



Supersaturated Zincate Solutions

W. Van Doorne and T. P. Dirkse*

Department of Chemistry, Calvin College, Grand Rapids, Michigan 49506

ABSTRACT

A study of supersaturated zincate solutions is made using light scattering and nuclear magnetic resonance techniques. The results indicate strongly that the excess zinc is present as a solute species rather than in a colloidal form. The solute species appears to be the same as that in solutions of ZnO in aqueous KOH, viz., $\text{Zn}(\text{OH})_4^{2-}$. There is no strong evidence to indicate the presence of other solute species.

When metallic zinc is treated anodically in aqueous KOH the surface often becomes dark in color and, if the treatment is continued long enough, a white solid precipitates from the solution. Both the white solid and the dark film on the metal are zinc oxide. Thus, the end product of the anodic treatment appears to be ZnO. However, ZnO is soluble in aqueous KOH. For some time it was believed that the solution from which the white solid precipitated was a saturated solution of ZnO in KOH. But further investigation (1) disproved this assumption. Instead, it was shown that the dissolved Zn(II) content of the electrolyte decreased and after about a year approached that of a saturated solution of ZnO. Meanwhile, a white solid continued to precipitate from the solution.

This phenomenon has been known for some 20 years and it is of significance for batteries containing a metallic zinc electrode and an aqueous KOH electrolyte. However, very little work has been done with these so-called "supersaturated" zincate solutions (szs).

A variety of evidence suggests that in a saturated solution of ZnO in aqueous KOH the dissolved Zn(II) species is primarily $\text{Zn}(\text{OH})_4^{2-}$ (2-4). Very little work has been done to determine the nature of the dissolved Zn(II) species in the szs. Dirkse (1) measured the emf of a zinc electrode in various szs and interpreted the results as indicating that $\text{Zn}(\text{OH})_4^{2-}$ is also the predominant species in szs. However, this suggestion has been called into question. It has been suggested, e.g., that the excess Zn(II) in the szs is in a colloidal form and there is evidence to support this, e.g., the slow precipitation of the excess Zn(II) as ZnO. Hampson *et al.* (5) on the basis of emf measurements concluded that the excess Zn(II) in szs is electrochemically inactive. A Raman spectra investigation (6) showed that the Zn(II) species in saturated solutions of ZnO in aqueous KOH is a tetrahedral zinc-hydroxy arrangement. With anodic treatment of zinc in a 40% KOH solution saturated with ZnO the dissolved Zn(II) content increased about 70%, but the area under a band typical of $\text{Zn}(\text{OH})_4^{2-}$ increased only about 12% and no new bands were observed. The conclusion is that about 1/6 of the excess Zn(II) is converted to

$\text{Zn}(\text{OH})_4^{2-}$. The nature of the remaining 5/6 was not determined.

In the early work with szs, it was observed (1) that the specific conductance of the solution decreased with increasing excess Zn(II). This may have been due to increased viscosity of the solutions and/or to replacement of OH^- ions by the zinc-hydroxy species.

In summary, on the basis of the work done to date it is not possible to describe precisely the nature of the excess Zn(II) in the szs. The work reported here was carried out in an attempt to gather more information about these szs solutions. Two techniques were used: (i) light scattering, and (ii) nuclear magnetic resonance (NMR). The light scattering technique may give information as to whether or not the Zn(II) in the szs is in a colloidal form. The NMR technique provides information about the environment of the protons in the solutions. This environment is averaged over all possible proton locations (i.e., in water, hydroxide ions, and Zn species). Because of rapid exchange of protons among these locations the NMR technique cannot distinguish between the various proton-containing species.

The initial investigation of the ZnO-aqueous KOH system by NMR techniques was reported by Newman and Blomgren (4). Their investigation covered a series of KOH concentrations ranging from 3.89 to 13.62 molal and ZnO concentrations nearly up to the saturation point for each of the KOH solutions. The analysis of Newman and Blomgren shows that the formulation $\text{Zn}(\text{OH})_4^{2-}$, as the primary Zn(II) species, is consistent with the chemical shift values. The present work employs a similar technique but extends the range of ZnO concentrations into those of the szs.

Experimental

The light scattering results were obtained by the use of a Coleman Universal spectrophotometer with a nephelometric attachment. The NMR spectra were obtained using a Jeolco MH60 spectrometer, operating at 60 MHz. Water was used as the external reference. After allowing time for obtaining temperature equilibrium in the sample, each spectrum was scanned five consecutive times.

Three stock solutions of KOH were prepared using reagent grade KOH. Saturated solutions of ZnO were made by dissolving the maximum of reagent grade

* Electrochemical Society Active Member.
 Key words: supersaturated zincate solutions, light scattering, nuclear magnetic resonance.

ZnO in each of the KOH solutions, followed by filtration through a Pyrex frit. Unsaturated solutions of varying ZnO concentrations were prepared by mixing appropriate amounts of pure KOH solution and the KOH solutions saturated with ZnO. A supersaturated Zn(II) solution was made by anodic oxidation of metallic zinc in a saturated ZnO solution. Solutions with varying degrees of supersaturation were made by mixing the saturated and supersaturated solutions in varying ratios. All zinc analyses were made by titration with EDTA.

Results and Discussion

Light scattering.—A saturated solution of ZnO in 2.8M KOH [0.13M in Zn(II)] was used as a reference and to set the galvanometer to 0. Next a szs solution [2.8M KOH + 0.35M Zn(II)] was placed in the same cuvette and the galvanometer then read 3%. This is within the experimental uncertainty associated with making these measurements. In a second run a saturated solution of ZnO [10.2M KOH + 1.12M Zn(II)] was placed in the cuvette and the galvanometer set to read 0. When a szs [10.2M KOH + 1.5M Zn(II)] was placed in the same cuvette the galvanometer read 0%. Thus, in both these cases the szs showed no or negligible increased light scattering compared to the saturated ZnO solutions. These results indicate the absence of colloidal material. It has been argued that the light scattering results are dependent on the refractive indices of the substances involved and that in these cases the refractive indices are such that even though there is colloidal material present no light scattering is observed. It has been observed under magnification that a pronounced refractive index change occurred around the zinc electrodes during discharge, *i.e.*, during anodic treatment (6, p. 34). This argument has been used often when solutions of ZnO in aqueous KOH are said to be optically clear. However, the fact that NMR results also support the absence of colloidal material (see below), seems to make it reasonable to state that the szs solutions contain no appreciable amounts of colloidal material.

Nuclear Magnetic Resonance.—All spectra showed a single peak for the external reference and a sharp, single, downfield peak for the KOH-ZnO solution. A typical scan is shown on Fig. 1.

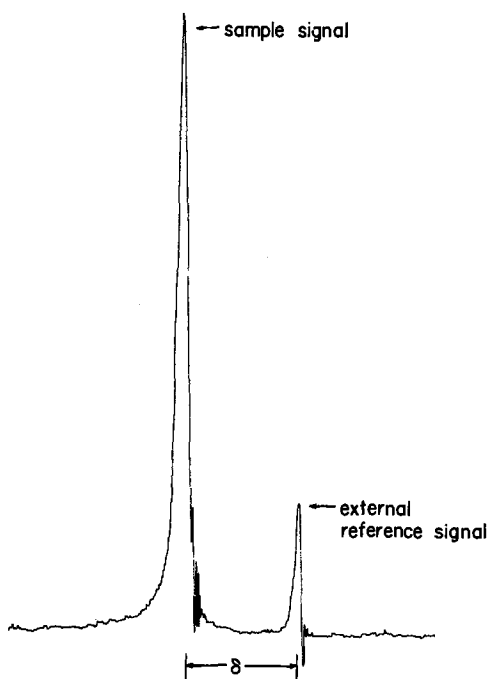


Fig. 1. Typical nuclear magnetic resonance scan

The five chemical shifts relative to water were measured for each sample and averaged to give the uncorrected chemical shift, δ . The standard deviation was 0.4 Hz for a typical set of five values.

Since an external reference was used, bulk susceptibility corrections were made using the equation given by Pople, Schneider, and Bernstein (7)

$$\delta = [(H - H_r)/H_r] + (2\pi/3)(\chi_{v,r} - \chi_v) \quad [1]$$

χ_{v1} and χ_v refer to the volume magnetic susceptibilities of reference and sample. χ values were obtained from the table given by Selwood (8) and it was assumed that the additivity law

$$\chi_v = \phi_1\chi_1 + \phi_2\chi_2 + \dots + \phi_n\chi_n \quad [2]$$

was obeyed. (ϕ represents the volume fraction of each component.)

The change in the chemical shift, δ , from that of the pure KOH solution, caused by the addition of ZnO, is defined as $\Delta\delta$.

As is shown in Fig. 2, $\Delta\delta$ increases with increasing Zn concentrations, and the slope of the lines increases with increasing KOH concentrations. The linearity of these plots, as has been observed by Newman and Blomgren (4), is consistent with the existence of a single Zn-containing species. Evidence from other authors suggests that this species is the tetra-coordinated ion $Zn(OH)_4^{2-}$ (2, 3).

Figure 3 gives a plot of $\Delta\delta$ vs. the increasing mole ratio of KOH to ZnO. In a similar graph, Newman and Blomgren found possible discontinuities in the two curves of lowest KOH concentrations (2.89 and 4.83M).

These discontinuities were tentatively attributed to second coordination sphere effects. Although our curve for the lowest KOH concentration (2.9M) also shows an increase at a mole ratio of about 11, we feel that this must be viewed with caution since the increase is less than twice the standard deviation of the δ -values, and may be due to normal statistical scatter.

In Fig. 2, 3, and 4 the dotted vertical line indicates the limit of normal solubility of ZnO in each of the KOH solutions. Neither Fig. 2 nor Fig. 3 shows a statistically significant discontinuity or change of slope on passing from the unsaturated into the supersaturated region. The absence of such a discontinuity is consistent with the view that in both the unsaturated and supersaturated regions only one type of Zn complex exists, namely $Zn(OH)_4^{2-}$.

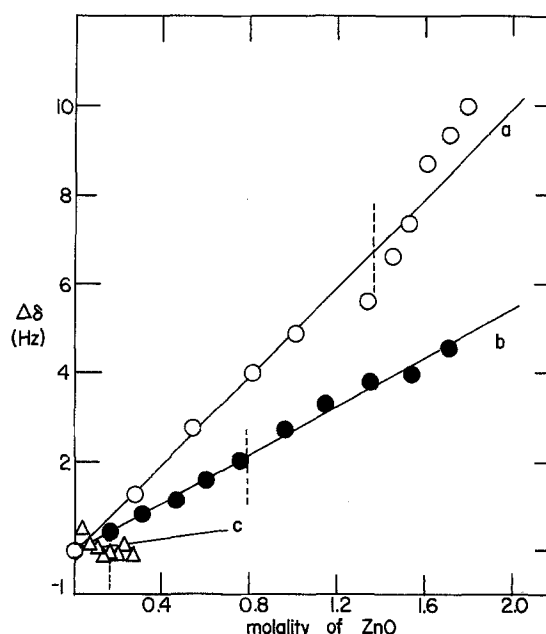


Fig. 2. Change in chemical shift with added ZnO at different base strengths: a, 12.2M KOH; b, 7.3M KOH; c, 2.9M KOH.

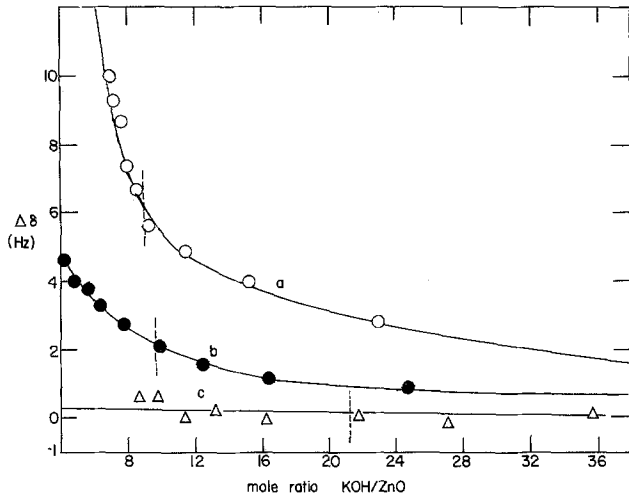


Fig. 3. Change of chemical shift with increasing mole ratio of KOH to ZnO at different base strengths: a, 12.2M KOH; b, 7.3M KOH; c, 2.9M KOH.

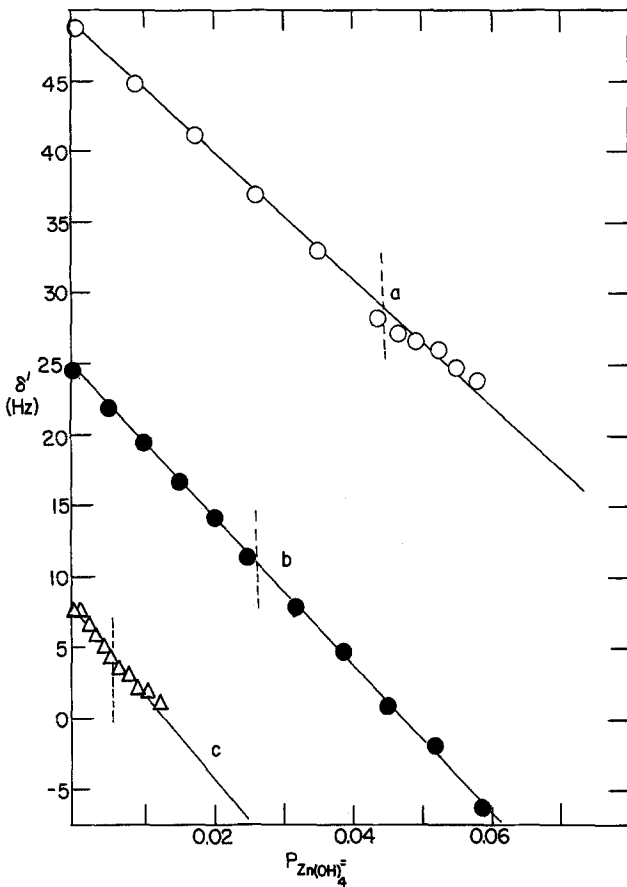


Fig. 4. Plot of δ' with increasing proton fraction of Zn(OH)₄²⁻ at different base strengths: a, 12.2M KOH; b, 7.3M KOH; c, 2.9M KOH.

The total chemical shift with respect to the reference signal may be expressed by the equation

$$\delta = P_{OH^-} \delta^{\circ}_{OH^-} + P_{Zn(OH)_4^{2-}} \delta^{\circ}_{Zn(OH)_4^{2-}} \quad [3]$$

in which the following definitions apply

δ = chemical shift corrected for bulk susceptibility

P_{OH⁻} = proton fraction of OH⁻ in solution

$$= (M_{KOH} - 2M_{ZnO}) / (M_{KOH} + 2 \times 55.51) \quad [4]$$

P_{Zn(OH)₄²⁻} = proton fraction of Zn(OH)₄²⁻ in solution

$$P_{Zn(OH)_4^{2-}} = 4M_{ZnO} / M_{KOH} + 2 \times 55.51 \quad [5]$$

δ^o_{OH⁻} = ratio of change of chemical shift with change in mole fraction of OH⁻ at infinite dilution

δ^o_{Zn(OH)₄²⁻} = ratio of change of chemical shift with change in proton fraction of Zn(OH)₄²⁻

The above definitions are identical to those used by Newman and Blomgren (4).

The value for δ^o_{OH⁻} found by Newman and Blomgren is 20.0 ppm or 1200 Hz.

This value was found by measuring the chemical shift, δ, vs. the proton fraction of OH⁻ ion and measuring the slope of the curve at zero concentration.

Both our values and those of Newman and Blomgren (4) show positive deviations from linearity which the latter authors have attributed to ion-pairing between the K⁺ and OH⁻ ions. The magnitude of this deviation should depend on the concentration of KOH and, since water solutions are strongly hydrogen-bonded, the deviation should also be temperature dependent (7, p. 400).

The differences in the deviation from linearity (Fig. 5) for identical KOH concentrations may be attributed to different spectrometer probe temperatures.

Newman and Blomgren do not report a temperature value. Ambient probe temperature in our instrument is 40° ± 2°C. In any case, the value of the slope of the curve extrapolated to zero concentration corroborates the value of 20.0 ppm for δ^o_{OH⁻}.

From the value of δ^o_{OH⁻} and the known KOH concentration the value of δ' may be calculated for each solution.

$$\delta' = P_{Zn(OH)_4^{2-}} \delta^{\circ}_{Zn(OH)_4^{2-}} = \delta - P_{OH^-} \delta^{\circ}_{OH^-} \quad [6]$$

A plot of δ' vs. P_{Zn(OH)₄²⁻} will then give as its slope, the value of δ^o_{Zn(OH)₄²⁻} (Fig. 4).

The following values were found:

Molality of KOH	δ ^o _{Zn(OH)₄²⁻} , ppm
2.9	-9.60
7.3	-8.60
12.2	-7.32

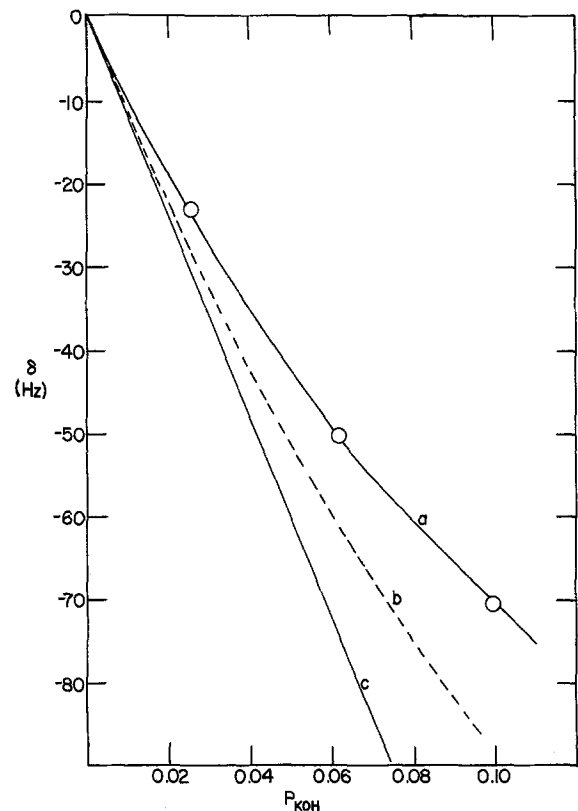


Fig. 5. Plot of proton resonance shift, δ, with increasing proton fraction of base: a, our values; b, approximate experimental values of Newman and Blomgren (4); c, slope of curves at P_{KOH} = 0. Used as values of δ^o_{KOH}.

In view of the small magnitude of the effect being measured and the uncertainty in the temperature, these values compare well with those found by Newman and Blomgren (4) which ranged from -6.44 to -6.04 ppm. Although our values are slightly higher, the change in $\delta_{\text{Zn(OH)}_4^{2-}}$ with changing KOH concentrations is similar, though somewhat more pronounced.

In calculating the data in Fig. 4, it was assumed that δ_{OH^-} has a constant value of 20.0 ppm. The error introduced by the deviations from this value (see Fig. 5) causes the nonzero intercepts of the curves in Fig. 4, but should not affect the slopes appreciably.

The plots of δ' vs. $P_{\text{Zn(OH)}_4^{2-}}$ do not show a significant deviation from linearity on passing from the unsaturated to the supersaturated region. In view of this, no difference in the zinc-containing species existing in those two regions is indicated. Should a second, different, zinc species exist in the supersaturated region, a change in slope might be expected.

If, for example, the excess zinc (above the normal limit of solubility) existed as simple Zn^{++} ions, the slope of the curves in Fig. 4 should approach zero in the supersaturated region. The species which cannot be eliminated by those arguments are other complexes of zinc containing 4 protons, namely, $\text{Zn(H}_2\text{O)}_2^{++}$ and $\text{Zn(OH)}_2(\text{H}_2\text{O)}$. The existence of these, however, is placed in doubt by the work of Fordyce and Baum (3).

Finally, the linearity of the plots in Fig. 4, and the lack of signal broadening in the spectra eliminate the possibility that the excess zinc exists as a colloid or suspended solid.

Acknowledgment

The work reported here was carried out with grants from the Aero Propulsion Laboratory of the United States Air Force, the United States Office of Naval Research, and the General Electric Company.

Manuscript submitted Feb. 26, 1974; revised manuscript received July 22, 1974.

Any discussion of this paper will appear in a Discussion Section to be published in the December 1975 JOURNAL. All discussions for the December 1975 Discussion Section should be submitted by Aug. 1, 1975.

Publications costs of this article were partially assisted by Calvin College.

REFERENCES

1. T. P. Dirkse, *This Journal*, **102**, 497 (1955).
2. T. P. Dirkse, *ibid.*, **101**, 328 (1954).
3. J. S. Fordyce and R. L. Baum, *J. Chem. Phys.*, **43**, 843 (1965).
4. G. H. Newman and G. E. Blomgren, *ibid.*, **43**, 2794 (1965).
5. N. A. Hampson, G. A. Herdman, and R. Taylor, *Electroanal. Chem.*, **25**, 9 (1970).
6. J. F. Jackovitz and A. Langer, "Zinc-Silver Oxide Batteries," J. J. Lander and A. Fleischer, Editors, Chap. 4, p. 29, John Wiley & Sons, Inc., New York (1971).
7. J. P. Pople, W. G. Schneider, and H. J. Bernstein, "High-Resolution Nuclear Magnetic Resonance," p. 81, McGraw-Hill Book Co., New York (1959).
8. P. W. Selwood, "Magnetochemistry," p. 78, Interscience Publishers, Inc., New York (1956).

The Sealed Nickel-Hydrogen Secondary Cell

Jose Giner*¹

Tyco Laboratories, Waltham, Massachusetts 02154

and James D. Dunlop*

COMSAT Laboratories, Clarksburg, Maryland 20734

ABSTRACT

A recently developed sealed nickel-hydrogen cell offers considerable promise to develop lightweight, long-life, rechargeable batteries. The most apparent advantages of this cell are its higher energy and power density as compared with other rechargeable systems including nickel-cadmium, lead-acid, and silver-zinc cells and the regenerative $\text{H}_2\text{-O}_2$ fuel cell. The energy density for lightweight 50 A-hr cells shown is 28 W-hr/lb. The cell enjoys a unique overdischarge protection mechanism which allows for long cycle life at high depth of discharge. Experimental data are presented to define the characteristics of the cell. Over 5000 high rate cycles have been completed on small 1.5 A-hr cells with good voltage performance. A 50 A-hr cell has completed to date over 800 cycles discharge to 70% of measured capacity in 1.2 hr.

A recently developed sealed nickel-hydrogen cell (1) offers considerable promise for the development of light, long-life, rechargeable batteries. This system competes favorably in many applications with such rechargeable systems as the lead-acid and nickel-cadmium (Ni-Cd) cells and with systems in the developmental stage, such as the regenerative $\text{H}_2\text{-O}_2$ fuel cells and Cd- O_2 cells. The most apparent advantages of the cell are its attractive energy and power densities for both charge and discharge. In addition, it shows high reliability, long cycle life,

storage life which is insensitive to the state of charge, considerable overcharge protection, and a unique overdischarge protection mechanism which makes it eminently suited for connecting cells in series. It also promises attractive low-temperature performance. The specific application of this system to synchronous satellite operation has already been discussed (2). In the following the characteristics of the cell are defined, based on experimental measurements, and the lightweight 66 W-hr (50 A-hr) cell design.

Description of the System

In its construction the nickel-hydrogen cell resembles the Ni-Cd cell, except that the cadmium electrode is replaced by a catalyst electrode capable of oxidiz-

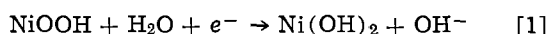
* Electrochemical Society Active Member.

¹ Present address: Giner, Inc., 144 Moody Street, Waltham, Massachusetts 02154.

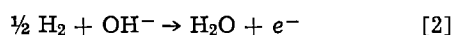
Key words: batteries, rechargeable batteries, nickel-hydrogen batteries, aerospace batteries.

ing hydrogen gas on discharge and evolving it on charge at low polarizations. Figure 1 is a schematic representation which shows the basic electrode arrangement for the cell. In this arrangement, the positive plates, the separators, and the electrolyte are identical to those used in the Ni-Cd cell, while the hydrogen electrode structure consists of Teflon-bonded platinum supported within a thin, fine mesh, Ni screen. A gas diffusion mesh Teflon screen is placed on the back side of each hydrogen electrode to facilitate hydrogen diffusion to the platinum electrode. The total electrode-electrolyte separator stack is surrounded by an atmosphere of hydrogen under pressure.

Under normal discharge conditions, the reaction on the positive electrode is



and, at the negative electrode

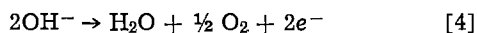


which results in the over-all cell reaction

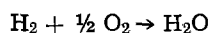


During charge, the reverse reactions occur. From reaction [3], it can be concluded that there is no water production or consumption during operation other than that caused by differences in the amount of water of crystallization in the different nickel hydroxides. As shown by Eq. [1] and [2], there are local water concentration changes at each electrode.

On overcharge, when most of the bivalent nickel oxide has been oxidized, oxygen is evolved according to the reaction



This oxygen reacts immediately at the abundant catalytic surface with an equivalent amount of the hydrogen (which is being produced at equivalent stoichiometric rates) according to



or is reduced at the negative electrode according to the reverse of reaction [4]. The Ni-H₂ cell is intrinsically positive electrode limited on charge because of the practically unlimited supply of water for the charging reaction at the negative electrode.

Cell reversal protection can be achieved by introducing a hydrogen precharge (i.e., an amount of hydrogen gas) in the cell while it is in the discharged state. Under these conditions, the cell becomes positive electrode limited on discharge. When all the trivalent nickel hydroxide has been reduced in the discharge part of the cycle and further current is passed, hydrogen is evolved on the nickel electrode surface (since it is extremely difficult to reduce nickel hydroxide to pure nickel under these conditions). The evolved hydrogen is compensated for by an equivalent amount of hydrogen which is oxidized at the hydrogen electrode.

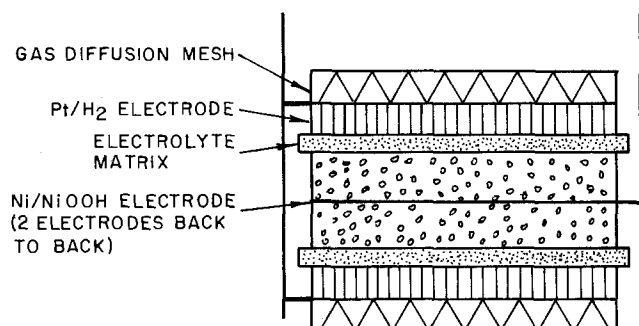


Fig. 1. Ni-H₂ cell configuration

Experimental Results

All experimental data presented were obtained using demountable heavy-walled pressure vessels. Two types of experimental cells were fabricated, a single 1.5 A-hr Ni-H₂ electrode cell, and multielectrode 5, 15, 25, and 50 A-hr cells. All of these cells used sintered nickel hydroxide positive electrodes, polypropylene separators, and Teflon-bonded platinum black negative electrodes, with a 30% KOH solution as electrolyte.

Single nickel hydroxide electrode cells (Fig. 1) were used to characterize electrochemical performance for cycle life, overcharge protection, temperature performance, and electrolyte management. Multielectrode cells (Fig. 2) were used to determine the effects of connecting a number of electrodes in parallel. In all cases the hydrogen gas was contained within the pressure vessel.

Parametric Data

The multielectrode cells were used to characterize the Ni-H₂ cell behavior in terms of temperature, pressure, and voltage with cycling. The cover of the heavy-walled container had an inlet tube to allow for hydrogen precharge filling and for pressure monitoring via a pressure transducer. The electrical feedthroughs were Ziegler-type plastic compression seals (3). A thermocouple was located in the cavity of the hydrogen electrode at the center of the electrode stack to determine the temperature under operating conditions. The thermocouple was encapsulated in polysulfone to avoid corrosion.

Conventional aerospace sintered nickel electrodes used in these cells were chemically impregnated and had a thickness of 0.76 mm and a measured flooded capacity of 0.12 A-hr/g. Two of these electrodes were used back to back to construct one positive electrode.

The hydrogen electrodes used in most cells were constructed from platinum black, bonded with Teflon, and pressed onto a thin nickel screen. Some of the electrodes had a porous Teflon backing on the gas side. A few cells used hydrogen electrodes consisting of a lightly platinized, graphite felt material (Energy Research Corporation proprietary electrode).

Pressure and voltage characteristics on cycling.—The pressure and voltage vs. time over a charge and discharge cycle are presented in Fig. 3. On charge at the C/1 rate,² the pressure increases linearly as hydrogen is evolved. The voltage rise at end of charge is

² The C/t rate is the rate in amperes for charging or discharging a cell, defined as the cell capacity in ampere-hours divided by the time, t, in hours (in this case, 1 hr).

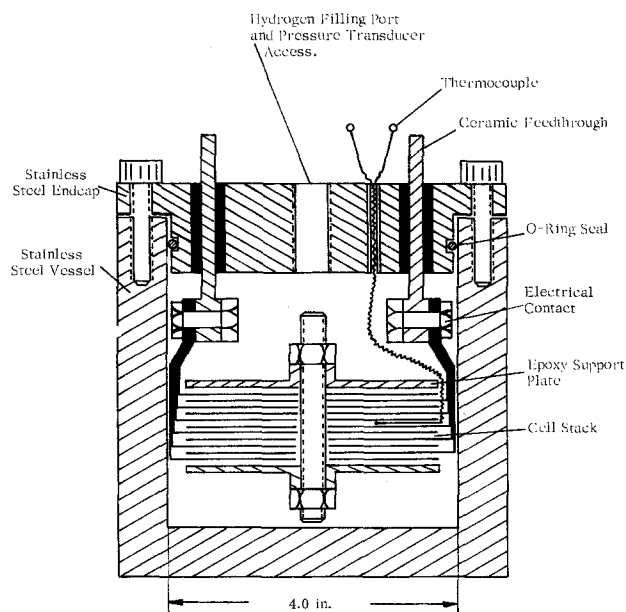


Fig. 2. Nickel/hydrogen test cell with 9.9 cm diam plates

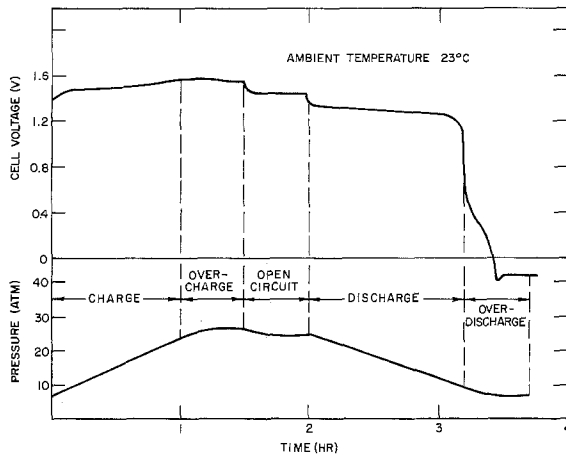


Fig. 3. Ni-H₂ cell pressure and cell voltage characteristics

caused by the onset of oxygen evolution at the nickel electrode. A slight voltage decrease observed during overcharge after O₂ evolution occurs is attributed to a temperature rise caused by O₂ and H₂ recombination. The pressure levels off and becomes constant. The partial pressure of oxygen measured during overcharge is less than 1% of the total cell pressure.

On discharge at the C/1 rate, the pressure decreases linearly as hydrogen is consumed. The voltage on discharge is characteristic of the nickel hydroxide electrode. A second plateau observed below 1V may be attributed either to reduction of chemisorbed oxygen on the positive electrode or to reduction of higher valent nickel. The cell voltage on discharge is not appreciably affected by the partial pressure of hydrogen at these temperatures and discharge rates.

During reversal on overdischarge of the positive electrode, the cell voltage reverses polarity and becomes slightly negative while the pressure levels off. This capability for continuous overdischarging of the cell with no adverse effects or pressure buildup is a unique feature of this cell.

Temperature characteristics.—Temperature data presented in Fig. 4 are for the thermocouple located in the center of the cell stack. On charge at a C/10 rate, the cell is slightly endothermic, and the cell temperature is practically constant. All of the power delivered to the cell on overcharge is dissipated as heat. Oxygen is evolved at the positive electrode, while hydrogen is evolved at the negative electrode in equivalent Faradaic rates. This oxygen and hydrogen react to form water (see Eq. [4] and [5]), causing the temperature to rise.

On discharge at the C/2 rate, part of the electrochemical energy is dissipated as heat, primarily because of polarization at the positive electrode which results in a temperature rise. A very high transient

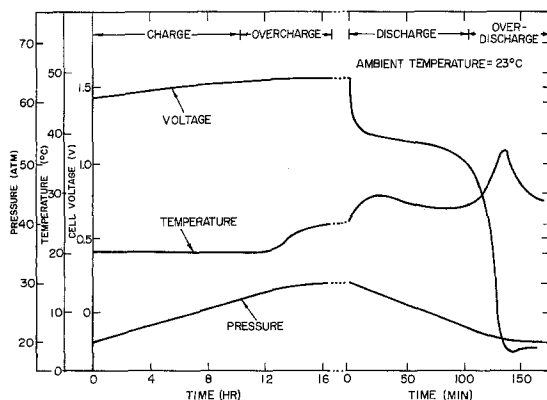


Fig. 4. Ni-H₂ cell temperature characteristics

temperature rise occurs at the end of discharge because of the high polarization at the positive electrode.

During reversal at the C/2 rate, the temperature decreases and stabilizes to a value lower than that observed on discharge. Hydrogen is generated at the positive electrode and consumed at the negative electrode with low polarization.

In general the thermal and temperature characteristics of the Ni-H₂ cell are very similar to those of the Ni-Cd cell with the exception of behavior on reversal.

Temperature effects on capacity.—The voltage vs. time discharge characteristics with temperature as a parameter are shown in Fig. 5. The cell has been overcharged by 60% at the C/10 rate and then discharged completely to 0V. From 0° to -10°C there is a significant loss in capacity and also above 40°C a significant loss is observed. As with an Ni-Cd system, the desirable temperature range of operation is from 0° to approximately 25°C. However, the Ni-H₂ cell does not have the low temperature limitation of the Ni-Cd cell attributed to the poor charge acceptance of the cadmium electrode.

Self-discharge.—The self-discharge characteristics for the Ni-H₂ cells standing on open circuit are shown in Fig. 6. Starting with a fully charged cell, the self-discharge can be directly related to a loss of hydrogen pressure. As shown in Fig. 6, the self-discharge, similar to that of a Ni-Cd cell, occurs in a diminishing exponential fashion; after one day of standing on open circuit, the cell retains approximately 80% of its full capacity. This self-discharge is attributable either to

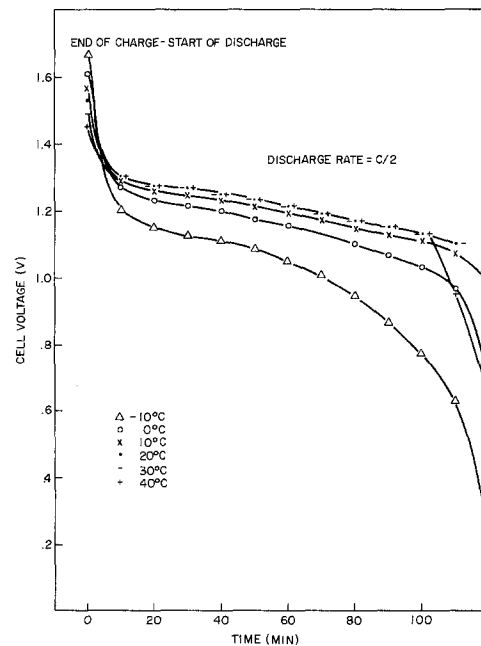


Fig. 5. Temperature effects on capacity

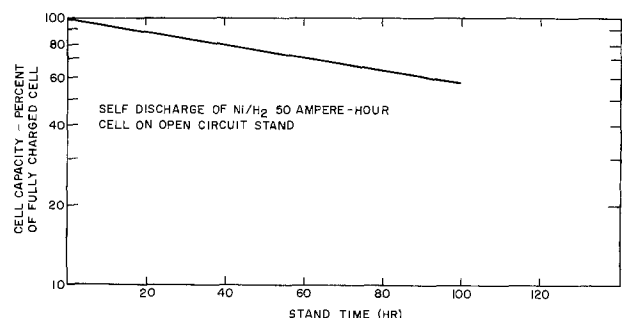


Fig. 6. Self-discharge characteristics

the direct reduction of Ni^{+3} to Ni^{+2} or to the reduction of chemisorbed oxygen on the nickel electrode.

Effects of charge and discharge rates.—Both the nickel hydroxide and the hydrogen electrodes are capable of high-rate charge and discharge. Figure 7 shows the cell voltage vs. the charge rate (up to the 5C rate) as a function of the state of charge of the positive electrode at room temperature. Figure 8 shows the cell voltage vs. the discharge rate (up to the 5C rate) as a function of the state of discharge.

Figure 9 shows the effect of the charge rate on charge acceptance. The charge acceptance was determined by charging the cell at different rates to return 5 A-hr of capacity to the cell and then discharging it at the C/1.2 rate to 1V. Maximum charge efficiency is achieved at the C/1 charge rate.

The effects of the rate of discharge on measured cell capacity after the cell is charged at the C rate to 33% overcharge are shown in Fig. 10. The capacity obtained on discharge at the 5C rate is only 10% less than that obtained at the C rate. Thus, in addition to providing a high energy density (approximately 66 W-hr/kg), the Ni-H₂ system has an excellent power density capability (over 300 W/kg).

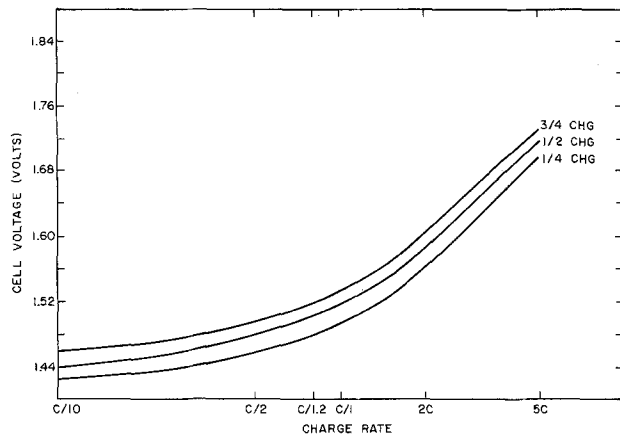


Fig. 7. Polarization on charge

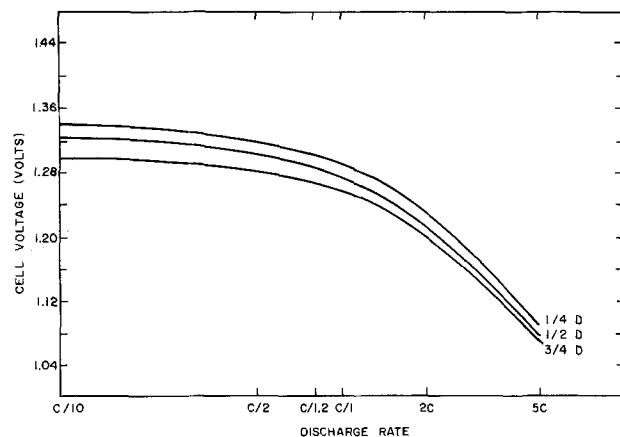


Fig. 8. Polarization on discharge

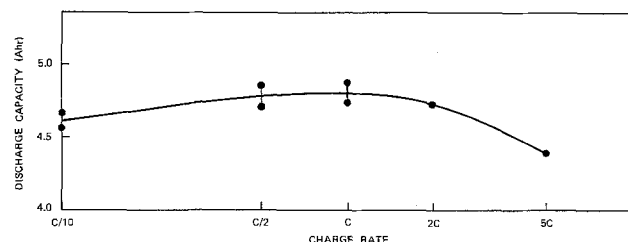


Fig. 9. Charge efficiency

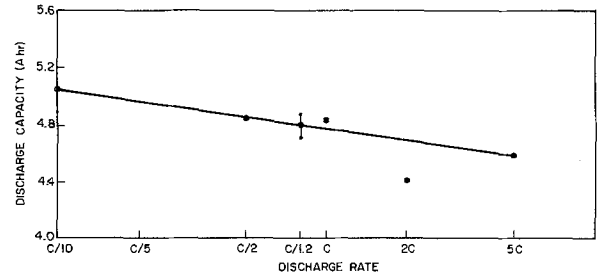


Fig. 10. Discharge rate effects on capacity

Cyclic Life Data

The nickel hydroxide electrode and the Teflon-bonded H₂ electrode are the two most stable electrodes developed for sealed secondary cells to date. Since the sealed Ni-H₂ cell is a recent development, the major failure mechanisms must still be determined. Data are presented for cyclic test results to date.

High-rate cycle test.—The purpose of this test is to evaluate different combinations of commercially available electrodes and separator materials in terms of cyclic life performance. Data are presented for five cells with electrode and separator materials identified in Table I. These cells are subjected to a 1 hr cycle test consisting of discharge for 26 min at a C/1.5 rate which corresponds to 28.6% depth of discharge (DOD) and charge for 34 min at a C/1.5 rate corresponding to 30% overcharge.

High-rate cycle test results.—Cell S/N 123 has completed over 5000 cycles to date. (Figure 11 shows the end-of-charge and end-of-discharge voltages for this cell.) The other cells have failed at 3000, 1674, 1068, and 468 cycles. The cells are considered to have failed when the discharge voltage drops below 1V.

Cell S/N 122 failed after 3000 cycles. The measured impedance of this cell increased from 70 mohm at the start of the test to over 200 mohm at failure. The increase in impedance results from a loss of electrolyte from the separator. Examination of the separator after failure revealed that the polypropylene had dried out and would not absorb electrolyte. Examination of the positive electrodes showed that they were still structurally sound, but that the thickness had changed from 0.76 to 1.16-1.30 mm.

This cell was rebuilt by using the same positive electrodes, but with a Hercules polypropylene separator and ERC Teflon-backed hydrogen electrodes. It has now completed 2000 additional cycles.

Cell S/N 115 failed after 1674 cycles. The hydrogen electrode in this cell did not have Teflon backing. The measured impedance increased from 70 mohm at the start of the test to 620 mohm at failure. Examination of the separator after failure again revealed that the polypropylene had dried out and would not absorb electrolyte. Examination of these positive electrodes showed

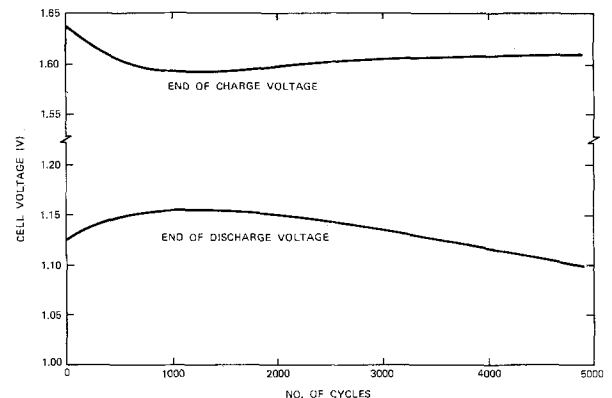


Fig. 11. Cyclic life performance of cell S/N 123

Table I. Electrode materials for use with polypropylene separators

Cell S/N	Nickel positive electrode	Separator	Negative
122	SAFT sintered nickel (slurry process) Nickel-plated perforated iron support Double electrodes back to back Each electrode 0.76 mm thick	Hercules polypropylene	ERC platinum and PTFE on nickel screen, Teflon backing
123	SAFT sintered nickel (slurry process) Nickel-plated perforated iron support Double electrodes back to back Each electrode 0.76 mm thick	Hercules polypropylene	ERC platinum and PTFE on nickel screen, Teflon backing
115	Eagle Picher sintered nickel (dry process) Nickel screen support Double electrodes back to back Each electrode 0.76 mm thick	Hercules polypropylene	ERC platinum and PTFE on nickel screen without Teflon backing
126	Eagle Picher sintered nickel (dry process) Nickel screen support Double electrodes back to back Each electrode 0.76 mm thick	Hercules polypropylene	ERC platinum on graphite without Teflon backing
127	Eagle Picher sintered nickel (dry process) Nickel screen support Double electrodes back to back Each electrode 0.76 mm thick	Hercules polypropylene	ERC platinum on graphite without Teflon backing
128	GE sintered nickel (slurry process) Nickel-plated perforated iron support Double electrodes back to back Each electrode 0.76 mm thick	Pellon polypropylene	ERC platinum and PTFE on nickel screen, Teflon backing
129	SAFT sintered nickel (slurry process) Nickel-plated perforated iron support Double electrodes back to back Each electrode 0.76 mm thick	Pellon polypropylene	ERC platinum and PTFE on nickel screen, Teflon backing

Table II. Electrode materials for use with nylon and potassium titanate separators

Cell S/N	Nickel positive electrode	Separator	Negative
130	SAFT double electrodes back to back Each electrode 0.76 mm thick	Nylon	ERC platinum and PTFE on nickel screen, Teflon backing
131	SAFT double electrodes back to back Each electrode 0.76 mm thick	Potassium titanate	ERC platinum and PTFE on nickel screen, Teflon backing
132	SAFT double electrodes back to back Each electrode 0.76 mm thick	Potassium titanate	ERC platinum and PTFE on nickel screen, Teflon backing
136	SAFT double electrodes back to back Each electrode 0.76 mm thick	Nylon	ERC platinum and PTFE on nickel screen, Teflon backing

that they also were still structurally sound, but that the thickness had changed from 0.76 to 1.16-1.30 mm.

Cells S/N 126 and 127 failed after 468 and 1068 cycles, respectively. These cells had the ERC graphite hydrogen electrodes without Teflon backing. Both failed because of loss of electrolyte, resulting in high impedance. These cells were rebuilt, S/N 126 with an ERC hydrogen electrode without Teflon backing and S/N 127 with an ERC hydrogen electrode with Teflon backing, using the same positive electrodes. These rebuilt cells have now completed over 3000 additional cycles and are still running (see Fig. 12).

Two new cells, cells S/N 128 and S/N 129, were built to evaluate the Pellon polypropylene separator material. The electrode and separator materials are identified in Table I.

Cell S/N 128 failed after 1488 cycles, again because of high impedance. The Pellon polypropylene was dried out and would not readily absorb electrolyte. This cell was rebuilt by changing the separator to Pellon nylon 2505. A significant improvement in voltage performance has been observed with the nylon separator (see Fig. 13).

Conclusions of the high-rate cycle test.—The thin graphite hydrogen electrodes and also the electrodes on nickel screen without Teflon backing have limited cycle lifetimes because of electrolyte entrainment, resulting in a loss of electrolyte from the separator. In addition, the polypropylene separators, both Hercules and Pellon, with wetting agents are becoming hydrophobic with cycling. Because of the problems with the polypropylene separator additives, cyclic tests have

been initiated to investigate nylon and potassium titanate separator materials (see Table II). The cells are subjected to a 3 hr cycle test consisting of discharge for 72 min at a C/1.5 rate to 85% DOD and charge for 1.8 hr at a C/1.96 rate to 15% overcharge. They are being cycled at a very deep DOD (85% of the measured capacity). To date they have completed 500 cycles demonstrating good voltage performance (see Fig. 14).

Cycle test data for the 50A-hr cell.—This cell electrode stack is similar in construction to the lightweight

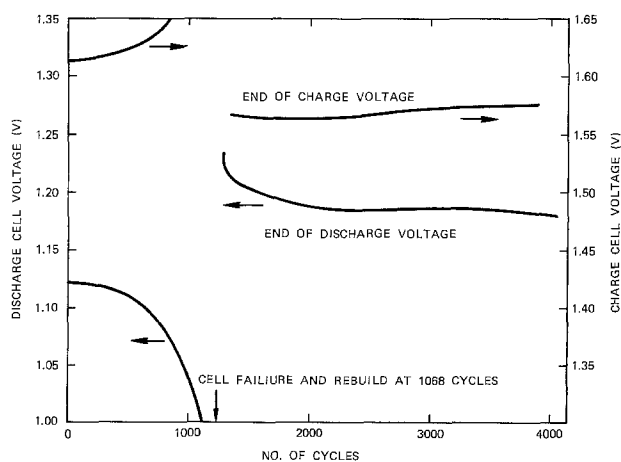


Fig. 12. Cyclic life performance of cell S/N 127

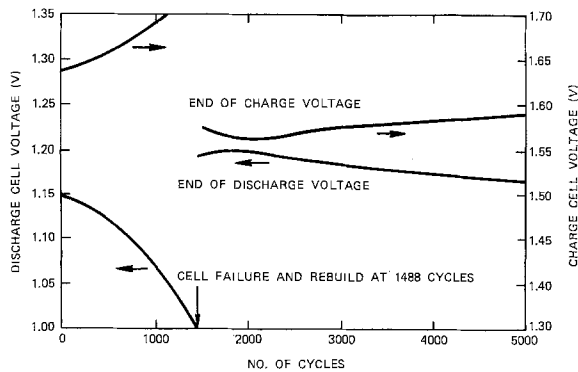


Fig. 13. Voltage performance of cell S/N 128 rebuilt with Pellon nylon 2505 separator.

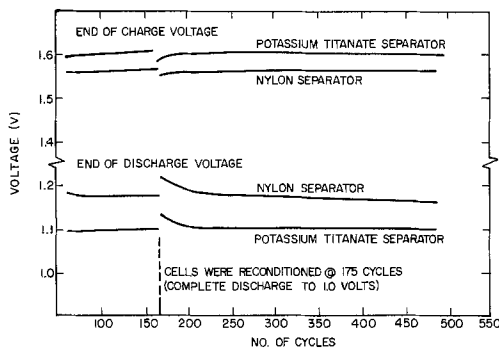


Fig. 14. Cyclic life performance of KT and nylon separator

prototype cells being fabricated. It has a 22 multi-electrode plate stack with the positive and negative electrodes connected in parallel. The hydrogen electrodes are Teflon-backed platinum and PTFE on nickel screen. SAFT aerospace positive electrodes, each 0.76 mm thick, are used back to back with the Hercules polypropylene separator.

Over 1000 cycles have been completed, demonstrating the ampere-hour turnover necessary to meet a 7 yr synchronous satellite mission (Fig. 15). A second 50 A-hr cell has now completed over 200 cycles on test. A positive SAFT nickel electrode has been manufactured specifically for this Ni-H₂ cell. Each nickel electrode is 0.96 mm thick; again they are used back to back to make one positive electrode, and all edges are coined. The cell has nylon separators.

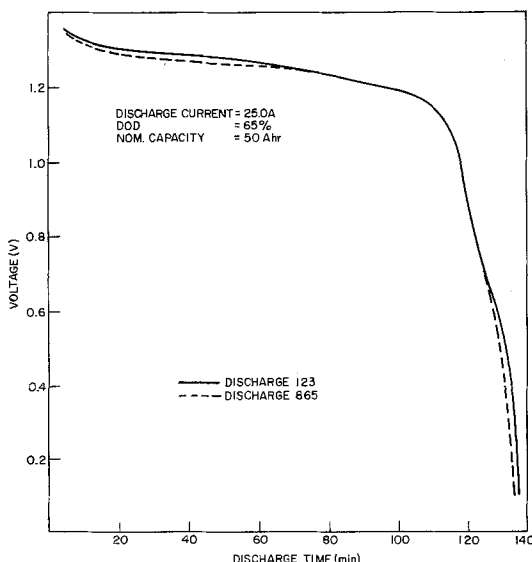


Fig. 15. Cyclic performance of the 50 A-hr cell

Lightweight Cell Design

For synchronous satellite applications, the cell design has been optimized for maximum energy density, subject to the practical restrictions discussed below.

A computer study has as the main variables cell capacity, capacity per unit area of the positive plates, cell diameter, and operating range of the cell pressure. The cell configuration for this study is a cylindrical single cell with the hydrogen contained within the pressure vessel. To characterize the electrode stack, state-of-the-art commercially available hydrogen electrodes, separators, gas diffusion screens, etc., are assumed. Inconel 625 is assumed to be the material used for the pressure vessel.

A practical cell design has been selected on the basis of the following criteria. The cell is sized to provide 66 W-hr (52 A-hr) of energy. The corresponding energy density for a cell of this capacity is 62-64 W-hr/kg (Fig. 16). Increasing the cell capacity does not significantly improve the energy density; however, if the cell capacity is reduced, there is a drop in energy density.

The cell capacity per unit area of the positive plates does have a significant effect on energy density (see Fig. 17). The practical limitations are the plate thickness that can be achieved in commercial production of the nickel plaque and the utilization of active material for thicker plates. For these reasons positive plates are used back to back in the fabrication of the multi-electrode cells.

Once the cell capacity is selected, the number of electrodes is dependent on the cell diameter selected. For the 66 W-hr cell the effect of the cell diameter and the current density on the energy density and the number of electrodes in the stack is shown in Fig. 18.

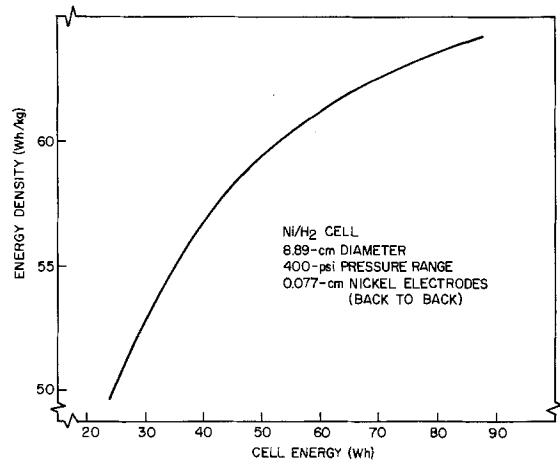


Fig. 16. Ni-H₂ cell, energy density vs. energy

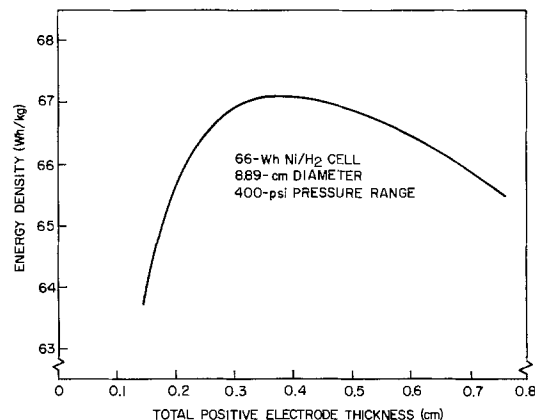


Fig. 17. Ni-H₂ cell, energy density vs. positive electrode thickness

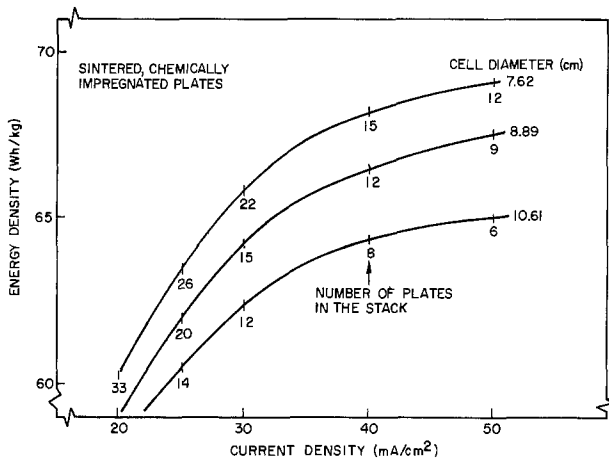


Fig. 18. Ni-H₂ cell, energy density vs. current density

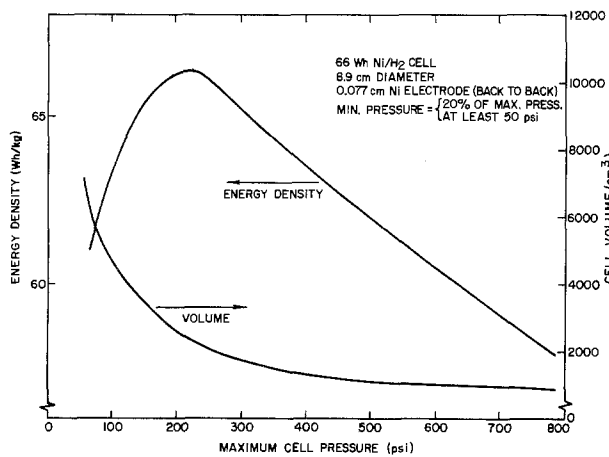


Fig. 19. Ni-H₂ cell, energy density vs. cell pressure

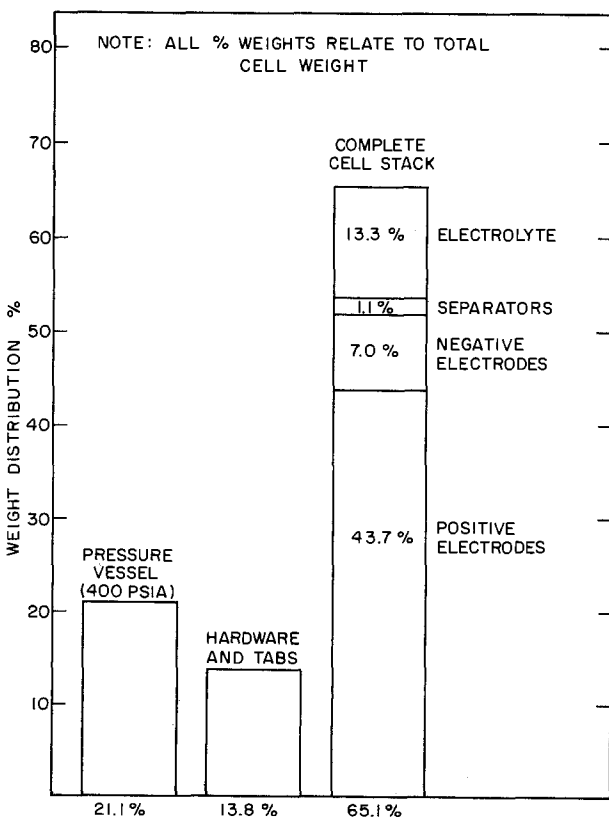


Fig. 20. Ni-H₂ cell, weight distribution

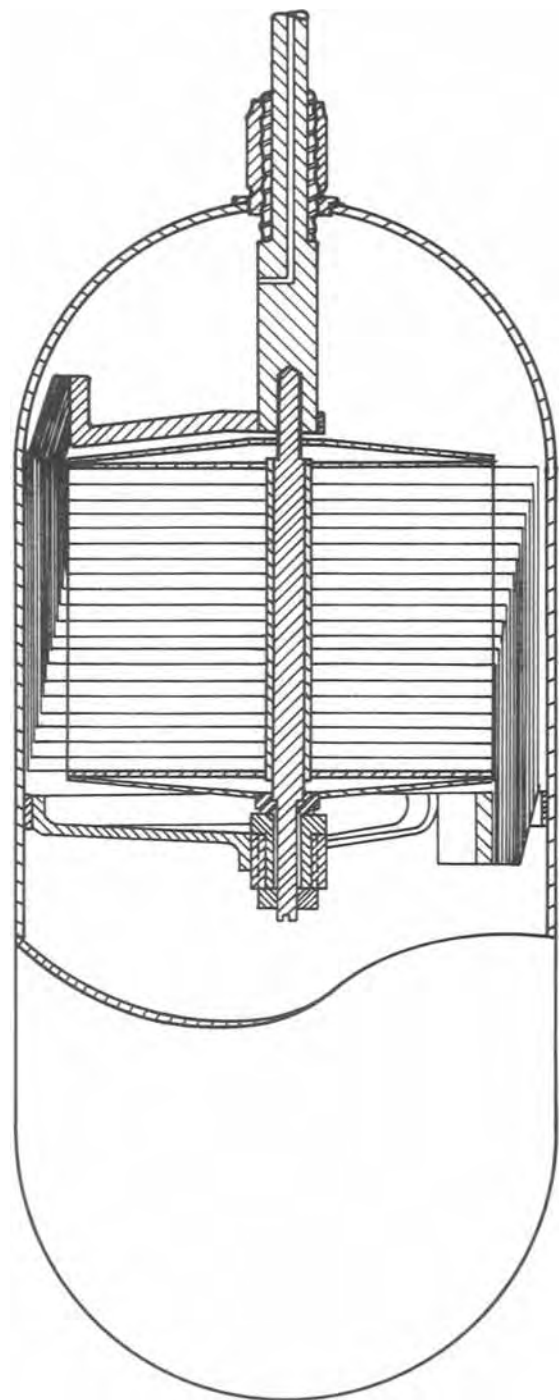


Fig. 21. Lightweight Ni-H₂ cell design

A diameter of 8.89 cm has been selected. At a current density of 25 mA/cm², the number of electrodes in the stack is 20. Decreasing the diameter makes it possible to achieve somewhat higher energy densities at the expense of an increased number of electrodes in the cell stack. The present design is a compromise between energy density and reliability.

The energy density and cell volume as functions of the maximum cell pressure are shown in Fig. 19 for an initial hydrogen pressure of 100 psi. A maximum pressure of 27 atm has been selected. Again, this is a trade off between maximum energy density and cell volume.

Figure 20 shows the weight breakdown for the 66 W-hr cell design. It should be noted that the weight of the nickel hydroxide electrodes is 44% of the total weight.

Lightweight Ni-H₂ cells are now being fabricated to the design shown in Fig. 21. Characteristics of the

sintered nickel electrodes are as follows:

thickness:	0.76 mm each,
	0.152 mm back to back
density:	3.25 g/cm ³
capacity:	0.12 A-hr/g (measured, flooded)
utilization:	96% (measured in electrode stack)
current density:	25 mA/cm ² (for 1.2-hr discharge)

This cell is designed to provide 66 W-hr at an energy density of 62-64 W-hr/kg.

The cylindrical pressure vessel is 8.89 cm in diameter by 19.9 cm high. The insulated feedthrough is a Ziegler plastic seal.

Conclusions

Experimental data presented from laboratory investigations demonstrate the capability of the Ni-H₂ system to meet the 7-10 year cyclic life requirements for a synchronous satellite application. In addition, the Ni-H₂ system has demonstrated performance characteristics superior to those of the Ni-Cd system in terms of higher overcharge capability, overdischarge capability, better low-temperature operation, and higher power density.

Lightweight cells have been designed and are now being fabricated. These cells are expected to demon-

strate three to four times the usable energy density of Ni-Cd cells. For an INTELSAT V (2 kW) satellite, this represents a potential weight reduction of 200-300 lb for the battery system.

Acknowledgments

The work discussed in this paper was supported by the International Telecommunications Satellite Organization (Intelsat). Lightweight cell (Fig. 21) was designed by Mr. L. Swette.

Manuscript submitted Dec. 20, 1973; revised manuscript received June 28, 1974.

Any discussion of this paper will appear in a Discussion Section to be published in the December 1975 JOURNAL. All discussions for the December 1975 Discussion Section should be submitted by Aug. 1, 1975.

Publication costs of this article were partially assisted by COMSAT Laboratories.

REFERENCES

1. James D. Dunlop, Jose Giner, Gerrit van Ommering, and Joseph F. Stockel, Patent pending.
2. J. F. Stockel, G. Van Ommering, L. Swette, and L. Gaines, in "Proceedings of the 7th Intersociety Energy Conversion Engineering Conference," San Diego, California, September 1972, p. 87.
3. E. J. McHenry and P. Hubbauer, *This Journal*, **119**, 564 (1972).

The Effect of Solvent on the Electrochemistry of Iron

A. L. Bacarella

Chemistry Division, Oak Ridge National Laboratory, Oak Ridge, Tennessee 37830

and A. L. Sutton

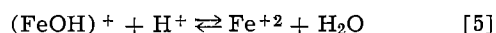
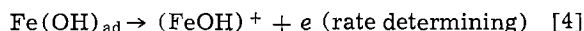
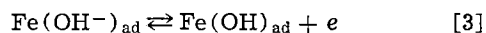
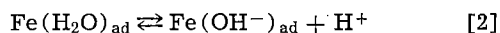
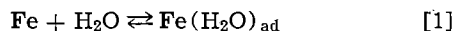
Chemical Technology Division, Oak Ridge National Laboratory, Oak Ridge, Tennessee 37830

ABSTRACT

A study was made of the electrochemical behavior of the active iron electrode in acidic ethanol-water media. The *pA* (*pH* in pure water solvent) and potential dependence of the iron dissolution and hydrogen evolution reactions were determined. The results of this investigation served to resolve the role of water in the iron dissolution mechanism. Basic to the proposed mechanism was the validity of an "absolute acidity scale" for EtOH-HOH solutions.

A study has been made of the electrochemical behavior of the active iron electrode in acidic ethanol-water media. The purpose of the investigation was to test the applicability of an "absolute acidity scale" postulated for ethanol-water (1), and in the application of the "acidity scale," to determine the kinetic order with respect to water and protons in the corrosion mechanism.

It has been shown by Kelly (2) and Bockris (3) that the steady-state anodic dissolution of zone-refined iron in aqueous acid sulfate solutions is characterized by a Tafel slope of 2/3 (2.303 RT/F), i.e., 40 mV/decade of current, and first order dependency on the hydroxyl ion activity. The results were interpreted in terms of the following mechanism



These equations take formal account of the simultane-

ous coverage of the surface by adsorbed water molecules, hydroxyl ions, and the surface intermediate Fe(OH)_{ad}, and lead to the kinetic expression

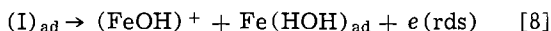
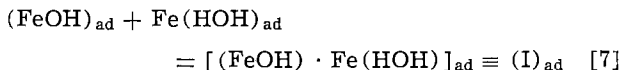
ous coverage of the surface by adsorbed water molecules, hydroxyl ions, and the surface intermediate Fe(OH)_{ad}, and lead to the kinetic expression

$$i = 2Fk_4^w (k_3^w k_2^w / a_{(\text{H}^+)}) k_{-3}^w k_{-2}^w \theta_1 \exp(3FE/2RT) \quad [6]$$

where $\theta_1 = (k_1^w a_w / (k_1^w a_w + k_{-1}^w))$ is the fraction of the total possible adsorption sites occupied by Fe(H₂O)_{ad}, a_w is the activity of water, and the k_i^w are the rate constants with infinitely dilute water solvent as the reference state. Since the infinitely dilute water solvent is the reference state for all solvent compositions including pure alcohol, the superscript "w" will be omitted in subsequent rate expressions.

In a subsequent paper, Kelly (4) reported on the results obtained for the iron dissolution and hydrogen evolution reactions on zone-refined iron in hydrogen-saturated sodium benzoate solutions (referred to as the inhibited system). The mechanism proposed for the iron dissolution reaction in the inhibited system involved the formation of an electrochemically active surface intermediate from the adsorbed anion, (FeB_z)_{ad} and (FeOH)_{ad}. Then by analogy with the inhibited system, an alternate mechanism for the non-inhibited system was proposed. If to the reactions

represented by Eq. [1]-[3] are added the reactions represented by Eq. [7] and [8]



where [8] is now the rate determining step, Eq. [6] becomes

$$i_+ = 2FK_3k_7k_3k_2/[k_{-7}k_{-3}k_{-2}(a_{\text{H}^+})] \\ \theta_1^2 \exp(3FE/2RT) \quad [9]$$

The steady-state current is now second order with respect to θ_1 , but remains unchanged with respect to pH and potential. In pure water $\theta_1 \sim 1$ and the effect of water on the anodic dissolution cannot be determined. The addition of ethanol to the aqueous acidic sulfate solution may provide a test for the alternate mechanisms as represented by Eq. [6] and [9]. However, changing the solvent system from HOH to EtOH-HOH introduces alternate reaction paths via other intermediates, e.g., $(\text{FeOEt})_{\text{ad}}$ and $\text{Fe}(\text{EtOH})_{\text{ad}}$, and also introduces a junction potential into the measured cell potential when the measurements are made with respect to the aqueous calomel reference electrode. In order to compare the rates at constant potential and with respect to the same reference state (infinitely dilute water solvent), the measurements must be made with respect to an aqueous reference electrode. Here, the saturated aqueous calomel electrode was chosen as the reference electrode. Since the aqueous calomel electrode is in a constant environment (saturated aqueous KCl), its potential is constant and independent of changes in the solution composition on the other side of the liquid junction. The term potential is used here as a contraction for potential difference, i.e., a Galvani potential difference, ${}^M\Delta S_1 \phi \equiv \phi_M - \phi_{S_1}$, between some point in the metal phase and some point S_1 in the solution phase. Although the absolute value of this potential cannot be determined, changes in this potential are obtained when the measurements are made with respect to some unchanging reference electrode. Here, however, the measured cell potential difference, $E^{\text{s}_{\text{cell}}}$, includes a liquid junction potential difference as well as the Galvani potential differences at the metal/solution interfaces, i.e.

$$(\phi_M - \phi_{\text{Hg}_2\text{Cl}_2/\text{Hg}} \equiv E^{\text{s}_{\text{cell}}} = (\phi_M - \phi_{S_1}) \\ + (\phi_{S_1} - \phi_{S_2}) + (\phi_{S_2} - \phi_{\text{Hg}_2\text{Cl}_2/\text{Hg}})$$

where $(\phi_M - \phi_{S_1}) \equiv E^{\text{s}_M}$ is the Galvani potential difference for the metal electrode, (Fe or Pt), $(\phi_{S_1} - \phi_{S_2}) \equiv -E^{\text{s}_L}$ the liquid junction potential difference between EtOH-HOH solvent and saturated aqueous KCl, and $(\phi_2 - \phi_{\text{Hg}_2\text{Cl}_2/\text{Hg}}) \equiv -E^{\text{s}_{\text{SCE}}}$ is the Galvani potential difference for the reference electrode. Therefore, $E^{\text{s}_{\text{Fe,Pt}}} = E^{\text{s}_{\text{cell}}} + E^{\text{s}_L} + E^{\text{s}_{\text{SCE}}}$, and changes in the Galvani potential for iron or platinum are obtained when the cell potential $E^{\text{s}_{\text{cell}}}$ is measured and the junction potentials E^{s_L} are known.

Junction Potentials

In solvents other than water it is useful to distinguish between two acidity measuring functions, pA and pH (5), defined as follows

$$pA = -\log a_+ = -\log c_{\text{H}^+} y^{\text{s}_{\text{H}^+}} f_{\text{H}^+} \quad [10]$$

$$pH = -\log a_{\text{H}^+} = -\log c_{\text{H}^+} y^{\text{s}_{\text{H}^+}} \quad [11]$$

where $y^{\text{s}_{\text{H}^+}}$ is the conventional molar lyonium ion activity coefficient in solvent S, and f_{H^+} is the "degenerate activity coefficient" for the transfer of proton from infinite dilution in solvent S to infinite dilution in H_2O (the reference state). The parameter f_{H^+} is also referred to as the "primary medium effect" term (6, 7). The pA function measures the actual proton

activity, a_+ , of the given solution, whereas pH measures the molar lyonium ion activity referred to the extremely dilute solution in the given solvent. Therefore, to correlate the rates of iron dissolution with respect to proton activity using the infinitely dilute water solvent, w , as the reference state, the pA of the solution must be measured. The pA can be obtained from a measurement of the emf of the Pt/ H_2 electrode in the EtOH-HOH solvent with respect to the saturated aqueous calomel electrode, SCE

Pt- H_2 (1 atm)/Soln. (X)

in EtOH-HOH/ E^{s_L} /KCl (sat. aq.) Hg_2Cl_2 -Hg [1']

where

$$pA = -\log a_+ = -\log c_{\text{H}^+} y^{\text{s}_{\text{H}^+}} f_{\text{H}^+} = -E^{\text{s}_{\text{Pt}}}/0.06 \quad [12]$$

where $E^{\text{s}_{\text{Pt}}} = E^{\text{s}_{\text{cell}(\text{Pt})} + E^{\text{s}_{\text{SCE}}} + E^{\text{s}_L}$. Again, however, for measurements in each solvent system S, the liquid junction potential E^{s_L} must be known, and this is known if values for f_{H^+} in each solvent can be determined. Grunwald (1, 8) and co-workers Gutbezahl and Berkowetz have determined the thermodynamic dissociation constants, (pK^{s}), of weak uncharged acids HA (acetic acid type) and cation acids HA^+ (ammonium type) in ethanol-water solvents. An extra-thermodynamic relationship, the activity postulate (9), was used to obtain values for the "degenerate" activity coefficient of the hydrogen ions, f_{H^+} . From a knowledge of f_{H^+} it was then possible to calculate the junction potentials in cells like (1'). Rearranging Eq. [12], the liquid junction potential

$$E^{\text{s}_L} = 0.06 \log (c_{\text{H}^+} y^{\text{s}_{\text{H}^+}} f_{\text{H}^+}) - (E^{\text{s}_{\text{cell}(\text{Pt})} + E^{\text{s}_{\text{SCE}}}) \quad [13]$$

where for dilute solutions, $y^{\text{s}_{\text{H}^+}}$ can be estimated from the Debye-Huckel limiting law, all other quantities on the right-hand side of Eq. [13] are known or measurable, and E^{s_L} may be calculated (1). Values of E^{s_L} as a function of EtOH-HOH composition are shown in Fig. 1. The measurements reported here are for a solution containing 0.5M H_2SO_4 , which is not dilute, but is constant for all solvents S. The assumption is made that the liquid junction potential is approximately independent of acid concentration to 0.5M acid. This assumption could lead to errors of about 0.1 pA units (5).

Aleksandrov and Izmailov (10, 11) obtained values for the "degenerate" activity coefficient of the hydrogen ion, f_{H^+} , which were not too greatly different from those of Grunwald and Gutbezahl. However, more recently, Popovych and Dill (12, 13) have obtained values which were greatly different. Liquid junction potentials calculated from these values were not only different in magnitude but also in sign. It will be shown later that these values are not consistent with the present study.

With this background and the values for E^{s_L} in Fig. 1, the analysis of the anodic dissolution of iron can be attempted. The experimental system can be represented as

(Pt or Fe) - H_2 (1 atm)/0.50M H_2SO_4

in EtOH-HOH// E^{s_L} //0.50M H_2SO_4

in HOH// E^{w_L} //KCl (sat. aq.) HgCl -Hg [2']

where $E^{\text{s}_L} + E^{\text{w}_L} = E^{\text{s}_L}$ and

$$E^{\text{s}_{\text{Fe}}} = E^{\text{s}_{\text{cell}(\text{Fe})} + E^{\text{s}_{\text{SCE}}} + E^{\text{s}_L} \quad [14]$$

$$E^{\text{s}_{\text{Pt}}} = E^{\text{s}_{\text{cell}(\text{Pt})} + E^{\text{s}_{\text{SCE}}} + E^{\text{s}_L}$$

where $E^{\text{s}_{\text{cell}(\text{Fe or Pt})}}$ is the experimental measured potential vs. the saturated aqueous calomel electrode. The calomel electrode becomes inoperable in solutions of

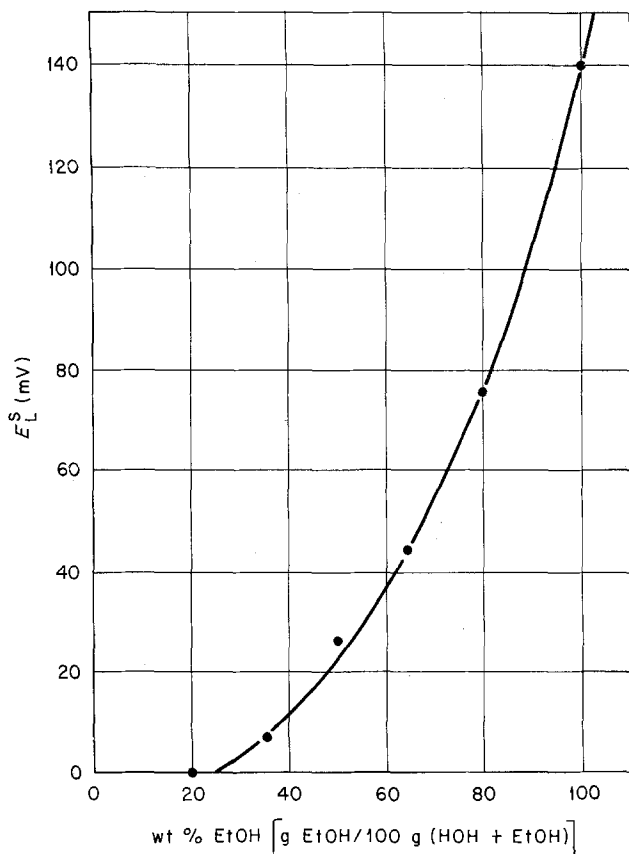


Fig. 1. Liquid junction potentials, E_L^S , between soln X in EtOH-HOH solvent and saturated aqueous KCl as a function of weight per cent EtOH in EtOH-HOH solvent.

high ethanol content due to plugging of the asbestos wick with KCl precipitation. According to [2'] a solution 0.5M H_2SO_4 in water was interposed between the calomel electrode and the ethanol-water solution. The liquid junction potential E_L^S now becomes the sum of the two junctions $E_L^{S_1}$ and $E_L^{S_2}$. Several measurements in cells like [1'] and [2'] showed that $E_L^S \sim E_L^{S_1} + E_L^{S_2}$ within about 5 mV. An additional iron electrode was included in the cell for the polarization measurements. The liquid junction potential E_L^S was constant and probably less than 5 mV (14).

Experimental

The high purity zone-refined iron¹ electrodes used in this investigation were cut from 1/4 in. rod stock and were 1/4 in. to 3/8 in. long. The electrodes were mounted in conventional Teflon electrode holders (15). The entire cell assembly was made from Pyrex glass and Teflon. The apparatus was designed so that the addition and removal of solution could be accomplished without opening the apparatus to the atmosphere. The test electrode compartment was a flat bottom cylinder made from a 55/50 TS ground glass joint. The ground surface was carefully removed by fire polishing. A glass jacket was provided for circulating water, so that the solution temperature could be maintained at $30.00^\circ \pm 0.03^\circ C$. The cap to the test electrode compartment was machined from Teflon and had seven convenience ports. The ports were 1/4 in. Teflon Swagelok fittings which were epoxied into holes drilled through the Teflon cap. One port provided for the delivery of H_2 saturated 0.5M H_2SO_4 in water. A glass tube passed from the bottom of the test electrode compartment (cell) through the walls of the water jacket, to a Teflon Nupro plastic valve,² diaphragm stem model. This tube and valve arrangement provided for solution sample removal for the electro-

metric Karl Fischer water analysis,³ and also for solution drainage, so that in conjunction with the solvent delivery facilities, varying EtOH-HOH compositions could be obtained. Ultrapure H_2 gas was provided by a Matheson generator. The H_2 gas passed successively through a presaturator containing 0.5M H_2SO_4 in absolute EtOH, a reservoir containing the 0.5M H_2SO_4 in absolute EtOH which is to be delivered to the electrochemical cell, the electrochemical cell, a reservoir containing the 0.5M H_2SO_4 in water, finally exiting to the atmosphere through a bubbler-trap which prevented back diffusion of atmospheric oxygen into the aqueous acid reservoir. Other ports in the test cell cap provided for the Fe test electrode, an Fe polarizing electrode for μA determinations, H_2 gas exit, and a Haber-Luggin capillary probe. Another glass tube for H_2 gas inlet passed through the wall of the water jacket near the top of the test cell and extended down to the bottom of the cell. An external saturated aqueous calomel electrode was used as a reference electrode in conjunction with the Haber-Luggin capillary probe. Flexible Teflon "spaghetti" tubing (1/8 in. or 1/4 in.) was used for convenient connections. A Teflon-coated bar magnet was used for stirring in the test cell.

The absolute ethanol and reagent grade sulfuric acid were used without further purification. The water was triply distilled. The iron electrodes were etched in 50/50 H_2SO_4 -water, rinsed in distilled water and ethanol, dried, then vacuum annealed at $800^\circ C$ for 12 hr at 10^{-7} Torr, and slow cooled. The annealed electrodes were again etched in 50/50 H_2SO_4 -water, rinsed in distilled water and ethanol, and transferred to the cell. In a typical experiment the iron electrodes were first exposed to the aqueous acid environment from one to several days, during which the solution was frequently replaced with fresh solution. As with Kelly (2), a well-behaved system exhibited no polarization hysteresis phenomenon, and this fact was used as the basic criterion by which the suitability of the system for investigation was determined. The solution was then drained and the 0.5M H_2SO_4 in absolute ethanol was delivered to the cell. Again, the above criterion was used for suitability for investigation. Usually, when no polarization hysteresis was observed in the aqueous environment, none was observed in the absolute ethanol environment. The absolute ethanol solvent composition was increased in water content by partial drainage of the cell and addition of the aqueous acid. When the "hysteresis" criterion was met in the aqueous and absolute ethanol environment, the solvent composition could be varied at will with increasing or decreasing water content, and no polarization hysteresis was observed at any intermediate solvent composition. Sometimes, polarization data on a given electrode were accumulated over a period of one week's time.

The polarizing currents were furnished by using the Research Model Anotrol Potentiostat in the galvanostatic mode. The currents were measured by recording the voltage drop across precision resistors in the polarizing circuit. The potentials were measured with a 610B Keithley Electrometer and recorded with a 10 mV Brown recorder.

Results

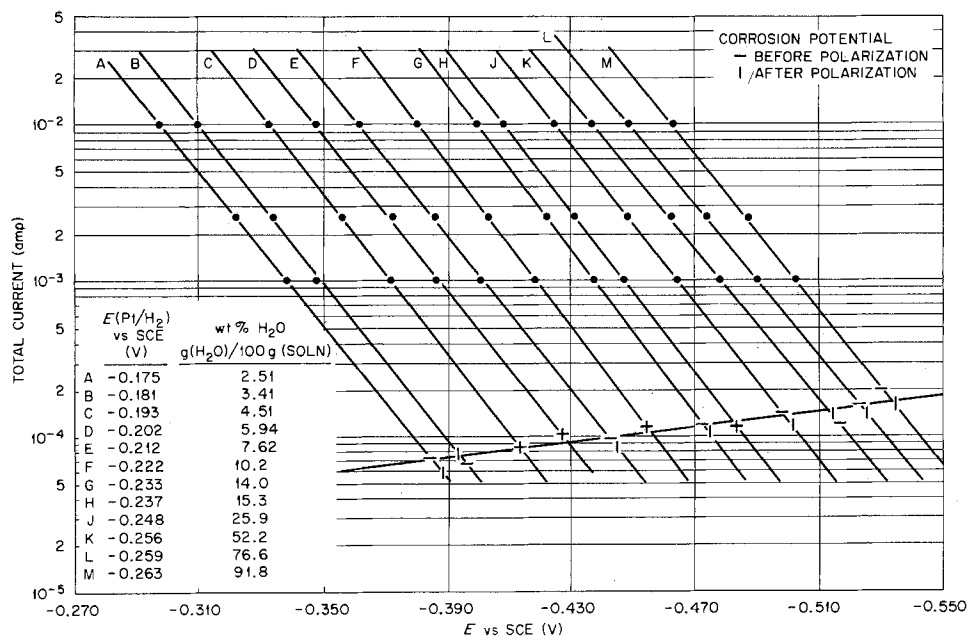
The anodic polarization data in the acidic ethanol-water environments are shown in Fig. 2. Here the total net dissolution current is plotted as a function of $E_{S_{cell}(Fe)}$ (i.e., the potential of the iron electrode vs. the saturated aqueous calomel electrode). The Tafel slope ($dE/d \log i$) = $2/3(2.3 RT/F)$, and is independent of solvent composition. This implies that in each solvent S, a mechanism similar to that in pure water prevails. The alphabetical listing reveals the sequence in which

¹ Prepared and analyzed by Materials Research Corporation.

² Manufactured by Swagelok.

³ The authors wish to express their appreciation to Dr. Richard Raridon of the ORNL Chemistry Division for the electrometric Karl Fischer water analysis.

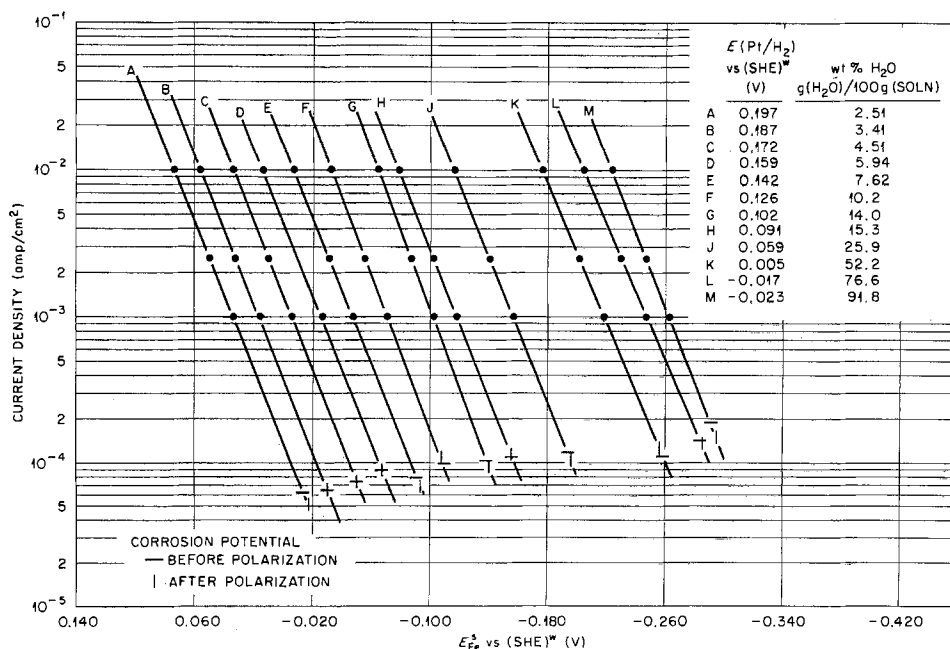
Fig. 2. Anodic polarization of iron in H_2 -saturated 0.50M H_2SO_4 in various EtOH-HOH solvents, $T = 30^\circ C$, electrode area 0.97 cm^2 .



the polarizations were made, starting generally with the least aqueous environment. The polarization in pure water was indistinguishable from the polarization in 91.8% water shown in Fig. 2. The pure water result was repeated numerous times, and was in excellent agreement with the results reported by Eichkorn, Lorenz, Albert, and Fischer (16) for zone-refined iron. Also included in Fig. 2 are the weight per cent H_2O (as $g[H_2O]/100g [soln]$), the potentials of the Pt- H_2 electrode vs. SCE and the corrosion potentials before polarization (horizontal slash) and after polarization (vertical slash). In Fig. 1 the liquid junction potentials between the acidic ethanol-water solution and the saturated aqueous KCl solution are plotted as a function of weight per cent H_2O in EtOH- H_2O solvent, where the weight per cent H_2O was calculated on the basis of $g(H_2O)/100g (EtOH + HOH)$. The weight per cent reported in Fig. 2 is calculated on the basis of $g(HOH)/100g (EtOH + HOH + H_2SO_4)$. Consequently to obtain values for the liquid junction potentials from Fig. 1, the Karl-Fischer determinations of the water content in Fig. 2 are corrected to weight per cent $(HOH)/100g (EtOH + HOH)$. For this calcula-

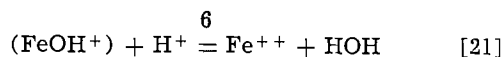
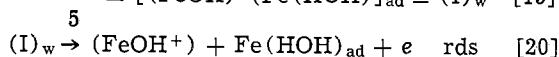
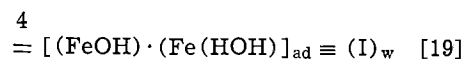
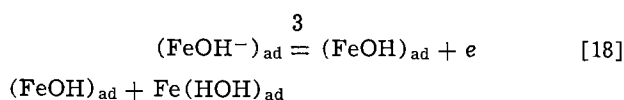
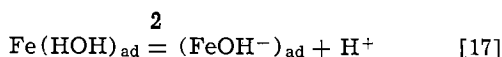
tion it was assumed that the density of the solution was the same as the density of the pure EtOH-HOH solvent at the Karl Fischer estimated water content. With these values for E^s_L , the results in Fig. 2 are re-plotted. Here, in Fig. 3, the polarizations are reported as current density (amperes/square centimeter) vs. the absolute potential of the iron electrode, $E^{s_{Fe}}$, i.e., the potential of the iron electrode in solvent S vs. the standard hydrogen electrode in water, $(SHE)^w$. Also included in Fig. 3 are the potentials of the Pt/ H_2 electrode vs. the $(SHE)^w$. At this point, it is probably worthwhile to emphasize that the measurement of the pA of the solutions, which is identically pH in pure water solvent, is defined according to Eq. [10]-[12]. The validity of such measurements is a test of the extra-thermodynamic postulates used for the estimation of the "degenerate" activity coefficients f_{H^+} , as a function of solvent composition. Such an application of the pA scale to inorganic reaction kinetics (in our case the corrosion of iron) has not heretofore been demonstrated. Unfortunately, the introduction of the measured pA values into the rate expression (to be derived for the EtOH-HOH solvent) does not provide

Fig. 3. Anodic polarization of iron in H_2 -saturated 0.50M H_2SO_4 in various EtOH-HOH solvents, $T = 30^\circ C$, electrode area 0.97 cm^2 .

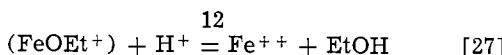
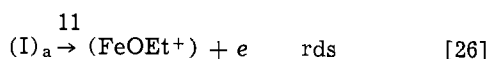
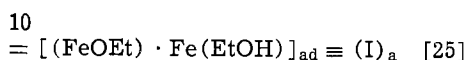
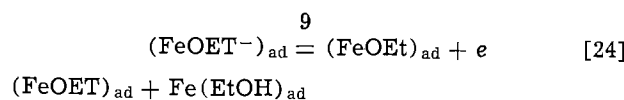
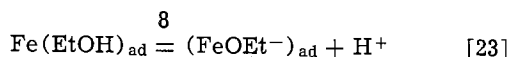
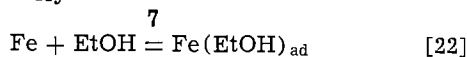


a direct test. In changing the solvent from pure water to EtOH-HOH, the activity of the water as well as the pA is changed, and some assumption must probably be made relating to the water activity, and presumably also to the activity of ethanol. It should be emphasized that the absolute potentials reported in Fig. 3 are based on the junction potentials provided by Grunwald and Gutbezahl. An interpretation of the results using the junction potentials provided by Popovych and Dill (12, 13) will be considered later.

The derivation of the rate expression for EtOH-HOH solvent follows very closely the mechanism proposed by Kelly (4) for the inhibited system. It is postulated that in pure EtOH the dissolution of iron proceeds by a mechanism similar to that in pure water, and in mixed solvents a simultaneous dissolution occurs by both water and alcohol, i.e., $i_+ = i_w + i_a$, where i_+ is the total net anodic dissolution current, and i_w and i_a are the currents due to water and alcohol, respectively. Equations [16]-[27] give a formal description of the mechanism proposed



and simultaneously



These equations take account of the simultaneous coverage by the several intermediates, where $[\text{Fe}(\text{HOH})_{\text{ad}}] = \beta\theta_1$, $[(\text{FeOH}^-)_{\text{ad}}] = \beta\theta_2$, $[(\text{FeOH})_{\text{ad}}] = \beta\theta_3$, $[(\text{I})_w] = \beta\theta_4$, $[\text{Fe}(\text{EtOH})_{\text{ad}}] = \beta\theta_5$, $[(\text{FeOEt}^-)_{\text{ad}}] = \beta\theta_6$, $[(\text{FeOEt})_{\text{ad}}] = \beta\theta_7$, $[(\text{I})_a] = \beta\theta_8$, and $a_+ = c_H + y^s_H + f_H^+$, where θ_i is the fraction of the total possible adsorption sites occupied by $[i]$, and the surface concentrations ($\beta\theta_i$), are expressed in moles/square centimeter, with β a proportionality constant, y^s_i the conventional molar activity coefficient in solvent S, and f_i the "degenerate" activity coefficient. The reference state for f_i is the infinitely dilute aqueous solvent for all solvent compositions including pure ethanol. A kinetic description of this mechanism in the steady state is given by Eq. [28]-[37]

$$\frac{i_w}{F} = \bar{k}_3[\beta\theta_2] - \bar{k}_{-3}[\beta\theta_3] + \bar{k}_5[\beta\theta_{1w}] \quad [28]$$

$$\beta \left(\frac{\partial \theta_{1w}}{\partial t} \right)_{\text{ss}} = 0 = \bar{k}_4[\beta\theta_3][\beta\theta_1] - \bar{k}_{-4}[\beta\theta_{1w}] - \bar{k}_5[\beta\theta_{1w}] \quad [29]$$

$$\begin{aligned} \beta \left(\frac{\partial \theta_3}{\partial t} \right)_{\text{ss}} = 0 = & \bar{k}_3[\beta\theta_2] - \bar{k}_{-3}[\beta\theta_3] \\ & - \bar{k}_4[\beta\theta_3][\beta\theta_1] + \bar{k}_4[\beta\theta_{1w}] \quad [30] \end{aligned}$$

$$\begin{aligned} \beta \left(\frac{\partial \theta_2}{\partial t} \right)_{\text{ss}} = 0 = & \bar{k}_2[\beta\theta_1] - \bar{k}_{-2}[\beta\theta_2][a_+] \\ & - \bar{k}_3[\beta\theta_2] + \bar{k}_{-3}[\beta\theta_3] \quad [31] \end{aligned}$$

$$\begin{aligned} \beta \left(\frac{\partial \theta_1}{\partial t} \right)_{\text{ss}} = 0 = & \bar{k}_1[a_w][(1 - \theta_T)] - \bar{k}_{-1}[\beta\theta_1] \\ & + \bar{k}_2[\beta\theta_1] - \bar{k}_{-2}[\beta\theta_2][a_+] - \bar{k}_4[\beta\theta_3][\beta\theta_1] \\ & + \bar{k}_{-4}[\beta\theta_{1w}] \quad [32] \end{aligned}$$

and similarly for dissolution by ethanol

$$\frac{i_a}{F} = \bar{k}_9[\beta\theta_5] - \bar{k}_{11}[\beta\theta_{1a}] \quad [33]$$

$$\begin{aligned} \beta \left(\frac{\partial \theta_{1a}}{\partial t} \right)_{\text{ss}} = 0 = & \bar{k}_{10}[\beta\theta_6][\beta\theta_4] \\ & - \bar{k}_{-10}[\beta\theta_{1a}] - \bar{k}_{11}[\beta\theta_{1a}] \quad [34] \end{aligned}$$

$$\begin{aligned} \beta \left(\frac{\partial \theta_6}{\partial t} \right)_{\text{ss}} = 0 = & \bar{k}_9[\beta\theta_5] - \bar{k}_{-9}[\beta\theta_6] \\ & - \bar{k}_{10}[\beta\theta_6][\beta\theta_4] + \bar{k}_{-10}[\beta\theta_{1a}] \quad [35] \end{aligned}$$

$$\begin{aligned} \beta \left(\frac{\partial \theta_5}{\partial t} \right)_{\text{ss}} = 0 = & \bar{k}_8[\beta\theta_4] - \bar{k}_{-8}[\beta\theta_5][a_+] \\ & - \bar{k}_9[\beta\theta_5] + \bar{k}_{-9}[\beta\theta_6] \quad [36] \end{aligned}$$

$$\begin{aligned} \beta \left(\frac{\partial \theta_4}{\partial t} \right)_{\text{ss}} = 0 = & \bar{k}_7[a_a][(1 - \theta_T)] - \bar{k}_{-7}[\beta\theta_4] \\ & - \bar{k}_8[\beta\theta_4][\beta\theta_6] + \bar{k}_{-8}[\beta\theta_5][a_+] \\ & - \bar{k}_{10}[\beta\theta_4][\beta\theta_6] + \bar{k}_{-10}[\beta\theta_{1a}] \quad [37] \end{aligned}$$

Here, a_w , a_a are the activities of water and alcohol, respectively, in the mixed solvent and a_+ is the "absolute activity" of the proton (*vide* Eq. [12]). The \bar{k} 's are again the electrochemical rate constants referred to the extremely dilute aqueous solvent as the reference state. Equations [28]-[37] reduce to the steady-state solution

$$\begin{aligned} \frac{i_+}{F} = \frac{i_w}{F} + \frac{i_a}{F} = & \frac{k_5}{[a_+]} \left(\frac{k_4}{k_{-4}} \frac{k_3}{k_{-3}} \frac{k_2}{k_{-2}} (\theta_1)^2 \right. \\ & \left. \exp \frac{3FE^s_{\text{Fe}}}{2RT} \right) + \frac{k_{11}}{[a_+]} \left[\frac{k_{10}}{k_{-10}} \frac{k_9}{k_{-9}} \frac{k_8}{k_{-8}} (\theta_4)^2 \exp \frac{3FE^s_{\text{Fe}}}{2RT} \right] \quad [38] \end{aligned}$$

$$\text{where } \theta_1 = \frac{1}{1 + \frac{k_{-1}k_7a_a}{k_1k_{-7}a_w}} \text{ and } \theta_4 = \frac{1}{1 + \frac{k_1k_{-7}a_w}{k_{-1}k_7a_a}}$$

Equation [38] assumes that the surface coverage is mostly adsorbed water and alcohol; $\theta_1 + \theta_4 \sim \theta_T$ and $\theta_T \sim 1$. In the detailed derivation of Eq. [38], $(\theta_1 + \theta_4) \sim 1$ implies $k_{-1}k_{-7} \ll k_{-1}k_7a_a + k_1k_7a_w$, and $k_{-1}k_{-7} \sim 0$. It is now further assumed that over the range of solvent composition studied $i_w \gg i_a$, leading to Eq. [39]

$$i_+ = \frac{k}{[a_+]} \left[\frac{1}{1 + \lambda' \frac{a_a}{a_w}} \right]^2 \exp \frac{3FE^s_{\text{Fe}}}{2RT} \quad [39]$$

$$\text{where } k = F \left(k_5 \frac{k_4}{k_{-4}} \frac{k_3}{k_{-3}} \frac{k_2}{k_{-2}} \right) \text{ and } \lambda' = \frac{k_{-1}k_7}{k_1k_{-7}}$$

It is assumed that the activity ratio $a_a/a_w = N_a/N_w$ where N_a and N_w are the mole fractions of alcohol and water, respectively. Further, it can be shown that $N_a/N_w = 18/46$ [weight per cent (EtOH)/weight per cent (HOH)] which leads to Eq. [40]

$$i_{+s} = \frac{k}{[a_+]} \left[\frac{1}{1 + \lambda \frac{w/o(\text{EtOH})}{w/o(\text{HOH})}} \right]^2 \exp \frac{3FE_{\text{Fe}}^s}{2RT} \quad [40]$$

The value for k in Eq. [40] was obtained from the results in pure water where $\frac{w/o \text{ EtOH}}{w/o \text{ HOH}} = 0$, and knowing k , the value for λ was a grand average value calculated from all data for solvent compositions ranging from ca. 10-50 w/o (HOH). In logarithmic form Eq. [40] becomes

$$\log(i_{+s}) = 3.1833 - E_{\text{Pt}}^s/0.06 + E_{\text{Fe}}^s/0.04 + 2 \log \left[\frac{1}{1 + 1.4R} \right] \quad [41]$$

where $R = w/o(\text{EtOH})/w/o(\text{HOH})$, $-\log(a_+) = -E_{\text{Pt}}^s/0.06$, $\log k = 3.1833$ and $\lambda = 1.4$. It should be recalled that the "absolute" acidity, $pA = -\log(a_+) = -E_{\text{Pt}}^s/0.06$. A plot of the experimental anodic current densities, (i_{+s}) , at constant potential $E_{\text{Fe}}^s = -0.222v \text{ vs. (SHE)}^w$, as a function of solvent composition, for the results reported in Fig. 3, is presented in Fig. 4. The calculated values in Fig. 4 were obtained from Eq. [41]. Also included in Fig. 4 are the results from another iron electrode of larger surface area. A better fit of the data would be obtained if λ was recalculated for each electrode. The value for λ is not expected to be the same for different electrodes since it is a ratio of rate constants. The experimental current densities reported in Fig. 4 were obtained analytically as follows. In pure water at $E_{\text{Fe}}^s = -0.222v$, the current density is 10^{-2} A/cm^2 , for which $\log(i_{+s}) = -2.0$. Therefore, it follows from Fig. 3 that

$$\log(i_{+s})_{E_{\text{Fe}}^s} = -2.0 \frac{(E_{\text{Fe}}^s)_{i_+} - (-0.222)}{0.040} \quad [42]$$

where $(i_{+s})_{E_{\text{Fe}}^s}$ is the anodic current density at solvent composition S and constant potential $E_{\text{Fe}}^s = -0.222v \text{ vs. (SHE)}^w$, $(E_{\text{Fe}}^s)_{i_+}$ is the potential of the iron electrode vs. (SHE)^w at $(i_{+s}) = 10^{-2} \text{ A/cm}^2$ and solvent composition S , and 0.040 is the anodic Tafel slope, $\partial(E_{\text{Fe}}^s)/\partial(\log i_{+s,a,+})$, at constant solvent composition S and proton activity, a_+ .

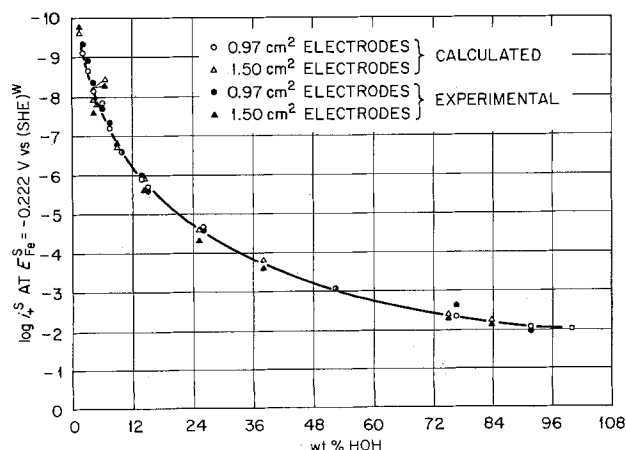


Fig. 4. Anodic current density for iron in H_2 -saturated 0.50M H_2SO_4 -EtOH-HOH as a function of weight per cent (HOH) at fixed potential, $E_{\text{Fe}}^s = -0.222v \text{ vs. (SHE)}^w$ at 30°C .

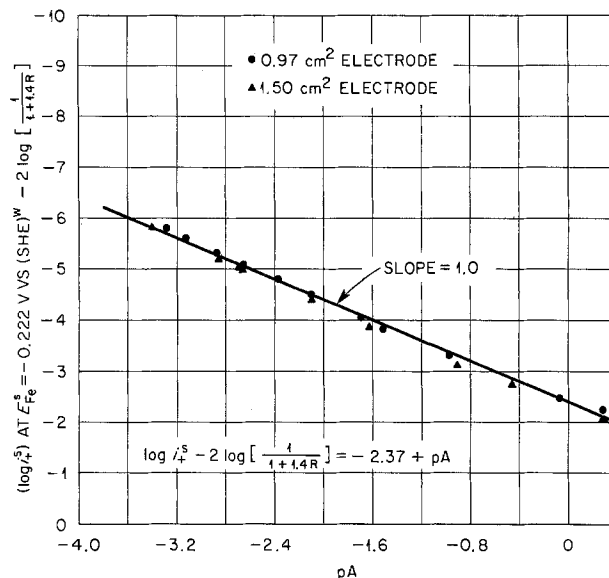


Fig. 5. The anodic current density for iron in H_2 -saturated 0.50M H_2SO_4 -EtOH-HOH as a function of pA at fixed potential, $E_{\text{Fe}}^s = -0.222v \text{ vs. (SHE)}^w$ at 30°C .

The calculated values for the anodic current density at constant $E_{\text{Fe}}^s = -0.222v$ are again presented in Fig. 5. The results are corrected for the solvent dependence, $2 \log \left(\frac{1}{1 + \lambda R} \right)$, and plotted as a function of $pA = -E_{\text{Pt}}^s/0.06$. According to Eq. [41]

$$\left(\frac{\partial \left[\log(i_{+s})_{E_{\text{Fe}}^s} - 2 \log \left(\frac{1}{1 + \lambda R} \right) \right]}{\partial pA} \right) = 1$$

if the reaction is first order in the reciprocal of the proton activity. The theoretical solid line drawn with unit slope provides an excellent fit to the data. Similarly, according to Eq. [41], after accounting for the coverage factor, and at constant anodic current density, the electrode potential should be a linear function of pA . The proportionality constant should be equal to -0.040 V/pA if the dissolution reaction is first order in the reciprocal of the proton activity. The electrode potential at constant anodic current density of 10^{-2} A/cm^2 is plotted as a function of pA in Fig. 6. The straight line drawn with a slope of -0.042 V/pA fits the data, further confirming the first order dependence and the coverage factor term.

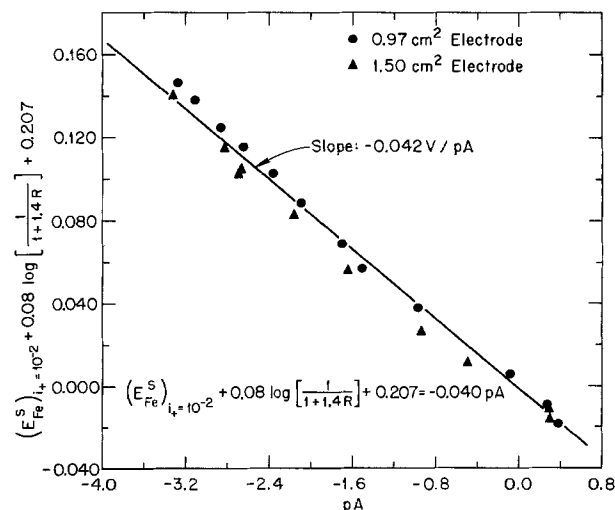


Fig. 6. The variation of the iron electrode potential in H_2 -saturated 0.50M H_2SO_4 -EtOH-HOH as a function of pA , at a constant anodic current density of $1 \times 10^{-2} \text{ A/cm}^2$, at 30°C .

The cathodic evolution of H_2 as a function of solvent has been investigated here to only a limited extent. The polarizations which have been made covered the range of solvent composition from pure water to about 98 w/o (EtOH), and have shown Tafel slopes, $(\partial E_{Fe}^{s_{Fe}} / \partial \log i^-)_{s,a,+}$, of 109–119 mV [approximately $2.3 (2 RT/F)$]. Since the results containing EtOH are similar to that which is observed in pure water solvent, it was postulated that the cathodic current was first order with respect to protons and that discharge occurred at both the adsorbed water sites, $Fe(H_2O)_{ads} \equiv \theta_1$, and at the adsorbed alcohol sites, $Fe(EtOH)_{ads} \equiv \theta_4$. A kinetic description of this mechanism is given by Eq. [43]

$$-\frac{(i^-)^s}{F} = k_w a + \theta_1 \exp \frac{-FE_{Fe}^{s_{Fe}}}{2RT} + k_a a + \theta_4 \exp \frac{-FE_{Fe}^{s_{Fe}}}{2RT} \quad [43]$$

where recalling the anodic dissolution mechanism

$$\theta_1 = \frac{1}{1 + \lambda R} \quad \text{and} \quad \theta_4 = \frac{\lambda R}{1 + \lambda R}$$

in the steady state. Again it is assumed that the rate via the aqueous mechanism is much greater than via the alcohol mechanism, and

$$-i^-^s = k_w a + \left(\frac{1}{1 + \lambda R} \right) \exp \frac{-FE_{Fe}^{s_{Fe}}}{2RT} \quad [44]$$

From Eq. [39] and [44] the corrosion potential and corrosion current as a function of pA and θ_1 may be obtained. It is recalled that at the corrosion potential, $E_{Fe}^{s_{Fe}(\text{corr})}$, $i^-^s = i^+^s = i^{s(\text{corr})}$, and therefore

$$\log i^{s(\text{corr})} - 5/4 \log \left(\frac{1}{1 + 1.4R} \right) + 3.562 = -1/2 pA \quad [45]$$

$$E_{Fe}^{s_{Fe}(\text{corr})} + 0.03 \log \left(\frac{1}{1 + 1.4R} \right) + 0.270 = -0.06 pA \quad [46]$$

The constants in Eq. [45] and [46] were obtained from the results in pure water where $R = 0$, $E_{Fe}^{s_{Fe}(\text{corr})} = -0.292 \bar{v}$ vs. (SHE)^w, $i^{s(\text{corr})} = 1.8 \times 10^{-4}$ A/cm², and $E_{Pt}^s = -0.022 \bar{v}$ vs. (SHE)^w. Figure 7 shows the corrosion current, $\log i^{s(\text{corr})}$, (corrected for coverage), as a function of pA , and the theoretical line with slope $-1/2$ provides a satisfactory fit to the data. Similarly, the corrosion potential, $E_{Fe}^{s_{Fe}(\text{corr})}$, (corrected for cover-

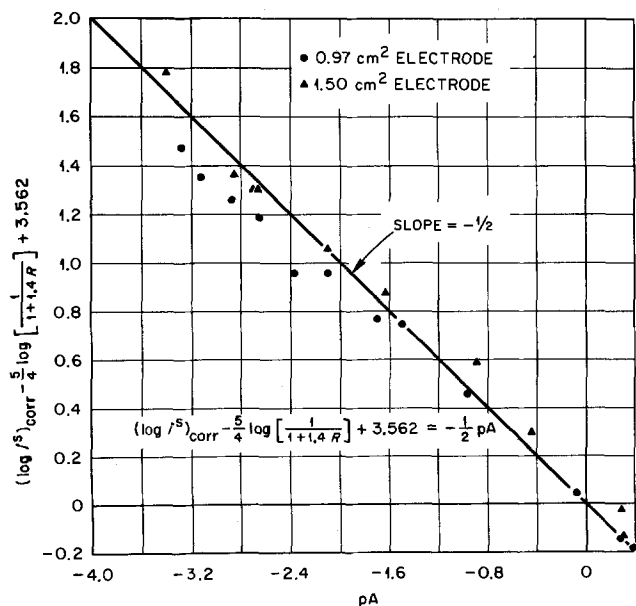


Fig. 7. The corrosion current for iron in H_2 -saturated 0.50M H_2SO_4 EtOH-HOH as a function of pA at $30^\circ C$.

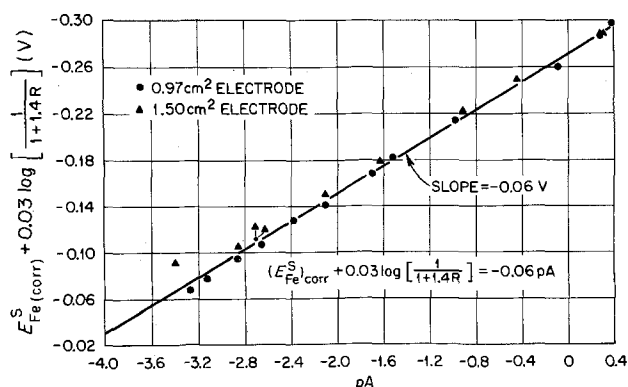


Fig. 8. The corrosion potential for iron in H_2 -saturated 0.50M H_2SO_4 EtOH-HOH as a function of pA at $30^\circ C$.

age) as a function of pA is shown in Fig. 8 and again the theoretical line with slope -0.060 provides an excellent fit to the data, i.e., $\partial(E_{Fe}^{s_{Fe}(\text{corr})} + 0.03 \log \theta_1) / \partial pA = -2.303 RT/F$.

Equation [46] can be written in terms of the experimentally measured cell potentials for Fe and Pt. In this form it is seen that the corrosion potential is independent of the liquid junction potential E_L .

$$E_{(cell\ Fe)corr}^s = -0.270 + E_{(cell)Pt}^s - 0.03 \log \left[\frac{1}{1 + \lambda R} \right] \quad [47]$$

The value $\lambda = 1.4$ (obtained from Eq. [40]) does indeed give good agreement between the calculated and the observed corrosion potentials. Using Eq. [47] a better value would be $\lambda = 1.8$. Alternatively, with this value of λ (say, gotten now from Eq. [47], Eq. [41] and [45] are better satisfied using Grunwald's (1) or Aleksandrov's and Izmailov's (10, 11) set of junction potentials rather than Popovych's (12, 13).

Accepting this value for λ from Eq. [47], a set of liquid junction potentials can be generated from Eq. [41]. Proton activities calculated using these experimentally determined junction potentials are compared with those estimated using the junction potentials of Grunwald and Gutbezahl (1), Aleksandrov and Izmailov (10, 11), and Popovych and Dill (13). A plot of these proton activities as a function of R is shown in Fig. 9. In this form, it is seen that the proton activities of Popovych and Dill are unacceptable.

Summary

Values for the junction potentials (1) between acidic EtOH-HOH solutions and saturated aqueous KCl were used to interpret the electrochemical polarization behavior of the active iron electrode in acidic EtOH-HOH solutions. The junction potentials were obtained from a correlation of the pK^s of organic acids in EtOH-HOH solvents. The correlation was based on the validity of the "activity postulate" of Grunwald and co-workers (1, 8).

The mechanism suggested by Kelly (4) for iron dissolution in hydrogen saturated sodium benzoate solutions (referred to as the inhibited system) was accepted with a few additional assumptions: the surface coverage was mostly adsorbed water ($Fe \cdot (H_2O)_{ad}$) and alcohol ($Fe \cdot (EtOH)_{ad}$), i.e., $\theta_1 + \theta_4 \sim 1$; there was a simultaneous dissolution by EtOH and HOH, with the dissolution rate by water much greater than by alcohol; and finally it was assumed that the ratio of the activity of alcohol to water was proportional to the weight per cent ratio. Thus, in a competition for active sites on the electrode surface, alcohol acts as a "relative" inhibitor. The decision to test this mechanism to the corrosion data was based primarily on the observation that the anodic Tafel slope, $(\partial E / \partial \log i^+)_{s,a,+} = 2/3 (2.303 RT/F)$, and was unchanged for all solvent compositions. Thus a mechanism (2, 3)

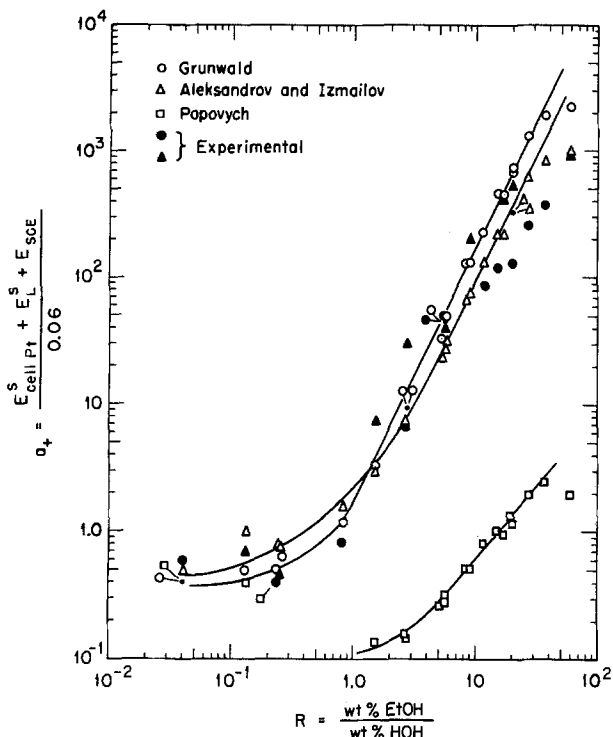


Fig. 9. The variation of proton activities, a_+ , as a function of $R = w/o \text{ EtOH}/w/o \text{ HOH}$; proton activities calculated using several sets of liquid junction potentials, E^S_L .

similar to that accepted for dissolution in water solvent was suggested. The further choice of the mechanism suggested by Kelly (4) for the inhibited system was based primarily on the better fit to the results for the anodic polarization with a second order dependency on coverage.

The cathodic polarizations gave a Tafel slope ($\partial E/\partial \log i_{-}$)_{s,a+} ~ 2 ($2.303 RT/F$), and was unchanged for all solvent compositions. On the basis of this observation, and to explain the observed variation of corrosion potential and corrosion current with solvent, it was postulated that the cathodic partial current was first order in both coverage, θ_1 , and the activity of the protons, a_+ .

Alternatively, accepting the corrosion mechanism, an "experimental" set of liquid junction potentials was generated. The proton activities, (a_+), calculated using these junction potentials were in much better agreement with those estimated using the values of

E^S_L from Grunwald and Gutbezahl (1) or Aleksandrov and Izmailov (10, 11) than with the proton activities calculated using the junction potentials proposed by Popovych (12) and Popovych and Dill (13).

Acknowledgment

The authors would like to express their appreciation to Dr. Eugene J. Kelly of the ORNL Chemistry Division for the many hours spent in discussions of this work, particularly relating to the final form of the rate expression. We also would like to thank Dr. Robert E. Meyer of the ORNL Chemistry Division for his many constructive criticisms.

This research was sponsored by the U.S. Atomic Energy Commission under contract with the Union Carbide Corporation.

Manuscript submitted July 27, 1973; revised manuscript received Aug. 12, 1974.

Any discussion of this paper will appear in a Discussion Section to be published in the December 1975 JOURNAL. All discussion for the December 1975 Discussion Section should be submitted by Aug. 1, 1975.

Publication costs of this article were partially assisted by Oak Ridge National Laboratory.

REFERENCES

1. B. Gutbezahl and E. Grunwald, *J. Am. Chem. Soc.*, **75**, 565 (1953).
2. E. J. Kelly, *This Journal*, **112**, 124 (1965).
3. J. O'M. Bockris, D. Drazic, and A. R. Despic, *Electrochim. Acta*, **4**, 325 (1961).
4. E. J. Kelly, *This Journal*, **115**, 1111 (1968).
5. A. L. Bacarella, E. Grunwald, H. P. Marshall, and E. Lee Purlee, *J. Org. Chem.*, **20**, 747 (1955).
6. R. G. Bates, "Determination of pH," pp. 189 et seq., John Wiley & Sons, Inc., New York (1964).
7. R. A. Robinson and R. H. Stokes, "Electrolyte Solutions," pp. 351 et seq., Butterworth & Co., (Publishers) Ltd., London (1959).
8. E. Grunwald and B. J. Berkowitz, *J. Am. Chem. Soc.*, **73**, 4939 (1951).
9. E. Grunwald and S. Winstein, *ibid.*, **70**, 846 (1948).
10. V. A. Aleksandrov and N. A. Izmailov, *Zh. Fiz. Khim.*, **32**, 404 (1958).
11. N. A. Izmailov and V. A. Aleksandrov, *ibid.*, **31**, 2619 (1957).
12. O. Popovych, *Critical Rev. Anal. Chem.*, **1**, 73 (1970).
13. O. Popovych and A. J. Dill, *Anal. Chem.*, **41**, 456 (1969).
14. G. Bianchi, G. Faita, R. Galli, and T. Mussini, *Electrochim. Acta*, **12**, 439 (1967).
15. R. E. Meyer, *This Journal*, **106**, 930 (1959).
16. G. Eichkorn, W. J. Lorenz, L. Albert, and H. Fischer, *Electrochim. Acta*, **13**, 183 (1968).

Accelerated Life Testing of Lead-Acid Industrial Motive Power Cells

N. J. Maskalick*

Westinghouse Research Laboratories, Pittsburgh, Pennsylvania 15235

ABSTRACT

Depth of positive grid corrosion is a regular and precise indicator of cell degradation during life testing of the subject lead-acid cells. Average corrosion depth at constant temperature is directly proportional to (time on cycle test)^{0.67} for Pb-5% Sb positive grids. The temperature dependence of the logarithm of the corrosion rate constant is employed to predict a room-temperature corrosion function. Lifetime at room temperature is then estimated to a predefined average depth of corrosion corresponding to actual failure in normal service. This test is capable of high precision predictions of cell lifetime in a period of 4-6 months, compared to 3-4 years in conventional testing.

The time required to test lead-acid cells is greatly shortened at high temperatures as was demonstrated by Willihnganz (1) in his work with cells on float service. He observed that the logarithm of the constant potential lifetime of lead-acid cells with lead-calcium positive grids increases linearly with the reciprocal absolute temperature, and that over-all positive plate growth can be plotted as a regular function of time on test. Cannone *et al.* (2) identified this functional dependence as parabolic for cells with pure lead, or lead-calcium positive grids, and as linear, for cells with lead-antimony positive grids. They extended and corroborated Willihnganz' work by demonstrating that the logarithm of the constant term in their derived positive plate growth functions is a linear function of the reciprocal absolute test temperature. They consequently specified a value of this constant for room temperature float service by log-linear extrapolation of high temperature results.

Cell life, and positive plate growth, in all of these prior experiments, must be considered to be directly related to over-all positive plate corrosion current and time. In the case of a constant voltage test, which was chosen to relate to the usage mode of cells in float service, over-all corrosion current does not remain constant but increases with surface roughness and decreases with the buildup of barrier (passivating) layers. This progress of corrosion with time (or the positive plate growth *vs.* time) is described by experimentally determined degradation functions employing a single temperature-dependent constant.

A test relating to the positive corrosion and lifetime expectancy of cells in cyclic charge-discharge service must differ from constant voltage operation as a matter of definition. The over-all positive grid corrosion in such cells varies with time in an even more complex manner.

This present work is a study of the temperature dependence of corrosion of lead-antimony alloy positive grids in cells in deep cycle service. As an investigation involved with direct and indirect measurements of corrosion depth as a function of time and temperature, it is designed to employ a testing cycle consisting of a constant-current, constant ampere-hour discharge, and a tapered-current, constant ampere-hour charge. This test routine, essentially a constant-coulombs per cycle (coulostatic) test, was chosen instead of a constant voltage schedule to reflect more faithfully the usage pattern of motive power cells.

The purpose of this paper is to describe experiments monitoring, directly and indirectly, the time and temperature dependence of the corrosion of lead-5%

antimony positive grids in specific industrial motive power cells on this fixed charge-discharge cycle routine. The test specifications employed (maximum temperature, depth of discharge, extent of overcharge) are selected from a prior unpublished study of stress parameter combinations by the author. These parameter levels are one of many possible compatible sets reflecting different types of service. One objective of the subject experiments was to produce a near maximum in cell degradation rate leading to failure comparable to field service and room-temperature bench testing. These accelerated test results are further applied to predict charge-discharge cycle lifetime for cells operating at room temperature.

Experimental

Charge-discharge cycling was conducted on a uniform group of 48 series-connected 5-plate industrial motive power cells equally divided among constant-temperature baths held at 60.0°, 70.2°, and 82.2°C. A 4 hr constant current discharge was set at 72 A-hr (90% of nominal capacity at the 6 hr rate). A 4 hr taper charge for all cells at 101 A-hr (140% of amount withdrawn) completed the cycle. The initial charging current was 101A, tapering logarithmically to 1A at 4 hr. Continuous cycling was carried out 5 days per week. All cells were given an equalizing charge of 2.0A throughout each weekend.

The test cells employed 1.280 sp gr H₂SO₄. Positive grids consisted of an alloy containing 4.83% Sb, 0.40% Sn, 0.075% As, and 0.055% Cu. These grids were approximately 14.8 cm wide, 25.2 cm high, and 0.62 cm thick at the outside frame as cast. Cured positive paste content of these grids was maintained at 1.41 ± 0.01 lb average deviation by avoiding both overpasting and underpasting. All positive plates were wrapped horizontally with Fiberglas yarn followed by Fiberglas mat; finally with a perforated PVC outer envelope. Such plates normally fail due to grid corrosion and disintegration rather than via active material loss or degradation. Cell capacities at room temperature (6 hr rate = 13.3A) were determined at 50-100 cycle intervals. Three cells were removed from each constant temperature bath at 50-100 cycle intervals for measurement of antimony content in the active material, over-all grid growth, and grid corrosion depth. Antimony content of both the positive and negative active material was determined by atomic absorption spectrophotometry. Samples for these analyses were obtained by removing active material from the entire plate, blending with a mortar and pestle, washing with water, then oven-drying to constant weight.

The dimension chosen to describe grid growth was the change in width of the positive grid at one-half of

* Electrochemical Society Active Member.

Key words: anodic, statistics, batteries, corrosion, oxidation.

plate height. Mean depth of corrosion of the positive grid was estimated from direct micrometer measurements of residual grid thickness along the outside frame of the chemically cleaned grid. Oxide film removal was accomplished with an aqueous stripping solution of 12% KOH containing 10g hydrazine sulfate per liter.

The estimated mean value of residual grid thickness was subtracted from the estimated mean thickness value (0.614 cm) of formed grids from cells in the same production run, but with no accelerated life test charge-discharge cycles. The precision of the resulting estimated mean depth of corrosion for the test grids was specified by employing tabulated values of the t statistic (3)

$$\text{precision} = \pm t_{\nu, 0.025} \sqrt{\frac{s^2}{n}}$$

where ν = degrees of freedom ($n - 1$), $t_{\nu, 0.025}$ = tabulated values for 95% confidence limits, s^2 = estimate of the variance of the data

$$\sum_n (y_i - \bar{y})^2 / (n - 1),$$

n = total number of observations in a sample, and y = observed values for corrosion depth.

The t statistic was similarly employed to determine precision of the curve describing the slope (E/R) of the plot of $\ln k$ vs. $1/^\circ\text{K}$, where R is the gas constant, and E is expressed as an activation energy. Over-all precision for the prediction of room temperature lifetime was related to the precision with which E could be specified. Details of the calculations are given in the Appendix.

Results

Periodic capacity data.—Cell capacities at room temperature (6 hr rate = 13.3A), taken at intervals during cycle life, were distributed over a range which revealed only a general trend toward capacity decay (Fig. 1a). Both positive and negative limitations were observed, as determined by individual electrode measurements vs. a $\text{Hg}/\text{Hg}_2\text{SO}_4$ standard electrode. Treatment of the data to obtain 95% confidence level estimates of the mean cell capacity resulted in improvement in precision of the capacity decay curve, but not

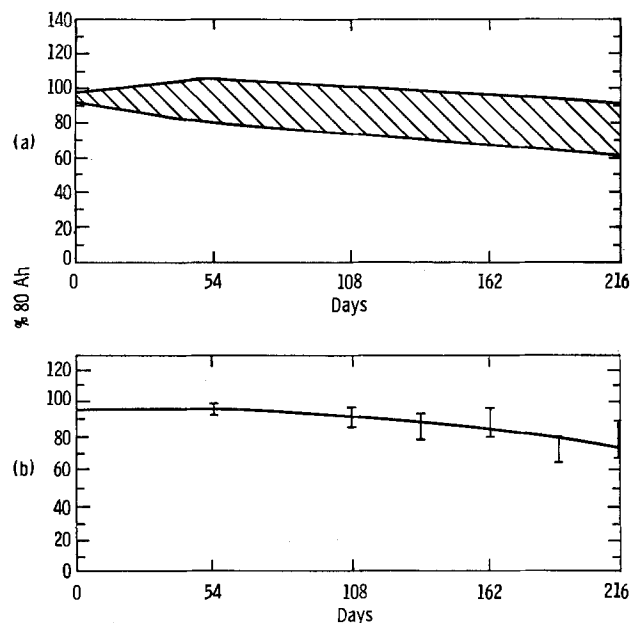


Fig. 1. Cell capacity vs. days on test at 60.0°C, room temperature capacity, 13.3A (nominal 6-hr rate).

enough to allow characterization leading to a lifetime prediction (Fig. 1b). These data did show, however, a general trend toward more rapid capacity decay with increasing test temperature. End-of-life capacity limitation was due to disintegration of the positive plate grid, leading to abrupt failure. For the 60.0°C cells this occurred beyond 216 days on test; it was not included on the curves of Fig. 1 due to the much lower confidence levels with which mean capacity values could be estimated for cells near end of life.

Periodic plate expansion data.—The positive plate expansion displayed a similar trend, with most highly expanded plates found in the highest temperature test bath. However, the results (Fig. 2) were mixed, precluding interpretation to yield any lifetime prediction.

Antimony migration.—The corrosion of the lead-antimony positive grid, accompanied by subsequent migration of soluble antimony-containing species, can be accurately monitored by direct periodic analysis of antimony pickup in the active material under ideal circumstances. Figure 3 demonstrates that test conditions are less than ideal, however, yielding antimony pickup curves showing such irregularities as concentration crossovers between discrete test temperatures and concentration maxima at approximately half-cycle life. No quantitative interpretation of these data was possible in terms of the experimental goal: prediction of room temperature cycle life. Qualitative interpretation is included in the Discussion section.

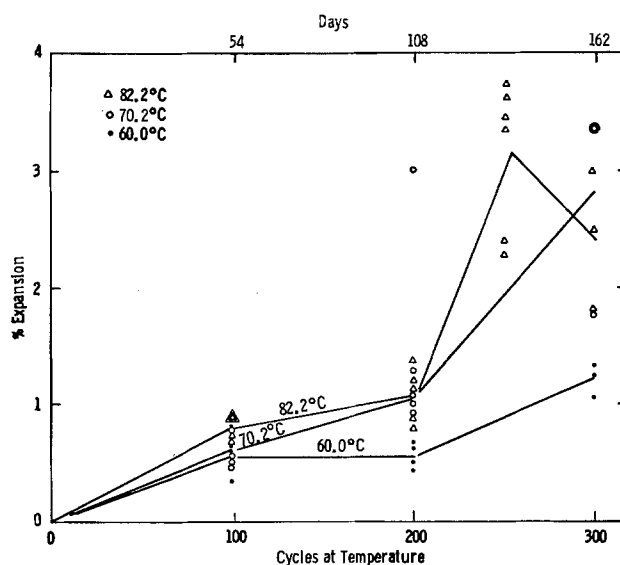


Fig. 2. Positive plate expansion during accelerated testing

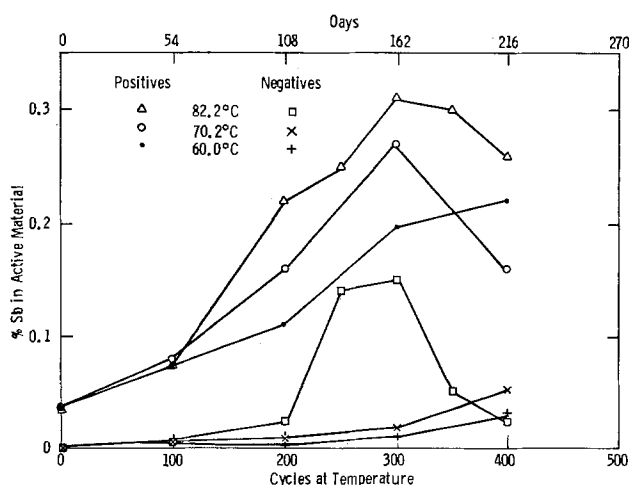


Fig. 3. Antimony absorption in PbO_2 (positive) and sponge Pb (negative).

Corrosion depth.—Residual grid thicknesses, after removal of corrosion layers, yielded estimates of mean corrosion depth. Initial measurements, involving a total of four measurements along the grid frame (Fig. 4), were insufficient to describe a precise corrosion depth vs. time curve. The average of 14 measurement points per grid improved precision of the estimated mean to ± 0.001 cm at a 95% confidence level. These estimates of the mean corrosion depth were plotted as points for purposes of curve fitting (Fig. 5).

The function corresponding to these curves was of the type

$$\text{Corrosion depth} = kt^x$$

where t = time on test (days) and, k = a temperature-dependent constant, with a sensitive response to temperature change such that $\log k$ is a linearly decreasing function of the reciprocal test temperature in degrees Kelvin. The best fitting value of the temperature-independent constant x , as determined by least squares approximation, is $x = 0.67$. Figure 6 illustrates this result and also specifies the k values corresponding to each test temperature, using $x = 0.67$.

The log-linear extrapolation of these k values (Fig. 7; Appendix D) leads to an estimate of 4.42×10^{-4} cm days $^{-0.67}$ for k at 25°C. The 95% confidence interval

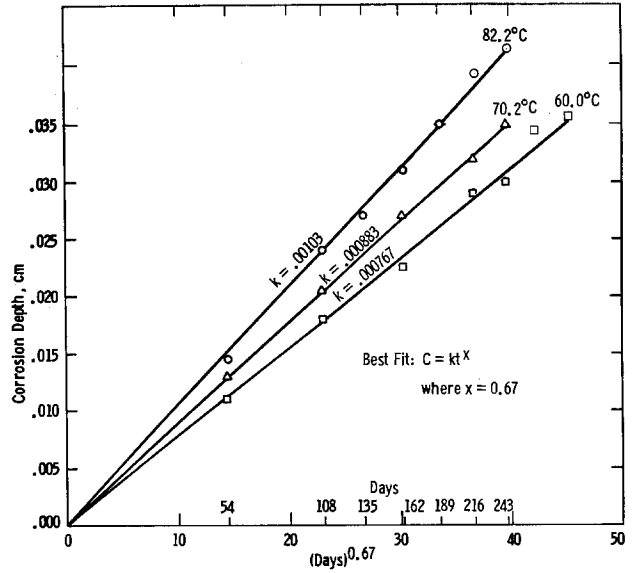


Fig. 6. Best fitting curve set at $C = kt^{0.67}$

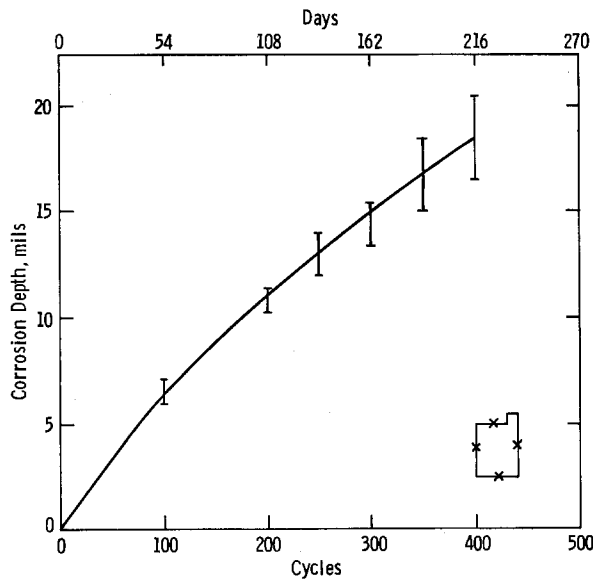


Fig. 4. Grid corrosion during accelerated testing, 82.2°C. Four-point grid thickness measurements, and 95% confidence limits for mean value corrosion depth.

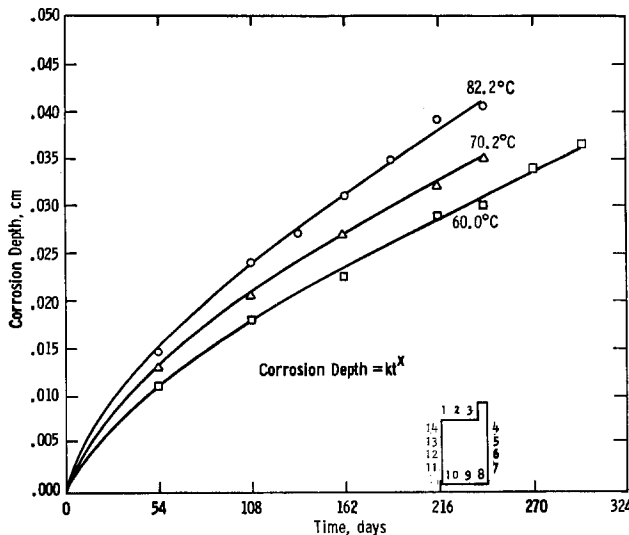


Fig. 5. Depth of grid corrosion vs. days on test. Minimum 14 points per grid.

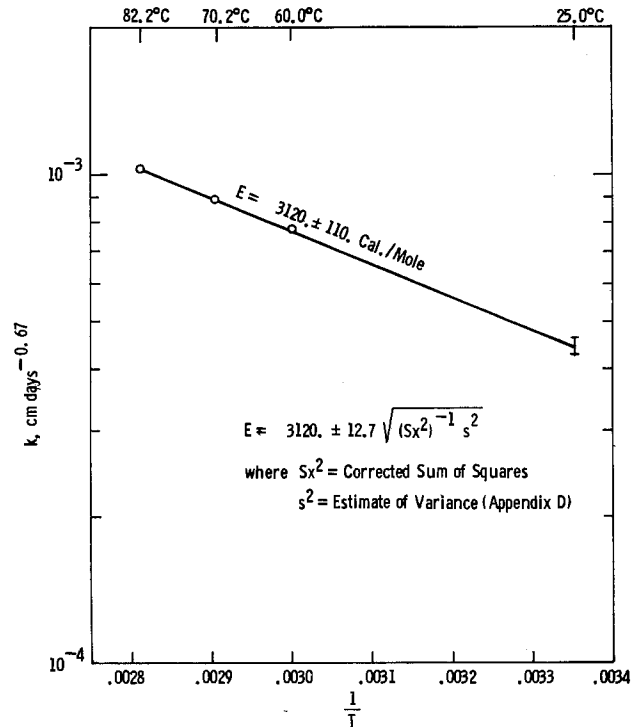


Fig. 7. Log-linear extrapolation of k

for this estimate would span from $k = 4.30 \times 10^{-4}$ to $k = 4.52 \times 10^{-4}$ cm days $^{-0.67}$.

A solution was obtained for estimated time at room temperature to corrode to a target depth of 0.035 cm for the charge-discharge cycle routine employed (Fig. 8; Appendix D). The target corrosion depth was estimated from corrosion measurements of similar plates bench-tested at room temperature according to interim federal specification W-B-00133B (GSA-FSS), performance test No. 2. In this test, and in field service, lifetime end-point is characterized by disintegration of the positive grid, the life-limiting component of the lead-acid cell on normal duty. In the accelerated test, the positive grid fails in the same manner. The extent of positive grid disintegration and the microscopic and crystallographic structure of the PbO_2 corrosion layers are equivalent to those which are found in cells cycled on long-term bench tests and cells in field service.

The assumption was made that casting quality for the room temperature, reference grids was substan-

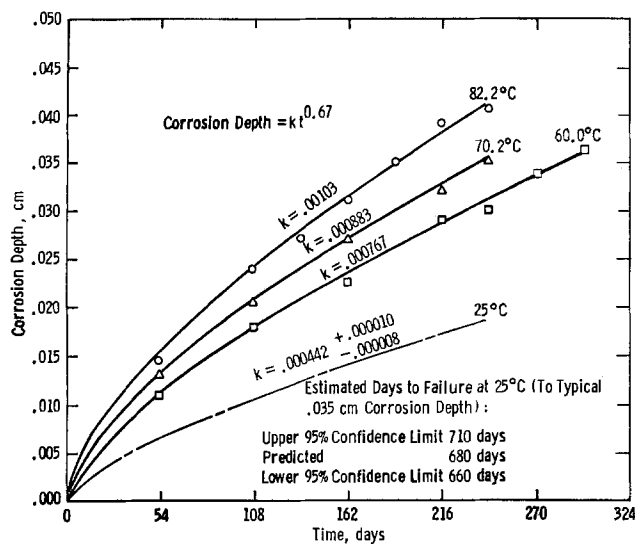


Fig. 8. Depth of corrosion vs. days on test

tially the same as for the group of positive castings employed in this accelerated test. This 0.035 cm depth of corrosion should, however, be viewed as a flexible target in a finalized life test, subject to changes reflecting casting quality, grid geometry, grid composition, etc. For this accelerated test, assuming practical equivalence with the reference grids, calculation yields a predicted lifetime of 680 days $\pm 4\%$, -3% . Converting to number of charge-discharge cycles, the corresponding 95% confidence statement is 1260 cycles $\pm 4\%$, -3% .

Discussion

Cell capacity vs. life.—During the test, some cells failed for reasons unrelated to the test objectives (shorts, loss of contact from lugs to posts, etc.). Also, progressive degradation evidence, specifically positive and negative plate voltages, did not consistently show that the positives were always failing preferentially. In cases of abrupt failure, such cells were removed, repaired, and returned to test if possible; if not, then removed permanently and disassembled to record temperature-dependent control parameter data (plate expansion, antimony migration, grid corrosion). In cases of gradual failure, lowest capacity cells were permanently removed and examined similarly at the programmed 50-100 cycle intervals. Although ultimate cell failure was due to sudden positive limitation, the capacity decline shown in Fig. 1 embodies substantial contributions from causes such as negative limitation, sediment and moss shorting, etc. Therefore, capacity curves, as taken on this test, are viewed as indicators of general cell performance, and not specific for the positive plate.

In all cases, however, the test was unaffected by these extraneous effects due to its inherent design, which called for exclusive monitoring of critical positive plate temperature-dependent control parameters. Thus, even if a cell had been abruptly removed for post failure, the critical data, e.g., grid corrosion, could be taken and employed as valid for that particular point in cycle life. Therefore, the progress of, e.g., grid corrosion during cycle life should be viewed as data collected on a partially selective, partially random basis.

Since the grids and plates were constructed as uniformly as possible, these data are considered to be representative of positive plate degradation for the entire group. Further, positive plate degradation is identified as the life-limiting mechanism in the lead-acid cell in deep discharge service. Consequently, the measured control parameters, particularly depth of corrosion, are viewed as related to critical normal service degradation, while cell capacity data is con-

fused by extraneous and less significant failure modes. These extraneous modes, though extremely temperature sensitive in themselves, do not affect the temperature dependence of corrosion of the positive grid.

Plate expansion vs. life.—Prior work in the literature had indicated that simple plate growth could be correlated with plate lifetime. Lander (4) cycled strips of Pb-6% Sb and Pb-4.5% Sn about typical positive plate potentials twice a day in 30% H_2SO_4 at 49°C. He measured regular increases in strip length with testing time, reporting up to 3% elongation. Cannone *et al.* (2), working with cells for telephone service in an elevated temperature range of 60°-93°C, showed that pure lead grids on constant potential charge expanded regularly in width in a parabolic fashion and that lead-antimony grids expanded along a linear curve.

The behavior of our lead-antimony grids was analogous to these two prior studies. However, because of the tendency of our grids to corrode completely through along fault lines, then to spring open abruptly, no smooth growth curve could be measured. If grid castings showing more regular growth are tested, direct nondestructive growth measurements could provide a lifetime prediction test with a minimum of test samples. An analysis of precision would be required, however, to establish the merit of this approach relative to the depth of corrosion approach.

Antimony migration vs. life.—Corrosion of lead-antimony positive grids in the lead-acid storage cell produces either PbO_2 or $PbSO_4$, depending on state of charge. Both are essentially insoluble, and remain in place in the positive plate. The antimony component of the grid alloy is quite soluble in H_2SO_4 , forming the anions $Sb(SO_4)_2^-$, $SbOSO_4^-$, and $Sb_3O_9^{3-}$, as proposed by Dawson *et al.* (5, 6). Adsorption of antimony on active material crystal surfaces is believed to occur, affecting crystalline growth habit on charge and discharge. Such adsorption is also viewed as the reason why antimony content of the positive active material increases so markedly with increased grid corrosion.

Anionic transfer to the sponge lead negative plate, and subsequent adsorption there leads to a lesser concentration buildup in the negative active material, compared with the positive, PbO_2 electrode. The well-known "poisoning" effect of Sb in the negative electrode is shown here to be associated with antimony accumulations well below antimony levels present in the positive plate. While positive plate voltages indicated that performance was virtually independent of antimony level, negatives showed decreasing voltages early in cycle life. Concentrations of antimony in the electrolyte itself are negligible, so that almost all antimony, though considered to be soluble, is associated with the solid phases of both electrodes.

If total antimony pickup in the active material can be determined, then, by direct analysis of the active material, a measure of grid corrosion would result. The irregularities found in the test are interpreted as being primarily due to inhomogeneous antimony levels in the cast grid alloy. Antimony-rich phases are known to be discrete entities in cast Pb-Sb alloys, existing in regions between the predominant, lower antimony grains. This work indicates, however, that a further change in composition occurs as corrosion strips away the outer surfaces of the cast grid, with significantly lower antimony concentrations found at levels approximately 0.025-0.030 cm below the surface. The peaks in the curves of antimony concentration vs. time on cycle life (Fig. 3) correspond to such a view.

In addition to these radial concentration gradients in the grid bar cross section and the concentration segregation inherent in the two-phase Pb-Sb alloy structure, a third effect is known to exist: the evolution of stibine gas, SbH_3 , from the negative electrode while the cell is in the charge mode, could reduce the estimate of grid corrosion depending on the efficiency

of stibine synthesis. This effect, in combination with the radial concentration model, accounts for negative curve slopes beyond 300 cycles.

Corrosion depth vs. life.—Test precision.—As the data of Fig. 5-8 demonstrate, the precision of this accelerated life test is considerably better than typical precision in lifetime prediction currently achieved in standard, long-time industrial testing ($\sim \pm 20\%$ at 95% confidence level). It is possible to identify the factors chiefly affecting precision from the derived corrosion function

$$C = \text{mean depth of corrosion} = k_{25^\circ\text{C}} t^x$$

when C is a targeted value, and being defined, does not limit precision. X , once derived, is employed as a constant which does not affect precision, only accuracy. This simplifying assumption is justified in the same way as other work, e.g., when ideally linear ($x = 1$) or ideally parabolic ($x = 2$) functions are assumed to describe phenomena. Therefore, only $k_{25^\circ\text{C}}$ has inherent limitations of precision when solving for t .

Examination of Eq. [A-9], Appendix D, shows that, if the temperatures are fixed, and precisely measured ($\pm 0.05^\circ\text{C}$) within the span of temperatures available in the test, then the estimate of the variance of the quantity $R \ln k$ (where $R = 1.9872$, the gas constant) and the degrees of freedom in the t statistic are the two factors influencing precision. In this three-temperature experiment (three degrees of freedom), two degrees of freedom are used up, due to the fact that, in solving for the least squares log-linear extrapolation of k , two unknowns, the slope E and the intercept $R \ln A$ are involved. Since this leaves only one degree of freedom to define the t statistic, the corresponding tabulated t statistic for 95% confidence limits is 12.7. Inspection of the t statistic tables shows that, for a four-temperature experiment, the term before the square root sign in the precision expression [A-9], is reduced to 4.3 since the t statistic can then be based on two degrees of freedom. For better precision, then, data should be grouped into four temperature groups. For industrial testing, which may involve only two temperatures, the cells should be grouped into equal samples of duplicate temperatures to yield at least four temperature groups, provided the variance of $R \ln k$ does not increase too rapidly.

The estimate of the variance of experimental values of $R \ln k$ with respect to the corresponding least squares values, $R \ln \hat{k}$

$$\frac{1}{n-2} \sum (R \ln k - R \ln \hat{k})^2$$

also decreases significantly as n , the total number of temperature groups, is increased from 3 to 4 or more. The difference term within the summation: (i) decreases with increasing accuracy in temperature measurement, (ii) decreases with increasing precision in temperature measurement, (iii) decreases with increasing uniformity of replication in the entire lot of positive plates employed in the test cell group, and (iv) decreases with increasing uniformity of replication of cell cycling parameters, e.g., A-hr discharge, A-hr charge, shape of charge curve.

If means can be found to avoid rapid negative sulfation, and thereby extend the temperature range of this test, precision can be further improved.

The corrected sum of squares in Eq. [A-9]

$$\sum \left(\frac{1}{T} \right)^2 - \frac{1}{n} \left(\sum \frac{1}{T} \right)^2$$

increases with increasing temperature range. Since this term is a denominator, it therefore increases the precision as the range of temperature increases.

The question arises: Why not collect the experimental corrosion depth data at a single temperature, pref-

erably at room temperature, and simply extrapolate the experimental room temperature curve to a targeted depth of corrosion? The answer is that this elevated temperature test magnifies the form of the corrosion function so that it can be identified and precisely specified at room temperature. Any room temperature experiment must be carried out nearly to end-of-life to achieve the same precision. Experience and analysis show that curves derived from direct room temperature measurements over the shorter period of time involved in this accelerated test lack the precision needed for satisfactory lifetime prediction. This is because, while the precision of the measurement data is constant, the actual values of corrosion depth decrease exponentially with decreasing absolute temperature.

Consequently, as an example, direct room temperature corrosion curves of differing grid alloys would be practically indistinguishable from each other; perhaps also even from a straight line over the first 200-300 charge-discharge cycles. Such room temperature curves are readily and precisely characterized with respect to k and x by extrapolation of high temperature experiments, thus revealing critical differences in calculated, room temperature, lifetime estimates.

It is appropriate to ask whether the predicted, room temperature, corrosion function has been experimentally demonstrated out to a point in cycle life where meaningful precision can be obtained. To make such a comparison it is assumed that the room temperature control cells will ultimately demonstrate the 0.035 cm mean depth of corrosion exhibited by the high temperature test groups and by prior bench testing of similar production cells. Three five-plate cells from the original test group, which were cycled at room temperature, obey the calculated corrosion function to within 0.001 cm at an estimated one-half cycle life to date, thus providing reasonable agreement of theory with experiment.

Testing time.—If subsequent test results on other types of cells and materials show that corrosion functions repeatedly turn out to be of the form

$$C = kt^x$$

then the taking of samples for corrosion depth measurements need not be conducted all along the curve, but merely at one point, sufficiently far along to permit acceptable precision in lifetime prediction. Given a test closely controlled as outlined above, with a group of cells all constituting faithful replicas of each other, excellent precision should be obtainable in 4-6 months testing time. However, any experiment with a different form of corrosion function would necessarily involve a full complement of cells being periodically extracted from test and measured to describe the exact form of the corrosion function until such time as actual failure occurs.

Number of specimens.—Five-plate cell variability is significant enough to require four or five such cells in each of four temperature groups for tests involving extraction from test and measurement at a single point in life ($c = kt^x$ assumed). As an alternative, the equivalent number of positive plates in fewer cells with more plates would serve the same purpose.

Asymmetrical upper and lower bounds in predicted life.—Adapting Eq. [A-8], Appendix D, to solve for k

$$\ln k = \frac{E \left(\frac{1}{T} \right) + R \ln A}{R}$$

it is evident that the upper and lower bounds obtained in the least squares estimate of E , at 95% confidence limits, yield a corresponding upper and lower bound expressed in $\ln k$; not k itself. As a consequence, translation of these derived limits, which are symmetrical

about $\ln k$, results in asymmetrical limits about k itself.

The significance of this lies simply in the Arrhenius model which was originally assumed (Eq. [A-5], Appendix D)

$$k = A \exp\left(\frac{b}{T}\right)$$

where it can be seen that any symmetrical uncertainties in either temperature or Rb ("activation energy") result in logarithmically related uncertainties in k .

As a practical application of this, it can be pointed out, for example, that temperature overestimation is more damaging to accuracy than temperature underestimation. Conceptually, the range of values of predicted life may be visualized as a probability distribution skewed to the right with the mode located to the left of the predicted value of lifetime.

"Activation energy," E .—The slope in Fig. 7 is characterized as an activation energy to conform to established practice and to provide a preliminary criterion for the identification of the type of rate control which prevails. It should be noted that true charge transfer activation energies generally lie in a range above 5000 cal/mole. At 3120 cal/mole, it is difficult to distinguish from the case of diffusion limitation. However, it is evident that the over-all effect of cyclic operation of the positive plate of these lead-acid storage cells is to bring about progressive anodization of the lead alloy current collector with the corrosion depth curve tending toward a diffusion-limited value (Fig. 8). E , then, may alternatively be viewed as related to a characteristic concentration overpotential.

Conclusions

High temperature charge-discharge cycle testing of lead-acid cells can yield a prediction of room temperature cycle life in as quickly as 4 months. The logarithm of cell lifetime decreases linearly with the absolute temperature.

Measurement of positive grid corrosion depth as a function of temperature yields a corrosion function characterized by one temperature-dependent constant. The value of this constant at room temperature is specified by a log-linear extrapolation. An experimental design employing 16 five-plate 80 A-hr cells at each of three different temperatures permits a +4%, -3% precision in lifetime prediction at a 95% confidence level.

This technique of elevated-temperature corrosion function analysis permits charge-discharge cycle life prediction capability of unprecedented precision and speed.

Acknowledgments

A. M. DiCroce and C. A. Hager assisted in conducting the tests. W. N. Ritchie and B. Terzic, of KW Battery Company, prepared and supplied all cells used in this program and helped to examine selected cell components against the background of their field experience. G. M. Jouris was consulted with respect to the statistical treatment of the data. J. T. Brown provided many stimulating technical discussions of the problem, particularly with respect to extrapolation theory.

Manuscript submitted May 31, 1974; revised manuscript received Aug. 13, 1974.

Any discussion of this paper will appear in a Discussion Section to be published in the December 1975 JOURNAL. All discussions for the December 1975 Discussion Section should be submitted by Aug. 1, 1975.

Publications costs of this article were partially assisted by Westinghouse Electric Corporation.

APPENDIX

A. Estimation of Mean Depth of Corrosion

Grid corrosion depth during cycle life was estimated by subtracting the average residual grid thickness

$$\bar{y} = \frac{1}{n} \sum_i^n y_i \quad [A-1]$$

from the average initial grid thickness (\bar{y}_0) after formation and initial capacity determination, then dividing by two. The mean value estimate of corrosion depth obtained in this way was characterized with respect to precision at a 95% confidence level by employing tabulated values of the t statistic (3) in the following expression

$$\frac{\bar{y}_0 - \bar{y}}{2} \text{ estimates } \eta = \text{mean value} \pm t_{\nu, 0.025} \sqrt{\frac{s^2}{n}}$$

where $t_{\nu, 0.025}$ = tabulated values for 95% confidence limits, ν = degrees of freedom ($n - 1$), n = total number of observations in a sample of grids, s^2 = estimate of the variance of the data

$$\frac{1}{n-1} \sum_i^n (y_i - \bar{y})^2,$$

and y = observed values for corrosion depth.

The number of observations, n , was increased until the 95% confidence level precision of the estimate of the mean value of corrosion depth approached 0.001 cm, comparing with the precision of the micrometer (0.0005 cm). To do this, up to 30 individual residual thickness measurements were made per grid.

B. Estimation of Power of t in Corrosion Depth Function

It was observed that the estimated mean grid corrosion depth obeyed a time and temperature-dependent function of the form

$$C = \text{corrosion depth (cm)} = kt^x \quad [A-2]$$

where k = a temperature-dependent constant, t = time (days), and x = a constant, with no apparent temperature dependence.

Taking logarithms

$$\log C = \log k + x \log t$$

In a least squares analysis of the data (7), x is given by

$$x = \frac{\sum \log t \log C - \frac{1}{n} (\sum \log t) (\sum \log C)}{\sum (\log t)^2 - \frac{1}{n} (\sum \log t)^2} \quad [A-3]$$

where n = the number of t data points.

The best fitting value of x was taken as the average x over all three temperatures employed in the test

$$\begin{aligned} X_{82.2^\circ\text{C}} &= 0.694 \\ X_{70.2^\circ\text{C}} &= 0.635 \\ X_{60.0^\circ\text{C}} &= 0.693 \\ \bar{X} &= 0.67 \end{aligned}$$

For purposes of precision analysis, this value, approximately 2/3, was considered to be a temperature-independent, constant exponent not affecting precision. A similar assumption is commonly employed in many curves which are arbitrarily fitted to strictly linear or quadratic models.

C. Estimation of "k" in Corrosion Depth Function

The constant k was then specified for each temperature by solving

$$\log k = \overline{\log C} - 0.67 \overline{\log t} \quad [A-4]$$

The results yielded three corrosion functions

$$\begin{aligned} 82.2^\circ\text{C}: C &= \text{corrosion depth (cm)} = 0.00103 t^{0.67} \\ 70.2^\circ\text{C}: C &= \text{corrosion depth (cm)} = 0.000883 t^{0.67} \\ 60.0^\circ\text{C}: C &= \text{corrosion depth (cm)} = 0.000767 t^{0.67} \end{aligned}$$

The adequacy of the model to represent the data is demonstrated by Fig. 6.

D. Determination of Precision of the Log-Linear Extrapolation of "k"

The decrease of k with respect to temperature conformed to an expression of the type

$$k = A \exp\left(\frac{b}{T}\right) \quad [\text{A-5}]$$

where T = absolute temperature ($^{\circ}\text{K}$) and A , b = constants.

The best fitting value of b was expressed as an activation energy, E cal/mol, by multiplying by the gas constant, $R = 1.9872 \text{ cal } ^{\circ}\text{K}^{-1} \text{ mole}^{-1}$.

Taking logarithms

$$R \ln k = R \ln A + E\left(\frac{1}{T}\right) \quad [\text{A-6}]$$

Least squares analysis leads to the following expression

$$E = \frac{\left(\sum \frac{R \ln k}{T}\right) - \frac{1}{n} \left(\sum \frac{1}{T}\right) \left(\sum R \ln k\right)}{\sum \left(\frac{1}{T}\right)^2 - \frac{1}{n} \left(\sum \frac{1}{T}\right)^2} \quad [\text{A-7}]$$

where $n = 3$ for this case involving three temperatures. $\ln A$ is obtained by straightforward substitution of average experimental data points, $(\bar{\quad})$, in [A-6]

$$\ln A = \frac{R \overline{\ln k} - E \left(\frac{1}{\bar{T}}\right)}{R} \quad [\text{A-8}]$$

permitting subsequent estimation of k at room temperature from [A-5].

The precision of the derived value of E is: 95% confidence level precision =

$$\pm t_{v,0.025} \sqrt{\frac{\sum (y - \hat{y})^2}{\left[\sum \left(\frac{1}{T}\right)^2 - \frac{1}{n} \left(\sum \frac{1}{T}\right)^2\right] \frac{1}{n-2}}} \quad [\text{A-9}]$$

where y = experimental value of $R \ln k$, \hat{y} = least squares predicted value of $R \ln k$, $\sum (y - \hat{y})^2$ = estimate of variance, and

$$\sum \left(\frac{1}{T}\right)^2 - \frac{1}{n} \left(\sum \frac{1}{T}\right)^2 = \text{corrected sum of squares.}$$

The maximum and minimum E values yield corresponding maximum and minimum predicted room temperature k values, from [A-5] and [A-8], in this case at a 95% confidence level.

E. Determination of the Precision of Room Temperature Lifetime Prediction

Maximum and minimum k values at room temperature are employed in [A-2], assuming 0.035 cm depth of corrosion, corresponding to field service and bench failure; solving for t . These room temperature, cycle lifetimes, therefore, represent the span of predicted values generated by 95% confidence level data.

REFERENCES

1. E. Willihnganz, *Electrochem. Technol.*, **6**, 338 (1968).
2. A. G. Cannone, D. O. Feder, and R. V. Biagetti, *Bell System Tech. J.*, **49**, 1279 (1970).
3. A. Hald, "Statistical Theory with Engineering Applications," pp. 388-397, John Wiley & Sons, Inc., New York (1960).
4. J. J. Lander, *This Journal*, **98**, 220 (1951).
5. J. L. Dawson, J. Wilkinson, and M. I. Gillibrand, *J. Inorg. Nucl. Chem.*, **32**, 501 (1970).
6. J. L. Dawson, M. I. Gillibrand, and J. Wilkinson, "The Chemical Role of Antimony in the Lead-Acid Battery," 7th International Power Sources Symposium, September 15-17, 1970, Brighton, England.
7. A. Hald, "Statistical Theory with Engineering Applications," pp. 528-549, 558-570, John Wiley & Sons, Inc., New York (1960).

The Existence of Multiple Steady States during Differential Aeration Corrosion

Richard Alkire* and George Nicolaidis**

Department of Chemical Engineering, University of Illinois, Urbana, Illinois 61801

ABSTRACT

A method of calculation has been developed for predicting the multiple steady-state current distributions which may exist along a metal surface undergoing localized attack by differential aeration corrosion. The calculational method is capable of finding all such multiple steady-state solutions. A compilation of those regions of parameter space within which highly localized attack is likely has been carried out for the model system.

Owing to differential aeration the local rate of corrosion along a metal surface may be highly nonuniform, especially if the metal exhibits passivity. The problem of determining the location and the local rate of corrosion attack corresponds to elucidating the details of the current flow between the anodic and cathodic regions which occur simultaneously on the metal surface. That is, one needs to know the current distribution. Whereas electrochemical current distribution problems originated in attempts to predict the over-all current-voltage behavior of electrolysis cells, such studies have also been conducted on corrosion-like configurations of fixed anode/cathode geometry

* Electrochemical Society Active Member.

** Electrochemical Society Student Member.

Key words: corrosion, differential aeration, current distribution, mathematical model, bipolar electrode.

as briefly reviewed in Ref. (1). More recently, current distribution calculations have been conducted on corroding systems wherein multiple electrochemical reactions occur on localized net anodic and cathodic areas, which coexist on adjacent regions of a single conductive surface. For simple configurations, such "bipolar" current density distributions may be computed once the system parameters have been specified (i.e., properties such as electrolyte conductivity, oxygen availability, electrode reaction kinetics, system geometry, etc.). Corrosion of rotating disks (2,3) has been shown to occur with nonuniform rates wherein one portion of the disk is passive while another portion corrodes actively. The study of aeration corrosion under barrier films of variable thickness (1,4,5) has shown that more than one steady-state

current distribution may be expected to exist for a single set of system parameters; some of these multiple steady-state corrosion distributions suggest the possibility of highly localized corrosion. However, the numerical methods employed in the foregoing studies were not well suited for determining how many such multiple solutions exist. Therefore the following investigation has been conducted with two goals in mind. First, a different computation method has been employed which is capable, for a given set of system parameters, of finding all possible steady-state current distributions. Second, a compilation has been carried out of all regions of parameter space within which highly localized corrosion may be anticipated for the model system under study. The results therefore contribute toward design of corrosion systems so as to avoid altogether those potentially hazardous situations where localized attack is likely.

Derivation of Model

The corrosion system to be investigated, shown in Fig. 1, is identical to that studied by other methods in Ref. (1). Readers may examine that reference for more extensive introductory remarks than are provided here. The metal is covered by an electrolyte-moistened barrier of locally variable thickness. Oxygen diffuses through the barrier layer to the metal surface, which corrodes. Both oxidation and reduction reactions occur everywhere along the corroding surface. In many cases, however, the local oxidation rate may exceed the local reduction rate, thus creating a local net anodic region. Similarly, local net cathodic regions may also arise. Electrical current flows in the barrier layer between the net anodic and the net cathodic regions which coexist along the metal surface. The buildup of corrosion products has not yet occurred to an appreciable extent. The simple situation shown in Fig. 1 has been modeled by a differential equation (1) subject to the following restrictions: (i) the corroding system is confined by two insulating planes as shown in Fig. 1; (ii) the potential within the corroding metal is uniform owing to the high conductivity of the metal phase; (iii) current flows in the barrier layer parallel to the corroding surface; (iv) oxygen diffuses through the barrier layer along paths which are perpendicular to the metal surface; (v) the barrier thickness varies with position in an exponential manner; and (vi) the concentration of ionic species is uniform.

Subject to these restrictions, the model system is assembled from Ohm's law (for flow of electrical cur-

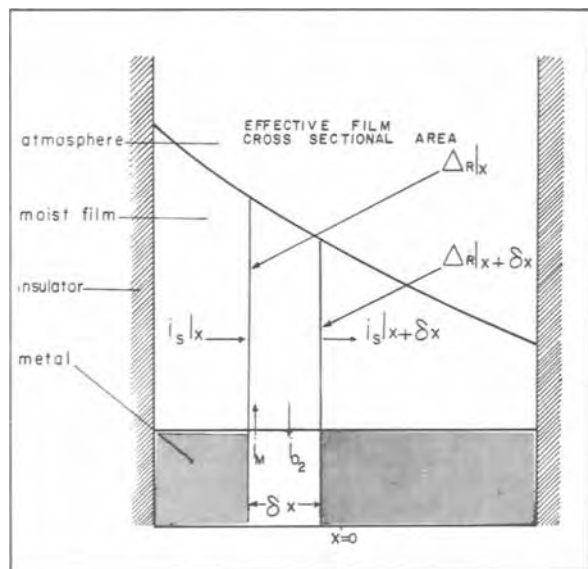


Fig. 1. System configuration for differential aeration corrosion study.

rent along the barrier layer), Fick's law (for diffusion of oxygen through the layer), a Tafel rate expression (for the oxygen reduction kinetics), and an active-passive rate expression (for the metal undergoing corrosive attack). Before proceeding it is suggested that interested readers review details concerning the derivation of the model as provided in Ref. (1). The equation of conservation of charge which models the system is

$$\frac{d^2\Phi}{dX^2} - (1 + \tanh X) \frac{d\Phi}{dX} = \frac{\xi}{(1 - \tanh X)} \left\{ \left[\frac{1 - \beta}{(\Phi - \Phi_R)^2} + \beta \right] \frac{1}{e^{\frac{\Phi - \Phi_R}{\sigma}}} - \left[\frac{\xi e^{-\alpha\Phi}}{\xi \Gamma e^{-X} e^{-\alpha\Phi} + 1} \right] \right\} \quad [1]$$

with boundary conditions

$$\frac{d\Phi}{dX} = 0 \text{ at } X = -\lambda \quad [2]$$

$$\frac{d\Phi}{dX} = 0 \text{ at } X = +\lambda \quad [3]$$

where the dimensionless variables are

$$X = \frac{x}{l}$$

$$\Phi = (V - \Phi_s) \frac{F}{RT}$$

$$C = \frac{c}{c^0}$$

$$\sigma = \left(\frac{F}{RT} \right)^2 s$$

$$\Phi_R = \frac{V_R F}{RT} \quad [4]$$

and the dimensionless system parameters are

$$\Gamma = \frac{a\delta_m}{4FDc^0}$$

$$\xi = \frac{Fl^2a}{RT\kappa\delta_R}$$

$$\zeta = \frac{k}{a} \quad [5]$$

The notation employed in the equation, boundary conditions, variables, and parameters, is the same as in Ref. (1) and is listed at the end of the text. Reading from left to right, the terms in Eq. [1] indicate that the electrical current flowing along the barrier layer suffers ohmic resistance (second derivative term) which varies locally with the film thickness (first derivative term). The bracketed term on the right side of Eq. [1] is the net local reaction rate, i.e., the local rate at which current flows into or out of the barrier layer. The local net reaction rate may be anodic or cathodic, depending on which partial reaction proceeds at the greater rate. For conditions of uniform corrosion, the right side of Eq. [1] would have the value of zero everywhere along the surface. On physical grounds, Eq. [1] therefore indicates that current flows into the barrier in the net anodic regions, flows along the moist layer while experiencing ohmic

resistance and cross-sectional strictions, and flows out of the barrier into the net cathodic regions.

A detailed discussion of the physical significance of the dimensionless parameters has been given in Ref. (1). In brief, the parameter Γ is related to the ease with which oxygen diffuses to the corroding surface. Small values of Γ correspond to rapid diffusion of oxygen so that the concentration along the metal surface would be essentially uniform, near the saturated value; large values of Γ correspond to slow diffusion rates. The parameter ξ characterizes the resistivity of the barrier layer and takes on small values when the barrier layer is highly conductive. The parameter λ is a measure of the difference in oxygen availability between one end of the surface and the other end; large values of λ correspond to large differential aeration and thereby enhance tendencies toward localized corrosion. Once again, the reader is urged to consult Ref. (1) for a more complete discussion of the model.

Method of Solution

Equation [1], along with its boundary conditions, was solved numerically with use of IBM 1800 and IBM 360 digital computers. The boundary value system was transformed to an initial-value system by introducing a guessed condition at one end and adjusting this condition until the required relation was satisfied at the other end (6). That is, Eq. [1] was re-cast into a pair of first-order differential equations. Integration of an initial-value problem was then carried out such that the boundary condition at the far end of the spatial interval was satisfied by inspection. The method proceeds by writing

$$\frac{d\Phi}{dX} = Y \quad [6]$$

hence Eq. [1] becomes

$$\begin{aligned} \frac{dY}{dX} - (1 + \tanh X)Y &= \frac{\xi}{(1 - \tanh X)} \left\{ \left[\frac{1 - \beta}{(\Phi - \Phi_R)^2} + \beta \right] \right. \\ &\quad \left. - \left[\frac{\xi e^{-\alpha\Phi}}{\xi \Gamma e^{-X} e^{-\alpha\Phi} + 1} \right] \right\} \quad [7] \end{aligned}$$

For initial conditions at $X = -\lambda$, Eq. [2] provides

$$Y = 0 \quad [8]$$

For the second initial condition at $X = -\lambda$, guess

$$\Phi = A \quad [9]$$

where A is a constant, which must be chosen with care. Equations [6] and [7] thus constitute two first-order equations having the unknown functions $\Phi(X)$ and $Y(X)$. The solution of this set, along with its initial conditions, is identical to the solution of Eq. [1], along with its boundary conditions, provided that the constant A is chosen such that

$$\frac{d\Phi}{dX} = 0 \text{ at } X = +\lambda \quad [3]$$

The procedure for integration therefore consisted of arbitrarily choosing a value for the constant A , and then integrating Eq. [6] and [7] by means of Runge-Kutta fourth-order formulas (7). Every value of A which satisfies Eq. [3] corresponds to a different steady-state current distribution.

As a check against numerical errors, integration was also carried out beginning at the opposite end of the spatial interval, i.e., beginning at $X = +\lambda$ and proceeding to $X = -\lambda$. Identical solutions were found for

the current distribution regardless of direction of integration. In addition, the iterative method of solution employed in Ref. (1) was always found to converge upon any desired solution provided that a reasonable trial distribution was provided. That is, three methods of calculation provided identical numerical results.

The advantage of the "shooting" method of calculation described here is that all multiple solutions may be found for a given set of parameter values. In clear contrast, the iterative method used previously (1) had the disadvantage that one could not know how many solutions existed, except by finding them. That is, one could not determine whether a certain solution actually disappeared in some region of parameter space or whether it merely became difficult to converge upon.

Results and Discussion

Calculations have been conducted in order to clarify the nature of the multiple steady-state current distributions predicted by the model system. In addition, a compilation has been carried out in order to indicate those regions of parameter space in which at least one steady-state current distribution indicates the likelihood of highly localized corrosion. Because the model is somewhat preliminary in nature, and because it has been investigated primarily as an intuitive aid, an exhaustive compilation has not been attempted. Parameter values which were not varied in the investigation are $\alpha = 0.5$, $\beta = 0.01$, and $\sigma = 0.15$. Except where otherwise stated, the parameter ξ has the value 0.5.

It is important to make a clear distinction between the number of algebraic roots of the right side of Eq. [1], and the number of solutions to the differential equation. Although up to three algebraic roots may be found on the right side, such information bears no direct relation to the number of solutions which the differential equation may exhibit. Analyses of even simple distribution equations have demonstrated that an infinite number of solutions may be found (8, 9). In a similar manner, steady-state, nonisothermal behavior of porous, spherical, catalyst pellets has been shown to have an infinite number of multiple steady-state conditions (10). Therefore one should not go under the expectation that a maximum of only three solutions are to be expected of Eq. [1].

In certain regions of parameter space, several classes of independent solutions of Eq. [1]-[3] have been found. For one set of system parameters, for example, Fig. 2 illustrates that for many values of A [i.e., the abscissa, $\Phi(-\lambda)$], the derivative at the far boundary [i.e., the ordinate, $d\Phi/dX(+\lambda)$] takes on values which may be nonzero. The model equations, however, are satisfied only for those situations for which the curve in Fig. 2 intersects the zero axis; each intersection point corresponds to a different steady-state current distribution. For the parameters used in Fig. 2, it is seen that thirteen multiple steady-state solutions are found. Some of the intersections are labeled (A, B, C, etc.) so that the solutions associated with them can be referred to in subsequent discussion.

It seems clear that all such solutions to the differential equation need not necessarily correspond to an observable steady-state condition of a physical system, even if that system is generally compatible with the approximations of the model. There are several reasons for which a mathematical solution may be regarded as physically unrealizable. First, a solution of the equation might predict a state of the system which is physically unstable to random disturbances. Although a stability analysis has not been conducted in this preliminary study, it should be mentioned that when multiple solutions exist as indicated in Fig. 2, it is frequently expected that the unstable solutions correspond to every other (i.e., alternate) intersection. Second, a solution may be improbable in the sense that the sequence of events necessary for the attainment of the steady state may be difficult to achieve. An informal discussion of the possible transient conditions

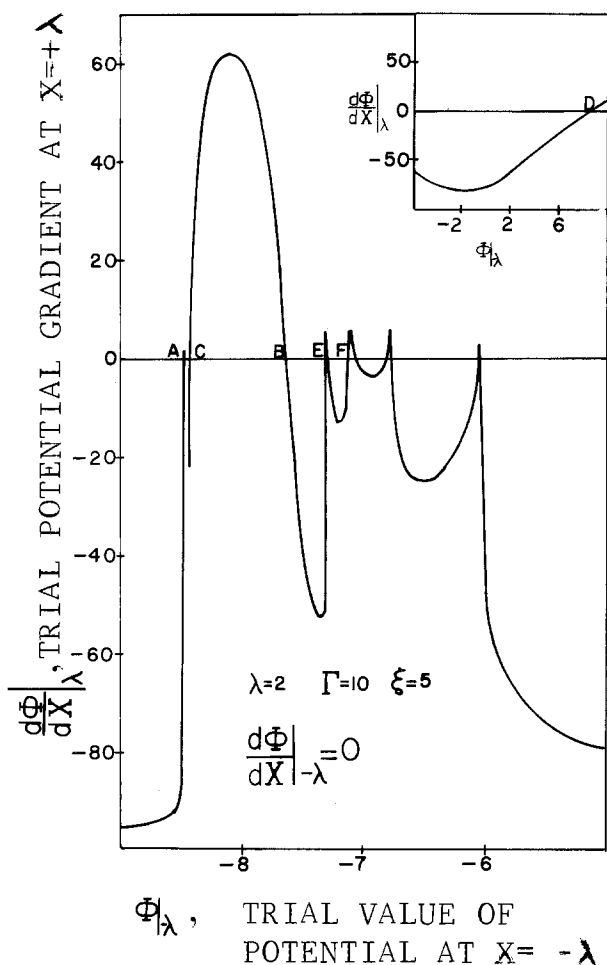


Fig. 2. Display of the existence of multiple solutions obtained by integrating Eq. [1] with a single set of system parameters. An independent solution exists at each intersection of the curve with the line.

that may lead to the various steady-state solutions is given below. Finally, a solution would be unrealistic if it depends strongly on one particularly weak approximation of the model. Such unrealistic solutions would be incompatible with data from a physical system, or with predictions of a more rigorous model.

The potential, current, and concentration distributions corresponding to the intersections A, B, C, and D of Fig. 2 are shown in Fig. 3. Figure 3 also corresponds to Fig. 3 of Ref. (1), and detailed discussion of the curves is contained therein. For Solution A, the metal is in the active potential range everywhere so that the local dissolution rate increases with decreasing layer thickness. Solution D represents a fully passive situation at a very positive potential. Solutions B and C exhibit intermediate behavior where one portion of the surface is passive while the rest is reactive. Solution B lies entirely on the decreasing branch of the anodic polarization curve whereas Solution C varies all the way from mildly reactive potentials to the passive potential region. One additional solution, denoted A', has general characteristics similar to the four solutions in Fig. 3. Solution A' is found at an intersection located between A and C in Fig. 2 (not drawn in for want of space) and yields distributions whose nature is in every respect intermediate between distributions corresponding to A and C. That is, the anodic rate distribution for A' usually includes a local maximum although the potential distribution has a smaller range than C.

The physical significance of the aforementioned five solutions will now be examined. The potential and anodic rate distributions of Solution A resemble closely the differential aeration corrosion of a nonpassivating

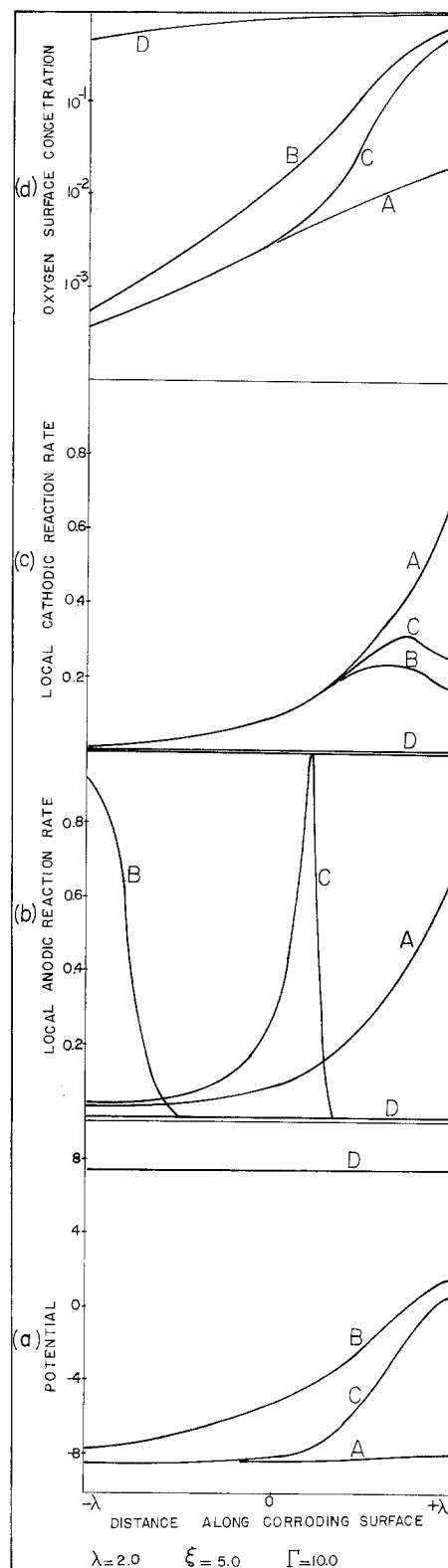


Fig. 3. Several distributions satisfying Eq. [1] were found for a single set of parameters. The curves labeled A, B, etc., comprise families of distributions which correspond to intersections A, B, etc., in Fig. 2. The distributions shown are: (a) potential of the metal relative to the solution, (b) anodic dissolution rate, (c) cathodic reduction rate, (d) oxygen concentration at the surface.

metal. Since range of potential is restricted to the active branch of the polarization curve, assumptions made in the model with regard to the passivating behavior of the metal have no influence. Therefore Solution A can be regarded as a stable and realistic situation which might be encountered in a physical system. For Solution D, the potential distribution is sufficiently removed from the active region that kinetic details

regarding active/passive transitions are inconsequential. The physical reasonableness of Solution D is clear, and fully passivated metal surfaces are commonly encountered.

If we assume that solutions corresponding to alternate intersections in Fig. 2 are unstable, then since A and D are clearly stable, A' and B will be unstable while C will be stable. Solution C is especially interesting since it indicates the likelihood of highly localized corrosion at intermediate positions under the barrier layer. Solution B appears to be unstable, perhaps because the potential distribution lies entirely on the decreasing branch of the polarization curve, a region of negative charge-transfer resistance. Because the nature of Solution B depends strongly on the negative-resistance region of the passivation curve, these solutions may be regarded as unrealistic (in the narrow sense defined above) insofar as they depend strongly on a rather weak aspect of the model. It therefore seems unlikely that Solution B would be observed in actual physical systems.

It is useful to postulate in an informal manner the transient conditions which might lead to the various steady-state solutions encountered thus far. For example, if the electrolyte is saturated with oxygen prior to formation of the barrier layer, the entire surface will passivate and the steady-state condition captured by the system would be expected to be Solution D. On the other hand, if the electrolyte is deaerated so that oxygen diffusion proceeds with great difficulty, then the steady-state condition may be attained before any part of the surface undergoes passivation, as in Solution A. For intermediate initial oxygen concentrations in the electrolyte, the oxygen might passivate a part of the metal surface at the thin side of the layer before a steady state is achieved. Then Solutions C, B, or A' might be exhibited, although the foregoing discussion has cast some doubt upon the attainment of B and A'.

We will now proceed to examine the remaining solutions encountered between B and D in Fig. 2. The number of such intersections was found to vary considerably with changes in the parameter values. In addition, these solutions are quite different from any solutions reported so far. Two such solutions, denoted E and F in Fig. 2, have been chosen for display. Figure 4(a) shows that the potential distributions for E and F exhibit maxima and minima, in clear contrast to Solution A' which is also shown. As a consequence, anodic dissolution rate distributions, shown in Fig. 4(b), are highly nonuniform and indicate that localized attack may proceed at more than one location along the surface. Solution E has two strong anodic rate maxima, while F has two strong maxima and one weakly anodic region at $X = -\lambda$. The cathodic reaction rate distributions, shown in Fig. 4(c), are similar for all three solutions. By comparing Fig. 4(b) and 4(c), it is realized that Solutions E and F indicate that several anodic regions exist along the corroding metal, each separated by a cathodic region. The oxygen concentration distribution for each solution is shown in Fig. 4(d). For all cases, the oxygen concentration tends to be highest at $X = +\lambda$, where the barrier layer is thinnest, and lowest at $X = -\lambda$, where the thick barrier impedes oxygen diffusion. The remaining six solutions indicated in Fig. 2 exhibit behavior similar to E and F, but have not been illustrated since they do not appear to contribute additional information.

In accord with the informal rule that alternate intersections in Fig. 2 correspond to stable solutions, one may conclude tentatively that Solutions E and F are stable. On the other hand, one may inquire as to what transient events would be required to arrive at the steady states given by E or F. It seems reasonable that highly novel start-up conditions would be required in order to capture Solutions E or F, and their likelihood of existence may be regarded as highly improbable in comparison with Solutions A, C, or D.

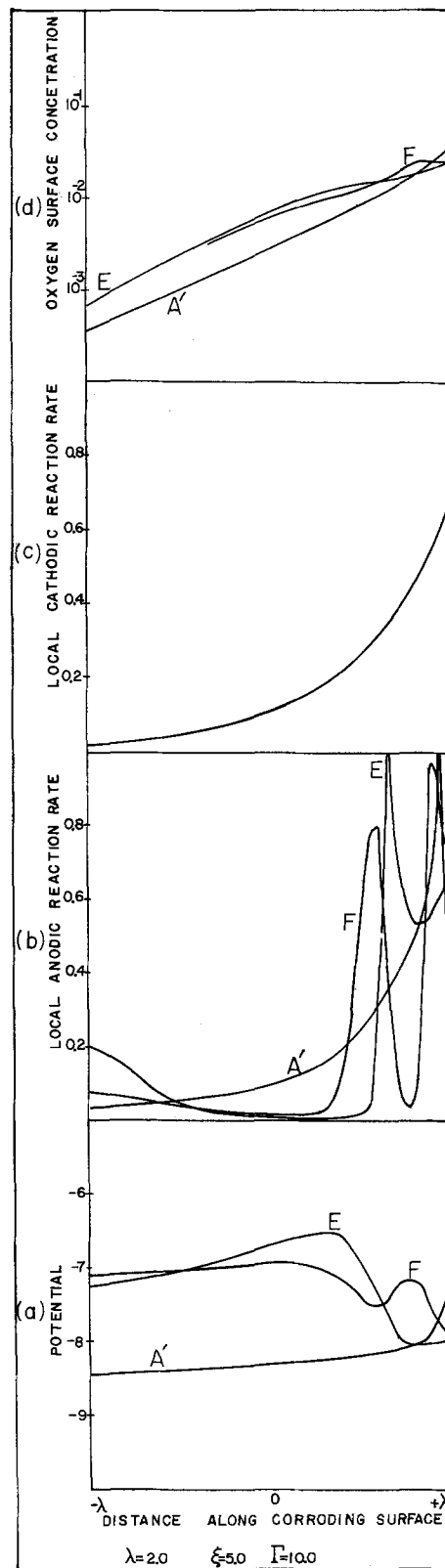


Fig. 4. Several distributions satisfying Eq. [1] were found for a single set of parameters. The curves labeled A', E, and F correspond to the solutions indicated in the text and in Fig. 2. The distributions shown are: (a) potential of the metal relative to the solution, (b) anodic dissolution rate, (c) cathodic reduction rate, (d) oxygen concentration at the surface.

As the system parameters are changed, the curve given in Fig. 2 moves up and down and also changes shape. As a consequence, points of intersection which correspond to different classes of solutions (A, B, C, etc.) may pass out of existence. For example, as parameter Γ is decreased, Solution A eventually merges with

A' and both disappear. As Γ is further decreased, Solutions B and C merge and disappear simultaneously. Such behavior also supports the contention that Solutions A' and B are unstable whereas A and C are stable.

The foregoing discussion has been directed at evaluating the mathematical model and computational method as well as gaining an understanding of a somewhat complex phenomenon. In what follows, the model is employed to indicate the regions of parameter space over which solutions with an unacceptable maximum local corrosion rate exist. In principle, the approach promises to be of value to corrosion engineers since the physical conditions corresponding to unacceptable regions may thereby be avoided through proper design.

Parameter values were compiled for which Solutions A and C indicated localized corrosion. In Fig. 5, the region between any of the two matching coded lines corresponds to the region where Solution C exists. For example, when $\lambda = 3$ and $\xi = 0.1$, localized corrosion by steady-state Solution C would be expected over the range $3 < \Gamma < 20$; outside of this range of Γ , Solution C is not found. The influence of parameter λ on the existence of C is also shown in Fig. 5. A large value of λ corresponds to a large differential aeration and thereby enhances tendencies toward localized corrosion. The region of existence of C is therefore markedly increased by an increase in λ .

The region of existence of Solution C is also influenced by the value of the parameter ξ which is the ratio of the cathodic rate constant to the maximum anodic current density at the "tip" of the passivation hump. Figure 6 illustrates, for $\lambda = 2$, the influence of parameter ξ . An increase in ξ corresponds to an increase in oxygen reactivity so that the surface concentration of oxygen would thereby be decreased. As a consequence, the range of Γ over which C exists is shifted to larger values in order to increase the ex-

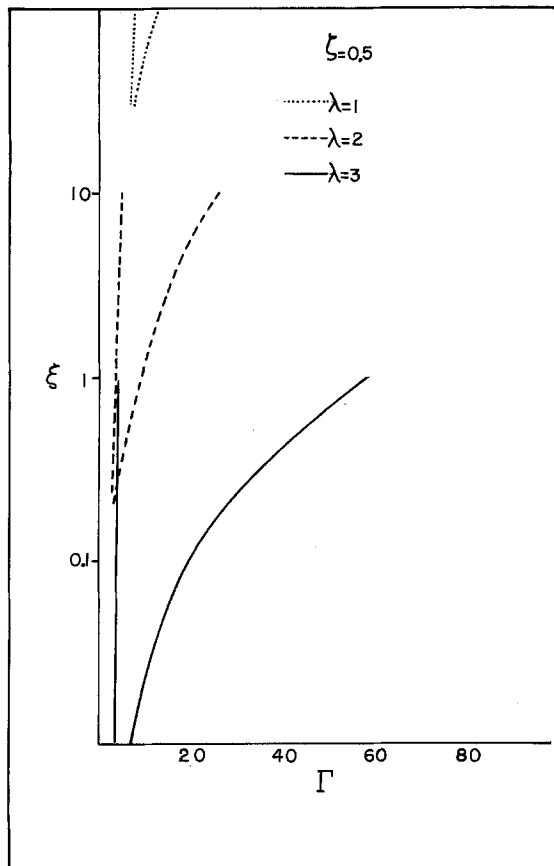


Fig. 5. Effect of differential aeration (parameter λ) on the existence of Solution C. The ξ - Γ region between any two matched coded lines is the region wherein Solution C exists.

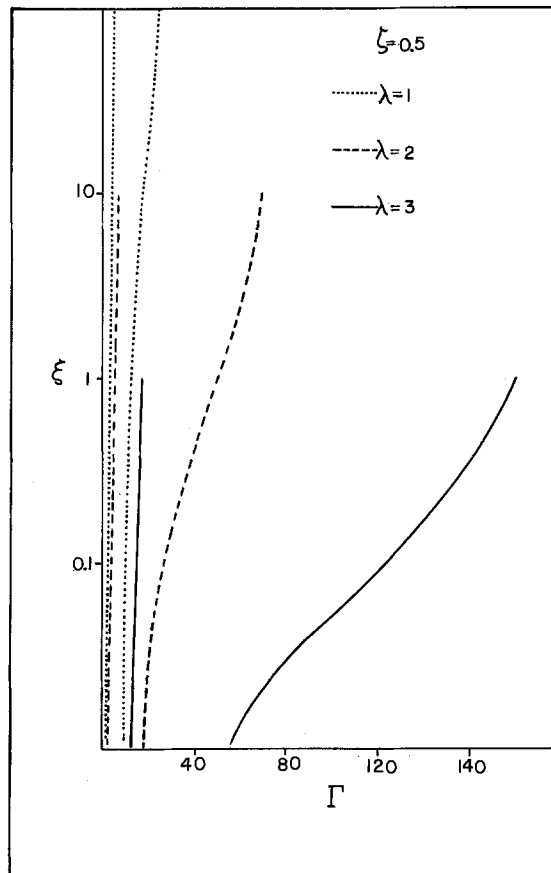


Fig. 6. Effect of differential aeration (parameter λ) on regions of parameter space where Solution A indicates highly localized attack.

tent of differential aeration, which is the sole driving force for localized corrosion in this system.

Comparison of the influence of parameters λ and ξ as shown in Fig. 5 and 7 indicates clearly that approximations regarding the geometric form of the barrier layer have a far more drastic effect than approximations regarding the reaction kinetics which are applied to the model. Therefore applications of the results of this study to systems of different geometry would appear to risk introducing significant errors.

Solution A corresponds to the situation where the metal corrodes in the active region everywhere so that the local anodic dissolution rate increases steadily with decreasing barrier layer thickness (1). Although no passivation occurs, highly nonuniform dissolution may nevertheless occur. The regions shown between the matching coded lines in Fig. 6 correspond to situations where the maximum dissolution rate exceeds the value 0.1a. It may be seen that the geometric parameter λ has a strong influence on the region of localized corrosion, similar to that shown in Fig. 5. On the other hand, the influence of the kinetic parameter ξ is essentially negligible and has not been displayed.

The existence of Solutions A' and B has always been found to lie within the range of existence of A and C as given by Fig. 5-7. The range of parameter space over which the remaining multiple solutions exist (excluding the passive solution, D) have not been compiled. In some cases, multipolar solutions having characteristics similar to E and F have been found which lie outside the envelopes of existence for Solutions A and C provided by Fig. 5, 6, and 7. On the other hand, arguments have already been presented regarding the improbability of attainment of steady states corresponding to the E- and F-type solutions which exhibit multipolar behavior. That is, the regions of parameter space indicated by Fig. 5-7 include all likely regions wherein highly localized corrosion rates have been found in the model system under

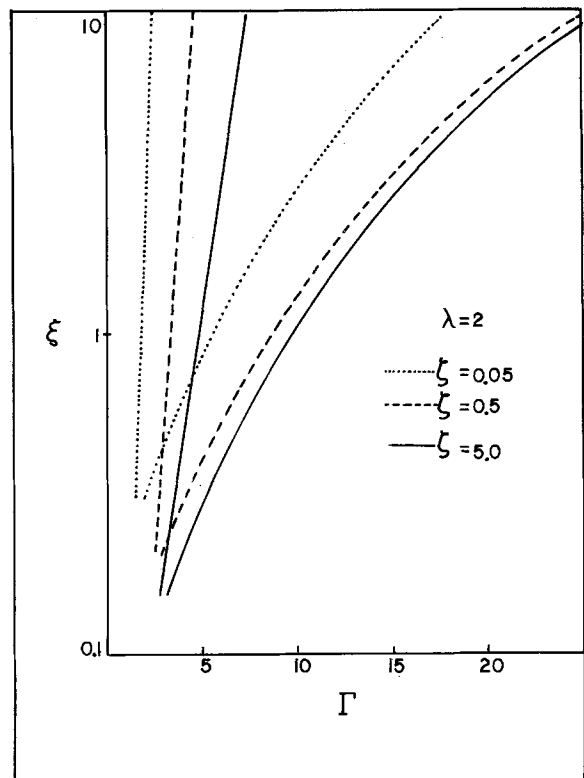


Fig. 7. Effect of the kinetic parameter ζ on regions of parameters space wherein Solution C exists.

study. Corrosion systems designed so as to lie outside these regions may therefore be expected to be unsusceptible to localized attack.

Conclusions

By determining the current distribution along a corroding surface, it has been possible to elucidate conditions under which highly localized corrosion is likely to occur in a simple model of differential aeration corrosion. Because the theoretical model is relatively straightforward, and because the underlying assumptions are relatively flexible, it is reasonable to expect that the foregoing transport phenomena approach may be extended to more complex situations of differential aeration corrosion as well as to other types of corrosion phenomena. The transport phenomena approach provides a route to predictive capabilities which has heretofore been lacking in corrosion design.

Owing to the active-passive behavior of the corroding metal incorporated in the model, multiple steady-state current distributions may exist for a single set of system parameters. The method of calculation employed above is capable of finding all of the multiple steady-state solutions. The method can therefore be used to seek out parameter regions where corroding systems would be susceptible to localized corrosion. The calculational method does not clarify the stability of the various multiple solutions in a rigorous manner but, by informal convention, suggests that Solutions A, C, and D are stable. Further, the method does not indicate which steady-state conditions would be attained following transient response from any given initial conditions; physical arguments, however, suggest that Solutions A, C, and D are most likely to be captured.

Several of the steady-state solutions exhibit multipolar behavior with up to three anodic and three cath-

odic regions distributed along the corroding surface. Current distributions of this type are not known to have been predicted in any previous investigation. However, the likelihood of observing such steady-state distributions in actual systems seems to be low in view of the unusual start-up conditions which would probably be required for their capture.

By developing dimensionless groups of system parameters, by investigating the response of the model to those parameters, and by developing a calculation method for finding all possible multiple solutions, the investigation provides a powerful intuitive grasp on the differential aeration corrosion phenomenon.

Acknowledgment

This study received partial support from the National Science Foundation via Grant NSF GK-36623.

Manuscript submitted Sept. 14, 1973; revised manuscript received July 19, 1974.

Any discussion of this paper will appear in a Discussion Section to be published in the December 1975 JOURNAL. All discussions for the December 1975 Discussion Section should be submitted by Aug. 1, 1975.

Publication costs of this article were partially assisted by the University of Illinois.

LIST OF SYMBOLS

a	maximum anodic current density, A/cm ²
c^0	oxygen concentration at barrier-atmosphere interface, g-mole/cm ³
D	oxygen diffusion coefficient, cm ² /sec
F	Faraday constant, 96,500 coulombs/g-equiv
k	oxygen reaction rate constant, A/cm ²
l	characteristics length, cm
R	gas constant, 8.31 joules/g-mole °K
T	temperature, °K
X	distance along corroding surface, x/l , dimensionless

Greek characters

α	transfer coefficient
β	anodic current density on passive plateau
δ_m	mass transport layer thickness at $X = 0$, cm
δ_R	effective cross-sectional area at $X = 0$, cm
ζ	kinetic parameter, k/a , dimensionless
κ	barrier electrolytic conductivity, (ohm cm) ⁻¹
λ	half-length of corroding surface, dimensionless
ξ	kinetic parameter, k/a , dimensionless
σ	characteristic width of passivation hump
Φ	potential, dimensionless

REFERENCES

1. R. Alkire and G. Nicolaidis, *This Journal*, **121**, 183 (1974).
2. I. Epelboin, C. Gabrielli, M. Keddam, J. Lestrade, and H. Takenouti, *ibid.*, **119**, 1632 (1972).
3. N. Vahdat and J. Newman, *ibid.*, **120**, 1682 (1973).
4. R. Alkire and G. Nicolaidis, Paper 101 presented at Electrochemical Society Meeting, Boston, Massachusetts, Oct. 7-11, 1973.
5. G. Nicolaidis, M.S. Thesis, University of Illinois, Urbana, Illinois, September 1973.
6. L. Fox, "Numerical Solution of Ordinary and Partial Differential Equations," Chap. 5, Addison-Wesley Publishing Co., Reading, Massachusetts (1962).
7. L. Lapidus and J. Seinfeld, "Numerical Solution of Ordinary Differential Equations," p. 65, Academic Press, New York (1971).
8. I. M. Gel'fand, *Am. Math. Soc. Translations*, **29**, 295 (1963).
9. H. Fujita, *Bull. Am. Math. Soc.*, **75**, 132 (1969).
10. I. Copelowitz and R. Aris, *Chem. Engr. Sci.*, **25**, 906 (1970).

Magnetic Properties of Anodic Oxide Coatings on Aluminum Containing Electrodeposited Co and Co-Ni

Satoshi Kawai

The Pilot Pen Company, Limited, Hiratsuka Works, Kanagawa, Japan

and Ryuzo Ueda

Department of Applied Physics, Waseda University, Tokyo, Japan

ABSTRACT

Cobalt and Co-Ni alloy were electrodeposited into the micropores of various kinds of anodic oxide films on aluminum. Fine granular metals precipitated on the barrier layer and formed columnar structures. Although the films of cobalt or nickel showed remarkable magnetic anisotropies perpendicular to the surface, the alloy films which consisted of approximately 50% cobalt showed a strong anisotropy along the horizontal direction. Coercive forces ranged from about 500 to about 1100 oe and the density of residual magnetization rose above 1000 gauss. The films may have applications in magnetic memories and recording devices.

When the surface of aluminum is anodized in some electrolytes, a film with micropores characteristic of the electrolytic conditions is formed (12). Asada (3) found that unsealed oxide coatings show peculiar colors when immersed in metal salt solutions after application of a.c. One of the authors (4) in a previous study observed that metallic nickel and nickel oxide were precipitated in the micropores when nickel sulfate was used as the electrolyte.

As cobalt has a larger saturation magnetization than nickel, deposits of cobalt and cobalt alloy are of particular interest for applications in magnetic devices. Zetner (5) reported that electrodeposited cobalt layers have a coercive force of 150-500 oe and a residual magnetization of 4000-8000 gauss, and that the coercive force could be increased to as high as 800 oe by the use of a.c. + d.c. during deposition. Morral (6) found that the magnetic properties of electrodeposited cobalt layers depend on bath temperature, current density, concentration of cobalt salt, ratio of a.c./d.c., and time of electrolysis.

Electrodeposited layers of Co-Ni alloy have a coercive force of 200-300 oe with remanence as high as 4000-8000 gauss. Zetner studied the relationship between the magnetic properties of Co-Ni alloy and electrolytic conditions and found that as pH varied from acid to neutral, the retentivity decreased, whereas the coercivity increased by about 50%. Furthermore, he indicated that a maximum coercivity and an excellent squareness ratio were obtained at about a 60% cobalt content in the deposited layer.

Endicott *et al.* (7) studied hardness and tensile strength of Co-Ni alloy deposits obtained from sulfamic acid baths under various conditions and found that the structure of the deposit affects the physical properties. In contrast to a columnar structure of the layers of pure cobalt and nickel, deposited layers of Co-Ni alloy have a lamellar structure with approximately 50% cobalt content, resulting in improved mechanical properties.

According to the phase diagram for Co-Ni alloys, the structures are β -phase at room temperature for a cobalt content of less than about 70%, and α -phase for the rest. Aotani (8) noted in his study of the structure of Co-Ni electrodeposits, using x-ray diffraction analysis, that the deposit obtained from an electrolyte solution of pH 1.2 showed fcc structure whereas those obtained from a bath of pH 6.3 included hcp at about 70% cobalt content.

Key words: anodizing, magnetic thin film, coercive force, remanence.

Experimental Procedures

Specimens were prepared by the following three methods, and the treatment conditions were as shown in Table I:

(i) Rolled aluminum sheets (99.99% in purity, $0.5 \times 500 \times 1000$ mm³ in size) were anodized in sulfuric acid, oxalic acid, chromic acid, phosphoric acid, sodium bisulfate, and sodium hydroxide [Table I (a)]. These oxide films were electrodeposited with cobalt in the sulfate solution [Table I (c)].

(ii) The oxide films made in sulfuric acid bath under various conditions [Table I (b)] were electrodeposited with cobalt in the sulfate solution [Table I (c)].

(iii) The anodic films formed in the sulfuric acid bath [Table I (d)] were electrodeposited with Co-Ni alloy for various ratios of cobalt and nickel in these sulfate solutions [Table I (e)].

Anodizing was carried out, with sufficient air stirring, either with a carbon plate as a counterelectrode for the oxalic acid and sodium hydroxide baths, or with a lead plate for the other electrolytes. When 15V

Table I. Bath compositions

Procedures	Remarks
Degreasing	5% NaOH, 80°C, 2 min
Desmut	5% HNO ₃ , 23°C, 1 min
(a) Anodizing	
Sulfuric acid	15% H ₂ SO ₄ , 0.1% Al, 1 A/dm ² , 21°C, 20 min
Oxalic acid	4% (COOH) ₂ , 0.1% Al, 1 A/dm ² , 35°C, 20 min
Chromic acid	5% CrO ₃ , 1 A/dm ² , 55°C, 40 min
Phosphoric acid	15% H ₃ PO ₄ , 1 A/dm ² , 30°C, 30 min
Sodium bisulfate	10% NaHSO ₄ · H ₂ O, 1.5 A/dm ² , 30°C, 20 min
Sodium hydroxide	0.5% NaOH, 2 A/dm ² , 15°C, 30 min
(b) Anodizing	
Sulfuric acid	5, 15, and 30% H ₂ SO ₄ , 0.1% Al 20° and 30°C 0.5, 1.0, and 2.0 A/dm ² 5, 10, 15, and 20 min
(c) Electrodeposition	
Cobalt	5% CoSO ₄ · 7H ₂ O, 2% H ₃ BO ₃ , pH 6.0 15V (50 Hz), 23°C, 10 min
(d) Anodizing	
Sulfuric acid	15% H ₂ SO ₄ , 0.1% Al, 1.5 A/dm ² , 21°C, 30 min
(e) Electrodeposition	
Co-Ni	4 ~ 0% CoSO ₄ · 7H ₂ O, 0 ~ 4% NiSO ₄ · 7H ₂ O, 2% H ₃ BO ₃ , 0.2% glycerine, 25°C, 20 min, 15V (50 Hz), pH 6.5
Sealing	1% Ni(CH ₃ CO ₂) ₂ · 4H ₂ O, 90°C, 20 min

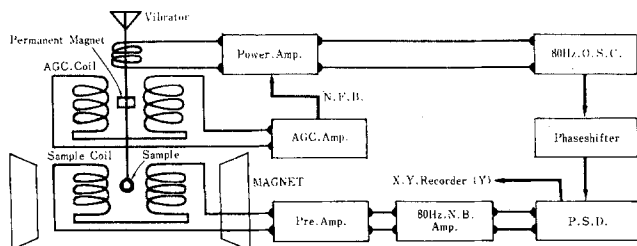


Fig. 1. Schematic diagram of sample vibrating magnetometer

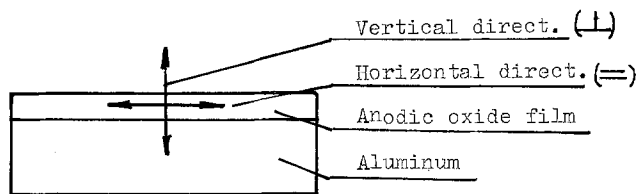


Fig. 2. Directions of magnetic anisotropies of anodic oxide film

a.c. was applied, about 5 A/dm² passed for a short time; after 5-10 sec a stationary current of about 1A/dm² was observed. The color of the oxide coating was brown at first, becoming black finally. After sealing, the specimens were wiped using a cotton cloth.

Specimens anodized in sulfuric and phosphoric acids were embedded in epoxy resin and sectioned to about 700Å using an ultrathin-film cutter. These sliced sections were then observed under an electron microscope.

For x-ray diffraction analysis, specimens anodized in sulfuric acid and electrodeposited with cobalt and Co-Ni alloy were immersed in 3% mercuric chloride solution and allowed to stand at room temperature for about 3 hr to strip the oxide. The stripped oxide films were washed, dried, and pulverized in an agar mortar.

The composition of the alloy deposited in the oxide films anodized in the sulfuric acid bath was determined by spectroscopic analysis. Specimens of 20 × 20 mm² were immersed in 5% sodium hydroxide solution at 30°C and the oxide films were stripped. The filtrate was boiled after adding hydrochloric acid, and the cobalt and nickel contents were determined using an atomic absorption spectrometer.

M-H hysteresis curves of the magnetic films were recorded with a vibrating magnetometer. A sample was vibrated along a direction vertical to the surface of the film; this made the measurement 50-500 times more sensitive than the usual automatic magnetometers. A schematic diagram of the apparatus is given in Fig. 1. Specimens in the form of a disk, 6 mm diameter were in sets of four on a quartz holder. The hysteresis loops along the horizontal and vertical direction were recorded to compare the magnetic anisotropies shown in Fig. 2.

Experimental Results

Figures 3 and 4 show electron micrographs of ultrathin sections of cobalt-deposited films anodized in sulfuric and phosphoric acids, respectively. The oxide film formed in sulfuric acid separated from the surface of the aluminum by a barrier layer. In the outer oxide film, columnar micropores about 100Å in diameter, about 400Å in distance from each other, and perpendicular to the surface were observed. These micropores were filled with fine granular deposits. In the phosphoric acid film, pillar-shaped deposits about 500Å in diameter were arranged nearly perpendicular to the surface at about 1000Å intervals.

From x-ray diffractometer analysis of the cobalt deposits, the structure was assigned as hcp α -Co ($a = 2.507\text{\AA}$, $c = 4.070\text{\AA}$) by reference to ASTM x-ray card 5-0727. In the case of Co-Ni alloy depositions, as the cobalt content decreased, the fcc crystal gradually appeared and the hcp structure disappeared. Figure 5 depicts the relationship between the calculated lattice constants and the cobalt content in the deposits.

The amount of cobalt and nickel deposited into the oxide film formed in the sulfuric acid bath is shown in Fig. 6.

The M-H hysteresis curves of the oxide films formed in various electrolytes and electrodeposited with the cobalt are shown in Fig. 7 (a)-(f). In these experiments, correction for the demagnetizing field of the quartz holder was made in advance.

With sulfuric acid, oxalic acid, and sodium bisulfate baths the cobalt-deposit layers showed strong magnetic anisotropies along the vertical direction with good squareness ratios but rather weak anisotropies along the horizontal direction. With chromic acid and sodium hydroxide baths, the anisotropies along the vertical direction were decreased. While with the phosphoric acid bath, this property along the horizontal direction was increased.

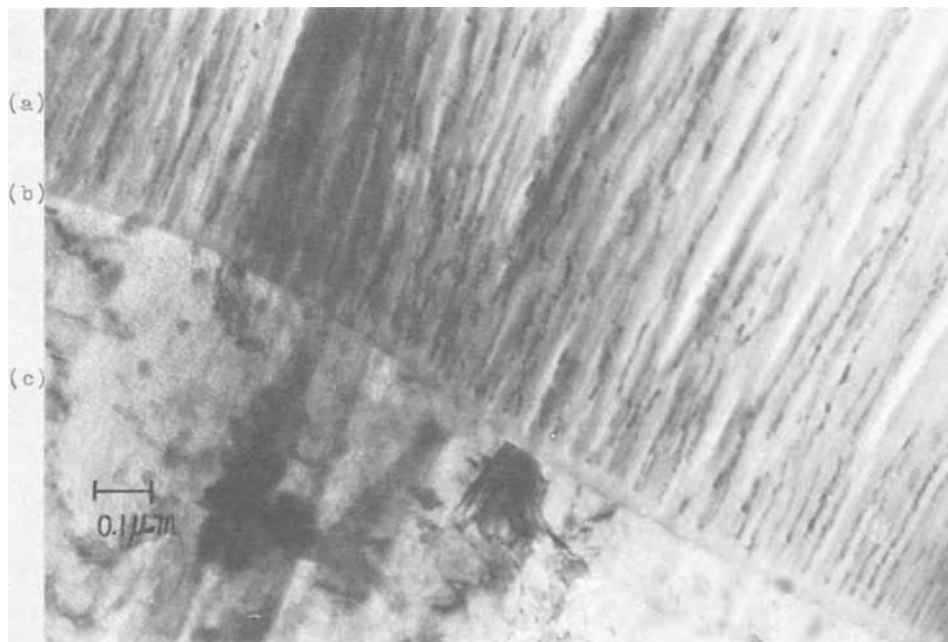
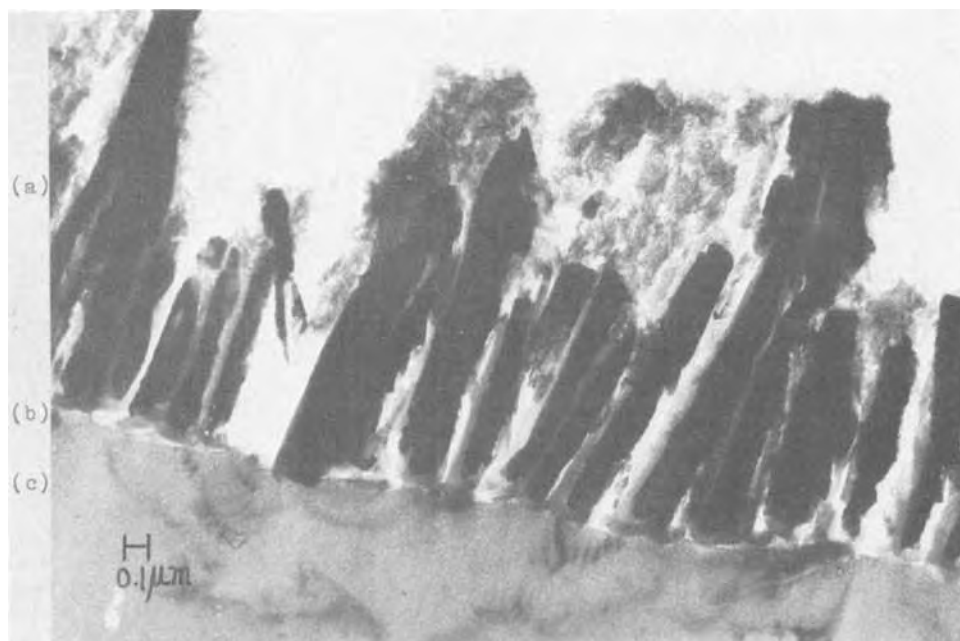


Fig. 3. Electron micrograph of ultrathin section film anodized in sulfuric acid and electrodeposited with cobalt. (a) Aluminum oxide film, (b) barrier layer, (c) aluminum.

Fig. 4. Electron micrograph of ultrathin section film anodized in phosphoric acid and electro-deposited with cobalt. (a) Aluminum oxide film, (b) barrier layer, (c) aluminum.



Coercive forces indicated are characteristic of each electrolyte. The values for the films anodized in sulfuric and oxalic acid baths were greater than 1000 oe, while low values of about 500 oe were obtained with the phosphoric acid bath.

In Fig. 8 coercivities of the films anodized in the sulfuric acid bath are given as a function of the anodizing time. The effects in various electrolytic conditions were also measured. Coercive forces along the horizontal direction varied little, while the vertical components increased with increasing electrolyte concentration and decreasing current density. However, these vertical coercive forces were reduced with anodizing time and converged to a definite value.

Similarly, the relation between the strength of the residual magnetizations and the anodizing time was measured. The strength along the horizontal direction increased with the anodizing time, this increase being more pronounced as the electrolyte concentration and current density increased. After calculating the film thickness using an empirical formula, the relationship between the residual induction and the film thickness was as shown in Fig. 9. Residual magnetization increased with film thickness, but approached a saturation value. A larger magnetization value was obtained for an electrolyte of 30% concentration than with one of 15%.

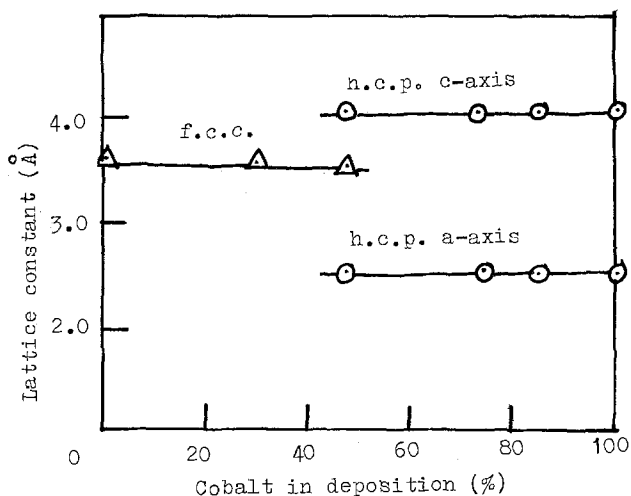


Fig. 5. Lattice constants of Co-Ni deposition onto anodic oxide films.

In general, the density of remanence, B , can be expressed as

$$B = 4\pi M/V$$

where M indicates the strength of remanence (emu) and V designates the volume of the magnetic film (cgs). Then, $0.01M$ for a disk 6 mm in diameter having a $10 \mu\text{m}$ film thickness gives a magnetic density of about 440 gauss, and $0.025M$ is calculated to be more than 1000 gauss.

From some typical hysteresis curves for Co-Ni alloy deposits in films anodized in the sulfuric acid bath, the relation between the cobalt contents in the deposit layers to the coercivities and retentivities are shown in Fig. 10 and 11, respectively.

The coercive forces along the vertical direction varied from about 750 oe at 100% nickel content to about 1100 oe at 100% cobalt content. On the other hand, the coercivities along the horizontal direction rapidly increased from a value of 300 oe for 100% nickel content to a maximum of about 1100 oe for

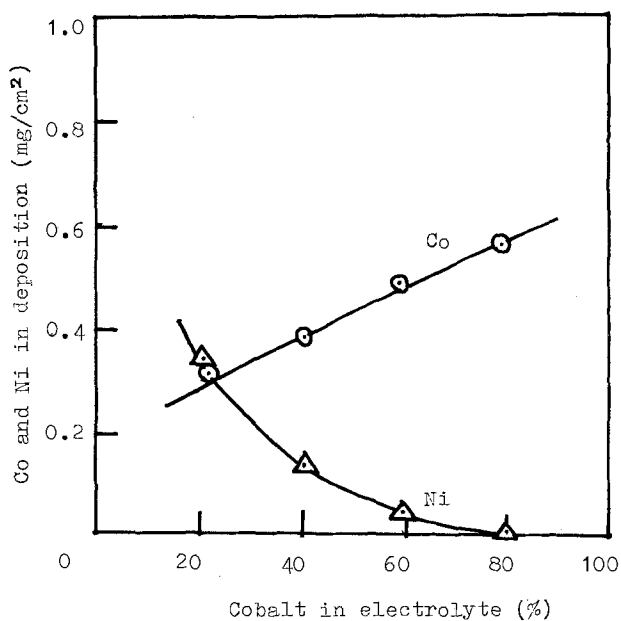


Fig. 6. Cobalt and nickel content between electrolyte and deposition.

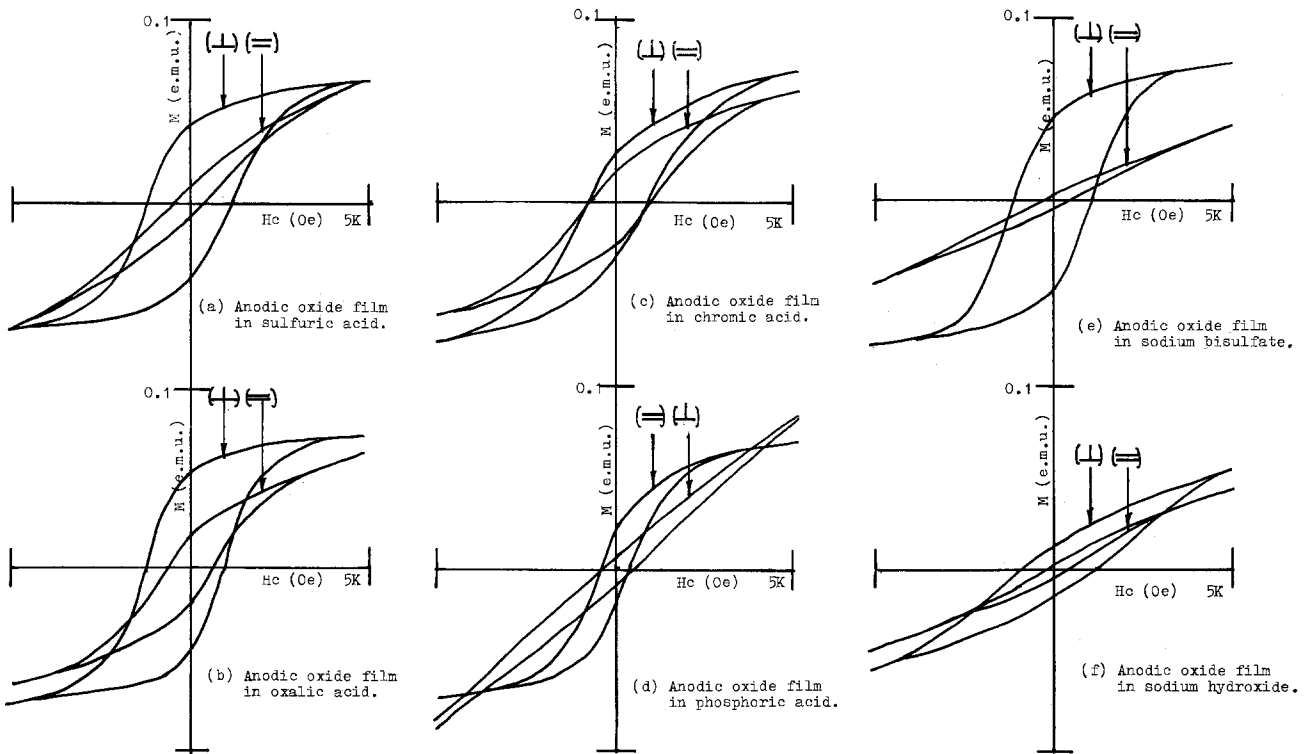


Fig. 7 (a)-(f). M-H hysteresis curves of oxide films anodized in various kinds of electrolytes and electrodeposited with cobalt

50% cobalt content, followed by a slight decrease to about 600 oe for 100% cobalt. The remanence strength along the vertical and horizontal directions showed a trend similar to that of the coercive forces, indicating a maximum value along the horizontal direction at about 50% cobalt content. The fact that the vertical and the horizontal magnetic properties reversed at around 50% content is considered to be an indication of some change in the structure of the deposited metal.

Magnetic Properties of Cobalt Deposits

The crystal orientation of the deposits has an influence on magnetic anisotropy. For α -Co with hcp structure, the axis of easiest magnetization has been measured to lie along the c-axis (9). Endicott and Knapp (7) demonstrated that electrolytic deposits obtained from cobalt salt solution show a columnar structure. Morral (6) indicated that the axis of easiest

magnetization of cobalt obtained from an electrolyte near neutral pH was vertical to the surface. Thus, with the columnar structure, magnetic anisotropy along the vertical direction may be attributed to crystal growth in a direction which is parallel to the c-axis. From these facts, cobalt crystals deposited in the micropores of anodic oxide films may be presumed to have similar structures.

Assuming a film thickness of 1 μ m, the ratio of the length to the diameter of the micropore will be 100:1. A needlelike structure of the metal deposit would result forming long unit magnetic domains. The magnetic anisotropy of the cobalt deposit may result not

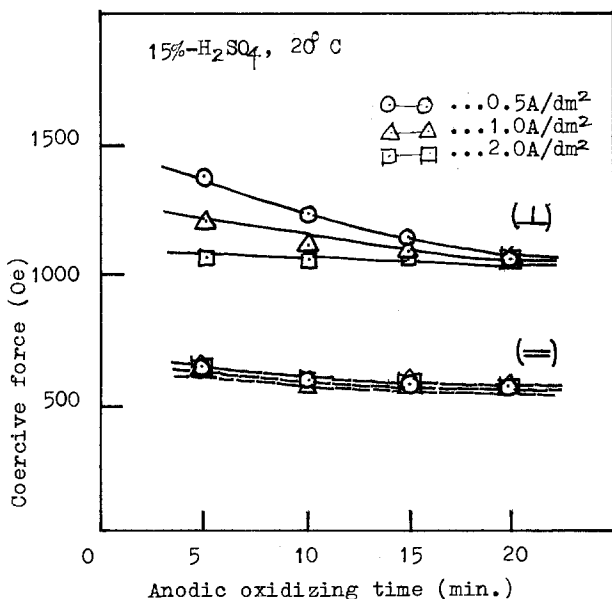


Fig. 8. Relations between remanences of electrodeposited layers and anodic oxidizing times.

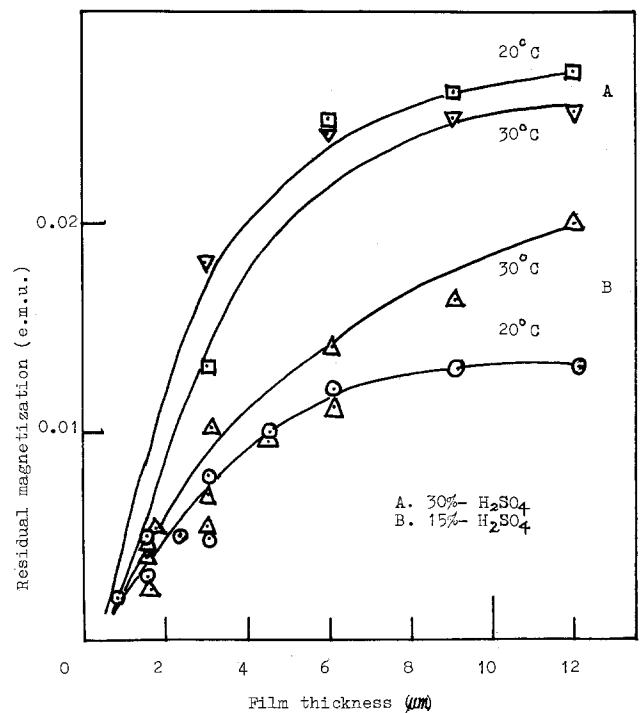


Fig. 9. Residual magnetizations vs. film thickness of anodic oxide films deposited with cobalt.

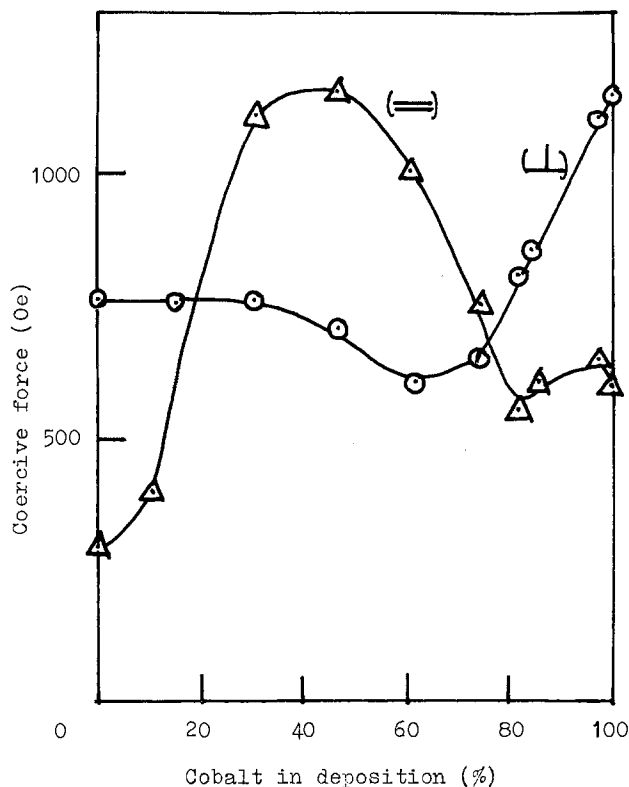


Fig. 10. Coercive forces of anodic oxide films electrodeposited with Co-Ni.

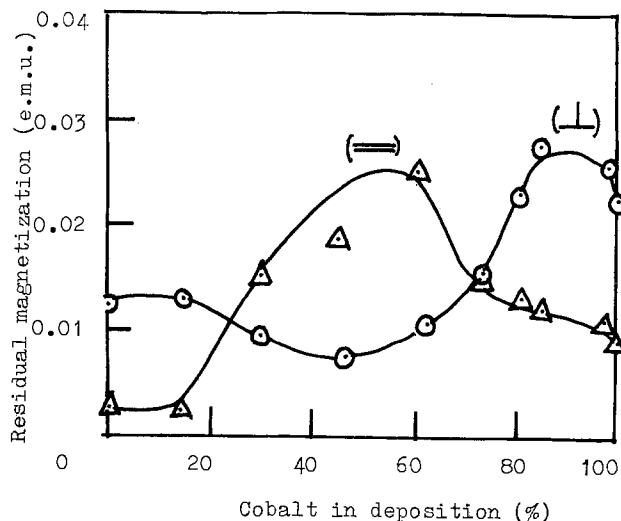


Fig. 11. Residual magnetizations of anodic oxide films electrodeposited with Co-Ni.

only from the orientation of the cobalt crystal particles but also by the effect of particle shape.

Anodic oxide films obtained from the chromic acid bath are reported to form zigzag micropores, which occurrence reduces the uniformity of deposition, resulting in a weaker magnetic anisotropy along the vertical direction than that obtained from the sulfuric acid bath. Magnetic films anodized in a sodium bisulfate bath are said to have properties similar to those in sulfuric acid, hence the identical hysteresis loop. Little is known about the film obtained from sodium hydroxide baths. Although the oxide film shows good adsorption of dyestuff, this indicates relatively large micropores in the film. From the magnetic properties of this film, the presence of an irregular pore struc-

ture similar to the chromic acid bath case can be expected.

The coercive forces of the films did not show any marked variation with electrolytic conditions, although the trend was observed that coercivities increased with concentration of the sulfuric solutions and decreasing current densities. According to Keller *et al.* (1), decreasing electrode potential has the effect of decreasing the cell diameter, and it may be accepted that variations in temperature and concentration of electrolyte influence the electrode potential. From these considerations, the diameter of micropores in this case should be reduced to a certain extent. The shorter the electrolysis time, the higher the coercivity obtained. This might be due to a greater uniformity of the micropore structure for thinner films.

The remanence strength became larger with increasing film thickness and electrolyte concentration. However, it reached a saturation value probably due to a definite amount of cobalt deposition in the micropores under the given operating conditions. On the other hand, the density of magnetization was smaller than the values obtained from the usual electrodeposition, and it is considered that there is some limitation of the amount of the density because the porosity of micropores is estimated to be about 10% of the whole volume of the oxide film.

Magnetic Properties of Co-Ni Alloy Deposits

An x-ray diffraction analysis of the Co-Ni alloy deposits revealed the presence of α -Co for the film having a cobalt content greater than about 50% and a fcc structure for the lower concentration. The magnetic anisotropy of these deposits rotated by 90° from the direction vertical to the horizontal at about 50% cobalt content.

The crystal orientation of metal grain in the films was not experimentally determined in this study, but the orientation of the metal deposit in the micropores should determine the magnetic anisotropy of the film. In the lamellar structure, as the direction of the crystal growth is parallel to the surface and the c-axis is easiest magnetization, the magnetic anisotropy of the oxide film develops to the horizontal direction of the surface, and this is regarded as crystal anisotropy.

The anodic oxide coatings deposited with magnetic metals provide not only a powerful means for study of the film structures, but also have potential applications for high bit density memories and recordings.

Acknowledgment

The authors thank Messrs. N. Shinohara and U. Sakai of the Pilot Pen Company, Limited for their help.

Manuscript submitted Feb. 11, 1974; revised manuscript received Aug. 7, 1974.

Any discussion of this paper will appear in a Discussion Section to be published in the December 1975 JOURNAL. All discussions for the December 1975 Discussion Section should be submitted by Aug. 1, 1975.

Publication costs of this article were partially assisted by The Pilot Pen Company, Limited.

REFERENCES

1. F. Keller, M. S. Hunter, and D. L. Robinson, *This Journal*, **100**, 411 (1953).
2. H. Akabori and T. Fukushima, *J. Electronmicroscopy (Tokyo)*, **13**, 162 (1964).
3. T. Asada, Jap. Pat. 310401 (1963).
4. S. Kawai and M. Mizusawa, *J. Metal Finishing Soc. Japan*, **20**, 272 (1969).
5. V. Zetner, *Plating*, **52**, 868 (1965).
6. F. Morral, *Metal Finishing*, **62**, 59 (1964).
7. D. W. Endicott and J. R. Knapp Jr., *Plating*, **53**, 43 (1966).
8. T. Aotani, *J. Inst. Metals Japan*, **B-14**, 55 (1950).
9. R. Bezorth, "Ferro-Magnetism," p. 555, D. Van Nostrand Co., Inc., Princeton, N.J. (1968).

Electrodeposition along the Air-Solution Interface

I. Experimental Investigation

R. A. Dilorio,¹ W. J. Newby,² and A. J. Sukava*

Chemistry Department, University of Western Ontario, London, Ontario, Canada

ABSTRACT

In the electrolysis of an acidified copper sulfate solution with a copper wire cathode located vertically along the axis of a cylindrical copper anode, addition of a small amount of norvaline to the solution causes a disklike deposit of copper to grow outwardly from the cathode and along the air-solution interface. Experiments show that this phenomenon is due mainly to a solid reaction product arising from air oxidation of the norvaline along the line of contact between the copper anode, air, and solution. This solid, presumably present in a highly subdivided state, migrates by surface diffusion from the anode to the cathode along the air-liquid interface, giving rise to nucleation sites that lead to the interfacial cathode growth. The mechanism is thought to involve a conductive surface film containing copper powder as a conducting medium. The rate of disk formation depends on the concentration of the norvaline, the area of anode surface along the air-solution interface, the acidity of the solution, the partial pressure of oxygen above the solution, and the rate of current flow. It does not depend very markedly on the concentration of the copper sulfate.

The results of preliminary experiments on the growth of a copper electrodeposit along the air-solution interface, caused by small concentrations of norvaline in the acid sulfate electrolyte, have been described in a previous publication (1). This unusual phenomenon was first noticed in this laboratory in the course of a study of excess deposit weights caused by various additives. It occurs when the acidified copper sulfate solution containing the norvaline is electrolyzed with a wire cathode positioned vertically along the axis of a cylindrical copper anode. The interfacial deposit consists of a disk-shaped growth of copper extending outwardly from the cathode along the liquid surface. The disk is sometimes radially asymmetric as a result of noncoincidence of the cathode position and the anode axis, with growth favored in the direction of greatest current flux.

As reported (1), the formation of the interfacial disk is always accompanied by a change in color of the copper sulfate solution to a blue-green, and by formation of a finely divided, black, suspended solid that settles on standing after electrolysis is stopped. Separation of the anolyte and catholyte by means of a porous thimble surrounding the wire cathode (Whatman cellulose extraction thimble as indicated by a--a in Fig. 1) prevents formation of the disk. Moreover, both the color change and the formation of black solid occur only in the electrode compartment outside the thimble, whether the outer cylindrical electrode is made the anode or the cathode. Obviously, these two effects are interdependent and not markedly affected by the electrode potential. They occur primarily at the electrode with the greater surface area.

Experiments showed that prior oxidation of the dissolved norvaline by air or oxygen in the presence of a copper surface (presumably as catalyst) is a primary requisite in giving rise to the interfacial disk. The color change and black solid are a result of this oxidation, and electrolysis of a solution containing these oxidation products produces the interfacial disk whether or not oxygen is excluded. If a freshly prepared norvaline-containing electrolyte is deaerated with nitrogen and then electrolyzed under a nitrogen atmosphere, none of these effects occur.

A more detailed study has now been made of this form of interfacial electrodeposition. The results of various experiments, some still preliminary in nature, are presented and discussed in this report.

Experimental Technique

The simple apparatus used in this study is illustrated in Fig. 1. The glass cell, fitted with a ground-glass cap as shown, had a total volume of about 100 mliters. A copper wire cathode, about 1 mm in diameter, was positioned approximately along the axis of a cylindrical copper anode with an inside diameter of about 3 cm. The cathode was immersed to a depth of about 4.9 cm when the cell contained 50 mliters of solution. An appropriate opening in the cell cap held the cathode in place and another opening provided access for the anode lead. Two other openings (not shown) provided for electrolysis under an atmosphere of nitrogen or oxygen as required.

Most of the anodes were made from ordinary commercial copper tubing. These anodes, as well as the wire cathodes, were heated to redness prior to use to destroy any possible organic contaminants that might have been present. They were then etched in nitric acid and washed and rinsed with distilled water. However, some of the anodes were prepared by electrodeposition of "pure" copper on cylindrical platinum gauze substrates, *i.e.*, using platinum electrodes and a copper sulfate electrolyte previously purified by passing through a column of activated charcoal. These anodes were not preheated since no organic additives were used in their formation.

The standard solution used in the disk-growth experiments contained 0.5M copper sulfate and 1.0M sulfuric acid, both reagent grade. The organic additives were also reagent grade, as obtained commercially. These were added without further purification to the freshly prepared standard electrolyte to give the desired concentration. The water used in the solutions was distilled twice with all-glass apparatus. It had a specific conductance of about 6×10^{-6} ohm⁻¹cm⁻¹.

All experiments were carried out at a constant applied current, using a Harrison regulated power supply, Model 6201-A. In most of the experiments, several cells containing different concentrations of organic additive were connected in series so that the same amount of charge flow occurred in each. The cell assembly was immersed to the solution level in a temperature-regulated bath maintained at $25^\circ \pm 0.05^\circ\text{C}$.

* Electrochemical Society Active Member.

¹ Present address: Colonel By Secondary School, Ottawa, Ontario, Canada.

² Present address: Alcan International Limited, Research Centre, Kingston, Ontario, Canada.

Key words: interfacial disk, anode effects, norvaline, copper powder, conductive film.

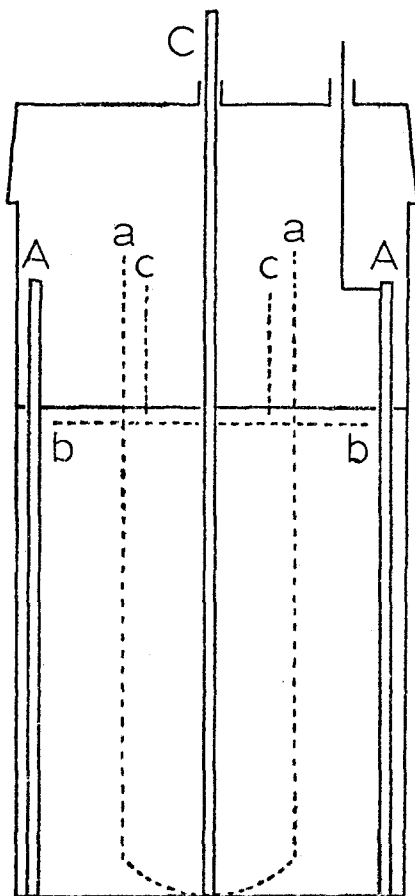


Fig. 1. Electrolysis cell. A, Cylindrical copper anode, about 3.0 cm ID; C, copper wire cathode, diameter about 1 mm; a --- a, porous cellulose thimble to separate anolyte and catholyte; b --- b, horizontal Parafilm or cellulose sheet to eliminate convection flow at the air-solution interface; c --- c, cylindrical Parafilm barrier to isolate the cathode region of the air-solution interface from the anode. Length of the cathode immersed with 50 mliter solution, 4.9 cm.

Results and Discussion

Figure 2 shows photographs of a typical cathode deposit obtained after prolonged electrolysis in the presence of a small amount of norvaline. The disklike deposit grew along the air-solution interface, during a given period of electrolysis and at a given current flow, to an extent dependent on the norvaline concentration. Typical data are shown in Fig. 3. At a constant current flow of about 45 mA, the optimum norvaline concentration was about 2.5×10^{-2} molar.³ Experiments with freshly prepared solutions always showed that the disk growth did not begin until after several hours of initial electrolysis. Furthermore, the results were qualitatively the same whether the anodes were made from "impure" commercial copper tubing or whether they were made by prior electrolysis of a "purified" copper sulfate electrolyte with deposition on cylindrical platinum substrates. The indication here is that possible minor impurities in the anode metal are of no apparent consequence in the disk growth process. The cathode and anode current efficiencies were about 100 and 83%, respectively.

Besides formation of the surface disk, the following additional effects were observed:

1. The initial blue color of the copper sulfate solution changed to a blue-green with about 24 hr of electrolysis.

³ In one experiment, a paper-thin layer of copper metal formed across the surface of the solution, causing a direct short between cathode and anode. Attempts to reproduce this extreme form of interfacial deposition were not successful, indicating that the conditions for maximum rate of disk growth are probably rather critical.



Fig. 2a. Copper cathode with interfacial disk. Top view. Diameter of disk, 2.0 cm

2. A small amount of finely divided black solid was found dispersed and suspended in the solution.

3. Finely divided copper powder was sometimes found at the bottom of the electrolysis cell, confirming Ibl's observation (2) that such powder forms at the cathode during electrolysis.

Inhibition of disk growth.—The decreased diameter of the copper disk with norvaline concentrations greater than 2.5×10^{-2} M (see Fig. 3) is probably due to some kind of inhibiting effect caused by the excess norvaline. This suggestion is based on the observation that the same effect was obtained by adding other structurally related organic compounds to the solution. For example, if the norvaline concentration was kept constant at 2.5×10^{-2} M, and if either N-acetyl norvaline or glycine was added, the effect was to decrease the disk growth. N-acetyl norvaline was found to cause a greater decrease in disk growth than glycine at the same concentration, indicating presumably that a large additional molecule has a greater inhibiting effect than a small one.

Disk growth and rate of current flow.—Figure 4 shows the effect of the rate of current flow on the size of the disk. In these experiments, the time of electrolysis was adjusted so that the same total charge passed through the solution in every case, with the initial concentration of norvaline being fixed at the optimum 2.5×10^{-2} M. The maximum rate of disk growth occurred under these conditions when the current, kept constant throughout, was about 60 mA.

Disk growth and convective flow.—In the cell shown in Fig. 1, the presence of the cellulose thimble a --- a

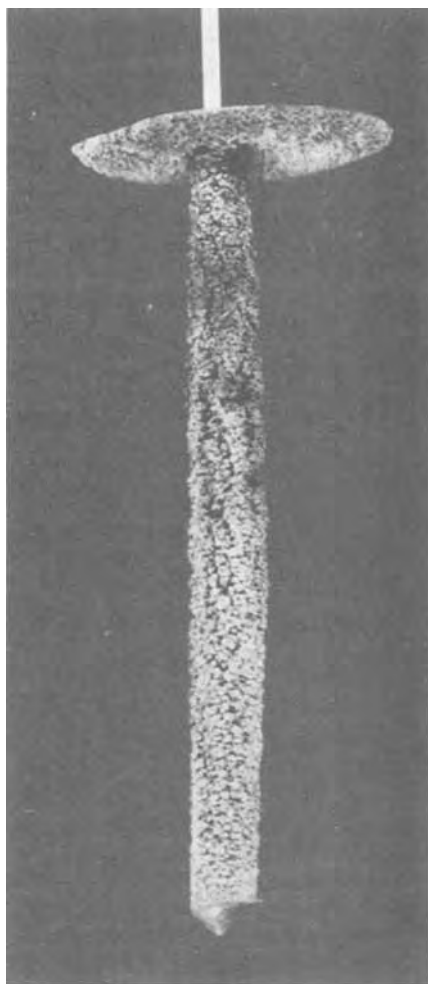


Fig. 2b. Copper cathode with interfacial disk. Bottom view

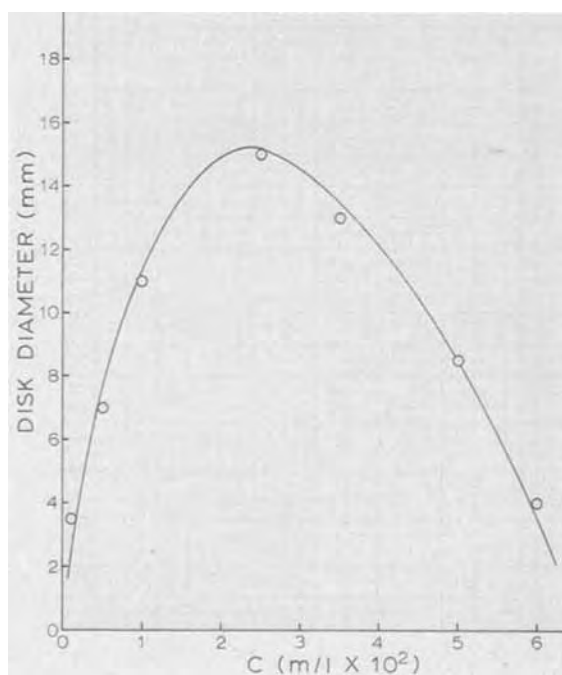


Fig. 3. Disk diameter vs. C , the initial molar concentration of norvaline. Time of electrolysis, 48 hr; current, 45 mA; temperature, 25°C.

can be expected to eliminate or at least substantially reduce the normal convective flow, which is upward

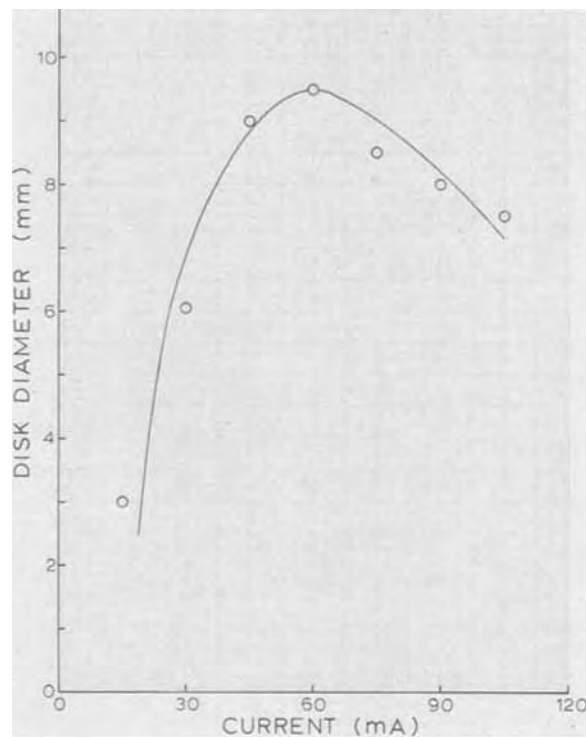


Fig. 4. Disk diameter vs. current. Norvaline concentration, $2.5 \times 10^{-2}M$; charge flow, 5200 coulombs; temperature, 25°C.

at the cathode and downward at the anode. Since this thimble prevents formation of the interfacial disk (1), experiments were designed to examine the role that convection might possibly play in the disk-growth mechanism. In some of these experiments, shortened, fully immersed thimbles were used such that they surrounded only the bottom 1-3 cm of the cathode. In others, pieces of cellulose cut from the thimbles were immersed in the solution in such a manner that they did not interfere with the convection stream. In every case, with the amount of cellulose being in excess of about 18 cm² of the thimble material, it was found that formation of the air-solution interfacial disk did not occur. Apparently the cellulose interferes with the disk-growth process by removing some soluble or colloidal active agent, possibly by adsorption.

Further evidence to support this view was obtained from experiments in which horizontal barriers were used to reduce or eliminate the normal convection (see b--b in Fig. 1). As was noted previously (1), formation of the interfacial disk is not prevented by a thin sheet of nonporous Parafilm (a waxy waterproof material obtained from the Fisher Scientific Company) attached to the cathode and located horizontally just below the solution line. However, similar horizontal barriers consisting of cellulose sheet (cut from Whatman extraction thimbles) do prevent the disk formation. Accordingly, since the convection stream cannot be affected very differently by these similar horizontal barriers, whether Parafilm or cellulose, then adsorption of a disk-growth agent by the cellulose is indicated. The convection stream as such is not an important factor in the disk-growth mechanism, except perhaps as an aid in keeping the disk-growth agent in suspension along the liquid surface.

Outgrowth at the bottom end of the cathode.—In the experiments with shortened cellulose thimbles, outgrowths sometimes appeared at the bottom end of the cathode and along the inner surface of the thimble (see Fig. 5). Evidence was found showing the presence of copper powder inside these fully immersed thimbles, indicating that decreased local turbulence due to reduced convection might be a factor in causing the powder to settle to the bottom. No copper powder

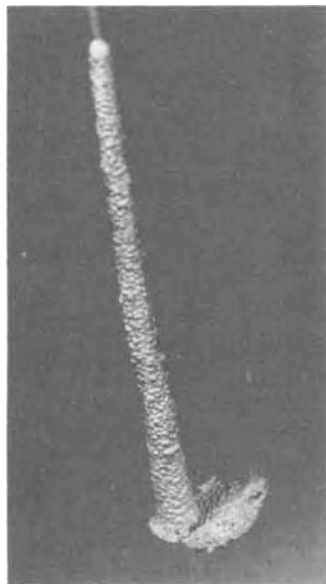


Fig. 5. Cathode growth with short, fully immersed, cellulose thimble, showing effect of settled solid and copper powder. Diameter of bottom outgrowth, 1.3 cm.

was found in any of the full-length thimbles that surrounded the cathode completely, and no such bottom-end growths occurred. Therefore, it seems evident and reasonable that copper powder is a factor in giving rise to the nucleation sites and conducting medium for the bottom outgrowth, if norvaline is present in the solution. It is also evident that a second factor required for the cathode outgrowths, whether at the bottom of a shortened thimble or at the air-solution interface, arises from an oxidation (1) of the norvaline at the anode.⁴ This is indicated by the behavior of the full-length cellulose thimble apparently acting as a barrier against the transport of some active powder-forming and outgrowth-producing agent to the cathode. Moreover, the anode reaction product is probably particulate in form, against which the cellulose can act as an effective and adsorptive screen. More conclusive evidence to support this view follows.

Role of the air-solution interface.—Since the cathode outgrowth along the air-solution interface is caused by effects arising initially at the anode, and since the convection stream is not the means of transport of the active agent to the cathode, experiments were done to test the possibility of transport of particulate material from anode to cathode by a diffusion mechanism operating along the liquid surface. A vertical Parafilm cylinder was used as a surface barrier (see c---c in Fig. 1). Because this cylinder, about 1.5 cm in diameter, extended into the solution to a depth of less than a millimeter, it did not interfere with the normal convection in the cell. It isolated the cathode only along the air-solution interface, and it prevented formation of the interfacial disk. Apart from this there was no other observable effect. The color change to blue-green and the formation of black solid occurred as before.

Obviously, transport of some kind of particulate material occurs along the surface of the solution, from anode to cathode, when norvaline is present during the electrolysis. It seems reasonable that this material is involved in the formation of a conductive film along the air-solution interface such that deposit nucleation can occur, and it is suggested that the interfacial conductivity probably arises from the presence in this film of metallic copper in a highly subdivided state. Copper powder can be expected to form along the

upper part of the cathode, as observed by Ibl (2), and to accumulate in the adjacent air-solution interface.

Material responsible for disk growth.—It was of interest to try to determine whether the color-change effects as well as the solid formed at the anode might be directly involved in the disk formation. Experiments with the cellulose thimbles and the Parafilm surface barriers, as already described, indicate that the material responsible is particulate in form.

It was found that if the suspended solid was removed from the electrolyzed solution by filtration through a fine sintered-glass funnel, and if the blue-green filtrate was then deaerated and electrolyzed under nitrogen, no disk formation occurred. Clearly, the disk-growth process requires the presence of the solid. (It was also found that if such a filtrate is electrolyzed in the presence of air, disk growth occurs after a few hours of such further electrolysis together with formation of more solid.) Other experiments then showed that if the solid obtained by filtering an electrolyzed norvaline solution is added to standard electrolyte containing no norvaline, and if this solution is deaerated and electrolyzed in the absence of oxygen, the interfacial disk is obtained and in a shorter period of time. The same result is obtained if the solid is first produced without electrolysis, that is, by sufficiently prolonged contact of the norvaline-containing electrolyte with air and a copper surface. (Copper turnings were used in these experiments.) Obviously, the dispersed solid is the only factor responsible for the disk growth, to the extent that the anode effects are concerned. The soluble color-affecting reaction products are not directly involved, indicating that the possible presence of dissolved copper-norvaline complexes is not important.

Particulate nature of the disk-forming agent.—A further indication that the material involved in the disk-growth mechanism is particulate in form came about in a different manner. An acid copper sulfate-norvaline solution was first electrolyzed for about 48 hr, during which the air-solution interfacial disk was formed. The electrolysis was then stopped and the system was left undisturbed for about 6 hr. After this period, during which the black solid settled to the bottom of the cell, the circuit was closed again for another 48 hr of electrolysis. The disk at the air-solution interface increased in size, but a second and larger disk now formed at the bottom along the glass-solution interface. A similar result was obtained if the solution was stirred by means of a steady stream of air flowing upward along the anode from a small capillary introduced into the cell. The effect was to decrease considerably the rate of disk formation at the air-solution interface, though not completely, and to cause a relatively rapid disk growth at the bottom end of the cathode (see Fig. 6). Obviously, the air stream causes coagulation and settling of the otherwise suspended solid to form a conducting medium along the bottom of the cell. [It should be noted at this point that a corresponding effect occurs in the disk growth along the upper surface of horizontal Parafilm sheets attached to the cathode at various depths, as observed previously (1), presumably because the solid then settles on these sheets during electrolysis due to reduced convection.]

Role of the anode.—Since the solid formed by air oxidation of norvaline is a primary cause of the disk growth at the cathode, and since this solid originates at the anode, experiments were done to examine the role of the anode in the oxidation mechanism. Variation in the area of anode surface in contact with the solution had no effect on the rate of growth of the interfacial disk, indicating that the oxidation of the norvaline does not occur on the immersed surface of the anode. Experiments were then done with a completely immersed anode, using a shortened copper cylinder such that the upper rim was immersed just below the

⁴ Whatever the detailed nature of the anode reaction, the effects are not stereospecific with respect to the norvaline. Experiments with the D and L forms alone gave the same results as the DL-norvaline routinely employed.

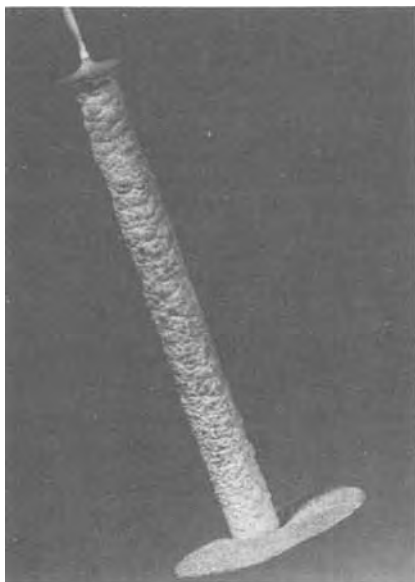


Fig. 6. Copper cathode with small interfacial disk, showing bottom outgrowth due to coagulation of solid by air flow past the anode. Diameter of bottom outgrowth, 1.9 cm.

solution line. No disk formation occurred and no color change or formation of black solid took place. Clearly, the air oxidation of norvaline at the anode occurs only along the line of contact between copper surface, air, and solution.

Dispersed solid and the oxidation reaction.—The results of preliminary and incomplete experiments indicate that a thorough study is required to examine the mechanism of air oxidation of norvaline at a copper surface, including in particular a detailed analysis of the solid and other possible products of the reaction. Roughly quantitative analyses showed that the composition of the solid material, which contains copper, varies from sample to sample. The solid is insoluble in ordinary organic solvents, indicating possibly a polymeric character. It is soluble in concentrated inorganic acids and, apart from a residue identified as copper powder, it dissolves also in dilute aqueous bases. (This evidence of copper powder in the dispersed solid reinforces our suggestion, or assumption, that conductivity of the interfacial film is probably due to metallic copper.) The base-soluble portion undergoes a nonreversible hydrolysis since a regenerated solid obtained on acidification no longer has the same organic composition as the original material. Nor does this regenerated solid have the disk-forming ability, presumably in part because it does not contain copper powder. However, analyses showed that about 30% by weight of the regenerated solid is copper, indicating that at least part of the copper in the original solid is present in combined or complexed form. This copper content, considerably greater than the amount found in the original material, about 5.5%, suggests strongly that the original solid is a mixture rather than a pure compound, with the combined copper presumably complexed in at least one component. Further study of the solid oxidation product was not attempted.

Formation of NH_3 and CO_2 .—Takajama *et al.* (3) have reported that amino acids undergo electrodecomposition to yield an aldehyde of one carbon less together with evolution of NH_3 and CO_2 . The oxidation of norvaline by air or oxygen in our experiments cannot be regarded as an electrodecomposition, since it occurs even in the absence of electrolysis, but it was nevertheless observed that NH_3 and CO_2 were produced, with the NH_3 appearing as ammonium ion in the acid solution. The results of various experiments

are presented here primarily as observations, without attempt at interpretation.

Analyses were done to determine the NH_3 and CO_2 produced as air, and then pure oxygen, was passed slowly through the cell and over the norvaline-containing solution. The NH_3 was determined after electrolysis by a standard Kjeldahl method, and the CO_2 was found by passing the gas stream during electrolysis through a solution of $\text{Ba}(\text{OH})_2$.

The rates of formation of NH_3 and CO_2 , with a given amount of norvaline present, were found to depend on the partial pressure of oxygen above the interface as shown in Fig. 7, the amount of each gas formed being approximately linear with time. It was also found that the rates of formation of NH_3 and CO_2 do not depend on the concentration of CuSO_4 , but that they do depend very markedly on the concentration of acid as shown in Fig. 8. Obviously, the rate of growth of the interfacial disk is correspondingly dependent on the acidity of the solution, and this in fact was observed. The maximum disk growth occurred with $2.5 \times 10^{-2}\text{M}$ norvaline when the H_2SO_4 concentration was about 1.0M. It was found as well that the production of NH_3 and CO_2 does not depend on the current, which is consistent with the observation that formation of the black solid occurs with equal facility in the absence of electrolysis. The reaction requires only an acidified norvaline solution, a copper surface, and air or oxygen at the interface.

It is interesting to note in Fig. 7 that the formation of NH_3 and CO_2 in our experiments does not take place in a one-to-one ratio, as would be the case if Takajama's observation regarding formation of an aldehyde were applicable to our system (3). Our data show that NH_3 and CO_2 are produced in a mole ratio of about four to one when norvaline in acid solution is oxidized by air or oxygen on a copper surface.

Experiments with other compounds.—Numerous experiments were done to see whether compounds other than norvaline are similarly capable of causing formation of the interfacial disk. Compounds structurally

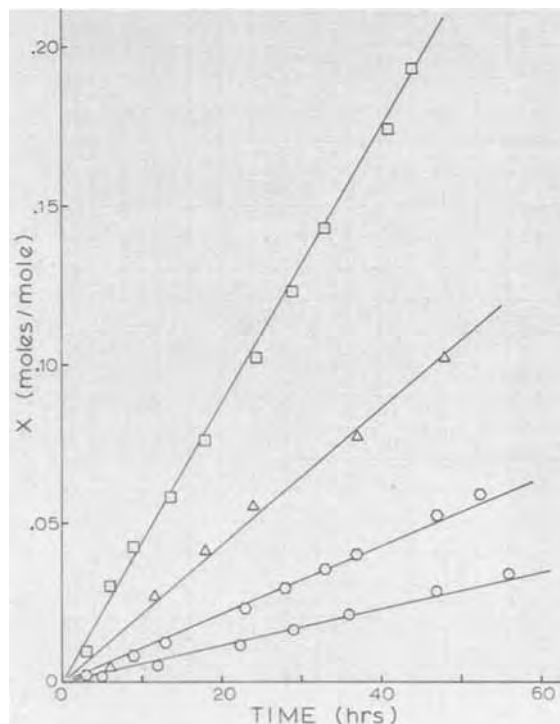


Fig. 7. X moles NH_3 and CO_2 produced per mole of norvaline present vs. time of electrolysis. Initial norvaline concentration, $2.5 \times 10^{-2}\text{M}$; current, 45 mA; temperature, 25°C. ○, CO_2 with air at the interface; ○, CO_2 with O_2 at the interface; △, NH_3 with air at the interface; □, NH_3 with O_2 at the interface.

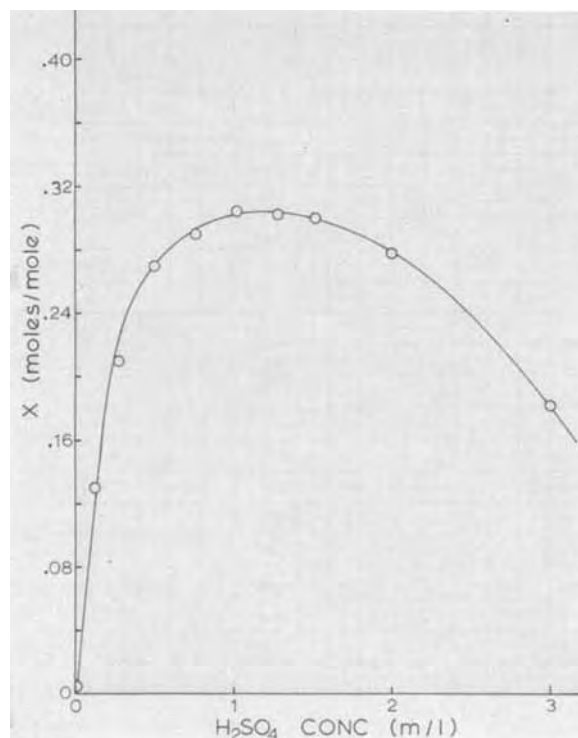


Fig. 8. X moles NH₃ produced per mole of norvaline present vs. molar concentration of H₂SO₄. Initial norvaline concentration, 2.5×10^{-2} M; time, 48 hr; temperature, 25°C.

and constitutionally related to norvaline were chosen. These were: norleucine, leucine, valine, α -aminobutyric acid, β -aminobutyric acid, α -aminooctanoic acid, and N-acetyl norvaline. The concentration of the additive, the acidity of the solution, and the time of electrolysis were all varied, but no condition was found such that disk formation occurred. Qualitative and quantitative tests showed that NH₃ was formed to a greater or lesser degree with all of these compounds, and a change in color of the solution was observed with some of them, particularly with norleucine and with α -aminooctanoic acid. However, unlike norvaline, none of them showed any formation of dispersed solid in observable amount. Obviously, the functional groups are not the only requirement for the formation of the solid and the interfacial disk. The length of the carbon chain appears to be a critical factor in the process.

Summary and Conclusions

1. In the electrolysis of an acid copper sulfate solution with a wire cathode surrounded by a cylindrical copper anode, addition of a small amount of norvaline causes a disk-shaped outgrowth to form on the cathode and along the air-solution interface.

2. The primary cause of this interfacial outgrowth is a solid oxidation product arising from reaction of the dissolved norvaline with air or oxygen at a copper surface, in this case the anode. Dissolved reaction products are not involved.

3. During the electrolysis, oxidation of the norvaline occurs only along the line of contact between copper anode, air, and solution.

4. Transport of the solid oxidation product from anode to cathode takes place by surface diffusion along the air-solution interface.

5. Cathode outgrowths can be produced along the bottom of the electrolysis cell by causing the otherwise suspended solid to settle.

6. Evidence of copper powder at the bottom of the cell in some experiments, and evidence of a copper-powder residue left on dissolving the solid reaction product in dilute bases, indicates that formation of the interfacial cathode outgrowths probably involves copper powder as a conducting medium.

7. In a group of eight structurally related amino acids, all examined under similar electrolytic conditions, only norvaline produced the interfacial cathode outgrowths.

Acknowledgments

Financial support from the National Research Council, Ottawa, in the form of a research grant, and also in the form of a scholarship to R.A.D., is gratefully acknowledged.

Manuscript submitted May 31, 1973; revised manuscript received July 29, 1974.

Any discussion of this paper will appear in a Discussion Section to be published in the December 1975 JOURNAL. All discussions for the December 1975 Discussion Section should be submitted by Aug. 1, 1975.

Publication costs of this article were partially assisted by the University of Western Ontario.

REFERENCES

1. A. J. Sukava, W. J. Newby, *et al.*, *Nature*, **220**, 574 (1968).
2. N. Ibl, *Helv. Chim. Acta.*, **37**, 1149 (1954).
3. Y. Takajama, T. Harada, and S. Miduno, *Bull. Chem. Soc. Japan*, **12**, 342 (1937).

Electrodeposition along the Air-Solution Interface

II. Metallographic Study

J. M. Trenouth,¹ R. A. Dilorio,² and A. J. Sukava*

Department of Chemistry, University of Western Ontario, London, Ontario, Canada

ABSTRACT

A metallographic examination was made of a cathode deposit formed along the air-solution interface of an acid copper sulfate electrolyte containing a small amount of norvaline. The photomicrographs indicate initial nucleation at the interface, presumably along a preexisting conductive film, followed by growth of the deposit downward toward the solution. No evidence was found of growth cones extending radially and horizontally from the cathode and along the interface.

The preceding paper (1) describes the results of some experiments on the mechanism by which a small amount of norvaline added to an acid copper sulfate electrolyte causes the cathode deposit to grow preferentially along the air-solution interface when electrolysis occurs with a wire cathode and a cylindrical copper anode. It is speculatively suggested that this particular form of electrodeposition occurs as a consequence of a conductive film formed along the surface of the solution. This film is thought to contain copper powder formed at the cathode, thus giving rise to initial deposit nucleation at or near the cathode but along the liquid surface.

The details of the growth habit of the interfacial disk are not revealed by the chemical investigation described in Part I (1). Moreover, it is not clear whether the assumed conductive film can be regarded as a pre-existing condition followed by the observed downward thickening of the interfacial deposit, due to nucleation only along its lower face, or whether a preferred horizontal growth occurs outwardly and radially from the cathode, along the air-solution interface, prior to the downward growth. To attempt a further elucidation of the mechanism, a brief metallographic examination of the interfacial deposit was carried out as part of the investigation. For this purpose, photomicrographs of deposit cross sections were produced and examined by one of us (J.M.T.) at the Structures and Materials Laboratory, National Aeronautical Establishment, National Research Council, Ottawa. The results are reported in this paper.

Specimen Preparation

Typical cathode deposits with the interfacial outgrowth were prepared as described in Part I (1). Various cross sections were then made for metallographic study, using standard techniques. Referring to Fig. 1a and b, longitudinal sections were made of the wire cathode and deposit in the region at the solution line and at the bottom end. A transverse section, made approximately midway, is represented in Fig. 1c. For the specimen examined, the interfacial disk-shaped deposit was detached readily from the electrode intact, enabling a separate cross section to be made of it as indicated in Fig. 2.

After sectioning, all specimens were coated with electroless nickel plating to preserve specimen edges and to prevent their rounding during subsequent grinding and polishing. All specimens were etched after polishing with either of the solutions A or B (Table I).

* Electrochemical Society Active Member.

¹ Present address: Structures and Materials Laboratory, National Aeronautical Establishment, National Research Council, Ottawa, Ontario, Canada.

² Present address: Colonel By Secondary School, Ottawa, Ontario, Canada.

Key words: interfacial disk, photomicrographs, growth cones, cone orientation.

Table I. Polishing solutions

Solution A	
H ₂ SO ₄ (conc)	1 mliter
H ₂ O ₂ (10%)	20 mliters
Followed by	
SnCl ₂ · 2H ₂ O	0.5g
CuCl ₂ · 2H ₂ O	1.0g
FeCl ₃ · 6H ₂ O	30.0g
HCl (conc)	42 mliters
C ₂ H ₅ OH	500 mliters
H ₂ O	500 mliters
Solution B	
H ₂ SO ₄ (conc)	1 mliter
H ₂ O ₂ (10%)	20 mliters
H ₂ O	21 mliters

Results and Discussion

Normal deposit.—The longitudinal and transverse sections of the electrode in Fig. 1, photographed under plane polarized light, show the wire with the copper deposit as it is normally formed. A variation in the structure of the deposit from the original substrate to the outer surface is evident, the deposit near the substrate having a columnar or conelike structure of the field-oriented type and that near the outer surface having an unoriented-dispersion type of structure. The crystallinity of the outermost deposit in this specimen is also considerably coarser than that near the original wire. These structural variations are presumably the result of a combination of factors including the gradu-

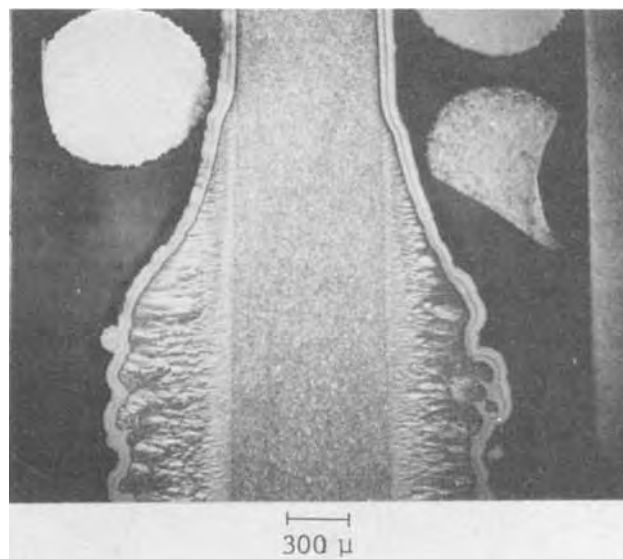


Fig. 1a. Longitudinal cross section of wire cathode and deposit at the solution line. Interfacial disk removed.

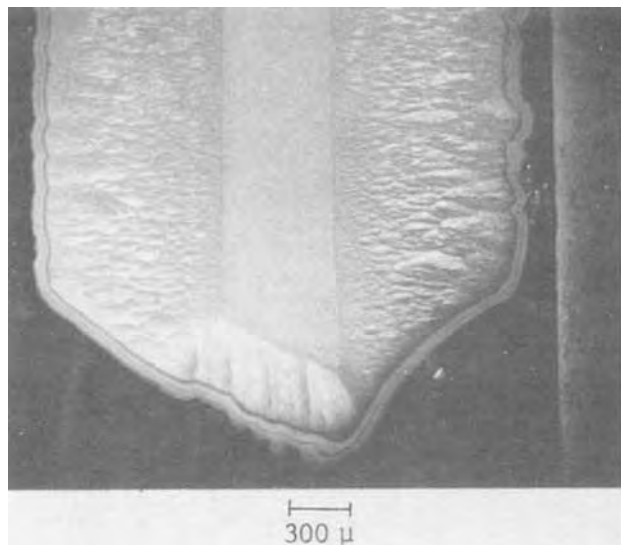


Fig. 1b. Longitudinal cross section of bottom end of wire cathode and deposit, showing vertical and horizontal growth cones.

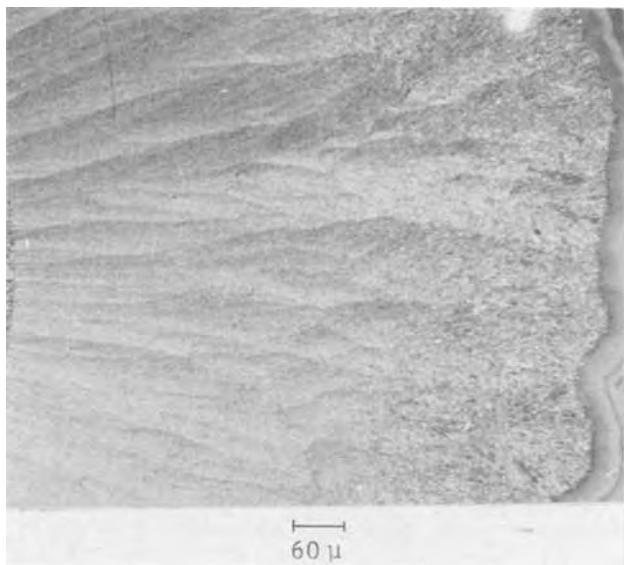


Fig. 1c. Transverse cross section of cathode deposit midway between solution line and bottom end. Part of the cathode wire substrate is visible on the left.

ally decreasing current density with increasing cathode area under constant current flow [see Part I (1)] and the presence of adsorbed components of the solution affecting the growth habit. These features were not always observed, however. In another specimen, the oriented columnar structure extended all the way to the outer surface, but only along the upper part of the cathode. The lower region showed a transition to the unoriented structure similar to Fig. 1. Examination showed that the oriented and unoriented internal structures are associated with relatively smooth and rough external surfaces, respectively.

The columnar structure evident in the longitudinal view in Fig. 1b is of particular interest in that it shows a discontinuity in direction of the growth cones at the bottom end of the electrode. The longitudinal section at the solution line where the interfacial disk was originally attached (Fig. 1a) showed only the horizontal columnar feature.

The conelike structure noted in all the sections of the deposit appears to be identical with that of vapor-deposited silicon carbide (2) and pyrolytic graphite

(3, 4). The growth cones are all of the continuously nucleated type shown schematically in Fig. 12 of Ref. (3) and as an actual deposit in Fig. 2B of Ref. (2). In the case of pyrolytic graphite, such continuous nucleation has been attributed to relatively large agglomerations of carbon being deposited with much finer particles (3). However, unlike the vapor deposits, the growth cones at the bottom end of the copper electrode shown in Fig. 1b are parallel with the axis of the electrode rather than perpendicular to the surface of deposition, and in place of continuous radiation of deposit around the corners at the electrode tip, there is an abrupt change from horizontal to vertical growth. If the direction of growth of the cones in the electrode deposit follows current flow lines as indicated by the deposit in Fig. 1c and that along the axis of the electrode in Fig. 1a and b, then the deposit at the electrode tip implies a discontinuous pattern of current flow lines at the corners of the tip.

Deposit at the air-solution interface.—In several instances, the interfacial disk-shaped deposit was only loosely held to the wire cathode, as was evident in its easy detachment enabling it to be lifted off along the wire. This suggests a primarily mechanical contact between the disk and the electrode rather than the presence of actual chemical bonds of the normal metallic type, as might be expected if the disk growth occurs and originates from a preexisting conductive surface film. On the other hand, it might be possible, although it appears less likely, that a thin or brittle interfacial deposit actually bonded to the wire at the meniscus could also result in the observed easy detachment of the disk.

The cross section of the interfacial disk shown in Fig. 2 reveals a columnar or conelike structure in all regions. This is just visible in the low-power micrograph of Fig. 2a taken in ordinary illumination but more clearly revealed when examined in polarized light and under greater magnification as shown in Fig. 2b and c. An enlarged view of one of the wings of the deposit is shown under ordinary illumination in Fig. 2d, slightly defocused to bring out the obvious laminar pattern in the deposit. The similarity of the structure of this copper deposit with those of silicon carbide (2) and pyrolytic graphite (3, 4) is apparent not only with respect to the growth cones perpendicular to the substrate surface but also with respect to the laminar pattern. The heavy line running midway through the deposit in Fig. 2d was probably caused by a current interruption leading to a discontinuity in the deposition process.

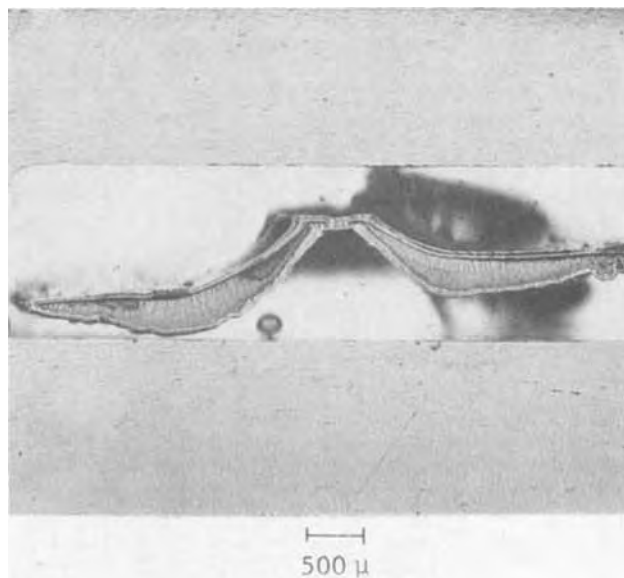


Fig. 2a. Vertical cross section of interfacial disk

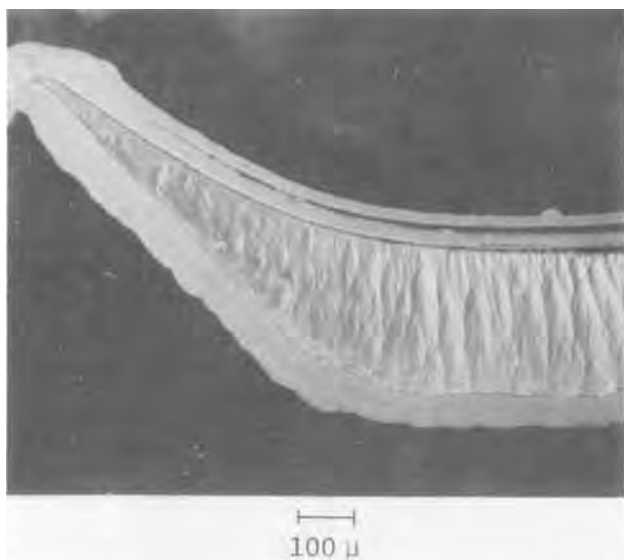


Fig. 2b. Vertical cross section of one wing of the interfacial disk under polarized light.

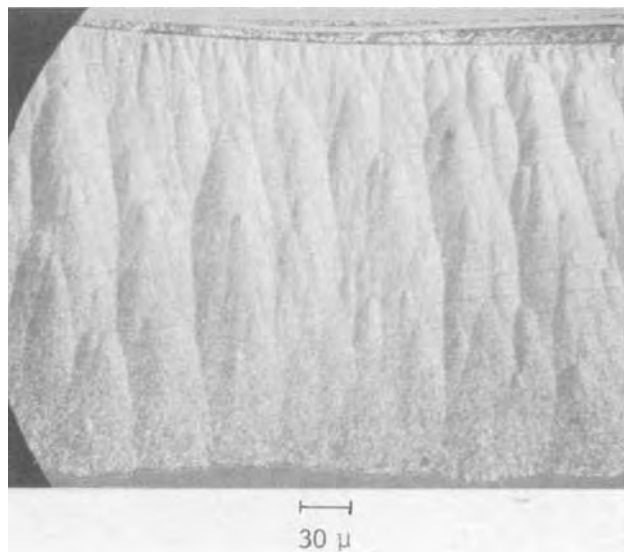


Fig. 2c. Vertical cross section of interfacial disk. Enlarged view under polarized light, showing columnar structure.

The orientation of the growth cones in the interfacial disk shown in Fig. 2 indicates that nucleation occurred at the surface of the electrolyte, along the air-solution interface. Growth perpendicular to this interface took place at all times, even within the meniscus. There is no evidence in the photomicrographs to indicate nucleation at the surface of the wire electrode with growth radiating out along the air-solution interface and perpendicular to the electrode axis. In fact, examination of Fig. 1a shows that the normal horizontal growth cones on the electrode just below the meniscus are prevented from continued growth by the downward-growing interfacial disk. Furthermore, the photomicrograph of the bottom end of the cathode in Fig. 1b seems to indicate that growth cones normally develop in a fixed orientation determined by the manner in which the growth begins, and that this orientation continues with the new cones as the deposit grows in a lateral direction. Presumably, the growth pattern of the interfacial disk is no exception.

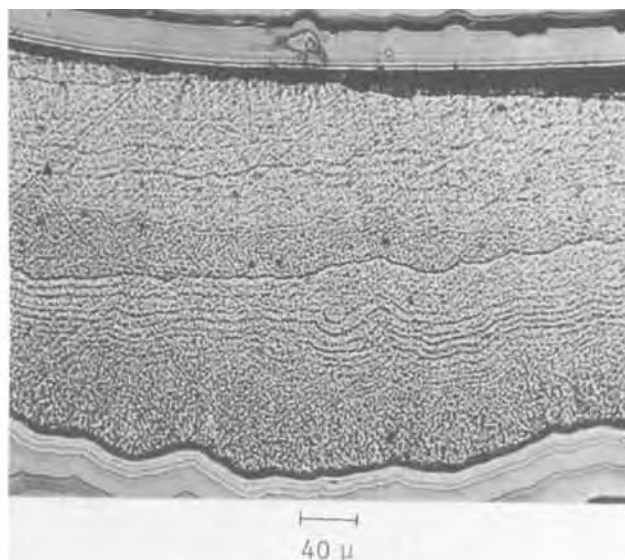


Fig. 2d. Vertical cross section of interfacial disk under ordinary illumination, showing laminar pattern.

Summary and Conclusions

1. Metallographic examination of cross sections of copper deposits formed at the cathode and along the air-solution interface, and caused by small amounts of norvaline in the acid copper sulfate electrolyte, shows growth cones extending downward from the interface into the solution.

2. The downward orientation of the growth cones, with no evidence of horizontal growth cones at the air-solution interface near the cathode, supports the view that deposit nucleation occurs at the liquid surface and that a conductive surface film is probably present as a preexisting condition for the nucleation.

3. The assumed conductivity of the interfacial film is considered to arise from the presence of copper powder formed at the cathode, in conjunction with reaction products arising from oxidation of the norvaline at the copper anode (1).

4. The disk-shaped deposit was sometimes easily detached from the cathode by lifting off along the wire, indicating mainly a mechanical contact with no particular metallic bond between the disk and the cathode wire. This is consistent with downward growth of the disk from a preexisting conductive surface film.

Acknowledgments

The financial support of the National Research Council, Ottawa, the use of the facilities of the Structures and Materials Laboratory, National Aeronautical Establishment, National Research Council, Ottawa, and, in particular, the preparation of the metallographic specimens by Mrs. Mary Grzedzielski, are all gratefully acknowledged.

Manuscript submitted May 31, 1973; revised manuscript received July 29, 1974.

Any discussion of this paper will appear in a Discussion Section to be published in the December 1975 JOURNAL. All discussions for the December 1975 Discussion Section should be submitted by Aug. 1, 1975.

Publication costs of this article were partially assisted by the University of Western Ontario.

REFERENCES

1. R. A. DiIorio, W. J. Newby, and A. J. Sukava, *This Journal*, **122**, 37 (1975).
2. T. D. Gulden, *J. Am. Ceram. Soc.*, **51** (8), 424 (1968).
3. L. F. Coffin, Jr., *ibid.*, **47** (10), 473 (1964).
4. S. Yajima and T. Hirai, *J. Mater. Sci.*, **4** (5), 416 (1969).

Electrode Kinetic Studies on Electro-organic Syntheses Involving Carbonium Ions

II. Anodic Oxidation of Acetate Ions in Presence of Dimethylformamide

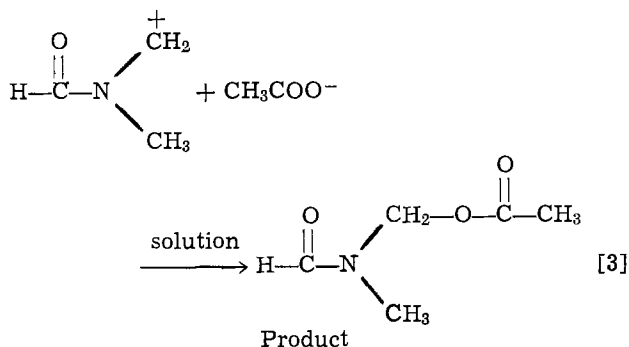
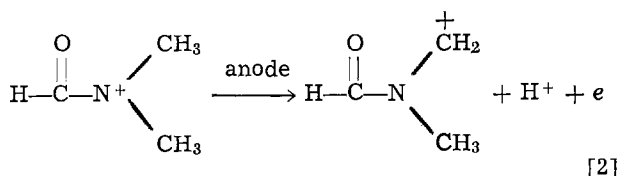
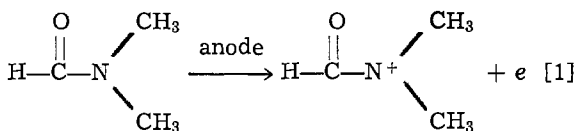
G. Bélanger,* C. Lamarre,* and A. K. Vijh*

Hydro-Quebec Institute of Research, Varennes, Quebec, Canada

ABSTRACT

The anodic oxidation of acetate ions in (nominally nonaqueous) glacial acetic acid and in glacial acetic acid-dimethylformamide solutions has been examined on platinum at various temperatures between 25° and 75°C. Potentiostatic and potentiodynamic techniques were used in conjunction with reaction product analysis by infrared and NMR. The real heat of activation at the reversible potential for the Kolbe reaction in glacial acetic acid is 53 kcal mole⁻¹. Also, acetate ions can undergo oxidation at low potentials (e.g., 0.45V vs. RHE) when the reaction is carried out at a high temperature (ca. 75°C). The oxidation of DMF is indicated around 1.1-1.5V at temperature above 55°C, both in potentiostatic and potentiodynamic profiles. The product analysis shows that oxidation of DMF also occurs at high potentials (e.g., 2.37V) in parallel to the Kolbe reaction. The product of DMF oxidation at this potential is N-acetoxymethyl N'-methylformamide; the coulombic efficiency for the formation of this product at 2.37V is about 5%.

In the first report (1) in this series of publications, anodic oxidation of acetate ions to methyl acetate, on a graphite electrode, was examined from an electrode kinetic point of view. The purpose of the present work was to investigate some aspects of the anodic oxidation of acetate ions in acetic acid in the presence of dimethylformamide (DMF) on a smooth platinum electrode. This has already been examined from a synthetic point of view by Ross (2) who suggests that the following reactions can occur



Recently, Ross *et al.* (3) have also reported some current potential studies, both steady-state and cyclic voltammetric, on the above system. The present work explores these electrode kinetic aspects in somewhat more detail, especially with regard to the effect of temperature on the reaction. In order to obtain this information, it was necessary also to investigate the tem-

perature effects on the oxidation of the acetate ions themselves, which has been examined previously only quite briefly (4).

Experimental

All experimental details except the following have been described recently (1).

Smooth platinum wires, sealed into Pyrex in open flame with subsequent thorough cleaning were used as the working electrodes. The platinum wire was 99.999% pure and was supplied by the Engelhard Industries Ltd. The DMF was Baker analyzed reagent.

The steady-state current-potential relationships were recorded by the automatic procedure described previously (5). All potential values refer to the hydrogen electrode in the same solution and are designated by the symbol, E_H .

Although the usual precautions to eliminate moisture from the acetate/acetic acid solutions were taken, the solutions must be presumed to contain traces of water since the experiments were not conducted in a controlled-atmosphere chamber.

For the analysis of reaction products, a large smooth platinum foil (10 cm²) was used for the galvanostatic electrolysis of a 1M DMF plus 1M potassium acetate in glacial acetic acid solutions. The current density used was 1.5 mA/cm² and the electrolysis was carried out for 5 days at 78°-79°C. The product was isolated and identified from its infrared and nuclear magnetic resonance (NMR) spectra by comparing with a known product synthesized chemically by the acetylation of N-hydroxymethyl N'-methylformamide, prepared as described previously (6).

Results and Discussion

Temperature effects in the anodic oxidation of acetate ions.—In Fig. 1, potentiostatic, steady-state current-potential curves for the anodic oxidation of 1M CH₃COOK in acetic acid at smooth platinum are presented for various temperatures. Although steady-state polarization curves were conducted at several temperatures for the determination of ΔH^* values (Fig. 2), the various Tafel plots shown in Fig. 1 and 4 depict only a few representative temperatures in order to avoid cluttering. These curves were corrected graphically for the iR drop. At the higher anodic potentials, there is little hysteresis between the ascending and descending curves. From these corrected current-

*Electrochemical Society Active Member.

Key words: Kolbe reaction, carbonium ions, electrosyntheses, DMF electro-oxidation, heat of activation.

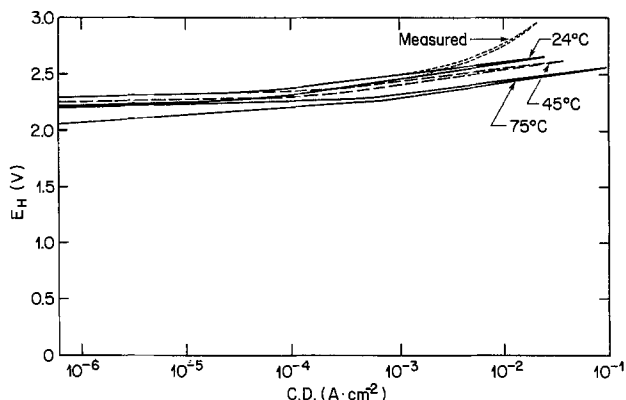


Fig. 1. Steady-state, potentiostatic current-potential relationships on smooth platinum in 1M CH₃COOK in CH₃COOH, at the shown temperatures. These curves were corrected for the ohmic drop in the solution. The 24°C curve illustrates the current-potential behavior with and without the ohmic corrections.

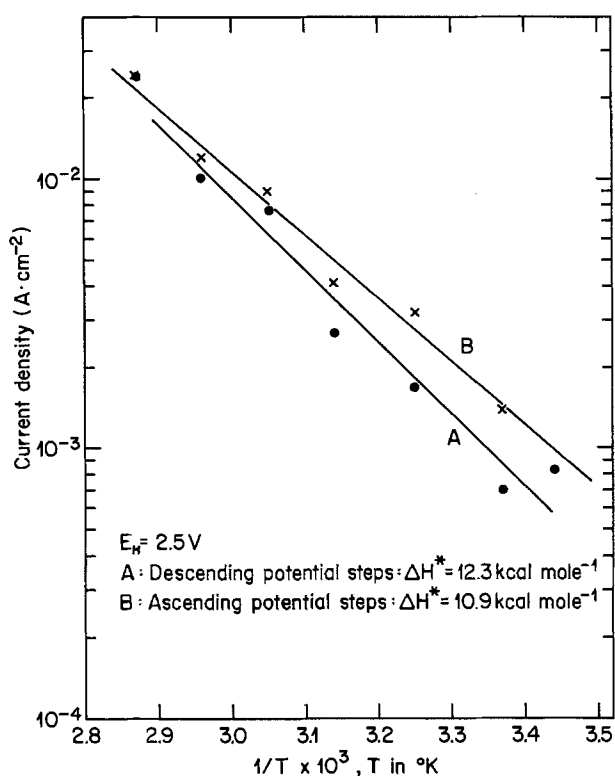


Fig. 2. Plots for the determination of ΔH^* , i.e., $(\partial \log i / \partial (1/T))_{E_H}$ values as deduced from the data in Fig. 1.

potential relationships, a Tafel correlation can be observed for at least two decades. In Table I, we present the experimental values of Tafel slopes and the transfer coefficient β for various temperatures. The latter is constant within the experimental error. The b values

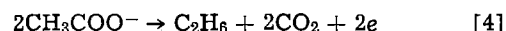
Table I. Tafel slopes in 1M CH₃COOK in glacial acetic acid solutions

Temp., °C	Ascending potential steps		Descending potential steps	
	b (exp), mV	β^*	b (exp), mV	β^*
24	150	0.39	125	0.47
35	140	0.44	105	0.58
45	135	0.47	113	0.55
55	150	0.43	118	0.55
65	150	0.45	133	0.50
75	137	0.50	125	0.55
	Avg: 0.45 ± 0.04		Avg: 0.53 ± 0.04	

* $\beta = 2.303RT/bF$.

for the ascending potential steps are greater than $2RT/F$. This high value of the Tafel parameter has also been observed for the Kolbe reaction (7) at low temperatures (25°C) and was accounted for by a barrier-layer film mechanism (7).

The apparent heat of activation ΔH^* can be evaluated from the log current density vs. $1/T$ relationships for a given potential as illustrated in Fig. 2. The slopes as obtained from a least square deviation treatment of the data give value of 11-12 kcal mole⁻¹ for the ΔH^* . This heat of activation does not, of course, refer to the value at the reversible potential for the over-all reaction of acetate oxidation



The apparent heat of activation at a given potential, ΔH^* , is related to the apparent heat of activation for the reaction at the reversible potential, ΔH^*_r , by the equation

$$\Delta H^*_r = \Delta H^* + \beta\eta F \quad [5]$$

where η is the value of the overpotential at which the ΔH^* value has been determined. The reversible potential for the acetate oxidation (i.e., Eq. [4]) in glacial acetic acid is $-1.05V$ (with reference to the reversible hydrogen electrode) (7). If the anodic oxidation of acetate, and hence the determination of ΔH^* is done at 2.5V (vs. RHE), as in Fig. 2, the value of the overpotential, η , becomes 3.55V for this case. By using this value of η and the experimental values of ΔH^* (at 2.5V) and β in Eq. [5], one obtains the value of $\Delta H^*_r \approx 47$ kcal mole⁻¹. This is the value of the heat of activation which is relevant to the process in reaction [4] since it refers to the reversible potential. Alternatively, one could have obtained the same value by determining the exchange current density, i_0 , values at various temperatures and then plotting $\log i_0$ vs. $1/T$; however, extremely long extrapolations needed to obtain i_0 values for the present case would make the values thus determined meaningless. The only approximation involved in our determination of ΔH^*_r value, as outlined above, is that the value of β is constant at various temperatures studied. Although the values of β in Table I are not exactly constant, they do not show a systematic variation with temperature and hence must be attributed to a normal scatter of experimental data within a fairly narrow range from which a mean constant value of β may be deduced, as in our calculation.

It is interesting to point out that from the value of the apparent heat of activation at the reversible potential, ΔH^*_r , one can estimate the real heat of activation, ΔH^*_R , for the Kolbe reaction in nonaqueous medium, i.e., for the reaction in Eq. [4]. This real heat of activation is given as (10)

$$\Delta H^*_R = \Delta H^*_r + \beta \Delta H^\circ$$

where ΔH° is the heat of the Kolbe reaction (Eq. [4]). This latter thermodynamic quantity has to be estimated from the heats of formation of CH_3COO^- solvated, C_2H_6 gas, and CO_2 gas. The last two quantities are available in standard handbooks. The value of the heat of formation of acetate ion in acetic acid has to be approximated to its value in aqueous solution which is -116.84 kcal mole⁻¹ (11). The validity of this approximation can be based on the near equality of free energy of formation of acetic acid in aqueous solution and its value in glacial acetic acid (7): the difference between these values is less than 4 kcal mole⁻¹. Since the heat of formation of the proton is defined as zero, one feels that the approximation for the ΔH° is sound. The ΔH° so obtained is equal to 13 kcal mole⁻¹ with an uncertainty of ± 5 kcal mole⁻¹ arising from the above assumption. Using the experimentally determined $\beta(0.45)$, the real heat of activation at the reversible potential, ΔH^*_R is estimated at 53 kcal mole⁻¹ with an estimated error of ± 3 kcal mole⁻¹.

It should be pointed out that the extremely high ($53 \text{ kcal mole}^{-1}$) value of ΔH^*_R for the Kolbe reaction (i.e., Eq. [4]) is consistent with other features of this reaction (7, 8) such as: very low exchange current densities, extremely high overpotentials needed to obtain a given rate of reaction, filming of the electrode and hence increase in the reaction resistance during the course of the reaction. No previous data, it is believed, are available for comparing the magnitude of our ΔH^*_R values.

An interesting temperature effect arises in the potentiodynamic profiles (Fig. 3). At a comparable sweep rate, the potentiodynamic profile at 75°C shows an additional anodic peak around 0.45V , which is not observed in the experiments carried out at a much lower temperature (24°C).

The appearance of the new anodic peak indicates that at high temperatures, a noticeable surface reaction between the surface oxides and the adsorbed organic (or its intermediates) occurs giving rise to the new anodic peak at 0.45V . This peak is similar to the one observed in the electrooxidation to CO_2 of other organic fuels, e.g., HCOO^- (9). This assignment of the peak would be consistent with the fact that at high temperatures, complete oxidation of the acetate ions to CO_2 does indeed occur at potentials below ca. 0.7V (4).

It has been observed that the peak at 0.45V appears only at low sweep rates (e.g., 50 mV sec^{-1}) whereas it tends to disappear at higher sweep speeds (e.g., 343 mV sec^{-1}). This would suggest that at faster sweep rates, the surface reaction between the oxide and the adsorbed organic does not have sufficiently long opportunity to pass enough charge needed to give rise to a pronounced anodic current peak.

Temperature effects in the anodic oxidation of acetate ions and DMF.—In the potentiostatic, steady-state current-potential curves (Fig. 4) obtained at various temperatures, it is observed that at potentials above 2.1V (i.e., at which the Kolbe reaction commences), there is little difference in the behavior in the presence or absence (Fig. 1) of DMF. At lower potentials, however, at temperature above ca. 55°C , new features appear which are presumably associated with the oxidation of DMF. The oxidation of DMF between 1.1 to 2.0V approximately, at 55°C and above, is suggested by

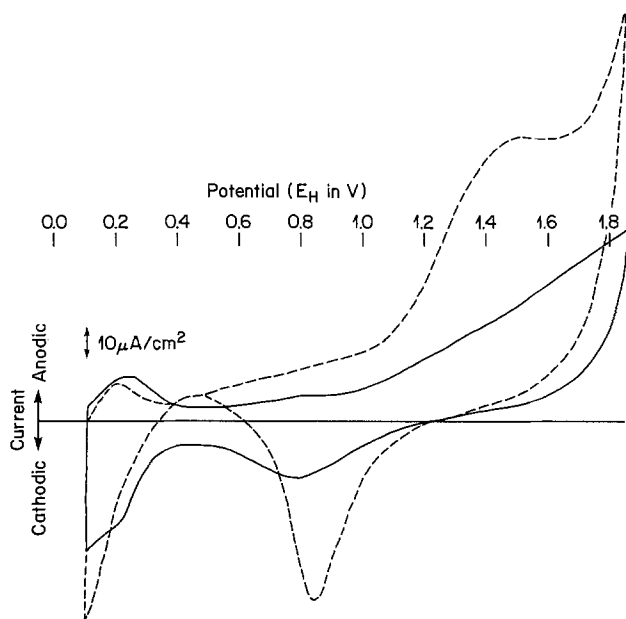


Fig. 3. Potentiodynamic profiles on smooth platinum in $1\text{M CH}_3\text{COOK}$ in CH_3COOH (also containing, presumably, traces of water). The solid line refers to the profile at 25°C whereas the dashed line is for 75°C . The new anodic peak around 0.45V may be noted at 75°C (sweep rate, 50 mV sec^{-1}).

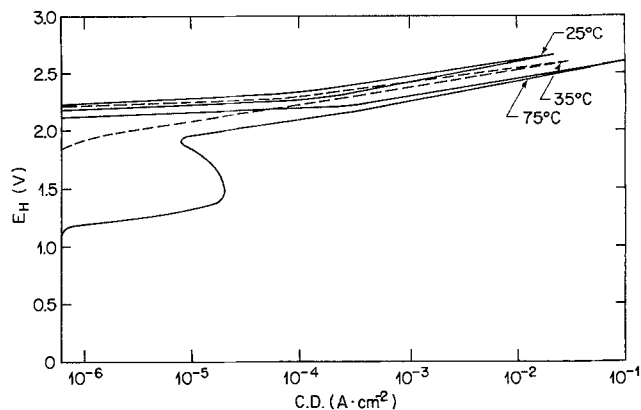


Fig. 4. Same as in Fig. 1 but now the solution made 1M in DMF

the new current inhibition regions appearing in Fig. 4. This type of inhibition inflections are not uncommon for electro-organic oxidations and have been discussed previously by Bagotskii (12), Conway and Gilroy (13), and others (14). The ΔH^* values for the DMF oxidation cannot be determined because of the absence of well-defined Tafel lines, at several temperatures, pertaining to the DMF oxidation (i.e., at potential below 2.0V). The ΔH^* values deduced from the Tafel lines (above 2.1V) in Fig. 4 are comparable to those obtained from Fig. 1 suggesting thereby that at high anodic potentials oxidation of the acetate is the predominant reaction even in the presence of DMF.

There are some pronounced effects of temperature on the potentiodynamic profiles obtained in solutions containing DMF (Fig. 5). At 25°C there is virtually no difference between this solution containing DMF and the profile obtained for potassium acetate in acetic acid. At 75°C , one clearly observes detailed structure in the profile, including the anodic peak around 0.5V . The

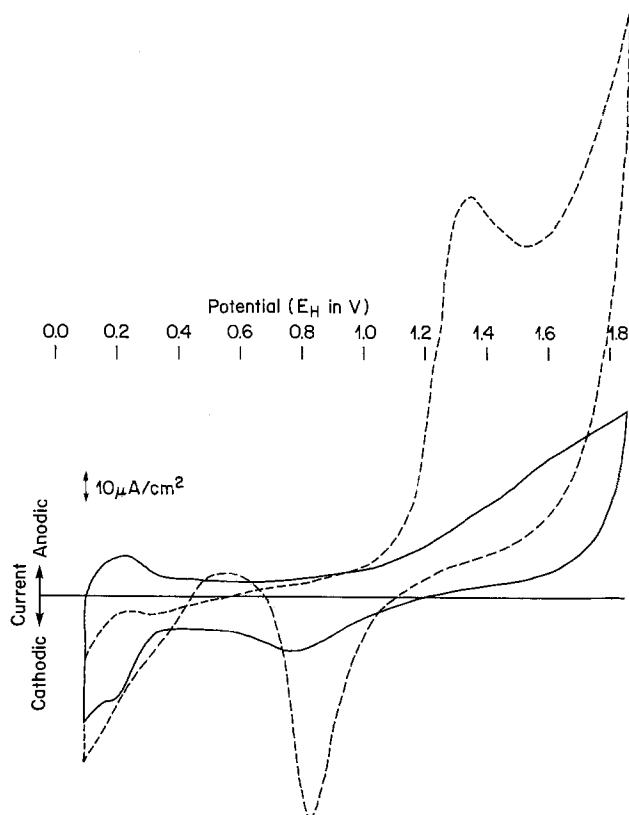


Fig. 5. Potentiodynamic profiles on smooth platinum in $1\text{M CH}_3\text{COOK}$ in CH_3COOH to which 1M DMF has been added. The solid profile is for 25°C whereas the dashed one is at 75°C (sweep rate, 50 mV sec^{-1}).

Table II. Tafel slopes in 1M CH₃COOK + 1M DMF in glacial acetic acid solutions

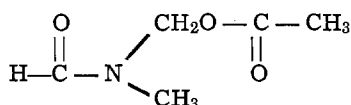
Temp, °C	Ascending potential steps		Descending potential steps	
	b (exp), mV	β	b (exp), mV	β
25	157	0.38	165	0.36
35	163	0.37	125	0.49
45	163	0.39	125	0.50
55	163	0.40	130	0.50
65	175	0.38	150	0.45
75	175	0.39	163	0.42
		Avg: 0.38 ± 0.01		Avg: 0.45 ± 0.06

peak at 1.35V is perhaps associated with the oxidation of DMF and the one at 0.55V may be attributed to the oxidation of acetate and of a product of the DMF oxidation.

This last hypothesis is confirmed by the fact that the peak at 0.5V increases in magnitude as the number of scans increases, and, as a function of time as shown in Fig. 6. This time effect is more pronounced in the presence of DMF than in the acetate-acetic acid solution. The increase in the anodic current at 0.5V, 1.3V, and higher potentials is concomitant with the diminution in the size of the oxide reduction peak at 0.85V; this oxide peak presumably originates from the presence of traces of water in the solution. The nature of the oxidized species at 0.5V cannot be ascertained but it could be an oxidation current of a byproduct of the DMF oxidation. The increase in current with time could indicate an accumulation of this byproduct in the solution. As the temperature is decreased to 25°C, after several potentiodynamic scanning experiments at 75°C, the peak at 0.5V is still observed which would confirm the suggestion of byproduct accumulation. Such evidence for the formation of this byproduct was not observed in the absence of DMF. For the acetate-acetic acid solution containing no DMF, the profiles at 25°C were identical in fresh solutions and in solutions in which experiments had already been conducted at 75°C.

The Tafel parameters determined from the upper (above 2.0V) part of the steady-state polarization curves are shown in Table II. The Tafel slopes are somewhat larger than those in the absence of DMF. In the potential range in which the reaction products can be practically determined (*i.e.*, the Tafel region), the Kolbe reaction proceeds with the simultaneous oxidation of DMF that could perhaps influence the Tafel slopes (see below).

The product isolated from the reaction solution after the galvanostatic electrolysis, was identified as N-acetoxymethyl N'-methylformamide



The refractive index, the infrared spectrum (2), and the NMR spectrum were identical with those for the same product synthesized by the acetylation of N-hydroxymethyl-N' methylformamide. The coulombic efficiency, assuming a two-electron process was found to be 5.2%. The main reaction at the potential of electrolysis (2.37V) is the Kolbe reaction. This confirms the results obtained by Ross *et al.* (3) where similar results were obtained at 25°C.

It may be added that in the anodic or cathodic charging curves triggered from the rest potentials (around 1.0V), in solutions containing DMF, no arrests were observed. This would indicate an absence of electroactive (*i.e.*, which can be deposited on, or stripped off from, the electrode in a transient) adsorbed species. Similarly, no arrests or inflections were observed in the fast (time of decay less than 1 sec) open-circuit potential decay profiles taken from various anodic potentials. In the slow (time of decay of

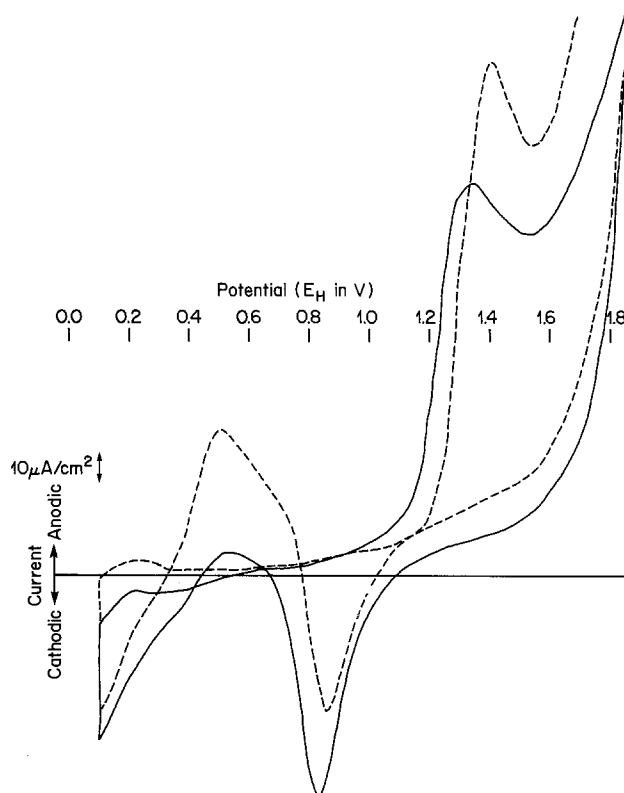


Fig. 6. Time effect for a 1M DMF and 1M CH₃COOK in CH₃COOH ($T = 75^\circ\text{C}$; sweep rate = 50 mV sec⁻¹). Curve B, (dashed profile), 5 single sweeps after curve A (solid profile) and 1 hr interval between these two curves.

the order of 1 min) open-circuit decay profiles, an "arrest" characteristic of the presence of a "depolarizer" was, however, observed in solutions with or without DMF. The "depolarization" effect must be associated with the relatively slow adsorption (or desorption) of intermediates (*e.g.*, traces of CH₃OH) that might be produced in an electro-oxidation such as the present one. It is obvious that open-circuit profiles such as these cannot be subjected to a meaningful analysis and are hence not shown here.

Conclusions

1. The apparent and the estimated real heats of activation (at the reversible potential) for the Kolbe reaction in acetate-glacial acetic acid solutions are 47 and 53 kcal mole⁻¹, respectively.
2. At temperatures above 55°C, the acetate ions tend to undergo anodic oxidation at potentials as low as 0.45V (RHE).
3. In the steady-state polarization curves of acetate-acetic acid-DMF solutions at smooth platinum, DMF undergoes oxidation between 1.1 and 1.5V at high temperatures (*e.g.*, 75°C). This behavior is also confirmed in the potentiodynamic profiles.
4. From the product analyses (which had to be carried out at high potentials in order to obtain reasonably high rates) at 2.37V, it is indicated that the oxidation of DMF proceeds parallel to the Kolbe reaction with a coulombic efficiency of the former equal to about 5%.

Acknowledgments

Thanks are due to Mr. Réal Jacques for his skillful contributions to the experimental manipulations, Mr. Yves Giguère for infrared analyses, Dr. Yvon Pépin, Chemistry Department, Université du Québec, at Montréal, for NMR analysis, and Mr. A. Bélanger for helpful discussions.

Manuscript submitted April 11, 1973; revised manuscript received Aug. 26, 1974.

Any discussion of this paper will appear in a Discussion Section to be published in the December 1975 JOURNAL. All discussions for the December 1975 Discussion Section should be submitted by Aug. 1, 1975.

Publication costs of this article were partially assisted by Hydro-Quebec Institute of Research.

REFERENCES

1. A. K. Vijh, *This Journal*, **119**, 679 (1972).
2. S. D. Ross, *Trans. N. Y. Acad. Sci., Series II*, **30**, 901 (1968); S. D. Ross, M. Finkelstein, and R. C. Petersen, *J. Am. Chem. Soc.*, **86**, 2745 (1964); **88**, 4657 (1966); *J. Org. Chem.*, **31**, 128 (1966).
3. E. J. Rudd, M. Finkelstein, and S. D. Ross, *J. Org. Chem.*, **37**, 1763 (1972).
4. D. F. A. Koch and R. Woods, *Electrochim. Acta*, **13**, 2101 (1968).
5. G. Bélanger, *This Journal*, **118**, 583 (1971).
6. C. H. Bramford and E. F. T. White, *J. Chem. Soc.*, **1959**, 1860.
7. A. K. Vijh and B. E. Conway, *Chem. Rev.*, **67**, 623 (1967).
8. B. E. Conway and A. K. Vijh, *Z. Anal. Chem.*, **224**, 149 (1967).
9. B. E. Conway, in "Progress in Reaction Kinetics," Vol. 4, G. Porter, Editor, Pergamon Press, Elmsford, N.Y. (1967).
10. B. E. Conway, "Theory and Principles of Electrode Processes," p. 108, The Ronald Press Co., New York (1965).
11. K. B. Harvey and B. Porter, "Introduction to Physical Inorganic Chemistry," p. 322, Addison-Wesley Publishing Co. Inc., Reading, Mass. (1963).
12. V. G. Bagotskii and Y. B. Vasilev, *Electrochim. Acta*, **9**, 869 (1964).
13. D. Gilroy and B. E. Conway, *J. Phys. Chem.*, **69**, 1259 (1965).
14. A. K. Vijh, *Can. J. Chem.*, **49**, 79 (1971); A. K. Vijh, "Electrochemistry of Metals and Semiconductors," p. 183, Marcel Dekker, New York (1973).

On the Electrochemical Nucleation of Silver on Different Crystal Orientations of Graphite

Ikram Morcos*

Hydro-Quebec Institute of Research, Varennes, Quebec, Canada

ABSTRACT

An attempt was made to determine experimentally the nucleation overpotential of silver on high-pressure, stress-annealed pyrolytic graphite as a function of crystal orientation, surface oxidation state, and solution composition using both galvanostatic and potentiostatic pseudo-steady-state current-potential relationships. Silver deposits on the edge orientation from silver perchlorate with a nucleation overpotential of about 30 mV but does not adhere to cleavage orientation at the conditions of the study. The deposition of silver takes place on both cleavage and edge orientations from silver cyanide solution and is accompanied with a nucleation overpotential of about 200 and 250 mV, respectively.

A knowledge of the magnitude of nucleation overpotentials of metals on graphite and carbon substrates is useful for both fundamental and applied aspects of electrodeposition. In spite of the progress made in understanding the kinetics of electronucleation (1-5), there is a lack of reliable data on the values of nucleation overpotentials of metals on graphite. Available information (1) appears to have been obtained under poorly defined experimental conditions and on carbon substrates with poorly defined surface structure and oxidation state. The present availability of high-pressure, stress-annealed pyrolytic graphite with well-oriented structure similar to that of single crystal material permits a more reliable determination of nucleation overpotentials. The results recently reported (7-8) on the electrochemical nucleation of mercury on the latter type of graphite are strongly in conflict with both theoretically predicted (6) and experimentally determined values on carbon samples used in previous work (9).

In the present work an attempt has been made to obtain some reliable values for the nucleation overpotential of silver on well-oriented (ZYH type) pyrolytic graphite. The effect of crystal orientation, surface oxide films, and solution composition has also been explored using both galvanostatic and potentiostatic pseudo-steady-state current-potential scanning methods. The effect of solution composition was explored by performing the study in solutions containing either simple salt (silver perchlorate in perchloric acid) or

complex salt (0.19N silver cyanide). Possible variations in the oxidation state of the graphite surface were examined by obtaining cathodic voltammograms in oxygen-free perchloric acid solutions.

Experimental Procedure

Galvanostatically controlled current-potential relationships were obtained by applying the circuit diagram shown in Fig. 1. A Tacussel function generator was used as a source of scanning voltage with a linear scanning rate of $1 \mu\text{A}/\text{sec}^{-1}$. A Wenking potentiostat (Type 68FR 0.5) was used to convert the scanning

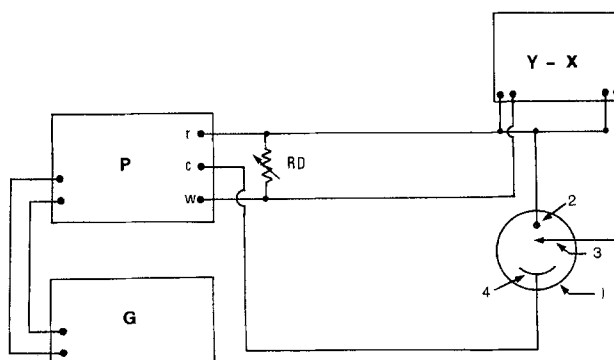


Fig. 1. Schematic diagram for the galvanostatic variation of current with potential. X-Y, X-Y recorder; G, function generator; P, potentiostat; RD, variable resistor; 1, electrochemical cell; 2, working electrode; 3, reference electrode; 4, counterelectrode.

* Electrochemical Society Active Member.

Key words: nucleation of silver, nucleation on graphite, graphite orientation and nucleation.

voltage into the applied galvanostatic current by connecting it (10) in the manner shown in Fig. 1. A Honeywell X-Y recorder was used to record the potential as a function of the current. Potentiostatically controlled current-potential relationships were obtained by connecting the potentiostat in the more conventional manner. The same potentiostatic method was applied to produce the cathodic voltammograms in perchloric acid solutions. All potentiostatic experiments were performed at a scan rate of 0.2 V/min^{-1} .

The electrochemical cell consisted of two compartments, one for the reference electrode and the other for both the working and counterelectrode. As a reference electrode a silver wire was used in silver perchlorate solution and a saturated calomel in both perchloric acid and silver cyanide solutions. The former reference electrode exhibited a potential of 0.666 V (NHE). In solutions containing silver ions two silver plates were used as a counterelectrode. In voltammetric experiments in perchloric acid the counterelectrode was a spectroscopic graphite rod to avoid contamination of the solution with silver ions. The rotating disk was applied throughout the work at a speed of 1600 rpm. Electrodes of both cleavage and edge orientations were machined and fitted to the Teflon coated steel shaft of the rotating disk assembly as described elsewhere (11). Solutions were prepared from AR quality salts and water triply distilled twice from a permanganate solution. All experiments were carried out in helium saturated solutions.

Results and Discussion

The electrodeposition of a metal on a foreign substrate with which it does not form mixed crystals involves the formation of a new phase, which, therefore, requires an energy of nucleation. The latter is provided by a nucleation overpotential which is necessary to bring the concentration in the double layer (12) to a certain supersaturation value.

Nucleation overpotential is experimentally well defined in galvanostatically controlled current-potential relationships. When the current is slowly increased, the overpotential with respect to a reference of the same metal in the test solution, will first increase rapidly at a low current density until the first layer of metal nuclei is deposited on the inert substrate. A further increase in the current density will cause a decrease in the overpotential as the deposition of the metal takes place on the same metallic surface and therefore results in a well-defined maximum. If, as in many cases, the reduction of the metal ion on the same metal substrate occurs reversibly, the increase in current density following the formation of the first layer of metal nuclei, in the absence of concentration polarization, will take place at an almost constant potential. Nucleation overpotential can then be defined as the difference between the maximum potential and that corresponding to the reduction of the metal ion at constant potential.

Figure 2 shows galvanostatically controlled current-overpotential relationships for the reduction of Ag^+ ion from helium-saturated silver perchlorate solution (0.05 N silver perchlorate in 1 N perchloric acid) on both cleavage and edge graphite orientations. No electrode pretreatment was applied after exposing the new surface. Both plots of Fig. 2 show well-defined maxima at overpotentials of -52 and -46 mV for cleavage and edge graphites, respectively. In the case of edge graphite the increase in current following the maximum occurs at a constant potential. The difference of 14 mV between that constant potential and the reversible reference is a slight activation polarization because of the high current density caused by the small true area of formed silver nuclei. Such is not the case with cleavage graphite where it is observed that the potential shows a linear increase with the increase in current. Figure 2 then clearly indicates that the nucleation and deposition of silver from a silver perchlorate solution occurs only on edge but not on

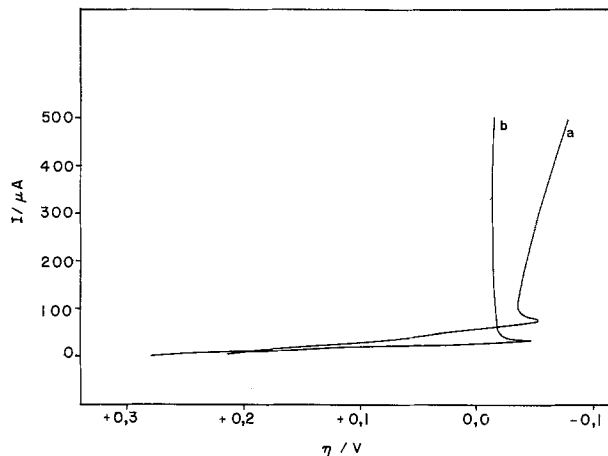


Fig. 2. Galvanostatic current-overpotential relationships for the reduction of Ag^+ ion from silver perchlorate on both cleavage and edge orientation of high-pressure, stress-annealed pyrolytic graphite. a, Cleavage graphite; b, edge graphite.

cleavage graphite. The appearance of the maximum in the case of cleavage graphite indicates that nucleation actually starts to take place on the surface, but, because of the lack of sufficient adhesion forces between the graphite surface and the formed nuclei, the process of nucleation is discontinued, the formed nuclei are removed, and the further reduction of silver ions continues to take place on the graphite surface. On the basis of the previously stated definition, nucleation overpotential, according to Fig. 2, is 32 mV in the case of edge graphite and 16 mV at the initial stage of nucleation in the case of cleavage graphite. These values are considerably smaller than a value of 100 mV reported in Ref. (1).

The observed difference in the activity of cleavage and edge orientations toward nucleation is consistent with the known differences in the chemical and electrocatalytic activity of both surfaces. Studies on the electroreduction of oxygen (11) on both surfaces have shown that edge graphite is much more electrocatalytically active than cleavage graphite. Furthermore the determination of cleavage graphite's surface tension (about 35 dynes/cm) (13) and the electrocapillary data obtained on the cleavage surface/electrolyte interface (14) indicates that ionic adsorption is strongly inhibited on that surface from aqueous solutions. The chemical and electrochemical inertness of cleavage orientation results from the lack of any unsatisfied valencies or polar surface structures. The atoms at the cleavage surface have satisfied valencies and are symmetrically arranged in rings parallel to the surface which are separated from successive carbon layers by only weak van der Waals forces. On the other hand, the edge orientation exposes different organic functional groups which can exist in different oxidation states.

Figure 2 indicates that the open-circuit potential of graphite in silver perchlorate solution is strongly shifted to more anodic values as compared with the corresponding reversible Ag/Ag^+ couple. The observed potential is probably a mixed one which consists of both the Ag/Ag^+ couple and the potential established between the surface organic functional groups and the hydrogen ions of the solution. Although only a very small number of these groups exists on the cleavage surface at sites of crystal defects, they can still have a similar effect on the open-circuit potential. Because these organic functional groups may exist in different oxidation states, it may be suggested that the maxima of Fig. 2 result from the reduction of a surface oxide rather than from the nucleation of silver on graphite.

The reduction of graphite's surface oxide can be identified with the appearance of peaks in cathodic voltammograms obtained in inert solutions. In two different studies (15-16), carried out on ordinary

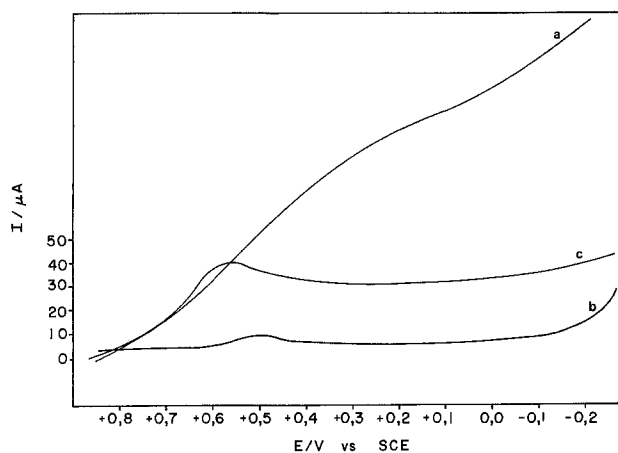


Fig. 3. Cathodic voltammograms on both cleavage and edge graphites in 1N HClO_4 . a, Cleavage graphite; b, edge graphite without pretreatment; c, edge graphite pretreatment in conc. HNO_3 .

pyrolytic graphite in 1M H_2SO_4 , it was reported that the oxide film formed by either chemical or electrochemical treatment is reduced at 0.5V (*vs.* SCE). The latter value is considerably more anodic than the potentials at which the maxima of Fig. 2 occur, and accordingly these maxima result from nucleation and not from the reduction of surface oxides. However, in order to confirm this latter conclusion it was considered necessary to obtain the cathodic voltammograms on the same graphite samples used in the present study and in perchloric acid rather than in sulfuric acid. Figure 3 shows the result of such experiments and it is seen that a small peak appears only in the case of edge graphite at 0.5V (*vs.* SCE). The absence of organic functional groups on cleavage graphite explains the absence of a well-defined peak in its voltammogram. The relatively large current observed on cleavage graphite probably results from charging of the double layer. When edge graphite is pretreated in concentrated nitric acid the peak becomes more prominent but still takes place at approximately the same potential. As a further confirmation, the galvanostatic current-potential relationships for the reduction of Ag^+ ion were obtained on both graphite orientations which were pretreated in concentrated nitric acid. Figure 4 shows that the section of the plots which is related to nucleation for both types of graphite is almost the same as that shown in Fig. 2. From this it is concluded that even when an oxide film is deliberately formed before the study of electro-

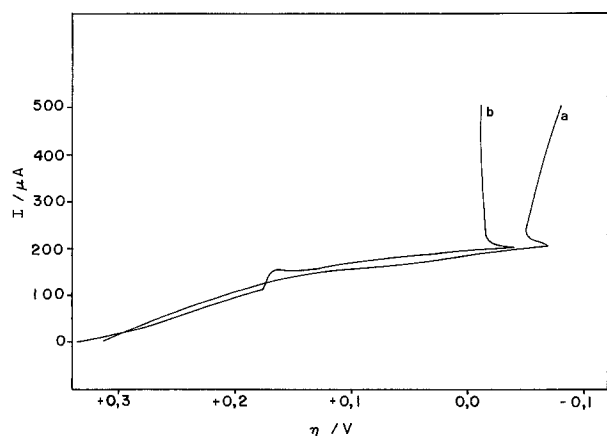


Fig. 4. Galvanostatic current-overpotential relationships for the reduction of Ag^+ ion from silver perchlorate on both cleavage and edge graphites which have been pretreated in conc. HNO_3 . a, Cleavage graphite; b, edge graphite.

chemical nucleation, reduction occurs at a potential more anodic than that corresponding to nucleation. The higher currents observed in Fig. 4 as compared to Fig. 2 at potentials more positive than that corresponding to nucleation are probably due to surface oxide reduction. Pretreatment in concentrated nitric acid oxidizes the cleavage surface and exposes the organic functional groups. Such formation and subsequent reduction of the organic functional groups on cleavage surface has probably resulted in the observed shift of the maximum overpotential into more negative potentials (compare Fig. 2a with Fig. 4a). It is probable that the reduction of such film activates the surface towards nucleation.

Figure 5 shows that nucleation overpotential of silver under potentiostatic conditions on both cleavage and edge graphite at the initial stage of deposition is 30 mV. This value is approximately the same as that determined by galvanostatic experiments on edge graphite. With the increase in current, the latter value shows only a slight increase because of the activation overpotential caused by the small true area but soon reaches a constant value. One observes, however, from Fig. 5 that this initial nucleation overvoltage in the case of cleavage graphite shows a linear increase with the increase in current for the reasons already mentioned in discussing the galvanostatic experiments.

The study of electrochemical nucleation on foreign substrates (particularly on an organic substrate such as graphite) is important in applied aspects of electrodeposition. This is because the important property of adhesion can be related to the magnitude of nucleation overpotential. It is known that conditions which favor microcrystalline deposits also favor the formation of new nuclei and better adhesion properties (17). The higher the nucleation overpotential the smaller is the grain size and therefore the stronger will be the adhesion between the deposited metal and the foreign substrate.

Such correlations between nucleation overpotential, adhesion, and grain size explain the common use of complex salts in industrial electrodeposition. Silver, for example, is deposited from alkaline silver cyanide solution. The much higher stability constant (5.6×10^{18}) of silver cyanide $[\text{Ag}(\text{CN})_2]^-$ results in a much less concentration of silver ions. Consequently a higher magnitude of nucleation overpotential is required to break the strong bonding forces and bring the ionic concentration into the required supersaturation value. Figure 6 compares the galvanostatic current-potential plots for the reduction of silver cyanide on both cleavage and edge orientations. The nucleation overpotential is well defined and is 0.2 and 0.25V on cleavage and edge, respectively. It is obvious that the silver nuclei under these conditions can adhere to the inert cleavage surface. The accompanying overvoltage provides the silver atoms with the required energy to form the metal-graphite bonding.

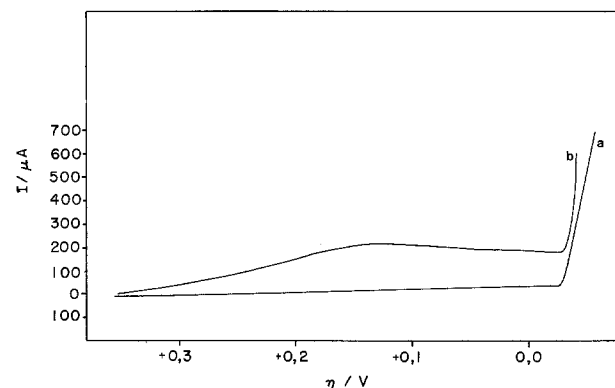


Fig. 5. Potentiostatic current-overpotential relationships for the reduction of Ag^+ ion from silver perchlorate on both cleavage and edge graphite. a, Cleavage graphite; b, edge graphite.

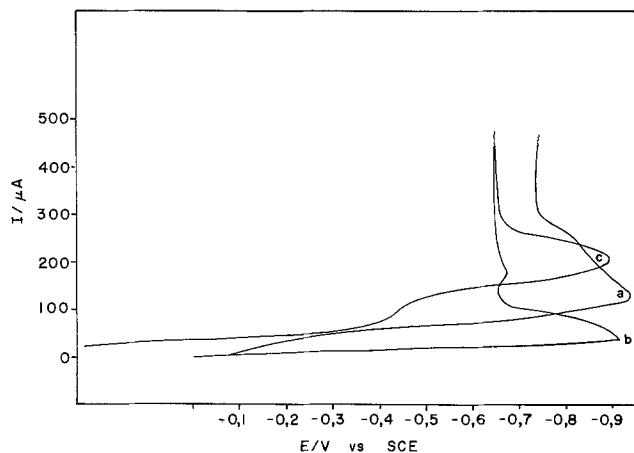


Fig. 6. Galvanostatic current-potential relationships for the reduction of $[\text{Ag}(\text{CN})_2]^-$ from silver cyanide solution on both cleavage and edge graphites. a, Cleavage graphite; b, edge graphite; c, edge graphite pretreated in conc. HNO_3 .

Acknowledgments

The author is grateful to Union Carbide Research Center, Parma, Ohio, for providing him with the graphite samples used in the present work and to Mr. G. Larochelle for his assistance in the physical realization of the investigation.

Manuscript submitted May 29, 1974; revised manuscript received July 30, 1974.

Any discussion of this paper will appear in a Discussion Section to be published in the December 1975

JOURNAL. All discussions for the December 1975 Discussion Section should be submitted by Aug. 1, 1975.

Publication costs of this article were partially assisted by Hydro-Quebec Institute of Research.

REFERENCES

1. M. Fleischmann and H. R. Thirsk, in "Advances in Electrochemistry and Electrochemical Engineering," Vol. III, P. Delahay and C. W. Tobias, Editors, Chap. 3, John Wiley & Sons, Inc., New York (1963).
2. D. J. Astley, J. A. Harrison, and H. R. Thirsk, *Trans. Faraday Soc.*, **64**, 192 (1968).
3. J. A. Harrison, *J. Electroanal. Chem.*, **36**, 71 (1972).
4. I. Markov, A. Boynov, and S. Toshev, *Electrochim. Acta*, **18**, 377 (1973).
5. P. Bindra, M. Fleischmann, J. W. Oldfield, and D. Singleton, *Discussions Faraday Soc.*, **56** (1973) (1973).
6. T. Erdey-Crüz and M. Volmer, *Z. Physik. Chem.*, **A157**, 182 (1931).
7. I. Morcos, *J. Electroanal. Chem.*, **50**, 373 (1974).
8. I. Morcos, *ibid.*, **54**, 87 (1974).
9. T. Erdey-Crüz and H. Wick, *Z. Physik. Chem.*, **162**, 63 (1937).
10. Operating Manual "121," Wenking Electronic Potentiostats, Brinkmann Instruments, Westbury, N.Y.
11. I. Morcos and E. Yeager, *Electrochim. Acta*, **15**, 953 (1970).
12. T. Erdey-Crüz, "Kinetics of Electrode Processes," p. 260, Wiley-Interscience, New York (1970).
13. I. Morcos, *J. Chem. Phys.*, **57**, 1801 (1972).
14. I. Morcos, *J. Phys. Chem.*, **76**, 2750 (1972).
15. G. Mamantov, D. B. Freeman, F. J. Miller, and H. E. Zittel, *J. Electroanal. Chem.*, **9**, 305 (1965).
16. K. F. Blurton, *Electrochim. Acta*, **18**, 869 (1973).
17. G. Milazzo, "Electrochemistry," p. 435 (English Edition) Elsevier Publishing Company, Amsterdam (1973).

Photoeffects at Polycrystalline Tin Oxide Electrodes

Hasuck Kim and H. A. Laitinen*

School of Chemical Sciences, University of Illinois at Urbana-Champaign, Urbana, Illinois 61801

ABSTRACT

The electrochemical behavior of thin-film polycrystalline tin oxide electrodes under subbandgap energy photoexcitation has been investigated. Photocurrents were dependent on the intensity of the light, wavelength, and the applied potential. The photocurrent spectrum showed a sharp decrease near the bandgap energy. This photocurrent is due to the oxidation of water in the electrolyte by holes at the permitted energy levels in the bandgap region. These energy states are formed by the presence of impurities, which are largely halides remaining from the preparation steps, grain boundaries, and adsorbed foreign molecules. A superficial hydrogen bonding interaction between oxide layers of SnO_2 and water molecules is proposed for the hydrated surface of tin oxide.

Long after the first photovoltaic effect was noticed by Becquerel, many investigators observed photocurrents at various electrode materials; such as mercury (1-3), elemental germanium (4), CdS (5), ZnO (6, 7), GaP (8), GaAs (9), and CuO (10). In all the semiconductor studies, single crystals were used. It was found that the bandgap energy illumination produced electron hole pairs which participated in the electrochemical process, i.e., electrons for the cathodic photocurrent in p-type electrodes, and holes for the anodic reaction in n-type materials. It was also found that the extra currents were due to the electrochemical decomposition of the electrode material under illumination.

* Electrochemical Society Active Member.

Key words: semiconductor, thin-film electrode, transparent electrode, photocurrent, tin oxide electrode.

One of the advantages of the use of a semiconductor electrode in the study of electrochemical reactions is the fact that the charge transfer processes occur only via the energy bands. Therefore, in the presence of organic dye in the electrolyte, charge transfer processes involving the excited states can be studied by observing dye sensitized photocurrents (11).

A semiconducting thin film of tin oxide on glass or quartz has shown some distinctive advantages over metals as an electrode in electrochemical investigations. Nearly metallic conductivity, optical transparency, high oxygen overvoltage, low background current, absence of any electrochemically active oxide layer, chemical durability, and excellent mechanical stability of the film made it possible to study many special electrochemical applications. Detailed applica-

tion of polycrystalline tin oxide material as an electrode can be found in Ref. (12).

Even though there are many applications and advantages in the use of tin oxide electrode, little attention has been paid to the nature and to the physical properties of the surface. Accordingly, this study of photoexcitation with radiation of energy less than the bandgap energy is one of a series (13, 14) to characterize the electrode surface.

Experimental

Reagents.—Chemicals used in this study were reagent grade and were used without further purification except where specifically noted. Stannic chloride, stannic bromide, hydrobromic acid, and tetrabutyltin were purified by vacuum distillation. Rhodamine B was recrystallized from ethanol. Solutions were made using laboratory distilled water which had been distilled twice.

Preparation of tin oxide electrodes.—The procedure in Mochel's patent (15) was generally followed. In addition to stannic chloride-hydrochloric acid, a stannic bromide-hydrobromic acid mixture was also used. The coating of tin oxide was obtained by blowing the spray mixture onto a hot quartz or glass substrate using a conventional all-glass atomizer. Each spray lasted for about 5 sec followed by a 3 min waiting period to prevent excessive cooling of the hot substrate. After each spray, the substrate was rotated clockwise by 90° to get a uniform thickness over the surface. The surface of the tin oxide film was then polished with Gamma polishing alumina¹ and Selvyt polishing cloth.¹ The commercial tin oxide coated glass (IRR) was used as substrate instead in the case of double coated electrodes. More details about the coating, polishing, and the cleaning, are given in Ref. (16).

The thickness of the coating was determined by measuring interference fringes (17) obtained by scanning the spectral region from 250-700 nm.

Construction of electrolyte cell.—The cell used for the photoexcitation studies on tin oxide is shown in Fig. 1. Its design was similar to that reported earlier (13), but it had a side flange and a side conical end as shown. The end of this side branch was polished flat. The electrical contact to the semiconductor electrode surface was made by a flat, highly polished copper "O" ring tightened firmly onto the electrode by three 4/40 machine screws and a Plexiglas support. A Teflon washer which provided both a tight seal between the cell and the electrode and defined the area of the electrode was placed tightly inside the metal "O" ring. To insure a good seal it was necessary to polish the Teflon washer on a plate of ground Lucite until a completely smooth surface was obtained. The area of the electrode was 0.124 cm².

¹ Buehler product, Evanston, Illinois.

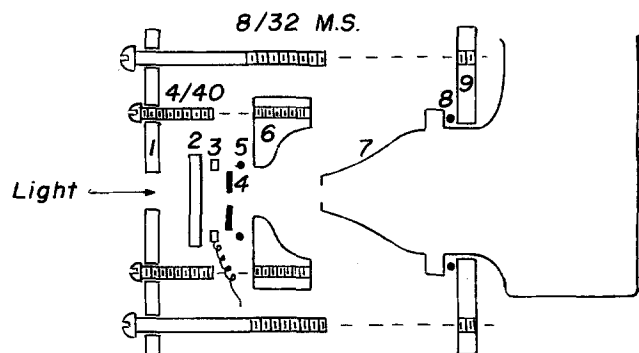


Fig. 1. Diagram of electrolytic cell. 1 and 9, Brass plates; 2, tin oxide electrode; 3, metal "O" ring with copper wire; 4, Teflon washer; 5 and 8, rubber "O" rings; 6, Plexiglas support; 7, all-glass electrolytic cell.

Photocurrent and photovoltage measurements.—The experimental setup is shown in Fig. 2. A saturated potassium chloride calomel electrode (SCE) with a porous Vycor junction was used as a reference electrode. A Luggin capillary filled with saturated potassium nitrate solution was placed between the reference Vycor junction and near the working electrode.

Under a constant applied potential, the SnO₂ electrode in contact with electrolyte was illuminated from the backside for a while; then the light path was interrupted manually with a metal sheet for the photocurrent measurement. The net change of current or voltage after it reached a steady-state value was taken as the photocurrent or photovoltage. The light source was a 100W xenon arc lamp with a Bausch and Lomb High Intensity Grating Monochromator (33-86-25-02).

Since the light intensity of the lamp was not uniform throughout the spectral region, the photocurrent was normalized to unit light intensity after the absolute intensity at each wavelength had been measured using a Hewlett-Packard Model 8334A Radiant Flux Detector with a Model 8330A Radiant Flux Meter.

Adsorption of rhodamine B.—C-14 labeled rhodamine B was prepared by condensation between *m*-diethylaminophenol and C-14-phthalic anhydride (18). A double coated tin oxide electrode was prepared by the same procedure as the electrodes used in the photoexcitation experiments. The electrode was first placed in a known concentration of labeled dye in 1M KNO₃ solution for a given time with or without applied potential, then was taken out. The electrode was washed thoroughly with distilled water using a wash bottle. Absolute ethanol (35 drops) was used to dissolve any adsorbed rhodamine B molecules from the electrode surface. Fifteen milliliters of scintillation liquid was then added to a counting vial in which 35 drops of ethanol had already been collected. Disintegration rates were counted using 2003 Packard Tri-Carb Liquid Scintillation Spectrometer seven times for 10 min each to achieve the desired S/N ratio.

Results and Discussion

Photocurrent measurements.—An increase of anodic residual current was observed by illumination with photoenergies which are less than the energy gap between the conduction and valence bands. The profile of photocurrent was dependent upon wavelength and applied potential. It decayed to a steady value after a sharp increase. Since the time constant of the electrode/electrolyte system was found to be 0.17-0.18 sec, while the photocurrent-time curve provided 0.3-1 sec, a simple charging-discharging of the double layer capacitance cannot be the total rate-determining process. It was also found that the photocurrent was directly related to the intensity of the light.

In order to find the most suitable surface for this study several different types of tin oxide material were examined. Since minority carriers, as mentioned before, play an important role in the photocurrent process (6), use of a poorly conductive electrode material is

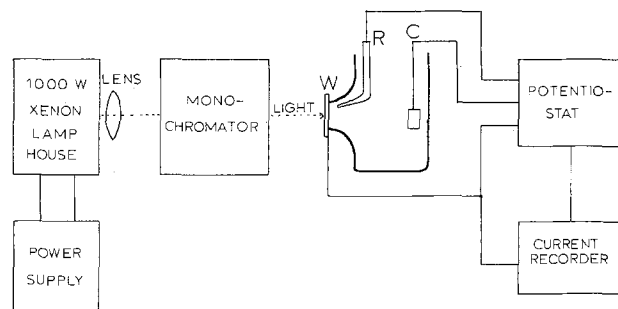


Fig. 2. Block diagram of experimental setup. W, Working electrode; R, reference electrode; C, counterelectrode.

desired. The source and nature of conductivity of "undoped" tin oxide film has been studied (16). Although the main source of conductivity is attributable to halides remaining after hydrolysis, the nonstoichiometry of tin oxide also contributes appreciably. A poorly conductive electrode can give a higher value of the ratio of the excess holes produced by photoenergy to major carrier concentration than a highly conductive electrode under the same light intensity. It also offers an electrode material with fewer impurities to cause additional complexities. But a large IR drop has to be considered when a highly resistive electrode is used. In order to eliminate this IR drop, a double coating technique was developed. The second layer of a highly resistive tin oxide film was obtained by use of non-doped stannic bromide on a commercial antimony-doped tin oxide surface. The thickness of the second layer was determined indirectly by measuring the thickness of another film obtained simultaneously on Pyrex substrate and was found to be about $0.4 \mu\text{m}$. It is quite possible that antimony in the first layer may diffuse to some extent into the second layer during the preparation step. This electrode, however, behaves like a highly resistive one at the electrode-electrolyte interface yet has a high conductivity to facilitate passage of electricity.

The double coated electrode prepared from stannic bromide, which has the most resistive surface among the electrodes, does give a higher photocurrent and a sharper slope than any other electrode. The sharper slope indicates a clear band separation, i.e., fewer impurities or energy states present between bands in the crystal structure. Therefore, double coated electrodes prepared with stannic bromide were used throughout this investigation.

Figure 3 shows a series of photocurrent spectra at different applied potentials obtained in $1M \text{KNO}_3$. The shapes of the spectra are similar. With an ideal tin oxide single crystal, the photocurrent would be noticeable only with bandgap energy illumination, corresponding to the energy at which electrons in the val-

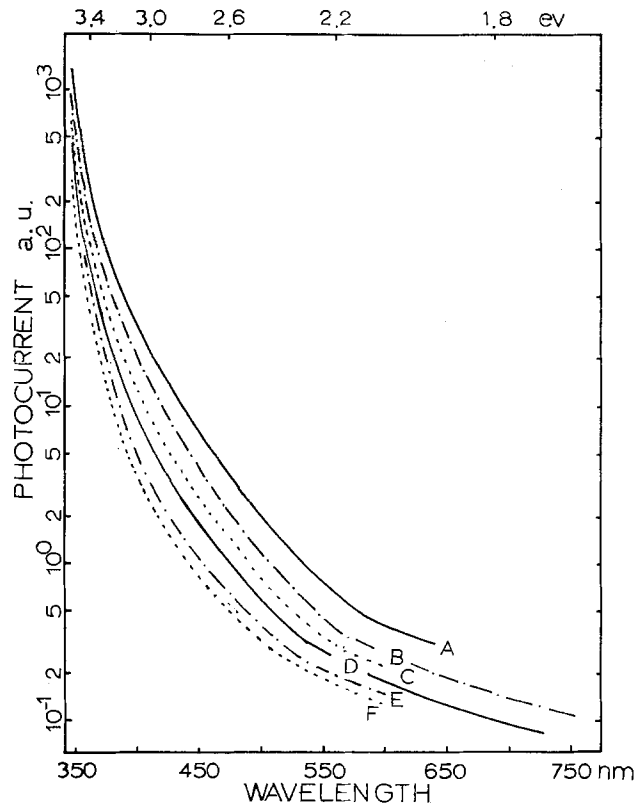


Fig. 3. Photocurrent spectra in $1M \text{KNO}_3$. $[\Delta\lambda] = 10 \text{ nm}$. Double coated electrode with SnBr_4 . a.u., Arbitrary units; A, at 1.3V vs. SCE; B, 1.1V; C, 0.9V; D, 0.7V; E, 0.5V; F, 0.4V.

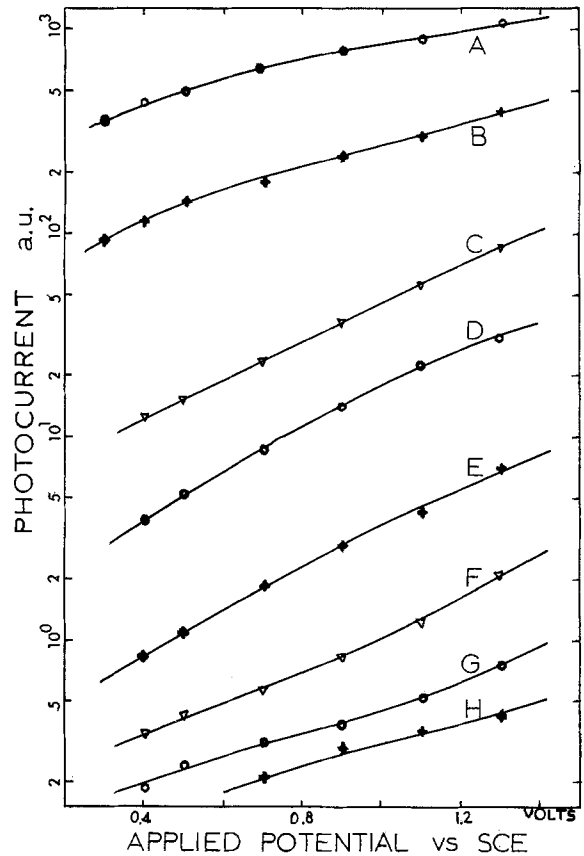


Fig. 4. Effect of applied potential on photocurrent in $1M \text{KNO}_3$. A, 350 nm; B, 360 nm; C, 380 nm; D, 400 nm; E, 450 nm; F, 500 nm; G, 550 nm; H, 600 nm.

ance band would be promoted to the conduction band, leaving holes behind. No electron hole pairs would be produced by illumination of energies less than the bandgap energy.

However, as shown in Fig. 3, the polycrystalline tin oxide electrode shows an appreciable photocurrent in wavelengths longer than 335 nm which corresponds to the bandgap energy of 3.7 eV. Therefore, there must be a number of energy states between bands. It is known that physical imperfections of a crystal, chemical impurities, grain boundaries (19), adsorbed foreign molecules, and surface states can introduce discrete energy levels into the forbidden gap much as donor and acceptor ions do in the case of a doped semiconductor.

We know there are "unintentionally added" bromides in the tin oxide electrode (16) which can be easily ionized at room temperature. These ionized donors introduce energy levels which are distributed according to Fermi-Dirac statistics. Therefore, the observed photocurrent near 350 nm decreases sharply.

As Fig. 4 shows, there is no saturation phenomenon as observed in single crystals of ZnO (6), SnO_2 (20), and CdS (1) with bandgap energy illumination in which the photocurrent is determined only by the diffusion rate of holes to the surface. In a polycrystalline material, holes produced by photoenergy could be recombined through the adjacent energy states before they reach the surface to participate in electrochemical processes.

The potential dependence of the charge transfer rate could be another reason for polycrystalline tin oxide electrodes not having a saturation phenomenon. The tunneling probability of an electron into the bulk of the electrode is governed by the shape of the energy barrier (14) and thickness of the space charge layer, which in turn primarily depends upon the density of charge carriers in the bulk and on the applied potential, since applying a different potential to a semiconductor electrode results only in a variation of the electrical potential difference in the space charge layer

without a major change in the Helmholtz double layer structure (21). Figure 5 reveals schematically the effect of applied potential on the potential energy diagram of semiconducting tin oxide. The tunneling probability or electron transfer coefficient would be much higher at the higher anodic potential than at a low anodic potential.

A change of the pH of the electrolyte, on the other hand, is believed to influence the Helmholtz layer, flatband potential, and surface hydroxyl groups. These changes occur at or near the electrode-electrolyte interface while the applied potential or electrode material can change the internal properties of the electrode.

HNO₃ and KOH were used to adjust pH values in order to eliminate any possible specific adsorption of buffer systems on the electrode surface. As shown in Fig. 6, a steady increase of the photocurrent in the range of pH from 3 to 10 can be explained by a continuous change of the flatband potential at a rate of 60 mV/pH unit (20).

A simple shift of the flatband potential by 60 mV/pH unit, however, cannot explain large changes of the photocurrent below pH = 3 and above pH = 10. In addition to the shift of the flatband potential, change of the charge transfer rate seems to take place due to the protonation and the formation of surface hydroxyl groups, respectively (see below). Even though this experiment had been done at a fixed applied potential, the shape of the potential energy curve, and thereby the space charge layer thickness, can be changed drastically by such surface changes.

Sensitized photocurrent.—In the presence of rhodamine B, an additional anodic photocurrent was observed and the photocurrent spectra were very similar to the absorption spectra of the dye as shown in Fig. 7. A similar phenomenon using various semiconducting electrodes has been observed (11, 22). The dye is electrochemically inactive in the dark in the region of the applied potentials. This additional photocurrent can be interpreted as a considerable increase of the number of carriers in the electronic energy states due to the adsorption of the dye molecules (23). A maximum conductivity has been observed in the course of photoconductivity measurements on ZnO single crystal (24) in the presence of adsorbed organic dye under absorption band illumination. Since the photocurrent is directly proportional to the rate of formation of carriers, there is a maximum population of carriers in the energy state corresponding to the absorption band of the dye.

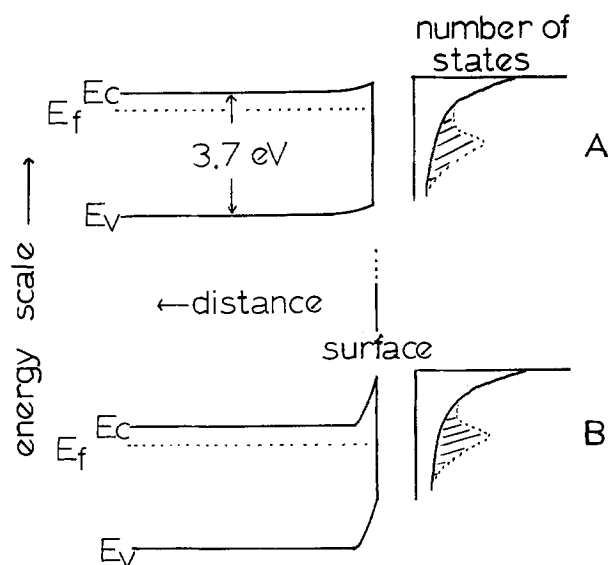


Fig. 5. Potential energy diagram of SnO₂ at the interface. A, Low anodic potential; B, high anodic potential; E_c, conduction band; E_f, Fermi energy level; E_v, valence band. Shaded areas are the energy states due to the presence of adsorption.

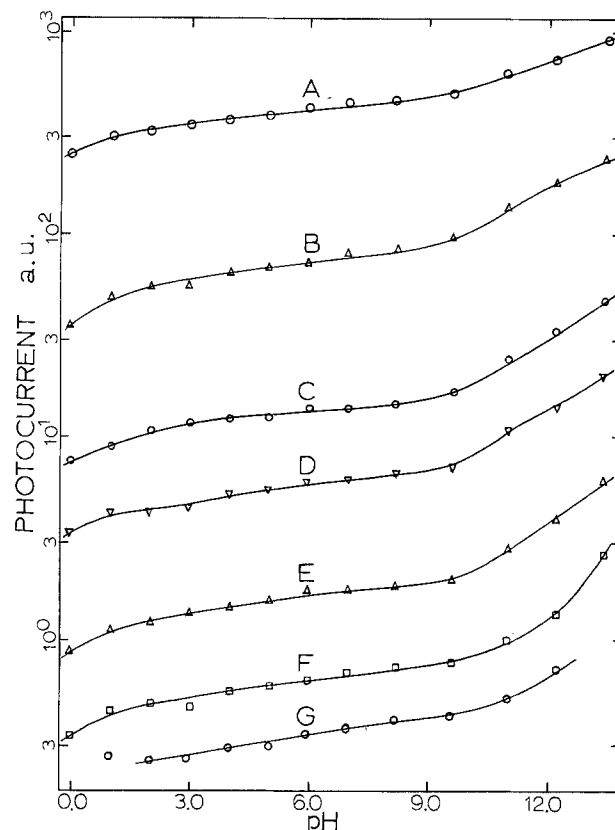


Fig. 6. Effect of pH on photocurrent at 0.7V vs. SCE. A, 360 nm; B, 380 nm; C, 400 nm; D, 450 nm; E, 500 nm; F, 550 nm; G, 610 nm.

The effect of applied potential on the sensitized photocurrent was very similar to the effect of applied potential on the photocurrent shown in Fig. 4. Again, no saturation was observed.

The sigmoid shape in Fig. 8 reveals a typical adsorption isotherm, and further evidence for the adsorption of rhodamine B at the tin oxide electrode surface has been provided by the radioactive carbon-14 labeling technique. The specific activity of C-14-rhodamine B was determined by relating the spectrophotometrically determined concentration to the counting rate.

The theoretical amount of a monolayer coverage was calculated, assuming 18Å as the diameter of rhodamine B molecule, to correspond to 3.93×10^{13} molecules/cm² or 6.53×10^{-11} mole/cm².

It was noticed that up to 99.5% of the adsorbed dye can be dissolved from the surface into ethanol in three successive washings, but water washings did not disturb the adsorbed dye. Adsorption of the dye appears to be very rapid because 4.2×10^{-11} moles/cm² (about two-thirds of theoretical monolayer coverage) of dye was observed after only 1 sec of immersion in $1.46 \times 10^{-4}M$ solution. Values between 5.8 and 6.9×10^{-11} moles/cm² were obtained after 2 and 10 min of immersion with or without polarization at applied potentials of 1.21 and -1.0V vs. SCE. About a monolayer coverage (5.9×10^{-11} moles/cm²) was also observed in the following way. The electrode was dipped into a $4.53 \times 10^{-6}M$ dye solution for 5 min, then it was taken out very slowly. There was no washing with water. This was done on the basis that the tin oxide was not easily wettable and that uniformly distributed solution layer 1 μm thick contained an amount of dye corresponding to less than 1% of a monolayer coverage. Actually there was only a little wetted area and the solution was efficiently taken away by an absorbing paper towel.

Photovoltage measurements.—A shift of rest potential by the bandgap energy illumination is due to the generation of excess hole electron pairs. The separation of photogenerated charge carriers of the different

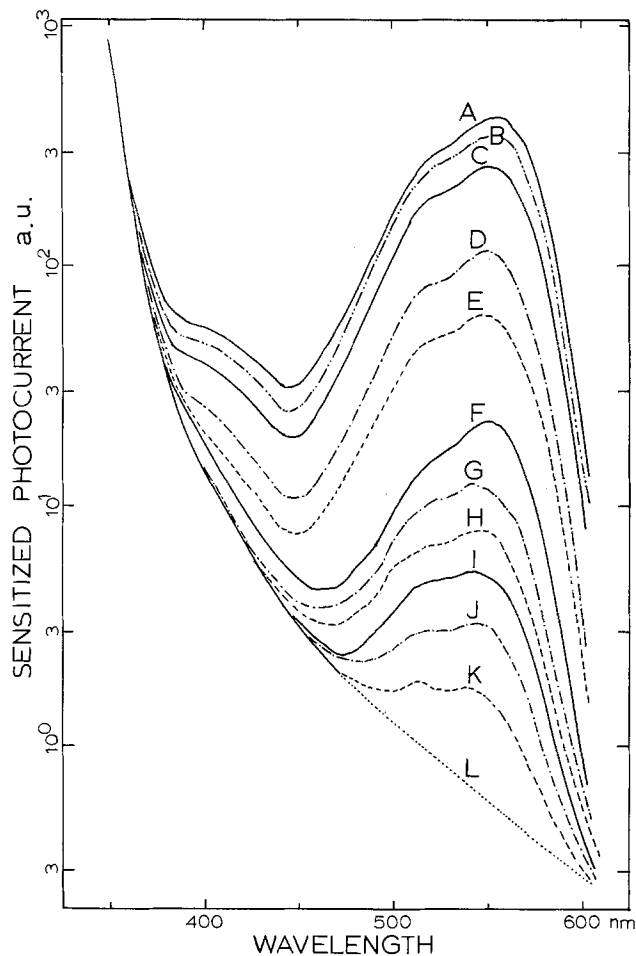


Fig. 7. Sensitized photocurrent by rhodamine B at 0.7V vs. SCE. $|\Delta\lambda| = 10$ nm. A, $2.434 \times 10^{-5}M$; B, 1/2A; C, 1/4A; D, 1/10A; E, 1/20A; F, 1/40A; G, 1/100A; H, 1/200A; I, 1/400A; J, 1/1000A; K, 1/2000A; L, 1M KNO_3 only.

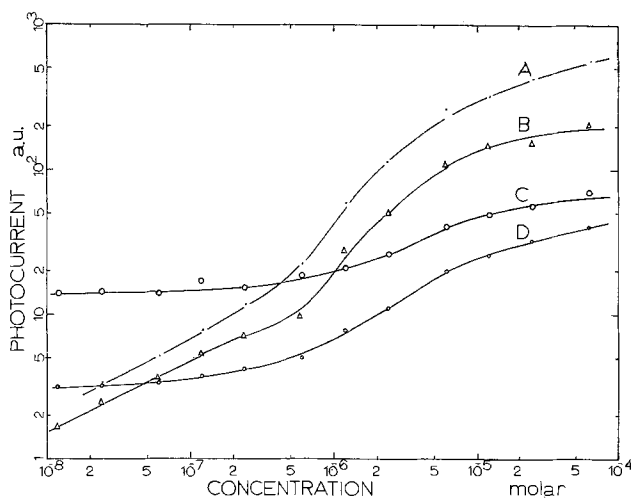


Fig. 8. Effect of rhodamine B concentration on sensitized photocurrent at 0.7V vs. SCE. A, At 550 nm; B, at 500 nm; C, at 400 nm; D, at 450 nm.

mobilities can also produce a photopotential (25). Both responses are known to be instantaneous because they are caused only by a nonequilibrium charge distribution.

When photoenergies of less than the energy gap were introduced on SnO_2 , a long rise and decay time was observed in an open circuit as shown in Fig. 9. The measured photovoltage depends very much on the previous history of the electrode and does not give reproducible values.

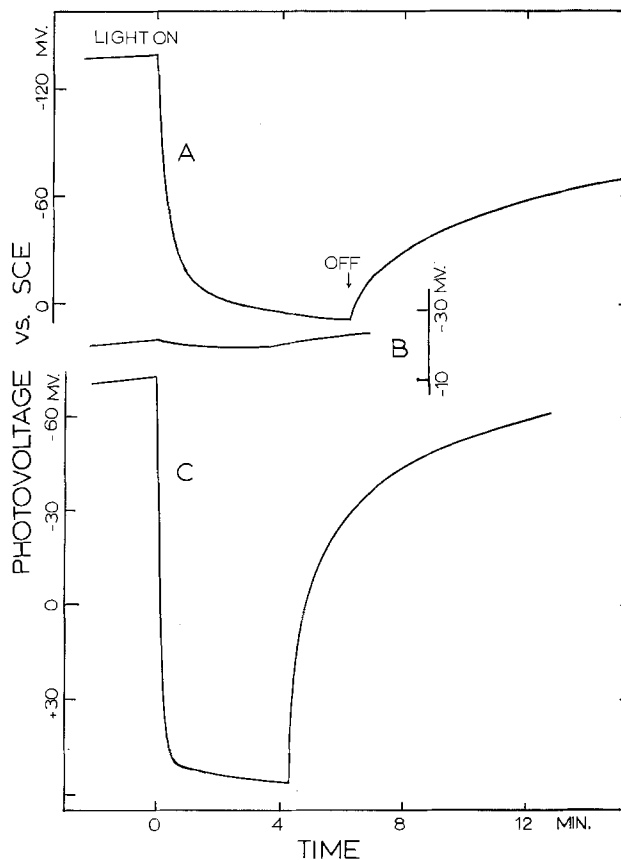


Fig. 9. Time dependence of photovoltage. A, 1M KNO_3 with 350 nm; B, 1M KNO_3 with 550 nm; C, $1.217 \times 10^{-5}M$ rhodamine B in 1M KNO_3 .

The slow response of photovoltage due to chemical process at the electrode surface was discussed in Ref. (6). In the open circuit measurement, there is no net current flow between the electrode and the electrolyte interface. But we already know that holes in the case of an n-type semiconductor are responsible for the anodic photocurrent. Therefore, electrons have to be consumed by means of a cathodic reaction at the reference electrode at the same rate as holes in the anodic reaction in order to get a quasi-steady-state response. The slow photovoltage response, therefore, is limited by the charge transfer rate at the electrode surface. It cannot simply be due to a pH change in solution, because the quantities of electricity are entirely inadequate for such changes at steady states. Moreover, the photovoltage was found to be insensitive to stirring.

The photovoltage spectrum which was obtained by measuring the photovoltages at each wavelength was very similar to the photocurrent spectrum. In the presence of rhodamine B, the photovoltage spectrum revealed a big hump corresponding to the absorption band around 550 nm. Therefore, the photovoltage measurement can also be used to determine the position of energy levels and the relative number of states in the surface level just as the photocurrent measurement can.

Surface hydroxyl groups.—The presence of hydroxyl groups on natural crystals of Bolivian cassiterite SnO_2 was first determined by infrared absorption near $3.07 \mu m$ (26). The electrochemical behavior of the tin oxide which had been immersed in 1M KNO_3 for 3 days after photoexcitation work is shown in Fig. 10, curve B. The cyclic voltammogram shows not only high background and photocurrent but also a decrease in oxygen overvoltage by as much as 0.5V. Polishing the electrode with alumina made only a small change; however, heating at $90^\circ C$ for 3 hr (curve C) did improve its behavior. After further heating at $115^\circ C$ for 24 hr (curve D), the electrode showed about the same volt-

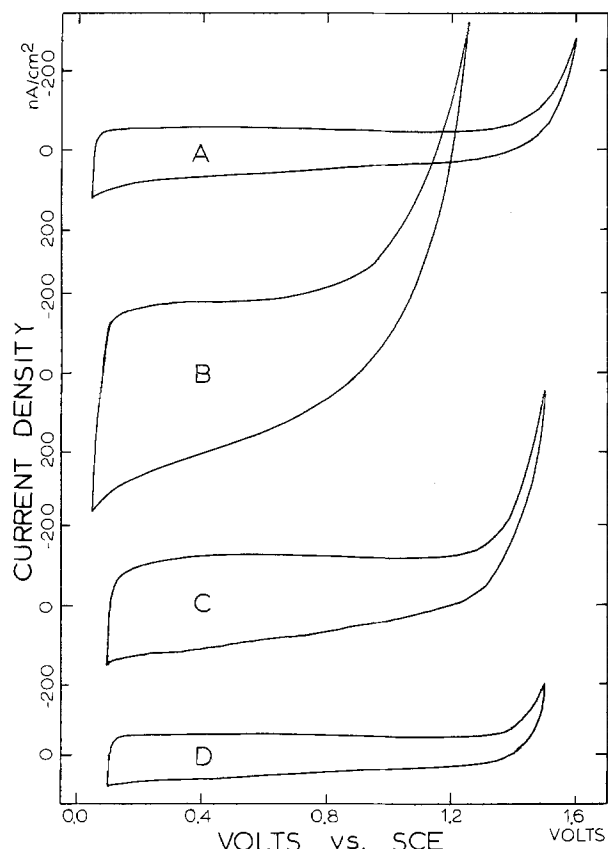
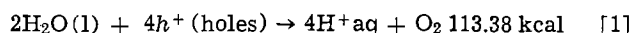


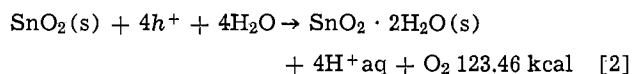
Fig. 10. Cyclic voltammograms of tin oxide electrode. Sweep rate = 20 mV/sec. A, Newly prepared electrode; B, 3 days old in 1M KNO_3 after photoexcitation work; C, dried at 90°C for 3 hr; D, dried at 115°C for 24 hr.

ammogram as shown by a newly prepared electrode. It is interesting that the wetting of the electrode surface is noticed even after polishing with alumina but not after heat-treatment. A new electrode is not wettable. Compared to the surface hydroxyl groups on silica or alumina which required much higher temperature and vacuum drying for complete removal, it seems very unlikely that such a gentle heat-treatment dehydrates a Sn-OH bond. A superficial hydrogen bonding interaction between oxide layers of SnO_2 and water molecules instead is proposed for the aging in the electrolyte. Presumably such an interaction is preserved under wet polishing conditions.

Proposed mechanism.—To determine whether the anodic decomposition of water or of the cassiterite lattice is energetically favorable we may compare the free energy changes of the reaction

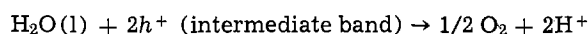
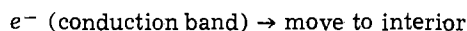
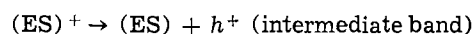
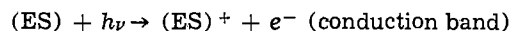


obtained from $\Delta G^\circ(\text{H}_2\text{O}) = -56.69 \text{ kcal/mole}$, and



obtained from $\Delta G^\circ(\text{SnO}_2(s)) = -124.2 \text{ kcal/mole}$, $\Delta G^\circ(\text{SnO}_2 \cdot 2\text{H}_2\text{O}(s)) = -227.5 \text{ kcal/mole}$, and $\Delta G^\circ(\text{H}_2\text{O})$ of reaction [2] requires more energy than reaction [1] by 10.08 kcal. Therefore, the decomposition of water is energetically favored. A prolonged experiment did not show any sign of decomposition of the electrode surface. The oxidation of water by photogenerated holes at TiO_2 electrodes also has been proposed (27).

Finally, the following scheme for the anodic photo-process at the tin oxide polycrystalline electrode is proposed



where (ES) represents the surface energy states due to the presence of impurities, defects, grain boundaries, and adsorbed molecules.

Acknowledgment

This research was supported by the National Science Foundation under grant GP 32847X.

Manuscript submitted Feb. 20, 1974; revised manuscript received Aug. 13, 1974. This was Paper 105 presented at the Houston, Texas, Meeting of the Society, May 7-11, 1972.

Any discussion of this paper will appear in a Discussion Section to be published in the December 1975 JOURNAL. All discussions for the December 1975 Discussion Section should be submitted by Aug. 1, 1975.

Publication costs of this article were partially assisted by the University of Illinois at Urbana-Champaign.

REFERENCES

1. R. Williams, *J. Chem. Phys.*, **32**, 1505 (1960).
2. H. Berg, *Naturwissenschaften*, **47**, 320 (1960).
3. M. Heyrovsky, *Nature*, **200**, 880 (1966).
4. G. C. Barker, A. W. Gardner, and D. C. Sammon, *This Journal*, **113**, 1182 (1966).
5. W. H. Brattain and C. G. B. Garrett, *Bell System Tech. J.*, **34**, 129 (1955).
6. H. Gerischer, *This Journal*, **113**, 1174 (1966).
7. F. Lohmann, *Ber. Bunsenges. Phys. Chem.*, **70**, 87 (1966).
8. R. Memming and H. Tributsch, *J. Phys. Chem.*, **75**, 562 (1971).
9. H. Gerischer, *Ber. Bunsenges. Phys. Chem.*, **69**, 578 (1965).
10. H. R. Schöppel and H. Gerischer, *ibid.*, **75**, 1237 (1971).
11. H. Gerischer and H. Tributsch, *ibid.*, **72**, 437 (1968); **73**, 850 (1969).
12. H. Kim, Ph.D. Thesis, University of Illinois, 1973.
13. H. A. Laitinen, C. A. Vincent, and T. M. Bednarski, *This Journal*, **115**, 1025 (1968).
14. D. Elliott, D. L. Zellmer, and H. A. Laitinen, *ibid.*, **117**, 1343 (1970).
15. J. M. Mochel, U.S. Pat. 2,564,707 (1951).
16. H. Kim and H. A. Laitinen, To be published.
17. E. A. Corl and H. Wimpfheimer, *Solid State Electron.*, **7**, 755 (1964).
18. P. Friedlaender, "Fortschritte der Teerfarbrikation und Verwandter Industriezweige," Vol. 2, pp. 68-72, Julius Springer, Berlin (1891).
19. R. G. Rhodes, "Imperfections and Active Centers in Semiconductors," pp. 259-270, Pergamon Press Oxford (1964).
20. F. Mollers and R. Memming, *Ber. Bunsenges. Phys. Chem.*, **76**, 469 (1972).
21. H. Gerischer, "Physical Chemistry an Advanced Treatise," H. Eyring, D. Henderson, and W. Jost, Editors, Academic Press, New York (1970).
22. R. Memming, *Photochem. Photobiol.*, **16**, 325 (1972).
23. D. R. Frankl, "Electrical Properties of Semiconductor Surface," pp. 186-194, Pergamon Press, Oxford (1967).
24. G. Heiland, W. Bauer, and M. Neuhaus, *Photochem. Photobiol.*, **16**, 315 (1972).
25. V. A. Myamlin and Yu. V. Pleskov, "Electrochemistry of Semiconductors," pp. 100-110, Plenum Publishing Corp., Inc., New York (1967).
26. E. E. Kohnke, *J. Phys. Chem. Solids*, **23**, 1557 (1962).
27. A. Fujishima and K. Honda, *Nature*, **238**, 37 (1972).

Light-Deflection Errors in the Interferometry of Electrochemical Mass Transfer Boundary Layers

F. R. McLarnon,* R. H. Muller,* and C. W. Tobias*

Inorganic Materials Research Division, Lawrence Berkeley Laboratory, and Department of Chemical Engineering, University of California, Berkeley, California 94720

ABSTRACT

The effect of light deflection on interferograms of electrochemical mass transfer boundary layers can result in substantial errors if interferograms are interpreted in the conventional way. Corrections in boundary layer thickness, interfacial concentration, and interfacial concentration gradient for the convection-free electrodeposition of Cu from aqueous CuSO_4 have been calculated to provide estimates for a wide range of experimental conditions.

Concentration profiles of single solutes in electrolytes near working electrodes can, in principle, be quantitatively observed by interferometric techniques. Such observations are useful in the study of transport processes and in the analysis of different measures designed to provide uniform accessibility and increased reaction rates at electrodes. Some of the advantages of interferometry compared to other means of observing boundary layers and local transport rates are: high resolution for concentration changes (typically 10^{-5}M) and, the possibility of continuous observation without disturbance (*e.g.*, of flow), not restricted to conditions of limiting current.

In the conventional interpretation of interferograms, local changes in the phase depicted by the interferogram are taken as a direct measure of local refractive index variations in the object. Such an interpretation is often not valid because it assumes that light travels along a straight line through the specimen. Refractive index variations normal to the propagation direction of the light beam produce a deflection of the beam (refraction, Schlieren effect) that results in two types of distortions in the interferogram: (i) Geometrical distortion due to displacement of the beam normal to its propagation direction. This effect falsifies conventional interpretation of distance on the interferogram and causes displacement of the apparent electrode/electrolyte interface. (ii) Phase distortion due to increased geometrical path length and passage of the beam through regions of varying refractive index. Quantitative concentration profiles, therefore, often cannot be derived by the conventional interpretation of interferograms.

Figure 1 schematically shows the trajectories of two light rays traversing a cathodic concentration boundary layer. Ray ABC is only slightly deflected and stays within the boundary layer over its path AB because it propagates near the edge of the boundary layer where the refractive index gradient is small. Ray DEF, which enters the electrolyte where the refractive index gradient is high, is deflected so much that it leaves the boundary layer at the intersection with line GH (and then travels along a straight line) before leaving the electrolyte at point E. A deflected ray will contribute to the interferogram only if it passes through the aperture of the objective lens. For instance, if ray DEF were to be deflected at any higher angle, it would not pass through the objective lens and, therefore, would not contribute to the interferogram. The corresponding part of the boundary layer would then not be visible on the interferogram.

Details of computational techniques, that have been developed to account for the effect of light deflection on interferograms of one-dimensional boundary layers, have been described elsewhere (1, 2). Suffice it to say that for any concentration profile, the shapes of

(double beam) interference fringes can now be calculated taking into account effects of light deflection. It has been found that distortions in the interferogram depend strongly on the position of the plane of focus of the imaging objective lens. Although for each concentration profile a plane of focus can be found (3) for which the location of the electrode surface is not distorted on the interferogram, it is preferable to use a more easily defined plane of focus at a fixed location and accept the resulting displacement of the electrode shadow. For the observation of cathodic boundary layers (to be considered here) we recommend (2) focusing on the inside of the cell wall on the light-entrance side of the cell, where suitable targets can be inscribed. (For anodic boundary layers, it would be preferable to focus on the inside of the cell wall on the light-exit side.)

It is the purpose of this paper to present calculations of light-deflection errors for the interferometric observation of boundary layers so that investigators may estimate errors to be expected under a wide range of experimental conditions.

Light-Deflection Errors

Figure 2 shows the experimental interferogram of a concentration boundary layer formed by constant-current electrolysis. Superimposed are the theoretical concentration profile, AE, derived by use of the Sand (4) equation, and an interference fringe, BF, computed from the concentration profile by taking light-deflection effects into account.

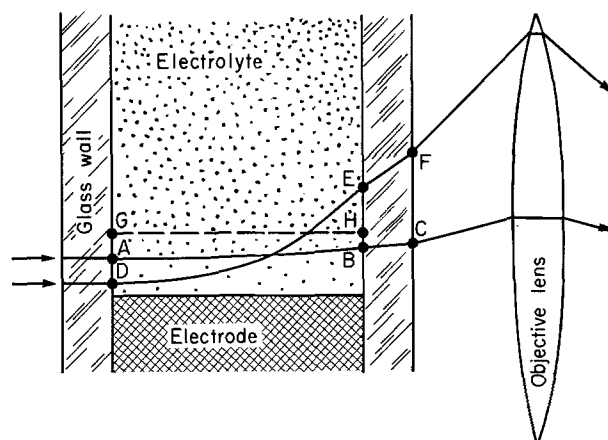
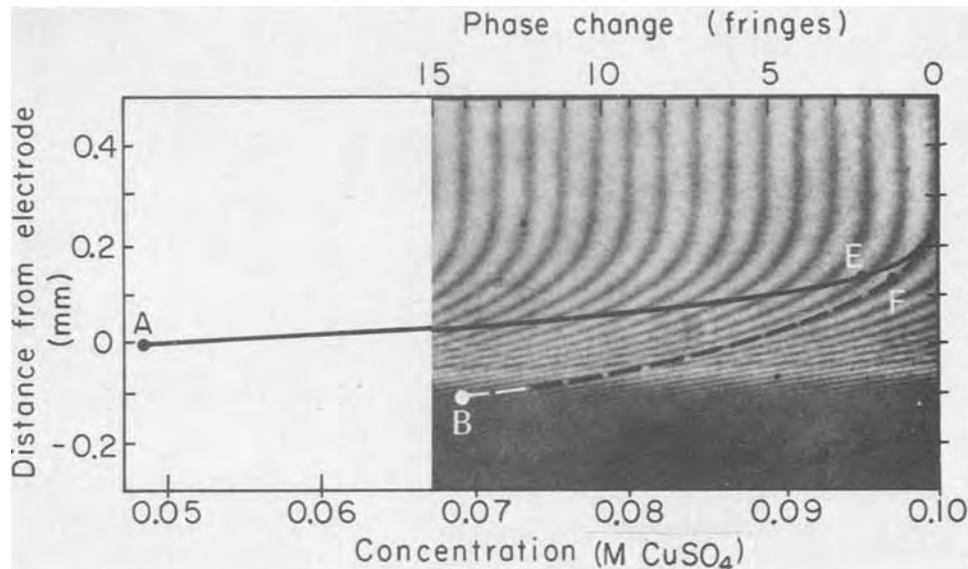


Fig. 1. Schematic of light ray trajectories in a cathodic concentration boundary layer: refractive index increases in the direction away from the electrode surface. ABC, trajectory of a ray that remains inside the boundary layer. DEF, trajectory of a ray that is deflected out of the boundary layer. GH, edge of the boundary layer.

* Electrochemical Society Active Member.

Key words: interferometry, refraction, diffusion, mass transfer.

Fig. 2. Experimental interferogram of a concentration boundary layer during galvanostatic deposition of copper on a 10 mm wide electrode. $i = 10.0 \text{ mA/cm}^2$, $C_b = 0.1 \text{ M CuSO}_4$, and $t = 10.0 \text{ sec}$. — Theoretical concentration profile AE corresponding to experimental conditions (calculated from Eq. [13]). - - - - Computed interference fringe BF corresponding to theoretical concentration profile. A, true interfacial concentration and position. B, apparent interfacial concentration and position. E, true (90%) boundary layer edge (position where $\theta = 0.9$). F, apparent boundary layer edge.



The ordinate on Fig. 2 denotes distance from the true (undistorted) image of the electrode surface. Local changes in the phase of transmitted light, visible as displacements of originally straight interference fringes, have been related to local concentration changes, as shown on the abscissa. The relationship has been based on the conventional interpretation of interferograms that assumes straight-line light propagation. Thus, local changes in phase have been linearly related to changes in concentration (or refractive index) at the corresponding point in the image.

If the interferogram was free of light-deflection effects, the interference fringes would follow the theoretical concentration profile AE. The figure illustrates that the apparent location B of the interface on the interferogram has receded from its original position A, identified by $y = 0$. Also, the apparent concentration change over the boundary layer is smaller than the true change.

Conventional interpretation of the interferogram in Fig. 2 would therefore lead to a boundary layer thickness that is too large. If we define the extent of the boundary layer as the region containing 90% of the concentration variation, the error e_t in boundary layer thickness can be defined in terms of the ordinates of the points shown in Fig. 2 as

$$e_t = (y_F - y_B) - (y_E - y_A)$$

Similarly, the apparent interfacial concentration is too high and the error can be formulated as a difference of abscissas

$$e_c = C_B - C_A$$

The interfacial concentration (refractive index) gradient is too low. The error can be represented by the difference in slope of the two curves at the interface

$$e_g = \left. \frac{dC}{dy} \right|_B - \left. \frac{dC}{dy} \right|_A$$

In addition to the above absolute errors in the interferometry of boundary layers, it is often desirable to estimate the relative errors. Such relative errors in boundary layer thickness, interfacial concentration, and interfacial concentration gradient, as shown in Fig. 8-13, are defined here as

$$\epsilon_t = \frac{e_t}{y_E}$$

$$\epsilon_c = \frac{e_c}{C_b - C_A}$$

$$\epsilon_g = \frac{e_g}{\left. \frac{dC}{dy} \right|_A}$$

Convection-Free Boundary Layers

Diffusion boundary layers free of convection effects offer a useful model for optical investigation since the concentration profiles are easily derived, and experimental results can serve to test the optical calculations. Convection-free transport conditions are common in electrochemical studies, and results can be used as a basis for convective transport studies.

The convectionless electrodeposition of a metal cation from a stagnant layer of an aqueous binary salt electrolyte is described by the time-dependent diffusion equation in one dimension¹

$$\frac{\partial C}{\partial t} = D \frac{\partial^2 C}{\partial y^2} \quad [1]$$

The current density is related to the interfacial concentration gradient by

$$i = \frac{zFD}{1 - t_+} \left. \frac{\partial C}{\partial y} \right|_{y=0} \quad [2]$$

For potentiostatic electrodeposition, the boundary conditions are

$$C = C_s \text{ at } y = 0, t > 0 \quad [3]$$

$$C = C_b \text{ at } t = 0, \text{ all } y \quad [4]$$

$$C = C_b \text{ as } y \rightarrow \infty \quad [5]$$

The solution, first obtained by Cottrell (5), is

$$\theta = \text{erf } \zeta \quad [6]$$

$$i = \frac{zF(\Delta C)}{1 - t_+} \sqrt{\frac{D}{\pi t}} \quad [7]$$

where erf ζ is the error function of dimensionless distance

$$\zeta = \frac{y}{2\sqrt{Dt}} \quad [8]$$

$\Delta C = C_b - C_s$ and the dimensionless concentration

$$\theta = \frac{C - C_s}{\Delta C} \quad [9]$$

For galvanostatic electrodeposition, the boundary conditions to Eq [1] are

$$\left. \frac{\partial C}{\partial y} \right|_{y=0} = \text{constant at } y = 0, t > 0 \quad [10]$$

¹ Concentration-independent diffusivity will be assumed. Solutions for variable diffusivity can also be obtained, although not in a convenient closed form.

$$C = C_b \text{ at } t = 0, \text{ all } y \quad [11]$$

$$C = C_b \text{ as } y \rightarrow \infty \quad [12]$$

The solution, first obtained by Sand (4), is

$$\theta = 1 + \sqrt{\pi} \zeta (1 - \text{erf } \zeta) - e^{-\zeta^2} \quad [13]$$

$$\Delta C = \frac{2i(1 - t_+)}{zF} \sqrt{\frac{t}{\pi D}} \quad [14]$$

Concentration profiles for use in the light-deflection analysis, with electrodeposition of Cu from aqueous CuSO₄ serving as a model, have been calculated. Equations [6] and [7] and Eq. [13] and [14] have been used in this computation. The interfacial concentration has been set C_s = 0, and the values of the bulk concentration were C_b = 0.01, 0.10, and 0.20M CuSO₄ (ΔC = 0.01, 0.10, or 0.20). For constant potential calculations, time *t* is varied to give different concentration profiles and interfacial mass flux rates. For constant current calculations, various current densities are used (substituting Eq. [2] into Eq. [10]) to give different concentration profiles and interfacial mass flux rates. (Note that specification of *i* and ΔC fixes *t* through Eq. [14].) A diffusion coefficient (6) *D* = 6 × 10⁻⁶ cm²/sec and Cu⁺⁺ transference number (7) *t*₊ = 0.36 (typical values for 0.1M CuSO₄ at 25°C) are used in all calculations. Representative concentration profiles employed in the optical analysis are shown in Fig. 3 and 4.

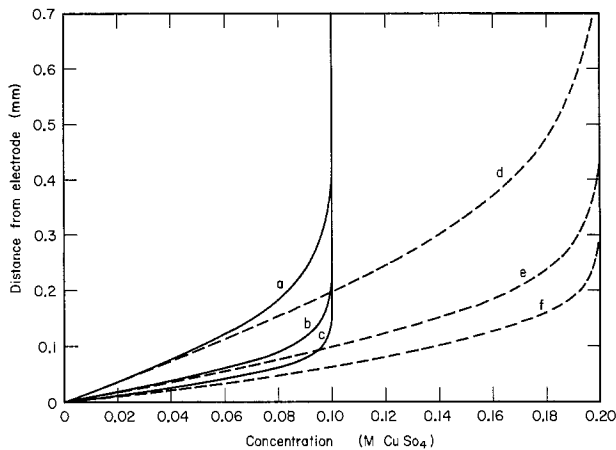


Fig. 3. Concentration profiles for potentiostatic conditions. — ΔC = 0.1M CuSO₄; - - - ΔC = 0.2M CuSO₄; a, *i* = 10.0 mA/cm², *t* = 17.5 sec; b, *i* = 20.0, *t* = 4.4 sec; c, *i* = 30.0, *t* = 1.9 sec; d, *i* = 10.0, *t* = 70.0 sec; e, *i* = 20.0, *t* = 17.5 sec; f, *i* = 30.0, *t* = 7.8 sec.

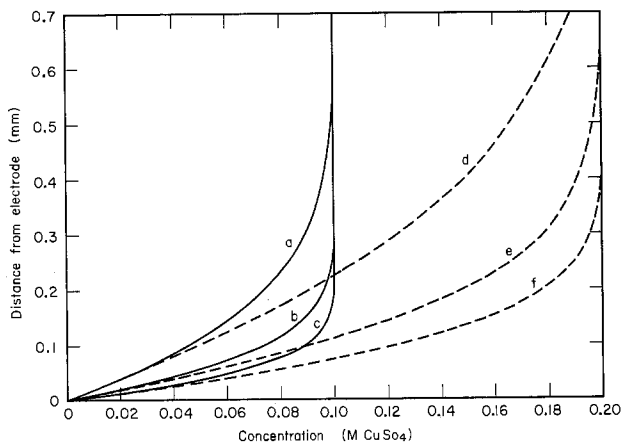


Fig. 4. Concentration profiles for galvanostatic conditions. ΔC and *i* designation as in Fig. 3. a, *t* = 43.2 sec; b, *t* = 10.8 sec; c, *t* = 4.8 sec; d, *t* = 172.7 sec; e, *t* = 43.2 sec; f, *t* = 19.2 sec.

Error Calculations

Cell dimensions and optical constants must be specified in order to compute interferograms from concentration profiles. The electrode, which is assumed here to fully occupy the space between the glass sidewalls, was assigned widths of 1.0, 2.5, 5.0, 10.0, and 20.0 mm. In order to model our experimental cell, the glass sidewalls were assumed to be 12.7 mm wide with a refractive index of 1.5231. However, refraction in the glass sidewalls has a negligible effect on light-deflection errors (3). Light of 632.8 nm wavelength is assumed incident parallel to the planar electrode surface and perpendicular to the glass sidewalls. The plane of focus is chosen as the plane where light enters the electrolyte. Electrolyte refractive index was experimentally found to be a linear function of CuSO₄ concentration at 632.8 nm wavelength and 25°C

$$n = 1.3311 + 0.029C \quad [15]$$

Interferograms similar to the dashed line in Fig. 2 are now calculated from concentration profiles using the above-mentioned computational technique (1).

Absolute errors in boundary layer thickness, interfacial concentration, and interfacial concentration gradient are shown in Fig. 5, 6, and 7, respectively, for a 10 mm wide electrode. Current density (interfacial refractive-index gradient) was chosen as abscissa because it is an easily measured variable. Note that a positive error means that the value of a variable on the interferogram is larger than the true value.

Relative errors in boundary layer thickness, interfacial concentration, and interfacial concentration gradient are shown in Fig. 8-13. Figures 8-10 also demonstrate the dependence of errors on concentration difference ΔC. The effect of electrode width is illustrated in Fig. 11-13.

Discussion

Figures 5-7 show that for a 10 mm wide electrode, the light-deflection errors depend strongly on current density and concentration difference ΔC and only weakly on the specific boundary condition (potentio-

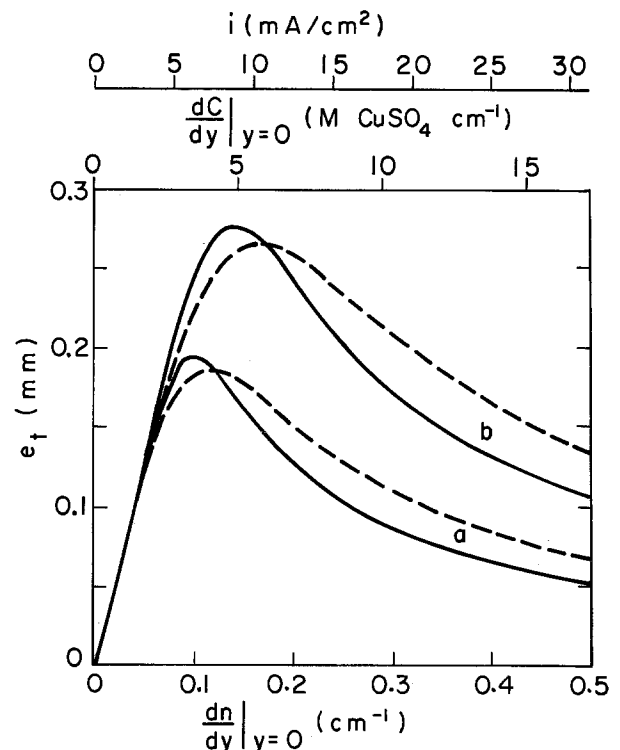


Fig. 5. Absolute error in boundary layer thickness. Electrode width = 10.0 mm. — potentiostatic boundary condition; - - - galvanostatic boundary condition; a, ΔC = 0.01M CuSO₄; b, ΔC = 0.10M CuSO₄; c, ΔC = 0.20M CuSO₄.

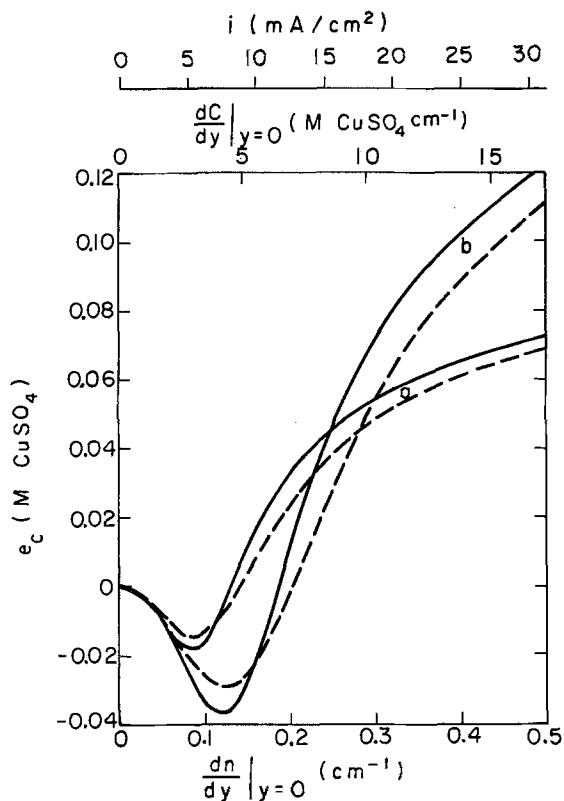


Fig. 6. Absolute error in interfacial concentration. Designations as in Fig. 5.

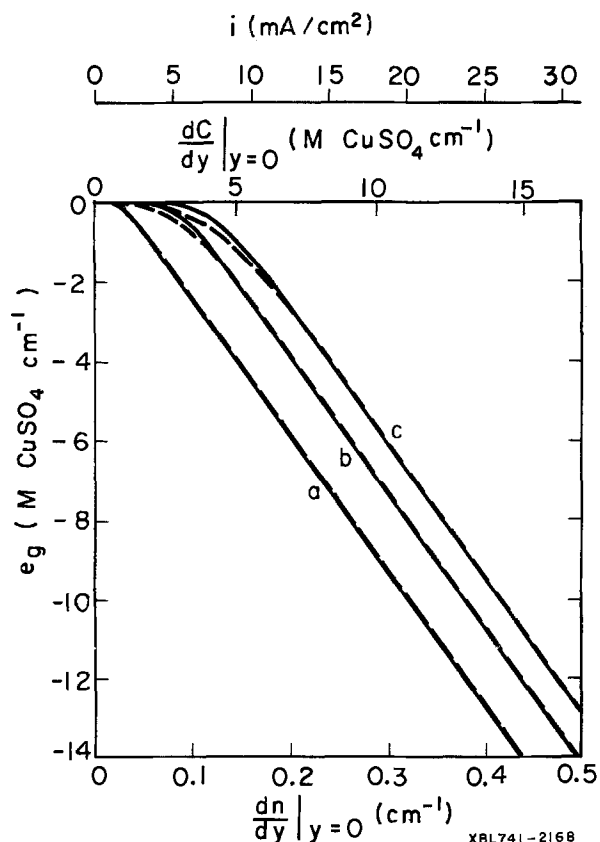


Fig. 7. Absolute error in interfacial concentration gradient. Designations as in Fig. 5.

static or galvanostatic). For current densities in the order of 1 mA/cm², the errors are independent of ΔC and boundary condition. The weak dependence on boundary condition can be ascribed to the similarity between the respective concentration profiles; com-

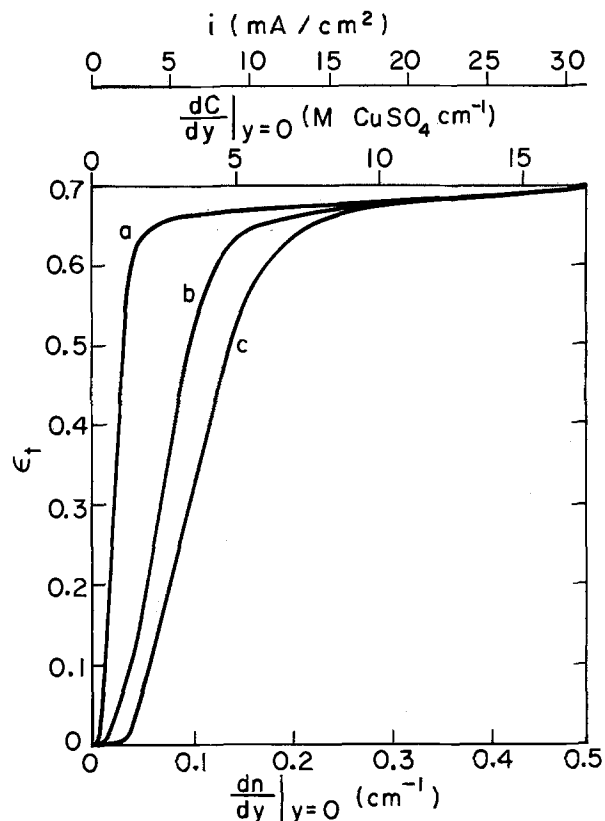


Fig. 8. Relative error in boundary layer thickness for various concentration differences. Electrode width = 10.0 mm, potentiostatic boundary condition. a, $\Delta C = 0.01M$ CuSO₄; b, $\Delta C = 0.10M$ CuSO₄; c, $\Delta C = 0.20M$ CuSO₄.

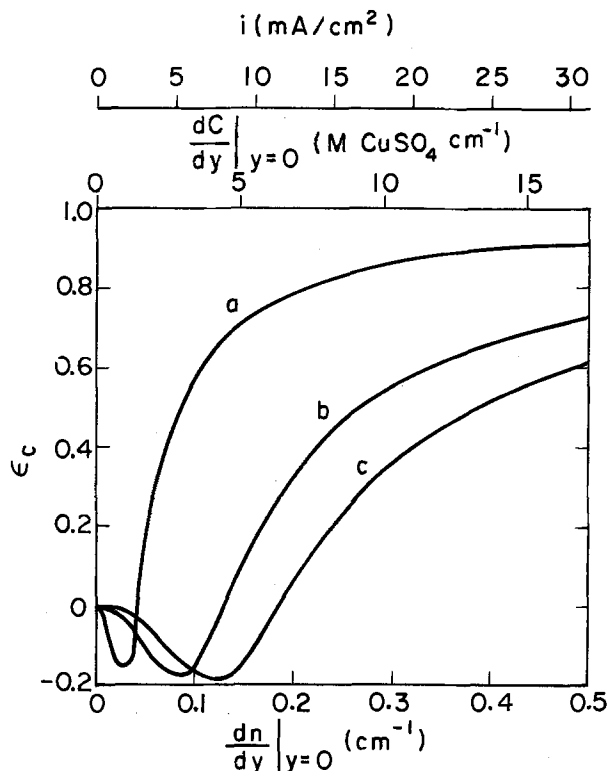
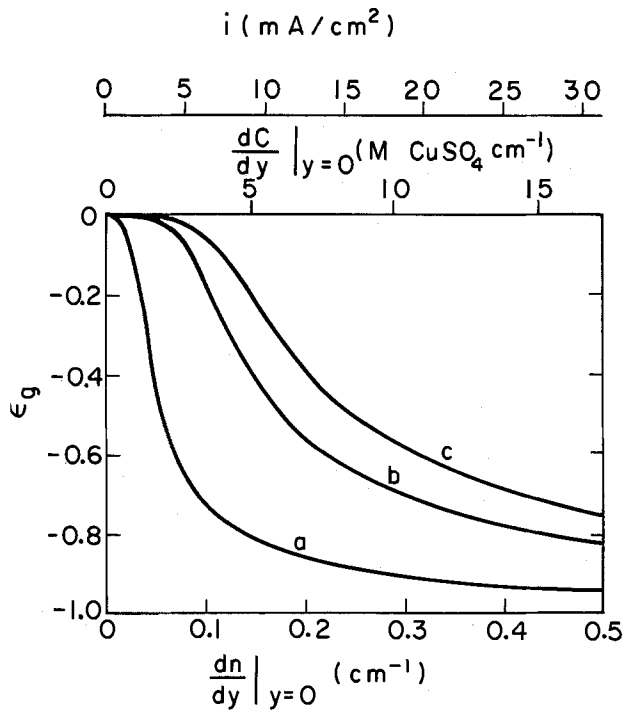


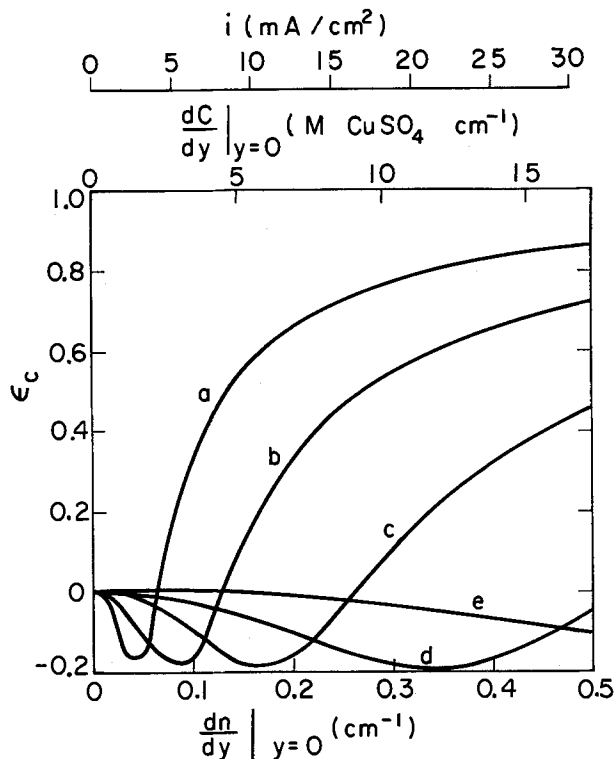
Fig. 9. Relative error in interfacial concentration for various concentration differences. Designations as in Fig. 8.

pare Fig. 3 and 4. Above about 2 mA/cm² for $\Delta C = 0.01M$ CuSO₄, about 7 mA/cm² for $\Delta C = 0.1M$, and about 10 mA/cm² for $\Delta C = 0.2M$, the light rays entering the boundary layer at the electrode surface are



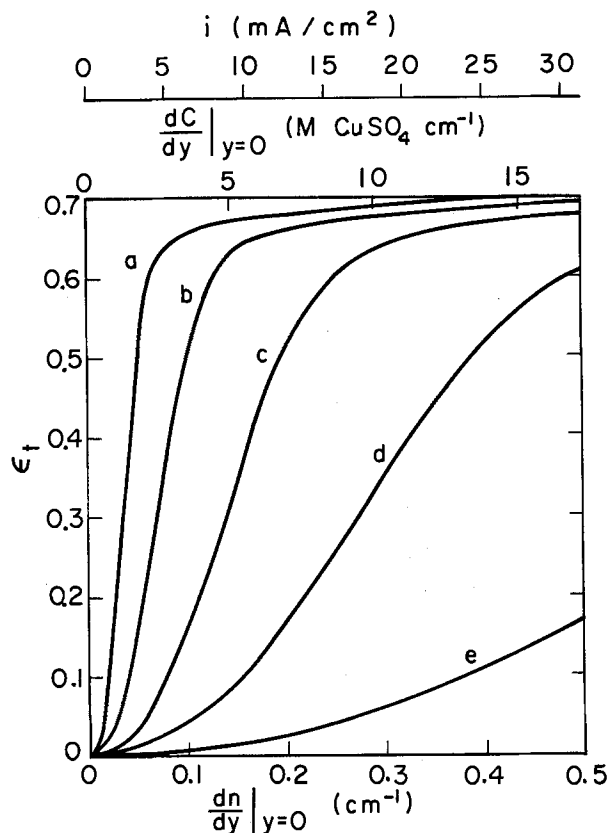
XBL741-2165

Fig. 10. Relative error in interfacial concentration gradient for various concentration differences. Designations as in Fig. 8.



XBL741-2163

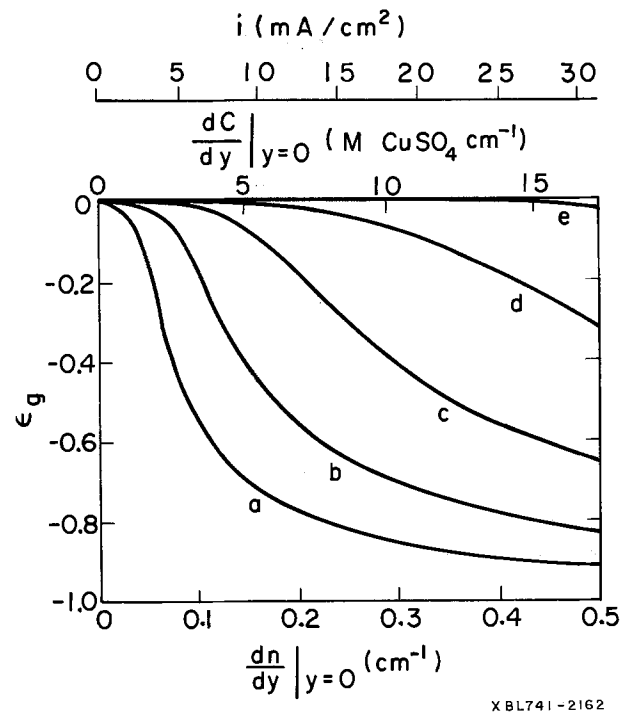
Fig. 12. Relative error in interfacial concentration for different electrode widths. Designations as in Fig. 11.



XBL741-2169

Fig. 11. Relative error in boundary layer thickness for different electrode widths. $\Delta C = 0.1M$ CuSO₄, potentiostatic boundary condition. a, electrode width = 20.0 mm; b, 10.0 mm; c, 5.0 mm; d, 2.5 mm; e, 1.0 mm.

deflected so much that they leave the boundary layer before they leave the electrolyte (as ray DEF in Fig. 1). This effect causes an error extremum in the curves of Fig. 5 and 6 and a knee in the curves of Fig. 7. The abrupt changes in the character of the error curves are due to the straight paths traversed by the deflected



XBL741-2162

Fig. 13. Relative error in interfacial concentration gradient for different electrode widths. Designations as in Fig. 11.

rays once they leave the boundary layer; at lower current densities the rays are continuously changing direction within the boundary layer. (Fig. 2 illustrates an interferogram in which rays entering the cell near the electrode surface are deflected out of the boundary layer.) As infinite current density is approached, the error in boundary layer thickness approaches zero, the error in interfacial concentration approaches ΔC , and the error in interfacial concentration gradient approaches negative infinity.

The trend toward apparent negative concentrations (i.e., on the interferogram) seen in Fig. 6, 9, and 12 is a result of the choice of focal plane position. For focus in the center of the cell, for instance, no such negative errors would occur.

Figures 8-10 show that, contrary to what one might expect, relative errors are generally smaller for larger concentration difference ΔC . However, for large concentration differences, interferogram interpretation can be impeded by crowding of the fringes near the interface.

Figures 11-13 show that similar to absolute errors derived analytically for constant concentration gradients of unlimited extent (3), relative errors strongly diminish with decreasing cell width, but are negligible only for electrodes thinner than a few millimeters.

Figures 5-13 can be used to estimate light-deflection errors in experimental interferograms if all deflected portions of the test beam are accepted by the objective lens. The maximum angle ϕ_{\max} of light deflection within a boundary layer is given by (2, 3)

$$\tan \phi_{\max} = \sqrt{\left(\frac{n_b}{n_s}\right)^2 - 1} \quad [16]$$

and the maximum angle of deflected light emanating from the specimen cell can be calculated by substituting numerical values of refractive index (e.g., Eq. [15] into Eq. [16]) and accounting for refraction in the glass sidewall. For example, the objective lens aperture must accept illumination at angles up to 1.59° for $\Delta C = 0.01M$ CuSO_4 , up to 4.65° for $\Delta C = 0.10M$, and up to 7.14° for $\Delta C = 0.20M$.

Conclusions

Light-deflection effects in the interferometry of electrochemical mass transfer boundary layers can lead to serious errors in the derivation of concentration profiles unless appropriate corrections in the interpretation of interferograms are employed. The magnitude of errors encountered may be estimated from the data presented in Fig. 5-13, but the accurate interpretation of interferograms with significant light-deflection effects requires individual optical analysis (2). Light-deflection errors are small (<10%) for small current densities (below 2.5 mA/cm^2 for a 1 cm wide electrode) or narrow electrodes (less than 2.5 mm for up to 10 mA/cm^2).

Acknowledgment

This work was conducted under the auspices of the U. S. Atomic Energy Commission.

Manuscript submitted March 19, 1974; revised manuscript received Aug. 12, 1974. This was Paper 352 presented at the San Francisco, California, Meeting of the Society, May 12-17, 1974.

Any discussion of this paper will appear in a Discussion Section to be published in the December 1975 JOURNAL. All discussions for the December 1975 Discussion Section should be submitted by Aug. 1, 1975.

Publication costs of this article were partially assisted by the Lawrence Berkeley Laboratory, University of California.

NOMENCLATURE

C	concentration (mole/liter)
C_b	bulk concentration (mole/liter)
C_s	interfacial concentration (mole/liter)
D	diffusion coefficient (cm^2/sec)
e_t	absolute error in boundary layer thickness (mm)
e_c	absolute error in interfacial concentration ($M \text{ CuSO}_4$)
e_g	absolute error in interfacial concentration gradient ($M \text{ CuSO}_4 \text{ cm}^{-1}$)
F	Faraday constant (coul/equiv)
i	current density (A/cm^2)
n	refractive index
n_b	bulk refractive index
n_s	interfacial refractive index
t	time after current (voltage) switch-on (sec)
t_+	cation transference number
y	distance from electrode (mm)
z	cation valence
ΔC	$C_b - C_s$ (mole/liter)
e_t	relative error in boundary layer thickness
e_c	relative error in interfacial concentration
e_g	relative error in interfacial concentration gradient
ξ	dimensionless distance (Eq. [8])
θ	dimensionless concentration (Eq. [9])
ϕ_{\max}	maximum angle of deflection within a boundary layer

REFERENCES

1. K. W. Beach, R. H. Muller, and C. W. Tobias, *J. Opt. Soc. Am.*, **63**, 559 (1973).
2. K. W. Beach, Ph.D. Thesis, University of California at Berkeley (1971).
3. R. H. Muller in "Advances in Electrochemistry and Electrochemical Engineering," R. H. Muller, Editor, Vol. 9, pp. 326-353, Wiley-Interscience, New York (1973).
4. H. J. S. Sand, *Phil. Mag.*, **1**, 45 (1901).
5. F. G. Cottrell, *Z. Physikal. Chem.*, **42**, 385 (1903).
6. W. G. Eversole, H. M. Kindsvater, and J. D. Peterson, *J. Phys. Chem.*, **46**, 370 (1942).
7. J. J. Fritz and C. R. Fuget, *ibid.*, **62**, 303 (1958).

Electrochemical Behavior of Rotating Iron Disks

Effect of Fe(III)

R. F. Tobias* and Ken Nobe*

School of Engineering and Applied Science, University of California, Los Angeles, California 90024

ABSTRACT

The electrochemical behavior of iron in deaerated H_2SO_4 containing ferric ions has been investigated with rotating disk electrodes. The rest potential and corrosion current of iron in 1N H_2SO_4 were not affected by variation in the angular velocity. On the other hand, the rest potential, E_m , and corrosion current of iron in 1N H_2SO_4 containing ferric ions varied with the ferric ion concentration, C , and the angular velocity of the iron disk, ω . E_m followed the relation

$$E_m = \text{constant} + 0.040 \log C + 0.020 \log \omega, \text{ volts}$$

The corrosion current of iron increased in the presence of ferric ions and was controlled by the diffusion of ferric ions. Diffusion coefficients of ferric and ferrous ions were determined: $D_{\text{Fe(III)}} = 5.2 \pm 0.3 \times 10^{-6}$ and $D_{\text{Fe(II)}} = 6.5 \pm 0.4 \times 10^{-6}$ cm^2/sec .

Metallic corrosion which is controlled by the diffusion of an electroreducible species in the solution can be studied conveniently with the rotating disk electrode technique. Previously, Makrides (1) examined the electrochemical behavior of rotating iron cylinders in $\text{H}_2\text{SO}_4\text{-Fe}_2(\text{SO}_4)_3$ solutions. He developed relationships between the rest potential (corrosion potential) and the ferric iron concentration and the rotation rate. In addition, he constructed anodic polarization curves from the rest potential-limiting diffusion current (ferric ion reduction) data, which was in good agreement with the experimental anodic polarization curve.

In this study the rotating disk electrode has been utilized to investigate the electrochemical behavior of iron in H_2SO_4 . The polarization and open-circuit characteristics of rotating iron disks in H_2SO_4 containing ferric sulfate at various rotation rates have been determined. In addition, the diffusion coefficients of ferric and ferrous ions have been determined from the limiting diffusion current densities for ferric and ferrous ion reduction, respectively. In contrast to the turbulent flow conditions in Makrides' studies with rotating cylinders (1), the rotating disk experiments were conducted within the laminar flow regime.

Experimental

The test electrodes were prepared from Ferrovac E iron rod stock which was turned down on a lathe to a diameter of either 1.25 or 0.65 cm. The rod was cut into 0.64 cm lengths with an Al_2O_3 abrasive cutoff wheel using water as a cutting lubricant. A Teflon sleeve was pressure-fitted about the cylindrical part of the electrode so that only the lower cross-sectional surface was exposed to the electrolyte. The outer diameter of the Teflon sleeve was 1.73 cm.

Before the test electrodes were mounted in the electrode assembly they were hand-polished with water-proof Al_2O_3 paper. Grit 240 was used initially to smooth out the rough surface, followed by 600 grit. After the polishing procedure the electrodes had a mirrorlike finish. The electrodes were then rinsed in water, wiped dry, placed in a Soxhlet column, and degreased with hot benzene for 4 hr. The degreased electrodes were annealed for 1 hr at 650°C and slowly cooled to room temperature under vacuum (pressure $<10^{-4}$ mm Hg). The finished electrodes were then stored in a desiccator until used.

The cell consisted of three parts: a separate compartment for the auxiliary electrode, the Pyrex jar, and the Teflon top. The Pyrex jar contained a ground glass joint, through which small amounts of a con-

centrated solution of $\text{Fe}_2(\text{SO}_4)_3$ or FeSO_4 were added to the solution from a precision burette equipped with a greaseless Teflon stopcock. The Teflon cell top had entry ports which provided space for the test electrode assembly, a Luggin capillary, a thermometer, a bubbler, and an entry to pass N_2 gas through the bottom and above the solution. The volume of electrolyte used was 1200 ml.

Analytical reagent grade chemicals and doubly distilled water were used to prepare the solutions. For the electrochemical studies of iron in the absence and presence of ferric sulfate, 1N H_2SO_4 was used for the supporting electrolyte. The ferric ion concentration was varied from 1.26 to 25.2 mM.¹ To determine limiting diffusion current densities for the reduction of ferrous ions, 0.5M sodium sulfate was used for the supporting electrolyte with the pH adjusted to 3.0 by addition of an appropriate amount of H_2SO_4 . The ferrous ion concentration was varied from 5.03 to 13.2 mM. After the electrolyte was placed in the cell, deaeration was accomplished by passing prepurified N_2 through the solution for at least 8 hr. All experiments were conducted at room temperature, $23^\circ \pm 1^\circ\text{C}$. All potentials are given with respect to a saturated calomel reference electrode (SCE).

The kinematic viscosity of the supporting electrolytes was measured with a Cannon-Ubbelohde semi-micro viscometer. For 1N H_2SO_4 , the kinematic viscosity was 0.973×10^{-2} cm^2/sec , while for the 0.5M sodium sulfate the kinematic viscosity was 1.088×10^{-2} cm^2/sec .

An Exact function generator Type 255 was used to drive a Wenking potentiostat for the potential sweep experiments. The potential-current data were recorded on a semilogarithmic scale by use of a Moseley Model 7561A logarithmic converter connected to a Moseley Model 7035AX-Y recorder.

The test sample was mounted in the electrode assembly. The iron electrode was washed with distilled water and then activated in 5N H_2SO_4 for 10 min. After activation, the sample was washed thoroughly with distilled water and then immersed in the cell solution. Then, cathodic potential sweeps were applied to the rotating disk electrode. In the preliminary experimental tests, sweep rates of 1, 10, and 100 mV/sec were investigated. Since the results of the two slower sweep rates were in good agreement, 10 mV/sec was selected for the experiments. After the hydrogen evolution reaction was determined by the first sweep, a known amount of ferric or ferrous sulfate was added to the cell from the burette. After the angular velocity

* Electrochemical Society Active Member.

Key words: corrosion, polarization, diffusion coefficients.

¹ Milligram ion.

was set to a specific value, the steady-state rest potential was recorded. Then, electroreduction experiments at one concentration were performed over the entire range of angular velocities selected before the concentration was increased to a new value.

A schematic diagram of the apparatus and the complete set of the experimental data are given elsewhere (2).

Results and Discussion

Fe-1N H₂SO₄ system.—In deaerated 1N H₂SO₄ solutions the steady-state rest potential (corrosion potential) of iron is -498 ± 8 mV and is not a function of the rotational velocity. The corrosion potential of iron is in reasonable agreement with Kelly (3) and with iron exhibiting Makrides' type i behavior (1) which exhibited an increase in corrosion potential with time from -550 mV to about a steady-state value of -515 mV.

The Tafel slope for hydrogen evolution, b_c , is 116 ± 8 mV/decade and is in good agreement with the values obtained by others (3-5). Makrides (1), on the other hand, reported lower values of the Tafel slope for the HER. The anodic Tafel slope, b_a , of 41 mV was also in good agreement with other workers (3, 4). Makrides (1), on the other hand, obtained values of about 60 mV for his type i electrodes.

The corrosion current, $I_{m,0}$, determined by extrapolation of the anodic and cathodic Tafel lines to the corrosion potential is 1.8×10^{-4} and 1.6×10^{-4} A/cm², respectively. $I_{m,0}$ can also be determined from the slope of the polarization, ϵ , vs. current density, I , plot in the region $\epsilon = 0$ as shown in Eq. [1].

$$I_{m,0} = \frac{b_a b_c}{2.303(b_a + b_c)} \left(\frac{dI}{d\epsilon} \right)_{\epsilon=0} \quad [1]$$

Equation [1], which was derived by Stern (6), is the basis of the polarization resistance method for the determination of the corrosion current. The $I_{m,0}$ value calculated from the polarization resistance plot for iron in 1N H₂SO₄ is 1.2×10^{-4} A/cm². The corrosion currents obtained in this study are in good agreement with those reported by Kelly (3) and Greene (7). Makrides (1) reports that the corrosion current obtained for his type i iron was 4.1×10^{-4} A/cm² by extrapolation of the cathodic Tafel line and the polarization resistance method and 5.6×10^{-4} A/cm² by extrapolation of the anodic Tafel line.

The electrochemical parameters of iron in 1N H₂SO₄ are summarized in Table I. These results are based on experiments with at least eight different electrodes.

Limiting diffusion currents for Fe(III) and Fe(II) reduction.—Typical cathodic polarization behavior of iron in 1N H₂SO₄ containing ferric ions at angular velocities varying from 625-4225 rpm is shown in Fig. 1. For this system at sufficiently large cathodic polarization the total cathodic current, I_c , consisted of the partial currents for the hydrogen evolution, I_H , and ferric ion reduction, $I_{Fe(III)}$, reactions. Makrides' results (1) indicate that the rate of ferric ion reduction on iron in acidic solutions is diffusion controlled. Thus

$$I_c = I_H + I_{Fe(III)} = I_H + I_L \quad [2]$$

where I_L is the limiting diffusion current.

Figure 2 represents a graphical description of the system. The cathodic polarization curves are given for

Table I. Electrochemical parameters of iron in 1N H₂SO₄

Rest potential (E_m)	-498 ± 8 mV (vs. SCE)
Corrosion current ($I_{m,0}$) (polarization resistance)	$1.2 \pm 0.3 \times 10^{-4}$ A/cm ²
Corrosion current ($I_{m,0}$) (anodic Tafel line extrapolation)	$1.8 \pm 0.3 \times 10^{-4}$ A/cm ²
Corrosion current ($I_{m,0}$) (cathodic Tafel line extrapolation)	$1.6 \pm 0.4 \times 10^{-4}$ A/cm ²
Anodic Tafel slope (b_a)	41 ± 3 mV/decade
Cathodic Tafel slope (b_c)	116 ± 8 mV/decade
Initial differential capacitance	42 ± 2 μ F/cm ²

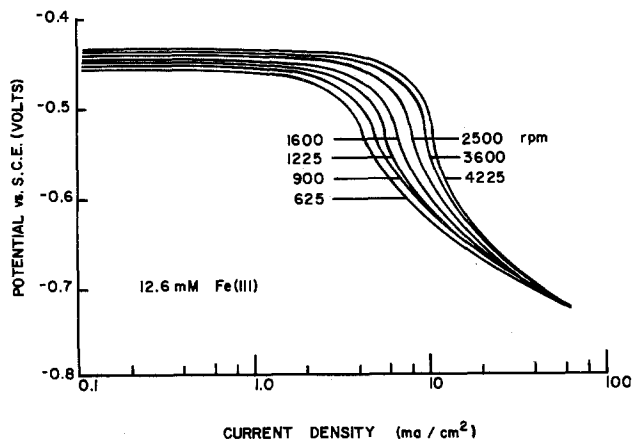


Fig. 1. Cathodic polarization of iron in 1N H₂SO₄ containing ferric ions.

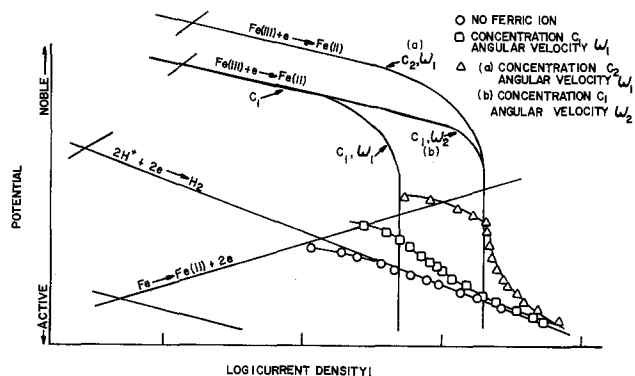


Fig. 2. Cathodic polarization of iron in absence and presence of ferric ions. Points represent calculated cathodic polarization data.

four different situations: first, in the absence of ferric ions; second, with ferric ion concentration, C_1 , and rotational velocity, ω_1 ; third, concentration, C_1 , and angular velocity, ω_2 ; fourth, concentration, C_2 , and angular velocity, ω_1 . For the case shown, $C_2 > C_1$ and $\omega_2 > \omega_1$. If the hydrogen evolution reaction is subtracted from the total cathodic current, the limiting diffusion current for the reduction of ferric ions is obtained. The square and triangle points shown in Fig. 2 represent cathodic polarization data constructed from the iron dissolution and the HER Tafel lines and the limiting diffusion currents for the reduction of ferric ions. The circle points represent cathodic polarization data constructed from the iron dissolution and the HER Tafel lines.

Figure 3 shows some typical results of the limiting current density for the reduction of ferric ions. These limiting currents were obtained in the following manner. First, before ferric ions were added to the sulfuric acid solution, the rate of hydrogen evolution on iron in 1N H₂SO₄ was determined. Then, with Eq. [2], the limiting diffusion currents for the reduction of ferric ions were obtained by subtracting the rate of the HER from the total measured current density obtained from the cathodic polarization curves of iron in solutions containing ferric ions as shown in Fig. 1.

The limiting current densities for the reduction of ferric ions vs. the square root of angular velocity are plotted in Fig. 4. A linear relationship is obtained in accord with the Levich equation for the limiting current density at a rotating disk electrode

$$i_L = 0.62 nFD^{2/3} \nu^{-1/6} \omega^{1/2} C \quad [3]$$

where the letters have their usual meaning.

Cathodic polarization measurements of iron in Na₂SO₄ (pH = 3) were conducted at various angular velocities in the absence (Fig. 5) and in the presence (Fig. 6) of ferrous ions. The observed limiting diffusion currents in Fig. 6 are the sum of the limiting dif-

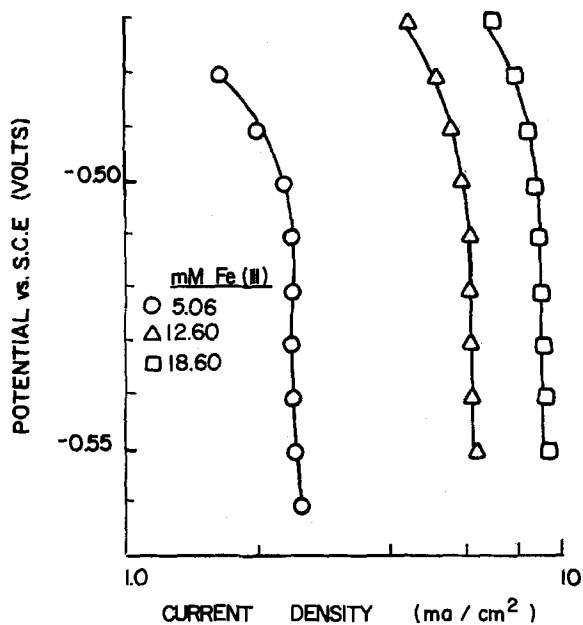


Fig. 3. Limiting diffusion currents for ferric ion reduction; $\omega = 1225$ rpm.

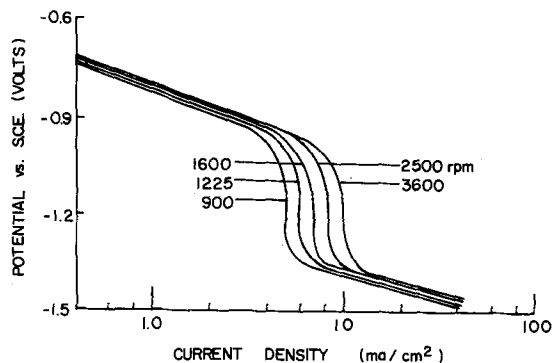


Fig. 5. Cathodic polarization of iron in $0.5M Na_2SO_4$ ($pH = 3$)

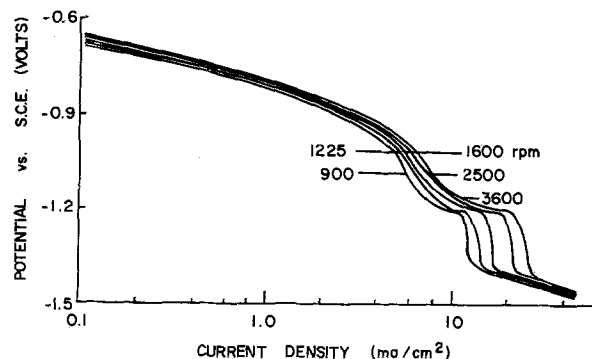


Fig. 6. Cathodic polarization of iron in $0.5M Na_2SO_4$ ($pH = 3$) containing ferrous ions (6.68 mM).

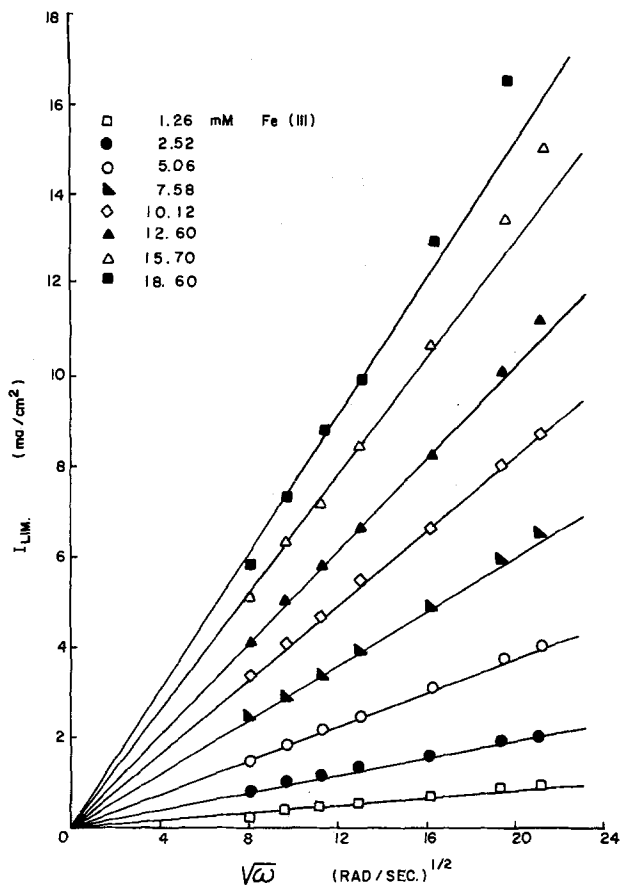


Fig. 4. I_L vs. $\sqrt{\omega}$ for ferric ion reduction

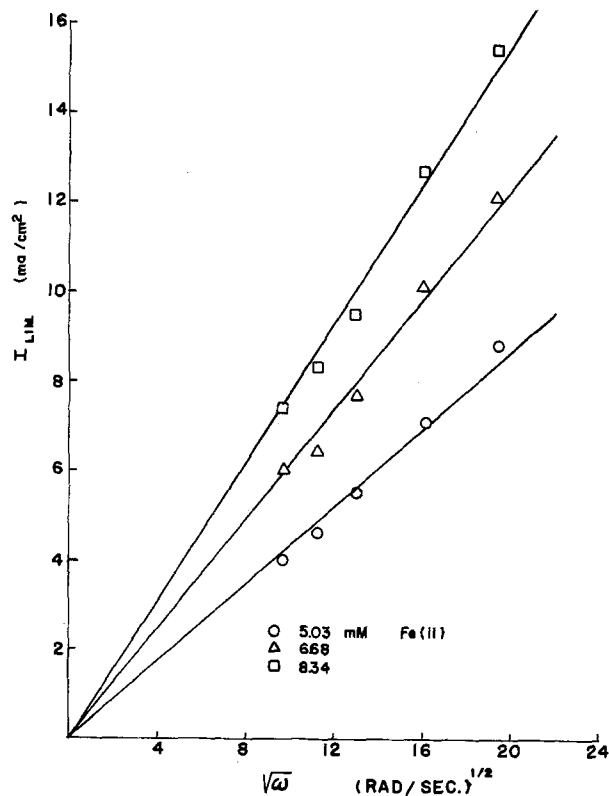


Fig. 7. I_L vs. $\sqrt{\omega}$ for ferrous ion reduction

fusion currents for hydrogen ion and ferrous ion reduction. The limiting diffusion currents for ferrous ion reduction are readily determined by subtracting the I_L for hydrogen ion reduction (Fig. 5) from the total diffusion current (Fig. 6). Figures 7 and 8 show the limiting diffusion current for the reduction of ferrous ions vs. the square root of the angular velocity and the concentration of the ferrous ions, respectively. In both plots Levich behavior is obtained.

Fe-1N H₂SO₄-Fe₂(SO₄)₃ system.—The rest potential behavior of iron in the presence of ferric ions showed

a marked dependence on both the concentration of ferric ions and the angular velocity of the iron disk. The data presented in Fig. 9 show the dependence of the rest potential on the concentration of the ferric ions over the range of angular velocities, 625–4225 rpm. ΔE_0 is defined as the rest potential of iron in the presence of ferric ions and at an angular velocity, ω , rela-

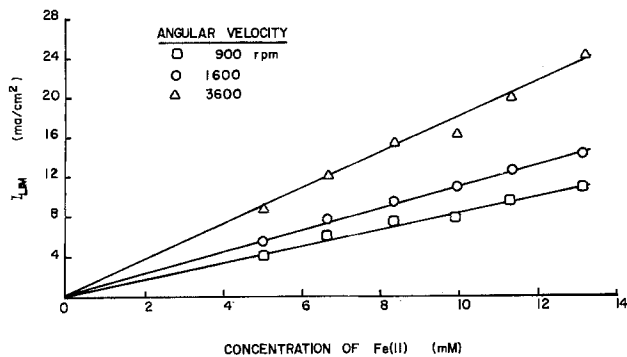


Fig. 8. I_L vs. concentration of Fe(II) for ferrous ion reduction

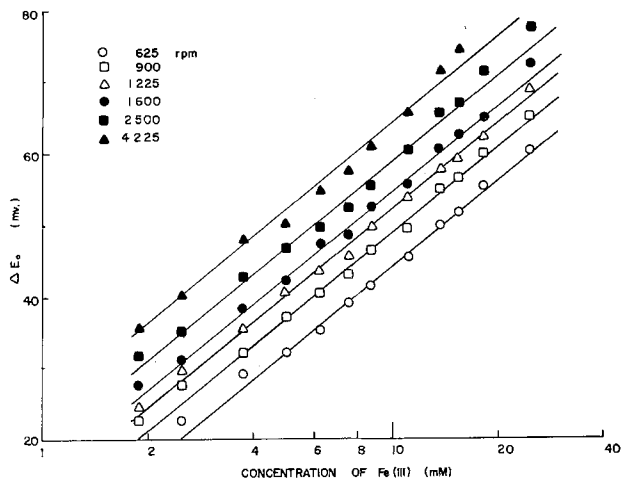


Fig. 9. ΔE_0 vs. concentration of Fe(III)

tive to the rest potential of iron in the absence of ferric ions.

For iron in an acidic media containing only reducible species, H^+ and H_2O , the corrosion current $I_{m,o}$ is

$$I_{m,o} = I_a = I_c \quad [4]$$

where I_a is the partial anodic process corresponding to iron dissolution and I_c is the partial cathodic process corresponding to the reduction of hydrogen ions.

For activation-controlled iron dissolution and HER, the total measured current for iron in H_2SO_4 can be represented by

$$I = I_{m,o} \left[\exp\left(\frac{\alpha_a n_a F \epsilon}{RT}\right) - \exp\left(\frac{-(1 - \alpha_c) n_c F \epsilon}{RT}\right) \right] \quad [5]$$

where the electrode kinetic parameters have their usual meaning. The first term on the right-hand side of Eq. [5] represents the rate of anodic dissolution of iron and the last term represents the rate of hydrogen evolution. The anodic dissolution term can be rearranged to obtain the Tafel equation

$$\epsilon_a = A + b_a \log I_a \quad [6]$$

If another easily reducible species is introduced into the solution (e.g., Fe^{+3}), the total cathodic current would consist of the sum of the rate of hydrogen evolution and the rate of reduction of the added oxidized species, i.e.

$$I_c = I_H + I_{ox} \quad [7]$$

When ferric ions are added to the iron-sulfuric acid system, the rate of ferric ion reduction is diffusion controlled as mentioned above. For this situation, $I_{ox} = I_L$, and the cathodic current can be expressed by Eq. [2]. For the conditions studied in this work

$$I_L \gg I_H \quad [8]$$

Thus

$$I_c \approx I_L \quad [9]$$

and at the rest potential, E_m

$$I_m = I_a = I_L \quad [10]$$

where I_m is the corrosion current of iron in H_2SO_4 containing ferric ions. Since the limiting diffusion current is independent of potential, the rest potential, E_m , is determined by the intersection of the anodic polarization curve and I_L .

The rate of iron dissolution in the absence of ferric ions at the rest potential, $E_{m,o}$, can be expressed as

$$I_{m,o} = I_a = i_{o,a} \left[\exp\left(\frac{\alpha_a n_a F}{RT} (E_{m,o} - E^e_a)\right) \right] \quad [11]$$

where E^e_a is the equilibrium potential of the Fe/Fe^{+2} reaction.

When ferric ions are added to the solution, the corrosion current can be expressed as

$$I_m = I_L = I_a = i_{o,a} \exp\left[\frac{\alpha_a n_a F}{RT} (E_m - E^e_a)\right] \quad [12]$$

where E_m is the rest potential of iron in the presence of ferric ions. The quantity, $(E_m - E^e_a)$, can be rearranged to

$$E_m - E^e_a = (E_m - E_{m,o}) + (E_{m,o} - E^e_a) = \Delta E_0 + (E_{m,o} - E^e_a) \quad [13]$$

where ΔE_0 is defined as the change in the rest potential with the addition of ferric ions to the H_2SO_4 solution. Equations [11] and [13] can be used to express Eq. [12] in the following form

$$I_m = I_L = I_{m,o} \exp\left[\frac{\alpha_a n_a F}{RT} \Delta E_0\right] \quad [14]$$

or rearrange Eq. [14]

$$\Delta E_0 = a' + b_a \log I_L \quad [15]$$

ΔE_0 can be expressed as a function of both the ferric ion concentration and the angular velocity by utilizing the Levich equation for I_L , Eq. [3]. Then, Eq. [15] becomes

$$\Delta E_0 = a + b_a \log C_{Fe(III)} + \frac{b_a}{2} \log \omega \quad [16]$$

Thus, ΔE_0 is shown to be a linear function of the logarithm of the ferric ion concentration with proportionality constant equal to the anodic Tafel slope obtained from anodic polarization experiments. The continuous lines in Fig. 9 have slopes of 40 mV/decade. Thus, the experimental data are consistent with Eq. [16], since a value of 41 mV for b_a was determined directly from anodic polarization measurements.

Figure 10 shows a plot of ΔE_0 vs. $\log \omega$ at constant ferric ion concentration. The experimental data fit the continuous lines well. The slopes of these lines are 20 mV/decade which is consistent with the $\frac{1}{2} b_a$ slopes predicted by Eq. [16].

Figure 2 indicates that a plot of ΔE_0 vs. I_L should give the anodic polarization curve for anodic dissolution of iron in H_2SO_4 . The effect of ferric ions on iron dissolution should be evident by comparing the anodic polarization curves obtained from the ΔE_0 vs. I_L plots and curves obtained by direct anodic polarization. Figure 11 provides such a comparison. The data points obtained by the two methods are in reasonable agreement indicating that the anodic polarization of iron in H_2SO_4 is not affected appreciably by the addition of ferric ions. These results are in accord with those obtained by Makrides (1) who showed that ferric ions had no specific effect on the anodic polarization of rotating cylindrical iron electrodes.

Since the corrosion rate is controlled by the limiting diffusion current for ferric ion reduction when ferric ions are introduced into the $Fe-H_2SO_4$ system, the cathodic Tafel slope is infinity ($b_c = \infty$). Then, Eq. [1]

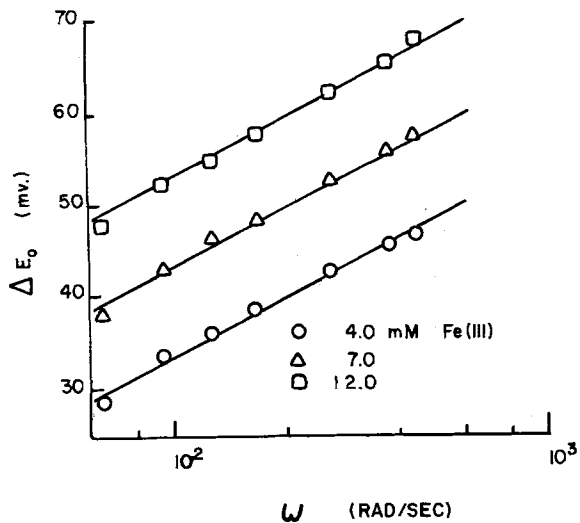


Fig. 10. ΔE_0 vs. $\log \omega$ plot

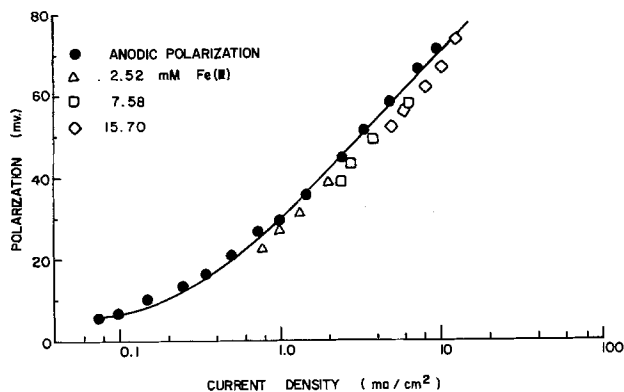


Fig. 11. Anodic dissolution of iron. Closed points represent anodic polarization data. Open points represent rest potential vs. I_L plots at various concentrations of Fe(III).

becomes

$$I_m = I_L = \frac{b_a}{2.303} \left(\frac{dI}{d\epsilon} \right)_{\epsilon=0} \quad [17]$$

Figure 12 shows typical linear plots of ϵ vs. I for small values of ϵ at a constant concentration of ferric ions. The corrosion current of iron at various angular velocities can be calculated from Eq. [17] and the slopes of these lines. Table II compares the corrosion

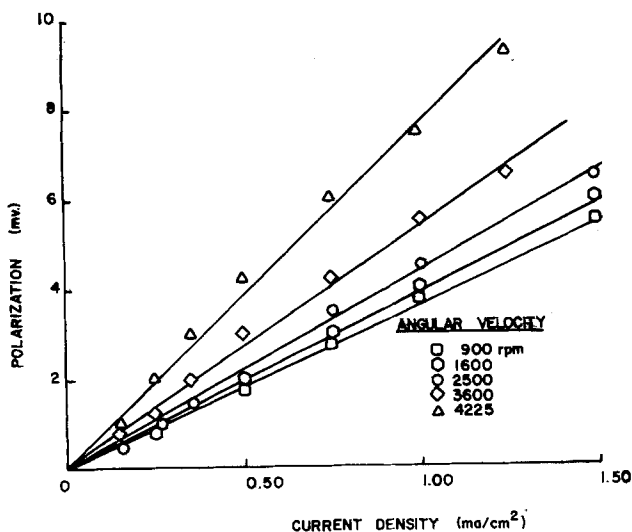


Fig. 12. Polarization resistance plot of iron in 1N H_2SO_4 and 7.5 mM Fe(III).

Table II. Corrosion currents of iron in acidic ferric sulfate solutions

Fe(III) conc, mM	Angular velocity, rpm	$\left(\frac{d\epsilon}{dI} \right)_{\epsilon=0}$	I_m (polarization), mA/cm ²	I_m (polarization), mA/cm ²
2.52	900	13.6	1.3	1.1
	1,600	11.6	1.5	1.5
	2,500	9.6	1.9	1.8
	3,600	8.2	2.2	2.2
	4,225	7.2	2.5	2.4
5.06	900	9.8	1.8	2.1
	1,600	7.0	2.6	2.7
	2,500	5.9	3.0	3.4
	3,600	5.0	3.6	4.0
	4,225	4.5	4.0	4.4
7.58	900	7.6	2.4	3.1
	1,600	5.4	3.3	4.1
	2,500	4.4	4.1	5.2
	3,600	3.9	4.6	6.1
	4,225	3.6	5.0	6.6
10.12	900	5.0	3.6	4.2
	1,600	3.8	4.7	5.2
	2,500	3.4	5.2	6.7
	3,600	3.0	6.0	8.2
	4,225	2.6	6.9	8.8
12.60	900	4.8	3.7	5.3
	1,600	3.1	5.8	6.7
	2,500	2.8	6.3	8.4
	3,600	2.2	8.3	10.2
	4,225	2.0	9.2	11.1

Table III. Diffusion coefficients of ferrous and ferric ions

Diffusion coefficient $\times 10^6$ (cm ² /sec)		Supporting electrolyte	Temp, °C	Reference
Ferric ion	Ferrous ion			
5.2 ± 0.3	6.5 ± 0.4	1N H_2SO_4	23	This work
4.5 ± 0.1	5.6 ± 0.2	0.5M Na_2SO_4	23	This work
3.92	4.21	1M H_2SO_4	25	8
		0.1M $HClO_4$	23	9
		1M $HClO_4$	25	10

currents obtained by the polarization resistance method and by the cathodic polarization method. In general, the corrosion currents obtained by cathodic polarization are larger than the corrosion currents obtained by the polarization resistance method. However, for the lower ferric ion concentrations the corrosion currents of iron determined by the two methods are in good agreement.

Diffusion coefficients of Fe(III) and Fe(II).—Diffusion coefficients of electroactive species can be readily determined from limiting diffusion current plots of rotating disk electrode experiments. The diffusion coefficients of ferric and ferrous ions were determined from the I_L vs. $\sqrt{\omega}$ and concentration plots as in Fig. 4, 7, and 8. These values are presented in Table III. For comparison, diffusion coefficients reported by several other workers (8-10) are also given in Table III.

Acknowledgments

This work was supported by the University of California sea water desalination program. One of us (R. F. T.) was a NASA predoctoral trainee during a part of this investigation.

Manuscript submitted March 21, 1974; revised manuscript received July 27, 1974.

Any discussion of this paper will appear in a Discussion Section to be published in the December 1975 JOURNAL. All discussions for the December 1975 Discussion Section should be submitted by Aug. 1, 1975.

REFERENCES

1. A. C. Makrides *This Journal*, **107**, 869 (1960).
2. R. F. Tobias, Ph.D. Dissertation, UCLA, March 1968.
3. E. J. Kelly, *This Journal*, **112**, 124 (1965).
4. J. O'M. Bockris and D. Drazic, *Electrochim. Acta*, **7**, 293 (1962).
5. T. Hurlen, *Acta Chem. Scand.*, **14**, 1533 (1960).
6. M. Stern and A. L. Geary, *This Journal*, **109**, 56 (1957).

7. N. D. Greene and G. A. Saltzman, *Corrosion*, **20**, 292t (1964).
 8. A. M. Baticle, F. Perdu, and P. Vennereau, *Compt. Rend. Acad. Sci. Paris*, **t264**, 12 (1967).

9. L. B. Anderson and C. N. Reilley, *J. Electroanal. Chem.*, **10**, 295 (1965).
 10. D. Jahn and W. Vielstich, *This Journal*, **109**, 849 (1962).

Double-Layer Capacity Determination of Porous Electrodes

William Tiedemann*

Globe-Union, Incorporated, Corporate Applied Research Group, Milwaukee, Wisconsin 53201

and John Newman*

Inorganic Materials Research Division, Lawrence Berkeley Laboratory, and Department of Chemical Engineering, University of California, Berkeley, California 94720

ABSTRACT

A method is presented for evaluating double-layer charging of porous electrodes. The maximum in the curve of $i\sqrt{t}$ vs. \sqrt{t} lends itself readily to experimental evaluation. Values of the double-layer capacity determined for the Pb and PbO₂ electrodes in sulfuric acid are in agreement with those reported in the literature.

A number of models have been developed for analyzing the behavior of porous electrodes, and various degrees of complexity have been taken into account. The transient charging of the double-layer capacity (1-5) is of interest first of all because it provides a comparison between experimental and theoretical results. The transient charging can also be used to advantage to measure the capacity per unit volume of the electrode. A measurement of the double-layer capacity reflects most directly the active surface area coherently connected electrically and therefore accessible for electrochemical consumption. Such results should be useful for the characterization of battery electrodes and may be especially valuable since the electrode is not destroyed and indeed need not be removed from the cell in which it is cycled.

Transient measurement of the double-layer capacity of porous electrodes, as opposed to integration of the current passed following a potential step, has the advantage of emphasizing the charging current relative to the faradaic current, which interferes with the measurement. Furthermore, the resistance-capacity time constant will be large for an electrode with a large surface area, and the transient measurement will then reduce the experiment time substantially.

Johnson and Newman (4) have shown that the current response of a porous electrode to a step change in the potential yields, under certain circumstances, a nearly constant value of $i\sqrt{t}$, the product of the current density and the square root of time. A plot of $i\sqrt{t}$ vs. \sqrt{t} yields a curve with a plateau. The curve is below this plateau value at short times because the ohmic resistance of the system prevents an infinite current density. At long times the curve again drops below the plateau value because the total capacity of the electrode begins to become saturated. The plateau value on a graph of this type is directly related to aC , the product of the specific interfacial area of the electrode and the double-layer capacity per unit area, and is independent of the thickness of the electrode. In this manner, Johnson and Newman inferred a value of $aC = 83.5$ farads/cm³ for their porous carbon electrode.

However, most battery electrodes (for example, Pb and PbO₂ electrodes in sulfuric acid) are so thin

that the ohmic limitation at short times overlaps with the approach to saturation at long times, and the plateau on the plot of $i\sqrt{t}$ vs. \sqrt{t} is reduced to a maximum whose magnitude now depends on the electrode thickness or an equivalent parameter. This maximum still deserves the focus of our attention in a simple method for inferring the double-layer capacity aC from the measured transient current response. The earlier part of the curve is governed by the ohmic resistance, not the capacity, and the latter part is subject to interference from faradaic reactions. (This difference between thick porous carbon electrodes and thin battery electrodes can be visualized graphically by referring below to Fig. 2, where basically $i\sqrt{t}$ is plotted against \sqrt{t} , although dimensionless variables are used. The parameter λ is inversely proportional to the electrode thickness, if the matrix conductivity is very high.)

Analysis

Figure 1 is a diagram of the equivalent circuit of the system. R_2 represents the resistance of the solution in the pores of the electrode; R_1 that of the electrode matrix. C is the double-layer capacity between the electrode matrix and the pore solution. R_s corresponds to the resistance in the solution between the porous electrode and the reference electrode while R_L

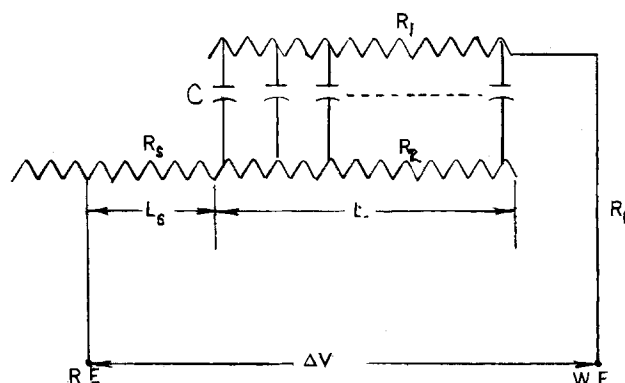


Fig. 1. Equivalent circuit of a porous electrode. The right side of the resistors represents a plane of symmetry in the center of the electrode.

* Electrochemical Society Active Member.

Key words: double-layer capacity, porous electrodes, lead-acid battery.

corresponds to the resistance in the leads and the current collector. For this system, Johnson and Newman (4) have related the Laplace transform of the current response to the Laplace transform of the applied potential. We make the following re-interpretation of their Eq. [20] (4) by including the resistance of the leads and that between the porous electrode and the reference electrode

$$R = \frac{L_s}{\kappa_s} + \frac{L}{\sigma + \kappa} + R_L \quad [1]$$

where L_s is the distance between the reference electrode and the porous electrode (κ_s being the conductivity of the medium between the two), L is the half thickness of a porous electrode with a counterelectrode opposite each face, σ is the effective conductivity of the matrix of the porous electrode, and κ is the effective conductivity of the pore solution. The terms in Eq. [1] have units of ohm-cm²; consequently, R_L is the lead resistance multiplied by twice the apparent cross-sectional area of a porous electrode with a counterelectrode opposite each face.

Thus, R is the effective resistance of the composite system and is subject to direct experimental determination as we shall discuss briefly. At zero time, the current cannot be infinite; it is limited by the effective resistance of the system

$$i|_{t=0} = \Delta V/R \quad [2]$$

where $i|_{t=0}$ is the peak current density at time zero and ΔV the applied potential step between the reference and working electrodes. Thus, R can be directly obtained from the initial current surge measured on an oscilloscope.

Let us consider the case of a highly conducting matrix, $\sigma \gg \kappa$ (for Pb and PbO₂ electrodes, $\sigma \approx 10^2$ and $\kappa \approx 0.1$ mho/cm). Posey and Morozumi (1) were the first to treat extensively double-layer charging of porous electrodes of finite thickness. They used a straight pore model and a highly conducting matrix. In an example involving the resistance between the working and reference electrodes, they inverted the Laplace transforms which are applicable to the system discussed in this paper. After some rearrangement the solution is

$$\frac{i\sqrt{\pi T}}{\Delta V} \frac{L}{\kappa} = 2\sqrt{\pi T} \sum_{n=1}^{\infty} \frac{\exp(-TX_n^2)}{1 + \lambda + \lambda^2 X_n^2} \quad [3]$$

where

$$T = \frac{t}{aCL} \frac{\kappa}{L} \text{ and } \lambda = \frac{R\kappa}{L} \quad [4]$$

aC is the double-layer capacity per unit volume of the electrode, and X_n is the positive root of cotangent $X_n = \lambda X_n$ [tabulated by Abramowitz and Stegun (6)]. In this result, no attempt has been made to account for faradaic reaction or concentration variations in the pore solution.

Since in our interpretation of the charging current we seek to emphasize the maximum in the curve of $i\sqrt{t}$ vs. \sqrt{t} , we plot in Fig. 2 the left side of Eq. [3] against \sqrt{T} . For $\lambda = 0$ the ordinate is a constant for short times. This corresponds to the plateau value discussed earlier, where

$$i\sqrt{t} = \Delta V \sqrt{aC\kappa/\pi} \quad [5]$$

At longer times, the value of $i\sqrt{t}$ begins to decrease as the charging wave penetrates to the center of the electrode. For $\lambda = 0$ the ohmic limitation at short times is not seen on this scale.

As the effective resistance in the circuit is increased ($\lambda > 0$), the instantaneous charging current is reduced, and the ordinate is initially zero. Providing the effective resistance is small enough, the ordinate may rise to the plateau predicted for $\lambda = 0$ after an initial transient period. As λ increases further, the

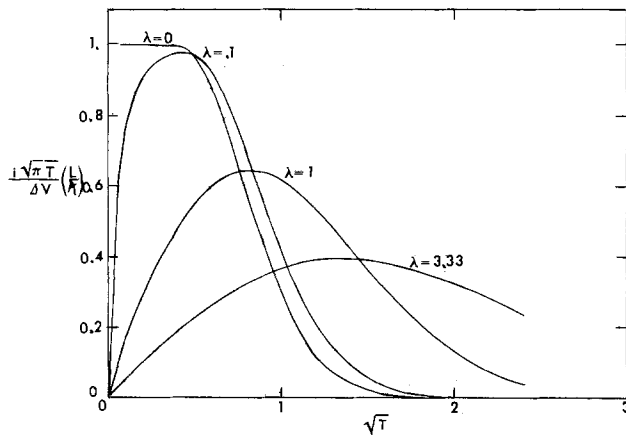


Fig. 2. Effect of the resistance-thickness parameter λ on the double-layer charging of a porous electrode.

value of the plateau (or maximum of the ordinate) decreases.

The lower initial charging currents postpone the time at which the electrode capacity begins to become saturated and the value of $i\sqrt{t}$ begins to decrease. Consequently, the time at which the plateau or maximum occurs increases with increasing λ . This maximum readily lends itself to experimental determination.

For interpretation of the charging current we need only the coordinates of the maxima shown in Fig. 2. This information is summarized in Fig. 3 by plotting against $1/\lambda$ the following three quantities: the ratio of the coordinates of the maximum (this quantity being independent of the value of the double-layer capacity), $1/T_{max}$ (the time at which the maximum occurs), and a dimensionless value of $i\sqrt{t}$ at the maximum.

Interpretation and Evaluation of Charging Curves

Utilization of the information contained in Fig. 3 requires prior knowledge of the effective conductivity, κ , of the solution contained in the porous electrode. De la Rue and Tobias (7) found that the effective conductivity of a dispersion of glass beads in electrolytes can be represented by

$$\kappa = \kappa_0 p^{1.5} \quad [6]$$

where κ_0 is the conductivity and p is the volume fraction of the continuous phase. The effective conductivity of a solution contained in a porous medium can be estimated with this equation by using the porosity for p . Alternatively, the conductivity can be measured directly. Romanova and Selitskii (8) have employed the porous electrode as an inert separator. The ohmic potential drop through the electrode is then equal to $i2L/\kappa$. The value of κ needs to be re-estimated or redetermined if the electrode structure changes sig-

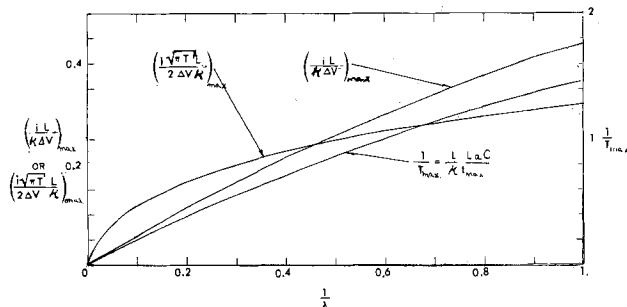


Fig. 3. Dependence of the coordinates of the maximum on the resistance-thickness parameter λ . Maximum refers to the maximum when $i\sqrt{t}$ is plotted against \sqrt{t} for the double-layer charging of a porous electrode with a step change in the applied potential.

nificantly on repeated cycling. However, it is possible to determine κ by replotting the information in Fig.

3. Multiplying the ordinate of Fig. 3, $\left(\frac{i}{\Delta V} \frac{L}{\kappa}\right)_{\max}$, by λ , we obtain $i_{\max}/i|_{t=0}$ (where i_{\max} refers to the value of the current density at the maximum in Fig. 2) which is plotted *vs.* $1/\lambda$ in Fig. 4. An oscilloscope trace of the current response to a voltage step will yield $i|_{t=0}$ directly, and a plot of $i\sqrt{t}$ *vs.* \sqrt{t} will give i_{\max} . The ratio of these two numbers will then yield a value of λ (which contains κ) as shown in Fig. 4. The measured value of the double-layer capacity is relatively insensitive to the value of κ when the resistance-thickness parameter λ is large.

An interesting sidelight of the results shown in Fig. 4 is that the value of κ determined in this manner can then be used to estimate the porosity of the electrode through the use of Eq. [6]. In this manner one may determine *in situ* the porosity of an electrode and follow its change through extended cycling tests.

The procedure used to extract the double-layer capacity per unit volume of electrode from the current response to a potential step can be stated as follows: (i) An oscilloscope trace of the current response of a porous electrode to a voltage step is obtained. (ii) The value of the current at time zero, $i|_{t=0}$, is recorded and a plot of $i\sqrt{t}$ *vs.* \sqrt{t} is made. The coordinates of the plateau or maximum of the resulting curve are recorded and yield i_{\max} and t_{\max} . (iii) If information is available concerning κ , one then uses the left-hand ordinate of Fig. 3 to obtain $1/\lambda$ which in turn is used to obtain T_{\max} , from the right-hand ordinate of Fig. 3. Using the definition of T_{\max} and the experimentally determined t_{\max} , one can calculate aC , the double-layer capacity per unit volume of electrode. (iv) If no information is available concerning κ , one first calculates $i_{\max}/i|_{t=0}$ and then obtains λ from the ordinate of Fig. 4. The value of aC can then be obtained as mentioned in (iii).

This value of aC is regarded to be a measure of the electrochemically accessible surface area of a macrohomogeneous porous electrode. A further division of the aC product requires either specific knowledge about the total interfacial surface area of the electrode

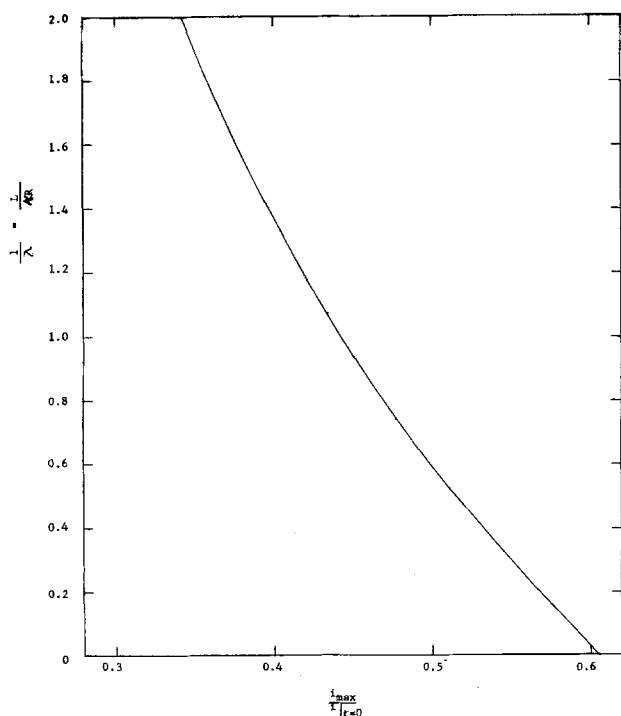


Fig. 4. Determination of the resistance-thickness parameter λ for a given set of i_{\max} and $i|_{t=0}$.

or a measurement of C on a flat surface. An approximate value of a can be obtained from a BET surface area determination and then a value of C calculated. This type of calculation should only be considered qualitative due to the uncertainty of the type of microstructure existing at any given site in a porous electrode. Also the measured BET surface area does not distinguish between electrochemically active and inactive areas. One may also question whether alterations in the specific surface area might not occur during the preparation of the electrode for the BET measurement.

Errors in Double-Layer Measurements

Geometric surface area.—A real porous electrode (e.g., a Pb or PbO₂ plate in the lead-acid battery) usually includes a grid support structure which, for practical purposes, does not contribute to the electrochemical capacity of the electrode but may occupy a significant portion of the electrode volume and geometric surface area. For many porous electrodes the active material is held in the grid support in the form of rectangular pellets, and it is the geometric area of these pellets which should be used in calculating the current density to be used in the treatment of the double-layer data. As grid support structures become more complicated, the specific area correction becomes more difficult leading to errors in the interpretation of the double-layer charging curves.

Electrode response time.—Most potentiostats have characteristic rise times of 1-10 μ sec; however, it is the electrical analog of the electrochemical system in question which usually is the limiting factor in determining the rise time for the system as a whole. Real porous electrodes contain specific surface areas of the order of 10^4 cm²/cm³ and thus unavoidably present a large RC time constant. When the rise time of the potentiostat becomes significant compared to 0.1 t_{\max} , one can expect errors to occur in the evaluation of the charging curves and the subsequent determination of aC . (We have examined the effect of the nonzero rise time of the potentiostat-electrode system by inverting the governing Laplace transform for an applied potential with an exponential approach to a constant value. While this is awkward for routine analysis of charging curves, it does provide an inexpensive alternative to the development of sophisticated electronics.)

Changes in electrode porosity.—For porous electrodes which undergo significant gassing, the effective conductivity of the solution within the electrode, κ , may change as a function of time (8). Also, the effective porosity of the electrode matrix may be altered by extended cycling. Therefore, it may be necessary to determine κ prior to performing a double-layer measurement.

Symmetry of the electrode.—Due to the manner in which real porous electrodes are fabricated (e.g., the Pb and PbO₂ electrodes), there may exist a lack of symmetry about the center line of the electrode. Therefore, one should measure the double-layer capacity with the reference electrode at several locations and on both sides of the porous electrode in question to determine what uncertainty is associated with the measurement.

Faradaic reactions.—The electrode has been assumed to be ideally polarizable. Small departures from this requirement will result in a charging current which does not decay to zero. In a plot of $i\sqrt{t}$ *vs.* \sqrt{t} the departure from a theoretical curve increases with time because the charging current is decreasing while the faradaic current is increasing. If the displacement is minor at large times, the effect on the coordinates of the maximum can safely be ignored. For battery electrodes which are selected to be highly reversible, one should minimize faradaic reactions by polarizing a fully charged electrode in the direction of further charge. (Actually, fully charged Pb and PbO₂ plates

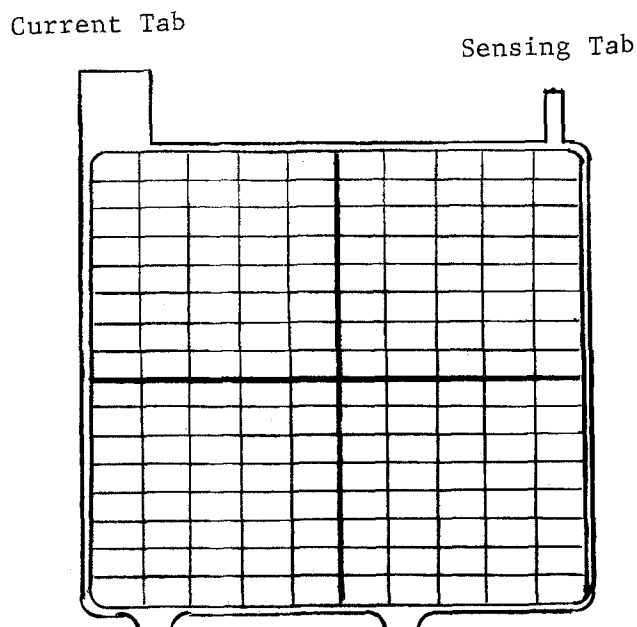


Fig. 5. Porous electrode with a lead grid.

can be polarized in the discharge direction because of the slow nucleation of PbSO_4 .)

Experimental

The electrodes investigated in this study were positive and negative plates manufactured for use in automobile batteries. These electrodes contained grids of a lead alloy (6% antimony) as current collectors (Fig. 5). Sensing leads were attached to the top of the grid opposite the electrode tab. The solution employed was 4.5M sulfuric acid. The physical parameters for each type of electrode are given in Table I. The total current, I , is divided by the geometric electrode area to obtain the current density, i . L is half of the electrode thickness given in Table I.

The cell (a polypropylene case, filled with 4.5M H_2SO_4) used for these measurements contained the electrode in question located symmetrically between two counterelectrodes. A Hg/HgSO_4 reference electrode was used for both the Pb and PbO_2 electrodes. A small capillary from the reference electrode compartment was positioned adjacent to each electrode.

Controlled potential measurements were made with a Wenking Model 6BTS1 potentiostat which was programmed with a Hewlett-Packard 3300A Function Generator. An input voltage divider was required for reproducible 1-4 mV square wave signals. The current response was recorded with a Tektronix 564 storage oscilloscope and/or a recorder fitted with a function converter which would automatically plot $i\sqrt{t}$ vs. \sqrt{t} .

The PbO_2 and Pb electrodes were held at 1.17 and -0.972V vs. a Hg/HgSO_4 reference electrode, respectively, for 12 hr after they had been electrochemically cycled. This time was provided to accommodate surface modifications which have been reported to occur within the first few hours after cycling (9-12). All double-layer measurements were performed at the above-mentioned potentials.

Table I. Physical parameters of the PbO_2 and Pb electrodes

Electrode	BET surface area ¹ ($10^4 \text{ cm}^2/\text{cm}^3$)	Porosity ¹	Electrode thickness (cm)	Geometric electrode area ² (cm^2)
PbO_2	20.5	0.56	0.2	241
Pb	2.5	0.63	0.15	241

¹ Determinations made at Globe-Union, Incorporated.

² Total geometric electrode area (both sides) minus grid area.

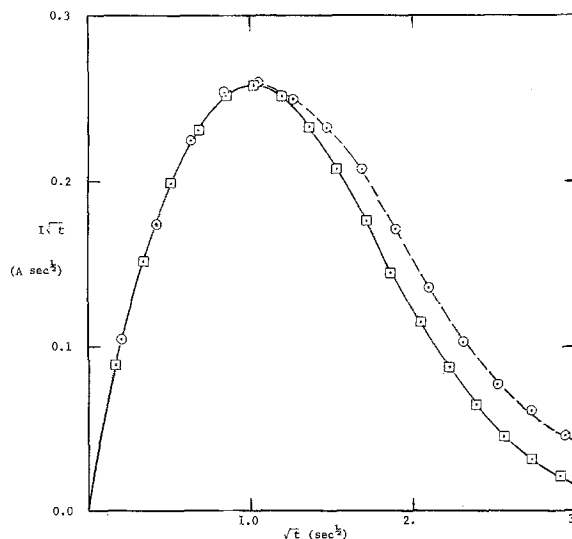


Fig. 6. Comparison of experimental and theoretical results for potentiostatic double-layer charging of a porous PbO_2 electrode. \odot , Experimental; \square , theoretical, Eq. [3]. $L = 0.095 \text{ cm}$, $\Delta V = 1.52 \text{ mV}$, area = 241 cm^2 , $\lambda = 0.768$, $aC = 26 \text{ farads/cm}^3$, temperature = 28°C .

Results and Discussion

Figure 6 shows a typical current response of a PbO_2 electrode to a voltage step and a subsequent display of $i\sqrt{t}$ vs. \sqrt{t} . Similar curves are obtained for the Pb electrode, only the time scale is two orders of magnitude smaller. The accuracy associated with the determination of aC for a given electrode is strongly dependent on the shape of the maximum in the $i\sqrt{t}$ vs. \sqrt{t} curve, a broad maximum implying a larger error. We therefore sought to make λ as small as possible by minimizing the effective resistance in the system (*i.e.*, reference electrode placed as close to the working electrode as possible, separate sensing leads). The magnitude of ΔV was selected more for its convenience (as long as faradaic currents and the potential dependence of the double-layer capacity were small) since the value of T_{max} is independent of the value of ΔV . The effective conductivity of the solution inside the porous electrode was determined using Fig. 4.

Entrapped gases were observed to increase the effective resistance of the electrode which prolonged the charging period. As a consequence, both electrodes were placed in a vacuum chamber and degassed before the measurements were performed. Since the PbO_2 electrode is continually gassing, there will always be some entrapped gases which are unavoidably included in the measurement. One might then consider the real value of aC to be higher than that found experimentally.

Since the electrodes being examined are commercial plates, there exists a certain degree of nonuniformity over the electrodes. The extent to which the position of the reference electrode reflects these nonuniformities was observed by determining aC at three locations on each electrode. As shown in Table II, the position of the reference electrode does reflect somewhat the nonuniformities of the electrodes; also, within the potential difference applied to each electrode, the double-layer capacity appears to be a constant. However, the difference between these values is of the same order of magnitude as the error associated with the double-layer measurement ($\sim 5\%$). One may conclude that the assumption of a macrohomogeneous electrode is valid within experimental error.

Using the information contained in Tables I and II, the double-layer capacity per unit area for the PbO_2 and Pb electrodes is 143 and $10 \mu\text{farads/cm}^2$, respec-

Table II. Double-layer capacity as a function of reference electrode position and applied potential

Electrode	Reference electrode position			Applied potential, mV		
	1 <i>aC</i> (farads/ cm ³)	2 <i>aC</i> (farads/ cm ³)	3 <i>aC</i> (farads/ cm ³)	2 <i>aC</i> (farads/ cm ³)	3 <i>aC</i> (farads/ cm ³)	4 <i>aC</i> (farads/ cm ³)
PbO ₂	30.2	28.4	29.2	30.2	30.4	30.7
Pb	0.254	0.238	0.248	0.252	0.246	0.250

Position 1, First quadrant, right side of electrode.
Position 2, First quadrant, left side of electrode.
Position 3, Second quadrant, right side of electrode.

tively. These values are in agreement with those reported in the literature (9-14) for electrochemically deposited PbO₂ and Pb on flat surfaces. However, it is realized that BET areas are a measure of the entire area available for gas adsorption and not the electrochemically active area. Therefore, the true double-layer capacity per unit area is higher than that calculated using areas determined by gas adsorption. The high observed value for PbO₂ may be due, in part, to a pseudocapacity. The term double-layer capacity has been used to mean interfacial capacity in a macroscopic sense and would include any capacity associated with the adsorption of charged species at the solution-matrix interface. It would exclude faradaic reactions which can be carried out in a steady state.

Conclusions

An interpretation of potentiostatic double-layer charging of porous electrodes has been presented. The emphasis on the maximum in the $i\sqrt{t}$ vs. \sqrt{t} curve results in experimental curves which lend themselves readily to the evaluation of the double-layer capacitance, and it is this quantity which directly reflects the active electrochemical connected area. It has been demonstrated that the values for the double-layer capacity determined on commercial-size battery electrodes are in agreement with that determined on small, flat experimental electrodes. This result is encouraging since one wishes to apply fundamental techniques in the study of large electrodes. We may also note that this procedure was used on two electrodes whose *aC* values differed by two orders of magnitude.

One application of this type of measurement will be in the determination of changes occurring in the active electrochemical surface area with cycling. Also, the effects of additives which alter surface morphology may be detected by their effect on the double-layer capacity.

The possibility of determining the effective conductivity of the solution inside the porous electrode, and thereby inferring something about the electrode porosity, may require carefully designed experiments.

Manuscript submitted April 25, 1974; revised manuscript received July 29, 1974.

Any discussion of this paper will appear in a Discussion Section to be published in the December 1975 JOURNAL. All discussions for the December 1975 Discussion Section should be submitted by Aug. 1, 1975.

Publication costs of this article were partially assisted by Globe-Union, Incorporated.

LIST OF SYMBOLS

<i>a</i>	specific interfacial area, cm ² /cm ³
<i>C</i>	double-layer capacity, farads/cm ²
<i>i</i>	current density, A/cm ²
<i>i</i> _{<i>t</i>=0}	peak current density at time zero given by Eq. [2], A/cm ²
<i>i</i> _{max}	current density at the maximum of $i\sqrt{t}$ vs. \sqrt{t} given in Fig. 2, A/cm ²
<i>L</i>	half-thickness of electrode, cm
<i>L</i> _s	separation distance between reference and working electrodes, cm
<i>p</i>	porosity
<i>R</i>	effective resistance given by Eq. [1], ohm-cm ²
<i>R</i> _L	resistance of leads and current collector, ohm-cm ²
<i>t</i>	time, sec
<i>t</i> _{max}	time of the maximum in the curve shown in Fig. 2b, sec
<i>T</i>	dimensionless time given by Eq. [4]
<i>T</i> _{max}	dimensionless time at the maximum shown in Fig. 2
ΔV	applied potential step, V
κ	conductivity of solution in porous matrix, mho/cm
κ_0	conductivity of bulk solution, mho/cm
λ	effective resistance-thickness parameter given by Eq. [4]
σ	conductivity of the porous electrode matrix, mho/cm
π	3.14159

REFERENCES

1. F. A. Posey and T. Morozumi, *This Journal*, **113**, 176 (1966).
2. R. de Levie, *Electrochim. Acta*, **8**, 751 (1963).
3. Robert de Levie, in "Advances in Electrochemistry and Electrochemical Engineering," Vol. 6, P. Delahay and C. W. Tobias, Editors, pp. 329-397, Interscience Publishers, Inc., New York (1967).
4. A. M. Johnson and John Newman, *This Journal*, **118**, 510 (1971).
5. L. G. Austin and E. G. Gagnon, *ibid.*, **120**, 251 (1973).
6. Milton Abramowitz and Irene A. Stegun, "Handbook of Mathematical Functions," NBS, p. 225, Dept. of Commerce, Washington, D.C. p. 225, (1964).
7. R. E. De La Rue and C. W. Tobias, *This Journal*, **106**, 827 (1959).
8. I. L. Romanova and I. A. Selitskii, *Elektrokhimiya*, **6**, 1776 (1970).
9. J. Burbank, A. C. Simon, and E. Willihnganz, in "Advances in Electrochemistry and Electrochemical Engineering, Vol. 8, P. Delahay and C. W. Tobias, Editors, pp. 157-252, Interscience Publishers, Inc., New York (1971).
10. J. P. Carr and N. A. Hampson, *Chem. Rev.*, **72**, 679 (1972).
11. J. P. Carr, N. A. Hampson, and R. Taylor, *J. Electroanal. Chem.*, **27**, 466 (1970).
12. J. P. Carr, N. A. Hampson, and R. Taylor, *ibid.*, **27**, 201 (1970).
13. P. Rüetschi, J. B. Ockerman, and R. Amlie, *This Journal*, **107**, 325 (1960).
14. E. Willihnganz, *ibid.*, **102**, 99 (1955).



Unified Approach to Cell EMF Calculations

David Gray*

Math/Science Division, Golden West College, Huntington Beach, California 92647

General Discussion

In calculating the emf of an electrochemical cell composed of two half-cell reactions, the usual procedure is to take the algebraic sum or difference (depending on convention) of the electrode potentials of the half-cells. In mathematical terms, this is expressed as

$$E_{\text{cell}} = E_{\text{ox}} \pm E_{\text{r}} \quad [1]$$

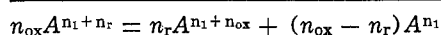
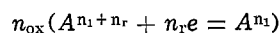
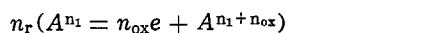
where E is the reversible or Nernst potential and the subscripts ox and r stand for oxidation and reduction half-cell, respectively. It will be shown in this paper that, while Eq. [1] is correct for most cases, it is not the general equation for cell emf calculations.

The only thermodynamic formula that will be necessary for this discussion is the well-known equation at constant temperature and pressure

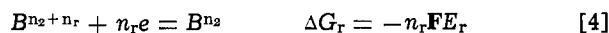
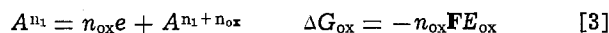
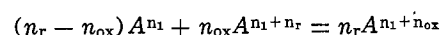
$$\Delta G = -nFE \quad [2]$$

where ΔG is the change in the Gibbs free energy, n is the change in the number of electrons, and F is the Faraday.

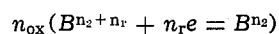
In general, if we consider two half-cell reactions, such as



or

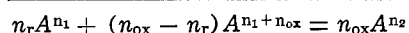
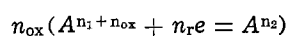


they may be combined to form a cell by the following procedure

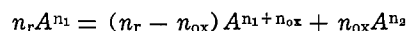


From thermodynamics, we can write that

$$\Delta G_{\text{cell}} = n_{\text{r}}\Delta G_{\text{ox}} + n_{\text{ox}}\Delta G_{\text{r}} \quad [8]$$



or



so that, from Eq. [2]

$$E_{\text{cell}} = \frac{n_{\text{r}}n_{\text{ox}}E_{\text{ox}} + n_{\text{ox}}n_{\text{r}}E_{\text{r}}}{n_{\text{cell}}} \quad [9]$$

Note that n_{cell} is the net cell electron change. It is obvious that

$$n_{\text{r}}n_{\text{ox}} = n_{\text{ox}}n_{\text{r}} \quad [10]$$

is true for all cases of cell formation. Thus, Eq. [9] may be written as

$$E_{\text{cell}} = \frac{n_{\text{r}}n_{\text{ox}}}{n_{\text{cell}}}(E_{\text{ox}} + E_{\text{r}}) \quad [11]$$

For cell calculations (case I, $A \neq B$) other than disproportionation reactions

$$n_{\text{cell}} = n_{\text{r}}n_{\text{ox}} \quad [12]$$

will be true, and Eq. [11] will reduce to Eq. [1].

Now, in disproportionation systems ($A = B$) there are two cases which will result in Eq. [12] and, therefore, Eq. [1] not being valid. If we set (case II)

$$n_1 = n_2 \quad [13]$$

$$n_{\text{r}} \neq n_{\text{ox}} \quad [14]$$

then we can rewrite Eq. [5], [6], and [7] as

$$n_{\text{r}}\Delta G_{\text{ox}} = -n_{\text{r}}n_{\text{ox}}FE_{\text{ox}} \quad [15]$$

$$n_{\text{ox}}\Delta G_{\text{r}} = -n_{\text{ox}}n_{\text{r}}FE_{\text{r}} \quad [16]$$

$$(n_{\text{ox}} > n_{\text{r}}) \quad [17a]$$

$$\Delta G_{\text{cell}} = -n_{\text{cell}}FE_{\text{cell}}$$

$$(n_{\text{r}} > n_{\text{ox}}) \quad [17b]$$

It is obvious that for this particular case there exists no general relationship between n_{cell} and $n_{\text{r}}n_{\text{ox}}$.

Or if we set (case III)

$$n_1 + n_{\text{ox}} = n_2 + n_{\text{r}} \quad [18]$$

$$n_{\text{r}}\Delta G_{\text{ox}} = -n_{\text{r}}n_{\text{ox}}FE_{\text{ox}} \quad [5]$$

$$n_{\text{ox}}\Delta G_{\text{r}} = -n_{\text{ox}}n_{\text{r}}FE_{\text{r}} \quad [6]$$

$$\Delta G_{\text{cell}} = -n_{\text{cell}}FE_{\text{cell}} \quad [7]$$

$$n_{\text{r}} \neq n_{\text{ox}} \quad [14]$$

then we can rewrite Eq. [5], [6], and [7] as

$$n_{\text{r}}\Delta G_{\text{ox}} = -n_{\text{r}}n_{\text{ox}}FE_{\text{ox}} \quad [19]$$

$$n_{\text{ox}}\Delta G_{\text{r}} = -n_{\text{ox}}n_{\text{r}}FE_{\text{r}} \quad [20]$$

$$(n_{\text{ox}} > n_{\text{r}}) \quad [21a]$$

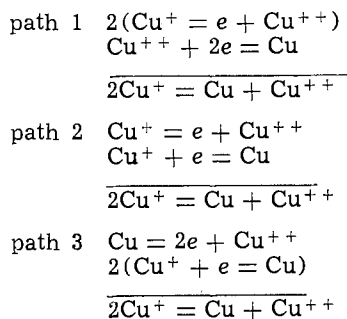
$$\Delta G_{\text{cell}} = -n_{\text{cell}}FE_{\text{cell}}$$

$$(n_{\text{r}} > n_{\text{ox}}) \quad [21b]$$

Once again, it is obvious that for this case there exists no general relationship between n_{cell} and $n_{\text{r}}n_{\text{ox}}$.

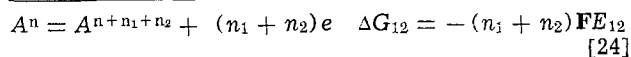
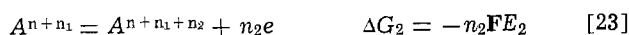
* Electrochemical Society Active Member.
Key words: cells, emf, potential.

Further, it should be noted that in cases II and III Eq. [1] will result in erroneous cell potentials (see examples). Thus, these generalized examples demonstrate that Eq. [11] and not [1] is the general equation for cell emf calculations. It is essential to remember



that addition of half-cell reactions, even to obtain a complete cell, means addition of ΔG or nE , but not of E alone (1). But as case I illustrates, most cell combinations are such that Eq. [12] can be used. For other disproportionation systems (i.e., $n_r = n_{ox}$), Eq. [12] and Eq. [1] will be valid.

For completeness, the method of combining half-cell reactions to form a new half-cell reaction will be included in this discussion. If we consider the following half-cell reactions



and since

$$\Delta G_{12} = \Delta G_1 + \Delta G_2 \quad [25]$$

we can write

$$E_{12} = \frac{n_1E_1 + n_2E_2}{n_1 + n_2} \quad [26]$$

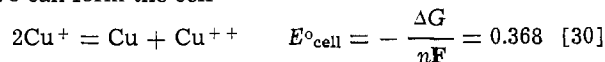
Specific Example

There are numerous examples which can be given to show that Eq. [1] is not always valid. Here one example will be assumed to be sufficient to show the general validity of Eq. [11].

If we take the following three half-cells (example 1) and their respective half-cell standard potentials (2)



we can form the cell



by three different paths:

$$E^\circ_{\text{path 1}} = \frac{2(-0.153) + 2(0.337)}{1} = 0.368\text{V}$$

(case III)

$$E^\circ_{\text{path 2}} = \frac{(-0.153) + 0.521}{1} = 0.368\text{V}$$

$$E^\circ_{\text{path 3}} = \frac{2(-0.337) + 2(0.521)}{1} = 0.368\text{V}$$

(case II)

If we had calculated these values by Eq. [1], E°_{cell} would have been 0.184V for paths 1 and 3, and 0.368V for path 2. This, in effect, would make E°_{cell} dependent on path, which it obviously is not. The important thing to note in this example is that n_{cell} has a definite and specific value which is determined by the over-all cell reaction and not by the half-cell reactions which make up the cell. In this example $n_{\text{cell}} = 1$ for all three paths

This example has been considered by Laitinen (3). However, he maintains the general validity of Eq. [1], which has been disproved in this discussion. Laitinen's book has been cited here because it is the only major textbook which discusses this problem at length.

One can now see that general use of Eq. [1] can make certain disproportionation systems path dependent, while Eq. [11] preserves the path independence of all cell emf calculations.

Manuscript submitted March 11, 1974; revised manuscript received ca. May 10, 1974.

Any discussion of this paper will appear in a Discussion Section to be published in the December 1975 JOURNAL. All discussions for the December 1975 Discussion Section should be submitted by Aug. 1, 1975.

REFERENCES

1. R. G. Bates, in "Treatise on Analytical Chemistry," Part 1, Vol. 1, I. M. Kolthoff and P. J. Elving, Editors, Chap. 9, Interscience Publishers, New York (1959).
2. W. M. Latimer, "Oxidation Potentials," 2nd ed., Prentice-Hall, Inc., Englewood Cliffs, N.J. (1952).
3. H. A. Laitinen, "Chemical Analysis," pp. 283-286, McGraw-Hill Book Company, New York (1960). See also W. H. Eberhardt, *J. Chem. Educ.*, **48**, 829 (1971); and D. A. Jenkins and D. J. Marks, *Educ. Chem.*, **2**, 213 (1965).

Relating Structural Variables of Porous Electrodes

T. Katan* and H. F. Bauman*

Materials and Structures, Lockheed Palo Alto Research Laboratory, Palo Alto, California 94304

The continued development of principles for electrode design [e.g., Ref. (1-3)] and the improvement of fabrication methods [e.g., Ref. (4-6)] must ultimately involve some specification of porous electrode structure. Yet, porous structures tend to elude physical description and relation of their electrochemically important (1-3) and geometrically derived variables such as specific surface area and porosity (7). Frequently, these variables are suspected to have mutual dependence, but it is not clear how a change in one variable will affect another.

It is our purpose here to show how the structural variables of battery and fuel cell electrodes can be specified and related by adapting a filamentary analog for porous structures. We also present practical values of these structural variables for typical electrodes.

The filamentary analog has been previously used by Everett and others in the study of adsorption processes (8). More complex models have been developed in other technical fields (9-13), but none of these appear to yield practical information of geometrical value so directly from a set of elementary equations.

Theoretical

In this approach a porous electrode is represented by a series of filaments, extending from one face of the mass to the other, which are assigned shapes and positions closely resembling the solid portions of an actual electrode. The filaments are assumed to have their ends situated at the centers of oppositely aligned unit squares in the electrode's facial planes and to individually occupy only the volumes contained between the squares. The unit squares have a side dimension x and comprise the grids of two matching Cartesian coordinate systems. As shown in Fig. 1, the pore parameter,¹ τ , is defined as the radius of an imaginary pore with a circular cross-sectional fitting between, and touching only at the ends of, any four adjacent, parallel filaments, each with an over-all solid radius, R , and tortuosity factor, τ . For shapes consisting of regular particles, each particle is assigned a volume, v , area, a , and length, L , along the filament through the electrode of thickness t and fractional void volume θ .

From the Pythagorean theorem, R and r are related with the side of the unit square, and, considering a single filament, an expression is written for the solid volume fraction $(1 - \theta)$. These two equations are then used together with the definition of specific surface area, A , i.e., the area of the particles per unit volume of electrode, to obtain a set of two equations relating r , R , τ , θ , A , a , v , and L

$$\frac{\tau}{(1 - \theta)} = \frac{(R + r)^2}{v/2L} \quad [1]$$

$$A = \frac{a(1 - \theta)}{v} \quad [2]$$

A third equation resulting from Eq. [1] and [2] also is useful

$$A = \frac{a\tau}{2(R + r)^2L} \quad [3]$$

For some structures, it is more accurate to treat the

filaments as pores; the forms of the equations are then unchanged but the meanings of the symbols become reversed. For such filamentary pores the dimensionless group $\tau/(1 - \theta)$ of Eq. [1] is directly related to the so-called effective diffusion coefficient (14). Unless otherwise noted, filaments will be considered in analyses as the solid portion of the structure.

The equations can be generalized if it is understood that $v = k_1 R^2 L$ and $a = k_2 R L$ for a given particle shape, where k_1 and k_2 are the applicable constants. Substitution into Eq. [1]-[3] yields, respectively, three corresponding equations relating the variables r , R , τ , θ , and A

$$\frac{\tau}{(1 - \theta)} = \frac{2}{k_1} \left(\frac{r}{R} + 1 \right)^2 \quad [4]$$

$$A = \frac{k_2 (1 - \theta)}{k_1 R} \quad [5]$$

$$A = \frac{k_2 R \tau}{2 (R + r)^2} \quad [6]$$

The constants k_1 and k_2 are altered only by a constant factor when particle shape is changed but are unchanged for all sizes of a given particle shape.

Results and Discussion

The set of three general equations suggests a natural division of structural variables into those which may be classified as either general, r , R , θ , τ , and A , or particulate, v , a , and L , and also suggests the use of certain groups of general variables, namely, $(R + r)$, r/R , $R/(R + r)^2$, and $(1 - \theta)$ which have practical significance. The variables $(R + r)$ and r/R are monotonically dependent on the defined pore parameter and hence, for typical τ and $(1 - \theta)$, on the effective pore radius for constant R ; $(R + r)$ and R/r are similarly dependent on filament (solid) size for constant r ; and $(1 - \theta)$ is the fractional solid volume. With the use of the general variables, the over-all effect on structure of suggested changes in design or fabrication becomes evident by considering, first, the relation of the general variables, and, second, the influence of particulate variables on the relation of the general variables.

General structural variables.—It is advantageous to examine plots of the general variables in some detail because the same dependences are found for all structures which can be represented by the filamentary analog. We may plot either R/r or $(r + R)$ vs. $(1 - \theta)$ for various τ from Eq. [1] or [4], A vs. R for various θ from Eq. [5], and A vs. τ for various $R/(R + r)^2$

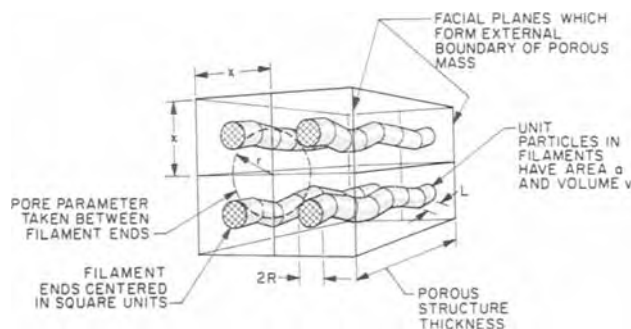


Fig. 1. Four volumetric units of electrode matrix with filaments showing effective dimensions.

* Electrochemical Society Active Member.

Key words: porous electrodes, porous structures, electrode design, batteries.

¹ The pore parameter, τ , is also useful because it is essentially equivalent to an "effective" pore radius excepting when τ and $1 - \theta$ become large i.e., when the average filament spacing at the interior differs appreciably from the assigned spacing of the ends.

from Eq. [6]. As a guide, we select Fig. 2 through 4 for electrodes constructed of uniform spheres, bonded together, where the filamentary analog is taken to consist of rows of touching spheres. Here, $v = 4/3\pi R^3 = k_1 R^2 L$, $a = 4\pi R^2 = k_2 R L$, and $L = 2R$, hence $k_1 = 2/3\pi$ and $k_2 = 2\pi$ in Eq. [4]-[6].

Particulate structural variables.—From Eq. [2] and [3], it can be seen that for a given set of general variables, A is increased linearly with increases in a/v or a/L . In fabrication this increase is usually accomplished by increasing surface roughness or by using filamentary particles having micropores. Ultimately, such increases in particle area become of limited practical use because of the onset of transport process limitations within the micropores (15). From Eq. [1] we see that the ratio v/L has the same influence as τ in shifting the curves of Fig. 2. The relation of particulate to general variables of porous structures is thus evident by Eq. [1]-[3]; the form of the relations of general variables always holds while these relations are changed by a proportionality constant with changes in the particulate variables as indicated above.

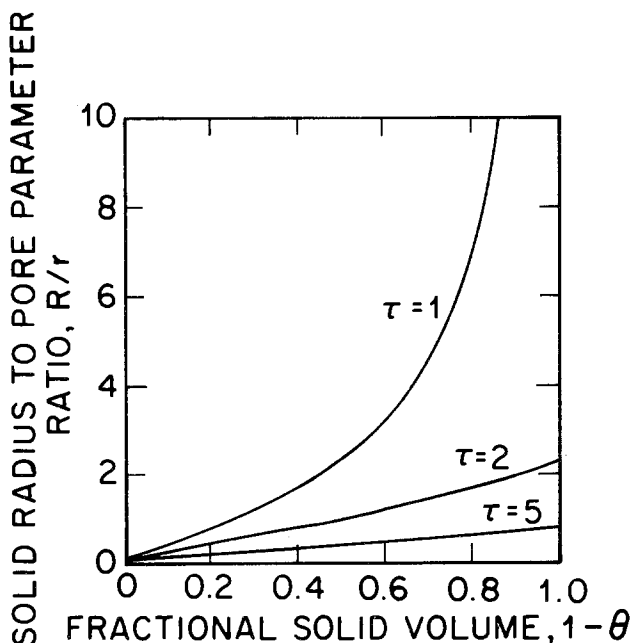


Fig. 2. Variation in ratio of effective solid radius to pore parameter for changes in fractional solid volume.

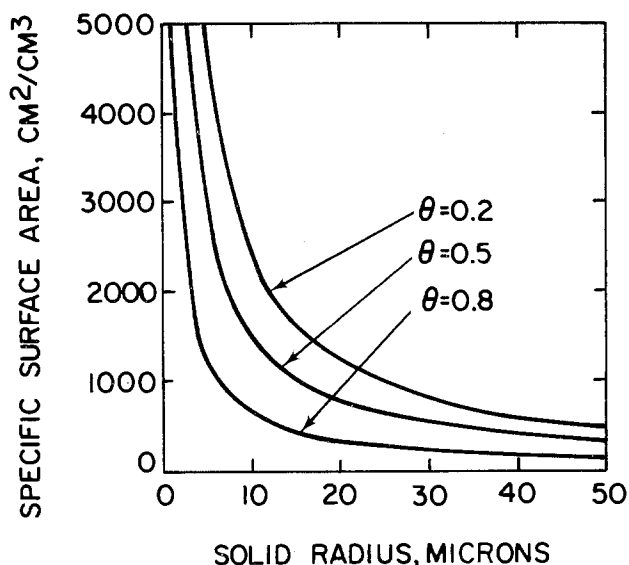


Fig. 3. Variation in specific surface area for changes in filament radius.

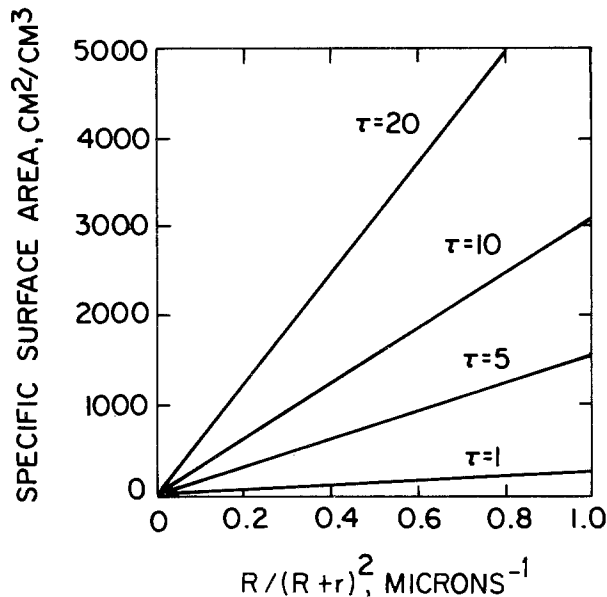


Fig. 4. Variation in specific surface area for changes in $R/(R+r)^2$.

Some applications.—Accuracy of the given equations is best for those structures whose void or solid portions are simply shaped or for those which closely resemble a filamentary network. For example, accurate relations should be obtained with many known practical structures which are structurally ordered, such as stacks of woven wire meshes or screens, bundles of parallel, uniform metal fibers (16), compacted short lengths of uniform metal fibers,² structures of sieved, bonded particles (5), metallized paper fiber structures (17), or uniform sphere beds (18). The latter three structures have been reported as experimental fuel cell and battery electrodes.

The filamentary analog for electrode structures should be selected so that the best correspondence in the representation is made, i.e., so that variables can be easily assigned. For example, with stacks of plain square weave screens, the wires in one direction could be taken as the principal filaments while wires perpendicular to these filaments should be considered as segments with specified area, divided and attached to the principal filaments at regular intervals. With more complex structures, it is useful to consider the porous mass to be divided into smaller, identical volume elements, equivalent to $x^3 t$ volumes, taken so that each volume element contains essentially the same geometrical configuration of filaments throughout the mass. In practice, we have found that some accuracy is retained with this method even with typical electrodes.

We have summarized in Table I the structural variables of four typical, more complex, electrode structures, giving the representations selected for the filamentary analog. For the given structures, r and R were determined by averaging several values measured from photomicrographs of polished metallographic cross sections taken with an optical microscope of the porous masses after impregnation with epoxy under vacuum, e.g., see Fig. 5a. Circles were fitted between the assumed filaments at a large number of randomly selected locations to obtain the average radius, r . Thickness of the assumed filaments, $2R$, was measured perpendicular to the filament direction, also at several randomly selected locations, as indicated in Fig. 5a. Photographs of a calibrated scale at the same magnification were used to ascertain distance.

Scanning electron microscopy, as shown in Fig. 5b, helped in selection of assumed filament shapes and direction. In Fig. 5b, the solid portions are visualized as approaching an ordered shape of interconnected

² "Feltmetal," prepared by Armour Research Foundation, Chicago, Illinois.

Table I. Structural variables of some porous electrodes

Material	Assumed structure of filament	Measured θ	Measured R (μm)	Measured r (μm)	Calc. A (cm^2/cm^3)	Calc. τ
Silver spheres ^a	Rows of spheres	0.373	18.6	6.30	1,010	1.1
Silver membrane ^b	Cylindrical	0.571	1.82	1.21	4,720	2.4
Porous nickel ^c	Cylindrical	0.823	0.979	4.48	3,470	3.4
Silver oxide ^d	Square pores	0.420	0.922	1.81	35,600	14.1

^a Silver spheres obtained in classified size from Metz Refining Company, Newark, New Jersey.

^b 0.002 in. thick porous silver plaques, Cat. No. FM-13-5, Selas Flotronic 5, Spring House, Pennsylvania.

^c Clevite nickel battery plaque, nickel screen not considered in 0.056 in. thick sheets, Clevite Corporation, Cleveland, Ohio.

^d Silver oxide electrodes, silver screen not considered in 0.040 in. thick sheets, Order No. 16-24587, The Eagle-Picher Company, Cincinnati, Ohio.

Table II. Surface areas obtained by different methods

Material*	Specific surface area (cm^2/cm^3)		
	Calc. from filamentary analog	BET	Stereometric analysis
Silver spheres	1,010	(1,260)	(695)
Silver membrane	4,720	4,690	4,700
Porous nickel	3,470	3,460	3,270
Silver oxide	35,600	31,100	—

* See Table I for material descriptions.

cylindrical filaments. For all of the complex structures, enough order could be detected to allow application of the filamentary analog method. Porosities were calculated from the measure weights of predetermined volumes of the specimens free of any supporting screen material and from the known densities of the void-free substances.

After the selection of a filamentary analog shape, A is calculated by Eq. [2], using the measured θ and R , and τ is calculated from Eq. [1] using the measured θ , R , and r . The average deviation in determined R and r values was less than $\pm 6\%$.

In Table II values are given of specific surface areas for the electrode materials determined by the filamentary analog representation (Table I), by the BET method (19), and by a stereometric method (20). The area of the specimen of silver spheres was too low to yield accurate analysis by the BET method to better

than $\pm 50\%$. The stereometric analysis with the spheres also failed to yield accurate analysis because of the inability of the used method of scanning to distinguish touching spheres from single spheres. On the other hand, for those cases where BET and stereometric methods are accurate, agreement with the filamentary analog values is to within $\pm 15\%$, which thus appears to be the limit of accuracy of the filament method for complex shapes. With simple shapes, accuracy is limited only by the accuracy in measurements of R and r as applied to Eq. [4]-[6].

Summary and Conclusions

A filamentary analog of a porous mass is mathematically developed to show how structural variables can be mutually related and act as a guide in evaluations of porous electrodes. Specific surface area, porosity, solid tortuosity, solid radius, and a pore parameter are related, and the influence of changes in solid filamentary particle volume, length, and area on these relations is shown. Accuracy of the filament method in estimating specific surface area was found to be within $\pm 15\%$ for complex electrode structures.

Acknowledgments

This work was supported in part by the Office of Naval Research. The work is a continuation of an earlier effort under National Aeronautics and Space Administration Contract NAS 3-11833.

Manuscript submitted March 29, 1974; revised manuscript received Aug. 12, 1974. This was Paper 353 presented at the San Francisco, California, Meeting of the Society, May 12-17, 1974.

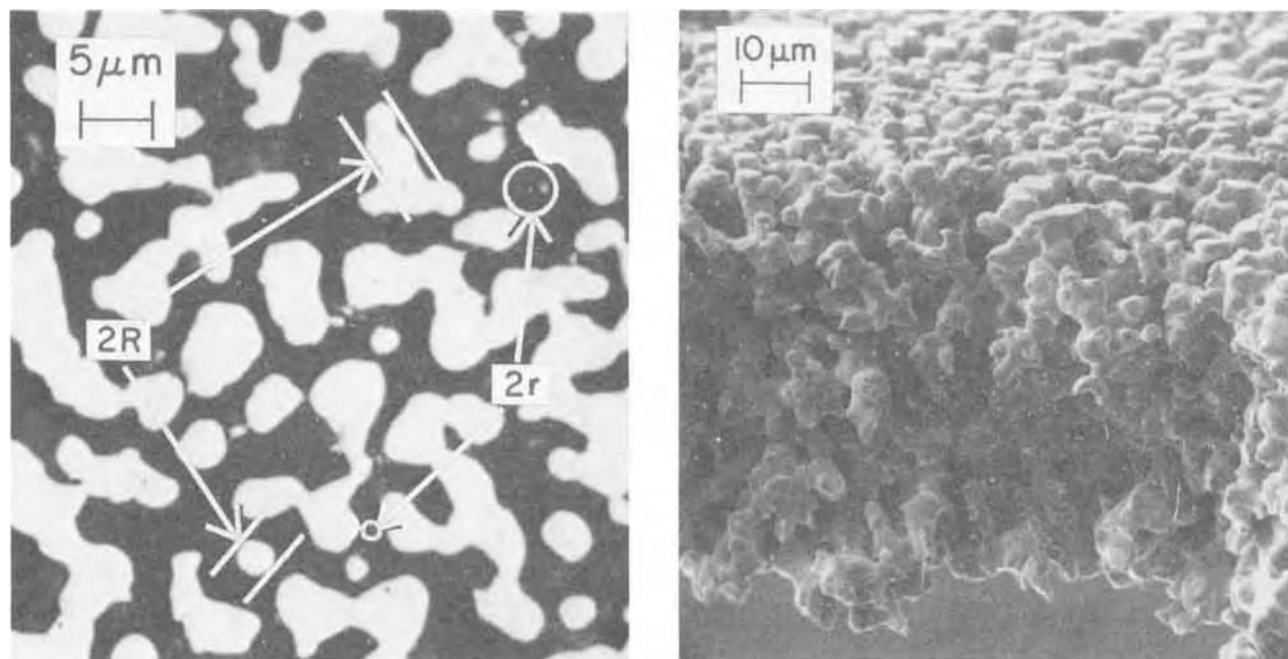


Fig. 5. Typical photomicrographs used for determining filament shape and size. a (left), Optical photomicrograph of polished, sectioned specimen of porous Flotronics silver membrane. Method of selecting r and R indicated. b (right), SEM photomicrograph of broken specimen of porous Flotronics silver membrane.

Any discussion of this paper will appear in a Discussion Section to be published in the December 1975 JOURNAL. All discussions for the December 1975 Discussion Section should be submitted by Aug. 1, 1975.

Publication costs of this article were partially assisted by Lockheed Palo Alto Research Laboratory.

LIST OF SYMBOLS

a	area of unit particle, cm^2
k_1, k_2	dimensionless constants depending only on particle shape
r	pore parameter, cm
t	electrode thickness, cm
v	unit particle volume, cm^3
x	side of square grid, cm
A	specific surface area, cm^2/cm^3
L	length of unit particle, cm
R	over-all radius of unit particle (filament), cm
τ	filament tortuosity or ratio of filament length to electrode thickness
θ	fractional void volume

REFERENCES

1. E. A. Grens *Ind. Eng. Chem., Fundamentals*, **5**, 542 (1966).
2. J. S. Dunning, D. N. Bennion, and J. Newman, *This Journal*, **118**, 1251 (1971).
3. D. Gidaspow and B. Baker, *ibid.*, **120**, 1005 (1973).
4. F. T. Bacon, *Electrochim. Acta*, **14**, 569 (1969).
5. E. Justi and A. Winsel, "Kalte Verbrennung," F. Steiner, Wiesbaden, Germany (1962).
6. D. J. Gordy, E. Luksha, and C. J. Menard, *This Journal*, **120**, 1447 (1973).
7. S. D. Holdsworth, *Chem. Process Eng.*, **44**, 184 (1963).
8. D. H. Everett, in "The Structure and Properties of Porous Materials," D. H. Everett and F. S. Stone, Editors, p. 95, Butterworth's Scientific Publications, London (1958).
9. A. J. De Bethune and R. L. Rowell, *J. Phys. Chem.*, **67**, 2065 (1963).
10. R. N. Foster and J. B. Butt, *A.I.Ch.E. J.* **12**, 180 (1966).
11. M. F. Johnson and W. E. Stewart, *J. Catalysis*, **4**, 248 (1965).
12. N. Wakao and J. M. Smith, *Chem. Eng. Sci.*, **17**, 825 (1962).
13. E. A. Mason, A. P. Malinauskas, and R. B. Evans III, *J. Chem. Phys.*, **46**, 3199 (1967).
14. C. N. Satterfield and T. K. Sherwood, "The Role of Diffusion in Catalysis," p. 15, Addison-Wesley Publishing Company, Inc., London (1963).
15. E. W. Thiele, *Ind. Eng. Chem.*, **31**, 916 (1939).
16. J. Sherfey, NASA TN D-6259, National Aeronautics and Space Administration, Washington, D.C., April 1971.
17. R. A. Botosan and T. Katan, *Electrochem. Technol.*, **5**, 315 (1967).
18. T. Katan, S. Szpak, D. N. Bennion, *This Journal*, **121**, 757 (1974).
19. S. Brunauer, P. H. Emmett, and E. Teller, *J. Am. Chem. Soc.*, **60**, 309 (1938).
20. E. E. Underwood, "Quantitative Stereology," p. 31, Addison-Wesley Publishing Company, Inc., London (1970).

Brief Communication



The Kinetics of Nickel Passivation

Adolf Pigeaud*

Department of Materials Science and Metallurgical Engineering, University of Cincinnati, Cincinnati, Ohio 45221

Passive surface conditions may be produced on metals and alloys by electrochemical polarization in the anodic region. The passive condition occurs as the result of a series of surface reactions which culminate in the deposition of a highly protective film. Such films usually consist of several very thin oxide phases parallel to, and in intimate contact with, the surface. Potentiostatic experiments are often performed to study the formation of these layers on sample metal electrodes in an electrochemical cell. Current is measured while potential is generally varied according to a controlled schedule of specified values. Unfortunately, this controlled variation in most potentiostatic experiments is selected without adequate regard for the reaction kinetics of the individual film formation processes. This is evident because the normal procedure usually is to vary the applied potential in stepwise fashion or to increase it monotonically during polarization even though individual reactions obviously still have not yet run their course.

In a recent study of pure Ni-polarization in 15N sulfuric acid, very fast and very slow current changes were investigated while potential across the total cell was maintained at a constant value throughout each experimental run. Oxide layers left on the surface from

previous experiments were removed before each new run by a kind of electropolishing technique in which vigorous oxygen evolution is enforced for about $\frac{1}{2}$ min. The sample is then allowed to come to its equilibrium rest potential in a fresh quantity of solution. A new run begins the moment a particular desired potential is applied across the total cell (i.e., from counterelectrode to working electrode without reference to any solution potential). Current data were obtained by means of two types of recorders: a light-beam oscillograph for the very fast initial changes and an $X(\log t) = Y$ recorder for the medium and very slow, long term changes. The current variable also extended over a wide range of values from about $100 \mu\text{A}/\text{cm}^2$ to over $1000 \text{ mA}/\text{cm}^2$. Hence "instantaneous" log converted values of current were the actually recorded variables for obtaining high frequency, wide band response. A large number of such isopotential experiments were run and in each case current behavior was followed for a considerable length of time, from 10 msec after startup to at least 17 min (1000 sec). Thus an enormous body of data was accumulated which proved too large and cumbersome to be handled by ordinary means of curve comparison. A powerful new method of analysis, using 3D-computer graphics, was then applied and a very revealing picture of the kinetics of nickel passivation resulted. Figure 1 illustrates this total kinetic

* Electrochemical Society Active Member.

Key words: polarization, kinetics, nickel, passivity.

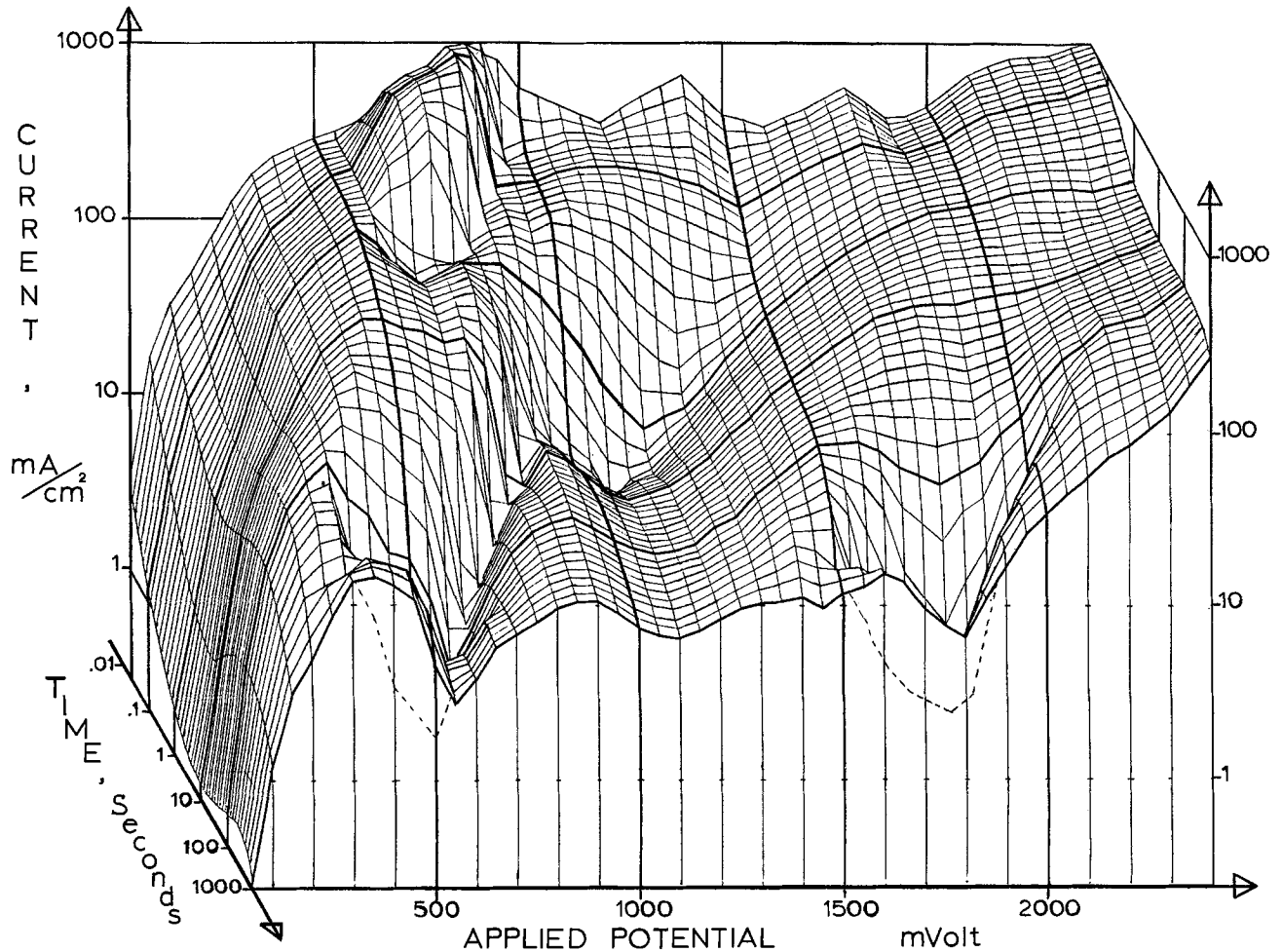


Fig. 1. Complete electrokinetic response in current-time-potential space of pure nickel polarized in 15N sulfuric acid

behavior as a complex surface in current-time-potential space. The surface was generated by manually converting the ($I-t$) analog data of each isopotential curve into digital form (e.g., some 2304 points were read) and these were then plotted as a three-dimensional perspective view from the side of the orthogonal current-potential plane. One should note that the ($I-E$) curves so obtained can never be directly generated in a real experiment since potential, of course, cannot be increased from 0 to 2400 mV in zero time.

To our knowledge this method of obtaining the complete "electrokinetic" response of a system while it polarizes is unique. The data were obtained both by a greatly improved instrumental method and a somewhat different operating procedure. Analysis of these data, in the form of a complex current-time-potential surface, moreover has proven powerful indeed. Originally the minima and maxima in the isopotential curves seemed to bear little relationship to known equilibria or to familiar reaction processes. After plotting in three dimensions, however, the extremes and inflections in these curves can be recognized as part of a larger system of ridges, saddle points, and valleys which have real meaning in terms of the various reactions that are likely to occur on the surface. Thus it has been possible, with the help of other visual and analytical evidence obtained during the experimental part of this program, to identify most of these features as being due to the formation on the surface of a number of colloidal hydroxides (1) and multiphase oxide layers.

Additional support for these conclusions came when it was realized that these data, which are basically kinetic in nature, can also be used to supply evidence of the momentary existence of thermodynamic equilibria during polarization. Namely when the saddle points and valleys of the complex surface are

projected onto the ($E-t$) base plane of Fig. 1 a kind of pseudo-Pourbaix diagram results which is illustrated in Fig. 2. This projection of the diffuse features of the complex surface in a different dimension suddenly allows one to fit rather precise straight-line boundaries to what were seemingly only vaguely defined regions of electrochemical stability. Single and dual phase layers which previously could only be inferred have also been added to this diagram which, it must be emphasized, shows stability with respect to a "time" frame of reference. When Fig. 2 is compared to a partial ver-

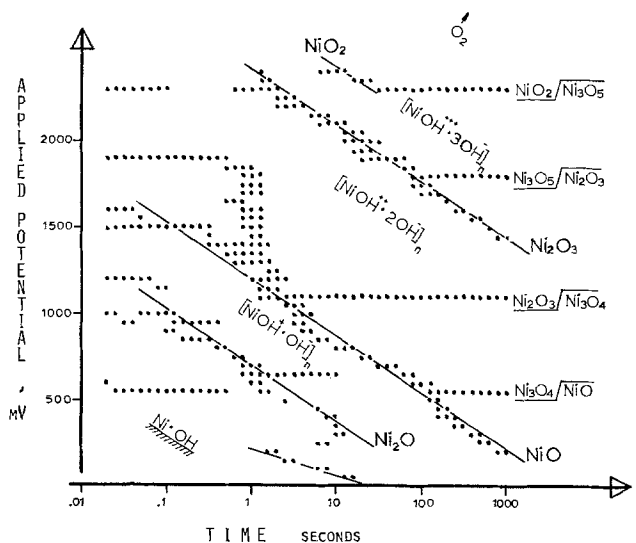


Fig. 2. Pseudo-Pourbaix diagram obtained directly from nickel polarization data.

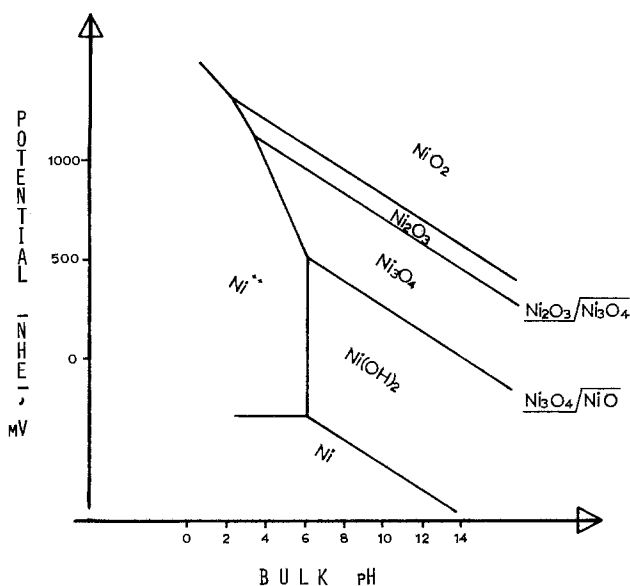


Fig. 3. Partial Pourbaix diagram of Ni-H₂O system

sion of the Pourbaix diagram for nickel, such as is shown in Fig. 3, the remarkable similarity between these two modes of expressing thermodynamic equilibria becomes apparent. In fact the almost 1:1 analogy between the phase boundaries in these two diagrams suggests that a simple inverse relationship must exist between polarization time and H⁺-ion concentration in the immediate vicinity of the polarizing metal surface (e.g., as compared to the bulk concentration). Such a relationship is not difficult to justify on theoretical grounds if one can assume a polarization model in which proton removal from the interface occurs at a constant electrophoretic rate of migration due to a constant electric field.

This means that a Pourbaix diagram, such as shown in Fig. 3 which is actually a composite of free energy

data obtained from many different sources, can now be obtained all at once by means of a single experimental procedure and also with respect to a more realistic time frame of reference. Furthermore, when completely developed, this procedure holds the promise of being able to yield detailed information on the various spinellike phases and multilayer combinations which may occur in protective films (e.g., on alloys) formed in real environments (e.g., in aqueous or organic solutions containing other cationic and anionic species).

Conclusion

An improved polarization and data analysis technique applicable to most metal/electrolyte systems has been developed which shows considerable promise as a new tool for the direct, time-dependent characterization of anodically deposited films.

Acknowledgment

The author wishes to thank Professor Clair M. Hulley, the developer of the generalized computer program, and Mr. Bob Hsieh for their assistance in running his data program on the IBM-1130 computer slaved to the Calcomp-718 curve plotter of the Electrical Engineering Department at the University of Cincinnati. The present communication will be followed by a more detailed theoretical and experimental paper on a new theory of metal/electrolyte polarization after the author has submitted it to the faculty of his Department in partial fulfillment of the requirements for the Ph.D. degree (1974).

Manuscript submitted May 16, 1974; revised manuscript received July 22, 1974.

Any discussion of this paper will appear in a Discussion Section to be published in the December 1975 JOURNAL. All discussions for the December 1975 Discussion Section should be submitted by Aug. 1, 1975.

REFERENCE

1. A. Pigeaud and H. B. Kirkpatrick, *Corrosion*, **25**, 209 (1969).

Erratum

In the paper "Additive Ternary Molten Salt Systems—Calculation of Phase Diagrams from Thermodynamic Data of Lower Order Systems" by Marie-

Louise Saboungi and Pierre Cerisier which appeared on pp. 1258-1263 in the October 1974 JOURNAL, Vol. 121, No. 10, Eq. [11] should read as follows

$$\begin{aligned}
 -\frac{A_m}{kT} = \ln Z_m = \ln Z_o + \sum_{i=1}^3 (g_i - 1) \left(\frac{\partial \ln Z_m}{\partial g_i} \right)_{g=1} \\
 + \frac{1}{2} \sum_{i=1}^3 \sum_{j=1}^3 (g_i - 1) (g_j - 1) \left(\frac{\partial^2 \ln Z_m}{\partial g_i \partial g_j} \right)_{g=1} \\
 + \sum_{i=1}^3 x_i \ln x_i + \dots
 \end{aligned}$$



Solid-State Ionics: High-Conductivity Solid Copper Ion Conductors: N,N'-Dialkyl (or Dihydro)-Triethylenediamine Dihalide-Copper(I) Halide Double Salts

Takehiko Takahashi* and Osamu Yamamoto

Department of Applied Chemistry, Faculty of Engineering, Nagoya University, Nagoya, Japan

ABSTRACT

New solid electrolytes with high copper ion conductivity at ambient temperature have been found in the system N,N'-dialkyl (or dihydro)-triethylenediamine dihalide-copper(I) halide in the composition range of 94-80 mole per cent (m/o) copper(I) halide. For example, the solid-state reaction product between copper(I) bromide 94 m/o and N,N'-dimethyl-triethylenediamine dibromide 6 m/o exhibited the conductivity of $0.035 \text{ (ohm-cm)}^{-1}$ at 20°C , which was essentially ionic. X-ray diffraction investigations indicated that these new solid electrolytes are unique and not the mixtures of their constituents.

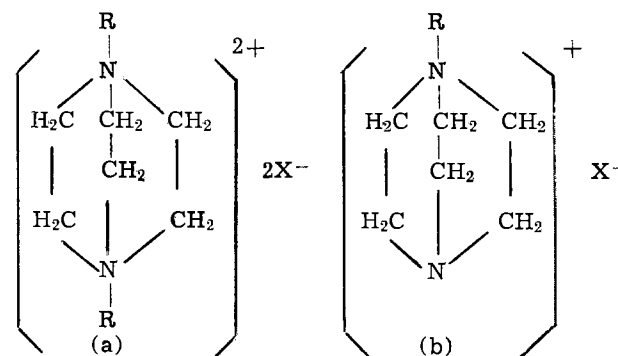
During the past decade, the electrical properties of high-conductivity solid electrolytes and their applications to electrochemical devices have been described by many authors (1). However, the high-conductivity materials reported previously have been mainly the silver ion or alkali ion conductors. Recently, promising results have been found by Takahashi, Yamamoto, and Ikeda (2), that N-alkyl (or hydro)-hexamethylenetetramine halide-copper(I) halide double salts exhibited high copper ion conductivities of 4×10^{-4} to $1.7 \times 10^{-2} \text{ (ohm-cm)}^{-1}$ at 20°C and their electronic conductivities were less than $10^{-10} \text{ (ohm-cm)}^{-1}$ at 100°C . Further investigations on copper ion conductors in our laboratory have revealed that the N,N'-dialkyl (or dihydro)-triethylenediamine dihalide-copper(I) halide double salts have the ionic conductivities of 2×10^{-3} to $4 \times 10^{-2} \text{ (ohm-cm)}^{-1}$ at 20°C .

Experimental

N,N'-dialkyl (or dihydro)-triethylenediamine dihalides, $\text{C}_6\text{H}_{12}\text{N}_2\text{R}_2\text{X}_2$ (R = H, CH_3 , C_2H_5 , X = Cl, Br, I), were prepared by mixing the ethanol solution of triethylenediamine (1,4-diazabicyclo 2,2,2 octane), $\text{C}_6\text{H}_{12}\text{N}_2$, and alkyl halides or hydrohalogenic acids. Triethylenediamine and alkyl halides used were manufactured by Tokyo Chemical Industry Company, and they were used without further purification. For example, to a solution containing 5g (0.045 mole) of triethylenediamine in 50 mliters of ethanol were slowly added 21g of a 50% methyl bromide (0.11 mole) solution in ethanol and the mixture was allowed to stand overnight at room temperature. After being filtered, the precipitate was dried in vacuo on P_2O_5 . By this method, five kinds of N,N'-dialkyl (or dihydro)-triethylenediamine dihalides, $\text{C}_6\text{H}_{12}\text{N}_2\text{2HCl}$, $\text{C}_6\text{H}_{12}\text{N}_2\text{2HBr}$, $\text{C}_6\text{H}_{12}\text{N}_2\text{2C}_2\text{H}_5\text{Br}$, $\text{C}_6\text{H}_{12}\text{N}_2\text{2HI}$, and $\text{C}_6\text{H}_{12}\text{N}_2\text{2CH}_3\text{I}$ were prepared. For the preparation of

all these precipitates, the mole ratio of alkyl halides (or hydro halogenic acids) to triethylenediamine was made larger than the stoichiometric ratio (2:1 mole ratio). N,N'-dimethyl-triethylenediamine dichloride was prepared as follows: triethylenediamine (25.5g) was added to a 7.3% ethanol solution of methyl chloride (422g). After standing for two days, methyl chloride gas was blown into the solution. The mixture was allowed to stand for seven days at room temperature, and after being filtered, the precipitate was dried in vacuo on P_2O_5 . The crystals obtained were recrystallized from ethanol.

Triethylenediamine has two nitrogen atoms in a molecule, and the following two types of quarternary alkyl triethylenediamine halide (a) and (b) may exist



where R is H, CH_3 , or C_2H_5 , and X is halogen. In this study, as the quarternary alkyl triethylenediamine halides were obtained using an excess amount of alkyl halide or hydrohalogenic acid, the chemical formulas of the obtained compounds were type (a) which are certificated by the analytical data shown in Table I. The analytical data agree well with the values calculated from the molecular form of $\text{C}_6\text{H}_{12}\text{N}_2\text{2RX}$. The decomposition temperature of these compounds are

* Electrochemical Society Active Member.

Key words: solid electrolyte; copper ion conductor; copper(I) halide; N,N'-dialkyl-triethylenediamine dihalide.

Table I. Analytical data of N,N' -dialkyl(or hydro)-triethylenediamine dihalides

Compound	Analysis						Decomposition temperature, °C
	Calculated			Found			
	C	H	N	C	H	N	
$C_6H_{12}N_2HCl$	38.9	7.6	15.1	39.1	7.4	15.2	167
$C_6H_{12}N_2CH_3Cl$	45.1	8.4	13.1	40.5	8.9	12.3	201
$C_6H_{12}N_2HBr$	26.3	5.1	10.2	26.1	4.9	10.1	232
$C_6H_{12}N_2CH_3Br$	31.8	6.0	9.3	31.6	6.0	9.6	218
$C_6H_{12}N_2C_2H_5Br$	36.4	6.7	8.5	36.8	6.6	8.5	216
$C_6H_{12}N_2HI$	19.6	3.8	7.5	19.2	3.7	7.3	247
$C_6H_{12}N_2CH_3I$	24.3	4.5	7.1	24.2	4.5	6.9	176

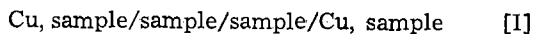
also shown in the table. Copper(I) halides were purified by recrystallizing in the corresponding hydrohalogenic acid.

The materials used for the conductivity and x-ray experiments were prepared by combining CuX with $C_6H_{12}N_2RX$. The appropriate quantities of both compounds were mixed with a small amount of ethanol and dried completely at about 80°C before being pressed to form a pellet under a pressure of 4000 kg/cm², and then heated in a sealed evacuated Pyrex vessel for 17 hr. The reactions were carried out below the decomposition temperatures of the corresponding $C_6H_{12}N_2RX$ shown in Table I, that is, at 160°C for the $CuCl-C_6H_{12}N_2HCl$ system, at 170°C for the $CuI-C_6H_{12}N_2CH_3I$ system, and at 190°C for the other systems. The resulting materials did not melt at these reaction temperatures, except for the $C_6H_{12}N_2HCl-CuCl$ system.

The electrical conductivity was measured by using a cell, Cu , sample/sample/ Cu , sample. The sample of about 0.8g was stacked between the mixture of powdered copper (325 mesh) and the sample (2:1 weight ratio), and pressed into a pellet of 13 mm diameter under a pressure of 4000 kg/cm². The pressed samples with copper electrodes were annealed for several hours at 100°-200°C, corresponding to the kind of sample, in oxygen-free nitrogen gas flow before being slowly cooled to room temperature in an oven. This treatment provides for removal of the excess halogen in the sample, thus avoiding a deficit of copper which will give hole conduction in addition to ionic (3). The resistance of the conductivity cell was measured by means of the Ando Denki conductance bridge using 1000 Hz. The frequency dependence of resistance was not observed for all samples investigated.

The method for determining the electronic conductivity was described previously in some detail (2). It was determined from the relation of the current density and the cell voltage for the cell, Cu /sample/graphite, upon passing a direct current.

The transport number of copper ion was measured by Tubandt's method. In order to reduce the electrode polarization, a mixture of powdered copper and the sample was used for the electrode, and the weight changes of the electrode and the sample of the cell of the type



were measured.

The x-ray diffraction patterns of the powdered samples were obtained at room temperature using conventional techniques with $CuK\alpha$ radiation.

Differential thermal analysis (DTA) was carried out for the sample which was sealed in a Vycor tube under vacuum. The heating rate was 3.5°/min. The decomposition temperature of samples was measured by thermogravimetric analysis (TGA), the heating rate of which was 3.3°C/min.

Results and Discussion

Electrical conductivity.—The effect of composition on the conductivity at room temperature was determined for the systems $C_6H_{12}N_2HCl-CuCl$, $C_6H_{12}N_2CH_3Cl-CuCl$, $C_6H_{12}N_2HBr-CuBr$, $C_6H_{12}N_2C_2H_5Br-CuBr$, $C_6H_{12}N_2CH_3Br-CuBr$, $C_6H_{12}N_2HI-CuI$, and $C_6H_{12}N_2CH_3I-CuI$.

Of these systems, the conductivity of the thermal reaction products of the $C_6H_{12}N_2HI-CuI$ system was comparable to or less than that of CuI . The other systems showed conductivities of 10^{-4} - 10^{-2} (ohm-cm)⁻¹ at room temperature in the composition range of 95-80 mole per cent (m/o) CuX . Figure 1 shows the electrical conductivities of the systems studied at 20°C as a function of the mole per cent of copper(I) halide. These curves show that the conductivity has a maximum at a certain content of copper(I) halide and decreases rapidly with decreasing the content of copper(I) halide. The maximum values of conductivity were obtained at 85 m/o $CuCl$ for the system $C_6H_{12}N_2HCl-CuCl$, at 80 m/o $CuCl$ for $C_6H_{12}N_2CH_3Cl-CuCl$, at 87.5 m/o $CuBr$ for $C_6H_{12}N_2HBr-CuBr$, at 94 m/o $CuBr$ for $C_6H_{12}N_2C_2H_5Br-CuBr$, at 85 m/o $CuBr$ for $C_6H_{12}N_2CH_3Br-CuBr$, and at 85 m/o CuI for $C_6H_{12}N_2CH_3I-CuI$. The highest conductivity of 4.9×10^{-2} (ohm-cm)⁻¹ at 20°C was found in the system $C_6H_{12}N_2HBr-CuBr$ at 87.5 m/o $CuBr$. This value of conductivity is about three times larger than that reported in our previous paper (2), in which the conductivity of 1.7×10^{-2} (ohm-cm)⁻¹ at 20°C was obtained in the system N -methyl-hexamethylenetetramine bromide-copper(I) bromide at 87.5 m/o $CuBr$. Further, the conductivity value is comparable to that of silver ion conductors which are obtained by combining silver iodide with organic ammonium iodides (4-6).

From the above results, it is recognized that in the systems $C_6H_{12}N_2RBr-CuBr$, the conductivity decreases successively with R being H , CH_3 , or C_2H_5 . This result suggests that the symmetry of organic ammonium halide may play a role to give the high conductivity compound. Triethylenediamine is known as a bicyclic cage compound, the stereo structure of which shows somewhat spherical symmetry, and the symmetry of the quaternary alkyl triethylenediamine ion gets worse with increasing the volume of R from H to C_2H_5 .

The temperature dependence of the electrical conductivities was determined for the samples in the

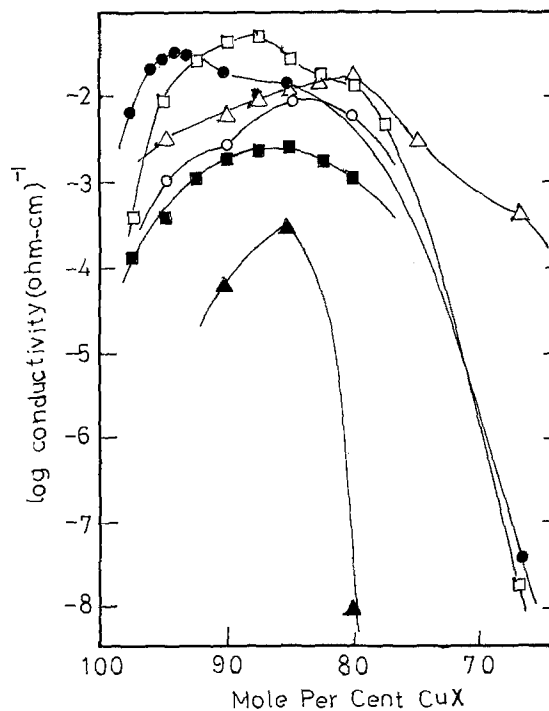


Fig. 1. Composition dependence of the electrical conductivity of the binary solid electrolyte systems $C_6H_{12}N_2HCl-CuCl$ (\circ), $C_6H_{12}N_2CH_3Cl-CuCl$ (Δ), $C_6H_{12}N_2HBr-CuBr$ (\square), $C_6H_{12}N_2C_2H_5Br-CuBr$ (\bullet), $C_6H_{12}N_2CH_3Br-CuBr$ (\blacktriangle), and $C_6H_{12}N_2CH_3I-CuI$ (\blacksquare) at 20°C.

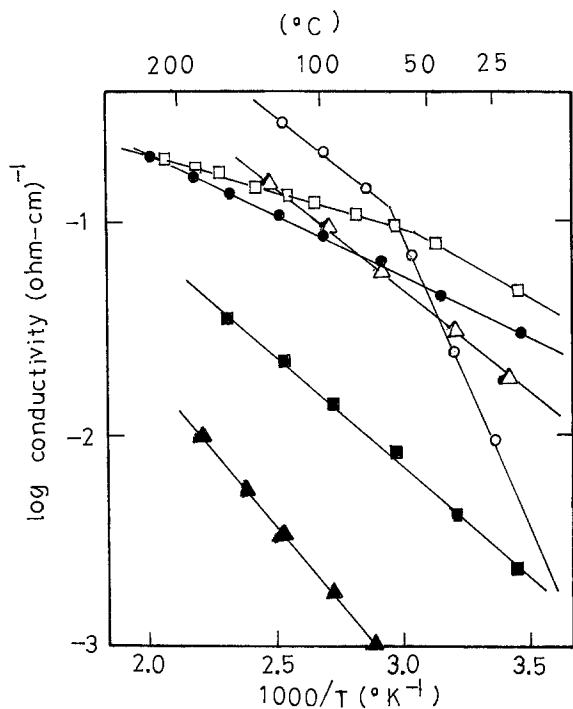


Fig. 2. Temperature dependence of the electrical conductivity of $17\text{CuCl}\cdot 3\text{C}_6\text{H}_{12}\text{N}_2\text{HCl}$ (\circ), $4\text{CuCl}\cdot \text{C}_6\text{H}_{12}\text{N}_2\text{CH}_3\text{Cl}$ (Δ), $7\text{CuBr}\cdot \text{C}_6\text{H}_{12}\text{N}_2\text{HBr}$ (\square), $47\text{CuBr}\cdot 3\text{C}_6\text{H}_{12}\text{N}_2\text{CH}_3\text{Br}$ (\bullet), $17\text{CuBr}\cdot 3\text{C}_6\text{H}_{12}\text{N}_2\text{C}_2\text{H}_5\text{Br}$ (\blacktriangle), and $17\text{CuI}\cdot 3\text{C}_6\text{H}_{12}\text{N}_2\text{CH}_3\text{I}$ (\blacksquare).

$\text{C}_6\text{H}_{12}\text{N}_2\text{RX}\cdot\text{CuX}$ system. The results of several temperature cycles are shown in Fig. 2. The log conductivity vs. the reciprocal of the absolute temperature curves for $4\text{CuCl}\cdot \text{C}_6\text{H}_{12}\text{N}_2\text{CH}_3\text{Cl}$, $47\text{CuBr}\cdot 3\text{C}_6\text{H}_{12}\text{N}_2\text{CH}_3\text{Br}$, $17\text{CuBr}\cdot 3\text{C}_6\text{H}_{12}\text{N}_2\text{C}_2\text{H}_5\text{Br}$, and $17\text{CuI}\cdot 3\text{C}_6\text{H}_{12}\text{N}_2\text{CH}_3\text{I}$ indicate that no phase transition occurs in the range of the temperature investigated. The activation energies calculated from these curves are 4.2 kcal/mole for $4\text{CuCl}\cdot \text{C}_6\text{H}_{12}\text{N}_2\text{CH}_3\text{Cl}$, 2.7 kcal/mole for $47\text{CuBr}\cdot 3\text{C}_6\text{H}_{12}\text{N}_2\text{CH}_3\text{Br}$, 5.6 kcal/mole for $17\text{CuBr}\cdot 3\text{C}_6\text{H}_{12}\text{N}_2\text{C}_2\text{H}_5\text{Br}$, and 4.8 kcal/mole for $17\text{CuI}\cdot 3\text{C}_6\text{H}_{12}\text{N}_2\text{CH}_3\text{I}$. The results for $17\text{CuCl}\cdot 3\text{C}_6\text{H}_{12}\text{N}_2\text{HCl}$ and $7\text{CuBr}\cdot \text{C}_6\text{H}_{12}\text{N}_2\text{HBr}$ exhibit an increasing activation energy at low temperature, which suggests that phase transitions occur near 65°C for $17\text{CuCl}\cdot 3\text{C}_6\text{H}_{12}\text{N}_2\text{HCl}$ and 50°C for $7\text{CuBr}\cdot \text{C}_6\text{H}_{12}\text{N}_2\text{HBr}$. However, $7\text{CuBr}\cdot \text{C}_6\text{H}_{12}\text{N}_2\text{HBr}$ is conductive at room temperature and has a low activation energy of 3.3 kcal/mole at 20°C . On the other hand, $17\text{CuCl}\cdot 3\text{C}_6\text{H}_{12}\text{N}_2\text{HCl}$ has a high activation energy of 13.5 kcal/mole at 20°C , and it indicates that the conductive phase transfers to a nonconductive phase below 65°C .

Electronic conductivity.—Though stoichiometric copper(I) halides exhibit ionic conduction predominantly, the existence of excess halogen or oxygen which corresponds to a deficit of copper causes hole conduction (3). Therefore, it is important to measure the electronic conductivity of the solid electrolyte containing copper(I) halides. The electronic conductivity of the $\text{C}_6\text{H}_{12}\text{N}_2\text{RX}\cdot\text{CuX}$ system was measured by Wagner's polarization method. The current vs. cell voltage curves for the cell, Cu/sample/graphite, showed a quasi-exponential increase of current in the temperature range of $100^\circ\text{--}200^\circ\text{C}$ for all samples investigated. Therefore, according to Wagner's theory, the hole conduction may be assumed to be dominant under this experimental condition. The electronic conductivities were calculated with the help of this theory. The temperature dependence of the electronic conductivity of $4\text{CuCl}\cdot \text{C}_6\text{H}_{12}\text{N}_2\text{CH}_3\text{Cl}$, $7\text{CuBr}\cdot \text{C}_6\text{H}_{12}\text{N}_2\text{HBr}$, $47\text{CuBr}\cdot 3\text{C}_6\text{H}_{12}\text{N}_2\text{CH}_3\text{Br}$, and $17\text{CuI}\cdot 3\text{C}_6\text{H}_{12}\text{N}_2\text{CH}_3\text{I}$ is shown in Fig. 3, compared to those of the copper(I) halides.

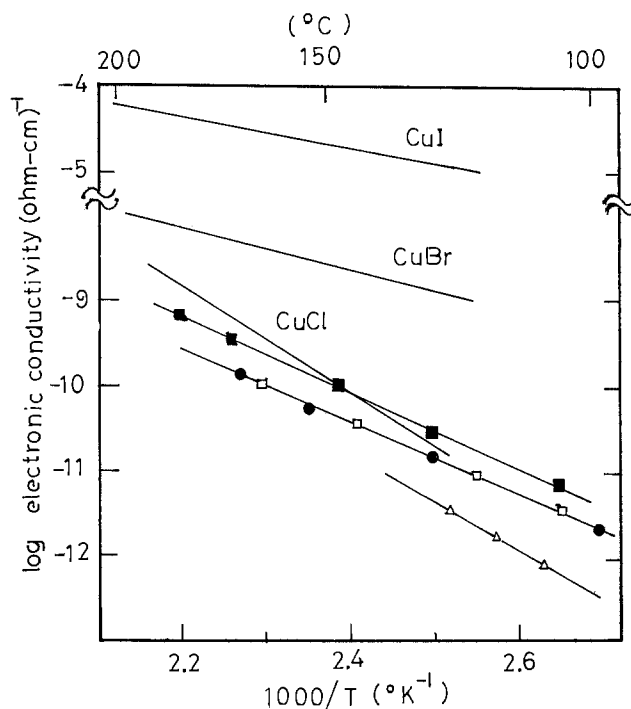


Fig. 3. Temperature dependence of the electronic conductivity of copper(I) halides, $4\text{CuCl}\cdot \text{C}_6\text{H}_{12}\text{N}_2\text{CH}_3\text{Cl}$ (Δ), $7\text{CuBr}\cdot \text{C}_6\text{H}_{12}\text{N}_2\cdot 2\text{HBr}$ (\square), $47\text{CuBr}\cdot 3\text{C}_6\text{H}_{12}\text{N}_2\cdot 2\text{CH}_3\text{Br}$ (\bullet), and $17\text{CuI}\cdot 3\text{C}_6\text{H}_{12}\text{N}_2\cdot 2\text{CH}_3\text{I}$ (\blacksquare).

The electronic conductivities of these new high conductivity materials are smaller than those of the corresponding copper(I) halides. At room temperature, the electronic conductivities of these materials were too small to measure with this method. Thus, it is concluded that the conduction in these new compounds is essentially ionic in nature.

Transport number measurements.—The ionic transport number in $47\text{CuBr}\cdot 3\text{C}_6\text{H}_{12}\text{N}_2\cdot 2\text{CH}_3\text{Br}$ was determined with the help of Tubandt's method. In order to reduce the electrode polarization, the measurement was carried out at 100°C . The direct current at the current density of $500\ \mu\text{A}/\text{cm}^2$ was passed through cell [I] over 21 hr. The total charge passed through the cell corresponded to the quantity of copper deposited at the cathode and dissolved at the anode; that is, the efficiencies of 102% at the anode and 100.5% at the cathode were obtained. This result indicates that the transport number of copper(I) ion is unity within the experimental error.

TGA and DTA.—The decomposition temperatures of these new, high copper ion conductivity materials were measured with the help of TGA, and the results are shown in Table II. All samples, except $17\text{CuCl}\cdot 3\text{C}_6\text{H}_{12}\text{N}_2\text{HCl}$, are stable up to 200°C . The $\text{N,N}'$ -dialkyl (or hydro)-triethylenediamine dihalide-copper(I) halide double salts are thermally more stable than the previously reported N -alkyl (or hydro)-hexamethylenetetramine-copper(I) halide double salts, which decomposed below 150°C .

Table II. Thermal data for $\text{N,N}'$ -dialkyl (or dihydro)-triethylenediamine dihalide-copper(I) halide double salts

Compound	Decomposition temperature, $^\circ\text{C}$	Melting point, $^\circ\text{C}$
$17\text{CuCl}\cdot 3\text{C}_6\text{H}_{12}\text{N}_2\text{HCl}$	120	112
$4\text{CuCl}\cdot \text{C}_6\text{H}_{12}\text{N}_2\text{CH}_3\text{Cl}$	222	199
$7\text{CuBr}\cdot \text{C}_6\text{H}_{12}\text{N}_2\text{HBr}$	206	300
$47\text{CuBr}\cdot 3\text{C}_6\text{H}_{12}\text{N}_2\text{CH}_3\text{Br}$	223	314
$17\text{CuBr}\cdot 3\text{C}_6\text{H}_{12}\text{N}_2\text{C}_2\text{H}_5\text{Br}$	234	196
$17\text{CuI}\cdot 3\text{C}_6\text{H}_{12}\text{N}_2\text{CH}_3\text{I}$	210	295

Further, DTA was carried out for these samples sealed in a Vycor tube. Each sample presented an endothermic peak which may be due to the melting of the sample. The melting points are also shown in Table II.

X-ray diffraction analysis.—The x-ray diffraction patterns were obtained at room temperature for the samples containing 95-50 m/o copper(I) halide in the system $C_6H_{12}N_2RX-CuX$. In the systems $C_6H_{12}N_2HCl-CuCl$ and $C_6H_{12}N_2CH_3Cl-CuCl$, the samples containing 90 and 85 m/o $CuCl$ showed the mixed patterns of $CuCl$ and a new compound. Samples containing 80 m/o $CuCl$ gave a pattern for a new single phase. In the $C_6H_{12}N_2HBr-CuBr$ system, the high-conductivity solid containing nearly 87.5 m/o $CuBr$ gave a single-phase pattern. Another two intermediate compounds were found at the composition of 66.7 and 50 m/o $CuBr$, which were poor conductors. In the $C_6H_{12}N_2CH_3Br-CuBr$ system, the sample containing 94 m/o $CuBr$, which exhibits the highest conductivity in this system, did not give a single-phase pattern but gave the patterns of two phases corresponding to a new compound and $CuBr$. However, a single-phase pattern was observed at the composition of 90 m/o $CuBr$, 66.7 m/o $CuBr$, and 50 m/o $CuBr$. In the $C_6H_{12}N_2HI-CuI$ system, only the peaks due to the starting materials were observed in the composition range of 90-50 m/o CuI . In the $C_6H_{12}N_2CH_3I-CuI$ system, three intermediate compounds were found at the composition of 85 m/o CuI , 66.7 m/o CuI , and 50 m/o CuI . The compound containing 85 m/o CuI is a high conductive solid electrolyte and the other compounds are poor conductors.

It was found from the x-ray investigation that the highest conductivity material in each system did not always give a single-phase pattern. This may be due

to the fact that the conductivity measurement is not precise enough to determine the exact formula of the compounds (4). However, it is concluded that the high-conductivity materials found in the $C_6H_{12}N_2RX-CuX$ systems are new compounds and not the mixtures of their constituents. The x-ray diffraction patterns of the new compounds were too complex to determine their crystal structures.

Conclusion

The high, copper ion conductivity and the low electronic conductivity were found in the N,N' -dialkyl (or dihydro)-triethylenediamine-dihalide-copper(I) halide double salts. The values of the conductivity are comparable to that of the previously reported quaternary ammonium iodide-silver iodide compounds.

Manuscript submitted May 20, 1974; revised manuscript received Aug. 7, 1974.

Any discussion of this paper will appear in a Discussion Section to be published in the December 1975 JOURNAL. All discussions for the December 1975 Discussion Section should be submitted by Aug. 1, 1975.

Publication costs of this article were partially assisted by the authors.

REFERENCES

1. "Physics of Electrolyte," J. Hladik, Editor, Academic Press, New York (1972).
2. T. Takahashi, O. Yamamoto, and S. Ikeda, *This Journal*, **120**, 1431 (1973).
3. J. B. Wagner and C. Wagner, *J. Chem. Phys.*, **26**, 1597 (1957).
4. B. B. Owens, *This Journal*, **117**, 1536 (1970).
5. B. B. Owens, J. H. Christie, and G. T. Tiedeman, *ibid.*, **118**, 1145 (1971).
6. M. L. Berardelli, C. Biondi, M. De Rossi, G. Fonseca, and M. Giomini, *ibid.*, **119**, 115 (1972).

Interface States and Fixed Charge as a Function of Small Changes in Orientation of (111) Silicon Wafers

Sigurd Wagner

Bell Laboratories, Holmdel, New Jersey 07733

and Edward I. Povilonis

Bell Laboratories, Murray Hill, New Jersey 07974

ABSTRACT

The orientation of a silicon substrate for integrated circuits frequently deviates from its nominal value. In this study the densities of the interface states (N_{SS}) and of the fixed charge (Q_{FC}) were determined as a function of small changes of the orientation. Metal-silicon dioxide-silicon capacitors were made on eleven silicon wafers oriented from -25 to $+173$ min of arc off the [111] direction toward the [011] direction. N_{SS} and Q_{FC} were derived from the high frequency and quasi-static capacitance-voltage characteristics. Both are independent of the orientation over the range examined with $N_{SS} = (4.4 \pm 1.3) \times 10^{10} \text{ cm}^{-2} \text{ V}^{-1}$, and $Q_{FC} = + (6.7 \pm 1.2) \times 10^{10} \text{ cm}^{-2}$.

Two types of electronic states, the interface states (N_{SS}) and the fixed charge (Q_{FC}) are located at the interface between silicon and silicon dioxide. The interface states exchange charge with the bulk of the semiconductor. Their equilibrium population depends on the position of the Fermi level at the interface. The fixed charge states do not alter their population when

the Fermi level scans the bandgap. Because of their contribution to the threshold voltage the densities of both types of states are important characteristics of insulated gate field effect devices.

One question about N_{SS} and Q_{FC} is whether they vary when the orientation of the silicon wafer deviates slightly from its nominal value. Silicon wafers for MOS integrated circuits may deviate by as much as one degree of arc from their nominal orientation (1).

Substrates for epitaxy are intentionally oriented off low index orientations by angles of the order of one degree (1). This is done to obtain epitaxial layers of good quality free of pyramidal growth. It is known that the "offset" in orientation is retained at the surface of the epitaxial layer. Another case where the effect of a small change in orientation is of interest is found in experiments on the effects of strain on the interface characteristics (2). Neither the existing theories about the origin of these states nor the published experiments on their orientation dependence answer the question.

No theory relates N_{SS} or Q_{FC} directly to the orientation of the interface. N_{SS} has been associated with unpaired localized electrons which could result from incomplete oxidation (3) or which may exist at misfit dislocations in the interface (4). N_{SS} has also been ascribed to lateral fluctuations of the interface potential due to charges distributed in the silicon dioxide (5), and to impurity atoms located at the interface (6, 7). Q_{FC} is believed to result from charges attached to incompletely oxidized silicon on the oxide side of the interface (8), or to strained regions at the interface (9). The fixed charge may be identical with charge in interface states located outside of the bandgap where net charging or discharging cannot take place.

One important aspect of both types of states is the dependence of their density on the crystallographic orientation of the SiO₂/Si interface. Maxima of N_{SS} [Ref. (10)] and of Q_{FC} [Ref. (8, 9, 11)] exist in the vicinity of {111} interfaces, and minima near {110} and {100}. Qualitatively these extrema can be correlated with the density of atoms in the first layer of a free surface of silicon. The existing data cannot be used for conclusions about the dependence of N_{SS} and Q_{FC} on small ($\sim 1^\circ$) changes in orientation. First, the densities of N_{SS} and Q_{FC} obtained in the previous studies (9, 10) are about five and ten times, respectively, higher than the lowest obtainable values. Second, in the published studies the spacing between experimental points ranges from 5 to 30 degrees of arc, and therefore does not offer sufficient resolution. We have measured N_{SS} and Q_{FC} of eleven samples oriented between -25 and $+173$ min of arc off the [111] direction toward the [011] direction, i.e., with the "zone axis" parallel to [011]. The (111) interface was selected to obtain comparatively large values of N_{SS} and Q_{FC} and concurrent low relative experimental errors. However, we did employ processing procedures to minimize these densities to the lowest values which can be attained for this orientation.

Experimental

One float zone grown [111] oriented $1\frac{1}{4}$ in. diameter p-type boron-doped ingot with a nominal resistivity of 0.46-0.55 ohm-cm was sawed into oriented wafers with successively increasing tilt off [111]. After a chemical etch and a Syton polish the orientation of the 14 mils (0.35 mm) thick wafers was determined by x-ray goniometry. After cleaning by a sequence of organic solvents, aqueous detergent solutions, acidic and oxidizing solutions, and by scrubbing, the wafers were prepared for oxidation by rinsing in deionized water and in dilute HF. All eleven wafers were then immediately brought into the very clean oxidation furnace. This furnace is made up of a double-walled, fused quartz tube within a silicon carbide liner. Gases enter the furnace through the inner quartz tube and flow back out through the annulus between the inner and the outer tube. All wafers were oxidized simultaneously for 100 min at 1000°C in a pure oxygen flux of 30 cm sec⁻¹, and subsequently annealed *in situ* in pure nitrogen at a flux of 30 cm sec⁻¹ for 30 min at 1000°C. After rapid cooling to room temperature, the SiO₂ film was etched to 0.0925 μ m in HF:H₂O = 1:15. Then high purity aluminum was evaporated from a sodium-free tungsten coil onto the wafers. A 30 mil (0.076 cm) diameter dot and guard ring pattern was

etched into the aluminum by standard photolithographic techniques. After a cleaning procedure, the back sides were aluminized, and the samples were annealed for 30 min at 400°C in pure hydrogen with a flux of 20 cm sec⁻¹.

The experimental setup used for the high frequency (1 MHz) and quasi-static (0.048 Vsec⁻¹) capacitance-voltage measurements is similar to that described by Lopez (12). The mobile charge in the SiO₂ was determined by the triangular voltage sweep technique (13) at 300°C with 0.048 Vsec⁻¹. In all measurements the guard ring was held at the voltage of the field plate.

The high frequency and quasi-static C-V curves were first evaluated for the doping profile, correcting for surface states (14)

$$N_A(x) = \left[\frac{2}{q\kappa_s\epsilon_0} \right] \left[\frac{1 - C_Q/C_{ox}}{1 - C_H/C_{ox}} \right] \left[\frac{d(1/C_H)^2}{dV} \right]^{-1}$$

where $N_A(x)$ is the net concentration of acceptors as a function of the distance x from the SiO₂/Si interface; q is the electronic charge, κ_s the relative dielectric constant of silicon, ϵ_0 is the permittivity of free space; C_Q , C_H , and C_{ox} are the quasi-static, the high frequency, and the maximum (oxide) capacitance, respectively; V is the voltage. For the numerical evaluation, points were taken off the C-V curves at 0.1V intervals.

The normalized flatband capacitance C_{FB}/C_{ox} was then calculated using the dopant concentration measured at $x = 0.1 \mu$ m, $N_A(0.1)$

$$\frac{C_{FB}}{C_{ox}} = \left[1 + \left[\frac{\kappa_{ox}^2 \epsilon_0 kT}{\kappa_s q^2} \right]^{1/2} \left[\frac{1}{t_{ox} N_A(0.1)^{1/2}} \right] \right]^{-1}$$

where κ_{ox} is the relative dielectric constant of SiO₂, k is the Boltzmann constant, T the absolute temperature, and t_{ox} the thickness of SiO₂.

The density of fixed charge, Q_{FC} , was determined from the difference between the ideal (ϕ_{MS}) and measured flatband voltage (V_{FB})

$$Q_{FC} = C_{ox}(\phi_{MS} - V_{FB})$$

(C_{ox} is the capacitance of the unit area of the SiO₂ layer.) It should be noted that this is a net charge made up of all ionized donor and acceptor states at the interface regardless of their location within or without the bandgap.

The density of interface states N_{SS} as a function of the interface potential ψ_s was derived from the difference between the quasi-static and the high frequency capacitance (15)

$$N_{SS}(\psi_s) = \frac{C_{ox}}{q} \left[\left[\frac{C_{ox}}{C_Q} - 1 \right]^{-1} - \left[\frac{C_{ox}}{C_{HF}} - 1 \right]^{-1} \right]$$

ψ_s was calculated by integration of the quasi-static capacitance with respect to applied voltage (16). The flatband voltage was taken as the lower limit

$$\psi_s(V) = \int_{V_{FB}}^V \left[1 - \frac{C_Q}{C_{ox}} \right] dV$$

Results

The mobile ionic charge in the SiO₂ films was uniformly low and ranged from 2 to 3 $\times 10^{10}$ cm⁻². It was too small to be determined by the bias-temperature stress technique which showed only the non-ionic "slow trapping" instability. A typical acceptor concentration vs. depth is shown in Fig. 1. The 5% accuracy limits (14) are denoted by $3L_B$ and $2L_B/\sqrt{u_B}$. L_B is the extrinsic Debye length and u_B is the bulk Fermi potential in units of kT/q . N_A drops from the bulk toward the interface as a consequence of the depletion of boron during the oxidation. N_A at $x = 0.1 \mu$ m is plotted against the orientation of the interface in Fig. 3c. This plot corresponds roughly to one of N_A vs. the position

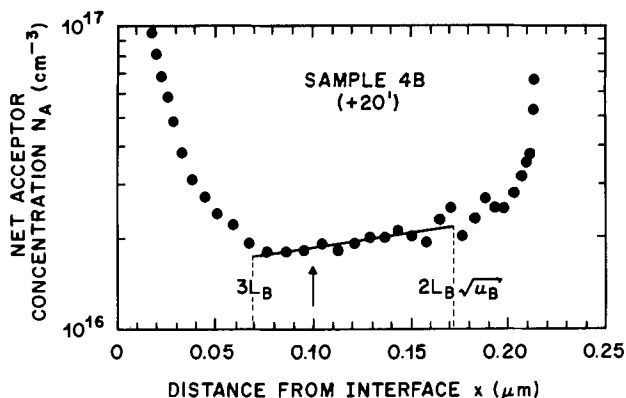


Fig. 1. Typical concentration profile of acceptors vs. distance from the SiO_2/Si interface. $3L_B$ and $2L_B\sqrt{u_B}$ denote the 5% error limits. The high values of N_A at $x < 3L_B$ and $x > 2L_B\sqrt{u_B}$ are artifacts of the capacitance-voltage technique.

in the original silicon ingot. $N_A(x = 0.1)$ is virtually constant at $(1.97 \pm 0.14) \times 10^{16} \text{ cm}^{-3}$.

Figure 2 shows a typical plot of the density of interface states vs. interface potential. The average of N_{SS} within $\pm 0.20\text{V}$ of the midgap potential is used to construct the plot of N_{SS} vs. the angle Φ , Fig. 3a. A least squares treatment of N_{SS} vs. Φ gives

$$N_{SS} = 4.60 \times 10^{10} - 0.0032 \times 10^{10} \times \Phi(\text{min}) \pm 1.31 \times 10^{10} \text{ cm}^{-2} \text{ V}^{-1}$$

The standard deviation corresponds to an uncertainty in the determination of $(C_Q - C_{HF})/C_{ox}$, at midgap potential, of $\pm 5 \times 10^{-3}$. An uncertainty of this order is usually encountered as a consequence of errors in the normalization of C_Q to C_{HF} in accumulation. Therefore we consider N_{SS} as constant within the experimental error

$$N_{SS} = (4.4 \pm 1.3) \times 10^{10} \text{ cm}^{-2} \text{ V}^{-1}$$

A least squares treatment of Q_{FC} vs. Φ (Fig. 3b) results in

$$Q_{FC} = 6.66 \times 10^{10} + 0.0002 \times 10^{10} \times \Phi(\text{min}) \pm 1.20 \times 10^{10} \text{ cm}^{-2}$$

Here the standard deviation corresponds to an uncertainty of 0.06V in the determination of the flatband voltage. Q_{FC} is thus virtually constant at $Q_{FC} = (6.7 \pm 1.2) \times 10^{10} \text{ cm}^{-2}$.

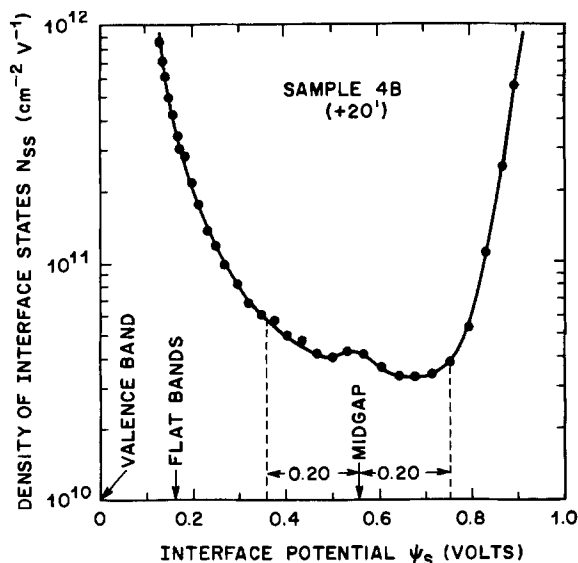


Fig. 2. Typical profile of the density of interface states vs. the interface potential. The average density within 0.20V of the midgap potential was used for further evaluation.

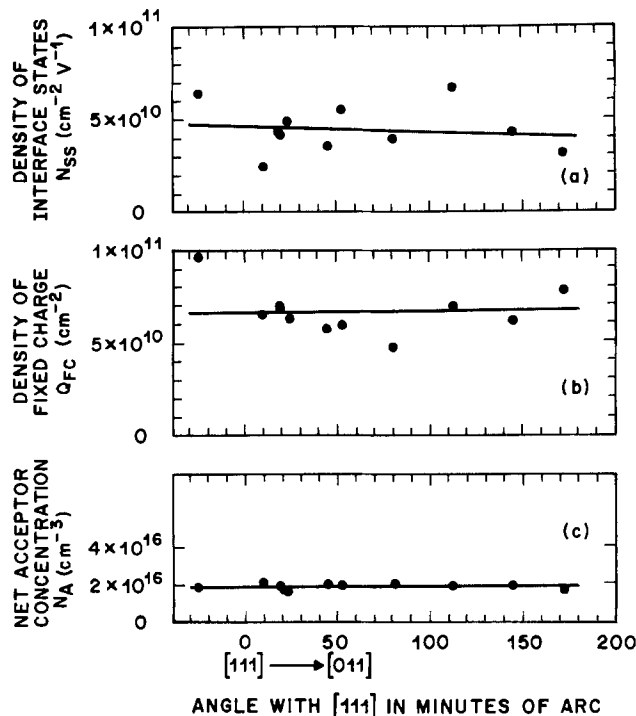


Fig. 3. (a) Density of interface states, (b) density of fixed charge, (c) acceptor concentration, all as a function of orientation.

Conclusion

The SiO_2/Si interfaces of eleven wafers, oriented within about 3° of the $[111]$ direction, were characterized. These orientations are typical for device material. The densities of the interface states and of the fixed charge were constant with $N_{SS} = (4.4 \pm 1.3) \times 10^{10} \text{ cm}^{-2} \text{ V}^{-1}$ and $Q_{FC} = +(6.7 \pm 1.2) \times 10^{10} \text{ cm}^{-2}$.

Acknowledgments

The authors wish to thank R. O. Miller and W. A. Sachs for slicing, polishing, and orienting the silicon wafers. They are indebted to D. V. McCaughan, B. C. Wonsiewicz, and J. R. Brews for valuable discussions.

Manuscript received March 7, 1974.

Any discussion of this paper will appear in a Discussion Section to be published in the December 1975 JOURNAL. All discussions for the December 1975 Discussion Section should be submitted by Aug. 1, 1975.

Publication costs of this article were partially assisted by Bell Laboratories.

REFERENCES

1. J. W. Carlson, *Solid State Technol.*, **16**, (11), 49 (1973).
2. D. V. McCaughan and B. C. Wonsiewicz, *J. Appl. Phys.*, **45**, 4982 (1974).
3. E. Kooi, "The Surface Properties of Oxidized Silicon," Springer, New York (1967).
4. G. F. Neumark, *Phys. Rev. Letters*, **21**, 1253 (1968).
5. A. Goetzberger, V. Heine, and E. H. Nicollian, *Appl. Phys. Letters*, **12**, 95 (1968).
6. S. Kar and W. E. Dahlke, *ibid.*, **18**, 401 (1971).
7. W. Fahrner and A. Goetzberger, *J. Appl. Phys.*, **44**, 725 (1973).
8. Y. Miura, *Japan. J. Appl. Phys.*, **4**, 958 (1965).
9. G. Abowitz, E. Arnold, and J. Ladell, *Phys. Rev. Letters*, **14**, 543 (1967).
10. E. Arnold, J. Ladell, and G. Abowitz, *Appl. Phys. Letters*, **13**, 413 (1968).
11. J. F. Delord, D. G. Hoffmann, and G. Stringer, *Bull. Am. Phys. Soc., Ser. 2*, **10**, 546 (1965).
12. A. D. Lopez, *Rev. Sci. Instr.*, **44**, 200 (1973).
13. N. T. Chou, *This Journal*, **118**, 601 (1971).
14. J. R. Brews, *J. Appl. Phys.*, **44**, 3228 (1973).
15. R. Castagné and A. Vapaille, *Surface Sci.*, **28**, 157 (1971).
16. C. N. Berglund, *IEEE Trans. Electron. Devices*, **ED-13**, 701 (1966).

Improved Dielectric Reliability of SiO₂ Films with Polycrystalline Silicon Electrodes

C. M. Osburn* and E. Bassous*

IBM Thomas J. Watson Research Center, Yorktown Heights, New York 10598

ABSTRACT

Time dependent dielectric breakdown of SiO₂ films in MOS structures is shown to be strongly dependent on the electrode material used. Polycrystalline silicon electrodes give substantially longer times to failure than do aluminum electrodes. The improvement is 3-4 decades at 300°C; and, because of the larger activation energy for wearout with poly-Si (2.4 eV) compared to Al (1.4 eV), the relative advantage would be 8-16 decades at room temperature. Although time to breakdown is a strong function of SiO₂ thickness when the electrode is Al, it is nearly independent of thickness for structures having poly-Si electrodes.

Increasing reliability requirements for MOSFET devices makes it desirable to optimize the selections of dielectric and electrode materials as well as processing conditions used to fabricate the gate region. Device failure due to gate oxide dielectric breakdown has been reported (1) as one failure mode. Because of its importance to over-all device reliability, several recent studies (2-9) have focused on the causes of time-dependent, dielectric degradation and breakdown in SiO₂ films. The electrode metal has been shown (6, 9) to be an important factor in determining the rate of dielectric deterioration.

MOS capacitor structures having polycrystalline silicon electrodes have previously been shown to exhibit (6) a more substantial resistance to dielectric degradation at high temperature than those utilizing reactive metals like Al or Mo. However, the earlier work only considered degradation during various post-metallization annealing treatments when no bias was applied; this study specifically extends that work to determine the influence of an electric field on wearout. Data are presented to show a thousandfold improvement of SiO₂ dielectric reliability due to breakdown, as a result of using positively biased poly-Si electrodes rather than aluminum. As such, it is the most reliable MOS system reported in studies to date, including those utilizing SiO₂ films grown in HCl-O₂ ambients (7). When stressed negatively, the poly-Si was only slightly more reliable than aluminum.

Experimental

The metal-oxide-semiconductor capacitors used here were fabricated on both n- and p-type silicon wafers (2 ohm-cm); oxide films were grown in oxygen at 1000°C. To avoid electrical shorts originating at the electrode perimeter due to definition of the electrodes using chemical etching processes, a thick, supporting oxide layer was first grown; 25 mil diameter holes were opened photolithographically; and the desired thin (200-700Å) oxide film was grown. The electrodes were fabricated by: chemical vapor depositing (CVD) 3000Å of poly-Si at 650°C using a mixture of SiH₄ and N₂; doping the poly-Si surface by reaction with POCl₃ vapor at high temperature; and, diffusing the phosphorus throughout the electrode at 1000°C using alternate dry-wet-dry oxygen ambients. Capacitance measurements were used to determine the optimal doping parameters: a high capacitance value indicated inadequately doped poly-Si while the appearance of a high flatband voltage signaled that the phosphorus had been driven too far into the oxide.

Two different dielectric breakdown measurements were made: voltage ramp breakdown (10) and ac-

celerated bias-temperature breakdown (6). With the former technique, many (typically 200) MOS capacitors on a wafer are stressed with a voltage ramp and the breakdown voltages (or fields) are recorded. In the second measurement, capacitors are stressed at constant electric field at elevated temperature (100°-400°C) and the times at which capacitor breakdown occurs are recorded: the largest value (t_{max}) has been shown (6) to be a good measure of the wearout time of an initially defect-free SiO₂ film.

Results and Discussion

Measurements of the breakdown voltages of MOS structures, having either poly-silicon or aluminum electrodes, by the ramping technique yielded statistically equivalent values: histograms of breakdown voltages were the same for both materials. Before reproducible silicon deposition and phosphorus-doping procedures were established, both abnormally high and low breakdown voltages were often observed using poly-Si structures. The high voltages were attributed to inadequate homogenization of the dopant in the electrode with attendant loss of voltage in this material due to the appearance of a depletion region. The low voltage values were probably caused by the large number of process steps involved and the subsequent higher chance of contamination, mask misalignment, and thermal stressing. Measurements on boron-doped poly-Si electrodes (11) also revealed carrier depletion unless the electrode homogenization was done at sufficiently high temperatures. Once the fabrication process was well controlled, it was repeatedly verified that ramp breakdown voltage values are the same for both contact electrodes. The high temperatures required to fabricate poly-Si electrodes does not degrade oxide quality once a reproducible Si deposition and doping procedure has been established.

During accelerated testing, however, the electrodes were found to play an important role. Compare the results for poly-Si and Al in Fig. 1, for stressing at 5 and 6 MV/cm at 300°C. The 300Å SiO₂ capacitors having poly-Si electrodes lasted 3 to 4 decades longer than the others. The wearout times (t_{max}) for the positive electrode bias case confirms that the ten-thousandfold improvement occurs over a wide range of applied electric fields (see Fig. 2). The maximum time to failure decreases almost exponentially with applied field; this dependence can be contrasted to a Peck's law behavior ($E \propto t^{-1/4}$) which was observed in other MOS samples (3, 4) which were intentionally contaminated with large amounts of mobile sodium. In contrast with the electrode biased negatively, t_{max} for poly-Si is only a factor of three larger than that for Al. For both polarities, the conduction current increases (often by several decades) prior to breakdown as shown earlier

* Electrochemical Society Active Member.

Key words: dielectric breakdown, silicon dioxide, silicon gates, reliability.

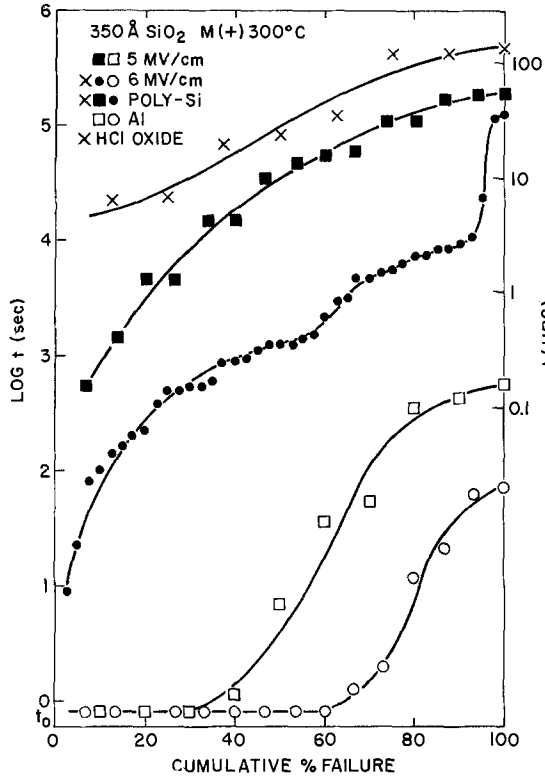


Fig. 1. Statistical failure times of 350Å SiO₂ films having either poly-Si or Al electrodes as measured at 300°C with positive electrode bias.

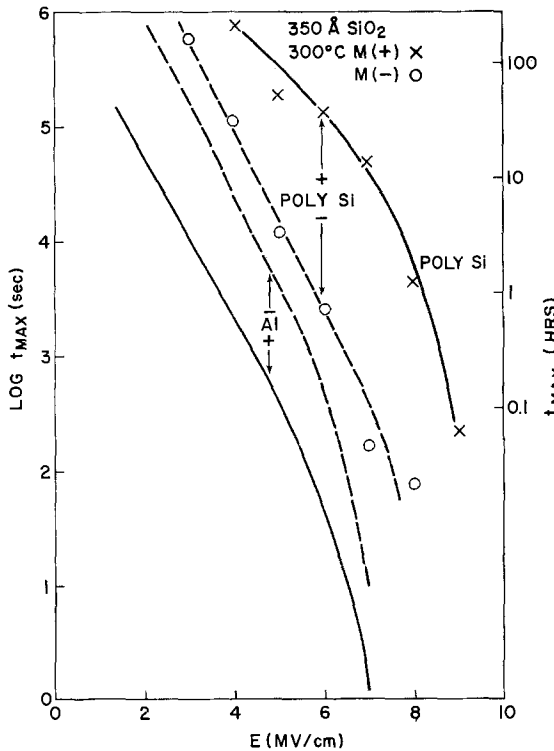


Fig. 2. Maximum time to failure as a function of applied field at 300°C for poly-Si and Al electrodes.

(6). The only difference between samples having poly-Si electrodes and those with Al is the time at which the current increases. The fact that with negative electrode bias Al and poly-Si have nearly equal wearout times, further shows that the wearout time depends on the anode material.

By plotting $\log t_{max}$ vs. $temperature^{-1}$, it was determined that the wearout times in both aluminum and poly-Si structures had a thermal activation energy of

1.4 eV for negative bias. With positive electrode bias, activation energies of 2.4 eV were observed with the poly-Si electrodes and 1.4 eV for aluminum (6) (see Fig. 3). The activation energy with poly-Si was so high that most of the points in Fig. 3 had to be extrapolated from plots of t_{max} vs. E at each temperature. In the absence of alternate wearout mechanisms, the activation energies coupled with the data of Fig. 2 would predict that poly-Si devices should last 10^8 - 10^{16} times longer than Al ones at 25°C.

Other processing conditions were then varied in order to further enhance the dielectric reliability. For example, improved reliability has been previously demonstrated (7) for aluminum-electroded structures when the SiO₂ was exposed to hydrogen at high temperatures. During standard processing of poly-Si structures here, hydrogen is present at two stages: (i) during CVD deposition of Si at 650°C, and (ii) during the phosphorus drive-in done in steam at 1000°C. An alternate phosphorus drive-in process, using dry oxygen alone, was tested and did not give significantly different breakdown characteristics than samples receiving the dry-wet-dry sequence. Formation of the SiO₂ in a 3% HCl/97% O₂ ambient was found to further enhance the dielectric integrity of poly-Si structures. The statistical occurrence of low field breakdown events (<0.8 MV/cm) in HCl oxides was less than half that for standard oxides. The wearout time improvement attributable to the HCl oxidation step was only apparent at moderate (~ 6 MV/cm) to low applied fields and could not be extensively studied because of the prohibitively long times to failure. At the higher fields, no substantial difference was noted for the two types of oxides.

Limiting failure times were measured as a function of oxide thickness (from 100-1500Å) and are com-

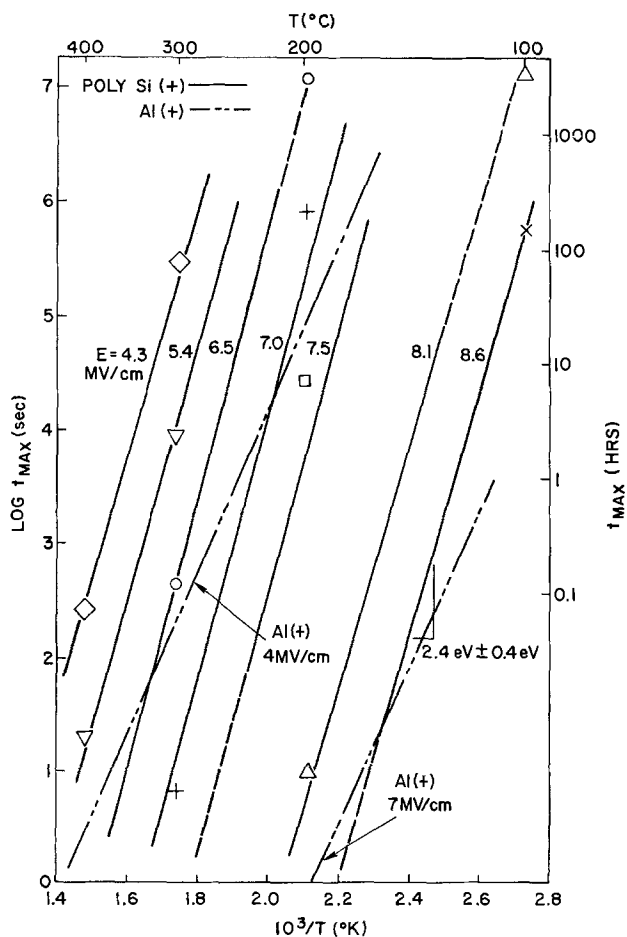


Fig. 3. Temperature dependence of wearout with positively biased poly-Si electrodes. The dashed lines go to points extrapolated from t_{max} vs. E plots at constant temperature.

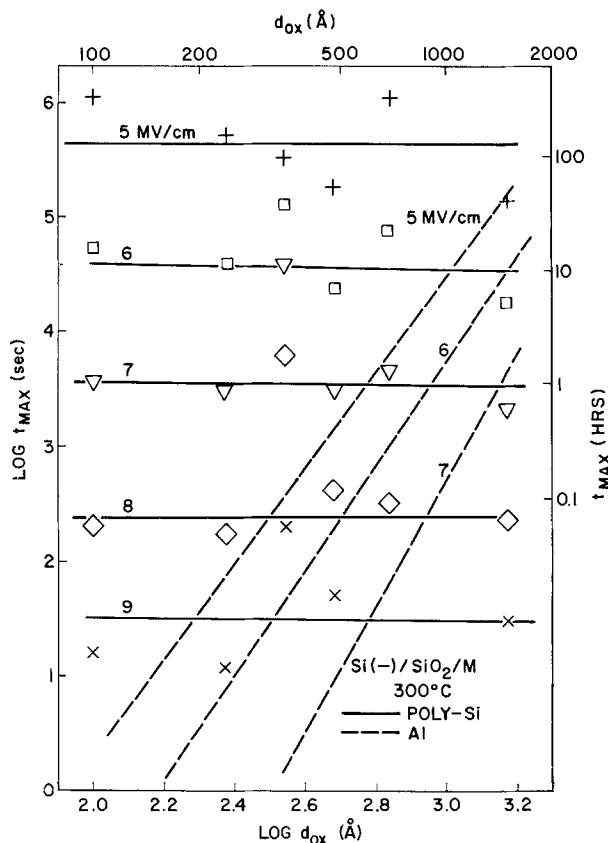


Fig. 4. Maximum time to failure as a function of oxide thickness for poly-Si electrodes biased positively at 300°C for different applied fields. The dotted lines represent the Al electrode data of Osburn and Chou (6).

pared to those using Al electrodes in Fig. 4. For some, as yet, unknown reason the scatter in the poly-Si results was greater than that for aluminum; nevertheless, it is apparent that wearout in poly-Si structures is nearly independent of oxide thickness. Thus poly-Si gates have three reliability advantages over aluminum: (i) under accelerated conditions, they are substantially longer lived, (ii) the activation energy for wearout is higher and hence they are comparatively more reliable at lower operating temperatures, and (iii) they are comparatively more reliable as the thickness of the dielectric is reduced.

Experiments were conducted to determine the source of the improved reliability of poly-Si devices. In one test, poly-Si was deposited on an oxide, doped and then stripped off with ethylene diamine-pyrocatechol solution (12); aluminum electrode dots were evaporated onto the oxide, and the wearout properties were characterized (see Fig. 5.) Even though the electrode was aluminum, the maximum time to failure was 2-20 times longer than with standard samples. Clearly, the silicon deposition and/or doping processes yield a longer lasting SiO₂ layer, regardless of electrode material. Nevertheless, for the positive bias case, the oxide improvement is only a small fraction of that seen with poly-Si electrodes; with a negative bias, on the other hand, the oxide improvement alone is often greater than the net improvement with poly-Si. Both electron microprobe and oxide etch rate measurements were made after doped silicon electrodes were stripped from SiO₂; phosphorus or a phosphosilicate glass (PSG) layer was not observed although neither technique is well-suited to detect a thin (10-20Å), dilute (1-3%) phosphorus-containing layer. In several instances, large flatband voltages (-1.5V) and hysteresis in C-V curves were observed. This might be attributed to phosphorus in the oxide (13, 14) as a result of overdoping the poly-Si. Dielectric wearout measure-

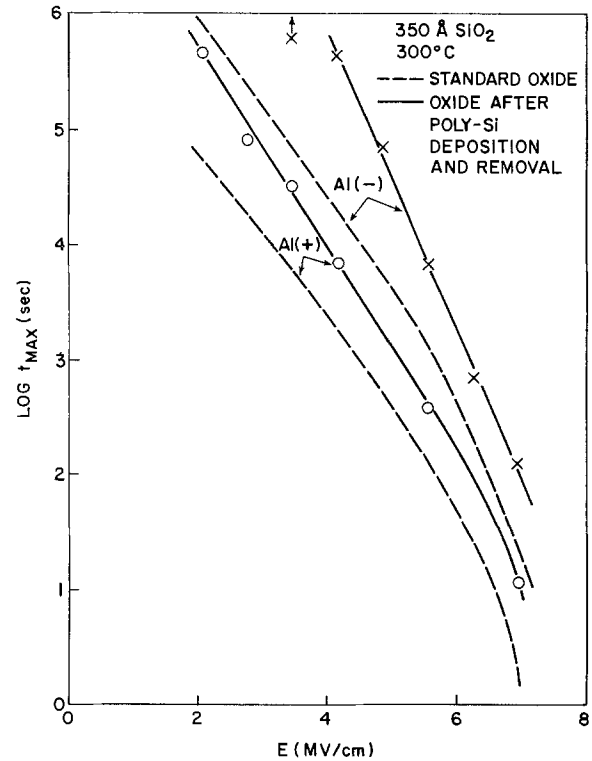


Fig. 5. Maximum time to failure as a function of applied field at 300°C for Al electrodes on standard oxides and on oxides from which doped poly-Si had been removed.

ments on SiO₂ films having different PSG layers suggest that a 50-100Å layer of 3-4% P₂O₅ would be required to give the oxide improvement that is seen after poly-Si removal.

Although several models can be proposed to account for the superior properties of poly-Si electrodes, they must all be considered speculative at this time. Poly-Si is much less reactive with SiO₂ than Al: poly-Si on SiO₂ has been shown (6) to withstand high temperature annealing better than Al on SiO₂; and aluminum injection and diffusion into SiO₂ were seen at relatively low temperature (15). Hydrogen introduced during silicon deposition or dopant drive-in contributes to the oxide integrity. A thin PSG layer or phosphorus-rich layer could also increase wearout time. Each individual model has serious drawbacks and a more complete knowledge of the mechanism of dielectric deterioration is needed to fully understand the source of the improvement seen here. Nevertheless, poly-Si electrodes can be used to fabricate MOS structures that have superior dielectric reliability.

Acknowledgments

The authors would like to thank J. Eldridge, H. Yu, and N. Chou for stimulating conversations during the course of this work. Sample preparation and measurement were aided by J. Kucza, M. Smyth, H. Lazari, V. Maniscalco, and D. Ormond.

Manuscript submitted April 30, 1974; revised manuscript received July 11, 1974.

Any discussion of this paper will appear in a Discussion Section to be published in the June 1975 JOURNAL. All discussions for the June 1975 Discussion Section should be submitted by Feb. 1, 1975.

The publication costs of this article have been assisted by IBM Corporation.

REFERENCES

- G. L. Schnable, H. J. Ewald, and E. S. Schlegel, *IEEE Trans. Reliability*, **R21**, 12 (1972).
- F. L. Worthing, *This Journal*, **115**, 88 (1968).

3. S. I. Raider, *Appl. Phys. Letters*, **23**, 24 (1973).
4. C. M. Osburn and S. I. Raider, *This Journal*, **120**, 1369 (1973).
5. T. H. DiStefano, *J. Appl. Phys.*, **44**, 527 (1973).
6. C. M. Osburn and N. J. Chou, *This Journal*, **120**, 1377 (1973).
7. C. M. Osburn, *ibid.*, **121**, 809 (1974).
8. N. Klein, *IEEE Trans. Electron Devices*, **ED-11**, 788 (1966).
9. N. J. Chou and J. M. Eldridge, *This Journal*, **117**, 1287 (1970).
10. C. M. Osburn and D. W. Ormond, *ibid.*, **119**, 591 (1972).
11. C. A. Neugebauer, J. F. Burgess, R. E. Joynson, and J. L. Mundy, *J. Appl. Phys.*, **43**, 5041 (1972).
12. R. M. Finne and D. L. Klein, *This Journal*, **114**, 965 (1967).
13. E. H. Snow and B. E. Deal, *ibid.*, **113**, 263 (1966).
14. J. M. Eldridge, R. B. Laibowitz, and P. Balk, *J. Appl. Phys.*, **40**, 1922 (1969).
15. H. L. Hughes, R. D. Baxter, and B. Phillips, *IEEE Trans. Nuc. Sci.*, **NS-19**, 256 (1972).

Curie Points of Electrodeposited Nickel Films

M. Ya. Popereka

Graduate School of Applied Science, The Hebrew University of Jerusalem, Israel

ABSTRACT

An abnormally low Curie temperature was observed in nickel films up to 50 μm thick, which were electrodeposited from sulfate solutions containing saccharin. In several cases this abnormal Curie point was 100° or more below that of pyrometallurgical bulk nickel. The phenomenon is explained by the formation of solid solutions of sulfur and carbon in nickel, saccharin being the main source of the sulfur and carbon.

It has been shown (1-5) that in very thin nickel films the Curie temperature is lower than it is in bulk samples of that metal (in the latter $\theta_K \cong 354^\circ\text{C}$). According to Neugebauer (4), this phenomenon is observed only up to thicknesses of 27Å, but Goureaux and Colombani (5) observed it in films as thick as 1000Å. The lowering of the Curie temperature in such thin films has been explained by the "thin film" state theories (7-9). Films of a thickness over 10³Å are considered theoretically as bulk samples; also, measurements have shown that the Curie points in such films do not differ from those measured in bulk samples (6).

This paper describes nickel films of thicknesses up to ~50 μm possessing abnormally low Curie temperatures. This property is not connected with the thin film state, since the films are too thick, but is, as is shown later, connected with the technology used for preparation of the films.

Experimental

Nickel films were electrolytically deposited from a solution of composition (in grams/liter): $\text{NiSO}_4 \cdot 7\text{H}_2\text{O}$, 294; H_3BO_3 , 30; and Rochelle salt, 25. Saccharin was added to the solution (1 g/liter unless otherwise indicated). Except in specified cases, the electrodeposition current density was 2 A/dm², the temperature of the solution 22°C, and pH 2.3. Polished copper rods of 2.2 mm diameter served as substrates.

The Curie points were measured by three methods. The first involved measurement of the dependence on temperature of the electric resistance by means of the automatically recording bridge-circuit. The second method was determination of the temperature at which the maximum differential magnetic permeability became zero (as observed by differential hysteresis loops displayed on the screen of an oscilloscope). The third method was based on the drop in value of the initial permeability near the Curie point; the initial permeability was measured using a device the main features of which are described in Ref. (11). In all cases, the rate of heating of the oven containing the sample was 5 deg/min and was held strictly constant. The temperature of the sample was, in all cases, controlled by a Chromel-Alumel thermocouple, graduated according to the melting points of gallium (99.999%), lead

and tin (both 99.99%). The results obtained by the three methods (of which the third was the most reliable and accurate) are shown in Fig. 1-3. No measurement exceeded the margin of errors indicated.

Results

As can be seen from the graphs, the Curie point in the films studied was, in a number of cases, lower than that in pyrometallurgical nickel (control measurements of the Curie point on the latter are represented by the dashed line in Fig. 2). In some cases, the Curie point dropped to 240°-250°C, i.e., to more than 100° below the "normal" value. Increasing the electrodeposition current density (Fig. 1) elevated the Curie temperature somewhat, bringing it nearer to its normal value. A similar effect could be obtained by superimposing a magnetic field along the substrate axis (Fig. 2) during the deposition of the film, and also by

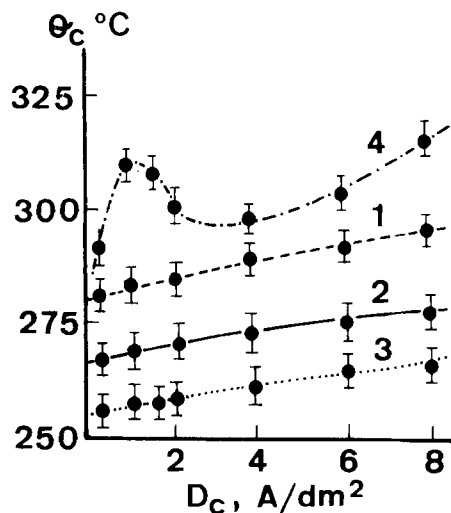


Fig. 1. Dependence of the Curie temperature of nickel films on the cathode current density. Curves 1, 2, 3: films deposited without the superposition of a magnetic field; curve 4: in field 975 Oe parallel to the substrate axis. The saccharin concentration in the solution (grams/liter) is: curve 1, 0.1; curve 2, 0.5; curves 3 and 4, 1.0. Film thickness, $10 \pm 0.2\mu$.

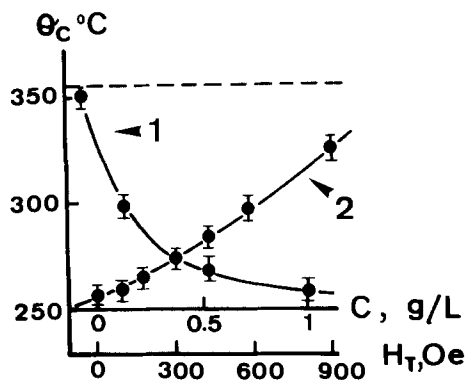


Fig. 2. Dependence of the Curie temperature of nickel films on the saccharin concentration in the solution (curve 1) and on the intensity of the technological magnetic field (curve 2). For curve 1, $H_T = 0$; for curve 2, $c = 1$ g/liter. The film thickness is $10 \pm 0.2\mu$.

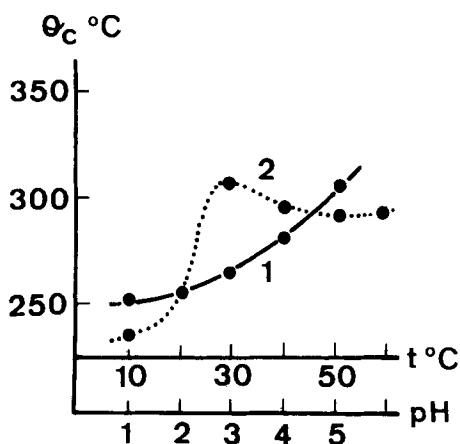


Fig. 3. Dependence of Curie temperatures of nickel film on the solution temperatures (curve 1) and on pH of the solution (curve 2). For curve 1, $\text{pH} = 2.3$; for curve 2, $t = 22^\circ$. The film thickness is $10 \pm 0.2\mu$.

raising the solution temperature (Fig. 3). On the other hand, an increase in the concentration of saccharin in the plating solution (Fig. 2) moved the Curie point away from that of a pyrometallurgical nickel. In the absence of saccharin, the Curie point of the nickel film electrodeposited from a sulfate bath was $\sim 352^\circ\text{C}$, *i.e.*, differing little from the value measured on a sample of pyrometallurgical nickel, of $\sim 354^\circ\text{C}$. The Curie point of a nickel film deposited from a solution containing $\text{NiCl}_2 \cdot 6\text{H}_2\text{O}$, 150 g/liter and H_3BO_3 , 30 g/liter, but containing no organic compounds, coincided with that of the sample of pyrometallurgical origin.

The results shown on the graphs can be supplemented by the following data. In the range of thicknesses from ~ 2 to $\sim 50 \mu\text{m}$, no substantial dependence has been discovered between the Curie points of the films and their thickness. The annealing of the films at 100°C (in a vacuum of $\sim 10^{-5}$ Torr for 3 hr) changed the Curie point very little (for example, for films deposited at 2 A/dm² in the presence of 1 g/liter saccharin, the change is from $\sim 260^\circ$ to $\sim 265^\circ\text{C}$), but an identical annealing at 500°C increased the Curie temperature to as great as 354°C , *i.e.*, to the normal value.

Discussion

The Curie temperature is a magnitude which is structure-sensitive only to a small degree. Factors such as difference in internal stresses, in concentration of defects, in grain size, etc., cannot account for such a large range of measured Curie points. The results described above enable us to assume that the anomalously low values of the Curie temperatures observed

are due to the codeposition of an alien material with the nickel, the main source of which is saccharin.

The assumption that the cause of the observed anomaly is the formation of a solid solution of the cathode hydrogen in the nickel (12) is contrary to the observed facts. Indeed, as shown in Ref. (13), with an increase in the saccharin concentration in the solution, the occlusion of hydrogen in the nickel film decreases; at the same time, the Curie point decreases from its normal value (Fig. 2, curve 1). Moreover, the nickel deposited from a chloride solution contains an amount of hydrogen approximately equal to that deposited from a sulfate solution, but in the first, the Curie point does not differ from its normal value, while in the second, it does. Thus, it is not hydrogen but other impurities that are responsible for the lowering of the Curie point.

As shown in Ref. (14) and (15), nickel films electrodeposited in the presence of a series of organic compounds, including saccharin, contain carbon (up to 0.2% by weight) and sulfur, the sulfur content generally exceeding that of the carbon. Formation of solid solutions of the elements in the nickel could be the cause of the observed phenomena.

It has been found in Ref. (16) that the Curie point of the solid solution of carbon in nickel decreases linearly with the increase in carbon content by $\sim 30^\circ$ /atom per cent ($\sim 0.2\%$ by weight). Hence, the presence of carbon in the films studied can account for a large part of the drop in the Curie point.

We have not found any mention of the influence of sulfur on the Curie point of nickel in the literature. It can be expected that the influence of sulfur is qualitatively identical to that of other nonferromagnetic elements [they all lower the Curie point of nickel by different degrees (4)]. Hence, we can ascribe the observed phenomenon to the joint effect of sulfur and carbon.

The above explanation falls in with the facts. With an increase in current density, the amount of sulfur and carbon in the film decreases (15), since metal grows at a higher speed while sulfur and carbon are being included into the growing layers of the metal at a constant speed. At the same time, the Curie point approaches its normal value (Fig. 1). Increasing the concentration of saccharin causes the amount of sulfur and carbon in the film to increase (15), and the Curie point is lowered from that of pure nickel (Fig. 2). The same correlation is observed for the other dependencies.

Some differences between the Curie points of films deposited without saccharin from a sulfate bath and those of pure nickel are probably due, as well, to the fact that a definite amount of sulfur from the sulfate, or carbon from the Rochelle salt, is incorporated into the film. Indeed, when the film is deposited from a chloride solution containing no sulfur or organic additives, it has a normal Curie point.

Annealing at a sufficiently high temperature (in our case $\sim 500^\circ\text{C}$) must lead to the disintegration of the solid solutions of sulfur and carbon in the nickel, hence the Curie acquires a normal value.

If the suggested explanation is correct, the conclusion may be drawn from curve 1, Fig. 2 that the superposition of a magnetic field during deposition of the film leads to a substantial decrease in the amount of alien material in the film.

Acknowledgment

The author wishes to express his gratitude to N. Suponyev and A. Ivanov who took an active part in the described experiments, and to Dr. I. Fried for her invaluable help in the preparation of the manuscript.

Manuscript received March 15, 1974.

Any discussion of this paper will appear in a Discussion Section to be published in the December 1975 JOURNAL. All discussions for the December 1975 Discussion Section should be submitted by Aug. 1, 1975.

REFERENCES

1. A. Colombani, G. Goureaux, and P. Huet, *J. Phys. Radium*, **20**, 303 (1959).
2. A. Colombani and G. Goureaux, *Compt. Rend.*, **248**, 380 (1959).
3. K. Kuwahara, *J. Phys. Soc. Japan*, **14**, 1247 (1959).
4. C. A. Neugebauer, *Phys. Rev.*, **116**, 1441 (1959).
5. G. Goureaux and A. Colombani, *Compt. Rend.*, **246**, 1979 (1958).
6. S. V. Vonsovskii, *Magnetizm*, Publ. "Nauka," Moscow (1971) (Russian).
7. M. J. Klein and R. S. Smith, *Phys. Rev.*, **81**, 378 (1952).
8. L. Valenta, *Izv. Akad. Nauk SSSR, Ser. Fiz.*, **21**, 879 (1957) (Russian); *English Transl., Bull. Acad. Sci. USSR, Phys. Ser.*
9. A. Corciovei, *J. Phys. Chem. Solids*, **20**, 162 (1961).
10. M. Prutton, "Thin Ferromagnetic Films," Butterworths, London (1961).
11. V. I. Berzhanski, G. A. Petrakovski, and V. N. Seleznev, Coll. "Tonkie magnitniye plionki, vychislitel'naya tekhnika i radiotekhnika," Vol. 2, p. 140, Krasnoyarsk Institut Fiziki (1970) (Russian).
12. H. Bauer and E. Schmidbauer, *Z. Phys.*, **164**, 307 (1961).
13. V. V. Reklite and Yu. Matulis, Coll. "Navodorozhivanie metallov i borba s vodorodnoy khrupkostyu," p. 158, Publ. Moskovskii Dom nauchno tekhnicheskoy propagandy, Moscow (1968) (Russian).
14. A. I. Bodnevas, A. V. Petrauskas, Yu. K. Viagis, and Yu. Yu. Matulis, Coll. "Issledovaniya v oblasti elektroosazhdeniya metallov," p. 9, Publ. Rintip, Vilnius (1968) (Russian).
15. D. S. Zheimite, A. I. Bodnevas, and Yu. Yu. Matulis, *ibid.*, p. 22.
16. F. C. Schwerer, *J. Appl. Phys.*, **40**, 2205 (1969).

Wavelength Dependence of PVA-Phosphor-Dot Photohardening

P. B. Branin and W. H. Fonger

RCA Laboratories, Princeton, New Jersey 08540

ABSTRACT

Dichromate-sensitized PVA coatings were exposed through 23V dot-aperture masks and several different absorption filters in order to study the dependence of dot growth and adherence upon exposure wavelength. For clear-resist coatings exposed under weak-absorption conditions, the hardening spectrum was proportional to the dichromate absorption spectrum. For coatings containing phosphor, the hardening spectrum was fairly flat and insensitive to the dichromate absorption spectrum; this different spectrum resulted because scattering increased the pathlengths of exposure light and led to strong-absorption conditions. With regard to phosphor-dot adherence, except at wavelengths below 350 m μ where phosphor bandgap absorption was strong, adherence was insensitive to the exposure wavelength, that is, to dichromate strong or weak absorption.

The photohardening of dichromate-sensitized polyvinyl alcohol (PVA) coatings, both with and without phosphor, was studied as a function of exposure wavelength. See Kosar (1) for a general review of dichromated colloids. Dichromate absorption spectra are shown in Fig. 1. These spectra were taken for (NH₄)₂Cr₂O₇-PVA aqueous solutions but are similar to K₂Cr₂O₇ solution spectra reported by Kortum (2) and Davies and Prue (3). The spectra show strong, broad, u.v. absorption bands peaking near 270 and 370 m μ plus a weak, blue-green absorption tail extending to 530 m μ . For acid solutions which emphasize Cr₂O₇⁻² over CrO₄⁻² ions, the u.v. bands are displaced to slightly shorter wavelength, the resolution between the bands is reduced, and the blue-green absorption tail is larger relatively.

O'Brien (4) and Koana (5) have reported photohardening rates of some dichromated colloids to be proportional to the rates at which photons are absorbed in dichromate ions, and this behavior is indicated for the PVA coatings studied here. However, this behavior does not make the hardening spectrum unique. Effective hardening spectra for coatings with and without phosphor were found to be different. The differences had to do with absorption conditions. For weak absorption, the hardening spectrum is proportional to the dichromate absorption spectrum; for strong absorption, it is flat and insensitive to the dichromate absorption spectrum.

Experimental

The phosphor used in these studies was Zn_{0.92}Cd_{0.08}S:Cu green phosphor (Z-910D). Slurries for the phosphor

coatings were prepared by ball-milling a stock of phosphor, PVA, and water from which final coating formulations were made by adding PVA, water, (NH₄)₂Cr₂O₇ sensitizer (1:10 relative to PVA), an acrylic resin, and a surfactant. For clear-resist coatings, the phosphor was eliminated and the water content adjusted, but the ratios of the remaining constituents were maintained the same.

The coatings were applied to 23V television faceplates using a stationary single-head slurry machine in a conventional rotating-tilting and final-spinout mode. Coating weight and uniformity were controlled by adjusting spinout speed and duration.

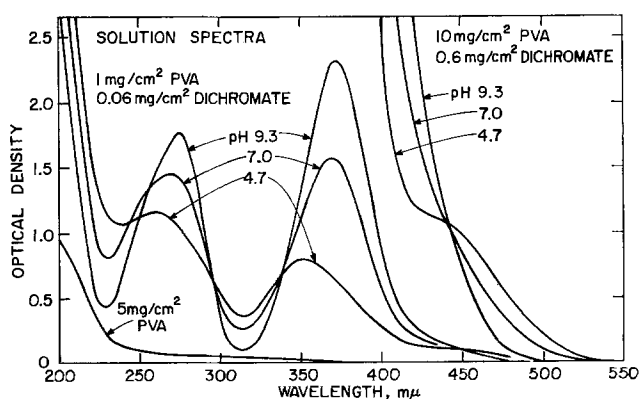


Fig. 1. Absorption spectra of (NH₄)₂Cr₂O₇-PVA aqueous solutions. The pH was adjusted with NH₄OH. These spectra were taken with a Cary Model 14 spectrophotometer.

Key words: phosphor-dot screening, photochemistry, PVA-hardening spectrum.

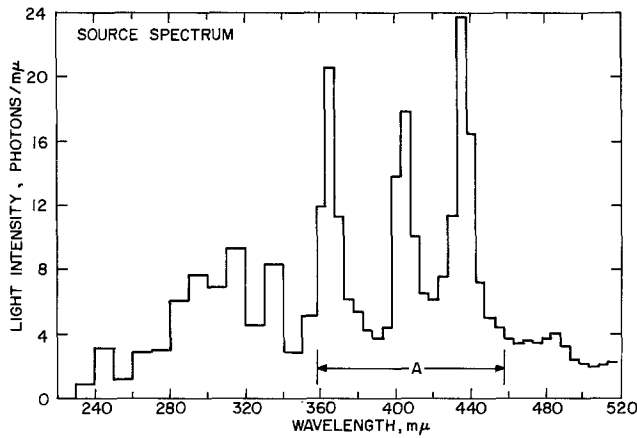


Fig. 2. Spectrum of the BH6-1 Hg capillary lamps used for the dot exposures. This spectrum contains strong Hg lines at 365, 404, and 436 mμ plus an underlying continuum. Normalization was made such that the 100 mμ interval labeled A contains 1000 photons.

The coatings were exposed in a single-position lighthouse equipped with a BH6-1 Hg capillary lamp and 100 mil quartz collimator. The spectrum of this source is shown in Fig. 2. The spectrum above 360 mμ was measured with a calibrated spectrometer. The spectrum below 360 mμ was adapted from vendor data (6) but was also roughly verified using some u.v. filters and the quantum counter liumogen (7). The coatings were exposed through a 23V dot-aperture mask plus several 2 × 2 in. absorption filters positioned below the mask as illustrated in Fig. 3. Exposures were made with the lighthouse lens package removed to provide high enough light intensity to offset low transmissions

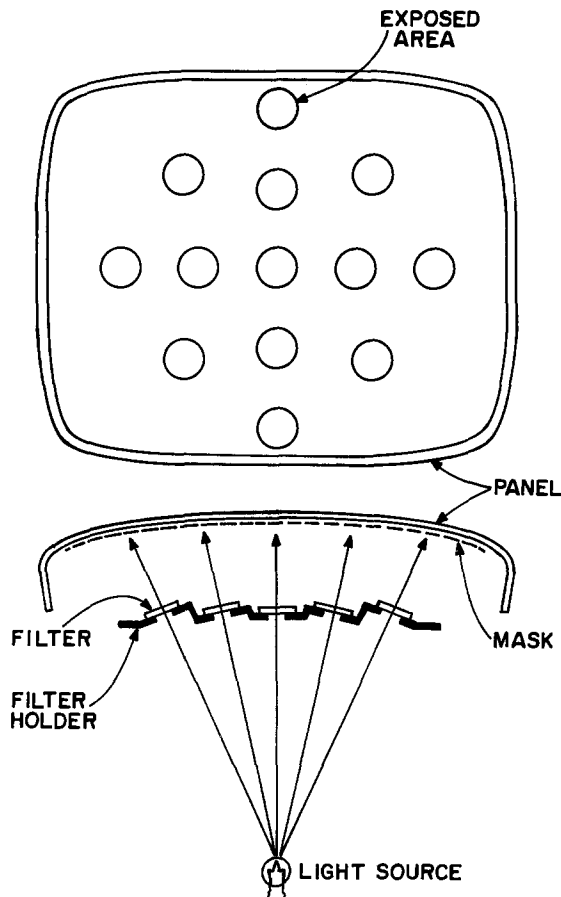


Fig. 3. Lighthouse arrangement used to make thirteen filtered exposures on 23V panels. The spacing between the mask and panel was 0.60 in.

of the filters, to avoid center-to-edge variations in the spectrum caused by the lens coating, and to preserve the source spectrum down to 230 mμ.

The transmissions of the absorption filters are shown in Fig. 4. Apart from a NiSO₄-solution cell used in the short u.v. region (240-350 mμ), the filters were Corning glass color filters of the 3, 7, and 0 series. The 3-series filters divide up the blue-green region of the spectrum. The remaining filters involved 7-series filters and divide up the u.v. region. The transmission of the 23V panel glass is also shown because it was an added filter for some exposures made through the panel.

After exposure, the dot patterns were developed on a rotating head in a water spray at 104°F and 17 psi for 30 sec.

Dot Growth with Exposure Time

The observed growth of dot diameters with exposure time is shown in Fig. 5 for 4.5 mg/cm² phosphor coat-

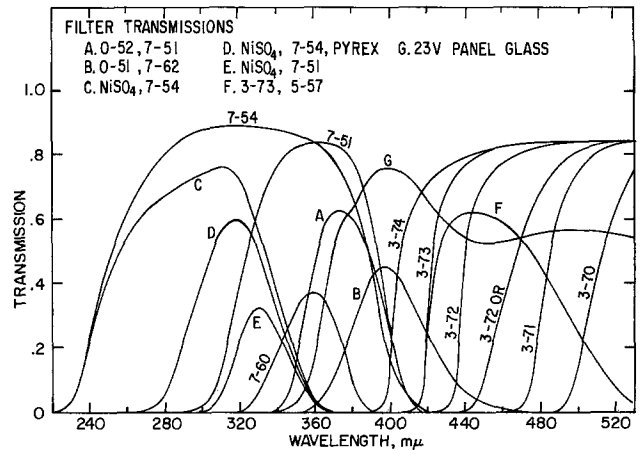


Fig. 4. Transmissions of the NiSO₄ and Corning filters used for filtered dot exposures; 3-72 OR was a particularly orange 3-72 filter.

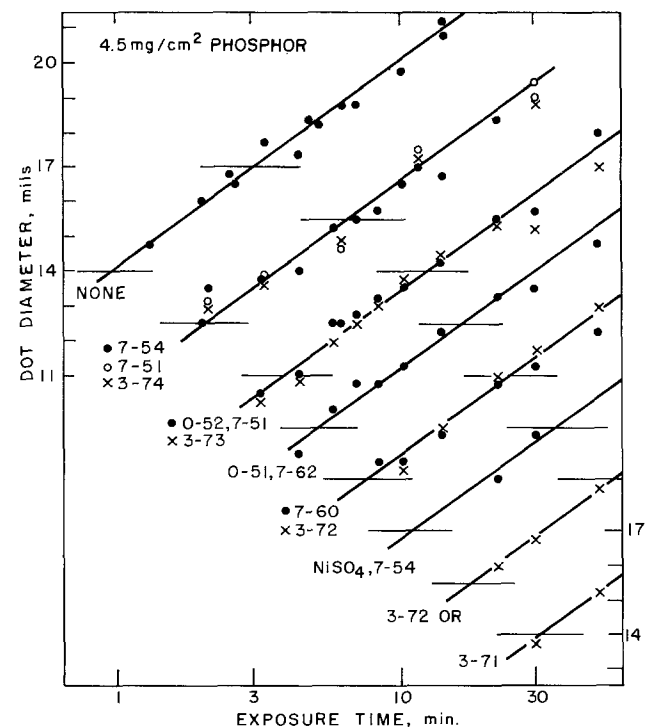


Fig. 5. Observed dot diameters vs. exposure time for 4.5 mg/cm² phosphor coatings exposed through various absorption filters. For the various sets of data, the two short horizontal lines mark the levels of 14- and 17-mil dot diameters. Exposure times have been corrected to constant light intensity.

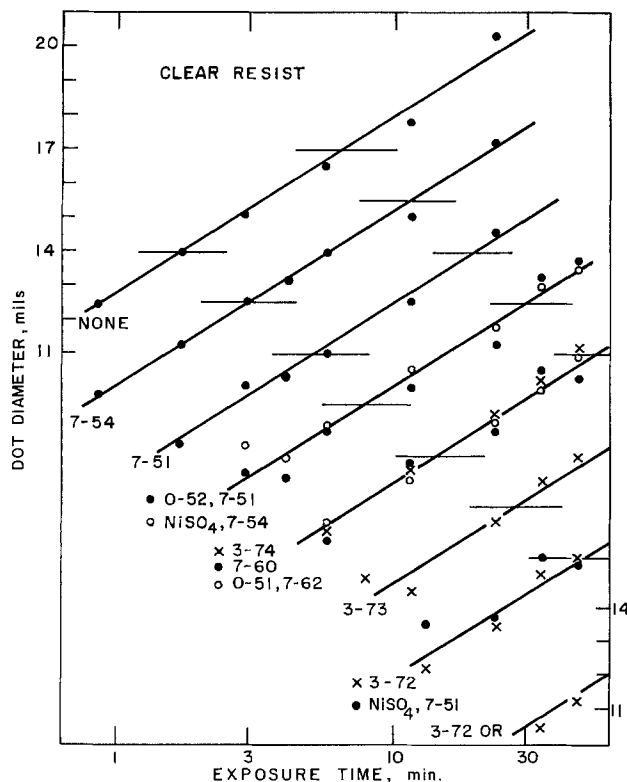


Fig. 6. Observed dot diameters vs. exposure time for clear-resist coatings.

ings. Exposures in the blue-green region through 3-series filters are shown by crosses and in the u.v. region through 7-series filters by dots. To avoid overlapping of data points, the ordinate scale is offset for the various sets of data, and the short horizontal lines show the 14-mil and 17-mil diameter levels. Dot diameters measured at the various filter positions (see Fig. 3) were corrected to center-panel values empirically. For the 23V panel mask used, 14 mils was the image size of center-panel mask holes projected from a point source, and 17 mils was the diameter of tangent tricolor dots.

For all exposures, dot diameter growth was approximately proportional to the log of the exposure time. Assuming that a fixed exposure level is needed for threshold photohardening, this behavior indicates that light intensity in the penumbra region decreased radially approximately exponentially. The slope of the D vs. $\log t$ lines shown in Fig. 5 corresponds to a radial $1/e$ distance of 1.30 mils.

Similar dot growth data for clear-resist coatings without phosphor are shown in Fig. 6.

Exposure times for the various filters were in different proportions for the phosphor and clear-resist coatings. That is, the hardening spectra for these

coatings were different. Relative to exposure times in the near-u.v. region (most 7-series filters) as a base, the phosphor coatings required longer exposure times in the short-u.v. region with the NiSO_4 , 7-54 filter and the 7-54 filter and shorter exposure times in the blue-green region (3-series filters). For example, exposure times for the short-u.v. NiSO_4 , 7-54, near-u.v. 7-60, and blue-green 3-73 filters were in that order for phosphor coatings but were in the reverse order for clear-resist coatings.

Since the slopes of the D vs. $\log t$ lines are fairly close in all cases, we will characterize hardening rates simply by the exposure times required to produce dots of a particular size, namely, 14 mils. These exposure times, T_{CR} , and $T_{4.5}$, and their ratios, $T_{CR}/T_{4.5}$, are listed in Table I. The ratios $T_{CR}/T_{4.5}$ are ≈ 6 in the blue-green region, ≈ 2 in the near-u.v. region, and ≈ 0.7 in the short-u.v. region where light is strongly absorbed in the phosphor bandgap.

The exposure times in Table I have been compared with simple, limiting hardening rates. Following behaviors reported for some other dichromated colloids (4, 5), we assume that, following absorption in dichromate ions at wavelength λ , the quantum efficiency for hardening $\eta(\lambda)$ is insensitive to λ . Hardening rates H_i are then proportional to the rates at which photons are absorbed in dichromate ions

$$H_i \propto \int d\lambda L(\lambda) t_i(\lambda) a(\lambda)$$

where $L(\lambda)$ is the source spectrum in photons per unit wavelength (Fig. 2), $t_i(\lambda)$ is the transmission of filter i (Fig. 4), and $a(\lambda)$ is the fraction of incident light absorbed in dichromate ions. For weak absorption $a(\lambda) \ll 1$, $a(\lambda)$ is proportional to the dichromate absorption constant $k(\lambda)$. For strong absorption $a(\lambda) \approx 1$, $a(\lambda)$ is insensitive to λ and can be omitted from the integrals.

The clear-resist dot exposures were made under weak-absorption conditions. Layer transmissions were ≈ 0.70 at the dichromate 370 $m\mu$ absorption peak. Thus, in the table, the clear-resist exposure times T_{CR} have been compared with the weak-absorption hardening rates $\int d\lambda L(\lambda) t_i(\lambda) k(\lambda)$. The products $T_{CR} \int d\lambda L t_i k$ decrease somewhat from shorter to longer wavelengths (from top to bottom in the table) but are relatively constant compared to the strong wavelength variation of the dichromate absorption constant $k(\lambda)$. Thus, the quantum efficiency $\eta(\lambda)$ was relatively constant, and the clear-resist hardening spectrum was approximately the dichromate absorption spectrum $k(\lambda)$.

In the integrals, $k(\lambda)$ was taken proportional to the dried-layer absorption spectrum shown in Fig. 7. This spectrum was taken for fresh, dried, clear-resist coatings deposited on 23V panels (transmission measurements possible down to 360 $m\mu$) and on 2×2 in. quartz slides. The resist had the same component ratios as the resist used in the clear-resist dot exposures, but the water content was reduced to give thicker coatings with absorption increased sixfold, as convenient for absorption measurements. The dried-

Table I. Observed exposure times T_{CR} and $T_{4.5}$ to make 14-mil dots for clear-resist and 4.5 mg/cm^2 phosphor coatings exposed through various absorption filters. These times are compared with weak- and strong-absorption hardening rates $\int d\lambda L t_i k$ and $\int d\lambda L t_i$, respectively. The source spectrum $L(\lambda)$ and the dichromate absorption spectrum $k(\lambda)$ are expressed in the arbitrary units used in Fig. 2 and 7, respectively.

Filter	T_{CR} , min	$T_{4.5}$, min	$T_{CR}/T_{4.5}$	$\int d\lambda L t_i k$	$T_{CR} \int d\lambda L t_i k$	$\int d\lambda L t_i$	$T_{4.5} \int d\lambda L t_i$
NiSO_4 , 7-54	7.8	11.0	0.71	325.0	2540.0	362.0	3980.0
NiSO_4 , 7-51	42.0			39.4	1650.0	64.0	
7-54	2.9	2.1	1.4	703.0	2040.0	770.0	1620.0
7-51	5.1	2.1	2.4	403.0	2060.0	470.0	990.0
None	1.7	0.95	1.8	1095.0	1860.0	1800.0	1710.0
7-60	14.0	7.8	1.8	115.0	1610.0	117.0	910.0
0-52, 7-51	8.2	3.9	2.1	219.0	1800.0	234.0	910.0
0-51, 7-62	14.0	5.2	2.7	93.0	1300.0	190.0	990.0
3-74	14.0	2.1	6.7	98.0	1370.0	581.0	1220.0
3-73	27.0	4.0	6.8	54.0	1460.0	446.0	1780.0
3-72	48.0	7.8	6.2	24.5	1180.0	261.0	2040.0
3-72 OR	≈ 140.0	18.0	≈ 8.0	7.7	≈ 1100.0	128.0	2300.0
3-71	> 200.0	≈ 30.0	> 6.0	2.5	> 500.0	69.0	≈ 2100.0

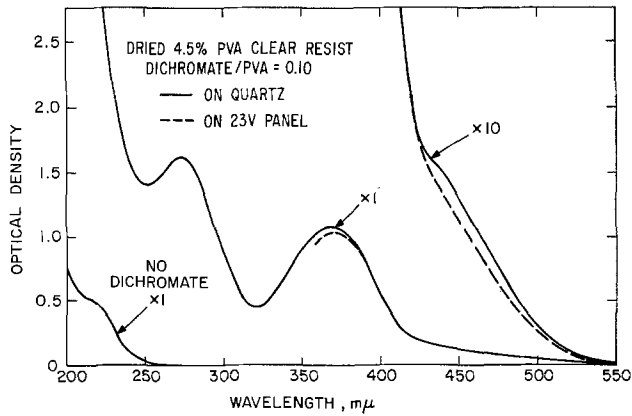


Fig. 7. Absorption spectra of dried, clear-resist coatings on a 23V panel and a 2×2 in. quartz slide. Substrate absorption has been subtracted out. Without dichromate sensitizer, absorption was negligible down to 250 $m\mu$. For the thinner clear-resist coatings used in the dot exposures, the optical densities were 1/6 times the values in this figure.

layer spectrum is similar to the dichromate solution spectra shown in Fig. 1 but is not identical to any one of these spectra. The position of the 370 $m\mu$ peak is typical of the neutral solution, but the relative size of the blue-green absorption tail is typical of the acid solution.

The phosphor exposure times $T_{4.5}$ in the table have been compared with the strong-absorption hardening rates $\int d\lambda L(\lambda) t_1(\lambda)$.¹ For the phosphor exposures, light scattering increased light pathlengths in the coatings and thereby enhanced absorption and hardening. In addition, dichromate absorption competed with phosphor absorption. For $\lambda < 350 m\mu$ (strong phosphor bandgap absorption), hardening was inefficient, and the product $T_{4.5} \int d\lambda L t_1$ was larger (NiSO₄, 7-54 filter). For $\lambda > 350 m\mu$ (phosphor Cu-impurity absorption), the products $T_{4.5} \int d\lambda L t_1$ were smaller and increased somewhat from shorter to longer wavelengths. Nevertheless, at these wavelengths, these products were relatively constant compared to the strong wavelength variation of the dichromate absorption constant, and the hardening spectrum of the phosphor coatings can be described as fairly constant and insensitive to the dichromate absorption constant.

For 4.5 mg/cm² phosphor coatings, one-half of the hardening capacity of BH6 light is contained in wavelengths above 400 $m\mu$, that is, in the region of dichromate weak, blue-green absorption. This result is evident from Fig. 5 where the hardening rates using the 7-54 and 3-74 filters were the same. The 7-54 and 3-74 filters are low-pass and high-pass filters, respectively, about the wavelength point 400 $m\mu$. See the filter profiles in Fig. 4.

Dot-growth curves similar to those shown in Fig. 5 and 6 were also obtained for 2 mg/cm² phosphor layers and for 4.5 mg/cm² phosphor layers exposed through the panel glass. In the latter cases, the penumbra shape at panel center was maintained as in normal exposures by using the same source-to-mask distance and the same effective mask-to-coating distance.² After correction for the panel-glass transmission at the exposure wavelength, these exposure times were

¹ For exposures with 3-series filters, the integrals $\int d\lambda L t_1$ were arbitrarily terminated at 518 $m\mu$ near the end of dichromate absorption. For a different termination point, these integrals would be somewhat different.

² For exposures through the panel, the light source and filters were maintained as in Fig. 3, and the coated panel was inverted. A formed mask cut from its frame was attached to the bottom (convex) side of the panel via standoffs of length $q_2 = 0.30$ in. The effective mask-to-coating distance was then $q_{eff} = q_1/n_1 + q_2$, where q_1 was the thickness of the panel glass and n_1 its index of refraction.

the same as for 4.5 mg/cm² phosphor coatings exposed in the normal way. That is, exposure times were the same for exposures from either side. For the 2 mg/cm² phosphor coatings, the wavelength dependence of the hardening rate was intermediate between the two wavelength dependences described above for clear-resist and 4.5 mg/cm² phosphor coatings.

Dot Adherence

Except for exposures in the short-u.v. region ($\lambda < 350 m\mu$) where phosphor bandgap absorption was strong and adherence poor, dot adherence was insensitive to exposure wavelength. Exposure with any filter above 350 $m\mu$ always led to adherence failure at exposures corresponding to 11-11½ mils dot diameter for clear-resist coatings, to 12-12½ and 15-16 mils for 2 and 4.5 mg/cm² phosphor coatings, respectively, and to 12-12½ mils for 4.5 mg/cm² phosphor coatings exposed through the panel.

The better phosphor-dot adherence for 2 mg/cm² coatings and for 4.5 mg/cm² coatings exposed through the panel is qualitatively explained by obvious gradings of exposure light intensity across the coatings. However, the insensitivity of dot adherence to dichromate strong 370 $m\mu$ or weak blue-green absorption seems surprising. We believe that, for the phosphor layers, gradings of light intensity across the layers were determined primarily by the scattering paths of the light and only secondarily by light absorption. In this way, the adherence could become insensitive to the dichromate absorption constant.

Conclusions

Relative to the photohardening rate in the dichromate strong 370 $m\mu$ absorption region, hardening in the dichromate weak blue-green absorption region was three times greater for 4.5 mg/cm² phosphor coatings than for clear-resist coatings. For the clear-resist coatings, exposures approximated weak-absorption conditions, and the hardening spectrum was proportional to the dichromate absorption spectrum. For the 4.5 mg/cm² phosphor coatings, exposures more nearly approximated strong-absorption conditions, and the hardening spectrum was fairly flat and insensitive to the dichromate absorption spectrum. For 4.5 mg/cm² phosphor coatings, one-half of the hardening capacity of BH6 light resides in blue-green wavelengths above 400 $m\mu$. Except at wavelengths below 350 $m\mu$ where phosphor bandgap absorption was strong, phosphor-dot adherence was insensitive to exposure wavelength, that is, to dichromate strong or weak absorption.

Manuscript received Aug. 23, 1974. This was Paper 122 presented at the San Francisco, California, Meeting of the Society, May 12-17, 1974.

Any discussion of this paper will appear in a Discussion Section to be published in the December 1975 JOURNAL. All discussions for the December 1975 Discussion Section should be submitted by Aug. 1, 1975.

Publication costs of this article were partially assisted by RCA Corporation.

REFERENCES

1. J. Kosar, "Light-Sensitive Systems," Chap. 2, John Wiley & Sons, Inc., New York (1965).
2. G. F. Kortüm, *Z. physik. Chem. (B)*, **33**, 243 (1936).
3. W. G. Davis and J. E. Prue, *Trans. Faraday Soc.*, **51**, 1045 (1955).
4. B. O'Brien, Jr., *J. Optical Soc. Am.*, **42**, 101 (1952).
5. Z. Koana, Intern. Congress of Photographic Science, Sect V, Sept. 1967.
6. Illumination Industries, Inc., Sunnyvale, Calif. 94086.
7. N. Kristianpoller and D. Dutton, *Appl. Optics*, **3**, 287 (1964).

Luminescence Properties of Thiogallate Phosphors

III. Red and White Emitting Phosphors for Flying Spot Scanner Applications

T. E. Peters

GTE Laboratories Incorporated, Waltham, Massachusetts 02154

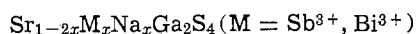
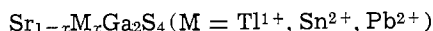
ABSTRACT

Ions with the ns^2 electronic configuration were investigated as activators in the $SrGa_2S_4$ host lattice. Phosphors activated with Sn^{2+} or Pb^{2+} were found to cathodoluminesce in the red spectral region and exhibit relative efficiencies (η_{cr} Rel.) of 1.1 and 4.6%, respectively. The Pb^{2+} phosphor has a short fluorescent decay time ($I_0/100 \sim 10^{-6}$ sec) and was found suitable for use as the red screen component in a flying spot scanner tube (FSST) employed as the transducer in color video playback. Coactivation of $SrGa_2S_4$ by Ce^{3+} and Pb^{2+} was found to result in a white-emitting phosphor that exhibits lower noise in FSST screens than is usually found when phosphor blends are employed.

The cathodoluminescence emission and decay properties of the Ce^{3+} activated alkaline earth thiogallates were reported earlier (1) with particular emphasis on factors governing the use of these materials in flying spot cathode-ray tubes. Phosphors activated with ions possessing the ns^2 electronic configuration (Tl^{1+} , Sn^{2+} , Pb^{2+} , Sb^{3+} , Bi^{3+}) are also of interest for use in this type of device because their fluorescence lifetime should be very short. As a consequence, these ions were also evaluated as activators in the $SrGa_2S_4$ host lattice, and this paper describes the cathodoluminescence emission and decay characteristics of the Pb^{2+} and Sn^{2+} activated, and Ce^{3+} - Pb^{2+} coactivated $SrGa_2S_4$ phosphors and discusses their application in flying spot scanner tubes (FSST) designed for use in color video playback systems.

Experimental

Phosphor preparation.—The phosphors described herein were synthesized according to the general formulas



by reacting mixtures of the previously prepared, high purity sulfides at 900° – $950^\circ C$ in a stream of H_2S . The activators were generally introduced at sufficiently high concentration to assure stoichiometry, and lower doping levels were achieved by dry dilution. Monovalent sodium was added as Na_2SO_4 , usually in excess of the stoichiometric amount, to serve as a mineralizer and provide charge compensation for the trivalent activators. Any sodium not incorporated in the $SrGa_2S_4$ host lattice was subsequently removed from the phosphor by washing with demineralized water. The Pb^{2+} and Sn^{2+} activated phosphors did not require valence compensation; consequently, the Na_2SO_4 was usually omitted and the higher reaction temperature was employed. In the case of Tl^{1+} , charge compensation was allowed to occur through a vacancy mechanism.

Measurements.—Standard analytical techniques were employed to monitor the purity and stoichiometry of the sulfide reagents and finished phosphors. X-ray powder diffraction was used to ascertain formation of the $SrGa_2S_4$ compound.

Emission spectra were recorded in terms of relative energy, and the relative cathode-ray efficiency values (η_{cr} Rel.) were obtained by comparing the integrated area under the spectral energy distribution curves to

that of selected thiogallate and NBS-1021 phosphors of known absolute efficiency.

Cathodoluminescence brightness levels of $SrGa_2S_4$:Pb were measured under conditions simulating those found in a color video playback system employing flying spot scanners (3). Phosphor-coated conducting glass slides were placed in a demountable CRT and excited with a 25 kV-100 μA electron beam which was scanned at the normal TV rate over a $5.7 \text{ cm} \times 7.6 \text{ cm}$ raster. The emission was detected by a Gamma photometer equipped with a Wratten No. 25 filter.

Cathodoluminescence decay times were measured by pulsing a 20 kV electron beam of a 12.7 cm diameter FSST at a rate of 60 Hz with a pulse duration of 100 nsec. The fluorescence was detected by a photomultiplier tube equipped with a Wratten No. 25 or 47B filter and displayed on an oscilloscope. Screen noise measurements were obtained by monitoring the change in emission intensity of the flying spot of light as it was scanned across the screen of a 12.7 cm FSST.

Results and Discussion

Of the ns^2 ions evaluated as activators only Sn^{2+} and Pb^{2+} produced visible emission at room temperature. The cathodoluminescence emission and decay characteristics of these materials are given in Table I, together with similar data for $Y_3Al_5O_{12}$:Ce (YAG:Ce) (2). The latter material is a fast decay phosphor that has been advanced as a replacement for the ZnO:Zn(P-24) screen in a version of the FSST employed as a playback transducer for color television. The radiant efficiency under cathode-ray excitation (η_{cr} Rel.) of the $SrGa_2S_4$:Pb (2 atom per cent [a/o]) is slightly higher than that of YAG:Ce while the $SrGa_2S_4$:Sn (1 a/o) phosphor has a lower efficiency.

The decay time (β) given in the last column of Table I is the time required for the fluorescence to decrease to $I_0/100$. This value has been found to be more significant for FSST phosphor evaluation than the fluorescence lifetime, τ -(decay to I_0/e), because it includes even the low level, long persistence components of the decay. The fluorescence intensity vs. time curve for the $SrGa_2S_4$:Sn phosphor exhibits a power law dependence ($I_0 \propto t^{-n}$), and its decay time is longer than that of the other phosphors which have essentially exponential decay curves (Fig. 1). The per-

Table I. Cathodoluminescence emission and decay characteristics of Sn^{2+} and Pb^{2+} activators

Phosphor	η_{cr} (%)	λ_{max} (nm)	Decay time, β (μsec)
$SrGa_2S_4$:Pb	4.6	595	1.24
$SrGa_2S_4$:Sn	1.1	680	>10.0
$Y_3Al_5O_{12}$:Ce	3.5	550	0.54

* Electrochemical Society Active Member.

Key words: video playback, fast decay phosphors, cathodoluminescent phosphors.

Table II. Decay time quenching in SrGa₂S₄:Pb

Pb (atom per cent)	Co (weight per cent)	Decay β (μ sec)	Relative red brightness	Mechanism used to increase decay rate
2	—	1.24	125	Concentration quenching
4	—	1.16	113	Concentration quenching
8	—	1.0	100	Concentration quenching
8	0.01	1.0	100	Transition metal quenching
8	0.1	0.98	98	Transition metal quenching

sistence of the SrGa₂S₄:Sn phosphor is long enough to eliminate it as a candidate for use in FSST screens; however, the decay of the Pb²⁺ activated phosphor is of a magnitude which would permit its use in systems employing electronic compensation (3).

The data in Table II shows that the decay time of SrGa₂S₄:Pb can be reduced slightly by concentration quenching. Although the reduction is slight, the effect appears to be real, with phosphors containing 8–10 a/o Pb consistently having decay times of 1 μ sec and those with lower Pb²⁺ concentrations having longer decay times. The reduction in decay attributed to concentration quenching is accompanied by a reduction in emission intensity (Table II) and a shift of λ_{\max} to lower energy.

Transition metal quenching, which produced a dramatic reduction in the decay time of the Ce³⁺ fluorescence in SrGa₂S₄:Ce, Na (1), is seen (Table II) to exert little influence on the fluorescence decay time of Pb²⁺ in the same host compound. This result is in agreement with that of other workers (4) who have shown that transition metal quenching does not alter the persistence of a phosphor whose fluorescence decays exponentially.

The efficiency and spectral energy distribution of the SrGa₂S₄:Pb phosphor make it particularly attractive for use in FSST's for color TV playback. This is shown in Fig. 2 which depicts the spectral energy distribution curves for YAG:Ce and SrGa₂S₄:Pb together with a spectral sensitivity curve (shaded) for a simulated red

detector of a video playback system. The detector sensitivity curve was generated from a convolution of the transmission curve for a Kodak No. 25 Wratten filter and the S-4 response curve of an RCA 931A phototube. The convoluted data was then normalized by setting the optimum detector output at 100. It is evident that the SrGa₂S₄:Pb emission is better matched to the detector's response than is the emission of YAG:Ce. This is important because most phototubes are relatively insensitive in the red spectral region and, as a consequence, the photocurrent generated by the red detector must be amplified to a much greater extent than that of the corresponding green and blue detectors.

For color video playback applications, FSST's that exhibit a uniform emission in the visible region of the spectrum are desirable. This effect can be achieved by blending the SrGa₂S₄:Pb with a blue-emitting phosphor such as SrGa₂S₄:Ce,Na (1), or by activating the SrGa₂S₄ host compound with both Ce³⁺ and Pb²⁺. The spectral energy distribution of the emission of FSST's prepared with the blended and single component thiogallate screens are compared to that of a commercial FSST (3) in Fig. 3. The tubes containing the thiogallate phosphors are seen to have a fairly uniform emission over the entire visible spectrum, while the commercial tube is deficient in the blue-green and red spectral regions.

The emission spectrum of the blended phosphor screen [Fig. 3(a)] can be altered to some extent by changing the ratio of its blue-to red-emitting components. Similar modifications in the spectral distribution of the single component screen [Fig. 3(b)] are best affected by altering the Ce³⁺ and/or Pb²⁺ concentration of the phosphor. This is illustrated in Fig. 4, where the trichromatic coefficients and blue (~450 nm)/red (~605 nm) peak intensity ratios (B/R) are given for SrGa₂S₄:Ce,Pb,Na phosphors activated with 4 or 8 a/o Pb and 0.03–0.5 a/o Ce. For materials with spectral distributions similar to that in Fig. 3(b) (viz., B/R \cong 1, $x \cong$ 0.35, $y \cong$ 0.33), the [Ce³⁺] should be in the vicinity of 0.1 a/o. When [Ce³⁺] increases much beyond this value, the blue emission band begins to dominate the fluorescence spectrum.

FSST's having the spectral distributions shown in Fig. 3 were evaluated in a color video playback system, and relevant data is reported in Table III. The data show the response of all three of the playback system's photodetectors to be significantly greater for the FSST's employing thiogallate screens. The fluorescence decay times for the thiogallate screens are somewhat longer than those exhibited by the blended phosphor screen of the commercial tube, but the longer decay times did not result in a noticeable deterioration in the televised picture. Screen noise for the blended thiogallate phosphor screen is equivalent to that of the Ca₂Al₂SiO₇:Ce-Y₃Al₅O₁₂:Ce screen, but the single component thiogallate screen is noticeably better in this respect.

Summary

Ions with the ns² electronic configuration were evaluated as activators in the SrGa₂S₄ host lattice. Under cathode-ray excitation, phosphors activated with Sn²⁺ or Pb²⁺ were found to fluoresce in the red spectral region with relative efficiencies (η_{cr} Rel.) of 1.1 and 4.6%, respectively. The Pb²⁺ activated phosphor was found to have a short fluorescence decay time

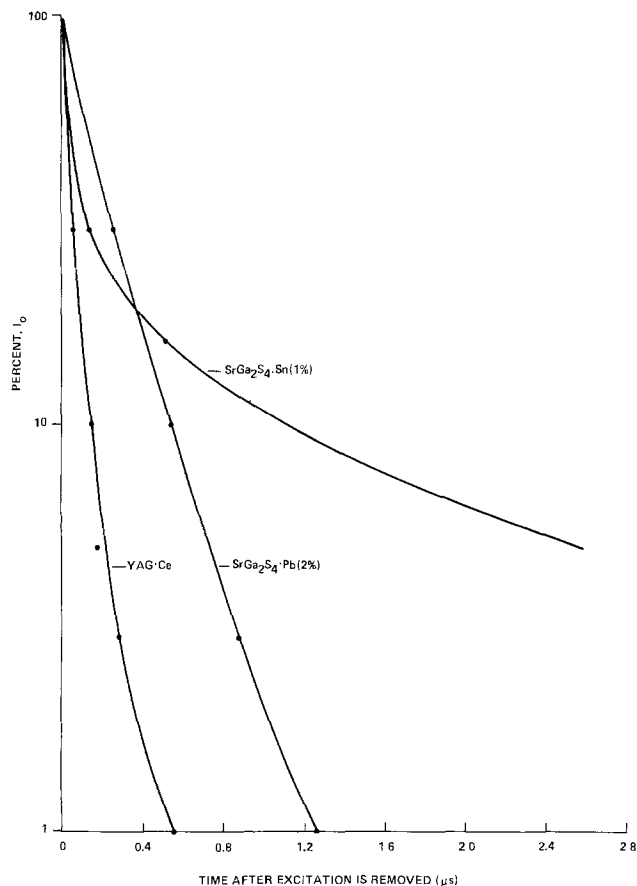


Fig. 1. Decay of fluorescence of red emitting phosphors

Fig. 2. Red detector response and spectral energy distribution of SrGa₂S₄:Pb and YAG:Ce.

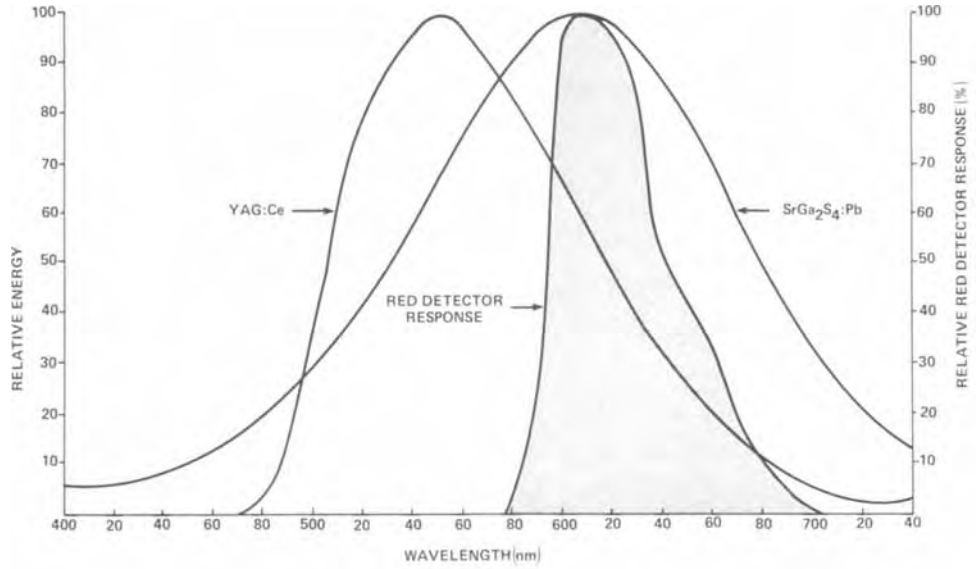


Fig. 3. Spectral energy distribution of FSST screens.

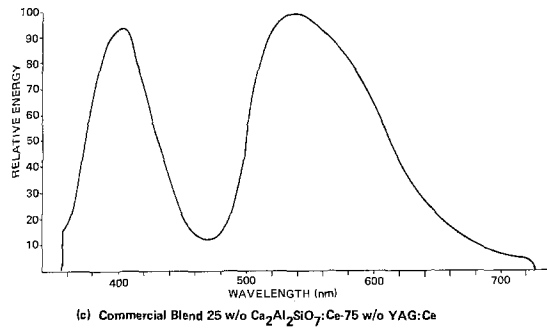
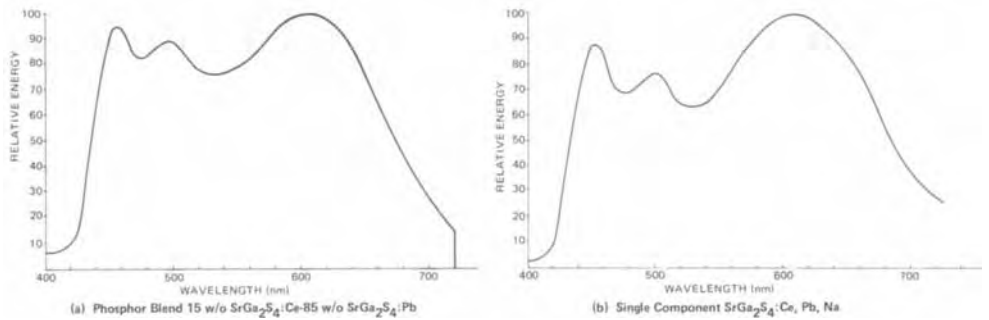


Fig. 4. Trichromatic coefficients and B/R ratios for SrGa₂S₄:Ce, Pb, Na phosphors.

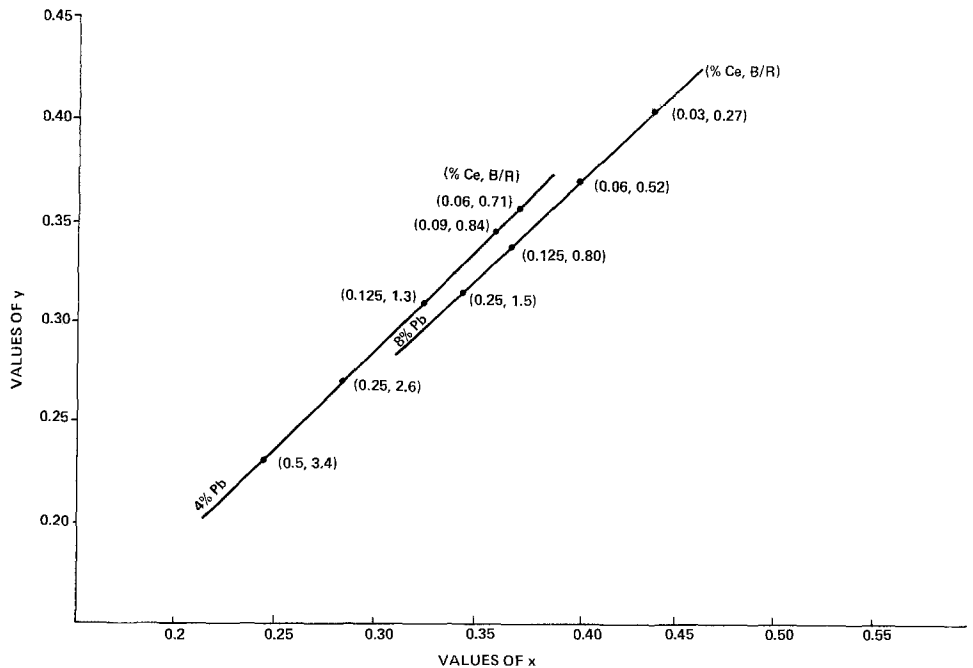


Table III. FSST's evaluation in color video playback system

Type tube	Screen composition	Relative photodetector response			Decay time, β (μ sec)		Screen noise (%)
		Blue	Green	Red	Blue	Red	
Experimental blended screen	15 w/o SrGa ₂ S ₄ :Ce,Na* 85 w/o SrGa ₂ S ₄ :Pb**	280	125	230	1.48	1.18	8
Experimental single component screen	100 w/o SrGa ₂ S ₄ :Ce,Pb,Na†	255	130	230	1.26	1.35	4
Commercial†† blended screen	25 w/o Ca ₂ Al ₂ SiO ₇ 75 w/o Y ₃ Al ₅ O ₁₂ :Ce	100	100	100	0.52	0.54	8

* 4 a/o Ce.

** 8 a/o Pb.

† 0.125 a/o Ce, 8 a/o Pb.

†† Ref. (5).

($I_0/100 \sim 10^{-6}$ sec) and was judged suitable for use as the red screen component in a FSST employed as a playback transducer for color television.

For color video playback applications, FSST's that exhibit a uniform emission in the visible region of the spectrum are desirable. This was achieved by blending the SrGa₂S₄:Pb phosphor with a blue emitting SrGa₂S₄:Ce,Na or by activating the SrGa₂S₄ host compound with both Ce³⁺ and Pb²⁺.

FSST's with screens containing the blended or single component thiogallate screens were found to elicit a substantially higher output from a playback system's photodetectors than a commercial tube with a screen composed of a Ca₂Al₂SiO₇:Ce-Y₃Al₅O₁₂:Ce phosphor blend. The single component thiogallate screen also exhibited lower screen noise than those of the thiogallate blend or the commercial phosphor mixture.

Acknowledgments

The author wishes to express his appreciation to T. Sisneros for brightness measurements, and to J. Ragu-

sin for technical assistance. Thanks are also due to K. Speigel, of GTE Sylvania Electronic Tube Division, who provided much of the decay data, and to F. Palilla and S. Natansohn for manuscript review.

Manuscript submitted May 13, 1974; revised manuscript received July 26, 1974.

Any discussion of this paper will appear in a Discussion Section to be published in the December 1975 JOURNAL. All discussions for the December 1975 Discussion Section should be submitted by Aug. 1, 1975.

Publication costs of this article were partially assisted by GTE Laboratories.

REFERENCES

1. T. E. Peters, *This Journal*, **119**, 1720 (1972).
2. G. Blasse and A. Brill, *Appl. Phys. Letters*, **11**, 53 (1967).
3. C. B. Neal and H. E. Smithgall, *IEEE Trans.*, **BTR-16**, 56 (1970).
4. W. Lehmann and F. M. Ryan, *This Journal*, **119**, 275 (1972).
5. H. Smithgall and K. Speigel, U.S. Pat. 3,566,012 (1971).

Rare Earth Doped Vitroceramics: New, Efficient, Blue and Green Emitting Materials for Infrared Up-Conversion

F. Auzel, D. Pecile, and D. Morin

Centre National d'Etudes des Télécommunications, 92220 Bagneux, France

ABSTRACT

New, efficient, vitroceramic hosts for rare earth luminescence are discussed. Their applications to infrared up-conversion are emphasized. Optimized compositions lead to an efficiency nearly twice as high as commercially available LaF₃:Yb:Er. As for infrared to blue efficiency, these vitroceramics are among the best compounds obtained so far. The easy preparation in air atmosphere is described. The excitation spectra have the advantage of being broader than usual for up-conversion phosphors. Kinetic studies present some puzzling behavior with respect to sample geometry; e.g., the rise time increases fourfold with sample thickness between 0.1 and 4.5 mm. Segregation of rare earths in the microcrystalline phase rather than in the glassy one is clearly shown which explains the high efficiencies.

Although the up-conversion processes by energy transfer between Yb³⁺ and Tm³⁺ or Er³⁺ were first discovered in a glass matrix (1), all the hosts reported to date are pure crystalline compounds (1-3). The main reason is that the fluorescence of rare earth ions is generally less efficient in a glass. Yet Auzel has shown that in the case of Er³⁺, the fluorescence emission at 0.54 μ is strongly enhanced with respect to glass inside the devitrified glass matrix (4); one then deals

Key words: glass ceramics, up-conversion, rare earths, infrared, energy transfer.

with a vitroceramic since large amounts of microcrystals are embedded in an amorphous structure.

The preparation, preliminary results about the structure, as well as up-conversion properties, of such vitroceramics are discussed. The general formula of these new materials is (Ln₂O₃, Yb₂O₃, PbF₂, M_nO_m) doped with oxides of erbium, thulium, holmium, or terbium with Ln = Y, La, Gd, or Lu and M being one of the following glass forming elements B, Si, P, Ge, or Te. According to the doping ion choice, either sequential or cooperative sensitization may be obtained.

Several glasses of different forming elements have been examined, but emphasis is given to the following example: (Yb_2O_3 , PbF_2 , GeO_2) doped either with Er_2O_3 or Tm_2O_3 .

From an efficiency point of view, such ceramics can be favorably compared with crystalline hosts. Furthermore, their shorter time response and their easy preparation make them particularly suitable for pulsed GaAs:Si diode excitation for LED applications. The fact that such materials can be cast, cut, and polished just as glasses may be also a further advantage over crystalline phosphors when large displays are considered.

On the other hand, several fundamental interesting aspects are shown. These matrices contain a large amount of oxygen, yet their green emission yield is as high as those obtained from the best oxygen-free YF_3 hosts. This fact is in contrast with what has been generally found in crystalline hosts (3). The trapping effect and radiative energy transfer between Yb^{3+} ions before nonradiative energy transfers take place, as recently evidenced (5), are particularly strong.

Experimental

Vitroceraamics composition and preparation.—The vitroceraamics are obtained by simply mixing together one or several of the following glass-forming oxides SiO_2 , GeO_2 , B_2O_3 , P_2O_5 , TeO_2 with lead fluoride and high purity rare earth oxides (99.999%). The mixture, contained in a platinum crucible with a cover, is heated and melted inside a muffle furnace at 1000°C for about 1 hr. The sample is then obtained by pouring the melt, in air, into a graphite mold of the desired form, the mold is maintained at about $300^\circ\text{--}400^\circ\text{C}$ for 4 hr for annealing purposes. A white compound with a glassy aspect is finally obtained.

The compositions ($\text{GeO}_2\text{--PbF}_2$):Yb, Er and ($\text{GeO}_2\text{--PbF}_2$):Yb, Tm are mainly discussed in this paper. These compositions have been optimized for infrared up-conversion under CW excitation. Under pulsed excitation, the optimization may be somewhat different since time constants vary with composition differently from efficiencies.

Spectroscopy and optical measurements.—Absorption and fluorescence spectra as well as excitation spectra are obtained with a Cary 17 spectrophotometer. The spectrometer has been modified, when used for fluorescence and excitation, by laboratory-made attachments. Only one beam is used with external excitation for fluorescence, and with internal excitation for excitation spectra.

The vitroceraamic samples are either optically polished plates of 50μ thickness or powders obtained by crushing the ceramics in a mortar and sieving to various sizes.

Efficiency comparison with other phosphors and fluorescence spectra are performed on powdered samples, whereas excitation spectra and absorption spectra are obtained from plate samples which are then compared with phosphor samples in forms of platelets of 80 mg/cm^2 sizes. This size is the optimum for relative up-conversion efficiency for an excitation through the phosphor samples. The details of the efficiency measurements have already been reported elsewhere (6).

Time constants are measured using a Texas Instruments TIXLI6 infrared emitting diode pulsed at 2A peak current with a 40 Hz repetition rate, the pulse width being usually 10 msec. The visible signal is collected from the same side as excitation, filtered by KG3, BG18 Shott glasses, detected by a photomultiplier, and fed directly to a storage oscilloscope.

The scanning electron microscope analysis has been obtained with a Cameca MEB 07 microscope to which has been added a cathodoluminescence attachment (7).

Results and Discussion

Comparative results for up-conversion efficiencies.—Several types of vitroceraamics with different glass-

Table I. Relative infrared green conversion efficiency for different glass-forming elements in vitroceraamics of the general formula (not optimized):

$$M_nO_m = 27.18\%; \text{PbF}_2 = 67.57\%; \text{Yb}_2\text{O}_3 = 4.85\%; \\ \text{Er}_2\text{O}_3 = 0.39\%; (\text{molar per cent})$$

Composition: M_nO_m	Efficiency relative to $\text{YF}_3\text{:Yb:Er} (= 100)$
B_2O_3	10
TeO_2	30
P_2O_5	70
SiO_2	65
GeO_2	70

forming elements have been prepared each having the same molar composition: $M_nO_m = 27.18\%$; $\text{PbF}_2 = 67.57\%$; $\text{Yb}_2\text{O}_3 = 4.85\%$; $\text{Er}_2\text{O}_3 = 0.39\%$. The relative efficiency is given in Table I. Except for B_2O_3 and TeO_2 , about the same results are obtained for the other glass-forming oxides: P_2O_5 , SiO_2 , and GeO_2 .

The compositions involving GeO_2 and SiO_2 were more thoroughly investigated. The relative ratios of GeO_2 and PbF_2 were systematically varied between 5 and 36% by weight leading to the results presented in Fig. 1, where the optimum $\text{GeO}_2/\text{PbF}_2 + \text{GeO}_2$ ratio is around 20%.

Optimization of Yb_2O_3 , Er_2O_3 , or Tm_2O_3 in the $\text{GeO}_2\text{--PbF}_2$ matrix are presented in Fig. 2 and 3 for the blue and green emissions, respectively. The optimum rare earth concentrations for blue are 25% Yb_2O_3 and 0.062% Tm_2O_3 ; the best ones for green are 10% Yb_2O_3 and 2% Er_2O_3 (weight per cent).

In Tables II and III, comparisons are made between our best vitroceraamics obtained so far, with RE fluoride phosphors. Comparison is made between powdered samples of the same particle size (about 50μ). But it should be noted that reducing vitroceraamics to powder of 50μ grain size decreases their efficiency by 75% with respect to the uncrushed ceramics or crushed ceramics with grains longer than 200μ . This effect of reduction of efficiency for powdered ceramics is not yet fully understood. It does not appear to be a lack of refractive index matching but seems closely linked to the effect of photon trapping as is shown below.

Comparisons are made under CW as well as pulsed excitation by using a figure of merit defined (8) as

$$M = \eta_n (1/2\pi\tau_1)$$

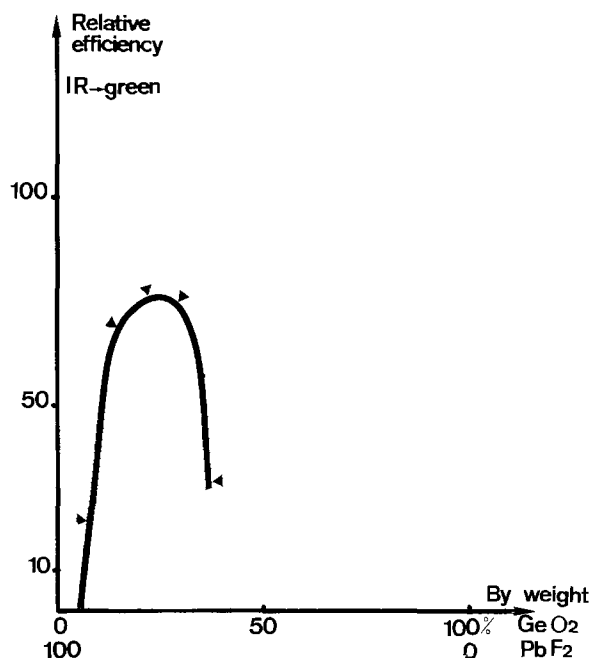


Fig. 1. Relative efficiency for infrared \rightarrow green conversion vs. $\text{GeO}_2/\text{PbF}_2$ ratio.

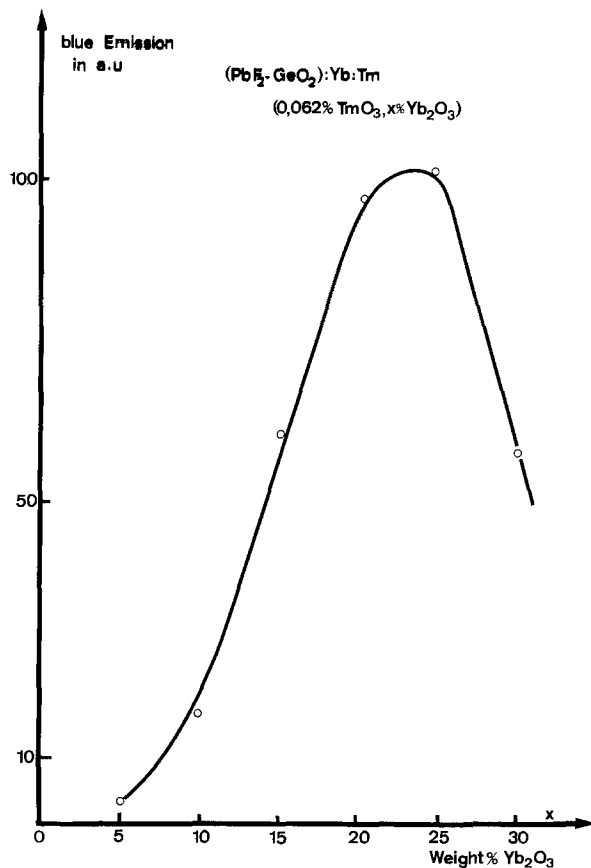


Fig. 2. Relative blue conversion efficiency vs. Yb^{3+} concentration for a $(PbF_2-GeO_2):Yb:Tm$ vitroc ceramic doped with 0.062% Tm_2O_3 .

where η_n is the efficiency as defined by the emitted power per square centimeter when 1 mW power per cm^2 at 0.97μ is falling on the sample; τ is the rise time of the emission as measured on the powder on the same side as excitation.

It is necessary to define the frame work of the time constant measurements for excitation and emission since the infrared photon trapping effect (5) due to $Yb^{3+} ({}^2F_{5/2} \rightarrow {}^2F_{7/2}) \rightleftharpoons Yb^{3+} ({}^2F_{7/2} \rightarrow {}^2F_{5/2})$ radiative transfer is particularly strong in this type of matrix. For example Fig. 4 presents the rise and fall times for the GeO_2-PbF_2 optimized-type vitroc ceramic; the measurements are made through samples of various thicknesses. A fourfold increase in rise time is found for thicknesses varying between 0.1 and 4.5 mm, and an

Table II. Comparison of efficiency and transient times for $Yb^{3+}-Er^{3+}$ doped materials

Sample Chemical formula powdered samples (ϕ 50 μ)	Infrared \rightarrow 0.55 μ conversion			
	Rise time τ_1 (msec)	Fall time τ_2 (msec)	Efficiency \dagger $\times 10^6$	Figure of merit $\times 10^3$ Hz
Vitroc ceramic No. 776 (CNET 1974) $(PbF_2-GeO_2):Yb-Er$ PbF ₂ 78%, GeO ₂ 22%, + 10% Yb ₂ O ₃ + 0.75% Er ₂ O ₃ (per cent by weight)	2	0.65	285	22.8
YF ₃ :Yb:Er (CNET 1972) $\dagger\dagger$ Y _{0.80} Yb _{0.18} Er _{0.01} F ₃	3.2	1.2	285	15
YF ₃ :Yb:Er (BTL 1970) $\dagger\dagger$ Y _{0.84} Yb _{0.15} Er _{0.01} F ₃	3.5	1.3	185	8.8
LaF ₃ :Yb:Er (GE 1970) $\dagger\dagger$ La _{0.80} Yb _{0.12} Er _{0.02} F ₃	4.25	1.6	165	7

\dagger Definitions are given in Ref. (8).

$\dagger\dagger$ The samples are discussed in Table X of Ref. (8) where a comparison between different samples from different origins at one point in their development is reported.

Table III. Comparison of efficiency and transient times for $Yb^{3+}-Tm^{3+}$ doped materials

Sample Chemical formula powdered samples (ϕ 50 μ)	Infrared \rightarrow 0.475 μ conversion			
	Rise time, τ_1 (msec)	Fall time, τ_2 (msec)	Relative efficiency	Relative figure of merit $\times 10^2$
Vitroc ceramic No. 774 (CNET 74) $(PbF_2-GeO_2):Yb-Tm$ PbF ₂ 78%, GeO ₂ 22% + 25% Yb ₂ O ₃ + 0.062% Tm ₂ O ₃	2.25	0.8	100	7
YF:Yb ₃ :Tm (CNET 1973) Y _{0.85} Yb _{0.346} Tm _{0.001} F ₃	3.25	1.4	100	4
YF:Yb:Tm (Tm _{0.003} Philips USA 1971) Y _{0.647} Yb _{0.35} Tm _{0.003} F ₃	3.25	1.7	37	1.4

increase of 3.4 times in decay time is found for the same thickness range. For larger thicknesses a time constant saturation takes place. This increase is due to the Yb^{3+} lifetime increase by resonance since the relation (9) $\tau_2 = Yb/2$ is found constant for any thickness: at 0.1 mm we have $\tau_{Yb} = 1.6$ msec or $\tau_{Yb}/2 = 0.8$ msec and τ_2 is found to be 0.9 msec; at 4.5 mm $\tau_{Yb} = 7$ msec and $\tau_{Yb}/2 = 3.5$ msec and τ_2 is found to be 3.4 msec. This effect has to be taken into account if one wishes to calculate transfer efficiencies from lifetime measurements.

This explains the reduction in efficiency when the vitroc ceramics are reduced to a powder. This hypothesis is based on the fact that τ_{Yb} is found to be lower for two samples of given thickness joined together, than for one of double thickness even if the two samples are bound by an index matching medium. In the same way, the efficiency cannot be restored for a powder using such a medium. If a space limited excitation is produced using a diaphragm, light emission of a ceramic wafer is obtained at a distance of about several millimeters from the diaphragm. This is the same average distance through which energy can migrate radiatively as indicated from lifetime curves in Fig. 4.

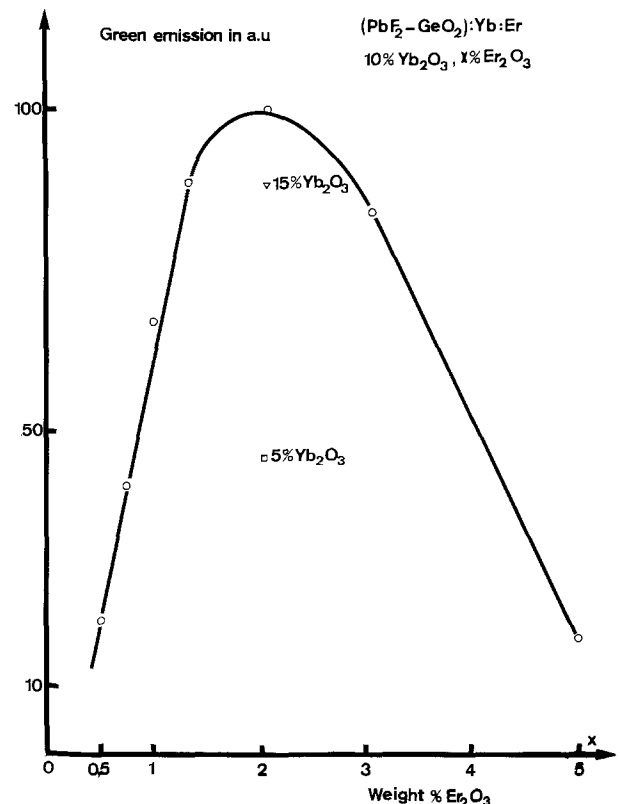


Fig. 3. Relative green conversion efficiency vs. Er^{3+} concentration for a $(PbF_2-GeO_2):Yb:Er$ vitroc ceramic.

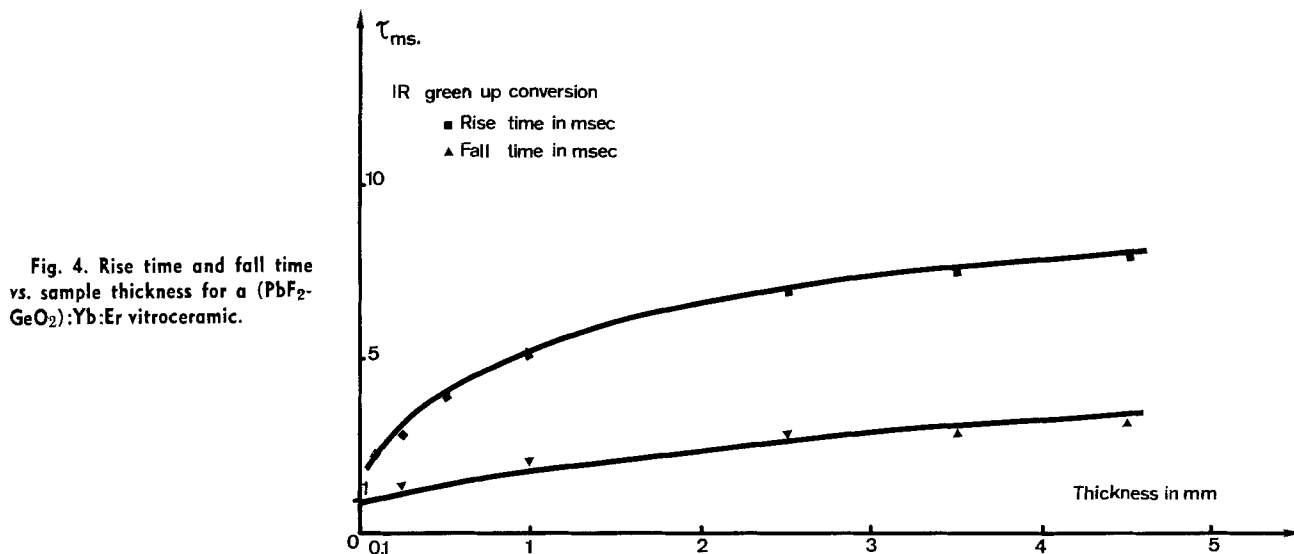


Fig. 4. Rise time and fall time vs. sample thickness for a $(\text{PbF}_2\text{-GeO}_2)\text{:Yb:Er}$ vitroc ceramic.

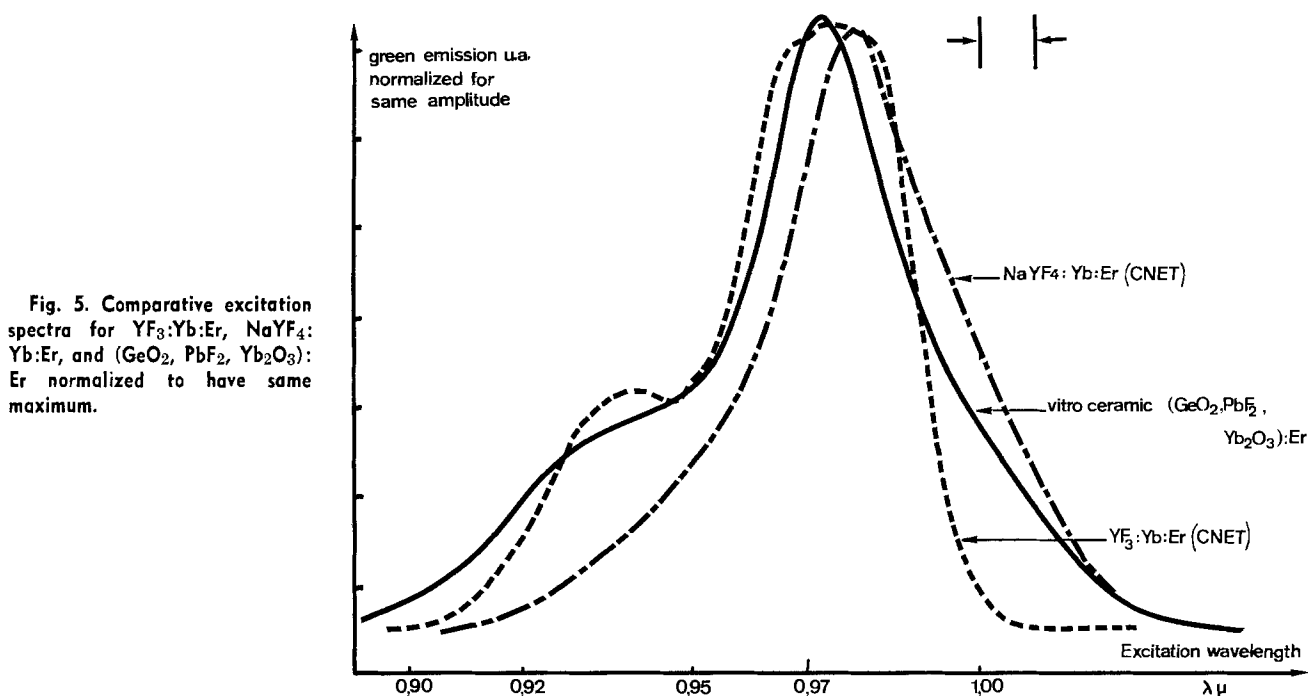


Fig. 5. Comparative excitation spectra for $\text{YF}_3\text{:Yb:Er}$, $\text{NaYF}_4\text{:Yb:Er}$, and $(\text{GeO}_2, \text{PbF}_2, \text{Yb}_2\text{O}_3)\text{:Er}$ normalized to have same maximum.

These results, in our view, indicate that the radiative transfer of Yb^{3+} energy is a necessary link for the efficiency of the up-conversion process and that the structure of the material plays a determinant role in that transfer. But we feel more work is necessary to assess these hypotheses. For LED applications, the optimum sample thickness was found to be around 300μ .

Comparative spectral results.—In order to compare the vitroc ceramics with classical up-conversion phosphors, excitation spectra are given in Fig. 5. The $\text{GeO}_2\text{-PbF}_2$ vitroc ceramic spectrum extends as far as the NaYF_4 one at longer wavelengths and somewhat farther than the YF_3 one at shorter wavelengths. Therefore excitation is possible with a GaAs laser at 0.9μ or a YAG:Nd laser at 1.06μ . As far as line width is concerned the general aspects of the excitation spectra are different; the vitroc ceramic shows fewer and broader lines. For instance, in Fig. 6, for the strongest line, the width is 20\AA as compared to 6\AA for $\text{YF}_3\text{:Yb:Er}$. Using the same excitation and detection conditions, the spectral peak intensity is stronger for YF_3 , which confirms the direct results of Table I. Similar results are presented in Fig. 7 for the blue emission. Approximately the same line width is found but the over-all splitting is stronger in ceramics.

The line widths of vitroc ceramics are much smaller than that usually found for the same emission in glass, 20\AA against 200\AA for a germanate glass. On the other hand the up-conversion efficiency is more than two orders of magnitude better than in a germanate glass (8). These two facts imply that the rare earths concentrate in the crystal phase rather than in the glass phase during the precipitation process; this segregation effect is evidenced below by the scanning electron microscope study. The Yb^{3+} concentration in the microcrystals is then higher than the one given by the bulk formula. This enhances the trapping effect found in these materials.

Another point of interest is the high efficiency and the high green/red emission ratio for hosts with such high oxygen concentration. The green/red energetic ratio for the vitroc ceramic is about 7 while for our best YF_3 , this ratio is 10, yet it is well known that the presence of oxygen in fluorides usually gives a lower green/red ratio and lower green efficiency (4). One hypothesis is that during the microcrystal precipitation process most of the oxygen of the melt is concentrated in the glassy phase rather than in the crystalline one; most of the oxygen present is necessary for the glassy phase to exist. Also as is well known, PbF_2 may act as a

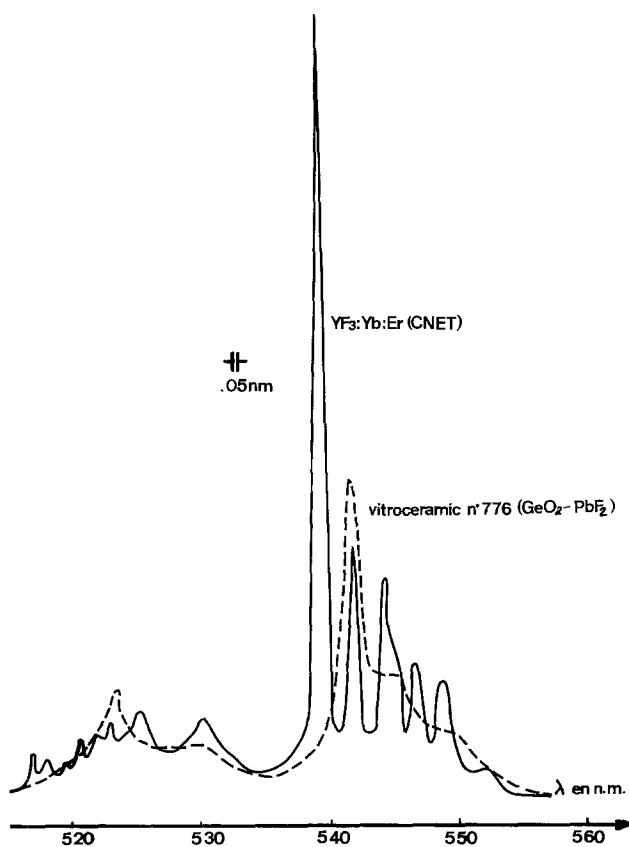


Fig. 6. Comparative green emission spectra of $YF_3:Yb:Er$ (CNET) and $(GeO_2, PbF_2, Yb_2O_3):Er$ vitroceraamics.

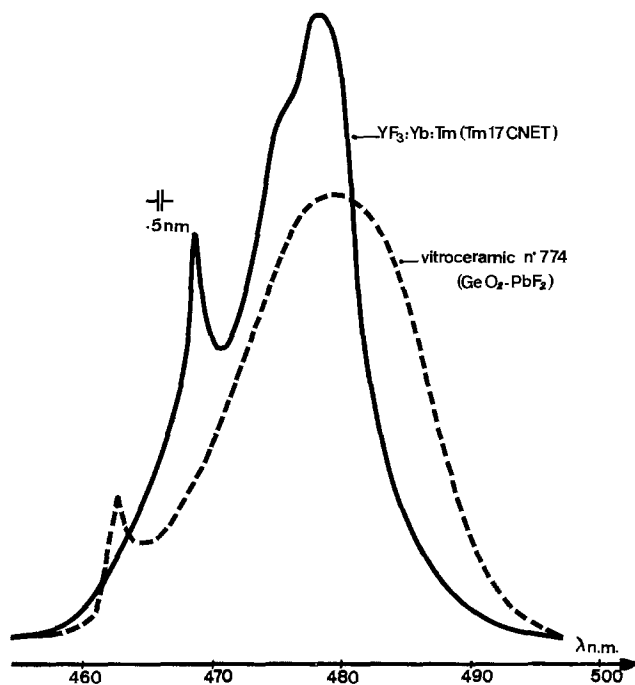


Fig. 7. Comparative blue emission spectra of $Yb_3:Yb:Tm$ (CNET) and $(GeO_2, PbF_2, Yb_2O_3):Er$ vitroceraamics.

scavenger for oxygen; this effect can also play a role to eliminate oxygen from the microcrystals. Yet this oxygen segregation hypothesis is not necessary if one considers a homogeneous distribution of constituents since the calculated Debye cutoff frequency is then 320 cm^{-1} , which according to Matsubara (10) predicts a green emission.

Relationship between spectroscopic results and microstructure.—The hypothesis that the rare earths (Yb, Er, or Tm) concentrate mainly in the microcrystal phase and germanium only in the glassy phase has been confirmed by the scanning electron microscope. Figure 8a presents the microcrystals (white) inside the glassy phase (dark) as obtained by back scattering of electrons. Figure 8b gives the same picture obtained by x-ray fluorescence of germanium (white) which shows that Ge is the main constituent of the glassy phase; on the other hand, when looking at x-ray fluorescence of ytterbium one obtains Fig. 8c which shows that Yb is essentially in the microcrystalline phase. The same results are obtained for the cathodoluminescence of erbium at 0.65μ as shown in Fig. 8d. When analyzing for lead by x-ray fluorescence, Fig. 8e is obtained which indicates that Pb is uniformly distributed.

Hence the glassy phase is probably a lead germanate whereas the microcrystalline phase (which is found to be homogeneous as shown on Fig. 9 by electron absorption) could be a fluoride of lead, ytterbium, and erbium. Attempts at producing good up-conversion efficiency by direct preparation of $PbF_2-YbF_3:Er$ microcrystals lead to an output of only 2% of the best vitroceraamics sample. The role played by the microstructure may be an explanation. Figure 10 shows a cathodoluminescence picture of the $0.65\mu\text{ Er}^{3+}$ emission at a lower magnification than the previous one. A long distance order ($\approx 200\mu$) is found for the microcrystalline structure; such long order cannot be obtained by a direct preparation of lead-ytterbium fluoride.

On the other hand, the decrease in up-conversion efficiency observed when crushing the ceramics into grains smaller than 200μ can be explained by the long distance order which is then destroyed and if one assumes that the radiative energy transfer migrates preferably along the microcrystal in the same way as in light-pipes, the behavior of these vitroceraamics could be understood.

Conclusions

We have presented here a new class of efficient materials for infrared up-conversion which has the advantages of easy preparation and good efficiencies. However their puzzling behavior requires more experiments for a clearer understanding.

In the vitroceraamics described, we have clearly demonstrated by up-conversion results as well as x-ray fluorescence and cathodoluminescence scanning microscopy that rare earth ions concentrate mainly in the precipitated microcrystals, which accounts for the high up-conversion efficiency.

Recently glass ceramics of quite different compositions have been demonstrated as replacements for glass laser materials (11, 12). But their lower fluorescence efficiency (12) and their broader emission line width (11) with respect to the glass of the same bulk composition is an indication that rare earth ions stay mainly in the glassy phase. The new high efficiency vitroceraamics presented here with the rare earth segregation in the microcrystals, should be a better prospect for glass ceramic laser materials than the previous ones, provided the microcrystal size could be reduced.

For display applications, the fact that such vitroceraamics can be cast, polished, and cut as glass, could lead to new ways to couple these solid phosphors to infrared sources. Seven segment displays, using the vitroceraamics as a substrate coupled with discrete diodes can be encompassed. Another advantage over powder phosphors is that multidielctric coatings (8) can be used easily with a glass substrate to capture the infrared radiation.

Acknowledgments

We are much indebted to J. Semo who performed the scanning microscope analysis, and to Dr. Müräu

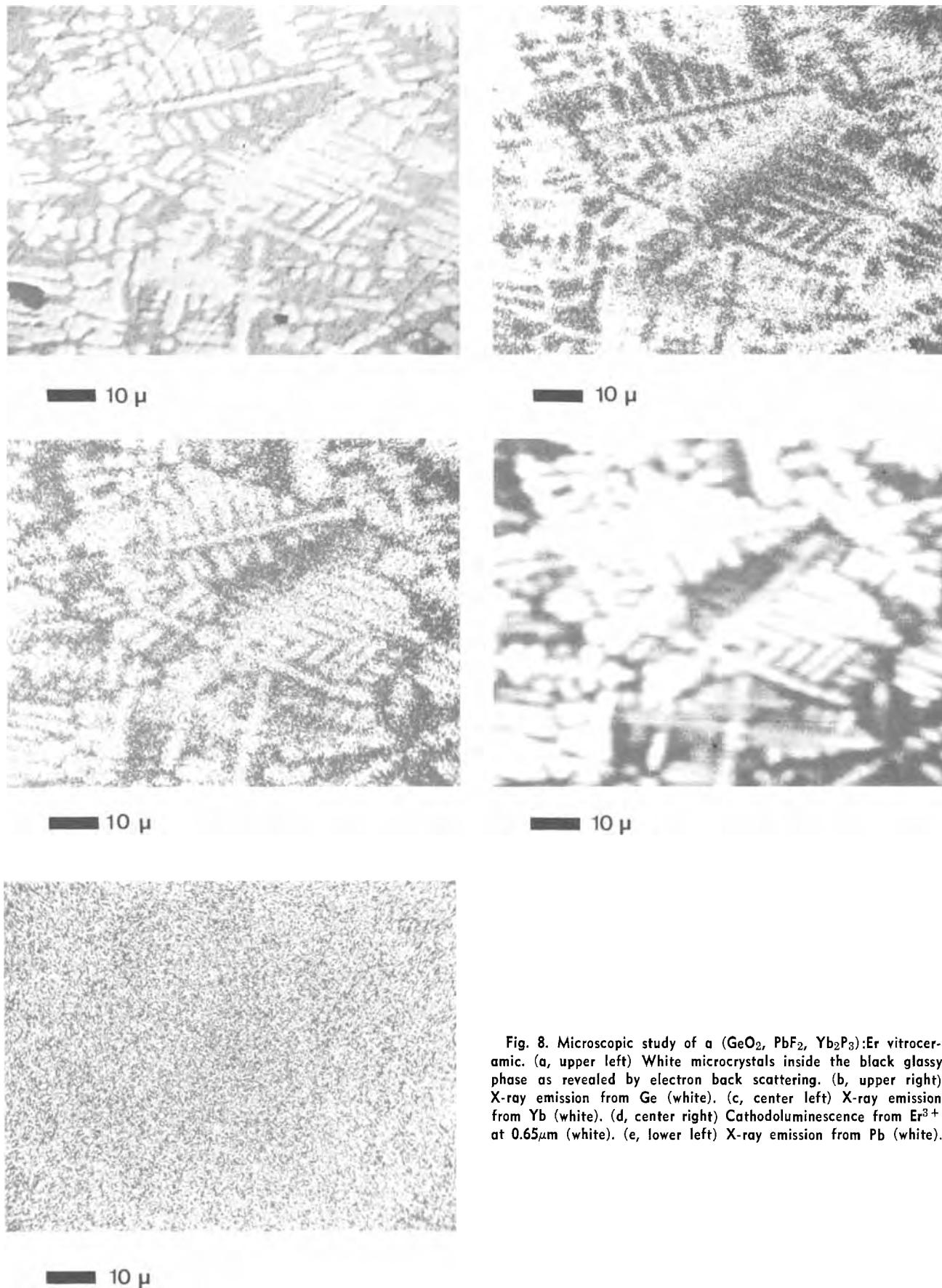


Fig. 8. Microscopic study of a $(\text{GeO}_2, \text{PbF}_2, \text{Yb}_2\text{P}_3):\text{Er}$ vitroc ceramic. (a, upper left) White microcrystals inside the black glassy phase as revealed by electron back scattering. (b, upper right) X-ray emission from Ge (white). (c, center left) X-ray emission from Yb (white). (d, center right) Cathodoluminescence from Er^{3+} at $0.65\mu\text{m}$ (white). (e, lower left) X-ray emission from Pb (white).

from North American Philips for kindly supplying the $\text{YF}_3:\text{Yb}:\text{Tm}$ sample for comparison. This work has been partially supported by D. G. R. S. T.

Manuscript submitted April 22, 1974; revised manuscript received Aug. 20, 1974. This was Paper 105 pre-

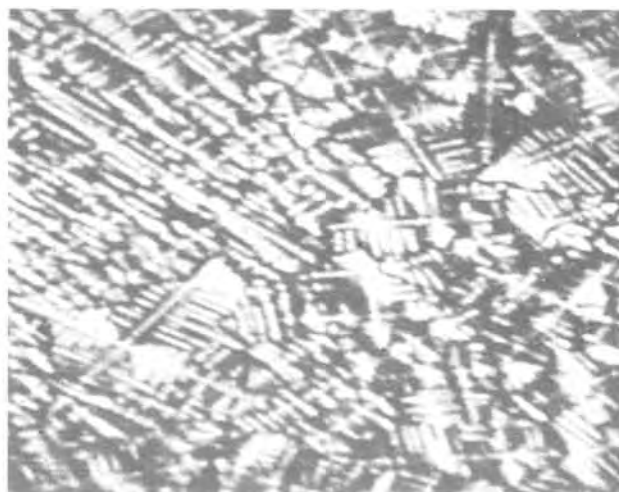
ented at the San Francisco, California, Meeting of the Society, May 12-17, 1974.

Any discussion of this paper will appear in a Discussion Section to be published in the December 1975 JOURNAL. All discussions for the December 1975 Discussion Section should be submitted by Aug. 1, 1975.



10 μ

Fig. 9. Microcrystals (dark) inside the glassy phase for a $(\text{GeO}_2, \text{PbF}_2, \text{Yb}_2\text{O}_3):\text{Er}^{3+}$ vitroc ceramic as revealed by electron absorption.



30 μ

Fig. 10. Long distance order inside a $(\text{GeO}_2, \text{PbF}_2, \text{Yb}_2\text{O}_3):\text{Er}^{3+}$ vitroc ceramic as revealed by Er^{3+} cathodoluminescence at 0.65μ .

REFERENCES

1. F. Auzel, *C. R. Acad. Sci. (Paris)*, **262**, 1016 (1966); *ibid.*, **263**, 819 (1966).
2. V. V. Ovsyankin and P. P. Feofilov, *Sov. Phys. JETP Letters*, **4**, 317 (1966); L. Esterowitz, J. Noonan, and J. Bahler, *Appl. Phys. Letters*, **10**, 126 (1967); R. A. Hewes and J. F. Sarver, *Phys. Rev.*, **182**, 427 (1969); R. L. Sommerdijk, *J. Luminescence*, **6**, 61 (1973); N. Menyuk, K. Dwight, and J. W. Pierce, *Appl. Phys. Letters*, **21**, 159 (1972); H. J. Guggenheim and L. F. Johnson, *Appl. Phys. Letters*, **15**, 51 (1969); J. E. Geusic, *et al.*, *J. Appl. Phys.*, **42**, 1958 (1971); F. W. Ostermayer, *Met. Trans.*, **2**, 747 (1971); L. G. Van Uitert, L. Pictroski, and W. H. Grodkiewicz, *Mater. Res. Bull.*, **4**, 777 (1969); N. M. P. Low and A. L. Major, *Mater. Res. Bull.*, **7**, 203 (1972); S. G. Parker and R. E. Johnson, *This Journal*, **119**, 610 (1972); T. Matsubara, *Japan. J. Appl. Phys.*, **10**, 1647 (1971); T. Kano, H. Yamamoto, and Y. Otomo, *This Journal*, **119**, 1561 (1972); J. P. Wittke, I. Ladany, and P. N. Yocom, *Proc. IEEE*, **58**, 1283 (1970).
3. P. C. Müräu and Z. Szilagyi, Paper 161 presented at Electrochemical Society Meeting, Cleveland, Ohio, Oct. 3-7, 1971.
4. F. Auzel, Thèse, Paris (1968).
5. F. Auzel and D. Pecile, *C. R. Acad. Sci. (Paris)*, **277**, 155 (1973).
6. F. Auzel and D. Pecile, *J. Luminescence*, **8**, 32 (1973).
7. J. Semo, Brevet Français BF 73-35044.
8. F. Auzel, *Proc. IEEE*, **61**, 758 (1973).
9. J. D. Kingsley, *J. Appl. Phys.*, **41**, 175 (1970).
10. T. Matsubara, *Japan. J. Appl. Phys.*, **11**, 1579 (1972).
11. C. F. Rapp and J. Chrysochoos, *J. Mater. Sci.*, **7**, 1090 (1972).
12. G. Muller and N. Neuroth, *J. Appl. Phys.*, **44**, 2135 (1973).

Poly(Vinylferrocene)—Conversion to an Oxidized Iron System Suitable for Use as a Semitransparent Hard Photomask

L. F. Thompson

Bell Laboratories, Murray Hill, New Jersey 07974

ABSTRACT

A novel technique for the production of iron oxide films from a polymer precursor is described. Films of poly(vinylferrocene) (PVFc) can be converted to iron oxide films in either a 200W oxygen plasma at room temperature or thermally in oxygen at 380°C. The thermal decomposition appears to be more suitable for routine use, and process parameters for this technique have been optimized. The thermal conversion has been studied using infrared, visible, and u.v. spectroscopy and a decomposition reaction proposed. The iron oxide films prepared from PVFc have chemical and physical properties similar to the iron oxide films prepared using the iron pentacarbonyl process. Films prepared from PVFc are presently being evaluated for use as semitransparent photolithographic masks.

The use of iron oxide for the fabrication of hard, semitransparent masks for use in the manufacture of integrated circuits is gaining rapid acceptance (1). Although the film material is primarily Fe_2O_3 , the exact structure is far more complicated than a pure Fe_2O_3 system. Iron oxide was chosen from a large group of transition metal oxides and mixed oxides as having the best combination of chemical and physical properties required for use as a transparent mask material (2). The relevant properties are given by Peters *et al.* (3) as: (i) <1% transmission in the 360-400 nm spectral region; (ii) >30% transmission at the sodium D line (589 nm); (iii) an etching rate compatible with conventional photolithographic processes and materials; (iv) in addition, the physical integrity of the film (hardness, abrasion resistance, etc.) must be sufficient to sustain the abuses of routine handling.

Three techniques are presently available for the deposition of thin films of iron oxide. The first is a chemical vapor deposition scheme using $\text{Fe}(\text{CO})_5$ developed by MacChesney *et al.* (4). Iron pentacarbonyl is thermally decomposed at temperatures in the 130°-200°C range in an oxidizing atmosphere ($\text{CO}_2 + \text{O}_2$) on glass substrates. Films prepared by this technique have excellent mask properties, and this is presently the technique of choice for mask film manufacture. The only substantial disadvantage of the procedure is using a poisonous compound, $\text{Fe}(\text{CO})_5$. A second deposition technique involving sputtering has been devised by Sinclair *et al.* (2,3) for depositing Fe_2O_3 films. The sputtering techniques used were conventional with the exception that it was found necessary to introduce $\text{CO}_2 + \text{O}_2$ as a discharge gas in order to increase the solubility of the deposited Fe_2O_3 films to an acceptable level for etching. The exact role that CO_2 plays is not clear, but it appears likely that the presence of iron carbonate in films leads to increased solubility (3). The sputtering technique produces films which meet all mask requirements with the only disadvantage being that the process is slow and requires expensive vacuum equipment. The third general procedure, one similar to the process described in this paper, involves the decomposition of an organometallic compound in an oxidizing atmosphere resulting in the deposition of a metal oxide film. Reid and Cukor (5) suggested that organo-iron compounds could be thermally decomposed in O_2 to Fe_2O_3 . Shelby and Cukor (6) decomposed nickel tetradecanoate and iron dodecanoate to Fe-Ni alloys at 500°C in a H_2 ambient.

Key words: iron oxide, photomasks, semitransparent masks, photolithography.

These films were subsequently used as x-ray standards and could be deposited with good reproducibility.

This paper describes a method for the deposition of an oxidized iron film using a high molecular weight, organometallic polymer as a precursor. This technique offers the advantage of being able to deposit uniform films of sufficient thickness to yield a useful mask material in one application. However, two or more thinner films may be applied if necessary to reduce defect densities.

Poly(vinylferrocene) (PVFc) has been synthesized by a number of workers (7-9). It has been shown that PVFc can be converted to Fe_2O_3 in an oxygen plasma and subsequently to Fe^0 capable of serving as a catalytic tract for selective electroless deposition of Cu, Au, and Ni (10). The disadvantage of plasma conversion lies in the time required to convert a 400 nm film to Fe_2O_3 . In preliminary studies it was found that in O_2 at 400°C, PVFc could be thermally converted in <30 min to an oxidized iron film possessing useful mask properties.

It should be noted that exact chemical composition of these films is difficult to ascertain. They are complex mixtures of Fe_2O_3 , Fe_3O_4 , $\text{Fe}(\text{CO}_3)_2$, and other inorganic iron compounds. Since any attempt to produce larger samples of material for subsequent analysis would significantly alter the physics and chemistry of the thin-film system and possibly yield a different conversion process and material, the exact structure remains undetermined.

The reaction scheme is shown in Fig. 1. The object of this study was to evaluate the oxidation of PVFc.

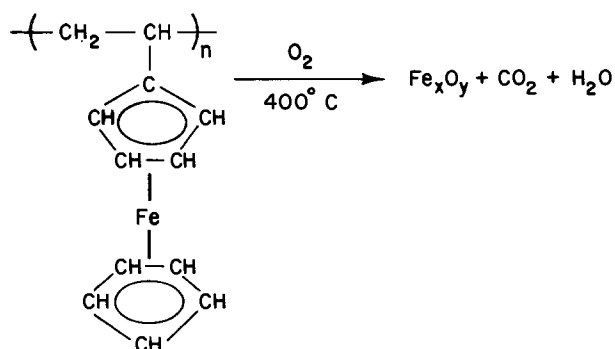


Fig. 1. Reaction scheme of the thermal oxidation of PVFc to Fe_2O_3 .

Experimental

PVFc deposition.—The PVFc used in this work was prepared by free radical bulk polymerization of vinyl ferrocene at 80°C (7, 8). The monomer, vinyl ferrocene, was purchased from Research Organics, Incorporated (ROC/FIC) and purified by vacuum sublimation (mp 50°-50.5°C). Azobisisobutyronitrile (AIBN) was used as a catalyst and was purified by recrystallization from methanol (mp 102°-103°C with slow decomposition). Vinyl ferrocene and 0.08% AIBN (by weight) were sealed in a glass tube under N₂. The vinyl ferrocene was melted and AIBN allowed to dissolve in it. The sealed tube was placed in a bath at 80° ± 0.5°C, and the polymerization was allowed to continue for 72 hr. The mixture solidified after about 12 hr. The tube was cooled in ice water, broken open, and the polymer dissolved in chlorobenzene. The PVFc was precipitated in cold methanol, recovered by filtration, and dried in a vacuum at 80°C for 24 hr. The polymer was dissolved in chlorobenzene (6-7% solids) and filtered to remove particulates by multiple passes through a 0.2 μ sintered silver filter prior to use. The substrates were spin coated with PVFc using standard photoresist techniques (11). All substrates used in this study were 1 in. diameter by 1/8 in. thick quartz disks which facilitated direct quantitative visible and ultraviolet (u.v.) absorption studies.

The visible-ultraviolet absorption spectra for Fe₂O₃ suitable for use as a photomask is well established (2) and is shown in Fig. 2 (dashed curve). The spectrum from 300 to 700 nm obtained with a Cary Model 14 spectrophotometer was used to follow the conversion of PVFc to Fe₂O₃.

Infrared studies were carried out using attenuated total reflection (ATR) with a Perkin-Elmer Model 631 spectrophotometer. The samples were coated on 5 mil aluminum foil and mounted against a KRS-5 plate for ATR studies. Spectrum assignments were made with the aid of known spectra.

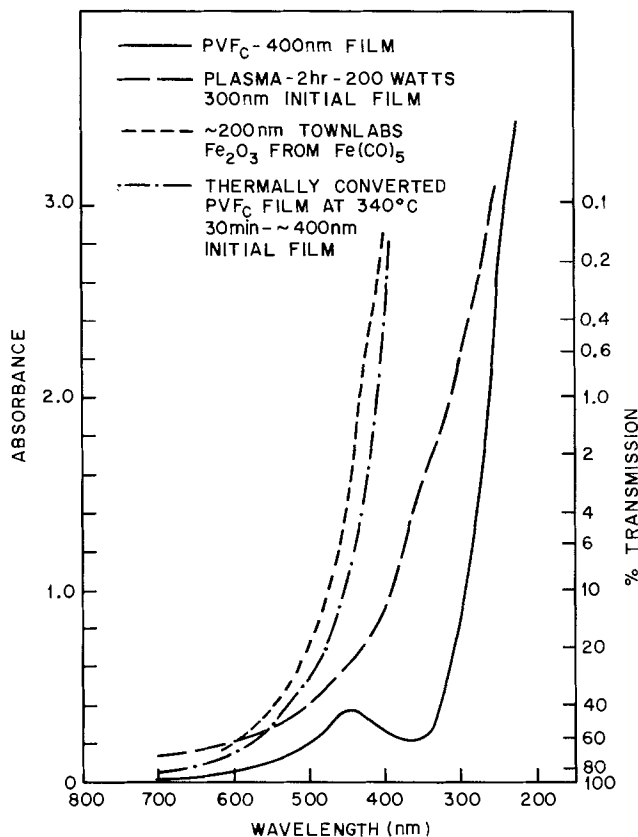


Fig. 2. 700-200 nm absorption spectra for PVFc and oxidized iron films.

Plasma conversion.—A 200W, 4 MHz radio frequency plasma was used to study plasma conversion of PVFc to Fe₂O₃. The degree of conversion was followed using visible u.v. spectroscopy to determine changes in absorption in the 360-400 nm region of interest. Although this does not yield precise information regarding structural changes, it does measure the primary parameter of interest for a semitransparent mask material.

Thermal conversion.—Thermal conversions were carried out in a 2 in. diameter tube furnace regulated to ±10°C with an O₂ flow rate maintained at ≈5 liters/min⁻¹. Infrared analysis and ultraviolet visible spectroscopy were then used to study the thermal conversion of PVFc.

Results and Discussion

The free-radical bulk polymerization of vinyl ferrocene as described yielded about 70% polymer in the 72 hr reaction time. The molecular weight of the polymer as determined by dilute solution viscosity was found to be ~80,000. Several separate batches of polymer were prepared with good reproducibility, although molecular weight varied by as much as ±20%. The yield never varied by more than 10%. A detailed study of the reaction parameter is presently underway. The polymer yielded uniform, defect-free films from a chlorobenzene solution.

Plasma oxidation.—It was found that in a 200W oxygen plasma, PVFc oxidized to an iron compound with a visible u.v. spectrum similar to that of Fe₂O₃ films prepared by the Fe(CO)₅ process. For complete conversion 3 hr or more were required. Figure 2 illustrates the spectrum of a 300 nm PVFc film which was oxidized in a plasma to an inorganic iron film. It is noted that the absorption is not adequate for mask purposes in the 300-400 nm region; however, if 400 nm of polymer is used, the absorption increases to an adequate level. This thickness can be achieved either by a single 400 nm coating or two sequential 200 nm coatings. The double coating technique has the advantage of reducing defects in the film at the expense of additional processing steps and time.

Plasma exposure time as a function of absorption (and per cent transmission) is shown in Fig. 3 at wavelengths of 600, 500, 400, and 350 nm. Note that the absorption in the 350 and 400 nm region increases rapidly as the oxidation proceeds, while in the 500 and 600 nm region absorption remains relatively unaffected. The plasma oxidation is complete after 3 hr. A slight decrease in absorption is noted after long exposures, probably due to sputter removal of material from the oxidized material. The oxidized films were soluble in cold 6-8M HCl and etched at about 1 μ min⁻¹ after

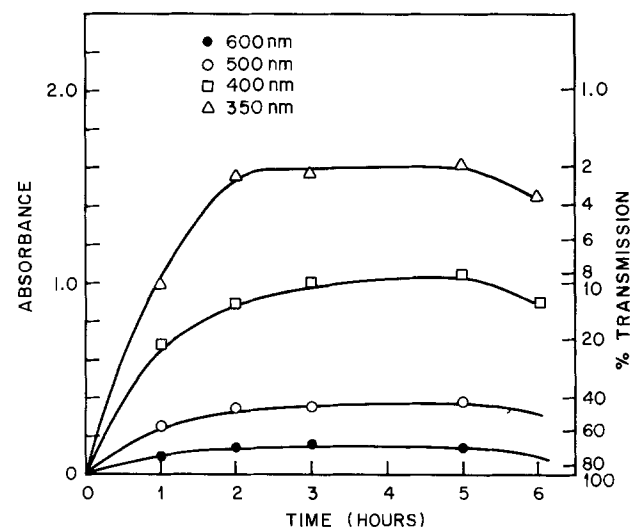


Fig. 3. Absorption as a function of time for the plasma conversion of PVFc with a 200W O₂ plasma.

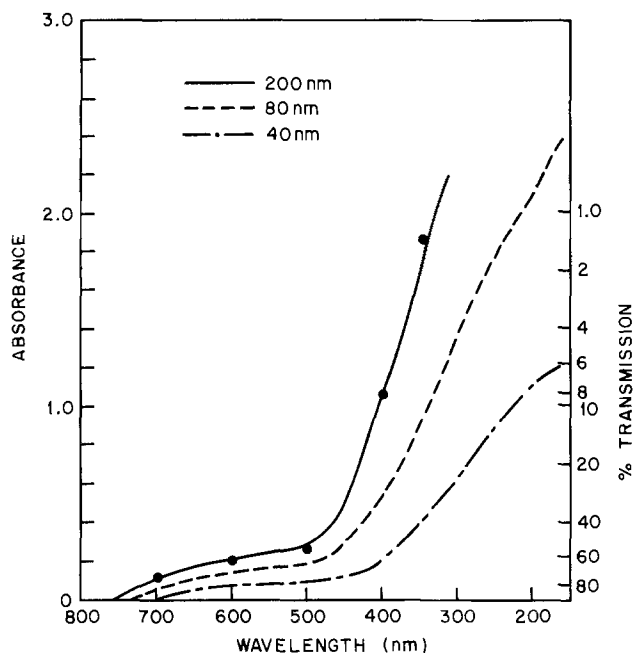


Fig. 4. 200-700 nm absorption spectra for the thermal conversion at 280°C of PVFc of three thicknesses.

complete plasma conversion. They became insoluble after a 450°C heat-treatment, although there were no noticeable absorption changes. Scanning electron microscopy (SEM) studies revealed no defects in the oxidized films that were not attributable to particulate inclusions in the precursor polymer film.

Thermal conversion.—It was found that thermal oxidation treatments at 400°C for 20-30 min in an oxygen atmosphere was sufficient to convert PVFc to a stable oxidized iron material. The optimum oxygen flow for the furnace used was ~ 5 liters/min⁻¹. However, flow rates are expected to be system dependent, they are not a critical parameter. Again the energy absorption in the visible u.v. region was used to optimize the conversion process since this is the primary property of concern in mask materials. Figure 4 shows the absorption spectra for three final film thicknesses. It should be noted that the thermal conversion is accompanied by a 50-60% decrease in film thickness.¹ It was found that to minimize the detrimental effects of film shrinkage, a programmed baking schedule was necessary. Figure 5A is a (SEM) micrograph of a 200

¹The thickness referred to in this study is final film thickness unless otherwise stated.

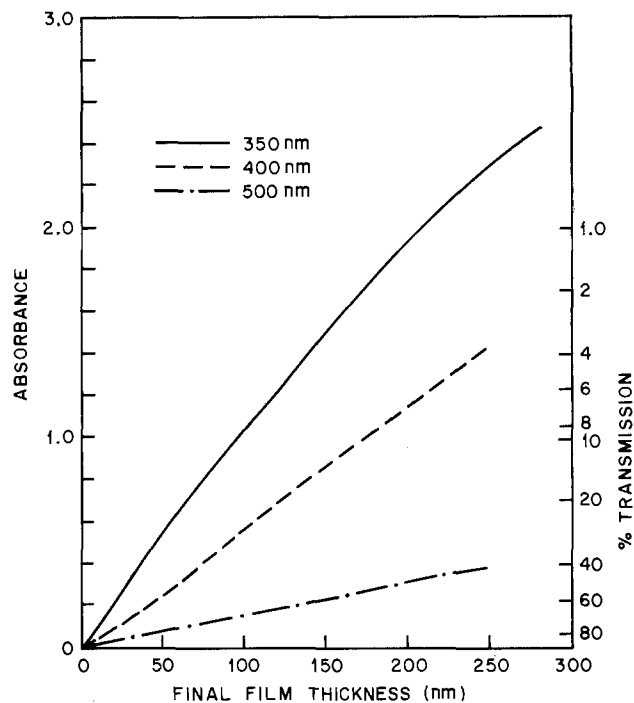


Fig. 6. Absorption as a function of thickness for PVFc films oxidized at 300°C for 30 min.

nm film which was baked in a preheated 400°C furnace. The broken areas shown were common on films treated in this way. However, when the baking schedule was started at room temperature and increased at $\sim 10^\circ\text{C}/\text{min}^{-1}$ rates, this catastrophic crazing effect was eliminated, and uniform films were then obtained (Fig. 5B).

It was found that ~ 200 nm of final film was necessary to give the desired absorption properties using thermal conversion. Figure 6 shows absorption as a function of film thickness for three wavelengths: 350, 400, and 500 nm. This film was converted with a $400^\circ \pm 10^\circ\text{C}$, 30 min baking schedule in which the temperature was increased from 22° to 400°C at $\sim 10^\circ\text{C}/\text{min}^{-1}$ and then held at $400^\circ \pm 10^\circ\text{C}$ for 30 min. The 200 nm final film thickness was achieved by converting a single coating of PVFc of an initial thickness of ~ 470 nm. As before, there are advantages in using two thin (~ 240 nm) coatings each followed by a bake, since the defect density will be less and the film should be more homogeneous throughout its thickness.

Both scratch resistance and adhesion were qualitatively compared to films deposited from $\text{Fe}(\text{CO})_5$. The adhesion (as per "scotch tape" test and epoxy pull

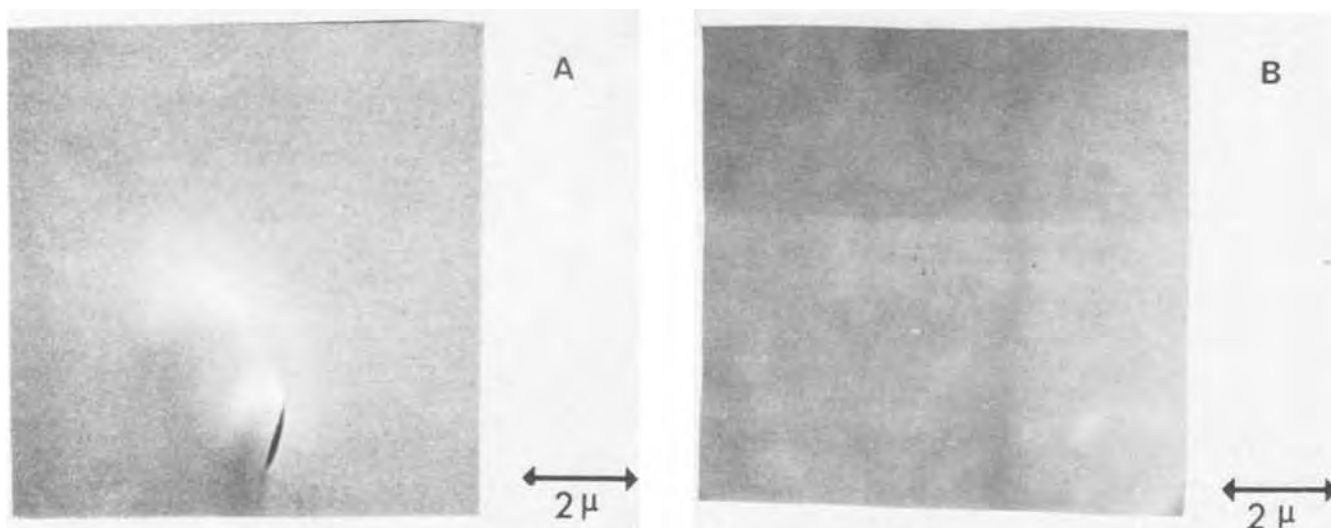


Fig. 5. SEM of thermally converted oxidized iron films

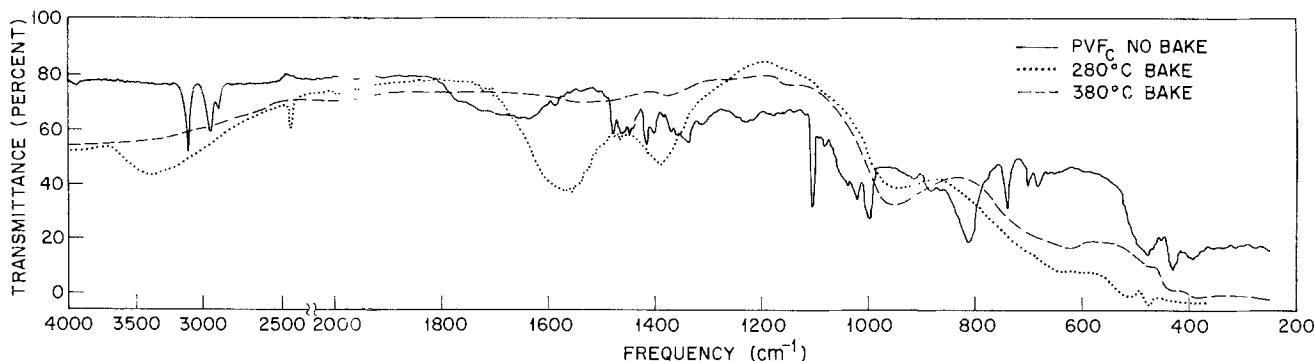


Fig. 7. Infrared spectra of a 400 nm polyvinylferrocene film baked at two temperatures, 200° and 400°C, for 30 min each

test) was in no case worse than the standard sample and exceeded that of the carbonyl film in most samples. The scratch resistance was comparable to the carbonyl standard. Precise defect density measurements are presently underway.

The conversion of PVFc to oxidized iron compounds involves considerable chemical changes in the film. Attenuated total reflectance (ATR) infrared spectroscopy was used to study the thermal oxidation of PVFc. A possible reaction spectra scheme is given in Fig. 1. Figure 7 shows three ATR spectra obtained using a 400 nm PVFc film. The spectrum of the film prior to baking is identical to those reported (8) for pure PVFc. The 250°C bake was sufficient to eliminate the general hydrocarbon structure of the original film. The C-H stretching bands in the 3225-2777 cm^{-1} region are probably the most sensitive and have completely disappeared. A broad peak centered about 3333 cm^{-1} is suggestive of bonded water, one of the decomposition products from the thermal oxidation of PVFc. The associated band at 1612 cm^{-1} also is suggestive of water. A large band at 1390 cm^{-1} has been assigned to the iron carbonate structure. The remainder of the spectrum is characteristic of Fe_2O_3 . After baking at 370°C for 30 min all traces of water and iron carbonate have disappeared and normal Fe_2O_3 spectrum remains. It should be noted that carbonate free material is still soluble in dilute HCl.

If these materials are fired above 450°C, the solubility in cold acids decreases until it becomes essentially zero. This has generally been attributed to crystallization of the iron oxide. It was found that the addition of 3% SnCl_2 to the 6M HCl increased the dissolution rate; however, this failed to facilitate solubility of normally insoluble material.

It should be emphasized that although results of the present investigation are internally self-consistent for this system, they deviate from results reported on other iron oxide systems (2,3). It is likely that in none of the three investigations was pure Fe_2O_3 being studied, and it is likely that complex mixtures of several iron compounds and possibly residual cyclic carbon skeletons were involved. Since in all of the studies it was the final properties, such as u.v. visible absorption, defect density, and solubility (etch rate), which were of primary consideration, it is not surprising that details of the fundamental chemistry have remained obscure. Care should be exercised in comparing the films made by the three techniques: $\text{Fe}(\text{CO})_5$, sputtered, and the polymer precursor system.

Conclusions

1. Poly(vinylferrocene) can be converted to an oxidized iron compound with properties similar to the films presently used to make semitransparent masks.
2. The PVFc may be oxidized with a 200W rf, oxygen plasma in 3 hr yielding a film with good mask

properties. The disadvantages of this procedure are the long times and expensive equipment necessary.

3. PVFc may alternatively be thermally converted in 30 min to a suitable mask material in an O_2 ambient at 400°C.

4. Infrared analyses indicates that conversion below ~280°C yields a product which contains appreciable amounts of carbonate and water.

5. Baking above 400°C removes all traces of CO_3^{++} and H_2O ; however, if 400°C is not exceeded, the films remain soluble in cold acids.

6. Scratch resistance and adhesion appear to be similar to the iron oxide films prepared by the pentacarbonyl process.

Acknowledgments

The author would like to acknowledge helpful conversations with W. Robert Sinclair, P. A. Turner, R. D. Heidenreich, and Gene Feit. He also thanks Betty Prescott for the spectroscopic studies and G. W. Kammlott for the x-ray diffraction studies. The plasma apparatus was used with the assistance of Frank Ryan. D. D. Bacon carried out the filtration and some thermal conversions, and E. P. Otocka provided the molecular weight data.

Manuscript submitted May 21, 1974; revised manuscript received Aug. 20, 1974.

Any discussion of this paper will appear in a Discussion Section to be published in the December 1975 JOURNAL. All discussions for the December 1975 Discussion Section should be submitted by Aug. 1, 1975.

Publication costs of this article were partially assisted by Bell Laboratories.

REFERENCES

1. M. V. Sullivan, *This Journal*, **120**, 545 (1973).
2. W. R. Sinclair, M. V. Sullivan, and R. A. Fastnacht, *ibid.*, **118**, 341 (1971).
3. F. G. Peters, W. R. Sinclair, and M. W. Sullivan, *ibid.*, **119**, 305 (1972).
4. J. B. MacChesney, P. B. O'Connor, and M. V. Sullivan, *ibid.*, **118**, 776 (1971).
5. F. J. Reid and P. Cukor, Abstract 127, p. 326, Electrochemical Society Extended Abstracts, Spring Meeting, Los Angeles, Calif., May 10-15, 1970.
6. W. B. Shelby and P. Cukor, *Anal. Chim. Acta*, **49**, 275 (1970).
7. J. C. Lai, T. Rounsfell, and C. U. Pittman, *J. Polymer Sci.*, **9**, 651 (1972).
8. M. G. Baldwin and K. E. Johnson, *ibid.*, **5**, 2091 (1967).
9. C. Aso, T. Kunitake, and T. Nakashima, *Makromol. Chem.*, **124**, 232 (1969).
10. L. F. Thompson and R. D. Heidenreich, Unpublished results (1971).
11. L. I. Maissel and R. Glang, "Handbook of Thin Film Technology," McGraw-Hill Book Co., New York (1970).

Optical Characterization of GaAs Layers Grown on Ge Substrates

Hiroyuki Kasano and Sigeyuki Hosoki

Central Research Laboratory, Hitachi Limited, Kokubunji, Tokyo, Japan

ABSTRACT

The structural quality of GaAs layers grown on Ge substrates has been optically characterized as a function of the distance d from GaAs-Ge interface along the growth axis, supported by electrical measurement and also by x-ray measurement. It is found that the degradation of the structural quality due to interface alloying and autodoping of Ge can be detected in the grown layers only within $\sim 3\mu$ from the interface, where the concentration of Ge involved would exceed 1×10^{17} atoms/cm³. However, the degradation caused by misfit dislocations extends as far as 80μ from the interface, in spite of the fact that the dislocation density decreases exponentially with increasing d . These misfit dislocations introduce quite effective nonradiative recombination centers in GaAs, which quench the luminescence intensity, L , in a form of $L = A \log(1 \times 10^6/N)$, where N is the density of these nonradiative recombination centers and A is a constant. If the GaAs layers are contaminated with Cu during the growth process, it is found that L is reduced in such a way that the constant A in the above equation is decreased.

In the commercial production of epitaxial layers of III-V compound semiconductors, such as GaAs and GaAs_{1-x}P_x, it is profitable to use Ge wafers as substrates. This is because Ge is superior to GaAs in wafer area and also in cost. However, heteroepitaxial growth of III-V compounds on Ge substrates causes degradation of the structural quality of the grown layers at the interface. This problem has been investigated in detail in the case of a GaAs-Ge system. The degradation includes misfit dislocations (1), interface alloying (2), autodoping of Ge (3), and the cross diffusions of Ge, Ga, and As (4). The structural quality of these GaAs layers has also been characterized by measurements on electron mobility (5) and the width of an x-ray rocking curve (6), but optical characterization has not yet been reported. Since crystal imperfections in GaAs crystals, such as dislocations (7) and precipitates (8), form deep levels and act as nonradiative recombination centers, structural quality can be studied by photoluminescence (PL) or cathodoluminescence (CL). Some works (5, 6) suggested that structural quality of these GaAs layers was rather improved in the bulk region of the epitaxial layer, more than 10μ from the heterojunction. It seems obvious that some portion of these improvements was due to an accommodation of the misfit by dislocation lines (9). However, little experimental work has been done to clarify the layer thickness dependence of the structural quality, which is an important factor for the practical use of Ge substrates.

The purposes of this study are: (i) to measure the distribution of crystal imperfections in these GaAs layers along the growth axis, (ii) to examine the influence of Ge involved in the GaAs epitaxial layers on the electrical and optical properties of the layers, and (iii) to examine the influence of other residual impurities on the optical properties of these GaAs layers. In order to achieve these purposes, the luminescence properties were observed at $\sim 80^\circ\text{K}$ under constant excitation level as a function of the distance, d , from Ge substrates. This conventional optical characterization, supported by x-ray topography, leads to the conclusion that degradation of structural quality due to misfit dislocations and residual impurity Cu (10) are important for the bulk properties of these GaAs layers. The concentration of Ge involved is estimated to be less than 1×10^{17} atoms/cm³ except for the interface

region, which is different from the case of GaAs_{1-x}P_x layers (11).

Experimental

GaAs was epitaxially grown on a (311) surface of a Ge substrate in the growth apparatus reported elsewhere (12) by using a GaAs-AsCl₃-H₂ system. The substrate, Ge, was doped with arsenic ($\rho = 3 \sim 5 \times 10^{-3}$ ohm-cm). The front face of the substrate was polished to a mirror surface and chemically etched with a solution of 1HF:1H₂O₂:1H₂SO₄ prior to use, whereas the back and side faces of the substrate were coated with a Si polycrystalline film (11). Unintentionally doped GaAs crystals ($n = 1 \sim 3 \times 10^{17}$ cm⁻³) and Te-doped ones ($n = 1 \times 10^{18}$ cm⁻³) were used as source materials for the epitaxy. The source and substrate temperatures adopted empirically were in the range of $750^\circ \sim 950^\circ\text{C}$ and $680^\circ \sim 720^\circ\text{C}$, respectively. Pd-diffused hydrogen and 7-nines pure AsCl₃ were used. The partial pressure of AsCl₃ was $0.5 \sim 3 \times 10^{-3}$ atm. GaAs layers, with a thickness of $20 \sim 180\mu$, were grown for 2-8 hr. All the grown layers had mirror-smooth surfaces except when the surface of the substrate was contaminated.

The doping profile in the grown layers was measured electrically along the growth axis, using both the point-contact breakdown (PCB) method and the d-c Van der Pauw technique (13) at a magnetic field of 4500 gauss. The measurement of PCB voltages, V_B , was carried out on a one-degree angle-lapped surface of the sample. The relation between the carrier concentration and V_B was calibrated beforehand by the C-V measurement on Schottky barriers formed on the as-grown surface. The PCB method is excellent for obtaining the profile of the carrier concentration near the interface. Electron mobility, as well as carrier concentration in the bulk region of GaAs layers was measured against the distance, d , from the interface by the d-c Van der Pauw technique. Prior to the Van der Pauw measurement, both the Ge substrate and the GaAs layer of $\sim 10\mu$ in thickness adjacent to the interface were removed by lapping. Indium alloys were used as ohmic contacts. In these cases, electrical measurement and chemical etching of the GaAs layer for only the as-grown surface side were alternatively repeated on the same sample. Fluctuation of layer thickness by etching was controlled within 10μ .

Photoluminescence (PL) was measured at 80°K to examine the optical influence of Ge on GaAs layers, using the Hg 3650Å line as an excitation source and a

Key words: misfit dislocations, cathodoluminescence, degradation of luminescence, nonradiative recombination, GaAs.

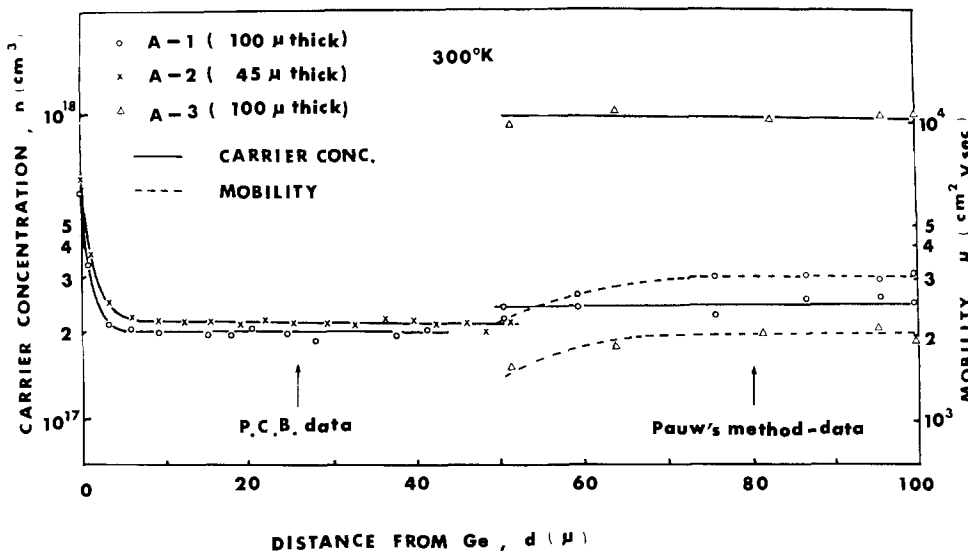


Fig. 1. Electrical properties of GaAs layers grown on Ge substrate, measured as a function of distance from the GaAs-Ge interface, d , at 300°K. The influence of Ge incorporated into GaAs layers is only observed in a region within $\sim 3\mu$ from the interface. The concentration of Ge involved is of the order of magnitude of 10^{16} atoms/cm³ or less beyond the interface region. The gradual decrease in mobility with decreasing d is caused by the crystal imperfections due to lattice mismatch.

33-86-40 Type spectrometer (Bausch and Lomb) coupled with a 7102 photomultiplier (Hamamatsu TV) as a detector. The excitation level of PL was kept constant for all samples. Since the PL intensity was observed to decrease drastically with reduction of the layer thickness, the intensity variation against d was further investigated using cathodoluminescence (CL) at 77°K. Operating conditions of CL were: accelerating voltage 30 kV, primary beam current 10^{-7} A, and beam spot diameter $1 \sim 3\mu$ for all samples. These conditions result in a quite high excitation level of luminescence, which is higher than that of the above-mentioned PL by several orders of magnitude. In this case, an EPU-2A Type spectrometer (Hitachi) coupled with a 7102 Type photomultiplier (Hamamatsu TV) was used as a detector. A step-etching technique was applied to each sample to vary d .

The dislocation density in GaAs layers, N , was measured against d by a transmission x-ray topograph using an Ag target. Prior to the measurement, the Ge substrates were removed by lapping, and GaAs layers with the desired thickness were obtained by using mechanical polishing and chemical etching. Samples with a different doping level and a different thickness were examined. Precipitates were observed in the GaAs layers near the interface using a transmission electron microscope. In this case, a hot H_2O_2 solution (5) was used as an etchant of the Ge substrate. After the Ge substrate was removed, the GaAs layer was carefully etched with a solution of $4H_2SO_4:1H_2O_2:1H_2O$ from only the as-grown surface side, in order to obtain the thin layer with a thickness of about 1000Å at the peripheral. These thin layers were bombarded with a 100 kV electron beam under a vacuum of 10^{-5} Torr.

In order to ascertain the origin of the acceptor-like residual impurities, a Cu-diffused GaAs sample was also prepared.

Results and Discussion

Influence of Ge incorporated into GaAs layers by autodoping process.—In this section, the influence of Ge incorporated into GaAs layers by the autodoping process is discussed.

Profiles of the carrier concentration, as well as those of mobility, were electrically measured and are shown in Fig. 1 as a function of d . The GaAs source crystals used for the epitaxial growth were an undoped one ($n = 2 \times 10^{17}$ cm⁻³, $\mu = 3000$ cm²/V·sec) for samples A-1 and A-2, and a Te-doped one ($n = 1 \times 10^{18}$ cm⁻³, $\mu = 2000$ cm²/V·sec) for sample A-3. It is found from Fig. 1 that the carrier concentrations in these layers are kept constant along the growth axis and are consistent with those in the GaAs source, except for the regions within $2 \sim 3\mu$ from the interface, where they are significantly high. These high

carrier concentrations are believed to be caused by Ge incorporated by the autodoping process, because the samples examined in this section were carefully prepared in an atmosphere kept as clean as possible to minimize the influence of residual impurities. This is supported by the following results obtained using a transmission electron microscope. A high density ($10^5 \sim 10^6$ cm⁻²) of precipitates with a diameter of $\sim 1\mu$ in the interface region was observed, and a typical example is shown in Fig. 2. Stacking faults were also observed to originate from some precipitates. However, no precipitate could be detected in layers a few microns apart from the interface. These results suggest that the Ga-Ge-As alloy (2) was partially produced only in regions within $2 \sim 3\mu$ from the interface as a result of relatively heavy incorporation of Ge by the autodoping process. The profiles of the carrier con-

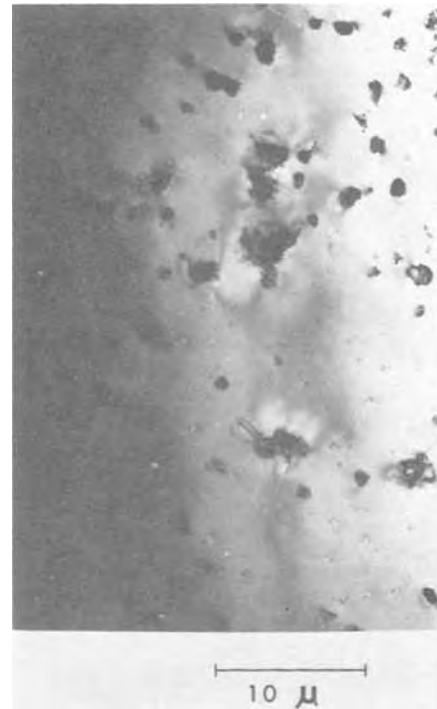
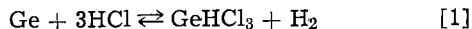


Fig. 2. A micrograph of the GaAs layer within $1 \sim 2\mu$ from the interface, obtained by using a transmission electron microscope. A high density ($10^5 \sim 10^6$ cm⁻²) of precipitates probably due to alloying are shown to exist. Prior to measurements, the Ge substrate was completely removed from the GaAs layer by chemical etching with hot H_2O_2 solution (5).

centration in Fig. 1 suggest that the Ge concentration in the GaAs layers is of the order of magnitude of 10^{16} atoms/cm³ or less except for the interface region, and that the impurity doping from the source materials is kept constant during the whole growth process.

The relatively low concentration of Ge in the bulk region of the GaAs layers was ascertained by the following thermodynamical consideration for the vapor etching process of Ge substrates and also by the results of photoluminescence measurement.

At the substrate temperatures adopted in this experiment, $680^\circ \sim 720^\circ\text{C}$, the predominant reaction between Ge and HCl is expressed as (14)



with the equilibrium constant, K_{Pl} , which was given by Miller *et al.* (14) as a function of temperature. In this case, the partial pressure of GeHCl_3 can be expressed by

$$P_{\text{GeHCl}_3} = \frac{1}{3} \left\{ P_{\text{HCl}(\text{GaAs})} - \left[\frac{P_{\text{HCl}(\text{GaAs})}}{6K_{\text{Pl}}} + \frac{\sqrt{\frac{P_{\text{HCl}(\text{GaAs})^2}{K_{\text{Pl}}^2} + \frac{4}{81K_{\text{Pl}}^3}}}{6} \right]^{1/3} + \left[-\frac{P_{\text{HCl}(\text{GaAs})}}{6K_{\text{Pl}}} + \frac{\sqrt{\frac{P_{\text{HCl}(\text{GaAs})^2}{K_{\text{Pl}}^2} + \frac{4}{81K_{\text{Pl}}^3}}}{6} \right]^{1/3} \right\} \quad [2]$$

where $P_{\text{HCl}(\text{GaAs})}$ is the equilibrium partial pressure of HCl over the GaAs source and equals $3P_{\text{AsCl}_3}/(1 + \sqrt[4]{K_{\text{P}}/P_{\text{As}_4}})$. The equilibrium constant of the $\text{GaAs-AsCl}_3\text{-H}_2$ system, K_{P} , has been calculated (11). By inserting the values of the growth parameters (the source temperature, the substrate temperature, and the partial pressure of AsCl_3) adopted in this experiment into the above equations, we get $P_{\text{GeHCl}_3} \lesssim 1 \times 10^{-6}$ atm. This value corresponds to a Ge concentration of 3×10^{18} atoms/cm³ in GaAs if the back-deposition rate of Ge is assumed to be 50%. Once the front face of the Ge substrate is covered with a GaAs layer, P_{GeHCl_3} may immediately drop by a few orders of magnitude. The net weight loss of Ge was measured after the grown layer was removed by chemical etching. None of the Ge was lost during the chemical etching process. The amount of the weight loss due to vapor etching was 0.05 ± 0.02 mg after a 5 hr run for a sample with an exposed surface area of 4 cm². This value is reasonable when compared with the calculated result, *i.e.*, the vapor etching of the Ge substrate with AsCl_3 is not so serious that the resultant incorporation of Ge will be reduced to less than 10^{17} atoms/cm³ in the bulk region of GaAs more than a few microns apart from the interface.

Photoluminescence spectra from the epitaxial layers are shown in Fig. 3. The data of a Ge-free sample (sample B) is included for comparison. Sample B was grown on a GaAs substrate in a different growth apparatus using a Ga source. There exist broad and intense low energy emission bands in addition to the near-gap emission band in every sample. The origin of these low energy bands is not well understood but is considered to be complexes associated with vacancies, such as a Ga vacancy-donor complex (15), because they appear in any bulk GaAs crystal containing various kinds of donors. Emission peaks due to Ge in n-GaAs are known to locate at 8380Å for the first acceptor level (16, 17), 8890Å for the second acceptor level (18), and $\sim 10,100\text{Å}$ for the donor level (16) at 77°K . Kressel *et al.* (18) reported

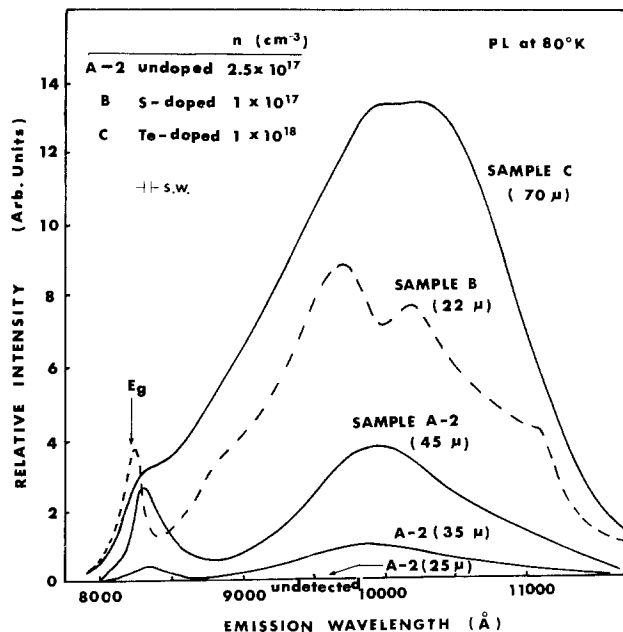


Fig. 3. Photoluminescence spectra at 80°K under constant excitation level. Samples A-2 and C were grown on Ge substrates, whereas sample B was grown on a GaAs substrate using a $\text{Ga-AsCl}_3\text{-H}_2$ system. The decrease of luminescence intensity is found in the case of A-2 as the layer thickness is reduced.

that the emission bands due to Ge could be detected in the PL spectra of GaAs if the Ge concentration exceeded 1×10^{17} atoms/cm³. However, none of them is observed in the PL spectra on the present samples. So, there is no evidence that samples A-2 and C are doped with Ge, although they are doped more heavily than sample B.

It is found in Fig. 1 that the electron mobility of the GaAs layers grown on the Ge substrates decreases gradually as d is reduced to less than 70μ , though the carrier concentration is invariant in this region. It is also found in Fig. 3 that luminescence intensity of sample A-2 decreases drastically with reducing d , whereas the spectrum is unchanged. The other samples grown on Ge substrates also showed similar results. Therefore, it is believed that these reductions in mobility and luminescence intensity were caused by the inhomogeneous distribution of crystal imperfections, and not by that of impurities. This problem is discussed in detail in the next section.

Influence of misfit dislocations.—In addition to the autoping of Ge and interface alloying, lattice mismatch at the GaAs-Ge interface also causes the degradation of the structural quality of the GaAs layers. In this experiment, the distribution of dislocations was investigated as a function of d , using a transmission x-ray topograph. Topographs were taken at different thicknesses of the GaAs layers as they were lapped and chemically etched from only their substrate sides. The result is shown in Fig. 4. It is found in Fig. 4 that the dislocation density, N , increases exponentially with decreasing d , which is similar to the case of GaP layers grown on GaAs substrates (19). Such a high density of dislocations and their exponential distribution could not be observed in GaAs layers grown on GaAs substrates. The value of N at the interface, $1 \times 10^6 \text{ cm}^{-2}$, obtained from Fig. 4 by extrapolation is consistent with that reported by Holloway *et al.* (1), $2 \times 10^6 \text{ cm}^{-2}$, for the sample grown at 750°C . As was suggested by Meieran (20), these dislocations are considered to have originated from the lattice constant mismatch between Ge and GaAs. These misfit dislocations, as is shown in Fig. 3, act as quite effective nonradiative recombination centers. On the other hand, the dislocations introduced by a four-point bending are less active recom-

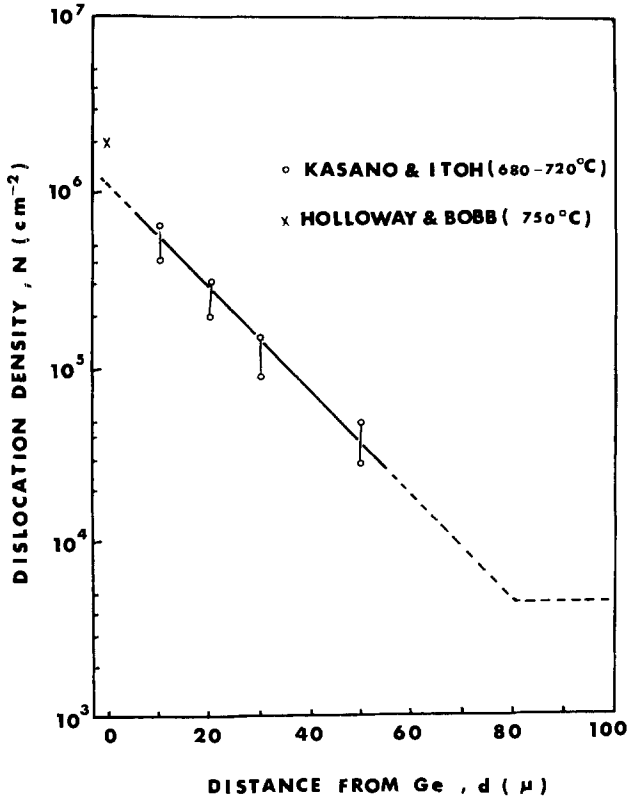


Fig. 4. Dislocation density of GaAs layers grown on Ge substrates, measured by using an x-ray topograph technique as a function of d . The dotted line is estimated from the result of the CL data shown in Fig. 5.

bination centers; Esquivel *et al.* (21) showed in the CL measurement for GaAs that only half of the initial intensity was quenched when high 10^6 cm^{-2} dislocations were introduced by bending. The decreasing rate of intensity is smaller than that observed in Fig. 3 by an order of magnitude. These differences in the decreasing rate may be caused by the impurity effect for dislocations; *i.e.*, grown-in dislocations associated with impurities act as effective nonradiative recombination centers (7, 22), whereas dislocations without impurity association do not do so (22). Therefore, a predominant part of the misfit dislocations in this experiment is considered to be associated with impurities, Ge, and other residual impurities.

In order to clarify the dependence of luminescence intensity, L , on the misfit-dislocation density, cathodoluminescence was measured at 77°K (23) as a function of d on several samples with different doping levels. The observed CL spectra consisted of only two emission bands as are shown in Fig. 6. They were the near-gap emission band peaked at $8230 \sim 8290 \text{ \AA}$ and the lower energy subband peaked at $\sim 9200 \text{ \AA}$. The intensity of both the bands varied with d as was shown in Fig. 5, though the spectra were unchanged as in the case of the above-mentioned PL. Figure 5 shows that L is nearly constant in a region of $d \cong 80 \mu$, but it decreases linearly with decreasing d in a region of $d < 80 \mu$ in any sample and in any emission band. At the interface ($d = 0$), L converges to zero. As the excitation level increased, L generally increased until saturation occurred, whereas L at the interface remained zero. From Fig. 4 and 5, L is given as a function of N by

$$L = L_s \log\left(\frac{N_0}{N}\right) / \log\left(\frac{N_0}{N_s}\right) = A \log\left(\frac{N_0}{N}\right), \quad (N_s \leq N \leq N_0) \quad [3]$$

where L_s is the saturated intensity at $\sim 80 \mu$, N_0 is

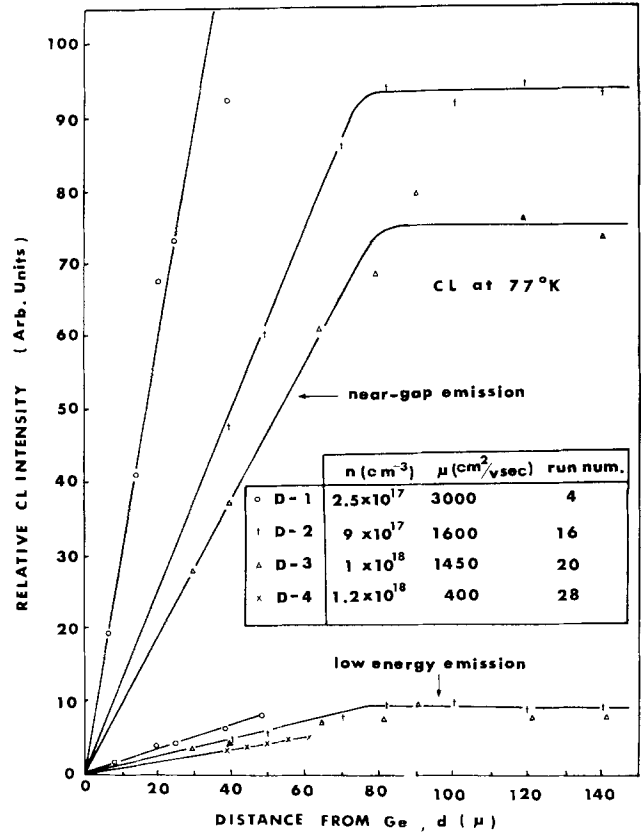


Fig. 5. Intensity variation of the cathodoluminescence from the GaAs layers grown on Ge substrates, measured as a function of d at 77°K. There are only two emission bands in the CL spectra, one of which is the near-gap emission with stronger intensity and the other is the low energy subband peaked at 9200 \AA with weaker intensity.

the density corresponding to $L = 0$, N_s is the density which gives L_s , and A is $L_s / \log(N_0/N_s)$. In this case, $N_0 = 1 \times 10^6 \text{ cm}^{-2}$, and $N_s \cong 5 \times 10^3 \text{ cm}^{-2}$. The excited pairs which are within a diffusion length, l , of the edge of the recombination center with the effective radius, r , will be drawn to this center, where they recombine nonradiatively via the continuum of states (24). It is noteworthy that the decrease of L is proportional to $\log N$, and not to N in the empirical Eq. [3]. The logarithmic dependence of L on N may be caused by the decrease of l as N increases. It has been established (25) that the lifetime of minority carriers, τ , in plastically deformed pure Ge is proportional to $1/N$. If l is simply defined as $\sqrt{D\tau}$, and the decrease of L is assumed to be proportional to $l^2 N$, the decrease of L becomes independent of N in pure Ge as suggested in the case of dislocations without impurity association in $\text{GaAs}_{1-x}\text{P}_x$ (22). However, the N dependence of τ becomes a more complicated form in the case where the dislocations are associated with impurities (25). The $D\tau$ is in this case proportional to $(1/N) \ln N$ based on Eq [3], though the mechanism is not clarified. The intensity saturation at $d \cong 80 \mu$ in Fig. 5 is probably caused by the "background" crystal imperfections, whose density is determined by the growth conditions. The dislocation density corresponding to this intensity saturation is estimated to be $\sim 5 \times 10^3 \text{ cm}^{-2}$ from Fig. 4. The results of Fig. 1, 3, and 5 indicate that the profile of misfit dislocations is explicitly obtained by measuring luminescence intensity under the constant excitation conditions along the growth axis. This results from the fact that the intentionally doped and/or unintentionally doped impurities are uniformly distributed except for the interface region.

As briefly mentioned above, the constant A in Eq. [3] can drastically vary from sample to sample. A

typical case is shown in Fig. 5. The D-series samples in Fig. 5 were grown using the same lot of AsCl_3 but a small amount of leakage existed in the gas line of the growth apparatus between the Pd diffuser and the AsCl_3 reservoir. By comparing the electrical properties of the D-series samples included in Fig. 5, it is found that the constant A becomes smaller in the sample with lower electron mobility, and that electron mobility becomes lower with the run number for the same lot of AsCl_3 . It was also observed that the emission bandwidth became broader for the samples with a smaller value of A . Sample D-4 is the extreme case, where no near-gap emission band but only the broad and weak subband peaked at $\sim 9200\text{\AA}$ was observed. This sample showed n-type conduction with the carrier concentration of $1.2 \times 10^{18} \text{ cm}^{-3}$, but mobility was only $400 \text{ cm}^2/\text{V}\cdot\text{sec}$. The growth conditions of D-4 were similar to those of other D-series samples except that the Pd diffuser was broken. The degradation of luminescence due to the decrease of A is obviously different from the degradation due to the misfit dislocations mentioned above. Both the bandwidth broadening and the relative increase of intensity of the low energy subband happen in this case. Hence, the origin of the decrease of A is deduced to be the contamination that occurred during the growth process. It should be emphasized that these contaminants also act as the origin of the low-energy subband. The details are discussed in the next section.

Influence of Cu on cathodoluminescence properties.—The CL properties of GaAs containing Cu are dealt with in this section, being correlated with the results obtained in the above section.

In the previous section, we have pointed out that the reduction of L due to the decrease of A is caused by contamination. The low electron mobility and the bandwidth broadening of the D-series samples suggest that the contaminants increase the compensation ratio of GaAs. It means that the contaminants act as acceptors in GaAs. We observed in this CL measurement at 77°K that the low energy subband was located at $\sim 9800\text{\AA}$ in Si-doped GaAs crystals and that luminescence intensity was not quenched in oxygen-doped semi-insulating GaAs crystals. They indicate that neither silicon nor oxygen is the contaminant in the present case. The peak position of the subband in this case, $\sim 9200\text{\AA}$ (1.35eV) at 77°K , is consistent with that of Cu-doped GaAs crystals, reported by Alferov *et al.* (26) using a photoluminescence technique. Hence, we can speculate the contaminant to be Cu, which can be easily introduced into III-V compounds during the

growth process and degrades the radiative efficiency (27).

In order to make sure of this assignment, a Cu-diffused GaAs sample was prepared, and the CL properties of this sample were measured. A Te-doped GaAs wafer ($n = 1 \times 10^{18} \text{ cm}^{-3}$) with a mirror-smooth surface (sample E) was dipped into a Cu_2SO_4 solution for 1 min and sealed in a quartz ampule at 1×10^{-5} Torr. The diffusion was carried out at 960°C for 20 min. Then, sample E was angle-lapped at 5° and its CL properties were measured as a function of the distance from the front surface along the wafer thickness, d . Figure 6 shows the CL spectra of samples D-2 and E (before and after Cu diffusion, respectively) near the front surface of the wafer. In sample E, the intensity of the near-gap band, L_G , became very weak and the relative intensity of the low energy subband against L_G , L_{Cu}/L_G , increased as a result of Cu diffusion. This result supports the above assignment that the degradation of luminescence with reduction of A was caused by Cu contamination. The reduction of luminescence intensity, as well as the enhancement of the relative intensity of the 1.35 eV band, was also reported for Cu-doped GaAs samples (28). As was predicted by Batavin *et al.* (28), the concentration of Cu involved can be estimated by measuring L_{Cu}/L_G . Figure 7 shows the variations of L_G and L_{Cu}/L_G along the wafer thickness in the sample E before and after Cu diffusion. The values of L_G and L_{Cu}/L_G are constant with d before Cu diffusion and it indicates a uniform distribution of unintentionally doped Cu impurity in the sample E. After Cu diffusion, both of them vary with d . It is found that the concentration of Cu dips near the center of depth, $d \simeq 450\mu$ as a result of Cu diffusion from both sides of the wafer surface. It is noticeable that the anomalous diffusion coefficient of Cu in GaAs (29) resulted in a rather high concentration of Cu even at the center of depth.

Next, the excitation current (I_B) dependence of L_G and L_{Cu} was observed. Figure 8 shows the I_B dependence of the CL intensities, L_G and L_{Cu} , of a GaAs layer near the front face of the Cu-diffused sample E. It is found that L_G is proportional to I_B^2 , whereas L_{Cu} is proportional to I_B . Rao-Sahib *et al.* (30) reported that CL intensity in p-GaAs was proportional to I_B^m ($1 \leq m \leq 2$) under the constant accelerating voltage, where $m = 1$ for low current region and $m > 1$ for high current region. A linear dependence of L on I_B was also observed by Casey *et al.* (31) in the Zn-O doped GaP, which was measured using an unfocused beam. These current dependences are reasonably ex-

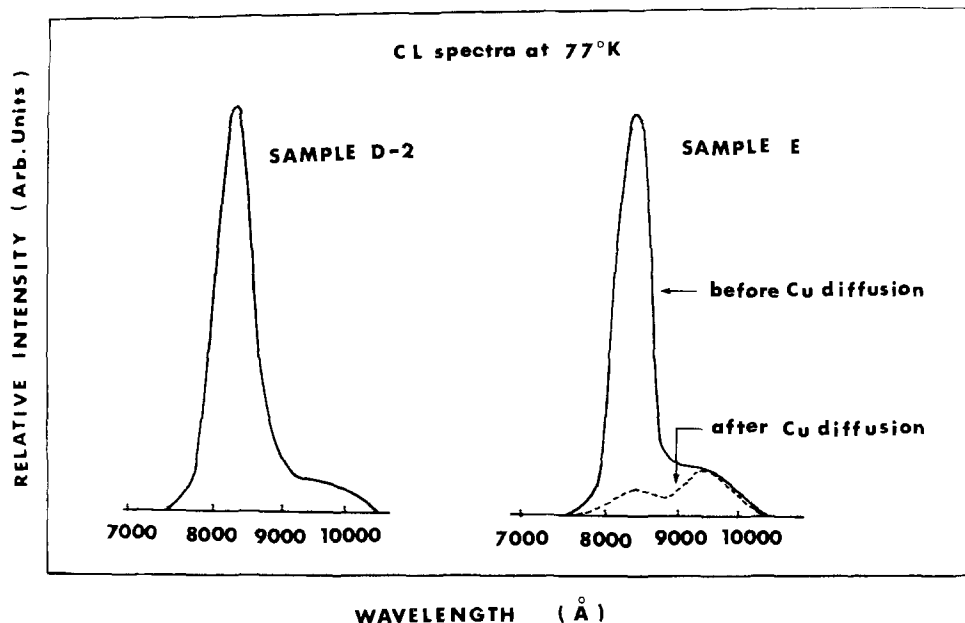


Fig. 6. Cathodoluminescent spectra of GaAs at 77°K , indicating the optical influence of Cu contaminants.

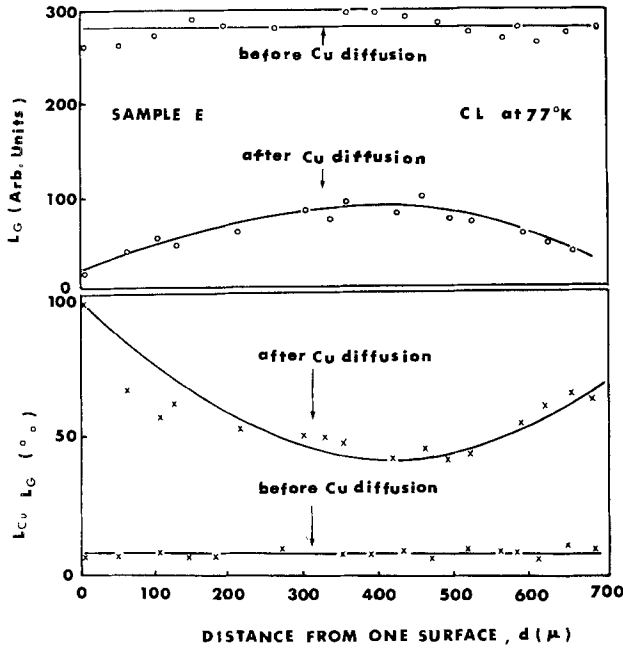


Fig. 7. Intensity variation of the cathodoluminescence of sample E before and after Cu diffusion along the wafer thickness, measured at 77°K. The figure shows that the concentration of Cu varies along the wafer thickness after Cu diffusion.

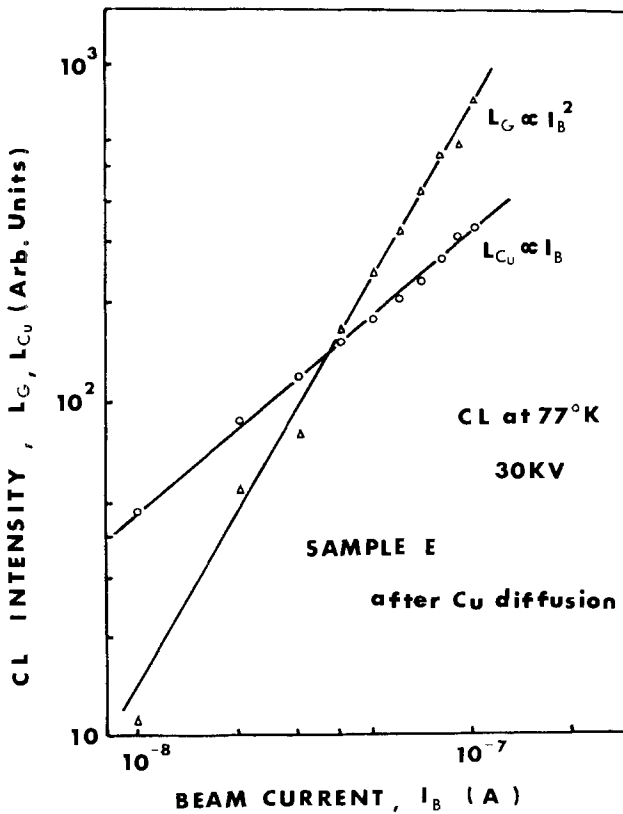


Fig. 8. Beam current dependence of the two emission bands at 77°K, measured under the constant accelerating voltage of 30 kV.

plained as follows. The density of free hole-free electron pairs, N_{pair} , created by electron beam excitation is given by (24)

$$N_{\text{pair}} = K \left(\frac{I_B}{S} \right) \left(\frac{E_P}{E_0} \right) F(\gamma, d) \quad [4]$$

where E_P/E_0 is the number of pairs created per incident electron, S the excited area, γ the back-scattering rate of the incident electron, d the effective penetration depth of the incident electron, and K the constant. Though F is given as the complicated form (32)

because of the nonuniform distribution of carrier generation with depth, it is considered that γ , d , and also F are kept nearly constant if the material, the accelerating voltage, and the flatness of the beam-incident plane are kept constant. As is well known, the radiative recombination rate of free electron-hole pairs under a constant excitation condition is given by the following equations

$$R_{\text{exc}} = \frac{np}{n_1^2} = \frac{(n_0 + \Delta n)(p_0 + \Delta p)}{n_1^2} R \quad [5]$$

where R is the radiative recombination rate at thermal equilibrium which was derived by van Roosbroeck and Shockley (33), n_1 the intrinsic carrier concentration, $\Delta n(\Delta p)$ a deviation of electron (hole) concentration from a thermal equilibrium value of $n_0(p_0)$ caused by the excitation, or N_{pair} . Since p_0 is much greater than n_0 in uncompensated p-type materials or vice versa in n-type ones, the following relation is approximately derived for p-GaAs from Eq. [4] and [5] under a constant accelerating voltage

$$R_{\text{exc}} \propto \Delta n(p_0 + \Delta p) \propto p_0 I_B + \alpha I_B^2 \quad [6]$$

where α is the constant. Equation [6] indicates that R_{exc} is proportional to I_B at low excitation levels where $p_0 \gg \Delta p$, whereas R_{exc} proportional to I_B^2 at high excitation levels or in a lightly doped p-type material where $\Delta p \gg p_0$ holds. This is the case of Rao-Sahib *et al.*

If GaAs is highly compensated, which is the case of sample E, a relation $p_0 \approx n_0$ holds and

$$R_{\text{exc}} \approx \frac{(p_0 + \Delta p)^2}{p_0^2} R = \left(1 + \frac{\Delta p}{p_0} \right)^2 R \quad [7]$$

At the excitation levels used in this experiment, $\Delta p \gg p_0$ holds in sample E. Hence, R_{exc} is proportional to I_B^2 in the case of near-gap emission, namely $L_G \propto I_B^2$.

The 1.35 eV subband was reported (26) to be due to the recombination between a free electron and a hole bound to the first acceptor level of Cu. In this case, the radiative recombination rate would be limited by the concentration of Cu in the first acceptor state, N^{A}_{Cu} , because of $p, n \gg N^{\text{A}}_{\text{Cu}}$, namely, the recombination rate is proportional to the product of $n \cdot N^{\text{A}}_{\text{Cu}}$. Hence, a relation $L_{\text{Cu}} \propto N_{\text{pair}} \propto I_B$ is obtained if $\Delta p \gg p_0$, which is the case shown in Fig. 8.

Summary

In this work the structural quality of the GaAs layers grown on the Ge substrates has been investigated as a function of distance from the GaAs-Ge interface, by measuring the photo- and cathodoluminescence properties at 77°K, as well as electrical properties at 300°K. The measurements using an x-ray topography and a transmission electron microscope were also carried out. At the interface, the structural quality of these GaAs layers was heavily degraded by misfit dislocations, interface alloying, and also by autodoping of Ge from the substrate, though the back-side faces of the substrate were coated with a Si polycrystalline film during the epitaxy. It is found that the influences of interface alloying and also autodoping of Ge on the electrical and optical properties of these GaAs layers are substantially neutralized in the regions more than a few microns apart from the interface. However, it is also found that structural quality of these GaAs layers less than $\sim 80\mu$ in thickness is affected by the misfit dislocations, though the dislocation density decreases exponentially with d . These misfit dislocations introduce quite effective nonradiative recombination centers in GaAs. It is noteworthy that luminescence intensity, L , is reduced by these nonradiative recombination centers according to the following experimental equation

$$L = A \log(N_0/N) + L_{\min}$$

where N is the density of these centers and $N \leq N_0$. In the case of the GaAs-Ge system, $N_0 \simeq 1 \times 10^6 \text{ cm}^{-2}$, $L_{\min} = 0$. Hence, by measuring the variation of L under the constant excitation conditions, the distribution of these centers can be easily estimated. The other factor which drastically reduces L is the residual impurities, especially Cu incorporated into GaAs during the growth process. The reduction of L due to Cu is found to occur as the decrease of A in the above equation. The distribution of Cu was estimated by measuring the distribution of the relative intensity of the 1.35 eV subband against the near-gap emission band, $L_{\text{Cu}}/L_{\text{C}}$, under the constant excitation conditions at 77°K. The dependence of the intensities of these two bands on the excitation level was also examined.

Acknowledgments

The authors are grateful to M. Tamura for his measurements using a transmission electron microscope, to Dr. S. Kishino for measurements using an x-ray topograph technique, to A. Doi for photoluminescence measurements, to S. Fukuhara for his technical assistance for cathodoluminescence measurements, and to K. Itoh for providing a part of the data of misfit-dislocation density. They would also like to thank Dr. J. Umeda, K. Kurata, and S. Tanimizu for their stimulating discussions and advice. They also wish to voice their appreciation of the support and encouragement given by Dr. H. Okano during the course of this experiment.

Manuscript submitted March 15, 1974; revised manuscript received July 29, 1974.

Any discussion of this paper will appear in a Discussion Section to be published in the December 1975 JOURNAL. All discussions for the December 1975 Discussion Section should be submitted by Aug. 1, 1975.

Publication costs of this article were partially assisted by Hitachi, Limited.

REFERENCES

1. H. Holloway and L. B. Bobb, *J. Appl. Phys.*, **39**, 2467 (1968).
2. H. Kasano and S. Iida, *Japan. J. Appl. Phys.*, **6**, 1038 (1967).
3. J. Grossman, *This Journal*, **110**, 1065 (1963).
4. W. Rice, *Proc. IEEE*, **52**, 284 (1964).
5. G. O. Radd, Jr. and D. L. Feucht, *Met. Trans.*, **1**, 609 (1970).
6. L. C. Bobb, H. Holloway, and K. H. Maxwell, *J. Appl. Phys.*, **37**, 4687 (1966).
7. K. H. Zschauer, *Solid-State Commun.*, **7**, 385 (1969).
8. H. Kressel, H. Nelson, S. H. McFarlane, M. S. Abrahams, P. LeFur, and C. J. Buiocchi, *J. Appl. Phys.*, **40**, 3587 (1969).
9. J. W. Matthews, S. Mader, and T. B. Light, *ibid.*, **41**, 3800 (1970).
10. T. N. Morgan, M. Pilkuhn, and H. Rupprecht, *Phys. Rev.*, **138**, A 1551 (1965).
11. H. Kasano, *Solid-State Electron.*, **16**, 913 (1973).
12. M. Aoki and H. Kasano, *Japan. J. Appl. Phys. Suppl.*, **39**, 234 (1970).
13. L. J. Van der Pauw, *Philips Res. Rept.*, **13**, 1 (1958).
14. K. J. Miller and M. J. Grieco, *This Journal*, **111**, 1099 (1964).
15. E. W. Williams, *Phys. Rev.*, **168**, 922 (1968).
16. H. Kressel, *J. Appl. Phys.*, **38**, 4383 (1967).
17. W. Schairer and W. Graman, *J. Phys. Chem. Solids*, **30**, 225 (1969).
18. H. Kressel, F. Z. Hawrylo, and P. LeFur, *J. Appl. Phys.*, **39**, 4059 (1968).
19. L. C. Luther, *Met. Trans.*, **1**, 593 (1970).
20. E. S. Meieran, *This Journal*, **114**, 292 (1967).
21. A. L. Esquivel, W. N. Lin, and D. B. Wittry, *Appl. Phys. Letters*, **22**, 414 (1973).
22. G. B. Stringfellow and P. E. Greene, *J. Appl. Phys.*, **40**, 502 (1969).
23. S. Hosoki and H. Okano, 6th Int. Conf. on X-ray Optics and Microanalysis, Osaka, 1972.
24. J. I. Pankove, "Optical Processes in Semiconductors," Prentice-Hall Inc., Englewood Cliffs, N. J. (1971).
25. G. K. Wertheim and G. L. Pearson, *Phys. Rev.*, **107**, 694 (1957).
26. Zh. I. Alferov, D. Z. Garbuzov, and E. P. Morozov, *Soviet Phys. Solid-State*, **8**, 2589 (1967).
27. A. A. Bergh, *IEEE Trans. Electron Devices*, **ED-18**, 166 (1971).
28. V. V. Batavin, V. M. Mikhaélyan, and G. V. Popava, *Soviet Phys. Semicond.*, **6**, 1616 (1973).
29. C. S. Fuller and J. M. Whelan, *J. Phys. Chem. Solids*, **6**, 173 (1958).
30. T. S. Rao-Sahib and D. B. Wittry, *J. Appl. Phys.*, **40**, 3745 (1969).
31. H. C. Casey, Jr. and J. S. Jayson, *ibid.*, **42**, 2774 (1971).
32. D. F. Kyser and D. B. Wittry, *Proc. IEEE*, **55**, 733 (1967).
33. W. van Roozbroeck and W. Shockley, *Phys. Rev.*, **94**, 1558 (1954).

Chemisorption Reactions on High Index ZnS Surfaces

W. R. Bottoms and D. B. Lidow

Princeton University, Princeton, New Jersey 08540

ABSTRACT

An attempt is made to determine the relative strength of interaction with an ambient for ZnS surfaces which differ only in the crystallographic perfection of the surface. Chemisorption reactions for a (110) crystal and a stepped high index ZnS surface with oxygen and carbon monoxide were monitored with low energy electron diffraction (LEED) and Auger electron spectroscopy (AES). The correlation of the dissociation and chemisorption activity with the disorder on these ZnS surfaces exhibits the importance of active sites in surface chemical reaction.

Various investigators have suggested that there exist certain "active sites" which are responsible for the chemical activity of catalysts (1). These "active sites" have generally been attributed to lattice defects and/or the topographic structure of a catalyst surface (2). Experimental investigations undertaken to determine the role of surface irregularities in the catalytic activity support an important role for surface imperfections in the chemical activity of these surfaces (2-4). In the present investigation an attempt is made to determine the relative strength of interactions with an ambient for ZnS crystal surfaces which differ only in the crystallographic perfection of the surface.

A (110) surface and a stepped high index face were prepared from a single ZnS crystal to insure identical bulk properties. Two independent experiments were performed upon these crystal faces to characterize the chemical activity of the edge states present upon the high index face using the nonreconstructed (110) surface as a control. In the first experiment, the two crystal faces were introduced separately into a 4-grid LEED-Auger device with a base pressure of 2×10^{-10} Torr. The surface composition and surface symmetries were then monitored with low energy electron diffraction (LEED) and Auger electron spectroscopy (AES). After cleaning the surfaces by argon ion bombardment and annealing, the crystal faces were subjected to various oxygen containing atmospheres and the chemical interaction was observed with LEED and AES. The second experiment exposed the same crystals, both faces mounted simultaneously in the system, to carbon dioxide containing atmospheres and similar LEED and AES observations were made. The results support the dominance of active sites in surface based chemical reactions.

Sample Preparation

The (110) surface, prepared by cleaving in air, exhibited a diffraction pattern upon room temperature pumpdown before any in vacuum processing. Auger spectra taken on these crystals before processing indicated the presence of oxygen, carbon, and chlorine in that order of abundance in addition to sulfur and zinc. These surface contaminants resulted in a poorly developed diffraction pattern and a sequence of annealing steps was undertaken to determine the desorption temperature for chemisorbed gases. The quality of the diffraction pattern showed no significant change until 580°C at which time there was a relatively abrupt change to a well-developed diffraction pattern. The development of the LEED pattern with annealing, illustrated in Fig. 1, indicates a relatively low binding energy for chemisorbed gases on the cleaved (110) surface of ZnS. Auger spectra taken after this high vacuum annealing confirm that the surface is relatively clean since no elements other than zinc, sulfur, and small amounts of carbon were detected. This carbon was almost completely removed by the argon ion bom-

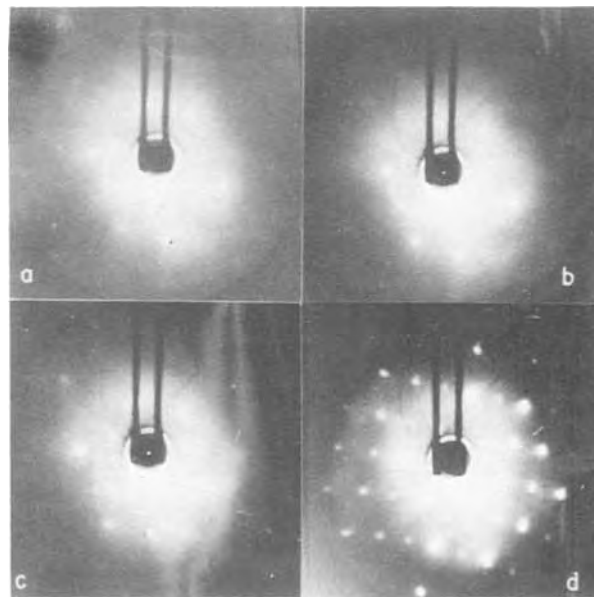


Fig. 1. Diffraction pattern of a (110) ZnS surface after cleaving in air, (a) no vacuum annealing, (b) 200°C for 10 min, (c) 500°C for 20 min, (d) 580°C for 10 min.

bardment and annealing sequence indicated in Table I before the dosing experiments.

Numerous experimentors have found that a high index crystal surface will, if given sufficient energy to initiate mass transfer, reorder itself into a surface of low index steps. These stepped or terraced surfaces have been observed by LEED for copper, germanium, gallium arsenide, uranium dioxide, and platinum (6). In the present study, a ZnS crystal was cut at a low angle to the (110) and chemically polished to provide such a stepped surface. This surface did not exhibit a diffraction pattern upon its first introduction into the vacuum system, and the argon ion bombardment

Table I. Preparation of the crystal faces

Random high index	(110)
Sawed at a low angle to the (110)	Cleaved
Chemically polished	Argon bombarded 41 hr
Annealed 30 min at 400°C*	Annealed 10 min at 1000°C*
Argon bombarded 20 hr	Annealed 10 hr at 600°C*
Annealed 45 min at 650°C*	Oxygen exposure of 1×10^{-4} Torr-sec
Oxygen exposure of 1×10^{-2} Torr-sec	Oxygen exposure of 10^{-2} Torr-sec
Oxygen exposure of 20 min at 1 atm	Oxygen exposure of 20 min at 1 atm
Annealed 30 min at 650°C*	Annealed 60 min at 600°C*

* Vacuum during annealing was maintained in the 10^{-9} Torr range.

Key words: chemisorption, defect states, zinc sulfide.

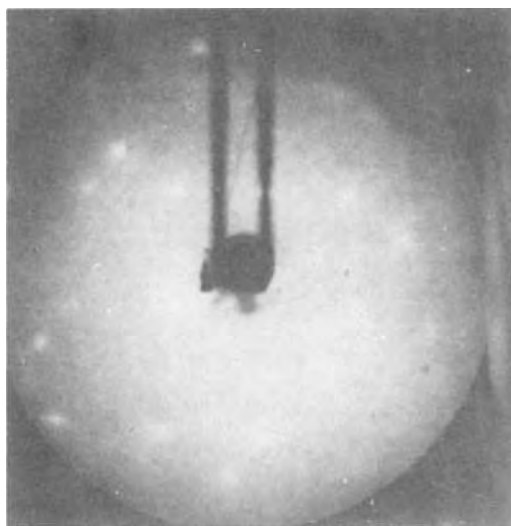


Fig. 2. Diffraction pattern of high index surface after cleaning by argon ion bombardment and annealing.

and annealing steps listed in Table I were necessary to obtain a diffraction pattern and a clean Auger spectrum. The LEED pattern observed on this surface (Fig. 2) was not characteristic of any major crystal plane, and there was evidence of small scale faceting. Streaking in the pattern due to an ordered array of steps is minimal, indicating the steps in the surface were not ordered over large areas (7). Auger spectra confirmed that this surface, after the in vacuum processing, was essentially atomically clean.

Experimental Results

The high index face, after in vacuum cleaning, was subjected to oxygen dosings ranging from 1×10^{-4} Torr-sec to 20 min at 1 atm. Auger data obtained after these oxygen exposures indicated substantial changes in the carbon concentration. The relative magnitude of the carbon Auger signal increased after each oxygen exposure with no indication of saturation as illustrated by Fig. 3. The source of this carbon is attributed to the high CO partial pressure (on the order of 20%) observed in this VacIon pumped system in the presence of oxygen. In addition to the increase in the carbon signal amplitude, there was a broadening of the peak. This broadening is attributed to chemical shifts due to the distribution of bonding configurations for the carbon atoms contributing to the spectra. Subsequent annealing caused the carbon Auger peak to decrease in width, indicating that the carbon remaining on the surface was predominantly in one valence state. The relative amplitude of carbon vs. oxygen Auger peaks increases with gas exposure indicating that the carbon on this surface is partially dissociated from the oxygen and the oxygen partially desorbed. This was also supported by the annealing behavior since the net result of the oxygen exposure on this surface after annealing was to increase rather than decrease the relative abundance of surface carbon.

Identical experiments were conducted on the cleaved (110) ZnS surface as a control. The entire ion clean-

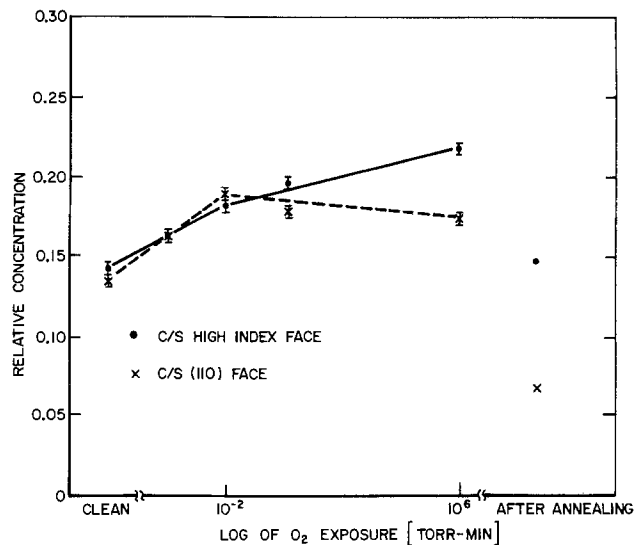


Fig. 3. Relative surface concentration of carbon on the (110) and high index surfaces of ZnS as a function of oxygen exposure.

ing, oxygen exposure, and annealing sequences were repeated as in the high index surface dosing experiment. It has been demonstrated (4, 5) that surfaces of some II-VI compound semiconductors can be rendered virtually inert to chemisorption by careful processing to remove surface imperfections. The ZnS (110) surface followed this pattern in the LEED, and AES data gave little evidence for chemisorption of CO or O₂ on the cleaved surface after that surface had been cleaned and ordered by the ion bombardment and annealing sequence in Table I. An increase in the carbon Auger signal was observed. However, the changes were reversible with annealing and the slight buildup observed was found to saturate after dosings of 10^{-2} Torr-sec of oxygen. Both the slight carbon amplitude change and saturation in the Auger signal upon oxygen exposure indicates that a low density of chemisorption sites were present upon the (110) face. These sites can be attributed to imperfections left in the surface by cleaving.

The high index face was introduced into the vacuum system for CO₂ exposures, mounted on the same sample holder with the low index crystal. Concentrations of carbon found upon the surface were removed by argon bombardment and gentle annealing to produce LEED patterns similar to that of Fig. 1d. Auger spectra confirmed a clean surface. After dosings in steps from 10^{-4} Torr-sec to 45 min at 1 atm of carbon dioxide, the high index face exhibited considerably higher carbon concentration than was observed on the (110) face. The carbon peak increase was not accompanied by an increase in the oxygen peak indicating dissociation as in the oxygen dosings. As before, this additional carbon was not loosely bound to the surface since upon annealing no decrease in the carbon Auger signal was observed (Table II). These results directly contrasted those obtained from the low index face. The CO₂ that adsorbed upon the (110) surface during the dosings was found to be loosely bound and both the oxygen and carbon Auger signals virtually disappeared during subsequent gentle annealing. Little ele-

Table II. Auger data/CO₂ dosings

	Random high index				110			
	$\frac{S}{Zn}$	$\frac{C}{S}$	$\frac{C}{Zn}$	$\Delta \frac{C}{S} (\%)$	$\frac{S}{Zn}$	$\frac{C}{S}$	$\frac{C}{Zn}$	$\Delta \frac{C}{S} (\%)$
Clean surface	11.6	0.059	0.667	—	14.1	0.078	1.11	—
After 45 min at 1 atm of CO ₂	10.2	0.052	0.526	-12	5.4	0.059	0.319	-24
After 24 hr anneal at 200°C*	2.4	0.093	0.222	+79	1.7	0.030	0.050	-51

* Vacuum during anneal was maintained in the 10^{-9} Torr range.

mental carbon was present since the carbon to oxygen peak ratio remained relatively constant throughout the dosings, indicating adsorption of a carbon-oxygen compound without surface dissociation.

Summary

The exposure to oxygen with a high partial pressure of carbon monoxide showed that chemisorption on the stepped surface was much faster than on the (110) surface. In addition, the stepped surface showed evidence of dissociation of the carbon monoxide which was never observed for the (110) face. Similar results were observed for carbon dioxide exposure in that a strong chemisorption and evidence of dissociation at the surface was observed for the stepped high index surface and not for the (110). This increased chemical activity can be explained in terms of active sites associated with edge states on the surface. The edges and corners present on the high index surface provide sites where the number of nearest neighbor and next nearest neighbor atoms is greater than on the clean and ordered low index surface. This results in an increase of the effective binding energy for chemisorption at certain "active sites." The correlation of the dissociation and chemisorption activity with the order of these ZnS surfaces exhibits the importance of "ac-

tive site" in surface chemical reactions on II-VI compounds.

Manuscript submitted Nov. 2, 1972; revised manuscript received ca. Jan. 15, 1974. This was Paper 287 presented at the Miami Beach, Florida, Meeting of the Society, Oct. 8-13, 1972.

Any discussion of this paper will appear in a Discussion Section to be published in the December 1975 JOURNAL. All discussions for the December 1975 Discussion Section should be submitted by Aug. 1, 1975.

REFERENCES

1. H. E. Grenga and K. R. Lawless, *J. Appl. Phys.*, **43**, 1508 (1972); W. S. Taylor, *Proc. Phys. Soc. (London)*, **A108**, 105 (1925).
2. B. Lang, R. W. Joyner, and G. A. Somorjai, *Surface Sci.*, **30**, 454 (1972).
3. A. Spilners and R. Smoluchowski, "Reactivity of Solids," p. 475, Elsevier, New York (1961).
4. S. Baidyaroy, W. R. Bottoms, and P. Mark, *Surface Sci.*, **29**, 165 (1972).
5. J. D. Levine, A. Willis, W. R. Bottoms, and P. Mark, *ibid.*, **29**, 144 (1972).
6. W. P. Ellis and R. L. Schwoebel, *ibid.*, **11**, 82 (1968); M. Henzler, *ibid.*, **19**, 159 (1970); G. E. Rhead and J. Perdereau, *ibid.*, **24**, 555 (1971); B. Lang, R. W. Joyner, and G. A. Somorjai, *ibid.*, **30**, 440 (1972).
7. J. E. Houston and R. L. Park, *ibid.*, **26**, 269 (1971).

Doping Profiles by MOSFET Deep Depletion C(V)

D. M. Brown,* R. J. Connery, and P. V. Gray

General Electric Company, Corporate Research and Development, Schenectady, New York 12301

ABSTRACT

Deep depletion MOS C(V) curves obtained by reverse biasing the junctions of MOSFET's are analyzed to produce N(X) doping profiles. Analytical techniques and possible errors are discussed together with experimental results obtained from samples on bulk, ion-implanted, and epitaxial Si wafers. Experimental results are compared with spreading resistance measurements. The simplicity of the method makes it suitable for rapid impurity profile research and process control applications.

Measurements of impurity profiles utilizing reverse biased capacitance C(V) measurements of diffused junction and Schottky barrier diodes have been described previously by many authors. Little use, however, has been made of MOS devices to provide doping profiles even though, as discussed by Nicollian *et al.* (1), information on the profile can be obtained closer to the surface by this method than by any other. The reasons for this, we believe, are based on a belief that the measurement techniques and required apparatus are complicated and there has been considerable concern about interface state errors in MOS doping profile determinations. Some of the techniques utilized in the past for Si profiling using MOS structures are discussed briefly below.

Because of minority carrier surface inversion, deep depletion is not easily obtainable using MOS capacitors at room temperature, and so specialized equipment and techniques have been required. Short pulses are usually used to measure the capacitance because the lifetime is usually too short to maintain the depleted state long enough to make a static measurement. Van Gelder and Nicollian (2) have used the pulsed high frequency technique to examine redistribution of impurities during thermal oxidation of Si. Slow voltage ramps can be applied to deplete the surface if the minority carrier lifetime is sufficiently long. Long lifetimes resulting in low minority carrier gen-

eration rates can be obtained by cooling the samples to 78°K and this has been utilized advantageously in the past. In fact, the analytical studies presented here indicate that accurate profile information can be obtained closer to the interface for low impurity concentrations by cooling the samples to 78°K. This has also been pointed out by Le Blanc *et al.* (3). A graphical analysis of low temperature (78°K) MOS deep depletion C(V) curves was used by Brown *et al.* (4) to detect B compensation in n-type Si. This method has also been more recently used by Adda and Clemens (5). A high frequency second harmonic technique has been described as a method of obtaining profiles with minimal interface state errors (1). Also, since the second harmonic technique directly measures the slope of the 1/C² vs. V curve used to determine N, one can use slower ramp voltages without introducing errors caused by minority carrier depletion "fill up." That is to say, only the second harmonic signal and total capacitance information are required to obtain N(X). Deep depletion information at large X may still require rather long lifetimes, however, if slow voltage ramps are used. This is also true of the technique utilized by Brews where the maximum depletion width was that occurring for minority carrier inversion at thermal equilibrium (6).

Method and Purpose

MOS deep depletion caused by minority carrier removal using an adjacent reversed biased diode in MOS

* Electrochemical Society Active Member.
Key words: N(X), MOS deep depletion, impurity profiles.

gate controlled diodes has been discussed by Grove and Fitzgerald (7). The purpose of this paper is to examine in detail the technique and possible errors and limitations of using deeply depleted MOS devices for impurity profiles.

This method has the advantage of the fact that static measurements can be made for a wide range of temperatures because the minority carrier depletion state is maintained as long as the depletion potential "well" produced by the reverse voltage, V_R , applied to the drain is "deeper" than that which can be produced by the gate bias. However, if the diode "well" potential, V_R , is "shallower," minority carriers will fill the gate bias well up to the bottom of the diode well. The maximum attainable depletion distance in this instance is therefore determined by the diode bias and for a uniform doping profile is given by (7)

$$X_{VR} \cong (2\epsilon_0 K_s V_R / qN)^{1/2} \quad [1]$$

Resultant $N(X)$ profiles for gate voltages which could produce "deeper" depletion wells than the adjacent diode well will therefore be incorrect. The surface potential produced by the MOS gate voltage on uniformly doped samples can be found from Eq. [5] below. For lightly doped samples ($N \leq 4 \times 10^{15}/\text{cm}^3$) and gate oxides about 1000\AA thick the deep depletion surface potentials are only a few volts less than the applied gate voltages.

Within the limitations discussed above, and subsequently within this paper, the impurity profile $N(X)$ can be obtained by using the familiar equations (2)

$$N = 2 \left/ \left(q\epsilon_0 K_s \frac{d}{dV} \left(\frac{1}{C^2} \right) \right) \right. \quad [2]$$

with X being obtained from

$$C_s = C_o C / (C_o - C) = \left(\frac{\epsilon_0 K_s}{X} \right) A \quad [3]$$

$$C_o = (\epsilon_0 K_{ox} / X_{ox}) A \quad [4]$$

where C is the measured capacitance, C_s the semiconductor space charge capacitance, C_o the oxide capacitance, X the depletion distance into the silicon, X_{ox} the oxide thickness, K_s and K_{ox} the dielectric constants of silicon and silicon dioxide, respectively, ϵ_0 the free space permittivity, and A the metal gate area. N is determined by finding ΔV and $\Delta(1/C^2)$ from the $C(V)$ data using a series of point-to-point evaluations. C_o is the measured majority carrier surface accumulation capacity. Combining C_o with the measurement of C in Eq. [3] gives X .

Errors in $N(X)$ caused by interface state densities of $1 \times 10^{12} \text{ cm}^{-2}$ have been examined previously (1, 6). Errors caused by interface states decrease for increasing measurement frequencies. However, for H_2 annealed samples, interface state densities are $\leq 10^{10}/\text{cm}^2$ and in these instances MOS profile measurements are valid for frequencies $\geq 10^6 \text{ Hz}$.

Analytical Study

Figures 1 through 4 represent analytical studies of the $N(X)$ analysis using computer simulated $C(V)$ sample data. This was done in order to test the data processing program and to examine the validity of the system under a wide variety of circumstances; theoretical "data" were calculated using equations given in the Appendix of Ref. (8). In all cases, a model using uniform phosphorous doping was assumed.

The salient feature of all these curves is the rapid rise in apparent $N(X)$ caused by majority carrier accumulation leading to the eventual flattening of the $C(V)$ curve as C_o is approached. This basic limitation of the MOS analysis is caused by the fact that the method is sensitive only to the rate of change of C vs. V and as such cannot determine the sign or nature of the space charge. This limitation, called the extrinsic Debye length limit, has been previously discussed in

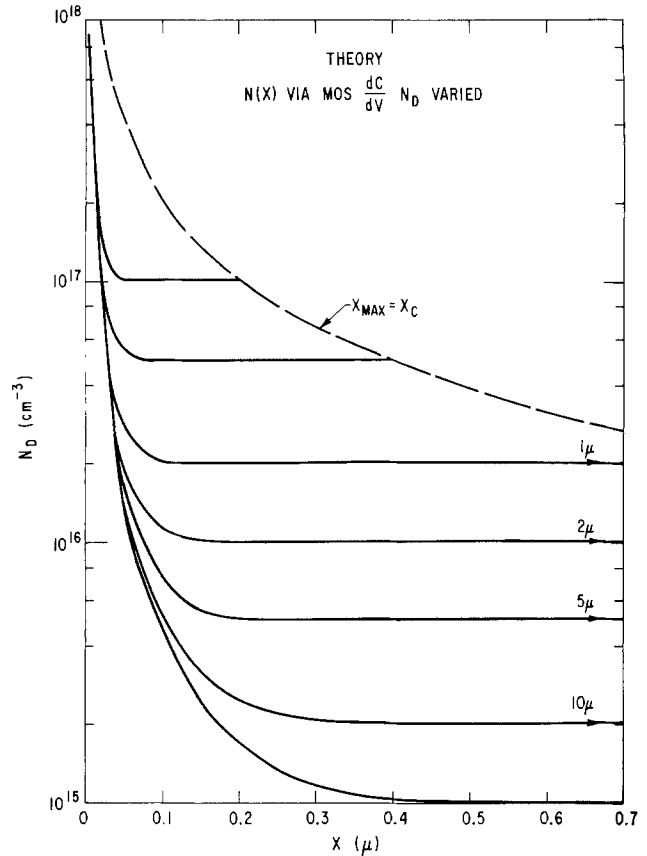


Fig. 1. Analytical $N(X)$ for uniform profiles for various donor concentrations. $X = X_c$ curve is limited by critical breakdown field $E_c = 3 \times 10^5 \text{ V/cm}$.

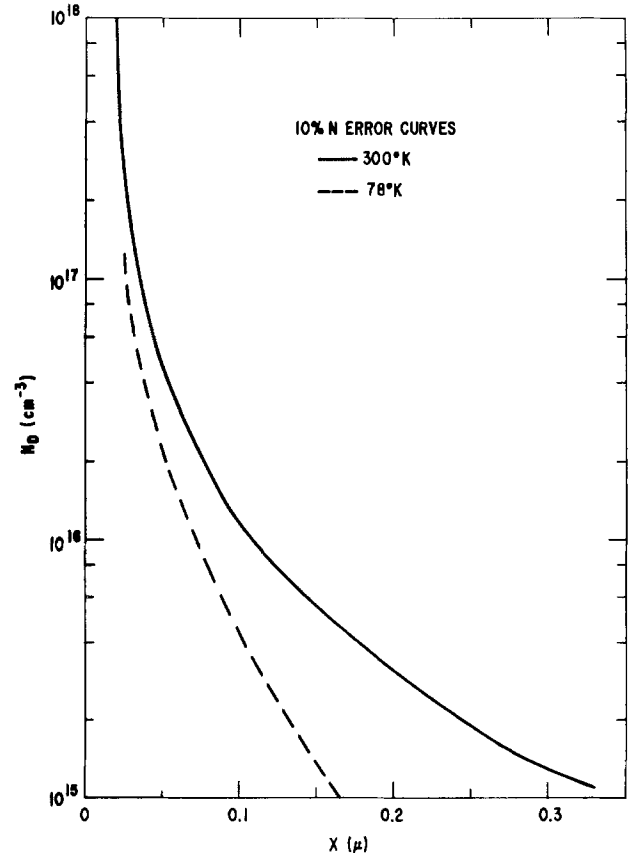


Fig. 2. 10% N error line blocking off valid analytical region to right of error line.

Ref. (1) and (3). Experimental errors caused by fixed value stray capacitances and errors in C_o are also con-

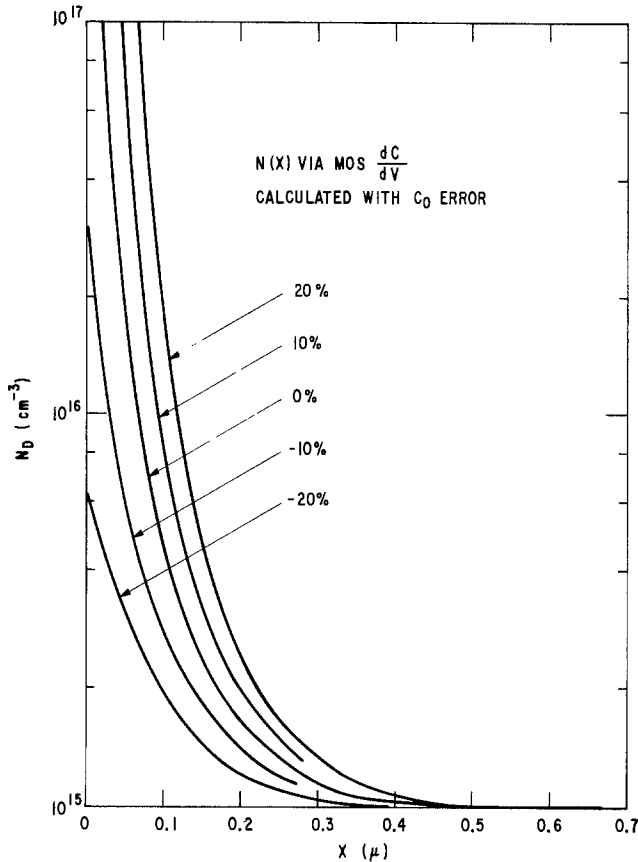


Fig. 3. $N(X)$ lines showing effects of errors in oxide capacitance C_0 .

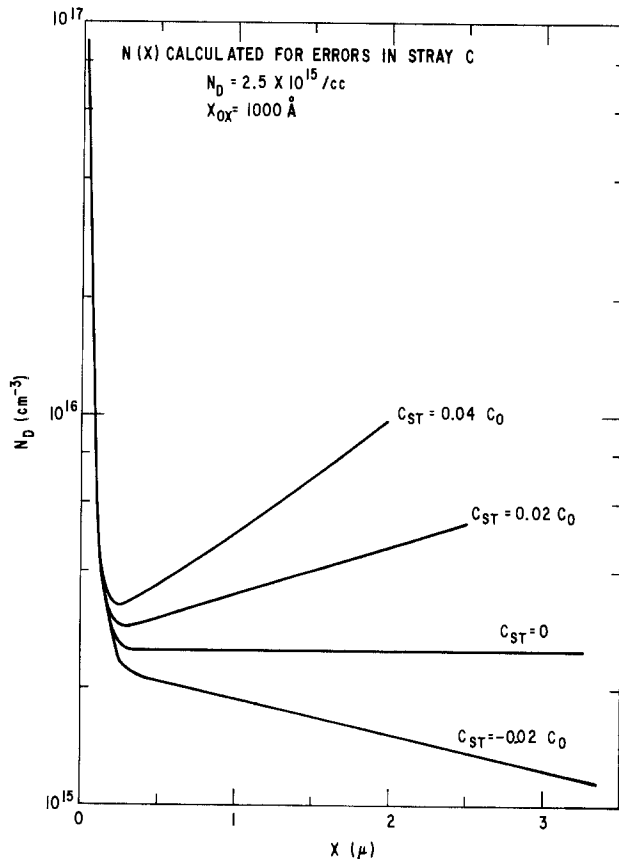


Fig. 4. $N(X)$ lines showing effects of errors in estimated stray capacitance, C_{ST} .

any cable capacitances and MOS chip capacitances which are not part of the active thin oxide gate region.

The $C(V)$ equations for MOS structures on uniformly doped n-type Si from accumulation through deep depletion (no minority carrier inversion) are given by

$$V(U_S) = (kT/q)(U_S - U_B) - Q_S/C_0 + \phi_{MS} \quad [5]$$

$$C_S(U_S) = \frac{q}{E_S} [A_c T^{3/2} F_{1/2}(U_S - E_G) - N_D(1 + 2 \exp(U_S + E_D - E_G))^{-1}] \quad [6]$$

where the surface field E_S is given by

$$E_S^2 = \frac{8\pi}{\epsilon_0 K_s} kT \left[A_c T^{3/2} \{ F_{3/2}(U_S - E_G) - F_{3/2}(U_B - E_G) \} + N_D \ln \left| \frac{2 + \exp(E_G - E_D - U_S)}{2 + \exp(E_G - E_D - U_B)} \right| \right] \quad [7]$$

These equations have been described in detail previously (8). U_S is the surface potential in kT units. The $N(X)$ analysis on these analytical $C(V)$ curves was carried out by the computer using Eq. [2] and [3].

The limitations caused by the surface accumulation of electrons can be estimated from Fig. 1 where the results for seven different uniform densities from 10^{15} to $10^{17}/\text{cm}^3$ are given. Clearly the method is valid only for depleted surfaces and since the depletion width depends on N_D , the region of validity can be blocked off with an error curve. A 10% N_D error curve generated by picking points at approximate X values where the measured $N(X)$ would be 10% above the flat profile concentration is shown in Fig. 2. $N(X)$ data to the right of this line have an accuracy better than 10%. Figure 2 shows that accurate profile information can be obtained closer to the surface of lightly doped samples by cooling the samples to 78°K.

Errors in C_0 can occur if, for instance, the gate is diode protected and C_0 has to be estimated from the shape of the experimental $C(V)$ curve near $V = 0$. In this instance, C was set as $C = (C_0 \pm \% C_0) C_S / ((C_0 \pm \% C_0) + C_S)$ and the analytical curves, Fig. 3, show that the errors in C_0 have to be relatively large to produce noticeable effects for small X . Errors in C_0 shift X values but do not change N because knowledge of N is independent of oxide thickness as seen in Eq. [2].

The errors introduced by unknown stray capacitances, however, are surprisingly large and have a large influence when the sample is in deep depletion and the total C is small. In this case, the error curves were calculated at a fixed donor density of $2.5 \times 10^{15}/\text{cm}^3$ assuming

$$C = \left(\frac{C_0 C_S}{C_0 + C_S} \right) \pm C_{ST}$$

where the positive and negative signs in front of the stray capacitance, C_{ST} , represent an over- and under-estimation of the stray capacitance, respectively. Experimentally the stray must be subtracted to obtain an errorless $N(X)$ analysis as represented by the curve labeled $C_{ST} = 0$ in Fig. 4. Small percentage errors in any assumed stray can cause considerable errors in $N(X)$ profiles as indicated. The best way to check on the estimated stray is to experimentally determine $N(X)$ for bulk samples where the profile is known to be flat. Once this is done, samples with unknown profiles can be measured using the same FET device geometry.

Experimental Techniques

Test samples.—P-channel MOSFET structures with minimum size source and drain diffusions were fabricated using the p-channel Mo gate (RMOS) technique described previously (9) using phosphorous doped 4

sidered below. Stray capacitances are all fixed value capacitances in parallel with the MOS gate caused by

ohm-cm bulk Si or approximately 2 ohm-cm epitaxial Si on (111) surfaces. Field oxides, 1.4μ thick, were grown in steam, and gate oxides, 1000\AA thick, were grown in dry oxygen. The processing sequence will not be described in detail. H_2 annealing using 10% H_2 in N_2 for 1 hr at 500°C was carried out near the end of the process to reduce the fast interface state density to $<10^{10}/\text{cm}^2$. Ti-Au was evaporated on the backside of the wafers to ensure a low resistance contact. Arsenic ion implants at dose levels of approximately $1 \times 10^{12}/\text{cm}^2$ using implant energies of 300 keV were included in some samples at a processing stage between gate oxidation and Mo gate deposition. Ion implanted Al gate MOSFET's with large area diffused source and drain junctions have also been successfully studied.

All the planar junctions of the devices studied here were about 1μ deep with resultant reverse breakdowns of about -30V .

The junctions of the MOSFET device were connected to a large negative voltage (approximately -30V) and gate capacitance data vs. gate voltage were obtained by applying a slow ramp voltage to the gate in conjunction with the a-c measurement frequency. This arrangement transforms the MOSFET into a surface depletion MOS gate controlled diode structure and the $C(V)$ curves are accordingly those of a deep depletion MOS structure.

Method I ($f = 1\text{ MHz}$).— $C(V)$ data were obtained using a Boonton Electronics Model 71A capacitance meter which operates at a frequency of 1 MHz. These data were logged using two digital voltmeters connected to an online data logging computer terminal. $N(X)$ was obtained using the dC^{-2}/dV equations and plotted on site using an X-Y recorder and digital point plotter. The experimental data were obtained using a simple probe station, and all equipmental stray capacitance was balanced out with the gate probe lifted. Any stray capacitance was, therefore, limited to that present in the chip caused by landing pads and Al runs over thick (approximately 1.4μ) field oxide.

All the results shown in Fig. 5-8 were obtained in this manner.

Method II ($f > 1\text{ MHz}$).—In order to verify the assumption that any small residual number of fast interface states in properly annealed samples does not introduce errors for a 1 MHz measurement frequency, a digital capacitance bridge capable of utilizing measurement frequencies $\cong 1\text{ MHz}$ was constructed. Be-

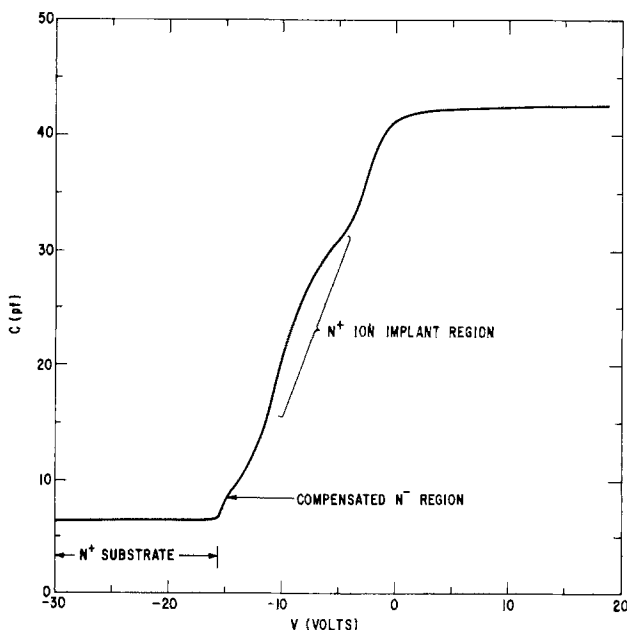


Fig. 5. Illustrative deep depletion $C(V)$ curve

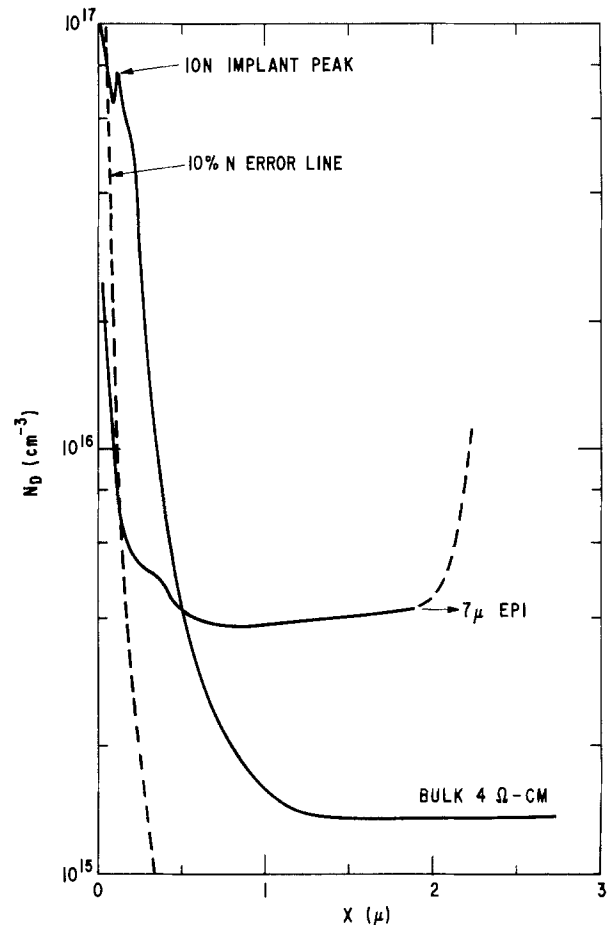


Fig. 6. $N(X)$ for bulk 4 ohm-cm ion implanted sample and $N(X)$ for lower resistivity epitaxial sample with ion implant. The sudden upward swing in the curve at large X is an indication of incomplete minority carrier removal occurring whenever the diode reverse bias is too small.

cause of the higher frequencies, the profiling was done utilizing packaged devices in order to eliminate lead inductance and ground loop effects. Careful measurements of stray capacitances contributed by the package, instrument probes, and test jig were carried out using empty packages. This stray capacitance was subtracted from each capacitance measurement through the use of an appropriate computer program which subsequently reduced the corrected $C(V)$ data to $N(X)$ data. Measurements at 1 and 10 MHz produced identical $N(X)$ profiles. Residual numbers of fast interface states are therefore deemed to be insignificant for 1 MHz profile measurements of properly annealed samples.

Device geometry.—Except for the expected parasitic effects discussed previously, device geometry did not appear to be a major factor. These effects were especially severe for the small Al gate FET's ($A = 6 \times 10^{-4}\text{ cm}^2$) which therefore required a stray capacitance subtraction as discussed in Method II above. Ideally the areas should be large ($A > 10^{-3}\text{ cm}^2$) and the junction gate overlap small. This was true of the self-aligned Mo gate structures ($A = 1.2 \times 10^{-3}\text{ cm}^2$) whose diffused junction regions were furthermore limited to a very small fraction of the gate's periphery.

Experimental Results

Some illustrative features of a specific ion implanted device constructed on a thin (approximately 2μ) epitaxial layer are illustrated in Fig. 5. Several features are significantly different from the usual exponentially shaped depletion curve: the ion implant region is observed as a rather large bulge at moderate voltages and the presence of the N^+ substrate is observed at

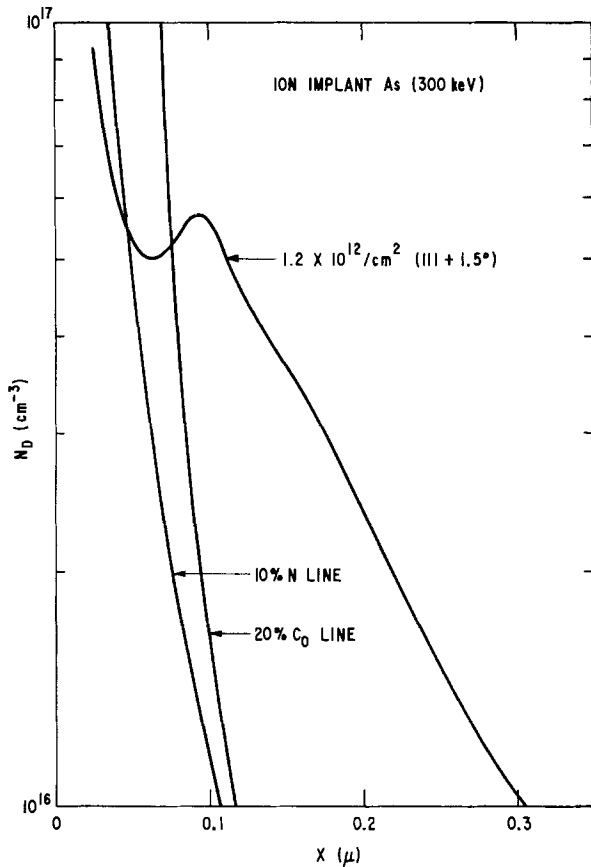


Fig. 7. As ion implant profile detail showing As ion implant peak and long tail.

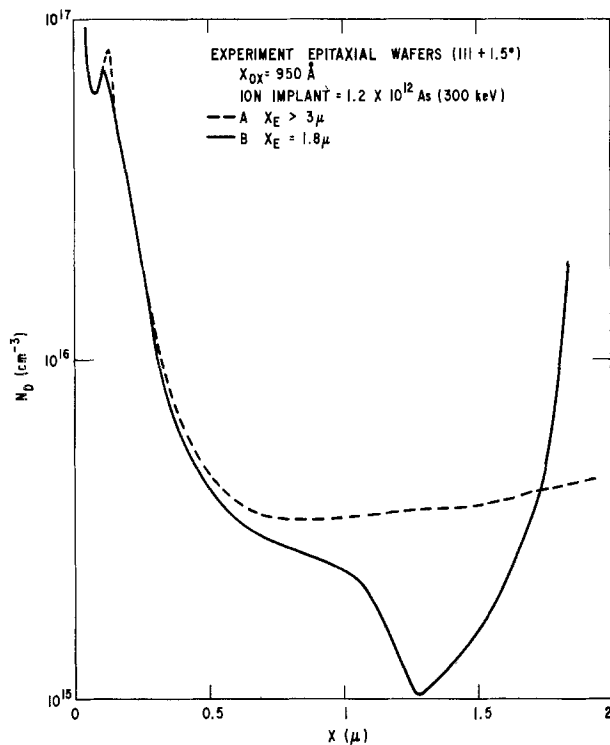


Fig. 8. $N(X)$ profiles for epitaxial layer samples. Profile B is for a complex sample whose $C(V)$ curve is given in Fig. 5. Profile shows ion implant peak, spurious high resistivity region at substrate interface, and epitaxial layer thickness. X_E means epitaxial layer thickness.

the highest voltages by the region where capacitance is independent of voltage. This particular sample contained a high resistivity region at the interface between the epitaxial layer and the N^+ substrate.

As indicated previously, the stray capacitance for the masks must be estimated with considerable accuracy and should be checked using samples where the profile and resistivity are known to be flat. A $N_D(X)$ profile of a 4 ohm-cm bulk sample is shown in Fig. 6. The measured donor concentration of $1.35 \times 10^{15}/\text{cm}^3$ for $1.5 \leq x \leq 3 \mu$ is within 10% of the bulk carrier concentration obtained from four-point probe measurements. The fact that this sample received a shallow As ion implant is unimportant for the calibration check of stray capacitance errors since these errors are maximum at large depletion distances.

The data for the lower resistivity epitaxial sample in Fig. 6 indicate an important feature of this profiling technique. As discussed earlier, data taken when the surface field produced by the gate voltage approaches and exceeds that produced by the diode bias give anomalous results because the surface is not then completely depleted. This feature is observed in a flattening out of the $C(V)$ curve at high gate voltages which produces the apparent rapid increase in $N(X)$. In some cases like this it was found that the maximum depth of accurate profiling was limited by the reverse breakdown voltage of the diode rather than by the critical field condition shown in Fig. 1. Nevertheless, this sample shows the phosphorous surface pileup produced by the field and gate oxidation sequences as indicated by the data for $x \leq 0.5 \mu$.

Figure 7 shows a more detailed As ion implant profile on a slightly off axis (111) surface. The concentration peak correlates well with the curves given by Gibbons (10) for an implant energy of 300 keV. The long As tail or shoulder is also apparent and has been described by others using the incremental sheet resistance technique or neutron activation analysis (11). The simplicity of our technique makes possible rapid analysis of such effects and provides useful information even though accurate analysis for very small X is limited by the N error line. It is also interesting to note that the As dose shown here is one order of magnitude less than the lowest dose in Ref. (11).

Figures 8 and 9 correlate the information obtained from our profiling technique and spreading resistance profiles of the same samples.¹ The electrical measurements on sample A indicate a nearly flat profile beyond the ion implant tail to a depth $> 2 \mu$ as verified by spreading resistance profiling. Sample B whose $C(V)$ curve is shown in Fig. 5 indicates an anomalous dip in donor concentration between 0.5 and 1.5μ . This was verified by the spreading resistance profile of this sample as shown in Fig. 9. It is interesting to note that before processing, the spreading resistance data on both these epitaxial layers indicated a flat profile. The anomalous dip for sample B was caused by boron acceptor level compensation produced by an outdiffusion of boron from the 0.01 ohm-cm Sb doped substrate during high temperature processing. Higher than normal B concentrations in these substrates were verified by the substrate crystal vendor. This identical B compensation phenomenon in n-type epitaxial layers grown on n-type substrates has been studied analytically by Langer and Goldstein (12). The information presented in Fig. 8 and 9 appears to represent the first published experimental observation of this effect.

Sample A of Fig. 8 shows a slight upward tilt of a supposedly flat profile. As indicated in Fig. 4 this usually is an indication of unaccounted for stray capacitances which adversely affect the shape of the curve for large depletion distances, because the depletion capacitances are becoming increasingly small for these samples. Larger samples or slight adjustments in the stray estimates using Method II are required for high accuracy in this region. This was carried out as shown in Fig. 10 and was compared with the spreading resistance profile data of this wafer. The spreading re-

¹ All spreading resistance profiles were obtained using the Automatic Spreading Resistance Probe Model ASR-100 manufactured by Solid State Measurements Incorporated.

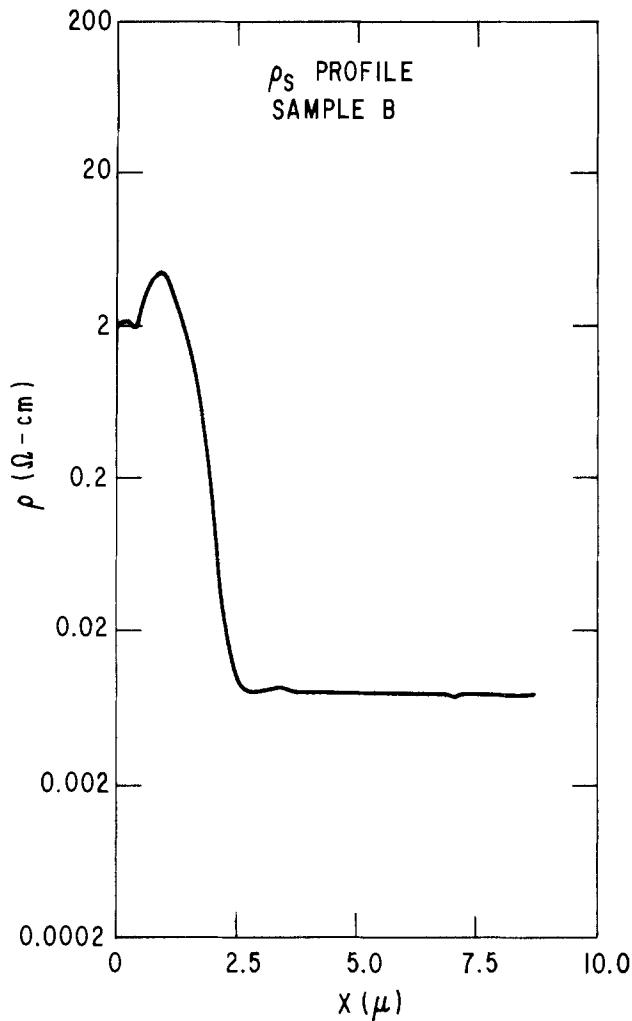


Fig. 9. Spreading resistance profile of sample verifying $N(X)$ results in Fig. 8 on sample B.

sistance data indicated a uniform epitaxial base concentration of $\leq 2.5 \times 10^{15}/\text{cm}^3$ ($\rho \geq 2$ ohm-cm) whereas the $N(X)$ profile in Fig. 10 indicates a base concentration of $3.5 \times 10^{15}/\text{cm}^3$ corresponding to a resistivity of 1.4 ohm-cm. The calibration of the automatic spreading resistance probe was subsequently found to be in error (13).

Discussion and Summary

An impurity profiling technique using minority carrier depleted MOS samples has been examined analytically and experimentally.

Minority carrier removal was accomplished by reverse biasing adjacent junction diodes. The resultant deep depletion $C(V)$ curves are easily analyzed to give $N(X)$. One advantage of the method is that simple $C(V)$ equipment employing slow voltage ramps can be used, since the deeply depleted state is maintained as long as the diode potential is larger than the surface potential produced by the MOS gate bias. This feature makes static measurements of the semiconductor space charge capacitance possible over a wide range of temperatures, since sample lifetime and minority carrier generation rates are unimportant.

Furthermore, it has been shown, as expected, that fast interface state errors are unimportant at measurement frequencies of 1-10 MHz in properly annealed samples, because no dispersive effects were observed over this range of frequencies.

The extrinsic Debye length limitation caused by majority carrier accumulation is shown by error plots as a function of concentration and temperature giving the minimum depth at which the technique is accurate. Profiling errors caused by stray capacitance effects and

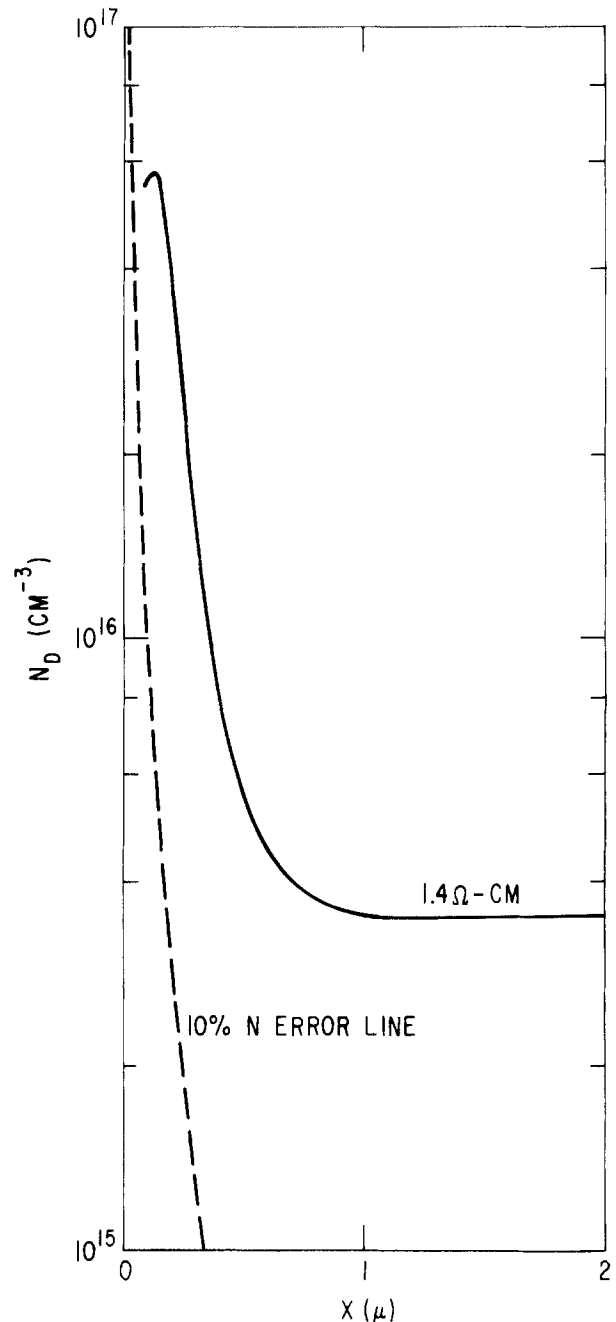


Fig. 10. Profile of sample using Method II in which small corrections for unknown stray were carried out.

errors in the MOS oxide capacitance have been detailed.

Experimental profiles obtained on different types of samples with ion implanted surfaces and using bulk and epitaxial wafers on compensated substrates have been presented showing the easy usefulness of the technique. The limitation in maximum depth caused by an insufficiently large drain bias, which results in minority carrier inversion at large gate voltages, has been pointed out. Some of the experimental results have been critically compared with spreading resistance profile measurements. The spreading resistance measurement is well suited to deeper profiles at even heavier impurity concentrations, whereas the major strength of this MOS profiling technique is its ability to measure profiles at shallower depths. The two methods, therefore, are good complements to one another especially when they have overlapping ranges of validity.

It is obvious that the MOS profiling technique presented here can be widely used for the study of diffusion phenomena, epitaxial layers, and ion implant pro-

files. Furthermore, it is a useful method to use for the measurement and control of the impurity profiles called for by certain types of MOS charge transfer devices.

Acknowledgments

The authors wish to thank L. F. Cordes for the use of his computer program for Method I and G. J. Charney for help with sample fabrication. M. Garfinkel's suggestions were most helpful, especially in indicating the proper use of the $C(V)$ equations for MOS $N(X)$ profiles. The ion implanted Al gate MOSFET's were supplied by D. Meyer.

Manuscript submitted April 8, 1974; revised manuscript received Aug. 22, 1974. This was Paper 270 RNP presented at the New York, New York, Meeting of the Society, Oct. 13-17, 1974.

Any discussion of this paper will appear in a Discussion Section to be published in the December 1975 JOURNAL. All discussions for the December 1975 Discussion Section should be submitted by Aug. 1, 1975.

Publication costs of this article were partially assisted by General Electric Company.

REFERENCES

1. E. H. Nicollian, M. H. Hanes, and J. R. Brews, *IEEE Trans. Electron Devices*, **ED 20**, 380 (1973).
2. W. Van Gelder and E. H. Nicollian, *This Journal*, **118**, 138 (1971).
3. A. R. LeBlanc, D. D. Kleppinger, and J. P. Walsh, *ibid.*, **119**, 1068 (1972).
4. D. M. Brown, P. V. Gray, P. R. Kennicott, and D. K. Hartman, Paper 338 RNP presented at Electrochemical Society Meeting, New York, N.Y., May 4-9, 1969; General Electric Report No. 69-C-168 (1969).
5. L. P. Adda and J. T. Clemens, Paper 52 presented at Electrochemical Society Meeting, San Francisco, Calif., May 12-17, 1974.
6. J. R. Brews, *J. Appl. Phys.*, **44**, 3228 (1973).
7. A. S. Grove and D. J. Fitzgerald, *Solid State Electron.*, **9**, 783 (1966).
8. D. M. Brown and P. V. Gray, *This Journal*, **115**, 760 (1968).
9. D. M. Brown, W. R. Cady, J. W. Sprague, and P. J. Salvagni, *IEEE Trans. Electron Devices*, **ED 18**, 931 (1971).
10. J. F. Gibbons, *IEEE Proc.*, **56**, 295 (1968).
11. F. N. Schwettman, *Appl. Phys. Letters*, **22**, 570 (1973).
12. P. H. Langer and J. I. Goldstein, *This Journal*, **121**, 563 (1974).
13. E. A. Taft, Private communication.

Electron-Beam Evaporated Al_2O_3 on Si

Philip C. Munro¹ and H. W. Thompson, Jr.

Purdue University, West Lafayette, Indiana 47907

ABSTRACT

Al_2O_3 is electron-beam evaporated onto n- and p-type silicon in an ion-pumped, high-vacuum environment. Fabrication parameters of substrate temperature, evaporation rate, and O_2 partial pressure are varied for optimization. The deposited films are annealed in several gas/temperature environment combinations for varying times. The resulting MOS structures are evaluated and an optimum process schedule is obtained. The deposited Al_2O_3 films have a relative dielectric constant of 8.0, a refractive index of 1.61, and breakdown field strengths exceeding 3×10^6 V/cm. Deposition rates of 100-500 Å/min onto substrates at 100°-200°C in an O_2 ambient of 2×10^{-5} Torr, followed by a 5-20 min anneal in N_2 at 550°C yield optimum insulator/interface characteristics. MOS devices so fabricated have surface-state densities in low 10^{11} states/cm²-eV range, hysteresis in the C-V characteristic of 0.1-0.2V, and flatband voltages in the range of $\pm 1V$.

Thin films of Al_2O_3 are being investigated for use with Si and other semiconductors in device and surface passivation applications. When compared to SiO_2 , Al_2O_3 has several advantages: (i) it has a higher density and therefore gives better hermetic sealing; (ii) it has shown superior radiation resistance (1, 2); (iii) its dielectric constant is twice that of SiO_2 ; (iv) it has shown better resistance to ion motion; and (v) p-type semiconductor surfaces (positive flatband voltage) have been obtained.

Films of Al_2O_3 have been deposited by pyrolysis (3, 4), plasma anodization (2, 5), RF sputtering (6, 7), and reactive sputtering (8, 9). Although several reports of vacuum-evaporated Al_2O_3 on Si have been published (10-14), no attempt to optimize the evaporation process or postdeposition anneals has been reported. It has been suggested that an added O_2 ambient during evaporation of Al_2O_3 improves the stoichiometry of the resulting films (13). This work provides data from Al- Al_2O_3 -Si samples fabricated by E-beam evaporation of Al_2O_3 in an O_2 ambient onto Si substrates from which such an optimization can be made. High frequency capacitance-voltage (CV) and quasistatic cur-

rent-voltage (IV) data are used to obtain insulator and insulator-semiconductor interface electrical characteristics including surface-state density, N_{ss} , flatband voltage, V_{FB} , and hysteresis.

Sample Fabrication

Substrate preparation.—Ten to fifteen ohm-centimeters (111) p- and n-type Si were used. Substrates were ultrasonically rinsed in trichloroethylene, acetone, methyl alcohol, and DI water. After cleaning in hot sulfuric and nitric acids, they were rinsed in dilute hydrofluoric acid. [Further details of sample fabrication and testing are given elsewhere (16).]

Square chips, 200 mils on a side, were coated for evaporation process optimization; whole wafers were coated for anneal optimization.

Al_2O_3 deposition.—The 99.998% pure Al_2O_3 tablets used for vacuum evaporation were obtained from Electronic Space Products, Incorporated. They were 10 mm in diameter and 7 mm thick and were contained in a water-cooled copper hearth during evaporation. Electron-beam spot sizes of about 5 mm were used during evaporations. O_2 was injected into the vacuum system at the base of a 5½ in. high by 2¾ in. diameter stainless steel chimney which was used to confine the evap-

¹ Present address: Youngstown State University, Youngstown, Ohio 44500.

Key words: Al_2O_3 , E-beam, MOS devices, oxide anneal, vacuum evaporation.

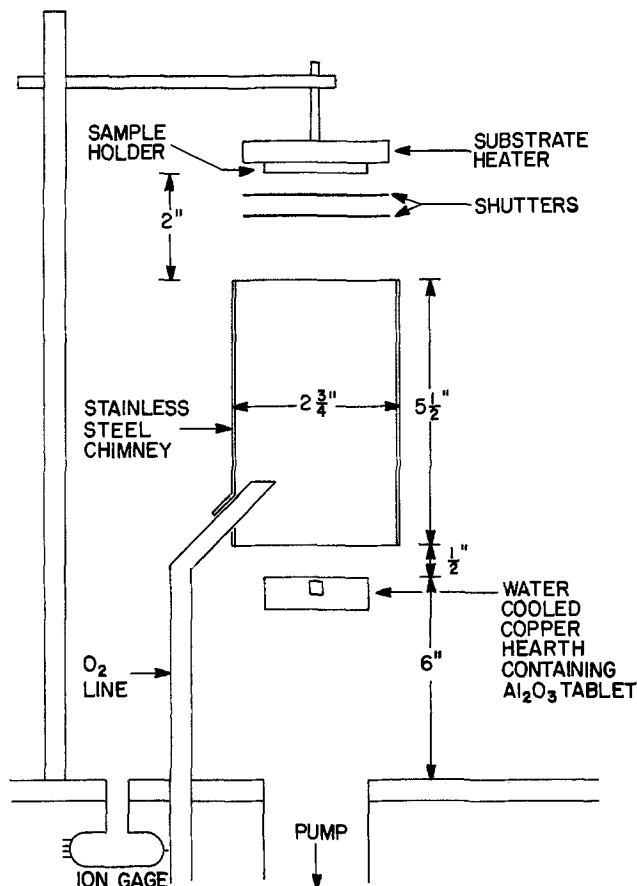


Fig. 1. Schematic layout of evaporation system

orant. System pressure was monitored at the base plate using an ion gauge. Figure 1 gives a diagram of the system showing relative placement of the substrate and the ion gauge.

The evaporations were carried out in a vac-ion system which included titanium sublimation onto a liquid-nitrogen cooled surface. Roughing was accomplished with an oil-free mechanical pump followed by sorption pumping. A 90° deflection electron gun was used to heat and evaporate the Al_2O_3 . An automatic pressure controller, driven by the ion gauge unit, controlled the O_2 leak into the system. The source of O_2 was J. T. Baker Zero-Gas oxygen with a stated hydrocarbon content of less than 0.5 ppm. No attempt was made to dry or otherwise further purify the O_2 gas.

The parameters which may affect the nature of the deposited Al_2O_3 films are substrate temperature, source-to-substrate distance, deposition rate, E-beam accelerating voltage, and system pressure. Two of these parameters were fixed while the other three were purposely varied.

The E-beam accelerating voltage was held essentially constant near 5.5 kV except for minor changes needed to obtain the required E-gun power variation. Source-to-substrate distance was set at 8 in. At this distance, deposition rates as low as 100-150 Å/min were possible.

The three deposition parameters varied were (i) system pressure, which was varied upward from the attainable base pressure to a maximum of 2×10^{-5} Torr with the controlled O_2 leak; (ii) substrate temperature, which was varied upward from room temperature with a resistive heater; and (iii) deposition rate, which was varied by changing the E-beam power.

The optimum deposition parameters were used to obtain Al_2O_3 -coated wafers for the study of postdeposition anneals. The significant anneal parameters are temperature, time, and ambient gas. Temperatures up to 800°C, times up to several hours, and N_2 , O_2 , and H_2 ambient gases were tested.

For the evaporation process study four pairs of n- and p-type Si chips were prepared simultaneously and then coated during a single vacuum system cycle. Each pair was coated separately by appropriately positioning two shutters.

For the anneal study, single wafers were coated and then scribed and broken into individual chips which were given different anneals.

Postdeposition processing.—Ohmic contacts consisted of plated electroless Ni for the n-type Si chips and evaporated Al for the p-type Si chips. The chips used for the evaporation optimization study were annealed for 5 min at 580°C in N_2 . This anneal also produced the Al-Si alloy necessary for the p-type Si ohmic contacts. After annealing, circular aluminum gate electrodes about 7 mils in diameter were evaporated through Cu-Be dot masks onto the Al_2O_3 film in a small diffusion pumped vacuum system. The samples were not annealed after the gate electrode deposition.

CV Measurements for Process Optimizations

The numerous high-frequency CV measurements required to evaluate the results were obtained with a semiautomatic measurement system which included a Boonton 71A Capacitance Meter, a triangular-wave generator (15), and an XY recorder. Where greater accuracy was required for detailed surface-state analyses, or where higher signal frequencies were desired, point-by-point measurements were obtained with a Boonton 33A Admittance Bridge. Semiautomatic sweep-voltage amplitudes were 8-10V peak-to-peak and the CV curves were recorded beginning at accumulation bias with typical sweep rates of 100-200 mV/sec. Three or more different gate electrodes were probed on each chip. A typical CV curve is shown in Fig. 2.

CV slope was measured graphically at flatband capacitance and was normalized with respect to accumulation capacitance (approximately equal to C_i). This normalization removed the effects of differences in electrode areas and small differences in insulator thicknesses. The normalized slope is expressed algebraically as $1/C_i \cdot dC_g/dV_g$. If one writes $C = C_g/C_i$ then the relation between CV slope and surface-state density in states/cm²-eV at flatband bias can be seen to be (17)

$$N_{ss} = \frac{C_i}{Aq} \left(\frac{q(1-C)C}{3kT \partial C / \partial V_g} - \frac{1}{1-C} \right) \Bigg|_{C_g = C_{FB}}$$

V_{FB} is the gate voltage at flatband capacitance and was measured on the more negative leg of a complete

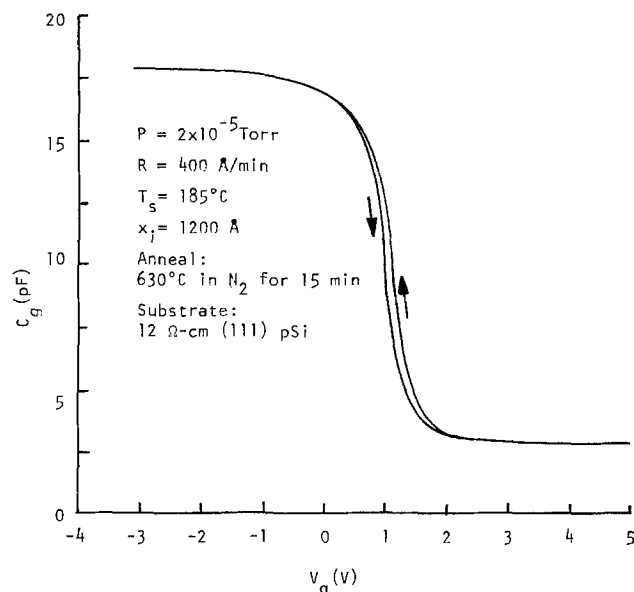


Fig. 2. A typical 1 MHz CV curve obtained with the semiautomatic measurement system.

CV curve for both n- and p-type Si samples. The ideal values of $V_{\text{FB}} = \frac{1}{q} \phi_{\text{ms}}$ are -0.05V for the n-type Si and -0.65V for the p-type Si samples. These values are calculated using an electron affinity of 4.0 eV for Si, work function of 4.2 eV for Al, and the appropriate fermi level positions for the Si used.

Hysteresis is the voltage difference between the two legs of a complete CV curve and was measured at flat-band capacitance.

Insulator Characteristics

The appearance of the deposited Al_2O_3 films was clear and of a color appropriate to the film thickness and refractive index. Only very slight nonuniformities in color were ever detected across a sample surface, and then only on large wafers with films of at least 3000\AA thickness.

No cracking or peeling occurred on any of the samples fabricated, even for film thicknesses to 6000\AA . The Al_2O_3 films showed no tendency to flake or peel away from the Si either before or after postdeposition anneals. Coated wafers of Si could be scribed on the coated surface with a diamond scribe and then broken into chips with no damage to the Al_2O_3 layer away from the scribe line. It was also observed that individual MIS capacitors which were destroyed by exceeding their breakdown field strengths had only local damage and no propagation of insulator damage away from the particular capacitor in question. Insulator breakdown field strength exceeded $3 \times 10^6\text{ V/cm}$.

Several Si samples with 3000\AA depositions of Al_2O_3 were evaluated by ellipsometry (courtesy of Delco Electronics). From these measurements, the refractive index of the evaporated Al_2O_3 was found to be 1.61. Si samples with 3000\AA films of Al_2O_3 were also used to obtain approximate values of the relative dielectric constant, k_i . Values of $k_i \approx 8.0$ were obtained. Similar values were obtained on several samples, some with no postdeposition anneals and others with a 15 min, 560°C anneal in N_2 . A somewhat higher value of $k_i \approx 8.5$ was obtained on another sample which had an additional anneal at 800°C in N_2 . These results for k_i parallel a similar and more detailed study of refractive index made by Woulbourn (18) on evaporated Al_2O_3 .

Results

Deposition parameter variations.—The results of bell jar pressure variations are presented in Fig. 3. For these samples, the directions of hystereses were consistent with an Al_2O_3 -Si interface trapping mechanism. The hysteresis was clockwise for n-type Si chips and counterclockwise for p-type Si chips. In addition to the data of Fig. 3, it was also noted that flatband voltage, V_{FB} , and CV hysteresis were more dependent on sweep voltage amplitude and rate for samples fabricated at the lower O_2 partial pressures. In fact, for Al_2O_3 deposited with zero O_2 leak, the hysteresis was about equal to the peak-to-peak sweep voltage, and the CV curves were very distorted. The dependence of V_{FB} and hysteresis on sweep rate and amplitude decreased considerably as the O_2 partial pressure during Al_2O_3 deposition increased.

Though results obtained at one value of a variable, such as O_2 pressure, generally differed from the results at another value of that variable, data for the best samples, fabricated under optimum conditions, were remarkably consistent. In almost all cases, C-V data from sample-to-sample within a group varied by less than 0.1V . Similarly, on samples fabricated using the optimum procedures hysteresis and flatband voltage show virtually no dependence on sweep voltage magnitude or rate.

Figure 4 presents deposition rate data. The directions of hystereses were again consistent with charge trapping at the Al_2O_3 -Si interface.

Figure 5 presents substrate temperature data. It was noted that Al_2O_3 deposited on 25°C chips showed more

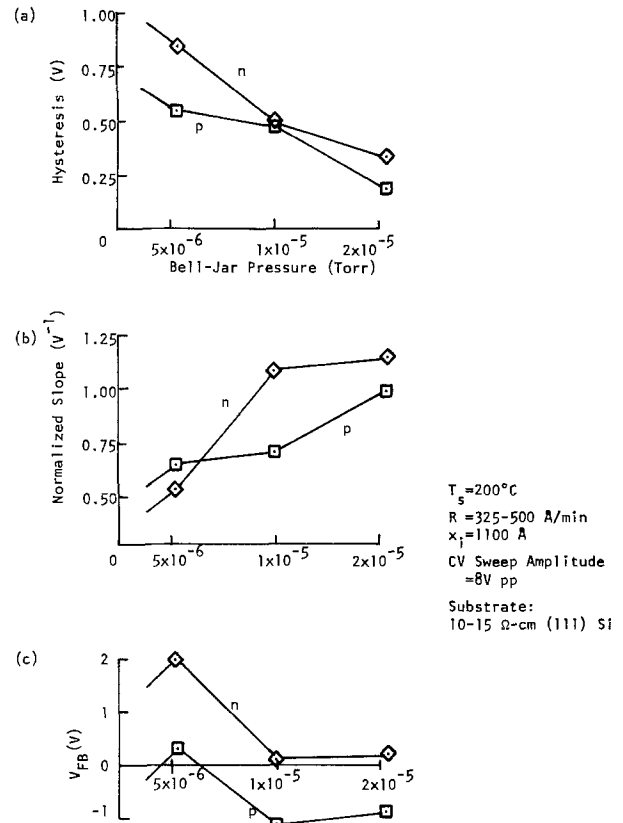


Fig. 3. CV results vs. the bell jar pressure during Al_2O_3 deposition on n- and p-type Si. The bell jar pressure was controlled with an O_2 leak.

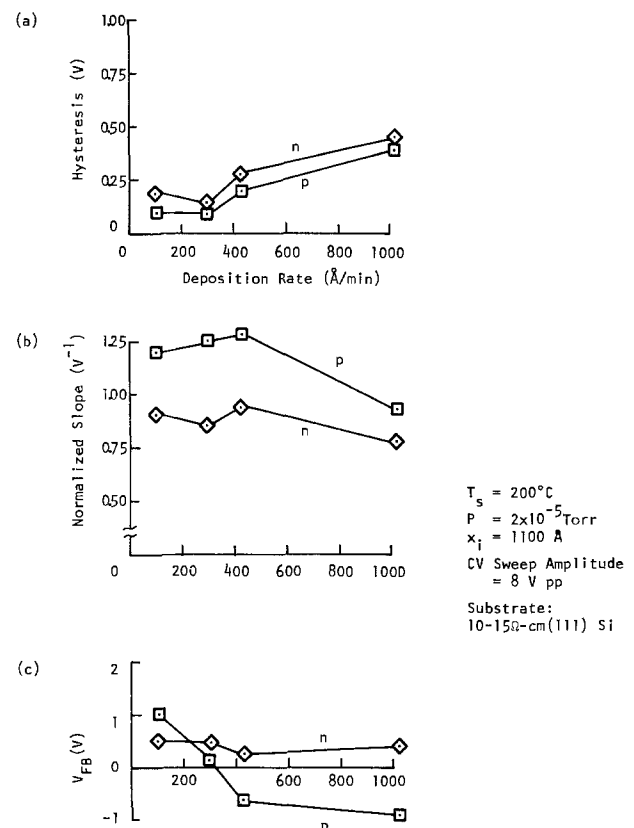


Fig. 4. CV results vs. the deposition rate during Al_2O_3 deposition on n- and p-type Si.

leakage and lower breakdown field strengths than those deposited at 100°C and higher. Except for the p-type Si chip coated at 25°C , directions of hystereses were consistent with charge trapping at the Al_2O_3 -Si interface.

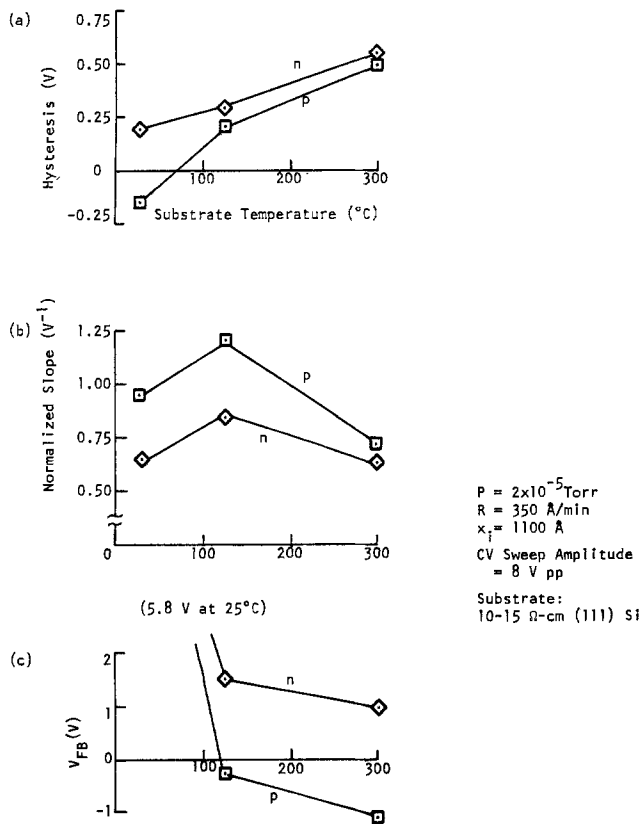


Fig. 5. CV results vs. the substrate temperature during Al_2O_3 deposition on n- and p-type Si.

Postdeposition anneal variations.—Different postdeposition anneals were tested on chips obtained from an Al_2O_3 -coated wafer. Several control chips were given no anneal whatever in order to establish the zero-time point in the anneal data. Most of the chips were annealed in N_2 for different times and at temperatures which are shown on the graphs of the resulting data (Fig. 6-8). They were processed in groups of four chips each. The chips within a given group were annealed at the same temperature but for different lengths of time.

Two chips were annealed in H_2 , and two in O_2 , at 550°C, and the results of those anneals are also shown

in the figures. Each H_2 anneal time includes 30 sec N_2 flushes at the beginning and end of the anneal.

Surface-state density.—Figure 9 shows surface-state density, N_{ss} , vs. energy measured from the center of the semiconductor bandgap for the sample whose semi-automatic 1 MHz CV curve is shown in Fig. 2. N_{ss} , as shown, was obtained from quasistatic IV measurements (19). An analysis of point-by-point high frequency CV measurements gave very similar results and is not shown here.

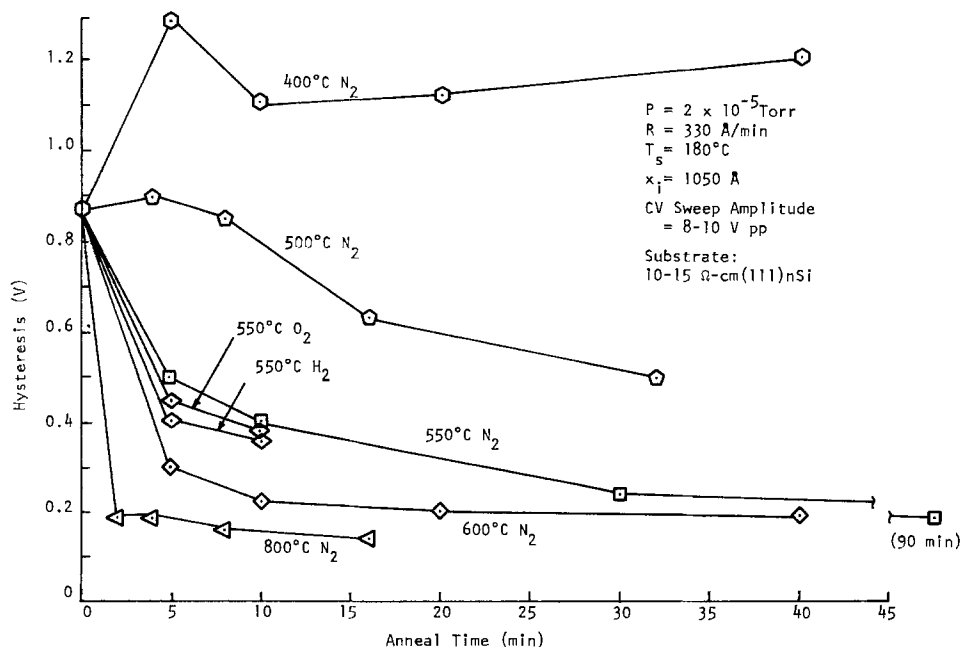
Discussion

The most favorable deposition and anneal parameters are chosen primarily to obtain minimum hysteresis, maximum normalized slope, and small or process controllable flatband voltage. In addition, deposition system constraints are considered, and observations of insulator leakage and breakdown influence the choice in some cases.

CV hysteresis is not always reported or denied in the literature, but it is a common occurrence where an insulating film is deposited, in contrast to those which are thermally grown (20). The mechanism of charge trapping and its relation to CV hysteresis has been discussed in the literature (21) and in particular for Al_2O_3 on Si (22, 23). Since the magnitude of hysteresis is an indication of trap density in the insulator (and of charge transport into and out of those traps), minimum hysteresis would be expected to coincide with the most favorable MIS conditions. It was also observed experimentally that smaller hysteresis coincided with a more stable surface potential to gate voltage relationship as the maximum sweep voltage magnitude was varied.

Deposition parameters.—Figure 3 shows the results of using different O_2 partial pressures during Al_2O_3 deposition. From these graphs and other similar experiments (24), it is evident that the higher values of bell jar pressure obtained with the controlled O_2 leak produce the most favorable CV results. Both hysteresis and slope have their best values at the highest bell jar pressure of 2×10^{-5} Torr, and the values of $|V_{FB}|$ are less than 1V at that pressure. Bell jar pressure was limited to 2×10^{-5} Torr due to increased difficulties when using an E-gun and a vac-ion system at much higher pressures. It should also be noted that the results in Fig. 3, and of previous experiments (24), show a similarity at the two higher pressures of 1 and 2×10^{-5} Torr, and therefore the improvement appears to saturate.

Fig. 6. CV hysteresis vs. post-deposition anneals.



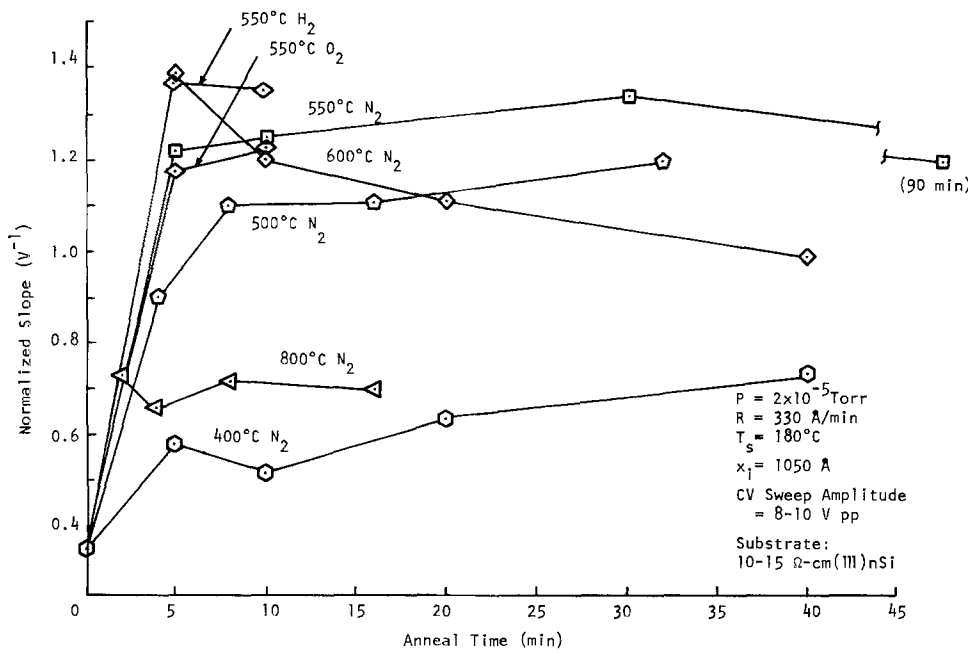


Fig. 7. CV normalized slope vs. postdeposition anneals.

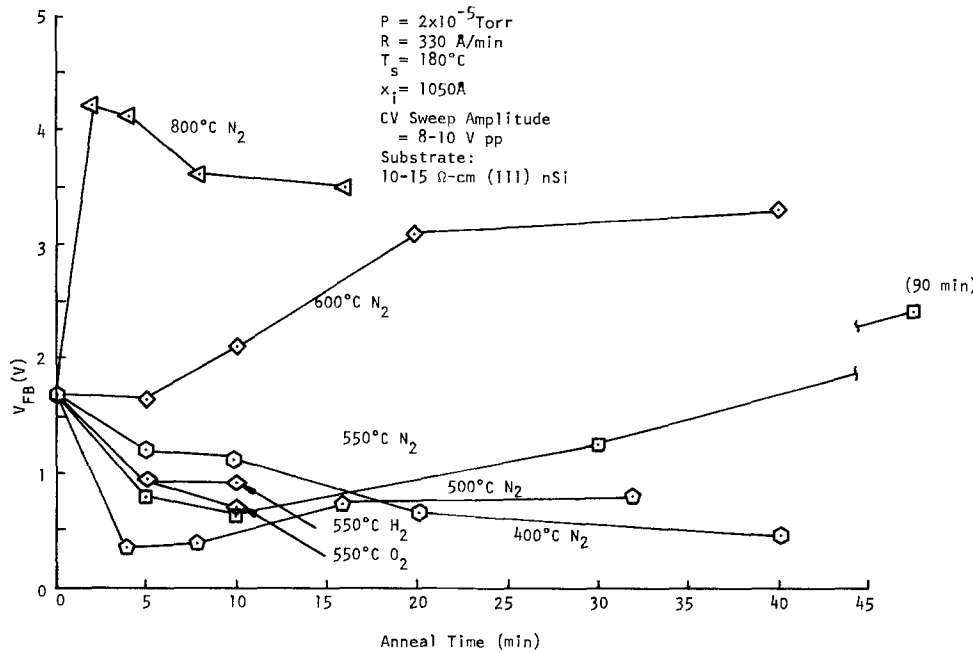


Fig. 8. CV flatband voltage vs. postdeposition anneals.

Figure 4 shows the results for different deposition rates and indicates that lower deposition rates give better results. Hysteresis of 0.1-0.2V is attainable and,

more importantly, is smallest at the lower deposition rates. Normalized slope is also at its preferred higher values at the lower rates. $|V_{FB}|$ is less than 1V at all of the deposition rates tested. Deposition rate is constrained at its lower values by the total time required to obtain a given film thickness. Because of this and the favorable results obtained at both of the two lowest rates tested, it is concluded that the preferred deposition rate is in the range of $300 \pm 200 \text{ \AA/min}$.

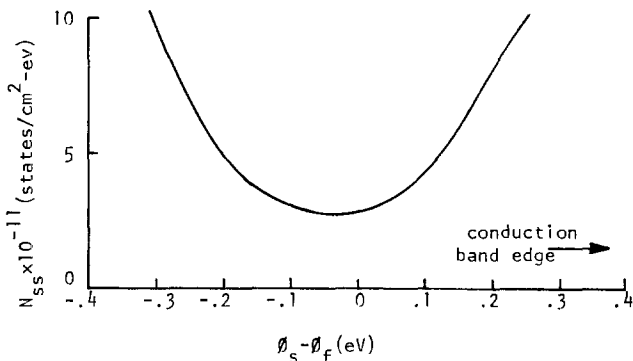


Fig. 9. Surface-state density vs. semiconductor bandgap energy measured from the center of the bandgap for the same sample whose 1 MHz CV curve is shown in Fig. 2.

Figure 5 gives results for different substrate temperatures. The increased leakage and much lower breakdown field strengths noted at 25°C may explain the "reverse" hysteresis obtained on the p-type Si chip. Such a reverse hysteresis could be due to charge injection from the metal gate, insulator polarization, or charge motion in the insulator. It is concluded that a substrate temperature in the range of 100°-200°C gives the best over-all results. CV slope is high, hysteresis low, and $|V_{FB}|$ is also low in that temperature range.

Summarizing these conclusions, the most favorable results with evaporated Al_2O_3 on Si are obtained by using an O_2 leak to hold the bell jar pressure near $2 \times$

10^{-5} Torr, a deposition rate of about 300 Å/min, and a substrate temperature near 150°C.

In addition to the conclusions drawn from each of the three Fig. 3-5, comparisons can also be made among the figures. These comparisons bring together the results of samples which did not have common predeposition, deposition, or postdeposition processings, in contrast to a set of samples whose results are given within each of the three figures. This comparison reveals excellent consistency in almost every case. Best values of hysteresis are in the 0.1-0.2V range with the p-type Si chips having slightly smaller hysteresis than the n-type Si chips. Best values of normalized slope are near 1.2/V for p-type Si chips and 0.9/V for n-type Si chips. Values of V_{FB} are near the range of -1 to +1V for chips which had the preferred deposition parameters. Furthermore, V_{FB} for p-type Si chips is more negative than for n-type Si chips (only Fig. 4c contains an exception), which is the proper tendency for the work function differences involved. However, the value of the difference is somewhat higher than the 0.6V work function difference expected for the doping levels used.

Postdeposition anneals.—Several researchers (18, 25-27) have suggested that amorphous Al_2O_3 transforms to polycrystalline Al_2O_3 at processing temperatures above 700°C. The decrease in slope and the increase in V_{FB} seen in Fig. 7 and 8, respectively, for anneals at 600° and 800°C may be related to such a transformation. The hysteresis, as shown in Fig. 6, continues to decrease as temperature is raised. This effect, too, is consistent with previous studies of Al_2O_3 reported in the literature. Hysteresis is apparently not affected by the amorphous-to-polycrystalline transformation.

From an examination of these figures, the optimum anneal appears to be 550°C for 5-20 min. In agreement with this research, Iwauchi and Tanaka (28) reported a favorable range of anneal temperatures (500°-600°C) above which surface-state densities increase. This may indicate a similarity between their O_2 -sputtered films and the present E-beam evaporated films. H_2 may offer some improvement over N_2 or O_2 , but the effect of the anneal appears to be due primarily to temperature and time, and not to the gas used. This suggests that evaporated Al_2O_3 may offer a good hermetic seal for semiconductor surfaces.

Summary and Conclusion

Al_2O_3 films produced by E-beam evaporation as described in this work have a relative dielectric constant of about 8.0, a refractive index of 1.61, and breakdown field strengths exceeding 3×10^6 V/cm. The Al_2O_3 films are clear, hard, and adherent. Coated samples can be scribed and broken with no propagation of damage in the Al_2O_3 coating. Optimum interface and insulator results require Al_2O_3 evaporation in an O_2 ambient with bell jar pressure near 2×10^{-5} Torr, a substrate temperature of 100°-200°C, and deposition rates below 500 Å/min. A postdeposition anneal of 5-20 min in N_2 at 550°C is also required. Such evaporations onto Si give interface-state densities in the low 10^{11} states/cm²-eV over the middle third of the Si energy bandgap, C-V hysteresis of 0.1-0.2V, and flatband voltages in the range of -1 to +1V.

It is concluded that Al_2O_3 deposited by E-beam evaporation as described is comparable to and therefore competitive with Al_2O_3 films produced by other methods such as pyrolysis or sputtering. Furthermore, vacuum deposition of Al_2O_3 is truly a low temperature process (100°-200°C, or in general any temperature) compared to pyrolytic depositions (400°C and up). The absence of gaseous ambients (except O_2) during vacuum depositions should result in purer Al_2O_3 films. The lack of excited plasmas near the sample and in the deposition system (cf. the case of sputtering) provides

a cleaner environment for the deposition and minimizes the possibility of semiconductor surface damage.

Acknowledgments

This work was supported in part by the National Science Foundation (MRL Program GH33574) and the Advanced Research Projects Agency (IDL Program DAHC-0213).

Manuscript submitted April 10, 1974; revised manuscript received Aug. 6, 1974.

Any discussion of this paper will appear in a Discussion Section to be published in the December 1975 JOURNAL. All discussions for the December 1975 Discussion Section should be submitted by Aug. 1, 1975.

Publication costs of this article were partially assisted by Purdue University.

LIST OF SYMBOLS

C_i	insulator capacitance
C_g	gate capacitance
V_g	gate voltage
ϕ_{ms}	metal-semiconductor work-function difference
T_s	substrate temperature during Al_2O_3 deposition
R	Al_2O_3 deposition rate
x_i	insulator (Al_2O_3) thickness
P	bell jar pressure during Al_2O_3 deposition

REFERENCES

- W. J. Dennehy, A. G. Holmes-Siedle, and K. H. Zaininger, *RCA Rev.*, **30**, 668 (1969).
- K. H. Zaininger and A. S. Waxman, *IEEE Trans. Electron. Devices*, **ED 16**, 333 (1969).
- M. T. Duffy and W. Kern, *RCA Rev.*, **31**, 754 (1970).
- L. H. Hall and W. C. Robinette, *This Journal*, **118**, 1624 (1971).
- F. B. Micheletti, P. E. Norris, and K. H. Zaininger, *RCA Eng.*, **16**, 48 (1970).
- C. A. T. Salama, *This Journal*, **117**, 913 (1970).
- P. K. Ajmera, M. A. Littlejohn, and J. R. Hauser, *ibid.*, **119**, 1421 (1972).
- T. Tanaka and S. Iwauchi, *Jap. J. Appl. Phys.*, **7**, 1420 (1968).
- T. Tanaka and S. Iwauchi, *ibid.*, **8**, 730 (1969).
- F. E. Cariou, V. A. Cajal, and M. M. Gajary, *IEEE Proc. Electron. Components Conf.*, **60** (1967).
- N. Mandani and K. G. Nichols, *J. Phys. D Appl. Phys.*, **3**, L7 (1970).
- R. A. Abbott and T. I. Kamins, *Solid State Electron.*, **13**, 565 (1970).
- D. Hoffman and D. Leibowitz, *J. Vacuum Sci. Technol.*, **8**, 107 (1971).
- C. C. Cheng, T. W. Kim, V. D. Deokar, and W. W. Granneman, *Bull. Am. Phys. Soc. Series*, **11**, **18**, 555 (1973).
- P. C. Munro and H. W. Thompson, Jr., *Rev. Sci. Instr.*, **43**, 1755 (1972).
- P. C. Munro, Ph.D. thesis, Purdue University, Dec. 1973.
- K. Lehovec, *Solid State Electron.*, **11**, 135 (1968).
- J. M. Woulbroun, Ph.D. thesis, Massachusetts Institute of Technology, Aug. 1963.
- M. Kuhn, *Solid State Electron.*, **13**, 873 (1970).
- D. R. Kerr, *8th Annual Proc. Reliability Phys.*, **1** (1970).
- F. P. Heiman and G. Warfield, *IEEE Trans. Electron Devices*, **ED 12**, 167 (1965).
- T. Tsujide, S. Nakanuma, and Y. Ikushima, *This Journal*, **117**, 703 (1970).
- S. Nakanuma, T. Tsujide, R. Igarashi, K. Onoda, T. Wada, and M. Nakagiri, *IEEE J. Solid-State Circuits*, **5**, 203 (1970).
- P. C. Munro, K. Sandgren, and H. W. Thompson, Jr., Presented at the Am. Vac. Soc. Great Lakes Regional Symposium, May 1971.
- M. T. Duffy and A. G. Revesz, *This Journal*, **117**, 372 (1970).
- K. Iida and T. Tsujide, *Jap. J. Appl. Phys.*, **11**, 840 (1972).
- J. A. Aboaf, *This Journal*, **114**, 948 (1967).
- S. Iwauchi and T. Tanaka, *Jap. J. Appl. Phys.*, **10**, 260 (1971).

Four-Point Probe Measurements on N-Type Silicon with Mercury Probes

P. J. Severin and H. Bulle

Philips Research Laboratories, Eindhoven, The Netherlands

ABSTRACT

With an instrument consisting of four mercury probes, simple, rapid, and nondestructive four-point probe measurements can be done on freshly etched n-type silicon samples. Measurements on bulk material and on thin layers with a conventional and with a mercury four-point probe are compared. The ratio of two current-voltage configurations is used as a figure of merit of the instruments. The precision is found to be about 2% and the systematic deviation from theory, which is supposed to be satisfied by a conventional four-point probe, amounts to about 8% for thin layers and much less on bulk material. A number of aspects which may affect the performance are discussed. Because the instrument has no penetrating probes it is particularly useful for very thin heterotype epitaxial layers and for shallow, ion implanted samples. Experiments have also been done on polycrystalline silicon, metallic glass, and conductive plastic layers.

It is generally felt that the economy of semiconductor device processing improves with increasing slice diameter, particularly for larger devices. However, this requires the pertinent slice properties to be uniform and deficient slices to be rejected at the earliest stage. These considerations form the basis for an ever increasing effort in material properties evaluation and characterization. In order to avoid losing material, thus adding to the cost, and to ensure measuring at the relevant spot, it is highly desirable for the methods to be nondestructive. They should also be rapid and simple in application. The purpose of this paper is to show how the peculiar properties of mercury on n-type Si can be used most efficiently for evaluation purposes with the four-point probe method. In this sense the present paper is a continuation of an earlier one on capacitance-voltage measurements (1), where it was stated also that a mercury contact is ohmic to well-cleaned, n-type Si. It will be followed by a paper on spreading resistance measurements, also with mercury probes (2).

The use and experimental results of mercury four-point probe measurements on bulk and thin layers of n-type Si are described below. The sources of error and the limits of applicability of the theory are also discussed. Practical conclusions are drawn and the perspectives for the mercury four-point probe are illustrated with more advanced results.

Mercury Four-Point Probe Measurements

A mercury probe with a single channel used for capacitance-voltage measurements has been described earlier (1). The mercury four-point probe (Hg-fpp) consists of four such holes and channels of identical construction at identical center-to-center distances $s = 3000 \mu\text{m}$. Details of the instrument are shown in Fig. 1. With the interchangeable lid (C, Fig. 1) various contact diameters can be used; the experiments described have been done with contact diameter $2A = 1020 \mu\text{m}$. The embodiment shown is one of the many possibilities. The four platinum wires (B, Fig. 1) should penetrate far enough into the channels to reduce contact resistance and should not be short circuited by mercury in the reservoir (D, Fig. 1). The channels are filled as follows. When the channels have been closed by a sample, the block is tilted and air pressure is applied. The surface of the Perspex block should not be too well polished so that air can escape and mercury can contact the sample. Thereupon the block is put into the horizontal position again. After

removing the air pressure enough mercury remains in the channels because they have been made slightly sloping. Now the instrument is ready to be used for four-point probe measurements.

To make an ohmic contact of mercury to silicon the surface should be carefully prepared. It should be freshly etched in HF, rinsed in deionized water, spin-dried, and subsequently left, until immediately before it is measured, top-side down closing a bottle filled with HF. As strictly speaking an ohmic contact is not required for fpp measurements, the storage stage can sometimes be skipped. The complete procedure is essential for mercury probe spreading resistance measurements (3), which will be discussed at length in a subsequent paper (2).

In the expression for the fpp resistance of a sample of resistivity ρ , thickness $d \gg s$, and infinite in lateral extent, the distance s figures with $R_{2314} = V_{23}/i_{14}$

$$R_{2314} = \frac{\rho}{2\pi s} \quad [1]$$

Hence the resistance R^H_{2314} measured with a Hg-fpp should be proportional to the resistance R^D_{2314} measured with any other, e.g., a Dumas fpp, with proportionality constant s_D/s_H . In Fig. 2 these two four-point probe resistance values are compared, and it is clear that this ratio does not depend on ρ over four decades of resistivity between 10^{-3} and 10^3 cm n-type

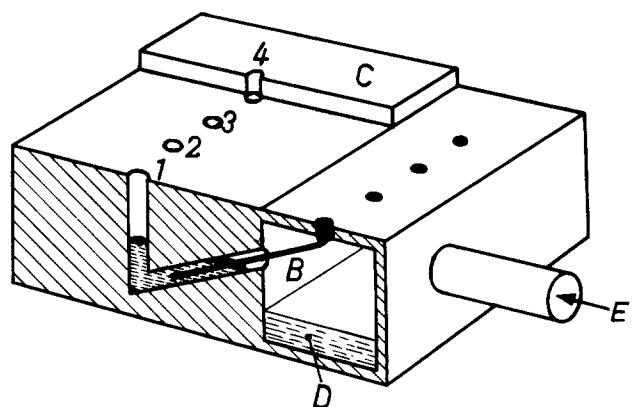


Fig. 1. The mercury four-point probe embodiment, shown schematically, cut through channel 1. Pressure is applied through E; the contact to the mercury is made with platinum wire B. Different contact diameters can be used with interchangeable cover C, shown cut through contact 4.

Key words: four-point probe, sheet resistance, silicon, mercury, epitaxy, polycrystalline, conductive layer, ion implanted layer.

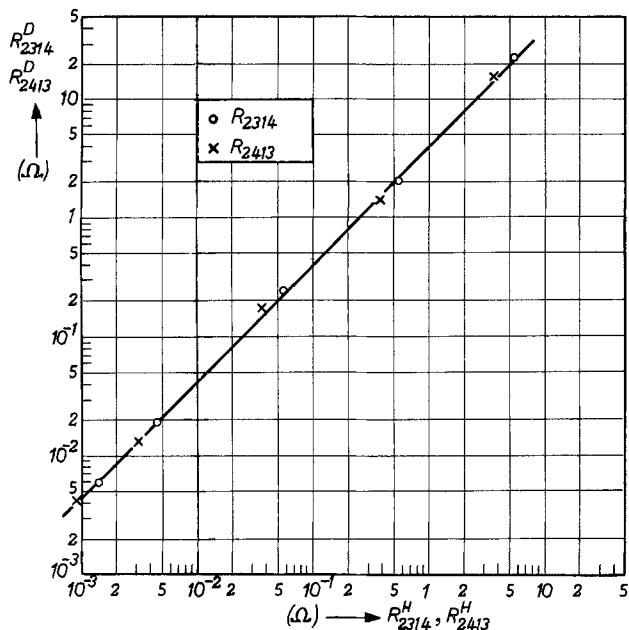


Fig. 2. The resistances R_{2314} (O) and R_{2413} (X) as measured with the mercury four-point probe plotted vs. the same parameters measured with a Dumas four-point probe, labeled H and D, respectively. The bulk sample data are given in Table I.

Si. As it has been explained elsewhere (4), two independent four-point probe measurements can be done by changing the probe order, the other one being for instance

$$R_{2413} = \frac{\rho}{2\pi s} 1.500 \quad [2]$$

This resistance has also been plotted in Fig. 2 for both probes because they should have the same proportionality constant and the measurement points should be on the same line. The ratio s_D/s_H has been calculated and it is found that for both sets the ratios are equal: 0.235 ± 0.022 for R_{2314} and 0.236 ± 0.020 for R_{2413} . This error is rather large, but, as shown in Table I, the two ratios correspond more closely by an order of magnitude on the same slice. It should be borne in mind that the slices are nonuniform and that the two probes measure at different spots and integrate over widely different surface areas. This difference is typical for each slice.

Because the ratio of the two independent four-point probe resistances depends on resistivity only to second order, it mainly characterizes the instrument. In Fig. 3 these two four-point probe resistance values are compared and plotted for both instruments. The ratio R_{2314}/R_{2413} should be equal to 1.500 for both types of fpp. Calculation of this ratio for all data points yields 1.461 ± 0.026 for the Hg- and 1.464 ± 0.034 for the Dumas-fpp. The departures from the average values are found to be statistically distributed over all samples, independent of resistivity. Hence the errors may be attributed to irreproducibilities in the performance of the instruments.

The fpp resistance of a thin layer of resistivity ρ , thickness $d \ll s$, and infinite in lateral extent

Table I. Ratios of R_{2314} and R_{2413} for Hg- and Dumas-fpp measured on bulk samples

ρ (mohm-cm)	$\left(\frac{R^H}{R^D}\right)_{2314}$	$\left(\frac{R^H}{R^D}\right)_{2413}$	$\left(\frac{R_{2314}}{R_{2413}}\right)^H$	$\left(\frac{R_{2314}}{R_{2413}}\right)^D$
9370	0.235	0.247	1.445	1.521
832	0.271	0.263	1.491	1.448
102	0.216	0.213	1.439	1.445
7.79	0.232	0.231	1.440	1.437
2.9	0.222	0.219	1.488	1.471

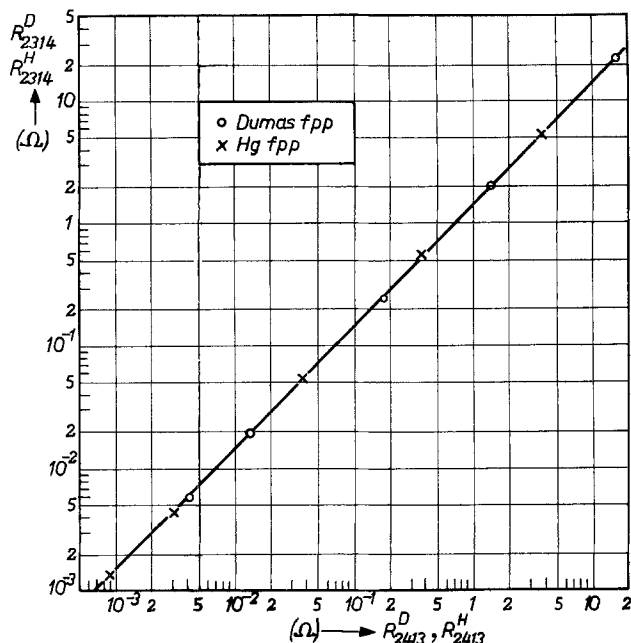


Fig. 3. The resistances R_{2314} , as measured with the mercury (X) four-point probe and with a Dumas (O) four-point probe, plotted vs. R_{2413} measured in the same way for the same samples as used in Fig. 2.

$$R_{2314} = \frac{\rho}{2\pi d} \ln 4 \quad [3]$$

is, to a first order, independent of the dimensions of the fpp. Hence the resistance as measured with a Dumas- and a Hg-fpp should be the same. In Fig. 4 the four-point probe resistances as measured with a Dumas- and a Hg-fpp are compared and are shown to be the same over four decades of substrate resistivities between 10^{-3} and 10 ohm-cm n-type Si. The ratio R_{2314}/R_{2413} has been measured twice with the two types of fpp on substrate slices. Typical results for a number of resistivities are presented in Table II. It is found that the reproducibility for both types of fpp is about equal; the two sets of data for both probes yield the same values which can be combined to 1.244 ± 0.015 for the Dumas- and 1.170 ± 0.029 for the Hg-fpp. The precision as measured on thin layers agrees closely

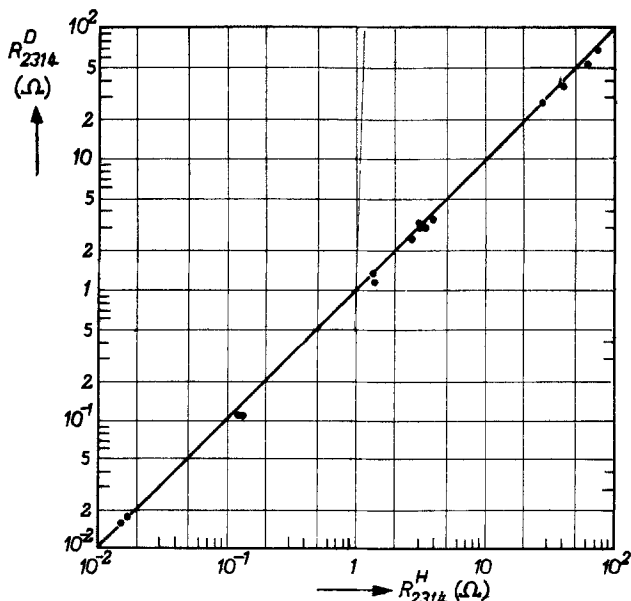


Fig. 4. The resistance R_{2314}^H as measured with mercury four-point probe plotted vs. R_{2314}^D as measured with a Dumas four-point probe for thin layers.

Table II. The ratio R_{2314}/R_{2413} for Hg- and Dumas-fpp measured twice on thin layers for a number of resistivities

ρ (ohm-cm)	$\left(\frac{R_{2314}}{R_{2413}}\right)^H$		$\left(\frac{R_{2314}}{R_{2413}}\right)^D$	
10^{-8}	1.173	1.153	1.237	1.237
10^{-9}	1.187	1.191	1.227	1.225
5×10^{-1}	1.119	1.115	1.231	1.260
3	1.205	1.199	1.241	1.243
7	1.164	1.164	1.248	1.270
10	1.176	1.182	1.270	1.243

with the precision obtained on bulk material for both probes.

The value of the ratio R_{2314}/R_{2413} has been introduced as a figure of merit of the instrument. The fpp resistance is directly affected both by nonuniformities in the sample and deficiencies of the instrument. The ratio is independent of the resistivity and the error in determining the ratio is due to the instrument deficiencies only. Because the two fpp resistances are about equally sensitive to the mainly mechanical irreproducibilities, the percentage of error of the ratio is about twice the percentage of error of the two fpp resistances.

The reproducibility of the Hg-fpp is excellent: removing and reapplying the Hg contact without displacing the slice produces identical readings, and when replacing it as well as possible on the same spot the error is within 1%. With the Dumas-fpp the reproducibility is about the same. The data presented in Fig. 2-4 are typically measured data and do not represent averages. Though, as will be shown below, the contact diameter, A , does not occur in the four-point probe formula, it is interesting to know its reproducibility. It turns out that A as measured under a microscope by pressing the mercury against a glass slide depends weakly on the applied pressure. At a controlled excess pressure of 150 Torr the diameter is reproducibly found to be 1020 μm . Work has been done with contacts 500 μm across, and smaller diameters down to 200 μm have been tried successfully.

From the measured data presented in the preceding section, referring to different spots on the same slice and on slices with different resistivities, it can be concluded that fpp measurements can be done with a precision of about 1% with the Dumas- and of about 2% with the Hg-fpp. There is no consistent indication of any influence of the resistivity of the sample.

Sources of Measurement Errors

The fpp method is probably the most familiar method in semiconductor evaluation. Generally, it is assumed that within the measurement precision the measured data are accurate with respect to the reference level set by the model and the ensuing theory. However, the data presented above show discrepancies with the theory worth discussing in greater detail.

In the model by which the mode of operation of an fpp is described, identical, nondamaging, circular contacts of diameter $2A$ are assumed, which can be neglected with respect to the identical probe center-to-center distances, s . The dependence of voltage, V , on distance, r , from the center of the current-carrying contact on a thin slice is given by

$$V_0 - V(r) = \frac{\rho i}{2\pi d} \ln \frac{r}{A} \quad [4]$$

where V_0 is the potential of the contact, and on bulk material by

$$V = \frac{\rho i}{2\pi A} \arcsin \frac{A}{r} \approx \frac{\rho i}{2\pi r} \quad [5]$$

Equation [4] is evidently valid only for $r \geq A$ and

the resistance R_m under the probe on a thin layer has been discussed (5) showing a complicated dependence on the contact resistance R_c and the sheet resistance R_s . Strictly speaking, this is valid only for a layer which is thin with respect to the probe diameter, whereas for fpp measurements the thickness is referred to the probe distance. In case $A < d$ in the direct vicinity of the probe, the potential drops according to Eq [5]. Because this is not of great importance with $r \gg A$, Eq [4] may be considered applicable from $r = A$ onwards. Allowing for the different probe center-to-center distances, s_{ij} , Eq. [3] and related resistances should read

$$\begin{aligned} R_{2314} &= \frac{\rho}{2\pi d} \ln \frac{s_{13}s_{24}}{s_{12}s_{34}} \\ R_{2413} &= \frac{\rho}{2\pi d} \ln \frac{s_{14}s_{23}}{s_{12}s_{34}} \\ R_{3412} &= \frac{\rho}{2\pi d} \ln \frac{s_{13}s_{24}}{s_{14}s_{23}} \end{aligned} \quad [6]$$

These equations have been derived, as usual, by adding the potential differences of the two probes due to currents flowing through each probe to infinity in opposite directions. This is not permitted when the potential is probed near the current source. For the mercury probe this could limit the applicability of Eq. [6].

It can easily be seen from Eq. [6] that whatever the probe contact diameters are, the three essentially different resistances on a uniform sample are always related by

$$R_{2314} = R_{2413} + R_{3412} \quad [7]$$

and that there is one independent ratio which, when all s are equal yields

$$\frac{R_{2314}}{R_{2413}} = 1.2619 \quad [8]$$

For bulk material the expressions corresponding to Eq. [6] are

$$\begin{aligned} R_{2314} &= \frac{\rho}{2\pi} \left(\frac{1}{s_{13}} - \frac{1}{s_{12}} + \frac{1}{s_{24}} - \frac{1}{s_{34}} \right) \\ R_{2413} &= \frac{\rho}{2\pi} \left(\frac{1}{s_{14}} - \frac{1}{s_{12}} + \frac{1}{s_{23}} - \frac{1}{s_{34}} \right) \\ R_{3412} &= \frac{\rho}{2\pi} \left(\frac{1}{s_{13}} - \frac{1}{s_{14}} + \frac{1}{s_{24}} - \frac{1}{s_{23}} \right) \end{aligned} \quad [9]$$

Equation [7] holds under all conditions and the ratio given in Eq. [8] equals 1.500. In real life with a mechanical fpp all values of s are never equal.

In the above considerations it has been assumed that the voltage probes reflect the potential directly below the center of the contact, i.e., they act as point contacts. It is worth considering under what conditions this simplification holds, particularly as the mercury probe contacts are 1000 μm across with $s = 3000 \mu\text{m}$. Any current drawn by the voltage probes can be neglected because voltmeters of 100 megohms input resistance are used. So the potential of the voltage probe is such that over the contact cross-section as much current flows into as out of the mercury. If the probe diameter is small with respect to the distance, this potential can be assumed to be the potential below the center of the probe. This would apply exactly when the sample has a rectangular shape and contacts take the form of strips; it could be easily calculated with the contacts on concentric circles, but an analysis for on-line circular contacts is virtually impossible. As long as no more detailed

theory is available, the voltage probes will be considered as point contacts.

This effect arises whatever the nature or magnitude of the resistance of the probe sample contact. A second effect is due to the finite value of the specific contact resistance R_c (ohm-cm²) or its voltage dependence. Because current flows through the contact, the same sample draws more current with a low contact resistance probe than with a high contact resistance probe; in other words the sample appears as lower resistivity material. A similar relation has been analyzed earlier for square and circular contacts used as spreading resistance probes (5). Because the main current then flows through these contacts, the theory cannot be directly applied, but the condition for negligible bypass, apart from a numerical factor of order unity, is roughly given by $R_s \ll R_c/A^2$ for thin layers and by $\rho \ll R_c/A$ for bulk samples. From mercury probe spreading resistance measurements on substrate material, to be reported in a subsequent paper (2), it follows that R_c is so low that these conditions are not met. Because, roughly, $R_c \sim \rho$, this applies equally over the resistivity range. When R_c is not very high and depends nonlinearly on ρ , the contacts may bypass the current through the sample to a different degree for various resistivity materials. A further complication may originate from a nonohmic characteristic of the voltage probe contact. When so high a potential is applied that the voltage drop over the diameter of a nonohmic contact in the material exceeds 25 mV, then the contact assumes a potential such that most of the contact draws reverse current. Moreover, the fpp resistance, as measured, turns out then to depend on the current. However, the current has, unless stated otherwise, been kept so low that the measured voltage is well below 25 mV, as advocated earlier (4).

In summary, the assumptions made in the theory are not completely met, firstly because current and probe contacts are not far enough apart to allow separation of the two current sources, secondly because the fairly large contact may partly short circuit the sample, and thirdly because R_c may depend on ρ and on the local voltage.

Discussion of Measurement Errors

From the data obtained from the experiments discussed above, conclusions could be drawn as to the precision of fpp measurements. The reproducibility on the same slices and on samples of different resistivity was tested particularly by using the ratio which depends on the uniformity of the slice to second order only. The data were arranged so as to be theoretically independent of any nonstatistically distributed influence. As the ratios did not show the expected values the theory was more carefully considered and some refinements were mentioned above. In this section the measurements related to these errors with respect to the true or theoretical value are discussed and some practical conclusions are drawn.

By way of example in Table III, the distances, s_{ij} , and probe radii, A_i , as measured under the microscope from a probes print of a Dumas-fpp are presented. From these data the ratio R_{2314}/R_{2413} is found to be 1.254 for thin layers and 1.486 for bulk material. When the two resistances are measured on two slices of widely different resistivity (10^{-2} and 10 ohm-cm n-type Si) and at two current levels, the results presented in Table IV are obtained. The ratios depend slightly on the resistivity and on the current. In actual practice the ratio is calculated regularly in this way and compared to the experimental value.

Table III. The probe center-to-center distances s_{ij} and probe radii A_i in micrometers as a practical example for a Dumas-fpp

$s_{12} = 629.2$	$s_{13} = 1259.0$	$A_1 = 19.2$	$A_3 = 25.0$
$s_{23} = 643.7$	$s_{24} = 1287.0$	$A_2 = 19.7$	$A_4 = 22.2$
$s_{34} = 653.4$	$s_{14} = 1907.8$		

Table IV. The ratios R_{2314}/R_{2413} for Hg- and Dumas-fpp on thin layers

	$\rho = 10^{-2}$ ohm-cm (10 mA)	$\rho = 10$ ohm-cm (22 μ A)	(220 μ A)
$\left(\frac{R_{2314}}{R_{2413}}\right)^D$	1.246	1.270	1.243
$\left(\frac{R_{2314}}{R_{2413}}\right)^H$	1.195	1.176	1.182

Disagreement is always less than 2% of either sign, so systematic bias error, which affects the accuracy, is not found. Therefore, the true value which is the reference with respect to which the accuracy is to be discussed, can be considered to be given in the theory above and as measured with a Dumas-fpp.

The Hg-fpp with identical probe center-to-center distance, s , satisfies the ideal conditions, and the ratio R_{2314}/R_{2413} for thin layers should be equal to 1.2619, which exceeds the experimental values given in Tables II and IV by about 8%. It is not clear to what extent this bias error (it has always been found to have the same sign) is due to R_{2314} or to R_{2413} . It is worth noting that in R_{2413} the potential difference V_{24} caused by current through probe 3 is always zero due to symmetry, whatever theoretical assumption is made. Supposing now that this bias error has the same influence on the voltage difference between two probes for each current probe, the value of R_{2314} as measured with a Hg-fpp should be increased by 12% to reach the true value measured with Dumas-fpp. From Fig. 4 it can be seen that this semiquantitative conclusion is substantiated by experiments.

The ratio s_D/s_H as measured on bulk samples hardly exceeds the theoretical value with $s_D = 630 \mu\text{m}$ and $s_H = 3000 \mu\text{m}$. The dependence on resistivity shown equally in $(R^H/R^D)_{2314}$ and $(R^H/R^D)_{2413}$ suggests some physical influence of the large area probes as discussed in the preceding section. It turns out to be an advantage of the ratio R_{2314}/R_{2413} that this resistivity-dependent effect also disappears. The experimental values of the ratio disagree with theory for both types of probe by equal amounts, not large enough with respect to the precision to be of any significance.

It would be worth investigating the influence of the ratio A/s on fpp measurements. In this paper it has been shown that the quite extreme ratio 1/6 produces results which can be interpreted in the same way and with the same amount of caution as conventional fpp measurements.

In conclusion a number of more advanced applications of the Hg-fpp are mentioned. The Hg-fpp is extremely useful for the assessment of very thin epitaxially grown heterotype silicon layers or shallow ion implanted samples, where conventional pointed probes cause substrate short circuit or even penetrate. It is found possible to measure silicon polycrystalline layers between 1000 and 2000 Å thick with resistivities between 0.06 and 2 ohm-cm. These layers are increasingly used as diffusion sources, vertical resistors, and MOS gate electrodes. Layers of Au Rd-oxide about 200 Å thick have been measured to yield a resistivity of about 1.6 mohm-cm. A reliable assessment of conductive plastic has also been made.

Manuscript submitted Jan. 22, 1974; revised manuscript received July 3, 1974. This was Paper 75 presented at the Chicago, Illinois, Meeting of the Society, May 13-18, 1973.

Any discussion of this paper will appear in a Discussion Section to be published in the December 1975 JOURNAL. All discussions for the December 1975 Discussion Section should be submitted by Aug. 1, 1975.

Publication costs of this article were partially assisted by Philips Research Laboratories.

REFERENCES

1. P. J. Severin and G. Poedt, *This Journal*, **119**, 1384 (1972).
2. P. J. Severin and H. Bulle, *ibid.*, **122**, 137 (1975).
3. P. J. Severin, Paper 75 presented at Electrochemical Society Meeting, Chicago, Illinois, May 13-18, 1973.
4. P. J. Severin, *Philips Res. Repts.*, **26**, 279 (1971).
5. P. J. Severin, *ibid.*, **26**, 359 (1971).

Spreading Resistance Measurements on N-Type Silicon Using Mercury Probes

P. J. Severin and H. Bulle

Philips Research Laboratories, Eindhoven, The Netherlands

ABSTRACT

With an instrument consisting of four mercury probes spreading resistance has been measured on n-type silicon bulk samples and thin layers without leaving any damage. With bulk samples the spreading resistance measured in a three-probe arrangement is found to be proportional to the resistivity without any indication of resistivity dependence of the proportionality constant between 10^{-3} and 10 ohm-cm. From repeated measurements it is concluded that the precision depends on the mechanical finish of the contact edge and can be as good as 3%. Upon comparison with the resistivity as measured with a conventional four-point probe, the mercury probe spreading resistance is found to be accurate within that error. The resistivity measured represents the average over about 1 mm², so that the resolving power of this instrument is intermediate between the resolving powers of conventional four-point and spreading resistance probes.

With thin layers a theory is used, in which the Hg-Si contact resistance is incorporated which is found to be almost proportional to the resistivity over the same four decades. It turns out to be small compared to the bulk spreading resistance, thus confirming the experiments on bulk material. Considering the cylinder resistance of an epitaxial n on n⁺ layer as an extra contribution to the contact resistance, with a mercury four-point probe and spreading resistance measurement the product ρd can be found.

A mercury probe has been applied successfully for capacitance-voltage measurements on n- and p-type silicon and various other semiconductors (1). The procedure which should be followed to prepare a silicon surface so that the contact to mercury is ohmic has been described earlier (2, 3). An instrument consisting of four mercury probes has been used for four-point probe measurements on n-type silicon and the attainable precision and accuracy have been discussed at length (3). It is the purpose of this paper to show how with mercury probes in a three-point probe arrangement spreading resistance measurements may be carried out.

This study is a continuation of Ref. (3) in the sense that the same mercury four-point probe accessory and the same bulk and substrate samples are used. Because a spreading resistance measurement is more exacting than a four-point probe measurement, the sample preparation should be more carefully executed.

The next section is devoted to the results on bulk samples. The results on thin layers, for which 230 μ m thick substrates for epitaxy have been used, are also presented in this paper. The theory needed to find the resistivity ρ and the contact resistance R_c from the measured data is recapitulated in the Appendix. In another section of this paper, a new method is outlined by which the product ρd for the top layer of thickness d of an n on n⁺ epitaxial structure can be determined. In the final section the use of the same mercury four-point probe accessory for four different purposes is summarized.

This paper will be followed by a fourth paper on rapid and simple pulsed MIS capacitance lifetime measurements with the same accessory.

Key words: silicon, epitaxial layer, thickness, resistivity, contact resistance, mercury, spreading resistance, four-point probe resistance.

It is worth stressing that this paper deals with n-type silicon only. Though the contact resistance of mercury to p-type silicon may be reduced by the use of suitable etches, it is not yet small enough for spreading resistance measurements.

Mercury Spreading Resistance Measurements on Bulk Samples

In a few years' time the spreading resistance technique has become an accepted and widely used tool in semiconductor evaluation. However, the theoretical value of the spreading resistance on a semi-infinite sample of resistivity with a probe of contact radius A

$$R_s = \frac{\rho}{4A} \quad [1]$$

is rarely found.

With hard metal probes, as discussed by Mazur and Dickey (4) and Keenan *et al.* (5), a contact resistance R_c is always found which generally is incorporated into the expression for spreading resistance as

$$R_s = k(\rho) \frac{\rho}{4A} \quad [2]$$

The factor $k(\rho) = 1 + 4A R_c/\rho$ is experimentally determined and Eq. [2] can be used only after calibration because $k(\rho)$ depends also on the particular probe properties.

One of the present authors (6) solved the same problem in a slightly different manner by using a softer steel probe. Then the contact can be described by a series spreading resistance due to a number, n , of microcontacts with average contact radius, a , acting in parallel as

$$R_s = \frac{\rho}{4A} + \frac{\rho}{4na} \quad [3]$$

It has been verified that R_s over four decades of resistivity is proportional to ρ . The magnitudes of the contributions of macro- and microcontacts are of the same order, which has an important bearing on the resolving power. In both approaches the precision and reproducibility of k and na are key conditions, the latter being the more relaxed one because only geometry is involved rather than ρ -dependent contact physics.

The main advantage of the spreading resistance method is the unparalleled resolving power, the information sampling depth being about equal to A which amounts to a few microns. Apart from the arguments given above an important drawback is that it is a destructive method. Furthermore, sophisticated vibration-free equipment is needed. In the experiments presented in this paper $A = 500 \mu\text{m}$, but it could easily be made 5 times smaller. The ensuing drop in resolving power is compensated by the fact that it is nondestructive, and that it can be done by simply switching the probe order after a mercury four-point probe measurement. Effectively, it offers a tool with resolving power intermediate between a metal spreading resistance probe and a four-point probe.

The same five bulk samples as used in the preceding paper (3) have been measured with mercury probes and the spreading resistance R_{2113} is plotted vs. the four-point probe resistance R_{2314} in Fig. 1. In the three-point probe arrangement chosen with center voltage-probe each of the four probes can be used as the common probe. No systematic difference turned out to exist. The spread arises from inhomogeneity of the sample and irreproducibility of the contacting process.

Working out the potential difference, V_{12} , measured due to current flow through probes 1 and 3, with the dependence on horizontal distance, r , from the probe center as

$$V(r) = \frac{\rho i}{2\pi A} \arcsin \frac{A}{r} \approx \frac{\rho i}{2\pi r} \quad [4]$$

it is found that

$$R_{2314} = \frac{\rho}{2\pi s}$$

and that

$$R_{2113} = \frac{\rho}{4A} \left(1 - \frac{A}{\pi s} \right) \quad [5]$$

With probe center-to-center distance $s = 3 \text{ mm}$ and A

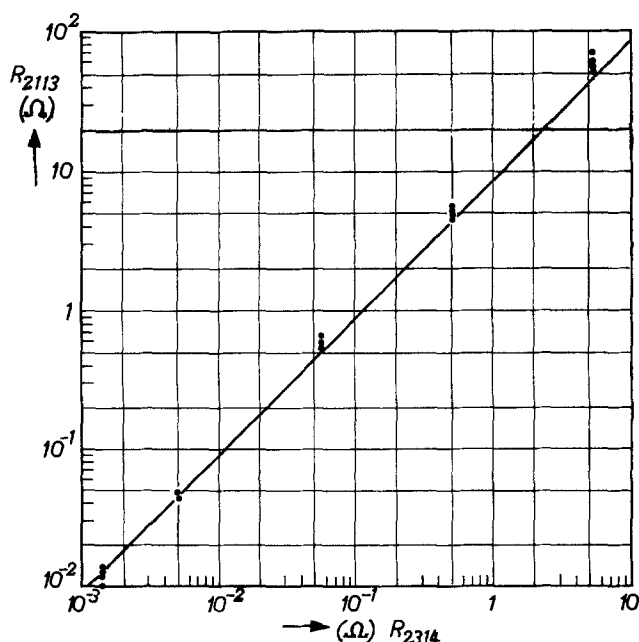


Fig. 1. The spreading resistance R_{2113} plotted vs. the four-point probe resistance R_{2314} , both measured with mercury probes, on bulk samples. The solid line represents $R_s = \rho/4A$, where 1 ohm corresponds to $\rho = 0.2 \text{ ohm-cm}$.

$= 0.5 \text{ mm}$ the term $A/\pi s$ equals 0.053 and the line in Fig. 1 is drawn so that $R_{2113}/R_{2314} = \pi s/2A = 9.42$.

It has been tacitly assumed above that any contact resistance is negligible. With specific contact resistance R_c' (ohm-cm²), Eq. [2] should in fact be written as

$$R_s = \frac{\rho}{4A} + \frac{R_c'}{\pi A^2} \quad [2a]$$

Anticipating the results of the next section where R_c' is determined, it can be verified that for $R_{2314} = 5.3$ and 1.4×10^{-3} ohms the corrections to R_{2113} would be 5 and 2×10^{-3} ohms, respectively, hence negligible on the logarithmic scale. Therefore, the spread of the measurement points cannot be due to differences in contact resistance.

In the experimental embodiment it turns out that the series resistance due to platinum lead, the platinum-mercury transition resistance, and the mercury channel resistance cannot be neglected for low resistivity specimens. The accurate value for each of the four channel series resistances, R_{ai} , can be determined with a platinum-coated, very low resistance specimen. The resistance R_{a1} which amounts to 65 ± 2 mohms, should be considered as a series resistance in the external circuit. It is evident from Fig. 1 that it seriously adds to the error for the low resistivity specimens.

It has been found that with removing and reapplying the mercury probes the measurement does not reproduce very well. Therefore, in order to test the reproducibility, the slice was removed, prepared again, and positioned at the same spot. The results of six measurements repeated in this way are presented in Fig. 2 for each of the four probes. It was found that the averages for each of the four probes are different by a few per cent and that each of these averages is subject to an error ranging from $\pm 3.1\%$ for probe 1 to $\pm 9.1\%$ for probe 2. From this experiment and further experience it should be concluded that repeated etching with HF does not affect the results. The performance of the probes probably depends on the quality of the mechanical finish of the hole and particularly on the absence of burrs at the contact edge. Upon averaging the 24 results of all four probes a value of 5.17 ohms is found with an error of $\pm 7\%$. With a Dumas four-point probe the area of measurement has been tested for nonuniformity, and it was found that measuring with a precision better than 1%, the resistivity ρ varied around the average value $\rho = 1.08 \text{ ohm-cm}$ by $\pm 4.4\%$. This value corresponds with Eq. [5] where a mercury probe measured $R_{2113} = 5.13$ ohms, hence well within the experimental error of the best probe.

In this way it has been proved that with a mercury probe it is possible to carry out spreading resistance measurements with a precision and accuracy of better than 3%.

Of course the value of the contact diameter $2A$ should be reproducible and precisely known: it is measured with a microscope by pressing the mercury against a glass slide. It has turned out that with increasing pressure the contact diameter first increases until the diameter of the hole has been reached then remains constant over a certain pressure range and finally increases again with increasing mercury pressure due to mercury penetrating between the Perspex and the sample. At a controlled pressure of 150 Torr the diameter is found to be reproducible and equal to the hole diameter within 1%. With a narrower channel the diameter of the contact increases with pressure over a longer range up to the hole diameter so that spreading resistance, contact resistance, and capacitance-voltage can be measured with the surface area as a continuous variable over about a factor of two.

Mercury Spreading Resistance Measurements on Thin Samples

The same measurement as described in the preceding section has been carried out on 230 μm thick substrate slices as used for epitaxy. A spreading resistance cor-

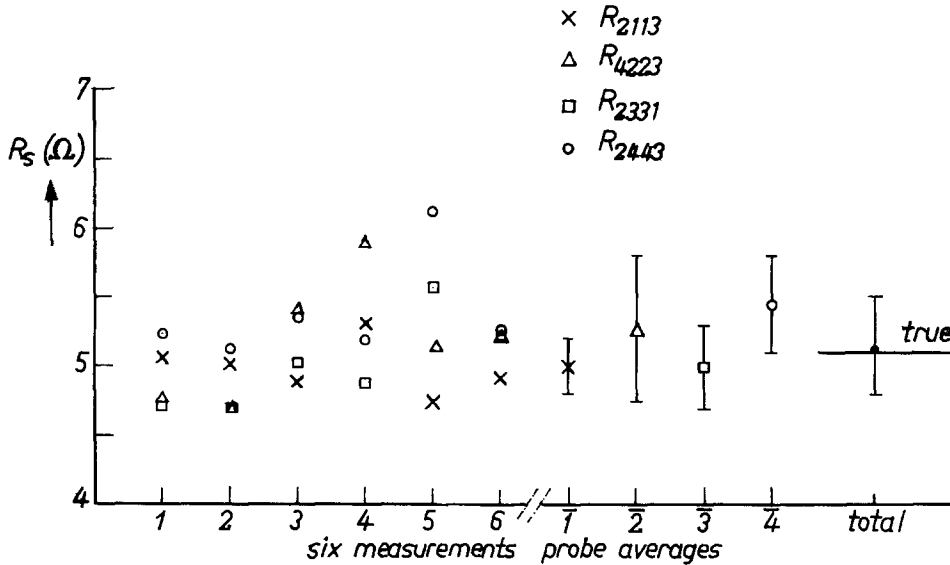


Fig. 2. The spreading resistance measurement on the same position on a 1.08 ohm-cm n-type Si bulk sample repeated 6 times. Each time data for four different common probes are obtained. The four averages and the total average are given separately; the true value $\rho = 1.08$ ohm-cm yields with Eq. [5] $R_{2113} = 5.13$ ohms, indicated by the horizontal bar.

rection formula for a thin layer on an insulating substrate based on a transmission-line model has been derived (7) and compared (10) to other models earlier. As recapitulated in the Appendix, the spreading resistance of the common probe (probe 1), with current probe (probe 4) and voltage probe (probe 2) is given by

$$R_{2114} = R_m + \frac{\rho}{2\pi d} \ln \frac{3s}{2A} \quad [6a]$$

with a four-point probe resistance

$$R_{2314} = \frac{\rho}{2\pi d} \ln 4 \quad [6b]$$

The resistance R_m is defined for a thin layer, $d \ll A$, as the difference between the contact potential V_o and the potential $V(A)$ at $r = A$ in the thin layer, divided by the current i_o . It is found to be equal to

$$R_m = \frac{\rho}{2\pi d} F(z) \quad [7]$$

with $F(z)$ plotted in Fig. 3, R_c' specific contact resistance in ohm-cm², $R_c = R_c'/\pi A^2$ and

$$z^2 = \frac{\rho A^2}{R_c' d} = \frac{\rho}{\pi d R_c} \quad [8]$$

For $s/A = 6$ the logarithmic factor in Eq. [6a] equals 2.197 and Eq. [6] and [7] can be recast into a form more suitable for calculation

$$F(z) = \frac{R_{2114}}{R_{2314}} 1.386 - 2.197 \quad [9a]$$

and

$$R_c = \frac{R_{2314}}{z^2} 1.443 \quad [9b]$$

The resistance R_m is plotted vs. R_{2314} in Fig. 4 and found to be almost proportional to ρ from 10 to 10⁻³ ohm-cm. This suggests, from Eq. [7], that z must be independent of ρ , hence that $R_c = R_c'/\pi A^2$ is proportional to ρ , as also shown qualitatively in Fig. 4.

It has been neglected in Eq. [9a] that in fact R_{2114} includes a term which refers to the local resistivity at probe 1 and a term which refers to the average value ρ between probes 1 and 4. The latter is represented adequately by the resistance R_{2314} .

In order to get the feel of the precision and accuracy involved let us consider a measurement of an 0.03 ohm-cm slice. We then find $R_{2114} = 4614$ mohms, $R_{2314} = 2702$ mohms, so that $R_m = 330$ mohms, $F(z) = 0.169$, $z = 6.45$, hence $R_c = 93.6$ mohms. It is clear that with these values of $F(z)$ and $\ln(3A/2s)$, the measurement conditions are very unfavorable: in order to find pre-

cise R_m within 10%, the values of R_{2114} and R_{2314} should be known within 1%. Because z hardly depends on ρ , this example is typical for the experiments described in this section. Because in this range $z \gg 1$, Eq. [9a] and [9b] can be simplified by the relation $F(z) = 1/z$.

As it is clear from Eq. [9a] and [9b], the measurement result is the contact resistance R_c . Usually quite some processing is involved in making an ohmic metal semiconductor contact, and R_c' , though not very reproducible, is considered as a figure of merit of the process. As long as R_c is small with respect to the bulk resistance of the device concerned, this is an unimportant aspect. However, the instrument described and the spreading resistance method are intended to serve evaluation purposes, viz., to measure the resistivity locally. From Eq. [9a] and [9b] it can be seen that $R_c(\rho)$ is finally the discriminating parameter which turns out not to be sufficiently precise and reproducible to yield ρ .

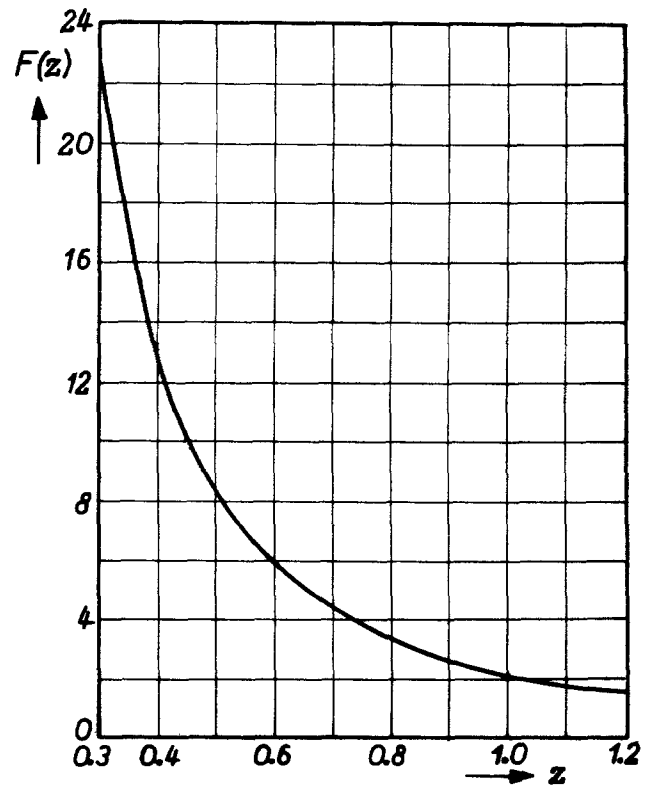


Fig. 3. The function $F(z)$ as used in Eq. [7] and defined in Eq. [A-8]

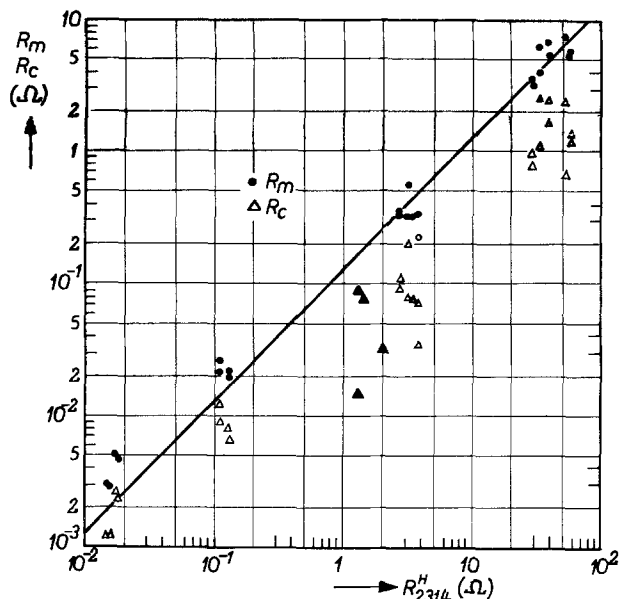


Fig. 4. The spreading resistance R_m (\bullet) and the ensuing contact resistance $R_c = R_c'/\pi A^2$ (Δ) on chem-mechanically polished silicon substrate slices vs. the Hg fpp resistance R_{2314}^H . For a 230 μm thick slice, 9.59 ohms corresponds to 1 ohm-cm; thickness variations $\pm 5\%$ are irrelevant on this scale. The contact resistance R_c (Δ) on epitaxial layers agrees with R_c measured on substrate material within the measurement error.

Spreading Resistance Measurement of an N on N⁺ Silicon Epitaxial Structure

The spreading resistance measurement discussed above can also easily be applied to measure the cylinder resistance R_y of an n-type silicon epitaxial layer on an n⁺ substrate

$$R_y = \frac{\rho d}{\pi A^2} \quad [10]$$

For a fpp measurement such a structure can be considered as being a single isolated n⁺ layer; with a 10 μm thick, 1 ohm-cm n layer on a 250 μm thick, 10^{-2} ohm-cm n⁺ substrate the sheet resistances are $\rho_e/d_e = 10^3$ ohms and $\rho_s/d_s = 0.4$ ohms, respectively. The thin resistance layer is of interest only for the spreading resistance probe because the real contact resistance R_c in series with the cylinder resistance R_y can be considered as an effective contact resistance R_{ce} in the sense as defined in the preceding section

$$R_{ce} = R_c + R_y \quad [11]$$

In using this formalism with R_m the contact radius, A , should be much larger than the layer thickness, d . This eliminates the use, without additional and doubtful correction, of the steel probes with $A = 10 \mu\text{m}$, applied for conventional spreading resistance mea-

surements (6, 7). For the above example, $R_y = 127$ mohms which, with the value $R_c \approx 60$ mohms to be found experimentally according to Fig. 4, should yield $R_{ce} \approx 200$ mohms.

It should be emphasized for this application of Eq. [9a] and [9b], that R_{2314} refers to the n⁺ substrate, that R_m is influenced by both the epitaxial layer R_{ce} and the substrate ρ/d , and that R_y refers to the epitaxial layer only. The meaning of the various parameters introduced is illustrated in Fig. 5.

It turns out that for conventional epitaxial structures the function $F(z)$ is near unity. Then $F(z)$ can be approximated for $z < 1.2$ within 1% and for $1.5 < z < 2$ within less than 4%, by

$$F(z) = \frac{2}{z^2} + 0.25 \quad [12]$$

whence Eq. [9a] and [9b] can be written as

$$R_{ce} = R_{2114} - 1.77 R_{2314} \quad [9c]$$

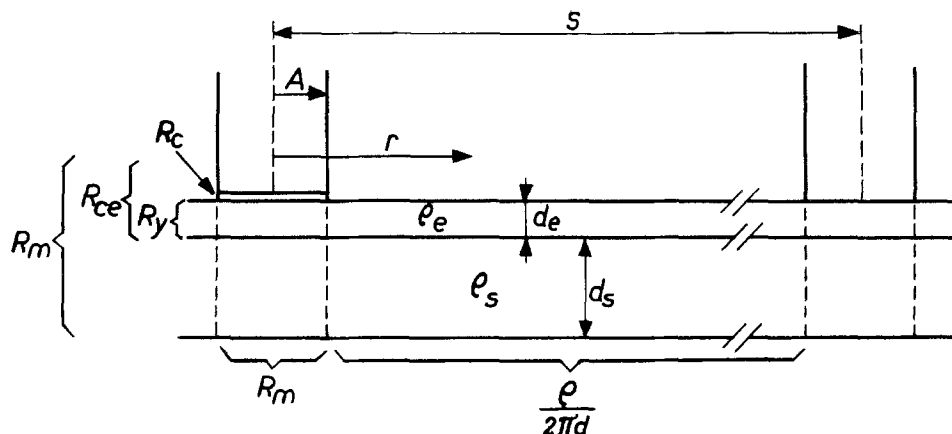
Physically this means that due to the epitaxial layer cylinder resistance the contact is dominated by the contact resistance R_{ce} , whereas the substrate sheet resistance is so small that there is a horizontal equipotential surface under the probe.

In order to show simply the feasibility of this technique, R_{ce} was first determined from the measured values R_{2314} and R_{2114} for a number of SiCl_4 -grown n on n⁺ structures. Thereupon the resistivity ρ was determined using Sze's and Irvin's curves (8); from the CV measured (1) dope concentration at a fixed depth of 4 μm , and with the IMI measured (9) thickness d , the value of R_y was calculated. It turned out then that R_y exceeded R_{ce} so that R_c was negative. Then a few structures were selected which were low doped and thin enough to be probed by the CV method (1) over the full depth of the epitaxial layer and the integral

$$R_y = \frac{1}{\pi A^2} \int_0^d \rho(x) dx \quad [13]$$

was determined. It was found that the IMI measured d includes a part of the transition layer which does not contribute at all to the cylinder resistance, and also that particularly for SiCl_4 grown slices, the dope concentration varies strongly with depth. Figures 6a and 6b show some typical profiles. Taking into account this real, reduced value of R_y a positive contribution due to contact resistance R_c was found. Some experimental data on the contact resistance of epitaxial layers measured in this way are presented in Table I and in Fig. 4. It is clear that the method can be used for evaluation purposes as described in the preceding section only when it is surely known that the dope atom concentration does not change with depth. This is the one restriction which hampers the use of the spreading resistance method for the evaluation of epitaxial layers, both with metal and mercury probes.

Fig. 5. The various parameters introduced for the measurement of the cylinder resistance on an n on n⁺ structure presented schematically.



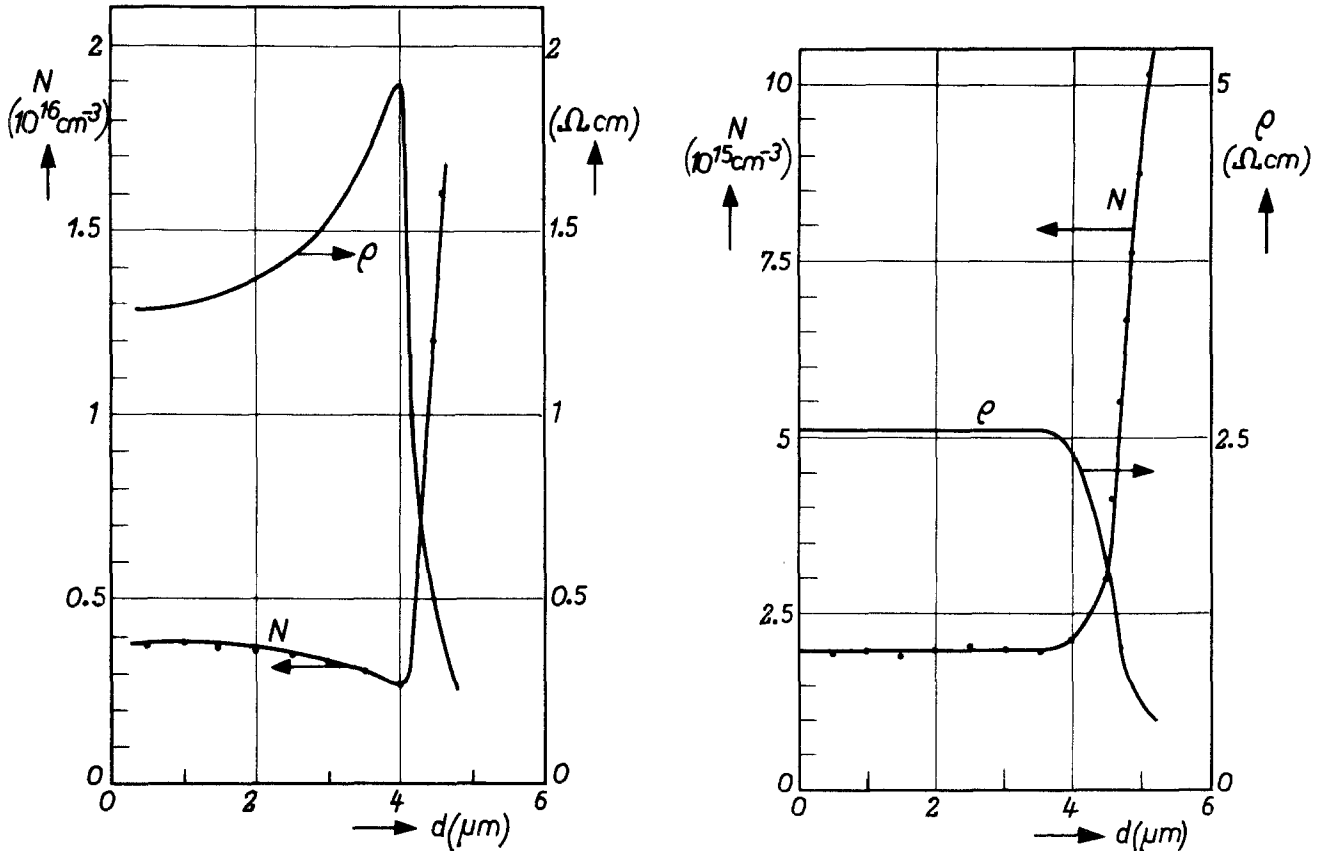


Fig. 6. The dope concentration N and ensuing resistivity ρ as a function of depth below the surface of an epitaxial n on n^+ structure. a, left: E2490-3, SiCl_4 -grown; b, right: Ril 1345, SiH_4 -grown. The IMI measured appropriately corrected thickness for a, left, 5.79 μm ; and b, right, 5.96 μm .

Summary and Conclusions

An instrument with four identical mercury probes can be used most efficiently for at least four kinds of measurements. First with one probe connected to a high frequency capacitance bridge, immediate, precise, and accurate capacitance-voltage measurements can be done on substrates and epitaxial layers. An n-type silicon specimen should be slightly oxidized; p-type silicon can be measured without special preparations (1). For routine measurements the bridge can be an automated instrument of which several types are commercially available. Agreement of fpp with CV measurement data, converted with Sze's and Irvin's curves (8) to resistivity, has been obtained for substrates to within a few per cent.

Second, a freshly etched n-type silicon sample can be fpp measured with this instrument without leaving any damage. Agreement with conventional fpp instruments is within a few per cent (3).

Third, a structure prepared as above can be spreading resistance measured with this instrument, and on bulk samples the resistivity agrees within a few per cent with the four-point probe data. The resolving power of about 1 mm makes the mercury spreading resistance probe an interesting instrument, where the fpp would be too coarse and the conventional spreading resistance would be too fine. In addition it leaves no damage. The spreading resistance measured on layers of thickness $d \lesssim A$ should be corrected. A theory

is used which integrates the effects of the contact resistance, R_c , into the final expression for the spreading resistance (7, 10). The parameters ρ/d and R_c are found in this way. When, as with conventional spreading resistance probe measurements, d has been obtained otherwise, the local value of ρ is found.

For an epitaxial n on n^+ structure tested in this way, the contact resistance consists of the cylinder resistance proportional to ρd and the real contact resistance in series.

It would be highly desirable to increase the precision of the method so that the contact resistance may be known from calibration, if necessary dependent on the surface preparation, in order to use the method for the determination of ρd of epitaxial layers.

Fourth, with the mercury probe a MIS diode can be made and pulse measured in order to evaluate simply and immediately the dope concentration directly below the surface and the bulk lifetime and surface recombination velocity. This will be the subject of a future paper.

Manuscript submitted Jan. 22, 1974; revised manuscript received July 3, 1974. This was Paper 75 presented at the Chicago, Illinois, Meeting of the Society, May 13-18, 1973.

Any discussion of this paper will appear in a Discussion Section to be published in the December 1975 JOURNAL. All discussions for the December 1975 Discussion Section should be submitted by Aug. 1, 1975.

Publication costs of this article were partially assisted by Philips Research Laboratories.

APPENDIX

A current i_0 enters a circular contact of radius A at potential V_0 on a thin layer of infinite extent, of thickness $d \ll A$ and resistivity ρ , shown in Fig. 5. The current i_0 leaves the structure through a contact at infinity at zero potential. The potential drops with r according to

Table I. The contact resistance R_c of mercury to n-type epitaxial silicon

Slice	ρ (ohm-cm) on surface	R_s (mohms)	R_c (mohms)
E 2490-3	1.31	76	31
Ril 1345	2.55	149	76
Ril 1286	1.20	55	13
Ril 1280	1.18	58	90

$$\frac{\partial V(r)}{\partial r} = -\frac{\rho}{2\pi d} \frac{1}{r} \quad \text{for } r \leq A \quad [\text{A-1}]$$

and the current $i(r)$ which passes through a cylinder increases below the contact as

$$\frac{\partial i(r)}{\partial r} = 2\pi r J(r) \quad [\text{A-2}]$$

because of the local voltage drop over the specific resistance R_c' given by

$$R_c' J(r) = V_o - V(r) \quad [\text{A-3}]$$

Writing $R_s = \rho/d$ and $\Lambda^2 = R_c'/R_s$, Eq. [A-1]-[A-3] can be combined to yield the differential equation

$$\frac{\partial^2 V}{\partial r^2} + \frac{1}{r} \frac{\partial V}{\partial r} - \frac{V - V_o}{\Lambda^2} = 0 \quad [\text{A-4}]$$

with solution in terms of the modified Bessel function of the first kind

$$V - V_o = a I_0 \left(\frac{r}{\Lambda} \right) \quad [\text{A-5}]$$

and hence

$$i = -\frac{2\pi d}{\rho} \frac{ra}{\Lambda} I_1 \left(\frac{r}{\Lambda} \right) \quad [\text{A-6}]$$

From the boundary condition $i = i_o$ at $r = A$ follows that with $z = A/\Lambda$ the potential drop over R_c at $z = 0$ equals

$$a = -\frac{\rho i_o}{2\pi d} \frac{1}{z I_1(z)} \quad [\text{A-7}]$$

and that the resistance R_m measured between the contact and a point very near $r = A$ given by

$$R_m = \frac{\rho}{2\pi d} \frac{I_0(z)}{z I_1(z)} = \frac{\rho}{2\pi d} \mathbf{F}(z) \quad [\text{A-8}]$$

The solution for $r > A$, where $J(r) = 0$ and $i = i_o$, follows from Eq. [A-1] as

$$V - V_o = \frac{\rho i_o}{2\pi d} \ln \frac{r_1}{r} \quad [\text{A-9}]$$

The solutions of Eq. [A-5] and [A-9] should be matched; it can easily be verified that

$$V_o - V = \frac{\rho i_o}{2\pi d} \left(\mathbf{F}(z) - \ln \frac{r}{A} \right) \quad [\text{A-10}]$$

In this way both the potential and its derivative, proportional to the current, are matched at $r = A$. A discrepancy which cannot be overcome is due to the fact that at $r = A$ the current density is maximum under the contact but vanishes at $r > A$. No doubt the approximation of J only perpendicular to the contact does not hold at the edge $r = A$, which affects the applicability of the theory less if $A \gg d$. The equation actually used in the measurement arrangement can be obtained from Eq. [A-10] by superposition of the two potential systems: current i_o enters through probe 1 and leaves at infinity and current i_o enters at infinity and leaves through probe 4. The ensuing logarithmic potential drop has experimentally been found to exist precisely.

REFERENCES

1. P. J. Severin and G. Poodt, *This Journal*, **119**, 1384 (1972).
2. P. J. Severin, Paper 75 presented at Electrochemical Society Meeting, Chicago, Ill., May 13-18, 1973.
3. P. J. Severin and H. Bulle, *This Journal*, **122**, 133 (1975).
4. R. G. Mazur and D. H. Dickey, *ibid.*, **113**, 255 (1966).
5. W. A. Keenan, P. A. Schumann, A. H. Tong, and R. P. Phillips, in "Ohmic Contacts to Semiconductors," B. Schwartz, Editor, p. 263, The Electrochemical Society Softbound Symposium Series, New York (1969).
6. P. J. Severin, *Solid State Electron.*, **14**, 247 (1971); NBS Special Publication 337, p. 224, 1970.
7. P. J. Severin, *Philips Res. Repts.*, **26**, 359 (1971).
8. S. M. Sze and J. C. Irvin, *Solid State Electron.*, **11**, 599 (1968).
9. P. J. Severin, *Appl. Opt.*, **9**, 2381 (1970); **11**, 691 (1972).
10. P. J. Severin, Symposium on Spreading Resistance Measurements, National Bureau of Standards, Gaithersburg, 1974.

Oxygen Ion Conduction of the Fluorite-Type $\text{Ce}_{1-x}\text{Ln}_x\text{O}_{2-x/2}$ (Ln = Lanthanoid Element)

Tetsuichi Kudo and Hidehito Obayashi

Central Research Laboratory, Hitachi, Limited, Higashi-koigakubo, Kokubunji, Tokyo, 185, Japan

ABSTRACT

The compounds $\text{Ce}_{1-x}\text{Ln}_x\text{O}_{2-x/2}$ (Ln = lanthanoid element) have been synthesized and the emf and resistivity measurements have been carried out between 400° and 1000°C. It is found that charge carriers of conduction in these compounds are oxygen ions above 600°C; the oxygen transference number being above 0.95 for all measured compounds. The resistivity value for $\text{Ce}_{0.77}\text{Gd}_{0.23}\text{O}_{1.885}$ is 15 ohm-cm at 750°C which compares with that of calcia stabilized zirconia at 1000°C. It is found that the dependence of the resistivity on temperature is described by

$$\rho = (\rho_o)_L \exp(\Delta E_L/kT) + (\rho_o)_H \exp(\Delta E_H/kT)$$

for most of the compounds, where the (ρ_o) 's and ΔE 's are empirically determined parameters. The activation energies of conduction are determined by the compounds' lattice constant so long as the dopant concentration is held constant. The activation energies increase as the dopant concentration x increases and ΔE_L and ΔE_H coincide at $x \cong 0.4$.

There have thus far been numerous studies on the ZrO_2 family oxygen ion conductive solid electrolytes (1-3). However, it seems that systems other than the

Key words: ionic conductor, solid electrolyte, cerium/lanthanoid oxide, solid solution.

ZrO_2 family have attracted less interest and that a systematic approach is lacking. Several compounds having oxygen ionic conduction have been reported by Singman (4), Mazelsky (5), and Iwahara (6). These solid electrolytes, however, exhibit poorer char-

acteristics both in resistivity and transference number compared with the ZrO_2 family.

Etsell and Flengas (7) published an excellent review on CeO_2 -base solid electrolytes as well as ZrO_2 -, ThO_2 -base and other solid electrolytes.

The CeO_2 family oxygen ion conductive solid electrolytes have been widely and systematically synthesized and their properties investigated in this paper. The compounds are represented in a general formula $Ce_{1-x}Ln_xO_{2-x/2}$ where Ln stands for the trivalent lanthanoid element ranging from Y, La, to Yb.

Experimental

Sample preparation.—The oxides CeO_2 (99.99% up, Shinetsu Kagaku K.K.) and Ln_2O_3 (99.9% up, Shinetsu Kagaku K.K.) were precisely weighed and mixed in an agar mortar. The mixture was pressed softly (0.5 t/cm^2) in a die and placed in an alumina boat. It was heated to 1300°C and kept at this temperature for 8 hr. The presintered sample did not show any foreign peaks other than fluorite-type compound $Ce_{1-x}Ln_xO_{2-x/2}$ in an x-ray diffraction pattern. The sample was then ground in an agar mortar to -325 mesh. When needed, 3 mole per cent (m/o) magnesium was added as $Mg(NO_3)_2$. As a binder 1 weight per cent (w/o) methyl cellulose was added and ground again to -40 to -60 mesh. The powder was pressed in a die at 3 t/cm^2 , then placed in a Pt-40% Rh basket and sintered at $1800^\circ \pm 20^\circ\text{C}$ for 2-3 hr in air. The sintered samples showed a porosity of less than 4% in all cases.

Oxygen ion transference number measurement.—The average oxygen ion transference number \bar{t}_{O-2} is given by

$$\bar{t}_{O-2} = \frac{E}{\frac{RT}{4F} \ln(p''_{O_2}/p'_{O_2})} \quad [1]$$

where symbol E stands for the observed emf of the cell

$$O_2(p'_{O_2}), Pt/Solid \text{ Electrolyte}/Pt, O_2(p''_{O_2}) \quad [2]$$

In the experiments reported here, $p''_{O_2} = 1 \text{ atm}$ and $p'_{O_2} = 0.21 \text{ atm}$.

For measurement of emf, a vertical type gas flow apparatus was made, whose schematic profile is shown in Fig. 1. A 20 mm diameter and 1-2 mm thick disk sample was sandwiched between silver packings to which ceramic tubes were attached. The silver packings ensure the gas tightness of the cell at elevated temperatures. The gas tightness was further ensured by a spring placed at the upper end of the ceramic tube. A rotary pump vacuum test was carried out before each run to test for gas tightness. An inner gas guide pipe was placed in both the upper and lower rooms so that both electrodes were exposed to fresh gas throughout each run. Oxygen gas was introduced into the upper room and air was introduced into the lower room.

Income gas flow rates were between 50 and 100 ml/min, and the gas was not preheated. Calculated linear flow rates for these conditions were around 0.5-1.0 cm/sec assuring that the gas is well heated to the equilibrium temperature of the furnace. The temperature of the sample was measured by a Pt-(Pt-Rh13) thermocouple and a cooling effect of incoming gas was proved to be negligibly small in the employed experimental conditions.

Resistivity measurement.—The electrical contacts were made using platinum paste electrodes to both sides of a disk sample. An a-c impedance bridge method was employed usually. An RC701 (Matsushita Electric) type frequency generator was used, and the bridge was an BV-Z-1 (Yokogawa Electric) type direct reading impedance bridge. The frequency used was 1 kHz. In the a-c measurements, the resistance of the platinum lead wire was compensated. In some

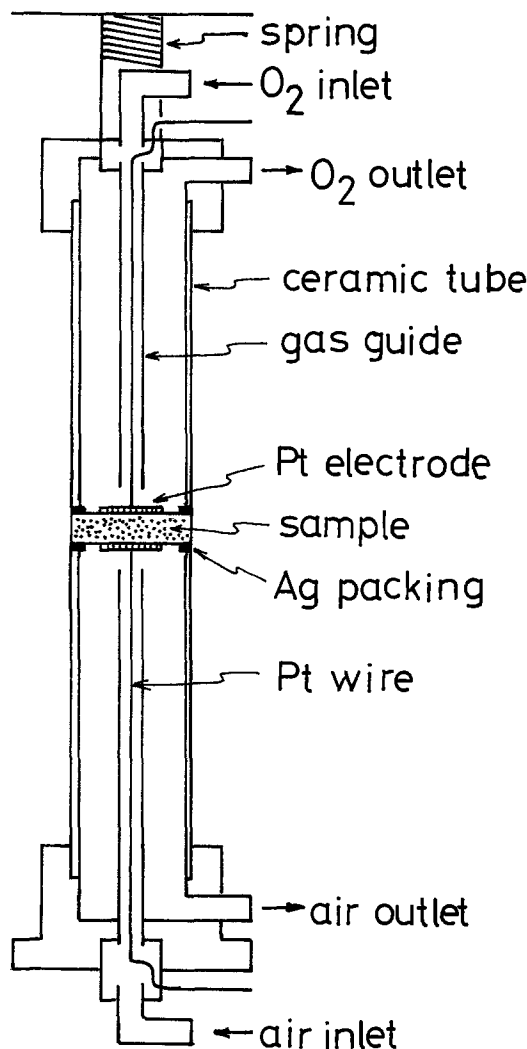


Fig. 1. Schematic drawing of emf measurement cell. The cell is placed in a vertical type furnace and the temperature is controlled within $\pm 2^\circ\text{C}$. EMF was measured by a potentiometer.

cases, d-c four-probe method was employed. In the d-c measurements, $30 \times 10 \times 5 \text{ mm}$ rod samples were used. Two platinum wires ($0.3 \text{ mm}\phi$) which work as the potential drop measurement probes were spanned on a flat and smooth alumina plate. The current flowing porous platinum paint electrodes were attached to far ends of the rod sample. This rod was placed on that plate and on the sample was another alumina plate on which a 100g platinum rod was placed. This rod was used to ensure the contacts between the sample and the spanned platinum probes. The potential drop between two probes during the constant current flow was measured by a potentiometric Hitachi QPD54 recorder. At the initial stage of this work, platinum wire probes were placed in 0.3 mm wide and 0.3 mm deep ditches surrounding the sample separated by 10 mm. However, it was assured that the above method gives the same result, therefore, we have changed to the easier method.

The uniformity of the temperature in the furnace was increased by covering a quartz tube with 1 mm thick nickel tube. At the same time, one end of the nickel tube was grounded so as to eliminate electric noises from the external field.

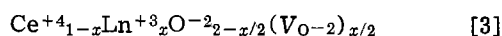
X-ray diffraction.—Usually, $Cu K_\alpha$ or $Fe K_\alpha$ radiation were used. The scanning speed was $2\theta/\text{min} = 1^\circ/\text{min}$. For the determination of lattice constants, diffractions from (620) and (533) planes were used when $Cu K_\alpha$ was employed while (422) and (511) planes were used when $Fe K_\alpha$ was employed. For some samples, high temperature x-ray diffraction measurements

were carried out at temperatures between room temperature and 1000°C.

DTA measurement.—DTA measurements were carried out using a Type M8006 macro DTA and a Type M8076 micro DTA apparatus (Rigaku-denki K.K.). Sample weights were 1.7-1.9g for macro and 10-50 mg for micro DTA measurements, respectively. The differential thermocouple used was Pt-(Pt-Rh13)-Pt thermocouple and one junction attached to reference (α -Al₂O₃) worked as temperature detecting thermocouple. Measurements were carried out between room temperature and 800°C and the speed of temperature rise was fixed to 20°C/min throughout all the measurements.

Result and Discussion

Crystal structure.—The compound CeO₂ has a fluorite-type cubic crystal structure. When trivalent lanthanoid ions Ln (Ln = Y, La, to Yb) replace the Ce ion sites of the fluorite lattice, the modified formula is generally expressed as



where V_{O-2} stands for the oxygen ion vacancy generated to compensate charges in the crystal.

The CeO₂-Ln₂O₃ system has a wide solid solution region of fluorite-type lattice and the compounds Ce_{1-x}Ln_xO_{2-x/2} show the pure fluorite lattice pattern up to ca. $x = 0.5$. The lattice constants of Ce_{1-x}Ln_xO_{2-x/2} ($x = 0.3$) are summarized in Table I. This table also contains several three component compounds, where the sum of the substituting components is $x = 0.3$. As seen from this table, the lattice constants decrease as the ionic radii of the substituting ions become smaller. When the system contains two kinds of substituting ions, the lattice constants fall into the intermediate values of two respective single-substituting ion cases. Thus it appeared that the lattice constant additivity rule holds in the system Ce_{1-x}Ln_xO_{2-x/2}.

Figure 2 shows the lattice constant change when the amount of Gd substitution was changed. Magnesia, like Ln₂O₃, dissolves into the lattice to form a solid solution. This was proven by the fact that the lattice constants of MgO-free compounds were larger than those of MgO-added compounds and the fact that there were no x-ray diffraction peaks comprising MgO. The saturation of lattice constant at $x \geq 0.4$ does not necessarily mean that the solubility limit exists at $x = 0.4$.

Bevan, Barker, and Martin (8) interpreted that this saturation is due to the Gd³⁺ ions and oxygen vacancies' strong interaction and that point defects are complexed. A similar phenomenon was observed by Brauer and Gradiger (9), and they also observed a

Table I. Lattice constants, ΔE_L and ΔE_H , and $(\rho_o)_L$ and $(\rho_o)_H$ of conduction for the compounds Ce_{1-x}Ln_xO_{2-x/2} ($x = 0.3$)

Ln ^(a)	Lattice ^(c) const (Å)	ΔE_L ^(d) (eV)	ΔE_H ^(d) (eV)	$(\rho_o)_L$ ^(d) (ohm-cm)	$(\rho_o)_H$ ^(d) (ohm-cm)
Y	5.398	1.12	0.91	8.5×10^{-5}	1.4×10^{-3}
La	5.503	0.94	0.81	7.3×10^{-4}	4.0×10^{-3}
Nd	5.460	0.96	0.81	3.0×10^{-4}	2.7×10^{-3}
Sm	5.442	0.98	0.78	2.5×10^{-4}	4.4×10^{-3}
Eu	5.433	1.03	0.81	8.3×10^{-5}	2.5×10^{-3}
Gd	5.428	1.05	0.84	1.6×10^{-4}	2.0×10^{-3}
Dy	5.406	1.12	0.88	5.8×10^{-5}	3.1×10^{-3}
Ho	5.398	1.13	0.93	6.5×10^{-5}	9.3×10^{-4}
Er	5.391	1.14	0.93	6.8×10^{-5}	1.0×10^{-3}
Yb	5.379	1.08	0.89	1.8×10^{-4}	2.1×10^{-3}
1Sm-4Ho ^(b)	5.408	1.11	0.89	9.6×10^{-5}	1.7×10^{-3}
4Sm-1Ho	5.434	0.99	0.81	2.2×10^{-4}	2.5×10^{-3}
1Sm-4Y	5.407	1.11	0.87	7.8×10^{-5}	1.8×10^{-3}
4Sm-1Y	5.434	1.00	0.80	2.4×10^{-4}	3.8×10^{-3}
1Dy-1Gd	5.417	1.03	0.87	1.6×10^{-4}	1.5×10^{-3}

^(a) Scandium does not form fluorite lattice with cerium.

^(b) Notations like 1Sm-4Ho mean the atomic ratio of Ln, thus, the exact formula for 1Sm-4Ho is Ce_{0.75}Sm_{0.0625}Ho_{0.24}O_{1.83}.

^(c) Lattice constant values are valid to the final digits.

^(d) Activation energies and (ρ_o) 's are valid within ± 0.5 of the final digits.

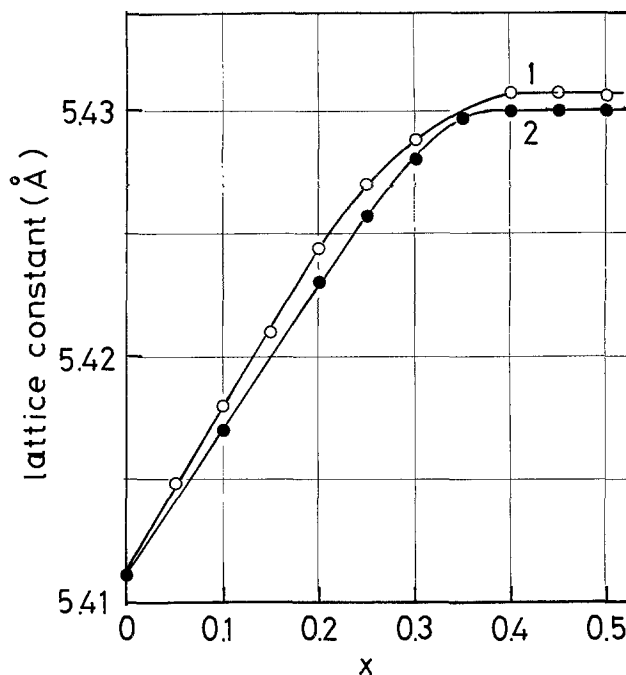


Fig. 2. Lattice constant change of Ce_{1-x}Gd_xO_{2-x/2} as Gd content is changed. Curves 1 and 2 represent data for MgO free and 3% MgO added samples, respectively.

sharp decrease of lattice constant at $x \geq 0.5$. As the fluorite lattice and the c-type Gd₂O₃ give quite similar x-ray diffraction patterns, it is difficult to determine the solubility limit precisely by this method. In our measurements, diffraction lines caused by the existence of superlattice in the compounds which could appear for c-type oxide, were not observed up to $x = 0.5$. Above this value, weak lines from superlattices were observed. Thus, it is reasonable to conclude that the system CeO₂-Gd₂O₃ keeps the fluorite lattice up to $x = 0.5$.

Figure 3 shows the lattice constant increase of the compounds Ce_{1-x}Gd_xO_{2-x/2} as the temperature is raised. The change of the lattice constant is almost linear regardless of composition, in the temperature range between room temperature and 1000°C. The average linear expansion coefficient of these compounds as calculated from Fig. 3 is $\beta = 12.6 \times 10^{-6} \text{ } ^\circ\text{C}^{-1}$ for the three compounds measured. The compounds Ce_{1-x}Gd_xO_{2-x/2} do not have any transitions

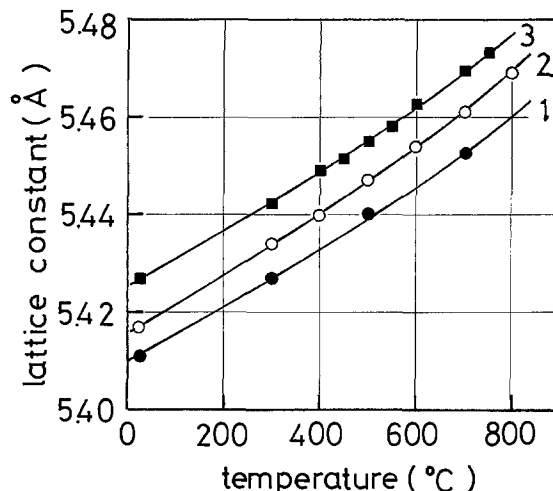


Fig. 3. Thermal expansion of lattice constants for Ce_{1-x}Gd_xO_{2-x/2}. Curves 1, 2, and 3 are for $x = 0, 0.1,$ and 0.2 . The average linear thermal expansion coefficient for these compounds are $12.6 \times 10^{-6} \text{ } ^\circ\text{C}^{-1}$.

observable by x-ray diffraction in this temperature range.

Oxygen ion transference number.—The charge carrier of the conduction is considered to be O^{-2} ion. In this section, results of oxygen ion transference number measurements are presented.

Figure 4 is the change of oxygen ion transference number as the temperature is changed. The emf measurement cell setup was expressed in Eq. [2].

At temperatures lower than 400°C , the resistivity is so high that it prohibits the emf measurements. The emf value deviated from the theoretical one at temperatures below $600^{\circ}\text{--}700^{\circ}\text{C}$ for all samples. The reasons were considered to be as follows. The porous platinum paste electrode does not function as a reversible oxygen electrode at lower temperatures, suggesting a reaction polarization becomes critical at these temperatures. In this sense, Fig. 4 does not show the correct transference numbers for these samples at temperatures below $600^{\circ}\text{--}700^{\circ}\text{C}$. Silver electrodes would have been better at lower temperatures as reversible oxygen electrodes. Above these temperatures, however, all the investigated compounds showed stable and reproducible emf values. The transference number for $\text{Ce}_{1-x}\text{Ln}_x\text{O}_{2-x/2}$ ($\text{Ln} = \text{Sm}$ and Dy) saturates at 0.95–0.96, whereas the other compounds containing Nd, Gd, and Er gave unity as their transference number. The reason of deviation of transference number from unity in the cases of the compounds containing Sm and Dy is not known yet, however, the porosities of the two samples were measured to be a little larger than the other samples suggesting there existed some open pores in these samples.

From these data and in view of the analogy of crystal structure with ZrO_2 , it was concluded that the charge carrier of conduction in $\text{Ce}_{1-x}\text{Ln}_x\text{O}_{2-x/2}$ in air is the oxygen ion.

Resistivity measurement.—Figures 5 and 6 show the relation between log resistivity and the reciprocal temperature for the compounds $\text{Ce}_{0.7}\text{Ln}_{0.3}\text{O}_{1.85}$ ($\text{Ln} = \text{Y}, \text{La}, \text{Eu}, \text{Sm}, \text{Gd}, \text{Dy}, \text{Ho}, \text{Er},$ and Yb). All plots show the two differing slope lines. Around the intersection of two lines, however, data deviated from linear lines toward the high resistivity side. The resistivity values of these compounds are very small (1/10 to 1/1000) compared with those listed by Etsell and Flengas (7). However, the resistivity measurements by a-c and d-c methods gave good agreement and they are quite reproducible as shown by the plots in Fig. 5 and 6, it is believed that our data represent true resistivities for these compounds.

Figure 7 shows the resistivity isotherms against lattice constant. In these plots, resistivity values ρ were

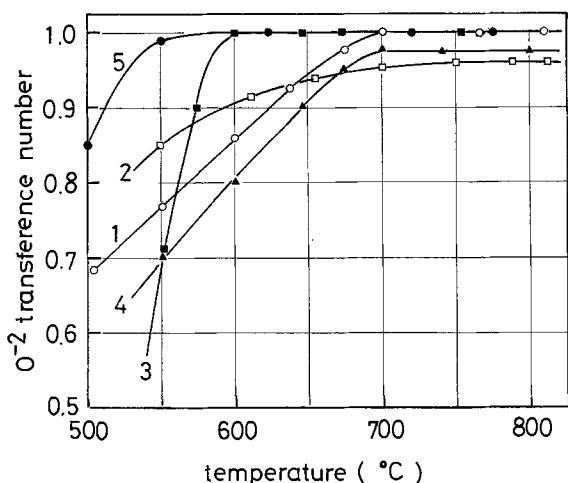


Fig. 4. Oxygen ion transference number of the compounds $\text{Ce}_{1-x}\text{Ln}_x\text{O}_{2-x/2}$ ($x = 0.3$). Curves 1–5 are for $\text{Ln} = \text{Nd}, \text{Sm}, \text{Gd}, \text{Dy},$ and Er .

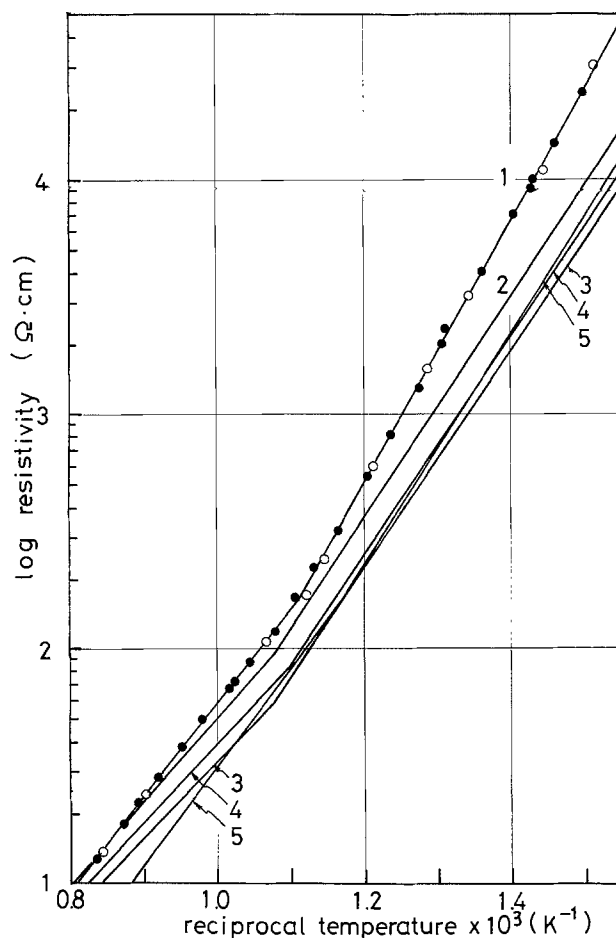


Fig. 5. Arrhenius plot of resistivity for the compounds $\text{Ce}_{1-x}\text{Ln}_x\text{O}_{2-x/2}$ ($x = 0.3$). Lines 1–5 are for $\text{Ln} = \text{Y}, \text{La}, \text{Nd}, \text{Sm},$ and Er . Filled circles are for rising temperature, and open circles are for lowering temperature measurements.

corrected in consideration of samples' porosity according to Juretschuke's formula (10)

$$\rho = \frac{1 - \epsilon}{1 + \frac{\epsilon}{2}} \rho_{\text{obs}} \quad [4]$$

where symbol ϵ stands for the porosity of samples. Each isotherm has its minimum resistivity value at a certain lattice constant. This provides a guideline for the minimization of the resistivity at various temperatures. For example, in order to get a low resistivity solid electrolyte at 800°C , it would be advisable to investigate the compositions whose lattice constants range from 5.43 to 5.44\AA . The fact that there exists a minimum resistivity value in the resistivity and lattice constant plot suggests the existence of a certain compensation rule between pre-exponential term ρ_0 and the activation energy ΔE in the Arrhenius-type formula.

The resistivity change of the compounds $\text{Ce}_{1-x}\text{Gd}_x\text{O}_{2-x/2}$ vs. temperature is shown in Fig. 8. At temperatures lower than 350°C , some samples showed small ΔE of conduction which suggested the onset of an electronic conduction; however, the data were lacking in reproducibility.

In the temperature range where the oxygen ionic conduction is predominant, the plot of resistivity vs. the reciprocal temperature could well be approximated by two linear lines. Similar results were obtained by Bauerle and Hrizo (11) for $(\text{ZrO}_2)_{0.90}(\text{Y}_2\text{O}_3)_{0.10}$. They proposed two hypotheses which yield such a temperature dependence; one being the vacancy trapping by yttrium ions, and the other, the grain boundary effect.

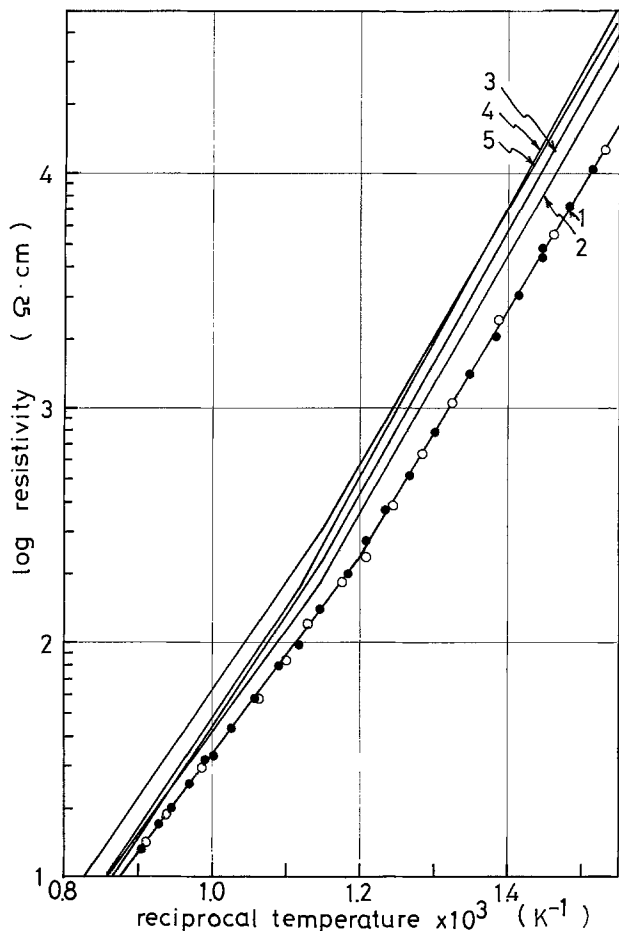


Fig. 6. Arrhenius plot of resistivity for the compounds $Ce_{1-x}Ln_xO_{2-x/2}$ ($x = 0.3$). Lines 1-5 are for Ln = Gd, Dy, Ho, Er, and Yb. Filled circles are for rising temperature, and open circles are for lowering temperature measurements.

These hypotheses are open to discussion, however, if the $\log \rho$ vs. T^{-1} relation was approximated by the two linear lines, it means that we assumed two Arrhenius-type formulas

$$\begin{aligned} \rho &= (\rho_o)_L \exp(\Delta E_L/kT) \quad \text{lower temp region} \\ \rho &= (\rho_o)_H \exp(\Delta E_H/kT) \quad \text{higher temp region} \end{aligned} \quad [5]$$

Then the temperature range could appropriately be divided into two regions, the boundary being the intersection point of the Arrhenius plot. The calculated (ρ_o) 's and ΔE 's are listed in Table I. The lower temperature region has a larger activation energy and the higher temperature region has a lower activation energy. The activation energy of CeO_2 -15% La_2O_3 as given by other workers are 14.7 (12) or 21.0 (4) kcal/mol (0.64 or 0.91 eV). Our results of activation energy for Ln doped compounds fall in the range of 0.77-0.93 eV for high temperature region conduction. Thus, data by Croatto and Mayer (12) seem to be too small. The calculated activation energies of conduction were interpreted in terms of lattice constant. The result is shown in Fig. 9.

The lattice constant a_o of $Ce_{0.7}Ln_{0.3}O_{1.85}$ changes in the range from 5.38 Å (Ln = Yb) to 5.50 Å (Ln = La). The activation energies of conduction ΔE_L and ΔE_H pass the maximum values at $a_o = 5.39$ Å, then they decrease as the lattice constant becomes larger. In the range where $a_o \geq 5.45$ Å, both activation energies ΔE_L and ΔE_H seem to be determined not by the kind of lanthanoid elements but by the value of lattice constant.

If the dopant concentration x is varied, the above discussion no longer holds. Figure 10 shows the activation energy change when the dopant concentration x

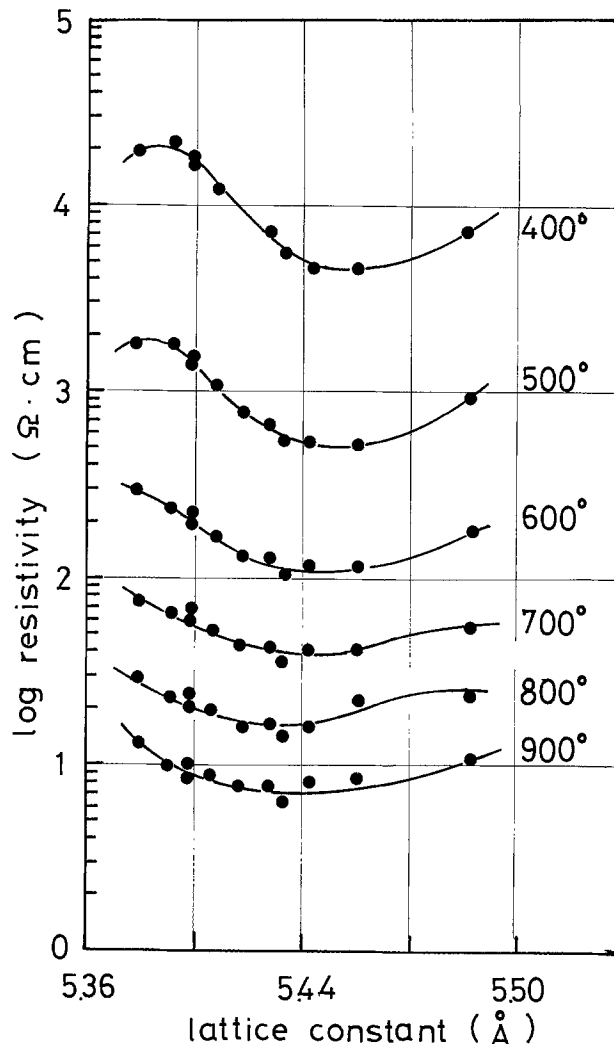


Fig. 7. Resistivity isotherms as summarized vs. lattice constant for the compounds $Ce_{1-x}Ln_xO_{2-x/2}$ ($x = 0.3$).

is varied for the compounds $Ce_{1-x}Gd_xO_{2-x/2}$ ($0 \leq x \leq 0.5$). As seen from this figure, the activation energy remains comparably constant in the range $x \leq 0.2$. The values increase rapidly as x is increased in the range where $0.3 \leq x \leq 0.4$. The sharp increase of activation energies in this range is paralleled by the saturation range of lattice constants. We suggested that interaction between vacancy-vacancy and vacancy-doped ion begins to start. Here, again this sharp increase could be attributed to this effect reducing the mobility of oxygen ion vacancies. Above $x = 0.4$, the activation energies of lower and higher temperature regions coincide and the value increases gradually as x is increased. Heyne (13) argues that in stabilized ZrO_2 , the conductivity increase cannot be interpreted by the simple concept of a conductivity proportional to the vacancy concentration. In CeO_2 base compounds, however, this concept can explain the increase of conductivity at least in the range $x \leq 0.2$.

As mentioned before, the cause of the existence of two activation energies of O^{2-} conduction is not known at present, however, it was observed by DTA measurements that the base line of the DTA curve deviates to the endothermic side at temperatures near 500°C for the compounds $Ce_{1-x}Gd_xO_{2-x/2}$ ($0 \leq x \leq 0.5$) suggesting an increase of the specific heat of the compounds. This increase does not necessarily mean the existence of transition in the crystal lattice as x-ray measurement revealed no pattern change between lower and higher temperatures. However, it seems likely that some higher order transition other than lattice type change occurs around 500°C and that this is the reason for the existence of kinks in the Arrhenius plots of

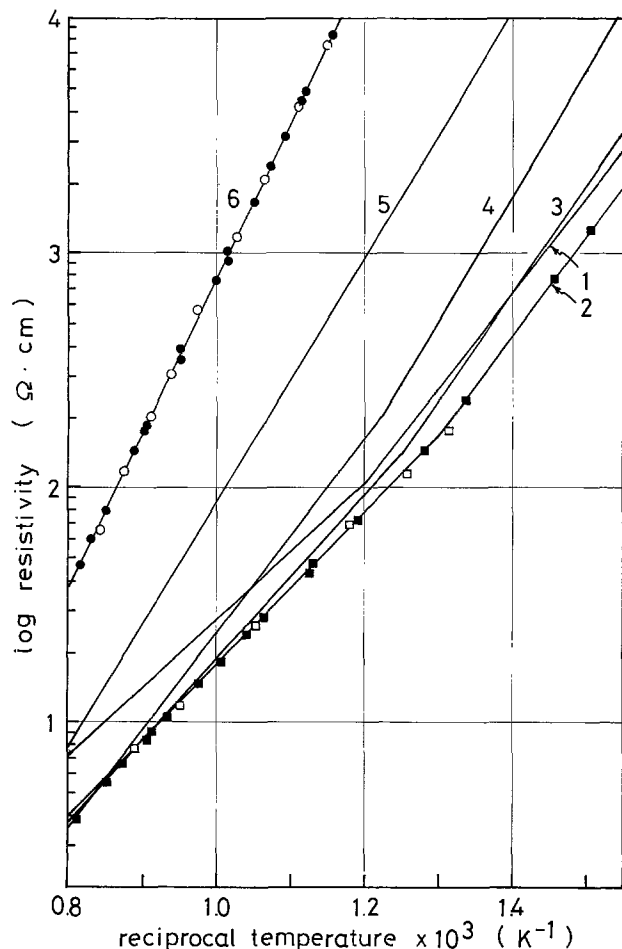


Fig. 8. Arrhenius plot of resistivity for the compounds $Ce_{1-x}Gd_xO_{2-x/2}$. Lines 1-6 are for $x = 0.1, 0.2, 0.25, 0.3, 0.4,$ and 0.5 . Filled plots are for rising temperature, and open plots are for lowering temperature measurements.

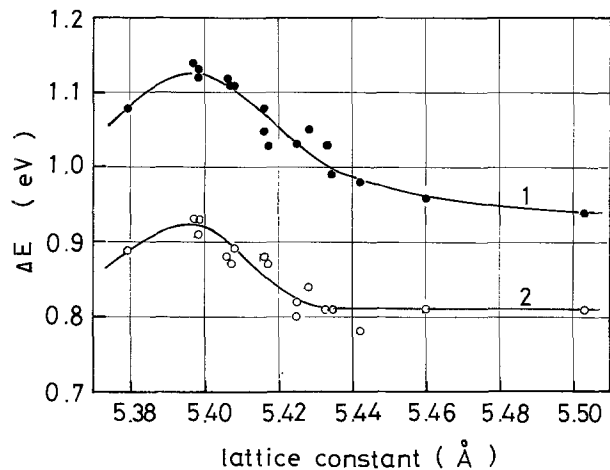


Fig. 9. Activation energy of oxygen ion conduction for the compounds $Ce_{1-x}Ln_xO_{2-x/2}$. Curves 1 and 2 are for low and high temperature regions.

resistivity. Further study is underway and the results will be published elsewhere.

Conclusion

The CeO_2 base fluorite-type solid solution $Ce_{1-x}Ln_xO_{2-x/2}$ ($Ln =$ lanthanoid element) can be characterized as a family of good conductive oxygen ion solid electrolytes. The following are the conclusions derived from this study.

1. The transference number of the oxygen ion as measured by an emf cell method using the oxygen concentration cell is greater than 0.95 at temperatures

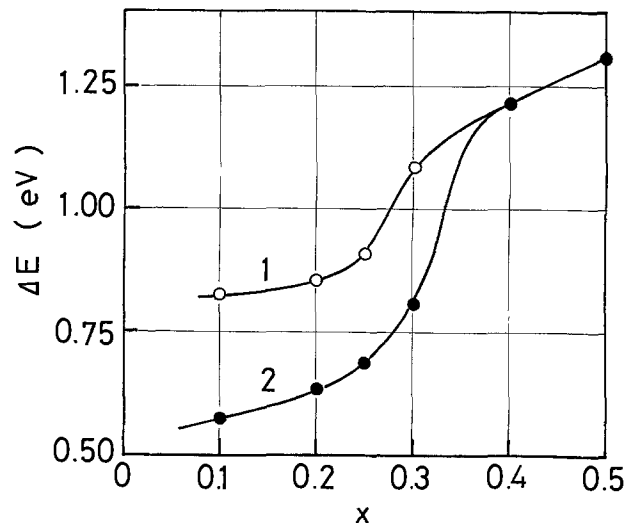


Fig. 10. Activation energy of oxygen ion conduction for the compounds $Ce_{1-x}Gd_xO_{2-x/2}$. Curves 1 and 2 are for low and high temperature regions. Above $x = 0.4$, both activation energies coincide.

above $600^\circ C$ for $Ce_{1-x}Ln_xO_{2-x/2}$ ($Ln = Nd, Sm, Gd, Dy,$ and Er).

2. The compounds $Ce_{1-x}Ln_xO_{2-x/2}$ ($x = 0.5$; $Ln = Y, La, Nd, Sm, Eu, Ho, Er,$ and Yb) are single phase fluorite-type solid solutions. The compounds containing Sc do not form a solid solution in the same range.

3. The Arrhenius type plot of resistivity is well approximated by two linear lines in the temperature range $T \approx 400^\circ C$. At lower temperatures electronic conduction is observed in some compounds. The resistivity of $Ce_{1-x}Ge_xO_{2-x/2}$ ($x = 0.23$) at $750^\circ C$ is 15 ohm-cm which rivals the value of calcia stabilized zirconia at $1000^\circ C$. The slope of the Arrhenius plot gives the activation energy of oxygen ion conduction, the value of which is determined by the dimension of the crystal lattice so long as dopant concentration x is kept constant. For $x = 0.3$, ΔE 's pass the maximum values at $a_0 = 5.39 \text{ \AA}$.

Acknowledgments

The authors wish to thank Dr. Y. Maki for his continuous encouragement and helpful discussions throughout this work.

Manuscript submitted Jan. 30, 1974; revised manuscript received June 24, 1974.

Any discussion of this paper will appear in a Discussion Section to be published in the December 1975 JOURNAL. All discussions for the December 1975 Discussion Section should be submitted by Aug. 1, 1975.

Publication costs of this article were partially assisted by Hitachi, Limited.

REFERENCES

1. C. Wagner, *Naturwissenschaften*, **31**, 265 (1943).
2. F. Z. Hund, *Z. Phys. Chem.*, **199**, 142 (1952).
3. H. Tannenberger, *Proc. Int. Etude Pile Comb.*, **III**, 19 (1965).
4. D. Singman, *This Journal*, **113**, 502 (1966).
5. R. Mazelsky, *ibid.*, **111**, 528 (1964).
6. H. Iwahara, *Denki Kagaku (Japan)*, **34**, 254 (1966).
7. T. H. Etsell and S. N. Flengas, *Chem. Rev.*, **70**, 339 (1970).
8. D. J. M. Bevan, W. W. Barker, and R. L. Martin, in "Proceedings of the 4th Conference on Rare Earth Research, Phoenix, Ariz. 1964," L. Eyring, Editor, p. 441, Gordon and Breach, New York (1965).
9. G. Brauer and H. Gradiger, *Z. Anorg. Allgem. Chem.*, **276**, 209 (1954).
10. H. J. Juretschke, *J. Appl. Phys.*, **27**, 838 (1956).
11. J. E. Bauerle and J. Hrizo, *J. Phys. Chem. Solids*, **30**, 565 (1969).
12. U. Croatto and A. Mayer, *Gazz. Chim. Ital.*, **73**, 199 (1943).
13. L. Heyne, *Electrochim. Acta*, **15**, 1251 (1970).

Charge Storage and Stoichiometry in Electron Beam Evaporated Alumina

Konrad M. Eisele

Institut fuer Angewandte Festkoerperphysik, Freiburg, Germany

ABSTRACT

Alumina films have been evaporated by means of an electron beam onto metal electrodes on ceramic substrates. A metal-oxide-metal structure has been subjected to an electric field and the resulting charge storage measured by recording the short circuit current. The charge storage has been related to the stoichiometry of the alumina film which in turn has been influenced by the beam power or by postdeposition treatment. The effect of electric field and temperature on the charge stored has been studied.

In a recent publication (1) aluminum oxide films have been examined for their ability to act as a barrier against alkali ion migration. This property makes such films useful as a passivation layer for integrated circuits. In these applications a low temperature process to generate the Al_2O_3 film is desirable. For this reason electron beam evaporation was considered.

It is known that this method yields Al_2O_3 films which are nonstoichiometric to various degrees. Hoffman and Leibowitz (2) showed that the stoichiometry can be regulated by controlling the potential of the substrate in such a way that secondary or reflected primary electrons coming from the hearth cannot build up charge which repels arriving oxygen ions. Whenever oxygen atoms emanate from Al_2O_3 under electron bombardment, part of these will be pumped away by the vacuum system and necessarily a certain lack of stoichiometry must result.

To study the electrical properties, especially charge storage as related to the stoichiometry of the oxide, we manufactured Al- Al_2O_3 -Al sandwiches by means of an electron gun.

The Metal-Alumina-Metal Capacitor

The active area of the device (Fig. 1) was 0.185 cm^2 , and the oxide thickness varied between 4,200 and 28,000 Å resulting in capacities from 150 to 24 pf/mm². The substrate was glazed ceramic. The structure was obtained by evaporating through nickel masks; no etching was employed. Four different metals were used as electrodes. The deposition rates of the aluminum oxide varied from 10 to 400 Å/min. The power of the electron beam determined the deposition rate but also the decomposition of the source material.

In view of Ref. (2) the quantity of stray electrons responsible for charge buildup increases with the power of the primary beam. In our arrangement the masking device as well as the bottom electrode was grounded, so that secondary or reflected primary electrons moved between points of equal potential, i.e., between the grounded hearth and the substrate.

At a power level of about 320W (4 kV, 80 mA) a blue glow appeared over the source material. The pressure in the vacuum system, usually in the low 10^{-6} Torr range, increased at this point indicating the liberation of oxygen from the aluminum oxide. With greater beam power the resulting Al_2O_3 film became increasingly darker in color. In addition the source material turned dark indicating loss of oxygen.

The influence of the electron beam acceleration voltage on the film composition was established by electron microprobe analysis and then correlated with the charge storage measurements. The index of refraction was derived from ellipsometer readings as being 1.762 compared to 1.765 for the bulk material and was the same for all samples. Electron diffraction analysis re-

vealed no crystallinity. The electrical measurements could not distinguish between films deposited at various substrate temperatures in the range from 670° to 77°K. The best films were able to withstand fields as high as $5 \times 10^6 \text{ V/cm}$.

Comparative measurements will be presented of two samples designated D₂ and D₄ representing the typical properties obtained with low and high beam power, respectively. For plate D₂ the evaporation of the Al_2O_3 was performed with low beam voltage (2.9 kV; 125 mA) and correspondingly low deposition rate (110 Å/min). The film was clear, of very low conductivity, and exhibited low charge storage. In contrast D₄ was deposited with high beam voltage (8 kV, 170 mA) at a rate of 410 Å/min which resulted in a dark film with a relatively high conductivity and charge storage. Between these extremes, various degrees of oxygen deficiency were produced.

Charge Storage in the Aluminum Oxide

Trap states have been encountered in various experiments with insulating films. They can store charge to change the space charge distribution in the insulator (3). Because the number of free electrons in an insulator is very small, a relatively small number of electrons getting trapped will suffice to change the charge distribution markedly.

One can assume that at a given temperature an equilibrium situation is established whereby a certain number of the traps are charged. If the metal-oxide-metal sandwich is now connected to a battery (Fig. 2), electrons will fill traps at the negative electrode and will leave them at the positive electrode. After the sample is disconnected the charge distribution is no longer in equilibrium. If the two metal electrodes are then

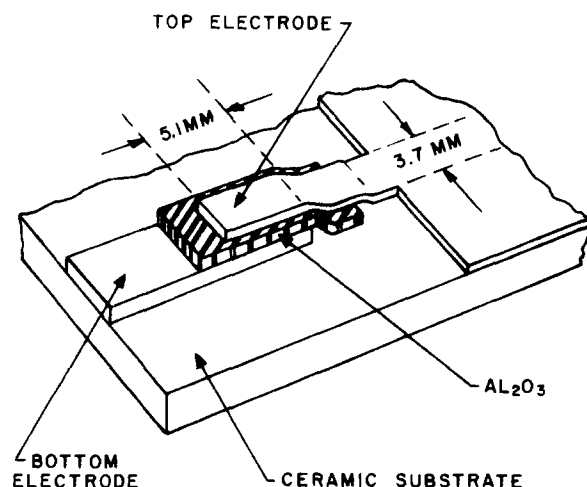


Fig. 1. Sample structure

Key words: Al_2O_3 films, stoichiometry, charge storage.

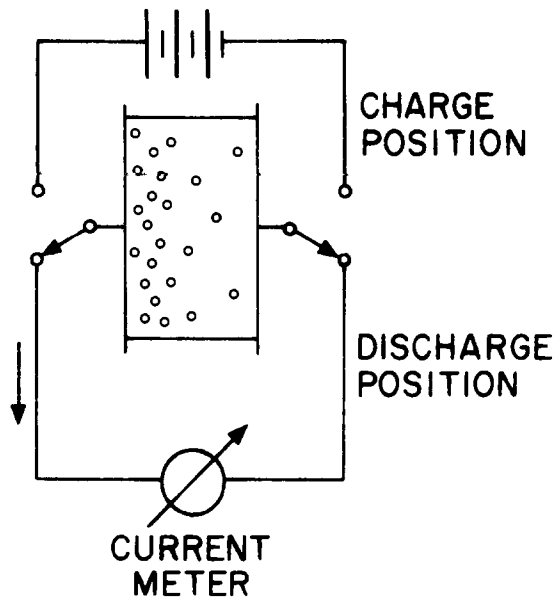


Fig. 2. Principle of charge storage measurement

shorted by an external conducting loop the electrons will flow in such a way as to restore equilibrium. This current was measured to investigate the number and the behavior of the trap states.

It is necessary to note that if the trapped charge was uniformly distributed in the oxide, no current would be measured in the outside loop. For this reason it is not entirely obvious that the measured current is proportional to the charge stored.

The following observation induced us to use this current as a representative quantity for investigating the alumina film. The stored charge increased measurably with the time the capacitor was connected to the voltage source but only during the first 30 min and stayed constant thereafter. Charging times of several hours did not equalize the charge distribution which would have resulted in a reduced or vanishing discharge current. There was also no saturation observed with increasing fields. In several attempts the voltage was increased to produce fields of 6×10^6 V/cm until breakdown occurred without the measured charge leveling off. In films that had low leakage up to high voltages, the increase of charge storage with voltage was close to linear. An example is presented in Fig. 3.

There have been cases (4) reported in which the charge distribution was opposite to the situation described here. But the reproducibility and the consistency with which we found the electron-injecting electrode always next to the volume of higher charge storage lead us to accept the current as a measure of the number of chargeable traps present.

For comparative measurements the voltage applied was 48V, the charging time was chosen to be 1 hr and so was the discharge time over which the current was integrated to determine the charge stored, although the discharge continued for several hours more. The contribution of the capacitive discharge to the recorded charge was not measurable because the RC product of the circuit was always $< 10^{-3}$ sec, too small to appear on the graph.

Four methods are available to influence the oxygen content of the film: (i) to evaporate at various oxygen pressures, (ii) to use different acceleration voltages on the electron beam, (iii) to control the substrate potential, and (iv) to heat the film in an oxidizing atmosphere. Table I lists the results of an experiment on three plates each with several capacitors. The film subjected to the most intensive oxidation process showed the least charge storage. Even more conclusive evidence is obtained when the same film is successively subjected to various degrees of oxidation. To this end the charge storage of a device was measured before and

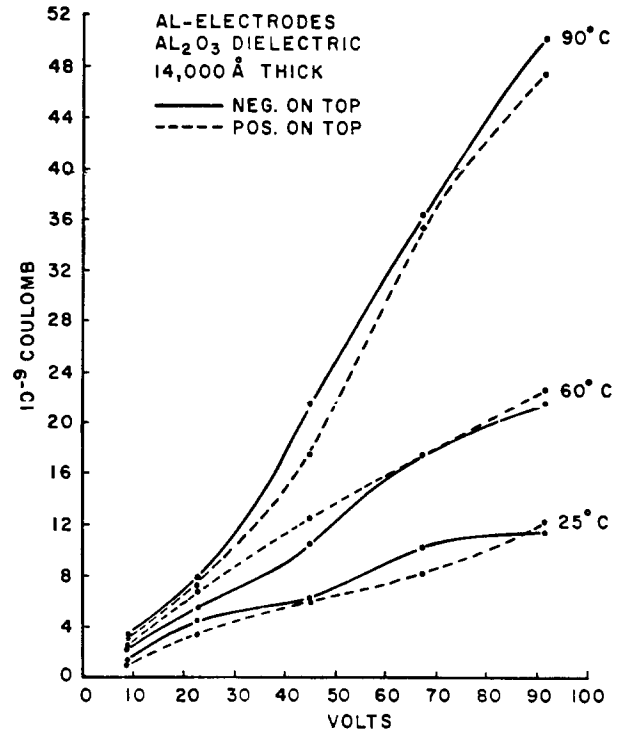


Fig. 3. Charge stored in dependence on voltage and temperature

after heating to 350°C in air for 6 hr. The average charge storage changed from 1440.8 to 165 nC. This change in storage capability supports the argument that the traps are associated with missing oxygen atoms.

To exclude the possibility of the heat-treatment alone reducing the traps, a plate was prepared on which the film was measured after manufacture, then fired at 380°C for 7 hr in dry hydrogen, and finally fired at 380°C for 7 hr in oxygen. The results for two samples are listed in Table II. No appreciable change was observed after the hydrogen firing, but the oxygen firing did reduce the trap density.

The dependence of the charge storage on temperature is shown in Fig. 3, which is typical of the many graphs plotted. When the dielectric is heated it stores considerably more charge than when cold. Conversely, when the film is cooled to liquid nitrogen temperature, charging or discharging of traps stops immediately. Discharge will continue after warm-up at the rate obtained prior to immersing the plate in the coolant. While

Table I. Effect of exposure to oxygen during and after deposition

	Thick-ness, Å	Charge stored $\times 10^9$ coulombs
Hot substrate		2393
High beam power	6890	
Vacuum 10^{-5} Torr		2335
Hot substrate		1151
High beam power	5400	889
O ₂ pressure 10^{-4} Torr		851
Plate fired at 400°C in oxygen	6860	12
		48

Table II. Test slide with aluminum electrodes and alumina dielectric 15,000 Å thick

Treatment after deposition of Al ₂ O ₃	Charge stored $\times 10^9$ coulombs
None	986
	776
Fired in dry H ₂	870
380°C, 7 hr	793
Fired in O ₂	270
380°C, 7 hr	266

the substrate is at liquid nitrogen temperature, no charge can be stored.

In many samples the charge storage was not symmetric with respect to polarity even though both electrodes were of the same material. Almost invariably the larger amount was stored when the negative electrode was on top, that is, near the oxide that had been deposited last. The source material has been subjected to electron bombardment for a longer time and consequently was more oxygen depleted.

Critical comparisons between various metal electrodes have to be made on the same slide. To this end a slide was prepared on which the bottom electrodes were all aluminum and only the top electrodes differed. They were of gold, copper, aluminum, and indium. The results are listed in Table III. Gold achieved the largest storage and aluminum the least. This was also evident from a slide (Table IV) in which the top and bottom electrode were of the same metal. Unfortunately the barrier heights of these metals against Al_2O_3 published by Hurst and Ruppel (5) do not explain the variation in charge storage. More recent measurements of the Al- Al_2O_3 -Al work function (6, 7), differ substantially from those of Hurst and Ruppel. For thermally oxidized aluminum Gundlach (6) measured 1.6-1.8 eV; for an aluminum electrode evaporated onto the oxide he measured values larger than 2.3 eV. Antula (8) also reports that the barrier in question depends on the process by which the Al_2O_3 film was made. This adds more complexity to the problem but may provide the key to the differences in conductivity of the various samples.

Under the assumption of the traps being distributed in the bandgap, Lindmayer (8) derived a 1/time dependence of the discharge current. Although we did find a 1/time dependence (Fig. 4) for some of the samples, a $1/t^m$ with $m = 0.35 \dots 0.44$ was frequently found.

D-C Measurements

As mentioned earlier, the insulating films of the plates D₂ and D₄ were produced with low and high beam voltage, respectively. Correspondingly their charge storage differed widely. D₂ stored 45 nC and D₄ 350 nC. These plates were chosen for the I-V measurements. A process considered relevant for the transport of electrons in the Al_2O_3 film is the Poole-Frenkel effect. The electrons tunnel into trap states from which they escape again by field-enhanced thermal excitation to be trapped again further down the field. This process repeats until the opposite metal electrode is reached. Following Mead's analysis (10) $\log I$ is plotted vs. $v^{1/2}$

Table III. Test slide with aluminum bottom electrode and alumina dielectric 6000 Å

Top electrode	Charge stored Top pos.	$\times 10^9$ coulombs Top neg.	Capacity, pf
Gold	2395 2449	2413 2874	2018
Copper	1705	1585 1899	1983
Indium	—	705	2015
Aluminum	391	341	1987

Table IV. Test slide with 6000 Å alumina film

Electrode material	Charge stored $\times 10^9$ coulombs
Gold-gold	75,630 67,760
Copper-copper	25,220 25,666
Indium-indium	25,160
Aluminum-aluminum	678 679

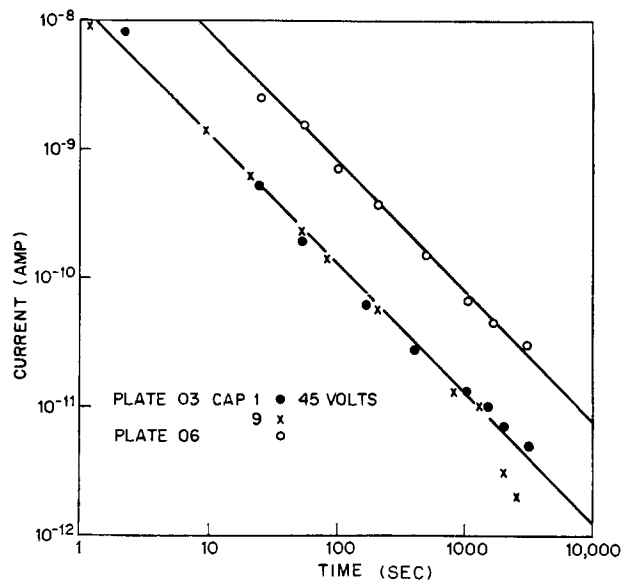


Fig. 4. Discharge current vs. time

in Fig. 5. The dashed line represents the slope obtained from the equation for space charge limited current using the static dielectric constant of $\epsilon = 8$. The corresponding current density is

$$J_1 = C_1 E \exp \{ (\beta v^{1/2} - q\phi) / kT \} \quad [1]$$

with

$$\beta = \sqrt{q^3 / \pi \epsilon \epsilon_0 d} \quad [2]$$

where C_1 is a constant, E the electric field, v the voltage, ϕ the depth of the trap potential well, q the electronic charge, and d the thickness of the film. If the current is controlled by the metal-insulator barrier rather than the bulk of the dielectric, the slope is half of the value in Eq. [2]. This is entered in Fig. 5 as a

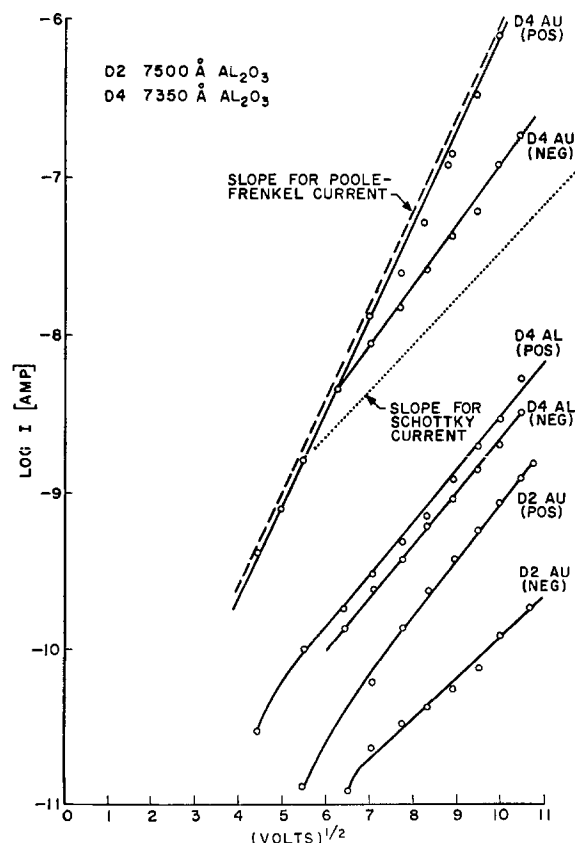


Fig. 5. Current-voltage characteristics

dotted line. For high fields the logarithm of the current followed a straight line. The current depended on the electrode material, the polarity, and it showed differences for oxides obtained under various conditions. Usually a dependence of current on polarity suggests an electrode-controlled transport mechanism. In the case presented here a sensitivity to polarity may be caused by differences in the oxide deposited at the beginning and the end of the evaporation as mentioned previously. The vertical position of the current-voltage curve is governed by the potential barrier ϕ and the density of the trap sites. The latter depends on the oxygen deficiency as derived from charge storage measurements. The slope of the straight section of the plot is controlled only by the dielectric constant and the thickness of the film. The question arises as to which dielectric constant should be used (11). The bulk dielectric constant of highly crystalline Al_2O_3 is as high as 13 from d-c to microwave frequencies and 3.1 at optical frequencies. The dielectric constants of these films were measured to be between 7.3 and 9.8, a difference too small to explain the differing slopes of the I-V characteristic in Fig. 5.

The current transport by means of trap states is temperature dependent as required by Eq. [1]. From charge storage measurements we recall that at some temperature below 0°C the movement in and out of traps was unmeasurable. Therefore, if we measure the dependence of the current on temperature we should find a corresponding behavior. This is indeed borne out by measurements plotted in Fig. 6. Below 260°K the current is independent of temperature as seen with sample D_6 which was typical of those measured over the available temperature range. Above 400°K the current rises steeply. The slopes of the straight portions of the current rise in Fig. 6 can be used to calculate the activation energy of the traps. To this end we write Eq. [1] as follows

$$\ln J = \ln C + \ln E - \frac{1}{T} \left(\frac{\beta v^{1/2}}{k} - \frac{q\phi}{k} \right)$$

where the term in brackets represents the slope of the

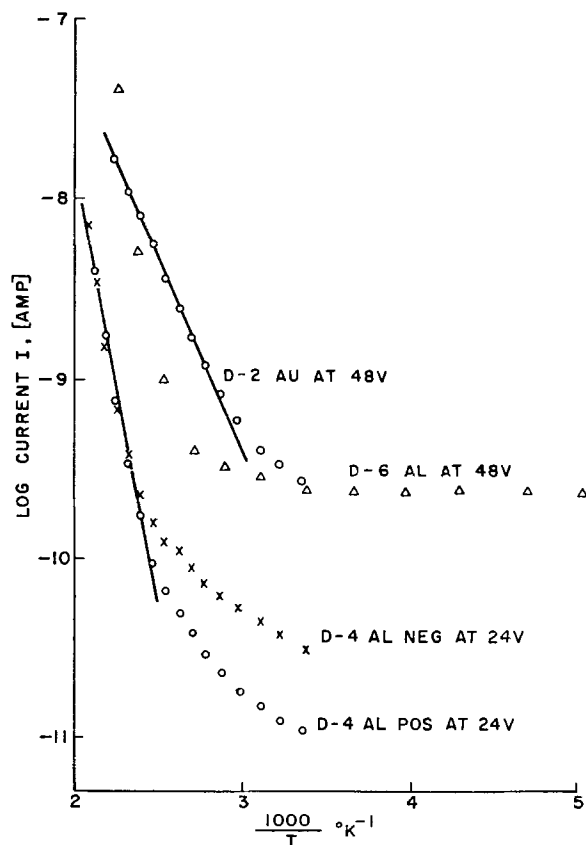


Fig. 6. Dependence of current on temperature

straight portion of the curve (D4) and the remaining terms the current for $1/T = 0$. Both numbers are obtained from the graph and yield $\phi = 1.08\text{V}$ and $C = 3.67 \cdot 10^{-4} \text{ A V}^{-1} \text{ cm}^{-1}$.

On the other hand we can write Eq. [1] as

$$\ln \left(\frac{J}{E} \right) = \ln C - \frac{q\phi}{kT} + \frac{\beta}{kT} \cdot v^{1/2}$$

and obtain from $\ln(J/E)$ for $V = 0$ again a value for ϕ by using the constant C calculated above. Sample D_4 on Fig. 5 follows most closely the characteristics of a Poole-Frenkel mechanism and was chosen for the calculation. The trap depth found from this measurement was $\phi = 1.13\text{V}$. The agreement with the ϕ from the thermal analysis is sufficiently good to permit the Poole-Frenkel conduction to be assumed relevant for the current transport in this alumina film.

At low temperatures thermal excitation cannot be part of the electron transport through the film. A process that depends only on the field is more appropriate. Electrons are tunneling from traps into other traps further down the field and eventually into the conduction band. The current is given by (13)

$$I_2 = C_2 E/E_0 \exp(-E_0/E)$$

where E_0 is a function of the energy level of the trap site and the effective electron mass. At liquid nitrogen temperatures the current depended linearly on the voltage and only above 10^6 V/cm did the current rise faster than ohmic.

Electron Microprobe Analysis

For this examination alumina films $0.30 \mu\text{m}$ thick were deposited with a beam current of 50 mA and the voltage set at various values between 3 and 7 kV . The material was Al_2O_3 pressed into pellets with a specified purity of 99.9% . The beam energy of the microprobe was 4 keV . The depth of the analyzed region was $0.17 \mu\text{m}$, the x-ray emergence angle 41° , and the density of the film 3.15 g/cm^3 . The peak-to-background ratios were for

	Typically	Best
Al	630/1	1026/1
O	38/1	80/1
Si	724/1	1682/1

the minimum detectability limits were for

	Typically	Best
Al	150 ppM	115 ppM
O	3000 ppM	1317 ppM
Si	160 ppM	90 ppM

In Fig. 7 the aluminum content in atomic per cent based on 12 analyses per point and the deposition rate is plotted vs. the beam power. The dashed line represents stoichiometric proportions allowing for an impurity of 0.14 atomic per cent (a/o) of silicon which was found in the average in all samples. An increase in aluminum content for the high beam power is apparent. This corroborates the conclusion that high beam power during evaporation of Al_2O_3 results in oxygen deficiency of the film; hence, its dark appearance and the large effect which annealing these films in oxygen had on the charge storage.

For the samples obtained with 4 and 5 kV beam voltage the microprobe has indicated less aluminum than would be expected for stoichiometric proportions. We cannot offer a simple explanation, but one could argue in the following manner: the dashed line in Fig. 7 would be at 40 a/o if the Al_2O_3 were absolutely pure. Because of the detected silicon content, the line has dropped to 39.86 . If there were other impurities not detected by the microprobe, the line would run even lower and then fall close to the measured points of aluminum. For very low evaporation rates (3 kV beam voltage) the source material turned dark slowly, but

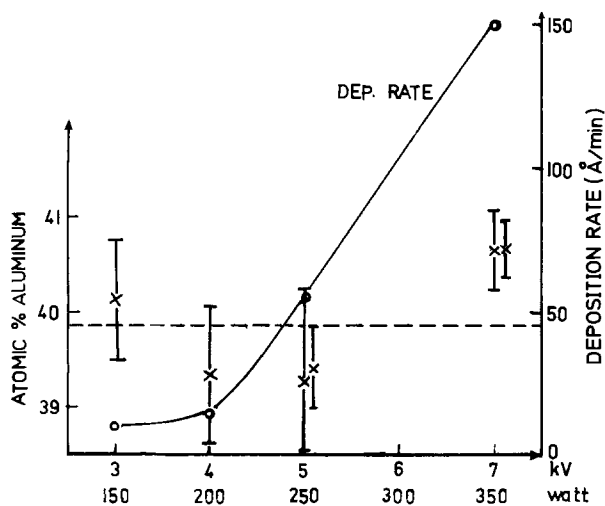


Fig. 7. The composition of the film and deposition rate for varying beam power.

because of the long times involved it became sufficiently oxygen depleted to result in poor films.

Summary

Aluminum oxide films deposited by an electron beam are aluminum rich; the degree of enrichment increasing the higher the beam power. The charge storage in the oxide is very sensitive to the degree of stoichiometry achieved. The charge storage capacity can be used to qualitatively grade the films and to study changes on postdeposition treatments. The d-c conductivity increases with decreasing oxygen content. For low conductivity, the oxide should be evaporated with a moderate beam power unless the method of Hoffman and Leibowitz is used. However, it is evident that even if electrons are prevented from striking and charging up the substrate, oxygen will still be lost through the pumping system and so not be available for complete stoichiometry of the oxide. Postdeposition heating in oxygen or air reduces both the charge storage capability and the conductivity as is expected from the trapping model used to interpret these experiments. There is a dependence on polarity due to the

loss of oxygen from the source material during the whole evaporation time. This means that the source material becomes increasingly aluminum rich during the deposition process. These particular properties may become of importance if electron gun evaporated Al_2O_3 finds application in the manufacture of integrated circuits. It would also be a means of obtaining electrets (14).

Acknowledgment

I gratefully wish to express my appreciation for the careful electron microprobe analysis of Mr. D. R. Wonsidler and the constructive criticism of Prof. N. Klein.

Manuscript submitted Jan. 17, 1974; revised manuscript received June 17, 1974.

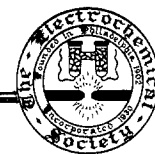
Any discussion of this paper will appear in a Discussion Section to be published in the December 1975 JOURNAL. All discussions for the December 1975 Discussion Section should be submitted by Aug. 1, 1975.

Publication costs of this article were partially assisted by the Institut fuer Angewandte Festkoerperphysik.

REFERENCES

1. R. A. Abott and T. I. Kamins, *Solid-State Electron.*, **13**, 565 (1970).
2. D. Hoffman and D. Leibowitz, *J. Vacuum Sci. Technol.*, **9**, 326 (1972).
3. D. A. Meyerhofer and S. A. Ochs, *J. Appl. Phys.*, **34**, 2535 (1963).
4. J. M. Calderwood and B. K. P. Scaife, *Proc. Roy. Soc.*, **269**, 217 (1971).
5. H. G. Hurst and W. Ruppel, *Z. Naturforsch.*, **19a**, 573 (1964).
6. K. H. Gundlach, in "Proc. of the International Symposium on Basic Problems of Thin Film Physics," Vandenhoeck and Ruprecht, Goettingen (1964).
7. S. R. Pollack and C. E. Morris, *J. Appl. Phys.*, **35**, 1503 (1964).
8. J. Antula, *Solid-State Electron.*, **9**, 825 (1966).
9. J. Lindmeyer, *J. Appl. Phys.*, **36**, 196 (1965).
10. C. A. Mead, *Phys. Rev.*, **128**, 2088 (1962).
11. S. M. Sze, *J. Appl. Phys.*, **38**, 2951 (1967).
12. M. O. Davies, Report Lewis Research Center, NASA, Feb. 1965.
13. A. G. Chynoweth, in "Progress in Semiconductors," Chap. 4, John Wiley and Sons, Inc., New York (1960).
14. L. W. Davies and R. E. Collins, *Electron. Letters*, **5**, 462 (1969).

Technical Notes



Synthesis of Rare Earth Oxysulfide Phosphors

Douglas W. Ormond*

IBM Thomas J. Watson Research Center, Yorktown Heights, New York 10598

and Ephraim Banks*

Department of Chemistry, Polytechnic Institute of New York, Brooklyn New York 11201

The rare earth oxysulfide phosphors have been of great interest recently due to their widespread applications in color television and in lighting (1, 2). Also these phosphor systems lend themselves easily to theo-

retical studies regarding luminescent mechanisms (3-5).

Though much information has been published about the synthesis of these compounds, a great deal has been deleted. This report describes the development of a clearly defined and reproducible method of synthesis of rare earth oxysulfides and phosphors derived from

* Electrochemical Society Active Member.

Key words: luminescence, phosphors, yttrium oxysulfide, lutetium oxysulfide, gadolinium oxysulfide, lanthanum oxysulfide.

them. The method involves the reaction of the sesquioxide with carefully controlled $N_2:H_2O:H_2S$ gas mixtures at temperatures near $1200^\circ C$.

There are numerous routes that will yield rare earth oxysulfides. Some of them are as follows: (i) partial hydrolysis of the sesquisulfide (6); (ii) reaction between oxide and hydrogen sulfide (7, 8); (iii) direct union of oxide and sesquisulfide (9); (iv) reaction of oxide with thioacetamide (10); (v) reduction of sulfates with carbon monoxide or hydrogen (11, 12); (vi) reduction of sulfates with an inert atmosphere which contained a small amount of hydrogen and hydrogen sulfide (8); and (vii) solid-state reaction utilizing a flux (13).

At the time of this investigation we were required to choose the proper synthesis route that would insure phosphors of the highest chemical purity, the reason being the ultrahigh resolution spectroscopy that was being performed on the final product by Sovers and Yoshioka (14, 15). With ultrahigh purity of the final product as the guiding factor, it was felt that the direct reaction between the rare earth (RE) oxides and hydrogen sulfide gas would be the best approach.

Eastman and Brewer (16, 17) have published many papers regarding RE oxysulfide preparation using dry H_2S firings. Hayes and Brown (8) used a similar approach. We started our investigation trying to reproduce these early works. One problem cropped up again and again. The problem was that the RE oxide would either be underfired (excess oxide left) or overfired (higher sulfide, discoloration present). Temperature, concentration of H_2S , moisture present, starting materials, and firing time were all too critical under the conditions stated in the literature; but by varying the concentration of H_2S and also the amount of H_2O present, we were able to control the reaction significantly. The water vapor kept the reaction from going too far and forming higher sulfides. In addition, the concentration of H_2S needed to be controlled. This was accomplished by mixing the H_2S with an inert gas, namely nitrogen.

Experimental Procedure

In order to insure dispersion of the activator in a homogeneous manner, the 99.999% pure rare earth oxides were dissolved in a minimum amount of nitric acid and then precipitated as the oxalates by slowly adding a 100% excess oxalic acid solution to the nitrate solution. The dried oxalates were then ignited to the oxides by firing in air at approximately $1000^\circ C$ for 2 hr. Tb- and Pr-containing oxides can be refired in dry H_2 to insure that the activator is in the +3 state.

A large variation of firing conditions was tried. Experimentation with a "dry" $N_2:H_2S$ type of arrangement quickly proved that the synthesis parameters involved, such as $N_2:H_2S$ ratio, firing temperature, firing time, and amount of charge in the firing vessel, were too critical. This procedure was usually too long and drawn out. It involved a series of firings to achieve the desired end product, Ln_2O_2S . Samples would usually be underfired (excess Ln_2O_3) or overfired (discoloration indicating higher sulfides).

In the former case, the remedy involved repeated "dry" $N_2:H_2S$ firings, while in the latter case, a wet N_2 firing yielding Ln_2O_3 , was prerequisite to subsequent "dry" $N_2:H_2S$ firings. Though the rare earths are often supposed to behave chemically in the same manner, La_2O_3 was exceptionally sensitive to overreacting to form some sort of higher sulfide. Y_2O_3 , Gd_2O_3 , and Lu_2O_3 were not found to be as sensitive in this regard.

To be able to control the oxysulfide synthesis more precisely several "wet" H_2S firings were tried. Water was introduced into the system by bubbling H_2S through a heated flask of water. The temperature of the water was held constant by means of a hot plate. Through temperature control, one is able to regulate the amount of water vapor being mixed with the H_2S , utilizing the temperature dependence of the vapor

pressure of water. Indeed, water was found to be effective in controlling the process.

Through a series of trial and error type experiments, close to optimum synthesis parameters were established for the general series of Ln_2O_2S phosphor systems, namely for La_2O_2S , Y_2O_2S , Gd_2O_2S , and Lu_2O_2S phosphors. During this final process, more water was added to the system, to extend the firing time of the reactions, thus allowing for better recrystallization to take place as indicated in Fig. 1. Also an even lower H_2S concentration was used since one experiment showed an increasing trend in brightness with lower H_2S concentration. The optimum conditions finally established for the general synthesis of Ln_2O_2S type phosphors are the following: nitrogen flow, $147.0 \text{ cm}^3/\text{min}$; H_2S flow, $35.0 \text{ cm}^3/\text{min}$; water temperature, $95^\circ \pm 2^\circ C$; firing temperature, $1150^\circ \pm 10^\circ C$; firing time, 1.5 hr; firing charge, approximately 2g; firing vessel, small $2 \times \frac{3}{8}$ in. quartz boat.

Results and Discussion

The criteria used to arrive at the most suitable synthesis conditions were twofold: one being the x-ray diffraction data and the other being the phosphor's luminescent properties.

X-ray powder diffraction patterns were taken of each sample (18). These patterns were obtained utilizing $Cu \text{ K}\alpha$ radiation and scanning down at a rate of $1^\circ/\text{min}$ from 60 to 20° . It must be noted that one may be easily misled in judging a sample's composition by x-ray diffraction alone. X-ray diffraction, as an analytical tool, is only good above about 5%, this figure becoming even larger in some cases, depending on the atomic scattering ability and crystallinity of the material (19, 20). It is, therefore, a common experience to obtain a powder pattern of a material which appears to be a single phase yet does in fact contain a second phase. Therefore, a second criterion was used to assess the variation in synthesis parameters, namely, the luminescent properties.

Both relative brightness of the photoluminescence and spectroscopic data were taken to evaluate the phosphors. Spectroscopic data showed that when the synthesis parameters were close to ideal the photoluminescence was completely due to $Ln_2O_2S:RE$ with no trace of $Ln_2O_3:RE$ fluorescence. The relative brightness of the photoluminescence was also recorded in order to peak the synthesis parameters toward producing an efficient phosphor. A Photovolt photomultiplier detection system was used to record the intensity of the total light output. Excitation was produced by a low

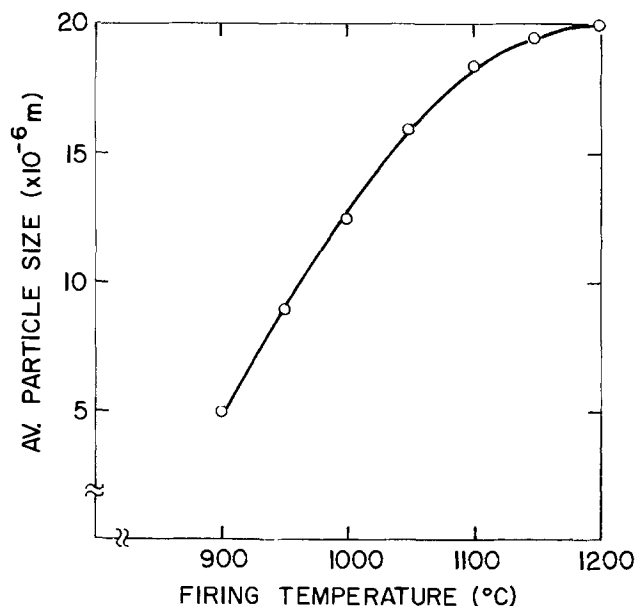


Fig. 1. Particle size vs. firing temperature

Table I. Processing parameters for $Y_2O_2S:Eu^{+3}$ (5 mole per cent)

A. Temperature series: dry H_2S , 1 hr firing time						
Temperature ($^{\circ}C$)	Body color	Relative brightness	X-ray analysis	Per cent weight gain	Per cent sulfur	Emission spectrum
1200	dark red gradual change	50.0	100% Y_2O_2S	7.61	14.2	100% Y_2O_2S
1100		43.7		6.71	12.5	
1000		37.5		6.43	12.0	
900		31.2		5.60	10.5	
800		23.6		4.78	8.9	
700		—	{ ~70% Y_2O_2S ~30% Y_2O_3	4.30	4.5	{ ~70% Y_2O_2S ~30% Y_2O_3
600	light red	—	{ ~90% Y_2O_3 ~10% Y_2O_2S	0.5	0.9	{ ~90% Y_2O_3 ~10% Y_2O_2S
B. Gas composition variations: with 50 $^{\circ}C$ H_2O temperature, 1/2 hr firing time at 1150 $^{\circ}C$						
$H_2S:N_2$ ratio	Body color	Relative brightness	X-ray analysis	Per cent weight gain	Per cent sulfur	Emission spectrum
1:9	White	85.2	100% Y_2O_2S	6.38	11.9	100% Y_2O_2S
1:4	White	85.0		7.33	13.7	
3:7	Tan	81.2		6.77	12.6	
C. Gas composition variations: with 95 $^{\circ}C$ H_2O temperature, 1 1/2 hr firing time at 1150 $^{\circ}C$						
$H_2S:N_2$ ratio	Body color	Relative brightness	X-ray analysis	Per cent weight gain	Per cent sulfur	Emission spectrum
1:9	White	93.7	100% Y_2O_2S	6.71	12.5	100% Y_2O_2S
1:4	White	100.0		7.10	13.3	
3:7	White	95.0		7.30	13.6	

pressure mercury vapor germicidal lamp. An ultraviolet filter, Corning No. 7-54, was used to allow only u.v. to pass through to the sample. A Wratten neutral density filter No. 0.5, was used to cut down on the light intensity to the detector.

The weight increases in going from oxide to oxysulfide were recorded for each sample to study possible correlations between relative brightness and nonstoichiometric oxysulfide. In addition, gravimetric analyses for sulfur and rare earth content were performed with the oxygen content taken as the difference between 100% and the sum of the rare earth and sulfur present. Table I shows representative data used to optimize processing parameters. Theoretically, in converting Y_2O_3 to Y_2O_2S , a net weight gain of 7.11% is expected. Overreaction produces a higher weight gain due to the formation of a higher sulfide, Y_2S_3 , as indicated by gravimetric analysis. Underreaction yields a mixture of Y_2O_3 and Y_2O_2S thus producing a lower net weight gain with reduced sulfur content. It can be seen from Table I that the optimal brightness results from a phosphor which is close to stoichiometric in composition.

Phosphors prepared by the aforementioned method had the following properties. The x-ray powder diffraction patterns obtained essentially agree with those found by Haynes and Brown (8). Low resolution spectroscopy showed that the photoluminescence was 100% that of $Ln_2O_2S:RE$. No trace of $Ln_2O_3:RE$ fluorescence was observed, although higher resolution spectroscopy, perhaps, would detect this type of photoluminescence in trace amounts. Also, no significant shifts in emission lines were detected in the $Ln_2O_2S:RE$ samples. Firing conditions seemed to affect only the relative intensity of the patterns and in no way affected the wavelength. The intensity of the emission spectra followed the same trend as that of the over-all relative brightness measurements in that all peaks seem to increase or decrease in the same relative proportion to each other.

Summary

Through a series of trial and error type experiments, close to optimum synthesis parameters were established for the general series of Ln_2O_2S phosphor system, namely for La_2O_2S , Y_2O_2S , Gd_2O_2S , and Lu_2O_2S phosphors. Starting at first with a dry H_2S ambient, then switching to a moist H_2S ambient, and then finally succeeding with a moist H_2S -nitrogen ambient, a successive chain of events led to the development of a clearly defined and reproducible method of synthesis of rare earth oxysulfides and the phosphors derived from them. The criteria used to arrive at the most

suitable synthesis conditions were twofold: one being the x-ray diffraction data and the other being the phosphor's luminescent properties. A gas-solid reaction was chosen to be the one most free of interfering foreign ions since careful theoretical work on the emission spectra was to be performed on the synthesized phosphors. The final method of synthesis involves the reaction of the rare earth sesquioxide with a carefully controlled $N_2:H_2O:H_2S$ gas mixture at a firing temperature of 1150 $^{\circ}C$ using approximately 2g of material placed in a small quartz boat.

Manuscript submitted April 1, 1974; revised manuscript received Aug. 9, 1974.

Any discussion of this paper will appear in a Discussion Section to be published in the December 1975 JOURNAL. All discussions for the December 1975 Discussion Section should be submitted by Aug. 1, 1975.

REFERENCES

- M. R. Royce, U.S. Pat. 3,418,246 (1968).
- P. N. Yocom, U.S. Pat. 3,418,247 (1968).
- F. C. Palilla, Paper 68 presented at Electrochemical Society Meeting, Dallas, Texas, May 7-12, 1967.
- M. R. Royce and A. L. Smith, Abstract 34, p. 94, Electrochemical Society Extended Abstracts, Spring Meeting, Boston, Mass. 5-9, 1968.
- R. E. Shrader and P. N. Yocom, *ibid.*, Abstract 35, p. 97.
- J. Flahaut and E. Attal, *Compt. Rend.*, **238**, 682 (1954).
- M. Picon and M. Patrie, *ibid.*, **242**, 516 (1956).
- J. W. Haynes and J. J. Brown, Jr., *This Journal*, **115**, 1060 (1968).
- L. Domange, J. Flahaut, and M. Guittard, *Compt. Rend.*, **249**, 697 (1959).
- H. A. Eick, *J. Am. Chem. Soc.*, **80**, 43 (1958).
- V. P. Surgutshii and V. V. Serebrennikov, *Russ. J. Inorg. Chem.*, **9**, 435 (1964).
- J. J. Pitha, A. L. Smith, and R. Ward, *J. Am. Chem. Soc.*, **69**, 1870 (1947).
- M. R. Royce, A. L. Smith, S. M. Thomsen, and P. N. Yocom, Paper 86 presented at Electrochemical Society Meeting, New York, N.Y., May 4-9, 1969.
- O. J. Sovers and T. Yoshioka, *J. Chem. Phys.*, **49**, 4945 (1968).
- O. J. Sovers and T. Yoshioka, *ibid.*, **51**, 5330 (1969).
- E. D. Eastman, L. Brewer, L. A. Bromley, P. W. Gilles, and N. L. Lofgren, *J. Am. Chem. Soc.*, **72**, 2248 (1950).
- E. D. Eastman, L. Brewer, L. A. Bromley, P. W. Gilles, and N. L. Lofgren, *ibid.*, **73**, 3896 (1951).
- W. H. Zachariasen, *Acta Cryst.*, **2**, 60 (1949).
- E. W. Nuffield, "X-Ray Diffraction Methods," John Wiley and Sons, Inc., New York (1966).
- B. D. Cullity, "Elements of X-ray Diffraction," Addison-Wesley, Inc., Reading, Mass. (1959).

Deposition Rate and Phosphorus Concentration of Phosphosilicate Glass Films in Relation to $O_2/SiH_4 + PH_3$ Mole Fraction

Miyoko Shibata and Katsuro Sugawara*

Hitachi, Limited, Semiconductor and Integrated Circuits Division, Kodaira, Tokyo, Japan

Phosphosilicate glass (PSG) films have been widely used in the passivation (1, 2), solid-to-solid diffusion (3, 4), insulation for multilevel interconnections (1), and protection of aluminum electrodes (1) in the field of semiconductor devices. In spite of these applications, few reports (5-10) have been published which systematically investigate the deposition rate and phosphorus concentration by changing the deposition parameters over a wide range. In this note, the dependence of O_2 to $SiH_4 + PH_3$ mole fraction on the deposition rate and phosphorus concentration during PSG film formation is reported.

A planetary-type CVD reactor (11) was used in this experiment. The bell jar was approximately 40 cm in diameter and 20 cm high. Clean silicon mirror-polished wafers, Czochralski-grown, boron-doped and (100)-oriented with resistivity of 30 ohm-cm, were placed on planetary rotation gears, then the bell jar was fixed and heating was effected. After reaching set temperatures of 300°, 350°, 400°, and 450°C, reaction was carried out by introducing SiH_4 (56 cm³/min), PH_3 (4 cm³/min), and O_2 (90-2000 cm³/min). The carrier gas was N_2 , and the total flow rate of 20 liters/min was maintained constant during deposition. The reaction time was set to obtain a PSG film of 3000-4000Å thickness. Thickness was measured by a "Talystep." The phosphorus concentration was determined by the sheet resistance after a predetermined diffusion in accordance with a calibration curve of sheet resistance and phosphorus concentration previously prepared by activation analysis. To determine the reacted SiH_4 concentration through the reactor system, the unreacted SiH_4 concentration of the vent gas was measured under the experi-

mental conditions. A Hitachi EPI-S2 infrared spectrometer was used for this purpose. Absorption spectra were taken in the ranges of 2200 cm⁻¹ and 900 cm⁻¹ (8); the peak of 930 cm⁻¹ was selected to avoid interference with the CO_2 peak near 2200 cm⁻¹. The transmittance through a 10 cm gas cell at the peak of 930 cm⁻¹ shows the reacted SiH_4 concentration.

As shown in Fig. 1, the deposition rate of PSG films exhibited a tendency of increase-maximum-decrease when the O_2 flow rate increased at the constant flow rate of SiH_4 and PH_3 . Mole fractions at these maximum ranges are approximately 3 at 300°C, 4-6 at 350°C, 8-12 at 400°C, and 14-22 at 450°C. The higher the temperatures of the deposition were, the larger the mole fractions and the wider the maximum range became. The phosphorus concentration rapidly increased with an increase of the O_2 flow rate, displaying a constant value at the maximum plateau range of the deposition rate, and then gradually increasing at the larger O_2 flow rate. The phosphorus concentration of the silicon wafers on which the PSG films were deposited, was determined after 30 min diffusion at 1100°C in dry nitrogen, using the calibration curve. Dependence of the oxygen mole fraction on the PSG film deposition is similar to that on CVD SiO_2 film formation (5-6, 9-10). At low $O_2/SiH_4 + PH_3$ ratio, increase in the deposition rate was found as the temperature decreased. This fact may be explained by smaller reaction rate in the hot zone; the increased deposition rate at lower temperature was brought as the result of difference between total reaction and reaction in the hot zone. The above-mentioned tendency was confirmed by the result of film thickness monitoring by a laser system (12).

Dependence of the oxygen mole fraction was also investigated in the case of various PH_3 flow rates. The oxygen flow rates were selected from 180 to 2000 cm³/

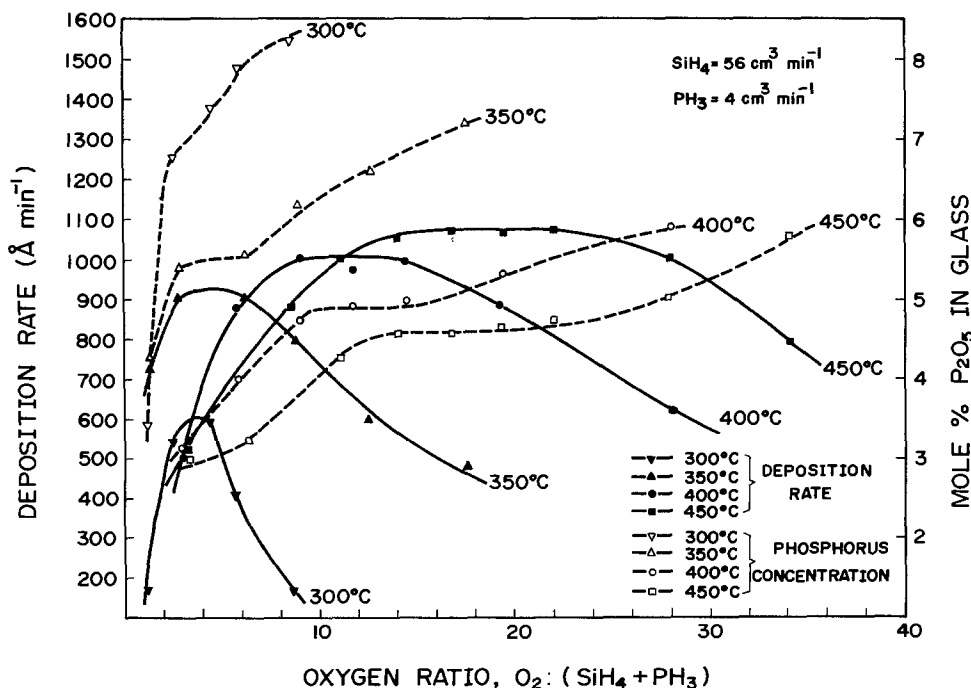


Fig. 1. $O_2:(SiH_4 + PH_3)$ mole fraction vs. deposition rate and phosphorus concentration of PSG films.

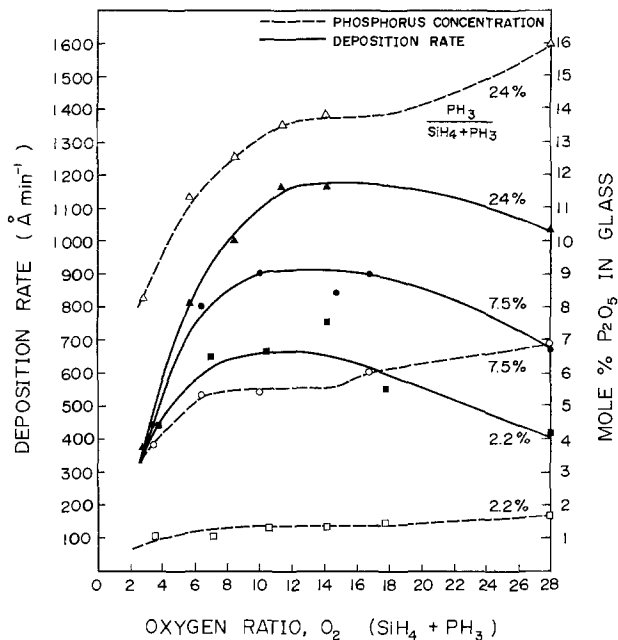


Fig. 2. Dependence of $O_2:(SiH_4 + PH_3)$ mole fraction on the deposition rate and phosphorus concentration of PSG films in various PH_3 flow rates. Deposition temperature: $400^\circ C$.

min at 1.8, 6.5, and 18.3 mole per cent (m/o) PH_3 . Deposition was carried out at $400^\circ C$. Figure 2 shows that both deposition rate and phosphorus concentration became plateau at approximately constant value, 8-12 of $O_2/SiH_4 + PH_3$.

The reacted per cent SiH_4 measured by the infrared absorption were plotted at various oxygen flow rates and deposition temperatures in Fig. 3. SiH_4-O_2 reaction was retarded as the oxygen flow rates increased. This retardation was remarkably noticeable when the film was deposited at the lower temperature. This result shows the same tendency as that of the undoped SiO_2 film formation (8).

The deposition rate and phosphorus concentration of PSG films formed by the $SiH_4-PH_3-O_2$ system was investigated in the temperature range of $300^\circ-450^\circ C$ by reaction with the $O_2/SiH_4 + PH_3$ mole fraction and the deposition temperature. The deposition rate showed a tendency of increase-maximum-decrease with increasing O_2 flow rates. This maximum plateau range became larger and wider with increasing deposition temperature. The phosphorus concentration was kept constant at this range.

Acknowledgment

The authors express their sincere gratitude to Mr. S. Nishida and Mr. H. Mishimagi for the most helpful discussions. Appreciation is also due to Dr. N. Nagasima and Miss H. Suzuki for the activation analysis of phosphorus in PSG films, and to Miss Y. Tsukamoto for assistance in the experimental work.

Manuscript submitted July 30, 1973, revised manuscript received July 8, 1974.

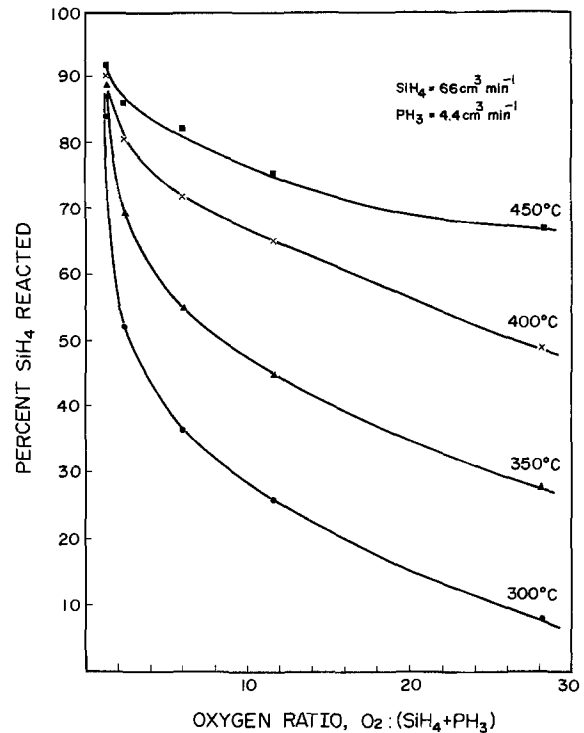


Fig. 3. $O_2:(SiH_4 + PH_3)$ mole fraction vs. per cent SiH_4 reaction in the over-all reactor, measured by infrared absorption.

Any discussion of this paper will appear in a Discussion Section to be published in the December 1975 JOURNAL. All discussions for the December 1975 Discussion Section should be submitted by Aug. 1, 1975.

Publication costs of this article were partially assisted by Hitachi, Limited.

REFERENCES

1. M. M. Schlacter, E. S. Schlegel, R. S. Keen, Jr., R. A. Lathlaen, and G. L. Schnable, *IEEE Trans. Electron Devices*, **ED-17**, 1077 (1970).
2. L. H. Kaplan and M. E. Lowe, *This Journal*, **118**, 1649 (1971).
3. A. W. Fisher, J. A. Amick, H. Hyman, and J. H. Scott, Jr., *RCA Rev.*, **29**, 533 (1968).
4. A. W. Fisher and J. A. Amick, *ibid.*, **29**, 549 (1968).
5. N. Goldsmith and W. Kern, *ibid.*, **28**, 153 (1967).
6. M. L. Hammond and G. M. Bowers, *Trans. Met. Soc. AIME*, **242**, 546 (1968).
7. W. Kern and R. C. Heim, *This Journal*, **117**, 562 (1970).
8. K. Strater, *RCA Rev.*, **29**, 618 (1968).
9. M. L. Barry, in "Chemical Vapor Deposition," John M. Blocher, Jr. and James C. Withers, Editors, p. 595, The Electrochemical Society Softbound Symposium Series, New York (1970).
10. B. J. Baliga and S. K. Gandhi, *J. Appl. Phys.*, **44**, 990 (1973).
11. W. Kern, *RCA Rev.*, **29**, 525 (1968).
12. K. Sugawara, T. Yoshimi, H. Okuyama, and T. Shirasu, in "Chemical Vapor Deposition," Gene F. Wakefield and John M. Blocher, Jr., Editors, p. 205, The Electrochemical Society Softbound Symposium Series, Princeton, New Jersey (1973).

Deposition Rate and Phosphorus Concentration of Phosphosilicate Glass Films in Relation to $\text{PH}_3/\text{SiH}_4 + \text{PH}_3$ Mole Fraction

Miyoko Shibata, Takeo Yoshimi, and Katsuro Sugawara*

Hitachi, Limited, Semiconductor and Integrated Circuits Division, Kodaira, Tokyo, Japan

Phosphosilicate glass films (PSG films) have been widely used for the fabrication of semiconductor devices, such as stabilization of electric characteristics, insulation of multilayer interconnection, and protection of aluminum electrodes. In spite of these wide uses, few papers have reported the detailed relation of wide range deposition parameters to the deposition rate and the phosphorus concentration (1-5). The authors reported that the deposition rate and the phosphorus concentration of the PSG films showed little variation when the films were formed under the proper mole fraction $\text{O}_2/\text{SiH}_4 + \text{PH}_3$, being dependent on the deposition temperature (5). In this range of $\text{O}_2/\text{SiH}_4 + \text{PH}_3$, the dependence of PH_3 flow rate on the deposition rate and the phosphorus concentration is reported.

The same CVD reactor used in the previous paper (5) was of planetary type (6). In this reactor, silicon mirror-polished wafers [(100) oriented and boron doped with resistivity of 30 ohm-cm] were charged, and the PSG films 3000-4000Å in thickness were deposited on the wafers by $\text{SiH}_4\text{-PH}_3\text{-O}_2$ reaction at the temperatures of 350°, 400°, and 450°C. Flow rates were: N_2 , 20 liters/min; SiH_4 , 56 cm^3/min ; O_2 , plateau range of the small, variable deposition rate and phosphorus concentration and being fixed at the temperatures, e.g., at 350°C, $\text{O}_2/\text{SiH}_4 + \text{PH}_3 = 5$, at 400°C, $\text{O}_2/\text{SiH}_4 + \text{PH}_3 = 12$, at 450°C, $\text{O}_2/\text{SiH}_4 + \text{PH}_3 = 18$; PH_3 , 0.7-14 cm^3/min . The thickness of the PSG films was measured by a "Talystep." The phosphorus concentration was determined by the sheet resistance in the previously prepared calibration curve between the phosphorus concentration by the activation analysis and the sheet resistance after the diffusion. To measure total amount of the reacted SiH_4 concentration with O_2 in the reactor, infrared gas absorption through a 10 cm gas cell was carried out, as reported in the previous paper (5). The reacted mole percentage of SiH_4 was detected by the transmittance of the cell, fixed at the absorption peak, 930 cm^{-1} of SiH_4 , using Hitachi EPI-S2.

Figure 1 shows the deposition rates of the PSG films under various PH_3 flow rates at the $\text{O}_2/\text{SiH}_4 + \text{PH}_3$ in the plateau range of the deposition rate. With increasing PH_3 flow rate, the deposition rate at 350°C shows a tendency of decrease-minimum-increase. After raising the deposition temperature in this experimental condition, the deposition rate became larger and showed the same tendency observed at 350°C. This was confirmed by the monitoring experiment using a 6328Å He-Ne laser system (7).

Figure 2 is the relation of $\text{PH}_3/\text{SiH}_4 + \text{PH}_3$ mole fraction to the phosphorus concentration in the PSG films, represented as $\text{P}_2\text{O}_5/\text{SiO}_2 + \text{P}_2\text{O}_5$ at the same experimental condition. With the increasing of the deposition temperature, P_2O_5 concentration in the PSG films decreased at the same $\text{PH}_3/\text{SiH}_4 + \text{PH}_3$ flow ratio. The similar result of decreasing dopant materials in films was obtained in the cases of P, As, and Sb doping for silicon epitaxial layers (8-9) and in AsH_3 and PH_3 doping for polycrystalline silicon films (10). In this temperature range PH_3 was almost completely reacted, while SiH_4 tended to increase the reaction rate with O_2 at the higher temperature as can be seen in Fig. 1 and

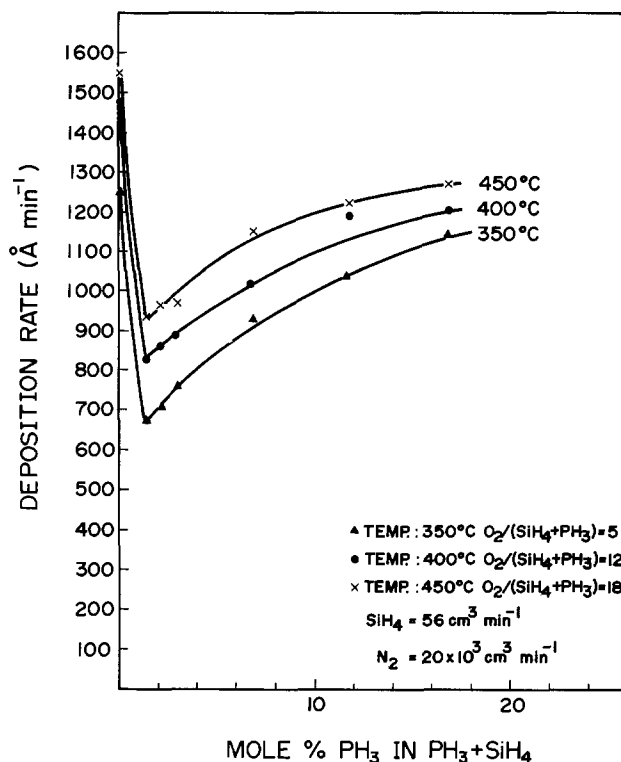


Fig. 1. Deposition rates of the PSG films vs. m/o PH_3 in $\text{SiH}_4 + \text{PH}_3$ in the plateau range of the deposition rate determined in terms of $\text{O}_2/\text{SiH}_4 + \text{PH}_3$ mole fraction.

in the infrared absorption in the previous paper (5). Therefore, the phosphorus concentration was diluted as a consequence of the increased SiH_4 reaction.

When the reaction was effected under various PH_3 flow rates at the deposition temperature of 400°C, the result of the reacted percentage SiH_4 measured by the infrared absorption method is shown in Fig. 3, in which the O_2 flow rate is indicated as a parameter. The reacted SiH_4 concentration became suppressed independently of O_2 flow rates when PH_3 was added up to 2-3 mole per cent (m/o). With further increasing of PH_3 flow rates, the reacted SiH_4 increased. This tendency was dominant at larger O_2 flow rates.

When the PSG films were formed by the $\text{SiH}_4\text{-PH}_3\text{-O}_2$ reaction, it was previously reported that there existed $\text{O}_2/\text{SiH}_4 + \text{PH}_3$ mole fraction, with little variation in the deposition rate and in the phosphorus concentration, and fixed at the deposition temperature. At this plateau range, the deposition rate showed the tendency of decrease-minimum-increase with increasing PH_3 flow rates. This tendency of the deposition rate was maintained in all reaction temperatures of this experiment.

Acknowledgment

The authors express their sincere gratitude to Mr. S. Nishida for his encouragement and helpful discussions, and to Miss Y. Tsukamoto for her assistance in the experimental work.

* Electrochemical Society Active Member.

Key words: $\text{SiH}_4\text{-PH}_3\text{-O}_2$ reaction, influence of PH_3 doping, infrared gas measurement, inhibiting reaction.

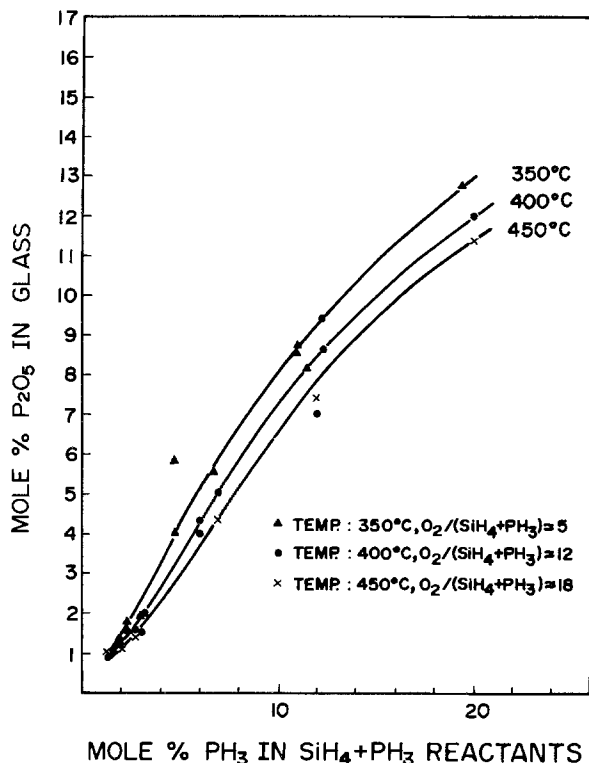


Fig. 2. M/o P₂O₅ in the PSG films vs. mole fraction PH₃ in SiH₄ + PH₃ reactants.

Manuscript submitted Oct. 19, 1973; revised manuscript received July 8, 1974.

Any discussion of this paper will appear in a Discussion Section to be published in the December 1975 JOURNAL. All discussions for the December 1975 Discussion Section should be submitted by Aug. 1, 1975.

Publication costs of this article were partially assisted by Hitachi, Limited.

REFERENCES

1. N. Goldsmith and W. Kern, *RCA Rev.*, **28**, 153 (1967).
2. M. L. Hammond and G. M. Bowers, *Trans. Met. Soc. AIME*, **242**, 546 (1968).
3. M. L. Barry, in "Chemical Vapor Deposition, Second International Conference," J. M. Blocher, Jr. and J. C. Withers, Editors, p. 595, Electrochemical Society Softbound Symposium Series, New York (1970).

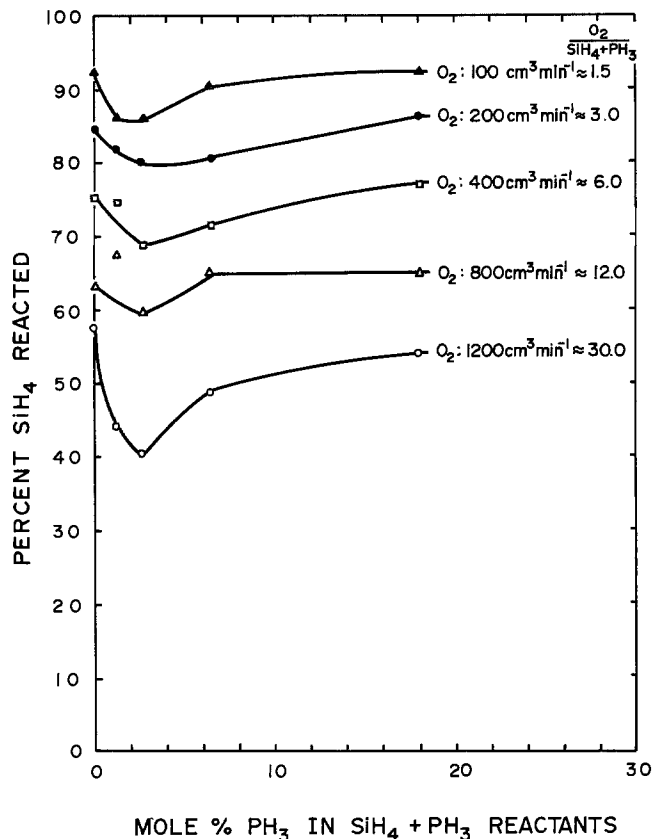


Fig. 3. Relation of m/o PH₃ to the total reacted SiH₄ concentration measured by the variation of transmittance through the infrared 10 cm gas cell.

4. B. J. Baliga and S. K. Ghandhi, *J. Appl. Phys.*, **44**, 990 (1973).
5. M. Shibata and K. Sugawara, *This Journal*, **122**, 155 (1975).
6. W. Kern, *RCA Rev.*, **29**, 525 (1968).
7. K. Sugawara, T. Yoshimi, H. Okuyama, and T. Shirasu, in "Chemical Vapor Deposition, Fourth International Conference," G. F. Wakefield and J. M. Blocher, Jr., Editors, p. 205, Electrochemical Society Softbound Symposium Series, Princeton, New Jersey (1973).
8. W. H. Shepherd, *This Journal*, **115**, 541 (1968).
9. T. B. Swanson and R. N. Tucker, *ibid.*, **116**, 1251 (1969).
10. F. C. Eversteyn and B. H. Put, *ibid.*, **120**, 106 (1973).



Electrochemical Behavior of the Perovskite-Type $\text{Nd}_{1-x}\text{Sr}_x\text{CoO}_3$ in an Aqueous Alkaline Solution

Tetsuichi Kudo, Hidehito Obayashi, and Tetsuo Gejo

Central Research Laboratory, Hitachi Limited, Higashi-koigakubo, Kokubunji, Tokyo, 185, Japan

ABSTRACT

The compounds $\text{Nd}_{1-x}\text{Sr}_x\text{CoO}_3$, which show high electrical conductivity, are electrochemically reduced in an aqueous alkaline solution to give rise to the oxygen deficient state $\text{Nd}_{1-x}\text{Sr}_x\text{CoO}_{3-\delta}$. The electrochemical redox reactions are reversible in the range $0 \leq \delta \leq x/2$. The electrode potentials of $\text{Nd}_{1-x}\text{Sr}_x\text{CoO}_{3-\delta}$ in a KOH solution have been measured as a function of δ . From these data and the measurements of potential change in the cathodic processes under constant current density, the oxygen ion diffusion constants have been calculated on the basis of a linear diffusion model of oxygen ions in the crystal, which was theoretically derived. The calculated diffusion constants at 25°C are 1.4×10^{-11} and 7.6×10^{-14} cm²/sec for $x = 0.2$ and $x = 0.5$, respectively. These values are very large as compared with ordinary oxides.

The compounds $\text{Nd}_{1-x}\text{Sr}_x\text{CoO}_3$ with the perovskite-type structure exhibit high electrical conductivity even at room temperature, and their specific conductivity is in the order of 10^0 - 10^4 ohm⁻¹ cm⁻¹ (1, 2). According to Heikes *et al.* (3), the large electrical conductivity is due to the delocalization of electrons among Co^{+3} -O²⁻- Co^{+4} network by the super exchange effect. Recently, these compound are taken notice of as electrode materials (4), especially as oxygen (or air) electrodes in an aqueous alkaline solution (5, 6).

It was suggested by the present authors' work (2) that these lanthanoid cobalt oxides with perovskite structure are ionic-electronic mixed conductors with large oxygen ion diffusivity compared with ordinary oxides and also with the electronic conductivity far greater than the ionic conductivity. From this point of view, the electrochemical behavior of $\text{Nd}_{1-x}\text{Sr}_x\text{CoO}_3$ in an aqueous KOH solution has been studied.

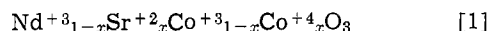
It is reasonable to consider that the oxygen ions in the crystal with perovskite structure are usually mobile, because many oxygen ion conductors with this structure have been reported (7, 8). The direct measurement of the oxygen ion diffusion constant is, however, almost impossible for the compounds with high electronic conductivity: The oxygen concentration cell method or the Wagner cell (9) method are proved inapplicable. Therefore, a new method to make use of the measurement of the potential change of the compound $\text{Nd}_{1-x}\text{Sr}_x\text{CoO}_3$ under the cathodic process was employed.

The diffusion constant can be calculated from the potential change by using a linear diffusion model of the compound, which was derived from a theoretical consideration.

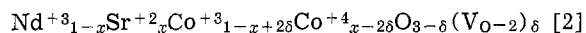
Theory

The electrode potential of $\text{Nd}_{1-x}\text{Sr}_x\text{CoO}_3$.—The valence setup of the compound $\text{Nd}_{1-x}\text{Sr}_x\text{CoO}_3$ is expressed as

Key words: perovskite-type oxides, electrode potential, diffusion constant, mixed conductor.

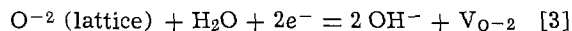


While this compound undergoes reduction, some of the oxygen ions are taken away from the crystal lattice and the valence set up becomes



where $\text{V}_{\text{O}-2}$ represents the oxygen ion vacancies and δ is a measure of the nonstoichiometry of the compound. Since the perovskite structure cannot be maintained if δ exceeds $x/2$, the discussion in the present paper is confined within the range $0 \leq \delta \leq x/2$.

When the compound is electrochemically reduced in an aqueous alkaline solution, the over-all reaction is



If the cathodic current of which integral is Q coulombs flows through 1g of the oxide concerned, the loss of oxygens ($\Delta\delta$) in this cathodic process is represented as

$$\Delta\delta = M \cdot \frac{Q}{2F} \quad [4]$$

where M represents the gram formula weight of $\text{Nd}_{1-x}\text{Sr}_x\text{CoO}_3$ and F represents the Faraday constant.

During this process, the concentration gradient of $\text{V}_{\text{O}-2}$ (or δ) in the crystal occurs, as schematically shown in Fig. 1. When the electric current is turned off, the relaxation of the concentration gradient formed by the current integral of Q coulombs sets in and continues until δ becomes uniform throughout the crystalline particles. If we consider the initial δ is zero, the value of δ in this relaxation state is $M \cdot (Q/2F)$.

The electrode potential of the compound $\text{Nd}_{1-x}\text{Sr}_x\text{CoO}_{3-\delta}$ regarding the electrochemical reaction represented by Eq. [3] can be written as

$$E = E^\circ - \frac{RT}{2F} \ln \frac{a_{\text{OH}^-}}{a_{\text{H}_2\text{O}}} + \frac{\Delta F(\delta)}{2F} \quad [5]$$

The symbol E° is the standard potential of an oxygen

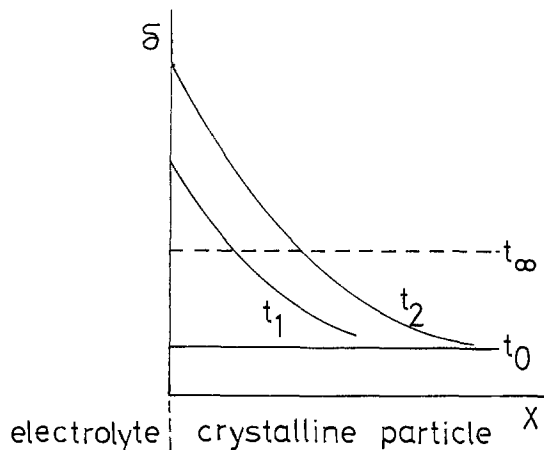
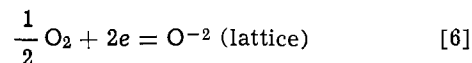


Fig. 1. Schematic diagram of the concentration gradient of oxygen ion vacancies formed in a particle of $\text{Nd}_{1-x}\text{Sr}_x\text{CoO}_{3-\delta}$. t_0 (initial level) $< t_1$ (under current passage) $< t_2$ (at which current turned off) $\rightarrow t_x$ (relaxation level).

electrode in basic solution (+0.401V vs. SHE), and $\Delta F(\delta)$ is the partial molar free energy change of the reaction



for the composition of the oxide $\text{Nd}_{1-x}\text{Sr}_x\text{CoO}_{3-\delta}$. The symbol E is, accordingly a function of δ in general, and its value vs. Hg/HgO reference electrode can be represented as¹

$$E(\delta) = 0.303 + \frac{1}{2F} \Delta F(\delta) \quad [7]$$

One can, therefore, determine the electrode potential as a function of δ by setting the relaxation level of δ (Fig. 1) at an appropriate value corresponding to the integral current Q as far as either the oxygen evolution from the crystal lattice or the dissolution into the lattice is negligible during the relaxation process. It was ascertained by TGA and DTA that these losses were negligible under the conditions that the temperature was lower than 150°C, the oxygen ambient to the electrodes was far less than 1 atm, and δ did not lie in the neighborhood of the critical value $x/2$.

Oxygen ion diffusion constant.—Let us consider a flat plate of thickness L . The electronic conductive material such as platinum net is attached to one side of the sample plate and molded with an oxygen free resin, the other side is directly contacted to an aqueous alkaline solution. When a cathodic current is applied to the plate, the oxygen ions at the surface of the sample are converted into OH^- ions according to Eq. [3] and a concentration gradient of oxygen ions across the plate is built up as shown in Fig. 2.

The diffusion equations associated with ion-electron mixed conductors have been derived by Hebb (10) and other workers (11, 12). Applying a similar treatment to the model of the present paper, one can obtain as a diffusion equation

$$\frac{\partial C_V}{\partial t} = \frac{\partial}{\partial X} \left(D \left(\frac{\partial C_V}{\partial X} - \frac{2eI}{kT} \frac{C_V}{\sigma_h} \right) \right) \quad [8]$$

Notations in Eq. [8] are: C_V , concentration of oxygen ion vacancies (cm^{-3}); D , diffusion constant of oxygen ion vacancies (cm^2/sec); σ_h , specific electronic conductivity ($\text{ohm}^{-1} \cdot \text{cm}^{-1}$); I , current density (A/cm^2); e , charge of electrons (1.60×10^{-19} coulomb); k , the Boltzmann constant (1.38×10^{-23} coulomb \cdot volt/deg); and T , absolute temperature, respectively. In the course of derivation of Eq. [8], the assumption that the σ_h is

¹ The standard potential for Hg/HgO couple is 0.098V. Thus, when alkaline concentration around the $\text{Nd}_{1-x}\text{Sr}_x\text{CoO}_{3-\delta}$ electrode and the reference electrode is same, Eq. [7] is directly derived from Eq. [5].

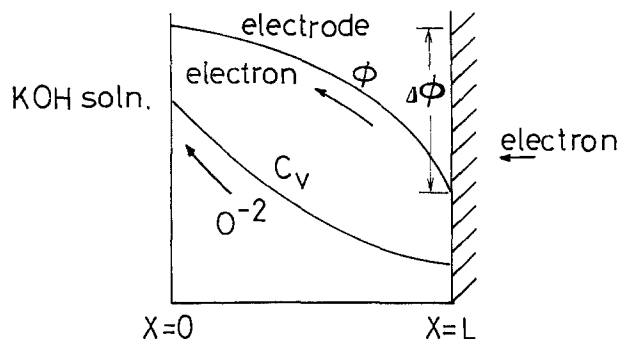


Fig. 2. Schematic diagram of a plain sheet $\text{Nd}_{1-x}\text{Sr}_x\text{CoO}_{3-\delta}$ electrode under a cathodic process. Arrows indicate the direction of electron and oxygen ion movements.

far greater than that of oxygen ions and the Townsend-Einstein relation were employed to eliminate the unobservable parameters. Equation [8] might be solved if the initial and the boundary conditions are given. These conditions under the constant current density process are

$$C_V(t=0, x) = C_V^* (= \text{constant}) \quad [9]$$

$$\left(\frac{\partial C_V}{\partial X} \right)_{x=0} = -\frac{I}{2eD} \quad [10]$$

$$\left(\frac{\partial C_V}{\partial X} \right)_{x=L} = 0 \quad [11]$$

The theoretical potential of the electrode at time t [$E_{\text{theo}}(t)$] is given by

$$E_{\text{theo}}(t) = E(C_V(t, x=0)) - \phi(t) \quad [12]$$

The first term of the right-hand side in this equation is the redox potential corresponding to C_V at the surface of the electrode, which is defined by Eq. [7]. The relation between C_V and δ in Eq. [7] is represented by

$$C_V = \frac{\delta}{v_c} \quad [13]$$

where v_c is the unit cell volume (cm^3) of the compound $\text{Nd}_{1-x}\text{Sr}_x\text{CoO}_{3-\delta}$. The symbol $\phi(t)$ is the potential change across the electrode which is shown in Fig. 2. These terms might be calculated from the solution of Eq. [8] as a function of the parameter D . It is consequently possible to determine the diffusion constant of oxygen ions, if we can find out the value of the parameter D which gives such potential variation that agrees with the observed one.

As Eq. [8] cannot be rigorously solved, we will hereafter treat the problem on the basis of the following approximations. Confining the problem in the case that the current density I is so small as to hold the relation

$$\frac{\partial C_V}{\partial X} \gg \frac{2eI}{kT} \cdot \frac{C_V}{\sigma_h} \quad [14]$$

and assuming the diffusion constant D is independent of C_V , Eq. [8] may be reduced to an ordinary form of the diffusion equation

$$\frac{\partial C_V}{\partial t} = D \frac{\partial^2 C_V}{\partial X^2} \quad [15]$$

Macey (13) gave the solution of this equation under the initial and boundary conditions substantially identical to the present case. Inserting Eq. [9], [10], and [11] into Macey's solution, $C_V(t, X)$ is expressed as

$$C_V(t, X) = C_V^* + \frac{I}{e} \sqrt{\frac{t}{D}} \left[\chi_1 \left(\frac{X}{2\sqrt{Dt}} \right) + \chi_1 \left(\frac{2L - X}{2\sqrt{Dt}} \right) + \chi_1 \left(\frac{2L + X}{2\sqrt{Dt}} \right) + \chi_1 \left(\frac{4L - X}{2\sqrt{Dt}} \right) + \chi_1 \left(\frac{4L + X}{2\sqrt{Dt}} \right) + \dots \right] \quad [16]$$

where the function χ_1 is defined by

$$\chi_1(x) = \int_x^\infty \left(\frac{2}{\sqrt{\pi}} \int_y^\infty e^{-t^2} dt \right) dy \quad [17]$$

The numerical value of χ_1 ranges from 0.564 at $X = 0$ to 0.0008 at $X = 2.2$. Thus the series in Eq. [16] is highly convergent, and assuming $L/\sqrt{Dt} \gg 1$, Eq. [16] can be reduced to

$$C_V(t, 0) = C_V^* + \frac{I\chi_1(0)}{e} \sqrt{\frac{t}{D}} \quad [18]$$

or using Eq. [13]

$$\delta_0(t) - \delta_0(t=0) = 0.564 \frac{v_c I}{e} \sqrt{\frac{t}{D}} \quad [18']$$

Since $\Phi(t)$ in Eq. [12] can be neglected as far as Eq. [14] holds, the electrode potential may be considered as a sole function of the surface vacancy concentration $C_V(t, x=0)$ or $\delta_0(t)$. It is therefore possible to estimate $\delta_0(t)$ by measuring the electrode potential change with time and then the diffusion constant of oxygen ion D can be calculated by Eq. [18'].

Experimental

Measurement of the electrode potential of $\text{Nd}_{1-x}\text{Sr}_x\text{CoO}_3$.—The compounds $\text{Nd}_{1-x}\text{Sr}_x\text{CoO}_3$ were obtained by sintering a homogeneous mixture of the component metal acetates at 900°C in air for 4 hr. The BET specific surface area of the powder oxides was about 5 m²/g. A half gram of specimen powder was weighed precisely to which 0.025g acetylene black and 0.025g of flaky graphite were added. The mixture was mixed in an agar mortar. Several drops of a 30 weight per cent (w/o) KOH solution were added to the powder mixture. The flaky graphite improves the affinity of the powder to the electrolyte. The specimen was charged into an acryl case shown in Fig. 3, and pressed from both sides, at which the platinum net current collectors were placed. Nitrogen gas was bubbled so as to make dissolved oxygen concentration be very

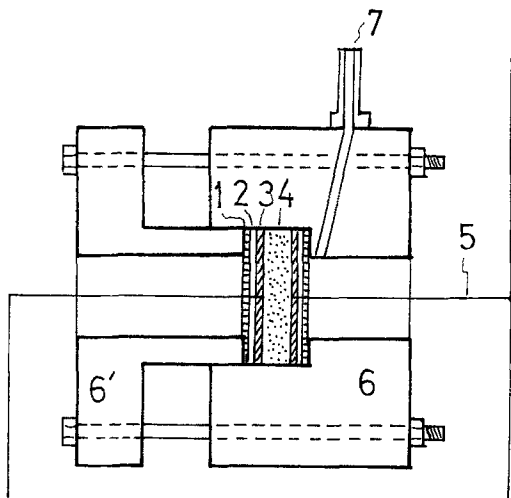


Fig. 3. Sample holder used for measurement of the electrode potential of $\text{Nd}_{1-x}\text{Sr}_x\text{CoO}_{3-\delta}$ as a function of δ . 1, perforated acryl plate; 2, filter paper; 3, platinum net; 4, mixed powder of $(\text{Nd}, \text{Sr})\text{CoO}_3$ and carbon; 5, platinum wire; 6, 6', acryl holder; 7, bubbling hole of N_2 gas.

small. The holder was soaked in a 30% KOH solution for 5 hr to make the contact between the sample and the electrolyte complete. Temperature of the solution was kept at $25^\circ \pm 1^\circ\text{C}$.

To make the oxidation of the sample perfect, *i.e.*, δ be zero, 1 mA of an anodic current was passed for 10 hr. Then 1 mA of a cathodic current was passed for a certain period. During this process the sample changes its composition from $\text{Nd}_{1-x}\text{Sr}_x\text{CoO}_3$ to $\text{Nd}_{1-x}\text{Sr}_x\text{CoO}_{3-\delta}$, according to Eq. [4]. The current density at the surface of oxide particles is calculated as $4 \times 10^{-2} \mu\text{A}/\text{cm}^2$; the current efficiency in this cathodic process can be considered to be almost 100%.

After the current is turned off, the cell potential rises gradually and saturates at a constant level regarded as the electrode potential of $\text{Nd}_{1-x}\text{Sr}_x\text{CoO}_{3-\delta}$. It took several hours to reach the saturation (or relaxation) level after the current was turned off. The potential was measured *vs.* Hg/HgO reference electrode by using a digital voltmeter of the input impedance greater than 10 megohms. A similar step was repeated to obtain the electrode potential as a function of δ ; δ can be changed by varying the current passing period.

Measurement of oxygen ion diffusion constant.—Disk preparation.—To the powder of the compounds $\text{Nd}_{1-x}\text{Sr}_x\text{CoO}_3$ prepared by the same method as in the above section, methyl cellulose (1% aqueous solution) was added as a binder and it was pressed in a die of 15 mm ϕ at the hydrostatic pressure of 700 kg/cm² to give a 2 mm thick disk. This disk was placed in an alumina die of 20 mm ϕ ; environment of the disk was filled with stabilized zirconia powder to prevent the disk from reacting with alumina. The die was put in a vertical type platinum resistance furnace and hot pressed under 350 kg/cm² at 1200°C for 3 hr. The obtained sample was lapped by several steps and polished finally by diamond paste. The surface area of the sample was considered to be the same as the geometrical one.

Measurement of oxygen ion diffusion constant.—The platinum net was attached to the one side of the disk sample as a current collector and was molded with an epoxy resin, the other side being exposed to a 30% aqueous KOH solution. A "H" type cell was used in this measurement as is shown in Fig. 4. The use of "H" type cell and bubble of nitrogen gas in both rooms of the cell protect the sample from the influence of oxygen. The potential change under the constant current cathodic process was measured *vs.* Hg/HgO reference electrode. The counterelectrode was

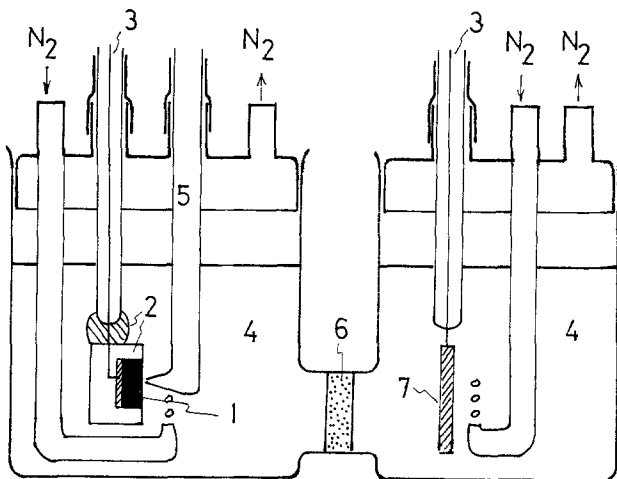


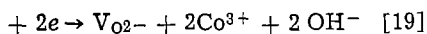
Fig. 4. Cell used for measurement of oxygen ion diffusion constant. 1, sample electrode (nonporous prepared by hot pressing); 2, epoxy molding; 3, platinum wire; 4, KOH solution; 5, salt bridge to the Hg/HgO reference electrode; 6, glass filter; 7, platinum counterelectrode.

platinum net, and the cell temperature was kept within $25^\circ \pm 1^\circ\text{C}$.

Results and Discussion

Electrode potential of $\text{Nd}_{1-x}\text{Sr}_x\text{CoO}_3$.—The potential of the $\text{Nd}_{1-x}\text{Sr}_x\text{CoO}_3$ ($x = 0.2$) after 5 hr soaking in an electrolyte is +90–100 mV vs. Hg/HgO. The potential becomes +510 mV after about 30 min of 1 mA anodic current passage. This value was considered to be the oxygen-evolving potential of the cell. The fact that about 30 min were needed to reach this potential may mean that the sample was already in a partially reduced state when it had been prepared. After passing an anodic current for 10 hr to make δ be essentially zero, the direction of the current was reversed. The profile of the potential decrease is shown in Fig. 5.

If all the cathodic current were due to the reaction



the potential would reach the hydrogen evolving potential (about -800 mV case of this cell) at the time when $2\delta/x = 1$ (i.e., 11.2 hr). However, the potential did not reach the hydrogen evolving potential even when $2\delta/x$ exceeded unity. Under the 1 mA of cathodic current, the hydrogen evolving potential was obtained when 120% of the theoretical capacity available from $\text{Nd}_{1-x}\text{Sr}_x\text{CoO}_3$ were discharged. The discrepancy between calculated and observed capacity of the cell increases with a decrease in the cathodic current. The reason may be that the residual dissolved oxygen in the electrolyte fills the oxygen ion vacancies generated through the cathodic process when the reduction of the oxide exceeds a certain critical level. This suggests that $\text{Nd}_{1-x}\text{Sr}_x\text{CoO}_{3-\delta}$ works as an oxygen electrode if sufficient amount of oxygen exists.

After 13 hr of cathodic process, the direction of the current was again reversed. The potential change in the anodic process is also shown in Fig. 5. In this process, the potential reached the level of oxygen evolution after 10 hr which being 90% of the theoretical value. The disagreement arose partly from the residual Co^{+4} and mainly from the situation that the surface of the particles reached the composition corresponding to the oxygen evolution potential (i.e., $\delta = 0$) faster than the inner part. The experimental results above reveal the reversibility of δ in the compound $\text{Nd}_{1-x}\text{Sr}_x\text{CoO}_3$ during the redox process.

The relation between the electrode potential and δ is shown in Fig. 6. The potential becomes nobler as Co^{+4} concentration increases; the value for $x = 0.5$

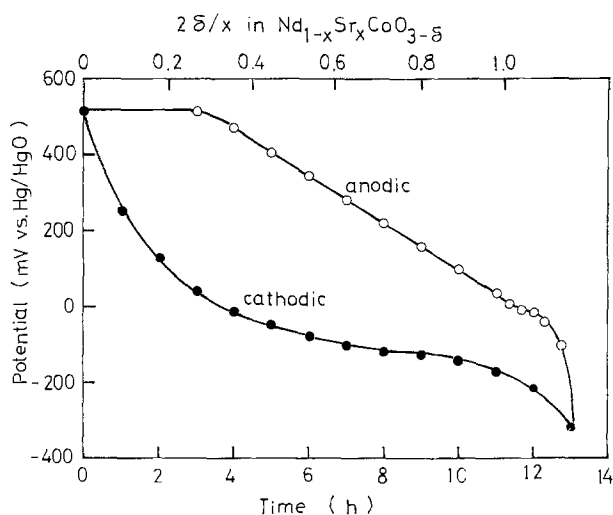


Fig. 5. Potential variation with time under the electrochemical redox processes in 30% KOH solution [$\text{Nd}_{1-x}\text{Sr}_x\text{CoO}_3$ ($x = 0.2$)]. The current employed was 1 mA for 0.5g of the sample.

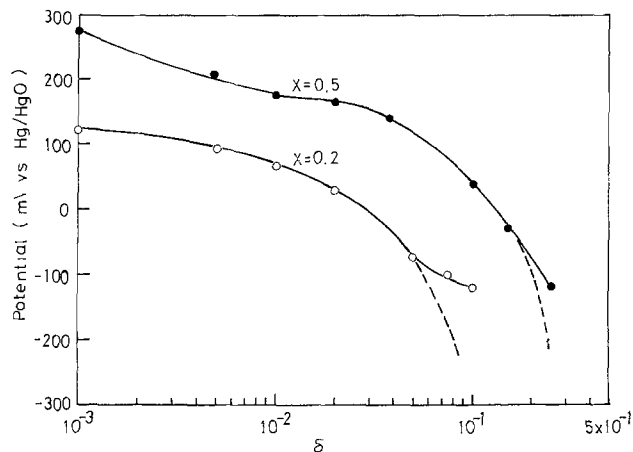


Fig. 6. The electrode potential as a function of δ in $\text{Nd}_{1-x}\text{Sr}_x\text{CoO}_{3-\delta}$.

is higher by 100–200 mV in the whole range of δ than the value for $x = 0.2$. Since the relation between the electrode potential $E(\delta)$ determined here as a function of δ and the partial free energy change of oxidation of $\text{Nd}_{1-x}\text{Sr}_x\text{CoO}_{3-\delta}$ holds as Eq. [7], the oxygen partial pressure in an equilibrium with this composition is expressed as

$$P_{\text{O}_2} = \exp \left[\frac{4F}{RT} (E(\delta) - 0.301) \right] (\text{atm}) \quad [20]$$

The equilibrium P_{O_2} obtained from TGA data was in a fair agreement with that calculated by Eq. [20].

Diffusion constant.—In the preceding discussion, the polarizations at the electrode/electrolyte interface, (the main portion of which may be the polarization arising from the activation process of the reaction of Eq. [3]) and the ohmic polarization were not taken into account. It is needed for the validity of the discussion that these polarizations be negligibly small. The check has been done by changing the pulse current in the range from 6 to 60 $\mu\text{A}/\text{cm}^2$ and observing the potential buildup process at the $\text{Nd}_{1-x}\text{Sr}_x\text{CoO}_3$ ($x = 0.2$) electrode by an oscilloscope. No significant profiles indicating the buildup of potential were found in the time constant range shorter than 2 sec. Time constants for ohmic polarization are in general very small as in the order of several microseconds and those for reaction polarization are of the several microseconds order. These results show that both polarizations are negligible in the range of current density employed in the present experiments.

The potential variations with time in the cathodic process were plotted in Fig. 7, for the samples $\text{Nd}_{1-x}\text{Sr}_x\text{CoO}_3$ ($x = 0.2$ and $x = 0.5$). The sample $x = 0.2$

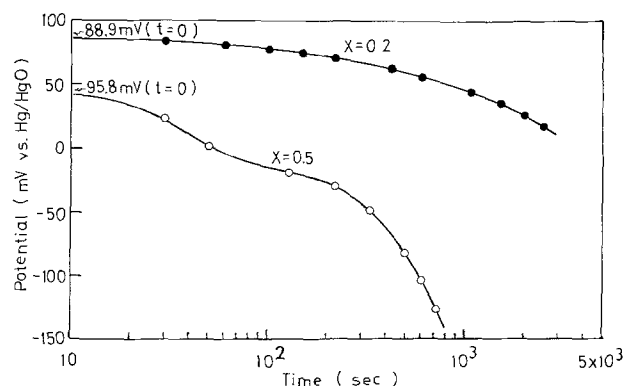


Fig. 7. The potential variations with time for the disk electrodes of $\text{Nd}_{1-x}\text{Sr}_x\text{CoO}_3$ under the constant current cathodic processes. The current densities for $x = 0.2$ and $x = 0.5$ are 6.0 and 9.8 $\mu\text{A}/\text{cm}^2$, respectively.

annealed from 800°C at which the platinum current collector had been attached showed the open-circuit potential of +88.9 mV, indicating δ in the electrode be 6.0×10^{-3} (cf. Fig. 6). It is reasonable to consider that the distribution of δ in the sample electrode was uniform since it was in the state which had been formed by a slow annealing from a higher temperature. The value of δ (6.0×10^{-3}) was considered to be appropriate (to start the experiment) because it was sufficiently small compared with the critical value (0.1 in this case). If the initial value of δ is as large as the critical value ($x/2$), the time range of measurement is restricted to a short period because δ cannot exceed $x/2$, and moreover the error of the diffusion constant to be calculated increases because the δ - E relation becomes inaccurate in the neighborhood of $x/2$ as shown in Fig. 5. According to this consideration, the cathodic current passage was started without any pretreatment for the sample $x = 0.2$. The current density was kept at $6.0 \mu\text{A}/\text{cm}^2$.

The sample $x = 0.5$, on the other hand, showed the open-circuit potential of +49.9 mV which corresponded to the δ value of 9.7×10^{-2} . This value lying near the tail of the curve in Fig. 6 ($x = 0.5$), the preliminary anodic current passage ($20 \mu\text{A}/\text{cm}^2$, 2 hr) was carried out to reduce δ in the sample. When the anodic current was turned off, the potential started to decay and saturated at 95.8 mV. This indicates that the pretreatment formed a substantially uniform distribution of δ , of which the value was considered to be 6.6×10^{-2} . The cathodic current passage was started from this state with the current density $9.8 \mu\text{A}/\text{cm}^2$.

From the x-ray diffraction, the volumes of single molecular nearly cubic unit cell of $\text{Nd}_{1-x}\text{Sr}_x\text{CoO}_3$ were given as 55.0×10^{-24} for $x = 0.2$ and $55.5 \times 10^{-24} \text{ cm}^3$ for $x = 0.5$, respectively. Thus Eq. [18'] for $x = 0.2$ and $x = 0.5$ can now be expressed as

$$\delta_0(t) - 6.0 \times 10^{-3} = \frac{1.16 \times 10^{-9}}{\sqrt{D}} \cdot \sqrt{t} \quad [21]$$

and

$$\delta_0(t) - 6.6 \times 10^{-2} = \frac{1.91 \times 10^{-9}}{\sqrt{D}} \cdot \sqrt{t}$$

respectively. It follows that the plot of $[\delta_0(t) - \delta_0(t=0)]$ vs. \sqrt{t} gives a straight line passing the origin and that the diffusion constant D can easily be calculated from the slope of the given straight line. Figure 8 shows these plots for $x = 0.2$ and 0.5.

The obtained diffusion constants of oxygen ions in $\text{Nd}_{1-x}\text{Sr}_x\text{CoO}_3$ are

$$D = (1.4 \pm 0.1) \times 10^{-11} \text{ cm}^2/\text{sec} \quad (x = 0.2)$$

and

$$D = (7.6 \pm 0.7) \times 10^{-14} \text{ cm}^2/\text{sec} \quad (x = 0.5)$$

at 25°C.² These values are presumably very large compared with ordinary oxides, while the direct comparison is impossible because the diffusion constant of oxygen ions in oxides at a low temperature has not been reported until now. However, the extrapolation

² These values are derived from regression analysis of Fig. 8.

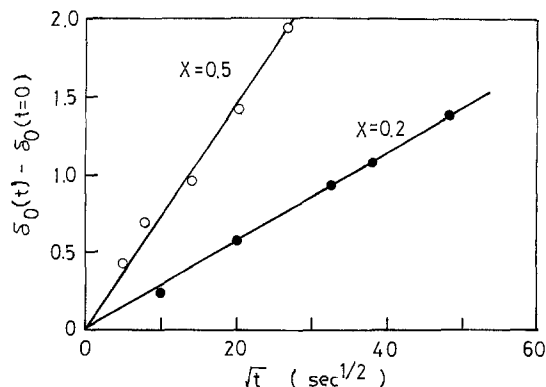


Fig. 8. The changes of δ at the surface of the electrode $[\delta_0(t) - \delta_0(t=0)]$ as plotted against square root of t . The plots for $x = 0.2$ and 0.5 are multiplied by 10^2 and 10 in the figure, respectively. Thus, for example, $[\delta_0(t) - \delta_0(t=0)]$ at $\sqrt{t} = 20 \text{ sec}^{1/2}$ should read 0.6×10^{-2} and 1.4×10^{-1} , respectively. The slopes give the oxygen ion diffusion constants (see text).

from the high temperature data (14) indicates, for an example, the oxygen ion diffusion constant in Y_2O_3 would be $10^{-19} \text{ cm}^2/\text{sec}$ at 25°C. The diffusion constant in $\text{ZrO}_2\text{-CaO}$ solid solution (15) can also be estimated to be in the order of $10^{-22} \text{ cm}^2/\text{sec}$ at 25°C while this solid solution is well known as a good oxygen ion conductor at a high temperature and its D at 1000°C is $10^{-7} \text{ cm}^2/\text{sec}$.

Manuscript submitted Oct. 10, 1973; revised manuscript received Oct. 7, 1974.

Any discussion of this paper will appear in a Discussion Section to be published in the December 1975 JOURNAL. All discussions for the December 1975 Discussion Section should be submitted by Aug. 1, 1975.

Publication costs of this article were partially assisted by Hitachi Limited.

REFERENCES

- G. H. Jonker, *Philips Res. Rept.*, **24**, 1 (1969).
- H. Obayashi, T. Kudo, and T. Gejo, *Japan. J. Appl. Phys.*, **13**, 1 (1974).
- R. R. Hikes, R. C. Miller, and R. Mazelsky, *Physica*, **30**, 1600 (1964).
- C. S. Tedmon, Jr., H. S. Spacil, and S. P. Mitoff, *This Journal*, **116**, 1170 (1969).
- D. B. Meadowcroft, *Nature*, **226**, 847 (1970).
- A. C. C. Tseung and H. L. Bevan, Abstract 8, p. 28, Electrochemical Society Extended Abstracts, Fall Meeting, Atlantic City, New Jersey, Oct. 4-8, 1970.
- W. van Gool, *Philips Res. Rept.*, **20**, 81 (1965).
- T. Takahashi and H. Iwahara, *Denki Kagaku*, **35**, 433 (1967).
- C. Wagner, *Z. Physik. Chem.*, **B21**, 25 (1933).
- M. H. Hebb, *J. Chem. Phys.*, **20**, 185 (1952).
- I. Yokota, *J. Phys. Soc. Japan*, **8**, 595 (1953).
- N. Valverde, *Z. Physik. Chem.*, **70**, S 128 (1970).
- H. H. Macey, *Proc. Phys. Soc.*, **52**, 625 (1940).
- M. F. Berard, C. E. Wirkus, and D. R. Wilder, *J. Am. Ceram. Soc.*, **51**, 643 (1968).
- W. D. Kingery, J. Pappis, M. E. Doty, and D. C. Hill, *ibid.*, **42**, 393 (1959).

Surface-Catalyzed Anodes for Hydrazine Fuel Cells

II. Lifetime Studies of Heat-Treated Nickel Boride Catalyzed Anodes

Stuart G. Meibuhr* and Robert F. Paluch

Electrochemistry Department, Research Laboratories, General Motors Corporation, Warren, Michigan 48090

ABSTRACT

The potential-time relationship of nickel boride catalyzed anodes for the electrochemical oxidation of hydrazine is different from that relationship for similarly catalyzed hydrogen anodes. The potential of freshly catalyzed, nickel boride hydrazine anodes exhibits a decay with time. Chemical, electrochemical, and microscopic analyses related the rate of boron loss from the anode to the rate of decay of the anodic potential. By subjecting the anode to a mild heat-treatment, considerable improvement in the life was achieved. Results are presented and a mechanism proposed to explain the data.

During work at these Laboratories, the potential of nickel boride (Ni_2B) catalyzed anodes for hydrazine fuel cells initially showed a decay with operating time. The decay occurred because the Ni_2B catalyst was being mechanically removed from the substrate by the evolved N_2 gas. Black catalyst particles were found in the electrolyte. This problem was overcome by depositing the catalyst on a Mond Ni substrate (1).

Later, when the anodes were operated at 0.2 A/cm^2 for times exceeding 8 hr, the resistance-free, anode-reference (A-R) potential (using a Hg/HgO reference electrode) showed another decay. On the average, this decay (to the arbitrary cutoff potential of -0.95V) occurred in about 60 hr of operating time, corresponding to about 220 hr of activation time (abbreviated as 60/220). The best times were 80/300 hr. This decay was not accompanied by the mechanical dislodgement of the catalyst particles.

This paper discusses the cause of this second potential decay, several ways to inhibit that decay, and the mechanism of catalyst failure causing that decay.

Experimental

Two types of experiments were performed. The first involved electrochemical lifetime studies with catalyzed anodes and the other involved measuring the surface area and determining the stoichiometry of nickel boride powders that had been subjected to various treatments.

Anode preparation.—Experimental details regarding the electroformation of the ribbed Ni substrates, the deposition of Mond 255 Ni powder, and its subsequent catalyzation with Ni_2B have been given before (1). The codeposition of the Mond Ni powder with electroplated Ni was performed at the optimum conditions as detailed previously (1), the maximum number of coulombs used was 1200 and stirring of the bath was limited to the first 10% of the total codeposition time.

Heat-treating of the freshly catalyzed anodes was performed in a tube furnace (ID = 70 mm, heated length = 0.44m, total tube volume = 0.00225 m^3) modified to operate over a temperature range from about 20° to about 300°C and to accept a flowing gas—dried air, air humidified at different temperatures, Ar, or Ar containing 6% H_2 . Anodes were also heat-treated under reduced pressure (about 100 Pa) in this same tube furnace.

The heat-treatment was performed in three sequential steps of flushing, heating, and finally cooling.

1. After the electrodes were positioned inside, the tube was flushed for 1 hr with Ar at 1.5 liters/min to remove the air.

2. After the first step was completed, the heating was begun. When the temperature reached the desired

value, the inert-gas flow was stopped and the flow of the desired gas was started, again at 1.5 liters/min for 1 hr.

3. After the appropriate heating step, the inert gas flow was again begun and the furnace was cooled. The anodes were exposed to the air only at room temperature.

Steps 1 and 3 were eliminated during the heat-treatment in air. When anodes were heat-treated under reduced pressure, step 1 consisted of 1 hr of pumping, step 2 consisted of heating while still maintaining the pumping, and finally, step 3 consisted of cooling under the reduced atmosphere.

Test procedure.—The catalyzed, heat-treated anodes (48 cm^2 active area) were prepared and tested in duplicate. They were operated against a Ni-plated, perforated steel sheet in the cell shown in Fig. 1, at a constant current density of 0.2 A/cm^2 . The electrolyte (5.7M [33%] KOH containing 1M [3.2%] N_2H_4) flow rate was about 16 times stoichiometric for this current

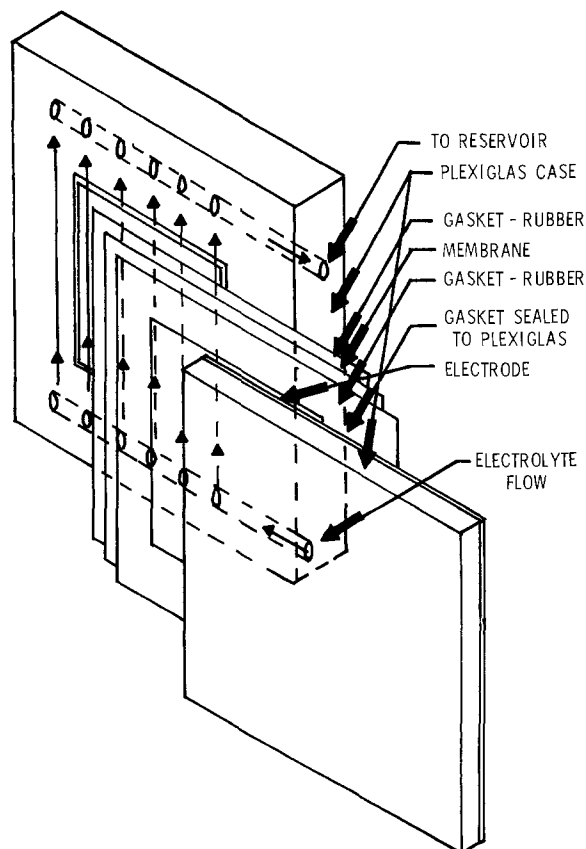


Fig. 1. Schematic diagram of test cell

* Electrochemical Society Active Member.

Key words: nickel-boride, hydrazine, anodes, fuel cells.

density; the electrolyte temperature was $31^\circ \pm 1^\circ\text{C}$. IR-free polarization data were taken regularly using a Kordes-Marko (2) bridge. The 5.7M KOH electrolyte was prepared by diluting 45% KOH-mercury-cell-liquor with deionized water. In all cases, the anode potentials were measured against the Hg/HgO reference electrode.

Scanning electron micrographs were made at low magnification of the Ni_2B surface before and after the electrochemical test. Chemical analyses of the KOH half-cell electrolyte were performed for the presence of boron at the conclusion of several electrochemical tests.

Preparation of nickel boride powder.—The nickel boride powder was prepared by chemical precipitation; a 5% solution of nickel acetate was added slowly to a stirred, 10% solution of NaBH_4 . An excess of NaBH_4 was used. The precipitate was washed well, filtered, and air dried for several days. This powder (about 1g) was spread thinly in a quartz boat that was then positioned in the tube furnace for the appropriate heat-treatment. The heating steps were the same as before.

Surface area determination.—All surface area determinations were made on the Numinco "Orr Surface-Area Pore-Volume Analyzer," Model MIC 103. The recommended procedure (3) was altered so that during the initial evacuation of the sample, no external heat was applied to accelerate the degassing. Thus, no heat was applied to the nickel boride powder samples except during the previous heat-treatment process. The surface area values were computer calculated from a simplified version of the program provided by the equipment manufacturer (3).

Soaking the powder in KOH.—After the surface area was determined (after the desired heat-treatment of step 2), a known weight of powder was soaked in 50 ml of hot (82°C) 33% KOH for 8 and finally for 64 hr at room temperature. The KOH was retained in a plastic beaker to eliminate any boron contamination from borosilicate glass beakers. This procedure was designed to simulate conditions existing during the electrochemical cell testing. These KOH solutions were subsequently analyzed for boron. The powders were washed to remove KOH and finally air dried for several days. The surface area was redetermined.

Differential thermal analysis (DTA).—All DTA data were obtained using a controlled atmosphere DTA system that permitted analyses to be performed at pressures from about 0.13 to about 2×10^5 Pa.

Results and Discussion

Freshly catalyzed anodes.—Freshly catalyzed Ni_2B anodes exhibited a time dependence in the anode potential as depicted in Fig. 2. The arbitrary cutoff potential was -0.95V ; the anode life is indicated in terms of two numbers—the first number designates the num-

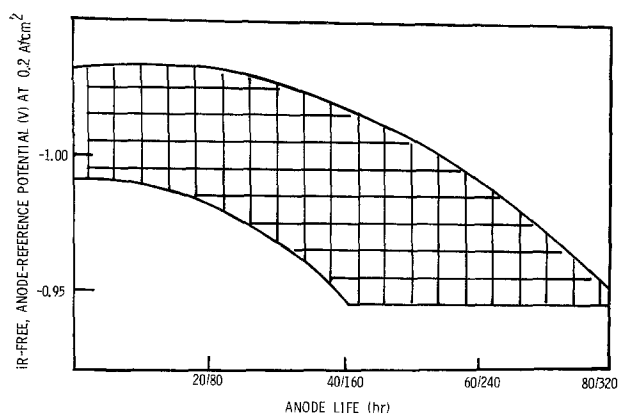


Fig. 2. Anode life (in hours) to an arbitrary cutoff potential of -0.95V (at 0.2 A/cm^2).

ber of hours the anode has operated at 0.2 A/cm^2 , whereas the second number designates the total number of hours the anode has remained in contact with the KOH (activation time), which includes both the load time and the time at open circuit. The total activation time was about four times longer than the operating time. The potential decayed to the arbitrary cutoff value within 60 hr of operating time on the average, corresponding to an activation time of 220 hr.

Figure 3 shows a representative sampling of the SEM micrographs taken of the Ni_2B surface before and after the electrochemical life test. The photomicrographs in the right column are of the freshly catalyzed Ni_2B surface, whereas those in the left column are of the Ni_2B surface after the life test. Figures 3G and 3H are side views of the electrodes and show the Ni sheet, the Mond particles, and the Ni_2B catalyst. Clearly, the photos in the left column show that there is a loss of material from the catalyst surface; the Ni_2B surface has become less dense, and the structure is more open than that depicted in the right column of photomicrographs. Since no black particles were evident in the KOH electrolyte during the electrochemical test, the shedding problem discussed before (1) was not the cause of the material loss. It appeared that the loss was by dissolution into the KOH.

To identify what was dissolving from the electrode, the KOH electrolyte was analyzed for boron and nickel at the end of the life test. No Ni was detected in the

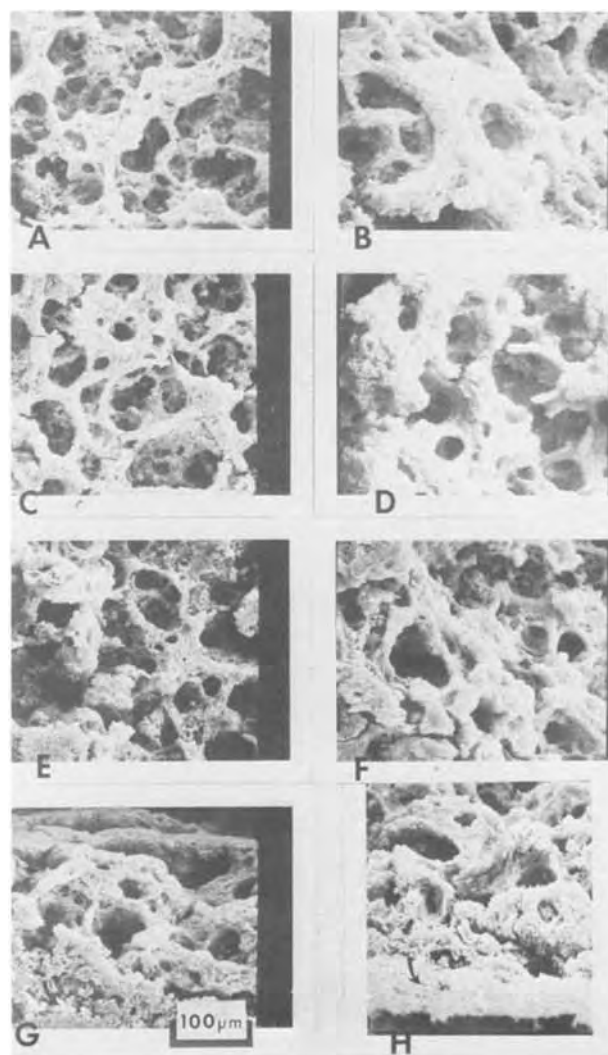


Fig. 3. Ni_2B -catalyst; magnification, 300X. A, B, top view, anodes No. 194 and 195; C, D, top view, anodes No. 187 and 188; E, F, top view, anodes No. 201 and 200; G, H, edge view, anodes No. 201 and 200. B, D, F, H, before electrochemical testing. A, C, E, G, corresponding anode after electrochemical testing.

Table I. Chemical analysis of the fuel cell electrolyte

Item	Anode No.	Boron ($\mu\text{g}/\text{ml}$)	Comments	Time	
				operating/ contact (hr/hr)	Rate of boron loss ($\mu\text{g}/\text{hr}$)
1	Blank	<0.1	33% KOH	—	—
2	227	3.6	Anode soaked in KOH for 8 days	—/196	0.018
3	212	4.0	Std anode, 2 kA/m ²	56/225	0.018
4	279	5.5	Std anode, 4 kA/m ²	58/230	0.019
5	—	5.9	Std anode, 2 kA/m ²	78/300	0.020
6	274	0.3	Heat-treated air, 93°C, 1 hr	20/64	0.005
7	274	1.5	Heat-treated air, 93°C, 1 hr	126/509	0.003
8	275	3.8	Heat-treated, 147°C, 1 hr	56/219	0.017

electrolyte. In Table I, items 1-5, which are results for freshly catalyzed anodes, demonstrate that boron was indeed being removed from the anode (item 3). The rate of boron lost (micrograms per hour of activation time) was independent of the operating current density or operating time. The same loss rate (about 0.018 $\mu\text{g}/\text{hr}$) occurred regardless of how the anode was operated: (i) only at open circuit, item 2; (ii) at 0.2 A/cm², items 3 and 5; (iii) at 0.4 A/cm², item 4. These results demonstrated that the boron loss was by a chemical dissolution mechanism. The rate of boron loss was closely associated with the rate of decay in the electrochemical potential of the anode during life testing.

A material balance on boron was made, understanding that (i) the catalyst formula was Ni₂B, (ii) there were 3 mg/cm² Ni₂B on the 48 cm² anode, (iii) the total electrolyte volume was 300 ml. The calculation showed that only about 5-15% of the boron initially on the anode was dissolved into the electrolyte. Consequently, it may be that the boron is lost only at the surface leaving behind an inactive surface for hydrazine oxidation.

Electron probe analysis failed to identify the presence of boron on the anode either before or after the life test. X-ray analysis showed no crystalline pattern for the nickel boride.

The surface area changes in nickel boride powder caused by the contact of the powder with hot KOH is presented in Table II as items 1 and 2. These samples are duplicate batches of powder, neither of which were heat-treated. Column 1 gives the initial surface area of the powder, column 2 tabulates the ratio of the surface area before heat-treatment to the surface area after a specified heat-treatment, column 3 presents the surface area of the specified powder after the KOH contact, column 4 lists the ratio of the surface area before the contact to the surface area after the contact, column 5 gives the absolute boron content of the KOH after contact with the powder, and finally column 6 presents the normalized value of the amount of boron lost per gram of powder. These data show that contacting the powder with KOH causes the surface area to increase about 2 $\frac{1}{4}$ times. This increase in the surface

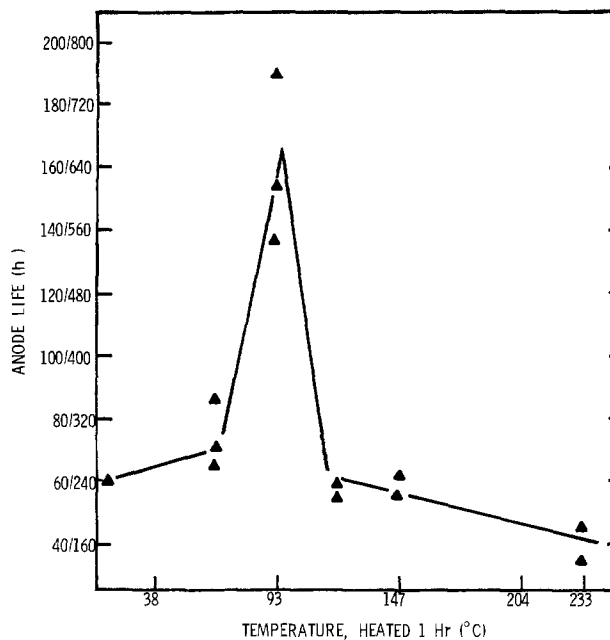


Fig. 4. Lifetime variation of heat-treated Ni₂B anodes using flowing, dry air.

area is consistent with what was seen in the SEM's of Fig. 3. The data of column 5 and 6 (Table II) agree with the data of Table I, items 2-5, that boron is leached out of the nickel boride material.

Anodes heat-treated in dry air.—Preliminary results showed that the operating lifetime of a Ni₂B catalyzed anode was significantly lengthened from 60 hr (60/220) to 160 hr (160/640) by a simple heat-treatment in air. The effect of different heat-treatment temperatures, to 233°C, on the life is displayed in Fig. 4. Despite some scatter in the data, it is clear that the optimum temperature for heat-treating Ni₂B catalyzed anodes in dry air is 93°C. The polarization curves are presented in Fig. 5 for the best performing heat-treated anode. The anodic polarization, curve A, remained unchanged for operating times exceeding 50 hr. At the 100 operating-hr time, the potential had fallen to that drawn as curve B. At the 180 operating-hr level, the potential had dropped to that given in curve C. This anode was in contact with the electrolyte for more than 700 hr.

The chemical analyses of the KOH electrolyte in contact with some of the heat-treated anodes are listed in Table I as items 6-8. These data show that the heat-treated anodes lose boron less rapidly than the non-heat-treated anodes. The rate of boron loss for anodes treated at 93°C was only 25% that for nontreated anodes. The boron loss rate for anodes treated at 147°C corresponded closely to that for nontreated anodes. These data support the hypothesis that the cause of the decay in the anodic potential during hydrazine oxidation of Ni₂B-catalyzed anodes is the loss of boron from the catalyst.

Table II. Nickel boride powder data

Item	Sample	1		3		5		Total B, mg/g of Ni ₂ B
		Initial surface area, m ² /g	Ratio	Surface area after KOH, m ² /g	Ratio	B content, mg/ml	mg/ml	
1	Batch 1 No ΔT	38.9	1.000	92.0	2.36	0.665	—	43.1
2	Batch 2 No ΔT	28.1	1.000	63.0	2.28	1.35	—	27.4
3	Batch 2 $\Delta T = \text{rm temp}/\text{H}_2/1 \text{ hr}$	25.6	0.91	34.6	1.36	0.975	—	26.3
4	Batch 2 $\Delta T = 93^\circ\text{C}/\text{H}_2/1 \text{ hr}$	26.0	0.905	44.4	1.71	0.975	—	18.1
5	Batch 2 $\Delta T = 147^\circ\text{C}/\text{H}_2/1 \text{ hr}$	24.2	0.86	51.2	2.12	1.57	—	31.0
6	Batch 1 $\Delta T = 233^\circ\text{C}/\text{H}_2/1 \text{ hr}$	28.8	0.74	69.4	2.49	1.40	—	31.3
7	Batch 2 $\Delta T = 300^\circ\text{C}/\text{H}_2/1 \text{ hr}$	21.7	0.772	41.5	1.92	—	—	—

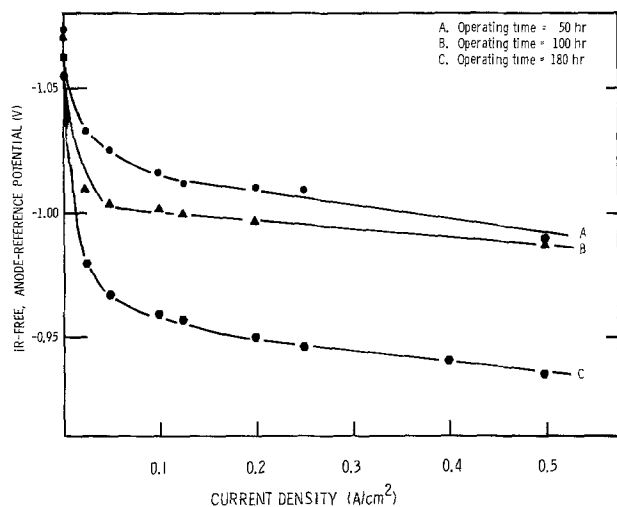


Fig. 5. Variation of the voltage vs. current density curve with time for a dry air, heat-treated, Ni_2B anode (No. 311).

In Fig. 6 are displayed the SEM micrographs showing the effect of temperature on the surface structure of the nickel boride. Parts A-C of Fig. 6 are micrographs of the nonheat-treated surface at three different magnifications; parts D-F are the micrographs of the nickel boride heat-treated at 93°C for 1 hr; and parts G-I are micrographs of the nickel boride treated at 233°C for 1 hr. The micrographs show that the nickel boride surface loses material when it is heated in dry air. This is most evident in the micrographs at low magnification in the left column.

At a heat-treating temperature of 233°C , considerably more material was lost than at 93°C . This loss must be considered excessive because the lifetime of the resultant anodes was well below that achieved for anodes treated at 93°C (see Fig. 4).

It is necessary to have a continuous flow of air over the anodes. In one experiment at 93°C in the tube furnace, no air was supplied to the system. Both ends of the furnace were open, however, so that air could diffuse through the tube. These two anodes had a very short operating life of about 20 hr (20/65) and had a poor initial operating anode-reference potential of about -0.97V .

The length of time that anodes are heat-treated is another important parameter. Table III presents the lifetime results for anodes treated at 93°C in flowing air for four different lengths of time. The data showed that (i) the 1 hr time yielded anodes with the best life, and (ii) the 16 hr time caused serious shortening in the life. The micrographs of Fig. 7 show surface changes that occurred in Ni_2B that was heated in flowing air at 93°C for times from 5 min to 2 hr. After heat-treatment for 2 hr (Fig. 7F), breaks in the Ni_2B surface have become evident, which are absent from the sample that was heat-treated for only 1 hr (Fig. 7E). It is evident that the optimum heat-treating conditions in dry air necessary to maximize the anode life are 93°C for 1 hr. Several possibilities exist to explain this improvement:

1. Some of the boron is removed during the heat-treatment yielding a stoichiometry that is more resistant to the KOH leaching of boron.

2. Surface oxides could form, which in turn make the surface more resistant to the KOH leaching of boron.

3. Some type of structural change occurs during the heat-treatment. With the present data, it is not possible to identify the mechanism involved in this heat-treatment stabilization of nickel boride catalyzed anodes for hydrazine oxidation.

Anodes heat-treated in a reducing atmosphere.—Heat-treating anodes in a reducing (6% H_2 in Ar) atmosphere has yielded anodes with an improvement of one to two orders of magnitude in lifetime. Figure 8 presents the lifetime data of three differently processed nickel boride catalyzed anodes. Curve A represents the average time decay of freshly catalyzed anodes (0.32 mV/hr decay rate). Curve B represents the average time decay of anodes treated in dry air at the optimum condition of 93°C for 1 hr (0.12 mV/hr decay rate). Curves C and C' represent the time decay for two anodes treated in the reducing atmosphere at 93°C for 1 hr (0.014 mV/hr decay rate). Thus the time decay for dilute H_2 treated anodes (to the cutoff voltage of -0.95V) is about one to two orders of magnitude less than for the untreated anodes.

The effect of different heat-treating temperatures (for 1 hr in the dilute H_2) on the life (defined similarly as for the air-treated anodes) is presented in Fig. 9. The circles represent data for anodes treated exactly as indicated by steps 1-3. The triangles correspond to data for anodes that were cooled in the same dilute H_2 gas that was used for heat-treating (used the same gas in steps 2 and 3); and the squares represent data for two anodes treated and cooled in 100% H_2 .

In Fig. 10 is plotted the effect of different heat-treating times (in 6% H_2 at 93°C) on the life of nickel boride anodes. The data from Fig. 9 and 10 show that the longest lived anodes were produced when the time in the flowing 6% H_2 stream was limited to 1 hr at a temperature of 93°C . The best life was also achieved when the cooling cycle was performed in Ar gas.

Anodes were also heat-treated under reduced pressure (100 Pa) at 93°C for 1 hr. The average lifetime of these anodes (before the cutoff potential was reached) was about 180/650 hr. This value is practically the same as that achieved by heat-treating anodes in air and considerably below the value achieved by heat-treating in a reducing atmosphere. The SEM micrographs of vacuum, heat-treated anodes appeared similar to the micrographs for air, heat-treated anodes. Anodes that were heat-treated in an inert atmosphere (100% Ar) at 93°C for 1 hr had a lifetime of about 300/1500 hr.

Several experiments were performed with nickel boride powders that were heat-treated in the reducing atmosphere at different temperatures. The data is presented in Table II, items 3-7. The value of the surface area measured after the heat-treatment was compared to the value measured before the treatment; the resultant ratios (column 2) are plotted in Fig. 11 as closed triangles. The open circles represent data from Jasinski (4); these powders were treated in vacuum for times varying from 2.5 to 17 hr. The closed circle represents data of Lindholm (5) for a nickel boride powder that was heat-treated in 100% H_2 for 1 hr. Although there is some scatter in the data, they do demonstrate that the surface area of nickel boride powders decrease with increased heating temperatures. Thus, the improved electrochemical performance evidenced for the H_2 -treated anodes cannot be ascribed to changes in surface area.

The surface area of freshly precipitated nickel boride powders that were soaked in KOH increased about $2\frac{3}{4}$ times (relative to their surface area before the immersion); see Table II, column 4, items 1 and 2. For powders that were heat-treated in 6% H_2 , this test caused the surface area to increase linearly with increasing temperature of heat-treatment (Fig. 12).

Table III. Effect of heat-treatment time

Heat-treatment time at 93°C (hr)	Operating time (> -0.95V) / contact time
0	26/74
$\frac{1}{2}$	43/175
1	160/600
4	50/198
16	12/28

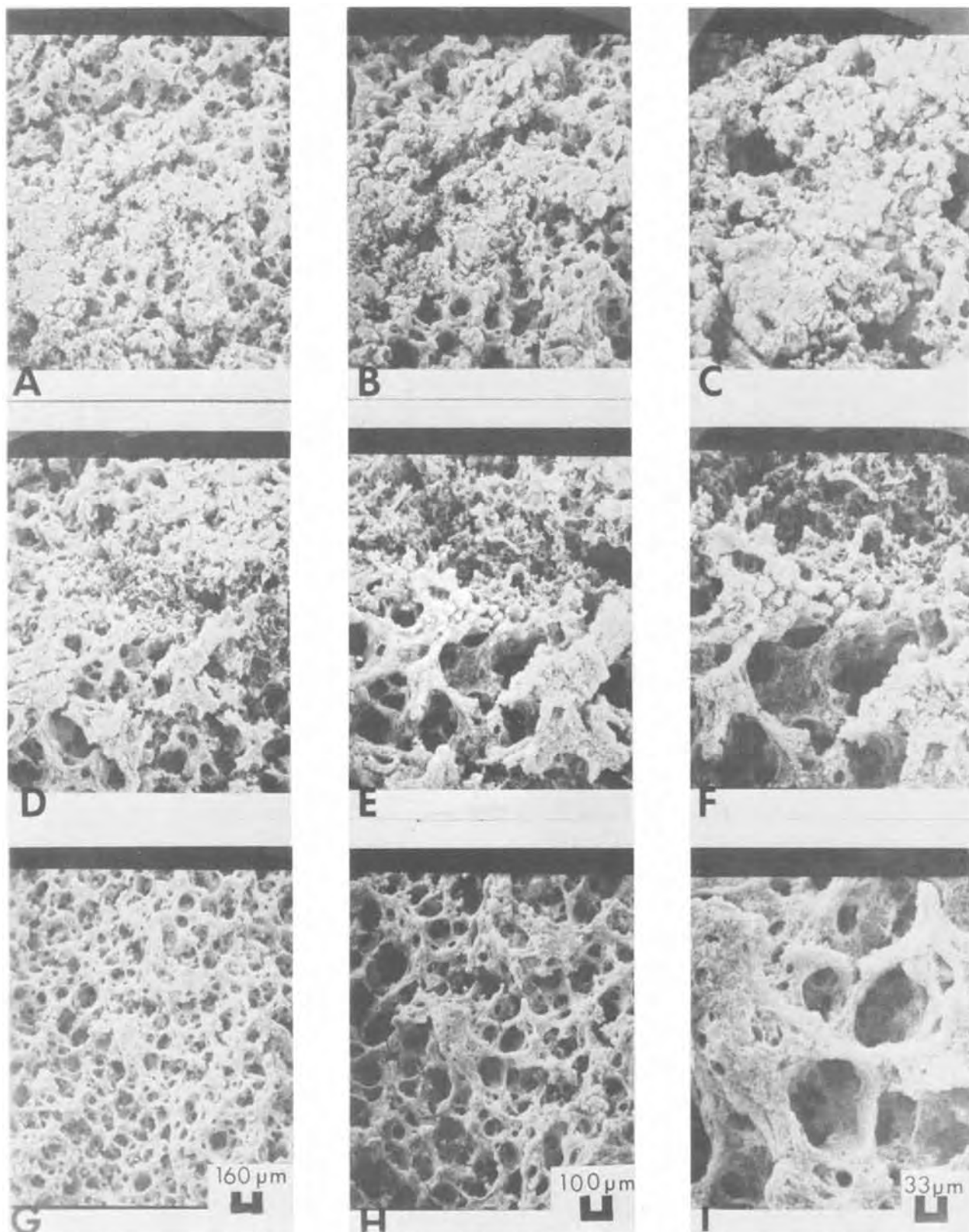


Fig. 6. Effect of temperature on Ni_2B catalyst. A, B, C, nonheat-treated; D, E, F, heated at 93°C for 1 hr; G, H, I, heated at 233°C for 1 hr. A, D, G, magnification, 60X; B, E, H, magnification, 100X; C, F, I, magnification, 300X.

Several reasons for the sudden decrease in the ratio for the powder heated at 300°C include (i) at 300°C there may occur sufficient physical changes such as sintering which leaves a surface that is more resistant to the subsequent chemical attack by the KOH; or (ii) sufficient chemical changes occur such as boron loss which leaves a surface that is more resistant to the subsequent chemical attack by the KOH.

The boron content of the KOH used in the immersion tests is listed in column 5 of Table II, and a normalized

value (to unit weight) is listed in column 6. The normalized boron loss is at its lowest value for the powder that was heat-treated in 6% H_2 for 1 hr at 93°C , the same conditions that have produced the longest lived nickel boride catalyzed hydrazine anode.

Analysis of a freshly precipitated powder for both nickel and boron showed the stoichiometry to be Ni_2B in agreement with the literature (5-7). Heat-treating the freshly precipitated powder in 6% H_2 at 93°C for 1 hr, caused the stoichiometry to become $\text{Ni}_2\text{B}_{0.67}$.

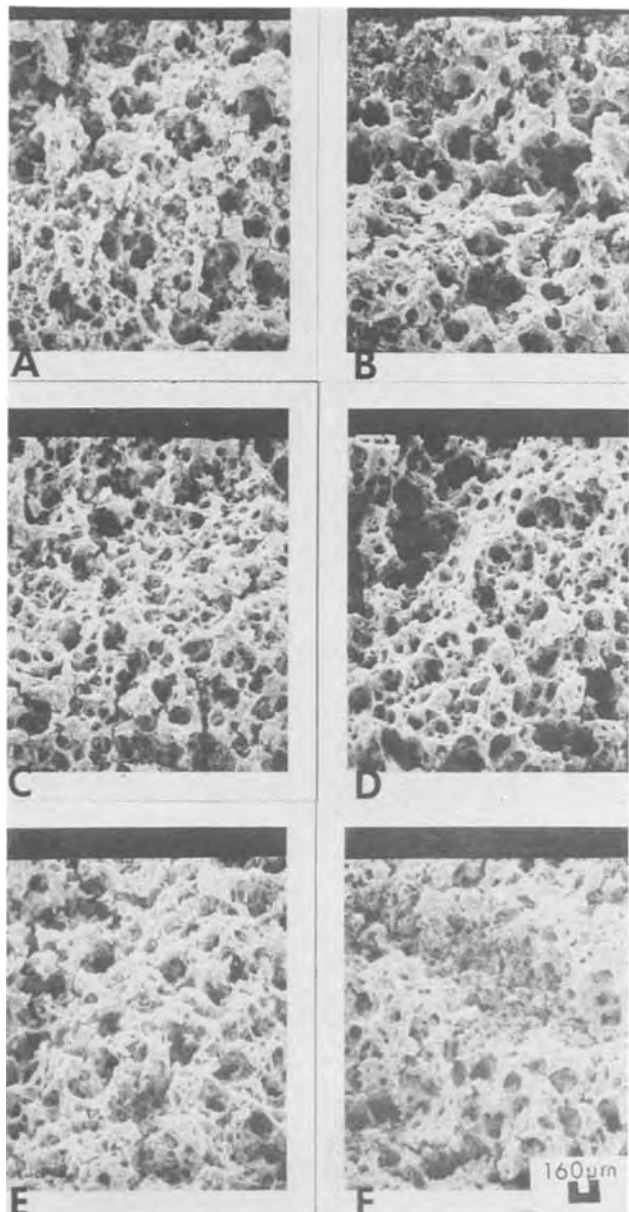


Fig. 7. The effect of heat-treatment time (in dry air) on the structure of Ni_2B at constant temperature (93°C). Magnification, 60X. A, $\Delta t = 0$ min; B, $\Delta t = 5$ min; C, $\Delta t = 10$ min; D, $\Delta t = 30$ min; E, $\Delta t = 60$ min; F, $\Delta t = 120$ min.

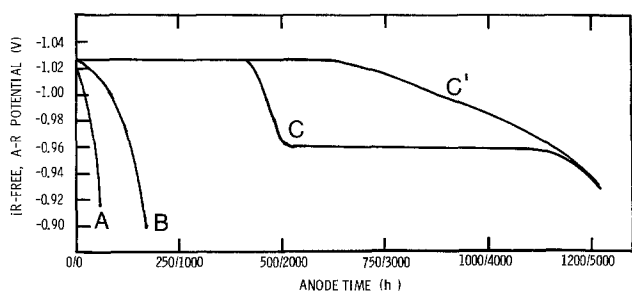


Fig. 8. Lifetimes of Ni_2B -catalyzed anodes. A, nontreated; B, heat-treated in flowing air at 93°C for 1 hr; C and C', heat-treated in flowing 6% H_2 at 93°C for 1 hr.

Differential thermal analysis was performed on nickel boride powder before and after different heat-treatments (in 6% H_2 in Ar atmosphere). Three DTA curves (run in 6% H_2 in Ar) are presented in Fig. 13. Curve A corresponds to the nonheat-treated material; five peaks were observed, occurring at 64°C (a), 120°C (b), $345\text{--}350^\circ\text{C}$ (c), 430°C (d), and 525°C (e). Curve B

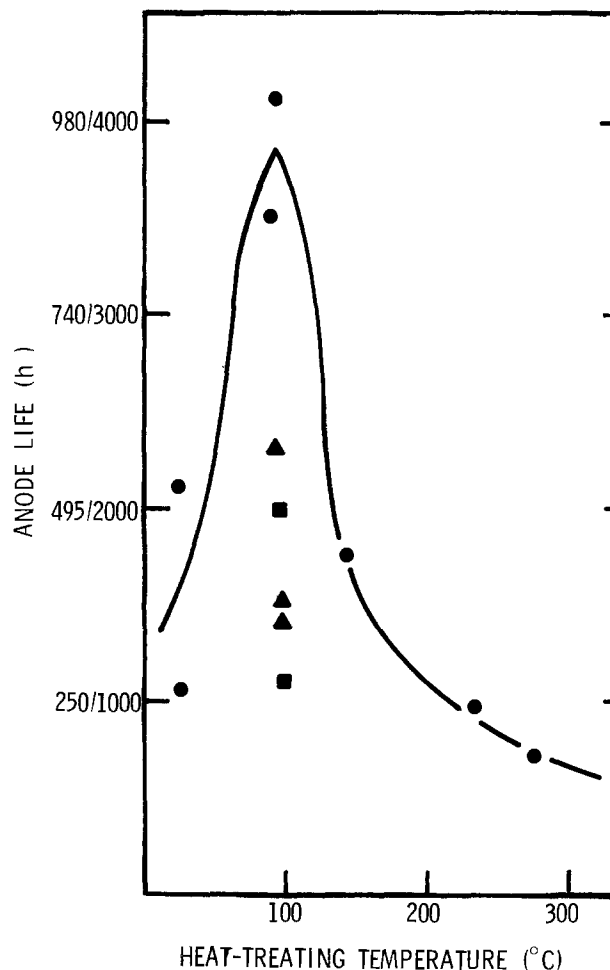


Fig. 9. Lifetime variation of heat-treated Ni_2B anodes in flowing H_2 as a function of heating temperature for a heating time of 1 hr. ●, Steps 1-3 followed; ▲, cooled in 6% H_2 ; ■, heated and cooled in 100% H_2 .

corresponds to a material that was heat-treated in 6% H_2 in Ar at 93°C for 1 hr. Two changes occurred in the DTA curve, peak (a) was eliminated and the ratio of heights of peaks (c) and (d) was reversed. Heat-treating the nickel boride to a higher temperature of 260°C for 1 hr in the 6% H_2 in Ar produced a material having the DTA curve represented by curve C. These curves imply that the Ni/B stoichiometry was altered by the specific heat-treatment. Analogous results were obtained when the nickel boride powder was heat-treated at 93°C for different times. Nonreproducible results occurred when an inert gas (N_2 or Ar) was used to blanket the sample during the DTA run.

Nickel boride powder was scrapped off anodes that had been under electrochemical testing for 450 and 2200 hr, and then DTA analysis was performed. The results are shown in Fig. 14; curve A corresponds to the catalyst material after 450 hr in contact with KOH and curve B, after 2200 hr. No characteristic nickel boride peaks were obtained with the latter material. It is obvious that contact with KOH altered the Ni/B stoichiometry of the catalyst. The elimination of peaks (c) and (d) (curve B) after 2200 hr contact with KOH occurred at about the same time that the iR -free anode-reference potential started to drop from its original value (curves C and C' of Fig. 8). It appears the two phenomena are related.

The chemical analysis of the nickel boride powders before and after a 6% H_2 heat-treatment and the SEM micrographs of heat-treated anodes showed that the heat-treatment process removed boron from the catalyst; and the KOH leaching of boron was retarded from the H_2 heat-treated nickel boride. Just as there were several possible explanations for the improved anode life by heat-treating in air, so are there several

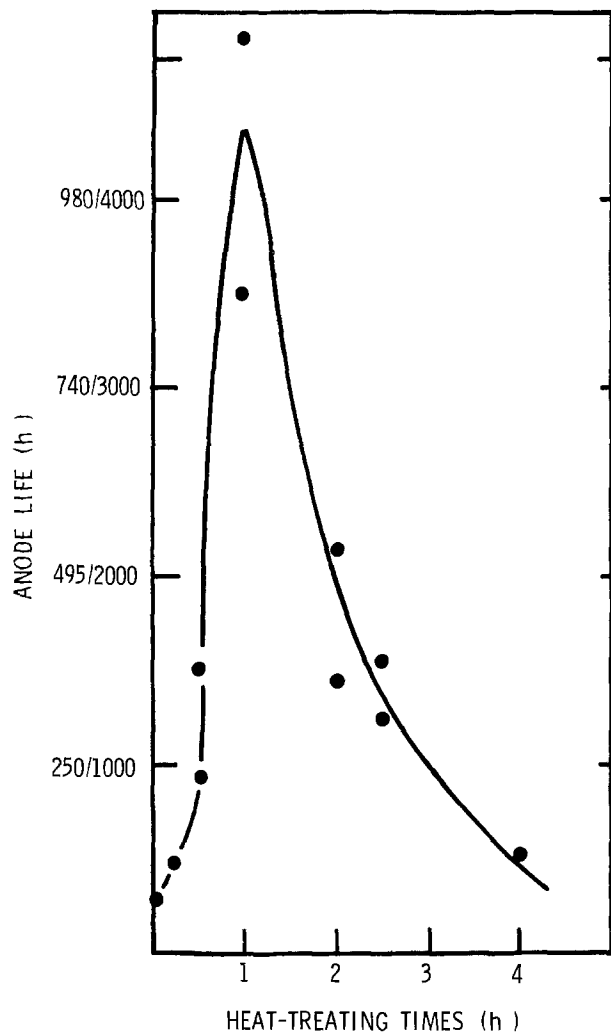


Fig. 10. Lifetime variation of heat-treated Ni_2B anodes in flowing 6% H_2 as a function of heating times at a temperature of 93°C .

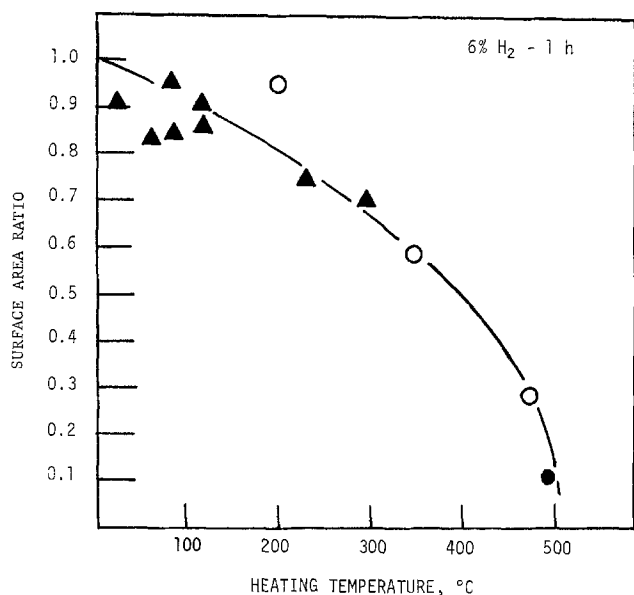


Fig. 11. Effect of the heating temperature on the relative surface area of nickel boride powders.

possible explanations for the 1-2 order of magnitude improvement in anode life caused by heat-treating in 6% H_2 . These include: (i) during the H_2 heat-treatment process, some of the boron is removed (perhaps by reaction with the H_2 to form volatile boron hydrides) leaving a Ni/B catalyst stoichiometry that is

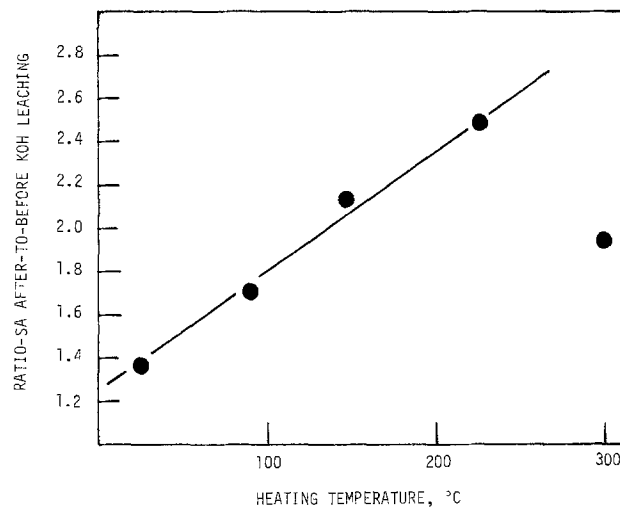


Fig. 12. Effect of the heating temperature on the relative surface area changes in nickel boride powders caused by KOH leaching.

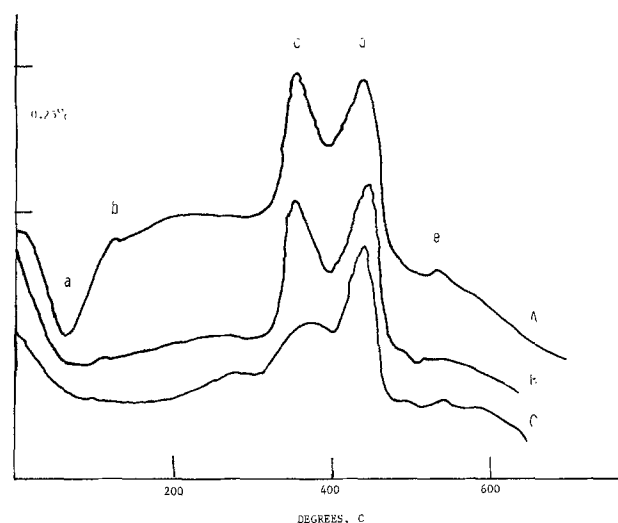


Fig. 13. DTA curves of nickel boride powder. Curve A, freshly precipitated powder; curve B, heat-treated in 6% H_2 (Ar) at 93°C for 1 hr; curve C, heat-treated in 6% H_2 (Ar) at 260°C for 1 hr.

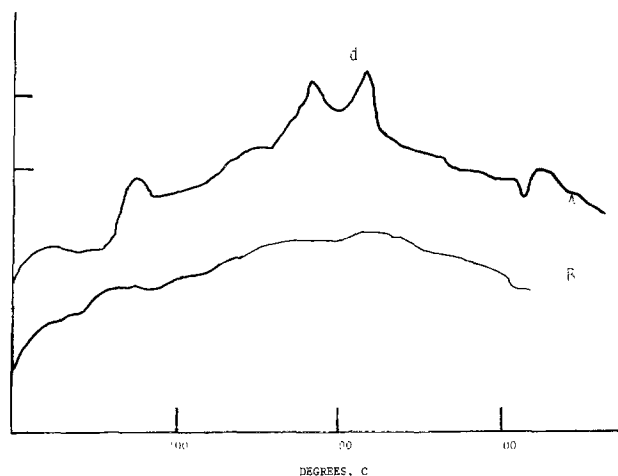


Fig. 14. DTA curves of nickel boride powder after contact with 33% KOH. Curve A, after 450 hr; curve B, after 2200 hr.

more resistant to attack by KOH and therefore capable of sustaining a current load at low overvoltage for prolonged times; (ii) during the heat-treatment process, surface oxides are removed by reduction with the H_2 followed by some sintering of the catalyst thereby rendering the catalyst more resistant to attack by KOH and therefore capable of sustaining a current load at

low overvoltage for prolonged times; (iii) during the heat-treatment process the surface could anneal (relieve stress).

Since the rate of potential decay of all the H₂-treated nickel boride catalyzed anodes was associated with the rate of boron loss from that catalyst, it appears that the first explanation is the most likely.

Manuscript submitted Jan. 28, 1974; revised manuscript received Aug. 12, 1974. This was Paper 341 presented at the San Francisco, California, Meeting of the Society, May 12-17, 1974.

Any discussion of this paper will appear in a Discussion Section to be published in the December 1975 JOURNAL. All discussions for the December 1975 Discussion Section should be submitted by Aug. 1, 1975.

Publication costs of this article were partially assisted by the General Motors Corporation.

REFERENCES

1. S. G. Meibuhr, *This Journal*, **121**, 1264 (1974).
2. K. Kordesch and A. Marko, *ibid.*, **107**, 480 (1960).
3. Operating Manual, Numinco, Apollo, Pennsylvania, Revised Nov. 1, 1964.
4. R. Jasinski, in "Fuel Cell Systems," G. J. Young and H. R. Linden, Editors, *Advances in Chemistry Series 47*, p. 95, American Chemical Society, Washington, D.C. (1965).
5. I. Lindholm, Paper presented at the SERAI Fuel Cell Symposium, p. 26, Brussels, June 1965.
6. R. Jasinski, C. McMullen, and L. Swette, Paper presented at the SERAI Fuel Cell Symposium, p. 38, Brussels, June 1965.
7. R. Paul, P. Buisson, and N. Joseph, *Ind. Eng. Chem.*, **44**, 1006 (1952).

Hydrogen Overpotential on Zinc Alloys in Alkaline Solution

T. S. Lee*¹

Union Carbide Corporation, Battery Products Division, Parma Research Laboratory, Cleveland, Ohio 44101

ABSTRACT

Hydrogen overpotential on uniformly prepared Zn alloys of Hg, Pb, and Cd in 9N KOH solution are measured. The effect of small amounts of iron evenly distributed in the sample on the overpotential of Zn-Hg and Zn-Pb alloys are also observed. Exchange current densities (I_0) and transfer coefficients (α) for the hydrogen evolution process on these surfaces are obtained.

Due to increased interest in using zinc electrodes in alkaline battery systems in the last decade, the behavior of zinc electrodes in alkaline media has been studied more in the past decade than ever before. Data on hydrogen overpotential on zinc in alkaline solution, which has both theoretical and practical interest, have appeared in the literature (1, 2). The data on zinc containing small amounts of impurities in alkaline media also have been published (3, 4). However, except for very sketchy reports (5), hydrogen overpotentials on uniformly prepared zinc alloys in concentrated alkaline solutions have not yet been reported. The present paper reports the measurement of hydrogen overpotentials on carefully prepared zinc alloys of Zn-Hg, Zn-Cd, Zn-Pb, Zn-Mn as well as Zn-Pb-Fe and Zn-Hg-Pb in 9N KOH solution at room temperature. It is believed that these will serve not only as scientific information but will also provide factual background for those who wish to use them to interpret zinc corrosion phenomena in alkaline systems (6).

Experimental

The cell used for the measurements is a modified H-type cell equipped as a closed system under a hydrogen atmosphere. It is made from epoxy-lined "Pyrex" so that the inner walls are highly alkaline-resistant. The details of the cell, the lining technique and tests for resistance to concentrated alkaline solution were reported previously (2).

The samples are prepared by alloying the high-purity zinc (99.999+%) with other pure metals. The purity of the other metals are as follows: mercury 99.996+%, lead 99.999+%, cadmium 99.999+%, manganese 99.99+%, and iron 99.99+%. The details of

making these alloys were reported elsewhere (4). In short, the alloys are prepared under inert atmosphere with great care to assure their uniformity and, simultaneously to avoid the introduction of any foreign materials. The final alloys are subjected to metallographic examinations and electron-microprobe analyses to determine their exact purity and uniformity.

The working electrodes are prepared from those alloys by cutting a piece from the center of the final casts.² The exposed area of this piece is about 1 cm²; the remainder is electrically insulated with the same epoxy used to line the cell. The electrode surface is prepared and treated by following the same procedure described before (2).

The counterelectrode is made from pure nickel and its area is about 8-10 times that of the working electrode in order to minimize the introduction of peroxide in the cell. The reference is a Hg/HgO electrode in contact with the same KOH solution as that in the cell. The concentration of the KOH is 9N.

The constant current is supplied by a Harrison Laboratories' Model 855C power supply through a variable power resistor in series. The potentials are measured by a Keithley Model 630 potentiometric electrometer, which has a minimum input resistance of 10¹⁸ ohm. All measurements are carried out at room temperature which is controlled at 25° ± 1°C. Measurements are carried out from the high current density to the low current density region and back again; this process is then repeated.

At each current density, the steady potential is obtained in a few minutes. Once the steady potential is reached, the electrode will stay at the same potential as long as ½ hr without any change. The data presented here are the average values of four runs. The deviation of each run from the average value is only a

* Electrochemical Society Active Member.

¹ Present address: Research and Development Laboratory, Drew Chemical Corporation, Parsippany, New Jersey 07054.

Key words: hydrogen overvoltage, hydrogen evolution process in alkaline solution.

² The alloys are all uniform from center to the skin, the reason for taking the center portion is to avoid the possible skin contamination during casting and handling.

few millivolts; there is no hysteresis in any of the runs. After the measurement, the electrodes are washed, dried, and examined under a microscope. The surface does not appear to have changed from its original appearance.

Results and Discussion

Hydrogen evolution on a zinc surface under imposed electric potential in alkaline solution is known to have the over-all reaction: $2\text{H}_2\text{O} + 2e = \text{H}_2 + 2\text{OH}^-$. The rate-determining step in this reaction is electron transfer. The transfer coefficient $\alpha = \frac{1}{2}$, and the hydrogen overpotential (η) for the reaction as shown previously (2) is

$$\eta = \text{const} + \frac{RT}{F} \ln A_{\text{H}_2\text{O}} A_{\text{OH}^-} - \frac{2RT}{F} \ln I$$

where A denotes the activity, I is the current density, and the other symbols have their usual meaning. At constant temperature and definite KOH concentration, the above equation reduces to the Tafel equation $\eta = a + b \log I$, where a and b are constants.

In the experiments, the hydrogen overpotentials are obtained by subtracting the reversible hydrogen potential from the measured potential. The reversible hydrogen potential in 9N KOH at 25°C, as both measured and calculated before (2), is -0.938V against a Hg/HgO electrode.

The hydrogen overpotentials of alloys of Zn-Hg, Zn-Cd, Zn-Pb, and Zn-Mn in 9N KOH are shown in Fig. 1-4, respectively, as a function of log current densities. In Fig. 1, one can see that all the mercury alloys have a higher hydrogen overpotential than that of pure zinc. The numerical value of the overpotential of Zn-2% Hg is higher than that of pure zinc and the Tafel slope is about the same as that of zinc. As the mercury content increases to 4 and 8%, the numerical

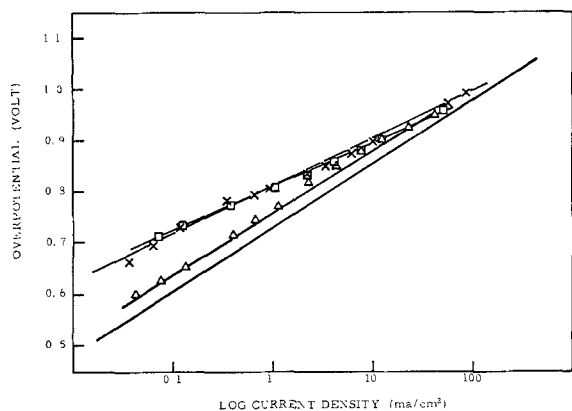


Fig. 1. Hydrogen overpotentials for Zn-Hg alloys. — Zn, Δ Zn-2% Hg, X Zn-4% Hg, \square Zn-8% Hg.

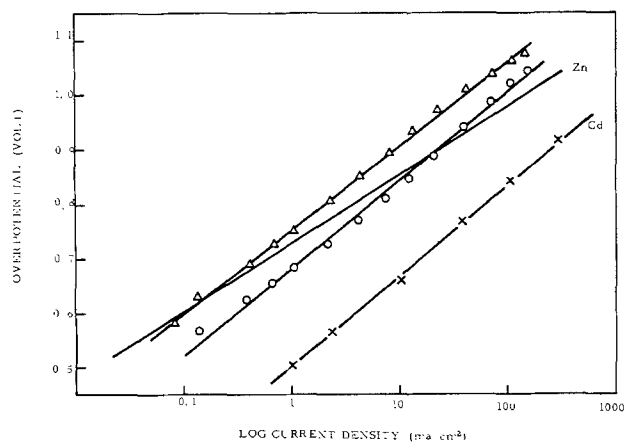


Fig. 2. Hydrogen overpotentials for Zn-Cd alloys. — Zn as well as Zn-0.05% Cd, \circ Zn-4% Cd, Δ Zn-8% Cd, X Cd only.

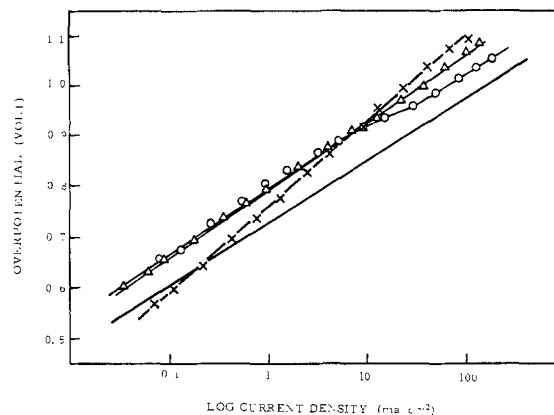


Fig. 3. Hydrogen overpotentials for Zn-Pb alloys. — Zn, \circ Zn-0.2% Pb, Δ Zn-0.8% Pb, X Zn-2.0% Pb.

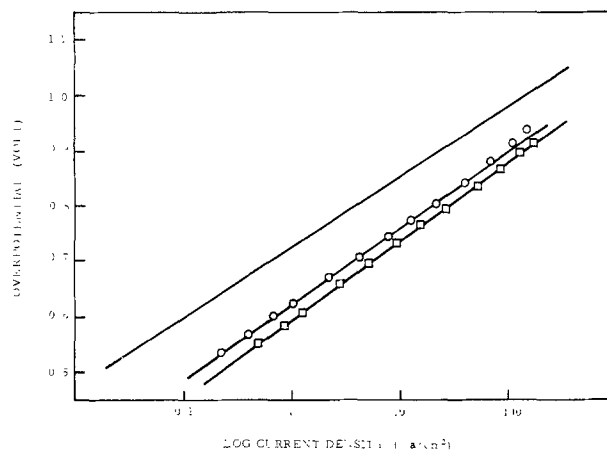


Fig. 4. Hydrogen overpotentials for Zn-Mn alloys. — Zn, \circ Zn-0.05 Mn, \square Zn-0.5-Mn.

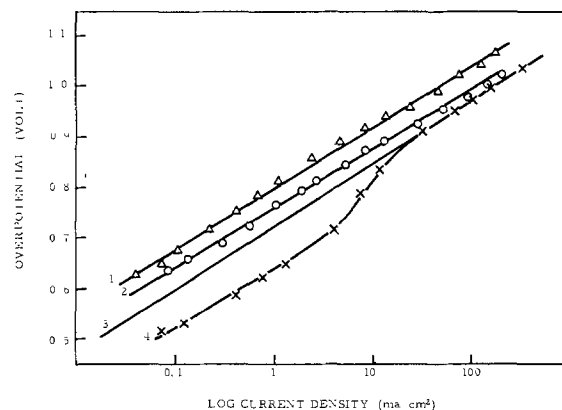


Fig. 5. Hydrogen overpotentials for tertiary Zn alloys. — Zn, X Zn-0.05% Fe, Δ Zn-2% Hg-0.2% Pb, \circ Zn-0.8% Pb-0.05% Fe.

values of hydrogen overpotential increase by more than 100 mV in the low current density region, while in the high current density region, the increase is not that much. This is due to the result of Tafel slope decrease as the mercury content in the sample increases. From the figure it looks as if the hydrogen overpotential data for the 4% Hg alloys are not much different from those for the 8% Hg alloys. However, by careful examination, one can see that the slope of the overpotential for the 8% Hg alloy is slightly smaller than that for the 4% Hg alloy. This may account for the slightly better corrosion protection of a zinc electrode with 8% Hg than that with 4% Hg in an alkaline electrolyte. This is schematically illustrated in Fig. 6. The anodic reaction of Zn/ZnO_2^- in alkaline solution is represented by curve a, which will not vary under

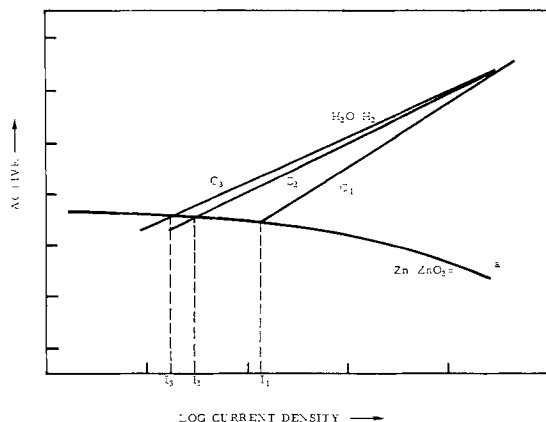


Fig. 6. Corrosion currents of zinc in alkaline solution with different slopes of $\text{H}_2\text{O}/\text{H}_2$ reaction.

the specific condition. The cathodic reaction of $\text{H}_2\text{O}/\text{H}_2$ is represented by the family of curves c_1 , c_2 , and c_3 . Curve c_1 represents the reduction of water on zinc surface. Curve c_2 is that of the cathodic reaction on the Zn-Hg surface and that of c_3 is the reaction on the Zn-Hg surface with a higher mercury content on the sample than that of c_2 . All the three curves intercept the curve of the anodic reaction $\text{Zn}/\text{ZnO}_2=$ at I_1 , I_2 , and I_3 , respectively. The numerical value of I_1 , I_2 , and I_3 are known as the corrosion currents of the respective surfaces in the KOH solution. The smallest numerical value of the three corrosion currents is I_3 . This is obtained as a result of the lowest slope of the water reduction on the metal surface. The experimental data shows that the higher the mercury content in the zinc alloy the lower the slope of the cathodic water reduction reaction. In Fig. 6 curve c_3 represents the cathodic reduction of water on the zinc surface containing the largest amount of mercury and shows the lowest corrosion current (I_3) of all curves.

Figure 2 shows the hydrogen overpotential plots for the cadmium alloys. As shown previously by (4), a small amount of Cd (0.05%) in Zn does not change the overpotential one way or the other. As the cadmium content increases to 4 and 8% in the alloys, the Tafel slope changes to that of cadmium. The hydrogen overpotential on Cd is reproduced in the figure for comparison. It appears that the cadmium alloy in the alkaline system behaves like cadmium but at a higher numerical value than that of pure cadmium. It is interesting to point out that the transfer coefficients (α) derived from the Zn-Cd alloys containing 4-8% cadmium are the same as those obtained from cadmium in 6N NaOH solution by Zhouldev and Stender (7) ($\alpha = 0.37$) and are not much different from those obtained in 1N HCl by Hickling and Salt (8) ($\alpha = 0.3$). The increase of the slope for the Zn-Cd alloy is the result of the cadmium component in the alloy. This might be due to a stronger adsorption of cations in the solution on the alloy surface than on pure zinc. The hydrogen overpotentials on lead alloys are plotted in Fig. 3. The slope of the overpotential on Zn-0.2% Pb is about the same as that of pure zinc; even the numerical value in the low current density region is larger than that in the high current density region, the overpotential on Zn-0.8% Pb is uniformly higher than that of zinc. As the lead content increases to higher

Table I. Electrochemical parameters for hydrogen evolution reaction on various Zn alloys surface in 9N KOH

Surface	Slope	α	I_0 (A/cm ²)
Zn	0.124	0.48	1.5×10^{-9}
Zn-2% Hg	0.116	0.51	2.7×10^{-10}
Zn-4% Hg	0.098	0.60	8×10^{-11}
Zn-8% Hg	0.086	0.69	6×10^{-12}
Zn-4% Cd	0.158	0.37	7×10^{-8}
Zn-8% Cd	0.154	0.37	1.5×10^{-8}
Zn-0.2% Pb	0.137	0.43	2×10^{-9}
Zn-0.8% Pb	0.134	0.44	1.3×10^{-9}
Zn-2% Pb	0.172	0.34	6.2×10^{-8}
Zn-0.05% Mn	0.138	0.43	5.1×10^{-8}
Zn-0.5% Mn	0.140	0.42	7.5×10^{-8}
Zn-2% Hg-0.2% Pb	0.125	0.48	6×10^{-10}
Zn-0.8% Pb-0.05% Fe	0.125	0.48	9×10^{-10}

percentages, as in Zn-2.0% Pb, the slope of the overpotential increases. This will cause the exchange current as well as the corrosion current to become larger than that of zinc which is less desirable than a lower percentage of lead with respect to corrosion protection. Figure 4 shows the plots for manganese alloys. It is evident that manganese in the alloy lowers the overpotential. The higher the numerical value of the overpotential. In Fig. 5, the interaction of one element with the other on the overpotential of the zinc alloy is shown. The 0.05% Fe introduced into zinc causes the overpotential decrease in the low current density region (curve 4). Where 0.8% Pb is added, however, the effect of iron is canceled (curve 2). The overpotential of the alloy Zn-0.8% Pb-0.05% Fe is uniformly higher than that of zinc. In other words, the effect of lead could mask the effect of iron. Curve 1 in Fig. 5 is the overpotential plot for Zn-2% Hg-0.2% Pb, which has a higher numerical value than either that of Zn-2% Hg or Zn-0.2% Pb.

The electrochemical parameters of the hydrogen evolution process are shown in Table I. Both the transfer coefficient (α) and exchange current (I_0) are derived from the Tafel plots.

Manuscript submitted March 4, 1974; revised manuscript received Sept. 20, 1974. This was Paper 346 presented at the San Francisco, California, Meeting of the Society, May 12-17, 1974.

Any discussion of this paper will appear in a Discussion Section to be published in the December 1975 JOURNAL. All discussions for the December 1975 Discussion Section should be submitted by Aug. 1, 1975.

Publication costs of this article were partially assisted by the Union Carbide Corporation.

REFERENCES

- Z. A. Iofa, L. V. Komlev, and V. S. Bagotskii, *Zh. Fiz. Khim.*, **35**, 1571 (1963).
- T. S. Lee, *This Journal*, **118**, 1279 (1971).
- T. I. Popova, V. S. Bagotskii, and B. V. Kabanov, *Zh. Prikl. Khim.*, **36**, 1743 (1963).
- T. S. Lee, *This Journal*, **120**, 707 (1973).
- S. Uno Falk and Alvin J. Salkind, "Alkaline Storage Batteries," p. 546, John Wiley & Sons, New York (1969).
- For example; F. Mansfeld and S. Gilman, *This Journal*, **117**, 1328 (1970).
- M. O. Zhouldev and V. V. Stender, *J. Appl. Chem. USSR*, **31**, 711 (1958).
- A. Hickling and F. W. Salt, *Trans. Faraday Soc.*, **36**, 1226 (1940).

Stress Corrosion Cracking of 4140 High Strength Steel in Aqueous Solutions

Aziz Asphahani* and H. H. Uhlig**

Department of Metallurgy and Materials Science,
Massachusetts Institute of Technology, Cambridge, Massachusetts 02139

ABSTRACT

The critical hardness value of 4140 steel is determined above which stress corrosion cracking (SCC) in boiling distilled water initiates within short times. Also the critical applied potentials are measured immediately below which SCC does not initiate. Cold work and various galvanic couples are evaluated. A reasonable mechanism of cracking is discussed.

The stress corrosion cracking (SCC) behavior of many high strength, low alloy steels stressed to 75% of their yield strength and exposed to a marine atmosphere was described by Phelps (1,2). Most steels with yield strengths below 180 ksi (125 kg/mm²) were resistant for at least 1000 days, some were resistant for this exposure period up to 210 ksi (148 kg/mm²), but all failed within days or months above this strength level. Yamamoto and Fujita (3) described a similar upper critical strength level for observed SCC of low alloy steels in water equal to 155-170 ksi (110-120 kg/mm²) yield strength, based on service data and laboratory tests. Although they reported that composition of a low alloy steel can also be a factor, their observed times to failure showed that strength level is the more important parameter determining susceptibility. They also showed that times to failure in water are appreciably shorter at elevated than at room temperatures; moreover, time to failure in 0.3% NaCl is a function of applied potential, as had been shown earlier for 12% Cr, 1% Mo, 0.3% V stainless steel in 3% NaCl by Phelps and Loginow (4) and for a 12% Ni maraging steel in sea water by Kirk, Covert, and May (5). Peterson *et al.* (6) using notched tensile bar specimens reported the potential range within which failure of H-11 steel [225 ksi yield strength (YS)] is inhibited for at least 160 hr in sea water.

Baker and Singletary (7), using U bend specimens of 4340 steel having a Rockwell hardness of R_c 51, confirmed shorter failure times in various aqueous solutions at above room temperature, and reported a marked pH and anion effect. Fujita and Yamada (8) and Okada (9) recently described the SCC behavior of various high strength steels in aqueous media, again emphasizing a critical yield stress range above which, but not below, susceptibility is observed; they also discussed metallurgical factors, mechanisms, and various protective measures. Gilchrist and Narayan (10) reported failures of stressed, high strength 0.83% C steel wires anodically or cathodically polarized; furthermore they showed that cold drawn wires were not immune and that cracks proceeded by either "active path" or by hydrogen cracking. Yamaoka and Wranglen (11) earlier reported failures of stressed, high strength 0.4% C low alloy steel whether anodically or cathodically polarized in water. Johnson and Wilner (12) employing precracked specimens of H-11 low alloy steel (230 ksi YS) showed that a given upper stress intensity factor insufficient to cause crack growth in dry argon was nevertheless adequate to cause crack growth in moist argon corresponding to as little as 0.1% relative humidity (r.h.). The rate of crack growth increased with partial pressure of H₂O up to 60% r.h., above which the rate leveled off.

It is the purpose of the present investigation: (i) to explore the critical potential range within which failures by SCC do not initiate, and the effect in this respect of some environmental factors and cold work, and (ii) to interpret presently known facts in terms of possible mechanisms.

Experimental

The present A.I.S.I. Type 4140 steel (0.43% C, 0.91% Cr, 0.23% Mo, 0.90% Mn, 0.32% Si, 0.024% S, 0.01% P, 0.15% Ni) in the form of 3/8 in. rod was made available by courtesy of Inland Steel Company. After rolling to 41 mil (1.0 mm) thick strip, specimens were sheared to the dimensions: 1 3/4 × 3/16 in. (4.5 × 0.5 cm), abraded, degreased, and pickled in 5 volume per cent (v/o) HNO₃ at 80°C for 3 min. They were then bent beyond the elastic limit to the form of a C having a span of 1 7/16 in. (3.7 cm). Bent specimens were held between porcelain insulators by remote spring loading, being subject, therefore, to constant flow stress up to the time a crack initiated. Total failure time was recorded by an electric clock. The assembly was submerged in boiling distilled water or in boiling aqueous salt solution contained in a flask fitted with a condenser. Boiling temperatures were preferred over lower temperatures because of corresponding shorter times to failure. For conditions of controlled potential, the flask was fitted with a glass frit-separated side arm which was located near the position of maximum bending of the test specimen and contained a saturated calomel reference electrode. Two auxiliary Pt electrodes 3 × 1 in. (7.6 × 2.5 cm) were placed at opposite sides of the specimen within the cell. To make electrical contact, an iron wire enclosed by closely fitting Teflon tubing was spot welded to one end of the specimen. A Wenking potentiostat controlled the applied potential throughout a test run. A sketch of the cell but with auxiliary electrodes outside the cell appeared in a previous publication (13).

The present test as applied to high strength steels is a measure primarily of conditions leading to crack initiation rather than crack growth. Although many arguments have been presented in favor of using precracked specimens and measuring crack growth, there are also valid arguments in favor of using smooth test specimens. A smooth test specimen stressed beyond the elastic limit has the advantage of conforming closely to conditions typical of practical structures which through surface scoring or assembly procedures are stressed locally beyond the elastic limit. Furthermore only a smooth specimen makes it possible to evaluate precise environmental conditions affecting failure, as well as the true operating potential range within which cracks are not initiated. By way of contrast in tests employing a precracked specimen, both electrolyte pH and composition within a deep fissure can vary greatly with time (14), and the

* Electrochemical Society Student Member.

** Electrochemical Society Active Member.

Key words: low alloy steels, critical potentials, decarburization, stress-sorption cracking, cold work, galvanic couples.

true potential at the apex of a deep crack is largely unknown.

It should also be pointed out that values of stress intensity K_{ISCC} below which cracks supposedly do not grow in a damaging environment are of doubtful value to most practical situations, including those involving high strength metals. Brown (15) referring to crack growth in precracked specimens of high strength steels exposed to sea water has stated that there does not appear to be a clear-cut threshold strength below which SCC does not occur. This conclusion is in contrast to that applying to the use of smooth specimens where a critical yield strength for SCC in water or moist air has been reported by more than one investigator, and which, moreover, correlates closely with field tests and with broad practical experience. In addition, as Peterson *et al.* (6) show, at high stress levels (such as are presently applied) the observed crack growth rate of high strength 4340 steel in sea water at room temperature can be as high as $\frac{1}{4}$ in. (0.6 cm)/min. Under these conditions, it is obviously more useful to study factors that prevent crack initiation, and it is these conditions with which the present paper is concerned.

Results

Effect of hardness.—Since high strength steels exposed to water are found to be subject to SCC only when they are heat-treated above a specific yield strength range (which can be interpreted in terms of hardness), it was important to determine whether the present laboratory test correlates with practical experience and with field tests. The 4140 steel specimens water quenched from 850°C attained high hardness and strength (R_c 53), but these on bending failed mechanically. Lower hardness values were obtained by tempering at 350°C or higher temperatures. Furnace-cooled specimens (in purified argon) were least hard, measuring about R_c 10. Tests in boiling distilled water showed that stressed water-quenched and tempered specimens (R_c 47) failed within the short time of 2 hr or less, but that furnace-cooled specimens did not fail within the maximum test period arbitrarily set at 200 hr. Averaged data (2 to 3 specimens) of Fig. 1 show that the critical hardness below which failure

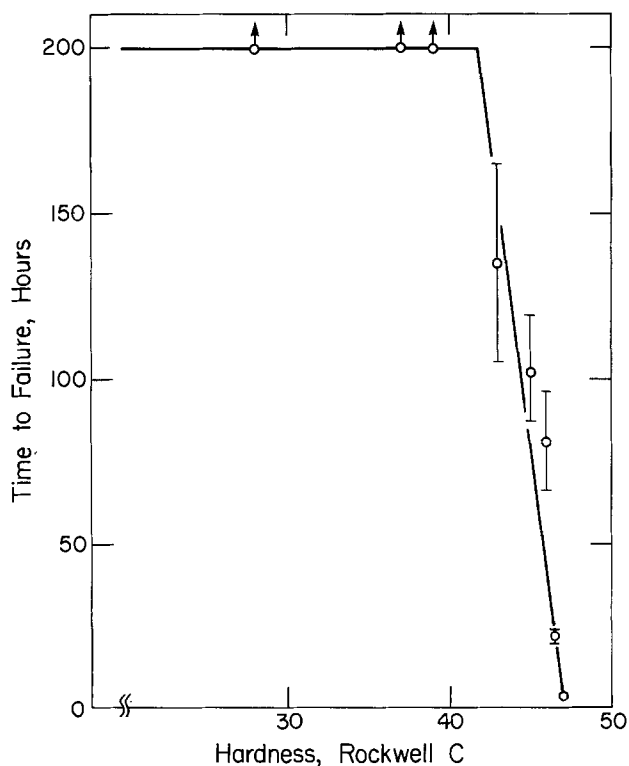


Fig. 1. Effect of hardness of 4140 steel on stress corrosion cracking in boiling distilled water.

times are >200 hr is about R_c 42. This value corresponds to a yield strength of 185 ksi (130 kg/mm²) which is close to the room temperature critical range established by Phelps through long time marine atmosphere tests (1, 2). The steep fall off of failure time with hardness confirms a critical range of hardness values above which SCC occurs. The lower level of hardness or yield strength corresponding to absence of SCC or very long expected life in a moist atmosphere can at best be estimated from broad practical experience; corrosion fatigue data of Lee and Uhlig (16) also contribute relevant information. They found no effect of moisture in air on the fatigue life of 4140 steel below the interpolated value of R_c 32-35 corresponding to a yield strength of 145-151 ksi (102-106 kg/mm²). This lower critical range is reasonably close to that reported by Yamamoto and Fujita (3) and by Okada (9).

A laboratory-prepared, relatively pure 1% Ni, 0.3% C steel tested in boiling distilled water had a critical hardness value of R_c 40 for >200 hr life; the corresponding value for a laboratory-prepared pure 1% Cr, 0.3% C steel was R_c 42. These values parallel that for 4140 steel and confirm that strength rather than composition is the important factor determining susceptibility of a steel to SCC in water.

The present accelerated test, therefore, provides a measure of susceptibility of low alloy steels to SCC in water and aqueous salt solutions. Average failure times of 4140 steel heat-treated to R_c 46 (205 ksi YS) and exposed to boiling 3% NaCl (57 hr) and to boiling 3% Na₂SO₄ (60 hr) are somewhat shorter than failure times in boiling water (81 hr), but the difference is not considered to be especially significant. The salt solutions have good electrical conductivity and were used to obtain values of the critical potential immediately below which otherwise susceptible steels do not undergo SCC failure at boiling temperatures for at least 200 hr, and probably for much longer times.

Effect of cold work and decarburization.—The effect of cold work was studied by cold-rolling steel previously water quenched from 850°C and tempered $1\frac{1}{2}$ hr at 420°C having a final hardness value for the cold-rolled material varying from R_c 43 for 25% reduction to R_c 46.5 for 60% reduction. It was feasible to cold-reduce steel so tempered to not more than 60% reduction of thickness. Cold-rolling was generally but not always beneficial. Specimens cold-rolled 60% reduction of thickness consistently did not fail in boiling distilled H₂O or in boiling 3% NaCl for the maximum test period. Failures, however, were observed in boiling 3% Na₂SO₄ within an average of 93 hr (4 specimens). Data are plotted in Fig. 2. The reason for the difference in behavior between NaCl and Na₂SO₄ test solutions was clarified by critical potential measurements to be described later.

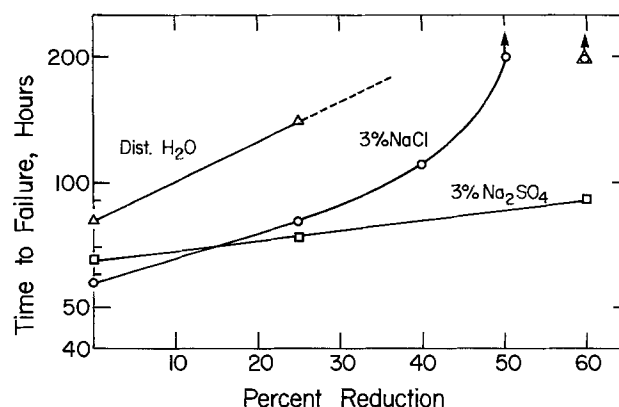


Fig. 2. Effect of cold-rolling parallel to long specimen direction of 4140 steel, R_c 43-46.5, on stress corrosion cracking in boiling aqueous solutions.

Table I. Effect of decarburized surface on susceptibility of 4140 steel to SCC in boiling distilled H₂O and to hydrogen cracking in 3% Na₂SO₄

Decarburization treatment	Rockwell hardness		Time to failure in boiling H ₂ O	Time of failure cathod. polarized in 3% Na ₂ SO ₄ + As ₂ O ₃ , 24 mA/cm ²	
	Surface	Core		Boiling	Room temp
1. Wet H ₂ 1000°C, 40 min, W.Q.	R _c 30	R _c 53	>200 hr (2)*	2.3 min (2)	5.5 min (2)
2. Wet H ₂ 760°C, 60 min, W.Q.	R _B 80	R _c 53	>200 hr (2)	2.0 min (2)	2.3 min (2)
3. Wet H ₂ 780°C, 60 min, W.Q., tempered 420°C, 20 min	R _B 74	R _c 46.5	>200 hr (2)**	>200 hr	15 min (2)
4. As in 3 but decarburized layer pickled off in 10% HNO ₃ , 85°C (loss of 15 mils spec. thickness)			52 hr (2)		

* Numbers in parentheses indicate number of specimen tested.

** Also no failure in boiling 3% NaCl and boiling 3% Na₂SO₄.

In a program to ascertain whether generation of hydrogen by the water-steel reaction may be the cause of cracking, as is thought to be the case by some investigators, specimens were prepared with a soft surface about 1-4 mils (0.03-0.1 mm) thick obtained by decarburization, allowing the core to remain at a hardness value above R_c 42 needed for susceptibility. The soft surface continues to react with water to form hydrogen, but would not supposedly initiate a crack. Such a surface was found to prevent failure, as is shown by data of Table I. These results confirm the observations of previous investigators (3, 17) who reported beneficial effects of a decarburized surface layer on SCC of high strength steels. The results of Table I also show that cathodically charging hydrogen onto decarburized specimens results in hydrogen cracking despite a soft surface. Two series of specimens failed by hydrogen cracking at room and at boiling temperature. A third series although failing at room temperature did not fail within 200 hr at boiling temperature, which may be explained by too little hydrogen entering the steel (better catalytic surface for 2H → H₂) at the higher temperature.

Along the same lines, if residual interstitial hydrogen in the steel were the cause of cracking, it should be possible to remove such gas by heating the specimen before applying stress. Three specimens immersed unstressed in boiling water for 25 hr, then stressed, failed within an average of 85 hr. Three additional specimens immersed unstressed for 100 hr failed within an average of 79 hr. Heating 3 specimens unstressed in air for 100 hr, then stressing and immersing in boiling water resulted in an average failure time of 86 hr. In absence of preimmersion in boiling water or previous heat-treatment in air at 100°C, the average failure time was 81 hr. All these times to failure are within the experimental variations of the test. They show that residual hydrogen in the steel, or hydrogen produced by the steel-water reaction, or heat-treatment at 100°C, are not apt to be important factors entering the cause of failure.

Critical potentials.—The importance of the critical potential relates to the decisive role it plays in determining whether or not SCC will initiate. Only a few millivolts either way accounts for initiation of damage or its absence. The significance of the critical potential in this regard was previously emphasized by data from this laboratory on SCC of austenitic (13, 18) and ferritic (19) stainless steels, and of mild steels (20) in nitrates and alkalis. For high strength steels, a similar well-defined critical potential is observed. However, because of the sensitivity of these materials to hydrogen cracking, a potential range usually beginning some tenths of a volt active to the critical potential can again lead to rapid failure. This gives rise to a potential interval within which protection is observed, as was shown by earlier data of Kirk *et al.* (5) for a maraging steel in sea water and by data of Peterson *et al.* (6) for 4340 steel in sea water. The effect of applied potential on time to failure in boiling 3%

Na₂SO₄ of 4140 steel water quenched from 780°C, tempered 20 min at 420°C, R_c 46, is shown in Fig. 3. The critical potential, referring to a life of >200 hr, appears at -0.658V, SCE, or -0.416V, SHE (neglecting liquid junction and thermal gradient potentials). The corrosion potential in this solution measured at the time of failure is equal to -0.63V, SCE, or -0.39V, SHE, which is noble to the critical value, accounting for spontaneous cracking in absence of an applied potential. The corresponding critical potential in boiling 3% NaCl (Fig. 4) is equal to -0.640V, SCE, or -0.398V, SHE, and a more noble corrosion potential equal to -0.61V SCE, or -0.37V, SHE, again accounts for spon-

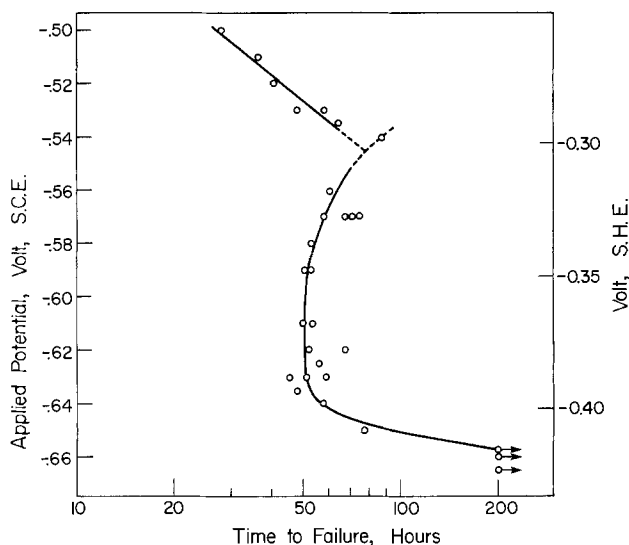


Fig. 3. Effect of applied potential on time to failure of 4140 steel, R_c 46, in boiling 3% Na₂SO₄.

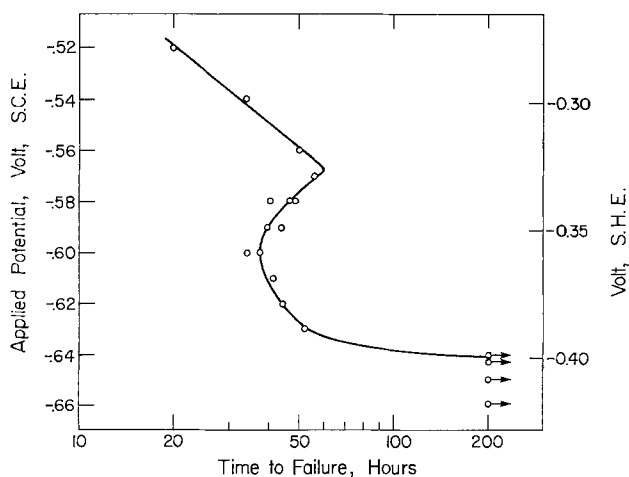


Fig. 4. Effect of applied potential on time to failure of 4140 steel, R_c 46, in boiling 3% NaCl.

Table II. Effect of cold-rolling on SCC of 4140 steel boiling solutions

Steel treatment	Critical pot. SHE, V		Corros. pot. SHE, V		Difference of pot., V		Time to failure, simple immersion, hr	
	3% Na ₂ SO ₄	3% NaCl	3% Na ₂ SO ₄	3% NaCl	3% Na ₂ SO ₄	3% NaCl	3% Na ₂ SO ₄	3% NaCl
W.Q. 783°C, temp'd. 420°C, 20 min, R _c 46	-0.416	-0.398	-0.388	-0.368	0.030	0.030	60 (3)	57 (2)*
W.Q., temp'd., cold-rolled 60%, parallel long spec. dimension, R _c 46.5	-0.398	-0.372	-0.393	-0.383	0.005	-0.010	93 (4)	>200 (2)

* Numbers in parentheses indicate number of specimens tested.

taneous failure. The critical potential was usually reproducible to ± 3 mV whereas the corrosion potential drifted with time and hence was reported only to the nearest 10 mV.

Critical potential data for steel cold-rolled 60% reduction parallel to the long specimen dimension show that the critical potential becomes more noble and the corrosion potential more active through cold-rolling, but that the corrosion potential is just noble to the critical potential in 3% Na₂SO₄ accounting for spontaneous cracking (Table II). This situation is opposite to that in 3% NaCl for which the corrosion potential remains active to the critical potential, accounting for resistance to failure.

These results demonstrate the sensitivity of failures by SCC to both critical potential and prevailing corrosion potential. This sensitivity is also shown by the inhibiting effects of alkalis and of orthophosphates. A shift of corrosion potential and critical potential accounts for lack of failure in boiling 3% NaCl at pH 11 and 12. Data are plotted in Fig. 5; pH values refer to room temperature. Because of inevitable drift of corrosion potentials with time, the cross-over of critical and corrosion potentials shown at about pH 9.3 may on the average occur within the pH range 9-10.

The inhibition of SCC by addition of 1% NaH₂PO₄ to boiling 3% NaCl adjusted to pH 6.4 is also accounted for by shift of potentials. In presence of phosphate the critical potential is moved 140 mV in the noble direction to -0.258V, SHE, and the corresponding corrosion potential is shifted 30 mV in the active direction to -0.40V, SHE. No failure occurs within the maximum test period of at least 200 hr.

Galvanic couples.—The importance of the critical potential to the observed SCC of high strength steels

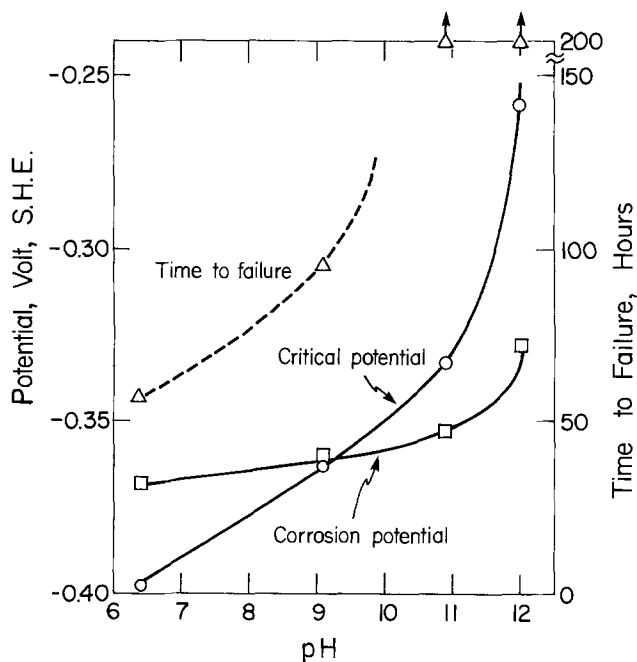


Fig. 5. Effect of pH of boiling 3% NaCl on critical and corrosion potentials, and on time to failure of 4140 steel, R_c 46.

leads to the prediction that coupling a steel to a more active metal of sufficient area to polarize the steel just active to its critical potential should be beneficial. At the same time, the potential must not be shifted into the still more active region where hydrogen cracking occurs. The latter form of damage is diminished at 100°C compared to room temperature because of less tendency for hydrogen to enter a cathodically polarized steel at above-room temperatures, but hydrogen cracking under some conditions can nevertheless occur at boiling temperatures, as our several tests showed. Results of galvanic couple tests in boiling 3% NaCl are summarized in Table III.

Discussion

The present laboratory results confirm that initiation of failure by SCC of low alloy carbon steels in water is sensitive largely to yield strength or hardness, and that failure times are much shorter at 100°C than at room temperature. A thin decarburized surface effectively protects a harder core ($>R_c$ 40) against SCC damage, but not against hydrogen cracking induced by cathodic polarization. It is also confirmed that cold-rolling can be beneficial, as is well known in the application of cold-drawn steel cables to bridge construction. A high pH aqueous environment (pH 11 or 12) at boiling temperature for which the corrosion potential tends to remain active (lack of passivity) is also beneficial. The latter observations on cold-rolling and pH are presently explained in terms of shifts of the critical potential for SCC and of the corrosion potential. Whenever the corrosion potential or applied potential falls active to the critical value, SCC does not initiate; in the reverse order failure is observed.

Properly chosen galvanic couples of adequate area can therefore be beneficial as data of Table III show. Phelps and Loginow (4) in their atmospheric tests found that Zn-rich paints and Al coatings are protective to high strength steels. On the other hand, Yamamoto and Fujita (3) found that couples of high strength steel with Mg or Zn in aerated water at room temperature were detrimental, but that couples with Cd, Sn, Pb, Mo, Al, and Cu were without effect. Peterson *et al.* (6) reported that Zn coupled to an 18% Ni maraging steel in sea water was detrimental, but that Cd was beneficial. The reported detrimental effect of Mg or Zn is probably a result of hydrogen cracking, an effect which is less likely with Cd because its corrosion potential is less active than either that of Zn or Mg, but active enough to polarize steel below its

Table III. Effect of galvanic coupling on SCC of tempered 4140 steel, R_c 46, in boiling 3% NaCl

Coupled to double area of	Pot. of couple V, SHE, after		Time to failure, hr
	1 hr	50 hr	
Zn	-0.81	-0.76	>230 (3)*
Cd	-0.57	-0.56	>230 (2)
0.1% Sn-Al alloy (commercial)	-0.81	-0.55	>230 (2)
None	(Crit. pot. = -0.398V)		57 (2)

* Numbers in parentheses indicate number of specimens tested.

critical potential. The successful use of Cd coatings on high strength steel aircraft landing structures is a practical illustration of a beneficial galvanic couple.

As the applied (cathodic polarization) or corrosion potential becomes increasingly active with respect to the critical potential higher rates of hydrogen discharge eventually cause hydrogen cracking, as has been demonstrated previously by many investigators (5, 6), and which has led to the opinion by some that all failures of high strength steels are caused by hydrogen. This opinion, however, although supported by some reported values of the activation energy for cracking similar to that for diffusion of hydrogen in iron, is not consistent with most of the facts. For example, our measurements show that hydrogen cracking occurs in equal or longer times at elevated compared to room temperature. Stressed, high strength, 4140 steel specimens cathodically polarized in 3% Na₂SO₄ saturated with As₂O₃ failed within minutes either at room temperature or at boiling temperature. These results are contrasted with SCC of specimens exposed to water or 3% Na₂SO₄ without polarization, failures of which occurred in <200 hr only at elevated temperatures. This fact plus the existence of a critical potential below which (active to) SCC is not observed conflict with any mechanism of cracking dependent upon hydrogen.

Anodic polarization, on the other hand, which in neutral or alkaline solutions understandably inhibits hydrogen discharge at a steel surface can nevertheless also cause hydrogen cracking. The surface accumulation of acid anodic corrosion products, e.g., FeCl₂ or FeSO₄, in sufficient amount generates hydrogen at the steel surface by local action. It is this factor that probably accounts for shorter times to failure in NaCl or Na₂SO₄ at potentials somewhat noble to the critical potential and at correspondingly increased anodic current densities, as shown in Fig. 3 and 4. Hydrogen cracking of the present high strength steel occurs in typically shorter times than does SCC. Hydrogen as the cause of cracking was also established for a cold-rolled ferritic 18-8 stainless steel stressed perpendicular to the rolling direction when anodically polarized in neutral NaCl solution, or when immersed unpolarized in saturated FeCl₂ (pH = 1) at room temperature (21). In this connection, Barth *et al.* (22) observed hydrogen permeation of an alloy steel anodically polarized in NaCl solution, as did Wilde (23) in similar measurements on a 12% Cr stainless steel. In both instances pits formed within which an anolyte of low pH could accumulate. It is likely that failure of an anodically polarized high strength steel reported by Yamooka and Wranglen (11) occurred by hydrogen cracking for similar reasons.

Hence the evidence of critical potential data is that hydrogen is not the likely cause of failure by SCC when 4140 steel is exposed to boiling water or to neutral aqueous solutions, but that it enters the mechanism of failure under conditions of pronounced cathodic or anodic polarization. The presence in the environment of cathodic poisons for the reaction $2H(ads) \rightarrow H_2$ consisting of, e.g., H₂S or As₂O₃, can serve to drive more hydrogen into the steel and hence extend the range of conditions under which hydrogen cracking occurs, but even in this situation, SCC can apparently occur independent of interstitial hydrogen.

There is additional evidence that SCC of 4140 and similar steels does not occur via a hydrogen cracking mechanism. They include the following observations over and above the evidence of temperature effects and the critical potential mentioned heretofore.

1. Cold work can considerably improve resistance of a carbon steel to SCC in water, but cold work does not similarly improve resistance to hydrogen cracking. The opinion is expressed, in fact, that cold work is detrimental to hydrogen cracking (24, 25). Obviously failures due to hydrogen cracking and those due to SCC do not have the same cause.

2. Failures by SCC in simple immersion tests occur as readily in distilled water as in dilute saline solutions. Although in saline media, acid anodic corrosion products can form within the confines of a notch or fissure, and in turn the acid environment in contact with steel can form damaging hydrogen, this is not an equally possible situation in distilled water. In water, the lowest possible pH within a notch is 7; it could also be higher corresponding to the pH of saturated Fe(OH)₂ equal to 9.5, but in neither of these environments is hydrogen generated to any appreciable extent.

3. A thin decarburized surface prevents SCC despite conditions that allow the Fe-H₂O reaction forming hydrogen to continue.

4. Inhibitors effective in preventing uniform corrosion are not always effective in preventing SCC. Furthermore, Baker and Singleterry (7) report that ammonium acetate, pH 6-7, added to 10% NaCl inhibited SCC of 4340 steel despite continuing visible corrosion.

5. Cold-rolled Type 301 stainless steel, which is transformed to ferrite by cold work, is resistant to SCC in atmospheric tests (1, 2). A low rate of reaction with water is not the reason, because corrosion-resistant martensitic or precipitation-hardening stainless steels fail readily in moist atmospheres above the same approximate critical yield strength range as do carbon steels. Severe cold work, as in the case of 4140 steel, is probably the important factor accounting for the observed resistance of Type 301 to SCC.

6. Failure by SCC occurs in moist air, including air of less than 50% relative humidity in which rusting is not observed over many years of exposure (26). Any hydrogen generated by exposure of steel to atmospheres of this kind is inconsequential.

The latter observation in moist air, plus the rapid cracking in distilled water in absence of an electrolyte, the important parameter of the critical potential below which SCC does not occur although uniform corrosion is not suppressed, and the beneficial effect of cold work despite an increased corrosion rate of cold-worked steel in low pH solutions are some of the evidence that "active path" cracking by electrochemical dissolution is also not a likely mechanism. Instead, reduction of metal bond strength by an adsorbate (stress-sorption cracking) is a third and probably the best possibility.

The likely adsorbate is the water molecule itself, since water alone can cause cracking of high strength carbon steels, martensitic and precipitation-hardening stainless steels, high strength aluminum and magnesium alloys (which are not susceptible to hydrogen cracking when cathodically polarized), high strength titanium alloys, and glass. This possibility is supported by adsorption-isotherm shaped curves reported by Johnson and Wilner (12) for crack growth rates of high strength steel as a function of the relative humidity of argon. It is also supported by the inhibiting effect of alkaline solutions, adsorbed H₂O presumably being displaced by OH⁻ ions which shift the critical potential in the noble direction. Phosphate ions may similarly displace water by interposing an adsorbed phosphate ion layer.

The critical potential according to the mechanism of stress-sorption cracking is interpreted as that value above which, but not below, damaging water molecules can adsorb in sufficient amount on appropriate surface defect sites at which cracks nucleate. Sites suitable for adsorption are generated only at high stress levels common to high strength steels; at lower yield strength levels, i.e., less than about 170 ksi, adsorbed H₂O no longer reduces bond strength sufficiently to initiate a crack although some adsorbed anions, e.g., NO₃⁻, can still do so causing SCC at strength levels common to mild steels. Initiation of cracks in 4140 steel by SCC occurs more readily at 100°C than at room temperature probably because formation of appropriate defect sites is favored at the

higher temperature. A similar situation exists for 18-8 stainless steel exposed to NaCl or MgCl₂ solutions, stress corrosion cracking being observed only at elevated temperatures.

The present facts lead to the conclusion, therefore, that at least two mechanisms enter observed failures by cracking of high strength steels. The one is hydrogen cracking, which occurs under circumstances that favor entrance of interstitial hydrogen into the steel, as occurs in acid pickling baths or electroplating operations or by interaction of steel with acid anodic corrosion products. The other is SCC in water and near-neutral or alkaline aqueous solutions which operates only at potentials noble to a critical value. The critical potential in turn is influenced by composition of the environment as well as by cold work of the steel. Failure times are not very sensitive to low alloy steel composition. The environment in addition to its influence on the corrosion potential apparently affects the extent to which H₂O adsorbs on a steel surface. The structure of steel and applied stress influence the nature and density of surface imperfection sites on which H₂O when adsorbed reduces metal atom bond strength sufficiently to nucleate a crack.

Summary

1. An accelerated test in boiling water or aqueous salt solutions employing a constantly stressed smooth specimen is well suited to measuring critical hardness, cold work, environmental factors, and the effect of applied potential on SCC of high strength steels.

2. The critical hardness value of 4140 steel, of 1% Ni, 0.3% C steel, and of 1% Cr, 0.3% C steel above which failure times by SCC in boiling water are short is in the range R_c 40-42 corresponding to a yield strength of 170-185 ksi (120-130 kg/mm²). This range lies close to that established by other investigators through laboratory tests, atmospheric service tests, and practical experience.

3. A thin decarburized soft surface over a core of hardness >R_c 40 effectively prevents initiation of SCC.

4. The critical potential of 4140 steel, R_c 46, immediately below which SCC does not initiate within at least 200 hr in boiling aqueous salt solutions is -0.40 to -0.42V, SHE.

5. Cold-working improves resistance to SCC in distilled water. Whether it is similarly beneficial in aqueous salt solutions depends on whether the critical potential is consistently noble to the prevailing corrosion potential.

6. Alkaline additions and orthophosphate additions to salt solutions inhibit against SCC by shifting potentials such that the critical potential remains noble to the corrosion potential.

7. Hydrogen cracking can occur with steel anodically or cathodically polarized at sufficiently high current densities in neutral aqueous NaCl or Na₂SO₄ solutions at boiling temperatures.

8. The over-all evidence suggests that in absence of polarization SCC occurs in distilled water or in neutral salt solutions independent of a hydrogen cracking mechanism.

Acknowledgment

This research was supported by the U.S. Army Research Office, Durham, North Carolina, to whom the

authors express their appreciation. One of us also wishes to acknowledge receipt of tuition assistance from C.N.R.S., Lebanon.

Manuscript submitted April 24, 1974; revised manuscript received Sept. 16, 1974. This was Paper 68 presented at the New York, New York, Meeting of the Society, Oct. 13-17, 1974.

Any discussion of this paper will appear in a Discussion Section to be published in the December 1975 JOURNAL. All discussions for the December 1975 Discussion Section should be submitted by Aug. 1, 1975.

Publication costs of this article were partially assisted by Massachusetts Institute of Technology.

REFERENCES

1. E. H. Phelps, in "Proc. 7th World Petroleum Congress," Spottesworde, Ballantyne Co., London (1967).
2. E. H. Phelps, in "Fundamental Aspects of Stress Corrosion Cracking," R. Staehle *et al.*, p. 398, Editors, Nat. Assoc. Corros. Engrs, Houston, Texas (1969).
3. S. Yamamoto and T. Fujita, in "Fracture," P. Pratt *et al.*, Editors, p. 425, Chapman-Hall, London (1969).
4. E. H. Phelps and A. W. Loginow, *Corrosion*, **16**, 325t (1960).
5. W. Kirk, R. Covert, and T. May, *Materials Eng. Quarterly, A. S. M.* (Nov. 1968).
6. M. Peterson, B. Brown, R. Newbegin, and R. Groover, *Corrosion*, **23**, 142 (1967).
7. H. Baker and C. Singleterry, *ibid.*, **28**, 340, 385 (1972).
8. T. Fujita and Y. Yamada, Conference on "Stress Corrosion Cracking and Hydrogen Embrittlement of Iron-base Alloys," Firminy, France (June 1973).
9. H. Okada, *Ibid.*
10. J. Gilchrist and R. Narayan, *Corrosion Sci.*, **11**, 281 (1971).
11. H. Yamaoka, and G. Wranglen, in "Current Corrosion Research in Scandinavia," H. Larinkari, Editor, pp. 128-132, Almquist and Wiksell, Stockholm (1965).
12. H. Johnson and A. Wilner, *Appl. Materials Res.*, **34** (Jan. 1965).
13. H. Lee and H. Uhlig, *This Journal*, **117**, 18 (1970).
14. B. F. Brown, C. Fujii, and E. Dahlberg, *ibid.*, **116**, 218 (1969).
15. B. F. Brown, in "The Theory of Stress Corrosion Cracking in Alloys," p. 186, J. Scully, Editor, North Atlantic Treaty Organization, Brussels, 1971.
16. H. Lee and H. Uhlig, *Met. Trans.*, **3**, 2949 (1972).
17. S. Ketcham, in "Stress Corrosion Cracking of Metals—A State of the Art," p. 82, ASTM Spec. Publ. 518, Philadelphia, Pa. (1972).
18. H. Uhlig and E. Cook, *This Journal*, **116**, 173 (1969).
19. R. Newberg and H. Uhlig, *ibid.*, **119**, 981 (1972).
20. H. Mazille and H. Uhlig, *Corrosion*, **28**, 427 (1972).
21. H. Uhlig and R. Newberg, *ibid.*, **28**, 337 (1972).
22. C. Barth, E. Steigerwald, and A. Troiano, *ibid.*, **25**, 353 (1969).
23. B. E. Wilde, *ibid.*, **27**, 326 (1971).
24. C. Carter, Conference on "Stress Corrosion Cracking and Hydrogen Embrittlement of Iron-base Alloys," Firminy, France (June 1973).
25. R. Treseder, *Ibid.*
26. H. H. Uhlig, "Corrosion and Corrosion Control," 2nd Ed., pp. 171-172, John Wiley & Sons, Inc., New York (1971).

A Study of Transient Corrosion in the Iron-Caustic System by Use of a Drop Weight Apparatus

R. B. Diegle^{*,1} and D. A. Vermilyea^{*}

Corporate Research and Development, General Electric Company, Schenectady, New York 12301

ABSTRACT

Repassivation current transients in the Fe-caustic system were measured after straining potentiostatically polarized electrodes with a drop weight apparatus, which could produce strains of about 5% in 1 msec. Peak current densities varied from 0.3 to 3.8 A/cm² depending on electrode potential, electrolyte concentration, and temperature, and initial film coverage was complete in less than 1 or 2 msec. The amount of corrosion accompanying passive film formation was not very sensitive to the above-mentioned electrochemical variables, and it ranged from 1×10^{-3} to 5×10^{-3} coulombs/cm². Repassivation was facilitated by additions to the test electrolyte of the anodic dissolution product HFeO₂⁻. The total corrosion up to 1 sec following straining was a strong function of potential, electrolyte concentration, and temperature, as was the quasi steady-state current density. The depth of corrosion 1 sec after straining ranged from twenty to several hundred angstrom units. The relevance of these results to several mechanistic models of caustic cracking is discussed.

The study of corrosion transients in alloy-corrodent systems exhibiting stress corrosion cracking (SCC) is of great importance in understanding the mechanism(s) of cracking. For instance, it has been proposed that susceptibility to SCC is in part determined by the amount of corrosion occurring after fracture of a protective passive film at the crack tip, and before repassivation occurs (1-4). Comparison of the effects of such pertinent electrochemical variables as electrode potential and electrolyte concentration on the kinetics of transient corrosion and on the rate of crack propagation during SCC should provide insight into this film rupture mechanism. Indeed, in a broader sense results can hopefully help determine the applicability to caustic SCC (CSCC) of the several types of models based on anodic dissolution, such as those involving periodic film rupture and intermittent crack advance (1-4), and others supporting uniform crack advance by corrosion at a continuously active crack tip (5, 6).

Although repassivation phenomena have been intensely investigated, relatively few studies have been made in systems which exhibit SCC. Recent exceptions are the studies of Beck (7), and Ambrose and Kruger (8, 9). Beck measured the repassivation rate of Ti in HCl electrolytes after specimen fracture, and he observed peak current densities of several amperes per square centimeter and initiation of repassivation in milliseconds due to monolayer oxide film formation. Ambrose and Kruger, using an abrasion technique called triboellipsometry (8), studied the repassivation of mild steel in NO₃⁻ and NO₂⁻ solutions (8), and of Ti in NO₃⁻ and Cl⁻ electrolytes (9). Again, large current transients resulted and repassivation began within several milliseconds after the cessation of abrasion.

This work is part of a continuing study designed to determine the validity of the film rupture theory of SCC as recently formulated (1, 2). The Fe-caustic system was chosen as a model for investigation of this theory because of the relative simplicity of electrode reactions which occur. Specific objectives were to determine the effects of such pertinent electrochemical variables as electrode potential, electrolyte concentration and temperature, and concentration of dihydroferrite ion, HFeO₂⁻, on the transient corrosion rate, and time required for initial film formation. A unique

drop weight apparatus was used to strain potentiostated Fe wire electrodes in NaOH electrolytes, and the ensuing repassivation current transients were monitored with oscilloscopes. Appropriate current-potential curves were generated so that comparison could be made between transient and relatively steady-state corrosion kinetics. Transient corrosion results are qualitatively similar to those of Beck and Ambrose and Kruger and strongly support an anodic dissolution mechanism of CSCC.

Experimental

Material.—Electrolytic grade 99.94% pure Fe was vacuum melted and cast into tapered ingots about 5 by 5 by 15 cm. These were hot forged in Ar to rod 0.25 cm diameter, which was then cold drawn with intermediate annealing to 0.127 cm diameter wire. Some wire containing 12% residual cold work was used in this condition; the rest was heated for about 24 hr in moist hydrogen. This heat-treatment not only served to anneal the wire, but it also decarburized it to a carbon level which minimized strain aging during subsequent elevated temperature straining experiments.

Current-potential curves.—The electrochemical cell used for polarization studies, Fig. 1, was constructed entirely of polytetrafluoroethylene to prevent attack by the concentrated caustic electrolytes. The thermistor and Nichrome windings permitted accurate temperature control, which was monitored with an iron-constantan thermocouple cemented inside a tube extending into the electrolyte and connected to a potentiometer. The Luggin probe, positioned to within 1 or 2 mm of the electrode, was connected to a 10% NaOH solution by plastic tubing containing a nylon wick. Potentials were measured *vs.* a room temperature saturated calomel electrode (SCE) connected to this solution by a second capillary, as shown.

Potentiodynamic potential sweeps were performed using a solid-state linear voltage-time function generator and a Wenking 68 TS1 potentiostat. Current in the counterelectrode circuit and electrode potential *vs.* the SCE were simultaneously measured with Keithley electrometers and recorded on a two channel L&N recorder. In one instance a potential stepping technique was used, with steps varied between 20 and 50 mV and current readings taken after 5 min at each potential.

In practice a 13 cm length of wire was acid etched for 2 min and electropolished 15 min in a room tem-

* Electrochemical Society Active Member.

¹ Present address: Battelle Columbus Laboratories, Columbus, Ohio 43201.

Key words: repassivation, stress corrosion, caustic cracking, film rupture.

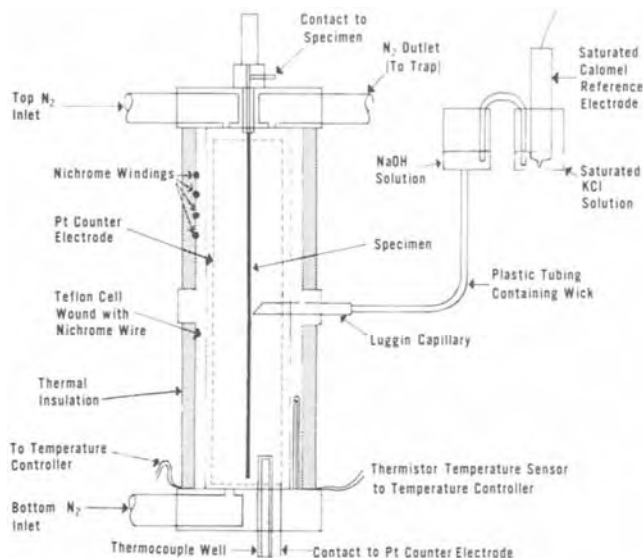


Fig. 1. Schematic cross section of cell used to study the polarization behavior of Fe in NaOH electrolytes.

perature mixture of 1300 mliters glacial acetic acid, 108 mliters 71% perchloric acid, and 41 mliters water at a current density of about 40 mA/cm². The cell was filled with electrolyte, which throughout this study was prepared from analytical reagent grade, carbonate-free NaOH and distilled water, after which the thoroughly rinsed wire was inserted. The electrolyte was heated to temperature and deaerated by bubbling ultrapure nitrogen through the lower inlet. When the open-circuit potential had reached the quite reproducible value characteristic of the electrolyte-temperature combination employed, the nitrogen flow was adjusted across the surface of the electrolyte. Next a potential sweep was begun from the rest potential and continued until the beginning of oxygen evolution; in most cases the sweep direction was reversed and the potential was returned to the initial value. Sweep rates of 0.6, 1.8, and 4.1 V/hr were used.

Certain current-potential curves were performed in electrolyte containing additions of the anodic dissolution product, dihypoferrite ion or HFeO_2^- . In these runs the electrolyte was previously charged with HFeO_2^- by dissolution of a dummy, high purity Fe electrode at -0.8V (SHE) until the desired number of coulombs of Fe had reacted, after which the wire electrode was quickly substituted and the potential sweep begun from the steady-state rest potential. The final concentration of Fe in the electrolyte was determined by volumetric analysis using EDTA and a standardized copper solution.

Repassivation transients.—The drop weight apparatus (DWA) used to generate unfiled electrode surface is shown in Fig. 2. A 13.6 kg (30 lb) weight was allowed to free-fall a distance of 137 cm and strike a collar threaded onto a 0.635 cm diameter steel shaft. The impact drove the collar-shaft-lower grip assembly downward through a preset distance of 0.635 cm in 1 msec, thereby creating 5% strain in the electrode at a strain rate of about 57 sec⁻¹. The shaft and lower grip were prevented from rebounding after full travel by two spring-loaded anti-rebound catches, which locked the lower grip into its lowest position after the initial displacement. The electrochemical cell used to surround the wire specimen was similar to that shown in Fig. 1 except that the electrode extended through both ends to permit insertion into the grips.

In practice a wire was etched in acid, rinsed, and lightly scribed with gauge marks defining that portion of the electrode submerged in the electrolyte after insertion into the cell. The cell containing the electrode and electrolyte was mounted in position in the DWA, the lower grip having been previously elevated from

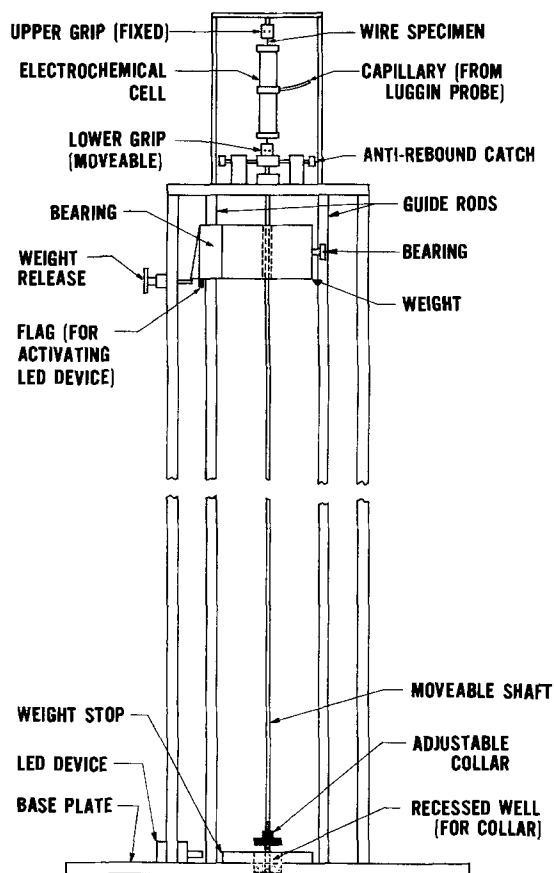


Fig. 2. Schematic drawing of the drop weight apparatus used to study repassivation behavior.

its fully extended position by 0.635 cm. Anti-rebound catches were engaged, the electrolyte was heated to temperature, and deaeration, if desired, was performed. When the rest potential was established the wire was polarized to the straining potential with a Wenking Model 66TS3 potentiostat (rise time of about 30 μsec). After a reasonably steady-state current had developed, the weight was dropped and the wire suddenly strained.

Current transients were recorded photographically from two oscilloscopes which measured the voltage drop across a 10 ohm precision resistor in the counter-electrode circuit. The oscilloscope sweeps were adjusted to monitor short (0-10 msec) and long (0-0.5 sec) current-time behavior. The sweeps were automatically triggered approximately 1 msec before the start of straining by interruption of a light emitting diode (LED) device with an opaque flag mounted on the weight. The total elongation which had occurred within the electrolyte was determined after each experiment by measuring the new gauge mark separation on the electrode.

Two points of interest should be made relative to this technique. As stated, full elongation of the electrode was accomplished in about 1 msec, which is sufficiently fast to permit study of the rapid transient corrosion kinetics characteristic of the Fe-caustic system. Second, auxiliary experiments showed that the velocity of the weight during its last 0.635 cm of travel was barely perturbed by the presence or absence of wire between the grips, indicating that the strain rate was essentially constant during the straining process.

Results

Current-potential curves.—It was desired to study current-potential behavior under relatively steady-state conditions for two reasons. First, such information permitted comparison of transient corrosion rates with more time-independent corrosion behavior. Sec-

ond, it provided a means for estimating the valence change of Fe during oxidation in NaOH as a function of potential.

The effects of NaOH concentration, temperature, and electrode potential agreed well with trends reported by earlier workers (10-12), and for this reason the polarization curves are not reported. Essentially, increasing electrolyte concentration and temperature accelerated the corrosion rate; this was especially true in the potential range in which CSCC occurs, namely, that encompassing the active and active-passive transition potentials. For example, at a susceptible potential of $-0.7V$ (SHE) and a sweep rate of $0.6 V/hr$, a 30-fold increase in current density resulted from changing the NaOH concentration from 20 to 50% at $85^\circ C$. An analogous 10-fold increase was observed in 35% NaOH due to raising the temperature from 50° to $105^\circ C$.

The influence of the anodic dissolution product on current-potential behavior is illustrated in Fig. 3. This product, assumed to be $HFeO_2^-$ from reference to potential-pH diagrams constructed for elevated temperatures (13-15), suppressed anodic dissolution. In fact, the region of active corrosion was completely eliminated by adding 11.6×10^{-3} mole/liter of iron as $HFeO_2^-$. In general the potential at which the minimum passive current occurred was moved in the negative direction, and the potential range over which passivity was observed was extended by several hundred millivolts. The passive current density increased with increasing concentration of $HFeO_2^-$ although the total effect was less than a factor of two. The additions also reduced current densities in the postpassive potential range, but again the effect was not large.

As expected, potential sweeps with 12% cold-worked Fe electrodes resulted in corrosion behavior almost identical to that of annealed Fe.

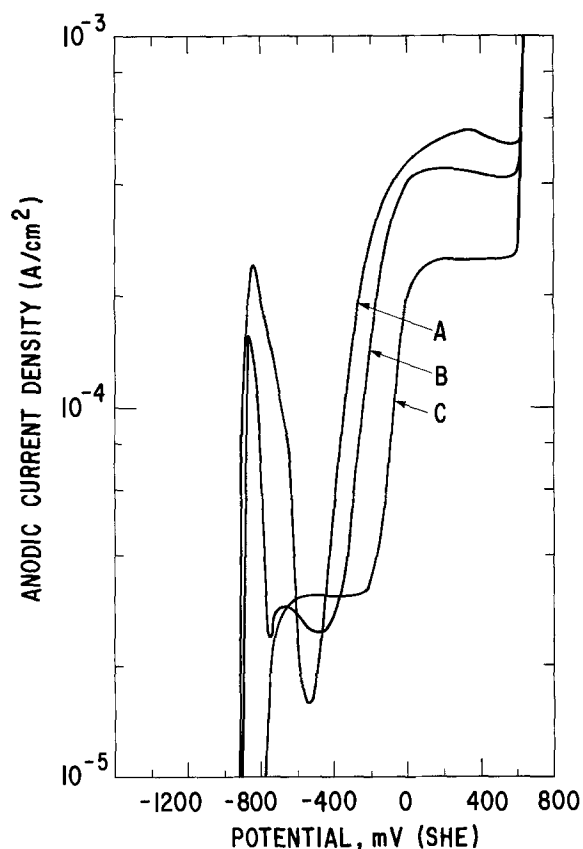


Fig. 3. Polarization behavior of Fe in 35% NaOH at $85^\circ C$ containing three concentrations of Fe as dihypoferrite ion. (Curves were generated by a potential stepping technique.) Potentials were not corrected for thermal and liquid junction errors. Curve A, none; curve B, $3.1 \cdot 10^{-3}$ mole/liter iron; curve C, $11.6 \cdot 10^{-3}$ mole/liter iron.

Repassivation transients.—The current values obtained from each oscillograph were converted to current density by dividing by the area change ΔA created during straining

$$\Delta A = 2\pi r(\Delta l) \quad [1]$$

where r is the wire radius after straining and Δl is the electrode elongation which occurred within the electrolyte. This equation is based on negligible ductility of the passive film, yet the assumption of perfect adherence requires that a small amount of film deformation occur. A representative pair of repassivation current transients obtained with the DWA are shown in Fig. 4. The peak anodic current density was $3.5 A/cm^2$, and throughout the runs it ranged from about 0.3 to $3.8 A/cm^2$ with higher values favored by positive potentials, concentrated electrolyte, and high test temperature. Initial film formation at the straining potential of $0V$ (SHE) occurred in less than about 1 msec, as seen by the rapid decrease in anodic current coincident with cessation of straining. The smaller peak observed 1.9 msec after the start of current rise, Fig. 4a, is thought to be caused by a slight flexure of the steel shaft and electrode at the instant the weight rebounded after impact. Transient corrosion rate was potential-dependent, as seen by comparing Fig. 4a with Fig. 5. The transient in Fig. 5, which was obtained at the rest potential of $-0.916V$ (SHE), is much broader than that obtained at $0V$ (SHE) and the rate of current decay is less. This type of current-time dependence is expected if the time required for initial film formation exceeds the straining time.

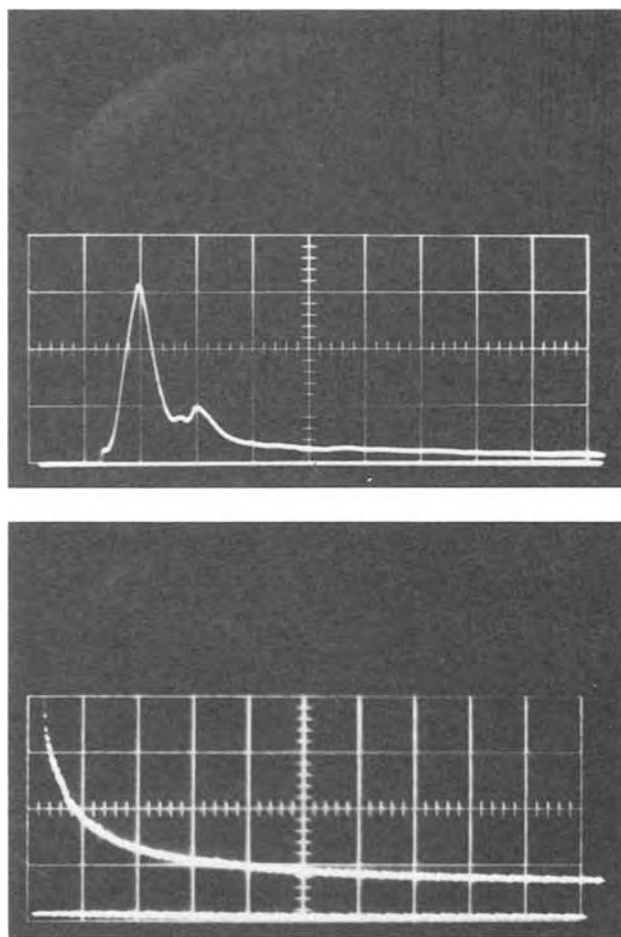


Fig. 4. Oscilloscopic anodic current transients obtained by straining in 35% NaOH at $85^\circ C$ at a potential of $0V$ (SHE). (a) One vertical division equals $0.2A$, one horizontal division equals 1 msec; (b) one vertical division equals $0.005A$, one horizontal division equals 50 msec.

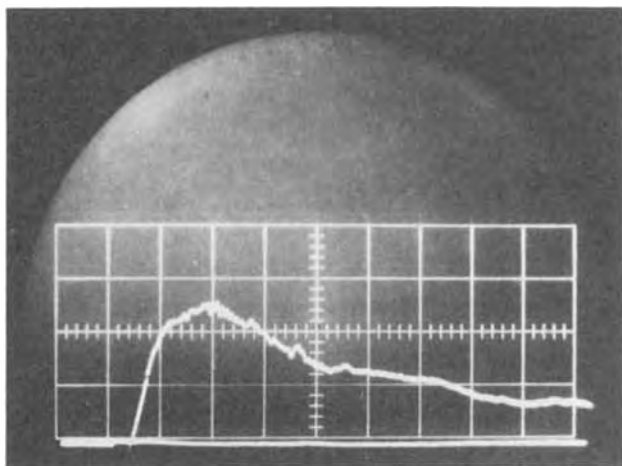
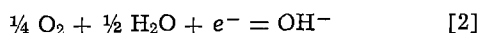


Fig. 5. Oscilloscopic anodic current transient obtained by straining in 35% NaOH at 85°C at the rest potential, $-0.916V$ (SHE). One vertical division equals $0.02A$, one horizontal division equals 1 msec.

Since one purpose of this work was to learn more about the nature of CSCC by studying transient corrosion behavior, data are presented as depth of corrosion *vs.* time curves. This manner of presentation is obviously more directly related to the kinetics of crack advance than, for example, illustration of current density-time relationships. Reduction of the current-time data was performed with the following assumptions: (i) no competing reactions occurred on the Fe electrode during repassivation that were comparable in rate to the repassivation process; that is, integration of the anodic current resulted in an accurate measure of the amount of Fe reacted; and (ii) exfoliation of the passive film did not occur during straining, an assumption which permitted calculation of the exposed area from elongation as shown in Eq. [1]. The first assumption is reasonable since the only other expected electrode reaction of any importance besides oxidation of Fe is reduction of O_2 in the electrolyte to OH^- according to the reaction



Simple theoretical calculations and preliminary experiments with deaerated and nondeaerated electrolytes confirmed that O_2 reduction decreased the measured charge transfer by a negligible amount, even in electrolytes which were not deaerated. Exfoliation was not expected due to the extremely thin nature of passive films grown for short times on Fe in NaOH solutions.

A functional relationship between current density and time after straining was obtained by noting that a plot of logarithm of current density *vs.* logarithm of time was linear for times greater than about 8 msec, Fig. 6. This relation was of the form

$$i = Kt^{-c} \quad [3]$$

in which K and c are constants. It is identical to that observed by Nagayama and Cohen for Fe passivated in a buffered borate electrolyte (16), except that in their work c was 1 and in this study c was always less than 1. The charge-time dependence was obtained by integrating Eq. [3] with respect to time to give

$$Q(t) = \frac{K}{1-c} [t^{1-c}]t_{\tau_0} \quad [4]$$

in which τ_0 is the shortest time at which Eq. [3] was obeyed; in this work it was taken as 8 msec, since a rather good fit to the data was obtained after about 8 msec had elapsed. The depth of corrosion as a function of time, $L(t)$, is thus given by the equation

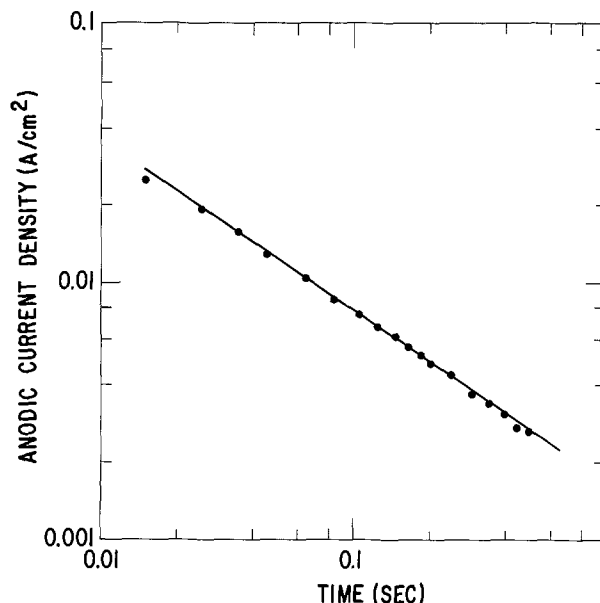


Fig. 6. Anodic current density as a function of time after straining in 35% NaOH at 50°C at a potential of $-0.500V$ (SHE).

$$L(t) = \frac{M}{nFd} \left\{ Q_0 + \frac{K}{1-c} [t^{1-c}]t_{\tau_0} \right\} \quad [5]$$

in which M , n , and d are the molecular weight (55.85), valence change, and density (7.87 g/cm³) of Fe, respectively, and F is the Faraday (96,500 coulombs). Q_0 , the charge transferred during the first 8 msec of repassivation, was determined by gravimetric integration of the 0-10 msec current transient to 8 msec from the start of straining. (Charge transfer from the double layer due to net reduction in electrode area after straining can be readily shown to be an insignificant fraction of the total charge passed, even that passed during the initial 10 msec.) The approach used to approximate the valence change n is explained in the Appendix.

Typical values of K , c , n , Q_0 , and the peak current density i_p observed during repassivation are presented in Table I. Note that over the range of potentials investigated the charge accumulated in the first 8 msec of repassivation varied by only a factor of about 4. Also, the constant c was considerably less than 1 in every instance.

The representative set of curves shown in Fig. 7, calculated from Eq. [5] and displayed to 1 sec after film rupture, illustrates the marked influence of potential on corrosion rate. [One second was chosen as the time to which total corrosion would be displayed because it is a reasonable interval between postulated film rupture events (1, 2).] For example, after 1 sec corrosion had proceeded to only about 27Å at the passive potential of $-0.5V$ (SHE), yet at the active potential of $-0.8V$ (SHE) it had progressed to 80Å. Note

Table I. Characteristic repassivation parameters obtained in 35% NaOH electrolyte at 85°C at various straining potentials

Straining potential (V vs. SHE)	K (A-sec/cm × 10 ⁻³)	c	n	Q ₀ (coulombs/cm ² × 10 ⁻³)	i _p (A/cm ²)
-0.916	7.02	0.50	2	1.22	0.27
-0.900	7.96	0.57	2	1.45	0.33
-0.880	14.36	0.31	2	1.73	0.45
-0.700	4.96	0.56	2	3.14	1.11
-0.600	2.08	0.74	2.5	2.95	1.79
-0.500	3.12	0.60	2.5	3.46	2.21
-0.500	2.22	0.69	2.5	2.96	1.97
-0.400	4.95	0.54	2.5	2.70	2.42
-0.300	4.35	0.64	2.5	3.81	2.54
-0.200	7.04	0.57	3	4.26	2.94
-0.100	8.75	0.56	3	5.11	3.32
0.000	11.04	0.52	3	4.95	3.58
+0.300	12.72	0.44	3	4.54	3.83

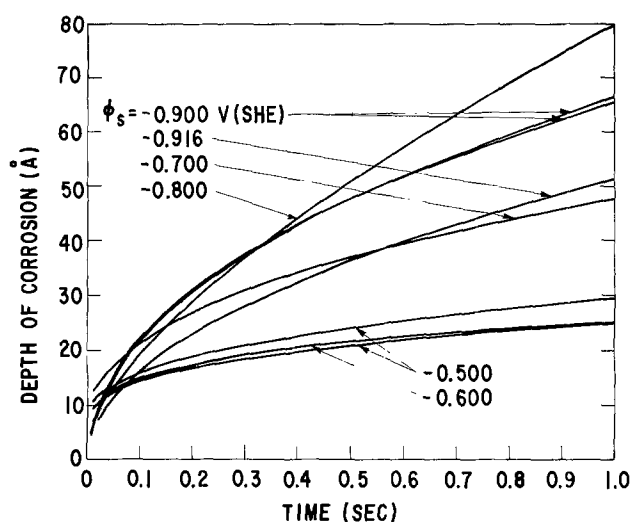


Fig. 7. Depth of corrosion as a function of time after straining and straining potential in 35% NaOH at 85°C. Potentials encompass the range in which CSCC occurs.

the appreciable corrosion rate at the rest potential, -0.916V (SHE).

Of particular interest is the rate of current decay at potentials in the postpassive region. CSCC of mild steel does not occur over most of this potential range, yet potentiodynamic polarization data suggested that transient corrosion rates at sufficiently positive potentials may exceed those in the CSCC potential range. This is indeed the case, as seen by comparing Fig. 8, in which a series of corrosion-time curves obtained at postpassive potentials is presented, with Fig. 7. The depth of corrosion extrapolated to 1 sec at potentials of $+0.1\text{V}$ (SHE) and greater equals or exceeds that measured at -0.8V (SHE). Also interesting is the observation that the transient corrosion rate is faster at potentials above about -0.1V (SHE) than at -0.7V (SHE), which is near the potential of greatest susceptibility for CSCC in this electrolyte (12, 17, 18).

The effect of electrolyte concentration on repassivation behavior is very potential dependent, as shown in Fig. 9. Changing the NaOH concentration from 20 to 50% increased the amount of corrosion after 1 sec from 19 to only 30 Å at -0.5V (SHE), but it jumped from about 23 Å to about 490 Å (not shown) at -0.8V (SHE), a remarkable effect.

An analogous correlation of potential with the effect of temperature is illustrated in Fig. 10. Again, at the passive potential of -0.5V (SHE) raising the temperature from 50° to 85°C increased the depth of corrosion

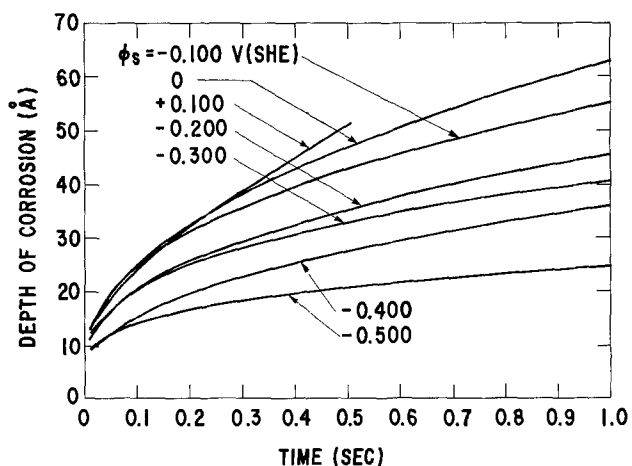


Fig. 8. Depth of corrosion as a function of time after straining and straining potential in 35% NaOH at 85°C. Potentials encompass the postpassive region of polarization behavior.

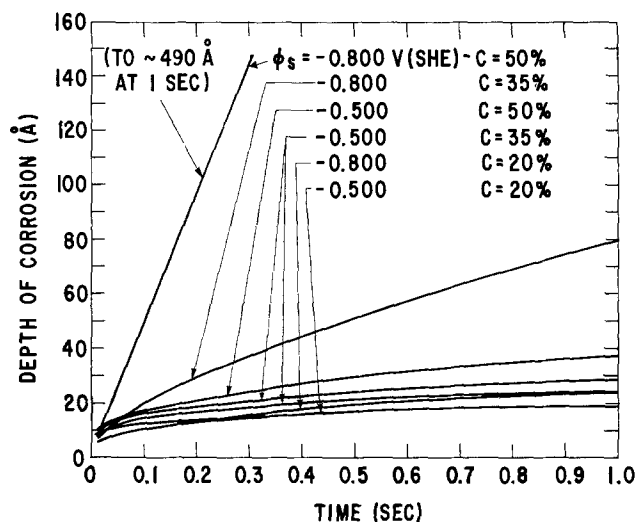


Fig. 9. Depth of corrosion as a function of time after straining for three concentrations of NaOH at 85°C. The potential -0.500V (SHE) corresponds to passive polarization behavior, while -0.800V (SHE) corresponds to active dissolution.

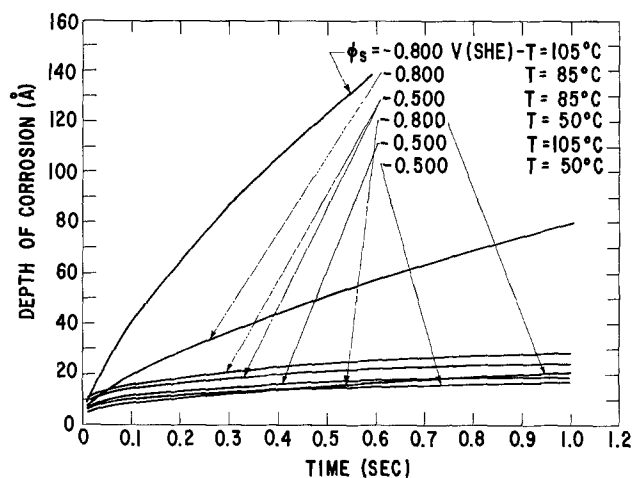


Fig. 10. Depth of corrosion as a function of time after straining in 35% NaOH at three temperatures. The potential -0.500V (SHE) corresponds to passive polarization behavior, while -0.800V (SHE) corresponds to active dissolution.

from 17 Å to about 27 Å; a further temperature rise to 105°C produced no further measurable increase. However, at -0.8V (SHE) the corrosion at 1 sec went from 20 Å at 50°C to 203 Å at 105°C.

The last effect of interest is the role of dihypoferrite ion in influencing repassivation. Figure 11 illustrates depth of corrosion-time curves calculated from data obtained in 35% NaOH at 85°C with and without prior addition of HFeO_2^- . (Somewhat different concentrations of HFeO_2^- were added from one run to another because of nonreproducibility in the anodic dissolution technique used to charge the electrolytes.) The potential dependence of the transient corrosion rate was qualitatively similar to that observed under more steady-state conditions; however, the addition of about 3.5×10^{-3} to 5.5×10^{-3} mole/liter of Fe as HFeO_2^- drastically reduced anodic dissolution at -0.8V (SHE) and below. The large current peaks occurring between about 0 and 3 msec still resulted, however, and the charge Q_0 was generally reduced by less than a factor of 2. The potential causing the most rapid corrosion rate was shifted from near the anodic peak potential of -0.8V (SHE) to about -0.7V (SHE), a potential which is within the passive region of the appropriate polarization curves in Fig. 3. This shift could be significant, since as previously stated the potential producing the fastest CSCC in 35% NaOH electrolyte is near -0.7V (SHE).

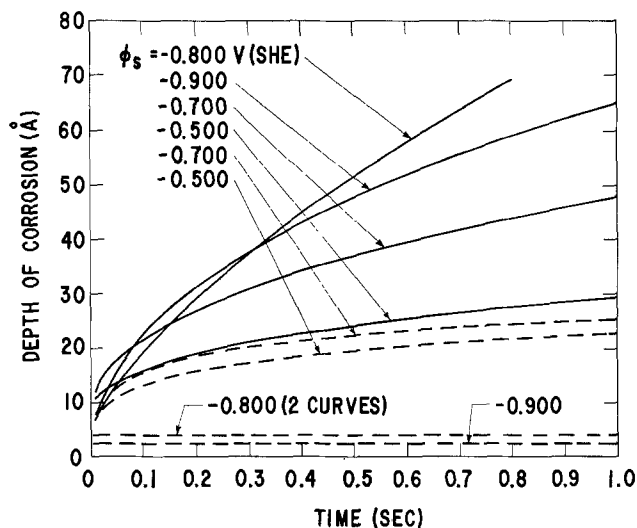


Fig. 11. Depth of corrosion as a function of time after straining and straining potential in 35% NaOH at 85°C with and without prior addition of iron as dihyperferrite ion. Solid curves, no iron added before straining; dashed curves, $3.4 \cdot 10^{-3}$ to $5.4 \cdot 10^{-3}$ mole/liter iron added before straining.

The presence of 12% residual cold work was found to have no detectable effect on the transient corrosion of Fe. Greater degrees of cold work were not investigated with the DWA since the electrodes fractured at very small strains.

Discussion

Current-potential curves.—As stated earlier in the paper, these curves were produced to enable comparison of the effects of environmental variables on transient vs. steady-state corrosion rates. The general shape of the current-potential curves of Fe in high pH electrolytes has been considered in detail elsewhere (10, 11, 19-26); therefore the curves obtained in this work are discussed only as they pertain to repassivation kinetics. Of some interest, however, is the effect of HFeO_2^- on polarization behavior, since it certainly exists in undetermined concentrations in crevices during CSCC. The effect of this ion was to suppress active dissolution and facilitate passivation, which supports the postulated mechanism of passivation as being one of precipitation of some type of film, perhaps $\text{Fe}(\text{OH})_2$ (19), when its solubility product near the electrode surface is exceeded during active corrosion. The rise in passive current density with increasing ion concentration possibly results from oxidation of divalent iron in solution to the trivalent state at higher potentials. Extension of the passive potential range to higher values and reduction of the current densities in the postpassive range may be due to a reduced rate of dissolution of the $\gamma\text{-Fe}_2\text{O}_3$ formed at these potentials due to the presence of HFeO_2^- .

Repassivation transients.—The internal reproducibility of this rapid straining technique was about $\pm 5\%$ after 1 sec of elapsed time. The absolute accuracy is certainly less, perhaps no better than 25%, due to uncertainties in electrode roughness factor and valence change of iron during oxidation, and because of the inaccuracy inherent with oscilloscopic measurements. Another factor of possible importance was hydrodynamics, although its influence was not investigated in this study. Since the method of data presentation requires accurate knowledge of the bare metal area produced by the DWA, supplementary film fracture experiments were conducted using the technique of Bubar and Vermilyea (27) to characterize passive film ductility. The fracture strains observed were of the order of 10^{-4} , indicating negligible film ductility and the validity of Eq. [1]. On the basis of internal reproducibility and the trends shown in Table I, it is

concluded that the DWA technique is sufficiently sensitive to study the effect on repassivation behavior of electrochemical parameters of major influence.

The most significant observations regarding the transient corrosion of Fe in caustic electrolytes is that the beginning of repassivation is quite rapid and is preceded by very little corrosion. Although anodic current densities reached a maximum of 3.8 A/cm^2 , Table I, they usually decreased to only a fraction of these peak values within about 3 msec. (These peak current densities were of course influenced by the strain rate applied by the DWA.) Immediate current decay after the end of straining at potentials about 0.05V more positive than the rest potential indicates the extremely rapid formation of a film which was very effective in reducing the subsequent corrosion rate. It is not known just how much film formed during this initial transient current flow for various reasons. For instance the identity and material properties of the film, including density and lattice parameter, were not determined, nor was the ratio of Fe going into solution to that forming film. However, an approximate calculation can be made as follows. If it is assumed that the initial film is Fe_3O_4 of density 5 g/cm^3 and lattice parameter 8.4\AA (17), then one monolayer would require 1.4×10^{-3} coulombs of Fe to react if it all went into film formation. Admittedly a rough estimate, this value compares favorably with the Q_0 's listed in Table I for repassivation at potentials in the active region. It is therefore proposed that initial current decay involves the rapid formation of one or two monolayers of a film of unknown identity, and that further corrosion consists of simultaneous film growth and dissolution.

Modeling the repassivation process.—To provide further understanding of the nature of initiation of repassivation in the Fe-caustic system, the repassivation process was modeled in the following way. In order to avoid the implied infinite current at zero time, Eq. [3] was modified to

$$i = K(\tau + t)^{-c} \quad [6]$$

in which τ is an adjustable parameter which ensures a finite current density at the instant of film fracture. It is proposed that during straining incremental film-free regions are continuously produced on the electrode surface, and that the total current I flowing after creation of an amount α of total exposed area can be obtained by integrating Eq. [6] to give

$$I = K \int_0^\alpha (\tau + t)^{-c} dA, \quad t \geq \tau_1 \quad [7]$$

in which τ_1 , the time at which straining is completed, is about 1 msec. Equation [7] can be transformed to

$$I = KdA/dt \int_0^t (\tau + t)^{-c} dt \quad [8]$$

The rate of creation of unfiled area, dA/dt , can be removed from under the integral because the strain rate is constant and the film is quite brittle. The integrated equation is

$$I = \frac{KdA/dt}{1-c} [(\tau + t)^{1-c}]_0^t, \quad t < \tau_1 \quad [9]$$

After straining has been completed, these small areas are still contributing current but no new ones are being created; therefore, the integration is performed from time $t - \tau_1$

$$I = \frac{KdA/dt}{1-c} [(\tau + t)^{1-c}]_{t-\tau_1}^t, \quad t > \tau_1 \quad [10]$$

Note that dA/dt is still included as a mathematical device, even though straining ceased at time τ_1 .

To illustrate the application of this model, data consisting of current-time combinations were taken from

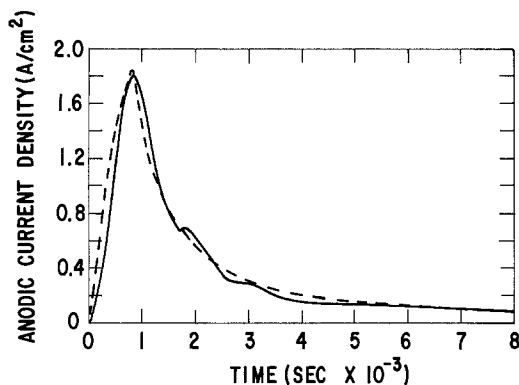


Fig. 12. Fit of Eq. [9] and [10] after dividing by ΔA (dashed curve), to experimental anodic current transient (solid curve) obtained in 35% NaOH at 85°C at a straining potential of $-0.600V$ (SHE).

a typical 10 msec transient and introduced into a curve-fitting computer program (28). A least squares fit produced the results shown in Fig. 12, converted to current density by dividing by the total area exposed ΔA . The good fit indicates that the model chosen provides a reasonably accurate picture of the straining process. The values of K and c giving good agreement, 3.21×10^{-5} A-sec/cm² and 1.62, are seen to differ substantially from the experimental values applicable at longer times and listed in the fifth column in Table I. This variation is substantiated by the lack of fit (not shown) between theory and experiment beyond 10 msec and is presumably caused by rapidly occurring changes in film properties which are not understood. The reduction in c could in part be due to the onset of film dissolution after several milliseconds, thus reducing the net rate of film thickening.

Relevance to CSCC mechanisms.—The repassivation transient data provide strong support for an anodic dissolution mechanism of CSCC for several reasons. Most significantly, the influence of potential, temperature, and NaOH concentration on transient corrosion kinetics are in good qualitative agreement with their effects on crack propagation rate. For example, it has been previously demonstrated that CSCC is accelerated by increasing the caustic concentration and electrolyte temperature [results reviewed in Ref. (19)], and in this work the transient corrosion rate was strongly accelerated in the same manner in the susceptible potential range. The influence of potential on transient corrosion is interesting, since below the passive potential the dependences of transient corrosion and CSCC rates on potential are very similar. Although the potential favoring the most rapid transient corrosion corresponds approximately to that at the active peak of the quasi steady-state polarization diagram, whereas that causing the fastest CSCC is in the more positive active-passive transition region, the effect of dihypoferrite ion is to shift the potential producing the most rapid transient corrosion to slightly higher values. In the postpassive potential region, however, the transient corrosion rate again increases (Fig. 8) in accord with polarization behavior, although CSCC is not observed in mild steels at these more positive values. [CSCC does occur at about -0.4 to $-0.1V$ (SHE) in temper-embrittled low alloy steels, Ref. (29-31).] Lack of susceptibility at postpassive potentials perhaps arises from the absence of a proper balance between active and passive corrosion rates, although an alternative explanation is suggested by the film rupture theory of Vermilyea (1). This is that the γ -Fe₂O₃ film present in this higher potential region may be more ductile than Fe₃O₄ film formed in the susceptible potential range, thereby promoting film thinning rather than fracture. Results from recent experiments indicate that indeed γ -Fe₂O₃ formed at high

potentials in NaOH electrolyte is more ductile than Fe₃O₄ produced at lower potentials.

These results are also helpful in a general evaluation of proposed mechanisms of CSCC. For example, if CSCC were caused by the stress-sorption mechanism of Uhlig (32), only about 1 msec would exist after film fracture for adsorption to occur before the electrode became film covered again. (That passivity is indeed caused by a discrete film and not an adsorbed layer of oxygen atoms is supported by the t^{-c} current density dependence at essentially the start of repassivation, a dependence which is often observed for film growth phenomena.) Assuming that an unfiled ledge of metal at least 1 atom wide, or about 3Å, must continuously exist at a slip step at the crack tip to permit adsorption of OH⁻ ions, the minimum rate of crack propagation would be equal to about 3×10^{-8} cm/10⁻³ sec or about 3×10^{-5} cm/sec. However, CSCC has been observed to proceed at rates of 10⁻⁷ cm/sec and less.

It has also been postulated that SCC proceeds due to active dissolution at an unfiled crack tip, the crack sides remaining passive (5, 6). More recently Hoar and Jones extended this proposed mechanism to include CSCC (33). It is not likely that the crack tip can remain bare during CSCC, since active corrosion in 35% NaOH at 85°C at the susceptible potential of $-0.7V$ (SHE) proceeds at the relatively large current density of about 1 A/cm², as shown in Table I. (Presumably higher strain rates with the DWA would produce even larger values.) A corrosion rate of 1 A/cm² corresponds to an electrochemical crack propagation rate of 3.7×10^{-5} cm/sec (for Fe = Fe⁺⁺), which again is considerably greater than many rates observed experimentally. Further discussion of the implication of this work to the results of Hoar and Jones will be presented in a future paper.

The data lend support to some type of film rupture mechanism of cracking, both because of the strong tendency for the electrode to remain film covered and because of the observed potential, temperature, and concentration dependences of the transient corrosion rate. For example, the depth of corrosion 1 sec after film rupture ranged from only about 20Å to several hundred angstroms as a result of appropriate changes in electrode potential and NaOH concentration. Although these distances are very small relative to the size of the plastic zone ahead of the crack tip, they nevertheless may be sufficiently large to cause enough plastic strain in the substrate after repassivation to produce successive film fracture as proposed by Vermilyea (1, 2). To further evaluate the applicability of this model data are needed describing the nature of the plastic strain gradient directly ahead of the crack tip during CSCC, as well as the fracture strain of the passive film.

Summary

Repassivation in the Fe-caustic system is characterized by peak anodic current densities on the order of 1 A/cm² following film fracture, with initiation of repassivation in milliseconds due to the formation of one or two monolayers of an unidentified reaction product film. The presence of 12% cold work in Fe did not affect repassivation kinetics, but the anodic dissolution product HFeO₂⁻ reduced the corrosion current flowing under both steady-state and transient corrosion conditions. In 35% NaOH transient corrosion was inhibited most markedly at potentials below those in the active-passive transition region of the steady-state polarization curve. The amount of corrosion occurring during the first 8 msec after film fracture, which was comprised mainly of that resulting from the large 3-5 msec current transient, ranged only between $1 \cdot 10^{-3}$ and $5 \cdot 10^{-3}$ coulombs/cm² for all conditions investigated. Corrosion accompanying the early stages of repassivation was therefore relatively insensitive to electrochemical variables. The total corrosion occurring at longer times, however, was

strongly influenced by these variables in a manner qualitatively similar to crack propagation rate during CSCC. This parallel behavior of corrosion and cracking kinetics was interpreted as supporting an anodic dissolution model of cracking. The strong tendency for repassivation suggests that, for the most part, the crack tip is covered by a passive film during crack propagation and that crack advance is the result of oxidation of Fe to form both film and soluble HFeO_2^- . The nature of the corrosion transients in the potential range promoting CSCC lend support to a film rupture theory (1-4), but the large transients occurring at postpassive potentials currently represent an anomaly. Recent results of work designed to measure the fracture strains and to compare the relative ductilities of Fe_3O_4 and $\gamma\text{-Fe}_2\text{O}_3$, and which will be reported in a future paper, will hopefully further the mechanistic understanding of CSCC.

Acknowledgments

Discussions with A. W. Urquhart and his assistance in the development of Eq. [9] and [10] are most appreciated.

This work was submitted to Rensselaer Polytechnic Institute in partial fulfillment of the requirements for the degree of Doctor of Philosophy by R. B. Diegle.

Manuscript submitted Jan. 14, 1974; revised manuscript received Sept. 16, 1974.

Any discussion of this paper will appear in a Discussion Section to be published in the December 1975 JOURNAL. All discussions for the December 1975 Discussion Section should be submitted by Aug. 1, 1975.

Publication costs of this article were partially assisted by General Electric Company.

APPENDIX

Method of Estimating the Valence Change of Iron as a Function of Potential During Repassivation

The technique used to estimate the valence change n is illustrated in Fig. A-1. The potential range en-

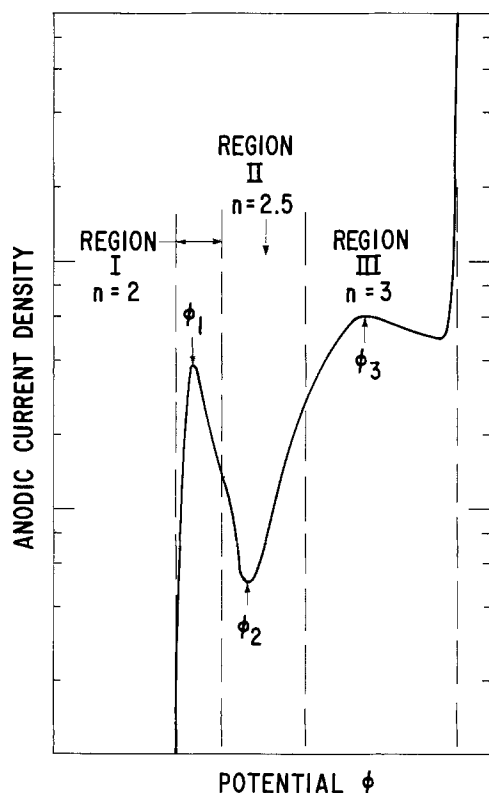


Fig. A-1. Schematic polarization curve showing the regions into which the experimental curves were divided and the valence assigned to each region.

compassing anodic current flow was divided into three regions based on the known behavior of Fe in high pH electrolytes. Region I is bounded by the rest potential and a potential midway between the active peak and passive potentials, ϕ_1 and ϕ_2 , respectively. A valence of 2 is assigned to Fe reacting in this range because of the stability of HFeO_2^- ion and the probable existence of a prepassive film of, perhaps, $\text{Fe}(\text{OH})_2$ (19). Regarding Region II, it has been shown that at a potential between ϕ_1 and ϕ_2 , Fe_3O_4 is stable but that $\gamma\text{-Fe}_2\text{O}_3$ is favored at higher potentials. This transition accounts for the increase in current flow at postpassive potentials and is presumably complete near the onset of the current plateau preceding oxygen evolution. An approximate valence for Region II would thus be between 2.67 and 3, except that some film dissolution is occurring. Therefore, an estimated average valence of 2.5 is assigned to Region II. A valence of 3 is ascribed to Region III due to the stability of $\gamma\text{-Fe}_2\text{O}_3$. This technique for estimating valence is self-consistent and not greatly in error, since the change of valence over the entire potential range investigated was only from 2 to 3.

REFERENCES

1. D. A. Vermilyea, *This Journal*, **119**, 405 (1972).
2. D. A. Vermilyea, Proc. International Conference on Stress Corrosion Cracking and Hydrogen Embrittlement of Iron Base Alloys, Firminy, France (1973), To be published.
3. H. L. Logan, *J. Res. Nat. Bur. Std.*, **48**, 99 (1952).
4. R. W. Staehle, Proc. International Conference on Stress Corrosion Cracking and Hydrogen Embrittlement of Iron Base Alloys, Firminy, France (1973), To be published.
5. J. C. Scully, *Corrosion Sci.*, **8**, 513 (1968).
6. R. N. Parkins, Proc. International Conference on Stress Corrosion Cracking and Hydrogen Embrittlement of Iron Base Alloys, Firminy, France (1973), To be published.
7. T. R. Beck, "The Theory of Stress Corrosion Cracking in Alloys," p. 64, J. C. Scully, Editor, NATO, Brussels (1971).
8. J. R. Ambrose and J. Kruger, *Corrosion*, **28**, 30 (1972).
9. J. R. Ambrose and J. Kruger, *This Journal*, In press.
10. J. Venczel and G. Wranglen, *Corrosion Sci.*, **4**, 137 (1964).
11. H. Grafen and D. Kuron, *Arch. Eisenhüttenw.*, **4**, 285 (1965).
12. M. J. Humphries and R. N. Parkins, *Corrosion Sci.*, **7**, 747 (1967).
13. H. E. Townsend, Jr., *ibid.*, **10**, 343 (1970).
14. V. Ashworth and P. J. Boden, *ibid.*, **10**, 709 (1970).
15. R. J. Biernst and R. G. Robins, *Electrochim. Acta.*, **17**, 1261 (1972).
16. M. Nagayama and M. Cohen, *This Journal*, **109**, 781 (1962).
17. M. J. Humphries and R. N. Parkins, Proc. of Conf., Fundamental Aspects of Stress Corrosion Cracking, NACE (1969), p. 384.
18. K. Bohnenkamp, *ibid.*, p. 374.
19. J. E. Reinhoehl and W. E. Berry, *Corrosion*, **28**, 151 (1972).
20. H. Grafen, *Werkstoffe Korrosion*, **20**, 305 (1969).
21. H. Grafen, *Corrosion Sci.*, **7**, 177 (1967).
22. D. de G. Jones, B. Case, and G. J. Bignold, Fourth International Congress on Metallic Corrosion, NACE (1967), p. 130.
23. W. M. M. Huybrechts, G. Van Osch, and A. Snel, *ibid.*, p. 127.
24. K. S. G. Doss, K. S. Rajagopalan, K. Balakrishnan, and K. Venu, Third International Congress on Metallic Corrosion, NACE (1969), p. 480.
25. A. K. Agrawal, K. G. Sheth, K. Poteet, and R. W. Staehle, *This Journal*, **119**, 1637 (1972).
26. R. L. Jones, L. W. Stratton, and E. D. Osgood, *Corrosion*, **26**, 399 (1970).
27. S. F. Bubar and D. A. Vermilyea, *This Journal*, **114**, 882 (1967).
28. M. J. D. Powell, *Computer J.*, **7**, 155 (1964).
29. J. F. Newman, To be published.
30. R. P. Harrison, D. de G. Jones, and D. V. Thornton, Presented at Conference on Mechanics and Mechanisms of Crack Growth, Cambridge (1973).
31. R. P. Harrison, D. de G. Jones, and J. F. Newman, Proc. International Conference on Stress Corro-

sion Cracking and Hydrogen Embrittlement of Iron Base Alloys, Firminy, France (1973), To be published.

32. H. H. Uhlig, "Corrosion and Corrosion Control,"

Chap. 7, John Wiley & Sons, Inc., New York (1963).

33. T. P. Hoar and R. W. Jones, *Corrosion Sci.*, **13**, 725 (1973).

The Na_2SO_4 -Induced Corrosion Properties of Ni-Base Superalloy Phases

Glauco Romeo*¹ and Douglas W. McKee

Research and Development Center, General Electric Company, Schenectady, New York 12301

ABSTRACT

The separate phases present in a Ni-base superalloy may offer different resistance to hot corrosion attack. Ni-Cr, Ni-Al, and Ni-Cr-Al alloys of composition corresponding, respectively, to the nominal γ matrix, the γ' phase, and a system of both these two phases, were coated with Na_2SO_4 and exposed to oxygen or $\text{H}_2\text{S-H}_2$ gas mixtures in the temperature range 850°-900°C. The corrosive attack was monitored with a recording microbalance. The results indicate that the degree and mechanism of corrosion of the above phases is markedly influenced by the nature of the environment and the composition of the oxide scales formed at the alloy surface. In general, the γ' phase appears to be a weak link in the over-all hot corrosion process.

The accelerated oxidation-sulfidation attack of nickel-base superalloys in the presence of sodium sulfate deposits is generally known as hot corrosion (1-6) and has been the subject of considerable investigation in the past two decades. The mechanism of hot corrosion has not yet been entirely clarified, and probably a generalized explanation for this type of phenomenon cannot be expected due to the variety of alloy compositions and environmental situations that can lead to similar corrosion morphologies. However, in the light of the available observations it is reasonable to assume that hot corrosion occurs by the combined action of (i) sulfur which diffuses rapidly into the alloy to produce a front of internally precipitated chromium sulfide particles that leaves the alloy matrix depleted in chromium, thus reducing its oxidation resistance (7, 8); and (ii) the Na_2SO_4 condensate which fluxes the normally protective oxides such as Al_2O_3 and Cr_2O_3 . The stoichiometry of the salt layer can be modified by the presence of some elements in the alloy such as molybdenum, vanadium, etc., thereby enhancing the oxide fluxing effect (3). If the sulfur potential at the scale-salt melt interface is raised by the onset of reducing conditions, the rate of corrosion can become catastrophic. In this case it is likely that sulfur diffusing into the alloy is the predominant factor of alloy degradation, particularly when its activity exceeds the equilibrium value for the formation of nickel sulfide which may be liquid at temperature (9, 10).

Although the bulk chemistry of the alloy and the role of the separate elemental components in causing accelerated attack has been thoroughly investigated (3, 4), scant attention has been paid so far to the possible correlation between alloy microstructure and corrosion rate. A recent note by Billingham *et al.* (11) points to this gap in the hot corrosion literature, suggesting that different heat-treatments of γ - γ' superalloys, by modifying the elemental partitioning between the different alloy phases, may result in satisfactory mechanical properties but may impair the surface stability of the alloy with respect to hot corrosion.

A nickel-base superalloy segregates into three or more phases (12). Of these the most important are (i)

the fcc γ -matrix, a solid solution rich in nickel and chromium and containing lesser amounts of other elements such as aluminum, titanium, etc.; (ii) an ordered intermetallic compound called γ' , primarily responsible for the high temperature strength of the alloy. This phase has the nominal composition of Ni_3Al , but it can be alloyed with other elements such as iron and titanium, and hence is more accurately denoted as $(\text{Ni,Fe})_3(\text{Al,Ti})$. Further, the chemical activity of the elements in the phase will be dependent on the composition of that phase. Finally, (iii) the other type of phase present in significant quantities in modern Ni-base superalloys are the carbides, which may exist in several forms, such as MC , M_7C_3 , M_{23}C_6 , etc., where M is the reactive metal in the carbide.

A priori, there is no reason to believe that these different phases, namely, the γ matrix, the γ' strengthener, and the carbides, will respond to a corrosive environment in the same way. Indeed, because of the wide spectrum of compositional difference between phases, it would be expected that they would respond quite differently in a hot corrosion environment. Because both sulfur diffusivity and ability to form a certain type of protective oxide (13) may vary considerably for the different phases present in a superalloy, it appeared useful to undertake a study in the temperature range 850°-1000°C of the hot corrosion behavior of some of the major phases present in a nickel-base superalloy, each phase being investigated separately in order to determine whether any of them could be a "weak link" in the alloy with respect to its hot corrosion resistance.

This paper reports part of the results of this study, with special emphasis on the behavior of the nominal γ and γ' phases in various environments that simulate oxidizing and reducing conditions.

Experimental

Specimen preparation and experimental techniques.—Alloys of composition [weight per cent (w/o)] Ni-35 Cr, Ni-20 Cr, Ni-13.3 Al, and Ni-10.4 Cr-13.5 Al were prepared by induction melting. The first two alloys simulate the chromium-enriched composition of the γ matrix, austenitic in a typical superalloy, the third alloy corresponds to the nominal γ' composition Ni_3Al , and the last alloy to a multiphase Ni-Cr-Al system containing both γ and γ' phases. The alloys were given

* Electrochemical Society Active Member.

¹ Present address: General Electric Company, Vallecitos Nuclear Center, Pleasanton, California 94566.

Key words: hot corrosion, sulfidation, gas turbines, nickel-chromium alloys.

Table I. Alloy preparation and treatment

Alloy composition (w/o)	Ingot preparation	Mechanical and thermal treatments
Ni-35 Cr	Melted, solidified, remelted and cast in Ar	Specimens annealed in vacuum for 3 hr at 1000°C
Ni-20 Cr	Melted and cast in Ar	Ingot forged to 0.575 in. thickness at 1100°-1175°C and rolled to 0.080 in. at 1100°C
Ni-10.4 Cr-13.5 Al	Ni-Cr melted in Ar at 1/3 atm, solidified and remelted in vacuum. Al added in Ar at 1 atm. Final casting in Ar	Used as cast
Ni-13 Al	Ni melted in Ar at 1/3 atm, solidified and remelted in vacuum. Al added in Ar at 1 atm. Final casting in Ar.	Ingots were heated to 1000°C and slices were hot cut

convenient heat and mechanical working treatments, according to their homogeneity and brittleness.

Table I shows a schematic of the alloy preparation and treatments. Due to the different ductility of the various alloys, test specimens for thermogravimetric analysis (TGA) were prepared by mechanical or electrical discharge machining of rectangular coupons approximately $15 \times 5 \times 1$ mm in size from rolled sheets or slices of the as-cast ingots. A suspension hole was drilled in each coupon. The specimens were wet ground through 600 grit silicon carbide papers and cleaned with acetone and methanol prior to each run. The surface area was computed by measuring the dimensions with a micrometer. The specimens were coated with a layer of sodium sulfate by spray deposition and drying with an infrared lamp. Most specimens were annealed for 4-6 hr in oxygen prior to coating them with sodium sulfate. This preoxidation treatment was intended to simulate the real condition of metal surfaces in gas turbines during salt deposition. It also provided a better adherence of the salt deposit to the oxide layer than to the bare metal.

The extent of the corrosive attack was monitored by means of a thermogravimetric apparatus (TGA). This consisted essentially of a recording microbalance, a reaction vessel for metal specimens, a temperature controlled furnace, and a set of flow meters to prepare gas mixtures. The microbalance was a Cahn RG Automatic Electrobalance with a capacity range of 1-2.5g and a sensitivity of 1 μ g. The balance was coupled with a digital data acquisition system, by means of which the voltage output of the balance could be punched directly on paper tape together with a time scale at preset time intervals. The tape was then processed automatically by a computer and the data could be displayed terminally as weight-gain vs. time plots. This greatly facilitated data collecting and analysis, especially for long term experiments. A more detailed description of the TGA can be found in a previous publication (14).

After most runs, samples of the corrosion products were submitted for x-ray diffraction analysis, and the specimens were mounted and cross-sectioned metallographically for examination of the corrosion scales with the light microscope. In some cases microprobe scanning of the cross sections was also carried out.

Choice of environmental parameters.—It is not feasible to define a single model environment for hot corrosion, because accelerated attack can occur in a great variety of situations. However, three types of environments were selected during the course of this study:

1. Sodium sulfate coatings exposed to H_2S-H_2 gas mixtures to simulate strong reducing conditions and high sulfur potentials.
2. Sodium sulfate coatings exposed to oxygen to simulate oxidizing conditions.
3. Gaseous atmospheres as described in types 1 and 2, but in the absence of sodium sulfate coatings.

Most experiments were carried out isothermally at 900°C. This temperature was selected as representative of an upper limit in current gas turbine operations and was sufficiently high for the sodium sulfate coatings to be present as a liquid film on the metal surface. The experiments were carried out with gases flowing at atmospheric pressure and flow rates of ~ 300 cm³/min corresponding to a linear velocity in the reaction cell of 0.5-1 cm/sec.

Crucible experiments with excess sodium sulfate.—A series of crucible experiments was also carried out with a range of Ni-Al (0-30 w/o Al) and Ni-Cr (0-20 w/o Cr) alloys, coupons of which were immersed in an excess (1g) of powdered sodium sulfate and heated in flowing air at 900°C. The resulting weight changes of these samples were measured in the Chevenard thermobalance described previously (6) as a function of the Al and Cr content of the alloy. The nominal and actual compositions of the alloy coupons used in these experiments are listed in Table II.

Results

Gamma matrix (nominal composition).—Two binary systems were used that simulated the fcc continuous matrix of Ni-base superalloys: Ni-35 w/o Cr and Ni-20 w/o Cr. Both of these systems belong to the range of existence of the γ phase at high temperature, according to the binary phase diagram (15), and correspond to an upper and medium value of chromium in solid solution with nickel.

Reducing conditions.—When Ni-35 Cr was exposed at 850°C to a 10% H_2S-H_2 gas mixture, the weight gain curve followed a pseudoparabolic trend, reaching a value of 58 mg/cm² after only 2½ hr. However, the reaction was not of a gas-solid type throughout the run because of the initial formation of a liquid nickel sulfide phase. Figure 1 shows a cross section of the specimen at the end of this experiment. The duplex scale consists of an external layer of Ni_3S_2 , which was molten at the temperature of the experiment, separated from the alloy by an inner layer of chromium sulfide. Grain boundaries in this inner layer offered a preferential path for the penetration of liquid nickel sulfide stringers (16), as evident in the micrograph. X-ray diffraction analysis indicated the composition of the chromium sulfide layer to be mainly Cr_3S_4 with traces of Cr_2S_3 . The stoichiometry of chromium sulfide can vary in the range CrS to Cr_2S_3 with the sulfur pressure (17). The composition Cr_3S_4 in particular can exist in a remarkably wide range of sulfur pressures (18).

X-ray analysis of the oxide scale grown at 900°C in oxygen at atmospheric pressure on a Ni-35 Cr alloy showed its composition to be predominantly Cr_2O_3 , with a few weak extraneous lines attributable to NiO and possibly a spinel. A test was then run to check whether this scale could provide a barrier to the formation of liquid nickel sulfide and consequent accelerated attack. Two specimens of Ni-35 Cr were pre-oxidized but only one of them was coated with ~ 2 mg/cm² of sodium sulfate. Both specimens were then treated with a 10% H_2S-H_2 mixture at 850°C. After a

Table II. Alloys used in crucible experiments

Nominal alloy composition (w/o)	Actual composition (w/o)
100 Ni	100 Ni
Ni-2 Al	Ni-1.8 Al
Ni-5 Al	Ni-4.9 Al
Ni-10 Al	Ni-9.7 Al
Ni-13 Al	Ni-13.3 Al
Ni-20 Al	Ni-19.5 Al
Ni-30 Al	Ni-29.3 Al
Ni-2 Cr	Ni-1.7 Cr
Ni-5 Cr	Ni-5.0 Cr
Ni-10 Cr	Ni-9.9 Cr
Ni-15 Cr	Ni-14.9 Cr
Ni-20 Cr	Ni-19.8 Cr

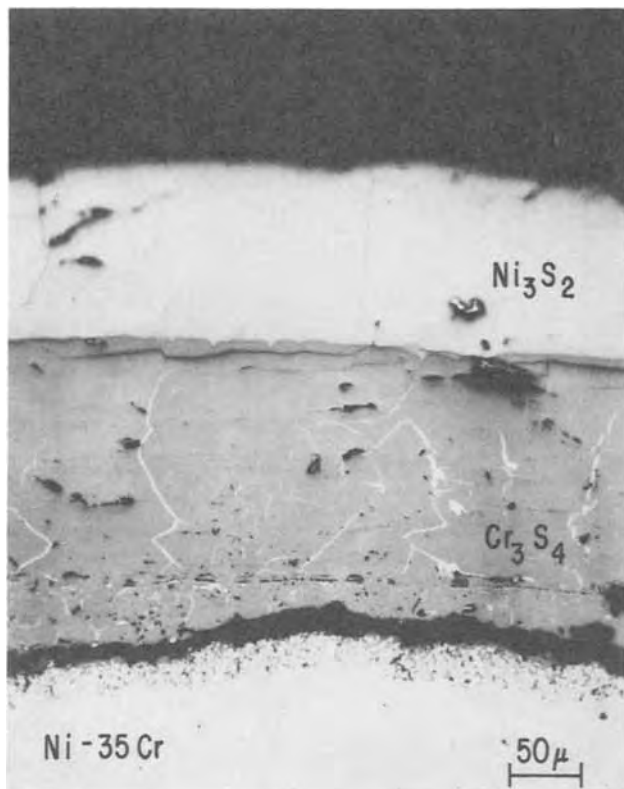


Fig. 1. Ni-35 Cr alloy treated at 850°C with a 10% H₂S-H₂ gas mixture for 2½ hr. The scale consists of an outer layer of nickel sulfide which was molten at temperature, and an inner layer of chromium sulfide.

brief induction period fast formation of liquid nickel sulfide resulted in both cases. The oxide layer did not offer significant protection against gaseous sulfidation and the sodium sulfate deposited onto the oxide did not accelerate substantially a situation which led to catastrophic attack.

Figure 2 shows an example of liquid sulfide formation over preoxidized salt-free Ni-35 Cr, where the liquid has dripped by gravity to the bottom of the specimen. Figure 3 shows the weight-gain curves for Ni-35 Cr specimens that were given different pretreatments and were subsequently exposed to a 10% H₂S-H₂ gas mixture.² While the extent of corrosion in Fig. 3 is of a comparable magnitude in the three cases after equal times, a larger induction period before the onset of fast sulfidation can be noticed for the specimen preoxidized and not coated with sodium sulfate. Most probably in this case a longer time was required for sulfur to diffuse through Cr₂O₃, whereas in the other two cases either Cr₂O₃ did not have time to reach a finite thickness or it was dissolved by a liquid film of Na₂SO₄-Na₂S mixture with which the specimen was coated. It should also be noted that hydrogen present in the H₂S-H₂ mixture readily reduces Na₂SO₄ to Na₂S at high temperature. Similar experiments have shown the same tendency for the Ni-20 Cr alloy to form liquid nickel sulfate when exposed to H₂S-H₂ atmospheres.

Oxidizing conditions.—A study was carried out on the effect of oxidizing conditions and cyclic oxidizing-reducing conditions on the nominal γ matrix composition, using oxygen at 1 atm throughout the run or alternating the main oxidation process with short periods of exposure to hydrogen. It is important to point out that in these conditions weight gain curves provide only an

² Here and in other kinetic plots no attempt will be made to interpret the curves in conformance to any quantitative rate law, because in most cases the corrosion scales lack entirely the uniformity and compactness which is required for such an analysis to be meaningful. However, the weight gain curves visualize the extent of the attack during the experiments and identify major changes in reaction mechanisms.

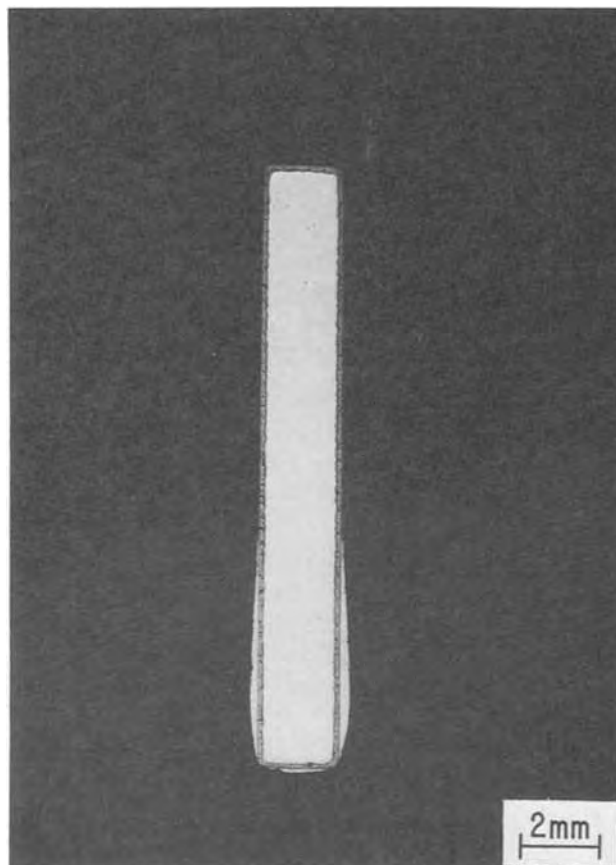


Fig. 2. Ni-35 Cr alloy preoxidized and subsequently sulfidized with a 10% H₂S-H₂ gas mixture at 850°C. Liquid nickel sulfide has dripped to the bottom of the specimen which was held vertically in the furnace.

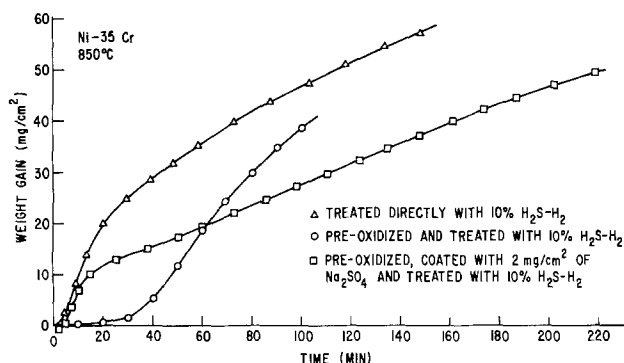


Fig. 3. Weight gain curves for a Ni-35 Cr alloy exposed at 850°C to a 10% H₂S-H₂ gas mixture after different pretreatments.

approximate indication of the extent of corrosion, since weight losses due to evaporation or reduction of sodium sulfate from the surface may be superimposed on weight gains due to formation of oxide and sulfide scales. Evaporation can be neglected, however, when reducing conditions with formation of liquid corrosion products result in a much faster rate of attack. In any case, metallographic measurements of metal recession can provide additional information on the depth of attack.

Ni-20 Cr preoxidized and coated with 10 mg/cm² of sodium sulfate was exposed to oxygen at 900°C for about 8 days. Figure 4 shows that within the first day the specimen gained less than 1 mg/cm², after which the weight loss due to evaporation of the sodium sulfate was greater than the weight gain due to oxidation. Relatively little weight gain has been reported by Goebel *et al.* (3) for a Ni-30 Cr alloy oxidized at 1000°C, and by Hardt *et al.* (19) for a Ni-20 Cr alloy oxidized at 905°C. However, in Goebel's case the alloy

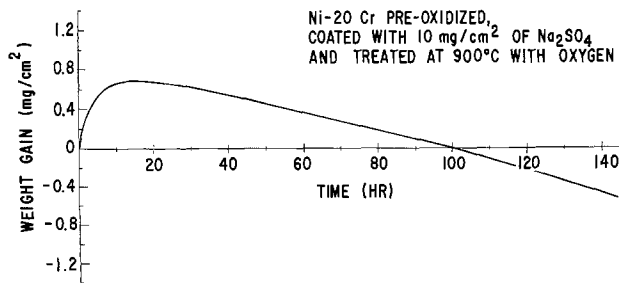


Fig. 4. Weight gain curve for a Ni-20 Cr alloy preoxidized, coated with 10 mg/cm^2 of Na_2SO_4 , and exposed to oxygen at 900°C . The weight loss of the specimen can be attributed mainly to evaporation of sodium sulfate.

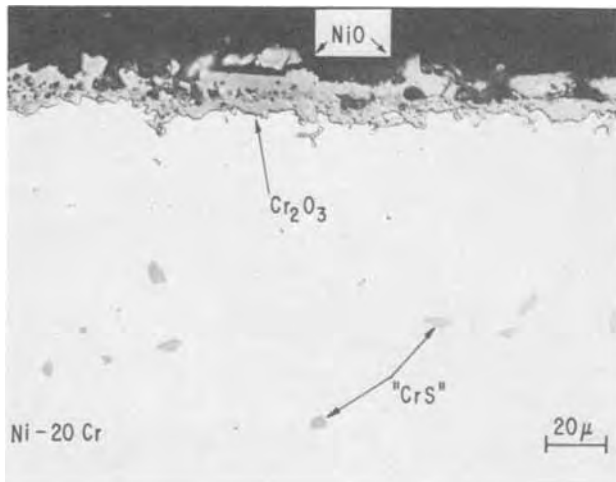


Fig. 5. Duplex oxide scale formed on a Ni-20 Cr alloy preoxidized, coated with 10 mg/cm^2 of Na_2SO_4 , and exposed to oxygen at 900°C for about 6 days. Some particles of chromium sulfide have precipitated within the alloy.

was coated with only 0.5 mg/cm^2 of sodium sulfate, and in Hardt's case with $1\text{--}3 \text{ mg/cm}^2$ of sodium sulfate. A much larger amount of salt in our case did not seem to alter significantly the corrosion rate, indicating that dissolution or penetration kinetics are limiting, rather than solubility effects. The same is true for a temperature increase of 100°C (from 900° to 1000°C).

At the end of the run the residual sodium sulfate exhibited a bright yellow color and the presence of sodium chromate was confirmed by x-ray analysis.

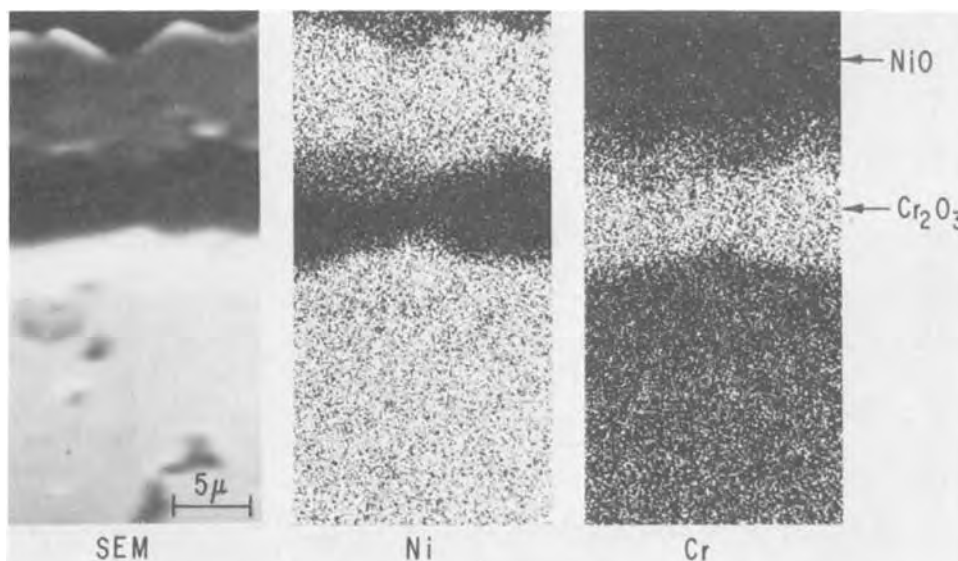


Fig. 6. Characteristic x-ray distribution for the duplex oxide scale formed on a Ni-20 Cr alloy preoxidized, coated with sodium sulfate, and exposed to oxygen at 900°C .

Light microscopy revealed a fairly compact external scale and internally precipitated particles of chromium sulfide (Fig. 5). X-ray mapping (Fig. 6) and diffraction analysis showed the upper portion of the scale to consist of NiO and the lower portion of Cr_2O_3 . The formation of sodium chromate, observed also by other authors, indicates reaction between sodium sulfate and initially present Cr_2O_3 layers. However, a considerable degree of protection for the alloy substrate is still provided by the scale, which appears to react only slightly with the sodium sulfate coating. It can be concluded that, by and large, the γ matrix presents a considerable resistance to hot corrosion due to sodium sulfate deposits, in purely oxidizing conditions.

The resistance of Ni-Cr alloys to corrosion by Na_2SO_4 under oxidizing conditions is also confirmed by the results of crucible tests carried out with a series of Ni-Cr specimens, immersed in excess salt in air at 900°C . As shown by the dashed curve of Fig. 7, in which the initial weight gain rate is plotted against alloy composition, the addition of chromium to nickel results in a steady decrease in corrosion rate with increasing chromium content, becoming very small at the nominal γ matrix composition of Ni-20 Cr. This behavior is in marked contrast to that of the Ni-Al alloy series, whose corrosion behavior is shown by the solid curve of Fig. 7 and is discussed further below.

Cyclic conditions.—The effect of cyclic oxidizing and reducing conditions was evaluated with Ni-20 Cr and Ni-35 Cr alloys by treating specimens alternatively with oxygen and hydrogen, to determine whether short term reduction stages would create conditions favorable to accelerated attack. The conditions used in these experiments were similar to those employed by Simons *et al.* (29). Figure 8 shows a weight gain curve for a specimen of Ni-20 Cr preoxidized, coated with 6 mg/cm^2 of sodium sulfate, and exposed at 900°C first to oxygen, then to hydrogen, and finally again to oxygen. During the reduction period the rapid weight loss of the specimen is due to the reactions: $\text{Na}_2\text{SO}_4 + 4\text{H}_2 \rightarrow \text{Na}_2\text{S} + 4\text{H}_2\text{O}$ and $\text{Na}_2\text{S} + 2\text{H}_2\text{O} \rightarrow 2\text{NaOH} + \text{H}_2\text{S}$. The presence of H_2S in the exhaust gases was confirmed with lead acetate paper strips.

The final oxidation stage resulted in an initial rapid weight gain, which most probably corresponds to re-oxidation of the residual Na_2S , followed by a steady state of very low weight gain during which a protective oxide layer is formed again and the corrosion proceeds very slowly. This behavior shows that the γ matrix offers the same resistance to hot corrosion both during continuous oxidation and when exposed to temporary reducing conditions, if the sulfur pressure at the gas-scale interface is not sufficient for the formation of liquid nickel sulfide. Indeed the morphology of

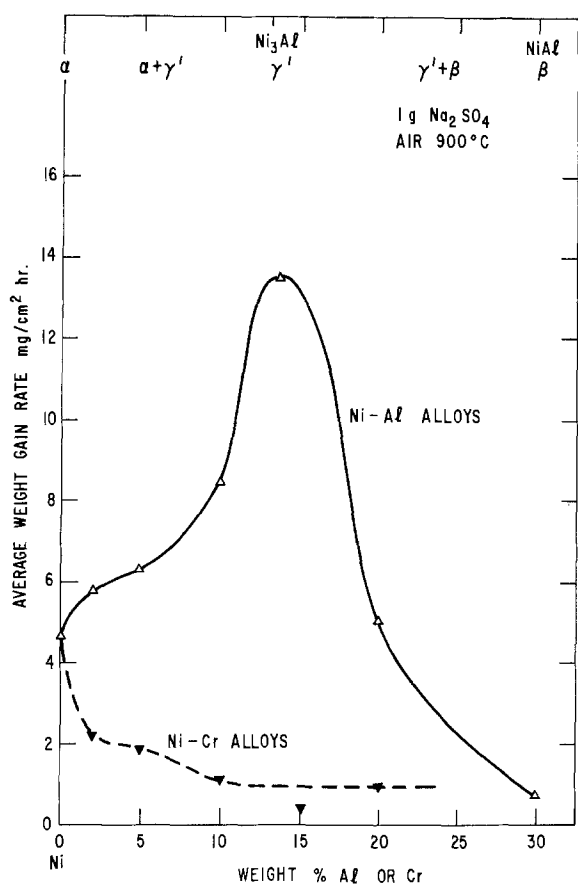


Fig. 7. Results of thermogravimetric tests carried out on Ni-Cr and Ni-Al alloys exposed to sodium sulfate in air, at 900°C.

the corrosion product is very similar in both cases with the sequence of base alloy, chromium sulfide, nickel-rich matrix, and nickel and chromium oxides indicated by the microprobe trace in Fig. 9. The Ni-35 Cr alloy showed a very similar behavior. It will be pointed out in a later section that alternate oxidizing-reducing conditions applied to a sodium sulfate coated two-phase ternary Ni-Cr-Al alloy seem to have induced accelerated attack after such a temporary re-

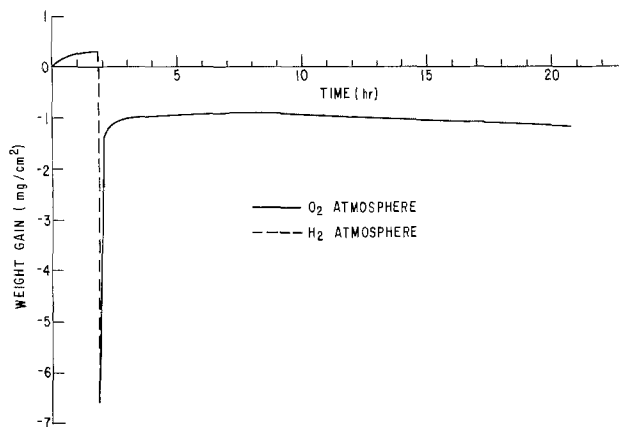


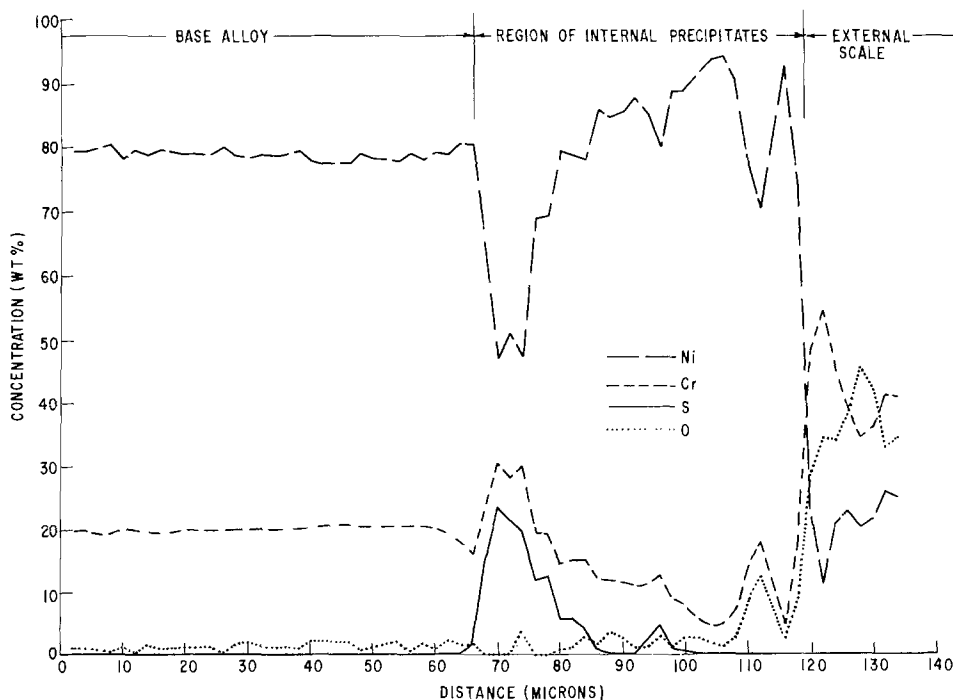
Fig. 8. Weight gain curve for a Ni-20 Cr alloy preoxidized, coated with 12 mg/cm² of Na₂SO₄, and exposed alternatively to oxidizing and reducing atmospheres at 900°C.

duction stage as that applied to the gamma phase above, most probably because hot corrosion is favored at areas of γ' phase.

Gamma prime (nominal composition).—Reducing conditions.—A specimen (a) of Ni₃Al was treated directly at 900°C with a 10% H₂S-H₂ gas mixture. After about 13 hr the weight gain amounted to only 2.5 mg/cm². X-ray analysis of the corrosion product indicated presence of Ni₃S₂ and some Al₂O₃. The latter compound probably formed because of oxygen impurity in the gas stream, and was responsible for the resistance of the specimen to sulfidation.

Another specimen (b) of Ni₃Al, preoxidized and coated with 9 mg/cm² of sodium sulfate, was treated with the 10% H₂S-H₂ mixture at 900°C. In this case the weight gain reached in 3½ hr, 11 mg/cm², indicating a marked acceleration of the corrosion process due most probably to removal from the metal surface of protective Al₂O₃ layers by the molten sodium sulfate. Figure 10 shows the weight gain curves for specimens (a) and (b). Figure 11 shows a portion of the scale formed on specimen (b). Microprobe scanning across this scale (Fig. 12) indicated an outer portion of nickel sulfide (Ni₃S₂) without any aluminum and an inner portion in which aluminum is present together with nickel sulfide. Once again the high cor-

Fig. 9. Distribution profile of elements for a Ni-20 Cr alloy preoxidized, coated with sodium sulfate, and exposed alternatively to oxidizing and reducing conditions.



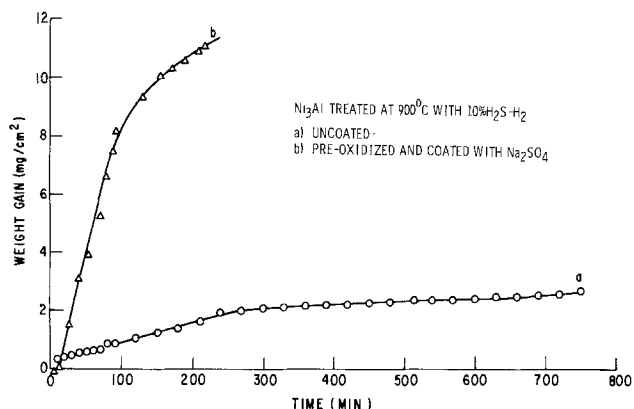


Fig. 10. Weight gain curves for a Ni-13 Al alloy treated with a 10% H₂S-H₂ gas mixture at 900°C: (a) uncoated specimen; (b) specimen preoxidized and coated with 9 mg/cm² of Na₂SO₄.

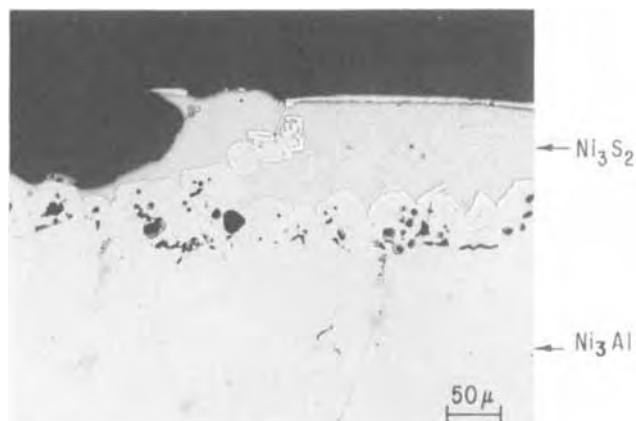


Fig. 11. Scale formed on a Ni-13 Al alloy preoxidized, coated with 9 mg/cm² of Na₂SO₄, and treated with a 10% H₂S-H₂ gas mixture at 900°C. The portion labeled as Ni₃S₂ was probably molten at reaction temperature.

rosion rate of the γ' phase coated with sodium sulfate and exposed to H₂S-H₂ mixtures can be explained by the initial formation of liquid nickel sulfide, which

subsequently reacts with aluminum to form aluminum sulfide. Formation of liquid nickel sulfide has indeed been observed with the hot-stage microscope on Ni₃Al specimens coated with sodium sulfate and exposed to sulfur-bearing atmospheres in reducing conditions. However, a comparison of the weight gain curves in Fig. 3 and Fig. 10 shows that the tendency to form liquid nickel sulfides when exposed to H₂S-H₂ atmospheres is much more pronounced with Ni-Cr systems than with Ni-Al systems.

The effect of reducing atmospheres on sodium sulfate deposited onto a γ' substrate was also studied in conditions of low sulfur potential in the gas phase. A specimen of Ni₃Al (c) was preoxidized, coated with 17 mg/cm² of Na₂SO₄, and exposed at 900°C to hydrogen. Reduction of the salt to Na₂S took place within an hour, after which no weight change was noticed. At the end of the run the specimen was rinsed with hot water and the insoluble portion of the washings treated with aqua regia. A residue (most probably Al₂O₃) remained insoluble after this treatment. Chemical analysis of the soluble portion showed a higher content of Al with respect to Ni (Al/Ni \approx 12). Again this would indicate a tendency for the aluminum oxide to dissolve in the Na₂SO₄-Na₂S layer. Figure 13-1 is a cross section of specimen (c) and shows that the corrosive attack is characterized by a front of internally precipitated particles. Most of these particles were removed by polishing, leaving behind a porous section. Figure 13-2 is a high magnification scanning electron micrograph of the porous area in Fig. 13-1. An electron beam was focused on a particle (point A) and in the alloy matrix (point B). The locally excited x-ray radiations were collected and analyzed by a solid-state detector. The corresponding spectrum is shown in Fig. 13-3, indicating that sulfur is present in particle A together with nickel and aluminum. Unfortunately oxygen cannot be identified directly by the solid-state detector and further analysis would be necessary to ascertain the nature of the internal precipitate. However, it is worth noticing that even though chromium is not present in the Ni₃Al phase, the presence of a sulfur-containing internal precipitate (a feature characteristic of hot corrosion) can still be detected.

Oxidizing conditions.—When a specimen of Ni₃Al (d) was preoxidized, coated with 5.5 mg/cm² of sodium sulfate, and treated at 900°C with oxygen, rapid

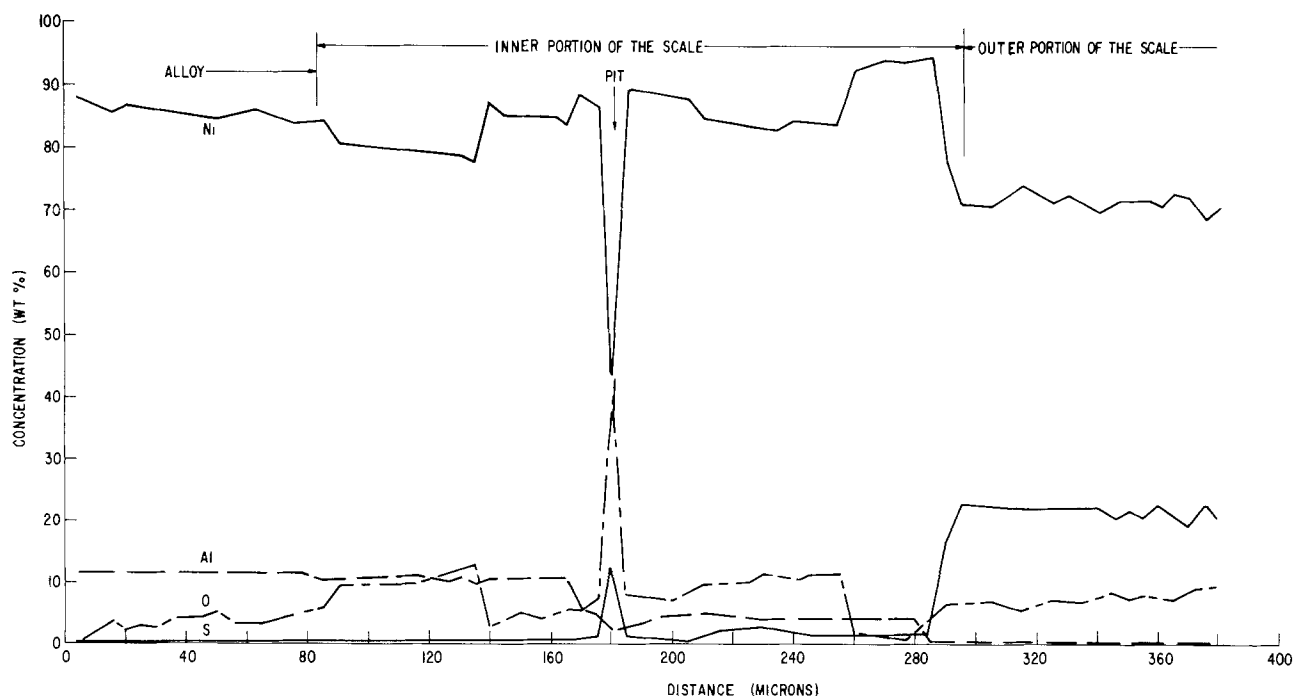


Fig. 12. Distribution profile of elements for a Ni-13 Al alloy preoxidized, coated with sodium sulfate, and treated with a 10% H₂S-H₂ gas mixture at 900°C.

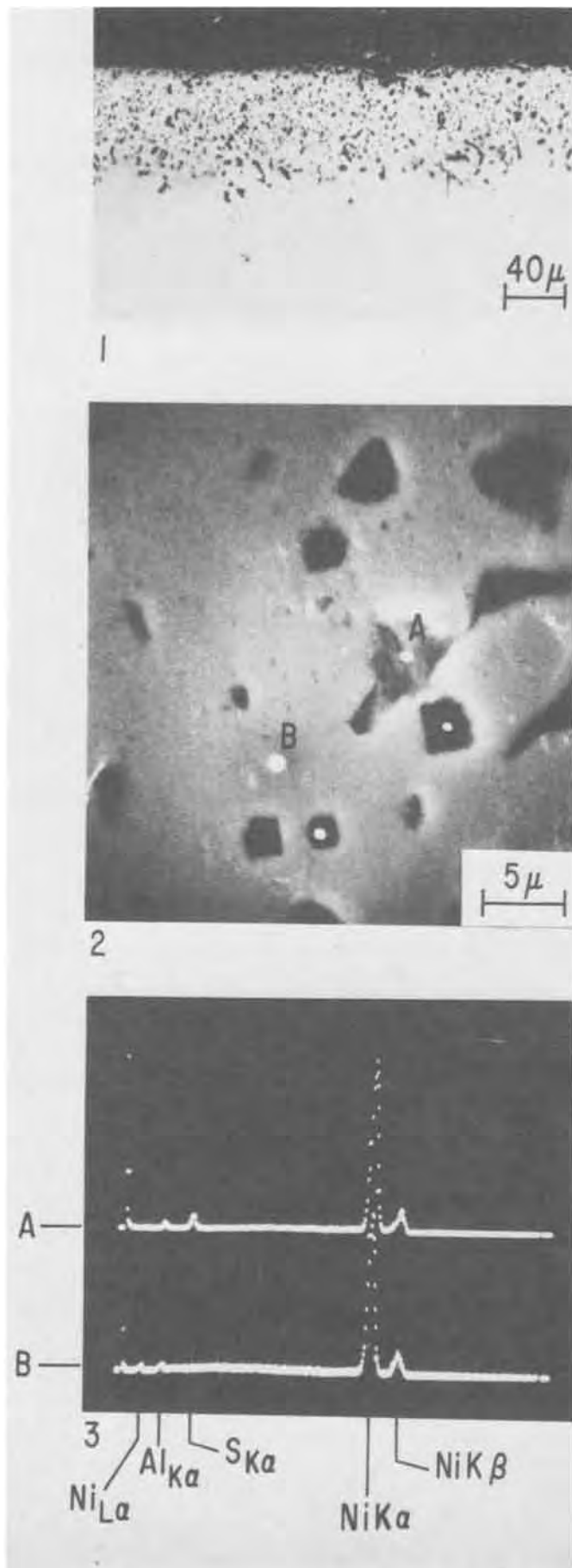


Fig. 13-1. Cross section of Ni-13 Al alloy preoxidized, coated with 17 mg/cm² of Na₂SO₄, and treated with hydrogen at 900°C for 4 hrs. 2. SEM micrograph of porous area shown in top micrograph. 3. X-ray spectrum of particle A shown in middle micrograph.

weight gain was observed in the first few minutes, followed by a continuous decrease in the reaction rate. The same experiment was repeated on a specimen which had not been preoxidized but had been coated with 11 mg/cm² of sodium sulfate (e). Similar results were obtained in this case and also with a specimen which was preoxidized and coated with 17 mg/cm² of sodium sulfate (f). Figure 14 shows the weight-gain curves for specimens d, e, and f.

The extent of the initial rapid attack appears to be roughly dependent on the amount of salt deposit. The presence of a preexisting oxide did not affect significantly the corrosion process. In all the three cases after about 10 hr the corrosion rate dropped to a negligible value. This behavior can be explained assuming that molten sodium sulfate acts initially as a flux for thin, protective oxide layers (mainly Al₂O₃). At a later stage the growth of thicker scales that offer partial protection to the metal substrate can take place.

Figure 15 shows the somewhat porous scale grown on specimen (e). X-ray analysis identified the presence of NiO as the predominant phase, plus a small amount of α-Al₂O₃. Microprobe scanning of the scale (Fig. 16) showed some evidence of sulfides, possibly of aluminum, at the metal-scale interface, while the scale profile appears to consist essentially of Ni and Al oxides. The growth of dark NiO crystals on the specimen surface has been frequently observed in the course of our experiments with Ni-base alloy coated with sodium sulfate and exposed to oxygen. Conceiv-

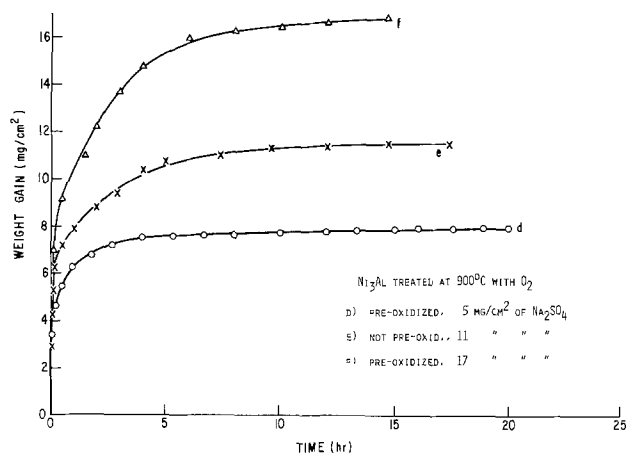


Fig. 14. Weight gain curves for a Ni-13 Al alloy exposed to oxygen at 900°C after the following pretreatments: (d) specimen preoxidized and coated with 5.5 mg/cm² of Na₂SO₄; (e) specimen not preoxidized but coated directly with 11 mg/cm² of Na₂SO₄; (f) specimen preoxidized and coated with 17 mg/cm² of Na₂SO₄.

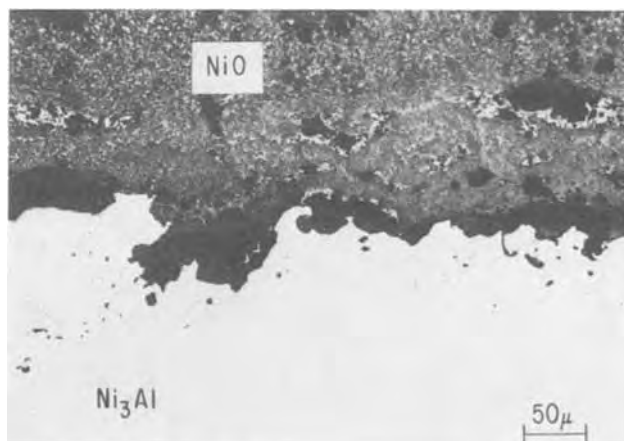


Fig. 15. Cross section of Ni-13 Al alloy coated with 11 mg/cm² of Na₂SO₄ and treated with oxygen at 900°C for 18 hr. A small amount of α-Al₂O₃ was detected in the main NiO porous scale.

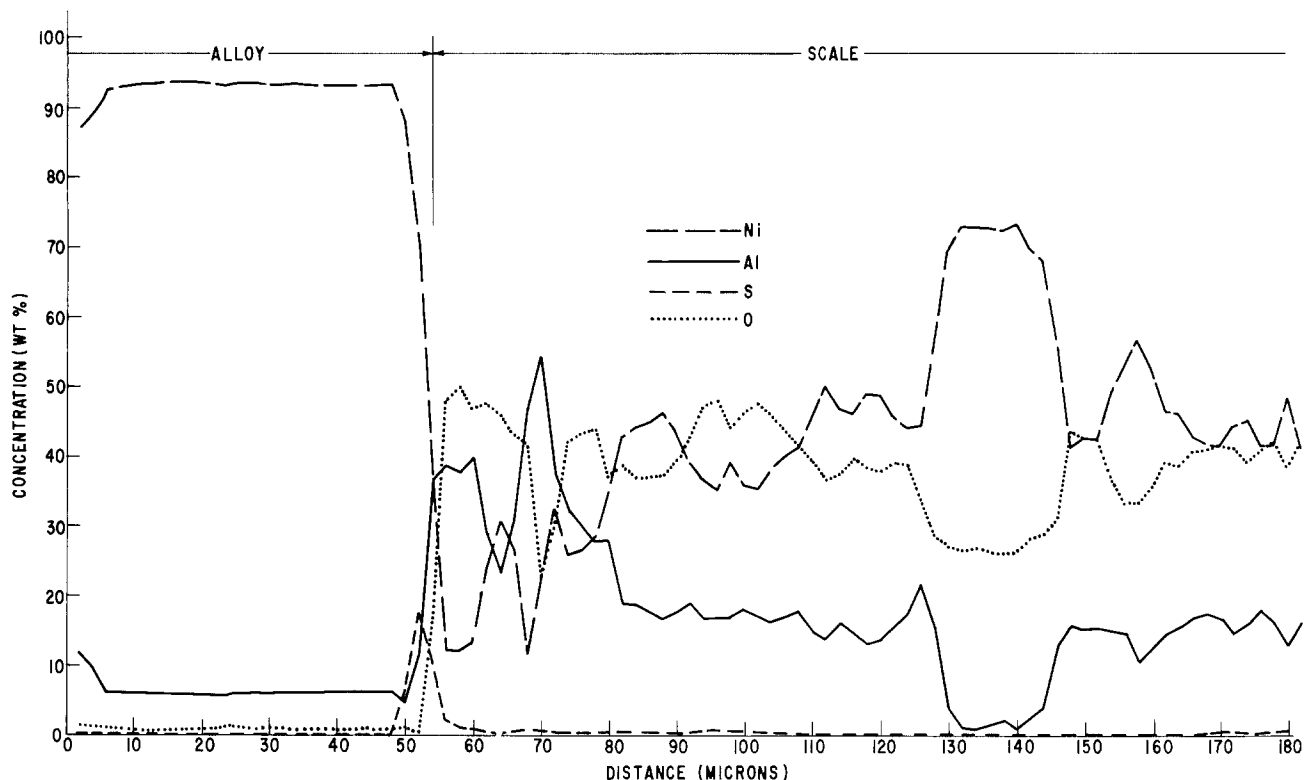


Fig. 16. Distribution profile of elements for a Ni-13 Al alloy coated with sodium sulfate and treated with oxygen at 900°C

ably the growth of thick and fairly coherent layers of NiO separates progressively the sodium sulfate film from the metal and results in a continuous slowdown of the corrosion rate for the Ni₃Al phase. This is also favored by the saturation of the salt film with corrosion products, which renders it less active in fluxing out the oxide scale.

The results of crucible experiments with a series of Ni-Al alloys exposed to excess molten Na₂SO₄ in an oxidizing atmosphere are summarized in Fig. 7. The solid curve shows the average initial corrosion rate (weight gain/cm² hr) at 900°C as a function of aluminum content of the alloy. On addition of Al to Ni, the corrosion rate under oxidizing conditions accelerates rapidly as the proportion of the γ' phase increases and becomes catastrophic at the nominal γ' composition, Ni₃Al. This alloy was reduced to a porous gray mass after exposure to excess Na₂SO₄ for a period of only 2 hr in air. Further additions of aluminum resulted in a decrease in corrosion rate as the proportion of the Ni-Al phase increased. The Ni-Al β phase itself (Ni-30 w/o Al) was remarkably resistant to attack and gained only 1 mg/cm² during a period of 4 hr in contact with the molten salt.

A multiphase Ni-Cr-Al system.—Studies of the behavior of a multiphase system were carried out on a Ni-10.4 Cr-13.5 Al (w/o). Taylor and Floyd (20) have shown that at temperatures approaching 1000°C this alloy composition can consist of up to four phases, namely the bcc solid solution of nickel in chromium (α), the fcc solid solution of chromium in nickel (γ), the ordered bcc NiAl phase (β), and the ordered fcc Ni₃Al phase (γ').

Reducing conditions.—A specimen of Ni-10.4 Cr-13.5 Al (a) treated at 850°C directly with a 10% H₂S-H₂ mixture reacted initially slowly, but after about 6 hr a breakaway took place in the weight gain curve and sulfidation proceeded at a linear rate for the rest of the run. X-ray analysis of the corrosion product indicated the presence mainly of Ni₃S₂, a mixed sulfide of chromium and aluminum,³ and a trace of α -Al₂O₃. The same scale composition was found in another speci-

men (b) coated with 1.3 mg/cm² of sodium sulfate and exposed at 850°C to the H₂S-H₂ mixture. Preoxidation of the alloy followed by isothermal treatment at 850°C with the H₂S-H₂ mixture resulted in a surprisingly low rate of attack (c). On the other hand, the same alloy preoxidized and coated with 2 mg/cm² of sodium sulfate after an initial treatment with oxygen underwent little corrosion, but was deeply attacked when subsequently exposed in isothermal conditions to the H₂S-H₂ mixture (d). The weight gain curves corresponding to these four experiments are summarized in Fig. 17.

A comparison between curve (a) and earlier data on corresponding untreated Ni-Cr alloys under sulfidation conditions (Fig. 3) indicates that addition of Al slows down remarkably the sulfidation rate of the γ matrix under reducing conditions. This is probably

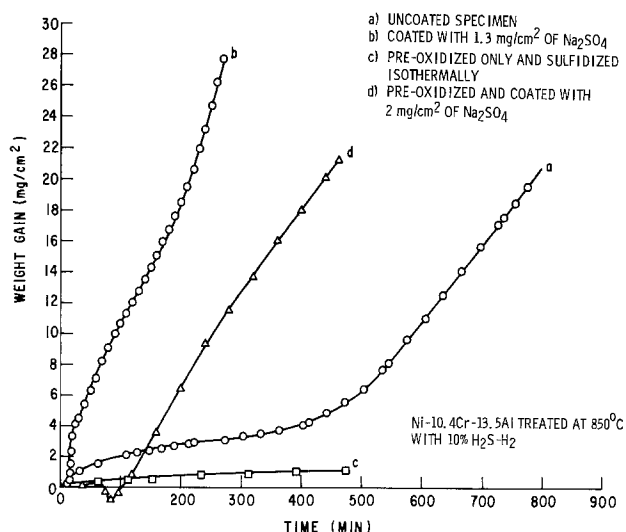
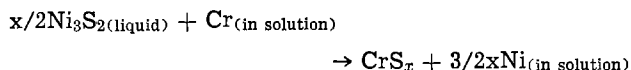


Fig. 17. Weight gain curves for a Ni-10.4 Cr-13.5 Al alloy exposed to a 10% H₂S-H₂ gas mixture at 850°C after the following pretreatments: (a) specimen untreated, (b) specimen coated with 1.3 mg/cm² of sodium sulfate, (c) specimen preoxidized, (d) specimen preoxidized and coated with 2 mg/cm² of sodium sulfate.

³ The compound Cr₂AlS₄ has a spinel structure ($a_0 \approx 9.9\text{\AA}$) and is referenced in Donnay (21).

due to the initial formation of oxides and sulfides of aluminum and chromium. Subsequent depletion of the alloy in these elements favors the formation of Ni_3S_2 and the reaction becomes much faster. Curve (c) in Fig. 17 shows the effect of a preexisting layer of oxide in reducing the initial sulfidation rate in the absence of destructive salt deposits. When instead sodium sulfate films remove protective oxides, the sulfidation process proceeds catastrophically, as exemplified by curves b and d in Fig. 17. The effect of sodium sulfate deposits is shown dramatically in Fig. 18, where the top and bottom micrographs correspond to the cross section of specimens (c) and (d), respectively. In the case of specimen (d) the presence of sodium sulfate has favored the growth of a much thicker scale of complicated morphology. Large polygonal particles of chromium sulfide are embedded in a scale of nickel and aluminum sulfide. The Ni_3S_2 was probably molten at reaction temperature, and chromium sulfide segregated from it, as suggested by Seybolt (8), according to the reaction



Oxidizing conditions.—A specimen of Ni-10.4 Cr-13.5 Al alloy was preoxidized, coated with 10 mg/cm^2 of sodium sulfate, and exposed to oxygen at 900°C . The specimen gained comparatively little weight for about three days, after which accelerated attack took place suddenly, as shown by curve a in Fig. 19. The experiment was repeated, and in the second case onset of accelerated attack occurred after 12 hr (curve b in Fig. 19). The sudden breakaway in the weight gain curves can again be related to the nature of the oxide scales preformed on the specimens and their rate of dissolution or penetration by the sodium sulfate melt. X-ray diffraction analysis indicated that the oxide scale formed in the absence of sodium sulfate deposits was a mixture of spinels of composition NiAl_2O_4 and NiCr_2O_4 . Differences in the thickness of the oxide layer due to small differences in surface preparation of the

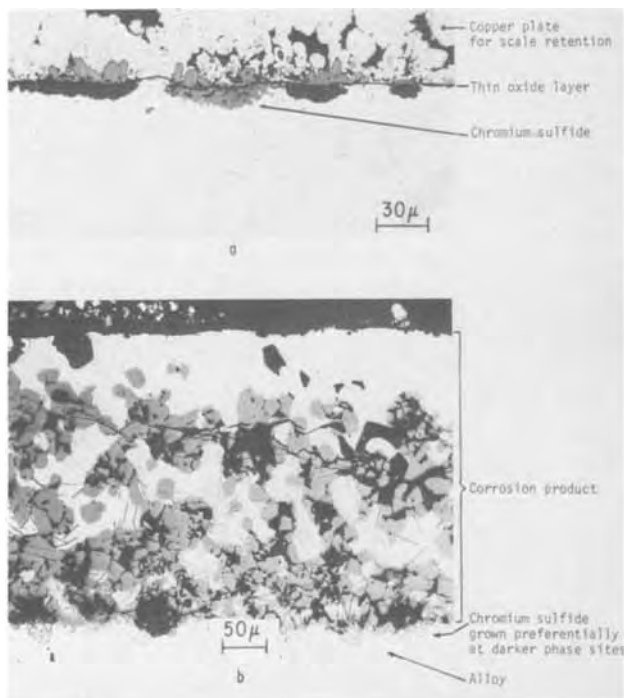


Fig. 18. Ni-10.4 Cr-13.5 Al alloy treated with a 10% $\text{H}_2\text{S}-\text{H}_2$ gas mixture at 850°C for 8 hr. (a) The specimen was preoxidized but not coated with sodium sulfate. A copper plate was used for retaining the relatively thin chromium sulfide layer. (b) Coating a preoxidized specimen with sodium sulfate produced deep attack and a complex morphology.

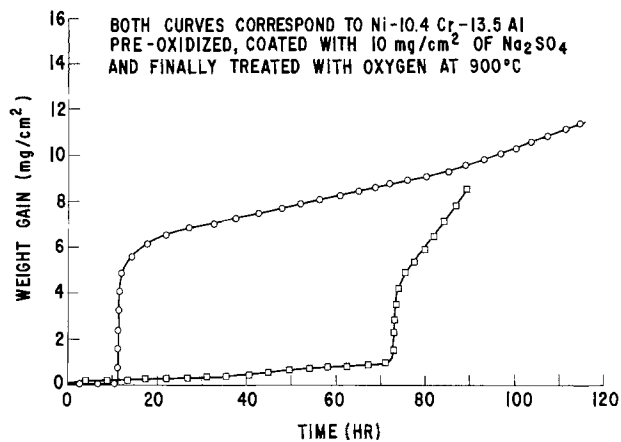


Fig. 19. Weight gain curves for two specimens of a Ni-10.4 Cr-13.5 Al alloy preoxidized, coated with 10 mg/cm^2 of Na_2SO_4 , and treated with oxygen at 900°C . An incubation period of varying length has preceded in both cases accelerated attack.

specimens may be responsible for the variation in the length of the incubation period prior to accelerated attack.

Figure 20 shows a Nomarski interference light micrograph of one of the specimens at the end of the run. The external scale was identified by x-ray diffraction as consisting of NiO and NiAl_2O_4 . As mentioned in the next section, internal precipitates of chromium sulfide can be noticed in the alloy surface layer, preferentially localized at the darker areas.

Cyclic conditions.—The effect of alternating oxidizing and reducing conditions was tested on the Ni-10.4 Cr-13.5 Al alloy by exposing to the sequence $\text{O}_2-\text{H}_2-\text{O}_2$ at 800°C a specimen preoxidized and coated with 5 mg/cm^2 of sodium sulfate. Figure 21 shows the corresponding changes in the weight gain curve. The weight loss due to the reduction of sodium sulfate by hydrogen is followed by an oxidation stage accelerated with respect to the initial one. The same experiment was repeated at 900°C and a similar weight gain curve was obtained. Figure 22 shows a cross section of the latter specimen. Again it can be noticed how the attack propagates preferentially at the darker γ' areas in the alloy, as mentioned in the previous section. Most probably, even at 800°C , a molten $\text{Na}_2\text{SO}_4-\text{Na}_2\text{S}$ film dissolved protective Al_2O_3 layers favoring sulfur penetration particularly at sites of higher grain boundary density. Subsequent oxidation resulted in the growth at a higher rate of a porous NiO scale. The microprobe trace in Fig. 23 shows that the external scale consists essentially of Ni and Cr oxides in its inner portion, while Al_2O_3 , which presumably formed at the very beginning of the run, also can be detected in its outer

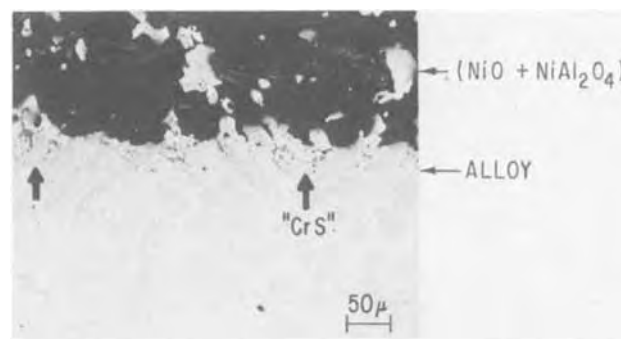


Fig. 20. Ni-10.4 Cr-13.5 Al alloy preoxidized, coated with 10 mg/cm^2 of Na_2SO_4 , and treated with oxygen at 900°C for about 4 days. A thick and porous scale consisting of NiO and NiAl_2O_4 has grown externally. The arrows indicate internal precipitates of chromium sulfide, localized preferentially at the darker phase within the alloy.

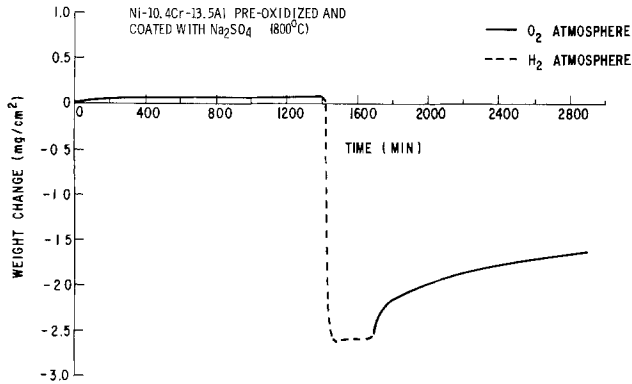


Fig. 21. Weight gain curve for a Ni-10.4 Cr-13.5 Al alloy pre-oxidized, coated with 5 mg/cm² of Na₂SO₄, and exposed alternately to oxidizing and reducing atmospheres at 900°C.

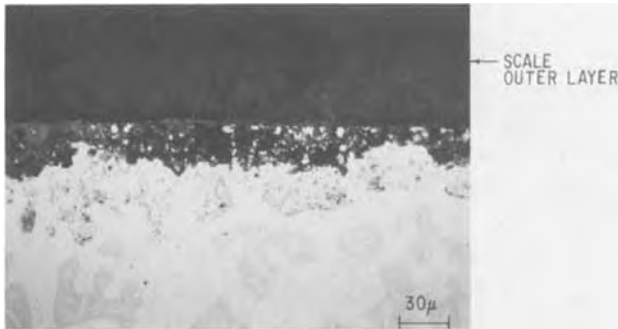


Fig. 22. Ni-10.4 Cr-13.5 Al alloy preoxidized, coated with 5 mg/cm² of Na₂SO₄, and treated at 900°C with the gas sequence O₂-H₂-O₂ for a total of 48 hr. Preferential attack can be noticed at the darker areas in the alloy.

portion. It may be noted that attack localized at the darker areas in the alloy was also observed when a specimen of Ni-10.4 Cr-13.5 Al coated with 16 mg/cm² of sodium sulfate was treated at ~870°C with a 10% CH₄-bal. N₂ mixture (Fig. 24). In this case, however,

methane instead of hydrogen acted as a reducing agent for sodium sulfate.

A comparison between the weight gain curve in Fig. 8 and Fig. 21 suggests that acceleration of the corrosion rate due to transient reducing conditions is more likely to occur when a multiphase system rather than a homogeneous γ matrix-type alloy is exposed to hot corrosion environments. A high density of preferential paths for the inward diffusion of sulfur appears to favor the formation of internal precipitates and consequent weakening of the alloy surface layer.

Discussion

In order to compare the behavior of the alloy phases that have been the object of this study, the discussion is divided into two sections pertaining, respectively, to the effect of reducing and oxidizing environments.

Reducing environments.—Reducing conditions, no matter whether the reducing agent is hydrogen, carbon, or partially uncombusted hydrocarbons (6), primarily result in increased sulfur potential at the metal-salt melt interface. Seen from a different standpoint, an increase in sulfur potential can occur when the composition of the salt melt is modified by the addition of elements such as molybdenum, tungsten, or vanadium (3). However, the magnitude of the effect can be different. While in the latter case fluxing of protective oxides is deemed responsible for catastrophic attack, the presence of reducing agents can both reduce oxide scales (22, 23) and by raising significantly the sulfur potential provide additional driving force for the diffusion of sulfur into the metal. If the activity of nickel in the alloy is sufficient to form continuously nickel sulfide, this will be in the molten state,⁴ thus further enhancing diffusion processes and fluxing of solid oxides such as NiO and Cr₂O₃.

In the course of this study the γ matrix phase showed a tendency to form liquid nickel sulfide whenever exposed to H₂S-H₂ atmospheres, regardless of the presence of a sodium sulfate deposit on the surface of the specimens. Furthermore, the existence of a pre-grown layer of Cr₂O₃ did not prevent the formation

⁴ The temperature of the eutectic nickel-nickel sulfide is 645°C.

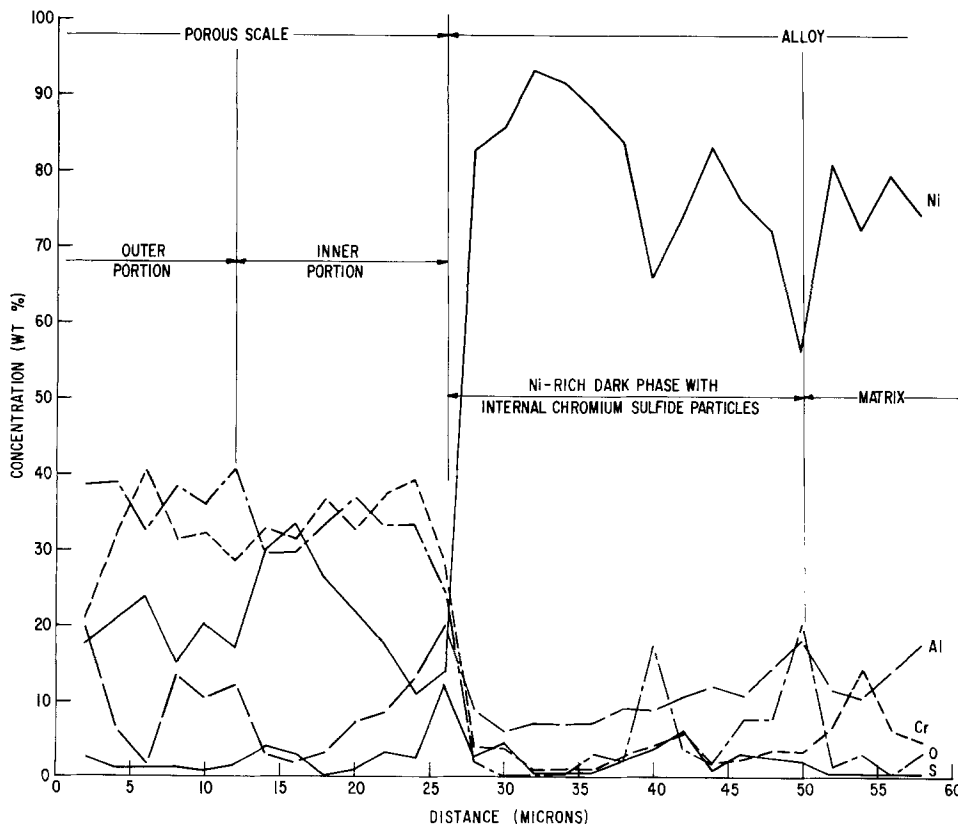


Fig. 23. Distribution profile of elements for a Ni-10.4 Cr-13.5 Al alloy preoxidized, coated with sodium sulfate, and exposed alternately to oxidizing and reducing atmospheres.

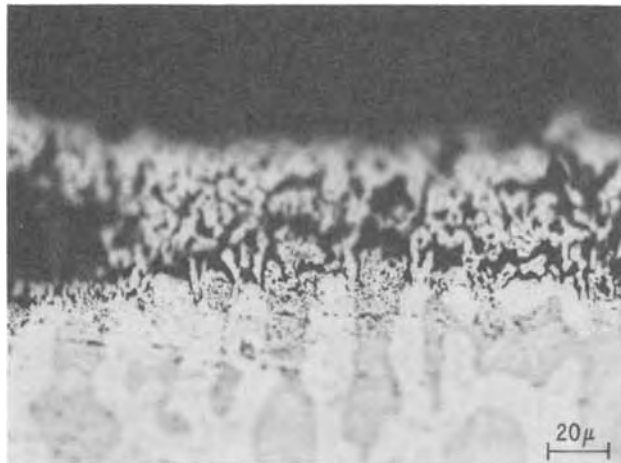


Fig. 24. Ni-10.4 Cr-13.5 Al alloy coated with 16 mg/cm² of Na₂SO₄ and treated with a 10% CH₄-N₂ gas mixture at 870°C for 3 hr. Localized attack can be noticed at the darker areas in the alloy.

of liquid nickel sulfide, but only increased the amount of time necessary for sulfur to diffuse through the chromium oxide barrier and reach the metal (24). Thus it appears that in a situation leading to local high sulfur potential the formation of liquid nickel sulfide is responsible for the catastrophic failure of the γ matrix phase.

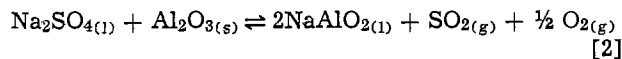
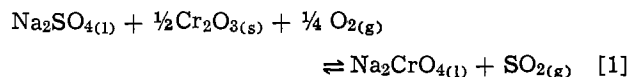
The results obtained in analogous conditions with specimens of nominal γ' composition exposed to H₂S-H₂ atmospheres show again the same tendency to form liquid nickel sulfide as the γ matrix, although to a lesser extent, as can be seen by comparing Fig. 3 and 10. Apparently, alloying the nickel with aluminum instead of chromium reduces the formation of liquid nickel sulfide. Since the activity of nickel in the γ matrix and the γ' phase are comparable (25, 26), we have not been able to find an explanation for this effect in thermodynamic terms.

It should be stressed that the extent of the corrosive attack for both γ matrix and γ' phases considered separately, bears a direct relationship to the magnitude of the sulfur potential continuously present at the metal-salt melt interface. The cyclic oxidation-reduction treatment of the γ matrix, in which the only sulfur available was that present in the limited sodium sulfate coating, did not lead to a significant acceleration of the reaction during the reduction and the subsequent oxidation stages. Of course, the presence of hydrogen sulfide in the gas phase in equilibrium with the salt melt would have resulted in a higher rate of attack during the reduction stage, by replenishing in the melt any sulfur consumed by the alloy.

When the γ matrix and the γ' phase are coexisting, as in the case of the Ni-10.4 Cr-13.5 Al alloy, the composition of the two phases can be different from the nominal composition, because to a limited extent aluminum can dissolve in the γ matrix and chromium in the γ' phase. Localized attack at γ' areas, characterized by the formation of internal chromium sulfide particles especially at higher sulfur potentials (Fig. 18, 22, and 24) can be due to segregation of chromium within the γ' areas, which by originating a higher grain boundary density would favor the inward diffusion of sulfur by a short-circuit mechanism. However, a detailed explanation of an alloy structure effect on hot corrosion would require systematic experiments, in particular on the $\gamma + \gamma'$ system at different γ/γ' volume ratios.

Oxidizing environments.—At very low sulfur potential, such as that present in stoichiometric sodium sulfate exposed to oxygen, the hot corrosion behavior of the γ matrix and the γ' phases is remarkably different. While the former appears to be extremely corrosion

resistant, the latter undergoes rapid attack in the initial stage of the reaction, followed by a progressive slowdown in corrosion rate. This behavior can be ascribed to a varying capability of the sodium sulfate melt to dissolve different oxides. From a thermodynamic standpoint, the composition of the gaseous atmosphere can influence the equilibria



since the corresponding equilibrium constants at a given temperature would be

$$K_{(1)} = P_{\text{SO}_2}/P_{\text{O}_2}^{1/4} \quad \text{and} \quad K_{(2)} = P_{\text{SO}_2} \times P_{\text{O}_2}^{1/2}$$

making the simplifying assumption that all condensed phases are at unit activity. Moreover, the rate of dissolution in the sodium sulfate melt may be different for Cr₂O₃ and Al₂O₃. In the case of the Ni-20 Cr alloy (γ matrix) formation of some sodium chromate took place during exposure to oxygen, as indicated by the presence of yellow deposits on the specimen at the end of the run. In this case reaction [1] was displaced toward the right by the absence of SO₂ in the gas phase. However, the rate of formation of new Cr₂O₃ was higher than its rate of dissolution in the molten salt, as shown by the presence of a continuous inner layer of Cr₂O₃ in the scale at the end of the run. In this case the outer layer of NiO may have also provided additional protection to the alloy. A similar composition for the oxide scale on Ni-Cr alloys has been reported by Giggins and Pettit (27).

In the case of the Ni-13 Al alloy (γ' phase) the porous oxide scale after oxidation in the presence of sodium sulfate deposits was identified as consisting mainly of NiO with traces of α -Al₂O₃. Pettit has reported that the oxidation product of a Ni-17 Al alloy at 1100°C in 0.1 atm oxygen consisted of a discontinuous layer of α -Al₂O₃ at the base of the scale, which consisted of NiO, NiAl₂O₄, and α -Al₂O₃ (28). Dissolution of the discontinuous Al₂O₃ layer in the melt would progressively deplete the alloy surface layer of aluminum, favoring the growth of a porous scale of NiO, which would eventually separate the salt film from the metal. In addition, saturation of the salt with corrosion products would decrease its effectiveness as a flux, thus slowing down the corrosion rate. It is conceivable that the initial phase of rapid attack would persist for a longer time, were a larger amount of sodium sulfate available for the dissolution of the oxide scale. The results of crucible tests shown in Fig. 7, in which Ni-Al coupons were immersed in excess molten sodium sulfate exposed to air, show that the γ' phase can indeed undergo total dissolution in the salt melt. By contrast the resistance of Ni-Cr alloys to this type of attack generally increases with increasing Cr content.

In the case of the Ni-10.4 Cr-13.5 Al alloy, in which the prevailing phases are γ matrix and γ' , the oxide scale formed at 900°C prior to exposure to sodium sulfate and oxygen was identified as a mixture of spinels NiAl₂O₄ and NiCr₂O₄. According to Giggins and Pettit (13) this ternary system at 1000°C should consist of only an external layer of Al₂O₃. Again, the rate of dissolution of the oxide scale in the salt melt can be the factor retarding accelerated attack of the alloy. In this case however, after fluxing of the oxide, the alloy microstructure may have favored inward diffusion of sulfur, thus making the alloy more susceptible to attack than the binary Ni-20 Cr alloy. This point of view is confirmed by the results of the experiments in which specimens were subjected alternatively to oxidizing and reducing conditions. In the case of the Ni-20 Cr alloy during the reduction stage the structure of the scale was not damaged extensively and could offer

protection against the increase in sulfur potential. The weight gain during the subsequent oxidation stage was then similar to the initial one. In the case of the Ni-10.4 Cr-13.5 Al alloy, the oxide scale was damaged by progressive dissolution in the salt melt during the initial oxidation stage. During the subsequent reduction stage diffusion of sulfur into the alloy was favored by the increase in sulfur potential. Sulfur diffusion may have also been enhanced by the microstructure of the alloy, if a higher density of grain boundaries was available at areas of γ' composition.

Conclusions

1. The hot corrosion resistance of an alloy is dependent on its chemistry and multiphase morphology, and the nature of the corrosive environment, in a very complex way, so that a generalized model for hot corrosion behavior is not yet possible.

2. The γ matrix phase is prone to catastrophic failure in severe hot corrosion environments characterized by high sulfur potentials. However, at low sulfur potentials such as those prevailing in a gas turbine environment, the γ matrix offers excellent corrosion resistance.

3. The γ' phase is susceptible to accelerated salt-induced hot corrosion under both reducing and oxidizing conditions. However, the comparison of weight gain data also shows that the γ' phase is much less resistant than the γ matrix to hot corrosion, under oxidizing conditions, and can be considered a weak link in the over-all corrosion process of a commercial Ni-base alloy.

4. Studies of (i) the rate of dissolution of Cr_2O_3 , Al_2O_3 , and spinel-type oxides in sodium sulfate melts, and (ii) alloy microstructure effects on the rate of sulfidation would significantly contribute to a better understanding of hot corrosion phenomena.

Acknowledgment

The authors are indebted to H. S. Spacil, C. S. Tedmon, Jr., R. E. Hanneman, and R. L. McCarron for useful discussion. The technical support of the Materials Characterization Operation staff of the General Electric R&D Center is also gratefully acknowledged. Part of this work was supported by the United States Department of Commerce under Contract No. 0-35510.

Manuscript received June 25, 1974.

Any discussion of this paper will appear in a Discussion Section to be published in the December 1975 JOURNAL. All discussions for the December 1975 Discussion Section should be submitted by Aug. 1, 1975.

Publication costs of this article were partially assisted by General Electric Company.

REFERENCES

1. "Hot Corrosion Problems Associated with Gas Turbines," ASTM Special Technical Publication No. 421 (1967).
2. J. Stringer, MCIC Report No. 72-08, Battelle-Columbus (1972).
3. J. A. Goebel, F. S. Pettit, and G. W. Goward, *Met. Trans.*, **4**, 261 (1973).
4. N. S. Bornstein and M. A. DeCrescente, *Corrosion*, **26**, 209 (1970).
5. A. M. Beltran and D. A. Shores, "Superalloys," C. T. Sims and W. C. Hagel, Editors, p. 317, John Wiley & Sons, Inc., New York (1972).
6. D. W. McKee and G. Romeo, *Met. Trans.*, **4**, 1877 (1973).
7. A. U. Seybolt, *Trans. AIME*, **242**, 1955 (1968).
8. A. U. Seybolt, General Electric Co., Corp. R&D Report No. 70-C-189 (1970).
9. D. W. McKee and G. Romeo, *Met. Trans.*, **5**, 1127 (1974).
10. D. W. McKee and G. Romeo, *ibid.*, In press (1975).
11. J. Billingham, J. Lauridsen, and R. E. Lawn, *Corrosion Sci.*, **13**, 623 (1973).
12. R. F. Decker and C. T. Sims, *Corrosion*, **26**, 33 (1970).
13. C. S. Giggins and F. S. Pettit, *This Journal*, **118**, 1782 (1971).
14. G. Romeo, E. Lifshin, M. F. Ciccarelli, and D. B. Sorensen, *Anal. Chem.*, **45**, 2444 (1973).
15. C. J. Bechtold and H. C. Vacher, *Trans. AIME*, **221**, 14 (1961).
16. G. Romeo and W. W. Smeltzer, *This Journal*, **119**, 1268 (1972).
17. F. Jellinek, *Acta Cryst.*, **10**, 620 (1957).
18. D. J. Young, W. W. Smeltzer, and J. S. Kirkaldy, *This Journal*, **120**, 1221 (1973).
19. R. W. Hardt, J. R. Gambino, and P. A. Bergman, in "Hot Corrosion Problems with Gas Turbines," ASTM Special Technical Publication No. 421, p. 64 (1967).
20. A. Taylor and R. W. Floyd, *J. Inst. Metals*, **81**, 451 (1952-1953).
21. J. D. H. Donnay and G. Donnay, Editors, "Crystal Data," 2nd ed., p. 955, American Crystal Association (1963).
22. S. K. Sharma, F. J. Vastola, and P. L. Walker, 10th Carbon Conference, Bethlehem, Pa., Paper No. RS-173 (1971).
23. W. L. Wheatfall, H. Doering, and G. J. Danek, Jr., in "Hot Corrosion Problems with Gas Turbines," ASTM Special Technical Publication No. 421, p. 206 (1967).
24. G. Romeo and H. S. Spacil, "High Temperature Gas-Metal Reactions in Mixed Environments," S. A. Jansson and Z. A. Foroulis, Editors, p. 299 TMS-AIME (1973).
25. R. Hultgren, R. L. Orr, P. D. Anderson, and K. K. Kelley, "Selected Values of Thermodynamic Properties of Metals and Alloys," p. 661, John Wiley & Sons, Inc., New York (1963).
26. R. E. Hanneman and A. U. Seybolt, *Trans. AIME*, **245**, 434 (1969).
27. C. S. Giggins and F. S. Pettit, *ibid.*, **245**, 2495 (1969).
28. F. S. Pettit, *ibid.*, **239**, 1296 (1967).
29. E. L. Simons, G. V. Browning, and H. A. Liebafsky, *Corrosion*, **11**, 505t (1955).

Electrochemical Reduction of Cr(III) in Molten LiCl-KCl Eutectic

Samuel C. Levy* and Frederick W. Reinhardt

Sandia Laboratories, Albuquerque, New Mexico 87115

ABSTRACT

The reduction of chromium(III) was studied in LiCl-KCl eutectic at 500°C by means of cyclic voltammetry. It has been shown to proceed via a two-step process to the metal. The intermediate Cr(II) species reacts with the solvent anions to form an insoluble compound, CrCl₂. The pseudo first-order rate constant for the chemical step is $0.028 \pm 0.008 \text{ sec}^{-1}$, while the heterogeneous rate constant for the charge transfer is $3.4 \pm 0.5 \times 10^{-2} \text{ cm sec}^{-1}$. The diffusion coefficient of Cr⁺³ was determined to be $0.5 \pm 0.1 \times 10^{-5} \text{ cm}^2/\text{sec}$ at 500°C. No adsorption of any species present in solution was found to occur on the vitreous carbon working electrode.

The lithium chloride-potassium chloride eutectic is one of the most commonly used electrolytes for thermal batteries (1). Thermal batteries developed at Sandia Laboratories principally use this electrolyte and a cathode (depolarizer) of calcium chromate (2). Although there has been much speculation as to the cathode mechanism, very little is known about this complex reduction. In order to gain an insight into the reactions occurring during the discharge of thermal batteries, we have begun a study of the electrochemical behavior of chromium in molten salts. This paper describes the results obtained with the compound CrCl₃ in LiCl-KCl at 500°C.

Experimental

The technique of cyclic voltammetry was used for this investigation. Voltammetric scans were made with a Tacussel Model PIT 20-2X potentiostat coupled to a Tacussel Model GSTP-2 function generator. The current voltage curves were recorded on a Moseley Model 7000 AM X-Y recorder.

The cell was fabricated from a 70-mm ID quartz 102/75 ball joint sealed on one end. The lid was made from the other half of the ball joint and had openings to accommodate three electrodes, a thermocouple, a gas bubbling tube, a gas inlet, and a tube for adding samples to the melt, which also served as the gas outlet.

A three-electrode circuit was used. The counter-electrode was a rod of Union Carbide spectroscopic grade graphite with one end immersed in the melt. The Ag/AgCl couple was chosen for the reference electrode because of its stability at elevated temperatures (3, 4). The reference electrode was prepared by placing 0.1M AgCl in LiCl-KCl solution in a Pyrex tube sealed at one end. A silver wire was then inserted through a hole in a cork placed into the other end. Use of Pyrex, which becomes conductive at elevated temperatures, as a container and electrolyte junction prevents contamination of the solution and results in an electrode that can be used many times.

Problems were encountered in fabricating the vitreous (glassy) carbon working electrode. All attempts to seal the rods in borosilicate glass resulted in a thin void between the glass and vitreous carbon. Use of these electrodes for cyclic voltammetric scans resulted in baselines having an appreciable slope, making it virtually impossible to analyze the waves. Finally, Beckwith Carbon Corporation, when contacted, suggested that a thin film of silicon deposited on the vitreous carbon would produce a welded bond with borosilicate glass.

Electrodes were fabricated from 1/8 in. diam rods which were centerless ground to a 0.120 in. diam circular cross section (area = 0.0729 cm²). One inch lengths were coated with a thin film (0.0005-0.005 in.) of silicon by decomposing silane on the carbon rod which was resistance heated (Fig. 1). A half-inch length of borosilicate glass (GSC-4) was then sealed to the coated rod by heating to the softening point. The end of the vitreous carbon rod protruding from the glass seal was force-fitted into a hole drilled into the end of a graphite rod. A Pyrex tube was then slipped over the graphite rod and sealed to the GSC-4 glass (5). A portion of the graphite rod was left extending as electrical contact. The vitreous carbon was ground flush with the glass and polished to a mirror finish (Fig. 2).

The electrolyte was prepared from Fisher certified reagent lithium chloride and potassium chloride. It was further purified by using a technique developed in this laboratory which is a combination of several techniques reported in the literature (6-8). Initially, the eutectic was heated under a hydrogen chloride atmosphere to 400°C. Hydrogen chloride was then bubbled through the melt for 24 hr. The temperature was then raised to 600°C and chlorine gas bubbled through the melt for 48 hr. Next, the temperature was lowered to 400°C and argon bubbled through the melt for 16 hr.

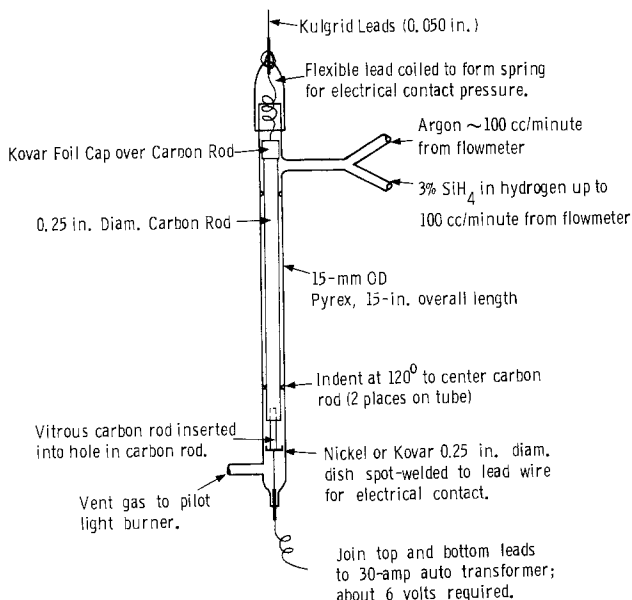


Fig. 1. Apparatus for silicon deposition

* Electrochemical Society Active Member.
Key words: chromium, molten salt, cyclic voltammetry.

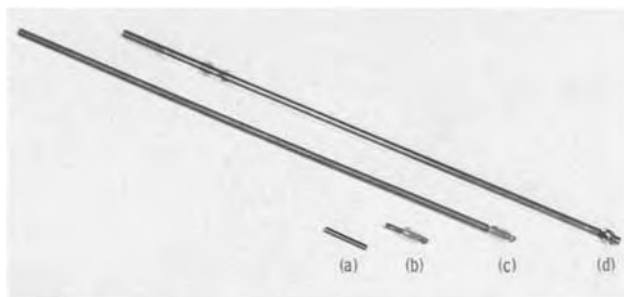


Fig. 2. Fabrication of vitreous carbon working electrode. (a) Vitreous carbon rod, (b) GSC-4 glass sealed to silicon-coated rod, (c) vitreous carbon inserted into hole in end of graphite rod, (d) completed electrode.

Finally, the electrolyte was cooled under an argon atmosphere and transferred to an argon-filled glove box.

Diamond Alkali Company anhydrous chromic chloride CrCl_3 was used without further purification.

The cell was assembled in an argon-filled glove box and then placed in a Hoskins furnace, Model FD104. Argon was continuously passed through the cell, and its temperature was maintained at 500°C with a Honeywell Versatronik SCR Trigger Temperature Controller, Model R7161J.

Results

Two reversible waves were obtained when scanning the LiCl-KCl-CrCl_3 system. They occurred at approximately $+0.2$ and -0.9V vs. the $\text{Ag}/0.1\text{M AgCl}$ reference electrode (Fig. 3 and 4). These potentials correspond to the reduction of Cr(III) to Cr(II) and of Cr(II) to Cr(0) (9). Each wave was studied individually at three concentrations of CrCl_3 (19.55, 32.29, and 40.55 mM) over a range of scan rates from approximately 0.008 to 0.8 V/sec .

$+0.2\text{V}$ peak.—For a reduction in which both the reactant and product are soluble, several relationships have been derived between the peak potential E_p (potential at maximum current), the half-peak potential $E_{p/2}$ (potential at one-half maximum current), the half-wave potential $E_{1/2}$ (occurs at a point 85.17% up wave), and n (the number of electrons involved in the

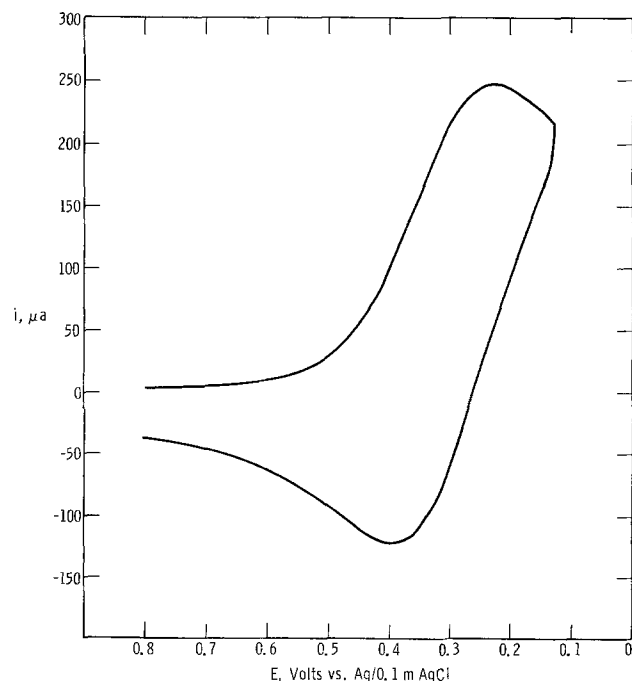


Fig. 3. Voltammogram for the reduction of Cr(III) to Cr(II) . 19.55 mM CrCl_3 , 0.1678 V/sec , 500°C .

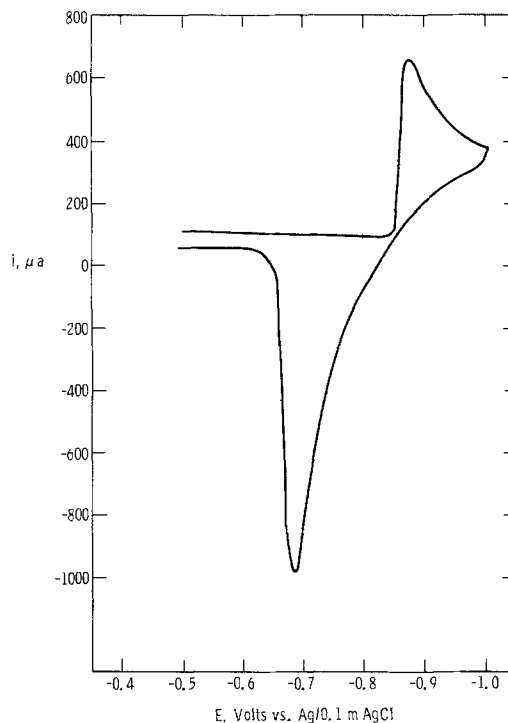


Fig. 4. Voltammogram for the reduction of Cr(II) to Cr(0) . 19.55 mM CrCl_3 , 0.0708 V/sec , 500°C .

charge transfer reaction) (10). They include the following

$$E_p = E_{1/2} - 1.109 RT/nF \quad [1]$$

$$E_{p/2} = E_{1/2} + 1.09 RT/nF \quad [2]$$

The value of n for this peak was calculated by both of the expressions at each sweep speed and concentration studied, using the values of E_p , $E_{p/2}$, and $E_{1/2}$ obtained from the individual current-voltage curves. The results are summarized in Table I.

We therefore conclude that one electron is transferred during this peak and that it represents the reduction of Cr(III) to Cr(II) .

Plots of peak current i_p vs. the square root of the voltage scan rate were linear at each concentration, indicating diffusion control for this process (11). A typical plot is shown in Fig. 5.

The diffusion coefficient of Cr^{+3} in LiCl-KCl at 500°C was calculated by use of the expression (12)

$$x = 1.67 \times 10^5 n^{3/2} A D^{1/2} C \quad [3]$$

In Eq. [3], n is the number of electrons transferred, A is the area of the electrode, D is the diffusion coefficient, C is the concentration, and x is the intercept at $v^{1/2} = 0$ of a plot of $i_p/v^{1/2}$ vs. $v^{1/2}$, i_p being the peak current and v the sweep speed in volts per second. Plots of $i_p/v^{1/2}$ vs. $v^{1/2}$ were made for each concentration studied and the intercepts determined by the method of least squares. Results are given in Table II.

To determine if the Cr^{+3} or Cr^{+2} species were adsorbed on the vitreous carbon electrode, plots of $i_p/v^{1/2}$ vs. v were constructed at each concentration. Since these graphs did not show a rapid increase with increasing scan rate, it was concluded that neither species was adsorbed (13).

Table I. Average value of n^* for $+0.2\text{V}$ peak

Concentration (mM)	Eq. [1]	Eq. [2]
19.55	1.01	0.99
32.29	0.99	1.04
40.55	1.03	1.00

* n average = 1.01 ± 0.02 .

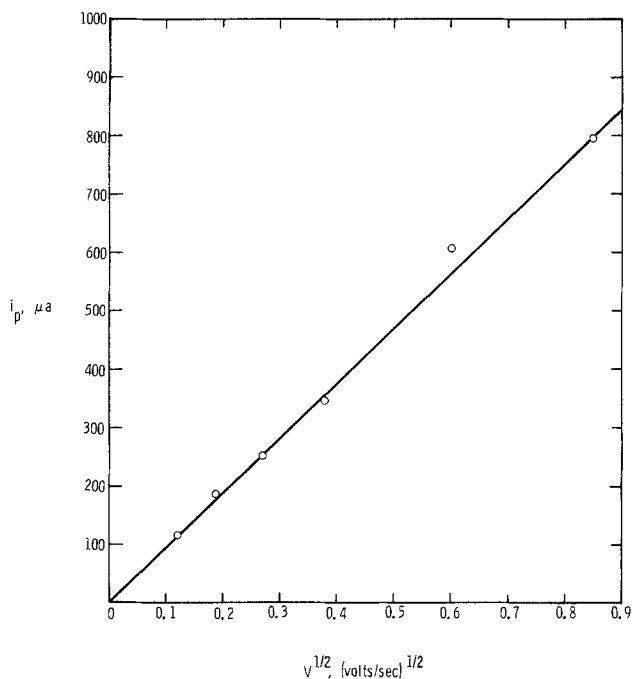


Fig. 5. Plot of i_p vs. $V^{1/2}$ for 32.29 mM CrCl_3

The diagnostic criteria of Nicholson and Shain (10) were used to determine the mechanism of the reaction $\text{Cr}^{+3} + e^- \rightleftharpoons \text{Cr}^{+2}$. First, the ratio of anodic to cathodic peak height i_a/i_c was calculated for each scan, using the empirical expression developed by Nicholson (14)

$$\frac{i_a}{i_c} = \frac{(i_a)_o}{(i_c)_o} + \frac{0.485 (i_{sp})_o}{(i_c)_o} + 0.086 \quad [4]$$

where $(i_a)_o$ and $(i_c)_o$ are the anodic and cathodic peak currents measured with respect to the zero current axis, and $(i_{sp})_o$ is the cathodic current at the switching potential (i.e., the potential at which the voltage scan is reversed) measured with respect to the zero current axis. The values of i_a/i_c were plotted vs. sweep speed (Fig. 6). An increase in this ratio with increasing sweep speed, leveling off at a value of 1.0, indicates the reversible charge transfer is followed by an irreversible chemical reaction. This behavior is caused by a difference in rates for the two reactions, the charge

Table II. Diffusion coefficient of Cr^{+3} in LiCl-KCl at 500°C

Concentration (mM)	$D^* \times 10^5 \text{ cm}^2/\text{sec}$
19.55	0.57
32.29	0.61
40.55	0.35

* D average = $0.5 \pm 0.1 \times 10^{-5} \text{ cm}^2/\text{sec}$.

Table III. Average value of k^* for reaction $\text{Cr}^{+2} + 2\text{Cl}^- \xrightarrow{k} \text{CrCl}_2$

Concentration (mM)	$k \text{ (sec}^{-1}\text{)}$
19.55	0.029
32.29	0.020
40.55	0.035

* k average = $0.028 \pm 0.008 \text{ sec}^{-1}$.

transfer being faster. At the slower sweep speeds, the reduced species, Cr^{+2} has time to react chemically before the scan is reversed and it can be reoxidized to Cr^{+3} . At faster speeds, all of the material is reoxidized before enough time has elapsed to allow the chemical reaction to proceed.

One possible irreversible chemical reaction which could occur in this system is the precipitation of CrCl_2 . To investigate this possibility, a saturated solution of CrCl_2 in LiCl-KCl was prepared at 500°C by adding excess solid to the melt and stirring for several hours by bubbling argon through the solution. It was then filtered through a fine glass frit at 500°C and the filtrate analyzed by atomic adsorption spectroscopy. A solubility of only 40 ppm (0.004%) was found. This indicates that the precipitation of CrCl_2 is very likely the irreversible chemical reaction that follows the reversible charge transfer.

A rate constant for the precipitation of CrCl_2 was calculated. Pseudo first-order kinetics were assumed since the Cr^{+2} is reacting with solvent anions. The rate constant k was determined for each scan from theoretical data giving the ratio of peak currents i_a/i_c as a function of $k\tau$, as calculated by Nicholson and Shain (10), where τ is defined as the time in seconds to go from the half-wave potential $E_{1/2}$ to the switching potential. Results are listed in Table III.

For waves having an anodic-to-cathodic peak current ratio of one, it is possible to calculate the hetero-

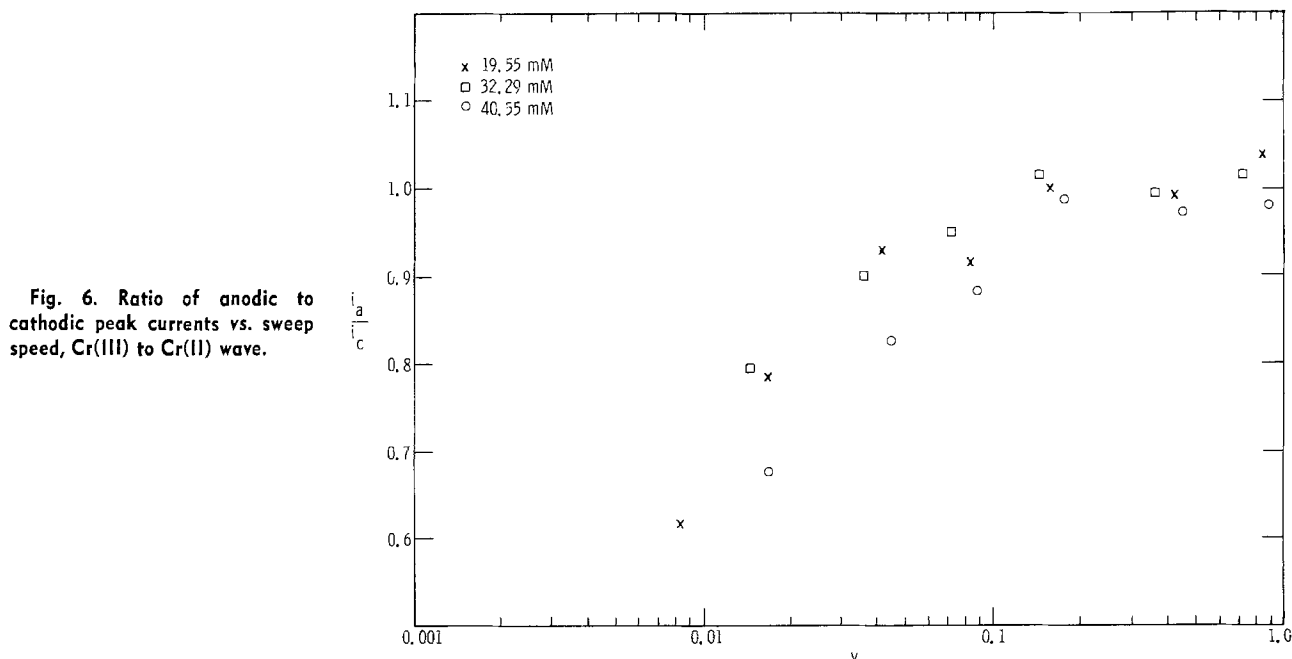


Fig. 6. Ratio of anodic to cathodic peak currents vs. sweep speed, Cr(III) to Cr(II) wave.

Table IV. Average value of k_h^* for reaction $\text{Cr}^{+3} + e^- \rightleftharpoons \text{Cr}^{+2}$

Concentration (mM)	$k_h \times 10^2 \text{ cm sec}^{-1}$
19.55	3.19
32.29	2.94
40.55	3.91

* k_h average = $3.4 \pm 0.5 \times 10^{-2} \text{ cm sec}^{-1}$.

geneous rate constant k_h for the charge transfer reaction, if the peak potential separation varies with the sweep speed. For the reaction $\text{Cr}^{+3} + e^- \rightleftharpoons \text{Cr}^{+2}$, a ratio of one was obtained for sweep speeds $>0.1 \text{ V/sec}$ (Fig. 6) and k_h was determined at these sweep speeds by the technique of Nicolson (15), using the following expression

$$\Psi = \gamma^\alpha k_h / \sqrt{\pi a D} \quad [5]$$

where α is the charge transfer coefficient, γ is the ratio of diffusion coefficients for the oxidized and reduced species [except for the unusual case of very large differences between D_o and D_R the quantity γ^α is very near unity, regardless of α (15)], $a = nFv/RT$, D is the diffusion coefficient of the oxidized species, and Ψ is dependent on the separation of the anodic and cathodic peak potentials for waves in which there is no competing chemical reactions (ratio of anodic to cathodic peak heights = 1). Data are given for the determination of Ψ from ΔE_p at 25°C .

Using the value of Ψ obtained from Nicholson's data corrected for temperature, and assuming $\gamma^\alpha = 1$, the heterogeneous rate constant was determined from each wave having $i_a/i_c = 1$. Results are given in Table IV. Use of this technique for the Cr^{+3} - Cr^{+2} system is discussed in a later section.

—0.9V peak.—For a reaction resulting in the deposition of a metal, several relationships between the number of electrons involved and voltage, current, and concentration have been derived (16, 17). These relationships, listed below, have been used to calculate the number of electrons transferred during the reaction represented by this peak

$$E_p - E_{p/2} = -0.7725 RT/nF \quad [6]$$

$$E_{p/2} = E^\circ + RT/nF \ln fC - \frac{0.0815 RT}{nF} \quad [7]$$

$$\log(i_p - i) = \frac{2.2 nF}{RT} E + \text{Constant} \quad [8]$$

Table V. Average value of n^* for —0.9V peak

Concentration (mM)	Eq. [6]	Eq. [8]
19.55	2.37	2.30
32.29	2.15	2.35
40.55	2.17	2.11

Volts/sec	Eq. [7]
0.007	2.02
0.036	1.91
0.071	2.25

* n average = 2.18 ± 0.15 .

where f is the activity coefficient and all the other symbols have their standard meanings. To use Eq. [7], a plot of $E_{p/2}$ vs. log concentration is required for each sweep speed. A straight line is obtained with a slope of $2.303 RT/nF$. Equation [8] assumes a constant activity of unity for the deposited metal, and was shown by Mamantov *et al.* (17) to be linear over the range of $0.7 i_p < i < 0.9 i_p$. This occurs because there is no metal present at the start of the wave. The activity is much smaller than unity and increases until the electrode is completely coated with the metal, resulting in the nonlinearity during the early portion of the wave (18). Values of n were calculated by each of the above methods. Slopes for Eq. [7] and [8] were calculated by the method of least squares. Results are given in Table V.

Thus, we conclude that $n = 2$, and this peak represents the reaction $\text{Cr}^{+2} + 2e^- \rightleftharpoons \text{Cr}^0$.

Plots of $i_p/v^{1/2}$ vs. v indicated that none of the species involved in this reaction are adsorbed on the vitreous carbon working electrode.

The mechanism of this reduction was studied by applying the diagnostic criteria of Nicolson and Shain (10). A plot of peak current divided by the square root of the voltage scan rate vs. voltage scan rate was relatively unchanged over the range of scan rates studied (Fig. 7), indicating a simple charge transfer with no coupled chemical reactions.

Discussion

Although the reaction $\text{Cr}^{+3} + e^- \rightleftharpoons \text{Cr}^{+2}$ appears to be completely reversible, as evidenced by the current-voltage curves obeying Eq. [1] and [2], it has in fact been shown to exhibit kinetic behavior. This can be

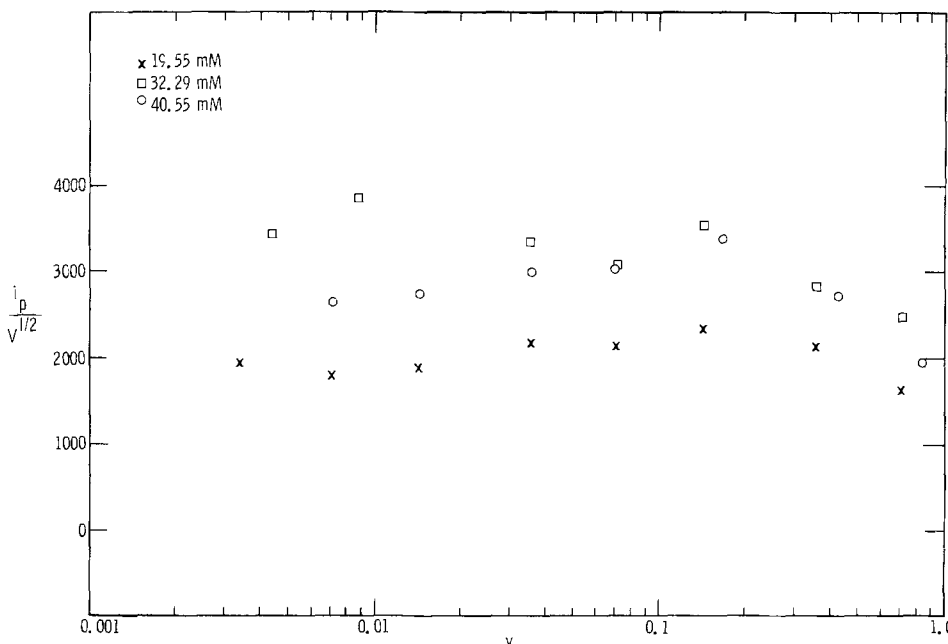
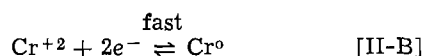
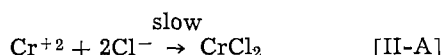
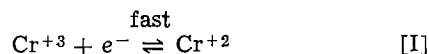


Fig. 7. Ratio of cathodic peak current to square root of sweep speed vs. sweep speed, Cr(II) to Cr(0) wave.

seen by the variation in peak potential separation with sweep speed. The heterogeneous rate constant calculated for this charge transfer reaction is fast enough that the deviation from reversibility is small. Thus, Eq. [1] and [2] are a close approximation for this system.

Conclusion

Chromium(III) is reduced to Cr(0) in LiCl-KCl eutectic at 500°C via a two-step process which is represented by the following scheme



If the potential is varied slowly enough, an appreciable portion of the Cr^{+2} will react with chloride ion via reaction [II-A]. Rapid changing of the potential, or maintaining the potential at a value negative to that required for reaction [II-B] will result in virtually all the Cr^{+3} being reduced to the metal, since this reaction is kinetically faster than the chemical one.

Acknowledgment

The authors are indebted to Dr. W. H. Smyrl and Dr. N. R. Armstrong for many helpful discussions during the course of this investigation. This work was supported by the United States Atomic Energy Commission.

Manuscript submitted Jan. 30, 1974; revised manuscript received Sept. 25, 1974. This was Paper 333 presented at the San Francisco, California, Meeting of the Society, May 12-17, 1974.

Any discussion of this paper will appear in a Discussion Section to be published in the December 1975 JOURNAL. All discussions for the December 1975 Discussion Section should be submitted by Aug. 1, 1975.

Publication costs of this article were partially assisted by Sandia Laboratories.

SYMBOLS

E_p	peak potential, V
$E_{p/2}$	half-peak potential, V
$E_{1/2}$	half-wave potential, V
n	number of electrons
R	gas constant, joules/° Kelvin-mole
T	temperature, ° Kelvin
F	Faraday's constant, coulombs/equivalent
i_p	peak current, μA
v	sweep speed, V/sec
x	intercept of a plot of $i_p/v^{1/2}$ vs. v

A	electrode area, cm^2
D	diffusion coefficient, cm^2/sec
C	concentration millimoles/liter (Eq. [3]), moles/liter (Eq. [7])
i_a	anodic peak current, μA
i_c	cathodic peak current, μA
$(i_a)_0$	anodic peak current with respect to the zero current axis, μA
$(i_c)_0$	cathodic peak current with respect to the zero current axis, μA
$(i_{sp})_0$	cathodic current at switching potential with respect to zero current axis, μA
τ	time to go from $E_{1/2}$ to switching potential, sec
k	pseudo first-order rate constant, sec^{-1}
k_h	heterogeneous rate constant for charge transfer reaction, cm/sec
γ	ratio of diffusion coefficients of oxidized and reduced species
α	charge transfer coefficient
a	nFv/RT
Ψ	a function, dependent on anodic and cathodic peak separations
f	activity coefficient
i	current, μA
E	potential, V

REFERENCES

1. C. W. Jennings, Sandia Laboratories, Albuquerque, New Mexico, SC-TM-70-829 (1971).
2. D. M. Bush, Sandia Laboratories, Albuquerque, New Mexico, SC-RR-69-497A (1972).
3. R. W. Laity, in "Reference Electrodes," D. J. G. Ives and G. J. Janz, Editors, Academic Press, New York (1961).
4. R. Littlewood, *Electrochim. Acta*, **3**, 270 (1961).
5. S. C. Levy and P. R. Farina, *Anal. Chem.*, To be published.
6. H. A. Laitinen, W. S. Ferguson, and R. A. Osteryoung, *This Journal*, **104**, 516 (1957).
7. J. B. Raynor, *Berichte der Bunsengesellschaft*, **67**, 360 (1963).
8. D. A. Nissen, Sandia Laboratories, Private communication.
9. J. A. Plambeck, *J. Chem. and Engr. Data*, **12**, 77 (1967).
10. R. S. Nicholson and I. Shain, *Anal. Chem.*, **36**, 706 (1964).
11. P. Delahay, "New Instrumental Methods in Electrochemistry," Interscience Publishers, New York (1954).
12. G. Mamantov and D. L. Manning, *J. Electroanal. Chem.*, **18**, 309 (1968).
13. R. H. Wopschall and I. Shain, *Anal. Chem.*, **39**, 1514 (1967).
14. R. S. Nicholson, *ibid.*, **38**, 1406 (1966).
15. R. S. Nicholson, *ibid.*, **37**, 1351 (1965).
16. W. K. Behl, *This Journal*, **118**, 889 (1971).
17. G. Mamantov, D. L. Manning, and J. M. Dale, *J. Electroanal. Chem.*, **9**, 253 (1965).
18. T. Berzins and P. Delahay, *J. Am. Chem. Soc.*, **75**, 555 (1953).

High Temperature Loss of Silica from Zircon and Refractory Silicates

R. A. Gardner¹

IBM System Products Division, East Fishkill Facility, Hopewell Junction, New York 12533

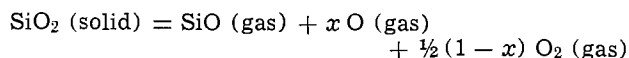
and R. C. Buchanan

IBM System Products Division, Kingston, New York 12401

ABSTRACT

Refractory silicates such as zircon, mullite, forsterite, etc. and silica are known to lose SiO₂ at high temperature and some, such as zircon, may undergo partial decomposition. This study examines some of the thermodynamic and kinetic factors which govern silicate stabilities. Sintering studies and weight loss determinations were used to determine the effects of temperature and ambient on the loss of SiO₂ from zircon. Results indicate the loss of SiO₂ as volatile SiO from zircon by a surface rate controlling mechanism. The major factors influencing this loss were found to be the oxygen partial pressure, temperature, and to some extent the particle size or surface area of the sample. Activation energies determined for the reaction of hydrogen with zircon were 82 kcal/mole for reaction with 99.999+ % H₂ containing 2 ppm H₂O and 121 kcal/mole for reaction with H₂ with a dew point of 24°C.

The importance of the loss of silica from solid silica and refractory silicates is evidenced by the number of investigations on this subject.² Silica can be lost from the surface of silica-containing materials by a number of mechanisms including direct volatilization of SiO₂ or reduction to form volatile silicon monoxide, SiO. The loss by direct volatilization involves, at least partially, the dissociation of silica according to a reaction such as



where x is the degree of dissociation of oxygen. Porter, Chupka, and Inghram (2) reported that the partial pressure of SiO over silica at 1900°K, for example, was 3.4×10^{-5} atm while the pressure of SiO₂ was only 1.0×10^{-7} atm. Under reducing conditions, the formation of SiO is even more dominant. A variety of reducing agents are capable of promoting the formation of SiO from silica or silicate materials. The most important of these are hydrogen, carbon, carbon monoxide, and silicon.

This study examines some of the thermodynamic and kinetic factors which govern silicate stabilities and loss of silica, particularly in reducing ambients. The kinetics and thermodynamics are discussed with emphasis on silica and zircon, ZrO₂·SiO₂.

Zircon Stability

The results of a number of investigations of the thermal stability of zircon are inconsistent in many cases. In a study of the phase relations in the ZrO₂-SiO₂ system, Zhirnova (3) determined the melting point of zircon to be 2430°C. The melting temperature, however, did not correspond to equilibrium conditions and had to be reached at a very high heating rate so that the decomposition at lower temperatures was not appreciable. Zhirnova did observe considerable decomposition at 1800°C. Zircon, however, does not have a true melting point; the compound melts by dissociation to its constituent oxides, zirconia and silica.

Striking differences exist in the literature as to the temperature of the onset of the dissociation. Dissociation temperatures as low as 1450°C and as high as

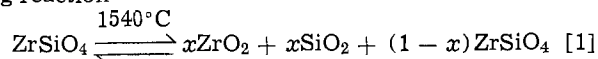
2000°C have been reported by Barlett (4) and by Matignon (5), respectively. Phase studies by Geller and Yavorsky (6) and by Geller and Lang (7) indicated dissociation at the incongruent melting temperature of 1775°C. The impurity content of the zircon samples can affect the dissociation temperature, as reported by Stott and Hilliard (8) who found that samples of 91.2% and 99.5% purity had dissociation temperatures of 1650°C and 1750°C, respectively. The addition of magnesia, MgO, to zircon can cause complete dissociation at 1240°C (9) with the formation of magnesium silicate and zirconium oxide.

The most detailed study of the thermal dissociation of zircon is that by Curtis and Sowman (10). In this study, the authors determined by x-ray diffraction the amount of dissociation present in zircon samples that had been heated for 2 hr at temperatures from 1540° to 1980°C in air and then quenched. The same procedure was followed for samples heated for 8 to 10 hr at temperatures of 1540°, 1650°, and 1760°C. They concluded that zircon begins to dissociate at approximately 1540°C, that the rate of dissociation increases rapidly as the temperature is increased to 1760°C, and that dissociation is complete after 6 hr at 1760°C.

Curtis and Sowman also concluded that the ZrO₂ and SiO₂ formed when zircon is dissociated at high temperatures, will recombine to again form zircon if some provision is made to prevent the loss of SiO₂ and if sufficient time is allowed during cooling. The maximum rate of reassociation occurred in the temperature range 1425°-1540°C. A similar result was obtained by Barlett (4) who found that zircon which had been completely dissociated reacted to form zircon again when heated for 3½ hr at 1450°C.

Chemical Reactivity of Silicates and Zircon

Most of the studies of the stability of zircon have been carried out in the presence of oxidizing atmospheres, under which condition zircon will decompose at temperatures above 1540°C according to the following reaction



A thermodynamic study of the formation of zircon from the oxides has been carried out by Matwejew and Agarkow (11). Extrapolation of their experimental data indicates that $\Delta G^\circ = 0$ at 1800°K (~1530°C), which is in good agreement with the ob-

¹ Present address: IBM General Products Division, San Jose, California 95193.

Key words: zircon, kinetics, silica, silicate, reduction.

² See, for example, the review by Toropov and Barzakovskii in Ref. (1).

servations of Curtis and Sowman. One can also estimate the dissociation temperature using the Gibbs-Helmholtz equation.

Using values of the enthalpies and entropies from thermodynamic tables (12, 13), the equation becomes

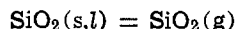
$$\Delta G^\circ = 15,360 - 8.48T \quad (1750^\circ - 1850^\circ \text{K})$$

so that

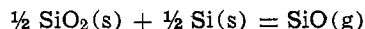
$$T = 1811^\circ \text{K} \text{ when } \Delta G^\circ = 0$$

Silica can be lost from the surface of pure silica, zircon or any refractory silicate by one or a combination of the following reactions:

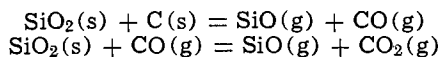
1. Vaporization



2. Silicon reduction



3. Carbon or carbon monoxide reduction



4. Hydrogen reduction



For the vaporization reaction the equilibrium vapor pressure is given by

$$\log P_{\text{SiO}_2} = -\Delta G^\circ / RT$$

where

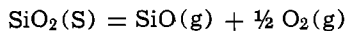
$$\Delta G^\circ = 127,200 - 36.0T^{(1)}$$

In cases where SiO_2 is part of a combined condensed phase, as in $\text{ZrO}_2 \cdot \text{SiO}_2$, then

$$P_{\text{SiO}_2}(\text{ZrO}_2 \cdot \text{SiO}_2) = a_{\text{SiO}_2} \cdot P_{\text{SiO}_2}(\text{SiO}_2, s, l)$$

a_{SiO_2} represents the activity of SiO_2 in the condensed phase.

The basic equation for reduction of silica by gaseous species such as hydrogen or carbon monoxide is



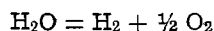
For this reaction

$$\log P_{\text{SiO}} = -\frac{\Delta G^\circ}{RT} - 0.5 \log P_{\text{O}_2}$$

and in a condensed phase, such as zircon

$$P_{\text{SiO}}(\text{ZrO}_2 \cdot \text{SiO}_2) = a_{\text{SiO}_2} \cdot P_{\text{SiO}}(\text{SiO}_2)$$

The partial pressure of the silicon monoxide thus depends on the activity of the silica in the condensed phase and on the oxygen partial pressure. Convenient methods for controlling the oxygen partial pressure are by controlling the ratios of hydrogen to water vapor and of carbon monoxide to carbon dioxide according to the equilibria



and

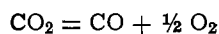


Figure 1 presents a thermochemical diagram for the Si-O system at 1800°K according to the method described by Kellogg (14) and by Gulbransen and Jansson (15). These diagrams are constructed such that the stability of condensed phases and the equilibrium pressures of the gaseous species can be read directly. The ordinates give the partial vapor pressures of the different gaseous species on a logarithmic scale. The dew points of particular $\text{H}_2/\text{H}_2\text{O}$ combinations are shown on the lower abscissa. The vertical line in the diagram separates the liquid and solid phases. The diagram clearly shows the effect of changes in the partial pressure of oxygen on the partial pressures of the SiO and SiO_2 phases.

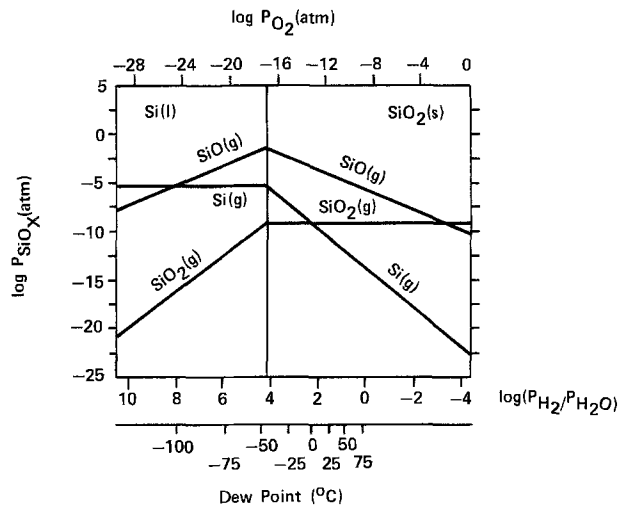


Fig. 1. Thermochemical diagram for the Si-O system at 1800°K

The reduction of SiO_2 by silicon has been extensively studied (16-22). Indeed, much of the thermodynamic data regarding reactions involving silicon monoxide has come from studies of this reaction. The evolution of SiO resulting from the reduction of SiO_2 by silicon is even more pronounced than reduction by hydrogen vapor as shown in Fig. 2 (after Toropov and Barzakovskii). This indicates that under conditions of reduction with hydrogen, the formation of SiO is more favorable than formation of Si.

Humphrey *et al.* (22) studied the reduction of SiO_2 by carbon with the results shown in Fig. 3a. It is seen that carbon is an extremely good reducing agent especially above 1400°C. Meyer (23) also found carbon to be an aggressive reducing agent; some of his results are shown in Fig. 3b. In the cases studied by Meyer and others (24, 25) it appears that the reduction of SiO_2 occurs whether or not the SiO_2 is present in the free state or in a chemically bound state, as in zircon or mullite, $3\text{Al}_2\text{O}_3 \cdot 2\text{SiO}_2$.

Kinetics of Silica Reduction

The rate of silica loss in reducing atmospheres has been studied by Schwerdtfeger (26), Crowley (27, 28) and more recently, by Gardner (29). Schwerdtfeger and Crowley determined the rate of silica loss by weighing fused quartz spheres and silica containing samples, respectively, before and after heat-treatment in reducing atmospheres, and they concluded that the rate of reduction in hydrogen is controlled by convective diffusion or mass-transfer from the reacting surface. This conclusion was based on the dependence of the rate of weight loss on hydrogen flow rates. The

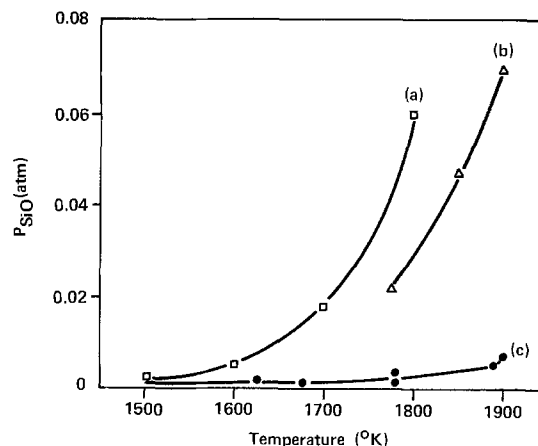


Fig. 2. Partial pressure of SiO as a function of temperature for (a) $\text{SiO}_2 + \text{Si}$ and (b) and (c) $\text{SiO}_2 + \text{H}_2$ according to the data of various authors (see Toropov and Barzakovskii).

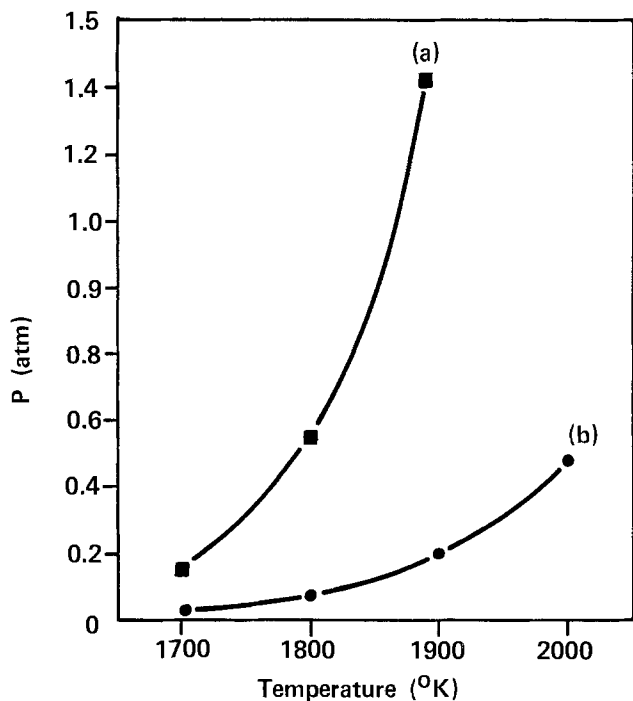


Fig. 3a. Partial pressure of (a) CO and (b) SiO as a function of temperature for decomposition of SiO₂ by Si and C. (a) P_{SiO} for the reaction $\frac{1}{2} \text{SiO}_2(\text{s}) + \frac{1}{2} \text{Si}(\text{l}) \rightarrow \text{SiO}(\text{g})$; (b) P_{CO} for the reaction $\text{SiO}_2 + \text{C}(\text{graphite}) \rightarrow \text{SiO}(\text{g}) + \text{CO}(\text{g})$ with the condition that P_{SiO} is fixed by the reaction $\frac{1}{2} \text{SiO}_2(\text{s}) + \frac{1}{2} \text{Si}(\text{l}) \rightarrow \text{SiO}(\text{g})$. [According to data of Humphrey (22)].

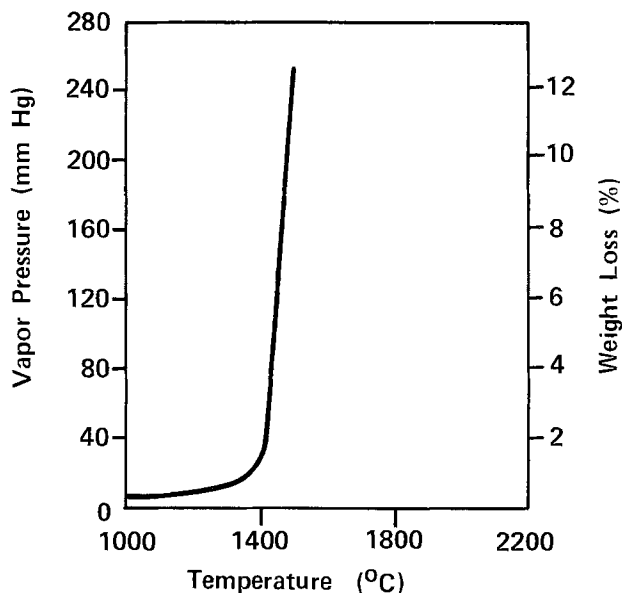


Fig. 3b. Vapor pressure of a mixture of graphite with quartz as a function of temperature [after Meyer (23)].

agreement between the theoretical and experimental rates, however, was not exact. Gardner has shown using a high temperature thermalgravimetric procedure that the rate of silica reduction in hydrogen closely obeys equations deduced on the basis of a reaction interface contracting inward from the sample surface. The velocity of the moving interface was found to depend primarily on temperature and the water vapor content of the ambient gas. The surface area of the reacting sample was also shown to be a factor in determining the rate of reduction.

Energy considerations have shown that for silicates in general there will be a significant driving force for reduction of SiO₂ to SiO and that the partial pressure of the silicon monoxide depends on several factors; the most important of these factors are temperature, the

activity of the SiO₂, and the partial pressure of oxygen (dew point in H₂/H₂O gas mixtures). Kinetic factors include temperature, oxygen partial pressure, surface area and, to some extent, the atmosphere flow rate.

Experimental

Kinetic studies were carried out using a high-temperature thermal gravimetric apparatus that has been described in detail elsewhere (29, 31). The apparatus used was a graphite-element furnace containing a high-purity aluminum oxide muffle and was capable of operating at temperatures up to 1700°C. A Cahn Model RG electrobalance was mounted above the furnace. The sample was contained in a molybdenum basket and suspended in the hot zone using a molybdenum wire. The system was purged before use with argon. Hydrogen with a purity of 99.999+ % and containing 2 ppm water vapor, as determined with a Beckman Trace Moisture Analyzer, was used as the reaction gas. The hydrogen flow rate was maintained at 1 cfh for experiments using water-saturated hydrogen (wet hydrogen) and at 4-5 cfh for experiments in non-saturated hydrogen (dry hydrogen). The low flow rate in wet hydrogen was used to ensure that the gas was saturated with water vapor. The dew point of the reaction gas was checked at the entrance to the furnace using a dew point hygrometer. The dew point in all the wet hydrogen experiments was 24°C. The range of the hygrometer was not broad enough to permit measurement of the dew point of the dry hydrogen.

The electrobalance used for the dynamic weight determinations was calibrated before each kinetic run with the empty sample basket and hangdown wire attached. The system was purged first with argon for 5-10 min and then with hydrogen for a minimum of 30 min prior to turning on power to the furnace. During the heating portion of the cycle, the gas was passed through a water bubbler at room temperature to saturate the gas. This was done to minimize the reduction of the zircon before the isothermal reaction temperature was reached. The furnace reached the preselected reaction temperature in approximately 40 min during which time the extent of reaction was generally less than 0.02% depending on the desired reaction temperature. Dry hydrogen was admitted when the desired temperature was reached and the reaction was allowed to proceed isothermally. Zero time was taken as the point when conditions become isothermal.

The zircon powder used for the kinetic studies was Zircopax from the TAM Division of National Lead Company. This powder has a mean particle size of 1.3 μm. Sample sizes were 100 ± 10 mg.

The samples used to evaluate the effects of hydrogen on the sintering of zircon had particle sizes of <1, 1.5, and 6 μm. These samples were from M&T Chemicals, Incorporated. The samples were prepared for sintering by mixing with solvents and a plasticized organic resin and then casting into 0.007 in. thick sheets by a conventional doctor-blade process. Ten sheets were laminated together and sintering samples were punched from the laminated stocks. The densities of the unfired samples were generally 2.35-2.45 g/cm³. The samples were then sintered for 3 hr at maximum temperature (see Fig. 9 and 10) in a molybdenum-element, elevator-hearth type furnace with a hydrogen ambient. The dew point of the hydrogen was maintained at approximately 25°C.

The sintered samples were polished by conventional methods and optical micrographs were prepared. Samples were also examined by x-ray diffraction using Cu K_α radiation; surface and bulk compositions were determined.

Ultraviolet spectroscopic analysis results for the zircon powders used are shown in Table I. Although no kinetic experiments were carried out with the M&T zircon powders, kinetic results would not be expected to be qualitatively different from those obtained with the TAM zircon powder.

Table I. U.V. spectroscopic analysis*

	Al	B	Ca	Cr	Fe	Ga	Mg	Mn	Na	Ni	Pb	V	Tl
M&T Milltrox	L	N.D.	0.05	N.D.	0.05	N.D.	0.003	0.001	<0.1	0.005	0.005	N.D.	0.1
M&T Ultrox 500	L	0.001	0.05	N.D.	0.05	N.D.	0.005	0.001	<0.1	0.005	0.005	N.D.	0.1
M&T Ultrox 1000	L	0.001	0.05	N.D.	0.05	N.D.	0.005	0.001	<0.1	0.005	0.005	N.D.	0.1
TAM Zircopax	L	0.001	0.05	0.001	0.03	N.D.	0.02	0.001	<0.1	0.003	0.005	0.001	0.1

* In weight per cent.
N.D. = not detected.
L = 0.1-1.0%.

Treatment of Kinetic Data

Kinetic data were treated according to the method described by Hancock and Sharp (30). The method involves preparation of plots of $\ln[-\ln(1-\alpha)]$ vs. \ln time (where α is the fraction reacted at time t) in order to determine the mechanism of the reaction. The slopes of such plots are diagnostic of the mechanisms of reactions which obey a number of solid-state kinetic equations. Determination of the slope, m , of $\ln[-\ln(1-\alpha)]$ vs. \ln time leads to identification of a function $f(\alpha) = kt$. When the function was identified which best fit the kinetic data, plots of $f(\alpha)$ vs. time were prepared and the rate constants, k , were determined from the slopes.

The fraction reacted, α , was determined by monitoring the weight of the reacting sample on a strip chart recorder running at a constant speed and comparing the weight at time t to the initial weight. The fraction reacted was calculated for zircon on the basis of the initial silica content and not on the total weight of zircon initially present.

Results and Discussion

Figures 4 and 5 present kinetic data in the form of $\ln[-\ln(1-\alpha)]$ vs. \ln time (hereafter referred to as "mechanism curves") for zircon samples reacted in "dry" hydrogen (i.e., pure hydrogen with no added water vapor) and "wet" hydrogen with a dew point of 24°C. The average slope for samples reacted in dry hydrogen is 1.18. This value is between the values of 1.07 or 1.11 and 1.24 expected for equations based on interface controlled reactions and zero order reactions, respectively. An interesting feature of the curves in Fig. 4 is that after the reaction reaches approximately 60% completion, the slopes of the curves begin to increase. The increase in slope is likely due to a contribution to the reaction mechanism of nuclei growth and interference phenomena during the later stages of the reaction.

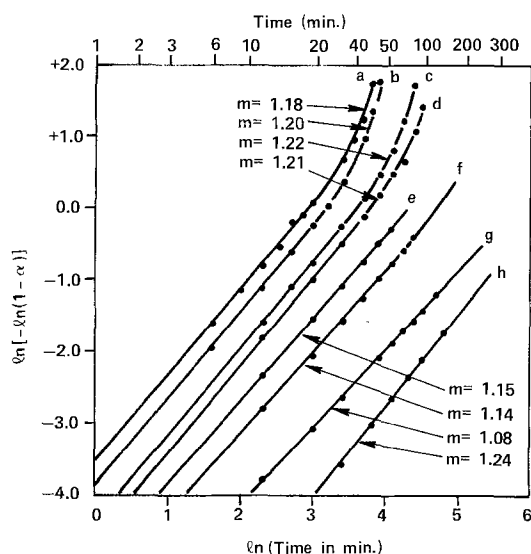


Fig. 4. Plots of $\ln[-\ln(1-\alpha)]$ vs. \ln time for zircon powder reacted in dry hydrogen. a, 1625°C; b, 1598°C; c, 1578°C; d, 1552°C; e, 1520°C; f, 1490°C; g, 1405°C; h, 136°C.

Figure 5 shows that slopes of mechanism curves for samples in wet hydrogen are considerably less than for samples reacted in dry hydrogen. The average value of 0.88 falls between the values of 1.07 or 1.11 expected for interface controlled reaction and 0.5-0.6 for diffusion controlled reactions. This probably indicates at least a partial dependence on diffusion phenomena. The reaction is primarily controlled by the movement of a reacting interface but it is possible that the reacting species may have to diffuse through a hydrated surface layer.

Previous studies of the kinetics of reduction of pure silica in hydrogen have shown that the reaction of SiO_2 with hydrogen closely obeys equations for the movement of a reacting interface. On the basis of the similarity of the reaction of hydrogen with pure silica, zircon, and other refractory silicates, the equation chosen to describe the kinetics of zircon reduction is the equation for phase-boundary controlled reactions.

For a sphere of radius r which reacts from the surface inward and where the reaction is controlled by the movement of the reaction interface at a constant velocity μ , the reaction can be described by

$$R_3(\alpha) = [1 - (1 - \alpha)^{1/3}] = (\mu/r)t$$

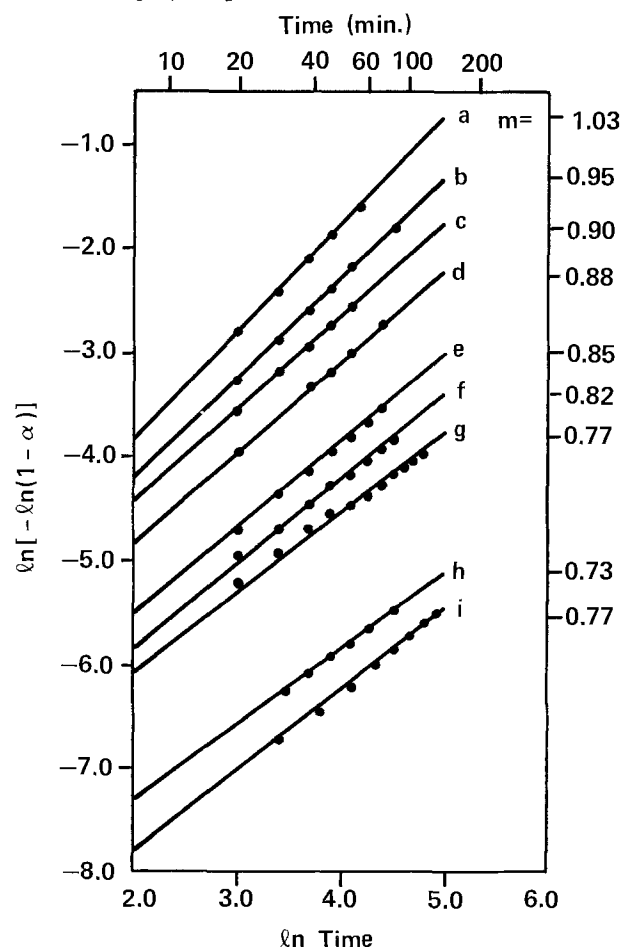


Fig. 5. Plots of $\ln[-\ln(1-\alpha)]$ vs. \ln time for zircon powder reacted in wet hydrogen (dew point = 24°C). a, 1625°C; b, 1598°C; c, 1578°C; d, 1552°C; e, 1520°C; f, 1490°C; g, 1445°C; h, 1405°C; i, 1360°C.

Plots of $R_3(\alpha)$ vs. time will be linear with a slope of (μ/r) if this equation effectively describes a particular reaction. Figures 6 and 7 present plots of $R_3(\alpha)$ vs. time for zircon samples reacted in dry and wet hydrogen, respectively. As can be seen from the figures, the plots are linear when the fraction reacted is less than approximately 0.60. This indicates fairly good

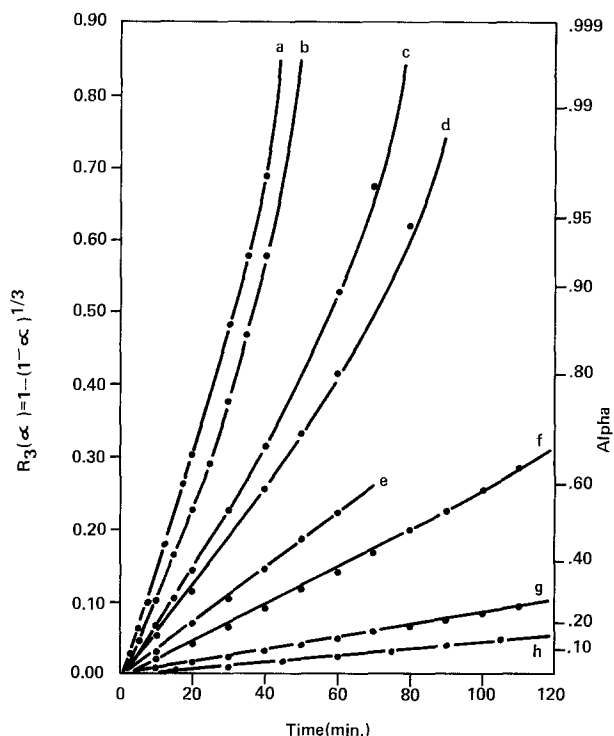


Fig. 6. $R_3(\alpha)$ vs. time for zircon powder reacted in dry hydrogen a, 1625°C; b, 1598°C; c, 1578°C; d, 1552°C; e, 1520°C; f, 1490°C; g, 1405°C; h, 1360°C.

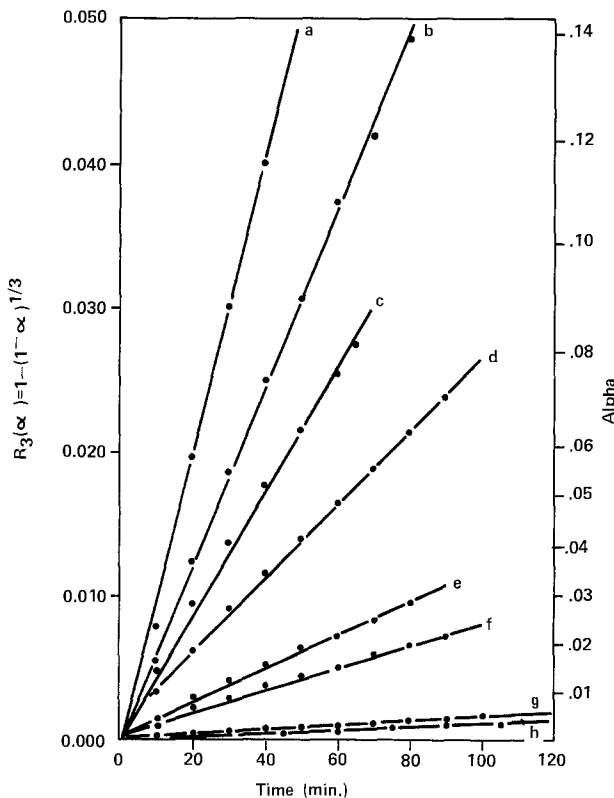


Fig. 7. $R_3(\alpha)$ vs. time for zircon powder reacted in wet hydrogen (dew point = 24°C). a, 1625°C; b, 1598°C; c, 1578°C; d, 1552°C; e, 1520°C; f, 1490°C; g, 1405°C; h, 1360°C.

agreement with the theoretical equation. The nonlinearity as the reaction proceeds toward near completion is likely due to the effect of nuclei growth and interference.

Arrhenius plots of the reaction rates vs. temperature are shown in Fig. 8, for zircon samples reacted in pure (dry) hydrogen and hydrogen saturated with water vapor. The activation energies are 82 and 121 kcal/mole for dry and wet hydrogen, respectively. The figure shows that the activation energies are constant throughout the temperature range studied (1360°-1630°C). The fact that zircon decomposes at about 1500°-1530°C to yield ZrO_2 and SiO_2 does not change the activation energy of the reaction of hydrogen with the silica. This indicates that the greatest energy barrier for the reaction is the energy required to break the silicon-oxygen bonds.

A previous study (28) has shown that the activation energies for the reduction of pure silica by dry and wet hydrogen were 85 and 135 kcal/mole, respectively. The observed value of 82 kcal/mole for reduction of silica in zircon is essentially the same as that for the reduction of pure silica. The lower observed value of 121 kcal/mole for reduction of zircon by wet hydrogen compared to the value of 135 kcal/mole for reduction of pure silica is probably due to the slightly lower affinity of the zircon surface for water compared to that of the pure silica surface.

The rates of reaction are slightly higher for the zircon powder studied than those observed for crystalline quartz. The rate of reduction of zircon in dry

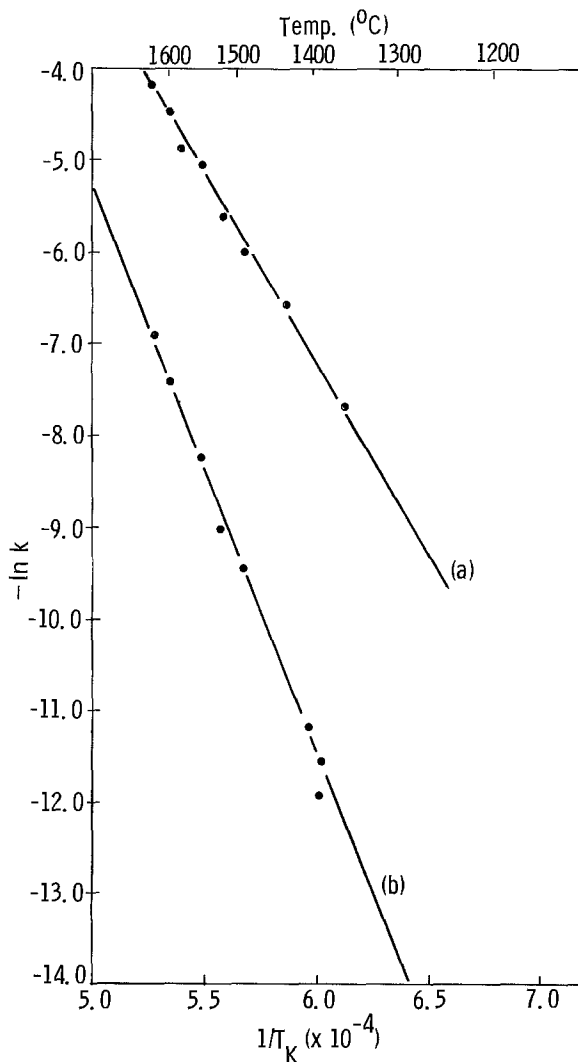


Fig. 8. Arrhenius diagram for calculation of activation energy. (a) Samples reacted in dry hydrogen; (b) samples reacted in wet hydrogen (dew point = 24°C).

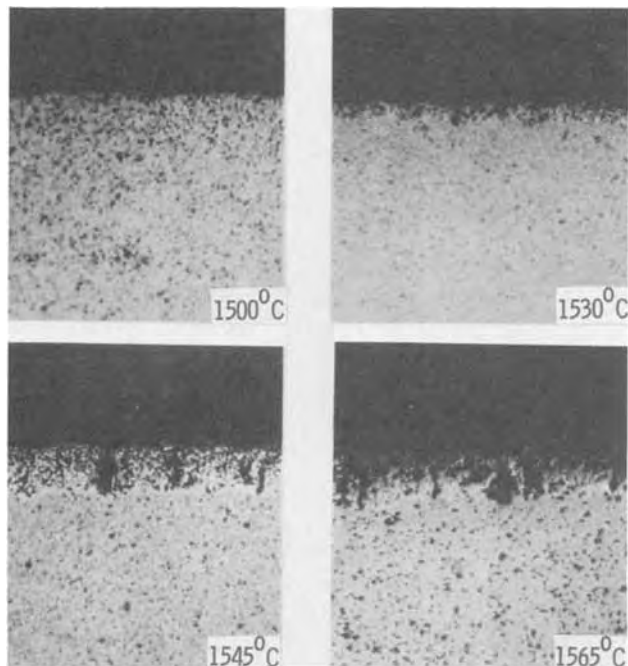


Fig. 9. Effect of hydrogen sintering temperature on surface decomposition for 1.5 μm zircon powder.

hydrogen at 1360°C, for example, is $4.62 \times 10^{-4} \text{ min}^{-1}$ while the observed rate for crystalline quartz powder was $3.63 \times 10^{-4} \text{ min}^{-1}$ (28). This relatively small difference in rate (in light of changes of several orders of magnitude with temperature) is most likely due to the difference in the surface areas of the powder samples.³

The previous discussion has been directed at elucidation of the reaction mechanism on a submicroscopic scale. Figure 9, however, presents photographs of zircon samples sintered in wet hydrogen (dew point $\cong 25^\circ\text{C}$) at various temperatures and these photographs show a reaction interface even on the microscopic scale. X-ray diffraction of the zircon samples shows the presence of monoclinic ZrO_2 on the surface of the samples when the sintering temperature is 1530°C or above. The ZrO_2 surface appears white in the photomicrographs of Fig. 9. The micrographs indicate that the zirconia surface is very porous. The actual reaction interface can be distinguished as the boundary between the white porous surface and the bulk of the sample.

Figure 10 shows the effect of particle size on the sintering of zircon and on hydrogen reduction. The samples were all sintered at 1545°C for 3 hr and the

³ The quartz powder used in that study was -325 mesh with a surface area of 1.3 m^2/g .

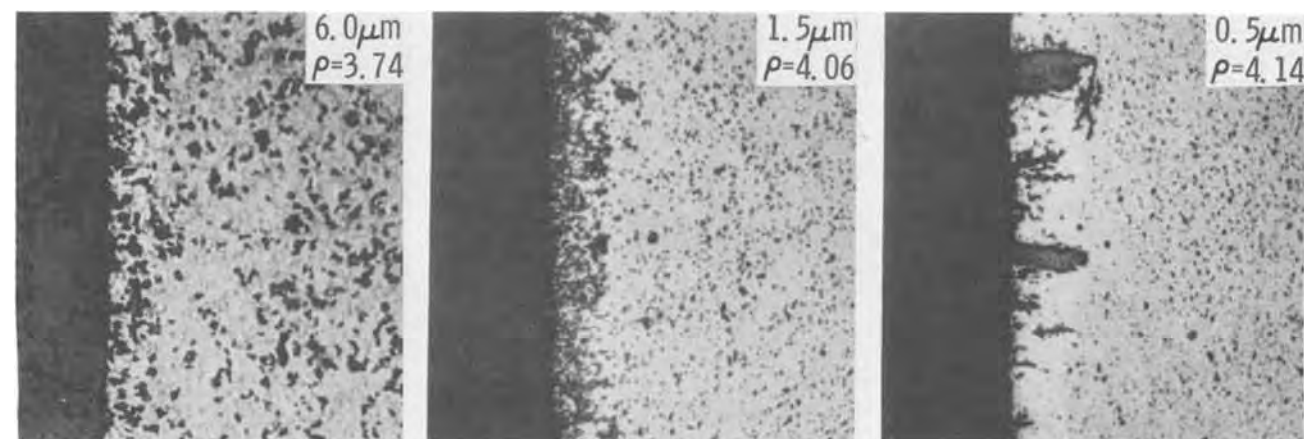


Fig. 10. Effect of particle size on decomposition at 1545°C in hydrogen

extent of the reduction is similar in each case. The ZrO_2 surface is clearly evident in the sample prepared from 0.5 μm zircon powder. In this case the ZrO_2 is fairly dense compared to the other samples except for some very large pores. Samples prepared from the 6.0 μm powder showed a zirconium dioxide surface as well as some internal ZrO_2 . The hydrogen gas apparently is able to easily diffuse through the porous zircon sample.

A practical result of these studies is the recognition of the fact that, in order to effectively sinter zircon in reducing atmospheres, the particle size of the zircon powder should be chosen to permit sintering at or below approximately 1500°C. Otherwise, considerable reduction can take place and prevent further sintering.

Conclusion

The rate of loss of silica from zircon surfaces by reduction in hydrogen has been shown to closely obey a function of α based on a model of a reaction interface contracting inward from the surface of the sample. The model, however, does not hold for the complete reaction. The reaction mechanism begins to change when approximately 60% of the available silica has been removed; above 60% reaction nuclei growth and interference phenomena become important. There is a difference in the reaction path when hydrogen containing water vapor is used as the ambient. This is evidenced by a change in the activation energy for reduction from 82 kcal/mole in dry hydrogen to 121 kcal/mole for reduction in hydrogen with a dew point of 24°C. This difference is likely due to adsorption of water on the zircon surface.

Manuscript submitted May 8, 1974; revised manuscript received Sept. 13, 1974.

Any discussion of this paper will appear in a Discussion Section to be published in the December 1975 JOURNAL. All discussions for the December 1975 Discussion Section should be submitted by Aug. 1, 1975.

Publication costs of this article were partially assisted by the IBM Corporation.

REFERENCES

1. N. Toropov and V. Barzakovskii, "High Temperature Chemistry of Silicates and Other Oxides," Special Report, Consultants Bureau, New York (1966).
2. R. F. Porter, W. A. Chupka, and M. G. Inghram, *J. Chem. Phys.*, **23**, 216 (1955).
3. N. Zhirnova, *Z. Anorg. Allgem. Chem.*, **218**, 193 (1934).
4. H. B. Barlett, *J. Am. Ceram. Soc.*, **14**, 837 (1931).
5. C. Matignon, *Compt. Rend.*, **177**, 1290 (1923).
6. R. F. Geller and P. J. Yavorsky, *J. Res. Nat. Bur. Std.*, **35**, 87 (1945).
7. R. F. Geller and S. M. Lang, *J. Am. Ceram. Soc.*, **32**, 157 (1949).
8. V. H. Stott and A. Hilliard, *Trans. Brit. Ceram.*

- Soc., **48**, 133 (1949).
9. W. R. Foster, *J. Am. Ceram. Soc.*, **34**, 302 (1951).
 10. C. E. Curtis and H. G. Sowman, *ibid.*, **36**, 190 (1953).
 11. G. M. Matwejew and A. S. Agarkow, *Silikat Tech.*, **20**, 86 (1969).
 12. J. Elliot, M. Gleiser, and V. Ramarkrishna, "Thermochemistry for Steelmaking," Vol. II. Addison Wesley, New York (1963).
 13. JANAF Thermochemical Tables, Second edition, Nat. Stand. Ref. Data Ser., Nat. Bur. Std. (U.S.), 37 (June 1971).
 14. H. H. Kellog, *Trans. Met. Soc. AIME*, **236**, 602 (1966).
 15. E. A. Gulbransen and S. A. Jansson, Paper presented at the International Conference on Heterogenous Kinetics at Elevated Temperatures, Philadelphia, Sept. 8-10, 1969.
 16. N. C. Tombs and A. J. E. Welch, *J. Iron Steel Inst.*, **172**, 69 (1952).
 17. H. Schafer and R. Hornle, *Z. Anorg. Allgem. Chem.*, **263**, 261 (1950).
 18. G. Grube and H. Speidel, *Z. Electrochem.*, **53**, 339 (1949).
 19. H. F. Ramstad and F. D. Richardson with Appendix by P. J. Bowles, *Trans. Met. Soc. AIME*, **221**, 1021 (1961).
 20. K. G. Gunther, *Glastech. Ber.*, **31**, 15 (1958).
 21. P. V. Gel'd and M. K. Kochnev, *Zh. Prikl. Khim.*, **21**, 1249 (1948).
 22. G. L. Humphrey, S. S. Todd, J. P. Coughlin, and E. G. King, *U.S. Bur. Mines Bull.*, 4888 (1952).
 23. O. Meyer, *Arch. Eisenhuettenw.*, **4**, 193 (1930).
 24. W. Eitel, "Silicate Science," Vol. V, pp. 183-184, Academic Press, New York (1966).
 25. E. Steinhoff, *Glastech. Ber.*, **33**, 86 (1960).
 26. K. Schwerdtfeger, *Trans. Met. Soc. AIME*, **236**, 1152 (1966).
 27. M. S. Crowley, *Bull. Am. Ceram. Soc.*, **46**, 679 (1967).
 28. M. S. Crowley, *ibid.*, **49**, 527 (1960).
 29. R. A. Gardner, *J. Solid State Chemistry*, **9**, 336 (1974).
 30. J. D. Hancock and J. H. Sharp, *J. Am. Ceram. Soc.*, **55**, 74 (1972).
 31. R. A. Gardner and W. R. Swiss, *Rev. Sci. Instr.*, **44**, 1428 (1973).

Electrohydrodimerization Reactions

IV. A Study of the Effect of Alkali Metal Ions on the Hydrodimerization of Several 1,2-Diactivated Olefins in DMF Solutions by Chronoamperometry and Chronocoulometry

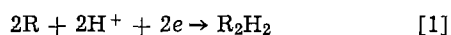
Mark J. Hazelrigg, Jr. and Allen J. Bard*

Department of Chemistry, The University of Texas at Austin, Austin, Texas 78712

ABSTRACT

The reduction of the activated olefins: dialkyl fumarates (alkyl = methyl, ethyl, butyl), ethyl cinnamate and cinnamionitrile in tetra-*n*-butylammonium iodide-dimethylformamide solutions in the absence and presence of Li⁺, Na⁺, and K⁺ was studied by double potential step chronocoulometric and chronoamperometric techniques, cyclic voltammetry, and controlled potential coulometry. The results in the absence of alkali metal ions confirmed the previous mechanism involving formation of the radical anion, R⁻, followed by dimerization; no evidence of appreciable adsorption of the parent olefin or R⁻ was found. The addition of alkali metal ion (M⁺) greatly increased the rate of the dimerization reaction and a mechanism based on formation of the ion pair, M⁺R⁻, followed by reaction of M⁺R⁻ with R⁻ or coupling of two M⁺R⁻ species is proposed based on an analysis of the kinetic data. The addition of Li⁺ also decreased the extent of polymer formation during bulk electrolysis experiments.

The mechanism of electrohydrodimerizations (1) (Eq. [1]) of activated olefins and related substances has been the subject of numerous investigations



in recent years. The mechanism which has emerged, based on chronoamperometric (2), rotating ring-disk electrode (3, 4), electron spin resonance (ESR) spectroscopic (5), linear scan voltammetric (6, 7), chronopotentiometric (8), and a-c polarographic (9) studies, is one in which the predominant pathway for many compounds (e.g., dialkyl fumarates, cinnamionitrile, α,β -unsaturated ketones) is an initial one-electron transfer at an electrode followed by dimerization of the electrogenerated radical ions (Eq. [2] and [3]), followed by protonation



* Electrochemical Society Active Member.

Key words: reductive coupling, electrolytic dimerizations, voltammetry, coulometry, ion pair formation.

Previous studies of electrohydrodimerizations of activated olefins have shown a strong effect on the electrochemical behavior on addition of alkali metal ions. Baizer (1, 10) for example, showed that the product ratios and reaction paths in reductive coupling depend upon the cation of the supporting electrolyte. Previous studies from this laboratory on the reduction of diethyl fumarate in *N,N*-dimethylformamide (DMF) solutions (2) showed that the addition of LiClO₄·3H₂O in millimolar concentrations to DMF solutions containing 0.44M tetra-*n*-butylammonium iodide (TBAI) caused the controlled potential coulometric n_{app} -value (where n_{app} is the number of faradays consumed per mole of electroactive species) to increase from 0.6 to 1.0, indicating an increase in the extent of formation of hydrodimer and a decrease in polymer formation. The addition of these small amounts of LiClO₄ also was found to increase the rate of the dimerization of the radical ions, although a quantitative study of this was not undertaken.

The alkali metal ion effect is most probably attributable to ion-pair formation between the alkali metal ion and the olefin radical anion. Ion-pair formation of

radical anions of organic compounds with metal ions in aprotic solvents has been of interest and has been studied using ESR and absorption spectroscopy (11), and polarography (12-15). Most of the previous electrochemical studies have been concerned with anions of aromatic quinones, nitrocompounds or carbonyl compounds. Very little work has been done with ion-pairs involving olefin anions. Ion-pairing affects the electrochemical reduction of organic compounds in different ways depending upon the electrochemical and chemical reactivity of the ion-pair. For the Nernstian reduction of neutral compounds which form stable radical anions, ion-pair formation causes a positive shift in $E_{1/2}$ or E_{pc} ; this shift in the reduction potential can be used to determine the ion-pair formation constant, K , (Eq. [4]) where ΔE is

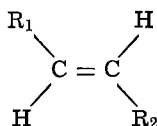
$$\Delta E = (RT/nF) \ln(1 + K[M^+]) \quad [4]$$

the shift in reduction potential, $[M^+]$ is the metal ion concentration, and K is the ion-pair formation constant. For example, Peover and Davis (12) found an ion-pair formation constant for the Li^+ -anthrasemiquinone ion-pair in 0.1M TEAP-DMF of 39 liters/mole using this method.

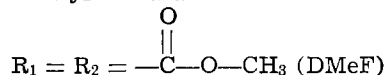
Ion-pair formation has also been shown to affect the rate of reactions following the electron transfer step. For example, Philp, Layloff, and Adams (16) found that Li^+ changes the electrochemical reduction pathway of benzil. In the absence of Li^+ , benzil is reduced in DMF solutions in 2 one-electron steps, while in the presence of Li^+ , it is reduced in an over-all single two-electron step. They proposed that a Li^+ -benzil ion-pair is formed which immediately undergoes a second electron transfer at potentials of the original first wave. Lasia (17) recently reported the effect of alkali metal ions on the rate of dimerization of phthalic aldehyde radical anion in DMF solutions using cyclic voltammetric techniques. He showed that the rate of disappearance of the radical anion increased by several orders of magnitude in the presence of alkali metal ion, with the rate of disappearance following the order $\text{Li}^+ > \text{Na}^+ > \text{K}^+$.

The work described in this paper was undertaken to investigate the role of the alkali metal ion in the dimerization reaction of activated olefin radical anions and to ascertain if the reaction mechanism in the presence of these metal ions was the same as in their absence. A second purpose of this investigation, since information about the kinetics of the over-all process was to be obtained by chronocoulometric techniques, was to see if any adsorption of parent species or intermediates takes place. The previous investigations all assumed in their data treatment the absence of adsorption and the occurrence of the dimerization reaction away from the electrode surface. Although the fit of the experimental data to theoretical models not involving adsorption was very good, we felt that chronocoulometric techniques utilizing digital data acquisition (18, 19) would be a more sensitive probe of adsorption. We have recently shown using chronocoulometry (20), that neither 9,10-diphenylanthracene nor its radical anion are appreciably adsorbed in DMF solutions at a platinum electrode.

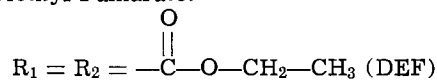
The substances investigated in this study were all activated olefins with the structure shown below



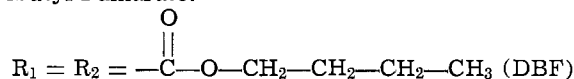
Dimethyl Fumarate:



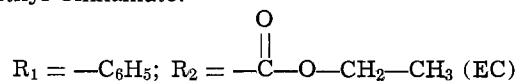
Diethyl Fumarate:



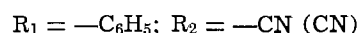
Dibutyl Fumarate:



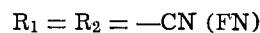
Ethyl Cinnamate:



Cinnamionitrile:



Fumaronitrile:



Double potential step chronoamperometric and chronocoulometric data were fit to theoretical models produced by digital simulation techniques (2), to obtain rate constants of the reactions following electron transfer.

Experimental

The general experimental techniques were the same as those reported previously (2); a detailed description is available (21).

Materials.—The solvent, dimethylformamide (DMF) (reagent grade, J. T. Baker Chemical Company) was purified by first storing over Linde Type 4A molecular sieves for 48 hr to remove the water, then storing over anhydrous cupric sulfate for 48 hr to complex dimethylamine. The solvent was then distilled from a small amount of molecular sieves and cupric sulfate using a 100 cm glass bead packed distillation column under a nitrogen atmosphere of 15 Torr using a reflux ratio of one. The middle 50% of the distillate was retained. This was stored under a helium atmosphere and used within three weeks of purification.

The supporting electrolyte, tetra-*n*-butylammonium iodide (TBAI) (polarographic grade, Southwestern Analytical Chemical Company, Austin, Texas) was vacuum dried and stored in a desiccator until use. Diethyl fumarate (DEF), cinnamionitrile (CN) (K. and K. Laboratories, Incorporated), and dibutyl fumarate (DBF) (Aldrich Chemical Company) were used as received. Dimethyl fumarate (K. and K. Laboratories, Incorporated) and fumaronitrile (FM) (Aldrich Chemical Company) were sublimed twice before use. Ethyl cinnamate (EC) (Aldrich Chemical Company) was vacuum distilled twice before use. Lithium perchlorate, lithium iodide, sodium iodide, and potassium iodide (reagent grade, J. T. Baker Chemical Company) were vacuum dried before use.

Apparatus.—The electrochemical cell used in the voltammetric studies was constructed from vacuum glassware and had a 25 ml capacity and contained a freeze-pump-thaw chamber and working, auxiliary, and reference electrode compartments. The auxiliary and reference electrode compartments were isolated from the working compartment by medium porosity glass frits. The cell contained four electrodes: a silver wire reference electrode, a platinum disk micro-electrode (0.013 cm²) for chronocoulometry, chronoamperometry, and cyclic voltammetry, a platinum gauze macro-electrode for preelectrolysis, and a platinum coil auxiliary electrode. A second cell, similar to the cell described above, was used for controlled potential electrolysis. This cell had a 50 ml capacity and an intermediate chamber between the working and auxiliary compartments to prevent contamination of the working electrode compartment by diffusion of products produced at the auxiliary electrode during bulk controlled potential electrolysis. The working electrode

in the coulometric experiments was a platinum wire gauze (2 cm by 10 cm).

The silver wire reference electrode in TBAI-DMF solutions was reproducible (less than 10 mV deviation) and was stable for more than 24 hr (less than 5 mV drift). Its use avoided the water and KCl contamination that sometimes results from an aqueous SCE and also showed a smaller amount of a-c pickup than cells in which a conventional SCE was employed.

Cyclic voltammetry and controlled potential coulometry experiments were performed with a PAR Model 170 Electrochemistry System (Princeton Applied Research Corporation, Princeton, N.J.). Positive feedback resistance compensation was employed. Double potential step chronoamperometry and chronocoulometry experiments were performed with a multipurpose instrument constructed from solid-state operational amplifiers previously described (22-24), and also employed positive feedback resistance compensation (25). The potential step was applied to the summing point of the potentiostat by a Wavetek Model 114 Function Generator. The length of the potential step was measured with a Beckman Berkley Model 7370 Universal Eput and Timer. Initial and final potentials for the potential steps were measured with a Fairchild Model 7050 Digital Voltmeter to an accuracy of ± 1 mV.

Data for the potential step experiments were taken using a PDP-12A computer system (Digital Equipment Corporation, Maynard, Massachusetts) and generally followed previously described digital data acquisition techniques [see (21, 23, 24, 26-29) and references therein]. Data sampling by the computer was synchronized to the potential step by amplifying the potential step and using it to trigger the real-time clock of the computer. The real-time clock in turn initiated data sampling at a rate determined by the computer program. The PDP-12A data acquisition program allowed sampling of 50 data points on the forward pulse and 50 points on the reverse one. These could be displayed, subjected to an internal least squares routine in studies of adsorption, listed, or printed as $i(2t_f)/i(t_f)$ or $Q(2t_f)/Q(t_f)$ where t_f is the forward pulse length, $i(t_f)$ and $Q(t_f)$ are the current and accumulated coulombs at t_f , respectively, and $i(2t_f)$ and $Q(2t_f)$ are these values at time $2t_f$.

Typical experimental procedure.—The platinum disk electrode was polished with AB ALPHA polishing alumina (Buehler Limited, Evanston, Illinois) before each experiment. The cell was assembled and pumped down on a vacuum line (10^{-5} Torr) for 1-2 hr. The supporting electrolyte was vacuum-dried in a transfer vessel. DMF was then vacuum transferred to the transfer vessel containing the supporting electrolyte to give a volume of 25 or 50 ml. After the supporting electrolyte dissolved, the solution was subjected to three freeze-pump-thaw cycles to remove any traces of oxygen. The solution was then vacuum-transferred to the electrochemical cell, brought to atmospheric pressure with high purity helium (99.995% Matheson Gas Products, La Porte, Texas), and allowed to equilibrate for 1 hr.

Liquid olefins and concentrated solutions of alkali metal ions were then added to the electrochemical cell as needed through a septum cap with the aid of syringes. Solid olefins were generally added with the supporting electrolyte in the transfer vessel. Concentrated alkali metal ion solutions were prepared in a vacuum vessel in a manner similar to that of the supporting electrolyte solution, except, that the DMF was freeze-pump-thawed several times both before and after the addition of the metal iodides. This was done to prevent the possibility of air oxidation of iodide to iodine in the presence of metal ions such as lithium.

Results

Theoretical models.—The method of obtaining kinetic and mechanistic information from the double potential step experiments generally followed that de-

scribed previously (2). Briefly, digital simulations (30) of the current (i) and coulombs (Q) flowing during a potential step to the limiting current plateau of the first reduction wave (production of R^- , Eq. [2]) and of i and Q during a reverse step back to the foot of the wave (oxidation of R^-) were carried out, for different values of the rate constant of the dimerization reaction, Eq. [3]. For completeness, other possible reaction sequences leading from R^- to hydrodimer were also considered; these are shown in Table I. Simulations employing 1000 iterations were used and tables of the normalized current and coulombs as functions of the dimensionless parameter $k_2 t_f C$ were generated. These were then used to generate tables of $i(2t_f)/i(t_f)$ and $Q(2t_f)/Q(t_f)$ as functions of $k_2 t_f C$. To fit the experimental data to the models, it is convenient to normalize these current and coulomb ratios and to represent these ratios as functions of a particular time when these ratios attain a certain value. The normalized ratios were obtained, as previously (2), i.e.

$$R_I = [i(2t_f)/i(t_f)]/0.2928 \quad [5]$$

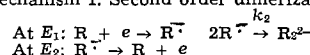
$$R_Q = \frac{[Q(2t_f)/Q(t_f)] - 0.414}{0.586} \quad [6]$$

so that R_I is 1 and R_Q is 0 in the absence of kinetic complications ($k_2 = 0$), with R_I decreasing to 0 and R_Q increasing to 1 for very large values of $k_2 t_f C$. In our previous work (2) we picked as the time reference point that value of $k_2 t_f C$ where $R_I = 0.5$, calling this point $t_{1/2}$ and using plots of R_I and R_Q vs. $t_{1/2}$ to determine the mechanism and the rate constant. Because we make greater use of the R_Q curves in the present work, we found it more convenient (and somewhat more diagnostic since the curves for the different possible mechanisms were more spread apart) to use as a reference point that where $R_Q = 0.4$; this value of $k_2 t_f C$ is designated as $T_{Q,4}$. A plot of R_I and R_Q vs. $T_{Q,4}$ is shown in Fig. 1 and, as an aid for others desiring to

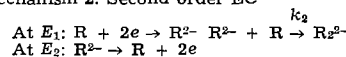
Table I. $R(Q)$ and $R(I)$ vs. $T_{Q,4}$ (up to eight $T_{Q,4}$ values) for four possible electrohydrodimerization mechanisms^(a)

$T/T_{Q,4}$	Mechanism 1		Mechanism 2		Mechanism 3		Mechanism 4	
	$R(Q)$	$R(I)$	$R(Q)$	$R(I)$	$R(Q)$	$R(I)$	$R(Q)$	$R(I)$
0.00	0.000	1.000	0.000	1.000	0.000	1.000	0.000	1.000
0.30	0.179	0.778	0.173	0.635	0.168	0.633	0.180	0.858
0.50	0.262	0.680	0.256	0.488	0.252	0.485	0.261	0.790
0.80	0.354	0.575	0.350	0.338	0.350	0.337	0.352	0.711
1.00	0.401	0.522	0.400	0.269	0.401	0.269	0.399	0.669
1.30	0.461	0.459	0.462	0.192	0.468	0.196	0.453	0.619
1.60	0.504	0.413	0.511	0.139	0.521	0.145	0.497	0.576
2.00	0.551	0.364	0.565	0.091	0.577	0.099	0.542	0.532
2.40	0.588	0.326	0.607	0.061	0.622	0.069	0.577	0.496
2.80	0.618	0.296	0.642	0.040	0.659	0.049	0.605	0.467
3.20	0.643	0.271	0.671	0.027	0.689	0.035	0.629	0.442
3.60	0.664	0.250	0.695	0.018	0.715	0.025	0.647	0.422
4.00	0.683	0.233	0.716	0.012	0.737	0.018	0.664	0.403
4.40	0.698	0.218	0.733	0.008	0.755	0.013	0.678	0.387
4.80	0.712	0.205	0.749	0.006	0.772	0.010	0.690	0.374
5.20	0.725	0.193	0.763	0.004	0.786	0.007	0.701	0.361
5.60	0.736	0.183	0.775	0.003	0.798	0.005	0.710	0.350
6.00	0.746	0.174	0.785	0.002	0.809	0.004	0.719	0.340
6.40	0.754	0.166	0.795	0.001	0.819	0.003	0.726	0.331
6.90	0.765	0.157	0.805	0.001	0.830	0.002	0.734	0.321
7.50	0.775	0.147	0.816	0.000	0.842	0.001	0.743	0.311
8.00	0.783	0.140	0.824	0.000	0.850	0.001	0.750	0.302

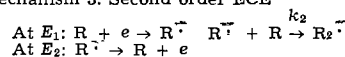
^(a) Mechanism 1. Second order dimerization [Mechanism V in (2)]



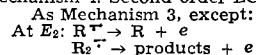
Mechanism 2. Second order EC [Mechanism III in (2)]



Mechanism 3. Second order ECE [Mechanism IV in (2)]



Mechanism 4. Second order ECE [Mechanism IVA in (2)]



Rate constants for each mechanism can be calculated by the following equations: Mechanism 1, $k_2 = 0.755/T_{Q,4}C$; Mechanism 2, $k_2 = 1.92/T_{Q,4}C$; Mechanism 3, $k_2 = 1.45/T_{Q,4}C$; Mechanism 4, $k_2 = 3.86/T_{Q,4}C$.

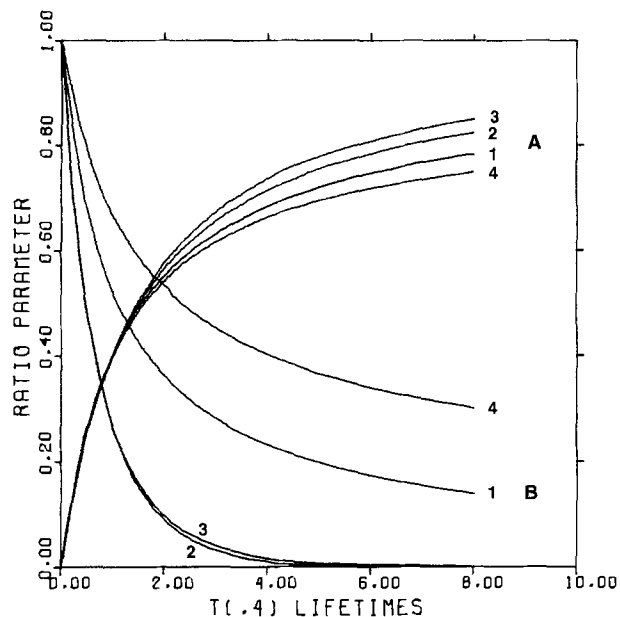
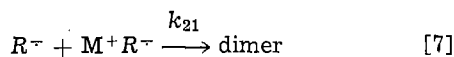


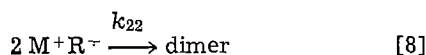
Fig. 1. Variation of the normalized coulomb (A) and current (B) ratio parameters as a function of $T_{Q,4}$ lifetimes for the different mechanisms considered.

use this procedure, the data is tabulated in Table I. In use the experimental R_1 and R_Q values are plotted against t_f , and the time axis then recalibrated in terms of $T_{Q,4}$ values. The fit of the experimental curve to the different model curves reveals the best mechanism, and the $T_{Q,4}$ value for that mechanism, knowing t_f and C , yields k_2 (Table I).

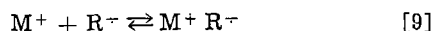
Models in the presence of alkali metal ions.—The results show (see below) that the hydrodimerization mechanism involves coupling of the radical anions (Mechanism 1) even in the presence of alkali metal ions. The involvement of alkali metal ion could proceed by ion pair formation, followed by reaction of ion pair with free radical anion



or by coupling of two ion pairs



If one assumes that these are the rate-determining steps, i.e., that ion pair formation and dissociation are so rapid, that reaction [9] can be considered at equilibrium



the over-all reaction velocity for the two paths can be obtained by combining the equilibrium constant expression for [9] (Eq. [10])

$$K = [M^+R^-]/[M^+][R^-] \quad [10]$$

with the rate expressions for [7] and [8]

$$v_7 = k_{21}[R^-][M^+R^-] \quad [11]$$

$$v_8 = k_{22}[M^+R^-]^2 \quad [12]$$

Taking the analytical concentration of radical anion as C_{R^-} (Eq. [13]), the concentration of ion pair

$$C_{R^-} = [R^-] + [M^+R^-] \quad [13]$$

is given by Eq. [14]

$$[M^+R^-] = \frac{K[M^+]}{1 + K[M^+]} C_{R^-} \quad [14]$$

and that of the free radical ion by Eq. [15]

$$[R^-] = C_{R^-}/(1 + K[M^+]) \quad [15]$$

Using these expressions in Eq. [11] and [12] yield

$$v_7 = \frac{k_{21}K[M^+]}{(1 + K[M^+])^2} C_{R^-} \quad [16]$$

$$v_8 = \frac{k_{22}K^2[M^+]^2}{(1 + K[M^+])^2} C_{R^-} \quad [17]$$

Both mechanisms show an over-all second order dependence on total radical anion concentration. The dependence on free metal ion concentration, in the limit $K[M^+] \ll 1$ (where Eq. [18] and [19] apply) is first order

$$v_7 = k_{21}K[M^+] C_{R^-} \quad [18]$$

$$v_8 = k_{22}K^2[M^+]^2 C_{R^-} \quad [19]$$

for the reaction in [7] and second order for that in [8]. The general over-all equation for the reaction rate under conditions where free radical ion coupling, and the ion-pair coupling reactions can all occur simultaneously is given by

$$v_{\text{over-all}} = \frac{k_2 + k_{21}K[M^+] + k_{22}K^2[M^+]^2}{(1 + K[M^+])^2} C_{R^-} \quad [20]$$

Electrochemical results in absence of alkali metal ions.—Cyclic voltammetric data for the different activated olefins are given in Table II. All compounds show behavior typical of a one-electron transfer followed by a following chemical reaction. In all cases the voltammograms become more reversible in appearance (e.g., show larger i_{pa}/i_{pc} -values) when either the scan rate is increased or the olefin concentration is decreased. In general the results for DEF and CN confirm those in earlier papers (2-3). Controlled potential coulometric reduction of these compounds was carried out at potentials beyond the first reduction peak; typical results are given in Table III. For the fumarates all show n_{app} -values smaller than one, with n_{app} -values smaller at higher (10 mM) concentrations than at lower (2.0 mM) ones. This has been attributed to a slow polymerization reaction initiated by the radical anions. For both EC and CN the n_{app} -values are much closer to one, suggesting considerably less polymerization occurs with these species.

Table II. Cyclic voltammetry results for activated olefins in absence of alkali metal ions^(a)

Compound	Conc (mM)	E_{pc} (V. vs. Ag.R.E.)	$E_{pc} - E_{pc/2}$ (mV)	$\frac{i_{pc}}{v^{1/2} C}$ $\mu A - sec^{1/2}$ V - mM	$E_{pc} - E_{pa}$ (mV)	$\frac{i_{pa}}{i_{pc}}$
DBF	1.49	-0.83	65	8.7	80	0.84
DEF	2.00	-0.82	60	9.3	85	0.73
DMeF	3.00	-0.78	63	10.9	80	0.50
EC	1.80	-1.25	70	9.9	90	0.60
CN	2.33	-1.25	61	10.9	80	0.41

^(a) All solutions were 0.20M TBAI in DMF with scan rate (v) of 200 mV/sec.

Table III. Controlled potential coulometry results for the reduction of activated olefins^(a)

Compound	Conc (mM)	E_{app1} (V. vs. Ag.R.E.)	n_{app}
DBF	2.00	-1.00	0.80
	10.7	-1.00	0.55
DEF	2.00	-1.00	0.85
	10.0	-1.00	0.60
DMeF	2.0	-1.00	0.82
	10.0	-1.00	0.63
EC	2.0	-1.40	0.96
	10.3	-1.40	0.91
CN	1.0	-1.40	0.99
	11.0	-1.40	0.82

^(a) 0.20M TBAI-DMF at Pt cathode.

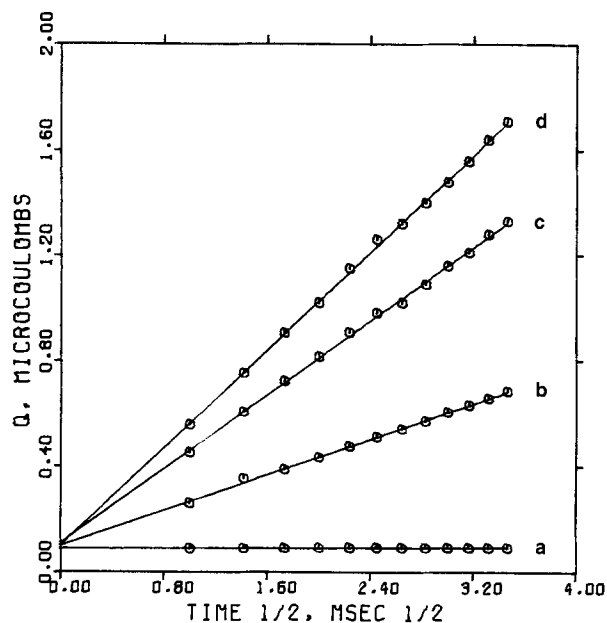


Fig. 2. Chronocoulometric data (Q vs. $t^{1/2}$) for dibutyl fumarate. The potential was stepped from -0.200 to -1.000 V vs. AgR.E. and the solution was $0.2M$ TBAI in DMF containing (a) 0, (b) 1.49, (c) 3.20, (d) 4.11 mM DBF.

Potential step chronocoulometry from the foot of the wave to the mass transfer limiting region in all cases produced linear Q vs. $t^{1/2}$ plots. Typical results are shown in Fig. 2; complete data are in Ref. (21). The intercepts and slopes for all of the compounds at several concentrations are given in Table IV. Analysis of the chronocoulometric data by the equation (18-20)

$$Q = Q_{dl} + nFA\Gamma + 2nFAC(D_0t/\pi)^{1/2} \quad [21]$$

shows that the intercept at $C = 0$ is the same as at higher concentrations of electroactive species, within $\pm 0.01 \mu C$. The maximum amount of adsorbed electroactive species is thus about $0.77 \mu C/cm^2$ or 8×10^{-12} mole/cm²; this corresponds to a maximum electrode coverage of 2-3%. The slopes are proportional to C in all cases. The linearity of the Q vs. $t^{1/2}$ plots also indicates that polymerization is not important during

Table IV. Chronocoulometric Q vs. $t^{1/2}$ intercepts and slopes^(a)

Concentration (mM)	Intercept (μC)	Slope ($\mu C/msec^{1/2}$)	Slope/ C ($\mu C \text{ msec}^{-1/2}/mM$)
Dibutyl fumarate ($E_i = -0.20V, E_f = -1.00V$)			
0	0.094	0.002	
1.49	0.100	0.169	0.113
3.20	0.112	0.350	0.109
4.11	0.101	0.463	0.112
Diethyl fumarate ($E_i = 0.40V, E_f = -1.00V$)			
0	0.083	0.002	
1.02	0.083	0.123	0.121
2.24	0.087	0.276	0.123
3.47	0.086	0.439	0.126
Dimethyl fumarate ($E_i = -0.40V, E_f = -1.00V$)			
0	0.087	0.002	
1.10	0.089	0.140	0.127
3.00	0.084	0.395	0.131
5.00	0.101	0.583	0.117
Ethyl cinnamate ($E_i = -0.80V, E_f = -1.40V$)			
0	0.082	0.001	
0.85	0.089	0.098	0.115
1.79	0.084	0.207	0.115
Cinnamionitrile ($E_i = -0.40V, E_f = -1.40V$)			
0	0.160	0.003	
1.54	0.160	0.210	0.136
3.12	0.159	0.389	0.125
4.80	0.152	0.544	0.113
6.41	0.170	0.738	0.115

^(a) Solutions were $0.20M$ TBAI in DMF. E_i is the initial potential and E_f the final potential, in V vs. AgR.E.

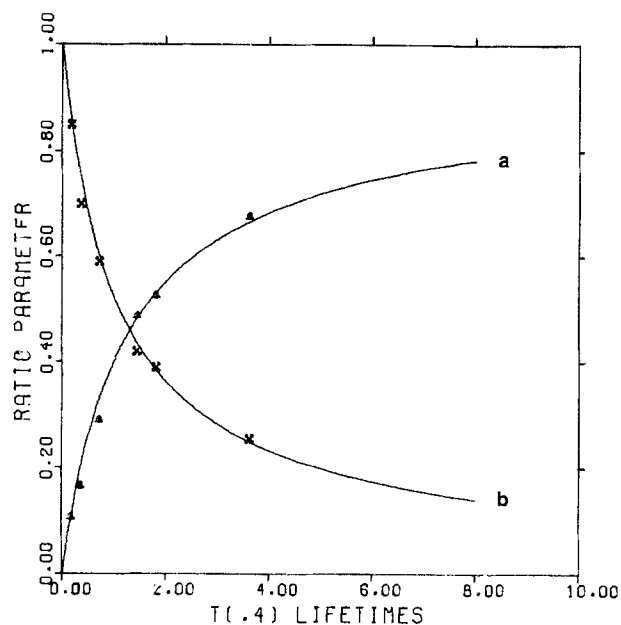


Fig. 3. Variation of the normalized coulomb (a) and current (b) ratio parameters as a function of $T_{Q,4}$ lifetimes for the reduction of 20.4 mM dibutyl fumarate in $0.20M$ TBAI-DMF solution. The points are experimental data and the lines are the simulation results for Mechanism 1 (radical anion dimerization).

the duration of the chronocoulometric experiment, since any appreciable extent of polymerization would consume parent species and lead to a nonlinear plot.

Mechanistic information was obtained by double potential step chronocoulometry and chronoamperometry, using the variation of $Q(2t_f)/Q(t_f)$ and $i(2t_f)/i(t_f)$ with the duration of the potential step, t_f , to obtain the ratio parameters R_Q and R_I and the $T_{Q,4}$ -value. These experimental R_Q and R_I vs. $T_{Q,4}$ curves were compared to the theoretical ones (Fig. 1) to establish the mechanism and determine the rate constant. Typical experimental data for DBF compared to theoretical curves for Mechanism 1 are shown in Fig. 3. The experimental values for the other compounds show essentially an equally good fit to Mechanism 1; complete data and curves are available (21). The experimental rate constants obtained for the dimerization from this data are listed in Table V. For those that have been determined before (DEF, DMef, CN) (2-5), the results here are in good agreement with previously reported values.

Electrochemical results in the presence of alkali metal ions.—Addition of alkali metal salts causes the cyclic voltammograms for the reduction of the olefins to change— E_{pc} shifts slightly in a positive direction and i_{pa}/i_{pc} is decreased; typical results are shown in Fig. 4. The positive shift in E_{pc} is in the order $Li^+ > Na^+ > K^+$, and can be attributed to ion pair formation of the radical anion with the metal ion and an increased rate of the following dimerization reaction. The current functions $i_{pc}/v^{1/2}C$ were similar to those without alkali metal ions and they decreased slightly with increasing scan rate. The anodic peak current, i_{pa} , was much smaller with alkali metal ions present, indicating a much faster following chemical reaction. For a given scan rate and metal ion concentration, the voltammograms showed larger i_{pa}/i_{pc} ratios when the olefin concentration was decreased, indicating a higher order following chemical reaction. For a given cyclic voltammetric scan rate, concentration of olefin, and concentration of metal ion, i_{pa}/i_{pc} increased in the order $Li^+ < Na^+ < K^+$. Thus the rate of the dimerization reaction is in the order $Li^+ > Na^+ > K^+ >$ no added alkali metal ion.

Controlled potential coulometry experiments were performed on solutions of dimethyl fumarate, diethyl fumarate, dibutyl fumarate, ethyl cinnamate, cinnam-

Table V. Rate constants for dimerization of several activated olefins obtained from double potential step chronoamperometric and chronocoulometric measurements^(a)

	Concentration (mM)	$T_{0.4}$ (sec)	k_2 (1/mole-sec)
Dibutyl fumarate	1.49	20.0	25
	10.1	3.30	24
	15.1	2.17	23
	20.4	1.38	26
			Avg = 25
Diethyl fumarate	7.0	2.30	47
	10.0	1.68	43
	10.0	1.66	44
	21.4	0.83	42
			Avg = 44
Dimethyl fumarate	3.00	2.07	1.2×10^2
	5.0	1.35	1.1
	10.0	0.62	1.2
			Avg = 1.2×10^2
Ethyl cinnamate	3.69	1.46	1.4×10^2
	5.55	0.905	1.5
	7.43	0.710	1.4
	9.26	0.585	1.4
			Avg = 1.4×10^2
Cinnamionitrile	1.26	0.673	8.9×10^2
	1.56	0.581	8.4
	1.88	0.455	8.8
	2.33	0.365	8.9
	3.78	0.223	8.9
	5.18	0.166	8.8
	5.82	0.152	8.5
	7.79	0.108	9.0
			Avg = 8.77×10^2

^(a) 0.2M TBAI in DMF; potential step program $E_1 \rightarrow E_2 \rightarrow E_1$ as in Table IV.

monitrile, and fumarionitrile in 0.20M TBAI-DMF with Li^+ , Na^+ , and K^+ ions added. Olefin concentrations ranged from 2.0 to 15.0 mM, while alkali metal ion (M^+) to olefin ratios up to ten to one were used. Typical n_{app} -values for solutions with 10 mM olefin and various $[\text{M}^+]/[\text{olefin}]$ ratios are shown in Table VI.

Experiments involving DBF, DEF, and DMeF with Li^+ added to the solution gave an n_{app} of 1.00 ± 0.03 when the $[\text{Li}^+]/[\text{olefin}]$ ratio was greater than four. The n_{app} decreased to the value obtained in the absence of alkali metal ion when the $[\text{Li}^+]/[\text{olefin}]$ ratio decreased. Experiments using LiI , LiClO_4 , and $\text{LiClO}_4 \cdot 3\text{H}_2\text{O}$ as the source of Li^+ all gave essentially the same n_{app} values. The electrolysis times of the anhydrous solutions containing alkali metal ions were 10-25% longer than the same solutions lacking M^+ under the same electrolysis conditions. Solutions with

Table VI. Typical controlled potential coulometry results for reduction of several activated olefins in the presence of Li^+ , Na^+ , or K^+ ^(a)

	DBF	n_{app} values DEF	DMeF	Fumaronitrile
$[\text{Li}^+]/[\text{olefin}]$				
6.0	0.98	1.02	0.97	0.43
4.0	1.00	0.99	0.99	
3.0	0.90	0.96	0.94	
2.0	0.89	0.91	0.91	
1.0	0.81	0.84	0.86	
0.0	0.55	0.60	0.63	0.41
$[\text{Na}^+]/[\text{olefin}]$				
10.0	0.53	0.63	0.60	0.37
4.0	0.57	0.59	0.59	
$[\text{K}^+]/[\text{olefin}]$				
10.0	0.58	0.62	0.64	0.42
4.0	0.57	0.65	0.61	

^(a) All solutions were 10.0 mM in olefin in 0.20M TBAI-DMF solution.

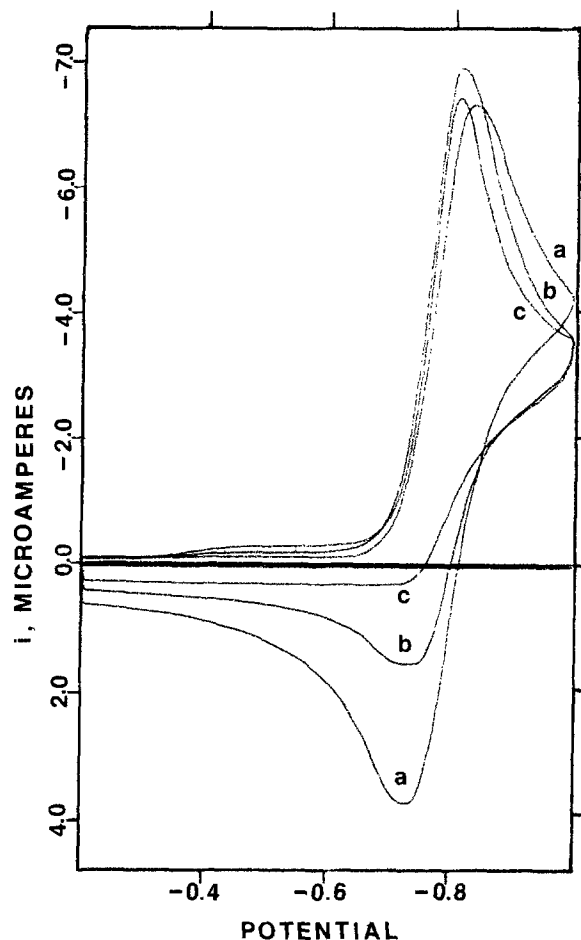


Fig. 4. Effect of Na^+ on the cyclic voltammetry of diethyl fumarate. The scan rate was 100 mV/sec and the DMF solution contained 0.20M TBAI, 1.49 mM DEF, and (a) 0, (b) 1.00 mM, (c) 12.0 mM NaI.

n_{app} -values close to one were colorless after the electrolysis, while solutions with n_{app} -values less than one had a yellow-brown color. During electrolysis with Li^+ present, a continuous formation of small bubbles was observed on the working electrode; the amount of these bubbles increased with increasing Li^+ concentration and were much more prevalent in the anhydrous solutions.

The n_{app} -values for the reduction of DMeF, DEF, and DBF were essentially unaffected by addition of Na^+ or K^+ , even with $[\text{Na}^+]$ or $[\text{K}^+]$ to $[\text{olefin}]$ ratios of 10/1 (film formation with DBF - K^+ solutions prevented an exhaustive electrolysis). Solutions containing Na^+ and K^+ were also characterized by a yellow-brown color after the electrolysis. The electrolysis times for solutions containing Na^+ and K^+ were three to five times longer than for solutions which did not contain alkali metal ions. We believe that a film of alkali metal hydroxide is formed during the electrolysis which partially blocks the electrode surface. This arises because the small hydrogen ion concentration that is present in solution is depleted in the vicinity of the electrode surface by the hydrodimerization reaction. When a small amount of water (0.1 ml per 50 ml DMF) was added as a weak proton source, the electrolysis times were reduced approximately 20%; however, they were still longer than the electrolysis times for solutions where no alkali metal ions were present. The water did not affect the n_{app} -values, but it did substantially increase the background current after electrolysis.

An NMR analysis was carried out on the electrolysis products for the reduction of DEF with Li^+ ($[\text{Li}^+]/[\text{DEF}] = 4.0$) and K^+ ($[\text{K}^+]/[\text{DEF}] = 6.0$) present. The NMR analysis could not be performed directly

on the electrolysis solution since the NMR spectra of the DMF and TBAI completely obscured the spectra of the electrolysis products. It was therefore necessary to extract the electrolysis products into methylene chloride, evaporate the methylene chloride and then obtain the NMR spectrum in carbon tetrachloride. The NMR of the electrolysis products were compared with those of pure samples of the hydrodimer (generously provided by Dr. M. Baizer of Monsanto, St. Louis, Missouri), diethyl succinate, and diethyl fumarate after they had undergone the same extraction process as the electrolysis products. The NMR spectrum of the Li^+ DEF electrolysis product was very similar to that of the pure hydrodimer, (1,2,3,4-tetraethyl butane tetracarboxylate); the electrolysis products, showed a small peak from unelectrolyzed DEF remaining in solution, and peaks from DMF carried over in the extraction. No singlet peak was observed at 7.50τ , indicating that no dihydro product (diethyl succinate), was formed during the electrolysis. The NMR of the K^+ -DEF electrolysis products gave spectra similar to that of the hydrodimer; however, each of the major peaks were split indicating several similar, but different, electrolysis products (e.g., hydrodimer and polymer). When the K^+ -DEF electrolysis products were vacuum distilled at 120°C , the distillate was a clear liquid (giving a hydrodimer NMR spectrum) while a brown tar remained in the distillation pot. The NMR spectrum of the brown tar exhibited the same number of peaks as the hydrodimer with slightly different chemical shifts. The NMR and n_{app} data indicate, in agreement with our previous results (2), that the polymerization reaction is eliminated and the hydrodimer becomes the only major electrolysis product upon addition of lithium ion, while, both sodium and potassium ions have no effect on the distribution of the final electrolysis products.

Electrolysis experiments were also carried out with fumaronitrile ($E_{\text{pc}} = -0.72\text{V}$ vs. AgR.E.) to see if alkali metal ions affected its reduction products in a manner similar to that for the fumarates. The n_{app} in the absence of alkali metal ions was found to be approximately 0.40, which indicates that a polymerization reaction involving parent molecules occurs. In this case the addition of Li^+ , Na^+ , or K^+ had no effect on the n_{app} -value. The electrolyses of cinnamionitrile and ethyl cinnamate were obscured by electrode filming and the electrochemical reduction of the metal ions to metal.

The experimental results for potential step chronocoulometry are summarized in Table VII; typical $Q - t^{1/2}$ curves in the absence and presence of LiI and DBF are shown in Fig. 5. The addition of alkali metal iodide causes the intercept to increase above that characteristic of the 0.2M TBAI-DMF solution. If we assume that there is no specific adsorption of cation at the initial potential (0.00V), then this increase can be attributed to rapid adsorption of the alkali metal ion at -1.00V requiring additional (negative) charge to compensate for these adsorbed positive ions. Under these conditions the relative extent of adsorption of alkali metal ion follows the order $\text{K}^+ > \text{Na}^+ > \text{Li}^+$.¹ The intercepts with the olefins present were essentially the same as those in their absence, indicating no appreciable adsorption of DBF and DEF.

Chronocoulometric Q vs. θ plots for the reverse potential step, while slightly perturbed by the hydrodimerization reaction, gave intercepts close to the value ($\pm 0.04 \mu\text{C}$) obtained for the forward step both in the absence and presence of DBF and DEF for all three alkali metal ions. This indicates that neither the radical anions produced nor any metal ion-radical anion ion-pair formed is appreciably adsorbed on the electrode surface.

¹ Another interpretation of the results, suggested by a reviewer, is adsorption of alkali metal ion at the initial potential which leads, through cooperative adsorption, to even greater adsorption of I^- and an initial increase in positive charge on the electrode.

Table VII. Chronocoulometric $Q - t^{1/2}$ intercepts and slopes^(a)

Olefin conc (mM)	Alkali metal ion conc (mM)	Intercept (μC)	Slope ($\mu\text{C}/\text{msec}^{1/2}$)
Dibutyl fumarate	LiI		
0	0	0.17	0.000
0	1.00	0.25	0.001
1.69	1.00	0.25	0.158
3.40	7.90	0.26	0.308
Dibutyl fumarate	NaI		
0	1.00	0.481	0.003
1.99	1.00	0.486	0.238
3.00	21.8	0.508	0.356
Dibutyl fumarate	KI		
0	1.00	0.602	0.003
1.50	1.00	0.605	0.154
3.20	11.1 ^(b)	0.465	0.222
Diethyl fumarate	LiI		
0	1.00	0.253	0.003
1.13	1.00	0.256	0.160
2.01	4.41	0.248	0.306
Diethyl fumarate	NaI		
0	1.00	0.481	0.004
1.49	1.00	0.492	0.179
2.94	8.00	0.509	0.352
Diethyl fumarate	KI		
0	1.13	0.609	0.002
3.32	8.77	0.618	0.398
6.02	12.9	0.629	0.763

^(a) Solutions were 0.20M TBAI in DMF, $E_1 = 0.000\text{V}$ and $E_2 = -1.000\text{V}$ vs. AgR.E.

^(b) Electrode filming occurred in DBF-KI solutions under these conditions.

Information about the reaction mechanism in the presence of alkali metal ions was again obtained by double potential step chronocoulometry and chronoamperometry, using the experimental R_0 , R_1 , and $T_{0.4}$ values to test theoretical models and obtain rate constants. Even in the presence of alkali metal ions, the results for reduction of DEF and DBF show the best fit with Mechanism 1 (dimerization of radical anions); typical experimental results are shown in Fig. 6. The over-all rate constants, k_{obs} , for the dimerizations as calculated from these results for different olefin and alkali metal ion concentrations are given in Table VIII. The reaction order with respect to alkali metal ion concentration was first estimated

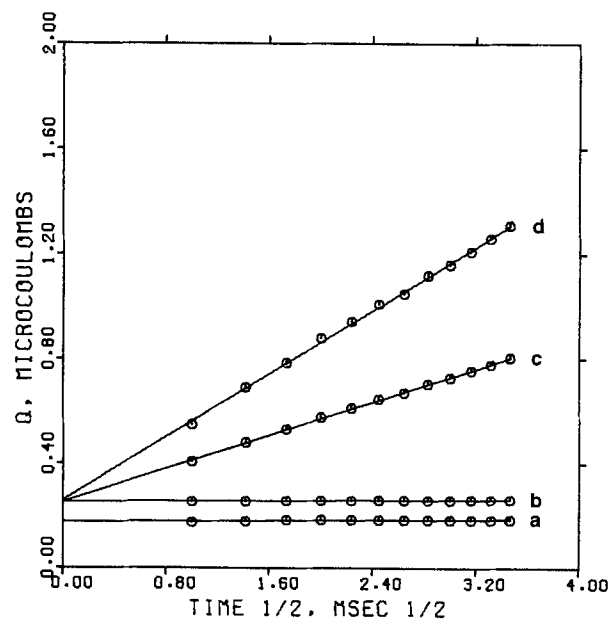


Fig. 5. Chronocoulometric data (Q vs. $t^{1/2}$) for dibutyl fumarate. The potential was stepped from 0.00 to -1.000V vs. AgR.E. and the DMF solution contained 0.20M TBAI and (a) 0 DBF, 0 LiI; (b) 0 DBF, 1.00 mM LiI; (c) 1.69 mM DBF, 1.00 mM LiI; (d) 3.40 mM DBF, 7.90 mM LiI.

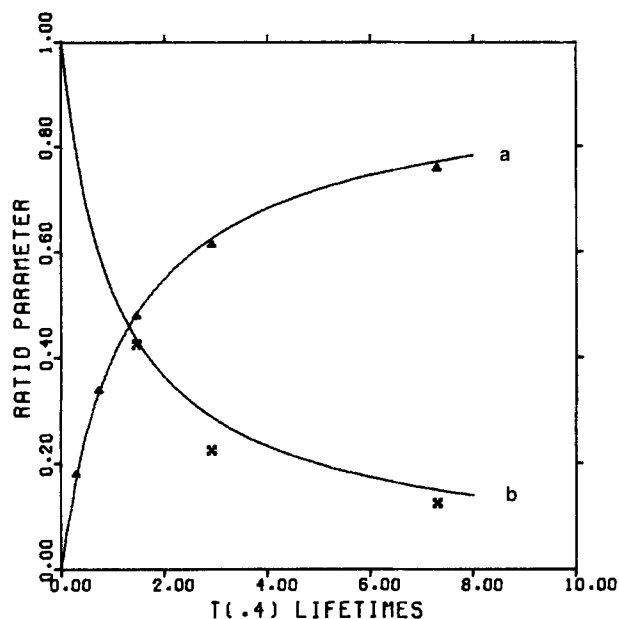


Fig. 6. Variation of the normalized coulomb (a) and current (b) ratio parameters as a function of $T_{0.4}$ lifetimes for the reduction of 0.95 mM diethyl fumarate with 3.81 mM Lil in 0.20M TBAI-DMF solution. The points are experimental data and the lines are the simulation results for Mechanism 1 (radical anion dimerization).

by plotting $\ln k_{\text{obs}}$ against $\ln [M^+]$; a typical plot is shown in Fig. 7. The slopes of these plots, i.e., the over-all reaction orders, using the data in Table VIII are for DEF: Li⁺, 1.08 ± 0.02 ; Na⁺, 1.07 ± 0.04 ; K⁺, 0.89 ± 0.03 and for DBF: Li⁺, 1.11 ± 0.03 ; Na⁺,

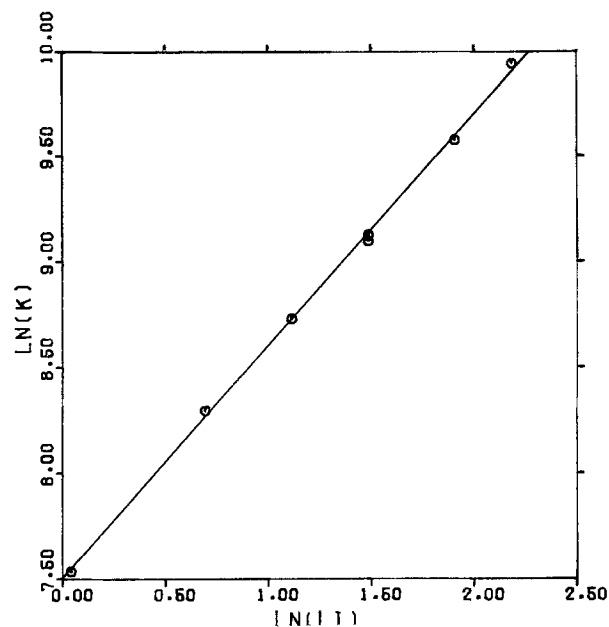


Fig. 7. Variation of $\ln k_{\text{obs}}$ with $\ln [Li^+]$ for the electroreduction of diethyl fumarate in 0.20M TBAI-DMF.

Table VIII. Rate constant for the dimerization of DBF and DEF radical anions in the presence of alkali metal ions^(a)

Olefin conc (mM)	Alkali metal ion conc [M ⁺], (mM)	$T_{0.4}$ (msec)	k_{obs} (l/mole-sec)	$k_{\text{obs}}/[M^+]$ (l ² /m ² -sec)
Dibutyl fumarate—Lithium iodide				
1.69	1.00	500.0	0.893×10^3	0.89×10^6
1.69	2.02	210.0	2.13	1.05
1.69	4.08	97.0	4.60	1.12
1.69	7.99	46.0	9.71	1.21
3.40	7.99	25.0	8.89	1.11
				Avg = 1.08×10^6
Dibutyl fumarate—Sodium iodide				
1.99	1.00	887.0	0.428×10^3	4.31×10^5
1.98	2.91	370.0	1.00	3.54
1.96	5.76	219.0	1.76	3.11
1.91	11.3	135.0	2.93	2.63
1.82	21.8	71.0	5.82	2.67
3.00	21.8	44.0	5.78	2.65
				Avg = 2.92×10^5
Diethyl fumarate—Lithium iodide				
1.13	1.04	857.0	1.87×10^3	1.79×10^6
1.13	2.00	167.0	4.00	2.00
1.13	3.04	108.0	6.19	2.03
1.13	4.41	73.0	9.15	2.07
2.01	4.41	42.0	8.94	2.03
2.01	6.72	26.0	14.4	2.14
2.01	8.90	18.0	20.8	2.33
				Avg = 2.05×10^6
Diethyl fumarate—Sodium iodide				
1.49	1.00	920.0	0.551×10^3	5.51×10^5
1.49	2.00	400.0	1.27	6.33
1.49	4.00	188.0	2.70	6.73
1.49	8.00	88.0	5.76	7.19
2.94	8.00	52.0	5.14	6.42
				Avg = 6.43×10^5
Diethyl fumarate—Potassium iodide				
3.42	1.13	1850.0	119	10.5×10^4
3.41	2.25	1280.0	176	7.78
3.40	3.36	855.0	260	7.74
3.36	5.56	513.0	438	7.88
3.32	8.77	365.0	623	7.10
3.31	12.9	266.0	858	6.64
6.02	12.9	149.0	840	6.50
				Avg = 7.27×10^4

^(a) All solutions contained 0.2M TBAI in DMF.

0.85 \pm 0.03. At ratios of M⁺ to olefin less than 0.8, a larger deviation from first order dependence on M⁺ was observed, because of the contribution to the over-all rate by the direct dimerization of the radical ions. Since the reactions were close to first order, the reaction mechanism most closely followed Eq. [7] and the appropriate kinetic expression is [16] or [18]. Thus the over-all rate constant, k_{obs} , is approximately $k_{21}K[M^+]$; the values of $k_{\text{obs}}/[M^+] \approx k_{21}K$ given in Table VIII are fairly constant, as expected. The ion-pair formation constant for DEF⁻ with Li⁺, Na⁺, and K⁺ cations was estimated by the cyclic voltammetric potential shifts on the DEF reduction wave with the addition of alkali metal ions. The observed potential shifts are a result of both ion-pairing and the increased dimerization rate. The potential shift due to the hydrodimerization reaction can be estimated by using the theory of cyclic voltammetry in the presence of a dimerization reaction (6, 31) and the rate constant calculated by chronocoulometry. Once this has been calculated, the shift due to ion-pairing can be extracted, and the ion-pair formation constant is then estimated using Eq. [4]. For example, for a solution containing 1.49 mM DEF and 8.00 mM Na⁺ a peak potential shift (compared to a solution in the absence of Li⁺) of 14 mV is observed. Of this, using the measured k_{obs} value of $5.8 \times 10^3 \text{ M}^{-1} \text{ sec}^{-1}$, 11 mV can be attributed to the following dimerization reaction. The residual 3 mV then yields an ion-pair formation constant K of about 6 M^{-1} . This procedure gives K-values of 29, 6, and 2 for ion-pairs of DEF⁻ with Li⁺, Na⁺, and K⁺, respectively. These values seem to be generally in line with previously determined values of association constants in DMF; for example Peover and Davies (12) report a K of about 39 M^{-1} for p-benzoquinone anion and Li⁺ while Lasia and Kalinowski (15) report K's of 120 and 41 for ion pairs of Li⁺ with fluorenone and indantrione radical anions, respectively. Using these K-values, a somewhat more detailed analysis of the kinetic data can be made. From the over-all rate expression for the reaction, Eq. [20], we find a k_{obs} given by Eq. [22]

$$k_{\text{obs}} = (k_2 + k_{21}K[M^+] + k_{22}K^2[M^+]^2)/(1 + K[M^+]^2) \quad [22]$$

Taking $K[M^+] = x$, this expression can be rearranged to

$$k_{\text{obs}}(1 + x)^2 - k_2 = k_{21}x + k_{22}x^2 \quad [23]$$

A plot of the left-hand side of [23] against x allows

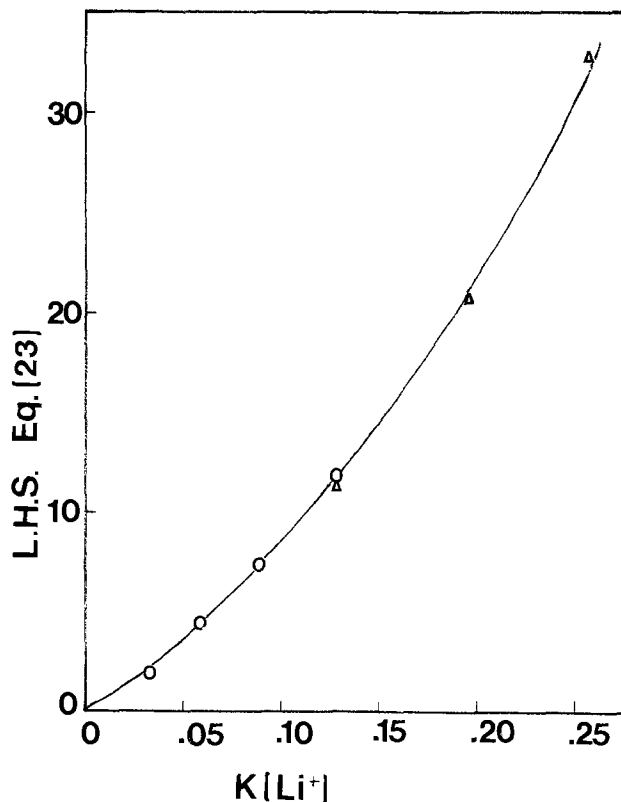


Fig. 8. Variation of lefthand side of Eq. [23] (equal to $k_{\text{obs}}(1 + K[\text{Li}^+]^2 - k_2)$) against $K[\text{Li}^+]$ with the data for the electroreduction of diethyl fumarate in 0.20M TBAI-DMF. The points are the experimental results at (○) 1.13 mM DEF and (△) 2.01 mM DEF and the line the calculated result with the rate constants listed in Table IX.

one to estimate the k_{21} and k_{22} -values; a typical plot for DEF-LiI is shown in Fig. 8. The values of k_{21} and k_{22} estimated by this procedure are given in Table IX. (A similar calculation for DBF, assuming the K -values for DBF^- are the same as DEF^- yields 3.2×10^4 and $5.7 \times 10^4 \text{ M}^{-1} \text{ sec}^{-1}$ for k_{21} with LiI and NaI, respectively). Extension of rate measurements to higher M^+ concentrations to obtain more reliable values for k_{22} were limited by the reaction becoming too fast to measure by our techniques for Li^+ , and the appearance of electrode filming in the case of Na^+ and K^+ .

We have assumed in this treatment negligible association of the metal ions with supporting electrolyte (I^-) ion. This appears to be in agreement with previous measurements on alkali metal ion iodides and perchlorates in DMF (12, 32). Several experiments were also performed using LiNO_3 or KNO_3 (instead of the iodides) in the 0.2M TBAI-DMF solvent on the electroreduction of DEF. While the second-order dependence in DEF and primarily first-order dependence in metal ion was still observed, the $k_{\text{obs}}/[\text{M}^+]$ values obtained (6.6×10^6 and $1.1 \times 10^6 \text{ M}^{-1} \text{ sec}^{-1}$ for LiNO_3 and NaNO_3 , respectively) were about twice those of the iodide salts. The reasons for these differences, which are well outside the experimental error limits of the measurements, are not clear, but

Table IX. Summary of rate constants for dimerization of diethyl fumarate in presence of alkali metal ions^(a)

System	K (M^{-1})	k_2 ($\text{M}^{-1} \text{ sec}^{-1}$)	k_{21} ($\text{M}^{-1} \text{ sec}^{-1}$)	k_{22}	$k_2 K$ ^(b)
DEF-LiI	29	44	6.2×10^4	2.4×10^5	1.8×10^6
DEF-NaI	6	44	9.3×10^4	9×10^5	5.6×10^6
DEF-KI	2	44	3.3×10^4	—	1.3×10^6

^(a) In 0.1M TBAI-DMF.

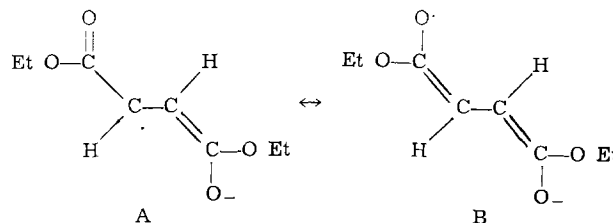
^(b) Compare to Table VIII, $k_{\text{obs}}/[\text{M}^+]$.

suggest that impurities (e.g., water of hydration), adventitiously added with alkali metal ion salt, may have an effect on the reaction rate.

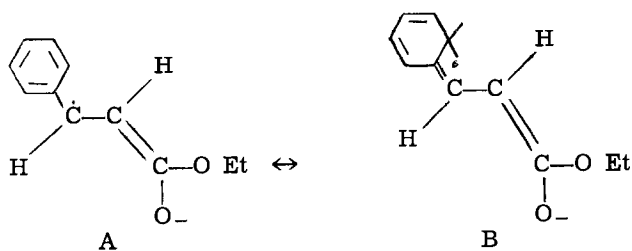
Discussion

The results generally show that reductive coupling of 1,2-diaactivated olefins involve dimerization of radical anions both in the absence and presence of alkali metal ions. Adsorption of the parent olefins or the radical ions does not appear to be an important step in the reaction sequence. The linearity of the $Q - t^{1/2}$ plots suggests that the polymerization reactions which are of importance on the controlled potential coulometric time scale, do not interfere with the short time voltammetric measurements. In agreement with the previous results (2) we have found that addition of Li^+ decreases the extent of polymerization on bulk electrolysis. The mode by which this occurs has not been established, however two possibilities appear reasonable. If the dimer dianion, R_2^{2-} , is ion-paired with Li^+ , it may be less reactive towards R and so show less polymerization. If this were the case, however, it is difficult to understand why Na^+ and K^+ have such a small effect on the coulometric results. A second possibility is that Li^+ increases the rate of protonation of R_2^{2-} . Li^+ is known to be quite acidic and hence coordinates strongly with traces of water in the DMF. This coordinated water will be a better proton donor than uncoordinated water and may be brought to close proximity to the dimer dianion by the ion-paired Li^+ . Na^+ and K^+ should show this effect to a much more limited extent. The increased acidity of water in the presence of Li^+ apparently does not cause appreciable protonation of the radical anion itself, since no evidence of the $2e$ reduction products was found. Additional evidence of the higher proton availability in the presence of Li^+ are the small bubbles observed during coulometry when Li^+ is present. These probably are caused by a small amount of H^+ -reduction at the electrode, concurrent with olefin reduction, forming some hydrogen gas bubbles. Electrode filming in the presence of the alkali metal ions, especially at higher concentrations can be attributed to the formation of insoluble hydroxides upon hydrolysis (i.e., deprotonation) of the aquated ions. Similar hydrolysis of metal ions and filming have been observed in nonaqueous solvents (33, 34).

The study also provides some new information on the dependence of radical anion dimerization rate on structure. For the dialkyl fumarates, the dimerization rate constant and diffusion coefficients decrease in the order $\text{Me} > \text{Et} > \text{n-Bu}$. Apparently, the bulkier the alkyl group, the slower is the movement through solution and the more hindered the dimerization reaction. The rate of dimerization of ethyl cinnamate (EC) radical anions ($140 \text{ M}^{-1} \text{ sec}^{-1}$), compared to that for DEF ($44 \text{ M}^{-1} \text{ sec}^{-1}$) may at first appear anomalously large, since EC can be considered to have a structure between DEF (2 $-\text{CO}_2 \text{Et}$ groups) and stilbene (2 phenyl groups), whose R^- dimerization rate is very slow. However, consideration of the resonance structures of the radical anions of the two compounds suggests that while DEF has several structures where electron density is not on the ethylenic carbon, e.g., structure



B, such structures are less probable for EC



Grypa and Maloy (35) recently also found a rate of disappearance of electrogenerated EC radical anion higher than that for DEF; their interpretation of the results differs from that given here, however.

The major conclusion of this study is that alkali metal ions increase the dimerization rate of radical anions by ion pair formation, thereby decreasing the electrostatic repulsion in the coupling of the bare anions. The reaction is predominantly first order in metal ion at low Li^+ and Na^+ and all K^+ concentrations, leading to a mechanism involving reaction of free radical anion with ion pair. At higher Li^+ and Na^+ concentrations coupling of two ion pairs becomes significant. Considering the results for DEF (Table IX) where fairly similar k_{21} -values are observed for the different alkali metal ions, we can speculate that the rate of the ion pair-radical anion reaction is roughly independent of metal ion and the different over-all rates observed depend upon different ion pair association constants. After this work was completed a note by Ryan and Evans (36) appeared in which the effect of Na^+ on DEF hydrodimerization in DMSO was investigated. Although the free anion dimerization rate in that solvent was much larger than that found in DMF, their values for k_{21} and k_{22} were remarkably close to those found in this study.

Acknowledgment

The support of the Robert A. Welch Foundation and the National Science Foundation (GP-31414X) is gratefully acknowledged.

Manuscript submitted July 29, 1974; revised manuscript received Sept. 16, 1974.

Any discussion of this paper will appear in a Discussion Section to be published in the December 1975 JOURNAL. All discussions for the December 1975. Discussion Section should be submitted by Aug. 1, 1975.

Publication costs of this article were partially assisted by The University of Texas at Austin.

REFERENCES

- M. M. Baizer, in "Organic Electrochemistry," M. M. Baizer, Editor, Chap. XIX, Marcel Dekker, Inc., New York (1973).
- W. V. Childs, J. T. Maloy, C. P. Keszthelyi, and A. J. Bard, *This Journal*, **118**, 874 (1971).
- V. J. Puglisi and A. J. Bard, *ibid.*, **119**, 829 (1972).
- V. J. Puglisi and A. J. Bard, *ibid.*, **120**, 748 (1973).
- I. B. Goldberg, D. Boyd, R. Hirasawa, and A. J. Bard, *J. Phys. Chem.*, **78**, 295 (1974).
- E. Lamy, L. Nadjo, and J. M. Savéant, *J. Electroanal. Chem.*, **42**, 189 (1973) and numerous references therein.
- E. Lamy, L. Nadjo, and J. M. Savéant, *ibid.*, **50**, 141 (1974).
- S. C. Rifkin and D. H. Evans, *This Journal*, **121**, 769 (1974) and references therein.
- J. W. Hayes, I. Ruzić, D. E. Smith, A. L. Booman, and J. R. Delmastro, *J. Electroanal. Chem.*, **51**, 269 (1974).
- J. P. Petrovich and M. M. Baizer, *This Journal*, **118**, 447 (1971).
- M. Szwarc, "Carbanions, Living Polymers and Electron Transfer Processes," Interscience, New York (1968); *Accts. Chem. Res.*, **2**, 87 (1969).
- L. Holleck and D. Becher, *J. Electroanal. Chem.*, **4**, 321 (1962); M. E. Peover and J. D. Davies, *ibid.*, **6**, 46 (1963).
- T. Fujinaga, K. Izutsu, and T. Normura, *ibid.*, **29**, 203 (1971).
- T. M. Krygowski, *ibid.*, **35**, 436 (1972); T. M. Krygowski, M. Lipsztajn, and Z. Galus, *ibid.*, **42**, 261 (1973); M. Lipsztajn, T. M. Krygowski, and Z. Galus, *ibid.*, **49**, 17 (1974).
- M. K. Kalinowski, *Chem. Phys. Letters*, **7**, 55 (1970); *ibid.*, **8**, 378 (1971); A. Lasia and M. K. Kalinowski, *J. Electroanal. Chem.*, **30**, 511 (1972).
- R. H. Philp, T. Layloff, and R. N. Adams, *This Journal*, **111**, 1189 (1964).
- A. Lasia, *J. Electroanal. Chem.*, **42**, 253 (1973).
- J. H. Christie, R. A. Osteryoung, and F. C. Anson, *ibid.*, **13**, 236 (1967).
- F. C. Anson, *Anal. Chem.*, **38**, 54 (1966).
- M. J. Hazelrigg and A. J. Bard, *J. Electroanal. Chem.*, **46**, 141 (1973).
- M. J. Hazelrigg, Jr., Ph.D. Dissertation, The University of Texas at Austin, 1973.
- F. C. Anson and D. A. Payne, *J. Electroanal. Chem.*, **13**, 35 (1967).
- D. A. Payne, Ph. D. Dissertation, The University of Texas at Austin, 1970.
- D. A. Payne and A. J. Bard, *This Journal*, **119**, 1665 (1972).
- E. R. Brown, D. E. Smith, and G. L. Booman, *Anal. Chem.*, **40**, 1141 (1968).
- G. Lauer and R. A. Osteryoung, *ibid.*, **40**, 30A (1968).
- G. Lauer, R. Abel, and F. C. Anson, *ibid.*, **39**, 765 (1967).
- R. A. Osteryoung, in "Electrochemistry," J. S. Mattson *et al.*, Editors, Chap. 11, Marcel Dekker, Inc., New York (1972).
- S. P. Perone, in "Electrochemistry," J. S. Mattson *et al.*, Editors, Chap. 13, Marcel Dekker, Inc., New York (1972).
- S. W. Feldberg, "Electroanalytical Chemistry," A. J. Bard, Editor, Vol. 3, Marcel Dekker, Inc., New York (1969).
- M. L. Olmstead, R. G. Hamilton, and R. S. Nicholson, *Anal. Chem.*, **41**, 260 (1969).
- (a) D. P. Ames and P. G. Sears, *J. Phys. Chem.*, **59**, 16 (1955). (b) P. G. Sears, E. D. Wilholt, and L. R. Dawson, *ibid.*, **59**, 373 (1955).
- I. M. Kolthoff and J. F. Coetzee, *J. Am. Chem. Soc.*, **79**, 1852 (1957).
- B. F. Myasoedov, I. S. Sklyarenko, and Yu. M. Kulyako, *Russian J. Inorganic Chem.*, **17**, 1541 (1972).
- R. D. Grypa and J. T. Maloy, Private communication.
- M. D. Ryan and D. H. Evans, *This Journal*, **121**, 881 (1974).

Effects of Procarbazine on Ti(IV) Reduction at the DME

John P. McCue* and John H. Kennedy**

Department of Chemistry, University of California, Santa Barbara, California 93106

ABSTRACT

Procarbazine, an anti-Hodgkin's disease drug, adsorbs on the dropping mercury electrode and causes the reduction of titanium(IV) to occur at more negative potentials. Only one wave due to titanium was observed even when the ratio of procarbazine to titanium was considerably less than one. These observations are interpreted as the formation of a titanium-procarbazine complex at the electrode surface which is then reduced.

In 1968 Carrol and Tullis (1) reported observations of titanium in leucocytes of peripheral blood and lymph nodes. McCue (2) confirmed these observations for peripheral blood and further showed them to be specific for the white cells of Hodgkin's and leukemia subjects. In the process of studying the chemical interactions between Ti(IV) and certain antineoplastic drugs, we found that procarbazine, an anti-Hodgkin's disease drug, was adsorbed on the dme and that upon addition of small amounts of procarbazine to Ti(IV) solutions the polarographic reduction wave of titanium was shifted to more negative potentials with an increase in reversibility for this electrochemical process. We now report a mechanistic interpretation of these and related observations.

In the past, the influence of surface active agents on reduction of metal ions at the dme have mainly been interpreted as kinetic effects (3). By setting up a "barrier" to the metal ion at the Hg surface the surfactant kinetically hinders or prevents the metal ion from undergoing reduction. A larger activation energy for reduction at the covered surface results, with little or no effect on the relative energies of the oxidized and reduced forms of the couple.

In terms of wave shapes and responses the effects of surfactants can be divided into two cases. The first case occurs when the metal ion is reversibly reduced in the absence of surfactant. The kinetic effect of addition of surface active agent to such metal ions is shown in Fig. 1a, and the theoretical explanation for this effect is schematically given in Fig. 2a. In this case $\Delta G^{\ddagger}_{\text{rev}}$ is small compared to $\Delta(\Delta G^{\ddagger}_{\text{rev}})$ so that for working potentials less than that required to activate path 2 only path 1 is electrochemically active. The net effect of surfactant is to decrease the available surface area at which the reduction can occur, and this results in a decrease in i_d for the polarographic wave (Fig. 1a). At any potential large enough to activate both paths, path 1 will be $e^{+\Delta(\Delta G^{\ddagger}_{\text{rev}})/nFV}$ times more electrochemically active than path 2; therefore when $\Delta G^{\ddagger}_{\text{rev}} \ll \Delta(\Delta G^{\ddagger}_{\text{rev}})$ the effect of path 2 is negligible, and no shift in $E_{1/2}$ is observed since the reaction occurs predominantly on the free surface. When the entire dme surface is covered with surfactant, only path 2 exists and the electrochemical process becomes slower and thus irreversible. If $\Delta(\Delta G^{\ddagger}_{\text{rev}}) < 3\Delta G^{\ddagger}_{\text{rev}}$ at ambient conditions, path 2 becomes significant and a small broadening or tilting of the polarographic wave occurs.

The second case occurs when the metal ion is irreversibly reduced in the absence of a surfactant. For this case $\Delta G^{\ddagger}_{\text{irrev}}$ is so large that the electrochemical reaction at the free surface is slow; when surfactant is added $\Delta(\Delta G^{\ddagger}_{\text{irrev}})$ is small (Fig. 2b). Thus, the electrochemical reaction at the covered surface (path 2) is

not negligible relative to the free surface (path 1). At applied potentials less than that required to activate path 2, the electrochemically active surface area is reduced similar to the reversible case. But unlike the reversible case, increasing the applied voltage significantly activates path 2. Since this path is more irreversible (i.e., greater activation energy) than path 1, the resultant polarographic wave is more irreversible (i.e., becomes broader as shown in Fig. 1b). These two

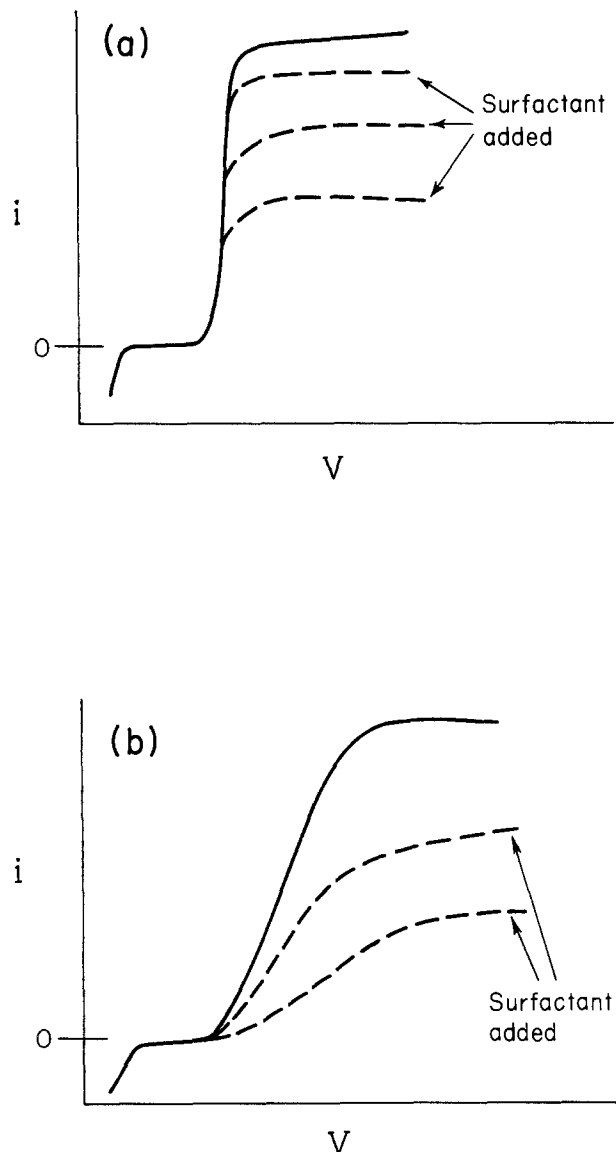


Fig. 1. Effect of surfactant on reduction of metal ion. (a) Reversible case and (b) irreversible case.

* Electrochemical Society Student Member.

** Electrochemical Society Active Member.

Key words: polarography, procarbazine, surface active agent, titanium, titanium-procarbazine complex.

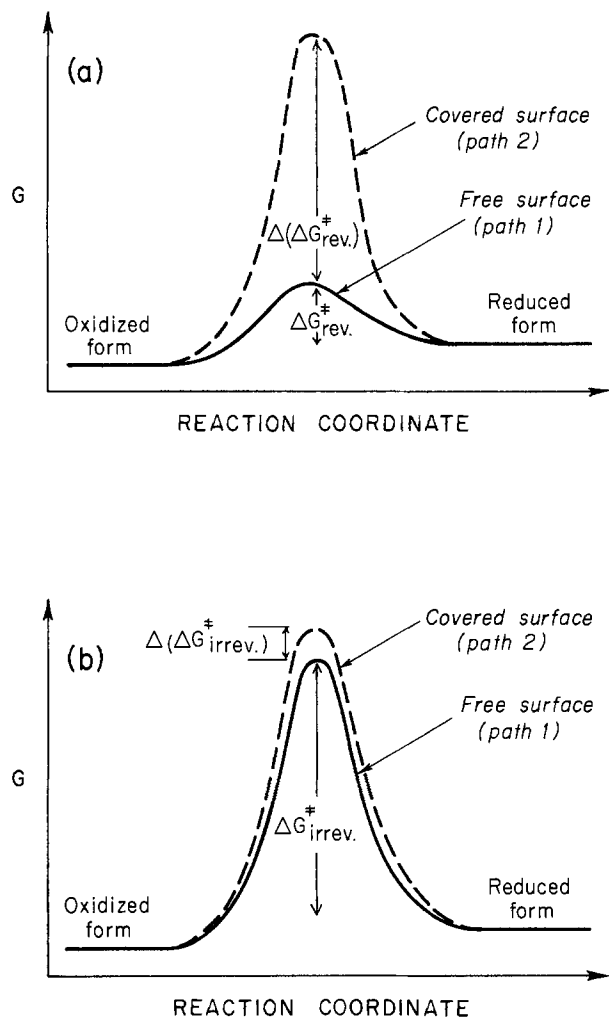


Fig. 2. Effect of surfactant on activation energy. (a) Reversible reduction in the presence of a surfactant and (b) irreversible reduction in the presence of a surfactant.

cases have been well documented (4-10), and their interpretation as kinetic effects are supported by theoretical calculations (11).

In contrast with the above observations, addition of the surface active agent procarbazine (at concentrations less than the metal ion) to Ti(IV) solutions causes a shift of the metal polarographic reduction wave to more negative potentials accompanied by an increase in the reversibility of the reduction process. Such behavior is identical to that seen (12) when a tenfold excess of complexing agent is added to a metallic depolarizer being monitored at the dme. Thus polarography of Ti(IV)-procarbazine mixtures displays features common to both surface active phenomena and metal ion complexation phenomena. These common features suggest that procarbazine below millimole concentration is adsorbed on the dme surface, the adsorption gives rise to a large procarbazine concentration at the surface, and that Ti(IV) at the surface reacts with this surface-concentrated procarbazine to produce a Ti(IV)-procarbazine complex for which reduction is more reversible than the Ti(IV) species in bulk solution. For such a process to occur certain critical conditions must be met, an investigation of these conditions is presented here.

Experimental

Stock aqueous solutions of Ti(IV) were prepared by adding 99.5% TiCl_4 (Matheson, Coleman and Bell) to concentrated HCl (Baker Analytical Grade) and diluting with deionized water. These solutions could then be diluted without hydrolysis if added to deionized water. When other chemicals were required in

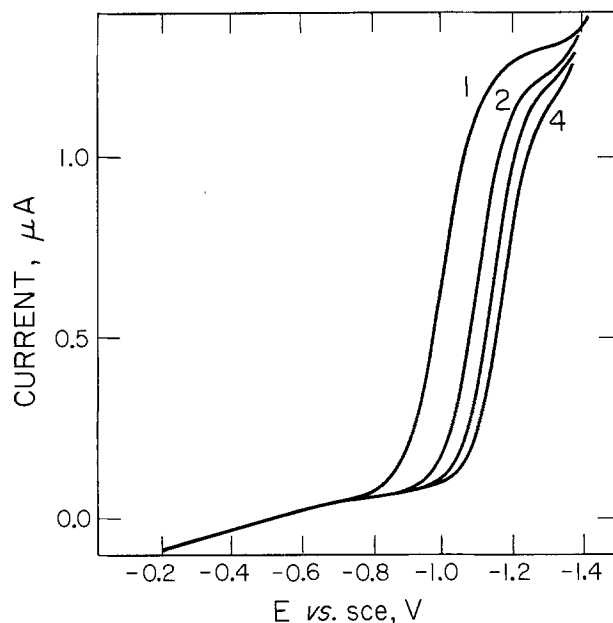


Fig. 3. Polarographic wave for 1, 20 ml of 0.6 mM Ti(IV) in 0.2M NaCl; 2, with addition of 0.5 ml of 2 mM procarbazine solution; 3, with addition of 1.0 ml of 2 mM procarbazine solution; and 4, with addition of 2.0 ml of 2 mM procarbazine solution. Drop time 1 sec and scan rate 5 mV/sec.

the titanium solutions they had to be added after dilution.

Procarbazine was supplied both as drug (Matulane®) and pure form by Roche Laboratories. Aqueous stock solutions were made by dissolving either source in deionized water with addition of HCl to pH 3.

Solutions were made basic by addition of NaOH or solid NaHCO_3 (Mallinckrodt-AR grade). pH was measured using a Beckman glass electrode No. 40498, and control during the polarographic experiments was accomplished by adjustment with HCl or NaOH initially and verification after the experiments. Buffer systems were not used because they would act as ligands for titanium and complicate the system further.

Polarography was accomplished with a "PAR-174 Polarographic Analyzer" equipped with a Houston Instruments "Omnigraphic-2000" X-Y recorder and a two electrode "H" cell with sce reference. Visible and u.v. spectroscopy was carried out with a Cary 14 Spectrometer.

Results and Discussion

When aliquots of 2 mM procarbazine solution were added to a 0.6 mM Ti(IV) solution, 0.2M in NaCl at pH 2, being monitored at the dme, Fig. 3 resulted. This behavior of the Ti(IV) polarographic wave was similar to the behavior of Cd^{+2} , Cu^{+2} , and Sn^{+2} ions in solution when a many-fold excess of complexing agent was added (13-15). However, for curve 3 in Fig. 3 for example the procarbazine-Ti(IV) molar ratio was 1:6, far below that normally required for a complexing agent to produce the observed $E_{1/2}$ shift of -0.095V . Accompanying the $E_{1/2}$ shifts were small reductions in i_d (Table I). Although this suppression of i_d indicated that procarbazine was probably adsorbed at the dme,

Table I. Decrease in diffusion current and $E_{1/2}$ shift for 0.6 mM Ti(IV) upon addition of procarbazine

Procarbazine, mM	i_d , ^(a) μA	$\Delta E_{1/2}$, V
0	0.85	0
0.01	0.82	-0.010
0.10	0.81	-0.095
0.20	0.80	-0.130

^(a) Corrected for dilution.

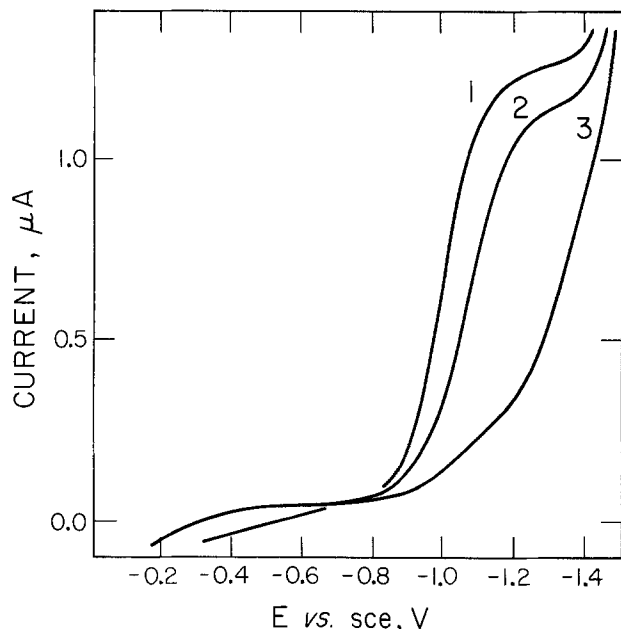


Fig. 4. Polarographic wave for 1, 20 ml of 0.6 mM Ti(IV) in 0.2M NaCl; 2, with addition of 0.5 ml of 2 mM Triton X-100 solution; and 3, with addition of 2.0 ml of 2 mM Triton X-100 solution. Drop time 1 sec and scan rate 5 mV/sec.

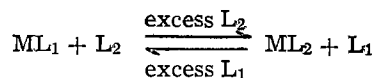
the change in slope for the Ti(IV) polarographic wave did not resemble that expected for a kinetically shifted wave (Fig. 4). When $E - E_{1/2}$ for the Ti-procarbazine system was plotted against $\log(i_d - i)/i$ the slope was 122.5 mV in the absence of procarbazine and 87.5 mV in the presence of procarbazine (0.1 mM procarbazine: 0.6 mM Ti(IV)). Thus, addition of procarbazine made the reduction of Ti(IV) appear more reversible, in contrast to the behavior expected for a kinetic phenomenon.

The above behavior can be explained by invoking a mechanism where (i) procarbazine adsorbs on the dme, (ii) Ti(IV) approaches the electrode and experiences a large procarbazine concentration with which it reacts to form a Ti(IV)-procarbazine complex, and (iii) this complex is reduced in a more reversible manner than the Ti(IV) in bulk solution.

The requirements made by this mechanism are:

1. The bulk [Ti(IV)] does not deplete the solution of free procarbazine.
2. The surface of the dme has reached maximum coverage with procarbazine by the time the depolarizer current is sampled.
3. The [procarbazine] at maximum coverage is sufficient to displace ligands from Ti(IV).
4. Ti(IV) forms a complex with procarbazine which is reduced more reversibly at the dme.

The first requirement can be met as a result of the observation that for ligand exchange reactions such as



the equilibrium favors complex formation with the ligand which is in excess, provided the stability constants are comparable. For the system described in this paper (i.e., procarbazine/Ti = 1/6) both the $[Cl^-]$ and $[H_2O]$ exceed procarbazine by at least 10^3 in bulk solution. Thus one could expect procarbazine to be primarily in its free form. This was experimentally confirmed by monitoring the u.v. spectrum of procarbazine as Ti(IV) was added. When Ti(IV) was added to a 0.2 mM solution of procarbazine a shoulder developed at 260 nm on the free procarbazine peak at 233 nm indicative of some complex formation, but the peak height at 233 nm decreased only slightly. Thus, it was found that even for tenfold excess of Ti(IV), procarbazine was predominantly in the free form.

Table II. Effect of procarbazine on the zinc polarographic wave

Metal ion	Concentration, mM	Procarbazine, mM	$i_d^{(a)}$, μA
ZnCl ₂ (H ₂ O) ₂ ²⁻	0.2	0.	1.04
		0.01	1.02
		0.10	0.97
		0.20	0.96

(^a) Corrected for dilution.

The second requirement involves adsorption of procarbazine on the dme. It also requires that the adsorption be fast enough so that the process is complete before the depolarizer current is sampled (i.e., less than 1 sec).

Suppression of i_d for Ti(IV) reduction upon addition of procarbazine could indicate that procarbazine was being adsorbed on the dme. However, if adsorption did occur, addition of procarbazine to other metal ion solutions should also show suppression of i_d . Thus, the behavior of Zn(II) upon addition of procarbazine was examined at the dme.

In the case of Zn(II), addition of procarbazine caused small decreases in i_d (see Table II) with a slight tilting of the polarographic wave (Fig. 5). In addition, the usual maximum observed for this solution disappeared upon addition of procarbazine to 0.01 mM. Such maximum suppression, reduction of i_d , and tilting of the polarographic wave are characteristic of adsorption by a surfactant. Thus, these results indicate that procarbazine was adsorbed on the dme.

With regard to the requirement that the adsorption be complete before the depolarizer current is sampled, Delahay and Trachtenberg (16) have experimentally shown that coverage is essentially complete within 1 sec for the surface active agents cyclohexanol, *n*-amyl alcohol and thymol, which was the time at which current was sampled in this study.

For the requirement that the procarbazine concentration at the surface be significantly larger than in the bulk solution, an order of magnitude calculation clearly shows that the concentration of adsorbed procarbazine at the electrode surface is significantly higher than the bulk concentration.

The quantity of surfactant adsorbed per cm² at time t before adsorption is complete at the dme is given

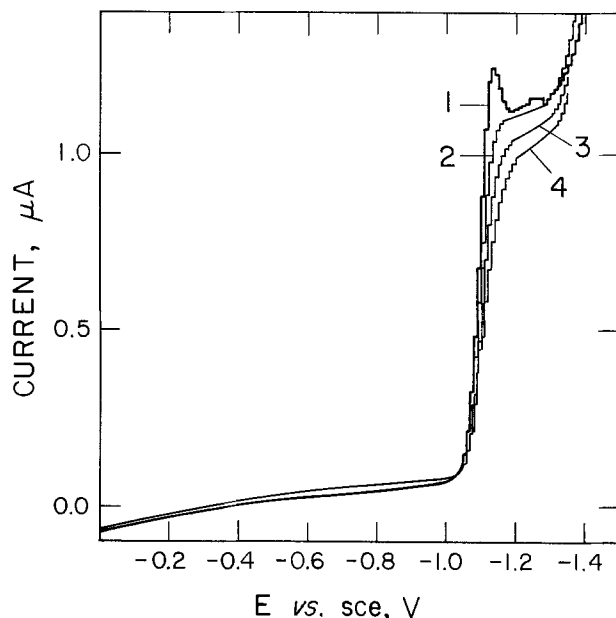


Fig. 5. Polarographic wave for 1, 20 ml of 0.2 mM ZnCl₂ in 10 mM HCl; 2, with addition of 0.1 ml of 2 mM procarbazine; 3, with addition of 1.0 ml of 2 mM procarbazine; and 4, with addition of 2.0 ml of 2 mM procarbazine. Drop time 1 sec and scan rate 5 mV/sec.

by (17)

$$\Gamma = 7.36 \times 10^{-4} [S] \sqrt{D_s} \sqrt{t}$$

If we assume that

$$\begin{aligned} D_s &= 10^{-5} \text{ cm}^2/\text{sec} \\ [S] &= 0.1 \text{ mM procarbazine} \\ t &= 1 \text{ sec} \end{aligned}$$

then

$$\Gamma = 2.3 \times 10^{-7} \text{ mmoles/cm}^2$$

If the double layer at the dme is assumed 1000Å then the concentration of surfactant within the electrolyte layer around the electrode will be

$$\begin{aligned} [S_{\text{adsorbed}}] &= 2.3 \times 10^{-7}/10^{-5} \text{ mmoles/cm}^3 \\ &= 23 \text{ mM} \end{aligned}$$

Thus the concentration of procarbazine at the surface is > 100 times that of the bulk solution, and ~ 30 times that of Ti(IV). Although this concentration gradient between bulk solution and the double layer is consistent with our model for the behavior of the Ti(IV) polarographic wave in the presence of small amounts of procarbazine, it does not establish that the procarbazine concentration at the electrode surface was large enough to form a Ti-procarbazine complex in the presence of Cl⁻ and H₂O. Therefore, it was necessary to examine chemically if a Ti-procarbazine complex formed in 10 mM procarbazine solutions. This was done by examining the stability of Ti(IV) against precipitation as TiO₂ in procarbazine solutions as the solution pH was increased. Ti(IV) will essentially precipitate completely as TiO₂ from aqueous solutions at or above pH 6 if no complexing agent is present to prevent attack on the metal by OH⁻. If an excess of complexing agent such as phosphate or citrate is present it will prevent such precipitation.

When Ti(IV) was mixed with procarbazine in a 13:1 procarbazine:Ti mM ratio at pH 2, no precipitation of TiO₂ was observed as the pH was increased to 12 by addition of NaOH. Similar experiments in which 0.02g NaHCO₃/ml of solution was used to increase the pH to 8.5 gave similar results. (When larger amounts of NaHCO₃ were used to increase the pH Ti(IV) precipitated quantitatively as the carbonate species.)

When the procarbazine to Ti(IV) ratio was 2:1 similar results to the above were observed for both addition of NaOH and NaHCO₃, but when the ratio was 1:1 partial precipitation of Ti(IV) occurred from the procarbazine solutions. These results clearly indicate that the procarbazine concentration at the dme surface in a solution of 0.1 mM bulk concentration is sufficient to form a Ti(IV)-procarbazine complex.

One further experiment exemplifies the role which procarbazine plays at the dme. It was observed that H⁺ ion reduction at pH 2 in the presence of procarbazine produced a "spike" shaped polarographic wave characteristic of strong adsorption of H⁺ at the electrode. When Ti(IV) was added in tenfold excess to the procarbazine solution the H⁺ reduction wave returned to a normal shape. Thus the presence of excess Ti(IV) eliminated the adsorption of H⁺ caused by procarbazine, indicating that a reaction between the metal and procarbazine occurred at the electrode surface.

Finally, it was necessary to show that the new waves observed when procarbazine was added to Ti(IV) solutions were due to a Ti-procarbazine complex. This was shown to be the case by following the behavior of these waves when the known Ti(IV) complexing agent H₃PO₄ was added to the Ti(IV)-procarbazine solutions. Since H₃PO₄ forms a strong complex with Ti(IV) which can be observed at the dme, incremental addition of H₃PO₄ to a Ti-procarbazine solution should increase the wave height of the known (18) Ti-phosphoric acid wave stepwise at the expense of the Ti-procarbazine wave height.

When 20 ml of 0.4 mM Ti(IV) solution, 0.257M in NaCl at pH 2, was mixed with 5 ml of 2 mM procarbazine solution the Ti(IV) reduction shifted from -0.990

to -1.130V vs. SCE, then upon addition of H₃PO₄ a new wave appeared near -0.4V with loss of wave height at -1.130V. When the H₃PO₄ concentration reached 1M, the wave at -1.130V disappeared with the appearance of a Ti-phosphoric acid complex wave at -0.420V (Fig. 6). These results showed that the wave which appeared upon addition of procarbazine to Ti(IV) solutions was due to a Ti-procarbazine complex.

The above mechanism also predicts the proper quantitative response of $E_{1/2}$ to addition of procarbazine. The general equation for the effect of a complexing agent on $E_{1/2}$ of an irreversible reduction of metallic depolarizer is given by (19)

$$E_{1/2}^c = E_{1/2}^s + \frac{RT}{\alpha n F} [\ln 0.886 k_e^0 \sqrt{t/D} - \ln(k_x k_{x-1} \dots k_{i+1}) - \ln[L]^{x-j}]$$

where the usual assumption has been made that only a ligand unsaturated metal species is electrochemically active, and this species is in equilibrium with all other metal-ligand species at the electrode surface. The half-wave potential of the complex, ML_x , is more negative than that of the free ion since the ion must first be liberated from the complex before it undergoes reduction. This requires energy and is reflected in a more negative $E_{1/2}$. From the above equation it is seen that a plot of $E_{1/2}$ against $\ln[L]$ will allow $x - j$ to be determined.

If L is adsorbed on the dme surface in linear proportion with addition of L to the bulk solution, then $[L] = a[L_0]$ where $[L_0]$ is the concentration of ligand in bulk solution, $[L]$ is the concentration at the surface, and a is a proportionality constant greater than one. Substituting these relationships into the above equation gives

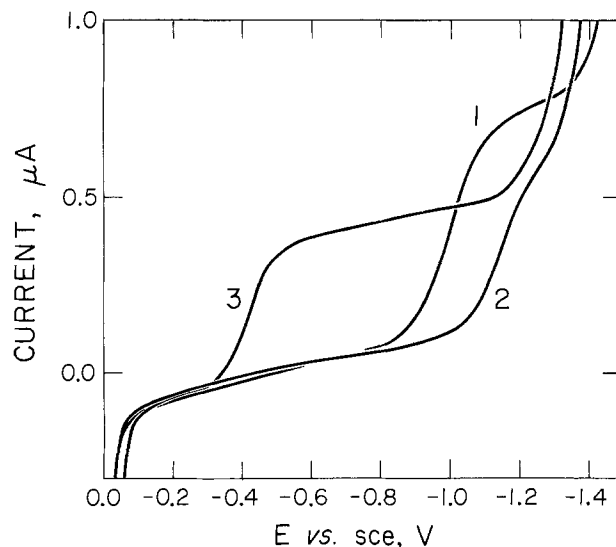


Fig. 6. Polarographic wave for 1, 0.4 mM Ti(IV) in 0.257M NaCl; 2, with addition of 5 ml of 2 mM procarbazine; and 3, with addition of 1 ml of 18M H₃PO₄. Drop time 1 sec and scan rate 5 mV/sec.

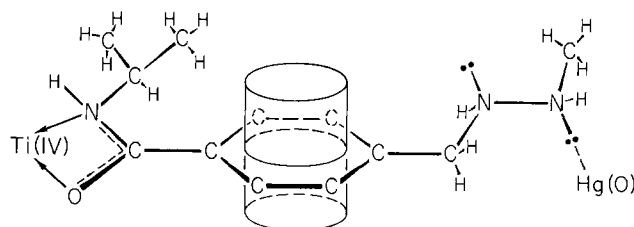


Fig. 7. Possible molecular configuration derived from to scale three dimensional models for a 1:1 Ti(IV)-procarbazine complex.

$$E_{1/2}^c = E_{1/2}^s + \frac{RT}{\alpha nF} [\ln 0.086 k_e^\circ \sqrt{t/D} - \ln K - (x - j) \ln a - (x - j) \ln [L_0]]$$

In using this equation it has been assumed that a steady-state condition was reached between the bulk metal ion concentration and the concentration of the complex ML_x in the double layer at the time the depolarizer current was sampled.

A plot of $E_{1/2}^c - E_{1/2}^s$ against $-\log[L_0]$ gives a slope of $2.3 RT/nF (x - j/\alpha)$. Such a plot constructed for the addition of small amounts of procarbazine to Ti(IV) solutions resulted in a slope of 91.66 mV and $x - j/\alpha = 1.554$. If $x - j = 1$, then $\alpha = 0.6436$, and our model is consistent with the observed shift in $E_{1/2}$; any other integer value of $x - j$ would lead to unrealistic values of α .

Thus we have found the experimental evidence to be consistent with our model for polarography of Ti(IV) in the presence of procarbazine. The adsorption of procarbazine on the dme allows its concentration to build up to at least 10 mM in the double layer, this double layer concentration is then sufficient to displace H_2O or Cl^- from the Ti(IV) species diffusing in from the bulk solution, and the new Ti-procarbazine complex formed in the double layer is the one involved in the electrochemical process at the dme. The nature of the electrochemical process itself, however, is not known. We are in the process of determining whether Ti(IV) dislodges procarbazine from the Hg surface or whether Ti(IV) is itself attached to the Hg surface through a procarbazine bridge. This latter case is possible because there are two coordination sites on procarbazine. The fact that this molecule has more than one coordination site of different chemical nature allows for both titanium complexation as well as adsorption. Finally, it should be pointed out that in the past most investigators have not looked at low levels of ligand concentrations and thus this effect may not be as rare as it appears.

Acknowledgment

We thank Roche Laboratories for supplying procarbazine samples.

Manuscript submitted July 8, 1974; revised manuscript received Oct. 18, 1974.

Any discussion of this paper will appear in a Discussion Section to be published in the December 1975 JOURNAL. All discussions for the December 1975 Discussion Section should be submitted by Aug. 1, 1975.

LIST OF SYMBOLS

a adsorption coefficient, has values greater than 1.
 α transfer coefficient, has values between 0 and 1.

E potential in volts
 $E_{1/2}^c$ half-wave potential for complex metal ion.
 $E_{1/2}^s$ half-wave potential for simple metal ion.
 F the Faraday
 G free energy
 G^\ddagger free energy of activation
 D diffusion coefficient of metal ion
 D_s diffusion coefficient of surfactant
 i current in μA
 j the number of ligands, L , coordinated to the electrochemically active metal species at the Hg surface
 k_n the stepwise equilibrium constants for formation of each complex ML_n in solution
 k_e° rate constant for the electron transfer process
 K over-all formation constant for ML_n
 $[L]$ concentration of ligand
 R gas constant
 $[S]$ concentration of surfactant
 t time in sec
 T temperature $^\circ K$
 X maximum number of ligands, L , coordinated to the metal species as it approaches the Hg surface
 Γ quantity of surfactant adsorbed at time t per cm^2 of the Hg drop surface

REFERENCES

1. K. G. Carrol and J. L. Tullis, *Nature*, **127**, 1172 (1968).
2. J. P. McCue, *Biochem. Med.*, **7**, 282 (1973).
3. J. Heyrovsky and J. Kuta, "Principles of Polarography," p. 299, Academic Press, New York (1966).
4. E. L. Colichman, *J. Am. Chem. Soc.*, **72**, 4038 (1950).
5. D. Hume and I. M. Kolthoff, *ibid.*, **72**, 4233 (1950).
6. T. Meites and L. Meites, *ibid.*, **73**, 1161 (1951).
7. A. A. Kryukova and M. A. Loshkarev, *Zh. Fiz. Khim.*, **30**, 2336 (1956).
8. M. A. Loshkarev and A. A. Kryukova, *ibid.*, **31**, 452 (1957).
9. M. A. Loshkarev and E. I. Dubyago, *ibid.*, **34**, 1430 (1960).
10. N. Tanaka, R. Tamanushi, and A. Takahashi, *Collection Czech. Chem. Comm.*, **25**, 3016 (1960).
11. J. Heyrovsky and J. Kuta, "Principles of Polarography," pp. 313-317, Academic Press, New York (1966).
12. J. Heyrovsky and J. Kuta, "Principles of Polarography," Chap. VIII, Academic Press, New York (1966).
13. B. E. Douglas, H. A. Laitinen, and J. C. Bailar, *J. Am. Chem. Soc.*, **72**, 2484 (1950).
14. H. A. Laitinen, E. I. Onstott, J. C. Bailar, Jr., and S. Swann, *ibid.*, **71**, 1550 (1949).
15. W. B. Schaap, J. A. Davis, and W. H. Nebergall, *ibid.*, **76**, 5226 (1954).
16. P. Delahay and I. Trachtenberg, *ibid.*, **80**, 2094 (1958).
17. J. Heyrovsky and J. Kuta, "Principles of Polarography," p. 305, Academic Press, New York (1966).
18. J. J. Lingane and J. H. Kennedy, *Anal. Chim. Acta*, **15**, 294 (1956).
19. J. Heyrovsky and J. Kuta, "Principles of Polarography," p. 222, Academic Press, New York (1966).

An Analysis of the Impedance of Polycrystalline Beta-Alumina

R. W. Powers* and S. P. Mitoff

General Electric Research and Development Center, Schenectady, New York 12301

ABSTRACT

A procedure is described in this paper for distinguishing in the measured electrical properties of polycrystalline β -alumina, the separate contributions of the grain boundaries and of the crystal, *i.e.*, the grain interiors. This separation is brought about through the use of a model for these properties. Certain quantitative consequences of the model are developed and compared with experimental results. For most sintered β -alumina ceramic, the electrical properties are determined more by the characteristics of the grain boundaries than by those of the interior of the grains.

Polycrystalline β -alumina is used in electrochemical devices to circumvent the deleterious high anisotropy in the electrical and mechanical properties of single crystals. Use of the polycrystalline ceramic does require, however, consideration of the effects of grain boundaries. A procedure is described here for distinguishing in the measured electrical properties of the ceramic, the separate contributions of the grain boundaries and of the crystal, *i.e.*, the interior of the grains. This separation is brought about through the use of a model for the electrical properties of β -alumina. Certain quantitative consequences of this model are developed and compared with experimental results.

Previous Work

The conductivity both of β -alumina single crystals and of polycrystalline ceramic has already received very considerable attention (1-15). Weber and Kummer reported that β -alumina exhibits high ionic conductivity, but no electronic conductivity (1). The ionic conductivity is due to the high mobility of sodium ions in planes perpendicular to the *c*-axis of the hexagonal structure. However, there is no conductivity parallel to the *c*-axis. They reported single-crystal specific resistivity values of 30 and 3.5 ohm-cm at room temperature and 300°C, respectively. Comparable values for polycrystalline ceramic prepared from single-crystal material was 250 and 18 ohm-cm. They attributed the difference to interface resistivity between the crystals of the polycrystalline material. The activation energy associated with the resistivity of single crystals was given as 3.8 kcal/mole (2).

Imai and Harata, on observing that the activation energy associated with conduction in sintered β -alumina was considerably larger than for single crystals, concluded that the conductivity of ceramic is governed by grain boundary conduction (4).

Jones and Miles found that the Arrhenius plot curved significantly below 200°C (5). Another activated process with a higher activation energy controlled the conductivity at lower temperatures. These authors speculated that this process was grain boundary contact resistance.

Whittingham and Huggins measured the conductivity of a single crystal from -150°C to 820°C (8). They found plots of $\log \sigma T$ to be linear in $1/T$ over this entire temperature interval. The conductivity was found to be 72 ohm-cm at 25°C. The activation energy was 3.79 kcal/mole. They reported the conductivity to be sensitive to the presence of moisture below 50°C.

Imai and Harata reported that the a-c conductivity of polycrystalline β -alumina increases with frequency but becomes independent of frequency above 5 MHz

at room temperature (12). However, Fally and associates found no frequency dependence up to 10^5 Hz at 300°C (14). Kennedy and Sammells found the conductivity to vary linearly with the square root of frequency at least up to 10 kHz on measurements with polycrystalline material at room temperature (13).

The Model

Grain boundaries in β -alumina can be viewed as almost a different material with resistive and dielectric properties distinct from those of the interior of the grains. Ionic charge is considered to pass successively through the grain interiors and the grain boundaries. These ideas are embodied in a model consisting of two resistors in series, each shunted by a capacitor (16). This particular representation is really appropriate only when evidence is present that the grain boundary resistivity is very large with respect to the crystal resistivity. When this situation occurs, one may consider the limiting case in which grains are in series with grain boundaries and parallel connections can be neglected. For the purpose of this study, it is convenient, but not necessary, to ignore the contribution of the capacitor shunting the crystal interior, which represents the crystal dielectric constant. Changes of impedance resulting from this capacitance will occur at frequencies higher than those studied here. Therefore, the simplified model, to be considered in detail below, is shown in Fig. 1.

If a specimen whose electrical properties can be so described is placed in series with a standard resistor and the combination energized with the output of a sine wave generator, the parameters characterizing the model can be determined from the variation of the observed impedance and phase angle with frequency. Certain relationships between these observable quantities can be used to determine the degree to which the electrical properties of β -alumina can be so modeled. The variation of the impedance with frequency for such a specimen is given by the expression

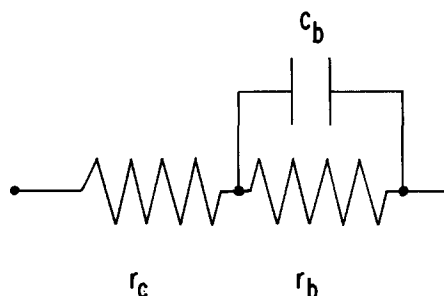


Fig. 1. Simplified model for the electrical properties of polycrystalline β -alumina.

* Electrochemical Society Active Member.

Key words: beta-alumina, solid electrolyte, electrical properties, grain boundary resistivity.

$$z = (r_c + r_b) \left[\frac{1 + \left(\frac{r_c}{r_c + r_b} \right)^2 (r_b C_b 2\pi f)^2}{1 + (r_b C_b 2\pi f)^2} \right]^{1/2} \quad [1]$$

where z is the measured impedance, f is the frequency, and the parameters r_c , r_b , and C_b are, respectively, the specific resistivity of grain interiors, the specific resistivity of the grain boundaries, and the specific capacity of the grain boundaries as shown in Fig. 1. This variation is shown in Fig. 2. There are two limiting levels of impedance, a low frequency one equal to $r_c + r_b$ and a high frequency one equal to r_c . Furthermore, at both very low and very high frequencies, the current through the specimen and the voltage developed across it are in phase. At intermediate frequencies, the current leads the voltage. This lead is maximum at that frequency corresponding to an inflection point on a plot of $\log z$ vs. $\log f$. This crossover frequency, analogous to the loss peak in dielectric relaxation measurements and indicated as f_c in Fig. 2, is that at which the impedance is the geometric mean of the low and high frequency limiting impedances, i.e., $z_c = \{r_c(r_c + r_b)\}^{1/2}$. The capacitance, C_b , can be obtained from this frequency, along with values for the limiting impedances, by means of the expression

$$C_b = \frac{1}{2\pi f_c r_b} \left[\frac{r_c + r_b}{r_c} \right]^{1/2} \quad [2]$$

Some other expressions are also useful in making detailed comparison with experiment. For example, the variation of the phase angle with frequency is

$$\tan \theta = \frac{r_b C_b 2\pi f}{1 + (r_c/r_b) \{1 + (r_b C_b 2\pi f)^2\}} \quad [3]$$

The maximum phase shift is

$$\tan \theta_{\max} = \frac{r_b}{2\{r_c(r_c + r_b)\}^{1/2}} \quad [4]$$

Experimental Techniques

Impedance data to be presented were obtained on β -alumina tubes about 1 cm in diameter and usually 7.5-10 cm in length. While a detailed description of the specimen fabrication procedure has recently been given, it will be outlined here (17). The starting material was a powder, indicated as XB-2 β -alumina by the manufacturer, the Aluminum Company of America. Into this powder, various additives such as yttria, magnesia, or zirconia were incorporated. Yttria was added by way of yttrium oxalate powder, magnesia via basic magnesium carbonate powder, and zirconia by wear of the grinding media used to reduce the particle size. After tumble mixing, the powder was calcined at 1400°C to decompose the oxalate and carbonate additives and to dry the powder. The calcined powder was then suspended in amyl alcohol.

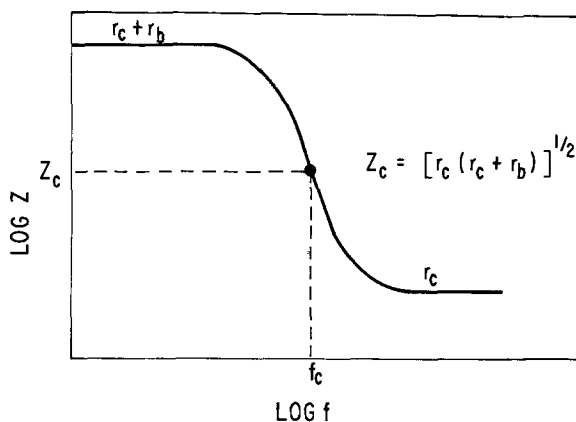


Fig. 2. Variation of impedance with frequency for simplified model.

The particle size was reduced either by ball or vibratory milling using either α -alumina or zirconia grinding media. The powder was formed in the shape of closed-end tubes using electrophoretic deposition. After removal from the forming electrodes, the green tubes were sintered in air at temperatures between 1700° and 1825°C.

Data are given in this paper on material of two different compositions. One contained 1 weight per cent (w/o) magnesia, 0.5 w/o yttria, and 1 w/o zirconia. The other differed only in the omission of yttria. Additives were incorporated mainly for the purpose of aiding densification during sintering. The composition of the as-received XB-2 powder is approximately 1.40 Na₂O·11 Al₂O₃, i.e., it contains a 40% excess of sodium oxide over that of the theoretical composition, Na₂O·11 Al₂O₃. According to Roth and Mitoff, this composition is that of the sodium-rich boundary of the single-phase field at 1725°C (18). Some sodium oxide is always lost during sintering. However, it is most unlikely that the composition dropped below 1.35 Na₂O·11 Al₂O₃ for the specimens on which data are given. This composition is well within the single-phase field.

The specimens were essentially without a preferred orientation. No phase other than hexagonal two-block β -alumina was evident from x-ray diffraction.

Impedance measurements were carried out using special jigs in which four 0.010 in. platinum rhodium wires were positioned circumferentially about the specimen at fixed distances along it. A photograph of one jig used at room temperature and below appears in Fig. 3. The 1/2 in. diameter Teflon polymer rods shown above and below the specimen were used to position the contact wires. To improve contact, the wires were wetted with very small quantities of a propylene carbonate solution, 0.6M in both NaI and iodine. For use at higher temperatures, the contact positioning rods were constructed of lava, and platinum bands were cathode sputtered circumferentially about the specimen to which contact was made with platinum wires. One junction of a thermocouple was placed inside the specimen tube in order to sense the temperature. For measurements at or below room temperature the resistivity jig was placed inside a 2 5/8 in. ID tubular brass housing which was placed in turn inside a controlled temperature Missimers environmental chamber. Measurements above room temperature were carried out in a simple wire-wound furnace.

The test circuit used for impedance measurements is shown in Fig. 4. The outer or current contacts were attached to a sine wave generator, the output amplitude and frequency of which could be varied, and to a multidecade resistance box, which served as a standard resistance. The voltage waveforms developed across the inner or voltage contacts to the specimen and across the resistance box were displayed on a dual beam oscilloscope. The impedance at some given

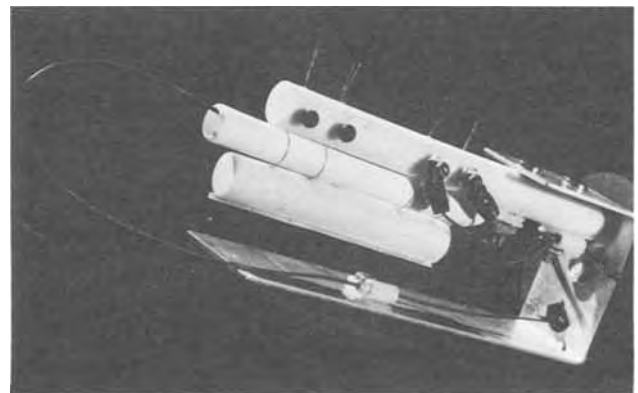


Fig. 3. Jig used for electrical measurements on β -alumina tubes

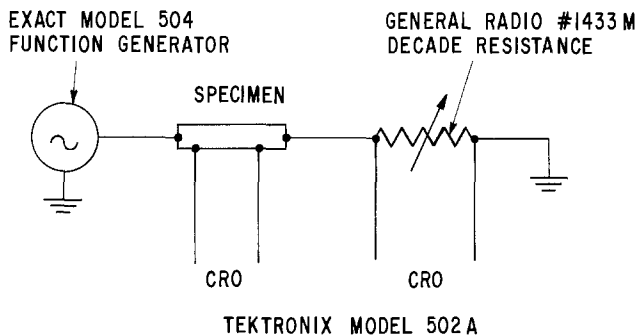


Fig. 4. Four point arrangement for measuring components of electrolyte impedance.

frequency was readily determined by adjusting the setting of the resistance box so that the amplitude of the voltage developed across it equaled that across the voltage contacts to the specimen. The phase lag was obtained from the horizontal displacement of the two waveforms in comparison with the displacement corresponding to one period.

This simple test arrangement was validated by carrying out measurements at frequencies ranging from 10 to 300,000 Hz on a simulated specimen constructed from high quality resistors and a capacitor. The measured impedances agreed with those calculated from the known values of the circuit elements using Eq. [1] to within 1.5% at all frequencies except at 30,000 Hz. Here a 3.5% discrepancy was encountered. Moreover, the value of C_b obtained with Eq. [2] differed from the true value by less than 5%.

The criterion for the suitability of contact to a specimen was that the phase angle at 10 Hz between the current through the specimen and the voltage between the two interior contact wires be no greater than one degree. It could usually be met except for two circumstances. The first arose when highly resistive surface layers formed on the specimen from exposure to the atmosphere. The second developed if the specimen was porous, causing absorption of the contact fluid and its removal from the contact wires. The problem was seldom encountered if the specimen density exceeded 3.15 g/cm³ and was nearly always present in specimens with densities less than 3.00 g/cm³.

The impedance values reported in this paper were found to be independent of the current level within approximately a per cent. For assurance on this point, it was routine to vary the current over a factor of about ten at each test temperature for every specimen. And on a few specimens, it was varied a thousand-fold. Indium amalgams were used to make electrical contact in preliminary work. The impedance values observed were the same, within experimental error, as those using a propylene carbonate solution of sodium iodide and iodine. Further, the data obtained using only platinum contacts were not distinguishable at room temperature and above from those using the propylene carbonate contact solution. These facts indicate that the impedance values presented were not compromised by polarization effects at the electrodes.

Measurements with the test arrangement described above are limited to frequencies somewhat less than a megahertz. This limitation is mainly due to the shunt capacitance of the multidecade resistance box serving as the reference resistor. Such capacitance causes the so-called a-c resistance to be less than the d-c value at higher frequencies. A simple criterion was developed to determine if the impedance measurements were compromised from this effect. It is based on the fact that the ratio of a-c to d-c resistance depends very sensitively on the frequency and setting of the resistance box. At higher frequencies after adjusting the reference resistance so that the voltage amplitude across the box equals that across the voltage

contacts to the specimen, the setting is reduced to one-half this value. If the amplitude is reduced correspondingly to one-half that across the specimen, the impedance measurement is considered valid. On the other hand, the extent to which the half-setting amplitude exceeds one-half that across the specimen provides an indication of the extent to which the measurement is compromised.

Experimental Results and Discussion

Plots of the logarithm of the specific impedance vs. the logarithm of the frequency are shown in Fig. 5 for five yttria-containing specimens which differed in the manner in which particle size reduction was carried out on the starting β -alumina powders. Ball milling was carried out using either α -alumina or zirconia grinding media for different lengths of time. The measurements were all carried out at room temperature. Below 100 Hz, the impedance does not vary with frequency. There is considerable variation, over a factor of 8, in the low frequency limiting value from one specimen to another. In contrast the impedance values for the different specimens almost converge around 10⁵ Hz and only range from 110-140 ohm-cm at this frequency. They appear to be approaching another plateau. Using a more precise method for treating impedance data described below, a value of 84 ohm-cm was obtained for this plateau at 25°C on two different β -alumina samples containing yttria. Since the high frequency plateau is associated with the resistivity of grain interiors, it should be compared with the resistivity of single crystals. Room temperature values of 30-72 ohm-cm have been reported on single crystals without additives. It might be expected that r_c values should be slightly larger than that for single crystals in easy conducting directions because the grains in the ceramic are randomly oriented with conducting paths somewhat longer as a consequence.

If values of the low frequency impedance plateau are to be associated mainly with the grain boundary resistance, then there should exist a good correlation between this value and the number of grain boundaries per unit length intersecting a line in the direction of the electric field. Ideally, a direct proportionality would be anticipated. However, because of the extreme tendency in β -alumina for a few grains to grow to very large size at higher sintering temperatures or longer sintering times, there is a problem with uniformity of current distribution. A direct proportionality consequently would be somewhat fortuitous. An illustration of this grain size variation is presented in Fig. 6 with a 500 \times photomicrograph of specimen 5P1-2. This correlation between grain boundary resistivity and the number of grain boundary intersections is presented in Table I for a series of four specimens all containing yttria. The grain size was altered by sintering at different temperatures. The number of grain boundary intersections per centim-

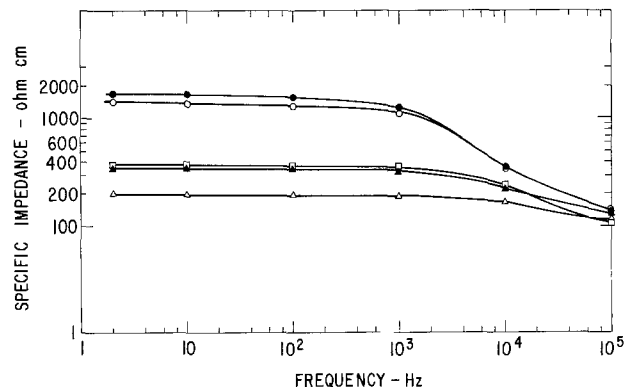


Fig. 5. Variation of impedance with frequency for several specimens.

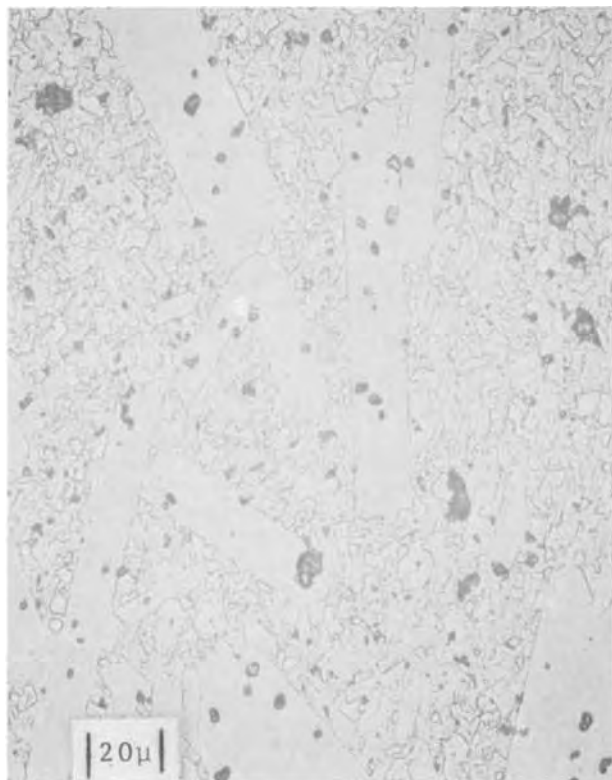


Fig. 6. Specimen 5P1-2. 500X

eter length was determined by counting the intersections of grain boundaries with random lines on either 250 or 500 \times micrographs. Since the crystal resistance makes only a small contribution to the low frequency limiting value of the impedance, a value of r_c of 84 ohm-cm determined on specimens 5P1-1 and 5P1-2, was used for all four specimens. The correlation is sufficiently good to give some confidence in the association of the value of the low frequency plateau with $r_c + r_b$.

The observation of some previous authors that plots of the logarithm of the product, temperature times conductivity, vs. reciprocal temperature are sometimes nonlinear can now be readily understood. The crystal resistance has a temperature coefficient differing considerably from that for the grain boundaries. Plots of $\log z$ vs. $\log f$ for specimen 5P1-1 at several temperatures ranging from -13° to 320°C are presented in Fig. 7. Similar plots obtained on a specimen of somewhat smaller grain size, 5P1-2, are shown in Fig. 8. From these data, values of r_c and r_b were determined over a range of temperatures. Since there still was a small variation in the impedance with frequency at low frequencies, an effect which increases with decreasing temperature, values of $r_c + r_b$ were obtained by linear extrapolation of plots of z vs. f to $f \rightarrow 0$. Similarly, values of r_c were obtained by linear extrapolation of plots of z vs. $1/f$ at high frequencies to $1/f \rightarrow 0$. The quantities $\sigma_c T$ and $\sigma_b T$ are presented on Arrhenius type plots in Fig. 9, where $\sigma_c = 1/r_c$, $\sigma_b = 1/r_b$, and T is the absolute temperature. The activation energy for conduction through the grain

Table I. Correlation of parameter r_b with number of grain boundaries per unit length intersected by random lines

Specimen	r_b , kohm-cm	Intersections per cm $\cdot 10^{-3}$	r_b /intersections per cm
5P1-1	1.33	0.81	1.64
5P1-2	1.88	2.25	0.84
5P1-3	2.2	2.75	0.80
5P1-5	6.9	3.5	1.97

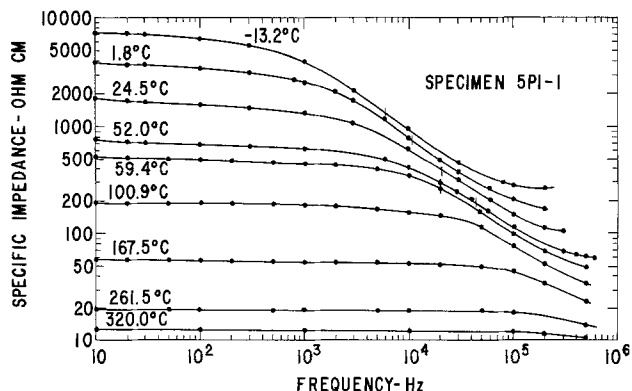


Fig. 7. Specific impedance vs. frequency curves for specimen 5P1-1.

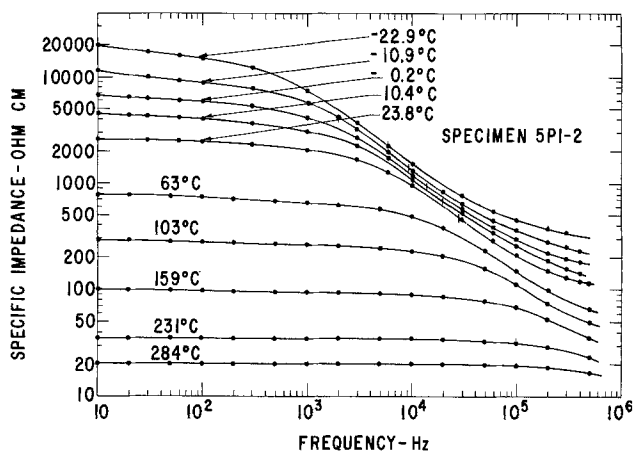


Fig. 8. Specific impedance vs. frequency curves for specimen 5P1-2.

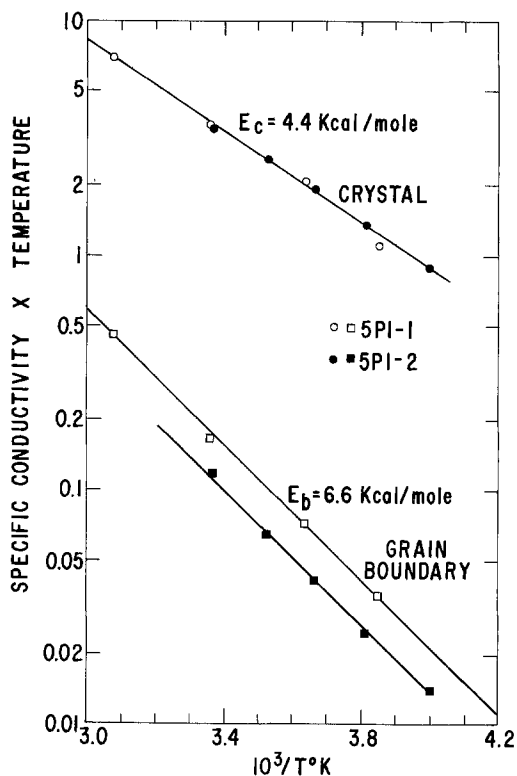


Fig. 9. Arrhenius plots for components of resistivity

interiors was nearly the same for both specimens and amounted to 4.4 kcal/mole. That for the grain boundaries on the other hand, amounted to 6.6 kcal/mole for both specimens. There can be considerable varia-

tion, however, in the measured activation energy for the grain boundary resistance from one specimen to another. A value as low as 5.1 kcal has been observed. This fact, perhaps, accounts for the considerably larger curvature on some plots of $\log \sigma_{\text{total}} T$ vs. $1/T$ reported previously than that observed by the present authors (5, 12). Here σ_{total} is the reciprocal of $r_b + r_c$.

There are still other grain boundary properties in addition to resistivity and its activation energy in which large variations are observed from one specimen to another. As shown in Fig. 10, the cross-over frequency is much larger at room temperature for specimen 6F10-2 than for the specimens on which data were presented above. The previous specimens contained 0.5 w/o yttria while this additive was absent from 6F10-2. Even at the highest frequencies, at which measurements would be made using the technique described in this paper, the impedance was only a little less than the low frequency limiting value. This fact, of course, implies a much smaller C_b value than for the other specimens. Measurements could not be extended above 300,000 Hz for reasons discussed above. Consequently, r_c values could not be measured on yttria-free specimens.

From Eq. [2], the cross-over frequency f_c is given by the expression

$$f_c = \frac{1}{2\pi C_b} \left(\frac{1 + \frac{r_c}{r_b}}{r_b r_c} \right)^{1/2}$$

It must shift to higher frequencies with increasing temperature because both r_c and r_b decrease with temperature. In contrast to the resistive parameters in the simplified model, the grain boundary capacitance varies hardly at all with temperature. On specimen 5P1-1 the parameter C_b was 0.020, 0.0213, 0.021, and 0.021 microfarads/cm at temperatures of -13.2° , 1.8° , 24.5° , and 52.0°C , respectively. On 5P1-2, this quantity was 0.0121, 0.0124, 0.0123, 0.0121, and 0.0126 microfarads/cm at temperatures of -22.9° , -10.9° , -0.2° , 10.4° , and 23.0°C , respectively. The temperature shift of f_c , indicated by vertical bars on the individual curves, is very evident in both Fig. 7 and 8 and imposes a practical limit on the temperature range over which r_c values can be obtained using the present experimental technique.

Some clarifications need to be made with regard to the units in which impedance measurements as well as the parameters r_c , r_b , and C_b , are expressed. The impedance of a specimen at a given frequency is obtained from a setting of the reference resistance box as described above. In analogy to the specific resistivity, the specific impedance is obtained simply from the product of this impedance and the ratio of effective cross-sectional area to distance between the voltage contacts. Similarly, the parameter r_c , the specific resistivity of the grain interiors, presents no dif-

ferences. However, the parameter r_b , although expressed in the units of specific resistivity, does not refer to a centimeter cube of grain boundary material. Rather it can be considered as the resistance of whatever grain boundaries are present in a specimen of 1 cm^2 cross section with the voltage drop measured over a 1 cm length. If r_c and r_b are expressed in units of ohm-centimeter, then from Eq. [2] the grain boundary capacitance must have units of farads/centimeter. It is possible, however, to get an order of magnitude estimate of the true grain boundary specific resistivity, ρ_b , from elementary considerations. Thus

$$r_b C_b = \left(\rho_b \frac{l}{A} \right) \left(\epsilon \epsilon_0 \frac{A'}{l'} \right)$$

where A is the effective cross-sectional area of the grain boundary normal to the electric field; l is the sum of the grain boundary thicknesses in the field direction; ϵ is the grain boundary dielectric constant; ϵ_0 is the permittivity of free space, $8.85 \cdot 10^{-14}$ farad/cm; A' is the effective area of grain boundary capacitor "plates"; and l' is the total thickness of such plates. If $A = A'$ and $l = l'$, then

$$r_b C_b = \rho_b \epsilon_0 \epsilon$$

Using values for r_b and C_b obtained on specimen 5P1-2 at room temperature and estimating ϵ to be about 5, one gets

$$\rho_b = 7.10^7 \text{ ohm-cm}$$

This value is roughly 10^5 times larger than r_c . The magnitude of this factor for β -alumina is the underlying reason for the subject given consideration in this paper and constitutes the basis for the simplified model as discussed above.

The most serious discrepancy between experimental data and predictions based on the simplified model is that the measured frequency interval between the low and high frequency impedance plateaus is larger than calculated. This fact is illustrated in Fig. 11 for specimen 5P1-1 at 52°C . This finding implies that the electrical properties of the grain boundaries cannot be described by a single set of r_b , C_b values, a result supported by measurements of the phase angle, also presented in Fig. 11. If the resistivity and dielectric constant of all grain boundaries are not identical, a satisfactory description requires a series of resistors, each shunted with its separate capacitor. At sufficiently low frequencies, the impedance of such a modified model would equal the sum of the individual grain boundary resistances plus that for the crystal as with the simplified model. The heterogeneity in the electrical properties of grain boundaries perhaps should not be too surprising because the various boundaries are oriented randomly with respect to the electric field and compositional variations from boundary to

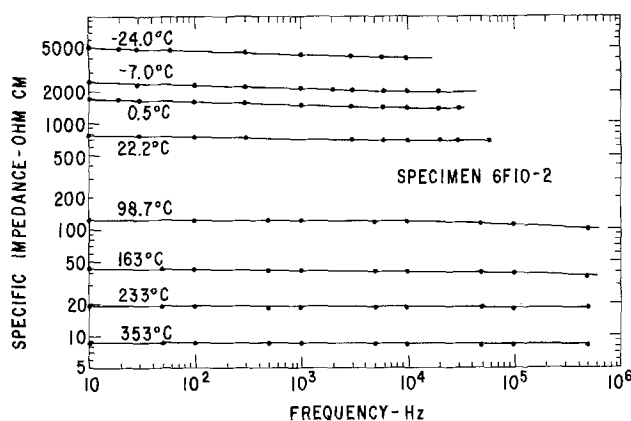


Fig. 10. Specific impedance vs. frequency curves for specimen 6F10-2.

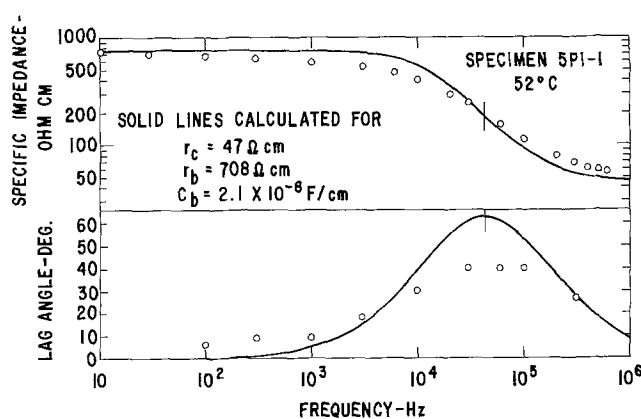


Fig. 11. Impedance and phase angle vs. frequency curves showing deviations from behavior of simplified model.

boundary are likely, due to the presence of impurities and additives.

The simplified model of the electrical properties of β -alumina ceramic shown on Fig. 1 is really that of a voltage divider for d.c. Consequently, when β -alumina is used in an electrochemical device, a large fraction of the applied voltage appears across the grain boundaries. This fraction does decrease, however, with increasing temperature. Assuming a typical β -alumina ceramic thickness of 1 mm, 10^8 grain boundaries per centimeter, a grain boundary thickness of 10^{-7} cm, and an applied voltage of 1V, all appearing across the grain boundaries, the electric field would be 10^5 V/cm. This value is sufficiently large for concern about the rapid decomposition of unstable substances which might be present in a boundary in contact with an electronic conductor. Such substances might be either additives or impurities. The cracking of β -alumina ceramic arising from sodium deposition into fine cracks may conceivably bear some association with the high fields present across grain boundaries.

Principal Conclusions

The simplified model of the electrical properties of β -alumina ceramic shown in Fig. 1 is a good first approximation but needs modification to take account of the heterogeneity of grain boundaries

The model helps place in perspective a number of findings of previous authors.

For most sintered β -alumina ceramic, the electrical properties are determined more by the characteristics of the grain boundaries than by those of the interior of the grains. Consequently, much of the voltage drop during current flow appears across the grain boundaries, giving rise there to very large electric fields.

Acknowledgments

The authors are indebted to E. Szymalak and R. N. King for experimental assistance and to Dr. G. A. Mellinger, P. D. DeTorres, and W. V. Olszewski for use of a Missimers furnace. A portion of this work was performed with the support of the Electric Power Research Institute.

Manuscript submitted April 22, 1974; revised manuscript received Aug. 20, 1974.

Any discussion of this paper will appear in a Discussion Section to be published in the December 1975 JOURNAL. All discussions for the December 1975 Discussion Section should be submitted by Aug. 1, 1975.

Publication costs of this article were partially assisted by General Electric Company.

REFERENCES

1. N. Weber and J. T. Kummer, Power Sources Conference Proc., Red Bank, N.J. 1967, p. 37.
2. Y. F. Yao and J. T. Kummer, *J. Inorg. Nucl. Chem.*, **29**, 2453 (1967).
3. R. H. Radzilowski, Y. F. Yao, and J. T. Kummer, *J. Appl. Phys.*, **40**, 4716 (1969).
4. A. Imai and M. Harata, Abstract No. 277, p. 673, Electrochemical Society Extended Abstracts, Spring Meeting, Los Angeles, California, May 10-15, 1970.
5. I. Wynn Jones and L. J. Miles, *Proc. Brit. Ceram. Soc.*, No. 19, p. 161 (1970).
6. L. J. Miles and I. Wynn Jones, *ibid.*, p. 179.
7. M. S. Whittingham and R. A. Huggins, *This Journal*, **118**, 1 (1971).
8. M. S. Whittingham and R. A. Huggins, *J. Chem. Phys.*, **54**, 414 (1971).
9. R. H. Radzilowski and J. T. Kummer, *This Journal*, **118**, 714 (1971).
10. D. S. Demott and P. Hancock, *Proc. Brit. Ceram. Soc.*, No. 19, p. 193 (1970).
11. R. D. Armstrong, T. Dickinson, and J. Turner, *This Journal*, **118**, 1135 (1971).
12. A. Imai and M. Harata, *Japan. J. Appl. Phys.*, **11**, 180 (1972).
13. J. H. Kennedy and A. F. Sammells, *This Journal*, **119**, 1609 (1972).
14. J. Fally, C. Lasne, Y. Lazennec, Y. LeCars, and P. Margotin, *ibid.*, **120**, 1296 (1973).
15. R. D. Armstrong, T. Dickinson, and J. Turner, *Electroanalytical Chem. and Interfacial Electrochem.*, **44**, 157 (1973).
16. S. P. Mitoff, chapter in "Fast Ion Transport in Solids," W. van Gool, Editor, North Holland American Elsevier Publishing Co., New York (1973).
17. R. W. Powers, Submitted to *This Journal*.
18. W. L. Roth and S. P. Mitoff, General Electric Co., Schenectady, N.Y., Corporate Research & Development Report No. 71-C-277, September 1971.

Thermodynamic Studies of Dilute Zinc Solutions in the Zn-Sn-Cd-Pb System at High Lead Concentrations

Z. Moser*¹ and W. Zakulski

Institute for Metal Research, Polish Academy of Sciences, Kraków, Reymonta 25, Poland

ABSTRACT

The activity coefficients of zinc were measured in the concentration range $0.03 < X_{Zn} < 0.1$ at temperatures in the range 714° – 877° K for lead-rich alloys in the quaternary system Zn-Sn-Cd-Pb with tin and cadmium mole fractions limited to $0.01 < X_{Sn} < 0.1$ and $0.01 < X_{Cd} < 0.1$. Measurements were of emf of concentration cells. Experimental values of $\ln \gamma_{Zn}$ were compared with values obtained from the Krupkowski formalism and from the Wagner formalism. In the latter instance two sets of values were generated, one set considering first-order interactions only and the other set considering both first- and second-order interactions. The comparisons show that the experimental data are reasonably described by both the Krupkowski approach and the Wagner approach with first-order interactions only. However, less satisfactory accord is obtained after inclusion of second-order interactions in the Wagner equations. The present results show that in the quaternary system strong negative self-interaction parameters, ϵ^{Zn}_{Zn} which lead to marked positive deviations from Raoult's law in the Zn-Pb binary system also lead to negative zinc-cadmium and zinc-tin interaction parameters in the quaternary system. This is in accord with earlier results on ternary systems.

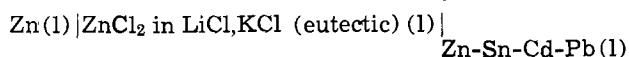
Determination of thermodynamic properties of dilute multicomponent systems is of interest from an industrial point of view but is also of fundamental interest in defining the predictability of solute-solute interaction parameters on the basis of a solute-solvent reference interaction. In this study the reference can be taken as a binary solution showing only strong positive deviations from ideal behavior. In a previous investigation (1) it was shown that in the case of ternary solutions where one binary pair exhibits extensive deviation from Raoult's law, the deviation influences in a predictable manner the thermodynamic properties of the ternary system. Zinc and lead form liquid solutions with strong deviations from Raoult's law. It has been experimentally demonstrated that negative values for interaction parameters ϵ^{Me}_{Zn} occur in ternary Zn-Me-Pb solutions where Me = Bi, Sb, Cd, Sn, and In. In all these Zn-Me binary systems a much smaller departure from ideality is observed than in the Zn-Pb system, and the original properties of Zn-Pb solutions are a decisive factor in the determination of the sign of the ternary interaction parameters ϵ^{Me}_{Zn} .

The main purposes of the present investigation were to find whether or not the strong negative self-interaction parameter, $\epsilon^{Zn}_{Zn} < 0$ in the Zn-Pb binary system is also decisive in quaternary solutions, to determine the influence of tin and cadmium additions on zinc activity, and finally to test Krupkowski's (2) and Wagner's (3) formalisms with experimental data. In Krupkowski's formalism the thermodynamic functions of a multicomponent system are evaluated from the activity coefficients of the constituent binary systems. Wagner's series expansion which represents the logarithm of the zinc activity coefficient as a sum of interaction parameters is simplified in the present system since the relation of $\ln \gamma_{Zn}$ vs. concentration of tin or cadmium in lead was found to be linear. The Wagner treatment may be applied with the assumption of first-order interactions only (model I) or with the assumption of both first- and second-order interactions (model II). It may be noted that Gluck and Pehlke (4, 5) have studied bismuth-rich ternary, quaternary, quinary, hexadic, and septenary solutions with dilute

zinc concentrations and have shown that in these systems the inclusion of second-order interactions is useful in predicting the activity coefficient of zinc.

Experimental Procedure

Zinc activities were determined by emf measurements on concentration cells of the type



Experimental details have been discussed in preceding papers (6, 7). Measurements were made with zinc mole fractions of $X_{Zn} = 0.03, 0.05, 0.07,$ and 0.1 and tin and cadmium mole fractions varying between 0.01 and 0.1 in the temperature range 714° – 877° K. For any given concentration, the experimental emf vs. temperature was found to be adequately described by a linear relationship, and the experimental data were fitted to such a relationship by the method of least squares. The resulting parameters with standard deviations are listed in Table I. Values from these linear relationships were taken at arbitrarily selected temperatures of $714^{\circ}, 805^{\circ},$ and 877° K and were converted to activity coefficients through the relation

$$\gamma_{Zn} = 1/X_{Zn} e^{-nEF/RT} \quad [1]$$

where γ_{Zn} and X_{Zn} are, respectively, the activity coefficient and mole fraction of zinc, n is the valence, F is Faraday's constant with a selected value of $23,066$ cal per volt per gram equivalent, E is the emf in volts, T is the temperature in Kelvin, and R is the gas constant. The experimental data are summarized in Table I. The uncertainties in the experimental emf's vs. temperature reflect uncertainties between 1 and 5% in $\ln \gamma_{Zn}$ at any given temperature at the 95% confidence level.

Interpretation of the Results by Krupkowski's Formalism

Values of $\ln \gamma_{Zn}$ from Eq. [1] are plotted in Fig. 1 through 4 as $\ln \gamma_{Zn}$ vs. X_{Sn} ($X_{Zn} = X_{Cd} = \text{const}$) and in Fig. 5 through 8 as $\ln \gamma_{Zn}$ vs. X_{Cd} ($X_{Zn} = X_{Sn} = \text{const}$). The ternary end points in Fig. 1 through 4 at $X_{Sn} = 0$ and in Fig. 5 through 8 at $X_{Cd} = 0$ are from previous papers on Zn-Cd-Pb (8) and Zn-Sn-Pb (9) systems, respectively. It can be seen from the extrapolations that the present data are in good accord with earlier data. In Fig. 1 through 8 the thin continuous line corresponds to $\ln \gamma_{Zn}$ values obtained by means of Krupkowski's formalism. According to Krupkowski's

* Electrochemical Society Active Member.

¹ Present address: Visiting Professor, Iowa State University, Ames Laboratory, USAEC, Ames, Iowa 50010.

Key words: concentration cell, liquid quaternary system, activity coefficient of zinc, interaction parameter.

Table I. Experimental data in the Zn-Sn-Cd-Pb liquid alloys

Alloy No.	X_{Zn}^*	X_{Sn}	X_{Cd}	X_{Pb}	Electromotive force, mV			$E_{mV} = -a + b T^{\circ}K^{**}$	$S(\bar{y})^{\dagger}$
					714°K	805°K	877°K		
1	0.0301	0.0100	0.0300	0.9299	21.976	38.704	51.939	= 109.271 + 0.18382T	0.52
2	0.0301	0.0299	0.0300	0.9100	22.166	39.621	53.431	= 114.786 + 0.19181T	0.58
3	0.0301	0.0500	0.0299	0.8900	26.298	42.812	55.879	= 103.279 + 0.18148T	0.42
4	0.0302	0.0700	0.0299	0.8699	28.399	45.637	59.276	= 106.854 + 0.18943T	1.09
5	0.0301	0.1000	0.0300	0.8399	33.928	50.545	63.692	= 96.448 + 0.18260T	—
6	0.0501	0.0100	0.0500	0.8899	7.692	23.341	35.722	= 115.087 + 0.17196T	—
7	0.0501	0.0299	0.0499	0.8700	9.852	25.690	38.222	= 114.420 + 0.17405T	—
8	0.0501	0.0500	0.0499	0.8500	12.926	28.570	40.947	= 109.818 + 0.17191T	—
9	0.0501	0.0700	0.0499	0.8300	13.810	29.096	41.190	= 106.128 + 0.16798T	—
10	0.0501	0.1000	0.0499	0.8000	18.753	34.008	46.078	= 100.942 + 0.16764T	—
11	0.0701	0.0100	0.0700	0.8499	2.577	15.733	26.142	= 100.646 + 0.14457T	0.26
12	0.0701	0.0298	0.0700	0.8301	5.762	18.650	28.847	= 95.362 + 0.14163T	—
13	0.0702	0.0500	0.0700	0.8098	8.616	20.443	31.224	= 100.098 + 0.14974T	—
14	0.0701	0.0700	0.0700	0.7899	9.331	23.142	34.069	= 99.033 + 0.15177T	0.62
15	0.0702	0.1000	0.0700	0.7598	11.925	25.364	35.998	= 93.526 + 0.14769T	—
16	0.1000	0.0100	0.0999	0.7901	—	6.747	17.342	= 111.717 + 0.14716T	—
17	0.1001	0.0299	0.0999	0.7701	—	9.840	21.049	= 115.482 + 0.15568T	0.43
18	0.1001	0.0499	0.1000	0.7500	—	11.680	21.173	= 94.451 + 0.13184T	—
19	0.1001	0.0700	0.1000	0.7299	1.401	13.728	23.482	= 95.325 + 0.13547T	—
20	0.1001	0.1000	0.1000	0.6999	4.541	16.683	26.290	= 90.728 + 0.13343T	—
21	0.0301	0.0300	0.0100	0.9299	21.885	38.107	50.943	= 105.400 + 0.17827T	0.20
22	0.0302	0.0300	0.0500	0.8398	23.614	41.288	55.268	= 115.045 + 0.19420T	—
23	0.0301	0.0300	0.0700	0.8699	25.891	43.381	57.219	= 111.340 + 0.19220T	—
24	0.0301	0.0299	0.0999	0.8399	28.389	44.840	57.856	= 100.688 + 0.18078T	0.35
25	0.0501	0.0500	0.0100	0.8899	10.496	24.980	36.439	= 103.137 + 0.15915T	0.33
26	0.0501	0.0500	0.0299	0.8700	10.527	26.367	38.900	= 113.759 + 0.17407T	0.36
27	0.0501	0.0500	0.0699	0.8300	12.570	28.192	40.553	= 110.002 + 0.17167T	0.40
28	0.0502	0.0500	0.0999	0.7999	14.349	30.015	42.410	= 108.566 + 0.17215T	0.13
29	0.0700	0.0700	0.0100	0.8500	4.853	17.933	28.281	= 97.770 + 0.14373T	0.39
30	0.0701	0.0700	0.0300	0.8299	6.150	18.188	27.729	= 98.482 + 0.13251T	0.22
31	0.0701	0.0700	0.0499	0.8100	7.572	20.678	31.047	= 95.258 + 0.14402T	—
32	0.0701	0.0700	0.0999	0.7599	11.176	23.705	33.618	= 87.127 + 0.13768T	—
33	0.1000	0.0999	0.0999	0.7302	1.564	11.855	19.996	= 79.158 + 0.11306T	0.08
34	0.1002	0.0999	0.0299	0.7700	2.171	13.437	22.351	= 86.222 + 0.12380T	—
35	0.1000	0.0999	0.0501	0.7500	2.899	14.708	24.051	= 89.757 + 0.12977T	—
36	0.1001	0.0999	0.0700	0.7300	3.384	15.154	24.466	= 88.965 + 0.12934T	0.45

* X_{Zn} , X_{Sn} , X_{Cd} , and X_{Pb} mole fractions weighed in basis. For repeated measurements, the mean values of all alloys for the same composition.

** a = intercept in the linear equation ($E_{mV} = -a + b T^{\circ}K$). b = slope of the line E_{mV} vs. temperature, mV/°K.

† $S(\bar{y})$ = standard deviation of the electromotive force.

method (2) the activity coefficients in binary systems take the form

$$\ln \gamma_j = \omega_{jk}(T) \left[(1 - X_k)^{m_{jk}} - \frac{m_{jk}}{m_{jk} - 1} (1 - X_k)^{m_{jk} - 1} + \frac{1}{m_{jk} - 1} \right] \quad [2]$$

$$\ln \gamma_k = \omega_{jk}(T) (1 - X_k)^{m_{jk}} \quad [3]$$

where γ_j , γ_k are activity coefficients of components j and k , $\omega_{jk}(T)$ is the function dependent on temperature, m_{jk} is the asymmetry coefficient independent of concentration, X_k is the concentration of the component k in molar fraction. Equation [2] is derived from Gibbs-Duhem equation ($X_k d \ln \gamma_k + X_j d \ln \gamma_j = 0$) assuming that Eq. [3] applied for component k . Values of $\omega(T)$ and m were obtained from experimental data for the constituent binary systems and are summarized in Table II. Using these data, following the notation $i = Zn, j_1 = Sn, j_2 = Cd, k = Pb(\text{solvent})$ and the procedure given in the Appendix the relation for $\ln \gamma_{Zn}$ in quaternary system is as follows

$$\begin{aligned} \ln \gamma_i = & -\omega_{ij_1} [(1 - X_i)^{m_{ij_1} - 2} X_i X_{j_1} - (1 - X_i)^{m_{ij_1} - 2} X_{j_1}] \\ & - \omega_{ij_2} [(1 - X_i)^{m_{ij_2} - 2} X_i X_{j_2} - (1 - X_i)^{m_{ij_2} - 2} X_{j_2}] \\ & - \omega_{ik} [(1 - X_i)^{m_{ik} - 2} X_i X_k - (1 - X_i)^{m_{ik} - 2} X_k] \\ & - \omega_{j_1 j_2} (1 - X_{j_2})^{m_{j_1 j_2} - 2} X_{j_1} X_{j_2} \\ & - \omega_{j_1 k} (1 - X_k)^{m_{j_1 k} - 2} X_{j_1} X_k - \omega_{j_2 k} (1 - X_{j_2})^{m_{j_2 k} - 2} X_{j_2} X_k \end{aligned} \quad [4]$$

The details of this procedure are also given in the paper (6) on the Zn-Sn-Cd-Bi system. Values of $\ln \gamma_{Zn}$ from Eq. [4] are compared with experimental values in Table III as well as in Fig. 1 through 8. From these comparisons it may be seen that the Krupkowski's formalism provides a quite reasonable approximation to the experimental data. The highest de-

viations from the experimental data occur at 714°K and at concentrations $X_{Zn} = X_{Sn} = 0.1$ and $X_{Zn} = X_{Cd} = 0.1$. These deviations result from the influence of immiscibility which occurs at these concentrations in the ternary systems Zn-Sn-Pb and Zn-Cd-Pb, respectively.

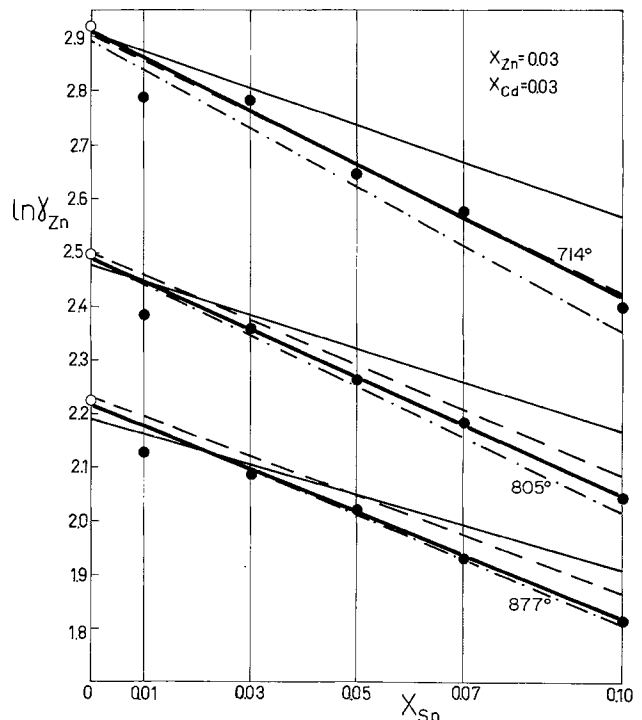


Fig. 1. $\ln \gamma_{Zn}$ vs. X_{Sn} dependence in Zn-Sn-Cd-Pb liquid solutions at 714°, 805°, and 877°K when $X_{Zn} = 0.03, X_{Cd} = 0.03$. —●— This study, ○ Ref. (8), ——— calculated from Krupkowski's Eq. [4], ····· calculated from model I Wagner's Eq. [8], —·—·— calculated from model II Wagner's Eq. [7].

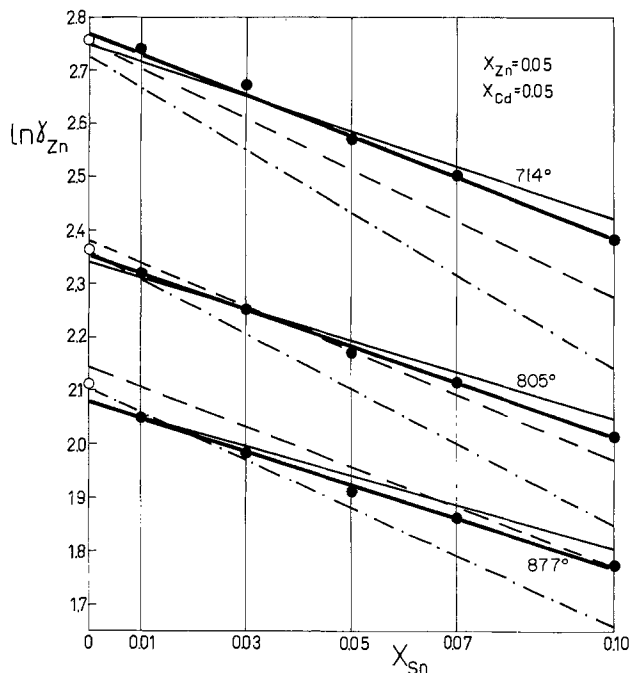


Fig. 2. $\ln \gamma_{Zn}$ vs. X_{Sn} dependence in Zn-Sn-Cd-Pb liquid solutions at 714°, 805°, and 877°K when $X_{Zn} = 0.05$, $X_{Cd} = 0.05$. —●— This study, ○ Ref. (8), ——— calculated from Krupkowski's Eq. [4], — · — calculated from model I Wagner's Eq. [8], · · · calculated from model II Wagner's Eq. [7].

Interaction Models

Following Wagner's suggestion (3) $\ln \gamma_i$ may be expanded in Taylor series for the quaternary system in the following form

$$\begin{aligned} \ln \gamma_i = \ln \gamma_i^0 &+ \left[X_i \left(\frac{\partial \ln \gamma_i}{\partial X_i} \right) + X_{j_1} \left(\frac{\partial \ln \gamma_i}{\partial X_{j_1}} \right) \right. \\ &+ \left. X_{j_2} \left(\frac{\partial \ln \gamma_i}{\partial X_{j_2}} \right) \right] + \left[\frac{1}{2} X_i^2 \left(\frac{\partial^2 \ln \gamma_i}{\partial X_i^2} \right) \right. \\ &+ \frac{1}{2} X_{j_1}^2 \left(\frac{\partial^2 \ln \gamma_i}{\partial X_{j_1}^2} \right) + \frac{1}{2} X_{j_2}^2 \left(\frac{\partial^2 \ln \gamma_i}{\partial X_{j_2}^2} \right) \\ &+ X_i X_{j_1} \left(\frac{\partial^2 \ln \gamma_i}{\partial X_i \partial X_{j_1}} \right) + X_i X_{j_2} \left(\frac{\partial^2 \ln \gamma_i}{\partial X_i \partial X_{j_2}} \right) \\ &\left. + X_{j_1} X_{j_2} \left(\frac{\partial^2 \ln \gamma_i}{\partial X_{j_1} \partial X_{j_2}} \right) \right] \quad [5] \end{aligned}$$

Equation [5] includes terms for both first- and second-order interactions. The notation is the same as used by Gluck and Pehlke (5) who were concerned with solute interactions of zinc in dilute solutions with molten bismuth. The first-order terms in Eq. [5] are

$$\left(\frac{\partial \ln \gamma_i}{\partial X_i} \right) = \epsilon_i^i \quad \text{self-interaction parameter in the system } i\text{-}k \text{ (solvent)}$$

$$\left(\frac{\partial \ln \gamma_i}{\partial X_{j_1}} \right) = \epsilon_i^{j_1} \quad \text{ternary-interaction parameter in the system } i\text{-}j_1\text{-}k$$

$$\left(\frac{\partial \ln \gamma_i}{\partial X_{j_2}} \right) = \epsilon_i^{j_2} \quad \text{ternary-interaction parameter in the system } i\text{-}j_2\text{-}k$$

and the second-order terms are

$$\left(\frac{\partial^2 \ln \gamma_i}{\partial X_i^2} \right) = \epsilon_i^{ii} \quad \text{second-order interaction parameter in the system } i\text{-}k$$

$$\left(\frac{\partial^2 \ln \gamma_i}{\partial X_{j_1}^2} \right) = \epsilon_i^{j_1 j_1} \quad \text{second-order direct ternary interaction parameter in the system } i\text{-}j_1\text{-}k$$

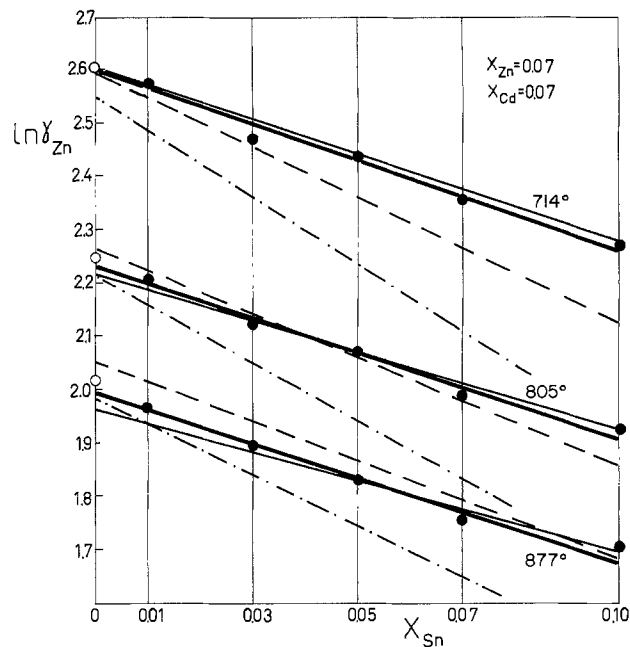


Fig. 3. $\ln \gamma_{Zn}$ vs. X_{Sn} dependence in Zn-Sn-Cd-Pb liquid solutions at 714°, 805°, and 877°K when $X_{Zn} = 0.07$, $X_{Cd} = 0.07$. —●— This study, ○ Ref. (8), ——— calculated from Krupkowski's Eq. [4], — · — calculated from model I Wagner's Eq. [8], · · · calculated from model II Wagner's Eq. [7].

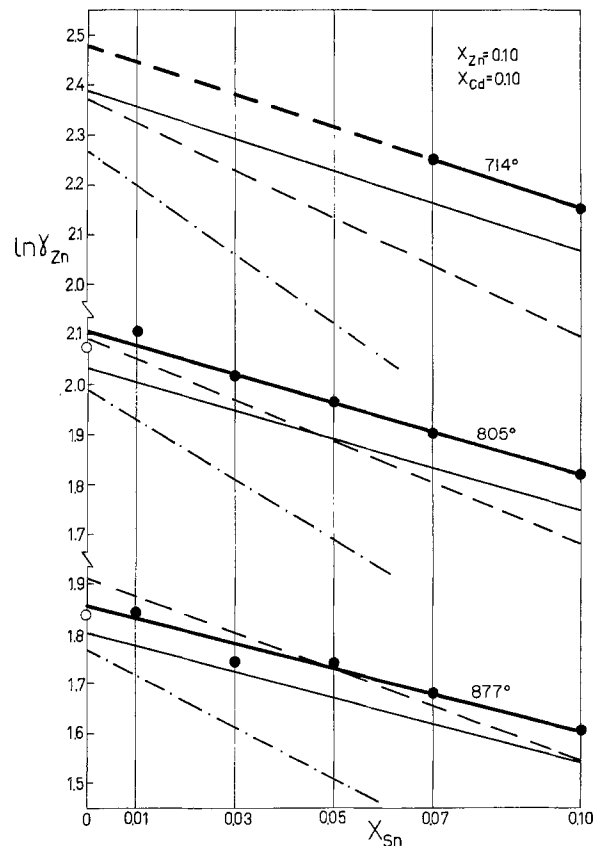


Fig. 4. $\ln \gamma_{Zn}$ vs. X_{Sn} dependence in Zn-Sn-Cd-Pb liquid solutions at 714°, 805°, and 877°K when $X_{Zn} = 0.10$, $X_{Cd} = 0.10$. —●— This study, ○ Ref. (8), ——— calculated from Krupkowski's Eq. [4], — · — calculated from model I Wagner's Eq. [8], · · · calculated from model II Wagner's Eq. [7].

$$\left(\frac{\partial^2 \ln \gamma_i}{\partial X_{j_2}^2} \right) = \epsilon_i^{j_2 j_2} \quad \text{second-order direct ternary interaction parameter in the system } i\text{-}j_2\text{-}k$$

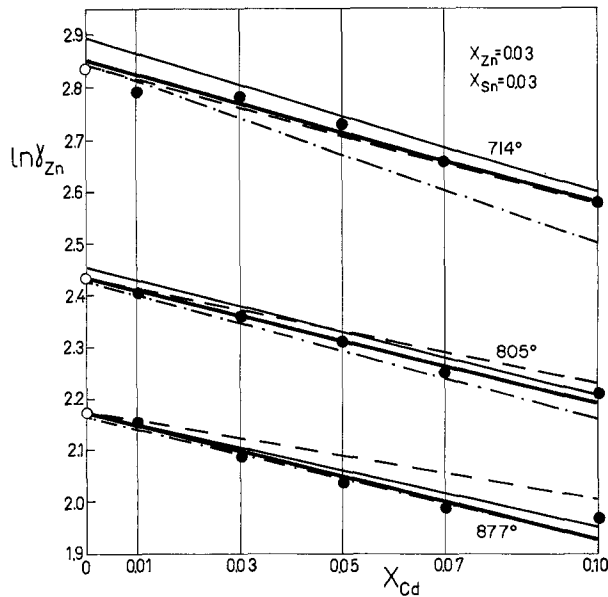


Fig. 5. $\ln \gamma_{Zn}$ vs. X_{Cd} dependence in Zn-Sn-Cd-Pb liquid solutions at 714°, 805°, and 877°K when $X_{Zn} = 0.03$, $X_{Sn} = 0.03$. —●— This study, ○ Ref. (16), — calculated from Krupkowski's Eq. [4], - - - calculated from model I Wagner's Eq. [8], - · - · - calculated from model II Wagner's Eq. [7].

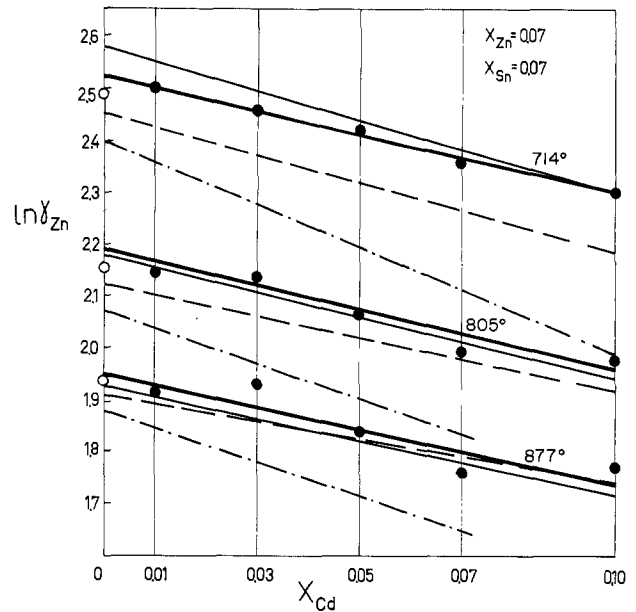


Fig. 7. $\ln \gamma_{Zn}$ vs. X_{Cd} dependence in Zn-Sn-Cd-Pb liquid solutions at 714°, 805°, and 877°K when $X_{Zn} = 0.07$, $X_{Sn} = 0.07$. —●— This study, ○ Ref. (16), — calculated from Krupkowski's Eq. [4], - - - calculated from model I Wagner's Eq. [8], - · - · - calculated from model II Wagner's Eq. [7].

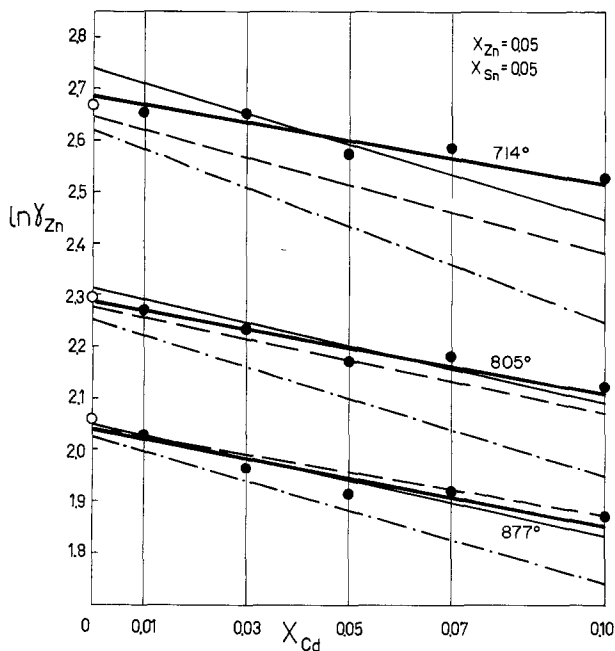


Fig. 6. $\ln \gamma_{Zn}$ vs. X_{Cd} dependence in Zn-Sn-Cd-Pb liquid solutions at 714°, 805°, and 877°K when $X_{Zn} = 0.05$, $X_{Sn} = 0.05$. —●— This study, ○ Ref. (16), — calculated from Krupkowski's Eq. [4], - - - calculated from model I Wagner's Eq. [8], - · - · - calculated from model II Wagner's Eq. [7].

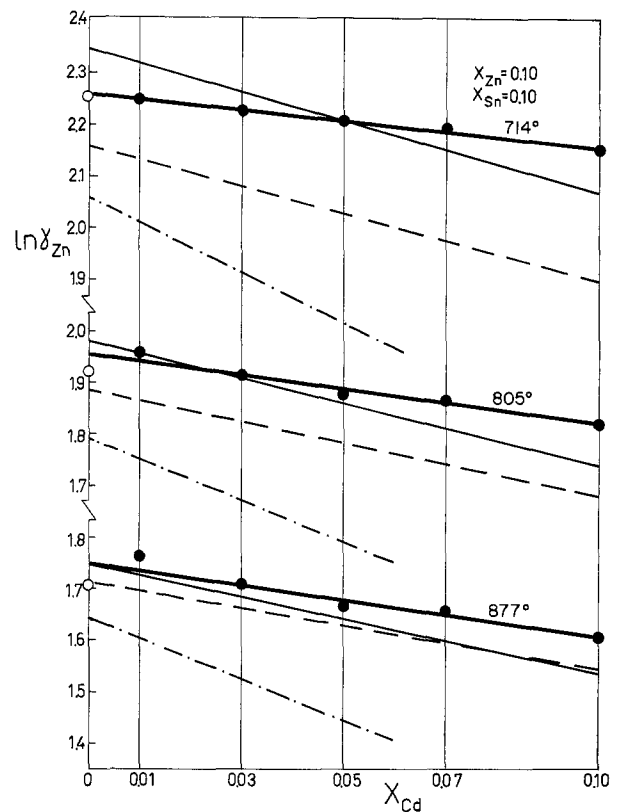


Fig. 8. $\ln \gamma_{Zn}$ vs. X_{Cd} dependence in Zn-Sn-Cd-Pb liquid solutions at 714°, 805°, and 877°K when $X_{Zn} = 0.10$, $X_{Sn} = 0.10$. —●— This study, ○ Ref. (16), — calculated from Krupkowski's Eq. [4], - - - calculated from model I Wagner's Eq. [8], - · - · - calculated from model II Wagner's Eq. [7].

$$\left(\frac{\partial^2 \ln \gamma_i}{\partial X_{i1} \partial X_{j1}} \right) = \epsilon_{i^1 j_1}^{j_1 i_1} \quad \text{second-order cross ternary interaction parameter in the system } i-j_1-k$$

$$\left(\frac{\partial^2 \ln \gamma_i}{\partial X_{i1} \partial X_{j2}} \right) = \epsilon_{i^1 j_2}^{j_2 i_1} \quad \text{second-order cross ternary interaction parameter in the system } i-j_2-k$$

$$\left(\frac{\partial^2 \ln \gamma_i}{\partial X_{j1} \partial X_{j2}} \right) = \epsilon_{i^1 j_2}^{j_2 j_1} \quad \text{indirect cross interaction parameter in the system } i-j_1-j_2-k$$

Equation [5] may be rewritten in the form

$$\begin{aligned} \ln \gamma_i = & \ln \gamma_i^0 + \left[X_{i1} \epsilon_{i^1}^{i_1} + \frac{1}{2} X_{i1}^2 \epsilon_{i^1 i_1}^{i_1 i_1} \right] + [X_{j1} \epsilon_{i^1 j_1}^{j_1 i_1} + X_{j2} \epsilon_{i^1 j_2}^{j_2 i_1}] \\ & + \left[\frac{1}{2} X_{j1}^2 \epsilon_{i^1 j_1}^{j_1 j_1} + \frac{1}{2} X_{j2}^2 \epsilon_{i^1 j_2}^{j_2 j_2} + X_{i1} X_{j1} \epsilon_{i^1 j_1}^{j_1 i_1} + X_{i1} X_{j2} \epsilon_{i^1 j_2}^{j_2 i_1} \right] \\ & + [X_{j1} X_{j2} \epsilon_{i^1 j_2}^{j_2 j_1}] \quad [6] \end{aligned}$$

Table IV. Values of binary, ternary, and quaternary interaction parameters at temperatures 714°, 805°, and 877°K

Parameter	T°K			Ref.
	714	805	877	
$\ln \gamma_{Zn}^0$	3.1	2.7	2.4	(9)
ϵ_{Zn}^{Zn}	-4.9	-3.7	-2.9	(9)
ϵ_{Zn}^{Sn}	-4.8	-4.1	-3.7	(16)
ϵ_{Zn}^{Cd}	-2.6*	-2.0	-1.6	(8)
ϵ_{Zn}^{SnZn}	-10.0 ± 2.0	-9.5 ± 2.0	-6.5 ± 1.5	This study
ϵ_{Zn}^{CdZn}	-10.0 ± 2.0	-10.0 ± 2.0	-15.0 ± 3.0	**
ϵ_{Zn}^{SnCd}	-10.0 ± 2.0	-9.5 ± 2.0	-9.0 ± 2.0	This study

* Extrapolated value from temperature range 805°-877°K.
 ** Calculated from Ref. (17).

erally good agreement with the experimental data. Also good agreement was obtained with Wagner's model I. Model II including interactions of second order seems applicable only for alloys with $X_{Zn} = 0.03$. The highest deviations (of order of about 30% in $\ln \gamma_{Zn}$) with respect to experimental data appear at temperatures near 714°K and at concentrations near $X_{Zn} = X_{Sn} = 0.10$ and $X_{Zn} = X_{Cd} = 0.10$; these high deviations are believed to result from the proximity to immiscibility range in the Zn-Pb system.

Investigation also indicates that the much stronger deviation from Raoult's law in the Zn-Pb system as compared with the Zn-Cd, Zn-Sn, Cd-Pb, Pb-Sn, and Cd-Sn binary systems plays a dominant role in determining the sign of interaction parameters in the quaternary Zn-Sn-Cd-Pb system. This result for the quaternary system is consistent with earlier observations (8, 9) on Zn-Cd-Pb and Zn-Sn-Pb ternary systems where the strong negative self-interaction parameter, $\epsilon_{Zn}^{Zn} < 0$, in the Zn-Pb binary system gives rise to negative interaction parameters, $\epsilon_{Zn}^{Cd} < 0$ and $\epsilon_{Zn}^{Sn} < 0$, in the respective ternary systems.

Acknowledgments

The authors are greatly indebted to Professor J. F. Smith from Iowa State University, Ames Laboratory, USAEC for helpful advice and for comment on the English text. The work reported in this paper was performed in part in the Ames Laboratory of the United States Atomic Energy Commission.

Manuscript submitted July 8, 1974; revised manuscript received Sept. 26, 1974. This was Paper 173 presented at the New York Meeting of the Society, Oct. 13-17, 1974.

Any discussion of this paper will appear in a Discussion Section to be published in the December 1975 JOURNAL. All discussions for the December 1975 Discussion Section should be submitted by Aug. 1, 1975.

Publication costs of this article were partially assisted by Iowa State University.

APPENDIX

In multicomponent systems the main assumption of Krupkowski's method (18) consists in the additivity of thermodynamic properties of the binary systems. His assumption is that the logarithm of an activity coefficient on an arbitrarily chosen component i of a solution may be represented by the sum

$$\ln \gamma_i = \sum_{\substack{j,k=1 \\ j \neq k}}^n [\ln \gamma_i]_{j,k} \quad [A-1]$$

where $[\ln \gamma_i]_{j,k}$ is the contribution which corresponds to j - k binary system

Accordingly Krupkowski obtains as solutions of the Gibbs-Duhem equation

$$\sum_{i=1}^n X_i d \ln \gamma_i = 0 \quad [A-2]$$

the following

$$\text{for } i \neq k \\ i \neq j \quad [\ln \gamma_i]_{j,k} = -\omega_{jk}(1 - X_k)^{m_{jk}-2} X_j X_k \quad [A-3]$$

$$\text{for } i = j \\ [\ln \gamma_j]_{j,k} = -\omega_{jk}(1 - X_k)^{m_{jk}-2} X_j X_k \\ + \frac{\omega_{jk}}{m_{jk} - 1} [1 - (1 - X_k)^{m_{jk}-1}] \quad [A-4]$$

$$\text{for } i = k \\ [\ln \gamma_k]_{j,k} = -\omega_{jk}(1 - X_k)^{m_{jk}-2} X_j X_k \\ + \omega_{jk}(1 - X_k)^{m_{jk}-2} X_j \quad [A-5]$$

Equation [A-3] shows the influence of thermodynamic properties of j - k binary solutions on the activity coefficient of the remaining component i in a multicomponent system. This equation is dependent on i only in the concentration term $(1 - X_k)$. The parameters ω and m are derived from binaries which do not include component i .

For a particular multicomponent system the components are enumerated as follows: $i = Zn$, $j_1 = Sn$, $j_2 = Cd$, and $k = Pb$; then for each binary system of the quaternary solutions there will be four relations according to Eq. [A-3]-[A-5]. For instance in the case of Zn-Sn system we have

$$[\ln \gamma_{Zn}]_{Zn-Sn} = -\omega_{ZnSn} [(1 - X_{Zn})^{m_{ZnSn}-2} X_{Zn} X_{Sn} \\ - (1 - X_{Zn})^{m_{ZnSn}-2} X_{Sn}] \quad [A-6]$$

$$[\ln \gamma_{Sn}]_{Zn-Sn} = -\omega_{ZnSn} \left\{ (1 - X_{Zn})^{m_{ZnSn}-2} \right. \\ \left. - \frac{1}{m_{ZnSn} - 1} [1 - (1 - X_{Zn})^{m_{ZnSn}-1}] \right\} \quad [A-7]$$

$$[\ln \gamma_{Cd}]_{Zn-Sn} = -\omega_{ZnSn} (1 - X_{Zn})^{m_{ZnSn}-2} X_{Zn} X_{Sn} \quad [A-8]$$

$$[\ln \gamma_{Pb}]_{Zn-Sn} = -\omega_{ZnSn} (1 - X_{Zn})^{m_{ZnSn}-2} X_{Zn} X_{Sn} \quad [A-9]$$

Finally Eq. [4] is obtained as a sum

$$\ln \gamma_{Zn} = [\ln \gamma_{Zn}]_{ZnSn} + [\ln \gamma_{Zn}]_{ZnCd} + [\ln \gamma_{Zn}]_{ZnPb} \\ + [\ln \gamma_{Zn}]_{CdPb} + [\ln \gamma_{Zn}]_{PbSn} + [\ln \gamma_{Zn}]_{CdSn} \quad [A-10]$$

In Eq. [A-10] the first term is equal to Eq. [A-6] and the three last terms equal $-\omega_{CdPb}(1 - X_{Cd})^{m_{CdPb}-2} X_{Cd} X_{Pb}$, $-\omega_{PbSn}(1 - X_{Pb})^{m_{PbSn}-2} X_{Sn} X_{Pb}$, and $-\omega_{CdSn}(1 - X_{Cd})^{m_{CdSn}-2} X_{Sn} X_{Pb}$, respectively. The parameters ω_{jk} and m_{jk} are determined from data for the respective j , k binaries and consequently reflect the influence of the binaries Cd-Pb, Pb-Sn, and Cd-Sn on the properties of the quaternary Pb-Sn-Cd-Zn alloys. The concentration terms $(1 - X_{Cd})$ and $(1 - X_{Pb})$ in the last three terms represent concentrations in the quaternary system.

REFERENCES

- Z. Moser, *Met. Trans.*, **2**, 2175 (1971).
- A. Krupkowski, *Bull. Acad. Polon. Sci. Lett.*, **1**, 15 (1951).
- C. Wagner, "Thermodynamics of Alloys," Addison Wesley Press, Cambridge, Mass. (1952).
- J. V. Gluck and R. D. Pehlke, *Trans. Met. Soc., AIME*, **239**, 36 (1967).
- J. V. Gluck and R. D. Pehlke, *ibid.*, **239**, 562 (1967).
- W. Ptak and Z. Moser, *This Journal*, **119**, 843 (1972).
- Z. Moser, *Arch. Hutnictwa*, **14**, 371 (1969).
- Z. Moser, Submitted to *Met. Trans.*
- Z. Moser and W. Zakulski, Submitted to *This Journal*.
- W. Ptak, *Arch. Gornictwa Hutnictwa*, **2**, 71 (1954).
- Z. Moser, *Bull. Acad. Polon. Sci., Ser. Sci. Tech.*, **19**, 45 (1971).
- L. Zabdyr, *Arch. Hutnictwa*, In print.
- R. Hultgren, R. L. Orr, P. D. Anderson, and K. K. Kelley, "Selected Values of Thermodynamic Properties of Metals and Alloys," John Wiley & Sons, New York-London (1963), also Supplement loose-leaf sheets (1968-1971).
- L. Zabdyr, *Arch. Hutnictwa*, **18**, 209 (1973).

15. J. M. Dealy and R. D. Pehlke, *Trans. Met. Soc. AIME*, **227**, 88 (1963).
 16. Z. Moser and W. Zakulski, *Arch. Hutnictwa*, **19**, 87 (1974).
 17. R. D. Pehlke, K. Okajima, and T. L. Moore, *This Journal*, **114**, 800 (1967).
 18. A. Krupkowski, *Bull. Acad. Polon. Sci., Ser. Sci. Tech.*, **17**, 87 (1969).

Electrochemical Reduction of Lithium Metavanadate in Lithium Chloride-Potassium Chloride Eutectic

R. B. Chessmore and H. A. Laitinen*¹

Department of Chemistry, University of Illinois at Urbana-Champaign, Urbana, Illinois 61801

ABSTRACT

Two reduction steps were observed in the electrochemical reduction of LiVO_3 in molten LiCl-KCl eutectic. The first reduction step produces an insoluble product which undergoes a chemical reaction with LiVO_3 to form insoluble LiV_2O_5 and Li_3VO_4 . The second reduction step produces insoluble LiVO_2 and Li_3VO_4 . LiVO_2 undergoes a number of chemical reactions with LiVO_3 to produce a mixture of solid compounds, one of which is LiV_2O_4 . VO_2 was found to react with LiVO_3 to produce LiV_2O_5 . The addition of oxide ion to the eutectic containing insoluble VO_2 resulted in the disproportionation of VO_2 to produce either Li_3VO_4 and V_2O_3 or Li_3VO_4 and LiVO_2 , depending on the oxide concentration.

The chemistry and electrochemistry of vanadium in molten salt systems has been partially studied by several groups. Van Norman and Osteryoung (1) found that metavanadate in a LiCl-KCl eutectic melt reacted with an excess of Na_2CO_3 to form orthovanadate as determined from the evolution of CO_2 . Molina (2) has described the absorption spectra of V(II) , V(III) , VO^{+2} , VO_3^- , and V_2O_5 , and gave a detailed discussion of the effect of adding oxide ion to either a V_2O_5 or VO^{+2} solution in LiCl-KCl eutectic melt. The standard potentials of V(II)/V(O) and V(III)/V(II) in a LiCl-KCl eutectic melt have been determined (3). Laitinen and Rhodes (4) studied the electrochemistry of V_2O_5 in LiCl-KCl eutectic melt and found that vanadium pentoxide was reduced to a mixture of a lithium-vanadium bronze and lithium vanadates. Shams El Din *et al.* (5) potentiometrically titrated metavanadate dissolved in molten LiCl-KCl , using Na_2O_2 as the titrant and an $\text{O}_2/\text{O}^{=}/\text{Pt}$ indicator electrode. The neutralization occurred in one step, forming orthovanadate in the melt. The electrochemistry of vanadyl ion in LiCl-KCl eutectic has been studied by Scrosati and Laitinen (6). These workers found that VO^{+2} is reduced in a one electron step to soluble VO^+ , followed by a fast chemical reaction to produce insoluble V_2O_3 and soluble V(III) .

In this study, chronopotentiometry, controlled potential electrolysis, chronopotentiometry with current reversal, and cyclic sweep voltammetry were used to investigate the electrochemical reduction of LiVO_3 in LiCl-KCl eutectic at 450°C .

Experimental

Reagents.—Anhydrous LiVO_3 and Li_3VO_4 were prepared by drying the research grade products (Lithium Corporation of America) at 150°C under vacuum for 24 hr. V_2O_3 and VO_2 were prepared according to the method given by Brauer (7). A method similar to that described by Holtzberg *et al.* (8) was used to prepare $\text{K}_4\text{V}_2\text{O}_7$. LiV_2O_5 was prepared by heating equal molar quantities of LiVO_3 and VO_2 in a quartz tube at 610°C

under an argon atmosphere for 24 hr and then at 650°C for an additional 24 hr. LiVO_2 was prepared by heating equal molar quantities of V_2O_3 and Li_2CO_3 in a platinum crucible to 600°C in a flow of hydrogen for 10 hr, then to 750°C for an additional 12 hr.

Chemicals other than those mentioned were reagent grade and were used without additional purification other than drying where required.

Molten salt procedures. The LiCl-KCl eutectic was obtained from Anderson Physics Laboratories, Incorporated, Champaign, Illinois, where it was prepared and purified by the method outlined by Laitinen *et al.* (9). The molten salt furnace and glassware associated with the molten salt apparatus have been previously described (10, 11). The procedures employed for cleaning glassware and handling the molten eutectic have been described in detail (11).

Electrochemical measurements.—A Pt(II)/Pt reference electrode was utilized in this work; its properties and construction have been described (12). Unless otherwise stated, all potentials are given with reference to a $\text{Pt(II)} (1M)/\text{Pt}$ electrode. A carbon electrode was used as a counterelectrode. The electrodes were constructed and cleaned according to the procedure outlined by Propp (13). Both the platinum disk electrodes used in the chronopotentiometric and cyclic sweep studies and the platinum flag electrodes were constructed by spot welding 2.5 cm of 26 gauge platinum wire to a platinum foil (3 cm^2). The electrode holders have been described by Propp (13). The construction of platinum disk electrodes have been described (11). A 2.5 cm length of 36 or 41 gauge platinum wire was spot welded onto the disks so they could be attached and detached from the electrode holder.

An indicator electrode whose construction has been described (11) was made from a 2.5 cm length of 3 mm diameter glassy carbon and was used in the amperometric titration of vanadium.

Steady-state voltammetric measurements were made with a Heath EUA19-2 Polarography Module combined with a Heath EUW-19A operational amplifier system stabilized by a Heath EUA-19-4 chopper stabilizer. A

* Electrochemical Society Active Member.

¹ Present address: Department of Chemistry, University of Florida, Gainesville, Florida 32611.

Key words: molten salts, cathodic processes, vanadium oxides.

Sargent recorder (Model S-82150) was used to record the current-voltage curves. A triangular sweep generator built by the Electronic Service Laboratory at the University of Illinois, in conjunction with a Wenking Potentiostat (Model 61RS) was used in the linear sweep studies. The Wenking potentiostat was also used for the constant potential electrolysis in preparative work. The constant current source employed for the chronopotentiometric studies has previously been described (13). A Tektronix 502A oscilloscope and a Tektronix C-12 camera were used to record the chronopotentiometric potential-time curves and the linear sweep current-voltage curves. A Sargent Model IV Coulometric Current Source was used for the generation of the Pt(II)/Pt reference electrode.

Analytical procedures.—In the preparative portion of this investigation, a number of routine analyses were performed to establish the composition of the electrode deposits. The deposits were washed with de-aerated water, dried, and dissolved in H_2SO_4 . A detailed procedure is given elsewhere (11).

Vanadium, as V(V) and/or V(IV), was quantitatively determined by an amperometric titration with Fe(II), utilizing a method similar to one developed by Rulfs *et al.* (14). Vanadium as V(IV) and/or V(III) was quantitatively determined by adding an excess of V(V) and amperometrically titrating with Fe(II). Lithium and potassium were determined by flame photometry. Chloride was determined by null point potentiometry as described by Malmstadt and Winefordner (15). The apparatus and detailed procedures for the various analyses are described elsewhere (11).

Results and Discussion

Chemistry of $LiVO_3$, Li_3VO_4 , and $K_4V_2O_7$.—There exists some confusion in the literature concerning anionic species of vanadium oxides and their solubility in LiCl-KCl eutectic (4). A brief study was, therefore, made to determine the solubility of lithium orthovanadate and potassium pyrovanadate in LiCl-KCl eutectic at 450°C.

Five mg of Li_3VO_4 was added to 12 ml of LiCl-KCl eutectic melt at 450°C. The melt solution was filtered after it had been stirred for 2 hr to allow equilibration. Analysis of the collected precipitate showed that only about 4% by weight of the Li_3VO_4 had dissolved. Taking into account the error in determining the volume of the compartment (approximately 5%), an upper limit of about 0.3 mM can be placed on the solubility of Li_3VO_4 in LiCl-KCl eutectic melt at 450°C. Ten mg of $K_4V_2O_7$ was added to 4.5 ml of LiCl-KCl eutectic melt. Part of the solid appeared to dissolve, and the melt solution took on a yellow color. The x-ray powder pattern of the precipitate matched the x-ray powder pattern of commercially obtained Li_3VO_4 . The results of the chemical analysis showed that about one-half of the total vanadium, on a mole basis, had dissolved in the LiCl-KCl eutectic melt. These results show that pyrovanadate is not stable in LiCl-KCl eutectic at 450°C, but decomposes to form soluble VO_3^- and a solid precipitate of Li_3VO_4 .

Voltammetry of $LiVO_3$.—Representative current-voltage curves of $LiVO_3$ dissolved in the eutectic are shown in Fig. 1. The reproducibility of these curves was poor because of the formation of insoluble products that caused the surface area of the electrode to change rapidly. Only general conclusions can be made concerning the process taking place. There appears to be a series of ill-defined reduction waves occurring before the maximum limiting current is reached at approximately -1.2V. A current-voltage curve in the positive direction (curve 2), after completion of a forward run, shows that there are several anodic processes. This indicates that there are several insoluble products formed during the negative scan and that these products can be oxidized during the positive scan. It may be possible that a single insoluble reduc-

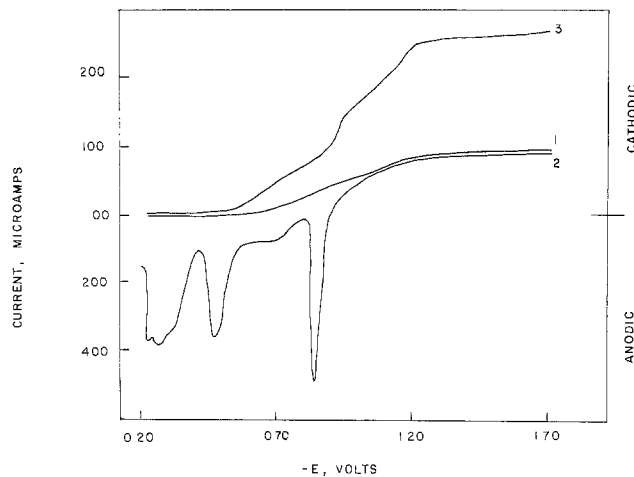


Fig. 1. Steady-state voltammogram of $LiVO_3$. Sweep rate 0.1 V/min. Curve 1, $7.25 \times 10^{-3}M$ $LiVO_3$; curve 2, reverse of curve 1; curve 3, 2.37×10^{-2} $LiVO_3$.

tion product undergoes oxidation via charge transfer and/or coupled chemical reactions to form other insoluble products which are further oxidized. The insoluble product(s) found during the negative scan are probably conductive since the current does not reach a limiting value and then decay as the applied potential becomes more negative.

Characterization of electrode deposits.—Samples of electrode deposits were prepared by constant potential electrolysis. No attempt was made to do an exhaustive electrolysis since stirring the melt solution caused part of the deposits to break away from the electrode surface. The deposits were analyzed for V, Li, K, and Cl by employing the methods previously described.

The x-ray powder pattern data of the deposit obtained at a potential corresponding to the first ill-defined wave, -0.620V, of curve 3 (Fig. 1), matched the γ phase LiV_2O_5 obtained by Galy and Hardy (17) and Hardy *et al.* (18). An x-ray diffraction powder pattern of a deposit that had been washed sparingly with de-aerated water matched that of LiV_2O_5 , except that diffraction lines of Li_3VO_4 were also present. The oxide ion released in the reduction of metavanadate to LiV_2O_5 precipitates VO_3^- as insoluble Li_3VO_4 . Table I summarizes the composition of three samples of deposits prepared under the previously given conditions. If the microequivalents of V(V), V(IV), and Li are mathematically converted to an equivalent weight of the metal oxide, as shown in Table IA, the sample weight can be completely accounted for in terms of Li_2O , V_2O_5 , and V_2O_4 .

The x-ray powder pattern data for a completely washed deposit obtained at -1.32V matched the pattern for $LiVO_2$ obtained by Rüdorff and Becker (19). An x-ray powder pattern obtained for an electrode deposit that had been sparingly washed was identical to that of $LiVO_2$, except that Li_3VO_4 diffraction lines were also present. The reduction of $LiVO_3$ occurring at -1.32V releases oxide ion which precipitates VO_3^-

Table I. Typical analysis of deposit obtained at -0.620V

A.						
	μ moles Li	mg Li_2O	μ moles V(V)	mg V_2O_5	μ moles V(IV)	mg V_2O_4
	23.30	0.348	23.06	2.097	23.01	1.908
	16.81	0.251	16.92	1.539	16.86	1.398
	18.21	0.272	18.24	1.659	18.21	1.510
B.						
	Sample wt mg	Total mg found	% wt found	Empirical formula		
	4.382	4.353	99.34	$Li_{1.01}V_{2.00}O_{5.01}$		
	3.210	3.188	99.31	$Li_{0.99}V_{2.00}O_{5.00}$		
	3.455	3.441	99.59	$Li_{1.00}V_{2.00}O_{5.00}$		

Table II. Typical analysis of deposit obtained at $-1.32V$

A.	$\mu\text{moles Li}^+$	mg Li_2O	millimoles V^{+3}	mg V_2O_3
	19.15	0.286	19.59	1.468
	12.48	0.186	12.27	0.920
	25.55	0.382	25.38	1.902

B.	Sample mg	mg found	% wt found	Empirical formula
	1.765	1.754	99.38	$\text{Li}_{10.06}\text{V}_{1.00}\text{O}_{1.00}$
	1.113	1.106	99.37	$\text{Li}_{11.01}\text{V}_{1.00}\text{O}_{2.01}$
	2.300	2.284	99.30	$\text{Li}_{11.01}\text{V}_{1.00}\text{O}_{2.00}$

as Li_3VO_4 . Table II summarizes the composition of three samples of the deposit obtained at $-1.32V$. The sample weight can be completely accounted for if the microequivalents of each metal are mathematically converted to an equivalent weight of metal oxide, as shown in Table IIA. This suggests that the oxidation occurring at $-0.83V$ (Fig. 1, curve 2) is the oxidation of LiVO_2 .

The steady-state voltammograms suggested that one or more intermediate reduction product exists between LiV_2O_5 and LiVO_2 . Deposits obtained at a potential corresponding to $-0.950V$ were bright green in color. The x-ray powder patterns of the sparingly washed deposit and the completely washed deposit were compared. The two patterns were identical except that the pattern of the sparingly washed deposit contained Li_3VO_4 diffraction lines. Table III shows the x-ray powder pattern data for a completely washed deposit obtained at $-0.950V$. A search of the literature did not reveal any x-ray powder patterns of vanadium compounds that matched that obtained for the deposit. A careful examination of the deposit under a microscope showed that the deposit was a mixture of solid products in the form of bright green, red, granular black, and needle-like blue-black crystals. Analysis of the deposits obtained at $-0.950V$ showed the deposit to contain V(V) V(IV), Li, K, and Cl. Attempts to use the analysis data to determine the various compounds that might be present in the deposit were futile. Only qualitative results could be obtained. The micromoles of Cl found were always less than either the micromoles of Li or K. This shows that even if the melt components were incorporated into the deposit, one or more of the compounds in the deposit actually contains Li and/or K. The micromoles of V(V) was always much less than the micromoles of V(IV), suggesting that the mixed deposit contains a very small amount of V(V) and relatively large amounts of V(IV), or that V(III) is also present in the deposit with the

Table III. X-ray diffraction data for a deposit obtained at $-0.950V$

d, Å	I/I ₀	d, Å	I/I ₀
7.93	s	1.83	s
6.31	m-s	1.79	vw
5.82	w	1.74	vw
5.33	vw	1.70	vw
5.05	vw	1.67	vw
4.68	w	1.61	w
4.18	w	1.59	w
3.97	s	1.53	vw
3.55	m	1.50	vw
3.34	m-s	1.48	vw
3.18	m	1.46	w
3.02	s	1.40	w
2.85	vw	1.36	w
2.75	vw	1.30	w
2.59	m	1.27	w
2.44	vw	1.15	vw
2.41	vw	1.14	vw
2.15	w-m	1.01	vw
1.98	w	1.01	vw
1.93	s	0.974	vw
		0.907	vw

vw = very weak.
w = weak.
m = medium.
s = strong.

microequivalents of V(V) being slightly larger than the microequivalents of V(III).

The x-ray powder pattern of the deposit obtained at $-0.800V$ was similar to that previously given for the deposit obtained at $-0.950V$, except diffraction lines that could be attributed to LiV_2O_5 were also found to be present. A similar experiment was repeated at $-1.03V$. The x-ray powder pattern of the deposit obtained at this potential was similar to that of the deposit obtained at $-0.950V$, except that diffraction lines of LiVO_2 were also found to be present. The appearance of the LiV_2O_5 and LiVO_2 lines in the powder patterns and the results of the chemical analysis show that the reduction of LiVO_3 in the potential range of -0.70 to $-1.20V$ produces a mixture of insoluble products on the electrode surface. Presumably, most or all of these products can be reoxidized electrochemically, as evidenced by the steady-state voltammograms.

Chemistry of the reduction products of LiVO_3 .—The results of the preceding section suggest that there may be a series of chemical reactions involving the solid reduction products, O^- and VO_3^- . Furthermore, since VO_2 is known to be insoluble in LiCl-KCl (2, 6), it was expected that the reduction of LiVO_3 would produce insoluble VO_2 . For these reasons, a study of the chemistry of LiV_2O_5 , VO_2 , and LiVO_2 in a melt solution containing either LiVO_3 or oxide ion was performed to reach a better understanding of the reduction of LiVO_3 .

A sample of LiV_2O_5 was placed in two compartments, one containing only LiCl-KCl eutectic, the other containing excess LiVO_3 in addition to the eutectic. The x-ray powder pattern and chemical analysis showed that both solids were LiV_2O_5 . From the experiments, it was concluded that LiV_2O_5 is stable in LiCl-KCl eutectic melt and in melt solution containing LiVO_3 .

At potentials intermediate to the formation of LiV_2O_5 and LiVO_2 , a mixture of insoluble compounds is formed. It was suspected that this mixture would contain mostly V(IV). No evidence as to the presence of VO_2 , which is known to be insoluble in LiCl-KCl , was found in the mixture of insoluble products. This suggested that VO_2 may react with VO_3^- in the melt and/or insoluble compounds containing an $\text{O}^-/\text{V(IV)}$ ratio greater than 2 may exist. Vanadyl compounds such as VOCl_2 and VOSO_4 are known to be soluble in LiCl-KCl eutectic and to slowly decompose to form insoluble VO_2 and soluble V(III) (6).

A sample of VO_2 was added to the melt. An x-ray powder pattern and analysis of the solid confirmed the results of Molina (2) and Scrosati (6) that VO_2 is stable and insoluble in LiCl-KCl eutectic melt at 450°C .

Similarly, 0.262 mM VO_2 was added to 0.444 mM LiVO_3 dissolved in about 4.5 ml of eutectic melt. There was an immediate reaction indicated by the yellow color of the melt solution decreasing in intensity and the black granular VO_2 changing to a blue-black needle-shaped solid. The x-ray pattern and chemical analysis of the solid showed it to be LiV_2O_5 . This result suggested that LiV_2O_5 may not be the first reduction product of VO_3^- , but rather the result of a chemical reaction between the first reduction product and VO_3^- . Since VO_2 reacts with VO_3^- to form LiV_2O_5 , soluble or insoluble V(IV) compounds containing an $\text{O}^-/\text{V(IV)}$ ratio greater than 2 would also be expected to undergo a chemical reaction with VO_3^- .

It was thought that $(\text{Li,K})_2\text{VO}_3$ might exist in LiCl-KCl eutectic melt at 450°C . Molina (2) has shown that the addition of O^- to a melt solution containing vanadyl ion precipitates VO_2 . This author found that further addition of oxide ion did not visually dissolve VO_2 . Results in this laboratory do not confirm the last observation. Equal moles of Li_2CO_3 and VO_2 were added to the eutectic. A reaction occurred as evidenced by the evolution of CO_2 . An x-ray powder pattern of the remaining solid showed only diffraction lines of

Li_3VO_4 and V_2O_3 . The analysis of the solid product, after Li_3VO_4 had been removed by washing, showed that the solid contained only V(III) and a small amount of Li . The sample weight could be completely accounted for in terms of a mixture of V_2O_3 and LiVO_2 . Inspection of the compartment showed the Pyrex glass of the compartment was badly etched from the carbonate. Li_2CO_3 and VO_2 in a mole ratio of $\text{Li}_2\text{CO}_3/\text{VO}_2$ equal to about 4, to offset the reaction of carbonate with the compartment walls, was added to the eutectic. An x-ray powder pattern of the resulting solid showed only LiVO_2 and Li_3VO_4 lines. Analysis of the solid after removal of Li_3VO_4 showed it to be LiVO_2 .

A number of conclusions can be reached from the preceding experiments. First, VO_2 is not stable in the presence of O^- , but disproportionates to form either V_2O_3 and Li_3VO_4 or LiVO_2 and Li_3VO_4 , depending on the concentration of oxide ion. Secondly, if the compound $(\text{Li,K})_2\text{VO}_3$ is the first reduction product of LiVO_3 , it would not be stable but would disproportionate to form insoluble LiVO_2 and Li_3VO_4 ; or, depending on time and concentration of VO_3^- , react with VO_3^- to form LiV_2O_5 and Li_3VO_4 .

If VO_3^- and LiVO_2 reacted in a mole ratio of one-to-one without the release of oxide, the product of the reaction would be $(\text{Li,K})_2\text{V}_2\text{O}_5$. Equal moles of LiVO_2 and LiVO_3 were added to the eutectic melt. A definite reaction occurred as evidenced by the appearance of a green solid. An x-ray powder pattern of the sparingly washed solid showed diffraction lines of Li_3VO_4 . This suggested that oxide ion is released in the reaction. Table IV shows the x-ray powder pattern of the completely washed solid. As can be seen, many of the diffraction lines that were present in the deposit obtained at -0.950V are also present in this x-ray powder pattern. The asterrated lines matched the x-ray powder pattern of LiV_2O_4 given by Rueter and Jackowsky (20). These data suggested that possibly one of the products of the reaction between VO_3^- and LiVO_2 in LiCl-KCl eutectic is LiV_2O_4 . A definite conclusion cannot be made owing to the presence of a mixture of compounds, some of which may have diffraction lines in common with LiV_2O_4 . Attempts to use the analysis data to determine the compounds in the solid proved futile.

A mole ratio of $\text{LiVO}_3/\text{LiVO}_2$ equal to 1.5 was added to the eutectic. The d spacings obtained from the x-ray powder pattern of the resulting solid were similar to those in Table IV, except the asterrated d spacings were less intense and diffraction lines of LiV_2O_5 were found to be present.

Chronopotentiometry.—A typical chronopotentiogram of LiVO_3 dissolved in LiCl-KCl eutectic melt is shown in Fig. 2A. Figures 2B and 2C show the effect of reversing the current along different portions of the cathodic wave.

Figure 2A shows there is only one reduction wave with a "linear" portion in the initial part of the wave.

Table IV. X-ray diffraction data for solid obtained from $\text{LiVO}_3\text{-LiVO}_2$ reaction

d, A	I/I_0	d, A	I/I_0
7.91	s	2.36	vw
5.78	vw	2.25	vw
*4.74	s	2.15	w
4.10	vw	*2.05	s
3.95	m	1.98	vw
3.55	w	1.93	m-s
3.32	m	1.83	m-s
3.01	s	1.79	vw
2.85	vw	1.74	vw
2.73	vw	1.61	w
2.60	w-m	*1.58	w-m
2.56	w	*1.45	m-s

vw = very weak.
w = weak.
m = medium.
s = strong.

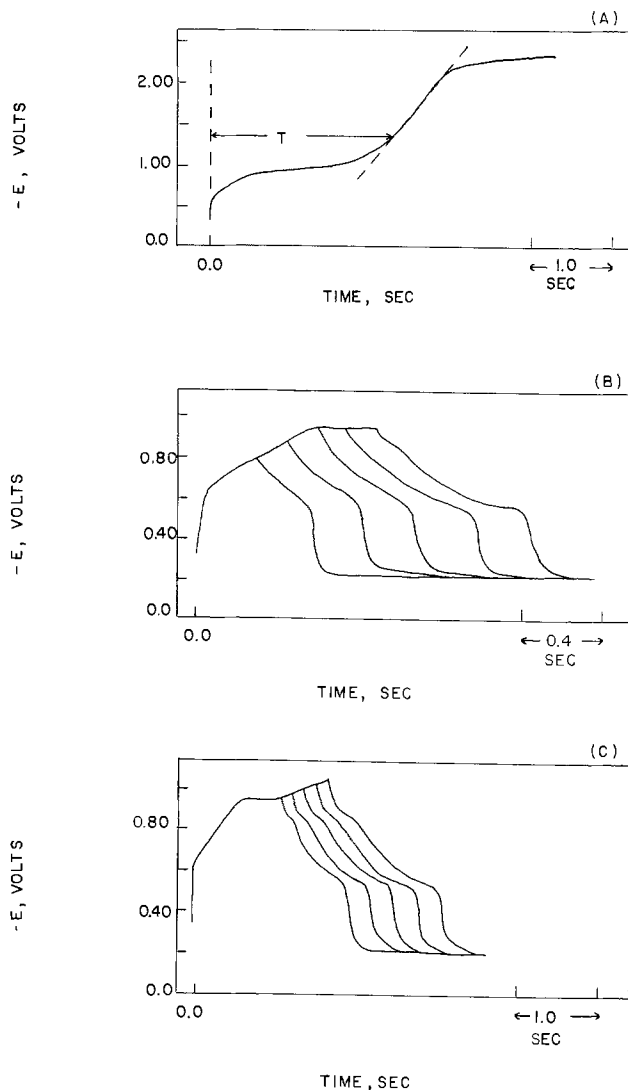


Fig. 2. (A) Typical chronopotentiogram of LiVO_3 [LiVO_3] = 4.66 mM, C.D., 0.880 mA/cm². (B, C) Typical chronopotentiograms of LiVO_3 with current reversal. [LiVO_3] = 4.66 mM, equal forward and reverse C.D. of 0.880 mA/cm².

Figures 2B and 2C show that if the current is reversed at a forward time that is still within the "linear" portion of the wave, only one reverse wave occurs at about -0.69V . If the current is reversed after the "linear" portion, there is a new oxidation wave occurring at about -0.86V and the wave that was seen at about -0.69V has become somewhat diffuse and shifted to a slightly less negative potential. The potential of about -0.86V is in good agreement with the observed oxidation potential of LiVO_2 seen in the steady-state voltammograms. The diffuse nature of the oxidation wave at the more positive potential could originate from a number of chemical complications previously mentioned.

A series of experiments was performed to verify that the oxidation occurring at about -0.86V was the oxidation of LiVO_2 . A melt solution containing 1 mg of VO_3^- was exhaustively electrolyzed by applying -1.32V . The x-ray powder pattern of the deposit matched that of LiVO_2 .

After exhaustively electrolyzing, a constant anodic current was applied, and the potential of the test electrode monitored with an x-y recorder. Two, and sometimes three, oxidation waves were seen occurring around -0.85 , -0.50 , and -0.41V . The ratios of the stripping transition times were not very reproducible and the oxidation at -0.41V was sometimes absent, and when it did occur, it was always much shorter than the other two waves. There was no solid remain-

ing on the electrode after the stripping had been completed.

The experiment was repeated but the stripping electrolysis was stopped when the transition time of the oxidation occurring at -0.86V was reached. An x-ray powder pattern of the black solid matched that of LiV_2O_4 (20).

From the results of these experiments, certain conclusions can be reached. The anodic process occurring at -0.86V is the oxidation of LiVO_2 to LiV_2O_4 . The oxidation at -0.50V is the oxidation of LiV_2O_4 . In the absence of VO_3^- and O^- , the oxidation product of LiV_2O_4 would presumably be VO_2 . The short transition time of the wave at -0.41V , compared to the transition times of the other two waves suggests that if the wave occurring at -0.41V corresponds to the oxidation of VO_2 , then either all the VO_2 produced from the oxidation of LiV_2O_4 is not on the electrode surface or that the oxidation of VO_2 does not produce all $\text{V}(\text{V})$. It should be pointed out that the stripping conditions in this experiment are different than those under normal chronopotentiometric conditions in that there was no VO_3^- or O^- present when the stripping was performed and that no cathodic electrolysis at less negative potentials had occurred before the deposition of LiVO_2 .

Returning to the chronopotentiometric experiment, the "linear" region exhibited some unusual properties with respect to the total transition time and the oxidation of LiVO_2 . The total number of coulombs passed in the "linear" region varied randomly between 500 and 600 microcoulombs/cm². If the total number of coulombs necessary to reach the total transition time was less than about 500 microcoulombs/cm², the total transition time was comprised entirely of the "linear" region. Current reversal under these conditions produced only one oxidation wave at about -0.69V . The oxidation wave of LiVO_2 was found to occur only after the forward number of coulombs had exceeded that amount needed to produce the "linear" region. After the "linear" region, the time at which the oxidation wave of LiVO_2 occurred depended upon the potential of the indicator electrode. If the potential of the indicator electrode was more positive than about -0.8V , no oxidation wave of LiVO_2 was seen. The reduction of VO_3^- to LiVO_2 appears to be related to the process occurring within the "linear" region and dependent upon the potential of the indicator electrode after the "linear" region. For an n value of 1, 200-500 microcoulombs/cm² of charge is normally required to form a monolayer coverage of the electrode. The amount of charge depends upon the unit cell parameters and the number of molecules of the reduced species per unit cell. The relationship between the "linear" region and the reduction of VO_3^- to LiVO_2 suggests that the platinum electrode has to be covered with a less reduced species than LiVO_2 before VO_3^- can be reduced to LiVO_2 .

By employing equal cathodic and anodic current densities, a number of current-reversals were performed along the total reduction wave. The ratio of the total reverse transition time, τ_R , to the forward electrolysis time, T_F , was about 0.87, regardless of the number of oxidation waves seen when the current was reversed. Once the oxidation wave of LiVO_2 was seen, the ratio of the transition times of the more positive diffuse oxidation wave to that of LiVO_2 decreased as the forward electrolysis time was increased. A limiting value for this ratio was never reached, even when the current was reversed at the forward transition time. The only conclusion that can be made is that most of the reduction products of VO_3^- , either from electrochemical reduction or chemical reduction/oxidation, are at the electrode surface and can be electrochemically oxidized.

At higher concentrations, lower current densities and short T_F , the ratio τ_R/T_F appeared to be somewhat smaller than 0.87. The oxidation wave still occurred

at about -0.69V . The ratio, however, approached 0.87 at larger T_F . Normally, the ratio had reached 0.87 before the oxidation wave of LiVO_2 was seen. This slight decrease in the ratio τ_R/T_F at short T_F suggested that VO_3^- might be removing the first reduction product from the electrode surface. In order to verify this supposition, a relatively large concentration of VO_3^- ($17.08 \times 10^{-3}\text{M}$) and a low current density ($4.4 \times 10^{-4}\text{ A/cm}^2$) were used. The ratio of τ_R/T_F varied from 0.3 to 0.63 for T_F ranging from 0.25 to 1.6 sec. The potential of the oxidation wave remained at about -0.69V . Smaller current densities caused the ratio τ_R/T_F to become even smaller. A similar effect was observed when the current density was kept constant and the concentration of VO_3^- was increased. The decrease of τ_R/T_F , when a relatively large concentration of VO_3^- exists at the electrode surface, shows that the first reduction product is not stable in the presence of VO_3^- . The first reduction product under normal chronopotentiometric conditions, therefore cannot be LiV_2O_5 . LiV_2O_5 was shown previously to be stable in the presence of VO_3^- . The simplest first reduction step that can be written is



Depending on time and VO_3^- concentration, this product would either disproportionate to LiVO_2 and Li_3VO_4 or react with VO_3^- to form LiV_2O_5 and Li_3VO_4 .

The Sand equation was tested by running duplicates of 5-7 C.D. at 5 different VO_3^- concentrations ranging from 1.78 to $17.09 \times 10^{-3}\text{M}$. It should be mentioned that these data were obtained in such a way that, in some cases, the total transition time was comprised entirely of the "linear" region and in other cases, the "linear" region was a small part of the total forward transition time. The Sand equation was found to be obeyed after correcting for residual impurities in the melt. The value of $I_0\tau^{1/2}/C$ was $0.234 \pm 0.002\text{ mA-sec}^{1/2}\text{ cm/mole}$, which gives a value of $0.76 \times 10^{-5}\text{ eq}^2\text{mole}^{-2}\text{cm}^2\text{sec}^{-1}$ for n^2D . Even though VO_3^- is not entirely reduced to LiVO_2 , the Sand equation is obeyed. This suggests the following type of mechanism may be occurring for the reduction of VO_3^- . VO_3^- is first reduced in a one electron step to form, on the electrode surface, a product which is not further reduced. VO_3^- is then, depending upon the surface coverage of the electrode and the potential, reduced in a 2-electron step to LiVO_2 . The oxide ion released would react with VO_3^- to form Li_3VO_4 . If this reaction were very rapid compared to the time of measurement, an apparent n value of 1 would be obtained. If the over-all apparent n value is 1, then D is found to be $0.76 \times 10^{-5}\text{ cm}^2/\text{sec}$. This estimate of D is rendered uncertain because it is not known whether oxide ion is released in the first reduction, nor are the rates of the reactions between VO_3^- and O^- and between VO_3^- and its own reduction products known. These reactions, if appreciable in extent, could lead to an apparent n less than 1, and an erroneously high value for D . Regardless of the chemical complications, however, $I_0\tau^{1/2}$ is a linear function of concentration.

Attempts were made to analyze the potential-time curves. The plots of $\log(\tau^{1/2} - T^{1/2})$ and $\log(\tau^{1/2} - T)/T^{1/2}$ vs. potential gave meaningless results, a behavior which was not surprising in view of the complex nature of the reduction of VO_3^- .

Cyclic sweep voltammetry.—Figures 3A-C, 4A-C, and 5A-B show typical cyclic sweep voltammograms of VO_3^- as the sweep rate is increased from 0.1 V/sec to 30 V/sec. There were no additional cathodic or anodic peaks in Fig. 3A when the switching potential occurred at more negative values. Figure 3A resembles the steady-state voltammograms in that several ill-defined waves are present on the negative scan and a number of stripping peaks appear in the positive scan. The potential of -0.865V for the oxidation peak is in good agreement with that assigned to the

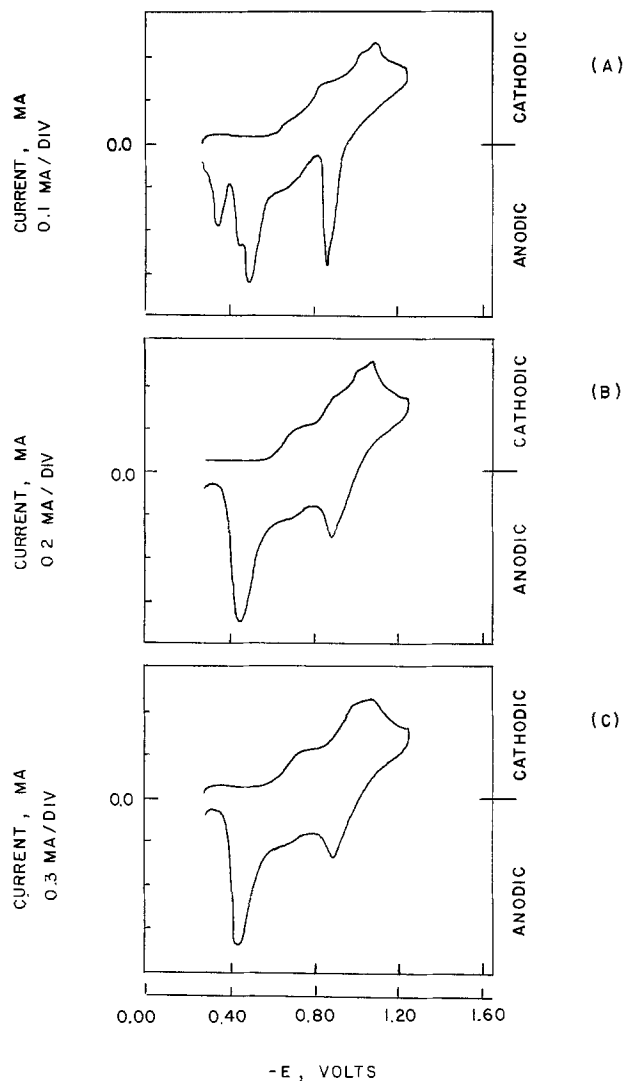


Fig. 3. Typical cyclic sweep voltammograms of LiVO_3 [LiVO_3] = 9.88 mM, switching potential = -1.25V , electrode area = 0.141 cm^2 . (A), Sweep rate 0.1 V/sec; (B), sweep rate 0.5 V/sec; (C), sweep rate 1.0 V/sec.

oxidation of LiVO_2 . As the sweep rate was increased (Fig. 3B-C), a number of effects could be seen. First, the reduction process became somewhat better defined in that only two apparent overlapping reductions were seen at about -0.77 and -1.05V . Second, on the negative scan, many of the stripping peaks had disappeared, indicating that several of the chemical reactions between VO_3^- , $\text{O}^=$, and the reduction products were no longer occurring. The stripping peak due to the oxidation of LiVO_2 was still seen at -0.89V . The peak at -0.45V agreed fairly well with that expected from chronopotentiometry for the oxidation of LiV_2O_4 . The shoulder occurring at about -0.67V appears to be due to the oxidation of the first reduction product observed in chronopotentiometry. As the sweep rate was further increased (Fig. 4A-C, 5A-B), the current due to the reduction occurring at about -0.77V increased with respect to the current for the reduction occurring at about -1.05V . Both peak potentials appeared to shift to more negative values. At 30 V/sec, only one broad reduction peak was seen at about -0.90V . There was also a dramatic change in the oxidation processes. The LiVO_2 oxidation peak and the LiV_2O_4 peak decreased and finally disappeared as the sweep rate was increased. Accompanying the disappearance of these two oxidation peaks was the appearance of an oxidation peak in the potential region of -0.60V . At 30 V/sec, only this one oxidation peak was seen. Changing the switching potential to a more negative value resulted in the reappearance

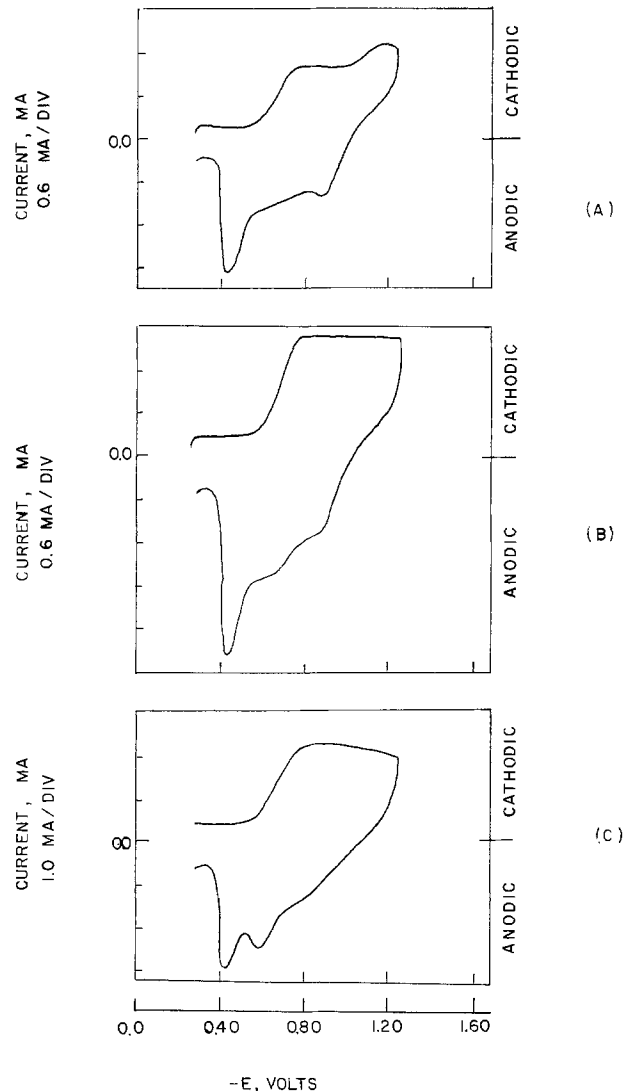


Fig. 4. Typical cyclic sweep voltammograms of LiVO_3 [LiVO_3] = 9.88 mM, switching potential = -1.25V , electrode area = 0.141 cm^2 . (A), Sweep rate 5.0 V/sec; (B), sweep rate 10.0 V/sec; (C), sweep rate 15.0 V/sec.

of the LiVO_2 and LiV_2O_4 oxidation peaks. No other reduction peak was seen.

The same trends were observed when smaller or larger concentrations were used. At smaller concentrations, the appearance of the one reduction and one oxidation peaks occurred at lower sweep rates while at larger concentrations, larger sweep rates were required. The sweep rate and concentration range were severely limited because of the interference of the reduction of impurities in the melt, charging current, and chemical reactions.

Plots of potential vs. $\log(i_p - i)$ and $\log(i_p - i)/i$ for the single reduction peak occurring at higher sweep rates produced curved lines. Either the process is kinetically controlled or the activity of the deposit is not constant. At the first appearance of only one reduction and oxidation peak, the number of coulombs passed in the reduction process was found to be between 400 and 500 microcoulombs/ cm^2 , regardless of the concentration of VO_3^- . This value is in good agreement with the number of coulombs contained in the "linear" region of the chronopotentiograms. The number of coulombs passed in reaching the peak potential was found to be about 130 microcoulombs/ cm^2 , corresponding to about 0.6 monolayer of VO_2 . The value 400-500 microcoulombs/ cm^2 is, therefore, somewhat high for monolayer coverage, suggesting that the deposit grew in lumps or clusters, so that a larger number of coulombs would need to be passed

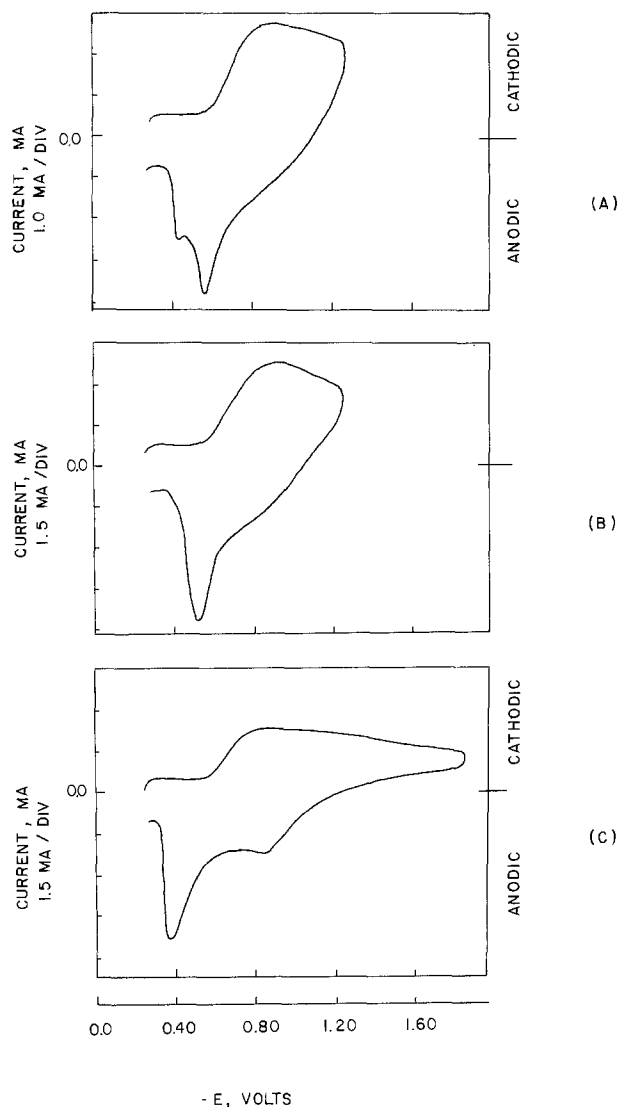


Fig. 5. Typical cyclic sweep voltammograms of LiVO_3 [LiVO_3] = 9.88 mM, electrode area = 0.147 cm^2 . (A), Sweep rate 20.00 V/sec, switching potential -1.25V ; (B), sweep rate 30.0 V/sec, switching potential -1.25V ; (C), sweep rate 15.0 V/sec, switching potential -1.85V .

before the electrode surface was completely covered. The relationship between the appearance of the electrochemical oxidation of LiVO_2 and the value 400-500 microcoulombs/ cm^2 suggests, as it did in the chonopotentiometric study, that VO_3^- is reduced to LiVO_2 only after the electrode surface has been covered with a less reduced product. If the surface had not been covered before the concentration of VO_3^- is zero at the electrode surface, no peak due to reduction of VO_3^- to LiVO_2 would be seen, regardless of the potential. However, if the surface was covered with the less reduced product the reduction would proceed once the reduction potential at which VO_3^- is reduced to LiVO_2 has been reached and its effect would be seen in the oxidation cycle by the appearance of the oxidation peak of LiVO_2 (-0.86V). At slower sweep rates, the electrode is covered with the less reduced species earlier in the scan and thus, a reduction peak of VO_3^- to LiVO_2 is seen. As the sweep rate is decreased further, a number of chemical re-

actions between VO_3^- and its reduction products start to occur.

The peak current increased as the sweep rate increased. Plots of peak current vs. the square root of sweep rate were scattered. The difference between the peak and half-peak potential for the single reduction wave was found to be on the order of 200 mV, as compared with 48 mV expected for a one electron, reversible deposition of a solid product at 450°C . White and Lawson (21, 22) have shown that submonolayer deposition has the effect of broadening the reduction peak, and thus leads to large differences between the peak and half-peak potential. The severe limitations on the sweep rate and concentration prohibited quantitative measurement of $E_{p/2}$ as a function of concentra-

Acknowledgment

Financial support of Ronald B. Chessmore by the National Science Foundation through a traineeship grant and by the Army Research Office, Contract Number US DA ARO D 31-124-72-G11 is gratefully acknowledged.

Manuscript submitted July 31, 1974; revised manuscript received Oct. 4, 1974.

Any discussion of this paper will appear in a Discussion Section to be published in the December 1975 JOURNAL. All discussions for the December 1975 Discussion Section should be submitted by Aug. 1, 1975.

Publication costs of this article were partially assisted by the University of Illinois at Urbana-Champaign.

REFERENCES

1. J. D. Van Norman and R. A. Osteryoung, *Anal. Chem.*, **32**, 398 (1960).
2. R. Molina, *Bull. Soc. Chim. France*, 301 (1961).
3. H. A. Laitinen and J. W. Pankey, *J. Am. Chem. Soc.*, **81**, 1053 (1959).
4. H. A. Laitinen and D. R. Rhodes, *This Journal*, **109**, 413 (1962).
5. A. M. Shams El Din, A. A. El Hosary, and A. A. A. Gerges, *J. Electroanal. Chem.*, **6**, 131 (1963).
6. B. Scrosati and H. A. Laitinen, *Anal. Chem.*, **38**, 1894 (1966).
7. G. Brauer, "Handbook of Preparative Inorganic Chemistry," Vol. 2, translated by Scripta Technic, Inc., Academic Press, New York (1965).
8. F. Holtzberg, A. Reisman, M. Berry, and M. Berkenblit, *J. Am. Chem. Soc.*, **78**, 1536 (1956).
9. H. A. Laitinen, R. Tischer, and D. Roe, *The Journal*, **107**, 546 (1960).
10. K. W. Hanck, Ph.D. Thesis, University of Illinois, 1969.
11. R. B. Chessmore, Ph.D. Thesis, University of Illinois, 1972.
12. W. S. Ferguson, Ph.D. Thesis, University of Illinois, 1956.
13. J. H. Propp, Ph.D. Thesis, University of Illinois, 1968.
14. C. L. Rulfs, J. J. Lagowski, and R. E. Bahr, *Anal. Chem.*, **28**, 84 (1956).
15. H. V. Malmstadt and J. D. Winefordner, *Anal. Chim. Acta*, **20**, 283 (1959).
16. D. R. Rhodes, Ph.D. Thesis, University of Illinois, 1961.
17. J. Galy and A. Hardy, *Bull. Soc. Chim. France*, 2808 (1964).
18. A. Hardy, J. Galy, A. Casalot, and M. Pouchard, *ibid.*, **4**, 1056 (1965).
19. W. Rüdorff and H. Becker, *Z. Naturforsch.*, **9**, 614 (1954).
20. B. Rueter and J. Jaskowsky, *Ber. Bunsenges. Physik. Chem.*, **70**, 189 (1966).
21. N. White and F. Lawson, *J. Electroanal. Chem.*, **25**, 409 (1970).
22. N. White and F. Lawson, *ibid.*, **26**, 113 (1970).

Transport Behavior and Raman Spectra of Electrolytes in Methyl Formate and Propylene Carbonate

H. V. Venkatesetty*

Honeywell Corporate Research Center, Bloomington, Minnesota 55420

ABSTRACT

The conductances of LiClO_4 , LiBF_4 , and LiAsF_6 in methyl formate and LiAsF_6 in propylene carbonate have been measured from dilute solution to very high concentration. Anomalous conductance behavior has been observed for the concentrated solutions of these salts in methyl formate. From conductance data, equivalent conductance at infinite dilution, ion-pair dissociation constant, and information on the formation of triple ions and more complex aggregates are obtained. The detectability of water in methyl formate and the effect of water on solvent spectrum are studied by Raman spectra. In concentrated solutions, ion-ion and ion-solvent interactions have been studied by Raman spectra.

Nonaqueous solvent systems are unique in that they provide a wide spectrum of macroscopic properties like the dielectric constant, wide liquid range, viscosity, and dipole moment. They also have specific microscopic properties like solvent molecular shape, solvent size, and different functional groups attached to them which can influence the behavior of solutes (1). The versatility of the nonaqueous electrolytes not only has led to new technologies but also to rapid advances in general theory of conductance (2). Recently different nonaqueous electrolyte systems, both organic and inorganic types, are being explored and some are being used with varying amounts of success with lithium anode and different kinds of cathode materials as high-energy density power sources (3-5). The mass transport properties of these electrolytes and electrolyte solution-electrode interactions can limit the efficiency and performance of the battery. It has been shown by Keller (6) in lithium-cupric fluoride battery with 1M LiClO_4 in propylene carbonate that the severe performance limitations encountered in regard to discharge rates can be attributed to mass transport limitations in the electrolytes.

Since more concentrated solutions of electrolytes ($\sim 1\text{M}$) are used in batteries wherever possible to minimize IR drop and most of the solvents have low dielectric constants, it is necessary to consider the formation of ion-pairs in these solvents even at low concentrations ($\sim 10^{-4}\text{M}$), and the formation of triple ions and more complex aggregates at higher concentrations. These complex equilibria can limit ionic transport processes particularly at low temperatures and thus affect battery operation. Unpublished results in the author's laboratory on the discharge characteristics of cells containing these electrolyte solutions have shown them to be potentially promising for high-energy density battery applications. The present studies were undertaken to determine the conductance behavior of LiClO_4 , LiBF_4 , and LiAsF_6 in methyl formate and LiAsF_6 in propylene carbonate over a wide concentration range and to obtain the Raman spectra for concentrated solutions of LiClO_4 , LiBF_4 , and LiAsF_6 in methyl formate which show anomalous conductance behavior. From conductance measurements such information as equivalent conductance at infinite dilution (Λ_0), ion-pair dissociation constant (K_d), and information on the formation of triple ions and more complex aggregates at higher concentration can be obtained. From Raman spectra

information on the effect of water on solvent structure and ion-solvent and ion-ion interactions in more concentrated solutions can be obtained.

Experimental

Methyl formate dried over Na_2CO_3 and distilled from P_2O_5 was used. It contained not more than 150 ppm of water as determined by gas chromatographic method and Karl Fischer titration. Propylene carbonate treated with CaO and distilled under vacuum contained no more than 120 ppm of water. The relative humidity of the dry room was about 4% and the dry box used in the author's laboratory with silica gel and with positive pressure of dry nitrogen showed a relative humidity of about 3% inside the box. Therefore all solutions were made in the dry room with precautions taken to eliminate any moisture contamination. The electrolytes LiClO_4 , LiBF_4 , and LiAsF_6 were the highest purity available (LiBF_4 and LiAsF_6 from Foote Mineral Company) and dried under vacuum at about 150°C for several hours and used without further purification. The electrolytes were assumed to be anhydrous and no moisture content was determined. Jones and Bollinger type conductance cells with bright platinum disk electrodes with cell constants varying from 0.2416 to 10.00 were used. All conductance measurements were made at $25^\circ \pm 0.05^\circ\text{C}$ with the conventional techniques to measure resistance with a General Radio bridge. Raman spectra were recorded with a Jarrell-Ash laser-Raman spectrometer (Model 25-300) having both He-Ne (6328Å) and Ar ion (4880Å) lasers (55 and 125 mW, respectively) as excitation sources. Pyrex glass Raman tubes (0.7 mm OD and 10 cm long) with optical flats as windows were filled with the solvent and solutions under dry conditions and sealed. The spectra were run two to three times to establish band positions. The region $2800\text{-}3900\text{ cm}^{-1}$ was examined for water frequencies.

Results and Discussion

AsF_6^- of LiAsF_6 is a noninterfering anion with low polarizability and spherical symmetry (7). Therefore, it should be interesting to compare its Raman spectrum and the conductance of LiAsF_6 in methyl formate with those of LiClO_4 and LiBF_4 .

The conductance measurements were made on LiAsF_6 in methyl formate covering a concentration range of 2M to $5 \times 10^{-4}\text{M}$, and in the case of LiClO_4 and LiBF_4 from 1.2 to $8 \times 10^{-4}\text{M}$ and for LiAsF_6 in propylene carbonate from 1.2 to $2 \times 10^{-4}\text{M}$. Plots of equivalent conductance (Λ) vs. log concentration for LiClO_4 and LiBF_4 in methyl formate are shown in

* Electrochemical Society Active Member.

Key words: methyl formate, propylene carbonate, electrolyte solutions, conductance, Raman spectra.

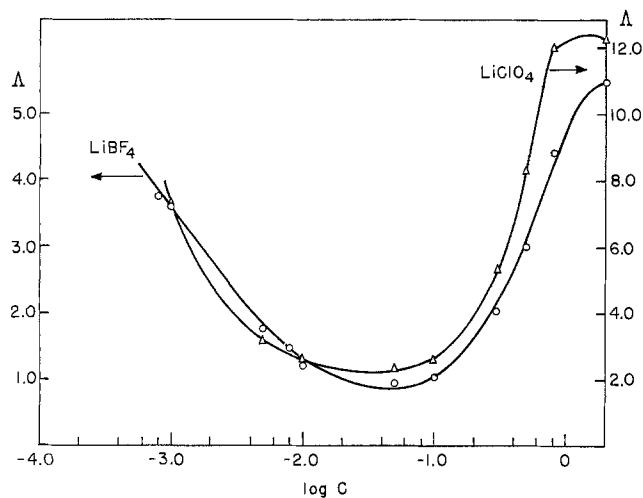


Fig. 1. Equivalent conductance vs. log concentration of LiClO_4 and LiBF_4 in methyl formate.

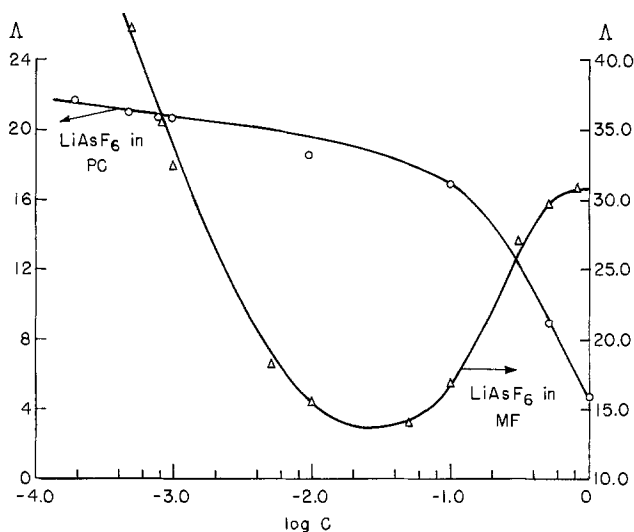


Fig. 2. Equivalent conductance vs. log concentration of LiAsF_6 in methyl formate and in propylene carbonate.

Fig. 1. Similar plots for LiAsF_6 in methyl formate and in propylene carbonate are shown in Fig. 2. It is interesting to note that LiAsF_6 as the most conducting salt shows a fairly high equivalent conductance at high dilution ($\Lambda = 42.4 \text{ cm}^2 \text{ ohm}^{-1} \text{ equiv.}^{-1}$ at $5 \times 10^{-4} \text{ M}$) and unusually high conductance at high concentration ($\Lambda = 21.2 \text{ cm}^2 \text{ ohm}^{-1} \text{ equiv.}^{-1}$ at 2 M) and the minimum in conductance appears at about 0.05 M ($\Lambda = 14.1$). In the case of LiClO_4 at high dilution, the measured equivalent conductance is much lower ($\Lambda = 7.3$ at $10 \times 10^{-4} \text{ M}$) whereas the equivalent conductance at high concentration is fairly high ($\Lambda = 12.4$ at 1.2 M) and the minimum occurs at around 0.05 M ($\Lambda = 2.3$). With LiBF_4 the conductances are lower over the entire concentration range indicating lower mobility ($\Lambda = 3.74$ at $8 \times 10^{-4} \text{ M}$ and $\Lambda = 5.46$ at 1.2 M) with the minimum occurring around 0.05 M ($\Lambda = 0.95$) as shown in Table I. In the case of LiAsF_6 in propylene carbonate, equivalent conductance decreases gradually with increasing concentration as expected for a solvent with high dielectric constant of 64.4 (1).

The plots of equivalent conductance vs. concentration shown in Fig. 1 and 2 and those of Λ vs. \sqrt{c} for all the three electrolytes in methyl formate and LiAsF_6 in propylene carbonate for more dilute solutions shown in Fig. 3, indicate that all these electrolytes behave as weak electrolytes with the formation of ion-pairs, triple ions, and more complex aggregates. For such solutions, the information on the limiting equivalent

Table I. Equivalent conductance at infinite dilution and dissociation constant for ion-pairs at 25°C

LiAsF_6 in MF*	LiAsF_6 in PC†	LiClO_4 in MF	LiBF_4 in MF
$\Lambda_0 = 71.5$ $K_d = 3.13 \times 10^{-4}$	$\Lambda_0 = 22.2$ $K_d = 11.8 \times 10^{-3}$	$\Lambda_0 = 16.6$ $K_d = 2.64 \times 10^{-4}$	$\Lambda_0 = 9.1$ $K_d = 2.4 \times 10^{-4}$
Log Λ vs. log C values			
Minimum conc (moles/liter)		Λ	Slope
LiAsF_6 in MF*	0.05	14.1	-0.45
LiAsF_6 in PC†	—	—	-0.5
LiClO_4 in MF	0.05	2.3	-0.46
LiBF_4 in MF	0.05	0.95	-0.45

* MF = Methyl formate.

† PC = Propylene carbonate.

conductance (Λ_0) and the dissociation constant (K_d) for the ion-pairs is important for understanding the ion-solvent and ion-ion interactions. The conductance data in the dilute region of the solution are expected to follow the Ostwald dilution law and the law of mass action. Approximating the activity coefficient of each ionic species unity as a limiting case, an equation of the form similar to that of Fuoss-Shedlovsky (8), except the function $S(z)$, can be conveniently applied. The equation is of the form

$$\frac{1}{\Lambda} = \frac{1}{\Lambda_0} + \frac{C\Lambda}{K_d(\Lambda_0)^2}$$

where Λ_0 is the limiting equivalent conductance and K_d is the dissociation constant. Plots of $1/\Lambda$ as a func-

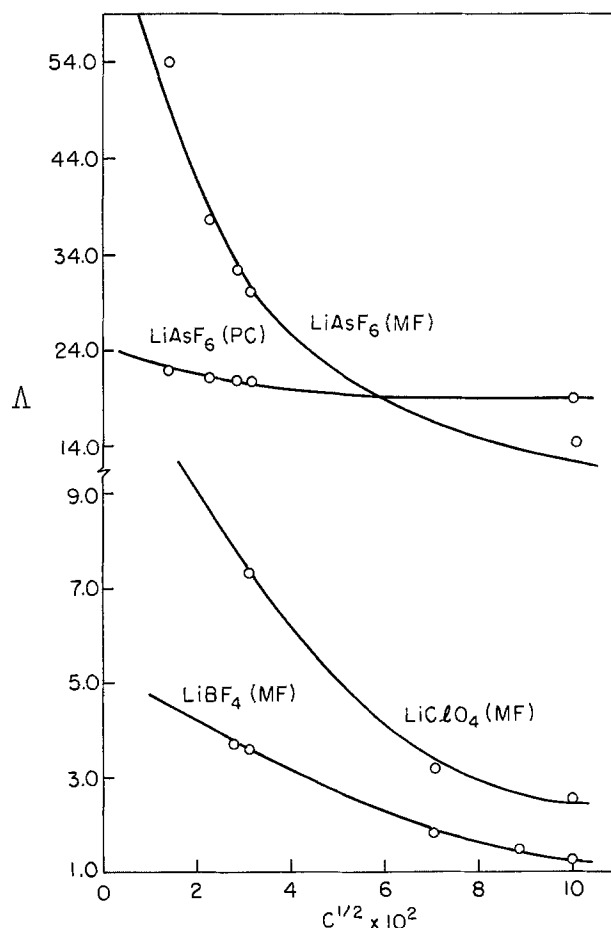


Fig. 3. Equivalent conductance vs. \sqrt{c} of concentration of LiAsF_6 , LiClO_4 , and LiBF_4 in methyl formate and LiAsF_6 in propylene carbonate.

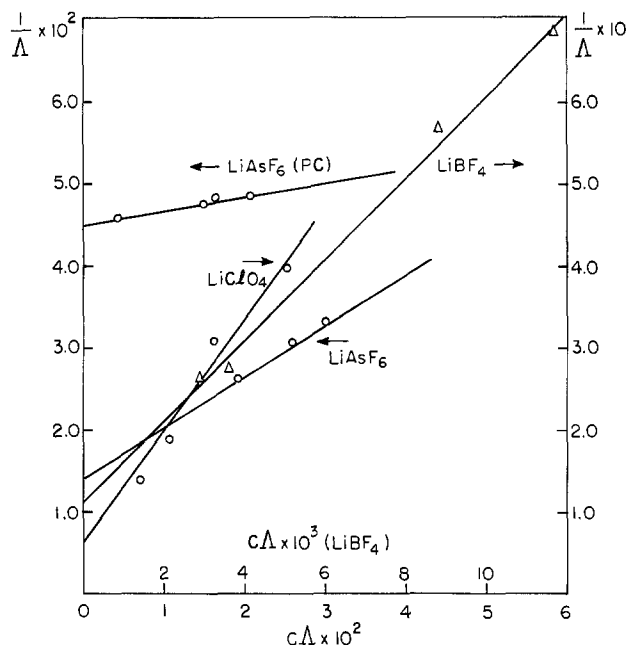


Fig. 4. $1/\Lambda$ vs. $C\Lambda$ plots of LiAsF_6 , LiClO_4 , and LiBF_4 in methyl formate and of LiAsF_6 in propylene carbonate.

tion of $C\Lambda$ for all the electrolytes in the two solvents gave straight lines as shown in Fig. 4. From the intercepts and the slopes, the limiting equivalent conductance(s) and dissociation constant(s) were obtained, respectively. These values are shown in Table I.

The Λ_0 value for LiAsF_6 in methyl formate is 71.5 and K_d 3.13×10^{-4} whereas in propylene carbonate Λ_0 is 22.2 and K_d is 11.8×10^{-3} . The higher value of Λ_0 can be attributed to the noninteracting nature of AsF_6^- ion and lower viscosity of methyl formate (1). Likewise the smaller value of Λ_0 in propylene carbonate can be attributed to higher viscosity and the higher value of K_d to the higher dielectric constant of propylene carbonate (1). In water at 25°C, the Λ_0 value for LiAsF_6 is 94.87 and is completely dissociated as expected (7). The lower values of Λ_0 for LiClO_4 (16.6) and LiBF_4 (9.1) shown in Table I can be attributed to considerable ion-solvent interactions in these systems. The K_d values are consistent with such interactions. When $\log \Lambda$ vs. $\log C$ plots are made for all these electrolytes the slope predicted for ion-pair formation, namely, $-\frac{1}{2}$ (9), is found for all the salts with minima occurring at 0.05M in methyl formate and shifting to a higher concentration in propylene carbonate, as shown in Table I.

The formation of triple ions and ion quadrupoles with increasing concentration of ionic salts in solvents of low dielectric constant has been treated theoretically by Fuoss and Kraus (9, 10). The increase in conductance with concentration after the minimum has been shown to be due to the formation of triple ions by coulombic interaction between the ion-pair and the ionic species. The equation describing this equilibrium is given by

$$\Lambda = \sqrt{\frac{K}{c}} \Lambda_0 + \frac{\sqrt{Kc}}{k} \Lambda_{03}$$

where K and k are the equilibrium constants for ion-pair and triple ion formation and Λ_0 and Λ_{03} have their usual significance (9, 10). Graphs of $\Lambda c^{1/2}$ vs. C in all these systems give straight lines indicating that such interactions do predominate.

The unusually high conductances observed for concentrated solutions of these salts in methyl formate can be explained partly due to large anions with low surface charge density and partly due to hydrolysis. Methyl formate solvent with a dielectric constant of 8.4 (1) has been found to show a dielectric constant of

27.4 ± 6.0 in 1.1M LiAsF_6 solution (11). The very low values of conductances and Λ_0 (9.1) observed for LiBF_4 in methyl formate are probably due to the dissociation of BF_4^- ion to BF_3 and F^- and the limited solubility of LiF ($3 \times 10^{-5}\text{M}$) in methyl formate (6).

Vibrational spectroscopy has been extensively used in molten salts and concentrated solutions of electrolytes in water to study ionic interactions. Unfortunately, very little such data are available on nonaqueous electrolytes of interest to battery technology. Janz and co-workers have used laser Raman spectroscopy to study ion-ion and ion-solvent interactions in concentrated solutions of silver nitrate in acetonitrile (12-14). Laser Raman spectroscopy has been used here to study the ion-ion and ion-solvent interactions in concentrated solutions of LiAsF_6 , LiClO_4 , and LiBF_4 in methyl formate which show anomalous conductance behavior.

Since the presence of water even in small quantity in the solvent (≥ 100 ppm) is detrimental to the stability and performance of a battery, it was decided to study the effect of water on the structure of the solvent. It was found that water in the solvent could be detected using Raman spectroscopy by the presence of a strong broad band appearing at a frequency of 3565 cm^{-1} due to symmetrical vibration (15) as shown in Fig. 5. Further, the presence of water can be detected only when the water content is larger than 1% by weight. In order to compare the spectra of solvent samples with different amounts of water in them, the height of the solvent CH_3 -symmetrical stretching peak appearing at a frequency of 2840 cm^{-1} , which does not change with water content, was used as an internal standard and compared to the height of the water peak at 3565 cm^{-1} . Therefore, when the ratio of the height of the water peak to the height of the standard solvent peak vs. weight per cent by water is plotted, the value of the ratio increases until a water content of 8.4% by weight is reached above which the value of this ratio remains constant as shown in Fig. 6. At higher concentration of water (11.67% by weight) on careful observation, a second layer below the methyl formate phase is seen. It is possible that this layer is already formed at smaller water concentrations. When these layers were separated and the spectra taken, it is found that the spectrum of the methyl formate phase

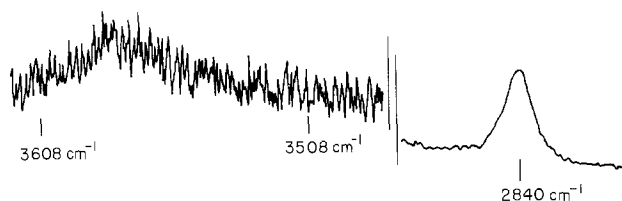


Fig. 5. Prominent water and methyl formate bands from Raman spectrum.

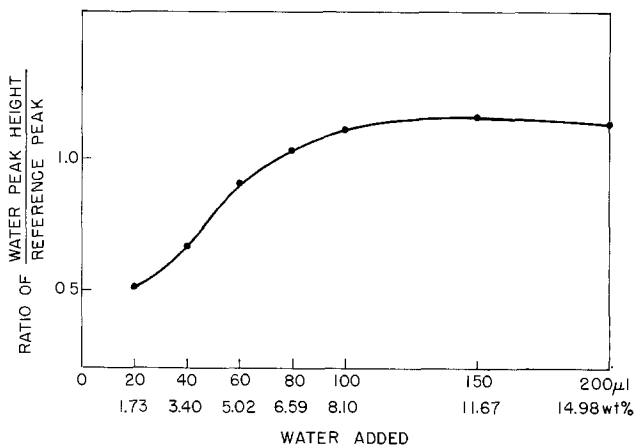


Fig. 6. Plot of the ratio of water peak height to the reference peak vs. the weight per cent water added.

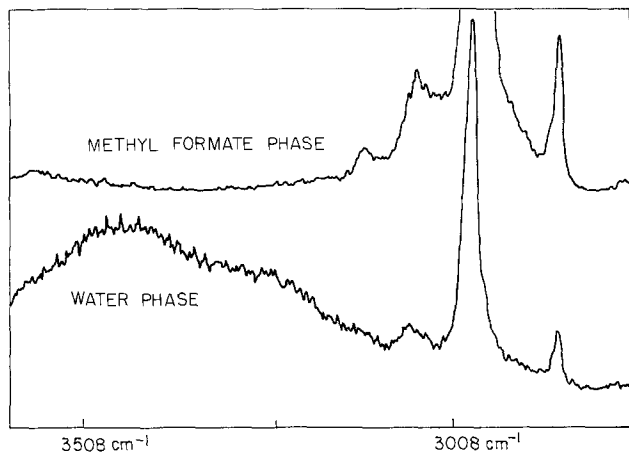


Fig. 7. Raman spectra of the methyl formate phase and the water phase.

is identical to the pure solvent whereas the spectrum of the water phase shows both the vibrations of the methyl formate and of the water modes. The carbonyl stretching band of methyl formate appearing at 1717 cm^{-1} in the pure solvent has shifted to lower frequency and the intense water peak has shifted from 3565 to 3444 cm^{-1} as shown in Fig. 7. These spectral changes can be interpreted in terms of interactions between the water molecules and the methyl formate molecules. The conclusion that can be drawn from this study is that a small quantity of water is soluble in methyl formate and it is possible that by strong interaction the carbonyl group of the solvent molecules induces a few bridges with the water molecules. Thus, it is possible that most of the soluble water in methyl formate is decoupled water and in the water phase most of the water is lattice water.

The Raman spectra of 2M LiAsF_6 in methyl formate have been obtained. The anion AsF_6^- with octahedral symmetry should give three Raman active fundamental vibrations (15). Three Raman frequencies are observed for solid related compounds (16). LiSbF_6 shows ν_1 at 668 cm^{-1} , ν_2 (double degenerate) at 558 cm^{-1} , and ν_3 at 294 cm^{-1} , whereas CsAsF_6 shows ν_1 at 685 cm^{-1} , ν_2 at 576 cm^{-1} , and ν_3 at 372 cm^{-1} (16) as shown in Table II. In the case of LiAsF_6 -methyl formate solution only two Raman frequencies are obtained ν_1 at 678 cm^{-1} and ν_3 at 344 cm^{-1} as shown in Table II where the degenerate mode ν_2 has been lifted. The lifting of the degenerate mode ν_2 can be attributed to interactions of the AsF_6^- ion with the solvent as well as the cation. Similar observations have been made by Janz and co-workers on acetonitrile-silver nitrate solutions (14) and aqueous lithium perchlorate solutions (17) which have been interpreted in terms of ion-ion and ion-solvent interactions.

An unperturbed perchlorate ion (ClO_4^-) with tetrahedral symmetry shows four Raman active vibrational modes; symmetric vibration, ν_1 , a doubly degenerate deformation, ν_2 , a triply degenerate vibration, ν_3 , and a triply degenerate deformation, ν_4 (15). The Raman spectrum of lithium perchlorate-methyl formate solution (1.2M) shows the expected four bands: ν_1 at 941 cm^{-1} , ν_2 at 457 cm^{-1} , ν_3 at 1125 cm^{-1} , and ν_4 at 632 cm^{-1} as shown in Table III. These frequencies when compared to those of molten lithium perchlorate (18) and solid lithium perchlorate (18) as shown in Table

Table II. Raman spectra of LiAsF_6 -methyl formate solution and related compounds

	$\nu_1(\text{cm}^{-1})$	$\nu_2(\text{cm}^{-1})$	$\nu_3(\text{cm}^{-1})$
CsAsF_6 (16)	685	576	372
LiSbF_6 (16)	668	558	294
$\text{LiAsF}_6\text{-MF}$ (1.2M)	678	—	344

Table III. Raman spectra of LiClO_4 -methyl formate solution and related systems

	$\nu_1(\text{cm}^{-1})$	$\nu_2(\text{cm}^{-1})$	$\nu_3(\text{cm}^{-1})$	$\nu_4(\text{cm}^{-1})$
$\text{LiClO}_4(\text{melt})$ (18)	953	466	1117 1162	635
$\text{LiClO}_4(\text{solid})$ (18)	965	464, 480	1063	621, 660
$\text{LiClO}_4(\text{Aq-soln})$ (19)	922	450	1110	620
LiClO_4 -methyl formate (1.2M)	941	457	1125	632

III show a shift to lower values indicating considerable ion-solvent interactions in methyl formate solution. The Raman spectrum of an aqueous solution of lithium perchlorate (19) shows that all four frequencies appear at lower values compared to those of lithium perchlorate-methyl formate solution as shown in Table III indicating that the ion-solvent interactions are stronger in the aqueous system as anticipated. The tetrafluoroborate ion BF_4^- with tetrahedral symmetry should show four Raman lines appearing in the frequency range of about $1000\text{-}350\text{ cm}^{-1}$ (20). However, LiBF_4 -methyl formate solution (1.2M) shows a band at 2130 cm^{-1} . It is possible that BF_4^- dissociates to BF_3 and F^- and BF_3 complexes with methyl formate while LiF with low solubility precipitates (6).

Acknowledgment

The author wishes to thank Professor G. J. Janz of Rensselaer Polytechnic Institute for Raman spectra and discussions and Dr. H. E. Heist for encouragement and Robert Dilloplane for experimental assistance. This work was carried out at Honeywell Power Sources Center, Horsham, Pennsylvania.

Manuscript submitted May 6, 1974; revised manuscript received Sept. 5, 1974. This was Paper 51 presented at the Boston, Massachusetts, Meeting of the Society, Oct. 7-11, 1973.

Any discussion of this paper will appear in a Discussion Section to be published in the December 1975 JOURNAL. All discussions for the December 1975 Discussion Section should be submitted by Aug. 1, 1975.

Publication costs of this article were partially assisted by Honeywell Incorporated.

REFERENCES

- "Nonaqueous Electrolytes Handbook," Vol. I and II, G. J. Janz and R. P. T. Tomkins, Editors, Academic Press, New York (1972) and (1973).
- R. M. Fuoss, L. Onsager, and J. F. Skinner, *J. Phys. Chem.*, **69**, 2581 (1965) and references quoted therein.
- A. N. Dey and M. L. B. Rao, Paper 53, and A. N. Dey Paper 54, presented at Electrochemical Society Meeting, Boston, Mass., Oct. 7-11, 1973.
- J. J. Auburn, K. W. French, S. I. Lieberman, V. K. Shah, and A. Heller, Paper 58, Electrochemical Society Meeting, Boston, Mass., Oct. 7-11, 1973.
- W. K. Behl, J. A. Christopoulos, M. Ramirez, and S. Gilman, Paper 59, Electrochemical Society Meeting, Boston, Mass., Oct. 7-11, 1973.
- R. Keller, *This Journal*, **117**, 1266 (1970).
- G. Atkinson and C. J. Hallada, *J. Phys. Chem.*, **64**, 1487 (1960).
- R. M. Fuoss and T. Shedlovsky, *J. Am. Chem. Soc.*, **71**, 1496 (1949).
- C. A. Kraus and R. M. Fuoss, *ibid.*, **57**, 1 (1935).
- R. M. Fuoss and C. A. Kraus, *ibid.*, **55**, 2387 (1933).
- R. Keller *et al.*, NAS3-8521, Rocketdyne, August 1969.
- K. Balasubrahmanyam and G. J. Janz, *J. Am. Chem. Soc.*, **92**, 4189 (1970).
- B. G. Oliver and G. J. Janz, *J. Phys. Chem.*, **74**, 3819 (1970).
- G. J. Janz, *J. Electroanal. Chem.*, **29**, 107 (1971).
- G. Herzberg, "Molecular Spectra and Molecular Structure," D. Van Nostrand Co. Inc., New York (1956).

16. G. M. Begun and A. C. Rutenberg, *Inorg. Chem.*, **6**, 2212 (1967).
 17. B. G. Oliver and G. J. Janz, *J. Phys. Chem.*, **75**, 2948 (1971).

18. W. H. Leong and D. W. James, *Australian J. Chem.*, **22**, 499 (1969).
 19. R. Fonteyne, *Nature*, **138**, 886 (1936).
 20. N. N. Greenwood, *J. Chem. Soc.*, **1959**, 3811.

Technical Note



Polarization of Mild Steel in Mixed $\text{NaNO}_3/\text{NaClO}_4$ Electrolytes

Der-Tau Chin^{*1}

Electrochemistry Department, Research Laboratories, General Motors Corporation, Warren, Michigan 48090

This communication describes an experimental measurement with a rotating mild steel¹ hemispherical electrode to see if there were convection effects on the steady-state polarization in mixed $\text{NaNO}_3/\text{NaClO}_4$ electrolytes. Details of the experimental measurement have been reported elsewhere (1). The results are shown in Fig. 1 (represented by the symbols \circ , Δ , \bullet , etc.) for three electrolyte compositions at various

rotational speeds. Nitrogen-saturated 4M (total anion strength) electrolytes at a constant temperature of $22^\circ \pm 2^\circ\text{C}$ were used for the tests; the pH of these electrolytes was maintained between 6 and 8 during the experimental runs. For comparison, steady-state polarization curves previously reported (1, 2) for the rotating mild steel hemispherical electrode in 4M NaNO_3 and 4M NaClO_4 are also plotted in the figure as the thick and the thin curves, respectively.

Figure 1 shows a difference between the present results and those reported previously by Hoare *et al.* (3, 4) for stationary mild steel beads in mixed $\text{NaNO}_3/\text{NaClO}_4$ electrolytes. These authors have found that

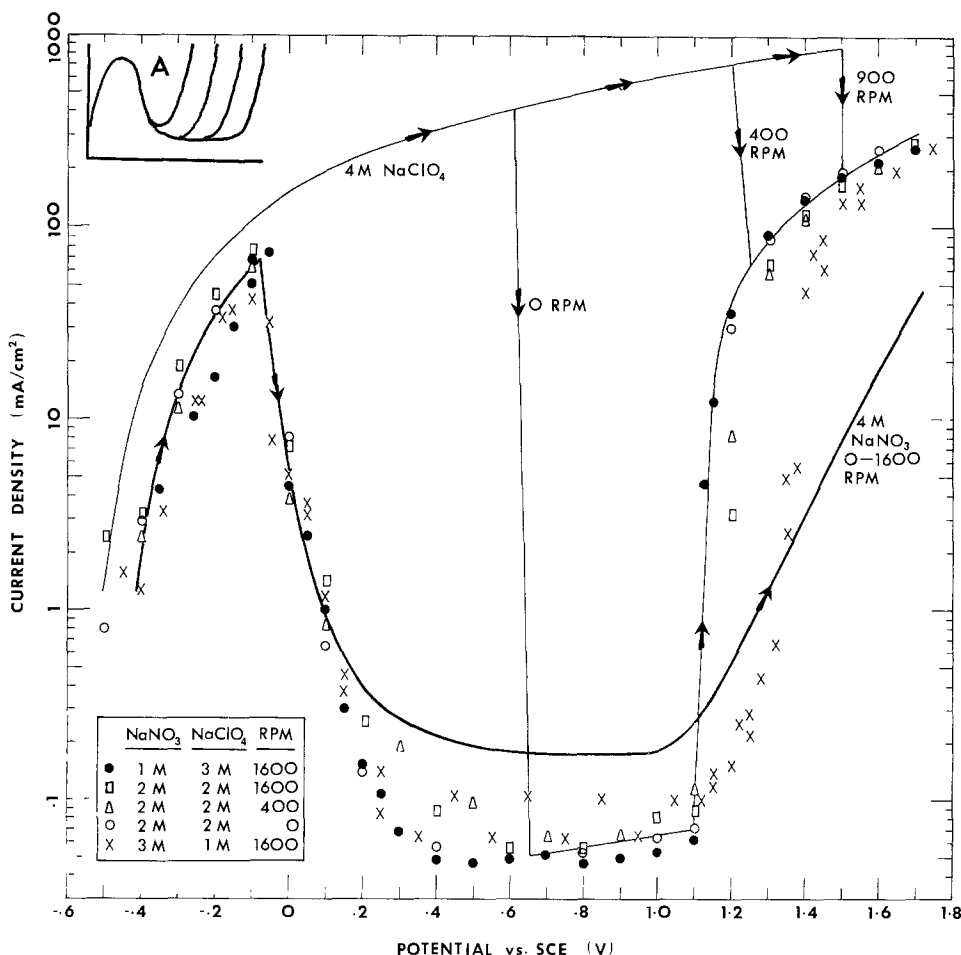


Fig. 1. Steady-state polarization of a rotating mild steel hemispherical electrode in mixed $\text{NaNO}_3/\text{NaClO}_4$ electrolytes. The data were taken at a constant temperature of $22^\circ \pm 2^\circ\text{C}$. For comparison, the results by Hoare *et al.* (3, 4) are sketched in inset A, in which the passive/transpassive transitional potential is a function of electrolyte composition.

the potential at which transition from the passive to the transpassive state began was a function of electrolyte composition (Fig. 1A). The transpassive potential began at less noble values with increasing concentration of perchlorate ions until a minimum potential of 0.3 V/SCE was reached at 67% perchlorate in a total 3M mixed $\text{NaNO}_3/\text{NaClO}_4$ electrolyte. The transpassive region then started at more noble potentials with further increase in perchlorate concentration.

In this study, the variation with the electrolyte composition is not as obvious. For all the compositions tested (ranging from 0% to 100% perchlorate), the transpassive region invariably starts at a potential of 1.1 V/SCE. The slope of the polarization curves at the very beginning of the transpassive region seems to vary with the composition. The curve for 4M NaNO_3 has the smallest slope, whereas the curve for 4M NaClO_4 has the sharpest transition from the passive to the transpassive states. The data for the mixed electrolytes exhibit a logical trend in that the slope of the transition falls between the two limits and increases with increasing perchlorate concentrations. Four other additional features can also be observed in the figure:

1. The electrode rotation had no effect on the polarization in the mixed electrolyte. The same is also true for the nitrate solution. For perchlorate, the active/passive transition potential occurs at more noble values with increasing rotational speed.

2. For potentials less than 0.2 V/SCE, the data for the mixed electrolytes fall exactly on the curve for 4M NaNO_3 . It seems that in this low potential region, only nitrate ions participate in the anodic processes; perchlorate serves only as the supporting electrolyte. There is no doubt that the passivation in the mixed electrolytes is initiated by nitrate ions.

3. In the passive region (from 0.2 to 1.1 V/SCE), the current density for the mixed electrolytes falls below that for NaNO_3 , and agrees with that for NaClO_4 . Apparently, in this region, the anode starts to adsorb perchlorate ions, which in turn reduce the passive current density to the level specified by the NaClO_4 curve. The nature of the protective film in the mixed electrolytes probably resembles that in the perchlorate solutions.

4. In the transpassive region (potentials greater than 1.1 V/SCE), the shape of the polarization curves for the mixed electrolytes closely resembles that of NaClO_4 rather than NaNO_3 even though the initial slopes are a function of electrolyte composition. For potentials greater than 1.5 V/SCE, the data points for all the mixed electrolytes seem to converge to a single curve represented by the polarization behavior in 4M NaClO_4 . It has been reported in previous studies (5, 6) that during the early transpassive state (below

the potential where the current density at the anode is less than 5000 mA/cm²), mild steel in nitrate solutions is covered with an electronically conductive oxide film, and the current is consumed solely in the oxygen evolution reaction at the oxide/electrolyte interface. Addition of perchlorate ion to nitrate solutions seems to greatly reduce the critical potential at which the oxide film begins to break apart and the underlying metal matrix starts to dissolve transpassively into the electrolyte.

In the present study, nitrogen-saturated 4M mixed electrolytes were used for the measurements, whereas Hoare *et al.* used oxygen-stirred 3M solutions. The solubility of O_2 in water at 25°C is 0.039 g/liter, or 0.0012M (7). It is questionable that the presence of this small amount of O_2 could reduce the onset of transpassive potential by up to 800 mV. The differences might be caused by variations in the composition of mild steels or the experimental methods used in the polarization measurements.

It is not known at the present time why the results of this study differ so much from those previously reported. The differences are of considerable importance to those working in this field. Hence, subtle, as yet unknown, factors can influence the results significantly—a fact which should be brought to the attention of future workers studying the fundamental nature of electrochemical machining.

Acknowledgment

The author wishes to thank J. D. Thomas, R. A. Foust, Jr., and K-W. Mao, also of the Electrochemistry Department, Research Laboratories, General Motors Corporation, for their helpful discussions and suggestions.

Manuscript submitted Aug. 6, 1974; revised manuscript received Oct. 7, 1974.

Any discussion of this paper will appear in a Discussion Section to be published in the December 1975 JOURNAL. All discussions for the December 1975 Discussion Section should be submitted by Aug. 1, 1975.

Publication costs of this article were partially assisted by the General Motors Corporation.

REFERENCES

1. D-T. Chin, *This Journal*, **119**, 1043 (1972).
2. D-T. Chin, *ibid.*, **119**, 1181 (1972).
3. J. P. Hoare and K-W. Mao, *ibid.*, **120**, 1452 (1973).
4. K-W. Mao, M. A. LaBoda, and J. P. Hoare, *ibid.*, **119**, 419 (1972).
5. D-T. Chin and A. J. Wallace, *ibid.*, **120**, 1487 (1973).
6. D-T. Chin and K-W. Mao, *J. Appl. Electrochem.*, **4**, 155 (1974).
7. A. Lange, "Handbook of Chemistry," McGraw-Hill Book Co., New York (1967).



Adsorption Isotherm of Iodide Ions on Copper Single Crystal Planes in Sulfuric Acid

S. M. Mayanna

Department of Chemistry, Central College, Bangalore University, Bangalore-1, India

Halide ions are both stimulators and inhibitors of corrosion of metals (1). Inhibitive anions are known to adsorb preferentially at metal/solution interfaces that are positive to the zero charge potential of the metal (2). Hackerman (3) has proposed an adsorption theory of corrosion inhibition in which adsorption is general in character and higher order of inhibitor efficiencies favor those inhibitors which exhibit chemisorption (4). An iodide ion can show strong interaction on the metal surface because of its high polarizability (5). Copper is an industrially important metal next to iron and the study of inhibition of acid corrosion of copper is a subject with tremendous technological significance. In view of the importance of specific adsorption to practical systems of corrosion, an attempt has been made to know the nature of interaction of iodide ions on copper single crystal planes during acid corrosion. The Langmuir adsorption isotherm has been applied to the adsorption of iodide ions on copper single crystal planes in 0.1N sulfuric acid, and heats of adsorption have been evaluated.

Solutions were prepared from freshly distilled and pre-electrolyzed AR sulfuric acid and recrystallized AR potassium iodide using triple distilled water; 99.999% copper (110), (100), and (111) planes with dislocation density of the order $10^6/\text{cm}^2$ were mechanically polished on 4/0 emery paper using ethyl alcohol as lubricant and then electropolished in 1:1 orthophosphoric acid (6) at a cell potential of 1.2V for 30 min. The dissolution was carried out in aerated 0.1N sulfuric acid with the desired amount of potassium iodide. The potentials of copper single crystal planes were recorded against a Hg/Hg₂SO₄ reference electrode using VTVM. The detailed experimental procedure has been given in a previous communication (7). Copper (110), (100), and (111) planes were dissolved in aerated unstirred 0.1N sulfuric acid containing various concentrations of iodide ions at different temperatures, and dissolution rates ($\text{mg}/\text{cm}^2/\text{hr}$) were evaluated. Iodide ions had significant effect on the dissolution rates of the crystal planes when its concentration was in between 10^{-6} and 10^{-4}M . The surface coverages (θ) of iodide ions on the crystal planes at different temperatures were evaluated from the dissolution rates using the equation (8)

$$\theta = 1 - P/P_0 \quad [1]$$

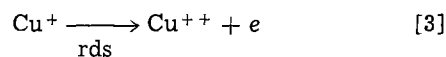
where P and P_0 were the dissolution rates with and without iodide ions, respectively. The surface coverage increased on increasing the concentration of iodide ions up to 10^{-4}M . The additional increase of iodide ions above 10^{-4}M did not increase the surface coverage further. Table I shows the effect of iodide ions on the surface coverage up to 10^{-4}M at 30°C . The values of C/θ were plotted against C (C being the concentration of iodide ions in the bulk of the solution) for various

Table I. Surface coverage of iodide ions on copper single crystal planes in sulfuric acid at 30°C

Sulfuric acid pH	Concentration of I ⁻ ions (M)	θ		
		(110)	(100)	(111)
1.0	1×10^{-6}	0.37	0.05	0.26
	5×10^{-6}	0.41	0.11	0.30
	1×10^{-5}	0.56	0.30	0.41
	5×10^{-5}	0.75	0.55	0.50
	1×10^{-4}	0.90	0.74	0.58

crystal planes at different temperatures. Figure 1 shows the variation of C/θ with C for all the crystal planes at 30°C . Heats of adsorption of iodide ions on copper (110), (100), and (111) planes were calculated (9) and these values were found to be 11.8, 13, and 15.2 kcal/mole, respectively.

The mechanism of the dissolution reaction of copper in acidic solution according to Bockris *et al.* (10) is as follows



The experimental data obtained recently (11) from our laboratory for copper single crystal planes in sulfuric acid with and without the presence of iodide ions are consistent with the above mechanism indicating that the second electron removal is the rate determining step. In the presence of iodide ions, the rate of the

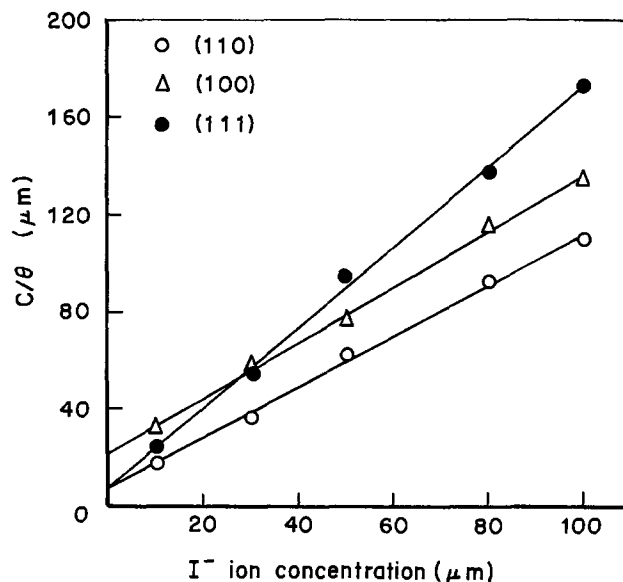


Fig. 1. Langmuir adsorption isotherm for adsorption of iodide ions on copper single crystal planes in sulfuric acid at 30°C .

Key words: surface coverage, inhibitors, adsorption isotherm, heat of adsorption.

dissolution reaction is decreased. However, the anodic Tafel slopes for copper single crystal planes in the absence and presence of iodide ions are the same. This indicates that the mechanism of the dissolution reaction on uninhibited and inhibited copper single crystal planes in sulfuric acid is the same.

The corrosion potential on ϕ scale (12) indicates the positive charge on the surface of the crystal plane and inhibition of acid corrosion by the adsorption of iodide ions at the reaction sites on the surface of the crystal plane. The dissolution rate of a metal depends on the number of available free reaction sites on the surface (13). If the above fact is valid, and assuming no interaction between the adsorbed ions (14) (at low values of θ), then the apparent dissolution rate of the inhibited copper single crystal plane is proportional to the number of reaction sites not covered by iodide ions. A correlation between θ and C can be achieved with the Langmuir adsorption isotherm

$$\theta = KC/1 + KC \quad [4]$$

Rearranging Eq. [4]

$$C/\theta = 1/K + C \quad [5]$$

Figure 1 is a plot of Eq. [5] and shows that the Langmuir adsorption isotherm correlates the experimental data. The values of heats of adsorption indicate that the iodide ion is strongly adsorbed on the copper single crystal planes. This is in agreement with the experimentally observed higher order of inhibitor efficiency of the iodide ions which is an important feature of chemisorption (15).

Acknowledgments

The work carried out was inspired by the late Professor T. H. V. Setty. The author wishes to express his gratitude to Professor M. Shadaksharaswamy, Head of the Department of Chemistry, Bangalore University, Bangalore, India, for his encouragement.

Manuscript submitted May 3, 1974; revised manuscript received July 10, 1974.

Any discussion of this paper will appear in a Discussion Section to be published in the December 1975 JOURNAL. All discussions for the December 1975 Discussion Section should be submitted by Aug. 1, 1975.

Publication costs of this article were partially assisted by Bangalore University.

REFERENCES

1. I. N. Putilova, S. A. Balezin, and V. P. Barannick, "Metallic Corrosion Inhibitors," p. 79, Pergamon Press, New York (1960).
2. C. P. De, *Nature*, **180**, 803 (1957).
3. N. Hackerman, "Comptes Rendus Symposium European 123 Sur Les Inhibiteurs De Corrosion," p. 99, University of Ferrara, Italy (1960).
4. N. Hackerman and R. M. Hurd, in "International Congress on Metallic Corrosion," L. Kenworthy, Editor, p. 166, Butterworths, London (1962).
5. J. M. West, "Electrodeposition and Corrosion Processes," 2nd ed., p. 123, Van Nostrand, Co., Ltd., London (1970).
6. P. A. Jacquet, *Metal Rev.*, **1**, 157 (1956).
7. S. M. Mayanna and T. H. V. Setty, *Indian J. Chem.*, **10**, 295 (1972).
8. Robert J. Chin and Ken Nobe, *This Journal*, **118**, 545 (1971).
9. S. J. Gregg, "The Surface Chemistry of Solids," p. 45, Chapman and Hall, Ltd., London (1951).
10. E. Mattsson and J. O'M. Bockris, *Trans. Faraday Soc.*, **55**, 1586 (1959).
11. S. M. Mayanna, A. K. N. Reddy, and T. H. V. Setty, Unpublished results.
12. L. I. Antropov, "Kinetics and Electrode Processes and Null Points of Metals," p. 5, C.S.I.R. Publications, India (1960).
13. T. P. Hoar and R. D. Holliday, *J. Appl. Chem.*, **3**, 502 (1953).
14. J. O'M. Bockris and D. Drazic, "Electrochemical Science," p. 65, Taylor and Francis, Ltd., London (1972).
15. N. Hackerman, E. S. Snavely, Jr., and J. S. Payne, Jr., *This Journal*, **113**, 677 (1966).

The Direct Radiometric Study of Electrosorption of Tritium Labeled Compounds Adsorption of Methanol on Gold Electrodes

Andrzej Wieckowski

Chemistry Department, University of Warsaw, Warsaw, Poland

"The main drawback (of radiometric methods) would seem to be the demand for electrodes of very large area. This restriction limits precision, limits the variety of metals which can be studied, and as yet does not allow measurements on smooth metals (to which most other methods have been applied)." This opinion of Perkins and Andersen (1) seems still to be valid in spite of the fact that some new methods have been elaborated since 1969 (2-4). As a way for improvement of the methods used for the study of adsorption of organic compounds, an application of tritium atoms as a labeling agent rather than ^{14}C may be suggested. However, owing to its low energy ($E_{\text{max}} = 18.6 \text{ keV}$), the β^- tritium radiation is strongly absorbed in adsorbent material which causes serious experimental problems. The working electrode must be prepared from a very thin layer of metals and use of a window counter (5) seems, in practice, to be impossible. This low penetrability of tritium radiation brings

Key words: electroadsorption, tritium labeled compounds, methanol, glass scintillator.

about, at the same time, the effective elimination of background counting (6). It should be noted that the presence of the background counting in the study of ^{14}C or ^{35}S labeled compounds has limited the range of applicability of radiometric methods.

Knowing the half thickness of ^3H radiation [$l_{1/2} = 0.28 \text{ mg}\cdot\text{cm}^{-2}$, (7)] we may estimate the maximum thickness of the layer of a metallic film which may be used for the adsorption study. For the case of Au or Pt electrodes, the practical thickness of the layer cannot be greater than ca. 2000Å. This value can be compared with the thickness of metallic films of OTE (optical transparent electrodes) described by von Benken and Kuwana (8) equal to ca. 100Å.

We have overcome the experimental difficulties by the use of a glass scintillator disk (NE 901, Nuclear Enterprises Limited) as a radiation detector. The metallic films were prepared by the vapor deposition of metals directly onto the scintillator surface. The tritium radiation transparent electrodes thus obtained will further be called TRTE.

Experimental

The sketch of the apparatus used, which is similar to the schemes previously reported (3, 4), is given in Fig. 1. Since Au was found to be poorly adherent to the scintillator surface, an oxide undercoating was first deposited. Lead dioxide produced the greatest improvement in film properties which is in agreement with von Benken and Kuwana's results (8). The thickness of PbO_2 was estimated to be about 100\AA and the thickness of Au, about 1100\AA . Gold films were mechanically stable, with the coating being removed only when hydrogen or oxygen were evolved or by immersion in concentrated acidic solutions. It was observed that after an exposure of the glass scintillators to daylight or white electric light, the strong excitation of the scintillator material occurred. It took several hours or more of keeping the scintillators in the dark to cool down their luminescence radiation. As a remedy, the annealing of the TRTE electrodes in an oven at 250°C was used. One hour of the annealing was quite enough to reduce the luminescence radiation to an acceptable level (ca. 20 counts per second). Moreover, it also improved the mechanical adherence of Au films (8). Further operations, which followed the annealing, were carried out using red electric light exclusively. During experiments, the electrochemical cell, the glass scintillator (TRTE), as well as the photomultiplier (Fig. 1), were placed in a lightproof box and all further operations were carried out outside the box.

Aqueous Na_2SO_4 (0.1M) solutions, used as a supporting electrolyte, were prepared from A.R. grade salt, recrystallized before use, and from threefold distilled water (the second distillation being made from alkaline permanganate solutions). The supporting electrolyte, before use, was preelectrolyzed on platinum elec-

trodes of high geometric area (ca. 30 cm^2) for several hours. A 1.35V cell, connected directly between the two electrodes, was used as a polarizing source (9). The inert gas passed through the preelectrolysis cell to purge volatile impurities from the solution, additionally stirred mechanically. The stream of the inert gas served also as a blanket to exclude any contact of the solution with the atmosphere. Purified and deoxygenated ($< 0.1\text{ ppm}$ of O_2) argon was used as the inert gas.

Tritium labeled methanol (methyl- ^3H) manufactured by "Amersham" (specific activity, $125\text{ mCi}\cdot\text{mmole}^{-1}$) and ^{14}C labeled methanol produced by "I.B.J.-Swierk" ($5\text{ mCi}\cdot\text{mmole}^{-1}$) were isotopically diluted to $10\text{ mCi}\cdot\text{mmole}^{-1}$ and $0.50\text{ mCi}\cdot\text{mmole}^{-1}$, respectively. A.R. grade methanol, purified further by the use of the method given in Ref. (10) was employed as a diluting agent. Since ^3H -methanol was labeled in methyl group, the exchange of ^3H with $^1\text{H}_2\text{O}$ could not be taken into account (11).

The remaining details concerning the experimental procedure were similar to those recently described for the case of the study of ^{14}C labeled compounds (4). The electrode potentials are referred to the hydrogen electrode in the same solution as the working (TRTE) electrode. At the beginning of every experiment, the alternate anodic-cathodic pulsing was imposed on the working electrode for several minutes to clean the Au surface. The electrode potential was controlled with a potentiostat (Radelkis, OH-404) and a valve voltmeter (Radelkis, OP-205) set. A conventional radiometric unit, equipped with a power supply, an amplifier, a scaler, and a printer ("Polon") was employed. The photomultiplier was cooled down to 2°C to reduce its thermal background.

All experiments were carried out at ambient temperature $25^\circ \pm 2^\circ\text{C}$. The bulk concentration of methanol was constant and equal to 10^{-2} M .

Results and Discussion

At first, the linearity of the radiometric unit was checked and the results are given in Fig. 2. Tritium labeled water (specific activity, $0.2\text{ mCi}\cdot\text{mmole}^{-1}$), added to the radioelectrochemical cell, was used as a calibrating agent. It may be seen that the linear dependence of the counting rates (N) on the specific activity of solution was obtained in the investigated range of c.p.s. (counts per second).

The dependence of the counting rates on time for adsorption and desorption of ^3H labeled methanol is given in Fig. 3. As the minimum of adsorption was

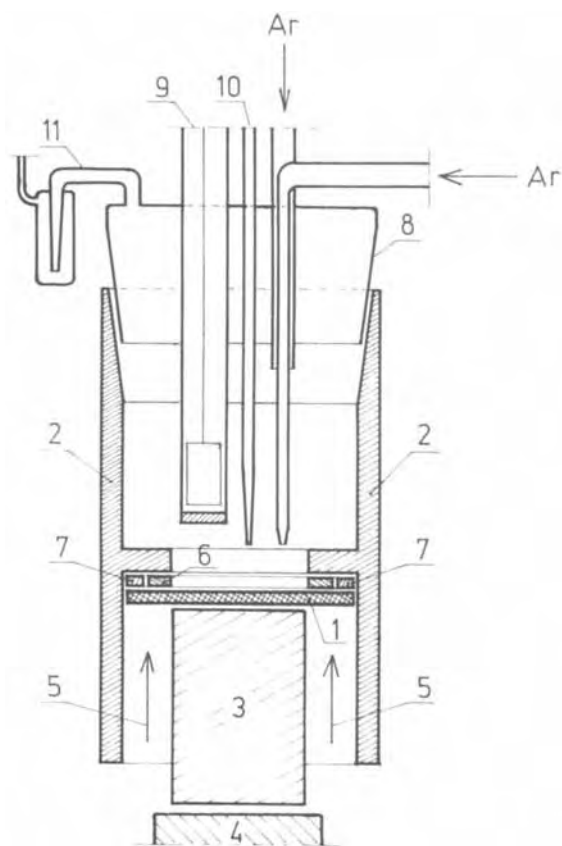


Fig. 1. Sketch of radioelectrochemical cell. 1, TRTE (tritium radiation transparent electrode); 2, Teflon frame; 3, light pipe; 4, photomultiplier (EMI-9514 S); 5, tightening; 6, Teflon gasket; 7, rubber gasket; 8, Kel-F sealed glass (Pyrex) ground joint; 9, counter-electrode (closed by fritted disk); 10, reference hydrogen electrode (Luggin capillary); 11, bubbler; Ar, inlets of argon.

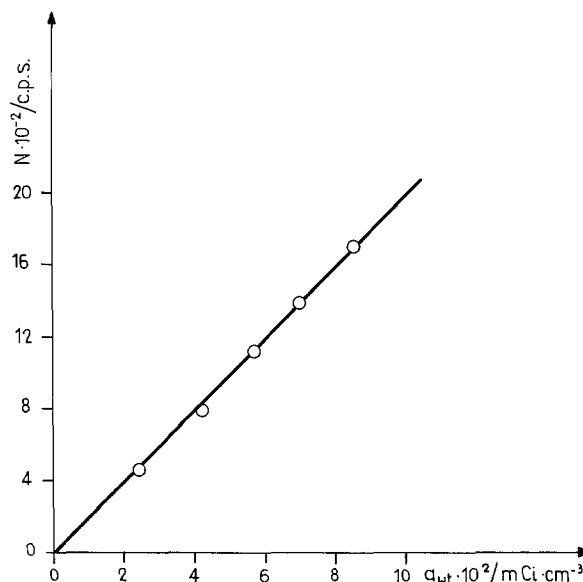


Fig. 2. The dependence of counting rates, N (counts per second) on the specific activity ($\text{mCi} \cdot \text{cm}^{-3}$) of tritium labeled water (the check of linearity).

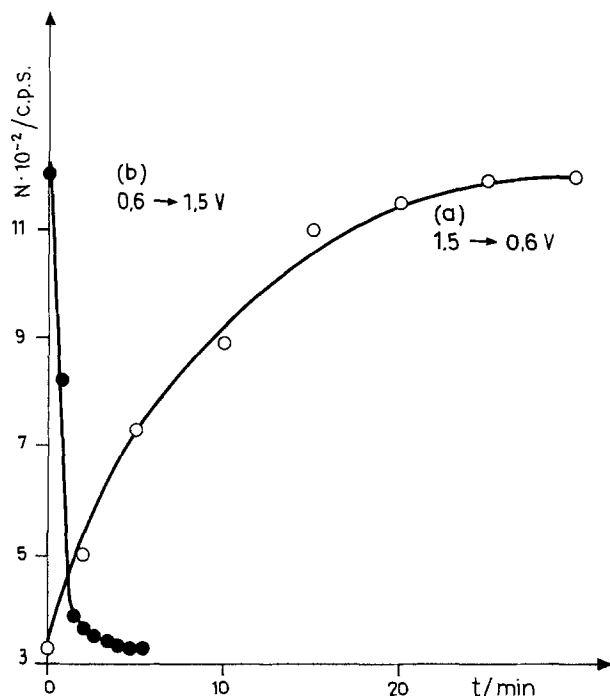


Fig. 3. The experiments with ^3H . The dependence of N (counts per second) on time for: (a) adsorption of methanol after potential step from 1.5 to 0.6V; (b) desorption of methanol (0.6 to 1.5V). The background of solution, $N_{\text{soln.}} = 325$ counts/sec.

found in the potential range: 1.3-1.7V, the electrode potential $E = 1.5\text{V}$ was chosen as a starting point. Slow adsorption at $E = 0.6\text{V}$ (Fig. 3a) and fast desorption (Fig. 3b) after the potential step from 0.6 to 1.5V may be seen in this figure.

In order to demonstrate the difference in using ^3H and ^{14}C as labeling agents some experiments with ^{14}C labeled methanol were also carried out. The results are given in Fig. 4. The curve "a" in this figure corresponds to the adsorption of ^{14}C labeled CH_3OH on the Au-glass scintillator electrode. The increase in counting rates was not observed within the experimental

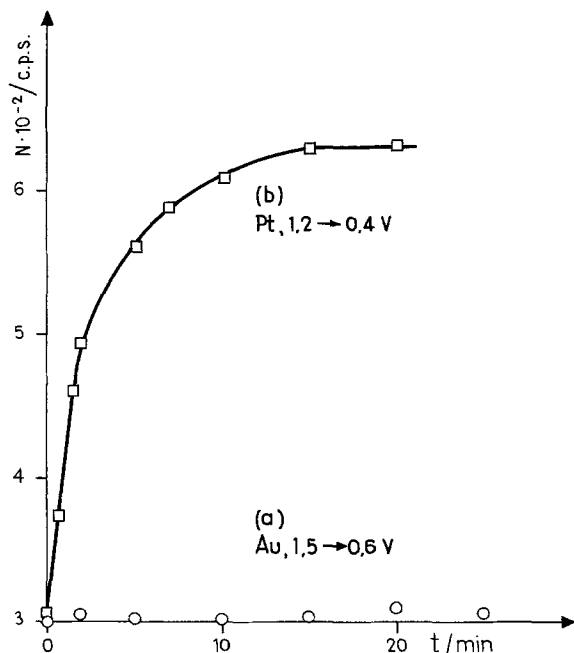


Fig. 4. The experiments with ^{14}C . (a) N (counts per second) vs. t plot for methanol adsorbed on the Au-TRTE after the potential step from 1.5 to 0.6V. (b) N (counts per second) vs. t plot for methanol adsorbed on platinized electrode of $R = 50$, after the step 1.2-0.4V. $N_{\text{soln.}} = 300$ counts/sec.

error. Adsorption of ^{14}C labeled methanol on a platinized electrode of a roughness factor $R = 50$ at $E = 0.4\text{V}$ is demonstrated in curve "b" of Fig. 4 (12). It should be noted that in both experiments with $^{14}\text{CH}_3\text{OH}$ the counting efficiency was kept practically the same.

The difference in the runs "a" and "b" in Fig. 4 can illustrate the importance of the roughness factor in radioelectrochemical investigations provided that the values of surface concentration of methanol intermediates adsorbed on Au and Pt electrodes are similar, which is a reasonable assumption. The difference in the plots "a" in Fig. 3 and "a" in Fig. 4 is considered as an evidence for the great improvement in the radiotracer method brought about by the use of ^3H instead of ^{14}C isotope in the study of the adsorption phenomena. This statement is enhanced by the fact that a very high increase in counts per second was observed for adsorption of ^3H labeled methanol contrary to the lack of the increase due to adsorption of $^{14}\text{CH}_3\text{OH}$. In the latter case, the radiometric method is unsuitable for the adsorption study. It must be stressed that besides the difference in the isotopic composition, the experimental conditions were in both cases exactly the same.

The main drawback of the tritium radiochemical method is its restriction to interactions of organic species with solid electrodes not involving the C-T breakage. It can be mentioned that such a process was observed during adsorption of methanol on smooth Pt electrodes (13).

For their good light output (28% of anthracene) and inert properties the glass scintillators can also fruitfully be used as detectors in the adsorption study of ^{14}C or ^{35}S labeled compounds on the electrodes of high R . Platinum adheres well to the scintillator surface, and the platinized electrodes can easily be obtained.

Further studies of electrosorption of tritium labeled compounds on the solid electrodes are in progress, and the results will be given soon.

Acknowledgments

The author is sincerely grateful to Professor J. Sobkowski for the encouragement of this work and for many valuable discussions. The help of Miss A. Jablonska in carrying out the measurements is greatly appreciated.

Manuscript submitted June 25, 1974; revised manuscript received Sept. 26, 1974.

Any discussion of this paper will appear in a Discussion Section to be published in the December 1975 JOURNAL. All discussions for the December 1975 Discussion Section should be submitted by Aug. 1, 1975.

REFERENCES

1. R. S. Perkins, and T. N. Andersen, in "Modern Aspects of Electrochemistry," J. O'M. Bockris, Editor, Vol. 5, Butterworth, London, (1969).
2. J. Solt, G. Horanyi, and F. Nagy, *Acta Chim. Acad. Sci. Hung.*, **63**, 385 (1970).
3. J. Sobkowski and A. Wieckowski, *J. Electroanal. Chem.*, **34**, 185 (1972).
4. A. Wieckowski and J. Sobkowski, *Roczniki Chem.*, **48**, 1351 (1974).
5. E. Blomgren and J. O'M Bockris, *Nature (London)*, **186**, 305 (1960).
6. H. Wróblowa and M. Green, *Electrochim. Acta*, **8**, 679 (1963).
7. N. G. Gusiev, "Spravochnik po radioaktivnom izluchieniyam," Moskwa (1956).
8. W. von Benken and T. Kuwana, *Anal. Chem.*, **42**, 1114 (1970).
9. J. O'M Bockris and S. Srinivasan, "Fuel Cells, Their Electrochemistry," McGraw-Hill Book Co., New York (1969).
10. H. A. Yugayev, "Khimicheskiye metody opredeleniya steroidnykh hormonov v biologicheskikh jidnostyakh," p. 116, Moskwa (1961).
11. A. I. Brodski, *Khimiya Izotopov*, Moskwa (1957).
12. A. Wieckowski, J. Sobkowski, and I. Szamrey, *Roczniki Chem.*, **48**, 77 (1974).
13. A. Wieckowski and J. Sobkowski, *J. Electroanal. Chem.*, Submitted for publication.



Doped Ceria as a Solid Oxide Electrolyte

H. L. Tuller¹ and A. S. Nowick

Henry Krumb School of Mines, Columbia University, New York, New York 10027

ABSTRACT

Ceria (CeO_2) doped with divalent or trivalent cations is a mixed conductor; conduction occurs predominantly by the motion of oxygen vacancies or by electrons, depending on the departure from stoichiometry. In order to establish the electrolytic domain (T vs. p_{O_2}) at which $(\text{CeO}_2)_{0.95}(\text{Y}_2\text{O}_3)_{0.05}$ behaves primarily as an ionic conductor with transference number $t_i \cong 0.99$, a careful study was made of the conductivity, σ , as a function of temperature and oxygen partial pressure, covering the p_{O_2} range of 10^0 - 10^{-22} atm in small steps. From these data the electrolytic domain was determined; it extends to about 10^{-13} atm at 600°C . When compared to calcia-stabilized zirconia (CSZ), doped ceria shows a higher conductivity, lower activation energy (0.76 eV) for anion vacancy migration, and absence of polarization effects to lower temperatures. These results indicate that doped ceria may be an attractive candidate for fuel cells and other applications at temperatures below those at which CSZ is useful.

There has been much interest in oxide materials which can serve as solid oxide-ion electrolytes for applications in oxygen concentration cells and in fuel cells (1, 2). The criteria to be met include: (i) a high anionic (*i.e.*, O^{2-} ion) mobility, and (ii) negligible electronic conductivity. Item (ii) is equivalent to the statement that the ionic transference number t_i must be close to unity, although the maximum acceptable value of $1 - t_i$ depends on the specific application. Relatively few oxides meet both of the above criteria. The two materials most often used as solid oxide electrolytes are ZrO_2 and ThO_2 , doped with divalent or trivalent cation impurities so as to introduce oxygen vacancies for charge compensation.

Ceria, CeO_2 , has the same (fluorite) structure as thoria and (doped) zirconia, but is different in that pure CeO_2 undergoes large departures from stoichiometry at elevated temperatures in a reducing atmosphere, with accompanying electronic conductivity (3). Although doped CeO_2 is often mentioned as showing predominantly ionic behavior (2, 4), the exact extent of the ionic vs. electronic contributions has not been well established. Generally, the tendency has been to regard it as unsuitable as an electrolyte material because of its electronic component. Nevertheless, Takahashi *et al.* (5, 2) have made t_i measurements of CeO_2 doped with La_2O_3 , using galvanic cell measurements, and have even tried this material in a fuel cell. The values for t_i that they obtain, however, generally fall in the range from 0.6 to 0.9, indicating a substantial electronic contribution.

In the present paper, it is intended to investigate the ionic transference number and electrolytic domain of doped CeO_2 . The term "electrolytic domain" refers here to the range of p_{O_2} and temperature at which t_i is greater than 0.99. The information will be obtained not through direct galvanic cell (emf) measurements, since these are deemed to be insufficiently

precise to obtain t_i values close to 1.0, but rather through measurement of conductivity, σ , as a function of p_{O_2} . Although such measurements have been performed earlier by Blumenthal *et al.* (6), one cannot obtain the type of quantitative information desired for present purposes from those measurements, primarily because of the existence of large gaps in the p_{O_2} range covered.

In the present work, with special care, it was possible to cover the entire range from $p_{\text{O}_2} = 1$ - 10^{-22} atm in sufficiently close steps to obtain the electrolytic domain with reasonable precision for the case of $(\text{CeO}_2)_{0.95}(\text{Y}_2\text{O}_3)_{0.05}$. In addition, some of the parameters which characterize ionic migration in CeO_2 are obtained. Finally, some experiments on polarization effects are reported.

Theory

Ionic conductivity.—It will be assumed that the only defect giving rise to ionic conductivity in CeO_2 is the doubly ionized oxygen vacancy, $V_{\text{O}}^{\bullet\bullet}$ [in the Kröger-Vink (7) notation]. If the concentration of these vacancies is denoted by n_v , we may write, for the ionic conductivity σ_i , the expression

$$\sigma_i = n_v q \mu_i \quad [1]$$

where $q = 2e$ is the (positive) charge on the vacancy and μ_i is its mobility, given by (8)

$$\mu_i = \frac{\nu a^2 q}{4kT} \exp(-\Delta G_i/kT) \quad [2]$$

Here ΔG_i is the free energy of activation for ionic motion, expressible in terms of an enthalpy of activation ΔH_i and entropy of activation ΔS_i by

$$\Delta G_i = \Delta H_i - T\Delta S_i \quad [3]$$

ν is a frequency factor and a is the lattice parameter of the cubic unit cell. ($a/2$ is the nearest neighbor oxygen spacing and, therefore, the jump distance of a vacancy.) Thus, in the semiempirical equation

¹ Present address: Physics Department, The Technion, Haifa, Israel.

Key words: ionic conductivity, cerium dioxide, solid electrolyte, point defects.

$$\sigma_i = \frac{C_i}{T} \exp(-E_i/kT) \quad [4]$$

the parameters E_i and C_i are given by

$$E_i = \Delta H_i \quad [5]$$

and

$$C_i = (\nu a^2 e^2/k) n_v \exp(\Delta S_i/k) \quad [6]$$

assuming that n_v is not temperature dependent.

The "activation energy" E_i is obtained in the usual way from a plot of $\log \sigma_i T$ vs. $1/T$. It should be noted that if instead, one plots $\log \sigma_i$ vs. $1/T$, a straight line will usually be obtained within experimental error, but its slope gives an apparent activation energy E_a given by

$$E_a = -\frac{d \ln \sigma_i}{d(1/kT)} = E_i - k\bar{T} \quad [7]$$

where \bar{T} is the average temperature over the range of the measurements.

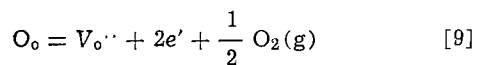
Two factors determine n_v , viz., charge compensation and nonstoichiometry. To produce vacancies by means of charge compensation we may dope with an aliovalent cation, e.g., CaO or Y_2O_3 . In this way we obtain one $V_o^{\cdot\cdot}$ for every molecule of dopant, since the Ca^{2+} and Y^{3+} ions enter the CeO_2 lattice as Ca''_{Ce} and Y'_{Ce} , respectively. Therefore

$$n_v = [Ca''_{Ce}] + \frac{1}{2} [Y'_{Ce}] \equiv n_M \quad [8]$$

that is, the quantity n_M defined here is the total effective dopant concentration. (It is defined so as to allow both Ca and Y to be present simultaneously; actually only one will be present in significant concentration at a time.) On the basis of Eq. [8] and [1], we expect that $\sigma_i \propto n_M$ and also, from Eq. [2]-[5], that E_i is independent of both n_M and the type of aliovalent dopant. Actually, this statement is only valid at low concentrations. In fact, for ceria, σ_i vs. n_M is linear up to a value of n_M corresponding to less than 4% oxygen vacancies, and then it shows a broad maximum as a function of dopant concentration (2, 6). In the case of $ThO_2:Y_2O_3$ the departure apparently takes place even earlier (9). Such results mean that defect interactions become important at high concentrations. In the case of $ZrO_2:CaO$, for example, it is well known that ordering effects take place (10). In the range where interactions are appreciable, the semiempirical relation [4] still holds, but the simple interpretations of E_i and C_i given by Eq. [5] and [6] no longer apply.

When vacancies are produced by departures from stoichiometry, one also obtains electronic defects which give rise to an electronic contribution to the conductivity, σ_e .

Nonstoichiometry and electronic conductivity.—The reaction which leads to nonstoichiometry is²



The electronic defect e' may be regarded as equivalent to the presence of a Ce^{3+} ion, or in defect notation, Ce'_{Ce} . The mass action equation which follows from the reaction [9] is, at low defect concentrations

$$n_v n_e^2 p_{O_2}^{1/2} = K_1(T) = K_{10} \exp(-\Delta H_1/kT) \quad [10]$$

in which n_e is the electron concentration, p_{O_2} the oxygen partial pressure, and ΔH_1 the enthalpy change of the reaction. In doped samples, we will be interested in the range where nonstoichiometry is small, specifically, $n_e \ll n_M$. Under these conditions $n_v \approx n_M$ and so from Eq. [10]

$$n_e = [K_1(T)/n_M]^{1/2} p_{O_2}^{-1/4} \quad [11]$$

² For large departures from stoichiometry, singly ionized vacancies can also be produced (11), but this complication can be ignored for the purposes of this paper.

In spite of the fact that $n_e \ll n_v$, however, the electronic conductivity

$$\sigma_e = n_e e \mu_e \quad [12]$$

can become appreciable because $\mu_e \gg \mu_i$. Since electrons migrate by a hopping mechanism (11), μ_e is given by

$$\mu_e = (b/T) \exp(-E_e/kT) \quad [13]$$

where E_e is a small activation energy. From Eq. [11] and [12], $\sigma_e \propto p_{O_2}^{-1/4}$. The total conductivity

$$\sigma \equiv \sigma_i + \sigma_e \quad [14]$$

is then clearly made up of a p_{O_2} -independent part, σ_i , and a part, σ_e , which is proportional to $p_{O_2}^{-1/4}$. This pressure dependence provides a convenient way to separate σ_i from σ_e and thereby to obtain the ionic transference number

$$t_i = \sigma_i/\sigma \quad [15]$$

The electrolytic domain.—The electrolytic domain is defined as the region, in a plot of $\log p_{O_2}$ vs. $1/T$ in which t_i is greater than some selected value (often 0.99) (12). Substituting [4] and [10] through [13] into Eq. [14] and [15], we obtain

$$\ln p_{O_2} = 4 \ln \left\{ \frac{t_i b e K_{10}^{1/2}}{C_i (1 - t_i) n_M^{1/2}} \right\} - 4 \left(\frac{\Delta H_1}{2} + E_e - E_i \right) \frac{1}{kT} \quad [16]$$

which shows that a plot of $\ln p_{O_2}$ vs. $1/T$ for a given t_i value gives a straight line whose negative slope is $(4/k)(\frac{1}{2}\Delta H_1 + E_e - E_i)$ and whose intercept depends on t_i and on the dopant concentration.

The straight line given by Eq. [16] separates the p_{O_2} - $1/T$ space into two regions, the region above the line being the domain for which t_i is greater than the selected value. From the intercept formula it is clear that, for t_i close to 1.0, the line shifts upward by close to 4 decades for every decade in $(1 - t_i)$; for example, in going from $t_i = 0.90$ to 0.99, the shift is 4.17 decades in p_{O_2} .

Experimental Methods

The specimens used in this study were fabricated from nominally pure CeO_2 powder (99.9% pure with respect to other rare earths). Analysis shows an aliovalent impurity content in the range 150-200 ppmw. Samples doped with Y_2O_3 or CaO were prepared by mechanically mixing appropriate amounts of Y_2O_3 or $CaCO_3$ powders with the CeO_2 . Cylindrical samples ($\frac{3}{4}$ in. diam \times 0.1 in. high) of the mixed powders were prepared by pressing in a steel die at 40,000 psi. The pressed specimens, covered by additional loose powder to minimize contamination and loss of dopant, were placed in high purity alumina holders and heated slowly to 1500°C in an argon atmosphere. They were held at this temperature for 12-14 hr. The densities of the samples so obtained were greater than 80% of theoretical density.

After samples were cut to size ($12 \times 5 \times 5$ mm³) electrodes were prepared using platinum paste (Englehard No. 6082) which was fired in air at 800°C to burn off the organic binder. Such electrodes are known (13) to be porous enough to allow the sample to come to equilibrium (with respect to oxygen) with the surrounding gas phase.

Measurements were carried out inside a quartz tube suspended inside a Kanthal-wound resistance furnace. Electric feedthroughs were mounted in a stainless steel cap from which four (15 mil) platinum leads ran to the specimen through insulating alumina tubes. Fine platinum wires (5 mil) were wrapped around the sample at both ends and at 1/3 and 2/3 of the length. The sample was then suspended by spot welding the sample leads to the heavier platinum wires contained in the alumina tubes. For improved contact, the area of contact between sample and wires was also coated

with several layers of platinum paste. A standard four-probe d-c technique was used to measure the conductivity. A fixed current was passed through the sample and the potential drop across the two center leads was measured with a Keithley Model 640 vibrating capacitor electrometer (input impedance of 10^{16} ohms). In addition, a-c measurements at 1592 Hz (10^4 rad/sec) were made with a Wayne-Kerr Model B221A universal bridge; results obtained by the two methods were essentially identical.

The sample temperature was measured by means of a Pt-Pt + 10% Rh thermocouple placed close to it, while the furnace was controlled to within $\pm 1^\circ\text{C}$ by another thermocouple placed close to the furnace windings.

Atmosphere control, ranging over 22 orders of magnitude in oxygen partial pressure, p_{O_2} , was achieved as follows. For the range $p_{\text{O}_2} = 1\text{--}10^{-4}$ atm $\text{O}_2\text{-Ar}$ mixtures were used, and for the range $10^{-4}\text{--}10^{-22}$ atm CO-CO_2 mixtures were used. The value of p_{O_2} of a CO-CO_2 mixture with known ratio CO/CO_2 can be calculated at any temperature using the well-known free energy values for the CO-CO_2 reaction (14). Fixed ratios of CO/CO_2 premixed and analyzed, were purchased from the Matheson Gas Company, but these mixtures were limited to CO/CO_2 ratios between 10^3 and 10^{-3} . The value for p_{O_2} for $\text{CO/CO}_2 = 10^{-3}$ is $\sim 10^{-12}$ atm, at 800°C . Thus, a gap of approximately 8 decades in p_{O_2} exists between the lowest available $\text{O}_2\text{/Ar}$ ratio and the least reducing CO/CO_2 . Since critical data fall within this gap, we have closed it by setting up a system for: (a) mixing the premixed $\text{CO/CO}_2 = 10^{-3}$ gas with pure CO_2 under controlled relative flow rates, and (b) monitoring the p_{O_2} level by means of a calcia-stabilized zirconia cell located in the hot zone close to the sample under study. The same technique was also used to span the gap between other premixed pairs of CO-CO_2 mixtures. In this way, it became possible to obtain p_{O_2} values from 1 to 10^{-22} atm in intervals as close as desired. Further details will be described in a later publication (11).

Results

Data for the variation of conductivity with temperature at $p_{\text{O}_2} = 1$ atm is shown in Fig. 1 for $(\text{CeO}_2)_{0.95}(\text{Y}_2\text{O}_3)_{0.05}$ and $(\text{CeO}_2)_{0.9}(\text{CaO})_{0.1}$. Good straight lines are obtained in the $\log \sigma T$ vs. $1/T$ plot for the range between 400° and 1000°C . In anticipation of the fact that the conductivity is almost entirely ionic in this range, the results for E_i and C_i (of Eq. [4]) are listed in Table I. Also shown, for comparison, in Fig. 1 are data (15) for calcia-stabilized zirconia

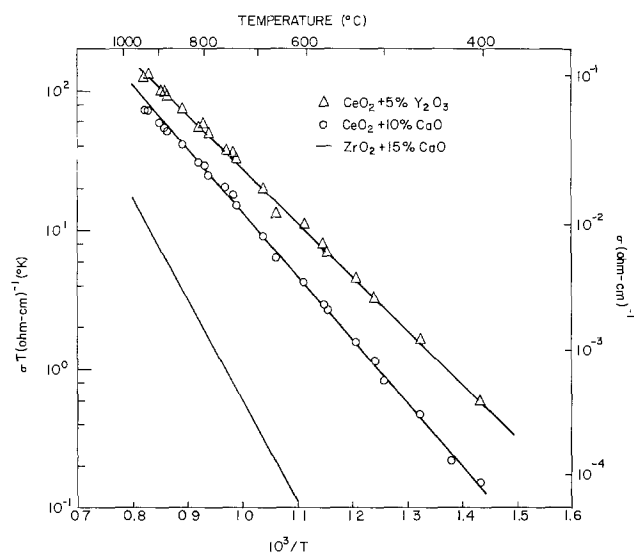


Fig. 1. Variation of conductivity with reciprocal absolute temperature for CeO_2 doped with 5% Y_2O_3 and with 10% CaO at 1 atm of oxygen, and comparison with data for calcia-stabilized zirconia.

Table I. Values of activation energy E_i and pre-exponential constant C_i for two compositions

CeO_2 doped with	E_i (eV) *	C_i ($\text{ohm-cm})^{-1} \text{ } ^\circ\text{K}$
5% Y_2O_3	0.76	1.95×10^5
10% CaO	0.91	5.25×10^5

* Uncertainty, ± 0.015 eV.

(CSZ), the conductivity of which is at least a decade lower than for the two doped ceria samples in the range $T < 900^\circ\text{C}$, and which has an activation energy $E_i = 1.3$ eV.

Figure 2 shows isothermal measurements on a 5% Y_2O_3 sample as a function of p_{O_2} in the range from 635° to 1150°C . For each isotherm the p_{O_2} range was covered in close enough intervals to obtain the range in which σ was independent of p_{O_2} as well as to observe the manner in which it increases with decreasing p_{O_2} . The constant σ region shrinks with increasing temperature and has practically disappeared by 1150°C . In accordance with Eq. [11], the increase of σ with decreasing p_{O_2} indicates the appearance of nonstoichiometric carriers. The nonstoichiometric component, *i.e.*, the difference between the total σ and the p_{O_2} -independent value, is shown as dashed lines in Fig. 2. Although there is some scatter, the slope of $1/4$, predicted by Eq. [11], fits the data in all cases. A similar $1/4$ power law has been found by Neumin *et al.* (16) for $\text{CeO}_2\text{:La}_2\text{O}_3$ and is also obtainable from the data given by Blumenthal *et al.* (6) for $\text{CeO}_2\text{:CaO}$, so that the relation may be regarded as well established. It is therefore reasonable to regard the p_{O_2} -independent conductivity as σ_i and the p_{O_2} -dependent part as σ_e .

On this basis, one may obtain t_i as a function of $\log p_{\text{O}_2}$ directly from the data of Fig. 2 as the ratio σ_i/σ where σ_i is the p_{O_2} -independent value. Such a plot is given in Fig. 3. The figure shows that t_i remains close to unity over a larger range of p_{O_2} , the lower the temperature.

In order to establish the electrolytic domain, we must be able to determine the p_{O_2} and T values at which a given t_i is obtained. For good precision it is convenient to select $t_i = 1/2$. For each temperature, the value of p_{O_2} at which $t_i = 1/2$, *i.e.*, $\sigma_e = \sigma_i$, was ob-

³ This is not quite true when the p_{O_2} -dependent part is much greater than the p_{O_2} -independent part, since nonstoichiometry introduces vacancies as well as electrons (Eq. [9]). Since $\mu_e/\mu_i \sim 20$ (11) in the temperature and composition range of interest, t_i will be ~ 0.05 even when all of the conductivity is due to nonstoichiometry.

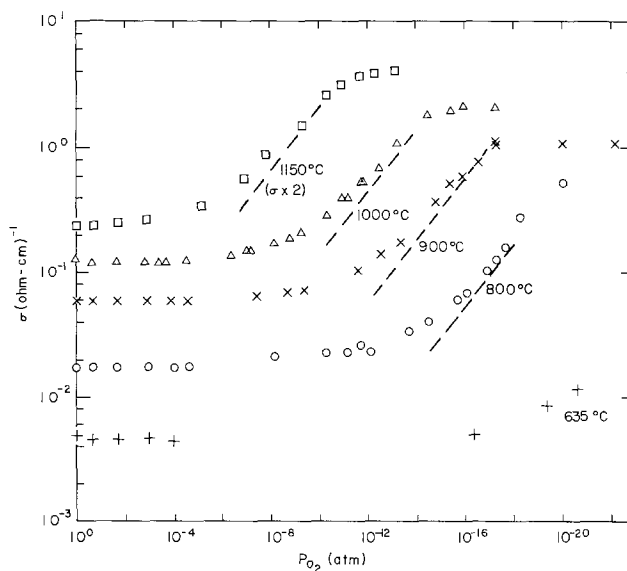


Fig. 2. Electrical conductivity as a function of p_{O_2} for a sample of $(\text{CeO}_2)_{0.95}(\text{Y}_2\text{O}_3)_{0.05}$ at five different temperatures. The dashed lines indicate the electronic component of the conductivity, σ_e .

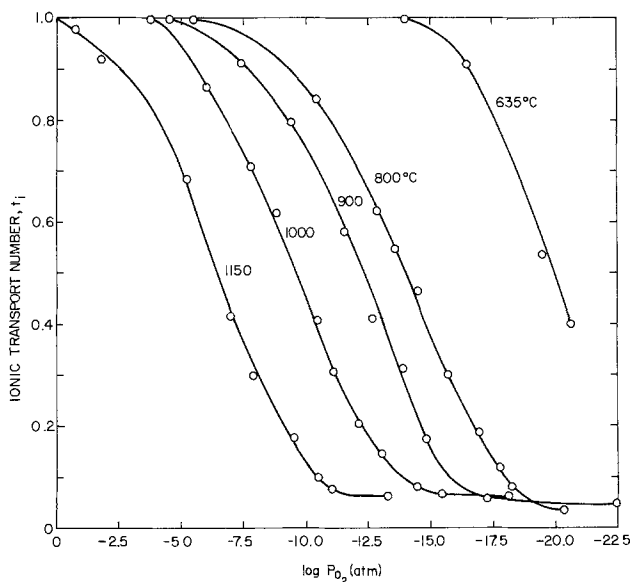


Fig. 3. The ionic transference number, t_i , as a function of p_{O_2} , as derived from Fig. 2 for various temperatures.

tained from Fig. 3. When plotted as $\log p_{O_2}$ vs. $1/T$ the results fall on a straight line, as shown in Fig. 4 and predicted from Eq. [16]. The same procedure was also followed for the case of $t_i = 0.9$. Although the data so obtained from Fig. 3 are less precise than that for the case of $t_i = 0.5$, the results shown in Fig. 4 strongly indicate that the domain line for $t_i = 0.9$ is parallel to that for $t_i = 0.5$, as expected from Eq. [16]. Also, while Eq. [16] predicts a shift in intercept of 3.8 decades in p_{O_2} between these two t_i values, the actual shift obtained is 4.0. It thus appears that the predictions of Eq. [16] are well confirmed. It therefore seems reasonable to use this equation to extrapolate beyond the range at which t_i can be directly estimated. In particular, the predicted domain line for $t_i = 0.99$ is shown as the uppermost line in Fig. 4. The region above this line is then the electrolytic domain for $(CeO_2)_{0.95}(Y_2O_3)_{0.05}$. It should be noted that, although this region is small at high temperatures, it increases rapidly with decreasing temperatures, reaching values as low as $p_{O_2} \sim 10^{-21}$ atm at $450^\circ C$.

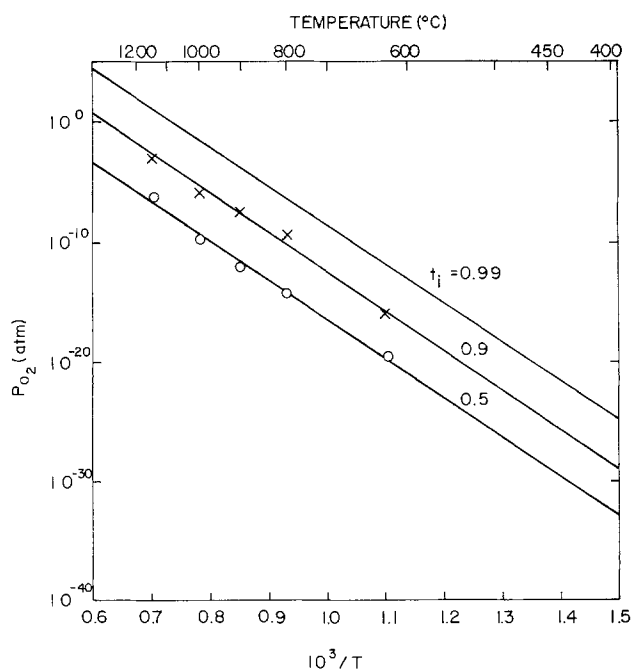


Fig. 4. Curves of p_{O_2} vs. T^{-1} at fixed values of t_i for $(CeO_2)_{0.95}(Y_2O_3)_{0.05}$. The upper curve, obtained by extrapolation, marks the boundary of the electrolytic domain ($t_i \cong 0.99$).

In Fig. 2, the points at $p_{O_2} = 1$ atm do not agree exactly with the data as a function of temperature shown in Fig. 1. It is believed that some of the discrepancies are due to the drastic expansions and contractions of the sample which occurred during the successive cycles of reduction and oxidation which were carried out. (Other samples have even shown evidence of cracking after such repeated cycling.) It is therefore believed that the temperature dependence of σ at a given p_{O_2} as obtained from Fig. 2 is not nearly as reliable as are the relative values of σ vs. p_{O_2} at each given temperature.

Aside from the question of the magnitude of t_i , the other factor that limits the utility of a material as a solid electrolyte is the onset of polarization. This factor usually sets the low temperature limit of usefulness of a given electrolyte. In order to determine at which level of current density significant polarization sets in, the voltage across a $(CeO_2)_{0.95}(Y_2O_3)_{0.05}$ sample was measured as a function of time when current was applied in steps. Figure 5 shows the results of some of these measurements at $635^\circ C$, first when the current is increased in steps of 1 mA and then in steps of 10 mA. The results show no evidence of polarization up to $I \sim 4$ mA (current density ~ 20 mA/cm²). On the other hand, at 10 mA, polarization is apparent. Such polarization behavior suggests the onset of ion blocking. Often the behavior is dependent on the type of electrodes used (17). In the present work, only the platinum paste electrodes (described in the Experimental Methods section) were used.

Discussion

Ionic mobility parameters.—Values of the activation energy E_i and pre-exponential constant C_i for the two doped materials studied are given in Table I. The 10% CaO specimen clearly falls in the range where interaction effects are important, as indicated by its composition being at about the value at which a maximum occurs in the plot of σ vs. n_M (6). Since E_i increases in the interaction range (10) it is not surprising that E_i for $(CeO_2)_{0.9}(CaO)_{0.1}$ is substantially higher than for

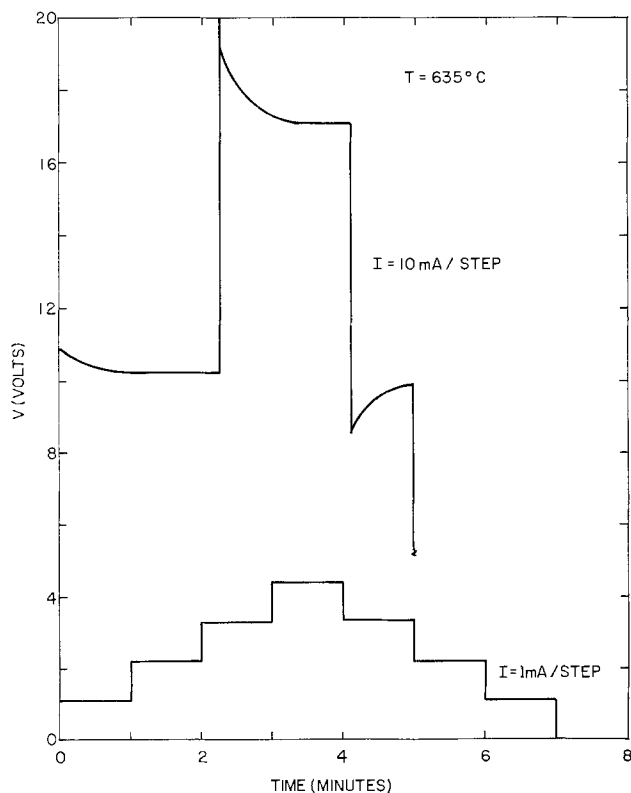


Fig. 5. The d-c potential across a sample of $(CeO_2)_{0.95}(Y_2O_3)_{0.05}$ at $635^\circ C$ as a function of time, when the current is applied and removed in steps of 1 or 10 mA.

(CeO₂)_{0.95}(Y₂O₃)_{0.05}. The latter composition may still fall in the range where interaction effects are small, and it is therefore interesting to compare it to results at still lower concentrations. Data for 1 and 2% CaO are available from Blumenthal *et al.* (6), although the range of temperature covered is smaller, and therefore the precision poorer, than that in the present work. In addition, the activation energies that they reported were obtained from plots of $\log \sigma$ vs. $1/T$ instead of $\log \sigma T$ vs. $1/T$, so that the additional correction given by Eq. [7] is required. In this way their "best value" is found to be 0.72 eV. This agrees with the present result of 0.76 eV to within experimental error.⁴ Accordingly, we may conclude that (i) interaction effects are relatively small in the 5% Y₂O₃ specimen,⁵ and (ii) the activation energy for migration of V_O^{••} in CeO₂ is close to 0.76 eV. This value is lower than the activation energy of about 0.85 eV obtained by Steele and Floyd (19) for oxygen self-diffusion in Y₂O₃-doped ceria, as well as the value of 0.86 eV obtained by Lay and Whitmore (20) for dielectric relaxation in CeO₂:CaO. (The latter represents the activation energy for migration of a vacancy which is associated with a Ca^{''}_{Ce}.)

Inserting the value of C₁ for (CeO₂)_{0.95}(Y₂O₃)_{0.05} into Eq. [6], we obtain for the effective frequency factor ν' (defined so as to include the activation entropy term)

$$\nu' = \nu \exp(\Delta S_i/k) = 1.4 \times 10^{13} \text{ sec}^{-1}$$

From this result, and the expectation that the attempt frequency ν falls in the mid 10¹² range, we may conclude that the entropy of activation is positive but not very large ($\Delta S_i/k \sim 0.7-1.8$).

Electrolytic domain and polarization.—In Fig. 4, it was demonstrated that the present method of separating σ_i and σ_e through measurement of σ vs. p_{O_2} can be used successfully to obtain the electrolytic domain. Equation [16] shows that the slope of the lines in Fig. 4 gives the energy $\frac{1}{2}\Delta H_1 + E_e - E_i$. The experimental value obtained is 1.61 eV. Using the values $E_i = 0.76$ eV from the present work, and $E_e = 0.3$ eV from Neumin *et al.* (16),⁶ we obtain $\Delta H_1 = 4.2$ eV for the energy of the reaction [9] (see Eq. [10]). The value for the same reaction energy ΔH_1 obtained in pure CeO₂ (11) is 4.7 eV, thus indicating that ΔH_1 may have decreased slightly with doping.

As remarked earlier, the domain of primarily electrolytic conduction ($t_i \geq 0.99$) for (CeO₂)_{0.95}(Y₂O₃)_{0.05}, though small near 800°C broadens rapidly with decreasing temperature. While the widely used calcia-stabilized zirconia (CSZ) has a wider range of electrolytic behavior at elevated temperatures (12) [e.g., down to $p_{O_2} = 10^{-15}$ atm at 1000°C, as against only 10⁻² for (CeO₂)_{0.95}(Y₂O₃)_{0.05}], it is well known (17) that its usefulness is limited by the onset of appreciable polarization below 800°-1000°C, as well as its low conductivity at these temperatures. Such factors limit the applicability of CSZ as a solid oxide electrolyte in a fuel cell to temperatures above 1000°C, and in an oxygen cell to temperatures above 800°C. The material (CeO₂)_{0.95}(Y₂O₃)_{0.05}, on the other hand, has a conductivity about 10 times larger than CSZ at 900°C (see Fig. 1) and, because of its smaller activation energy, this factor increases to nearly 100 at 600°C. Accordingly, the question of whether doped CeO₂ can be useful as a solid oxide electrolyte, by comparison to CSZ, then centers on whether polarization for CeO₂ is absent to lower temperatures. The results of Fig. 5 provide evidence that this is indeed the case, showing that at 635°C polarization is completely negligible to current densities of 20 mA/cm² and higher. Similar results were obtained for CeO₂:La₂O₃ by Takahashi *et al.*

⁴ For both the 1 and 2% CaO specimens, the plot of Blumenthal *et al.* could indeed have been drawn slightly steeper.

⁵ Further evidence in support of this statement comes from comparing T vs. p_{O_2} plots at constant t_i from the present work with data from reference 6 (18).

⁶ A similar value for E_e was also obtained by the present authors for pure CeO₂ (11).

(5), who also found significant polarization for CSZ already at 800°C for current densities less than 1 mA/cm².

Takahashi *et al.* also carried out preliminary measurements using CeO₂:La₂O₃ as an electrolyte in a fuel cell at 1000°C and obtained a maximum output of 0.17W. They concluded that the output was limited by the low value of t_i at that temperature. However, now that the electrolytic domain is established, it is clear that fuel cells utilizing doped ceria as the electrolyte are more likely to be successful at lower temperatures, when operating with fuels which generate oxygen partial pressures within the allowable domain.

Acknowledgment

This work was supported in part by the Advanced Research Projects Agency and by the National Science Foundation. This paper is based on part of a dissertation submitted by H. L. Tuller for the degree of D.Eng.Sci. at Columbia University, December 1973.

Manuscript submitted June 21, 1974; revised manuscript received Sept. 17, 1974.

Any discussion of this paper will appear in a Discussion Section to be published in the December 1975 JOURNAL. All discussions for the December 1975 Discussion Section should be submitted by Aug. 1, 1975.

REFERENCES

1. K. Goto and W. Pluschkell, in "Physics of Electrolytes," Vol. 2, p. 540, J. Hladik, Editor, Academic Press, London (1972).
2. T. Takahashi, in "Physics of Electrolytes," Vol. 2, p. 989, J. Hladik, Editor, Academic Press, London (1972).
3. P. Kofstad, "Nonstoichiometry, Diffusion, and Electrical Conductivity in Binary Metal Oxides," Wiley-Interscience, New York (1972).
4. L. D. Yushina and S. F. Pal'guyev, in "Electrochemistry of Molten and Solid Electrolytes," Vol. 2, p. 74, M. V. Smirnov, Editor, Consultants Bureau, New York (1963).
5. T. Takahashi, K. Ito, and H. Iwahara, in "Proc. Journées Int. d'Etude des Piles à Combustible II," p. 42, S.E.R.A.I. Bruxelles (1965).
6. R. N. Blumenthal, F. S. Brugner, and J. E. Garnier, *This Journal*, **120**, 1230 (1973).
7. F. A. Kröger and H. J. Vink, *Solid State Phys.*, **3**, 310 (1956).
8. See, for example: L. W. Barr and A. B. Lidiard, in "Physical Chemistry X. Solid State," W. Jost, Editor, Academic Press, New York (1970); E. Barsis and A. Taylor, *J. Chem. Phys.*, **48**, 4362 (1968).
9. M. F. Lasker and R. A. Rapp, *Z. Physik. Chem. N.F.*, **49**, 198 (1966).
10. R. E. Carter and W. L. Roth, in "Electromotive Force Measurements in High Temperature Systems," p. 141, C. B. Alcock, Editor, American Elsevier, New York (1968).
11. H. L. Tuller and A. S. Nowick, To be published.
12. J. Patterson, in "Physics of Electronic Ceramics," Vol. 1, Chap. 5, L. L. Hench and D. B. Dove, Editors, Marcel Dekker, New York (1971).
13. R. A. Rapp and D. A. Shores, in "Techniques of Metals Research," Vol. 4, Part 2, p. 123, R. A. Rapp, Editor, Interscience, New York (1970).
14. D. D. Wagner, J. E. Kilpatrick, W. G. Taylor, K. S. Pitzer, and F. D. Rossini, *J. Res. Nat. Bur. Std.*, **34**, 143 (1945).
15. W. D. Kingery, J. Pappis, M. E. Doty, and D. C. Hill, *J. Am. Ceram. Soc.*, **42**, 393 (1959).
16. A. D. Neumin, S. F. Pal'guyev, and V. N. Chebotin, in "Electrochemistry of Molten and Solid Electrolytes," Vol. 2, p. 79, M. V. Smirnov, Editor, Consultants Bureau, New York (1963).
17. L. Heyne, in "Mass Transport in Oxides," J. B. Wachtman and A. D. Franklin, Editors, p. 149, Nat. Bur. Std. Special Publ. 296 (1968).
18. H. L. Tuller and A. S. Nowick, in "Proc. 9th University Conf. on Ceramic Science," Plenum Press, To be published.
19. B. C. H. Steele and J. M. Floyd, *Proc. Brit. Ceram. Soc.*, No. 19, p. 55 (March 1971).
20. K. W. Lay and D. H. Whitmore, *Phys. Status Solidi (b)*, **43**, 175 (1971).

Anodic Dissolution of N-Type Gallium Arsenide under Illumination

Akio Yamamoto and Soichi Yano

Electrical Communication Laboratories,
Nippon Telegraph and Telephone Public Corporation, Tokai, Ibaraki, Japan

ABSTRACT

An experimental study has been made of the anodic dissolution of n-type GaAs under illumination. In the dark, the dissolution potential depended on the carrier concentration and the surface orientation of the sample. By illuminating the surface of the sample, the dissolution potential became less noble and its dependence on carrier concentration and surface orientation became small with increasing light intensity. Samples were electropolished under the condition that the surface orientation dependence of the dissolution potential was scarcely observed. In electroetching under illumination, flat-bottomed holes were obtained and the etched depth was controlled with an accuracy better than $0.1 \mu\text{m}$. Under illumination, a damaged surface exhibited less dissolution than that of an undamaged surface. With the introduction of surface damage to selected regions of the substrates by nitrogen bombardment, selective etching without the use of protective masks has been carried out.

The recent development of GaAs electronic devices demands new technologies of integrated circuits. For etching and shaping operations in integrated circuit technology, it becomes desirable to apply electrochemical processing.

Several authors (1-4) have discussed the anodic behavior; Nuese and Gannon (5) have described selective etching of GaAs. Anodic dissolution of n-type GaAs has not been widely studied as compared with p-type GaAs.

It is well-known that electropolishing of n-type semiconductors requires supplying extra holes. Gerischer (6) has described electrochemical behavior of n-type semiconductors under illumination. Harvey (3) has shown a surface profile of an n-type GaAs electrode following anodic dissolution under illumination. Regarding electropolishing or electroetching, however, few discussions have been made of anodic dissolution of n-type GaAs. The present paper discusses anodic dissolution and electroetching of n-type GaAs under illumination.

The experimental work was done in two parts. First, the measurements of I - V characteristics were performed carefully to obtain the dependence of carrier concentration and crystal orientation on dissolution rate. The second part was done to research the general features of electroetching and as the result of that to obtain the effects of defects and damage on dissolution rate.

Experimental

The apparatus used for the study of anodic dissolution of n-type GaAs under illumination is schematically illustrated in Fig. 1. The anodic current was pulsed at a frequency of 5 Hz and with a 10% duty ratio. Measurements of potential were made of the GaAs electrodes against a saturated calomel electrode.

GaAs samples were illuminated with monochromatic light with a wavelength of $0.8 \mu\text{m}$ in the measurements of I - V characteristics. For the study of electroetching, an incandescent lamp was used for illumination. The light intensity at the sample surface was calibrated in degrees by a silicon photocell positioned in place of the sample without an electrolyte. One degree in arbitrary unit corresponded to $10 \mu\text{W}/\text{cm}^2$.

For the electrolyte, a solution composed of $2.5(10)^{-2}$ mol/liter NaOH and $1.0(10)^{-3}$ mol/liter EDTA was employed. The chemicals used were all of reagent

grade. The electrolyte was kept at $25^\circ \pm 1^\circ\text{C}$, and dry N_2 gas was slowly bubbled during experiments.

The GaAs wafers were cut from single-crystal rod grown by the horizontal Bridgeman method, and were mechanically lapped with a SiC slurry and then polished with fine abrasive alumina ($0.3 \mu\text{m}$ particle size). After being degreased and rinsed with deionized water, they were chemically polished in a solution composed of $3\text{H}_2\text{SO}_4$ (conc), $1 \text{H}_2\text{O}_2$ (30%), and $1 \text{H}_2\text{O}$. The respective surface planes were adjusted within $\pm 0.5^\circ$ of the desired orientation.

The following treatments were made for the samples used for the measurements of I - V characteristics. To ensure good electrical contacts, indium containing gold (10 weight per cent) was evaporated to one side of the wafers at room temperature and then annealed in H_2 at 350°C for 15 min. The other side of the wafers was polished again in the above-mentioned solution before measurements.

The wafers had carrier concentrations in the range from 10^{16} to 10^{18}cm^{-3} , and had either $\langle 100 \rangle$, $\text{Ga}\langle 111 \rangle$, or $\text{As}\langle 111 \rangle$ orientations.

Samples were fixed by a sample holder illustrated in Fig. 2. The wafer was cemented with an adhesive wax to the Teflon electrode holder and coated with paraffin. The exposed area of the GaAs surface was between 0.002 and 0.010cm^2 . The electrodes were connected to the outer circuit by using an electrically conducting lubricant.

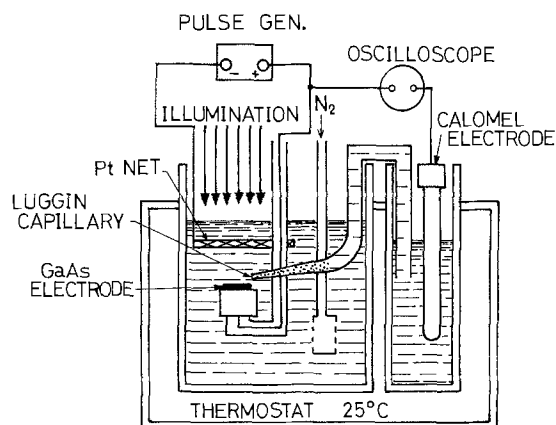


Fig. 1. Schematic arrangement of electrolytic cell

Key words: GaAs, anodic dissolution, illumination, electroetching, selective removal.

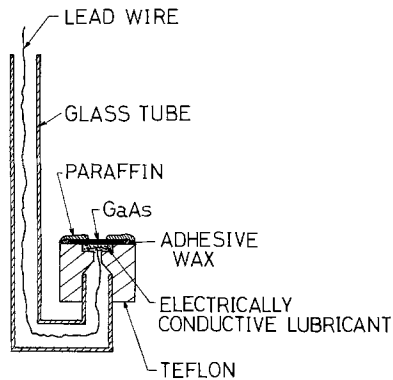


Fig. 2. Cross section of sample holder

Results and Discussion

First, measurements of the I - V characteristics of n -type GaAs are described and discussed. Second, the etching behavior of n -type GaAs illuminated with incandescent light is described. Finally, the observed effects of surface damage on the anodic dissolution of n -type GaAs under illumination are shown.

I - V characteristics of n -type GaAs electrodes.—The GaAs electrode potential was measured as a function of current density on $\langle 100 \rangle$ -oriented samples with carrier concentrations of $5.3(10)^{16} \text{ cm}^{-3}$ (undoped) and $2.2(10)^{18} \text{ cm}^{-3}$ (Te doped). For comparison, the same measurements were carried out on $\langle 100 \rangle$ -oriented Zn-doped p -type samples with carrier concentrations of $7.0(10)^{17} \text{ cm}^{-3}$ and $1.7(10)^{19} \text{ cm}^{-3}$.

When a pulsed current of 5 Hz and 10% duty ratio was employed, the potential became thoroughly stable and highly reproducible. At current densities between 10^{-2} and 1 mA/cm^2 , no film formation and no gas evolution were observed on the surface.

The results are summarized in Fig. 3. The n -type samples showed current saturation. The p -type samples were readily dissolved and large currents were drawn at few volts. One can see in Fig. 3 that a dissolution rate ratio of p -type GaAs to n -type GaAs is the order of more than 10^2 at a potential of about zero volt. This presents the possibility of selective removal of only p -type from p - n structures (7).

The carrier concentration dependence of I - V curves for p -type samples were hardly observed. On the other hand, the I - V curves for n -type electrodes remarkably depended on carrier concentration. In the dark,

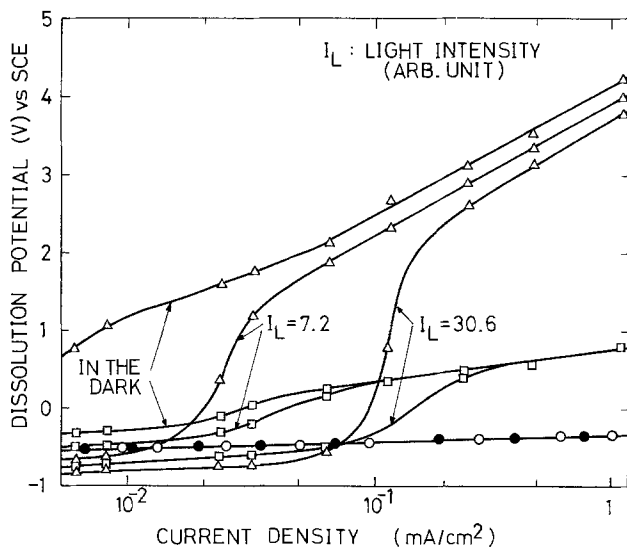


Fig. 3. Dissolution potential-current density curves for various GaAs electrodes with different types and carrier concentration: \circ , p -type $7.0(10)^{17} \text{ cm}^{-3}$; \bullet , p -type $1.7(10)^{19} \text{ cm}^{-3}$; Δ , n -type $5.3(10)^{16} \text{ cm}^{-3}$; \square , n -type $2.2(10)^{18} \text{ cm}^{-3}$.

the n -type sample of $5.3(10)^{16} \text{ cm}^{-3}$ exhibited nobler dissolution potential, i.e., lower dissolution rate than that of $2.2(10)^{18} \text{ cm}^{-3}$. We can not explain the fact, as in the case of heavily doped n -type Ge (8) or Si (9), that the n -type sample with higher carrier concentration is more reactive in anodic dissolution than that with the lower doping by taking account of only their hole concentration in the bulk. Since n -type GaAs of 10^{16} - 10^{18} cm^{-3} has few holes in the bulk, the diffusion from the bulk cannot be a sufficient source of holes. Consequently, holes involved in the dissolution process in the dark were probably generated in the space-charge region of the semiconductor (10).

For p -type samples, there was no difference between the I - V curves in the dark and those under illumination. For current densities below about 2 mA/cm^2 , the Tafel relation held and the slope was about 96 mV/decade .

Illumination caused an increase in the saturation current density of the I - V curves for n -type samples. The saturation current density was proportional to the incident light intensity. Above the saturation current density, the potentials under illumination were closely similar to that in the dark. Since the shift of dissolution potential to a less noble value by illumination was larger for the sample of $5.3(10)^{16} \text{ cm}^{-3}$ than for the sample of $2.2(10)^{18} \text{ cm}^{-3}$, the dissolution potential of the former was less noble than that of the latter above a certain value of light intensity. Figure 4 shows plots of dissolution potential at constant current density vs. light intensity. The dissolution potential of the sample of $5.3(10)^{16} \text{ cm}^{-3}$ was drastically shifted toward a less noble value in the low region of light intensity. The linear relationship between the potential and the logarithm of light intensity (6) held for the sample of $5.3(10)^{16} \text{ cm}^{-3}$ only in the higher region of light intensity, while this relationship held for the sample of $2.2(10)^{18} \text{ cm}^{-3}$ over the whole range of light intensity we examined. Thus, the behavior of the samples in anodic dissolution depended remarkably on the carrier concentration in the low region of the light intensity. The differences in dissolution potential between both samples became smaller with increasing light intensity. Therefore, the carrier concentration dependence is considered to disappear when the dissolution process of the samples is controlled fully by holes generated

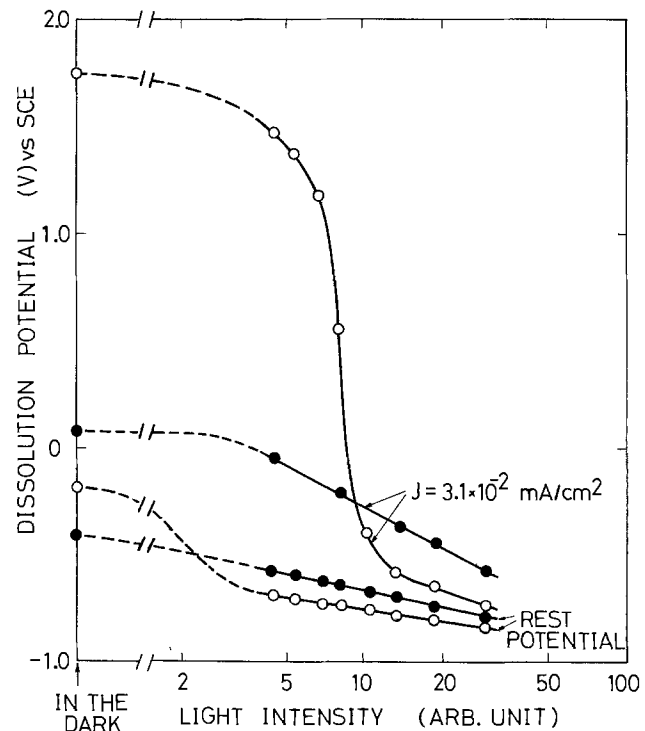


Fig. 4. n -type GaAs dissolution potential vs. light intensity at constant current densities: \circ , $5.3(10)^{16} \text{ cm}^{-3}$; \bullet , $2.2(10)^{18} \text{ cm}^{-3}$.

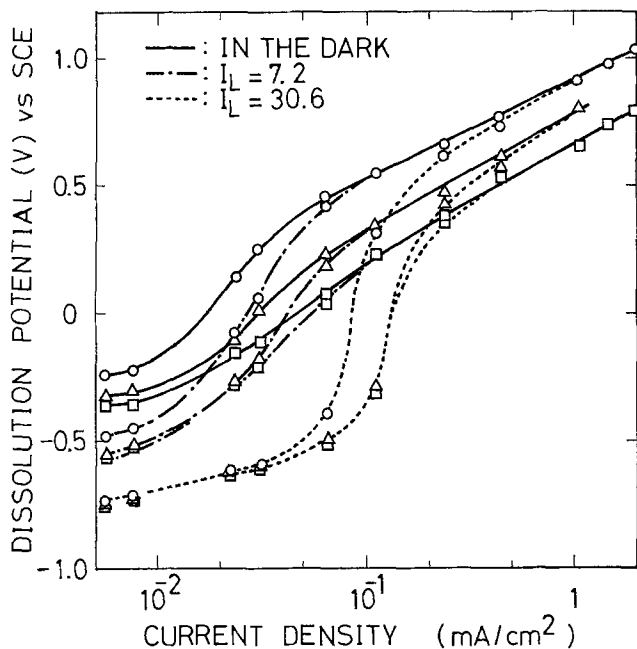


Fig. 5. Surface orientation dependence of dissolution potential-current density curves for n-type GaAs of $2.2(10)^{18} \text{ cm}^{-3}$: \circ , Ga(111); \square , As(111); \triangle , (100).

by incident light. This leads to the conclusion that it is possible to electroetch uniformly n-type GaAs samples containing different dopant concentrations by illuminating the surface strongly.

Figure 5 shows the surface orientation dependence of the I - V curves. The samples employed had carrier concentration of $2.2(10)^{18} \text{ cm}^{-3}$ and (100), Ga(111), and As(111) planes. In the dark, appreciable differences in dissolution potential existed. The order of magnitude of dissolution potential was Ga(111) >

(100) > As(111). By illuminating the surface, the dissolution potential became less noble and the differences among the three planes decreased with increasing light intensity. Under strong illumination, the dissolution potential of the three planes was almost identical at low current densities. These results indicate that the dependence of the dissolution rate on the surface orientation becomes smaller with increasing dissolution rate by illumination.

For p-type GaAs electrodes, the dependence of dissolution potential on the surface orientation was explained by the extent of surface coverage of the $\text{Ga}(\text{OH})_3$ which showed little solubility in alkaline solution (4). The fact that the dissolution rate of n-type GaAs can be increased by illumination shows that the dissolution reaction of n-type GaAs is limited by the supply of holes. Therefore, it is unsuccessful for n-type GaAs to explain the surface orientation dependence of the dissolution rate by taking account of coverage of the $\text{Ga}(\text{OH})_3$ layer on the surface. It is suggestive that its dependence is due to the difference in the habit of crystal planes.

No appreciable changes were observed on the surface after the short times needed for measurement of the I - V curves. Appreciable changes occurred, however, when anodic dissolution was carried out for more than 1 hr. Figure 6 shows the etch patterns on (100) planes of n-type GaAs resulting from anodic dissolution in various conditions. In the dark, etch pits parallel to the $\langle 110 \rangle$ direction appeared over the whole range of current densities employed [Fig. 6(a) and (c)]. Under strong illumination, the etch pits were similarly produced at high current density [Fig. 6(b)], but not produced at low current density [Fig. 6(d)]. From the results shown in Fig. 5 and 6, one can see that the formation of the etch pits depends on the differences in dissolution potential among three planes; that is, no pits were produced and samples were electropolished under the condition that the differences in dissolution potential among the three planes were small. Even under strong illumination, the pits were pro-

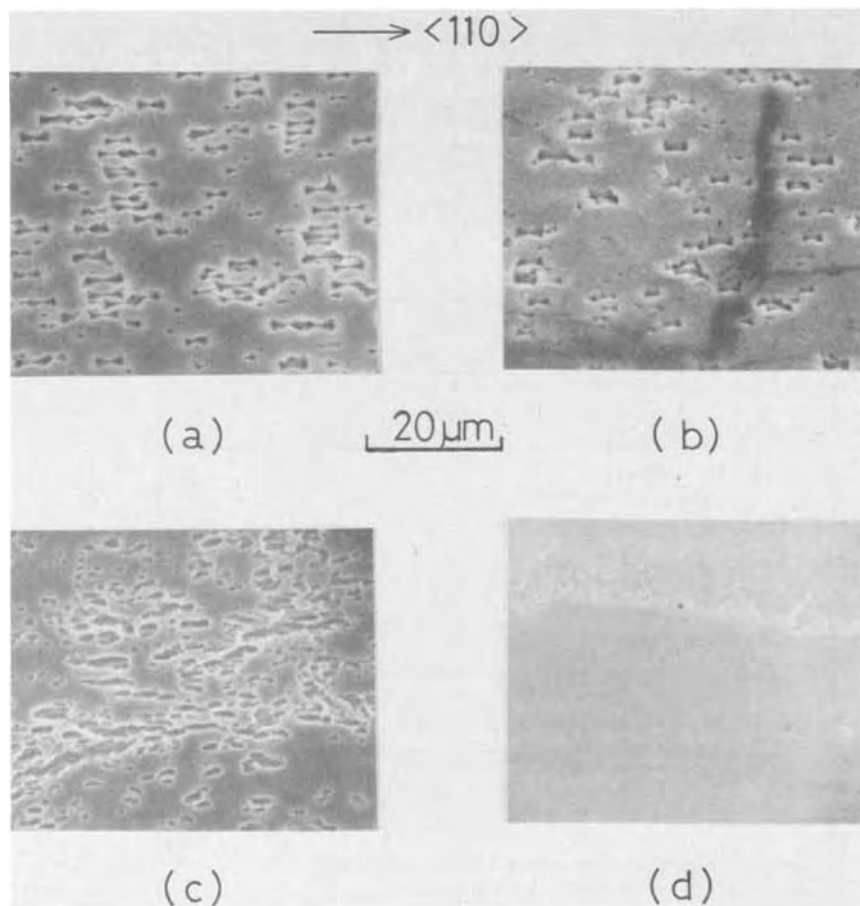


Fig. 6. SEM photographs of surfaces of n-type GaAs with (100) plane after anodic dissolution at various conditions. (a) $J = 2.0 \text{ mA/cm}^2$, in the dark; (b) $J = 2.0 \text{ mA/cm}^2$, $I_L = 30.6$; (c) $J = 3.1(10)^{-2} \text{ mA/cm}^2$, in the dark; (d) $J = 3.1(10)^{-2} \text{ mA/cm}^2$, $I_L = 30.6$.

duced only when differences in dissolution potential existed.

When anodic dissolution was further carried out on the surface as shown in Fig. 6(a), there was little remaining of the original plane and other planes appeared as shown in Fig. 7. The planes that remained after extensive etching were those that exhibited the smallest dissolution rate. Since their identification was hard to achieve, it was not clear whether these planes were the Ga(111) planes or other planes of high index (3).

As described, the effects of illumination were not always observed on the anodic dissolution of n-type GaAs. The light intensity and the current density are very important parameters for the study of the effects of illumination on the anodic dissolution of semiconductors.

Electroetching of n-type GaAs.—As described in the previous section, the n-type GaAs was electropolished by illuminating the surface. As those experiments were performed at relatively low current densities, etch rates were fairly small. It is desirable to obtain etch rates of, at least, $1 \mu\text{m/hr}$. To find a practical range of electroetching, anodic dissolution of n-type GaAs was studied at current densities in the range of $1\text{--}20 \text{ mA/cm}^2$. In order to obtain the dissolution potential in the range -0.5 to -1.0V vs. SCE , samples were illuminated with incandescent light of intensities in the range $3(10)^3\text{--}10^4$ (arbitrary unit, see in Experimental section). Under these experimental conditions, no film formation and no gas evolution were observed on the surface.

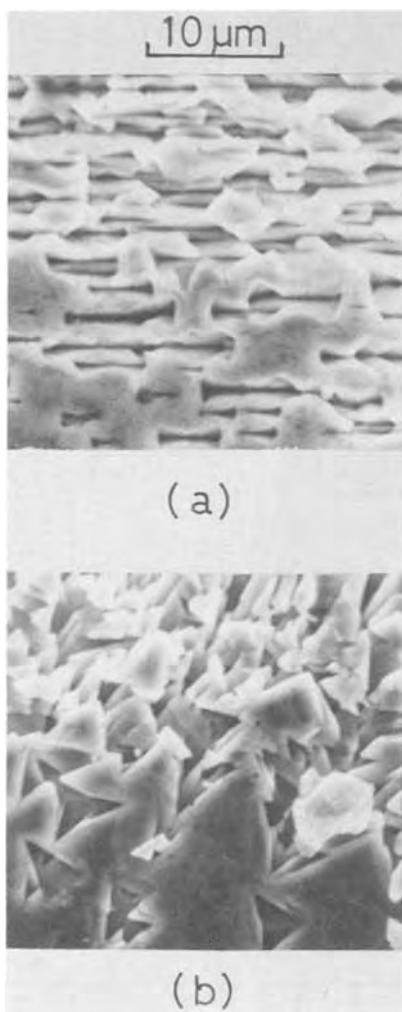


Fig. 7. Etch patterns after anodic dissolution prolonged on (a) (100) plane, and (b) As(111) plane.

A surface roughness and an etched depth were measured by Dektak (an instrument for mechanical measurement of roughness and waviness, manufactured by Sloan Corporation¹).

Surface profiles of the samples with (100) planes after anodic dissolution are shown in Fig. 8. Current densities were roughly divided into three regions. The terms region I, region II, and region III will from now on be used to refer to the three regions, low, intermediate, and high current densities, respectively. At low current densities (region I), the surfaces were roughly etched, that is, there existed unetched areas [Fig. 8(a)]. At high current densities (region III), deep etch pits were produced [Fig. 8(c)]. Between region I and region III (region II), the surfaces were etched uniformly [Fig. 8(b)]. Figure 9 shows SEM photographs of the surfaces shown in Fig. 8. As seen in Fig. 9(a), anodic dissolution revealed a multitude of defect structures in region I. The unetched areas corresponded to the portions that involved defects. When a linear scratch mark was made mechanically on the chemically polished surface, the dissolution scarcely proceeded on the damaged part, as shown in Fig. 10. These observations suggest that the presence of defects or damage leads to a decrease in reactivity of the surface under illumination. No defect structures were observed in regions II and III. The sensitivity for the defects decreased with increasing current density. With increasing light intensity, regions II and III shifted to higher current densities and consequently region I became wide. These are summarized in Fig. 11. From the above results, we concluded that the defects became more sensitive to selective etching with increasing light intensity. The effects of defects or damage on anodic dissolution are discussed in detail in the next section.

The etch pits produced in region III were different in shape and distribution from the pits observed in the measurements of the $I\text{--}V$ characteristics. The pits produced in region III were caused by the local breakdown of the surface voltage barrier, as in the case of n-type Si (11). These results suggest that the surface orientation dependence of the dissolution rate was sufficiently small in these experimental conditions. The lack of uniformity in etched depth was due to the inhomogeneity of the crystals employed.

¹ Sloan Instruments Corporation, 535 East Montecito Street, Santa Barbara, California 93100.

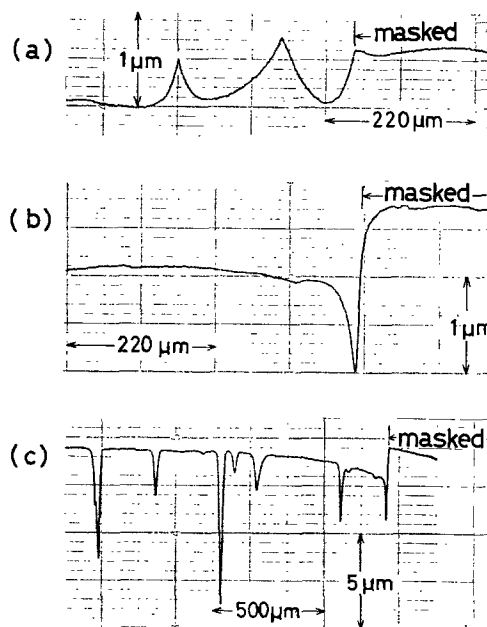


Fig. 8. Surface profiles of n-type GaAs with (100) plane after electroetching at various current densities. (a) $J = 1.2 \text{ mA/cm}^2$, (b) 4.7 mA/cm^2 , (c) 11.5 mA/cm^2 .

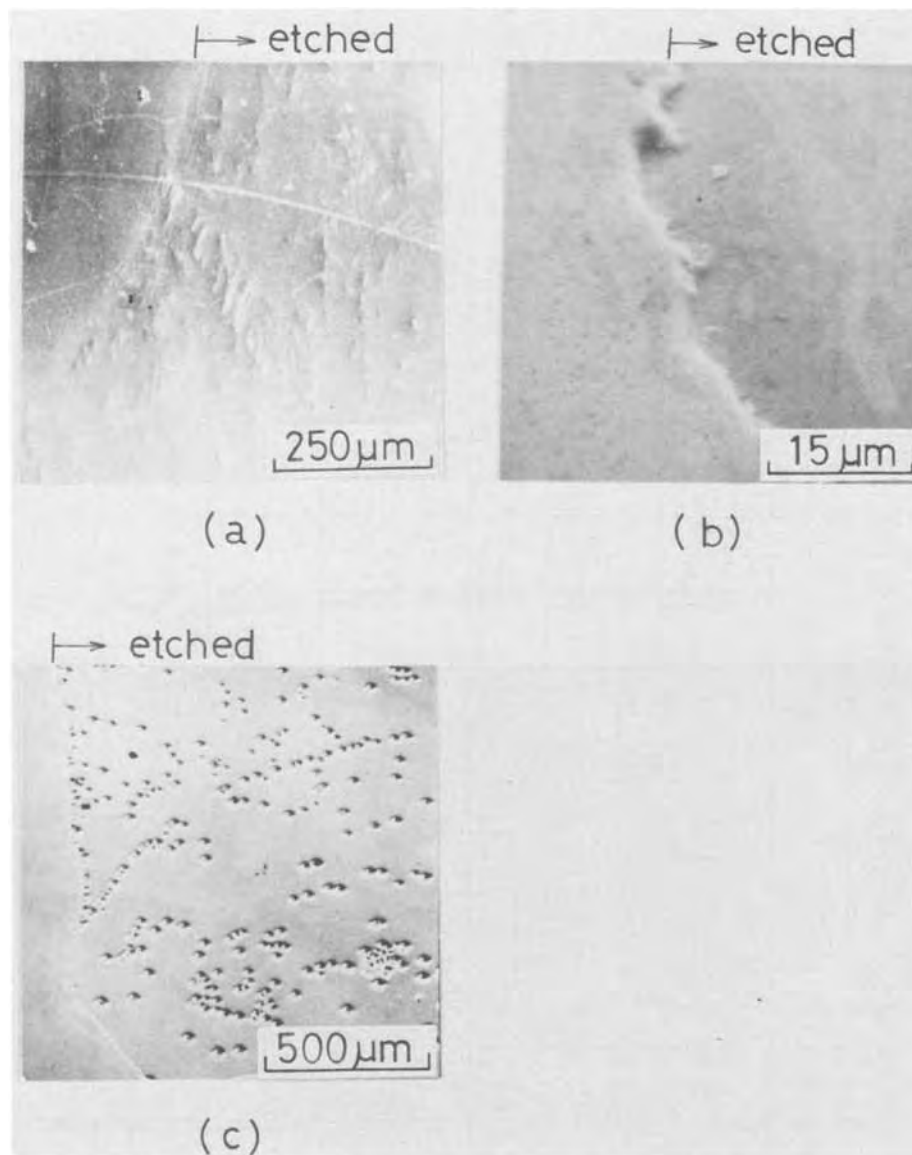


Fig. 9. SEM photographs of the surfaces shown in Fig. 8.

Samples were etched more deeply near the mask edge than at the center of the holes in regions II and III (see Fig. 8). Shaw (12) observed such an "edge effect" in the chemical selective etching of GaAs substrates and suggested that the edge effect was caused by the surface diffusion of etchant molecules along the mask. In the present investigation, the above edge effect was not influenced by stirring the electrolyte. When black wax (for example picene wax) which shielded the incident light was employed as a mask instead of paraffin, the edge effect was scarcely observed as shown in Fig. 12. In this case, the surface diffusion of etchant molecules had no effects on the edge effect, but the diffusion of holes generated by the incident light through the layer of paraffin did.

Under the experimental conditions in region II, an etched depth as a function of integrated current was measured on the samples with (100) and Ga(111) planes. The results are summarized in Fig. 13. The experimental plots were in good agreement with the theoretical data calculated by assuming that the current efficiency was 100% and the electron number was 6 (3). Figure 13 shows that etched depths can be controlled with accuracy better than $0.1 \mu\text{m}$.

Behavior of damaged surfaces and selective removals without using protective masks.—As described in the previous section, the presence of defects or damage led to a decrease in dissolution rate of the surface under illumination. To clarify the behavior of damaged surface, anodic dissolution was studied on samples having various pretreatments.

Figure 14 shows the I - V curves of n-type GaAs samples polished chemically, polished mechanically, and bombarded with nitrogen-ions at room temperature. In the dark, the surfaces damaged by mechanical polishing or N-ion bombardment exhibited less noble dissolution potentials than that of the undamaged surface. This fact indicates that the presence of damage leads to an increase in reactivity of the surface atoms in the dark (11, 13). By illuminating the surface, the dissolution potential of the undamaged surfaces were shifted to more active values. The shift of the potential increased with increasing light intensity. The dissolution potential of damaged surfaces, however, was scarcely changed by illumination. Consequently under strong illumination, the undamaged surfaces were more reactive than the damaged surfaces. The difference in dissolution rate between the damaged surface and the undamaged one increased with increasing light intensity. This result explains the fact, shown in Fig. 11, that the defects became more sensitive with increasing light intensity.

The dissolution potential under illumination at a constant current density as a function of distance from the surface for various pretreatments is shown in Fig. 15. No change in dissolution potential was observed when the original surface was chemically polished. In the case of the samples treated with mechanical polishing and N-ion bombardment, however, the potential was extremely noble at the surface and became less noble with distance from the surface. The dissolution potential of the samples with various pretreatments

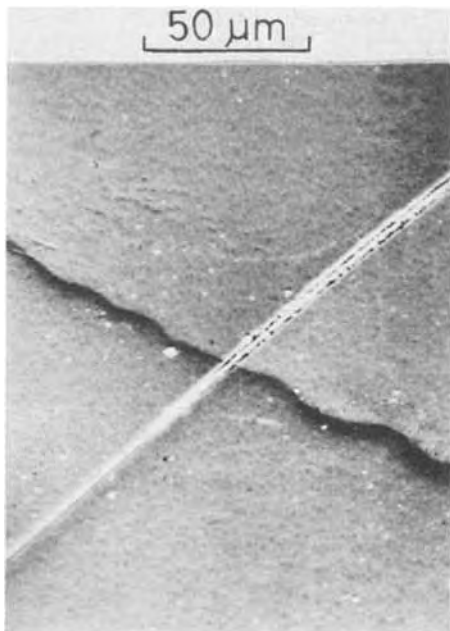


Fig. 10. Linear scratch mark made mechanically on the chemically polished surface.

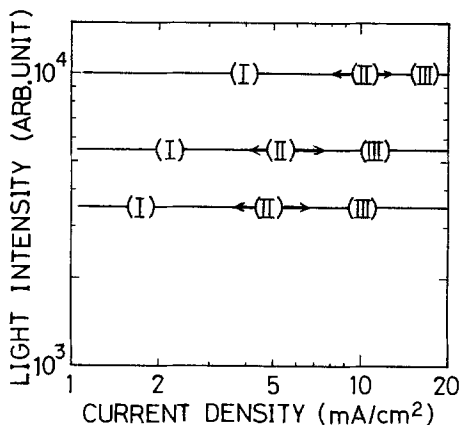


Fig. 11. Light intensity dependence of etched surface character (see text for details).

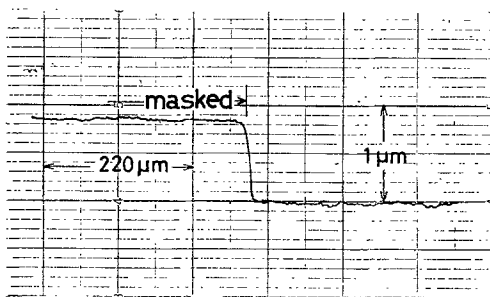


Fig. 12. Etched step obtained by employing picene wax as a protective mask.

almost coincided with the value of the chemically polished sample at a distance longer than about 0.5 μm from the surface.

The fact that the effects of illumination on the damaged surface were scarcely observed indicates that there existed few holes generated by the light. Further, this means either that the damaged surfaces had little incident light or that excess holes generated by the incident light recombined almost immediately. The former is less probable because a remarkable difference in reflection coefficient of light was not observed between the damaged surface and the undamaged one (13). Therefore we may conclude that, although holes

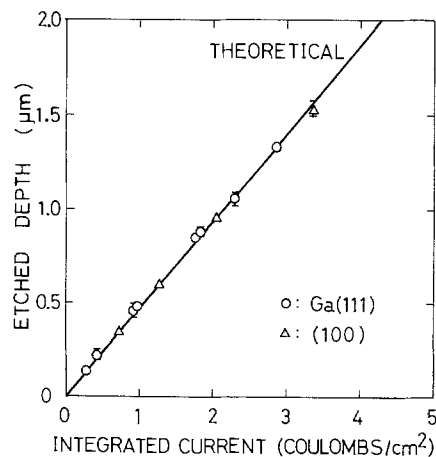


Fig. 13. Etched depth vs. integrated current for n-type GaAs electrodes with (100) and Ga(111) planes.

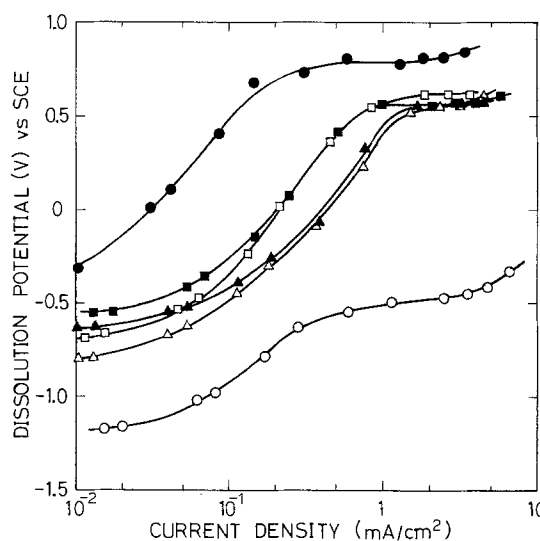


Fig. 14. Dissolution potential-current density curves for n-type GaAs electrodes with different surface pretreatments. Open symbols, under illumination; solid symbols, in the dark; ○, ● polished chemically; □, ■ polished mechanically with abrasive alumina (0.3 μmφ); △, ▲ bombarded with 10¹⁵ atoms/cm² 20 keV nitrogen ions.

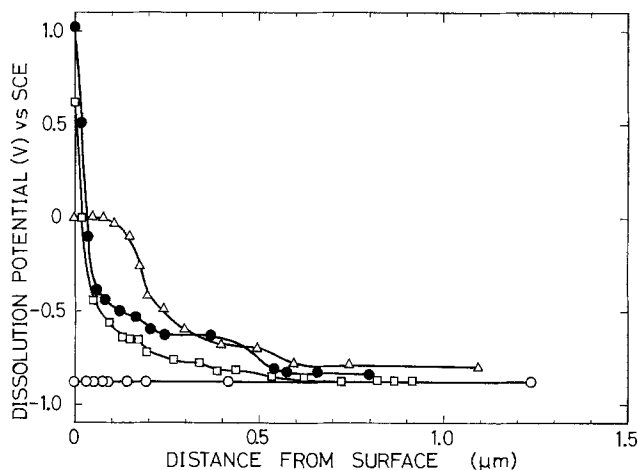
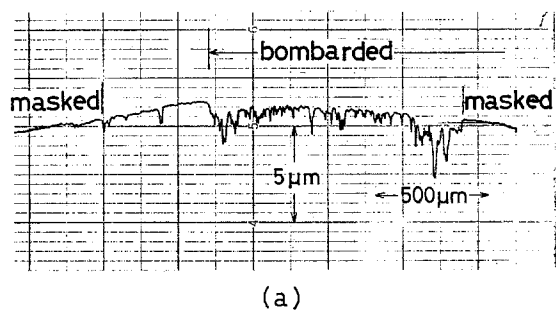


Fig. 15. Dissolution potential of (100) surface of n-type GaAs under illumination as a function of distance from the surface for various surface pretreatments. ○, Polished chemically; ●, polished with abrasive alumina (0.3 μmφ); □, polished with abrasive alumina (0.05 μmφ); △, bombarded with 10¹⁵ atoms/cm² 20 keV nitrogen ions.

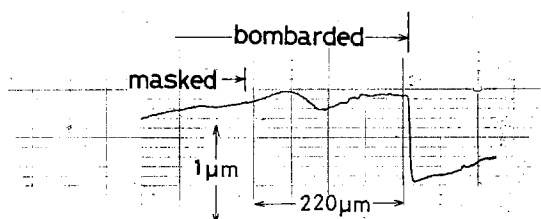
were generated, they recombined swiftly through many defects. Further discussion of this matter should be given on the basis of a better understanding of the actual nature of the damaged surface layer.

Selective removal of n-type GaAs substrates without using protective masks was attempted. The substrates were bombarded in selected areas with approximately 10^{15} atoms/cm² 20 keV nitrogen ions at room temperature. Figure 16(a) and (b) show surface profiles of the samples following anodic dissolution in the dark and under illumination, respectively. In the dark, the area bombarded with N-ions was etched more deeply. As expected from the results shown in Fig. 14, on the other hand, the unbombarded area was selectively removed under illumination. As the thickness of the damaged layer was a function of the applied voltage for ions (14), the step depth produced in the dark was determined by the applied voltage for ions. Therefore, once the damaged layer had been removed the surface became very rough and the dissolution proceeded on the unbombarded area as shown in Fig. 16(a). Under illumination, the removal proceeded uniformly and the step depth was controlled with little dependence of the thickness of damaged layer because the damaged layer acted as the protective mask. It is evident that the selective removal under illumination was more selective by about ten times than that in the dark. This is readily expected from the results shown in Fig. 14.

An attempt was made to anodically etch semi-insulating GaAs (Cr-doped, 10^6 ohm-cm). Etching behavior of the above samples was similar to that of n-type GaAs except that the enhancement of etch rate near the mask edge was more remarkable. Figure 17 shows the selective removal under illumination on a Cr-doped GaAs substrate bombarded with N-ions selectively.



(a)



(b)

Fig. 16. Surface profiles of n-type GaAs substrates bombarded with 10^{15} atoms/cm² 20 keV nitrogen ions following electroetching (a) in the dark, and (b) under illumination.

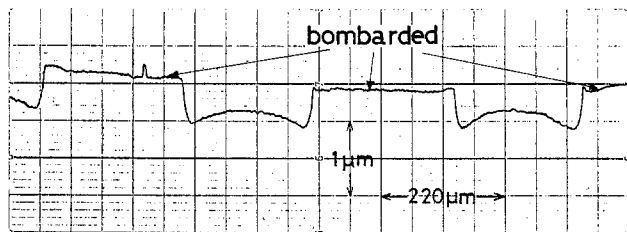


Fig. 17. A selective removal made on Cr-doped GaAs substrate

As described above, by the electroetching under illumination (without using protective masks) various etch patterns have been produced on the GaAs substrates to which surface damage was selectively introduced. This technique is powerful for the fabrication of semiconductor devices with ion bombardments or ion implantations.

Summary

Anodic dissolution of n-type GaAs under illumination was experimentally studied.

Samples in the dark exhibited different dissolution rates depending on the carrier concentration and on the surface orientation. One of the samples with higher doping levels exhibited a larger dissolution rate. The Ga(111) plane showed smallest dissolution rate among the (100), Ga(111), and As(111) planes. Etch pits parallel to the $\langle 110 \rangle$ direction were produced on (100) planes in the dark. When the surface was illuminated, the saturation current density increased in proportion to the incident light intensity. Below the saturation current density, the dissolution rate of the samples increased and the dependence of dissolution rate on the carrier concentration and on the surface orientation became small with increasing light intensity. Under the condition that the differences in dissolution rate were scarcely observed among the (100), Ga(111), and As(111) planes, no pits were produced and samples were electropolished. Above the saturation current density, the dissolution rate was hardly changed from the value in the dark by illumination and the etch pits similar to that observed in the dark were produced even under strong illumination.

In the electroetching under illumination, three different etched profiles were obtained at current densities in the range 1-20 mA/cm². At low current densities, a multitude of defect structures were observed. At high current densities, deep etch pits caused by the local breakdown of the surface voltage barrier were observed. Samples were etched uniformly by employing suitable light intensity and current density. The sensitivity for defects in anodic dissolution increased with decreasing current density and with increasing light intensity. The current density required to etch the surface uniformly was a function of the light intensity. Etched depths were controlled with accuracy better than 0.1 μ m.

Damaged surfaces dissolved faster than undamaged surfaces in the dark. Under illumination, undamaged surfaces dissolved faster than damaged surfaces because of the small change in the dissolution rate of damaged surfaces by illumination. By utilizing the difference in dissolution rate between an area damaged by N-ion bombardment and an undamaged area, various etch patterns were produced without using protective masks. This method was applicable to semi-insulating GaAs.

Acknowledgment

The authors wish to thank Dr. K. Nakagawa and Dr. K. Kudo for their helpful suggestions.

Manuscript submitted Oct. 16, 1973; revised manuscript received Sept. 6, 1974.

Any discussion of this paper will appear in a Discussion Section to be published in the December 1975 JOURNAL. All discussions for the December 1975 Discussion Section should be submitted by Aug. 1, 1975.

Publication costs of this article were partially assisted by Nippon Telegraph and Telephone Public Corporation.

REFERENCES

1. H. C. Gatos and M. C. Lavine, *This Journal*, **107**, 427 (1960).
2. H. Gerischer, *Ber. Bunsengesellschaft Physik. Chem.*, **69**, 578 (1965).

3. W. W. Harvey, *This Journal*, **114**, 472 (1967).
4. M. E. Straumanis, J. P. Krumme, and W. J. James, *ibid.*, **115**, 1050 (1968).
5. C. J. Nuese and J. J. Gannon, *ibid.*, **117**, 1094 (1970).
6. H. Gerischer, *ibid.*, **113**, 1174 (1966).
7. R. L. Meek and N. E. Schumaker, *ibid.*, **119**, 1148 (1972).
8. R. Gereth and M. E. Cowher, *ibid.*, **115**, 645 (1968).
9. R. L. Meek, *ibid.*, **118**, 437 (1971).
10. R. L. Meek, *Surface Sci.*, **25**, 526 (1971).
11. M. V. Sullivan, D. L. Klein, R. M. Finne, L. A. Pompliano, and G. A. Kolb, *This Journal*, **110**, 412 (1963).
12. D. W. Shaw, *ibid.*, **113**, 958 (1966).
13. K. Vedam and S. S. So, *Surface Sci.*, **29**, 379 (1972).
14. J. F. Gibbons, E. O. Hechtel, and T. Tsurushima, *Appl. Phys. Letters*, **15**, 117 (1969).

Steady-State Anodic Leakage Current in Barrier-Type Aluminum Oxide Films

Peter G. Anderson and Owen F. Devereux*

Department of Metallurgy and Institute of Materials Science, University of Connecticut, Storrs, Connecticut 06268

ABSTRACT

When aluminum is polarized potentiostatically in a barrier-forming electrolyte, such as aqueous ammonium tartrate, the current passed diminishes steadily to a low value commonly termed the leakage current. This value is not stable, but increases gradually, attaining a constant value after many hours. The dependence of this steady-state current on potential has been studied for aluminum electrodes in 1M aqueous ammonium tartrate at pH 7 and test temperatures of 30°, 50°, and 70°C. In the overpotential range of approximately 50-80V, current is independent of overpotential, while exponential dependence of the anodic current on overpotential is seen at lower overpotentials, with a significant reverse contribution below approximately 20V. The values of both forward and reverse exponential coefficients are extremely anomalous in comparison to normal Tafel slopes. Above approximately 80V, current increases rapidly with potential until breakdown occurs.

During the potentiostatic formation of barrier-type anodic oxide films on "valve" metals the anodic current is seen to decrease monotonically to a minimum value, commonly termed the "leakage current." For aluminum anodized in an electrolyte conducive to barrier film formation, such as neutral aqueous ammonium tartrate, this minimum is reached in a matter of minutes. However, this leakage current is not stable, but gradually increases, attaining a stable value only after many hours. A similar effect is seen if the value of the applied potential is reduced after the leakage current has stabilized. There is then a marked reduction in the anodic current, with a new minimum value being observed after a period of several minutes. Again, however, this value is not stable, but increases at an accelerating rate with a higher, apparently stable value being attained after many hours. This is apparently a distinct phenomenon from that observed by several previous investigators (1-8), in which a transient current response is seen following an abrupt change in applied potential or an interruption in the application of an anodic potential. Such transients have durations of the order of minutes, two to three orders of magnitude shorter than the time required for establishment of a stable leakage current, and have been attributed to a relaxation process involving the conducting ions in the oxide (9, 10).

Research on valve metal electrodes has been extensively reviewed (9-17); therefore, it is necessary only to refer to those aspects of previous work that directly pertain to the establishment of a stable leakage current through the anodic oxides formed on such electrodes. Much earlier work was stimulated by the rectifying properties of valve metal electrodes. Van Geel (18, 19) and Taylor and Haring (20) attributed this behavior to the occurrence of a p-n junction with-

in the anodic oxide, while Saski proposed a p-i-n junction (21). The latter observation is somewhat supported by the results of Heine and Pryor (22), who, in studying anodic aluminum oxide, found an n-type region adjacent to the metal, a p-type region near the electrolyte, and a less-defective oxide in the intermediate region. Dewald (23), on the basis of their rectifying and photovoltaic characteristics, has treated anodic films on valve metals as semiconducting electrodes. On the other hand Vijn (24) has indicated that there may be many cases that are not amenable to this treatment, citing a variety of possible occurrences at the oxide-electrolyte interface that may lead to masking of the high bandgap of the oxide. In such cases Tafel behavior would be seen, but with an anomalous slope. Smith (25) regarded current to be limited by the rate of carrier injection at the oxide-electrolyte interface, anodic polarization causing electron injection by oxygen evolution and cathodic polarization causing hole injection by hydrogen evolution. Although the difference in behavior of these carriers would explain rectification, Smith (26) later attributed rectification to the presence of structural defects such as electrolyte-filled pores formed during anodizing. Vermilyea (27) and Young (12) have espoused a similar view in attributing rectification to "weak spots" in the oxide film. Inherent in this thought is the view that the oxide is essentially nonconducting, and that significant current is passed only at structural defects.

In the cases cited above the current passed by a valve metal electrode has been, sometimes tacitly, assumed to be electronic, an obvious assumption in view of the high mobility of electronic defects and the commonly held belief that an anodic film reaches terminal thickness coincident with attaining the leakage current, thereby obviating the need for considering ionic current. It is not clear, however, that this assumption is valid. For example, Hunter and Towner

* Electrochemical Society Active Member.

Key words: electronic current, polarization, transients.

(28) observed growth of a porous oxide during prolonged anodizing of aluminum in aqueous ammonium tartrate subsequent to the formation of a barrier oxide layer of terminal thickness. Under the conditions of their experiment the porous film grew at a constant rate of $175 \text{ \AA}\cdot\text{hr}^{-1}$ and the leakage current remained at a constant value of $15 \mu\text{A}\cdot\text{cm}^{-2}$. Using a density of $3.0 \text{ g}\cdot\text{cm}^{-3}$ for the porous film (29), 56% of the leakage current was necessary to account for the porous oxide growth and, therefore, was necessarily ionic. Plumb (30) evaluated the coulometric efficiency of barrier layer formation on aluminum and found that only a portion of the leakage current could be accounted for by electronic flow, measured as oxygen evolution. Smith (31) obtained results similar to those of Hunter and Townner but, in addition, measured the dissolution of aluminum in the anodizing electrolyte. He found that, for anodizing times up to 90 min, ionic flow, evaluated as the aluminum found as oxide plus that in solution, was equal to the cell current, i.e., that there was no indication of a significant electronic contribution to the leakage current.

It is apparent that the distinction commonly made between formation of "barrier" layers and of "porous" layers on valve metal electrodes is one of degree and not of kind, a view expressed explicitly by others (14, 16, 32). Thus for prolonged anodizing of valve metals in an electrolyte conducive to barrier layer formation it is necessary to consider those processes which contribute to the current passed during the formation of a porous film (16). These include as ionic processes both the steady-state growth of a porous oxide film and the steady-state dissolution and the reformation of the barrier oxide film. The distinction between these processes may be somewhat arbitrary and both may involve both anionic and cationic transport (9). Electronic processes may involve any of several possible electrode reactions resulting in injection of electrons or holes at the oxide-electrolyte interface; electronic processes at the metal-oxide interface are energetically unlikely to be rate limiting (25).

Experimental

Specimens were prepared from 99.999% pure aluminum rod (Leico Industries, Incorporated). Small cylinders were finish-machined, axially drilled and tapped for mounting, and mechanically polished. Residual stresses were relieved by heating in argon to 345°C and furnace cooling. Each cylinder, on use, was incorporated into a specimen assembly as described by Greene (33). The assemblies were subsequently cleaned by immersion in an aqueous solution containing 3% nitric acid and 80% phosphoric acid for 15 min, followed by an ultrasonic rinse in double-distilled water (34).

Anodizing and polarization studies were conducted in 1M solutions of reagent grade ammonium tartrate in double-distilled water, adjusted to pH 7 by titration with a dilute ammonium hydroxide solution. These solutions were stored under nitrogen to hinder carbon dioxide absorption, and were discarded periodically during the experiments.

The test cell was that described by Greene (33), employing the aluminum specimen as working electrode, two platinum counterelectrodes, and a saturated calomel reference electrode. The latter employed a salt bridge with a Luggin-Haber probe adjacent to the working electrode. The cell was continuously purged with nitrogen through a fritted glass inlet tube, and the entire apparatus was contained in a constant temperature bath. Potentials of less than 10V were applied with a Wenking potentiostat, Model 68TS3, with the potential of the working electrode measured relative to the reference electrode; potentials greater than 10V were applied with a constant voltage d-c power supply, Raytheon Model QHD 100-2 or Hewlett-Packard Model 6299A, and were measured relative to the counterelectrodes. The applied potential and the anodic

current were measured with electrometers, Keithley Models 602 and 615.

All specimens were initially anodized at $1 \text{ mA}\cdot\text{cm}^{-2}$ in the 1M tartrate solution at the test temperature, 30° , 50° , or 70°C , until a specimen potential of 30V was reached (22). The potential was then held constant until a stable leakage current obtained, a condition defined by zero observable variation in current over a period of time. The total duration of this initial anodizing was several hours. On reaching a constant leakage current, the specimen potential was reduced to -1V SCE , at which the specimen was slightly anodic, and held until the current reached a stable value, recorded as characteristic of that potential. The specimen potential was then increased (made more anodic) in a series of potential steps; during each step the specimen potential was held constant until the stable leakage current at that potential was established. When imminent anodic breakdown became apparent the procedure was reversed and the specimen potential was reduced in sequential steps, with the stable leakage current again being recorded.

Results

The overpotential of an electrode is defined by Young (35) as the difference between two values of the electrode potential measured relative to the electrolyte: that when the electrode reaction is proceeding at a finite rate under given conditions minus that when the electrode is at equilibrium under the same conditions. The former, v_{exp} , is the experimentally measured electrode potential relative to the reference electrode; the latter, v_0 , is the value of the electrode potential when zero current is flowing in the external circuit, obtained by extrapolation or by computation on the basis of thermodynamic equilibrium (26, 35, 36). Extrapolation did not provide reliable values of v_0 due to the paucity of data taken at very low current values and to lack of *a priori* knowledge of the form of the current-voltage characteristic. Hence v_0 was calculated according to the afore-cited procedure, using the data of Kubachewski *et al.* (37), and taking into account the temperature, pH, and, for values of $v_{\text{exp}} \leq 10\text{V}$, the calomel reference electrode. The equilibrium condition was computed for the reaction between aluminum and water to produce Al_2O_3 and gaseous hydrogen. To some extent this is an arbitrary choice justified by a lack of detailed knowledge of the interfacial reaction kinetics; however, the correction to the measured potentials is modest and probably not very sensitive to the reaction selected. Values of v_0 are listed in Table I. Except as noted, the data herein are reported in terms of anodic overpotential, $v = v_{\text{exp}} - v_0$. Current values are reported as current density, the specimen area being determined from its geometry.

A series of current vs. time curves is shown in Fig. 1, representing the change in current following a reduction of the specimen potential from the initial formation potential to a new value. Initially a large reduction in current is seen, involving several orders of magnitude in a time span of less than 1 hr. Subsequent to this initial drop the current increases nearly exponentially with time until a new, stable value is reached. The magnitude of the initial decrease and the rate of recovery are dependent on the value of the overpotential, as seen in Fig. 1, and were also observed to be sensitive to the exact manner in which the reduction in overpotential was accomplished. With respect to the latter observation the behavior shown in

Table I. Calculated values of v_0

Ref. electrode	Temperature, $^\circ\text{C}$		
	30	50	70
SCE, V	-2.16	-2.18	-2.20
Pt/ H_2 , V	-1.92	-1.96	-1.99

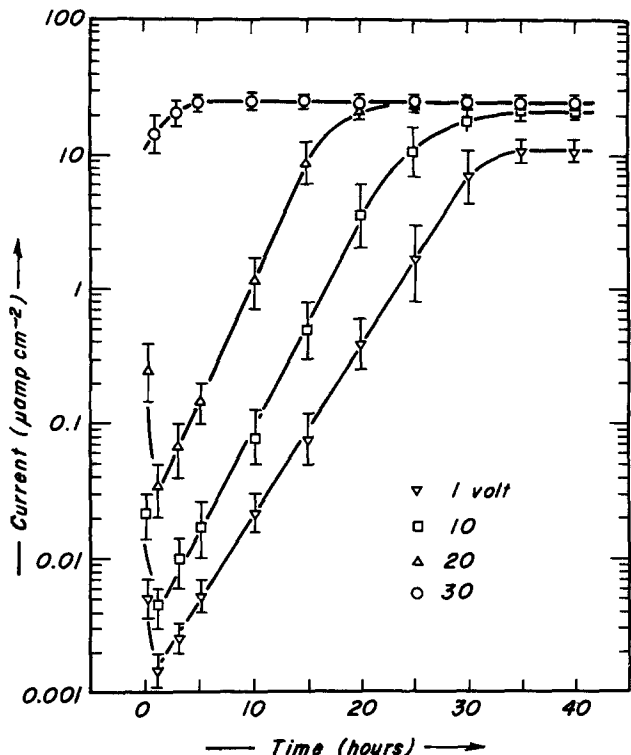


Fig. 1. Average current vs. time for aluminum electrodes anodized at 30V in 1M ammonium tartrate (30°C, pH 7), then reduced to stated potential at $t = 0$.

Fig. 1 may be regarded as "typical." The steady-state current did not appear to be thus affected.

Figure 2 shows the current-voltage characteristics for three specimens at 30°C, each obtained as described in the preceding section. The curves have been separated for clarity; although there is some hysteresis, scatter

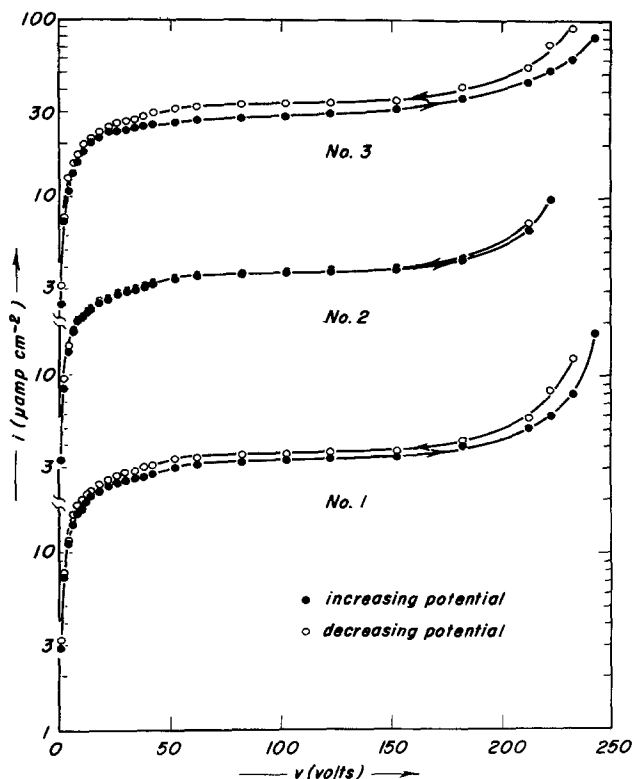


Fig. 2. Stable current vs. anodic overpotential for three different aluminum specimens anodized in 1M ammonium tartrate (pH 7) at 30°C, showing curves both for increasing potential and decreasing potential.

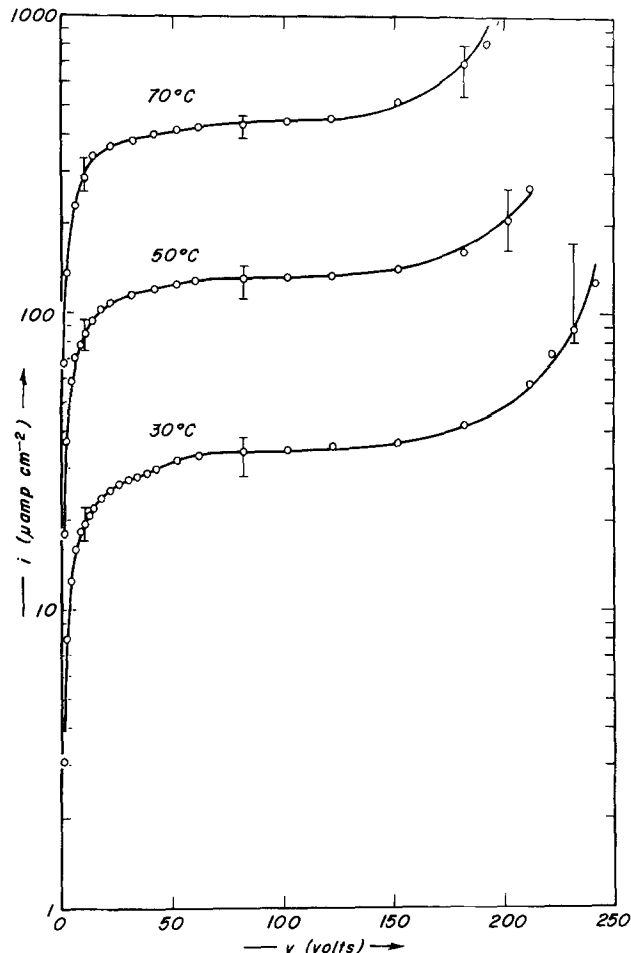


Fig. 3. Average stable current vs. anodic overpotential for aluminum anodized in 1M ammonium tartrate (pH 7). Error bars typical.

from a given curve is slight. Averaged values of the stable current in the tartrate environment are shown in Fig. 3 as a function of the overpotential for the three experimental temperatures. Typical error bars are shown for selected potentials representing, again, variation between specimens rather than uncertainty in a given measurement. Experimental variation is of the order of $\pm 13\%$ at low overpotentials, $\pm 10\%$ in the middle potential range, and increases to $\pm 30\%$ only in the region just preceding breakdown.

In the region of (relatively) low overpotentials, $0 \leq v \leq 50V$, the anodic current approaches exponential dependence on the overpotential as the electrode is made more anodic. The averaged data in this region are accurately described by

$$i = i_0(e^{v/b_a} - e^{-v/b_c}) \quad [1]$$

While in Eq. [1] b_a resembles an anodic Tafel constant, divided by 2.303; b_c , the analogous cathodic constant; and i_0 , an exchange current density (38), this comparison is inappropriate due to the markedly anomalous values of these constants as seen in Table II and to the dissimilarity between this process and

Table II. Empirical values of parameters for Eq. [1], [2], and [3] (Anodized aluminum electrode, aq. 1M ammonium tartrate, pH 7)

	Temperature, °C		
	30	50	70
$i_0, \mu A\text{-cm}^{-2}$	22	99	350
b_a, V	137	215	310
b_c, V	5.98	5.87	5.78
$i_s, \mu A\text{-cm}^{-2}$	34	130	440
v_a, V	255	245	215
c	5	5	6

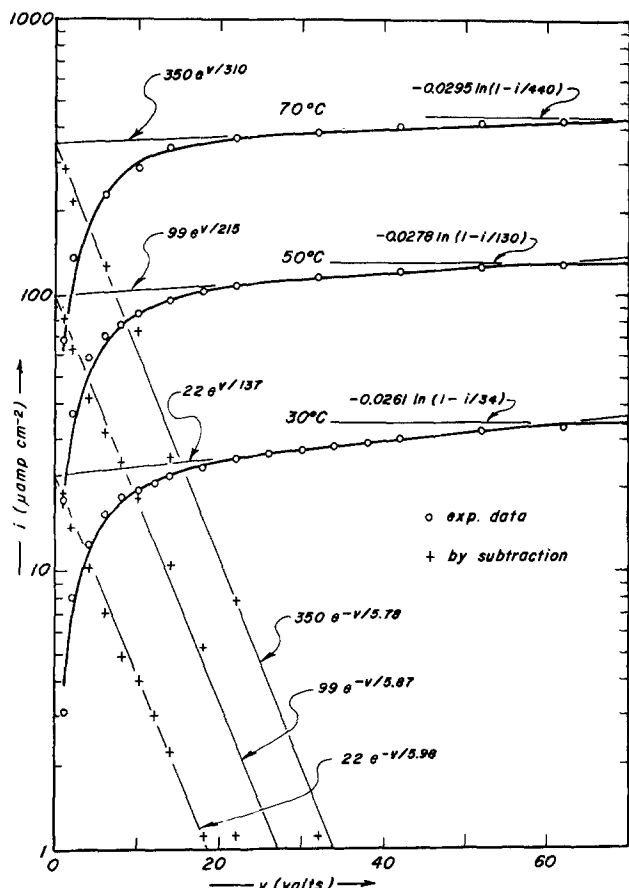


Fig. 4. Anodic and cathodic contributions, and saturation current of anodic anodized aluminum electrodes in 1M ammonium tartrate (pH 7).

those traditionally described by the Tafel relation. This region is analyzed in detail in Fig. 4, showing graphical evaluation of the three constants at each experimental temperature. Above 50V the behavior changes abruptly, with a limiting current, i_s , being attained. The current-overpotential behavior in this region resembles that of a simple electrode experiencing concentration polarization (38)

$$v = b_a \ln(i/i_0) - RT/F \ln(1 - i/i_s) \quad [2]$$

The saturation current, i_s , is readily chosen by inspection. On increasing the overpotential the current does not remain constant, however, but at overpotentials greater than approximately 80V increases ever more rapidly with potential. Behavior in this region closely follows

$$i = \frac{i_s}{1 - (v/v_a)^c} \quad [3]$$

derived empirically for avalanche phenomena (39). The parameters v_a and c are readily determined from the applicable data by plotting $\log(1 - i_s/i)$ vs. $\log v$. The curves in Fig. 3 were drawn according to Eq. [1], [2], and [3] using the values of the empirical parameters given in Table II.

Discussion

It is well established that during potentiostatic anodizing of valve metals in appropriate electrolytes growth of barrier-type oxide terminates at a thickness in proportion to the applied potential difference. The average field in such films is thus independent of the applied potential difference, neglecting any potential drops other than that across the barrier oxide, and for aluminum in aqueous ammonium tartrate is of the order of $(13 \text{ A}\cdot\text{V}^{-1})^{-1}$ or $7.7 \times 10^6 \text{ V}\cdot\text{cm}^{-1}$ (29). This field represents a steady state in which a finite ionic

flow through the barrier oxide occurs in equilibrium with the rate of dissolution of the barrier oxide at the oxide-electrolyte interface (16). A portion of the dissolved oxide is precipitated as porous oxide (16, 28, 31). Ionic flow through the oxide is clearly dependent on the field within the oxide as well as the concentration gradient, while the rate of dissolution is dependent on the field near the oxide-electrolyte interface. The functionality in the latter case is not established (16). The simplest explanation of Haas's data (29) is that the field is homogeneous throughout the oxide and that transport processes other than a field-dependent diffusional flow are unimportant. In such a model the ionic contribution to the terminal leakage current would necessarily be independent of the applied potential difference. This, alone, is not in conflict with the data shown in Fig. 2 and 3 inasmuch as the observed variation in total current could be attributed to electronic processes. However, the minimum ionic current that must flow in this system to maintain the observed porous film growth is of the order of $8 \mu\text{A}\cdot\text{cm}^{-2}$ (28, 31), substantially higher than the minimum total current observed. It is, thus, feasible to conclude that the steady state is substantially different from the state of films previously studied as cited in the foregoing. Maximum anodizing times previously reported were of the order of 90 min (31), approximately the time required to reach the current minimum in the transient reported in Fig. 1.

At present there are virtually no data concerning the morphology, defect structure, and transference numbers characteristic of steady-state films grown in barrier-forming electrolytes, providing a very poor base on which to propose a model. Young (12) has derived an expression for the field in an anodic film at steady state, assuming that the current is ionic and diffusion limited. Neither restriction may be justified, *a priori*, in this case. Butler (40) has discussed the equilibrium distribution of potential and space charge in oxide on the basis of Boltzmann statistics; Devereux and deBruyn (41) have provided detailed solutions to the Poisson-Boltzmann equation that may be applied to this case. However, the expected Boltzmann distribution of charge in highly polarized anodic films is trivial; in the presence of very large potential differences necessarily all carriers in the film will reside at the film boundaries. The field within the oxide will then be constant, with a discontinuity at each boundary, and smaller in magnitude than the apparent average field. This is possible only to the extent that a barrier to carrier flow across the interface exists. In the absence of such a barrier there would be no buildup of interfacial charge and the field within the oxide would be simply equal to the potential difference across the film divided by the film thickness.

The authors have assumed in interpreting the i - v characteristics depicted in Fig. 2 and 3 that they are not an artifact of specimen preparation. That is, an obvious interpretation of the substantially constant current region between overpotentials of approximately 50 and 150V is that the current is governed by a field that is independent of applied potential, *i.e.*, film thickness is proportional to overpotential. The diminished current below 50V could be interpreted as a manifestation of the initial equilibration of the electrode at 30V (overpotential ≈ 32 V). If the barrier layer formed in this operation were assumed capable only of growing, when higher anodic overpotentials are applied, and not thinning under the action of lower overpotentials, then clearly the small currents at low overpotentials would be due to a reduced field in the oxide. This does not appear to be the case, however. Not only does the onset of the constant current region occur at a significantly higher overpotential than 32V, but the reversibility of the process as shown in Fig. 2 clearly demonstrates that the stable leakage current is determined only by the overpotential and is independent of the potential history of the specimen. This observation

admits to two interpretations: either the film assumes a thickness characteristic of the applied overpotential and independent of the potential history, or the leakage current is independent of specimen thickness. In support of the former interpretation, Fig. 5 shows transmission electron micrographs of a film formed at an overpotential of 32V and a similar film subsequently stabilized at 12V. Clearly in the latter case a thinning process has occurred which may loosely be described as a growth and coalescence of pores. Although such thinning in neutral tartrate environments has not been previously observed, it appears to be a logical extension of similar processes that have been noted in acidic media (16, 42, 43). Not only has pore formation been noted in neutral tartrate electrolytes (28, 32), especially under current decay conditions (44), but, as previously noted, a number of authors find the anodic behavior of aluminum in "barrier-forming" electrolytes entirely similar to that in "pore-forming" electrolytes except for the rate at which pore development occurs (14, 16, 32). It is suggested that the proposed barrier layer thinning on reduction of the anodic overpotential occurs by an unbalance of the equilibrium, existing at steady state, between growth and dissolution of the barrier layer. This may result in the initia-

tion and growth of pores into the barrier layer, or to the deepening of existing pores by dissolution of the barrier layer at the bases of such pores. The status of porous layer formation at steady state has not yet been established. Goruk *et al.* (9), citing Renshaw's (45) work in citrate environments, expect pore formation to be dependent on current density. Hoar and Yahalom (32) note that pores initiate only when the field at the surface drops to a low enough value to permit protons to enter the film against the field. This is entirely consistent with barrier layer thinning by pore formation when the overpotential is reduced, but leaves open the question of porous layer growth over and above that required for barrier layer thinning. The authors do not regard the extent of the porous layer as an important issue in the present context, however, since the pores are highly conductive and, thus, can have little direct effect on leakage current.

The authors thus propose that the i - v behavior shown in Fig. 2 and 3 is characteristic of a barrier layer whose thickness is determined by the applied overpotential. The functional relation between thickness and overpotential is nonobvious, however, except in the intermediate potential region, approximately 50-150V, where the current is substantially independent of potential. In this region it is logical to propose that the barrier layer thickness is proportional to the overpotential and that interfacial potential drops (*i.e.*, "space" charge effects as discussed previously) are negligible. Under these circumstances the field in the oxide would be independent of potential and a diffusion-limited leakage current would be constant, consistent with observation. As the overpotential is reduced, however, any potential differences across either oxide interface would become increasingly significant, especially if these differences are substantially independent of the overpotential as would be the case if local equilibrium exists at the interfaces. Thus the field in the oxide would no longer be constant, but would decrease with the potential, yielding a reduced diffusion current in agreement with observation. While the form of the i - v characteristics below 50V is not amenable to easy interpretation, the two exponential terms clearly arise from simultaneous occurrence of both forward and reverse conduction and are consistent in form with either a field-dependent diffusion-limited process, as discussed above, or a potential-dependent interfacial transfer process as current limiting. In either case the exponential coefficients are anomalous with respect to expected values. The authors are presently unable to offer a discussion based on potential-dependent interfacial transfer processes that offers as many points of consistency with observation as does the proposal that current is field dependent and diffusion limited.

Zahavi and Yahalom (46-48) have examined anodic breakdown of oxide films in considerable detail, viewing it as an avalanche process initiated at the oxide-electrolyte interface at adequately high potentials. Full scale avalanching is preceded by short-lived sporadic discharges at the interface; presumably this phenomenon gives rise to the marked increase in anodic current in the overpotential region preceding failure and described by Eq. [3].

The temperature dependence of the exponential coefficients, b_a and b_c , is shown in Fig. 6; it, as well as the magnitudes of the constants, is anomalous in comparison to Tafel behavior. Young (49, 50) has discussed at length anomalies in the Tafel slopes observed during growth of anodic films on niobium and has attributed them to space charge effects arising from a nonuniform distribution of cations "frozen-in" during film formation. In view of the distinction between growth and steady state, however, as well as the greater degree of anomaly seen in the present study, such an explanation would not seem directly applicable.

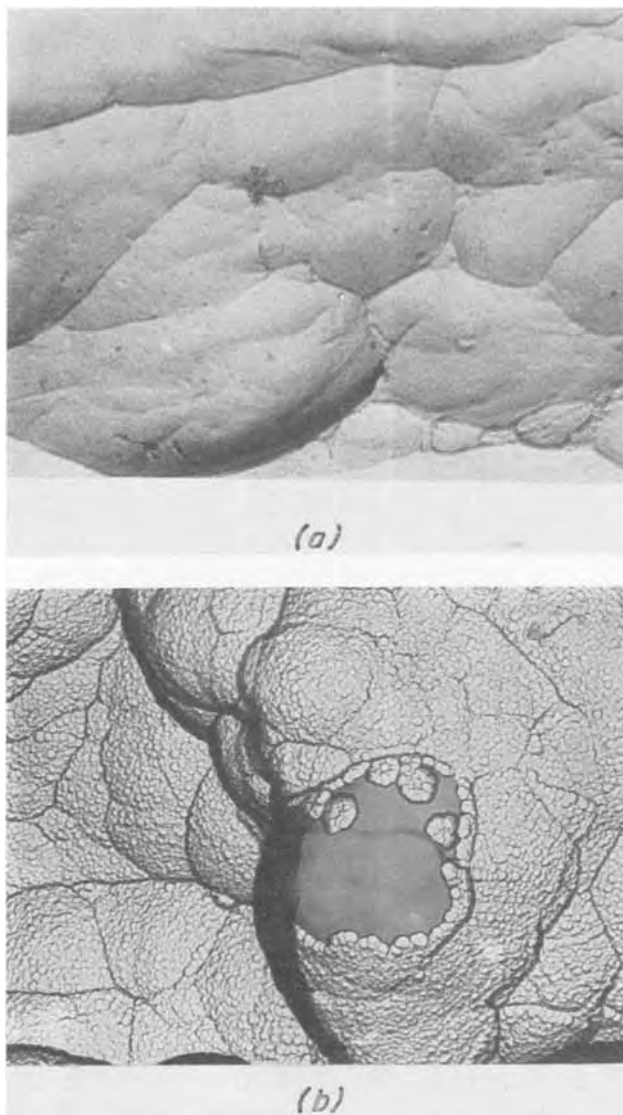


Fig. 5. Transmission electron micrographs of the anodic oxide formed on aluminum in 1M ammonium tartrate at 30°C on anodizing (a, upper) for 45 min at 30V (\approx 32V overpotential) and (b, lower) at 10V (12V overpotential) until steady state obtained. Magnification 23,500X.

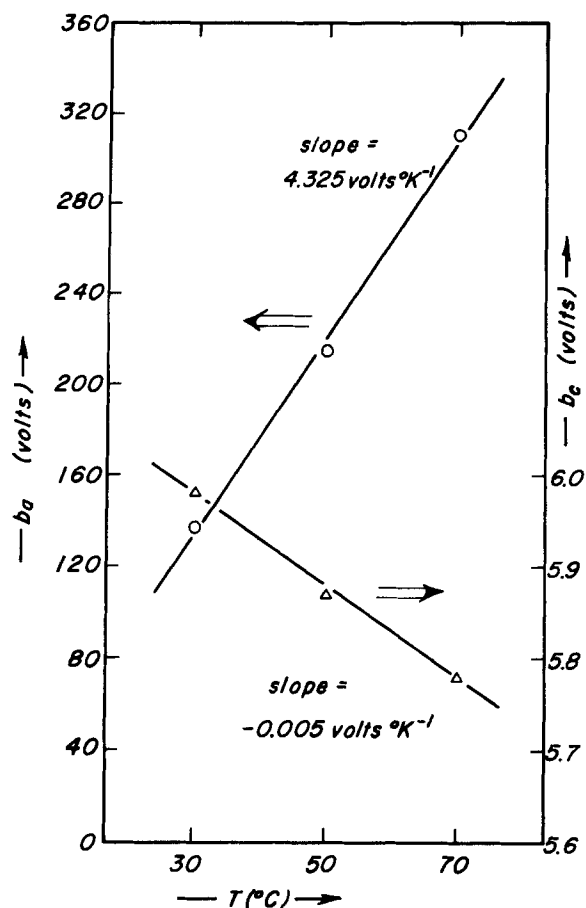


Fig. 6. "Anodic" and "cathodic" exponential coefficients vs. temperature.

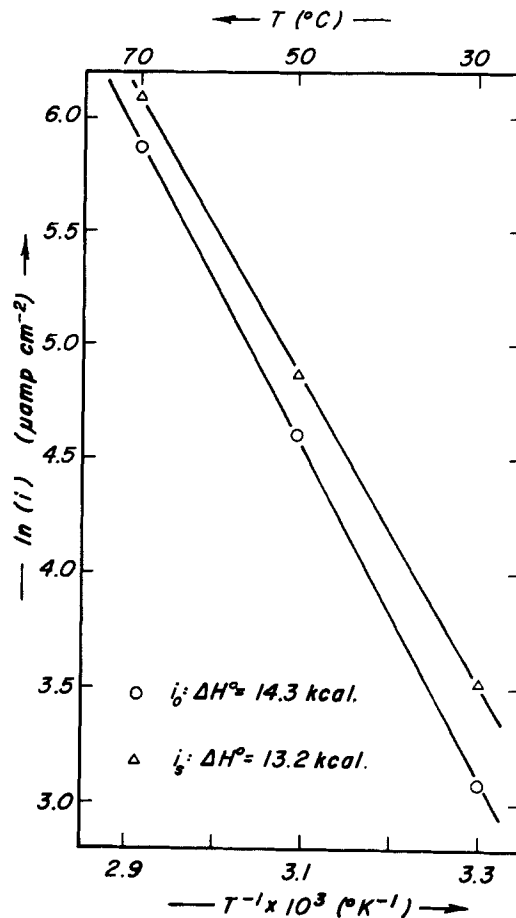


Fig. 7. Arrhenius plot of "exchange current," i_o , and "saturation current," i_s .

Arrhenius plots for the "exchange current," i_o , and the "saturation current," i_s , are shown in Fig. 7. The Arrhenius slope for each process should represent the sum of the enthalpy of formation of the carrier and that for the activated state of the carrier pertaining to that process. Values of 14.3 and 13.2 kcal-g-atom⁻¹ are seen for the exchange current and the saturation current, respectively. These values are essentially identical, suggesting that the same transport mechanism is limiting in both the low and intermediate potential regions. Furthermore, the values are small in comparison to the bandgap of the oxide, 7 eV (160 kcal) (51) suggesting that the carrier state is ionic rather than electronic. In the light of the foregoing discussion the authors propose that the current-limiting mechanism at steady state is ionic diffusion over the anodic overpotential range of 0 to approximately 80V and that, while above 50V the field is substantially constant independent of overpotential, at lower overpotentials the field is significantly reduced by charge polarization within the oxide.

Acknowledgments

The authors express their appreciation to the National Science Foundation for its generous support through grants No. GK 20017, "The Role of Environment in the Mechanical Behavior of Passive Films," and No. GH 35580, "Environment-Affected Properties of Oxide Films as Related to Defect Structure." Numerous supporting statistical and regression computations were carried out using the facilities of the University of Connecticut Computer Center. The authors gratefully acknowledge the contributions of Professors M. A. Melehy and J. H. Tripp, Departments of Electrical Engineering and of Physics, respectively, University of Connecticut, derived through several lengthy discussions, as well as those of the anonymous reviewers for this JOURNAL, which enabled a substantial improvement in the discussion.

Manuscript submitted Aug. 1, 1973; revised manuscript received Sept. 6, 1974.

Any discussion of this paper will appear in a Discussion Section to be published in the December 1975 JOURNAL. All discussions for the December 1975 Discussion Section should be submitted by Aug. 1, 1975.

Publication costs of this article were partially assisted by The University of Connecticut.

REFERENCES

1. D. A. Vermilyea, *This Journal*, **104**, 427 (1957).
2. L. Young, *Proc. Roy. Soc. (London)*, **A263**, 395 (1961).
3. L. Masing and L. Young, *Can. J. Chem.*, **40**, 903 (1962).
4. L. Young, *This Journal*, **111**, 1289 (1964).
5. M. J. Dignam and P. J. Ryan, *Can. J. Chem.*, **46**, 535 (1968).
6. M. J. Dignam and P. J. Ryan, *ibid.*, **46**, 549 (1968).
7. D. F. Taylor and M. J. Dignam, *This Journal*, **120**, 1299 (1973).
8. D. F. Taylor and M. J. Dignam, *ibid.*, **120**, 1306 (1973).
9. W. S. Goruk, L. Young, and F. G. R. Zobel, in "Modern Aspects of Electrochemistry," J. O'M. Bockris, Editor, No. 4, p. 176, Plenum Press, New York (1966).
10. M. J. Dignam, in "Oxides and Oxide Films," J. W. Diggle, Editor, Vol. 1, p. 91, Marcel Dekker, Inc., New York (1972).
11. J. P. Hoar, in "Modern Aspects of Electrochemistry," J. O'M. Bockris, Editor, No. 2, p. 262, Butterworths, London (1959).
12. L. Young, "Anodic Oxide Films," Academic Press, New York (1961).
13. D. A. Vermilyea, in "Advances in Electrochemistry and Electrochemical Engineering," P. Delahay and C. Tobias, Editors, Vol. 3, p. 211, Interscience Publishers, Inc., New York (1963).
14. J. W. Diggle, T. C. Downie, and C. W. Goulding, *Chem. Rev.*, **69**, 365 (1969).

15. S. Tajima, in "Advances in Corrosion Science and Technology," M. G. Fontana and R. W. Staehle, Editors, Vol. 1, p. 229, Plenum Press, New York (1970).
16. G. C. Wood, in "Oxides and Oxide Films," J. W. Diggle, Editor, Vol. 2, p. 167, Marcel Dekker, Inc., New York (1973).
17. J. W. Diggle, *ibid.*, p. 281.
18. W. Ch. van Geel, *Physica*, **17**, 761 (1951).
19. W. Ch. van Geel, *Halbleiterprobleme*, **1**, 291 (1955).
20. R. L. Taylor and H. E. Haring, *This Journal*, **103**, 611 (1956).
21. Y. Sasaki, *J. Phys. Chem. Solids*, **13**, 177 (1960).
22. M. A. Heine and M. J. Pryor, *This Journal*, **110**, 1205 (1963).
23. J. F. Dewald, in "Semiconductors," N. B. Hannay, Editor, ACS Monograph 140, p. 727, Reinhold Publishing Corp., New York (1959).
24. A. K. Vijh, in "Oxides and Oxide Films," J. W. Diggle, Editor, Vol. 2, p. 1, Marcel Dekker, Inc., New York (1973).
25. A. C. Smith, *Can. J. Phys.*, **35**, 1151 (1957).
26. A. C. Smith, *ibid.*, **37**, 591 (1959).
27. D. A. Vermilyea, *J. Appl. Phys.*, **27**, 963 (1956).
28. M. S. Hunter and P. F. Towner, *This Journal*, **108**, 139 (1961).
29. G. Haas, *J. Opt. Soc. Am.*, **39**, 532 (1949); J. D. Edwards, *Proc. ASTM*, **40**, 14 (1940).
30. R. C. Plumb, *This Journal*, **105**, 498 (1958).
31. R. D. Smith, M.S. Thesis, University of Connecticut, (1974).
32. T. P. Hoar and J. Yahalom, *This Journal*, **110**, 614 (1963).
33. N. D. Greene, "Experimental Electrode Kinetics," R.P.I., Troy, New York (1965).
34. J. M. Adrus and R. Petit, in "Anodized Aluminum," ASTM STP No. 388 (1965).
35. L. Young, *Trans. Faraday Soc.*, **53**, 841 (1957).
36. D. A. Vermilyea, *This Journal*, **101**, 389 (1954).
37. O. Kubachewski, E. Li. Evans, and C. B. Alcock, "Metallurgical Thermochemistry," 4th ed., Pergamon Press, New York (1967).
38. M. Stern and A. L. Geary, *This Journal*, **104**, 56 (1957).
39. R. P. Nanavati, "An Introduction to Semiconductor Electronics," McGraw-Hill Book Co., New York (1967); S. L. Miller, *Phys. Rev.*, **99**, 1234 (1955).
40. J. N. Butler, *J. Chem. Phys.*, **35**, 636 (1961).
41. O. F. Devereux and P. L. DeBruyn, "Interaction of Plane Parallel Double Layers," M.I.T. Press, Cambridge, Mass. (1963).
42. J. P. O'Sullivan and G. C. Wood, *Proc. Roy. Soc. (London)*, **A317**, 511 (1970).
43. T. A. Libsch and O. F. Devereux, *This Journal*, **121**, 400 (1974).
44. A. J. Brock and G. C. Wood, *Electrochim. Acta*, **12**, 395 (1967).
45. T. A. Renshaw, *This Journal*, **108**, 185 (1961).
46. J. Zahavi and J. Yahalom, *Electrochim. Acta*, **16**, 89 (1971).
47. J. Yahalom and J. Zahavi, *ibid.*, p. 603.
48. J. Yahalom, in "Oxide-Electrolyte Interfaces," R. S. Alwitt, Editor, p. 289, The Electrochemical Society Softbound Symposium Series, Princeton, N. J. (1973).
49. L. Young, *Trans. Faraday Soc.*, **52**, 502 (1956).
50. L. Young, *ibid.*, p. 515.
51. J. J. Lander, in "Semiconductors," N. B. Hannay, Editor, ACS Monograph 140, p. 50, Reinhold Publishing Corp., New York (1959).

Fluorescence of Eu^{3+} in Sodium Phosphotungstate Glasses

R. Reisfeld, H. Mack, A. Eisenberg, and Y. Eckstein

Department of Inorganic and Analytical Chemistry, The Hebrew University of Jerusalem, Jerusalem, Israel

ABSTRACT

Sodium phosphotungstate glasses of various ratios of $\text{P}_2\text{O}_5/\text{WO}_3$ were doped by 1.0 weight per cent Eu^{3+} . Fluorescence spectra were measured on excitation to 394 and 464 nm. On excitation to 394 nm the ratio of ${}^5\text{D}_0 \rightarrow {}^7\text{F}_2/{}^5\text{D}_0 \rightarrow {}^7\text{F}_1$ emissions and the amount of splitting of the ${}^5\text{D}_0 \rightarrow {}^7\text{F}_1$ transition are dependent on composition of the glass and conditions of glass preparation. It is concluded that two different types of Eu^{3+} sites exist in phosphotungstate glasses. One type is this in which Eu^{3+} is surrounded by phosphate and tungstate tetrahedra at random. In the other type, Eu^{3+} is incorporated into microcrystallites. It is shown that Eu^{3+} may serve as a spectroscopic probe for microphase separation. It is also suggested that phosphotungstate glasses doped by Eu^{3+} can substitute Eu^{3+} -doped tungstate crystals for fluorescence purposes.

Tungstate crystals doped by rare earth ions are known to be good laser materials. Recently, it has been shown by the present authors (1, 2), for series of rare earth doped different oxide glasses, that the glasses have similar optical characteristics as the crystals, the main difference being in the inhomogeneous broadening and higher oscillator strengths. In most glasses studied, the excitation of the rare earth ions is achieved by direct absorption to the electronic levels of the dopant, while in the case of tungstate crystals, transfer of excitation energy from the matrix is also observed. The latter process can increase the brightness of fluorescence.

It was the purpose of this work to prepare tungstate glasses which were expected to have some of the optical properties of tungstate crystals. Technically, preparation of such glasses is much easier than that of the corresponding crystals. Since pure tungstate glasses are

very unstable, and an addition of P_2O_5 is highly effective in stabilizing and widening the glass forming region (3), mixed sodium-phosphotungstate glasses, containing Eu^{3+} ions, were prepared.

Experimental

The starting materials were WO_3 (Hopkin and Williams, Limited), Na_2HPO_4 analytical "Frutarom," and Eu_2O_3 (Molycorporation) 99.99% purity. Glasses containing 1 weight per cent (w/o) of Eu^{3+} and varying concentrations of WO_3 , Na_2O , and P_2O_5 were prepared by melting the mixture at 950°-1050°C in a platinum crucible in air. The various concentrations of the oxides in the mixture are given in Table I. The melting times varied from 9 to 120 min. The melts were either quenched rapidly (henceforth called fast cooling rate) or allowed to cool slowly in the crucible until the liquid became viscous and then poured on the tile (henceforth referred to as slow cooling rate). The time of heating and the rate of cooling as well as the rela-

Table I. Relative concentration of WO_3 , P_2O_5 , and Na_2O in the starting mixtures

WO_3 (w/o)	WO_3 (m/o)	Na_2O (m/o)	P_2O_5 (m/o)
50	28.0	48.0	24.0
60	37.3	41.8	20.9
63	40.0	40.0	20.0
65	42.7	38.2	19.1
66	43.3	37.8	18.9
67	44.5	37.0	18.5
68	45.7	36.2	18.1
69	47.5	35.0	17.5
70	48.1	34.6	17.3
72	50.5	33.0	16.5
75	54.4	30.4	15.2
78	58.6	27.6	13.8
80	61.9	25.4	12.7

Mean error ± 0.2 .

tive concentrations of WO_3 and $\text{Na}_2\text{O} \cdot \text{P}_2\text{O}_5$ affect the emission characteristics of Eu^{3+} as a result of microphase separation.

Results and Discussion

The emission spectrum of Eu^{3+} was measured by excitation at 394 and 464 nm. These bands have the highest intensity in the excitation spectrum of ${}^5\text{D}_0 \rightarrow {}^7\text{F}_j$ emission of Eu^{3+} . The emission spectrum of Eu^{3+} in glasses with varying ratios of WO_3 to $2\text{Na}_2\text{O} \cdot \text{P}_2\text{O}_5$ is presented in Fig. 1. As seen from this figure, on excitation at 394 nm differences are observed between glasses containing 68 and 75 w/o of WO_3 in the ratio of the relative intensities of ${}^5\text{D}_0 \rightarrow {}^7\text{F}_2$ (at 613 nm) to ${}^5\text{D}_0 \rightarrow {}^7\text{F}_1$ (at about 590 nm) and in the splitting of these transitions.

For the sake of the arguments which will be applied below, we defined the resolution of the ${}^5\text{D}_0 \rightarrow {}^7\text{F}_1$ transition as the sum of the areas of the two components of this transition divided by the minimum intensity between them. In the case of glass, where no distinct splitting was observed (e.g., 68 w/o WO_3 in Fig. 1), the ${}^5\text{D}_0 \rightarrow {}^7\text{F}_1$ transition was resolved into two gaussians peaking at the same wavelengths as those of ${}^5\text{D}_0 \rightarrow {}^7\text{F}_1$ transition in the sample containing 75 w/o WO_3 , where we observed a defined splitting (presented in Fig. 1). The resolution between the two gaussians was done as described above. At 464 nm, no splitting is observed and the ratio of ${}^5\text{D}_0 \rightarrow {}^7\text{F}_2/{}^5\text{D}_0 \rightarrow {}^7\text{F}_1$ remains constant with the changing of the concentrations of WO_3 . The ratio and resolution for glasses of varying amounts of WO_3 prepared at constant temperature (1050°C), constant heating time (60 min), and slow cooling rate are given in Table II for excitation at 394 nm.

Table II. Dependence of the ${}^5\text{D}_0 \rightarrow {}^7\text{F}_2/{}^5\text{D}_0 \rightarrow {}^7\text{F}_1$ and the spectral resolution of ${}^5\text{D}_0 \rightarrow {}^7\text{F}_1$ transition on the WO_3 content (after 60 min of heating at 1050°C and slow cooling rate).
Excitation 394 nm.

WO_3 (w/o)	${}^5\text{D}_0 \rightarrow {}^7\text{F}_2$	Reso- lution	
	${}^5\text{D}_0 \rightarrow {}^7\text{F}_1$		
60	10.47	2.0	glass
63	8.42	2.0	
65	6.62	4.0	
66	5.52	4.6	microcrystallites
67	9.92	2.0	
68	10.16	2.0	glass
69	10.74	2.0	
70	4.67	3.19	
72	2.90	4.76	microcrystallites
75	3.02	9.00	
78	3.02	4.02	
80	9.15	1.57	

High ratio of $\frac{{}^5\text{D}_0 \rightarrow {}^7\text{F}_2}{{}^5\text{D}_0 \rightarrow {}^7\text{F}_1}$ and low resolution are characteristic of a glass.

Low ratio of $\frac{{}^5\text{D}_0 \rightarrow {}^7\text{F}_2}{{}^5\text{D}_0 \rightarrow {}^7\text{F}_1}$ and high resolution are characteristic of microphase separation.

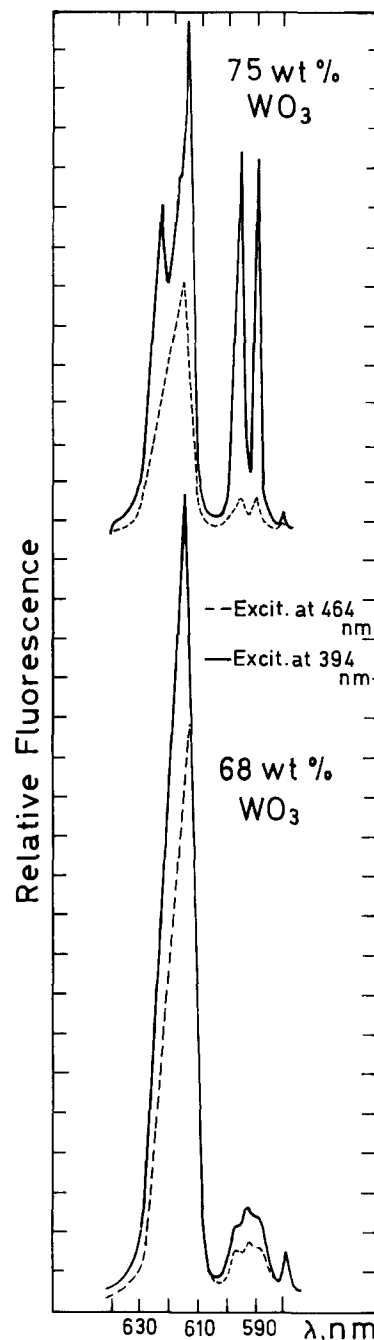


Fig. 1. Emission spectra of 1 w/o Eu^{3+} in $x\text{WO}_3 \cdot \gamma(2\text{Na}_2\text{O} \cdot \text{P}_2\text{O}_5)$ glasses. The ratio of peak areas of $\text{Eu}^{3+} {}^5\text{D}_0 \rightarrow {}^7\text{F}_2/{}^5\text{D}_0 \rightarrow {}^7\text{F}_1$ transitions under 394 nm excitations which are given in Table II and Table III is 3 for the 75 w/o WO_3 sample and 10.16 for the 68 w/o WO_3 sample. The resolution of the ${}^5\text{D}_0 \rightarrow {}^7\text{F}_1$ transition in the two samples is 9 and 2, correspondingly.

The differences in the emission spectra of Eu^{3+} produced by the two different excitation wavelengths is explained by the existence of different types of Eu^{3+} sites in the tungstate glass. One type of Eu^{3+} site is that in which the ion is surrounded by phosphate tetrahedra and tungstate octahedra intermixed at random. Such an arrangement is typical for glasses, hence the site symmetry is the lowest, as evident by the high ratio between ${}^5\text{D}_0 \rightarrow {}^7\text{F}_2/{}^5\text{D}_0 \rightarrow {}^7\text{F}_1$ transitions and the highest inhomogeneous broadening. The ${}^5\text{D}_0 \rightarrow {}^7\text{F}_2$ is known to be "hypersensitive" on the site symmetry in which Eu^{3+} is incorporated as it is originated from forced electric dipole transition, while ${}^5\text{D}_0 \rightarrow {}^7\text{F}_1$ is a magnetic dipole transition and much less sensitive on site symmetry. This picture is similar to that of Eu^{3+} in phosphate glasses (4).

We suggest that the other type of Eu^{3+} site, for which the ratio of ${}^5\text{D}_2 \rightarrow {}^7\text{F}_2/{}^5\text{D}_0 \rightarrow {}^7\text{F}_1$ transition is

Table III. Optical properties of Eu^{3+} in sodium phosphotungstate glasses as a function of preparation conditions. Excitation 394 nm.

WO ₃ (w/o)	Heating time (min)	Temper- ature (°C)	Cooling rate		${}^5\text{D}_0 \rightarrow {}^7\text{F}_2$ ${}^5\text{D}_0 \rightarrow {}^7\text{F}_1$	Reso- lution	$\Delta\nu^*$ (cm ⁻¹)
			fast	slow			
50	7	950	X		7.2	2.0	377
	11	950		X	8.3	2.0	
68	14	1000	X		1.9	9.7	51
	17	1000		X	1.9	9.1	51
	60	1000		X	8.8	2.4	375
72	10	950	X		3.2	5.9	50
	10	950		X	3.5	6.0	43
	60	950		X	4.5	3.9	47
	90	950		X	10.2	2.0	373
75	12	950	X		2.4	7.3	65
	10	950		X	2.4	7.4	65
	50	1000	X		11.7	2.0	377
	50	1000		X	3.5	6.8	79

* $\Delta\nu$ is the half-bandwidth of the short wavelength component of $\text{Eu } {}^5\text{D}_0 \rightarrow {}^7\text{F}_1$ transition for the microcrystallites and half-width of the unresolved ${}^5\text{D}_0 \rightarrow {}^7\text{F}_1$ band for the glasses.

about 3-6.5, is Eu^{3+} incorporated into microcrystallites of tungstate. This suggestion is based on the similarity of the emission spectra of Eu^{3+} excited at 394 nm to Eu^{3+} -doped $\text{Na}_{0.5}\text{Y}_{0.5}\text{WO}_4$ crystals (5). As seen from Table III, the half-bandwidth of the short wavelength component of the ${}^5\text{D}_0 \rightarrow {}^7\text{F}_1$ transition of Eu^{3+} in such tungstate crystallites is about 50 cm^{-1} compared to the half-bandwidth of this unresolved band in glasses which is about 380 cm^{-1} . A similar increase of the bandwidths with increasing randomness of the Eu^{3+} sites has been also observed by Van Uitert: 1.5 and 5 cm^{-1} in pure CaWO_4 and 4 and 11 cm^{-1} in $\text{Na}_{0.5}\text{Y}_{0.5}\text{WO}_4$ for the $\text{Eu}^{3+} {}^5\text{D}_0 \rightarrow {}^7\text{F}_2$ transition (5). The fact that even in the polycrystallites of Eu^{3+} tungstates the smallest ratio of ${}^5\text{D}_0 \rightarrow {}^7\text{F}_2/{}^5\text{D}_0 \rightarrow {}^7\text{F}_1$ transitions observed was 2.9 indicates that the polycrystallites do not possess a center of inversion, and thus resemble Eu^{3+} -doped tungstate crystals (5).

At 394 nm excitation, the fluorescence of Eu^{3+} in the crystallite sites is predominant, while at 464 nm excitation the fluorescence of Eu^{3+} in the glass forms makes the main contribution. At about 400 nm, the tungstate has an absorption edge and, therefore, at this excitation the Eu^{3+} ions embedded in the crystallites are mainly excited (probably by energy transfer from tungstate to Eu^{3+}). At 464 nm, the Eu^{3+} is excited directly into its electronic levels and since the oscillator strengths of the glass are higher than that of the crystals, the emission from the glass is predominant. The higher oscillator strength of Eu^{3+} in glasses are due to the forbidden $f \leftrightarrow f$ transitions which are more permissible as a result of the total absence of symmetry in glass. At the appropriate concentration of WO_3 , when only a glass structure exists, there was no difference in the spectral behavior of Eu^{3+} in the two excitations.

The appearance of microcrystallites should depend on conditions which promote crystallization, such as (i) a definite ratio of WO_3 to $2\text{Na}_2\text{O} \cdot \text{P}_2\text{O}_5$, (ii) slow

cooling rate at which an equilibrium can be achieved between the glass and the microcrystallites, and (iii) the doped microcrystallites may be formed by diffusion of Eu^{3+} into the tungstate phase when the temperature is low and the time insufficient for a thorough mixing of the glass and the crystalline phases. This can be observed in all concentrations of WO_3 (with the exception of a 50 w/o WO_3 mixture), since it is not an equilibrium process.

The influence of melting conditions on the appearance of microcrystallites, as reflected by a small ratio of ${}^5\text{D}_0 \rightarrow {}^7\text{F}_2/{}^5\text{D}_0 \rightarrow {}^7\text{F}_1$ transitions, high resolution and a small half-bandwidth of the ${}^5\text{D}_0 \rightarrow {}^7\text{F}_1$ band when excited at 394 nm, is summarized in Table II and Table III. From Table II we see that at conditions in which an equilibrium may be achieved, the only limiting factor for the appearance of the microcrystallites is the ratio between WO_3 and $2\text{Na}_2\text{O} \cdot \text{P}_2\text{O}_5$. The concentration regions of the glass phase and microcrystallite phase are marked in Table II. From Table III we conclude that the conditions for glass or microcrystallite formation are the following: If the concentration ratio of WO_3 to $2\text{Na}_2\text{O} \cdot \text{P}_2\text{O}_5$ is characteristic for glass, then after proper heating time, which is needed for achieving the equilibrium, a glass will be formed. This time is 11 min for a 50 w/o WO_3 mixture and 50-60 min for mixtures containing 68-72 w/o WO_3 . At concentrations of WO_3 in which the equilibrium conditions favor the appearance of microcrystallites, a slow cooling rate will enable it to reach an equilibrium and microcrystallites will be formed. This can be seen in the mixture containing 75 w/o WO_3 (Table III).

In summary, the fluorescence spectra of Eu^{3+} can serve as a probe for the indication of microphase separation and the materials presented in this work can, in some cases, substitute in tungstate crystals.

Acknowledgment

This work was supported by the Israel National Council of Research and Development.

Manuscript submitted April 26, 1974; revised manuscript received July 15, 1974. This was Paper 108 presented at the San Francisco, California, Meeting of the Society, May 12-17, 1974.

Any discussion of this paper will appear in a Discussion Section to be published in the December 1975 JOURNAL. All discussions for the December 1975 Discussion Section should be submitted by Aug. 1, 1975.

Publication costs of this article were partially assisted by The Hebrew University of Jerusalem.

REFERENCES

1. R. Reisfeld, *J. Res. Nat. Bur. Std.*, **76A**, 613 (1972).
2. R. Reisfeld, *Structure and Bonding*, **13**, 53 (1973).
3. H. Rawson, "Inorganic Glass-Forming Systems," p. 207, Academic Press, London (1967).
4. R. Reisfeld, R. A. Velapoldi, and L. Boehm, *J. Phys. Chem.*, **75**, 3980 (1971).
5. L. G. Van Uitert, in "Luminescence of Inorganic Solids," P. Goldberg, Editor, p. 465, Academic Press, New York (1966).

Crystal Growth and Steady-State Segregation under Zero Gravity: InSb

A. F. Witt,* H. C. Gatos,* M. Lichtensteiger,
M. C. Lavine, and C. J. Herman

Massachusetts Institute of Technology, Cambridge, Massachusetts 02139

ABSTRACT

It was established that ideal, diffusion-controlled, steady-state segregation, never accomplished on earth, was achieved during the growth of Te-doped InSb crystals in Skylab. Surface tension effects led to nonwetting conditions under which free surface solidification took place in confined geometry. It was further found that, under forced contact conditions, surface tension effects led to the formation of surface ridges (not previously observed on earth) which isolated the growth system from its container. In addition, it was possible, for the first time, to identify unambiguously: the origin of segregation discontinuities associated with facet growth, the mode of nucleation and propagation of rotational twin boundaries, and the specific effect of mechanical-shock perturbations on segregation. The results obtained prove the advantageous conditions provided by outer space. Thus, fundamental data on solidification thought to be unattainable on earth because of gravity-induced interference are now within reach.

Structural and compositional control during solidification of materials is impeded by gravity-induced effects in the melt. Thermal gradients necessary for crystal growth lead, in the presence of gravitational forces, to thermal convection which in general causes uncontrolled variations in the solidification rate and in diffusion boundary layer thickness; such variations lead directly to periodic and/or random microscopic and macroscopic segregation inhomogeneities. Furthermore, in the presence of gravity, establishing steep thermal gradients, frequently required to prevent constitutional supercooling, is often impossible and consequently interface breakdown is unavoidable.

Gravity effects are, thus, primarily responsible for the present lack of reliable solidification data and the existing gap between theory and experiment. Consequently, crystal growth and associated segregation phenomena are still based on empiricism, and the properties and performance of solids are not at their theoretical limits.

Gravity-free conditions made accessible through the space program provide a unique opportunity to obtain reliable crystal growth data and, therefore, to advance our quantitative understanding of solidification processes; in addition this program makes possible the exploration and assessment of the potential of outer space for materials processing.

Indium antimonide was chosen for the presently reported Skylab experiment because its relatively low melting point (525°C) made the experiment compatible with the available electrical power. In addition, chemical etching, the only high-resolution technique available, at the time, for the study of segregation inhomogeneities on a microscale, had been developed on InSb to its most advanced level.

The experiments performed during the Skylab-III and -IV missions included the growth of undoped, tellurium-doped, and tin-doped indium antimonide. The present report is concerned primarily with results obtained on tellurium-doped InSb.

Objectives

The objectives of growing Te-doped InSb in Skylab were to assess the advantages of zero-gravity environment, to obtain basic data on solidification, and to explore the feasibility of electronic materials processing in outer space. Thus, the experiment was designed to

achieve solidification under diffusion-controlled, steady-state conditions and to investigate the associated growth and segregation behavior on a micro- and macro-scale. Direct comparison of growth and segregation on earth and in space was to be achieved by melting and resolidifying in space a portion of each crystal growth on earth.

Experimental Approach

Crystal growth apparatus.—The InSb growth experiment was carried out in the "multipurpose furnace" (Fig. 1). The furnace provided for three tubular cavities into which three stainless steel cartridges containing the crystal growth assemblies were inserted. Heat levelers, lateral heat-shields, and the heat extractor plate insured controlled heat flow from the heating element to the heat extractor plate through the crystal. Melting was initiated at the end of the crystal (to be referred to as hot end), located inside the heating element and the crystal-melt interface was advanced to the desired position (back-melting) by appropriate power input. Regrowth, in turn, was achieved by controlled power reduction.

Crystal preparation and assembly.—Indium antimonide used for ground-based tests and the Skylab experiment was synthesized in the Electronic Materials Laboratory at M.I.T. The single crystals for the experiment were pulled from the melt in the $\langle 111 \rangle$ direction by the Czochralski technique. The as-grown crys-

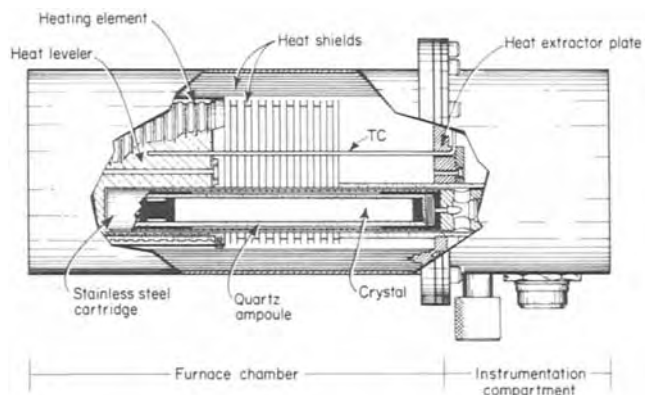


Fig. 1. Sketch of the multipurpose furnace employed for the InSb growth experiment in Skylab.

* Electrochemical Society Active Member.

Key words: segregation (dopant), crystal growth, gravity effects, solidification.

tals (approximately 1.8 cm in diameter and 17 cm long) were centerless ground to a diameter of 1.4 cm, and cut to a length of 11 cm. The cylindrical crystals were etched in modified CP-4, 3 parts (48%) HF + 5 (conc) HNO₃ + 3 (glacial) CH₃COOH + 10H₂O, to remove surface damage and reduce their diameter to the desired value. Each crystal was subsequently inserted between graphite spacers into a quartz ampul of 3 mm wall thickness. The diameter of every crystal was 0.13 mm smaller than the inside diameter of its ampul.

The spacer at the hot end had a peripheral cylindrical cavity to provide additional space for the melt in case unforeseen surface tension effects under zero gravity conditions resulted in increased clearance between the regrown crystal and the quartz wall; the cylindrical graphite spacer at the other end of the crystal (to be referred to as cold end) was designed to enhance heat transfer from the crystal to the heat extractor plate. The crystals were positioned in the ampuls so that their B <111> direction coincided with the regrowth direction.

All ampuls were repeatedly flushed with purified helium and evacuated to 10⁻⁷ Torr prior to sealing. The crystals were anchored near their cold end to the ampuls by means of a small depression in the quartz wall formed by local heating of the evacuated ampuls.

Each sealed ampul was encapsulated in an evacuated stainless steel cartridge; one set of three cartridges containing an undoped crystal, a Te-doped crystal (~10¹⁸/cm³), and a heavily Sn-doped crystal (~10²⁰/cm³) was used for the zero gravity growth experiment (Skylab-III mission). A second set intended for backup purposes was eventually used in an unscheduled additional experiment in space (Skylab-IV mission). A sealed ampul and its metal cartridge used in the Skylab experiment are shown in Fig. 2.

Crystal growth procedure in space.—Skylab-III mission experiment.—The samples were inserted into the multipurpose furnace and back-melting was initiated by turning on the power. The desired back-melting was achieved in 120 min. Then the system was kept at temperature for a period of 60 min (thermal soak), to achieve thermal equilibrium in the system and homogenization of the melts.¹ Subsequently, a cooling rate of 1.17°C/min was established by controlled power reduction at intervals of 14.4 sec. Four hours after initiation of regrowth the power was turned off and passive cooling to the ambient temperature took place. The thermal history of the growth system (hot-end temperature) obtained from a Chromel/Alumel thermocouple in the furnace is shown in Fig. 3.

Skylab-IV mission experiment.—The remelting and thermal soaking procedure was identical with that of the Skylab-III experiment. However, in this, originally

¹ A soaking period of 180 min was originally specified for this purpose; however, an inadvertent power shortage necessitated the reduction of the soaking period to 60 min.

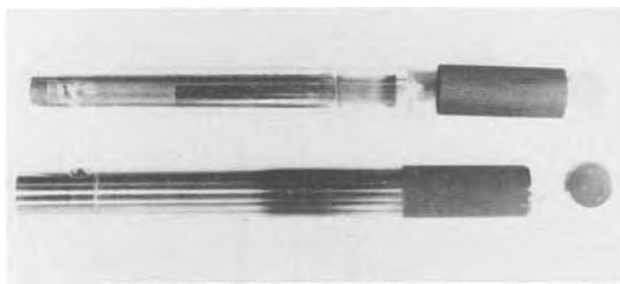


Fig. 2. Top: Quartz ampul containing InSb crystal used in the Skylab experiment; the cold-end graphite spacer, the earth-grown crystal segment, the space-grown segment, and the hot-end graphite spacer with a peripheral cavity are seen from left to right; at extreme right is graphite sleeve positioned between ampul and the metal cartridge. Bottom: Stainless steel cartridge in which ampul was encapsulated.

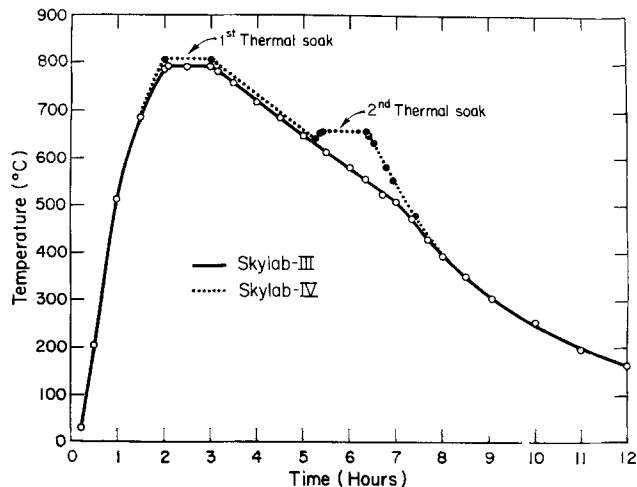


Fig. 3. "Hot-end" temperature cycles for Skylab-III and Skylab-IV experiments as obtained from a Chromel/Alumel thermocouple.

unscheduled, experiment the growth system was subjected to a mechanical shock by striking the furnace assembly at a predetermined time; furthermore, the constant cooling rate of 1.17°C/min was interrupted 140 min after initiation of regrowth and a second thermal soaking period of 60 min was introduced by maintaining the furnace power at a constant level. The power was subsequently turned off and the system was allowed to reach ambient temperature (see Fig. 3). These changes in the growth procedure were intended to provide time reference markings in the crystal and to obtain data on the dependence of transient segregation on growth rate.

Results and Discussion

Morphological characteristics.—The extent of regrowth achieved during the Skylab experiment was virtually the same for all crystals (about 6 cm) and in excellent agreement with theoretical calculations and ground-based testing; in each crystal the regrowth interface was clearly delineated (see for example Fig. 2).

All crystals were separated from their containers, without affecting their morphological characteristics, by dissolving the quartz ampuls in 48% HF.

The Te-doped InSb crystals grown in the two Skylab missions are discussed individually since they exhibit seemingly significant differences in morphological characteristics.

Tellurium-doped InSb grown in Skylab-III.—This crystal was of the same diameter as the earth-grown segment (seed); two portions of the crystal corresponding to the early and late stages of growth are shown in Fig. 4 and 5, respectively. The surface of the

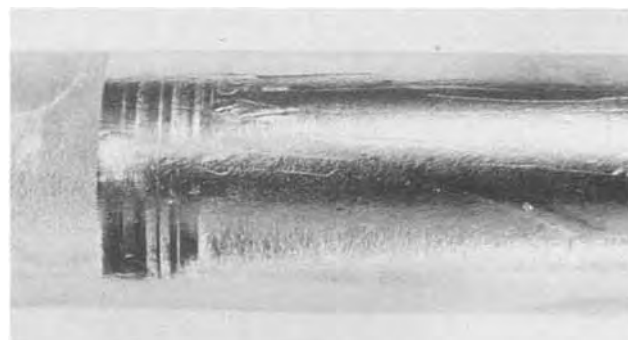


Fig. 4. Te-doped crystal grown during Skylab-III mission. Note initial growth interface (left-hand side), rotational twin bands, and surface ridges propagating along the growth direction; the diameter of the space-grown segment is the same as that of the earth-grown segment. Magnification 4.9×.

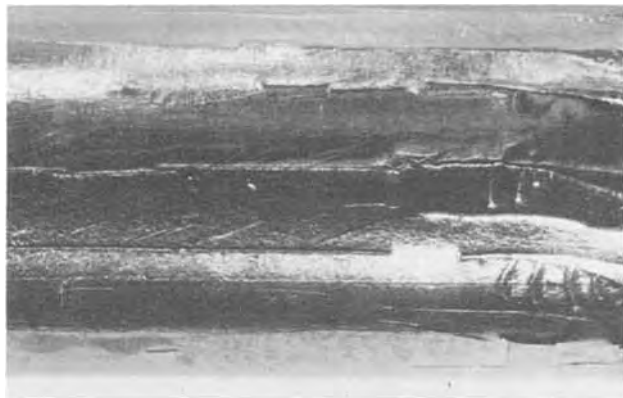


Fig. 5. Part of the Te-doped crystal, grown during Skylab-III mission, 3.7-5.9 cm from the initial regrowth interface. Surface ridges broaden and branch out at the late stages of growth (right-hand side). Magnification 6.8 \times .

crystal has a dull appearance which indicates that during growth it did not establish contact with the confining quartz wall. This conclusion is reinforced by the absence of the peripheral cavities which generally characterize growth under confined geometry.²

The surface of the regrown crystal in the vicinity of the seed (Fig. 4) exhibits several bands of differing width oriented normal to the growth direction. These bands were identified as the external boundaries of rotational twins (see below) which are frequently encountered in InSb grown in the $\langle 111 \rangle$ direction.

Conspicuous in Fig. 5 is the presence of irregularly spaced "surface ridges" oriented preferentially in the direction of growth (left to right). The ridges are shiny at the top indicating contact with the quartz wall; they are, on average, 25 μm high and increase in width toward the hot end of the crystal. Over the last 10 mm of the crystal the ridges become irregular and branch out. The regions between the ridges exhibit, in general, the characteristics of growth from free (unconfined) melts. In some isolated areas inclined lines, which have the appearance of stress-induced defects, originate at the surface ridges. These defects were shown to be confined to the surface region and to have no detectable effects on the growth and segregation behavior of the system. To the authors' knowledge, the phenomenon of surface ridge formation has not been previously observed in solidification under confined geometry; it is further discussed below.

Tellurium-doped InSb grown in Skylab-IV.—As seen in Fig. 6, regrowth, following the thermal soaking period, proceeds (left to right), in this case, first with decreasing and then essentially constant crystal diameter. With continuing growth the crystal diameter

² It is of interest to note that the surface of the Sn-doped and undoped crystals grown in Skylab was shiny and exhibited peripheral cavities indicating intimate contact (wetting) of the melt with the confining quartz wall.

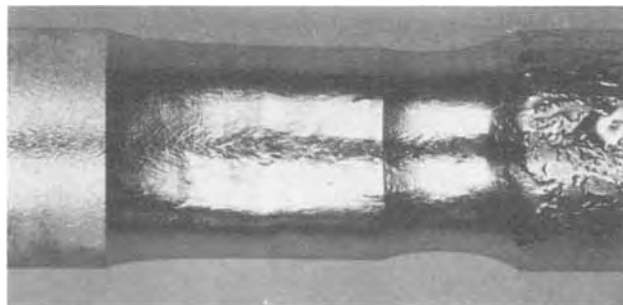


Fig. 6. Te-doped crystal grown during the Skylab-IV mission; note decrease in crystal diameter upon initiation of growth; surface ridges appear on right-hand side after crystal diameter reaches its maximum constant value. Magnification 4.8 \times .

decreases again, then increases and assumes a constant value of 12.8 mm (right-hand side of Fig. 6) which is the same as that of the ID of the confining quartz ampul. (The reasons for the differences in diameter between the two Te-doped crystals in the early stages of regrowth are discussed below.)

From volume considerations, it is concluded that the increase of the crystal diameter coincides in time with the initial contact of the melt with the graphite spacer at the hot end of the quartz ampul. Since crystal growth over the first 30 mm proceeded with a decreased diameter, and solidification of InSb is accompanied by a volume expansion of 12.9%, the volume available to the residual melt is less than during the Skylab-III experiment at the same time in growth. Thus, toward the final stages of solidification some melt was ultimately forced into the peripheral cavity available in the hot-end graphite spacer. Indium antimonide solidified in the spacer cavity weighed 2.52g. Accordingly, the total available volume for the melt in the ampul itself (excluding the volume of the cavity in the graphite spacer) was occupied after the crystal had reached a length of 34 mm, i.e., 5 mm after the crystal diameter reached its maximum value. Since the clearance between the spacer and the quartz wall was less than 0.25 mm, the melt was under substantially increased pressure during the last 25 mm of growth. This increased pressure, however, did not lead to forced wetting between the melt and the quartz wall since contact between the crystal and the wall remained confined to the surface of the irregularly spaced ridges as in the Skylab-III crystal.

The surface characteristics of the crystal grown with a diameter smaller than the ID of the ampul are typical of free-surface solidification. They are identical with those encountered between the surface ridges in the Skylab-III crystal and are similar to those observed on crystals grown by the Czochralski technique on earth.

Figure 7 shows the surface characteristics of the crystal portion grown with constant reduced diameter at a distance of about 10 mm from the initial regrowth interface; the surface irregularities are the same as those commonly observed in nonfaceted crystal growth from the melt. In addition, randomly spaced lines oriented normal to the $\langle 111 \rangle$ growth direction are visible. These lines are not continuous over the whole periphery and are confined to the three relatively flat portions of the crystal surface. They are not present on the centrally located "white" band which was identified as a rotational twin (see also below).

The crystal portion with a reduced diameter does not exhibit surface ridges observed on the previously discussed crystal; surface ridges do appear as the crystal diameter increases and approaches the value of the ID of the ampul. Details of surface ridge patterns are

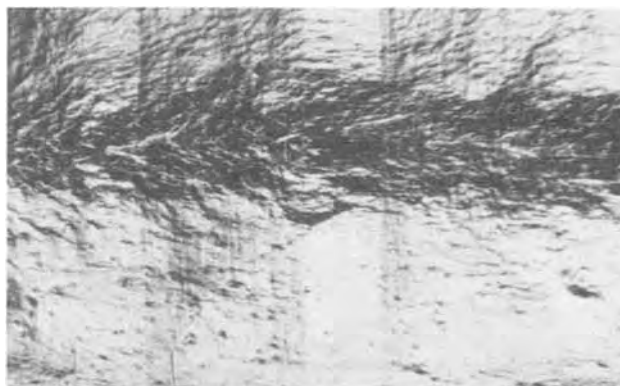


Fig. 7. Part of Te-doped crystal shown in Fig. 6; surface characteristics are typical for unconfined solidification; note random distribution lines normal to the growth direction; rotational twin is visible (white band). Magnification 19 \times .

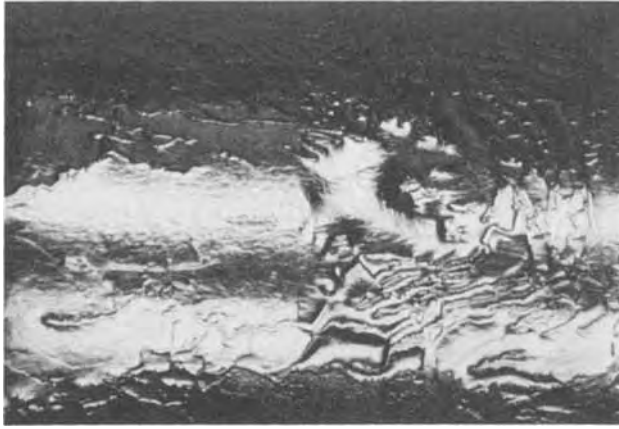


Fig. 8. Surface ridge patterns formed after crystal reached maximum constant diameter during Skylab-IV experiment; note discontinuity in surface morphology associated with second thermal soaking (see text). Magnification $21\times$.

shown in Fig. 8. The ridges in this crystal are of the same height as those on the crystal grown in Skylab-III ($\sim 25\ \mu\text{m}$). Here again they have no measurable effect on growth and segregation in the bulk of the crystal; they appear, however, less oriented along the growth direction and more branched. From the propagation patterns of these ridges, it is concluded that they are not the result of anomalous solidification, but, rather, that they are formed on the melt prior to solidification.

So far all attempts to account for ridge formation on the basis of known phenomena, such as wetting and convection induced by surface tension gradients, have met with fundamental inconsistencies.

Bulk characterization.—The bulk characterization of the space-grown crystals was aimed primarily at the growth and segregation behavior employing various analytical techniques. For this purpose the crystals were sectioned as shown in Fig. 9.

Dopant segregation.—The analysis of dopant segregation by high resolution differential etching was carried out on longitudinal sections of (211) surface orientation (see Fig. 9). All crystal sections were polished with Syton and etched for 40 sec in a solution of $1\text{HF}(48\%)$ and $1\text{CH}_3\text{COOH}$ (glacial) + 1KMnO_4 (saturated aqueous solution); they were subsequently rinsed, dried in purified nitrogen, and studied by means of interference contrast microscopy.

Dopant segregation during growth under the influence of gravity and under zero gravity conditions is evident in Fig. 10 where a portion of earth-grown (upper part) and space-grown crystal (lower part)

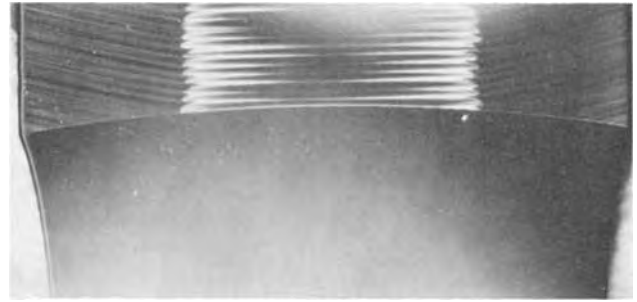


Fig. 10. Etched cross section (under dark field illumination) of crystal grown during Skylab-IV mission; space-grown region (bottom), in contrast to earth-grown region (top), exhibits no compositional inhomogeneities. Magnification $12\times$.

is shown. It is further seen that the regrowth interface morphology, established during thermal soaking, is concave (viewed from the melt). The sharp demarcation line separating the earth- and space-grown segment is the result of an abrupt decrease in Te concentration which is dictated, for initial regrowth, by the thermodynamic characteristics of the system, i.e., the distribution coefficient, k_0 of Te in InSb is less than one ($k_0 = C_S/C_L < 1$, where C_S and C_L are the concentration of Te in the solid and the melt, respectively).

The microscopic segregation behavior for the peripheral and the central part of the crystal in the vicinity of the regrowth interface is shown in Fig. 11 and 12, respectively. Pronounced segregation fluctua-

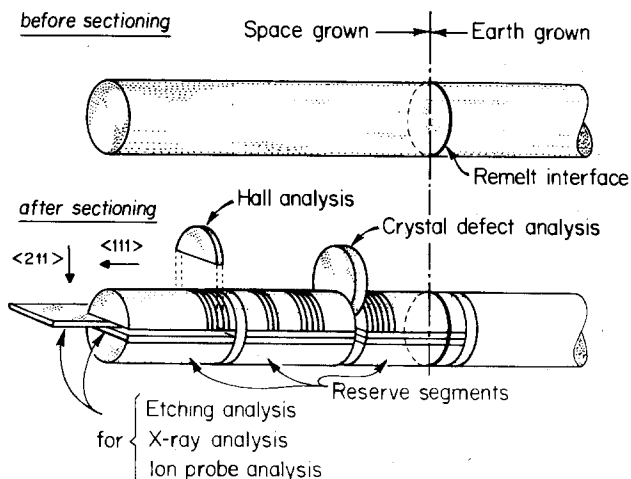


Fig. 9. Sectioning scheme for analysis of space-grown crystal

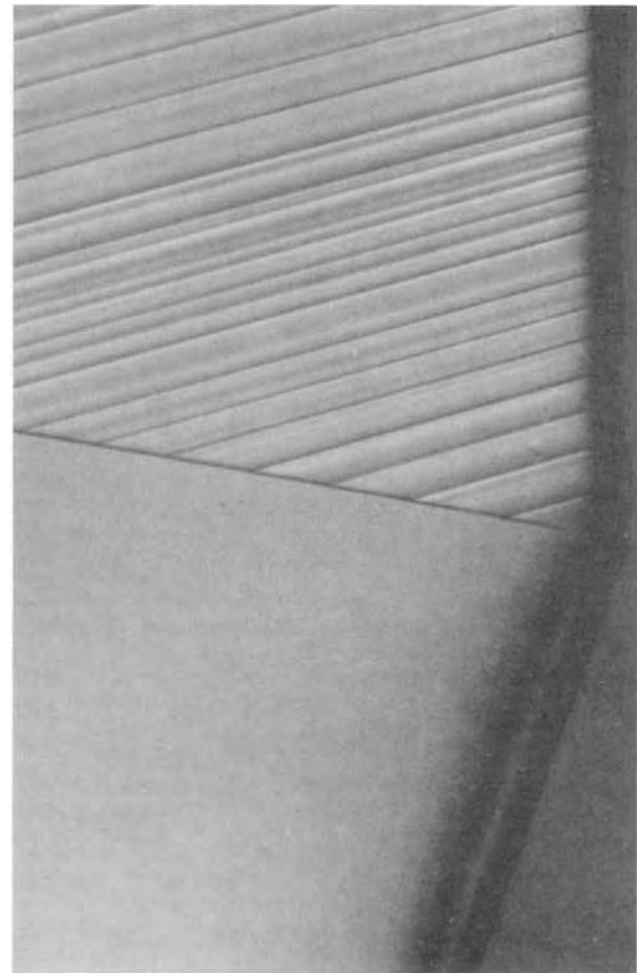


Fig. 11. Dopant segregation characteristics near the periphery of initial regrowth interface (right-hand side of Fig. 10). Magnification $300\times$.

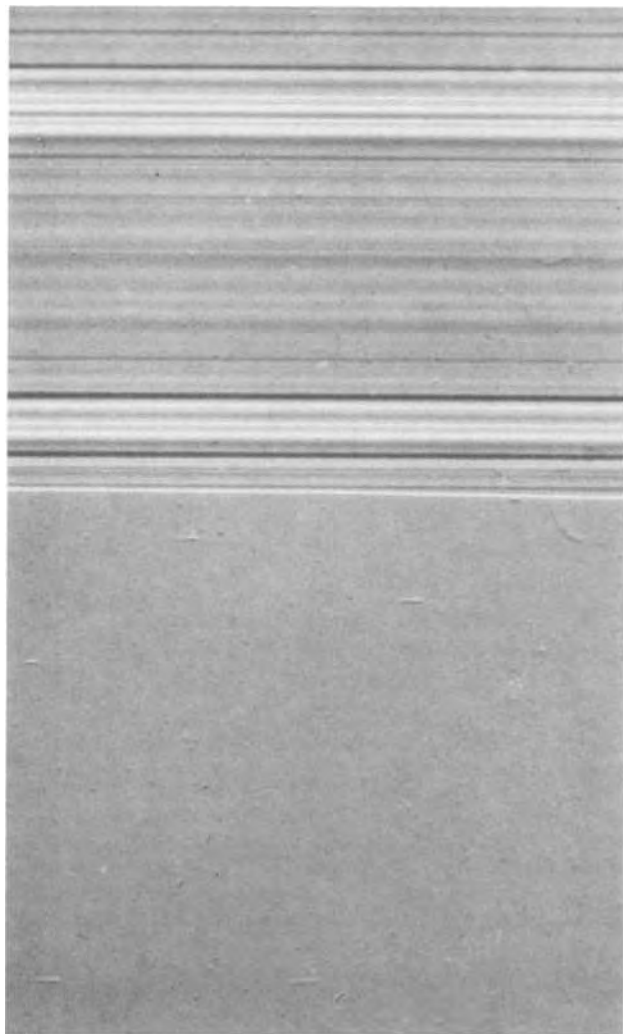


Fig. 12. Dopant segregation characteristics near the central region of initial regrowth interface of crystal grown during Skylab-IV mission. Magnification $580\times$.

tions (compositional inhomogeneities) in the earth-grown segment reflect irregular variations in growth conditions which are due to rotation effects (Czochralski pulling) and to uncontrolled gravity-induced thermal convection in the melt. No microscopic compositional fluctuations are present in the crystal segment grown in space. The segregation behavior in the equivalent region of the crystal grown during the Skylab-III mission was identical to the behavior presented above.³

According to theory, the area of the space-grown region shown in Fig. 12 must be part of a segregation transient (not revealed by etching) over which the dopant concentration increases continuously until, in the absence of convection, it reaches the same value as that of the dopant concentration present in the bulk of the melt; at this point steady-state segregation conditions are established and the dopant concentration in the solid remains constant except at the very terminal stage of solidification.

Quantitative dopant segregation analysis.—Since one of the major objectives of the Skylab experiment was to achieve steady-state segregation, quantitative dopant concentration analysis of the transition region was undertaken by means of Hall-effect measurements and ion-microprobe scanning.

Hall-effect measurements were carried out by the Van der Pauw technique on square samples measuring

³ The use of Czochralski-grown seed material was necessitated because no single-crystal seed material can be obtained by the gradient freeze technique in confined geometry due to pronounced volume expansion during solidification.

$2 \times 2 \times 0.5$ mm. Silver contacts were evaporated at the four corners of each sample and were annealed at 350°C for 2 hr to ensure ohmic behavior. Subsequently, gold wire leads were soldered with indium onto the contacts. More than thirty individual Hall-effect measurements (at different field strengths) were carried out on each sample to optimize the validity of the data. The reproducibility of the results was better than 1%. Twelve successive crystal slices were cut from the crystal grown in the Skylab-III mission as shown in Fig. 9. Two adjacent Hall-effect samples were chosen from each slice, in most instances near the central part of its straight edge. From some slices the Hall-effect samples were taken adjacent to the central location since twin or grain boundaries were present.

The compositional (carrier) profile together with the corresponding resistivity and carrier mobility obtained at 77°K are shown in Fig. 13. (Room temperature data, as expected, were found to be similar to those shown in Fig. 13 in view of the relatively high level of carrier concentration.)

The carrier concentration curve (N_{space}) in Fig. 13 shows clearly the decreased dopant concentration in the initial part of the space growth region, as predicted from theory; it delineates further the transient region in which the dopant concentration increases steadily and reaches its maximum value at a distance of about 0.5 cm from the regrowth interface. Beyond this distance the dopant concentration remains constant for the entire crystal length analyzed (5 cm). It is, thus, shown that steady-state segregation and homogeneous dopant distribution were achieved under zero gravity conditions.

In the ground-based tests performed in an identical experimental configuration and under "stabilizing thermal gradients," the dopant profile (N_{earth}) indicates clearly a steadily increasing dopant concentration, as seen in Fig. 13, which reflects the presence of slow convection caused by unavoidable lateral thermal gradients. The adverse effects of this type of convection cannot be revealed by high resolution etching, since no abrupt fluctuations in composition take place.

The ratio of the dopant concentration in the initially grown region and in the steady state-grown region is a direct measure of the equilibrium distribution coefficient, k_0 , which cannot be reliably determined on earth. Unfortunately, the low spatial resolution of Hall-effect measurements does not permit, at this time,

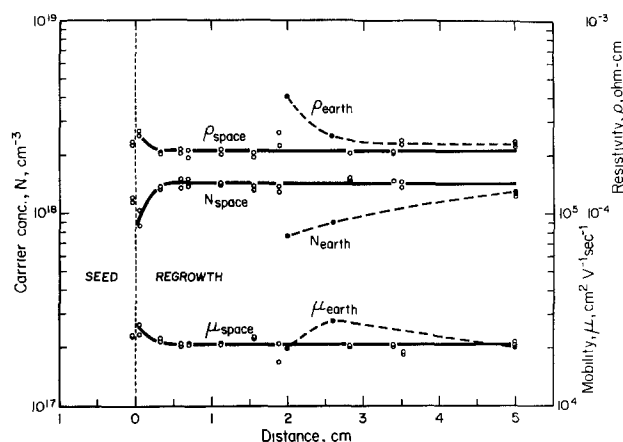


Fig. 13. Carrier (dopant) concentration profile obtained from Hall-effect measurements for Te-doped crystal grown during Skylab-III mission (N_{space}) and for Te-doped crystal grown during ground-based testing. The position of the original regrowth interface for both crystals is indicated by the vertical dashed line. Due to the presence of many twin and grain boundaries in the InSb grown during the ground-based testing, no meaningful Hall-effect measurements could be carried out in the vicinity of the regrowth interface.

the accurate determination of k_0 . From the width of the region of transient segregation and the associated compositional change, the diffusion coefficient of the dopant in the melt can be determined, provided the microscopic growth rate is known and constant; this condition was not met in the present experiment, since only the nominal growth rate is known.

It should be pointed out that the observed variation in carrier concentration between adjacent Hall samples is not surprising since extensive twinning took place in this InSb crystal. In addition to twinning, growth under confined geometry leads to high dislocation densities which account for the measured, relatively low, carrier mobilities. It is of interest to note that in the crystal grown during the Skylab-IV mission, with a smaller diameter than that of the quartz ampul (unconfined solidification) the dislocation density was found to be 40% smaller than that in the earth-grown segment.

The compositional profile in the Skylab-III crystal was in parallel subjected to ion microprobe analysis since this technique was expected to provide a similar sensitivity as the Hall-effect measurements but a resolution in the micron range. The results obtained are consistent with the Hall-effect measurements; however, due to the relatively low yield of sputtered Te ions, the linear resolution and accuracy were found to be limited. Thus, the precision of the ion-microprobe analysis with a scanning beam of $25\ \mu\text{m}$ was only of the order of $\pm 16\%$.

Intentionally introduced segregation discontinuities.—As pointed out earlier, the growth process during the Skylab-IV mission was perturbed 90 and 140 min after initiation of the cooling cycle by a mechanical shock and by an arrest of cooling, respectively; the cooling arrest was sustained for a period of 60 min. These perturbations were intended to introduce time reference markers in the crystal and to study their specific effect on segregation behavior under steady-state conditions.

Etching analysis of the crystal revealed the presence of only two distinct segregation discontinuities manifested as curved lines, extending over the entire cross section of the crystal, 15 and 28.8 mm from the initial regrowth interface. As seen from the sketch in Fig. 14, the first discontinuity coincides with an abrupt decrease in crystal diameter and is of relatively low intensity as viewed in interference contrast. The second discontinuity was formed after the crystal had reached its maximum constant diameter and is very pronounced, as seen in Fig. 15.

The nature of these segregation discontinuities was investigated by double beam interferometry. As seen in Fig. 16a, the first perturbation (15 mm from the initial regrowth interface) resulted in a small and localized increase in tellurium concentration; on the other hand, the second perturbation (Fig. 16b) resulted in a pronounced segregation discontinuity (decrease) which persisted for an extended period of time. Thus, this second discontinuity is unambiguously identified as a transient segregation region associated with regrowth following thermal soaking, while the first, short-lived, segregation discontinuity is attributed to the mechanical shock.

Identification of the two segregation discontinuities permits their use as time markers for the determination of average microscopic growth rates in two different portions of the crystal. Thus, the average growth rate from the initial regrowth interface to the first discontinuity, 90 min into growth, is found to be $2.8\ \mu\text{m}/\text{sec}$ and the growth rate from the first to the second discontinuity is $4.6\ \mu\text{m}/\text{sec}$. The average growth rate over the first 2.88 cm of growth (see Fig. 14) is $3.4\ \mu\text{m}/\text{sec}$.

The above growth behavior is consistent with theory: for the thermal configuration in the multipurpose furnace the thermal gradient in the melt is expected to decrease with continuing solidification and

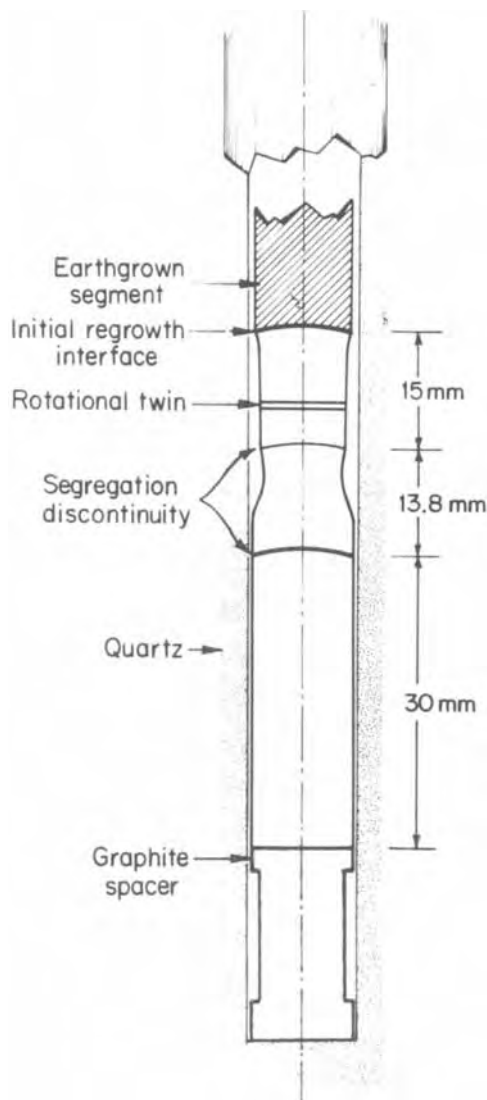


Fig. 14. Cross section of crystal grown during Skylab-IV mission

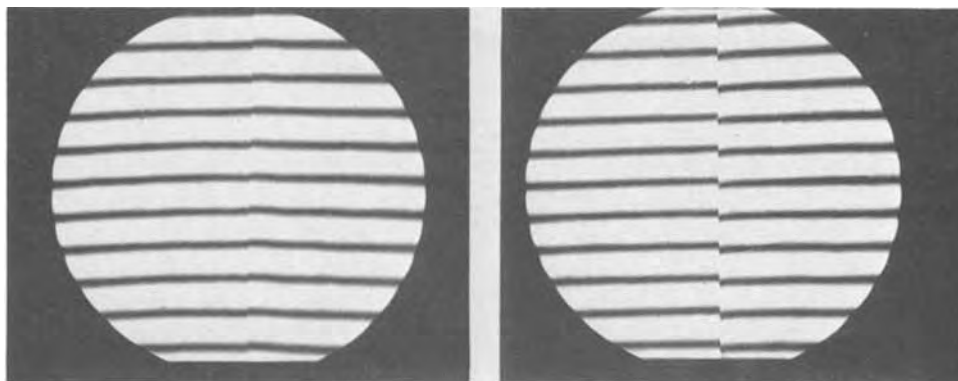


Fig. 15. Dopant segregation discontinuity caused by cooling arrest and thermal soaking during growth in Skylab-IV mission. Magnification $400\times$.

consequently the growth rate must correspondingly increase.

It is of interest to note that the fringe deflection at the second compositional discontinuity (Fig. 16b) is constant over the entire crystal diameter. Since the fringe deflection is proportional to the concentration change across the discontinuity and since the dopant concentration in the initial regrowth portion at the discontinuity (following thermal soaking) must be constant across the crystal diameter, it must be concluded that the tellurium concentration in the crystal above the discontinuity, which is constant along the

Fig. 16. Double beam interferograms of segregation discontinuities as revealed by etching (a, left) caused by mechanical shock and (b, right) caused by regrowth after thermal soaking (see text).



growth axis (fringes parallel to the growth axis), must also be constant in the radial direction.

Crystal morphology.—As discussed earlier, the surface morphological characteristics of both space-grown crystals indicate that the Te-doped InSb melt does not wet the confining quartz wall. Accordingly, the contact angle between the seed and the melt at the peripheral contact line is controlled by the interfacial tensions of the three phases involved and the meniscus of the melt (which determines the shape of the growing crystal) becomes a function of the radius of curvature of the crystal-melt interface. The decrease in crystal diameter observed during the early stages of growth in the Skylab-IV experiment (Fig. 6) is, thus, a direct consequence of the pronounced concave configuration of the crystal-melt interface (as viewed from the melt) brought about by the thermal characteristics of the system.

The ensuing gradual change to constant crystal diameter reflects the decrease in lateral heat transfer (due to the increasing distance of the growing crystal from the quartz wall) which results in an increase of the radius of curvature of the regrowth interface. The second decrease in crystal diameter, which coincides with the intentional, mechanical-shock perturbation, is attributed to a deformation of the melt (stretching toward the hot end) which established a melt meniscus leading to decreasing crystal diameter. The subsequent increase in the diameter of the crystal is due to the fact that the volume available to the growth system becomes limited.

In the Skylab-III experiment the radius of curvature of the initial growth interface was significantly larger than in the Skylab-IV experiment, apparently due to inadvertent differences in the heat transfer characteristics of the two cartridges; accordingly, the crystal diameter in the Skylab-III experiment conformed to the size of the confining quartz wall.

Peripheral facet effect.—Basic thermodynamic parameters are responsible for the fact that during growth of InSb in the $\langle 111 \rangle$ direction a facet is generally formed at the growth interface. Since facet formation is associated with kinetic supercooling, the facet is centrally located at convex interfaces and peripherally at concave interfaces (as viewed from the melt). It is generally believed that dopant segregation within facets is controlled by the lateral layer growth rate which is sensitive to thermal perturbations and gravity-induced convection.

Consistent with the above considerations, peripheral facet formation is observed in both space-grown crystals (Fig. 17) since in both experiments the growth interface assumed concave morphology (Fig. 14). The well-defined segregation discontinuities on the facet grown region cannot, however, be explained on the basis of thermal and/or convective perturbations in the melt since segregation in the nonfaceted bulk of the crystals was found to be homogeneous.

The observed segregation effects in the peripheral facet can be explained by considering that kinetic

supercooling for peripheral facet formation assumes its highest value at the outermost part of the growth interface, which thus becomes the location with the highest probability for nucleation of lateral layer growth. Under these conditions, any perturbation, such as a vibration or the arrival of a foreign particle at the peripheral three-phase contact line may trigger nucleation of lateral layer growth and, thus, result in the formation of the observed segregation discontinuities. Their magnitude (intensity) is seen to decrease with decreasing supercooling from the periphery to the interior. Furthermore, depending on their magnitude, the facet segregation discontinuities extend more or less into the adjacent off-facet region; accordingly, it must be concluded that a finite amount of kinetic supercooling is associated with growth adjacent to facet regions. There is some evidence that the randomly spaced lines visible on the surface of the grown crystal (Fig. 7) correspond to the external boundaries of the presently discussed facet segregation discontinuities.

It should be pointed out that the same type of facet segregation discontinuity has been observed superimposed on compositional inhomogeneities in facet regions of earth-grown InSb; their origin could not, however, be explained.

Rotational twinning.—The bands of varying width appearing on the left-hand side of the crystal grown during the Skylab-III experiment (Fig. 4) were identified as the external boundaries of $(\bar{2}11)$ rotational twins. Each band is the result of two consecutive rotations by 60° of the (111) plane normal to the growth direction.

Analysis of the rotational twins on etched crystal segments of (211) surface orientation (Fig. 18) shows that some propagate across the entire crystal, some terminate within the crystal, and others deteriorate to grain boundaries, eventually leading to breakdown of the single-crystal matrix.

In view of the concave interface morphology, nucleation during growth is essentially restricted to the outermost peripheral part of the growth interface, as

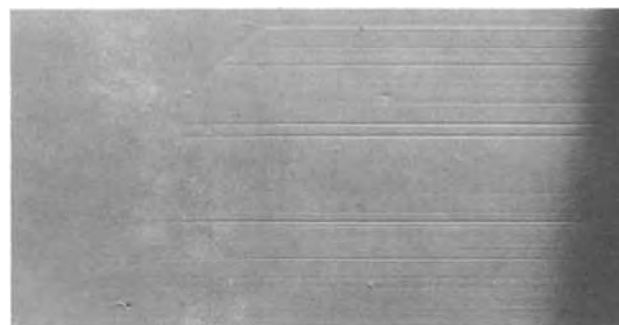


Fig. 17. Peripheral facet growth with segregation discontinuities in crystal grown during Skylab-IV mission. Magnification $300\times$.

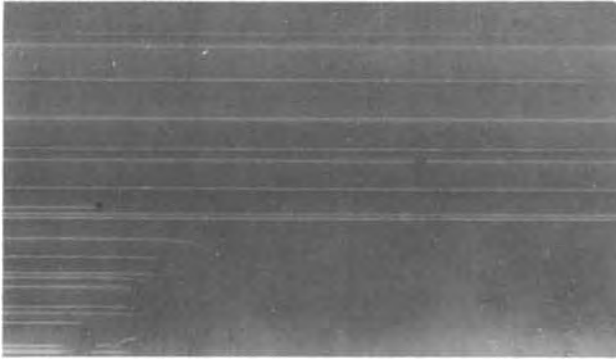


Fig. 18. Cross section of crystal grown during Skylab-III mission exhibiting rotational twinning (see also Fig. 5). Magnification $12\times$.

discussed previously. Rotational twin formation initiated by a nucleus having a 60° misorientation within the growth plane can thus be explained as the result of misoriented nucleation at the crystal periphery.

Because of inherent thermal asymmetry in the multipurpose furnace, the concave growth interface morphology is to some extent inclined to the growth direction. Therefore, any misoriented nucleus formed at the lowest part of the three-phase contact line (periphery of the growth interface) encounters no constraints in propagating and results in the formation of a twin boundary which crosses the entire crystal. Nucleation at any higher part of the periphery, however, can propagate only through part of the crystal, since a varying fraction of the plane of propagation has solidified already in the original orientation. Considering that a twin boundary cannot terminate within the crystal, its direction of propagation must change to form a curved grain boundary which may either terminate at a subsequently nucleated twin boundary or lead to a polycrystalline matrix (see Fig. 18). It is of interest to note that the tendency of twin formation is strikingly reduced (only one rotational twin was observed) in the crystal grown with reduced diameter during the Skylab-IV experiment.

Summary

The present InSb experiment proves unambiguously the uniqueness of zero-gravity conditions for obtaining fundamental data on crystal growth and segregation associated with solidification. Furthermore it demonstrates striking advantages of processing materials in space.

Specifically the following results and conclusions were obtained for the first time:

Ideal steady-state growth and segregation (exclusively diffusion controlled) were achieved leading to three-dimensional chemical homogeneity on a microscale over macroscale dimensions (several centimeters in the present case); the transient segregation profile was determined; limitations in the experimental arrangement and in the presently available microanalytical techniques do not permit, at this time, the extraction of fundamental data pertinent to solidification.

Surface tension effects led to phenomena previously never observed and theoretically not predicted: the Te-doped melt, not wetting the quartz wall, solidified with a free surface (unconfined) configuration. Under

forced contact conditions, the growth system remained essentially isolated from its container through the formation of narrow surface ridges. It was also shown that surface tension effects in space remained localized on the surface and did not affect growth and segregation in the bulk.

In the absence of convective interference it was possible to identify segregation discontinuities associated with facet growth and to explain their origin on the basis of spurious nucleation. The absence of convective interference permitted, further, the determination of the mode of nucleation (formation of misoriented nuclei at the three-phase boundary line) and propagation of rotational twinning.

A mechanical-shock perturbation intentionally introduced during growth was identified in the crystal and found to cause a localized increase in dopant segregation; this dopant discontinuity was used as a time reference for the determination of the average macroscopic growth rate.

On the basis of the present results it is apparent that fundamental data necessary for bridging the gap between theory and experiment can be reliably obtained in the absence of gravity and that outer space presents a unique opportunity to science and technology.

Acknowledgments

The authors wish to express their appreciation to the National Aeronautics and Space Administration, and particularly to the Staff at the Marshall Space Flight Center for their uncompromising efforts, cooperation, and enthusiastic support during all stages of the experiment. They are indebted to Dr. K. M. Kim for carrying out much of the ground-based testing, to Drs. J. R. Carruthers and J. Colbey for stimulating discussions, and to Mr. W. J. Fitzgerald and J. Baker for their skillful assistance with the characterization program. Finally, the authors are grateful to Dr. R. K. Lewis and the CAMECA Instruments, Incorporated, for their generosity in carrying out Ion-Microprobe Analyses of the crystal.

Manuscript submitted June 20, 1974; revised manuscript received Aug. 23, 1974.

Any discussion of this paper will appear in a Discussion Section to be published in the December 1975 JOURNAL. All discussions for the December 1975 Discussion Section should be submitted by Aug. 1, 1975.

Publication costs of this article were partially assisted by Massachusetts Institute of Technology.

BIBLIOGRAPHY

The following bibliography is intended to provide pertinent background information.

- J. C. Brice, "The Growth of Crystals from Liquids," North-Holland Publishing Co., Amsterdam (1973).
- B. Chalmers, "The Principles of Solidification," John Wiley & Sons, Inc., New York (1964).
- J. J. Gilman, Editor, "The Art and Science of Growing Crystals," John Wiley & Sons, Inc., New York (1963).
- P. F. Kane and G. B. Larrabee, "Characterization of Semiconductor Materials," McGraw-Hill Book Co., New York (1970).
- R. A. Laudise, "The Growth of Single Crystals," Prentice-Hall, Inc., Englewood Cliffs, N.J. (1970).
- W. G. Pfann, "Zone Melting," 2nd ed., John Wiley & Sons, Inc., New York (1966).
- D. P. Woodruff, "The Solid-Liquid Interface," Cambridge University Press, New York (1973).

Properties of SiO₂ Grown in the Presence of HCl or Cl₂

Y. J. van der Meulen*, C. M. Osburn,* and J. F. Ziegler

IBM T. J. Watson Research Center, Yorktown Heights, New York 10598

ABSTRACT

Effects associated with the incorporation of chlorine during the thermal growth of SiO₂ (500-1400Å) on <100> Si are investigated as a function of additive species (HCl, Cl₂), additive concentration, and oxidation temperature (900°-1150°C). Chlorine profiles are measured mainly by nuclear backscattering spectroscopy, and oxide thicknesses and refractive index changes by ellipsometry. The highest chlorine concentrations in unannealed oxides always occur at the Si-SiO₂ interface. Under otherwise similar conditions, the use of Cl₂ results in higher, more evenly distributed chlorine levels (up to 1.2×10^{21} at cm⁻³). The incorporated chlorine is gradually removed by annealing at temperatures in excess of 1100°C, as well as under conditions where further oxide growth takes place without the presence of HCl or Cl₂. Additional oxide formation in steam effectively removes all the incorporated chlorine. MOS capacitors made from oxides grown in HCl or Cl₂ show fixed charge levels lower than 10^{11} cm⁻² and mobile charge levels less than 10^{10} cm⁻². When biased at high fields (>6 MV/cm) significant shifts in the flatband potential of Si were observed. Chlorine-grown oxides exhibit positive and negative shifts attributed to a mobile species; the smaller negative shifts in HCl oxides are attributed to interface states. Other electrical data of intentionally Na-contaminated HCl oxides suggest that only a constant fraction of the Na is trapped.

Recent reports on the beneficial electrical effects (1-8) of small additions of chlorine-containing species to the oxidative atmosphere during the thermal oxidation of silicon wafers have in turn led to studies in which the effects of the additive on the oxide growth were examined (9-12). It was thus found (11) that changes occur in the SiO₂ growth rate which are quite complex and depend not only on the additive species used (HCl, Cl₂) but also on the oxidation temperature. Of major concern with respect to the long-term dielectric stability is whether chlorine or its compounds are actually incorporated into the growing oxide layer; some analytical results published on this subject (9, 10, 13) point to the presence of substantial amounts of chlorine, and also indicate a surprisingly high mobility of these chlorine atoms in the dielectric matrix under the conditions present during Auger electron analysis (9). The purpose of this article is to present results of a more detailed and quantitative analysis of the incorporation of chlorine into SiO₂ during thermal oxidation of silicon, as well as on some electrical properties of such oxides.

Experimental

For our studies chem-mechanically polished silicon wafers ([100]-oriented, 1¼ in. diameter, p- and n-type, 2 ohm-cm) were used. They were cleaned by a standard process (14); usually subjected to a clean-up oxidation to remove surface damage in oxygen at 1050°-1100°C to form ~ 2000Å of SiO₂; re-cleaned; blown dry in filtered, purified nitrogen; and placed in a double-walled quartz oxidation tube through which the oxidizing mixture was passed.

Thin SiO₂ films (500-1400Å) were grown on these wafers at temperatures ranging from 900° to 1150°C, in dry-oxygen containing up to 9 volume per cent (v/o) HCl (HCl oxides) or 3 v/o Cl₂ gas (Cl₂ oxides). The HCl and Cl₂ were 99.99+ % pure. In most cases an effort was made to obtain films of approximately 1000Å; this was an almost optimum thickness for analysis by nuclear backscattering spectrometry. In some cases, the O₂-HCl, or O₂-Cl₂ gas mixture was used only during an initial or a final stage of the oxidation proc-

ess before or after a regular oxide was grown in pure O₂ in another furnace. Relatively little attention was given to the use of H₂O as the oxidant as it has been reported (1, 13) that oxides grown in H₂O-HCl or H₂O-Cl₂ do not show any improvement over regular steam-grown oxides. However, some experiments were performed in which HCl or Cl₂ oxides were further oxidized in steam before being analyzed for the presence of Cl in the film. It has been found (11) that the oxidation process in quartz furnace tubes can be influenced by lingering traces of HCl and especially of Cl₂ long after additions to the oxidant have been halted. When using a particular furnace tube, it was therefore always subjected to an overnight bake in nitrogen at high temperature (1100°-1150°C) to ensure the removal of traces of earlier additives.

The effectiveness of the HCl additions in removing impurities was also demonstrated in the following way: the inside of a high purity quartz furnace tube, that had been used for six months, was rinsed with acid to remove deposits at several locations and the resultant solutions were analyzed by emission spectroscopy. Significantly higher amounts of impurities were detected downstream, close to the mouth of the furnace tube. A typical result is listed in Table I. This shows the effectiveness of the removal from the hot zone of metals as halides, that condense at the cooler end of the tube. However, it also illustrates the contamination risk present in the area through which wafers normally are loaded and unloaded.

Oxide thicknesses were measured ellipsometrically following earlier reported procedures (14). It has been

Table I. Analysis of film deposited at cool end of HCl oxidation tube.*

(Amounts are given as a percentage of the total cationic content of the film.)

> 10%	0.1-9.9%	Trace
Cu	Ni	B
Na	Fe	Mn
	Cr	Sn
	Al	Ga
	Ti	Ca
	Mg	Ag

* High Purity Quartz containing 300 ppm Re, 10 ppm Al, 3 ppm Cu, and 3 ppm Mg.

* Electrochemical Society Active Member.

Key words: chlorine incorporation, nuclear backscattering spectroscopy, flatband voltage shift.

demonstrated (15) that the SiO₂ thickness can also be obtained directly from the nuclear backscattering spectrum by integration of the oxygen or silicon signal. Because of the fact that rather thin SiO₂ films were used in the present investigation, and in view of possible distortion of the oxygen signal at 2.6 MeV, the ellipsometric determination was thought to be more reliable. It was found that the oxides formed were generally quite homogeneous in thickness across a wafer (to within 1-2%); nonuniformities were encountered only in Cl₂ oxides grown at temperatures in excess of 1000°C. From the ellipsometric measurements on oxides with thicknesses ranging from 1000-1400Å, we could also determine with a high degree of accuracy the influence of the halide additive on the oxide refractive index. The results indicate systematic variations, not only as a function of additive concentration but also as a function of the oxidation temperature (Table II). The latter variations may be due to a difference in stress built-in during cooling; the shifts from a standard value with halide concentration are thought to be real, and not caused by an increase in surface roughness or by a slight optical absorption in the dielectric film. They probably are caused by a slight change in the density of the SiO₂ film, as a function of the growth conditions. Shifts measured in the Cl₂ oxides were more ambiguous since corrosion of the silicon surface did sometimes occur visibly at oxide thicknesses around 1000Å.

Auger analyses (9) showed instabilities in the profile of the incorporated chlorine and eventual desorption into the vacuum of the AES system. Further data were obtained using x-ray fluorescence spectroscopy (XFS), electron microprobe analysis (EMA), and nuclear backscattering spectroscopy (NBS). In all cases, particular care was taken to check for transient effects such as were found in the Auger experiments. However, no indication of the occurrence of such instabilities was found. Sometimes, wafers oxidized at the same time were evaluated by several analytical and electrical techniques. However, NBS was most extensively used, because of its rather unique ability to determine both quantitatively and nondestructively an impurity profile as a function of depth into the oxide. Hence, a somewhat detailed description of its application to the present case is given in the next section. Results of the various analyses are given in the later sections of this article.

Nuclear backscattering spectroscopy.—Several review articles on the use of this technique have recently been published (16, 17). The essential features pertaining to the analysis of thin oxides are shown in Fig. 1. The insert displays schematically the elastic collision between a ⁴He ion projectile and a target nucleus, which results in the backscattering of the ⁴He toward a semiconductor detector that gives a signal proportional to the energy of the impinging ion. The Cl impurity atoms are heavier than the SiO₂ matrix atoms, so they absorb less energy. Thus the ⁴He ions backscattered from Cl atoms are more energetic than those scattered by Si or O atoms. These

Table II. Shift in oxide refractive index (Δn) as a function of halide addition and temperature, relative* to the index obtained after oxidation in 100% O₂ at 1000°C

Halide, v/o	Refractive index change, Δn		
	900°C	1000°C	1150°C
3	+0.0029	0	-0.0035
4.5	-0.0001	-0.0020	-0.0045
9	-0.0004	-0.0035	-0.0055
0.5		-0.0018	
2		-0.0079	

* It should be noted that the absolute value obtained at 1000°C in 100% O₂ ($n = 1.4715$) may depend slightly on the instrument used.

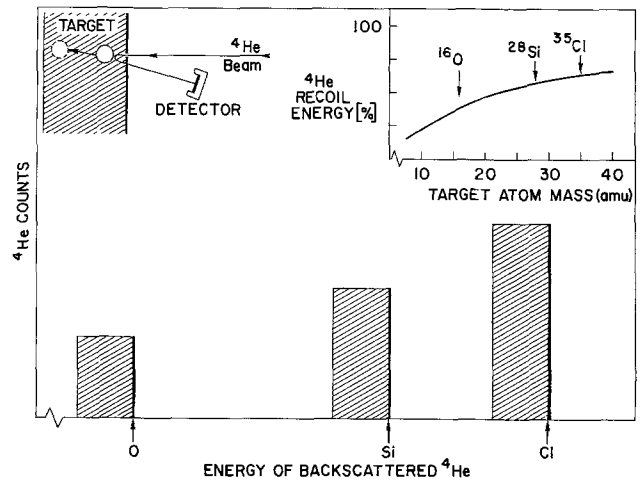


Fig. 1. Relative energy of backscattered ⁴He atoms as a function of the target nuclei.

major energy changes allow a differentiation between Cl, O, and Si in the target. Smaller changes in ⁴He energy are used to obtain impurity depth profiles. At 2.6 MeV, the ⁴He ion moves much faster than the target electrons, making the target matrix appear as an electron sea. When traversing this matrix, the ⁴He projectile loses a small, but detectable amount of energy which can be converted to sampling depth by using tables of specific energy loss of ⁴He ions in matter (18).

Since the target is a compound, Bragg's rule (19) must be used in the energy loss determination. The applicability of Bragg's rule to SiO₂ has recently been verified experimentally to within a few per cent (20). However, it was found during the present investigation, that reliable depth values of the Cl impurity could be confirmed by using the technique of Chu *et al.* (21). As shown in Fig. 2, the depth δx_{Cl} is calculated from

$$\delta x_{Cl} = d_{SiO_2} (\delta E_{Cl} / \Delta E_{Cl}) \quad [1]$$

where d_{SiO_2} is the ellipsometrically determined film thickness, δE_{Cl} is the energy difference between the Cl signal from the surface (cf. Fig. 2) and that from a depth x in the film, and ΔE_{Cl} is the energy difference between the Cl signals from the surface and from the bottom of the SiO₂ film. Values of ΔE_{Cl} can be calculated from the value of ΔE_{Si} measured in the same spectra

$$\Delta E_{Cl} = \Delta E_{Si} ([S]_{Cl} / [S]_{Si}) \quad [2]$$

where the $[S]$ factors (22) may be easily calculated from tables (18). For backscattering from Si or Cl target atoms in an SiO₂ matrix the ratio of the $[S]$ factors is near unity ($[S]_{Cl} / [S]_{Si} = 1.01$) and rela-

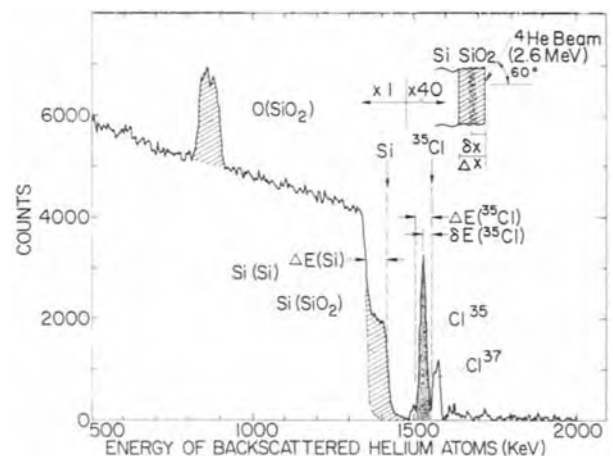


Fig. 2. Spectral distribution of ⁴He atoms backscattered from a thin SiO₂ film (Cl doped) on a Si substrate.

tively insensitive to errors in the absolute energy loss values.

Experimentally, a ^4He incident energy of 2.6 MeV kept the Cl and Si signals well separated provided that the SiO_2 thickness did not greatly exceed 1000Å. This thickness still permitted an oblique angle of incidence ($\phi = 60^\circ$) of the beam onto the target, which doubled the apparent thickness and thus increased the accuracy of the Cl profile. It was noted in an earlier study (10) that the analysis of ^4He backscattering profiles of Cl in SiO_2 is complicated by the isotope ratio in natural Cl ($^{35}\text{Cl}:^{37}\text{Cl} = 76:24$). At the high values of the incident energy used in the present investigation, the two Cl isotopes can be separated into individual profiles. To obtain the impurity distribution use was made mainly of the ^{35}Cl profile, corrected for isotopic abundance. With the 17 keV detector resolution of the instrument used, it is estimated that the final depth resolution of the spectra was approximately 200Å.

Results and Discussion

HCl oxides.—Analysis by NBS of HCl oxides always results in similarly shaped chlorine concentration profiles, regardless of the SiO_2 thickness, the growth temperature, or the ambient HCl concentration during oxidation. A typical example of a measured profile and the evaluation in terms of constituent signals is shown in Fig. 3. The chlorine concentration is lower than the limit of detection (approximately 3×10^{19} at. cm^{-3}) in the top of the layer and then increases toward a maximum near the Si-SiO₂ interface. It seems evident that chlorine is incorporated directly at the Si-SiO₂ interface during oxidation. During further oxide growth, as the distance between the previously trapped chlorine and this interface increases, the chlorine is slowly released and perhaps replaced by oxygen atoms. As discussed before, an upper thickness limit of approximately 1100-1200Å exists above which SiO_2 films can no longer be analyzed for chlo-

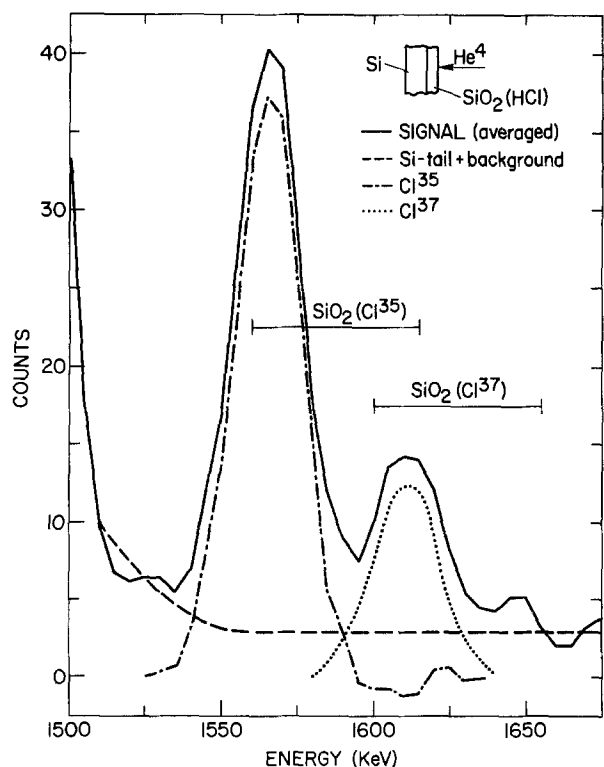


Fig. 3. Chlorine distribution as a function of depth in an HCl oxide (1150°C, 9 v/o HCl, 780Å). The measured signal has been separated into background and chlorine isotope profiles. The calculated energy range for both chlorine isotopes in the oxide film is indicated. Note: In all figures, the energy of the ^4He atoms backscattered from a given isotope decreases as the distance to the SiO_2 -vacuum interface increases.

rine with NBS. Our data therefore do not permit quantitative conclusions on the Cl-incorporation over a wide range of oxide thicknesses. However, it was found elsewhere, using XFS, that the total amount of chlorine incorporated in HCl-oxides grown at 1000°C is roughly proportional to the film thickness (165-4240Å) (23). From the observed shape of the Cl concentration profile, we conclude that this correspondence cannot simply be explained on the basis of a larger number of sites available to chlorine atoms. It also has to reflect a higher level of incorporation at the Si-SiO₂ interface and perhaps a slower rate of removal of the incorporated species as the oxide thickness increases. Such an increasing chlorine concentration is consistent with the silicon surface corrosion that is observed only underneath much thicker oxides (11-13). The parallel reactions of the O₂ and the HCl with the silicon apparently compete kinetically, and as the oxygen flux decreases with increasing SiO_2 thickness more chlorine is incorporated. The subsequent removal of chlorine is caused by the greater thermodynamic stability between the Si-O and Si-Cl bonds. Finally, the concept of a relatively high mobility of the chlorine carrying species during growth of HCl oxides is in agreement with the results of other experiments described later in this paper.

Regardless of the angle of incidence (ϕ) of the exciting beam upon the target sample, the backscattered helium atoms were analyzed and counted in energy increments of 5 keV. For different angles of incidence these sampling intervals therefore correspond to different thicknesses. Analysis of a number of HCl oxides at $\phi = 0^\circ$ and 60° showed the maximum concentration to be higher by a factor 1.5-1.7 for the smaller sampling increments ($\phi = 60^\circ$). This illustrates the steepness of the maximum in the chlorine concentration as a function of position in the oxide layer. Peak chlorine concentrations ($\phi = 60^\circ$) and average concentrations are listed in Table III as a function of oxidation temperature and ambient HCl concentration.

Cl₂ oxides.—NBS profiles of Cl₂ oxides show the chlorine distribution to be less prominently peaked than was the case for the HCl oxides. In fact, a number of analyses indicate a distribution that is homogeneous within the margin of error (Fig. 4). This is the main qualitative distinction between Cl₂ and HCl oxides, but it leads once again to the conclusion that incorporation takes place upon formation of the oxide. Analysis results for peak and average chlorine concentrations are listed in Table IV. A comparison with Table III shows that the incorporation of chlorine in Cl₂ oxides takes place at a much higher level, especially if the additive concentrations are considered. The more homogeneous distribution in this group of oxides can also be gauged from these tables.

The wider, more even chlorine distribution in Cl₂ oxides (as compared with HCl oxides) indicates a slower rate of removal of incorporated chlorine during further growth. As is seen below, annealing in N₂ leads to similar behavior for both types of oxide, and additional growth in steam reduces the original oxide chlorine level effectively to zero in all cases. Thus, the higher rate of removal in the HCl oxides may well reflect the presence of appreciable amounts of H₂O in

Table III. Chlorine content of oxides grown in O₂-HCl ambients and analyzed by nuclear backscattering spectroscopy. E = 2.6 MeV; $\phi = 60^\circ$

Oxid. temp (°C)	\bar{P}_{HCl} (v/o)	d_{SiO_2} (Å)	[Cl] _{max} (at. cm^{-3})	[Cl] _{avg} (at. cm^{-3})
900	9	880	$< 3 \times 10^{19}$	—
1000	3	1030	$< 3 \times 10^{19}$	—
1000	9	1050	1.18×10^{20}	2.5×10^{19}
1050	9	813	1.7×10^{20}	7.5×10^{19}
1100	9	894	5.7×10^{20}	1.6×10^{20}
1150	3	928	3.3×10^{20}	1.2×10^{20}
1150	9	922	8.4×10^{20}	2.4×10^{20}

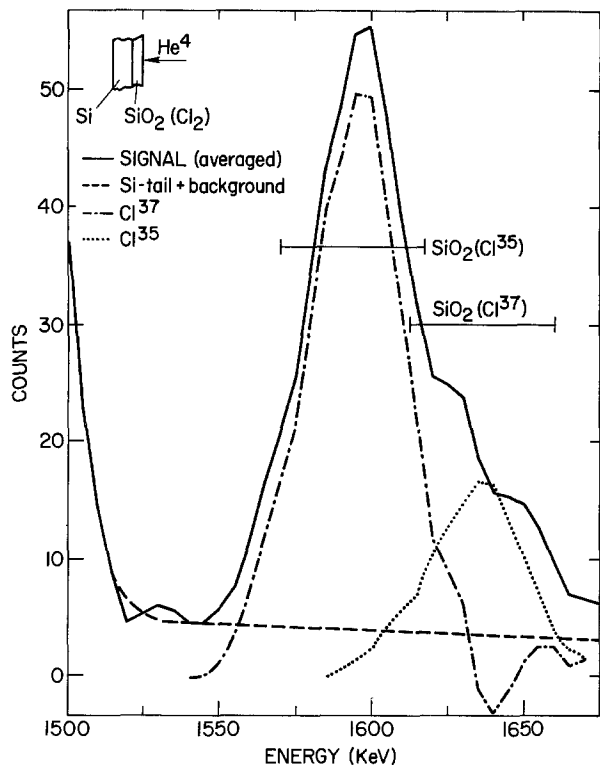


Fig. 4. Chlorine distribution in a Cl₂ oxide (1000°C, 2% Cl₂, 640Å). The measured signal has been separated into background and chlorine isotope profiles. Calculated energy ranges are indicated by horizontal bars.

the oxidizing ambient, even though the oxide growth rate itself does not seem to be affected (11).

Annealing experiments.—It has been reported (24) that annealing of HCl oxides in an inert ambient at temperatures in excess of 1100°C results in a loss of Na neutralization in such films. To correlate such effects with the actual degree of chlorine incorporation, NBS profiles were obtained for Cl₂ and HCl oxides of comparable thickness (~1000Å) before and after various annealing treatments in vacuum and in N₂. It was found that vacuum annealing for 60 min at 100°C did not result in a measurable decrease in oxide chlorine concentrations, and such treatments were not pursued any further. High temperature annealing results are shown in Fig. 5 (HCl oxides) and 6 (Cl₂ oxides). In both cases little if any significant decrease in the chlorine profile is seen to occur after annealing for 60 min at 1100°C. Annealing at 1200°C, however, results in the loss of approximately 50% of the built-in chloride, while at the same time the original profile is considerably changed in shape. Even if allowance is made for some uncertainty in the as-measured profiles, it appears that the chlorine originally incorporated closest to the Si-SiO₂ interface is removed most efficiently in the HCl oxides. Kriegler has argued that proximity of built-in chlorine to that interface is a precondition for Na neutralization, and it is therefore not surprising that such annealing at 1200°C causes a complete loss of passivating properties of the oxide.

Table IV. Chlorine content of oxides grown in O₂-Cl₂ ambients and analyzed by nuclear backscattering spectroscopy. E = 2.6 MeV; φ = 60°

Oxid. temp (°C)	\bar{P}_{Cl_2} (v/o)	d_{SiO_2} (Å)	[Cl] _{max} (at. cm ⁻³)	[Cl] _{avg} (at. cm ⁻³)
900	2	1155	2.2×10^{20}	1.7×10^{20}
1000	0.5	995	3.2×10^{20}	1.7×10^{20}
1000	2	914	6.0×10^{20}	4.4×10^{20}
1150	2	~550	1.2×10^{21}	1.2×10^{21}

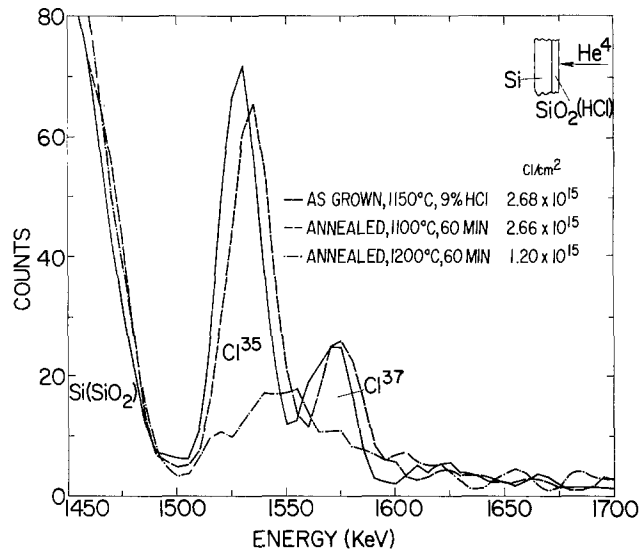


Fig. 5. Chlorine distribution in a HCl oxide (1150°C, 9% HCl, 920Å) before and after annealing for 60 min at 1100° and 1200°C.

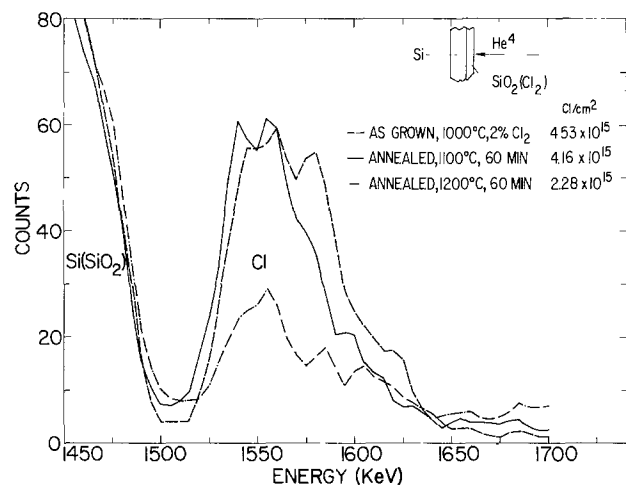


Fig. 6. Chlorine distribution in a Cl₂ oxide (1000°C, 2% Cl₂, 975Å) before and after annealing for 60 min at 1100° and 1200°C.

Sequential growth studies.—In an effort to better understand chlorine motion through the SiO₂ films, a number of oxides were grown in two steps, i.e., the oxidative ambient and (sometimes) temperature were changed by transferring the sample to a different furnace after an initial oxidation. The conditions are listed in detail in Table V. It must be recalled that oxide growth occurs at the Si-SiO₂ interface so that the outer oxide is formed in the first step.

Samples 1-4 were prepared to explore possible differences in chlorine incorporation when HCl or Cl₂ are added during only part of the oxide growth process. When the initial oxide is grown in 100% O₂ (sam-

Table V. Overview of sequentially grown oxides

Sample No.	Step 1			Step 2			
	T ₁ (°C)	Ambient (v/o)	d ₁ (Å)	T ₂ (°C)	Ambient (v/o)	d ₂ (Å)	d _{tot} (Å)
1	1150	100 O ₂	900	1150	91 O ₂ + 9HCl	108	1008
2	1000	100 O ₂	800	1000	98 O ₂ + 2Cl ₂	72	872
3	1150	91 O ₂ + 9HCl	776	1000	100 O ₂	453	1229
4	1000	98 O ₂ + 2Cl ₂	702	1000	100 O ₂	373	1075
5	1150	91 O ₂ + 9HCl	787	1000	100H ₂ O	252	1039
6	1000	98 O ₂ + 2Cl ₂	627	1000	100H ₂ O	448	1075

ples 1 and 2), the chlorine was found to be incorporated in the general area of the oxide layer grown during the second step. Little qualitative difference is therefore observed between the chlorine profile in sample 1 and that in the regular HCl oxides discussed earlier. On the other hand, the distinction is obvious for the films grown with Cl₂ added to the ambient: the chlorine in sample 2 is located only in the part of the oxide that is closest to the Si-SiO₂ interface, whereas in regular Cl₂ oxides the incorporation takes place over a much wider range. Experimental broadening of the profiles makes it difficult to judge whether incorporation in samples 1 and 2 has occurred solely within the second layer. Assuming, however, that this is indeed the case, it is calculated that for the HCl oxide (Cl)_{avg} = 5.6 × 10²⁰ at. cm⁻³ and for the Cl₂ oxide (Cl)_{avg} = 6.1 × 10²⁰ at. cm⁻³. These concentrations do compare closely to the values of [Cl]_{max} measured on one-step oxides grown under the same conditions (Tables II and III). Measurements on samples 3 and 4 which had their final oxidation take place in 100% O₂ showed that the chlorine incorporated during the first oxidation step followed the SiO₂-Si interface during the second step and afterward was located mainly in the layer grown in this last step. Considerable loss of chlorine to the atmosphere did apparently occur (60-70%), since the concentrations calculated on basis of the amount detected and the width of the first layer were quite low.

Samples 5 and 6 were grown to greater thickness in steam after the initial growth in O₂ + HCl or O₂ + Cl₂. This caused the chlorine to be removed almost completely (>90%). This process apparently proceeds quite rapidly as the time necessary to grow the additional (steam) oxide was relatively short: 2½ min for sample 5, 4 min for sample 6.

Electrical analysis.—To gain insight into the electrical effects associated with chlorine incorporation in SiO₂, two types of experiments were performed. In the first group, otherwise uncontaminated oxide samples were grown in O₂ + HCl or O₂ + Cl₂, metallized, and tested by MOS capacitance-voltage techniques. In the second series of experiments such oxides were intentionally contaminated with Na in an effort to relate the halogen incorporation quantitatively to sodium neutralization efforts reported earlier (3, 4, 13, 24, 25).

The electrical stability of the silicon surface potential under bias was measured to determine the effects of the incorporated chlorine. Capacitance-voltage plots are an excellent measure of the concentration of charged species and their spatial distribution in silicon dioxide (26). As such they are very sensitive to charge motion. In order to make these measurements, an array of aluminum capacitor dots was evaporated onto the silicon dioxide. Oxides grown in either HCl or Cl₂ show exceptionally low oxide charge (<10¹¹ charges/cm²). As previously reported (5, 13), these oxidation additions have proven effective in reducing the charge levels obtained with oxidation in pure O₂.

Under bias at room temperature, however, the Cl₂ oxides were electrically unstable. Both positive and negative flatband voltage shifts were seen and they were of opposite sign as the applied electrode voltage. These shifts were indicative of considerable mobile charge (~10¹² charges/cm²) and they were much larger than the mobile charge levels (<10¹⁰/cm²) normally found. The fact that positive as well as negative voltage shifts were seen demonstrated: (i) that the charges must have originated from the bulk of the oxide film rather than at an interface, and (ii) that both negative and positive charges were involved. Apparently neutral centers were initially present within the oxide and were ionized by the applied voltage. Charge of one sign moved in the field in order to give the dipole charge that resulted in a flatband voltage shift. Unfortunately it was not possible with these measurements to determine the sign of the mobile

species. It was noted that the level of mobile charges (as calculated from the ratio of the flatband voltage shift to the oxide thickness) seen here was ~10¹² cm⁻² and thus considerably less than the amount of incorporated Cl (~10¹⁶/cm²). Either only a small fraction of the Cl becomes charged under bias or the separation of positive and negative charges is extremely small. For instance, 10¹⁶ charges/cm² with positive and negative centers 0.1Å apart would give the same flatband voltage shift as 10¹² charges/cm² that were 1000Å apart. If the charge separation were actually less than an angstrom one might expect a very significant relaxation when the applied field is removed. Some relaxation is indeed seen but many hours are required for the flatband voltage shift to decay even 10-20%. Furthermore with the Cl uniformly incorporated, the separation between positive and negative centers would be small regardless of the separation of the charge centroids, and some relaxation might be expected in any case.

As a test of field-induced chlorine motion, metal (Pt)-oxide (Cl₂ oxide)-silicon capacitor structures were biased while *in-situ* backscattering profiles were measured. No Cl shift was detected with fields of ±6 MV/cm even though electronic currents and flatband voltage shifts were substantial.

The transient flatband voltage was monitored to help determine the kinetics of charge ionization and motion in Cl₂ grown oxides. A typical flatband shift vs. (time)^{1/2} is given in Fig. 7 for several applied bias voltages. The Al(-) bias polarity was chosen for most measurements to keep any positively charged contaminants like Na⁺ at the metal-SiO₂ interface where they do not contribute to the flatband voltage. With this bias, a positive flatband shift corresponds to the negative charge center being closer to the silicon than the positive center. A negative flatband voltage shift cannot be explained by charge motion under the influence of the applied field and is commonly referred to as a negative bias instability; models have been proposed (27-30) to account for this behavior, but very little is known about it. The abscissa is (time)^{1/2} since both diffusion-limited (26) and emission-limited processes (30-32) should give linear plots with this scale. Clearly the observed behavior is very complex; nevertheless it is qualitatively reproducible in Cl₂ grown oxides. The magnitudes of the shifts are merely larger when more Cl₂ is incorporated during oxidation. At a moderately high applied voltage (60V in Fig. 7) we observe a negative shift, primarily occurring at short time. At very high voltages the flatband voltage initially increases with time. When an intermediate voltage is used the flatband first goes negative and then positive like the lower curve in Fig. 8. Instead of continuing to increase indefinitely or saturate at higher voltages, ΔV_{FB} decreases at long times. The onset and the rate of this decrease is accelerated by higher applied voltage. This final mode is characterized by distorted

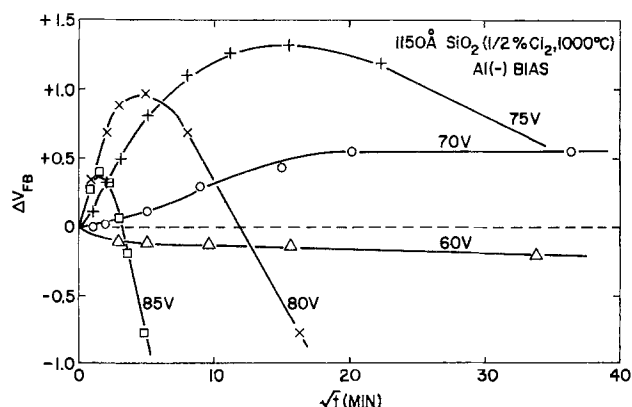


Fig. 7. Time dependence of the flatband voltage shift for an 1150Å SiO₂ film (1000°C, 0.5% Cl₂). The aluminum electrode was biased negatively.

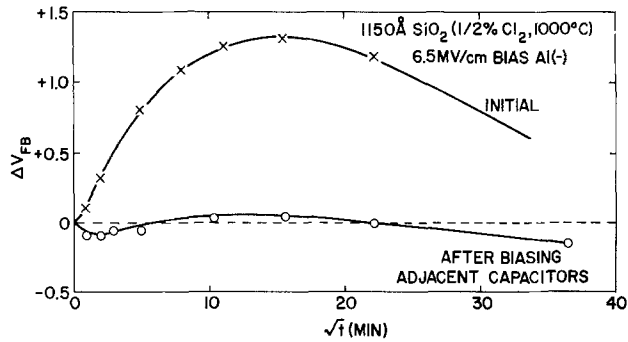


Fig. 8. Change in flatband voltage transient as a result of stressing capacitors adjacent to the capacitor of interest.

rather than parallel shifts in the capacitance-voltage curves. This distortion is characteristic of interface state generation. Thus the flatband voltage of Cl oxides has three components: an initial negative or delayed positive shift, a positive shift, and a negative voltage shift with time. The first component is most pronounced at moderately high fields (6 MV/cm) and the last at very high fields (8 MV/cm). The mechanism of the first component is unknown; mobile charge motion can explain the second; and interface state generation dominates the third.

In addition to having very complex kinetics, the flatband voltage of Cl₂ oxides exhibits a proximity effect. Measurements were made of individual capacitors (32 mils diameter) in a larger array (intercapacitor spacing was 80 mils). Flatband voltage shifts were reproducible provided that a capacitor on a virgin wafer was tested even after several months of room temperature storage. When several capacitors on a wafer were biased, however, the flatband shifts were greatly reduced in magnitude (see Fig. 8). Note that all three components of the flatband instability are still present after adjacent capacitors had been biased. This effect was first observed with Na neutralization measurements on HCl oxides. Metal-oxide-semiconductor capacitors on freshly prepared wafers were able to neutralize large amounts of sodium ($\sim 10^{13}/\text{cm}^3$); however, very little was neutralized ($\sim 10^{12}/\text{cm}^2$) on wafers where adjacent capacitors were biased. Again storage could not explain the effect; it was a direct result of the bias.

On the other hand, the flatband voltage shifts seen with HCl grown oxides were all negative (see Fig. 9). The shifts could be extremely large but did not become appreciable unless a very high electric field was applied (over 6 MV/cm for the extreme case of a film grown in 9% HCl at 1150°C). More thorough examination of the C-V curves showed considerable distortion; the method of Gray and Brown (33) was used to confirm the generation of interface states during this high field biasing. At the low fields typically encountered

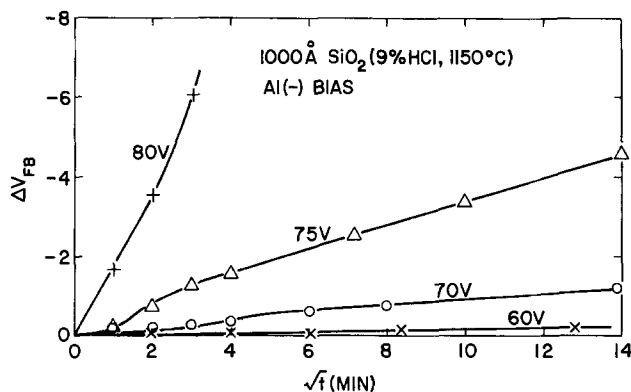


Fig. 9. Time dependence of the flatband voltage shift for a 1000 Å SiO₂ film (1150°C, 9% HCl). The aluminum electrode was biased negatively.

with FET gate dielectrics (~ 2 MV/cm), HCl oxides were no less stable than conventionally grown oxides.

Sodium neutralization in halogen grown oxides was studied for the purpose of establishing a possible correlation with the amount of incorporated chlorine. Several important and previously unreported observations were made. First, different methods to measure the amount of neutralized sodium gave different results. For example, flatband voltage shifts after a bias-temperature stress gave different values for the amount of neutralized Na than did reversible charge time ($Q-t$) measurements of the mobile charge after initially neutralizing some of the charge. Second, using ($Q-t$) measurements, the amount of neutralized and immobile sodium appeared to be a fixed fraction of the total amount present. In 9% HCl oxides grown at 1150°C only about 1/3 of the total sodium was immobile from 10^{12} - 10^{14} Na⁺·cm⁻². Even though sodium might be neutralized (as measured by C-V) it is not necessarily immobile (since $Q-t$ reveals the presence of mobile charged species) and still presents a potential stability problem. Limited data suggest that the effect of oxidation temperature and halogen concentration is merely to change the ratio of immobile to total sodium. This finding is in sharp contrast with the hypothesis that the halogen oxides contain a certain number of trapping sites and all sodium is neutralized until the Na concentration exceeds the trap concentration. The qualitative results of Kriegler showing the degree of neutralization to increase with halogen concentration and oxidation temperature were verified; the immobile Na concentration ($Q-t$ measurements) does indeed increase with the peak Cl concentration. However, this increase appears to be sublinear and the amount of neutralized Na is never more than a small fraction of the amount of chlorine incorporated (<1%). Based on these and earlier data it is apparent that the sodium neutralization is a complex phenomenon and requires more information before a meaningful model can be postulated.

Summary

A study was made of the chemical and electrical properties of thin SiO₂ films (500-1400 Å) grown at temperatures ranging from 900°-1150°C under addition of small amounts of HCl (0-9 v/o) or Cl₂ (0-2 v/o) to the oxygen ambient. Chlorine is known to be incorporated into such oxides and it was found that the oxide refractive index depends on the growth conditions.

Nondestructive measurement of the chlorine concentration profile took place by nuclear backscattering spectroscopy using He⁴ ions as the bombarding species. Under otherwise similar growth conditions (time, temperature, additive concentration), more than ten times as much chlorine was incorporated into Cl₂ oxides than into HCl oxides. For both additives incorporation increased with oxidation temperature and percentage added. No chlorine incorporation could be measured in the silicon substrate ($[\text{Cl}] < 3 \times 10^{19} \text{ cm}^{-3}$). The highest average oxide concentration was 5 atomic percent in a sample grown in 2% Cl₂ at 1150°C. In HCl oxides the maximum concentration is found at the Si-SiO₂ interface; as the distance from this interface increases, a rapid decrease in the concentration occurs and the oxide near the surface contains little if any chlorine. In Cl₂ oxides, on the other hand, the peak at the Si-SiO₂ interface is much broader and it appears as if a fairly even distribution exists throughout most of the film. Accordingly, peak and average concentrations are quite similar for Cl₂ oxides, but not for HCl oxides.

Annealing in N₂ shows that the incorporated chlorine is slowly removed at temperatures between 1100° and 1200°C. Experiments in which HCl or Cl₂ was present only during part of the oxidation process show the chlorine to disappear from the oxide very rapidly by subsequent oxidation in steam.

Electrical measurements were made on MOS capacitors using HCl or Cl₂ oxides. At low applied fields, such oxides had lower charge levels than control oxides; at high fields (> 6 MV/cm) different types of electrical instability were observed. One type was ascribed to a mobile species in Cl₂ oxides. Interface state generation also contributed to the instability at very high fields (> 8 MV/cm). Sodium neutralization was monitored in Na-contaminated HCl oxides by measuring the amount of mobile charge; the results indicated that only a fixed fraction of the sodium is trapped regardless of the initial concentration.

Manuscript submitted April 19, 1974; revised manuscript received Aug. 19, 1974.

Any discussion of this paper will appear in a Discussion Section to be published in the December 1975 JOURNAL. All discussions for the December 1975 Discussion Section should be submitted by Aug. 1, 1975.

Publication costs of this article were partially assisted by IBM Corporation.

REFERENCES

1. P. H. Robinson and F. P. Heiman, *This Journal*, **118**, 141 (1971).
2. R. S. Ronen and P. H. Robinson, *ibid.*, **119**, 747 (1972).
3. R. J. Kriegler, *Appl. Phys. Letters*, **20**, 449 (1973).
4. R. J. Kriegler, Y. C. Cheng, and D. R. Colton, *This Journal*, **119**, 388 (1972).
5. H. Chen and J. W. Hile, *ibid.*, **119**, 223 (1972).
6. H. Severi and G. Soncini, *Electron. Letters*, **8**, 402 (1972).
7. D. R. Young and C. M. Osburn, *This Journal*, **120**, 1578 (1973).
8. C. M. Osburn, *ibid.*, **121**, 809 (1974).
9. N. J. Chou, C. M. Osburn, Y. J. van der Meulen, and R. Hammer, *Appl. Phys. Letters*, **22**, 380 (1973).
10. R. L. Meek, *This Journal*, **120**, 308 (1973).
11. Y. J. van der Meulen and J. G. Cahill, *J. Electron. Mater.*, **3**, (1974).
12. K. Hirabayashi and J. Iwamura, *This Journal*, **120**, 1595 (1973).
13. R. J. Kriegler, in "Semiconductor Silicon 1973," Howard R. Huff and Ronald R. Burgess, Editors, p. 363, The Electrochemical Society Softbound Symposium Series, Princeton, N. J. (1973).
14. Y. J. van der Meulen, *This Journal*, **119**, 530 (1972).
15. M. H. Brodsky, D. Kaplan, and J. F. Ziegler, *Appl. Phys. Letters*, **21**, 305 (1972).
16. M.-A. Nicolet, J. W. Mayer, and I. V. Mitchell, *Science*, **177**, 841 (1972).
17. W. K. Chu, J. M. Mayer, M.-A. Nicolet, T. M. Buck, G. Amsel, and F. Eisen, *Thin Solid Films*, **17**, 1 (1973).
18. T. F. Ziegler and W. K. Chu, Nuclear and Atomic Data Tables (to be published).
19. W. H. Bragg and R. Kleeman, *Phil. Mag.*, **10**, 5318 (1905).
20. J. E. Baglin and J. F. Ziegler, *J. Appl. Phys.*, **45**, 1413 (1974).
21. W. K. Chu, B. L. Crowder, J. W. Mayer, and J. F. Ziegler, *Appl. Phys. Letters*, **22**, 490 (1973).
22. I. V. Mitchell, M. Kamoshida, and J. W. Mayer, *J. Appl. Phys.*, **42**, 4378 (1971).
23. R. Gdula, Private communication.
24. R. J. Kriegler, *Thin Solid Films*, **13**, 11 (1972).
25. R. J. Kriegler and T. F. Devenyi, "Reliability Physics 1973," p. 153, IEEE, New York, N. Y.
26. E. H. Show, A. S. Grove, B. E. Deal, and C. T. Sah, *J. Appl. Phys.*, **36**, 1664 (1965).
27. D. Goetzberger and H. E. Nigh, *Proc. IEEE*, **54**, 1454 (1966).
28. B. E. Deal, M. Sklar, A. S. Grove, and E. H. Show, *This Journal*, **114**, 266 (1967).
29. Y. Miura and Y. Matukura, *Jap. J. Appl. Phys.*, **5**, 180, 582 (1966).
30. S. R. Hofstein, *Solid State Electron.*, **10**, 657 (1967).
31. S. R. Hofstein, *IEEE Trans. Electron Dev.*, **ED-13**, 222 (1966).
32. J. M. Eldridge and D. R. Kerr, *This Journal*, **118**, 986 (1971).
33. P. V. Gray and D. M. Brown, *Appl. Phys. Letters*, **8**, 31 (1966).

Bipolar Charging of Low Density Polyethylene under Corona Discharges

I. B. Jordan

Université Laval, Québec, Canada G1K 7P4

ABSTRACT

Low density polyethylene films 25-100 μm thick were corona-charged between parallel-plane electrodes under d-c fields ranging from 0.4 to 2 MV/cm. These films were studied for their electret properties in air at atmospheric pressure and room temperature by measuring the external residual field 1 min after charging. Observations show that there is a limit to the dipole effect in polyethylene depending upon the charging voltage and upon the delay of measurement after charging. This limit is determined by an increase of the rate of injected charge decay with the initial charge density.

Charge trapping in polymers can be achieved by a variety of methods; among them are thermal procedures (1), simultaneous application of heat and an electric field, application of a breakdown field (2), electron bombardment, and corona discharge (3). Application of corona discharge under high electric stress is of more practical interest in the case of low density polyethylene because of the use of this material as a high voltage insulation and its deterioration under corona discharges. Low density polyethylene offers no advantage from the point of view of electret production because of its relatively low stability (4).

Key words: electret, polyethylene, charge, corona, air.

Experiments

The observations reported here were made on thin films (25, 50, and 100 μm thick) of commercial low density polyethylene having a density of 0.92 g/cm³ and a melting point of about 115°C. An infrared transparency spectrum of the material is shown in Fig. 1. Samples 5 \times 5 cm were placed between circular electrodes 3.7 cm in diameter (Fig. 2). An insulating ring spacer was inserted between the upper electrode and the film for most of the measurements. Several films could be charged simultaneously, as shown in Fig. 3. After charging for a given period of time, the insulating spacer was removed, the upper electrode was

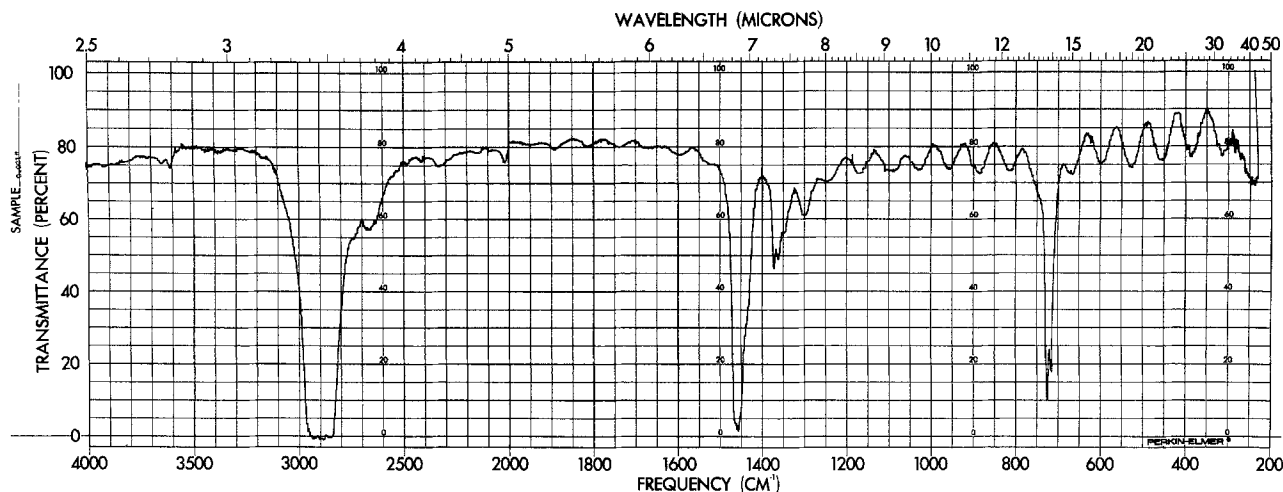


Fig. 1. Infrared spectrum of a sample of polyethylene film 25 μm

brought into contact with the film, and the electrodes were externally short-circuited for 30 sec. Then the residual field was measured at the polymer surface using an electrostatic fieldmeter (Monroe Electronics). Measurement of desorption current was made with a sensitive d-c meter (Boonton Electronics).

All investigations were carried out in air at atmospheric pressure, room temperature (22°-24°C), and a relative humidity of about 25%.

Results

Measurements were first made with an insulating ring 37 μm thick inserted between the sample and the upper electrode. The residual field measured after charging increased with duration of applied voltage, with a time constant of the order of 10 min. This constant did not change appreciably with sample thickness; therefore a charging time of 15 min was used in all further tests. The infrared spectra have shown that the decrease in transparency resulting from corona-induced oxidation did not exceed 5%.

The exposure time having been determined, the dependence of the residual field upon the charging voltage was investigated. The residual field, as measured 1 min after voltage removal, initially increased with charging voltage, reaching a maximum value (Fig. 4) which depended upon the sample thickness, and thereafter decreased. Maximum field was not influenced significantly by the insulating spacer thickness. However higher corona pulses were observed with longer gaps, leading more easily to sample breakdown under higher stresses. The residual field did not change when the sample was charged without a spacer, but the number of the sample breakdowns was as high as in the case of thicker dielectric inserts.

For obvious reasons it is very difficult to make a direct study of an air layer sandwiched between a polyethylene film and a metal electrode. Capacitance measurements can however give valuable information about the mean thickness of this layer. For this purpose silver electrodes were vacuum deposited on both sides of a 25 μm -thick sample. The capacitance between these electrodes, measured at 1 kHz, was in accordance

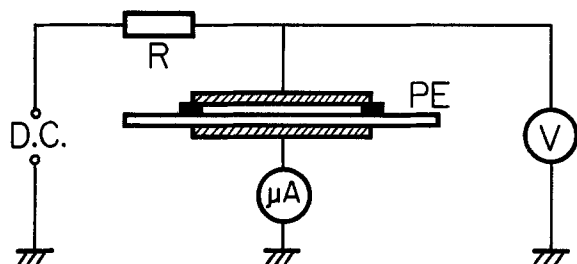


Fig. 2. Circuit for charging polyethylene samples

with the sample thickness and dielectric constant, and did not change significantly when a sample was subjected temporarily to a high electric stress. The behavior of a polyethylene film sandwiched between plain brass electrodes was completely different. First, the measured capacitance was 3.5 times lower than in the previous case. This could be attributed to the presence of air layers having an average thickness of 12 μm on each side of the film. Second, the thickness of these layers decreased to 7 μm when a sample was put under 2 kV for a few seconds.

Residual field was not influenced by the electrode material as far as tests with brass, steel, and aluminum electrodes may be considered conclusive. However, it was influenced by surface smoothness; higher charge

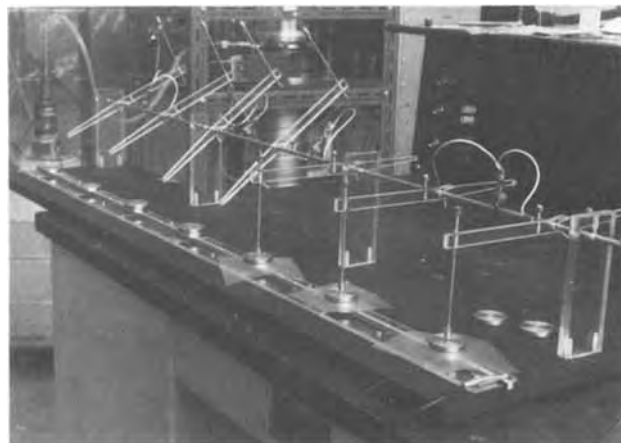


Fig. 3. Experimental setup

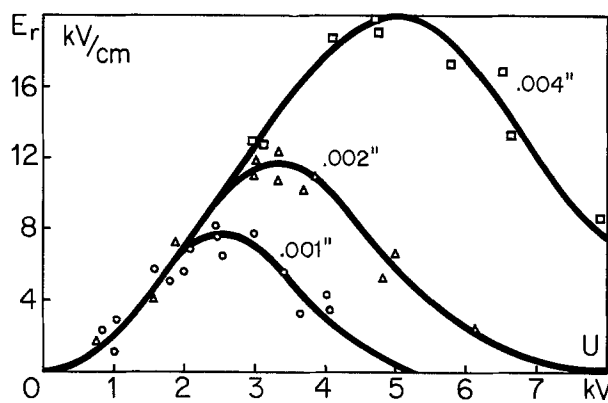


Fig. 4. Residual field E_r as a function of applied voltage U , for three thicknesses of polyethylene film.

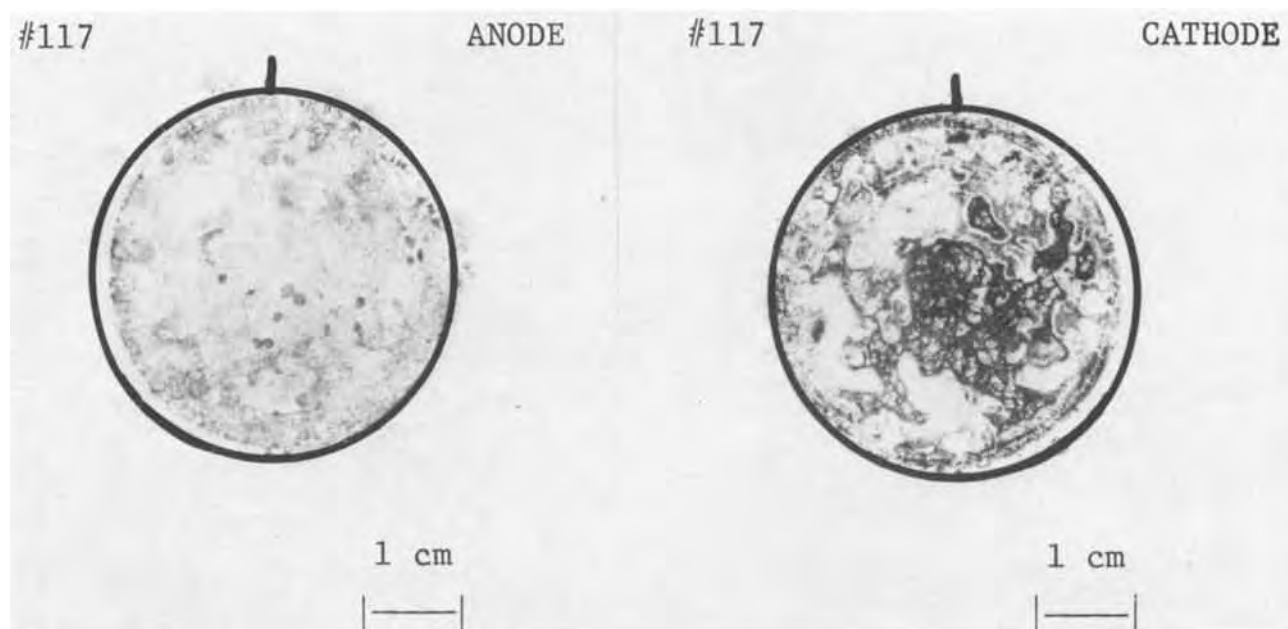


Fig. 5. Lichtenberg figures of both surfaces of a 50 μm thick sample. Formation voltage, 4 kV

densities were for the most part obtained with rough electrode surfaces.

Finally, the temperature influence was investigated. Electrodes and samples were kept under voltage for 15 min at constant elevated temperatures, ranging between 25° and 80°C, then cooled rapidly to ambient temperature before voltage removal and sample short-circuiting. This process did not yield any higher residual fields, despite the fact that the charging current increased from $5 \cdot 10^{-10}\text{A}$ at 25°C to $2 \cdot 10^{-6}$ at 80°C (film 25 μm under 2 kV). However a large scatter of values was observed.

It became clear therefore that the residual field is the result of charge injected by corona discharges. The charging was not symmetrical. At lower voltages (on the rising slope of curves in Fig. 4) the positive homocharge prevailed, whereas at higher voltages (on the falling slope) the opposite was true in most of the cases.

In order to get further insight into the charging mechanism, Lichtenberg dust figures of both surfaces were made with a mixture of Neon Red and Saturn Yellow fluorescent pigments of Day-Glo Color Corporation. An orthochromatic film was used for the photographs (Fig. 5). The black surfaces (red in reality) correspond to negatively charged regions, whereas the gray half-tones correspond to positive areas (yellow on a color film). The pictures show the heterogeneity of the charging process. Both surfaces display the presence of positively and negatively charged regions. However the prevailing charge on a given side had the same polarity as the adjacent electrode during the charging process.

Two additional investigations were undertaken to explain the peculiar form of the residual field curves (Fig. 4): a study of temporal field decay, and a measurement of desorption current transients. Results of the first study are shown in Fig. 6. The charge decay depends evidently on charging voltage, and different curves may cross each other. This phenomenon was discovered by Ieda, Sawa, and Shinobara (5) in polyethylene samples with small amounts of surface active agents.

Results of the second study are given in Fig. 7. The discharging current of samples charged under voltages below 2 kV flowed in a direction opposite to the direction of the charging current, whereas a current inversion was observed in samples subjected to higher stresses. The voltage corresponding to the appearance of homocurrent depended upon the electrode surface

condition. For smoothly polished electrodes the current reversal appeared only at higher voltages. With rough electrodes the homocurrent was observed even after charging at 1.5 kV.

Discussion

When a low density polyethylene film is inserted between parallel-plate electrodes, two air layers about 10 μm thick usually remain trapped between the film and metal electrodes. Thicknesses of these layers decrease under applied voltage due to attractive electrostatic forces between electrodes. These air layers are of course far from being uniform and their heterogeneity probably increases with the beginning of corona activity as could be deduced from the dust figures (Fig. 5). This activity appears at a potential difference close to Paschen's minimum, since the pd value under atmospheric pressure is close to critical. Below corona onset the desorption current transients (Fig. 7) exhibit only the presence of heterocharges. These charges are deposited on the polyethylene surface and also at the interfaces between amorphous and crystalline regions

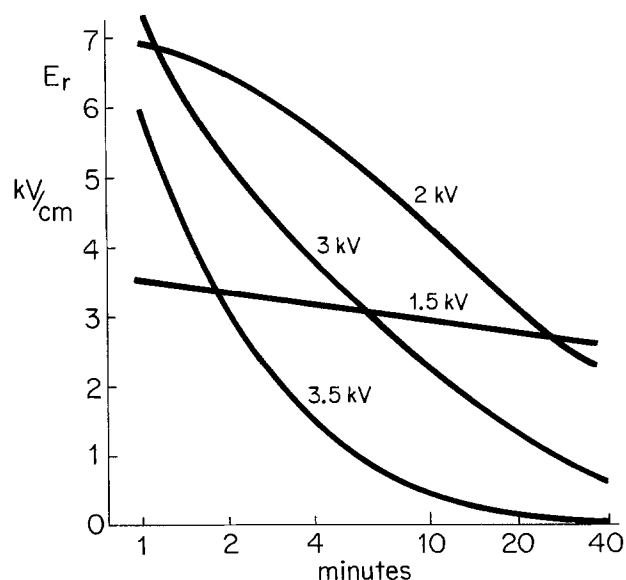


Fig. 6. Field decays at polyethylene samples 25 μm thick after charging under various voltages. Charging time of 15 min followed by 30 sec of short-circuiting.

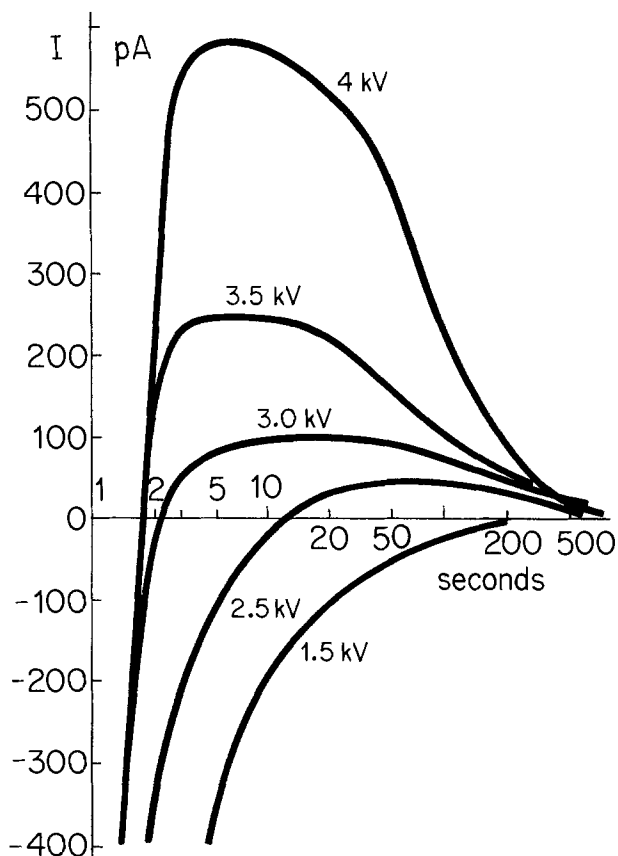


Fig. 7. Desorption current transients of polyethylene samples 25 μm thick after charging under various voltages.

of polymer (low density polyethylene under investigation was about 50% amorphous).

Charge injection from ionized air layers became important under voltages exceeding 1 kV (in our investigations the onset voltage was independent of sample thickness). This was manifested by the appearance of a residual field (Fig. 4) and by desorption current inversion (Fig. 7). Figure 7 shows that amplitude of the homocurrent increases exponentially with applied voltage. Therefore the charge densities and the residual field should also increase with the voltage. But the

homocurrent in samples subjected to high stress reaches its peak in a few seconds after voltage removal and then decreases with a rate depending upon applied voltage. Figure 6 indicates that the higher the charging voltage and the initial injected charge density, the faster is the residual field decay. Therefore the residual field measured 1 min after voltage removal reaches its maximum as shown in Fig. 4 and then decreases again. There is also a second factor limiting the residual field increase in thicker samples, air ionization at the sample surface.

Conclusions

Investigation of desorption current of corona charged low density polyethylene shows two distinct charging processes: heterocharge moving towards electrodes after short-circuiting, and homocharge injected by corona discharges in air and moving through polymer after external field removal. Under low stress, only heterocharge is observed. At higher voltages the homocharge becomes dominant. Drift of this charge is strongly influenced by initial charge density; it decays more rapidly when the initial injected charge density is high. This phenomenon, and crossing of field decay curves (Fig. 6), are responsible for the peculiar form of residual field curves (Fig. 4) measured some time after charging voltage removal. Density of injected homocharge depends upon the corona activity and indirectly upon the electrode surface condition.

Manuscript submitted June 19, 1973; revised manuscript received Aug. 14, 1974.

Any discussion of this paper will appear in a Discussion Section to be published in the December 1975 JOURNAL. All discussions for the December 1975 Discussion Section should be submitted by Aug. 1, 1975.

Publication costs of this article were partially assisted by Université Laval.

REFERENCES

1. F. Gutmann, *Rev. Mod. Phys.*, **20**, 457 (1948).
2. G. M. Sessler and J. E. West, *J. Appl. Phys.*, **43**, 922 (1972).
3. R. A. Creswell and M. M. Perlman, *ibid.*, **41**, 2365 (1970).
4. R. A. Creswell, M. M. Perlman, and M. A. Kabayama, in "Dielectric Properties of Polymers," F. E. Karasz, Editor, p. 295, Plenum Press, New York (1972).
5. M. Ieda, G. Sawa, and U. Shinobara, *Japan J. Appl. Phys.*, **6**, 793 (1968).

High Resolution Tungsten Patterning Using Buffered, Mildly Basic Etching Solutions

T. A. Shankoff and E. A. Chandross

Bell Laboratories, Murray Hill, New Jersey 07974

ABSTRACT

Prior to this work, commonly available chemical etches for tungsten were difficult to use for high resolution patterns because of their incompatibility with available positive and negative photoresists. Rapid attack by basic hydrolysis made the use of positive resists impossible and the use of negative resists difficult. It was found that solutions of $K_3Fe(CN)_6$ which were buffered in the mildly basic pH range of 7.5-9.5 etch tungsten as fast as the previously used highly alkaline $KOH-K_3Fe(CN)_6$ etches (pH 13-14) but are far better in the practical fabrication of tungsten-based integrated circuits. These etches can be used to delineate patterns of high resolution (1-2 μm range) limited only by the photolithography, with no evidence of failure of either positive or negative photoresists.

Until the present time practical chemical etches for tungsten have involved strongly alkaline solutions of an oxidizing agent, e.g., H_2O_2 in aqueous NH_3 (1) or $K_3Fe(CN)_6$ in aqueous KOH (2). The use of any metal as a conductive layer in a semiconductor device is dependent on pattern definition using standard photolithographic technology. Previous etchants suffered from either low etch rates at room temperature and/or too rapid attack of the photoresist material. All commonly available positive photoresists are rapidly hydrolyzed in aqueous alkaline solution, e.g., whereas AZ-1350 is actually dissolved away at pH 14 in less than 1 min, it loses its insulating ability at pH 12 in 1-2 min through loss of adhesion. Thus, for example, in recent work (3) it was found that the $KOH-K_3Fe(CN)_6$ system was unusable for defining circuits if the photoresist (both positive and negative) was exposed to the solution for as little as half a minute. Even KMER and KTFR fail during this time in the 5% KOH solution recommended (3). Since chemical etching rates were reported to be in the order of 30 \AA sec^{-1} , for practical purposes this system is unattractive. Because of this, electrochemical etching techniques have been used to obtain etching rates commensurate with resist lifetime in the $KOH-K_3Fe(CN)_6$ system (3).

Our approach to this problem was to seek a means of reducing the basicity of tungsten etching solutions to a range compatible with long protective lifetimes for both negative and positive photoresists, and yet maintain chemical etching as a viable means of tungsten pattern delineation.

Experimental

Reagents, materials, and equipment.—All reagents used were of the highest purity commercially available. Deionized water was used for all experimental work. Etchants were generally not filtered prior to employment.

The following equipment was used in the work: Coleman Model 37A pH Meter for all pH measurements; Cary Model 14 for spectroscopic work; Headway Research Photoresist Spinner EC101; Thayer and Chandler Airbrushes, Models C and E; and Teflon-coated tweezers for all etching rate data.

Etching techniques.—Samples of SiO_2/Si (0.5 cm^2) overcoated with tungsten (2500 \AA : resistivity 15-25 $\mu\text{ohm-cm}$) were etched by rapid hand agitation using 40 mliters of etchant in a 50 mliter beaker. The etching end point was taken as the visual disappearance of the last trace of tungsten from the sample.

Key words: tungsten etching, tungsten photolithography, tungsten metallization, tungsten processing.

High resolution etching of $1\frac{1}{4}$ in. wafers was done by spraying etchant with a Thayer and Chandler Model C or E Airbrush, using 25-50 lb in.⁻² air pressure, onto a photoresist (AZ-111 or KMER) patterned tungsten coated SiO_2/Si wafer spun at 100-1500 rpm on a Headway Model EC101 Photoresist Spinner. The airbrush was held 4-6 in. above and was centered on the wafer. Towards completion of etching the sample was inspected visually and etched for 5-10 sec intervals to completion. Final microscopic observation prior to resist removal was always made to ensure complete etching. Etching was stopped with distilled water and the sample was dried by spinning at 7000-8500 rpm. Two inch diameter wafers were etched in a similar manner with excellent results across a wafer. To compensate for the increased area, several spray nozzles (each covering a portion of the wafer) are directed at the rotating wafer.

Analytical.—It was found that 5.7 moles of $K_3Fe(CN)_6$ reacted with one mole of tungsten by determining the maximum weight of tungsten metal powder which could be dissolved in an etching solution. By using the molar extinction coefficient (4) of 290 at the $Fe(CN)_6^{-4}$ absorption maximum of 3250 \AA it was found that 0.1M $Fe(CN)_6^{-3}$ yielded 0.096M $Fe(CN)_6^{-4}$ in the exhausted etchant. Acidification of the exhausted etchant according to the method in Remy (5) produced the faintly yellow precipitate characteristic of the simple tungstate anion WO_4^{-2} .

Results

Development of buffered chemical etchants.—It has been established (6) that tungsten metal is passive to chemical attack in acid solution. More recently, data have been obtained (7) which show that the metal is electrochemically inactive at $pH \leq 6$ and undergoes oxidation at $pH \geq 6.5$. There are exceptions to this finding (8, 9), however; for example, concentrated aqueous $HF-HNO_3$ solutions attack the metal readily. Practically speaking it is clear that chemical etches for tungsten should operate in alkaline solutions. The important question is: How alkaline does the etching solution need to be in order to support tungsten oxidation and dissolution?

The initial set of experiments was directed at determining the minimum KOH concentration which could be used in the conventional $KOH-K_3Fe(CN)_6$ system with satisfactory etching results. The etch rate data for the system are presented in Fig. 1. It is seen that relatively rapid etching can be done by this system, but only at high pH values. When the pH is reduced to anything approaching a value compatible with positive

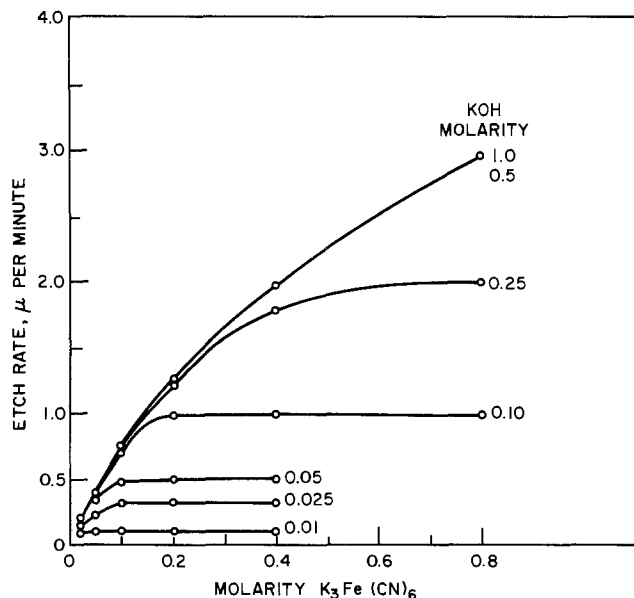


Fig. 1. Plot of tungsten etch rate vs. $K_3Fe(CN)_6$ concentration for various KOH concentrations.

photoresist stability ($pH < 12$, $< 0.01M$ KOH), very slow rates are obtained. Moreover, we found that samples etched in 0.01–0.025M KOH, 0.05–0.8M $K_3Fe(CN)_6$ solutions showed very nonuniform etching; etching always tends to occur from a photoresist-tungsten edge into a feature so that fine resolution patterns are lost before coarse features are resolved. In Fig. 2, a photomicrograph of an Ealing test chart etched into tungsten which was protected by $0.5 \mu m$ KMER using 0.02M KOH–0.5M $K_3Fe(CN)_6$ as the etchant, it can be seen that much metal remains in the very coarse 30 and $40 \mu m$ lines while the fine sets of lines are resolved. Moreover, overetching of the 2.0, 1.5, and $1.3 \mu m$ lines in the upper left of the pattern has become evident.

The trends evident in Fig. 1 make it obvious that further pH reduction by dilution of the strong base, KOH, would be futile. We felt that a reasonable approach at this point was to substitute weak bases for KOH in order to assess the effects of further pH reduction. A common practice for improving etch capacity while maintaining constant concentrations of certain etchant components is to include complexing agents for the metal in question. Ethylenediamine (en) was selected for the dual role of pH reduction and complexation. Even though there is a dearth of reported

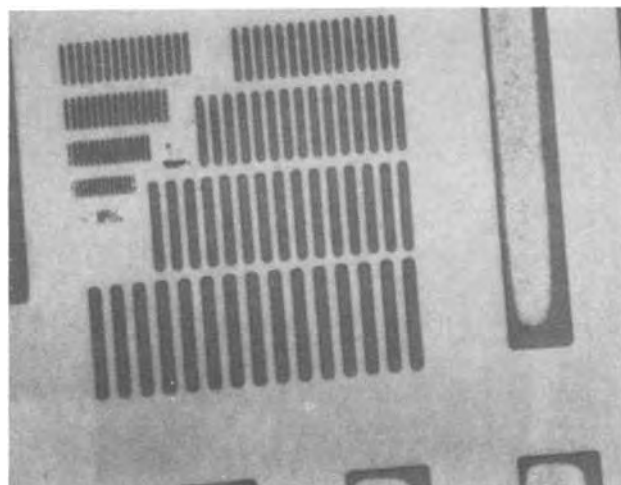


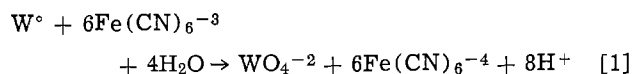
Fig. 2. Photomicrograph of an Ealing test pattern etched into tungsten using an etchant composed of 0.02M KOH and 0.5M $K_3Fe(CN)_6$. Note tungsten remaining in 30 and $40 \mu m$ lines and overetched small features.

amine- W^{+6} chemistry (W^{+6} is formed in the etch process) it was hoped that this strong ligand for inorganic cations might facilitate etching by complexing transiently formed species intermediate between W^0 and W^{+6} .

It was found that a solution of 0.01M $K_3Fe(CN)_6$ brought to pH 12 with en (1M) etches tungsten at the rate of $4600 \text{ \AA min}^{-1}$, compared with a pH 12 KOH- $K_3Fe(CN)_6$ rate of $1000 \text{ \AA min}^{-1}$. The data in Table I were obtained in an attempt to understand further the role of a weak base in the ferricyanide etching of tungsten. It can be seen that there is a fairly constant etch rate at pH 12 for the weak bases.

It was found that lowering the pH by dilution of the weak base leads to much the same result as reducing the pH by decreasing the KOH concentration; etch rates rapidly fall to very low values and nonuniform etching once again becomes a problem. It was subsequently discovered that etching rates of weak base-ferricyanide etchants could be maintained at a high level, while the pH is drastically reduced, by partially neutralizing the base with an acid to produce a buffered etching solution. This important finding is evident in the data tabulated in Table II, which shows the etch rate to be independent of pH over the range from unbuffered weak base (en at pH 12) to a pH value as low as 7.5, for constant $K_3Fe(CN)_6$ concentration. The same holds true for other common weak bases. There seems little reason to attempt to replace ferricyanide with an alternative oxidant. The innocuous nature of this chemical coupled with the lack of other oxidants which function adequately in basic solution governed this decision.

Mechanism of etching.—A logical explanation of the above results can be advanced by considering the chemistry of tungsten removal by a basic oxidizing solution. We can write Eq. [1]¹ for the etching of tungsten metal by an aqueous ferricyanide solution at any pH



It is obvious from Eq. [1] that the generation of H^+

¹ That 6 moles of $K_3Fe(CN)_6$ react for each mole of W^0 and that $Fe(CN)_6^{-4}$ is quantitatively formed in the redox reaction from $Fe(CN)_6^{-3}$ has been verified by the use of gravimetric and spectroscopic analysis. The presence of a simple tungstate (WO_4^{-2}) after oxidation as opposed to some more complex meta- or paratungstate has been established experimentally according to standard analytical procedure (5).

Table I. Etch rate data at pH 12 for aqueous 0.1M $K_3Fe(CN)_6$ solutions of several bases

Base	Molarity	Etch rate (\AA min^{-1})
1. NH_3	5.0	5800
2. Ethylene diamine	1.0	4600
3. Piperidine	0.2	4800
4. KOH	0.01	1000

Table II. Etch rate as a function of pH for aqueous 0.1M $K_3Fe(CN)_6$ solutions initially 1M in ethylene diamine (pH 12)

pH*	Rate (\AA min^{-1})
12.0	4600
11.0	5000
10.0	4800
9.0	4500
8.5	4300
8.0	4600
7.7	4800
7.5	4000
7.3	3300
7.1	1400
6.9	600

* The pH was lowered by the gradual addition of HCl to the etchant.

locally at the tungsten surface will potentially lead to acid passivation of tungsten. If sufficient base is present to neutralize the acid generated by dissolution of the metal the surface will remain active. The important factor is the ability of the etching solution to neutralize the acid and maintain the pH at a high enough value to prevent passivation. This does not depend on the hydroxide ion concentration but depends only on the concentration of Bronsted base and the rate at which the protons are removed from the metal-solution interface. Thus at a given pH a high concentration of weak base (e.g., an amine) may, depending on the kinetics, be much more effective than the corresponding low concentration of OH^- . Buffered solutions are effective because they have a high capacity for absorbing protons while maintaining the pH essentially constant. The buffering suppresses the hydrolysis of the weak base, thus keeping the OH^- concentration low while the solution still has a large capacity for rapidly neutralizing acid.

Description of representative systems.—We have studied several prototype etching systems which are based on the developmental work just described. Our initial work on the buffered systems was with en-HAc- $\text{K}_3\text{Fe}(\text{CN})_6$ maintained above the obvious passivation limit seen in Table II. We subsequently substituted HCl since a strong acid provides larger buffer capacity in the basic range than a weak one, when coupled with a weak base. The etch rate data presented in Fig. 3 are for various permutations of concentration for the system en-HCl- $\text{K}_3\text{Fe}(\text{CN})_6$ at pH 8.0. Remember that raising the pH to higher values has no effect upon the etch rates in these systems. The data in Fig. 4 are for

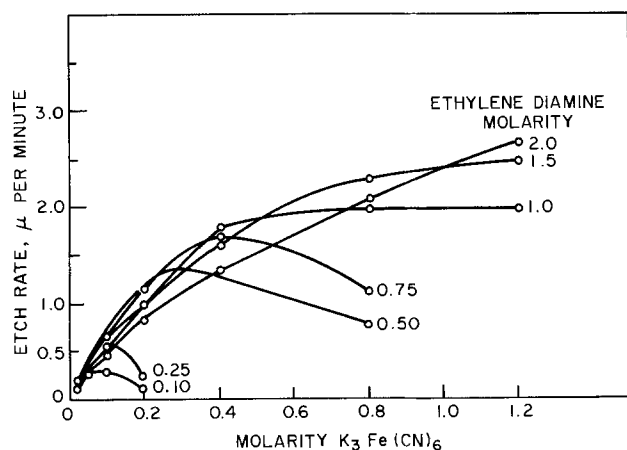


Fig. 3. Plot of tungsten etch rate vs. $\text{K}_3\text{Fe}(\text{CN})_6$ concentration for various ethylene diamine concentrations at pH = 8.0.

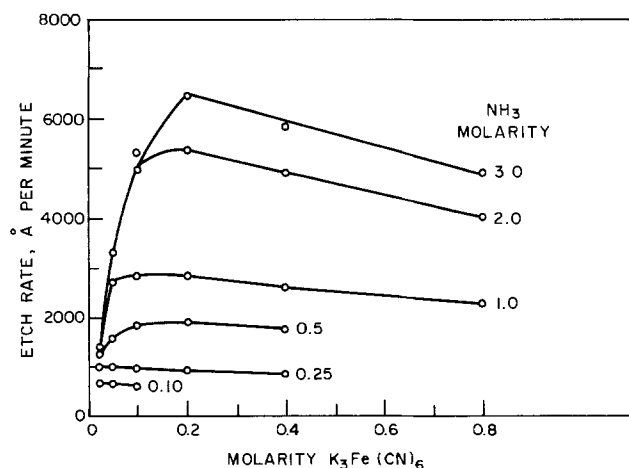


Fig. 4. Plot of tungsten etch rate vs. $\text{K}_3\text{Fe}(\text{CN})_6$ concentration for various NH_3 concentrations at pH = 8.0.

the closely related system $\text{NH}_3\text{-HCl-K}_3\text{Fe}(\text{CN})_6$, or $\text{NH}_3\text{-NH}_4\text{Cl-K}_3\text{Fe}(\text{CN})_6$, also maintained at pH 8.0.

In an attempt to determine whether a conventional inorganic buffer system could be substituted for the buffered amine systems, we obtained rate data for the $\text{KOH-KH}_2\text{PO}_4\text{-K}_3\text{Fe}(\text{CN})_6$ system at pH 8.0. These data are given in Fig. 5. The parameter of buffer concentration refers to the molarity of KH_2PO_4 in the solution. Note, that to achieve pH 8, it is necessary to add 0.92 moles of KOH to each mole of KH_2PO_4 . While the etch rates for this system do not approach those for en-HCl- $\text{K}_3\text{Fe}(\text{CN})_6$ or even those for $\text{NH}_3\text{-NH}_4\text{Cl-K}_3\text{Fe}(\text{CN})_6$, this system has important advantages which recommend it for routine tungsten etching. In the first place the weak amine base systems are unstable and some formulations must be used within 1-2 hr of preparation. Secondly, the etch rates are constant over a wide range of buffer and $\text{K}_3\text{Fe}(\text{CN})_6$ concentration, which is not the case for the en and NH_3 systems. Thus, this system is less sensitive to error in etchant preparation than the others. It is obvious that the employment of related weak bases and inorganic buffering systems should yield similar results.

Discussion

Mechanism.—It is not completely clear why the etch rate data behave as they do. It is readily seen that the maximum etching rate obtainable for a given base at constant base concentration follows the base ionization constants or base strengths without exception: $\text{KOH} > \text{piperidine} > \text{en} > \text{NH}_3 > \text{HPO}_4^{2-}$ (HPO_4^{2-} is the base in the $\text{KOH-KH}_2\text{PO}_4$ system) $>$ pyridine. While this is the case, the differences in rate cannot be quantitatively explained on this basis alone. We can make quantitative rate comparisons on the systems as follows: KOH , en, NH_3 , HPO_4^{2-} , pyridine, have relative rates of 200:60:10:3:1. For example, KOH is said to be three times as effective as en because the maximum etch rate possible for 0.1M KOH at any $\text{K}_3\text{Fe}(\text{CN})_6$ concentration is $10,000 \text{ Å min}^{-1}$ while that for 0.1M en is 3000 Å min^{-1} (see Fig. 1 and 3). The ionization constants and relative ionization (at 1 molar concentration) are 1 (100%), 9×10^{-5} (1%), 1.5×10^{-5} (0.4%), 10^{-7} (0.03%), and 1.4×10^{-9} (0.004%) for KOH , en, NH_3 , HPO_4^{2-} , and pyridine, respectively. The relative rates of 60:10:3:1 for the weak bases are reasonable when compared to the ionization percentages which might be interpreted as reflecting the importance of free OH^- to etching. As a group, however, the weak bases have rates close to the completely ionized KOH . Thus while the etch rates for weak bases are within a factor of three of that obtained for KOH , the absolute OH^- concentration is only 1% of that of the KOH solution. As emphasized above it is the dynamic ability of the solution to neutralize protons which is important rather than the absolute OH^- concentration. The amines are not quite as effective as is OH^- , as judged from the rate data, and this difference may be due to small differences in the rates of reaction with the actual acidic species.

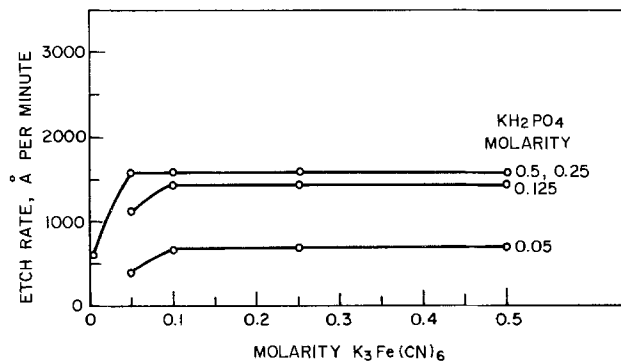


Fig. 5. Plot of tungsten etch rate vs. $\text{K}_3\text{Fe}(\text{CN})_6$ concentration for various KH_2PO_4 concentrations at pH = 8.0.

The similarity of the rates for mono- and difunctional amines suggests that coordination of metal ions is not important in the dissolution of tungsten. If it were so, en would be expected to be much more effective than the monofunctional amines. Further, we measured the etching rate vs. $K_3Fe(CN)_6$ concentration for 0.5M solutions of KOH, piperidine, en, and ammonia. The maximum rate in the amine solutions was highest for piperidine which is the strongest base of the three amines. This result suggests that coordination is not important in the dissolution of tungsten.

Etchant composition.—It is our observation that as long as the etch rate curves are in the ascending region of etch rate, then any etchant composition is useful and apparently equivalent as far as etching patterns are concerned. Once the concentration of $K_3Fe(CN)_6$ gets too far in excess of the base concentration needed to support tungsten dissolution then nonuniform and unpredictable etching results. Thus, for example, 0.5M en neutralized to pH 8 with HCl can be used with good results only up to 0.2M $K_3Fe(CN)_6$. Beyond this point the oxidation proceeds faster than surface depassivation and hard to remove oxidation products, which impede the etching process, become evident. This observation is consistent with our early finding that 0.01M KOH solutions produce nonuniform etching. In the case of the KOH- KH_2PO_4 - $K_3Fe(CN)_6$ system which has a wide region of constant etch rate, these problems do not show up as clearly as in the weak systems having steep etch rate curves.

Since the etch rate data above pH 7.5 show no significant dependence on pH and since the etchants can easily be prepared to ± 0.1 pH unit, then the use of the etchant at some pH safely above 7.5 is suggested, e.g., pH 8.0. The KOH- KH_2PO_4 - $K_3Fe(CN)_6$ system exhibits long shelf life if the etchant is stored in an amber bottle and its activity is assured if its pH remains above 7.5. Certain of the more concentrated en-HCl- $K_3Fe(CN)_6$ and NH_3 - NH_4Cl - $K_3Fe(CN)_6$ etchants are quite unstable, while the more dilute compositions (etch rates $< 10,000 \text{ \AA min}^{-1}$) should be used within a few hours of preparation.

We have included typical etching results in Fig. 6. Figure 6a shows the AZ-111 photolithograph and etching of an Ealing test pattern using 0.25M KH_2PO_4 , 0.24M KOH, and 0.1M $K_3Fe(CN)_6$, while Fig. 6b shows a CCD-L pattern etched using 0.5M en, 0.5M HCl, and 0.1M $K_3Fe(CN)_6$. The finest resolved Ealing line is 1.25μ in the photolithograph, while the smallest feature in the CCD-L pattern is 2.5μ wide. Tungsten samples 2500Å thick were etched using the spinning wafer spray etching technique described in the next section.

Etching technique.—Unless there is uniform exchange of etching products with fresh etching solution at the metal surface, obvious nonuniform etching occurs which is especially evident on 2 in. wafers. Every attempt must be made to minimize this nonuniformity consistent with the size of a device feature and the degree of undercutting that one can tolerate. Thus, where overetching of a 10μ m feature in a 2000Å thick tungsten film by 100% will hardly be noticeable, the same treatment of a 3μ m feature may be unwarranted.

We have found that while coarse patterns in the 25μ m range can be etched using almost any technique that one chooses, 1-10 μ m devices are best etched by spraying. We further suggest that some attempt be made to minimize spray pattern nonuniformities. Our best results have been obtained using single or multiple atomizing spray nozzles either centered on (1 nozzle) or uniformly distributed (> 1 nozzle) over a wafer rotating 4-6 in. beneath the nozzle(s). Generally, one can achieve results with undercutting of no greater than 0.25μ m per feature edge in 3500Å thick tungsten films across a 2 in. wafer.

Etching rates.—The etch rates presented here are for beaker hand-agitated etching at room temperature of small samples of sputter deposited tungsten films. They

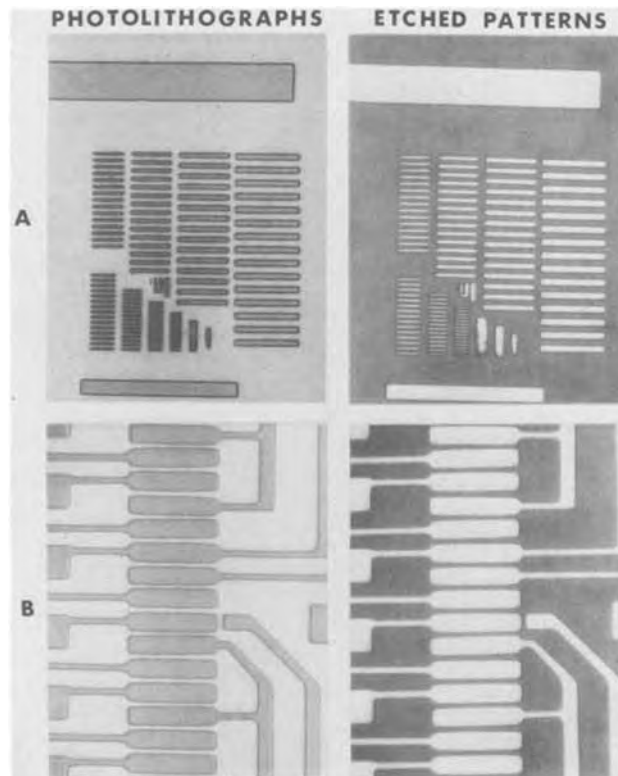


Fig. 6. Typical patterns etched into 2500Å of tungsten and initial photolithography. A, Ealing test pattern etched using 0.25M KH_2PO_4 -0.24M KOH-0.1M $K_3Fe(CN)_6$; smallest resolved set is 1.25μ m. B, CCD-L metallization pattern etched using 0.5M ethylene diamine-0.5M HCl-0.1M $K_3Fe(CN)_6$; gaps are 2.5μ m wide.

should be used only as a guide since etch rates vary with technique. In general those which involve the most vigorous movement of etchant to and from the metal surface produce the fastest etch rate. Thus, for example, certain spray techniques give rates 3-5 times as fast as those reported in this memorandum. We have found that in the range 20° - 45° C a 10° C rise in temperature approximately doubles the etch rate.

An etchant composition which furnishes adequate rate commensurate with the tungsten thickness being etched and ample time for unhurried etching is suggested for routine work.

Selection of photoresists.—There has been no evidence of degradation of any photolithograph either by direct attack or by loss of adhesion at feature edges using any of the prototype systems described earlier (pH 8). All photoresists, both positive and negative, are apparently satisfactory.

Summary

It has been found that a method of achieving satisfactory tungsten etching solutions is to replace the strong base in the KOH- $K_3Fe(CN)_6$ etching system by a buffer solution. This solution can be of any composition that functions in the mildly basic pH range (7.5-9.5). Thus buffered solutions obtained by neutralization of a weak base by a strong acid or by reaction of a strong base with a mono-basic weak acid (KOH- KH_2PO_4) are effective. We have shown that the etching rate in these systems generally follows the ionization constant or base strength.

As long as there is sufficient H^+ absorbing capacity in a particular etching solution the rate of etching depends only on the concentration of oxidant, $K_3Fe(CN)_6$. If this criterion is satisfied, uniform and reliable tungsten etching is easy to achieve. If the ability to absorb H^+ formed in tungsten oxidation becomes insufficient, then the oxidation is no longer the rate determining step and nonuniform, unpredictable etching occurs

owing to buildup of hard-to-dissolve oxidation products at the etching surface.

The three prototype systems studied [en-HCl-K₃Fe(CN)₆, NH₃-NH₄Cl-K₃Fe(CN)₆, and KOH-KH₂PO₄-K₃Fe(CN)₆] are all capable of excellent etching of high resolution tungsten device circuits as long as the selected composition meets the criterion of H⁺ absorbing capacity. We tend to favor KOH-KH₂PO₄-K₃Fe(CN)₆ (even though it furnishes the lowest etching rates) for general work owing to its long shelf life and relative independence of component concentrations. Where speed is required or thick tungsten samples (> 5000Å) must be etched, then the en-HCl-K₃Fe(CN)₆ system is recommended, provided the user is aware of the short shelf life of the etchant.

The gentle nature of K₃Fe(CN)₆ coupled with the near-neutral pH of etchant operation makes these systems completely compatible with all presently available photoresists.

Acknowledgment

We wish to thank J. L. Bartelt for suggesting the advantages of strong acids for buffering amines.

Manuscript submitted Dec. 21, 1973; revised manuscript received Sept. 9, 1974.

Any discussion of this paper will appear in a Discussion Section to be published in the December 1975 JOURNAL. All discussions for the December 1975 Discussion Section should be submitted by Aug. 1, 1975.

Publication costs of this article were partially assisted by Bell Laboratories.

REFERENCES

1. J. Drobek and V. E. Hauser, Bell Labs. Memorandum, 1969.
2. C. J. Smithells, "Tungsten," p. 121, Chapman and Hall, Ltd., London (1952).
3. W. Kern and J. M. Shaw, Paper 71 presented at the Electrochemical Society Meeting, Washington, D.C., May 9-13, 1971.
4. J. A. Ibers and N. Davidson, *J. Am. Chem. Soc.*, **73**, 476 (1951).
5. H. Remy, "Treatise on Inorganic Chemistry," p. 178, Elsevier Publishing Co., New York (1956).
6. T. Moeller, "Inorganic Chemistry," pp. 879 ff., John Wiley & Sons, Inc., New York (1952).
7. D. M. MacArthur, Bell Labs. Memorandum, 1971.
8. F. A. Cotton and G. Wilkinson, "Advanced Inorganic Chemistry," p. 933, Interscience Publishers, Inc., New York (1966).
9. P. K. Skurkiss and D. M. MacArthur, Bell Labs. Memorandum, 1972.

Metal Vapor Effects on Chemical Reactions in an Argon Plasma

Paul Meubus*

Department of Applied Sciences, Université du Québec à Chicoutimi, Chicoutimi, Quebec, Canada

ABSTRACT

In order to illustrate the effect of metal vapors on chemical reactions carried out at high temperatures, the example has been taken of propane cracking in an argon plasma, yielding acetylene. The reaction takes place in the homogeneous phase, in the presence of iron vapor. Molar ratios propane/argon of 1.5 and 6.0% have been used, associated with 0.25, 0.75, and 1.00% iron/argon molar ratios. It is observed that the reaction temperatures required for obtaining the maximum conversion of propane into acetylene are considerably lowered in the presence of iron vapor, attaining then 3200°-4200°K while, all other conditions being equal, except for the presence of iron vapor, these temperatures are of the order of 5000°-6500°K. The latter conditions also lead to maximum conversions of propane into acetylene which are of the order of 40% while these conversions attain 100% when iron vapor is present. Possible mechanisms are suggested, relating the results observed either to a catalytic effect generated by condensing iron particles, or to a photosensitization process by which excited iron vapor emissions around 3000.7 and 5328.5Å contribute to the stabilization of acetylene and C₂H precursor during the quenching stage, thus avoiding the decomposition of these species into solid carbon and hydrogen.

It is the purpose of this study to show by an example how a metallic vapor may alter the chemical kinetics of a given reaction taking place in a plasma gas. The case investigated is the formation of acetylene from propane cracking in the presence of iron vapor, the plasma matrix being argon. Acetylene production from lower hydrocarbons like methane, ethane, and propane have been studied and the reaction kinetics is well known (1, 2) so that possible changes brought by the introduction of iron vapor are more easily evaluated.

Iron is supplied to the argon stream by means of an iron wire 1 mm in diameter, which is introduced into the plasma gas at a given rate. Propane is then injected into the resulting mixture and a small plasma volume is delimited within which the average temperature is recorded by means of the hydrogen lines H_α and H_β. Reacted gas samples are then drawn through a cooled probe for gas chromatography analy-

sis. An interpretation of the results observed is given, based on catalytic effects resulting from the condensation of the metal vapor, and also based on possible photosensitization effects related to the iron spectroscopic emissions around 3000.7 and 5328.5Å as explained later in the text.

Apparatus and Mode of Operation

The power supply, control panels, and plasma torch have been described elsewhere (3). As shown in Fig. 1, the reactor is made up of a plasma torch and of a set of cooled copper probes used for metal injection (G), propane injection (H), and reacted products sampling. The probes G and H are provided with a welded tungsten refractory tip whose purpose is to facilitate injection of the metal and propane into the plasma gas. The iron injection rate is adjusted by means of a controlled speed driving wheel entraining an iron wire 1 mm in diameter. The wire emerges through the cooled probe G within the plasma where it evaporates and turbulent mixing occurs so that

* Electrochemical Society Active Member.

Key words: argon plasma, metal vapors, chemical reactions, photochemical effects, catalytic effects.

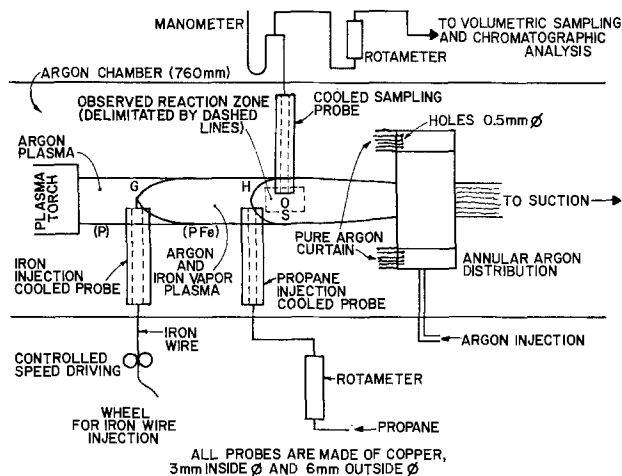


Fig. 1. Plasma reactor

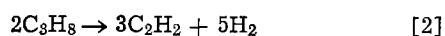
about 3 cm downward from G, a homogeneous mixture of argon-iron vapor is available within which propane is injected at a given rate.

The probes are installed in such a way that their vertical axis of symmetry is contained in the vertical plane of symmetry of the plasma jet (which is of cylindrical symmetry) and they are positioned at, respectively, 0.7 (G), 3.8 (H), and 4.8 cm (sampling probe) from the plasma torch outlet. The probes' tips horizontal surfaces (for G and H) coincide with the horizontal plane of symmetry of the plasma. This positioning of the probes ensures an adequate reproducible plasma surrounding the injection parts. While in operation, three sections may be distinguished in the plasma: (i) an argon section (P), (ii) an argon + iron vapor plasma (PFe), and (iii) the reaction zone within which a small volume S can be delimited, care being taken that chemical equilibrium is attained at the prevailing temperature. Temperatures are recorded by means of spectroscopic measurements related to the atomic hydrogen lines H_{α} and H_{β} , using the well-known lines intensity ratio method (4).

Also, reacted gas samples are withdrawn through a cooled probe always under the same negative pressure and gas flow rate so that the quenching conditions can be accurately controlled. The samples are analyzed for acetylene and H_2 which are, for all practical purposes, the only gas constituents found in all cases as products of reaction. A Pye Unicam 104 with a 20% Squalane on Chromosorb P column is used for flame ionization detection of the hydrocarbons, while a Fisher Hamilton 29 supplied with a Molecular sieve $13\times$ determines the hydrogen content of the sample. Since the refractory tips already mentioned provide conditions of homogeneous region within the considered reactor volume S, the following relation can be written

$$\frac{\text{moles } C_2H_2}{\text{moles } C_2H_2 + \text{moles } H_2} = \frac{\text{moles } C_2H_2}{\text{mole } C_3H_8} \quad [1]$$

a value of 1.5 for this ratio being equivalent to 100% C_2H_2 yield for the reaction



where the acetylene and hydrogen concentrations are obtained from a sample analysis for a given test, the total content of hydrogen being used for the determination of the initial amount of propane. In order to avoid any contamination of the plasma flame by-products of reaction that may accumulate in the surrounding chamber, an annular distributor supplies a certain of pure argon around the reaction site (see Fig. 1).

Before starting an experiment, the chamber was filled with argon and the pressure was maintained at

760 mm Hg. The plasma argon flow rate was kept constant at 0.2 g-moles/min while, respectively, 0.3×10^{-2} and 1.2×10^{-2} g-moles/min propane were used. Variable amounts of iron were injected in the pure argon section P (Fig. 1), ranging from 5×10^{-4} up to 19×10^{-4} g-moles/min iron, calculated on the basis of iron wire feed rate. While sampling the products of reaction, the quenching rate was adjusted until optimum acetylene yield was obtained. The adjustment was made by means of suction application and the flow rate of gas withdrawn was obtained from a rotameter reading thus avoiding any misleading conclusion resulting from pressure reading alone.

Results

The optimum quenching conditions were found practically equivalent in all cases and resulted in quenching times of about 10^{-3} sec. The argon flow rate was 2×10^{-1} g-moles/min. The values given for iron injection rates are those corresponding to the iron wire speed and they are discussed later.

With a propane flow rate of 0.3×10^{-2} g-moles/min in 0.20 g-moles/min argon, an injection of 5.0×10^{-4} g-moles/min of iron resulted in an acetylene yield approaching 100% propane conversion, the latter never exceeding 40% without added iron. Further, the most favorable temperature for the production of acetylene achieved was reduced from 6500° to 3500°K. When the iron rate was increased to 19×10^{-4} g-moles/min, the maximum yield dropped back to 40% propane conversion into acetylene at a temperature of 4500°K. The data from these experiments are presented in Fig. 2 and Table I.

When a propane flow rate of 1.2×10^{-2} g-moles/min in 0.2 g-moles/min argon was used, the addition of 5×10^{-4} , 15×10^{-4} , 19×10^{-4} , and 0 g-moles/min iron resulted in temperatures for maximum acetylene yield obtention of, respectively, 3000°, 3800°, 4200°, and 5000°K, the propane conversion into acetylene attaining nearly 100% for all the iron flow rates used, against 65% when no iron was present in the reacting medium. As a result, and within the limits of the experimental conditions, the higher propane flow rate used was related to lower optimal tempera-

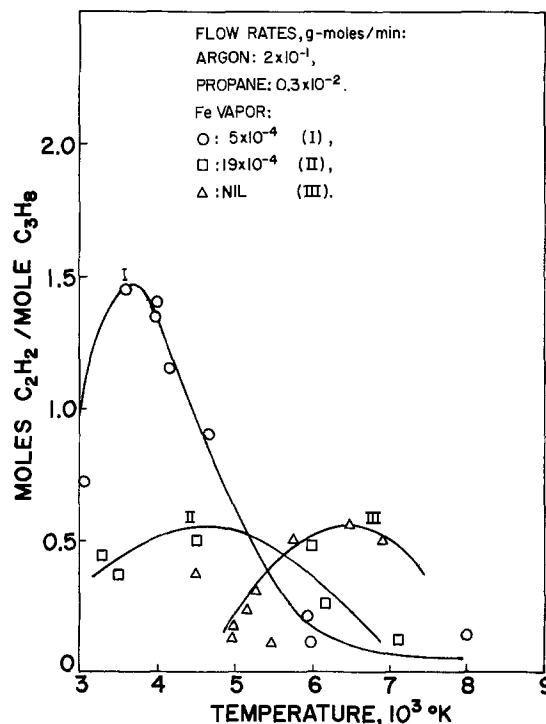


Fig. 2. Effect of iron vapor concentration on C_2H_2 formation from C_3H_8 cracking: 1.5% C_3H_8 in argon, 0.25% Fe (curve I), 1.0% Fe (curve II), 0% Fe (curve III).

Table I. Propane conversion into acetylene at various propane and Fe injection rates into argon

Reaction temperature, °K	Flow rate, g-moles/min		% Constituents in argon (argon basis)		Conversion	
	C ₃ H ₈	Fe	C ₃ H ₈	Fe	moles C ₂ H ₂	C ₃ H ₈ converted C ₃ H ₈ initial × 100
					mole C ₃ H ₈ (Eq. (1))	
3000	0.3 × 10 ⁻²	5 × 10 ⁻⁴	1.5	0.25	0.70	47
3700	0.3 × 10 ⁻²	5 × 10 ⁻⁴	1.5	0.25	1.45	97
4000	0.3 × 10 ⁻²	5 × 10 ⁻⁴	1.5	0.25	1.40	94
4000	0.3 × 10 ⁻²	5 × 10 ⁻⁴	1.5	0.25	1.35	90
4200	0.3 × 10 ⁻²	5 × 10 ⁻⁴	1.5	0.25	1.15	77
4700	0.3 × 10 ⁻²	5 × 10 ⁻⁴	1.5	0.25	0.90	60
5900	0.3 × 10 ⁻²	5 × 10 ⁻⁴	1.5	0.25	0.20	13
5900	0.3 × 10 ⁻²	5 × 10 ⁻⁴	1.5	0.25	0.10	7
3300	0.3 × 10 ⁻²	19 × 10 ⁻⁴	1.5	1.00	0.45	30
3500	0.3 × 10 ⁻²	19 × 10 ⁻⁴	1.5	1.00	0.35	23
4500	0.3 × 10 ⁻²	19 × 10 ⁻⁴	1.5	1.00	0.50	33
6000	0.3 × 10 ⁻²	19 × 10 ⁻⁴	1.5	1.00	0.45	30
6300	0.3 × 10 ⁻²	19 × 10 ⁻⁴	1.5	1.00	0.25	17
7200	0.3 × 10 ⁻²	19 × 10 ⁻⁴	1.5	1.00	0.10	7
3300	1.2 × 10 ⁻²	5 × 10 ⁻⁴	6.0	0.25	1.50	100
3500	1.2 × 10 ⁻²	5 × 10 ⁻⁴	6.0	0.25	1.25	84
3800	1.2 × 10 ⁻²	5 × 10 ⁻⁴	6.0	0.25	1.45	97
3900	1.2 × 10 ⁻²	5 × 10 ⁻⁴	6.0	0.25	1.35	90
4300	1.2 × 10 ⁻²	5 × 10 ⁻⁴	6.0	0.25	0.60	40
5300	1.2 × 10 ⁻²	5 × 10 ⁻⁴	6.0	0.25	0.25	17
5800	1.2 × 10 ⁻²	5 × 10 ⁻⁴	6.0	0.25	0.20	13
3400	1.2 × 10 ⁻²	15 × 10 ⁻⁴	6.0	0.75	1.35	90
3800	1.2 × 10 ⁻²	15 × 10 ⁻⁴	6.0	0.75	1.10	74
4100	1.2 × 10 ⁻²	15 × 10 ⁻⁴	6.0	0.75	1.35	90
5000	1.2 × 10 ⁻²	15 × 10 ⁻⁴	6.0	0.75	0.65	44
5800	1.2 × 10 ⁻²	15 × 10 ⁻⁴	6.0	0.75	0.40	27
7000	1.2 × 10 ⁻²	15 × 10 ⁻⁴	6.0	0.75	0.25	17
3300	1.2 × 10 ⁻²	19 × 10 ⁻⁴	6.0	1.00	0.70	47
3500	1.2 × 10 ⁻²	19 × 10 ⁻⁴	6.0	1.00	1.10	74
4300	1.2 × 10 ⁻²	19 × 10 ⁻⁴	6.0	1.00	1.35	90
4600	1.2 × 10 ⁻²	19 × 10 ⁻⁴	6.0	1.00	1.35	90
4800	1.2 × 10 ⁻²	19 × 10 ⁻⁴	6.0	1.00	1.30	87
5000	1.2 × 10 ⁻²	19 × 10 ⁻⁴	6.0	1.00	0.90	60
6000	1.2 × 10 ⁻²	19 × 10 ⁻⁴	6.0	1.00	0.40	27

tures required for maximum acetylene yield at the various iron flow rates tested, the temperature drop being around 500°K for equivalent iron flow rate conditions.

Finally, it was observed that the iron injection rate did not affect, for all practical purposes, the maximum acetylene yield (nearly 100%) obtained when keeping a propane flow rate of 1.2×10^{-2} g-moles/min, while a drop in maximum yield from around 100% down to 40% was observed, using a propane flow rate of 0.3×10^{-2} g-moles/min with, respectively, 5×10^{-4} and 19×10^{-4} g-moles/min iron. Figures 3, 4, and 5 show the results described while Table I summarizes the data from these experiments.

In order to obtain reference conditions, a number of experiments were carried out with respective pro-

pane flow rates of 0.3×10^{-2} , 0.7×10^{-2} , and 1.2×10^{-2} g-moles/min in 0.20 g-moles/min argon, no iron being used. In this way, a curve was derived showing the increase in maximum acetylene yield at decreasing maximum temperatures when the propane flow rate was increased. At about 3000°K (extrapolated), a maximum of 73% propane conversion into acetylene is obtained. This should be the limiting value attainable for nearly pure propane in the homogeneous phase at atmospheric pressure, and a molar ratio carbon over hydrogen (C/H₂) equal to 0.75 (corresponding

Table II. Propane conversion into acetylene at various propane injection rates into argon

Test conditions: argon flow rate;
 2×10^{-1} g-moles/min, atmospheric pressure

Reaction temperature, °K	C ₃ H ₈ feed in argon, g-moles/min	% C ₃ H ₈ in argon	Conversion	
			moles C ₂ H ₂ mole C ₃ H ₈ [Eq. (1)]	C ₃ H ₈ converted C ₃ H ₈ initial × 100
3100	1.2 × 10 ⁻²	6.0	0.60	40
3300	1.2 × 10 ⁻²	6.0	0.70	47
3500	1.2 × 10 ⁻²	6.0	0.80	53
3800	1.2 × 10 ⁻²	6.0	0.95	63
4300	1.2 × 10 ⁻²	6.0	0.98	65
4700	1.2 × 10 ⁻²	6.0	1.00	67
5400	1.2 × 10 ⁻²	6.0	0.85	57
6300	1.2 × 10 ⁻²	6.0	0.75	50
4600	0.7 × 10 ⁻²	3.5	0.60	40
4800	0.7 × 10 ⁻²	3.5	0.50	33
5300	0.7 × 10 ⁻²	3.5	0.75	50
6300	0.7 × 10 ⁻²	3.5	0.80	53
6900	0.7 × 10 ⁻²	3.5	0.65	43
7700	0.7 × 10 ⁻²	3.5	0.42	28
4500	0.3 × 10 ⁻²	1.5	0.35	23
5000	0.3 × 10 ⁻²	1.5	0.10	67
5000	0.3 × 10 ⁻²	1.5	0.20	13
5100	0.3 × 10 ⁻²	1.5	0.25	17
5400	0.3 × 10 ⁻²	1.5	0.30	20
6500	0.3 × 10 ⁻²	1.5	0.55	37
7000	0.3 × 10 ⁻²	1.5	0.50	33
7000	0.3 × 10 ⁻²	1.5	0.40	27
7700	0.3 × 10 ⁻²	1.5	0.42	28
9000	0.3 × 10 ⁻²	1.5	0.25	17

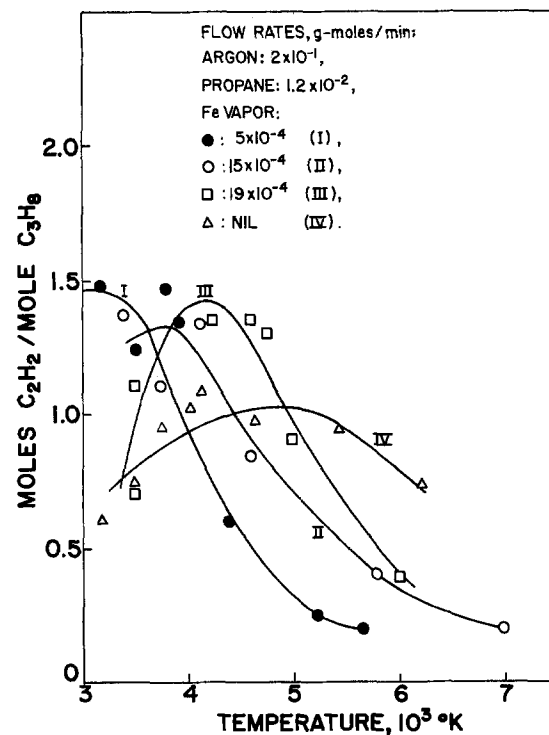


Fig. 3. Effect of iron vapor concentration on C₂H₂ formation from C₃H₈ cracking: 6.0% C₃H₈ in argon, 0.25% Fe (curve I), 0.75% Fe (curve II), 1.0% Fe (curve III), 0% Fe (curve IV).

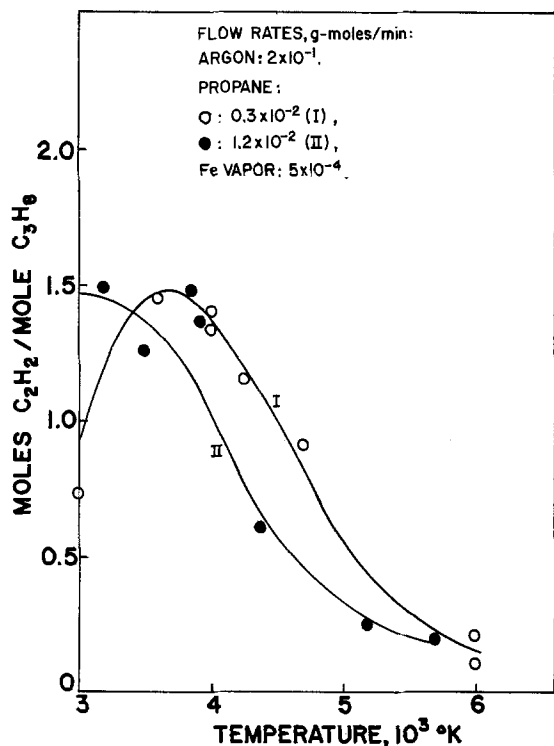


Fig. 4. Effect of 0.25% Fe on C_2H_2 formation from C_3H_8 cracking with, respectively, 1.5% (curve I) and 6.0% (curve II) propane in argon.

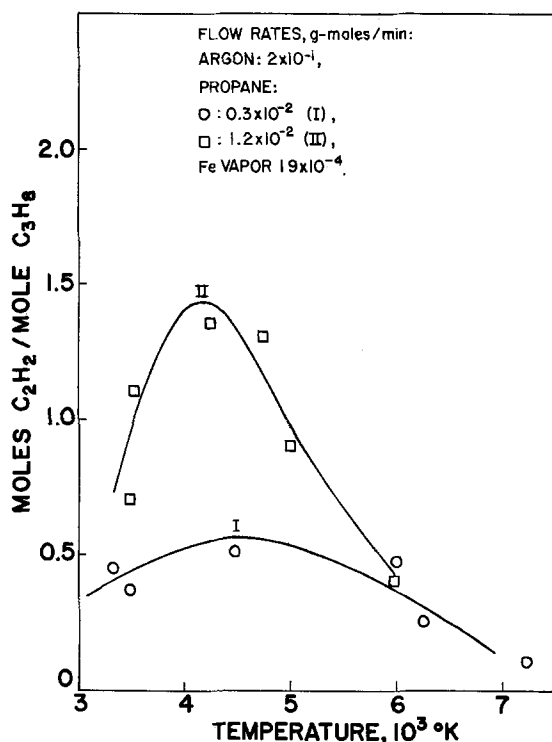


Fig. 5. Effect of 1.0% Fe on C_2H_2 formation from C_3H_8 cracking with, respectively, 1.5% (curve I) and 6.0% (curve II) propane in argon.

to propane). Such a conclusion is derived from the slow variation of maximum acetylene yield as a function of optimal temperature and propane flow rate, and also from the fact that the sublimation temperature of carbon is 3200°K for a pure C-H₂ system at atmospheric pressure and $C/H_2 = 0.75$ (1). This limiting value of 73% conversion should be compared with a nearly 100% conversion in the presence of iron vapor. The representative curves are shown in Fig. 6.

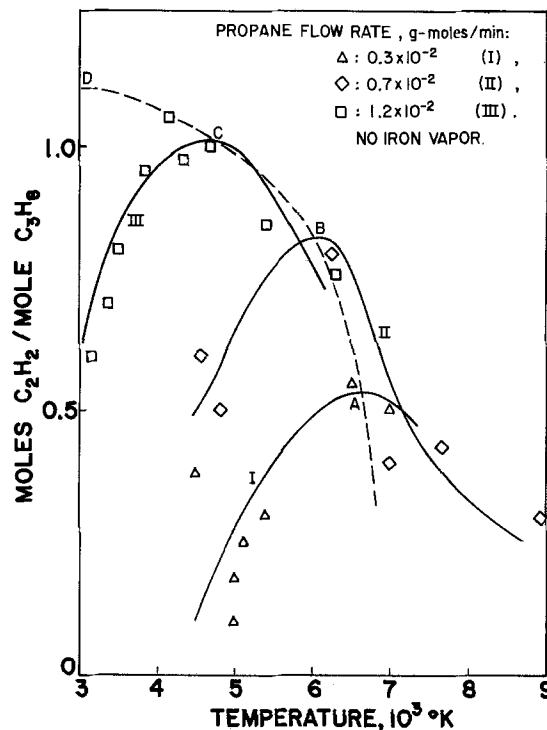
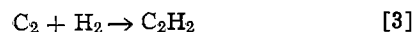


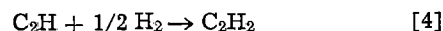
Fig. 6. Effect of C_3H_8 concentration in argon on C_2H_2 formation from C_3H_8 cracking. Argon flow rate: 0.2 g-moles/min. Propane % in argon: 1.5 (curve I), 3.5 (curve II), 6.0 (curve III).

Discussion

Suggested reactions.—Equilibrium composition calculations have been made for the carbon-hydrogen system above 2000°K (1, 2, 5), considering a large range of total pressures and C/H₂ molar ratios. The plasma formed consists, in the homogeneous phase (the one we are interested in here), of the polymeric forms of carbon vapor C₁, C₂, and C₃, of atomic and molecular hydrogen, as well as of a number of radicals and molecules. The main reactions leading to the formation of acetylene should be

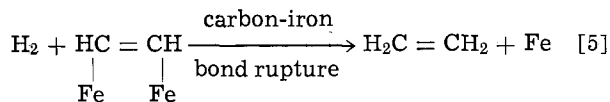


and a quench mechanism has been postulated (1) whereby C₂H should act as a precursor for C₂H₂ formation so that

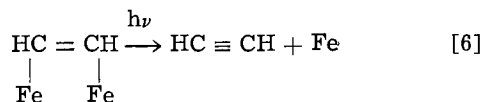


Reverting back to Fig. 2 and 3 related to propane flow rates of 0.3×10^{-2} g-moles/min and 1.2×10^{-2} g-moles/min, it is observed that the maximum acetylene yields occur, as an average, at 3200°K and 4200°K when, respectively, 5×10^{-4} and 19×10^{-4} g-moles/min iron vapor are injected into the reacting medium. However, reference to the work of Baddour and Blanchet (1, 5) leads to the conclusion that for the conditions of the present study (atmospheric pressure; $C/H_2 = 0.75$), acetylene is nearly maximum at 3200°K , its concentration being about two times higher than C₂H. On the other hand, the precursor C₂H goes through a maximum at 4200°K , being at least an order of magnitude higher than the acetylene concentration. Taking these facts into account, some possible mechanisms for the reaction involved are now suggested.

Catalytic effects resulting from condensed iron particles.—Acetylene is liable to be adsorbed on the {100} and {110} planes of face-centered cubic metals of which γ iron is an example. Desorption should then proceed through hydrogenation (6) and formation of ethylene. Thus, for a carbon-metal bond, one obtains

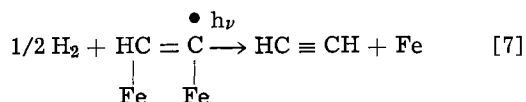


However, very small amounts of ethylene are found in the products of reaction so that if any catalytic process of the kind described is susceptible to occur, acetylene could be desorbed, for instance, by the catalyst surface irradiation with photons of the appropriate energy, the desorption taking place at a temperature low enough for avoiding subsequent decomposition of acetylene



As a matter of fact, there is a growing interest in this type of mechanism on the catalytic effects of metals and metal oxides (7).

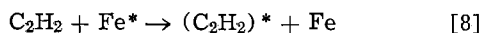
Considering now the case of C_2H which has been related to maximum acetylene yields obtained around 4200°K , a reaction similar to that described by Eq. [6] can be considered, except that desorption should now occur by partial hydrogenation



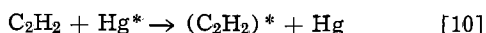
Equations [6] and [7] are the distinct reactions which should explain the variations of maximum yield obtained when, respectively, acetylene or C_2H predominate in the system. Equation [7] is a function of hydrogen concentration and should therefore be favored by an increase in propane flow rate, thus explaining why, for a given amount of iron present, the reaction implying C_2H leads to higher yields when the propane flow rate is raised from 0.3×10^{-2} up to 1.2×10^{-2} g-moles/min. On the other hand, acetylene stabilization from conditions prevailing around 3200°K should not depend on hydrogen concentration, following Eq. [6] and therefore, should not be affected by propane flow rate (Fig. 2 and 3).

It should be pointed out that the γ iron crystalline form is obtained between 906° and 1401°C , the fusion temperature of iron being 1530°C . Below and above this temperature range, the α iron body-centered cubic form is obtained, which is less liable to lend itself to acetylene adsorption. While it is doubtful that the γ form be always obtained, it may be expected that the rapid quenching rate will introduce defects in the particles structure, making them suitable for the adsorption processes involved.

Possible photochemical effects resulting from the presence of iron vapor.—By analogy with observed photosensitization effects occurring between acetylene and mercury atoms (8, 9), it is possible to consider a photochemical energy exchange process, generated by appropriate iron lines, which may oppose the decomposition of an acetylene molecule during the quenching process so that the yield of propane conversion into acetylene is improved. For instance, the reaction leading to an excited state of the acetylene molecule could occur if the iron excitation state is high enough. Thus



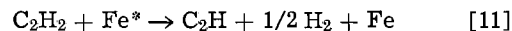
The similar reaction



has been proposed earlier (8), using the 2537\AA mercury radiation as the excitation source. The energy coupling takes place by means of a photosensitization effect. In the case of the present study, for reaction

temperatures of 3200° – 4200°K , the short u.v. emission from iron vapor is not high enough for allowing any resonant energy interchange since the latter should occur for acetylene at 1540\AA and downward (10). As a result, if Eq. [8] describes an actual situation, here again energy should be exchanged by a process of photosensitization.

Another photosensitization reaction between iron and acetylene is suggested by a similar reaction studied in the case of mercury (8)



Reaction [11] could also oppose the decomposition of acetylene into solid carbon and hydrogen. From Ref. (1) one obtains, for C_2H_2

$$\Delta H^\circ_{(0)f} = 54.33 \text{ kcal/g-mole} \quad [12]$$

(2.36 eV)

$$\Delta H^\circ_{(3200)f} = 48.36 \text{ kcal/g-mole} \quad [13]$$

(2.09 eV)

and, if the energy transfer during photosensitization is entirely used for internal energy increase of the acetylene molecule, then photons are required whose associated wavelength is

$$\lambda_1 = \frac{hc}{E_1} = \frac{6.62 \times 10^{-27} \times 3.0 \times 10^{10}}{2.36 \times 1.602 \times 10^{-12}} \times 10^8 \quad [14]$$

$$\lambda_1 = 5330\text{\AA}$$

This value is purely indicative of the excitation level required by iron vapor and emissions of higher energy are available from iron vapor at the prevailing temperatures.

$\Delta H^\circ_{(0)f}$ for the radical C_2H may be obtained from chemical bond strength considerations (11), while data from Bauer and Duff (12) are used for an approximate evaluation of $\Delta H^\circ_{(4200)f}$. Then

$$\text{C}_2\text{H} \quad \Delta H^\circ_{(0)f} = 95.5 \text{ kcal/g-mole} \quad [15]$$

(4.14 eV)

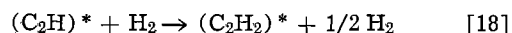
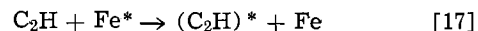
and

$$\Delta H^\circ_{(4200)f} = 90.0 \text{ kcal/g-mole} \quad [16]$$

(3.91 eV)

From the heats of formation given in [13] and [16], the enthalpy of reaction for Eq. [11] should be approximately 51.6 kcal/g-mole at 3200°K . As a result, the wavelength associated with the photons required for reaction [11] to take place should be of the same order of magnitude as the one related to the photons required for Eq. [8], both reactions taking place around 3200°K .

Considering now the case where the radical C_2H prevails in the medium at around 4200°K , a mechanism could be written on the basis of a similar structure between the radical and acetylene, with the possible formation of an iron complex

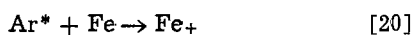


de-excitation taking place at a temperature low enough so that the decomposition reaction into solid carbon and hydrogen does not take place. Referring to [15], and assuming that the photosensitizing energy is absorbed only for increase in internal energy, the wavelength corresponding to the photons required for Eq. [17] should be

$$\lambda_2 = \frac{hc}{E_2} = \frac{6.62 \times 10^{-27} \times 3.0 \times 10^{10}}{4.14 \times 1.602 \times 10^{-12}} \times 10^8 = 3000\text{\AA} \quad [19]$$

A number of iron lines are emitting with a fairly high intensity around the wavelengths defined in rela-

tions [14] and [19] and two representative lines of these groups are observed at 5328.5 and 3000.7Å. The assumed photosensitization effects imply energy transfer by means of collisions between excited iron atoms and acetylene molecules as well as C₂H radicals. It may be conceived that, while the gas is withdrawn for sampling, it is still exposed to plasma radiation (Fig. 1) since most of the quenching takes place at the inlet of the sampling probe where iron is present up to 0.13% (vapor pressure at 1800°C) at 1800°C. The cooled iron vapor can be excited, prior to conveying its energy: (i) by resonance absorption of 3000.7 and 5328.5Å photons emitted from the plasma, and (ii) by collision with metastable argon atoms (12) resulting in reactions of the kind (Penning effect)



In view of the experimental results obtained, it seems that high iron vapor concentrations favor the formation of acetylene at higher temperatures (around 4200°K), this indicating that an emissive power high enough in quanta of wavelength 3000.7Å is required for allowing the occurrence of reaction [17]. On the other hand, such an emission density is probably liable to decompose acetylene instead of exciting the molecule, thus decreasing the probability of acetylene formation. This should explain, to a certain extent, the curves appearing on Fig. 2-5, the effect of propane flow rate variation at 4200°K being understood from Eq. [18].

Propane cracking in an argon plasma without iron vapor.—The experimental results show that an increase in propane flow rate increases the conversion into acetylene and decreases the temperature required for maximum conversion. In this case, the yield is essentially a question of quenching rate keeping the acetylene and C₂H precursor formed at high temperature from decomposition into solid carbon and hydrogen. In this respect, the amount of hydrogen present at the start of the quenching process will affect the quenching rate since it is well known that around 4000°K down to 2000°K, the thermal conductivity of hydrogen considerably increases (13). A higher initial propane flow rate results in higher concentrations of hydrogen present in the gas mixture at elevated temperatures, thus improving optimal quenching conditions with resulting higher optimal quenching conditions with resulting higher acetylene yields. However, the hydrogen effect is limited to an upper propane concentration value beyond which no further change is observed in acetylene yield.

These considerations lead to a possible interpretation of Fig. 6 which, in conjunction with Fig. 2-5 also shows that the maximum possible acetylene yield remains around 30% below the maximum value (nearly 100% yield) obtained when cracking is carried out in the presence of iron vapor.

Spectroscopic considerations.—The assumption has been raised in this work of photochemical excitation of iron vapor in relationship with photosensitization reactions involving acetylene and the C₂H radical. It is of interest to evaluate the power emitted from excited iron at 3000.7 and 5328.5Å since these emissions or similar ones could be responsible for part of the effects observed.

The emission intensity for a given spectral line can be written (4)

$$I = \frac{2}{3} \times 10^{16} \frac{hc gf N_0 e^{-E/kT}}{\lambda^3 Z_0(T)} \quad [22]$$

or, in terms of quanta emission rate

$$Q = \frac{2}{3} \times 10^{16} \frac{gf N_0 e^{-E/kT}}{\lambda^2 Z_0(T)} \quad [23]$$

N_0 being here a function of temperature and concentration P of the total number of particles for a given species (iron in this case) injected into the plasma gas. The function $Z_0(T)$ in Eq. [22] or [23] can be evaluated from the energy levels related to the atomic species whose concentration is N_0 and the latter is obtained from the following equations, first ionization only being considered

(a) Saha equation

$$\frac{N_+ N_e}{N_0} = K = 2 \frac{Z_+(T)}{Z_0(T)} \left(\frac{2\pi m_e kT}{h^2} \right)^{3/2} e^{-E_i/kT} \quad [24]$$

(b) Species conservation

$$N_+ + N_0 = P \quad [25]$$

(c) Assumption of first ionization only

$$N_+ = N_e \quad [26]$$

From Eq. [24], [25], and [26], one obtains with the restriction that $N_0 \leq P$

$$N_0 = \left[\frac{(K + 4P)^{1/2} - K^{1/2}}{2} \right]^2 \quad [27]$$

which is then substituted in Eq. [22] or [23] with the appropriate constants for the given electronic transitions. As a result, I or Q may be obtained for a number of temperatures.

Applying these calculations to the present study, emission power for iron at 3000.7Å and 5328.5Å was calculated, at various temperatures, for an argon flow rate of 0.2 g-moles/min and iron vapor flow rates p , respectively, equal to 10^{-5} , 10^{-4} , and 1.5×10^{-3} g-moles/min. The total iron particles concentration P (atoms + ions) per cm³ of plasma gas was calculated from

$$P = \frac{6.02 \times 10^{23} \times 273}{0.2 \times 22,400} \frac{p}{T} \quad [28]$$

The value for E_i in Eq. [24] related to iron as well as the energy levels for atomic and singly ionized iron required for calculating $Z_0(T)$ and $Z_+(T)$ were obtained from Ref. (14) and Table III shows the values of $Z_0(T)$, $Z_+(T)$, and K for various temperatures. The other spectroscopic parameters required for iron were taken from Ref. (4). Then

$$Q_1 = \frac{2}{3} \times 10^{16} \times 156 \times \frac{1}{(5328.5)^2} \frac{N_0 e^{-\frac{3.23 \times 11,600}{T}}}{Z_0(T)} \quad [29]$$

Table III. Partition functions for atomic and singly ionized Fe. Equilibrium constant for the reaction: $\text{Fe} \rightarrow \text{Fe}^+ + e$

Temperature, °K	Partition functions		Equilibrium constant, K , $\text{Fe} \rightarrow \text{Fe}^+ + e$
	Atomic Fe, $Z_0(T)$	Singly ionized Fe, $Z_+(T)$	
1,000	15.756	19.626	3.345×10^{-20}
1,500	17.953	24.290	1.192×10^{-6}
2,000	19.466	28.194	8.305
2,500	20.737	31.493	1.150×10^5
3,000	21.969	34.344	6.960×10^7
3,500	23.252	36.874	6.956×10^9
4,000	24.634	39.185	2.242×10^{11}
4,500	26.148	41.358	3.382×10^{12}
5,000	27.825	43.455	2.990×10^{13}
5,500	29.695	45.525	1.789×10^{14}
6,000	31.785	47.608	7.972×10^{14}
6,500	34.120	49.733	2.828×10^{15}
7,000	36.724	51.920	8.384×10^{15}
7,500	39.619	54.187	2.151×10^{16}
8,000	42.824	46.544	4.905×10^{16}
8,500	46.357	58.998	1.015×10^{17}
9,000	50.234	61.554	1.937×10^{17}
9,500	54.469	64.214	3.452×10^{17}
10,000	59.055	66.980	5.807×10^{17}

and

$$\lambda_2 = 3000.7 \text{ \AA}$$

$$Q_2 = \frac{2}{3} \times 10^{16} \times 46 \times \frac{1}{(3000.7)^2} \frac{N_0 e^{-\frac{-4.20 \times 11,600}{T}}}{Z_0(T)} \quad [30]$$

The results obtained for Q_1 and Q_2 at various temperatures and iron flow rates are shown in Fig. 7 and 8. The same figures also indicate that, at the average iron flow rates used in the present study, the rate of quanta emitted following Eq. [29] and [30], at, respectively, 3200° and 4200°K, should be of the order of 10^{20} quanta/cm³-sec. The maximum amount of acetylene or C₂H present in the reaction medium amounts to approximately 10^{15} particles/cm³. As a result, a quantum efficiency of around 0.1%, for the proposed photochemical mechanisms, should be sufficient, this including particles concentration and capture cross-section effects, the latter being not known. It should be mentioned that all the iron used is not actually introduced into the plasma and some preliminary work made in this laboratory should indicate that between 1 and 10% of the iron is incorporated in the plasma.

Conclusion

The cracking reaction of propane in an argon plasma at atmospheric pressure has been studied in the presence of iron vapor. Comparing the results obtained with those related to mixtures of argon and propane alone, all conditions being identical except for the presence of iron vapor, it is observed that the reaction temperature required for maximum yield is considerably decreased, dropping from 5000° to 6500°K when

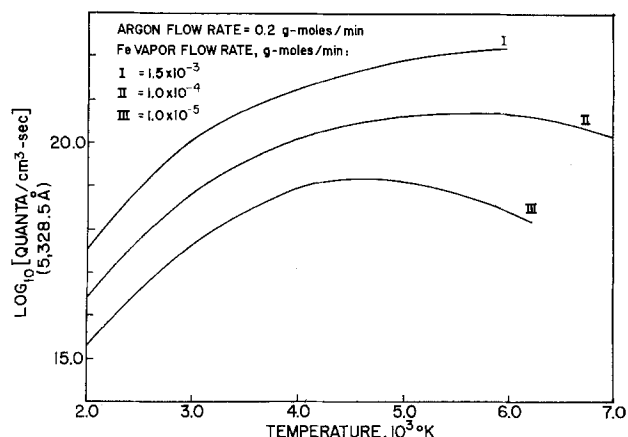


Fig. 7. Neutral Fe 5328.5 Å emission as a function of temperature and iron vapor flow rate in argon.

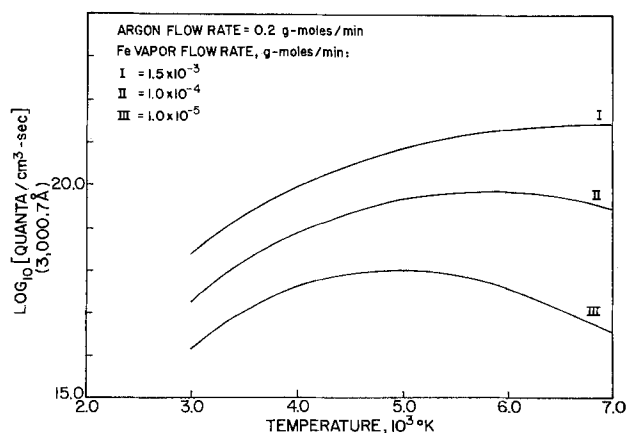


Fig. 8. Neutral Fe 3000.7 Å emission as a function of temperature and iron vapor flow rate in argon.

iron vapor is not present, down to 3200° to 4200°K in the presence of this metal vapor and depending on the latter concentration as well as on the initial propane flow rate adopted. In most cases when iron is present, except for small propane and high iron vapor flow rates, the acetylene yield is nearly 100%, while the maximum attainable propane conversion without iron is of the order of 70%.

An interpretation of the results obtained is given in terms of catalytic effects resulting from the minute condensing iron particles. Also, by analogy with mercury photosensitization effects in relationship with the acetylene molecule, an energy transfer mechanism is suggested which involves resonance energy absorption by the iron vapor during the cooling stage, or iron vapor excitation by metastable argon atoms, followed by energy exchange through particles collision. Iron emission around 3000.7 and 5328.5 Å should be responsible for enhanced acetylene production from, respectively, excited acetylene species and, for instance, excited complex [C₂H-iron]* molecules. De-excitation should occur at temperatures low enough for avoiding the decomposition of acetylene into solid carbon and hydrogen. The results observed could be the consequence of a combination of the mechanisms proposed, although further work is required for casting more light on the actual mechanisms involved.

Acknowledgment

The author is indebted to the National Research Council of Canada and to the Ministry of Education of the province of Quebec (Canada) for grants received during the course of this work.

Manuscript submitted Feb. 11, 1974; revised manuscript received Aug. 9, 1974. This was Paper 262 presented at the Boston, Massachusetts, Meeting of the Society, Oct. 7-11, 1973.

Any discussion of this paper will appear in a Discussion Section to be published in the December 1975 JOURNAL. All discussions for the December 1975 Discussion Section should be submitted by Aug. 1, 1975.

Publication costs of this article were partially assisted by the Centre du Moyen Nord (Université du Québec à Chicoutimi).

SYMBOLS

\AA	angströms
c	velocity of light, cm/sec
e	base of Napierian logarithms
E	excitation energy level, ergs or eV
f	oscillatory strength
g	statistical weight
h	Planck's constant 6.62×10^{-27} erg-sec
H	atomic hydrogen symbol
H	enthalpy, kcal/g-mole
I	emission rate intensity, erg/sec-cm ³
k	Boltzmann's constant, 1.38×10^{-16} erg/°K
K	Saha constant, cm ⁻³
m	mass of particle, g
M	second or third body
N	number of particles/cm ³
p	iron vapor flow rate, g-moles/min
P	defined by Eq. [20], particles/cm ³
Q	quanta emission rate, quanta/cm ³
R	gas constant, kcal/g-mole-°K
T	temperature, °K
$Z(T)$	partition function

Greek symbols

λ	wavelength, cm or angströms
ν	frequency, sec ⁻¹
$\Delta H^\circ(T)_f$	heat of formation, kcal/g-mole or eV/g-mole, at T °K and standard conditions

Subscripts

i	pertaining to ionization
e	pertaining to electrons
n	1 or 2
$+$	first ionization level
0	atomic level
1	pertaining to 5328.5 Å Fe atomic line
2	pertaining to 3000.7 Å Fe atomic line

Superscripts

- ° standard state
- excited state

REFERENCES

1. R. F. Baddour and J. L. Blanchet, *I & EC Process Design Development*, **3**, 258 (1964).
2. J. L. Blanchet, J. R. Parent, and P. A. Courtois, *Can. J. Chem. Eng.*, **45**, 264 (1967).
3. P. Meubus, *Chem. Eng. Sci.*, **27**, 2117 (1972).
4. W. J. Pierce, WAD Technical Report 59-346, Wright Patterson Air Force Base, Ohio (February 1960).
5. J. L. Blanchet, Thesis, Chem. Eng. Dept, M.I.T. (1963).
6. J. M. Thomas and W. J. Thomas, "Introduction to the Principles of Heterogeneous Catalysis," p. 396, Academic Press Inc. Ltd., London (1967).
7. J. M. Thomas and W. J. Thomas, *ibid.*, p. 287.
8. H. E. Gunning and O. P. Strausz, "Isotopic Effects and the Mechanism of Energy Transfer in Mercury Photosensitization," *Advances in Photochemistry*, p. 242. Interscience Publishers, New York (1963).
9. E. W. R. Steacie, "Atomic and Free Radicals Reactions," p. 423, Reinhold Publishing Corp., New York (1954).
10. W. C. Price, *Phys. Rev.* **47**, 444 (1935).
11. S. Glasstone and D. Lewis, "Elements of Physical Chemistry," pp. 92-93, D. Van Nostrand Co., New York (1960).
12. A. Czernichowski, J. Chapelle, and F. Cabannes, *C. R. Acad. Sci. Paris*, **E. 270**, 54-57, Serie B (Jan. 5, 1970).
13. F. Bosnjakovic and W. Springe, "Progress in International Research on Thermodynamic and Transport Properties" 2nd Symposium on Thermodynamic Properties, Princeton Univ., Princeton, N. J. (1962).
14. C. E. Moore, "Atomic Energy Levels," Nat. Bur. Std. 467, Washington, D. C. (1949).

The Activities and Activity Coefficients of Tin and Indium in Their Amalgams at High Temperature

N. Koura*¹

*Department of Industrial Chemistry, Faculty of Science and Technology,
Tokyo University of Science, Noda, Chiba, Japan*

and M. Mukai*

Department of Electrochemistry, Faculty of Engineering, Tokyo Institute of Technology, Meguro, Tokyo, Japan

ABSTRACT

Activities and activity coefficients of indium and tin in their amalgams were determined by means of potentiometric measurements in the temperature region 150°-200°C. The equilibrium potential of indium amalgam was far less noble than that of tin amalgam. In the case of tin amalgam, the activity coefficient decreased rapidly with temperature, but the difference between the normal amalgam potential and the standard electrode potential, E^* , was kept practically constant. On the other hand, in the case of indium amalgam the activity coefficient was kept nearly constant, but the value of E^* increased fairly. The temperature dependence of the activity coefficient was discussed in relation to the type of the amalgamation reaction. Indium amalgam was considered as a simple mixture of indium and mercury and tin amalgam was regarded as a complex such as Sn_xHg_y which was dissolved in a simple mixture of tin and mercury.

In previous papers (1-9), we studied manufacturing processes for production of high purity tin and indium from tin ores containing a small amount of indium and from electrolytic baths containing indium ions used for electrolytic refining of tin. A fused salt electrolysis with amalgam, which is performed in a fused salt electrolyte by the use of an amalgam as an anode and the pure metal as a cathode, was proposed as a new metallurgical method of production of high purity indium from a mixed amalgam of tin and indium (7-9). Through these investigations it was found that the potential of indium amalgam was far less noble than that of tin amalgam at high temperature (180°C) in fused salt, while indium amalgam was more noble than tin amalgam in aqueous solution at room temperature. Therefore, only indium was dissolved by the anodic reaction into the fused salt from the mixed amalgam of tin and indium, whereas only tin was dissolved in an aqueous solution at room temperature. Thus, it was suggested that amalgamated metals behaved in a different manner at high temperature from those at low

temperature. Activities and activity coefficients of indium (10-13) and tin (14-16) in their amalgams at around room temperature have been measured by many workers. However, they have scarcely been investigated at high temperature except a few reports (15, 17).

The present work deals with determination of activities and activity coefficients of indium and tin in their amalgams at high temperature. The results were compared with those obtained at around room temperature and the thermodynamic properties of indium and tin amalgams are discussed.

Experimental

Materials and apparatus.—Metals used in this study were 99.99% purity. Chemicals were guaranteed reagents.

A Pyrex H-type cell (Fig. 1) was used for potentiometric measurements. The amalgam and fused indium well were connected with platinum wire. Emf measurements were carried out in the temperature region 150°-200°C in a bath thermostated within $\pm 0.5^\circ\text{C}$. A universal digital meter Type 2502 (internal resistance $> 10^9$ ohm, Yokogawa Electric Works) was employed in all potential measurements.

* Electrochemical Society Active Member.

¹ Present address: Argonne National Laboratory, Argonne, Illinois 60439.

Key words: tin amalgam, indium amalgam, activity coefficient, high temperature.

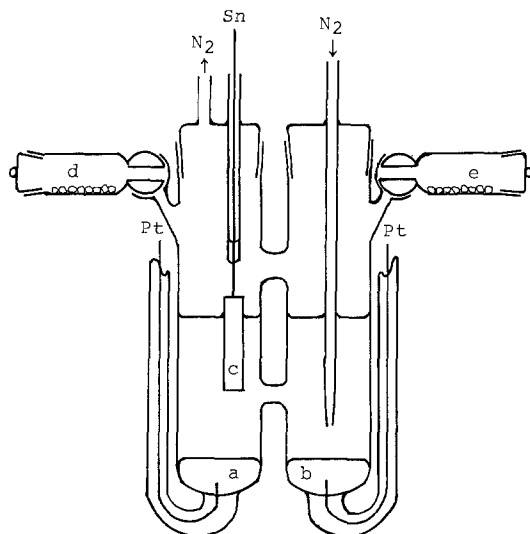


Fig. 1. Schematic diagram of H-cell. In the case of tin amalgam, mercury is used for a and b, tin for c, d, and e. In the case of indium amalgam, mercury is used for b and indium for a and e. Both c and d are not in use.

Experimental procedure.—Anhydrous indium (I) chloride was prepared with indium metal and mercury (I) chloride by the method of Clark (18). Aluminum chloride was reduced to powder in a dry-box, and then heated for 15 hr at 90°C *in vacuo* to remove hydrogen chloride and moisture (8). Powdered sodium chloride was dried for 2 hr at 250°C and tin(II) chloride for 2 hr at 100°C *in vacuo*. The fused salts consisting of 51.6 mole per cent (m/o) aluminum chloride, 43.8 m/o sodium chloride, and 4.6 m/o indium(I) chloride and of 53.5 m/o aluminum chloride, 45.5 m/o sodium chloride, and 1.0 m/o tin(II) chloride were used as cell electrolytes for potentiometric measurements of indium and tin amalgams, respectively. These salts were preheated in bubbling nitrogen for 10 hr at 180°C in order to form a single phase and to remove a very small amount of hydrogen chloride. These were cooled to room temperature and reduced to powder, and then charged into the legs of the emf cell under a nitrogen atmosphere.

Indium was cut to obtain the fresh surface with a grease-free stainless steel cutter and then used as soon as possible. Tin was degreased with benzene and methyl alcohol, and then rinsed with concentrated sulfuric acid for 30 sec. It was then rinsed with distilled water and methyl alcohol and dried *in vacuo* immediately before use.

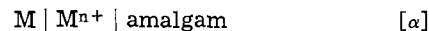
Under a nitrogen atmosphere, all emf measurements were carried out in a cell containing electrodes of a pure metal of tin or indium and an amalgam of a known concentration of tin or indium. The amalgam was produced by dissolving weighed metallic tin or indium (d or e in Fig. 1) in mercury (a or b in Fig. 1) under a nitrogen atmosphere after the salts were fused, and agitated for 10 min.

Results and Discussion

Activities and activity coefficients of indium and tin in their amalgams.—The activity (a_{M-Hg}) and activity

coefficient (γ_{M-Hg}) of a metal M in the amalgam at high temperature were measured by applying the method of Butler (11).

The cell is described as



The electromotive force (E_{M-Hg}) of the cell is given by Eq. [1]

$$\begin{aligned} E_{M-Hg} &= [E_{M-Hg}^{\circ} - (RT/nF) \ln (a_{M-Hg}/a_{M^{n+}})] \\ &\quad - [E_M^{\circ} - (RT/nF) \ln (1/a_{M^{n+}})] \\ &= (E_{M-Hg}^{\circ} - E_M^{\circ}) - (RT/nF) \ln a_{M-Hg} \quad [1] \end{aligned}$$

E_{M-Hg}° and E_M° denote the normal amalgam potential and the standard electrode potential, respectively. As long as the composition of the fused salt and the temperature are kept constant, ($E_{M-Hg}^{\circ} - E_M^{\circ}$) is given as a constant. Therefore, Eq. [1] is reduced to

$$E_{M-Hg} = E^* - (RT/nF) \ln a_{M-Hg} \quad [2]$$

$$= E^* - (RT/nF) \ln X_{M-Hg} \cdot \gamma_{M-Hg} \quad [2']$$

where E^* is a constant and X_{M-Hg} the mole fraction of the amalgam. Equation [2'] is rearranged to

$$E_{M-Hg} + (RT/nF) \ln X_{M-Hg} = E^* - (RT/nF) \ln a_{M-Hg} \quad [3]$$

E_{M-Hg} is determined against X_{M-Hg} at a constant composition and temperature of the fused salts. The value of the left-hand side of Eq. [3] is plotted against X_{M-Hg} . If γ_{M-Hg} is defined to approach unity at the infinitely dilute amalgam, the extrapolation of the amalgam concentration toward zero gives the value of E^* . Thus the activity and activity coefficient of a metal in the amalgam are calculated by Eq. [4].

$$a_{M-Hg} = X_{M-Hg} \cdot \gamma_{M-Hg} = \exp(nF/RT) (E^* - E_{M-Hg}) \quad [4]$$

Activities and activity coefficients of indium and tin in their amalgams obtained at 150°, 160°, 180°, 190°, and 200°C are listed in Tables I and II. In order to visualize the change of the activities with temperature values of a_{Sn-Hg} determined in this work are shown in Fig. 2 together with those² of Bonnier *et al.* (14) and a_{In-Hg} in Fig. 3 together with values of Butler (11). In the case of tin amalgam as shown in Fig. 2, the activities and activity coefficients became extremely small at high temperature. It was also seen from Fig. 2 that γ_{Sn-Hg} was nearly constant at a given temperature below 50°C, because the curve of X_{Sn-Hg} vs. a_{Sn-Hg} was approximately linear at the temperature. In the case of indium amalgam (Fig. 3), the activities and activity coefficients changed very little with temperature (especially at low concentration). Therefore, it is seen from these results that the temperature coefficient of γ_{M-Hg} depended upon the amalgamated metals.

The temperature dependence of activity coefficients and thermodynamic properties of amalgams.—It is considered that the remarkable difference of the temperature dependence of γ_{In-Hg} and γ_{Sn-Hg} is favorable to separate indium from a mixed amalgam of tin and indium by means of the fused salt electrolysis with

² The values may be smaller if they are calculated by our method.

Table I. Activities and activity coefficients of indium in the amalgam

X_{In-Hg}	160°C			180°C			190°C			200°C		
	E_{In-Hg} (mV)	a_{In-Hg}	γ_{In-Hg}	E_{In-Hg} (mV)	a_{In-Hg}	γ_{In-Hg}	E_{In-Hg} (mV)	a_{In-Hg}	γ_{In-Hg}	E_{In-Hg} (mV)	a_{In-Hg}	γ_{In-Hg}
0.0180	228.0	0.0179	0.995	239.8	0.0178	0.986	245.0	0.0178	0.988	250.8	0.0176	0.978
0.101	151.3	0.140	1.39	159.7	0.138	1.37	163.3	0.138	1.37	167.1	0.137	1.36
0.256	108.5	0.441	1.72	116.7	0.416	1.63	121.0	0.398	1.56	124.2	0.394	1.54
0.471	63.4	1.48	3.14	68.3	1.44	3.06	71.1	1.39	2.96	74.4	1.34	2.84
0.700	22.0	4.49	6.41	25.7	4.29	6.13	28.0	4.10	5.86	29.0	4.07	5.82
0.807	7.8	6.57	8.14	11.1	6.23	7.73	12.3	6.08	7.54	13.8	5.91	7.33
E^* (mV)		78.0			82.5			84.3			86.2	

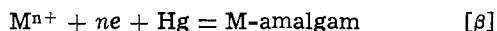
Table II. Activities and activity coefficients of tin in the amalgam

$X_{\text{Sn-Hg}}$	$E_{\text{Sn-Hg}}$ (mV)	150°C			160°C			180°C			200°C		
		$a_{\text{Sn-Hg}}$	$\gamma_{\text{Sn-Hg}}$	$E_{\text{Sn-Hg}}$ (mV)	$a_{\text{Sn-Hg}}$	$\gamma_{\text{Sn-Hg}}$	$E_{\text{Sn-Hg}}$ (mV)	$a_{\text{Sn-Hg}}$	$\gamma_{\text{Sn-Hg}}$	$E_{\text{Sn-Hg}}$ (mV)	$a_{\text{Sn-Hg}}$	$\gamma_{\text{Sn-Hg}}$	
0.0111	24.0	0.0121	1.09	31.5	0.00883	0.795	35.7	0.00872	0.786	40.4	0.00842	0.759	
0.0506	12.7	0.0225	0.445	16.1	0.0202	0.398	19.4	0.0201	0.398	23.1	0.0197	0.389	
0.0950	11.2	0.0245	0.257	12.4	0.0246	0.259	15.5	0.0246	0.259	19.4	0.0236	0.249	
0.273	6.0	0.0325	0.119	7.3	0.0323	0.118	10.0	0.0326	0.119	13.1	0.0322	0.118	
0.451	2.6	0.0392	0.0870	3.8	0.0390	0.0865	7.0	0.0380	0.0842	10.1	0.0373	0.0826	
0.700	$\approx 0^a$	—	—	0.3	0.0471	0.0672	1.6	0.0501	0.0716	4.5	0.0491	0.0701	
0.850	$\approx 0^a$	—	—	$\approx 0^a$	—	—	$\approx 0^a$	—	—	$\approx 0^a$	—	—	
E^* (mV)		-56.4			-56.7			-56.8			-56.9		

^a The value of saturated amalgam with excess solid tin present.

amalgam. In the following section the difference is discussed on the basis of thermodynamics.

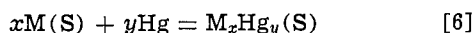
If the reaction of a metal ion with a mercury electrode is described as follows



the electrode potential (E'_{M-Hg}) is generally represented as follows (19)

$$E'_{M-Hg} = E^o_{M-Hg} - (RT/nF) \ln (a_{M-Hg}/a_{M^{n+}}) \\ = E^o_M + E_s + (RT/nF) \ln a_{\text{sat}} + (RT/nF) \ln a_{M^{n+}} \\ - (RT/nF) \ln a_{M-Hg} \quad [5]$$

where a_{sat} denotes the activity of a saturated amalgam with the metal M. E_s is defined as $-\Delta F/nF$ provided that the change in free energy of the following reaction is given as $-\Delta F$



where S represents a solid state and M_xHg_y a compound of metal M with mercury. In addition, E_s is regarded as the electromotive force of a cell which consists of electrodes of a metal and an amalgam saturated with the metal; $M | M^{n+} | M\text{-amalgam}(\text{sat})$. If the equilibrium potential of the reaction [β] is measured against the electrode potential of the metal M and if the temperature and the composition of the fused salt are equal to those in the cell [α], the following equation is derived from Eq. [2] and [5]

$$E'_{M-Hg} - E^o_M - (RT/nF) \ln (1/a_{M^{n+}}) = E_{M-Hg} \quad [7]$$

Insertion of Eq. [7] into Eq. [5] leads to

$$E_{M-Hg} = E_s + (RT/nF) \ln a_{\text{sat}} - (RT/nF) \ln a_{M-Hg} \quad [8]$$

Therefore, from Eq. [2] and [8] we obtain

$$E^* = E_s + (RT/nF) \ln a_{\text{sat}} \quad [9]$$

Values of E_{M-Hg} and E^* for indium amalgam and tin amalgam were determined, and are listed in Tables I and II. The values of E^* , ($E^* - E_{M-Hg}$), $\exp(nF/RT)$ ($E^* - E_{M-Hg}$) and ratio of a_{M-Hg} (temperature change, 30°C) at the mole fraction of 0.0111 for tin amalgam and of 0.0180 for indium amalgam are shown in Table III. In the case of tin amalgam the activity ratio was given as 1.39, while the ratio was 1.01 for indium amalgam. The value of a_{M-Hg} was greatly affected by E^* as shown in Table III.

In the case of indium amalgam the change of E^* with temperature was close to that of E_{In-Hg} . However, in the case of tin amalgam the change of E^* was extremely smaller than that of E_{Sn-Hg} . These tendencies were observed over the whole range of the amalgam concentration studies as shown in Tables I and II. Then it is concluded that the difference between the changes of activities (or activity coefficients) of indium and tin in their amalgams with temperature was due to the variation in the change of E^* of these amalgams with temperature. Such a conclusion was confirmed by the temperature dependence of E^* between 25° or 30°C and 180°C, which is shown in the third column of Table IV. The change in E^* with temperature for indium amalgam is extremely larger than that for tin amalgam.

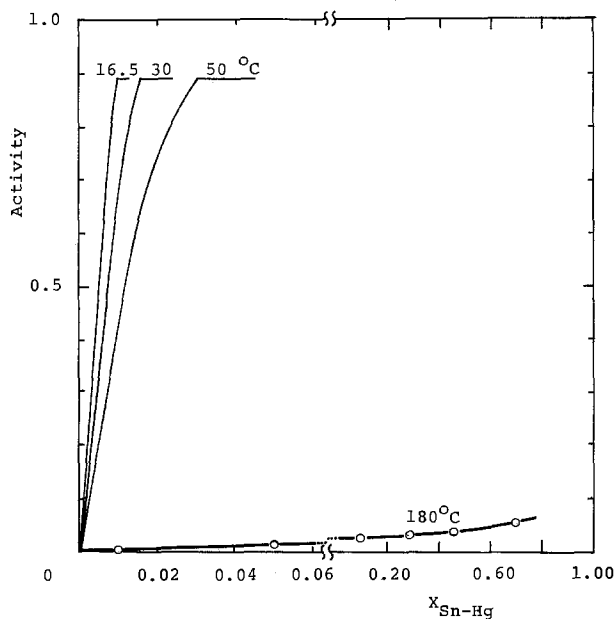


Fig. 2. Activities of tin in the amalgam. — Bonnier et al. (14), —○—○— present work.

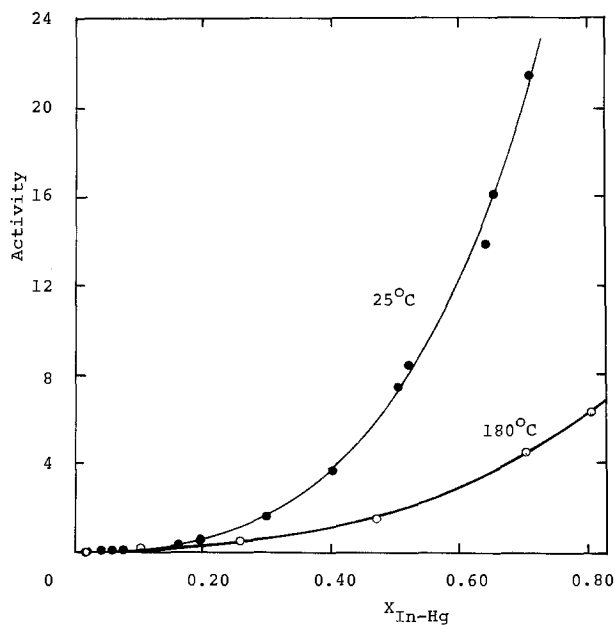


Fig. 3. Activities of indium in the amalgam. —●—●— Butler (11), —○—○— present work.

Table III. Measured and calculated values of each term at a given temperature

Amalgam (X_{M-Hg})	Temp. (°C)	E^* (mV)	E_{M-Hg} (mV)	$E^* - E_{M-Hg}$ (mV)	$\exp(nF/RT)$ $\times (E^* - E_{M-Hg})$	Ratio of a_{M-Hg} (temp. change, 30°C)
Tin amalgam (0.0111)	150	-56.4	+24.0	-80.4	0.0121	1.39
	180	-56.8	+35.7	-92.5	0.00872	
Indium amalgam (0.0180)	160	+78.0	+228.0	-150.0	0.0179	1.01
	190	+84.3	+245.0	-160.7	0.0178	

In order to consider the change in E^* with temperature, $(RT/nF) \ln a_{sat}$ and E_s at 25°, 30°, and 180°C were calculated by the use of Eq. [9] and are listed in Table IV. The change in E_s for both tin and indium amalgams with temperature were very small, i.e., 3.1 and 0.1 mV, respectively. Furthermore, the values of E_s for indium and tin amalgams were approximately zero at both 25° or 30°C and 180°C.

Types of amalgamation reactions of indium and tin amalgams.—Information obtained above is discussed separately on indium and tin amalgams.

1. *Indium amalgam.*—Thermodynamic properties of indium amalgam observed are summarized as follows: (i) The change of a_{In-Hg} with temperature was very small at a given concentration (especially at low concentration). (ii) E_s was practically zero and independent of temperature. (iii) E^* varied with temperature.

From the Gibbs-Helmholtz equation, we lead to

$$\begin{aligned} \Delta H &= \Delta G + T[\partial(-\Delta G)/\partial T] \\ &= -T^2[\partial(\Delta G/T)/\partial T] \end{aligned} \quad [11]$$

When the relation $\Delta G = RT \ln (a_1/a_2)$ is inserted into Eq. [11] and a differential version is used, the change of the activity ratio with temperature is represented as the following equation

$$d \ln (a_1/a_2)/dT = -\Delta H/RT^2 \quad [12]$$

where a_1 and a_2 are activities, and $\Delta H = \Delta H_2 - \Delta H_1$. Subscripts show the states 1 and 2. Since the change of the activity of indium in the amalgam with temperature is very small, we obtain

$$\Delta H \approx 0 \quad [13]$$

On the other hand, Kirchhoff's law gives the following relationship

$$\Delta H_T = \Delta H_0 + \int_0^T \Delta C_p dT \quad [14]$$

Combining Eq. [13] with [14], we obtain

$$\int_0^T \Delta C_p dT \approx 0 \quad [15]$$

According to Kubaschewsky (20) ΔC_p 's of indium and mercury are very small and independent of temperature, i.e., 7.24³ and 6.61 cal/deg-mol, respectively. Thus, it is expected that ΔC_p of indium amalgam is also small provided that there is no special interaction between indium and mercury in the amalgam. Therefore, it seems reasonable to assume that indium amalgam is a simple mixture of indium and mercury. In addi-

³ As an amalgamated indium is liquid, a value of fused indium is quoted. This value is nearly independent of temperature below 527°C.

Table IV. Calculated values of each term at a given temperature by using Eq. [9]

Amalgam	Temperature (°C)	E^* (mV)	$(RT/nF) \ln a_{sat}$ (mV)	E_s (mV)
Tin amalgam	30 ^a	-56.2	-54.7	-1.5
	180	-56.8	-58.4	+1.6
	25 ^b	+26.3	+26.4	-0.1
Indium amalgam	180	+82.5	+82.5	0

^a Calculated from data of Bonnier et al. (14).

^b Calculated from data of Butler (11).

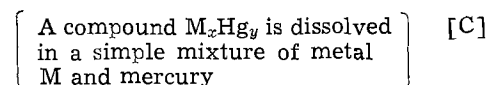
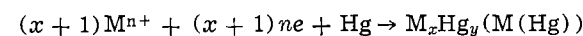
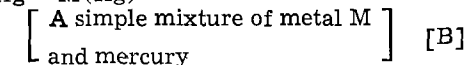
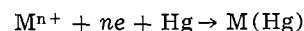
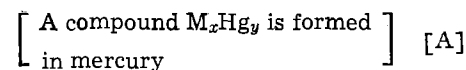
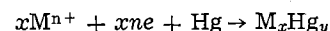
tion, this assumption satisfactorily explains the property (ii), because it is considered from Eq. [15] that both the value of ΔF^4 and the change with temperature are small.

Bros (21) and Kleppa (22) found that ΔH of indium amalgam was approximately constant against temperature. Butler (11) assumed that indium amalgam was a regular solution in his study of ΔS of indium amalgam at room temperature. These studies support our consideration. Thus, it is concluded that indium amalgam is the simple mixture of indium and mercury.

2. *Tin amalgam.*—The thermodynamic properties of tin amalgam are summarized as follows. (i) E_s was nearly equal to zero and varied very little with temperature. (ii) γ_{Sn-Hg} was approximately constant with the concentration change at a constant temperature below 50°C. (iii) γ_{Sn-Hg} largely changed with temperature. (iv) E^* was practically independent of temperature.

As shown in Fig. 2, a_{Sn-Hg} varied largely with temperature. Therefore, it would be expected that ΔF and ΔH of tin amalgam varied largely with temperature. Kozin (15) found that the change in ΔF of tin amalgam with temperature was large. The fact that E_s was nearly independent of temperature is inconsistent with these results. According to the general treatment (19) as stated in the previous section, all metal atoms in a saturated amalgam must exist as M_xHg_y . However, indium amalgam can be regarded as a simple mixture of indium and mercury rather than In_xHg_y as we pointed out. Smallman (23), Halder (24), and Folley (25-27) reported that Tl_2Hg_5 was formed in a simple mixture of thallium and mercury and the amount of Tl_2Hg_5 varied with the temperature and concentration of thallium amalgam. Namely, all metal atoms in an amalgam do not always exist as M_xHg_y . In such cases results obtained may not be satisfactorily interpreted by the general treatment.

The amalgamation reactions of metals may be divided into three types as follows



where mercury exists in large excess. Compounds of tin with mercury such as $SnHg_2$, $SnHg$, Sn_2Hg , Sn_3Hg , Sn_4Hg , and Sn_5Hg were reported and heat capacities of these compounds were estimated to be large (28). Hinzner (29) also suggested that Sn_xHg_y is formed when tin dissolves in mercury. Therefore, if it is assumed that the amalgamation reaction of tin belongs to the type (C), i.e., Sn_xHg_y exists in $Sn(Hg)$, and moreover, that a large portion of tin exists as Sn_xHg_y , we can conclude that: (I) $-\Delta H$ of tin amalgam largely changes with temperature, because a complex com-

⁴ It should be noted that ΔG can be rewritten in terms of ΔF at constant pressure and volume. Therefore, in the following section, discussion is made in terms of ΔF instead of ΔG .

pound such as Sn_xHg_y has a large heat capacity and in general the heat capacity of such a compound is a function of temperature (20), and (II) $\gamma_{\text{Sn-Hg}}$ is practically independent of the concentration of tin amalgam [the property (ii)], because a large portion of tin in the amalgam exists as Sn_xHg_y and the interaction between Sn_xHg_y and Sn_xHg_y may be much smaller than that between Sn and Sn in the amalgam.⁵ However, $\gamma_{\text{Sn-Hg}}$ is slightly affected with the concentration change, because tin in the amalgam may not exist entirely as Sn_xHg_y and the interaction between Sn_xHg_y and Sn_xHg_y is not negligible. These tendencies may become strong at high temperature.

From the above (I), it is considered that $\gamma_{\text{Sn-Hg}}$ decreases rapidly with temperature [the property (iii)]. Thus, the results can reasonably be explained by assuming that the amalgamation reaction of tin belongs to type [C].

As described above, the fact that indium is separated from the mixed amalgam of tin and indium is attributed to the wide variation of $\gamma_{\text{Sn-Hg}}$ and to the approximately constant $\gamma_{\text{In-Hg}}$ with temperature. It can also be concluded that the difference is ascribed to the different amalgamation reaction type, i.e., indium amalgam belongs to type [B] and tin amalgam to type [C]. On the other hand, it should be noted that the temperature dependence of E^* (i.e., $E^{\circ}_{\text{M-Hg}}$) has a great influence on that of $E_{\text{M-Hg}}$. Because $E_{\text{M-Hg}}$ is affected not only by the change of $\gamma_{\text{M-Hg}}$ (and $a_{\text{M-Hg}}$) with temperature but also by the change of $E^{\circ}_{\text{M-Hg}}$ with temperature as described by the following equation

$$E_{\text{M-Hg}} = E^{\circ}_{\text{M-Hg}} - (RT/nF) \ln(a_{\text{M-Hg}}/a_{\text{Mn}+}) \quad [16]$$

The relationship of the temperature dependence of E^* to the amalgamation reaction type is under investigation, and the results will be published shortly.

Conclusion

The reason why indium is separated effectively from a mixed amalgam of tin and indium by means of the fused salt electrolysis with amalgam was investigated. The potential of indium amalgam was far less noble than the potential of tin amalgam at high temperature, because $\gamma_{\text{Sn-Hg}}$ decreased rapidly with temperature (and E^*_{Sn} was kept practically constant), while $\gamma_{\text{In-Hg}}$ was approximately constant (and E^*_{In} increased fairly). From the temperature dependence of the activity coefficient, we concluded that indium amalgam is the simple mixture of indium and mercury (type [B]), whereas tin amalgam contains a complex such as

⁵ It is known that metal M in an amalgam is very active and compound M_xHg_y in the amalgam is stable (30).

Sn_xHg_y dissolved in a simple mixture of tin and mercury (type [C]).

Manuscript submitted Feb. 21, 1973; revised manuscript received Aug. 16, 1974.

Any discussion of this paper will appear in a Discussion Section to be published in the December 1975 JOURNAL. All discussions for the December 1975 Discussion Section should be submitted by Aug. 1, 1975.

Publication costs of this article were partially assisted by the Tokyo Institute of Technology.

REFERENCES

1. N. Koura and M. Mukai, *J. Mining Met. Inst. Japan*, **84**, 1089 (1968).
2. N. Koura and M. Mukai, *ibid.*, **85**, 85 (1969).
3. N. Koura and M. Mukai, *J. Metal Finishing Soc. Japan*, **20**, 6 (1969).
4. N. Koura and M. Mukai, *J. Mining Met. Inst. Japan*, **86**, 99 (1970).
5. N. Koura and M. Mukai, *ibid.*, **86**, 919 (1970).
6. N. Koura and M. Mukai, *Japan Pat.*, 45-427 (1970).
7. N. Koura and M. Mukai, *Fused Salt*, **13**, 186 (1970).
8. N. Koura and M. Mukai, *J. Mining Met. Inst. Japan*, **87**, 33 (1971).
9. N. Koura and M. Mukai, *Japan Pat.*, 46-2734 (1971).
10. N. Sundén, *Z. Elektrochem.*, **57**, 100 (1953).
11. J. N. Butler, *J. Phys. Chem.*, **68**, 1828 (1964).
12. L. F. Kozin, *Trans. Inst. Khim. Nauk, Akad. Nauk Kaz. S.S.R.*, **9**, 71 (1962).
13. L. F. Kozin, *ibid.*, **9**, 81 (1962).
14. E. Bonnier *et al.*, *Compt Rend.*, **255**, 2432 (1962).
15. L. F. Kozin *et al.*, *Zh. Neorgan. Khim.*, **8**, 2556 (1963).
16. V. F. Sergeeva *et al.*, *ibid.*, **10**, 1955 (1965).
17. G. R. B. Elliot, *This Journal*, **115**, 1143 (1968).
18. R. J. Clark *et al.*, *J. Am. Chem. Soc.*, **80**, 4764 (1958).
19. I. Tachi, "Polarography," Iwanami Shoten, Publisher, Tokyo (1956).
20. O. Kubaschewsky *et al.*, "Metallurgical Thermochemistry," The Pergamon Press Ltd., England (1958).
21. J. P. Bros, *Compt Rend.*, **260**, 3935 (1965).
22. O. J. Kleppa *et al.*, *J. Phys. Chem.*, **61**, 1120 (1957).
23. R. E. Smallman *et al.*, *Act. Met.*, **4**, 611 (1956).
24. N. C. Halder *et al.*, *J. Phys. Chem.*, **45**, 1259 (1966).
25. W. T. Folley *et al.*, *Can. J. Chem.*, **41**, 1782 (1963).
26. W. T. Folley *et al.*, *ibid.*, **42**, 2607 (1964).
27. W. T. Folley *et al.*, *ibid.*, **42**, 2749 (1964).
28. National Research Council of U.S.A., "International Critical Table of Numerical Data, Physics, Chemistry and Technology," McGraw-Hill Book Co., Inc., New York (1926).
29. F. W. Hinzner *et al.*, *J. Phys. Chem.*, **67**, 2424 (1963).
30. M. Mukai and N. Koura, *J. Mining Met. Inst. Japan*, **82**, 35 (1966).



Effect of the Rate of Cooling on the Emission of CaS:Ce Phosphor

D. R. Vij and V. K. Mathur

Department of Physics, Kurukshetra University, Kurukshetra, India

Calcium sulfide phosphors are among the earliest phosphors to be synthesized in the laboratory. The bright emission and persistent afterglow of these phosphors led to their extensive investigations by the "Lenard School" (1). However, due to inadequate techniques employed in their synthesis, the resulting phosphors were of poor reproducibility and were found to be unstable against atmospheric carbon dioxide and water vapor. Successful attempts have since been made to synthesize calcium sulfide phosphors which are stable as well as reproducible (2-4).

We have been able to synthesize (5) a stable and reproducible CaS:Ce phosphor from CaSO₄. The reduction of CaSO₄ by carbon and the incorporation of activator (Ce) in the host lattice of CaS is achieved in a single process of firing at a comparatively lower temperature of 900°C in the presence of a flux. Later it was discovered by us that due to the hygroscopic nature of the flux it absorbed water vapor from the atmosphere and thereby impaired the emission properties of the phosphor. Surprisingly enough the flux could be removed by washing with water, and the phosphor product thus obtained did not show any deterioration in its emission properties even after a few weeks exposure to the atmosphere.

We have studied thermoluminescence (5), thermally stimulated conductivity (6), and spectral characteristics (7) of these phosphors. The emission of CaS:Ce phosphor consists of a green and a yellow band. It was observed (7) that at lower concentration of cerium, the green emission is predominant, while at higher concentration, the yellow emission is enhanced at the expense of green emission. Lehmann and Ryan (8), however, state that the intensity ratio of the two bands is independent of all preparational parameters. These authors synthesized the CaS:Ce phosphors by the method of Wachtel (4) and further found that the addition of chlorine enhances very much the emission of the phosphor. Smith (9) succeeded in synthesizing these phosphors without the addition of any flux (in our method, a flux is essential for the synthesis of the phosphor) or even without the addition of any chlorine, which according to Lehmann is an essential ingredient for their bright emission. Smith observed the effect of a varying Ce⁺⁺⁺ concentration on the emission similar to the one reported by us (7) but unlike the observations of Lehmann and Ryan (8).

We wish to report here the effect of the rate of cooling of the charge after firing, which is one of the interesting parameters (10) among many found to affect the emission of the CaS:Ce phosphor.

Experimental

The CaS:Ce phosphor was synthesized by the method developed by Bhawalkar (11). A charge was prepared by mixing 5g of CaSO₄·2H₂O powder with 1.5g of an-

hydrous Na₂SO₄. An appropriate quantity of carbon, slightly in excess of that needed to reduce CaSO₄ completely, was added to this charge. Cerium was added in the form of a solution of Ce(NO₃)₃·6H₂O in triply distilled water. The percentage of Ce was varied from 0.02 to 1.0 by weight of CaSO₄·2H₂O.

After proper mixing, the whole charge was fired in a Salamander graphite crucible at 900°C in a muffle furnace for 2 hr. Additional carbon was fired in a separate crucible in the muffle furnace to create a reducing atmosphere in the furnace. Finally, after firing, the mass was crushed to a fine powder. Flux was removed by washing of the powder in boiling double distilled water for 2-3 min, and it was dried at 150°C. The phosphor thus prepared was found to be stable and unaffected by the moisture in the atmosphere.

CaS:Ce (0.08%) was the most intense green emitting phosphor (10). The effect of rate of cooling after proper firing was evaluated on this sample. After firing of the above mentioned charge for 1 hr, the whole mass was brought out of the furnace, crushed to powder to ensure proper reduction in the interior volume of the charge. At this stage, it was divided into two parts and again placed in the furnace in two separate crucibles. After firing for one more hour, the charge of one of the crucibles was brought out and crushed immediately. If this is not done and the charge is allowed to cool as such, the outer crust of the mass would cool down while the interior volume of the hot mass still remains at high temperature. By crushing, the whole mass cools homogeneously at a faster rate. The other part of the phosphor placed in another crucible was left as such in the furnace. It was cooled with the average rate of 50°C/hr.

To observe the emission, the samples were excited by short wave UVS-12 lamp which predominantly emits 3650Å radiations. The emission was observed with the help of a constant deviation spectrometer, to which was attached a photomultiplier tube, Type 1P21. For TL studies, the phosphor was excited to saturation using u.v. radiations. The heating of the phosphor was started after 90 sec of decay. The rate of heating was 0.25°C/sec. The resulting TL was measured with the help of 1P21 photomultiplier. The details of experimental setup are described elsewhere (5).

Results

The emission spectra of slow and fast cooled samples of CaS:Ce (0.08%) are shown in Fig. 1. As is obvious from the curves, the slow-cooled sample exhibits brighter emission (see curve-I, Fig. 1) than the fast-cooled one (see curve-II, Fig. 1). Both the bands in the green and yellow regions are of higher intensity in the slow cooled sample.

In Fig. 2 the thermoluminescence curves of the two samples are plotted. In this case the effect of rate of cooling is opposite to that of emission, i.e., the slow-cooled sample gives rise to low intensity of TL (see

Key words: green emission, thermoluminescence, alkaline-earth sulfides, luminescence.

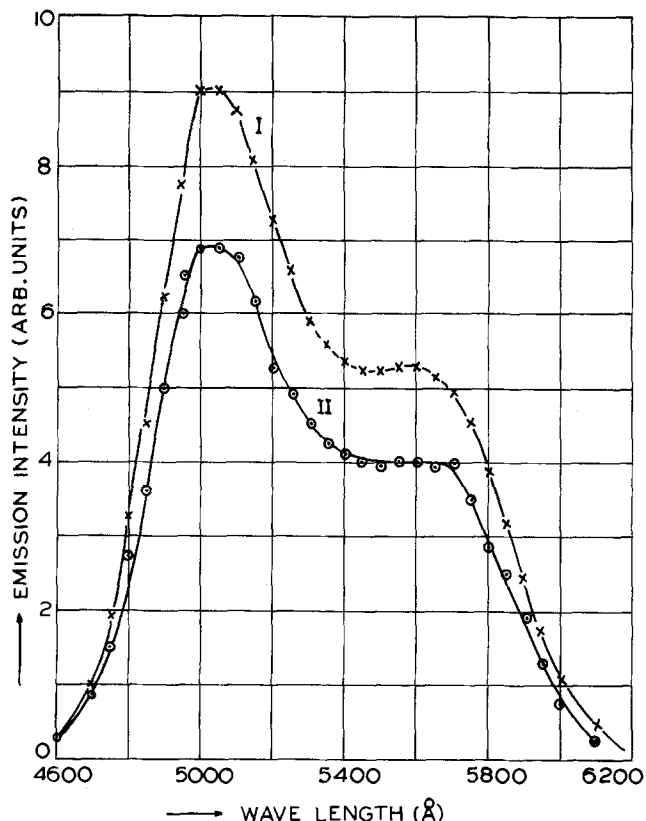


Fig. 1. Emission spectra of fast- and slow-cooled $\text{CaS:Ce}(0.08\%)$ phosphor. (X)-curve-I, slow-cooled sample; (O)-curve-II, fast-cooled sample.

curve-I, Fig. 2) as compared to the fast-cooled one which emits higher intensity of TL (see curve-II, Fig. 2).

Discussion

At the temperature of firing the lattice has a large density of defects which tends to "freeze" during fast cooling. It is well known that these defects give rise to trapping centers in sulfide phosphors. On the other hand if the phosphor is cooled slowly, the lattice would have sufficient time to adjust itself and come to an equilibrium state corresponding to that particular temperature. This results in a smaller density of defects and consequently of traps. The above mentioned facts are borne out by the thermoluminescence studies reported in Fig. 2. It is seen that the area under the glow curve of the fast-cooled sample (curve-II) is more than the area under the glow curve of the slow-cooled sample. It may therefore, appear that the smaller density of defects in a slow-cooled sample results in well-defined luminescent centers increasing thereby the probability of radiative transitions. Therefore, it appears that for higher emission efficiency, the samples should be cooled very slowly.

Acknowledgments

The authors wish to acknowledge the keen interest shown by Prof. N. Nath during the course of these

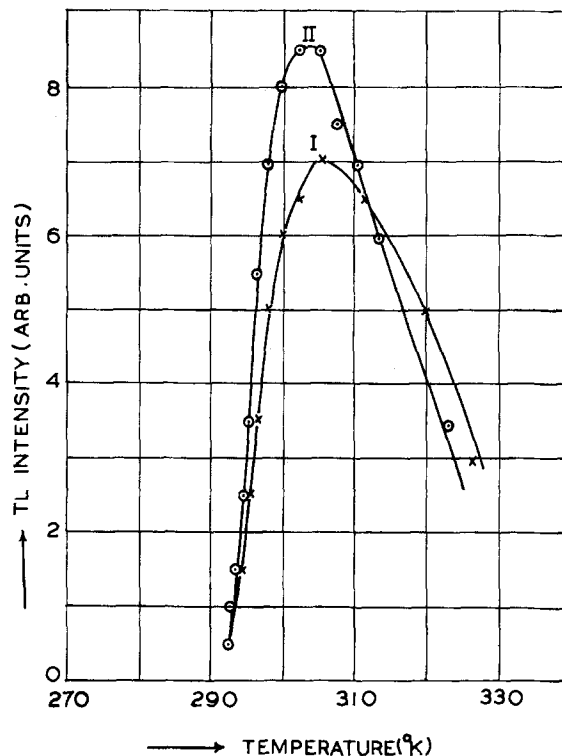


Fig. 2. TL of slow- and fast-cooled $\text{CaS:Ce}(0.08\%)$ phosphor. (X)-curve-I, slow-cooled sample; (O)-curve-II, fast-cooled sample.

studies. One of the authors (D.R.V.) also acknowledges the financial assistance from the Council of Scientific and Industrial Research, India, in the form of a Senior fellowship during the tenure of the work.

Manuscript submitted July 8, 1974; revised manuscript received Sept. 15, 1974.

Any discussion of this paper will appear in a Discussion Section to be published in the December 1975 JOURNAL. All discussions for the December 1975 Discussion Section should be submitted by Aug. 1, 1975.

REFERENCES

1. P. Lenard, F. Schmidt, and R. Tomaschek, "Handbuck der Exp. Phys.," Vol. 23 (1928).
2. R. Ward, *Trans. Electrochem. Soc.*, **93**, 171 (1948).
3. O. Sorge, Thesis, Technical University, Berlin (1959).
4. A. Wachtel, *This Journal*, **107**, 199 (1960).
5. D. R. Vij and V. K. Mathur, *Indian J. Pure Appl. Phys.*, **6**, 67 (1968).
6. D. R. Vij and V. K. Mathur, *ibid.*, **6**, 646 (1968).
7. D. R. Vij and V. K. Mathur, *ibid.*, **7**, 638 (1969).
8. W. Lehmann and F. M. Ryan, *This Journal*, **118**, 477 (1971).
9. A. L. Smith, Private communication.
10. D. R. Vij, Ph.D. Thesis, Kurukshetra University, India (1974).
11. D. R. Bhawalkar, *Saugar Univ. J. (India)*, **1**, 209 (1951-1952).

Infrared-to-Visible Conversion in $\text{YOF:Yb}^{3+}, \text{Ho}^{3+}$ and $\text{YF}_3:\text{Yb}^{3+}, \text{Ho}^{3+}$ Phosphors

J. Wojciechowski, I. Pawelska, R. Grodecki, and L. Szymanski

Institute of Electron Technology, Al. Lotnikow 32/46, Warsaw, Poland

In recent years there has been much interest in phosphors that emit visible radiation when excited with infrared radiation from Si-doped GaAs electro-luminescent diode source (1).

These phosphors, in general, contain Yb^{3+} ions absorbing infrared radiation of about $1 \mu\text{m}$ and transferring excitation in two or more sequential steps to activator ions.

The most frequently used sensitizer-activator systems are: for green and red radiation, $\text{Yb}^{3+}-\text{Er}^{3+}$, and for blue radiation, $\text{Yb}^{3+}-\text{Tm}^{3+}$. Green radiation can

Key words: anti-Stokes luminescence, $\text{Yb}^{3+}-\text{Ho}^{3+}$ system, excitation processes, visible emission.

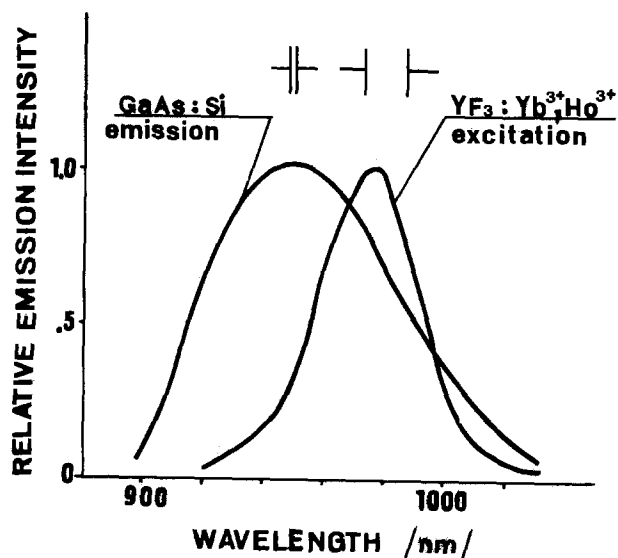


Fig. 1. Excitation spectrum of $\text{YF}_3:\text{Yb}^{3+}, \text{Ho}^{3+}$ compared with emission spectrum of Si-GaAs diode.

also be obtained with $\text{Yb}^{3+}-\text{Ho}^{3+}$ system, but the efficiency of Ho^{3+} activated phosphors is smaller in comparison with Er^{3+} activated phosphors. This is the reason why the $\text{Yb}^{3+}-\text{Ho}^{3+}$ system is the object of investigation only in a small number of papers (2, 3) and processes of energy transfer, stepwise excitation, and radiation deexcitation are not fully explained.

In this paper some comments on the dynamics of infrared-to-visible conversion in the $\text{Yb}^{3+}-\text{Ho}^{3+}$ system are given and also some advantages of Ho^{3+} activated phosphors are shown.

Experimental Procedures

Samples of phosphors were made according to the usual methods. As starting materials very high purity oxides were used: Y_2O_3 (6N), Yb_2O_3 (5N), and Ho_2O_3 (4N).

$\text{YOF:Yb}^{3+}, \text{Ho}^{3+}$ phosphor was made according to the method described by Matsubara (4) and $\text{YF}_3:\text{Yb}^{3+}, \text{Ho}^{3+}$ phosphor was made in a similar manner, but in this case the possibility of oxidation was thoroughly eliminated. The temperature in a furnace was about 1100°C . Ho^{3+} activated phosphors were compared with $\text{YF}_3:\text{Yb}^{3+}, \text{Er}^{3+}$ phosphor prepared in the same way. As a rule samples of composition $\text{Y}_{0.80}\text{Yb}_{0.198}\text{Ho}_{0.002}\text{OF}$, $\text{Y}_{0.80}\text{Yb}_{0.198}\text{Ho}_{0.002}\text{F}_3$, and $\text{Y}_{0.80}\text{Yb}_{0.19}\text{Er}_{0.01}\text{F}_3$ were used.

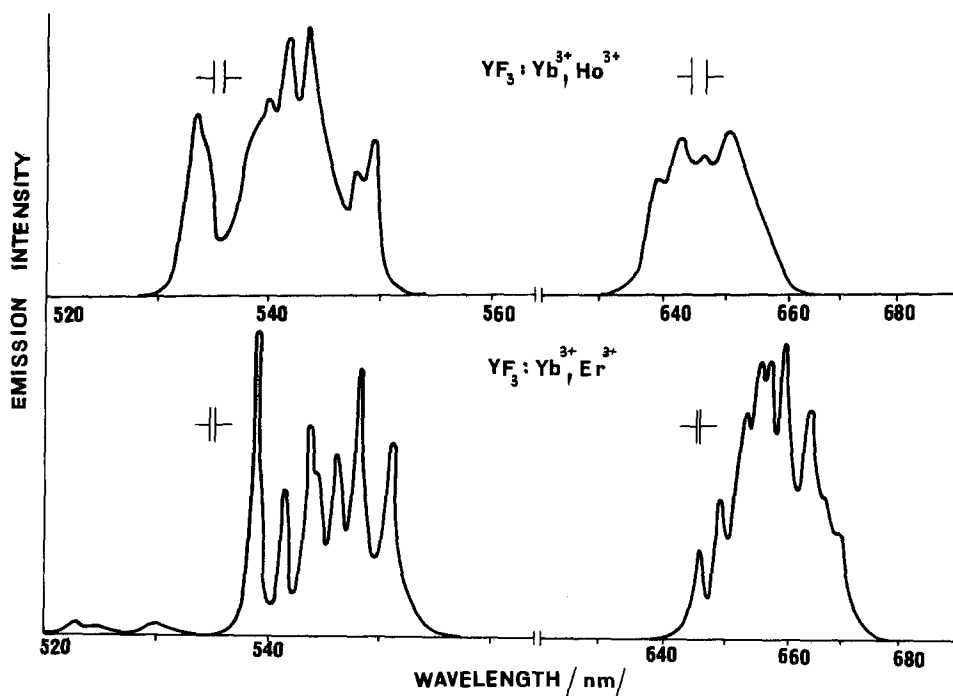
As an infrared radiation pump source, an Si-doped GaAs diode was used, with 2% efficiency and peak emission at 950 nm.

The excitation source for infrared excitation spectra was 800W tungsten-iodine light source.

Results and Discussion

The excitation spectrum of $\text{YF}_3:\text{Yb}^{3+}, \text{Ho}^{3+}$ for green emission is shown in Fig. 1. The excitation resolution is indicated. In Fig. 1 also shown is the emission spectrum of the Si-GaAs diode.

Fig. 2. Visible radiation spectra of $\text{YF}_3:\text{Yb}^{3+}, \text{Ho}^{3+}$ and $\text{YF}_3:\text{Yb}^{3+}, \text{Er}^{3+}$.



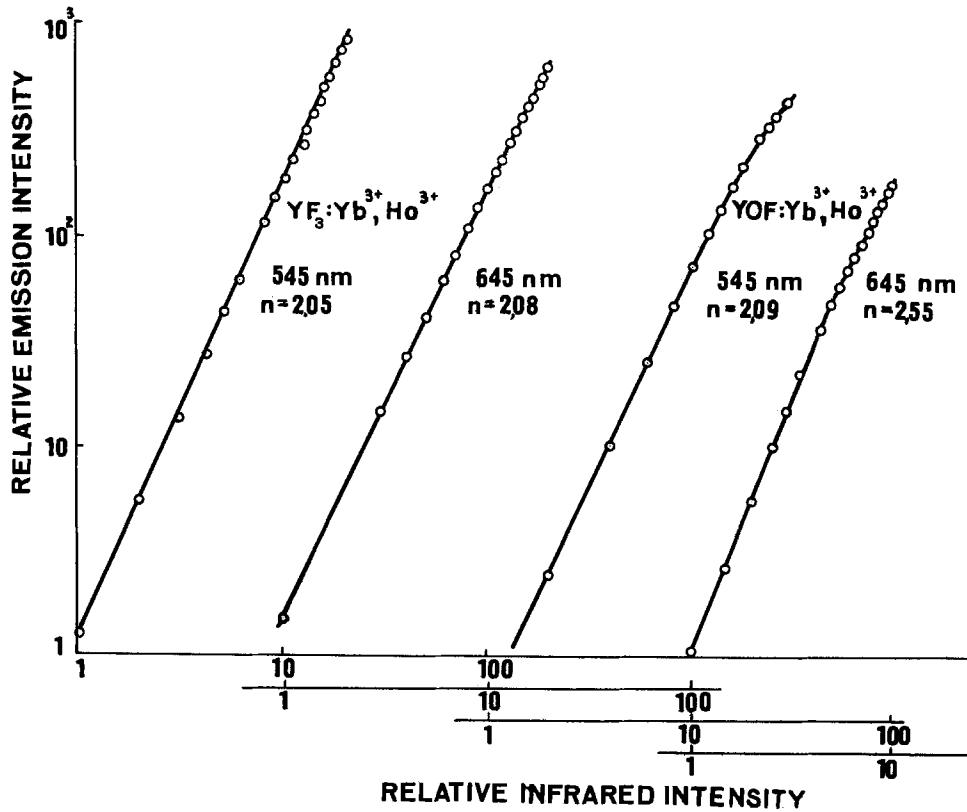


Fig. 3. Dependence of green and red emission from YF₃:Yb³⁺, Ho³⁺ and YOF:Yb³⁺, Ho³⁺ on Si-GaAs infrared pump intensity.

The excitation spectrum consists of a narrow band, with peak at 975 nm. Investigation of other compositions YOF:Yb³⁺, Ho³⁺ and YF₃:Yb³⁺, Er³⁺ indicates that this property is generally true for all systems in-

vestigated. Differences in shape of infrared excitation spectra are very small.

Visible radiation spectra of phosphors excited by the Si-doped GaAs diode are shown in Fig. 2. In upper

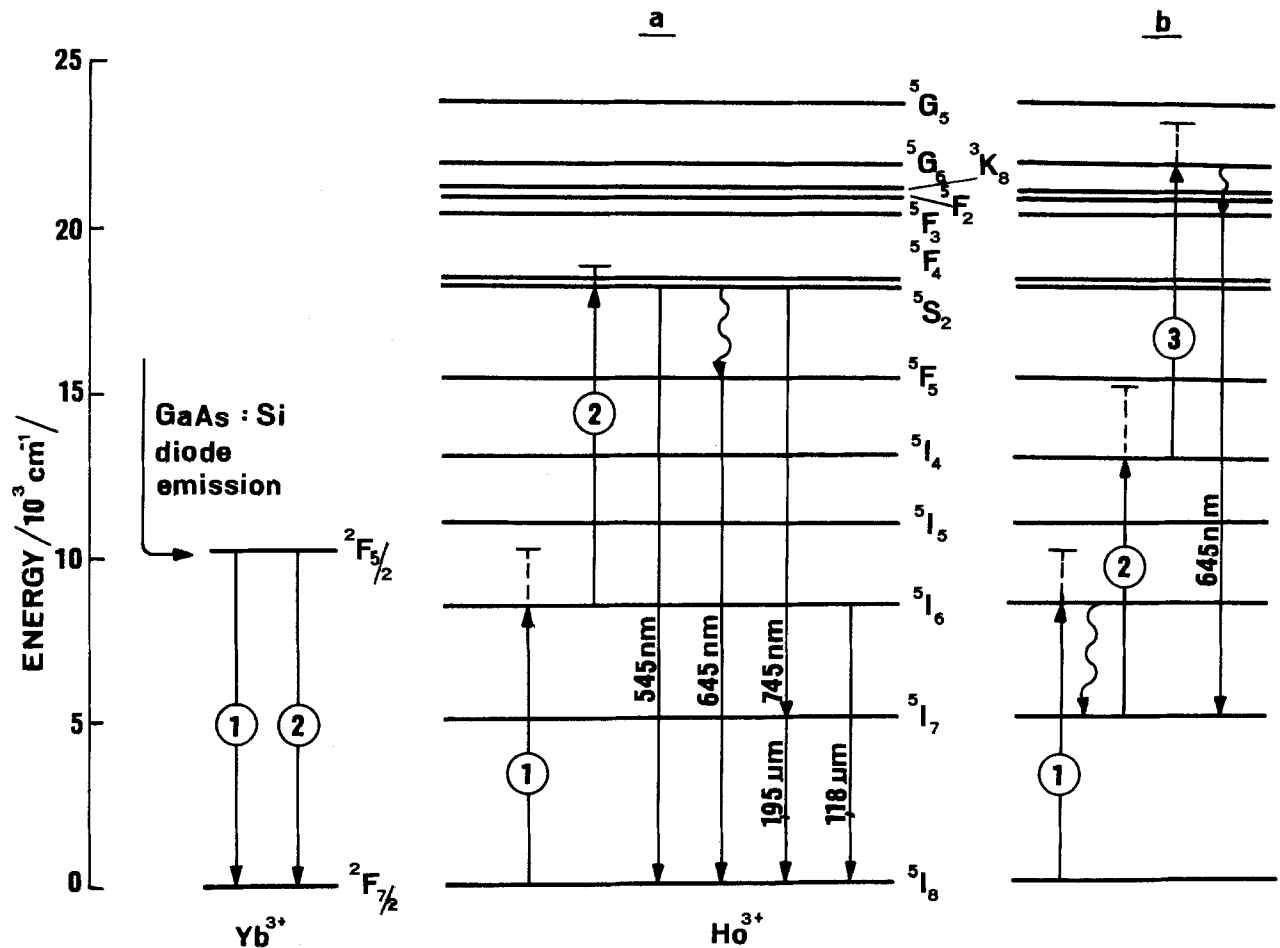


Fig. 4. (a). Infrared-to-visible conversion in YF₃:Yb³⁺, Ho³⁺. (b). Three-photon excitation of red emission in YOF:Yb³⁺, Ho³⁺.

part of this figure radiation spectra of $\text{YF}_3:\text{Yb}^{3+},\text{Ho}^{3+}$ are given, in lower part, that of $\text{YF}_3:\text{Yb}^{3+},\text{Er}^{3+}$. In all cases strong green emission is observed.

In $\text{YF}_3:\text{Yb}^{3+},\text{Ho}^{3+}$ phosphor the green emission is in a series of lines between 530 nm and 555 nm, near the peak of the normal eye sensitivity. Some weak lines (not to scale on Fig. 2) are also observed near 645 nm.

The intensity of green and red emission varies almost proportionately to the square of the infrared pump power (Fig. 3). This indicates that the excitation process involves two successive transfers of energy from Yb^{3+} ions, as shown in Fig. 4a. A phonon-assisted transfer from Yb^{3+} to the $^5\text{I}_6$ state of Ho^{3+} is followed by second transfer exciting Ho^{3+} to the $^5\text{S}_2, ^5\text{F}_4$ states. Green emission arises from transitions from the $^5\text{S}_2$ state to the $^5\text{I}_8$ ground state. Weak red emission arises according to the $^5\text{F}_5 - ^5\text{I}_8$ transition.

Visible emission is accompanied by very weak emission in the infrared, near 745 nm, 1.18 μm and 1.95 μm . Emission at 745 nm arises from transitions from $^5\text{S}_2$ to $^5\text{I}_7$ state. Emission at 1.18 μm is given as a radiative decay to the ground state from $^5\text{I}_6$, after first energy transfer from Yb^{3+} ion. Intensity of this radiation varies linearly with infrared pump intensity. Emission at 1.95 μm corresponds to the transition from $^5\text{I}_7$ to $^5\text{I}_8$ and can arise as a consequence of multiphonon transition from $^5\text{I}_6$ to lower lying state or can be combined with 745 nm radiation.

In $\text{YOF}:\text{Yb}^{3+},\text{Ho}^{3+}$ phosphor the visible spectra are similar in shape, in comparison with $\text{YF}_3:\text{Yb}^{3+},\text{Ho}^{3+}$ spectra, but in the oxyfluoride the dependence of emission intensity on infrared pump power gives a slope of about 2.55 for the red emission. This indicates contributions from both two- and three-photon processes.

The most probable three-photon excitation process of red emission is shown in Fig. 4b. The first step of excitation is from $^5\text{I}_8$ to $^5\text{I}_6$ and then a multiphonon decay to $^5\text{I}_7$ follows. After the next two steps of excitation shown in Fig. 4b the 645 nm emission results from the $^5\text{F}_3$ to $^5\text{I}_7$ transition.

Another three-photon excitation process can also be considered which would be followed by excitation of higher lying states, e.g., $^5\text{G}_4$ and $^5\text{G}_5$. But probably such is not the case because visible and ultraviolet radiation at wavelengths shorter as 530 nm is not observed. Such blue and ultraviolet light in the Yb^{3+} -

Er^{3+} system was observed by Johnson and his co-workers (5) as the consequence of the three- and four-photon excitation.

Next, from our measurements of emission spectra the red-to-green ratio of the emission can be estimated. The red-to-green ratio of the emission from $\text{YF}_3:\text{Yb}^{3+},\text{Er}^{3+}$ is about 35 times greater than the red-to-green ratio of the emission from $\text{YF}_3:\text{Yb}^{3+},\text{Ho}^{3+}$ and about 4 times greater than the ratio of the emission from $\text{YOF}:\text{Yb}^{3+},\text{Ho}^{3+}$. Accordingly, the radiation from $\text{YF}_3:\text{Yb}^{3+},\text{Ho}^{3+}$ seems pure green, whereas the radiation from $\text{YF}_3:\text{Yb}^{3+},\text{Er}^{3+}$ is slightly yellower. The possibility of obtaining pure green emission seems advantageous in some technical applications.

It is worth adding here that in $\text{YOF}:\text{Yb}^{3+},\text{Ho}^{3+}$ phosphor the green-to-red ratio of the emission does not depend on Yb^{3+} concentration, as it is seen in $\text{YOF}:\text{Yb}^{3+},\text{Er}^{3+}$ phosphor (4).

Acknowledgments

The authors would like to thank Professor B. Paszkowski and Dr. B. Mroziewicz for encouragement in work and fruitful discussions. They thank Dr. B. Darek for offering some Si-GaAs diodes. The valuable technical assistance of Mr. M. Grabinski is also acknowledged.

Manuscript submitted May 22, 1973; revised manuscript received Sept. 16, 1974.

Any discussion of this paper will appear in a Discussion Section to be published in the December 1975 JOURNAL. All discussions for the December 1975 Discussion Section should be submitted by Aug. 1, 1975.

REFERENCES

1. L. F. Johnson, H. J. Guggenheim, T. C. Rich, and F. W. Ostermayer, *J. Appl. Phys.*, **43**, 1125 (1972).
2. R. K. Watts, *J. Chem. Phys.*, **53**, 3552 (1970).
R. K. Watts and W. C. Holton, *Solid State Commun.*, **9**, 137 (1971).
R. K. Watts and H. J. Richter, *Phys. Rev.*, **B4**, 1584 (1972).
3. V. V. Ovsyankin and P. P. Feofilov, *Opt. Spektroskopija*, **31**, 944 (1971).
4. T. Matsubara, *Japan J. Appl. Phys.*, **10**, 1647 (1971).
5. L. F. Johnson, J. E. Geusic, H. J. Guggenheim, T. Kushida, S. Singh, and L. G. Van Uitert, *Appl. Phys. Letters*, **15**, 48 (1969).

The Influence of Leakage Current on Concentration Profile Measurements

P. Kramer, C. de Vries, and L. J. van Ruyven

Semiconductor Development Laboratory, N. V. Philips' Gloeilampenfabrieken, Nijmegen, Netherlands

The capacitance-voltage technique (CV) is a standard method for obtaining the profile of electrically active impurities in semiconductors (1). The method has been automated to create the possibility of routine materials evaluation (2, 3) and many investigators have studied the necessary corrections to obtain the true impurity concentration as a function of depth (4, 5). Besides the above corrections which have a more fundamental nature, Copeland has calculated the correction necessary for test samples consisting of a Schottky barrier test diode on a wafer, due to the extension of the depletion layer under reversed bias (6).

This report describes an additional requirement of a practical nature arising from the reverse current irregularities, quite commonly observed in Schottky

diodes (7), prepared by an evaporated metal dot or a confined mercury column (8). Although in most cases the magnitude of the reverse current stays well within the limits for correct measurements (9), it will be shown that even then sudden changes can alter the result substantially. This effect can be in particular very misleading if the samples themselves have large variations in impurity concentration, as is the case in ion implanted material.

Any experimental arrangement requires of course a second contact, which introduces a series resistor with or without a parallel capacitor (see Fig. 1). This series resistor acts as a d-c voltage divider and therefore its value should be small compared to the resistive part of the test diode impedance (9). This requirement, which can be written in conductance form as $G_d/G_s \ll 1$, is usually fulfilled. Therefore the apparent car-

Key words: impurity profile, diode-capacitance, leakage current, series resistance, silicon.

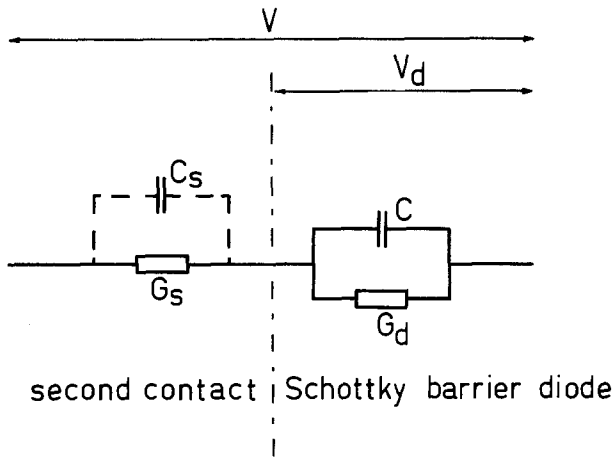


Fig. 1. Diagram of a reversed diode. C = capacity, G_d = parallel conductance, G_s = series conductance.

rier density does not need to be corrected for this small error in voltage, but a sudden change in the sample conductance itself in combination with this series conductance can cause substantial errors. It can be shown that the final result is strongly dependent on the derivative of the conductance with respect to voltage.

The static conductances G_s and G_d give rise to a small difference between V and V_d , being the applied voltage and the true voltage over the Schottky barrier diode (see Fig. 1). Consequently the ratio between V and V_d differs from unity according to

$$V = \left(1 + \frac{G_d}{G_s}\right) V_d \quad [1]$$

Differentiation of Eq. [1] yields

$$\frac{dV}{dV_d} = 1 + \frac{G_d}{G_s} + \frac{V_d}{G_s} \cdot \frac{dG_d}{dV_d} \quad [2]$$

The real carrier density N_d should be derived from

$$N_d = C^3 \frac{dV_d}{dC} \cdot \frac{1}{q \epsilon_0 \epsilon_r A^2} \quad [3]$$

in which q is the electron charge, $\epsilon_0 \epsilon_r$ the semiconductor permittivity, and A the diode area. However, assuming $C \ll C_s$, the actual experiment yields

$$N = C^3 \frac{dV}{dC} \cdot \frac{1}{q \epsilon_0 \epsilon_r A^2} \quad [4]$$

because only V can be read from the instrument. If we define N_d/N as the relative error in carrier density we can write, by combining [2], [3] and [4]

$$\frac{N_d}{N} = \frac{1}{1 + \frac{G_d}{G_s} + \frac{V_d}{G_s} \cdot \frac{dG_d}{dV_d}} \quad [5]$$

Equation [5] demonstrates that in addition to the G_d/G_s -correction a third term $\frac{V_d}{G_s} \cdot \frac{dG_d}{dV_d}$ should be taken into account. The effect of this term on the final result will be an abrupt increase and decrease in the apparent carrier density at a sudden change in the slope of the leakage current vs. voltage.

A number of silicon slices were analyzed with the aid of an inhouse developed doping profile plotter (10). This plotter measures the capacitance C of a mercury-silicon junction (8) as a function of an exponentially increasing blocking voltage V . An analog computer derives dC/dt and dV/dt and uses these values to calculate the concentration N according to Eq. [4]. The concentration and the leakage current are displayed simul-

taneously on a double beam X-Y-oscilloscope as a function of blocking voltage or depth, which enables the interaction between apparent concentration and leakage to be studied. The capacitance measurement is carried out with a phase sensitive detector circuit; the measuring voltage amounts to 25 mV rms with a frequency of 10 MHz. The blocking voltage ramp has a repetition frequency of 10 Hz and a peak value of 150V.

In Fig. 2 the concentration N and the leakage current I vs. blocking voltage V are given for a mercury contact on a 13μ thick 1.4 ohm-cm N-type epitaxial layer on an N^+ substrate, as displayed by the plotter. It appears that a marked peak in the N -curve coincides with a sharp step in the leakage current curve. In this case the back contact on the slice was about 1 cm^2 of silver paste (Leitsilber 100 of Degussa) with a resistance of about 100 ohms, which may represent the major part of the series conductance G_s , which thus becomes 10^{-2} ohm^{-1} . The back contact has a capacitance of about $2 \times 10^4\text{ pF}$.

As can be seen from Fig. 2, the static conductance just below 14V (arrow) equals $G_d = 65\ \mu\text{A}/14\text{V} = 4.65 \times 10^{-6}\text{ ohm}^{-1}$. The step at 14V gives an increase ΔI of $70\ \mu\text{A}$, resulting in a static conductance $G_d = 135\ \mu\text{A}/14\text{V} = 9.65 \times 10^{-6}\text{ ohm}^{-1}$ just above 14V, hence G_d is increased by an amount dG_d of $5.3 \times 10^{-6}\text{ ohm}^{-1}$. Assuming from the scope picture that this increase occurs over a voltage increment dV_d of 10 mV, dG_d/dV_d becomes $5.3 \times 10^{-4}\text{ ohm}^{-1}\text{ V}^{-1}$. Substituting these values in Eq. [5] it follows that $N_d/N = 0.57$. Considering the N -value of about 4×10^{15} at $V = 10\text{V}$ equal to N_d , N should increase at the leakage step to about 7×10^{15} over an increment of 10 mV. Experimentally, the increase is slower than predicted (see Fig. 2) due to the time constant of the analog computer. Similarly, the sudden decrease of dG_d/dV_d on the top of the leakage step determines the shape of the trailing edge of the concentration peak.

Figure 3 represents a 109 ohm-cm homogeneous P-type slice. The leakage current I begins abruptly at $V = 6\text{V}$ (arrow), which causes a very pronounced peak in the N -curve. At the right-hand side of this

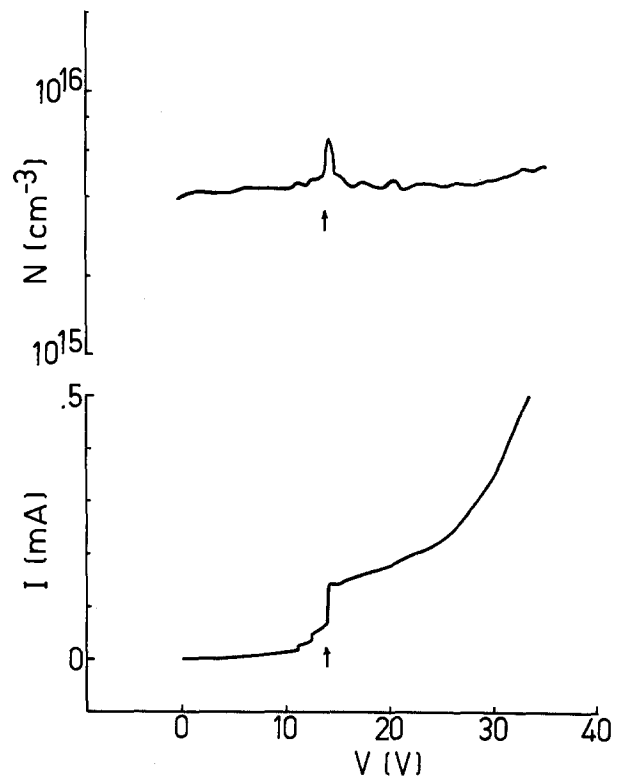


Fig. 2. Curves of apparent concentration N and leakage current I vs. blocking voltage V for a mercury contact on a 1.4 ohm-cm N-type epitaxial layer on an N^+ substrate.

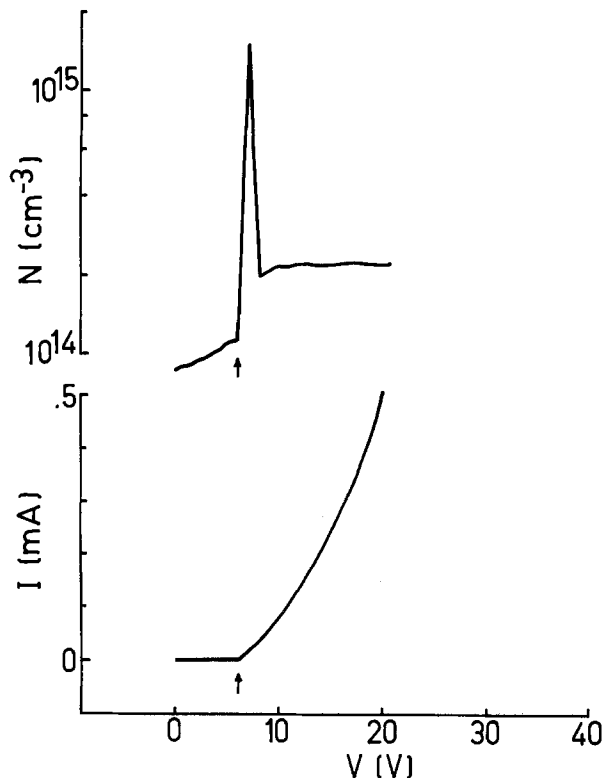


Fig. 3. N and I vs. V curves for a 109 ohm-cm homogeneous P-type slice.

peak the level of N is markedly higher than on the left, which is caused by the persistent increase of G_d at higher voltages. An additional proof of the correlation between the apparent concentration peak and the step in the leakage characteristic is the observation that in case of instability both phenomena always occur simultaneously along the X-axis.

Experiments with a simulating circuit have shown a quantitative confirmation of the phenomenon. This circuit was built up from linear resistors (G_s and G_d), a linear capacitor (C_s), and a low leakage diode (C) according to Fig. 1. G_d was switched on and off at certain values of V , using a mercury switch.

As a result of this study we conclude that an important source of error can be detected if the experimental arrangement is made such that large values of the derivative of the parallel conductance with respect to voltage can be observed. The simultaneous display of the carrier profile and the leakage current turns out to be a practical solution.

Acknowledgments

We would like to express our appreciation to Dr. J. J. Goedbloed and Dr. C. van Opdorp for stimulating discussion and critical comments.

Manuscript submitted March 1, 1974; revised manuscript received Aug. 2, 1974.

Any discussion of this paper will appear in a Discussion Section to be published in the December 1975 JOURNAL. All discussions for the December 1975 Discussion Section should be submitted by Aug. 1, 1975.

Publication costs of this article were partially assisted by N. V. Philips' Gloeilampenfabrieken.

REFERENCES

1. C. O. Thomas, D. Kahng, and R. C. Manz, *This Journal*, **109**, 1055 (1962).
2. J. A. Copeland, *IEEE Trans. Electron. Devices*, **ED-16**, 445 (1969).
3. P. J. Baxandall, D. J. Colliver, and A. F. Fray, *J. Phys. E.*, **4**, 213 (1971).
4. D. P. Kennedy, P. C. Murley, and W. Kleinfelder, *IBM J. Res. Develop.*, **12**, 399 (1968).
5. R. A. Moline, *J. Appl. Phys.*, **42**, 3553 (1971).
6. J. A. Copeland, *IEEE Trans. Electron. Devices*, **ED-17**, 404 (1970).
7. A. M. Cowley, *Solid-State Electron.*, **12**, 403 (1970).
8. P. J. Severin and G. J. Poedt, *This Journal*, **119**, 1384 (1972).
9. A. M. Goodman, *J. Appl. Phys.*, **34**, 329 (1963).
10. C. de Vries, To be published.

The Origin of the Cubic Rate Law in Zirconium Alloy Oxidation

G. P. Sabol

Westinghouse Research Laboratories, Pittsburgh, Pennsylvania 15235

and S. B. Dalggaard*

Westinghouse Nuclear Fuel Division, Pittsburgh, Pennsylvania 15230

The pretransition corrosion kinetics of zirconium and zirconium-based alloys at temperatures of less than about 400°C have been reported (1-3) to deviate from the ideal parabolic behavior characteristic of diffusion control through a thickening homogeneous scale barrier. Reviews of the pertinent work describing the corrosion kinetics have been presented (4, 5), and it appears that the observed rates approach cubic behavior. Moreover, in an extensive test program, Kass (3) has shown that the pretransition kinetics of Zirca-loy-2 and -4 are cubic for corrosion in pressurized water in the temperature range studied, 232°-316°C. In this note it is postulated that these cubic kinetics are accounted for by involving mass transfer along grain boundaries and a steadily increasing grain size of the oxide with increasing film thickness.

* Electrochemical Society Active Member.

Key words: zirconium, corrosion, kinetics, cubic, crystallites.

It appears clear from the literature that diffusion of oxygen through the oxide film takes place along preferred paths (6-8), and that these regions of high diffusivity are probably crystallite or grain boundaries (7, 8). From an analysis of $^{17}\text{O}_2$ tracer diffusion profiles, Cox and Pemsler (7) have found that the diffusion coefficient of oxygen in ZrO_2 along grain boundaries is greater than that for lattice diffusion by a factor of about 10^4 at 400°-500°C. They conclude, therefore, that all of the oxygen transported through the oxide film during oxidation migrates along grain boundaries and no more than 0.01% is transported via lattice diffusion.

Assuming grain boundary migration as the controlling mechanism, then ideal parabolic kinetics would apply only if the grain boundary area per unit volume of oxide is independent of oxide thickness. However, such is not the case. Recently, the microstructure

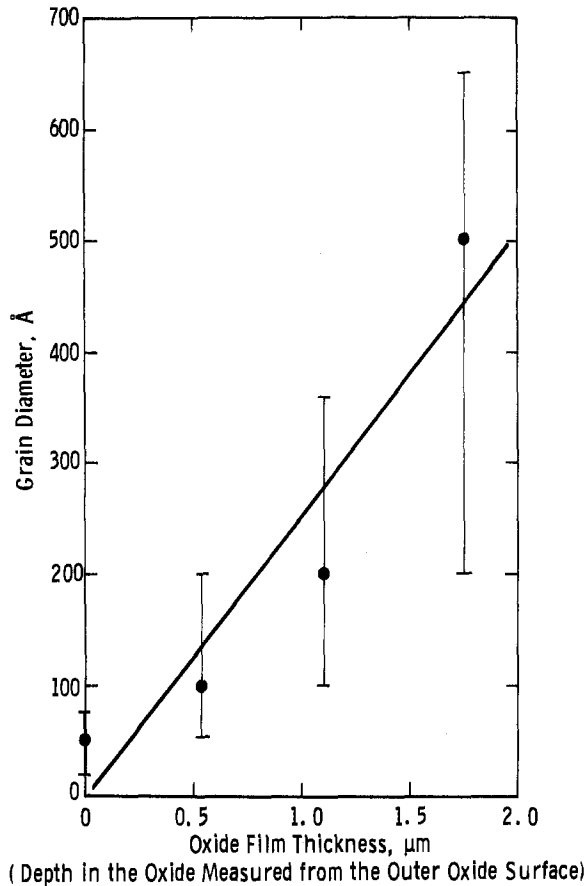


Fig. 1. Grain diameter of the oxide as a function of position in the oxide in the pretransition region for Zircaloy-4. Data taken from Ref. (9) for samples exposed in 360°C water.

of oxide films formed on zirconium alloys has been characterized (9). The grains of the initially formed film were observed to be approximately 50Å or less in diameter, and to retain this size throughout continued exposure in the corrosive environment. This observation is at variance with Cox's suggestion (8, 10) that growth of ZrO_2 crystallites in the oxide by recrystallization may have accounted for variations in the oxidation rate law. Upon increase of the oxide thickness layer crystallites were observed to form at the actively growing metal-oxide interface, and the grain size reached about 500Å at the interface as the film thickness reached 2 μm, the approximate end of the pretransition regime. A plot of the pretransition data reported previously (9) is shown in Fig. 1. The points represent the average grain size of the oxide, and the bars represent the range of sizes observed. Although the data are of insufficient strength to establish the exact relationship between grain size and film thickness, linear behavior is indicated and, therefore, a linear relationship was assumed for sim-

plicity and the line drawn accordingly. Coupling these data with the observation that oxygen migration through the oxide film during low-temperature oxidation takes place primarily along grain boundaries, then, in fact, the kinetics should deviate from parabolic and would be ideally cubic if the linear relationship between grain size and film thickness is valid.

The cubic kinetics can be derived quite easily by setting the rate of film thickening, dx/dt , to be inversely proportional to the integrated resistance to mass transport. In this instance, as the diffusion paths are the grain boundaries, the specific resistance to mass flow is proportional to the film thickness, because the grain boundary area decreases linearly with increasing thickness. Thus, the integrated resistance becomes the square of the film thickness, and the rate of film thickening is given by

$$\frac{dx}{dt} = \frac{k}{x^2}$$

This yields cubic behavior. The actual kinetics would deviate from cubic depending upon the exact relationship between grain diameter and film thickness. Also, volume diffusion at the larger grain size would contribute to deviations. Nevertheless, the present interpretation and analysis lend credence to the postulate that the widely observed cubic rate law in zirconium alloys may be accounted for by progressive increase in the grain size of the oxide.

Manuscript submitted April 3, 1974; revised manuscript received Aug. 23, 1974.

Any discussion of this paper will appear in a Discussion Section to be published in the December 1975 JOURNAL. All discussions for the December 1975 Discussion Section should be submitted by Aug. 1, 1975.

Publication costs of this article were partially assisted by the Westinghouse Electric Corporation.

REFERENCES

1. E. A. Gulbransen and K. F. Andrew, *J. Metals*, **1**, 515 (1949).
2. A. A. Kiselev, V. A. Myshkin, A. V. Kozhevnikov, S. I. Korolev, and E. G. Shorina, "Corrosion of Reactor Materials," Vol. II, p. 67, IAEA, Vienna (1962).
3. S. Kass, *J. Nucl. Mater.*, **29**, 315 (1969).
4. K. Hauffe, "Oxidation of Metals," p. 228, Plenum Press, New York (1965).
5. B. G. Parfenov, V. V. Gerasimov, and G. I. Venediktova, "Corrosion of Zirconium and Zirconium Alloys," p. 42, translated from Russian, Israel Program for Scientific Translations Ltd., AEC-tr-6978 (1969).
6. B. Cox, *This Journal*, **108**, 24 (1961).
7. B. Cox and J. P. Pemsler, *J. Nucl. Mater.*, **28**, 73 (1968).
8. B. Cox, *ibid.*, **29**, 50 (1969).
9. G. P. Sabol, S. G. McDonald, and G. P. Airey, ASTM-STP 551, p. 435 (1974).
10. B. Cox, *J. Nucl. Mater.*, **25**, 310 (1968).



Conductance-Viscosity Studies on Some Moderately Concentrated Nonaqueous Electrolyte Solutions from -50° to 125°C

II. Solutions of Pr_4NBr , Bu_4NBr , and Bu_4NI in Propylene Carbonate

J. F. Casteel, J. R. Angel, H. B. McNeeley, and P. G. Sears*

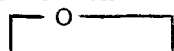
Department of Chemistry, University of Kentucky, Lexington, Kentucky 40506

ABSTRACT

Matching conductance, viscosity, and density data at 25° intervals between -50° and 125°C have been determined and analyzed for moderately concentrated solutions of three quaternary ammonium halides in propylene carbonate. Detailed results are presented for the fitting of experimental data as functions of molal concentration and temperature to appropriate equations by computer least squares procedures. Calculated results related to moles of solvent displaced per mole of solute and also apparent molal volumes indicate the lack of significant ion-solvent interactions in the solutions of the quaternary ammonium salts in propylene carbonate. Additionally, conductance-viscosity products and activation energies of viscous flow and conductance have been calculated and discussed. Throughout the broadly varying experimental conditions over the 175°C range, the conductances of the three salts have been found to be fairly closely proportional to the fluidity, or reciprocal of the viscosity, of the medium.

Conductances and viscosities of moderately concentrated solutions of Bu_4NI , KSCN , and NH_4Br in *N,N*-dimethylformamide from -50° to 125°C were dealt with in the first article in this series (1). As a supplementary, parallel investigation on other nonaqueous electrolyte solutions over the unusually broad 175°C range, the present conductance-viscosity study relates to solutions of three quaternary ammonium halides in propylene carbonate, a solvent which like DMF has received much attention during the last 15-20 years.

Propylene carbonate or 4-methyl-1,3-dioxolan-2-



one, $\text{H}_3\text{C}-\text{CH}-\text{CH}_2-\text{O}-\text{C}=\text{O}$, symbolized by PC, is a commercially available cyclic ester which has become established as a promising electrolytic solvent (2). It has a liquid range extending from -49° to 241°C and is a good solvent for most quaternary ammonium salts, selected alkali metal salts, and organic compounds. PC as a dipolar, aprotic liquid has the following physical properties at 25°C : dielectric constant, 64.9 (3); viscosity, 2.513 cP (4); density, 1.1995 g cm^{-3} (5); dipole moment, 4.94 debyes (6); Kirkwood correlation factor, 1.01 (3).

Other studies dealing with conductances and viscosities of both dilute and concentrated solutions of electrolytes in PC have been reported or summarized (2, 4, 7-10), but none of these have significantly overlapped with the scope of this work. The quaternary ammonium salts were selected primarily because they were found to be among the most soluble common salts in PC at -50°C . The major objective of this study, other than obtaining extensive and valuable new data, was

to thoroughly examine and compare matching conductance and viscosity characteristics of moderately concentrated solutions of electrolytes in PC over a very broad temperature range.

Experimental

PC (Eastman practical grade) was purified through two fractionations at ~ 1 mm using a 1m distillation column packed with 6 mm porcelain saddles, each time retaining the middle 75% of the distillate. Values determined for the physical properties of the finally retained PC are in good agreement with comparable data reported by other investigators (4, 5).

Eastman grade Pr_4NBr , Bu_4NBr , and Bu_4NI were dried overnight in a vacuum oven at 45°C and used without further purification. Exploratory solubility determinations revealed that the approximate upper working limits for solubilities in PC at -50°C were 10, 12, and 10 weight per cent (w/o) for Pr_4NBr , Bu_4NBr , and Bu_4NI , respectively. Solutions were prepared in glass-stoppered flasks on a weight basis, in 2% by weight increments of solute, in sufficient quantities to permit separate portions of each solution to be used for the determinations of conductance, viscosity, and density.

The equipment and other procedural details are described in the preceding article (1). All determinations were made in duplicate or triplicate with very good precision except in six cases of conductance or viscosity determinations at the lowest temperatures where differences as great as 1% were observed. Mean values of the experimental data were fitted to various equations with an IBM 360/65 computer using double precision Fortran IV programming. Usually normal least squares analyses were performed; in a few cases, however, a nonlinear least squares program of the type

* Electrochemical Society Active Member.

Key words: density, propylene carbonate, activation energy, apparent molal volume, ion-solvent interactions.

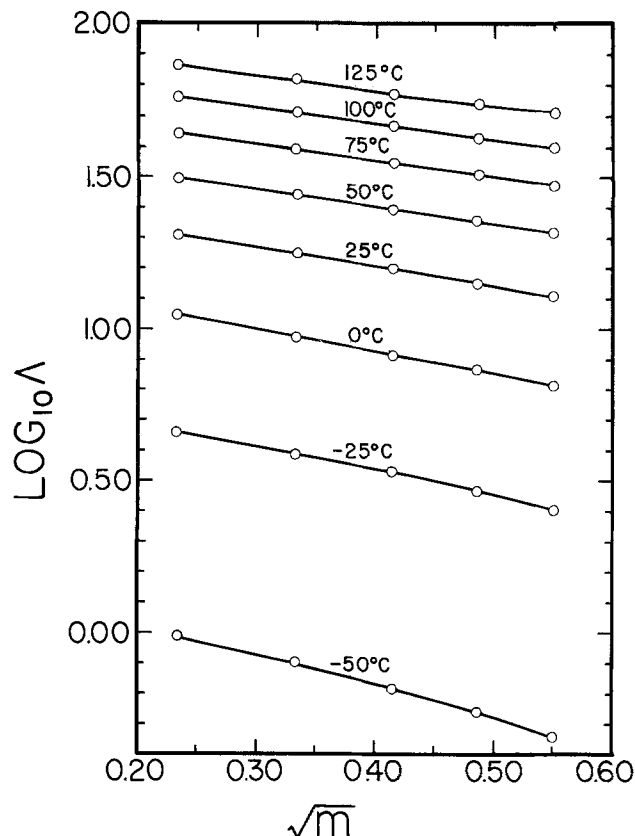


Fig. 1. Logarithm of molar conductance vs. square root of molality for solutions of Bu_4NI in PC.

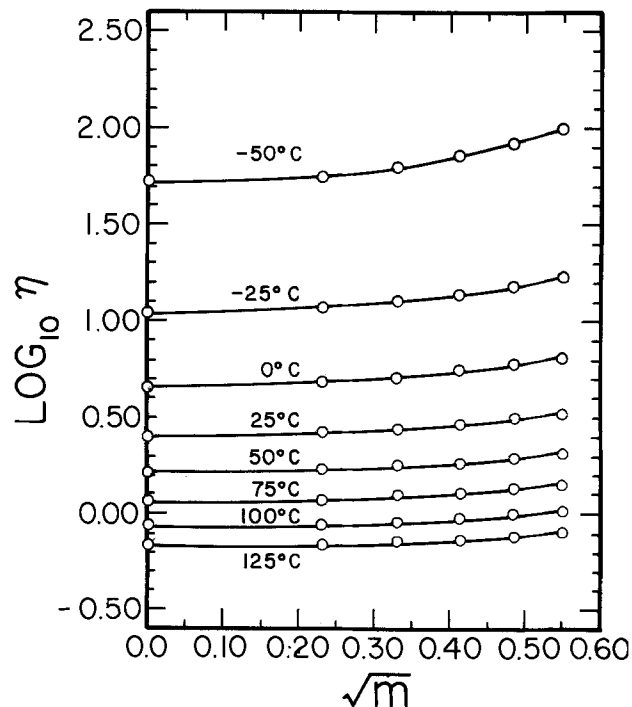


Fig. 2. Logarithm of viscosity vs. square root of molality for solutions of Bu_4NI in PC.

partial molar volumes or other appropriate quantities such as volume displacements which are related to ion-solvent effects. Though fairly accurate density data were determined in this study, the small differences between the densities of the solutions and the solvent (usually $<0.0100 \text{ g cm}^{-3}$) precluded the calculation of partial molar volumes which were meaningful to more than two or three significant figures. Alternatively,

Jasinski (2) has shown that density data may be used for quantitatively determining the displacement of solvent by solute in solution. The displacement tends to be large if the solvation energy is low and/or the sizes of the ions are large. The moles of solvent (PC) displaced per mole of solute, symbolized by Δ , may be calculated using the following equation

$$\Delta = 1000(\rho_0 - \rho)/M_1C + M_2/M_1 \quad [2]$$

The symbols in this and other equations are defined below in a List of Symbols.

Values of Δ calculated for the various solutions at -50° , 25° , and 125°C are summarized in Table IV. Through observation of the data in this table, three trends in the values of Δ are readily apparent: for any solute at a given temperature, there is little change in Δ with concentration; at a given temperature, Δ increases significantly with increasing sizes of ions; and, for a given salt, Δ decreases noticeably with increasing temperature.

The Δ values in Table IV can be converted to apparent molal volumes for the solute by multiplying the Δ values at -50° , 25° , and 125°C by 79.7, 85.1, and $93.4 \text{ cm}^3/\text{mole}$ (PC), respectively. The resulting value of $320 \text{ cm}^3/\text{mole}$ for Bu_4NBr in its most concentrated solution in PC at 125°C is identical with the value calculated by dividing the gram molecular weight of Bu_4NBr by the density of molten Bu_4NBr at 125°C (12). Such behavior is characteristic of an ideal solution in which exact additivity of volumes of components occurs. Using extrapolated density data for supercooled liquid Bu_4NI at 125°C (12), the calculated apparent molal volume for Bu_4NI at 125°C is $329 \text{ cm}^3/\text{mole}$, which is 1.3% less than the experimental value of $333 \text{ cm}^3/\text{mole}$.

From a slightly modified approach, experimental values for the apparent molal volumes of Pr_4NBr and Bu_4NBr in their most concentrated solutions in PC at 25°C are 238 and 305 cm^3 , respectively, which are 5-7% higher than those calculated by dividing the gram molecular weights by available densities of the salts as solids at 25°C (13). These results suggest slight expansion effects accompanying dissolution of such a salt in PC.

The comparisons of experimental and calculated apparent molal volumes for the quaternary ammonium salts in PC indicate an absence of contraction effects which are characteristic of strong ion-solvent interactions. This finding is not surprising, however, since other investigators have previously commented that PC not only closely approximates an "ideal structureless dielectric" solvent (14), but also has poor solvating ability with respect to anions and large cations (15). A conclusion that there is an absence of significant ion-solvent interactions for the solutions of quaternary ammonium salts in PC is completely consistent with the observed results. If the solute ions simply displace the solvent in solution without strong interactions, the values of Δ would be proportional to

Table IV. Moles of propylene carbonate displaced per mole of solute (Δ)

Solute	m	Δ		
		-50°C	25°C	125°C
Pr_4NBr	0.0765	2.82	2.79	2.62
	0.1550	2.81	2.80	2.63
	0.2380	2.84	2.79	2.63
	0.3200	2.87	2.79	2.63
	0.4115	2.86	2.79	2.63
Bu_4NBr	0.0635	3.55	3.59	3.40
	0.1236	3.60	3.60	3.41
	0.1930	3.63	3.59	3.41
	0.2645	3.65	3.58	3.39
	0.3433	3.66	3.59	3.42
	0.4122	3.65	3.59	3.42
Bu_4NI	0.0542	3.85	3.77	3.53
	0.1109	3.83	3.74	3.54
	0.1725	3.83	3.74	3.56
	0.2359	3.84	3.74	3.56
	0.3012	3.82	3.74	3.57

sizes or volumes of the ions and independent of the solute concentration as observed. Furthermore, the value of Δ for such a salt in PC would be expected to decrease with increasing temperature if the temperature coefficient of the density or molar volume for PC were greater than that for the salt, which is substantiated by a comparison of the temperature coefficients for the densities of PC and Bu_4NBr as liquids.

The small decrease in solution density with increasing molality indicates that Pr_4NBr , Bu_4NBr , and, below 100°C , Bu_4NI are less dense than PC. For Bu_4NI -PC solutions at 100°C , and as has been previously observed for KPF_6 -PC solutions at 25°C (2), the density does not change with concentration providing evidence that the densities of the solute and solvent are equal. In the specific case in this study, Bu_4NI and PC each have a density of 1.1204 g cm^{-3} at 100°C .

The densities for the PC salt solutions as a function of temperature are described excellently by the following quadratic expression

$$\rho = a + bt + ct^2 \quad [3]$$

Parameters relative to fitting the density data to Eq. [3], along with corresponding very small deviations, are compiled in Table V.

Solutions of the quaternary ammonium salts in PC have fairly low viscosities ranging from 0.7 to 3.7 cP as the temperature decreases from 125° to 25°C . For 0° through -50°C , however, the viscosity increases very abruptly with decreasing temperature. The $0.4122M$ Bu_4NBr solution has a viscosity of 139.7 cP at -50°C , which is 165 times greater than its viscosity at 125°C . This probably results from the thermal energies of the constituent species in solution being too weak to counteract strong dipole-dipole and other electrostatic interactions which would account for high viscosities at low temperatures. Plots of $\log \eta$ vs. $1/T$ for three solutions of Bu_4NI in PC, which are typical of all solutions in this study, are shown in Fig. 3. It may be observed from this figure that the similarly shaped plots are nonlinear and that their slopes increase slightly with increasing molality of electrolyte.

Because of the abruptness of the change in viscosity at the lower temperatures in conjunction with the much smaller rate of change in viscosity over the upper 100°C range, it was challenging to find a suitable viscosity-temperature relationship to which the viscosity data could be closely fitted over the entire 175°C range. After other relationships were found to be essentially inapplicable or less than satisfactory, the following equation which was used in the preceding study (1) was employed again not only because of its superior applicability but, importantly, also for theoretical and computational reasons

Table V. Parameters for density data fitted to Eq. [3]

Molality	a	b $\times 10^8$	c $\times 10^6$	Per cent deviation	
				Mean	Maximum
Pr_4NBr					
0.0000	1.22637	-1.0718	7.71	0.04	0.05
0.0765	1.22456	-1.0641	12.48	0.03	0.06
0.1550	1.22279	-1.0595	18.48	0.03	0.05
0.2380	1.22079	-1.0431	16.86	0.04	0.08
0.3200	1.21872	-1.0212	11.81	0.04	0.07
0.4115	1.21671	-1.0127	15.52	0.03	0.07
Bu_4NBr					
0.0635	1.22323	-1.0712	16.38	0.03	0.05
0.1236	1.21991	-1.0607	19.33	0.03	0.07
0.1930	1.21638	-1.0441	17.24	0.03	0.05
0.2645	1.21278	-1.0315	21.05	0.03	0.05
0.3433	1.20924	-1.0165	15.90	0.03	0.06
0.4122	1.20616	-1.0123	20.38	0.04	0.05
Bu_4NI					
0.0542	1.22532	-1.0622	9.62	0.03	0.04
0.1109	1.22464	-1.0520	7.33	0.02	0.04
0.1725	1.22354	-1.0422	7.43	0.02	0.06
0.2359	1.22259	-1.0296	4.86	0.02	0.04
0.3012	1.22159	-1.0237	8.86	0.03	0.06

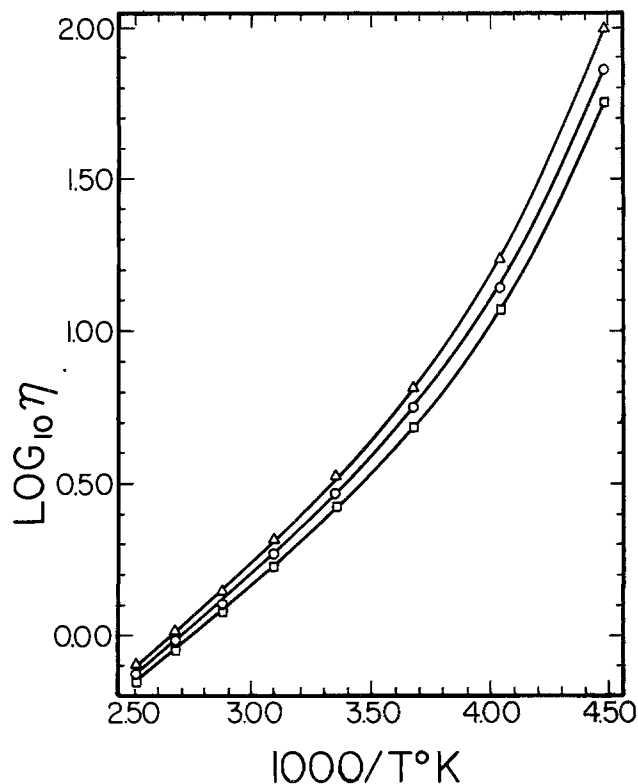


Fig. 3. Logarithm of viscosity vs. $1/T$ for typical solutions of Bu_4NI in PC. Key to symbols: squares, $0.0542M$; circles, $0.1725M$; triangles, $0.3012M$.

$$\eta = \exp(\alpha + \beta/T + \gamma/T^2 + \delta/T^3 + \epsilon/T^4) \quad [4]$$

The fitting of the viscosity data to Eq. [4], for which parameters and deviations are given in Table VI, is good considering the breadth of both the temperature

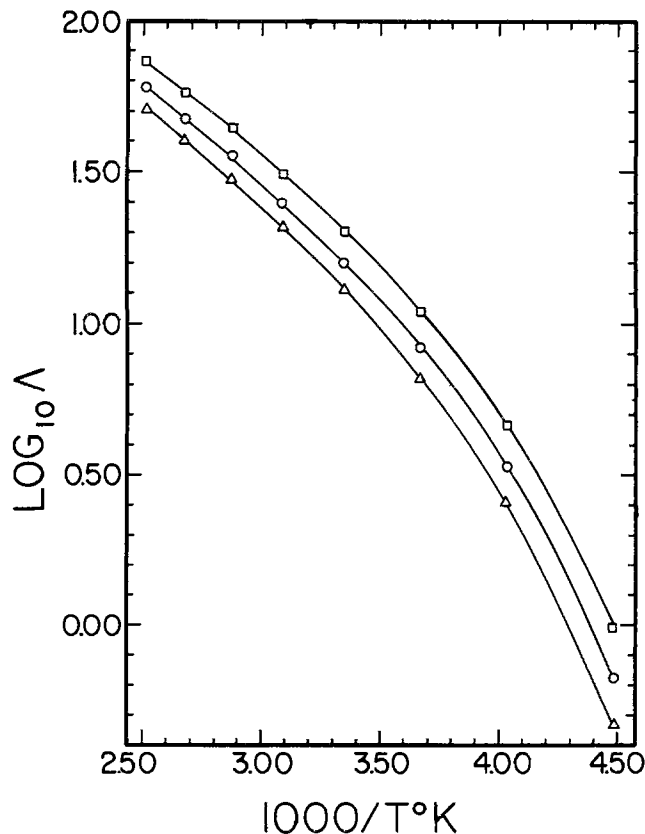


Fig. 4. Logarithm of molar conductance vs. $1/T$ for typical solutions of Bu_4NI in PC. Key to symbols: squares, $0.0542M$; circles, $0.1725M$; triangles, $0.3012M$.

and viscosity ranges. The average deviation between calculated and experimental values in each case is $\leq 0.84\%$; the maximum deviation frequently is less than 1% and never exceeds 1.40%.

Plots of $\log \Lambda$ vs. $1/T$ for the same three solutions of Bu_4NI in PC are presented in Fig. 4. The plots are similarly shaped and nonlinear, with their slopes increasing slightly with increasing molality of Bu_4NI . Obviously, the plots in Fig. 3 and 4 are closely, but inversely, related. Such behavior is typical for systems in which molar conductance is closely, but reciprocally, related to viscosity.

Molar conductances, like viscosities, vary greatly over the 175°C range but in an inverse manner. It was, therefore, logical to fit molar conductance data as a function of temperature to the following expression

$$\Lambda = \exp -(\alpha' + \beta'/T + \gamma'/T^2 + \delta'/T^3 + \epsilon'/T^4) \quad [5]$$

Parameters for fitting Λ values to Eq. [5], together with deviation data, are listed in Table VII. The average deviation between calculated and experimental values in each case $\leq 0.99\%$; the maximum deviation never exceeds 1.60%. Generally, these results are satisfactory and essentially equivalent to those obtained in the analysis of the viscosity data in terms of Eq. [4].

The deviations for fitting η and Λ data for the PC systems to Eq. [4] and [5] are somewhat larger than those resulting from parallel analyses of data for DMF systems discussed previously (1). This is explained in major part by greater temperature coefficients for η and Λ and experimentally less precise determinations on the PC salt solutions.

Conductance-viscosity (or Walden) products decrease 10-15% with increasing temperature over the 175°C range for any solution and, at any temperature, decrease 20-25% with increasing concentration in the 0.05-0.41M range. The general trends in the variation of conductance-viscosity products agree well with observations for other systems (1, 2, 16).

Activation energies of viscous flow and conductance also provide valuable comparison information about conductance and viscosity (or viscous flow) when these are considered as rate processes. In view of common expressions for E_{vis} and E_{con} in conjunction with the temperature relationships for η and Λ used in this study (Eq. [4] and [5]), E_{vis} and E_{con} may be calculated using the following relationships

$$E_{\text{vis}} = Rd(\ln \eta)/d(1/T) \\ = R(\beta + 2\gamma/T + 3\delta/T^2 + 4\epsilon/T^3) \quad [6]$$

$$E_{\text{con}} = -Rd(\ln \Lambda)/d(1/T) \\ = -R(\beta' + 2\gamma'/T + 3\delta'/T^2 + 4\epsilon'/T^3) \quad [7]$$

Values of E_{vis} based on Eq. [6] show an approximate broad range of 2,800-10,300 cal; values of E_{con} based on Eq. [7] show a comparable range of 2500-9700 cal. Table VIII contains values of E_{vis} and E_{con} at -50° , 25° , and 125°C for three solutions of each of the salts in PC. As found previously for the DMF systems, the values of E_{vis} and E_{con} generally increase with increasing salt concentration and decreasing temperature. Corresponding values of E_{vis} and E_{con} do not differ very much, but, in every case, $E_{\text{vis}} > E_{\text{con}}$. Values of

Table VI. Parameters for viscosity data fitted to Eq. [4]

Molality	α	β	γ	$\delta \times 10^{-9}$	$\epsilon \times 10^{-11}$	Per cent deviation	
						Mean	Maximum
Pr₄NBr							
0.0000	0.76756	-5318.470	3660755	-0.9062973	0.8695432	0.25	0.61
0.0765	6.54423	-12642.35	7110288	-1.617842	1.414256	0.45	0.99
0.1550	7.22435	-13423.22	7467669	-1.692408	1.476453	0.57	1.26
0.2380	8.32177	-14713.89	8044602	-1.805393	1.561224	0.59	1.33
0.3200	8.46606	-14954.36	8196973	-1.844174	1.598455	0.56	1.25
0.4115	7.04280	-13002.92	7236851	-1.639634	1.442794	0.55	1.17
Bu₄NBr							
0.0635	2.64175	-7426.182	4548339	-1.069798	0.9836807	0.25	0.41
0.1236	4.23197	-9475.717	5539361	-1.279364	1.149583	0.28	0.50
0.1930	7.32458	-13416.17	7412374	-1.669407	1.452808	0.28	0.56
0.2645	6.27025	-12111.40	6836456	-1.559485	1.379614	0.26	0.48
0.3433	3.32003	-8504.017	5230706	-1.248810	1.163228	0.18	0.33
0.4122	5.83792	-11554.28	6604911	-1.519737	1.363831	0.37	0.62
Bu₄NI							
0.0542	5.82287	-11347.41	6327857	-1.421572	1.237776	0.24	0.55
0.1109	7.18097	-12762.27	6865729	-1.507669	1.288149	0.57	0.87
0.1725	10.98977	-17321.29	8902711	-1.907896	1.582566	0.84	1.33
0.2359	10.18850	-16607.70	8702474	-1.890049	1.586631	0.80	1.16
0.3012	7.18967	-12851.20	6984639	-1.548004	1.339579	0.71	1.40

Table VII. Parameters for molar conductance data fitted to Eq. [5]

Molality	α'	β'	γ'	$\delta' \times 10^{-9}$	$\epsilon' \times 10^{-11}$	Per cent deviation	
						Mean	Maximum
Pr₄NBr							
0.0765	4.34873	-14095.71	7500202	-1.651989	1.411258	0.57	1.32
0.1550	6.88928	-17165.35	8949089	-1.953293	1.646553	0.57	1.28
0.2380	6.44169	-16431.78	8586634	-1.876517	1.590701	0.58	1.29
0.3200	7.27707	-17437.95	9079701	-1.982100	1.676258	0.58	1.23
0.4115	4.66638	-13971.14	7416595	-1.632364	1.408155	0.58	1.27
Bu₄NBr							
0.0635	-2.29265	-5749.668	3633526	-0.8671760	0.8233493	0.32	0.77
0.1236	0.41714	-9092.510	5227708	-1.200671	1.082891	0.17	0.28
0.1930	-0.77383	-7419.221	4419974	-1.029994	0.9530992	0.25	0.51
0.2645	0.77980	-9295.521	5309576	-1.216245	1.101173	0.32	0.63
0.3433	-0.95967	-6976.747	4209984	-0.9878280	0.9296256	0.21	0.49
0.4122	-0.73524	-7217.012	4338265	-1.019256	0.9612879	0.38	0.87
Bu₄NI							
0.0542	1.47762	-10325.60	5662444	-1.256826	1.095952	0.35	0.54
0.1109	5.32457	-14773.24	7606588	-1.627196	1.358169	0.66	1.13
0.1725	8.23163	-18248.54	9188025	-1.942796	1.593807	0.85	1.41
0.2359	10.39471	-20894.22	10421540	-2.193918	1.784891	0.99	1.60
0.3012	8.94107	-18975.49	9524906	-2.011221	1.651095	0.85	1.48

Table VIII. Energies of activation of viscous flow and conductance* and their ratios for selected solutions and temperatures

Molality	-50°C			25°C			125°C		
	E_{vis}	E_{con}	E_{vis}/E_{con}	E_{vis}	E_{con}	E_{vis}/E_{con}	E_{vis}	E_{con}	E_{vis}/E_{con}
				Pr ₄ NBr					
0.0765	8990	8744	1.028	3574	3504	1.020	2822	2504	1.127
0.2380	9574	9407	1.018	3742	3668	1.020	2829	2523	1.121
0.4115	9960	9630	1.034	3939	3860	1.020	2909	2616	1.112
				Bu ₄ NBr					
0.0635	8538	8366	1.021	3629	3546	1.023	2801	2602	1.076
0.1930	9417	8844	1.065	3761	3684	1.021	2846	2646	1.076
0.4122	10289	9661	1.065	4067	3962	1.027	2994	2739	1.093
				Bu ₄ NI					
0.0542	8502	8259	1.029	3587	3543	1.012	2743	2541	1.079
0.1725	8931	8797	1.015	3765	3723	1.011	2628	2463	1.067
0.3012	9357	9257	1.011	3928	3898	1.008	2838	2529	1.122

* In calories.

E_{vis}/E_{con} , as shown in Table VIII, are quite close to unity.

Generally, the results of this conductance-viscosity study involving moderately concentrated solutions of three quaternary ammonium halides in PC over a 175°C range reflect that the magnitude of molar conductance is fairly closely related to the fluidity, or reciprocal of the viscosity, of the medium. Activation energies of viscous flow and conductance also have been found to be almost equal for each PC salt solution over the relatively broad spectrum of experimental conditions. The results for the quaternary ammonium halides in PC especially closely parallel those obtained previously for solutions of Bu₄NI in DMF.

Acknowledgment

This work was supported in major part by Themis Contract DAA-69-C-0366.

Manuscript submitted Aug. 6, 1973; revised manuscript received Sept. 10, 1974.

Any discussion of this paper will appear in a Discussion Section to be published in the December 1975 JOURNAL. All discussions for the December 1975 Discussion Section should be submitted by Aug. 1, 1975.

Publication costs of this article were partially assisted by the University of Kentucky.

LIST OF SYMBOLS

PC	propylene carbonate
Pr	n-propyl
Bu	n-butyl
Λ	molar conductance, $\text{ohm}^{-1} \text{cm}^2 \text{mole}^{-1}$
η	absolute viscosity of solution, cP
cP	centipoise
t	temperature, °C
T	temperature, °K
R	molar gas constant, $\text{cal mole}^{-1} \text{deg}^{-1}$
E_{vis}	activation energy of viscous flow, cal
E_{con}	activation energy of conductance, cal
ρ	density of solution, g cm^{-3}
ρ_0	density of solvent, g cm^{-3}
Y	general variable in Eq. [1]
M	molality, mole kg^{-1}

κ	specific conductance, $\text{ohm}^{-1} \text{cm}^{-1}$
Δ	moles of solvent displaced per mole of solute
M_1	molecular weight of solvent, g-mole^{-1}
M_2	molecular weight of solute, g-mole^{-1}
C	concentration of solute in mole liter^{-1}
exp	exponential to base e
ln	logarithm to base e
log	logarithm to base 10
c_1, c_2, c_3, c_4	constants in Eq. [1]
a, b, c	constants in Eq. [3]
$\alpha, \beta, \gamma, \delta, \epsilon$	constants in Eq. [4] and [6]
$\alpha', \beta', \gamma', \delta', \epsilon'$	constants in Eq. [5] and [7]
DMF	N,N-dimethylformamide

REFERENCES

1. T. V. Rebagay, J. F. Casteel, and P. G. Sears, *This Journal*, **121**, 977 (1974).
2. R. Jasinski, "Advances in Electrochemistry and Electrochemical Engineering," Vol. 8, pp. 253-333, John Wiley and Sons, Inc., New York (1971).
3. R. Payne and I. E. Theodorou, *J. Phys. Chem.*, **76**, 2892 (1972).
4. M. L. Jansen and H. L. Yeager, *ibid.*, **77**, 3089 (1973).
5. M. Salomon, *ibid.*, **73**, 3299 (1969).
6. R. Kempa and W. H. Lee, *J. Chem. Soc.*, 1936 (1958).
7. R. Jasinski, "High-Energy Batteries," pp. 128-130, Plenum Press, New York (1967).
8. L. M. Mukherjee and D. P. Boden, *J. Phys. Chem.*, **73**, 3965 (1969).
9. L. M. Mukherjee, D. P. Boden, and R. Lindauer, *ibid.*, **74**, 1942 (1970).
10. M. L. Jansen and H. L. Yeager, *ibid.*, **78**, 1380 (1974).
11. W. E. Wentworth, *J. Chem. Educ.*, **42**, 96 (1965); *ibid.*, **42**, 162 (1965).
12. J. E. Lind, Jr., H. A. A. Abdel-Rehim, and S. W. Rudich, *J. Phys. Chem.*, **70**, 3610 (1970).
13. A. K. R. Unni, L. Elias, and H. I. Schiff, *ibid.*, **67**, 1216 (1963).
14. H. L. Friedman, *ibid.*, **71**, 1723 (1967).
15. H. L. Yeager, J. D. Fedyk, and R. J. Parker, *ibid.*, **77**, 2407 (1973).
16. P. G. Sears and L. R. Dawson, *J. Chem. Eng. Data*, **13**, 124 (1968).

Standard Free Energies of Formation of Metal Fluorides by Solid Electrolytic Galvanic Cell Method

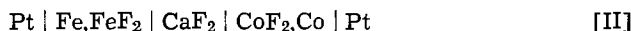
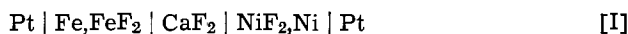
I. Metal Difluorides

G. Chattopadhyay, M. D. Karkhanavala, and M. S. Chandrasekharaiah

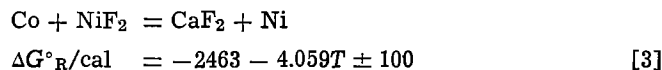
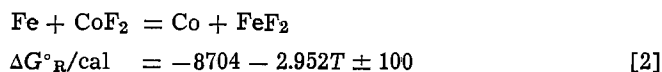
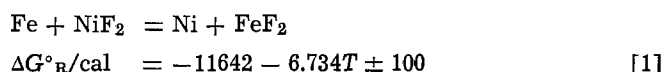
Chemistry Division, Bhabha Atomic Research Centre, Trombay, Bombay 400085, India

ABSTRACT

Measurements of ΔG°_f of FeF_2 , CoF_2 , and NiF_2 employing single crystals of CaF_2 as the solid electrolyte are presented. From the emf data between 850° and 1050°K of the following cells



the ΔG°_R for the corresponding reaction was calculated



Combining these results with the best available literature value of $f\Delta G^\circ_T(\text{NiF}_2)$, the ΔG°_f of FeF_2 and CoF_2 were calculated.

$$f\Delta G^\circ_T(\text{NiF}_2)/\text{cal mole}^{-1} = -156079 + 36.33T \pm 500 \quad \text{[4]}$$

$$f\Delta G^\circ_T(\text{CoF}_2)/\text{cal mole}^{-1} = -158542 + 32.27T \pm 600 \quad \text{[5]}$$

$$f\Delta G^\circ_T(\text{FeF}_2)/\text{cal mole}^{-1} = -167721 + 29.60T \pm 600 \quad \text{[6]}$$

The solid electrolyte galvanic cell (SEGC) method is now firmly established as an invaluable source of reliable thermodynamic data for materials at high temperatures (1). SEGC measurements based on CaF_2 as the fluoride ion conducting electrolyte have great potentialities in alloy thermochemistry. The d-block (transition) metal fluorides in general are stoichiometric compounds compared to the significantly nonstoichiometric oxides of the corresponding metals. Hence, the activity data evaluated from the fluoride cells will have smaller uncertainties due to the smaller nonstoichiometry of the coexisting binary compound.

Availability of accurate thermodynamic data for a set of metal fluorides to be used as reference electrodes is a primary requirement before this method can be utilized for alloy activity measurements. Thermodynamic data for such fluoride systems are scant and not very reliable (2). Hence it was decided to investigate three such reference electrode systems, *viz.*, Fe, FeF_2 , Co, CoF_2 ; and Ni, NiF_2 . The results are presented here

Experimental

Electrolyte.—The electrolyte was a rectangular piece ($16 \times 15 \times 8$ mm) of single crystal, optical grade CaF_2 (Isomet Corporation). The two parallel surfaces were polished flat with carborundum papers before use in each cell assembly. The polished surfaces were transparent.

Materials.—Anhydrous NiF_2 and CoF_2 (Ozark-Mahoning Corporation, total metallic impurities < 200 ppm) were mixed with equal amounts of the respective metal sponge (Chemistry Division, BARC. < 100 ppm metallic impurities) and pressed into pellets. An-

Key words: fluoride electrolyte, free energies, cobalt fluoride, ferrous fluoride, nickel fluoride.

hydrous FeF_2 was prepared by fluorination of iron sponge (Johnson-Matthey specpure, impurities < 10 ppm) and then mixed with excess iron powder and pressed into pellets. The phases present were characterized by x-rays before and after the experiment. Usually the green pellets were heated in a stream of anhydrous HF and argon before use. To check whether there was any reaction between CaF_2 and FeF_2 , NiF_2 , or CoF_2 , mixtures of CaF_2 and the respective fluorides were heated in argon for 24 hr and then examined by x-ray diffractometry. No new phases or change in the intensities of CaF_2 peaks were observed indicating the absence of mixed crystal formation or any substantial mutual solubility. Egan and Hues (3) also did not observe any saturation between CoF_2 and CaF_2 .

Ultrapure argon gas (> 99.95%) was purified further by passing sequentially over Drierite, anhydrous $\text{Mg}(\text{ClO}_4)_2$, a column of copper oxide, and copper at 500°C, a molecular sieve trap refrigerated in a dry ice bath, a bed of titanium sponge at 750°C, and finally through another molecular sieve trap refrigerated with dry ice before admitting into the cell. The residual oxygen concentration after purification was below the detectable level by either gas chromatography or mass spectrometry. All connections were made by using oxygen-free high conducting copper tubings with brazed joints. A glass capillary flowmeter connected to the exit side of the cell not only indicated the gas flow rate but also prevented the back diffusion of air into the cell. The details of the flow meter is given elsewhere (4).

Furnace.—Kanthal A wire (1 mm) wound non-inductively on a recrystallized alumina tube (600 mm long, 40 mm diameter) together with another ancillary heater for end heat loss compensation provided an iso-

thermal zone ($\pm 1.0^\circ\text{C}$) of 5 cm long near the center of the furnace. A SCR proportional temperature controller (Eurotherm type PID) maintained the set temperatures within $\pm 1.0^\circ$ for several hours. All temperatures were measured with a calibrated Pt-Pt 10% Rh thermocouple placed close to the electrolyte.

Cell assembly and measuring procedure.—A schematic view of the cell assembly, which was designed to separate the two electrode chambers and to minimize the fused silica surface exposed to the fluoride vapors, is shown in Fig. 1.

The two electrode chambers were separated by pressing the recrystallized alumina tube (A) against the polished surface of the electrolyte block (B). Inner electrode pellet (C) with the platinum disk was placed inside this tube and pressed against the electrolyte surface by means of an alumina tube (D) and a mild steel plug (E). The other electrode pellet (F) with the lead wire connections was pressed against the outer surface of the electrolyte by means of a stainless steel disk (G). This disk was held in position by three stainless steel or nickel wires (H) which were passed through the disk. The tension in these wires was maintained by three stainless steel springs at the cold end of the cell. This entire assembly was placed inside a fused silica tube. The two electrode chambers were separately flushed with purified argon.

The polished electrolyte piece and the electrode pellets were placed separately inside Pyrex tubes and evacuated to 10^{-5} Torr at ambient temperature for several hours to remove all surface adsorbed moisture and they were then kept sealed in a tube until required. The cell assembly was evacuated to 10^{-1} Torr and refilled with purified argon several times in each series before the furnace was brought to its desired temperature. An argon flow rate of 1.5–2.0 liter/hr was usually maintained during the heating and cooling cycle. The emf was recorded over 1–4 hr at each set temperature. Each cell was subjected to several heating and cooling cycles lasting for several days. Revers-

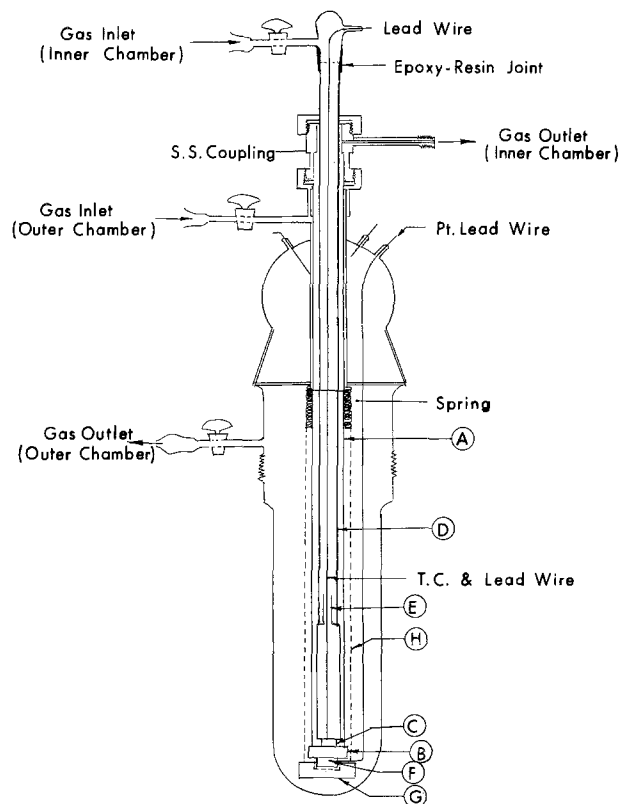


Fig. 1. Cell assembly. A, Outer alumina tube; B, electrolyte; C, electrode (1); D, inner alumina tube; E, mild steel plug; F, electrode (2); G, stainless steel disk; H, stainless steel wire.

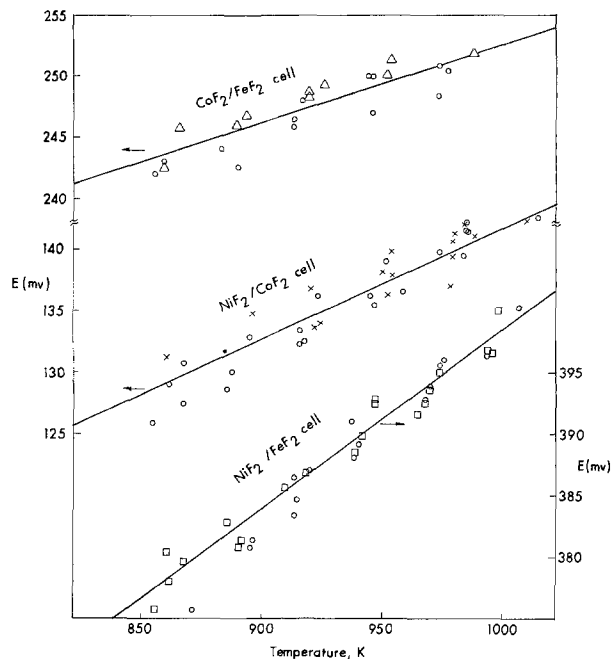


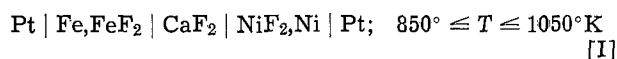
Fig. 2. Emf vs. temperature plot

ibility of the electrode processes was established in the usual way (1).

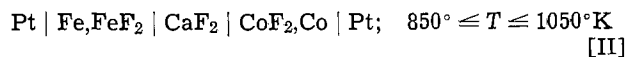
A thin nickel sheet was placed coaxially on the outside of the silica tube and was earthed to prevent any a-c pickup during the emf measurements. A high input impedance ($> 10^{12}$ ohms) vibrating reed electrometer (Vibron Model 33C) as well as a precision microvolt potentiometer (Leeds and Northrup K5 with electronic d-c null detector) were employed to measure the emf values with a precision better than ± 0.2 MV.

Results and Discussion

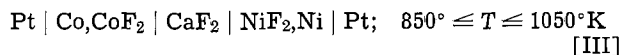
The emf of the cells [I], [II], and [III] were measured and the results were expressed by a linear expression using the least squares method. The uncertainties quoted are the standard deviation in E . The temperature dependence of the emf is presented in Fig. 2.



$$E_{\text{I}}(\text{mV}) \pm 2.0 = 252.4 + 14.60 \times 10^{-2}T \quad \text{[1]}$$



$$E_{\text{II}}(\text{mV}) \pm 2.0 = 188.7 + 6.40 \times 10^{-2}T \quad \text{[2]}$$



$$E_{\text{III}}(\text{mV}) \pm 2.0 = 53.4 + 8.80 \times 10^{-2}T \quad \text{[3]}$$

The internal consistency among the data is excellent as may be seen by comparing the values in the second column of Table I with the corresponding values in the fifth column of Table I.

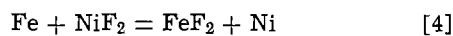
From the measured emf data, the $\Delta G^\circ_{\text{R}}$ for the following net cell reactions were calculated assuming

Table I. Emf values at some selected temperatures

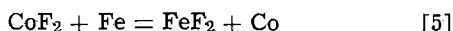
T/K	emf (mV)	$E_{\text{I}} \pm 2$	$E_{\text{II}} \pm 2$	$E_{\text{III}} \pm 2$	$(E_{\text{II}} + E_{\text{III}}) = E_{\text{I}}^{\text{calc.}} \pm 4$
1000		398	253	141	394
		385*	240*	111*	351*
900		384	246	133	379
		377*	241*	113*	354*

* Calculated from Skelton and Patterson data (8).

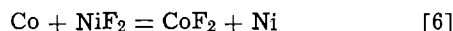
negligible solid solutions



$$\Delta G^\circ_{\text{I}}/\text{cal} = -11642 - 6.734 \pm 100; 850^\circ \leq T < 1050^\circ\text{K} \quad [4A]$$



$$\Delta G^\circ_{\text{II}}/\text{cal} = -8704 - 2.952T \pm 100; 850^\circ \leq T \leq 1050^\circ\text{K} \quad [5A]$$



$$\Delta G^\circ_{\text{III}}/\text{cal} = -2463 - 4.059T \pm 100; 850^\circ \leq T \leq 1050^\circ\text{K} \quad [6A]$$

Paucity of reliable enthalpy and entropy data for the anhydrous metal difluorides precludes any direct comparison of these $\Delta G^\circ_{\text{R}}$. Only for $\text{NiF}_2(\text{s})$, are $f\Delta H^\circ_{298}$ data available from combustion calorimetry (5), as well as low temperature (6) and high temperature (7) heat capacity data. The best available data are $f\Delta H^\circ_{298}(\text{NiF}_2) = -157.2 \pm 0.4 \text{ kcal mole}^{-1}$ (5) and $S^\circ_{298} = 17.59 \pm 0.2 \text{ eu}$ (6). Combining these data with the high temperature drop calorimetric results (7), the following expression was calculated for the $f\Delta G^\circ_{\text{T}}(\text{NiF}_2)$

$$f\Delta G^\circ_{\text{T}}(\text{NiF}_2)/\text{cal mole}^{-1} = -156079 + 36.33T \pm 500 \quad [7]$$

Expressions [4A] and [7] yielded

$$f\Delta G^\circ_{\text{T}}(\text{FeF}_2)/\text{cal mole}^{-1} = -167721 + 29.60T \pm 600 \quad [8]$$

Similarly, Eq. [7] and [6A] gave

$$f\Delta G^\circ_{\text{T}}(\text{CoF}_2)/\text{cal mole}^{-1} = -158542 + 32.27T \pm 600 \quad [9]$$

The uncertainty in these free energy data is essentially the uncertainty involved in calculating $f\Delta G^\circ_{\text{T}}(\text{NiF}_2)$. The experimental inaccuracy in the galvanic cell measurement is much less.

When this work was almost complete, Skelton and Patterson (8) recently reported some of their galvanic cell measurements of metal fluorides. The emf values calculated from their data for the three cells at 900° and 1000°K are also shown in Table I. Besides this report, data for only cell [I] are available to a limited extent. Lofgren and McIver (9) and Bones, Markin, and Wheeler (10) have reported emf values of $375 \pm 2 \text{ mV}$ and $374 \pm 3 \text{ mV}$, respectively, for the cell [I] at 873°K. A value of $384 \pm 2 \text{ mV}$ was calculated from the equation given for the emf of the same cell by Bagshaw (11) compared to $380 \pm 2 \text{ mV}$ obtained in the present work. Vecher and Rogach (12) have reported emf data they have measured for the cell $\text{Pt}|\text{Mo}|\text{Fe},\text{FeF}_2|\text{CaF}_2|\text{NiF}_2,\text{Ni}|\text{Mo}|\text{Pt}$ from which a value of $85.2 \pm 2.6 \text{ mV}$ was calculated at 873°K. These discrepancies are difficult to account for except that galvanic cell measurements with all fluoride cells require experimentally much more care than the corresponding solid oxide galvanic cell measurements (9, 10).

A probable explanation for the discrepancies may be the difference in the details of cell arrangement, particularly in the separation of the two electrode chambers. Skelton and Patterson (8) have used an open cell stacked pellet assembly where the possibility of gas phase interaction exists.

In the present work as well as in that of Lofgren and McIver (9), and Bones *et al.* (10), the two electrodes were isolated from each other. In those experiments where some gas was able to leak from cathode chamber to anode as a result of some misalignment, the emf was unsteady. This indicates the necessity of isolating the electrode chambers in fluoride cells.

The relative reliability of data from different investigators can best be established by an internal consistency test by measuring the emf of two cells against a common third electrode. Such measurements have not always been reported. The internal consistency check was made in the present work (Table I) and was shown to be good. But as can be seen from the calculated data (Table I), the results of Skelton and Patterson (8) do not fulfil this requirement indicating some source of systematic error. (E_{I} measured is not in agreement with their $E_{\text{I}}^{\text{calc.}} = (E_{\text{II}} + E_{\text{III}})$.) It is rather difficult to account for the extremely low value for cell [I] reported by Vecher and Rogach (12). In view of the excellent internal consistency in the present work, the data reported here for $\text{NiF}_2(\text{s})$ and $\text{FeF}_2(\text{s})$ are considered more reliable.

Acknowledgment

We thank our colleagues, Shri O. M. Sreedharan for his assistance in some of the experimental work and Shri A. S. Kerker for his help in the fabrication of the cell assembly and the gas purification train. We would like to acknowledge our indebtedness to Dr. M. V. Ramaniah, Head, Radiochemistry Division, and his colleagues and to Dr. T. K. Das of Chemistry Division for permitting us to utilize their hydrofluorination/fluorination setup for the preparation of fluorides.

Manuscript submitted April 26, 1974; revised manuscript received Sept. 16, 1974.

Any discussion of this paper will appear in a Discussion Section to be published in the December 1975 JOURNAL. All discussions for the December 1975 Discussion Section should be submitted by Aug. 1, 1975.

REFERENCES

1. D. A. Shore and R. A. Rapp, in "Techniques of Metal Research," Vol. IV, Part 2, R. A. Rapp, Editor, pp. 123-192, John Wiley & Sons, Inc., New York (1970).
2. JANAF Thermochemical Tables, 2nd ed., D. R. Stull and H. Prophet, Editors NSRDS-NBS 37, (1971).
3. J. J. Egan and R. J. Hues, *Z. Phys. Chem.*, **49**, 38 (1966).
4. O. M. Sreedharan, S. R. Dharwadkar, and M. S. Chandrasekharaiah, BARC Report No. I 239 (1973).
5. E. Rudzitis, E. H. van Deventer, and W. N. Hubbard, *J. Therm. Eng. Data.*, **12**, 133 (1967).
6. J. W. Stout, *J. Chem. Phys.*, **23**, 1284 (1955).
7. J. S. Binford and T. H. Hebert, *J. Chem. Therm.*, **2**, 407 (1970).
8. W. H. Skelton and J. W. Patterson, *J. Less Common Metals*, **31**, 47 (1973).
9. N. L. Lofgren and E. J. McIver, U.K. At. Energy Authority, **AERE-R**, 5169 (1966).
10. R. J. Bones, T. L. Markin, and V. J. Wheeler, *Proc. Brit. Ceram. Soc.*, **9**, 51 (1967).
11. A. N. Bagshaw, *Russ. J. Phys. Chem.*, **46**, 939 (1972).
12. R. A. Vecher and L. M. Rogach, *ibid.*, **44**, 865 (1970).

The Free Energy of Formation of Iridium Oxide by Solid Electrolyte Galvanic Cell

E. S. Ramakrishnan,¹ O. M. Sreedharan, and M. S. Chandrasekharaiah

Chemistry Division, Bhabha Atomic Research Centre, Bombay 400085, India

ABSTRACT

The ΔG°_f of $\text{IrO}_2(\text{s})$ was determined in the range of 950°–1170°K from the measured emf data of the cell



and the best available data of $\Delta G^\circ_f <\text{NiO}>$. The value of $\Delta G^\circ_f <\text{IrO}_2>$ so calculated from the emf of the cell is

$$\Delta G^\circ_f <\text{IrO}_2>/\text{cal mole}^{-1} \pm 400 = -56760 + 40.41T$$

The enthalpy and the entropy of formation of $\text{IrO}_2(\text{s})$ calculated by the second law method at a mean temperature of 1048°K were respectively

$$\Delta H^\circ_{f,1048} <\text{IrO}_2>/\text{cal mole}^{-1} = -56760 \pm 400$$

$$\Delta S^\circ_{f,1048} <\text{IrO}_2>/\text{cal mole}^{-1} \cdot \text{K}^{-1} = -40.4 \pm 0.4$$

Platinum-iridium alloys have better mechanical properties compared with pure platinum and hence they are substituted for platinum in many high temperature applications. But the stability and the volatility of IrO_2 and IrO_3 alter the alloy composition during use and thereby affect the strength of the alloy. Accurate thermodynamic data for these iridium compounds at high temperatures would enable one to estimate the iridium loss and make appropriate correction in the alloy composition. The presently available entropy and enthalpy data for $\text{IrO}_3(\text{g})$ (1-3) and for $\text{IrO}_2(\text{s})$ (4) have large uncertainties which render them unsuitable for this purpose.

The solid oxide electrolyte galvanic cell method has proved to be superior to other methods for obtaining the ΔG°_f for oxides directly at high temperature (5, 6). High sensitivity and better precision and accuracy are the attractive features of this method. The value of $\Delta G^\circ_f <\text{IrO}_2>$ as a function of temperature was determined between 875° and 1175°K by employing calcia stabilized zirconia (CSZ) as the oxide electrolyte. The results shown below serve to supplement the preliminary data which were published earlier (7).

Experimental

Materials.— $\text{IrO}_2(\text{s})$ was prepared by oxidizing iridium powder (Johnson-Matthey specpure quality, total metallic impurities < 200 ppm, mostly other platinum group metals) in dry oxygen at 1273°K for 80 hr. The resulting product was shown by x-ray diffractometry to be essentially $\text{IrO}_2(\text{s})$ with only one or two weak lines of $\text{Ir}(\text{s})$. The (Ir, IrO_2) electrode pellets made by cold compacting of Ir and IrO_2 (1:1) mixture by weight did not yield reproducible emf data on thermal cycling. Hence a second batch of electrode pellets was made by merely pressing the oxidized sample into disks of 6 mm diameter and 2 mm thick (10 tsi). Sintering them in argon at 775°K for 12 hr before use served to generate the Ir phase *in situ*. The x-ray diffractometric analysis of these sintered pellets established the presence of both Ir and IrO_2 phases.

Cu , Cu_2O , and Ni , NiO reference electrodes were prepared from equimolar powder mixtures of each metal and its oxide. Disks of 6 mm diameter and 1.5 mm thick (10 tsi) were first cold-pressed and then sintered in evacuated, sealed silica tubes for 24 hr at 1200°K.

Pellets of 15 mole per cent (m/o) calcia stabilized zirconia electrolyte (10 by 2 mm thick) were prepared

by first decomposing the coprecipitated oxalate in air and then pressing the resultant powder into the disks of required size. The green pellets were first sintered in air at 1700°K for about 750 hr followed by an additional heating of 1 hr at 2100°K. The sintered pellets were polished to a mirror finish with corosil paper before use. In addition, a CSZ tube obtained from Zircoa Corporation (12 in. long, 3/8 in. ID and closed end flat) was used to partially separate the two electrode chambers in all measurements involving $\text{IrO}_2(\text{s})$.

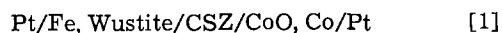
Argon of initial purity >99.95% was further purified by passing it sequentially through anhydrous $\text{Mg}(\text{ClO}_4)_2$, copper oxide (750°K), a trap cooled by dry ice, titanium sponge (500°K), and another trap cooled by dry ice before admitting it into the cell. The flow was regulated at 1-1.5 liters/hr by a calibrated capillary flow meter.

Apparatus and measurement procedure.—A Pt-Rh alloy wire wound noninductively on a sintered alumina tube (16 in. long, 1.5 in. ID) served as the furnace whose temperature was regulated to $\pm 0.5^\circ\text{K}$ by a SCR controlled proportional controller. The cell assembly was always placed in the 2.0 in. long isothermal zone near the center. The temperature of the system was measured by placing a calibrated platinum-platinum 10 weight per cent (w/o) rhodium alloy thermocouple close to the electrolyte pellet.

An open cell stacked pellet assembly, modified to some extent by the electrolyte tube in some runs, was adopted for emf measurement. The emf was measured with the Leeds and Northrup K-5 potentiometer and Leeds and Northrup 9834 d-c null detector as well as the high input Vibron 33-C electrometer. Each cell was subjected to several heating and cooling cycles and the emf was recorded in both heating and the cooling sequences. Emf measurements were continued for several days in each case. The reversibility of the electrode processes was ascertained in each case by momentarily polarizing the electrodes in the usual way and observing that the original emf was restored within 10 min. For each series the initial equilibration at the highest temperature required from 3 to 4 hr; however, on subsequent changes of temperature, equilibrium emf values were achieved as soon as thermal equilibrium was attained.

Results and Discussion

The reliability of the setup was ascertained first by measuring the emf of the following cells



¹ Present address: Department of Atomic Energy, University of Bombay, Bombay, India.

Key words: oxide electrolyte, iridium oxide, free energy.

Pt/Co, CoO/CSZ/NiO, Ni/Pt [2]

Pt/Fe, Wustite/CSZ/NiO, Ni/Pt [3]

The emf data for each cell was expressed by a linear expression

$$E_1/(\text{mV}) \pm 1.0 = 88.0 + 8.20 \times 10^{-2}T; \\ 1175^\circ \leq T \leq 1375^\circ \text{K} \quad [4]$$

$$E_2/(\text{mV}) \pm 1.0 = 17.5 + 6.20 \times 10^{-2}T; \\ 1175^\circ \leq T \leq 1375^\circ \text{K} \quad [5]$$

$$E_3/(\text{mV}) \pm 1.0 = 102.4 + 14.30 \times 10^{-2}T; \\ 1175^\circ \leq T \leq 1375^\circ \text{K} \quad [6]$$

These show very good agreement with the published data as well as an excellent internal consistency of the measurements (Table I).

After establishing reliability, the $\Delta G^\circ_f <\text{IrO}_2>$ was evaluated from the measured emf of the cell

Pt/Ir/Ni, NiO/CSZ pellet/CSZ tube/IrO₂, Ir/Pt [7]

between 875° and 1175°K. The partial isolation of the two electrode chambers by the CSZ tube was a necessity without which the gas phase interaction made the emf measurement impossible. This probably was the result of the rather high oxygen dissociation pressure of $<\text{IrO}_2>$ (about 10^{-3} atm near 1273°K). A schematic diagram of the cell assembly is shown in Fig. 1.

Five different series of measurements were made. Series A and B (Ir, IrO₂) electrodes made from equal amount mixtures of the oxide and the metal were used. In series A (Ir, IrO₂) pellets made from equal weight mixtures were placed inside the CSZ tube with the Ni, NiO pellet outside it. This cell gave continuously falling emf values, differing by as much as 10-15 mV at the same set temperature within 1½ hr, and eventually reaching almost zero emf at the end of 24 hr of measurement. In series B, the positions of the electrode pellets were interchanged. Though it improved the readings, the emf values at a given set temperature still decreased with time and the cell did not yield reproducible values on thermal cycling. So these data were not included in the free energy calculation. In the remaining three series (C, D, and E), (Ir, IrO₂) pellets of the second batch were used which gave satisfactory results and each cell gave reproducible emf's extending over 5-6 days. Tables II and III present the typical emf data. The least squares treatment of the data yielded the expression

$$E_7/(\text{mV}) \pm 3.5 = 597.9 - 0.0038T; 920^\circ \leq T \leq 1175^\circ \text{K} \quad [8]$$

The emf values and their scatter increased excessively when the temperature was below 920°K. Consequently, values below 920°K were not included in the determination of $\Delta G^\circ_f <\text{IrO}_2>$. The plot of emf vs. T shows a distinct break in the slope around 920°K (Fig. 2).

Table I. The emf values for the following cells at selected temperatures: E_I , Fe, Fe_{0.95}O/CSZ/CoO, Co; E_{II} , Co, CoO/CSZ/NiO, Ni; E_{III} , Fe Fe_{0.95}O/CSZ/NiO, Ni

emf	Temperature, °K				Remarks
	1323	1273	1223	1173	
E_I (mV) ±1.0	196.5	192.4	188.3	184.2	This work
	191	189	188	186	Ref. (10)
E_{II} (mV) ±1.0	96.5	93.4	90.3	87.2	This work
	96.6	93.2	89.8	86.4	Ref. (11) std. dev. = ±0.63
	98.0	94.0	90.0	86.0	Ref. (12) std. dev. = ±2.0
	100.5	97.0	93.5	90.0	Ref. (10) (Combining their FeO/NiO and FeO/CeO data)
E_{III} (mV) ±1.0	296.6	284.4	277.2	270.1	This work
	291.0	286.0	281.0	276.0	Ref. (13)
$(E_I + E_{II}) = (E_{III}) \pm 2.0$	293.1	285.8	278.7	271.4	This work

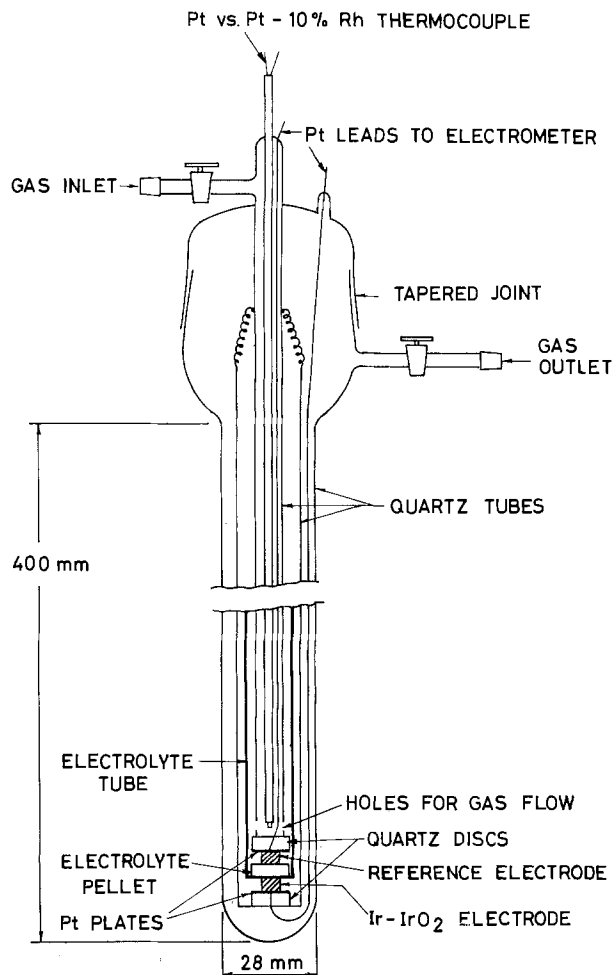
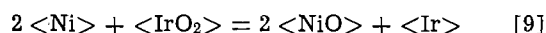


Fig. 1. The cell assembly

The large scatter in the experimental data below this temperature rendered the calculation of slope at lower temperature rather uncertain.

The net chemical reaction of cell [7] for the passage of 4 Faradays of electricity is



The available literature data show insignificant mutual solid solution between $<\text{Ni}>$ and $<\text{NiO}>$ or $<\text{Ir}>$ and $<\text{IrO}_2>$. Hence

Table II. The emf data for the cell Ni, NiO/CSZ/IrO₂, Ir

Run No.	Temperature (°K ± 0.5°)	emf (mV)*	Run No.	Temperature (°K ± 0.5°)	emf (mV)*
C-1	1019.0	588.0, 592.0	D-11	913.0	618.0, 620.0
C-2	1073.0	592.8, 593.0	D-12	1048.0	597.6, 598.0
C-3	1132.5	593.4, 594.2	D-13	998.0	596.4, 596.2
C-4	895.7	605.8, 605.6	D-14	943.0	604.6, 604.8
C-5	966.0	599.7, 600.0	D-15	1063.1	598.0, 598.8
C-6	1015.0	596.7	D-16	1121.0	597.6
C-7	1076.2	593.9, 592.4	E-1	1007.0	592.9, 590.0
C-8	1071.0	592.8, 592.5	E-2	898.0	610.8, 612.4
C-9	1131.0	589.3	E-3	961.4	594.6, 592.8
C-10	1016.5	594.1, 593.7	E-4	1009.5	586.8
C-11	915.0	598.8, 599.6	E-5	956.0	589.2, 598.8
C-12	988.0	596.2, 594.2	E-6	1131.0	590.7, 591.0
D-1	1049.2	593.9, 594.8	E-7	1013.0	590.4, 590.2
D-2	982.0	590.3, 590.7	E-8	1127.0	590.0, 594.6
D-3	983.0	591.5, 591.3	E-9	1066.0	591.9, 591.7
D-4	918.4	592.4, 590.8	E-10	1132.0	595.4, 595.0
D-5	983.0	591.2, 592.0	E-11	1023.0	590.2, 591.7
D-6	923.0	590.0, 591.4	E-12	950.0	593.6
D-7	1076.0	598.4, 599.0	E-13	1132.0	595.2, 595.0
D-8	891.0	623.0, 636.0, 632.0	E-14	961.0	593.2, 593.6
D-9	998.2	603.0	E-15	1131.0	595.8, 594.2
D-10	1046.0	593.3, 593.9			

* The two readings of emf were the lowest and the highest during a recording of 1-1½ hr at any one temperature.

Table III. The emf data for the cell Cu, Cu₂O/CSZ/IrO₂ Ir

Run No.	Temperature (°K ± 0.5°)	emf (mV)*	Run No.	Temperature (°K ± 0.5°)	emf (mV)*
F-1	958.9	328.6, 326.4	F-14	996.7	305.3, 302.3
F-2	1048.0	313.4, 308.8	F-15	1041.5	309.6, 300.5
F-3	1043.0	305.0, 306.4	F-16	957.0	320.0
F-4	896.4	359.0, 356.0	F-17	1036.6	303.0, 302.4
F-5	903.0	354.9, 354.0	G-1	1029.0	309.6, 310.0
F-6	1094.1	317.7, 313.0	G-2	958.0	326.3, 326.9
F-7	1087.4	312.0, 314.0	G-3	965.0	327.3
F-8	1087.0	313.0, 312.9	G-4	1071.5	313.3, 312.8
F-9	929.0	345.0, 344.0	G-5	1135.9	315.9, 316.3
F-10	1096.0	314.3, 313.2	G-6	1025.5	305.7, 308.3
F-11	928.8	344.0, 344.6	G-7	1083.1	312.6
F-12	1095.0	326.0, 313.2	G-8	1135.3	318.2, 318.9
F-13	1090.9	312.8, 310.9	G-9	1973.0	312.4

* The two readings were the lowest and the highest during a recording period of 1-1½ hr at any set temperature.

$$\Delta G^{\circ}_f < \text{IrO}_2 > = 2\Delta G^{\circ}_f < \text{NiO} > + 4F(E_7) \quad [10]$$

Kellogg (8) recently reevaluated the thermochemical data for <NiO> and <Cu₂O> and the following linear expression for the $\Delta G^{\circ}_f < \text{NiO} >$ was calculated from his tabulation

$$\Delta G^{\circ}_f < \text{NiO} > / \text{cal mole}^{-1} \pm 50 = -56000 + 20.38T; \quad 900^{\circ} \leq T \leq 1350^{\circ} \text{K} \quad [11]$$

Substituting this expression for $\Delta G^{\circ}_f < \text{NiO} >$ and the expression [8] for the emf in Eq. [10] and rearranging yields

$$\Delta G^{\circ}_f < \text{IrO}_2 > / \text{cal mole}^{-1} \pm 400 = -56760 + 40.41T; \quad 920^{\circ} \leq T \leq 1175^{\circ} \text{K} \quad [12]$$

The enthalpy and the entropy of formation of IrO₂(s) at 1048°K (the mean temperature of measurement) calculated by the second law method was

$$\Delta H^{\circ}_f, < \text{IrO}_2 >, (1048^{\circ} \text{K} / \text{cal mole}^{-1}) = -56760 \pm 400 \quad [13]$$

$$\Delta S^{\circ}_f, < \text{IrO}_2 >, (1048^{\circ} \text{K} / \text{cal K}^{-1} \cdot \text{mole}^{-1})$$

$$= -40.4 \pm 0.4 \quad [13A]$$

A linear extrapolation of Eq. [12] yields 1404.6°K as the temperature at which oxygen dissociation pressure becomes one atmosphere. This temperature is in good agreement with directly measured values of 1396°, 1373°, and 1378°K reported respectively by Schafer and Heitland (2), Cordfunke and Meyer (3), and Bell, Tagami, and Inyard (4). Bell *et al.* (4) have measured the dissociation pressure of IrO₂ by tensiometry and have calculated the enthalpy and the entropy of formation of IrO₂(s) at a mean temperature of 1300°K as $-54.0 \pm 1.5 \text{ kcal mole}^{-1}$ and $-39.2 \pm 1.5 \text{ cal mole}^{-1} \text{ K}^{-1}$, respectively. They also have estimated ΔC°_p for the formation of IrO₂(s) by combining C°_p values of Ir(s) and O₂(g) given by Kelley and an estimated C°_p for IrO₂. Assuming this ΔC°_p to be constant in the range of 1300°-1048°K, the ΔH°_f and ΔS°_f of IrO₂(s) at 1048°K was calculated to be $\Delta H^{\circ}_f = -54.95 \pm 1.5 \text{ kcal mole}^{-1}$ and $\Delta S^{\circ}_f = -40.06 \pm 1.5 \text{ cal mole}^{-1} \text{ K}^{-1}$. There is an excellent agreement between their entropy of formation and the data from present investigation (Eq. [13A]). But the $\Delta H^{\circ}_f, 1048^{\circ} \text{K} < \text{IrO}_2 >$ calculated from emf data is nearly 1.8 kcal more negative than the corresponding enthalpy data of Bell *et al.* This is also reflected in the slightly higher dissociation temperature (1404.6°K) compared to their calculated value of 1378°K. The uncertainties involved in the tensiometric measurements are reflected in the spread of nearly 25°K in the temperature of dissociation of IrO₂(s) among the three investigators (2-4), all of whom employed essentially the same experimental technique.

To verify the consistency and the reliability of the measurement, the $\Delta G^{\circ}_f < \text{IrO}_2 >$ was determined with the (Cu, Cu₂O) reference electrode by employing the cell configuration

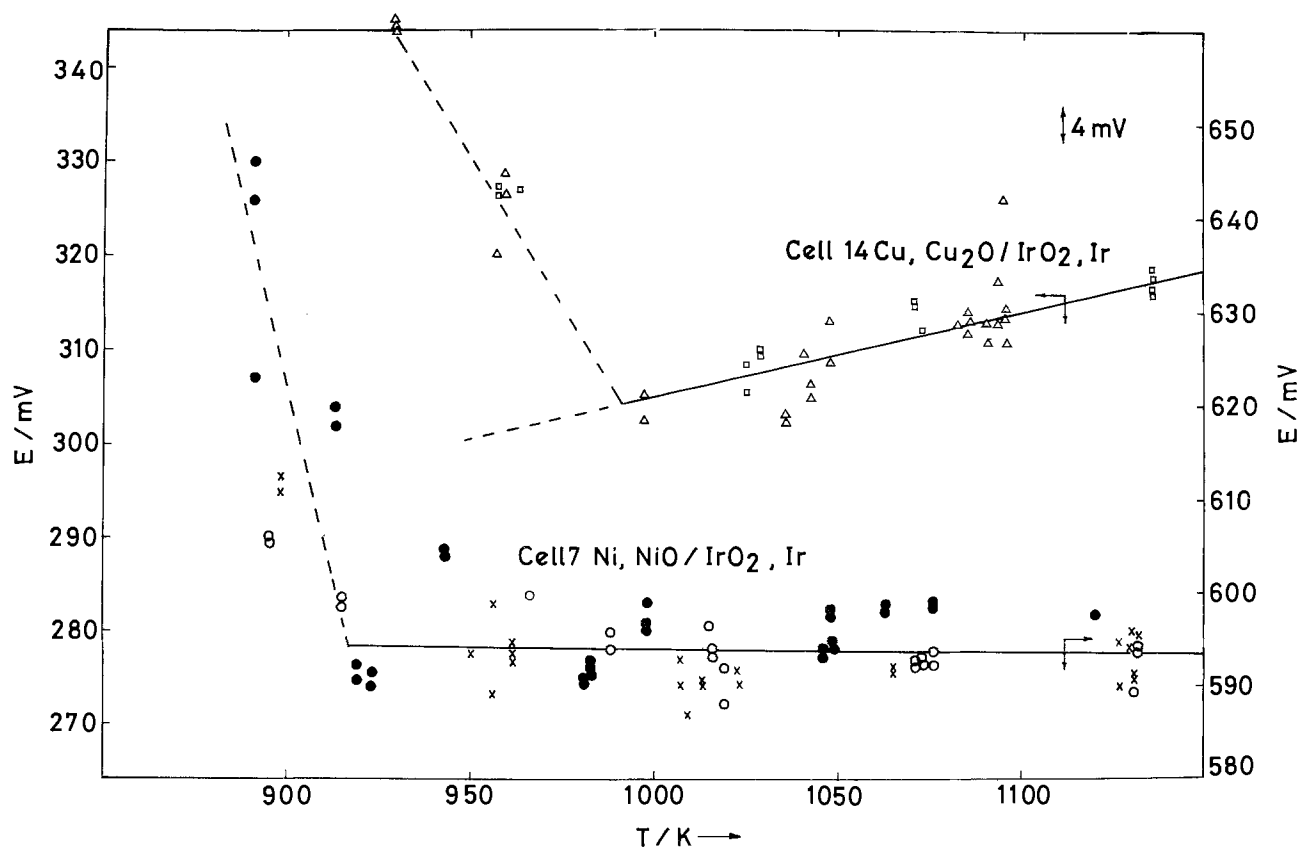
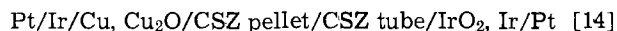


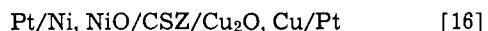
Fig. 2. Emf vs. temperature plot for cell [7] (bottom) and cell [14] (top). ○, Series C; ●, series D; ×, series E; △, series F; □, series G.

between 970° and 1175°K. The least squares treatment of the data gave the expression

$$E_{14}(\text{mV}) \pm 4.0 = 236.0 + 7.85 \times 10^{-2}T$$

$$970^\circ \leq T \leq 1175^\circ\text{K} \quad [15]$$

The internal consistency of the emf measurements was checked by the direct measurement of the emf of the cell



in the temperature range of 950°-1275°K. The emf of this cell was found to be

$$E/\text{mV} \pm 2.0 = 364.0 - 8.0 \times 10^{-2}T$$

$$950^\circ \leq T \leq 1275^\circ\text{K} \quad [17]$$

Combining the emf of cell [7] and cell [14] would yield the expression

$$(E_7 - E_{14}) \pm 7.5 \text{ mV} = 361.9 - 8.23 \times 10^{-2}T \quad [18]$$

for the emf of cell [16]. Thus the internal consistency was established to be good. For example, at 1000°K, expression [18] would yield a value of 279.6 ± 7.5 mV while the corresponding value calculated directly from Eq. [17] is 284.0 ± 2 mV.

The best available value for $\Delta G^\circ_f <\text{Cu}_2\text{O}>$ (8) between 1000° and 1275°K can be expressed as

$$\Delta G^\circ_f <\text{Cu}_2\text{O}>/\text{cal mole}^{-1} \pm 100 = -39848 + 17.04T \quad [19]$$

From Eq. [15] and [19], the following expression for the $\Delta G^\circ_f <\text{IrO}_2>$ was calculated

$$\Delta G^\circ_f <\text{IrO}_2>/\text{cal mole}^{-1} \pm 500 = -57984 + 41.30T \quad [20]$$

in good agreement with that calculated from the (Ni, NiO) reference (Eq. [12]).

The reproducibility of emf data for cell [7] below 920°K and for cell [14] below 950°K was poor. Besides, in both cases the temperature dependence of emf changed abruptly below these temperatures indicating a possible transformation in the IrO₂ phase. The exact nature of this transformation is not known. A DTA investigation of the IrO₂ pellet indicated a small endotherm peak around 950°K at a heating rate of 36°C/min but not at smaller heating rates. This may be due to any transformation in the IrO₂ phase since none of the other phases involved are known to exhibit any phase transformation. Because of this possible transformation no attempt was made to extrapolate the enthalpy and the entropy data to 298°K.

When this work was completed, a report appeared in the literature (9) in which the $\Delta G^\circ_f <\text{IrO}_2>$ was also measured employing SEGC. Kleykamp and Paneth (9), however, have employed (Fe, Wustite) as the reference and apparently stacked open cell arrangements. They gave the following expression for the free energy data

$$\Delta G^\circ_f <\text{IrO}_2> = (-61.66 \pm 0.741) + (43.26 \pm 0.956)T$$

$$\text{kcal/mole} \quad [21]$$

The agreement is not good. For example, at 1048°K, the $\Delta G^\circ_f <\text{IrO}_2>$ calculated from Eq. [21] will be (-16.32 ± 0.85) kcal/mole compared with a value of (-14.41 ± 0.40) kcal/mole obtained from Eq. [13] and [13A].

The discrepancy may perhaps be attributable to difference in the experimental details of the two measurements. Kleykamp and Paneth (9) have used

(Fe, Fe_{0.95}O) as the reference electrode and yttria doped thoria as the electrolyte. It is generally known (14) that Wustite may react with the electrolyte and form YFe₂O₄ resulting in mixed potential. Secondly, with this reference electrode, the oxygen potential difference is very large and complications (15) may arise due to oxygen transport, particularly in view of relatively high oxygen dissociation pressure of IrO₂. Thirdly, the p-type semiconduction is observed in YDT at P_{O₂} > 10⁻⁵ atm (16) which is within the oxygen dissociation pressure of IrO₂(s) in this temperature range. The internal consistency of the emf data was not established with one more reference electrode as is normally done. Hence, their more negative free energy of formation (nearly 2 kcal) data may not be acceptable. The break in the emf vs. temperature below 920°K which is observed in this investigation is not reported so far. In view of these considerations, the free energy of formation data reported here for IrO₂(s) is considered more reliable.

Acknowledgment

The authors thank Dr. J. Shankar, Emeritus Scientist, BARC, for his encouragement and Dr. M. D. Karkhanavala, Head, Chemistry Division for his suggestions and criticism. We wish to express our indebtedness to many of our colleagues, especially to Shri A. S. Kerkar in the fabrication of the apparatus. One of the authors, E. S. Ramakrishnan, gratefully acknowledges the financial assistance provided by the Department of Atomic Energy, Government of India, by the offer of a predoctoral fellowship during this work.

Manuscript submitted April 26, 1974; revised manuscript received Sept. 18, 1974.

Any discussion of this paper will appear in a Discussion Section to be published in the December 1975 JOURNAL. All discussions for the December 1975 Discussion Section should be submitted by Aug. 1, 1975.

REFERENCES

1. C. B. Alcock and G. W. Hooper, *Proc. Roy. Soc.*, **A254**, 551 (1960).
2. H. Schafer and H. J. Heitland, *Z. Anorg. Allgem. Chemie.*, **304**, 249 (1960).
3. E. H. P. Cordfunke and G. Meyer, *Rec. Trav. Chim.*, **81**, 495 (1962); **81**, 670 (1962).
4. W. E. Bell, M. Tagami, and R. E. Inyard, *J. Phys. Chem.*, **70**, 2048 (1966).
5. B. C. H. Steele, in "Electromotive Force Measurements in High Temperature Systems," C. B. Alcock, Editor, pp. 1-27. Institute of Mining and Metallurgy, London (1968).
6. D. A. Shores and R. A. Rapp, in "The Techniques of Metal Research," Vol. 4, Part II, R. A. Rapp, Editor, pp. 122-189, John Wiley & Sons, Inc., New York (1971).
7. E. S. Ramakrishnan, *Scripta Met.*, **7**, 305 (1973).
8. H. H. Kellogg, *J. Chem. Eng. Data.*, **14**, 41 (1969).
9. H. Kleykamp and L. J. Paneth, *J. Inorg. Nucl. Chem.*, **35**, 477 (1973).
10. K. Kiukkola and C. Wagner, *This Journal*, **104**, 379 (1957).
11. C. B. Alcock and G. P. Stavropoulos, *J. Am. Ceram. Soc.*, **54**, 436 (1971).
12. M. F. Lasker and R. A. Rapp, *Z. Phys. Chem. (Frankfurt)*, **49**, 198 (1966).
13. B. C. H. Steele and C. B. Alcock, *Trans. AIME*, **233**, 1359 (1965).
14. W. L. Worrell, *Proc. Symp. Thermodynamics*, Vol. 1, IAEA, Vienna (1966).
15. M. Sato, in "Research Techniques for High Pressures and High Temperatures," G. C. Ulmer, Editor, pp. 63-64, Springer Verlag, Berlin (1971).
16. M. Sato, *ibid.*, p. 57.

Conductivity and Crystal Structure of $(C_5H_5NH)_5Ag_{18}I_{23}$ A Two-Dimensional Solid Electrolyte

S. Geller, P. M. Skarstad, and S. A. Wilber

Department of Electrical Engineering, University of Colorado, Boulder, Colorado 80302

ABSTRACT

The solid electrolyte pentapyridinium 18-silver iodide, $(C_5H_5NH)_5Ag_{18}I_{23}$, has a crystal structure which allows the Ag^+ ions to move in only two dimensions, perpendicular to its hexagonal *c*-axis. The structure consists of face-sharing iodide tetrahedra which provide a network of pathways for diffusion of the Ag^+ ions. Planes of (formally) $[(C_5H_5NH)_3I]^{2+}$ groups, which occupy a considerable proportion of the crystal space, block the motion of Ag^+ ions in the *c*-axis direction. Crystals of $(C_5H_5NH)_5Ag_{18}I_{23}$ belong to space group $P\bar{6}2m(D_{3h}^{3-})$ with lattice constants $a = 13.62 \pm 0.02$, $c = 12.58 \pm 0.02 \text{ \AA}$, and the unit cell contains one formula unit. There are 55 tetrahedral sites for the Ag^+ ions in seven crystallographically nonequivalent sets of sites; as expected, the distribution of Ag^+ ions over these sites is markedly nonuniform. The low specific conductivity of this solid electrolyte is consistent with its two-dimensionality.

The origin of electrolytic conductivity in true solid electrolytes, especially halogenides and chalcogenides, has been propounded in several papers (1-6). To at least some extent, the physical properties of a crystalline solid are related to its structure, by which we mean the arrangement and types of atoms in the material. In the case of solid electrolytes, this relation is vividly recognized when one examines their crystal structures.

The main characteristics of a true solid electrolyte¹ are (i) a large ratio of available sites for the mobile cations (current carriers) to the number of available cations, and (ii) networks of passageways resulting from the face-sharing of anion polyhedra. There are corollaries to these: if the available sites are comprised of two or more crystallographically nonequivalent sets, then almost certainly the distribution of the carriers over the available sites will not be uniform. It should be clear that if sites are not crystallographically equivalent, they cannot be energetically equivalent, and of course, the distribution of carriers will depend on the site energy differences. Simplicity and numerous interconnections of passageways will give higher specific conductivities; $RbAg_4I_5$ which has the highest room temperature specific (electrolytic) conductivity (7, 8) has the best network of passageways (1). The passageways should be interconnected, preferably in three dimensions to facilitate the movement of the carriers. The larger the proportion of crystal space occupied by these channels, the smaller will be the restriction on the motion of the carriers.

Contrary to some views, it is misleading to refer to the sites for the carriers in true solid electrolytes as "defects." A Na^+ or Cl^- missing from its appropriate site, or one or the other in an (inappropriate) interstitial position in a $NaCl$ crystal at thermodynamic equilibrium, is rightly called a "defect." An ideal $NaCl$ crystal is one which has none of these defects. On the other hand, an ideal solid electrolyte of the type discussed here is characterized by cation disorder. The probability of occupancy within a set of crystallographically equivalent sites is exactly the same for each of the sites in the set, whereas the probabilities of occupancy of sites in crystallographically nonequivalent sets are very likely to be different. On the average, there will always be a large number of empty sites in an ideal solid electrolyte. Electrolytic conductivity in a crystal of $NaCl$ is in a real sense accidental,

Key words: solid electrolyte, silver ion conductor, conductivity, crystal structure.

¹ For discussion purposes, we refer specifically to mobile cation solid electrolytes.

resulting from annihilation and creation of defects that would not be present in an ideal crystal. Electrolytic conductivity in a true solid electrolyte is an inherent property of the crystal resulting from the nature of the crystal structure as described in the preceding paragraph.

There are now two known solid electrolytes in the pyridinium iodide- AgI system. Details on $(C_5H_5NH)-Ag_5I_6$ have been published (4, 5). The other, namely, $(C_5H_5NH)_5Ag_{18}I_{23}$, is the subject of this paper. The particularly interesting feature of $Py_5Ag_{18}I_{23}$ ² is that it is a two-dimensional solid electrolyte. In this respect, it has some relation to the β -aluminas (9), which to date are the only other reported two-dimensional solid electrolytes.

The paper contains two main parts, one concerned with the results of conductivity measurements, the other the crystal structure determination. Finally, we hope to bring out the relation between the structure and the observed conductivity.

Conductivity

Experimental.—The pyridinium iodide was kindly given to us by Dr. B. B. Owens. The silver iodide was Research Organic-Inorganic Chemical Company, Grade A.R., advertised to be 99.9% AgI . All the conductivity measurements were made on pellets of polycrystalline material. The polycrystalline compound was made by weighing appropriate amounts of pyridinium iodide and silver iodide into an agate mortar (total weight, approximately 4g), mixing well, and forming a 3/8 in. pellet of the material by compressing at 50 tsi. The pellet was sealed into a tube filled with argon and the tube placed in an oven at 85°C for 5 days. The tube was opened, the pellet reground and reformed, resealed into a tube filled with argon, and again placed in the oven at 85°C for about 2 days. An x-ray powder photograph of the specimen was taken with $CuK\alpha$ radiation to check for extraneous phase.

The density of the material was determined by measuring the length and diameter of a good pellet and weighing the pellet. Values of 4.23-4.26 g/cm^3 were obtained. Good pellets were obtained with some difficulty. The description of the procedure for making the pellet is long and tedious so we will omit it with the thought that anyone doing this kind of work will have a personal technique (possibly better than ours) for producing a good pellet. It is important, of course, that the density be close to the x-ray density (4.32 g/cm^3

² We use the convention $(C_5H_5NH)^+ \equiv Py^+$.

for this material as will be shown later), that the edges of the pellet be sharp, and that there be no cracks in it.

The equipment (Fig. 1) used to measure the conductivity is somewhat similar to that used by Mrgudich (10) in his measurements of conductivity of AgI. The pellet is mounted between two silver electrodes with mercury amalgamated surfaces. The four high-wattage resistors mounted directly on the aluminum bar supporting the electrode assembly heat the specimen by conduction through the aluminum support sleeve and pyrophyllite electrical insulating sleeve. Temperature is controlled by a variable d-c power supply and measured with the thermocouple inside a small cavity in the end of one of the electrodes.

A one kHz, ± 25 mV square wave signal was applied by means of a potentiostatic circuit³ (8, 11) (Fig. 2) which also provides an output proportional to the current flowing through the load. The potentiostat maintains the load output at the same voltage as that of the input reference signal regardless of the instantaneous load current. The operational amplifier is a Type 307, which can provide peak currents of approximately 15 mA. The two measuring outputs from the potentiostat are connected to the Tektronix 5A19N differential amplifier plugged into a Tektronix Type 5103N oscilloscope. Measurements of current are made alternately with load output across the pellet and with the load output across a precision 10 ohm resistor. Correction (1.03 ohms) was made for the resistance of leads and electrodes. Contact resistance was found to be negligible; measurements made on specimens of different thicknesses resulted in good agreement of $\log \sigma T$ vs. $1/T$ plots.

Results.—A plot of \log specific conductivity multiplied by absolute temperature (σT) vs. reciprocal temperature is given in Fig. 3. At room temperature, the conductivity is 0.008 (ohm-cm)⁻¹, about an order of

³ For application to polarization measurements, the potentiostatic circuit can also produce positive or negative voltage steps of 0.1V with 6 μ sec rise/fall time imposed on a bias of 0.2V. Contact bounce noise is eliminated by using a mercury-wetted relay in the stepping circuit.

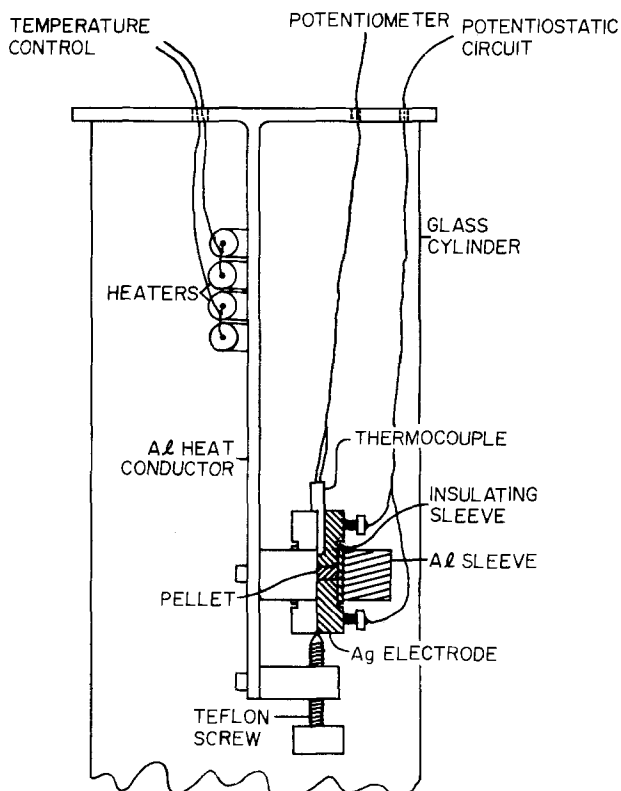


Fig. 1. Heater and electrode assembly for conductivity measurements. Part of the electrode assembly is sectioned to show the arrangement of the sample pellet between the electrodes.

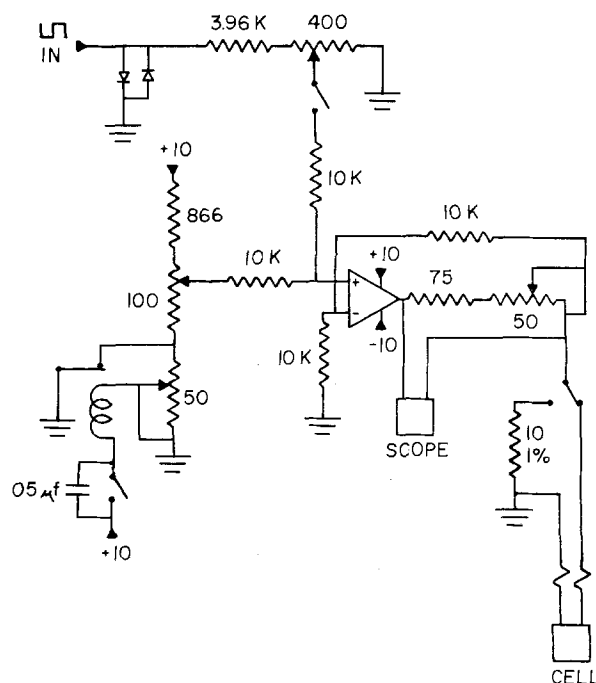


Fig. 2. Potentiostatic circuit

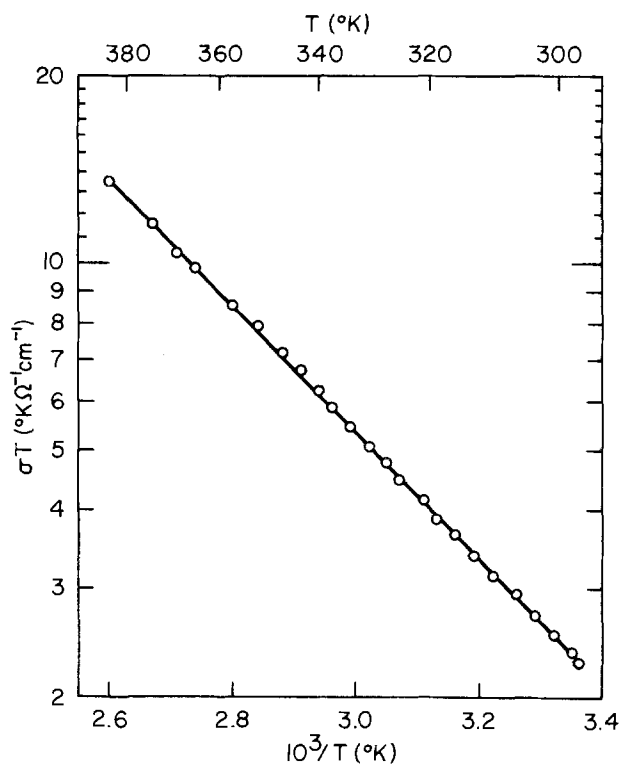


Fig. 3. Specific conductivity multiplied by temperature vs. reciprocal temperature for $Py_5Ag_{18}I_{23}$.

magnitude lower than that, 0.077 (ohm-cm)⁻¹, of $(C_5H_5NH)Ag_5I_6$ (5). The slope of $\log \sigma T$ vs. $1/T$ (Fig. 3) gives an average Ag^+ ion activation enthalpy of motion of 4.6 kcal/mole or 0.21 eV, about the same as for the high temperature ($> 50^\circ C$) region of $(C_5H_5NH)Ag_5I_6$ (5).

Crystal Structure

Experimental.—Crystals of $(C_5H_5NH)_5Ag_{18}I_{23}$ were grown by Espinosa using the gel method [see Ref. (12)]. X-ray photographs taken with a Buerger precession camera show that crystals of $(C_5H_5NH)_5Ag_{18}I_{23}$ have diffraction symmetry 6/mmm. There are no sys-

tematically absent reflections, implying that the crystal structure belongs to one of the following space groups (13): $\overline{P}6m2(D_{3h}^1)$, $\overline{P}62m(D_{3h}^3)$, $P622(D_{6h}^1)$, $P6mm(C_{6v}^1)$, $P6/mmm(D_{6h}^3)$.

A crystal was ground to a sphere of 0.10 mm radius with a sphere grinder (14) similar to that described by Schuyff and Hulscher (15). [Both are modifications of the Bond sphere grinder (16)]. The crystal was aligned along the *c*-axis. Initial lattice constants were determined from the precession camera photographs and refined after mounting on the single-crystal diffractometer. The lattice constants are $a = 13.62 \pm 0.02$, $c = 12.58 \pm 0.02 \text{ \AA}$. The unit cell contains one $(C_5H_5NH)_5Ag_{18}I_{23}$; the formula weight is 5261.002; the cell volume is 2021.0 \AA^3 . These give an x-ray density of 4.32 g/cm^3 . As mentioned above, values of measured density were $4.23\text{--}4.26 \text{ g/cm}^3$ in good agreement with the x-ray value.

The intensity data were collected with a Buerger-Supper diffractometer operated automatically with a Nova 1200 computer. Interface between computer and diffractometer and the programming was carried out in our laboratory by S. L. Langer. $MoK\alpha$ radiation and balanced Zr and Y filters were used. The data collected were those of independent reflections included between $2\theta = 10^\circ$ and 45° . Each reciprocal lattice point was scanned at a rate of $2.5^\circ/\text{min}$ over the range $(1.50 + 0.5 \text{ Lp})$ degrees, where Lp is the Lorentz-polarization-Tunell factor (17). Background counts were taken at the beginning and at the end of the scan interval at $1/6$ the scan time of each scan.

Intensities of data beyond $2\theta = 45^\circ$ were not significant. Within the range $10^\circ \leq 2\theta \leq 45^\circ$, 729 independent reflections were measured; of these, 190 were below the 200 count threshold.

Some of the data processing is done by the Nova computer. The final output on paper tape and the teletype printout consists of the relative squares of the structure amplitudes for both the Zr and Y filters. These results are processed with the CDC 6400 computer to give the net relative squares of the structure amplitudes. The corrections on the intensity data are those for background, absorption, and Lorentz-polarization-Tunell factor.

The linear absorption coefficient, μ , of $(C_5H_5NH)_5Ag_{18}I_{23}$ for $MoK\alpha$ radiation is 140 cm^{-1} ; from which

for $R = 0.10 \text{ mm}$, $\mu R = 1.40$. For the data used, the difference between maximum and minimum absorption correction is 7.9%.

Determination and refinement of the structure.—As indicated in the beginning of this paper, we know that a solid electrolyte must have face-sharing polyhedra formed by the anions. Further, we know that the iodides tend to form icosahedra⁴ with an iodide at the center. At first, we were under the impression that the formula contained one less AgI than it finally turned out to have. This is another case [see Ref. (3)] in which the solution of the crystal structure led to the correct formula.

After consideration of all the probable space groups, a model was devised in space group $\overline{P}62m$ in which 22 iodide ions form a two-dimensional network of face-sharing tetrahedra. Packing considerations require that three of the pyridinium ions lie in cavities in the iodide structure centered at positions $3g$ with $x \approx 0.63$ (13, p. 296). Two rotationally disordered pyridinium ions lie on the $\overline{6}$ axes at $z \approx \pm 0.20$. This arrangement was seen to leave space for an additional iodide ion at $(0, 0, 1/2)$. As a starting point for the refinement the 18 silver ions were assumed to be distributed uniformly over sites near the centers of the 55 iodide tetrahedra of the model structure. (It should be emphasized however, that we knew that finally the distribution would not be uniform.) The pyridinium ions on the $\overline{6}$ axes are required to be rotationally disordered by the site symmetry of positions $2e$ of the space group (Table II). Thus to simplify the calculation, the pyridinium ring was approximated by a regular hexagonal ring of carbon atoms with C—C distance equal to 1.39 \AA [see Ref. (4)]. The "bisecting"⁵ orientation (Fig. 4a) was first assumed by analogy with the structure of $(C_5H_5NH)Ag_5I_6$ (4); again packing considerations make this orientation more probable than the "parallel" orientation or than further rotational disorder. In the "bisecting" orientation, the ring is defined by atoms in position $12l$ at $(x, 2x, z)$, $x \approx 0.059$. The *x*-parameter could not be refined, but it was allowed to vary; it was never significantly different from the starting value. The *z*-parameter was refined.

⁴ This is not the case for $(C_5H_5NH)Ag_5I_6$, however.

⁵ The "bisecting" orientation is the one in which the hexagonal *a* and *b* axes bisect the line joining two carbon atoms.

Fig. 4. a. Top view of iodide ion arrangement in $Py_5Ag_{18}I_{23}$; the pyridinium ions (stippled) on the hexagonal axes are also shown. b. Top view of Ag^+ ion paths in $Py_5Ag_{18}I_{23}$; the equilibrium Ag^+ ion sites (located at or near iodide tetrahedra centers) are shown; \times indicates connection between upper and lower halves of the Ag^+ path network within the conducting layer; see also Fig. 4d. c. Side view of the iodide arrangement in $Py_5Ag_{18}I_{23}$; the pyridinium ions (stippled) in the $\pm 1/2c$ levels of the unit cell are shown; these together with the I^- ions at $\pm(0, 0, 1/2)$ block movement of Ag^+ ions in the *c*-axis direction. d. Side view of the Ag^+ ion paths in $Py_5Ag_{18}I_{23}$.

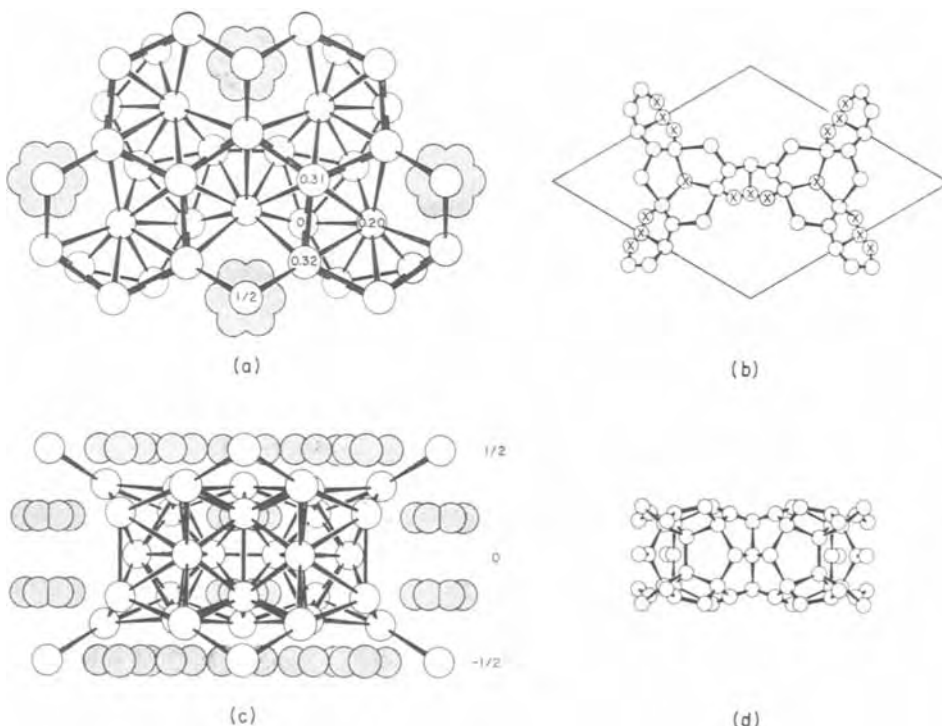


Table I. Final values of I⁻ and Ag⁺ ion parameters^(a)

Ion	Position	Multiplier	x	y	z	10 ⁴ β ₁₁ ^(b)	10 ⁴ β ₂₂	10 ⁴ β ₃₃	10 ⁴ β ₁₂	10 ⁴ β ₁₃	10 ⁴ β ₂₃
I ⁻	1b	1/12	0	0	1/2	92 (5)	= 10 ⁴ β ₁₁	168 (13)	= 10 ⁴ × ½β ₁₁	0	0
I ⁻	4h	1/3	2/3	1/3	0.3132 (4)	76 (2)	= 10 ⁴ β ₁₁	58 (3)	= 10 ⁴ × ½β ₁₁	0	0
I-A	6i	1/2	0.3050 (3)	0	0.3239 (4)	111 (3)	73 (3)	82 (3)	= 10 ⁴ × ½β ₂₂	35 (2)	0
I-B	6i	1/2	0.6349 (3)	0	0.1984 (2)	95 (2)	73 (2)	50 (2)	= 10 ⁴ × ½β ₂₂	-6 (2)	0
I ⁻	6j	1/2	0.4575 (4)	0.1689 (3)	0	105 (4)	84 (3)	60 (2)	50 (3)	0	0
Ag ⁺	3f	0.15 (3)	0.5371 (20)	0	0	215 (30)	244 (98)	62 (13)	= 10 ⁴ × ½β ₂₂	0	0
Ag ⁺	4h	0.15 (1)	2/3	1/3	0.0855 (17)	141 (16)	= 10 ⁴ β ₁₁	144 (23)	= 10 ⁴ × ½β ₁₁	0	0
Ag ⁺	6i	0.09 (3)	0.4311 (38)	0	0.1573 (73)	191 (66)	355 (145)	331 (116)	= 10 ⁴ × ½β ₂₂	7 (50)	0
Ag ⁺	6j	0.15 (3)	0.4715 (28)	0.3854 (71)	0	129 (25)	228 (70)	124 (25)	96 (31)	0	0
Ag ⁺ A	12l	0.42 (2)	0.4460 (9)	0.2067 (10)	0.2237 (9)	138 (11)	124 (11)	115 (9)	37 (7)	-4 (9)	16 (8)
Ag ⁺ B	12l	0.53 (2)	0.5056 (7)	0.1185 (7)	0.2143 (5)	92 (7)	125 (9)	91 (6)	13 (5)	12 (5)	15 (6)
Ag ⁺ C ^(c)	12l	0.01	0.6380	0.1994	0.1321						

^(a) Numbers in parentheses are standard errors and pertain to the last digit in all cases.

^(b) The expression for the thermal factor is $\exp - (h^2\beta_{11} + k^2\beta_{22} + l^2\beta_{33} + 2hk\beta_{12} + 2hl\beta_{13} + 2kl\beta_{23})$.

^(c) Positional parameters for the Ag(I)c site are calculated values for the point equidistant from the four iodides defining the tetrahedron. The multiplier given for this site was determined by difference.

The orientation of the pyridinium ions on the $z = \frac{1}{2}$ plane was indicated by the shape of the cavity (see Fig. 4a) formed by the surrounding iodide ions. The centers of the pyridinium rings are almost directly above and below the iodide ions in positions I(i)B (Table I), and the two mirror planes of the pyridinium ion coincide with the mirror planes of the space group (13, p. 296). The shape of the pyridinium ion (18) is very close to that of the cavity in the proper orientation; thus the nitrogen atoms lie near the iodide atoms in the $z = \frac{1}{2}$ level. For clarity, the pyridinium ions in these cavities have been omitted from Fig. 4a.

Positional parameters for the atoms in the ordered pyridinium ions were derived from the structure of this ion in pyridinium chloride (18). In the calculations these pyridinium ions (excluding hydrogen atoms) were considered to be rigid bodies (19) centered at positions 3g: $(x, 0, \frac{1}{2}; 0, x, \frac{1}{2}; \bar{x}, \bar{x}, \frac{1}{2})$; x converged to the value 0.628, with a standard error of 0.004.

The refinement was carried out by iterative least squares calculations (20).⁶ In the refinement, the Ag⁺ ion multipliers⁷ were varied (for determination of the Ag⁺ ion distribution) as well as all possible positional and anisotropic thermal parameters (with the aforementioned restrictions on the pyridinium ions). It was not possible to vary all parameters at once in the early stages of the calculations because of substantial parameter interaction (21), particularly between Ag⁺ ion multipliers and thermal parameters. In most of the iterations, refinement was facilitated by constraining the total Ag⁺ ion content to 18 per unit cell. In the final cycle, this constraint was removed and all parameters were varied except scale factors and positional and thermal parameters of Ag(I)c. The final value of the Ag(I)c multiplier was 0.05 with limits of error ± 0.06 . This implies that the Ag⁺ ion occupancy of this site is not significantly different from zero. The remaining multipliers for the Ag⁺ ion sites converged to the values shown in Table I. These total 1.49; when

⁶ A version of the basic ORFLS program (20) modified by J. A. Ibers and R. J. Doedens was used.

$$^7 \text{Multiplier} = \frac{\text{number of atoms in particular set of positions}}{\text{number of equipoints in general set of positions}}$$

multiplied by 12, the number of points in general positions, we obtain 17.9 Ag⁺ ions per unit cell. In Table I, we have arbitrarily assigned to Ag(I)c the multiplier 0.01 to bring the total Ag⁺ ion content per unit cell to 18. The achievement of convergence of the iodide and Ag⁺ ion parameters and of the correct Ag⁺ ion content, the latter without constraint, gives additional confidence in the general model proposed for solid electrolytes (see above).

The final value of the discrepancy factor $R = \Sigma |F_o| - |F_c| / \Sigma |F_o|$, where F_o is the observed and F_c the calculated structure amplitude, is 0.065 and the standard deviation of a structure amplitude with unit weight is 1.39. Excluding scale factors, pyridinium ion parameters and parameters of the nearly empty Ag(I)c sites, 68 variable parameters were fitted to the data.

In the least squares calculations, the atomic scattering factors used were those of Cromer and Waber (22); correction was made for the real parts of the anomalous dispersion (23). The observed data were weighted according to the formula

$$\sigma = \frac{1}{\sqrt{w}} = 1 + 0.025 [F_o - 15.0 + |F_o - 15|] + 10 \exp(-F_o/15)$$

A table showing the comparison between the observed and calculated structure amplitudes is available.⁸ Tables I and II list the final values of the structure parameters.

Interionic distances.—Interionic distances and standard errors calculated (24) from the refined coordinates and the final variance-covariance matrix of the least squares calculation are given in Table III. To facilitate the understanding of the structure, the surroundings of each crystallographically independent

⁸ See NAPS document No. 02500 for 6 pages of supplementary material. Order from ASIS/NAPS c/o Microfiche Publications, 440 Park Avenue South, New York, N.Y. 10016. Remit in advance for each NAPS accession number. Make checks payable to Microfiche Publications. Photocopies are \$5.00. Microfiche are \$1.50. Outside of the United States and Canada, postage is \$2.00 for a photocopy or \$0.50 for a fiche.

Table II. Final parameter values for atoms in pyridinium ions

Ion	Atom	Position	x	y	z	β ₁₁	β ₂₂	β ₃₃	β ₁₂ ^(a)
Pyridinium 1 ^(b)	C, N	12l	0.059	0.118	0.176 (7)	0.016	= β ₁₁	0.020	= ½β ₁₁
Pyridinium 2 ^(c)	N	3g	0	-0.275 (4)	½	8.0 ^(d)			
	C1	6k	0.105	-0.270 (4)	½	8.0 ^(d)			
	C2	6k	0.100	-0.376 (4)	½	8.0 ^(d)			
	C3	3g	0	-0.469 (4)	½	8.0 ^(d)			

^(a) For pyridinium 1, β₁₂ = β₂₃ = 0. Also see note (b), Table I.

^(b) Two pyridinium 1 ions are centered at positions 2e on the $\bar{6}$ axes with minimum symmetry 3m.

^(c) Three pyridinium 2 ions are centered at positions 3g on the mirror plane at $z = \frac{1}{2}$ with minimum symmetry mm.

^(d) Isotropic thermal parameter B(Å²).

Numbers in parentheses are standard errors and pertain to the last digit in all cases.

Table III. Interionic distances and standard errors

Atom types and positions (No.)	Distance, Å(σ)	Atom types and positions (No.)	Distance, Å(σ)	Atom types and positions (No.)	Distance, Å(σ)
Nearest I ⁻ neighbors of I(b)		Tetrahedron about Ag(i) site		Tetrahedron about Ag(l)B site, continued	
I(b)-I(i)A	(6) 4.708(4)	Ag-I(i)A	(1) 2.71(8)	-I(j)	(1) 4.720(5)
Nearest I ⁻ neighbors of I(k)		-I(i)B	(1) 2.82(5)	I(i)A-I(i)B	(1) 4.762(6)
I(h)-I(i)A	(3) 4.746(3)	-I(j)	(2) 2.92(6)	-I(j)	(1) 4.630(5)
-I(i)B	(3) 4.574(3)	I(i)A-I(i)B	(1) 4.762(6)	I(i)B-I(j)	(1) 4.788(5)
-I(j)	(3) 4.720(5)	-I(j)	(2) 4.630(5)	Tetrahedron about Ag(l)C	
Nearest I ⁻ neighbors of I(i)A		I(i)B-I(j)	(2) 4.788(5)	Ag-Z(h)	(1) 2.82 ^a
I(i)A-I(b)	(1) 4.708(4)	I(j)-I(j)	(1) 3.984(8)	-I(i)B	(1) 2.82 ^a
-I(h)	(2) 4.746(3)	Tetrahedron about Ag(j) site		-I(j)	(1) 2.82 ^a , (1) 2.82 ^a
-I(i)B	(1) 4.762(6), (2) 4.881(4)	Ag-I(i)B	(2) 2.83(1)	I(h)-I(i)B	(1) 4.574(3)
-I(j)	(2) 4.630(5)	-I(j)	(1) 2.86(8), (1) 2.87(4)	-I(j)	(2) 4.720(5)
Nearest I ⁻ neighbors of I(i)B		I(i)B-I(i)B	(1) 4.993(6)	I(i)B-I(j)	(1) 4.280(4), (1) 4.788(5)
I(i)B-I(h)	(2) 4.754(3)	-I(j)	(2) 4.280(4), (2) 4.788(5)	I(j)-I(j)	(1) 4.500(7)
-I(i)A	(1) 4.762(6), (2) 4.881(4)	I(j)-I(j)	(1) 4.500(7)	Nearest neighbor Ag ⁺ sites	
-I(i)B	(1) 4.993(6)	Tetrahedron about Ag(l)A site		(Jump distances)	
-I(j)	(2) 4.280(4), (2) 4.788(5)	Ag-I(h)	(1) 2.84(1)	Ag(i)-Ag(i)	(2) 2.45(8)
Nearest I ⁻ neighbors of I(j)		-I(i)A	(1) 2.79(1)	-Ag(j)	(2) 1.12(8)
I(j)-I(h)	(2) 4.720(5)	-I(i)B	(1) 2.89(1)	Ag(h)-Ag(h)	(1) 2.15(4)
-I(i)A	(2) 4.630(5)	-I(j)	(1) 2.88(1)	-Ag(l)C	(3) 1.76 ^a
-I(i)B	(2) 4.280(4), (2) 4.788(5)	I(h)-I(i)A	(1) 4.746(3)	Ag(i)-Ag(f)	(1) 2.45(8)
-I(j)	(1) 3.984(8), (2) 4.500(7)	-I(i)B	(1) 4.574(3)	-Ag(l)B	(2) 1.58(4)
Tetrahedron about Ag(f) site		-I(j)	(1) 4.720(5)	Ag(j)-Ag(f)	(1) 1.12(8)
Ag-I(i)B	(2) 2.83(1)	I(i)A-I(i)B	(1) 4.881(4)	-Ag(l)C	(2) 2.18 ^a
-I(j)	(2) 2.99(2)	-I(j)	(1) 4.630(5)	Ag(l)A-Ag(l)B	(1) 1.76(2)
I(i)B-I(i)B	(1) 4.993(6)	I(i)B-I(j)	(1) 4.280(4)	-Ag(l)C	(1) 2.22 ^a
-I(j)	(4) 4.788(5)	Tetrahedron about Ag(l)B site		Ag(l)B-Ag(i)	(1) 1.58(4)
I(j)-I(j)	(1) 3.984(8)	Ag-I(h)	(1) 2.916(8)	-Ag(l)A	(1) 1.76(2)
Tetrahedron about Ag(h) site		-I(i)A	(1) 2.749(8)	-Ag(l)C	(1) 1.88 ^a
Ag-I(h)	(1) 2.86(2)	-I(i)B	(1) 2.93(1)	Ag(l)C-Ag(h)	(1) 1.76 ^a
-I(j)	(3) 2.812(9)	-I(j)	(1) 2.936(7)	-Ag(j)	(1) 2.18 ^a
I(h)-I(j)	(3) 4.720(5)	I(h)-I(i)A	(1) 4.746(3)	-Ag(l)A	(1) 2.22 ^a
I(j)-I(j)	(3) 4.500(7)	-I(i)B	(1) 4.574(3)	-Ag(l)B	(1) 1.88 ^a

^aDistances involving the Ag(l)C site were calculated for the position equidistant from the four iodides defining the tetrahedron.

atom are given, even though considerable repetition occurs.

Following the order given in Table III, the iodide ions have 6, 9, 8, 10, and 11 near neighbor iodide ions and, respectively, 5, 3, 4, 2, and 2 near neighbor pyridinium ions. Thus, considering only the large iodide and pyridinium ions, the coordination numbers of the iodide ions are 11, 12, 12, 12, and 13. The average iodide-iodide distances, in the same order, and their limits of error (3σ) are 4.849 ± 0.012 , 4.682 ± 0.012 , 4.529 ± 0.015 , 4.680 ± 0.012 , and 4.708 ± 0.012 Å. For comparison, the nearest neighbor I-I distance in zinc-blende type AgI (25) is 4.59 Å. Average I⁻-I⁻ distances in the seven crystallographically nonequivalent tetrahedra range from 4.588 to 4.703 Å. One I⁻-I⁻ distance I(j)-I(j) across the vertical mirror plane of the space group is unusually short, 3.984(8) Å. The remaining I⁻-I⁻ distances range from 4.280(4) to 4.993(6) Å.

Average Ag⁺-I⁻ distances in the crystallographically nonequivalent iodide tetrahedra range from 2.82 ± 0.18 to 2.91 ± 0.05 Å. Four of the seven mean Ag⁺-I⁻ distances are significantly longer than the value 2.80 Å in the zinc-blende type AgI; none is shorter. Those with average distance significantly longer are Ag(i)A, Ag(l)B, Ag(h), and Ag(f) which are occupied 42, 53, 45, and 60% of the time, respectively. The three other silver sites have lower occupancies; consequently higher error limits are associated with their Ag⁺-I⁻ distances.

Each pyridinium ion on the \bar{c} axis is surrounded by thirteen iodide ions and one symmetry related pyridinium ion. These pyridinium rings are 4.4(2) Å apart along the c-axis (Fig. 4c). Among the thirteen iodides surrounding a pyridinium is the one at (0, 0, 1/2), which lies 4.07 Å from the center of the pyridinium ring with I-(C, N) distances of 4.30(8) Å. Three I(i)A and three I(i)B iodides form a puckered hexagonal ring about this pyridinium; distances to nearest carbon (nitrogen) atoms are 3.56(4) and 3.843(7) Å, respectively. The remaining six iodide ions surrounding the pyridinium

are I(j) ions lying in the mirror plane at $z = 0$; the nearest I-(C, N) distance is 4.65(4) Å.

The pyridinium ions on the $z = 1/2$ plane are surrounded by 13 iodide ions. I(i)B ions lie directly above and below the centers of the rings. Distances from ring atoms to nearest surrounding iodides are C-I(i)A, 3.8 Å; C-I(b), 3.7 Å; C-I(i)A, 3.6 Å; N-I(b), 3.7 Å.

Description of the structure.—See Fig. 4. Eighteen of the twenty-three iodide ions lie at the vertices of four hemi-icosahedra. These occur in two pairs, each pair sharing a (triangular) face in the basal hexagonal plane. Four of the iodide ions lie in the centers of what would be the complete icosahedra. The basal plane I⁻ ions are in positions 6j, while the remaining vertices of the hemi-icosahedra are occupied by I⁻ ions in two sets, A and B of positions 6i. The ions at centers occupy positions 4h. The twenty-third iodide ion is not involved in the icosahedra or in any way with the passageways for the Ag⁺ ions. In fact, this situation is thus far unique in AgI-based solid electrolytes.

An icosahedron has twenty triangular faces, and the hemi-icosahedron, ten. Thus the I⁻ ions on the three-fold axes, in positions 4h, form ten I⁻ ion tetrahedra in each hemi-icosahedron, for a total of forty iodide tetrahedra. These tetrahedra provide the three sets of 12l and the one set of 4h Ag⁺ ion sites. Fifteen tetrahedra are formed between the hemi-icosahedra providing the 6i, 6j, and 3f sets of Ag⁺ ion sites. Thus there is a total of 55 tetrahedra for 18 Ag⁺ ions per unit cell.

The arrangement of tetrahedra is such that they form a network of passageways (1-6) which extends throughout the crystal essentially parallel to the (001) plane. The Ag⁺ ions can migrate through these passageways in a manner similar to those described in previous papers (1-6). Sequences may be found by examination of Fig. 4 and Table III. Every Ag⁺ ion passageway through the crystal includes at least two of the Ag(l)C positions in each unit cell. Passageways can be found which bypass each of the six other symmetry sets of equilibrium Ag⁺ positions.

As in the cases of other AgI-based solid electrolytes, not all the tetrahedra share all their faces with other tetrahedra. Table III shows that the Ag(l)A tetrahedron shares one face with an Ag(l)B tetrahedron and one with an Ag(l)C tetrahedron; the remaining faces open to pyridinium ions. The Ag(l)B tetrahedron shares faces with only three other tetrahedra: those of Ag(l)A, Ag(l)C, and Ag(i). Ag(i) and Ag(j) tetrahedra each share faces with only three other tetrahedra. Ag(l)C, Ag(h), and Ag(f) tetrahedra share faces with four other tetrahedra.

The equilibrium Ag^+ ion sites near the centers of the iodide tetrahedra are shown in Fig. 4b and d; the lines connecting the sites indicate jumps through the faces of the tetrahedra shown in Fig. 4a and c. Positions indicated by x in Fig. 4b are connections between the upper and lower identical halves (related by the mirror plane at $z = 0$) of the Ag^+ network within the conducting layer. While the multiply-connected nature of the network in directions perpendicular to the c-axis is evident in Fig. 4a and b, the complete absence of connections across the mirror planes at $z = \frac{1}{2}$ is clearly shown in Fig. 4c and d. Layers of formal composition $[(C_5H_5NH)_3I]^{2+}$ are interposed (at $z = \frac{1}{2}$) between conducting slabs; there are no passageways for Ag^+ migration across these layers. Thus Ag^+ ions are confined to passageways within two-dimensional slabs of the structure.

Alternatively, the iodide structure can be regarded as composed of quasi-icosahedra with iodides at eleven vertices centered about the 6j iodides. Atoms of the pyridinium ions on the $\bar{6}$ axes lie near the twelfth vertices of completed icosahedra. Since 6j iodides occupy both center and vertex positions of any icosahedron, successive icosahedra interpenetrate, the center of one being a vertex of the next. These interpenetrating icosahedra form slabs which extend throughout the crystal; all the iodide tetrahedra in the structure lie within these slabs. The icosahedral arrangements and the predominance of tetrahedra in the iodide structure suggest a similarity of the conducting region of this solid electrolyte to alloy structures even if not the full analogy observed for $RbAg_4I_5$ with β -Mn(1). Parts of two quasi-icosahedra are apparent in Fig. 4c on either side of the central mirror plane; twofold axes of these polyhedra are approximately normal to the plane of the figure.

Discussion

We have now presented the details on the results of conductivity measurements and of the crystal structure determination. Both are necessary to a clear understanding of the behavior of this solid electrolyte. Unfortunately the crystals are too small to enable us to make quantitative directional conductivity measurements on them. However, because thus far all halogenide and chalcogenide solid electrolytes adhere to the model propounded (1-6), we can infer from the crystal structure that $(C_5H_5NH)_5Ag_{18}I_{23}$ is a two-dimensional solid electrolyte.

For the hexagonal crystal, we have (26) that the conductivity

$$\sigma = \sigma_1 \sin^2 \theta + \sigma_3 \cos^2 \theta$$

where θ is the angle between the direction in which the conductivity is being measured and the c-axis, σ_1 is the conductivity in the basal plane, and σ_3 is the conductivity along the c-axis. The average of $\sin^2 \theta$ over a hemisphere is $2/3$, from which, because $\sigma_3 = 0$, $\sigma_1 = 1.5 \langle \sigma \rangle$. Thus for $(C_5H_5NH)_5Ag_{18}I_{23}$, $\sigma_1 = 0.012$ (ohm-cm) $^{-1}$ at room temperature.

It is of interest to compare briefly the other solid electrolyte in the PyI-AgI system, namely $(C_5H_5NH)Ag_5I_6$ (4, 5), with the one discussed here. A top view of the crystal structure of $(C_5H_5NH)Ag_5I_6$ at $-30^\circ C$ is shown in Fig. 5. As the temperature increases, Ag^+ ions increasingly move into the tetrahedra which are empty in this figure. $PyAg_5I_6$ has three-dimensional passageways for Ag^+ ion diffusion; details

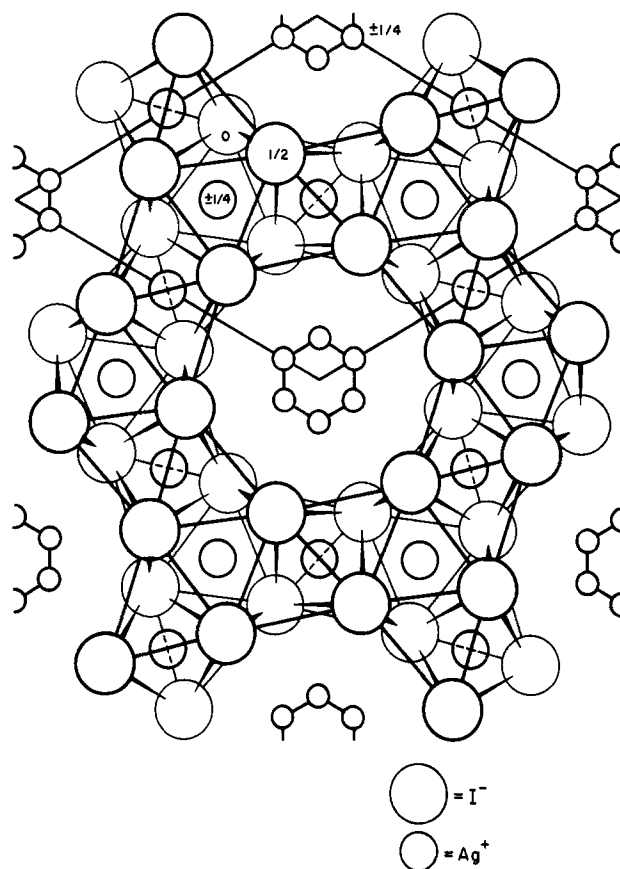


Fig. 5. Top view of the crystal structure in $PyAg_5I_6$ at $-30^\circ C$. As temperature increases, Ag^+ ions increasingly move into the tetrahedra which are empty in this figure [from Ref. (1)].

on these passageways have been given elsewhere (4, 5). At room temperature, the conductivity is 0.077 (ohm-cm) $^{-1}$ (5), almost an order of magnitude higher than that, 0.008 (ohm-cm) $^{-1}$, of $Py_5Ag_{18}I_{23}$. However, at $50^\circ C$, $PyAg_5I_6$ has a transition from a region of low disorder to a region of high disorder, where the average enthalpy of activation of motion, h_m , is 0.21 eV. This is the value found for the average enthalpy of activation of motion of $Py_5Ag_{18}I_{23}$ between room temperature and $100^\circ C$. At $55^\circ C$ the average specific conductivities of $PyAg_5I_6$ and $Py_5Ag_{18}I_{23}$ are 0.29 and 0.015 (ohm-cm) $^{-1}$, respectively. Sodium β -alumina, a material which is also a two-dimensional solid electrolyte, does not attain a high conductivity until relatively high temperature; at $100^\circ C$, for example (27), $\sigma_1 = 0.077$ (ohm-cm) $^{-1}$; for $Py_5Ag_{18}I_{23}$ it is 0.05 (ohm-cm) $^{-1}$.

The two-dimensional solid electrolyte implies lower concentrations of Ag^+ ions and equilibrium sites. In $Py_5Ag_{18}I_{23}$ these are, respectively, 0.89 and 2.72×10^{22} cm $^{-3}$, whereas in $PyAg_5I_6$ they are 1.07 and 3.65×10^{22} cm $^{-3}$. The lower values for $Py_5Ag_{18}I_{23}$ occur simply because the crystals must contain ions or atoms which block the motions of the current carriers in one of the crystal dimensions. The solid electrolyte, $RbAg_4I_5$, which has the highest room temperature conductivity (7, 8), has a ratio of Ag^+ ions to equilibrium sites of $16/56$ or 0.287 , whereas the ratio for $PyAg_5I_6$ (at temperatures $> 50^\circ C$) is $10/34$ or 0.294 and for $Py_5Ag_{18}I_{23}$, $18/55$ or 0.327 .

Another way to look at this is to compare the relative space occupied by the face-sharing polyhedra for the two crystals. Table IV gives the volume of each tetrahedron associated with each crystallographically nonequivalent Ag^+ ion site in $Py_5Ag_{18}I_{23}$. The net volume occupied by all the face-sharing tetrahedra is 638.3 \AA^3 ; this is 31.6% of the total volume of the unit cell and therefore of the crystal.

Table IV. Tetrahedral site occupancy and volume

Site	Number of jumps*	Occupancy, %	Volume tetrahedron, Å ³
Ag(f)	4	60	11.83
Ag(h)	4	45	11.51
Ag(i)	3	18	11.19
Ag(j)	3	30	11.27
Ag(l)A	2	42	11.62
Ag(l)B	3	53	12.23
Ag(l)C	4	1	11.32

* See Table III for jump distances.

In PyAg_5I_6 , the volumes at room temperature are: for the f-type tetrahedron 11.74\AA^3 ; for the m-type tetrahedron 10.70\AA^3 ; and for the octahedron 40.32\AA^3 . The total space occupied by the polyhedra is $(6 \times 11.74 + 24 \times 10.70 + 4 \times 40.32)\text{\AA}^3 = 488.5\text{\AA}^3$. The unit cell volume is 931.2\AA^3 ; thus the face-sharing polyhedra which provide the passageways for Ag^+ ion diffusion occupy 52.5% of the unit cell volume and therefore of the crystal. This may be slightly misleading, because the octahedra have 3.4 and 3.8 times the volumes of f- and m-type tetrahedra, respectively. Perhaps the octahedra are not that much more important than the tetrahedra, although they do form straight channels along the c-axis. However, the tetrahedra alone occupy 35.1% of the unit cell.

The volume of a regular tetrahedron is $0.11785a^3$ where a is the side. A side of 4.59\AA (an I-I distance in zinc-blende type AgI) gives a volume of 11.40\AA^3 . In $\text{Py}_5\text{Ag}_{18}\text{I}_{23}$, the weighted average volume of the tetrahedra is 11.62\AA^3 . In PyAg_5I_6 the average volume of the tetrahedra alone is 10.92\AA^3 . The volume of the m-tetrahedron is very small; even at 125°C it is still only 11.18\AA^3 , accounting perhaps for the low occupancy of these sites even at higher temperatures. For example, at room temperature, 23°C , these sites are only about 5% occupied, and at 125°C , only about 18% (5).

In RbAg_4I_5 (1), there are three different types of tetrahedra: one of multiplicity 8, the other two of multiplicity 24. The volumes are 11.87, 12.41, and 11.52\AA^3 . The total space occupied by the 56 tetrahedra is 669.3\AA^3 which is 47.1% of the volume of the unit cell. $[(\text{CH}_3)_4\text{N}]_2\text{Ag}_{13}\text{I}_{15}$ has eight crystallographically different sets of tetrahedra (3). In this case we will estimate the net volume occupied by the tetrahedra. There is small variation in the total volume if we assume an average volume of between 11.6 and 11.9\AA^3 . The net volume of the tetrahedra in the triply primitive cell will vary from 1427 to 1464\AA^3 . The volume of the triply primitive cell is 3748.1\AA^3 and the space occupied by the face-sharing tetrahedra is estimated to be 38.1-39.1%.

The above indicates that the conductivity is related to the total volume occupied by the diffusion pathways. In Table IV, there is an indication that there is a direct relation between tetrahedron size and occupancy; however, this relation does not hold well for RbAg_4I_5 . Occupation of next nearest neighbor Ag^+ ion sites must also play a role. As to the magnitude of the conductivity, simplicity of the network and the existence of bottlenecks must also be important.

Conclusions

The crystal structure of $(\text{C}_5\text{H}_5\text{NH})_5\text{Ag}_{18}\text{I}_{23}$ shows that it is a two-dimensional solid electrolyte. Such a solid electrolyte is apt to have a substantial amount of crystal space occupied by the ions or atoms which block diffusion. As a result, the conductivity of such materials is inherently low.

Put positively, the results and comparisons given here demonstrate that three-dimensional pathways for

diffusion of the ionic carriers are most favorable for high conductivity solid electrolytes. Simplicity of the network and numerous pathways apparently enhance the conductivity.

Acknowledgment

This work was supported by the National Science Foundation Grant GH37102.

Manuscript received Aug. 19, 1974.

Any discussion of this paper will appear in a Discussion Section to be published in the December 1975 JOURNAL. All discussions for the December 1975 Discussion Section should be submitted by Aug. 1, 1975.

Publication costs of this article were partially assisted by the National Science Foundation.

REFERENCES

1. S. Geller, *Science*, **157**, 310 (1967).
2. H. Wiedersich and S. Geller, in "The Chemistry of Extended Defects in Non-Metallic Solids," L. Eyring and M. O'Keefe, Editors, pp. 629-650, North-Holland Publishing Co., Amsterdam (1970).
3. S. Geller and M. D. Lind, *J. Chem. Phys.*, **52**, 5854 (1970).
4. S. Geller, *Science*, **176**, 1016 (1972).
5. S. Geller and B. B. Owens, *J. Phys. Chem. Solids*, **33**, 1241 (1972).
6. S. Geller, in "Fast Ion Transport in Solids/Solid State Batteries and Devices," W. vanGool, Editor, pp. 607-616, North-Holland/American Elsevier, Amsterdam-London (1973).
7. B. B. Owens and G. R. Argue, *Science*, **157**, 308 (1967); J. N. Bradley and P. D. Greene, *Trans. Faraday Soc.*, **63**, 424 (1967).
8. D. O. Raleigh, *J. Appl. Phys.*, **41**, 1876 (1970).
9. For a review, see J. T. Kummer, in "Progress in Solid State Chemistry," Vol. 7, pp. 141-176 H. Reiss and J. O. McCaldin, Editors, Pergamon Press, Oxford (1972).
10. J. N. Mrgudich, *This Journal*, **107**, 475 (1960).
11. H. V. Malmstedt, C. G. Enke, and E. C. Toren, Jr., "Electronics for Scientists," pp. 369-370, W. A. Benjamin, Inc., New York (1963).
12. H. K. Henisch, "Crystal Growth in Gels," The Pennsylvania State University Press, University Park, Pa. (1970).
13. N. F. M. Henry and K. Lonsdale, Editors, "International Tables for X-ray Crystallography," Vol. I, Kynoch Press, Birmingham (1969).
14. P. B. Crandall, *Rev. Sci. Instr.*, **41**, 1895 (1970).
15. A. Schuyff and J. B. Hulscher, *ibid.*, **36**, 957 (1968).
16. W. L. Bond, *ibid.*, **22**, 344 (1951).
17. J. S. Kasper and K. Lonsdale, Editors, "International Tables for X-ray Crystallography," Vol. II, pp. 266-267, Kynoch Press, Birmingham (1967).
18. C. Rerat, *Acta Cryst.*, **15**, 427 (1962).
19. C. Scheringer, *ibid.*, **16**, 546 (1963).
20. W. R. Busing, K. O. Martin, and H. A. Levy, Oak Ridge National Lab. Report ORNL-TM-305 (1962).
21. S. Geller, *Acta Cryst.*, **14**, 1026 (1961).
22. D. T. Cromer and J. T. Waber, *ibid.*, **18**, 104 (1965).
23. D. T. Cromer, *ibid.*, **18**, 17 (1965).
24. W. R. Busing, K. O. Martin, and H. A. Levy, Oak Ridge National Lab. Report ORNL-TM-306 (1964).
25. R. W. G. Wyckoff, "Crystal Structures," Vol. 1, pp. 110, 186, Interscience Publishers Inc., New York (1963).
26. J. F. Nye, "Physical Properties of Crystals," pp. 25-26, Oxford University Press, New York (1969).
27. A. Imai and M. Harata, Paper 277 presented at Electrochemical Society Meeting, Los Angeles, Calif., May 10-15, 1970; see also, Ref. 9.

Two New Silver Electrolytes of Possible Use in Solid-State Batteries

Bruno Scrosati,* Francesco Papaleo, and Gianfranco Pistoia

Laboratorio di Chimica Fisica ed Elettrochimica, Università di Roma, Rome, Italy

and Mario Lazzari

Centro di Studio sui Processi Elettrodici del C.N.R., Istituto di Elettrochimica, Politecnico di Milano, Milan, Italy

ABSTRACT

Two new silver solid electrolytes, having high ionic conductivity, have been found in the systems $\text{AgI-Ag}_3\text{AsO}_4$ and $\text{AgI-Ag}_3\text{VO}_4$. The most remarkable advantage of these electrolytes is their excellent stability in iodine and moisture. The possibility of using these solid ionic conductors in silver-iodine solid-state batteries has also been investigated.

Recently Takahashi and co-workers (1) reported the discovery of silver solid conductors based on the combination of silver iodide with silver oxyacid salts. In particular they studied the systems $\text{AgI-Ag}_3\text{PO}_4$, $\text{AgI-Ag}_4\text{P}_2\text{O}_7$, and $\text{AgI-Ag}_2\text{WO}_4$ finding intermediate compounds which have the characteristics of high ionic conductivity silver solid electrolytes with average structures. The properties of these electrolytes are summarized in Table I.

The electrolytes are of interest for practical applications since they show a much greater stability in moisture and iodine atmosphere than RbAg_4I_5 , which is the silver ion conductor with the highest conductivity at room temperature and has been so far the electrolyte used the most in the development of solid-state batteries (2, 3). Therefore we considered it important to extend the study examining the systems $\text{AgI-Ag}_3\text{AsO}_4$ and $\text{AgI-Ag}_3\text{VO}_4$. In both the systems, intermediate compounds, at 80 mole per cent (m/o) AgI , having high ionic conductivity, have been ascertained by conductivity and x-ray studies. The electrochemical properties of these two new solid electrolytes and their possible use in solid-state batteries have been investigated and the results are reported in this work.

Experimental

Silver iodide was prepared by precipitation, gradually adding an aqueous solution of KI to a solution of AgNO_3 . The resulting product was washed several times with distilled water and acetone and then dried under nitrogen. Silver arsenate was prepared by precipitation, mixing an aqueous solution of $\text{Na}_2\text{HAsO}_4 \cdot 7\text{H}_2\text{O}$ with a solution of AgNO_3 . The precipitate was washed with distilled water and acetone and dried under nitrogen. The x-ray diffraction patterns of Ag_3AsO_4 so obtained agreed with those reported in the literature.

Silver vanadate was obtained following the procedure of Moser and Brandl (4). An aqueous solution of AgNO_3 was added to a saturated solution of NH_4VO_3 also containing CH_3COONa and concentrated ammonia. After precipitation, the solution was boiled to remove excess of NH_3 . The precipitate was washed with distilled water and acetone and then dried under nitrogen at 110°C for 20 hr. The composition was ascertained by silver chemical analysis using the Volhard method.

All the chemicals used were reagent grade type.

The new phases were obtained by intimately mixing weighed amounts of AgI and Ag_3XO_4 , where X was

* Electrochemical Society Active Member.

Key words: silver iodide-silver arsenate and silver iodide-silver vanadate solid electrolytes, solid-state batteries.

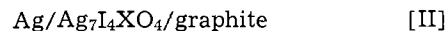
As and V. The mixture was melted under vacuum or dry nitrogen and cooled at room temperature. The resulting products were ground and pressed at 2500 kg/cm^2 into pellets of 1.16 cm^2 surface with an average thickness of 0.15 cm for the electrochemical measurements.

The total conductivity was determined using as electrodes mixtures of silver and electrolyte (1/2 weight ratio), according to a procedure generally adopted in solid electrolyte technology to reduce contact polarizations. The resistance of the resulting cells of the type



was measured with a 1 kHz impedance bridge.

The electronic conductivity was checked with Wagner's method and analysis (5), polarizing the cell



under voltages less than the decomposition potential of the electrolytes with the graphite acting as the blocking electrode.

The silver transport number in both the new solid conductors was obtained by Tubandt's method (6) using a cell composed of separable layers. Also in this case, to reduce contact resistance, electrodes formed by a mixture of silver and the electrolyte were used.

The solid-state batteries were assembled by pressing the electrolyte and a thin layer of the cathode into a single pellet. This pellet was placed in a plastic container, having gold-plated terminals, to which was then added a mixture of silver and the electrolyte (anode), also in form of a pressed pellet. As cathode, the iodine-perylene ($\text{I}_2\text{-P}$, 1/1 mole ratio) charge transfer complex, obtained with a method already described (7), was used.

The polarization and discharge curves were obtained and recorded using standard equipment.

Results and Discussion

Takahashi and co-workers (1) stated that in the system $\text{AgI-Ag}_3\text{AsO}_4$ there are no high conductivity

Table I. Properties of silver solid conductors of the silver iodide-silver oxyacid salt type at 25°C , reported by Takahashi and co-workers (1)

Electrolyte	Color	Total conductivity (ohm-cm^{-1})	Activation energy (kcal/mole)	Silver transport number
$\text{Ag}_7\text{I}_4\text{PO}_4$	Orange	0.019	3.8	0.998 ± 0.005
$\text{Ag}_{10}\text{I}_5\text{P}_2\text{O}_7$	Yellow	0.09	3.3	0.999 ± 0.005
$\text{Ag}_6\text{I}_4\text{WO}_4$	Yellow	0.047	3.6	0.994

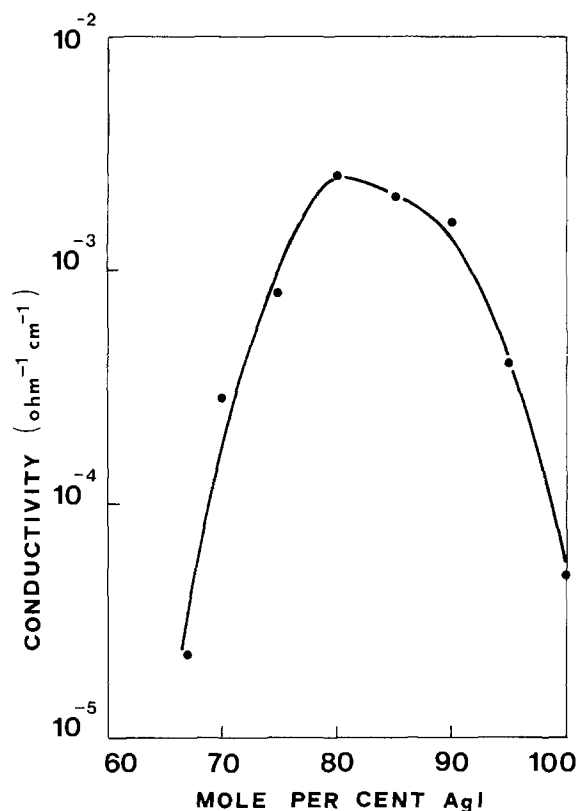


Fig. 1. Composition dependence of the specific conductivity in the system AgI-Ag₃AsO₄ at 25°C.

compounds. No explanation or experimental data however were given to support what has appeared to us an anomalous behavior considering the similarities between the PO₄³⁻ and the AsO₄³⁻ groups. We therefore reexamined the system and found an intermediate compound having high conductivity, as indicated by the maximum, at 80 m/o AgI, in the conductivity-composition plot reported in Fig. 1.

Results of x-ray analysis of this compound, which may be tentatively written as Ag₇I₄AsO₄, confirm the conductivity evidence, since the most intensive lines of AgI and Ag₃AsO₄ are not present in the pattern, as shown in Table II.¹

The Arrhenius plot of Ag₇I₄AsO₄, shown in Fig. 2,

¹Note added in proof: It has to be mentioned, however, that the x-ray spectra are of difficult interpretation since the peaks are very broad. This could indicate a glass-like structure for the electrolytes.

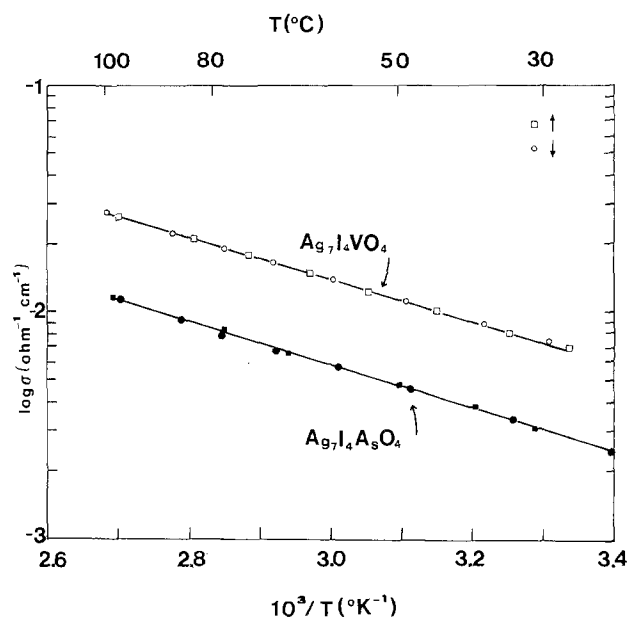


Fig. 2. Temperature dependence of the specific conductivity of Ag₇I₄AsO₄ and of Ag₇I₄VO₄.

is linear in the temperature range from 20° to 100°C. At 25°C the conductivity is 0.004 (ohm cm)⁻¹. From the slope of the plot an activation energy of about 4 kcal/mole is obtained. This value is typical of solid conductors having an "average structure" in which the mobile ions are statistically distributed in a large number of sites in the lattice. To determine the nature of the mobile ions, Tubandt's method was used (6). The results obtained from a series of samples under various conditions and reported in Table III show that the ionic conductivity through Ag₇I₄AsO₄ is solely due to silver ion movements.

The fact that the silver transport number is one is an indication that the electronic contribution of the total conductivity of Ag₇I₄AsO₄ is low. This has been further confirmed by Wagner's analysis (5). The results obtained indicated that the electronic conductivity of the electrolyte is less than 10⁻⁸ (ohm cm)⁻¹ at 25°C.

The decomposition potential of the electrolyte was determined from the current-voltage curve, reported in Fig. 3, of a cell similar to cell [II], with the graphite electrode maintained positive. The results are reported in Table IV, where the properties of Ag₇I₄AsO₄ are summarized.

Table II. Powder x-ray patterns for the systems AgI-Ag₃AsO₄ and AgI-Ag₃VO₄ (only the most intensive lines are reported)

Ag ₃ AsO ₄ *		Ag ₇ I ₄ AsO ₄		Ag ₃ VO ₄		Ag ₇ I ₄ VO ₄		γ-AgI*	
d(Å)	I	d(Å)	I	d(Å)	I	d(Å)	I	d(Å)	I
3.07	3	3.63	8	4.58	4	3.62	5	3.75	10
2.74	10	2.93	5	2.88	10	3.00	5	2.30	6
2.50	5	2.73	10	2.75	10	2.83	5	1.96	3
1.64	3	2.48	6	2.54	6	2.71	8		
		2.38	4			2.58	10		
		2.29	6						

* Data for Ag₃AsO₄ and γ-AgI from ASTM Cards No. 6-0493 and 9-399, respectively.

Table III. Typical silver transport number results in Ag₇I₄XO₄ electrolytes at 25°C

Electrolyte	Current density (mA/cm ²)	Changes in mass (mg)				Ag deposited in coulometer	Silver transport number
		Anode	Electrolyte	Cathode			
Ag ₇ I ₄ AsO ₄	0.05	-3.4	-0.2	+3.1	3.2		
Ag ₇ I ₄ AsO ₄	1.0	-14.2	+0.1	+14.0	14.1		
Ag ₇ I ₄ AsO ₄						1.01 ± 0.03	
Ag ₇ I ₄ VO ₄	0.15	-11.85	-0.4	+11.10	11.46		
Ag ₇ I ₄ VO ₄	0.20	-5.1	+0.2	+4.65	4.83		
Ag ₇ I ₄ VO ₄						1.01 ± 0.03	

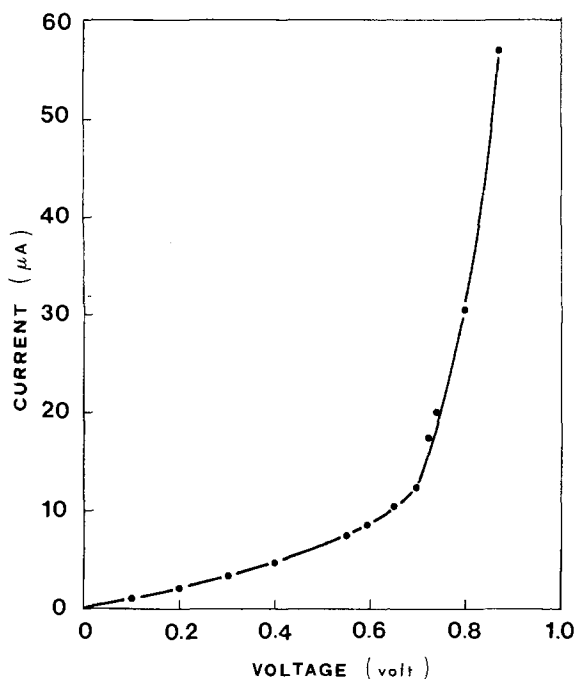


Fig. 3. Decomposition potential of $Ag_7I_4AsO_4$ at $25^\circ C$

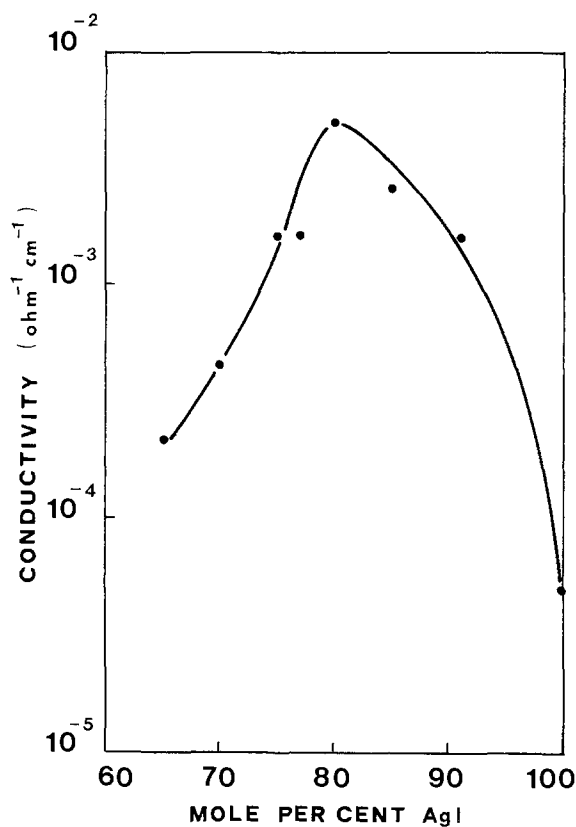


Fig. 4. Composition dependence of the specific conductivity in the system $AgI-Ag_3VO_4$ at $25^\circ C$.

Also in the silver iodide-silver vanadate system there is an intermediate compound with high conductivity, as shown by the maximum of $0.007 (ohm-cm)^{-1}$, at

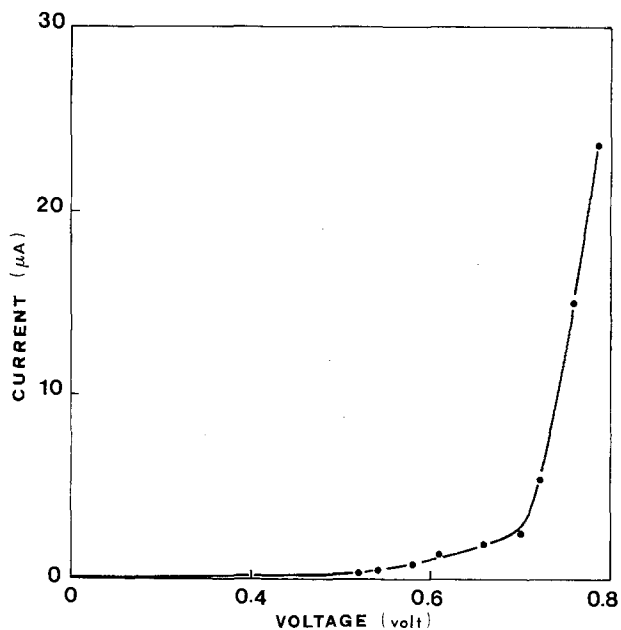


Fig. 5. Decomposition potential of $Ag_7I_4VO_4$ at $25^\circ C$

about 80 m/o AgI , in the conductivity-composition plot reported in Fig. 4. The existence in the $AgI-Ag_3VO_4$ system of a new electrolyte, which may be tentatively written as $Ag_7I_4VO_4$, was also ascertained by x-ray analysis (see Table II).

From the Arrhenius plot of the electrolyte, linear in the temperature range from 20° to $100^\circ C$ (see Fig. 2), an activation energy of about 4 kcal/mole is derived. This value implies that $Ag_7I_4VO_4$ also has an average structure.

The charge carrier in the electrolyte has been determined as being silver ion by Tubandt's method (6). Typical results, reported in Table III, indicate in fact that the silver transport number is one within the experimental error. The ionic character of the conductivity of $Ag_7I_4VO_4$ has been confirmed by the low value of the electronic contribution, $10^{-8} (ohm-cm)^{-1}$ at $25^\circ C$, found by Wagner's analysis (5).

From the current-voltage curve of a cell similar to cell [II], shown in Fig. 5, the decomposition potential of the electrolyte has been determined. Its value is reported in Table IV, where the properties of $Ag_7I_4VO_4$ are summarized.

The conductivity of the two new electrolytes here described is lower than that of the solid conductors listed in Table I, but is high enough to make $Ag_7I_4AsO_4$ and $Ag_7I_4VO_4$ of interest for practical applications. This interest is increased by the great stability shown by the electrolytes in moisture and iodine atmosphere. An example of this excellent behavior is the fact that the resistance of a cell similar to cell [I], maintained in an atmosphere of more than 60% humidity, did not show appreciable changes for several days. Furthermore in Fig. 6 are shown the changes in resistance of cells of the type



The resistance initially increases about 15% and then stabilizes to a constant value. A cell similar to [IV], having $RbAg_4I_5$ as electrolyte, would have shown, for the same period of time, a progressive increase in

Table IV. Properties of $Ag_7I_4XO_4$ silver solid electrolytes at $25^\circ C$

Electrolyte	Color	Density at 2.5 kg/cm ² (g/cm ³)	Total conductivity (ohm-cm) ⁻¹	Electronic conductivity (ohm-cm) ⁻¹	Silver transport number	Decomposition potential (V)
$Ag_7I_4AsO_4$	Red-violet	5.3	0.004	10^{-9}	1.01 ± 0.03	0.68
$Ag_7I_4VO_4$	Orange-brown	5.0	0.007	10^{-8}	1.01 ± 0.03	0.70

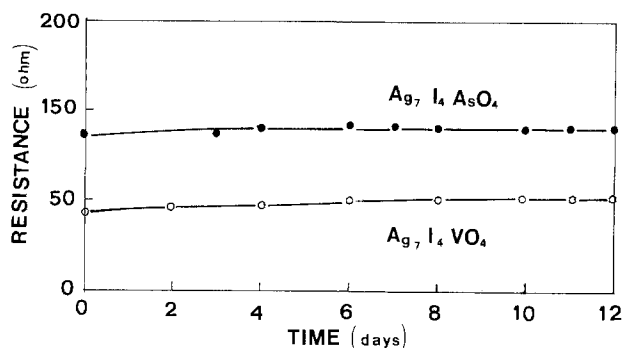


Fig. 6. Changes of resistance of cell [IV] at 25°C

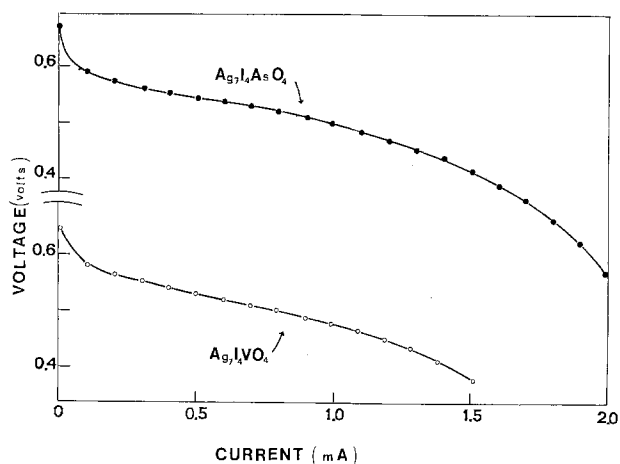
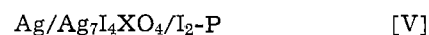


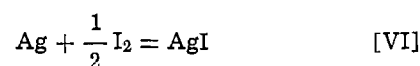
Fig. 7. Polarization curve of cell [V] at 25°C

resistance up to 200% (1). The reason for this difference is probably that in these electrolytes there is not the solubility and diffusion of iodine which was found in RbAg_4I_5 (8). Furthermore the new silver conductors here reported should be, at room temperature, thermodynamically more stable than silver rubidium iodide, which undergoes a water-catalyzed decomposition reaction below 27°C (9). To ascertain this definitely, thermodynamic studies, such as the emf of formation cells and phase diagrams, should be carried out for the $\text{Ag}_7\text{I}_4\text{XO}_4$ electrolytes. These studies are in progress in our laboratory.

The applicability of $\text{Ag}_7\text{I}_4\text{AsO}_4$ and $\text{Ag}_7\text{I}_4\text{VO}_4$ for the development of silver-iodine solid-state batteries has been tested by assembling the cell



which had, both in the case of arsenate and vanadate, an open-circuit voltage (OCV) of 0.67V at 25°C. This value may be compared with the thermodynamic one (0.687V at 25°C) related to the process



considering the reduced iodine activity in the cathode (7).

The polarization curves, shown in Fig. 7, indicate that cell [V] may sustain discharge current densities of the order of 1 mA/cm² without serious polarization. The feasibility of $\text{Ag}_7\text{I}_4\text{AsO}_4$ and $\text{Ag}_7\text{I}_4\text{VO}_4$ in solid-state power sources is finally confirmed by the typical discharge curves of cell [V], reported in Fig. 8 and 9. The structure and the energetic characteristics of these batteries are reported in Table V. The specific energy density is low, as is typical of solid-state power sources (2). It must be kept in mind, however, that batteries [V] have been assembled only as laboratory

Fig. 8. Typical discharge curves of the cell $\text{Ag}/\text{Ag}_7\text{I}_4\text{AsO}_4/\text{I}_2\text{-P}$ at 25°C.

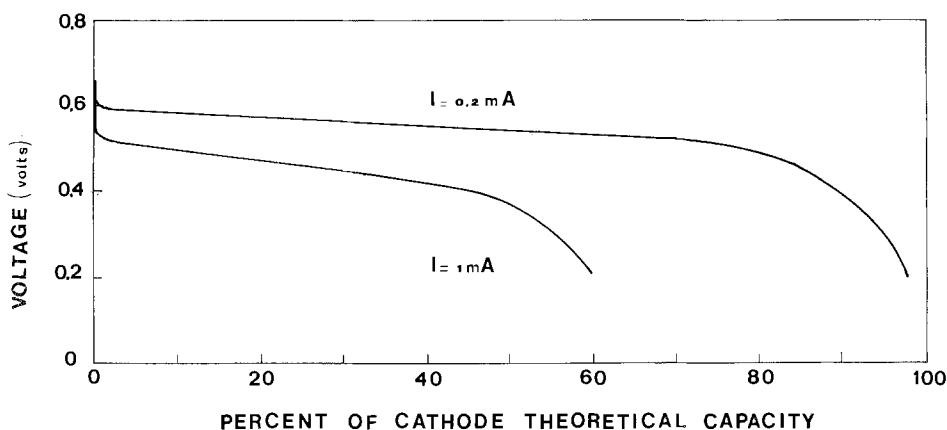


Fig. 9. Typical discharge curves of the cell $\text{Ag}/\text{Ag}_7\text{I}_4\text{VO}_4/\text{I}_2\text{-P}$ at 25°C.

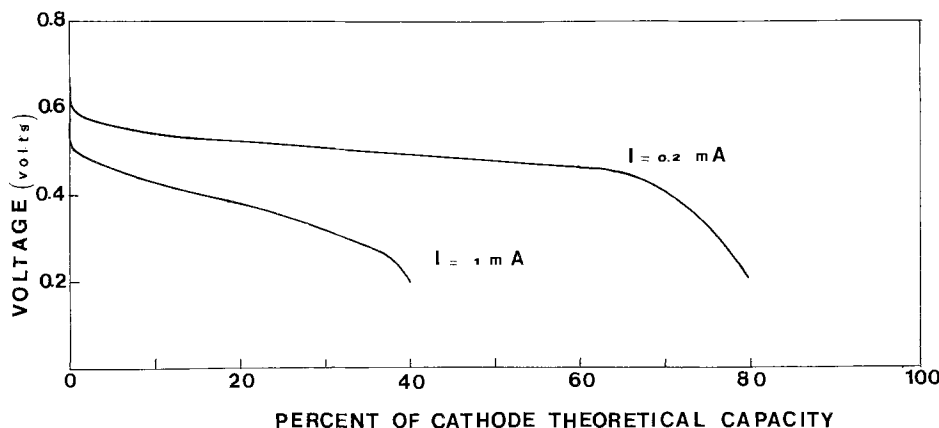


Table V. Dimensions and energetic characteristics of cell [V] at 25°C*

Type of cell	Total thickness (cm)	Anode thickness (cm)	Total weight (g)	Anode weight (g)	Specific energy density (W-hr/kg)	Volumetric energy density (W-hr/cm ³)
Ag/Ag ₇ I ₄ AsO ₄ /I ₂ -P	0.17	0.07	1.2	0.6	~1.1	~6 × 10 ⁻³
Ag/Ag ₇ I ₄ VO ₄ /I ₂ -P	0.12	0.04	0.9	0.3	~1.1	~8 × 10 ⁻³

* The cell surface is 1.16 cm².

prototypes and, therefore, their performances may certainly be improved by optimization of the cell's geometry. This was of course beyond the scope of this work which was carried out primarily to examine the electrochemical properties of the intermediate, highly conductive compounds in the systems AgI-Ag₃AsO₄ and AgI-Ag₃VO₄.

Acknowledgment

This work has been supported by the Consiglio Nazionale delle Ricerche (C.N.R.).

Manuscript submitted Aug. 7, 1974; revised manuscript received Oct. 14, 1974. This was Paper 21 presented at the New York, New York, Meeting of the Society, Oct. 13-17, 1974.

Any discussion of this paper will appear in a Discussion Section to be published in the December 1975 JOURNAL. All discussions for the December 1975 Discussion Section should be submitted by Aug. 1, 1975.

Publication costs of this article were partially assisted by the Consiglio Nazionale delle Ricerche.

REFERENCES

1. T. Takahashi, S. Ikeda, and O. Yamamoto, *This Journal*, **119**, 477 (1972); **120**, 647 (1973).
2. B. B. Owens, "Advances in Electrochemistry and Electrochemical Engineering," P. Delahay and C. W. Tobias, Editors, Vol. 8, Wiley-Interscience, New York (1971).
3. B. Scrosati, *J. Appl. Chem. Biotechnol.*, **21**, 223 (1971).
4. L. Moser and O. Brandl, *Monatsh. Chem.*, **51**, 169 (1929).
5. C. Wagner, *Z. Elektrochem.*, **60**, 4 (1956).
6. C. Tubandt, *Handbuch Exp. Phys.*, **12**, 383 (1932).
7. B. Scrosati, M. Torroni, and A. D. Butherus, "Power Sources 4," D. H. Collins, Editor, p. 453, Oriol Press (1973).
8. R. D. Armstrong, T. Dickinson, H. R. Thirsk, and R. Whitfield, *J. Electroanal. Chem.*, **34**, 47 (1972).
9. L. E. Topol and B. B. Owens, *J. Phys. Chem.*, **72**, 2106 (1968).

Critical Potentials for Stress Corrosion Cracking of 63-37 Brass in Ammoniacal and Tartrate Solutions

H. Uhlig,* K. Gupta,* and W. Liang*

Department of Metallurgy and Materials Science,
Massachusetts Institute of Technology, Cambridge, Massachusetts 02139

ABSTRACT

The critical potentials below which SCC of 63-37 brass does not occur in a cupric ammonium test solution are measured as a function of pH, dissolved Cu concentration, and in the presence of the inhibiting ions: Cl⁻ and Br⁻. They are also measured in presence of various metal ammonium complexes other than the Cu complex and for alkaline tartrate solution. Possible mechanisms are discussed.

Many papers have appeared proposing mechanisms for stress corrosion cracking (SCC) of brass since the time of the first reference (1) in 1906 mentioning the phenomenon itself. To this day, the various proposed viewpoints differ widely, and the search continues. The situation has not been helped by some investigators who occasionally confuse intergranular corrosion, not requiring a tensile stress, with stress corrosion cracking which does. For example, moist sulfur dioxide, SO₂, is sometimes stated as causing SCC of brass, but it probably causes slower intergranular corrosion instead, which, so far as the accumulated evidence shows, operates by a different mechanism. Lynes (2), for example, listed several corrosive media including acid sulfates and chlorides that cause slow intergranular corrosion of brass. but he demonstrated that rapid SCC occurs only in electrolytes containing cupric complexes of ammonia. This

was true whether or not a given solution causes intergranular corrosion in absence of stress.

Pickering and Byrne (3) recently described the appearance of cracks in dynamically strained 70-30 brass in acid sodium sulfate solution anodically polarized to 0.24V (SHE) which they reported to be an instance of SCC. There was no cracking at constant applied load. Although having the outward appearance of SCC, it is suspected that their observation instead is still another example of intergranular corrosion accelerated by anodic polarization and made visible by the widening of surface grain boundaries during plastic deformation of the metal. It would seem to be a reasonable conclusion that whenever a corrosive medium induces intergranular corrosion in absence of stress (e.g., brass in acid salts) the appearance of surface cracks in dynamic strain tests should not be taken as unequivocal evidence of stress corrosion cracking.

The apparent intergranular stress corrosion cracking of pure Cu in 15N aqueous NH₃ + 2.5 g/liter of

* Electrochemical Society Active Member.

Key words: brass, ammoniacal solutions, tartrate solutions, inhibitors, stress-sorption cracking.

Cu reported by Pugh *et al.* (4) was repeated and interpreted as intergranular corrosion not requiring stress by Uhlig and Duquette (5). The reported SCC of 99.9% Cu wires, 0.254 mm diameter, stressed beyond the elastic limit in 0.05N cupric acetate by Escalante and Kruger (6) may have still another interpretation. Either the observed oxide cracking was an instance of SCC, as was reported, or it represented alternatively a weakening of the highly stressed thin cross section of metal by its gradual conversion into Cu_2O which then failed mechanically. A reported longer failure time of their 99.999% Cu specimens when thicker (although still thin) in cross section (0.71 mm), suggests that mechanical failure probably describes the situation. This interpretation is also supported by the well-established fact that heavy sections of Cu sheet as used in practice may oxidize but are not observed to undergo SCC when exposed to acetate solutions.

The various theories proposed to explain SCC of α -brass include: (i) electrochemical dissolution of alloy along "active paths" at the base of a notch or crack (7-9); (ii) progressive fracture of an oxide or other type reaction product film covering the alloy surface (9-13); or (iii) reduction of metal bond strength by an adsorbate (14, 15), called by one of us "stress-sorption cracking" (16). Some authors have placed emphasis on metallurgical factors such as dislocation arrays as being responsible for crack-sensitive paths (8, 17), whereas others have emphasized that factors of the environment such as pH or applied potential determine whether the observed fracture path is intergranular or transgranular (15, 18). Over and above such detail, it is important to recognize, as Lynes emphasized, that the usual stress corrosion cracking of brass, if it is to occur at all, requires a specific environment, limited, by and large, to ammonia and the amines, or in some instances to nitrogen oxides and nitric acid vapors which convert by reaction with the brass surface to corresponding ammonium compounds (19). Johnson and Leja (14) showed in addition that bona fide intergranular stress corrosion cracking can occur in alkaline citrates and tartrates, which, like ammonia, form copper complexes. Otherwise, the commonly encountered electrolytes, no matter how corrosive, are not likely to cause stress corrosion cracking.

As in the case of austenitic and ferritic stainless steels (20-22), of mild steel (23), and of high strength low alloy steels (24), there exists a critical potential below which SCC of brass does not occur in an otherwise damaging environment. The significance of such a potential to the previously proposed mechanisms of SCC for brass needs evaluation. Critical potentials are presently measured and interpreted for a variety of ammoniacal solutions and also for a tartrate solution; in addition, attention is directed to the question of whether Cu in solution is required for SCC, or whether other ammonium complex ions can be equally damaging.

Experimental

Material for test specimens consisted of cold-rolled (20% reduction) commercial 63-37 brass supplied by courtesy of Bridgeport Brass Company. The analysis is: 62.65% Cu, 0.01% Sn, 0.012% Pb, 0.023% Fe, 0.01% Cd, balance Zn. The sheet 0.041 in. (0.104 cm) thick was sheared to specimens measuring $1\frac{3}{4} \times 3/16$ in. (4.5×0.5 cm). After smoothing the edges with 600 grade emery paper, the specimens were degreased in boiling benzene, then pickled in 45 volume per cent (v/o) HNO_3 for 30 sec at room temperature. They were bent beyond the elastic limit into the form of a C having a final span of $1\frac{7}{16}$ in. (3.7 cm) and held to this dimension between insulating holders of the zirconium test apparatus at constant flow stress as maintained by remote spring loading. Failure times were recorded by an electric clock. The test apparatus was similar to that described earlier for measuring stress

corrosion cracking of stainless steels (21) and hydrogen cracking of ferritic alloys (25).

The test solutions were made up of stock solutions of CuSO_4 and $(\text{NH}_4)_2\text{SO}_4$ mixed just prior to the test. The composition conformed approximately to that recommended earlier by Mattsson (18), and by Johnson and Leja (14) for producing minimum failure times; it consisted of 0.05M CuSO_4 and 1.0M $(\text{NH}_4)_2\text{SO}_4$ of pH 6.5 adjusted using NH_4OH . Solutions at room temperature were usually stirred mildly by bubbling air through them.

Controlled potential runs made use of a Wenking potentiostat connected to a saturated calomel reference electrode via a salt bridge to the test solution. The salt-bridge capillary was located near the maximum bend of the test specimen. The electrical connection to the specimen was made by a Teflon coated copper wire fastened to the specimen through a hole drilled at one end. Two platinum electrodes located on either side of the test specimen served as auxiliary electrodes. In general, the critical potential below which failure by SCC did not occur for at least 50-100 hr was reproducible to within 5 mV. The corrosion potential measured by simple immersion of the stressed or unstressed specimen (no difference) was usually recorded at the time of failure.

Results

The effect of pH on times to failure is shown in Fig. 1. A minimum in the region of pH 6.5 confirms previous data reported by Johnson and Leja (14).

The effect of applied potential on failure times at pH 6.5 is shown in Fig. 2. The critical potential below which failure does not occur within at least 50 hr is 0.095V SHE or -0.147 V SCE. This value is consistent with limited and more approximate values reported by Sircar *et al.* (15) and by Lahiri *et al.* (26). It also approximates the value reported for 70-30 brass in 15N aqueous NH_3 by Pugh and Green (27).

Minimum time to failure is observed at 0.27V SHE. At more noble potentials, time to failure again increases, reaching >50 hr at about 0.31V. At the latter potential an appreciable anodic current density causes uncertainty in the potential measurements because of high alloy dissolution rates and consequent thinning of the specimens, contrary to the situation at 0.095V where dissolution of the specimen is suppressed by the accompanying cathodic current.

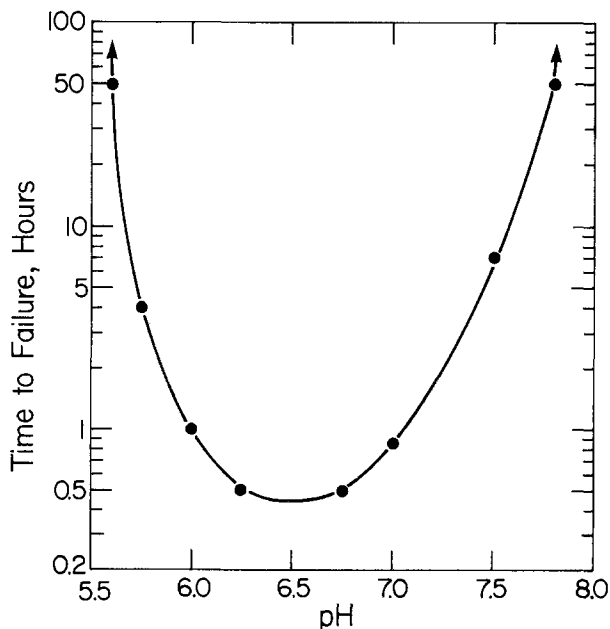


Fig. 1. Effect of pH of 0.05M CuSO_4 , 1M $(\text{NH}_4)_2\text{SO}_4$ on time to failure of 63-37 brass at room temperature.

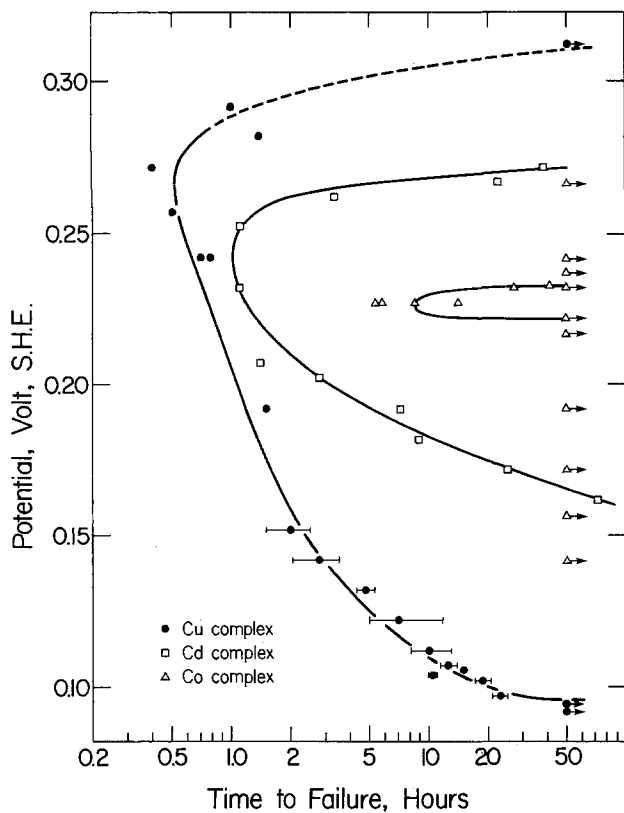


Fig. 2. Effect of applied potential on time to failure in 0.05M CuSO_4 , CdSO_4 , or CoSO_4 , 1M $(\text{NH}_4)_2\text{SO}_4$, pH 6.5 at room temperature.

At moderately higher pH values, the corresponding critical potentials as well as the corrosion potentials are shifted to less noble values, as shown in Fig. 3. As shown later, and also by previous measurements for the stainless (20-22) and carbon (23, 24) steels, should the corrosion potential become active to the corresponding critical potential, failure is not observed. According to Fig. 3, this situation is projected to a pH of about 8 and is supported by corresponding long times to failure at pH 7.8, as shown in Fig. 1. At pH values below 6.0, it is likely that the corrosion potentials fall outside the potentials for minimum failure time. This could not be checked because measurements

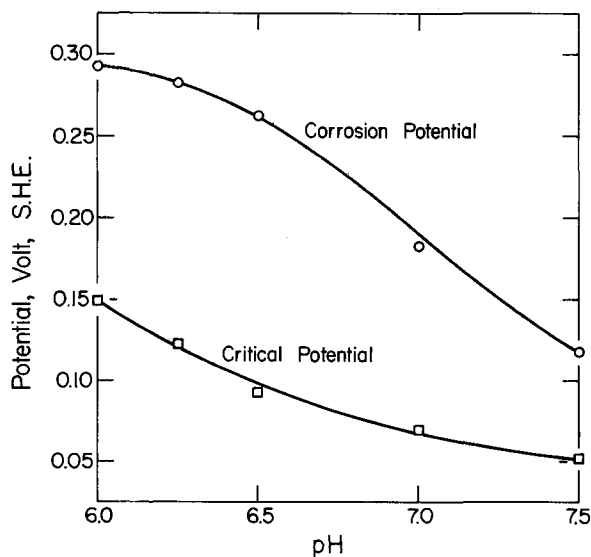


Fig. 3. Effect of pH of 0.05M CuSO_4 , 1M $(\text{NH}_4)_2\text{SO}_4$ on critical potential and corrosion potential at room temperature.

of critical potentials in the acid range are obscured by a high uniform anodic dissolution rate of the alloy, and hence are not reported.

The effect of annealing the present cold-rolled brass (20% reduction) at 300°C for 1 hr is to shift the critical potential in the noble direction by about 18 mV without much change in the short times to failure. However, severe cold-rolling (20-93% reduction) is reported by Edmunds (28) to appreciably increase the resistance of 70-30 brass to failure when stressed either parallel or perpendicular to the rolling direction. Robertson *et al* (29) reported a similar beneficial effect on SCC resulting from cold-working a 1.9% Ni, 0.6% Si-Cu alloy tested in ammonia. The effect of severe cold-rolling on the critical potential could not be checked using the present thin gauge material; these measurements remain to be done.

The effect of higher temperatures is to decrease times to failure in accord with an approximate Arrhenius relationship (Fig. 4). The apparent average activation energy is 10 kcal/mole corresponding more likely to a chemical rather than to a diffusion limiting process in the solution. This value agrees with that of 9.9 kcal/mole reported by Pugh *et al.* (30) for 70-30 brass in a so-called tarnishing solution consisting of 8 g/liter Cu in 15N aqueous NH_3 . Johnson and Leja (14) reported for 69.5% Cu-30.5% Zn brass in 0.04M Cu, 1.5M total NH_3 , pH 6.8 solution, a variable activation energy ranging from 4 to 11.5 kcal/mole.

The times to failure in 1M $(\text{NH}_4)_2\text{SO}_4$, pH 6.5 as a function of dissolved Cu are shown in Fig. 5. The effect of decreasing Cu concentration is to shift the critical potential in the noble direction and the corrosion potential in the active direction (Fig. 6). The extrapolated values show an intersection at 0.003M CuSO_4 indicating that, at this concentration and below, spontaneous cracking of brass in simple immersion tests is not expected nor is it observed. Decreasing copper concentration increases failure times, in accord with data previously reported by Althof (31) and by many subsequent investigators. The reason for the dependence on dissolved Cu concentration is now made clear in terms of converging critical and corrosion potentials.

Addition to the ammonium sulfate test solution of various cations which form ammonium complexes and variation of the Cu concentration but keeping total metal concentration at 0.05M, has no appreciable ef-

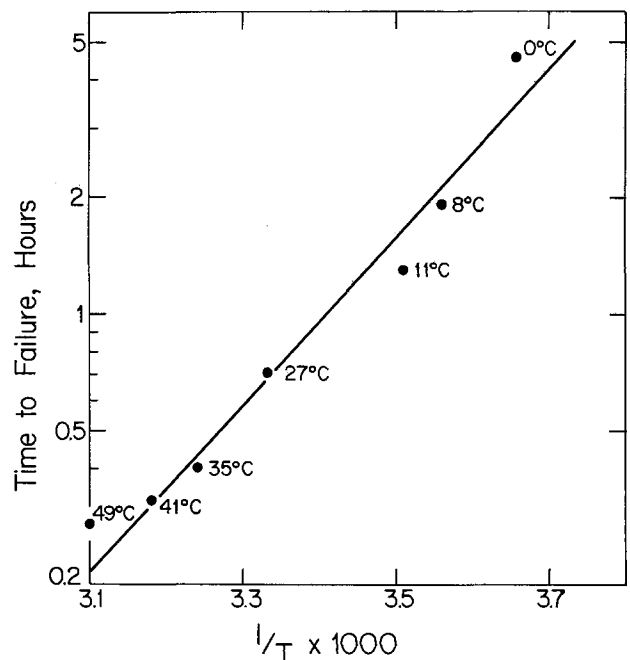


Fig. 4. Effect of temperature on time to failure in 0.05M CuSO_4 , 1M $(\text{NH}_4)_2\text{SO}_4$, pH 6.5.

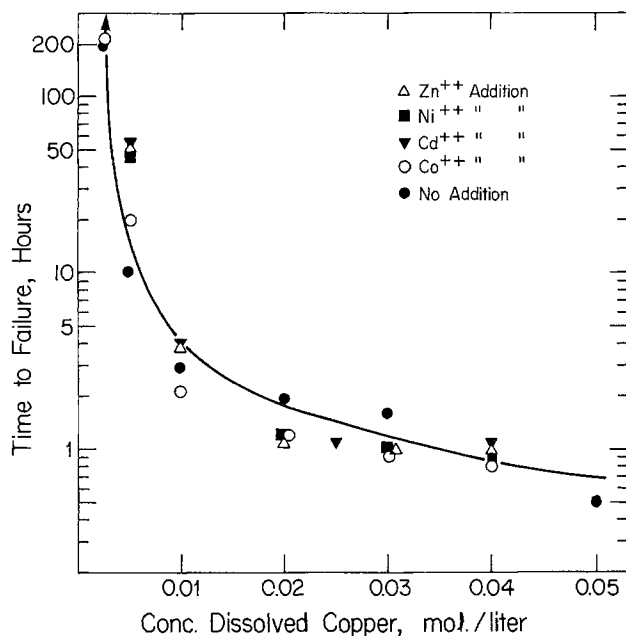


Fig. 5. Effect of dissolved copper in presence of other metal sulfates on time to failure in 1M $(\text{NH}_4)_2\text{SO}_4$, pH 6.5 at room temperature. Total metal concentration is maintained at 0.05M, except for the solutions containing Cu only.

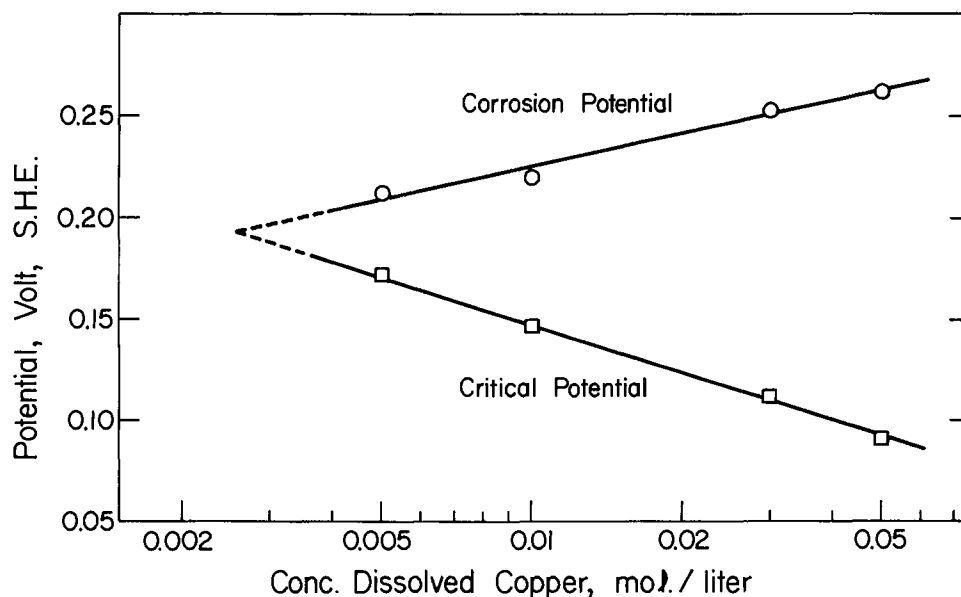
fect on times to failure (Fig. 5). Furthermore, 0.05M of any such extraneous cation in absence of dissolved Cu does not spontaneously induce SCC. Extraneous cations, however, are able to induce failure under conditions of anodic polarization with or without occasional renewal of the test solution in order to avoid accumulation of Cu salts. The data supposedly show, as Pugh and Green (27) concluded earlier from results obtained in a copper-free ammoniacal test solution, that SCC of brass occurs in absence of dissolved Cu provided that the prevailing potential is favorable. However, the noble values of the favorable potentials, accompanied by continuous anodic dissolution of the brass, makes it impossible to avoid accumulation of dissolved Cu at the specimen surface. This is also true of measurements made in the present non-Cu ammonium complex solutions, hence dissolved Cu in some amount is present in all instances at the time of fail-

ure. Whether dissolved Cu is or is not necessary to failure, the apparent critical potentials in the initially Cu-free solutions, in absence of other factors, should all be approximately the same, but, in fact, they are not. It appears, therefore, that failures can occur independent of an initially dissolved Cu concentration, but not independent of whatever heavy metal ammonium complex is present. It is found, for example, that the critical potentials for 0.05M Zn^{++} or Cd^{++} in 1M $(\text{NH}_4)_2\text{SO}_4$, pH 6.5 solutions are both about 0.16V SHE, but for 0.05M Co^{++} it is 0.22V SHE. The corresponding critical potential for 0.05M Ni^{++} , for which the $(\text{NH}_4)_2\text{SO}_4$ concentration was reduced to 0.5M in order to avoid precipitation of Ni salts, is 0.14V. Data for the Cd^{++} and Co^{++} test solutions are included in Fig. 2. For Co^{++} test solution, the damaging potential region is so narrow that it is easily missed experimentally. Anodic protection (>50 hr) occurs only 10 mV above the critical potential at and below which cathodic protection is observed. For Cd^{++} test solution, a similar spread of potential between cathodic and anodic protection is equal to 110 mV and for the Cu^{++} test solution it is still greater and equal to 215 mV.

It was found that some anions, e.g., Cl^- and Br^- , added to the usual test solution inhibit the cracking process. Acetate, NO_3^- , and ClO_4^- ions, on the other hand, have less or no inhibiting effect, as shown in Fig. 7. The effect of Cl^- and Br^- is to shift the critical potential in the noble direction, and the corrosion potential in the active direction. The approximate concentration observed at the merger of the two potentials corresponds to the optimum minimum concentration of halide ion imparting inhibition (Fig. 8). The optimum minimum concentration for NaCl is 0.04M and for NaBr it is only 0.005M.

It was also of interest to determine whether SO_4^{--} is an inhibitor in view of the report by McKinney and Hermance (32) describing failure of Ni-brass telephone exchange components by SCC in the Los Angeles atmosphere known to be high in nitrogen oxides and nitrates, but not in New York City where the higher sulfate content of the atmosphere presumably inhibits similar failures. The failure time of brass in 0.05M $\text{Cu}(\text{NO}_3)_2$, 2M NH_4NO_3 , pH 6.5 was 0.85 hr, and with added 1M Na_2SO_4 , it was 0.70 hr, showing no inhibition. It is possible, therefore, that SO_4^{--} actually inhibits the reduction of NO_3^- to NH_4^+ by the corrosion reactions occurring on a brass surface, the presence of NH_4^+ being necessary to SCC. This possibility deserves investigation.

Fig. 6. Effect of CuSO_4 concentration in 1M $(\text{NH}_4)_2\text{SO}_4$, pH 6.5 on critical and corrosion potentials.



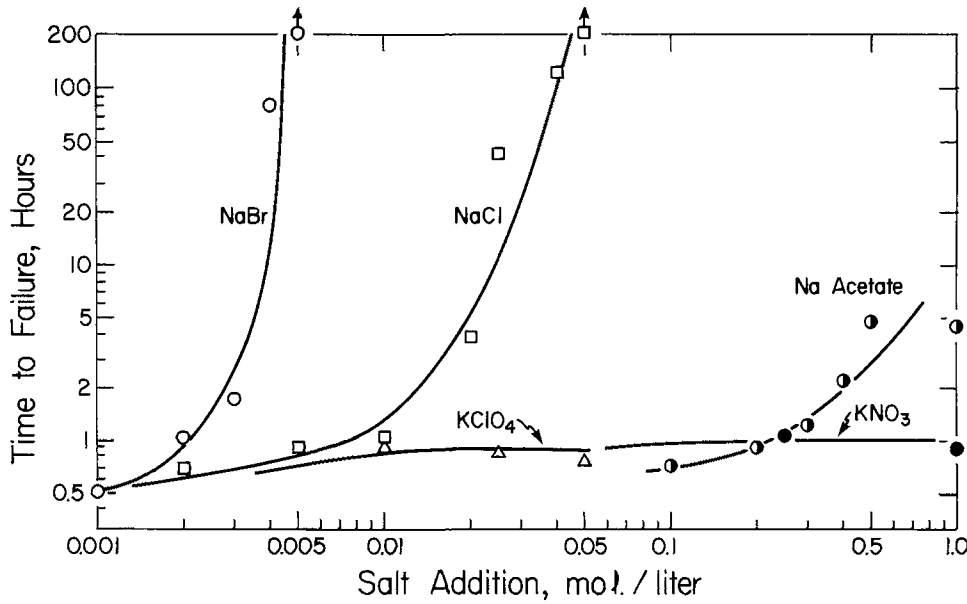


Fig. 7. Effect of various anions on time to failure in 0.05M CuSO_4 , 1M $(\text{NH}_4)_2\text{SO}_4$, pH 6.5 at room temperature.

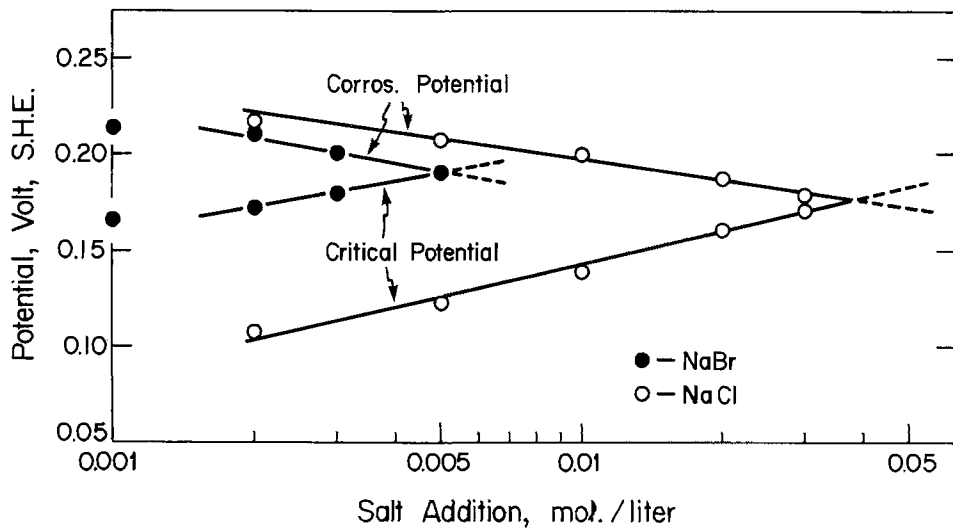


Fig. 8. Effect of NaCl and NaBr additions to 0.05M CuSO_4 , 1M $(\text{NH}_4)_2\text{SO}_4$, pH 6.5 on critical and corrosion potentials at room temperature.

Finally, data of Fig. 9 show that brass in alkaline tartrates also exhibits a critical potential for SCC, the value being considerably more active than that in am-

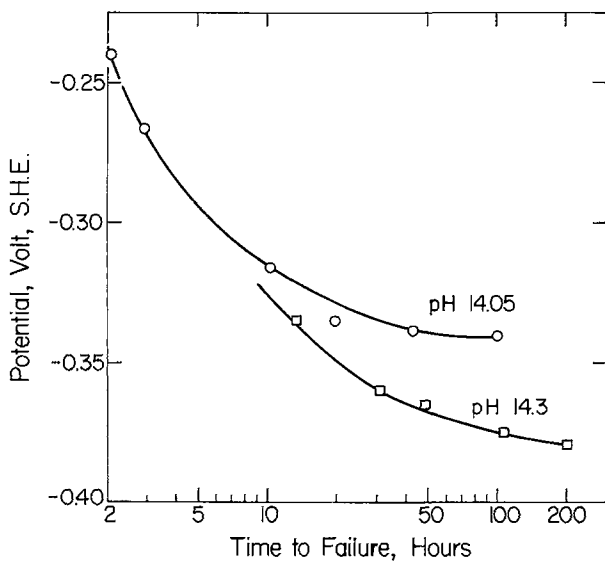


Fig. 9. Effect of applied potential on time to failure in 0.04M CuSO_4 , 0.5M potassium tartrate at two pH values.

moniacal solutions. Hence cathodic protection is also possible in tartrate solutions. The values of pH were measured using the glass electrode and hence are only approximate. The alkaline error was reduced, but not eliminated, using potassium instead of sodium tartrates and hydroxides. Qualitatively, an increase in alkalinity of the tartrate solution shifts the critical potential in the active direction.

Discussion

It is quite clear that similar to the situation for stainless steels, high strength steels, and mild steels, brass resists spontaneous stress corrosion cracking if the corrosion potential is active to the critical potential. The prevailing potential, alternatively, can be noble to the potential region above which the time to failure again increases (anodic protection). Rapid anodic dissolution of brass may occur simultaneously in the noble region, particularly in the presence of appreciable dissolved Cu.

The critical potential is affected by cold-work of the brass, and by pH, dissolved Cu concentration, and by presence of inhibiting anions. Analogous to other metal systems, it is probably also affected by temperature. Brass undergoing SCC in alkaline tartrate solutions similarly exhibits a critical potential below which failure does not occur within at least 200 hr and probably for much longer times.

The present evidence indicates that dissolved Cu^{++} or some other heavy metal ammonium complex in

some amount is required for the observed failures. This conclusion is supported by the small amount of dissolved Cu^{++} (0.003M, Fig. 5) needed for spontaneous failure, and the continuing dissolution of brass at potentials required for failure in non-Cu complex test solutions, all of which are noble to the corrosion potentials. It is also supported by differing critical potentials for failure depending on whether the available ammonium complex contains Cu^{++} , Cd^{++} , Zn^{++} , Ni^{++} , or Co^{++} . Failures are observed in each solution only if the corrosion potential or applied potential is noble to the critical value. It appears that the Cu^{++} complex is the most damaging of the various heavy metal complexes in view of its least noble critical potential, and the ineffectiveness of other complexes in presence of the Cu^{++} complex to change the time to failure (Fig. 5). Necessity for the presence of NH_4^+ has been demonstrated by early investigators and most recently by Lynes (2) and by Sircar *et al.* (15). The two notable exceptions are Cu complex-forming alkaline tartrates and citrates (14).

The effect of increasing pH above 6.5 is to shift corrosion and critical potentials resulting in an increase of times to failure. At a pH of 6.5 the prevailing corrosion potential coincides with the potential corresponding to minimum failure time (Fig. 2 and 3).

The halide ions Cl^- and Br^- added to the test solution are more effective inhibitors than perchlorates, acetates, sulfates, and nitrates probably because the halide ions or their complexed species more readily adsorb on the metal surface. The marked inhibiting action of small amounts of halide ion is to shift the critical potential in the noble direction and the corrosion potential in the active direction. The latter shift is in accord with a decreased activity of Cu^{++} caused, directly or indirectly, by ionic complexing involving Cl^- or Br^- . Regarding the critical potential, it should be noted that the effect of the inhibiting anions for SCC of mild steel and 18-8 stainless steel is similarly to shift the critical potentials of these metals in the noble direction (20, 23). The explanation for the consistent behavior of inhibitors in this respect is important to any relevant proposed mechanism of SCC. Hoar and Booker (7) earlier found an inhibiting effect of Cl^- on SCC of brass but did not offer an explanation other than to suggest that the surface oxide in its presence was seemingly less compact.

It is difficult to explain the observed critical potentials and the effect of inhibiting anions on the basis of an oxide film fracture model. For example, when the visible oxide film was pickled off presently stressed brass specimens in 6N HCl at room temperature for 1 min after exposure for either 0.5, 1.0, 2.4, 3.5, or 5 hr to the usual composition Cu^{++} test solution of pH 7.5 (average time to failure is 7 hr), then washed and re-exposed to the same test solution without removal from the test apparatus, there was no major change of failure time. The average total time gradually increased from 7.0 hr for unpickled specimens to 9.1 hr for pickled specimens previously exposed to the test solution for 5 hr. Any fracture of a thick oxide film is obviously unimportant to the mechanism. Supposed fracture of a thin oxide film is also not plausible in light of absence of SCC just below the critical potential of 0.095V SHE, and its occurrence slightly above this potential. The latter value of potential has no obvious relation to the formation or reduction of Cu_2O by the Pourbaix diagram for Cu (33). Moreover, the potential-pH diagram for Cu as modified by Mattsson (18) and by Hoar and Booker (7) does not account for the effect of increasing dissolved Cu concentration and of increasing pH on observed shift of the critical potential in the active direction. If the estimated thermodynamic activity or other properties of alloyed Zn are invoked to move the equilibrium boundaries in the required direction, any such explanation is obviously not relevant to an explanation of the

susceptibility of Cu alloys not containing Zn, *e.g.*, those containing Si, Ni, Sb, As, Al, or P (34).

The relevance of the critical potential to incidence or absence of SCC also casts doubt on any "active path" or metal dissolution model. Uniform corrosion of brass continues just above or below the critical potential, as data of Pugh and Green show (27). If the critical potential is equated to a specific minimum corrosion rate at and above which cracks initiate and grow, it becomes difficult to explain why this supposed rate should be decreased and the critical potential increased by the presence of a small amount, 0.04M, of chloride or by only 0.005M bromide. Both halide ions form soluble Cu-Zn corrosion products and do not inhibit uniform corrosion of Cu or Zn. Furthermore, it is not plausible to interpret the reduced susceptibility of severely cold-worked brass in terms of a reduced corrosion rate brought about by cold-work.

As in the proposed explanations for SCC of stainless steels, high strength steels, and mild steels, adsorption of the environment on appropriate surface defect sites accompanied by reduction of metal bond strength comes closest to explaining the available facts. This model and the evidence for its support have been discussed in detail in previous publications (35, 36). Johnson and Leja (14) and Sircar *et al.* (15) also favored an adsorption mechanism. It is assumed, accordingly, that surface adsorption on stressed brass of a damaging ammonium complex containing Cu^{++} or another heavy metal ion occurs in sufficient amount above the critical potential, and its corresponding desorption occurs below. Desorption may again take place at still more noble potentials, as is dramatized by the SCC behavior of brass in the Co^{++} test solution. Potentials at which relevant adsorption or desorption takes place understandably varies with the type of ammonium complex. The metal bond breaking process by the adsorbed complex is considered to be analogous to that responsible for nucleation and growth of cracks in, for example, stressed β -brass exposed to moist air (37), in stressed high strength steels exposed to pure H_2 at 1 atm (38), or to moist argon (39), in stressed α -brass exposed to liquid Hg, or in stressed austenitic stainless steels exposed to hot chlorides. If this concept also applies to the present situation, more facts must be made available to clarify which of the possible ammonium complexes containing Cu are the damaging species. It may be one of the well-known stable complexes described in the literature, or, instead, it may be a metastable reaction product of the test solution with brass, the composition of the reaction product being potential dependent. The damaging species presumably must have an over-all apparent negative charge within the damaging potential region because of the more pronounced susceptibility to SCC at potentials just noble to the critical value. Hence, although stable copper complexes are normally positively charged, the responsible species may adsorb accompanied by or combined with an anion or anions. The same situation applies to SCC by Cu complexes involving tartrates and citrates. The inhibiting function of Cl^- and Br^- , accordingly, is probably one of displacing the damaging species by non-damaging adsorbed Cl^- and Br^- or their complexed species. This competitive adsorption process is favored less at more noble applied potentials, a higher concentration of halide ion being necessary for inhibition under these conditions. Competitive adsorption involving Cl^- ions, it should be recalled, was also proposed as describing the inhibiting behavior of extraneous anions in the pitting corrosion of stainless steels (40), aluminum (41), and Ni-Cu alloys (42). However, it should not be concluded from this apparently parallel behavior that the mechanism of SCC necessarily depends on initial pitting corrosion. Adsorption sites for the two processes are quite different, involving a stressed lattice in the one instance, but not in the other.

In accord with the mechanism of stress-sorption cracking, the accountable imperfection network is usually concentrated along grain boundaries or, in the case of transgranular cracking, along the slip planes of stressed α -brass. They mark the sites on which preferred adsorption of the damaging ammonium complex occurs, resulting in cracking. Which direction the crack follows is determined in part by alloy composition and by the degree of cold-work, both affecting imperfection networks, and also by factors of the environment, such as pH. The latter determines the nature of specific Cu complexes in competition with OH⁻ or other ions available to adsorb on one type of imperfection network over that of another.

A suitable imperfection network is not usually generated in plastically deformed pure Cu, but it is favored by increasing amounts of alloyed Zn. The properties of alloyed Zn, in this regard, are shared by many other alloyed components (34), chemically unrelated as mentioned earlier, which also induce susceptibility. In other words, it is not so much the supposed film-forming or electrochemical properties of alloyed components that induce susceptibility as it is the probable effect of such components on suitable imperfection networks generated during tensile stressing of the alloy.

Along the same lines, shorter failure times at above-room temperatures suggest that, at least in part, more favorable imperfection networks are generated in brass at the higher temperatures. This is analogous to the situation in austenitic stainless steels exposed to MgCl₂ solution which fail by SCC only above room temperature.

Conclusions

1. It is confirmed that minimum failure time of 63-37 brass in 0.05M CuSO₄, 1M (NH₄)₂SO₄ test solution occurs at pH 6.5.

2. The critical potential in the above test solution below which failure time is > 50 hr is 0.095V SHE. This value is shifted in the active direction by increasing pH and by increasing dissolved Cu concentration.

3. The activation energy for SCC in the above test solution is 10 kcal/mole.

4. The minimum dissolved Cu⁺⁺ concentration for spontaneous cracking of 63-37 brass in 1M (NH₄)₂SO₄ is 0.003M. Above this concentration the corrosion potential is noble; below it is active to the critical potential.

5. Sodium chloride and sodium bromide, at least 0.04 and 0.005M, respectively, added to the test solution are effective inhibitors of SCC. They shift the critical potential in the noble and the corrosion potential in the active direction; inhibition occurs when the two potentials merge or cross.

6. An ammonium complex containing Cu or some other heavy metal is necessary in some amount for SCC of brass to occur in the (NH₄)₂SO₄ test solution. This conclusion is reached from (i) the very small concentration of dissolved Cu (0.003M) needed for spontaneous cracking, (ii) the continuing uniform corrosion of brass supplying Cu⁺⁺ at the noble potentials required for failures in initially Cu-free solutions, and (iii) the distinctly different critical potentials for failures in some of the Cu⁺⁺, Cd⁺⁺, Zn⁺⁺, Ni⁺⁺, and Co⁺⁺ ammonium complex test solutions.

7. The critical potential in 0.04M potassium tartrate, pH 14, is -0.34V SHE, becoming more active at a higher pH.

8. The present results are interpreted in terms of reduction of metal bond strength by adsorption of a Cu-containing or other heavy metal ammonium complex on appropriate defect sites along grain boundaries or slip planes.

Acknowledgment

This research was supported by the U.S. Army Research Office, Durham, North Carolina, to whom the authors express their appreciation. They also wish to

acknowledge the help of Donald Hixson in obtaining some of the data.

Manuscript submitted Aug. 14, 1974; revised manuscript received Nov. 4, 1974.

Any discussion of this paper will appear in a Discussion Section to be published in the December 1975 JOURNAL. All discussions for the December 1975 Discussion Section should be submitted by Aug. 1, 1975.

Publication costs of this article were partially assisted by the Massachusetts Institute of Technology.

REFERENCES

1. E. Sperry, *Brass World*, **2**, 39 (1906). [Quoted by D. Thompson, in "Stress Cracking of Metals—A State of the Art," p. 39, ASTM Special Publication 518, Philadelphia, Pa. (1972).]
2. W. Lynes, *Corrosion*, **21**, 125 (1965).
3. H. Pickering and P. Byrne, *ibid.*, **29**, 325 (1973).
4. E. Pugh, W. Montague, and A. Westwood, *Corrosion Sci.*, **6**, 345 (1966).
5. H. Uhlig and D. Duquette, *ibid.*, **9**, 557 (1966).
6. E. Escalante and J. Kruger, *This Journal*, **118**, 1062 (1971).
7. T. Hoar and C. Booker, *Corrosion Sci.*, **5**, 821 (1965).
8. D. Tromans and J. Nutting, *Corrosion*, **21**, 143 (1965).
9. E. Pugh, in "The Theory of Stress Corrosion Cracking in Alloys," J. Scully, Editor, North Atlantic Treaty Org., Brussels (1971).
10. A. Forty and P. Humble, *Phil. Mag.*, **8**, 247 (1963).
11. A. McEvily and A. Bond, *This Journal*, **112**, 131 (1965).
12. S. Birley and D. Tromans, *Corrosion*, **27**, 297 (1971).
13. B. Syrett and R. Parkins, *Corrosion Sci.*, **10**, 197 (1970).
14. H. Johnson and J. Leja, *Corrosion*, **22**, 178 (1966).
15. S. Sircar, U. Chatterjee, M. Zamin, and H. Vijayendra, *Corrosion Sci.*, **12**, 217 (1972).
16. H. Uhlig, in "Physical Metallurgy of Stress Corrosion Fracture," T. Rhodin, Editor, pp. 1-17, Interscience, New York (1959).
17. A. Forty, in "Fundamental Aspects of Stress Corrosion Cracking," R. Staehle, A. Forty and D. van Rooyen, Editors, p. 64, National Association of Corrosion Engineers, Houston, Texas (1969).
18. E. Mattson, *Electrochim. Acta*, **3**, 279 (1961).
19. H. Uhlig and J. Sansone, *Mater. Protect.*, **3**, 21 (1964).
20. H. Uhlig and E. Cook, *This Journal*, **116**, 173 (1969).
21. H. Lee and H. Uhlig, *ibid.*, **117**, 18 (1970).
22. R. Newberg and H. Uhlig, *ibid.*, **119**, 981 (1972).
23. H. Mazille and H. Uhlig, *Corrosion*, **28**, 427 (1972).
24. A. Asphahani and H. Uhlig, *This Journal*, **122**, 174 (1975).
25. J. Marquez, I. Matsushima, and H. Uhlig, *Corrosion*, **26**, 215 (1970).
26. A. Lahiri and T. Banerjee, *Corrosion Sci.*, **8**, 895 (1968).
27. E. Pugh and J. Green, *Met. Trans.*, **2**, 3129 (1971).
28. G. Edmunds, in "Symposium on Stress Corrosion Cracking of Metals," p. 67, ASTM-AIME, Philadelphia, Pa. (1945).
29. W. Robertson, E. Grenier, W. Davenport, and V. Nole, in "Physical Metallurgy of Stress Corrosion Fracture," T. Rhodin, Editor, p. 273, Interscience, New York (1959).
30. E. Pugh, J. Craig, and A. Sedriks, in "Fundamental Aspects of Stress Corrosion Cracking," R. Staehle et al., Editors, p. 118, National Association of Corrosion Engineers, Houston, Texas (1969).
31. F. Althof, *Z. Metallk.*, **36**, 177 (1944).
32. N. McKinney and H. Hermance, in "Stress Corrosion Testing," Special Technical Publication No. 425, p. 274, A.S.T.M., Philadelphia, Pa. (1967).
33. M. Pourbaix, "Atlas of Electrochemical Equilibria in Aqueous Solutions," p. 387, Pergamon Press, New York (1966).
34. D. Thompson and A. Tracy, *Trans. Am. Inst. Mining Met. Eng.*, **185**, 100 (1949).
35. H. H. Uhlig, in "Fundamental Aspects of Stress Corrosion Cracking," R. Staehle et al., Editors, pp. 86-91, National Association of Corrosion Engineers, Houston, Texas (1969).

36. H. H. Uhlig, Submitted paper and also discussions of papers by R. N. Parkins and R. Staehle in Conf. on Stress Corrosion Cracking and Hydrogen Embrittlement of Iron-base Alloys, held at Firminy, France, June 1973.
37. A. Bailey, *J. Inst. Metals*, **87**, 380 (1959).
38. G. Hancock and H. Johnson, *Trans. Am. Inst. Mining Met. Eng.*, **236**, 513 (1966).
39. H. Johnson and A. Wilner, *Appl. Mater. Res.*, **4**, 34 (1965).
40. H. Leckie and H. Uhlig, *This Journal*, **113**, 1262 (1966).
41. H. Bühni and H. Uhlig, *Corrosion Sci.*, **9**, 353 (1969).
42. T. Koizumi and H. Uhlig, *This Journal*, **121**, 1137 (1974).

On the Anodic Oxidation of Molybdenum

C. M. Daly and R. G. Keil*

Department of Chemistry, University of Dayton, Dayton, Ohio 45469

ABSTRACT

The anodic oxidation of molybdenum in an acetic acid solution has been studied with regard to the nature of the formed film and the kinetics of film growth. Faradaic methods, ATR spectroscopy, and "open-current" transient methods were utilized. A comparison was made between the anodic oxide film formed on molybdenum and vanadium. The anodic film on molybdenum was found to contain molybdenum in an oxidation state less than +6.

The purpose of this study was to investigate the chemical nature and certain physical properties of anodic molybdenum oxide films formed in a nonaqueous anodizing solution. Young (1) has reported that the hexavalent oxides are not readily soluble in acid solution and when subjected to anodic polarization in acid solution the metals form passivating films of the oxides. Some metals, (e.g., molybdenum and vanadium) do not yield an insoluble anodic oxidation product when anodized in aqueous media and such a film can only be formed in nonaqueous solutions (2). Young has also reported that it is not clear whether anodic metal oxide films might contain cation valencies less than the highest common one.

Recently Johnson *et al.* (3) have studied the mechanism of the anodic dissolution of molybdenum in aqueous sulfate solution as a function of pH and salt composition. An anodic dissolution mechanism was proposed which involved the prior oxidation of surface films of molybdenum(V) oxide to MoO₃ and subsequent dissolution by hydrolyzation. This entire mechanism is based, of course, upon the availability of sufficient free water to form soluble molybdic acid.

In addition, Arora and Kelly (4) formed anodic oxide films on molybdenum for radiochemical depth distribution studies. In that work they utilized a nonaqueous solvent reported earlier by Keil and Salomon (2) which had been successfully employed to grow anodic oxide films upon vanadium metal. They make the *a priori* assumption that the anodic oxide formed is in fact molybdenum trioxide. Earlier results have prompted us to make a comparative study of the nature of anodic films upon vanadium and molybdenum using this rather unusual anodizing solution, acetic acid-water-borax.

In this present work, we study the nature of the film on molybdenum using Faradaic methods, attenuated total reflectance (ATR) spectroscopy, and electrical properties of the molybdenum oxide film by use of open-circuit transient analysis. The anodic oxidation of several metals (5-8) has been studied using this method. We were particularly interested in this study, to compare the results obtained through the anodic oxidation of molybdenum with those of vanadium.

Experimental

High-purity (> 99.9%), single-pass, zone-refined molybdenum metal in wire and foil form was used for

this work. The molybdenum, obtained from both Materials Research Corporation and Alpha Chemicals, was mounted by methods previously described (2). The molybdenum surface was prepared for anodization by first polishing with a series of emery polishing papers (4, 3, 2, 0, 2/0, 3/0, and 4/0) followed by wet aluminum oxide powder polishing (15.0, 5.0, and 1.0 μ) on a rotating felt wheel. The finest aluminum oxide powder utilized was 1.0 μ micropolish. Subsequently the electrode was washed first for 15 sec with 1:1 water-nitric acid (70% assay) solution, then with acetone, dried in a stream of nitrogen gas, and immersed in the anodizing solution. In this work we used an acetic acid solution 2.0M in water and 0.02M in sodium tetraborate. The solution had a conductivity of 79 μ (ohm-cm)⁻¹. These studies were carried out at 25°C. An ambient of nitrogen was maintained in the reaction flask and the anodizing solution was degassed prior to use.

Under galvanostatic conditions current densities not less than 379 μ A/cm² were used. For the open-circuit transient studies a pair of Philbrick SP102 operational amplifiers were used for galvanostat and voltage follower. The output of the voltage follower, which accomplished a power gain, was then fed into the input terminals of a Sanborn Model 7701B oscillographic recorder. These amplifiers operate over a range of ± 100 V. All potentials were recorded relative to the saturated calomel reference electrode. For the studies at high current densities, an analog to digital converter data collection system was employed. The voltage *vs.* time data was fed into the computer via an audio coupler. Overpotentials were calculated from observed voltages by subtracting the value of the open-circuit potential. Apparent current densities were obtained by dividing the observed current by the macroscopic surface area of the anode.

Faradaic studies.—In an effort to obtain the upper limit of the average valence of the molybdenum ion within the anodic film, quantitative measurements of the charge passed and the amount of molybdenum oxidized were made. The results obtained using this method include gassing, if any, which would result in the actual valence state being substantially lower.

The amount of molybdenum metal present in the anodic oxide was determined using the colorimetric method of Ayres and Tuffly (9) as reported by Snell and Snell (10). The method involved the determination as molybdate in the hexavalent state by phenylhydra-

*Electrochemical Society Active Member.

Key words: anodic oxidation, molybdenum, transients, structure.

zine hydrochloride. The following modifications were incorporated: (a) approximately 0.02g of potassium meta-periodate (KIO_4) were added to the phenylhydrazine hydrochloride before boiling took place in order to oxidize the molybdenum present to the hexavalent state, (b) the film was quantitatively dissolved by immersing the electrode in 0.5 ml of ammonium hydroxide. A constant current of 2500 μA was used and films were grown to a maximum of 56V. Due to the small surface area of the electrode (0.664 cm^2) consecutive runs were made in the anodizing solution for a cumulative time of approximately 300 sec. The anodizing solution was not changed during these consecutive runs but the electrode was removed after each thin film growth and the stripping modification in part (b) above was employed. After the completion of enough runs to reach the time of 300 sec the anodizing solution was removed and reduced to approximately 10 mliters by boiling. This reduced solution was then combined with the ammonium molybdate formed in the stripping process and added to the phenylhydrazine hydrochloride solution. The per cent transmittance was measured at 505 nm in a Perkin-Elmer double beam spectrophotometer. The apparent oxidation state of anodically oxidized molybdenum, defined as the ratio of number of Faradays to grow the film to the number of moles of molybdenum found in the film plus anodizing solution, was then calculated.

ATR spectroscopy.—Infrared spectra were obtained utilizing a Wilk's single beam ATR attachment equipped with a KRS-5 prism. An important step in anodizing (in those instances where a permanent film was desired) was that the specimens be dried with a stream of dry gas (we used nitrogen) immediately following removal from the anodization cell. The molybdenum anodic oxide films, like vanadium, are unstable. This instability is evidenced by changes in the uniformity of the interference colors and occur approximately 15 sec after removal from the anodizing solution if it is kept in a moist atmosphere. This instability is inherent to the oxides of V and Mo and not to the electrolyte. Films formed on Nb or Ta in our laboratory in this electrolyte have the same stability as films formed on these metals using boric acid-borax solutions.

Results

Anodic oxidation in this anodizing solution results in an anodic film which exhibits intense interference colors. The film interference colors observed at various formation potentials are shown in Table I for potentiostatic film growth. Anodization under potentiostatic conditions produced films whose minimum final leakage current was 0.5-1.5 mA/cm^2 and from which some film dissolution did occur even during film growth.

Faradaic studies to obtain an upper valence limit of the molybdenum ion within the anodic film were conducted under galvanostatic conditions. Massive gassing at the anode did not occur. However, it is possible that small amounts of gas were produced. This would cause the actual oxidation state of the metal within the film to be less than the apparent oxidation state. Results showed that the average apparent oxidation state of molybdenum within the film equaled 5.50. It should be pointed out that complete development of the colorimetric complex between the dissolved molybdenum

film and phenylhydrazine hydrochloride was not obtained unless periodate was first added to the film solution to be analyzed. The periodate ion oxidizes the molybdenum quantitatively to the Mo(VI) oxidation state.

Additional insight into the nature of the anodic molybdenum film can be gained by viewing the ATR spectra for films produced potentiostatically. Figure 1 shows the ATR spectra of the anodic film as a function of formation voltage. For comparison the spectra published for MoO_3 by Nyquist (11) is given in Fig. 1. Note that there is a definite absorbance of the anodic films at about 1000 cm^{-1} in agreement with the published spectra for MoO_3 but that the broad band centered at 850 cm^{-1} in the standard is either not present or shifted markedly to higher energies in the spectra of the anodic oxide films. We should note that we are comparing a probably amorphous film with a crystalline standard.

The oxide film can be considered to be the dielectric medium of a capacitor whose plates are composed of the substrate metal and the anodizing solution. Under galvanostatic conditions the film carries current in some manner. During an open-circuit transient the differential equation describing the system becomes

$$i + C \, dV/dt = 0 \quad [1]$$

which relates the ion current through the film, i , with the film capacitance, C , and the voltage decay rate, dV/dt . Measurement of V as a function of t experimentally enables one to determine the equation of dV/dt and ultimately a definitive expression of i as a function of V . Earlier work (5-7) has established that an expression between voltage and time of the form

$$V = k - V_0 \ln(t + \theta) \quad [2]$$

can lead to a field-assisted ionic migration growth mechanism in which the mobile ions jump periodic potential energy barriers. The quantities θ , V_0 , and k are parameters which are determined by the particular transient and its initial conditions. For molybdenum, the voltage-time transient fit an equation of the above form. Analysis of the voltage-time trace was performed with the assistance of a digital computer. The computer was fed voltage *vs.* time data. It then performed the following functions: (a) it chose from

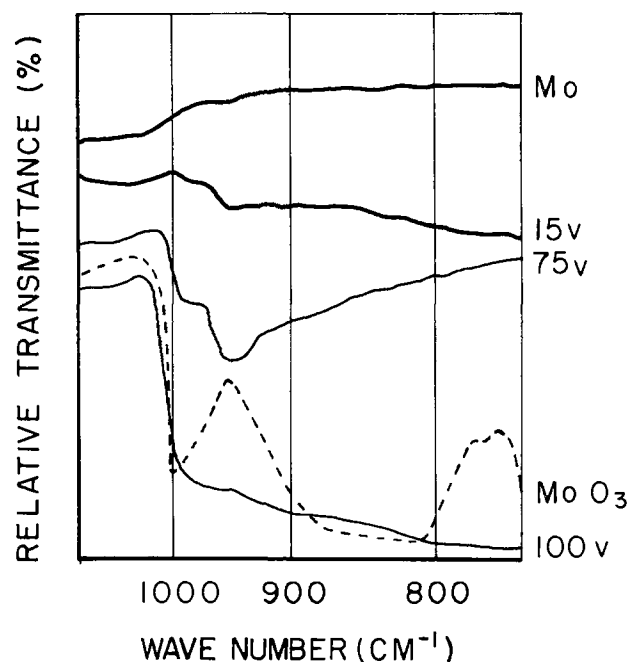


Fig. 1. ATR spectra of anodic oxide films at various formation voltages.

Table I. Observed interference colors at various formation voltages

Formation voltage, V	Film interference color
6-10	Light yellow
15	Steel blue
25	Light blue
35	Yellow-green
45	Violet
55	Deep violet
65	Emerald green

a very large selection the value of θ which produced a minimum standard deviation of all data points when the data were subjected to a linear least square analysis, and (b) it printed out values of k , θ , V_0 , and the standard deviation. It can be shown (8) that manipulation of Eq. [2] can ultimately yield as a final result relating i and V , an equation of the form

$$i = i_0 \exp(V/V_0) \quad [3]$$

where the exchange current density $i_0 = CV_0 \exp(-k/V_0)$.

The point is that an equation of this form is the mathematical consequence of the differential equation describing the system and the experimental voltage-time profile. Here i_0 and V_0 are experimentally determined parameters whose dimensions are the same as i and V , respectively. If time zero equals the commencement of the transient, the transients fit Eq. [2] for times corresponding to 80% of the potential decay at a current density of $3794 \mu\text{A}/\text{cm}^2$ and 60% of the potential decay at 1897 and $379 \mu\text{A}/\text{cm}^2$. Figure 2 shows the relationship between the parameter V_0 and the formation potential. For a given formation current density, V_0 is a linear function of the formation potential and all lines nearly pass through the origin. The slope of each line is obviously a function of the formation current density and decreases with increasing current density.

From data analysis, we learned that the value of θ required to fit the transient data to Eq. [3] is quite small, with values ranging from essentially zero to as high as 0.2. A typical value is 0.001. Generally, θ increased with the formation potential of the film. Small values are not unexpected because of the relatively large formation current densities and $\theta = CV_0/i_e$. Figure 3 shows the relationship between the reciprocal capacitance and the formation potential. The reciprocal capacitance is related to θ by the equation $1/C = V_0/i_e\theta$, where i_e equals the film formation current.

Discussion of Results

The results of the Faradaic studies show conclusively that the metal ions in the anodic molybdenum oxide film cannot quantitatively be present in the +6 oxida-

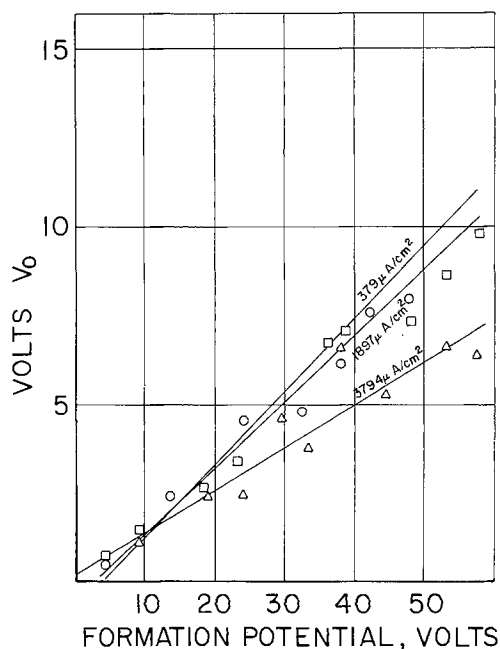


Fig. 2. Dependence of V_0 on formation potential for molybdenum in anodizing solution. The formation current density was $379.4 \mu\text{A}/\text{cm}^2$ for the data represented by \square , $1897 \mu\text{A}/\text{cm}^2$ for the data represented by \circ , and $3794 \mu\text{A}/\text{cm}^2$ for the data represented by \triangle .

tion state. This point was accentuated by the fact that full development of the molybdenum-phenylhydrazine hydrochloride was not achieved unless prior to complexation some periodate ion was added. Thus, some of the molybdenum must be present in an oxidation state less than +6 within the film. Also any oxygen evolution (not observed under galvanostatic conditions) would require still lower metal ion valencies. Johnson *et al.* (3) in a study on anodic dissolution of Mo in aqueous acid media postulated that dissolution is probably accomplished through a hydration reaction to form $\text{MoO}_3 \cdot \text{H}_2\text{O}$ (or molybdic acid H_2MoO_4). They further postulated that Mo metal when placed in solution forms a film of approximate composition Mo_2O_5 that completely covers the metal surface. They also noted that the conductive Mo_2O_5 is converted to MoO_3 upon anodic polarization. A major conclusion they made, and with which we agree, is that an equilibrium probably exists between MoO_3 and a lower oxide. We suggest the results from Faradaic experiments and the ATR spectroscopy possibly point to the presence of a lower oxidation state as a major film constituent. Ho and Ord (12) recently followed the formation of mixed inner and outer anodic layer on iron with a following ellipsometer in neutral borate electrolyte. Prediction of our anodic oxidation product upon thermodynamic grounds is further complicated because of the nature of our electrolyte, a difficulty we experienced in earlier work with vanadium (2). The activity of water in the acetic acid solution has not been determined and renders thermodynamic consideration using Pourbaix-type pH vs. E (SHE) diagrams (13) difficult. We suggest our data (Faradaic and spectroscopic) at the very least indicate an amorphous film nature and possibly the presence of oxides other than MoO_3 . Care must be exercised in these spectral comparison however because we are comparing a probably amorphous (3) film material with a crystalline standard.

An exponential dependence of the current density through the oxide film on the overpotential can be interpreted in terms of an activation-energy-controlled process (1). The theoretical relation for such a process, in the high-field case, is given in its simplest form by

$$i = 2an\nu \exp(-U/kT) \exp(qaE/kT) \quad [4]$$

where a is the half-jump distance of the activation barrier, n the density of charge carriers, ν the frequency of the oscillating ions, U the activation energy for the process, q the effective charge on the mobile ions, and E the electric field at the activation barrier. The other symbols have their usual meanings. Assuming the field at the activation barrier is equal to the average electric field, a comparison of Eq. [3] and [4] may be made which yields the relationship

$$V_0 = (kT/qa)D \quad [5]$$

Thus, V_0 is proportional to the thickness of oxide layer, D .

The experimental data presented here verify a model of this type. Figure 2 shows that the values of V_0 are linearly proportional to the formation potential for a given formation current density over a wide range of values and the lines nearly intersect the origin. This result indicates that a high-field conduction process limits the current through the layer. Data taken for

Table II. Apparent oxidation state of molybdenum anodic oxidation product for various formation voltages grown at a current density of $3762 \mu\text{A}/\text{cm}^2$

Formation voltage, V	Total molybdenum, μmoles	Total charge passed, $\mu\text{Faradays}$	Apparent oxidation state
37.7	1.605	8.945	5.57
38.3	1.725	8.658	5.02
45.96	1.51	7.727	5.12
53.85	1.41	7.909	5.61
55.75	1.32	8.101	6.16

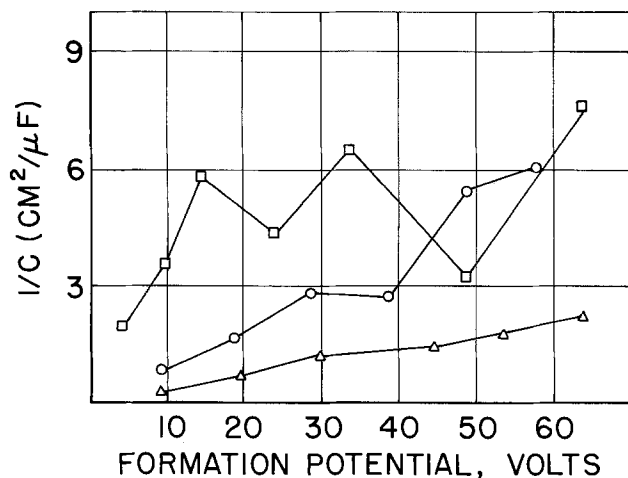


Fig. 3. Dependence of the reciprocal capacitance on formation potential. The formation current density was $379.4 \mu\text{A}/\text{cm}^2$ for the data represented by \square , $1897 \mu\text{A}/\text{cm}^2$ for the data represented by \circ , and $3794 \mu\text{A}/\text{cm}^2$ for the data represented by \triangle .

different formation current densities fall on lines of differing slopes, indicating that the field in the layer depends on the formation current density. The field in the dielectric may increase with increasing formation current density because of an increase in the ion jump distance at higher formation current densities. For films grown potentiostatically the current decreased to some limiting value which we called the "leakage" current. Our results indicate that the final "leakage current" under potentiostatic conditions equaled $0.5\text{--}1.5 \text{ mA}/\text{cm}^2$. We presume this is due primarily to a steady-state dissolution of the anodic oxide. Analysis of the electrolyte verifies that some molybdenum is dissolving during film growth. This result is in agreement with those found for vanadium (8). Inspection of the reciprocal capacitance plot, Fig. 3, shows severe scatter of points. Perhaps this is due to the fact that we were using high current densities and consequentially obtained very small values of θ or it may indicate some film porosity.

The results of this investigation on molybdenum are similar to those obtained in an earlier work on vanadium (8). Both metals when subjected to anodic polarization in the acetic acid-water-sodium tetraborate so-

lution, yield a protective film exhibiting intense interference colors rather than anodic dissolution. The anodizing solution is probably unique and works because the water activity is significantly reduced on account of strong intermolecular interactions with acetic acid dimer molecules. Perhaps a comparative study of, say, niobium in aqueous and acetic acid borax solutions would be informative.

The film on molybdenum is not quantitatively MoO_3 , but probably exists as a mixed oxide. Ionic conduction during film growth proceeds by the mechanism of field-assisted barrier migration.

Acknowledgment

The authors wish to thank the University of Dayton Office for Graduate Studies and Research for the support of this work.

Manuscript submitted July 18, 1974; revised manuscript received Oct. 21, 1974.

Any discussion of this paper will appear in a Discussion Section to be published in the December 1975 JOURNAL. All discussions for the December 1975 Discussion Section should be submitted by Aug. 1, 1975.

Publications costs of this article were partially assisted by the University of Dayton.

REFERENCES

1. L. Young, "Anodic Oxide Films," Academic Press, London and New York (1961).
2. R. G. Keil and R. E. Salomon, *This Journal*, **115**, 628 (1968).
3. J. W. Johnson, C. H. Chi, C. K. Chen, and W. J. James, *Corrosion*, **26**, 238 (1970).
4. M. A. Arora and Roger Kelly, *This Journal*, **119**, 270 (1972).
5. D. J. DeSmet and M. A. Hopper, *ibid.*, **116**, 1184 (1969).
6. J. L. Ord, *ibid.*, **112**, 46 (1965).
7. J. L. Ord and D. J. DeSmet, *ibid.*, **116**, 762 (1969).
8. R. G. Keil and K. Ludwig, *ibid.*, **118**, 864 (1971).
9. G. H. Ayres and B. L. Tuffly, *Anal. Chem.*, **23**, 304 (1951).
10. F. D. Snell and C. T. Snell, "Colorimetric Methods of Analysis," D. Van Nostrand Co., Inc., New York (1959).
11. R. A. Nyquist and R. O. Kagel, "Infrared Spectra of Inorganic Compounds," Academic Press, New York (1971).
12. F. C. Ho and J. L. Ord, *This Journal*, **119**, 139 (1972).
13. M. Pourbaix, "Atlas of Electrochemical Equilibria," p. 272, Pergamon Press, Elmsford, N. Y. (1966).

Nitrogen Diffusion in Zirconium Nitride

J. G. Desmason¹ and W. W. Smeltzer*

Department of Metallurgy and Materials Science, McMaster University, Hamilton, Ontario, Canada, L8S 4M1

ABSTRACT

Diffusion of nitrogen in $ZrN_{0.93}$ plates obtained by direct nitridation of 99.995 weight per cent zirconium sheets at 1150°C was studied using the ^{15}N gas-solid exchange technique. These specimens were characterized by chemical analyses, density, lattice parameter, and structural measurements. The diffusion anneals were performed at a nitrogen pressure of 220 Torr and at temperatures in the range 1000°-1200°C. The tracer diffusion coefficient can be expressed as $D^*(cm^2/sec) = 4.08 \times 10^{-6} \exp -36,600/RT$. These results when compared to determinations of the chemical diffusion coefficients obtained from Zr nitriding kinetics demonstrate that nitrogen transport in the polycrystalline solid at temperatures less than 1200°C is associated with a short-circuit diffusion mechanism.

Diffusion studies on metal nitrides have been a subject of limited interest. Indeed, diffusion coefficients have been reported for only a few transition metal nitrides which are chemical coefficients for nitrogen diffusion except for uranium mononitride where tracer diffusion coefficients are available for both nitrogen and the metal species. The purpose of this investigation, accordingly, was to determine the nitrogen tracer diffusion coefficient in zirconium mononitride and to compare this determination to diffusivities obtained from models for the nitridation of zirconium (1-6) and the sintering of this nonstoichiometric compound (7).

Experimental

Sample preparation.—ZrN plates, $2.5 \times 1.5 \times 0.025$ cm, were prepared by nitriding zone-refined Zr sheets, 99.995 weight per cent (w/o) pure, in research grade nitrogen, < 1 ppm O_2 , held at 1150°C and 1 atm pressure for periods of 4 weeks. Careful precautions were taken to prevent insofar as possible oxygen contamination of the solids. The Pt boat containing the Zr specimens chemically polished in a 5 volume per cent (v/o) HF-45 v/o HNO_3 aqueous solution was covered with a Zr foil and surrounded with Zr gettering chips.

Sample characterization.—ZrN exists over a broad composition range corresponding to $ZrN_{0.55}$ - $ZrN_{1.0}$ (8). The composition of the plates was computed from the weight gain during nitridation, the result being checked by chemical analyses. Nitrogen analysis was conducted using Bollman's modified Kjeldahl method in which the dissolving medium is a stannous-phosphoric acid reagent (9). The zirconium content was deduced from the weight of ZrO_2 obtained by reacting a ZrN sample in oxygen for 24 hr at 1000°C.

The structure was characterized by a combination of metallography, lattice parameter, and density measurements. Specimens mounted in room-setting epoxy resin were polished to 1μ diamond paste with kerosene as lubricant. The HF- HNO_3 etchant was used to reveal grain boundaries. X-ray diffraction traces were made in the high angle region at $1/4^\circ$ per min using 4° slits and Ni-filtered Cu radiation. The lattice parameters were calculated from the (331), (420), (422), (440), and (511) peaks. In some cases the Debye-Scherrer powder x-ray method was used. Densities were determined by the pycnometric method using xylene as the reference liquid.

Diffusion experiments.—Diffusion rates were determined at constant temperature from the decrements of the ^{15}N isotope concentration in the isotopically enriched nitrogen atmosphere. These experiments were carried out in the apparatus shown in Fig. 1. The Pt-

Rh reaction chamber, Fig. 2, was equipped with two winches, one for lowering and raising the quartz crucible containing ZrN powder for oxygen getting and the other for lowering the Pt crucible containing the ZrN plates to undergo nitrogen exchange. The space between the Pt-Rh and mullite tubes was also gettered of oxygen by means of Zr foil. Following are the precautions taken to prevent oxygen contamination of the ZrN plates. The crucibles, each containing 500 mg of ZrN were introduced into the upper section of the reaction chamber. After nitrogen purging and evacuation of the system, an aliquot of 96 atom per cent (a/o) ^{15}N enriched nitrogen was introduced into the reaction chamber to a pressure of 10-15 Torr. Sufficient normal nitrogen was then admitted to give a pressure of 220 Torr when the system was heated to the diffusion temperature. Argon was introduced into the outer chamber at a slightly smaller pressure. The furnace was then brought up to 850°C and the quartz crucible containing ZrN and the Zr foil lowered into the furnace zone for 12 hr to permit getting of residual oxygen. The temperature was subsequently increased to that for the diffusion run, the quartz crucible raised from the reaction zone, and two 1 cm^3 gas samples collected to measure the initial ^{15}N concentration. Immediately afterwards the Pt crucible containing the ZrN plates was lowered into the hot zone, the zero time taken when the crucible reached this zone. Gas samples subsequently collected at suitable intervals were analyzed by the mass spectrometric technique.

Tracer diffusion coefficients D^* were calculated from the equation of Carman and Haul (10)

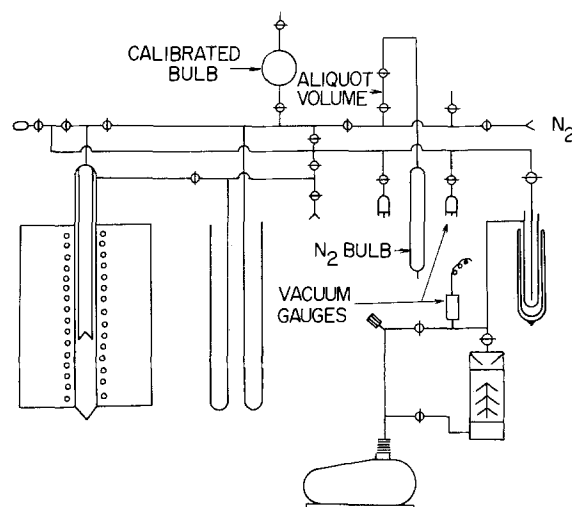


Fig. 1. General schematic diagram of the diffusion apparatus

* Electrochemical Society Active Member.
¹ Present address: Laboratoire de Chimie Minérale et Cinétique Hétérogène, Université de Limoges, 87100 Limoges, France.
Key words: zirconium nitride, nitrogen diffusion, lattice and short-circuit diffusion.

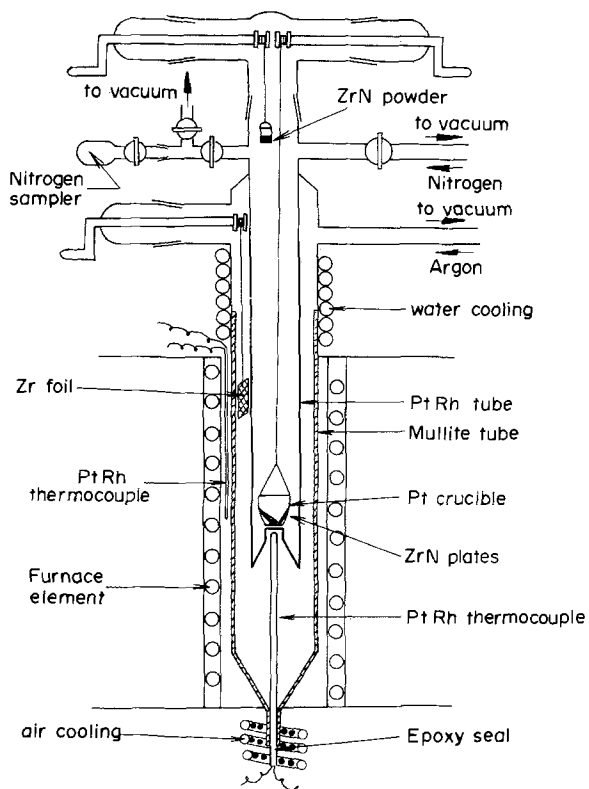


Fig. 2. Reaction chamber and assembly of the diffusion apparatus.

$$\frac{C_t - C_s}{C_g - C_s} = e \operatorname{erfc} \frac{\sqrt{\tau}}{\lambda} \quad [1]$$

where $\tau = D^*t/l^2$. Here, C_t , C_s , and C_g represent the atom fraction of ^{15}N in the atmosphere at time t , in the solid at time zero (taken as the natural abundance 0.0037), and in the atmosphere at time zero, respectively, l is the half thickness of a ZrN plate, and λ is the ratio of the total mass of nitrogen in the gas phase to that in the solid.

Results

ZrN specimens, which exhibited the golden yellow color of this compound, were in the metal excess range at the atom ratio $\text{N/Zr} = 0.93 \pm 0.01$. The lattice parameter, Table I, calculated from diffractometer traces was used to compute the x-ray density given by the expression

$$d_x (\text{g/cm}^3) = \frac{nM}{Na^3} \quad [2]$$

where M is the molecular weight of $\text{ZrN}_{0.93}$, N is Avogadro number, a is the lattice parameter, and $n = 4$ is the number of metal atoms in the NaCl-type unit cell. The estimate given in Table I for the fraction of vacant sites in the zirconium sublattice from the small difference of 0.67% between the x-ray and pycnometer densities is questionable (8). Literature data invariably show that $d_x > d_p$, which has been attributed to structural defects such as voids in the polycrystalline solid or the influence of oxygen as an impurity on the defectiveness of the metal sublattice (8, 11, 12).

A smooth surface finish could not be obtained on cross sections of ZrN due to its brittleness. Etching re-

Table I. Densities and vacancy concentration in $\text{ZrN}_{0.93}$ plates at 23°C

d_p (pycnometer density) (g/cm ³)	a (lattice parameter) (Å)	d_x (x-ray density) (g/cm ³)	V_N (a/o)	V_{Zr} (a/o)
7.180 ± 0.008	4.5755 ± 0.0007	7.228	7.62	0.66

vealed grains of variable size in the 10-30 μ range as demonstrated in Fig. 3. Surface examination of the plates showed the existence of small protuberances delineating polygonal surfaces.

In each diffusion run, three or four plates having a total mass close to 500 mg were placed in an inclined position with intervening space in the Pt crucible. Blank runs at 1000° and 1100°C without plates showed no measurable nitrogen exchange. The runs were carried out at temperatures in the range 1000°-1200°C and at 220 Torr nitrogen pressure. Plots of D^*t/l^2 vs. time for periods up to 10 hr are given in Fig. 4. Since the plots were linear, diffusion was assumed to be the rate-determining step. The tracer diffusion coefficients were

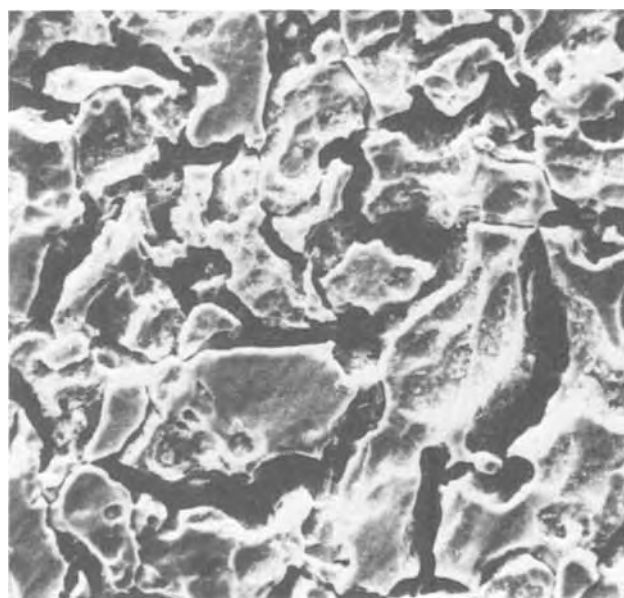


Fig. 3. Etched cross section of $\text{ZrN}_{0.93}$ plate (Magnification $\times 695$).

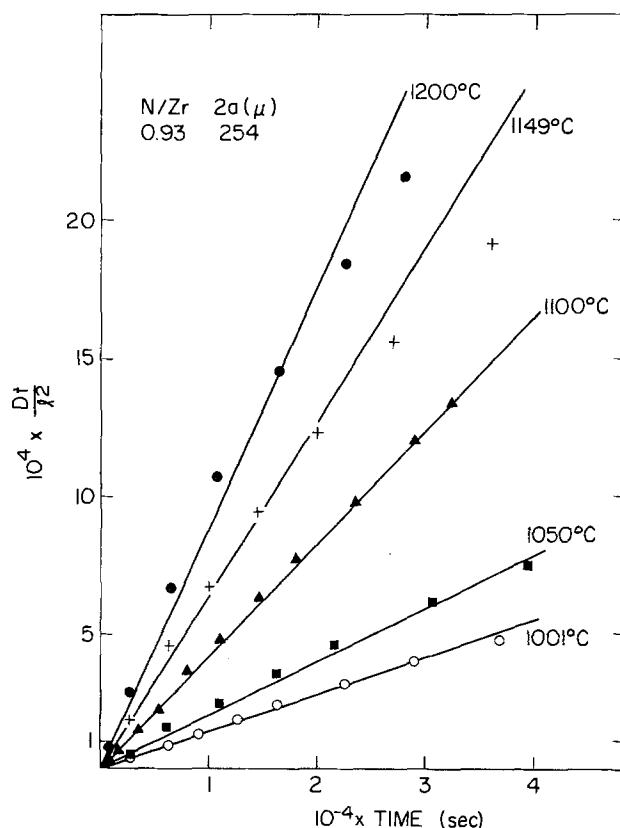


Fig. 4. Experimental results for ^{15}N diffusion in $\text{ZrN}_{0.93}$ plates

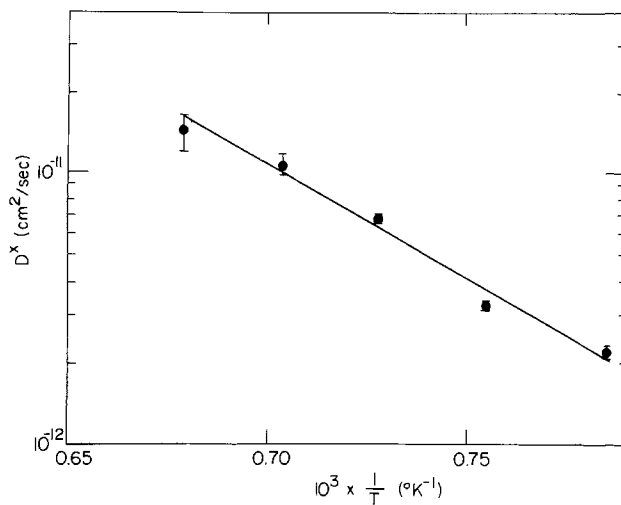


Fig. 5. Arrhenius plot of the nitrogen tracer diffusion coefficient for $ZrN_{0.93}$.

calculated from the slopes of the best lines and an Arrhenius plot of these evaluations is shown in Fig. 5. The expression for this diffusivity is

$$D^* (\text{cm}^2/\text{sec}) = 4.08^{+88.2}_{-3.9} \times 10^{-6} \exp \left(- (36,600 \pm 4500)/RT \right) \quad [3]$$

where the limits are at the 95% confidence level.

The ZrN plates were not discolored during exposures up to 10 hr. At longer times they developed a brownish-green color which darkened with increasing exposure. Powder x-ray photographs contained no new lines but the diffractometer traces of the surface showed a very small extra peak corresponding to the maximum intensity peak of monoclinic ZrO_2 .

Discussion and Conclusions

Preparation of ZrN from the metal was carried out under conditions typical of those used in investigations on the nitriding kinetics of zirconium. Since zirconium diffusion is negligible, several investigators (1-5) have analyzed the parabolic kinetics for the nitrogen uptake governing the growth of the ZrN surface layer in terms of unidirectional two-phase ($T < 862^\circ\text{C}$) or three-phase ($T > 862^\circ\text{C}$) volume diffusion models to obtain an average value for the chemical diffusion coefficient. These values are recorded in Table II and shown by Arrhenius plots in Fig. 6. There are also included diffusivities calculated from the nitriding of $ZrN_{0.76}$ wires (6) and the sintering of ZrN wires of various compositions (7). In this latter investigation, the effective diffusion coefficient determined from the growth of the neck radii and a sintering model was assigned to nitrogen diffusion. The present determination of the tracer diffusivity agrees approximately with several of the

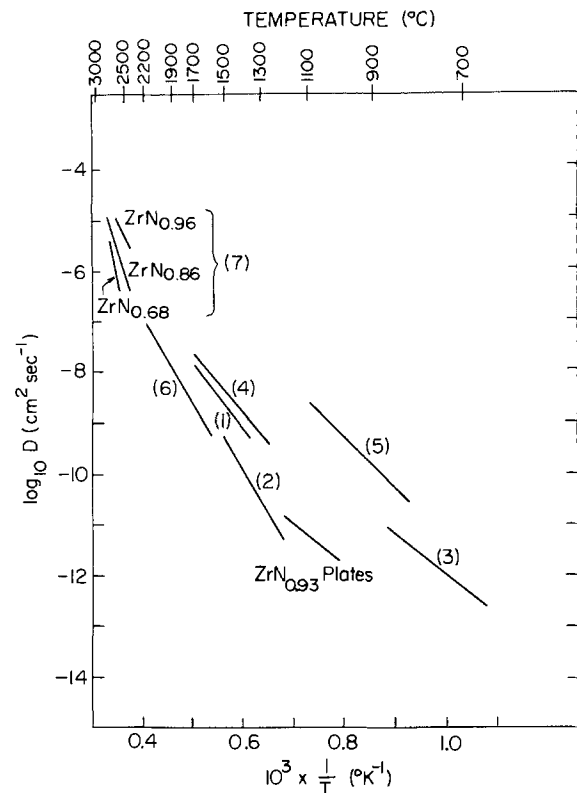


Fig. 6. Present results and those reported in the literature for nitrogen diffusivities of zirconium nitride. The numbers in parentheses refer to the references.

chemical diffusivities obtained from nitriding of the metal. Despite the discrepancies in the determinations, one can conclude that the activation energy and pre-exponential factor for the diffusivities obtained from the different types of measurements increase with increasing temperature. Also, the diffusivities calculated from the sintering results are characterized by an appreciable concentration dependence.

The nitrogen deficiency in the NaCl structured $ZrN_{0.93}$ is essentially caused by the presence of vacancies in the nitrogen sublattice (Table I). One can, therefore, reasonably assume that the zirconium sublattice is fixed and that transport of nitrogen occurs via nitrogen vacancies. Using a Darken-type diffusion analysis for this solid (2, 13, 14), the chemical diffusion coefficient \tilde{D} can be related to the intrinsic coefficient D and the tracer diffusion coefficient D^* by

$$\tilde{D} = D = D^* (\partial \ln a_N / \partial \ln x) \quad [4]$$

In this relationship, a_N and x are the nitrogen activity and the nitrogen-to-zirconium atom ratio, respectively.

Table II. The nitrogen tracer (D^*), chemical (\tilde{D}), and self-effective (D_{eff}) diffusion coefficients for ZrN expressed in Arrhenius form: $D = D_0 \exp -Q/RT$

Material	Diffusion coefficient	Temperature range ($^\circ\text{C}$)	D_0 (cm^2/sec)	Q (kcal/mole)	Method	Ref.
ZrN	\tilde{D}	650-850	7.87×10^{-5}	35.9	Nitriding kinetics	3
ZrN	\tilde{D}	1250-1700	6.0×10^{-2}	60.0	—	1
ZrN	\tilde{D}	1260-1720	1.69×10^{-2}	53.66	—	4
ZrN	\tilde{D}	800-1100	2.5×10^{-2}	44.2	—	5
ZrN	\tilde{D}	1200-1500	3.12	79.4 ± 6.0	—	2
$ZrN_{0.76}$	D	1600-2200	7.5×10^{-1}	78.3	Diffusion saturation	6
$ZrN_{0.83}$	D_{eff}	2550-2700	3.5×10^{12}	245.0	Sintering kinetics	7
$ZrN_{0.88}$	D_{eff}	2400-2750	7.9×10^5	150.0	—	7
$ZrN_{0.96}$	D_{eff}	2400-2600	2.6×10^2	97.0	—	7
$ZrN_{0.93}$	D^*	1000-1200	4.08×10^{-6}	36.6	Isotope tracer	This work

In the absence of data on the nitrogen activity as a function of nonstoichiometry one cannot evaluate the activity term in Eq. [4]. Kohlstedt *et al.* (14) have provided, nevertheless, pertinent conclusions on the influence of the carbon activity gradient on carbon diffusion in TiC which exhibits the same type of crystallography and nonstoichiometry as ZrN. The contribution to the activation energy for diffusion from the activity term was estimated to be only ~ 6 kcal/mole in comparison to the total activation energy for chemical or tracer diffusion of the order of 100 kcal/mole. They, therefore, suggest that when differences of many kcal/mole are reported between the activation energies of \tilde{D} and D^* , like diffusion evaluations from metal carburizing and single-crystal tracer results, the explanation resides in the role of short-circuit diffusion paths in the polycrystalline solid formed rather than in the chemical activity term of Eq. [4].

These conclusions are also consistent with the findings on the nitrogen diffusional properties of ZrN. The evaluation of the tracer diffusivity and those for the chemical diffusivity from metal nitridation investigations at temperatures less than 1200°C were obtained from results on polycrystalline ZrN formed from the metal. This latter temperature is ~ 0.4 of the melting point of ZrN. Consequently, the low values of the activation energy in the range of 35-45 kcal/mole represent this energy for nitrogen short-circuit diffusion through low resistance structural paths such as ingrown dislocations and grain boundaries. The transition of this energy to values in the 50-80 kcal/mole range at temperatures between 1200° and 2200°C accordingly represents the decreasing influence of short-circuit diffusion as the activation energy becomes that for nitrogen transport by lattice diffusion according to a vacancy mechanism. The activation energies larger than 100 kcal/mole and the high pre-exponential factors obtained above 2200°C in sintering studies, along with the fact that these parameters decrease as stoichiometry is approached, suggest an increasing contribution of Zr diffusion in the mass transport process in the initial sintering of this material (7). Thus the relatively large discrepancies in the nitrogen diffusion coefficients over the lower temperature range results from the different polycrystalline structures of the ZrN solid in each investigation.

Acknowledgments

This work was taken from the thesis of J. G. Desmaison submitted to McMaster University in partial fulfillment of the requirements for the M.Sc. degree in Materials Science. He wishes to acknowledge the financial support of the National Research Council of Canada.

Manuscript submitted April 30, 1974; revised manuscript received Oct. 4, 1974.

Any discussion of this paper will appear in a Discussion Section to be published in the December 1975 JOURNAL. All discussions for the December 1975 Discussion Section should be submitted by Aug. 1, 1975.

Publication costs of this article were partially assisted by McMaster University.

REFERENCES

1. V. S. Eremeyev, Y. M. Ivanov, and A. S. Panov, *Izv. Akad. Nauk SSSR, Metal.*, No. 4, 262 (1969).
2. S. K. Iyer, Ph.D. Thesis, University of Pennsylvania, Philadelphia, Pa. (1971).
3. C. J. Rosa and W. C. Hagel, *This Journal*, **115**, 467 (1968).
4. Y. V. Levinskii, S. S. Kiparisov, and Y. D. Stroganov, *Izv. Vysshikh Uchebn. Zavedenii, Tsvetn. Met.*, **13**, 91 (1970).
5. J. Paidassi and R. Le Delliou, *C. R. Acad. Sci. Paris, Ser. C*, **272**, 249 (1971).
6. I. I. Spivak, *Izv. Akad. Nauk SSSR, Neorg. Mater.*, **5**, 1138 (1969).
7. R. A. Andrievskii, I. I. Spivak, and K. L. Chevasheva, *Poroshkovaya Met., Akad. Nauk Ukr. SSR*, **8**, 65 (1968).
8. E. K. Storms, *M.T.P. Int. Rev. Sci., Inorg. Chem., Ser. I*, **37** (1972).
9. D. H. Bollman, *Anal. Chem.*, **44**, 887 (1972).
10. P. C. Carman and R. A. W. Haul, *Proc. Roy. Soc., London*, **A222**, 109 (1954).
11. A. S. Shevchenko, R. A. Andrievskii, V. P. Kalinin, and R. A. Lyutikov, *Poroshkovaya Met., Akad. Nauk Ukr. SSR*, **10**, 89 (1970).
12. E. I. Smagina and V. S. Kutsev, *Zh. Fiz. Khim.*, **37**, 1813 (1963).
13. S. K. Iyer and W. L. Worrell, "7th International Symposium on Reactivity Solids," Bristol, J. S. Anderson, N. W. Roberts, and F. S. Stone, Editors, p. 294, Chapman and Hall, London (1972).
14. D. L. Kohlstedt, W. S. Williams, and J. B. Woodhouse, *J. Appl. Phys.*, **41**, 4476 (1970).

Anodic Phenomena in Cryolite-Alumina Melts

I. Overpotentials at Graphite and Baked Carbon Electrodes

E. W. Dewing* and E.Th. van der Kouwe¹

Arvida Research Centre, Aluminum Company of Canada, Limited, Arvida, Province of Quebec, Canada

ABSTRACT

A method is described for measuring the potential of a working carbonaceous anode with respect to an aluminum reference electrode. The correction for resistance drop is determined by measuring the apparent resistance with a superimposed alternating current and a Kelvin bridge, and at the same time measuring the amplitude of the second harmonic voltage generated, which also gives the Tafel slope. For graphite the Tafel slope is found to be 0.295, but the exchange current varies from 1.5 mA-cm⁻² for current densities below 0.1 A-cm⁻² to 5 mA-cm⁻² above 0.5 A-cm⁻². The effect is attributed to changing CO/CO₂ ratio in the gas generated. For baked carbons the same value of the Tafel slope is found, although it applies over a restricted range of current density, and the overpotentials are lower than for graphite. The sheath of gas bubbles rising around the electrode distorts the current flow so that overpotentials at a fixed geometric current density vary with size and shape of the electrode.

One may wonder why yet another paper should be needed on overpotentials at carbon and graphite electrodes in cryolite-alumina melts in view of the amount of competent work already existing. [Thonstad (1) has given numerous references which there is no point in repeating here.] The justification is that we have applied a fresh technique, have obtained a novel result, and have revealed some problems which are, perhaps, more serious than had generally been realized.

The design of an apparatus for such measurements is dictated very largely by the nature of the electrode materials to be investigated. Commercial carbon anodes are made from a petroleum coke aggregate with particles up to 1 cm in diameter; if the surface of a test electrode is to be statistically representative it must have dimensions of the order of 4 cm, and the surface area will be 30-40 cm². Since commercial cells work at up to 1 A-cm⁻², and it is desired to extend the laboratory work substantially higher, this means that a current of at least 80A is required. There is, unfortunately, no small reference electrode (the equivalent of a Luggin capillary) which can be used, owing to problems with materials of construction; the physically bulky types available must be kept at a distance from the working electrode (to avoid disturbing the current distribution) and this leaves a sizable resistance drop to correct for. If a precision of, say, 10 mV is aimed at, then with 80A total current the resistance must be measured with a precision of about 10⁻⁴ ohm. This, in fact, turns out to be the major problem. The resistance must be measured at the same time as the cell potential, since it is obviously dependent on the gas bubbles and may be expected to vary with the d-c current; the only possible approach is by superposition of an a-c current and the measurement of the apparent a-c resistance by means of a bridge. This quantity, and previous workers seem to have ignored the fact, contains also the Faradaic resistance of the electrode, and the only way we have found to eliminate it is to go one step further and measure the degree of harmonic distortion of the a-c voltage (i.e., the generation of the second harmonic). Thanks to modern instrumentation this is now relatively easy, and, as is shown below, it not only solves the resistance problem but generates valuable information in its own right.

* Electrochemical Society Active Member.

¹ Present address: South African Atomic Energy Board, Private Bag X256, Pretoria, South Africa.

Key words: cryolite, alumina, graphite, carbon, overpotential, Faradaic rectification, Tafel slope.

Theory

Let the potential V of an electrode be a function, $f(I)$, of the current I . Then the potential at a current $I + h$ (where $h \ll I$) is given by Taylor's series as

$$f(I + h) = f(I) + hf'(I) + \frac{h^2}{2}f''(I) + \dots \quad [1]$$

If a small sinusoidal current is superimposed on the direct current, then h can be replaced by $\delta \sin \omega t$, where δ is the amplitude and ω the frequency of the superimposed current. Equation [1] thus becomes

$$f(I + \delta \sin \omega t) = f(I) + \delta \sin \omega t \cdot f'(I) + \frac{\delta^2}{2} \sin^2 \omega t \cdot f''(I) + \dots \quad [2]$$

The alternating component of the potential is obtained by subtracting the potential corresponding to the d-c current alone and is

$$V_{\text{alt}} = f(I + \delta \sin \omega t) - f(I) = \delta \sin \omega t \cdot f'(I) + \frac{\delta^2}{2} \sin^2 \omega t \cdot f''(I) + \dots \quad [3]$$

If the substitution $\sin^2 \omega t = (1 - \cos 2 \omega t)/2$ is made this becomes

$$V_{\text{alt}} = \delta \sin \omega t \cdot f'(I) + \frac{\delta^2}{4} f''(I) - \frac{\delta^2}{4} \cos 2 \omega t \cdot f''(I) \dots \quad [4]$$

The apparent resistance as observed at the fundamental frequency is simply $f'(I)$ (obtained by dividing the first term in Eq. [4], which is the only one at the fundamental frequency, by the sinusoidal current, $\delta \sin \omega t$). The second term represents Faradaic rectification, but is much too small to observe in the presence of the pseudorandom fluctuations in potential caused by the evolution of gas bubbles. The third represents a sinusoidal voltage of twice the fundamental frequency and amplitude $\sigma = (\delta^2/4)f''(I)$.

Suppose now that, over a limited range of current density (i) and time, the Tafel equation

$$V = a + b \ln i \quad [5]$$

may be used. By this we mean that, over the range of current densities covered by the excursions of the superimposed a.c., and for the time for several such oscillations to take place, the values of a and b are effectively constant. We can replace i , the current

density, by I/A , where I is the total current and A is the effective surface area, again assumed constant for a short period of time, and we can add a resistance term IR , so that

$$V = f(I) = a + b \ln I - b \ln A + IR \quad [6]$$

Differentiation gives successively

$$f'(I) = b/I + R \quad [7]$$

and

$$f''(I) = -b/I^2 \quad [8]$$

It is important to note that A , the effective area, has disappeared from both these derivatives, and R , the resistance, from the second. Experimental values of the second harmonic amplitude (σ) can be obtained, and hence $f''(I)$ from

$$f''(I) = 4\sigma/\delta^2 \quad [9]$$

If Tafel's law is applicable a plot of $\log(4\sigma/\delta^2)$ vs. $\log I$ should have a slope of -2 . Once this is established a value of b is calculated; this in turn can be used to correct the apparent resistance for the term b/I to give R (Eq. [7]), and finally IR can be subtracted from the measured V to give the electrode potential.

If Tafel's law is not verified on the log-log plot, then the Faradaic resistance must be determined by numerical integration of the experimental values of $f''(I)$.

We wish to emphasize that, complex though this procedure may be, we are not aware of any other experimental method of determining R . (In principle it can be done by going to frequencies high enough that the Faradaic resistance is short-circuited by the electrode capacity, but it seems that, with the high d-c current densities used here, frequencies of the order of 500 kHz would be necessary, and, with the low values of resistance to be measured, the problem of pickup in the loop formed by the anode and reference electrode leads and the melt seems to be insuperable.)

Experimental

All experiments reported here were made in a melt saturated with alumina at temperatures between 960°-980°C. About 800g of aluminum was added to 3 kg of melt except for two runs where a 20 weight per cent (w/o) Cu alloy was used. The graphite crucible containing the melt was 20 cm OD, 15 cm ID, and 20 cm high, and was heated in a resistance furnace. Temperatures were obtained before a run from a Chromel-Alumel thermocouple immersed in the melt. The temperature had to be watched closely to avoid cooling and crystallization of alumina on the electrode.

Details are given in Fig. 1. The working electrode was screwed onto a 1.6 cm diam copper rod attached higher up to a copper tube. A new anode had the form of a 3.75 cm diam cylinder with a hemispherical end, and a total immersed area of about 50 cm². Due to consumption the anode became somewhat conical in shape, and the average value of D_1 and D_2 was taken as the diameter of the cylinder. The diameter of the hemisphere was taken as D_2 . An Inconel rod (2 mm diam) was imbedded in the anode and ran parallel to the copper tube to serve as a potential lead.

The reference electrode consisted of a 0.7 cm ID alumina tube containing aluminum and a tungsten rod (1.5 mm diam) as lead. An opening was cut in the side facing the anode.

The electrical circuit is shown in Fig. 2. The d-c rectifier power supply, capable of giving 1000A at 5V, was connected, via a 0.388 mHenry choke, and a 0.5 mohm current measuring shunt across the cell. In the low current range a 1 ohm resistance was included in the circuit to extend the control steps of the power supply. A potential divider (ratio 100:1100 ohm) reduced the voltage between the anode and reference electrode to bring it within the range of the

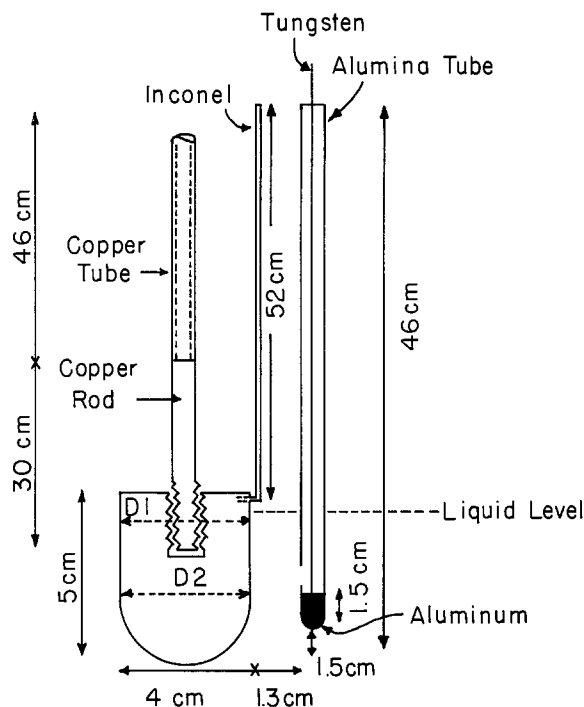


Fig. 1. Dimensions of anode and reference electrode

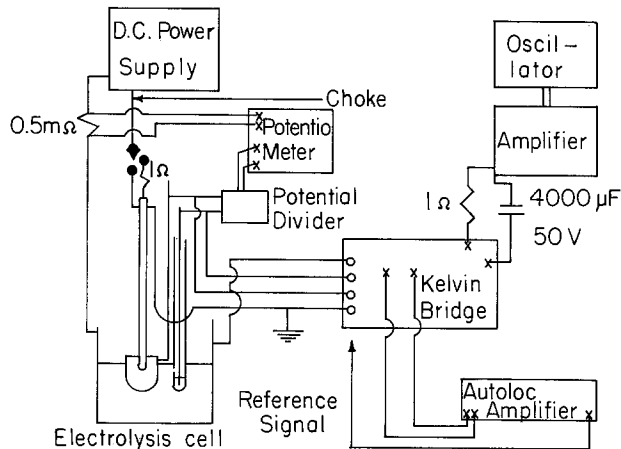


Fig. 2. Electrical circuit

potentiometer used to measure both it and the drop across the shunt.

A modified Kelvin bridge was used to measure the apparent resistance. Its power supply was a Heathkit oscillator and amplifier. To prevent d.c. going through the amplifier a 4000 μF capacitor was placed in series, as was also a 1 ohm resistor to protect the bridge from overloading. The input did not exceed 5V rms. It was essential that the lead to the cell shown in Fig. 2 as grounded should have the lowest practical resistance, and a 60 cm length of 6 gauge flexible cable was found suitable. It was connected to the copper tube supporting the electrode. The bridge was checked against a known resistor and found to give reliable results for frequencies up to 1.5 kHz.

The heart of the a-c measuring system was a phase-sensitive, frequency locked amplifier.² This instrument, which has a maximum sensitivity of 10 μV full scale deflection (fsd), is given a reference signal of the frequency of interest, and thereafter is sensitive only to that frequency, ignoring other frequencies, d.c., and random noise. The sole interference comes from odd harmonics of the reference frequency, but they were of

² Keithley Instruments Incorporated, 28775 Aurora Road, Cleveland, Ohio 44139, Model 840 Autoloc amplifier.

no concern in this work. By turning a switch the instrument can be operated at twice the frequency of the reference signal, thereby making it ideal for the second harmonic measurements.

The reference signal was taken across the standard resistor (usually 1 ohm) in use in the Kelvin bridge; this ensured that the phase taken as standard was that of the a-c current going through the cell. The magnitude of the current (rms) was next fixed (at either 1 or 0.3A, depending on the d-c current) by using the Autoloc amplifier to measure the drop across the same resistor. Following this the amplifier was used in place of the galvanometer of the bridge.

A run consisted of a series of about 20 voltage, current, resistance, and second harmonic measurements. Each run was started by applying the high currents first, thereby obtaining a steady-state surface. The current densities varied from about 3 to 0.01 A-cm⁻².

The resistance measurements were straightforward. The Autoloc amplifier was set to zero phase angle so that it would not respond to any inductive or capacitive components of the impedance, and the bridge was balanced to give zero signal. The second harmonic amplitude was measured across the galvanometer terminals after the bridge was balanced. In this way any second harmonic component contained in the input current was balanced out. The measurement was made at phase angles of 0°, 90°, 180°, and 270° to eliminate interference as far as possible. No successful measurements could be obtained at the highest d-c currents.

After a series of measurements, the current was reversed and run at about 5-10A for a minute or two to depolarize the electrode. The apparent resistance was then measured, and the current was returned to its normal direction. About 20A were passed for a few minutes before taking the electrode out of the bath; if this was not done it was hard to see where the immersion line was. When it was cold the dimensions of the electrode were measured.

Measurements were made on grade ATJ graphite and on baked carbon electrodes of the type used in Soderberg cells. They were made from petroleum coke aggregate heat-treated in a nitrogen atmosphere at 1250° and 1400°C, bonded with pitch, and finally baked at 970°C.

Treatment of Results

Resistances measured on the Kelvin bridge were in the vicinity of 0.01 ohm, and consequently sometimes lay in the X1 range of the bridge and sometimes in the X0.1 range. Despite the fact that tests with known resistors showed that there was no discrepancy on passing from one range to another, it was noticed that results with cells often did show a jump associated with the change of range. To check on this the a-c current and voltage were measured directly with the Autoloc amplifier, and the resistance was calculated to compare with bridge reading. It was found that the resistances on the X1 range were correct while those on the low range were in error, although measurements made with reversed d-c current seemed to be correct. The reason for this behavior is not known, but all measurements made on the low range have been eliminated from the final results.

The amplitude of the second harmonic component was measured across the galvanometer terminals of the bridge in order that the second harmonic distortion existing in the input waveform (~2%) should be balanced out, but owing to the dividing action of the bridge resistors, the full amplitude was not present across the galvanometer terminals. The magnitude of the factor (measured amplitude/input amplitude) was determined by applying a known voltage across the potential input of the bridge and measuring the voltage between the galvanometer terminals. The factor was found to vary from 0.990 to 0.908, depending on the bridge setting.

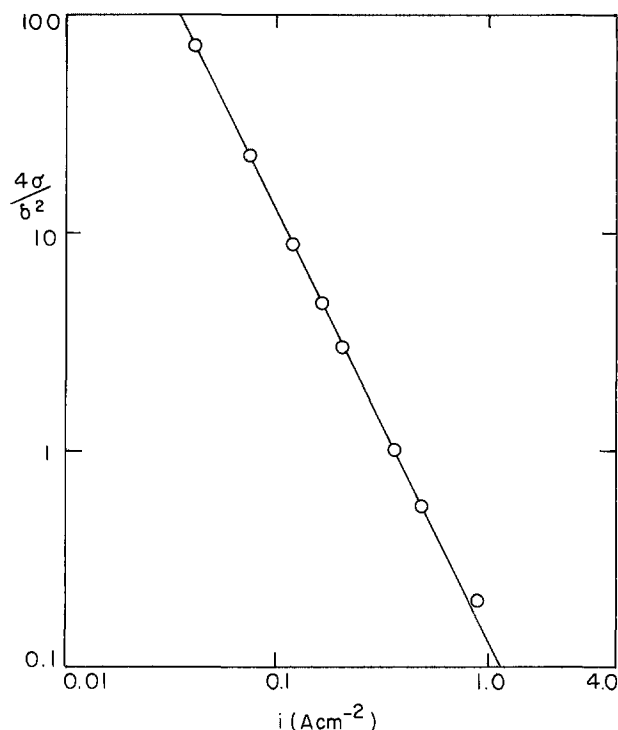


Fig. 3. Second harmonic amplitude (σ) as a function of d-c current density for ATJ graphite.

It was assumed that the genuine part of the second harmonic signal was reversed in sign when the phase was changed 180°. By subtracting algebraically, any part which was not reversed was eliminated. This was done for the 0°-180° pair and the 90°-270° pair, and they were then added vectorially. The resultant was corrected for the calibration factor and the quantity $4\sigma/\delta^2$ found. (Note that a factor of $\sqrt{2}$ is necessary to go from rms values as measured to amplitudes.)

Results

Figure 3 shows, on a log-log plot, values of the quantity $4\sigma/\delta^2$ as a function of current density for one of the runs with graphite. The expectation of a straight line of slope -2 , indicating Tafel behavior, is borne out; in this case the statistical value is -1.935 with a standard error of ± 0.014 , and the corresponding value of b (Eq. [8] and [9]) is 0.1291 ± 0.0039 . The results of the eight runs with graphite are given in Table I. In only one of them was the slope statistically different from -2 (-1.886 ± 0.011). For ease of comparison with the other runs the exchange currents have nonetheless been calculated with a constant value of b (see below). The arithmetic mean value of the slopes is -1.964 with a standard deviation of ± 0.048 . This value obviously does not differ significantly from -2 , so that Tafel behavior is proven.

Table I. Values of the slope of the log-log plot and b for graphite

Slope	\pm Standard error	b	\pm Standard error
-1.987	0.024	0.1512	0.0032
-1.999	0.024	0.1169	0.0023
-2.027	0.019	0.1159	0.0017
-1.935	0.014	0.1291	0.0039
-1.915	0.094	0.1460	0.0083
-1.991	0.013	0.1210	0.0016
-1.886	0.011	*	—
-1.971	0.011	0.1176	0.0014
Mean: -1.964		Mean: 0.1282	

* Since the slope is statistically different from -2 , no value of b is calculated

The arithmetic mean value of b is 0.128 with a standard deviation of ± 0.015 . Whereas the standard deviation of the slopes is comparable with the standard error of individual values, the standard deviation of b is four times greater than the individual standard errors. This implies that the values of b are genuinely different from one another.

With the baked carbon electrodes a different situation is encountered. Whereas with graphite the second harmonic results were independent of frequency in the range 50-520 Hz (the results reported were obtained at 520 Hz), with carbon the values show a frequency dependence, and furthermore the log-log plot is not straight over so wide a range. Figure 4 shows the results of three runs at each of two frequencies for the 1200°C carbon; the straight line is that for graphite. At 49 Hz the results are identical to those for graphite above about 0.7 A-cm⁻²; at 520 Hz there are deviations both above and below this value. Measurements on the 1400°C carbon were made only at 50 Hz. The deviations (Fig. 5) are markedly less in the low current range than for the 1200° material.

Turning now to the electrode potentials after correction for the resistive drop, Fig. 6 shows the results for graphite, and Fig. 7 those for baked carbons; they are generally similar but about 100 mV lower. Since the melts were saturated with Al₂O₃ the reversible potential (for production of CO₂) is readily calculated from the JANAF Tables (2) as 1.19V at 970°C. Two lines, both with the slope $b = 0.128$ derived from Table I, have been drawn. Although each line fits reasonably well over a range of current densities, it is apparent that there is a discontinuity between 0.2 and 0.5 A-cm⁻². This implies that there is a change of exchange current in this region. The exchange currents are plotted in Fig. 8; they have been calculated from the potentials with the average value of b instead of the individual ones since small differences in b make large differences in i_0 . The exchange current rises from about 1.5 mA-cm⁻² for currents below 0.1 A-cm⁻² to about 5 mA-cm⁻² for currents above 0.5 A-cm⁻². The two runs made with the 20 w/o Cu alloy show somewhat higher exchange currents.

Discussion

It would be very easy, in the absence of the value of b from the second harmonic measurements, to

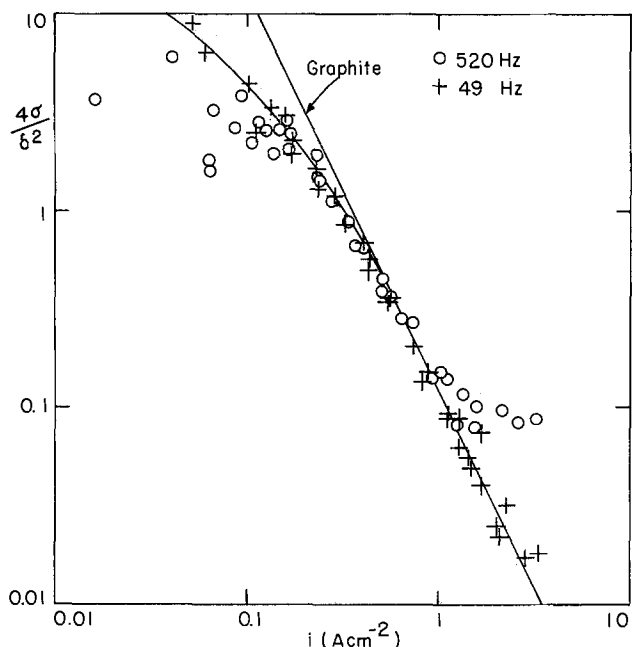


Fig. 4. Second harmonic amplitude (σ) as a function of d-c current density for 1200°C carbon.

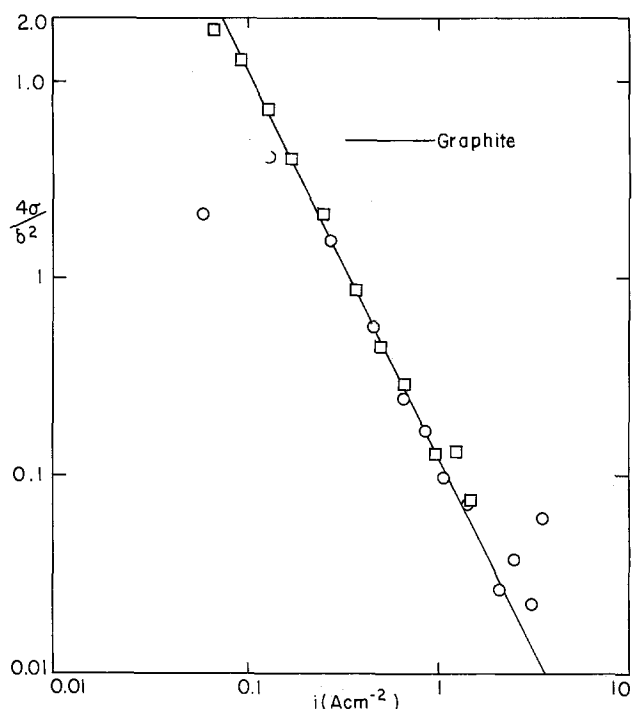


Fig. 5. Second harmonic amplitude (σ) at 50 Hz as a function of d-c current density for 1400°C carbon.

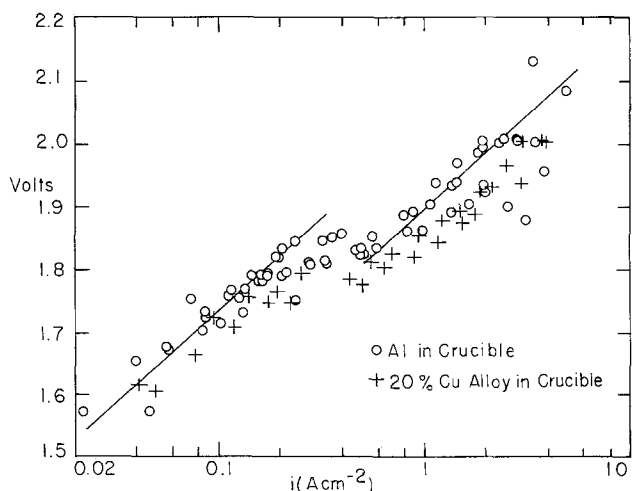


Fig. 6. Current-potential curve for ATJ graphite

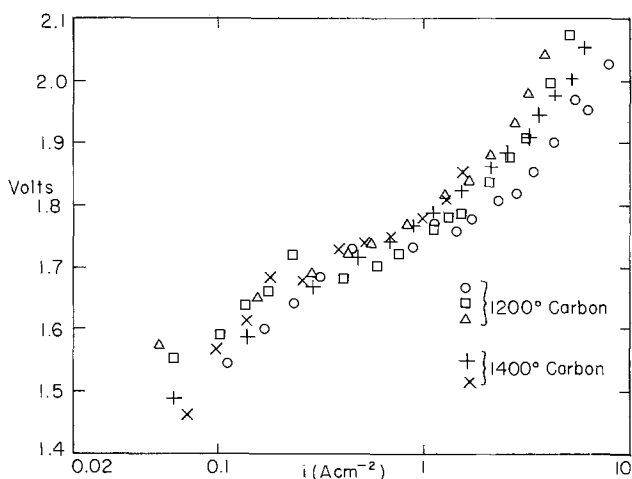


Fig. 7. Current-potential curves for baked carbons

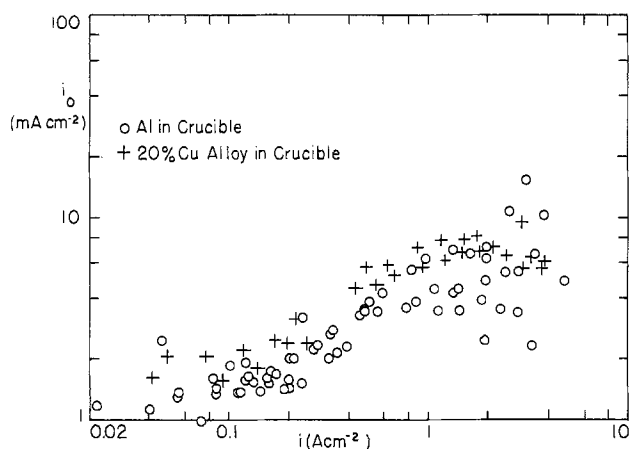


Fig. 8. Exchange current density as a function of current density for ATJ graphite.

draw a straight line of much flatter slope through the points of Fig. 6. This kind of effect is probably the reason for the disparate values of b appearing in the literature.

The decision to add metallic aluminum to the crucible was taken because preliminary experiments had shown that if this was not done quite erratic results were obtained. It is not possible with the present equipment to operate in the absence of aluminum since it is inevitably formed during the electrolysis, and adding it initially was the best way to control the situation. It is, however, quite possible that it is responsible for the change of exchange current shown in Fig. 8. Since there is aluminum in the melt, there will be dissolved aluminum in the melt, and this gives rise to CO in the gas by the familiar mechanisms responsible for loss of current efficiency. The fraction of CO in the gas will depend on how fast CO₂ is being generated electrolytically; the higher the current the more CO₂ will be available to dilute the CO. It is known that CO is strongly adsorbed on carbon surfaces and acts as a catalytic poison. Studies of the rate of oxidation of carbon by gaseous CO₂ (3) have shown that adsorbed CO inhibits the reaction, and the overpotential measurements of Richards and Welch (4) also showed higher values when the CO content of the gas surrounding the anode was increased. One therefore suspects that the lower exchange current at low current densities is due to the adsorption on the surface of CO produced by reaction of CO₂ with dissolved aluminum. The fact that higher exchange currents are found when an Al-Cu alloy (which will reduce the amount of Al in solution) is used tends to confirm the hypothesis.

The reproducibility of the results obtained with graphite (excluding those from the two runs with the Cu alloy) is shown in Table II. The individual points on the current-voltage curves were interpolated linearly to convenient values of current; no attempt was made to smooth the curves before doing so, although it is quite possible that it would improve reproducibility if a satisfactory procedure could be evolved.

On examining the results for the baked carbons another effect was noticed. The run marked in Fig. 7 with circles is conspicuously low. On seeking what was different, it turned out that it was an electrode

Table II. Interpolated anode potentials for graphite anodes

i (A-cm ⁻²)	Mean V	± Std deviation
1.0	1.871	0.043
0.5	1.830	0.010
0.2	1.810	0.017
0.1	1.738	0.019

which had been used several times, and consequently it had a much reduced surface area. This called into question the whole concept of plotting potential against current density. In fact, inspection showed that less scatter was obtained by using total current as the abscissa and not bringing in the area at all.

To try and clarify the situation the data on the 1200° carbon were fitted by regression analysis to the equation

$$\log(\text{total current}) = a_0 + a_1V + a_2V^2 + a_3 \log A \quad [5]$$

where A is the electrode area, and the value of a_3 was found to be 0.309 ± 0.057 . The proper variable to take is thus

$$\text{total current}/(\text{area}^{0.309})$$

and Fig. 9 shows the result. The scatter is substantially reduced.

The discovery of this area effect raises a number of questions. In the first place, What causes it? The most likely answer seems to lie with the gas bubbles. Although the technique used corrects the voltage for the effect of the electrical resistance caused by the gas around the anode, there is no way of correcting for the fact that the bubbles screen part of the electrode, and that the current distribution is not uniform. Presumably the current concentrates toward the bottom and is limited toward the top by the sheath of gas rising around the electrode. Under these circumstances, an increase in area by lowering the electrode further into the melt may have little effect, since the new surface is at the top and it is largely screened. The data available are not adequate to carry the analysis beyond this purely qualitative picture. It seems that Piontelli and his colleagues have observed a similar effect (5).

The second point which is raised, since we are apparently dealing with a scale effect, is how one transfers the results of laboratory experiments to industrial cells. At the same time, if the gas is having such effects on small, vertical electrodes where it can escape easily, it must be having a drastic influence under a large horizontal industrial anode. At this point, it looks as if study of gas bubbles and how they behave may be of much more practical importance than the overpotentials themselves.

From Fig. 7 it would obviously be impossible to say that there was any significant difference in overpotential between the two baked carbons. From Fig. 9, where the scatter is less, it looks as if there might be, in some ranges of current density. However, in the range 0.5-1.0 A-cm⁻² used in practice (6.5-13 on the scale at the bottom of Fig. 9) any difference is marginal. Exact statistics are hard to apply, but 20 ± 20 mV would be a fair estimate.

The value of b obtained (0.128 if the Tafel equation is expressed in natural logarithms, 0.295 if in

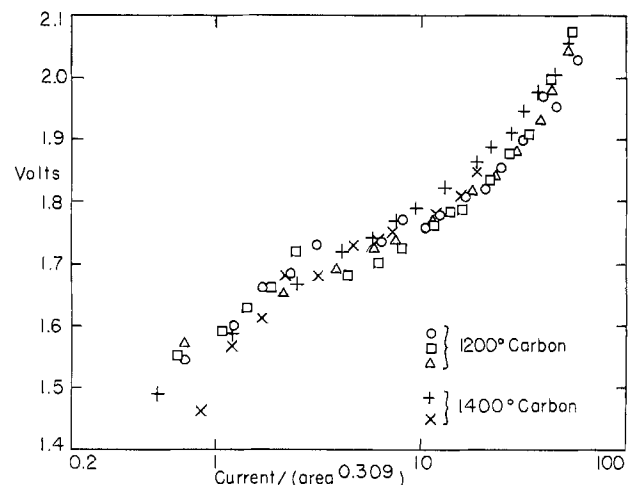


Fig. 9. Current-potential curves for baked carbons

\log_{10}) applies to both graphite and the baked carbons used, and, since it was obtained by a method not affected by the presence of gas bubbles, should be of fundamental significance.

Manuscript submitted March 7, 1974; revised manuscript received Oct. 15, 1974.

Any discussion of this paper will appear in a Discussion Section to be published in the December 1975 JOURNAL. All discussions for the December 1975 Discussion Section should be submitted by Aug. 1, 1975.

Publications costs of this article were partially assisted by Aluminum Company of Canada, Limited.

REFERENCES

1. J. Thonstad, *Electrochim. Acta*, **15**, 1569 (1970).
2. JANAF Thermochemical Tables, 2nd ed., NSRDS-NBS 37, U.S. Bureau of Standards, Washington, D.C. (1971).
3. E. T. Turkdogan and J. V. Vinters, *Carbon*, **8**, 39 (1970).
4. N. E. Richards and B. J. Welch, "Proc. First Australian Conference on Electrochemistry," p. 901, Pergamon, London (1964).
5. U. Ducati, 2nd Czech. Aluminium Symposium, Banska Bystrica (1972).

The Iodate-Iodine Electrode

Mechanism, Standard Potentials, Related Thermodynamic Data

R. D. Spitz

Dow Badische Company, Freeport, Texas 77541

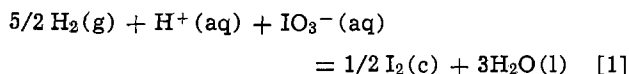
and H. A. Liefbafsky*

Department of Chemistry, Texas A&M University, College Station, Texas 77843

ABSTRACT

The standard potential of the iodate-iodine electrode enters into the calculation of many other thermodynamic data. The following new values of this E° have been measured: 1.1942V at 25°C, 1.1903V at 37.5°C, 1.1863V at 50°C with an estimated uncertainty ($\pm 0.0002V$) improved about tenfold over earlier values. Calculated values of related thermodynamic data are given. Agreement, established in 1905, of electrochemical and chemical values for the equilibrium constant of the Dushman reaction has been restored and extended. Thermodynamic difficulties inherent in the cells studied have been successfully handled by approximation-extrapolation methods. The investigation was carried out with the following mechanism as a guide. The electron-transfer steps at the reversible iodate-iodine electrode are assumed to be identical with those at the reversible iodine-iodide electrode. At the former electrode these electron-transfer steps are assumed to be accompanied by the chemical steps that participate in the Dushman reaction.

The standard potential E° for the reaction

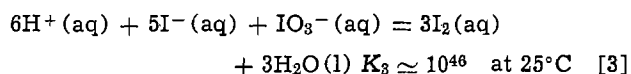


is the standard potential of the iodate-iodine electrode; it is also the voltage reading for the cell



operating reversibly under standard conditions with elimination of the potential difference at the junction of the aqueous electrolytes. The early value of E° at 25°C by Sammet (1) has been superseded by that of Lundberg, Vestling, and Ahlberg (2), which is $1.195 \pm 0.002V$. There appear to be no reliable values for other temperatures.

This standard potential has been used to establish thermodynamic data for iodate ion (2), and it has been combined with that of the iodine-iodide electrode (and with other data) to give the equilibrium constant of the Dushman reaction



This electrochemical determination of K_3 was carried out by Sammet (1), who obtained results at 25°C that agreed to about 10% with the K_3 that he chemically

determined. An uncertainty of 0.002V in E° means an uncertainty of about 50% in K_3 . The new value of E° spoils the good agreement Sammet found in his classic investigation. Further work is needed, not only to show how closely a complex equilibrium constant like K_3 can be established by these two methods, but also to obtain results for temperatures other than 25°C.

The last matter has become important because the oscillatory decomposition of hydrogen peroxide (3, 4), which is being reinvestigated at 50°C, involves the Dushman reaction. For this and the reasons preceding, an extensive study of the iodate-iodine electrode was made at 25°, 37.5°, and 50°C.

Experimental

Chemicals of the best grade obtainable were used without further purification.

To eliminate the risk of reaction between H_2 and IO_3^- , a cell with liquid junction is mandatory. In Ref. (2), this junction was static, being formed in a three-way stopcock. With the stopcock open, the junction was reproducible and relatively stable; with the stopcock closed, voltage readings changed in a few minutes, probably because of changes in the thin liquid film. In comparative experiments, we found a flowing junction (5) to give steady, reproducible values and to be preferred over a static junction.

Experiments proved the desirability of equilibrating the iodate electrolyte with crystalline iodine outside the cell. Equilibration for at least 24 hr with stirring on a hot plate at 50°C was adopted as standard practice.

* Electrochemical Society Active Member.

Key words: electrode mechanism, iodate-iodine electrode, thermodynamic data, Dushman reaction.

Each cell compartment contained dual, platinized electrodes, each about 1 cm² in area. Voltage differences between electrodes in the same compartment were about 0.0001V when cells were at thermostat temperature, which was controlled to less than $\pm 0.1^\circ\text{C}$.

For reasons to be discussed, temperature-cycling of the cells in the thermostat was used to ensure reliable voltage readings. When each cell compartment and the two electrolyte reservoirs had been filled at the initial thermostat temperature of 50°C, electrolyte flow was started to set up the liquid junction. Voltage readings were then made with a Corning® Model 101 Digital Electrometer, this being a solid-state voltmeter with an input impedance of 10¹⁴ ohms, which was standardized frequently against a new, saturated Weston standard cell. The cell voltage was monitored until it became steady to within $\pm 0.0001\text{V}$ over at least an hour. This usually occurred some 10 or 12 hr after the cell had been filled. With a satisfactory cell voltage established at 50°C, the thermostat temperature was lowered to 37.5°C, and the voltage monitoring was repeated to establish the cell voltage at the lower temperature. This typically required 12 hr. Next, the cell voltage at 25°C was similarly obtained. At 25°C, the equilibrating period was sometimes 24 hr long. For most of the final cells, the temperature sequence was then reversed to obtain another set of voltage readings at 37.5° and 50°C. In general, the second reading at each temperature checked the first to within 0.0001V, which is conclusive evidence that the readings were satisfactory. See Fig. 1.

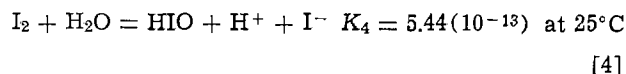
Difficulties. Mechanism

The evaluation of E° for the iodate-iodine electrode is beset with the following difficulties: the liquid-junction potential; the fact that HIO₃ is an intermediate electrolyte, neither weak nor strong (details later); uncertainties in activity coefficients; and unreproducibility of voltage readings, especially at low iodic acid concentrations. Consequently, values of E° , instead of being identical, are different for different iodic acid concentration. With increasing dilution, the first three difficulties can become less serious; but voltage unreproducibility then made reliable measurements impossible: results at 0.001M HIO₃ were not considered worth reporting in Ref. (2). To resolve this dilemma, a new approach is needed.

The voltage unreproducibility must be due to sluggishness of reaction, chemical, electrochemical, or both, at the iodate-iodine electrode. Reaction mechanisms at electrodes so complex as this are never certain. Nevertheless, some sort of picture is needed. The picture that follows did guide us to experimental conditions under which the iodate-iodine electrode was more nearly reversible so that voltage readings were improved.

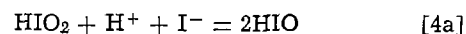
Iodine and iodate do not react with each other. Yet kinetic studies have shown the existence of various

compounds, intermediate between I₂ and IO₃⁻ in oxidation number and with oxygen covalently bonded to iodine; for example, HIO, HIO₂, H₂I₂O₃, HI₃O, I₃O₂⁻, and I₂O₂ are all needed (6) to explain the kinetics of the reverse Dushman reaction, Eq. [3]. None of these oxygenated species is likely to exchange electrons reversibly (that is, with great ease) at an electrode. Still, one cannot have complete equilibrium unless each species in the system is at its equilibrium concentration. We therefore postulate that the equilibrium concentration of each oxygenated iodine species is established chemically as in the Dushman reaction. The hydrolysis of iodine, namely



is rapid enough (7) in both directions so that reaction [4] is always at equilibrium (8). For present purposes, it is permissible to simplify the kinetic picture by considering HIO, HIO₂, and IO₃⁻ to be the only significant oxygenated species, and by assuming that they react only with I⁻ and H⁺.

The iodine-iodide electrode is known to be highly reversible (9). This leads to the following mechanism for the iodate-iodine electrode. The electron-transfer processes at the two electrodes are identical and involve no oxygenated species. Complete equilibrium is established at the iodate-iodine electrode through the participation of steps characteristic of the Dushman reaction. To illustrate: one step is



The occurrence of reaction [4a] will shift the equilibrium of reaction [4]. When this happens, [I₂] and [I⁻] will change, and these concentration changes will affect the electron-transfer processes at the electrode.

This picture relies upon the reactions of I⁻, a species that appears neither in reaction [1] nor in the Nernst equation for the iodate-iodine electrode. The picture is nevertheless reasonable. Suppose a saturated iodine solution at 25°C is made 0.1M in HIO₃. Prior to the HIO₃ addition, [I⁻] will be near 10⁻⁶M (Eq. [4]). At complete equilibrium in the cell, [I⁻] will have decreased to, say 10⁻⁹M (Eq. [3]). This reduction in concentration will have been brought about in large part by the forward Dushman reaction at a rate (10) given by

$$-d[\text{IO}_3^-]/dt = -1/5 d[\text{I}^-]/dt \\ = 1.2(10^4)[\text{H}^+]^2[\text{IO}_3^-][\text{I}^-] \text{ mol l}^{-1} \text{ min}^{-1} \quad [5]$$

When [H⁺] = [IO₃⁻], this rate is evidently proportional to [HIO₃]³. It is near 10⁻⁸ mol IO₃⁻ per liter per minute when [I⁻] is near 10⁻⁹M and [HIO₃] is 0.1M. The net rate will of course be much less near equilibrium as the reverse reaction also comes into play. Note that Eq. [5] was actually established at iodide concentrations near 10⁻¹⁰M, which lends credibility to the present discussion. Note also that the [HIO₃]³ proportionality means a very low forward rate in dilute iodic acid solutions, which is probably the reason for the voltage unreproducibility encountered at [HIO₃] = 0.001M (2).

With increasing temperature, the equilibria in reactions [3] and [4] are shifted so as to increase the concentrations of iodine reaction products such as I⁻ and HIO. It is reasonable to suppose that the concentrations of other intermediate products (e.g., HIO₂) also increase when this happens. Suppose complete equilibrium exists at an iodate-iodine electrode at 50°C, and the temperature is lowered to 37.5°C. Suppose that the concentrations of the various intermediate compounds readjust themselves slowly to the reduced equilibrium values at the lower temperature. Until they reach these reduced values, the voltage of the cell will be above its equilibrium value for 37.5°C. The same consideration applies when the temperature is subse-

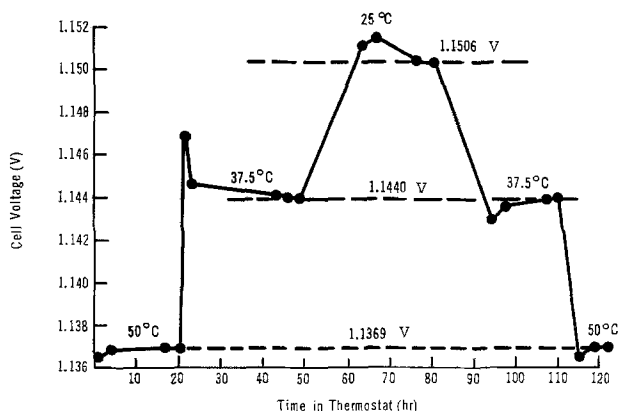
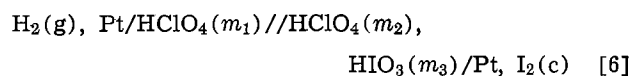


Fig. 1. Final voltage readings as established by temperature-cycling.

quently lowered from 37.5° to 25°C. It applies in reverse when the temperature is subsequently raised, first to 37.5° and then back to 50°. The behavior just described is actually found; see Fig. 1. This further evidence of slowness of reaction increases confidence in final voltage readings (such as 1.1369 and 1.1440V in Fig. 1) established by temperature-cycling.

Equation [5] shows that increasing $[H^+]$ is the most effective way of increasing the rate of the forward Dushman reaction. It is also evident that complications caused by the liquid junction, by activity coefficients, and by the weakness of HIO₃ will all disappear if $[IO_3^-]$ can be made low enough. The first feature of our approach is to replace cell [2] by cell [6], which is



where the concentrations in this and all subsequent cells are molalities (mols solute/kg H₂O) with $m_1 = m_2 + m_3$ in all final experiments. The second feature is to make a series of cell measurements in which m_3 is varied. The third feature is temperature-cycling, already discussed. In this way, we obtain at each temperature a series of measured voltages that are corrected to unit fugacity of hydrogen to give values called E_c . The fourth feature is the calculation, in various ways, of approximate standard potentials called E°_1 . The fifth feature is the extrapolation of these E°_1 data to $m_3 = 0$ to give the final E° , which is the standard potential for a hypothetical cell in which the only electrolyte at appreciable concentration is HClO₄ at molality m_1 .

For the iodate-iodine compartment, the postulated mechanism consists of the iodine-iodide electrode reactions combined with the chemical steps characteristic of the Dushman reaction. This mechanism is in accord with the results of the following experiments: (i) Cells with $m_1 = 0.1$ reach their final voltage readings much more quickly than cells with $m_1 = 0.01$, other things equal. (ii) The reaching of final voltage readings was not appreciably speeded by early operation of the iodate-iodine electrode as a low-current-density anode or cathode; such efforts might be expected to fail if the only electrochemical processes are those of the iodine-iodide electrode, which is highly reversible (9). (iii) The addition of I⁻ to generate I₂(c) within the cell gave evidence of the presence of intermediate products (e.g., HIO₂) similar to that in Fig. 1. For such a cell, the voltage readings increased steadily until, after 5 hr, they passed those of a cell that was comparable except for having the iodate electrolyte equilibrated as usual with I₂(c). The explanation: when I⁻ is added, it is rapidly removed according to Eq. [5]. As this occurs, HIO₂ is generated; rapidly at first, more slowly as $[I^-]$ decreases. The reduction of $[HIO_2]$ to its final equilibrium value is slow enough so that it still exceeds this value at 5 hr and beyond. The excess in $[HIO_2]$ does not occur unless I⁻ is initially added. The cell thus treated has the higher voltage reading so long as this excess exists.

Experimental Results and Extrapolations

Any attempt to calculate E° rigorously from the E_c values is, in our opinion, less likely to give reliable results than the approximation-extrapolation method now to be described. At each temperature, E°_1 is calculated in four ways from E_c at each m_3 , and each series of calculated values is plotted against m_3 as abscissa. Extrapolation to $m_3 = 0$ then permits selection of the final E° from a consideration of the intercepts on the ordinate axis. The four methods of calculation are

$$1. \quad {}_1E^{\circ}_1 = E_c + (RT/5F) \ln [H^+] [IO_3^-] (\gamma_{\pm})^2_{HClO_4} \quad [7]$$

$$2. \quad {}_2E^{\circ}_1 = E_c + (RT/5F) \ln (H^+) (IO_3^-) (\gamma_{\pm})^2_{HClO_4} \quad [8]$$

where

$$(H^+) = [H^+] - (HIO_3) \quad [9]$$

$$(IO_3^-) = [IO_3^-] - (HIO_3) \quad [10]$$

and

$$K_{11} = (H^+) (IO_3^-) (\gamma_{\pm})^2_{HClO_4} / (HIO_3) \quad [11]$$

Evidently, the second approximation introduces a correction for the weakness of HIO₃. Brackets denote analytical ("total") concentrations of the enclosed substances; parentheses enclose calculated actual concentrations. The activity coefficient of HIO₃ is taken as unity.

$$3. \quad {}_3E^{\circ}_1 = E_c + (RT/5F)$$

$$\ln [(H^+)^6 {}_1 (IO_3^-) (\gamma_{\pm})^2_{HClO_4} / (H^+)^5 {}_H] \quad [12]$$

The subscript I identifies the iodate-iodine compartment of the cell, and the subscript H identifies the hydrogen compartment. Owing to the weakness of HIO₃, $(H^+)_I$ is less than $(H^+)_H = m_1 = 0.1$. Consequently, the voltage is reduced below what it would have been were HIO₃ as strong an electrolyte as HClO₄.

$$4. \quad {}_4E^{\circ}_1 = {}_3E^{\circ}_1 - E_L \quad [13]$$

Here E_L is the potential at the liquid junction calculated for each cell according to MacInnes (11). Fortunately, E_L is small; it ranges from 0.0023V for $m_3 = 0.05$ to less than 0.0001V for $m_3 = 0.001$.

The following values of $(\gamma_{\pm})_{HClO_4}$ were used, all for $m_1 = 0.1$: 0.803 (25°C); 0.799 (37.5°C); 0.795 (50°C). The first is the accepted value for 25°C (12), which was assumed to vary with temperature according to the Debye-Hückel limiting law to give the other two values.

The dissociation constants of HIO₃ were calculated from

$$\log K_{11} = 634.9/T - 2.911 \quad [14]$$

(T , thermodynamic temperature) which is the equation for the least squares line corresponding to results in the literature (13-16).

The experimental results and the approximate standard potentials are given in Table I.

The variation of E°_1 with m_3 is gratifyingly small. The extrapolations will accordingly give reliable standard potentials. To show this, the E°_1 values at 50°C for all four approximations are plotted in Fig. 2. The last three methods give lines converging on 1.1863V = E° at 50°C to within 0.0002V (estimated). The first method, which neglects the weakness of HIO₃, must be disregarded.

Table I. Corrected voltage readings, E_c , and approximate standard potentials, E_1

m_3 , mol HIO ₃ /kg·H ₂ O	E_c , V	${}_1E_1$, V	${}_2E_1$, V	${}_3E_1$, V	${}_4E_1$, V
Temperature, 25.0°C					
0.05	1.1617	1.1912	1.1934	1.1969	1.1951
0.04	1.1608	1.1914	1.1935	1.1964	1.1949
0.03	1.1598	1.1919	1.1939	1.1960	1.1950
0.02	1.1576	1.1918	1.1937	1.1951	1.1944
0.01	1.1533	1.1911	1.1929	1.1936	1.1932
0.005	1.1510	1.1923	1.1941	1.1944	1.1942
0.001	1.1387	1.1883	1.1900	1.1941	1.1900
Temperature, 37.5°C					
0.05	1.1556	1.1864	1.1890	1.1932	1.1911
0.04	1.1547	1.1867	1.1892	1.1925	1.1909
0.03	1.1539	1.1874	1.1898	1.1923	1.1911
0.02	1.1517	1.1874	1.1897	1.1914	1.1905
0.01	1.1478	1.1872	1.1894	1.1902	1.1898
0.005	1.1449	1.1880	1.1901	1.1905	1.1903
0.001	1.1348	1.1865	1.1886	1.1887	1.1886
Temperature, 50.0°C					
0.05	1.1499	1.1820	1.1851	1.1899	1.1876
0.04	1.1487	1.1820	1.1850	1.1889	1.1870
0.03	1.1480	1.1829	1.1858	1.1887	1.1873
0.02	1.1460	1.1832	1.1859	1.1879	1.1869
0.01	1.1424	1.1834	1.1860	1.1870	1.1865
0.005	1.1387	1.1836	1.1861	1.1866	1.1864
0.001	1.1298	1.1837	1.1861	1.1862	1.1862

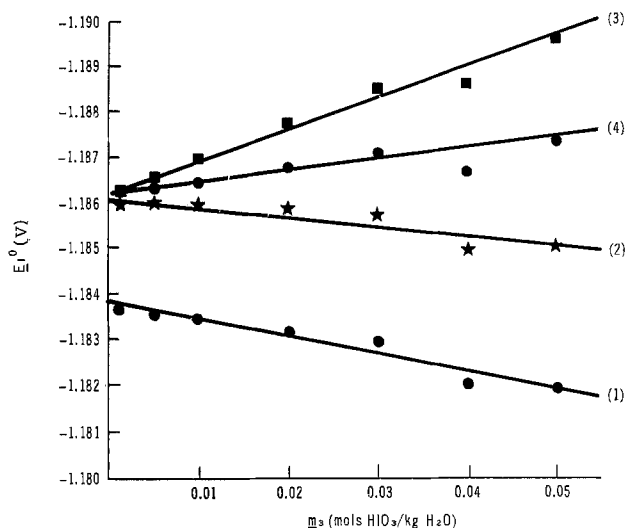


Fig. 2. Extrapolation of approximate standard potentials at 50°C to establish $E^\circ = 1.1863 \pm 0.0002V$.

At the lower temperatures, values of $4E^\circ_1$ at $m_3 = 0.001$ diverged from the chosen straight line by 0.0042V at 25°C and 0.0034V at 37.5°C. This divergence was attributed to sluggishness of reaction not observed at 50°C. It will be remembered that Lundberg *et al.* regarded results for 0.001M HIO₃ at 25°C as too unreplicable to report (2).

The results of the extrapolations are given in Table II. At 25°C, the final E° is within the limits, $E^\circ = 1.195 \pm 0.002V$, of Ref. (2); but the estimated uncertainty is tenfold smaller.

Derived Thermodynamic Data

Cell reaction.—Derived data and explanatory notes for reaction [1] appear in Table III.

Dushman reaction.—For reaction [3]

$$\Delta G^\circ[3] = \Delta G^\circ[1] - 5\Delta G^\circ[16] - 3\Delta G^\circ[17] \quad [15]$$

where the bracketed numbers identify reactions, and the two reactions not yet mentioned are

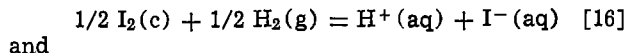


Table II. Values of E° from various approximation-extrapolation procedures for the cell $H_2(g)$, Pt/HClO₄//HIO₃/Pt, I₂(c)

Approximation	E° (V)		
	25.0°C	37.5°C	50.0°C
1	1.1924	1.1882	1.1838
2	1.1941	1.1903	1.1862
3	1.1941	1.1903	1.1863
4	1.1942	1.1903	1.1863
Final E°	1.1942 ^(a)	1.1903 ^(a)	1.1863 ^(a)

^(a) Estimated uncertainty: $\pm 0.0002V$.

Table III. Thermodynamic functions for reaction [1]

Temperature, °K	ΔG° , cal/mol IO ₃ ⁻	ΔH° , cal/mol IO ₃ ⁻	ΔS° , cal/K·mol IO ₃ ⁻
298.15	137,697	148,559	-36.44
310.65	137,248	148,565	-36.44
323.15	136,785	148,559	-36.44

NOTES

- $\Delta G^\circ = -nFE^\circ$. E° from experimental measurements of E_c .
- $\Delta S^\circ = nF\partial E^\circ/\partial T$. Quotient is slope of least squares line through values of E° plotted against absolute temperature. Variation of ΔS° with T too small to be detected.
- $\Delta H^\circ = \Delta G^\circ + T\Delta S^\circ$.
- As is customary, calculated values are reported to more places than is warranted by the estimated uncertainty in the experimental data (Table II).



Thermodynamic data for these reactions are given in Tables IV and V, and the data for reaction [3] appear in Table VI.

We must now see how well the new K_3 values agree with those from the chemical determinations by Sammet (1). His chemical determinations, unlike his electrochemical determinations, of K_3 could probably not be improved upon today. When adequate time to reach chemical equilibrium is allowed (Sammet found 5-10 weeks at 25°C and 6-8 days at 60°C to suffice), the chief experimental uncertainty in the chemical determinations is in the determination of $[I_2(aq)]$ at equilibrium. For Sammet's experiments

$$K_3 = [I_2(aq)]^3 / (K_{19}/K_{20})^5 (H^+)^6 (IO_3^-)^6 (\gamma_{\pm})^{12} {}_{HIO_3} \quad [18]$$

where the two previously undefined equilibrium con-

Table IV. Standard potentials and standard Gibbs energy changes for reaction [16]

Temperature, °K	E° (V)		ΔG° (cal/mol I ⁻)	
	Thermochemical	Electrochemical	Thermochemical	Electrochemical
298.15	+0.5383	+0.5355	-12,413	-12,349
310.65	+0.5361	+0.5333	-12,363	-12,299
323.15	+0.5339	+0.5312	-12,313	-12,249

NOTES

- Thermochemical data calculated in usual way from standard enthalpies of formation and standard entropies of reactants and products in reaction [16]. Data accepted as definitive were used (17).
- At 298.15°K, E° is Latimer's value (18). For the other temperatures, E° values are calculated from this datum and from the thermochemical value of ΔS° . See Note 2, Table III. Corresponding ΔG° values obtained as in Note 1, Table III. This procedure should give the best results as the thermodynamic entropy data (17) are more reliable than the heats of formation.
- The thermodynamic value of E° at 298.15°K exceeds the electrochemical by 0.0028V, an amount considered greater than the uncertainty in the latter. The thermodynamic ΔH°_f for I⁻ is -13.60 \pm 0.20 kcal/mole. This uncertainty corresponds to $\pm 0.0087V$ in E° . Perhaps the data in Ref. (16) should be reevaluated.
- The ΔG° values in the table are also ΔG°_f values for iodide ion.

Table V. Solubility of iodine, reaction [17]

Temperature, °K	Solubility (mols/liter) $\times 10^8$		ΔG° , cal/mol I ₂ (aq)
	Gross	Corrected	
298.15	1.3317	1.3151	-3930
310.65	1.9570	1.9277	-3859
323.15	2.7914	2.7460	-3787

NOTES

- Gross solubility as measured. The smoothed data conform to the equation: $\log s = -(1.239 \times 10^3/T) + 1.279$.
- The true concentration of dissolved iodine, $I_2(aq)$, is less than the gross solubility owing to reaction [4] and to the formation of I₃⁻; that is, $[I_2(aq)] = s - [HIO] - [I_3^-]$. Equilibrium constants from Ref. (8) were used in calculating the corrections.

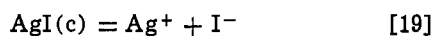
Table VI. Standard Gibbs energy changes and equilibrium constants for reaction [3]

Temperature, °K	ΔG° (El) cal/mol IO ₃ ⁻	ΔG° (Th) cal/mol IO ₃ ⁻	K_3 (El)	K_3 (Th)
298.15	-63,842	-64,162	6.27×10^{46}	1.08×10^{47}
310.65	-63,854	-64,174	8.37×10^{44}	1.41×10^{45}
323.15	-63,859	-64,179	1.54×10^{43}	2.54×10^{43}

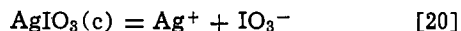
NOTES

- ΔG° values calculated according to Eq. [15]. Equilibrium constants from $\Delta G^\circ = -RT \ln K_3$.
- Values labeled (El) are based on electrochemical data for reaction [16]. See Table IV. We prefer these values.
- Values labeled (Th) are based on thermochemical data for reaction [16]. See Table IV.
- As average values for the temperature range shown above, we have calculated:
 ΔH° (El) = 63,639 cal/mol IO₃⁻; ΔS° (El) = -0.68 cal/K·mol IO₃⁻;
 ΔH° (Th) = 63,959 cal/mol IO₃⁻; ΔS° (Th) = -0.68 cal/K·mol IO₃⁻.

stants are for the reactions

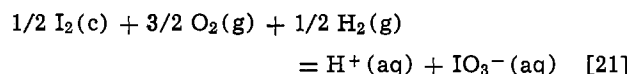


and



used by Sammet as a means of establishing a calculable $[I^-]$. Note that a change of 1% in $(\gamma_{\pm})_{\text{HIO}_3}$ in Eq. [18] changes K_3 by about 12%. We have reevaluated Sammet's chemical results at 25° and 60°C, using the best values (13) of $(\gamma_{\pm})_{\text{HIO}_3}$ extrapolated as necessary. (Details on request from R. D. Spitz.) The results: $K_3 = 4.59(10^{46})$ at 25°C, the mean of 9 determinations in which $[\text{HIO}_3]$ ranged from 0.046 to 0.132M; $K_3 = 1.80(10^{42})$ at 60°C. Extrapolation to this temperature of the K_3 values in Table IV gives $K_3(\text{El}) = 7.9(10^{41})$ and $K_3(\text{Th}) = 1.3(10^{42})$. Comparison of these values with the new Sammet result, and a similar comparison for 25°C (Table VI) shows good agreement throughout. The comparison does not establish whether the electrochemical (El) or the thermochemical (Th) data for reaction [16] are to be preferred; see Notes 2 and 3 of Table VI.

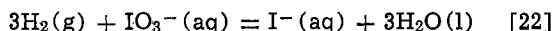
Other derived thermodynamic data.—The Gibbs energy of formation of $\text{IO}_3^-(\text{aq})$ is the standard Gibbs energy change in the reaction



which is obtainable from ΔG° for reaction [1] and that for the formation (17) of $\text{H}_2\text{O}(l)$. The calculated result: $\Delta G^\circ_f = -32,373$ cal/mol $\text{IO}_3^-(\text{aq})$ at 25°C, in satisfactory agreement with the earlier value (2) of $-32,251$ cal.

The analogous calculation of ΔS°_f for $\text{IO}_3^-(\text{aq})$ gave 22.5 cal/deg/mol $\text{IO}_3^-(\text{aq})$, to be compared to thermochemically determined values (19) of 26.9 and 27.7 in the same units. It is well known that voltage measurements cannot often compete with heat-capacity measurements in establishing entropy changes.

Finally, by methods analogous to those used above, calculations were made for the reaction



The results for 25°C: $\Delta G^\circ = -150,110(\text{Th})$ and $-150,046(\text{El})$ cal/mol $\text{IO}_3^-(\text{aq})$ and $E^\circ = 1.0849\text{V}(\text{Th})$ and $1.0844\text{V}(\text{El})$. As before, the results depend on whether the thermochemical or the electrochemical value for ΔG°_f of I^- is used. The voltages are evidently standard potentials of the iodate-iodide electrode.

SYMBOLS

F	Faraday constant, 23,060.8 cal volt ⁻¹ equiv ⁻¹
T	thermodynamic temperature, °K
m	molality, mols solute per kg H ₂ O
(A)	actual concentration of A, molality
[A]	analytical ("total") concentration of A, molality, except when mols/liter, or M, is specified
E _c	voltage reading corrected to unit fugacity of H ₂ , V

iE°_1	approximate standard potential calculated by <i>i</i> 'th method, V
E_L	potential at liquid junction, V
E°	standard potential, V
R	gas constant, 1.98717 cal/K · mol
n	number of Faradays
K_i	equilibrium constant for <i>i</i> 'th reaction
K	unit of thermodynamic temperature
$(\gamma_{\pm})_{\text{HA}}$	mean ionic activity coefficient of HA

Acknowledgment

We thank the Robert A. Welch Foundation and the Dow Badische Company for financial support. We thank Professors D. W. Brooks and J. K. Gladden for lending us equipment.

Manuscript submitted March 2, 1973; revised manuscript received Oct. 7, 1974.

Any discussion of this paper will appear in a Discussion Section to be published in the December 1975 JOURNAL. All discussions for the December 1975 Discussion Section should be submitted by Aug. 1, 1975.

Publication costs of this article were partially assisted by Dow Badische Company.

REFERENCES

- V. Sammet, *Z. Physik. Chem.*, **53**, 665 (1905).
- W. O. Lundberg, C. S. Vestling, and J. E. Ahlberg, *J. Am. Chem. Soc.*, **59**, 264 (1937).
- J. H. Woodson and H. A. Liebhafsky, *Anal. Chem.*, **41**, 1894 (1969), and earlier references there given.
- I. Matsuzaki, J. H. Woodson, and H. A. Liebhafsky, *Bull. Chem. Soc. Japan*, **45**, 3317 (1970).
- A. B. Lamb and A. E. Larson, *J. Am. Chem. Soc.*, **42**, 229 (1920).
- A. Skrabal, *Z. Elektrochem.*, **40**, 232 (1934).
- M. Eigen and K. Kustin, *J. Am. Chem. Soc.*, **84**, 1355 (1962).
- J. D. Burger and H. A. Liebhafsky, *Anal. Chem.*, **45**, 600 (1973).
- G. N. Lewis and M. Randall, "Thermodynamics" pp. 427-430, McGraw-Hill Book Co., New York (1923).
- R. Furuichi, I. Matsuzaki, R. Simic, and H. A. Liebhafsky, *Inorg. Chem.*, **11**, 952 (1972).
- D. A. MacInnes, "The Principles of Electrochemistry," p. 232, Reinhold Publishing Co., New York (1939).
- R. A. Robinson and O. J. Baker, *Trans. & Proc. Roy. Soc. N.Z.*, **76**, 250 (1946).
- A. D. Pethybridge and J. E. Prue, *Trans. Faraday Soc.*, **63**, 2019 (1967).
- E. Abel, O. Redlich, and P. Hersch, *Z. Physik. Chem.*, **107A**, 112 (1934).
- R. M. Fuoss and C. A. Krauss, *J. Am. Chem. Soc.*, **55**, 476 (1933).
- N. C. C. Li and Y. Lo, *ibid.*, **63**, 397 (1941).
- CODATA Bull, No. 5, December, 1971, ICSU CODATA Central Office, Frankfurt, West Germany.
- W. M. Latimer, "Oxidation Potentials," 2nd ed., p. 63, Prentice Hall, New York (1952).
- W. O. Lundberg and W. M. Latimer, *J. Am. Chem. Soc.*, **56**, 858 (1934).

Electro-Oxidation of Organic Compounds I

Oxidation of Benzaldehydes at the Dropping Mercury Electrodes

W. James Bover* and Petr Zuman**

Department of Chemistry, Clarkson College of Technology, Potsdam, New York 13676

ABSTRACT

Benzaldehydes substituted in the meta and para positions with both electron-donating and electron-withdrawing substituents react with hydroxide ions and form geminal diol anions in a reaction $\text{ArCHO} + \text{OH}^- \rightleftharpoons \text{ArCH}(\text{OH})\text{O}^-$. The height of the anodic waves, recorded with d-c and pulse polarography, decreases with decreasing pH in the shape of a dissociation curve. This has been interpreted as due to the electro-oxidation of the anion $\text{ArCH}(\text{OH})\text{O}^-$ preceded by the above acid base equilibrium. The source of the second oxygen in the electrolytic formation of benzoic acids in alkaline media is thus the hydroxide ion. Based on the shape of the dissociation curve, oxidation of the dianion $\text{ArCH}(\text{O})_2^{2-}$ seems improbable. Under the assumption that the acid-base reaction behaves like a volume reaction, values of rate constants for the anion formation and cleavage were calculated. Half-wave potentials of anodic waves are a linear function of Hammett substituent constants σ .

Benzaldehyde undergoes oxidation by chemical reagents relatively easily (1) but the information on electro-oxidation is rather limited (2). For benzaldehyde in sulfuric acid solutions using a platinum anode, yields of about 30% of benzoic acid were reported (3). As reasons for the observed low yields, further oxidation of the side-chain and oxidative substitution on the ring were considered (3), as well as formation of polymers (3, 4). The formation of the latter was seemingly suppressed when the electrolysis was carried out in an aqueous solution of sodium benzene sulfonate using a nickel electrode in the presence of a cupric oxide catalyst where a 58% yield was found (5). However, under these conditions, competition with the Cannizzaro reaction has been assumed. Considerably higher yields of anisic acid have been reported (6) for the oxidation of anisaldehyde on a platinum electrode in aqueous sulfuric acid solutions.

The above studies have been carried out under applied current conditions. In another study using controlled potential electrolysis Lund (7) observed on current-voltage steps obtained in solutions of anisalcohol in acetonitrile using a platinum anode two anodic waves and proved that the more positive wave (at +1.63V) corresponded to the oxidation of anisaldehyde. It was also observed that the anisaldehyde wave disappears upon addition of pyridine. No preparative oxidation had been performed at potentials more positive than 1.63V and no evidence for the product formed was given (7).

Polarographic anodic waves of pyridine-4-carboxaldehyde, 2- and 4-nitrobenzaldehyde, 4-cyanobenzaldehyde, and 4-dimethylaminobenzaldehyde in aqueous solutions containing 10-20% ethanol in 0.1-1.0N sodium or potassium hydroxide solutions with a dropping mercury electrode were first reported by Volke (8). These studies were later (9) extended to ten substituted benzaldehydes. It has been proved that the polarographic anodic waves, observed in 0.04-1.8M potassium hydroxide, correspond to a two-electron irreversible process. These authors (9) neither described any change in the limiting current with hydroxide ion concentration (which proved to be essential for the interpretation of the mechanism), nor were aware of the establishment of the equilibria between benzaldehydes and hydroxide ions in homogeneous solutions (10, 11).

In the preliminary communication (8), anodic peaks obtained with linear sweep voltammetry were reported

which were observed in solutions containing benzaldehydes when a vibrating platinum electrode was used. The presence of such peaks was offered (8) as a proof that mercury salt formation can be excluded as the interpretation of the anodic process. Nevertheless, these anodic peaks have been shown (9) to correspond to oxidation of ethanol, used as cosolvent.

The mechanism of anodic oxidation of benzaldehydes can be considered as speculative. In particular, the source of the second oxygen atom in the resulting benzoic acid has been rather uncertain. Fichter (3) assumed electrolytic formation of atomic oxygen as the oxidizing species, and a radical mechanism (4) was also considered. In the absence of dissolved oxygen in deaerated acetonitrile solution "the formation of carboxyl groups is dubious" (7). The polarographic study (9) assumed electrochemical oxidation of mercury and a surface chemical oxidation of the benzaldehyde involving $\text{HgO} \cdot \text{OH}^-$.

In the present study we aimed at a contribution to the mechanism of the electro-oxidation of aromatic aldehydes, in particular with respect to the source of the second oxygen atom. Since the anodic waves were observed (8, 9) in alkaline media, it seemed essential to decide whether the addition of hydroxide ions to the benzaldehydes according to equation $\text{ArCHO} + \text{OH}^- \rightleftharpoons \text{ArCH}(\text{OH})\text{O}^-$ with $K = [\text{ArCH}(\text{OH})\text{O}^-] / [\text{ArCHO}][\text{OH}^-]$ [which has been proved to occur in alkaline homogeneous solutions (10, 11)] plays also a role in the generation of the electroactive species, the conjugate base.

The pK values of the studied benzaldehydes (10) together with the preliminary experiments indicated the need to carry out further experiments on electro-oxidation in strongly alkaline solutions in order to achieve conditions under which at least part of the benzaldehyde exists in the form of the conjugate base. For this purpose it was necessary to define the acidity in these strongly alkaline solutions and to find a suitable reference cathode.

Although the acidity scale H^- corresponding to the loss of a proton in concentrated solutions of hydroxides is known (12), it could be used only as a first approximation in the studied reaction which involves the addition of a hydroxide ion. Since the acidity scale (J_-) corresponding to such conditions has not been available from equilibrium data, a new acidity scale J_- has been established (11), based on our values of the dissociation constants K . This acidity function describes the acidity in aqueous sodium hydroxide solutions (up to 13M) for reactions involving addition of a hydroxide ion to a neutral molecule. The use of substituted benz-

* Electrochemical Society Student Member.

** Electrochemical Society Active Member.

Key words: d-c polarography, pulse polarography, acid-base equilibria, hydroxide ion addition, geminal diol anion, benzoic acid, structural effects, substituent effects, Hammett equation.

aldehydes as indicators for the establishment of the acidity function J_- makes this function particularly useful for the study of the effect of acidity on reactions of benzaldehydes and their electrode reactions.

As the reference electrode (cathode) for oxidations in strongly alkaline solutions, a carbon rod electrode immersed in a concentrated sodium hydroxide solution proved (13) most useful in obtaining reproducible anodic waves of substituted benzaldehydes and other related compounds.

Experimental

All of the d-c and differential pulse polarographic curves were recorded on a PAR Model 174 Polarographic Analyzer (Princeton Applied Research Corporation, Princeton, New Jersey) with a Hewlett-Packard 7004B X-Y Recorder. The a-c polarographic curves were recorded on the Cambridge Polarographic Analyzer 82P (Cambridge, England). The capillary employed in these electrochemical experiments with a dropping mercury electrode had the following characteristics: an outflow velocity of 2.49 mg/sec at a 100 cm head of mercury with a natural drop time of 3.18 sec. All capillary characteristics were determined at zero potential (short circuit) in a nondeaerated solution of 1.0M sodium hydroxide in the cell employed for the polarographic measurements.

Current-voltage curves with a rectangular voltage polarization were recorded with the PAR 174 and with a commutator switching device constructed according to the principle suggested by Kalousek (14) and the scheme proposed by Nemeč and Holub (15) (the device is referred to as a Kalousek commutator). Cyclic voltammograms were obtained with a triangular function generator built by the courtesy of R. N. Adams, which provided a scanning rate range from 250 to 2000 V/min⁻¹. The resulting voltammetric curves were followed on a Tektronic Type 564B Storage Oscilloscope using Type 3A9 and 2A63 Differential Amplifiers and permanently recorded by tracing the curve on graph paper.

A modified Kalousek cell as described in a previous communication (13) was employed for all electrochemical measurements. The reference electrode was a spectroscopic grade carbon rod immersed in either 1.0 or 5.0M sodium hydroxide.

A Corning Digital 112 Research pH-Meter with a combination Sargent glass-calomel electrode (S-30072-15) was employed for pH measurements of the buffers used in the experiments (the meter was standardized using 0.01M borax and saturated calcium hydroxide, pH 9.180 and 12.343, respectively, at 25°C).

A minicomputer (modified PDP-8, Digital Equipment Corporation, Maynard, Massachusetts) and an IBM 360/40 computer were used for the multiparametric curve fitting analyses (16).

Spectrophotometric experiments were performed on a Unicam SP800-A (Pye-Unicam, Cambridge, England) recording spectrophotometer. Matched fused quartz cells (10 mm sample path) were employed in a thermostated cell holder which was maintained at 25 ± 0.1°C by a Mark F. J. (Haake, Berlin) thermostat pump circulator.

Chemicals and solutions.—Most of the aldehydes were supplied by the Aldrich Chemical Company (Milwaukee, Wisconsin). The compounds were checked for purity by recording the relevant melting or boiling points and by recording a gas-liquid chromatogram of an ether solution of the aldehyde.

Preparation of benzaldehyde stock solutions and of the various sodium hydroxide solutions followed the procedures described previously (13). The phosphate buffers pH 10.8 and 11.9 were prepared from an 0.05M dipotassium hydrogen phosphate solution titrated with various portions of 0.1M hydroxide, and the bicarbonate buffers pH 9.9-10.8 were prepared by titration of an 0.05M solution of sodium bicarbonate with 0.1M sodium hydroxide. Piperidine (pK_a 11.12) buffers were

also prepared for use in the pH range between 10.2 and 12.0, but their use was limited by the dependence of the oxidation differential pulse current on the concentration of piperidine in the buffer.

Working procedures.—*Polarographic current-voltage curves.*—Most d-c and differential pulse polarographic measurements were carried out in solutions that were 2 × 10⁻⁴M in aldehyde and contained 2% ethanol. These solutions were prepared by pipetting 0.2 ml of the ethanol stock solution of the aldehyde to 9.8 ml of sodium hydroxide just prior to placing the solution in the polarographic cell. The solution was then deaerated with a stream of nitrogen for a period of 2 min.

The half-wave potentials of anodic waves in 0.1, 0.25, 1.0, 2.0, 4.0, 6.0, and 9.0M sodium hydroxide were measured against the half-wave potential of phthiocol (2-hydroxy-3-methylnaphthoquinone) to avoid corrections for changes in liquid junction potential. Half-wave potentials of the pilot compound were proved to be independent of sodium hydroxide concentration and the compound to be stable except in the most concentrated hydroxide solutions. But even in 9M sodium hydroxide waves can be recorded and half-wave potentials measured. Cathodic waves of phthiocol were recorded before and after the recording of the anodic waves of a series of benzaldehydes for each concentration of sodium hydroxide.

Measurement of the half-wave potential of the reduction wave of phthiocol in 0.1N sodium hydroxide against a SCE made it possible to express the half-wave potentials of the anodic waves of benzaldehydes vs. SCE (Table I). This procedure was checked by using thallium(I) ions as an internal standard in 1.0M sodium hydroxide. The values of half-wave potentials of the anodic waves of benzaldehydes used by these two independent procedures were practically identical.

The differential pulse polarographic current-voltage curves were recorded using an applied pulse (ΔE) of 25 mV at a scan rate of 2 mV/sec⁻¹ and a controlled (forced) drop time of 2.0 sec. Under the condition that (using the PAR-174) the parameters, drop time, potential scan rate, and pulse voltage are kept constant for each run in a pH series, the peak current, Δi_{max} , is directly proportional to the concentration of electroactive species (17, 18). The applied potential was driven from negative to positive values so as to avoid mercury salt contamination of the electrode surface which results when the electrode is polarized at potentials more positive than the initial anodic current rise.

The cyclic voltammograms were recorded for m-cyanobenzaldehyde in 1.0M sodium hydroxide at a scan rate of 12 V/min⁻¹. The Kalousek commutator technique was used for m-cyano- and m-chlorobenzaldehydes in hydroxide solutions at a switching frequency of 1 Hz with the auxiliary potential set on the plateau of the anodic wave. The a-c polarographic curves were recorded in 1.0M sodium hydroxide with an alternating voltage of 10 mV rms at a scan rate of 0.4 mV sec⁻¹ and a forced drop time of 1.0 sec.

Results

D-C polarographic curves.—The anodic waves for the substituted benzaldehydes were initially observed in alkaline solutions with d-c polarography using a drop-

Table I. Half-wave potentials of substituted benzaldehydes as a function of sodium hydroxide concentration

Benzaldehyde ^[NaOH]	$E_{1/2}$ (vs. SCE)						
	9.0	6.0	4.0	2.0	1.0	0.25	0.1
3,5-Cl ₂	-0.525	-0.509	-0.506	-0.469	-0.429	-0.360	-0.302
3,4-Cl ₂	-0.529	-0.516	-0.518	-0.484	-0.429	—	—
3-Cl	-0.510	-0.487	-0.481	-0.448	-0.391	-0.308	-0.259
4-Cl	-0.478	-0.501	-0.476	-0.419	-0.362	-0.275	-0.229
3-OCH ₃	-0.485	-0.478	-0.454	-0.397	-0.332	-0.252	-0.207
H	-0.446	-0.456	-0.430	-0.357	-0.295	-0.223	-0.193
4-CH ₃	-0.456	-0.446	-0.424	-0.335	-0.272	-0.205	-0.167
4-OCH ₃	-0.422	-0.386	-0.346	-0.291	-0.234	-0.171	-0.129

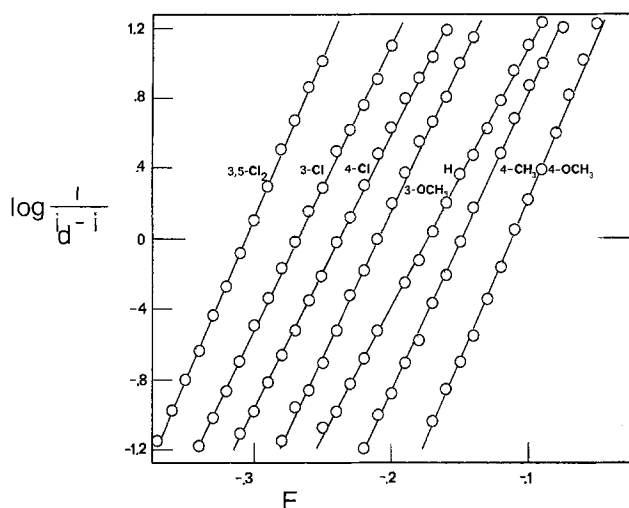


Fig. 1. A plot of the $\log i/(i_d - i)$ for the rising portion of the anodic wave vs. the potential (in volts vs. carbon reference electrode) for substituted benzaldehydes. The solutions were all $2 \times 10^{-4}M$, 2% ethanol and 1.0M sodium hydroxide at 25°C.

ping mercury electrode and a carbon rod reference electrode as previously described (13). Well-developed waves, enabling measurement of both wave-heights and half-wave potentials were obtained for most aldehydes in 0.1-9.0M solutions of sodium hydroxide [cf. Fig. 2, Ref. (13)]. Anodic waves were well separated from the initial anodic current rise due to oxidation of mercury and were proved irreversible by cyclic voltammetry and the Kalousek commutator technique.

This has been further confirmed by logarithmic analysis (Fig. 1) which shows a linear plot of $\log i/(i_d - i)$ as a function of potential with a slope corresponding to βn_b values which vary from 0.86 to 1.08 (Table II).

A decrease of the anodic limiting current at sodium hydroxide concentrations of 1-4M is due to an increase in viscosity (η), as proved from a practically constant value of the product $i(\eta)^{1/2}$. At still higher sodium hydroxide concentrations, the limiting current decreases somewhat more than would correspond to an increase in solution viscosity. This additional decrease which is similar for various substituted benzaldehydes is not in the shape of a dissociation curve. Moreover, the limiting current of benzaldehyde remains diffusion controlled as shown by a linear dependence on the square root of mercury pressure in both 6 and 10M sodium hydroxide, which show, nevertheless, a small negative intercept.

When sodium hydroxide solutions more dilute than about 0.25M and buffers of lower pH values were stud-

Table II. Parameters of the anodic process of substituted benzaldehydes

Benzaldehyde	0.058 ^a	$dE_{1/2}$ ^b	0.058 ^b
	$dE/d \log i/(i_d - i) = \beta n_b$	dpH (V)	$dE_{1/2}/dpH = \beta n_b$
3,5-Cl ₂	1.044	0.113	0.52
3,4-Cl ₂		0.113	0.52
3-Cl ^c	0.96 (0.87) ^d	0.127	0.46
4-Cl	0.91	0.130	0.45
3-OCH ₃	0.99	0.130	0.45
H	0.86	0.134	0.43
4-CH ₃	1.07	0.133	0.44
4-OCH ₃	1.08	0.127	0.46

^a βn_b obtained from the slope of $\log i/(i_d - i)$ vs. E for the rising portion of the anodic wave in 1.0M NaOH recorded automatically (Fig. 1).

^b From the slope of $E_{1/2}$ vs. pH plot (Fig. 5).

^c For m-chlorobenzaldehyde the following values were found at varying sodium hydroxide concentrations: [OH]: 0.5, 1.0, 1.7, 3.0, 4.0, and 6.0M; βn_b : 0.88, 0.92, 1.09, 0.98, 1.02, and 1.04.

^d The current values at varying potentials for the log analysis were measured potentiometrically (point by point) using a three-electrode system.

ied, a shift of the anodic waves to more positive potentials was observed. Since this shift with pH was greater than the shift of the current rise due to mercury dissolution, the waves became less well developed at lower pH values. Below certain pH values (characteristic for each substituted benzaldehyde) the anodic wave was no longer observed. For benzaldehydes with electropositive substituents (e.g., p-methyl or p-methoxy) it was hardly possible to decide whether the absence of the anodic wave was solely due to a potential shift to more positive values than the initial current rise, or whether a decrease in the wave-height occurred as well. For the benzaldehydes with electronegative substituents (e.g., m-nitro or m-chloro, Fig. 2) a decrease in wave-height was indicated on the d-c current-voltage curves, but quantitative measurements were difficult.

An attempt has been made to determine the wave-height of m-nitrobenzaldehyde at pH 11.5-10 by multiparametric curve fitting analysis (16). Even when this approach proved qualitatively the decrease of the limiting current with decreasing pH, uncertainty of the treatment was too large to permit a decision among the possible shapes of the i -pH plot. The main source of uncertainty was the change in the course of the residual current in the presence of the benzaldehyde, which made simple subtraction of the residual current for the pure buffer solution insufficient.

Differential pulse polarography.—To confirm the decrease of the current at lower pH values and to obtain reliable values for current, differential pulse polarographic curves (17, 18) of solutions of benzaldehydes were recorded and the peak currents, Δi_{max} , were obtained which were measurable with sufficient accuracy to considerably lower pH values than it was possible to measure the limiting currents of d-c polarographic curves (Fig. 3).

To correct differential pulse polarographic curves which are close to the current rise due to mercury dissolution (last two curves, Fig. 3) for the residual current, use has been made of the symmetry of the peak and the practical independence of the half-width of the peak on peak-height.

Using the construction of the whole peak based on current values accurately measured at more negative potentials (curve 3, Fig. 3), it was possible to obtain

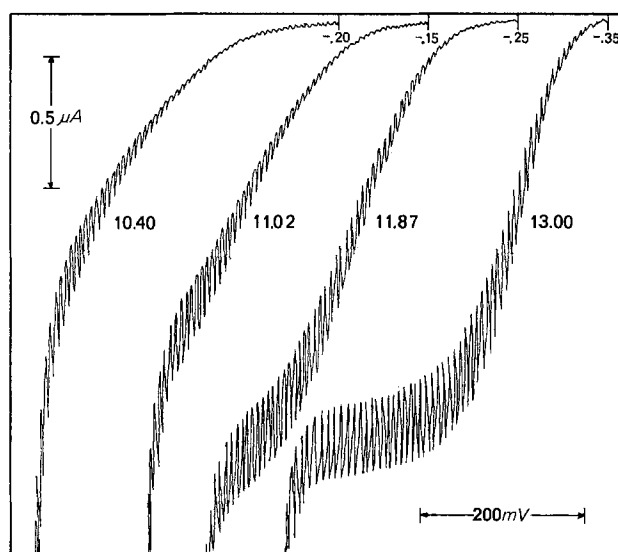


Fig. 2. The dependence of the d-c polarographic current voltage curves on pH for the oxidation of m-nitrobenzaldehyde at the indicated pH values in carbonate (10.40) phosphate (11.02, 11.87) buffers and in 0.1M sodium hydroxide (13.00). All solutions were $2 \times 10^{-4}M$ in aldehyde and contained 2% ethanol at 25°C. The voltage scanning started from the negative potentials to more positive values.

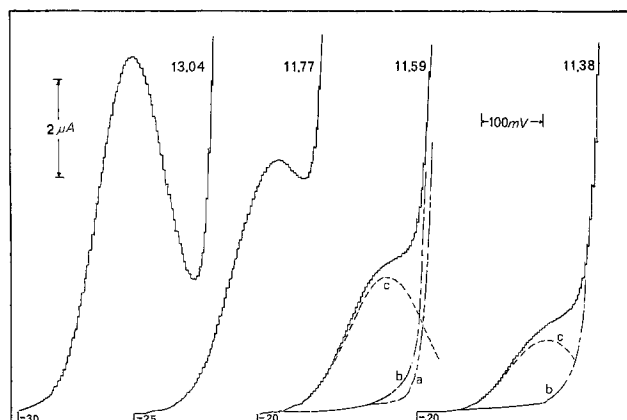


Fig. 3. The dependence of the differential pulse polarographic current-voltage curves for the oxidation of *p*-chlorobenzaldehyde on pH in solutions of 0.1M sodium hydroxide (pH 13.04) and phosphate buffers (pH 11.77, 11.58, 11.38). The voltage scanning started from the negative to more positive values at the rate of 2 mV/sec. The broken curves correspond (b) to the residual current due to the buffer alone; and (c) to the current resulting from the subtraction of curve (a) from the total limiting current. All solutions were 2×10^{-4} M in aldehyde and contained 2% ethanol at 25°C.

well-reproducible values of Δi_{\max} even for less well-developed curves.

Current-pH plots.—Reliable values of Δi_{\max} , expressed relative to $(\Delta i_{\max})_d$ obtained at sufficiently high pH, show a decrease with decreasing pH in the shape of a monobasic acid dissociation curve (Fig. 4a). When $\log \Delta i_{\max}/[(\Delta i_{\max})_d - \Delta i_{\max}]$ was plotted against pH (Fig. 4b), a linear plot with unit slope was obtained.

Analogous plots, i.e., $i/i_d = f(\text{pH})$, are commonly used for the treatment of d-c polarographic currents governed by a rate of an antecedent chemical reaction (19). The theory of such currents for differential pulse polarography has not yet been developed. To prove empirically the possibility of using $\Delta i_{\max}/(\Delta i_{\max})_d$ instead of i/i_d for interpretation of pH dependences two approaches have been used: plots of $\Delta i_{\max}/(\Delta i_{\max})_d$ and

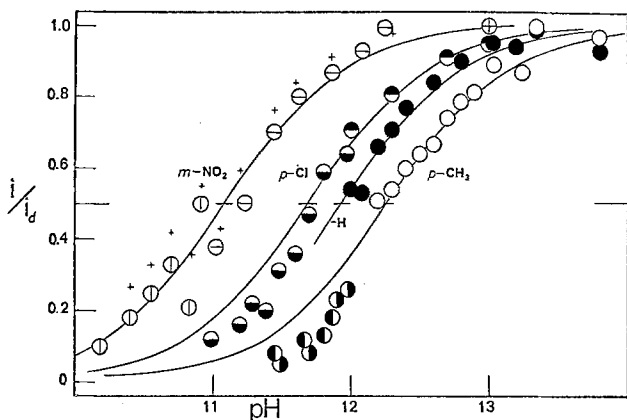


Fig. 4a. The dependence of the differential pulse peak current as a fraction of the corresponding diffusion current on pH for some substituted benzaldehydes. The experimental points represent data obtained for *p*-tolualdehyde in sodium hydroxide (○) and phosphate buffers (●); for benzaldehyde in sodium hydroxide (●) and phosphate buffers (●); for *p*-chlorobenzaldehyde in sodium hydroxide (●) and phosphate (●) buffers; for *m*-nitrobenzaldehyde in sodium hydroxide (⊕), phosphate (⊖), and carbonate (⊙) buffers. All solutions were 2×10^{-4} M in aldehyde and contained 2% ethanol at 25°C. The solid curves have a shape corresponding to a theoretical dissociation curve for a monobasic acid. The values (+) shown on the *m*-nitrobenzaldehyde curve correspond to those current values obtained with d-c polarography.

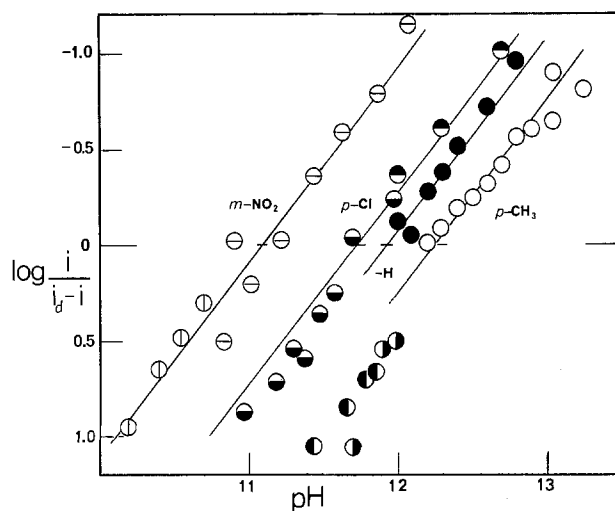


Fig. 4b. The dependence on pH of the $\log(i/i_d - i)$ where i is the peak current at a given pH and i_d the corresponding diffusion peak current in solutions described in Fig. 4a for some benzaldehydes. The straight lines of unit slope represent the theoretical slope for a monobasic acid dissociation. Symbols for points are the same as in Fig. 4a.

\overline{i}/i_d against pH have been compared for current-voltage curves of benzoylacetone, which correspond to an irreversible reduction process accompanied by an antecedent volume acid-base reaction (20). Both plots have been found to have the same shape and inflection points (pK'). Furthermore, benzaldehydes, like *m*-nitrobenzaldehyde where the current in the pH region for which the decrease of the current with pH occurred was measurable both by differential pulse ($\Delta i_{\max}/(\Delta i_{\max})_d$) and \overline{i}/i_d , fitted reasonably well a single, continuous curve when plotted vs. pH (Fig. 4a). Hence the use of $\Delta i_{\max}/(\Delta i_{\max})_d$ for treatment in expressions derived for \overline{i}/i_d has been substantiated as a first approximation.

Even when we are aware that the differential pulse peak current can also decrease due to a change in the value of the transfer coefficient and the heterogeneous rate constant of the electrode process, all the facts mentioned above indicate that the rate of the chemical reaction is the predominant factor governing the decrease of the anodic current.

Comparison of the curves in Fig. 4a and 4b shows that values of $\Delta i_{\max}/(\Delta i_{\max})_d$ obtained in phosphate or bicarbonate buffers show deviations toward smaller currents when compared with the theoretical curves plotted to fit values obtained in sodium hydroxide solutions. When recorded in phosphate buffers of constant pH, the value of Δi_{\max} decreased with increased phosphate concentration.

Half-wave and peak potentials.—From a comparison of the anodic waves of several benzaldehydes using both d-c and differential pulse polarography under identical experimental conditions, an empirical relationship between the half-wave potential ($E_{1/2}$) and the peak potential (E_p) has been found, viz., $E_p \approx E_{1/2} + 0.025\text{V}$.

Plots of $E_{1/2}$ and E_p values vs. J_- show three linear sections (Fig. 5). At the lowest and highest pH (or J_-) values a pH independent section is observed; in the intermediate pH range a shift to more positive potentials with decreasing pH occurs. Slopes of this linear section are tabulated in Table II.

The half-wave potentials of substituted benzaldehydes in 1.0 and 2.0M sodium hydroxide [where they are all dependent on concentration of hydroxide ions with practically identical value of $dE_{1/2}/dpH$ (Table II)] are a linear function of Hammett substituent constants σ_x (Fig. 6). The reaction constants in 1.0M ($\rho\pi^A = -0.225\text{V}$, $r = 0.994$, $SD_\rho = 0.011$) and 2.0M ($\rho\pi^A =$

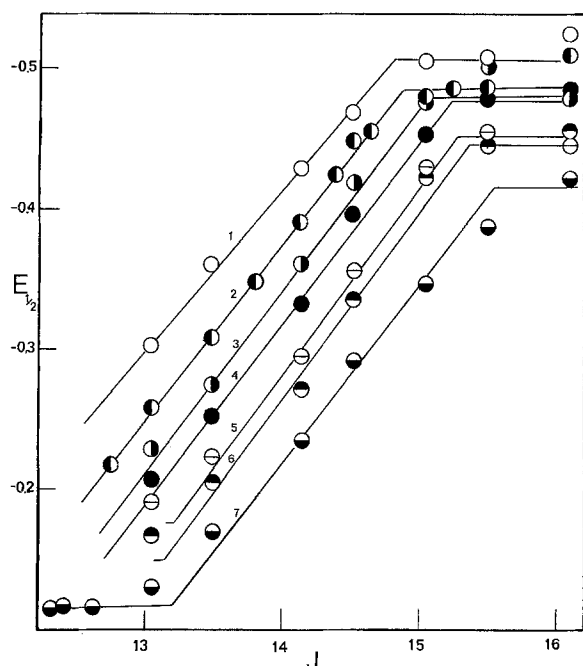


Fig. 5. The half-wave potentials for the anodic polarographic waves are plotted as a function of the acidity function J_- for (1) 3,5 dichloro-; (2) 3-chloro-; (3) 4-chloro-; (4) 3-methoxy-; (5) unsubstituted; (6) 4-methyl-; and (7) 4-methoxy-benzaldehydes. Potentials are reported vs. the SCE, and the solutions were $2 \times 10^{-4}M$ in aldehyde and contained 2% ethanol at $25^\circ C$.

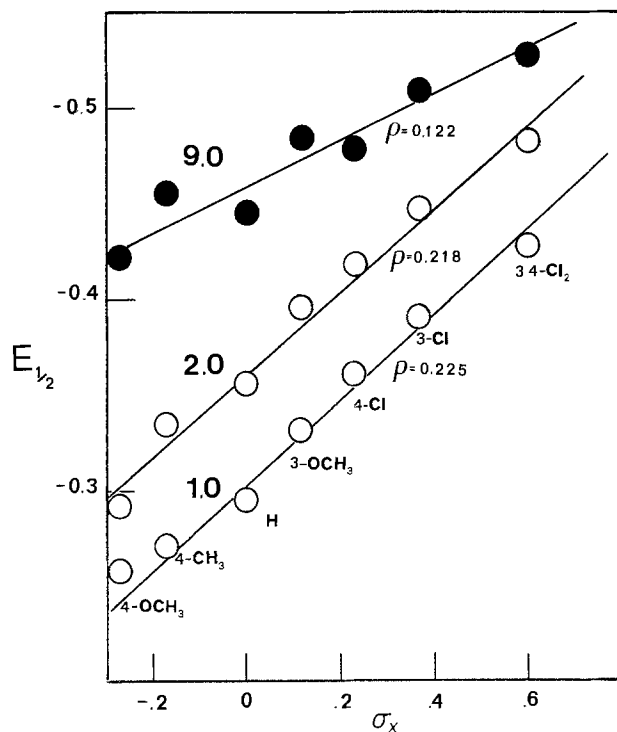


Fig. 6. The dependence of the half-wave potentials for the anodic waves of substituted benzaldehydes in 1.0, 2.0, and 9.0M sodium hydroxide on the Hammett substituent constants, σ_x . All solutions were $2 \times 10^{-4}M$ in aldehyde and contained 2% ethanol. The potentials are reported vs. SCE with $E_{1/2}^H = -0.294$ for benzaldehyde.

$-0.218V$, $r = 0.990$, $SD_p = 0.014$) are consequently practically identical.

The half-wave potentials in 9M sodium hydroxide (where J_- is equal to 15.97), in an acidity region where all the half-wave potentials are independent of

sodium hydroxide concentration (Fig. 5), are also a linear function of Hammett substituent constants σ_x (Fig. 6). The linear plot corresponds to a reaction constant $\rho_{\pi^B} = -0.122V$ ($r = -0.954$, $SD = 0.014$). The lower value of the correlation coefficient reflects the smaller value of the reaction constant, but the correlation can be considered good.

Spectrophotometric studies.—Spectrophotometric determinations of equilibrium constants (K) of the reaction $ArCHO + OH^- \rightleftharpoons ArCH(OH)O^-$ have been described elsewhere (10). Recent attempts to determine the second dissociation constant (K_2) corresponding to the formation of a dianion in a process of the type $ArCH(OH)O^- \rightleftharpoons ArCH(O^-)_2 + H^+$ were unsuccessful even for nitrobenzaldehydes, which have the lowest pK_1 value of the compounds studied (12.79 for para and 13.07 for meta). Hence for nitrobenzaldehydes the value of pK_2 must be at least more than two pK units larger than pK_1 .

Discussion

Electroactive forms.—The presence of anodic oxidation waves in alkaline media only (Fig. 2), the decrease of their wave-height with decreasing pH in the shape of a dissociation curve (Fig. 4), and the shift of their half-wave potentials with pH (Fig. 5) indicate that the species $ArCHO$, which predominates in solutions of benzaldehydes at lower pH values, is not the electroactive form. The fact that mercury does not participate in the anodic process in mercury salt formation has been confirmed by irreversibility of the electrode process as proved by cyclic voltammetry and the Kalousek commutator technique. The absence of mercury in the electrolysis products (13) also confirmed this view.

On the other hand, inflection points of polarographic dissociation curves (pK') roughly parallel the pK values obtained spectrophotometrically for the addition of hydroxide ions (10) (Table III). It has been thus deduced that the species $ArCH(OH)O^-$, the formation of which in alkaline media has been recently proved (10, 11), seems to be the electroactive species which undergoes oxidation to benzoic acid. It was nevertheless necessary to consider the oxidation of the dianion of the geminal diol [$ArCH(O^-)_2$] as an alternative reaction path.

The pH dependence of the limiting current and in particular the dependence of the inflection points pK' on structure of the aldehyde cannot be brought into agreement with the proposed (9) mechanism involving oxidation by $HgO \cdot OH^-$.

The shift of the polarographic dissociation curve to lower pH values than the spectrophotometrically obtained dissociation curve (10), as demonstrated by the smaller values of pK' than pK (Table III) as well as by the kinetic character of the anodic wave when $i < 0.2 i_d$, indicates that the height of the anodic waves at $pH < pK$ does not correspond to the equilibrium concentration of the electroactive anion in the bulk of the solution, but rather to the rate of formation of this anion (kinetic current).

Reaction scheme.—The simplest reaction scheme, which would be in agreement with the spectrophotometric evidence (10, 11) and would explain the observed change in current with pH (Fig. 4), is a set of reactions [1]

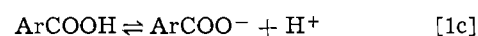
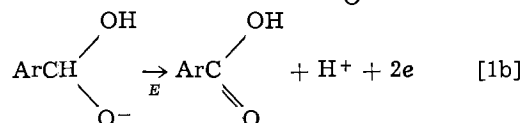
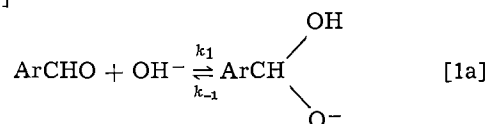


Table III. Equilibrium constants ($K_1 = [\text{ArCH}(\text{OH})\text{O}^-][\text{H}^+]/[\text{ArCHO}]$) determined spectrophotometrically (pK_{spec}), polarographic dissociation constants ($pK' = \text{pH}$ at which $i = 0.5 i_d$), and rate constants of the reaction $\text{ArCHO} + \text{OH}^- \xrightleftharpoons[k_{-1}]{k_1} \text{ArCH}(\text{OH})\text{O}^-$ at 25°C for substituted benzaldehydes (X-ArCHO) and aromatic heterocyclic aldehydes

X	Sodium hydroxide solutions					Buffers ^b		
	σ_x	pK_{spec}^a	pK'	$\log k_1^c$	$\log k_{-1}$	pK'	$\log k_1^c$	$\log k_{-1}$
4-NO ₂	0.78	12.79	10.48	5.65	4.44	10.80	5.01	3.80
3,5-Cl ₂	0.74 ^d	13.09 ^e	10.65	5.61	4.70	10.86	5.19	4.28
3-NO ₂	0.70	13.07	10.67	5.56	4.63	11.08	4.73	3.80
3,4-Cl ₂	0.60 ^d	13.81 ^e	11.08	5.47	5.28	10.85	5.93	5.74
3-Cl	0.37	13.92	11.24	5.25	5.17	11.45	4.84	4.76
4-Cl	0.23	14.44	11.58	5.10	5.54	11.72	4.82	5.26
3-OCH ₃	0.11 ^g	14.61	11.70	5.03	5.64			
-H	0	14.90	11.93	4.86	5.76			
3-CH ₃	-0.07	15.00	12.03	4.76	5.76			
4-CH ₃	-0.17	15.39	12.23	4.75	6.14			
4-OCH ₃	-0.27	15.96	12.57	4.64	6.60			
Furfural		14.77 ^f	12.30	3.99	4.76			
Thiophene-2-carboxaldehyde		15.11 ^f	12.20	4.53	5.64			
5-Br-thiophene-2-carboxaldehyde		14.64 ^g				11.42	5.62	6.26

^a W. J. Bover and P. Zuman, Ref. (10).

^b Values determined from data obtained in phosphate or carbonate buffers.

^c Values obtained from pK_{spec} and pK' .

^d σ_x values.

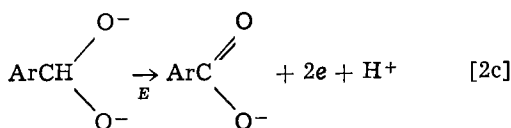
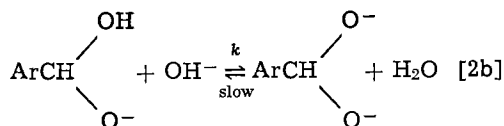
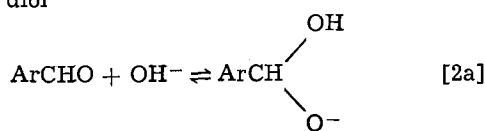
^e Determined by Th. J. Pouw.

^f Determined by K. Bratin.

^g Determined by W. J. Scott.

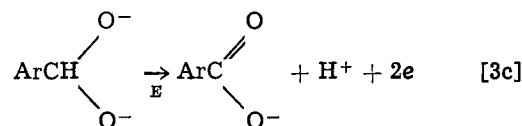
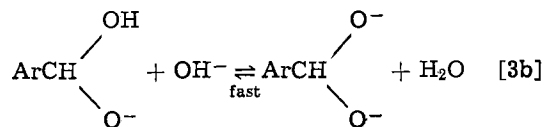
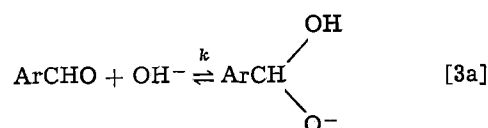
In this system the rate of the addition of the hydroxide ion governs the limiting current of the anodic wave, until at sufficiently high sodium hydroxide concentrations the current becomes diffusion controlled.

The scheme will, nevertheless, be compared with two alternative schemes, [2] and [3], where the electroactive form, yielding the benzoic acid as proved by controlled-potential electrolysis (13) is the dianion of the geminal diol



In scheme [2] the slow step would be the abstraction of a proton from an -OH group which does not seem to be in agreement with the experience with similar types of reactions.

Alternatively scheme [3] can be considered



where the addition of the hydroxide ions is the slow step.

When the general treatment for acid-base reactions preceding the electrode process proper (21) is applied to schemes [1]-[3], in all cases the current (i) expressed as a fraction of the diffusion current (i_d) decreases with decreasing pH in the shape of a dissociation curve. The shape of this curve depends on the scheme and on the relative magnitude of the equilibrium constant K_1 characterizing reactions [1a], [2a], and [3a] and the pH at which the polarographic wave is one-half of the diffusion current (pK'). Equations for individual schemes are summarized in Table IV to-

Table IV. Equations for the dependence of current (i) on pH for reaction schemes [1]-[3] for $pK_2 > pK_1$

Scheme	Equation	Conditions	$d \log (i/i_d - i)$
			$d \text{ pH}$
[1]	$i/i_d = \frac{0.866 \sqrt{k_1 K_w^2 K_1} / [\text{H}^+]}{1 + 0.866 \sqrt{k_1 K_w^2 K_1} / [\text{H}^+]} \frac{1/[\text{H}^+]^2}{1/[\text{H}^+]^2}$		1
[2]	$i/i_d = \frac{0.866 \sqrt{k_1 K_w^2 K_2}}{1/K_1 + 1/[\text{H}^+]} \frac{1/[\text{H}^+]^2}{1 + 0.866 \sqrt{k_1 K_w^2 K_2} / [\text{H}^+]^2}$	$\left\{ \begin{array}{l} pK' \gg pK_1 \\ pK' \ll pK_1 \end{array} \right.$	$\left\{ \begin{array}{l} 1 \\ 2 \end{array} \right.$
[3]	$i/i_d = \frac{0.866 \sqrt{k_1 K_w^2 K_1 K_2}}{1 + K_1/[\text{H}^+]} \frac{1/[\text{H}^+]^{3/2}}{1 + 0.866 \sqrt{k_1 K_w^2 K_1 K_2} / [\text{H}^+]}$	$\left\{ \begin{array}{l} pK' \gg pK_1 \\ pK' \ll pK_1 \end{array} \right.$	$\left\{ \begin{array}{l} 1/2 \\ 3/2 \end{array} \right.$

gether with the slopes of the respective dissociation curves expressed as $d \log(i/i_d - i)/dpH$. In all the systems studied it was assumed that $pK_1 \ll pK_2$, as is observed experimentally (11).

Since in all experimentally accessible cases the value of pK' was smaller than pK_1 , only the shapes of the dissociation curves for the condition $pK' \ll pK_1$ need to be considered. As the observed dissociation curves all have a slope $d \log(i/i_d - i)/dpH = 1.0$ (Fig. 4b), schemes [2] and [3] which would require steeper dissociation curves with slopes of 1.5 or 2 can be excluded. Hence the pH dependence of the limiting current of the anodic wave indicates that the monoanion of the geminal diol $ArCH(OH)O^-$ is the electroactive form and the working hypothesis (13), that the electroactive form is the dianion, seems less probable.

There is, nevertheless, some evidence available that the detailed mechanism might be more complex than described by scheme [1]. When the value βn_b , obtained from logarithmic analysis of the rising portion of the anodic wave (column 1, Table II) is compared with the value of βn_b obtained from the pH dependence of half-wave potentials (column 3, Table II) under an assumption of the transfer of one hydroxide ion prior to the electrode process proper, a considerable difference is found. It cannot be excluded even when the process appears to be over-all irreversible, that the proton evolution in the electrode process proper affects the half-wave potential, e.g., that the proton abstraction in scheme [1b] precedes the electron uptake. The participation of the electrode surface, proposed by Manousek and Volke (9) as an antecedent step, cannot be excluded in the proton abstraction step.

Further support for the validity of scheme [1] can be found in the shape of the plot of half-wave potentials as a function of pH. It has been shown recently (22) that a plot consisting of three linear sections as observed in Fig. 5 (with two pH independent sections at the lowest and highest pH values and a linear pH dependent section in the intermediate pH range) corresponds only to systems involving the transfer of one proton or hydroxide ion prior to the electron uptake. Mechanisms which involve two proton transfers (e.g., H^+, H^+, e, e or H^+, e, H^+, e) show plots with four linear sections (with intersections corresponding to the two pK values involved).

In analogy with systems involving antecedent proton transfer and reduction of the conjugate acid (22), it is possible to derive equations for half-wave potentials of systems involving antecedent reaction with hydroxide ions and oxidation of the conjugate base

$$E_{1/2} = E^\circ - \frac{RT}{\beta n_b F} \ln 0.886 k_e^\circ (t/D)^{1/2} - \frac{RT}{\beta n_b F} \ln \frac{K}{K + [H^+]} \quad [4]$$

where $K = K_1 K_w$ and other symbols have the usual

meaning. For $[H^+] \gg K$ then

$$E_{1/2} = E^\circ - \frac{RT}{\beta n_b F} \ln 0.886 k_e^\circ (t/D)^{1/2} - \frac{RT}{\beta n_b F} \ln \frac{K}{[H^+]} \quad [5b]$$

or

$$E_{1/2} = \text{const.} + \frac{RT}{\beta n_b F} (pK - pH) \quad [5b]$$

Similarly at $[H^+] \ll K$

$$E_{1/2} = \text{const.} = E^\circ - \frac{RT}{\beta n_b F} \ln 0.886 k_e^\circ (t/D)^{1/2} \quad [6]$$

Finally, in the pH region where the height of the limiting current decreases with decreasing pH (i.e., at sufficiently low pH values) expression [7] applies

$$E_{1/2} = E^\circ - \frac{RT}{\beta n_b F} \ln \frac{k_e^\circ}{(k_1 D)^{1/2}} \quad [7]$$

where k_1 corresponds to the rate of the addition of the hydroxide ion. Equations [6] and [7] correspond to the pH region where the half-wave potentials are pH independent at low (Eq. [7]) and at high (Eq. [6]) pH values. Equation [5] describes the shift of the half-wave potential in the intermediate pH range. The pH^* values at which right-hand sides of Eq. [7] and [5] are equal corresponds to the value of pK' (i.e., to the pH where $i = i_d/2$). Experimentally found pH^* values were in agreement with pK' values (Table III) for those few compounds for which the value of pH^* was experimentally accessible.

The pH values at which the right-hand sides of Eq. [5] and [6] are equal correspond to the pK value of the antecedent acid-base equilibrium, independent of the characteristics of the electrode, the diffusion coefficient, and the value of k_e° .

A comparison of the $pK_{E_{1/2}}$ values obtained from the $E_{1/2}$ -pH plots with those values obtained spectrophotometrically (pK_{spec}) (Table V and Fig. 5) shows a small difference for the unsubstituted compound, the para-methyl and para-methoxy benzaldehyde, but larger differences for other substituted aldehydes. This can be attributed to the difference in the value of the equilibrium constant in the bulk of the solution and in the electric field of the electrode.

Further evidence in support of scheme [1] is the comparison with homogeneous oxidations. The geminal diol anion, proposed in scheme [1] as the oxidizable species, was considered (23, 24) as a reactive intermediate in manganate and permanganate oxidations of benzaldehydes in alkaline media, as well as of furfural at pH 11.5-13.5 by permanganate (25). The oxidation of strongly hydrated aliphatic aldehydes, like fluoral or chloral, is assumed at pH > 6 also to take place via the geminal diol anion (26, 27).

Moreover, as the oxidations are similarly strongly affected by electron withdrawing groups, the chemical

Table V. Values of equilibrium and rate constants for the reaction $RCHO + OH^- \xrightleftharpoons[k_{-1}]{k_1} RCH(OH)O^-$. Comparison of values calculated from data obtained polarographically ($E_{1/2}$ -pH plots), (i/i_d -pH plots), and spectrophotometrically

Benzaldehyde	pK		log k_1		$\Delta E_{1/2}^\circ$	log k_{-1}	
	$pK_{\text{spec}}^{a,d}$	$pK_{E_{1/2}}^b$	from pK_{spec}, pK'^d	from $pK_{E_{1/2}}, pK'$		from pK_{spec}, pK'^d	from $pK_{E_{1/2}}, pK'$
3,5-Cl ₂	13.09	14.82	5.61	7.34		4.70	8.16
3-Cl	13.92	14.87	5.25	6.21	6.48	5.17	8.16
4-Cl	14.44	14.08	5.10	5.74		5.54	6.82
3-OCH ₃	14.61	15.24	5.03	5.66		5.64	6.90
H	14.90	15.30	4.86	5.26		5.76	6.56
4-CH ₃	15.39	15.37	4.75	4.73	5.11	6.14	6.07
4-OCH ₃	15.96	15.55	4.64	4.23	5.55	6.60	5.87

^a Values obtained spectrophotometrically.

^b From intersection of the $E_{1/2}$ -pH plot.

^c Using Eq. [10].

^d From Table III.

homogeneous oxidation in alkaline solutions shows a large value of Hammett reaction constant (23, 24) ($\rho = 1.83$ at pH 12.6). Furthermore, the participation of phosphate and carbonate buffers observed for electro-oxidation has been found (24) also for permanganate oxidation.

Furthermore, addition of a free electron pair of a negatively charged oxygen to the carbonyl double bond in scheme [1] is analogous to the addition of the oxygen of a chromate ion (28, 29) and the proposed intermediate in the chromate oxidation is a derivative of a geminal diol. Moreover, both in scheme [1] and in the chromate oxidation the carbon-hydrogen bond cleavage occurs in the rate-determining step. Position of the hydration equilibria for benzaldehydes has been used also as an argument in the interpretation of substituent effects on chromate oxidation of substituted benzaldehydes (30).

Finally, the oxidation of aldehydes by hydrogen peroxide in alkaline media was interpreted as involving the attack of hydrogen peroxide on geminal diol anion (31).

Solution phenomena.—Deviations of current from the theoretical dissociation curves observed in phosphate and carbonate buffers and the decrease of current with increasing buffer concentration indicate that these buffer components react with aldehydes to produce electroinactive compounds. The possibility of addition of phosphate or carbonate anions cannot be excluded and will be studied in more detail. Sensitivity toward the effect of phosphates increases with the increasing electropositivity of the substituent on benzaldehyde (Fig. 4), *i.e.*, the deviations are greater for *p*-methyl than for *p*-chlorobenzaldehyde. For these reasons only the currents measured in sodium hydroxide solutions were taken into consideration for the calculations of the rate constants.

Similarly, currents in sodium hydroxide solutions more concentrated than 4.0M were not considered in finding the best value of the diffusion current (i_d). Since deviations from $i\eta^{1/2} = \text{constant}$ in such solutions showed a similar trend for all aldehydes studied, interaction of anions formed with the excess of sodium ions, *e.g.*, to form ion pairs, seems less probable. Changes in the activity of water and changes in the structure of the solvent as well as the structure-breaking properties of concentrated sodium hydroxide solutions can affect the validity of the Stokes-Einstein relation on which the equation $i\eta^{1/2} = \text{constant}$ is based.

Rate constants.—To calculate rate constants of reaction [1a] from measurements of polarographic currents, the equation for i/i_d (Table IV) is transformed to Eq. [8]

$$\begin{aligned} \log k_1 &= pK - 2pK' + pK_w - \log t_1 - 2 \log 1.15 \\ &= pK_1 - 2pK' - \log t_1 - 2 \log 1.15 \end{aligned} \quad [8]$$

where pK_1 is the value for the equilibrium constant of reaction [1a] expressed as

$$K_1 = [\text{ArCH(OH)O}^-] [\text{H}^+] / [\text{ArCHO}]$$

and t_1 is the drop time. Hence to calculate the rate constant k_1 , it is necessary to determine the polarographic dissociation constant pK' which is defined as $\text{pH} = pK'$ for $i/i_d = 0.5$ (*i.e.*, inflection points of curves in Fig. 4a or the *pH* value at which the logarithm term in Fig. 4b becomes equal to zero).

Values of pK' based on measurements with d-c and differential pulse techniques at $t_1 = 2$ sec are summarized in Table III. When the comparison was restricted to those values of pK' obtained in solutions of sodium hydroxide, a linear correlation with the Hammett substituent constants σ_x was found with a reaction constant $\rho = 1.87$ ($r = 0.995$).

The calculation of the value of k_1 for the rate constant of the addition of hydroxide ions to benzaldehydes by means of Eq. [8] can be carried out in two ways: either the pK' value is used in combination with

the spectrophotometrically determined value of pK_{spec} or with the polarographically determined value of $pK_{E_{1/2}}$, obtained from the $E_{1/2}$ -*pH* plot. When data are restricted to those obtained in sodium hydroxide solutions, both sets of rate constants ($\log k_1$) are a linear function of substituent constants σ_x . The values of the reaction constants ρ are nevertheless different ($\rho = 0.95$ when pK_{spec} values are used and $\rho = 2.94$ using $pK_{E_{1/2}}$ values). Values of k_1 calculated from current measurements in phosphate or carbonate buffers show no correlation with substituent constant σ_x .

From the value of k_1 and the measured value of pK it was possible to calculate the value of the rate constant k_{-1} for the reverse reaction by means of Eq. [9]

$$\log k_{-1} = \log k_1 + \log K_w + pK \quad [9]$$

Similarly as in the previous case, either $pK_{E_{1/2}}$ or pK_{spec} values can be used in the computation of the values of k_{-1} by means of Eq. [9]. The values of $\log k_{-1}$ obtained in both cases were a linear function of Hammett substituent constants σ_x , but according to the choice of $pK_{E_{1/2}}$ or pK_{spec} in connection with Eq. [9] the values of $\log k_{-1}$ show either a positive or a negative value of the reaction constant, ρ .

Calculation of the rate constant of the addition reaction k_1 can also be carried out by an independent procedure. As has been shown (22), it is possible to use the difference ($\Delta E_{1/2}$) between the values of the half-wave potentials in the two *pH* regions, where the half-wave potentials are *pH* independent and follow Eq. [6] and [7], by means of Eq. [10]

$$\Delta E_{1/2} = \frac{RT}{\beta n_b F} \ln 0.886 (k_1 t_1)^{1/2} \quad [10]$$

The values obtained for those compounds where experimental data could have been obtained at low enough *pH* values, where the half-wave potentials become *pH* independent are presented in Table V.

The positive value of the reaction constant ρ found for the addition of hydroxide ions to benzaldehydes for values of k_1 obtained using pK_{spec} or $pK_{E_{1/2}}$, which indicates an increase in reactivity with increasing electronegativity of the substituent, is in agreement with the prediction made by Hammett (32) for reactions involving a nucleophilic attack.

Absence of a precedent makes it impossible to predict the sign of the reaction constant ρ for the reverse reaction with rate constant k_{-1} . Hence it is impossible to deduce whether the use of K_{spec} or $K_{E_{1/2}}$ leads to a more reliable value for k_{-1} . This choice between the use of the two equilibrium constants can be made only after some of the values for k_1 or k_{-1} are determined by independent, *e.g.*, relaxation, techniques.

Sensitivity to substituent effects.—Sensitivity of individual quantities characterizing the acid-base and electrochemical properties of benzaldehydes are expressed by the values of the individual reaction constants, ρ (Table VI).

The susceptibility of half-wave potentials of the oxidation of benzaldehydes to substituent effects, expressed by the negative value of the reaction constant ρ_π (Table VI), is similar to that observed for the majority of reductions (33), which also show negative values of the reaction constant ρ_π . Thus the introduction of a substituent, *e.g.*, a *p*-cyano group, which makes the reduction of the aldehydic group easier (*i.e.*, causes a potential shift to more positive values) results also in a more facile oxidation (*i.e.*, causes a shift to more negative potentials). Nevertheless, an opposite effect, shown by a positive value of the reaction constant ρ_π , would be expected for oxidations where the electron transfer was potential determining, as reported for oxidations of alcohols, phenols, or hydrazines (33). It is thus possible to assume that hydrogen abstraction is potential determining in reaction [1b], similarly as in homogeneous oxidations (28, 29).

Table VI. Summary of the values of reaction constants and corresponding correlation coefficients for various Hammett relationships

Constant (vs. σ)	No. of aldehydes studied n	Reaction constant ρ	Correlation coefficient r
pK_{spec}	15	2.76	0.994
$pK_{E_{1/2}}$	7	0.74	0.957
pK^*	8	1.42	0.976
$\log k_1$ (using pK_{spec})	5 ^a	0.95	0.964
(using $pK_{E_{1/2}}$)	7 ^a	2.94	0.995
$\log k_{-1}$ (using pK_{spec})	5 ^a	-1.82	+0.972
(using $pK_{E_{1/2}}$)	7 ^a	2.50	0.936
$(E_{1/2}^{\text{A}} - E_{1/2}^{\text{B}})$	n	$\rho\pi$	r
1.0M NaOH (Region A)	7	-0.225V	+0.994
2.0M NaOH (Region A)	7	-0.218V	+0.970
9.0M NaOH (Region B)	7	-0.122V	+0.954

^a Values restricted to data obtained in sodium hydroxide solutions only.

The difference between the value of the $\rho\pi^{\text{A}}$ observed in the pH range where half-wave potentials are pH dependent and the value of $\rho\pi^{\text{B}}$ found at such high sodium hydroxide concentrations ($[\text{OH}^-] \gg K_1$) that it was pH independent, is due to the fact that $\rho\pi^{\text{A}}$ involves the dependence of the acid-base equilibrium constants pK on structure (as expressed by the reaction constant ρ). Relationship [11] will be derived and discussed in some detail elsewhere (34)

$$\rho\pi^{\text{A}} = \rho\pi^{\text{B}} - \frac{RT}{\beta n_b F} \rho \quad [11]$$

Conclusions

The source of the second oxygen atom in the electro-oxidation of benzaldehydes to yield benzoic acid, which was a source of some confusion and uncertainty (3, 4, 7, 9) has been proved to be the hydroxide ion. The addition of hydroxide ion takes place in a reaction preceding the electrode process proper.

Such a mechanism would make oxidations of benzaldehydes in nonaqueous media by this mechanism impossible. The effects of organic solvents on the values of acidity functions J_- are currently being studied to make an extension of the study of oxidations to these media possible.

The principle of allowing only the smallest structural change in the course of an electrode process would indicate that the dianion $\text{ArCH}(\text{O})_2^{2-}$ rather than the anion $\text{ArCH}(\text{OH})\text{O}^-$ would be the electroactive form. The oxidation of the monoanion namely involves a dissociation of the benzoic acid following the electron transfer process. Furthermore, it has been suggested (35) that dianions of the type $\text{ArCH}(\text{O})_2^{2-}$ are reactive in some homogeneous reactions of aldehydes. Nevertheless, the shape of the pH dependence of the limiting current strongly indicates that it is the monoanion $\text{ArCH}(\text{OH})\text{O}^-$ which is the electroactive form. This is supported by the shape of the $E_{1/2}$ -pH plots.

Such oxidation processes should not be restricted to benzaldehydes. Extension to heterocyclic aldehydes and anions of strongly hydrated aldehydes and ketones is under study. The assumption that the acid-base process is a volume reaction will be verified by comparison with rate constants of the addition reaction studied by stop-flow and relaxation techniques.

It is rather satisfying that the proposed mechanism is in accordance with mechanisms (23-31) suggested for homogeneous chemical oxidation of benzaldehydes by oxidizing reagents like chromic acid, permanganate, or hydrogen peroxide. It is a further contribution to the observation that chemical and electrochemical reactions under conditions where adsorption is not predominant follow a similar pattern.

Acknowledgment

The authors wish to thank the Princeton Applied Research Corporation (Princeton, New Jersey) for the loan of the PAR Model-174 Polarographic Analyzer. This work was supported by the 1972 Edward Weston Fellowship of The Electrochemical Society and the 1972-1973 Western Publishing Company Fellowship sponsored by the Technical Association of the Graphic Arts which were awarded to one of the authors (W.J.B.). This paper was presented in part at the North Eastern Regional Meeting of the American Chemical Society (Buffalo, September 1971).

Manuscript submitted June 14, 1973; revised manuscript received Sept. 26, 1974. This was Paper 176 presented at the Chicago, Illinois, Meeting of the Society, May 13-18, 1973.

Any discussion of this paper will appear in a Discussion Section to be published in the December 1975 JOURNAL. All discussions for the December 1975 Discussion Section should be submitted by Aug. 1, 1975.

REFERENCES

- H. S. Verter, in "The Chemistry of Carbonyl Group," Vol. 2, J. Zabicky, Editor, p. 136, Interscience Publishers, New York (1970).
- N. L. Weinberg and H. R. Weinberg, *Chem. Rev.*, **68**, 449 (1968).
- F. Fichter and E. Uhl, *Helv. Chim. Acta*, **3**, 24 (1960).
- A. I. Shlygus and N. B. Kondrikov, *Uch. Zap. Dal'nevost. Univ.*, **58** (1966); *C.A.*, **69**, 32449 (1968).
- R. McKee and J. Heard, *Trans. Electrochem. Soc.*, **65**, 301 (1934).
- F. Fichter and H. Ris, *Helv. Chim. Acta*, **7**, 803 (1924).
- H. Lund, *Acta Chem. Scand.*, **11**, 491 (1957).
- J. Volke, *J. Electroanal. Chem.*, **10**, 344 (1965).
- O. Manoušek and J. Volke, *ibid.*, **43**, 365 (1973).
- W. J. Bover and P. Zuman, *J. Chem. Soc., Perkin* **11**, 1972 (1973).
- W. J. Bover and P. Zuman, *J. Am. Chem. Soc.*, **95** 2531 (1973).
- C. H. Rochester, "Acidity Function," Academic Press, New York (1970).
- W. J. Bover, *This Journal*, **120**, 33C (1973).
- M. Kalousek, *Coll. Czech. Chem. Commun.*, **13**, 105 (1948).
- L. Němec and I. Holub, Unpublished results.
- L. Meites and L. Lampugnani, *Anal. Chem.*, **45**, 1317 (1973).
- E. P. Parry and R. A. Osteryoung, *ibid.*, **37**, 1634 (1965).
- J. H. Christie, J. Osteryoung, and R. A. Osteryoung, *ibid.*, **45**, 210 (1973).
- J. Heyrovský and J. Kůta, "Principles of Polarography," p. 339, Academic Press, New York (1965).
- G. Nigli, D. Barnes, and P. Zuman, *J. Chem. Soc. B*, 688 (1970).
- J. Koutecký, *Chem. Listy*, **47**, 9 (1953); *Coll. Czech. Chem. Commun.*, **18**, 597 (1953).
- M. Heyrovský and S. Vavříčka, *J. Electroanal. Chem.*, **36**, 203 (1972).
- K. B. Wiberg and R. Stewart, *J. Am. Chem. Soc.*, **77**, 1786 (1955).
- R. Stewart, in "Oxidation in Organic Chemistry," Part A, K. B. Wiberg, Editor, p. 54, Academic Press, New York (1965).
- F. Freeman, J. B. Brant, N. B. Hester, A. A. Kamgo, M. L. Kasner, T. G. McLaughlin, and E. W. Paull, *J. Org. Chem.*, **35**, 982 (1970).
- R. Stewart, in "Oxidation in Organic Chemistry," Part A, K. B. Wiberg, Editor, p. 58, Academic Press, New York (1965).
- R. Stewart and M. M. Mocek, *Can. J. Chem.*, **41**, 1160 (1963).
- K. B. Wiberg, *J. Am. Chem. Soc.*, **76**, 5371 (1954).
- K. B. Wiberg, in "Oxidation in Organic Chemistry," Part A, K. B. Wiberg, Editor, p. 172, Academic Press, New York (1965).
- J. Roček, *Tetrahedron Letters*, **5**, 1 (1959).
- E. Abel, *Z. Physik. Chem. N.F.*, **7**, 101 (1956).

32. L. P. Hammett, "Physical Organic Chemistry," p. 174, McGraw-Hill Book Co., New York (1940); H. H. Jaffe, *Chem. Rev.*, **53**, 191 (1953).
33. P. Zuman, "Substituent Effects in Organic Polarog-

- raphy," Plenum Publishing Corp., New York (1967).
34. W. J. Bover and P. Zuman, Unpublished results.
35. J. Hine and G. F. Koser, *J. Org. Chem.*, **36**, 1348 (1971).

Low Temperature Studies of Electrochemical Kinetics

I. Cyclic Voltammetry of Diethyl Fumarate

Roman D. Grypa*¹ and J. T. Maloy**

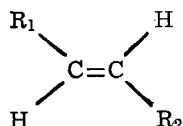
Department of Chemistry, West Virginia University, Morgantown, West Virginia 26506

ABSTRACT

Descriptive, low temperature, cyclic voltammetry studies have been conducted upon diethyl fumarate (DEF) in dimethylformamide (DMF). Temperature variations down to 200°K reveal three, interrelated, reduction processes. The first and second correspond to the formation of DEF^- and DEF^{2-} ; the third is attributed to the reduction of a dimeric product of the initial reduction. Temperature reduction inhibits the formation of this dimeric product while enhancing the availability of DEF^- for reduction to DEF^{2-} . The extensive formation of DEF^{2-} at reduced temperatures appears to be accompanied by a filming of the electrode surface. This suggests that polymerization may proceed through DEF^{2-} and may actually be inhibited by the dimerization process. The addition of water enhances the third reduction peak; it also decreases the available cathodic potential range so that this peak becomes lost in background at room temperature. Temperature reduction increases the available potential range so that products of the water-accelerated electrohydrodimerization reaction may be studied.

The electrohydrodimerization (EHD) reactions of 1,2-diaactivated olefins have been studied by many investigators. These EHD reactions are of synthetic interest because they are generally regarded as the first step in the formation of the "living" polymer (1). Recent studies (2-4) have also indicated that these reactions may also be used to electroinitiate certain cyclizations.

The olefins used in these studies are of the form



where R_1 and R_2 are electron withdrawing groups; these compounds are easily reduced in aprotic media to form relatively stable radical anions.

Baizer and co-workers (1, 2) have carried out numerous studies on these EHD (or electrolytic reductive coupling) reactions on various diaactivated olefins. From their voltammetric studies, they determined that the initial reduction of the olefin involved a one-electron transfer to form the radical anion of the parent olefins. Baizer also used macroelectrolysis (2) to find that these diaactivated olefins could be used to form cyclic compounds after the dimer dianion was protonated to form the hydrodimer anion. The yields and distributions obtained were highly dependent on the reaction conditions employed.

Bard and co-workers have extensively investigated the possible mechanistic path of the EHD reaction of diethyl fumarate ($\text{R}_1 = \text{R}_2 = -\text{CO}_2\text{Et}$; hereafter designated DEF) using double potential-step chronoamperometry (5) and studies of different diaactivated olefins at a rotating ring-disk electrode (6). Using working curves obtained through digital simulation,

they investigated the path of the reaction and proposed that the EHD reaction of DEF proceeded by a second-order dimerization mechanism. This is contradictory to the results reported by Baizer *et al.* (1), where they presumed the probable mechanistic path to be a second-order electrochemical-chemical-electrochemical mechanism. Further experiments conducted by Bard and Puglisi (6) on different olefins indicated that the second-order dimerization mechanism can be applied to other olefins, so that it is not unique to DEF.

Saveant *et al.* (7) have carried out extensive studies on the EHD reaction of several olefins in nonaqueous solvents to study the kinetics involved in the electrochemical reduction using linear sweep voltammetry. Their results indicated that the dimerization (radical-radical coupling) of two radical anions occurred after an initial one-electron transfer. They measured the variation of the cathodic peak potential of the first reduction peak with respect to the scan rate, the bulk olefin concentration, and the amount of proton source added to these systems. From their observations of the variation of the cathodic peak potential with respect to the scan rate and bulk olefin concentration, they determined that the reaction was not first order, but some type of "bimolecular reaction." The rate-determining step in the EHD reaction for diaactivated olefins was determined to be the radical coupling of the two radical anions. This conclusion was similar to the one reached by Bard.

Recent investigations by Klemm *et al.* (3, 4) on the electroreduction of some α,β -unsaturated esters of cinnamic acid, substantiated Baizer's observation that the EHD reaction could be used to synthesize cyclic compounds. On the basis of product analysis, they have proposed that these isolated cyclic compounds were formed by a Dieckmann cyclization of the hydrodimer anion.

Voltammetric studies reported by Bard (5) also indicate that at room temperature DEF exhibits $i_p/v^{1/2}$ behavior characteristics of a dimerization mechanism (8). In his earlier voltammetric studies Baizer observed a marked increase in $i_p/v^{1/2}$ behavior for ethyl cinna-

* Electrochemical Society Student Member.

** Electrochemical Society Active Member.

¹ Present address: Fertilizer and Chemical Division, Agway, Inc., Ithaca, New York 14850.

Key words: low temperature electrochemistry, electrohydrodimerization, reductive coupling, electrochemical dimerizations.

mate (EC; above structure with $R_1 = -C_6H_5$ and $R_2 = -CO_2Et$) at slow scan rates. (It appears that the caption for Figure 2 in Ref. (1) is in error; from the associated text it appears that the current function decreases with increasing scan rates for EC.) Since this behavior is characteristic of a first-order electrochemical-chemical-electrochemical process, Baizer proposed that the dimerization of EC might be complicated by an additional (first-order) process leading to an electroactive product. No variation in scan rate brought about the resolution of these two competing processes purported to involve the radical anion of EC. The development of low temperature electrochemical techniques by Van Duyne and Reilley (9-11) appeared to offer a means by which these two competing homogeneous reactions could be resolved, provided that the activation energy associated with one of the processes was significantly different from that of the other. This work was initially undertaken, then, in an attempt to resolve the apparent mixed mechanism associated with EC, but not with DEF.

A detailed rate and mechanism study of the low temperature electrochemistry of EC is the subject of a future communication. Because the EHD reactions of DEF had been well studied at room temperature, DEF was selected as an ideal compound to use in the initial experiments extending low temperature techniques to the study of EHD reactions. Since recent interest has been focused on the products of the EHD reaction, these initial experiments were designed to study the complete voltammetry of the DEF system. Temperature reduction has been shown to extend the available background potential limits of the solvent supporting electrolyte system (9); therefore, this technique permits the observation of electrochemical activity at potentials unobtainable conventionally. The results of the cyclic voltammetry experiments employed to characterize the products of the reduction of DEF at a variety of experimental temperatures constitute the remainder of this work.

Experimental

Apparatus.—The electrochemical cell used for low temperature cyclic voltammetry (and subsequent double potential-step chronocoulometry) studies is shown in Fig. 1. The cell was designed with a planar 0.008 cm^2 platinum working electrode, a platinum foil counterelectrode, and a silver wire quasi-reference electrode (QRE). The counterelectrode was made from a rectangle of platinum foil which was wrapped around the outside of a fritted glass cylinder, and attached to a nickel-tungsten lead passing through a 10/30 standard taper inner joint with a detachable con-

ductor. The QRE sat in a glass tube which was connected to the cap of the electrochemical cell. Thus, both reference and working electrodes were separated by glass tubing to prevent them from coming into contact with each other or the counterelectrode in the course of any experiments.

The cap of this electrochemical cell consisted of a 40/50 standard taper outer joint designed to hold all three electrodes. In addition, it supported the QRE compartment which in turn supported a fritted glass electrolysis compartment, used to separate the working and counterelectrodes. Sealed within this cap was the QRE compartment which was sealed to the base of the QRE joint. The tip of this tube was bent upward and sealed in the center of the bottom of the fritted glass electrolysis compartment in such a manner that the tip extended up into the compartment. The opening on this drawn tip had an inner diameter of 1 mm. When the cell was fully assembled, the distance between the drawn tip and the planar working electrode was approximately 2 mm. This distance was minimized to reduce the uncompensated resistance in the cell.

A double-walled cooling cryostat was constructed from Pyrex so that its inner wall extended above its outer wall to support a machined brass cap; the space between the walls of the cryostat was evacuated. A hole was drilled in the center of the cap to hold the cell firmly in the cryostat and the walls of this hole were lined with a rubber gasket to prevent any damage to the cell. Three smaller holes were drilled in the cap and fitted with copper tubing to serve as entrance and exit ports for the precooled nitrogen gas and thermocouple well.

A cooling system was constructed from a Matheson Gas Products No. 604 flowmeter, a 1900 mliter Dewar flask, a copper cooling coil, and the cooling cryostat. A 3 in. copper cooling coil was prepared from $\frac{1}{4}$ in. copper tubing. Nitrogen gas was passed from a needle valve through the flow meter into the copper cooling coil which was immersed in liquid nitrogen contained in the 1900 mliter Dewar flask. (Some experiments were conducted at higher than ambient temperatures; to achieve these temperatures, warm water was used instead of liquid nitrogen in this Dewar flask.) After leaving the cooling coil, the cooled nitrogen passed through a glass wool insulated column into the cooling cryostat. The temperature was regulated by adjusting the flow of the nitrogen gas through this system, and monitored by a copper-constantan thermocouple placed either in the cooling cryostat or in the cell.

Thermocouple voltages were amplified from the millivolt level with a noninverting operational amplifier (WC1741) equipped with a trimpot variable resistor so that an exact 1000-fold amplification could be achieved. A Systron Donner multimeter, Model 7050, was connected to the output of the circuit to provide the digital readout of temperature. The amplifier was calibrated with a Heath standard voltage source, Model EU-80A, to assure the linearity of the millivolt converter.

The Princeton Applied Research Model 170 Electrochemistry System was used in all electrochemical experiments. A Perkin-Elmer, Model 137, infrared spectrometer and a Varian T-60 nuclear magnetic resonance spectrometer were used to obtain infrared and NMR spectra of the compounds used.

Reagents.—Highly purified chemicals were required for these electrochemical experiments; therefore, the solvent, supporting electrolyte, and compounds used in these studies were purified and stored carefully. Spectroquality *N,N*-dimethylformamide (DMF), used as the solvent, was obtained from Fisher Scientific Company, and was purified and stored by the method described by Huret and Maloy (12). Purity was determined through electrochemical experiments. Polarographic grade tetra-*n*-butyl ammonium iodide (TBAI), the supporting electrolyte, was supplied by Southwestern Analytical Chemicals, Inc. TBAI was

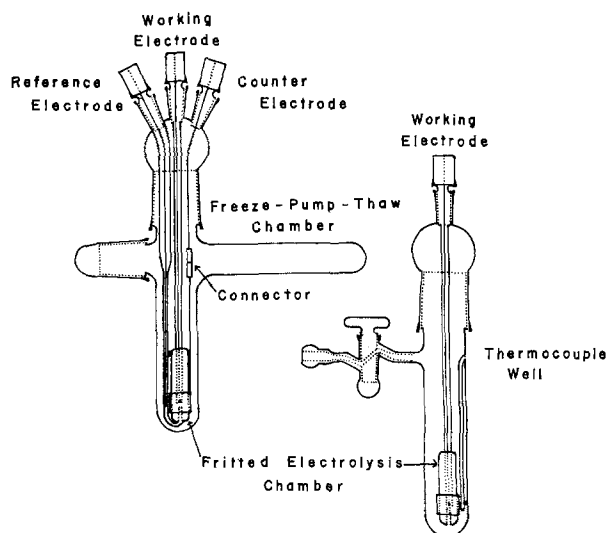


Fig. 1. Electrochemical cell

used as received and was stored in a desiccator over Drierite. Diethyl fumarate (DEF) was purchased from Aldrich Chemical Company. It was used as received (99+ % pure) and was stored in a desiccator over Drierite. The purity was assured by infrared and NMR spectroscopy. Prepurified nitrogen and 99.995% pure helium were obtained from Air Products and Chemicals, Inc. Both were used as received. These two gases were used in the course of sample and cell preparations. Ordinary house nitrogen was used as the cooling gas and it was not purified because it never came in contact with the sample.

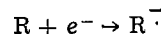
Procedure.—In a typical run, the cell was vacuum-dried and weighed so that concentrations could be determined gravimetrically; in all experiments 0.26–0.27M TBAI was used. After the supporting electrolyte had been dried in the cell, DMF was added to the evacuated cell from an air-tight storage flask under a slight positive pressure of helium. The resulting solution was subjected to five freeze-pump-thaw cycles to remove dissolved oxygen. Sample preparations were then carried out in a glove bag. A DEF solution of known concentration was prepared using the DMF-TBAI solution as the solvent, and an aliquot of this was injected into the remaining solution in the cell. In this manner, 1–5 mM DEF solutions were prepared. The cell was finally evacuated to $\sim 10^{-3}$ Torr, placed in the cryostat, and allowed to stand to permit the solution levels on either side of the fritted surface to equilibrate.

The rest potential of the solution was determined at each experimental temperature by a null balance technique. Positive feedback voltage compensation was used for resistance compensation in the cell. This was set at each current range setting used at every experimental temperature. Single scan and repetitive scan cyclic voltammetry (CV) experiments were performed at a variety of temperatures. After each CV experiment, the solution was allowed to equilibrate for a few minutes to reestablish initial conditions at the electrode.

Results and Discussion

Variable temperature CV experiments were run on all samples. Some especially interesting results were obtained when the entire potential range was scanned. Figure 2 illustrates a number of CV scans which were obtained for the DEF system at different temperatures and scan rates. It can be seen that three significant

reduction processes may occur, depending on the scan rate and temperature. At 295°K, the first reduction peak occurred at $-0.80V$ vs. Ag-QRE, in agreement with the potential reported by Bard (5); the other two principal reduction peaks occurred at -1.68 and $-1.90V$ vs. Ag-QRE, respectively. (A fourth peak may just be detected at potentials slightly positive of the second principal peak at higher temperatures. The height of this peak relative to the first principal peak does not appear to change with changing temperature over the range in which it may be detected; at lower temperatures, however, the second principal peak becomes larger so that this minor peak could not be detected even if the species responsible for it was present in the vicinity of the electrode. This peak has been tentatively assigned to an impurity present in the DEF or a product of the DEF reduction that it is not affected by temperature changes. Because its role in the low temperature electrochemistry of DEF has been judged to be minor, this peak is not discussed further herein.) A decrease in the experimental temperature to 203°K, shifted the first reduction peak to $-1.04V$ vs. Ag-QRE and the second reduction peak to $-1.90V$ vs. Ag-QRE; the third reduction peak was completely eliminated. These absolute potentials are not too significant because only a silver wire was used as the reference electrode, and no attempt was made to thermostat the reference electrode at room temperature. However, in all of these samples, the first peak corresponds to the well-established, one-electron reduction of the parent olefin R, to form the olefin anion radical



The dependence on scan rate and temperature on the formation of the second and third reduction peak is also evident in this figure. At room temperature, a decrease in the scan rate decreases the formation of the product of the second reduction wave and enhances the formation of the third reducible species. A decrease in the experimental temperature enhances the formation of the product of the second reduction wave and decreases the formation of the third reducible species; the species responsible for the third reduction wave apparently disappears at very low temperatures; simultaneously the second reduction wave becomes almost as large as the first wave.

The presence of the third reduction wave only at temperatures where the dimerization rate is rapid

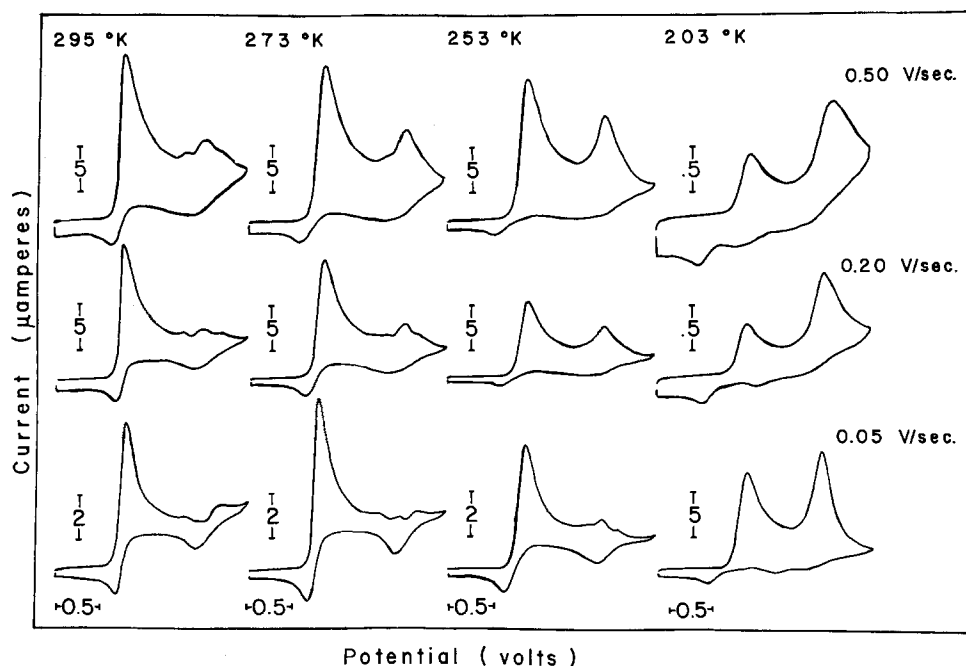
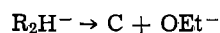
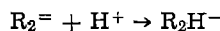
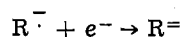


Fig. 2. Complete potential scan cyclic voltammograms for DEF at various temperatures and scan rates. The solution was 3.84 mM in DEF.

seems to indicate that this is due to the reduction of an electroactive product of the dimer dianion, possibly the hydrodimer anion, R_2H^- , such as the one proposed by Baizer (2) or the cyclic compound 2,3,4-tricarboethoxycyclopentane-1-one (C) in a manner similar to that recently suggested by Klemm and Olson (4) through the proposed mechanism



However, lowering of the experimental temperature decreases the dimerization rate and stops the formation of this third reducible species. This permits sufficient radical anion, $R^{\cdot-}$, to populate the diffusion layer to be further reduced to the dianion, R^{2-} , which is shown by the second reduction wave; that is



This may occur extensively only at reduced temperatures.

Table I shows the dependence of the three reduction processes on the scan rate and temperature for the DEF system. A comparison between the cathodic and anodic peak current heights for the first reduction wave reveals that the peak current ratios which are obtained upon a complete potential scan are different than those obtained when a potential scan is run just past the first reduction peak. The fraction of radical anion which dimerizes to form the cyclic product may be estimated from the value $1 - (i_{pa1}/i_{pc1})$ provided that these peak current ratios are obtained from a potential scan just past the first reduction wave. It may be noted that as the scan rate is increased or the temperature is lowered, the amount of radical anion undergoing dimerization decreases. This is accompanied by a simultaneous increase in the second reduction wave and a decrease in the third reduction wave. The peak current ratios obtained from a complete potential scan indicate that the radical anions formed in the reduction are precursors of the other reducible species. The i_{pa1}/i_{pc1} ratios are considerably less for the complete potential scan than they are for the po-

tential scan just past the first reduction wave. When the potential is scanned just past the first reduction wave, a decrease in the temperature increases the i_{pa1}/i_{pc1} ratio toward a maximum value of 1.0. The rate of reaction governing the disappearance of the radical anion is sufficiently reduced to allow the radical anion to be oxidized back to the parent olefin. However, when a complete potential scan is run, this regular increase is not observed. The third reduction process does not occur at low temperatures, but the products of the second reduction do not undergo oxidation on the reverse scan. This loss of radical anion at low temperature scans through the second reduction process indicates that this process is probably due to the reduction of the radical anion to the dianion; since the dianion (or products formed from it) does not undergo oxidation back to the radical anion, this low temperature reduction removes the otherwise stable radical anion from the diffusion layer.

At high temperatures and slow scan rates, when the amount of dimerization is extensive, the i_{pc2}/i_{pc1} ratio is small. As the extent of dimerization decreases, the i_{pc2}/i_{pc1} ratio increases and the i_{pc3}/i_{pc1} ratio decreases. This occurs when the scan rate is increased or the temperature is lowered. These observations support these contentions: (i) a product of the dimerization reaction is responsible for the third reduction wave, and (ii) when the amount of dimerization is extensive, very little radical anion remains in the diffusion layer to be further reduced to the dianion. If this analysis is correct, $(i_{pc3}/i_{pc1})/(1 - (i_{pa1}/i_{pc1}))$ should be an approximate measure of the concentration of the species reduced in the third reduction process relative to the concentration of radical anion available from the first reduction for its formation. [This suggestion is valid only if the peak-to-peak time (t_c) for the cyclic voltammetry just past the first reduction wave is similar to the peak-to-peak time (t_c') in the linear sweep voltammetry between the first and third peaks. These times are shown in Table I. At large values of t_c , $d(i_{pa1}/i_{pc1})/dt_c$ is ca. -0.002 sec^{-1} ; thus, a 5 sec difference between t_c and t_c' represents an error of ~ 0.01 in the estimation of i_{pa1}/i_{pc1} in the long time linear sweep voltammetry experiment. Similarly, when t_c is

Table I. Cyclic voltammetry data for a 3.84 mM solution of DEF showing the effect of temperature and scan rate variations on the peak current heights^(a)

Temperature, T (*K)	Scan rate v (V/sec)	$i_{pa1}^{(b)}$		t_c (sec) ^(c)	$i_{pa1}^{(d)}$		i_{pc2} i_{pc1}	i_{pc3} i_{pc1}	t_c' (sec) ^(e)	$1 - (i_{pa1}/i_{pc1})^{(b)}$
		i_{pc1}			i_{pc1}					
314	0.10	0.44 ^(f)		—	(g)	(h)	0.21	0.13	11.2	0.38
	0.20	0.55 ^(f)		—	(g)	(h)	0.13	0.02	5.5	0.29
	0.50	0.74 ^(f)		—	(g)	0.06	0.02	0.02	2.2	0.06
295	0.02	0.35		62.5	0.37	(h)	0.16	0.10	51.0	0.25
	0.05	0.42		24.6	0.38	(h)	0.12	0.06	20.4	0.21
	0.20	0.60		6.1	0.29	(h)	0.06	0.01	5.3	0.03
253	0.02	0.42		64.5	0.45	(h)	0.10	0.02	52.0	0.17
	0.05	0.49		25.6	0.37	(h)	0.06	0.02	20.4	0.04
	0.20	0.76		6.4	0.19	(h)	0.24	—	—	(h)
203	0.02	0.67		62.0	0.16	(h)	0.76	—	—	(h)
	0.05	0.83		24.9	0.10	(h)	0.81	—	—	(h)
	0.20	0.96		6.2	0.30	(h)	1.40	—	—	(h)
295 ⁽⁴⁾	0.02	0.34		60.5	0.32	(h)	(j)	—	—	(j)
	0.05	0.39		23.8	0.24	(h)	(j)	—	—	(j)
	0.20	0.50		5.4	0.35	(h)	0.12	—	4.6	0.24
253 ⁽⁴⁾	0.02	0.40		64.0	0.41	(h)	0.17	0.07	51.0	0.16
	0.05	0.55		25.6	0.34	(h)	0.10	0.01	20.4	0.03
	0.20	0.69		6.4	0.13	(h)	0.29	0.01	5.1	0.03
218 ⁽⁴⁾	0.02	0.47		60.5	0.31	(h)	0.30	0.01	51.0	0.03
	0.05	0.71		24.0	0.14	(h)	0.45	—	—	(h)
	0.20	0.85		6.0	0.14	(h)	0.70	—	—	(h)

(a) The solvent was 0.26M TBAI in DMF. A 0.008 cm² platinum working electrode area was used.

(b) Peak current ratios for the first reduction wave from cyclic voltammograms scanning just past the first reduction wave.

(c) Peak-to-peak time for cyclic voltammetry scans just past the first reduction wave.

(d) Peak current ratios for the first reduction wave from cyclic voltammograms scanning to background.

(e) Peak-to-peak time for linear sweep voltammetry between peak 1 and peak 3.

(f) Peak current ratios estimated from plot of $\frac{i_{pa1}^{(b)}}{i_{pc1}}$ vs. $1/T$.

(g) Baseline cathodic currents greater than those observed on the forward scan were observed on reverse scan. This may be caused by adsorbed hydrogen formed on the electrode during the temperature-facilitated breakdown of the solvent system at more negative potentials.

(h) No peak observed in cyclic voltammograms.

(i) Solution contained 53 mM water.

(j) Cathodic peak superimposed upon the breakdown wave of the solvent-supporting electrolyte.

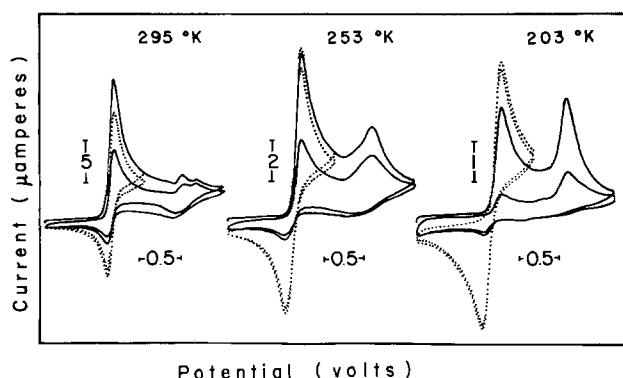


Fig. 3. Repeated scan cyclic voltammetry for DEF at various temperatures. The same DEF solution was used throughout; identical scan rates were employed at each temperature. —, Complete potential scan;, potential scan just past the first reduction wave.

small, $d(i_{pa1}/i_{pc1})/dt_c$ is ca. -0.01 sec^{-1} . Typical differences between t_c and t_c' indicate that the error in estimating i_{pa1}/i_{pc1} in the linear sweep voltammetry experiment never exceeds 0.02 through this approximation.] At high temperatures and slow scan rates, even when no current is detected for the second reduction process, the ratio in the last column of Table I never exceeds 0.5. This, of course, would be expected if the third reduction wave is attributed to the one-electron reduction of a dimeric product of the electro-generated radical anion.

It also appears that the loss of the third peak at low temperatures is accompanied by the loss of the reversible oxidation of the radical anion and the possible formation of a film on the electrode surface. Figure 3 shows repetitive CV scans to a potential just past the first reduction peak superimposed on those run on a complete potential scan. If a potential scan is carried out to a potential which is just past the first reduction process and repetitive CV scans are run, the difference between the cathodic peak current on the first scan and that of the second scan is very small compared to the difference which is observed when a complete CV scan is run in the repetitive mode for the same system. A decrease in the experimental temperature clearly enhances this effect and apparently results in the deposition of a slowly dissolving species on the electrode surface. In the absence of exhaustive electrolysis experiments aimed at product determination, it is unknown whether this species is a saturated hydrocarbon formed by the protonation of the monomer dianion or whether a polymer is being formed.

In Table II evidence is presented that dianion formation results in extensive deposition of product on the electrode surface. This table shows the effect of repeated CV scans on the height of the first cathodic

Table II. Variation of cathodic peak current with repeated cyclic scans at various temperatures for a 3.84 mM solution DEF

Temperature, T (°K)	Scan rate ν (V/sec)	i_{pc1}'		$i_{pc1}'^{(a)}$ i_{pc1}
		$i_{pc1}'^{(a)}$ i_{pc1}	$i_{pc1}'^{(b)}$ i_{pc1}	
295	0.20	0.77	0.51	0.34
	0.50	0.83	0.45	0.46
	1.00	0.88	0.49	0.44
253	0.20	0.92	0.42	0.54
	0.50	0.95	0.22	0.77
	1.00	0.95	0.15	0.84

(a) Cathodic peak current ratio for the first reduction wave from cyclic voltammograms scanning just past the first reduction wave.
(b) Cathodic peak current ratio for the first reduction wave from cyclic voltammograms scanning to background.

wave. The first column gives the ratio of the first cathodic peak on the second scan i_{pc1}' , to that on the first scan, i_{pc1} when the potential scan is carried out just past the first reduction peak. A decrease in temperature results in an increase in this ratio. In the second column, the same ratio is shown for a scan past the peak potential for dianion formation. This decreases with decreasing temperature. At any temperature or scan rate this ratio is reduced when dianion formation occurs. This is illustrated in the third column where the relative change in peak ratio due to dianion formation is given. This effect could be caused either by the depletion of the parent olefin because of the chemical irreversibility of dianion formation, or the deposition of a product of the dianion on the electrode surface. The latter is a distinct possibility; at low temperatures, the initial peak current is not restored when the solution is stirred. Only extensive standing results in the restoration of the initial first wave peak current. This observation would be expected if the formation of the dianion resulted in a slowly dissolving product film on the electrode surface. [This behavior is also illustrated in the full scan cyclic voltammogram at 203°K in Fig. 3. This was obtained after a preliminary potential excursion had resulted in the second process. Even though several minutes had passed between the preliminary voltammogram and the one shown in Fig. 3, the initial current peak was still not restored to the value obtained in the short scan voltammogram. This same effect probably accounts for some of the difficulty encountered in obtaining meaningful peak current ratios at low temperatures. In at least one instance (cf. Table I), it is assumed that prior-run filming decreased the magnitude of i_{pc1} relative to that of i_{pc2} so that the ratio of the latter to the former exceeded 1.0. This behavior was observed only at low temperatures when short (ca. 5 min) time intervals passed between successive runs.]

Single CV scans just past the first reduction process were also run on this system. In general, an increasing peak separation between i_{pc1} and i_{pa1} was observed as the temperature was lowered. The magnitude of the peak separation (ΔE_p) is shown in Table III in units of RT/F . Increasing peak separation with temperature reduction is to be expected if the reduction of the parent olefin proceeds by a quasi-reversible electron transfer (9). This could also be attributed to

Table III. Typical cyclic voltammetry data for the first reduction wave for a 3.84 mM solution of DEF at various temperatures^(a)

Temperature, T (°K)	Scan rate ν (V/sec)	$\frac{\Delta E_p}{(RT/F)}$	$\left(\frac{i_{pc1}}{C}\right)\left(\frac{T}{V}\right)^{1/2}$
295	0.10	2.0	108
	0.20	2.3	105
	0.50	2.9	93
	1.00	3.6	101
253	0.10	5.7	86
	0.20	6.4	83
	0.50	7.4	80
	1.00	8.3	85
223	0.10	8.0	45
	0.20	8.6	45
	0.50	9.6	45
	1.00	11.0	46
203	0.10	11.0	24
	0.20	11.8	24
	0.50	13.7	24
	1.00	15.5	24
295 ^(b)	0.10	2.5	103
	0.20	2.9	105
	0.50	3.7	101
	1.00	4.3	110
253 ^(b)	0.10	3.3	65
	0.20	4.1	60
	0.50	5.1	62
	1.00	5.9	67
218 ^(b)	0.10	4.4	35
	0.20	5.3	35
	0.50	6.6	37
	1.00	7.3	37

(a) The solution was 0.26M TBAI in DMF. The platinum working electrode was 0.008 cm².
(b) The solution contained 53 mM water.

increased cell resistance at lower temperatures; however, "full" iR compensation was employed in all voltammetry experiments at every temperature, and uncompensated iR has been judged to be only a secondary cause of this effect. (One reviewer has suggested that incomplete iR compensation may be the primary cause of the increase in ΔE_p at reduced temperatures and has reported some difficulties in achieving complete compensation with cells employing a QRE in his own laboratory. This is also a distinct possibility in the work reported herein.) The results in Table III also show the dependence of i_{pc1} upon scan rate. At fixed temperature, an increase in scan rate, v , increases i_{pc1} but generally results in a decrease in the (i_{pc1}/C) $(T/v)^{1/2}$ ratio, although this decrease was not found to be strictly monotonic with increasing scan rate (cf. representative data in Table III). A decrease of 15-18% in this ratio at constant temperature has been cited as a diagnostic criterion for a dimerization mechanism (7, 13), and this range is typical of the maximum amount of decrease observed with this system. Since the peak ratios in Table III have been temperature-normalized, the differences observed at different temperatures reflect the variation in the diffusion coefficient of DEF with decreasing temperature.

The addition of water to the DMF measurably decreases the usable potential range. At room temperature, water breakdown occurs near the potential where the third reduction process occurs. However, a decrease in temperature sufficiently displaces the breakdown of water to a more negative potential to allow the observation of the third reduction peak.

Water was added to the DMF to determine the effect of a proton source on the reduction of DEF. Figure 4 shows a series of CV scans run in DMF-H₂O over a variety of temperatures. Superimposed on these are CV run in anhydrous DMF. The addition of water increases the relative height of the third reduction peak; this indicates that the formation of the dimeric product is enhanced by the addition of a proton source. The differences between the cathodic peak currents for the first reduction wave in the DEF system in the presence and absence of water is probably due to extensive prior run filming of the electrode that occurs

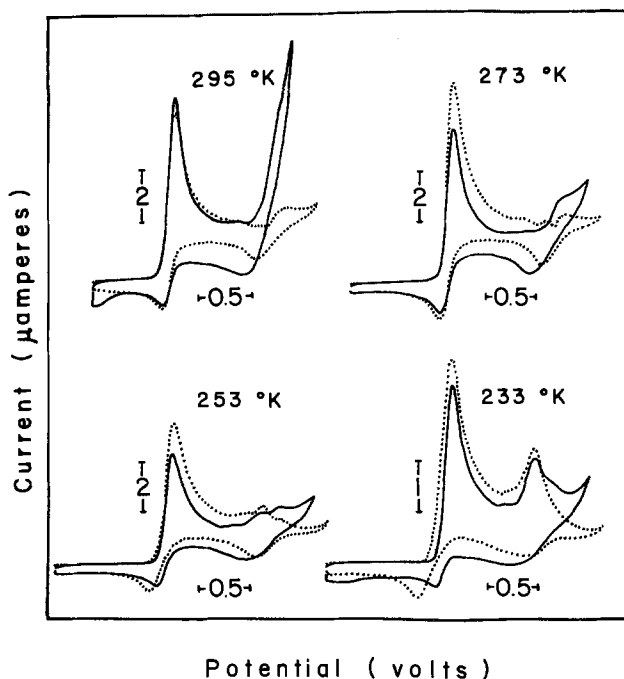


Fig. 4. Effect of water addition on the cyclic voltammetry of DEF. The same DEF solution was used throughout, but different scan rates were employed at different temperatures. —, Solution contained 53 mM water;, anhydrous solution.

following the formation of the dianion in the presence of additional water. That the addition of water clearly enhances the formation of a dimeric product is shown by the increase of the $(i_{pc3}/i_{pc1})/(1 - (i_{pa1}/i_{pc1}))$ ratio listed in the last column in Table I for the DMF-H₂O system compared to the anhydrous DMF system at similar scan rates; still, under no conditions is a value greater than 0.5 observed. However, as the experimental temperature is lowered, the extent of the third reduction process also decreases, while the relative height of the second reduction wave increases. This implies that even though water addition decreases the available potential range, the over-all rate of dimerization may be substantially increased through the addition of the proton source; the reduction of temperature allows the products of the dimerization to be observed before the dimerization reaction is stopped.

The dependence of i_{pc1} on scan rate is similar to that of DEF in anhydrous DMF as shown in Table III. Water addition also decreases the peak separation between the cathodic and anodic peak currents for the first reduction wave.

Conclusion

This work has shown the feasibility of temperature reduction in the study of processes involved in the EHD reactions of DEF. Temperature and scan rate variations have clearly indicated that the formation of the dimeric species inhibits the formation of the DEF dianion. When the dianion is formed, extensive deposition of a product formed from the dianion seems to occur on the electrode surface. If this product film is a polymeric form of DEF, then it would seem that the dimerization reaction, once regarded as the first step in the formation of the polymer, actually inhibits polymerization. This could mean that the product distribution in a bulk electrolysis is temperature dependent; at high temperatures, one would expect extensive dimer formation, while at lower temperatures the formation of a polymer may be anticipated. Variable temperature bulk electrolysis studies are presently being initiated to investigate the temperature dependence of product distribution.

The addition of water increases the rate of the EHD reaction of DEF. It appears that other slow EHD reactions in the absence of water could be forced to react rapidly by water addition. Temperature reduction may significantly retard the rate of proton reduction so that the cathodic background current for these systems may be displaced toward negative potentials at lower temperatures. Evidence presented above indicates that the cathodic range in the presence of water is easily extended by temperature reduction. Thus, water-accelerated EHD reactions may be studied effectively at reduced temperatures. This seems especially important in the study of the product of the third reduction process and its role in subsequent reactions. Since the formation of the species responsible for this reduction is enhanced by water addition, temperature reduction may prove to be essential in the study of this species.

No evidence is presented herein that any observable change in DEF reaction mechanism occurs at reduced temperature. The hitherto proposed dimerization mechanism for DEF appears operative at all temperatures on the basis of the limited CV data presented. Thus, the DEF system should provide a good basis for comparison with the low temperature electrochemical behavior of the EC system. These comparisons will be made in the second paper in this series.

Acknowledgment

The authors wish to thank Rein Valdna who constructed the vacuum cell and cryostat used in this research. Acknowledgment is made to the Donors of the Petroleum Research Fund administered by the American Chemical Society, for the support of this research.

Manuscript submitted May 14, 1974; revised manuscript received Oct. 2, 1974.

Publication costs of this article were partially assisted by The Petroleum Research Fund.

Any discussion of this paper will appear in a Discussion Section to be published in the December 1975 JOURNAL. All discussions for the December 1975 Discussion Section should be submitted by Aug. 1, 1975.

REFERENCES

1. J. P. Petrovich, M. M. Baizer, and M. R. Ort, *This Journal*, **116**, 743 (1969).
2. J. P. Petrovich, M. M. Baizer, and M. R. Ort, *ibid.*, **116**, 749 (1969).
3. L. H. Klemm, D. R. Olson, and D. V. White, *J. Org. Chem.*, **36**, 3740 (1971).
4. L. H. Klemm and D. R. Olson, *ibid.*, **38**, 3390 (1973).
5. W. V. Childs, J. T. Maloy, C. P. Keszthelyi, and A. J. Bard, *This Journal*, **118**, 829 (1971).
6. V. J. Puglisi and A. J. Bard, *ibid.*, **119**, 829 (1972).
7. E. Lamy, L. Nadjo, and J. M. Saveant, *J. Electroanal. Chem.*, **42**, 189 (1973).
8. M. I. Olmstead, R. G. Hamilton, and R. S. Nicholson, *Anal. Chem.*, **41**, 260 (1969).
9. R. P. Van Duyne and C. N. Reilley, *ibid.*, **44**, 142 (1972).
10. R. P. Van Duyne and C. N. Reilley, *ibid.*, **44**, 153 (1972).
11. R. P. Van Duyne and C. N. Reilley, *ibid.*, **44**, 158 (1972).
12. T. M. Huret and J. T. Maloy, *This Journal*, **121**, 1178 (1974).
13. C. P. Andrieux, L. Nadjo, and J. M. Saveant, *J. Electroanal. Chem.*, **26**, 147 (1970).

Technical Note



The Effect of Cathodic Treatment on Nickel Dissolution

B. MacDougall and M. Cohen*

Division of Chemistry, National Research Council of Canada, Ottawa, Ontario, Canada K1A 0R9

In recent years, numerous workers have reported two (or more) current peaks associated with the anodic dissolution of nickel in aqueous solutions using both polarization and transient techniques (1-7). A variety of possible explanations have been put forward to account for the existence of more than one current peak for the $\text{Ni} \rightarrow \text{Ni}^{2+} + 2e$ reaction, but have not

been fully substantiated. In the course of an investigation of nickel dissolution in neutral (8) and acid solutions, this multiplicity of current peaks for nickel dissolution was occasionally observed and prompted a study of the relationship between the anodic behavior of nickel and the state of the electrode surface before anodic polarization.

Figure 1(a and b) shows the effect of various cathodic treatments on the subsequent anodic potentiody-

* Electrochemical Society Active Member.

Key words: anodic dissolution, passivity, nickel oxide.

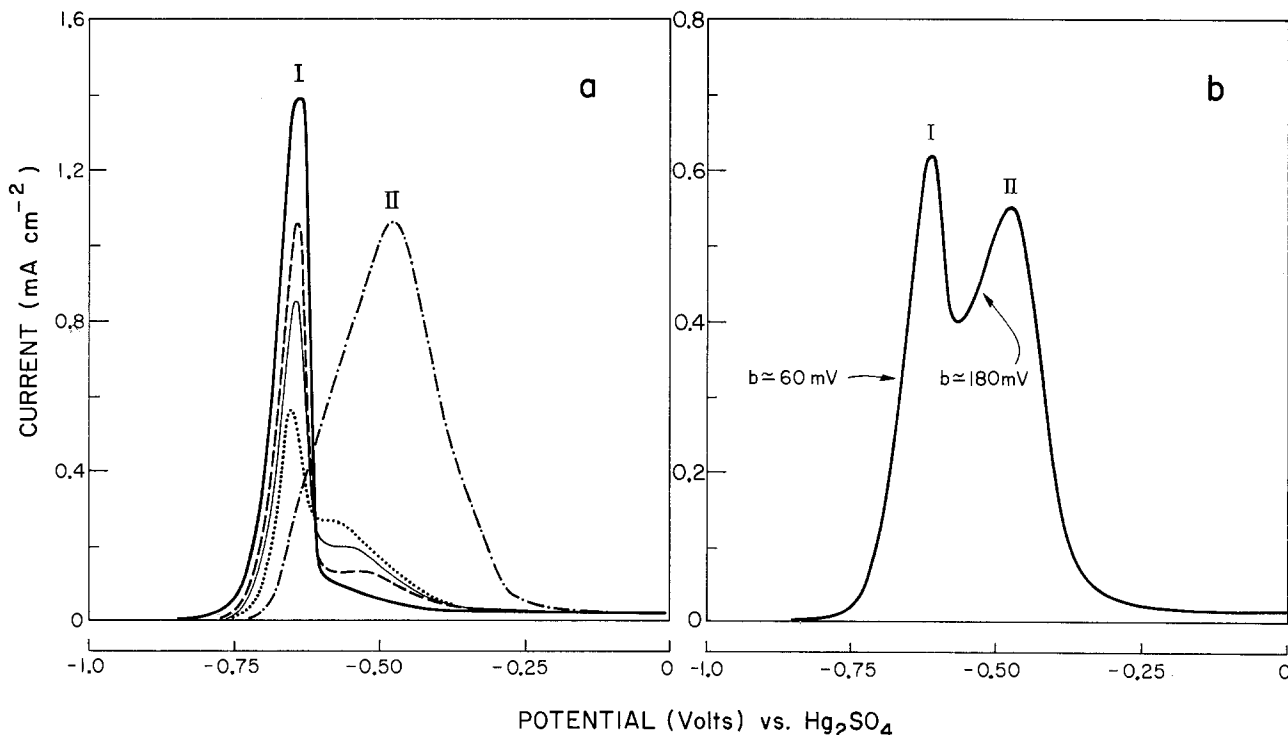


Fig. 1. a, Anodic potentiodynamic profiles at $S = 4 \text{ mV/sec}^{-1}$ on electropolished polycrystalline Ni electrodes in pH 3.0 Na_2SO_4 solutions after various cathodic treatments: a(—), 5 min at -1.0V with no N_2 bubbling (the same profile is obtained even after 2 hr of cathodic reduction); b(---), 5 min at -1.0V with light N_2 bubbling; c(—), 5 min at -1.0V with vigorous N_2 bubbling; d(. . .), 10 min at -1.0V with vigorous N_2 bubbling; e(—), 1 hr at -1.0V with moderate N_2 bubbling. All potentials quoted in this paper are referred to the Hg_2SO_4 electrode ($+0.665\text{V}$ with respect to the standard reversible hydrogen electrode). b, As in (a) above but after 20 min at -1.0V with vigorous N_2 bubbling.

dynamic sweep behavior of electropolished nickel [see Ref. (8)] in a 0.15N Na_2SO_4 (certified ACS)- H_2SO_4 solution of pH 3.0. Longer times of cathodic treatment in stirred acid solution or more rapid solution stirring at constant time increases the potential range over which nickel dissolves anodically and, as seen in Fig. 1b, another current peak (i.e., II) is clearly resolved.¹ Figure 1a shows peak II growing from a slight shoulder on peak I in curve (a) to become the predominant peak in curve (e) with peak I now only a shoulder in this latter case. Analysis of the solutions for nickel showed that the charge under both anodic peaks is due to nickel dissolution. An increase in the time and bubbling rate during cathodic treatment shifts the potential of passive film formation to more anodic values with a corresponding increase in the area of peak II. In the absence of N_2 bubbling during the cathodic treatment, the anodic sweep profile displays only a very small peak II, as shown in Fig. 1a (curve a), and is found to be independent of the cathodic reduction potential (even up to -1.6V) and time of cathodic polarization. The increased activity of the electrode

¹ The appearance and size of peak II is, however, independent of solution stirring during the anodic sweep itself.

and growth of peak II is therefore not due to more complete reduction of the prior oxide on electropolished nickel [cf., Ref. (8)].

Reflection electron diffraction was used to investigate the state of a nickel single crystal surface after the various prior cathodic treatments which gave rise to the subsequent anodic profiles in Fig. 1a. Anodic sweep experiments on the Ni (111) after these cathodic treatments give results similar to those in Fig. 1a for polycrystalline nickel. Figure 2(a-d) shows the diffraction patterns from an electropolished nickel (111) electrode before and after cathodic reduction for 1 hr in a pH 3.0 Na_2SO_4 (certified ACS) solution with no N_2 bubbling. Cathodic reduction of electropolished nickel in this solution at -1.0V leaves the surface oxide-free, and upon exposure to the air during transfer to the diffraction apparatus an oxide film forms which has the same diffraction characteristics as the film on electropolished nickel (8). This is also the case for cathodic reduction with light N_2 bubbling for short time periods (< 15 min) or in the absence of N_2 bubbling for extended periods of time (e.g., several hours). With more vigorous N_2 bubbling during the cathodic treatment, the resulting diffraction pattern depends

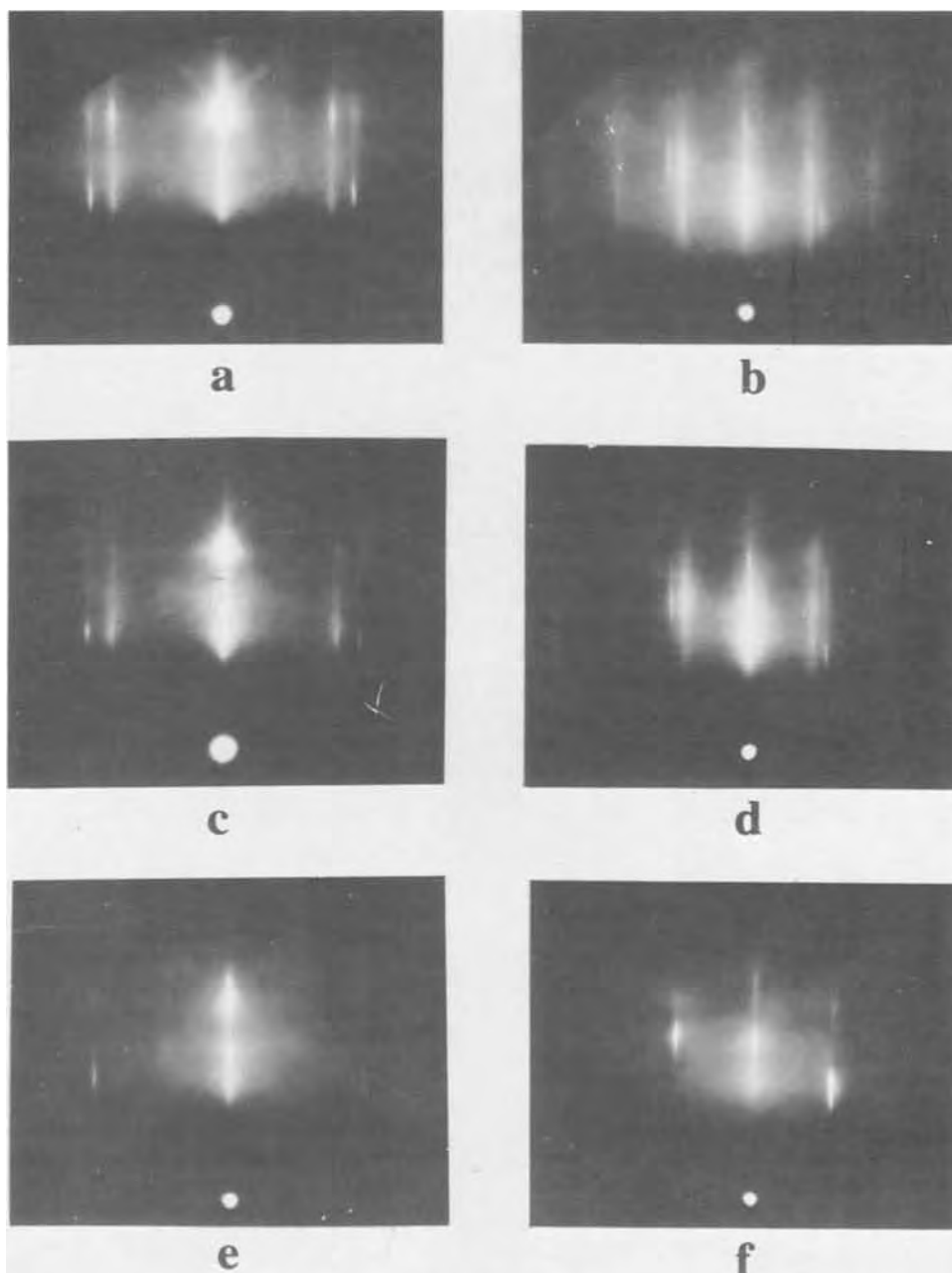


Fig. 2. Reflection electron diffraction patterns from a (111) nickel single crystal, in both the $\langle 112 \rangle$ and $\langle 110 \rangle$ directions, after various electrochemical treatments: (a and b), electropolished in H_2SO_4 ; (c and d), cathodic reduction in an unstirred pH 3.0 Na_2SO_4 solution at -1.0V with the results being independent of time of polarization; (e and f), cathodic reduction in a vigorously stirred pH 3.0 Na_2SO_4 solution (certified ACS) at -1.0V for 1 hr.

on the time but not on the cathodic polarization potential. The increased rate of N_2 bubbling in conjunction with long reduction periods results in a diminishing of intensity of the NiO reflections so that there is an almost complete loss of these reflections after ca. 1 hr of cathodic polarization with vigorous N_2 bubbling, as shown in Fig. 2(e and f).

The electron diffraction results in Fig. 2(e and f) indicate that there has been a substantial decrease in the amount of highly epitaxed NiO after cathodic reduction in rapidly stirred solutions and air exposure, and the possibility exists that the oxide has still formed on the surface but in an amorphous configuration. However, oxygen K_{α} x-ray emission spectroscopy shows that the amount of surface oxide represented by the diffraction pattern of Fig. 2(e and f) was ca. 65% lower than that on electropolished nickel. It would therefore appear that both the nature and extent of peak II during the anodic sweep and the amount of oxide formed by air exposure after cathodic treatment are related to and controlled by the surface coverage of some impurity acting as a blocking agent. Indeed impurity adsorption from solution onto the oxide-free nickel surface is a diffusion controlled process which would be accelerated by N_2 bubbling during cathodic reduction, as is the case here. During a series of potentiodynamic sweeps on a contaminated nickel surface, the effects of the impurity diminish during each successive anodic sweep, i.e., peak II diminishes and peak I becomes predominant, the impurity being removed as Ni dissolves. The time involved during the cathodic sweep at 4 mV/sec^{-1} (ca. 4 min for the range in Fig. 1a) is not sufficient to allow large amounts of impurity to diffuse from the solution to the surface again. Although it has previously been shown (9) that large amounts of impurities in the metal itself may extend the potential range of metal dissolution, the present problem is one of adsorption from solution on a high purity nickel metal.

Possible sources of impurity in solution would be the water, acid (H_2SO_4), or salt (Na_2SO_4). The water used in these experiments was prepared by distillation of distilled water from a Corning Still² which employs a quartz heating tube. The same results were obtained with water distilled from alkaline permanganate or passed through a series of ion and carbon exchange cartridges. When a pH 3.0 H_2SO_4 solution was used without any added Na_2SO_4 or a pH 3.0 $HClO_4$ solution with 0.15N $NaClO_4$ (ACS grade), cathodic reduction with vigorous N_2 bubbling even for several hours did not affect the oxide reflections on subsequent air-exposure. Impurities in the ACS grade Na_2SO_4 would thus appear to be responsible for contamination of the nickel electrodes. Indeed, electron diffraction showed that when ultrapure Na_2SO_4 was used there was no detectable diminishing of oxide reflections even after cathodic reduction for several hours with vigorous N_2 bubbling. Anodic sweeps in the ultrapure Na_2SO_4 solution, after a cathodic treatment which would have given a greatly enhanced peak II in certified ACS Na_2SO_4 , instead gave an approximately 30% decrease in peak I but no corresponding increase in peak II, i.e., the potential of passivation was not shifted. The diminishing of peak I in this case is probably associated with what one might call the "ordinary" solution impurity which adsorbs during long time reduction with vigorous N_2 bubbling, even in the pure solutions, and which

acts as a surface blocking agent. This latter impurity does not prevent formation of either the highly epitaxed air-formed film on air exposure nor the passive film on nickel during anodic polarization and is therefore different from the more specific impurity in certified ACS Na_2SO_4 . Cathodic reduction for shorter times ($\leq 1/2$ hr) with N_2 bubbling in the ultrapure Na_2SO_4 solution results in a decrease of peak I of less than 5% and this treatment can therefore be used to produce uncontaminated starting surfaces.

X-ray emission was used to analyze the various nickel surfaces and their films in an attempt to identify the impurity. No significant impurities were detected by the technique on any of the nickel surfaces. No sulfur was detected on either clean or contaminated surfaces (limit of detection is $0.005 \mu\text{g/cm}^{-2}$) and the carbon content was $< 0.01 \mu\text{g/cm}^{-2}$ (i.e., close to the limit of detection) on all surfaces.

An anodic sweep such as that in Fig. 1b can be obtained with the certified ACS Na_2SO_4 where there is good separation between the two peaks, even after peak II has grown considerably. From this sweep profile the Tafel slope for nickel dissolution during peak I is ca. 60 mV, i.e., nickel is dissolving from a film-free surface region. However, the Tafel slope of peak II is ca. 180 mV and this may be due to nickel dissolution through a barrier-layer film, e.g., the impurity and/or oxide which has begun to grow. A true passive film forms at higher anodic potentials and nickel dissolution practically ceases. Replica electron microscopy of the nickel specimens after considerable nickel dissolution via peak II shows a general roughening of the surface but no pitting is detected. This shows that the specific impurity from the ACS Na_2SO_4 does not act like chloride ion to give localized corrosion and supports the view of nickel dissolution in peak II through a modified barrier-layer type film. This work indicates that the anodic polarization curve of clean nickel has a single sharp dissolution peak and that the extension of the potential range of active nickel dissolution with possible resolution of multiple peaks is probably due to adsorbed impurities.

Manuscript submitted Sept. 19, 1974; revised manuscript received Nov. 4, 1974.

Any discussion of this paper will appear in a Discussion Section to be published in the December 1975 JOURNAL. All discussions for the December 1975 Discussion Section should be submitted by Aug. 1, 1975.

Publication costs of this article were partially assisted by the National Research Council of Canada.

REFERENCES

1. J. L. Weininger and M. W. Breiter, *This Journal*, **110**, 484 (1963).
2. I. A. Gindin, L. N. Jagupolskaja, W. K. Aksenow, and Ja. D. Starodubow, *Corrosion Sci.*, **13**, 967 (1973).
3. L. N. Yagupolskaya and B. A. Mouchan, *Proc. 4th Intern. Congress on Metal. Corrosion*, p. 473, Amsterdam (1969).
4. M. Daguene, M. Froment, and M. Keddah, *J. Microscopie*, **5**, 569 (1966).
5. N. D. Greene, *Proc. 1st Intern. Congress on Metal Corrosion*, p. 113, London (1962).
6. Y. M. Kolotyarkin, *Zashchito Metal.*, **3**, 131 (1967).
7. H. J. Ratzler-Scheibe and H. G. Feller, *Electrochim. Acta*, **18**, 175 (1973).
8. B. MacDougall and M. Cohen, *This Journal*, **121**, 1152 (1974).
9. G. A. DiBari and J. V. Petrocelli, *ibid.*, **112**, 99 (1965).

² Corning Glass Works, Water Distillation Apparatus Model AG-2.

Infrared Reflectance Spectra (IRRS) of Anodic Oxide Films on Pure Tantalum Formed in Phosphoric Acid

Tsutomu Takamura* and Hirochika Kihara-Morishita

Toshiba Research and Development Center, Tokyo Shibaura Electric Company, Limited,
1 Komukai-Toshiba-cho, Saiwai-ku, Kawasaki, 210 Japan

In previous work, we measured the IRRS of the anodic oxide film of Ta formed in dilute nitric acid and suggested that the growth of the oxide phases was dependent on the forming voltage and that the chemical structure of the film might be changed at around 100V (1). No nitrate anion was incorporated.

When, however, the anodic oxide film is formed in phosphoric acid, the incorporation of phosphorus atoms in the oxide film has been reported by several authors (2-4). Randall *et al.* showed that the content of phosphorus was dependent on both the phosphoric acid concentration of the electrolyte and the current density of anodization (2, 5).

If the amount of incorporated phosphate anion is not low, we can detect it by IRRS. One of the purposes of the present study is to determine the amount of phosphorus incorporated as functions of the forming voltage, the film thickness, and the phosphoric acid concentration of the electrolyte, which will be the aid of the analysis of the formation mechanism.

The authors' purpose is to ascertain the previous findings that both the growth rates of the oxide phases and the chemical structure of the film were dependent on the forming voltage or the film thickness irrespective of the electrolyte and the concentration of the solution.

A thin Ta rolled plate of 99.97% purity was polished chemically with a mixture of concentrated hydrofluoric acid, sulfuric acid, and nitric acid and anodized at a constant current density of 1.0 mA/cm² in various concentrations of phosphoric acid aqueous solution. When the voltage reached a desired value, the electrolysis circuit was turned off. The specimens were rinsed with distilled water carefully and dried at room temperature *in vacuo*. IRRS were recorded on a Nihon Bunko (JASCO) IR spectrophotometer in connection with equipment specially designed for the reflection measurement (1) in dried air with an incident angle of 45°. The number of reflections were six.

IRRS of the anodic oxide films on Ta obtained at various forming voltages are shown in Fig. 1. The anodic films gave rise to an intense and very broad absorption band in the region around 900 cm⁻¹, which, by a Gaussian band decomposition (6), could be resolved into three components as seen in Fig. 1. The three components, *i.e.*, 925, 860, and 800 cm⁻¹ were always observed for all the oxides irrespective of electrolyte composition, but the 1110 cm⁻¹ band was observed only with phosphate, phosphonate, or phosphinate present. In general, inorganic phosphate gives rise to a band due to ν PO₄ in the 1120-1080 cm⁻¹ region (7, 8). Accordingly, the band at 1110 cm⁻¹ will be assigned to be ν PO₄ of PO₄⁻³ group. Of the three

bands in the 1000-750 cm⁻¹ region, there are two possibilities of the assignment, *i.e.*, due to the deformation of Ta-OH bond or the stretching of Ta-O band. The former is not probable since no evidence of the presence of O-H group was found in the 3 μ m region. On the other hand, the three bands were always observed with a number of Ta anodic oxide films formed in various electrolytes. Therefore, the three bands in the region were assigned to the stretching vibration mode of Ta-O bond. Of course, no band due to the Ta-O deformation mode is expected in these wave number regions (9).

Figure 2 shows how the optical density of each resolved band changes depending on forming voltage or film thickness of the film. As clearly seen in the figure, intensities of the two bands, *i.e.*, 925 and 800 cm⁻¹ bands increase linearly with the increase of the anodization voltage, and accordingly, of the film thickness. The rates of their increase, however, change in the 70-90V region where the rates become slow, which were already seen on the anodic oxide formed in dilute nitric acid (1). The intensities of both bands were independent of the concentration of phosphoric acid.

Several causes may be considered for the explanation of these changes in the rates of intensity increase: (i) the change of the chemical structure of the film, (ii) the slowing down of the growth rates of the oxide phases in the film, (iii) the change of complex dielectric constant of the film due to the variation of strain

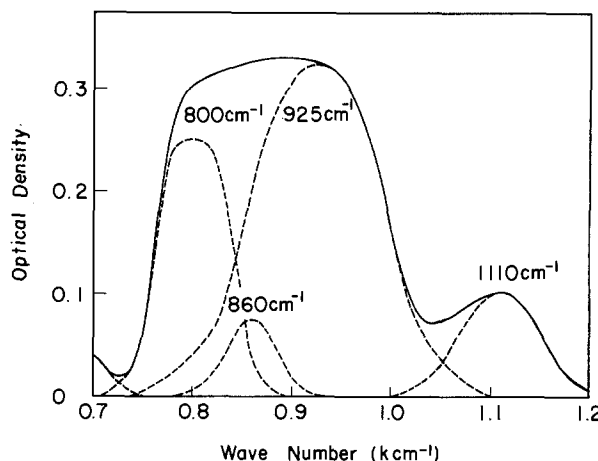


Fig. 1. IRRS and four component absorption bands appearing in the wave number region of 700-1200 cm⁻¹ for the anodic oxide films formed on pure tantalum plate which were anodized at 1.0 mA/cm² to 300 V in 1.0 × 10⁻²N H₃PO₄ aqueous solution at 20°C.

* Electrochemical Society Active Member.

Key words: anodic film, chemical structure, infrared spectra, phosphate inclusion, tantalum oxides.

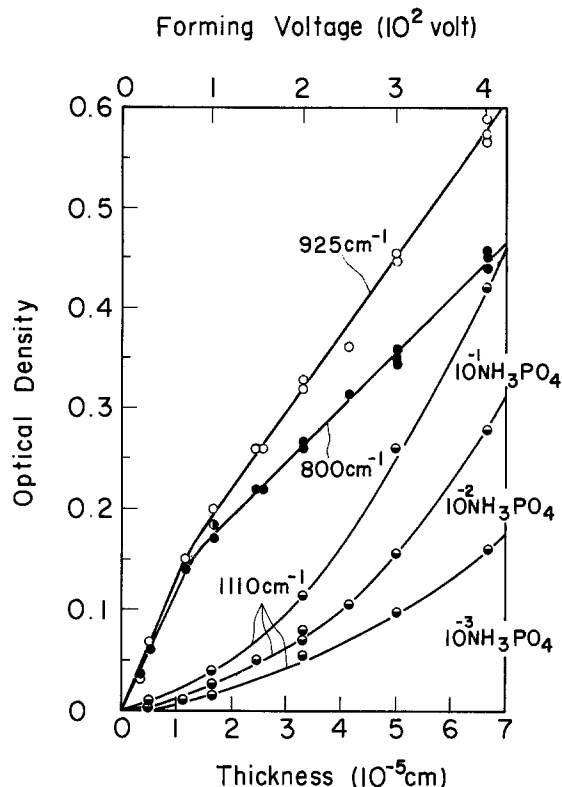


Fig. 2. Dependency of the optical density of each absorption band on the forming voltage and the film thickness of the tantalum anodic oxide film. Three components (925, 860, and 800 cm^{-1}) were examined. The intensity was dependent on $[\text{H}_3\text{PO}_4]$ of anodizing bath. Higher concentration bath gave higher intensity. Therefore three lines were obtained for one absorption.

in the film (10, 11). Further investigation is necessary to determine which cause given above is actually working.

The 1110 cm^{-1} band was intensified more rapidly when the forming voltage was increased (Fig. 3). The band intensity increased linearly against the square of the forming voltage or the film thickness. At constant voltage, it increased logarithmically against the phosphate concentration. At the same time, the 610 cm^{-1} band increased in a similar manner to the 1110 cm^{-1} band. Consequently, these bands will indicate the corresponding phase will contain phosphate.

Manuscript submitted Aug. 7, 1974; revised manuscript received ca. Oct. 18, 1974.

Any discussion of this paper will appear in a Discussion Section to be published in the December 1975 JOURNAL. All discussions for the December 1975 Discussion Section should be submitted by Aug. 1, 1975.

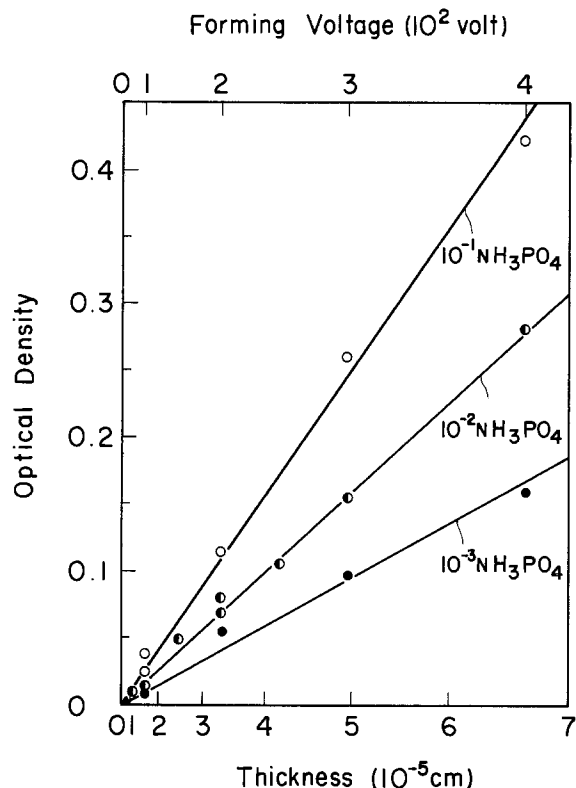


Fig. 3. Quadratic plots of the forming voltage or the film thickness of the tantalum anodic oxide film against the optical density of the 1110 cm^{-1} absorption band.

Publication costs of this article were partially assisted by The Tokyo Shibaura Electric Company, Limited.

REFERENCES

1. H. Kihara-Morishita, T. Takamura, and T. Takeda, *Thin Solid Films*, **6**, R29 (1970); *Denki Kagaku*, **39**, 417 (1971).
2. J. J. Randall, Jr., W. J. Bernard, and R. R. Wilkinson, *Electrochem. Acta*, **10**, 183 (1964).
3. R. E. Pawel, J. P. Pensler, and C. A. Evans, Jr., *This Journal*, **119**, 24 (1972).
4. D. M. Smyth, *ibid.*, **113**, 1271 (1966).
5. C. J. Dell'Oca and L. Young, *ibid.*, **117**, 1545 (1970).
6. J. Pitha and R. N. Jones, "Optimization Method for Fitting Curves to Infrared Band Envelopes," *NRC Bulletin No. 12*, Nat. Res. Coun. Canada, Ottawa (1968).
7. E. Steger and W. Schmidt, *Ber. Bunsenges. Phys. Chem.*, **68**, 102 (1964).
8. F. A. Miller and C. H. Wilkins, *Anal. Chem.*, **24**, 1253 (1952).
9. T. A. Sidorov, *Zh. Fiz. Inst. Akad. Nauk SSSR*, **12**, 236 (1960).
10. A. T. Fromhold, Jr., *Surface Sci.*, **22**, 396 (1972).
11. W. Jaenicke, "Passivierende Filme und Deckschichten," H. Fischer, *et al.*, Editors, p. 160, Springer-Verlag, Berlin (1956).



A Study of the Diffusion of Oxygen in Alpha-Zirconium by Means of Nuclear Microanalysis

D. David and G. Amsel*

Groupe de Physique des Solides de l'École Normale Supérieure (L.A. C.N.R.S. No. 17), 75005 Paris, France

and P. Boisot¹ and G. Béranger²

Laboratoire de Métallurgie Physique (L.A. C.N.R.S. No. 177), Université Paris-Sud, 91405 Orsay, France

ABSTRACT

Polycrystalline zirconium samples were oxidized in pure oxygen under atmospheric pressure at temperatures ranging from 700° to 845°C and for times up to 400 hr. The diffusion of oxygen in the metal, beneath the oxide layer formed, was studied using a direct quantitative method of analysis based on the observation of the nuclear reaction $O^{16}(d,p)O^{17x}$. It was found that at a given temperature the oxygen concentration profiles, referred to the oxide-metal interface, may be superimposed after scaling by a factor \sqrt{t} . The results may be fitted assuming a concentration independent diffusion coefficient D , the oxygen concentration at the oxide-metal interface being constant and nearly equal to the saturation value, around 30 atom per cent. An activation energy $Q = (49 \pm 1)$ kcal/mole was found for the process. Identical results were obtained in air, showing that, at atmospheric pressure, nitrogen in the air plays a negligible role in the dry corrosion of zirconium.

Zirconium, like other metals such as titanium and hafnium, can form interstitial solid solutions containing large amounts of oxygen (1). Hence, in addition to the formation of an oxide layer (zirconia), the thermal oxidation of zirconium also gives rise to a simultaneous diffusion of oxygen into the metal matrix beneath the oxide. A complete study of the oxidation of zirconium requires these two phenomena to be separated. For the full understanding of the phenomena on the atomic scale, one has to know the profile of the oxygen concentration within the metal as a function of both time and temperature. It is the purpose of this paper to study with a direct method these concentration profiles and the corresponding diffusion process.

Several authors have attempted to establish oxygen profiles in zirconium. Most of the early investigations were based on an indirect determination of the oxygen contents obtained by measuring the microhardness (2-6), or the parameters of the hexagonal Zr lattice (7). However, recent measurements have shown that the relationships between oxygen concentration and both microhardness (8-10) and lattice parameters (11-12) are strongly nonlinear and for the first case not even one to one; thus, the results obtained by these methods have a qualitative character only. In some works the concentration profiles were determined by using more quantitative methods. Thus, Ericsson *et al.* (8) have measured the concentration of zirconium

in the Zr-O solid solution by means of an electron probe analyzer and obtained, by difference, the concentration profile of oxygen. Their precision was ± 2 atom per cent (a/o); hence amounts of oxygen below 2 a/o could not be detected. More recently Quataert and Coen-Parisini (13) have studied directly the oxygen concentrations by means of an ion probe analyzer. In order to convert their data into depth profiles they had to assume the sputtering rate and ionization probability to be independent of oxygen concentration; moreover they did not attempt an absolute concentration calibration, interpreting only normalized profiles to extract the diffusion coefficient D ; finally, due to nonuniform erosion across the ion beam spot their sensitivity for low oxygen contents at depths larger than about $2\sqrt{Dt}$, i.e., 2 a/o, was very poor. However, Ref. [8] and [13] contain the first reliable data from direct measurements of oxygen in the metal matrix, in the 600°-900°C temperature range.

Resorting to an ingenious method Pemsler (14) measured oxygen profiles by observing the rate of dissolution, during an anneal under vacuum at 510°C, of anodic oxide layers deposited on polished sections of specimens, previously oxidized at 850°C. He has assumed that the quantity of oxygen diffused during the anneal under vacuum was, at each point, proportional to $C_s - C$, where C_s represents the saturation concentration of the Zr-O solid solution and C the oxygen concentration to be measured. The quantity of oxygen diffused at each point was deduced from the decrease in the thickness of the anodic layer during the anneal under vacuum, which could be estimated from the change in color of this layer. The concentration profiles so obtained were of the error function type. In interpreting his results, Pemsler must assume that,

* Electrochemical Society Active Member.

¹ Present address: Creusot-Loire, Unité carbures, 71200 Le Creusot, France.

² Present address: Université de Technologie de Compiègne, Division Matériaux, Département de Génie Mécanique, 60206 Compiègne, France.

Key words: oxidation, oxygen diffusion, zirconium, diffusion coefficient, temperature, microhardness, lattice parameters, nuclear microanalysis.

after an anneal of 145 min at 510°C, the solid solution Zr-O is saturated at the anodic oxide-metal interface, and that the coefficient of diffusion at this temperature is known and does not depend on oxygen concentration. This method therefore cannot give profiles without *a priori* assumptions; moreover it lacks sensitivity at low concentrations, below about 8 a/o. It gives hence semiquantitative results in terms of the value of C_s which is not measured directly. As will be shown below, several of Pemsler's assumptions are confirmed by the present work: his simple method might hence prove very useful, the more so that it allows one to observe, under the microscope, single grains and to estimate crystal orientation effects on diffusion.

In the frame of a study, using O^{17} as a tracer, of the self-diffusion of oxygen in zirconia growing on zirconium, Cox and Roy (15) have estimated the diffusion coefficient of oxygen in the metal beneath at 400° and 500°C. They used the nuclear reaction $O^{17}(He^3, \alpha)O^{16}$ to detect and locate O^{17} as a function depth. It appears that such nuclear techniques are best suited for direct and absolute concentration measurements for depth profile determinations. For heterodiffusion there is no need to use oxygen isotopes, as O^{16} (99.758% natural abundance) may be readily detected. We resorted to such a method in this work.

The general principles of microanalysis by the direct observation of nuclear reactions have been described in Ref. (16) as applied to O^{16} and O^{18} and more recently in Ref. (17), which contains most of the experimental details on the techniques used here. Specific applications to the study of diffusion processes in zirconium were described in Ref. (18), to which we shall refer here systematically, and which contains the first typical results on oxygen diffusion profiles in zirconium obtained by our group. The $O^{16}(d, p)O^{17x}$ reaction was used. This reaction presents high cross sections below 1 MeV bombarding energies and a low energy accelerator may be used, thus simplifying the experimental setup to some extent. These techniques have been applied also to a study of the physical properties of the Zr-O solid solution, like microhardness (9, 19), lattice parameters (12, 19), and density.

Experimental

Specimen preparation.—Specimens of rolled Kroll zirconium containing 600 ppm of oxygen have been used. The precise analysis of the impurities is given in Ref. (18). As the initial state of the metal surface has a considerable influence on the kinetics of oxidation (20, 21), a detailed study of various methods of surface preparation was carried out (22). The standard treatment chosen according to this work is briefly described.

Specimens measuring $15 \times 10 \times 2$ mm were polished mechanically under water and then polished chemically in a fluonitric bath (HNO_3 60%, HF 5%, H_2O 35%) for 20 sec. They were then annealed at 800°C for 2 hr in a vacuum of 10^{-6} Torr; a second chemical polishing, similar to the previous one, was then applied, its aim being the elimination of the metal layer contaminated by the diffusion of oxygen during the anneal (22). It must be noticed that such a polishing treatment leaves a superficial oxide layer of about 60Å (22). The oxygen concentration in the bulk of the metal is then the same as the concentration before the treatment (600 ppm), while the grain size is well defined and of the order of 25 μm .

The specimens so prepared were oxidized in pure oxygen under atmospheric pressure, at temperatures of 700°, 750°, 810°, and 845°C, for times up to 400 hr. The treatments were carried out with an automatically stabilized ADAMEL furnace of type Chevenard-Journier in a 5 cm internal diameter quartz tube. Temperature uniformity in the vicinity of the sample was better than $\pm 2^\circ C$ in a 5 cm long zone. The temperature was measured with a precision of the order of one degree using a Chromel-Alumel thermocouple

placed near the sample and a MECI pyrometer-potentiometer Type ESPM. Periodic readings indicated $\pm 1^\circ C$ long term stability. Ten identical specimens were prepared for each treatment condition: they were ground off to various depths, as in Ref. (18). The depths thus reached were characterized by measuring the decrease of weight of the sample, ΔM , per unit surface, after each grinding operation (see below).

Nuclear analysis.—The general features of the method may be found in Ref. (16-18). We shall summarize here briefly the experimental conditions and describe in more detail a procedure which improves the precision for high oxygen concentrations.

The ground off specimens were bombarded by a 900 keV, 1 μA , beam of deuterons from the 2 MeV Van de Graaff accelerator of the Ecole Normale Supérieure. The beam spot size was 1 mm. The energy spectra of the protons from the reaction $O^{16}(d, p)O^{17x}$ were registered at 165° by means of a 3 cm² surface barrier detector at 10 cm. Elastically scattered deuterons were stopped with a 12 μm thick Mylar absorber.

As shown in Ref. (17), the protons contributing to the spectrum originate from the first microns of the sample; the decrease with depth of the oxygen concentration is practically negligible over this surface region for the relatively deep diffusions considered here. Hence the spectra are characteristic of the surface concentration C of the sample under study. Thus one may obtain a series of couples of values ($C_j, \Delta M_j$) for each treatment, from which the profile $C(x)$ may be deduced for the values x_j corresponding to ΔM_j .

The first step consists in calculating C from the spectra. C is conveniently expressed as the oxygen to zirconium atomic ratio O/Zr . If $\beta = O/(Zr + O)$ is the usual "atom per cent" concentration, we have

$$C = \frac{O}{Zr} = \frac{\beta}{1 - \beta} \text{ and } \beta = \frac{O}{Zr + O} = \frac{C}{1 + C} \quad [1]$$

Figure 1 shows a typical proton spectrum from a Zr-O solution; it represents the number of counts N_i in channel i which corresponds to a fixed energy interval ΔE around the energy E_i . It may be shown (17), that if the statistical spread involved in the proton detection process is neglected, we have

$$N_i = C \Delta x n_{Zr} \sigma[\theta, E_d(x_i)] K \quad [2a]$$

where x_i is the mean depth corresponding to E_i , Δx the mean depth interval corresponding to ΔE , n_{Zr} is the number of Zr atoms per cm³, $E_d(x_i)$ the mean energy of the incident deuterons at depth x_i , [$E_d(O)$ is the bombarding energy], $\sigma(\theta, E_d)$ the differential cross section at detection angle θ and energy E_d , and K a constant depending on the counting conditions. The spectrum presents a plateau near its peak, which corresponds, according to Eq. [2a] to $800 < E_d < 900$ keV, where $\sigma(\theta, E_d)$ is practically constant (16); the fall of the spectrum is due to the decrease of $\sigma(\theta, E_d)$ at lower energies. In the plateau region

$$N_i = C \Delta x n_{Zr} K' \quad [2b]$$

K' being constant. In fact n_{Zr} depends on C due to the expansion of the Zr-O solution with increasing oxygen content. Δx is related to the energy loss of deuterons and protons produced by the zirconium and oxygen atoms on their path: it depends hence on C . We may write Eq. [2b] in the form

$$N_i = C \Delta x(o) n_{Zr}(o) K' f(C) \quad [2c]$$

with

$$f(C) = \frac{\Delta x(C) n_{Zr}(C)}{\Delta x(o) n_{Zr}(o)}$$

For low values of C , $f(C) = 1$ and C may be deduced directly from the "plateau height" H (i.e., the mean value of the N_i in the plateau region). For high C

1555

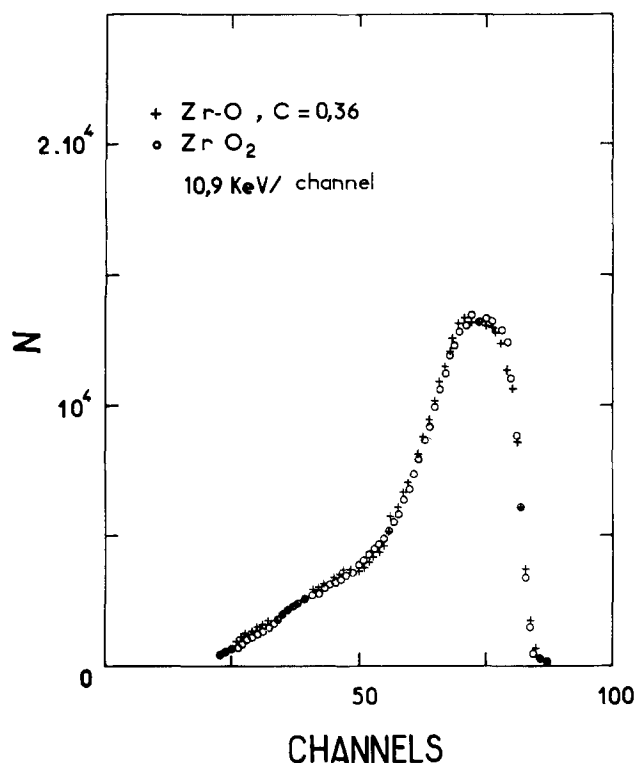


Fig. 1. Normalized experimental spectra obtained for thick thermally grown zirconia (10 μm) and for a Zr-O solid solution, respectively. Conditions: 10.9 keV/channel, the maximum energy of the protons at detection is 1195 keV, corresponding to channel 82.

values Eq. [2c] yields an uncorrected value $C_u = Cf(C)$, which corresponds to neglecting the effect of oxygen on the slowing down of the particles. C is then found by solving this equation, according to $C = g(C_u)$. The corresponding calculations are shown in Appendix A. Figure 2 shows this correction curve; the correction is appreciable for $C > 0.15$, i.e., $\beta > 0.14$.

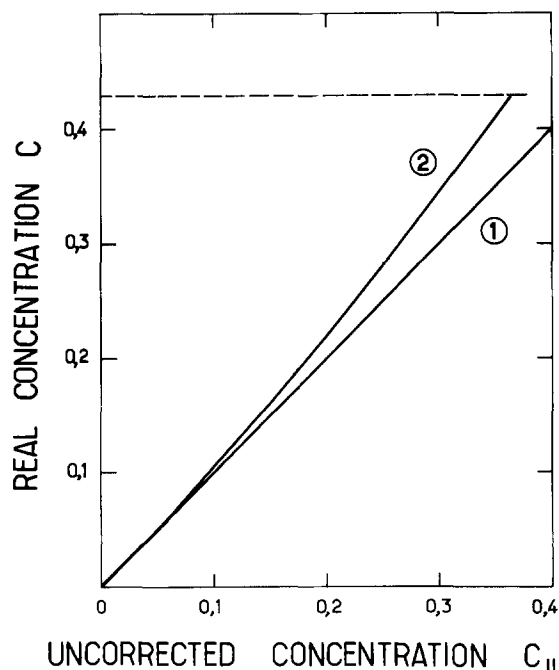


Fig. 2. Curve $C = g(C_u)$ relating the real concentration (oxygen to zirconium atomic ratio), corrected for the stopping power of oxygen, to the uncorrected concentration (curve 2). Curve 1 is the bisectrix of the quadrant, traced for the sake of comparison.

Absolute calibration was achieved by using a reference standard prepared by anodic oxidation of tantalum in well-defined conditions (17, 23). The oxygen content n_s of such an oxide layer is known to within about 2% (24). The standard used here, about 1100Å thick, contained $6 \cdot 10^{17}$ oxygen atoms per cm^2 . The total counting corresponding to the standard is, the energy loss in the film being small

$$N_s = n_s K \sigma [\theta, E_d(o)] = n_s K' \quad [3]$$

Hence dividing [2c] by [3] and inserting the plateau height H for N_1

$$\frac{H}{N_s} = \frac{C_u}{n_s} \Delta x(o) n_{Zr}(o) \quad [4]$$

This equation allows one to calculate C_u with a precision depending on statistics (for H and N_s) and on the knowledge of $\Delta x(o) n_{Zr}(o)$. The latter is calculated in Appendix B. Appendix C contains an improved calibration method. It was estimated that the relative error on the absolute concentrations C is about 3%. Relative values of C may be compared to within about 1%, not including statistics.

It should be emphasized that this oxygen analysis technique is background free [except for possible contaminations by light nuclei like F^{19} , N^{14} ; see Ref. (16 and 17)]. The sensitivity limitation is physical: it is due to the presence of a 60Å thick spontaneous oxide on the samples, whatever their oxygen content. This fixes the lower limit of sensitivity for oxygen concentration measurements in zirconium to the order of 50 ppm; 1000 ppm concentrations may already be measured to within 3%, as stated above. Counting rate is hardly a problem: most of the measurements require some minutes only.

Finally it should be noted that the low energy part of spectra like that of Fig. 1 may depend on C , if the energy loss parameters for O and Zr do not vary with energy in constant proportion. This was investigated experimentally by recording a spectrum from a thick zirconia target: the result, represented in Fig. 1, shows that the spectrum is nearly identical to that from a Zr-O solution, although the O/Zr ratio varied from 0.36 to 2. This shows that the shape of the spectra does not depend on C . Hence the area as well as the plateau height of the spectra may be used as a relative measure of C ; this improves statistics and simplifies the measurements.

Depth scales.—The depths will be measured from the metal-oxide interface. Let ΔM_s be the total mass per cm^2 of the Zr-O solution ground off from a sample, $X(t, T)$ the thickness of the oxide after a treatment time t at temperature $T^\circ K$, M_x the weight of this oxide per cm^2 . We have $\Delta M = M_x + \Delta M_s$. We shall first take as a measure of depth the mass m of zirconium per cm^2 of the Zr-O solution ground off. m is independent of the Zr-O density, which varies with C . Let $C(m)$ be the corresponding profile; we have

$$\Delta M_s = \int_0^m [1 + aC(m)] dm \quad [5a]$$

with $a = 16/91.22 = 0.175$ (mass ratio). Let $\hat{C}(\Delta M)$ be the experimental profile in the ΔM coordinate, $\hat{C}(\Delta M) = C(m)$. By differentiation

$$\frac{d\Delta M_s}{dm} = 1 + aC(m) = 1 + a\hat{C}(\Delta M) = \frac{d\Delta M}{dm}$$

Integrating

$$m = \int_{M_x}^{\Delta M} \frac{d\Delta M}{1 + a\hat{C}(\Delta M)} \quad [5b]$$

Equation [5b] was integrated numerically by summation using the measured values C_j , ΔM_j for $\hat{C}(\Delta M)$.

$X(t,T)$ was measured for each t,T value with a microscope and M_x calculated using the density 5.6 for zirconia.

Let us suppose that a curve $C_1(m_1)$ may be deduced from a curve $C_0(m)$ by simply multiplying m by α , i.e., $m_1 = \alpha m$. Then $C_1(m_1) = C_0\left(\frac{m_1}{\alpha}\right)$. The corresponding ΔM_S^1 is, from [5a]

$$\Delta M_S^1 = \int_0^{m_1} [1 + \alpha C_1(m_1)] dm_1 = \alpha \int_0^{m_0} [1 + \alpha C_0(m)] dm$$

Thus

$$\Delta M_S^1 = \alpha \Delta M_S^0 \quad [6]$$

Hence for profiles having the same shape a single integration of Eq. [5b] yields a universal new depth scale. This simplifies the calculations as will be seen.

The relation between the geometrical depth x and m is

$$m = \mu_{Zr} \int_0^x n_{Zr}[C(x)] dx$$

μ_{Zr} being the mean mass of the zirconium atom. In what follows the dependence of n_{Zr} on C will be neglected. In fact it was shown (12, 19) that the volume associated to each Zr atom in the Zr-O solution varies only by 1.9% for $0 \leq C \leq C_s$. Hence we shall deduce

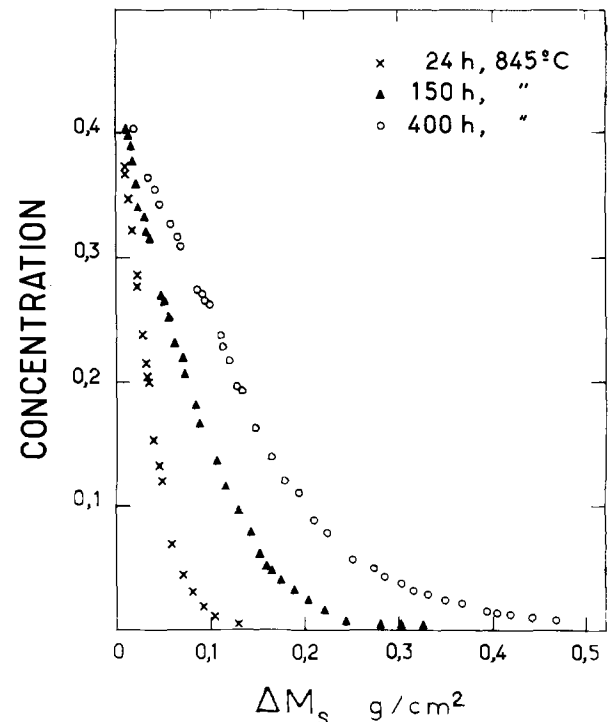
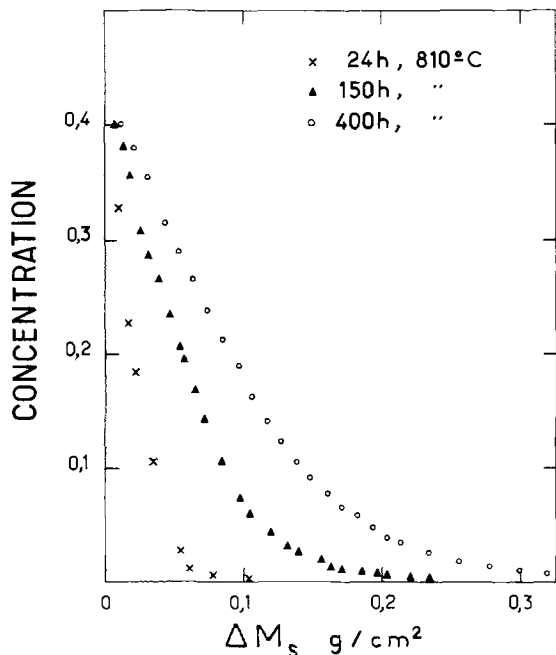
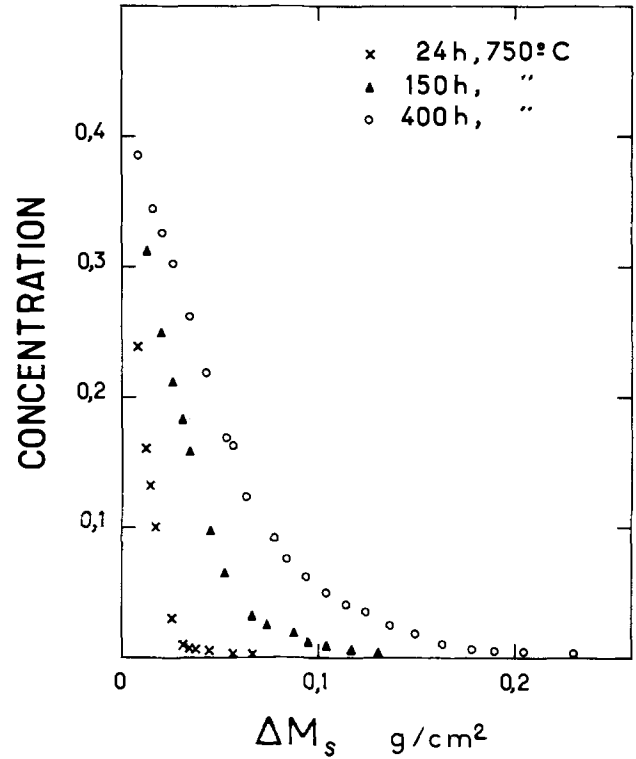
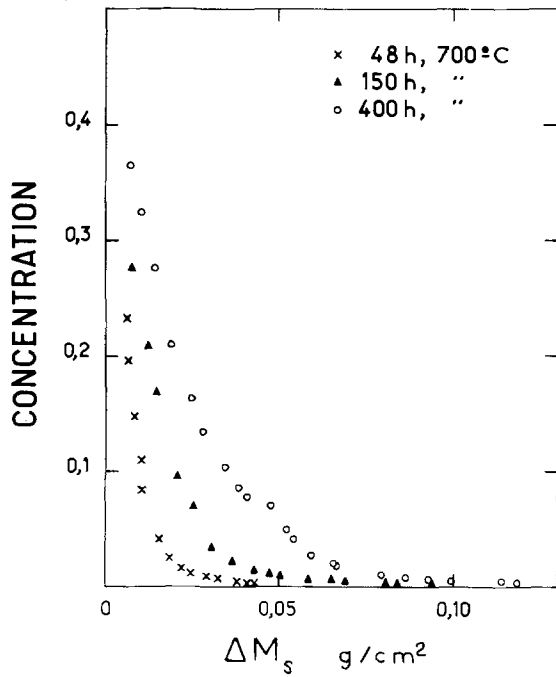


Fig. 3. Concentration profiles for various conditions expressed as a function of ΔM_S , the mass per cm^2 of the ground off Zr-O solution. For low C values $0.1 g/cm^2$ is equivalent to 154μ .

x from m simply by using the density 6.5 for zirconium. In fact the only reason to introduce the x scale explicitly is for giving diffusion coefficients in the usual units of cm^2/sec .

$C(x)$, expressed in atom per cm^3 , may be calculated similarly. It should be noted that an advantage of expressing C in O/Zr units is that the latter are independent of the depth scale chosen.

It may be noted at this stage that the quantity $\Delta x(C)n_{\text{Zr}}(C)$ in Eq. [2c] is just equal to $\Delta m/\mu_{\text{Zr}}$ and is hence independent of $n_{\text{Zr}}(C)$. The calibration does not depend on densities: from the nuclear point of view the physical state of the target has no influence; the density fixes only the geometrical depth scale. This again shows that m is the natural depth scale for profiles obtained by nuclear methods.

Results and Discussion

Figure 3 shows the experimental results as a function of the ground off mass ΔM_s . Except at 700°C , the penetrations are large with respect to the grain size (0.1 g/cm² of zirconium content being equivalent to 154 μm). All curves decrease toward the initial concentration C_0 of 600 ppm, i.e., 3×10^{-3} atom oxygen per zirconium. A scaling of the mass scale by \sqrt{t} leads to well superimposed profiles at all temperatures as illustrated in Fig. 4 for one set of curves. One single depth correction for oxygen content was hence made at each temperature, according to the remark above. The resulting profiles ($C - C_0$) as a function of m/\sqrt{t} are shown in Fig. 5. These curves illustrate clearly a first important result: the diffusion process under study has a parabolic character.

It was next investigated whether these reduced profiles may be fitted with a single calculated curve according to the classical expression of the concentration profile

$$\frac{C - C_0}{C_s - C_0} = \frac{\text{erfc} \frac{x + x_0}{2\sqrt{Dt}}}{\text{erfc} \frac{x_0}{2\sqrt{Dt}}} \quad [7]$$

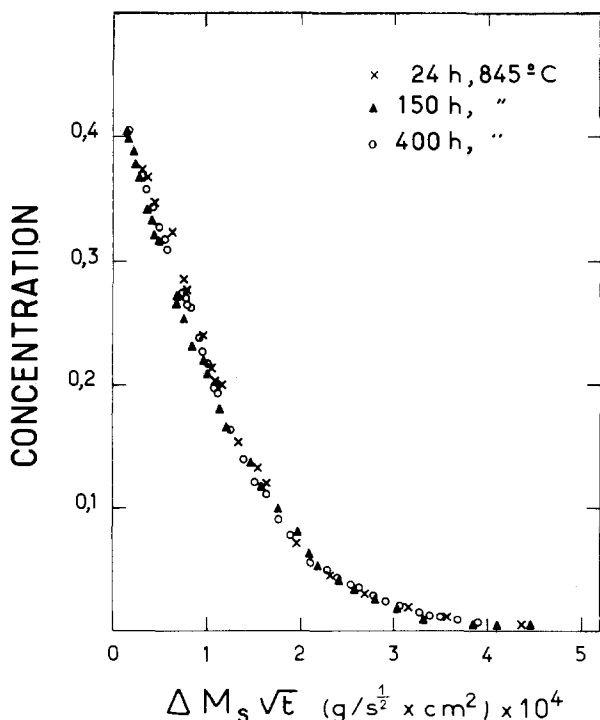


Fig. 4. A typical set of concentration profiles expressed as a function of the reduced coordinates $\Delta M_s/\sqrt{t}$. The \sqrt{t} law is clearly well followed.

This equation is derived assuming a constant diffusion coefficient in the metal and that the thickness of metal x_0 , incorporated into the oxide developing from the surface varies like \sqrt{t} at each temperature [see Jost (25) and Ref. (18)]. The latter assumption is known not to hold in the case of zirconium as the early stage of the oxidation process is not parabolic (6). From the measurements of the oxide thicknesses $X(t, T)$ performed as mentioned above it was established that the variations with time of the corresponding oxide mass per cm^2 $M_X(t, T)$ may be fitted by an expression of the form

$$M_X(t, T) = M_0(T) + \Gamma(T) \sqrt{t} \quad [8]$$

for large enough t . We shall postulate in what follows that Eq. [7] may be applied to our results with

$$x_0 = \gamma(T) \sqrt{t} \quad [9]$$

where $\gamma(T)$ is relative to the mass per cm^2 of zirconium corresponding to $\Gamma(T)$ (which relates to the mass per cm^2 of oxide). $\gamma(T)$ is expressed in $\text{g}/\text{sec}^{1/2} \times \text{cm}^2$ of zirconium. This postulate implies that, at that start of the oxidation, a thin oxide layer is quickly formed, with thickness around $M_0(T)$, while little oxygen diffuses into the metal beneath. Typical values of $M_0(T)$ are around 4 μm . While we cannot state that this assumption is precisely valid, it appeared to be consistent with our results.

Using Eq. [9], Eq. [7] may be written, at a given temperature T

$$\frac{C - C_0}{C_s - C_0} = \frac{\text{erfc} \left(\frac{x}{2\sqrt{Dt}} + \frac{\gamma}{2\sqrt{D}} \right)}{\text{erfc} \frac{\gamma}{2\sqrt{D}}} \quad [10]$$

This equation was used to fit the profiles of Fig. 5, using the experimental values of γ listed in Table I. The values of C_s and D corresponding to the best fit are also listed in this table. It appears that Eq. [10] is well obeyed. The following comments may be made:

(i) A constant diffusion coefficient, for concentrations up to saturation, is compatible with the results. It seems, according to these detailed measurements, that the departures from the erfc behavior reported in the previous publications of Ref. (9, 18, and 19) are not confirmed. This is due mainly to the detailed corrections applied here for the oxygen stopping power in the Zr-O solution.

(ii) The concentration at the metal-oxide interface is nearly independent of time and temperature, C_s ranging from 0.421 to 0.429. It is most probable that C_s is a constant, the spread being within experimental errors. The corresponding mean value is $C_s = 0.424$, i.e., 29.8 a/o. This is in good agreement with the zirconium-oxygen equilibrium diagram (26, 27); this shows in turn, that during oxidation near-equilibrium prevails at the metal-oxide interface.

(iii) The quantity $\psi = \gamma/2\sqrt{D}$ decreases with T from 1.9 to 0.8: hence there is no universal curve describing the profiles at various temperatures. The total

Table I. Parameters used in Eq. [10] to fit the concentration profiles in Fig. 5*

Temperature, °C	$\gamma \times 10^{16}$, g/sec ^{1/2} cm ²	C_s	$D^{(a)} \times 10^{12}$, cm ² /sec	$D^{(b)} \times 10^{12}$, cm ² /sec
700	11.7	0.423	9.2	7.2
750	18.2	0.421	37	39
810	20.2	0.423	125	140 ^(c)
845	25.8	0.429	256	300 ^(c)

* With $C_0 = 3 \cdot 10^{-3}$.

^(a) Present measurements.

^(b) Results of Quataert and Coen-Porisini (13).

^(c) Corrected for 810° and 845°C from 800° and 850°C.

D is given in the usual cm^2/sec units for easy comparison; x was deduced from m using the density 6.5 for zirconium.

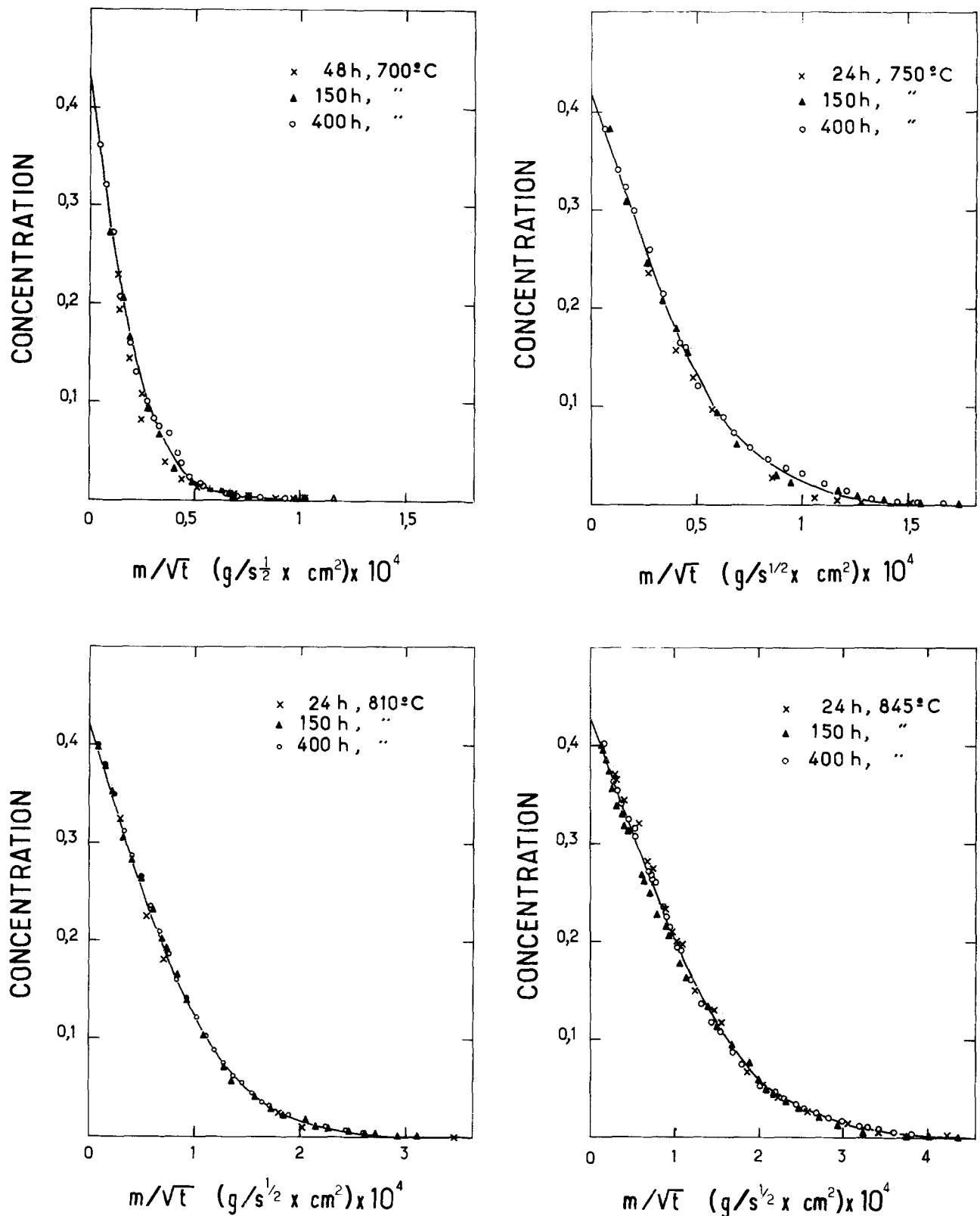


Fig. 5. Concentration profiles expressed as a function of the reduced coordinates m/\sqrt{t} . The initial oxygen concentration C_0 was subtracted. The solid lines represent the best fit in the reduced coordinate scale, calculated according to Eq. [10], from which the D values were deduced.

mass $M(t)$ of oxygen which is present in the metallic phase is readily calculated to be

$$M(t) = 2\sqrt{Dt} (C_s - C_0) \frac{\text{ierfc } \Psi}{\text{erfc } \Psi} \quad [11]$$

The last factor is due to the growth of the oxide and varies here from about $0.4\sqrt{\pi}$ to $0.6\sqrt{\pi}$; the value $\sqrt{\pi}$ corresponds to $\psi = 0$, i.e., no oxide growth (simple diffusion with constant surface concentration).

(iv) Taking into account the various sources of errors, the values of D given in Table I are known with a relative precision of $\pm 10\%$. The values of D are plotted as a function of $1/T$ in Fig. 6. The resulting straight line indicates that a single mechanism of diffusion predominates in the temperature range considered; this is with high probability bulk diffusion, as grain boundary diffusion was shown to predominate mainly below 650°C (2, 6).

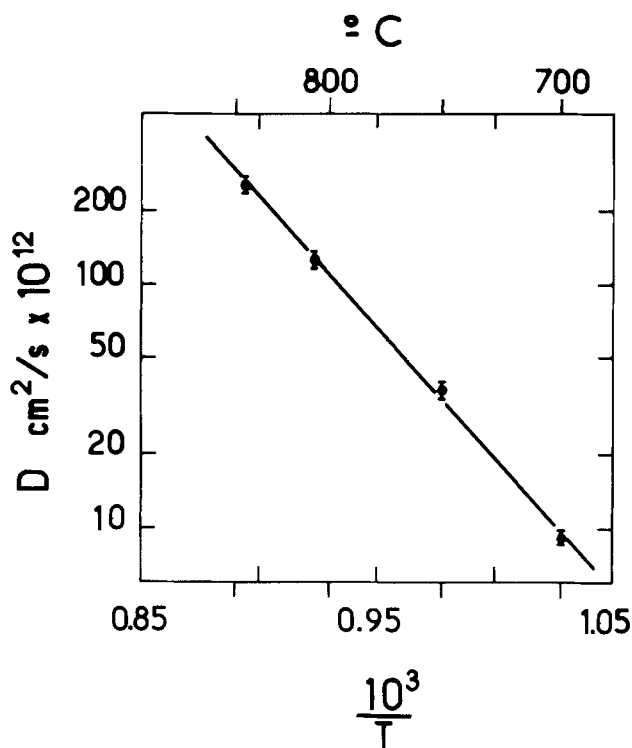


Fig. 6. Variation of the logarithm of the diffusion coefficient D with the reciprocal of the absolute temperature. The error bars correspond to an estimated 10% relative precision.

The temperature dependence of D was fitted with the expression

$$D(T) = D_0 e^{-Q/RT} \quad [12]$$

The best fit yields

$$Q = 49 \text{ kcal/mole}, D_0 = 1 \text{ cm}^2/\text{sec}$$

The errors on Q and D_0 may be conveniently discussed as follows. Let ΔQ be the error on Q and \bar{Q} be its true value, $Q = \bar{Q} \pm \Delta Q$ and \bar{D} be the true value of D , $D = (1 \pm \epsilon)\bar{D}$, ϵ being the relative precision on D . From Eq. [12]

$$\bar{D}(1 \pm \epsilon) = D_0 e^{\pm \Delta Q/RT} e^{-\bar{Q}/RT}$$

If the range of T around its central value T_0 is narrow enough, which is the case here, we may write

$$D_0 = \bar{D} e^{+\bar{Q}/RT_0} (1 \pm \epsilon) e^{\pm \Delta Q/RT_0} \quad [13]$$

We see that the error on D_0 is very large and dominated by the factor $e^{\pm \Delta Q/RT_0}$, which may easily be of the order of 3 (in our case $RT_0 \approx 2.1$ kcal/mole). Hence the extreme values of D_0 may often differ by one order of magnitude, although D is known with reasonable accuracy. This is due to the fact that D_0 is obtained by a long range extrapolation on the logarithmic scale.

In the present work it has been estimated, considering the 10% precision on $D(T)$, that $\Delta Q = 1$ kcal/mole. Hence the final result is

$$Q = (49 \pm 1) \text{ kcal/mole}$$

$$D_0 = 1 \times (1.8)^{\pm 1} \text{ cm}^2/\text{sec}$$

i.e.

$$0.55 < D_0 < 1.8 \text{ cm}^2/\text{sec}$$

It should be emphasized that the errors on Q and D_0 are by no means independent but related by Eq. [13].

Equation [13] explains why the spread of the published data on D_0 is so huge, from 0.2 to 200, as reported by Quataert and Coen-Porisini (13). When examining the published data, large values of D_0 appear to be associated with large values of Q . As an example let us analyze the data from Ref. (13)

$$D_0 = 15 \text{ cm}^2/\text{sec}, Q = 54.7 \text{ kcal/mole}$$

If we assume that the true value of Q is 49 kcal/mole, so as to compare to our result, D_0 must be divided by $e^{2.7} = 14.9$. This yields $D_0 = 1$, exactly our value. It appears hence that the measured values of D should be compared, rather than D_0 and Q , the latter containing often large errors, depending much on the analysis of the data performed by the authors. A similar remark has been made by Kidson (28) in his excellent review of diffusion process in zirconium, who observed that published D_0 and Q values may differ considerably, while "individual D values are in close agreement." The D values of Ref (13) are listed in Table I, for sake of comparison. The agreement is good, except for a somewhat smaller value at 700°C and somewhat larger at 845°C: this explains the higher value of Q reported in this reference. Taking into account that the result of Ref (13) was obtained by a direct method, but with some problems for precise calibration (as discussed above), we may conclude that our results are in satisfactory agreement with recent literature, while the precision is likely to be higher. The comparison with the values reviewed by Kidson (28) is also satisfactory, the various D_0 values reported being within a factor of 2 equal to ours, when the correction for Q is made as above.

It should be recalled at this point that many authors found a plateau in the microhardness-depth curve measured on such oxygen diffused zirconium samples (3, 4, 8, 14). In Ref. (9 and 19) the authors have shown that these plateaus do not correspond to any accident in the concentration-depth curve. This was confirmed again in the present measurements in great detail, the effect being due to a nonlinear relationship between the O/Zr ratio and microhardness (9).

It should be noted, that according to Pemsler (29) D depends markedly on the crystallographic orientation of the zirconium sample. In our case the samples were polycrystalline, but with a recrystallization texture after rolling which is characterized by a preferential orientation of the $\{1,0, \bar{1},0\}$ planes at 32° with respect to the plane of rolling, the $\langle 1,1, 2,0 \rangle$ direction being parallel to the rolling direction (30). The results reported here are hence associated with this texture.

From practical point of view, when studying thermal oxidation of zirconium as a corrosion process, it is most important to know what happens when the heat-treatment is performed in air instead of pure oxygen. Figure 7 displays a typical result for samples treated for 24 hr at 810°C in air and in pure oxygen at atmospheric pressure. The concentration profiles of oxygen appear to be identical within experimental error. It appears hence that nitrogen plays no role in the oxidation of zirconium in the above-mentioned conditions. This was further confirmed by analyzing both the oxides formed and the metal beneath for nitrogen contamination, using the highly sensitive $N^{14}(d,\alpha)C^{12}$ nuclear reaction (31). No detectable N^{14} was observed in the bulk of the samples, a surface contamination of about 0.05 $\mu\text{g}/\text{cm}^2$ being measured on all samples whether heat-treated or not. It should be noticed that this result was by no means trivial, as according to Croset and Velasco (32), large amounts of nitrogen may be dissolved in tantalum thin films heated in nitrogen containing traces of oxygen. After an initial strong dissolution of nitrogen the latter is rejected and is replaced by oxygen from the traces in the gas, even if the latter represent only 1 ppm nitrogen may hence play an important role when zirconium undergoes corrosion in nitrogen gas containing low concentrations of oxygen. This point merits further investigation.

In conclusion it appears that nuclear microanalysis proves to be a highly powerful method for measuring oxygen depth profiles in metals like zirconium. The technique may be readily extended to depth profiles of other light elements like nitrogen or fluorine. Work

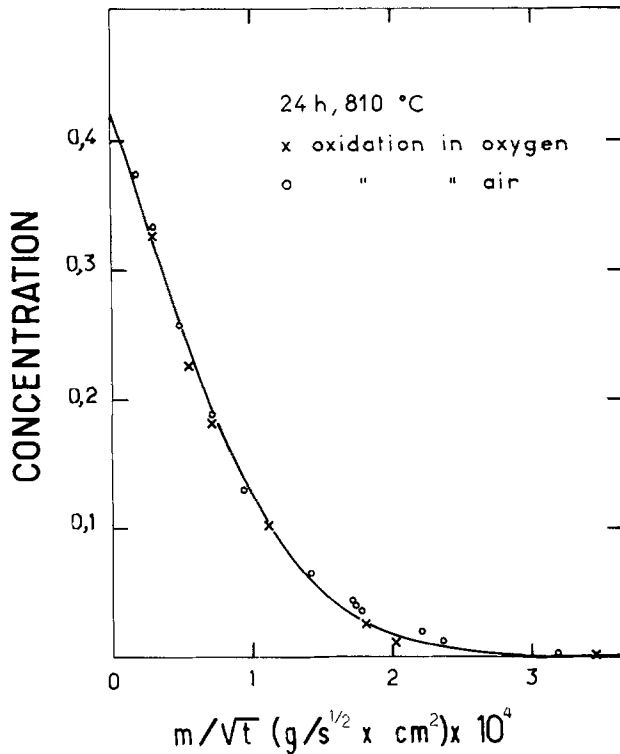


Fig. 7. Comparison of oxygen diffusion profiles represented as in Fig. 5 in zirconium oxidized in identical conditions in pure oxygen and in air.

is in progress for studying oxygen diffusion phenomena in titanium.

Acknowledgments

The authors wish to thank Professor P. Lacombe for fruitful discussions during the early stage of this work. This work was supported by the Centre National de la Recherche Scientifique (RCP No. 157), the DRME, and the DGRST.

Manuscript submitted July 15, 1974; revised manuscript received Sept. 27, 1974.

Any discussion of this paper will appear in a Discussion Section to be published in the December 1975 JOURNAL. All discussions for the December 1975 Discussion Section should be submitted by Aug. 1, 1975.

Publication costs of this article were partially assisted by Centre National de la Recherche Scientifique.

APPENDIX

A. Calculation of $C = g(C_u)$

From Eq. [2c] it is seen that $f(C)$ is independent of the absolute value of the channel width ΔE , as it is a ratio of quantities proportional to ΔE . Hence the energy calibration (amplifier gain, influence of Mylar absorber, etc.) has no influence. Let ϵ_0^d and ϵ_0^p be the atomic stopping powers of oxygen for deuterons and protons in the vicinity of the energies involved (bombarding energy for d, energy at emission for p), ϵ_z^d and ϵ_z^p similar quantities for zirconium. The ϵ will be considered as energy independent for the plateau region. The energy loss for the incident deuterons up to depth x is (applying Bragg's rule for compounds)

$$\Delta E_d = x n_{Zr} (\epsilon_z^d + C \epsilon_0^d) \quad [A-A-1]$$

A deuteron reacting at energy E_d gives rise, toward the angle θ , to a proton with energy E_p , $E_p = k(E_d)$, according to the kinematics of the reaction. k is nearly linear, so $E_p = AE_d + B$ and the incoming deuteron energy loss gives rise to a loss $\Delta E_p^{in} = A\Delta E_d$. The outgoing proton undergoes a further loss

$$\Delta E_p^{out} = \frac{x}{|\cos \theta|} n_{Zr} (\epsilon_z^p + C \epsilon_0^p) \quad [A-A-2]$$

where $x/|\cos \theta|$ is the outgoing proton path length, assuming the sample to be perpendicular to the beam (17). The over-all loss is

$$\Delta E_p = \Delta E_p^{in} + \Delta E_p^{out} = x n_{Zr} \left[A (\epsilon_z^d + C \epsilon_0^d) + \frac{1}{|\cos \theta|} (\epsilon_z^p + C \epsilon_0^p) \right] = x n_{Zr} S(C) \quad [A-A-3]$$

As this relation is linear in x , we may substitute Δx to x

$$\Delta x(C) n_{Zr}(C) = \frac{\Delta E_p}{S(C)} \quad [A-A-4]$$

As ΔE_p is proportional to the channel width ΔE

$$f(C) = \frac{S(O)}{S(C)} = \frac{1}{1 + \lambda C} \quad [A-A-5]$$

where λ depends on a ratio of the stopping powers for O and Zr. λ may be calculated using published stopping powers. We used the values of Williamson *et al.* (33). We get $\lambda = 0.42$.

Thus, from [A-A-5]

$$C_u = C f(C) = \frac{C}{1 + \lambda C}$$

and

$$C = g(C_u) = \frac{C_u}{1 - \lambda C_u} \quad [A-A-6]$$

An error $d\lambda$ on λ leads to an error dC on C according to

$$\frac{dC}{C} = \frac{1}{C} \frac{\partial C}{\partial \lambda} d\lambda = \frac{\lambda C}{(1 + \lambda C)^2} \frac{d\lambda}{\lambda} \quad [A-A-7]$$

For $C = 0.4$ this gives $dC/C = 0.12 d\lambda/\lambda$, *i.e.*, less than 1% even for $d\lambda/\lambda = 8\%$. Hence the error due to the correction itself is negligible.

B. Calculation of $\Delta x(o) n_{Zr}(o)$

From Eq. [A-A-4] this quantity is $\Delta E_p/S(o)$. The ΔE_p corresponding to the channel width ΔE may be measured directly by varying the accelerator energy (*i.e.*, changing physically E_p) and observing the corresponding change in channels for the proton peak from a thin anodic oxide target. $S(o)$ is calculated from the data of Ref. (33). The latter cannot be taken *a priori* to be known to within less than 8%. This uncertainty dominates all others and the absolute calibration for C is precise to within at least 8%.

C. Improving Absolute Calibration

As shown in Fig. 1 the spectra for a Zr-O solution near saturation and for ZrO_2 have the same shape; this indicates that λ is practically constant in a wide energy domain, although the individual values of ϵ vary with energy. In addition it is found from Fig. 1 that the ratio of the plateau heights of the two spectra is in a good agreement with the values calculated using the above λ and concentrations determined as described. This suggests that Eq. [A-A-6] is valid up to $C = 2$, *i.e.*, for zirconia. If this assumption is made, zirconia may be taken as a standard reference, known to within a negligible error. The error on C is then only due to an error on λ . For calculating the corresponding formula let us call H_0 the plateau height for ZrO_2 , H that for an unknown sample. From Eq. [4]

$$\frac{C_u}{C_u^0} = \frac{H}{H_0} = h$$

We have, as $C = 2$

$$C_u^0 = \frac{2}{1 + 2\lambda}$$

and as $C_u = C_u^0 h$, we get

$$C = \frac{2h}{1 + 2\lambda(1 - h)} \quad [\text{A-C-1}]$$

Let us examine the effect of an error on λ . One calculates readily

$$\frac{dC}{C} = \lambda \frac{2 - C}{1 + 2\lambda} \frac{d\lambda}{\lambda} \quad [\text{A-C-2}]$$

For C around 0.4 this yields $dC/C:0.44 d\lambda/\lambda$. An 8% error on λ yields 3.5% on C . In fact λ , being a ratio, is better known than that. We may conclude that a 3% precision on C is surely achieved. This is the precision we shall assume in this paper. It should be emphasized that this calibration technique is universal, and allows one to achieve absolute measurements without the need for thin film oxygen standards. The results obtained here with the latter confirm our confidence in this technique. The method may be readily extended to other metals like hafnium, tantalum, titanium, etc.

REFERENCES

1. D. Whitwham, J. Paidassi, and J. Herenguel, "L'oxydation des métaux," Vol. II, chap. X, par J. Benard, Gauthier-Villars, Paris (1964).
2. M. Davis, K. R. Montgomery, and J. Standring, *J. Inst. Metals*, **89**, 172 (1961).
3. J. Debuigne, *Métaux-Corrosion-Industries*, **43**, 89, 186, 235 (1967).
4. G. R. Wallwork, W. W. Smeltzer, and C. J. Rosa, *Acta Met.*, **12**, 409 (1964).
5. R. Darras, H. Loriers, and P. Baque, *J. Nucl. Mat.*, **17**, 79 (1965).
6. G. Beranger, Thesis, Paris (1967) and Note C.E.A. No. N1130 (1970).
7. G. Sainfort, R. Jacquesson, and P. Laurent, "Proc. 2ème Colloque de Métallurgie," Saclay (1958) P.U.F. Paris.
8. T. Ericsson, G. Östberg, and B. Lehtinen, *J. Nucl. Mat.*, **25**, 322 (1968).
9. G. Amsel, G. Beranger, P. Boisot, D. David, B. De Gelas, and P. Lacombe, *C.R. Acad. Sci., Paris*, **267 C**, 301 (1968).
10. A. Dubertret, J. Debuigne, and P. Lehr, *C.R. Acad. Sci., Paris*, **262 C**, 1571 (1966).
11. B. Holmberg and T. Dagerhamn, *Acta Chem. Scand.*, **15**, 919 (1961).
12. P. Boisot and G. Beranger, *C.R. Acad. Sci., Paris*, **269 C**, 587 (1969).
13. D. Quataert and F. Coen-Porisini, *J. Nucl. Mat.*, **36**, 20 (1970).
14. J. P. Pemsler, *This Journal*, **111**, 381 (1964).
15. B. Cox and C. Roy, *J. Electrochem. Technol.*, **4**, 121 (1966).
16. G. Amsel and D. Samuel, *Anal. Chem.*, **39**, 1689 (1967).
17. G. Amsel, J. P. Nadai, E. D'Artemare, D. David, E. Girard, and J. Moulin, *Nucl. Inst. Methods*, **92**, 481 (1971).
18. G. Amsel, G. Beranger, B. De Gelas, and P. Lacombe, *J. Appl. Phys.*, **39**, 2246 (1968).
19. P. Boisot, G. Beranger, D. David, and G. Amsel, Proc. 4th Intern. Congr. Metallic Corrosion, Amsterdam, (1969), edited by "National Association of Corrosion Engineers," U.S.A., (1972), p. 367.
20. E. A. Gulbransen and F. K. Andrew, *J. Metals*, **101**, 339 (1954).
21. B. De Gelas, G. Beranger, and P. Lacombe, *J. Nucl. Mat.*, **29**, 1 (1969).
22. G. Amsel, D. David, G. Beranger, P. Boisot, B. De Gelas, and P. Lacombe, *ibid.*, **29**, 144 (1969).
23. G. Amsel, C. Cherki, G. Feuillade, and J. P. Nadai, *J. Phys. Chem. Solids*, **30**, 2117 (1969).
24. G. Amsel, C. Ortega, S. Rigo, and J. Siejka, To be published.
25. W. Jost, "Diffusion in Solids, Liquids, Gases," p. 71, Academic Press, New York (1960).
26. R. F. Domagala and D. J. McPherson, *J. Metals*, **6**, 238 (1954).
27. E. Gebhardt, H. D. Seghezzi, and W. Durrschnabel, *J. Nucl. Mat.*, **4**, 255 (1961).
28. G. V. Kidson, *Electrochem. Technol.*, **4**, 193 (1966).
29. J. P. Pemsler, *Nucl. Metals*, **105**, 315 (1958).
30. H. Demars and P. Lehr, *C. R. Acad. Sci.*, **253**, 2688 (1961).
31. G. Amsel and D. David, *Rev. Phys. Appl.*, **4**, 383 (1969).
32. M. Croset and G. Velasco, *J. Vacuum Sci. Technol.*, **9**, 165 (1972).
33. C. F. Williamson, J. P. Boujot, and J. Picard, Tables of range and stopping power of chemical elements for charged particles. C E A Report R3042 (1966).

Preparation and Stabilization of Anodic Oxides on GaAs

S. M. Spitzer,* B. Schwartz,* and G. D. Weigle

Bell Laboratories, Murray Hill, New Jersey 07974

ABSTRACT

Anodic oxidation of GaAs is examined and a technique for growing full surface oxides $\approx 8600\text{\AA}$ thick is reported. Anodization in a hot, concentrated (30%) H_2O_2 electrolyte of $\text{pH} = 2$ using self-anodizing metal contacts is found to yield uniform oxides with a refractive index of 1.8 and a growth rate ranging from 22 to 50 $\text{\AA}/\text{V}$. The as-grown oxide will etch in HCl and H_2O . Chemical stability of this oxide is enhanced with baking in dry nitrogen and after 2 hr at 250°C , H_2O will no longer etch the oxide; after 1 hr at 600°C , HCl , HF , HNO_3 , NH_4OH will not etch the oxide but hot H_3PO_4 will etch the oxide. The oxide is an amorphous, vitreous film which crystallizes to $\beta\text{-Ga}_2\text{O}_3$ after several hours at 800°C . A thin ($<100\text{\AA}$) graded, oxide-GaAs interface was found to grow at anodization potentials $>100\text{V}$ and for heat-treatment at temperatures greater than 400°C for 1 hr. The oxide exhibits excellent adherence to the substrate, has good match with the thermal coefficient of expansion of GaAs, and forms a relatively strain-free interface. Since GaAs is consumed during anodization, this provides a technique for surface cleaning using an oxide growth-strip step. Enhanced device reliability is expected to result by utilization of the oxide growth-strip-regrowth cycle during device fabrication, since this will remove contamination from the surface. The findings here enumerated, coupled with ease of oxide growth, suggest ready implementation to a GaAs planar technology.

The growth of amorphous native oxides on compound semiconductors has recently been demonstrated (1, 2), and has been shown to have beneficial passivation effects (3, 4). It has therefore become necessary to expand both our understanding and our technological capabilities to determine the extent to which we can apply these oxide growth concepts to device fabrication techniques. In a recent paper (5), the anodization of GaAs in aqueous H_2O_2 solutions was discussed and application to mesa formation for waveguides and double heterostructure lasers were described. In this paper, we show the results of additional studies on a similar anodization system. We describe how the range of oxide thickness has been extended from the 3000\AA previously reported, to greater than 8000\AA . We also describe how both the physical and chemical characteristics change with heat-treatment. In addition, a technology is presented which permits full surface anodization, and utility of this oxide as both a surface evaluation tool and a surface cleaning and protection method. Potential device applications of this emerging anodic oxide technology are also discussed.

Experimental Procedure

The anodization process used here is similar to the technique described earlier (2), but has been extended to allow: (i) anodization with either a constant voltage source (maximum current limit) or a constant current source (maximum voltage limit); (ii) variation of the temperature of the anodization bath from room temperature to the boiling point of 30% H_2O_2 ($\approx 106^\circ\text{C}$); and (iii) use of self-anodizing Al-Ni wire or Al tweezers rather than Pt to contact the anode (semiconductor) sample.

The anodization bath consisted of an aqueous solution of 30% H_2O_2 , which was buffered to a pH of 2.0 ± 0.5 with H_3PO_4 for standard oxide growth conditions.

Anodization studies were performed on (100)- and (111)-oriented GaAs wafers, which were p-type with a net Zn acceptor concentration in the $1\text{-}5 \times 10^{18}/\text{cm}^3$ range or n-type with a net Si donor concentration in the $0.5\text{-}5 \times 10^{17}/\text{cm}^3$ range. The samples were lapped with $0.3\ \mu\text{m}$ alumina in H_2O and $75\ \mu\text{m}$ was then etched [the arsenic face for (111)-oriented samples] with a bromine methanol solution for a final wafer thickness of $0.3\ \text{mm}$.

* Electrochemical Society Active Member.

Key words: oxidation, compound semiconductors, device technology.

The wafers were thoroughly degreased using trichlorethylene and acetone soxhlet cycles, followed by a water and methanol rinse prior to anodization. At this point oxides were grown in a hot peroxide solution under constant voltage or constant current conditions. Room temperature oxides were also grown to provide reference samples. A drying procedure, that of heating in dry nitrogen for 2 hr at 250°C , was established to stabilize the oxide films.

Oxide thickness and index of refraction were measured with an ellipsometer at 6328\AA using procedures described for similar studies of the oxidation of GaP (2). Oxide thickness was also measured with a Taly-step¹ by comparing the step height of photoresist protected oxide stripes (6) with respect to the GaAs surface, thus producing an independent thickness measurement.

Sample anodization.—During the early anodization studies only partial oxidation of the surface area was possible because the GaAs sample was clamped in Pt tweezers and the sample was immersed in the bath to a depth such that the Pt did not contact the solution. When considering the effects of surface tension and vibration of the solution, a significant portion of the semiconductor sample did not anodize. This problem became particularly severe when small samples were used, such as 6 mm square double-heterostructure laser slices. Furthermore, the effects of high electric field and uncontrollable pH at the air-liquid interface generate a nonuniform oxide band parallel to this interface. Thus the unanodized and nonuniform portions of the wafer were wasted. One of the first problems solved was the development of a means of achieving "full surface" sample anodization, using a metal to contact the semiconductor which itself can be immersed in the electrolytic bath and will self-anodize. In (3% Al), Ni, Al-Ni, and Al were found to anodize quickly, forming a high resistivity oxide which eliminates any shunt path to the solution, thus permitting semiconductor anodization. Silver was found to be unsuitable because the Ag_2O_3 so formed is soluble in the anodization bath and the silver contact dissolves before the semiconductor is anodized to any appreciable thickness. The results on aluminum were particularly interesting because this self-passivating effect stops oxide growth leaving a thin brittle oxide on the Al. This oxide then cracks easily under slight mechanical pressure, thus

¹ Taylor-Hobson Company.

allowing good electrical contact to be made to the underlying metal. Such a self-anodizing metal can be affixed to the back of a sample with wax, as shown in Fig. 1. In the case of higher resistivity samples, where current spreading can be a problem or where a full surface back contact is desired (as in MOS samples), a full back surface aluminum or aluminum overlay metallization can be evaporated to act as a sealant for the anodization. For rapid processing, however, the technique used predominantly throughout this series of experiments was to hold the sample with Al-tipped tweezers and then immerse the sample and tweezers tip in the bath as shown schematically in Fig. 2. In this manner, all but about 2 mm² of the surface was anodized, and problems associated with the air-liquid interface were eliminated.

Oxidation

The mechanism of anodization of GaAs is thought to involve an ionic drift process, wherein the ionic ox-

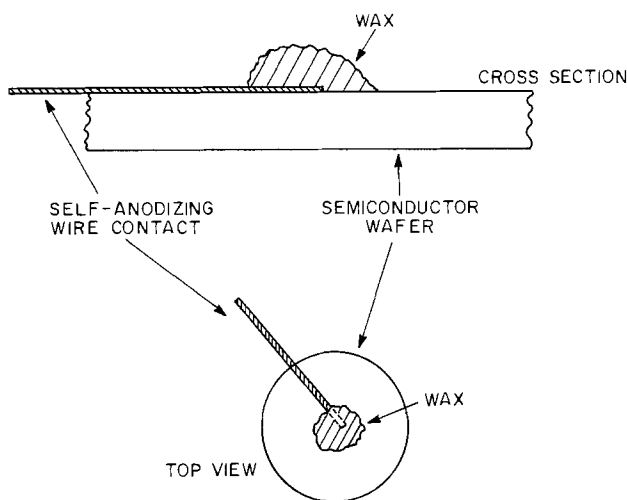


Fig. 1. Technique for full surface oxide growth using a self-anodizing metal contact.

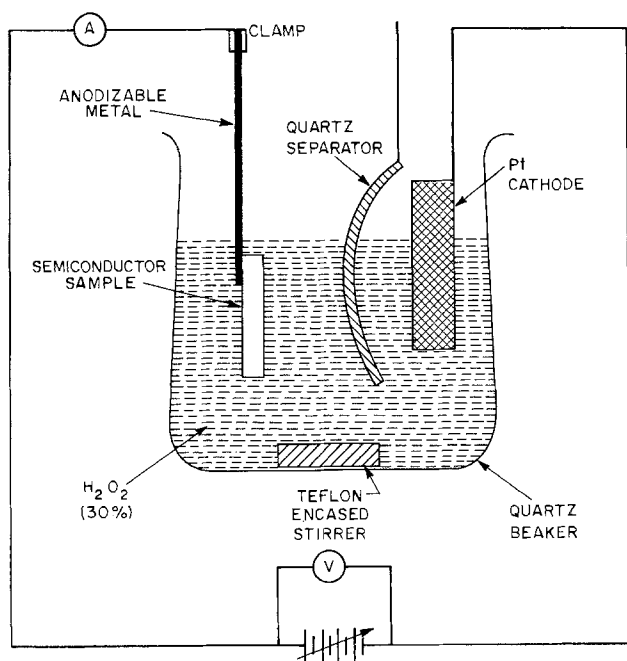


Fig. 2. Schematic of anodization system using self-anodizing contact for full surface oxide growth at room temperature and at 100°C.

drifts through the oxide to reach the oxide-semiconductor interface where the oxidation actually takes place. The partially oxidized gallium (e.g., Ga⁺¹) is now influenced by the electric field in the oxide and starts to drift toward the oxide-electrolyte interface. During its migration, or at least soon after it reaches the oxide-electrolyte interface, the gallium is oxidized further to the Ga⁺³ state, where it finally stabilizes.² Therefore, under steady-state conditions, there is charged oxidant moving inward from the electrolyte and charged reductant moving outward from the semiconductor. The assumption is also made that the arsenic oxidizes to its fully stable state (probably As⁺³) and becomes stationary, being bonded to its neighboring oxygen atoms.

Since ionic conductivity is known to be strongly temperature dependent, the logical step in an attempt to increase the ultimate oxide thickness was to raise the temperature of the anodization bath (9). The effect of temperature on the "ultimate" oxide thickness is interpreted as being related primarily to two factors: increased ionization in solution and enhanced drift mobility. The influence of temperature on ionization in solution is well known and for most inorganic acids, the ionization constant increases with increasing temperature; hydrogen peroxide as an inorganic acid shows this property (10), and therefore the concentration of ionic oxidant is increased in solution.

Drift mobility of the ionic oxidant is strongly temperature dependent; the ionic drift rate follows an $\exp(-E/kT)/T$ dependence (11), a rapidly increasing function between room temperature and 100°C. One might also expect enhanced diffusion of species in solution at elevated temperature, but this effect is not believed to be an important contributor to the increased oxide thicknesses. Sample conductivity also has a role in the ionic processes required for anodization. Intrinsic (undoped) samples exhibit a strong temperature-conductivity dependence and oxide growth is enhanced at elevated temperature due to this effect. The conductivity of extrinsic samples ($> 10^{16}/\text{cm}^3$) however, is temperature insensitive from room temperature to 100°C, and thus would not contribute to increased oxide growth.

An increase in oxide growth was indeed observed for this hot-peroxide system, and the dependence of oxide thickness on anodization voltage for boiling-peroxide growth is shown in Fig. 3; also included are data for room temperature growth (5). Note that for biases less than 100V the hot-peroxide thickness dependence is linear at approximately 22 Å/V, 20% greater than the room temperature growth. However, at higher voltages, the growth becomes superlinear with voltage approaching 50 Å/V at 180V, more than 2½ times the room temperature growth. The thickest as-grown oxide prepared to date has been 8600Å at ~180V.

Oxide thickness was measured with both the Talystep and ellipsometer because of the interpretational problems reported with the ellipsometry data for room temperature anodizations at biases greater than 150V (5). For the high temperature anodizations at biases less than 100V, agreement was found between the two measurement techniques. The index of refraction of the oxide was measured as $n = 1.8$, identical with the value obtained for room temperature anodization. However, analysis of ellipsometric data for the high temperature oxides, grown at biases greater than 100V, yielded an apparent index of refraction which increased with anodization voltage, up to $n \approx 3.2$ at 190V. Thus, the calculated oxide thickness appeared to decrease with increasing voltage. Because these were clearly anomalous results, Talystep measurements were made which showed that the oxide thickness monotonically increased with applied bias. These results clearly show that the model of a uniform oxide and abrupt in-

² Studies on the composition of the grown oxide (7) show non-uniformities of composition similar to those found in anodized GaP (8).

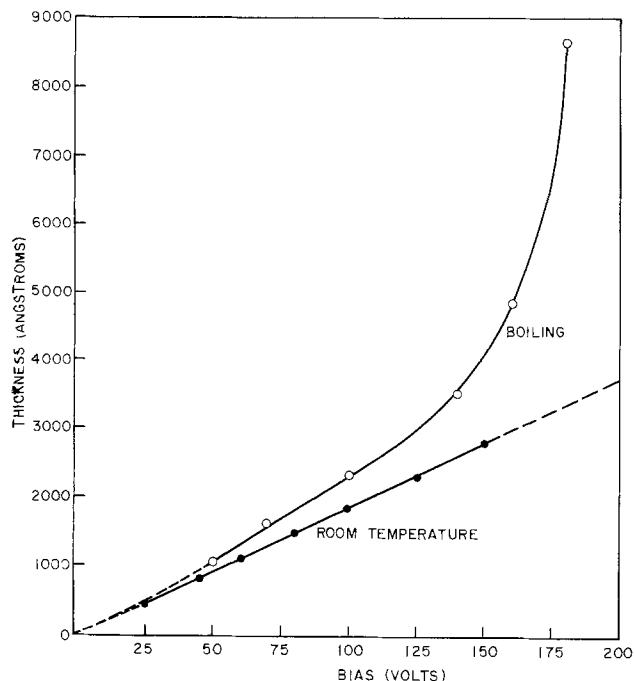


Fig. 3. Oxide thickness produced vs. anodization potential for room temperature and boiled anodization.

interface used in the ellipsometric analysis is no longer valid.

It is postulated that a grading of composition at the semiconductor-oxide interface occurs at high bias conditions. Some additional corroborating evidence for the existence of such an interface region is presented below.

Oxidized samples were examined using a phase-contrast microscope at $160\times$, and the two interfaces (i.e., semiconductor-oxide and oxide-air) could be brought into focus separately. Oxides produced by hot-anodization at 140V were smooth and shiny and of apparent uniform color throughout (Fig. 4a); oxides formed at higher voltages exhibited a dull and/or grainy texture as seen in Fig. 4b. Careful microscopic examination of the dull and of the grainy oxides showed a grainy region forming deep within the oxide; although the oxide-air surface still appears to be smooth in both cases. This grainy region deep in the oxide film, shown clearly in Fig. 4b, grows and becomes more clearly defined with increasing bias, until the entire film becomes very hazy and nonuniform in color with the

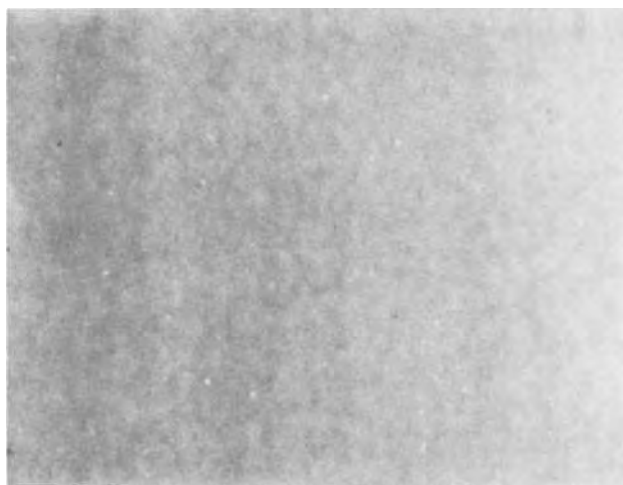


Fig. 4a. Microphotograph of semiconductor-oxide interface of 2200Å thick oxide produced by hot anodization at 140V. Note uniform texture. (Original magnification $160\times$.)

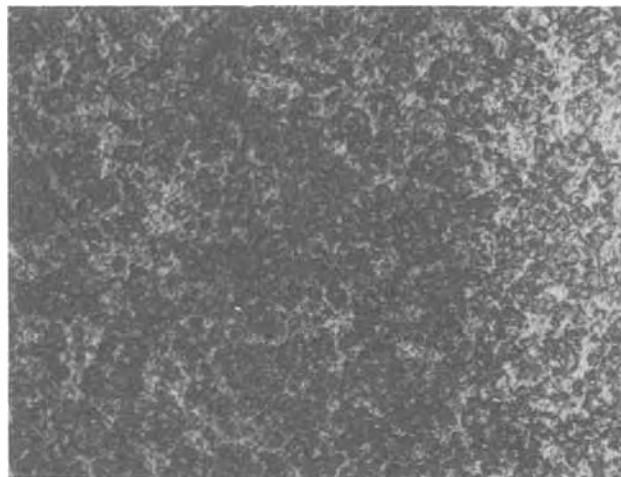


Fig. 4b. Microphotograph of semiconductor-oxide interface of oxide $> 8600\text{\AA}$ thick produced by hot anodization at 190V. Grainy detail is readily apparent. (Original magnification $160\times$.)

appearance of patches of color randomly distributed.

Since this structure is voltage dependent and the surface looks as though it may have been decorated by electrical breakdown, an attempt to increase anodization voltage while maintaining shiny, high quality oxides was made by increasing the voltage in step increments during anodization. The reasoning behind this approach was to prestress the oxide with bias less than 140V, then to slowly increase the bias as the oxide thickness increases. A typical step cycle was to anodize for 5 min each at 120, 140, and 160V, and this approach was indeed successful: oxides produced at biases up to 160V were shiny and uniform in color, at biases up to 180V were shiny but gray, and at bias greater than 190V the oxides were again dull and grainy. It should be noted that this voltage step-increment technique is actually a linear piece-wise approximation to a constant current anodization process. Samples have been anodized using both a constant current and constant voltage source, and the following similarities have been observed. In both cases final oxide thickness seems to depend only on the applied bias. In the constant voltage mode, oxide thickness is predetermined by the applied voltage and if the series resistance between the anode and cathode is not exceedingly high, the oxide grows quickly (5-10 min) (5) and is reasonably unchanged if left in the anodic cell for longer times. In the constant current density mode, power must be cut off at some predetermined voltage, otherwise oxide growth will continue as long as the bias continues to be applied to maintain the current level in the system.

Oxide Properties

It was reported that for anodization of GaP a bake-dry cycle was necessary to remove waters of hydration incorporated during oxide growth (2). Oxide layers on GaAs show no change in thickness after oxide growth and after bake cycles up to 400°C . It was thus determined that the procedure used for GaP does not necessarily apply for GaAs. It was observed, however, that when wafers were rinsed in water subsequent to anodization, the water would lightly etch the oxides. However, a dry-bake cycle was found to completely stabilize the oxide with respect to water etching. Thus, for all data presented here unless otherwise indicated, the oxides have been baked for 2 hr in a dry nitrogen ambient immediately following anodization.

The anodic oxide on GaAs is readily etched in HCl solutions; the oxide etch rate vs. HCl concentration in H_2O is shown in Fig. 5 for room-temperature anodized oxides; oxides anodically grown in boiling-peroxide exhibited similar etch rates. These data were obtained by first determining the oxide step height with the Talystep, and then measuring the time required to etch

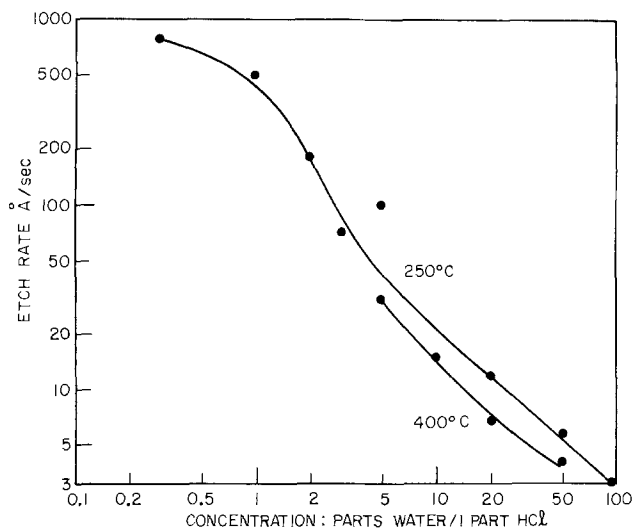


Fig. 5. Oxide etch rate determined by complete removal of a 2000Å room temperature oxide as a function of HCl concentration. Samples were heat-treated at 250°C for 2 hr and at 250°C for 2 hr and 400°C for 1 hr to evaluate chemical stability.

to the GaAs surface. The etch rate for oxides baked at 250°C range from approximately 1000 Å/sec in concentrated HCl to 3 Å/sec in 1:100 concentrated HCl to water.

In anticipation of possible high temperature use of these native oxides on GaAs, several physical properties have been examined at elevated temperatures. The etch rate following a 400°C-1 hr bake is also plotted on Fig. 5; note the enhanced chemical stability of the oxide as evidenced by the decreased etch rates. Furthermore, after baking at 600°C, the observed etch rate is less than 1 Å/sec, *i.e.*, below measurable limits even in concentrated HCl. Oxides baked at high temperature do not seem to etch in HCl, HNO₃, HF, NH₄OH, or NaOH; only hot, concentrated H₃PO₄ seems to remove the oxide. The oxide thickness of a room temperature grown, 2000Å thick film was measured after growth, and after sequential bake cycles each at 1 hr at temperatures up to 650°C. These data, plotted in Fig. 6, show virtually no thickness change up to 400°C, but above 450°C, the oxide thickness decreased until only approximately 50% of original thickness remained at 650°C. At 550°C and above, some graininess was observed in the oxide, analogous to the grainy appearance at the interface observed under high bias conditions. Etching studies have also shown that after baking at 400°C, the last 100Å of oxide (*i.e.*, at the semiconductor-oxide interface) has a granular appearance and does not etch easily. Thus, the interface region develops both at high anodization bias and after a baking cycle at 400°C and above. The thickness of this interface region appears to be less than 100Å, and is extremely difficult to remove via etching.

The data showing change in oxide thickness with heat-treatment might suggest structural changes in the native oxide. X-ray diffraction studies on the as-grown oxide as well as after sequentially heating it in dry N₂ for 2 hr at 250°C, 2 hr at 600°C, 2 hr at 700°C, and 10 min at 800°C showed no detectable crystallization, *i.e.*, the film remained amorphous. However, after 1 hr at 800°C a pattern started to develop indicating the presence of β -Ga₂O₃ in small quantities in the glass film. Following 2 hr at 800°C, transmission electron microscopy identified the presence of small grains (200-500Å) of β -Ga₂O₃ distributed in between large grains (2000Å) of an unidentifiable crystalline phase, all encased in an amorphous medium. Whiskers growing from the semiconductor-oxide interface up through the oxide were also observed. After 4 hr at 800°C the entire film crystallized and flaked off the surface of the GaAs.

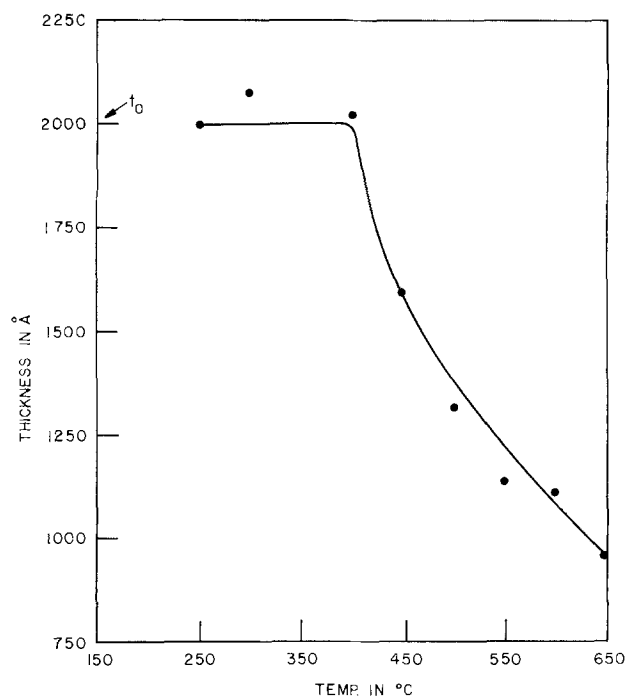


Fig. 6. Oxide thickness as a function of heat-treatment after 1 hr at each given temperature. Oxide originally grown at room temperature and 100V.

Clearly this crystallization is a dynamic process dependent on time and temperature.

Another important physical property is oxide adherence to the substrate. As-grown oxides and oxides heat-treated up to 700°C for 1 hr all passed the "Scotch tape test." Only when crystallization occurred, after exposure to 800°C for several hours, did the film become brittle and lift from the semiconductor. A preliminary study was made to determine if oxide growth would induce strain in the GaAs substrate, or if potential mismatch in the thermal coefficients of expansion would induce strain after temperature cycling. A piece of GaAs was cleaved and viewed through crossed polarizers under an infrared microscope before and after oxide growth, and again after heat-treatment to 600°C for 1 hr; no strain induced birefringence was observed, indicating at least no gross strain to be present. However, a more sensitive measurement using the technique of automatic Bragg angle control must be made before these strain results are conclusive.

Device Application

The native anodic oxide can be used as a mask for chemical etching, previously described for the formation of passive optical waveguides and mesas suitable for double-heterostructure (DH) lasers (5). There are, of course, many other potential uses and in this section we describe some applications of the oxide in terms of general processing schemes as well as several particular device applications.

Since oxide growth rates are dependent on the anodic current density, oxide uniformity is dependent on sample conductivity or carrier concentration. Thus, an oxide grown on a semiconductor with nonuniform lateral doping (Fig. 7a) will exhibit color bands or fringes (as shown in Fig. 7b) with the thicker oxides growing on more highly doped areas. Oxide growth is also a sensitive function of crystalline perfection, so that some epitaxial growth defects are clearly delineated during oxide growth (seen in Fig. 7b) (9). This is proving to be a simple, yet valuable, surface evaluation technique in the DH laser fabrication technology.

During anodization, approximately 2/3 of the oxide thickness represents GaAs material consumed (5). This provides a controllable technique for sectioning thin

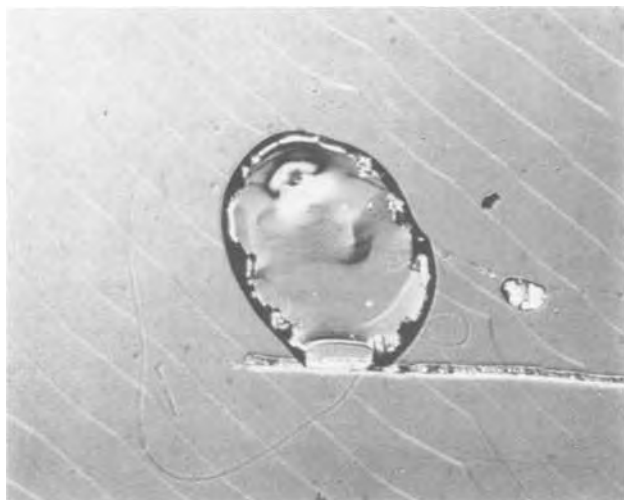


Fig. 7a. Photomicrograph of as-grown p-type LPE layer on GaAs substrate. (Original magnification $160\times$.)

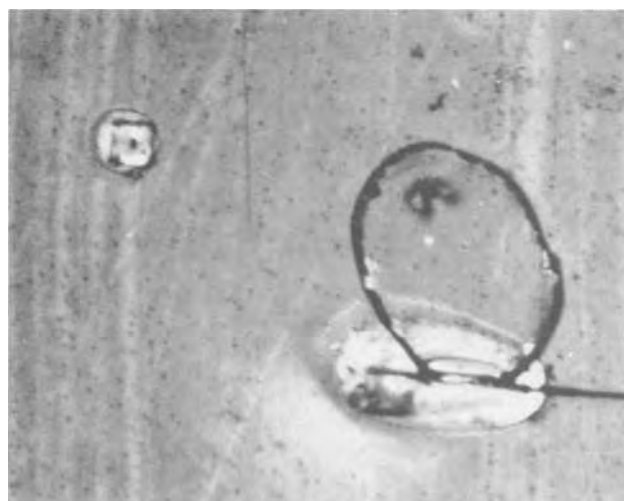


Fig. 7b. Photomicrograph of same area of p-LPE layer after anodic oxidation at 100V. Striated regions indicate nonuniformities in carrier concentration, while ring-like, splotchy areas decorate epi-layer defects. (Original magnification $160\times$.)

parallel layers for material analysis and semiconductor profiling. This technique also provides an excellent scheme for semiconductor surface cleaning: a predetermined semiconductor surface layer up to approximately 5000\AA thick can be removed by oxidation followed by an HCl strip. Aside from being a superior cleaning technique to that of organic solvent cleaning, this technique will remove surface damage which may have been caused during prior processing steps if this damage penetrates less than the thickness of GaAs consumed during anodization. Such cleaning is useful in device fabrication to keep contamination from active regions, to minimize surface leakage, and to provide more reliable low resistance contacts. This technique can be extended to provide surface protection as well as cleaning. If an anodization step is performed after certain processing steps, including the initial materials preparation step of epitaxial layer growth or diffused layer formation, the oxide will keep the semiconductor surface clean from contamination until the next processing step. Measurements of oxides on GaP (12) indicate this oxide does act as an effective mask against mobile ionic species (including Na^+) and on GaAs (13) against the diffusion of atomic Zn. Thus, a further advantage may be obtained in that the native oxide should passivate the semiconductor surface and offer improved device reliability.

One class of devices that may become feasible utilizing this anodization process is the MOS family. In particular, the p- and n-channel insulated gate field effect transistor (IGFET) could be fabricated using the anodic oxide as the gate insulator. An experiment is now in progress to explore these possibilities. Another class, diffused junction devices, can be optimized using well-controlled selective area diffusion (13) along with a diffusion damage buffer (13) as a result of the anodically grown oxides. The sectioning technique provides a fabrication technology for yet another class, mesa or quasi-planar. This mesa geometry can be particularly useful for lasers and LED diode arrays especially where junction isolation and current confinement are required.

The technology of anodic oxidation of GaAs may be very useful in the GaAs-GaAlAs double heterostructure laser technology. The oxidation process seems well suited to the design of new laser structures and the improvement of laser reliability and lifetime. However, discussions of these details will be covered in future efforts.

Summary

1. A technique has been developed permitting the growth of a native oxide on GaAs to an as-grown thickness of up to 8600\AA . The oxides formed by anodization with biases to 180V in a boiling H_2O_2 -aqueous solution have an index of refraction, $n = 1.8$, and exhibit excellent adherence to the substrate. The growth-bias dependence of such oxides has been measured and found to range from 22 to 50 $\text{\AA}/\text{V}$.

2. A method for obtaining full surface anodization has been described which allows for more economical use of the semiconductor material, more uniform and repeatable anodizations, as well as eliminating problems at the surface of the solution and of premature oxide breakdown at the air-liquid interface.

3. The anodic oxide was found to exhibit enhanced chemical stability with heat-treatment. The as-grown oxide etches in HCl, and also etches slowly in H_2O . After being baked in dry N_2 , the HCl etch rate was unchanged, but H_2O would no longer etch the oxide. Following a bake at 400°C , the observed HCl etch rate decreased, and after a high temperature bake, HCl would no longer etch the oxide at any appreciable rate. A "standard" bake cycle of 250°C for 2 hr was incorporated to prevent water etching; no oxide thickness change was observed following this bake.

4. Gallium arsenide is consumed during anodization at a rate of $2/3$ of the oxide thickness growth rate. This technique can be utilized for lateral sectioning and to profile the material, as well as to clean the semiconductor surface via a growth-strip step.

5. A region at the semiconductor-oxide interface with optical and chemical properties differing from both the semiconductor and oxide has been identified using the ellipsometer and chemical etching. This interface is produced when anodizing at biases greater than 150V and can also be produced by heat-treatment at 400°C for 1 hr.

Clearly the most important outcome of this study is the recognition of the potential of this oxide to develop a planar GaAs technology, and the multitude of new device structures such a technology implies.

It has been found that this native oxide acts as a diffusion mask against Zn (13). It is also a barrier against moisture and may act as a barrier to many different atomic species. This oxide is compatible with standard photolithographic processing, will serve as an etching mask, has good adherence, and forms a relatively strain free, high integrity interface with the semiconductor. The ease of oxide formation, coupled with the technology developed here, suggest an interesting and active future for the GaAs-native oxide system.

Acknowledgments

We wish to thank R. L. Hartman for his assistance with strain measurements, Mrs. M. H. Read for x-ray

diffraction analysis, P. Petroff for transmission electron microscopy, and Miss M. Brastad for the data on etching the baked oxide in H_3PO_4 . We thank M. Kuhn for his encouragement and many helpful suggestions along the way. We also thank R. W. Sadowski and M. C. Nelson for sample cutting and polishing, and D. L. Deppen for photoresist processing.

Manuscript submitted April 3, 1974; revised manuscript received Sept. 6, 1974. This was Paper 70 presented at the San Francisco, California, Meeting of the Society, May 12-17, 1974.

Any discussion of this paper will appear in a Discussion Section to be published in the December 1975 JOURNAL. All discussions for the December 1975 Discussion Section should be submitted by Aug. 1, 1975.

Publication costs of this article were partially assisted by Bell Laboratories.

REFERENCES

1. B. Schwartz, *This Journal*, **118**, 657 (1970).
2. B. Schwartz and W. J. Sundburg, *ibid.*, **120**, 576 (1973).

3. R. L. Hartman, B. Schwartz, and M. Kuhn, *Appl. Phys. Letters*, **18**, 304 (1971).
4. B. Schwartz, J. C. Dymont, and S. E. Haszko, IV International Conference on GaAs and Related Compounds, Boulder, Colorado, Sept. 25-27, 1972.
5. R. A. Logan, B. Schwartz, and W. J. Sundburg, *This Journal*, **120**, 1385 (1973).
6. R. L. Field, Jr., Internal communication.
7. L. C. Feldman, J. M. Poate, F. Ermanis, and B. Schwartz, *Thin Solid Films*, **19**, 81 (1973).
8. J. M. Poate, T. M. Buck, and B. Schwartz, *J. Phys. Chem. Solids*, **34**, 779 (1973).
9. M. Kuhn, Personal communication.
10. M. G. Evans and N. Uri, *Trans. Faraday Soc.*, **45**, 224 (1949).
11. S. Glasstone, K. J. Laidler, and H. Eyring, "The Theory of Rate Processes," McGraw-Hill Book Co., New York (1941).
12. S. M. Spitzer, B. Schwartz, and M. Kuhn, *This Journal*, **120**, 669 (1973).
13. S. M. Spitzer, B. Schwartz, and G. D. Weigle, *ibid.*, **121**, 820 (1974).

Vapor Deposition of GaP for High-Efficiency Yellow Solid-State Lamps

Bruce W. Wessels*

General Electric Corporate Research and Development, Schenectady, New York 12301

ABSTRACT

Nitrogen-doped gallium phosphide has been epitaxially deposited on GaP substrates by chemical vapor deposition using phosphine, hydrogen chloride, and gallium as reactants. The morphology of the epitaxial layers and the electroluminescence of the Zn-diffused diodes were investigated as a function of substrate temperature, Ga source temperature, and reactant concentration. It was found that by decreasing the $PH_3/GaCl$ ratio at which the material was grown, the electroluminescence of the diodes prepared from the material shifted to longer wavelengths as a result of increased nitrogen incorporation. Minority carrier lifetime for the n-type epitaxial material was measured by the diode reverse-recovery technique. For diffused diodes, the reciprocal of the minority carrier lifetime is directly proportional to the $PH_3/GaCl$ ratio at which the material was prepared. Possible recombination centers consistent with lifetime-ambient composition behavior are the Si-O complex or Ga vacancy complex. Quantum efficiencies for the encapsulated yellow light emitting diodes with a mesa structure were as high as 0.15% at 20 A/cm² and 0.24% under pulsed operation at 100 A/cm².

One of the most important materials for the fabrication of efficient solid-state lamps is GaP. By suitably doping GaP grown by liquid phase epitaxy (LPE), lamps which emit red (Zn-O doped) and green (N-doped) light have been made. Recently, it has been observed that by increasing the nitrogen doping level in GaP to greater than 1×10^{19} atoms/cm³, yellow electroluminescence can be obtained (1). Efficient yellow lamps, however, are not easily prepared from GaP LPE material because of formation of GaN in the melt at high N concentrations (2). A growth technique that allows the preparation of GaP with efficient yellow and yellow-orange emission is vapor phase epitaxy (VPE).

Although quantum efficiencies of 0.1% have been observed for yellow Zn-diffused GaP VPE devices, further improvements are required. One area where advances can be made is in the epitaxial growth. In the present work, growth conditions, including reactant partial pressure, growth and source temperatures, have been studied for the Ga-HCl- PH_3 - H_2

vapor-growth system and related to the morphology of the epitaxial material as well as to its electroluminescent properties. In addition, the dependence of the space charge current for diffused diodes, the minority carrier lifetime, and quantum efficiency were investigated as a function of the $PH_3/GaCl$ ratio at which the epitaxial material was grown. As a result of this study, yellow light emitting diodes with the highest quantum efficiency yet reported for GaP VPE devices have been prepared.

Experimental

Apparatus.—The system used for vapor phase GaP epitaxial growth was similar to that described by Tietjen and Amick (3) for the deposition of III-V compounds from Group V hydrides, Group III metals, and HCl. A schematic diagram of the reactor is given in Fig. 1. The reactor chamber consists of a high-purity synthetic quartz tube, with stainless-steel piping leading to it. The quartz reactor was placed in a three-zone resistance heated furnace.

Reactant gases included electronic grade HCl, a 5% mixture of electronic grade phosphine in UHP hydrogen, and palladium-diffused hydrogen as the carrier

* Electrochemical Society Active Member.

Key words: gallium phosphide, vapor phase epitaxy, electroluminescence, minority carrier lifetime.

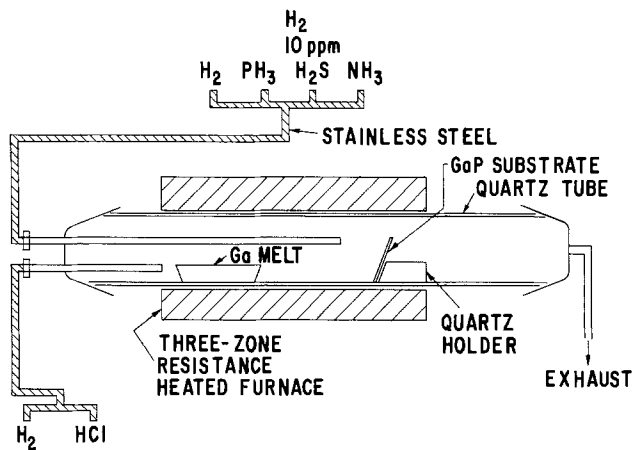


Fig. 1. Schematic diagram of vapor deposition apparatus

gas. A mixture of 10 ppm hydrogen sulfide in hydrogen was used to dope the epitaxial layers n-type to a level of $3 \times 10^{16}/\text{cm}^3$. Nitrogen doping of the layers was achieved by incorporating electronic grade ammonia into the gas stream. Elemental Ga of 6 nines' purity was the metallic source. Epitaxial layers were grown on LEC grown gallium phosphide wafers, oriented 10° off the (100) plane. Before deposition the wafers were lapped, chemically polished, and then etched in 3:1:1, $\text{H}_2\text{SO}_4:\text{H}_2\text{O}:\text{H}_2\text{O}_2$. Subsequently, the wafers were rinsed in deionized water and inserted into the reaction chamber after drying in N_2 .

Typical growth conditions consisted of a gallium source temperature of $880^\circ\text{--}930^\circ\text{C}$ and a substrate temperature of $780^\circ\text{--}840^\circ\text{C}$. The phosphine and hydrogen chloride flow rates were 1.5 and $3.0\text{--}7.5 \text{ cm}^3/\text{min}$, respectively, with a total hydrogen flow rate of $650 \text{ cm}^3/\text{min}$. The furnace was profiled so that there were two regions of differing temperature gradients: a flat zone at which the Ga source was placed, and a region with an $8^\circ\text{C}/\text{cm}$ temperature gradient where the substrate was placed. Growth rates for a HCl input concentration of $4.0 \text{ cm}^3/\text{min}$, a source temperature of 890°C , and substrate temperature of 800°C were of the order of $0.3 \mu/\text{min}$.

The following reactions have been found to occur for a similar vapor-hydride system (4). Gaseous HCl reacts completely ($>98\%$) with the gallium source in the metal zone to form gallium monochloride. Phosphine partially decomposes near the deposition zone to form the species P_2 and P_4 . Subsequently, at the deposition zone gallium monochloride reacts with phosphorus and hydrogen to form GaP and the by-product HCl. An important feature of the present system as compared to the $\text{Ga-PCl}_3\text{-H}_2$ system (5) is that the relative amount of Ga to P in the ambient can be readily varied making it possible to study the effects of stoichiometry on the properties of epitaxial GaP.

Diodes were prepared from the VPE material by diffusing zinc from a saturated source of ZnP_2 in a closed tube. Diffusions were done at 775°C for 3 hr, which yielded junction depths of about 5μ . The diffused material was scribed into chips $1.45 \times 10^{-3} \text{ cm}^2$ in area, which were then bonded to gold headers with tin. Direct contact was made to the diffused p-side with a 1-mil gold wire. Mesa diodes were constructed by the method described by Logan *et al.* (2).

Measurements.—Electroluminescent spectra for the diodes were obtained using a Spex monochromator with an RCA C31034 photomultiplier tube. The nitrogen concentration, N , of the epitaxial layers was determined by measuring the room temperature absorption coefficient at 5540 \AA (A line) and relating it to the nitrogen concentration with the expression $\alpha = \sigma N$ where σ , the absorption cross section, equals $5 \times 10^{-17} \text{ cm}^2$ (2). The absorption cross section has been corrected in keeping with the work of Lightowlers *et al.*

(6). The external quantum efficiencies of the solid-state lamps were determined using an integrating sphere. Minority carrier lifetime was measured using the diode reverse-recovery technique of Kingston (7). For the Zn-diffused p^+n structure the lifetime measured by this method is essentially the minority carrier hole lifetime.

Results

It was found that the morphology, electroluminescent spectral characteristics, and minority carrier lifetime were affected by a number of growth parameters. These parameters included the partial pressures of the reactants, dopant concentrations, source and substrate temperatures, and substrate orientation.

Temperature effects.—The morphology of the epitaxial layers was extremely sensitive to the gallium source temperature. Figure 2 shows the morphology of the epitaxial layers grown at a gallium source temperature of 930°C . A stacking fault density of the order of $10^6/\text{cm}^2$ was observed at the surface of the as-grown layers. Upon lowering the source temperature 30°C the density of the stacking faults decreased to less than $10^3/\text{cm}^2$.

The electroluminescent spectra of diodes prepared from material grown at various source temperatures also differed as shown in Fig. 3. Spectrum 1 was observed for diodes fabricated from material grown at

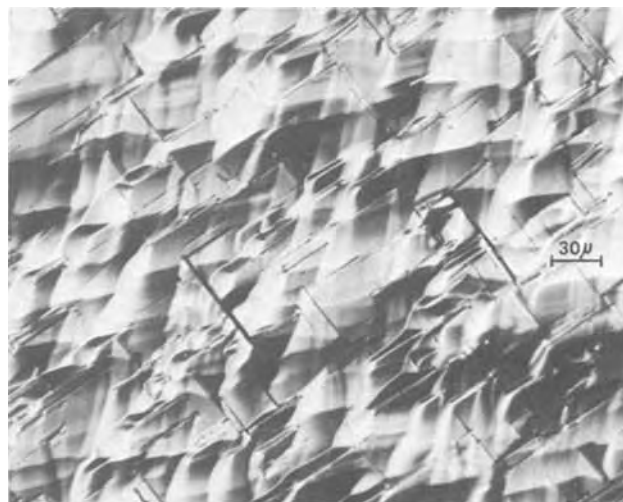


Fig. 2. Morphology of GaP epitaxial layer grown at a gallium source temperature of 930°C .

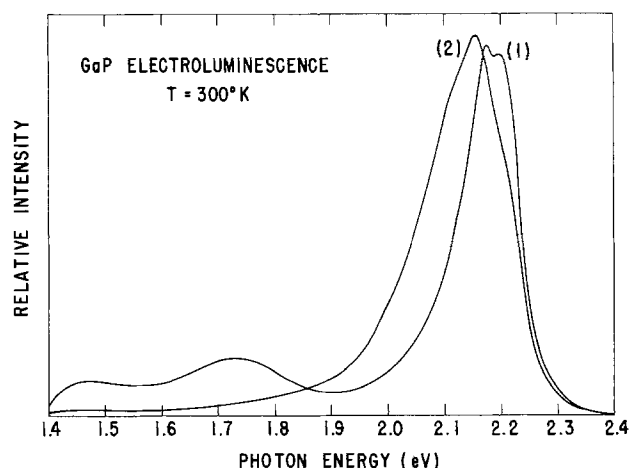


Fig. 3. Electroluminescent emission spectra at 300°K of GaP diodes prepared from material grown with a Ga source temperature of 930°C (spectrum 1) and a Ga source temperature of 900°C (spectrum 2).

a gallium source temperature of 930°C and a high stacking fault density. A relatively large red emission quantum efficiency of 4.4×10^{-5} resulting from zinc-oxygen pair recombination was noted for these diodes. However, for diodes fabricated from material prepared with a Ga source temperature of 900°C and low stacking fault densities (spectrum 2 in Fig. 3) a substantially reduced red emission efficiency of 1.6×10^{-5} was observed. This result suggests that oxygen may play a role in the formation of stacking faults in GaP vapor epitaxial material. The oxygen contamination probably results from the decomposition of the SiO₂ reaction chamber whose decomposition rate increases with increasing source temperature (8).

In addition to the source temperature, the GaP substrate temperature also affected epitaxial morphology. At a substrate temperature of 840°C and a PH₃/GaCl ratio of 0.3 an essentially featureless morphology was observed for the epitaxial layers. But, as the substrate temperature decreased, hillocks began to form as shown in Fig. 4, with hillock concentrations as high as 50/cm² having been observed. The hillocks in themselves are not deleterious to the luminescent efficiency of the material; but it was noted that the leakage current of diodes fabricated from material with a high hillock density is large.

Orientation and layer thickness effects.—Substrate orientation was found to be a critical parameter for achieving high nitrogen incorporation without degradation of epitaxial layer morphology. High nitrogen concentration could not be obtained for growth on the (111) orientation without severe hillock formation. However, when growth was performed upon crystals which were 10° off the (100) plane, high concentrations of nitrogen could be incorporated into the GaP without excessive morphological changes. In fact, nitrogen concentration as high as 4×10^{19} atoms/cm³ could be obtained with this orientation.

In contrast to previous work (9), it was observed that the quantum efficiency of the grown material was relatively insensitive to the thickness of the layers. Layers as thin as 17μ have been prepared in this study with the resulting diodes having quantum efficiencies similar to those prepared from layers with a thickness of ten times that amount.

Reactant concentration.—It was observed that by changing the molar ratio of PH₃/GaCl in the reactor ambient for a constant phosphine input, both the morphology and luminescent characteristics of the epitaxial layers could be altered. For PH₃/GaCl ratios of 0.5 or less it was noted that when the PH₃/GaCl ratio was decreased, the concentration of hillocks increased. This finding agrees with observations in

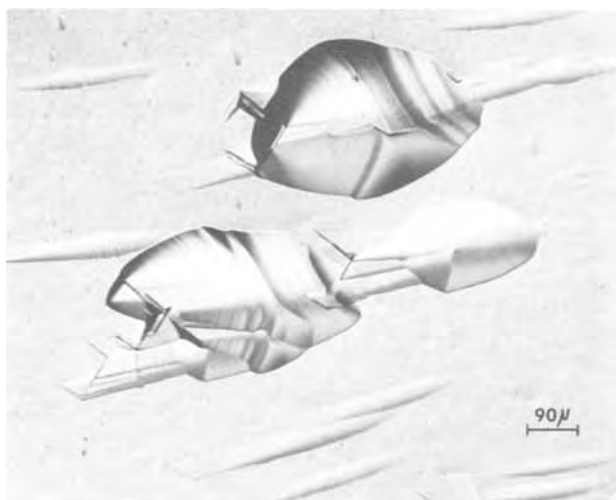


Fig. 4. Morphology of GaP epitaxial layer grown at a substrate temperature of 800°C.

Table I. Effect of PH₃/GaCl ambient ratio on nitrogen concentration epitaxial layer

Sample No.	PH ₃ :GaCl	N conc in layer	Emission peak, eV
1	1:1.3	8×10^{17} cm ⁻³	2.21
2	1:3.5	4.4×10^{18} cm ⁻³	2.16
3	1:7.1	1.1×10^{19} cm ⁻³	2.10

other hydride growth systems, since similar increases in hillock density with increased III/V gaseous species ratio have been observed in the epitaxial growth of GaAs (10) and GaAs_xP_{1-x} (11).

More significantly, it was found that by varying the PH₃/GaCl for a constant ammonia input, the amount of nitrogen incorporated into the epitaxial layers could be varied. A low PH₃/GaCl ratio gave layers with large nitrogen concentration, as reported in Table I. Consequently, the spectral characteristics of diodes prepared from grown material could be modified by changing the PH₃/HCl ratio. Figure 5 shows that the electroluminescent spectra of diodes shifted to longer wavelengths due to increased nitrogen content as the PH₃/GaCl ratio was decreased.

The minority carrier lifetime, a quantity that is directly proportional to the quantum efficiency, was measured by the reverse-recovery technique on diodes prepared from n-type material grown at different PH₃/GaCl ratios. As shown in Fig. 6, it was found that the reciprocal of the minority carrier lifetime τ was proportional to the PH₃/GaCl ratio. Moreover, the diode current at a forward bias of 1.5V was investigated as a function of PH₃/GaCl ratio at which the n-type material was grown, and was also found to be proportional to the PH₃/GaCl ratio as shown in Fig. 6. To insure that the changes in the diode current resulted from bulk generation-recombination of carriers and not surface leakage, diodes of different areas were fabricated. It was observed that the current density was essentially independent of area, thus indicating a bulk recombination effect.

For forward biases up to 1.7V, the current-voltage characteristics of the diodes could be fitted with the expression for pure space-charge current, I_{sc} , given by (12)

$$I \approx I_{sc} = \frac{\pi}{2} \frac{n_i k T W}{\tau_s (V_d - V)} \exp \frac{eV}{2kT} \quad [1]$$

where n_i is the intrinsic carrier concentration, V_d the built-in potential, W the space charge width, and τ_s the effective carrier lifetime in the space charge region. For a constant dopant concentration, the only

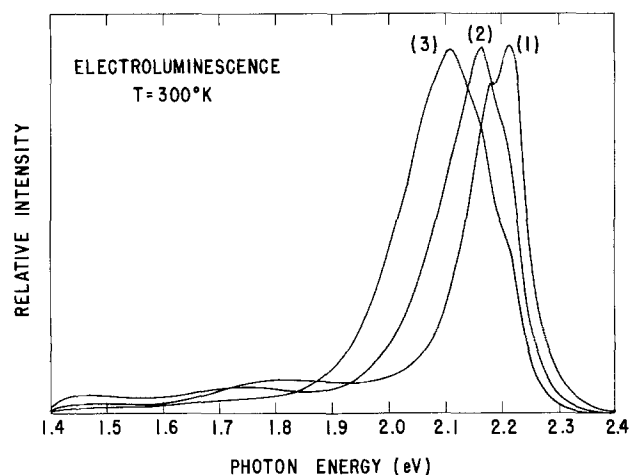


Fig. 5. Electroluminescent emission spectra at 300°K of GaP diodes prepared from material grown with different PH₃/GaCl ratios in the ambient, but at a constant ammonia partial pressure. PH₃/GaCl ratios are given in Table I.

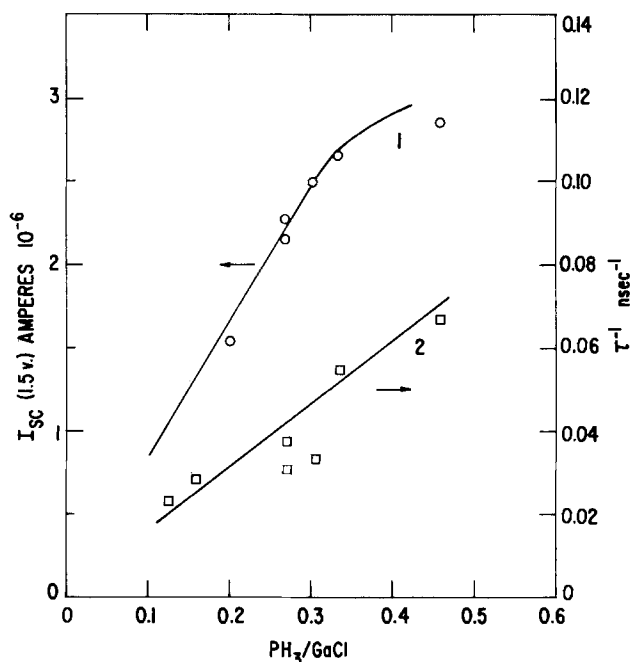


Fig. 6. Dependence of space charge current, I_{sc} , at a forward bias of 1.5V and the reciprocal of the minority carrier lifetime τ on PH_3/GaCl ratio at which the vapor epitaxial material was prepared.

parameter in Eq. [1] which is dependent on material preparation conditions is the lifetime. Thus the observed changes in the diode current with PH_3/GaCl ambient ratio are also due to the dependence of lifetime on the growth ambient.

In support of the increase of the nonradiative lifetime with decreasing PH_3/GaCl ratio, the reciprocal of the electroluminescent quantum efficiency was found to increase with increasing PH_3/GaCl ratio as shown in Fig. 7. However, instead of a simple monotonic relationship between η^{-1} and the PH_3/GaCl ratio, a superlinear dependence was observed. This super-

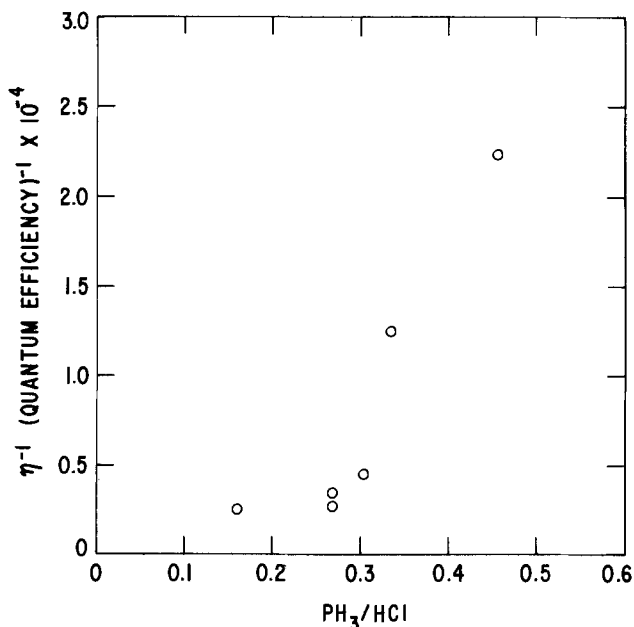


Fig. 7. The reciprocal of electroluminescent quantum efficiency as a function of PH_3/GaCl ratio at which the n-type epitaxial material was grown. The quantum efficiency was measured at 13 A/cm².

linearity indicates that in addition to the decrease in minority carrier lifetime with increased PH_3/GaCl there is also an increase in the radiative lifetime. The observed increase in radiative lifetime is consistent with the dependence of nitrogen recombination center concentration on PH_3/GaCl ratio reported in Table I.

Electronic properties.—With the VPE technique, net donor concentrations, $N_D - N_A$, of $2 \times 10^{15}/\text{cm}^3$ have been obtained for unintentionally doped epitaxial material. Minority carrier hole lifetimes of 70 nsec have been observed in heavily nitrogen-doped material with a net donor concentration of $3 \times 10^{16}/\text{cm}^3$. Quantum efficiencies for encapsulated mesa yellow light emitting diodes with a characteristic spectrum of Fig. 8 are 0.15% at 20 A/cm². With pulsed operation, efficiencies of 0.24% have been obtained at 100 A/cm² in the better diodes, as shown in Fig. 9.

Discussion

For a single dominant recombination center, the reciprocal of the low-level recombination lifetime is given by (13)

$$\tau^{-1} = CN_{nr} \quad [2]$$

where N_{nr} is the number of recombination centers and C the capture constant. Thus the increase in the reciprocal of the minority carrier lifetime and the space charge current with PH_3/GaCl ratio or P/Ga ratio results from an increase in the generation-recombination center density. The identity of these predominantly nonradiative centers N_{nr} is not known; however, there are several possible candidates.

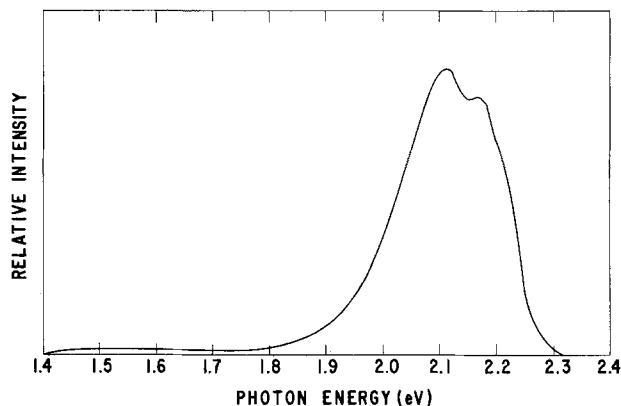


Fig. 8. Electroluminescent spectra at 300°K of a yellow solid-state lamp prepared from VPE material. Current density was 6.9 A/cm².

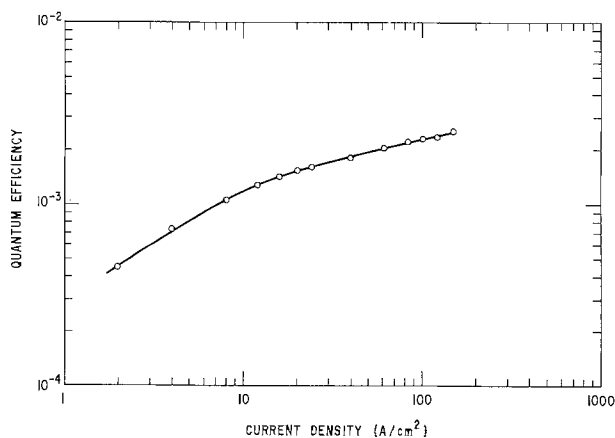


Fig. 9. EL quantum efficiency as a function of current density for a yellow encapsulated solid-state lamp, with a mesa structure.

One type of recombination center previously found to be important in liquid-encapsulated Czochralski GaP (14) and LPE GaP (15) is the gallium vacancy. The concentration of gallium monovacancies is directly proportional to the P/Ga growth ambient ratio, which is the same concentration dependence noted for the unknown recombination center observed in this study. This concentration dependence, however, does not uniquely define the center involved, inasmuch as other centers associated with the gallium vacancy, such as gallium vacancy complexes or substitutional impurities on Ga sites, are also consistent with the observed lifetime-ambient behavior.

Two other possible recombination centers in VPE GaP are Si and Si-O complexes, since both of these species are inadvertently present in the ambient as a result of decomposition of the quartz reactor. Furthermore, both have been cited as effective recombination centers in LPE GaP (16, 17). Evidence in support of Si being important in VPE material is given by the findings of Okamoto *et al.* (18) on the Ga-As-HCl-H₂ system for the growth of GaAs, where they observed that by increasing the As/Ga ratio, the unintentional silicon donor concentration increases in the epitaxial layer.

To further support silicon or silicon complexes acting as the primary (nonradiative) recombination center in GaP, the work of Smith and Abbott (16) on minority carrier lifetimes in LPE GaP can be cited. In their studies, Smith and Abbott noted that the lifetimes decreased for increasing Si dopant concentration (16). They attributed this decrease in lifetime to the acceptor Si (silicon on the phosphorus site) acting as a recombination center. Their conclusion, however, is inconsistent with that of Bachrach *et al.* (17) who found, on studies of deliberately silicon-doped GaP LPE layers, that even at relatively high concentration (10¹⁸/cm³) of silicon in the layers, minority carrier lifetimes of 200 nsec could be obtained. Bachrach *et al.* observed that only when GaP layers were simultaneously doped with silicon and oxygen were marked decreases in the lifetimes noted. Consequently, they attributed the decreased lifetime to Si-O complexes.

The present study also suggests that silicon as an acceptor is not the major generation-recombination center insofar as it was observed that the number of centers increased with increasing P/Ga ratio in the ambient. On the other hand, the concentration of silicon acceptors should decrease with increasing P/Ga ratio, as a result of the incorporation of silicon acceptors being dependent on the concentration of phosphorus vacancies. Therefore, a center involving Si on a gallium site such as the Si donor-O complex rather than a silicon acceptor is more likely to be a major recombination center in VPE material.

In view of the experimental evidence, it is not yet possible to resolve which specific impurity is the primary generation-recombination center responsible for decreased lifetime and increased space charge current in diodes fabricated from VPE material grown at high P/Ga ratios. However, it can be concluded from this study that the recombination center involves the Ga site.

Summary

1. A high gallium source temperature resulted in epitaxial GaP with a high stacking fault density and

an increased red emission in the electroluminescent spectra.

2. Decreasing the P/Ga ratio in the ambient or decreasing the substrate temperature resulted in epitaxial layers with large hillock densities.

3. By varying the P/Ga ratio in the ambient the amount of nitrogen incorporated in the epitaxial layers could be controlled. It was found that the lower the P/Ga ratio the greater the nitrogen concentration.

4. Relatively long minority carrier lifetimes of 70 nsec and decreased space charge current could be obtained by fabricating diodes from epitaxial material grown at low P/Ga ratios in the ambient. The decrease in the space charge current and the increase in the lifetimes are probably associated with a decrease in the number of Si-O complexes or gallium vacancy complexes incorporated into the layers.

Acknowledgments

The author wishes to thank P. Menditto and F. C. Mall for technical assistance. Discussions with J. D. Kingsley, D. T. F. Marple, and J. F. Womac are greatly appreciated.

Manuscript submitted June 17, 1974; revised manuscript received Oct. 4, 1974. This was Paper 210 presented at the New York, New York, Meeting of the Society, Oct. 13-17, 1974.

Any discussion of this paper will appear in a Discussion Section to be published in the December 1975 JOURNAL. All discussions for the December 1975 Discussion Section should be submitted by Aug. 1, 1975.

Publication costs of this article were partially assisted by General Electric Company.

REFERENCES

1. R. Nicklin, C. D. Mobsby, G. Lidgard, and P. B. Hart, *J. Phys. C*, **4**, L344 (1971).
2. R. A. Logan, H. G. White, and W. Weigmann, *Solid-State Electron.*, **14**, 55 (1971).
3. J. Tietjen and J. A. Amick, *This Journal*, **113**, 7 (1966).
4. V. Ban and M. Ettenberg, *J. Chem. Phys. Solids*, **34**, 1119 (1973).
5. W. G. Oldham, *J. Appl. Phys.*, **36**, 2887 (1965).
6. E. C. Lightowers, J. C. North, and O. G. Lorimor, *ibid.*, **45**, 2191 (1974).
7. R. H. Kingston, *Proc. Inst. Radio Engrs.*, **42**, 829 (1954).
8. M. E. Weiner, *This Journal*, **119**, 496 (1972).
9. J. W. Burd, Govt. Technical Report AFML-TR-73-89.
10. J. K. Kennedy and W. D. Potter, *J. Crystal Growth*, **19**, 85 (1973).
11. T. Y. Wu, *ibid.*, **21**, 85 (1974).
12. C. T. Sah, R. N. Noyce, and W. Shockley, *Proc. IEEE*, **45**, 1228 (1957).
13. J. S. Blakemore, "Semiconductor Statistics," Pergamon Press, New York (1962).
14. A. S. Jordan, A. R. Van Neida, R. Caruso, and C. K. Kim, *This Journal*, **121**, 153 (1974).
15. I. Ladany and H. Kressel, *RCA Rev.*, **33**, 517 (1972).
16. B. L. Smith and M. Abbott, *Solid-State Electron.*, **15**, 361 (1972).
17. R. Z. Bachrach, O. G. Lorimor, L. R. Dawson, and K. B. Wolfstirn, *J. Appl. Phys.*, **43**, 5098 (1972).
18. H. Okamoto, S. Sakata, and K. Sakai, *ibid.*, **44**, 1316 (1973).

Very High Efficiency GaP Green Light Emitting Diodes

O. G. Lorimor, P. D. Dapkus, and W. H. Hackett, Jr.

Bell Laboratories, Murray Hill, New Jersey 07974

ABSTRACT

GaP green light emitting p-n junction material with an average quantum efficiency for uncontacted diced diodes in air at 7 A/cm² of 0.101% has been reproducibly grown in a vertical dipping system using a modified overcompensation process. This value corresponds to an average efficiency of 0.16% for epoxy encapsulated mesa diodes, which is 60% higher than previously obtained. Mesa diode efficiencies as high as 0.230% at 5 A/cm² and 0.67% at ~300 A/cm² were obtained. The low current value is the highest reported to date while the high current value is equal to the highest previously reported. These efficiencies were obtained through the introduction of several modifications in the previous overcompensation growth procedure. It was determined that a large cooling interval, from 900° to 700°C, with a corresponding decrease in the temperature at which the p-n junction is formed (850°C) was the most important modification that resulted in the efficiency improvement. Minority carrier lifetime measurements revealed spatial variations of the lifetimes in both n- and p-layers. The lifetimes increased with decreasing growth temperature, indicating that LPE growth temperatures as low as possible should be used. Typical values were $\tau_h = 200$ nsec and $\tau_e = 100$ nsec at the junction. An analysis of the exit gas from the LPE growth system lets one estimate that as much as ~5 ppm O₂ could typically be present in the LPE growth system. Deliberate additions of small oxygen concentrations >10 ppm to the inlet gas produced a pronounced reduction in the quantum efficiency and minority carrier lifetimes while oxygen additions ≤ 10 ppm had no effect on the efficiency or lifetimes.

A considerable effort has been devoted over the past three years to improving the quantum efficiency of GaP green light emitting diodes (LED's) and to understand the operation of the device (1, 2). As a result of this work p-n junction material has been reproducibly grown with electroluminescent (EL) quantum efficiencies of encapsulated mesa diodes averaging 0.1% at 5 A/cm² (1). This material has been extensively characterized with respect to doping levels, N concentrations, minority carrier lifetimes (τ_e , τ_h), diffusion lengths (L_e , L_h), and bulk luminescent efficiency. For example, in 0.1% p-n junction material typical values of τ_e and τ_h are 40 and 100 nsec, respectively, with corresponding bulk efficiencies of 0.3 and 0.06% (2). These lifetimes and efficiencies are limited by nonradiative recombination which competes in parallel with bound exciton recombination on the N site.

In order to achieve these efficiencies and lifetimes in our vertical "dipping" liquid phase epitaxial (LPE) growth system (3), it was essential to eliminate oxygen from the system (4). The inlet gas lines were carefully constructed to be as leak free as possible. Because of this leak-free gas system, the efficiencies were independent of whether or not a sodium trap (4) (oxygen getter) was used. The growth system itself was designed to contain no "dead" air spaces which could act as virtual leaks. To minimize oxygen contamination resulting from loading, the growth system was flushed overnight with H₂ after loading and prior to growth.

The overcompensation procedure used to obtain these efficiencies (1) was one where both the n- and p-layers were grown in a single run. A Te,N doped n-layer was first grown by cooling the melt from 900° to 880° or 870°C. After n-growth, without removing the seed from the melt, Zn was added to the melt to overcompensate the Te. The Zn,N layer was then grown by further cooling to 830° or 820°C.

Recently with the dipping system some very long minority carrier lifetimes have been obtained; values

of τ_h ranged from 300-800 nsec for net donor concentrations from $1-3 \times 10^{17}$ cm⁻³. By varying the growth procedure (5), lifetimes up to 1000 nsec were obtained in undoped, but n-type layers. The cause for these longer lifetimes was unknown but it was speculated that they were due, at least partly, to a general improvement in the growth technique which presumably resulted in a lowering of the O₂ contamination. The relative contribution of each of the variations in the growth procedure (5) was also unknown. The work described herein was initiated with two objectives; to determine, if possible, the origin of the longer lifetimes and to grow p-n junction material incorporating these lifetimes which should be reflected in higher EL efficiencies.

Experimental

The LPE layers were grown in an open flow dipping system which has been in continual use in the GaP green LED optimization program (1-3). The new growth cycle (5), hereafter termed "modified," adopted for this work incorporates a number of procedural changes from the "overcompensation" procedure (1) used previously. Table I enumerates the differences in these two growth procedures. In the present work, the Ga+P melt is placed in a Si₃N₄ coated quartz crucible which in turn is located at the bottom of a freshly cleaned furnace tube. Both the seed and source holders were graphite with the seed holder tube being hollow as previously described. The Si₃N₄ coating of the quartz crucible was used to eliminate oxygen contamination resulting from the reduction of the quartz by the Ga. The graphite holders were to accelerate the loss of oxygen from the melt through the formation of CO. The first grown layer, which is a low doped n-layer, is grown by cooling a melt intentionally doped only with N from 900° to 850°C at a rate of 30°C/hr. Upon reaching 850°C, 0.14 atom per cent (a/o) Zn is dropped into the melt through the hollow seed holder tube while the furnace is held at constant temperature for ½ hr to uniformly distribute the Zn in the melt. The p-layer is then grown by cooling from 850° to

Key words: GaP, LED, GaP-oxygen.

Table I. Comparison of the "overcompensation" growth procedure with the "modified" procedure adopted for this work. Growth parameters other than these remained unchanged

Growth parameter	Overcompensation	Modified
Crucible material	Quartz	Si ₃ N ₄ coated quartz
Seed and source holders	Quartz	Graphite
Cooling interval: n-layer	900° → 880° or 870°C	900° → 850°C
p-layer	880° or 870° → 830° or 820°C	850° → 700°C
Overnight anneal	None	700°C
n-Layer: dopants	Te, N	—, N
N _d -N _a	1-2 × 10 ¹⁷ cm ⁻³	< 1 × 10 ¹⁷ cm ⁻³
p-Layer: dopants	Zn, N	Zn, N
N _a -N _d	5-10 × 10 ¹⁷ cm ⁻³	5-10 × 10 ¹⁷ cm ⁻³

700°C at 30°C/hr. During the p-growth (at ~775°C) Zn is again dropped into the melt, this time with no interruption in the cooling. This second Zn addition is to insure that the net acceptor concentration at the surface is high enough for good electrical contacts.¹ Upon reaching 700°C the LPE layers were annealed in the Ga+P melt for ~14 hr (overnight). During the entire growth cycle, with the exception of the anneal, the seed was continually being stirred while in the melt to promote more uniform growth. The ambient gas consists of H₂ plus 1.5 × 10⁻³ atm of NH₃ which is unchanged from that used previously. This ammonia addition to the gas stream results in a N concentration in the GaP of 2 × 10¹⁸ cm⁻³ as measured by optical absorption (1, 4, 8). Since the n-layer is not deliberately doped, the resulting net donor concentration varied considerably, viz., $\approx 5 \times 10^{15} < (N_d - N_a) < 1 \times 10^{17} \text{ cm}^{-3}$. In the p-layer, N_a-N_d varied from 5 × 10¹⁷ to 1 × 10¹⁸ cm⁻³ at the p-n junction.

In order to evaluate the relative importance of these changes in the growth cycle from the previous "overcompensation" procedure (1), the changes were sequentially eliminated. These include either a quartz or graphite crucible instead of the Si₃N₄ coated quartz crucible, quartz seed and source holders instead of graphite, variations in the cooling intervals, and the elimination of the anneal. Interspersed with these runs were runs using the complete "modified" procedure to insure the constancy of the system. The effect of each of these changes on the electroluminescent efficiency and minority carrier lifetime was assessed. From these experiments the relative importance of each change was determined.

Most of the quantum efficiency measurements were made on uncontacted diced diodes (9) in air at ~7 A/cm². Experience has shown that efficiencies measured in this manner are ~60% of epoxy encapsulated mesa diodes operated at the same current density (9). Equivalent mesa diode efficiencies can be calculated by multiplying the uncontacted diced diode efficiencies by ~1.6. Epoxy encapsulated mesa diodes (10) were fabricated only in the cases of a particularly high uncontacted die efficiency or when measurements at current densities larger than 7 A/cm² were desired.

All efficiencies were measured on a pulsed basis in a close coupled cavity. At current densities < 30 A/cm², 15 μsec pulses were used; at current densities > 30 A/cm², 1 μsec pulses. The narrower pulses were used at the higher current densities to avoid heating during the pulse. Pulses narrower than 1 μsec were not used so as to keep the pulse width much larger than the characteristic response time of the diode (~ largest minority carrier lifetime), thus insuring that a quasi-steady-state distribution of carriers would be obtained during the pulse.

The net donor or acceptor concentrations, |N_d-N_a|, were determined from capacitance measurements of

¹ Zn loss in the open flow dipping system and the relative behavior of n- and p-type distribution coefficients (6, 7) has always resulted in a decrease in the net acceptor concentration from the p-n junction toward the surface. This decrease in N_a-N_d is a large effect in the layers grown over the wide temperature interval used in this work.

Schottky barrier diodes on an angle-lapped surface (11). The minority carrier lifetimes were determined from a measurement of the green photoluminescent decay time using the 4880Å line from an argon ion laser for excitation (12). The laser power was adjusted so that the generated minority carrier density was comparable to that produced by a diffusion current of ~1-10 A/cm² through a p-n junction. The minority carrier lifetime measurements as a function of depth were made on the same angle-lapped sample that was used for the |N_d-N_a| measurements.

The diffusion length measurements were performed in a Cambridge "Stereoscan" scanning electron microscope. The measurements are made by scanning a focused electron beam across a polished surface perpendicular to the junction on a 15 × 15 mil die. The diffusion lengths are determined from the functional dependence of the induced junction current with scan distance across the junction (13). The electron beam excitation levels were also adjusted to provide carrier densities equivalent to diffusion current densities of ~1-10 A/cm² through a p-n junction.

A Varian Model 1532b gas chromatograph was used to analyze the entrance and exit gases of the LPE growth systems during the course of this study. Two molecular sieve 5A columns, one 20 ft × 1/8 in. operating at 50°C and the other 3 ft × 1/8 in. at ~90°C were used. With these two columns the concentrations of the commonly observed unintentionally present gases O₂, N₂, CH₄, and CO could be simultaneously and quantitatively measured at sub-ppm levels in 1 atm of H₂. The chromatograph was quantitatively calibrated for CO, O₂, CH₄ and N₂ by the use of an exponential dilution flask (14). A known volume of sample gas is injected into the flask, also of known volume V, resulting in an initial concentration, C₀. After injection, the concentration of sample gas in the flask decays as C₀ exp (-Ft/V) where F is the flow rate through the flask of a carrier gas. Periodically sampling the effluent gas with the chromatograph gives the quantitative calibration. For the four previously mentioned gases, concentrations less than 1 ppm could easily be measured under the experimental conditions used in this study. Additional work on the application of chromatography to the analysis of LPE systems is given elsewhere (15).

Results

The quantum efficiencies of the devices which were fabricated from this material are presented first followed by a more detailed characterization yielding the minority carrier lifetimes and diffusion lengths. These parameters were studied as a function of the growth procedure to determine the critical growth parameters. Finally, in an effort to determine the effects on the efficiency of small amounts of O₂ in the gas stream the results of a gas analysis study of oxygen contamination are presented.

Quantum efficiency.—Twenty-one p-n junctions were grown over a 5 month period using the modified overcompensation procedure described earlier. Figure 1 compares the efficiencies of these junctions to those grown by the former overcompensation process (1). Each data point in Fig. 1 is the average efficiency of

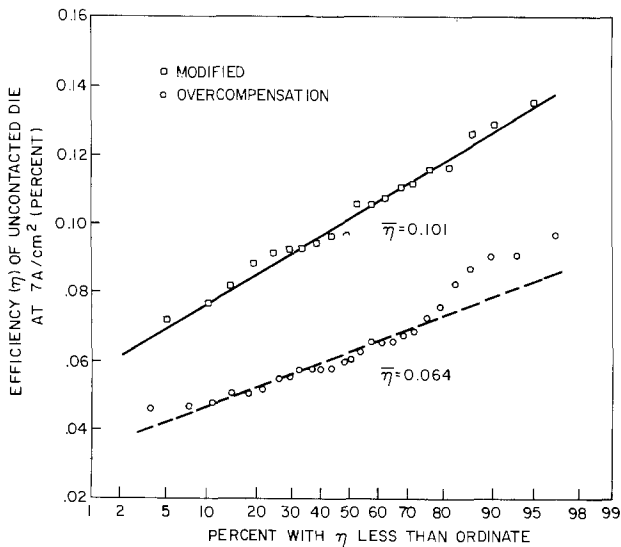


Fig. 1. Comparison of electroluminescent quantum efficiencies of uncontacted die in air at 7 A/cm² for the former overcompensation procedure and the present modified overcompensation procedure. Each data point is the average of ~6 diodes. The equivalent epoxy encapsulated mesa diode efficiency is higher by ~60%.

~6 uncontacted diced diodes fabricated from a single p-n junction sample. Prior to this work, the overcompensation process most reproducibly yielded the highest efficiencies we were able to obtain. The average efficiency of the overcompensated junctions is 0.064% while that of the modified process is 0.101%. This is a ~60% increase in average efficiency. Consequently, the modified procedure has resulted in a significant efficiency improvement.

Mesa diodes were fabricated from a number of the more efficient crystals and their efficiencies measured at higher currents. Figure 2 shows the efficiency for three of these epoxy encapsulated mesa diodes as a function of current. A value of 0.67% at ~300 A/cm was observed for 1-623 which is the highest value we achieved. This efficiency is essentially equal to the highest value (0.7%) reported to date by Ladany and Kressel (16). The doping density in the n-layer of diode 1-623 is $\sim 6 \times 10^{15} \text{ cm}^{-3}$ while that in 2-576 is $9 \times 10^{16} \text{ cm}^{-3}$. For comparable diffusion lengths, conductivity modulation of the lower doped n-layer in diode 1-623 is expected to result in an enhanced current dependence of the efficiency (17).

For most device applications the low current efficiency is a much more relevant parameter than the high current values. Figure 2 also shows the current dependence of the diode 1-628 with the highest effi-

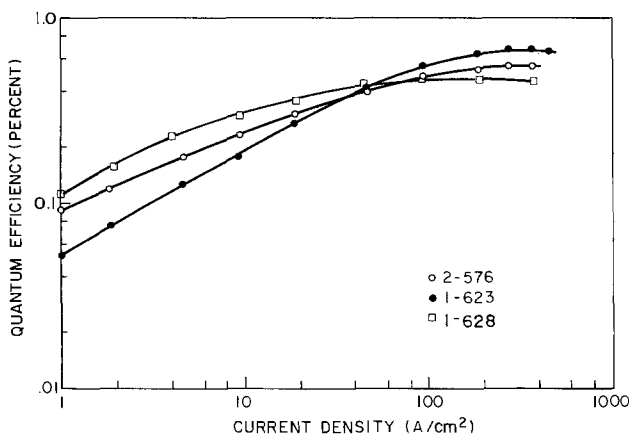


Fig. 2. Quantum efficiency as a function of current density for three high efficiency epoxy encapsulated mesa diodes.

ciency measured at $\sim 5 \text{ A/cm}^2$ which was 0.230%. This is the highest efficiency at this low current density reported to date. The average extrapolated mesa diode efficiency of the junctions grown by the modified overcompensation process is $\sim 0.16\%$ at 5 A/cm^2 .

The modified overcompensation process used to achieve these results utilizes several changes in the growth procedure from the former overcompensation process. However, since these changes were simultaneously incorporated into the growth procedure, the relative importance of each was unknown. Consequently, a series of crystal growth runs were made where these changes were systematically eliminated in order to study their relative importance.

Table II presents a summary of the efficiencies of uncontacted diodes for the combinations of quartz, graphite, and Si₃N₄ coated quartz which were used. None of the other growth parameters, e.g., doping levels, the cooling interval, and the annealing cycle were changed. The efficiencies of the material grown with these combinations of materials are judged to be essentially the same. Thus, the high efficiencies do not appear to be unique to only Si₃N₄ coated quartz plus graphite in contact with the melt, but can be achieved in an all quartz or graphite LPE system.

Several growth runs were made using narrow cooling intervals as previously reported (1) or eliminating the annealing cycle, but using the Si₃N₄ coated quartz crucibles and graphite seed holder. Table III compares the quantum efficiencies of these p-n junctions with those grown by the modified process. From this data we conclude that the anneal did not appear to cause the increase in efficiency but increasing the cooling interval did. Consequently, we conclude that the primary new factor in the present growth cycle resulting in the higher efficiencies is the longer cooling intervals and the associated lower growth temperature of the p-n junction.

In the early part of this work the LEC substrate doping levels varied from $1.6\text{--}7 \times 10^{17} \text{ cm}^{-3}$. An interesting correlation was noted between the quantum efficiency and doping density of the substrate for the modified overcompensation growths. This correlation is depicted in Fig. 3. The quantum efficiency shows a general decrease from ~ 0.1 to $\sim 0.04\%$ as the LEC doping level increases from 2 to $7 \times 10^{17} \text{ cm}^{-3}$. When this correlation was observed, the use of LEC wafers with $N_d\text{--}N_a > 3 \times 10^{17} \text{ cm}^{-3}$ was discontinued. Thus there are less data at these higher LEC doping levels. One should note that this effect was observed only for p-n junctions grown in one particular manner in our dipping system and on slices from a single ingot,

Table II. Quantum efficiencies of uncontacted diced diodes for p-n junctions grown with differing materials in contact with the melt while holding the growth cycle optimum

Crucible material	Seed holder material	Number of growth/runs	Avg η	Max η
Si ₃ N ₄ coated quartz (modified procedure)	Graphite	21	0.101 ± 0.018	0.136
Si ₃ N ₄ coated quartz	Quartz	6	0.082 ± 0.034	0.147
Quartz	Quartz	2	0.100 ± 0.023	0.124
Graphite	Graphite	7	0.088 ± 0.033	0.129

Table III. Quantum efficiencies of uncontacted diced diodes for material grown by various growth cycles using Si₃N₄ coated crucibles and a graphite seed holder

	Cooling interval (°C)	n-layer p-layer	Number of growth/runs	Avg η	Max η
Modified	50°	150°	21	0.101 ± 0.018	0.136
Narrow cooling intervals	30°	50°	3	0.078 ± 0.007	0.087
Modified without anneal	50°	150°	2	0.109 ± 0.007	0.116

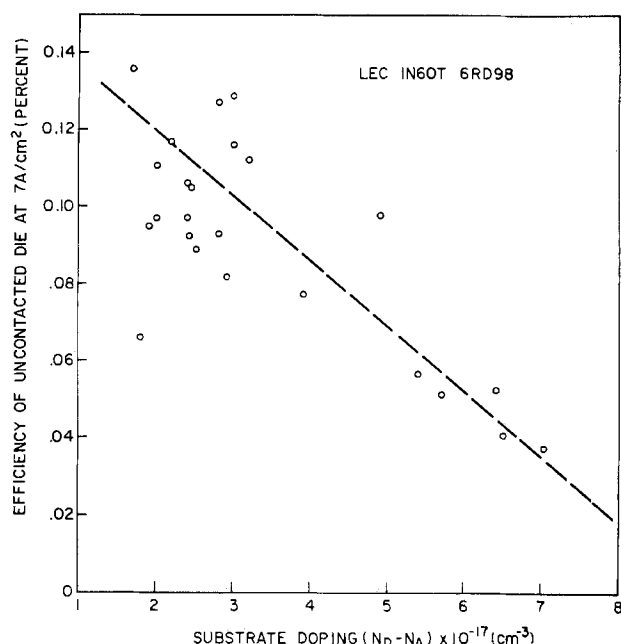


Fig. 3. Average electroluminescent efficiency of uncontacted die in air at 7 A/cm for junctions grown by the modified overcompensation procedure as a function of substrate doping density.

6Rd98. The generality of this effect in other growth systems and for other ingots is not known. However, a survey of p-n junctions previously grown in the Murray Hill crystal growth models laboratory uncovered a similar but less pronounced effect (18).

In an effort to determine the cause for the low efficiencies at higher LEC doping densities, optical absorption measurements were made on the LEC slices. An enhanced absorption of $\alpha \sim 10 \text{ cm}^{-1}$, was found at the energy of the green emission in the higher doped slices. However, the work of Joyce *et al.* (19, 20) indicates that this additional absorption alone can account for only part of the observed efficiency decrease. The minority carrier lifetimes in the LPE layers were generally found to be independent of substrate doping density.²

Minority carrier lifetimes and diffusion lengths.—A number of these high efficiency p-n junctions were characterized by a measurement of the minority carrier lifetimes and diffusion length. Table IV shows a summary of these parameters for four of these samples which ranged in efficiency from 0.136 to 0.077%. Typically the minority carrier lifetimes (τ_h) and diffusion lengths (L_h) in the n-layer near the junction range from 200–250 nsec and 6.5–8 μ , respectively. These values are significantly larger than $\tau_h \approx 100$ nsec and L_h which was typically found previously at the lowest doping levels used in the overcompensated junctions (1). Likewise in the p-layer $\tau_e = 120$ –180 nsec at the p-n junction with $L_e = 5$ –6 μ . Previously these parameters were ~ 40 nsec and 3.5–4 μ , respectively, at com-

² In an LEC ingot, the dislocation density often exceeds $1 \times 10^5 \text{ cm}^{-2}$ and increases from seed-to-tail which is the same direction as $N_d - N_a$ increases (21). Recently it has been shown that the efficiency becomes markedly reduced as the dislocation density becomes $> 2 \times 10^5 \text{ cm}^{-2}$ (22). Consequently we may speculate that this efficiency decrease is due to the effects of increasing dislocation density.

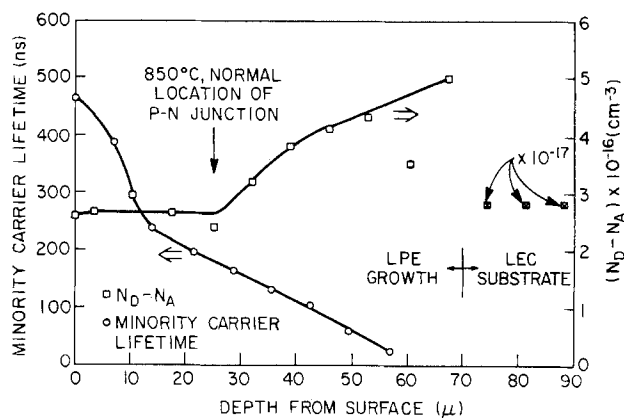


Fig. 4. Minority carrier lifetime and net donor concentration as a function of depth in a layer intentionally doped only with N.

parable doping densities (1, 2). Thus the present material has significantly longer lifetimes and diffusion lengths than the former material which are reflected by higher bulk efficiencies. The present increase in electroluminescent efficiency is a direct result of these longer lifetimes.

The lifetime measurements also revealed significant variations of τ with depth in the LPE layers. Figure 4 shows the spatial dependence of the minority carrier lifetime and the net donor concentration for an n-layer grown over the temperature interval 900°–700°C. This layer was grown with exactly the same growth procedure as that used for the modified p-n junctions except that no Zn was added to the melt. However, the interruption of the cooling at 850°C provided a doping discontinuity that was revealed by photoetching. Consequently, the location where the p-n junction would have been if Zn had been added was identifiable. In the first grown part of the layer near the n-LPE: n-LEC interface, the lifetime is quite short, < 100 nsec.

(Measurements of the minority carrier lifetime cannot be made closer than 3 diffusion lengths from a junction or a LPE-LEC interface.) At the normal location of the p-n junctions the lifetime has increased to (~ 150 –200 nsec) which is close to that typically measured on the n-side of a junction. However the lifetime increases rapidly from the 850°C location toward the surface (700°C) reaching a value of ~ 450 nsec at the surface. A similar spatial dependence of the lifetime was observed in all of the n-layers which were examined. Corresponding measurements in p-type material were more difficult as the layers were generally thinner (~ 30 –40 μ). However several thick layers were examined and they also showed an increase in lifetime from the initial growth region (850°C) toward the surface of the layer (700°C). The lifetimes were typically ~ 100 nsec near the junction and 200–250 nsec at the surface. The increase in lifetime with decreasing temperature most likely results from a general reduction in impurity incorporation or a decrease in the native defect, e.g., gallium vacancy (23), concentration.

In the former overcompensation process the p-n junction was formed at temperatures varying from 880° to 870° instead of the present 850°C. From Fig. 4,

Table IV. Representative minority carrier lifetimes and diffusion lengths

Sample	η (%)	$N_d - N_a$ (cm^{-3})	$N_a - N_d$ (cm^{-3})	L_e (μ)	L_h (μ)	τ_e (nsec)	τ_h (nsec)
1-594	0.136	6.0×10^{18}	4.2×10^{17}	5.9	6.8	125	250
1-603	0.097	1.7×10^{18}	6.0×10^{17}	5.3	7.9	—	210
1-617	0.129	7.6×10^{18}	1.1×10^{18}	4.8	6.8	185	200
1-600	0.077	3.3×10^{18}	5.3×10^{17}	5.5	6.6	85	110

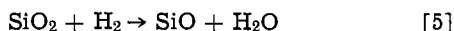
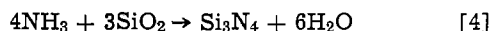
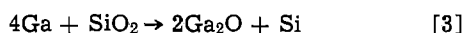
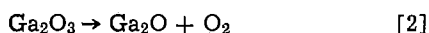
it can be deduced that this 20°-30°C temperature difference can result in lifetimes larger by as much as a factor of 2 for the 850°C junction. Consequently, it appears that the lower p-n junction formation temperature presently used is an important factor in the longer, near junction lifetimes measured in the n-layers. Likewise we feel that the longer lifetime in the p-layer is also largely due to the lower growth temperature used for p-growth.

Gas analysis.—A gas chromatograph has been used to monitor the impurity gases found in both the entrance and exit gases of the LPE growth system. The entrance gas, $H_2 + NH_3$, was found to contain less than 1 ppm O_2 . However, our gas chromatograph is unable to measure small concentrations of H_2O vapor. A direct measurement for H_2O using other instruments was not attempted due to many experimental difficulties at low concentrations (24). Thus any oxygen present as H_2O in either the entrance or exit gases is not detected.

Oxygen present in the LPE system during growth would be converted to H_2O by reacting with the ~ 1 atm of H_2 in the hot growth system



making a measurement of O_2 in the exit gas meaningless. However, the possibility of internally liberated oxygen from high temperature reactions such as



makes it desirable to obtain a measure of the oxygen in the exit gas during growth and not before or after growth with the system cold. Consequently, it was decided to make use of the reaction



and deduce the oxygen concentration from a measurement of the CO concentration. Thus a measure of the oxygen both from internally generated sources and $O_2 + H_2O$ in the entrance gases would be obtained. The graphite seed holder, which is dipped into the melt, was used as the source of C in reaction [6].

Using the free energies from the JANAF thermochemical tables (25), the ratio of equilibrium CO to H_2O partial pressures in 1 atm of H_2 is 37 at 925°C and 11 at 825°C. Thus, for temperatures $> 800^\circ C$ most of

the H_2O which is present would be converted to CO at equilibrium. However, because of the relative small amount of graphite (only the seed or source holder) which is present in the hot zone of the LPE growth system, it may be expected that much less than the equilibrium concentration of $O_2(H_2O)$ would be converted to CO, which in fact, is the case. When a much larger amount of graphite and lower flow rates were used, more, but still only a small fraction, of the $O_2(H_2O)$ was converted to CO. It appears that a much larger surface area of the graphite and perhaps improved gas flow patterns in the system would be required to approach equilibrium. Consequently, a measurement of the CO concentration in the exit gas provides a relative measure of the oxygen contamination only as long as the other experimental conditions are unchanged.

Figure 5 shows the concentration of CO in the exit gas as a function of time for growth run 2-579 which was a "modified" growth. Also indicated on the figure is the approximate melt temperature during the run. Data taken on several other modified LPE runs showed CO concentrations at corresponding times that were the same within a factor of 2. Thus, it is felt that these CO concentration data are representative for a typical LPE growth run in this system.

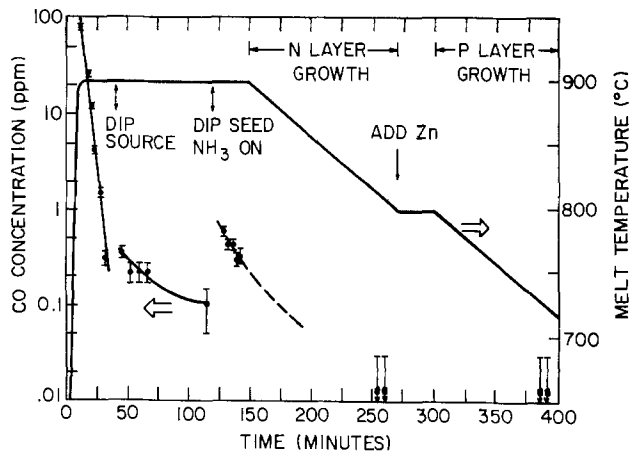


Fig. 5. Carbon monoxide concentration in the exit gas from the LPE growth system and the melt temperature as a function of time for a typical LPE growth run.

Immediately after heating the melt to the initial growth temperature, the CO concentration is quite high, over 100 ppm, and falls to less than 1 ppm in approximately a half hour. This large initial concentration of CO is attributed to outgassing of the melt and adsorbed O_2 or H_2O on the LPE system baking out and being partially converted to CO. A smaller increase in CO appears when the seed is lowered into the hot zone of the growth system and dipped into the melt. However, by the time LPE growth is initiated the CO concentration has dropped to ~ 0.2 to 0.3 ppm. As is discussed later, this CO concentration could represent up to several ppm of oxygen present in the LPE growth system during growth. The CO concentration decreases still further to a level below the limit of detectability (0.03 ppm) during growth. This continual decrease during growth is observed even when a constant oxygen concentration is added to the inlet gas. Thus this continual CO decrease during growth is attributed to a decreasing percentage of the oxygen being converted to CO as the temperature is lowered and not to a decreasing oxygen concentration in the LPE system.

Several standard LPE runs were made with small deliberate oxygen additions to the inlet gas stream while keeping all other experimental conditions the same. Figure 6 shows the resultant electroluminescent efficiencies and CO concentrations in the exit gas as a function of the oxygen addition to the inlet $H_2 + NH_3$ gas. The two data points at zero oxygen addition are the first and fifth (last) crystal growth runs in this series. The minority carrier lifetimes of the junctions grown with no and ~ 10 ppm O_2 additions were typical

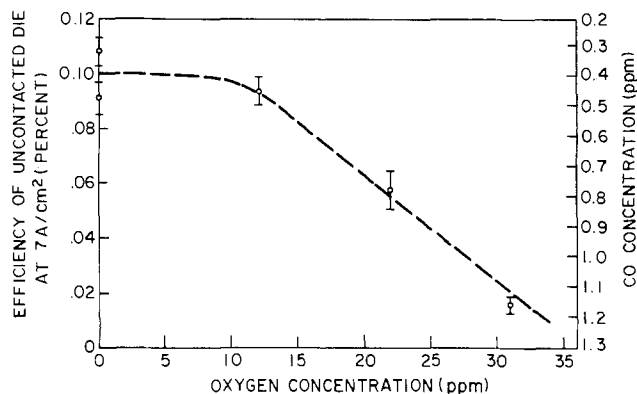


Fig. 6. Average efficiency of uncontacted die in air at 7 A/cm² and carbon monoxide concentration in the exit gas from the LPE system as a function of the oxygen concentration added to the inlet gas.

of those found in high efficiency diodes. The lifetimes in the junctions grown with > 10 ppm O_2 additions are significantly lower. The efficiency is essentially unaffected for oxygen additions < 10 ppm. This behavior

implies that an effective oxygen level up to ~ 10 ppm exists at all times in the growth system or that another nonradiative center is present in the GaP at levels such that a reduction in the oxygen below ~ 10 ppm is ineffective in increasing the efficiency. The CO concentrations shown in Fig. 6 are those measured during the early part of n-layer growth where the CO concentration should be most representative of the oxygen addition. The low CO concentrations compared to that expected from the oxygen additions are attributed to a large departure from thermodynamic equilibrium. For none and 12 ppm oxygen additions, 0.4 ppm of CO was observed in the exit gas which is within a factor of two of the data shown in Fig. 5. This implies that several ppm of O_2 may be present during a modified growth run. At higher concentrations of oxygen the CO concentration increases as expected.

These estimated levels are significantly larger than the O_2 concentration (< 1 ppm) measured in the $H_2 + NH_3$ entrance gas. Thus it appears that efforts to further improve the efficiency through reductions in the oxygen contamination will involve the elimination of small (a few ppm at the most) oxygen concentrations.

Conclusions

GaP green light emitting p-n junction material with quantum efficiencies for uncontacted diced diodes in air at 7 A/cm² of 0.101% has been reproducibly grown in a vertical dipping system using a modified over-compensation procedure. This represents a 60% efficiency increase from that previously obtained by over-compensation. Although the present results were obtained through the introduction of several modifications in the growth procedure, it was determined that a large cooling interval, 900°-700°C, with a corresponding decrease in the temperature at which the p-n junction was formed, was the single, most important modification. Epoxy encapsulated mesa diodes fabricated from some of the better p-n junction material had quantum efficiencies as high as 0.230% at ~ 5 A/cm² and 0.67% at ~ 300 A/cm². This low current efficiency is the highest observed to date while the high current value essentially equals the highest that has been previously measured by Ladany and Kressel (16).

A correlation between the EL quantum efficiency and the LEC doping density for p-n junctions grown on LEC ingot 6Rd98 was observed. The efficiency of uncontacted die decreased from ~ 0.1 to $\sim 0.04\%$ as the substrate doping level increased from 2 to 7×10^{17} cm⁻³. This decrease is likely due to the increased dislocation density in the LEC crystals which has been observed to accompany the increase in N_d-N_a within an ingot.

Minority carrier lifetime measurements as a function of depth revealed significant variations throughout the layers. The lifetime of the n-layers was typically ~ 200 nsec at the p-n junction and decreased toward the n-LPE-n-LEC junction. N-layers grown down in temperature to 700°C typically had lifetimes on the surface of 400-500 nsec. P-layers showed a similar lifetime variation of from ~ 200 nsec on the surface which decreased to ~ 100 nsec near the p-n junction. This general behavior of increasing lifetime with lower temperature of LPE growth suggests that one should form the p-n junction at a temperature even lower than the 850°C used in this study. Still longer near junction lifetimes which should be found would be reflected in a higher electroluminescent efficiency. However, the low solubility of P below 850°C makes LPE growth much below this temperature difficult.

An analysis of the exit gas from the LPE growth system showed that as much as ~ 5 ppm O_2 levels could be present in the LPE growth system during

growth. Deliberate additions of small oxygen concentrations to the inlet gas showed no change in efficiency or lifetimes for O_2 concentrations < 10 ppm. For concentrations > 10 ppm pronounced reductions in both the efficiency and lifetimes resulted. This is the first data that have shown quantitatively the effects of small O_2 additions on the quantum efficiency.

Acknowledgments

The authors are indebted to R. H. Saul and R. W. Dixon for valuable discussions and encouragement during the course of this work. We wish to thank S. E. Haszko and G. W. Kammlott for assistance with the SEM measurements. Thanks are also due to T. E. McGahan and L. B. Hooker for experimental assistance and to V. Wohlheiter for coating the quartz crucibles with Si_3N_4 . Discussions with M. E. Weiner on thermodynamic considerations were also much appreciated.

Manuscript submitted July 8, 1974; revised manuscript received Oct. 2, 1974.

Any discussion of this paper will appear in a Discussion Section to be published in the December 1975 JOURNAL. All discussions for the December 1975 Discussion Section should be submitted by Aug. 1, 1975.

Publication costs of this article were partially assisted by Bell Laboratories.

REFERENCES

- O. G. Lorimor, W. H. Hackett, Jr., and R. Z. Bachrach, *This Journal*, **120**, 1424 (1973).
- P. D. Dapkus, W. H. Hackett, O. G. Lorimor, G. W. Kammlott, and S. E. Haszko, *Appl. Phys. Letters*, **22**, 227 (1973).
- O. G. Lorimor, L. R. Dawson, R. Z. Bachrach, D. D. Roccasecca, and R. G. Sobers, *This Journal*, **118**, 292C (1971).
- R. A. Logan, H. G. White, and W. Wiegmann, *Solid State Electron.*, **14**, 55 (1971).
- N. E. Schumaker, R. Z. Bachrach, and P. D. Dapkus, Private communication.
- R. H. Saul and W. H. Hackett, Jr., *This Journal*, **117**, 921 (1970).
- R. H. Saul and W. H. Hackett, Jr., *J. Appl. Phys.*, **41**, 3554 (1970).
- E. C. Lightowers, J. C. North, and O. G. Lorimor *ibid.*, **45**, 2191 (1974).
- W. H. Hackett, Jr., O. G. Lorimor, and J. M. Ralston, Private communication.
- H. C. Casey, Jr., L. C. Luther, O. G. Lorimor, A. S. Jordan, and M. Kowalchik, *Solid State Electron.*, **15**, 617 (1972).
- T. E. McGahan and W. H. Hackett, Jr., *Rev. Sci. Instr.*, **41**, 1182 (1970).
- R. Z. Bachrach and O. G. Lorimor, *J. Appl. Phys.*, **43**, 500 (1972).
- W. H. Hackett, Jr., R. H. Saul, R. W. Dixon, and G. W. Kammlott, *ibid.*, **43**, 2857 (1972).
- C. H. Hartmann and K. P. Kimick, Pittsburgh Conference on Analytical Chemistry and Applied Spectroscopy, March 1965.
- D. D. Roccasecca, R. H. Saul, and O. G. Lorimor, *This Journal*, **121**, 962 (1974).
- I. Ladany and H. Kressel, *Proc. IEEE*, **60**, 1101 (1972).
- P. D. Dapkus, W. H. Hackett, Jr., W. B. Joyce, and O. G. Lorimor, Work in progress.
- R. H. Saul, Private communication.
- W. B. Joyce, R. W. Dixon, R. Z. Bachrach, and D. A. Sealer, *J. Appl. Phys.*, **45**, 2229 (1974).
- R. Z. Bachrach, W. B. Joyce, and R. W. Dixon, *ibid.*, **44**, 5458 (1973).
- S. F. Nygren, C. M. Ringel, and H. W. Verleur, *This Journal*, **118**, 306 (1971).
- W. A. Brantley, O. G. Lorimor, P. D. Dapkus, S. E. Haszko, and R. H. Saul, *J. Appl. Phys.* (Submitted).
- A. S. Jordan, A. Von Neida, R. Caruso, and C. K. Kim, *This Journal*, **121**, 153 (1974).
- H. S. Knight and F. T. Weiss, *Anal. Chem.*, **34**, 749 (1962).
- JANAF Thermochemical Tables, Published by the U.S. Department of Commerce, 1965.

Oxide Growth on Etched Silicon in Air at Room Temperature

S. I. Raider,* R. Flitsch, and M. J. Palmer

IBM System Products Division, East Fishkill Facility, Hopewell Junction, New York 12533

ABSTRACT

Oxide growth on etched silicon wafers at room temperature was studied as a function of etching procedure, wafer orientation, dopant concentration, and exposure to ultraviolet light. An impurity film was rapidly deposited on the silicon surface after etching with hydrofluoric acid. Impurity adsorption was distinguished from oxide growth by x-ray photoelectron spectroscopy (ESCA). The impurity film greatly reduced the initial oxide growth rate when compared with oxide growth on a cleaved silicon surface. The thickness of oxide films formed on etched surfaces was determined and compared using ESCA and ellipsometry.

The interaction of silicon with oxygen on atomically clean silicon surfaces has been described (1). The silicon surface for these studies is generally prepared in ultra-high vacuum at elevated temperatures. A related problem of practical importance in semiconductor processing is the growth of oxide films at room temperature on etched silicon single-crystal substrates (2-4). Ellipsometric measurements of film growth have been used to describe oxide growth kinetics on silicon after an initial film is rapidly formed (2, 4). Changes in ultra-thin film thickness were determined from ellipsometric data by employing the index of refraction of silicon dioxide and treating the films as oxides. These films were not characterized although Archer (2) noted that an impurity layer, which could be removed with organic solvents, was present in addition to an oxide film after exposure to air for 24 hr. Recent Auger studies of etched silicon surfaces also indicated the presence of both carbon and oxygen (5-8). The present work describes the growth rate of an oxide at room temperature for a silicon surface prepared by etching in HF and covered with adsorbates.

X-ray photoelectron spectroscopy, or ESCA (electron spectroscopy for chemical analysis), is used here to complement ellipsometric measurements of ultra-thin film formation on etched silicon surfaces. ESCA is particularly well suited as a technique for examination of oxide films $\leq 100\text{\AA}$ thick and can provide analytical and bonding data in terms of photoemitted electron line intensities and binding energies. The basis of the ESCA technique is the excitation of the electronic structure of an atom by x-rays and the analysis of the kinetic energies of the photoemitted electrons. The mean free paths of the monoenergetic, inelastically scattered photoelectrons are $< 30\text{\AA}$ in the 1 keV energy range. Contributions to a photoelectron line intensity decrease exponentially with distance from the film surface. Photoelectrons excited from core levels are mainly atomic in character but are subject to shifts in binding energy caused by the chemical environment of the atoms. By comparing ESCA and ellipsometric data, the films formed on etched silicon at room temperature are characterized and those factors which affect oxide growth are determined.

Experimental

Sample preparation.—Silicon dioxide films, 2000Å thick, were grown in dry oxygen at 1050°C on chem-mech polished silicon wafers. The substrates used were $\langle 100 \rangle$, p-type, 2 ohm-cm, although $\langle 111 \rangle$ orientations, n-type silicon and different resistivity wafers were also examined. The 2000Å films were generally etched at 25°C for 30 sec in freshly prepared HF diluted with an equal volume of deionized water. A variety of etching procedures were used in attempts to

reduce transfer of contaminants to the silicon surface and for comparisons with reported results. Pendant HF was removed either by rinsing in deionized water for about 10 min until the water resistivity reached 16 megohm-cm or by drying with nitrogen gas without solvent rinsing or by other procedures described below.

Film growth on etched silicon was allowed to occur in air in clean hoods in our oxidation laboratory. The temperature and relative humidity in this area remained at $25^\circ \pm 2^\circ\text{C}$ and 30-50%, respectively.

Impurities were adsorbed on sample surfaces either during processing or during exposure to the laboratory environment. Attempts were made to remove the adsorbed contaminants by rinsing in solvents or by heating at different temperatures in nitrogen gas. Oxidants in the nitrogen gas caused some modification of the oxides. Heating with quartz-iodine lamps in vacuum (10^{-7} Torr) reduced the level of surface contamination without modifying the oxides.

Oxide growth rates were determined using groups of wafers exposed to similar environments from which samples were randomly selected for examination by ellipsometry and ESCA. Etched wafers were stored either in metal containers, in plastic containers, or in deionized water. They were either exposed to room fluorescent lighting, 2537Å ultraviolet light (Mineralight, UltraViolet Products, Inc.), or were kept in the dark. Unless explicitly stated, wafers were exposed to air in the dark or in red filtered light. Etched wafers were split into halves and comparisons were made on the same wafer in studies of the effect of light on film growth rates. Cleaved samples were formed by fracturing 2 ohm-cm, p-silicon slugs, essentially along the $\langle 111 \rangle$ plane, either in air, deionized water, or deionized water containing 1% isopropanol.

Ellipsometry.—The thicknesses of films formed on silicon substrates were determined using a Rudolf ellipsometer. All data points were measured in two zones with the quarter-wave plate at 45.00°, at a wavelength of 5461Å and with an angle of incidence of 70.00°. For ultra-thin films on silicon substrates, the thicknesses were evaluated using the measured value of Δ and by assuming an index of refraction (n) of 1.47. A change in the imaginary part of the silicon refractive index [0.028 (9, 10)] affects the Δ value and, therefore, the ellipsometric film thickness value for a very thin oxide film; the real part of the index (4.076) will almost exclusively shift the Ψ value and not alter film thickness (11). An alternate value of 0.042 (12) has been assigned to the imaginary part of the silicon refractive index. Use of this value would decrease measured film thicknesses about 1.5Å.

Changes in ellipsometric measurements upon exposure of freshly prepared surfaces to air at 25°C in a darkened room indicated that film formation was occurring. The rate of impurity film growth on a 24Å

* Electrochemical Society Active Member.

Key words: native oxide, x-ray photoelectron spectroscopy (ESCA), ellipsometry, oxidation.

silicon dioxide film was about 0.05Å/min (assuming $n = 1.47$) during the first hour, followed by a much slower subsequent growth. Impurity film growth on freshly etched silicon, which rapidly formed about 7Å of film prior to the first ellipsometric measurement, was about 0.03Å/min during the first hour of exposure to air. Ellipsometer measurements were therefore made within 3 min after the surfaces were prepared.

ESCA.—ESCA has previously been described by Siegbahn *et al.* (13). An AEI photoelectron spectrometer with a magnesium anode in the x-ray source ($K\alpha_{12}$ radiation = 1253.6 eV) was employed in this work. About 10 to 20 min were required for preparing and mounting a sample of appropriate size and for evacuating the spectrometer sample chamber. Spectral data were obtained at a pressure of $<10^{-6}$ Torr from samples 0.2×0.5 in. A broad kinetic energy scan (1300 eV) of the sample was first obtained at 2 eV/sec. The kinetic energies of the photoelectron lines of interest were then scanned at a rate of 0.02 eV/sec. All data were referenced to the Au $4f^{7/2}$ line at 83.8 eV (14). The electron binding energies were determined to ± 0.1 eV by subtracting the kinetic energies of the emitted photoelectrons and a spectrometer correction from the energy of the incident x-rays; i.e.

$$E_b = E_{x\text{-ray}} - E_{\text{kinetic}} - E_{\text{spectrometer correction}}$$

The silicon dioxide binding energy data were corrected for a shift of +0.3 eV which was presumably due to charging (15). The magnitude of this shift was found to be independent of oxide thickness in the thickness range under consideration.

Estimates of the thickness of oxide films formed in air at room temperature were made from comparisons of photoelectron line intensities with intensity data extrapolations of O 1s and Si 2p photoelectron lines in silicon dioxide films oxidized at 850°C (16). The detection limit for an element decreases with film but is about 0.1 monolayer at the film surface. Therefore, trace impurities which might be observed in Auger and backscattering spectra after etching silicon are not detected by ESCA.

The carbon line, C 1s, was monitored on all samples examined. Wagner (17) has reported that the specific intensities of the O 1s and C 1s photoelectron lines are in the ratio of about 2:1. The number of carbon atoms in a given volume of amorphous carbon film is about twice the number of oxygen atoms in a similar volume of silicon dioxide film. A 10Å thick carbon impurity film, assumed to be amorphous carbon, contains $9.0\text{--}10.5 \times 10^{15}$ carbon atoms/cm³ whereas a 10Å thick silicon dioxide film contains about 4.5×10^{15} oxygen atoms/cm³. A carbon impurity film was therefore considered to be equal in thickness to an oxygen film with the same photoelectron line intensity.

Comparison of ellipsometric and ESCA measurements.—Reference oxide thicknesses were obtained from ellipsometric measurements of silicon dioxide films formed at 850°C by oxidation with 1% oxygen in nitrogen. The precision of these ellipsometric measurements is $\pm 1\text{Å}$.

Changes in ellipsometric data of oxides or etched silicon exposed to atmospheric pressure occur rapidly relative to changes in the ESCA spectra obtained in vacuum. Therefore, ellipsometric measurements of film thickness were made immediately after sample preparation and were followed with ESCA measurements on the same wafer. Discrepancies can exist with respect to the thickness of films and oxides formed on etched silicon at room temperature. These may be related to desorption of volatile surface contaminants in the ESCA vacuum chamber which contribute to the film thickness measured by ellipsometry and/or adsorption of organic impurities in the ESCA spectrometer.

Both techniques provide average measurements of macroscopic sample areas. Discontinuities in ultra-

thin oxide films formed a room temperature in the presence of surface contaminants generally cannot be discerned using these techniques. The consistency and reproducibility of the ESCA and ellipsometric data obtained, however, permit conclusions to be reached concerning oxide growth at room temperature, despite the small differences in measured film thicknesses.

Results and Discussion

Freshly etched silicon wafers.—Typical ESCA spectra of the elements observed on a thermally grown silicon dioxide film are shown in Fig. 1a and are compared in Fig. 1b with elements observed in the spectrum of a freshly etched 2 ohm-cm $<100>$ silicon wafer. The spectra indicate the presence of oxygen (O 1s), carbon (C 1s), and silicon (Si 2p) photoelectron lines with binding energies of 532.5, 284.3, and 99.3 eV, respectively. An additional Si 2p line found at 103.7 eV, which corresponds to silicon in the silicon dioxide film (Fig. 1a), is not detected in the etched silicon spectrum (Fig. 1b).

The contaminants always found in ESCA spectra of etched silicon surfaces are carbon and oxygen. Fluorine is present in the ESCA spectrum only if a sample is etched and dried without a deionized water rinse. No detectable difference in the ellipsometric film thickness 7–8Å is observed when the etched sample is immediately dried or first rinsed in deionized water for 10–15 min.

The O 1s and Si 2p oxide line intensities on etched silicon (Fig. 1b) indicate that the film thickness of 7.4Å measured by ellipsometry does not correspond to an oxide film thickness. By extrapolation from thermally grown silicon dioxide data to be described elsewhere (16), the O 1s line intensity in Fig. 1b corresponds to an oxide film $<2\text{Å}$ thick or $<10^{15}$ oxygen atoms/cm². This oxygen line may either be due to oxygen bound to silicon or is associated with oxygen in species adsorbed or incorporated in impurities on the etched surface. Little can be deduced from the oxygen binding energy since no significant O 1s shift is observed for the weak, broad line shown in Fig. 1b from the O 1s line in Fig. 1a.

Significant differences in the concentration of oxygen present on freshly etched silicon surfaces have been observed. Chang (8) has estimated, from Auger spectral line intensities, that $2\text{--}5 \times 10^{15}$ oxygen atoms/

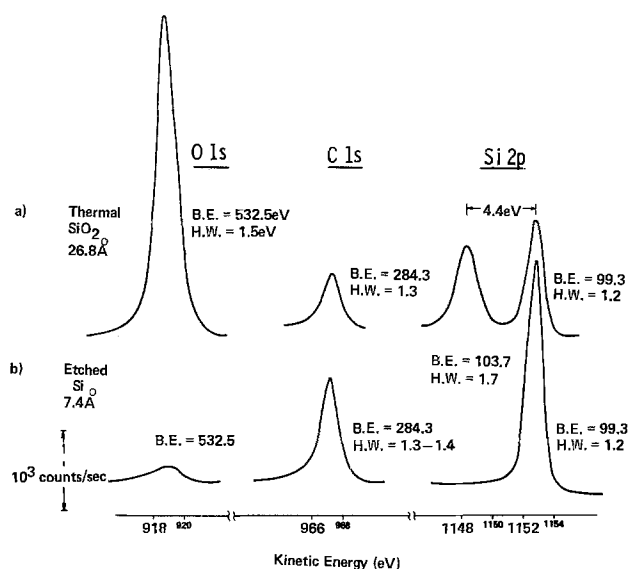


Fig. 1. Binding energies and relative line intensities for O 1s, C 1s, and Si 2p ESCA photoelectron lines (a) from silicon dioxide film grown at 850°C and (b) from a freshly etched silicon surface. Film thicknesses are determined by ellipsometry.

cm² are present on his etched, unheated silicon samples which is more oxygen than we observe with ESCA. Charig and Skinner (5) have published an Auger spectrum of unheated, cleaned silicon which appears nearly free of oxygen. We have repeated the etching procedure used by Charig and Skinner but no change was found in the result shown in Fig. 1b for the ESCA oxygen line intensity.

Carbon contamination on the etched silicon surface.—Carbon was always identified on all ESCA spectra. Particular attention was therefore given in an attempt to determine its source and its influence on the room temperature oxidation of etched silicon wafers.

Carbonaceous contaminants may be chemisorbed on our etched silicon samples, together with more volatile impurities, prior to insertion into the ESCA spectrometer. These contaminants contribute to the ellipsometric film thickness. Henderson (7) has observed that etching silicon with HF enhances carbon contamination and has suggested that the carbon impurity is co-deposited within the oxide phase during the etching step. Alternately, organic impurities may be exchanged with adsorbed HF at the etched silicon surface during the deionized water rinse. Other workers (8) have observed carbon contamination on etched silicon, even in oil-free vacuum systems, which suggests that a part of the carbon film may be transferred to the etched silicon samples prior to insertion into the ESCA spectrometer. In addition, carbon contamination may be attributed partly to oil backstreaming from the spectrometer vacuum pumps.

In order to reduce carbon contamination prior to insertion into the ESCA vacuum system, the silicon was etched in distilled HF solution, in distilled diluted (1:10) HF solution, in HF solution pretreated with crushed silicon to getter carbon (18), and in gaseous HF. The etched samples were either rinsed for 10 to 15 min in deionized water and then dried, immediately spun dry in a nitrogen ambient, immersed into distilled acetone to remove HF (2), or immediately rinsed in a carbon tetrachloride solution saturated with iodine. Very little change from samples etched in nondistilled HF, rinsed in deionized water, and dried in nitrogen gas was detected in most of the ESCA spectra. A small decrease in the carbon line intensity was observed when using the distilled acetone rinse. A decrease in ellipsometric thickness was also noted after rinsing in acetone (7.7–6.8Å) which is consistent with Archer's observations (2). Iodine was detected on the sample rinsed in carbon tetrachloride saturated with iodine in addition to the normally observed oxygen and carbon line intensities. The silicon bonding energy was unaffected by this rinse, but the oxygen line was shifted to a lower binding energy (532.0 eV) and the carbon was shifted to a higher binding energy (285.5 eV). The ellipsometric thicknesses of these films ranged from 30 to 40Å.

The ellipsometric film thicknesses of etched silicon were generally not changed by the different etching procedures used. It is not known whether these treatments had any effect on the carbon contamination present at the surface. Part of the nonvolatile carbon contamination on an oxide surface appears to originate from inside the spectrometer after the ellipsometric measurement is made. Transferring the sample in and out of the roughing pump insertion lock section of the spectrometer increases the ellipsometric film thickness. In addition, the sample is contaminated with carbon while in the ESCA vacuum chamber. On an etched silicon sample, an estimated carbon film thickness of 4.5–5.5Å (about $4-6 \times 10^{15}$ carbon atoms/cm²) is initially present, which increases to about 7Å after several hours in the ESCA vacuum chamber. Chang (8) has observed less carbon ($2-20 \times 10^{14}$ carbon atoms/cm²) in Auger spectra of etched, unheated silicon samples. Less carbon remains adsorbed under vacuum once an oxide surface is formed than on freshly etched silicon surface. After insertion into the ESCA spec-

trometer, a carbon film on an oxide surface is estimated at be 2–3Å thick initially and increases to about 5Å after 15 hr. The initial carbon film thickness can be reduced to about 1Å by minimizing the sample time in the roughing pump section of the insertion lock and by direct insertion into the ESCA vacuum chamber. A decrease of only about 1Å in carbon impurity level is detected by direct insertion of an etched silicon sample into the ESCA vacuum chamber. The additional carbon adsorbed during insertion into the spectrometer completely masked any improvements which may have been achieved by purification of the etchant or modifications of the etching procedure.

Oxidation and film growth on etched silicon surfaces.—Film growth on etched silicon wafers in air at 25°C exposed to room light was monitored both by ESCA and ellipsometry. Changes in the spectrum of the Si 2p line in the oxide with time are shown in Fig. 2 together with the corresponding ellipsometric changes in film thickness. The baseline of the silicon spectra is the spectrum of a freshly etched silicon surface. For comparison, the Si 2p line from a thermal oxide spectrum is shown in Fig. 2. The magnitudes of the shifts in the oxide binding energies from that of the silicon substrate binding energy, designated by δ , are given in Fig. 2. These shifts in binding energy will be discussed in a subsequent paper (19). The data for the increases in film thickness (ellipsometry) as a function of time on an etched silicon surface are summarized in Fig. 3 together with the estimated oxide thicknesses (ESCA). The initial oxide growth process as determined from ESCA spectra extrapolates back to the origin and has an oxide thickness dependency proportional to the logarithm of the oxidation time. Upon increasing the exposure time of the etched silicon surface to air, the intensity of the Si 2p oxide line is

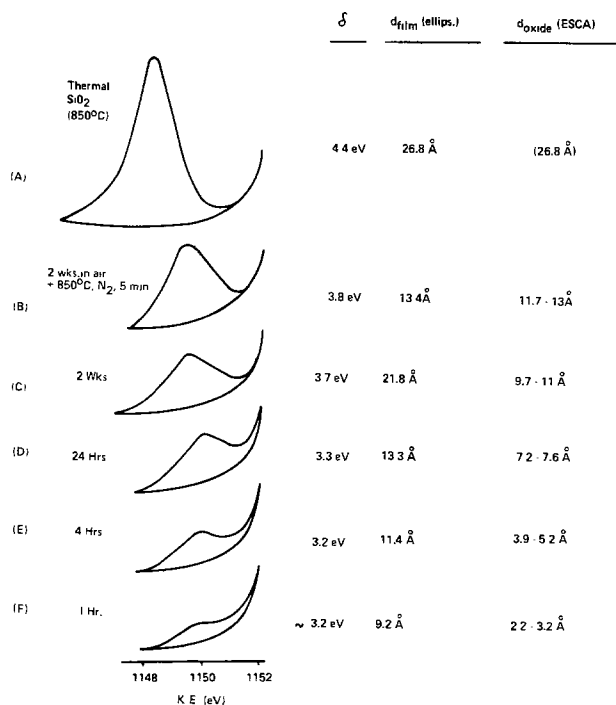


Fig. 2. Changes in the Si 2p oxide ESCA line as a function of exposure time to air at room temperature (samples C through E). The baselines correspond to the spectrum from a freshly etched silicon surface. Spectrum B is sample C exposed for 2 weeks to air followed by an anneal in nitrogen at 850°C for 5 min. Spectrum A is a silicon dioxide film 27Å thick grown in oxygen at 850°C. The difference in binding energies between the maxima of the Si 2p substrate and oxide lines are represented by δ values. The range in oxide thickness is based on estimates using both the Si 2p and O 1s line intensities.

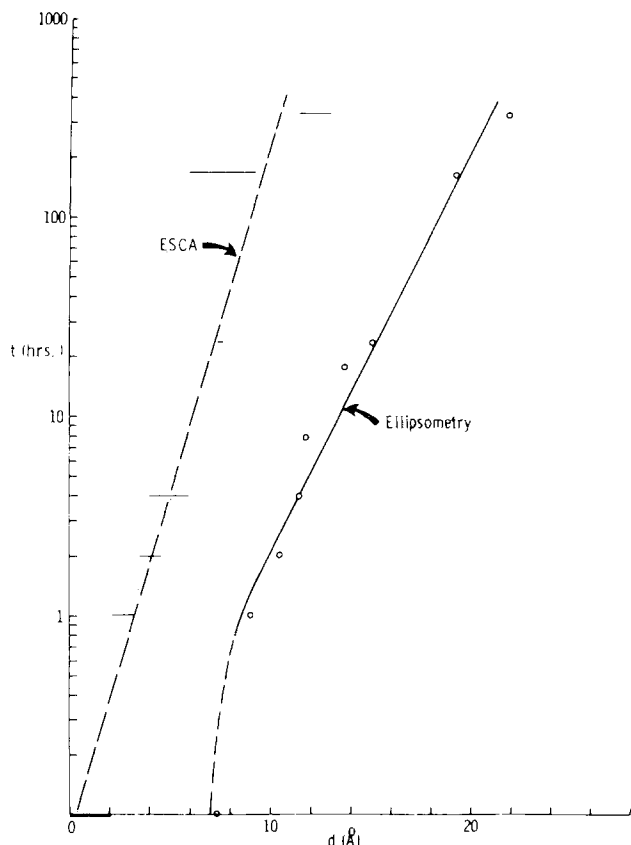


Fig. 3. Ellipsometric and ESCA thickness data plotted as a function of the logarithm of the time of exposure of etched samples to air at room temperature.

increased and its binding energy is shifted toward that of thermally grown oxide films. After exposure to air for 2 weeks, both the binding energy and the line intensity were still significantly different from that of the thermal oxide. After a 1 year exposure to air at room temperature, negligible additional change in the oxide binding energy or line intensity was observed. From this data and the cleavage experiments described below, an equilibrium oxide film thickness for oxide growth at room temperature in air is estimated to be $<14\text{\AA}$. This value is considerably lower than previous indications which were based on ellipsometric measurements (2,4).

Oxide growth and impurity adsorption occur simultaneously on etched silicon wafers during exposure to air at room temperature. The difference between an ellipsometric film thickness and estimated film thickness (ESCA) is often too large to be accounted for by nonstoichiometry or densification of the oxide film. Volatile contaminants are presumably adsorbed from air and desorbed in vacuum and contribute to increase the ellipsometric film thickness relative to the estimated ESCA film thickness.

Heating an oxide to 850°C for 5 min in nitrogen at 1 atm pressure was found to remove the adsorbed species from the oxide surface. Milder conditions were sought to remove the adsorbed contaminants from oxide surfaces formed in air at 25°C . Samples were rinsed in various solvents or heated to 200°C in nitrogen for 5 min. Although some scatter is observed, the results given in Table I are characteristic of the changes in ellipsometric film thickness found on different quarters of the same wafer as a function of sample treatment. Solvent rinses (aqueous, organic) reduce the film thickness. An additional decrease is observed by heating at 200°C . However, a significant additional decrease in adsorbed contaminants is obtained by heating the sample at 850°C . It has been reported (8) that a temperature of $>800^\circ\text{C}$ is required to remove the carbon adsorbed on silicon.

Table I. Effect of solvent rinses and heating on ellipsometric film thickness of films formed on etched silicon

	Etched Si, \AA	SiO_2 (thermal), \AA
t_0	7.2	27
Air; R.T.	18 (5 weeks)	33 (4 months)
Solvent rinse	17	30
200°C , N_2 , 5 min	16	—
850°C , N_2 , 5 min	12	27
	(ESCA: $d_{\text{oxide}} = 12$)	(ESCA: $d_{\text{SiO}_2} = 27$)

Closer agreement is obtained between ESCA and ellipsometry with regard to oxide thickness after heating the exposed etched samples at 850°C in nitrogen. For example, when the etched sample left in air for 5 weeks is heated at 850°C in nitrogen at 1 atm pressure for 5 min, a decrease in ellipsometric thickness from 18 to 12\AA is observed. A second example, shown in Fig. 2, indicates that the oxide film thickness (ESCA) increased due to oxygen impurities in the nitrogen gas stream (1-5 ppm) from 10 to 12\AA and a small increase in the silicon binding energy of 0.1 eV was detected. Negligible changes in the ESCA spectra were observed for exposed samples after heating at 850°C in vacuum for 15-20 min. The observed difference in binding energies between silicon dioxide and oxides formed in air at 25°C is not related to densification of the oxide film, since similar binding energies are not obtained even after heating at 850°C .

Oxidation of cleaved silicon surfaces.—Silicon single crystals cleaved in air form oxide films more rapidly than do etched silicon wafers. For example, the thinnest oxide film observed on a cleaved silicon surface was 5-7 \AA thick after 5-10 min exposure to air. This thickness was estimated from ESCA spectra taken 15-20 min after cleaving the sample. If exposure to air is increased about 10 min, the estimated oxide film thickness is 10-12 \AA . For comparison, etched silicon wafers with either $\langle 100 \rangle$ or $\langle 111 \rangle$ orientations possess oxide films only 2-3 \AA after 1 hr exposure to air. After 3 and 24 hr of exposure of the cleaved sample to air, the estimated oxide thickness is 11-13 \AA . Each of the cleaved samples exposed to air and then examined by ESCA contained carbon contamination on the silicon surface similar in thickness to carbon on etched oxide surfaces.

Cleavage of the silicon crystal either in deionized water or in deionized water containing an intentionally added organic impurity both significantly reduce the rate of oxidation on the clean surface even in the absence of HF. For example, a sample cleaved in deionized water containing 1% isopropanol, dried, and then examined by ESCA about 5-10 min after cleavage possessed an oxide film 1-2 \AA thick. The cleaved silicon oxidation results are summarized in Table II.

As is shown by the cleavage experiments, an oxide can readily grow on a clean silicon surface in air at room temperature. Etching in HF results either in HF or other impurities to be adsorbed on the silicon surface and reduce the rate of oxide growth. The adsorbed impurities provide a barrier to the initial oxidation of the etched silicon surfaces. Deionized water,

Table II. Oxide growth on cleaved silicon samples

Cleavage ambient	Exposure time (to ambient)	d_{ox} (estimated), \AA
Air	5-10 min	5-7
Air	20 min	10-12
Air	3 hr	11-12
Air	24 hr	11-13
DI H_2O	5-10 min*	3-4
1% isopropanol in DI H_2O	5-10 min*	1-2

* A 0.5-1 min exposure to aqueous media (to simulate HF etch step) followed by drying, mounting the sample on a holder, and insertion into the spectrometer. Temperature: 24°C .

which contains organic impurities in the ppm range, reduces the rate of oxide growth on cleaved samples with respect to air. Roikh *et al.* (20) have shown that water vapor in air increases the rate of oxidation of silicon at room temperature when compared with dry air. It is the presence of impurities on the sample surface or in the deionized water which limits the oxide growth rate on silicon rather than the reactivity of water with silicon at room temperature. Isopropanol (1%) in the deionized water further reduces, but does not eliminate, oxide growth.

Factors affecting oxide growth rates on etched silicon.—Oxide growth rates on etched silicon wafers at room temperature were examined by ellipsometry and ESCA as a function of wafer orientation, dopant type and concentration, exposure to ultraviolet light, and storage in deionized water. Typical ellipsometric data are shown in Fig. 4 for growth rates in air on p-type silicon surfaces. Ellipsometric results indicate that a freshly etched $\langle 111 \rangle$ oriented wafer surface possesses $\leq 5\text{\AA}$ of film. The ESCA spectra of these surfaces are identical and indicate the presence of $< 2\text{\AA}$ of oxide. The C 1s line intensities on $\langle 111 \rangle$ and $\langle 100 \rangle$ etched silicon surfaces are equal. After exposure to air in the dark (in a metal container), both ellipsometry and ESCA indicate that an oxide is forming somewhat more rapidly on the $\langle 111 \rangle$ surface than on the $\langle 100 \rangle$ surface. This initial difference in oxidation rate may be related to the difference in thickness of the impurity film adsorbed on the silicon surfaces in air.

The dopant concentration in the silicon substrate affects the oxidation of an etched silicon surface (21). Similar ellipsometric and ESCA results were obtained for growth on p-type (boron) and n-type (phosphorus) silicon wafers as a function of dopant concentration. Lightly doped ($\sim 5 \times 10^{14}/\text{cm}^3$) silicon wafers appear to exhibit the same film growth rate as do the 2 ohm-cm ($\sim 5 \times 10^{15}/\text{cm}^3$) wafers. However, heavily doped 10^{-3} ohm-cm silicon wafers with about 10^{20} dopant atoms/ cm^3 oxidize more readily than the 2 ohm-cm wafers. For example, freshly etched 10^{-3} ohm-cm wafers possess an ellipsometrically measured film 8.5-10Å thick and an estimated (ESCA) initial oxide thickness of 2-4Å. In contrast to the results of Ritter *et al.* (22) which indicated that an anomalously thick oxide layer formed in air on etched, p-type 10^{-2} ohm-cm silicon, p-type 10^{-2} ohm-cm

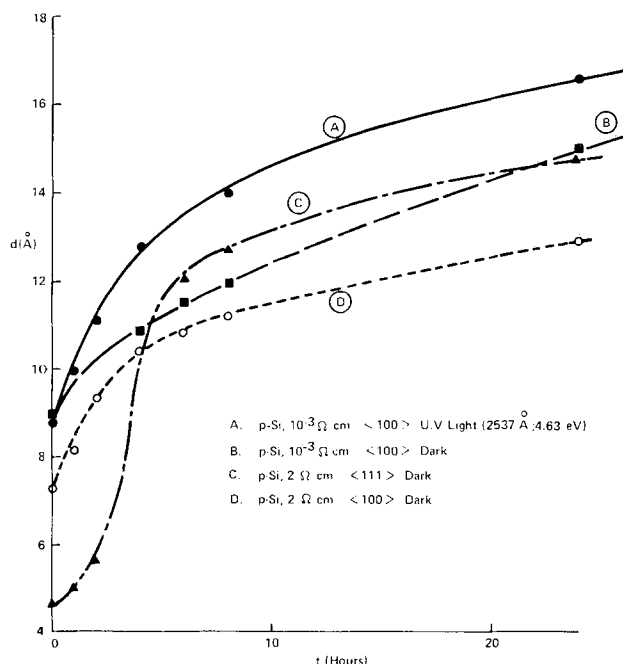


Fig. 4. Film growth rates on etched silicon wafers at room temperature measured by ellipsometry.

($10^{19}/\text{cm}^3$) silicon wafers exhibit an intermediate growth rate between that of 2 and 10^{-3} ohm-cm silicon. The rate of subsequent oxide growth in air is more rapid on the heavily doped silicon and is indicated by both ellipsometry and ESCA. It is suspected that differences in impurity adsorption on highly doped silicon surfaces and changes in the reactivity of the heavily doped silicon both contribute as causes for the enhanced oxidation.

Immersion of freshly etched silicon wafers into non-agitated, deionized water at room temperature generally reduced the rate of oxide growth when compared with growth in air. As previously indicated, oxidation of cleaved surfaces also occurs less readily in deionized water than in air. In a static system, the growth of an oxide film on an etched silicon wafer often proceeded at a normal rate only after an induction period. This induction period was occasionally observed for etched wafers immersed in deionized water or for rinsed wafers contained in a closed plastic container. For example, no changes in ellipsometric film thickness from the t_0 measurement were observed for a period of 6-10 hr for samples contained in a closed container. Once oxide growth was initiated, subsequent oxidation within the container occurred at a normal rate. When an etched wafer is rinsed in stirred deionized water, the rate of oxidation is increased. Bubbling nitrogen or oxygen gas through the deionized water also increased the rate of oxidation.

The etched silicon surface is hydrophobic due to the presence of Si-F bonds (23) or adsorbed HF. Covalent organic impurities, present in the deionized water in trace quantities, are preferentially adsorbed on the silicon as the HF goes into solution. These impurities apparently form a barrier film which inhibits aqueous oxidation of the silicon. Water or oxygen permeation into this barrier is enhanced by agitation of the system. Modification of the adsorbed barrier film by coadsorption of water or ionic species from solution can make the surface of the sample appear hydrophilic.

The frequency distribution of laboratory fluorescent lighting extends into the near ultraviolet. Exposure to this light accelerated the oxide growth rate on etched silicon when compared with oxide growth in the dark. The effect of ultraviolet light on oxide growth is shown in Fig. 4 using light with a wavelength of 2537Å. Irradiated films were compared with films grown in the dark after 3 weeks by ellipsometry and ESCA when an oxide has nearly reached its equilibrium thickness in air in the dark. Results in Table III indicate that both the total film and estimated oxide thicknesses are greater after exposure to ultraviolet light than after growth in the dark. The extent to which oxidation is modified by ultraviolet irradiation is much less than is indicated by ellipsometric measurements. The ESCA spectrum indicated that the exposed wafers possessed a significant increase in the thickness of the carbon impurity film on the oxide surface. Multiple carbon lines rather than the single carbon line normally observed suggested that the adsorbed carbon film was modified due to photolysis at the silicon surface. This result suggests that an organic film is present on the silicon surface prior to insertion into the ESCA spectrometer. The presence of ozone or heating of the wafer during exposure were experimen-

Table III. Effect of ultraviolet light on oxide growth in air

Technique	Measurement of	UV (2537Å), Å	Dark, Å
Ellipsometry	Total film thickness	44.5	17.8
ESCA	Estimated oxide thickness	15-16	11

Temperature, 25°C.
Exposure time: 3 weeks.

tally eliminated as possible causes for the increase in oxide thickness.

Cabrera (24) has reported that ultraviolet irradiation enhances the oxidation of aluminum and Oren and Ghandhi (25) have made similar observations for oxidation of silicon at elevated temperatures. However, Fehlner (26) has recently noted that ultraviolet irradiation of silicon under clean, dry conditions does not affect silicon oxidation. It remains to be determined whether our observations of the enhanced oxidation of silicon are related only to irradiation of silicon with ultraviolet light or to irradiation in the presence of impurities.

Summary

Impurities are rapidly adsorbed on moderately doped substrates after etching in HF. The film present on a freshly etched silicon surface and measured by ellipsometry is primarily an impurity film rather than an oxide film. A Si 2p oxide photoelectron line is not detected on a freshly etched silicon surface. The intensity of an oxygen photoelectron line for a substrate etched and then rinsed in deionized water indicates that $<2\text{\AA}>$ of oxide is present. A difference in surface behavior is observed between a freshly etched silicon wafer and an oxidized wafer. More carbon is initially adsorbed on an etched surface than on a surface with oxide present. It is likely that $<0.1>$ monolayer of silicon dioxide (detection limit of ESCA) forms on a freshly etched silicon surface rinsed in deionized water and exposed to air and that the oxygen detected in the ESCA spectra is largely from adsorbed oxidized impurities. Oxide film thicknesses on etched silicon surfaces, as well as oxide growth rates, are therefore overestimated by ellipsometry.

The initial oxide growth rates on etched silicon surfaces in air or water at room temperature are lower than on cleaved silicon surfaces. HF etching enhances the rate of impurity adsorption on a silicon surface relative to the rate of surface oxidation. An induction period is sometimes observed during which oxide growth does not occur on etched silicon but it is not observed once oxidation is initiated. The thickness of the impurity layer on etched silicon is decreased after oxidation is initiated and its effect on the rate of subsequent oxidation of silicon is also decreased.

A number of factors affect the rate of oxide growth on etched silicon at room temperature. An increased oxide growth rate is observed if the substrate dopant (n- or p-type) concentration is $\geq 10^{19}/\text{cm}^3$. The oxide growth rate in air is greater on $<111>$ oriented substrates than on $<100>$ surfaces. Ultraviolet light (2537Å) also increases the oxide growth rate in air. However, the major effect of ultraviolet irradiation is to increase the nature and film thickness of the carbon impurities at the silicon surface presumably by a mechanism different from that of adsorption in the dark. The equilibrium oxide thickness in air at room temperature is less than 14Å unless the substrate dopant concentration is greater than $10^{19}/\text{cm}^3$ or the substrate is exposed to u.v. light during oxidation.

Acknowledgments

We are grateful to F. W. Anderson, A. Berman, D. L. Klein, W. A. Pliskin, and B. H. Vromen for many helpful discussions.

Manuscript submitted April 1, 1974; revised manuscript received Oct. 14, 1974. Portions of this paper were presented as Paper 357RNP at the Miami Beach, Florida, Meeting of the Society, Oct. 8-13, 1972.

Any discussion of this paper will appear in a Discussion Section to be published in the December 1975 JOURNAL. All discussions for the December 1975 Discussion Section should be submitted by Aug. 1, 1975.

Publication costs of this article were partially assisted by IBM Corporation.

REFERENCES

1. B. A. Joyce and J. H. Neave, *Surface Sci.*, **27**, 499 (1971).
2. R. J. Archer, *This Journal*, **104**, 619 (1957).
3. J. T. Law, *J. Phys. Chem. Solids*, **4**, 91 (1958).
4. F. Lukes, *Surface Sci.*, **30**, 91 (1972).
5. J. M. Charig and D. K. Skinner, *ibid.*, **15**, 277 (1969).
6. B. A. Joyce, J. H. Neave, and B. E. Watts, *ibid.*, **15**, 1 (1969).
7. R. C. Henderson, *This Journal*, **114**, 772 (1972).
8. C. C. Chang, *Surface Sci.*, **23**, 283 (1970).
9. R. J. Archer, *J. Opt. Soc. Am.*, **52**, 970 (1962).
10. K. Vedam, W. Knausenberger, and F. Lukes, *ibid.*, **59**, 64 (1969).
11. Y. J. van der Meulen, *This Journal*, **119**, 530 (1972).
12. J. Shewchun and E. C. Rowe, *J. Appl. Phys.*, **41**, 4128 (1970).
13. K. Siegbahn, C. Nordling, A. Fehman, R. Nordberg, K. Hamrin, J. Hedman, G. Johansson, T. Bergman, S.-E. Karlsson, and I. Lindberg, "ESCA—Atomic, Molecular and Solid State Structure Studied by Means of Electron Spectroscopy," Almquist and Wiksells, Uppsala, Sweden (1967).
14. G. Johansson, J. Hedman, A. Berndtsson, M. Klasson, and R. Nilsson, *J. Electron Spectrosc.*, **2**, 295 (1973).
15. D. J. Hnatowich, J. Hudis, M. L. Perlman, and R. C. Ragaini, *J. Appl. Phys.*, **42**, 4883 (1971).
16. R. Flitsch and S. I. Raider, *J. Vacuum Sci. Technol.*, **12**, 299 (1975).
17. C. D. Wagner, *Anal. Chem.*, **44**, 1050 (1972).
18. A. Goodman, Private communication.
19. S. I. Raider and R. Flitsch, To be published.
20. I. L. Roikh, S. G. Belitskaya, and V. V. Ordynskaya, *Izv. Akad. Nauk SSSR*, **8**, 1525 (1972).
21. C. C. Chang and G. Quintana, *J. Elect. Spect. Rel. Phen.*, **2**, 363 (1973).
22. J. C. Ritter, M. N. Robinson, B. J. Faraday, and J. L. Hoover, *J. Phys. Chem. Solids*, **26**, 721 (1965).
23. R. K. Iler, "The Colloid Chemistry of Silica and Silicates," Cornell University Press, Ithaca, New York (1955).
24. N. Cabrera, *Rev. Met.*, **45**, 86 (1948); *Phil. Mag.*, **40**, 175 (1949).
25. R. Oren and S. K. Ghandhi, *J. Appl. Phys.*, **42**, 792 (1971).
26. F. P. Fehlner, *This Journal*, **119**, 1723 (1972).

Simple Theoretical Estimates of the Schottky Constants and Virtual-Enthalpies of Single Vacancy Formation in Zinc-Blende and Wurtzite Type Semiconductors

J. A. Van Vechten*¹

Bell Laboratories, Murray Hill, New Jersey 07974

ABSTRACT

Phillips and Van Vechten have shown that, because of the high valence electron density in diamond type semiconductors, their vacancies may properly be treated as macroscopic cavities. With this model one may estimate the enthalpy of neutral vacancy formation, $\Delta H(V^x)$, as simply the surface energy of the cavity. Values of $\Delta H(V^x)$ are known for Si and Ge and are 10% less than the theoretical estimates. Here this model is extended to zinc-blende and wurtzite type crystals. The virtual-enthalpies of formation $\Delta H(V_A^x)$ and $\Delta H(V_B^x)$ are calculated for 17 common semiconductors. Difficulties in analyzing empirical data which arise from the ionization of the vacancies and their interaction with other defects are noted. However, for CdS, where the data are adequate, the empirical values are about 12% less than those calculated.

Phillips and Van Vechten have noted (1,2) that the Wigner-Seitz atomic radius, r_w , is much greater than the inverse of the Thomas-Fermi screening wave number, k_s , in the diamond type semiconductors

$$k_s(\text{Si})r_w(\text{Si}) = 3.5, \quad k_s(\text{Ge})r_w(\text{Ge}) = 3.6 \quad [1]$$

Moreover, the surface energy of a metal, E_s , results from the spilling of electronic charge density into the vacuum, where it is not compensated by the positive charge of the ion cores, because the electronic wave functions cannot be abruptly terminated by a finite potential (3, 4). This spilled charge distribution decays as $\rho_0 \exp(-rk_s)$. One expects the range of effects which produce the surface energy of a semiconductor to be similar to or slightly shorter than in the case of a metal (1). Furthermore, because all the lattice sites of a diamond type crystal may be treated as equivalent sites, the macroscopic volume to be associated with a single atomic vacancy is exactly one atomic volume, Ω

$$\Omega = a^3/8 = 4\pi r_w^3/3 \quad [2]$$

where a is the lattice constant. Therefore, if the single vacancy is regarded as a macroscopic cavity of volume Ω , the range over which the surfaces of this cavity would seem poorly defined in a microscopic sense is small compared with the total dimensions of the vacancy. Thus, it was concluded that a single atomic vacancy in a diamond type semiconductor may properly be treated as a macroscopic cavity and the enthalpy of neutral vacancy formation, $\Delta H(V^x)$, may be estimated as its surface area times its surface energy

$$\Delta H(V^x) = \hat{A}E_s \quad [3]$$

To evaluate $\Delta H(V^x)$, one should note that the equilibrium shape of a cavity in a diamond type crystal is not a sphere, but an octahedron with only (111) surfaces, and that E_s is not isotropic (2, 5, 6). The enthalpy or internal energy per unit area of the (111) surfaces, $E_s(111)$, is less than that of any other surface. Thus, if the vacancy has the same equilibrium shape as a macroscopic cavity in the same material, we have

$$\Delta H(V^x) = \hat{A}_s E_s(111) \quad [4]$$

* Electrochemical Society Active Member.

¹ Present address: IBM Thomas J. Watson Research Center, Yorktown Heights, New York 10598.

² Note that the values quoted in Ref. (1) differ slightly from those in Eq. [13] because proper account was not made for the surface entropy.

Key words: defects, stoichiometry, nonradiative recombination, GaP, CdS.

where \hat{A}_s is the surface area of an octahedron of volume Ω

$$\hat{A}_s = 1.1826 \hat{A}_\alpha \quad [5]$$

and $\hat{A}_\alpha = 4\pi r_w^2$ is the area of the Wigner-Seitz sphere. It has been noted (2) that the observed Jahn-Teller distortion of V_{Si^x} and V_{Si^+} corroborates the assumption that its macroscopic shape is octahedral.

Gilman obtained an empirical estimate for $E_s(111)$ of Si from an irreversible crack-propagation experiment (7). However, similar experiments have not been reported for other semiconductors so it is necessary to make theoretical estimates. It was proposed (1, 2) that

$$E_s(\text{ijk}) = E_s^m(\text{ijk}) + E_s^b(\text{ijk}) \quad [6]$$

where $E_s^m(\text{ijk})$ is the contribution from long-ranged, metallic forces (3, 4) and $E_s^b(\text{ijk})$ is the contribution from short-ranged, directional covalent forces (8). [Note that the energy of the covalent bond is here reckoned as the extra cohesive energy of the covalent phase relative to the metallic phase of the same composition rather than as the total cohesive energy relative to free atoms (8). This covalent energy is calculated in the manner of Hume-Rothery by comparing the electronic band structures of the semiconducting and metallic phases.]

Because both theoretical and experimental values are available for the surface tension of liquid metals (3, 4), it seems wise to relate E_s^m to the surface tension and to test the proposed relation with the case of Si. It is assumed that $E_s^m(111)$ is just the surface enthalpy per unit area, H_s^l , of the metallic liquid phase of Si corrected for difference in density between the solid and liquid phases. The value of H_s^l is obtained from measurements of the surface tension, F_s^l , of the liquid, which is indeed the surface free energy per unit area

$$F_s^l = H_s^l - TS_s^l \quad [7]$$

where T denotes temperature and S_s^l is the surface entropy per unit area, $S_s^l = -dF_s^l/dT$. The generally accepted values for Si at $T^F = 1685^\circ\text{K}$ are $F_s^l(\text{Si}, T^F) = 734 \text{ erg/cm}^2$ and $S_s^l(\text{Si}, T^F) = 0.09 \text{ erg/cm}^2$ (9-11) so that $H_s^l(\text{Si}, 1685^\circ\text{K}) = 887 \text{ erg/cm}^2$. Taking the density of the liquid phase to be 15.3% greater than the solid (8) and the theoretical result that H_s^l vary as the $-5/6$ power with density, one estimates

$$E_s^m(111, \text{Si}) = H_s^l / (1.153)^{5/6} = 788 \text{ erg/cm}^2 \quad [8]$$

The contribution from short-ranged, directional covalent forces, $E_s^b(\text{ijk})$, to each of the two surfaces

formed as a crystal is cleaved is just

$$E_S^b(\text{ijk}) = N_S^b(\text{ijk}) E_b/2 \quad [9]$$

where $N_S^b(\text{ijk})$ is the number of broken bonds per unit area of (ijk) surface and $E_b = E_b(T)$ is the energy of each covalent bond relative to the metallic phase. [A rather complete discussion of $E_b(T)$ is given in Ref. (8) where calculated values are successfully compared with experiments.] For Si at 77°K, one finds

$$E_S^b(111, \text{Si}, 77^\circ\text{K}) = 116 \text{ erg/cm}^2 \quad [10]$$

so that the calculated value of the total (111) surface energy is

$$E_S(111) = 904 \text{ erg/cm}^2 \quad [11]$$

This value may be compared with Gilman's value, 1240 erg/cm², which should be an overestimate of the true value because it was obtained from an irreversible process (7). Because the source of this overestimate is the failure to allow for relaxation processes on the newly cleaved surfaces, a crude estimate of its magnitude would be that it is the same fraction of $E_S(111)$ as the Jahn-Teller relaxation is of $\Delta H(V_{\text{Si}^x})$. The Jahn-Teller relaxation energy for V_{Si^x} is roughly 1 eV (2), and the net value of $\Delta H(V_{\text{Si}^x}) \cong 2.4$ eV so, by this criterion, the true empirical value is $E_S(111) = 2.4 \times 1240/3.4 = 875$ erg/cm². Therefore, the agreement with theory is considered to be acceptable.

From the above considerations, one may estimate $\Delta H(V)$ for diamond type crystals as³

$$\Delta H(V^x, T) = \beta_8 E_S^m(111) + 4E_b(T) \quad [12]$$

if empirical values for E_S^1 are known as they are for Si and Ge (9-11). [Note that the factor 4 follows from the fact that there are four broken bonds about the vacancy and the full energy of the bonds must be ascribed to $\Delta H(V^x)$. One should also note that S_S^1 does not vary greatly from one liquid metal to another (10, 11).] For Si and Ge at their respective melting points one calculates

$$\Delta H(V_{\text{Si}^x}, T^F) = 2.66 \text{ eV}, \quad \Delta H(V_{\text{Ga}^x}, T^F) = 2.21 \text{ eV} \quad [13]$$

Empirical values may be obtained from quenching experiments (12-14). However, one should take proper account of the ionization state of the vacancies at high temperatures and of the finite quenching rate when these experiments are analyzed (15-17). The empirical values are

$$\Delta H(V_{\text{Si}^x}) = 2.4 \pm 0.2 \text{ eV}, \quad \Delta H(V_{\text{Ga}^x}) = 2.0 \pm 0.2 \text{ eV} \quad [14]$$

so that this macroscopic model seems to overestimate the true values of $\Delta H(V^x)$ by about 10%.⁴ One should expect such an overestimate to occur because the charge density spilling into the vacancy cavity will overlap along the edges and at the apexes. Thus, these portions of the surface should have a lower energy than the corresponding free surfaces at infinite separation.

³ Note that $\Delta H(V^x)$ refers to the process in which one lattice site is added to the crystal so that an atom from the bulk moves to the surface leaving a neutral vacancy in the bulk and causing the sample to expand by one atomic volume. No atom is removed to the vapor in this process, which is commonly denoted $\text{O} = V^x$. [See Kröger (15), p. 313.]

⁴ As the creation of a vacancy produces four broken bonds about the vacant site and as there are twice as many bonds as atoms in the Si structure, it is often noted that Pauling's notion of the additivity of bond energies would lead one to estimate $\Delta H(V^x)$ as twice the heat of atomization or for Si, 9.3 eV. This is far more than the observed values which generally run between 0.5 and 1.0 times the heat of atomization for most materials. In the present discussion the bond energy E_b is far less than half the heat of atomization because it denotes only the energy resulting from the short-ranged, directional covalent forces. [See Ref. (8).] Of course, there is no direct relation between $\Delta H(V^x)$ and the heat of atomization because the vacancy creation process does not involve removing an atom from the sample, but it is worth noting that the relaxation of atomic positions concomitant with the establishment of the equilibrium shape of the vacancy cavity corresponds to a substantial reduction in the long-range contributions to $\Delta H(V^x)$ from the value that would obtain in an unrelaxed lattice. See the discussion of the Jahn-Teller distortion in Ref. (2).

Extension of Theory to Zinc-Blende and Wurtzite Crystals

The lattice constants of GaAs, ZnSe, and CuBr are nearly the same as that of Ge because all these elements occur in the same row of the periodic table (18). For this reason they have nearly the same valence electron density, bulk, and surface plasmon frequencies. Therefore, the use of the macroscopic model to treat vacancies in zinc-blende or wurtzite type crystals is as well justified as its use with diamond type crystals.

Because zinc-blende and wurtzite crystals will contain both anion and cation vacancies, V_B and V_A , one must establish some criterion for the relative size of these two species. It is here assumed that the dimensions of a vacancy cavity are proportional to the tetrahedral covalent radius, r_c , of the relevant element according to the table of Van Vechten and Phillips (18). Then by simple geometry, one finds the effective Wigner-Seitz radius of A is

$$r_w(A) = (16/\pi\sqrt{3})^{1/3} r_c(A) = 1.433 r_c(A) \quad [15]$$

Then the area of, for example, an octahedral cavity of appropriate size may be calculated using Eq. [5].

At this point we may make a qualitative observation about the agreement of theory with experiment. Consider the relative energy of neutral cation and anion vacancies which may be discussed in terms of their virtual-enthalpies of formation, $\Delta H(V_A^x)$ and $\Delta H(V_B^x)$. [We recognize that only the Schottky constant enthalpy

$$H_S(\text{AB}) = \Delta H(V_A^x) + \Delta H(V_B^x) \quad [16]$$

is a true enthalpy defined in terms of a true chemical potential, but that it is both permissible and convenient to calculate the virtual-enthalpies of vacancies in these compound crystals in a manner analogous to that used with elemental crystals. These virtual-enthalpies are then used in the proper structure element analysis of the thermodynamics of compounds developed by Kröger, Stieltjes, and Vink (19).⁵ Because there is only one type of bond in these AB crystals, the short-range or broken bond contribution is the same to $\Delta H(V_A^x)$ as to $\Delta H(V_B^x)$. Therefore, the difference between the two is only in the long-range contribution, $\beta_8 E_S^m(111)$ of Eq. [12], which is proportional to r_w^2 . Thus, the present theory predicts that $\Delta H(V^x)$ will be larger for the component with the larger r_c .

If differences in the enthalpies of ionization, $\Delta H_I(V_A^-)$ and $\Delta H_I(V_B^+)$, and of the activities in the liquid or vapor phase are neglected, then the ionized vacancies of the smaller element should be more numerous at the maximum of the solidus. Thus, by considering only vacancy contributions to the defect induced extrinsic carrier concentration of undoped material, one predicts the material to be n-type if $r_c(A) > r_c(B)$ and to be p-type if $r_c(A) < r_c(B)$. In Table I are listed the carrier types and radius ratios of the II-VI compounds. It is commonly believed that the carrier type that may be obtained in these compounds is limited by a vacancy self-compensation mechanism, although antistructure defects, A_B^- or B_A^+ , may also be important. [See the accompanying paper (23).] In any event, the comparison in Table I shows perfect agreement between prediction and observation.⁶ The same correlation occurs in III-V crystals although most of these can be doped to either type with impurities; undoped GaSb is p-type, while GaP and GaN are n-type. The author knows of no exception to this rule.

⁵ Note that real values have been measured for the virtual-enthalpies in several virtual reactions in some alkali-halide and silver-halide crystals. See Ref. (20-22).

⁶ A similar correlation was observed by Mandel (24) who used Pauling's table of covalent radii and ascribed the cause to differences in ΔH_I for V_A and V_B . However, that hypothesis was discredited by Kröger (25), and the correlation was not exact. The latter point is further evidence for the superiority of the table of covalent radii in Ref. (18) over the earlier table of Pauling when these are applied to semiconductors.

Table I.

Compound AB	$r_c(A)/r_c(B)$	Conductivity type
ZnO	1.81	n only
CdS	1.25	n only
CdSe	1.15	n only
ZnS	1.09	n only
ZnSe	1.00	n + p
CdTe	1.00	n + p
MgTe	0.93	p only
ZnTe	0.87	p only
BeTe	0.69	p only

In order to make quantitative estimates of $\Delta H(V^x)$, one must determine the shape of the vacancy cavity and the value of the appropriate surface energy. In contrast to diamond, Si and Ge, the equilibrium shape of zinc-blende type crystals is in general the rhombohedral-dodecahedron, which has only (110) surfaces. It is commonly assumed that this distinction results from the fact that the unreconstructed (110) surface has an equal number of anion and cation surface atoms whereas unreconstructed (111) [and (100)] surfaces have only one type of surface atom. Therefore, it seems likely that the distinction between diamond and zinc-blende equilibrium shapes results from Coulomb interactions across several unit cells of surface atoms that would not be operative on the surfaces of a neutral vacancy. Furthermore, the author is unaware of any determination of the Jahn-Teller distortion about V_A^x or V_B^x in a zinc-blende crystal which could serve to settle the question of the shape of the cavity, but the geometry of the lattice seems to favor the octahedral shape of vacancies in Si and Ge (2). Finally, there seems to be no measurements of $E_S(110)$ for zinc-blende crystals like those of Gilman for Si $E_S(111)$ (7), so that it is not possible to test any proposed relation between F_S^1 and $E_S(110)$ as was done for $E_S(111)$ in Eq. [11]. Due to the above considerations, it is here assumed that V_A^x and V_B^x have the same octahedral shape as V_{Si}^x and V_{Ge}^x and that the same relation holds between the surface tension of the stoichiometric liquid, $F_S^1(A_{0.5}B_{0.5})$, and the effective $E_S(111,AB)$ on the surface of the V_A^x or V_B^x cavity.

Thus, we have

$$\begin{aligned} \Delta H(V_A^x) &= \bar{f}_S(A) E_S^m(111) + 4E_b(AB) \\ \Delta H(V_B^x) &= \bar{f}_S(B) E_S^m(111) + 4E_b(AB) \end{aligned} \quad [17]$$

where $\bar{f}_R(A)$ and $\bar{f}_S(B)$ are defined in terms of $r_c(A)$ and $r_c(B)$ by Eq. [5] and [15]. Values of E_S^m are here calculated using the theory of Schmit and Lucas to calculate H_S^1 with the same parameters for the surface plasmon cutoff (3, 4) and of the change in density upon melting and S_S^1 as are observed for Si. (Schmit and Lucas calculated H_S^1 for 53 metals within 15% of experiment.) The resulting values are shown in Table II.

In Table II, calculated values are also shown for the surface tension of the stoichiometric liquid at T^F , $F_S^1(A_{0.5}B_{0.5}, T^F)$. Although it would seem to be easily possible to measure F_S^1 using the method of Sugden (26, 27), only a few measurements have been reported (28, 29) and these generally refer to a nonstoichiometric liquid which is in equilibrium with the solid under some convenient growth condition. Thus, for example, the calculated value for $F_S^1(Al_{0.5}Sb_{0.5}, 1353^\circ K) = 531$ erg/cm² cannot be compared with the reported value, 480 erg/cm² (28), until more information about the experiment is supplied.

Although the values in Table II are appropriate for the crystal at T^F , the variation of the calculated values with temperature is not large. This is because the coefficients of thermal expansion of these crystals are so small that the electron density varies less than 2%. Thus, the dominant term, $\bar{f}_S E_S^m$, varies less than 2%. The temperature variation of the covalent term, $4E_b(T)$, is given in Ref. (8).

Comparison with Experiment

The analysis required to determine $\Delta H(V_A^x)$ and $\Delta H(V_B^x)$ from experimental data is rather more involved than that required to determine $\Delta H(V^x)$ for elemental semiconductors (15-17). As with Si and Ge, one must take account of the ionization state of both types of vacancies at the high temperature, T_h , at which an equilibrium is established and of the escape and agglomeration of these vacancies during the finite time required to cool the sample from T_h to the temperature where measurements are made. As with V_{Si} and V_{Ge} , both V_A and V_B may be expected to form complexes with impurities, C_A and C_B , during the quench so that any ionization energies observed at low temperature must be ascribed to C_A and C_B rather than to V_A and V_B . [The ionization energies $\Delta H_I(V_A^-)$ and $\Delta H(V_B^+)$, etc., can only be determined if simple, single vacancies can be produced near $T = 0^\circ K$ as by electron irradiation.]

The problem of analyzing the data for AB crystals is worse than that with elemental semiconductors because one should expect the vacancies to interact with antisite defects, A_B and B_A (23). If the crystal is grown off-stoichiometry, say with an excess of A, then the excess may be accommodated in the lattice as V_B or A_B or interstitial A_i . It seems that the concentration of interstitials [A_i] is significant only for elements of valence $Z_A = 1$, i.e., the alkali and noble metal impurities. Elements with $Z_A = 2$ may occur as interstitials in a concentration sufficient to affect atomic diffusion but they are more commonly found on substitutional sites(30). Except for cases like O in Si where a compound is formed, [A_i] is negligible when $Z_A > 2$. However, the virtual enthalpies of formation of antisite defects, $\Delta H(A_B^x)$ or $\Delta H(B_A^x)$, are comparable with $\Delta H(V_B^x)$ and $\Delta H(V_A^x)$ (23). Moreover,

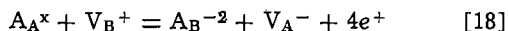
Table II.

Compound AB	$r_w(A)$ A	$r_w(B)$ A	T^F °K	$H_S^1(AB)$ calc, erg/cm ²	$F_S^1(A_{0.5}B_{0.5}, T^F)$ calc, erg/cm ²	$\bar{f}_S(A)E_S^m(111)$, eV	$\bar{f}_S(B)E_S^m(111)$, eV	$4E_b(T^F)$, eV	$\Delta H(V_A^x)$, eV	$\Delta H(V_B^x)$, eV
SiC	1.680	1.109	2810	1546	1290	3.59	1.57	1.35	4.94	2.92
AlAs	1.762	1.755	2013	814	631	2.08	2.07	0.68	2.76	2.75
AlSb	1.762	2.013	1535	654	531	1.67	2.18	0.63	2.30	2.81
GaN	1.755	1.030	2791*	1428	1174	3.62	1.25	1.48	5.10	2.73
GaP	1.755	1.616	1740	879	721	2.23	1.89	0.75	2.98	2.64
GaAs	1.755	1.755	1511	802	664	2.03	2.03	0.56	2.59	2.59
GaSb	1.755	2.013	985	659	569	1.67	2.20	0.36	2.03	2.56
InP	2.013	1.616	1343	731	609	2.44	1.57	0.60	3.04	2.17
InAs	2.013	1.755	1216	681	570	2.27	1.73	0.34	2.61	2.07
InSb	2.013	2.013	809	571	497	1.91	1.91	0.21	2.12	2.12
ZnO	1.755	0.971	1975	1369	1189	3.47	1.06	1.94	5.41	3.00
ZnS	1.755	1.615	2196	896	696	2.27	1.93	1.20	3.47	3.13
ZnSe	1.755	1.755	1788	797	634	2.02	2.02	1.07	3.09	3.09
ZnTe	1.755	2.013	1563	666	524	1.70	2.22	0.84	2.54	3.60
CdS	2.013	1.615	1825	738	572	2.46	1.59	1.10	3.56	2.69
CdSe	2.013	1.755	1512	669	531	2.23	1.70	0.95	3.18	2.65
CdTe	2.013	2.013	1365	570	446	1.90	1.90	0.85	2.75	2.75

* Calculated in Ref. (8).

while V_B acts as a donor, A_B will be an acceptor so that the two native defects resulting from an excess of A will compensate each other.

The charge compensation of V_B^+ with A_B^- or A_B^{-2} will occur not only at T_h but also as the sample cools. At T_h the equilibrium concentrations of neutral vacancies $[V_B^x]$ and neutral antisite defects $[A_B^x]$ will be different functions of the partial vapor pressures, P_A and P_B , over the sample (31). However, as the sample is cooled the equilibrium with the vapor is broken and vacancies and antisite defects may be interchanged by reactions of the type



which will occur every time a vacancy migrates to a nearest neighbor site.

$[V_B^+]$ and $[A_B^-]$, $[A_B^{-2}]$, etc., will always be affected by the position of the Fermi level, E_F . They may interact through the charge compensation mechanism to keep the E_F in the gap even though the deviation from stoichiometry may be significant. The author proposes that this effect is the resolution of the paradox that deviations from stoichiometry in GaP produce electrically active "shunt-path killer centers" although they have little effect on the carrier concentration either at T_h or at room temperature (32).

To the author's knowledge, the only case for which adequate information has been obtained to determine $\Delta H(V_A^x)$ and $\Delta H(V_B^x)$ properly is that of CdS (33). Kumar and Kröger have concluded that $\Delta H_S(\text{CdS}) \approx 5.6$ eV while an analysis of their data similar to that illustrated for GaP in the following paper (23) implies $\Delta H(V_{Ca}^x) \approx 3.15$ eV and $\Delta H(V_S^x) \approx 2.45$ eV. These values may be compared with the present theory, Table II, $\Delta H_S(\text{CdS}) = 6.25$ eV, $\Delta H(V_{Ca}^x) = 3.56$ eV and $\Delta H(V_S^x) = 2.69$ eV. We see that the theoretical values are about 12% greater than the empirical values in each case. This compares very favorably with the 10% theoretical overestimate found for $\Delta H(V_{Si}^x)$ and $\Delta H(V_{Ge}^x)$ in Eq. [13] and [14].

We should expect all of the theoretical estimates in Table II to be comparably reliable, i.e., 5-20% overestimates, and far more reliable than estimates made by fitting data with a naive van't Hoff plot that neglects ionization states, escape, and interactions.

Added Note

After completion of this work the author was made aware of detailed studies of the surface tension of liquid GaSb (34) and liquid InSb (35) as a function of composition and temperature. For the 50% Ga-50% Sb liquid 10°K above T^F , the apparent values are: $F_S^l = 454$ erg/cm²; $S_S^l = 0.112$ erg/cm² deg.; $H_S^l = 566$ erg/cm². These values differ somewhat from those assumed in the present calculation and would imply $\Delta H(V_{Ga}^x) = 1.79$ eV and $\Delta H(V_{Sb}^x) = 2.25$ eV, which are 10% less than the values in Table II.

Within the Schmit-Lucas theory (3, 4), one may expect H_S^l to be less for a partially ionized liquid than for an elemental liquid of the same valence electron density because interband transitions would be more effective in cutting off the plasmons. However, the magnitude of this effect may not be as large (10%) as the apparent experimental values suggest. It was found that F_S^l varies a factor of 2 across the Ga-Sb composition range so that one should expect the composition of the surface to deviate from that of the bulk in such a way as to minimize the free energy of the system. Furthermore, an unexplained peak in $F_S^l(x)$ is found at the 50% composition.

The situation in liquid InSb is similar to that in GaSb and the discrepancy between apparent values of F_S^l and Table II are somewhat less. However, the data on the temperature variation, which is required to obtain S_S^l and H_S^l , is not sufficiently accurate to discuss a correction.

The author is indebted to Dr. A. S. Jordan for bringing this data to his attention.

Manuscript submitted May 14, 1974; revised manuscript received Sept. 9, 1974.

Any discussion of this paper will appear in a Discussion Section to be published in the December 1975 JOURNAL. All discussions for the December 1975 Discussion Section should be submitted by Aug. 1, 1975.

Publication costs of this article were partially assisted by Bell Laboratories.

REFERENCES

1. J. C. Phillips and J. A. Van Vechten, *Phys. Rev. Letters*, **30**, 220 (1973).
2. J. A. Van Vechten, *Phys. Rev. B*, **10**, 1482 (1974).
3. J. Schmit and A. A. Lucas, *Solid State Comm.*, **11**, 415, 419 (1972).
4. J. Schmit and A. A. Lucas, *Collect. Phen.*, **1**, 127 (1973). See also J. Harris and R. O. Jones, *Phys. Letters*, **46A**, 407 (1974).
5. C. Herring, in "Structure and Properties of Solid Surfaces," G. Gomer and C. S. Smith, Editors, p. 5 and especially pp. 24-30, University of Chicago Press, Chicago (1953).
6. R. A. Swalin, "Thermodynamics of Solids," p. 223, Wiley-Interscience, New York (1972).
7. J. J. Gilman, *J. Appl. Phys.*, **31**, 2208 (1960).
8. J. A. Van Vechten, *Phys. Rev. B*, **7**, 1479 (1973).
9. B. N. Oscherin, *Izv. Akad. Nauk. SSSR Neorgan. Materialy*, **6**, 1165 (1970) (Trans: *Inorganic Materials*, **6**, 1014 (1970)).
10. O. A. Timofeevicheva and P. P. Pugachevich, *Dokl. Akad. Nauk SSSR*, **124**, 1093 (1959).
11. J. R. Carruthers, Private communication.
12. R. A. Logan, *Phys. Rev.*, **101**, 1455 (1956).
13. A. Hiraki, *J. Phys. Soc. Japan*, **21**, 34 (1966).
14. L. Elstner and W. Kamprath, *Phys. Status Solidi*, **22**, 541 (1967).
15. F. A. Kröger, "The Chemistry of Imperfect Crystals," p. 325, North Holland, Amsterdam (1964).
16. R. R. Hasiguti and S. Motomiya, in "Radiation Effects in Semiconductors," J. W. Corbett and G. D. Watkins, Editors, p. 39, Gordon and Breach, London (1971).
17. J. A. Van Vechten and C. D. Thurmond, To be published.
18. J. A. Van Vechten and J. C. Phillips, *Phys. Rev. B*, **2**, 2160 (1970).
19. F. A. Kröger, F. H. Stieltjes, and H. J. Vink, *Philips Res. Rept.*, **14**, 557 (1959).
20. R. W. Davidge, *Phys. Status Solidi*, **3**, 1851 (1963).
21. K. L. Kliewer, *J. Phys. Chem. Solids*, **27**, 705 (1966).
22. K. L. Kliewer and L. S. Koehler, *Phys. Rev.*, **157**, 685 (1967).
23. J. A. Van Vechten, *This Journal*, **122**, 000 (1975).
24. G. Mandel, *Phys. Rev.*, **134**, A1073 (1964).
25. F. A. Kröger, *J. Phys. Chem. Solids*, **26**, 1717 (1965).
26. S. Sugden, *J. Chem. Soc.*, **121**, 858 (1922).
27. P. P. Pugachevich and V. B. Lazarev, *Russian J. Phys. Chem.*, **34**, 1228 (1960).
28. B. N. Oscherin, *Izv. Akad. Nauk SSSR Neorgan. Materialy*, **6**, 1165 (1970).
29. M. Ya. Dashevskii, G. V. Kukuladze, V. B. Lazarev, and M. S. Mirgalovskaya, in "Growth of Crystals," Vol. 8, p. 85, Consultants Bureau, New York (1969).
30. H. C. Casey, Jr., in "Atomic Diffusion in Semiconductors," D. Shaw, Editor, p. 351, Plenum Press, London (1973).
31. F. A. Kröger and H. J. Vink, in "Solid State Physics," Vol. 3, p. 307, F. Seitz and D. Turnbull, Editors, Academic Press, New York (1956).
32. A. S. Jordan, A. Von Neida, R. Caruso, and C. K. Kim, *This Journal*, **121**, 153 (1974).
33. V. Kumar and F. A. Kröger, *J. Solid State Chem.*, **3**, 387 (1971).
34. M. Ya. Dashevskii, G. V. Kukuladze, V. B. Lazarev, and M. S. Mirgalovskii, *Izv. Akad. Nauk SSSR Neorgan. Materialy*, **3**, 1561 (1967), (Trans: *Inorganic Materials*, **3**, 1360 (1967)).
35. V. B. Lazarev and M. Ya. Dashevskii, *ibid.*, **1**, 1901 (1965) (Trans: *ibid.*, **1**, 1720 (1965)).

Simple Theoretical Estimates of the Enthalpy of Antistructure Pair Formation and Virtual-Enthalpies of Isolated Antisite Defects in Zinc-Blende and Wurtzite Type Semiconductors

J. A. Van Vechten^{*1}

Bell Laboratories, Murray Hill, New Jersey 07974

ABSTRACT

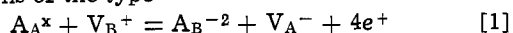
The few theoretical treatments which have been successful in predicting the thermodynamic parameters of substitutional impurities are examined for their implications regarding antisite defects, B_A or A_B , and antistructure pairs, B_AA_B in AB semiconductors. All such theories predict a large concentration of $B_AA_B^x$, especially in III-V's. All predict that B_A^+ or B_A^{+2} and A_B^- or A_B^{-2} should be important to the properties of III-V's. Results of the Phillips-Van Vechten dielectric two-band model are presented for 23 common semiconductors. These are combined with results for vacancies in the accompanying paper to give a detailed account of native defects in GaP both during crystal growth and as the sample cools. The existence curve is calculated and compared with experiment. The interaction between vacancies and antisite defects is invoked to explain why deviations from stoichiometry have slight effects on carrier concentration but large effects on luminescent efficiency.

An antisite defect in a compound crystal, AB, may be an atom of element A which occupies an anion (B-type) lattice site, A_B , or a B-atom which occupies a cation (A-type) lattice site, B_A . (It seems that the terms "antisite" and "antistructure" are used interchangeably in the literature.) An antistructure pair, B_AA_B , would result from interchanging two nearest neighboring atoms in the perfect zinc-blende or wurtzite structure.

Although these defects have always been enumerated among the varieties of native defects in the standard text books (1, 2), the author has been unable to find any previous estimates of the enthalpy changes in the crystal concomitant with their formation.

However, A_B and B_A may be viewed as special cases of substitutional impurities in the AB crystal. A few theoretical treatments of the thermodynamics of substitutional impurities and of their distribution coefficients have been presented which achieve reasonable success in semiconductors (3-6). Therefore, the author here applies preexisting theory for impurities, particularly that of the dielectric two-band model developed by Phillips and Van Vechten (7-9), to the antistructure defect problem.

Despite the fact that appreciable concentrations of antisite defects (10, 11) and, in particular, antistructure pairs (12, 13) have been reported in several materials, it seems that they are often ignored when experimentalists seek to analyze their data. It is shown that there is no basis in theory for the assumption that antistructure defects may be neglected in III-V and SiC crystals. Moreover, the insensitivity of carrier concentration to significant deviations from stoichiometry (14, 15) may be explained in terms of compensation between vacancies and antisite defects which may occur both at the growth temperature, T_h , and during the cooling of the sample. It is noted that vacancies may be converted to antisite defect-vacancy complexes by reactions of the type



which will occur every time a vacancy migrates to a nearest neighbor site. (The superscript x denotes the

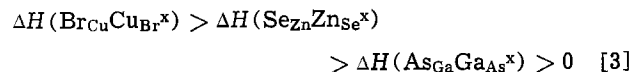
neutral state of the species.) Such an explanation resolves some paradoxes that arise if one assumes that deviations from stoichiometry may result only from differences in the concentrations of anion and cation vacancies, $[V_B]$ and $[V_A]$. An example of this would be the case of the "shunt-path killer centers" in GaP (14, 15).

Neutral Antistructure Pairs

The enthalpy and entropy of formation of a neutral antistructure pair, $\Delta H(B_AA_B^x)$ and $\Delta S(B_AA_B^x)$, are defined by the reaction



corresponding to the interchange of the two atoms in a unit cell of the crystal. Obviously, $\Delta H(B_AA_B^x)$ and $\Delta S(B_AA_B^x)$ are both zero for elemental crystals like Si and Ge. One would expect their values to be roughly proportional to the ionicity of the compound or the electronegativity difference between A and B (4, 7-9, 16). Thus one should expect, for example



It is easy to estimate $\Delta H(B_AA_B^x)$ using Pauling's table of elemental electronegativities, X_A and X_B , and his rules for the heat of formation of covalent bonds (16). The formula for either the zinc-blende or the wurtzite structure is

$$\Delta H(B_AA_B^x) = 6(X_A - X_B)^2 Z(A)/4 \text{ eV} \quad [4]$$

where $Z(A)$ is the valence of the cation. The factor $Z(A)/4$ appears because, according to Pauling, there are $Z(A)$ bonds "resonating" among 4 ligands to the nearest neighboring atoms. The factor 6 appears because 6 of the 7 A-B ligands attached to these two atoms are replaced by 3 A-A ligands and 3 B-B ligands.

The values obtained from Eq. [4] are presented in Table I, where they are compared with values calculated using the dielectric two-band model (4, 7-9) and treating $B_AA_B^x$ as a pair of impurities, B_A and A_B . In this model one considers two contributions to the excess heat of mixing, $\Delta H(I_x A_{1-x} B)$, of a substitu-

^{*} Electrochemical Society Active Member.

¹ Present address: IBM Thomas J. Watson Research Center, Yorktown Heights, New York 10598.

Key words: defects, stoichiometry, nonradiative recombination, GaP, CdS.

Table I.

Crystal AB	$\Delta H(\text{B}_A\text{A}_B^x)$ Pauling, eV	$\Delta H(\text{B}_A\text{A}_B^x)$ Van Vech- ten, eV	Crystal AB	$\Delta H(\text{B}_A\text{A}_B^x)$ Pauling, eV	$\Delta H(\text{B}_A\text{A}_B^x)$ Van Vech- ten, eV
SiC	2.21	0.89	InN	7.61	5.53
BN	4.50	1.98	InP	0.72	1.30
BP	0.05	0.24	InAs	0.41	0.90
BA _s	0.00	0.12	InSb	0.18	0.54
AlN	10.13	5.06	ZnO	10.83	11.40
AlP	1.62	1.11	ZnS	2.43	3.19
AlAs	1.13	0.74	ZnSe	1.92	2.51
AlSb	0.72	0.38	ZnTe	0.75	1.74
GaN	8.82	4.77	CdS	1.92	3.34
GaP	1.13	1.06	CdSe	1.47	2.67
GaAs	0.72	0.70	CdTe	0.48	1.87
GaSb	0.41	0.40			

tional impurity, I, on the A sublattice of the AB host crystal at a mole-fraction concentration x (4)

$$\Delta H(\text{I}_x\text{A}_{1-x}\text{B}) = \Delta H_0(\text{I}_x\text{A}_{1-x}\text{B}) + \Delta H_e(\text{I}_x\text{A}_{1-x}\text{B}) \quad [5]$$

The contribution ΔH_0 is that produced by the reduction of the various optical bandgaps, which results from the disorder of the crystal potential concomitant with alloying. These bandgaps are a measure of the separation of valence electron wave functions into bonding (valence band) states and antibonding (conduction band) states so that their reduction reduces the covalent bonding contribution to the cohesive energy of the material. A predictive theory for this effect has been published and compared with optical data for a wide range of pseudobinary alloys (17, 18). The comparison of this theory with empirical liquidus and solidus curves is given in Ref. (4-6).

The second term in Eq. [5], $\Delta H_e(\text{I}_x\text{A}_{1-x}\text{B})$, is the contribution produced by the effect of the excess or deficit of electrons contributed to the crystal due to the difference in valence between I and the atom it replaces, A in this case. Thus

$$\Delta H_e(\text{I}_x\text{A}_{1-x}\text{B}) = [I](E_F - H_V)(Z(I) - Z(A)) \quad [6]$$

for donor impurities, $Z(I) > Z(A)$, or

$$\Delta H_e(\text{I}_x\text{A}_{1-x}\text{B}) = [I](H_C - E_F)(Z(A) - Z(I)) \quad [7]$$

for acceptor impurities, $Z(I) < Z(A)$ and with corresponding formulas for $\Delta H_e(\text{AB}_{1-x}\text{I}_x)$. In Eq. [6] and [7], $E_F - H_V$ and $H_C - E_F$ denote the enthalpy differences between the Fermi level and the valence and conduction bands, respectively. In obtaining Eq. [6] and [7], it was assumed (4) that, under the conditions for which equilibrium is obtained while growing the crystal, the dominate ionization state of the impurity had charge $-e(Z(I) - Z(A))$. Thus, the distribution coefficients calculated in this way were those of the fully ionized species; if the neutral state is the dominate species during growth, then $\Delta H(\text{I}_x\text{A}_{1-x}\text{B})$ will not contain this contribution and the distribution coefficient for the neutral species would be calculated (4).

Because the nearest neighbor antistructure pair B_AA_B^x is neutral within the unit cell, it clearly should be treated as a neutral complex with the corresponding $\Delta H_e = 0$. Thus, for the dielectric two-band model

$$\Delta H(\text{B}_A\text{A}_B^x) = \lim_{x \rightarrow 0} ((\Delta H_0(\text{B}_x\text{A}_{1-x}\text{B}) + \Delta H_0(\text{AB}_{1-x}\text{A}_x))/x) \quad [8]$$

Comparing the value calculated with Eq. [8] with those of Pauling's theory, Eq. [4], in Table I, we see that there are significant differences in the estimates for several compounds, but general agreement as to the over-all magnitude of $\Delta H(\text{B}_A\text{A}_B^x)$. For SiC, all the III-V's except GaN, and several II-VI's, both estimates of $\Delta H(\text{B}_A\text{A}_B^x)$ are substantially less than the Schottky constant enthalpy for vacancy pairs or even the virtual-enthalpy of single vacancy formation (19, 20). Therefore, both theories predict that the antistructure pair will be the most common native defect in stoichiometric material.

One may ask if there is any viable theory which predicts substantially larger values for $\Delta H(\text{B}_A\text{A}_B^x)$ in these materials. The answer seems to be no. The theory of Stringfellow (5, 6) makes the same separation as that at Eq. [5] for the separation of the excess heat of mixing into one contribution, ΔH_e , due to the excess or deficit of electrons provided by I and one other contribution, ΔH_0 , due to other effects. Stringfellow treats ΔH_e , in effectively the same manner as Ref. (4) so his $\Delta H_e = 0$ for B_AA_B^x also. Rather than calculating the optical spectrum of the alloy and deducing ΔH_0 therefrom, Stringfellow estimates this contribution from the lattice strain resulting from the difference in covalent radius between I and the atom it replaces. (He uses Pauling's table of tetrahedral covalent radii.) Under those assumptions the estimates of $\Delta H(\text{B}_A\text{A}_B^x)$ are much less than either of those in Table I. For example, one obtains $\Delta H(\text{As}_{\text{Ga}}\text{GaAs}^x) = 0.008$ eV and $\Delta H(\text{C}_{\text{Si}}\text{SiC}) = 0.16$. As such values are implausibly small, one concludes that Stringfellow's treatment should be restricted to pseudobinary alloys and single donor or acceptors, as he has done (6, 7).

Weiser also separated the excess heat of mixing into two contributions (3), ΔH_s and ΔH_b . The term ΔH_s is a lattice strain term of the same general magnitude as Stringfellow's ΔH_0 , although it is calculated differently. The term ΔH_b resulted from the difference between the unstrained bond energies of A-B bonds and either I-B or B-I bonds. Thus, when applied to the antistructure pairs, this term should be the heat of formation of the A-B bonds, just as with Pauling's theory, Eq. [4]. Therefore, Weiser's theory yields values only slightly larger than those listed for Pauling in Table I.

Having concluded that all reasonable estimates of $\Delta H(\text{B}_A\text{A}_B^x)$ are small, let us take the case of GaAs, for which both the dielectric theory and Pauling's theory agree that $\Delta H(\text{As}_{\text{Ga}}\text{GaAs}^x) \approx 0.70$ eV, and consider the experimental evidence. If we assume that

$$\Delta S(\text{B}_A\text{A}_B^x) = 0 \quad [9]$$

then the equilibrium concentration of these antistructure defects would be $2 \times 10^{19}/\text{cm}^3$ at 1100°K and 2×10^{15} at 500°K. However, because they are neutral within the unit cell, they should not be prominent in the luminescence or absorption spectra and will not effect the carrier concentration. It seems that the first report and tentative identification of a concentration, $[\text{As}_{\text{Ga}}\text{GaAs}] \approx 5 \times 10^{19}/\text{cm}^3$, was made by Goldstein and Almeleh in 1963 on the basis of electron paramagnetic resonance (EPR) studies (12). Blanc, Bube, and Weisberg made a very good case for this identification and magnitude of concentration with a series of thermally stimulated current, photo- and dark-Hall effect, thermal conductivity, absolute density, and lattice constant experiments in 1964 (13). Furthermore, it is observed that the mobility of high resistivity GaAs is about an order of magnitude less than can be accounted from analysis (21, 22) of the known impurity concentrations and the band structure, which is firmly established. The $\text{As}_{\text{Ga}}\text{GaAs}^x$ defect should be expected to have a small cross section for electron scattering so that $[\text{As}_{\text{Ga}}\text{GaAs}^x] \approx 2 \times 10^{19}/\text{cm}^3$ would easily account for this discrepancy. Indeed, the theory of van Roosbroeck and Casey for transport in the relaxation regime (23) requires a large concentration of neutral defects to successfully account for observations on high resistivity GaAs (23, 24).

Because the masses of Ga and As are so similar, one should not expect $\text{As}_{\text{Ga}}\text{GaAs}^x$ to produce a local phonon mode, which would be observed in the infrared spectrum. However, for GaP one would expect $\text{P}_{\text{Ga}}\text{GaP}^x$ to produce three local modes, one about 24 cm^{-1} above the optic modes and two in the gap between optic and acoustic modes (25). The infrared spectrum of GaP contains several such features which have never been firmly identified.

Isolated Antisite Defects

One would expect the isolated antisite defects B_A and A_B to act as donors and acceptors, respectively. While they might be fairly deep in SiC, in III-V and II-VI compounds they will probably be multiply ionizable with the first level comparable with the effective mass value. Therefore, in intrinsic GaAs the dominant charge states of the isolated antisite defects are most likely As^{+2} and Ga^{-2} .

The neutral antistructure pair $As_{Ga}Ga_{As}^x$, which was discussed in the previous section, may be thought of as the nearest neighbor bound pair of As_{Ga}^{+2} and Ga_{As}^{-2} . The binding energy of such a pair, ΔH_{BA} as defined by the reaction $B_A^{+\Delta Z} + A_B^{-\Delta Z} = B_A A_B^x$, ΔH_{BA} , where $\Delta Z = Z(B) - Z(A)$, might be approximated as the electrostatic energy of the ions on the unperturbed lattice

$$\Delta H_{BA} = -\Delta Z^2 e^2 / r_0 \tilde{\epsilon}(r_0) \quad [10]$$

where e is the charge of the electron, r_0 is the normal bond length (nearest neighbor distance), and $\tilde{\epsilon}(r_0)$ is value of the spacial dielectric function at r_0 . Calculations of $\tilde{\epsilon}(r)$ find that it is approaching the optical dielectric constant (the square of the index of refraction), $\epsilon(\infty)$, as r approaches the normal bond length, r_0 , but its value is changing rapidly with r at this point (26, 27). Therefore, although $4e^2/r\epsilon(\infty) = 2.2$ eV for GaAs would be a firm lower limit for the magnitude of $-\Delta H_{BA}$, substantially larger values are also quite plausible.

Because of the uncertainty involved in the evaluation of Eq. [10], as well as the question of the adequacy of the approximation that there is no lattice distortion or central cell correction, it seems wise to continue to rely on the theory for substitutional impurities which was found successful in predicting alloy phase diagrams and distribution coefficients (4-6). According to the theories of Stringfellow and of Van Vechten

$$-\Delta H_{BA} = \Delta H_e(B_A^{+\Delta Z}) + \Delta H_e(A_B^{-\Delta Z}) \quad [11]$$

where $\Delta H_e(B_A^{+\Delta Z})$ and $\Delta H_e(A_B^{-\Delta Z})$ are just the electronic contributions to the excess heat of mixing, Eq. [6] and [7], per defect

$$\Delta H_e(B_A^{+\Delta Z}) = \Delta Z(E_F - H_v) \quad [12]$$

$$\Delta H_e(A_B^{-\Delta Z}) = \Delta Z(H_c - E_F) \quad [13]$$

(It appears that the quantities ΔH_e in Eq. [12] and [13] are contributions to the virtual-enthalpies of the corresponding structural units rather than to true enthalpies defined by true chemical potentials. However, as shown by Kröger, Stieltjes, and Vink, this procedure is both permissible and convenient as long as they are always used in combinations corresponding to real processes (28)².) With Eq. [12] and [13], Eq. [11] reduces to

$$-\Delta H_{BA} = \Delta Z H_{cv} \quad [14]$$

where H_{cv} is the enthalpy of the forbidden bandgap at the appropriate temperature. For GaAs at high temperatures, one estimates $-\Delta H_{AsGa}(As_{Ga}Ga_{As}) = 3.0$ eV in this way as compared with 2.2 eV obtained by using $\epsilon(\infty)$ for $\tilde{\epsilon}(r)$ in Eq. [10].

Now the total virtual-enthalpy of an isolated antisite defect will be

$$\begin{aligned} \Delta H(B_A^{+\Delta Z}) &= \Delta H_0(B_A) + \Delta H_e(B_A^{+\Delta Z}) \\ \Delta H(A_B^{-\Delta Z}) &= \Delta H_0(A_B) + \Delta H_e(A_B^{-\Delta Z}) \end{aligned} \quad [15]$$

Because ΔH_e is generally much larger than ΔH_0 , one predicts that antistructure pairs, $B_A A_B$, will be much more numerous than either isolated defect B_A or A_B in stoichiometric material.

² Note that real values have been measured for the virtual-enthalpies in several virtual reactions in some alkali-halide and silver-halide crystals. See Ref. (29-31).

The values of $\Delta H_0(B_A)$ and $\Delta H_0(A_B)$ calculated with the dielectric two-band model are given in Table II. In order to obtain ΔH_e , one must know ΔH_{cv} and E_F . The value of ΔH_{cv} at T_h , the temperature of the equilibration, may be deduced from the values (9) of the forbidden bandgap at $T = 0$, $\Delta E_{cv}(0)$, and the variation with temperature of this free energy (32, 33). The value of E_F must be deduced from the condition of neutrality and by considering the ionization of all species present.

Comparison with Experiment

One will note in Table II that the virtual-enthalpy to place an atom on the site of a larger atom is found to be less than the virtual-enthalpy to place the larger atom on the site of the smaller atom. Thus, $\Delta H_0(S_{Zn}) < \Delta H_0(Zn_S)$ and $\Delta H_0(Te_{Zn}) > \Delta H_0(Zn_{Te})$, for example. Because S_{Zn} and Te_{Zn} are donors while Zn_S and Zn_{Te} are acceptors, this effect will produce a tendency toward n-type conductivity in cases for which $r_c(A) > r_c(B)$ and toward p-type conductivity in case for which $r_c(A) < r_c(B)$. (Here, r_c is the tetrahedral covalent radius.) It is shown in the accompanying paper (20) that the virtual-enthalpies of single vacancy formation produce the same tendency to correlate anion to cation radius ratio with normal (undoped) conductivity type and that, if the Van Vechten-Phillips table of tetrahedral covalent radii (34) is used, the agreement with experiment is exact.

However, one may distinguish the effect of differences between $\Delta H(V_A^-)$ and $\Delta H(V_B^+)$ from those resulting from a difference between $\Delta H(B_A^+)$ and $\Delta H(A_B^-)$ if one can determine the deviation from stoichiometry at the maximum of the solidus. For example, in normal, n-type GaP and ZnO, the material is found to be deficient in P and O respectively (15, 35) so that V_P^+ and V_O^+ must be more numerous than P_{Ga}^{+2} and O_{Zn}^{+4} . On the other hand, for normal, p-type GaSb, the material is found to be deficient in Sb so that Ga_{Sb}^{-2} must be more numerous than V_{Ga}^- (10, 11). By comparing Eq. [15] and Table II with the values of $\Delta H(V_A)$ and $\Delta H(V_B)$ given in Table II of the accompanying paper (20), we see that these three empirical conclusions are in agreement with the predictions of the present theory because under intrinsic growth conditions: for ZnO, $\Delta H(V_O^x) = 3.0$ eV $< \Delta H(O_{Zn}^{+4}) \simeq 13.8$ eV; for GaP, $\Delta H(V_P^x) = 2.6$ eV $< \Delta H(P_{Ga}^{-2}) = 2.9$ eV; for GaSb, $\Delta H(V_{Ga}^x) = 2.0$ eV $> \Delta H(Ge_{Sb}^{-2}) = 0.9$ eV.³ In general, the theory predicts that vacancies will be more important in wide bandgap semiconductors and isolated antisite defects will be more important in small bandgap semiconductors.

In order to compare theory and experiment quantitatively, let us consider the particular case of GaP. The virtual-enthalpies of neutral vacancy formation are given in Table II of Ref. (20) as

$$O = V_{Ga}^x; \Delta H(V_{Ga}^x) = 2.98 \text{ eV}$$

$$O = V_P^x; \Delta H(V_P^x) = 2.64 \text{ eV} \quad [16]$$

³ In general, $\Delta H(V^x)$ is greater than the relevant enthalpy, that of the ionized vacancy, but, as values for the enthalpy of ionization are lacking, the point can be made with $\Delta H(V^x)$.

Table II.

Crystal AB	$\Delta H_0(B_A)$, eV	$\Delta H_0(A_B)$, eV	Crystal AB	$\Delta H_0(B_A)$, eV	$\Delta H_0(A_B)$, eV
SiC	-0.06	0.96	InN	2.53	3.00
BN	1.37	0.61	InP	0.42	0.89
BP	0.49	-0.25	InAs	0.33	0.57
BA _s	0.57	-0.46	InSb	0.27	0.27
AlN	2.38	2.68	ZnO	5.98	5.43
AlP	0.50	0.60	ZnS	1.45	1.74
AlAs	0.45	0.30	ZnSe	1.25	1.25
AlSb	0.36	0.02	ZnTe	0.96	0.78
GaN	2.07	2.71	CdS	1.48	1.86
GaP	0.38	0.68	CdSe	1.25	1.42
GaAs	0.35	0.35	CdTe	0.94	0.94
GaSb	0.08	0.32			

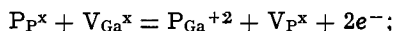
These may be combined with the virtual-enthalpies in the present Table II

$$\Delta H(\text{GaP}^{-2}) = 0.38 \text{ eV} + 2(H_c - E_F) \cong 2.9 \text{ eV} \quad [17]$$

for $E_F - H_v = H_c - E_F \cong 1.25 \text{ eV}$ under intrinsic growth conditions, and similarly

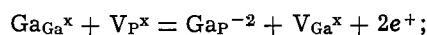
$$\Delta H(\text{P}_{\text{Ga}^{+2}}) = 0.68 \text{ eV} + 2(E_F - H_v) \cong 3.2 \quad [18]$$

With these one can estimate the real enthalpies of the real reactions



$$\Delta H = 0.44 \text{ eV} + 2 \Delta H_{\text{cv}} \quad [19]$$

where the e^- 's are taken to be in the conduction band, and



$$\Delta H = 0.72 \text{ eV} + 2 \Delta H_{\text{cv}} \quad [20]$$

However, in order to estimate the solidus curve of GaP (14, 15), it is necessary to determine the virtual-enthalpies of the virtual processes

$$\text{Ga}(1) = \text{Ga}_{\text{Ga}}; \Delta H_f^0(\text{Ga}, \text{GaP}) \quad [21]$$

$$\text{P}(1) = \text{P}_{\text{P}}; \Delta H_f^0(\text{P}, \text{GaP}) \quad [22]$$

where Ga(1) and P(1) denote the pure, elemental (liquid) Ga and P at the same temperature, T_h , as the sample. Of course, the enthalpy of formation of GaP at T_h , $\Delta H_f^0(\text{GaP})$ is a real enthalpy related to Eq. [21] and [22] by

$$\Delta H_f^0(\text{GaP}) = \Delta H_f^0(\text{Ga}, \text{GaP}) + H_f^0(\text{P}, \text{GaP}) \quad [23]$$

By combining Eq. [21] and [22] with Eq. [16], we may complete defect incorporation equations

$$\text{Ga}(1) = \text{Ga}_{\text{Ga}} + \text{V}_{\text{P}^x}; \Delta H(\text{V}_{\text{P}^x}) + \Delta H_f^0(\text{Ga}, \text{GaP}) \quad [24]$$

$$\text{P}(1) = \text{V}_{\text{Ga}^x} + \text{P}_{\text{P}}; \Delta H(\text{V}_{\text{Ga}^x}) + \Delta H_f^0(\text{P}, \text{GaP}) \quad [25]$$

$$\text{Ga}(1) = \text{V}_{\text{Ga}^x} + \text{GaP}^{-2} + 2e^+; \Delta H(\text{V}_{\text{Ga}^x}) + \Delta H_f^0(\text{Ga}, \text{GaP}) + \Delta H(\text{GaP}^{-2}) + 2H(e^+) \quad [26]$$

$$\text{P}(1) = \text{P}_{\text{Ga}^{+2}} + \text{V}_{\text{P}^x} + 2e^-;$$

$$\Delta H(\text{V}_{\text{P}^x}) + \Delta H_f^0(\text{P}, \text{GaP}) + \Delta H(\text{P}_{\text{Ga}^{+2}}) + 2H(e^-) \quad [27]$$

In [26] and [27] the enthalpy per carrier would be $H(e^+) = E_F - H_v$ and $H(e^-) = H_c - E_F$ if the carriers are taken to be in the bands.

In order to determine the values of $\Delta H_f^0(\text{Ga}, \text{GaP})$ and $\Delta H_f^0(\text{P}, \text{GaP})$ for a given set of equilibrium conditions, i.e., to apportion $\Delta H_f^0(\text{GaP})$ between the anion and cation lattice sites, let us consider the process by which one atom of Ga and one atom of P are removed from the pure elements to infinity and then placed on the proper lattice sites of the crystal. As is well known, the partial pressures of the elemental vapors over their pure liquids, $p(\text{Ga}^0)$ and $p(\text{P}^0)$, are related to the enthalpy and entropy of vaporization, ΔH_v and ΔS_v , as

$$\ln(p_{\text{Ga}^0}/p_r) = -\Delta H_v(\text{Ga}^0)/kT_h + \Delta S_v(\text{Ga}^0)/k \quad [28]$$

$$\ln(p_{\text{P}^0}/p_r) = -\Delta H_v(\text{P}^0)/kT_h + \Delta S_v(\text{P}^0)/k \quad [29]$$

where p_r is a reference pressure and the superscript zero denotes the pure element. Let us simply extend these formulas to the partial pressures and single adsorption reactions over the stoichiometric liquid

$$\ln(p_{\text{Ga}^{\text{GaP}^1}}/p_r) = -\Delta H_v(\text{Ga}^{\text{GaP}^1})/kT_h + \Delta S_v(\text{Ga}^{\text{GaP}^1})/k \quad [30]$$

$$\ln(p_{\text{P}^{\text{GaP}^1}}/p_r) = -\Delta H_v(\text{P}^{\text{GaP}^1})/kT_h + \Delta S_v(\text{P}^{\text{GaP}^1})/k \quad [31]$$

Thus subtracting [28] from [30] and [29] from [31]

$$kT_h \ln(p_{\text{Ga}^{\text{GaP}^1}}/p_{\text{Ga}^0}) = \Delta H_v(\text{Ga}^0) - \Delta H_v(\text{Ga}^{\text{GaP}^1}) - T_h(\Delta S_v(\text{Ga}^0) - \Delta S_v(\text{Ga}^{\text{GaP}^1})) \quad [32]$$

$$kT_h \ln(p_{\text{P}^{\text{GaP}^1}}/p_{\text{P}^0}) = \Delta H_v(\text{P}^0) - \Delta H_v(\text{P}^{\text{GaP}^1}) - T_h(\Delta S_v(\text{P}^0) - \Delta S_v(\text{P}^{\text{GaP}^1})) \quad [33]$$

Obviously the sum of [32] and [33] must be the free energy of formation of liquid GaP, $\Delta H_f^0(\text{GaP}) - T_h \Delta S_f^0(\text{GaP})$, because this combination of these virtual processes is the formation process. Now, in the practical experiment (14, 15) one has the GaP crystal in contact with a Ga-P liquid of variable composition and the vapors are in contact with this liquid. Thus, the prevailing partial pressures vary with the liquid composition primarily because of the entropy factor in the liquid chemical potentials. Therefore, in order to make a meaningful separation of $\Delta H_f^0(\text{GaP})$ and $\Delta S_f^0(\text{GaP})$ for the crystal, we postulate that the apportionment of ΔH_f^0 for the crystal is the same as that of the stoichiometric liquid. Then, we may reduce Eq. [32] and [33] to

$$\begin{aligned} \Delta H_f^0(\text{Ga}, \text{GaP}) / \Delta H_f^0(\text{P}, \text{GaP}) \\ = \ln(p_{\text{Ga}^0}/p_{\text{Ga}^{\text{GaP}^1}}) / \ln(p_{\text{P}^0}/p_{\text{P}^{\text{GaP}^1}}) \\ = \ln(a^1(\text{Ga}, x_{\text{P}} = 0.5)) / \ln(a^1(\text{P}, x_{\text{P}} = 0.5)) \quad [34] \end{aligned}$$

where $a^1(\text{Ga}, x_{\text{P}} = 0.5)$ and $a^1(\text{P}, x_{\text{P}} = 0.5)$ are the activities of Ga and P in this liquid. The formula to separate ΔS_f^0 is entirely analogous. [As usual, for Ga

$$a^1(\text{Ga}) = x^1(\text{Ga})\gamma^1(\text{Ga}) \quad [35]$$

where $x^1(\text{Ga})$ is the atom fraction of Ga in the liquid and $\gamma^1(\text{Ga})$ is its activity coefficient, and the corresponding equation holds for P.]

Let us accept Thurmond's evaluation of the activity coefficients throughout the Ga-P liquid system (36) and Jordan *et al.*'s (14) values $\Delta H_f^0(\text{GaP}) = -1.34 \text{ eV}$ and $\Delta S_f^0 = -7.19 \text{ k}$ at $T_h \approx 1400^\circ \text{C}$. At the 50-50 liquid composition Thurmond found $\gamma^1(\text{Ga}) = 0.68$ and $\gamma^1(\text{P}) = 1.00$ so that $a(\text{Ga}) = 0.34$ and $a(\text{P}) = 0.50$. Thus, from Eq. [34] we conclude

$$\Delta H_f^0(\text{Ga}, \text{GaP}) = -0.82 \text{ eV}, \Delta S_f^0(\text{Ga}, \text{GaP}) = -4.38 \text{ k} \quad [36]$$

$$\Delta H_f^0(\text{P}, \text{GaP}) = -0.52 \text{ eV}, \Delta S_f^0(\text{P}, \text{GaP}) = -2.81 \text{ k} \quad [37]$$

In order to estimate the entropy of the real reactions [24]-[27], it is assumed that the virtual entropies of both V_{Ga^x} and V_{P^x} , Eq. [16], are the same as the best estimates (37, 38) of $\Delta S(\text{V}_{\text{Si}^x})$ and $\Delta S(\text{V}_{\text{Ge}^x})$

$$\Delta S(\text{V}_{\text{Ga}^x}) = \Delta S(\text{V}_{\text{P}^x}) = k \ln 3 = 1.10 \text{ k} \quad [38]$$

This value corresponds to an assumption that the Jahn-Teller distortion about V_{Ga^x} and V_{P^x} is 3-fold degenerate, as it is for V_{Si^x} , and that any contribution to $\Delta S(\text{V}^x)$ due to a shift in lattice mode frequencies (37-39) is negligible. The latter point is supported by recent infrared and Raman studies of lattice modes in defect zinc-blende structure crystals like In_2Te_3 (40). The entropy of the fully ionized antisite defect will be taken to be

$$\Delta S(\text{B}_A^{+\Delta Z}) = \Delta S(\text{A}_B^{-\Delta Z}) = \Delta Z \Delta S_{\text{cv}}(\text{AB}) \quad [39]$$

where ΔS_{cv} is the entropy of the forbidden gap corresponding to the enthalpy ΔH_{cv} (33). Thus, the entropy of the antisite defect is treated in exact analogy to the treatment of its enthalpy at Eq. [15] and as previously assumed by Stringfellow and by Van Vechten (4-6). For GaP one finds (32-33)

$$\Delta S(\text{P}_{\text{Ga}^{+2}}) = \Delta S(\text{GaP}^{-2}) = 2\Delta S_{\text{cv}}(\text{GaP}) = 12.9 \text{ k} \quad [40]$$

Therefore, we calculate the enthalpies and entropies of the real reactions [24]-[27] to be

$$\text{Ga}(1) = \text{Ga}_{\text{Ga}} + \text{V}_{\text{P}^x}; \Delta H = 1.8 \text{ eV} \quad \Delta S = -3.3 \text{ k} \quad [41]$$

$$\text{P}(1) = \text{V}_{\text{Ga}^x} + \text{P}_{\text{P}}; \Delta H = 2.5 \text{ eV} \quad \Delta S = -1.7 \text{ k} \quad [42]$$

$$\begin{aligned} \text{Ga}(1) = \text{V}_{\text{Ga}^x} + \text{GaP}^{-2} + 2e^+; \\ \Delta H = 2.5 \text{ eV} + 2\Delta H_{\text{cv}}, \quad \Delta S = 9.6 \text{ k} \quad [43] \end{aligned}$$

$$P(1) = P_{\text{Ga}^{+2}} + V_{\text{P}}^x + 2e^-;$$

$$\Delta H = 2.8 \text{ eV} + 2\Delta H_{\text{cv}}, \quad \Delta S = 11.2\text{k} \quad [44]$$

The above reactions are not adequate to describe the data obtained by measuring the deviations from stoichiometry (14, 15). Indeed, one should not expect them to be adequate because it seems unlikely that the vacancies are predominately in their neutral state during the growth process. Consideration of both the enthalpy and the entropy of ionization argue for this point. It is known that vacancies in Si and Ge have both acceptor and donor states within the gap (38, 41). Near $T = 0^\circ\text{K}$ these levels are deeper than half the gap and, for Si, the values are established within about 0.2 eV; expressing the ionization enthalpy, $\Delta H_{\text{I}}(V_{\text{Si}})$, in terms of ΔH_{cv} (38-41)

$$\Delta H_{\text{I}}(V_{\text{Si}^-}) = 0.52 \Delta H_{\text{cv}}; \quad \Delta H_{\text{I}}(V_{\text{Si}^{-2}}) = 0.9 \Delta H_{\text{cv}};$$

$$\Delta H_{\text{I}}(V_{\text{Si}^+}) = 0.7 \Delta H_{\text{cv}} \quad [45]$$

Therefore, if E_{F} is at midgap near $T = 0^\circ\text{K}$, the predominate charge state is V_{Si}^x . However, at high temperatures at least one charged state is more numerous than V_{Si}^x for any value of E_{F} (38). This is evidenced by numerous charge state effects in impurity diffusion and defect annealing experiments (42-44). This results from the entropy of ionization, $\Delta S_{\text{I}}(V_{\text{Si}})$, which causes the free energy of the levels to vary with temperature so that they become progressively shallower and actually cross at about 800°K ; to a good approximation

$$\Delta S_{\text{I}}(V^-) = \Delta S_{\text{I}}(V^{-2}) = \Delta S_{\text{I}}(V^+) = \Delta S_{\text{cv}} \quad [46]$$

for Si and Ge (38) and should also hold for $V_{\text{A}}^x = V_{\text{A}}^- + e^+$ and $V_{\text{B}}^x = V_{\text{B}}^+ + e^-$ in the AB semiconductors.

Although, for reasons to be discussed, it is difficult to identify and measure the vacancy ionization levels in most III-V crystals, including GaP, various levels have been measured in several II-VI's especially CdS (45-47). In CdS the two V_{S} donor levels are rather shallower than the two V_{Cd} acceptor levels

$$\Delta H_{\text{I}}(V_{\text{S}}^+) = 0.07 \Delta H_{\text{cv}}; \quad \Delta H_{\text{I}}(V_{\text{S}}^{+2}) = 0.10 \Delta H_{\text{cv}}$$

$$\Delta H_{\text{I}}(V_{\text{Cd}}^-) \approx 0.2 \Delta H_{\text{cv}}; \quad \Delta H_{\text{I}}(V_{\text{Cd}}^{-2}) \approx 0.7 \Delta H_{\text{cv}} \quad [47]$$

Comparing Eq. [47] with [45] it is evident that the values of ΔH_{I} , relative to ΔH_{cv} , decrease with increasing ionicity of the materials considered and seem to show an asymmetry between V_{A} and V_{B} , which may be related to the sizes of the atoms (48). Because P, like S, is smaller than the cation, one may expect the decrease in the ΔH_{I} 's for V_{P}^+ to be greater than for V_{Ga}^- . However, in the absence of such size effects, one would expect the acceptor states to be shallower than the donor states, as in Si, because vacancies increase the number of lattice sites and thus the number of band states without increasing the number of electrons. In view of the above, the author's present best guess is⁴

$$\Delta H_{\text{I}}(V_{\text{Ga}}^-) = 0.2 \Delta H_{\text{cv}}, \quad \Delta H_{\text{I}}(V_{\text{P}}^+) = 0.2 \Delta H_{\text{cv}} \quad [48]$$

with $\Delta H_{\text{I}}(V_{\text{Ga}}^{-2})$ and $\Delta H_{\text{I}}(V_{\text{P}}^{+2})$ equal to or greater than ΔH_{cv} .

In Fig. 1 we see the existence curve for GaP calculated with the thermodynamic parameters for both vacancies and antisite defects⁵ compared with experi-

⁴The only way to obtain a detectable concentration of simple, single vacancies at low temperature from which the ΔH_{I} 's could be determined is by electron irradiation at liquid nitrogen temperatures or below. Such experiments, Esposito and Loferski (49), show that the vacancies produced act as nonradiative recombination centers and do not produce luminescence. One might conclude that they are shallower than the ~ 1 eV deep luminescence centers which they quench. It seems that photocapacitance measurements immediately after low temperature irradiation will yield the best estimates of $\Delta H_{\text{I}}(V_{\text{Ga}}^-)$ and $\Delta H_{\text{I}}(V_{\text{P}}^+)$.

⁵This problem may be treated with an approximate, graphical treatment [Kröger and Vink (50)]. However, because both types of ionized defects may be present in comparable concentrations in the region of interest, a computer program which obtains consistency between the assumed Fermi level and the condition of neutrality by iteration was employed.

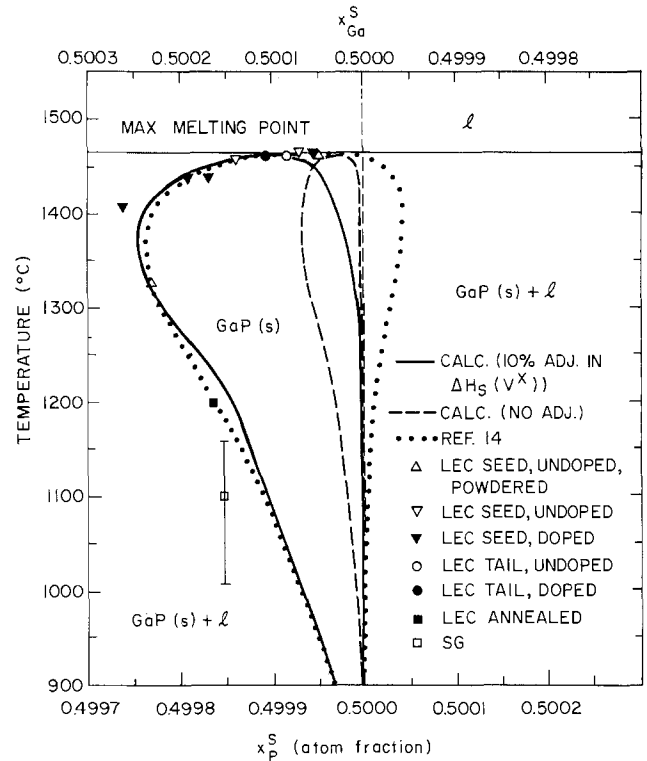


Fig. 1. The existence curve of GaP as calculated and according to the data of Jordan *et al.* (14). LEC and SG denote the data points of samples grown by liquid-encapsulation Czochralski and solution methods. The dotted curve was obtained in Ref. (14) by assuming that only simple, neutral vacancies are present and fitting the resulting four parameters to the data. It is noted that the Schottky entropy thus inferred is implausibly large. The dashed curve is calculated from theory considering vacancies and antisite defects in several ionization states without any adjustment except a reasonable estimate of the defect ionization levels. The full curve results from adjusting only the calculated virtual enthalpies of neutral vacancy form by 10% in accord with empirical results for Si, Ge, and CdS and with the expected theoretical overestimate noted in Ref. (20).

ment (14). It is noted that this nonadjusted curve is substantially narrower than the experimental data indicate. However if the assumed values for $\Delta H(V_{\text{Ga}}^x)$ and $\Delta H(V_{\text{P}}^x)$ are each reduced by 10%, so that Eq. [41] and [42] become

$$\text{Ga}(1) = \text{Ga}_{\text{Ga}} + V_{\text{P}}^x; \quad \Delta H = 1.5 \text{ eV}, \quad \Delta S = -3.3\text{k} \quad [41a]$$

$$P(1) = V_{\text{Ga}}^x + P_{\text{P}}; \quad \Delta H = 2.2 \text{ eV}, \quad \Delta S = -1.7\text{k} \quad [42a]$$

while the parameters of the antisite defects remain unchanged, then an excellent fit to the data is obtained. (The parameters and results of this existence curve are listed in Table III). We recall that it was necessary to reduce the values of $\Delta H(V_{\text{Si}}^x)$ and $\Delta H(V_{\text{Ge}}^x)$ by 10% and those of V_{Cd} and V_{S} in CdS by 12% in order to attain agreement with experiment and that this order of an overestimate should be expected of the macroscopic cavity model (20, 38).

The fit to experiment obtained with this choice of parameters is certainly not unique. One could invoke V_{Ga}^{-2} and V_{P}^{+2} and vary the antistructure and neutral vacancy parameters in a number of ways to obtain curves that fit the data within experimental accuracy. Indeed, Jordan *et al.* obtained (14) the dotted curve in Fig. 1 by assuming that the only defects present were neutral vacancies and fitting the parameters to the data. The Schottky enthalpy and entropy that they inferred in this way were $\Delta H_{\text{S}}(\text{GaP}) = 3.84$ eV and $\Delta S_{\text{S}}(\text{GaP}) = 10.1\text{k}$ as contrasted with the present (adjusted) estimates, $\Delta H_{\text{S}}(\text{GaP}) = 5.06$ eV, $\Delta S_{\text{S}}(\text{GaP}) = 2.2\text{k}$. While it may be argued that Jordan *et al.*'s estimate of $\Delta H_{\text{S}}(\text{GaP})$ is plausible, their estimate of ΔS

Table III.

x_{Ga^+} , a/o	Temp, °K	a_{Ga}	a_P	Δ^* , * 10^{-5}	$[V_{Ga^-}]$, $10^{17}/cm^3$	$[V_{P^+}]$, $10^{17}/cm^3$	$[GaP^{-2}]$, $10^{17}/cm^3$	$[P_{Ga^{+2}}]$, $10^{14}/cm^3$
6	1433	0.020	0.984	0.1	3.6	4.8	0.0	11.1
10	1475	0.036	0.987	0.3	6.3	8.1	0.0	12.7
20	1600	0.080	0.940	1.1	19.4	27.2	0.1	33.3
30	1675	0.144	0.842	2.7	35.7	53.8	0.5	38.5
40	1730	0.225	0.705	5.4	50.5	81.3	2.1	32.6
45	1735	0.271	0.617	6.8	50.4	97.9	3.7	21.6
50	1738	0.340	0.500	9.2	46.3	111.0	7.3	11.7
55	1735	0.437	0.374	13.1	36.5	129.0	14.9	5.2
58	1730	0.471	0.341	14.4	32.8	132.0	17.8	3.9
60	1725	0.535	0.297	16.9	28.0	142.0	23.9	2.6
64	1711	0.625	0.227	20.8	19.5	154.0	34.0	1.3
70	1675	0.750	0.161	23.6	11.0	155.0	43.6	0.4
80	1600	0.919	0.087	23.3	3.5	137.0	48.1	0.1
90	1480	0.964	0.037	14.6	0.6	81.4	31.7	0.0
94	1433	1.000	0.0203	13.5	0.2	73.3	30.2	0.0

* $\Delta^* \equiv (x_{Ga^+} - 0.5)$.

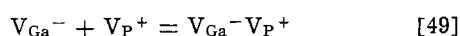
seems to be much too great to be assigned neutral vacancies (37-39) and may be taken as evidence that the defects present are mostly ionized under growth conditions.⁶ It would seem that one must assume this in order to understand why the defects are electrically active "shunt-path killer centers" at room temperature.

Defect Reactions as the Crystal Cools

The calculation just described estimates the concentrations of simple defects in equilibrium with the liquid under growth conditions. (See Table III.) These concentrations of defects will not be in equilibrium amongst each other, let alone with the exterior of the crystal, at room temperature. Because the defects will migrate about the sample as the crystal cools, one must expect their concentrations to tend toward a new equilibrium at a lower temperature.

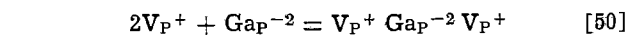
To appreciate the prevalence of defect redistribution processes, let us make the conservative estimate that the enthalpy of single vacancy migration in GaP is about 2.0 eV, as compared with 1.3 and 1.0 eV for Si and Ge (38, 39, 52) and about 1.6 eV for GaAs (53), and let us take the entropy of vacancy migration to be 4.1k, as in Si and Ge (38, 39). Then, taking the jump attempt frequency (approximately the Debye frequency) to be $10^{13}/sec$, one estimates the jump rate to be $4 \times 10^7/sec$ at $1400^\circ K$ and $5 \times 10^4/sec$ at $1000^\circ K$. As a typical crystal cools from 1050° to $950^\circ K$ in 600 sec (54), a simple vacancy would pass through more than 10^8 lattice sites in that period. Because, according to the present analysis, most of the vacancies are ionized and the concentration of charged impurities is at least $10^{14}/cm^3$ while the concentrations $[GaP^{-2}]$ and $[P_{Ga^{+2}}]$ were typically 10^{18} and $10^{14}/cm^3$ during growth and $[GaP^{-2} P_{Ga^{+2}}]$ dipolar pairs were $10^{19}/cm^3$, simple vacancies will constantly be encountering other defects with which they may form bound complexes. It seems certain that the internal equilibrium between the various point defects and their complexes is closely maintained down to temperatures well below $1000^\circ K$. Therefore, relative concentrations of simple point defects and defect complexes will be governed by the appropriate law of mass action relations down to quite moderate temperatures. At room temperature, almost all the vacancies present should be tied up in complexes.

To determine the ultimate fate of the simple point defects introduced during growth, several types of complexes amongst them should be considered. It seems likely that the most common complexes will be those which have no net charge because these would have the greatest binding energy. In addition to the formation of the nearest neighbor complex

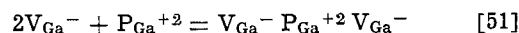


second neighbor complexes such as

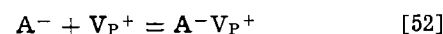
⁶ In the experiments discussed in Ref. (14) there was no way to determine whether the defects introduced were neutral or ionized but compensated (51).



and

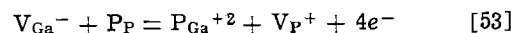


may be important. Indeed, a simple point charge model predicts that the binding energy of reactions [50] and [51] would be 2.02 times that of [49], $e^2/r\epsilon$. Because GaP^{-2} is likely to be the most common double acceptor present, Eq. [50] is probably the most important processes trapping V_{P^+} . The interaction of V_{P^+} with a single acceptor impurity, A^-

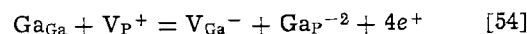


should have about the same binding energy as [49] and thus would not be competitive with [50].

Now, the concentrations of positively charged and negatively charged simple point defects introduced during growth are in general, not equal. Therefore, the concentrations of some type of simple point defect would be exhausted as reactions [49]-[52] proceed during the cooling unless other reactions occur which interchange one type of point defect for another. Consider the reactions

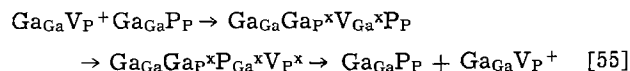


and



which will occur every time a vacancy migrates to a nearest neighbor site. Obviously, such reactions act to compensate the sample and prevent the Fermi level from approaching either band edge during the cooling.

It seems most unlikely that the activation energy for [53] and [54] could be so large that they would not occur during cooling at a rate sufficient to prevent $[P_{Ga^{+2}}]$ and $[GaP^{-2}]$ from being depleted while $[V_{Ga^-}]$ and $[V_{P^+}]$ are still large. One may estimate the rate of this process by considering one channel for single vacancy migration



(The requisite electronic reactions are assumed to occur instantaneously on the scale of atomic motion and are neglected here.) The activation enthalpy for this process would be

$$\Delta H_m^*(V_{P^+}, GaP) = \Delta H_m(V, IV) + \Delta H_O(GaP) \approx 2.0 \text{ eV} \quad [56]$$

where the asterisk denotes the specific channel [55] and $\Delta H_m(V, IV)$ denotes the enthalpy of single vacancy migration in a hypothetical group IV elemental crystal equivalent to GaP with respect to the homopolar (covalent) portions of the crystal potential. [Presumably, $\Delta H_m(V, IV) \approx \Delta H_m(V^*, Si) \approx 1.3 \text{ eV}$ for GaP (52).] This crude estimate corresponds with the value assumed above and also corresponds with Lang and Kimerling's empirical estimate for vacancy migration in GaAs (53). Although the entropy of this channel

may be too low for it to dominate the atomic diffusion, it is obviously rapid enough to maintain the equilibrium among $[V_{Ga}^-]$, $[P_{Ga}^{+2}]$, $[V_P^+]$, and $[GaP^{-2}]$.

Consequently, one would expect reactions such as [50], [51], [53], and [54] to proceed as the crystal cools until almost all the vacancies that were introduced during growth are tied up in neutral complexes such as $V_{Ga}^- P_{Ga}^{+2} V_{Ga}^-$ and $V_P^+ GaP^{-2} V_P^+$, and perhaps $V_{Ga}^- P_{Ga}^{+2} GaP^{-2} V_P^+$ and more complex species. The tendency of the vacancies and antisite defects to produce such complexes amongst themselves rather than to compensate impurities, e.g., Eq. [52], would explain the relative insensitivity of room temperature carrier concentration to deviations from stoichiometry (14) as well as the propensity of such deviations to produce electrically active "shunt path killer centers."

Summary

It has been shown that all viable theories (3-6, 16) which may be applied to predict the concentrations of antistructure pairs, $B_A A_B^x$, and of antisite defects, B_A^+ and A_B^- , imply that these should be significant in zincblende and wurtzite semiconductors. It is concluded that a proper account of the antisite defects is crucial to an understanding of the properties of III-V semiconductors. The theoretical estimates of the dielectric two-band model (7-9) for antisite defects have been combined with those of the macroscopic cavity model for vacancies (20) to show that the available data on the existence curve and electrical properties of GaP can be successfully accounted for with physically and chemically reasonable parameters by taking account of the interaction between these defects.

Acknowledgment

The author is pleased to acknowledge the advice and encouragement of Dr. C. D. Thurmond.

Note added in proof: The vacancy-antisite defect complex $V_{Ga}^- P_{Ga}^{+2} V_{Ga}^-$ proposed above as the "shunt path killer center" in GaP would constitute a cylindrical defect oriented in a $\langle 110 \rangle$ direction one atom in diameter and having a length corresponding to 3 second nearest neighbor sites, i.e., $3a/\sqrt{2}$, where a is the usual lattice constant. It appears that such defects have been observed directly in LEC GaAs by a direct lattice imaging electron microscopy technique (55).

Manuscript submitted May 14, 1974; revised manuscript received Sept. 9, 1974.

Any discussion of this paper will appear in a Discussion Section to be published in the December 1975 JOURNAL. All discussions for the December 1975 Discussion Section should be submitted by Aug. 1, 1975.

Publications costs of this article were partially assisted by Bell Laboratories.

REFERENCES

1. F. A. Kröger, "The Chemistry of Imperfect Crystals," p. 406 and especially p. 411, North-Holland, Amsterdam (1964).
2. R. A. Swalin, "Thermodynamics of Solids," 2nd Edition, p. 318, Wiley-Interscience, New York (1972).
3. K. Weiser, *J. Phys. Chem. Solids*, **7**, 118 (1958).
4. J. A. Van Vechten, *Phys. Rev. B*, **7**, 1479 (1973).
5. G. B. Stringfellow, *J. Phys. Chem. Solids*, **33**, 665 (1972), and to be published (1974).
6. G. B. Stringfellow, *This Journal*, **119**, 1780 (1972).
7. J. C. Phillips, "Bonds and Bands in Semiconductors," Academic Press, New York (1973).
8. J. A. Van Vechten, *Phys. Rev.*, **182**, 891 (1969).
9. J. A. Van Vechten, *ibid.*, **187**, 1007 (1969).
10. F. J. Reid, R. D. Baxter, and S. E. Miller, *This Journal*, **113**, 713 (1966).
11. Y. J. Van Der Meulen, *J. Phys. Chem. Solids*, **28**, 25 (1967).
12. B. Goldstein and N. Almeleh, *Appl. Phys. Letters*, **2**, 130 (1963).
13. J. B.anc, R. H. Bube, and L. R. Weisberg, *J. Phys. Chem. Solids*, **25**, 225 (1964).
14. A. S. Jordan, A. Von Neida, R. Caruso, and C. K. Kim, *This Journal*, **121**, 153 (1974).
15. A. S. Jordan, R. Caruso, A. Von Neida, and M. E. Weiner, *J. Appl. Phys.*, To be published 1974.
16. L. Pauling, "The Nature of the Chemical Bond," p. 93, Cornell University Press, Ithaca, N. Y. (1960).
17. J. A. Van Vechten and T. K. Bergstresser, *Phys. Rev. B*, **1**, 3351 (1970).
18. O. Berolo, J. C. Woolley, and J. A. Van Vechten, *ibid.*, **8**, 3794 (1973).
19. F. A. Kröger "The Chemistry of Imperfect Crystals," p. 418, North-Holland, Amsterdam (1964).
20. J. A. Van Vechten, *This Journal*, **122**, 423 (1975).
21. D. L. Rode and S. Knight, *Phys. Rev. B*, **3**, 2534 (1971).
22. A. Y. Cho and H. C. Casey, Jr., *J. Appl. Phys.*, **45**, 1258 (1974); D. L. Rode, Unpublished.
23. W. van Roosbroeck and H. C. Casey, Jr., *Phys. Rev. B*, **5**, 2154 (1972).
24. H. J. Queisser, H. C. Casey, Jr., and W. van Roosbroeck, *Phys. Rev. Letters*, **26**, 551 (1971); H. J. Queisser, Private communication.
25. A. S. Barker, Jr., R. Berman, and H. W. Verleur, *J. Phys. Chem. Solids*, **34**, 123 (1973); A. S. Barker, Private communication.
26. G. Srinivasan, *Phys. Rev.*, **178**, 1244 (1969).
27. J. P. Walter and M. L. Cohen, *Phys. Rev. B*, **2**, 1821 (1970).
28. F. A. Kröger, F. H. Stieltjes, and H. J. Vink, *Philips Res. Rept.*, **14**, 557 (1959); Ref. 1, p. 502.
29. R. W. Davidge, *Phys. Status Solidi*, **3**, 1851 (1963).
30. K. L. Kliewer, *J. Phys. Chem. Solids*, **27**, 705 (1966).
31. K. L. Kliewer and L. S. Koehler, *Phys. Rev.*, **157**, 685 (1967).
32. Y. P. Varshni, *Physica*, **34**, 149 (1967).
33. C. D. Thurmond, To be published.
34. J. A. Van Vechten and J. C. Phillips, *Phys. Rev. B*, **2**, 2160 (1970).
35. D. G. Thomas, *J. Phys. Chem. Solids*, **3**, 229 (1957).
36. C. D. Thurmond, *ibid.*, **26**, 785 (1965).
37. A. Seeger, in "Radiation Effects in Semiconductors," J. W. Corbett and G. D. Watkins Editors, p. 29, Gordon and Breach, London (1971).
38. J. A. Van Vechten and C. D. Thurmond, *Bull. Am. Phys. Soc.*, **19**, 211 (1974); To be published.
39. R. A. Swalin, *J. Phys. Chem. Solids*, **18**, 290 (1961).
40. E. Finkman and J. Tauc, *Phys. Rev. Letters*, **31**, 890 (1973).
41. G. D. Watkins, in "Effects Des Rayonnements Sur Les Semiconductors," p. 97, Dunod, Paris (1965); J. A. Naber, C. E. Mallon, and R. E. Leadon, in "Radiation Damage and Defects in Semiconductors," J. E. Whitehouse, Editor, p. 26, The Institute of Physics, London (1973).
42. L. C. Kimerling, H. M. DeAngelis, and C. P. Carnes, *Phys. Rev. B*, **3**, 427 (1971).
43. L. C. Kimerling and C. P. Carnes, *J. Appl. Phys.*, **42**, 3548 (1971).
44. L. C. Kimerling, H. M. DeAngelis, and J. W. Diebold, *Bull. Am. Phys. Soc.*, **19**, 210 (1974).
45. V. Kumar and F. A. Kröger, *J. Solid State Chem.*, **3**, 387 (1971).
46. Ho Bin Im and R. H. Bube, *J. Appl. Phys.*, **39**, 2908 (1968).
47. D. C. Look and J. M. Meese, *Radiation Effects*, **22**, 229 (1974).
48. G. Mandel, *Phys. Rev.*, **134**, A1073 (1964).
49. R. M. Esposito and J. J. Loferski, "Ninth International Conference on the Physics of Semiconductors," p. 1105, Nauka, Moscow (1968).
50. F. A. Kröger and H. J. Vink, in "Solid State Physics," Vol. 3, p. 349, F. Seitz and D. Turnbull, Editors, Academic Press, New York (1956).
51. A. S. Jordan, Private communication.
52. J. A. Van Vechten, *Phys. Rev. B*, **10**, 1482 (1974).
53. D. V. Lang and L. C. Kimerling, To be published.
54. C. D. Thurmond, Private communication.
55. J. B. Van der Sande and E. T. Peters, *J. Appl. Phys.*, **45**, 1298 (1974).

Epitaxial Growth by Solid-State Diffusion

T. Gabor and G. H. Dierssen*

3M Company, St. Paul, Minnesota 55133

ABSTRACT

It was demonstrated that CdS can be grown epitaxially by exposing opposite faces of a CdS wafer to cadmium and sulfur vapors, respectively, and thus causing countercurrent diffusion of the cadmium and sulfur to the opposite faces where they form CdS by reaction with the vapor. The effects of substituting zinc for the cadmium vapor, and in another experiment selenium for the sulfur vapor, were also investigated. In the two-component system, good quality single crystal was obtained while in the three-component system void formation was prevalent.

In conventional crystal growth the reactants are brought to the substrate either in a gas or in a liquid phase. Some disadvantages inherent in this approach may be overcome by bringing the reactants to the surface by solid-state diffusion through the substrate itself. One can visualize the driving force being a temperature gradient and/or concentration gradients. Due to the widespread interest in CdS and to its ready availability in single crystalline form, this compound was selected as a model crystal for the experiments; cadmium and sulfur were diffused countercurrently through CdS. The above-described growth by countercurrent diffusion was also combined with exchange reactions. In one experiment zinc was substituted for the cadmium, and in another selenium for the sulfur, thus leading to the $\text{CdS} \rightarrow \text{ZnS}$ and $\text{CdS} \rightarrow \text{CdSe}$ reactions.

Experimental

The substrates were obtained by wafering a 19 mm diameter cylinder of CdS. To allow optimum utilization with the given shape of the boule, the axis of the cylinder was selected to coincide with the $\langle 10\bar{1}3 \rangle$ direction. After etching in concentrated HCl for 4 min, the final thickness was 1.4-1.6 mm. On some of the wafers, circular-shaped tantalum markers were deposited by sputtering. The wafers were placed, as shown in Fig. 1, sandwiched between two reservoirs; one containing the Group II, the other the Group VI element.

To decrease the rate of vapor transport of the substrate CdS components to the cool ends, the cross-sections of the reservoirs were decreased by sealing capillary tubes with an about 0.5 mm diameter bore into the neck of each reservoir.

Evacuation was performed at room temperature and the ampules were sealed at 10-45 μm .

A typical temperature profile is shown in Fig. 1. The experimental conditions and thermodynamic data are

* Electrochemical Society Active Member.

Key words: crystal growth, cadmium-sulfur system, zinc-cadmium-sulfur system, cadmium-sulfur-selenium system.

listed in Table I. The temperature range as recorded over the reservoirs (columns 3 and 6), and the corresponding vapor pressures of the elements (columns 4 and 7) calculated by the formulas of Shiozawa and Jost (1) are listed. Table I also lists the substrate temperature (column 8), the corresponding equilibrium constants (column 9), and the duration of the experiments (column 11). Columns 10, 12, and 13 are discussed below.

Inspection of the system after cooling to room temperature revealed that in all cases a tight seal formed between the substrate and the metal reservoir. However, the chalcogen reservoir was never altogether tight and some sulfur or selenium was found after the experiments between the reservoirs and the outer tube at the cold ends. However, sufficient chalcogen remained in the reservoir throughout the experiments to insure the desired chalcogen vapor pressure.

Results

Some characteristics of the specimens are collected in Table II, while further details are given in the following.

In experiment I, the section of the wafer between the two reservoirs became curved, the cadmium-exposed face being convex and the sulfur-exposed face concave. The data given in columns 2 and 3 of Table II were obtained by measuring the curvature with a traveling microscope along four parallel lines on the polished cross section. The measurements showed that the thickness within the reservoir varied from 1.7 to 1.9 mm, while the original wafer was 1.61 mm thick. The wafer outside the reservoirs retained its original thickness. Reflection x-ray diffraction indicated plastic deformation with a maximum angle of 7° .

In experiment II both the substrate temperature and the sulfur pressure were lowered. Under these conditions, the plane-parallelity of the wafer was retained. One segment of the cadmium exposed surface after experiment II is shown in Fig. 2. The rough surface on

Fig. 1. Schematic drawing of experimental apparatus and temperature profile. The vertical and horizontal dimensions are on a different scale. The wafer diameter was 19 mm.

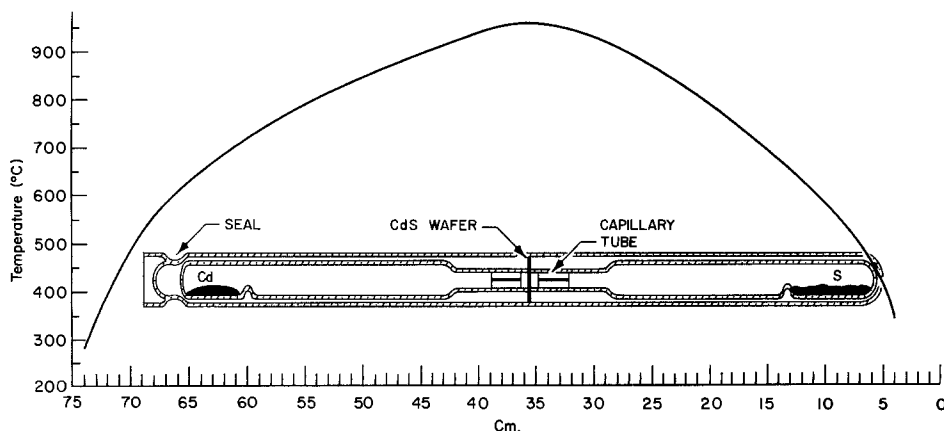


Table I. Experimental conditions and corresponding thermodynamic data

(1)	(2)	(3)	(4)	(5) Vapor sources		(6)	(7)
Expt.	Group II			Group VI			
		°K	Atm.			°K	Atm.
I	Cd	993-903	0.59-0.18	S		993-843	11.0-4.8
II	Cd	973-873	0.46-0.11	S		813-688	3.4-0.6
III	Zn	1043-933	0.21-0.04	S		923-783	10.2-2.4
IV	Cd	963-923	0.43-0.24	Se		1083-963	4.0-1.1

(1)	(8)	(9)	(10)	(11)	(12)	(13)
Expt.	Substrate			Time (min)	Real pressure (atm)	
	°K	K_p	P_{II} (atm)		P_{II} (on VI-side)	P_{VI} (on II-side)
I	1223	2.4×10^{-4}	4.8×10^{-3}	9,600	7.2×10^{-5} - 1.1×10^{-4}	1.6×10^{-7} - 1.8×10^{-6}
II	1173	6.1×10^{-5}	2.0×10^{-3}	24,000	3.3×10^{-5} - 7.7×10^{-5}	1.8×10^{-8} - 3.0×10^{-7}
III	1223	1.7×10^{-5}	1.8×10^{-4}	12,000	5.2×10^{-7} - 1.1×10^{-6}	6.2×10^{-11} - 1.5×10^{-9}
IV	1233	3.2×10^{-4}	5.9×10^{-3}	17,400	1.6×10^{-4} - 3.0×10^{-4}	5.6×10^{-7} - 1.8×10^{-6}

Table II. Growth characteristics

(1) Exp.	(2) Growth (mm) II-side	(3) Growth (mm) VI-side	(4) Mtlis.	(5) Crystallinity	(6) Morphology	(7) Consistency
I	0 to +0.9	0 to -0.7	CdS	Single	Curved	Bulk
II	+0.008	-0.1	CdS	Single	Straight	Bulk
III	+0.04	+0.2	ZnS	Poly (growth into S-reservoir single)	Straight	Porous except growth on S-side
IV	0	+0.3	CdSe	Single (few large grains)	Straight; protrusions at wall of Cd reservoir	Porous

the left is where a tantalum marker was deposited. Both the smooth surface on the right and the rectangular crystallites within the tantalum-marked area are 8 μ m higher. The sulfur-exposed face was 0.1 mm lower than the ring which was in contact with the reservoir wall.

In experiment III one side of the wafer was exposed to zinc instead of cadmium vapor. This led to a considerable change in the shape of the specimen. The faces within the reservoirs were relatively flat, but they advanced 0.04 mm into the zinc reservoir and 0.19 mm into the sulfur reservoir. This latter growth is visible at the top right of the polished cross section shown in Fig. 3a and at a higher magnification in Fig. 4. To reveal different characteristics, the two micrographs of Fig. 3 were taken with varying angles of reflected light. The two traces of the planar surfaces on each side of the wafer indicate areas where the original geometry of the wafer was retained due to contact with the reservoir walls. The volume of the wafer outside the reservoirs (below the vertical traces in the micro-

graphs) increased considerably, growing from the original 1.53 mm thickness to a maximum of 1.93 mm. The position of the reservoirs was not centered, hence the different levels at which the straight traces on the opposite faces are found.

As indicated by the white color, most of the specimen was transformed into ZnS. There remained a weak yellow tinge on the face exposed to the sulfur reservoir. This layer was too thin to be revealed in the cross section. However, significant amounts of single-crystalline CdS were present in a narrow layer along the faces of the wafer outside the reservoirs, and the

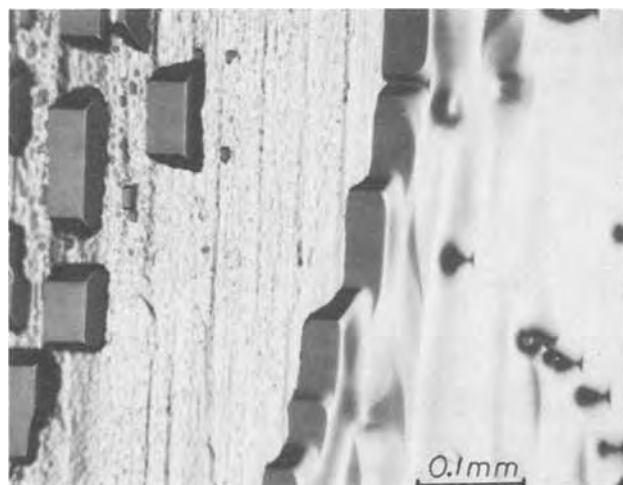


Fig. 2. Smooth surface (right) and tantalum-marked area (left) on cadmium-exposed face after experiment II.

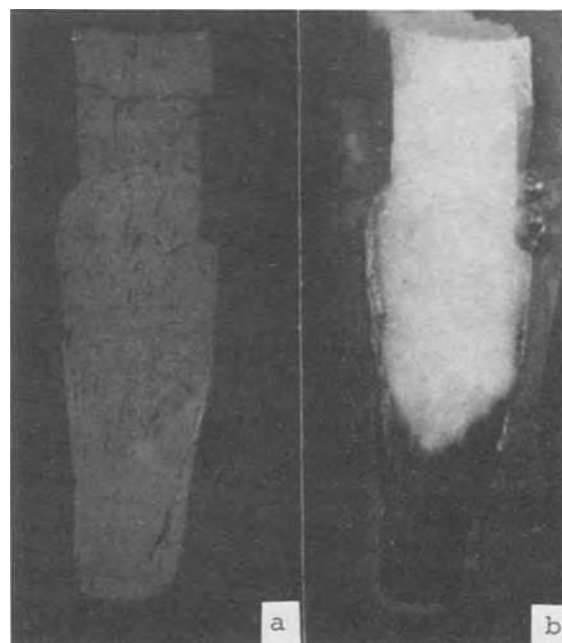


Fig. 3. Polished cross section of part of wafer after experiment III. Photographed at two different illuminations. At the top right of (a), the growth into the sulfur reservoir can be seen. The dark color in (b) indicates CdS, while the ZnS is white.

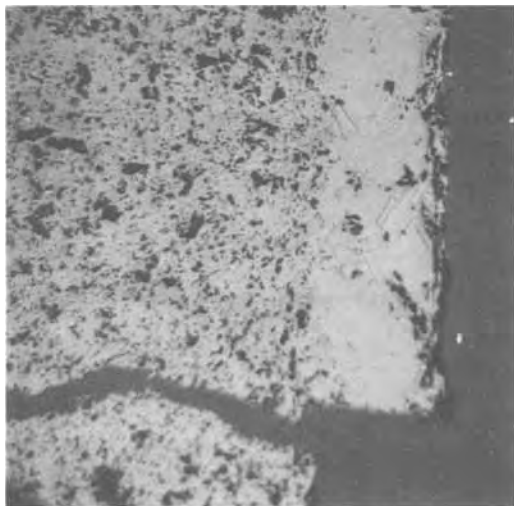


Fig. 4. The top right of Fig. 3 at a higher magnification. The growth on the sulfur-exposed face is single crystalline. The black areas are due to voids.

original CdS was retained at the rim, as is shown by the dark contrast in Fig. 3b. The Cd:Zn atomic ratio was determined by an electron probe and was found to be 1.5 on the face exposed to the sulfur reservoir, 0.003 in the area which was in contact with the reservoir wall and 58.3 on the surface of the wafer outside the reservoirs.

Crystallinity of the ZnS was studied in the cross section by optical microscopy (oriented facets on chemical polishing) and by Laue back reflection measurements. Pronounced single crystallinity was revealed in the material which grew into the sulfur reservoir (Fig. 4) and in narrow layers paralleling the CdS on the surface of the wafer outside the reservoirs. Single crystallinity improved as the measurements were taken closer to the rim (further away from the reservoirs). Even where not single crystalline, the material was found to be textured.

In experiment IV, the sulfur in the reservoir was replaced by selenium. By observing the polished cross section (Fig. 5) of the wafer, one is led to believe that a contour similar to the one shown in Fig. 3 would have formed had sublimation not taken place preferentially on the side facing the hotter of the two reservoirs (selenium). The uniform dark color of the specimen shows that transformation into CdSe has taken place.

A large void runs across the whole wafer roughly parallel to the exposed faces within the reservoirs and bends toward the cadmium reservoir outside the reservoirs. Numerous smaller voids and channels, most of which are perpendicular to the traces of the exposed faces, are also present as is illustrated in the composite micrograph of Fig. 6. In a layer starting somewhat below the original selenium-exposed surface and continuing up to the final surface on that side, the material is spongy and contains pores of irregular shape and size.



Fig. 5. Polished cross section of wafer after experiment IV. The convex-appearing side (top) was exposed to the selenium vapors.



Fig. 6. Selected area of Fig. 5 at higher magnification. The pores in the layer grown on the selenium-exposed face are irregularly shaped while in the original wafer they are perpendicular to the faces.

Etching of the cross section revealed that the wafer consisted of one large crystal and a few grains.

Discussion

As diffusion rates increase with increasing wafer temperatures, it is advantageous to work at high temperatures. However, the sublimation rate also increases with temperature, as the equilibrium constant, K_p , in the equation $K_p = p_{II} \times p_{VI}^{1/2}$ is temperature dependent. The values of p_{II} calculated for the theoretical case of congruent vaporization when $p_{II} = 2 p_{VI}$ are listed in column 10 of Table I. However, the group II and group VI reservoirs established high p_{II} and p_{VI} values, and thereby decreased sublimation due to a decrease in the equilibrium pressures of p_{VI} and p_{II} , respectively. Due to the square root relationship, an increase in p_{VI} led to a smaller decrease in p_{II} (Table I, column 12) than did the reverse, (column 13), hence the net growth on the cadmium-exposed faces in experiments I and II. The high temperature and sulfur pressure in experiment I led to plastic deformation. This deformation and possible sublimation from the wafer precluded the accurate determination of the solid-state flux. However, one can calculate that the minimum 0.2 mm growth corresponded to a flux of 2×10^{14} sulfur atoms/cm² sec.

In experiment II, growth is indicated not only by the 8 μ m height difference between the tantalum-marked area and the rest of the surface, but also by the smoothness of the surface. The original etched wafer, and also the sulfur-exposed face (where sublimation exceeded growth by solid-state diffusion) were both strongly faceted. Assuming that no material was lost by sublimation on the cadmium-exposed face and that, except for the rectangular crystallites, no growth occurred over the tantalum-marked area, one may calcu-

late that the solid-state flux of sulfur was 10^{13} atoms/cm² sec. The rectangular crystallites probably grew through local discontinuities (e.g., cracks) in the tantalum film.

Numerous studies have been performed on the diffusion in CdS of one of the constituent elements at a time. Still, the mechanism is not yet completely understood (2, 3). When the crystal is in equilibrium with high sulfur pressures, cadmium is thought to be transported as V_{Cd}'' and sulfur as S_i^x (2). However, in case of high cadmium pressures, there is disagreement on whether the mobile species is Cd_i^{\cdot} or $Cd_i^{x\cdot}$ and whether the dominant defect is $V_s^{\cdot\cdot}$ or $Cd_i^{\cdot\cdot}$ (2-4). Also, sufficient information is not available on the interaction between various defects and their effect on concentrations and mobilities. The present case is even more complex, as diffusion mechanisms must continuously change across the specimen, reaching the limiting cases at the two surfaces where the wafer is in equilibrium with high cadmium and high sulfur pressures, respectively. Thus, in case of cadmium transport, there must be a region within the wafer where the mobile species change from V_{Cd} to Cd_i . In this region one would expect to find material with relatively low cadmium defect concentration and thus this region may limit the magnitude of the flux (i.e., the rate of crystal growth on the sulfur exposed face). Similar argument may be applied to the sulfur flux.

Exchange reactions in II-VI compounds have been studied by several authors (5-7). Just as in the case of binary compounds, the situation in the present work was again made more complex by the exposure of opposite faces to p_{II} and p_{VI} vapors. Also, in addition to having to consider the numerous defect species and mobile species as in the case of the binary system, one also has to consider the fact that while the exchange reaction is taking place, one of the elements has to diffuse to the surface and either form a compound there with the vapor or sublime off. For example, at the beginning of experiment III, the cadmium is expected to have sublimed into the zinc reservoir when it was replaced by zinc. However, as the ZnS-CdS interface advanced into the wafer, an ever larger fraction of the cadmium diffused toward the sulfur exposed surfaces, "uphill" along a cadmium concentration gradient in the direction of a decreasing chemical potential (8), as the chemical potential of cadmium had its lowest value where the CdS was in contact with the sulfur vapors. Part of the cadmium reacted with the sulfur forming an epitaxial CdS deposit. One may speculate that cadmium, zinc, and sulfur all moved both as interstitials and as vacancies depending on the existing local activities of zinc and sulfur.

In experiment III, zinc diffused not only toward the sulfur reservoir but also toward the rim of the wafer. As both faces of the wafer outside the reservoirs were exposed to sulfur vapors, zinc displaced cadmium internally and deposited the Cd ions as CdS on both faces. Hence the increase in thickness outside the reservoirs (0.4 mm) was twice that of the increase within the reservoirs (0.2 mm). As ZnS and CdS are mutually soluble in all proportions (9), it is expected that the interface during the exchange reaction was diffuse. Once a critical ZnS concentration was reached, the volume decrease (20% on complete transformation) must have led to the nucleation of voids and the formation of a microcrystalline phase. The varying degrees of crystallinity found makes one believe that the orientation and size of the ZnS crystallites depended on their rate of growth, rapid growth leading to finer grain size. Hence the best crystallinity appeared furthest away from the zinc reservoir. The higher crystallographic quality of the material grown outside the volume of the original wafer makes one believe that the diffu-

sion of zinc through ZnS was a slower process than the diffusion accompanying the CdS \rightarrow ZnS transformation.

In experiment IV, the CdS \rightarrow CdSe transformation should lead to a 10% increase in volume. The formation of voids shows that the out-diffusion of sulfur and cadmium took place faster than the in-diffusion of cadmium and selenium from their respective reservoirs. As the presence of a larger ion on a lattice site is known to favor association with a vacancy (10), one may postulate that Se_s^x was associated with V_{Cd} . Thus, movement of the interface toward the cadmium reservoir facilitated the out-diffusion of cadmium toward the selenium reservoir via a vacancy flux. If the sulfur vacancy flux moving toward the cadmium reservoir was larger than the flux due to the "uphill" diffusion of sulfur (see argument advanced for experiment III) which was displaced by selenium, then the agglomeration of vacancies can account for the formation of voids. A significant fraction of the voids must have agglomerated along a plane parallel to the faces of the wafer; however, numerous other voids, most of them elongated in the direction perpendicular to the faces (thus favoring vapor transport) also formed. As contact with the walls of the reservoirs locally prevented the in-diffusion of vacancies (i.e., the out-diffusion of material), void formation was less pronounced between the opposite walls of the reservoirs.

The present work proved the feasibility of epitaxial growth in case of compound semiconductors by solid-state diffusion. The slow rate of growth in case of a binary system and void formation in case of exchange reactions may limit the practicality of the approach.

Acknowledgment

We thank H. E. Mishmash for the electron probe examination, W. E. Thatcher for the x-ray examinations, and Prof. Robert A. Rapp (Ohio State University) for very helpful discussion.

Manuscript submitted March 14, 1974; revised manuscript received Sept. 20, 1974. This was Paper 26RNP presented at the San Francisco, California, Meeting of the Society, May 12-17, 1974.

Any discussion of this paper will appear in a Discussion Section to be published in the December 1975 JOURNAL. All discussions for the December 1975 Discussion Section should be submitted by Aug. 1, 1975.

Publication costs of this article were partially assisted by the 3M Company.

REFERENCES

1. L. R. Shiozawa and J. M. Jost, "Research on Improved II-VI Crystals", ARL 71-0017, Contract No. F33615-68-C-1601-P002 (Jan. 1971).
2. V. Kumar, "Self Diffusion and the Defect Structure of Cadmium Sulfide," University Microfilms (1971); V. Kumar and F. A. Kröger, *J. Solid State Chem.*, **3**, 387, 406 (1971).
3. D. A. Stevenson, "Atomic Diffusion in Semiconductors," D. Shaw, Editor, p. 487 *et seq.*, Plenum Publishing Company, New York (1973).
4. D. Shaw, *Phys. Status Solidi (b)*, **60**, K45 (1973).
5. E. T. Handelman and W. Kaiser, *J. Appl. Phys.*, **35**, 3519 (1964).
6. H. H. Woodbury and R. B. Hall, *Phys. Rev.*, **157**, 641 (1967).
7. J. Zimja, *Acta Phys. Polonica*, **A40**, 435 (1971).
8. L. S. Darken and R. W. Gurry, "Physical Chemistry of Metals," p. 462, McGraw-Hill Book Co., New York (1953).
9. L. Indradev, J. Van Ruyven, and F. Williams, *J. Appl. Phys.*, **39**, 3344 (1968).
10. G. D. Watkins, "Intrinsic Defects in II-VI Compounds," ARL 73-0163, Contract No. F33615-72-C-1505, p. 19, (Nov. 1973).



Gallium Migration Through Contact Metallizations on GaP

W. A. Brantley,¹ B. Schwartz,* V. G. Keramidis, G. W. Kammlott, and A. K. Sinha

Bell Laboratories, Murray Hill, New Jersey 07974

The thickness of the native oxide film which can be grown on GaP is increased considerably if the semiconductor has a chemically nonreactive, ohmic contact to provide a site for the cathodic component of the oxidation-reduction reaction (1). However, the contacts to GaP cannot be characterized as nonreactive with respect to the oxidation process. Formation of gallium and phosphorus oxides on the gold-based ohmic contacts (2, 3) to GaP during galvanic oxidation (1) has been established from electron microprobe analysis (4). It is believed that the presence of oxides on the surfaces of the contacts could be the cause of subsequent bonding difficulties.

There are several possible mechanisms by which gallium and phosphorus might arrive at the surfaces of the ohmic contacts: (i) migration through the metallizations during the contact alloying or during the galvanic oxidation process, (ii) surface diffusion, (iii) transport through the oxidizing solution, and (iv) as a consequence of the dicing process or subsequent etching. Of these possibilities, it is suspected that (ii) is not a major transport mechanism, and (iii) was demonstrated not to be significant by a controlled experiment in which there was no gallium transport to a gold wire immersed adjacent to the semiconductor in the oxidizing solution. Support for mechanism (i) is available from several experiments. An SiO₂ layer was found on gold films evaporated on silicon substrates, after heating at relatively low temperatures (< 300°C) in an oxidizing ambient; during the heating, silicon atoms were assumed to migrate through the gold film (5). Rapid dissolution of gallium into thin platinum films on GaP at 250°C has recently been detected by x-ray diffraction (6), and evidence for gallium migration through thin gold and platinum films on GaAs at temperatures above 250°C has been obtained by 2 MeV ⁴He⁺ ion backscattering experiments (7). Nakatsuka *et al.* (8) observed that evaporated gold films on GaAs and GaP melted at temperatures considerably below the known (9) Au-GaAs eutectic temperature and proposed that this melting occurs at a gallium-rich composition; the unknown Au-GaP eutectic temperature is expected to be greater than the Au-GaAs eutectic temperature since the melting point of GaP exceeds that of GaAs by 200°C.

These collective results suggest that the metallization-semiconductor interface can be metallurgically reactive at temperatures considerably below binary eutectic values. Nevertheless, even if GaP melts to yield a gallium-rich liquid at the gold film interface, it is not evident how much of the contact film participates in the alloying process. Furthermore, because the GaP contacts are relatively thick (~ 1.5 μm), it was considered unlikely that gallium and phosphorus would migrate through the entire contacts.

In this work, the origin of the gallium and phosphorus on the surfaces of the contacts to GaP has been investigated by means of secondary ion mass spec-

trometry² (SIMS). This technique can provide (i) in-depth mass spectrometric analyses and (ii) ion image displays of sputtered secondary ions generated by a high energy primary ion beam impinging on the specimen (10-12). With these options, a relative chemical composition profile with depth can be obtained (provided no artifacts are introduced due to relative sputtering yields of the various components of the metallizations) or the area uniformity for a particular species at a given depth can be observed. For the present experiments, the primary sputtering beam consisted of ~5.5 keV O₂⁺ ions, and the secondary ion beam was apertured so that only the signal from the

central ~70 μm region of the ~ 200 μm diameter "burn" was detected. A rapid sputtering rate of ~90 Å/sec through the gold films was employed; this burn rate was subsequently established from determination of crater depths by both interference fringe and Talysurf measurements.

Contact metallizations (2, 3) were deposited by electron gun evaporation on <111>-oriented GaP wafers. The p-contact consisted of a Be-Au alloy, and these films were deposited on p-type GaP having $N_A - N_D \sim 5 \times 10^{17} \text{ cm}^{-3}$. The n-contact consisted of a Si-Au alloy, and these films were deposited on n-type GaP

having $N_D - N_A \sim 3 \times 10^{17} \text{ cm}^{-3}$. The films were nominally ~1.5 μm thick, and some specimens were subsequently alloyed for 5 min at 600°C in a forming gas atmosphere to obtain ohmic contacts. In addition, a reference specimen consisting of a pure gold film ~1 μm in thickness on a quartz substrate was prepared.

Examination of ⁶⁹Ga⁺ profiles through numerous alloyed metallizations indicates that extensive gallium migration does occur through the ohmic contacts. Although ³¹P⁺ profiles indicate that some phosphorus migration through the contacts also occurs, the SIMS apparatus has much lower sensitivity for phosphorus than gallium (as positive secondary ions), and only the gallium migration has been investigated in detail. Absolute gallium concentrations within the metallizations cannot be established by secondary ion mass spectrometry due to lack of appropriate chemical standards for comparison and possible different sputtering rates for the various gold matrices. Only the presence of gold was detected in the alloyed contacts by x-ray diffraction (13). However, the β-phase (14) between gold and gallium [~21 atomic per cent (a/o) Ga] has been detected near the metallization-GaP interface by transmission electron microscopy (15). For thinner (~0.5 μm thick) Be-Au films alloyed with GaP at 600°C, preliminary x-ray diffraction analyses suggest that compounds between beryllium and gold (possibly Au₃Be and Au₂Be) also form (13).

Although absolute gallium concentrations cannot be established, relative comparisons of the extent of gallium migration can be obtained. The gallium signals from the various specimens are compared at some arbitrary depth such as 1000 Å, where the metallization

* Electrochemical Society Active Member.

¹ Present address: Department of Dental Materials, School of Dentistry, Marquette University, Milwaukee, Wisconsin 53233.

Key words: ohmic contacts, compound semiconductors, secondary ion mass spectrometry.

² SMI 300, Cameca Instruments, Incorporated, Elmsford, New York 10523.

matrix is still gold but the near-surface signal enhancement (12,16) arising from the presence of a surface gallium oxide is no longer significant. The $^{69}\text{Ga}^+$ signals at an estimated 1000Å depth, normalized to a value of unity for the reference specimen, are summarized in Table I. Although the data are not sufficiently precise to warrant comparisons among the several members of each GaP specimen group, the great differences between the groups do permit order of magnitude comparisons. Accordingly, Table I is presented in a decade format where each entry is the logarithm of the upper limit for the decade; for example, an entry of 2 corresponds to a normalized gallium signal lying between values of 11 and 100.

Considerably lower gallium signals from the reference gold film on quartz and from the unalloyed films, compared to the alloyed films, prove that the source of the gallium near the surface of the ohmic contacts is the underlying GaP and that the overwhelming portion of the migration takes place during the alloying process for the contacts. Some gallium migration evidently also occurs during the contact deposition. (The reference specimen was investigated subsequent to several metallizations on GaP to allow ample opportunity for gallium contamination of the SIMS specimen chamber.) Variation over half an order of magnitude in deposition rate, while inducing considerable changes in microstructure of the films, did not significantly alter the extent of the gallium migration. Excessive gallium signals throughout the alloyed films precluded determination of area uniformity of the gallium migration. However, examination of Ga^+ ion images from a specimen where an additional unalloyed gold film was deposited over an underlying alloyed film indicates that the migration probably is not uniform. In addition, preliminary experiments suggest that the near-surface gallium level in contact metallizations may be increased an order of magnitude by the dicing process. Extensive gallium migration through gold-based ohmic contacts to GaAs also has been found during the present SIMS investigation.

It is possible that gallium migration during the alloying heat-treatment is beneficial to the formation of ohmic contacts to GaP. The beryllium or silicon contact dopants used to provide degenerate doping of GaP

are both Ga-site substitutional impurities whose incorporation should be favored by an excess of gallium vacancies in GaP at the metal-semiconductor interface. The role of phosphorus vacancies in the GaP arising from the phosphorus migration is not known although competition between phosphorus and gallium vacancies might be expected for the amphoteric silicon dopant. (Analogous considerations would be applicable for contacts to GaAs.) On the other hand, it is recognized that the presence of gallium and phosphorus oxides at the surface of the contacts can cause problems with device bonding.

Acknowledgment

The authors acknowledge the assistance of several individuals during this investigation. R. K. Lewis and B. Autier of Cameca Instruments, Incorporated performed the SIMS experiments. C. R. Paola established deposition procedures and prepared the reference specimen. Some of the specimens were kindly provided by P. E. Fraley and J. J. Bastek. The authors are particularly grateful to Mrs. M. H. Read for the x-ray diffraction analyses and to T. T. Sheng and P. M. Petroff for the transmission electron microscopy.

Manuscript submitted June 27, 1974; revised manuscript received Sept. 23, 1974.

Any discussion of this paper will appear in a Discussion Section to be published in the December 1975 JOURNAL. All discussions for the December 1975 Discussion Section should be submitted by Aug. 1, 1975.

Publication costs of this article were partially assisted by Bell Laboratories.

REFERENCES

1. B. Schwartz and W. J. Sundberg, *This Journal*, **120**, 576 (1973).
2. N. E. Schumaker and G. A. Rozgonyi, *ibid.*, **119**, 1233 (1972).
3. J. M. Ralston, *J. Appl. Phys.*, **44**, 2635 (1973).
4. K. Yoshida and D. R. Wonsidler, Unpublished research.
5. A. Hiraki, E. Lugujo, and J. M. Mayer, *J. Appl. Phys.*, **43**, 3643 (1972).
6. V. Kumar, Unpublished research.
7. A. K. Sinha and J. M. Poate, *Appl. Phys. Letters*, **23**, 666 (1973).
8. H. Nakatsuka, A. J. Domenico, and G. L. Pearson, *Solid-State Electron.*, **14**, 849 (1971).
9. M. B. Panish, *This Journal*, **114**, 516 (1967).
10. J. V. DiLorenzo, R. B. Marcus, and R. Lewis, *J. Appl. Phys.*, **42**, 729 (1971).
11. J. V. DiLorenzo, *This Journal*, **118**, 1645 (1971).
12. J. M. Morabito and R. K. Lewis, *Anal. Chem.*, **45**, 869 (1973).
13. M. H. Read, Private communication.
14. C. J. Cooke and W. Hume-Rothery, *J. Less-Common Metals*, **10**, 42 (1966).
15. T. T. Sheng and P. M. Petroff, Private communication.
16. R. K. Lewis, J. M. Morabito, and J. C. C. Tsai, *Appl. Phys. Letters*, **23**, 260 (1973).

Table I. Gallium migration through metallizations on GaP

Metallization*	Relative $^{69}\text{Ga}^+$ signal at 1000Å depth†
Gold on quartz substrate (reference specimen)	0
As-deposited n- or p-contact	2
Alloyed n- or p-contact	5-6

* Each GaP metallization group consists of several specimens.

† These values are logarithms of the upper limit of the decade(s) within which the relative Ga^+ signal values lie. For example, a value of 2 corresponds to a relative signal between 11 and 100. All the relative Ga^+ signals are normalized to the reference specimen whose near-surface Ga^+ signal has been assigned a value of unity (and thus a logarithm of 0).

Some Effects of "Trichloroethylene Oxidation" on the Characteristics of MOS Devices

Gilbert J. Declerck,¹ Takeshi Hattori,² Gerald A. May, Jacques Beaudouin, and James D. Meindl*

Stanford Integrated Circuits Laboratory, Stanford, California 94305

The use of phosphosilicate glass (PSG) as a stabilizing film on top of thermally grown SiO₂ has become almost a universal step in integrated circuit processing (1). It is well known that PSG getters sodium ions and acts as a barrier against sodium ion drift through silicon dioxide, thereby stabilizing the threshold voltage of MOS transistors. It is also well known that PSG has several undesirable effects, among which are polarizability and phosphorus penetration through the oxide to the silicon-SiO₂ interface. The PSG stabilization is also thought to bring about an increase in surface-state density, rendering it objectionable for CCD and related processes.

In an effort to circumvent the need for PSG, it has been found that the use of a chlorine-bearing species (Cl₂, HCl, or C₂HCl₃) in an oxidizing ambient can have both the gettering and passivating effects of PSG, without its more insidious side effects. The gettering effect is due to the chlorine in the oxidizing atmosphere preventing positive alkaline ions from being introduced into the growing oxide through the formation of volatile chloride compounds (2). Chlorine incorporated into the oxide also has a passivating effect against sodium drift. One possible explanation is that sodium ions are immobilized by the chlorine ions (3). Another explanation is that the sodium ions are still penetrating through the oxide but have no effect on the silicon surface potential because they become neutralized in an interaction with a chlorine-associated species near the interface (4). In any event, proper introduction of chlorine into the oxidizing atmosphere eliminates the necessity of postoxidation PSG stabilization.

Until recently, most procedures have introduced chlorine into the oxidizing atmosphere in the form of HCl. This method has several drawbacks associated with it. HCl is a very dangerous acid and cannot be handled easily. In addition, it can be very corrosive in the presence of small amounts of water vapor, causing etching of the quartz and stainless steel chambers associated with the usual oxidation furnace and exhaust systems. Because of these deleterious effects, a more manageable chlorine source has been sought. Lately, the use of trichloroethylene (TCE) has been reported to be an effective agent for reducing positive ion instabilities (5). It has some distinct advantages over HCl in that it is much easier to handle and is far less corrosive.

The purpose of this work is to further investigate the use of TCE for improving MOS structures. HCl grown oxides have not only shown improved electrical stability, but also high minority carrier lifetime (6, 7) and very low surface-state densities (8). Because these effects are also assumed to be related to the gettering action of the chlorine, measurements of these quantities were performed on TCE oxide samples as well, and the results are presented in this work. Beside an increase of minority carrier lifetime, as already reported before (6), we also found long storage times, low surface-state densities, and low noise characteristics. It may be expected that TCE oxides have great

potential for high transfer efficiency CCD's requiring low surface-state densities and high storage times. In addition, it can also be very useful for MOS circuits, and particularly for low noise transistors.

Experimental Procedure

MOS capacitors with and without TCE were fabricated on n-type (100)-substrates. As a comparative standard, oxides were grown at 1200°C for 14 min in a dry oxygen flow of 1500 cm³/min in a 50 mm quartz tube. TCE oxides were grown under the same conditions, but with varying flows of dry nitrogen through a bubbler filled with TCE. To insure good reproducibility, this flow was established 30 min prior to actual oxidation. The temperature of the bubbler was constant at 34°C within a few degrees. All wafers were given a 2 min nitrogen anneal before pulling them from the oxidation furnace. To avoid interface and lattice stresses, the pull rate was approximately 1 min. The wafers were then metallized on both sides by means of a tantalum filament evaporation system and capacitors were made using standard photolithography. Portions of each sample were annealed at 450°C in forming gas for 30 min or at 500°C in wet nitrogen for 10 min. Our results showed no difference between the two low temperature annealing steps.

Several samples of MOS capacitors using the procedure described above were prepared. Measurements of flatband voltage yielded the fixed oxide charge which was in the low 10¹⁰ cm⁻² range for all TCE samples. Bias temperature stress was performed at 200°C for 10 min with a field of 2 × 10⁶ V/cm and the resulting flatband voltage shift was measured. Storage times were found by pulsing the capacitors from accumulation into deep depletion (9-12). Fast surface-state densities were measured by the quasistatic C-V method (13, 14). All of the measurements were performed on both the standard oxide samples and the TCE oxide samples.

Next, MOS transistors were fabricated using a standard p-channel process. The run was divided into three groups according to the type of gate oxidation. The first group had a TCE oxide. The second had a standard thermal oxide with no phosphorus stabilization. The third group had a standard oxide with the usual phosphorus stabilization. All of these samples were metallized by electron-gun evaporation. The noise performance of each of the three groups was then compared.

Results

Oxidation rate.—It has been reported that in the presence of HCl or Cl₂ the oxidation rate of silicon is increased (15). The principal reasons are an enhanced diffusion of O₂ and H₂O in these oxides and an enhanced reaction at the silicon-SiO₂ interface (16). We have found that in the presence of TCE the oxidation rate is also increased, as shown in Fig. 1. Oxide thickness is plotted vs. the amount of N₂ flow through the TCE bubbler. The data show the same parabolic dependence on TCE flow that has been previously seen for HCl (15). The same graph has been reproduced through several runs, so that it may be concluded that the TCE oxide thickness is predictable when the oxidation parameters are known. It should be mentioned that a TCE-N₂ flow over 150 cm³ is

* Electrochemical Society Active Member.

¹ Permanent address: Laboratory Fysica en Elektronica van de Halfgeleiders, Katholieke Universiteit Leuven, Belgium.

² Permanent address: Sony Corporation Research Center, Japan.

Key words: surface-state density, storage time, low-frequency (1/f), noise, electrical stability, gettering.

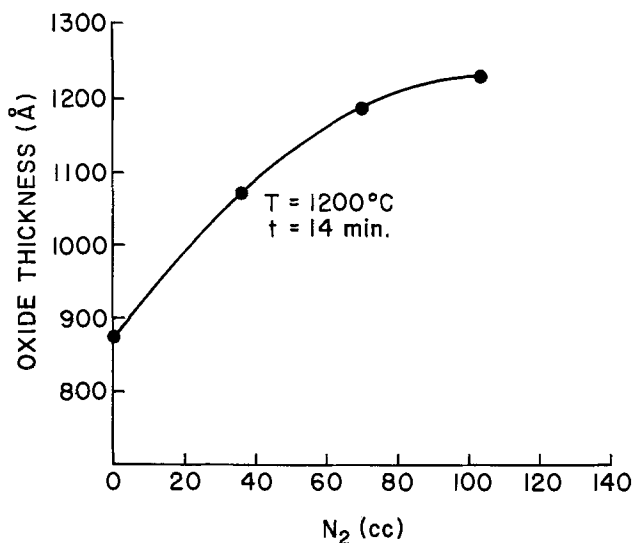
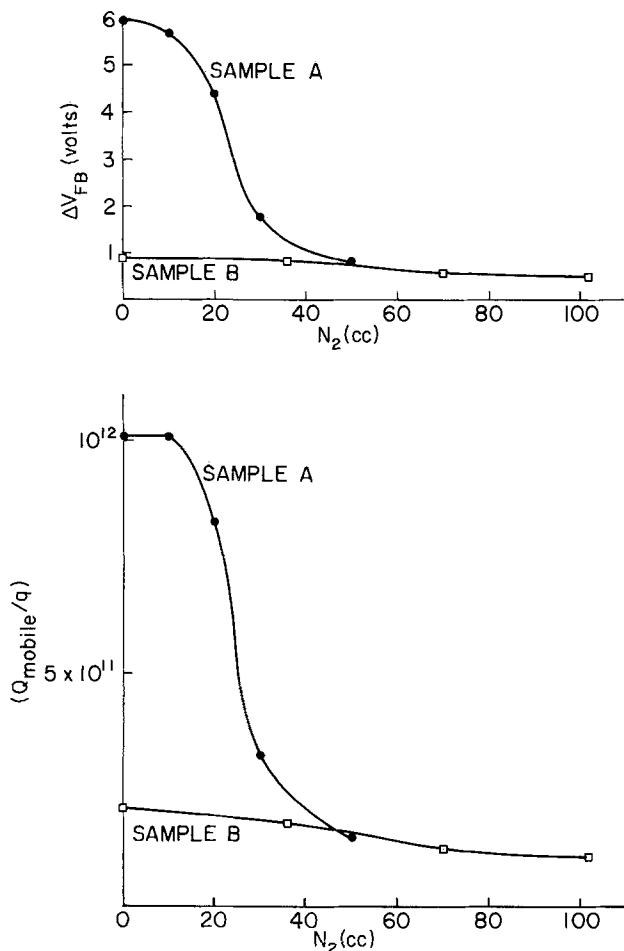


Fig. 1. Oxide thickness vs. TCE flow

probably too high because these oxides were very leaky and no oxide thickness or other parameters could be measured.

Stability.—The effect of TCE on the change in flat-band voltage after bias temperature stress is shown in Fig. 2. As the oxide thickness of each sample is different, the measured shift provides the actual mobile oxide charge from the relation $Q_{\text{mobile}} = C_{\text{ox}}\Delta V_{\text{FB}}$. The results are also plotted in Fig. 2. This figure shows that the magnitude of the mobile charge is strongly dependent on the amount of TCE in the oxidizing atmosphere.

Fig. 2. Flatband shift (ΔV_{FB}) and mobile oxide charge (Q_{mobile}/q) vs. TCE flow.

Sample A is typical for a wafer contaminated with about 1×10^{12} mobile ions per cm^2 . The contamination probably occurred during metallization (evaporation from tantalum filament). The ΔV_{FB} exhibits a strong thresholdlike behavior vs. TCE flow (15). About $60 \text{ cm}^3 \text{ N}_2\text{-TCE}$ is necessary to reduce ΔV_{FB} to a minimum of 0.5V.

Sample B was measured on wafers metallized after the metallization system had been cleaned. The total amount of mobile ions is reduced to about 1×10^{11} per cm^2 in the standard sample. However, at the $60 \text{ cm}^3 \text{ N}_2\text{-TCE}$ flow there remains a ΔV_{FB} of 0.5V. It is unlikely that this shift is due to mobile sodium ions, because the same shift is also seen on very clean electron-gun metallized samples. Furthermore, if the temperature of the B-T experiment is lowered to 150°C , the shift is negligible (less than 0.1V).

Storage time.—Another noteworthy effect of TCE is the increase in capacitor storage time over that of the standard thermal oxide. This effect is shown in Fig. 3. It should be noted that the substrate doping was $1\text{-}2 \times 10^{15}/\text{cm}^3$, the oxide thickness was about 1000Å , and the capacitors were pulsed from accumulation (+2V) to deep depletion (−7V). These parameters influence the storage time, so that it is important to keep them in mind when comparing different experiments. Storage times for our standard oxides are less than a few seconds, while for moderate flows of TCE the storage time was consistently above 1 min. For large TCE flows the storage time decreases. No attempt is made here to derive bulk lifetime in a quantitative fashion, since recent reports (12) have shown that lifetime is not so easily predictable from storage time, as previously thought (9-11). However, it is still true that longer storage times give a qualitative indication that the combined effect of bulk generation rate (inversely proportional to bulk lifetime) and of surface generation rate (proportional to surface-state density and to surface-state capture cross section) is slower.

Surface states.—Fast surface-state densities were measured by the quasistatic C-V method (13, 14). A plot of the fast surface-state density vs. TCE flow is shown in Fig. 4. It should be brought to mind that these samples were metallized by evaporation from a tantalum filament. The figure shows that the surface-state density for the standard oxide, without any form of stabilization, is about $2\text{-}3 \times 10^{10} \text{ eV}^{-1} \text{ cm}^{-2}$. This low value can be attributed to the high temperature nitrogen step after oxidation and to the wet nitrogen or forming gas anneal after metallization. However, by the use of moderate flows of TCE, surface-state densities can be reduced below $10^{10} \text{ eV}^{-1} \text{ cm}^{-2}$. Exact measurements below this value are limited by the sensitivity of the quasistatic C-V method (14). Further experiments using, e.g., the Nicollian-Goetzberger con-

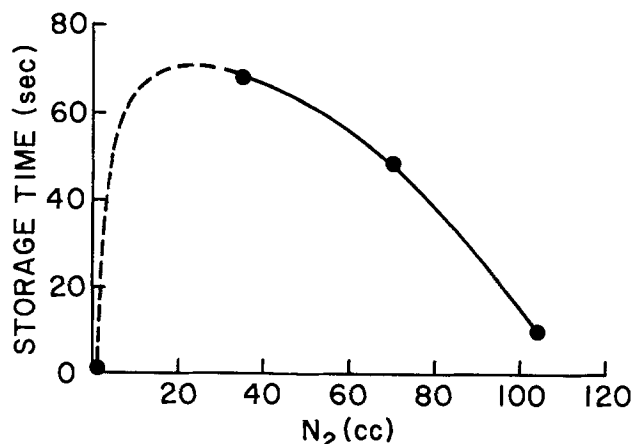


Fig. 3. Storage time vs. TCE flow

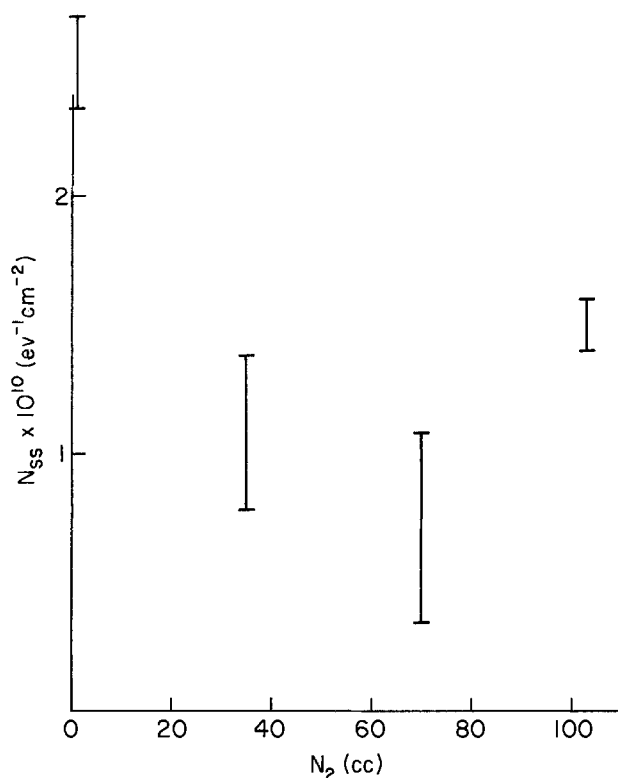


Fig. 4. Surface-state density vs. TCE flow

ductance technique are needed to accurately determine these values.

Samples made without TCE but metallized with electron-gun evaporation had measured surface-state densities in the same range as the best TCE samples. At the same time these "electron-gun" samples show very little sodium contamination in our bias temperature stress measurements. It is known that very clean samples having little sodium contamination will have a correspondingly small surface-state density when using appropriate annealing techniques. This could explain the fact that the surface-state densities in samples with electron beam evaporated metal were as low as in TCE samples with filament evaporated metal.

MOS transistor fabrication.—As mentioned in the experimental procedure, p-channel transistors using TCE oxides were fabricated. The gate oxides of these transistors were grown using an N_2 -TCE flow of 50 cm^3 . This flow was chosen because previous measurements on the MOS capacitors had shown that it was nearly the optimum value for small flatband shift, long storage times, and low surface-state densities. The gate oxide thickness of both the standard and the TCE transistors was kept equal by adjusting the oxidation time for the standard transistors. The metallization was performed by an electron-gun evaporation.

Measurements of the low-frequency (1/f) noise in the saturation region of the MOS transistor were compared between the TCE samples and the standard samples. Some of the standard devices were carried through the standard phosphorus stabilization (1050°C for 10 min in the phosphorus deposition furnace, but with the $POCl_3$ source off). Noise measurements were interpreted in terms of the input-referred noise voltage e_n which has been shown by many authors (17) to have a frequency dependence in the saturation region given by

$$e_n^2 \propto \frac{N_{ss} t_{ox}^a}{A f} F(V_{GS} - V_T) \quad [1]$$

where N_{ss} = surface-state density; $eV^{-1} cm^{-2}$; t_{ox} =

gate oxide thickness; $A = WL$ of the device, where W is the channel width and L is the channel length; and $1 < a < 2$. $F(V_{GS} - V_T)$ is a function describing a weak (linear or logarithmical) dependence of e_n on the effective gate voltage $V_{GS} - V_T$ (17). e_n has the dimensions of V/\sqrt{Hz} .

Figure 5 gives a plot of the input-referred noise voltage vs. frequency for the TCE sample, the P_2O_5 -stabilized sample, and the standard sample without P_2O_5 . The drain current was 1 mA at $V_{DS} = 10V$. All the samples show the characteristic 1/f dependence up to about 10^5 Hz. Beyond this point, the channel current noise predominates. The noise voltage for the TCE and standard samples without P_2O_5 was the same, while the P_2O_5 -stabilized sample has a noise voltage between 4 and 10 times greater. It must be mentioned that this comparison is only true for the standard P_2O_5 stabilization employed here. Using lower temperatures and shorter times for the stabilization yields lower surface-state densities (18). However, these stabilization techniques are much more difficult to apply than the TCE method described here.

Referring to the noise voltage equation, we may conclude that the difference in surface-state densities between the devices is at least one and maybe two orders of magnitude. By a quasistatic C-V measurement N_{ss} was proven to vary on the P_2O_5 -stabilized samples between $5 \times 10^{10} eV^{-1} cm^{-2}$ and a few $10^{11} eV^{-1} cm^{-2}$. Consequently, the noise measurements given here also indicate that on the other samples (TCE and standard without P_2O_5), the density is significantly less than $10^{10} eV^{-1} cm^{-2}$.

Figure 6 shows the dependence of noise voltage on drain current for the TCE sample. Figure 7 gives the variation of noise voltage with current at 1 kHz measuring frequency. The rise of the 1/f noise at higher current levels can be explained by the function $F(V_{GS}$

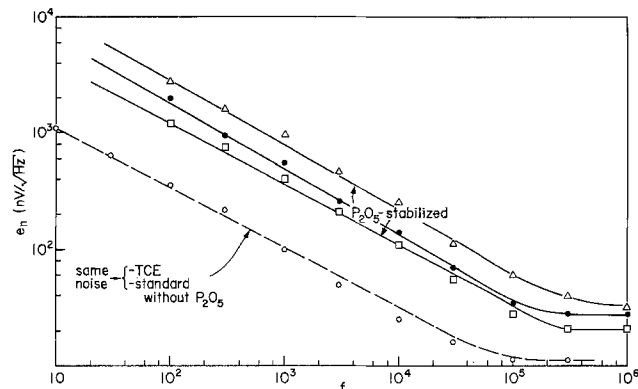


Fig. 5. Input-noise voltage (e_n) vs. frequency at $I_D = 1$ mA and $V_{DS} = 10V$.

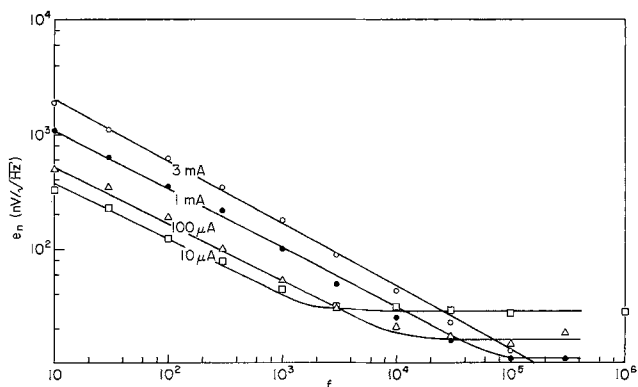


Fig. 6. Input-noise voltage (e_n) vs. frequency for TCE sample at different bias currents.

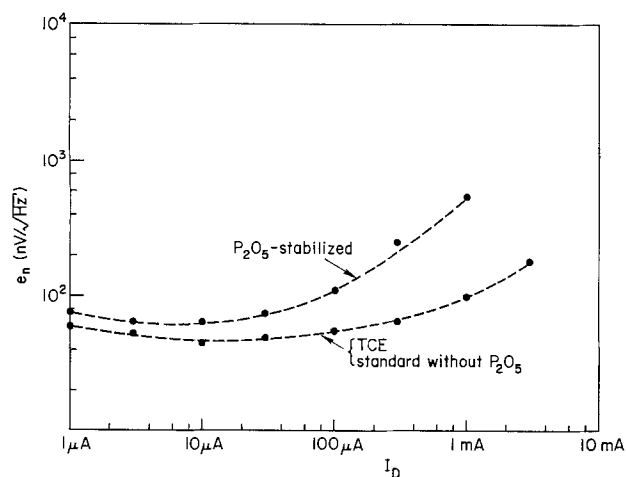


Fig. 7. Input-noise voltage (e_n) vs. current at $f = 1$ kHz

$-V_T$) in Eq. [1] or can be due to an increase in surface-state density near the bandedges. It is seen that the increase in $1/f$ noise is less pronounced on the TCE and standard samples without P_2O_5 . The small rise at lower currents is due to an increase in channel resistance thermal noise.

As a last point, we would like to compare our noise results with published low noise data. Looking at Fig. 6 and 7 we see that the 1 mA bias current used in Fig. 5 was not lying in the optimum low noise region. A noise voltage of 15-20 nV/\sqrt{Hz} , found by Ronen (17) at 1 kHz and at 1 mA on specially designed transistors with $W = 1600 \mu m$ is regarded to be an extremely low noise result. This value must be compared with the 60 nV/\sqrt{Hz} that we found at 150 μA on our transistors with $W = 250 \mu m$ (because of the change in current levels with smaller W/L and assuming about the same channel length). When the area factor is considered in Eq. [1], it is clear that the 60 nV/\sqrt{Hz} must be divided by a factor of two or three, which brings us to a value comparable to Ronen's figure. Using the TCE technology, and optimizing the geometry, very good low noise transistors can be made.

Conclusion

The TCE capacitors we fabricated showed good stability, long storage times (>1 min), and low surface-state densities (a few $10^9 eV^{-1} cm^{-2}$). A strong indication that these characteristics are maintained through a complete processing schedule has been given by the successful fabrication of low noise MOS transistors. Further work should be done in evaluating storage times, transfer efficiency and dark currents on

charge coupled devices, and MOS image sensors processed using the TCE technology.

In addition, the increased oxidation rate is helpful in keeping the \sqrt{Dt} products small, by allowing oxides to be grown at lower temperatures. A careful study of TCE oxides grown by a wet/dry oxidation schedule at lower temperatures ($\sim 900^\circ C$) would be interesting for DMOS and related devices, in which high temperature oxidations may not be desirable.

Acknowledgments

The authors wish to thank the staff of the Stanford Integrated Circuits Laboratory for their helpful discussions and technical assistance.

Manuscript submitted June 7, 1974; revised manuscript received Oct. 7, 1974.

Any discussion of this paper will appear in a Discussion Section to be published in the December 1975 JOURNAL. All discussions for the December 1975 Discussion Section should be submitted by Aug. 1, 1975.

Publication costs of this article were partially assisted by Stanford Integrated Circuits Laboratory.

REFERENCES

1. P. Balk and J. M. Eldridge, *Proc. IEEE*, **57**, 1558 (1969).
2. R. J. Kriegler, in "Semiconductor Silicon 1973," H. R. Huff and R. R. Burgess, Editors, p. 363, The Electrochemical Society Softbound Symposium Series, Princeton, N. J. (1973).
3. R. D. Baxter, "Investigation of Impurities in Thermally Grown SiO_2 ," for Naval Air Systems Command, Department of the Navy, by Battelle Memorial Institute, Columbus Laboratories, Columbus, Ohio 43201 (Jan. 1973).
4. R. J. Kriegler, *Appl. Phys. Letters*, **20**, 449 (1972).
5. Mao-Chieh Chen and John W. Hile, *This Journal*, **119**, 223 (1972).
6. D. R. Young and C. M. Osburn, *ibid.*, **120**, 1578 (1973).
7. P. H. Robinson and F. P. Heiman, *ibid.*, **118**, 141 (1971).
8. M. Severi and G. Soncini, *Electron. Letters*, **8**, 402 (1972).
9. S. R. Hofstein, *IEEE Trans. Electron Devices*, **14**, 785 (1967).
10. Frederick P. Heiman, *ibid.*, **14**, 781 (1967).
11. D. K. Schroder and J. Guldberg, *Solid-State Electron.*, **14**, 1285 (1971).
12. Thomas W. Collins, *IEEE Trans. Electron Devices*, To be published.
13. M. Kuhn, *Solid-State Electron.*, **13**, 873 (1970).
14. R. Van Overstraeten, G. Declerck, and G. Broux, *This Journal*, **120**, 1785 (1973).
15. R. J. Kriegler, Y. C. Cheng, and D. R. Colton, *ibid.*, **119**, 388 (1972).
16. K. Hirabayashi and J. Iwamura, *ibid.*, **120**, 1595 (1973).
17. R. S. Ronen, *RCA Rev.*, **34**, 280 (1973).
18. G. Declerck, R. Van Overstraeten, and G. Broux, *Solid-State Electron.*, **16**, 1451 (1973).

On the Technique and Evaluation of Angle-Beveling Silicon Epitaxial Layers

P. J. Severin, H. Bulle, G. Poodt, and J. D. Wasscher

Philips Research Laboratories, Eindhoven, Netherlands

For advanced applications of epitaxially grown structures the dope concentration profile and the extent of the concentration gradient between substrate and epitaxial layer are of paramount importance. In order to study these properties with surface probing techniques the interior should be exposed by beveling the slice. The method this paper is focused on, is the spreading resistance technique (1), which is accepted now as a very powerful tool for investigating epitaxially grown structures. Recently also the electroreflectance method was reported (2) to yield promising results when applied to an angle-polished junction. Also the capacitance-voltage (3) and the voltage breakdown methods (4) can be used on beveled structures to profile the junction.

Any technique integrates over a certain length and for obtaining a large resolving power in-depth the bevel angle should be as small as possible. This implies, however, that for precise correlation between horizontal position and depth below the original surface the departure from ideal flatness of the slice is taken into account. This note deals with the preparation and evaluation of small bevel angles down to $1/2000$. It is concerned with basically known tools and techniques: lapping jigs, polishing procedures, the interference microscope and interferometers. However, in order to fully and correctly exploit the possibilities of the spreading resistance and other methods, on a bevel these techniques should be very critically and carefully applied.

The preparation and evaluation procedures are intimately connected. The use of the polishing jig is described in the next section. In semiconductor device technology patterns are optically imaged on a slice which therefore should be sufficiently flat. A laser-operated interferometer developed originally to study this surface topography of a silicon slice, is briefly sketched in the third section. Its use in conjunction with the polishing jig for evaluating the local bevel angle, taking into account any departures from perfect flatness of the slice, is explained in the fourth section. It is also shown that by tilting the slice differences in height as low as 60\AA can be measured.

Preparation of the Bevel

Conventional angle-lapping jigs have been used for bevel and stain measurements at relatively large angles by Bond and Smits (5, 12), Fuller and Ditzenberger (6), Gutsche (7), Kane and Larrabee (8), and Herff and Roeder (9). The reliability of these instruments is limited by mechanical tolerances: the play increases with use because it cannot be avoided that powder penetrates between inner and outer cylinders during the lapping process. Moreover, the angle can be measured on the interferometer only before lapping. Here we first describe a more stable and versatile tool, shown schematically in Fig. 1, which matches well the interferometer to be described later.

The piston A to which the slice S is attached can slide without play in the holder B and can be fixed at any height and position by screw C. This assembly rests on three balls on the support ring D and can be moved with respect to the support by two screws E. With one screw the assembly can be tilted about the axis between the other screw and the third ball. In this way the angle between the axes of B and D can be varied in a simple and precise way. The holder B

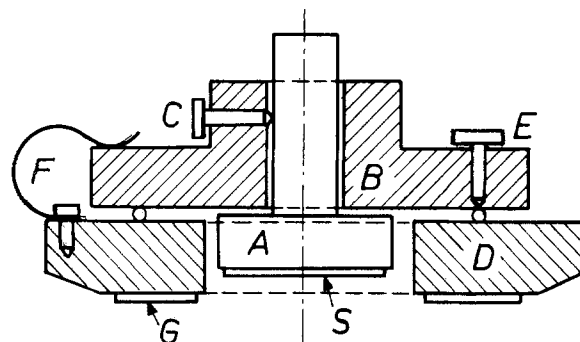


Fig. 1. Schematic view of the angle-polishing jig. The slice S is waxed to the piston A, which fits tightly into holder B and can be clamped with screw C. With the screws E the slice can be tilted with respect to the support D, which rests on pieces of silicon G.

and the support D are held in position by three resilient clamps F. A basically similar device used for polishing parallel optical flats is described by Bennett and Wilson (10). The jig rests on a number of pieces of silicon G glued to the support D. Hence during lapping and polishing no foreign particles are produced and because their total surface area of about 10 cm^2 is much larger than the area to be beveled, the pressure and rates are constant during the process. The slice is mounted on the piston A in a thick layer of beeswax by heating. When it is allowed to cool slowly, the slice assumes its equilibrium position.

The lapping and polishing is done on a machine¹ on which the slice is subjected to three different motions. The slice is lapped on a glass plate through a slurry of water and Al_2O_3 ² for a few minutes under a load of 1500g and then thoroughly rinsed with water. The subsequent polishing is done on a disk³ into which diamond paste⁴ can be embedded under supply of water. After polishing, which takes about 2 min, at a few times higher speed the roughness is reduced sufficiently to make the surface mirror-like. At this stage the surface shows some pits and scratches due to deep lapping damage, but usually the polishing process is not continued. It has been found that there is about a 20% difference in spreading resistance between touched and nontouched parts. Because profiles are measured generally on a logarithmic scale, this difference in calibration is unimportant.

The Interferometer

A bevel of relatively steep slope and mirror surface quality can easily be evaluated with an interference microscope which typically covers under $100\times$ magnification a field of view of $1500\text{ }\mu\text{m}$ diameter. In order to obtain a reliable value for the slope at least a dozen contour lines should be visible, which implies that the slope should be steeper than $1/250$ if the reference plane covers half the field of view. It has been found that for very steep angles reliable results can be obtained. However, for smaller angles the slice turns out not to be flat enough to unambiguously define its slope with respect to the reference flat. Moreover, the method

¹ Kent Mk2, Engis Limited, Mailstone, England.

² 303.5 size 12-18 μm .

³ Hyprocel Pa-W*, Slough Products, Bruxelles.

⁴ Type C, size 0-3 μm , H. Struers Chemiska Lab., Copenhagen, Denmark.

Key words: angle-beveling, silicon, thin layer, interferometer.

is time consuming and it is impossible to obtain an over-all impression. In this section an instrument of greater field of view is described with which the untouched part of the surface of a beveled slice can be seen and used as a horizontal reference in determining the slope of the bevel.

The optical layout of this interferometric instrument which is not at all critical, is shown in Fig. 2. A HeNe laser (1) operating at 6328Å at about 2 mW power level provides an extremely monochromatic, coherent, relatively intense, and narrow light beam. The light is incident on a diffuser (3), which serves as an intense and monochromatic light source. Via a semireflecting mirror (5) the enlarged-diameter parallel beam is incident on the polished side of the silicon slice (7) which is positioned face to face with a semireflecting optical flat (8), about 1 cm thick. The fringe system arising from multiple interference at the positions of appropriate slice-flat distance is imaged by a lens (9) onto a screen, a television camera, or a photographic camera (10). As the light turns out to be still so coherent that speckles can be seen, the diffuser (3) is mounted on a motor axis which revolves sufficiently fast that they disappear. In Fig. 2 the slice is shown resting on the back side with an optical flat at a few millimeters distance, adjusted with three screws to be more or less parallel to the polished side of the slice. The instrument can also be used with the polished side down and the support G resting on the optical flat. The angle with the optical flat is adjusted with the screws E.

The distance between two contour lines corresponds to a height difference equal to $\lambda/2 = 0.316 \mu\text{m}$ and the resolving power is about one fifth of this difference. In the next section it will be shown how this can be improved by an order of magnitude to be about 60Å.

Evaluation of Bevel Angle

In general a slice is not flat and, although the bevel as produced may be flat, local thickness of a beveled epitaxial layer plotted vs. horizontal position may not be a straight line. Typical surface topographs of silicon slices can be seen in Fig. 3. Usually the contour lines show a maximum or a minimum, manifested by closed lines, and sometimes saddle points.⁵ The radius of curvature of an extremum is roughly between 2 and 20m for 250 μm thick Si slices. Hence the slope may change over 5 mm by an angle 1/500. However, with the procedure described such variations in slope do

⁵ This implies that concavity measured as a standard routine (11) and commonly called bowing or dishing, does not adequately describe the topography of silicon slice. This has been neglected in the ASTM test for thickness of epitaxial layers in silicon by angle bevel and stain technique (12).

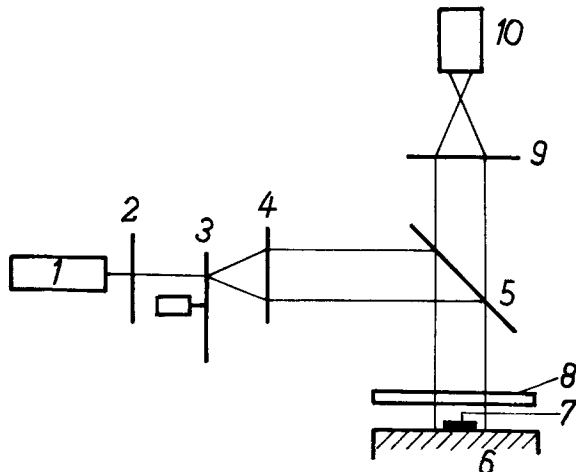


Fig. 2. The layout of the interferometer with the slice placed polished side up: laser (1), mirror (5), diffuser (3), lenses (2, 4, 9), optical flat (8), slice (7), (television) camera (10). With the slice fixed to the jig, the jig rests on the optical flat and the light is incident from below.

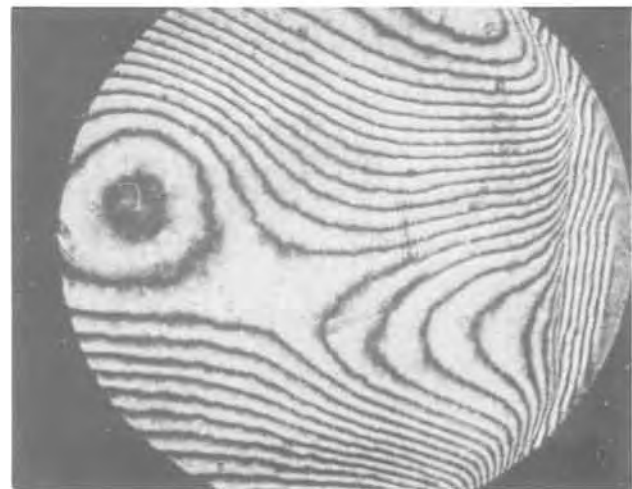
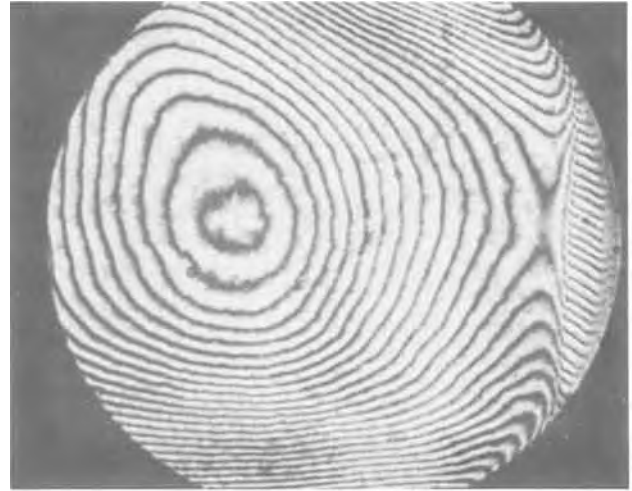


Fig. 3. Typical topographs of silicon slices. On the right-hand side of the reference flat the aluminum support is visible, which also reflects.

not present a real problem because the profiles of both the original surface and the polished beveled surface can be measured accurately.⁶ To produce a bevel the slice is mounted on the jig of Fig. 1 and the mirror (8) of Fig. 2 is placed on top of the silicon pieces G of the jig. Using the screws E the piston A is adjusted such that on the television monitor a pattern arises with easily recognizable features. This pattern is photographed. Then the desired angle is adjusted with

⁶ Sometimes the curvature is so strong that the camera does not resolve the contour lines at a few millimeters from the center. Such slices cannot successfully be beveled and should be rejected for IC processing as well.

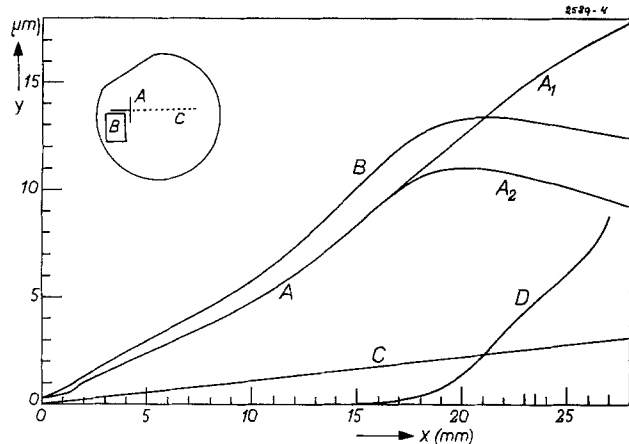


Fig. 4. Profiles of the original surface (A), of the beveled surface (B) and the depth below the surface (D). The auxiliary line C is the difference between the left-hand sides of A and B. When the right-hand side of B is corrected by the difference C, the line A_2 is found. The difference between A_1 and A_2 yields curve D which represents the true depth below the original surface. In the inset the scratch mark A, the patch of paper B and the spreading resistance track C are shown.

screws E and the piston is lowered until the slice touches the optical flat and is fixed again with screw C. After lapping and polishing, the slice is positioned again such that the pattern on the nontouched part of the slice compares well to the photograph made earlier and photographed again. Then the bevel angle is determined from the two photographs under the microscope as described in detail below. Of course, the pattern on the slice before beveling is arbitrary, because it only serves the purpose of providing a reference to the position of the beveled surface by means of the nontouched part adjusted to show identical patterns in both situations.

In practice the procedure runs as follows. A mark, labeled A in the inset of Fig. 4, is scratched on the slice. In order to see this mark on the photograph a small rectangular patch of paper, noted B in Fig. 4, is glued to the slice. The slice is adjusted to such an angle with the optical flat that a number of closely spaced interference fringes perpendicular to the track C is visible, and photographed (Fig. 5a). This slope may correspond to the desired angle, otherwise the desired angle is adjusted, the patch of paper is removed, and

the slice is beveled. As before, a patch of paper is glued on the slice and the slice is adjusted as well as possible in the same position as before beveling and photographed (Fig. 5b). Then, from the photographs the profiles along the track to be made, are measured and plotted. Of course it will not be possible to reproduce precisely the pattern on the nontouched part. This is shown clearly in Fig. 4, where curve A represents the profile as measured on the original photograph. After beveling, the profile labeled B is measured, which is different from the original one, though the left-hand side nontouched parts should be identical. This arises from the fact that the angles with respect to the optical flat in the two cases were slightly different. This can be corrected by pivoting curve B around the origin so that A and B are coincident. The difference between curve A and the first part of curve B turns out to be, as expected, a straight line, labeled C. Extrapolating this correction, due to a slightly different tilt of the slice, over the range where the slice has been beveled, the true surface profile curve A_2 is obtained from the measured curve B. The difference between curve A_1 and A_2 , plotted as a curve labeled D, is the true depth below the original surface. Due to the surface topography and the nature of the polishing process, there is no linear relation between depth and horizontal position. Therefore some method to obtain a curve like curve D of Fig. 4 is definitely indispensable for precise and accurate work, in which the local thickness should be precisely and accurately known.

A particularly interesting application of this technique in which tilt is used to increase the resolving power of details in height, runs as follows. The slice is positioned almost parallel to the optical flat (Fig. 6a) and the positions of the fringes are plotted as curve A in Fig. 7. Thereupon the slice is tilted (Fig. 6b) and the positions of the fringes are plotted again. From this plot a vertical distance increasing linearly with horizontal position corresponding to the tilt angle should be subtracted, yielding curve B in Fig. 7. The number of observation points has been increased with the slope. In this way details in height structure are revealed which cannot be obtained with the conventional interference contrast microscope. In the example shown the slice has been tilted by about $1/1000$ and vertical details as small as 60\AA can be resolved. This can be decreased further. Of course, there is no reduction of the horizontal scale so that this technique could be considered to be a nontouching version of the moving stylus method.

Manuscript submitted March 15, 1974; revised manuscript received Nov. 26, 1974.



Fig. 5. Topograph of a slice adjusted before beveling (a, left) and after beveling (b, right). A small rectangular patch of paper glued on the slice, serves as a starting point for the photographic analysis and spreading resistance measurements.

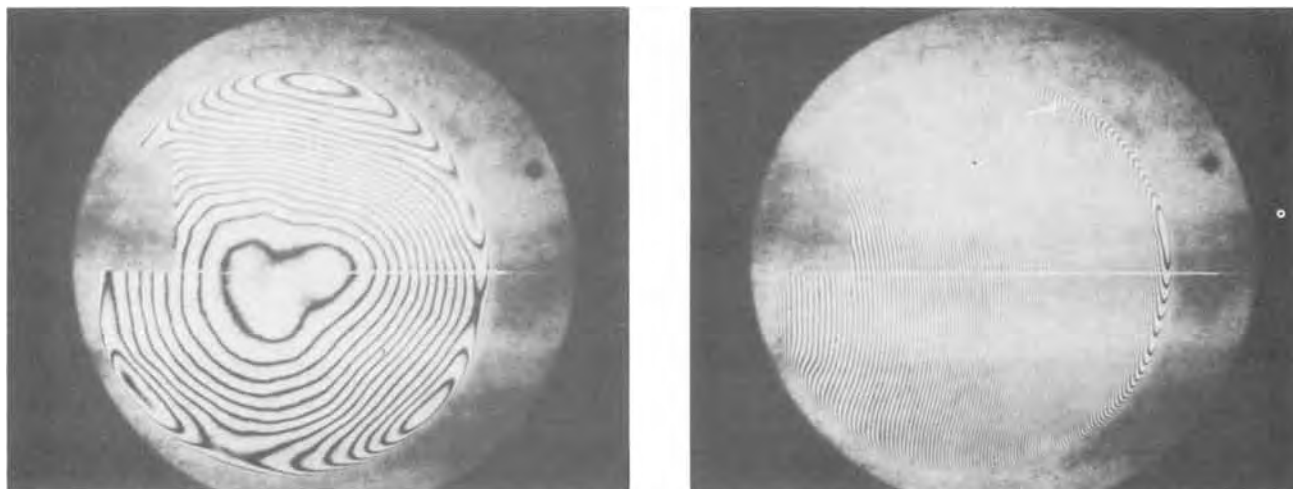


Fig. 6. Topograph of a silicon slice adjusted to be almost parallel (a, left), and under an angle of about $1/1000$ (b, right) to the optical flat.

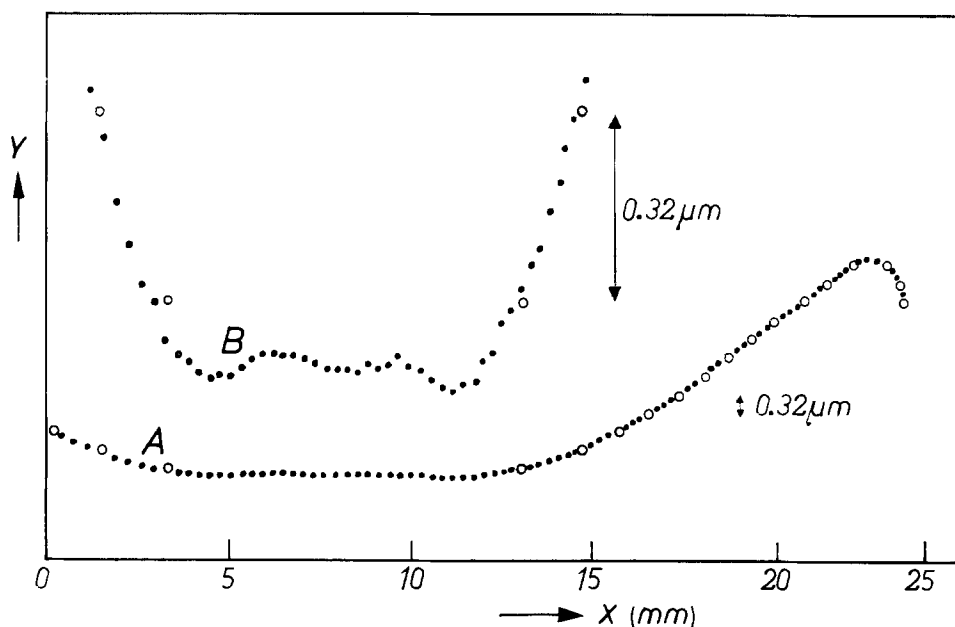


Fig. 7. The position of the fringes measured on the topograph shown in Fig. 6a yields curve A (○). The position of the fringes measured on the topograph shown in Fig. 6b yields curve B (●) after a vertical distance linearly related to the horizontal position has been subtracted. The closed circles have been drawn in curve A after curve B had been obtained. Note that the vertical scales for curves A and B differ by a factor 10.

Any discussion of this paper will appear in a Discussion Section to be published in the December 1975 JOURNAL. All discussions for the December 1975 Discussion Section should be submitted by Aug. 1, 1975.

Publication costs of this article were partially assisted by Philips Research Laboratories.

REFERENCES

1. P. J. Severin, *Solid-State Electron.*, **14**, 247 (1971).
2. R. Sittig and W. Zimmerman, *Phys. Status Solidi*, **A12**, 663 (1972).
3. P. J. Severin and G. Poodt, *This Journal*, **119**, 1384 (1972).
4. Yu. P. Boitsov, V. J. Prokhorov, and V. T. Mashekin, *Instr. Exp. Techn.*, **5**, 1292 (1970).
5. W. L. Bond and F. M. Smits, *Bell System Tech. J.*, **35**, 1209 (1956).
6. C. S. Fuller and J. A. Ditzenberger, *J. Appl. Phys.*, **27**, 544 (1956).
7. H. W. Gutsche, 6th IEEE Microelectronics Symp., Clayton (1967).
8. Ph. F. Kane and G. B. Larrabee, "Characterization of Semiconductor Materials," McGraw-Hill Book Co., New York (1970).
9. K. Herff and E. Roeder, *Praktische Metallografie*, **9**, 615 (1972).
10. G. A. Bennett and R. B. Wilson, *J. Sci. Instr.*, **43**, 669 (1966).
11. Monsanto Evaluation Standards, Monsanto Electronic Materials, St. Peters, Missouri, 1973, No. 16-ME-005-0472.
12. ASTM Book of Standards, part 8, F110-72.

The Use of Metalorganics in the Preparation of Semiconductor Materials

VI. Formation of IV-VI Lead and Tin Salts

H. M. Manasevit* and W. I. Simpson

Rockwell International Corporation, Electronics Research Division, Anaheim, California 92803

The ever-increasing interest in the use of IV-VI compounds, particularly PbTe and $Pb_{1-x}Sn_xTe$, for IR detectors and the success demonstrated in the use of metalorganics in preparing III-V and II-VI compounds and alloys (1) prompted a study to extend the metal-organic chemical vapor deposition (CVD) technique to the preparation of IV-VI compounds also. Growth studies were performed on PbTe and on single-crystal insulating substrates transparent in the visible part of the spectrum. The transparent substrates were used in order to help in determining the onset of crystal growth as evidenced by a darkening of the substrate and to facilitate optical studies and microprobe analyses of the crystals formed. These substrates included mechanically polished Al_2O_3 , $MgAl_2O_4$, and BaF_2 , and freshly cleaved (in air) MgO, NaCl, CaF_2 , and BaF_2 . BaF_2 was the primary insulator used in these investigations since in thin wafer form it is transparent to 11-12 μm radiation, is more stable than NaCl at temperatures $\sim 625^\circ C$, and matches the thermal expansion of the IV-VI's relatively closely (2).

The metalorganic compounds used in this study, some of their pertinent properties, and the suppliers are listed in Table I.

The Pb, Sn, and Te compounds were used as received in stainless steel bubblers except for purging with H_2 carrier gas prior to use in film growth experiments. The bubblers were maintained at room temperature during film growth. Pd-purified H_2 at a total flow of about 10 liters/min was used as the carrier gas in the deposition experiments. H_2S and H_2Se were at a minimum purity of 99.5 and 98.0%, respectively (Matheson Gas Products, East Rutherford, New Jersey).

BaF_2 and CaF_2 were purchased from the Harshaw Chemical Company (Solon, Ohio). Rockwell polished single-crystal BaF_2 windows and BaF_2 and CaF_2 wafers cleaved from 1 in. diameter rods were used as substrates. Cleaving into (111)-oriented substrate blanks was performed just prior to use in a film growth experiment. The $\alpha-Al_2O_3$ was Czochralski material from Union Carbide Corporation (San Diego, California) and polished by Insaco (Quakertown, Pennsylvania). The $MgAl_2O_4$ was produced and polished by Union Carbide Corporation. The NaCl and MgO were single crystals that were cleaved just before use.

The PbTe substrates were all wafers sawed from crystals obtained from Electronic Materials Corpora-

tion (Pasadena, California) and polished in our laboratory (3). A slice of $Pb_{0.80}Sn_{0.20}Te$ was also obtained from this vendor for use as a standard for electron microprobe (EM) analysis of film composition. The probable accuracy of the composition was quoted by the supplier as ± 1 mole per cent (m/o) as measured by the x-ray lattice parameter method.

Elemental scans by the EM were used to determine that the films formed were free of major impurities and consisted of the desired elemental constituents. Electrical measurements ranged from conductivity-type determinations with a thermoelectric probe to measurements of the carrier mobility and concentration in the films by the van der Pauw technique (4) at both room temperature and $77^\circ K$. Ohmic contact was made to the film usually by pressing small beads of In metal onto the film surface. Optical data to provide bandgap (and thus composition) information were obtained from transmittance scans made with a Beckman Model IR-5A infrared double-beam spectrophotometer.

The reactor used for this work was similar to the vertical quartz tube used in previous studies at Rockwell of III-V and II-VI film growth by the metal-organic CVD process (5-7). Measurements of the temperature of film deposition were accomplished by means of an infrared radiation thermometer (Infrared Industries Model TD-6B) used to sense the temperature of the SiC-coated pedestal through the wall of the quartz reactor tube.

Because it was noticed early in the studies that DMTe reacted with a hot BaF_2 surface, presumably forming BaTe, most of the subsequent compound growth studies involved premixing the reactants prior to their introduction into the reactor (except as noted). After film growth, the Group IV metalorganic reactant flows were stopped, and the film was maintained at the growth temperature in flowing H_2 and the Group VI containing gas for 1 min. The DMTe or hydride flow was then stopped, and the rf field was switched off.

PbTe Growth using Tetraethyllead (TEPb) or Tetramethyllead (TMPb) and Dimethyltellurium (DMTe)

Both TEPb and TMPb when mixed with DMTe and pyrolyzed in H_2 at temperatures as low as $475^\circ C$ led to the formation of PbTe. The initial experiments were performed with TEPb, which was more readily available than the reportedly "unstable" TMPb (8), and

* Electrochemical Society Active Member.

Key words: heteroepitaxy, IV-VI compounds, PbTe, $PbSnTe$, CVD.

Table I. Metalorganic compounds used for CVD experiments

Compound	Formula	Supplier*	Melting point ($^\circ C$)**	Boiling point ($^\circ C$)**	Reported vapor pressure**
Tetramethyllead	$(CH_3)_4Pb$	A.P. and S.C.	-27.5	110	10 mm at $4.4^\circ C$
Tetraethyllead	$(C_2H_5)_4Pb$	A.P.	-135	198-202	10 mm at $78^\circ C$
Tetramethyltin	$(CH_3)_4Sn$	A.P.	-53	78	10 mm at $-20.6^\circ C$
Tetraethyltin	$(C_2H_5)_4Sn$	Org.	-112	179.5-181.5	10 mm at $73^\circ C$
Dimethyltellurium	$(CH_3)_2Te$	A.P. and S.C.	-10 (-150)	82	—

* A.P. = Alfa Products, Beverly, Massachusetts; S.C. = Strem Chemical, Inc., Danvers, Massachusetts; Org. = Orgmet, Inc., East Hampstead, New Hampshire.

** D. R. Stull, *Ind. Eng. Chem.*, 39, 517 (1947); see also "Handbook of Organometallic Compounds," H. C. Kaufman, Editor, D. Van Nostrand Co., New Jersey (1961).

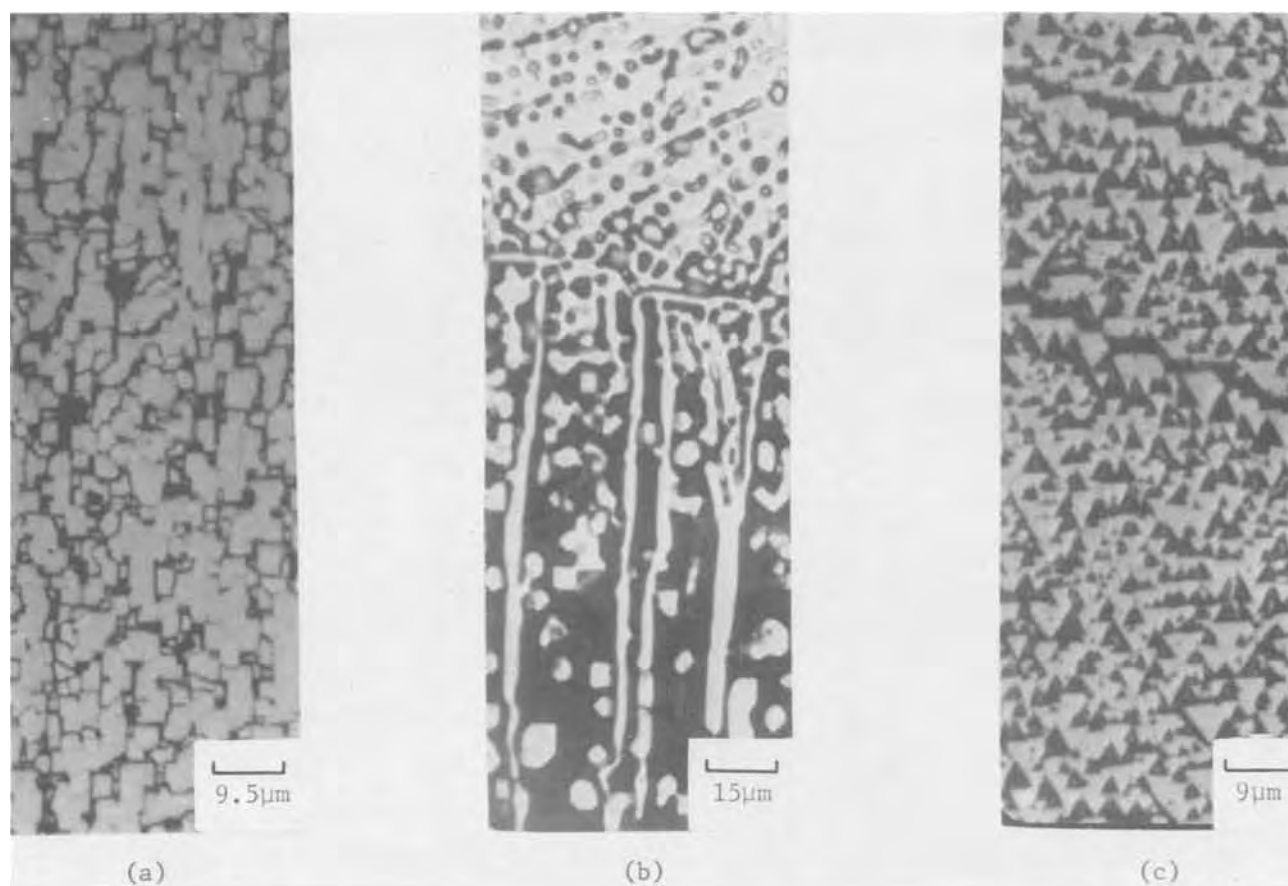


Fig. 1. Ordered growth of PbTe on cleaved (a) (100)MgO, (b) (100)NaCl, and (c) (111)BaF₂

conditions were established for growth of PbTe on BaF₂, MgO, NaCl, (0001)Al₂O₃, and (111)MgAl₂O₄.

The crystallographic ordering of the overgrowths shown in Fig. 1 suggested that epitaxy of PbTe had been obtained on cleaved (100)-oriented MgO, (100)-oriented NaCl, and (111)-oriented BaF₂ at film growth temperatures of 500°-525°C. Cleavage steps on the NaCl surface tended to act as scavengers for the film nuclei. The PbTe film on NaCl also displayed a "worm-like" structure, perhaps caused by an erosion of the NaCl surface in H₂ prior to being completely covered with PbTe. A 7.5 μm thick overgrowth on BaF₂ (Fig. 1c) displayed the trigonal structure usually associated with (111) growth.

Growth phenomena on Al₂O₃ and MgAl₂O₄ were different from those obtained on the other substrates. Crystallite growth was obtained on (0001)Al₂O₃ and (111)MgAl₂O₄ under film growth conditions which led to continuous film growth on BaF₂. Most of the crystallites were highly ordered on (0001)Al₂O₃ surfaces (see Fig. 2). They displayed a threefold specular reflection during rotation while the film was growing. By changing the deposition procedure slightly, that is, introducing TEPb into the reactor first, DMTe next, and then the TEPb-DMTe mixture, a continuous film on both (0001)Al₂O₃ and (111)MgAl₂O₄ was formed, as shown in Fig. 3. It was assumed that a first deposit, presumably of Pb, was converted to PbTe by the DMTe, and that subsequent growth of PbTe took place preferentially at nucleation sites produced in the previous steps. The true nature of this growth process has not yet been determined. Films at least 5 μm thick did not peel or pop off the substrates, in spite of the considerable tension generated by the large differences in thermal expansion coefficients

$$\begin{aligned} [\alpha_{\text{PbTe}} = \sim 27 \times 10^{-6}/^{\circ}\text{C}; \quad \alpha_{\text{Al}_2\text{O}_3} = \sim 8 \times 10^{-6}/^{\circ}\text{C}; \\ \alpha_{\text{MgAl}_2\text{O}_4} = 7.5 \times 10^{-6}/^{\circ}\text{C}] \quad [\text{Ref. (2)}] \end{aligned}$$

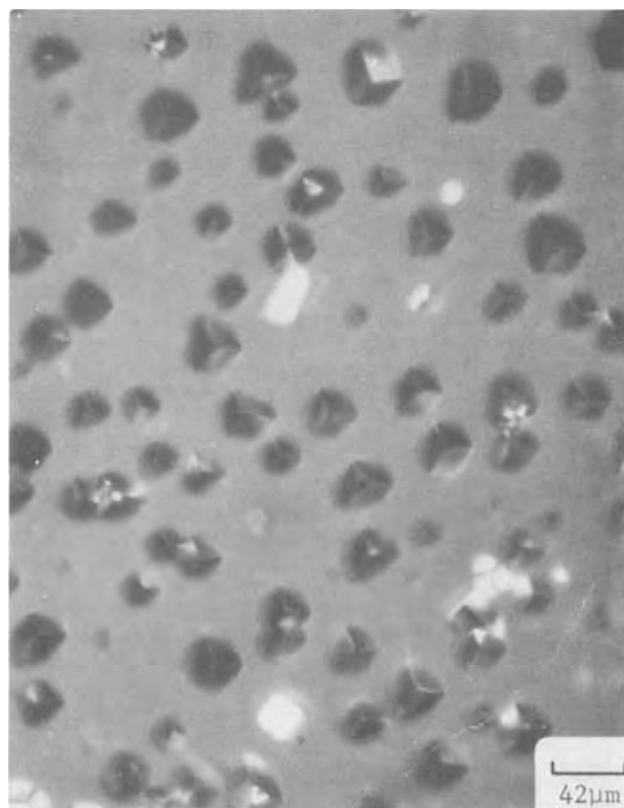


Fig. 2. Highly ordered PbTe crystallite growth on (0001)Al₂O₃

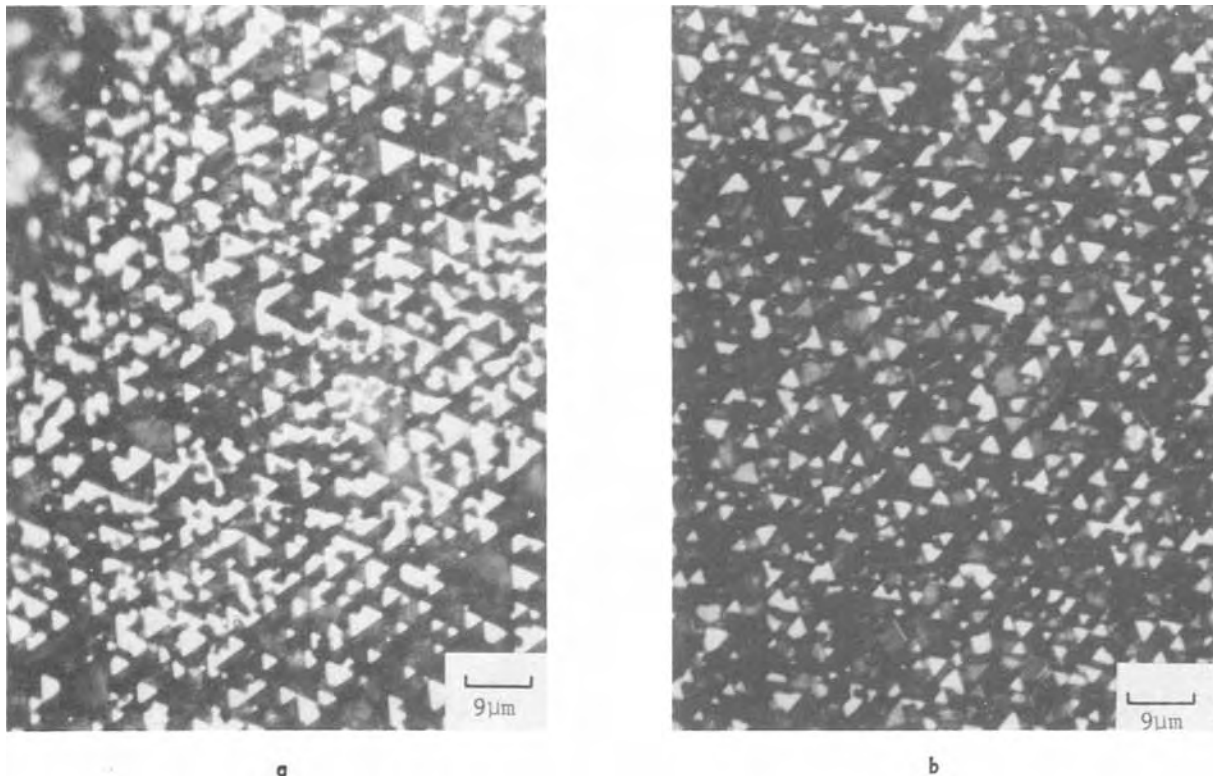


Fig 3. PbTe growth on (a) (0001)Al₂O₃ and (b) (111)MgAl₂O₄, after nucleating the film growth with Pb deposit. (Film thickness $\sim 3 \mu\text{m}$)

X-ray measurements established the relationships shown in Table II. Although the (111)PbTe and BaF₂ planes are parallel, 60° azimuthal rotation in the (111) plane is observed for these cubic materials. A 30° azimuthal rotation is noted for $\sim(111)$ PbTe on (111)MgAl₂O₄.

Optical transmittance scans made on the PbTe films indicated a bandgap energy of $\sim 0.33 \text{ eV}$ at room temperature, which is in agreement with other published values (9, 10).

Studies using the lower boiling tetramethyllead (TMPb) in place of TEPb as the source of Pb were found to be quite beneficial; PbTe growth rates at $\sim 575^\circ\text{C}$ increased from $\sim 4\text{--}5 \mu\text{m/hr}$ (when the flow through the TEPb was 1 liter/min) to values up to about $60 \mu\text{m/hr}$ (when the flow through the TMPb was $400 \text{ cm}^3/\text{min}$). When the H₂ flow rates through TMPb and DMTe were adjusted to provide a flow ratio of about 1.3:1, a high quality p-type film of PbTe was grown at 625°C on a cleaved (111)BaF₂ substrate. The $13.8 \mu\text{m}$ thick film displayed the following electrical properties at room temperature: mobility (μ) = $632 \text{ cm}^2/\text{V}\text{-sec}$; hole concentration (p) = $1.7 \times 10^{18} \text{ cm}^{-3}$. For a flow ratio of about 3:1 and a growth rate of $\sim 32 \mu\text{m/hr}$, an n-type film was grown. At room temperature, a mobility of $900 \text{ cm}^2/\text{V}\text{-sec}$ was measured for the $16 \mu\text{m}$ thick film with a carrier concentration (n) of $5.3 \times 10^{16} \text{ cm}^{-3}$; at 77°K , $\mu = 22,500 \text{ cm}^2/\text{V}\text{-sec}$ and $n = 4.3 \times 10^{16} \text{ cm}^{-3}$. At higher TMPb-DMTe flow ratios (6:1) deposits on BaF₂ were formed with meshlike structures which appeared to be composed of needles and molten metal intermixed.

Table II. Epitaxial relationships for PbTe growth on Al₂O₃, MgAl₂O₄, and BaF₂

Parallel planes	Parallel directions
(111)PbTe// (0001)Al ₂ O ₃	$[\bar{1}10]$ PbTe// $[\bar{1}2\bar{1}01]$ Al ₂ O ₃
$\sim(111)$ PbTe// (111)MgAl ₂ O ₄	$[2\bar{1}1]$ PbTe// $[\bar{1}01]$ MgAl ₂ O ₄
(111)PbTe// (111)BaF ₂	$[\bar{1}10]$ PbTe// $[0\bar{1}1]$ BaF ₂

Growth of Pb_{1-x}Sn_xTe Films using TEPb or TMPb, DMTe, and Tetraethyltin (TESn)
By pyrolyzing three-component mixtures of TEPb or TMPb, DMTe, and TESn in H₂, epitaxial films of

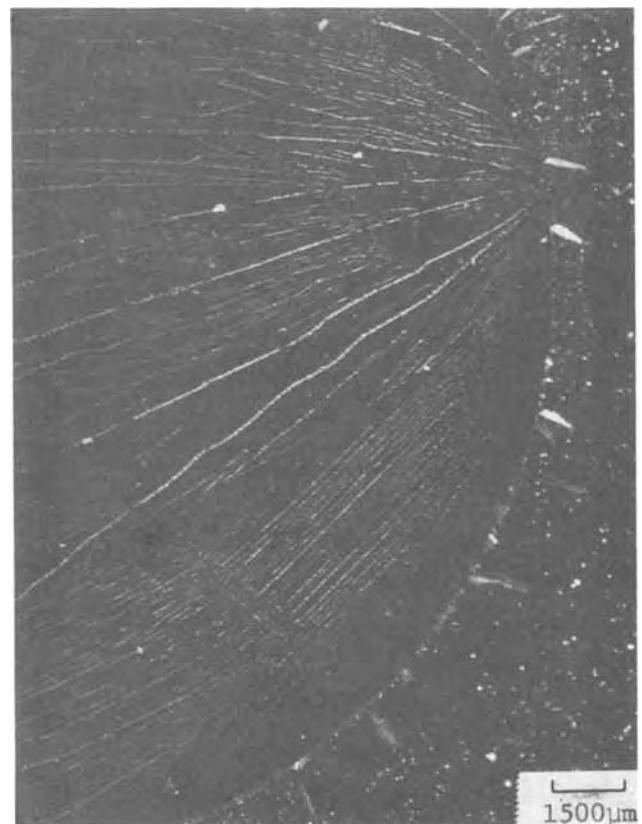


Fig. 4. Thick Pb_{0.8}Sn_{0.2}Te film on substrate of cleaved (111)-oriented BaF₂ (substrate is resting on SiC-covered C pedestal).

$Pb_{1-x}Sn_xTe$ were readily formed at $\sim 550^\circ\text{--}625^\circ\text{C}$ on (100)PbTe and cleaved (111)BaF₂ substrates. In these experiments, films with values of x up to 0.4 were produced. Growth rates of 6–8 $\mu\text{m/hr}$ were realized at 550°C for $Pb_{0.8}Sn_{0.2}Te$ when flows of 1 liter/min were used to transport the TEPb or flows of 50 cm^3/min were used for the TMPb, with the concentration of TESn essentially constant at a H₂ flow of 3 liters/min. At 625°C , the growth rate of the alloy was $\sim 20 \mu\text{m/hr}$ with the TESn flow at 2 liters/min.

Polished (111)BaF₂ surfaces, which were found to be generally not amenable to the growth of good quality PbTe nor $Pb_{1-x}Sn_xTe$, also seemed to suffer from the same type of atmospheric contamination that prevented good film growth on cleaved (111)BaF₂ surfaces that were exposed to the laboratory atmosphere for a few minutes. However, polished (100)BaF₂ was sufficient in many cases for the growth of almost featureless (100)-oriented PbTe and $Pb_{1-x}Sn_xTe$ films.

Films with $x \sim 0.2$ on cleaved (111)BaF₂ were p-type as grown, with room temperature resistivities (ρ) $\approx 2 \times 10^{-3}$ ohm-cm, hole concentrations (p) $\approx 5 \times 10^{18}$ cm^{-3} , and mobilities (μ) ≈ 570 $\text{cm}^2/\text{V-sec}$; at 77°K , $\rho \approx 2.5 \times 10^{-4}$ ohm-cm, $p \approx 7 \times 10^{18}$ cm^{-3} , and $\mu \approx 3500$ $\text{cm}^2/\text{V-sec}$, properties consistent with those measured in some films of this composition grown by a two-source vacuum deposition method (11). Additional electrical and device properties of these films will appear elsewhere (12).

The growth of very thick ($\sim 100 \mu\text{m}$) epitaxial $Pb_{0.8}Sn_{0.2}Te$ films on cleaved (111)BaF₂ substrates resulted in spike formation at the periphery of the substrate, and cleavage steps on the surface were clearly revealed (Fig. 4). Figure 5 illustrates the nature of some of the crystal spikes that emanated from the edges. The "shingled" effect was common on these growth spikes. Many of the crystals seemed to grow in a helix form and to possess a hollow interior. The growth habit of these crystals could be the basis of an interesting study.

A film of $Pb_{0.8}Sn_{0.2}Te$ grown to a thickness of $\sim 100 \mu\text{m}$ on polished (100)PbTe possessed a heavily textured surface. It was characterized by a number of prominent crystallographic "out-croppings" similar to those occurring in thick films grown on BaF₂. A photomicrograph of the surface of such a thick (100)-oriented film is shown in Fig. 6.

Studies using Tetramethyltin (TMSn) as a Source of Sn

Tetramethyltin (TMSn) was evaluated as a possible source of Sn in place of TESn, in order to determine if films of composition $Pb_{0.8}Sn_{0.2}Te$ could be grown at high growth rates using the lower boiling (more volatile) TMSn. Several experiments using the TMSn, however, demonstrated that at $550^\circ\text{--}600^\circ\text{C}$ the efficiency of Sn formation from TMSn is inferior to that from TESn; even at relatively high flow rates of car-

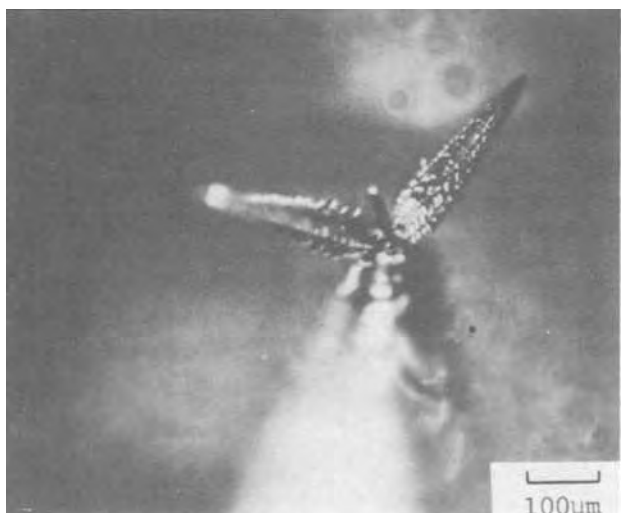
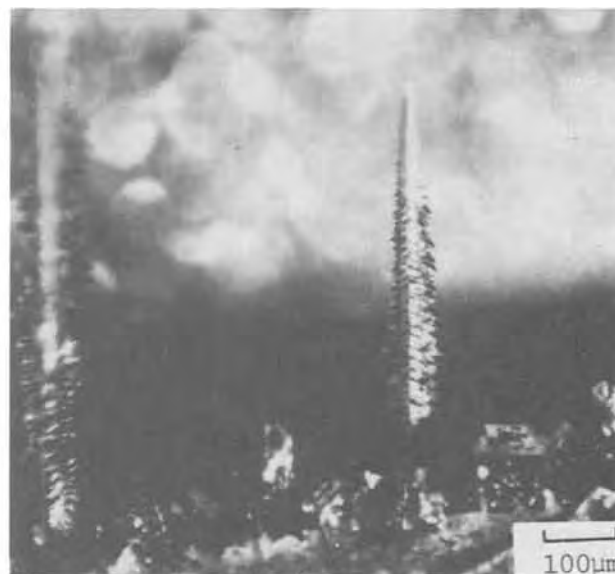
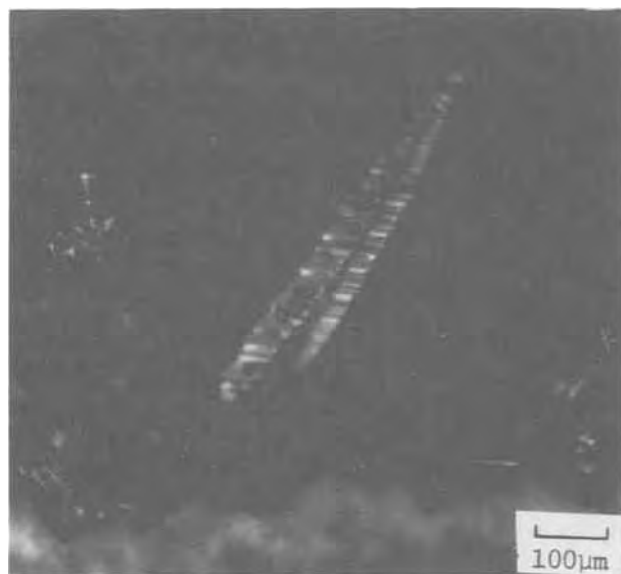


Fig 5. Various crystallite growth forms found around periphery of $Pb_{0.8}Sn_{0.2}Te$ deposit on BaF₂ shown in Fig. 4.

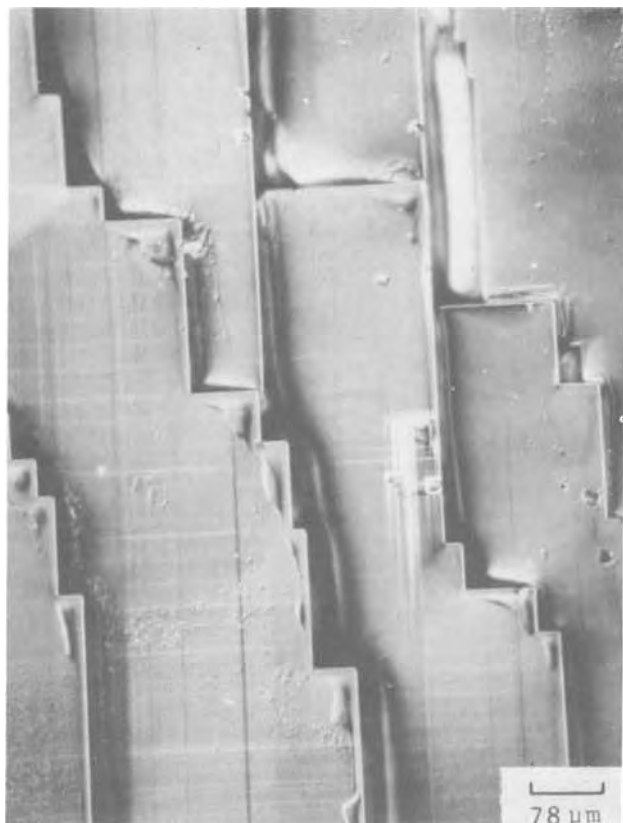


Fig. 6. Surface of (100)-oriented p-type $\text{Pb}_{0.8}\text{Sn}_{0.2}\text{Te}$ film ($\sim 100 \mu\text{m}$ thick) grown on polished (100)PbTe substrate.

rier gas through the TMSn ($200 \text{ cm}^3/\text{min}$) alloys with $x > 0.1$ did not readily form.

Growth of PbS and PbSe

Single-crystal continuous films of PbS and PbSe were grown on cleaved (111)BaF₂, cleaved (111)CaF₂, and (0001)Al₂O₃ by pyrolyzing TMPb-H₂S and TMPb-H₂Se mixtures, respectively, at $\sim 550^\circ\text{C}$. Film growth and coverage on Al₂O₃ was much more uniform and extensive than that obtained for PbTe growth on Al₂O₃. For growth rates of 0.1-0.3 $\mu\text{m}/\text{min}$ films as thick as 25 μm possessed a purple cast. Scanning elec-

tron microscope (SEM) photographs taken normal to the surface revealed the nature of the surface of a few films that were grown during these preliminary studies. Pyramidal growth is displayed (Fig. 7) by these PbS and PbSe films on (0001)Al₂O₃ and (111)BaF₂. Needle growth was observed on the edges of BaF₂ substrates when thick films were grown, as occurred for PbTe and Pb_{1-x}Sn_xTe.

PbS and PbSe showed the same epitaxial relationships toward (0001)Al₂O₃ and (111)BaF₂ as did PbTe, and growth on (111)CaF₂ paralleled that obtained for PbTe on (111)BaF₂, including the 60° azimuthal rotation in the (111) plane.

Growth of Sn-VI Films

Some preliminary experiments were also made to determine if reaction of TESn with DMTe, H₂S, and H₂Se would lead to Sn-VI compound formation. In all experiments, the H₂ flow through the TESn was kept constant at 2 liters/min. The flow through DMTe and the H₂S and H₂Se flows were arbitrarily set at 75, 25, and 50 cm^3/min , respectively.

At 625°C , some ordered growth of SnTe was obtained on the substrates examined, cleaved (111)BaF₂, and polished (100)PbTe. Considerable trigonal structure usually associated with (111) growth was obtained on the BaF₂, particularly near the edges of the substrate (see Fig. 8a). Growth on (100)PbTe produced the array of islands shown in Fig. 8b. Large crystallites with parallel faces and, in some cases, prominent hollow centers grew at the edges of the PbTe substrates under these less-than-optimum growth conditions (Fig. 8c).

The nature of the growth of the S and Se chalcogenides of Sn, which possess an orthorhombic structure, was not like that of cubic SnTe. Tin sulfide films, $\sim 3 \mu\text{m}$ thick, grown at 550°C simultaneously on cleaved (111)BaF₂ and (111)CaF₂ tended to peel from the BaF₂ but adhered to the CaF₂. At 500°C , tin selenide grew as crystallites on BaF₂. An orienting influence of the substrate is suggested by the parallelism and 60° symmetry displayed by many of the crystallites (Fig. 9). In the early growth stages the films possessed a yellow-orange color; thicker films were gray (13). Both compounds nucleated poorly on (0001)Al₂O₃. It was not determined if the Sn was in the divalent or quadrivalent state. It was presumably in the former because of the reducing atmosphere used. Further studies in the growth of the Sn chalcogenides are contemplated.

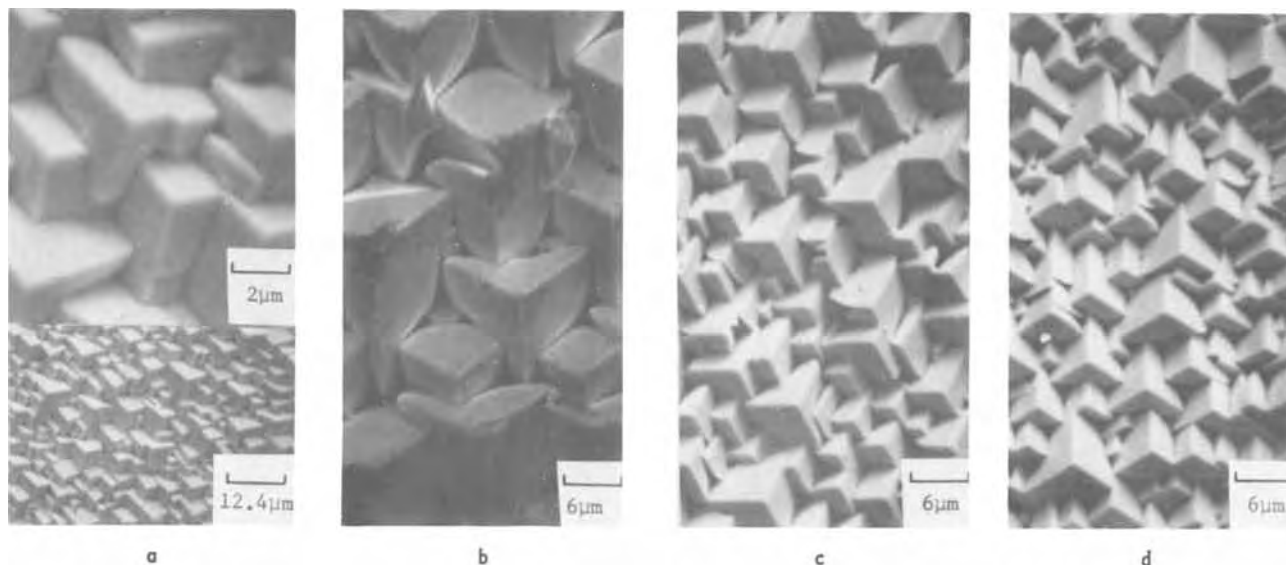
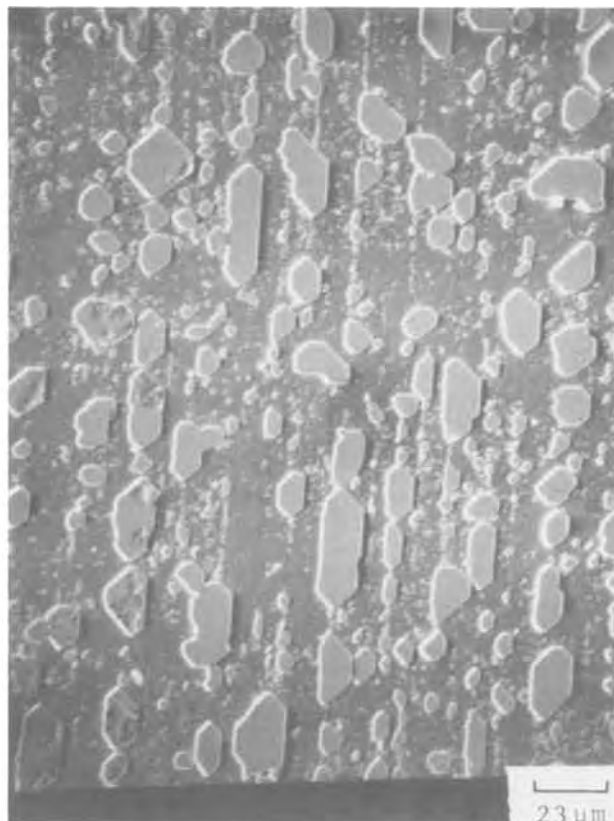


Fig. 7. SEM photographs of (a) PbS/(0001)Al₂O₃ (7.4 μm thick film); (b) PbSe/(0001)Al₂O₃ ($\sim 32 \mu\text{m}$ thick film); (c) PbS/(111)BaF₂ ($\sim 20 \mu\text{m}$ thick film); (d) PbSe/(111)BaF₂ ($\sim 25 \mu\text{m}$ thick film).



a



b



c

Fig. 8. SnTe growth (a) near top edge of cleaved (111) BaF₂; and (b) near the center and (c) at the top edge of a (100)-oriented PbTe substrate.

Conclusion

The metalorganic CVD process has been extended to include the formation of films of a number of Pb and Sn-Group VI compounds and alloys. Epitaxial films of PbTe, Pb_{1-x}Sn_xTe, PbS, and PbSe have been grown to date on substrates such as PbTe, BaF₂, Al₂O₃, and MgAl₂O₄. Tin chalcogenides were also formed. Tetraethyllead or tetramethyllead was used as the source of Pb, tetraethyltin for Sn, dimethyltellurium for Te, and H₂S and H₂Se as the sources of S and Se, respectively.

The as-grown Pb_{1-x}Sn_xTe films were p-type; PbTe films could be grown either p- or n-type by controlling the ratio of the reactants in the gas phase and the growth temperature. For the same carrier concen-

tration range, the Hall mobilities of the films are comparable to those grown by vacuum deposition processes.

Acknowledgments

The authors are grateful to their associates in the Rockwell Electronics Group for assistance with these investigations: J. P. Wendt for measurement of the electrical properties of the films; R. F. Cunningham for the electron microprobe analyses; J. E. Coker and G. W. Johnson for sawing and polishing the PbTe substrates; and L. A. Moudy, Dr. J. L. Kenty, and R. E. Johnson for x-ray and scanning electron microscope examination of some of the films. We also acknowledge the support of Dr. J. L. W. Pohlmann of the Night Vision Laboratory who monitored the cited contract and Dr. R. P. Ruth for reviewing the manuscript.

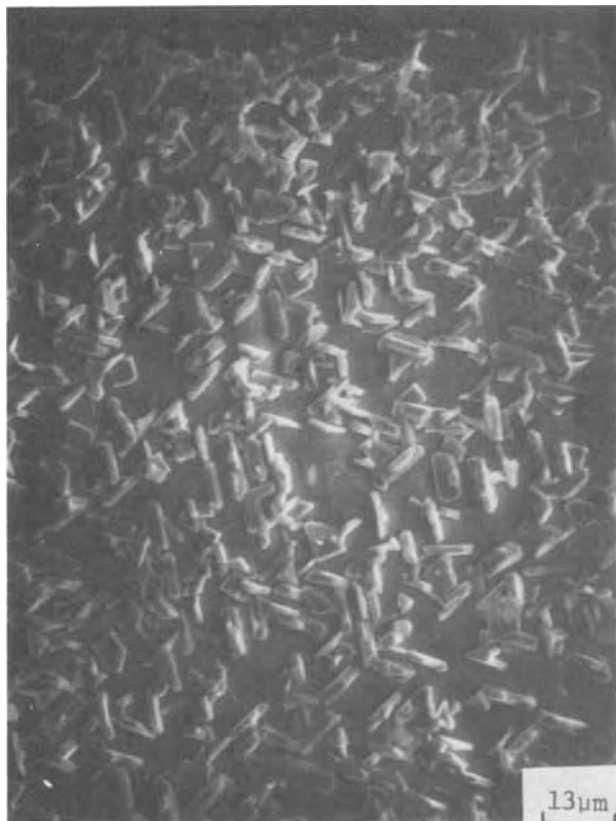


Fig. 9. Tin selenide growth on cleaved (111)BaF₂ (SEM photograph).

This work was supported in part by the Night Vision Laboratory USAECOM, Fort Belvoir, Virginia, under Contract No. DAAK02-73-C-0080.

Manuscript submitted July 30, 1974; revised manuscript received Nov. 5, 1974. This was Paper 12RNP presented at the San Francisco, California, Meeting of the Society, May 12-17, 1974.

Any discussion of this paper will appear in a Discussion Section to be published in the December 1975 JOURNAL. All discussions for the December 1975 Discussion Section should be submitted by Aug. 1, 1975.

Publication costs of this article were partially assisted by Rockwell International.

REFERENCES

1. H. M. Manasevit, *J. Crystal Growth*, **13/14**, 306 (1972).
2. H. M. Manasevit, *ibid.*, **22**, 125 (1974).
3. J. E. Coker, *This Journal*, **116**, 1352 (1969).
4. L. J. van der Pauw, *Philips Res. Rept.*, **13**, 1 (1958).
5. H. M. Manasevit and W. I. Simpson, *This Journal*, **116**, 1725 (1969).
6. H. M. Manasevit and W. I. Simpson, *ibid.*, **118**, 644 (1971).
7. H. M. Manasevit, F. M. Erdmann, and W. I. Simpson, *ibid.*, **118**, 1864 (1971).
8. S. E. Cook, Private communication, Ethyl Corp., Baton Rouge, La.
9. J. N. Zemel, J. D. Jensen, and R. B. Schoolar, *Phys. Rev.*, **140**, A330 (1965).
10. W. W. Scanlon, *J. Phys. Chem. Solids*, **8**, 423 (1959).
11. H. Holloway, E. M. Logothetis, and E. Wilkes, *J. Appl. Phys.*, **41**, 3543 (1970).
12. H. M. Manasevit, F. A. Pizzarello, R. P. Ruth, and W. I. Simpson, Submitted to *J. Electron. Mater.*
13. A. G. Mikolaichuk, Ya I. Dutchak, and D. M. Freik, *Sov. Phys. Cryst.*, **13**, 490 (1968).

Brief Communications



Ohmic Contacts to Al-Implanted ZnSe

B. K. Shin,¹ D. C. Look,² and Y. S. Park

Aerospace Research Laboratories, Wright-Patterson Air Force Base, Ohio 45433

The production and characterization of ohmic contacts is an important part of semiconductor technology. In this paper we report the formation of ohmic contacts on ZnSe, by evaporating or sputtering Au or Pt onto the Al-implanted, n-type substrate. Although these metals normally form rectifying Schottky barriers on n-type ZnSe, such barriers are precluded if the implanted layer is degenerate. An advantage of Au or Pt contacts is that much higher operating temperatures are possible than with the commonly used In or Ga.

The Al implantation was carried out at 90 keV to a dose of 10^{15} ions/cm² at room temperature.³ The substrate was a high-resistivity ($\sim 10^9$ ohm-cm) crystal cut to expose the (110) face. Before implantation, the surface was mechanically polished and chemically

etched at 90°C for 1 min in a mixture of 2 parts H₂SO₄ and 3 parts saturated aqueous solution of K₂Cr₂O₇, followed by a 20 sec rinse in a boiling 25% solution of NaOH. In a previous paper (1) it was reported that crystals implanted in such a manner and annealed in evacuated fused-silica ampuls for 4 hr at 900°C showed nearly degenerate electrical characteristics, with an effective electron mobility of about 4 cm²/V-sec and an effective sheet carrier concentration of about 10^{15} cm⁻². When unimplanted samples and samples implanted with Ar ions were annealed under the same conditions, they remained highly resistive. This showed that the Al implantation was essential for the production of the conductive layer, i.e., neither the annealing alone nor the radiation damage produced by Ar ions were sufficient to appreciably change the conductivity of the original substrate. The thickness of the implanted and annealed conductive layer was roughly checked by the use of the etch described above. This etch removes about 50 Å/sec from unimplanted ZnSe at room temperature and the rate for implanted ZnSe

¹Permanent address: Systems Research Laboratories, Incorporated, Dayton, Ohio 45440.

²Permanent address: Department of Physics, University of Dayton, Dayton, Ohio 45469.

Key words: metal-semiconductor contacts, contact resistance, ion implantation.

³The ion implantation was done at NASA Langley Research Center.

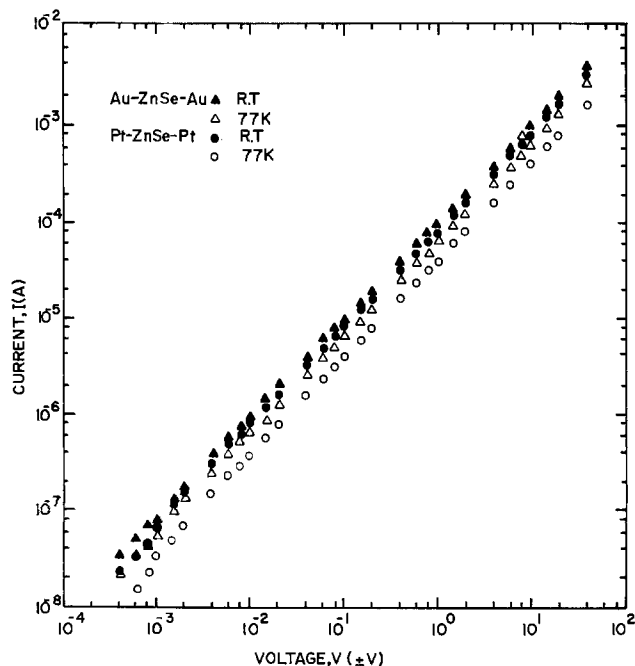


Fig. 1. I - V characteristics of Au and Pt contacts on Al-implanted, annealed ZnSe at 77° and 300°K.

is probably about the same. It was found that etching for about 1000 sec was necessary to reduce the conductivity to that of the original substrate. This suggests that the implanted layer, after annealing, was about 5 μm thick, giving an average doping concentration of about 10^{18} - 10^{19} cm^{-3} . Such a concentration is consistent with the observed nearly degenerate electrical characteristics.

Two Au (or Pt) contacts, of 0.1 cm diameter, were evaporated (or sputtered) 0.35 cm apart on the implanted, annealed surface. Current vs. voltage measurements were carried out at 77° and 300°K, over a voltage range of 4×10^{-4} -40V. The magnitude of the current was the same for both voltage polarities. The results are plotted in Fig. 1. Both Au and Pt contacts were found to be ohmic over five decades of voltage; however, the Pt did show some departure from ohmic behavior below 1 mV. The contact resistance, R_c , was determined from the relationship

$$R_c = \frac{1}{2} (R - R_{\square} L/W) \quad [1]$$

where $R \equiv V/I$, R_{\square} is the sheet resistivity [denoted by ρ' in Ref. (1)], L is the contact spacing, and W is the sample width. The results of this calculation are presented in Table I, but it must be emphasized that Eq. [1] is only approximate with our contact geometry. For comparative purposes we also list the contact re-

Table I. Contact properties of Al-implanted annealed ZnSe

Contact metal	Temperature (°K)	R_{\square} (kohm/ \square)	R (kohm)	R_c (kohm)	ρ_c (ohm-cm ²)
Au	300	8.76	10.40	2.13	16.72
	77	14.10	16.10	3.10	24.33
Pt	300	13.70	12.60	0.95	7.45
	77	28.50	25.40	1.60	12.56

sistivity (2), $\rho_c \equiv R_c A_c$, where A_c is the effective contact area, taken in this case to be just the actual contact area. It is seen that $\rho_c \approx 10$ -20 ohm-cm² for contacts produced in the manner described above.

The small temperature dependence of ρ_c suggests that a tunneling mechanism dominates the thermionic emission. For tunneling in a Schottky barrier at low temperatures and low bias voltages ($V \ll E_b/q$), ρ_c is dominated by (3, 4) $\exp(E_b/E_{\infty})$ where E_b is the effective barrier height, and $E_{\infty} \equiv (\hbar q/2) (N/\epsilon m^*)^{1/2}$. Here N is the doping density (assumed equal to the carrier concentration), ϵ is the specific permittivity, and m^* is the effective mass. If $N \approx 10^{18}$ - 10^{20} cm^{-3} , then E_b must be about 0.1-1 eV, a reasonable range, to give the right order of magnitude for ρ_c . However, this model would predict linear I - V characteristics only for $V \lesssim E_{\infty}/q$, and since $E_{\infty} = 20$ -200 meV for $N = 10^{18}$ - 10^{20} cm^{-3} we would not expect linear behavior above about 100 mV. The fact that such behavior is observed even at 10V suggests that the barrier becomes completely transparent in both forward and reverse bias conditions when a highly doped shallow layer having a surface carrier concentration of $\sim 10^{15}$ cm^{-2} is formed.

Acknowledgments

This work was performed by one of the authors (B.K.S.) under Contract No. F33615-72-C-1099 supported by the Aerospace Research Laboratories, and by another of the authors (D.C.L.) under Contract No. F33615-71-C-1877 supported by the Aerospace Research Laboratories.

Manuscript submitted Feb. 11, 1974; revised manuscript received Oct. 30, 1974.

Any discussion of this paper will appear in a Discussion Section to be published in the December 1975 JOURNAL. All discussions for the December 1975 Discussion Section should be submitted by Aug. 1, 1975.

Publication costs of this article were partially assisted by the Department of the Air Force.

REFERENCES

1. B. K. Shin, Y. S. Park, and D. C. Look, *Appl. Phys. Letters*, **24**, 435 (1974).
2. H. H. Berger, *This Journal*, **119**, 507 (1972).
3. F. A. Padovani and R. Stratton, *Solid-State Electron.*, **9**, 695 (1966).
4. C. Y. Chang, Y. K. Fang, and S. M. Sze, *ibid.*, **14**, 541 (1971).

The Semiconductive Property of Gamma-Ferric Oxyhydroxide

Katsumi Kaneko and Katsuya Inouye

Department of Chemistry, Faculty of Science, Chiba University, Chiba, Japan

The recent investigations by Cohen *et al.* on the passive films deposited upon iron or platinum from neutral ferrous sulfate solution (1) or ferrous perchlorate solution (2) strongly suggest that the composition of these films corresponds to crystalline γ -FeOOH. It appears that the electrical properties of FeOOH-type oxides have not been studied extensively, although the

Key words: passive film on iron, γ -FeOOH, electrical conductivity.

ultimate characteristics of such substances should have pregnant implications for the function of surface films.

In the preceding study on the electrical properties of ferric oxyhydroxides (3), the present authors found that α -, β -, and γ -FeOOH are semiconductors which show d-c conductivity in the order of 10^{-9} ohm⁻¹ cm⁻¹ and high-frequency (7 MHz) conductivity of 10^{-6} - 10^{-7} ohm⁻¹ cm⁻¹ and which probably have negative carriers. The appropriate value of conductivity ob-

tained for each ferric oxyhydroxide was in the order: γ -FeOOH > β -FeOOH > α -FeOOH. These facts were further utilized to discuss the conduction mechanism based on the crystallographic structure of each compound.

In the course of further study, particular changes in the conductivity were observed with respect to the temperature and the oxygen pressure, more markedly for γ -FeOOH than for α -FeOOH and β -FeOOH. Pure α - and β -FeOOH crystals were prepared as described in the preceding report (3) by the hydrolysis of ferric sulfate and ferric chloride solutions respectively at suitable pH ranges. γ -FeOOH was obtained by warming at 60°C for 50 min a solution of 500 ml 0.2M ferrous chloride, 100 ml 2M hexamethylenetetramine, 13.5 ml concentrated HCl, and 100 ml 1M sodium nitrite. The resulting precipitate was washed thoroughly and dried at 100°C for 3 hr for α - and β -FeOOH, and at 60°C for 10 hr for γ -FeOOH. Specimens formed as disks of crystals under a pressure of 150 kg/cm² were set between electrodes in a glass cell, evacuated at 10⁻⁵ Torr, and thus held for 14 hr at the different temperatures of 100°, 110°, 125°, and 140°C. After this pretreatment, the conductivity was determined over the temperature range from -170° to 140°C and various frequencies. For the samples pretreated at 125° and 140°C, the effect of oxygen on the conductivity was examined at 30°C and various total pressures over the range 10⁻²-10⁺² Torr.

It was found that the logarithm of conductivity is proportional to the reciprocal of experimental temperature for each oxyhydroxide. The dependence of $\log \sigma$ on $1/T$ was almost identical for α - and β -FeOOH irrespective of the pretreating temperature, whereas that for γ -FeOOH varied with the pretreating temperature. Moreover, γ -FeOOH pretreated at 125° and 140°C revealed two different slopes of the temperature dependence of d-c conductivity, as shown in Fig. 1, which gave the activation energies of ca. 0.1 eV at the lower temperature region and 0.3-0.4 eV at the higher temperature region. It may thus well be that γ -FeOOH has two conduction mechanisms depending on the temperature. The dividing temperature between the two

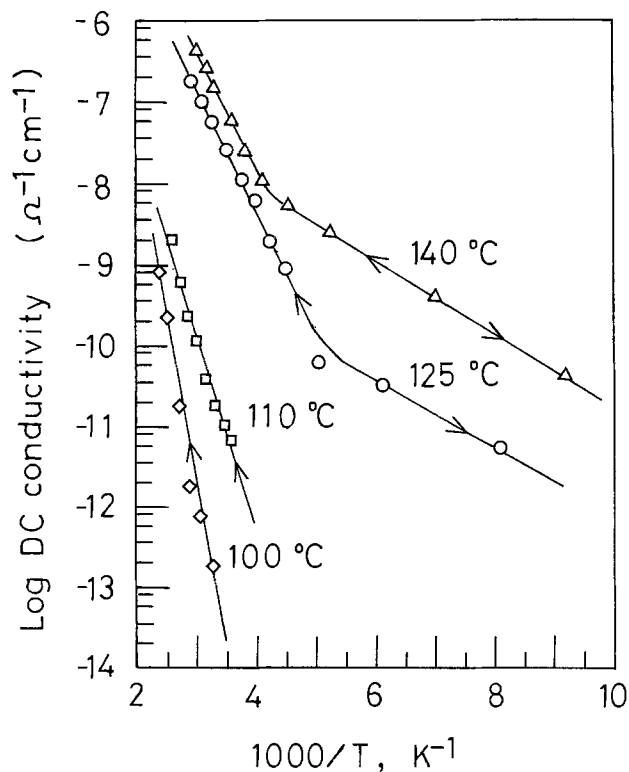


Fig. 1. Temperature dependence of d-c conductivity for γ -FeOOH preheated at different temperatures.

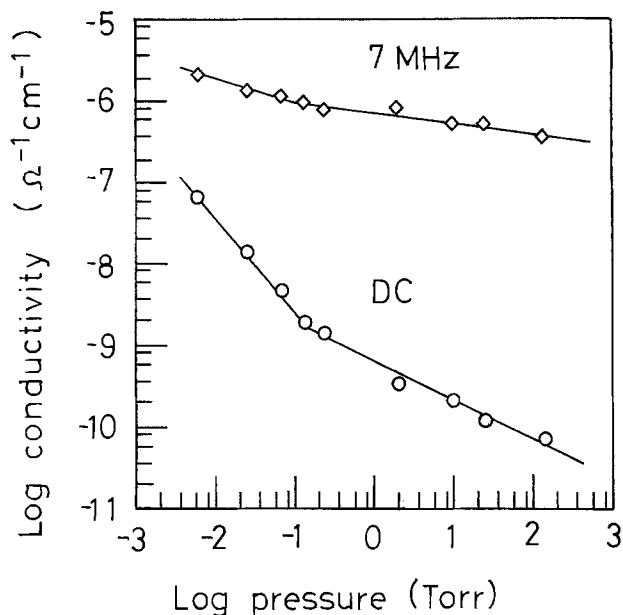


Fig. 2. Decrease of conductivity with oxygen pressure for γ -FeOOH at 30°C preheated at 125°C for 14 hr under 10⁻⁵ Torr.

mechanisms is higher for the 140°C pretreatment than for the 125°C one. The activation energy for the low pretreatment temperature appears to decrease with increasing pretreatment temperature; it could not be determined whether a change in mechanism occurs at these temperatures (100° ~ 110°C), because the conductivity was too low to measure.

The conductivity decreased generally with the oxygen pressure for each oxyhydroxide, but the relationship was most noticeable for γ -FeOOH as shown in Fig. 2, which shows the relationship between the logarithms of conductivity and oxygen pressure for γ -FeOOH pretreated at 125°C. In this figure, two different slopes are observed in both the d-c conductivity and the high-frequency conductivity with a borderline at approximately 0.1 Torr.

These observations may testify that the baking and evacuation of γ -FeOOH in particular result in the formation of oxygen defects in crystals, making the movement of electrons more facile presumably by the increase in mobility. It is interesting that the changes in Fig. 1 were almost reversible with increasing and decreasing temperatures. By irradiating γ -FeOOH with electron beam at 50 kV for not less than 10 min in the vacuum of 10⁻⁵ Torr, the electron diffraction pattern corresponding to (200) became diffuse and faint, indicating possibly the destruction of intra-lamellar lattices of γ -FeOOH crystals. The sharpness of diffraction pattern was recovered by cooling the sample.

It is very likely therefore that γ -FeOOH has a particularly sensitive and mobile structure and the characteristics recognized may be pertinent to the stationary stability of the passive state of iron surfaces.

The detailed results of this experiment will be published elsewhere.

Manuscript submitted Sept. 5, 1974; revised manuscript received Oct. 17, 1974.

Any discussion of this paper will appear in a Discussion Section to be published in the December 1975 JOURNAL. All discussions for the December 1975 Discussion Section should be submitted by Aug. 1, 1975.

Publication costs of this article were partially assisted by Chiba University.

REFERENCES

1. J.-L. Leibenguth and M. Cohen, *This Journal*, **119**, 987 (1972).
2. M. Cohen and K. Hashimoto, *ibid.*, **121**, 42 (1974).
3. K. Kaneko and K. Inouye, *Bull. Chem. Soc. Japan*, **47**, 1139 (1974).



A Polarization Cell for Organic Electrolytes

G. A. Capuano*

Department of Chemistry, University of Quebec in Montreal, Montreal, Quebec, Canada

and W. G. Davenport

Department of Mining and Metallurgical Engineering, McGill University, Montreal, Quebec, Canada

ABSTRACT

An all-glass cell for studying the polarization behavior of organic electrolytes has been developed. The cell is completely enclosed so that the tests can be carried out in isolation from atmospheric moisture. Cathode overvoltages are measured by means of a metal vs. ion reference electrode situated behind the cathode and a 0.8 mm diameter Luggin capillary drilled through the cathode to its working face. Two side reference electrodes are also affixed into the cell. The cell has been tested using a CuSO_4 , H_2SO_4 aqueous electrolyte and an ethyl benzene-toluene 1:1 (50 weight per cent AlBr_3) organic electrolyte. The aqueous tests indicated that the cathode overvoltage can be determined and reproduced by three independent measurement techniques. Tests with the organic electrolyte have led to consistent Tafel plots which indicate that the cell can be successfully used for corrosive, high viscosity organic electrolytes.

A number of alkyl benzene- AlBr_3 electrolytes have been developed for the plating of aluminum onto metal substrates (1-4). The mechanisms of plating from these electrolytes are not well known, and as a first step in understanding the plating process, an investigation into cathode overvoltages was undertaken. A polarization cell with which overvoltages can be measured while the electrolyte is isolated from the atmosphere was developed specifically for this purpose.

* Electrochemical Society Active Member.

Key words: alkyl benzene electrolytes, aluminum plating, organic electrolytes, overvoltages, polarization cell.

The cell was constructed from glass rather than an organic polymer (plastic) so that it can be used for a wide range of organic electrolytes without fear of contaminating the solution with the container material. It is the object of this paper to describe the design of the polarization cell and its testing and use.

The Cell

The polarization cell is described in Fig. 1, 2, 3, and 4. It consists of a cylindrical glass body with the working electrodes occupying the cross section of the cell, at each end. A reference electrode is situated behind the

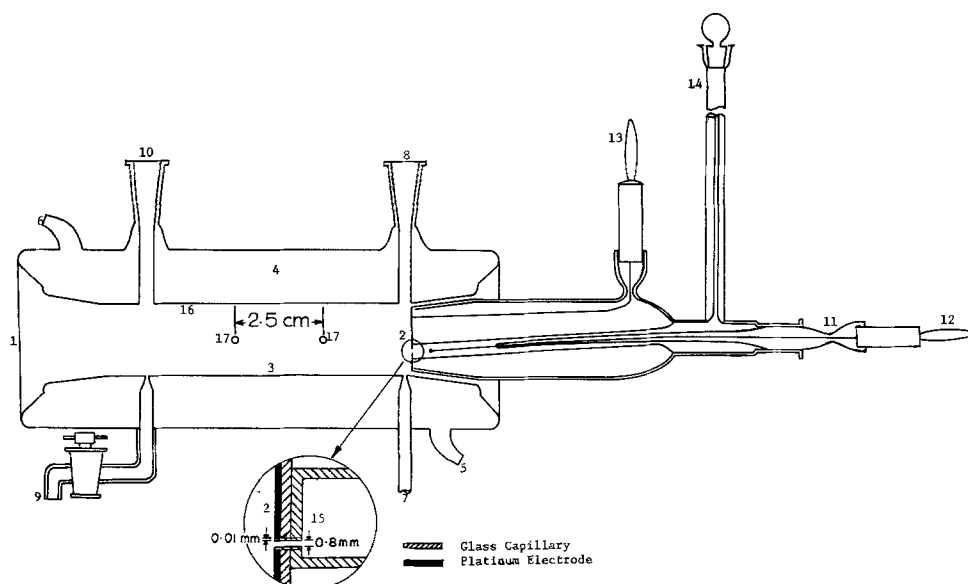


Fig. 1. Section of the polarization cell. 1, Metallic anode; 2, cathode; 3, cell body; 4, water cooling chamber; 5, water inlet; 6, water outlet; 7, inert gas inlet; 8, inert gas outlet; 9, emptying tube; 10, filling tube; 11, back reference electrode; 12, reference electrode electrical connection; 13, cathode electrical connection; 14, gas escape tube to permit filling reference electrode; 15, Luggin capillary behind active cathode; 16, electrolyte; 17, lateral reference electrodes.

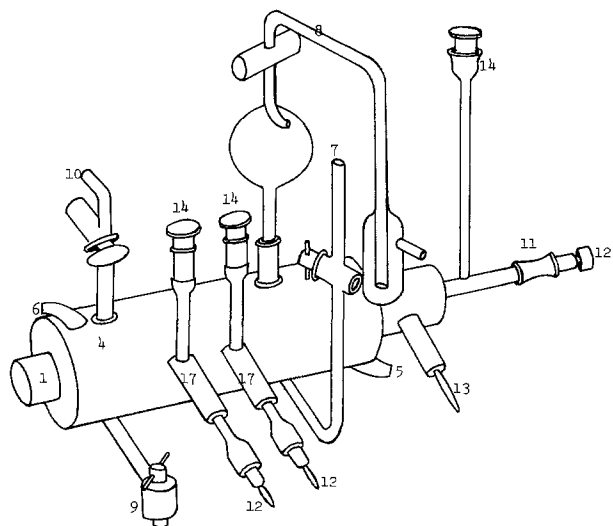


Fig. 2. Spacial view of the polarization cell (see Fig. 1 legend for details).

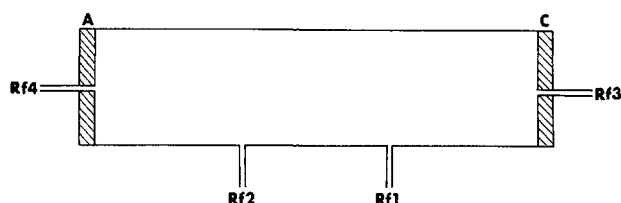


Fig. 3. Sketch showing the positions of the electrodes in the polarization cell.

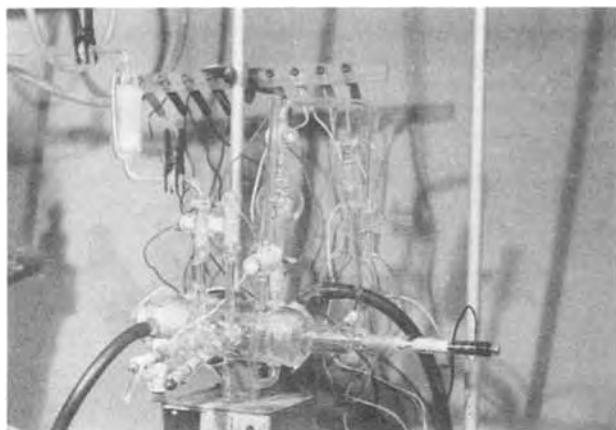


Fig. 4. Photograph of polarization cell with electrical and cooling connections made.

cathode, and it penetrates to the front through a 0.8 mm glass-lined hole (Luggin capillary). The reference electrode is the metal *vs.* ion type, in which the metal is that being plated and the ions are those in the electrolyte. Since the back reference electrode and the working electrode (cathode) are the same material, the dynamic potential difference between them (assuming no *IR* drop or concentration polarization) represents the cathode polarization for any given plating condition.

Comparison with previous cells.—The back electrode design of the present cell is similar to that used by Piontelli (5, 6) for aqueous electrolytes. Piontelli suggests that of all the capillary systems, this configuration provides a minimum of electrical field distortion at the cathode surface. One problem with the Luggin capillary technique is, however, that it introduces a resistance error between the tip of the capillary and

the working face of the cathode. In the case of the reference electrode used in the present cell this manifests itself in an electrolyte resistance which is roughly equivalent to the thickness of the glass lining of the hole through the cathode (0.01 mm).

This resistance problem has been attacked in several ways by other workers, principally Eisenberg (7), and Cahan (8), who also reviews the criteria of good polarization cell design. Eisenberg (7) studied cathode polarization for LiCl-AlCl₃-propylene electrolytes using side reference electrodes in a polypropylene cell. However, this method is subject to concentration polarization errors if the electrolyte is not evenly stirred throughout the cell. It must, therefore, be regarded only as an indirect measurement technique.

Cahan (8) employed a Teflon cell with a thin conical or horizontal slot around the circumference of the cathode surface in place of a Luggin capillary. This design eliminates current distortion at the cathode surface due to the reference electrode and it permits estimation of the resistance error between the cathode and the reference electrode. Cahan's measurements show that the error in this cell is equivalent to about a 0.02 mm column of liquid which is of the same order as that in the present cell (≈ 0.01 mm). The thickness of the horizontal slot can be varied in the Cahan cell, a facility which can be important when stable potentiostatic control is required. Thus the Cahan cell has a number of desirable features. Unfortunately it requires machining during its fabrication which means that its container material is restricted to Teflon or other polymer materials.

Many organic electrolytes will attack polymers so that prior to the development of the present cell it was decided that glass is the only completely satisfactory material. As it turned out this was a propitious choice because Teflon is slowly attacked by the alkyl benzene electrolytes. With an all-glass construction, a back reference electrode connected to the cathode surface via a glass-walled capillary through the cathode, appeared to be the best system of measurement from the points of view of minimizing current distortion and the resistance error.

Experimental

The components of the experimental cell are presented in detail in Fig. 1. The cell consists of a cylindrical glass body, 2 cm in diameter and 7.5 cm long, built within a thermostatically controlled ($\pm 0.1^\circ\text{C}$) water chamber. The anode is a rod of the metal under study, machined to fit the 24/40 T glass joint of the cell. The electrolyte is stirred by means of a micromagnetic Teflon-covered bar. Grease is avoided in all joints and connections of the cell, and Teflon leaves are employed where necessary.

The cathode is a platinum disk, 0.5 mm thick (Fig. 1) and 1.8 cm diameter, affixed by melted glass onto a 24/40 T glass joint. The electrical connection to the power supply is through a platinum wire welded to the back of the cathode.

A 0.8 mm hole was drilled through the platinum disk and its supporting glass joint half way between the center and the border of the disk. This hole (2-3 mm long) provides the connection between the reference electrode and the front of the cathode. It is the actual Luggin capillary of the reference electrode. The side of the hole was insulated by melting a drop of glass into the hole followed by forcing a 0.8 mm diameter needle through it. Microscopic examination showed that the walls were 0.01-0.015 mm thick after this operation. The final step in completing the cathode and back reference electrode system was to weld a receptacle for the reference electrode into the hollow 24/40 T joint (Fig. 1).

The metallic part of the back reference electrode is either a 1 mm diameter platinum wire freshly plated with the metal under study or a 1 mm wire of the

metal under study. It is placed 0.75 cm from the main body of the electrolyte (Fig. 1). Moving the electrode tip ± 0.25 cm from this point was found to have no effect on the polarization measurements. Two auxiliary side reference electrodes are equispaced between anode and the cathode.

The auxiliary apparatus for the cell consists of a potentiostat Type 20 PRT-10X which is used to supply constant current, and a high impedance digital millivoltmeter Type ARIES 1000 with an accuracy of 0.1% of the full scale reading which is used to measure the potential across the electrodes. An ammeter Type MAR 298 with an accuracy of 0.1% of the full scale reading is used for the measurement of current density. These instruments are all "Tacussel" design (TechnEurope, Montreal).

Testing the cell.—The usefulness and accuracy of the cell were tested with (i) an aqueous solution 1N in CuSO_4 , 1N in H_2SO_4 using a copper anode and copper-plated platinum reference electrodes; and (ii) an organic electrolyte, ethyl benzene-toluene 1:1 by volume with 50 weight per cent (w/o) AlBr_3 , using an aluminum anode and aluminum reference electrodes.

The copper sulfate electrolyte was used to evaluate the consistency of the back and side reference electrodes in determining cathode overvoltages. This electrolyte is much more easily prepared and handled than the organic electrolyte and it was, therefore, the first electrolyte studied in the cell. The subsequent organic electrolyte tests used only the back reference electrode and the performance of the cell was evaluated for this system on the basis of the consistency and reproducibility of the measured overvoltages. The results were also compared on the basis of a standard Tafel plot.

Procedures.—The basic experiments for both the aqueous and organic tests were started by filling the cell with prepared electrolyte (an outline of the preparation is appended at the end of the paper), followed by a brief period of plating the particular metal onto the cathode and the back and side electrodes. This was accomplished by connecting the cathode and reference electrodes in turn as the cathode. Once this procedure was complete, the electrodes were connected in their proper working and measuring circuits and normal plating was begun under controlled current density conditions. The potential measurements were made after 1 min of plating at each preset current density.

Measurements and interpretation.—The measurements taken for the copper sulfate electrolyte were (Fig. 3): $E_{(C-Rf3)}$, $E_{(C-Rf1)}$, $E_{(Rf3-Rf1)}$, $E_{(Rf1-Rf2)}$, where the E values represent the difference in potential between the respective electrodes as indicated in Fig. 3.

The results were interpreted on the basis of the following considerations.

(i) Since for each system all the electrodes are of the same metal and since the electrolyte composition is uniform throughout the cell due to its stirring system; then the static potential of each electrode is the same, i.e.

$$e_A = e_C = e_{Rf1} = e_{Rf2} = e_{Rf3} \quad [1]$$

(ii) E_C , the dynamic potential of the cathode during current flow is $e_C + \eta_C$ where η_C is the cathode overvoltage. In the absence of concentration gradients in the cell, as is assumed here, η_C is due entirely to the electrode reactions themselves.

(iii) Thus the potential difference between C and Rf3 (the back reference electrode) during current flow is given by

$$E_{(C-Rf3)} = (e_C + \eta_C) - e_C = \eta_C \quad [2]$$

which means that the overvoltage is measured directly, assuming there is no IR drop between the cathode surface and the Luggin capillary.

(iv) Similarly

$$E_{(C-Rf1)} - E_{(Rf3-Rf1)} = e_C + \eta_C - e_{Rf1} + IRel_{(C-Rf1)} - [e_{Rf3} - e_{Rf1} + IRel_{(Rf3-Rf1)}] \quad [3]$$

where $IRel_{(C-Rf1)}$ and $IRel_{(Rf3-Rf1)}$ are the IR voltage drops in the electrolyte between C and Rf1 and between Rf3 and Rf1, respectively. In this case the cathode C, and Rf3 are essentially at the same position so that the two IR drops cancel and

$$E_{(C-Rf1)} - E_{(Rf3-Rf1)} = \eta_C \quad [4]$$

It can be seen that measurements (iii) and (iv) provide two independent methods of determining η_C . In addition, η_C can be obtained from measurements of $E_{(C-Rf1)}$, $E_{(Rf1-Rf2)}$, and f , the ratio of the electrolyte resistances between C and Rf1 and between Rf1 and Rf2. From these measurements

$$E_{(C-Rf1)} - E_{(Rf1-Rf2)} \cdot f = e_C + \eta_C - e_{Rf1} + IRel_{(C-Rf1)} - [e_{Rf1} - e_{Rf2} + IRel_{(Rf1-Rf2)}]f \quad [5]$$

from which

$$E_{(C-Rf1)} - E_{(Rf1-Rf2)} \cdot f = \eta_C \quad [6]$$

f was determined in preliminary experiments during which a few milliamperes of current were passed through the cell between the anode and Rf3. The resistances were determined from the current flow and the measured voltages between the pertinent electrodes. For our specific cell, f has the value of 1.10.

In summary then, measurements of four potential differences and a preliminary determination of the relative resistances between electrodes provides three independent methods of determining the cathode overvoltage. In testing the cell, these three determinations were employed to check the reproducibility and internal consistency of the polarization measurements.

Test Results

Cathode overvoltage, copper sulfate system.—The cathode overvoltages for the aqueous electrolyte as determined¹ by Eq. [2], [4], and [6] are presented in Table I. It can be seen that the values are in good agreement (within $\pm 3\%$) for the three independent determinations. It can be noticed that the overvoltages obtained by Eq. [6] become slightly larger than those of Eq. [2] at the high current densities. This may be the result of a slight concentration gradient in the cell due to imperfect stirring. If such a concentration gradient exists, then Eq. [1] becomes

$$e_C = e_{Rf3} = e_{Rf1} + \eta_G = e_{Rf2} + \eta_G \quad [7]$$

where η_G is the concentration polarization due to the difference in cation concentration between the electrodes C, Rf3 and Rf1, Rf2 (assuming the latter are at the same concentration as a result of the stirring system). Equation [6] then becomes

$$E_{(C-Rf1)} - E_{(Rf1-Rf2)} \cdot f = \eta_C + \eta_G \quad [8]$$

and since

$$\eta_C = E_{(C-Rf3)} \quad [2]$$

then

$$\eta_G = E_{(C-Rf1)} - E_{(Rf1-Rf2)} \cdot f - E_{(C-Rf3)} \quad [9]$$

¹ Small residual static potentials were observed before and after each test. For purposes of calculation these were subtracted from their equivalent dynamic potential. They were not significant at current densities above 2 mA cm^{-2} .

Table I. Calculated cathode overvoltages, aqueous electrolytes 300°K

Current, mA	Current density, mA/cm ²	η_C (mV)			η_G (mV)
		Eq. [2]	Eq. [4]	Eq. [6]	
1.0	0.4	-9.4	-8.7	-8.8	+0.6
2.0	0.8	-30.7	-30.2	-31.3	-0.6
4.0	1.6	-77.8	-77.8	-78.0	-0.2
8.0	3.2	-90.4	-90.2	-89.4	+1.0
16.0	6.4	-116.1	-117.0	-114.9	+1.2
20.0	8.0	-117.4	-117.4	-120.3	-2.9
24.0	9.6	-117.8	-117.9	-123.0	-5.2
30.0	12.0	-119.1	-119.6	-125.1	-6.1

Table I shows this effect and it indicates that η_G never became more than 5% of η_C during the testing. The factor η_G does not come into Eq. [2] and [4].

Table I indicates, therefore, that the overvoltage determinations in the cell are reproducible by three independent measurement techniques, and that the cell can be used with confidence. Calculations using Eq. [6] are not, however, as satisfactory as those using Eq. [2] and [4] because a concentration polarization error may be introduced.

Cathode overvoltage, organic system.—The applicability of the cell for use with organic electrolytes was tested by determining cathode overvoltages for the ethyl benzene-toluene-AlBr₃ system at several temperatures and current densities. The measured variable was $E_{(C-RF_3)}$ which directly gives η_C (Eq. [2]). The polarization behavior of the ethyl benzene-toluene-AlBr₃ system had not been studied prior to this work so that the only method of testing the consistency of the experimental data was by means of a Tafel plot of η_C vs. $\log i_C$ (cathode current density).

This plot (Fig. 5) gave a series of parallel lines in which η_C consistently decreases with increasing temperature. The lines also appear to straighten above η_C values of 20 mV. This would be expected if the Tafel equation

$$\eta_C = A - B \log i_C \quad [10]$$

is obeyed, i.e., if the controlling electrode mechanism is charge transfer.

The organic electrolyte data are, therefore, internally consistent leading to the conclusion that the cell is suitable for organic polarization studies. It has subsequently been used to examine a number of alkyl benzene-AlBr₃ electrolytes.

Discussion

The cell was found to be specifically suitable for electrolytes which must be protected from the atmosphere and which tend to be contaminated by polymer container materials. High viscosity electrolytes such as ethyl benzene-toluene-AlBr₃ solutions can also be handled quite readily.

As was pointed out at the beginning of this paper, the main defect of the cell design is the IR voltage drop between the tip of the Luggin capillary of the back reference electrode and the working face of the cathode. This has not been taken into consideration in Table I or Fig. 5.

The distance between the capillary tip and the cathode surface is the thickness of the glass wall. The magnitude of the IR voltage error can be estimated by the equation

$$E_{IR} = \frac{i_C \delta}{K} \quad [11]$$

where i_C is the current density, δ is the glass wall thickness, and K is the specific conductance of the electrolytes. This calculation is equivalent to considering that the Luggin tip is at a distance δ in front of the cathode (9).

Thus with an ethyl benzene-toluene-AlBr₃ electrolyte ($K = 4 \times 10^{-3} \text{ ohm}^{-1} \text{ cm}^{-1}$) and a glass thickness of 0.001 cm, the values of E_{IR} from Eq. [11] are 1.25, 2.5, and 4 mV at current densities of 5, 10, and 15 mA/cm², respectively. The actual values of E_{IR} are likely to be considerably less than these calculated values because the capillary tip is displaced horizontally rather than in front of the cathode, and because of the edge effect which tends to slightly increase the potential around the cathode hole due to field distortion (10, 11). In any case the error does not significantly alter the results shown in Fig. 5.

The cell can also be used for anode polarization but this aspect of its operation has not been tested.

Conclusions

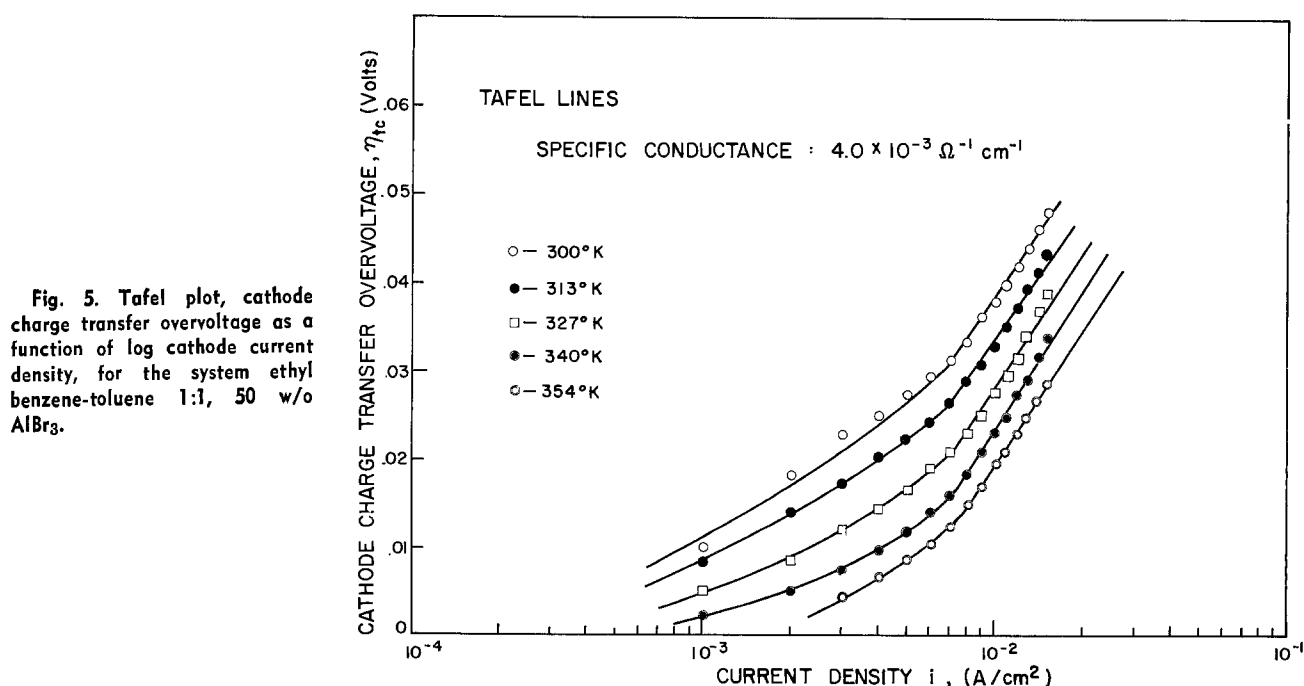
1. A cell has been developed for studying the polarization characteristics of organic electrolytes. The cell is specifically useful for electrolytes which must be protected from the atmosphere and which should not be exposed to organic materials of construction.

2. The cell employs a back reference metal vs. metal ion electrode, and two side electrodes. By this arrangement cathode overvoltages can be measured by three independent techniques to check the consistency of the cell operation.

3. The cell has been tested successfully with an aqueous copper sulfate solution and with an organic ethyl benzene-toluene-AlBr₃ electrolyte.

Acknowledgments

The authors wish to thank the National Research Council of Canada and the Defence Research Board of Canada for financial support of this work. The authors also wish to thank Dr. R. Minto for his valuable suggestions and Mr. R. Striegler for his technical assistance.



Manuscript submitted July 30, 1973; revised manuscript received Sept. 18, 1974.

Any discussion of this paper will appear in a Discussion Section to be published in the December 1975 JOURNAL. All discussions for the December 1975 Discussion Section should be submitted by Aug. 1, 1975.

APPENDIX

Electrolyte Preparation

1. Aqueous electrolyte, copper sulfate, sulfuric acid: reagent grade. Copper anode: electrolytic copper 99.994% Cu, Canadian Copper Refiners Company, Limited, Montreal. The electrolyte was prepared from triple distilled water and it was deoxygenated by bubbling with dry nitrogen for 15 min, *in situ*.

2. Organic electrolyte, AlBr_3 : prepared from high purity aluminum and bromine (2). Ethyl benzene: practical grade, Eastman Organic Chemicals, Rochester, New York. Toluene: commercial grade, Esso Imperial Oil Company, Montreal. Aluminum anode: ALCAN 1S 99.9% Al. The conductivity of the electro-

lyte was adjusted up to $4 \times 10^{-3} \text{ ohm}^{-1} \text{ cm}^{-1}$ by bubbling HBr through the solution (2).

REFERENCES

1. G. A. Capuano and W. G. Davenport, *This Journal*, **118**, 1688 (1971).
2. G. A. Capuano and W. G. Davenport, *Plating*, **60**, 251 (1973).
3. G. A. Capuano and W. G. Davenport, U. S. Pat. 3,775,260 (1973).
4. G. A. Capuano and W. G. Davenport, Canadian Pat. 945,935 (1974).
5. R. Piontelli and G. Poli, *Gazz. Chim. Ital.*, **78**, 717 (1948).
6. R. Piontelli, *Z. Elektrochem.*, **55**, 128 (1951).
7. M. Eisenberg, R. E. Kuppinger, and K. M. Worig, *This Journal*, **117**, 577 (1970).
8. B. D. Cahan, Z. Nagy, and M. A. Genshaw, *ibid.*, **119**, 64 (1972).
9. S. Barnartt, *ibid.*, **108**, 102 (1961).
10. S. Barnartt, *ibid.*, **99**, 549 (1952).
11. R. Piontelli, *Gazz. Chim. Ital.*, **83**, 357, 370 (1953).

Primary Sodium Batteries with Beta-Alumina Solid Electrolyte

F. G. Will* and S. P. Mitoff

General Electric Corporate Research and Development, Schenectady, New York 12301

ABSTRACT

The principal characteristics of a new class of high-energy density primary batteries are described. These batteries employ sodium beta-alumina as a solid electrolyte membrane that separates the reactants, sodium-mercury amalgam as the anode, and halogens, water, or air as the oxidants. The batteries operate at or near ambient temperatures and produce very high cell voltages and energy densities. They have an essentially nondetectable rate of self-discharge, and shelf and operating times of ten years appear feasible. A present limitation is their low power drain capability. The operating features of the sodium-mercury amalgam anode, the cell polarization characteristics, and the discharge behavior of cells employing various liquid cathodes are described.

In certain applications of primary batteries, such as in heart pacemakers, electronic watches, automatic exposure cameras, etc., very long life as well as small size and weight are the overriding considerations while the attainable power levels are only of secondary importance.

The useful life of conventional primary batteries, for example, silver-zinc, mercury-zinc, and dry cells, is limited by systematic self-discharge mechanisms, passivation phenomena, or spontaneous events, such as internal electrode shorting. Self-discharge mechanisms include mainly the diffusion of soluble active material from one electrode to the other and electrode dissolution accompanied by gas evolution. Typical values for the specific energy and energy density of aqueous-type primary batteries are 90-130 W-hr/kg (40-60 W-hr/lb) and 350-600 W-hr/dm³ (6-10 W-hr/in.³).

Batteries employing organic electrolytes attain considerably higher energy densities than these. However, they share with batteries using aqueous electrodes a noticeable rate of self-discharge which is usually caused by a finite solubility of the cathode.

Primary batteries with beta-alumina solid electrolyte offer a combination of unique features not readily attainable with liquid electrolyte batteries. Most significant among these are very low self-discharge rate, high cell voltage, and very small size and weight. The

essentially nondetectable rate of self-discharge results from using a solid ionic conductor, sodium beta-alumina (1, 2). This solid electrolyte acts as an ideal membrane, permitting only the migration of sodium ions and certain other monovalent cations (3) while completely preventing the permeation of anions and neutral reactants. Furthermore, there is no electrode dissolution or electrode shorting similar to that often encountered in aqueous electrolytes. Since the electronic conductivity of sodium beta-alumina is also very low (4), the usual self-discharge mechanisms are virtually absent and primary batteries with beta-alumina as the electrolyte inherently have the potential of achieving very long life. A disadvantage of such batteries is the comparatively low ionic conductivity of the solid electrolyte at or near ambient temperature. Typically, the room temperature conductivity of sodium beta-alumina is two to three orders of magnitude lower than that of the best aqueous electrolytes. As a result, the power densities attainable at room temperature with primary batteries employing beta-alumina are significantly lower than those common for aqueous-type batteries.

In this paper, consideration will be given to the general characteristics of primary sodium cells with beta-alumina as the solid electrolyte and halogens, oxygen, or water as the oxidants. After describing some general aspects of cell operation, the sodium-mercury amalgam anode, common to all of the primary bat-

* Electrochemical Society Active Member.

Key words: primary batteries, solid electrolyte batteries, sodium-halogen batteries, sodium amalgam, beta-alumina.

teries considered here, is discussed in some detail. The polarization curves of cells employing cathodes of bromine, iodine, oxygen, and water are presented and, lastly, the discharge behavior of cells with bromine and iodine cathodes is discussed.

Experimental

The experiments were carried out in simple glass cells. Figure 1 shows a schematic of the cell design. The anode consists of a disk of sodium beta-alumina ceramic sealed into a closed-end glass tube containing a sodium-mercury amalgam for room temperature operation. A Kovar alloy wire is sealed into the glass tube and contacts the reductant. The cathode half-cell design depends upon the oxidant used. Shown in Fig. 1 is the design for use with halogens or water as the oxidant. In these cases, the reactants are liquid and a metal screen or graphite felt serves as a current collector. Suitable metals include tantalum, niobium, and platinum for use with the halogens and nickel, iron, or platinum for use with water. The halogens are dissolved in suitable solvents, such as water or organic solvents. When water is used as the oxidant, small amounts of solutes are added, such as NaOH or Na₂CO₃, to establish initial conductivity. The catholyte is contained in a vented glass vessel. For experiments with sodium/air cells, a polypropylene felt was used to contain the electrolyte between the beta-alumina disk and a Teflon-polymer bonded platinum electrode. Aqueous solutions of NaOH or Na₂CO₃ served as the electrolyte.

The sodium beta-alumina disks have the chemical composition Na₂O · 9Al₂O₃ with 1% MgO and 0.5% Y₂O₃ as additives. They are prepared by pressing the blended beta-alumina and oxide powders at room temperature and sintering in air at 1830°C. Further details on the preparation can be found in Ref. (2). The sintered disks have a diameter of 1 cm and thickness of 0.1 cm. Their density is 3.18 g/cm³ or 98% of theoretical, they are nonpermeable to helium and have a conductivity of 10⁻³ ohm⁻¹ cm⁻¹ at 25°C.

The anodes were prepared by vacuum-distillation of sodium into the anode half-cell and sealing under vacuum. In those cases where sodium-mercury amalgams were prepared, the sodium was distilled into the appropriate amount of mercury in the half-cell. All reactants used were reagent-grade.

Results and Discussion

General aspects of cell operation.—During cell discharge, the following reactions take place at the electrodes

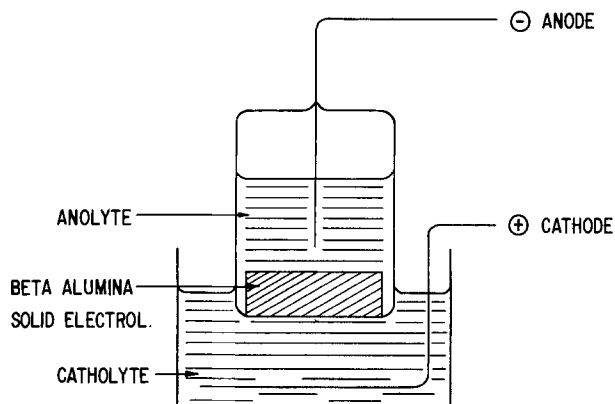
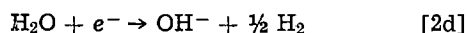
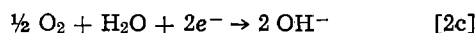
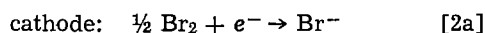
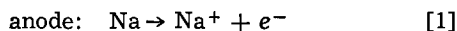
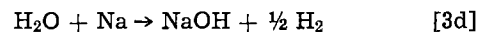
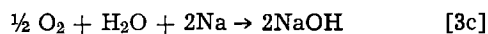
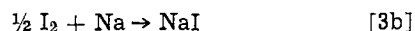


Fig. 1. Cell schematic

Sodium ions, generated at the sodium amalgam/beta-alumina interface, migrate through the solid electrolyte into the catholyte. As anions cannot permeate through the solid electrolyte, the solute concentration in the catholyte increases in accordance with the cell reactions



During cell discharge, there is a major volume decrease in the anode compartment due to sodium leaving the anode, but only relatively minor volume changes occur in the cathode compartment due to salt formation. Typically, the volume of the catholyte increases for reactions [3a]-[3c] by 5-15% and decreases for reaction [3d] by 3-5%, owing to hydrogen evolution. The precise numbers depend upon the desired concentration range of the solute or whether precipitation of solid reaction products, such as NaBr, is allowed to occur.

Sodium-mercury amalgam anode.—For cell operation at or near room temperature, pure sodium is unsuitable for all but very small power densities. Sodium is solid below 97.5°C, and the diffusion of sodium in the solid state is very slow. The self-diffusion coefficient at 25°C is only 5 · 10⁻⁹ cm²/sec (5). The problem of slow diffusion is circumvented by using sodium-rich mercury amalgams as the anode. These amalgams are at least partly liquid at the cell operating temperature. The diffusion coefficient of sodium in liquid mercury is more than three orders of magnitude larger than in solid sodium, that is 8 · 10⁻⁶ cm²/sec at 22°C (6).

The phase diagram of the sodium-mercury system is shown in Fig. 2. The initial amalgam composition in the fully charged condition of the cell preferably lies in the range of 70-90% sodium by weight. At these high sodium concentrations, the fraction of liquid phase becomes very small; at lower concentrations, the weight and volume penalty due to the mercury becomes very noticeable. Cell operation is not feasible at temperatures below 21.5°C, which corresponds to the

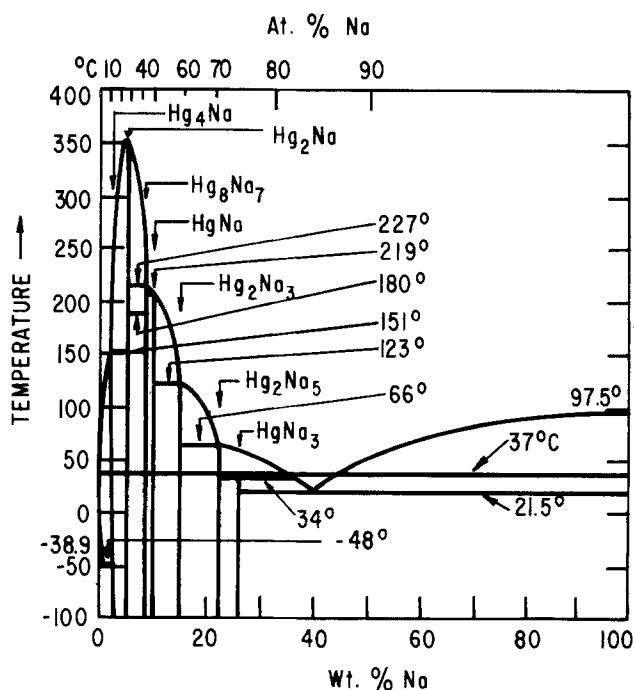


Fig. 2. Phase diagram of sodium-mercury system [from C. J. Smithells, "Metal Reference Book," Vol. 1, p. 399, Interscience Publishers, New York (1955)].

freezing point of the eutectic composition at 39.8% sodium. During cell discharge at constant temperatures above 21.5°C, one proceeds in the phase diagram on a horizontal line from right to left as sodium is ionized and leaves the anode compartment. The proportion of liquid to solid-phase increases until the all-liquid part of the diagram is reached. The end of useful cell discharge is determined by that sodium content which corresponds to the formation of solid intermetallic compounds as evident from the phase diagram. For example, at an operating temperature of 37°C, the end of discharge corresponds to a final sodium content of 38%.

The effect of initial sodium content (fully charged condition) on the electrode capacity per unit weight and volume is shown in Fig. 3 for operation at 37°C. The capacity values decrease from the theoretical limits 1.16 A-hr/g and 1.13 A-hr/cm³, calculated for pure sodium assuming 100% utilization, to zero in the trivial case where the initial sodium content in the amalgam is equal to the final content of 38%. For a starting composition of 90% sodium, the capacity values are 0.97 A-hr/g and 1.04 A-hr/cm³, while for a 70% Na/30% Hg amalgam, the values are 0.60 A-hr/g and 0.81 A-hr/cm³. Thus, for equal electrode capacity, the weight penalty due to the use of amalgams instead of pure sodium amounts to between 20 and 94% and the volume penalty to between 9 and 40%.

The sodium content and the fraction of liquid phase in the sodium-mercury amalgam as a function of the depth of discharge are plotted in Fig. 4. The curves refer to 37°C operation and initial amalgam compositions of 90, 80, and 70% Na by weight. Complete discharge corresponds to an amalgam composition of 38% Na. The fraction of liquid phase at the beginning of discharge amounts to 18, 36, and 54% for initial composition of 90, 80, and 70% Na. The fraction of liquid phase increases steeply during cell discharge, and the amalgams become completely liquid at 96, 92, and 85% depth of discharge.

Cathode operation.—The kinetics of halogen reduction (Eq. [2a] and [2b]) and, in particular, oxygen reduction (Eq. [2c]) and hydrogen evolution in aqueous solutions have been the subject of numerous studies. Comparatively little information is published on halogen reduction in nonaqueous solutions. This applies especially to the study of very concentrated halogen solutions. Highly concentrated halogen solutions are desirable from a standpoint of optimizing the energy density of the cell. However, the use of high halogen concentrations leads to precipitation of solid reaction products (NaBr, NaI) as the salt solubility is exceeded during discharge.

Salt precipitation has been observed on both the graphite current collector and the beta-alumina surface. Different crystal morphologies have been identified, depending upon the nature and amount of solvent, the nature of the substrate, and the current density. Conditions have been identified under which the effect of crystal formation on cathode polarization is small

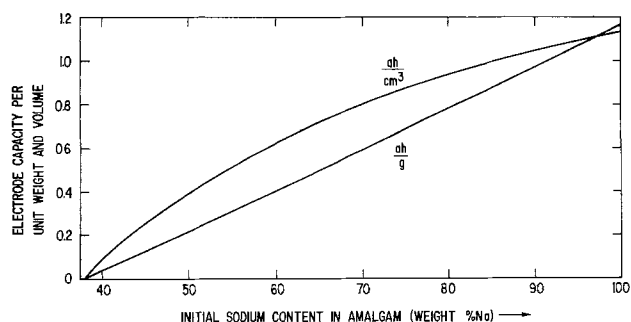


Fig. 3. Effect of initial sodium content in amalgam on electrode capacity per unit weight (A-hr/g) and unit volume (A-hr/cm³) for 37°C operation.

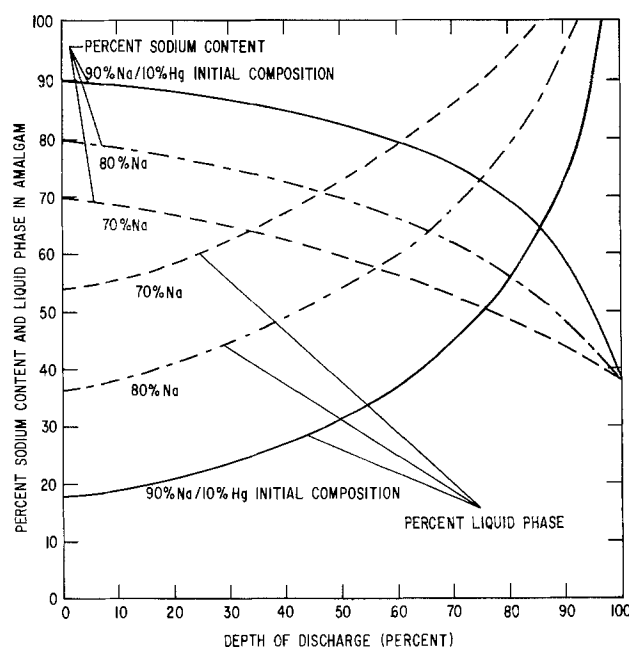


Fig. 4. Fraction of sodium content and of liquid phase in the amalgam as a function of the depth of discharge; 37°C operation; initial amalgam compositions 90, 80, and 70% Na by weight.

compared to other sources of polarization. More details about crystal formation will be published in a subsequent paper (7).

By far the largest contribution to cathode polarization derives from the polarization of the interface beta-alumina/catholyte. A study of this interfacial polarization has been undertaken (7, 8) and will be published separately.

Cell polarization.—Current-voltage curves for four different sodium-mercury amalgam primary cells at 25°C are shown in Fig. 5. The anode in all of these cases consists of a 70% Na/30% Hg amalgam by weight. The catholytes consist of 1 g-atom Br₂ dissolved in an aqueous solution of 1N NaBr (curve a), 1 g-atom I₂ dissolved in a solution of 1 mole NaI per liter of propylene carbonate (curve b), an air-saturated 1N NaHCO₃ solution (curve c), and a 1N NaOH solution (curve d). Current collectors consist of Pt screens or TFE-bonded porous Pt (curve c).

The observed open-circuit voltages for the Na/Br₂ and Na/NaOH cells correspond within 30 mV to the thermodynamically expected values of 3.78 and 1.89V.

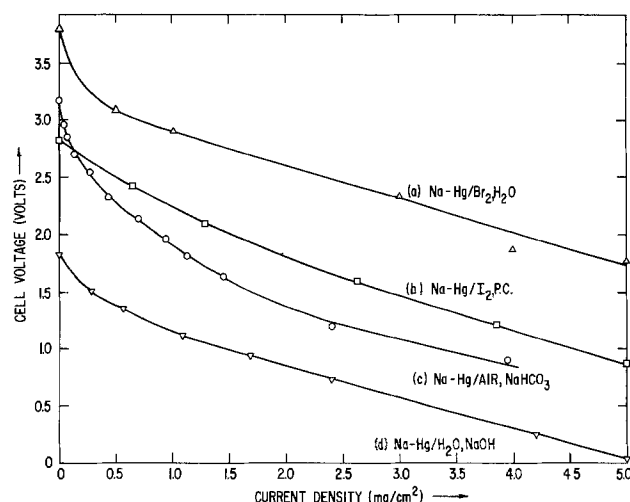


Fig. 5. Current-voltage curves for sodium-mercury amalgam primary cells with various cathodes at 25°C.

The open-circuit voltage for the Na/I₂, P.C. (propylene carbonate) cell is 2.83V or 0.52V lower than calculated for an aqueous solution. This reflects the different energy of solvation in the organic as compared to the aqueous solvent (9). The open-circuit voltage of the Na/air cell is 3.18V which is approximately 0.3V lower than the calculated value for the pH of 1N NaHCO₃ solution. This discrepancy is caused by the oxygen electrode and is usually interpreted in terms of mixed potentials involving couples such as O₂/H₂O, O₂/H₂O₂, and Pt-O/H₂O (10).

At low current densities, all four cells show the effects of an activation-controlled process. Independent investigations (7, 8), using a reference electrode in the beta-alumina, have shown that the interface beta-alumina/catholyte is the source of this polarization. Its magnitude depends upon the pretreatment of the beta-alumina and the nature of the solvent.

At higher current densities, the curves in Fig. 5 become straight lines with slopes which are nearly identical for all four cells. The discharge behavior in this range of currents is determined by the ohmic resistance of the beta-alumina solid electrolyte. The slopes correspond to a unit area resistance of 300 ohm-cm² which translates into a resistivity of 3000 ohm-cm for the beta-alumina thickness of 0.1 cm. This value for the resistivity is three times larger than resistivities calculated from four-probe alternating current measurements made at a frequency of 10 kHz. Part of this discrepancy is due to intergranular resistances in the polycrystalline solid electrolyte which are shunted by capacitances (11).

Another part has been found to derive from the diffusion of small amounts of water into the surface layers of the beta-alumina. This effect exists even when propylene carbonate is used as a solvent in an open cathode half-cell such as shown in Fig. 1 since propylene carbonate absorbs water from the environment.

In all cases reported in this paper, water was present only in the cathode compartment of primary cells. Under these conditions, the beta-alumina used in this study (2) undergoes only slow changes in electrical resistivity, but the mechanical integrity remains unaffected. Some cells have now been operating for 3 years and continue to discharge. If, on the other hand, water is present in the anode compartment, the ceramic electrolyte fails mechanically within a few hours or weeks, depending upon the magnitude of the current density. Increasing current density enhances the rate of failure. While it is known that hydronium ions enter beta alumina (12), the detailed effects of this process are as yet unknown.

Cell discharge as a function of time.—The curves in Fig. 5 are initial polarization curves, obtained at low depths of discharge. At larger depths of discharge, the effect of crystal formation often becomes evident in increased cell polarization, especially in the case of very concentrated halogen solutions. Figure 6 shows the cell voltage as a function of discharge time at a constant current density of 0.1 mA/cm² and 25°C for various halogen cells. The discharge voltages are smaller than those shown in Fig. 5 for the same current density. This is due to the use of beta-alumina of slightly different composition and pretreatment, resulting in higher ohmic and interfacial losses. The discharge times are expressed as depth of discharge on the abscissa of Fig. 6 to accommodate all curves with quite different discharge times on a single graph. Cell discharge was limited by the exceedingly small volume of catholyte, only 6 · 10⁻³ cm³, used in these cells. By choosing such small amounts of catholyte, a full cell discharge could be accomplished in times varying from 2 to 24 hr.

Curves 1 and 2 in Fig. 6 refer to 1 g-atom Br₂ per liter of a saturated solution of NaBr in water (curve 1) and in propylene carbonate (curve 2). For the aqueous solution, about 65% of the Br₂ originally present is

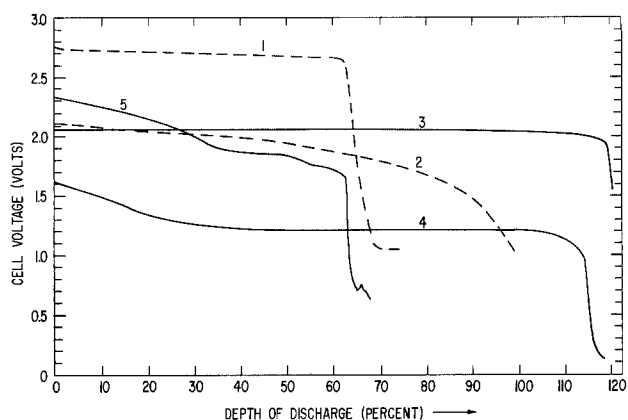


Fig. 6. Cell voltage as a function of depth of discharge for sodium-mercury amalgam cells at 0.1 mA/cm² and 25°C. Curve 1, 1N Br₂ in NaBr-saturated H₂O; curve 2, 1N Br₂ in NaBr-saturated propylene carbonate; curve 3, 2N I₂ in NaI-saturated H₂O; curve 4, 2N I₂ in NaI-saturated PC; curve 5, 80% I₂/20% H₂O by weight.

reduced, whereas nearly 100% is reduced in propylene carbonate solution. The balance of the Br₂ in the aqueous solution has been lost by evaporation. Losses by evaporation are less significant in the propylene carbonate solution due to the lower vapor pressure of Br₂ above such solutions. The actual discharge times were 121 and 144 min for the aqueous and propylene carbonate solutions, respectively. The discharge voltage is consistently smaller in the propylene carbonate solution due to the different solvation energy as compared to aqueous solutions and decreases visibly during cell discharge, whereas the voltage for the aqueous solution remains relatively constant. Microscopic examination reveals that this different behavior is caused by different morphologies of the crystal layers growing on the beta-alumina surface.

Curves 3 and 4 in Fig. 6 refer to catholytes prepared from 2 g-atoms I₂ per liter of a saturated solution of NaI in water (curve 3) and propylene carbonate. These cathodes discharged for nearly 3 hr to yield essentially theoretical capacity. The finding that, in fact, more than 100% depth of discharge appears to be obtained is explained by the difficulty in determining the minute amount of catholyte, only 6 · 10⁻³ cm³, to a better accuracy than 20-25%. The discharge curve in aqueous solution is remarkably flat while a continuously decreasing discharge voltage is observed in propylene carbonate solution. This behavior is similar to that found in the Br₂-containing solutions, and different crystal morphologies are again the reason for the observed behavior.

Curve 5 in Fig. 6 is obtained with a catholyte consisting of a mixture of 80% I₂ and 20% H₂O by weight. The mixture contains solid I₂ and I₂ dissolved in H₂O. This catholyte discharged for nearly 24 hr, yielding about 65% depth of discharge. Titration for undischarged I₂ yielded less than 2% of the originally present I₂. The balance was lost by evaporation.

The foregoing cell discharge tests establish the feasibility of discharging halogen cathodes containing very concentrated halogen solutions to large depths of discharge. However, only very small solution volumes were used in these experiments to achieve reasonably short discharge times. These studies lead to the formation of only very thin crystal layers and cannot be expected to represent the discharge behavior of cells with many years life. The long-term discharge performance and other detailed characteristics of sodium-amalgam/bromine cells, with 10 yr design life, are described in Ref. (7).

Cell performance characteristics.—A summary of the more significant performance characteristics of primary cells employing cathodes of bromine, iodine, air, and water is presented in Table I.

Table I. Summary of cell performance characteristics at 25°C

Cell couple	Open-circuit voltage (V)	Voltage at 0.1 mA/cm ² (V)	Specific energy		Energy density	
			W-hr/kg theor.	W-hr/kg practical	W-hr/dm ³ theor.	W-hr/dm ³ practical
Na-Hg/Br ₂ , H ₂ O	3.77	3.5	1026	330-440	557	240-330
Na-Hg/Br ₂ , P.C.	3.34	3.1	910	330-440	492	150-200
Na-Hg/I ₂ , H ₂ O	3.25	3.0	579	220-330		
Na-Hg/I ₂ , P.C.	2.82	2.8	502	170-260		
Na-Hg/O ₂ , NaHCO ₃	2.90	2.8	1553	660		
Na-Hg/H ₂ O, NaOH	1.85	1.7	991	440		

The theoretical values for specific energy and energy density were calculated on the basis of an initial amalgam composition 90% Na/10% Hg and 90% by weight halogen in the catholyte. The "practical" values are computed optimum values for current densities not exceeding 0.1 mA/cm². These values take into account all cell components such as the beta-alumina electrolyte, cell casing, and current collectors. Sodium amalgam/bromine cells with a stored energy corresponding to 350 W-hr/kg and 295 W-hr/dm³ have actually been operated to depths of discharge up to 45%, simulating 4½ yr operating life.

Conclusions

Primary batteries employing sodium beta-alumina as a solid electrolyte membrane, sodium-mercury amalgam as the anode, and halogens, air, or water as the cathodes are feasible for operation at or near room temperature with a combination of unique features: Essentially nondetectable rate of self-discharge, long shelf and operating life, and very high cell voltages and energy density. Limitations of these cells are their inability to perform at large power levels and at temperatures below 21°C. For sodium amalgam/bromine cells, open-circuit voltages of 3.8V and operating voltages of 3.5V at 0.1 mA/cm² have been obtained. Cells have been built with a stored energy corresponding to 350 W-hr/kg and 295 W-hr/dm³ and operated to depths of discharge up to 45%, simulating 4½ yr operating life.

Acknowledgment

We gratefully acknowledge the active help of H. J. Hess in obtaining some of the data presented here. We

also thank General Electric's Battery Business Department and Medical Systems Division for their support.

Manuscript submitted Oct. 3, 1974; revised manuscript received ca. Nov. 25, 1974. This was Paper 39 presented at the Boston, Massachusetts, Meeting of the Society, Oct. 7-11, 1973.

Any discussion of this paper will appear in a Discussion Section to be published in the December 1975 JOURNAL. All discussions for the December 1975 Discussion Section should be submitted by Aug. 1, 1975.

Publication costs of this article were partially assisted by the General Electric Company.

REFERENCES

1. J. T. Kummer *et al.*, U.S. Pat. 3,404,035 (Oct. 1968).
2. R. J. Charles and S. P. Mitoff, U.S. Pat. 3,607,435 and 3,607,436 (Sept. 1971).
3. Y.-F. Yu Yao and J. T. Kummer, *J. Inorg. Nucl. Chem.*, **29**, 2453 (1967).
4. N. Weber and J. T. Kummer, Annual Power Sources Conf. Proc., 1967, p. 37.
5. N. H. Nachtrieb, E. Catalano, and J. A. Weil, *J. Chem. Phys.*, **20**, 1185 (1952).
6. M. v. Stackelberg and V. Toome, *Z. Elektrochem.*, **58**, 226 (1954).
7. F. G. Will, R. R. Dubin, and H. J. Hess, Paper 40 presented at Electrochemical Society Meeting, Boston, Massachusetts, Oct. 7-11, 1973.
8. F. G. Will and K. Kalapis, M.S. thesis of K. Kalapis, University Bonn, Germany, To be published.
9. L. Fischer, G. Winkler, and G. Jander, *Z. Elektrochem.*, **62**, 1 (1958).
10. J. P. Hoare, "The Electrochemistry of Oxygen," p. 32, Interscience Publishers, New York (1968).
11. R. W. Powers and S. P. Mitoff, *This Journal*, **122**, 226 (1975).
12. H. Saalfeld, *Ber. Deutschen Keramischen Ges.*, **45**, 212 (1968).

Structural Transformations of the PbO₂ Active Material during Cycling

A. C. Simon,* S. M. Caulder,*¹ and J. T. Stemmler¹

Electrochemistry Branch, Naval Research Laboratory, Washington, D. C. 20375

ABSTRACT

A combined optical and scanning electron microscope study of the PbSO₄/PbO₂ electrode has revealed changes in the PbSO₄ crystallography and the tendency of PbO₂ to form a network during life cycle tests. It was found that during cycling a definite coralloid structure developed. The mode of deposition and crystal form of the PbSO₄ crystals changed with increasing cycle life.

In a previous paper (1) certain observations were made concerning the structural changes that occurred in the PbO₂ electrode during cycling. These changes

were observed with the optical microscope. Samples of the positive, or PbO₂/PbSO₄ electrode, of the lead-acid battery were examined, in both the charged and discharged state, at various points in the cycle life. Properly prepared samples (2) were sectioned and polished so that the microstructure could be examined in the section. It was found that plates having radically different microstructures after curing and forming were

* Electrochemical Society Active Member.

¹ International Lead Zinc Research Organization Research Associate at Naval Research Laboratory.

Key words: lead dioxide, lead-acid battery, coralloid microstructure, porous electrode structure, lead sulfate, anodic film microstructure.

all transformed into almost identical structures in less than 50 cycles. This led to the conclusion that the structure developed during cycling was independent of either the method used to cure the plates, or to accomplish their formation.

While the microstructure of the formed electrode was usually rather dense and contained only very small voids, after a few cycles the voids became much larger and the material surrounding the voids at first became more dense and compact, but later disintegrated into very loosely joined particles. From this it was concluded that gas bubbles, formed during the last stages of the charge process, forced apart the active material to form channels during their escape to the surface. In the early cycles it was assumed that this pressure pushed the active material that formed the walls of these channels into the more dense than original state that was found with microscopy. At a later stage, when the walls became thinner due to the considerable loss of active material that was washed away as sediment, the gas escaped by breaking through the existing walls into adjacent channels.

More recently, examinations made with the scanning electron microscope, SEM, together with reevaluation of some of the earlier optical microscope observations, and consideration of other recently discovered properties of the PbO_2 active material, has led to a considerably different concept of the active material structure and the manner of its formation.

Compilation of Various Observations and Their Significance

Observations with the SEM.—Samples for the SEM examination were obtained by subjecting positive electrodes to capacity charge-discharge operation for a total of 56 cycles, at which point failure was complete. Discharges were made at 35.9 mA/cm^2 , charges at 14 mA/cm^2 in an excess of 1.28 sp gr acid. The system was positive limited so that both charge and discharge of the positive electrode was complete. The positive plate voltages were checked by means of a $\text{PbO}_2/\text{PbSO}_4$ reference electrode. Samples were obtained for examination at the end of formation and after 10, 20, 30, 40, and 50 cycles. To avoid the artifacts occurring at the plate surface, examination was made upon the rough cross sections obtained by breaking the plate into small portions. The accuracy of the observations made on the above samples was checked by additional examination of commercial plates which had received various numbers of SAE type cycles.

The SEM observation revealed the same uniform closely packed active material structure after formation that had been seen in the optical microscope studies. The exposed surfaces were smooth and exhibited very little detail, other than an occasional basic sulfate crystal that had not been completely converted to PbO_2 (Fig. 1).

With an increasing number of cycles it was apparent that larger voids were being formed but the structure that was being developed was not clearly revealed in the charged electrode until after 30 deep cycles (Fig. 2).

In the case of examination of the discharged, or reduced, plate, the structure was even more evident, mainly because of the manner in which the lead sulfate crystals clustered along the branches of the interdependent parts (Fig. 3). It was clear that this coraloid structure was the three-dimensional counterpart of the void-filled structures observed, after cycling, with the optical microscope (Fig. 4). The connected but involuted nature of the structure was not evident in cross sections taken for optical microscopy, nor was the extensive surface porosity that was revealed by SEM examination. The three-dimensional structure seen in Fig. 2 is definitely not the result of gas action. Study of many such areas has made it clear that the structure is an interconnected and continuous entity of a very extensive nature. The voids are incidental to

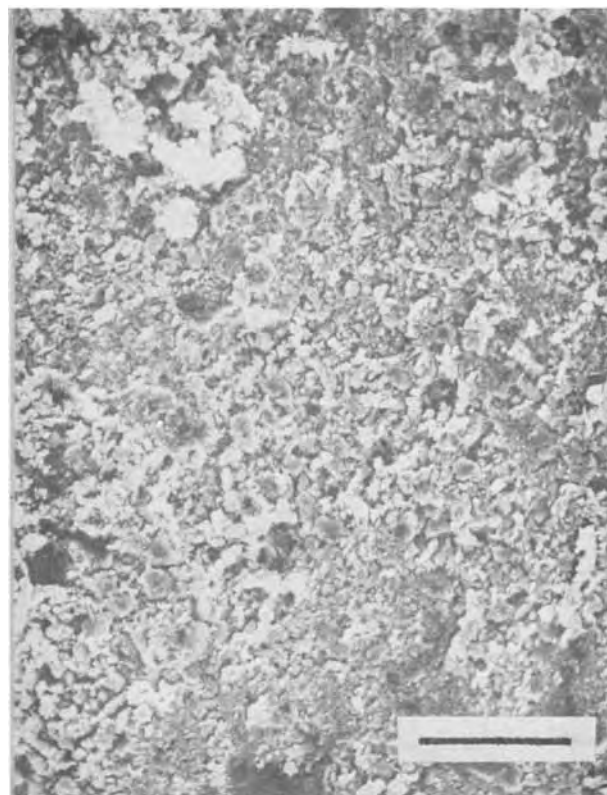


Fig. 1. Interior section of a formed positive plate. As seen with the SEM. Scale length = $20 \mu\text{m}$.

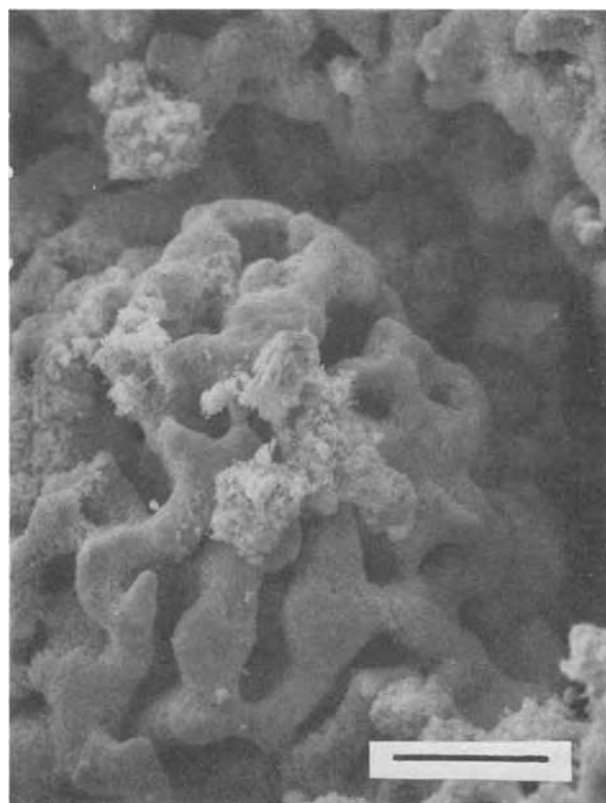


Fig. 2. Coraloid structure developed in the charged PbO_2 active material after 40 capacity discharges. As seen with the SEM. Scale length = $20 \mu\text{m}$.

its formation and are not the cause. The porous and detailed fine structure that is shown along the branches indicates that no extensive and violent turbulence of



Fig. 3. Coralloid structure in the discharged active material (PbSO_4 crystals) after 40 discharges. As seen with the SEM. Scale length = 20 μm .

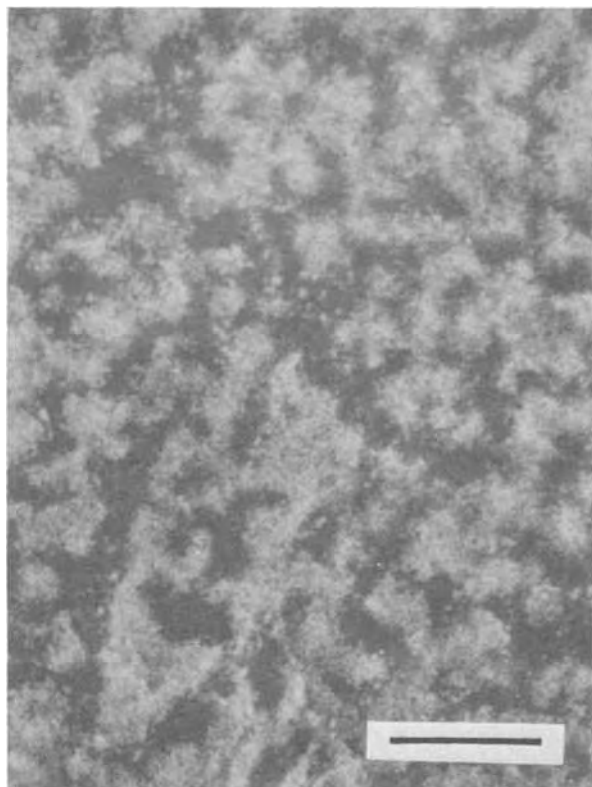


Fig. 4. Coralloid structure as seen in polished cross section of positive plate, using optical microscopy. Light material is PbO_2 , dark spaces represent voids in the plate. Scale length = 40 μm .

Although operating conditions had been different, there was a parallelism in the structural changes that occurred in the above capacity discharge experiments, and those that took place in plates that had received SAE type cycling. It was evident that the same structural changes had taken place in both cases but that these changes had occurred much more rapidly under the conditions where the cell was completely discharged at each cycle.

Evidence for the presence of electrochemically active and inactive forms of PbO_2 .—It has been found that electrochemically active and inactive forms of PbO_2 coexist in the positive active material of the lead acid battery (3, 4). Studies with nuclear magnetic resonance (NMR) have shown that electrochemically prepared samples of PbO_2 have hydrogen present in at least two configurations, while chemically prepared samples showed only one hydrogen-containing species. The chemical nature of the hydrogen species common to both the chemical and electrochemical preparations is not yet clear. The hydrogen-containing species found in the electrochemically prepared samples was determined not to be present as water. Its exact chemical makeup is also not clear. The relaxation curves resulting from perturbations of this hydrogen bonding are different for the chemically and electrochemically prepared PbO_2 . It has been found that the relaxation curves of the electrochemically prepared material more and more resemble that of the chemically prepared form as the electrochemical type is cycled (4). Since it is well known that chemically prepared PbO_2 is unsuited for the manufacture of active material because it does not develop capacity and cycle properly, it can be assumed to be relatively inert to electrochemical action. It is significant that the electrochemically prepared PbO_2 , after considerable cycling, apparently develops the NMR curves of the chemically prepared form, with an accompanying loss of capacity.

Relevant observations from optical microscopy.—In studies with the optical microscope (5) residual particles of PbO_2 were always found within the crystals of lead sulfate formed during discharge (Fig. 5). The reason for this residue was puzzling. Before the knowledge was available that an active and inactive form of PbO_2 were both present in the active material, it could only be assumed that PbO_2 was somehow encapsulated within the growing PbSO_4 crystals before dissolution of the PbO_2 structure could be completed. Most logically this could occur as some parts of the PbO_2 structure became electrically isolated by prior dissolution of its connecting network with other portions. However, it was realized that this explanation was not entirely satisfactory because the PbO_2 particles within the PbSO_4 crystals appeared to have fairly uniform distribution, both throughout the active material and within the PbSO_4 crystals as well (Fig. 5). Moreover, the particles were relatively isolated from one another and did not occur as agglomerates, as one would expect if portions of the PbO_2 structure became isolated. It is now evident that these embedded particles are the inactive form of PbO_2 .

Another observation resulting from optical microscopy was that the recharge process, the oxidation of PbO_2 , began with the growth of the residual encapsulated PbO_2 particles. Many observations were made of electrode sections in various stages of recharge and it was found that a significantly large number of the embedded PbO_2 particles were surrounded by void areas within the PbSO_4 crystal, indicating dissolution of the surrounding PbSO_4 during the growth of the PbO_2 particle. In periods of discharge similar voids surrounding the PbO_2 particles were never found within the PbSO_4 crystals. Moreover it was very frequently observed that dissolution of PbSO_4 crystals during charge resulted in a splitting into smaller crystals. Such splitting was the result of preferential dissolution around PbO_2 particles of such alignment

the electrolyte has occurred in the vicinity, as would be the case if gas bubbles had been generated that were sufficiently violent to cause channeling.

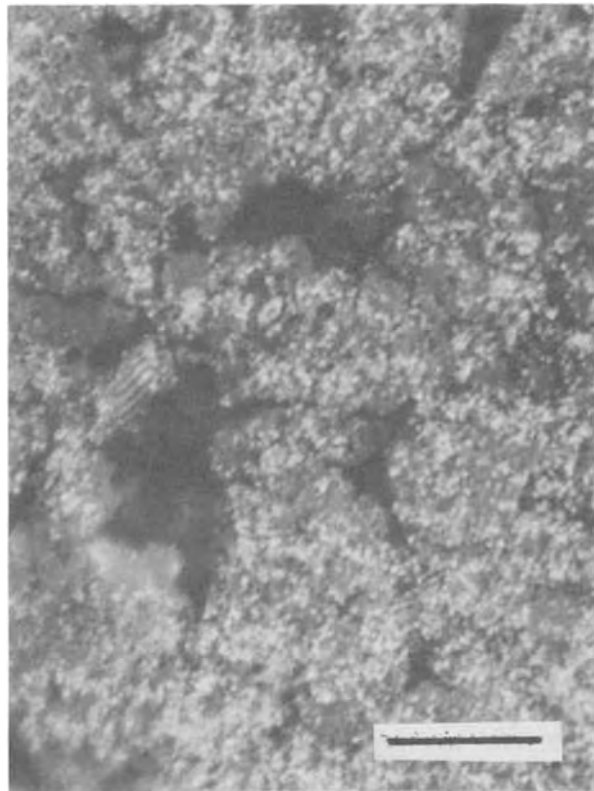


Fig. 5. Discharged plate, cross-sectioned PbSO_4 crystals containing large amounts of unreacted PbO_2 particles. Light gray PbSO_4 crystals, of regular outline, contain bright particles of PbO_2 encapsulated within their structure. Darkest areas are voids in the active material. As seen with the optical microscope. Scale length = 10 μm .

as to cause separation of a large PbSO_4 crystal into several smaller ones, each surrounded by a chain of PbO_2 particles that were growing and merging into one another.

It could not be determined if this was the only mechanism of growth, since it was also possible that the dissolution of PbSO_4 crystals in a given area might also contribute to growth of PbO_2 at a more distant point. However, it was indicated that the embedded residual particles of PbO_2 initiated the growth of the PbO_2 resulting from the next charge cycle, by providing nuclei for the crystallization process of the PbO_2 .

One further point of observation was that these nucleating PbO_2 particles were not always at what appeared to be the surface of the PbSO_4 crystal. Often the embedded particle, with its significant surrounding void space, appeared to occur deep within the crystal, as judged from the cross section. The possibility exists that the PbSO_4 crystal allowed migration of the reacting ions to the deeply embedded site, but it seems more likely that what appeared in section to be one crystal might in actuality have been two or more, joined along faces not visible in the section, or that the apparently deeply buried PbO_2 particle might have actually been at the surface in a plane either above or below that which was sectioned.

Conclusions

It can therefore be reasonably concluded that these embedded PbO_2 particles that remain at the end of discharge are the inactive form of PbO_2 that is resistant to reduction to PbSO_4 , although still fully capable of acting as nuclei for the crystallization of the active form.

Examination of discharged plates show that, even at the first discharge, there is a large amount of residual PbO_2 embedded in the lead sulfate crystals, even

though this is the first reduction of the PbO_2 that was created in the forming process. It seems safe to assume that the electrolytic formation has not resulted in PbO_2 that is 100% in the active form.

The clearly defined coralloid structure that develops after a period of cycling can therefore be explained upon the basis of a "memory" pattern that remains from cycle to cycle and that originates in the presence of inactive particles of PbO_2 .

Assuming the initial presence of inactive PbO_2 particles, uniformly distributed throughout the active material matrix, it is possible to imagine the release of these inactive particles as the surrounding active form of PbO_2 is dissolved during the discharge process. These particles will then settle upon all available surfaces and, while a small portion may be lost from the plate, a larger portion will settle upon the surfaces of growing PbSO_4 crystals, to be subsequently encapsulated. Other of the inactive particles so released will settle upon remaining PbO_2 , to be again released as this substrate is further dissolved. The continuation of this process will tend to concentrate the majority of the inactive particles in or on the lead sulfate crystals and there will, of course, be none left in the voids created by the dissolution of the active PbO_2 .

On the initiation of the next charge cycle the inactive particles in the surface of the lead sulfate act as nuclei for the growth of the active PbO_2 and, as these PbO_2 particles enlarge and PbSO_4 dissolves, further particles are uncovered which will also enlarge and grow together in the sites where PbSO_4 crystals had been formed. There is no tendency for the PbO_2 to extend for any great distance into the spaces left void in the previous discharge, so that these remain defined. With the next cycle of discharge the PbSO_4 crystals will tend to congregate more closely on the existing PbO_2 structure and as the active portion of the PbO_2 dissolves, the inactive portion will tend to be concentrated even more in the areas where the PbO_2 structure of the previous charge was located. The void areas surrounding this network will therefore slightly enlarge.

By a continuation of this charge-discharge cycling a well-defined PbO_2 coralloid structure eventually emerges, which can be repetitively reproduced on each charge cycle, by reason of the residual inactive PbO_2 particles which it contains.

The observed coralloid PbO_2 structure appears to be of an ideal construction for a porous electrode. From optical microscopy of sections it was learned that its convolutions have a very dense PbO_2 core, which should provide the maximum of strength and electrical conductivity in such an interwoven structure. At the same time the surfaces of the convolutions are found to consist of many small joined particles that present an enormous surface area, of great porosity. The much larger voids that occur between the convolutions of the PbO_2 structure would seem able to provide free flow of electrolyte and to insure that an adequate amount is present at the reacting surfaces.

However, the loss of capacity is already in an advanced stage when the coralloid structure reaches its most perfect form. There are two possible explanations for this that are immediately evident. It is noted that when a positive plate is cycled, particularly at higher discharge rates and to a low terminal voltage, there is a continual change in the method of PbSO_4 crystal deposition as the cycling continues. On initial discharge cycles, the PbSO_4 crystals deposit in considerable disorder, with crystals of a considerable size range piled haphazardly upon one another. The result is a porous PbSO_4 layer and one that probably reaches a considerable thickness before it is able to passivate the remaining PbO_2 (Fig. 6). As cycling continues, however, the crystals become more uniform in size and are arranged so that they appear to be tightly interlocked, with little or no porosity visible between the crystals (Fig. 7). It is evident that such a struc-

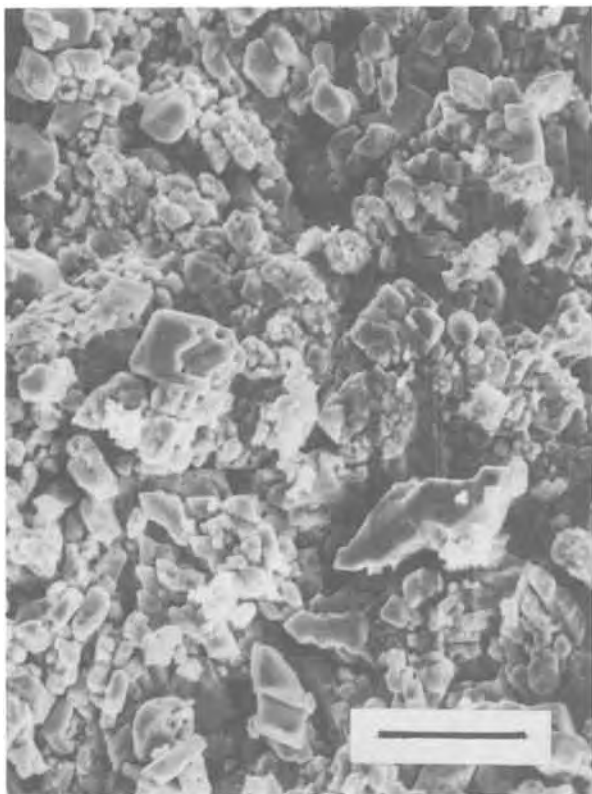


Fig. 6. Appearance of PbSO_4 crystals deposited on the coralloid structure after the 5th capacity discharge. As seen with the SEM. Scale length = 20 μm .

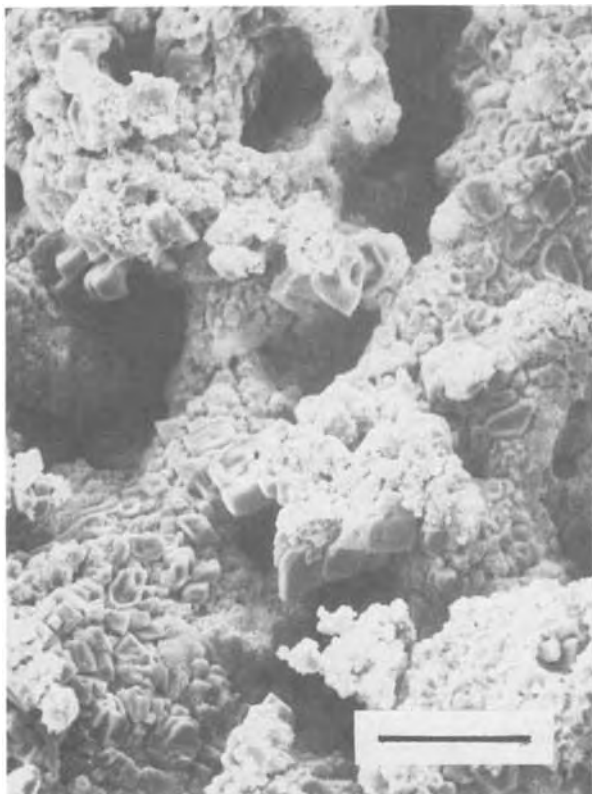


Fig. 7. Very closely packed and dense layer of PbSO_4 crystals deposited on the coralloid structure after the 15th capacity discharge. As seen with the SEM. Scale length = 20 μm .

ture can passivate the underlying PbO_2 much sooner than was the case in earlier cycles. Correlation between capacity loss and the occurrence of this over-

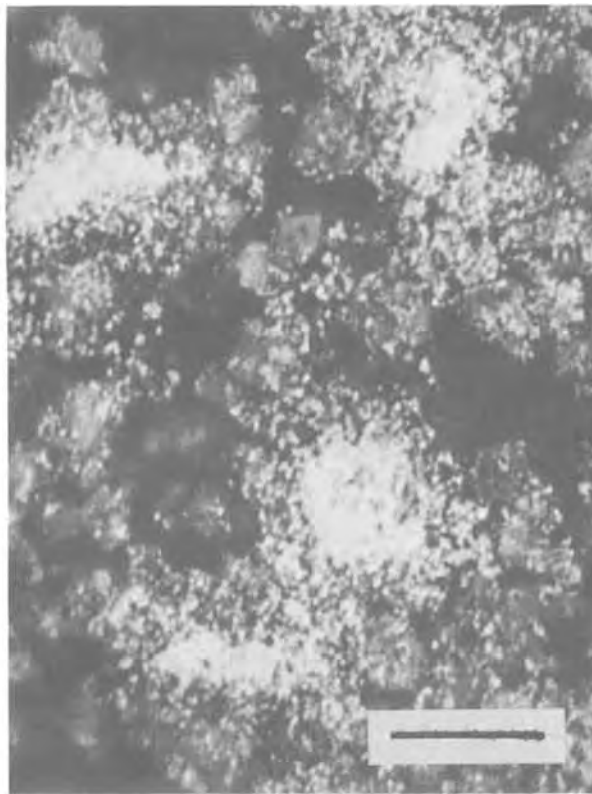


Fig. 8. Cross sections of convolutions of the coralloid structure of a discharged plate, as seen with optical microscope. Very bright areas are at the centers of the convolutions and show dense packing of the remaining PbO_2 within the PbSO_4 crystal envelope. Cross section is made perpendicular to the long axis of convolution growth. Scale length = 10 μm .



Fig. 9. Same area as Fig. 8, but with polarized illumination. Dark areas corresponding to bright areas of Fig. 8 are in reality slate gray or black, and, as can be seen, are surrounded by a layer of PbSO_4 crystals. Scale length = 10 μm .

lapped, tightly packed PbSO_4 film is good, which lends credibility to this explanation.

Another possibility is that the occurrence of the coralloid structure is itself the cause of the loss of capacity. It has been found that the individual convolutions of the coralloid structure, while porous on the outside, have a very dense core structure. This is illustrated in Fig. 8. This photomicrograph, of a discharged plate, shows a cross section of several coralloid convolutions, at right angles to their long axis. The bright, nearly featureless areas are the remaining densely packed PbO_2 at the center of the convolutions. These are surrounded by light gray material that consists of cross sections of PbSO_4 crystals. These can be seen more clearly in Fig. 9, the same area but seen by polarized light. The bright material in Fig. 8, which looks black in Fig. 9, could be either electrochemically active or inactive PbO_2 . The point to be made, however, is that a relatively large amount of PbO_2 remains at the end of discharge, either because of the passivation by the PbSO_4 crystals that surround it, or because the material may be the inactive form of PbO_2 , or because the PbO_2 , although electrochemically reactive, is so densely compacted that extensive reaction becomes difficult. This compacted condition seems to be directly related to the development of the coralloid structure. Unfortunately the centers of the coralloid convolutions appear to be dense at some portions of cycle life and porous at others, under conditions not yet defined. For this reason correlation between the dense structure and loss of capacity has not been found.

It is also possible that the increasing amount of the inactive form of PbO_2 may be the sole cause of capacity loss. This might also explain the gradual break up of the coralloid structure that is observed toward

the end of cycle life. It may be that the increasing amount of this inactive form provides so many nucleation centers that very small PbO_2 crystals of the active species are formed, that are incapable of joining to form the aggregates responsible for the coralloid structure.

In any case, the observations recorded here are considered of sufficient importance to warrant further investigation of the coralloid structure and of the inactive form of PbO_2 , as these observations may lead to methods for increasing battery life, energy density, and capacity.

Acknowledgments

The authors express their appreciation to the Naval Research Laboratory and the International Lead Zinc Research Organization for their joint support and for permission to publish this report.

Manuscript submitted Sept. 10, 1974; revised manuscript received Nov. 5, 1974.

Any discussion of this paper will appear in a Discussion Section to be published in the December 1975 JOURNAL. All discussions for the December 1975 Discussion Section should be submitted by Aug. 1, 1975.

Publication costs of this article were partially assisted by the Naval Research Laboratory.

REFERENCES

1. A. C. Simon and S. M. Caulder, *This Journal*, **118**, 659 (1971).
2. A. C. Simon and E. L. Jones, *ibid.*, **102**, 279 (1955).
3. S. M. Caulder, J. S. Murday, and A. C. Simon, *ibid.*, **120**, 1515 (1973).
4. S. M. Caulder and A. C. Simon, *ibid.*, **121**, 1546 (1974).
5. A. C. Simon, C. P. Wales, and S. M. Caulder, *ibid.*, **117**, 987 (1970).

Conduction Characteristics of Polycrystalline Lead Fluoride

C. C. Liang* and A. V. Joshi*

P. R. Mallory and Company, Incorporated, Laboratory for Physical Science, Burlington, Massachusetts 01803

ABSTRACT

The effect of the aliovalent cation dopants on the ionic conduction characteristics of the polycrystalline lead fluoride was studied in the temperature range between 25° and 350°C in order to determine the predominate mobile species in both α - PbF_2 and β - PbF_2 . It was found that the activation energy of motion was 11.6 ± 0.6 kcal/mole for α - PbF_2 and 14.3 ± 0.6 kcal/mole for β - PbF_2 . Doping with YF_3 did not result in a change in the value of the activation energy for either α - PbF_2 or β - PbF_2 . However, the activation energy of motion for the KF-doped α - PbF_2 was 8.9 ± 0.3 kcal/mole and that for the KF-doped β - PbF_2 was 4.1 ± 0.3 kcal/mole. It was concluded from these results that Frenkel disorder is predominate in the lead fluoride lattice. The interstitial fluoride ions are the principal mobile species in the nominally pure as well as the YF_3 -doped α - and β - PbF_2 and the fluoride ion vacancies are the principal mobile species in the KF-doped α - and β - PbF_2 .

The solid electrolyte properties of lead fluoride in both orthorhombic form (α - PbF_2) and cubic form (β - PbF_2) was investigated by Kennedy, Miles, and Hunter (1). It was found as in the early work by Tubandt (2) that the conductivity of lead fluoride is predominately due to the fluoride ions. Furthermore, Kennedy *et al.* (1) reported that the activation energy of movement for the mobile species was about 0.5 eV in both forms.

Although Kennedy *et al.* (1) suggested a fluoride ion vacancy transport mechanism in both α - PbF_2 and

β - PbF_2 , the conduction mechanism has not been investigated in detail.

In the present investigation the effect of aliovalent cation dopants on the conduction characteristics of lead fluoride were studied in order to elucidate a mechanism for the transport process of the fluoride ions.

Experimental

Material preparation.—Alpha Inorganics lead fluoride (99.9+%) was used in this study without further purification. Potassium fluoride and yttrium fluoride (ROC-RIC) were used as the dopants. They were dried before use by heating in an evacuated flask at about 130°C for several hours then transferred to a

* Electrochemical Society Active Member.

Key words: lead fluoride, ionic conductivity, ionic conduction mechanism, solid electrolyte.

Vacuum Atmospheres dry box under a helium atmosphere. The oxygen and moisture content in the dry box was always maintained below 15 parts per million (ppm). All the sample preparation and measurements were conducted in the dry box.

In order to prepare the potassium- or yttrium-doped lead fluoride a stock solid solution was prepared by melting a well-blended powder mixture of PbF_2 and KF or YF_3 in a mole ratio of 98 to 2 at about 350°C . The resulting clear melt was quenched to ambient temperature and pulverized by means of a Fisher mechanical grinder. The dilution of the doped lead fluoride was accomplished by similar procedures.

It was noted that the doped lead fluoride obtained by quenching the melt to ambient temperature was in the cubic form. However, the orthorhombic form could be obtained by grinding the cubic form of the doped lead fluoride in the mechanical grinder for about two hours or by pressing the powder in a steel die at 100,000 psi at room temperature then pulverizing the pressed pellet using the mechanical grinder.

Conductivity measurement.—The total conductivity of the nominally pure and doped PbF_2 in both orthorhombic and cubic form was measured at various temperatures. Lead electrode [containing 10 weight per cent (w/o) of electrolyte] or graphite electrodes were used in the conductivity cells. The $\text{Pb}/\text{PbF}_2/\text{Pb}$ or graphite/ PbF_2 /graphite conductivity cells were fabricated according to the following procedures:

A weighed amount of lead fluoride powder was prepressed at 4000 psi in a 0.6 in. diameter steel die. While the prepressed pellet remained in the steel die the electrode powder was placed on both sides of the pellet, the total assembly was pressed at 100,000 psi to form the conductivity cell.

Inasmuch as the cubic form lead fluoride could be converted to the orthorhombic form at pressures above 30,000 psi (1) a conductivity cell for the cubic form lead fluoride could not be fabricated by the pressing of the cubic lead fluoride powder. In order to obtain a conductivity cell of lead fluoride in the cubic form the orthorhombic lead fluoride conductivity cell was heated to about 350°C . Since the cubic lead fluoride has a lower density than the orthorhombic lead fluoride, the conversion of $\alpha\text{-PbF}_2$ to $\beta\text{-PbF}_2$ would result in a volume expansion of the pellet. This volume expansion often caused cracking of the pellet as noted by Kennedy *et al.* (1). Nonetheless, it was reported (1) that the rate of interconversion is highly temperature dependent and the temperature where the phase transition is observed depends on the heating rate. It was found during our investigation that in order to avoid cell cracking due to the volume expansion upon conversion of $\alpha\text{-PbF}_2$ to $\beta\text{-PbF}_2$ the temperature of the sample must be increased gradually. A rate of $1^\circ\text{C}/\text{min}$ was found to be sufficient to convert the lead fluoride from the orthorhombic form to the cubic form without fracturing the pellet.

The geometric area of the lead fluoride pellet was calculated from the diameter and the thickness was determined by measuring a lead fluoride pellet of the same weight formed under similar conditions but without the electrodes.

The conductivity of the pellet was determined from the resistance of the conductivity cell which was held in a lava cell holder and measured by means of a General Radio conductance bridge at 1000 Hz. Resistance measurements were also made with square wave excitation from 1,000 to 10,000 Hz of a bridge constructed from Helipot precision potentiometers. A Tektronix Type E differential preamplifier made possible the application of only 3 mV peak to peak to the sample. Same results were obtained using both techniques.

A Blue M Model M10A resistance furnace was used to maintain the temperature of the conductivity cell above ambient.

X-ray diffraction analysis.—The x-ray diffraction patterns of the nominally pure and doped lead fluoride

were obtained at room temperature using a Philips diffractometer with $\text{CuK}\alpha$ radiation through a Ni filter.

Transference number measurement.—The transference numbers of F^- in the YF_3 -doped $\alpha\text{-PbF}_2$ were determined at 110°C using the Tubandt method. A $\text{Pb}/\alpha\text{-PbF}_2/\alpha\text{-PbF}_2/\alpha\text{-PbF}_2/\text{graphite}$ cell was used for the measurement. The weight change in both the $\text{Pb}/\alpha\text{-PbF}_2$ and the $\alpha\text{-PbF}_2/\text{C}$ pellets after the passage of a current was used to determine the transference number. An Electronics Measurements M-621 constant current supply was used to provide the current for electrolysis. The electrolysis was carried out at a constant current of 1 mA for exactly 80 hr. A silver coulometer was used to measure the total number of coulombs used for the electrolysis. The weights of the pellets in the cell were weighed using a Mettler H15 balance before and after the electrolysis.

Results

The x-ray diffraction patterns showed that the lead fluoride pellet formed from the commercial powder material was in the orthorhombic form ($\alpha\text{-PbF}_2$). No impurity was found by the x-ray diffraction analysis. Nonetheless, some impurities were found by spectrographic analyses. The impurity contents are shown in Table I. The conversion to the cubic $\beta\text{-PbF}_2$ was accomplished by heating the pellet gradually to about 350°C . Once the $\beta\text{-PbF}_2$ was formed it remained stable at room temperature and pressure. Kennedy *et al.* (1) found that the room temperature equilibrium potential of the $\text{Pb}/\beta\text{-PbF}_2/\text{KF}_{\text{aq}}/\alpha\text{-PbF}_2/\text{Pb}$ cell was +1.7 mV and suggested that $\beta\text{-PbF}_2$ was in fact more stable than $\alpha\text{-PbF}_2$ at room temperature and pressure.

Figure 1 shows the temperature dependence of the total conductivity for the nominally pure lead fluoride in both α and β forms. Inasmuch as the electronic conductivity is negligible compared with the ionic conductivity in lead fluoride (1,3) the data shown in Fig. 1 may be regarded as characteristic for ionic conduction. It was noted that the conductivity of lead fluoride was generally independent of the electrode material. Similar results were obtained when either graphite or lead was used as the electrodes in the conductivity cells. The conductivity of $\beta\text{-PbF}_2$ was higher than that of $\alpha\text{-PbF}_2$ at the same temperature. However, similar activation energies for conduction were found for both $\alpha\text{-PbF}_2$ in the temperature range between 25° and 300°C and $\beta\text{-PbF}_2$ in the temperature range between 25° and 350°C . It is noted that Kennedy *et al.* (1) concluded from their conductivity measurements that both forms of lead fluoride exhibited the same activation energy of movement. Nonetheless, the values of the activation energy calculated from the data shown in Fig. 1 were 11.6 ± 0.6 kcal/mole for $\alpha\text{-PbF}_2$ and 14.3 ± 0.6 kcal/mole for $\beta\text{-PbF}_2$. It is most likely that these activation energies were for the mobility of the conducting species inasmuch as the conductivity was measured at relatively low temperatures (1). No attempt was made to study the conduction characteristics in the intrinsic region.

Table I. Results of spectrographic analysis of the commercial $\alpha\text{-PbF}_2$

Impurity	Concentration, parts per million (ppm)
Al	10.0
Ag	8.0
Bi	40.0
Ca	10.0
Cu	7.0
Cr	0.5
Fe	75.0
Mg	1.0
Mn	1.0
Mo	5.0
Ni	2.0
Sn	6.0
Si	20.0
Sr	0.7
Tl	5.0

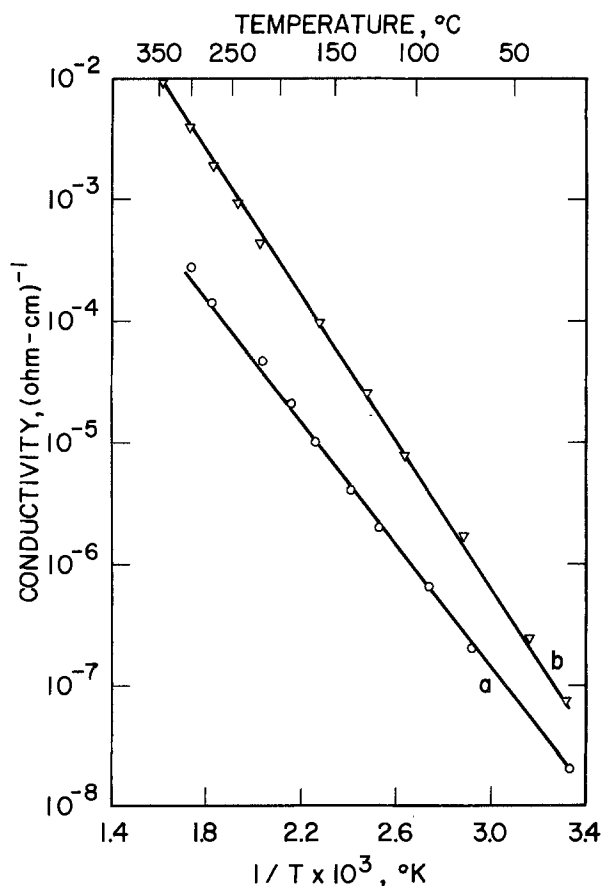


Fig. 1. The temperature dependence of the total conductivity of polycrystalline lead fluoride. a, α -PbF₂; b, β -PbF₂.

The conduction characteristics of both forms of lead fluoride were altered by doping with potassium fluoride. The conductivity was increased substantially by the incorporation of potassium fluoride in the lead fluoride lattice. Furthermore, a substantial decrease in activation energy was observed for both α -PbF₂ and β -PbF₂ upon doping with KF.

Figures 2 and 3 show that the conductivity of the doped lead fluoride at room temperature increased linearly with the potassium fluoride concentration up to 1 mole per cent (m/o). Figures 4 and 5 show the temperature dependence of the conductivity for the KF-doped lead fluoride in comparison with that for the nominally pure lead fluoride in both forms. These results showed that the inclusion of potassium fluoride

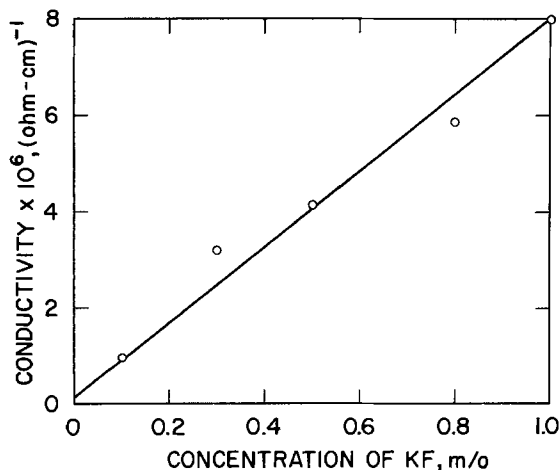


Fig. 2. The effect of KF dopant on the conductivity of α -PbF₂ at $25^\circ \pm 2^\circ\text{C}$.

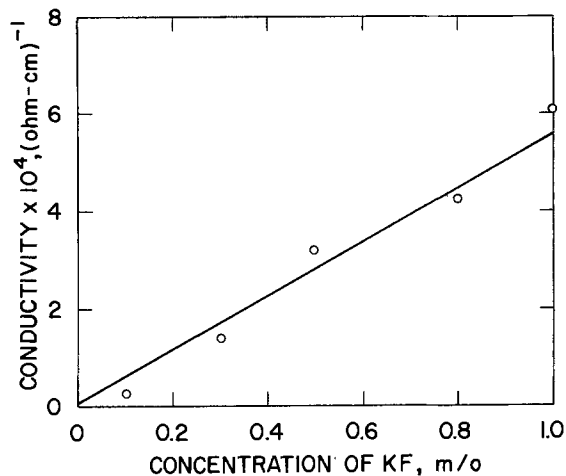


Fig. 3. The effect of KF dopant on the conductivity of β -PbF₂ at $25^\circ \pm 2^\circ\text{C}$.

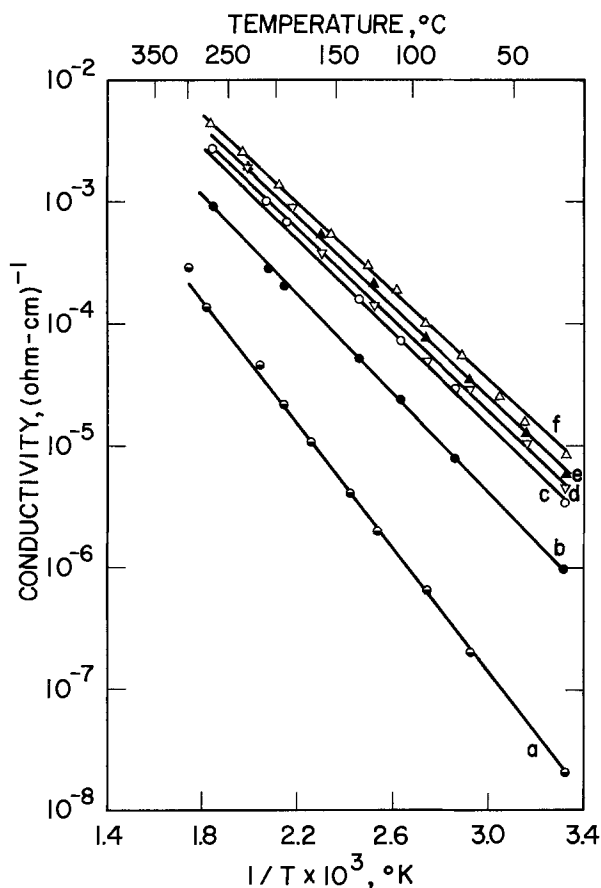


Fig. 4. The temperature dependence of the total conductivity of polycrystalline α -PbF₂. a, Nominally pure; b, 0.1 m/o KF; c, 0.3 m/o KF; d, 0.5 m/o KF; e, 0.8 m/o KF; f, 1 m/o KF.

changed the activation energy of mobility from 11.6 ± 0.6 kcal/mole to 8.9 ± 0.3 kcal/mole for α -PbF₂ and from 14.3 ± 0.6 kcal/mole to 4.1 ± 0.3 kcal/mole for β -PbF₂. The change in the activation energy indicated a change in the conduction mechanism. It was known from the transference number measurements (1, 2) that the ionic conductivity of lead fluoride was predominately due to the fluoride ions. The transport of fluoride ions are either via interstitials or via vacancies. The effect of doping on the transport mechanism was shown by the change in activation energy. In order to determine whether the interstitial or the vacancy was the prevailing mechanism, the effect of trivalent cations on the conduction characteristics of lead fluoride was also investigated. It was found that

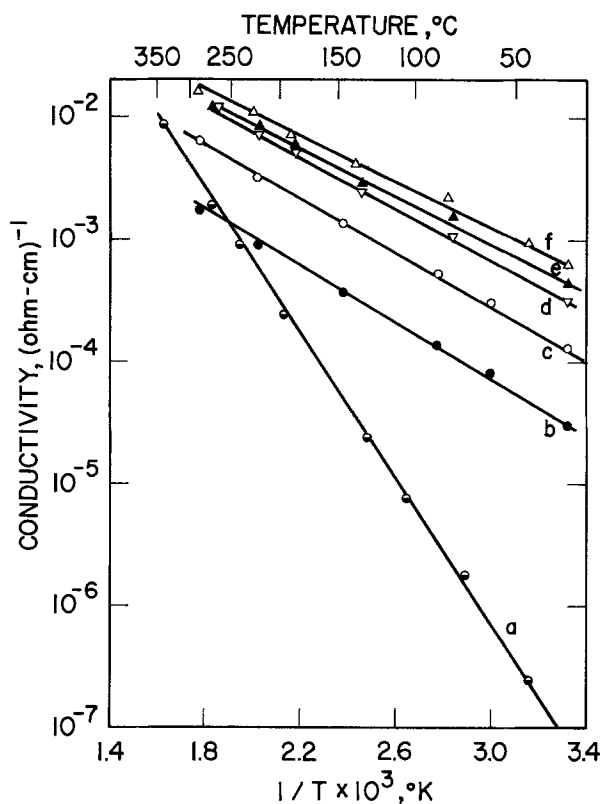


Fig. 5. The temperature dependence of the total conductivity of polycrystalline β -PbF₂. a, Nominally pure; b, 0.1 m/o KF; c, 0.3 m/o KF; d, 0.5 m/o KF; e, 0.8 m/o KF; f, 1 m/o KF.

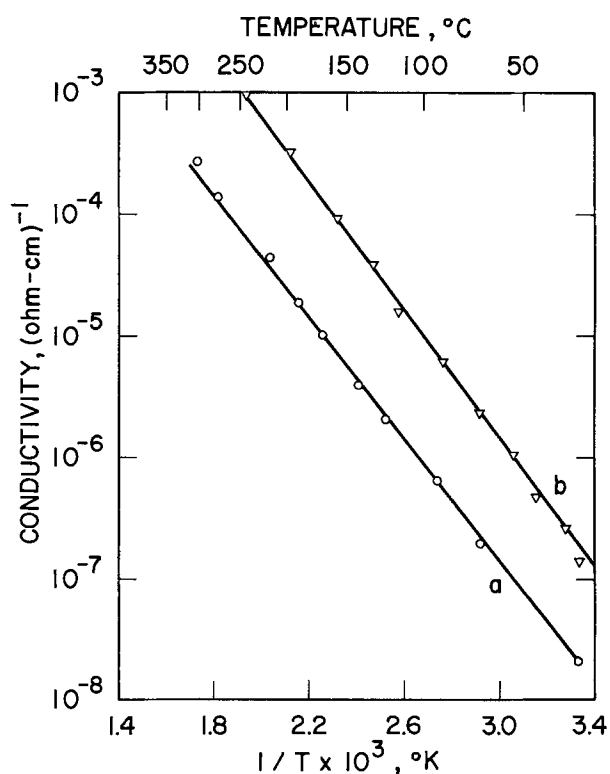


Fig. 6. The temperature dependence of the total conductivity of polycrystalline α -PbF₂. a, Nominally pure; b, 0.3 m/o YF₃.

the conductivity of PbF₂ was increased by doping with YF₃. However, the activation energy for the conduction process remained the same as shown by Fig. 6 and 7. These results indicated that the conduction mechanism was not affected by the incorporation of the trivalent yttrium ions.

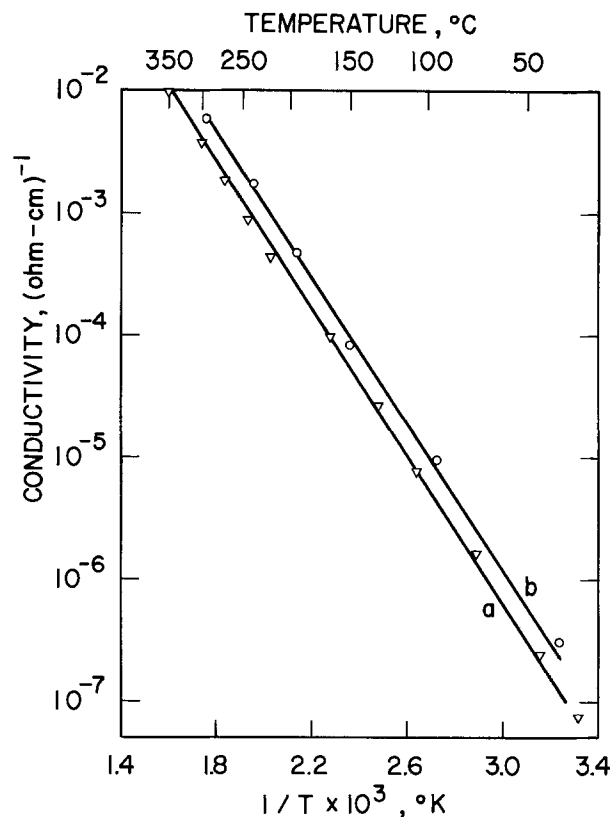


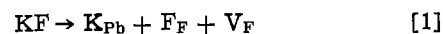
Fig. 7. The temperature dependence of the total conductivity of polycrystalline β -PbF₂. a, Nominally pure; b, 0.3 m/o YF₃.

The transference number of the fluoride ion in the yttrium-doped α -PbF₂ was determined using the Tubandt method at 110°C. A value of 0.94 ± 0.02 was obtained as shown in Table II.

Discussion

Inasmuch as lead fluoride is an anionic conductor (1, 2), either the fluoride ion vacancy and interstitial fluoride ion pairs (Frenkel disorder) or the lead ion and fluoride ion vacancies (Schottky disorder) are the predominate defects. In the case of Frenkel disorder, the fluoride ion vacancies and/or the interstitial fluoride ions may be the mobile species; in the case of Schottky disorder the fluoride ion vacancies are the mobile species.

It is known (4) that the cubic lead fluoride has Frenkel defects. Accordingly, the interstitial fluoride ions and the fluoride ion vacancies are the intrinsic point defects. Upon doping with KF and YF₃, the fluoride ion vacancies and the interstitial fluoride ions are generated respectively as shown by the following equations



Where K_{Pb} denotes the potassium ion at a lead ion site in the lattice with an effective charge of -1 , Y_{Pb}

Table II. Transference number measurement on the 0.3 m/o YF₃-doped α -PbF₂ at 110°C.

Electrode	Weight before electrolysis, g (including the weighing bottle)	Weight after electrolysis, g (including the weighing bottle)	Weight change
α -PbF ₂ /graphite pellet	82.0383	82.0032	-0.0351
Middle α -PbF ₂ pellet	82.2547	82.2521	-0.0026
Pb/ α -PbF ₂ pellet	83.7969	83.8339	+0.0370

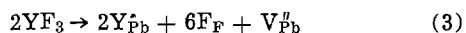
Current = 1 mA.
Total change = 288.0 coulombs.
Transference number of the fluoride ion, $t_{\text{F}^-} = 0.94 \pm 0.02$.

the yttrium ion at a lead ion site with an effective charge of +1, F_F , V_F , and F_i represent respectively the fluoride ion at a fluoride ion site, the fluoride ion vacancy with an effective charge of +1 and the interstitial fluoride ion with an effective charge of -1.

Our experimental results showed that upon doping with KF the conductivity of β -PbF₂ was increased substantially. Furthermore, Fig. 5 shows that the activation energy of motion is decreased from 14.3 ± 0.6 kcal/mole for the nominally pure β -PbF₂ to 4.1 ± 0.3 kcal/mole for the KF doped β -PbF₂. These results indicate a difference in conduction mechanisms. In view of Eq. [1] we conclude that the predominate mobile species in the KF-doped β -PbF₂ are fluoride ion vacancies while that in the nominally pure β -PbF₂ are interstitial fluoride ions.

These conclusions are also supported by the conduction characteristics of the YF₃-doped β -PbF₂. Upon doping with YF₃ the concentration of the interstitial fluoride ions was increased resulting in a conductivity increase for β -PbF₂. Nonetheless, the activation energy of motion remained unchanged indicating common mobile species which are interstitial fluoride ions (Eq. [2]). Accordingly, in the cubic form for lead fluoride the activation energy for the mobility of interstitial fluoride ion is 14.3 ± 0.6 kcal/mole and that of the fluoride ion vacancy is 4.1 ± 0.3 kcal/mole.

For the orthorhombic α -PbF₂ we have considered both the Frenkel and the Schottky disorders. In the situation where Frenkel disorder prevails it has been shown in Eq. [1] and [2] that fluoride ion vacancies and interstitial fluoride ions are generated by doping with KF and YF₃ respectively. In the situation where Schottky disorder is the predominate defect structure, doping with KF also results in an increase in the fluoride ion vacancy concentration as shown in Eq. [1]. The inclusion of YF₃ in α -PbF₂ with Schottky disorder will generate the lead ion vacancies as shown in the following equation



where Y_{Pb} and V_{Pb} represent respectively the yttrium ion at a lead ion site with an effective charge of +1 and the lead ion vacancy with an effective charge of

-2. However, results from the transference number measurements (Table II) showed that the YF₃-doped α -PbF₂, same as the pure lead fluoride (1, 2) is an anion conductor. Furthermore, from the activation energy shown in Fig. 6 it is noted that the same transport mechanism prevails in the YF₃-doped and the nominally pure α -PbF₂. Therefore, we concluded that lead ion vacancies cannot be the principal conducting species. Furthermore, if Schottky disorder were the predominate defect structure then the mobile species would be the fluoride ion vacancies in both the nominally pure and the KF-doped α -PbF₂. However, Fig. 4 shows that the activation energy of motion for the nominally pure α -PbF₂ is different from that for the KF-doped α -PbF₂ indicating different mobile species in the two α -PbF₂ under discussion. Therefore, it is unlikely that Schottky disorder is predominate in α -PbF₂.

Our experimental data would indicate that (i) two mobile species are present in α -PbF₂ (Fig. 1, 4, and 6) and (ii) both of the mobile species transport fluoride ions (Table II). Therefore, we concluded that Frenkel disorder is also predominate in α -PbF₂ as in β -PbF₂. Accordingly, in α -PbF₂ the activation energy for the mobility of the interstitial fluoride ion is 11.6 ± 0.6 kcal/mole and that for the mobility of the fluoride ion vacancy is 8.9 ± 0.3 kcal/mole.

Manuscript submitted Oct. 1, 1974; revised manuscript received Dec. 5, 1974.

Any discussion of this paper will appear in a Discussion Section to be published in the December 1975 JOURNAL. All discussions for the December 1975 Discussion Section should be submitted by Aug. 1, 1975.

Publication costs of this article were partially assisted by P. R. Mallory and Company, Incorporated.

REFERENCES

1. J. H. Kennedy, R. Miles, and J. Hunter, *This Journal*, **120**, 1441 (1973).
2. C. Tubandt, *Z. Anorg. Chem.*, **115**, 105 (1921).
3. A. V. Joshi and C. C. Liang, *J. Phys. Chem. Solids*, In press.
4. J. Schoonman, G. J. Dirksen, and G. Blasse, *J. Solid State Chem.*, **7**, 245 (1973).

Growth of Oxide Films at Pt Anodes at Constant Current Density in H₂SO₄

A. Damjanovic, A. T. Ward, B. Ulrick, and M. O'Jea

Xerox Corporation, Webster Research Center, Webster, New York 14580

ABSTRACT

Constant current charging curves from 10^{-6} to 10^{-1} A-cm⁻² are used to study the mechanism of growth of anodic oxide films at platinum in H₂SO₄ solutions. At any constant current density the potential initially changes linearly with time. In this linear region no O₂ is evolved. The linear region is followed by a region in which potential changes logarithmically with time while oxygen evolution becomes the predominant reaction. The thickness of the oxide films at which the transition occurs depends on the applied current density but for all current densities it is less than 10Å. Both in the linear and the logarithmic region the ellipsometric thickness-time relationships essentially parallel the V-t relationships. The rate of growth is described by $i = i_0 \exp [\alpha(V - V_0)/d]$ where d is the thickness and V_0 the potential at which oxide film starts to grow. From the transfer coefficient α , that is equal to 158 Å-V⁻¹, it was deduced that the oxide phase is composed of divalent platinum ions, i.e., the oxide phase is PtO. It is suggested that the rate-determining step is a process at the metal/oxide interface rather than a process at the oxide/solution interface or a process within the bulk of oxide. The distribution of the potential between the oxide film and the double layer is discussed. It is shown that the potential difference across the solution double layer is constant for the growth at current densities examined here. This is possible if the electrochemical reaction in the double layer is fast.

The nature of the "oxygen containing films" at platinum electrodes at potentials anodic to about 0.7V vs. hydrogen electrode has been the subject of numerous recent studies (1-20). Views of various workers range from "... the film is all absorbed oxygen..." (13)—even at potentials as high as 2.2V and for coverages over 2.5 oxygen atoms per platinum atom in the surface,—to "... it is a phase oxide..."—particularly above 1.0V. The latter potential was taken to represent, somewhat arbitrarily, a border between potential regions of chemisorbed oxygen (from about 0.7-0.95), and oxide phase (9, 21) (above about 1.0V). Electrochemical or chemical evidence alone was not sufficient to resolve the problem. It is only in recent studies, particularly those based on reflectance and ellipsometric measurements (3-6), low energy electron diffraction (22), and field ion spectroscopy (23) that conclusive evidence was provided favoring the view that above 1.0V "... the film is made of an oxide of platinum forming a definite phase..." (6) while below about 1.0V "... the film is composed of [reversibly (21)] chemisorbed oxygen species" (4, 6). The latest evidence, both from the ellipsometric studies and Auger spectroscopy (24) indicated that divalent platinum constituted the oxide phase. This is in agreement with an early finding of Anson and Lingane (1) that the chemically stripped anodic oxide films correspond mostly to PtO.

Due probably to this divergence of views regarding the "nature" of the oxygen-containing films, little attention has been paid to the analysis of the kinetics and mechanisms of the anodic film growth at platinum. This is sharply contrasted to the extensive work of anodic oxide formation on valve metals, or on metals "known to passivate," such as nickel or iron. Reddy, Genshaw, and Bockris (5) have concluded from their steady-state ellipsometric measurements that the oxide films at platinum grow by "a place exchange mechanism" leading to the direct logarithmic law of growth. Vetter and Schultze (15) examined the rate of growth as a function of time at various constant potentials; from their data it is evident that the same law of growth holds for oxide film grown at constant potentials. For polarization at constant current density,

however, Vetter and Schultze (16) have observed a different law of growth; it can be described by the well-known Mott's equation for growth of oxide films in the presence of a high electric field within an oxide film.

In the present study we have examined the kinetics of oxide film growth at platinum anodes at the early stages of polarization with various constant current densities, and analyzed the mechanism of growth in the potential region in which no significant oxygen evolution occurs.

Experimental

An all-Pyrex, two-compartment cell used in present experiments was similar to a cell previously described (25). A platinum wire test electrode (diameter = 0.5 mm) was "sealed" at one end into a soft glass tube that fitted a Beckman stopcock closing the main compartment. Geometrical area of the electrode was 0.5 cm². Stated purity of the metal was better than 99.999%. The solution was made with triple-distilled water (with two distillations in an all quartz system) and Analar grade H₂SO₄. Final cleaning of the cell and electrodes was made *in situ* with triple-distilled water and then acid solutions of the same concentrations as used in subsequent experiments.

Prior to any measurement a test electrode was abraded with polishing papers (ending with 40), and then after extensive washing was subjected to a few high (~2.0V) anodic pulses (10-30 sec) followed by cathodic (0.0V) pulses (20-60 sec). The roughness factor of electrodes was determined by capacitance measurements in the potential region close to 0.5V, and current densities were corrected for the roughness of the electrodes.

A potentiostat (Tacussel PRT 40-1X) connected for a galvanostatic mode of operation was used. Potentials of the test electrode with respect to a hydrogen electrode in the same solution were measured with an electrometer (Keithley 610) and recorded with time on a strip-chart recorder (Mosley 1100). For high current densities and fast rise of potentials, an oscilloscope (Tektronix, Type 564 with 2A63 differential amplifier and 612 oscilloscope camera) was used.

In a few experiments, a rotating disk platinum electrode with a concentric ring electrode was used to de-

tect the early stages of oxygen evolution. After a constant current was applied to the test electrode, first oxygen gas evolved at the disk electrode was quantitatively detected (as a function of time) at the ring electrode kept at 0.5V. Solution in these experiments was saturated with argon.

Finally, in as yet preliminary experiments, the early stages of oxide growth at platinum at a constant current density were followed with time by an automatic ellipsometer (Rudolf Research Inc. Automatic Ellipsometer). The thickness of oxide film was determined *in situ* upon reflection of polarized light from a mirror-polished platinum disk electrode (diameter = 12 mm). The cell used in this work was similar to those described by other workers (26). All experiments were performed at room temperature. Potentials refer to hydrogen electrode in the same solution (HE).

Results

Preliminary experiments.—At prerduced electrodes in solutions saturated with oxygen under 1 atm pressure a potential close to 0.98V was readily established in less than 1 min. In argon-saturated solutions an unstable, slowly drifting potential in the region 0.3-0.7V was observed. When a constant current is applied to an electrode at rest a linear $V-t$ region is observed at potentials above 1.0V. This linear region is followed by a region in which the potential changes only very slowly with time (Fig. 1). This region does not, however, represent a steady state: in this region too the potential increases with time, but now according to a direct logarithmic rather than a linear law. The logarithmic dependence extends to at least $2 \cdot 10^4$ sec (Fig. 2). Irrespective of whether a constant current is applied to an electrode in oxygen- or argon-saturated solution the slopes of the charging curves in the linear region were the same above 1.0V. For this reason, only the data obtained in oxygen-saturated solutions are presented here.

Vigorous stirring of the solution by bubbling, or rotation of a disk electrode, had no effect on the $V-t$ curves. This result shows that the mechanism of anodic film growth at platinum does not follow the dissolution-precipitation path. Finally, a test was made to ascertain whether mechanical damage of the electrode surface, which could result from polishing, affected the polarization behavior of the electrodes. No significant change in the $V-t$ curves was detected at mechanically polished as compared to initially flamed (presumably annealed) electrodes providing the electrodes were treated by alternative anodic-cathodic pulses and the correction for roughness factor was made. Electrodes were always prerduced prior to an experiment by potentiostating in the potential region 0.4-0.5V for a few minutes. When an electrode was not well reduced, the rate of change of potential was high

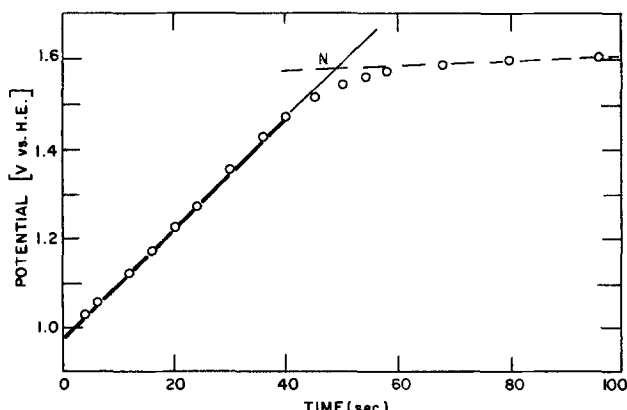


Fig. 1. Change of potential with time of polarization with constant current density $i = 1.82 \cdot 10^{-5} \text{ A}\cdot\text{cm}^{-2}$. Solution $2N \text{ H}_2\text{SO}_4$. The linear region is followed by a quasi steady state.

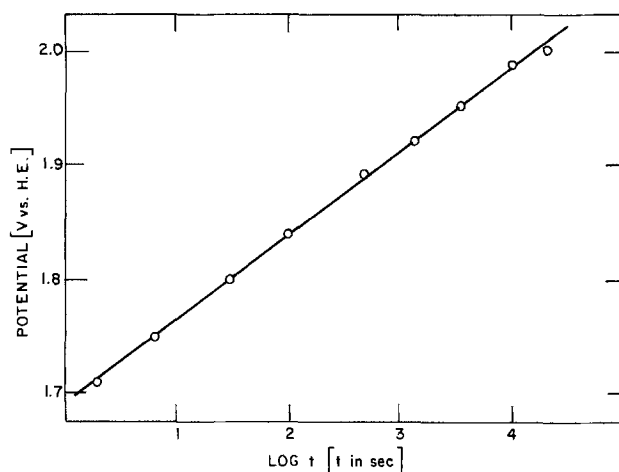


Fig. 2. Change of potential with time during the extended growth of oxide film. $i = 5.5 \cdot 10^{-4} \text{ A}\cdot\text{cm}^{-2}$. Solution $2N \text{ H}_2\text{SO}_4$.

and not reproducible. The electrolyte was frequently replaced with fresh solution to avoid possible contamination with H_2O_2 .

Charging curves at constant current densities.—A series of charging curves for different constant current densities ranging from about 10^{-6} - $10^{-1} \text{ A}\cdot\text{cm}^{-2}$ are plotted vs. total charge, q , in Fig. 3. These curves are obtained in $2N \text{ H}_2\text{SO}_4$ solution. Identical data with respect to HE are obtained in 0.1 and 0.01N solutions. A linear dependence of V on q is evident in all charging curves at or above $10^{-6} \text{ A}\cdot\text{cm}^{-2}$. Charging curves below $10^{-6} \text{ A}\cdot\text{cm}^{-2}$ frequently exhibit a shoulder around 1.2-1.3V, after which the potential increases linearly with time.

The linear $V-t$ relationship has frequently been reported (14, 16-18, 27, 28) and is interpreted to represent the buildup of an oxygen-containing film at electrodes without oxygen evolution. The rotating disk-ring electrode assembly offers here an additional proof for this. When a constant current is applied across the disk electrode no current is detected at the ring electrode for as long as the potential of the disk remained in the linear $V-t$ region (29). Accordingly, all, or at least the major part of the current at the disk goes for formation of oxygen film. Only close to, or after the knee in the $V-t$ curves (cf., N in Fig. 1) oxygen starts to evolve at the disk and is detected at the ring electrode. At this point the ring current increases rapidly and soon reaches the value that corresponds almost completely to the current at the disk electrode. Addi-

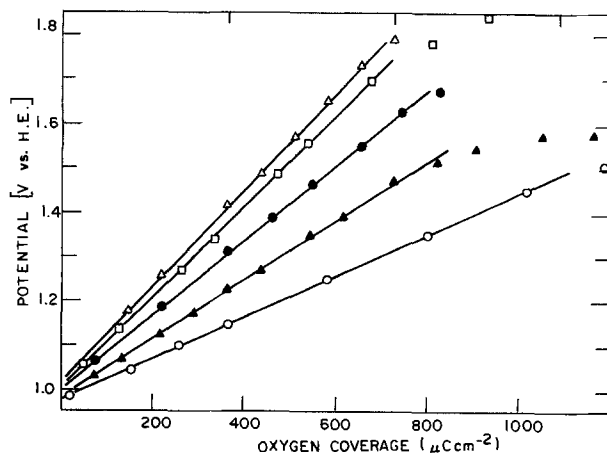


Fig. 3. Linear change of potential with oxygen coverage at initial stages of oxide growth at different constant currents of polarization. Δ , $3.6 \cdot 10^{-2}$; \square , $1.8 \cdot 10^{-2}$; \bullet , $5.5 \cdot 10^{-4}$; \blacktriangle , $1.8 \cdot 10^{-5}$; and \circ , $7.3 \cdot 10^{-7} \text{ A}\cdot\text{cm}^{-2}$. Solution $2N \text{ H}_2\text{SO}_4$.

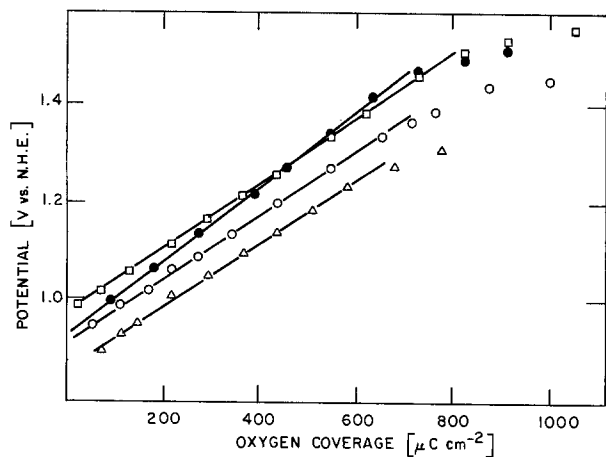


Fig. 4. Initial, linear change of potential with coulometric thickness at $1.8 \cdot 10^{-5} \text{ A}\cdot\text{cm}^{-2}$ in: Δ , 0.01; \circ , 0.1; and \square , 2N H_2SO_4 solutions. \bullet , $1.8 \cdot 10^{-4} \text{ A}\cdot\text{cm}^{-2}$ in 0.1N H_2SO_4 .

tional experiments verified that the response of the ring electrode was fast so that the "delay" in the ring current was due only to the "induction" period for oxygen evolution at the disk electrode.

pH dependence.—The effect of pH is shown in Fig. 4, where the V - q curves at a given current density in solutions of different pH are plotted. In this figure the potentials refer to NHE. There is a strong dependence of the position of the V - q lines on pH, but the slopes of the charging curves at a given current density are not affected by pH. For any constant charge, q , and current density, i , the potential with respect to NHE changes by about -60 mV per unit of pH, i.e.

$$\left(\frac{\partial V}{\partial \text{pH}}\right)_{q,i} \approx -2.3 RT/F \quad [1]$$

Ellipsometric determination of film thickness.—The changes in azimuth and ellipticity associated with the changes in the electrode surface from the initial, freshly reduced film-free state¹ to the final anodically oxidized state were used to calculate the change ($\Delta_0 - \Delta$) in the relative phase retardation, Δ , between components of the light polarized perpendicular and parallel to the plane of incidence, respectively. This change was used to calculate the mean film thickness, d , using Drude's approximation,² [$(\Delta_0 - \Delta) = kd$], a relationship valid for films thin compared with the wavelength of light.

The optical constants ($n_1 = 2.80$; $n_2 = 1.94$; $\kappa_2 = 4.36$) used here to calculate thickness were taken from the work of Kim, Paik, and Bockris (6) who determined these parameters entirely from ellipsometric data. Here, n_1 is the refractive index of the film, and n_2 and κ_2 are the refractive index and absorption constant, respectively, of the platinum substrate. With angle of incidence $\phi = 75^\circ$, corrected for refraction through the cell windows and wavelength $\lambda = 5460 \text{ \AA}$, the constant k in Drude's equation is calculated as 0.263 \AA^{-1} . The film thicknesses are then typically less than 10 \AA , and the use of Drude's equation is justified.

Ellipsometric data revealed a linear change of Δ with time, t , during the initial stages of polarization at constant current density. The variation of Δ or d vs. t at different applied current density is somewhat obscured due to the scatter of data and the narrow region of accessible current densities for ellipsometric work. However, the Δ - t , or d - t relationships essentially

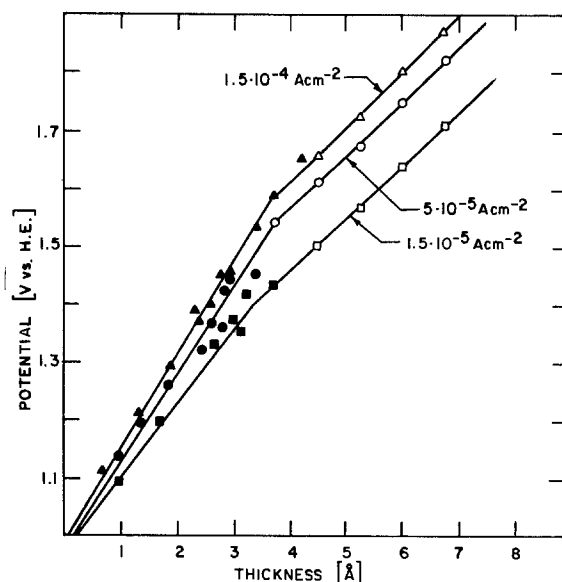


Fig. 5. The dependence of potential on ellipsometric thickness in the initial linear (full symbols) and subsequent logarithmic growth (open symbols) of oxide films. \blacksquare and \square , $1.5 \cdot 10^{-5}$; \bullet and \circ , $5 \cdot 10^{-5}$; and \blacktriangle and \triangle , $1.5 \cdot 10^{-4} \text{ A}\cdot\text{cm}^{-2}$. Solution 2N H_2SO_4 .

parallel the V - t relationships both in the linear V - t and the logarithmic growth region. When Δ or d is plotted against V , linear relationships appear for both growth regions as shown in Fig. 5. Here, only the growth in the linear region is discussed; the discussion of the extended growth region is deferred to a subsequent paper.

Discussion

Since in the linear V - q (or V - t) region all the current is used to build up an oxide film (with no significant losses to corrosion or oxygen evolution) the kinetic data in this region appear particularly suitable for the study of the mechanism of initiation and growth of the anodic oxide films at platinum. Only in this region do oxides grow under controlled and ideal conditions of constant current density. Once oxygen starts to evolve, or becomes a major product in the over-all reaction, oxides continue to grow but now at a much reduced and no longer constant rate. As is discussed later, the observed linear change of the potential with time represents the change of the potential across the oxide film only, the potential across the double layer being constant for a constant current density. Once oxygen starts to evolve the total potential difference across the electrode is expected to rearrange and redistribute across the oxide film and the double layer. The new distribution will now be controlled by the major on-going reaction, the oxygen evolution reaction, and no longer directly by the growth of the oxide film. Though in this region most of the current is used for oxygen evolution, the observed potential change still represents the change in the thickness of the oxide film (25). The analysis of the oxide growth, however, becomes more complex since both the current for oxide growth and the potential difference across the oxide film change with time (25, 30). Under potentiostatic conditions too, the mechanistic analysis of oxide growth is rather complex since again both the potential difference across the oxide film and the current density for oxide growth (or O_2 evolution) change simultaneously with time. In this paper the rate of growth is analyzed for the initial, linear region before the onset of oxygen evolution.

The rate equation of oxide growth.—The most significant aspect of the present results, and the one which is characteristic for the mechanism of growth, is that the $(\partial V/\partial q)_i$ slopes increase linearly with logarithm of the applied current density. The linear relationship extends for over several decades of cur-

¹ The film-free condition exists under potentiostatic conditions at 0.5V HE. At 0.98V the phase retardation was somewhat lower reflecting the presence of adsorbed species on the electrode.

² The assumption implicit in Drude's approximation is that the refractive index of the film is independent of thickness. Since the adsorbed layer and the film ultimately formed may not have similar refractive index the Drude assumption will lead to a small but constant error in calculated thicknesses.

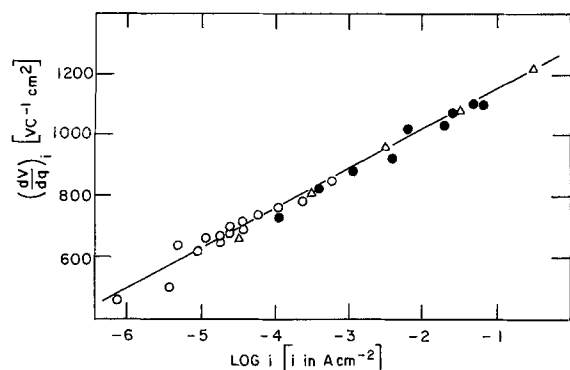


Fig. 6. The dependence of slopes in V - q diagrams on current density. ●, Oscilloscope recording; ○, recording with a mechanical recorder. Solution $2N$ H_2SO_4 , △, Data of Vetter and Schultze (16) in $1N$ H_2SO_4 solution.

rent density (Fig. 6). In Fig. 6 in addition to many data obtained in the present work, data from the work of Vetter and Schultze (16) are included for comparison. The latter data are, however, scaled to the present data by a factor of 1.3 to compensate for the difference in electrode roughness. The fact that a single scaling factor brings both the position and slopes of $(\partial V/\partial q)_i$ vs. $\log i$ to overlap, justifies in itself the scaling procedure. From Fig. 6 one obtains

$$\left(\frac{\partial V}{\partial q}\right)_i = c \ln i + b \quad [2]$$

with $c = 57$ $V\text{-cm}^2\text{-C}^{-1}$, and $b = 1280$ $V\text{-cm}^2\text{-C}^{-1}$ when i is in $A\text{-cm}^{-2}$. Writing $b = -c \ln i_0$ with i_0 as a constant, [2] transforms to

$$\left(\frac{\partial V}{\partial q}\right)_i = c \ln \frac{i}{i_0} \quad [3]$$

From Fig. 2, the dependence of potential on logarithm of current density at any constant charge, q , is obtained (Fig. 7). From Fig. 7 it follows that

$$\left(\frac{\partial V}{\partial \ln i}\right)_q = aq \quad [4]$$

With a equal to 62 $V\text{-cm}^2\text{-C}^{-1}$. It is convenient to convert q into average thickness, d , of the oxide film according to $d = r q$ where r is a conversion factor.

At constant pH and temperature, V is a function of $\ln i$ and d , only, i.e.

$$V = V(\ln i, d) \quad [5]$$

and from [3] and [4] one obtains

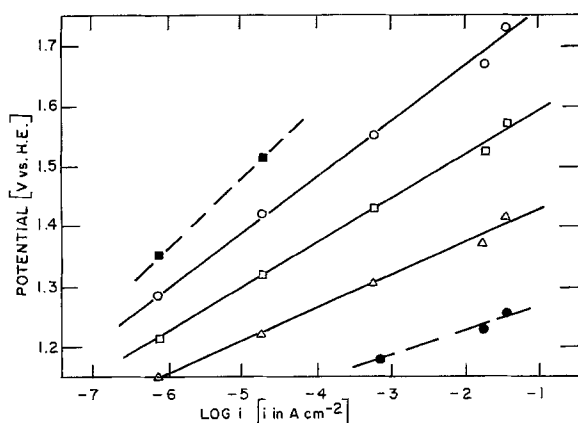


Fig. 7. "Tafel slopes" for oxide growth at constant thickness of oxide film. ■, 800; ○, 655; □, 510; △, 365; and ●, 220 $\mu\text{C-cm}^{-2}$. Solution $2N$ H_2SO_4 .

$$dV = (ad/r) \partial \ln i + (c/r) \ln (i/i_0) \partial d \quad [6]$$

Integration of [6] yields

$$i = i_0 \exp \left[\frac{\alpha(V - V_0)}{d} \right] = i_0 \exp \left[\frac{\alpha \Delta V_{of}}{d} \right] \quad [7]$$

Here, V_0 is the potential at $d = 0$, and ΔV_{of} the potential difference across the oxide film. Factor $\alpha (= r/a)$ is the transfer or field coefficient as it is sometimes called. It follows that $a = c$, in fair agreement with the experimental data.³ Constant i_0 , the exchange current density for oxide growth, is equal to $1.8 \cdot 10^{-10}$ $A\text{-cm}^{-2}$.⁴ Further, an inspection of Fig. 3, as well as of Fig. 1 in the paper of Vetter and Schultze (16), shows that the intercepts increase slightly with current density. The linear V - q lines intercept at a negative value of charge. This charge is associated with oxygen adsorption before the onset of oxide film formation [about $130 \mu\text{C-cm}^{-2}$ (4)]. Since the coverage with adsorbed oxygen at oxide electrodes (38) is only 0.02-0.03 all the oxygen ions adsorbed on the oxide-free surface are used in the very initial formation of the oxide film before the linear V - q relationship is established.

Tafel slopes.—It has been the practice to call the V - $\log i$ lines in Fig. 7 the Tafel lines, and the $(\partial V/\partial \log i)$ slopes, the Tafel slopes. The slopes increase with increasing thickness in accordance with [4]. They approach zero for $d = 0$. Ord and Ho (18) have determined Tafel slopes for oxide growth over a range of potentials (or thicknesses) by interrupting the growth at a constant polarization current (of $10 \mu\text{A-cm}^{-2}$) at various times of polarization and analyzing the open-circuit self-discharge transients. With this technique the Tafel slopes are found to be proportional to the (ellipsometric) thickness of the oxide film and to extrapolate to zero value at about 1.0V (or more precisely at 0.98V), the potential that corresponds to the onset of oxide growth. Vetter and Schultze (16) also have examined the kinetics of oxide growth under galvanostatic conditions. In their work, galvanostatic, anodic, or cathodic pulses of various current densities (all $\geq 10^{-4}$ $A\text{-cm}^{-2}$) were superimposed over a basic anodic charging curve (of $20 \mu\text{A-cm}^{-2}$) at different points on the curve, that is, at different thickness of the oxide film. From these superimposed pulses, they determined overvoltages for different superimposed current densities, and calculated both anodic and cathodic Tafel relationships. Again, the anodic slopes increase linearly with the (coulometric) thickness of the oxide film. However, the slopes $b = b^0(1 + a + \theta)$, assume a constant value ($b^0 = 36$ mV) when coverage (θ) approaches zero.

The constant $b^0 a_+ / (2q_{H_2})$ calculated with their data for $a_+ (=1)$ and $q = \theta \cdot 2q_{H_2}$, where q_{H_2} is coverage with hydrogen ($=210 \mu\text{C-cm}^{-2}$), is 86 $V\text{-cm}^2\text{-C}^{-1}$. This value should compare with 57 $V\text{-cm}^2\text{-C}^{-1}$ of the present work. In view of the different experimental procedures, the agreement appears satisfactory.

Mechanism of oxide growth and transfer coefficient.—Following Mott (31) and Cabrera and Mott (32), the rate of growth of oxide films in the presence of a high field is given by

$$i = k \exp \left[- \frac{Q - ne^{-\lambda E}}{kT} \right] \quad [8]$$

where Q is the activation energy in the absence of the electric field, E , given by $\Delta V_{of}/d$, n and λ are valence and distance from initial position of an (interstitial) cation to its position in the activated state (the half-jump distance), respectively, and e^- is the unit charge.

³ In contrast to c , the a parameter is affected by parallel displacement of V - t curves. Consequently, the c parameter is more accurate. In the following we place $a = c = 57$ $V\text{-cm}^2\text{-C}^{-1}$.

⁴ Vetter and Schultze (16) give $i_0 = 10^{-10}$ $A\text{-cm}^{-2}$. The discrepancy is apparently due to the different experimental procedure (superposition of galvanostatic pulses) used by Vetter and Schultze in obtaining i_0 .

Other symbols have their usual significance. We use this Mott formalism to analyze the experimental data. From [7] and [8]

$$\frac{\partial^2 V_{of}}{\partial \ln i \partial d} = \frac{kT}{ne^{-\lambda}} = \frac{1}{\alpha} \left[\frac{a}{r} \right] \quad [9]$$

This derivative is proportional to the slope of $(\partial V/\partial q)$ vs. $\log i$ in Fig. 6, and is readily obtained if the conversion factor, r , is known. This factor can be calculated for a given stoichiometry or structure of the surface oxide. Early chemical (1), as well as the most recent ellipsometric (6, 7) and Auger spectroscopy (24) evidence indicates that the anodic layer is made of divalent Pt-oxide, i.e., PtO. No data on crystal structure of PtO appears to be available. From the x-ray density of Pt₃O₄, which is probably close in density to PtO, the conversion factor is equal to $9 \cdot 10^3 \text{ \AA} \cdot \text{cm}^2 \cdot \text{C}^{-1}$. With this factor, α is calculated as $158 \text{ \AA} \cdot \text{V}^{-1}$. From [9] and with $\alpha = 158 \text{ \AA} \cdot \text{V}^{-1}$, $n\lambda$ is equal to 3.99\AA , and for $n = 2$, i.e., for Pt²⁺ as the carrier of the ionic current, λ is about 2.0\AA . This is a reasonable value for the half-jump distance in platinum oxides.⁵ If one assumes that $n = 4$ (i.e., PtO₂ structure), and with $\alpha \approx 90 \text{ \AA} \cdot \text{V}^{-1}$ calculated for PtO₂, λ becomes impossibly small ($\sim 0.6\text{\AA}$). Similarly, if $n = 1$ (e.g., a kind of suboxide structure), λ becomes too large to correspond to reality. The analysis of the transfer coefficient led, therefore, to the same conclusion as ellipsometry or Auger spectroscopy: the anodic oxide films at platinum above about 1.0V vs. HE are made of divalent Pt ions, i.e., the oxide phase is PtO.

According to the original Mott's model of oxide growth, interstitial cations are formed in a rate-determining step at the metal/oxide interface and diffuse in the high field to the surface of oxide film. Other models or reaction steps besides the formation of interstitials at the metal/oxide interface may be assumed and are suggested in the literature to be rate determining (16, 33, 34). For instance, a positive vacancy may be created at the oxide/solution interface by pulling out a metal ion in the first layer of the oxide and placing it over the surface where it forms with O⁼ or OH⁻ a new element of the oxide phase. The positive vacancy then migrates in the field toward the metal/oxide interface. At the interface it is filled by a metal ion from the surface of the metal whereby a vacancy in the metal surface is formed. If the surface vacancy is filled with an oxygen atom from the oxide phase a negative vacancy is created in the oxide which then diffuses toward the oxide/solution interface. In this simple example both positive and negative vacancies in a cooperative way participate in the transport of charge and matter through the oxide film (though not necessarily in equal proportions).⁶ If $i_+ \approx i_-$, the over-all rate is given by Vetter and Schultze in a form that is similar to

$$i = \sqrt{i_+ i_-} = \text{const exp} \left[\frac{(n_+ e^{-\lambda_+} + n_- e^{-\lambda_-}) \Delta V_{of}}{2kTd} \right] \quad [10]$$

Here, (+) and (-) stand for positive and negative valencies, respectively. Since $\lambda_+ \approx \lambda_-$, the rate equation reduces to [8] when $n_+ \approx n_-$. For $n_+ \neq n_-$, α in Tafel slopes (cf., Eq. [9]) will be a multiple of $e^{-\lambda}/kT$ only when $n_+ + n_-$ is even. The same equation as [8] is obtained also for diffusion across the oxide film as rate-determining step.

If the growth occurs along two parallel but independent paths, it is expected that the rates for these two paths are sufficiently different so that the over-all rate is still controlled by a single path and rate-determining step. If the rates along the two paths are comparable then unless $n_1 \lambda_1 = n_2 \lambda_2$ no linear

change of potential with thickness is expected for a constant current growth of oxide films. The observed linear V - t relationships at platinum, and the simple factor for the field coefficient $\alpha = \left[2 \frac{e^{-\lambda}}{kT} \right]$ points,

therefore, to a simple mechanism of growth with a single reaction path. Moreover, since the observed law of growth holds from the earliest stages of growth when the coverages with oxygen are less than 1 and therefore the diffusion within the oxide film is not as yet operative, the rate-determining step is a process at the metal/solution, initially, and subsequently at the metal/oxide interface. The process at the oxide/solution interface is not expected to be the rate-determining step. It would require a change in the activation energy (and hence in i_0) as the oxide film grows from a monolayer to a multilayer. No such change is observed.

Finally, a comment about the nature of the oxide films and the relation of the nature of the films to the type of the ionic current in the oxide growth. The low angle electron diffraction revealed (22) that the oxide films on platinum have some degree of arrangement or crystallinity, though they still may be classified as "amorphous." Were the oxides crystalline, the ionic current will be due to the transport, via point defects (interstitials or vacancies), of cations only since their ionic radius is so much smaller than that of an oxygen ion. If oxides are, however, amorphous the possibility may arise that anions participate in the ionic current. It is now known that anionic current may even dominate in the anodic growth of oxides at tantalum, niobium, zirconium, and some other metals (35). With respect to structures, these oxides when amorphous are classified as glassy or network formers (33). A network of channels extends through these structures, so that large anions can easily move through these channels, and therefore anionic current is possible. Anodic oxides at platinum are not network formers if for no other reason than because of their stoichiometry, and the transport through the oxides is expected to be by cations only.

Potential distribution across the metal-solution interface.—The kinetics of oxide growth according to the model discussed here depends on ΔV_{of} rather than on the observed difference in potential ΔV . The potential difference ΔV between metal and solution is divided into the potential difference across the oxide film, ΔV_{of} , and across the double layer, ΔV_{dl} , i.e.

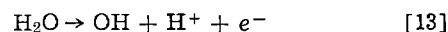
$$\Delta V = \Delta V_{of} + \Delta V_{dl} \quad [11]$$

Here, ΔV is linearly related to the measured potential, V . These partial potential differences adjust themselves in such a way that for any thickness of the oxide film, the (ionic) current across the oxide film, i_{og} , equals that across the double layer, i_{dl} . The dependence of ΔV_{dl} on current density and thickness of oxide film is now discussed.

It is reasonable to assume that ΔV_{dl} depends on current density in a usual way as

$$\Delta V_{dl} = f(i) = \frac{RT}{\gamma F} \ln (i_{dl}/i_{o,dl}) \quad [12]$$

Here, γ is the transfer coefficient for a reaction across the double layer, e.g., for



and $i_{o,dl}$ is the exchange current density for such a reaction. With [12] into [7] it follows that

$$\frac{d}{\alpha} \ln (i_{og}/i_0) = \Delta V - \frac{RT}{\gamma F} \ln (i_{dl}/i_{o,dl}) \quad [14]$$

where i_{og} is equal to i_{dl} . Equation [14] requires that at any constant current ΔV changes linearly with d and that slopes $d\Delta V/dd$ increase with applied current den-

⁵ For Pt₃O₄, the distance between two Pt or two O atoms is about 3.9\AA . These are also distances between interstitial positions. Half-jump distance is then approximately 1.95\AA .

⁶ Vacancies in the surface of metal may either diffuse into the bulk or upon accumulation cause the interface to collapse.

sity, as observed in present experiments. However, it requires also that the intercepts on the V -axis increase with increasing current density. For [13] as rate-determining step, γ is $\frac{1}{2}$ and the intercept should shift about 120 mV toward higher potentials for any tenfold increase in current density. Such shift is not observed. If a step that follows [13] is rate determining, γ is larger than $\frac{1}{2}$, and smaller shifts would be expected. Even then the shift will easily be detected when current density changes by few orders of magnitude. For instance, for $\gamma = 2$ the shift would be 150 mV when current density changes by five orders of magnitude as in present experiments. Larger values for γ are not reasonable since only two electrons are involved in charge transfer of the over-all reaction ($\text{H}_2\text{O} \rightarrow \text{O} + 2\text{H}^+ + 2e^-$). It is concluded, bearing in mind the qualification provided by Eq. [12], that ΔV_{dl} is a constant independent of applied current density, i.e.

$$\Delta V_{dl} = \text{constant} \neq f(i) \quad [15]$$

Now, if ΔV_{dl} is a function of d , for instance due to some catalytic effects, Eq. [7] would read

$$\frac{d}{\alpha} \ln(i/i_0) = \Delta V - f(d) \quad [16]$$

and for a constant current density one obtains

$$\left(\frac{\partial \Delta V}{\partial d} \right)_i = \frac{1}{\alpha} \ln(i/i_0) + \frac{df(d)}{dd} \quad [17]$$

Since $(\partial \Delta V / \partial d)_i = \text{constant}$, $df(d)/dd$ is either a constant independent of applied current density or zero, i.e.

$$\Delta V_{dl} = f(d) = md + V_0' \quad [18]$$

With [18] the rate equation, [7], reduces to an expression of the same form as [7] but with different values for i_0 and ΔV_0 , and no conclusion is possible regarding the dependence of ΔV_{dl} on d . However, irrespective of whether ΔV_{dl} is dependent or independent on i_{dl} , since the latter current density was found (30) to be invariant with d , it follows that $\Delta V_{dl} \neq f(d)$. The change of electrode potential, ΔV , with time during the constant rate of growth reflects then the change in ΔV_{of} . This is possible only if the reaction across the double layer is fast, i.e., $i_{0,dl} \gg i_{dl}$. It may be noted that the first discharge step such as that given by Eq. [13] was reported to be fast both in anodic oxidation of hydrocarbons (36) and in oxygen evolution at platinum (30, 37).

pH dependence.—The observed pH dependence apparently reflects the change with pH of the potential at which oxides start to grow. Only when the field in the double layer of as yet unoxidized platinum surface reaches certain critical values, platinum atoms are pulled out with a significant rate from their regular position in the lattice of the metal. The potential corresponding to this field is then pH dependent. It simply follows the change with pH of the potential of zero charge. If so, the rate of growth itself is not (directly) dependent on pH. This will be the case if the reaction across the double layer is fast and the rate of oxide growth is controlled by a process at the metal/oxide interface (or initially before oxides are formed at the metal/solution interface), as it is suggested in the present study.

Manuscript submitted Aug. 20, 1974; revised manuscript received Nov. 1, 1974.

Any discussion of this paper will appear in a Discussion Section to be published in the December 1975 JOURNAL. All discussions for the December 1975 Discussion Section should be submitted by Aug. 1, 1975.

Publication costs of this article were partially assisted by Xerox Corporation.

REFERENCES

1. F. C. Anson and J. J. Lingane, *J. Am. Chem. Soc.*, **79**, 4901 (1957).
2. S. Gilman, *Electrochim. Acta*, **9**, 1025 (1964).
3. W. Böld and M. Breiter, *ibid.*, **5**, 145 (1961).
4. M. L. B. Rao, A. Damjanovic, and J. O'M. Bockris, *J. Phys. Chem.*, **67**, 2508 (1963).
5. A. K. N. Reddy, M. A. Genshaw, and J. O'M. Bockris, *J. Chem. Phys.*, **48**, 671 (1968).
6. S. H. Kim, W. Paik, and J. O'M. Bockris, *Surface Sci.*, **33**, 617 (1972).
7. W. Visscher, *Optik*, **26**, 402 (1967).
8. R. Parsons and W. Visscher, *J. Electroanal. Chem.*, **36**, 329 (1972).
9. H. Angerstein-Kozłowska, B. E. Conway, and W.B.A. Sharp, *ibid.*, **43**, 9 (1973).
10. S. D. James, *This Journal*, **116**, 1681 (1969).
11. S. W. Feldberg, C. G. Enke, and C. E. Bricker, *ibid.*, **110**, 826 (1963).
12. S. Shibata and M. P. Sumino, *Electrochim. Acta*, **16**, 1089 (1971).
13. T. Biegler and R. Woods, *J. Electroanal. Chem.*, **20**, 73 (1969).
14. R. Thacker and J. P. Hoare, *ibid.*, **30**, 1 (1971).
15. K. J. Vetter and J. W. Schultze, *ibid.*, **34**, 131 (1972).
16. K. J. Vetter and J. W. Schultze, *ibid.*, **34**, 141 (1972).
17. S. Schuldiner and T. B. Warner, *This Journal*, **112**, 212 (1965).
18. J. L. Ord and F. C. Ho, *ibid.*, **118**, 46 (1971).
19. H. Wroblowa, M. L. B. Rao, A. Damjanovic, and J. O'M. Bockris, *J. Electroanal. Chem.*, **15**, 139 (1967).
20. A. Damjanovic and M. L. B. Rao, in "18th Annual Power Sources Conference," p. 3, PSC Publications Committee (1964).
21. A. Damjanovic, in "Modern Aspects of Electrochemistry," J. O'M. Bockris and B. E. Conway, Editors, Vol. 5, p. 369, Plenum Press, New York (1969).
22. S. Shibata, *Electrochim. Acta*, **17**, 395 (1972).
23. C. C. Schubert, C. L. Page, and B. Ralph, *ibid.*, **18**, 33 (1973).
24. W. C. Johnson and L. A. Heldt, *This Journal*, **121**, 34 (1974).
25. A. Damjanovic, A. T. Ward, and M. O'Jea, *This Journal*, Submitted for publication.
26. Y. C. Chiu and M. A. Genshaw, *J. Phys. Chem.*, **73**, 3371 (1969).
27. H. A. Laitinen and C. G. Enke, *This Journal*, **107**, 773 (1960).
28. S. Gilman, in "Electroanalytical Chemistry," A. J. Bard, Editor, Vol. 2, p. 111, Marcel Dekker, Inc., New York (1967).
29. L. Harris, Private data.
30. A. Damjanovic and B. Jovanovic, *This Journal*, Submitted for publication.
31. N. F. Mott, *Trans. Faraday Soc.*, **43**, 429 (1947).
32. N. Cabrera and N. F. Mott, *Rept. Prog. Phys.*, **12**, 163 (1949).
33. F. P. Fehner and N. F. Mott, *Oxidation of Metals*, **2**, 59 (1970).
34. See: L. Young, "Anodic Oxide Films," Academic Press, London and New York (1961).
35. J. A. Davies, B. Domeij, J. P. S. Pringle, and F. Brown, *This Journal*, **112**, 675 (1965).
36. H. Wroblowa, B. J. Piersma, and J. O'M. Bockris, *J. Electroanal. Chem.*, **6**, 401 (1963).
37. J. W. Schultze and K. J. Vetter, *Electrochim. Acta*, **18**, 889 (1973).
38. K. J. Vetter and J. W. Schultze, *Ber. Bunsenges. Phys. Chem.*, **77**, 945 (1973).

The Codeposition of Copper and Arsenic from $\text{H}_2\text{SO}_4\text{-CuSO}_4\text{-As}_2\text{O}_3$ Solutions

Electrochemical Formation of Copper Arsenides

Jacques Dewalens, Luc Heerman,¹ Luc Van Simaey

Laboratory of Inorganic Chemistry, University of Louvain, 37, Schapenstraat, 3000 Louvain, Belgium

ABSTRACT

The induced codeposition of copper and arsenic from $\text{H}_2\text{SO}_4\text{-CuSO}_4\text{-As}_2\text{O}_3$ solutions (50-500 g/liter H_2SO_4) leads to the formation of copper arsenides. The codeposition potential at 50°C is $0.200 \pm 0.010\text{V}$ (NHE), almost independent of electrolyte composition. Potentiostatic E - i curves exhibit two waves for solutions with molar ratios $\text{Cu}/\text{As} > 2.25$. This is explained by induced codeposition with maximum induction as a limiting factor by which is understood that deposition of one arsenic atom as copper arsenide requires neutralization of at least two copper ions (corresponding to formation of Cu_2As , the arsenic richest phase observed). The phases $\text{Cu}_{5-x}\text{As}_2$, $\beta\text{-Cu}_{3-x}\text{As}$, Cu_6As , and the α -phase (solid solution) are obtained as pure single phases. The phase $\alpha\text{-Cu}_{3-x}\text{As}$ which normally can be obtained only by thermal synthesis at high pressures was also obtained pure. Cu_2As , on the contrary, was found only in mixtures with other phases, mainly $\text{Cu}_{5-x}\text{As}_2$. Some of the products formed could not be identified.

The phase diagram of the copper-arsenic system has been recently reviewed (1) (Fig. 1). Copper arsenides can be synthesized from copper and arsenic compounds by precipitation from aqueous solution (2) and from the elements by solid-state diffusion at high temperatures (3-5). In this paper some results on the codeposition of copper and arsenic as copper arsenides from $\text{H}_2\text{SO}_4\text{-CuSO}_4\text{-As}_2\text{O}_3$ solutions are reported with special emphasis on the electrochemical factors governing the formation of the different phases present in the deposits. This work originated from a study of the codeposition of copper and arsenic under the conditions prevailing during certain stages of the electrorefining of copper. Although the principal objective of this study was thus not the electrochemical synthesis of copper arsenides, the results presented here may very well possess some preparative potentialities. It is interesting to note that copper arsenides are good electronic conductors as was shown by electrical measurements on thermally prepared products (6).

Experimental

Reagents and solutions.—Solutions were prepared from analytical grade As_2O_3 (Merck), As_2O_5 (Union Chimique Belge), $\text{CuSO}_4 \cdot 5\text{H}_2\text{O}$ (Union Chimique Belge), and H_2SO_4 (Merck). Solutions contained 500 g/liter H_2SO_4 unless indicated otherwise. Deionized water was used throughout. Purified nitrogen was passed through the solutions to remove dissolved oxygen. During the experiments solutions were kept under inert atmosphere by passing nitrogen over the electrolytes to avoid possible air oxidation of the products deposited on the cathode. All experiments were performed at 50°C unless indicated otherwise.

Solubility of As_2O_3 in sulfuric acid solutions.—In a preliminary series of experiments the solubility of As_2O_3 in concentrated sulfuric acid solutions, eventually with addition of copper sulfate or As_2O_5 , was investigated. Solutions were prepared at about 90°C, rapidly cooled down to the desired temperature, and analyzed daily over a period of three weeks (see below). From the results in Fig. 2, it is clear that As_2O_3 easily forms supersaturated solutions and part of this work was performed with such solutions.

X-ray diffraction revealed that the precipitates in equilibrium with the solutions consist of claudetite

(monoclinic As_2O_3) for solutions containing sulfuric acid either with or without addition of copper sulfate. Addition of As_2O_5 , however, increases the solubility of As_2O_3 and leads to the precipitation of arsenolite (cubic As_2O_3).

It must be noted that the solubilities of As_2O_3 found in this work, about 4 g/liter As(III) at 25.0°C and 7.5 g/liter As(III) at 50.0°C, are somewhat lower than those reported previously by Anderson and Story (7) but are in good agreement with recently determined values (8).

Cell and electrodes.—Experiments were performed in a glass cell containing approximately 1000 ml of electrolyte. The electrode assembly consists of a 2×2.5 cm² cathode flanked on either side by two 5×5 cm² anodes. Either platinum or copper electrodes were used in this work, the anodes being made of the same material as the cathode. Just prior to the measure-

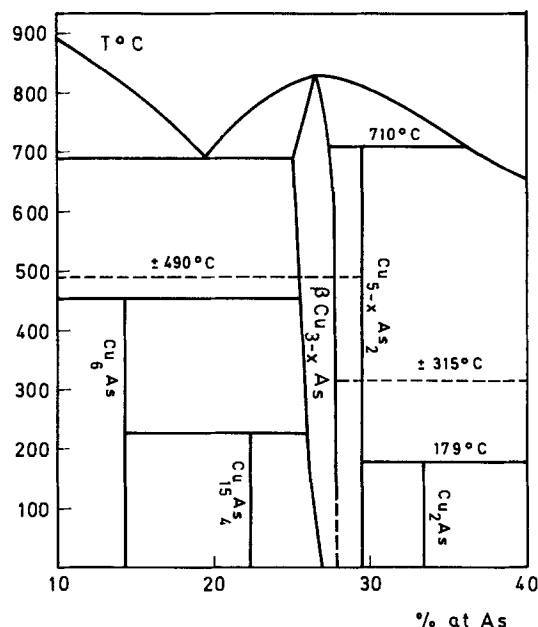


Fig. 1. Phase diagram of the copper-arsenic system (after Naud and Priest).

¹ Present address: Laboratory of Radiochemistry, Katholieke Universiteit Leuven, Celestijnenlaan 200F, 3030 Heverlee, Belgium.

Key words: codeposition, copper, arsenic, copper arsenides.

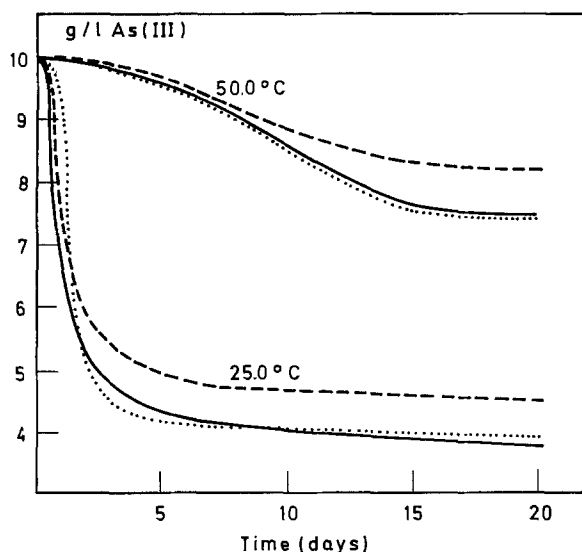


Fig. 2. Solubility of As_2O_3 in concentrated sulfuric acid solutions; initial concentration 10 g/liter As(III) (26.4 g/liter As_2O_3) 500 g/liter H_2SO_4 ; — 500 g/liter H_2SO_4 , with addition of 10 g/liter copper ions; - - - - - , 500 g/liter H_2SO_4 , with addition of 15 g/liter As(V).

ments, cathodes of electrolytic copper sheet were dipped for 1 min in 1:1 nitric acid, rinsed with distilled water, and transferred immediately to the polarization cell. In some cases, copper electrodes were prepared by depositing a thin layer of copper on electrolytic copper sheet from a solution of the same composition as used for the measurements but without addition of As_2O_3 . The results obtained with both types of copper electrodes were essentially the same but electrodeposited electrodes gave a somewhat better reproducibility. Most experiments were performed without stirring of the solution (natural convection), otherwise solutions were gently stirred with a Teflon-coated magnetic stirring bar.

Electric circuit and measurements.—*E-i* curves were recorded using a conventional galvanostatic or potentiostatic circuit. The most reliable results were obtained, however, by the potentiostatic method since very often stable potentials could not be obtained at constant current density. Potentiostatic *E-i* curves were recorded at a sweep rate of 34.4 mV/min starting from the rest potential in the cathodic direction. Potentials were measured vs. SCE with a bridge filled with the test solution. Experimental potential values are converted to normal hydrogen scale (NHE). Electrolysis at constant potential was performed with a potentiostat provided with an integrating coulometer. For all experiments a constant charge, about 5×10^3 coulombs, was passed through the polarization cell.

Analytical methods.—The products formed on the cathode were stripped from the electrode and washed with deionized water, alcohol, and ether. Samples were dissolved in a mixture of concentrated HNO_3 and H_2SO_4 and this solution was evaporated until the appearance of white fumes. Attempts to determine arsenic in the presence of copper by atomic absorption analysis were unsuccessful (9). Therefore, arsenic was separated from the solution by adding hydrazine sulfate to a 5 mliter sample, distilling as AsCl_3 after addition of 50 mliters conc HCl, and collecting the gases in 250 mliters of a solution containing about 250 g/liter NaOH. This distillation was repeated twice and arsenic was determined in the distillate by iodometric titration. Copper was determined by EDTA titration.

The formation of arsine, AsH_3 , was detected by placing a filter paper moistened with a 5% alcoholic solution of HgCl_2 in the gas stream (10). No attempt was

undertaken for quantitative determination of this (poisonous) compound.

X-ray diffraction analysis.—X-ray diffraction patterns of the products formed on the cathode were taken with a Philips-Norelco unit using nickel filtered CuK_α radiation. Products were identified with respect to the X-ray Diffraction Powder Data File (11), except Cu_2As which was recently described by Naud and Priest (1).

Results

E-i curves recorded for solutions containing different concentrations of As_2O_3 in the absence of copper ions in the electrolyte for platinum or copper electrodes are shown in Fig. 3. The hydrogen evolution proceeds with considerable overvoltage at platinum electrodes in solutions containing As_2O_3 , the deposition potentials shifting toward more negative potentials with increasing concentration. The effect of arsenic compounds on the hydrogen evolution reaction has been reported earlier (12). The hydrogen evolution reaction is accompanied by the formation of arsine. The standard free energy of formation of this compound has been reevaluated as $\Delta G^\circ_f = 26.0$ kcal/mole (13), considerably lower than the value $\Delta G^\circ_f = 42.0$ kcal/mole previously reported in the literature (14). Taking this new value the formation of arsenic becomes possible at potentials about 0.23V more positive than the values calculated by Pourbaix (15). On copper electrodes, the hydrogen evolution reaction for the base solution, i.e., no As_2O_3 present in solution, proceeds with higher overvoltage than observed for platinum electrodes, as could be expected. Addition of As_2O_3 to the electrolyte, however, has relatively little effect on hydrogen overvoltage in comparison with the effect found for platinum electrodes. Gas evolution is accompanied by the formation of a thin layer of copper arsenide on the electrode, the composition of which was not identified with certainty.

If electrolysis was continued over extended periods of time at constant current density, at least 20 hr at 10 mA/cm², the formation of a colloidal brick-red precipitate in the solution was observed. This precipitate possibly consists of solid hydrogen arsenides such as As_2H_2 or As_2H_4 , the existence of which has been reported in the literature (16).

E-i curves were then recorded for solutions containing either a constant concentration of copper ions with various additions of copper ions. Some typical curves are shown in Fig. 4-5. Strong potential oscillations were

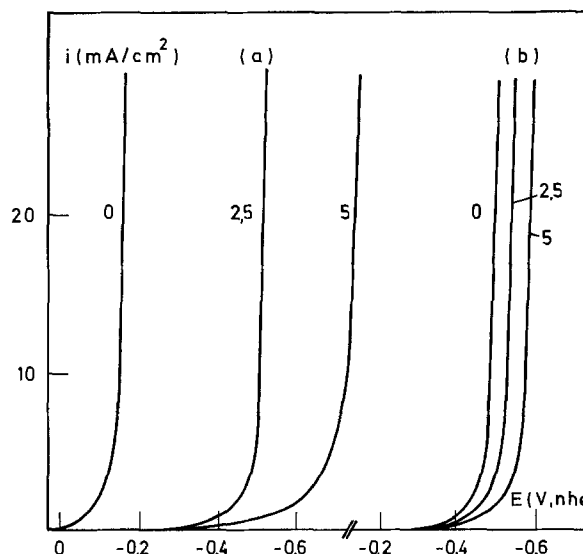


Fig. 3. (a) *E-i* curves for hydrogen evolution reaction on platinum electrode in presence of As(III); 500 g/liter H_2SO_4 , 50°C, arsenic concentration indicated for each curve. (b) Same as (a), copper electrode.

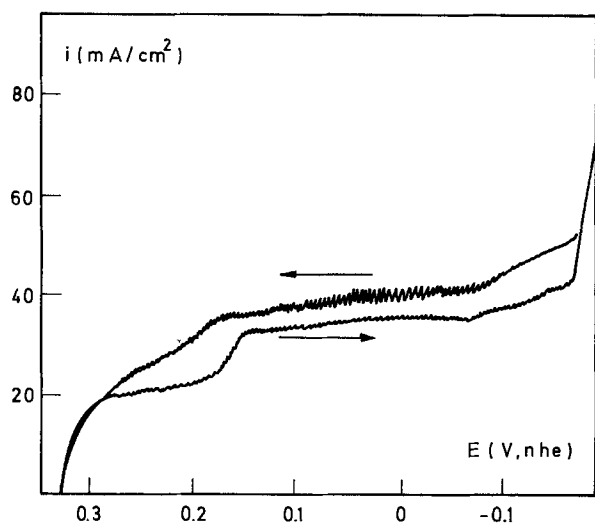


Fig. 4. Potentiostatic E - i curve for solution containing 500 g/liter H_2SO_4 , 5 g/liter As(III), 20 g/liter copper ions, copper electrode, 50°C, sweep rate 34.4 mV/min.

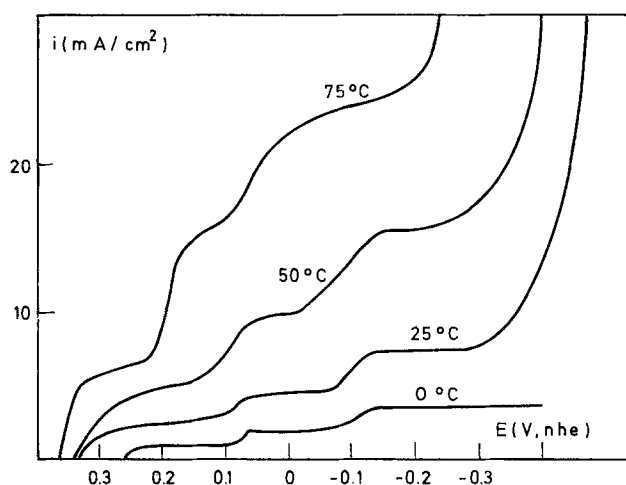


Fig. 5. Potentiostatic E - i curves at different temperatures for solution containing 500 g/liter H_2SO_4 , 5 g/liter As(III), 5 g/liter copper ions, copper electrode, sweep rate 34.4 mV/min.

observed during galvanostatic measurements in the potential region of the second wave and specially in the potential region of the third wave. Therefore the curves in Fig. 5 have been somewhat idealized. The E - i curves exhibit either two or three waves, depending on the experimental conditions. The first wave corresponds to the deposition of copper metal but at potentials of about +0.200V (NHE) a second wave appears. In the potential region of this second wave, copper and arsenic are codeposited with formation of copper arsenides as was shown by x-ray diffraction studies, the composition of these compounds being discussed later. The exact potential at which the deposition of copper arsenides starts was determined by electrolysis at controlled potential and x-ray analysis of the cathodes. In this way the codeposition potential was found to be $0.200 \pm 0.010V$ (NHE), independent of bath compositions (copper ion concentration was varied between 0.5 and 20 g/liter and arsenic concentration between 2.5 and 10 g/liter).

The appearance of the third wave depends on the bath composition, or, more specifically, on the molar copper/arsenic ratio in the electrolyte. This is shown in Fig. 6 where the heights of the first and second waves are plotted as a function of the copper ion concentration for a constant arsenic content of the solution. For solutions with a molar ratio Cu/As > 2.25 only two waves are observed and the height of the second wave

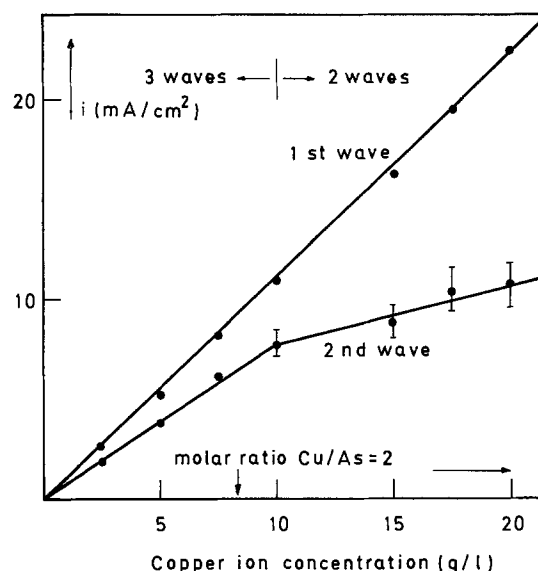


Fig. 6. Height of first and second waves as a function of copper ion concentration for solutions containing 500 g/liter H_2SO_4 and 5 g/liter As(III), copper electrode, 50°C.

becomes almost independent of the copper ion concentration. For solutions with a molar ratio Cu/As < 2.25 three waves are observed and the height of the second wave increases linearly with the copper ion concentration. From the temperature dependence of the height of the different waves shown in Fig. 5, the activation energy was calculated as about 4.5 kcal/mole for all three waves, indicating the diffusional nature of the processes involved.

Similar results were obtained for solutions containing 50 or 200 g/liter H_2SO_4 . The products formed on the cathode were subjected to chemical analysis allowing decomposition of the E - i curves as shown in Fig. 7. The results clearly indicate that the second wave is only due to deposition of arsenic, copper being deposited at the limiting current of the first wave. Whereas arsine formation is almost negligible in solutions for which two waves only are observed, this process becomes much more important in solutions with a higher relative arsenic concentration, thus solutions for which three waves are observed. In the latter case the beginning of the third wave coincides with gas evolution at the electrode. Semiquantitative tests have shown that the gas evolved at the electrode at the beginning of

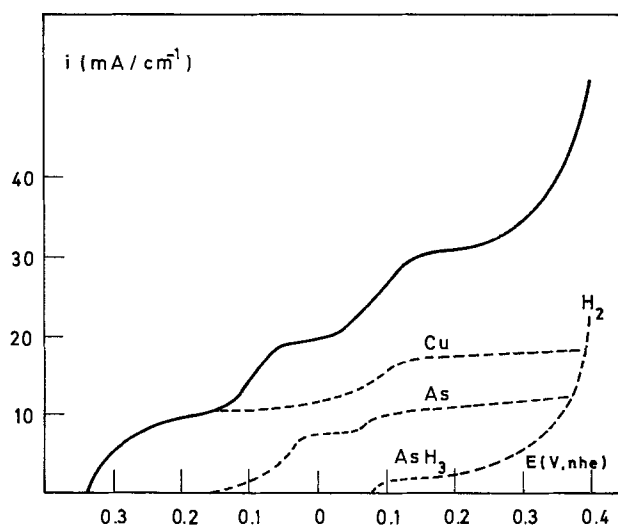


Fig. 7. Decomposition of E - i curve into partial curves for solution containing 500 g/liter H_2SO_4 , 5 g/liter As(III), 5 g/liter copper ions, 50°C.

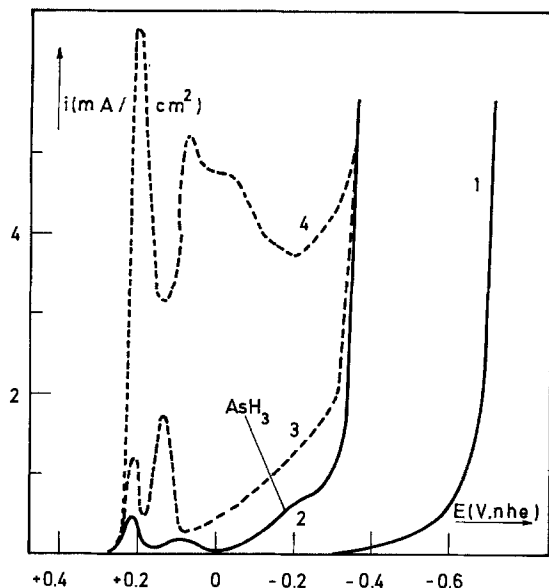


Fig. 8. Potentiostatic E - i curve for As(III) reduction on copper arsenide electrodes in absence of copper ions in the electrolyte; 500 g/liter H_2SO_4 , 5 g/liter As(III), 50°C. Curve 1, platinum; curve 2, $Cu_{5-x}As_2$ ($Cu_{2.4}As$); curve 3, β - $Cu_{3-x}As$; curve 4, Cu_6As ; sweep rate 34.4 mV/min.

the third wave consists mainly of arsine. This was also confirmed by voltametric measurements on arsenic reduction on copper arsenide electrodes prepared by electrolysis shown in Fig. 8. Whereas hydrogen evolution starts at about $-0.300V$ (NHE), the formation of arsine is already observed at much more negative potentials, about $-0.100V$ (NHE). The two reduction peaks at more positive potentials cannot be explained with certainty but are eventually due to the deposition of amorphous elemental arsenic or to the charging of the copper arsenide with arsenic, leading to the formation of a compound with a higher arsenic content.

The results presented thus far naturally lead to the conclusion that the codeposition of copper and arsenic is a case of induced codeposition in the terminology of Brenner (17), *i.e.*, codeposition under such conditions where one of both elements (arsenic) cannot be deposited in the absence of the other (copper). Indeed, in the presence of copper ions, trivalent arsenic is reduced at $+0.200V$ (NHE) with formation of copper arsenides, whereas in the absence of copper ions arsenic can be reduced only to arsine. This must be coupled with the finding that the arsenic richest phase observed in the deposits by x-ray diffraction is Cu_2As . This fact necessitates the concept of a maximum induction, by which is understood, as applied to the present case, that at least two copper ions must be discharged to make deposition of one arsenic atom as copper arsenide possible. In this way it is easily understood that only two waves are observed for solutions containing excess copper ions, *i.e.*, ratios $Cu/As > 2$. The second wave corresponds to a true diffusion limiting current since all the arsenic arriving at the electrode surface is reduced to copper arsenide and its concentration at the electrode surface is zero, explaining also the formation of trace amounts only of arsine. This is not the case however for solutions containing excess arsenic, *i.e.*, ratios $Cu/As < 2$, for which three waves are observed. In this case the reduction of arsenic as arsenide is limited by the slow mass transfer of copper ions to the electrode and the concentration of arsenic species at the electrode surface is not zero. The excess therefore can be reduced as arsine. The experimental results clearly indicate that the appearance of the third wave is associated with the presence of excess arsenic in solution. It is well known that gas evolution leads to an increased mass transfer to the electrode (18, 19). Therefore, the evolution of

arsine enhances the transport of copper ions and arsenic species to the electrode and this explains the increase of the partial curves for copper and arsenic in the potential range of the third wave. The fact that the transition from two to three waves does not occur exactly at the ratio $Cu/As = 2$ can be explained by the experimental fact that Cu_2As is never obtained pure but always in mixtures with the phase $Cu_{5-x}As_2$.

The composition of the deposits can be calculated from the partial currents of copper and arsenic. At the limiting current plateau of the second wave, the composition of the deposits can be represented by $Cu_{2.15}As$ as calculated from the left side of Fig. 6 (three waves) while the copper content of the deposits increases to a composition of about Cu_6As at the extreme right side of Fig. 6 (two waves). Of course, if working at current densities below the limiting current of the second wave, the copper content can reach still higher values, as is clear also from the partial curves of Fig. 7, especially if the Cu/As ratio in the bath is high.

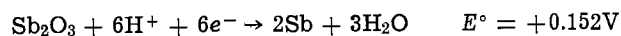
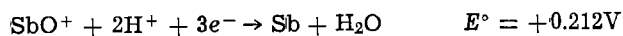
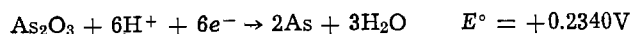
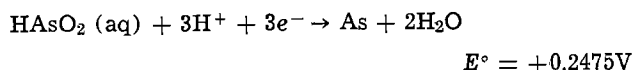
With this discussion in mind, the formation of different phases in the deposits as observed by x-ray diffraction can be discussed more easily. In the most general way it can be stated that the formation of different phases is determined mainly by the concentration of copper ions and arsenic species at the electrode surface, *i.e.*, by the bath composition. A survey of the various phases found in the deposits is given in Table I. Although often a mixture of different phases was obtained, all the phases described in Table I could be obtained pure under the proper experimental conditions, with exception of Cu_2As . The phase Cu_2As , recently described by Naud and Priest (1), can be obtained by selective wet oxidation of phases with a higher metal content (1, 2) or by leaching of copper-rich arsenides in concentrated sulfuric acid (20) but could not be obtained either by precipitation methods or by direct synthesis from the elements. It must be noted furthermore that not all the products formed on the electrode could be identified with respect to the ASTM Powder Diffraction Data File (10). At the beginning of the second wave, *i.e.*, at potentials $+0.200V$ (NHE), the deposition of metallic copper is accompanied by the formation of two unidentified phases containing arsenic, one phase (X) being obtained from solutions with relative high copper ion concentrations, the other phase (Y) being obtained from solutions with relative low copper ion concentrations. At slightly more negative potentials, $+0.190V$ (NHE), these products can be obtained without deposition of

Table I. Summary of various phases obtained by codeposition of copper and arsenic from H_2SO_4 - $CuSO_4$ - As_2O_3 solutions

1. Cu_2As	Arsenic richest phase obtained by codeposition; never obtained pure, always in mixtures with $Cu_{5-x}As_2$; previously obtained by selective wet oxidation (1, 2) or leaching (20) of metal-rich copper arsenides.
2. $Cu_{5-x}As_2$	Composition range $Cu_{2.10}As$ - $Cu_{2.45}As$; phase most frequently obtained from solutions with high relative arsenic concentrations (three waves), specially at limiting current of second and third wave; according to Naud and Priest (1), the domain of homogeneity of the orthorhombic (low temperature) form corresponds to $Cu_{2.40 \pm 0.03}As$.
3. β - $Cu_{3-x}As$	Composition range $Cu_{2.59}As$ - $Cu_{3.10}As$; domain of homogeneity at 300°C corresponds to $Cu_{2.60}As$ - $Cu_{2.85}As$ (1); domain of homogeneity at 25°C estimated as $Cu_{2.60}As$ - $Cu_{2.70}As$ but phases with slightly higher copper content than $Cu_{3.0}As$ can be obtained (21); obtained from solutions with excess arsenic (three waves) in potential region before reaching limiting current of second wave and from solutions with excess copper ions (two waves).
4. α - $Cu_{3-x}As$	Frequently obtained in mixtures with $Cu_{5-x}As_2$; occasionally pure in conditions where normally β - $Cu_{3-x}As$ would be expected; normally only prepared by thermal synthesis at high pressures (22).
5. X	Not identified with respect to ASTM Powder Diffraction File; solutions with excess copper ions (two waves); 0.200-0.190V (NHE); see text.
6. Y	Not identified with respect to ASTM Powder Diffraction File; solutions with excess arsenic (three waves); 0.200-0.199V (NHE); see text.
7. Cu_6As	Phase ϵ (Cu_6As - Cu_4As); this phase is not yet very well known, see Naud and Priest (1); composition range $Cu_{6.03}As$ - $Cu_{6.10}As$.
8. Phase α	Solid solution containing up to 7 a/o arsenic (23).

metallic copper. Both products are crystalline as is shown by their x-ray spectra but are not really stable, i.e., after removal from the electrode the x-ray pattern is characteristic for a mixture of metallic copper with a little β -Cu_{3-x}As. This indicates that both products must be rich in copper as could be expected from the ratio of the partial currents of copper and arsenic at their formation potential although precise determination of the composition of these products has not been possible. Deposition from solutions with high relative arsenic concentrations (three waves) at the limiting current of the second wave and in the entire potential range of the third wave almost always yields formation of the phase Cu_{5-x}As₂, eventually in mixtures with some Cu₂As and β -Cu_{3-x}As or α -Cu_{3-x}As. This is easily understood since under these conditions the effect of maximum induction is maximal. The domain of homogeneity of the phase Cu_{5-x}As₂ (orthorhombic low temperature form) at room temperature was estimated by Naud and Priest (1) as Cu_{2.40} ± 0.03As. It has not been possible by any means (x-ray diffraction after thermal treatment, washing with organic solvents) to show the presence of elemental arsenic in the deposits. Therefore it seems not unlikely that the domain of homogeneity of the phase Cu_{5-x}As₂ can be extended to much higher arsenic contents by electrochemical synthesis, although the presence of amorphous arsenic in the deposits cannot be totally excluded. The phase β -Cu_{3-x}As was obtained by deposition from solutions with high relative arsenic concentrations in the potential range preceding the limiting current of the second wave and also from solutions with high relative copper ion concentrations. The phase α -Cu_{3-x}As which was found frequently in mixtures with other phases, mainly Cu_{5-x}As₂, was occasionally obtained pure under such conditions where normally β -Cu_{3-x}As should be expected. It is interesting to note that normally the phase α -Cu_{3-x}As can be obtained only by thermal synthesis at high pressures (22). Deposition from solutions with high relative copper ion concentrations (two waves) always leads to the formation of copper-rich phases such as β -Cu_{3-x}As, α -Cu_{3-x}As, Cu₆As (phase ϵ ; composition range found in this work Cu_{6.03}As-Cu_{9.10}As) and even the α -phase [solid solution containing up to 7 atom per cent (a/o) arsenic]. With the foregoing discussion in mind, it is obvious that there are no sharp changes in composition at the points corresponding to a compound of specific composition, but rather a gradual transition from one phase to another and, intermediary, the coexistence of several (generally two) phases.

Finally, some comparison can be made between the codeposition of copper and arsenic as described in this paper and some data on the codeposition of copper and antimony reported by Raub (24, 25). The standard electrode potentials of arsenic and antimony



are rather close to the standard electrode potential of copper



Raub (24) studied the codeposition of copper and antimony from cyanide baths in which copper is far less noble than antimony, being 0.7 to over 1V more negative. The copper-antimony system is then of the regular type, characteristic for systems where the deposition potentials are far apart, the classic example of the regular type being the copper-bismuth system described in detail by Brenner (26). Raub (24) also studied the codeposition of copper and antimony from

ammoniacal baths eventually with addition of Rochelle salt, in which copper is more noble than antimony, the difference of deposition potentials being of the order of 0.5V. Raub (24) found that the copper content of the alloys deposited from such ammoniacal baths showed almost no variation with the metal percentage of copper in the bath although the metal percentage varied by a factor of 2.5. Brenner (25) calls this lack of a trend unique among alloy plating baths. The same lack of a trend is now also observed for the copper-arsenic system. Indeed, taking again the data of the left side of Fig. 6, the composition of the deposit, corresponding to Cu_{2.15}As [68.5 weight per cent (w/o) copper], remains constant if the concentration of copper in the bath is varied fourfold from 2.5 to about 10 g/liter.

Although the data of Fig. 6 are obtained for a constant bath concentration of arsenic, the composition of the deposit remains constant as the ratio copper/arsenic in the bath, Cu/As < 2. In this paper, the phenomenon was explained by maximum induction. A comparison of the standard potential of copper and arsenic shows that codeposition should readily occur in acid solutions at the potentials where the formation of copper arsenides was observed. Therefore, the term induction refers to the kinetic impossibility of depositing elemental arsenic rather than to the thermodynamic impossibility. The free energy of formation of the copper arsenides is then not a prime factor governing the composition of the deposits and it is easily understood that the composition of the alloys is determined only by the bath composition for solutions with molar ratios Cu/As > 2, i.e., the composition of the alloys is diffusion controlled.

In sharp contrast however with the findings in this paper for the copper-arsenic system, Raub (24) observed that the copper content of the alloys with antimony became independent of the copper percentage in the bath for a composition at the copper-rich side of the phase diagram (about 5 w/o copper; α -phase). The results of Raub (24) can be explained by an induced codeposition of copper and antimony whereby, at least in principle, several reasons can be imagined why only the α -phase is obtained. The most plausible explanation seems to be that only the α -phase has a sufficiently large energy of formation to cause a sufficient shift of the deposition potential of the alloy.

Little information is available on the energy of formation of copper antimonides or arsenides: the heat of formation of Cu₃Sb, 2.5 kcal/mole, is rather low when compared with the heat of formation of Cu₃As, 25.6 kcal/mole (27). No information is available on the energy of formation of the α -phases although the explanation given here seems to be corroborated by the *E-i* curves given by Raub (25), this point being discussed already by Brenner (25) who supposed the formation of an intermetallic compound. It would certainly be advisable to repeat at least part of Raub's experiments (24) at controlled potential and, as already noted by Brenner (25), the codeposition of copper and antimony probably would be easier from acid solutions.

Acknowledgment

The authors wish to express their sincere thanks to Prof. Dr. R. Breckpot for his advice. One of the authors (J. D.) is indebted to the I.R.S.I.A., Belgium, for the award of a research scholarship.

Manuscript submitted Jan. 22, 1974; revised manuscript received July 15, 1974. This was Paper 144 presented at the Boston, Massachusetts, Meeting of the Society, Oct. 7-11, 1973.

Any discussion of this paper will appear in a Discussion Section to be published in the December 1975 JOURNAL. All discussions for the December 1975 Discussion Section should be submitted by Aug. 1, 1975.

Publication costs of this article were partially assisted by the University of Louvain.

REFERENCES

- J. Naud and P. Priest, *Mat. Res. Bull.*, **7**, 783 (1972).
- P. Priest, Ph.D. Thesis, U.C.L., Louvain, 1973.
- R. D. Heyding and G. J. G. Despault, *Can. J. Chem.*, **38**, 2477 (1960).
- R. Juza and K. von Benda, *Z. Anorg. Chem.*, **357**, 238 (1968).
- V. Liebisch and K. Schubert, *J. Less. Common Metals*, **23**, 231 (1971).
- L. J. Pauwels, G. Maervoet, and R. Vervaeke, *Z. Anorg. Allgem. Chem.*, **397**, 307 (1973).
- E. Anderson and L. G. Story, *J. Am. Chem. Soc.*, **45**, 1102 (1923).
- C. Feneau, Private communication.
- M. Hamels, Private communication.
- W. Scott, "Standard Methods of Chemical Analysis," D. Van Nostrand Co., Inc., New York (1939).
- ASTM Powder Diffraction Data File, American Society for Testing Materials, X-ray Dept., Philadelphia.
- J. O'M Brockris and B. E. Conway, *Trans. Faraday Soc.*, **45**, 989 (1949).
- S. R. Gunn, W. L. Jolly, and G. Green, *J. Phys. Chem.*, **64**, 1334 (1960).
- W. M. Latimer, "Oxidation Potentials," 2nd Ed., p. 113, Prentice Hall, New York (1952).
- M. Pourbaix, "Atlas d'Equilibres Electrochimiques," p. 516, Gauthier-Villars, Paris (1963).
- P. Pascal, Editor, "Nouveau Traité de Chimie Minérale," Vol. XI, p. 90, Masson, Paris (1958).
- A. Brenner, "Electrodeposition of Alloys," Vol. I, p. 76, Academic Press, New York (1963).
- N. Ibl., *Chem. Ingr. Tech.*, **35**, 353 (1963).
- L. J. J. Janssen and J. G. Hoogland, *Electrochim. Acta*, **15**, 1013 (1970).
- J. Dewalens, L. Heerman, and L. Van Simaey, *Bull. Soc. Chim. Belges*, **82**, 711 (1973).
- J. Naud, Private communication.
- J. Bolfa, *C. R. Acad. Sci., Serie C*, **230**, 103 (1950).
- W. B. Pearson, "Handbook of Lattice Spacings and Structures of Metals and Alloys," p. 570, Pergamon Press, London (1958).
- E. Raub, *Z. Erzbergbau Metallhüttenw.*, **5**, 155 (1952); for a discussion of these results, see Ref. (25).
- A. Brenner, "Electrodeposition of Alloys," Vol. II, pp. 560 ff., Academic Press, New York (1963).
- A. Brenner, *ibid.*, Vol. II, pp. 578 ff.; see also numerous examples in Vol. I.
- O. Kubasschewski, E. Evans, and C. B. Alcock, "Metallurgical Thermochemistry," Pergamon Press, Inc., New York (1967).

Fabrication of Beta-Alumina Tubes by Electrophoretic Deposition from Suspensions in Dichloromethane

John H. Kennedy* and Alain Foissy

Department of Chemistry, University of California, Santa Barbara, California 93106

ABSTRACT

Thin-walled tubes of β -alumina (0.03-0.1 cm thick) have been produced by electrophoresis using a suspension of 1μ β -alumina powder in dichloromethane. Trichloroacetic acid was added to facilitate particle charging. The particles were negatively charged and were deposited on graphite rod mandrels. Density of the material after sintering ranged from 2.9 to 3.1 g/cm³, and conductivities in good agreement with pressed powders were measured. Sodium-sulfur cells were constructed and operated using electrophoretic tubes as the electrolyte.

The phenomenon of electrophoresis has been known since 1809 with the work of F. F. Ruess although it was not until 1879 that H. von Helmholtz (1) introduced the concept of the double layer to explain electrophoretic mobility. Electrophoresis has since become an important tool in biochemistry, physiology, and medicine. Electrophoretic deposition of ceramic powders is of much more recent origin. In 1962, Avgustinik *et al.* (2) and in 1969 Andrews *et al.* (3) reported on the deposition of Al₂O₃ in various media such as ethanol and acetone. In the last few years the use of electrophoresis for obtaining ceramic bodies has increased with the work of Boncoeur and Carpentier (4), and especially noteworthy is the research on β -alumina depositions. Lazennec and Fally (5) patented methods for forming thin-wall tubes of zirconia and β -alumina using nitromethane and acetone/ethanol as solvent media, while Powers (6) reported on β -alumina deposition from various alcohols.

Basically, electrophoretic deposition of a powder suspended in a solvent depends on the powder's ability to become charged either positively or negatively. Three mechanisms for this generation of charge have been proposed: (i) an unequal transfer of positive or negative ions from the surface of the solid to the liquid;

(ii) a preferential adsorption of ions on the solid particles from the liquid medium; and (iii) an orientation of dipolar molecules present on the surface of the solid particle. These three mechanisms give rise to an electric double layer at the particle surface and to a potential difference across the phase boundary. Stern (7) proposed a model in which the double layer is divided into two parts; the first part consists of counterions attracted to the charged surface, and these ions are located in the "Stern layer" which has the thickness of about one solvent molecule. The second part is mobile and is called the diffuse layer. The potential difference between the solid surface and the Stern layer is called the "Stern potential" while the potential difference between the Stern layer and the bulk solvent is called the "zeta potential."

When an electric field is applied the solid particles move with their Stern layer, and thus, electrokinetic studies are directly related to the zeta potential. If we assume that the double layer acts as an electric capacitor, the electrophoretic velocity is given by

$$v = \frac{\zeta E \epsilon}{4\pi\eta}$$

where ζ is the zeta potential, E is the potential gradient, ϵ is the dielectric constant of the medium, and η is the viscosity of the medium. The deposition rate is

* Electrochemical Society Active Member.
Key words: beta-alumina, electrophoresis, ionic conductivity, sodium/sulfur cell, solid electrolyte.

basically the product of electrophoretic velocity and concentration of the particles in the suspension.

Although electrophoretic velocity is a primary consideration, other variables play an important role and, for example, Powers reported that depositions of β -alumina could only be obtained from solvents having dielectric constants in the range 12-24 (6).

Experimental

Beta-alumina (Alcoa 325 mesh) was ground for 2 weeks in an aluminum oxide ball mill to achieve particle sizes of about 1μ . Ethylene glycol (10 drops in 400g of β -alumina) was employed as a grinding aid. No α - Al_2O_3 from wear was detected in the final powder by x-ray diffraction. After grinding the powder was kept in an oven at 110°C .

Dichloromethane (MC and B), analytical reagent quality, was used without further purification. All other chemicals were also analytical reagent grade and used without further purification.

Suspensions of pure β -alumina were made by adding 40g (unless otherwise stated) of the ground material to 500 ml of dichloromethane and 1-12g of trichloroacetic acid. The mixture was placed in a ball mill for about 12 hr. Other methods of mixing the materials were tried but no change in deposition rate was noted.

Suspensions of doped β -alumina were prepared by first mixing β -alumina powder with 2 weight per cent (w/o) MgO and 2 w/o Na_2CO_3 in a ball mill for 12 hr. The mixture was heated for 10 hr at 1200°C and then used as above for preparing suspensions.

Figure 1 shows the setup for electrophoretic depositions. A 400 ml beaker served as a container, and a stainless steel screen basket served as the negative electrode. The basket geometry also helped to prevent stream lines. The positive electrode was a graphite (Union Carbide Corporation) rod (0.25 in. diameter) and was rotated at 60 rpm. The suspension itself was stirred continuously with a magnetic stirrer. During the deposition, the voltage was controlled with a variable power supply (100-500V), and the current was monitored. Except for the study of yield with voltage, all depositions were carried out with an applied voltage of 200V. Deposition time varied from 30 to 300 sec. A series of suspensions in which all variables were held fixed gave a deposit weight range of $\pm 2\%$ from the mean.

After electrophoresis the tubes formed on the graphite rods were allowed to air-dry for one day. The green density was not measured because the tubes were still on the graphite mandrel. Qualitatively, the deposits made at high acid concentration appeared

more porous than those obtained at low acid concentrations. The rods were then placed in coarse β -alumina powder and heated at 800°C for 3 days to burn out the graphite. The tubes of β -alumina were cleaned with compressed air to remove ashes and were kept at 110°C until sintered. The tubes were 3-4 cm long with an internal diameter of 0.6 cm and a wall thickness of 0.03-0.10 cm.

Sintering of undoped material was carried out at 1700°C for 1.5-2 hr while sintering of doped material was accomplished at 1750°C for 5 hr. It was reported previously (8) that the presence of MgO decreased the rate of sintering. During sintering in an air atmosphere the tubes were completely covered with coarse β -alumina powder to provide a sodium oxide pressure and avoid any loss of sodium content. No α -alumina or sodium aluminate was detected by x-ray diffraction on the sintered materials. The average grain size was about 20μ , and the highest density deposits exhibited some elongated grains about 100 - 200μ in length.

Sodium analysis was carried out using atomic absorption after ion exchanging the β -alumina with molten silver nitrate as reported previously (8).

Results

Grinding.—Two suspensions were prepared containing 40g β -alumina, 1g trichloroacetic acid, and 500 ml of dichloromethane. One of the suspensions was mixed by grinding in the ball mill for 12 hr and yielded $0.6\text{ g/cm}^2\text{-min}$ of β -alumina electrophoretic deposit. The second suspension was mixed merely by stirring and yielded only $0.1\text{ g/cm}^2\text{-min}$. Thus, the grinding/mixing technique gave a suspension which deposited 6 times faster than the same suspension without this procedure. The process aided in generating the necessary charged particles, *i.e.*, established a large zeta potential which increased electrophoretic velocity. It may have also affected the viscosity of the suspension to a small degree.

Voltage.—The role of voltage on the rate of electrophoretic deposition was studied using a suspension containing 40g β -alumina, 4g trichloroacetic acid, and 500 ml of dichloromethane. The yield as a function of applied voltage is shown in Fig. 2. As expected from the equation for electrophoretic velocity, a straight line was obtained. The slope was $1.87 \times 10^{-3}\text{ g/cm}^2\text{-min}\cdot\text{V}$. These results are consistent with those obtained with MgO (2).

Deposition time.—It was observed that there was a small decrease in current during deposition. However, the rate of deposition was essentially constant ($\pm 3\%$). Suspensions containing 1g trichloroacetic acid deposited at $0.59\text{ g/cm}^2\text{-min}$ while suspensions containing 6g trichloroacetic acid deposited at $0.96\text{ g/cm}^2\text{-min}$

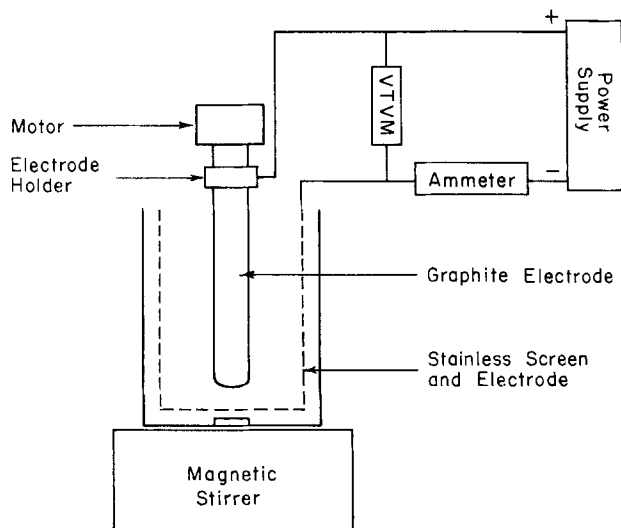


Fig. 1. Experimental setup for electrophoresis

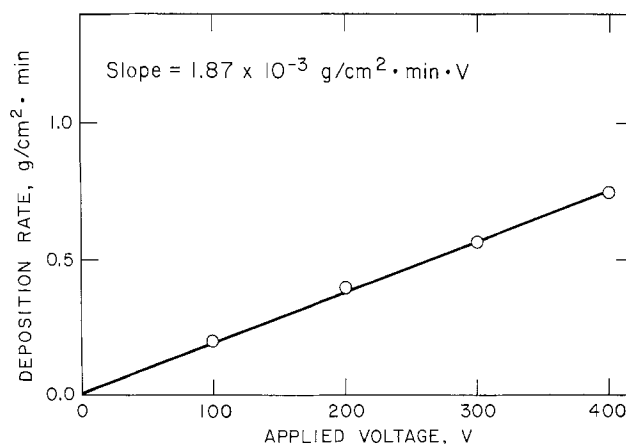


Fig. 2. Electrophoretic yield as a function of voltage. Suspension contained 40g β -alumina, 4g trichloroacetic acid, and 500 ml dichloromethane.

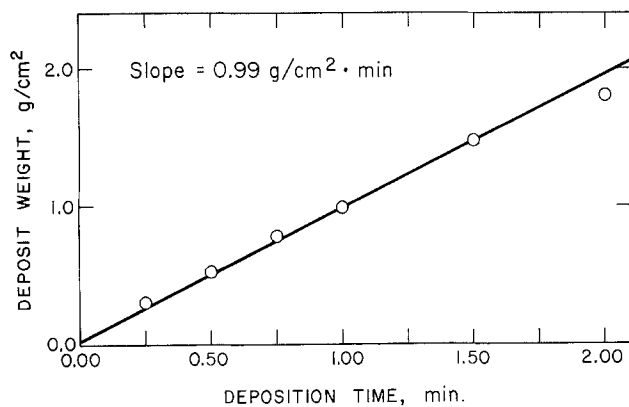


Fig. 3. Electrophoretic yield as a function of time. Suspension contained 40g β -alumina, 6g trichloroacetic acid, and 500 ml dichloromethane, 200V applied voltage.

(Fig. 3). This again is consistent with the results obtained with MgO (2).

Acid concentration.—With suspensions of β -alumina in dichloromethane it was necessary to add an acid, and trichloroacetic acid gave the best results. When no acid was present the suspensions tended to flocculate rapidly and settle. Addition of 1g of acid to this suspension immediately stabilized it. However, with this small amount of acid, deposition was slow (or did not occur at all in some cases). Benzoic acid did not stabilize the suspension nearly as well and deposits could not be made. Large amounts of acid, > 10g trichloroacetic acid, again resulted in little or no deposition. The best deposits were obtained when 2-6g of trichloroacetic acid were added to the suspension (Table I).

Presence of water.—To observe the influence of water on the electrophoretic deposition a suspension containing 40g β -alumina, 6g trichloroacetic acid, 500 ml dichloromethane, and 1 ml water was prepared. The water formed a new phase which disappeared after the grinding/mixing procedure. A deposition using this suspension was flaky and adhered poorly to the graphite. The deposit also had a wet appearance and cracked during drying. Occasionally this type of behavior was observed with supposedly dry suspensions and was attributed to traces of moisture introduced inadvertently.

Density of deposit.—Densities were measured by the hydrostatic method using toluene. Weight/volume measurements, used for pellets, were considered to be inaccurate here because of the uncertainty in measur-

ing the tube thickness. The values ranged from 2.9 to 3.1 g/cm³, but no marked correlation could be found between density variation and deposition or sintering conditions. This density range was the same as that found for sintered pellets which gave high electrical conductivity (8).

Conductivity of deposits.—Silver electrodes were vacuum deposited on the β -alumina tubes which were then placed in the apparatus shown in Fig. 4. Measurements were made in a nitrogen atmosphere to prevent oxidation of the silver electrodes, and measurements were made from 25°-600°C. Arrhenius plots were made as shown in Fig. 5. Tubes sintered for 1.5 hr had activation energies of about 4.9 kcal/mole while those sintered for 2 hr exhibited activation energies of about 4.3 kcal/mole. These values are consistent with those obtained by Kennedy and Sammells for sintered pellets (8). The resistivity of the electrophoretic tubes at 300°C was about 25 ohm-cm which agrees well with other data for polycrystalline material (9). Doped β -alumina did not give appreciably different results which was surprising based on previous studies with pressed pellets and may reflect that additional sodium and magnesium did not deposit with the β -alumina even though they were present in the suspension. Sodium analyses showed no increase over undoped β -alumina suspensions. Additional doping studies will be pursued in the future.

Results are summarized in Table I. It can be seen that high acid concentrations resulted in tubes of low density and very high resistivity. Otherwise no correlation was noted between electrophoresis conditions and the properties of the tubes obtained. The resistivities at 25°C were unusually low for undoped material although the sodium contents were quite high and

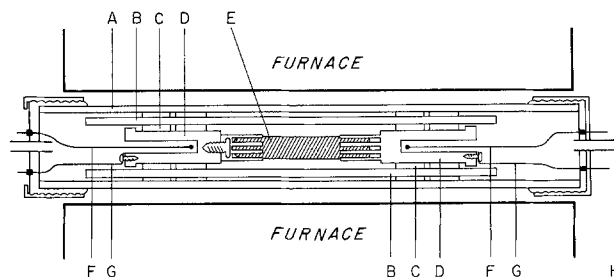


Fig. 4. Experimental setup for conductivity measurements. A, Pyrex tube; B, connecting rods; C, transit holder; D, sample holder; E, β -alumina sample; F, thermocouple; G, electrical connections; H, gas inlet and outlet.

Table I. Properties of beta-alumina electrophoretic tubes

Designation	Tri-chloro-acetic acid (g)	Density ¹ (g/cm ³)	Na ₂ O ¹ (w/o)	Resistivity ¹ [ohm-cm (25°C)]
A2-626	2	2.98	6.44	314
A2-630	2	3.09	7.26	
A2-522	2	2.95		500
A4-51	4			400
A4	4	3.05	8.63	
A6-617	6	3.04	7.02	
A6-72	6	2.98	6.44	425
A6-617	6	2.95	6.30	
A6-617	6		6.95	2,450
A6-522	6	2.92		126
AD-624 ²	6	2.94	6.60	570
AD-617 ²	6	2.94	7.25	570
AD-624 ²	6	2.97		1,120
A8-717	8	2.85	5.37	7,518
A10-619a	10	2.86	7.23	~40,000
A10-619b	10	2.85		4,520
	12	no deposit		

¹ Since the tubes were used for various experiments all measurements could not be made on all tubes. Tubes were sintered for 2 hr at 1700°C.

² Doped β -alumina containing 2 w/o MgO, 2 w/o Na₂CO₃. Tubes were sintered for 5 hr at 1750°C.

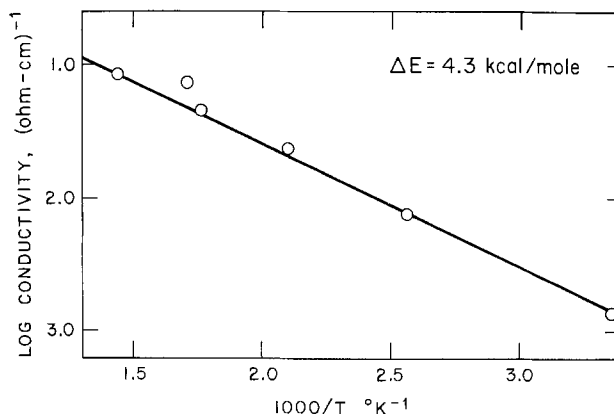


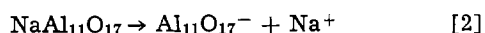
Fig. 5. Conductivity of electrophoretic beta-alumina tube as a function of temperature. Suspension contained 40g β -alumina, 6g trichloroacetic acid, and 500 ml dichloromethane. Tube sintered for 2 hr at 1700°C.

could account for the relatively high conductivities found for the electrophoretic tubes.

Sodium-sulfur cells.—Although the primary objective of this project was the fabrication of high density, high conductivity β -alumina tubes, it was only natural to attempt to use the tubes for sodium-sulfur cells. The experimental setup is shown in Fig. 6 and was fabricated from Type 304 stainless steel. After heating to 300°C in a dry box the cathode chamber was filled with a mixture of 2.3g sulfur and 1.5g graphite, and the anode compartment was filled with 1g molten sodium. An open-circuit voltage of 2.12V was observed and was stable for several weeks in the dry box. A load curve is shown in Fig. 7. The apparent internal resistance was 104 ohms which is considerably higher than the 1 ohm resistance of the electrolyte calculated from the a-c conductivity. This added resistance was attributed to the graphite-sulfur mixture and its contact with the β -alumina. This resistance increased with time which supports the hypothesis of contact resistance since tube resistances were stable. In any event the tubes appeared suitable for sodium-sulfur cells, and, in fact, showed no visible damage after 2 weeks use at 300°C.

Discussion

Powers (6) proposed two possible mechanisms for the generation of charged β -alumina particles



The first gives rise to positively charged particles which would migrate to the cathode. The presence of

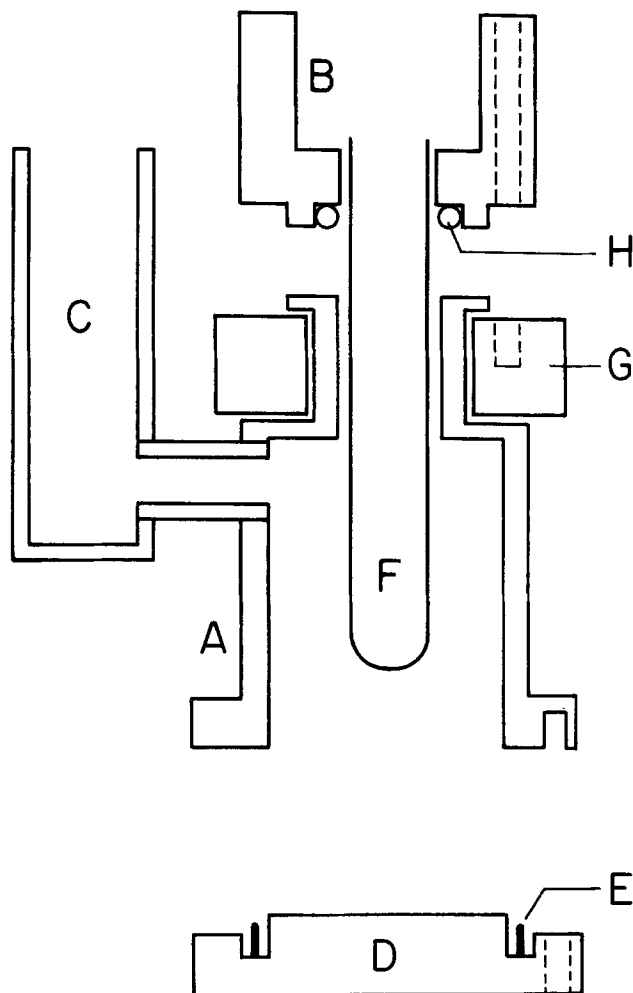


Fig. 6. Experimental setup for sodium-sulfur cell operated in dry box. A, Sulfur and graphite compartment; B, sodium container; C, sulfur addition tube; D, bottom plate; E, aluminum o-ring; F, β -alumina tube; G, nonconductive ceramic; H, Viton o-ring.

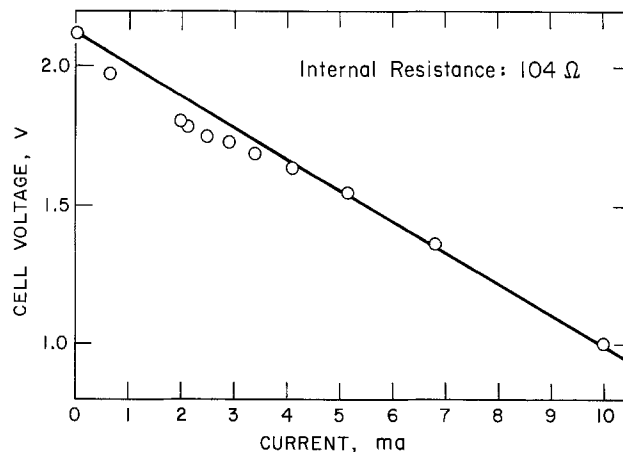


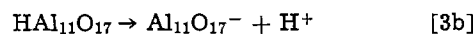
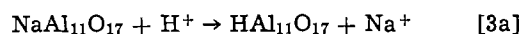
Fig. 7. Load curve for sodium-sulfur cell at 300°C

acid would be necessary for this mechanism. This effect was observed by Lazennec and Fally (5). The second mechanism requires no acid and yields negatively charged particles which would migrate to the anode. This was the type of behavior reported by Powers.

Our own studies showed that under certain conditions positively or negatively charged particles could be obtained, and indeed in some cases no deposits were obtained. We found that the presence of acid was necessary for electrophoretic depositions, and yet the particles were negatively charged. It should be kept in mind that the solvent used in these studies (dichloromethane) has a dielectric constant of 9 which is at the low end of the range suggested by Powers (6). Our choice was made before Powers' study was available, and was made on the basis of good suspension characteristics, i.e., the suspensions were stable for long periods of time. Thus, charge production in the pure solvent may be marginal and the presence of acid improved charge generation.

It should also be remembered that generation of charged particles is only part of the story. The Stern layer moves with the particle, and thus, it is the zeta potential which is the determining factor. In the usual case, the charge on the particle is partially neutralized, but in special cases complete neutralization or even reversal of charge can occur (10). Thus, it is conceivable that even by mechanism [1] the particle with its Stern layer could be negatively charged if the acid anion is a surfactant in the system. In the case of trichloroacetic acid this probably does not occur, but cannot be overlooked.

Another explanation of our results which appears more plausible is that the charging of β -alumina particles is kinetically slow. This would help explain why long mixing/grinding procedures were necessary. It could also explain the need for acid by proposing a catalytic role for H^+



In this proposed mechanism H^+ ion-exchanges with Na^+ , and it is the acid form which dissociates in dichloromethane to give negatively charged particles. The ion-exchange properties of β -alumina are well known (9). A minimum amount of acid would be required to give charged particles, while too high an acid content would allow mechanism [1] to compete and also tend to decrease the zeta potential by adsorption of H^+ in the Stern layer. The presence of proton-form β -alumina on the grain surface could also lead to the high resistivity results reported in Table I for high acid concentrations.

Obviously, one cannot prove or disprove these hypotheses by comparing results obtained by three different research groups all working in different solvent systems. More work needs to be done in this area especially since the product, β -alumina shapes by elec-

trophoretic deposition, has excellent physical and electrochemical properties.

Acknowledgment

The authors acknowledge financial support of this project by the National Science Foundation, Grant No. GH-37144.

The authors acknowledge helpful discussion with Mr. James Akridge and one of the authors (A.F.) expresses appreciation to Professor G. Robert, Faculté des Sciences de Besançon, France, for his advice and encouragement.

Manuscript submitted Aug. 12, 1974; revised manuscript received Nov. 12, 1974.

Any discussion of this paper will appear in a Discussion Section to be published in the December 1975 JOURNAL. All discussions for the December 1975 Discussion Section should be submitted by Aug. 1, 1975.

Publication costs of this article were partially assisted by the University of California.

REFERENCES

1. H. L. von Helmholtz, *Wied. Ann.*, **7**, 337 (1879).
2. A. I. Avgustinik, V. S. Vigdergauz, and G. I. Zhuravlev, *J. Appl. Chem. (USSR)*, **35**, 2090 (1962).
3. J. M. Andrews, A. H. Collins, D. C. Cornish, and J. Dracass, *Proc. Brit. Ceram. Soc.*, **12**, 211 (1969).
4. M. Boncoeur and S. Carpentier, *Ind. Ceram.*, **648**, 79 (1972).
5. Y. Lazennec and J. Fally, *Fr. Demande*, 2,092,845, March 3, 1972.
6. R. W. Powers, General Electric Co. Rept. No. 73CRD289, October 1973.
7. O. Stern, *Z. Elektrochem.*, **30**, 508 (1924).
8. J. H. Kennedy and A. F. Sammells, *This Journal*, **119**, 1609 (1972).
9. J. T. Kummer, *Progr. Solid State Chem.*, **7**, 141 (1972).
10. D. J. Shaw, "Electrophoresis," pp. 10, 11, Academic Press, New York (1969).

Catalysis in Nickel Electroless Plating

M. Lelental

Research Laboratories, Eastman Kodak Company, Rochester, New York 14650

ABSTRACT

The kinetics of the metal deposition from electroless plating baths has been studied. In addition, transition metal doped nickel electroless plating baths have been formulated which exhibit increased rates of metal deposition. Among all dopants examined, copper proved to be most effective. Addition of 10-20 mole per cent copper to a nickel-dimethylamineborane electroless plating bath leads to a considerable increase in the rate of metal deposition. This increase is due to the deposition of Ni-Cu alloys of a significantly improved catalytic activity in comparison with pure nickel. X-ray photoelectron spectroscopy has been employed to demonstrate the autocatalytic nature of the nickel deposition process. It is proposed that this improvement arises because the presence of copper leads to the promotion of weak chemisorption of hydrogen on the catalytic surface.

Nickel electroless plating baths have found widespread industrial applications. Numerous studies involving the use of additives such as stabilizers, surfactants, and brighteners have been reported (1-3). Feldstein has also studied the effect of complexing agents used in such baths on plating rates (4). In addition, nickel electroless plating solutions incorporating other metal ions which deposit nickel alloys have been formulated (5, 6). Such mixed electroless plating baths have been employed to alter the physical and chemical properties of the metal deposit. The most commonly employed catalyst for the initiation of deposition of metal from electroless plating baths is palladium.

Most of the work dealing with these electroless plating processes has been of an empirical nature dealing with bath formulations and measured electrical and magnetic properties of the metal deposits. The detailed mechanism of the deposition process remains, however, uncertain. It is generally accepted that deposition from these thermodynamically unstable but kinetically stable plating baths is an autocatalytic process. An intriguing question in this respect involves the possible role of the palladium catalyst in advanced stages of the plating process. With the development of modern probes for surface analysis such as Auger and photoelectron spectroscopy it is now possible to determine if palladium diffusion to the surface of the metal deposit occurs in these plating processes.

The present paper describes the use of x-ray photoelectron spectroscopy to elucidate the autocatalytic nature of nickel electroless plating initiated by palladium catalyst. In addition, the kinetics of metal deposition from nickel electroless plating solutions doped

with various transition metal ions have been studied. The amount of dopant ranged from the ppm level for the noble metals up to 50 mole per cent (m/o) for Group VIII on 1B metals. Deposition of nickel alloys characterized by different electronic properties allows the evaluation of electronic effects on the catalytic activity of alloys in such plating processes.

Experimental

The palladium catalyst used in this work was prepared as thin metal films deposited on microscope slides by the vacuum evaporation technique of Hamilton and Logel (7). The rate of metal deposition was determined using ground-glass microscope slides (18.6 cm²) with a palladium coverage of 1.4×10^{-6} g/cm². Dopants were added to the plating bath as received from the supplier without further purification. Purity of the materials used as dopants ranged from 99.9 to 99.999%. Selection of dopants was based on their known behavior as hydrogenation catalysts, as well as on expected electronic effects due to the formation of nickel-dopant alloys. An appropriate amount of a complexing agent was added with the dopant in order to keep the metal-to-ligand ratio constant. A nickel pyrophosphate electroless plating bath of the following composition has been used for the majority of doping experiments

NiCl ₂ · 6H ₂ O	25 g/liter
Na ₄ P ₂ O ₇ · 10H ₂ O	50 g/liter
Adjust pH to 10.5 with NH ₄ OH	
Dimethylamineborane	10 g/liter

Compositions of the deposits, as well as amount of deposited metal, were determined using atomic absorption spectroscopy and neutron activation analysis after dissolution of the deposits in aqua regia. The thickness of the Ni deposits were then calculated from these coverage values (milligrams per square centimeter). The distribution of a dopant in the deposits was examined by Auger spectroscopy.

Results and Discussion

Surface examinations of nickel deposits.—In order to be able to interpret the results of the doping experiments, it was necessary to determine the role of the original palladium catalyst in an advanced stage of nickel electroless plating. Particularly, it seemed important to establish the autocatalytic character of the nickel deposition process. Although it is widely accepted that deposited nickel is a catalyst for the continuation of electroless plating, it is possible that palladium diffuses through the nickel layer and thereby participates in a catalytic surface reaction even in an advanced stage of plating. This would require a completely different approach to the doping of the nickel electroless plating baths. Therefore, it was necessary to establish the behavior of the palladium catalyst during the course of nickel electroless plating. For this purpose nickel deposits of different thicknesses (10–250 Å) have been prepared using as a catalyst palladium nuclei evaporated on ground-glass substrates. The amount of palladium on the top surfaces of the deposits has been determined using photoelectron spectroscopy (ESCA, Fig. 1).

The disappearance of the Pd-ESCA signal after deposition of a 200 Å thick layer of nickel indicates that palladium does not diffuse during the course of nickel electroless plating. It should be emphasized that the sensitivity of the ESCA measurement allows the determination of as little as 3% of the original Pd coverage used in the experiment described. Taking into account that the ESCA half-thickness layer of nickel for Pd-3d electrons is equal to approximately 30 Å, one would expect a noticeable Pd signal in the case of a 250 Å thick nickel sample if the palladium had diffused through the nickel layer. The distribution of palladium in the thick nickel coatings was also examined using Auger spectroscopy. Results of the Auger examinations fully support previous ESCA observations. Results of surface examinations of nickel deposits clearly indicate that palladium does not diffuse through the nickel layer and prove the autocatalytic character of nickel electroless plating. This implies that the course of the nickel electroless plating depends to a great extent on the catalytic properties of the deposit.

Doping of nickel electroless plating baths.—Dopants used in this work can be divided into two categories.

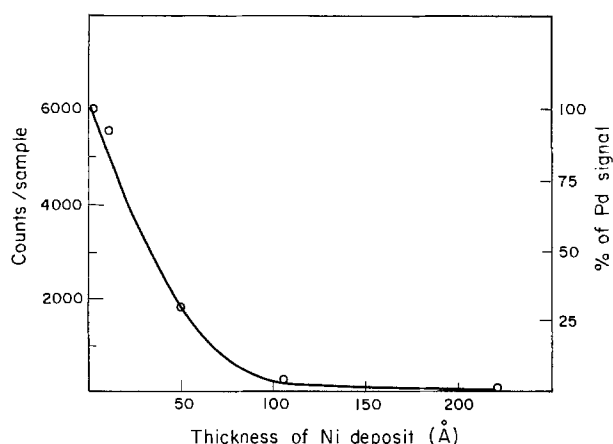


Fig. 1. ESCA examination of Ni deposits prepared by palladium-catalyzed nickel electroless plating.

The first group constitutes the platinum-group metals, as well as the IB-group metals that were added to the nickel electroless plating bath in trace amounts in relation to the concentration of nickel (Table Ia). The second group comprises other metals expected to affect the properties of nickel electroless plating baths that were added in an amount considerably greater than the dopants listed in Table Ia (Table Ib).

Among the dopants listed in Tables Ia and Ib, copper seems to be most interesting. Addition of copper to the nickel electroless plating bath leads to a significant increase in the plating rate. Addition of copper to the nickel also leads to the considerable change of the electronic properties of the deposits and allows one to interpret the behavior of nickel electroless plating baths on the basis of theory of catalysis. Therefore, copper was studied in considerable detail.

Copper-doped nickel electroless plating baths.—The unexpected increase in the activity of nickel electroless plating baths caused by the addition of copper ions is reflected in a considerable increase in the rate of metal deposition. Figure 2 shows the rate effect as a function of composition of the bath, and Fig. 3 gives the rate effect in terms of the alloy composition caused by the baths depicted in Fig. 2.

Figures 2 and 3 indicate that the increase in the activity of nickel electroless plating baths caused by the addition of copper ions is not limited to the one type of bath. Nickel solutions containing different complexing agents, such as organic amines (ethanolamine), carboxylic acids (gluconic acid or citric acid), as well as inorganic complexing agents (sodium pyrophosphate-ammonia), exhibit similar change in activity after the addition of copper ions.

The acceleration factor, defined as the ratio of the rate of deposition of Ni-Cu alloy to the rate of deposition of pure nickel, changes with the copper content in the solution. For room-temperature plating it is a maximum at 15–20 (m/o) of copper in the nickel electroless plating bath. This corresponds to 30–50 m/o

Table Ia. Effects of Group VII and IB dopants*

Dopant (X)				
Element	Concentration in the solution (m/o × 10 ⁻⁴)	Concentration in the deposit (m/o)	Rate of the (Ni + X)* deposition**	Stability***
Pt-(Na ₂ PtCl ₄)	50-2000	0.30-1.22	↓	G
Ir-(IrBr ₄)	100-2000	0.14-1.41	↓	G
Rh-(RhCl ₃)	10-200	0.065-0.436	Constant	GP
Ru-(RuCl ₃)	100-2500	0.020-0.066	Constant	G
Au-(KAuCl ₄)	3-500	0.0006-0.00052	Constant	GP
Ag-(AgNO ₃)	80-400		Constant	P

* (Ni + X) - Na₂P₂O₇ - 1% DMAB.

** ↑ = higher than for Ni electroless plating; ↓ = lower than for Ni electroless plating.

*** G = good (above 30 min at room temperature); GP = good to poor (10-30 min at room temperature); P = poor (less than 10 min at room temperature).

Table Ib. Effects of Group VIII and IB dopants

Dopant (X)				
Element	Concentration in the solution (m/o)	Concentration in the deposit (m/o)	Rate of the (Ni + X)* deposition**	Stability***
Co	10-50	20.9-60.0	↑	G
Zn	2.5-50	8.6-21.0	↓	G
W	10-50	—	Constant	G
Fe	10-50	—	↓	G
Cu	2.5-50	8.8-100	↑	G

* See Table Ia.

** See Table Ia.

*** See Table Ia.

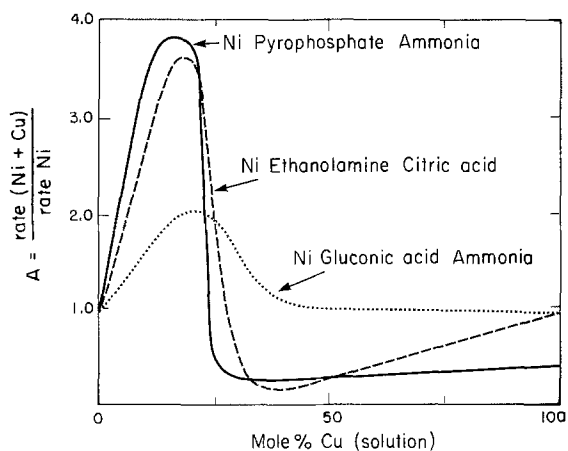


Fig. 2. Activity of Cu-doped Ni electroless plating baths (21°C, 10 min plating).

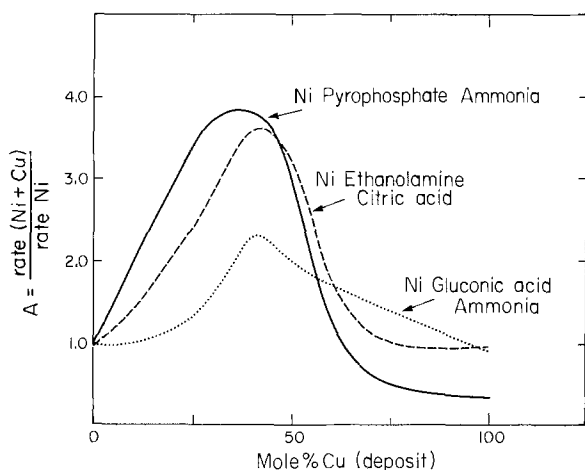


Fig. 3. Activity of Cu-doped Ni electroless plating baths as a function of deposit composition (21°C, 10 min plating).

copper in the deposit. The increase in the rate of plating due to the addition of Cu(II) ions to the nickel bath is more pronounced in the advanced stage of the process (Fig. 4).

These observations seem to indicate strongly that the increased activity of Ni-Cu electroless plating baths is due to the formation of more catalytically active deposits composed of nickel-copper alloys. This can be interpreted on the basis of the Dowden-Reynolds d-band theory for the activity of hydrogenation

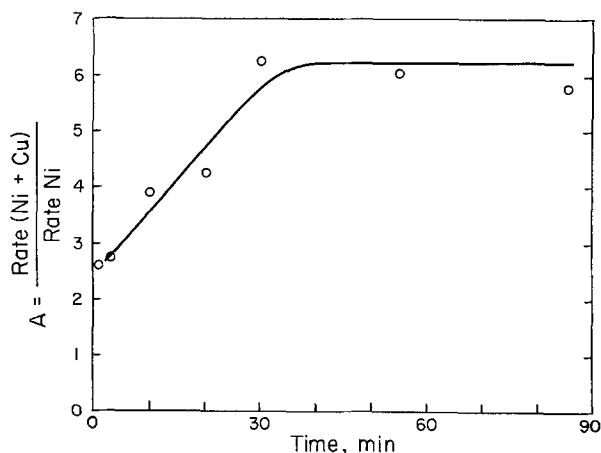
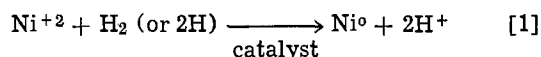
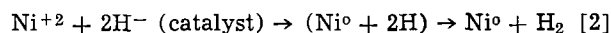


Fig. 4. Effect of Cu dopant on activity of Ni electroless plating bath in different stages of the plating (Ni-Cu-pyrophosphate-ammonia, 21°C, 90 m/o Ni-10 m/o Cu).

catalysts (8). This theory takes into account the differences in electronic properties of nickel and nickel-copper alloys. It is widely accepted that molecular or atomic hydrogen, or hydride ion bound to the catalytic surface, is the active intermediate during the course of nickel electroless plating. Feldstein (9) has shown that hydrogen gas formation in alkaline medium is proportional to the rate of metal deposition in such Ni electroless plating solutions. According to Brenner (10) the actual reductant for nickel is hydrogen acting by heterogeneous catalysis at the catalytic surface as follows



Mechanisms suggesting hydride ions as the reducing intermediate have been proposed by Hersch (11) and later modified by Lukes (12) (Eq. [2])



Both these mechanisms imply that the interaction of one or another form of hydrogen with a catalytic surface takes place during the course of nickel electroless plating. This would indicate a certain similarity between catalytic hydrogenation reactions and nickel electroless plating. This analogy allows the interpretation of the catalytic properties of the deposits formed during electroless plating on the basis of the theory of catalysis developed for hydrogenation reactions. The catalytic activity of transition metals has been ascribed to their d-band holes. The technique of alloying transition metals with IB metals to decrease their d-band hole density and hence control their catalytic activity has been utilized by numerous workers (13-20). Thus, the activity of the transition metals for the hydrogenation reaction should diminish with increasing IB metal content, falling to zero with the alloy composition corresponding to the filled d-band. Magnetic susceptibility measurements of Ni-Cu alloys indicate that the number of d-band holes decreases linearly with increasing copper content, falling to zero at approximately 60 atom per cent (a/o) copper (21). However, the correlation between d-band holes and catalytic activity, in some cases, is not satisfactory. Sachtler has partly explained this difficulty by noting that bulk and surface composition, as well as electronic properties, can differ appreciably (14).

The homogeneity of the Ni-Cu deposits formed by electroless plating has been examined using Auger spectroscopy. The sputtering profile of nickel in a $\sim 1.5\mu$ thick (83 m/o Ni; 17 m/o Cu) nickel-copper deposit is shown in Fig. 5. No significant differences in the nickel content as a function of depth have been observed. This would indicate that there is no substantial enrichment of the top surface with copper as has been observed by Sachtler (14) in the case of Ni-Cu films prepared by vacuum deposition.

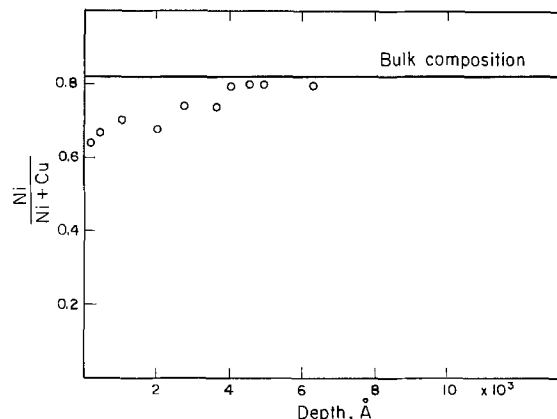


Fig. 5. Sputtering profile of Ni in a Ni-Cu deposit

Boron is often present in electrolessly plated nickel when amine boranes or sodium borohydride is used as the reducing agent (22). Auger examinations of Ni and Ni-Cu coatings revealed no boron. Also, analysis of Ni and Ni-Cu deposits carried out in these Laboratories excluded the possibility of a boron content greater than 1% in these deposits. Therefore, it is not expected that change in the catalytic activity of the deposits is caused by change in boron content. However, Auger spectroscopy demonstrated a carbon content of about 10 m/o throughout the Ni-Cu deposit. This can be interpreted as resulting from occluded dimethylamine. A detailed description of the Auger analysis of such Ni deposits is described elsewhere (23).

Change in the concentration of reducing agent affects the rate of metal deposition to the same degree in Ni, as in Ni-Cu electroless plating baths (Fig. 6).

As is indicated in Fig. 6, the acceleration factor A does not change significantly in the range of DMAB concentrations most commonly used for nickel electroless plating.

Catalytic properties of Ni-Cu alloys.—A number of investigations have been undertaken to elucidate the influence of the electronic structure of alloys, particularly nickel-copper systems, on catalytic activity since the proposal of the d-band theory by Dowden and Reynolds (8). There have been pronounced discrepancies between activity pattern expected on the basis of the d-band theory and experimental results reported for nickel-copper alloy catalysts. The theory states that the catalytic activity of transition metal IB-group metal catalysts should decrease with increased content of IB-group metal. This decrease is expected on the basis of the decrease of d-band holes with the addition of IB-group metal to the transition metal catalyst. However, Russell (24), Emmett (25), and Takeuchi (26) have reported that maximum catalytic activity of nickel and nickel-copper catalysts for hydrogenation reactions is found in some cases in the alloy region and that it is approximately ten times as active as pure nickel. Hall and Emmett (18) reported that for the hydrogenation of ethylene over a series of nickel-copper alloys a large promoting effect of chemisorbed hydrogen on the reaction rate in the copper-rich range was observed. These promoted alloys were more active than pure nickel. Recently Roberti (15) postulated that the increased activity of nickel-copper alloys is caused by weakening of the metal-adsorbate bond. Takeuchi (17) reported that the heat of adsorption of hydrogen on nickel and nickel-copper catalysts changes monotonically with the composition of alloy from 27 kcal/mole for pure nickel to 13 kcal/mole in the case of 75 a/o Cu alloy. This can be interpreted on the basis of the complexity of the hydrogen chemisorption processes. There is definite evidence that more than one type of chemisorption of hydrogen is possible, the difference being mainly in the strength of adsorbant-adsorbent bond. The decrease in the heat of

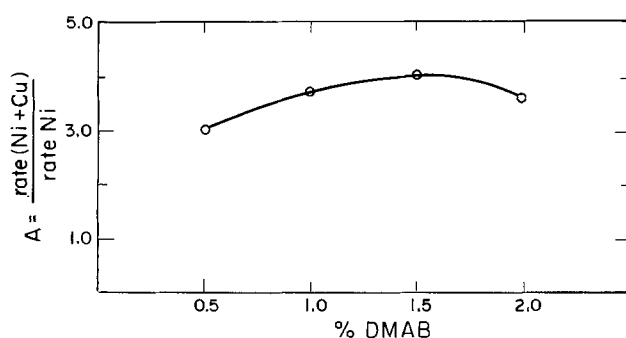


Fig. 6. Activity of Cu-doped Ni electroless plating bath as a function of DMAB concentration (Ni-Cu-pyrophosphate-ammonia, 21°C, 90 m/o Ni-10 m/o Cu).

H_2 chemisorption observed by Takeuchi can be explained by taking this fact into account. The chemisorption of hydrogen on the various nickel-copper alloys was investigated in detail by Sinfelt *et al.* (19). The presence of two forms of chemisorbed H_2 (*i.e.*, strongly and weakly chemisorbed hydrogen) was observed by these workers. They reported that with nickel catalyst the amount of weakly adsorbed hydrogen is small compared to the total adsorption. But the fraction of weakly adsorbed hydrogen increases considerably when a small amount of copper is added to the nickel. They concluded that the addition of copper to nickel decreases markedly the average strength of adsorption of hydrogen (*i.e.*, strongly adsorbed hydrogen becomes a much smaller fraction of the total). The composition of the Ni-Cu alloys produces similar effects on the weak chemisorption of hydrogen and the catalytic activity of these alloys in electroless plating processes (Fig. 7). Assuming that hydrogen or hydride ion chemisorbed on the catalytic surface is the active intermediate involved in the reduction of Ni and Cu ions in electroless plating it is likely that the kinetics of metal deposition depends on the strength of the "hydrogen"-catalyst bond. The data presented in Fig. 7 suggest that the increase in the rate of electroless plating observed for Ni-Cu alloys is related to the promotion of weak chemisorption of hydrogen by incorporation of copper in the nickel catalyst. Although the mechanism of the promotion of weak chemisorption by the addition of copper to the nickel catalyst is not fully understood, there is a widespread belief that chemisorption and catalysis are not determined by collective (*i.e.*, bulk) properties of the catalyst, such as the filling of its d-band, but by the chemical properties of its surface atoms. These properties are affected to a great extent by the neighboring atoms. In coordination chemistry, it is well known that metal ligand bond strength is influenced in a very pronounced way by the other ligands in the coordination sphere. This is a second-order effect similar to that which should be expected for chemisorption by metals and metal alloys. Wise's (27) interpretation of the fact that the catalytic properties of transition metals, as well as the weak adsorption of hydrogen, are enhanced by the addition of IB-group metal is based on the hypothesis that catalytic action is related to the promotion of an electron to a localized band. According to Wise, d orbitals of transition metals are split into two groups, *i.e.*, e_g and t_{2g} . For the interpretation of the catalytic properties of Ni-Cu alloys, it is relevant that the narrow Ni e_g band with its high density of states will be more readily filled than the relatively broad t_{2g} band by the introduction of s electrons from

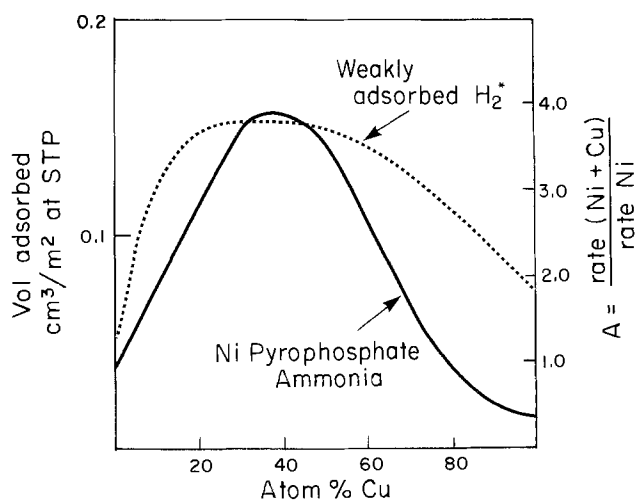


Fig. 7. The effect of composition of Ni-Cu alloys on weak chemisorption of hydrogen and catalytic activity of these alloys in electroless plating. *Sinfelt *et al.* (19).

copper. The selective filling of one of these subbands at a certain alloy composition may be responsible for the observed change in the relative amounts of strongly and weakly chemisorbed intermediates, as well as for the maximum catalytic activity observed at a fixed alloy composition. This would strongly imply the existence of a bond for adsorbed intermediates that energetically is most favorable for catalytic reaction.

Conclusions

The observed increase in the activity of nickel electroless plating baths resulting from the addition of copper ions manifested by an increased rate of metal deposition should be interpreted on the basis of the generally accepted mechanism of nickel electroless plating. The increased activity of Ni-Cu electroless plating baths is due to the increased catalytic activity of the deposited Ni-Cu alloys. It is proposed that this increased catalytic activity is related to the promotion of weak chemisorption of hydrogen due to the addition of copper to the nickel deposit. The role of hydrogen intermediates in the nickel electroless plating process, as well as chemisorption of hydrogen on Ni and Ni-Cu surfaces, has been discussed. There seems to be a correlation between the increased activity of these baths and the promotion of weak chemisorption of hydrogen by the deposited Ni-Cu alloys. This seems to imply that the rate of Ni and Ni-Cu electroless plating is a function of the strength of the binding in the weak state of adsorption state.

Acknowledgments

I wish to thank Dr. R. C. Baetzold and Messrs. J. E. Moore and R. E. Mack for ESCA and Auger spectroscopic examinations of Ni and Ni-Cu deposits.

Manuscript submitted Sept. 9, 1974; revised manuscript received Nov. 12, 1974.

Any discussion of this paper will appear in a Discussion Section to be published in the December 1975 JOURNAL. All discussions for the December 1975 Discussion Section should be submitted by Aug. 1, 1975.

Publication costs of this article were partially assisted by the Eastman Kodak Company.

REFERENCES

1. N. Feldstein and P. R. Amodio, *This Journal*, **120**, 110 (1970).
2. N. Feldstein, *Solid State Tech.*, **87** (1973).
3. G. Salvago and P. L. Cavallotti, *Plating*, **59**, 665 (1972).
4. N. Feldstein, *RCA Rev.*, **31**, 317 (1970).
5. P. Cavallotti and G. Salvago, *Electrochem. Metal*, **3**, 23 (1968).
6. F. Pearlstein and R. F. Weightman, *Electrochem. Technol.*, **6**, 427 (1968).
7. J. F. Hamilton and P. C. Logel, *Thin Solid Films*, **16**, 49 (1973).
8. D. A. Dowden and P. Reynolds, *Disc. Faraday Soc.*, **8**, 184 (1950).
9. N. Feldstein and T. S. Lancsek, *This Journal*, **118**, 869 (1971).
10. A. Brenner and G. Riddell, *J. Res. Nat. Bur. Std.*, **37**, 31 (1946).
11. P. Hersch, *Trans. Inst. Metal Finishing*, **33**, 417 (1955).
12. R. M. Lukes, *Plating*, **51**, 969 (1964).
13. G. C. Bond, "Catalysis by Metals," Academic Press, New York (1962).
14. W. M. H. Sachtler and Van der Plank, *Surface Sci.*, **18**, 62 (1969).
15. A. Roberti, V. Ponec, and W. M. H. Sachtler, *J. Catal.*, **28**, 381 (1973).
16. T. J. Plunkeit and J. K. A. Clarke, *J. Chem. Soc.*, **68**, 60 (1972).
17. T. Takeuchi, M. Sakaguchi, and I. Miyashi, *Bull. Chem. Soc. Japan*, **35**, 1390 (1962).
18. W. K. Hall and P. H. Emmett, *J. Phys. Chem.*, **63**, 102 (1959).
19. J. H. Sinfelt, J. L. Carter, and D. J. C. Yates, *J. Catal.*, **24**, 283 (1972).
20. T. A. Spooner and J. K. A. Clarke, *Ber. Bunsenges. Phys. Chem.*, **76**, 1187 (1972).
21. J. H. Shulman and J. S. Cho, *Surface Sci.*, **2**, 245 (1964).
22. G. O. Mallory, *Plating*, **58**, 319 (1971).
23. R. C. Baetzold and R. E. Mack, *J. Catal.*, In press.
24. E. G. Alexander and W. W. Russell, *ibid.*, **4**, 184 (1965).
25. J. S. Campbell and P. H. Emmett, *ibid.*, **7**, 252 (1967).
26. T. Takeuchi, Y. Tezuka, and O. Takayasu, *ibid.*, **14**, 126 (1969).
27. H. Wise, *ibid.*, **10**, 69 (1968).
28. R. C. Baetzold, Private communication.

The Electrophoretic Forming of Beta-Alumina Ceramic

R. W. Powers*

General Electric Company, Research and Development Center, Schenectady, New York 12301

ABSTRACT

The forming or shaping of beta-alumina ceramic is usually difficult with conventional ceramic processing. In this paper, electrophoretic deposition is shown to be an operationally simple, rapid, and reliable technique for forming a wide range of beta-alumina shapes required in electrochemical devices. The following topics are discussed in detail: the basis for selection of a suitable vehicle for holding beta-alumina particles in suspension, the control of electric charge on the particles, the milling of starting powder to provide a small particle size with minimum contamination by wear of the grinding media, the deposition procedure, and the removal of electrophoretic deposits from forming mandrels. Finally, some properties are given for sintered ware formed by electrophoretic deposition.

The high ionic conductivity of beta-alumina and the use of this material as electrolyte in sodium-sulfur cells were made known about 7 years ago (1). The conductivity arises from the rapid migration of monovalent cations, e.g., sodium, in loosely packed planes

of oxygen atoms (2). These conducting planes are sandwiched at approximately 11Å intervals between spinel blocks consisting of four closely packed layers of oxygen atoms with aluminum in interstitial positions. In contrast to the large conductivity in the conducting planes, that perpendicular to these planes is very low. The mechanical properties of beta-alumina are likewise very anisotropic. Cleavage occurs readily

* Electrochemical Society Active Member.
Key words: beta-alumina, ceramic processing, electrophoretic deposition, electrophoretic forming.

parallel to the conducting planes but not across such planes. Consequently, to obtain strong isotropic material for use in electrochemical devices, fine-grained polycrystalline ceramic is required. The forming or shaping of polycrystalline beta-alumina ware is difficult with most conventional ceramic processing techniques. This paper is mainly concerned with the use of electrophoretic deposition for this purpose. The background considerations to an operationally simple, reliable, versatile procedure are described in some detail.

Fabrication of ceramic ware usually follows a three-step procedure. The first involves preparation of powder of the composition required in the end product or one which transforms to such a composition during subsequent processing. The second step involves shaping or forming of the powder into a shape similar to that required in the end product. Finally, this "green" ware is heated to high temperatures. In this sintering step, the material shrinks, porosity is greatly reduced, and mechanical strength along with other required properties is developed. Although the main concern of this paper is with the second of these steps, that of forming, certain aspects of powder preparation and of sintering are discussed, particularly as they pertain to electrophoretic forming.

Although the phenomenon of electrophoresis—the motion of electrically charged particles in an electric field—has been known for over 160 years, its use in the forming of ceramic ware is a development of the past few years. Some highlights in the history of this development, which really constitute the basis of our present capability, are indicated in Table I.

An important advantage of electrophoretic deposition for ceramic forming is that of high throwing power. Another is the short deposition times required. Most of the ware discussed in this paper were deposited in about 1 min. A third important advantage of electrophoretic forming is its versatility. A wide variety of shapes are possible. "Tooling" is relatively simple. Only the mandrels on which the deposit is laid down require precision machining.

Two important properties of beta-alumina that relate to processing were described above: the anisotropy of the electrical conductivity and of the mechanical strength. Among its other properties that especially need to be taken into account for electrophoretic forming is its limited stoichiometric range. Sodium beta-alumina always contains sodium oxide in excess of that corresponding to the composition of the ideal structure, $\text{Na}_2\text{O} \cdot 11\text{Al}_2\text{O}_3$. It is really not a compound in the strict chemical sense, but rather a phase of

rather narrow compositional range. According to Roth and Mitoff, the single-phase field at 1725°C extends from $1.2 \text{Na}_2\text{O} \cdot 11\text{Al}_2\text{O}_3$ to $1.4 \text{Na}_2\text{O} \cdot 11\text{Al}_2\text{O}_3$ (8). Its hard and abrasive nature creates problems in reduction to sufficiently small particle size without undue contamination from abrasion of the grinding media. The thermal shock resistance is high. Beta-alumina powders absorb considerable quantities of water. Concentrations in excess of 3 weight per cent (w/o) have been found by the author in powders as received from the supplier.

Experimental Procedures

The forming operation in the fabrication of beta-alumina ware by electrophoretic deposition can be subdivided into three separate steps: (i) reduction of the particle size of the starting powder and charging of the individual particles in suspension in a suitable organic liquid; (ii) deposition of the beta-alumina particles onto a mandrel; and (iii) removal of the deposit from the mandrel. Problems are associated with each of these steps. They are discussed here after the experimental procedures used in this work have been described.

Starting powders.—Most work has been carried out with two commercially available beta-aluminas: Monofrax H beta-alumina from the Carborundum Company and XB-2 beta-alumina powder from Aluminum Company of America. The nominal compositions of these materials are given in Table II. Monofrax H beta-alumina, a fused product, is generally available in the form of bricks. These were jaw crushed, ball milled dry with alpha-alumina balls, and then screened to provide powder in the range of $44\text{--}105\mu$. Alcoa XB-2 beta-alumina, a calcined product, was obtained in the form of a fine powder. Additives, of the order of 1 w/o, were often added to the as-received material. These included, for example, additional soda by way of anhydrous sodium carbonate as well as magnesia from basic magnesium carbonate. Furthermore powders with soda contents corresponding to those in β'' -alumina have also been deposited satisfactorily. Appropriate quantities of the additives in powder form were mixed thoroughly with the beta-alumina powder by tumble mixing for 24–48 hr. The resulting mixture of powders was calcined in an oxygen atmosphere for 24 hr at 1400°C . Such calcined material served as the starting powder for the deposition work.

Suspension preparation.—In this work, reduction in size of the starting powder and electrical charging of the particles were carried out simultaneously by milling under the vehicle, i.e., the organic liquid in which the beta-alumina particles are suspended during deposition. Three different kinds of milling (ball, vibratory, and jet) were examined in the course of this work. While the greatest effort was given to ball milling, some very satisfactory results have also been obtained with vibratory milling. Particle size reduction by jet milling, before dispersion in the vehicle, was not satisfactory.

Table I. Important previous events in the development of electrophoretic forming

Date	Contributor(s)	Contribution	Reference No.
1809	F. F. Ruess	Discovery of phenomenon of electrophoresis	
1879	H. von Helmholtz	Concept of double layer. Equation delineating factors affecting electrophoretic mobility.	
1927	S. E. Sheppard	Rubber deposition from latex. Deposition into angled recesses.	(3)
1939	J. H. DeBoer H. C. Hamaker E. J. W. Verwey	Use of organic liquids as vehicles. Deposition of micron-size particles for coatings. Ballmilling used for particle size reduction. Theory of electrophoretic deposition.	(4-5)
1969	J. M. Andrews A. H. Collins D. C. Cornish J. Dracass	Forming of 5 mm thick alpha-alumina radomes	(6)
1971	Y. Lazennec J. Fally J. Leboucq	Forming of closed-end zirconia and beta-alumina tubes by combination of electrophoretic deposition and hydrostatic pressing	(7)

Table II. Typical chemical analyses for commercially available beta-alumina

Designation: Source:	Monofrax H Carborundum Co.	XB-2 Alcoa
w/o Na_2O	5.59	7.30
Li_2O	n.i.	0.01
K_2O	n.i.	0.01
MgO	0.05	n.i.
CaO	0.10	0.03
Fe_2O_3	0.08	0.03
Ga_2O_3	n.i.	0.01
SiO_2	0.18	0.02
TiO_2	0.03	n.i.

n.i. means not indicated in manufacturer's literature.

Both ball and vibratory milling have been carried out in 32 oz wide-mouth polyethylene bottles as received from the supplier without use of special cleaning procedures. Their use as mill jars reduces contamination since any abraded material is burned out during sintering. These containers were half-filled with grinding media, either 1100g of alumina media or 1800g of zirconia. When suspensions were ball milled, the volume of the vehicle was 200 ml. However, for some experiments with vibratory milling, the vehicle volume was increased to 300 or 400 ml. The amount of starting powder in the charge ranged from 35 to 300g.

Ball milling was done on a Model 764 AV Norton jar mill, while vibratory milling was carried out with a Sweco Model M18L55 mill.

Deposition.—Deposition in electrophoretic forming is carried out by applying a d-c voltage between the mandrel and a counterelectrode, both immersed in the beta-alumina suspension. Following the initial stages of this work, the containers for the suspension were made to serve also as counterelectrodes. They are usually made of an 18-8 stainless steel.

Photographs of several mandrels with their corresponding suspension containers appear in Fig. 1 and 2. In Fig. 1, a mandrel for forming open-end tubes up to 8 in. long is shown in the foreground. Mandrels for forming cylindrically shaped objects must be tapered slightly to facilitate removal of the deposit after drying. The other mandrel shown is for forming closed-end tubes up to 4.5 in. long. Mandrels for forming 3 cm disks and a pocket-shaped article are shown in Fig. 2. The Teflon polymer ring shown with the disk mandrel is used to shape the electric field. Its use permits a deposit of uniform thickness over the face of the disk. Only relatively scratch-resistant materials have been used for mandrel construction. Nickel, 18-8 stainless steel, and 36-Invar have all proved satisfactory. Mandrels are usually buffed to obtain smooth surfaces.

Considerable attention must be given to the materials allowed to contact the suspension in order that the charge on the beta-alumina particles not be adversely affected. Difficulties were encountered with paper masking tape as well as silicone rubber. Also

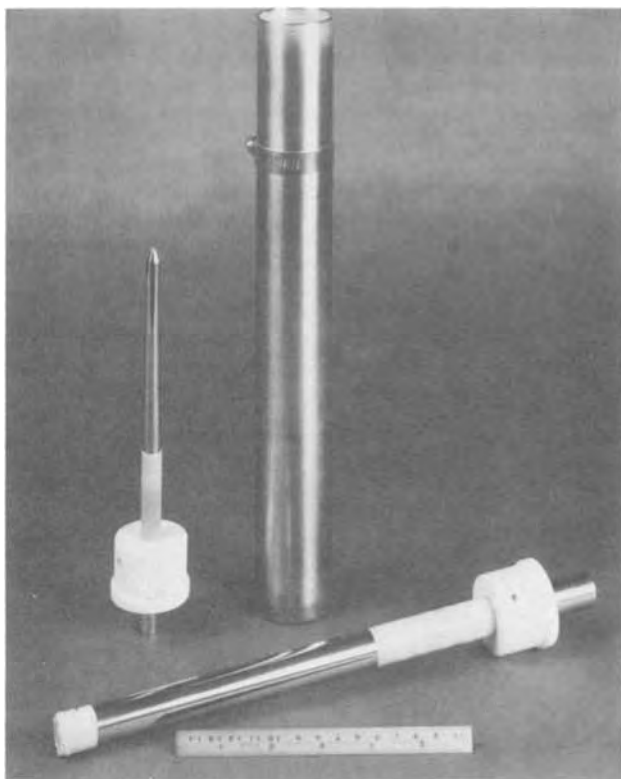


Fig. 1. Mandrels and suspension container for forming tubes

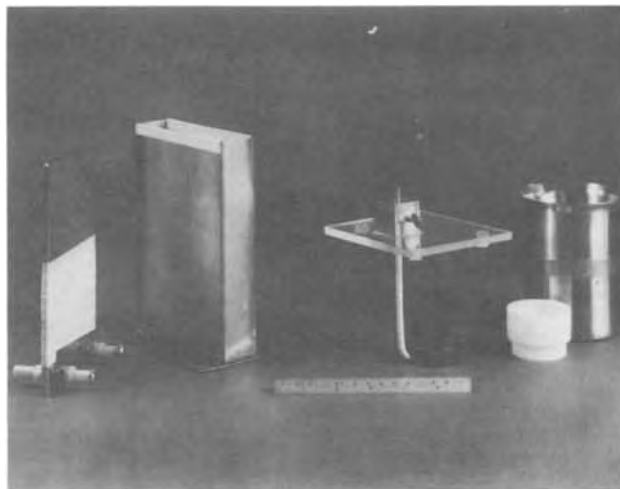


Fig. 2. Apparatus for forming disks and pocket-shaped pieces

polymethylmethacrylate containers were found to affect adversely the charge on the particles. Borosilicate glass containers are innocuous, however.

A d-c high-voltage supply has been used to apply voltages in the range 200–1000V between the mandrel and counterelectrode. Such voltages correspond to fields at the electrode surface between 280 and 1400 V/cm for the tube mandrels as shown on Fig. 1. At present, it is the practice to use the highest fields permitted by the power supply. This procedure usually reduces deposition times to about 1 min and makes stirring of the suspension unnecessary during deposition. However, were the deposition extended over several minutes, stirring would be needed to avoid excessive settling of the beta-alumina particles in suspension. Suspensions are vigorously stirred with a magnetic stirring bar before a deposition.

The very simple electrical circuit used for electrophoretic forming is shown in Fig. 3. In essence, the series combination of deposition cell, current meter, current recorder, and charge integrator is placed across the d-c power supply. A high impedance voltmeter indicates the cell voltage. As a safety precaution, the suspension container which surrounds the forming

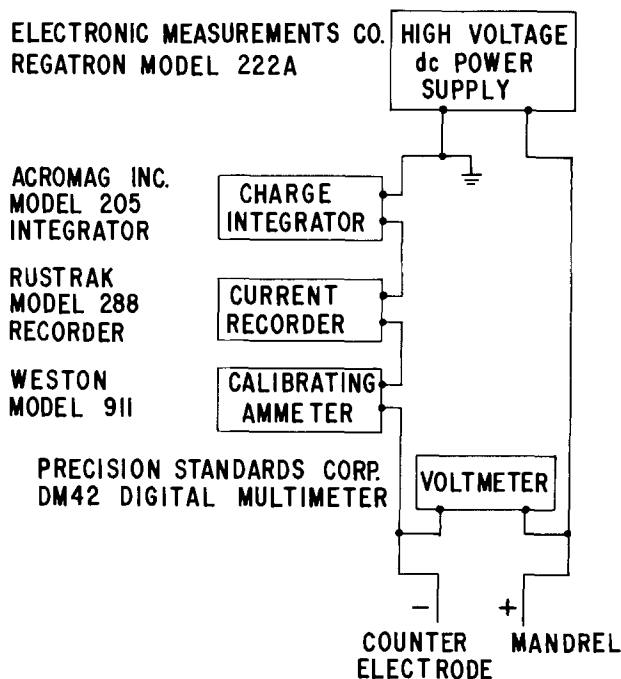


Fig. 3. Circuit diagram for electrophoretic deposition

mandrel is maintained at or very near ground potential.

Sintering.—Sintering of green beta-alumina ware has been carried out on alpha-alumina saggars in molybdenum-wound furnaces. The saggars are heated inside a dense alpha-alumina tube filled with either an oxygen or an air atmosphere. This protects the ware from the hydrogen atmosphere which needs to envelop the furnace muffle to prevent oxidation of the molybdenum winding. Sintering has been done between 1700° and 1825°C.

Problem Areas in Electrophoretic Forming

The first operation in electrophoretic forming, the preparation of a suitable suspension, is critical since it involves three problem areas all of which require considerable attention. They include selection of a suitable organic liquid in which the beta-alumina particles can be suspended during deposition, control of electric charge on the particles, and the techniques by which milling of the particles is carried out. In contrast, the second operation, the deposition process itself, is more straightforward. Likewise, the final operation, the removal of the deposit from the forming mandrel, also involves relatively simple considerations.

Selection of a suitable vehicle for dispersion of beta-alumina particles.—The electrical conductivity of a number of suspensions is shown in Fig. 4 as a function of the dielectric constant of the vehicle with which the suspension was prepared. In each case, the suspension contained 35g of fused beta-alumina powder suspended in 200 ml of the vehicle. The suspensions had been ball milled for 16 hr with alpha-alumina grinding media. The conductivities were measured in a concentric cylinder arrangement and were computed from the dimensions of the deposition cell, the voltage drop, and

the initial current before any appreciable quantity of deposit covered the forming electrode.

Two features on Fig. 4 are noteworthy. The first is that, in general, the conductivity increases rather sharply with the dielectric constant of the vehicle, approximately seven orders of magnitude rise for a change in the dielectric constant from 2 to 40. The second and perhaps more surprising feature is that electrophoretic deposits were obtained only from vehicles with dielectric constants in the range from about 12 to 25 as indicated by the filled circles on the figure.

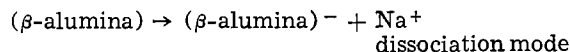
As discussed in the following section, the predominant charging mode for the beta-alumina particles is assumed to be dissociation of sodium cations. The absence of deposition from vehicles such as benzene or p-dioxane is consistent with this interpretation as their low dissociating power would not likely give rise to effective particle charging. On the other hand, mainly practical considerations limit use of vehicles of high dielectric constant. Their high conductivity is further enhanced by ohmic heating during the passage of current. Deposits formed from vehicles with dielectric constants slightly below 25 (for example, from ethanol) tended to be very fluid and to slide off the mandrels. In some instances, this situation made determination of the existence of a deposit very difficult although usually this behavior was accompanied by a sudden large increase in current for constant applied cell potential. Anodic film formation on mandrels was also noted with vehicles of high dielectric constant.

The importance of the dielectric constant in the selection of a vehicle was confirmed by the observation of beta-alumina deposits from an equal volume mixture of methanol and p-dioxane although deposition did not occur from these liquids separately. In other experiments, deposition was obtained from a technical grade methyl acetate, containing approximately 15% methanol but not from the reagent grade ester.

Following initial experiments with a large number of vehicles and mixtures of vehicles, nearly all subsequent work was carried out with n-amyl alcohol (pentanol-1). Its dielectric constant, ϵ , is 13.9. With it, neither the formation of anodic films on the mandrels nor that of fluid deposits is observed. Since reagent grade material is sold by a number of manufacturers, a reproducible vehicle is readily available. Finally, n-amyl alcohol is relatively nontoxic. It has been used as an industrial solvent for many years (9).

Control of electric charge on beta-alumina particles.—As indicated on Fig. 4, no electrophoretic deposits were obtained with ethyl acetoacetate ($\epsilon = 15.4$). Nor were any found with ethylene diamine ($\epsilon = 14.2$) nor with water/p-dioxane mixtures with compositions corresponding to dielectric constants in the range 12 to 25. With pyridine ($\epsilon = 16.3$), a deposit was obtained with the mandrel negative whereas with all the other vehicles used in the survey experiments, results from which are shown in Fig. 4, deposits appeared on the positive electrode. Clearly, then, there are some complications in controlling the surface charge on beta-alumina particles.

Charging modes for beta-alumina.—The results of many experiments are consistent with the hypothesis that there are two very different charging modes for beta-alumina. One, as mentioned above, is the dissociation of sodium ions to give rise to a negatively charged particle. Thus,



However, another mode is the adsorption of protons or conceivably other cations which lead to positively charged particles. Thus,

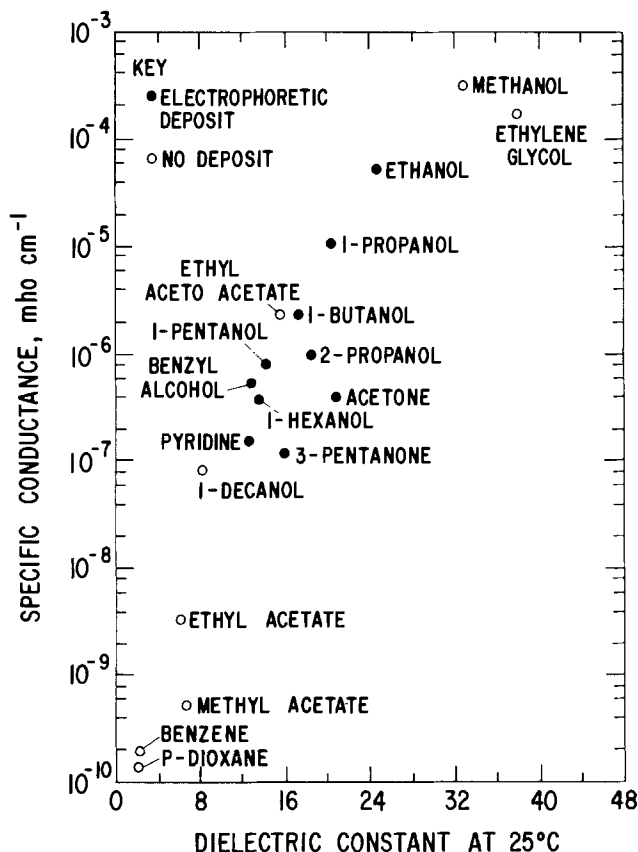
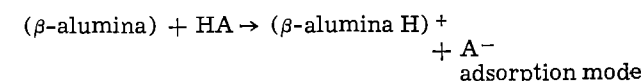


Fig. 4. The electrical conductivity of suspensions vs. the dielectric constant of their vehicles.

Proton donors might be water or organic acids such as benzoic or stearic acid.

The two charging modes are competitive. For nearly all the work discussed in this paper, dissociation was used as the predominant mode. However, the negative charge on the beta-alumina particles prepared from a fused block can be neutralized by the addition of a few tenths of a per cent water to the n-amyl alcohol vehicle, as made evident by the absence of a deposit. And, usually with 1/2% water in the vehicle, the particles are positively charged. The absence of a deposit with ethyl acetoacetate and ethylene diamine and a deposit on the negative electrode with pyridine likely resulted from the presence of small amounts of water in these vehicles. The addition of about 1% benzoic or stearic acid (based on beta-alumina) will also give rise to positively charged particles. The Marcoussis group of Compagnie Generale d'Electricité have, in fact, used proton adsorption as the predominant charging mode in their electrophoretic deposition work with both zirconia and beta-alumina (7). The activator used was benzoic acid. Likewise, very recently Kennedy and Foissy have used trichloroacetic acid in a methylene chloride vehicle to obtain beta-alumina particles with a positive charge (10). The existence of competing charging modes for electrophoretic particles is not unique to beta-alumina. Very similar phenomena are found with certain micas. For example, pyrophyllite particles can be charged negatively by dissociation of potassium ions as well as by adsorption (11).

Effects of water.—In addition to charge neutralization and charge inversion described above, there are actually a number of other effects of water on the behavior of beta-alumina/n-amyl alcohol suspensions. With suspensions which are "excessively dry" as defined more precisely below, very smooth, uniform deposits can be obtained which, however, undergo creep for several minutes after removal from the suspensions. In extreme cases, 50-90% of the deposit may flow off the mandrels. Fortunately, there is a level of water content, not difficult to reproduce experimentally, over which very satisfactory, smooth, uniform deposits can be obtained. Charge neutralization and inversion are obtained with larger additions, at concentrations of about 0.2 and 0.5%, respectively, using fused beta-alumina powder. With still larger amounts of water, e.g., 5%, charge neutralization occurs a second time as deposits are not obtained. Where there is but a small amount of deposition, near the neutralization point, the suspensions appear flocculated. Deposits are weak. The suspensions settle more rapidly and give rise to a sediment about twice as voluminous as from suspensions yielding good deposits. Most of these phenomena can be understood qualitatively in terms of a theory of electrophoretic deposition proposed by Hamaker and Verwey (5). A very clear review of this theory has been given by Troelstra (12).

Suspensions of beta-alumina appear ideally suited for illustrating the stability aspects of suspensions. Since two opposing charging mechanisms are known, wide variations in the repulsive force between particles are possible. For example, negatively charged particles with very strongly repulsive interactions are available through the use of nearly water-free n-amyl alcohol suspensions. Such suspensions give rise to deposits that undergo viscous flow off the mandrels as described above. Neutral suspensions or those of particles with weakly repulsive interactions carrying either positive or negative charge can be obtained by addition of appropriate quantities of water. These latter are examples of flocculating suspensions. Vehicles other than n-amyl alcohol can also be used. It would appear that a beta-alumina suspension of intermediate stability, i.e., one stable at larger interparticle separation distances, are most desirable for electrophoretic deposition.

Practical control of water content.—The treatment to be given a beta-alumina powder to control the water

concentration depends strongly on its porosity. That of low porosity, such as obtained by crushing and grinding fused beta-alumina bricks, does not require further drying if stored in dry, tightly capped polyethylene containers. In fact, if such powder is dried overnight in a vacuum oven at 220°C, deposits are obtained which undergo viscous flow. On the other hand, calcined beta-alumina powder is a much more porous material. Drying in air at temperatures somewhat in excess of 600°C is required to remove sufficient water so that a satisfactory negative charge is developed on the particles. Normally, drying is accomplished simultaneously with the 1400°C calcination operation described above. Weight losses of 3.0-3.5% in excess of those attributable to additive decomposition are measured with this powder on calcination. These losses arise mostly from water contained in the as-received powder. Such dried calcined powders are stored in tightly capped polyethylene bottles and redried in a vacuum oven at 200°C overnight immediately before use. Also, in order to achieve reproducible deposits, considerable care need be exercised to use clean, dry, grinding media. Most lack of reproducibility in early work was traced subsequently to insufficient attention to this point. The n-amyl alcohol is used as received without further drying.

Milling problem.—The milling or grinding of beta-alumina/n-amyl alcohol suspensions is carried out for two very different purposes: to develop a suitable charge on the particle surfaces, and secondly, to facilitate production of dense ware during sintering. Beta-alumina powders are charged positively when first placed in n-amyl alcohol, presumably as a result of water adsorption from the atmosphere. During milling, this charge is first neutralized, and subsequently, a negative charge develops after 2-8 hr, depending on the powder, grinding media, and the method of milling. A limitation of the dissociative charging mode is that beta-alumina particles must not be removed from the suspension before deposition, after milling to small particle size. Otherwise, a positive charge is acquired which then is most difficult to neutralize by further milling. Consequently, whatever contamination is introduced into the suspension from media wear will likely be incorporated in the electrophoretic deposit.

The gist of the milling problem is the need to develop techniques to produce an adequately small particle size in an exceedingly hard and abrasive substance without incurring appreciable wear of the grinding media. There can be various deleterious effects from such wear. For example, silica, often present in alpha-alumina grinding media to improve the wear resistance, will increase the electrical resistivity of beta-alumina (13). Moreover, the addition of alpha-alumina itself to the beta-alumina by grinding media wear effectively decreases the sodium oxide concentration. If such contamination is sufficient to lead to a second phase on sintering, the ware will often crack during cooling to room temperature.

A more rational approach to the milling problem can be made from an understanding of the factors affecting the rate of grinding and the rate of media wear. Both were found to depend strongly on the nature of the powder undergoing grinding, the type of grinding, and the grinding media. The grinding rate is also markedly dependent on the size of the particles undergoing milling while the wear rate is also a sensitive function of the concentration of beta-alumina particles in suspension.

The fact that the milling rate of beta-alumina powder depends greatly on the method of preparation of that powder is illustrated with scanning electron micrographs shown in Fig. 5. Inspection indicates that calcined beta-alumina powder can be reduced to a smaller size in 4 hr of ballmilling than fused beta-alumina powder in 5 hr.

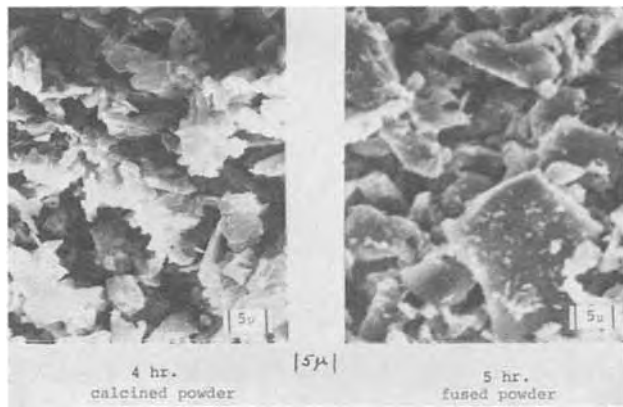


Fig. 5. Scanning electron micrographs of different powders, ball-milled with 91% Al_2O_3 .

The micrographs of Fig. 5 also illustrate the fact that ballmilling to about 10μ size can be accomplished in only a few hours. However, more protracted milling times are required to reduce the size to only a few microns. This fact is true for vibratory milling as well as for other media such as zirconia. On the other hand, the wear of the grinding media is nearly proportional to the milling time for both ball and vibratory milling. This is shown for vibratory milling with zirconia media in Fig. 6.

A comparison of micrographs also indicates the more rapid grinding achieved by vibratory milling. This fact is confirmed by data on the degree of sintering attained on ceramic that had been milled under different conditions as indicated in Table III. The density of completely sintered beta-alumina lies between 3.25 and 3.26 g/cm^3 . All the specimens, on which data are given in this table, were deposited electropherically in the form of closed-end tubes and subsequently sintered at 1800°C . Data are given for several specimens from suspensions similarly prepared in order to indicate the degree of reproducibility in the density and wear measurements. Examples are 5H3-5 and 5K1-2; 5G2-1 and 5H2-2; 5F3-3 and 5L1-1. Wear of the grinding media is expressed in Table III as a fraction of the amount of beta-alumina present in suspension.

An important point with regard to particle size is also brought out by data in this table. Specimens 5F3-3, 5F3-4, and 5F3-5 were the third, fourth, and fifth tubes deposited respectively from suspension 5F3.

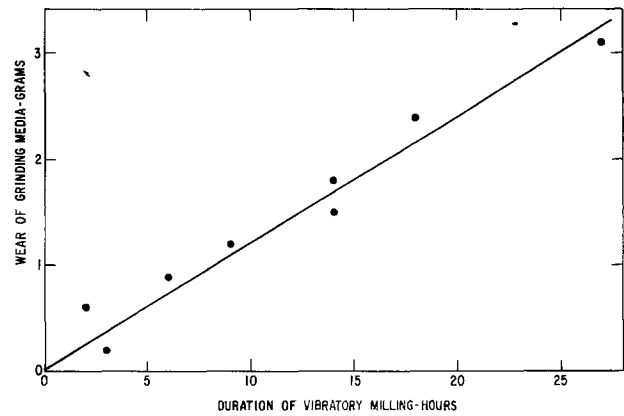


Fig. 6. Wear of 1800g 0.5 in. zirconia cylinders in vibratory milling 150g modified calcined powder suspended in 300 ml n-amy alcohol.

Neither in this series, nor in others, have systematic trends in sintered density been observed with the order in which tubes were deposited from a suspension. A trend should be observed if there was any substantial preferential deposition by particle size, as reported previously for alpha-alumina (6). Such a preferential deposition might also be indicated by differences in microstructure between the inner and outer walls of electropherically deposited, sintered tubes. This has never been observed.

Data in Table III also demonstrate the more rapid milling and lower wear rate of zirconia compared to alpha-alumina media. This fact is also brought out in Table IV in which wear data are collated for a number of different alpha-alumina media as well as for zirconia. Also shown is the need for some silica in alpha-alumina grinding media in order to keep wear at tolerable levels. Alumina balls containing 91% alumina were selected over other alumina media as the best compromise between wear rates and risk of contamination by silica.

Wear rates, unlike milling rates, depend rather strongly on the concentration of the suspensions as indicated on Fig. 7. The reduced rates with more concentrated beta-alumina suspensions should be noted. The advantages to milling more concentrated suspensions are really twofold. Not only is the absolute amount of wear product reduced, but in addition, it is diluted with a larger amount of beta-alumina. The

Table III. Optimum density of sintered beta-alumina for various milling conditions

Specimen designation	Suspension preparation	Milling conditions			Density (g/cm^3)	% wear of media	
		Type	Media	Time (hr)			
5H3-5	200g modified calcined powder + 0.25g aluminum stearate milled in 200 ml n-amy alcohol. After milling suspension diluted with 200 additional ml of vehicle.	Vibro	91% Al_2O_3 balls	24	3.184	1.4	
5K1-2	Same as 5H3-5	Vibro	91% Al_2O_3 balls	24	3.184	1.1	
5K2-4	Same as 5H3-5	Vibro	91% Al_2O_3 balls	48	3.226	3.2	
5K3-4	Same as 5H3-5	Vibro	91% Al_2O_3 balls	72	3.236	5.0	
5F2-1	150g modified calcined powder + 0.188g aluminum stearate milled in 300 ml n-amy alcohol.	Vibro	Zirconia cylinders	6	3.143	0.6	
5G2-1	Same as 5F2-1	Vibro		14	3.212	1.0	
5H2-2	Same as 5F2-1	Vibro		14	3.234	0.9	
5G1-3	Same as 5H3-5	Vibro		14	3.206	0.8	
5F3-3	Same as 5F2-1	Vibro		18	3.252	1.2	
5F3-4	This specimen deposited from same suspension as 5F3-3.	Vibro		18	3.231		
5F3-5	Same as 5F3-4	Vibro		18	3.250		
5L1-1	Same as 5F2-1	Vibro		18	3.243	1.2	
3R1-2	110g modified fused powder + 0.138g aluminum stearate milled in 200 ml n-amy alcohol.	Ball		91% Al_2O_3 balls	16	3.000	2.8
4P3-1	100g modified calcined powder + 0.125g aluminum stearate milled in 200 ml n-amy alcohol.	Ball		91% Al_2O_3 balls	12	3.087	2.0
5D3-2	Same as 5H3-5	Ball	ZrO_2 cylinders	63.5	3.175	1.4	

Table IV. Wear data for various grinding media

Data set A			
Wear of 1100g of media in ballgrinding 35g of fused powder in 200 ml n-amyl alcohol for 16 hr			
99.5%	alpha-alumina balls 3/8 in. diam., supplier A		43g
99.5%	alpha-alumina balls 1 cm diam., supplier B		18g
91%	alpha-alumina balls (6% SiO ₂) 1/2 in. diam.		10g
85%	alpha-alumina cylinders 1/2 in. x 1/2 in. (11% SiO ₂)		9g
Data set B			
Wear in ballgrinding 100g calcined powder in 200 ml n-amyl alcohol for 16 hr			
91%	alpha-alumina balls (1100g)		2.9g
ZrO ₂	Cylinders 1/2 in. x 1/2 in. (1800g)		0.9g

highest concentration milled was 200g of beta-alumina per 200 ml n-amyl alcohol. A "suspension" of this concentration behaves as a wetted solid prior to milling although it becomes fluid after several minutes of milling. It must be diluted to about 100g/200 ml after milling to avoid problems with viscous flow following electrophoretic deposition.

In the course of studying the effect of additives on wear of grinding media, aluminum tristearate was found to improve the smoothness of electrophoretic deposits. The effect is illustrated in the photograph shown in Fig. 8. The center tube was deposited from a suspension without aluminum stearate. Admittedly, the difference is more pronounced for deposits derived from fused powder than from calcined powder. The finding is of some importance. Wholly apart from appearance, a smooth surface on an electrophoretic deposit facilitates inspection for flaws such as cracks or holes.

Miscellaneous problems associated with deposition.—A mixture of topics falls within this heading including a discussion of the factors affecting the yield in electrophoretic deposition as well as practical methods for controlling the dimensions of ware, factors affecting the green density, and some specialized problems occurring with the forming of flatware.

Factors influencing yield.—Hamaker showed sometime ago that yield or amount of electrophoretic deposition is given by the expression

$$y = a \int \mu F C A dt$$

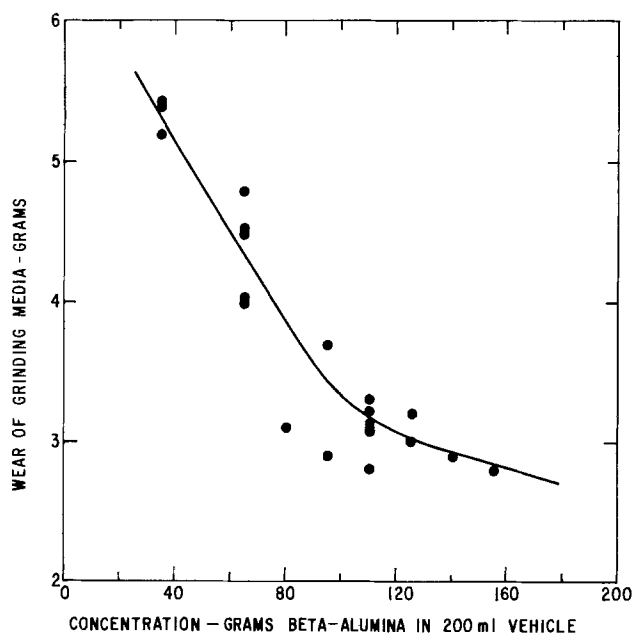


Fig. 7. Wear of 1100g 0.5 in. diameter 91% alumina balls in ballmilling various concentrations of modified fused powder for 16 hr.

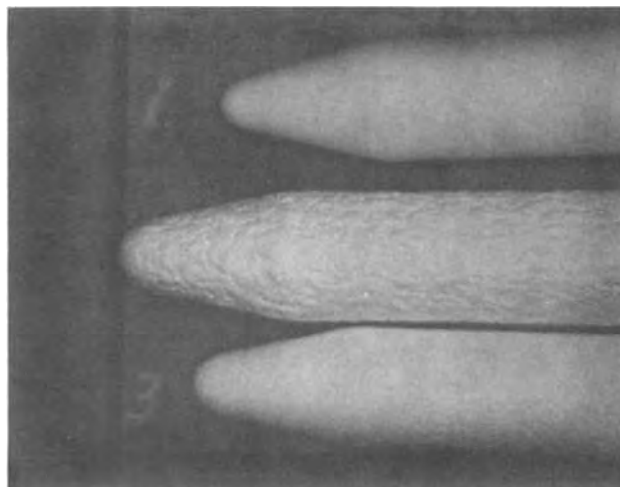


Fig. 8. The effect of aluminum stearate on the smoothness of beta-alumina deposits.

Here μ is the electrophoretic mobility, the velocity of a particle in a unit field of 1 V/cm; F is the electric field; C is the concentration of particles in grams per cubic centimeter; A is the electrode area; and t is the time (14). The coefficient, a , takes account of the possibility that not all particles which migrate to the electrode may deposit. Hamaker's expression has been confirmed by later work (15).

If a number of depositions are carried out successively from a suspension onto nearly identical mandrels for equal times at constant cell voltage, the yield, and correspondingly the wall thickness, decline because of the drop in concentration of beta-alumina. The simple technique used in this work to hold the thickness constant in successive depositions was to increase the time to maintain the product, Ct , invariant. Information on the measured masses of 18 closed-end tubes, six from each of three suspensions prepared in the same manner and deposited according to this scheme, is indicated in Table V below. It should be noted in these examples that over 80% of the beta-alumina had been deposited from the suspensions. However, there is usually noticeable degradation in the quality of deposits for more than about 70% depletion.

For deposition onto identical mandrels using the same fields and deposition times, the mass of the first deposit from a suspension is a good measure of the electrophoretic mobility of the suspended particles. The data presented in Table V are illustrative of beta-alumina powder containing 1% magnesia and 1% zirconia as additives. Vibratory milling of the suspensions had been carried out for 18 hr with zirconia grinding media. The deposit thickness was approximately 1.5 mm after sintering. Since the electrophoretic mobility

Table V. Variations in mass of electrophoretically deposited tubes

Depositions were carried out at 990V from suspension containing 100g calcined beta-alumina powder per 200 cm³ n-amyl alcohol

Suspension		a	b	c
Tube No.	Deposition time, sec	Mass, g	Mass, g	Mass, g
1	44	13.90	13.78	13.63
2	48	13.96	13.05	13.60
3	54	13.61	13.89	13.71
4	64	13.97	14.06	13.96
5	77	14.05	13.90	14.05
6	105	13.70	13.93	14.11
Average mass		13.87	13.77	13.84
Standard deviation		0.17	0.36	0.22
Standard deviation as % of mass		1.2	2.6	1.6

does depend somewhat on the powder composition as well as on the particle size, i.e., on the milling time, cell voltage and deposition times would require adjustment for powders of other compositions and particle sizes as well as for other deposit thicknesses.

Green density.—An important parameter affecting the degree of sintering is the density of ware in the green state. Two factors which exert a noticeable influence on the green density are the concentration of beta-alumina and the concentration of aluminum stearate. This is demonstrated in Fig. 9 where green densities are plotted as a function of the cell voltage. For both fused and calcined beta-alumina powder, there are clear indications of the advantage of using higher concentrations to obtain larger green densities. The densities achieved with calcined powder were slightly greater than with the fused starting material. Depositions are not usually carried out, however, with concentrations of beta-alumina powder much in excess of 100g/200 ml vehicle because of problems with viscous flow after deposition. Aluminum tristearate concentrations of 0.12%, based on the amount of beta-alumina, are normally used since this concentration is nearly as effective as larger ones in improving the smoothness of deposits. Furthermore, green densities obtained with this concentration are not much less than those obtained in the absence of aluminum stearate. Suspensions for which green density data are presented in Fig. 9 were milled with alpha-alumina media. Somewhat higher green densities, typically 1.74 g/cm³, are obtained with zirconia media, likely as a result of finer grinding.

Various deposit configurations.—The versatility of electrophoretic deposition as a forming technique for beta-alumina ceramic is illustrated in Fig. 10. Here are shown a number of items of green ware: closed-end tubes of different lengths, an open-end tube 6 in. long and 0.75 in. diameter, a 3 cm disk, and a pocket-shaped piece.

Some special problems with the forming of disks and other flat ware.—When electrophoretic deposition occurs on a polished disk mandrel, the thickness of the deposit is generally greater at the edge than at the center. For example, one green disk was only 1.04 mm thick at the center, but 1.40 mm near the edge. The variation in deposit thickness can be nearly eliminated by the use of an insulating Teflon polymer sleeve which fits around the edge of the mandrel, as shown in Fig. 2. The sleeve shapes the electric field and gives rise to a nearly uniform current density over the elec-

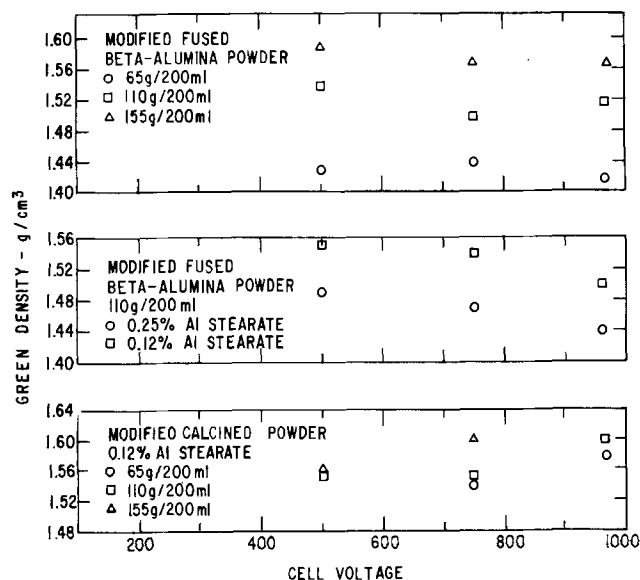


Fig. 9. Dependence of green density on cell voltage

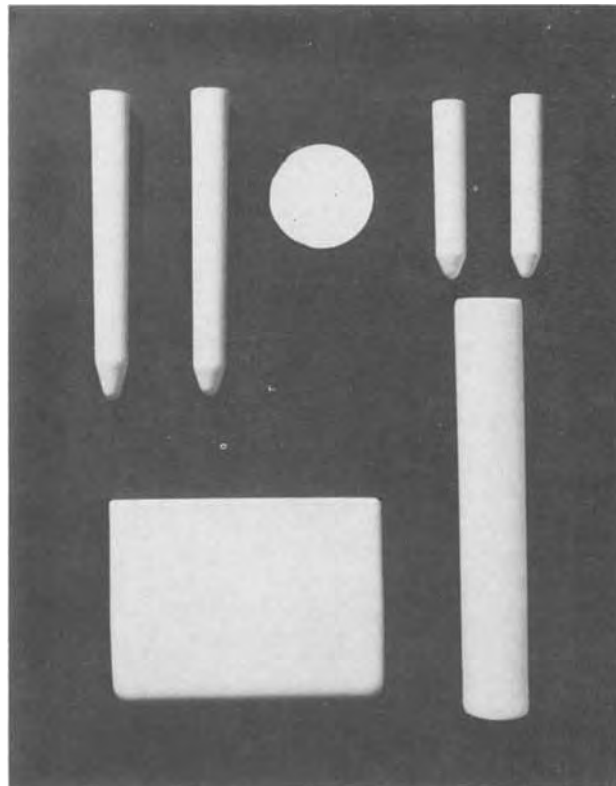


Fig. 10. Green ware formed by electrophoretic deposition

trode face. The fact underlying this design is that the current density over a disk will be uniform, regardless of the shape or position of the counterelectrode, if the insulating sleeve extends above the surface of the electrode a distance of at least the disk radius (16). A green disk formed using the Teflon polymer sleeve was 1.70 mm thick at the center and 1.72 mm at the edge. Beta-alumina disks, which are at least 1.5 mm thick, warp little during sintering.

Removal of electrophoretic deposits from mandrels.—The need for removal of deposits from mandrels after forming involves some problems not encountered in the use of electrophoretic deposition for coating purposes. These problems have been treated in very different ways in previous applications of electroforming. Andrews, Collins, Cornish, and Dracass removed alpha-alumina ogives from aluminum formers with a polyvinyl chloride sheath metallized on its outer surface and dusted with talc on its inner surface (6). This sheath covered the former during deposition and subsequently, deposit and sheath together were slid off the aluminum former. On the other hand, Lazennec, Fally, and Leboucq removed zirconia and beta-alumina closed-end tubes from aluminum mandrels after air-drying and isostatic pressing (7). The working hypothesis underlying the work described in this report was that satisfactory removal of deposits depends on the nearly complete elimination of vehicle from the deposit. This hypothesis originated from the commonplace observation that soil, mainly an aqueous suspension of aluminosilicates, adheres to smooth metal surfaces much less tenaciously when dry. Experience has indicated the need for only slight modifications in this hypothesis. Two kinds of problems are encountered in securing the satisfactory release of green beta-alumina deposits from mandrels: those related to sticking and those associated with cracking.

Release of green deposits in the form of closed-end tubes can usually be accomplished after drying overnight in air at room temperature. At most, 24 hr are needed. However, up to 3 days of drying may be required for the 3 mm thick deposits formed on larger

mandrels such as the one for forming pocket-shaped pieces. Despite careful drying, deposits from suspensions containing aluminum stearate in excess of about 0.25%, based on the amount of beta-alumina, often cannot be removed from mandrels in one piece. These findings raise the question whether the deposit adherence noted by previous groups may have been caused by the presence of binders in the deposit. Andrews, Collins, Cornish, and Dracass in their electroforming work with alpha-alumina used 0.5% dewaxed shellac in their preferred formulation while Lazennec, Fally, and Leboucq used up to 2% of a polycarbonate in their work with zirconia.

Comparison of present process with that developed previously.—It seems appropriate to conclude this discussion of the problems in the electrophoretic forming of beta-alumina ware with a brief comparison of the features of the process described in this paper with one described previously (7). This comparison is indicated in Table VI.

The Properties of Sintered Beta-Alumina Deposits

The properties of sintered beta-alumina depend on details associated with each of the three major fabrication steps, the preparation of starting powders, the forming of green ware, and finally, the sintering procedure. A brief description of this final operation used with beta-alumina green ware formed by electrophoretic deposition was given in a previous section of this paper. Only an indication of the range of properties that can be obtained will be given here.

When sintering is carried out at temperatures between 1700° and 1825°C for times ranging from a few minutes to a few hours in either an air or an oxygen atmosphere, densities ranging from 2.98 to 3.26 g/cm³ are obtained on single-phase material. These values correspond to residual closed porosity from 10 to less than 1%. Microstructures of three different specimens, all based on calcined starting powder, are shown on Fig. 11. A very coarse-grained structure from a specimen with a density of 3.15 g/cm³, appears in part A. The more or less rounded dark spots on the photomicrograph indicate pores while those with straight sides likely indicate the position of grains which were removed during mechanical polishing prior to etching in phosphoric acid. The micrograph for a specimen of high density (3.24 g/cm³) and small grain size is shown in part B while one, also of small grain size but with high porosity, is shown in part C. The density of this third specimen was only 2.98 g/cm³. While this specimen was not leak tight to helium, other specimens of this low density have been tight.

D-c specific resistivities as low as 105 ohm-cm and as high as 26,000 ohm-cm have been measured at room temperature. While a small grain size is desirable for mechanical strength and uniformity of current dis-

tribution, the lowest specific resistivities are usually observed with specimens of large grain size. Consequently, a compromise must be sought between these conflicting requirements. A more rational basis for this compromise is considered in another paper (17).

Summary

In this study, electrophoretic deposition was examined as a method for forming green beta-alumina ware. Ceramic articles are often fabricated in a three-step procedure: (i) the preparation of starting powders, (ii) the forming of such powder into a compact shape similar to that required in the final product, and (iii) the sintering of this green ware to reduce porosity and to develop other necessary properties. For beta-alumina, the second step of this sequence is difficult with conventional ceramic processing. Electrophoretic deposition offers the advantages of speed and versatility, making available a variety of shapes with a minimum of precision tooling. Deposits are essentially without a preferred orientation.

The electrophoretic forming operation in turn is also comprised of three main steps: (i) the preparation of a suitable suspension of powder dispersed in a vehicle, i.e., organic liquid; (ii) the deposition of the powder from the suspension onto a mandrel using an electric field; and (iii) removal of the green deposit from the mandrel. The first of these steps is crucial. Three major problem areas were identified with it: (i) the selection of a suitable vehicle in which to suspend the beta-alumina particles, (ii) control of the charge on these particles, and (iii) milling of the particles to effect a suitable charge and to produce the fine size required for high densification on sintering. Problems associated with the other two steps were of a more straightforward nature.

Selection of vehicle for dispersing beta-alumina particles.—With the predominant charging mode used in this study, satisfactory electrophoretic deposits are obtained only with vehicles with dielectric constants in the range 12-25. Most work has been carried out using n-amyl alcohol as the vehicle because its dielectric constant is 13.9 at 25°C. Furthermore, neither the formation of anodic films nor that of fluid deposits is a problem with it. This alcohol is available as reagent grade material from a number of manufacturers. Finally, this vehicle is relatively nontoxic.

Charge control of beta-alumina suspensions.—Two different competing charging modes are known for beta-alumina. Negative charging, the predominant mode used in this study, arises from dissociation of sodium ions from the particles. On the other hand, positively charged particles can be obtained by adsorption of protons from water or organic acids such as stearic or benzoic. Suitable charging is mainly a matter of controlling the water content of the suspension. A variety of phenomena have been encountered depending on this water concentration. These can be generally understood in terms of the Hamaker-Verwey theory of electrophoretic deposition.

Milling problem.—This problem comes about from the need to mill an exceedingly hard, abrasive substance to about 1 μ size particles with very little contamination of the suspension by the wear products of the grinding media. The preferred practice at this time involves: (i) the use of a more friable beta-alumina; (ii) the use of a very high powder concentration during milling, e.g., 100-200g beta-alumina in 200 ml. vehicle; (iii) vibratory milling being preferred over ballmilling because of its speed and the somewhat lower wear of the grinding media; (iv) zirconia media being used in preference to those of alpha-alumina. If slight contamination of the suspension by zirconia is intolerable, 91% alpha-alumina grinding balls are used. Smoother electrophoretic deposits are obtained

Table VI. Comparative features of present process and that developed previously

Feature	Previous work	This paper
Charging mode for particles	Proton adsorption	Dissociation of Na ⁺
Activator used	Benzoic acid	None
Charge on particles	Positive	Negative
Vehicle	CH ₃ NO ₂ /CHCl ₃ mixture	N-amyl alcohol
Binder	Diphenol polycarbonate	None
Cell voltage	300-500V	300-1000V
Hydrodynamic conditions during deposition	Mandrel rotated and suspension stirred	No stirring during deposition
Method used to remove deposits from mandrels	Drying followed by isostatic pressing	Drying

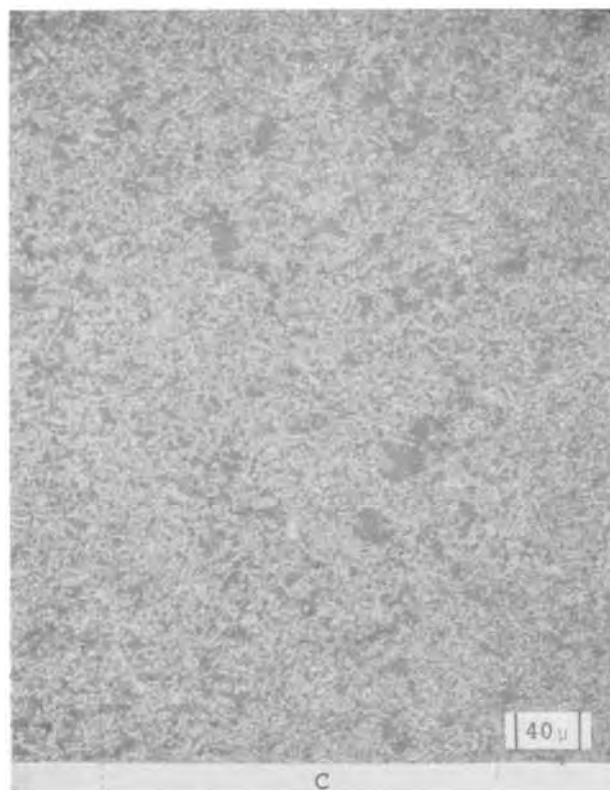
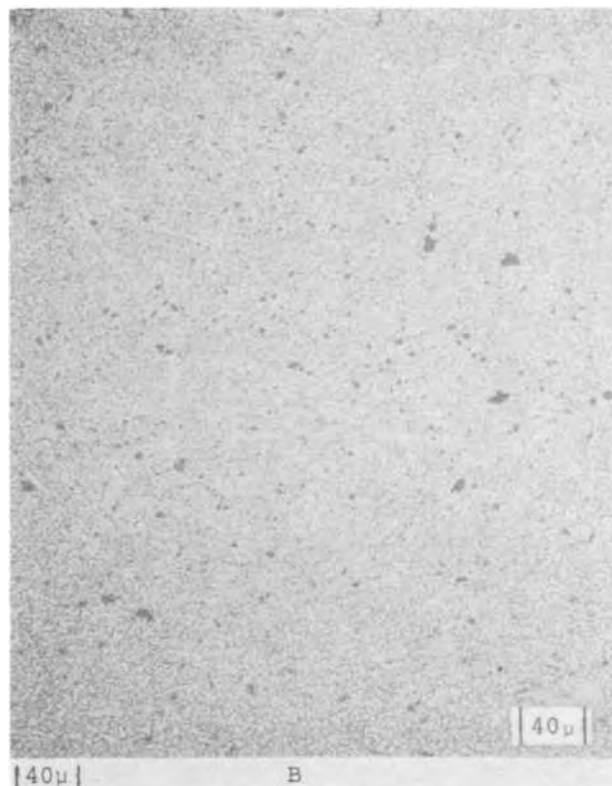
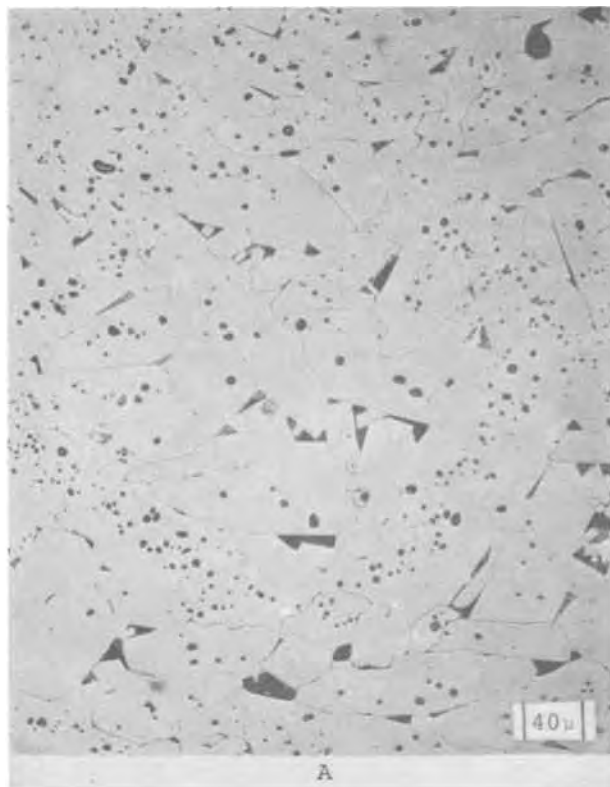


Fig. 11. Various microstructures observed with ware formed electrophoretically.

on milling with ca. 0.12% aluminum tristearate in the suspension.

Assorted problems with deposition.—More nearly constant ware thicknesses can be obtained on successive deposition from a suspension if the deposition time is extended to maintain the product of deposition time and beta-alumina concentration a constant. Green densities were found to increase with the beta-alumina concentration of the suspension and to decrease with the aluminum tristearate concentration. Disks of uniform thickness can be deposited electrophoretically

through the use of an insulating Teflon polymer ring fitting about the face of the disk-mandrel.

Removal of deposits from mandrels.—Deposits can be taken from slightly tapered mandrels after thorough removal of the vehicle either by air-drying or by accelerated drying in a vacuum oven.

A wide variety of properties can be obtained with electrophoretically deposited ware, depending mainly on the sintering conditions but also to some extent on the nature of the starting powders as well as on details concerned with the forming operation.

Acknowledgments

The author is indebted to many friends and colleagues for their numerous suggestions and help which greatly accelerated the progress of this study. He feels particularly indebted to S. P. Mitoff, R. A. Giddings, R. S. Owens, E. Szymalak, R. N. King, and C. R. Seaward. The scanning electron micrographs are the work of M. D. McConnell and M. F. Ciccarelli.

Manuscript submitted Aug. 12, 1974; revised manuscript received Nov. 18, 1974. This was Paper 50 presented at the New York, New York, Meeting of the Society, Oct. 13-17, 1974.

Any discussion of this paper will appear in a Discussion Section to be published in the December 1975 JOURNAL. All discussions for the December 1975 Discussion Section should be submitted by Aug. 1, 1975.

Publication costs of this article were partially assisted by the General Electric Company.

REFERENCES

1. N. Weber and J. T. Kummer, *Proc. Ann. Power Sources Conf.*, **21**, 37 (1967).
2. Y. Yao and J. T. Kummer, *J. Inorg. Nucl. Chem.*, **29**, 2453 (1967).
3. S. E. Sheppard, *Trans. Electrochem. Soc.*, **52**, 47 (1927).
4. J. H. DeBoer, H. C. Hamaker, and E. J. W. Verwey, *Rec. Trav. Chim.*, **58**, 662 (1939).
5. H. C. Hamaker and E. J. W. Verwey, *Trans. Faraday Soc.*, **36**, 180 (1940).
6. J. M. Andrews, A. H. Collins, D. C. Cornish, and J. Dracass, *Proc. Brit. Ceram. Soc.*, **12**, 211 (1969).
7. Y. Lazennec, J. Fally, and J. Leboucq, French Pat. Addition 95.549 (1971); Y. Lazennec and J. Fally, French Pat. 2.092.845 (1972); J. Fally, C. Lasne, Y. Lazennec, Y. LeCars, and P. Margotin, *This Journal*, **120**, 1296 (1973).
8. W. L. Roth and S. P. Mitoff, Private communication.
9. D. W. Fassett and Don D. Irish, Editors, "Industrial Hygiene and Toxicology," Interscience Publishers, New York (1963).
10. J. H. Kennedy and A. Foissy, Submitted to *This Journal*.
11. C. Kiefer, *Bull. Soc. Franc. Ceram.*, **2**, 24 (1949).
12. S. A. Troelstra, *Philips Tech. Rev.*, **12**, 293 (1951).
13. J. T. Kummer and N. Weber, U.S. Pat. 3,404,036 (1968).
14. H. C. Hamaker, *Trans. Faraday Soc.*, **36**, 279 (1940).
15. C. G. A. Hill, P. E. Lovering, and A. L. G. Rees, *ibid.*, **43**, 407 (1947).
16. R. W. Powers, *Electrochem. Technol.*, **5**, 429 (1967).
17. R. W. Powers and S. P. Mitoff, *This Journal*, **122**, 226 (1975).

A Method for Characterizing the Structure of Hydrophilic Porous Gas Diffusion Electrodes

Christer Morén

Department of Chemical Technology, Royal Institute of Technology, 100 44 Stockholm 70, Sweden

ABSTRACT

An apparatus, the dilactres cell, has been developed for determining structure parameters on operating porous gas diffusion electrodes. The experimental values of these parameters have been compared with the predictions of the thin-film model where all forms of polarization are present. The experimentally obtained polarization curves are within 15% of the computed ones for Ni-electrodes operating on air in 5M KOH at 50°C with Ag as catalyst.

Various models have been proposed for porous gas diffusion electrodes with different types of reactant and product transport as well as different liquid configurations.

The simple pore model was developed by Austin *et al.* (1), who proposed that reactant gas dissolves in the electrolyte and diffuses to the electrode surface near the three-phase boundary of solid-liquid-gas. The simple pore model has also been studied by Srinivasan, Hurwitz, and Bockris (2).

The thin-film model was postulated by Will (3, 4). Will studied the mechanism of ionization of molecular hydrogen on partially immersed Pt electrodes in acidic solutions. He experimentally proved the existence of an electrochemically active electrolyte film. The effects of activation control were neglected and an arbitrary film thickness parameter was utilized for calculating the current. Austin (5) and Lindström (6) postulated that the walls of the gas filled pores in a gas diffusion electrode are covered by a thin electrolyte film.

Grens *et al.* (7) as well as Bennion and Tobias (8, 9) took into account the activation polarization in their calculations. Iczkowski (10) formulated an electrolyte film mechanism for a hydrogen gas diffusion electrode. Rockett and Brown (11) made a theoretical analysis of a single pore coated with a thin film of electrolyte

and compared it with data from nickel electrodes operating on oxygen in 80% KOH. Numerical calculations were carried out by Srinivasan and Hurwitz (12) for a thin-film model in the case where all forms of polarization are present, varying the kinetic and physical parameters. Lindström (13) and Lindholm *et al.* (14) correlated the electrochemical activity with the electrolyte film resistance.

A meniscus model was introduced by Bockris and Cahan (15) who observed a meniscus with a finite contact angle on Pt electrodes in H₂SO₄.

Pshenichnikov (16) considered wide film-covered pores, the walls of which were penetrated by electrolyte filled micropores.

Katan and Grens II (17) studied the influence of differential pressure on electrode activity for oxygen cathodes made up of beds of uniform silver spheres. The extent and nature of this dependence they explained through use of the concept of pendular and funicular liquid configuration in the pore space of the electrode.

The statistical concept of porous structure was adapted by Markin *et al.* (18) as well as by Micka (19-21), who considered a macrohomogeneous system on which he applied a statistical model based on the assumption that the electrode reaction proceeds on active centers, distributed statistically in a large number over the entire volume of the operating layer.

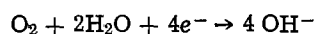
Key words: porous gas electrodes, hydrophilic, tortuosity, film resistance, differential pressure.

According to the film model the walls in the gas filled pores are covered by a thin electrolyte film. The reaction gas diffuses to the electrode surface and reacts there so that electrons are transferred from, or to, the electrode. In addition ionic current transport must proceed along these films.

Mass transport is often the primary cause of polarization in air and oxygen cathodes. This polarization can be attributed to one or more of the transport steps: diffusion of oxygen molecules in the gas phase, diffusion of oxygen molecules in the liquid phase, diffusion or migration of hydroxyl ions in the liquid, and diffusion of water in the liquid phase.

Lindström (13) characterized the electrochemical structure with the aid of certain parameters, mainly the pore size distribution, film area, film perimeter, film thickness, interstice tortuosity, and film tortuosity. He determined these parameters on single porosity gas electrodes. The measurements were performed in separate stages with different sets of apparatus. The dilatometry measurements were not performed with the electrodes operating as cathodes. According to the film resistance measurements he had to provide the coarse pore layer with a fine pore layer on both sides, with the gas being supplied to a ring arranged around the periphery. The principal disadvantages of these methods are that the physical measurements are carried out separately while there is no current flow.

Most theoretical treatments assume that the concentration of electrolyte is constant in the liquid films in porous electrodes. In oxygen and air electrodes there is always a concentration of the electrolyte in the films due to water removal and formation of hydroxyl ions on account of the reaction



The concentration of electrolyte is counteracted by diffusion of water in the gas phase as well as in the liquid, but the water vapor transport is counteracted by convective diffusion of oxygen in the gas phase toward the electrolyte side.

Lindholm (23) investigated the dilution of electrolyte with increasing current density for hydrogen electrodes. For oxygen electrodes Micka (24) calculated the concentration of KOH in the pores according to the model of porous electrodes of second order. His calculations were based on approximate solutions yielding rather high concentrations which attained saturation. In another paper (25) he used more exact transport equations resulting in lower concentration gradients.

The purpose of this paper was to determine certain structure parameters and their influence on the behavior of operating air cathodes, *i.e.* with current flow. For this purpose a special apparatus was developed, the so-called dilactres cell, which stands for: DILatometry, ACTivity, and film RESistance. In the dilatometry measurements, the penetration of gas into the electrode at varying differential pressures was investigated. From these data, the film area and film thickness were calculated. The activity measurements gave the polarization curve. In the film resistance measurements, the voltage drop in the electrolyte film was measured, when an ionic current was forced through the film network. After necessary corrections the effective specific resistance (ohm-cm) in the film was obtained, based on the current per unit cross-sectional area of the electrode. This film resistance is a very important factor since together with the current distribution in the pore, it determines the ohmic potential drop in the electrolyte film. Even the film tortuosity was calculated from the resistance values.

The experimental polarization curves have been compared with the predictions of the thin-film model, as proposed by Srinivasan and Hurwitz (12).

General Experimental Arrangement

The apparatus consisted of the dilactres cell, air pressure and flow regulation equipment, and monitor-

ing instrumentation. The arrangement is shown in Fig. 1-3. Figure 1 is a schematic diagram of the apparatus with electrical connections. The probe is pulled out to make the drawing clearer. Figure 2 shows the electrical circuits. In Fig. 3 the relations between the probe, working electrode, and reference electrodes during film resistance measurements are shown.

Dilactres cell.—The dilactres cell consisted of a turned out block of polymethylmethacrylate, PMMA. The working and counterelectrodes were kept at a fixed distance by means of a distance element, made from PMMA, so that a definite volume of electrolyte was kept between the electrodes. At the top of the cell a riser, consisting of a thin calibrated glass tube equipped with a movable graduated scale, was inserted for dilatometry measurements. A canal was milled around the electrolyte compartment and con-

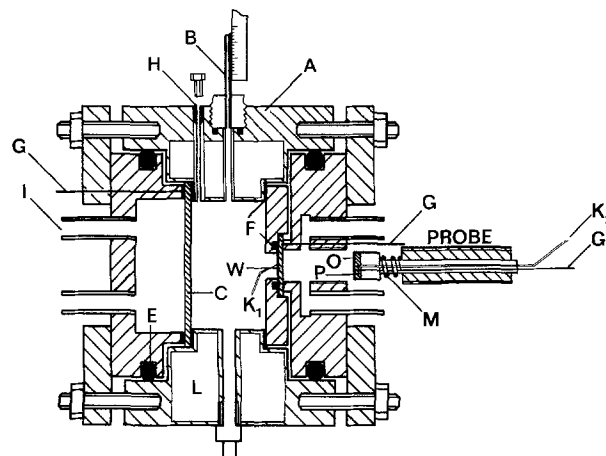


Fig. 1. Schematic diagram of the dilactres cell. A, Main body; B, electrolyte riser; C, counterelectrode; E, O-rings; F, gaskets; G, current collectors; H, venthole; I, gas inlets and outlets; K, reference electrode capillaries; L, thermostated water; M, spring; O, separator; P, probe electrode; W, working electrode.

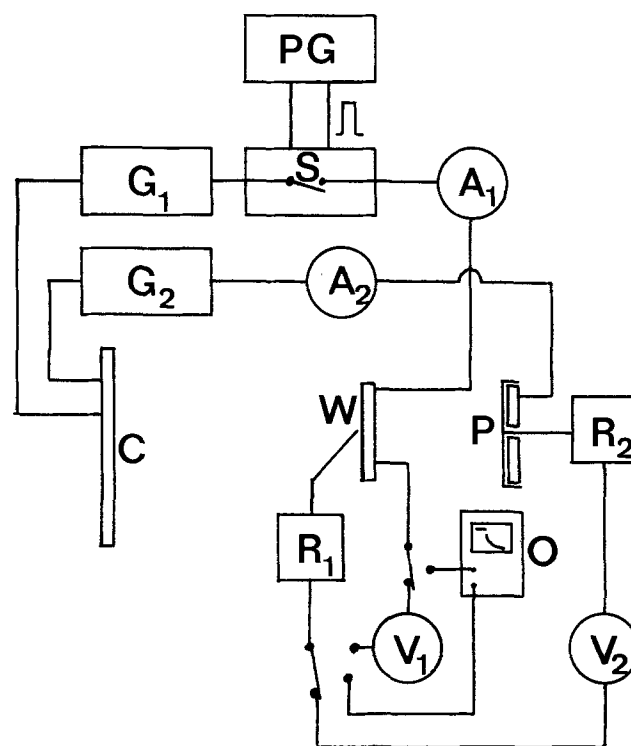


Fig. 2. Diagram of the electrical circuits. A, Ammeters; C, counterelectrode; G, galvanostats; O, oscilloscope; P, probe electrode; PG, pulse generator; R, reference electrodes; S, electronic switch; V, digital voltmeters; W, working electrode.

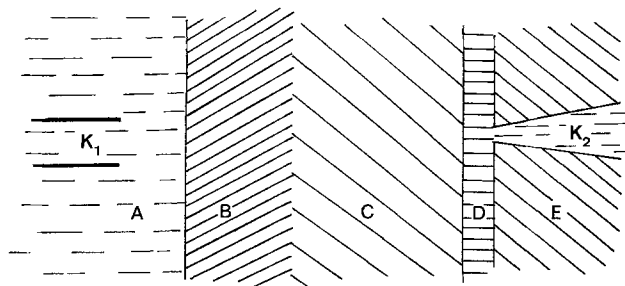


Fig. 3. Relations between the probe, working electrode, and reference electrodes during film resistance measurements. A, Bulk electrolyte; B, fine pore layer of the working electrode; C, coarse pore layer of the working electrode; D, separator; E, probe electrode; K, reference electrode capillaries.

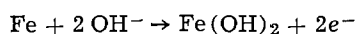
ected to a thermostat controlled waterbath. The whole cell assembly was inserted into a temperature controlled air bath. A thermocouple was placed inside the cell in the electrolyte to check the settings of the temperature regulators, and data collection was never started until the bulk electrolyte attained 50°C to assure temperature equilibrium.

Working and counterelectrodes.—The working electrodes, called A, B, and C, respectively, were hydrophilic double layer gas diffusion electrodes. From each type of electrode, A, B, and C, three 20.5 × 11.7 cm electrodes were manufactured. From each of these plates two electrodes were punched with external surface areas, exposed to the electrolyte, of 16 cm² and 1 cm², respectively, so that a total of 18 electrodes were investigated. Three large electrodes were chosen in order to study the structure homogeneity from plate to plate and two smaller sizes were investigated in order to check a possible bulging of the electrode, when the differential pressure was applied. It was also a check on the functioning of the distance element.

The fine pore layers were identical for the three electrode types and consisted of a 0.029 cm thick sintered Ni-layer with a porosity of 0.43 and a mean pore radius, r_{mf} , of 1.15×10^{-4} cm. The fine pore layers contained no catalyst. The coarse pore layer of electrode A was a sintered Ni-layer with a porosity, U , of 0.74 and a thickness, L , of 0.051 cm. The mean coarse pore radius, r_2 , was 5.84×10^{-4} cm. Electrode B was a compressed version of electrode A with a porosity of 0.63 and L equaling 0.034 cm. r_2 was 2.11×10^{-4} cm. Electrode C was identical to A except for the coarse pore layer thickness which was 0.068 cm. The silver catalyst content in the coarse pore layers was 9.3% by weight.

L was determined on electrode cross sections in a scanning electron microscope. r_2 and r_{mf} have been defined as the pore radii, when half the fraction of the electrode void volume was displaced by Hg in the Hg-porosimeter. The porosity was determined both by Hg-porosimetry and by weighing electrodes manufactured without fine pore layers.

Counterelectrodes identical to the working electrode were not possible to use during the dilatometry measurements, because anodic gas evolution would arise when the electrodes were loaded. Because of this difficulty a porous Fe-electrode was chosen as counterelectrode. The thickness and external surface area were 0.26 cm and 16 cm², respectively. It was discharged according to



Reference electrodes.—The capillary K_1 in Fig. 1 was inserted through the wall of the cell and connected to a Hg/HgO reference electrode kept at 50°C in the thermostated air bath. The tip of the Luggin capillary was placed in the bulk electrolyte about 0.5 mm from the working electrode. The very fine capillary K_2 in Fig. 1 was inserted through the probe, see

below, to the outer surface of the probe electrode and connected to another Hg/HgO reference electrode in the air bath. The electrolyte in the latter reference electrode could be forced out into the capillary, when the probe was withdrawn from the working electrode surface, by means of an applied N₂-pressure.

Pressure and flow regulation.—The air was obtained from the laboratory air system. It passed through an oil filter and was dried with Mg(ClO₄)₂ before use.

The air pressure was kept constant at the gas side of the working electrode by means of a precision reducing valve from Drägerwerk Lübeck. The pressure was measured with a mercury manometer. The differential pressure read on the manometer was corrected with the electrolyte column pressure in the dilatometry riser.

A nitrogen differential pressure of 40.9 cm of H₂O was applied to the counterelectrode in order to avoid electrolyte leakage out into the gas room. It was necessary to apply this pressure merely because the electrode holder was designed to accept gas diffusion electrodes as counterelectrodes.

Electrolyte.—Five molar KOH at 50°C was used as bulk electrolyte throughout the whole investigation. It was prepared as 5.06M KOH at 20°C from reagent grade KOH-pellets and distilled water.

Experimental Procedure

Dilatometry measurements.—These were performed in order to determine the electrolyte film area and the film thickness. The circuit, as shown in Fig. 1, was used to measure the penetration of gas into the working electrodes at varying differential pressures. The amount of expelled electrolyte was read off to the nearest half-scale division on the riser, which corresponds to 2.7×10^{-3} cm³ of liquid for the large riser used with the 16 cm² electrodes and 5.9×10^{-4} cm³ of liquid for the small riser used with the 1 cm² electrodes.

In order to investigate the influence from the counterelectrode discharge on the dilatometry measurements, the 16 cm² counterelectrode was discharged together with both 1 and 16 cm² air electrodes during a time equaling the dilatometry test time. The cathodic current density was varied between 0 and 0.2 A/cm² and the differential air pressure was kept constant at P_{max} . The volume change by time in the riser was measured as a function of current density on the cathode. For low current densities, any change of the electrolyte height in the riser was not observed. For higher current densities a very slow continuous rise of the electrolyte was noticeable. For a cathodic current density of 0.2 A/cm² the rising speed, on an average for the three electrode types, amounted to 1.1×10^{-2} cm³/5 min (2 scale divisions/5 min) for the 16 cm² cathodes and 3.0×10^{-4} cm³/5 min (0.5 scale divisions/5 min) for the 1 cm² cathodes. This very slow rising, which corresponds to density differences between Fe and Fe(OH)₂, removal of H₂O from the electrolyte due to cathodic reaction, removal of H₂O by the gas stream, and a possible temperature increase were easily separated from the rapid rise, when the air pressure was changed in the dilatometry measurements.

During the dilatometry measurements the differential air pressure was increased stepwise up to a pressure, P_{max} , where no further penetration of gas was observed.

With the aid of the equations derived below it is possible to calculate the film area and the mean film thickness from the dilatometry measurements. The equations are essentially based on the model for the interstice network as introduced by Lindström (13). An increase of dP for a differential pressure, P , results in a further gas penetration, dW , corresponding to a cross section with an area equal to $dW/L \cdot s$ and the film perimeter dN . If the contact angle is denoted

θ and the surface tension σ , the balance between the capillary force and the differential pressure can be expressed by

$$dN \cdot \sigma \cdot \cos \theta = P \cdot \frac{dW}{L \cdot s} \quad [1]$$

where L is the thickness of the coarse pore layer and s is the interstice tortuosity, see Eq. [6] below. Lindström used L instead of $L \cdot s$ in Eq. [1], but the use of the latter quantity seems more plausible. Dilatometry experiments give $W = f(P)$ from which

$$dW = f'(P) dP \quad [2]$$

Combining Eq. [1] and [2] gives

$$dN \cdot \sigma \cdot \cos \theta = P \cdot f'(P) \cdot \frac{dP}{L \cdot s} \quad [3]$$

Integration gives

$$N \cdot L \cdot s = \frac{1}{\sigma \cdot \cos \theta} \int_0^P P \cdot f'(P) dP \quad [4]$$

The contact angle was supposed to be zero degrees. The surface tension was calculated from literature data (22) given at 25°C. The temperature coefficient was supposed to equal the temperature coefficient for pure water. Neglecting the pressure influence, σ was found to be 8.48×10^{-2} cm of H₂O·cm (= 83 dyne/cm) at 50°C for 5M KOH.

The film area A^* was calculated as

$$A^* = N \cdot L \cdot s / a \quad [5]$$

where a is the external electrode area. A^* equals the film area per unit of external electrode area (cm²/cm²). The mean film thickness FT was calculated as the volume of the electrolyte film at P_{\max} divided by the total film area. Figure 4 shows $A^* = f(P)$ and in Table II the A^* values at P_{\max} are tabulated.

Activity measurements.—The cell permitted measurements of the electrode activity, i.e., recording polarization curves. For this purpose current was supplied from a Wenking Potentiostat, operated galvanostatically, and measured with an Unigor 1P ammeter. The working electrode potential vs. the Hg/HgO reference electrode was measured with a digital multimeter MN-124 from Schneider Electronique. The IR drop between the tip of the reference capillary and the electrode surface was recorded on an SS-5157 Synchroscope oscilloscope, when the current was interrupted. A rapid electronic switch was built at our laboratory for this purpose. It was triggered by a pulse generator

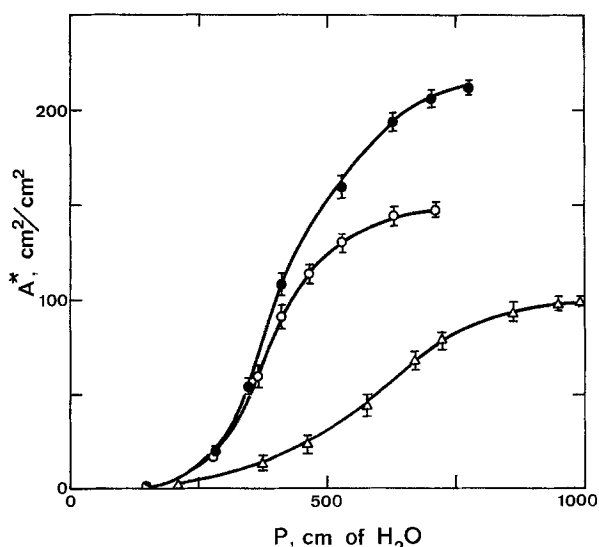


Fig. 4. Electrolyte film area as a function of the differential air pressure at 50°C. ○, electrode A; △, electrode B; ●, electrode C.

PG 56 from Advance Instruments. All polarization curves were corrected for this IR drop, which never exceeded 2% of the total polarization.

Before recording the polarization curves the electrodes were activated during 10 cycles with a constant current density of 0.025 A/cm² at a differential air pressure of 410 cm of H₂O. Each cycle consisted of 2 hr of oxidation plus 1 hr of reduction.

The potential vs. Hg/HgO as a function of the differential air pressure was determined stepwise from 40 cm of H₂O to P_{\max} for a constant current density of 0.025 A/cm², see Fig. 5. Polarization curves were determined in the current density range 0–0.2 A/cm², see Fig. 6.

The electrode homogeneity was confirmed with the activity measurements, in that, no significant activity differences existed between the large and small electrodes.

Film resistance measurements.—To get an idea of the ion transport along the electrolyte film, the film resistance, Z' , see below, was measured. Together with the current distribution the film resistance determines the ohmic potential drop in the film. The interstice and film tortuosities were also determined. The interstice tortuosity, s , is the effective tortuous length for the current to traverse through the coarse pore layer when this layer is completely soaked with electrolyte divided by the coarse pore layer thickness. In the same way the film tortuosity, f , is the effective tortuous length for the current to traverse through the film network in the coarse pore layer divided by the coarse pore layer thickness. The expression for the interstice tortuosity is derived in the following manner. If an electric current flows through an electrolyte path of uniform cross section, the resistance of the path is given by

$$R' = \frac{e \cdot L'}{a'} \quad [7]$$

where e = the electrolyte resistivity (ohm-cm); L' = the length of the electrolyte path (cm); and a' = the cross sectional area of the electrolyte path (cm²).

If the electrolyte resistance is measured through a completely drowned porous body with a thickness L'' and an outer surface cross-sectional area of a' , the resistance will be higher than was R' , the resistance of the electrolyte alone since (i) the mean length of path traversed by the current is longer and (ii) the cross-sectional area which is available to current flow is smaller. Let the effective tortuous length through the porous body traversed by the current by L'' , and the apparent cross-sectional area of the electrolyte saturated porous body, available to current flow be a'' , then

$$R'' = \frac{e \cdot L''}{a''} \quad [8]$$

Dividing Eq. [8] by [7]

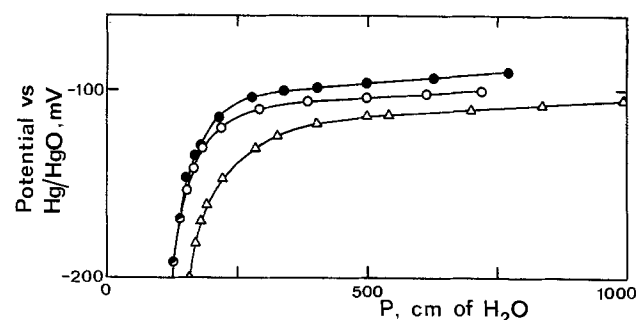


Fig. 5. Potential of the working electrode vs. Hg/HgO as a function of the differential air pressure at a constant current density of 0.025 A/cm² at 50°C. ○, Electrode A; △, electrode B; ●, electrode C.

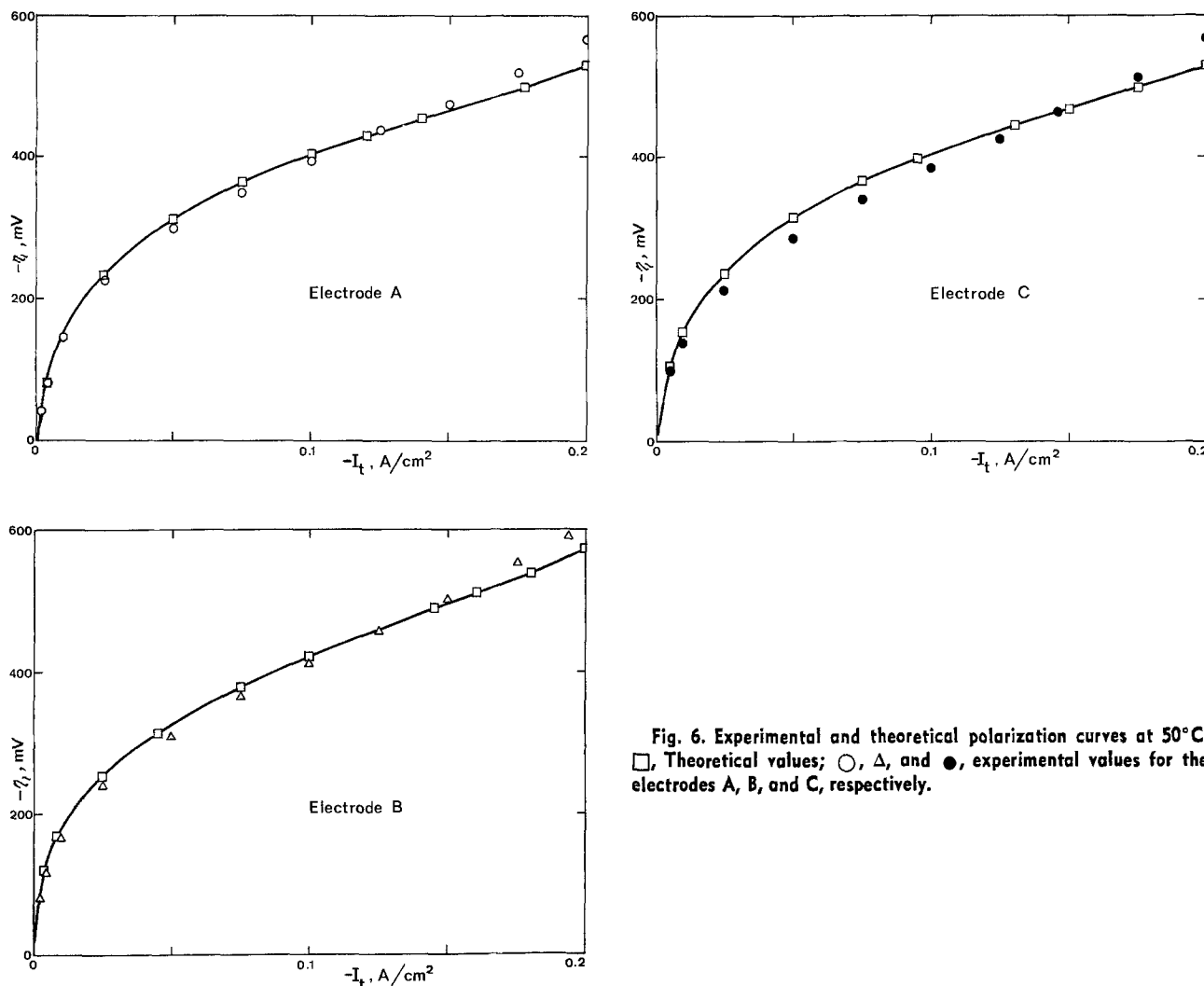


Fig. 6. Experimental and theoretical polarization curves at 50°C. □, Theoretical values; ○, △, and ●, experimental values for the electrodes A, B, and C, respectively.

$$\frac{R''}{R'} = \frac{L''/L'}{a''/a'} \quad [9]$$

The ratio L''/L' is defined as the interstice tortuosity s . The ratio a''/a' may be designated as τ . If the resistivity factor R''/R' is called G , substituting in Eq. [9] gives

$$G = s/\tau \quad [10]$$

If $s \cdot \tau = U$, where U is the porosity, then substitution in Eq. [10] gives

$$G = s^2/U \text{ or } s = \left(\frac{Z^0}{e} \cdot U \right)^{1/2} \quad [11]$$

where

$$G = Z^0/e \text{ and } Z^0 = \frac{\Delta V_s}{I \cdot L} \text{ (ohm-cm)} \quad [12]$$

ΔV_s = potential drop in the liquid, filling the coarse layer, with corrections made for the potential drop in the separator, fine pore layer (see below), and the IR drop in the bulk electrolyte from the electrode surface to the Luggin capillary tip, (V); I = probe current density (A/cm^2); L = thickness of the coarse pore layer (cm).

The film tortuosity factor is calculated in an analogous way as

$$f = \left(\frac{Z'}{e} \cdot \frac{FT \cdot A^*}{L} \right)^{1/2} \quad [13]$$

where the effective specific film resistance is

$$Z' = \frac{\Delta V_f}{I \cdot L} \text{ (ohm-cm)} \quad [14]$$

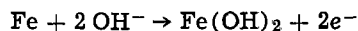
ΔV_f is measured in the same way as ΔV_s , but P equals the maximum differential pressure P_{max} .

U in Eq. [11] is the fraction of the coarse pore layer volume occupied by electrolyte, when the electrode is completely soaked.

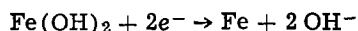
$\frac{FT \cdot A^*}{L}$ in Eq. [13] is the fraction of the coarse

pore layer volume occupied by the electrolyte film at P_{max} . The film resistance measurements were carried out by means of a special probe, see Fig. 1-3. The main probe body was made of PMMA. A porous iron electrode with current collector was attached to the front of the probe. The diameter of the hole in the tip of the probe reference capillary (see above) was less than 0.1 mm in order to diminish as far as possible the influence from the capillary on the current distribution in the vicinity of the tip. The probe reference electrode (K_2 in Fig. 1) was connected to the reference electrode (K_1) in the bulk electrolyte via a digital voltmeter from Schneider Electronique. To avoid electronic contact between the probe and the working electrode, a microporous separator, Dynel Acropor WA, covered the probe electrode surface. Before use the probe electrode was soaked with KOH and oxidized for 3 hr with a current corresponding to 70% of the useful capacity. When the film resistance measurements were performed the probe was pressed against the gas side of the working electrode and current was allowed to pass between the probe electrode and the counterelectrode. The probe current density was $0.015 A/cm^2$ and the potential drop between K_1 and K_2 was measured. After the necessary corrections, see below, for the potential drop in the separator, fine pore layer, and bulk electrolyte between K_1 and the working electrode surface,

the film resistance was calculated according to Eq. [14]. Because of the low exchange current density for the oxygen reduction on the working electrode, the resistance of the electrolyte film is much less than the resistance of the charge-transfer reaction so that no electrode reaction occurs in the working electrode due to current flow between the probe and the counter-electrode, *i.e.*, only ionic current flows through the working electrode. During the film resistance measurements the counterelectrode reaction was



and the probe reaction was



For low differential air pressures the probe disturbed the activity of the working electrode, but this disturbance was eliminated with increasing pressure and was below 1% for $P = 410$ cm of H_2O and not detectable at P_{max} . For differential pressures less than P_{max} the gas filled pores were shunted with soaked pores, *i.e.*, the measured apparent film resistance was a pure film resistance only for $P = P_{\text{max}}$. The working electrode current density was varied between 0 and 0.05 A/cm^2 during the film resistance measurements with no significant change of the Z' values. Neither was any change observed when the probe size was changed from 0.33 to 1.00 cm^2 .

Corrections for the voltage drop in the fine pore layer of the working electrode and in the electrolyte filling the separator were made in the following way. Three electrodes of different thicknesses solely consisting of fine pore layers without any catalyst were prepared and tested with a probe current density of 0.015 A/cm^2 , see Table III. The potential drop in the electrolyte filling the fine pore layer was not changed when P was increased up to P_{max} . This potential drop is supposed to be a linear function of the electrode thickness. This leads to finding the least squares solution of an overdetermined system of three linear equations

$$\begin{aligned} \Delta V_1 + 0.051 \cdot \Delta V_2 &= 5.3 \\ \Delta V_1 + 0.073 \cdot \Delta V_2 &= 6.9 \\ \Delta V_1 + 0.087 \cdot \Delta V_2 &= 7.95 \end{aligned}$$

ΔV_1 = the potential drop in the probe separator (mV) and ΔV_2 = the potential drop/cm of the fine pore electrode thickness (mV/cm).

The equation system above is rewritten as

$$\begin{aligned} \Delta V_1 + 0.051 \cdot \Delta V_2 - 5.3 &= r_1 \\ \Delta V_1 + 0.073 \cdot \Delta V_2 - 6.9 &= r_2 \\ \Delta V_1 + 0.087 \cdot \Delta V_2 - 7.95 &= r_3 \end{aligned}$$

Minimizing $(r_1^2 + r_2^2 + r_3^2)$ gives the solution

$$\begin{aligned} \Delta V_1 &= 1.54 \text{ mV} \\ \Delta V_2 &= 73.61 \text{ mV/cm} \end{aligned}$$

with a root-mean-square error of 9.16×10^{-3} . This leads to a potential drop of 3.7 mV in the 0.029 cm thick working electrode fine layer plus probe separator. Figure 7 shows the apparent film resistance as a function of the differential air pressure and Table II shows s and f for the three electrodes A, B, and C.

Theoretical Model

The experimental results have been compared with the thin-film model according to Srinivasan and Hurwitz (11) where all forms of polarization are present.

The basic assumption in the thin-film model is that a thin film of liquid is spread over and in contact with the solid phase in the pore (Fig. 8). It is assumed that the thickness of the film is constant along the pore and small compared with the radius of the pore. It is further assumed that all the current is generated on the electrode surface in the film region.

A reaction sequence of the following type is assumed for this model: (i) diffusion of the reactant

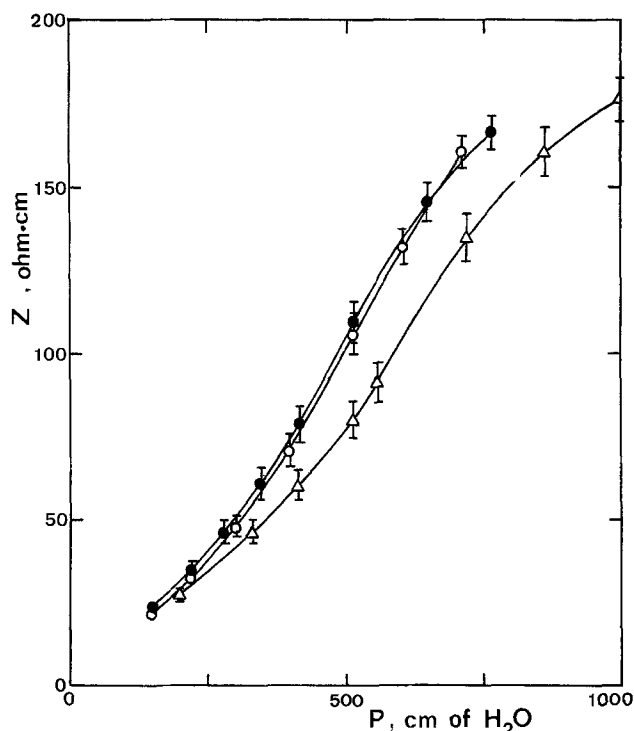


Fig. 7. The apparent film resistance as a function of the differential air pressure at 50°C . \circ , Electrode A; Δ , electrode B; \bullet , electrode C.

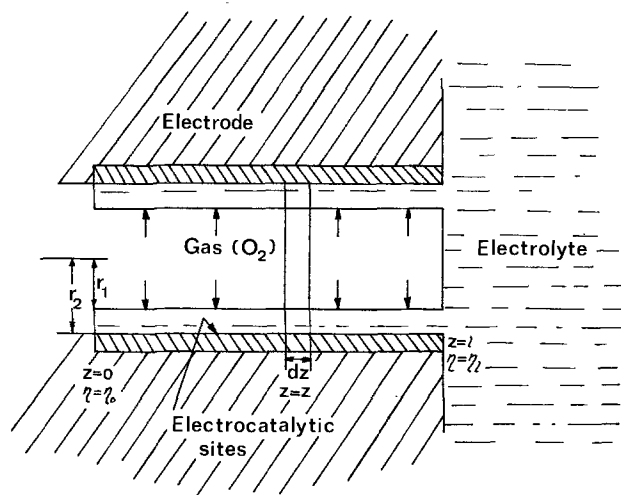


Fig. 8. Schematic representation of a single pore of a porous gas diffusion electrode using the thin-film model. Thickness of film is largely exaggerated.

gas from the outer end of the porous electrode to the gas/electrolyte interface; (ii) dissolution of reactant gas in the electrolyte at the gas/electrolyte interface; (iii) radial diffusion of the dissolved gas through the electrolyte film; (iv) electroadsorption of dissolved reactant gas at the electrode $(\text{O}_2)_{\text{ads}}$; (v) charge-transfer reaction of $(\text{O}_2)_{\text{ads}}$ to give $(\text{O}_2^-)_{\text{ads}}$; (vi) charge-transfer reaction of $(\text{O}_2^-)_{\text{ads}}$ to give products; (vii) diffusion of products away from the electrode and migration of ions through the film.

It is assumed that step (v) is the activation controlling intermediate step at the electrode.

The rate of the electrode reaction in an element dz of the electrode is given by

$$di = 2\pi r_2 dz i_0 \left[\exp\left(\frac{\eta F}{2RT}\right) - \frac{C}{C_0} \exp\left(-\frac{\eta F}{2RT}\right) \right] \quad [15]$$

Table I. Physical parameters determined before the dilactres measurements were performed

Electrode type	$L \times 10^2$, cm	$r_2 \times 10^4$, cm	$r_{mf} \times 10^4$, cm	Porosity U
A	5.1	5.84	1.15	0.74
B	3.4	2.11	1.15	0.63
C	6.8	5.85	1.15	0.74

where i_0 is the exchange current density (current/internal surface area) of the electrode reaction when the concentration of the reactant at the electrode is C_0 . The current i is cathodic, hence $i < 0$ and $\eta < 0$. η is the sum of activation and concentration overpotentials. The symmetry factor is assumed to be $\frac{1}{2}$. The average potential drop in the element, dz , is expressed by

$$d\eta = i \frac{dz}{\kappa\pi(r_2^2 - r_1^2)} \quad [16]$$

where κ is the specific conductivity of the electrolyte ($\kappa = 1/e$). In order to ascertain the concentration C at the electrode surface in the steady state, Srinivasan and Hurwitz assumed that the reactant gas has a flux only in the r direction and that the reactant is only consumed at the electrode surface

$$di = 2\pi r dz DnF \left(\frac{\partial C}{\partial r} \right) \quad [17]$$

Integrating Eq. [17] using the boundary condition that at

$$r = r_1 \quad C = C_0 \quad [18]$$

gives

$$C = C_0 - \frac{1}{2\pi DnF} \left(\frac{di}{dz} \right) \ln \left(\frac{r_1}{r_2} \right) \quad [19]$$

Using Eq. [19] in Eq. [15]

$$\frac{di}{dz} = 2\pi r_2 i_0 \left[\exp \left(\frac{\eta F}{2RT} \right) - \left\{ 1 - \frac{1}{2\pi DnFC_0} \left(\frac{di}{dz} \right) \ln \left(\frac{r_1}{r_2} \right) \right\} \exp \left(-\frac{\eta F}{2RT} \right) \right] \quad [20]$$

Rearranging Eq. [20]

$$\frac{di}{dz} = \frac{4\pi r_2 i_0 \sinh \left(\frac{\eta F}{2RT} \right)}{1 + \frac{r_2 i_0}{DnFC_0} \ln \left(\frac{r_2}{r_1} \right) \exp \left(-\frac{\eta F}{2RT} \right)} \quad [21]$$

Differentiating Eq. [16] with respect to z

$$\frac{d^2\eta}{dz^2} = \frac{di}{dz} \cdot \frac{1}{\kappa\pi(r_2^2 - r_1^2)} \quad [22]$$

Combining Eq. [22] and [21] gives

$$\frac{d^2\eta}{dz^2} = \frac{[4r_2 i_0 / \kappa(r_2^2 - r_1^2)] \sinh \left(\frac{\eta F}{2RT} \right)}{1 + \frac{r_2 i_0}{DnFC_0} \ln \left(\frac{r_2}{r_1} \right) \exp \left(-\frac{\eta F}{2RT} \right)} \quad [23]$$

Making the substitutions

$$\frac{\eta F}{2RT} = y \quad [24]$$

and

$$\frac{z}{l} = x \quad [25]$$

Eq. [23] reduces to

$$\frac{d^2y}{dx^2} = \frac{a \cdot \sinh(y)}{1 + b \exp(-y)} \quad [26]$$

where

$$a = \frac{2r_2 i_0 l^2 F}{\kappa RT (r_2^2 - r_1^2)} \quad [27]$$

$$b = \frac{r_2 \cdot i_0}{DnFC_0} \ln \left(\frac{r_2}{r_1} \right) \quad [28]$$

In terms of the dimensionless parameters x and y , the current generated from $z = 0$ to $z = z$ is given by

$$i_z = 2\kappa\pi(r_2^2 - r_1^2) \frac{RT}{lF} \left(\frac{dy}{dx} \right)_{x=z} \quad [29]$$

and the total current generated from $z = 0$ to $z = l$ by

$$i_t = 2\kappa\pi(r_2^2 - r_1^2) \frac{RT}{lF} \left(\frac{dy}{dx} \right)_{x=1} \quad [30]$$

Equation [26], which is a second order differential equation, is not possible to solve analytically in the general case. It was replaced by a system of two first order equations and solved numerically employing the Runge Kutta technique. The calculations were conducted on an IBM 360/75 computer with FORTRAN IV programming.

The only unknown parameter was the exchange current density. The value of i_0 was curve fitted to 6×10^{-6} A/cm² of internal surface area for all the tested electrodes.

The physical parameters determined before the dilactres method was applied are listed in Table I and the parameters determined with the dilactres method are listed in Table II. The effective pore length, l , in the model was calculated at $f \cdot L$.

The D , C_0 , and κ -values for 5-9M KOH at 50°C are listed in Table IV.

D , the diffusion coefficient of oxygen in KOH solution and C_0 , the solubility of oxygen in KOH, were calculated from data given by Davis, Horvath, and Tobias (26). D was calculated taking into account the deviations in temperature and viscosity from literature data. C_0 was calculated taking into consideration the different P_{max} values, the varying atmosphere pressure, and the water vapor pressure variation with film electrolyte concentration. The electrolyte conductivity was measured in our laboratory with 5-9M KOH.

In Fig. 6 the theoretical and experimental polarization curves are compared. The D , C_0 , and κ values are calculated for a constant electrolyte concentration of 5M KOH in the film. The theoretical current density, I_t (A/cm² of external surface area) was calculated as

$$I_t = i_t \frac{A^*}{2\pi r_2 l} \quad [31]$$

and $\eta = \eta_l$ at $z = l$

Theoretical polarization curves were also calculated for a hypothetical case where the electrolyte concen-

Table II. Parameters determined with the dilactres method

Electrode type	s	A^* , cm ² /cm ²	$FT \times 10^6$, cm	$Z' \times 10^{-2}$, ohm-cm	f
A	1.12 ± 0.02	143.9 ± 3.3	11.95 ± 0.22	1.61 ± 0.05	2.23 ± 0.05
B	1.39 ± 0.02	98.3 ± 2.7	22.90 ± 0.30	1.77 ± 0.06	3.28 ± 0.07
C	1.21 ± 0.01	209.3 ± 2.8	16.03 ± 0.15	1.67 ± 0.05	2.75 ± 0.04

Table III. Values from the determination of the potential drop in the fine pore layer and probe separator. Probe current density = 0.015 A/cm²

Single fine pore layer thickness × 10 ² , cm	Potential drop, mV
5.1	5.3
7.3	6.9
8.7	7.95

Table IV. *D*, *C*₀, and *κ*-values used in the theoretical model

KOH conc., molarity	<i>D</i> × 10 ⁵ , cm ² /sec	<i>κ</i> , ohm ⁻¹ -cm ⁻¹	<i>C</i> ₀ × 10 ⁸ , mole/cm ³		
			A	B	C
5.0	1.62	0.92	5.19	5.91	5.36
5.5	1.53	0.93	4.43	5.01	4.53
6.0	1.45	0.95	3.72	4.20	3.81
6.5	1.37	0.99	3.10	3.52	3.20
7.0	1.30	1.03	2.60	2.93	2.66
7.5	1.22	1.04	2.18	2.48	2.25
8.0	1.15	1.02	1.83	2.08	1.89
8.5	1.08	0.99	1.55	1.74	1.59
9.0	1.00	0.96	1.27	1.45	1.32

Table V. Comparison between the experimental and theoretical film resistance values

Electrode type	Experimental values <i>Z'</i> _{mean} , ohm-cm	Theoretical values <i>Z'</i> , ohm-cm
A	161	155
B	177	187
C	167	169

tration varied linearly from 5M at the fine pore layer/coarse pore layer intersection to 9M at the gas side of the coarse pore layer, but the curves were almost identical to the curves with constant electrolyte concentration. Maximally they differed a few millivolts for the largest current density.

In Fig. 9 the theoretical current distribution relations for three different *I*_t-values are shown for the electrodes A, B, and C. The theoretical ΔV_f -values, ΔV_{ft} , used to calculate the theoretical *Z'*-values, were calculated according to Eq. [16] as

$$\Delta V_{ft} = \frac{i_t f L}{\kappa \pi (r_2^2 - r_1^2)} \quad [32]$$

Table V shows the experimental *Z'*-values compared with the theoretical ones.

Discussion

In this study measurements were performed on porous gas diffusion electrodes in order to determine

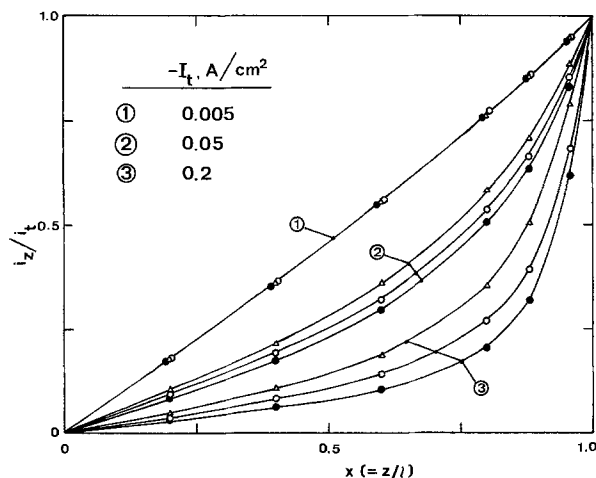


Fig. 9. Theoretical current distribution relations for three current densities. ○, Electrode A; △, electrode B; ●, electrode C.

certain structure parameters and their influence on the behavior of these electrodes.

Regarding the absence of hysteresis when the differential air pressure was increased and decreased, respectively, indicates an "open structure" without ink-pot pores. The similarity between the dilatometry curves for the 16 and 1 cm² unloaded electrodes indicates rather homogeneous structures of the working electrodes. The similarity between the dilatometry curves when the electrodes were loaded indicates that the influence from the counterelectrodes could be neglected, after correction of the very slow continuous rise in the riser under current load, since the same counterelectrode size was used during all the experiments and consequently they were differently loaded without influencing the dilatometry curves.

The absence of differences in the dilatometry curves when the working electrodes were loaded from 0 to 0.2 A/cm² also indicates that for $P < P_{max}$ the liquid filled pores still have electrolyte concentrations nearly equaling the bulk electrolyte concentration. If that were not the case the curves in Fig. 4 should be shifted toward higher *P*-values, because the surface tension increases with increasing electrolyte concentration. The effect is certainly counteracted by increasing the differential pressure, but this effect is much smaller than the former. Regarding the investigated coarse pore layer thicknesses, the current was found not to be proportional to the thickness of the coarse pore layer. An electrode with a thin coarse pore layer (electrode A) generates more current per centimeter thickness than an electrode with a thick coarse pore layer (electrode C), which indicates that electrode C is utilized less effectively than electrode A despite the fact that electrode C has a much larger *A**-value.

The differential pressure required for funicular-pendular transition according to Katan and Grens II (17) was calculated. This pressure is well above the maximum differential pressure used in this investigation. This is confirmed by the fact that the activities in Fig. 5 do not decrease as the differential pressure is increased. However, it is hard to compare the highly regular silver sphere beds used in Ref. (17) with the pressed and sintered electrodes used in this investigation.

The rather low probe current density, 0.015 A/cm², used during the film resistance measurements was chosen in order to make sure that the electrolyte resistivity did not change to any great extent as a consequence of an increase in electrolyte concentration within the pores with increased probe current density. The fact that probe current densities of 0.005 and 0.010 A/cm² resulted in the same film resistance, within the confidence limits, was taken as a proof of a rather constant electrolyte resistivity. However, the confidence interval of *Z'* allows for a possible resistivity change corresponding to a concentration increase from 5 to about 6M KOH in the pores, because the changes in the resistivity with increased electrolyte concentration in this concentration range are rather small. A comparison between the interstice tortuosity values, *s* (Table II), shows that *s* is slightly increased when the thickness of the coarse layer is increased, which indicates that the average angle of the electrolyte filled interstices against the electrode surface increases, when ionic current is allowed to flow through the completely soaked electrode (A vs. C). The average angle is also increased when the coarse layer is compressed (A vs. B).

The relatively high film tortuosity values, *f* (Table II), can be attributed to the presence of narrow passages in the film network, the effect of which is more pronounced when the electrode is compressed.

The film resistance was investigated in order to estimate the resistance of the film network to hydroxyl ion transfer. The thin film of electrolyte has a relatively high effective specific resistance mainly due to its narrow cross section. This resistance directly in-

fluences the effective mass transport of ion by making the latter more difficult.

The experimental Z' -values are of about the same magnitude as the resistance values predicted by the thin-film model (Table V). Noticeably electrode B has the greatest Z' -value despite its thicker film. This depends to a large extent on its relatively large effective pore length, $f \cdot L$.

Due to lack in proportionality between activity and coarse pore layer thickness, one might expect that only a small portion of the pore length is utilized for generation of the main part of the current. This is supported by the theoretical current distribution relations (Fig. 9) where approximately 50% of the current is generated in 10% of the pore length for a current density of 0.2 A/cm². This effect is more pronounced the higher is the value of the current density. Due to this mass transport effect, expressed by the Z' -values, higher current densities are supposed to concentrate the reaction toward the pore end, i.e., toward the bulk electrolyte side of the pore. This also explains the small calculated activity differences mentioned above, when a linear concentration gradient was supposed to exist along the pore. So the way a large Z' -value influences the performance is not so much by increasing the ohmic polarization as by reducing the reaction zone.

The differences between the experimental and theoretical polarization curves in Fig. 6 at higher current densities can be partly explained by a possible blocking of the pores by nitrogen and lowering of the oxygen partial pressure inside the pore, which has not been accounted for in the model. This partial pressure lowering has the effect of extending the region of activity by lowering of the generated current at every point along the pore.

A higher KOH concentration than calculated in the reaction zone close to the fine pore layer also results in higher polarization due to lowering of the D and C_0 -values.

It is obvious that one way of improving the electrodes in the high current density range, due to bad utilization of the effective pore length, would be to make the electrodes thinner, thereby reducing the internal mass transport. By doing so A^* is also reduced so these effects must be optimally balanced.

Conclusion

The dilactres method as described here has proved to be a valuable tool for the characterization of hydrophilic gas diffusion electrodes. The method allows determination of the structure parameters: interstice tortuosity, film tortuosity, effective specific film resistance, effective pore length, mean film thickness, and film area on operating electrodes.

These structure parameters were put into the equations according to the thin-film model. The experimental and calculated polarization curves as well as the experimental and calculated film resistance values are in relatively good agreement, indicating that the thin-film model rather appropriately describes the operation of the investigated electrodes in a practical current density range.

In conclusion, the structure parameters determined with the dilactres method seem to form a good base for optimization of hydrophilic porous gas diffusion electrodes.

Acknowledgment

The author wishes to acknowledge the financial support of this project by the Swedish Board of Technical Development and Professor Olle Lindström for initiation of the work and helpful discussions and suggestions. He also wishes to express his gratitude to the members of the Swedish National Development Company who manufactured the electrodes at the authors request.

Manuscript submitted March 1, 1974; revised manuscript received July 26, 1974.

Any discussion of this paper will appear in a Discussion Section to be published in the December 1975 JOURNAL. All discussions for the December 1975 Discussion Section should be submitted by Aug. 1, 1975.

Publication costs of this article were partially assisted by the Royal Institute of Technology, Sweden.

LIST OF SYMBOLS

A^*	film area, cm ² /cm ² of external surface area
a	see Eq. [27]
a'	cross-sectional area in Eq. [7], cm ²
a''	cross-sectional area in Eq. [8], cm ²
b	see Eq. [28]
C	O ₂ concentration at the electrode surface, g-mole/cm ³
C_0	equilibrium O ₂ concentration at the gas/electrolyte interface, g-mole/cm ³
D	diffusion coefficient of O ₂ in KOH, cm ² /sec
e	electrolyte resistivity, ohm-cm
F	Faraday's constant, 96,500 coulomb/g-equiv
FT	mean film thickness, cm
f	film tortuosity
G	s/τ in Eq. [10]
I	probe current density, A/cm ²
I_t	current density, A/cm ²
i_0	exchange current density, A/cm ² of internal surface area
i_t	total current generated from $z = 0$ to $z = l$, A
i_z	current generated from $z = 0$ to $z = z$, A
L	thickness of the coarse pore layer, cm
L'	length of electrolyte path in Eq. [7], cm
L''	length of electrolyte path in Eq. [8], cm
l	effective pore length = $f \cdot L$, cm
N	film perimeter, cm
n	number of electrons taking part in the electrode reaction, g-equiv/g-mole
P	differential air pressure, cm of H ₂ O
P_{\max}	maximum differential air pressure, cm of H ₂ O
R	gas constant, 8.314 joules/g-mole °K
R'	resistance in Eq. [7], ohm
R''	resistance in Eq. [8], ohm
r_1	$r_2 - FT$, cm
r_2	mean coarse pore layer radius, cm
r_{mf}	mean fine pore layer radius, cm
s	interstice tortuosity
T	temperature, °K
U	porosity of coarse pore layer
W	volume of gas in the coarse pore layer, cm ³
ΔV_1	potential drop in the probe separator, mV
ΔV_2	potential drop/cm of the fine pore electrode thickness, mV/cm
ΔV_f	potential drop in Eq. [14], V
ΔV_{ft}	potential drop in Eq. [32], V
ΔV_s	potential drop in Eq. [12], V
x	z/l , dimensionless
y	$\eta F/2RT$, dimensionless
Z	apparent film resistance ($P < P_{\max}$), ohm·cm
Z'	effective film resistance ($P = P_{\max}$), ohm·cm
Z_0	see Eq. [12], ohm-cm
z	coordinate in Fig. 9, cm

Greek Characters

η	polarization, V
η_l	polarization at $z = l$, V
κ	specific conductivity of electrolyte (= $1/e$), ohm ⁻¹ ·cm ⁻¹
σ	surface tension, cm of H ₂ O·cm
τ	a''/a'
θ	contact angle

REFERENCES

- L. G. Austin, M. Ariet, R. D. Walker, G. B. Wood, and R. H. Comyn, Report AD 602276 (November 1964).
- S. Srinivasan, H. D. Hurwitz, and J. O'M. Bockris, *J. Chem. Phys.*, **46**, 3108 (1967).
- F. G. Will, *This Journal*, **110**, 145 (1963).
- F. G. Will, *ibid.*, **110**, 152 (1963).
- L. G. Austin, Report AD-296229 (November 1962).
- O. Lindström, *Tek. Tidskr.*, **23**, 593 (1963).
- E. A. Grens II, R. M. Turner, and T. Katan, *Advan. Energy Conversion*, **4**, 109 (1964).
- D. N. Bennion and C. W. Tobias, *This Journal*, **113**, 589 (1966).
- D. N. Bennion and C. W. Tobias, *ibid.*, **113**, 593 (1966).
- R. P. Iczkowski, *ibid.*, **11**, 1078 (1964).

11. J. A. Rockett and R. Brown, *ibid.*, **113**, 207 (1966).
12. S. Srinivasan and H. D. Hurwitz, *Electrochim. Acta*, **12**, 495 (1967).
13. O. Lindström, *Energy Conversion*, **8**, 33 (1968).
14. I. Lindholm and I. Jonsson, *This Journal*, **116**, 1150 (1969).
15. J. O'M. Bockris and B. D. Cahan, *J. Chem. Phys.*, **50**, 1307 (1969).
16. A. G. Pshenichnikov, *Dokl. Akad. Nauk SSSR*, **148**, 1121 (1963).
17. T. Katan and E. A. Grens II, *This Journal*, **118**, 1881 (1971).
18. V. S. Markin, Y. A. Chizmadzhev, and Y. G. Chirkov, *Dokl. Akad. Nauk SSR*, **150**, 596 (1963).
19. K. Micka, *Coll. Czech. Chem. Commun.*, **30**, 2288 (1965).
20. K. Micka, *ibid.*, **31**, 3623 (1966).
21. K. Micka, *Electrochim. Acta*, **12**, 1273 (1967).
22. P. M. Dunlop and S. R. Faris, *Nature*, **196**, 1312 (1962).
23. I. Lindholm, Paper presented at the "Deuxièmes Journées Internationales d'Etude des Piles à Combustible, Bruxelles" (1967).
24. K. Micka, *Coll. Czech. Chem. Commun.*, **34**, 3205 (1969).
25. K. Micka, *ibid.*, **38**, 1911 (1973).
26. R. E. Davis, G. L. Horvath, and C. W. Tobias, *Electrochim. Acta*, **12**, 287 (1967).

Low Temperature Studies of Electrochemical Kinetics

II. Double Potential Step Chronocoulometry of Ethyl Cinnamate and Diethyl Fumarate

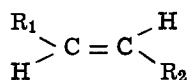
Roman D. Grypa^{*.1} and J. T. Maloy^{**}

Department of Chemistry, West Virginia University, Morgantown, West Virginia 26506

ABSTRACT

Low temperature studies of the double potential step chronocoulometry (DPCC) behavior of ethyl cinnamate (EC) and diethylfumarate (DEF) have been conducted. The results have been compared with working curves obtained using digital simulation. At fixed concentration, both EC and DEF appear to undergo electrohydrodimerization through a radical anion dimerization mechanism at all temperatures employed (203°-316°K). Comparisons at different concentrations (C_B) reveal that the $Q(2t_f)/Q(t_f)$ behavior of DEF is a smooth function of $t_f C_B$, while that of EC is a smooth function of $t_f C_B^{1/2}$. Since the gross low temperature cyclic voltammetry of EC and DEF is identical, an ecc mechanism is proposed to account for this discrepancy in behavior with changes in C_B . On the basis of a radical ion dimerization mechanism, the rate constants for DEF and EC at 25° are 45 and 225 liters/mole-sec, respectively; activation energies are 4.6 and 6.2 kcal/mole.

In a previous paper (1), low temperature studies of the cyclic voltammetry of diethyl fumarate (DEF) were presented in an attempt to form some generalizations about the temperature dependence of the electrochemical processes associated with the electrohydrodimerization (EHD) reactions of deactivated olefins



In that paper, it was observed that either two or three reduction processes occur, depending on the temperature: at high temperature only the reduction of the parent olefin and a dimeric product are observed, even though the second one-electron reduction of the olefin occurs at a potential intermediate to that of the two processes observed; at low temperature both one-electron reductions of the parent olefin may be observed because the temperature reduction has inhibited the dimerization reaction; at intermediate temperatures all three processes occur.

Extensive mechanistic studies have been conducted with DEF ($R_1 = R_2 = -CO_2Et$) using a variety of techniques. Double potential step chronoamperometry studies (2) have established that the EHD reaction of DEF probably proceeds through the dimerization of two radical ions; this judgment has been rendered on the basis of a comparison of experimental current-time data with working curves generated for a variety of

proposed mechanisms using digital simulation techniques. The rate constant for the dimerization reaction at 25°C has been found to be 37 liters/mole-sec and the energy of activation has been estimated to be 4.5 kcal/mole using a two-point fit. Thus, DEF has been extensively characterized by voltammetric and chronoamperometric techniques; it is well suited as a model compound with which others may be compared.

Early room temperature voltammetric studies (3) of ethyl cinnamate (EC; above structure with $R_1 = -C_6H_5$ and $R_2 = -CO_2Et$) revealed the possibility of an additional chemical complication not observed in the DEF system. While DEF exhibits the characteristic 15-18% decrease in $i_p/v^{1/2}$ with increasing scan rate as predicted for a dimerization mechanism (4), EC exhibits a marked increase in $i_p/v^{1/2}$ ratio at slow scan rates. Since this behavior would be characteristic of a first-order ecc mechanism, it was suggested that the dimerization of EC was influenced by this second kinetic perturbation; thus, two processes have been assumed to be in direct competition for the electro-generated radical ion of EC. These differences have been discussed previously (1). Low temperature electrochemistry (5) appeared to offer some hope of resolving this mixed mechanism so that one of the proposed reaction routes could be enhanced at the expense of the other. This study was initiated, then, in the hope that the activation energies of these two purported processes were sufficiently different to permit their resolution. This objective was not attained. However, extensive double potential step chronocoulometry (DPCC) studies performed on the DEF and the EC system at several different temperatures and concentrations reveal that there is a significant difference be-

* Electrochemical Society Student Member.

** Electrochemical Society Active Member.

¹ Present address: Fertilizer and Chemical Division, Agway, Inc., Ithaca, New York 14850.

Key words: low temperature electrochemistry, electrohydrodimerization, cyclic voltammetry, reductive coupling, digital simulation.

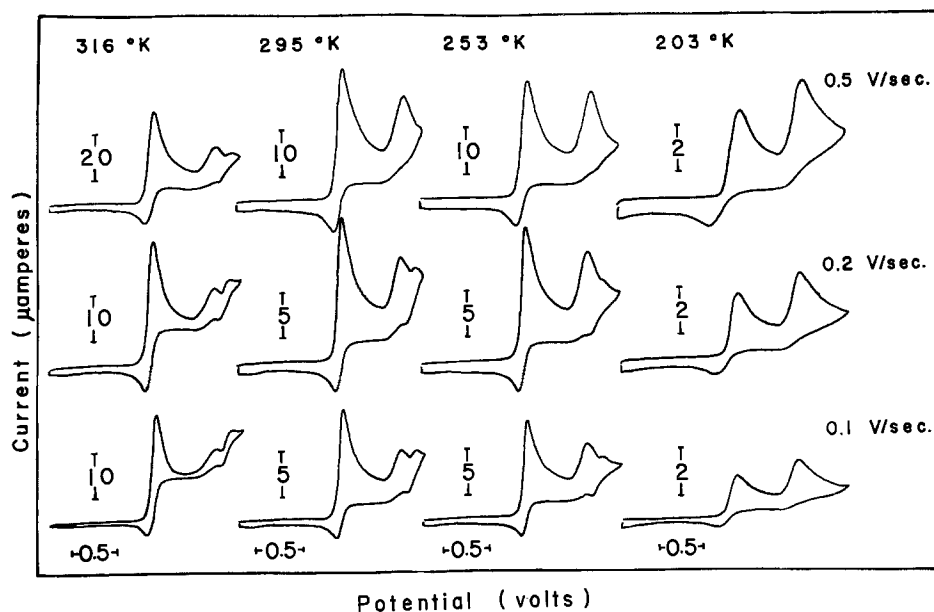


Fig. 1. Complete potential scan cyclic voltammograms for a 3.63 mM solution of EC at various temperatures and scan rates.

tween the two systems, while low temperature cyclic voltammetry (CV) studies indicate that some aspects of the two systems are very similar. These experiments and a discussion of their implications constitute the remainder of this work.

Experimental

Reagents, apparatus, and procedure have been discussed previously (1). Reagent grade ethyl cinnamate was supplied by Eastman Organic Chemicals; it was vacuum distilled at 123°C and 4 Torr and the middle 80% was stored in a desiccator prior to use. All electrochemical experiments were performed with a Princeton Applied Research Model 170 Electrochemical System using a positive feedback voltage to compensate for cell resistance at all temperatures. DPCC experiments were run at a variety of temperatures using initial and final potentials selected on the basis of CV experiments so that the electrode reaction proceeded under diffusion limiting conditions at all times. The duration of the interval between the initial and final potential step, t_f , was varied between 0.25 and 50 sec.

Voltammetry of Ethyl Cinnamate

Low temperature CV studies were performed on several dimethylformamide (DMF) solutions containing EC and using tetra-*n*-butyl ammonium iodide

(TBAI) as the supporting electrolyte. Figure 1 shows a series of complete CV scans obtained for the EC system at various temperatures and scan rates. As in the case of DEF, as many as three reduction processes occur depending on the scan rate and the temperature. At 295°K, these three reduction processes occurred at -1.24 , -1.86 , and -2.05 V vs. Ag-QRE. (The silver wire quasi-reference electrode was immersed in the DMF-TBAI solution at the temperature of the run.) Decreasing the experimental temperature to 203°K eliminated the third reduction peak and shifted the first two reduction peaks to -1.35 and -2.05 V vs. Ag-QRE, respectively; the second reduction peak grew to become almost identical to the first reduction peak at low temperatures. If the experimental temperature was increased to 316°K, a decrease in the scan rate increased the size of the third reduction peak so that it approached one-half the height of the first reduction peak. At the same time, a decrease in scan rate decreased the size of the second reduction peak. This behavior is analogous to that of DEF.

Table I shows the dependence of the three reduction processes for the EC system upon the scan rate and temperature. A decrease in temperature increases the anodic to cathodic peak current ratio obtained for the first reduction wave from CV scanning just past the first reduction wave; at low temperatures, this ratio

Table I. Cyclic voltammetry data for a 3.63 mM solution of EC showing the effect of temperature and scan rate variation on the peak current heights^(a)

Temperature, T (°K)	scan rate, v (V/sec)	$i_{pa1}^{(b)}$		t_c (sec) ^(c)	$i_{pa1}^{(d)}$		i_{pc2}	i_{pc3}	t'_c (sec) ^(e)	i_{pc3}/i_{pc1}	$1 - (i_{pa1}/i_{pc1})^{(f)}$
		i_{pc1}	i_{pc1}		i_{pc1}	i_{pc1}					
316	0.05	0.28 ^(f)	—	—	(g)	0.19	0.29	15.8	0.43		
	0.10	0.39 ^(f)	—	—	(g)	0.24	0.20	8.3	0.33		
	0.20	0.48 ^(f)	—	—	(g)	0.24	0.12	4.3	0.23		
295	0.05	0.36	21.2	0.28	(g)	0.23	0.13	16.2	0.20		
	0.10	0.47	10.6	0.30	(g)	0.28	0.08	8.3	0.15		
	0.20	0.54	5.3	0.33	(g)	0.35	0.04	4.2	0.09		
253	0.05	0.52	20.4	0.40	(g)	0.39	0.01	16.6	0.02		
	0.10	0.67	10.1	0.37	(h)	0.50	(h)	—	(h)		
	0.20	0.75	5.1	0.35	(h)	0.55	(h)	—	(h)		
203	0.05	0.85	20.2	0.44	(h)	0.86	(h)	—	(h)		
	0.10	0.91	9.4	0.38	(h)	0.85	(h)	—	(h)		
	0.20	0.95	4.7	0.34	(h)	0.83	(h)	—	(h)		

(a) The solvent was 0.26M TBAI in DMF. A 0.008 cm² platinum working electrode area was used.

(b) Peak current ratios for the first reduction wave from cyclic voltammograms scanning just past the first reduction wave; concentration of ethyl cinnamate was 4.15 mM.

(c) Peak-to-peak time for cyclic voltammetry scans past the first reduction wave.

(d) Peak current ratios for the first reduction wave from cyclic voltammograms scanning to background.

(e) Peak-to-peak time for linear sweep voltammetry between peak 1 and peak 3.

(f) Estimated peak current ratios for the first reduction wave from a plot of $\frac{i_{pa1}^{(b)}}{i_{pc1}}$ vs. $1/T$.

(g) Baseline cathodic currents greater than those observed on the forward scan were observed on the reverse scan.

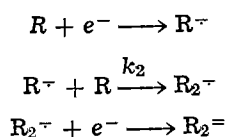
(h) No peak was observed in cyclic voltammogram.

approaches a maximum value of 1.0, indicating that the kinetic perturbation is inhibited at reduced temperature. However, anodic to cathodic peak current ratios obtained from CV scanning the entire potential range do not approach this maximum. At low temperatures, the height of the second reduction peak approaches that of the first reduction peak. If one goes to high temperatures, the ratio of the height of the third reduction peak to that of the first reduction peak increases as the scan rate is decreased. This ratio never exceeds 0.5 at high temperatures and slow scan rates. The arguments applied previously (1) to the DEF system can be applied to the EC system also; therefore, the $(i_{pc3}/i_{pc1})/(1 - (i_{pa1}/i_{pc1}))$ ratio should be an approximate measure of the relative concentration of the species involved in the third reduction with respect to its radical anion precursor. This ratio should not exceed 0.5 (even in the absence of the second peak) if the third wave is due to the one-electron reduction of a dimeric product; that this is true is even more obvious in the case of EC than it was with DEF.

A summary of the CV data for the first reduction wave of EC at various temperatures is shown in Table II. Since resistance compensation was employed throughout, most of the increase in peak separation as the temperature is lowered may be attributed to the quasi-reversibility of the EC reduction (5). It may also be due to incomplete iR compensation because a QRE was employed (1). This effect with EC is not as pronounced as it is with DEF. The $(i_{pc}/C)(T/v)^{1/2}$ behavior shown is not unlike what one would expect for a dimerization mechanism; at scan rates lower than those in Table II, however, higher $(i_{pc}/C)(T/v)^{1/2}$ ratios were obtained at 295°K than would be expected in a simple dimerization.

Digital Simulations

Three different types of EHD mechanisms were considered possible in this study. The first was a second-order ece mechanism



where the parent olefin is reduced at the electrode surface to form the radical anion, which reacts with incoming olefin in the rate-determining step to form a mononegative dimer which undergoes subsequent reduction at the initially applied potential to form the dimer dianion. The second was a second-order ec mechanism

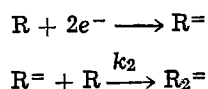
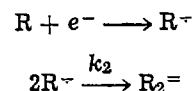


Table II. Typical cyclic voltammetry data for the first reduction wave for a 4.15 mM solution of EC at various temperatures^(a)

Temperature, T (°K)	Scan rate, v (V/sec)	$\frac{\Delta E_p}{(RT/F)}$	$\left(\frac{i_{pc1}}{C}\right)\left(\frac{T}{v}\right)^{1/2}$
295	0.10	1.4	108
	0.20	1.4	106
	0.50	1.5	95
	1.00	1.9	105
253	0.10	1.7	80
	0.20	2.2	76
	0.50	2.5	70
	1.00	3.2	70
223	0.10	2.5	49
	0.20	3.4	46
	0.50	4.7	51
	1.00	5.9	43
203	0.10	4.9	28
	0.20	6.1	26
	0.50	7.4	24
	1.00	9.0	23

^(a) The solvent was 0.26M TBAI in DMF. The platinum working electrode area was 0.008 cm².

where the olefin undergoes an initial two-electron reduction to form the monomer dianion; this is followed by reaction with incoming olefin to produce the dimer dianion. The third was a second-order dimerization mechanism



in which the olefin undergoes an initial one-electron transfer to form the radical anion; this is followed by reaction with another radical anion to produce the dimer dianion. In each of these mechanisms, only the radical anion is regarded as electroactive after the second potential step.

Working curves for the kinetically perturbed DPCC experiment have been obtained through previously published digital simulation techniques (2). The simulation employed predicts the effect of both diffusion and chemical reactions on the measured current and charge parameters; it is generally accurate within ordinary electrochemical uncertainty (~1%). Figure 2 illustrates the working curves obtained for the three, second-order EHD reactions considered. Each of these working curves shows the variation of the ratio of the charge at time $2t_f$ to that at time t_f as a function of the logarithm of the product of the initial electrolysis time and the bulk concentration of olefin in solution, C_B . Variations in the shape of these curves are due to the mechanistic perturbation experienced by the formation of the radical anion of the deactivated olefin. The top curve represents the DPCC results expected in the second-order ece mechanism; the middle curve is that expected for the second-order ec mechanism; the bottom curve shows that expected for the dimerization mechanism. These working curves may be compared with data obtained experimentally to elucidate the reaction mechanism. The shape of best fit determines the preferred mechanism; thus the radical anion dimerization mechanism is indicated by lower experimental charge ratios at longer times. The dotted lines in Fig. 2 show the co-ordinates when $k_2 t_f C_B$ is 1.0. Thus, the second-order rate constant may be obtained conveniently from the reciprocal of the $t_f C_B$ product at the particular charge ratio indicated for each mechanism. For the second-order radical anion dimerization mechanism, the rate constant is the reciprocal of that $t_f C_B$ product which gives a charge ratio of 0.69.

Double Potential Step Chronocoulometry Studies

Variable temperature DPCC experiments were run on different concentrations of DEF and EC to deter-

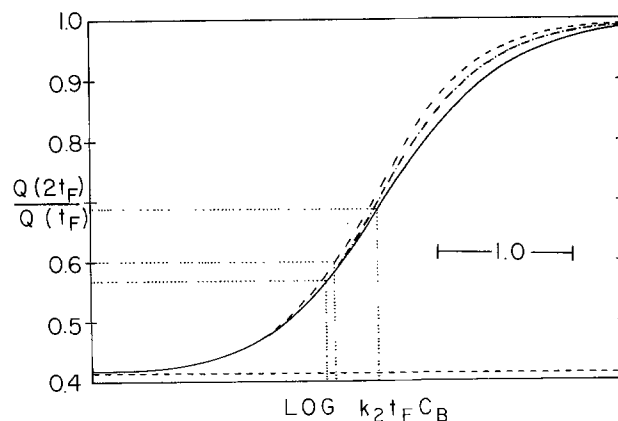
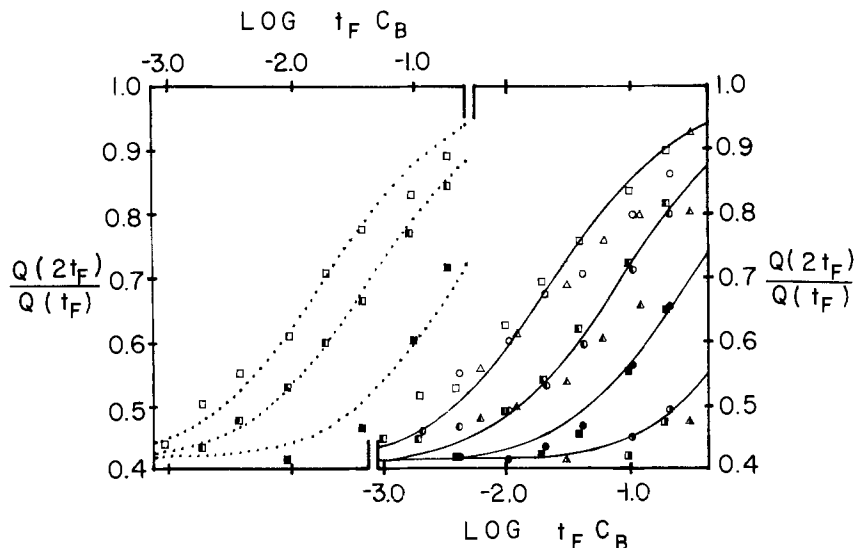


Fig. 2. Working curves obtained for double potential step chronocoulometric experiments from digital simulations. (—) second-order ece mechanism; (---) second-order ec mechanism; (· · ·) second-order dimerization mechanism. Dotted lines show $Q(2t_f)/Q(t_f)$ when $k_2 t_f C_B = 1.0$ for each mechanism. The dashed line indicates the behavior expected in the absence of kinetic perturbation.

Fig. 3. Fitting experimental data for DEF to a second-order dimerization working curve. (—) Anhydrous DMF solution; (.....) DMF contained 53 mM solution of water. Experimental temperature: (Δ \circ \square) 295°K; (\triangle \bullet \blacksquare) 253°K; (\blacktriangle \bullet \blacksquare) 223°K (anhydrous DMF), 218°K (in DMF-H₂O); (\triangle \bullet \blacksquare) 203°K. DEF concentration: (\blacksquare \blacksquare \blacksquare \square) 3.84 mM; (\bullet \bullet \bullet \circ) 4.19 mM; (\blacktriangle \blacktriangle \blacktriangle \triangle) 12.19 mM.



mine rate constants for each sample at different temperatures. Rate constants were determined by comparison of experimental charge ratios with theoretical working curves obtained from digital simulations.

Figure 3 illustrates fitting experimental data obtained at different temperatures to the simulated radical anion dimerization working curves for various concentrations of DEF. Attempts to fit the experimental charge ratios to either the second-order ec or ece working curves were unsuccessful because neither of these mechanisms agreed with the experimental data at both large and small charge ratios. At room temperature the rate constants obtained in this study agreed remarkably with previously reported kinetic data for the DEF system obtained using chronoamperometry (2). A reduction in temperature did not result in any observable change of the radical anion dimerization mechanism, as shown by the smooth fit of the experimental data to the simulated working curve. Only a decrease in the rate constant was obtained, as noted by the positive shift of the experimental points as the temperature was lowered.

The addition of a proton source to the DEF system caused no observable change in the apparent radical anion dimerization mechanism. This is shown on the left side of Fig. 3. These points give reasonable agreement with the dimerization working curve at all temperatures. Moreover, the addition of a proton source increases the rate constants for this system.

The decrease in rate constants with decreasing temperature is shown in Table III. A 100-fold decrease is obtained by reducing the experimental temperature from 295° to 203°K. The presence of 53 mM water increases the rate constant for DEF from 45 to 58 liters/mole-sec at 295°K. However, these rate constants also decrease as the experimental temperature is lowered.

Rate constants obtained from the DPCC experiments provide a valid method to determine the activation energy, E_a , of this radical anion dimerization reaction.

Figure 4 shows a plot of $\log k_2$ vs. $1/T$ used to determine the activation energy of these systems. A linear relationship is obtained by plotting the temperature dependence of experimental rate constants in this manner. Curve C represents the plot obtained for the DEF system. Curve B, that for DEF-H₂O, also exhibits a linear relationship. That these two lines are parallel indicates that these two systems have identical activation energies. The relatively small activation energies determined in this manner are shown in Table III; these agree well with that reported previously (2).

A somewhat different behavior can be observed when one compares the experimental data obtained for

Table III. Summary of second-order rate constants obtained from double potential step chronocoulometry experiments run at different temperatures

Compound	Temperature, T (°K)	k_2 (liters/mole-sec)	E_a (kcal/mole)
DEF	295	45	4.6
	273	30	
	253	13	
	223	3.6	
DEF-H ₂ O ^(a)	203	0.7	4.7
	295	58	
	273	40	
	253	24	
EC ^(b)	218	4.7	6.2
	295	225	
	273	100	
	253	41	
	223	8.3	
	203	1.8	

^(a) Solution contained 53 mM water.

^(b) Data obtained using 4.15 mM solution.

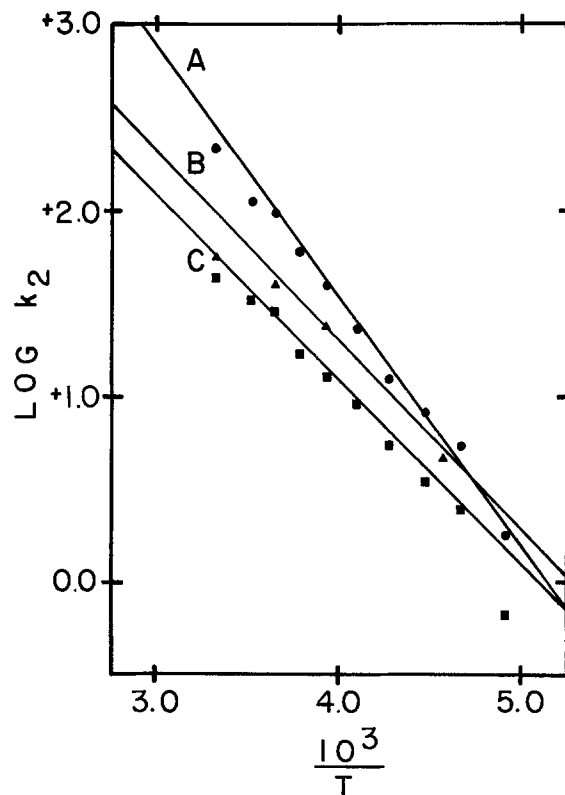


Fig. 4. Variation of rate constant with temperature. Curve A (\bullet) EC in DMF; curve B (\blacktriangle) DEF in DMF-H₂O; curve C (\blacksquare) DEF in DMF.

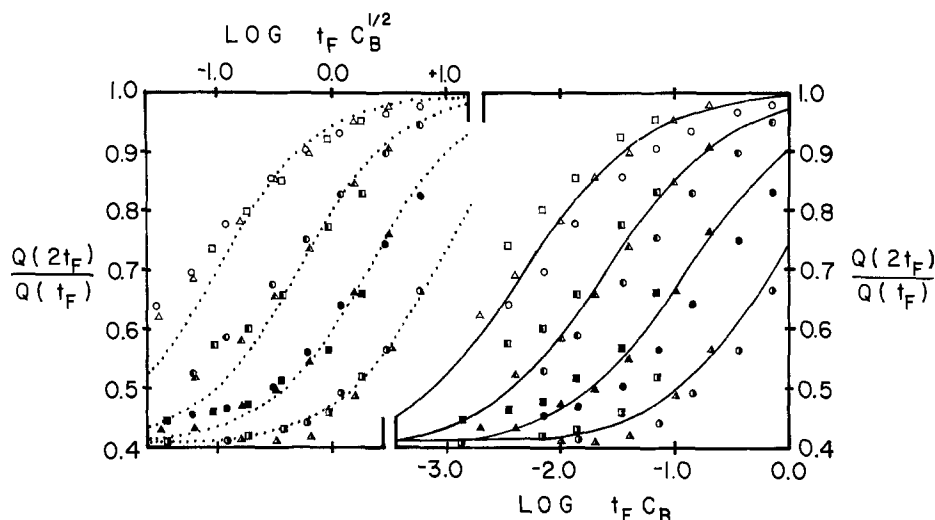


Fig. 5. Fitting experimental data for EC to simulated working curves. (—) Second-order working curve; (.....) 3/2-order working curve. Experimental temperature: (Δ \circ \square) 295°K; (\blacktriangle \bullet \blacksquare) 253°K; (\triangle \circ \square) 203°K. EC concentration: (\blacksquare \blacksquare \square) 1.43 mM; (\blacktriangle \blacktriangle \triangle) 4.15 mM; (\bullet \bullet \bullet \circ) 14.89 mM.

the EC system with that obtained for the DEF system. The right-hand side of Fig. 5 illustrates that it is much more difficult to fit a radical anion dimerization working curve to this data. Charge ratios obtained from solutions having different bulk olefin concentrations do not appear to be the same smooth function of the $t_F C_B$ product as the charge ratios obtained for the DEF system appear to be. That is, one can fit a radical anion dimerization working curve through experimental data for a specific concentration, but no one line can be fit through the experimental data for a variety of concentrations. This effect does not appear to be due to the expected scatter of the experimental data. Close scrutiny of the data reveals that there is a regular variation in these plots with increasing bulk EC concentrations. (This was not observed in the case of DEF.) This suggests that the charge ratio for EC might be shown as a smooth function of $t_F C_B^j$ (where $j \neq 1$); of course, this would have mechanistic implications because the over-all order of the reaction could be expressed (2) as $j + 1$.

Several different values of j were tried in an attempt to show the charge ratio for EC as a smooth function of $t_F C_B^j$. The best agreement of different concentrations at all temperatures was obtained by plotting these experimental points as a function of $t_F C_B^{1/2}$. (This implies that the rate-determining sequence is of 3/2 order over-all.) The curves to the left in Fig. 5 represent this. The dotted curves represent working curves for the 3/2-order reaction obtained through digital simulation. In these simulations, it was merely assumed that the conversion of R^- to electroinactive product occurred by a 3/2-order step

$$\frac{d[R^-]}{dt} = -k[R^-]^{3/2}$$

The agreement in shape with the 3/2-order reaction is reasonable at all temperatures. The effect seems genuine; its meaning is open to interpretation.

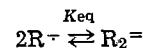
Although low temperature DPCC studies were done with the hope of resolving a reported mixed mechanism, this expectation was not realized. Rate constants obtained by fitting the EC system to a second-order dimerization mechanism, therefore, are not strictly reliable. The rate constants measured at fixed concentration are probably proportional to the actual rate constants so that the activation energies determined in this manner are valid. For EC, curve A in Fig. 4 exhibits a greater slope than that for DEF and consequently, EC has a higher activation energy associated with it.

If one (improperly) assumes that EC reacts according to a second-order dimerization mechanism, it may be shown that the reaction of the anion of EC proceeds more rapidly than that of DEF. This may be seen in Table III; at room temperature, EC has a rate constant of 225 liters/mole-sec compared to one of 45 liters/mole-sec for DEF. As in the studies involving DEF, these rate constants decrease about 100-fold by lowering the experimental temperature to 203°K.

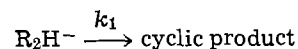
Discussion

Even though it was not possible to resolve any mixed mechanism for the EC system by temperature reduction, sufficient information has been obtained by comparing DEF and EC to raise some fundamental questions about the mechanism of EHD reactions. The DPCC experiments outlined above indicate clearly that the dimerization of EC does not exhibit the same concentration dependence as that of DEF, which is believed to proceed through radical anion coupling. On the other hand, low temperature CV experiments have established that the two compounds exhibit similar gross voltammetric behavior. There is reason to suspect that a cyclic product like that recently reported by Klemm and Olson (7) for EC results when DEF undergoes an EHD reaction also (1). Thus, whatever mechanism is invoked, it must account both for differences and similarities between the two compounds. In addition, it should account for the fact that the bulky EC radical ion reacts faster than the more compact DEF radical ion while experiencing a greater barrier to activation than the DEF ion experiences.

An appealing compromise exists in the invocation of an ecc mechanism not unlike that recently discussed by King (8). This mechanism would suggest that the initial step in the EHD reaction is a rapidly established equilibrium between two radical anions and a dimer dianion



Protonation of R_2^{2-} would result in R_2H^- which then could undergo a first-order cyclization reaction in the rate-determining step



This mechanism has the distinct advantage of appearing to be first order if K_{eq} is large while appearing to be second order if K_{eq} is small. An intermediate equilibrium constant results in an apparent reaction order somewhere between first and second order as observed

in the case of EC. [The necessary conditions for this are discussed in detail in Ref. (8).] Those mechanisms already reported as proceeding through a second-order dimerization pathway may only appear to do so because K_{eq} is small.

This line of reasoning has some intuitive appeal. The substitution of a C_6H_5 group in EC for a CO_2Et group in DEF would probably increase the delocalization of the unpaired electron in the radical anion. This would tend to minimize the repulsive forces inhibiting dimerization, so that one would expect a larger equilibrium constant for EC than for DEF. Thus, the over-all rate of dimerization for EC may be faster than that of DEF and need not be of second order. If one believes that the rate-determining step is the cyclization reaction, this argument may also be applied to aid in the understanding of the difference in activation energies obtained. If this scheme is operative, the barrier to ring closure would be expected to be less in a CO_2Et -substituted compound like DEF than in a C_6H_5 -substituted compound like EC, due to the added steric hindrance offered by the phenyl rings in the latter compound.

Of course, at this point, any discussion of an ecc mechanism of this sort is speculative. Other ecc mechanisms involving some sort of equilibrium step could exhibit the same 3/2-order dependence. Examples of these include: (i) the reaction of R and R^- in the equilibrium step, followed by the catalytic regeneration of R through the reaction of R_2^- with more R^- to produce R^- ; and (ii) the parallel *trans* dimerization of R^- occurring simultaneously with *cis-trans* isomerization (the equilibrium step) followed by *cis-trans* dimerization. Neither of these mechanisms lead to the formation of the cyclic compound observed by Klemm and Olson in the rate-determining step, however. Regardless of the mechanism, none of the working curves simulated for this paper take the initial equilibrium

into account. This step is, nevertheless, eminently amenable to treatment using digital simulation techniques. These simulations are presently underway and it is expected that their results will be the topic of a future communication.

Acknowledgment

Acknowledgment is made to the Donors of the Petroleum Research Fund, administered by the American Chemical Society, for the support of this research. This work was presented as Paper 322 at the 25th Annual Pittsburgh Conference on Analytical Chemistry and Applied Spectroscopy, Cleveland, Ohio, March 1974.

Manuscript submitted June 3, 1974; revised manuscript received Oct. 2, 1974.

Any discussion of this paper will appear in a Discussion Section to be published in the December 1975 JOURNAL. All discussions for the December 1975 Discussion Section should be submitted by Aug. 1, 1975.

Publication costs of this article were partially assisted by the Petroleum Research Fund.

REFERENCES

1. R. D. Grypa and J. T. Maloy, *This Journal*, **122**, 377 (1975).
2. W. V. Childs, J. T. Maloy, C. P. Keszthelyi, and A. J. Bard, *ibid.*, **118**, 874 (1971).
3. J. P. Petrovich, M. M. Baizer, and M. R. Ort, *ibid.*, **116**, 743 (1969).
4. M. I. Olmstead, R. G. Hamilton, and R. S. Nicholson, *Anal. Chem.*, **41**, 260 (1969).
5. R. P. Van Duyne and C. N. Reilley, *ibid.*, **44**, 142 *ibid.*, **44**, 153 (1972); *ibid.*, **44**, 158 (1972).
6. R. J. Lawson and J. T. Maloy, *ibid.*, **46**, 559 (1974).
7. L. H. Klemm and D. R. Olson, *J. Org. Chem.*, **38**, 3390 (1973).
8. E. L. King, *J. Chem. Ed.*, **51**, 186 (1974).

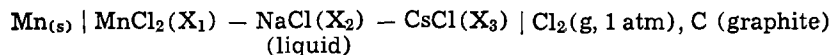
Charge Asymmetrical Ternary Molten Salt Systems: Theory of Dilute Solutions

Donald R. Sadoway* and S. N. Flengas**

Department of Metallurgy and Materials Science, University of Toronto, Toronto, Ontario, Canada M5S 1A4

ABSTRACT

The thermodynamic properties of dilute solutions of MnCl_2 in the ternary system $\text{MnCl}_2\text{-NaCl-CsCl}$ have been investigated by the measurement of the reversible emf of the formation cell



The partial molar properties of MnCl_2 have been found to be in good agreement with values predicted by the complex-ion model reported in previous publications from this laboratory (1-3). In the present paper it is shown that these rather involved expressions reduce to useful, simple equations of the form

$$(\Delta Z)_{123} = (1 - t) (\Delta Z)_{12} + t(\Delta Z)_{13}$$

where Z represents either an integral or a partial molar property. The ternary solution is denoted by the subscripts 1,2,3, while the two binaries, each containing the reactive-metal chloride, are denoted by 1,2 and 1,3; t is a concentration variable. It is also shown that the following expression applies to the activity of the reactive-metal chloride (component 1) in solution

$$(a_1)_{123} = (a_1)_{12}^{1-t} \cdot (a_1)_{13}^t$$

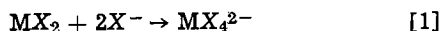
For dilute solutions obeying Henry's law, the activity coefficients are given by

$$(\gamma_1)_{123} = (\gamma_1^0)_{12}^{X_2} \cdot (\gamma_1^0)_{13}^{X_3}$$

where $(\gamma^0)_{i,k}$ is the Henrian activity coefficient in the binary i,k and X_k is the mole fraction of k present in the ternary solution, providing that X_1 in the ternary 1,2,3 is the same as that in the two binary solutions 1,2 and 1,3.

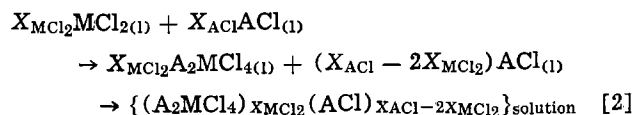
Previous work in this laboratory has shown that the thermodynamic (1-3) and transport (4) properties of molten salt solutions consisting of a divalent-metal chloride and an alkali-metal chloride may be explained by a thermodynamic model which is based on the existence of tetrahedrally coordinated complex ions.

The complex ions are thought to form by reactions of the type



The present treatment of complexing in fused salts follows postulates previously cited (1-4).

The process of mixing X_{MCl_2} moles of MCl_2 with X_{ACl} moles of ACl in a binary system $\text{MCl}_2\text{-ACl}$, where $X_{\text{MCl}_2} + X_{\text{ACl}} = 1$ and $0.33 > X_{\text{MCl}_2} > 0$, may be represented by the following two-step mechanism



The first of these reactions represents the formation of the pure complex compound, while the second represents the mixing process.

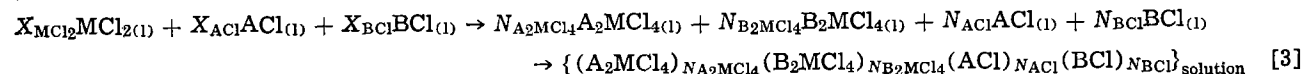
The detailed derivation of the expressions which describe the concentration dependence of the enthalpy of mixing and of the entropy of mixing in the $\text{MCl}_2\text{-ACl}$ binary systems has been given elsewhere (2). The

expressions have been found to represent to a high degree of accuracy the concentration dependence of the calorimetrically determined enthalpies of mixing reported by Papatheodorou and Kleppa (5-7) and by McCarty and Kleppa (8) in the reactive-metal chlorides $\text{MnCl}_2\text{-ACl}$, $\text{FeCl}_2\text{-ACl}$, $\text{CoCl}_2\text{-ACl}$, $\text{NiCl}_2\text{-ACl}$, $\text{MgCl}_2\text{-ACl}$, and $\text{CdCl}_2\text{-ACl}$, where A represents Li , Na , K , Rb , and Cs .

The corresponding mixing reactions and the relevant expressions for the concentration range $1.0 > X_{\text{MCl}_2} > 0.33$ also may be found elsewhere (1-3). These equations are not required for the purposes of the present study.

The partial molar properties of the $\text{MnCl}_2\text{-ACl}$ systems were investigated in this laboratory (2) by an emf method, and their concentration dependence was found to be in excellent agreement with that predicted by the model. The expressions include a number of interaction parameters which have been shown (1, 2) to depend on the ionic radii of the species present in the various systems.

Further development of the model (3) has shown that the expressions for two binary systems such as $\text{MCl}_2\text{-ACl}$ and $\text{MCl}_2\text{-BCl}$, where A and B are two different alkali-metal cations, may be expanded to predict the enthalpy of mixing of the combined ternary system $\text{MCl}_2\text{-ACl-BCl}$. In this case the process of mixing X_{MCl_2} moles of MCl_2 with X_{ACl} moles of ACl and X_{BCl} moles of BCl , where $0.33 > X_{\text{MCl}_2} > 0$ and $X_{\text{MCl}_2} + X_{\text{ACl}} + X_{\text{BCl}} = 1$, may also be represented by a two-step mechanism



The important thing to note is that the over-all solution reaction is split into two steps. The first involves the formation of pure complex species, while the second represents the mixing process.

* Electrochemical Society Student Member.

** Electrochemical Society Active Member.

Key words: manganese chloride, complex formation, electromotive potential, thermodynamic properties.

In the Appendix the expressions which describe the concentration dependence of the integral enthalpy and entropy of mixing are given. It should be noted that the interaction parameters which appear in these equations are those representing the constituent binary systems $MnCl_2$ - $NaCl$ and $MnCl_2$ - $CsCl$.

The model for ternary solutions, so far, has been tested with respect to only a few available calorimetric data on integral enthalpies of mixing (3) for concentrated solutions.

In the present investigation the partial molar properties of dilute solutions composed of $MnCl_2$ and various proportions of $NaCl$ and $CsCl$ have been investigated by an emf method involving the use of manganese chloride formation cells.

The mathematical expressions which describe the concentration dependence of the partial molar properties, and, particularly, their behavior in dilute solutions have been derived. The experimental results for partial molar enthalpies of mixing and activities of $MnCl_2$ are in excellent agreement with the theory even in the dilute concentration range where all the partial molar properties acquire limiting values. The ternary system $MnCl_2$ - $NaCl$ - $CsCl$ was chosen as a test system because the $MnCl_2$ - $NaCl$ binary system shows only moderate deviations from ideality, while the $MnCl_2$ - $CsCl$ system is a highly reactive system with pronounced negative deviations from ideality. For example, the minimum integral molar enthalpy of mixing in the former is -1.8 kcal, compared to -5.3 kcal in the latter (5). Accordingly, the prediction of the behavior of such a ternary system should represent a severe test of any significant thermodynamic model.

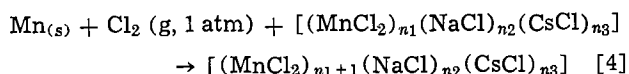
Experimental

The electromotive force was measured for the cell represented schematically as



In order both to establish electrical contact and to prevent the diffusion of chlorine gas to the manganese electrode, the cell consisted of two compartments joined by an asbestos diaphragm. Its fabrication is described elsewhere (15).

The cell reaction may be written as



where the n 's denote mole number.

The cell emf is related to the activity of manganese dichloride by the Nernst equation

$$E = E^\circ - \frac{RT}{2F} \ln a_{MnCl_2} \quad [5]$$

where R is the ideal gas constant, equal to 1.987 cal/mole- $^\circ K$, T is the temperature in Kelvins, F is the Faraday constant, equal to $23,060$ cal/volt-equivalent, and E° is the standard formation cell potential of pure liquid $MnCl_2$ in volts at the same temperature T . The values of E° used in this study were previously determined in this laboratory (2).

The preparation of materials and cell design have been described elsewhere (2). The main improvement in the present apparatus was the use of vacuum-cast manganese rods as electrodes. These were 40 mm long and 6 mm in diameter connected to either platinum or tungsten leads. All emf's reported in the present work have been corrected for thermoelectric voltages determined experimentally.

The tube furnace used was wound with Kanthal wire. It had a 2 in. zone over which the temperature varied by $1^\circ K$. Melt depths never exceeded 1 in. Actually, temperature profiles were measured in several melts, and variations of the order of only $0.5^\circ K$ were

found. A grounded Inconel sheath was placed between the cell wall and the furnace tube to eliminate induced emf's from the a-c field of the furnace windings. Cell potential did not vary as power to the furnace was switched on and off.

In order to test for reversibility, all cells were subjected to a polarization test using an external dry cell. About 1 mA was passed through the experimental cell for approximately 60 sec. Cell voltages returned to within 0.5 mV of their values before perturbation less than 15 sec after the external dry cell had been disconnected. This observation was the same regardless of the polarity of the applied voltage.

The fact that voltages were reproducible over a period of 24 hr was also a demonstration of the cell's reversibility.

Results

Table I displays measured cell emf's which have been expressed as least squares lines of the form $E = a - bt$, where E is the cell potential in volts and T is temperature in Kelvins. Melt compositions are expressed in terms of both principal mole fractions, X_i , and the corresponding ternary concentration variables, y and t , defined as

$$t = X_{CsCl} / (X_{NaCl} + X_{CsCl}) \quad [6]$$

$$y = X_{NaCl} + X_{CsCl} = 1 - X_{MnCl_2} \quad [7]$$

Plots of cell potential *vs.* temperature are shown in Fig. 1 a-c. The concentrations of the solutions studied are shown on the inset composition triangle. An increase in the value of t from zero to unity at constant y represents a change in the composition of the solvent from $NaCl$ -rich to $CsCl$ -rich. The plots are linear and demonstrate that at a given concentration level of

$MnCl_2$, as the $CsCl$ concentration of the melt increases, the cell potential also increases.

Figure 2 shows emf isotherms at $810^\circ C$ displayed on a plot of cell potential *vs.* $\log_{10} X_{MnCl_2}$ at various values of t . Experimental data are plotted, and the lines drawn through these points represent the best straight lines having a "two-electron" slope of $-RT/2F$. Also included in the figure are measurements performed previously in this laboratory (2) on concentrated binary solutions of $MnCl_2$ - $NaCl$ and $MnCl_2$ - $CsCl$. It may be seen that the results of the present study are consistent with those of Kucharski and Flengas (2) and reveal the anticipated extension to dilute solutions.

Table II displays partial molar enthalpies of mixing, partial molar entropies of mixing, activities, and activity coefficients of $MnCl_2$ calculated from the experimental results. The pertinent formulas are also given in the table.

Discussion

The Appendix traces the method by which the previously derived expressions [1]-[3], which describe the concentration dependence of an integral or a partial molar property in binary and ternary fused salt systems, may be reduced to useful simple equations of the form

$$(\Delta Z)_{123} = (1 - t)(\Delta Z)_{12} + t(\Delta Z)_{13} \quad [8]$$

where Z represents any such property. The ternary solution is denoted by the subscripts 1, 2, 3, while the two constituent binary solutions are denoted by the subscripts 1, 2 and 1, 3. Component 1 is always the divalent metal chloride, and t is the concentration variable defined by Eq. [6].

It is worth noting that although the general expression, Eq. [8], was derived on the assumption of tetrahedrally coordinated complexes of the type

Table I. Summary of experimental results

X_{MnCl_2}	X_{NaCl}	X_{CsCl}	y	t	$E = a - bT$ (V)		
					a (V)	b ($\times 10^3$ V/ $^{\circ}K$)	$\sigma_{E,T}^{**}$ ($\times 10^3$ V)
0.01	0.99	0.00	0.99	0.00	2.4102	0.2244	0.5
0.0293*	0.9707	0.00	0.9707	0.00	2.4057	0.2720	0.7
0.0981*	0.9019	0.00	0.9019	0.00	2.4078	0.3309	0.4
0.01	0.7425	0.2475	0.99	0.25	2.4694	0.2421	0.2
0.03	0.7275	0.2425	0.97	0.25	2.4560	0.2713	0.6
0.05	0.7125	0.2375	0.95	0.25	2.4823	0.3310	0.6
0.01	0.495	0.495	0.99	0.50	2.5288	0.2473	0.4
0.03	0.485	0.485	0.97	0.50	2.5095	0.2771	1.4
0.05	0.475	0.475	0.95	0.50	2.5381	0.3327	0.3
0.01	0.2475	0.7425	0.99	0.75	2.5808	0.2600	0.4
0.03	0.2425	0.7275	0.97	0.75	2.6036	0.3354	0.8
0.05	0.2375	0.7125	0.95	0.75	2.5982	0.3568	1.3
0.01	0.00	0.99	0.99	1.00	2.6435	0.2897	0.4
0.0319*	0.00	0.9681	0.9681	1.00	2.6428	0.3198	0.7
0.0981*	0.00	0.9019	0.9019	1.00	2.6193	0.3662	0.8

* $E^{\circ} = 2391.7 + 0.4043T \log_{10} T - 0.3729 \times 10^{-4} T^2 - 1.138 \times 10^8 T^{-1} - 1.7308T$ mV where $923^{\circ}K < T < 990^{\circ}K$.

* $E^{\circ} = 2376.6 + 0.2721T \log_{10} T - 0.78 \times 10^{-5} T^2 + 7.32 \times 10^8 T^{-1} - 1.3510T$ mV where $990^{\circ}K < T < 1200^{\circ}K$.

* Reference (2).

** Standard error of estimate.

A_2MCl_4 , the corresponding treatment for complexes of the type $AMCl_2$ and A_2MCl_6 yields Eq. [8]. The compounds $KAg(CN)_2$ (9) and K_2ZrCl_6 (10) are examples of nontetrahedrally coordinated complexes. In addition, similar treatment of the previously derived thermodynamic relationships in the concentration range $1.0 > X_{MCl_2} > 0.33$ also yields Eq. [8]. Hence, Eq. [8] appears to be of general applicability in expressing the relationship between the thermodynamic properties of binary and ternary fused salt systems containing a reactive component.

If Z is taken to represent the partial molar enthalpy and entropy of component 1, \bar{H}_1 and \bar{S}_1 , the relationship $RT \ln a_1 = \Delta\bar{H}_1 - T\Delta\bar{S}_1$ and Eq. 8 yield the following expression for the activity of MCl_2 in a ternary system

$$(a_{MCl_2})_{123} = (a_{MCl_2})_{12}^{(1-t)} (a_{MCl_2})_{13}^t \quad [9]$$

Equation [9] is valid when X_{MCl_2} has the same value in the ternary solution 1, 2, 3, as in the binary solutions 1, 2 and 1, 3. Equation [9] may be written in terms of activity coefficients as

$$(\gamma_{MCl_2})_{123} = (\gamma_{MCl_2})_{12}^{(1-t)} (\gamma_{MCl_2})_{13}^t \quad [10]$$

In very dilute solutions γ_{MCl_2} becomes independent of composition. As X_{MCl_2} approaches zero in a ternary

solution, $(1-t) \rightarrow X_{ACl}$, $t \rightarrow X_{BCl}$ and Eq. [10] may be written as

$$(\gamma_{MCl_2})_{123} = (\gamma^{\circ}_{MCl_2})_{12} X_{ACl} \cdot (\gamma^{\circ}_{MCl_2})_{13} X_{BCl} \quad [11]$$

where $(\gamma^{\circ}_{MCl_2})_{12}$ and $(\gamma^{\circ}_{MCl_2})_{13}$ represent the limiting values of γ_{MCl_2} at infinite dilution in the MCl_2 - ACl and MCl_2 - BCl binary systems, respectively, and X_{ACl} and X_{BCl} represent the mole fraction of ACl and BCl , respectively, in the ternary solution. Thus, with values of only the Henrian activity coefficient of MCl_2 in the two appropriate binary systems, Eq. [11] is able to estimate values of the activity coefficient of MCl_2 anywhere in the dilute region of the ternary system.

Table II shows a comparison between values of γ_{MCl_2} determined experimentally in the present study and values of γ_{MCl_2} calculated by Eq. [11]. For these calculations the values of γ_{MCl_2} at $X_{MCl_2} = 0.01$ in the appropriate binary solutions served as values for $(\gamma^{\circ}_{MCl_2})_{ik}$. Good agreement is obtained between observed and predicted values.

Figures 3a and b show plots of $\log \gamma_{MCl_2}$ vs. t in the systems $NiCl_2$ - $NaCl$ - KCl (12) and $CoCl_2$ - $NaCl$ - KCl (13), studied by Hamby and Scott, and $MnCl_2$ - $NaCl$ - $CsCl$, studied in the present investigation. The linear-

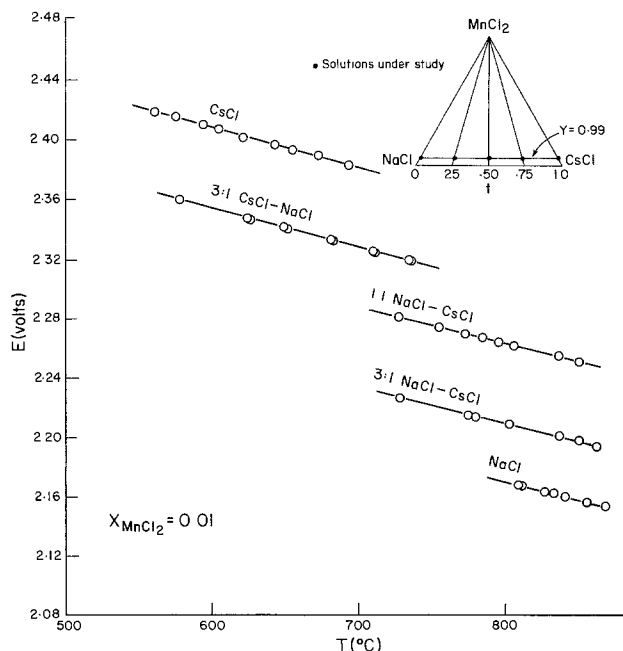


Fig. 1a. Temperature dependence of emf in the system $MnCl_2$ - $NaCl$ - $CsCl$ at $X_{MnCl_2} = 0.01$.

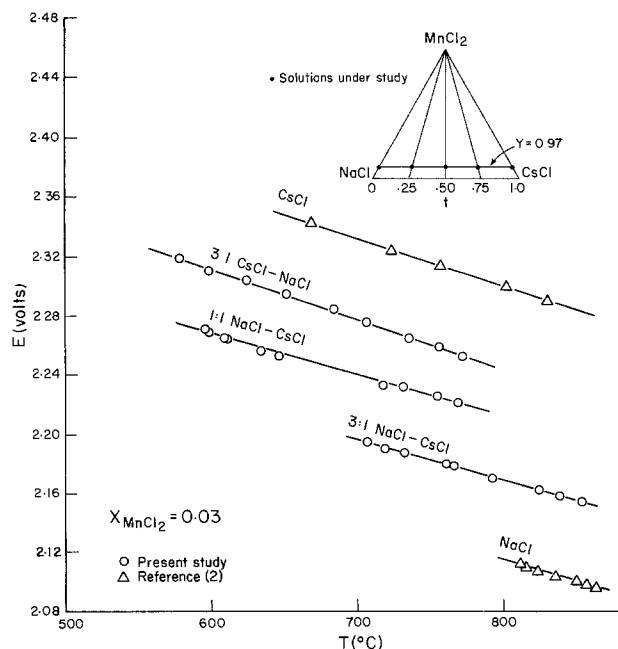


Fig. 1b. Temperature dependence of emf in the system $MnCl_2$ - $NaCl$ - $CsCl$ at $X_{MnCl_2} = 0.03$.

Table II. Partial molar properties of $MnCl_2$ in the ternary system $MnCl_2$ - $NaCl$ - $CsCl$

X_{MnCl_2}	t	$\overline{\Delta H}_{MnCl_2}^*$ (kcal) (observed)	$\overline{\Delta H}_{MnCl_2}$ (kcal) (calculated Eq. [A-6])	$\overline{\Delta S}_{MnCl_2}^{**}$ (cal/mole-°K) (observed)	$a_{MnCl_2}^{***}$ (observed)	a_{MnCl_2} (calculated Eq. [9])	$\gamma_{MnCl_2}^{***}$ (observed)	$\gamma_{MnCl_2}(\sim)$ (calculated Eq. [11])
0.01	0.00	-7.2	-7.0	9.06	3.99×10^{-4}	3.76×10^{-4}	3.99×10^{-2}	—
0.0293(x)	0.00	-6.9	-7.0	6.87	1.25×10^{-3}	1.26×10^{-3}	4.25×10^{-2}	—
0.0981(x)	0.00	-6.9	-6.7	4.27	4.70×10^{-3}	4.72×10^{-3}	4.79×10^{-2}	—
0.01	0.25	-9.6	-9.6	8.47	1.48×10^{-4}	1.60×10^{-4}	1.48×10^{-2}	1.54×10^{-2}
0.03	0.25	-9.2	-9.6	7.13	5.00×10^{-4}	3.86×10^{-4}	1.67×10^{-2}	1.68×10^{-2}
0.05	0.25	-10.3	-9.5	4.35	9.48×10^{-4}	9.54×10^{-4}	1.90×10^{-2}	1.83×10^{-2}
0.01	0.50	-12.3	-12.3	8.26	5.47×10^{-5}	5.06×10^{-5}	5.47×10^{-3}	5.78×10^{-3}
0.03	0.50	-11.4	-12.2	6.93	1.87×10^{-4}	1.53×10^{-4}	6.23×10^{-3}	6.42×10^{-3}
0.05	0.50	-12.7	-12.1	4.39	3.60×10^{-4}	3.00×10^{-4}	7.20×10^{-3}	7.12×10^{-3}
0.01	0.75	-14.8	-14.9	7.65	2.04×10^{-5}	2.24×10^{-5}	2.04×10^{-3}	2.17×10^{-3}
0.03	0.75	-15.7	-14.8	4.25	7.03×10^{-5}	7.86×10^{-5}	2.34×10^{-3}	2.45×10^{-3}
0.05	0.75	-15.5	-14.6	3.30	1.37×10^{-4}	1.45×10^{-4}	2.74×10^{-3}	2.77×10^{-3}
0.01	1.00	-17.6	-17.5	7.24	7.55×10^{-6}	7.30×10^{-6}	7.55×10^{-4}	—
0.0319(x)	1.00	-17.5	-17.4	4.99	2.37×10^{-5}	2.37×10^{-5}	7.42×10^{-4}	—
0.09871(x)	1.00	-16.4	-16.7	2.88	1.15×10^{-4}	1.15×10^{-4}	1.17×10^{-3}	—

$$* \overline{\Delta H}_{MnCl_2} = -2F \left(\frac{\partial(E - E^0)/T}{\partial(1/T)} \right)_{P, n_{NaCl}, n_{CsCl}}$$

$$** \overline{\Delta S}_{MnCl_2} = 2F \left(\frac{\partial(E - E^0)}{\partial T} \right)_{P, n_{NaCl}, n_{CsCl}}$$

$$*** \ln a_{MnCl_2} = - \frac{2F}{RT} (E - E^0), \text{ where } a_{MnCl_2} = \gamma_{MnCl_2} X_{MnCl_2}$$

(x) Reference (2).

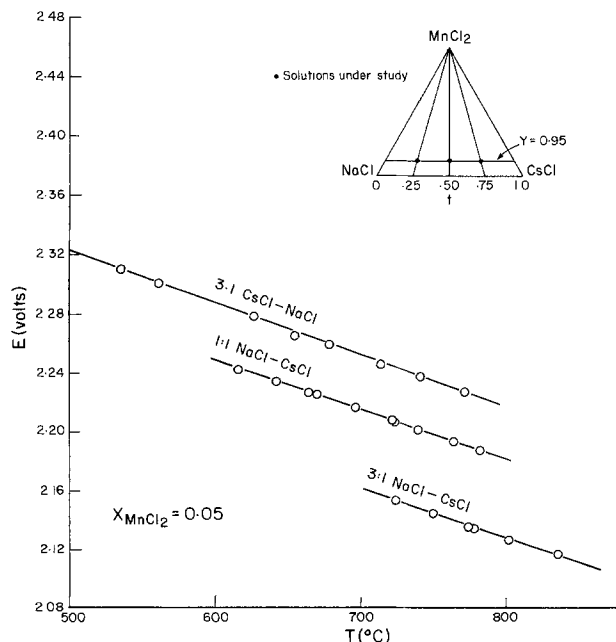
(\sim) Values of γ_{MnCl_2} in the two binary systems:

$$(\gamma_{MnCl_2})_{12} = 3.99 \times 10^{-2}; (\gamma_{MnCl_2})_{13} = 7.55 \times 10^{-4}$$

ity of these curves demonstrates the validity of Eq. [10] even for concentrated solutions. Figure 3b also includes data from the study by Pelton and Flengas (14) of the $AgCl$ - $NaCl$ - $RbCl$ system. As expected, Eq. [10] is obeyed in this system, although $AgCl$ is not a divalent transition-metal chloride and is not known to form tetrahedrally coordinated complexes.

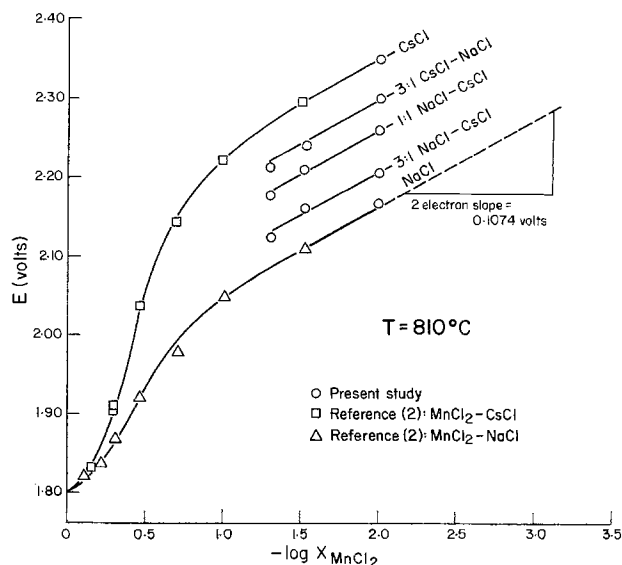
The integral enthalpies of mixing in the binary systems, $MnCl_2$ - $NaCl$ and $MnCl_2$ - $CsCl$, as well as those in the ternary system, $MnCl_2$ - $NaCl$ - $CsCl$, have been measured calorimetrically in this laboratory (12). Figure 4 shows plots of ΔH_{mix}^{int} vs. t at various fixed concentrations of $MnCl_2$. The linearity of these curves demonstrates the validity of the "t-fraction average" rule proposed herein.

The least squares analysis of these data revealed linearity to 99.9% confidence limits. It should be noted that Eq. [A-5] is observed in solutions highly concentrated in $MnCl_2$.

Fig. 1c. Temperature dependence of emf in the system $MnCl_2$ - $NaCl$ - $CsCl$ at $X_{MnCl_2} = 0.05$.

The partial molar enthalpies of $MnCl_2$ in the binary systems $MnCl_2$ - $NaCl$ and $MnCl_2$ - $CsCl$ have been measured in this laboratory by an emf method (2). In the present study $\overline{\Delta H}_{MnCl_2}$ has been determined for dilute solutions in the ternary system, $MnCl_2$ - $NaCl$ - $CsCl$. Figure 5 shows a plot of $\overline{\Delta H}_{MnCl_2}$ vs. t for $X_{MnCl_2} = 0.01$. By statistical analysis this curve is found to be linear within 99.9% confidence limits, as expected from the theoretical treatment.

Thus, by the use of Eq. [A-5], [A-6], [10], and [11] the thermodynamic behavior of $MnCl_2$ in the ternary solution, $MnCl_2$ - $NaCl$ - $CsCl$, is completely characterized by expressions which contain thermodynamic quantities representing only the binary solutions, $MnCl_2$ - $NaCl$ and $MnCl_2$ - $CsCl$. Table II also includes partial molar enthalpies and activities predicted by the theory. The binary data used for these calculations, with the exception of values for ΔS_R , were those determined by Kucharski and Flengas (2) in their emf study of the binary systems, $MnCl_2$ - $NaCl$ and $MnCl_2$ - $CsCl$. Values for ΔS_R in the present study were determined from

Fig. 2. Concentration dependence of emf in the system $MnCl_2$ - $NaCl$ - $CsCl$ at $810^\circ C$.

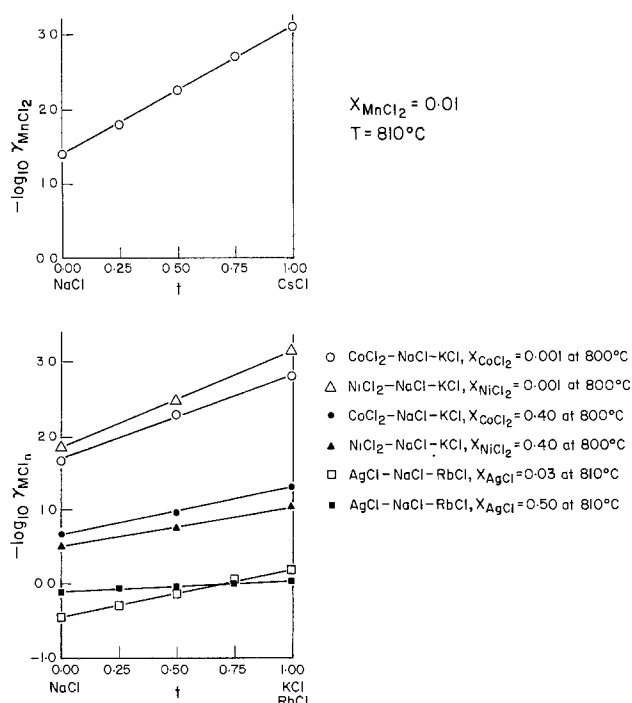


Fig. 3. Concentration dependence of activity coefficient in some ternary systems: (a, top) $\text{MnCl}_2\text{-NaCl-CsCl}$ and (b, bottom) $\text{CoCl}_2\text{-NaCl-KCl}$; $\text{NiCl}_2\text{-NaCl-KCl}$; AgCl-NaCl-RbCl .

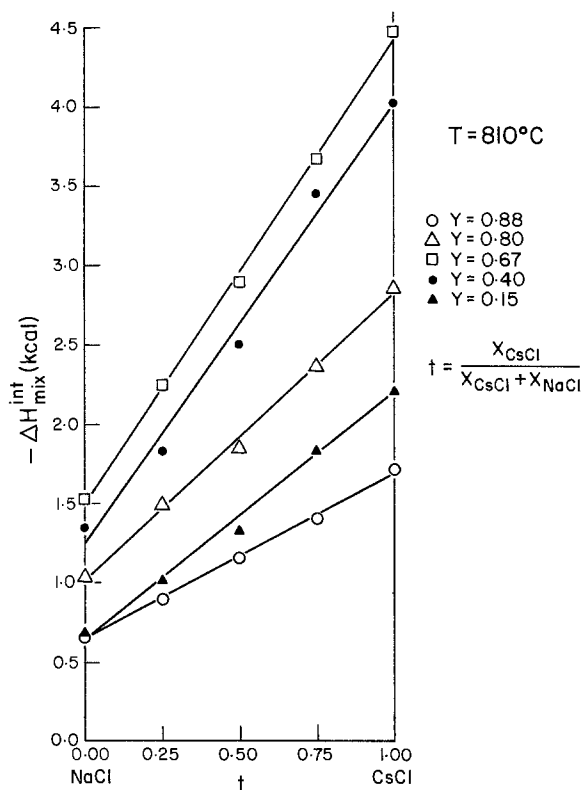


Fig. 4. Concentration dependence of the integral enthalpy of mixing in the system $\text{MnCl}_2\text{-NaCl-CsCl}$ at 810°C .

the slope of a plot of $\log \gamma_{\text{MnCl}_2}$ vs. $1/T$ in the appropriate binary systems.

Conclusions

The treatment of binary and ternary fused salt solutions in terms of a thermodynamic model has led to the derivation of simple expressions which relate the thermodynamic properties of ternary fused salt solu-

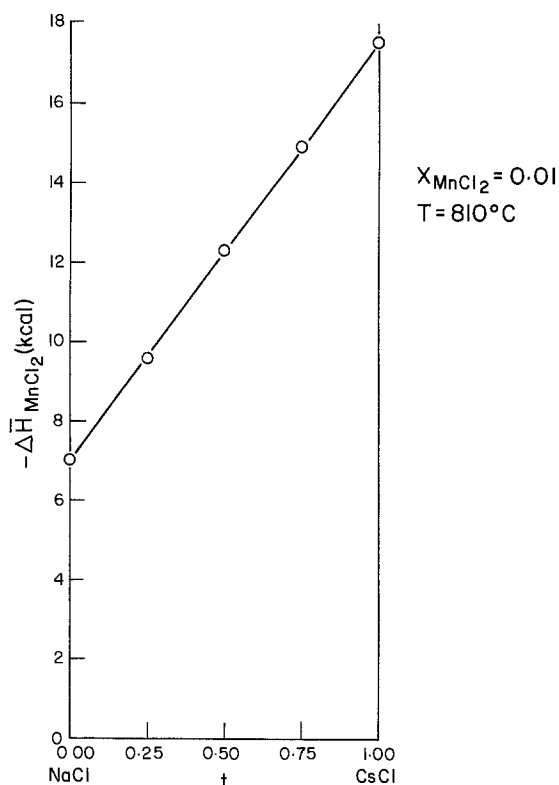


Fig. 5. Concentration dependence of the partial molar enthalpy of mixing of MnCl_2 in the system $\text{MnCl}_2\text{-NaCl-CsCl}$ at 810°C .

tions to the properties of constituent binary solutions. The relationship in generalized form is summarized by Eq. [8] which contains only experimentally determinable quantities and which may be used without detailed knowledge of the thermodynamic model.

Limiting laws for dilute solutions have also been derived. The expressions have been verified by the results of the present investigation of the system $\text{MnCl}_2\text{-NaCl-CsCl}$, as well as by the results of several other ternary systems in the literature. The applicability of these expressions to a range of systems suggests that the structural model on which the derivations are based is physically meaningful.

Acknowledgment

The financial assistance to one of the authors (D.R.S.) by the Steel Company of Canada in the form of a Stelco Graduate Research Fellowship in Metallurgy is gratefully acknowledged.

Manuscript submitted Sept. 10, 1974; revised manuscript received Nov. 7, 1974.

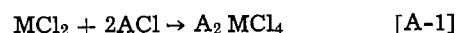
Any discussion of this paper will appear in a Discussion Section to be published in the December 1975 JOURNAL. All discussions for the December 1975 Discussion Section should be submitted by Aug. 1, 1975.

Publication costs of this article were partially assisted by the University of Toronto.

APPENDIX

Expressions for the Thermodynamic Properties of Ternary Solutions of the Type $\text{MCl}_2\text{-ACl-BCl}$ Derived from the Complex Ion Model (3)

For a melt having the primary composition X_{MCl_2} , X_{ACl} , and X_{BCl} , where $0 < X_{\text{MCl}_2} < 0.33$, the reactions



produce new species.

The expression which describes the concentration dependence of the enthalpy of mixing in the ternary system $\text{MCl}_2\text{-ACl-BCl}$ has been derived elsewhere (3).

For a solution of composition $0 < X_{\text{MCl}_2} < 0.33$ the molar integral enthalpy of mixing is given by

$$\begin{aligned} \Delta H_{\text{mix}}^{\text{int}} = & (1-y)[(1-t)(b_R)_{12} + t(b_R)_{13}] \\ & + \frac{(1-y)^2(2-3y)}{(2y-1)^2} [(1-t)(2b_1 + b_2)_{12} \\ & + t(2b_1 + b_2)_{13}] + \frac{2(3y-2)^2(1-y)}{(2y-1)^2} \\ & [(1-t)(2b_1 + b_2)_{12} + t(2b_1 + b_2)_{13}] \\ & - \frac{(1-y)(3y-2)^2}{(2y-1)^2} [(1-t)(3b_1 + b_2)_{12} \\ & + t(3b_1 + b_2)_{13}] + \frac{2(1-y)^2(3y-2)}{(2y-1)^2} \\ & [(1-t)(b_1 + b_2)_{12} + t(b_1 + b_2)_{13}] \quad [\text{A-3}] \end{aligned}$$

By a rearrangement of terms Eq. [A-3] is further reduced to

$$\begin{aligned} \Delta H_{\text{mix}}^{\text{int}} = & (1-y)[(1-t)(b_R)_{12} + t(b_R)_{13}] \\ & + \frac{(3y-2)(1-y)}{(2y-1)^2} \{(3y-2)[(1-t)(b_1)_{12} \\ & + t(b_1)_{13}] + (2y-1)[(1-t)(b_2)_{12} + t(b_2)_{13}]\} \quad [\text{A-4}] \end{aligned}$$

where the interaction parameters b_R , b_1 , and b_2 are defined by equations 14 and 18 of Ref. (2) and have values determined in the appropriate binary system.

The substitution of y by its equivalent, $1 - X_{\text{MCl}_2}$, in Eq. [A-4] followed by factoring and comparison of the resulting expression with the corresponding expressions for the binary systems yields the much simpler relationship

$$\begin{aligned} \{\Delta H_{\text{mix}}^{\text{int}}(X_{\text{MCl}_2}, t)\}_{123} = & (1-t)\{\Delta H_{\text{mix}}^{\text{int}}(X_{\text{MCl}_2})\}_{12} \\ & + t\{\Delta H_{\text{mix}}^{\text{int}}(X_{\text{MCl}_2})\}_{13} \quad [\text{A-5}] \end{aligned}$$

which is valid when the concentration of MCl_2 in the ternary solution 1, 2, 3 is the same as that of the two constituent binary solutions, 1, 2 and 1, 3. The expressions for $\Delta H_{\text{mix}12}^{\text{int}}$ and $\Delta H_{\text{mix}13}^{\text{int}}$ are given by equation 19 of Ref. (2).

Partial differentiation of Eq. [A-4] followed by rearrangement of terms yields the result

$$\begin{aligned} \{\Delta \bar{H}_{\text{MCl}_2}(X_{\text{MCl}_2}, t)\}_{123} = & (1-t)\{\Delta \bar{H}_{\text{MCl}_2}(X_{\text{MCl}_2})\}_{12} \\ & + t\{\Delta \bar{H}_{\text{MCl}_2}(X_{\text{MCl}_2})\}_{13} \quad [\text{A-6}] \end{aligned}$$

The integral entropy of mixing may also be treated as the sum of two terms: an internal entropy change associated with reactions [A-1] and [A-2] and a configurational entropy change due to the mixing of the products of these reactions. Since it is assumed that there is no interaction between A_2MCl_4 and B_2MCl_4 , the internal entropy change is given by

$$\Delta S^{\text{internal}} = (1-y)[(1-t)(\Delta S_R)_{12} + t(\Delta S_R)_{13}] \quad [\text{A-7}]$$

where $(\Delta S_R)_{12}$ and $(\Delta S_R)_{13}$ are the molar entropies of formation of pure A_2MCl_4 and B_2MCl_4 , respectively. The configurational term is given by

$$\Delta S^{\text{configurational}} = -R[N_i \sum \ln N_i] \quad [\text{A-8}]$$

where N_i is the ionic fraction of species i and the summation is extended over all ionic species present in the reacted system.

Accordingly, the molar integral entropy of mixing in the ternary system $\text{MCl}_2\text{-ACl-BCl}$ for the composition range $0.33 > X_{\text{MCl}_2} > 0.0$ is given by

$$\begin{aligned} \Delta S_{\text{mix}}^{\text{int}} = & (1-y)[(1-t)(\Delta S_R)_{12} + t(\Delta S_R)_{13}] \\ & - R[(1-t) \ln(1-t) + t \ln t \\ & + \frac{(1-y)}{(2y-1)} \ln \frac{(1-y)}{(2y-1)} + \frac{(3y-2)}{(2y-1)} \ln \frac{(3y-2)}{(2y-1)}] \quad [\text{A-9}] \end{aligned}$$

Rearrangement of terms, substitution of $y = 1 - X_{\text{MCl}_2}$, and comparison of the expression for the binary systems yields the much simpler expression

$$\begin{aligned} \{\Delta S_{\text{mix}}^{\text{int}}(X_{\text{MCl}_2}, t)\}_{123} = & (1-t)\{\Delta S_{\text{mix}}^{\text{int}}(X_{\text{MCl}_2})\}_{12} \\ & + t\{\Delta S_{\text{mix}}^{\text{int}}(X_{\text{MCl}_2})\}_{13} \quad [\text{A-10}] \end{aligned}$$

Partial differentiation of Eq. [A-10] followed by substitution of $y = 1 - X_{\text{MCl}_2}$ gives

$$\begin{aligned} \Delta \bar{S}_{\text{MCl}_2} = & (1-t)(\Delta S_R)_{12} + t(\Delta S_R)_{13} \\ & - R \ln \frac{X_{\text{MCl}_2}(1-2X_{\text{MCl}_2})}{1-3X_{\text{MCl}_2}} \quad [\text{A-11}] \end{aligned}$$

The logarithmic term may be factored to give

$$\begin{aligned} \Delta \bar{S}_{\text{MCl}_2} = & (1-t) \left[(\Delta S_R)_{12} - R \ln \frac{X_{\text{MCl}_2}(1-2X_{\text{MCl}_2})}{(1-3X_{\text{MCl}_2})^2} \right] \\ & t \left[(\Delta S_R)_{13} - R \ln \frac{X_{\text{MCl}_2}(1-2X_{\text{MCl}_2})}{(1-3X_{\text{MCl}_2})^2} \right] \quad [\text{A-12}] \end{aligned}$$

Comparison of Eq. [A-12] with equation 47 of Ref. (2) gives

$$\begin{aligned} \{\Delta \bar{S}_{\text{MCl}_2}(X_{\text{MCl}_2}, t)\}_{123} = & (1-t)\{\Delta \bar{S}_{\text{MCl}_2}(X_{\text{MCl}_2})\}_{12} \\ & + t\{\Delta \bar{S}_{\text{MCl}_2}(X_{\text{MCl}_2})\}_{13} \quad [\text{A-13}] \end{aligned}$$

These equations demonstrate that the values of the integral and partial molar enthalpies and the integral and partial molar entropies of mixing in a ternary solution are the "t-fraction average" of the corresponding properties in the two constituent binary solutions having the same MCl_2 concentration as the ternary solution.

REFERENCES

1. S. N. Flengas and A. S. Kucharski, *Can. J. Chem.*, **49**, 3971 (1971).
2. A. S. Kucharski and S. N. Flengas, *This Journal*, **119**, 1170 (1972).
3. S. N. Flengas and J. M. Skeaff, *Can. J. Chem.*, **50**, 1345 (1972).
4. A. S. Kucharski and S. N. Flengas, *This Journal*, **121**, 1298 (1974).
5. G. N. Papatheodorou and O. J. Kleppa, *J. Inorg. Nucl. Chem.*, **33**, 1249 (1971).
6. G. N. Papatheodorou and O. J. Kleppa, *Inorg. Chem.*, **10**, 872 (1971).
7. G. N. Papatheodorou and O. J. Kleppa, *J. Inorg. Nucl. Chem.*, **32**, 889 (1970).
8. F. G. McCarty and O. J. Kleppa, *J. Phys. Chem.*, **70**, 1249 (1966).
9. S. N. Flengas and Sir Eric Rideal, *Proc. Roy. Soc. A*, **223**, 443 (1956).
10. R. L. Lister and S. N. Flengas, *Can. J. Chem.*, **43**, 2947 (1965).
11. J. M. Skeaff, Ph.D. thesis, University of Toronto, Toronto, Ontario, Canada (1971).
12. D. C. Hamby and A. B. Scott, *This Journal*, **115**, 704 (1968).
13. D. C. Hamby and A. B. Scott, *ibid.*, **117**, 319 (1970).
14. A. D. Pelton and S. N. Flengas, *ibid.*, **118**, 1307 (1971).
15. A. D. Pelton and S. N. Flengas, *ibid.*, **117**, 1130 (1970).

The Triangular Voltage Sweep Method for Determining Double-Layer Capacity of Porous Electrodes

IV. Porous Carbon in Potassium Hydroxide

E. G. Gagnon*

Electrochemistry Department, General Motors Research Laboratories, Warren, Michigan 48090

ABSTRACT

Triangular sweep voltammetry data for a number of commercially available carbons in 31 weight per cent KOH are discussed. A capacity minimum of $10 \mu\text{f}/\text{cm}^2$ was observed about 0V vs. Hg/HgO for five carbon blacks. Results indicated that the carbon blacks with internal structure were completely wetted; results with one activated carbon having fine micropores ($<25\text{\AA}$) indicated partial wetting. Experimental methods for minimizing faradaic current and distributed capacity effects are discussed.

Many electrochemical processes involve porous electrodes. To optimize porous electrode design for specific applications, it is necessary to know how much of the internal structure of the porous electrode is actually used during the reaction. Although the BET surface area method is often used for this purpose, it does not always give a reliable estimate of the surface area available for electrochemical reaction. One method of determining the wetted surface area available for electrochemical reactions involves a measurement of the double-layer capacity (DLC) of the electrode-electrolyte interface using the triangular voltage sweep (TVS) technique (1). However, complicating effects may arise with porous electrodes due to distributed capacity (i.e., nonuniform reactions through the electrode) and faradaic current (2). These effects must be eliminated or at least minimized. This paper shows how the TVS technique was used to determine the wetted surface area of several commercially available carbons in KOH.

Theory

Faradaic currents are often caused by processes which are complex and difficult to describe mathematically (e.g., removal of impurities on the electrode surface or the adsorption of species present in the solution). Distributed capacity effects arise when the exterior surface of the porous electrode charges or discharges faster than the interior. An increase in the resistance of the electrolyte in the pores of the electrode enhances this effect. Four cases of interest have been previously discussed (2) for the TVS method and some of the essential features pertinent to this study are summarized in Fig. 1. The triangular sweep voltammetry data for the cases discussed apply to potential regions where the capacity is constant.

It has been demonstrated (2) that faradaic currents can be eliminated, or at least minimized, by testing at lower temperatures. [A precise definition of what is meant by low temperature depends upon the physical properties of the porous electrode and the electrolyte (3).] At lower temperatures, distributed capacity effects can become quite serious. Likewise, the use of high surface area materials can give rise to severe distributed capacity effects, even at room temperature. The principal equations describing this effect are summarized below. In the absence of faradaic current, the current-time curve in region abc (Fig. 1C) can be predicted from

$$i(L) = \beta_1 k C' \quad [1]$$

$$\beta_1 = f_1(\psi, t/\rho_e C' L) \quad 0 \leq \beta \leq 1$$

$$\psi = L\lambda/d$$

and the current-time curve is region cde (Fig. 1C) can be predicted (3) from

$$i(L) = \gamma k C' \quad [2]$$

$$\gamma = f_2(\psi, t/\rho_e C' L) \quad 1 \geq \gamma \geq -1$$

where $i(L)$ is the current density at the face of the porous electrode; k is the sweep rate; C' is capacity based upon the geometric area of the electrode thickness, L ; λ is the labyrinth factor; d is the distance between the tip of the Luggin capillary and the surface of the test electrode; t is time; ρ_e is the effective specific resistance of the electrolyte in the pores of the electrode.

Predicted and experimental results (2, 3) have shown that as time decreases, or as the specific resistance of the electrolyte increases, distributed capacity effects become more severe.

The electrical double-layer at the electrode-electrolyte interface has a thickness of only a few angstroms in concentrated electrolytes and therefore follows the microcontours of the surface. Thus the DLC of the electrode is proportional to surface area at least in potential regions where capacity is constant and faradaic current and distributed capacity effects are negligible. With high surface area materials, severe distributed capacity effects can arise (see Eq. [1] and [2]), but the effects can often be minimized experimentally.

Experimental

Materials.—Five commercially available carbon blacks and one activated carbon were used. Table I gives the specific BET surface area of each carbon and the percentage of internal surface estimated using

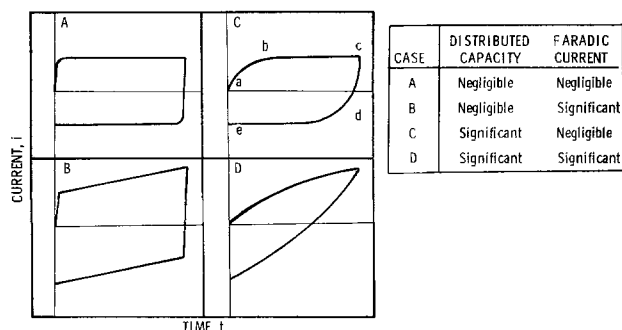


Fig. 1. TVS results illustrating distributed capacity and/or faradaic current effects in potential regions where capacity is constant.

* Electrochemical Society Active Member.

Key words: double-layer capacity, triangular voltage sweep, porous electrodes, carbon structures.

Table I. Properties of carbon types

Sample	Material	Avg. particle diameter (m μ)	Surface area	
			BET, m ² /g	Internal %
A	Colloidex-5	29	85	0
B	Conductex SC	17	145	0
C	Conductex 950	21	245	45
D	Raven 30	27	82	0
E	Vulcan XC-72	30	230	56
F	Norit-A	Unknown	910	Unknown

$$\frac{A_{\text{BET}} - A_d}{A_{\text{BET}}} \times 100$$

where A_{BET} is the BET surface area and A_d is the surface area calculated from the average particle size dimensions and a volume-to-area ratio of $(4/3\pi r^3)/4\pi r^2 = r/3$ where r is the average particle radius. Table II gives the source of the carbons used and the heat-treatments used to stabilize the carbon properties by removing impurities and increasing the electrical conductivity. Each carbon was supported on unpressed porous nickel MetNet (4) disks having a geometric area of 9.6 cm². The MetNet disks were dipped for several minutes into suspensions of carbon and reagent grade isopropyl alcohol (10g carbon/400 ml IPA). The electrodes were then air-dried at 100°C.

Procedures.—Details of the electrochemical cell, the Teflon test electrode holder, and preparation of the solutions are given elsewhere (5). An Hg/HgO [31 weight per cent (w/o) KOH] reference electrode with a Luggin capillary was used. The complete cell and the reference electrode were assembled in a constant-temperature cabinet. Prior to all testing, the electrolyte was equilibrated at the test temperature for periods of at least 18 hr. After the electrodes were immersed in the KOH, they were potentiostated at -0.50V vs. Hg/HgO for several hours to consume the dissolved oxygen in the pores of the electrode; no other precautions were taken to deaerate the KOH.

Triangular voltage sweeps (TVS) were performed using a potentiostat in conjunction with a signal generator; an X-Y recorder plotted current as a function of potential, from which capacities were calculated. In all of the tests, small voltage excursions of 140 mV were used to minimize transient faradaic currents in order to determine capacity solely as a function of potential. Experimental conditions were selected to allow the individual voltammetry sweeps to superimpose, giving an envelope of potential vs. current. Capacities were calculated from

$$C = i/k$$

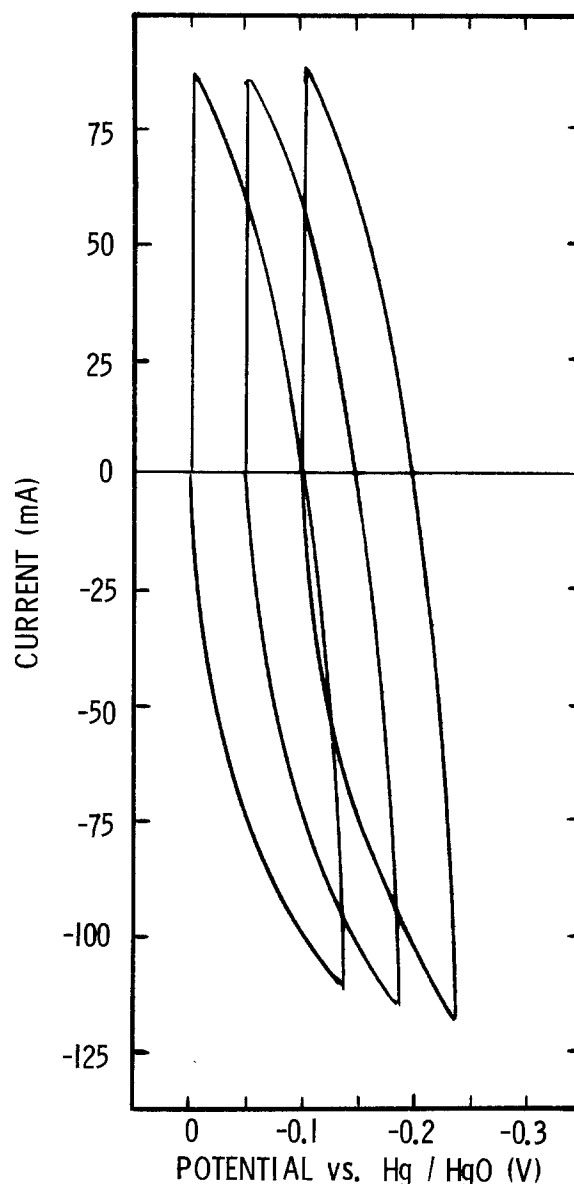
where C is capacity (farads), i is current (mA), and k is sweep rate (mV/sec).

Results and Discussion

Carbon blacks.—Proper experimental conditions had to be determined for each carbon black. For example, Fig. 2 shows a composite of three single TVS curves for 82 mg of sample E (Table III) supported on MetNet in 31 w/o KOH at 21°C. Each sweep begins at a different potential, covers a voltage excursion of 140

Table II. Identification of commercially available carbons

Sample	Type	Source	Process	Heat-treatment		
				Temp. (°C)	Time (hr)	Environment
A	Black	Columbian	Furnace	1000	2.5	H ₂
B	Black	Columbian	Furnace	1200	2.5	H ₂
C	Black	Columbian	Furnace	1000	2.5	N ₂
D	Black	Columbian	Furnace	1200	2.5	H ₂
E	Black	Cabot	Furnace	1000	2.5	H ₂
F	Acti- vated	American Norit Co.	Steam and CO ₂ ac- tivation	1200	2.5	H ₂

Fig. 2. TVS results for sample E at 21°C; $k = 60$ mV/sec

mV, and has the same sweep rate of 60 mV/sec. The results show severe distributed capacity effects (Fig. 1C) with perhaps some additional contributions of faradaic current (Fig. 1D). Decreasing the sweep rate by an order of magnitude to 6 mV/sec (Fig. 3) markedly reduces the distributed capacity and faradaic current effects. Only a small faradaic current effect is

Table III. Capacity data for carbon types¹

Sample	Weight (mg)	Temperature (°C)	Minimum capacity, C_{min} ² (farads)
A	65.5	21	0.78
	65.5	-46	0.75
B	61.6	21	0.81
	131.9	21	3.12
D	122.1	21	0.81
	77.3	21	0.62
E	77.3	-46	0.59
	82.1	21	1.87
	82.1	-46	1.70
	30.6	21	0.72
F	30.6	-46	0.75
	76.5	21	3.42 ²
	46.5	21	1.56 ²

¹ All capacity values were determined using a sweep rate of 6 mV/sec except for sample F which required a sweep rate of 0.6 mV/sec.

² After soaking in KOH for 2 days.

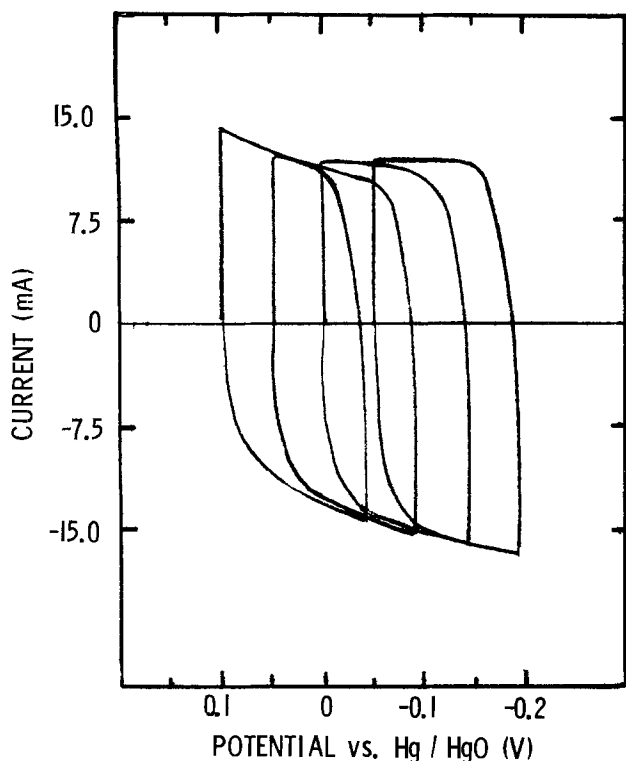


Fig. 3. TVS results for sample E at 21°C; $k = 6$ mV/sec

seen in the cathodic direction. The voltammetry data superimpose to form an envelope of potential *vs.* current where the minimum in the vicinity of 0V *vs.* Hg/HgO (anodic direction) corresponds to a capacity, C_{\min}^a of 1.87f or $C^* = 9.9 \mu\text{f}/\text{cm}^2$, based upon the BET surface area of the carbon. The effect of lowering the temperature to -46°C , while keeping the sweep rate at 6 mV/sec is seen in Fig. 4. At the lower temperature faradaic current is markedly reduced (compared to the 21°C data, Fig. 3), but distributed capacity effects are slightly enhanced; the capacity minimum, C_{\min}^a is 1.70f or $C^* = 9.3 \mu\text{f}/\text{cm}^2$ and are slightly lower than the 21°C values.

To determine the reliability of the capacity data, a different loading of sample E was tested. If capacity is constant and both faradaic current and distributed capacity effects are negligible, a plot of capacity *vs.*

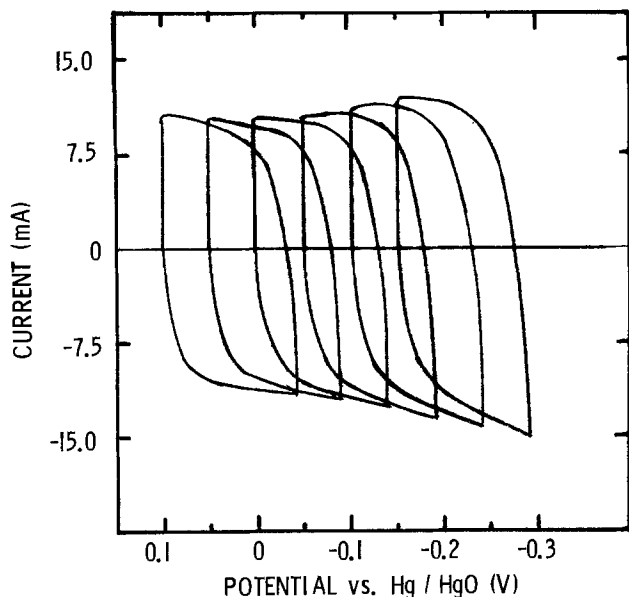


Fig. 4. TVS results for sample E at -46°C ; $k = 6$ mV/sec

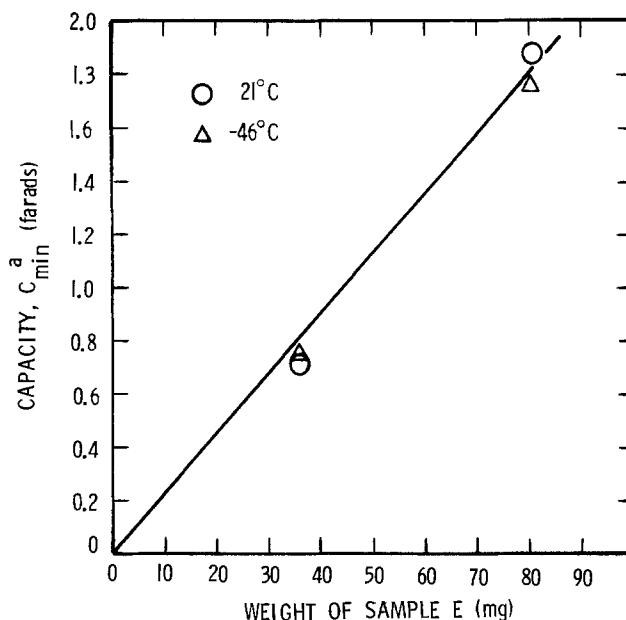


Fig. 5. Capacity *vs.* weight of sample E at 21°C and -46°C ; $k = 6$ mV/sec.

sample weight should be linear. Figure 5 shows such a plot to be linear giving an average capacity, C^* , of $9.8 \mu\text{f}/\text{cm}^2$ (based upon the BET surface area of $230 \text{m}^2/\text{g}$).

Figure 6 shows a near parabolic dependency of current (hence capacity) with potential for sample E at -46°C ; similar results were also observed for the other carbons tested.

Table III gives a compilation of capacity values obtained for all of the carbons tested; included are values obtained at 21° and -46°C and for different loadings wherever possible. Figure 7 shows that the plot of C_{\min}^a *vs.* BET surface area using all of the carbon black data is linear with a slope of $9.6 \mu\text{f}/\text{cm}^2$. This average value is in good agreement with results by Soffer and Folman (6) where integral capacities of 10.7 and $9.5 \mu\text{f}/\text{cm}^2$ were found for blocks of porous carbon.

Two of the carbon blacks had internal structure (samples C and E), whereas the others did not (Table I). Results in Fig. 7 suggest that the internal structures of samples C and E were completely wetted by the KOH, and that the technique gives a reliable estimate of the wetted surface area available for electrochemical reaction.

The capacity-potential curves in the region of the minimum (Fig. 6) take the form of a shallow parabola and are similar in shape to results reported by Randin and Yeager (7) using stress annealed pyrolytic graphite. The capacity at the minimum ($\sim 10 \mu\text{f}/\text{cm}^2$) is also lower than that of metallic electrodes under similar conditions [*i.e.*, approximately $30 \mu\text{f}/\text{cm}^2$ (1, 2) for

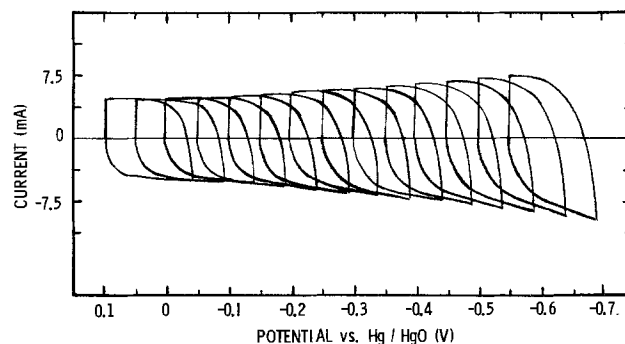


Fig. 6. Effect of potential with sample E at -46°C ; $k = 6$ mV/sec.

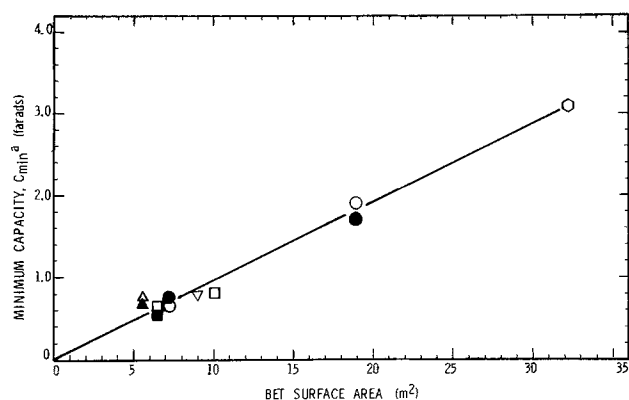


Fig. 7. Minimum capacity vs. BET surface area for commercially available carbon blacks. \triangle Sample A at 21°C; \blacktriangle sample A at -46°C; ∇ sample B at 21°C; \circ sample C at 21°C; \square sample D at 21°C; \blacksquare sample D at -46°C; \circ sample E at 21°C; \bullet sample E at -46°C.

silver and nickel in 31 w/o KOH]. Since carbon is a semiconductor and has a space charge region, the observed capacity at an electrode-electrolyte interface should reflect this property. Thus, in concentrated electrolytes where diffuse double-layer effects can be considered negligible, one would expect that

$$\frac{1}{C^*} = \frac{1}{C_{DL}} + \frac{1}{C_{sc}} \quad [3]$$

where C_{DL} is the ionic double-layer capacity and C_{sc} is the space charge layer capacity. A rough estimate of C_{sc} for the carbon blacks is $15 \mu\text{f}/\text{cm}^2$ using $C_{DL} = 30 \mu\text{f}/\text{cm}^2$ and $C^* = 10 \mu\text{f}/\text{cm}^2$. The C_{sc} value is higher than that reported by Randin and Yeager (7) for stress annealed pyrolytic graphite and is subject to some question. On the other hand, one would not expect carbon blacks to behave the same as pyrolytic graphite. Bauer *et al.* (8) have reported vast differences in capacity data for pyrolytic graphites as a function of electrode preparation. C_{sc} is known to vary in a hyperbolic cosine manner with potential (9) which would explain the parabolic shape observed in the vicinity of the capacity minimum (Fig. 6). Therefore, regardless of the precise value of C_{sc} , it does appear to contribute to the capacity of the carbon-electrolyte interface as suggested in Eq. [3], tending to give a lower apparent capacity than that normally seen with metallic electrodes.

Activated carbon.—The capacity of sample F (Table III), an activated carbon with a specific BET surface area of about $910 \text{ m}^2/\text{g}$ (after heat-treatment, Table II) increased with soak time and leveled off at a steady value after 2 days of immersion; a different loading showed the same type of behavior. (In general, with the carbon blacks a steady value was achieved within hours of immersion and in some cases within minutes.) Capacities at the minimum (Table III) were about 45% of the values expected assuming that activated carbon has the same specific double-layer capacity as carbon blacks. This indicates that the internal structure of the activated carbon may not have been completely wetted by the KOH. A pore size distribution for sample F shows that about 42% of the material has pore sizes less than 25\AA , whereas for the carbon blacks, most of the pores are in the range of $20\text{--}60\text{\AA}$. It would appear that below a certain critical pore size, the internal microporous structure of the activated carbon is not readily accessible to the KOH. This might also account for the slower rate of wetting experienced with the activated carbon than with the carbon blacks.

Conclusions

Capacity data determined using the triangular voltage sweep technique were used to estimate the wetted

surface area of a variety of commercially available carbons.

A capacity minimum of $10 \mu\text{f}/\text{cm}^2$ was observed in the vicinity of $0\text{V vs. Hg}/\text{HgO}$ for all of the five carbon blacks. The low value compared to metallic electrodes was explained in terms of a contribution due to a space charge layer which exists in semiconductors. Likewise, semiconductor theory was used to explain a near-parabolic dependence of capacity on potential.

Results indicated that the carbon blacks which had some internal structure were completely wetted by the KOH.

Severe distributed capacity effects were observed especially with some of the higher surface area materials. The effects were consistent with that predicted using a previously developed model (3) and therefore could be minimized using suitable experimental techniques.

Capacity data for the one high surface area activated carbon tested indicated that about 45% of the internal structure of the material was not accessible to the KOH. This was presumably due to the presence of very fine micropores which exist in some activated carbons ($<25\text{\AA}$).

Acknowledgments

I wish to thank Professor E. Yeager of Case Western Reserve University and Dr. R. R. Witherspoon of General Motors Research Laboratories for helpful discussions during the course of this work.

Manuscript submitted May 13, 1974; revised manuscript received Nov. 12, 1974. This was Paper 36 presented at the New York, New York, Meeting of the Society, Oct. 13-17, 1974.

Any discussion of this paper will appear in a Discussion Section to be published in the December 1975 JOURNAL. All discussions for the December 1975 Discussion Section should be submitted by Aug. 1, 1975.

Publication costs of this article were partially assisted by General Motors Corporation.

LIST OF SYMBOLS

A_{BET}	BET surface area, m^2/g
A_d	surface area calculated from the average size dimensions of the carbon particles, m^2/g
C	capacity, farads
C'	capacity based upon the geometric area of the electrode, $\mu\text{f}/\text{cm}^2$
C_{min}^a	anodic capacity minimum, farads
C^*	capacity per BET surface area, $\mu\text{f}/\text{cm}^2$
C_{DL}	ionic double-layer capacity, $\mu\text{f}/\text{cm}^2$
C_{sc}	space charge layer capacity, $\mu\text{f}/\text{cm}^2$
d	distance between the tip of the Luggin capillary and the surface of the electrode, cm
i	current, mA
$i(L)$	current density at the face of the electrode, mA/cm^2
k	sweep rate, mV/sec
L	electrode thickness, cm
r	average particle radius, m
t	time, sec
β_1	dimensionless parameter between 0 and 1, which is a function of $(\psi, t/\rho_e C' L)$
γ	dimensionless parameter between +1 and -1, which is a function of $(\psi, t/\rho_e C' L)$
ψ	dimensionless parameter $(L\lambda/d)$
λ	labyrinth factor
ρ_e	effective specific resistance of the electrolyte in the pores of the electrode, ohm-cm

REFERENCES

1. E. G. Gagnon, *This Journal*, **120**, 1052 (1973).
2. E. G. Gagnon, *ibid.*, **121** 512 (1974).
3. L. G. Austin and E. G. Gagnon, *ibid.*, **120**, 251 (1973).
4. S. Katz, U.S. Pat. 3,694,325, Sept. 26, 1972
5. E. G. Gagnon, Abstract 354, p. 845, Electrochemical Society Extended Abstracts, Spring Meeting, San Francisco, California, May 12-17, 1974. To be published in *This Journal*.

6. A. Soffer and M. Folman, *J. Electroanal. Chem.*, **38**, 25 (1972).
7. J. P. Randin and E. Yeager, *ibid.*, **36**, 257 (1972).
8. H. B. Bauer, M. S. Spritzer, and P. J. Elving, *ibid.*, **17**, 299 (1968).
9. J. O'M. Bockris and A. K. N. Reddy, "Modern Electrochemistry," Vol. 2, p. 816, Plenum Press, New York (1970).

Brief Communications



Accelerated Corrosion Test to Determine the Continuity of Thin Oxide Films on Aluminum

Neil T. McDevitt and William L. Baun

*Air Force Materials Laboratory, Mechanics and Surface Interactions Branch,
Wright-Patterson Air Force Base, Ohio 45433*

Over the past year the aircraft industry has been studying more closely the anodization of aluminum alloys as a surface preparation of structural adhesive bonding. The technical application of the anodization of aluminum that produces a thick ($>2.5 \mu\text{m}$) surface oxide, that resists weathering and deterioration, are well known (1). However, in order for an adhesive to form an integral bond with the metal adherend, the surface oxide layer has to be thin compared to films formed by present day procedures. Consequently, very little information has been generated on thin ($<0.2 \mu\text{m}$) anodic oxide films on aluminum. The quality of this thin oxide film will determine the amount of corrosion protection the aluminum metal will receive and, therefore, add to the durability of the formed adhesive bond. In this case, quality will be determined by the continuity of the surface oxide film over the area anodized. Present day test methods usually rely on salt spray exposure or immersion in sodium chloride solution to determine the protection offered by a surface oxide film. These tests normally require some 16-50 hr to perform (2). In order to study a large number of different electrolytes with varying anodization parameters, it would be essential to have a test that would require less time and equipment than the above procedures.

This paper describes the use of the iodine-methanol technique (3) and its ability to determine the continuity of thin anodic oxide films. This technique has been used extensively for isolating oxide films from aluminum. The chemistry of the primary reaction involves the attack of iodine-methanol solution on aluminum and its alloys, with no quantitative indication of any attack on the surface aluminum oxide hydroxide (AlOOH). Ideally then, this solution may be used to determine cracks, flaws, or porosity of thin oxides generated by various methods. Utilizing the above reaction, a solution containing 5g iodine/100 ml absolute methanol, in a covered petri dish, can determine the continuity of a film within 1-8 hr, which we define here as an accelerated corrosion test (ACT). With this method, a number of electrolytes, along with various anodization parameters, may be studied in a relatively short period of time in order to achieve a thin oxide film having maximum continuity. Two drawbacks of the ACT solution are: (i) the main product of the reaction (aluminum methoxide) is insoluble in anhydrous methanol, and (ii) trace amounts of water sig-

nificantly slow the rate of reaction of the solution with aluminum. The first drawback must be avoided since the insoluble product will precipitate on the sample surface and hinder the attack of the solution on the aluminum. In the second case, small amounts of water allow the aluminum methoxide to be soluble, but the different trace amounts of water picked up by atmospheric contamination vary the reaction rate enough so as to make time studies for two different sets of samples uncorrelatable.

One inch square specimens of 2024 aluminum 0.063 in. thick are used for the experimental anodization studies. After anodization, the specimens are placed flat in a 5.5 in. diameter petri dish with 200 ml of ACT solution. When test specimens are placed in the same 200 ml solution, and oxide films are of the same comparable thickness, information concerning the continuity of the different films is readily obtained and correlatable. Figure 1 shows the results of an ACT solution on various surface preparations. The specimens A, C, and D are 2024 clad aluminum. The specimens B, E, and F are 2024 bare aluminum. A and B were treated with an FPL etch solution for 10 min at 62°C . C and E were anodized in a 0.01M phosphoric acid electrolyte while D and F were anodized in a 0.03M phthalic acid electrolyte. These specimens were anodized at 25V at room temperature. Barrier layer oxides were formed in both cases. The oxide thickness for the specimens shown in Fig. 1 is between 0.03 and $0.04 \mu\text{m}$. Specimens A and B were in the solution for 1 hr. It is quite apparent that the discontinuities in B are so large that the entire oxide film has been lost due to the attack on the aluminum metal. The continuity of the anodic oxide on C and D appears to be good, while E is moderate and F is only fair. These specimens were in the ACT solution for a period of 2 hr. Some preliminary results on the comparison of the ACT solution with outdoor exposure studies are shown in Fig. 2. All specimens are 2024 clad aluminum. A and C were anodized at 50V in an 0.2M ammonium oxalate electrolyte, while B and D were anodized at 20V in an oxalic-sulfuric acid mixture each in 0.1M concentrations. A and B were exposed to the ACT solution for 2 hr. The A specimen showed poor oxide film continuity and the B specimen can be rated as moderate. The C and D specimens were exposed to atmospheric conditions on the North Florida Gulf Coast for 60 days. It is apparent that the same ratings assigned to A and B can be given to C and D. The area below the dotted line on C and D

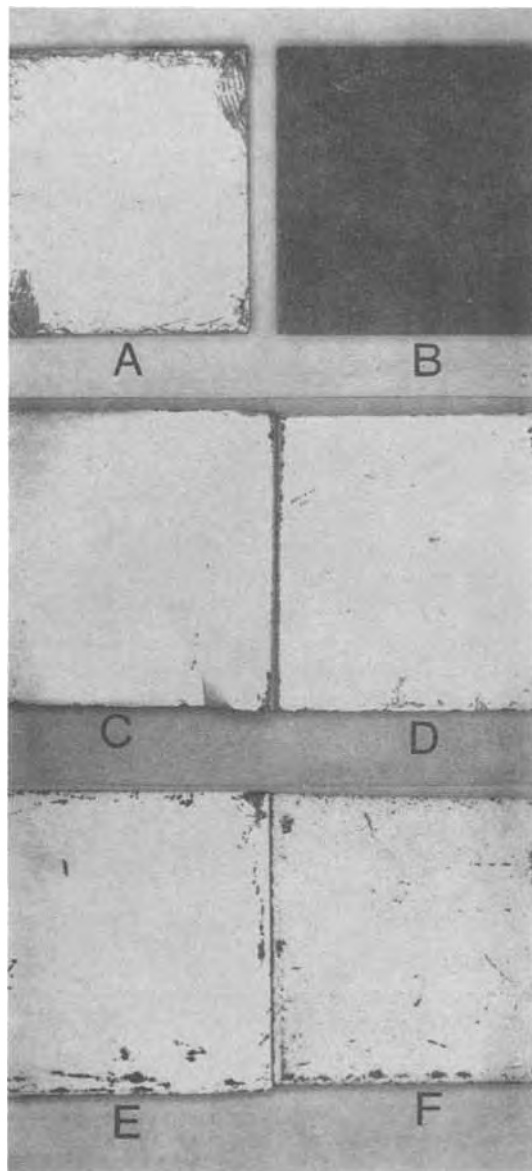


Fig. 1. Accelerated corrosion test comparison of various surface oxide preparations. A and B, FPL etch, exposed 1 hr. C and E, 0.01M H_3PO_4 anodize; D and F, 0.03M phthalic acid anodize, exposed for 2 hr.

was unexposed due to the clamp holding the specimens to a board.

The results of these experiments show that the iodine-methanol solution will determine the continuity of thin oxide films in a short period of time. The preliminary investigation of the comparison of ACT with outdoor exposure indicates there may be some corre-

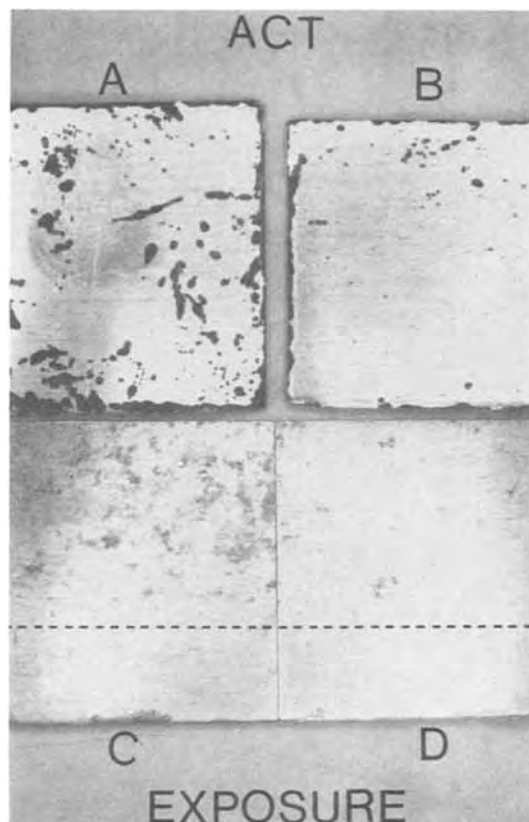


Fig. 2. Comparison of ACT with outdoor exposure. A and C, 0.2M ammonium oxalate anodize; B and D, 0.1M mixture oxalic-sulfuric anodize. ACT exposure for 2 hr; outdoor exposure 60 days.

lation, however, many more data points will have to be obtained to reach a firmer conclusion. The authors emphasize that the chemistry of this solution must be understood so that the term corrosion, as used in this paper, pertains only to an attack on the unexposed aluminum metal due to cracks, flaws, or porosity in the surface oxide film.

Manuscript received Oct. 24, 1974.

Any discussion of this paper will appear in a Discussion Section to be published in the December 1975 JOURNAL. All discussions for the December 1975 Discussion Section should be submitted by Aug. 1, 1975.

Publication costs of this article were partially assisted by the Department of the Air Force.

REFERENCES

1. G. H. Kissin, "The Finishing of Aluminum," Reinhold Publishing Corp., New York (1963).
2. M. A. Heine, D. S. Keir, and M. J. Pryor, *This Journal*, **112**, 24 (1965).
3. M. J. Pryor and D. S. Keir, *ibid.*, **102**, 370 (1955).

Mechanism of Reduction of the Fluorographite Cathode

M. Stanley Whittingham*

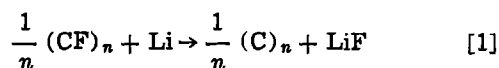
Corporate Research Laboratories, Exxon Research and Engineering Company, Linden, New Jersey 07036

Graphite has a layered structure which on reaction with fluorine at elevated temperatures gives the compound $(CF)_n$ in which the graphite lattice loses its

* Electrochemical Society Active Member.
Key words: ternary phase, high energy density battery, carbon fluoride, cathode.

aromatic character and electronic conductivity (1). Ebert (2) has shown that the six membered carbon rings take up the boat configuration with the fluorine atoms between the carbon layers. The spacing between these layers expands from 3.35 to $\sim 5.8\text{\AA}$ on reaction. This carbon monofluoride is used as the cathode of

lithium high energy density batteries utilizing organic electrolyte systems (3-6). The postulated reaction during discharge is



for which the calculated voltage obtained from the free energy of formation of LiF, -139.2 kcal/mole (7), and the heat of formation of $(\text{CF})_n$, -46.7 kcal/mole (8), is around 4.0V . However, in use the open circuit voltage (OCV), $\sim 2.8\text{V}$ (5), is markedly less than this theoretical value. Tiedemann recently proposed (5) that the OCV of this electrode can be interpreted as a mixed potential resulting from the anodic reaction of the solvent coupled with the cathodic reaction of the fluorographite. The object of this paper is to suggest an alternative hypothesis in which the open circuit voltage is determined not by the formation of lithium fluoride and graphite but rather by an intermediate product of the reaction.

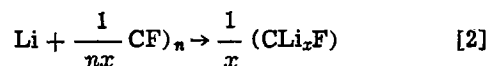
Wood *et al.* (8) determined that the C-F bond energy in $(\text{CF})_n$ is 115 kcal/mole. This high energy of the covalent bond dictates an extremely small diffusion coefficient for the fluorine; this is borne out in the need of high temperatures, $\sim 450^\circ\text{C}$, for its formation from carbon and fluorine (9). This can be contrasted with the small energy of formation of the bromine compound, C_8Br , and its ready preparation at ambient temperatures (10). It is thus unlikely that the fluorine will be able to diffuse to the edges of the basal planes rapidly enough to maintain the observed discharge currents. It is therefore proposed that the lithium ion diffuses between the layers of the graphite lattice to react with the fluorine forming a ternary compound of composition (CLi_xF) where $x < 1$. This intermediate then disproportionates to give lithium fluoride and graphite.

To test this hypothesis fluorographites of composition $\text{CF}_{0.85}$ and $\text{CF}_{1.1}$ obtained from Marchem, Incorporated were reacted with 1M solutions of lithium and sodium naphthalides in tetrahydrofuran for 24 hr. The samples turned almost immediately from their white to a black color showing that electrons are being returned to the graphite lattice on reduction of the naphthalide to naphthalene. X-ray analysis of the products of reaction was performed on a Philips diffractometer using Cu K_α radiation. For the lithium product diffraction lines were found for d values of 9.35 , 4.69 , and 3.12\AA . These can be associated with a lattice spacing between the graphite planes of 9.35\AA . For sodium the spacing was 9.45\AA . That this expansion of the lattice was not due to the intercalation or other reactions of the polar solvent or naphthalene was shown following Armand's procedure (11) using n -butyl lithium dissolved in a nonpolar solvent, hexane. Identical x-ray data were obtained and octane was the organic reaction product. Backtitration of the residual naphthalide or n -butyl lithium indicated a stoichiometric reaction of the alkali with the fluorine. Thus $\text{CF}_{0.85}$ and $\text{CF}_{1.1}$ reacted with 0.89 and 1.07 moles of n -butyl lithium, respectively.

The expansion of the crystalline lattice from the 5.8\AA spacing of the $(\text{CF})_n$ structure to the 9.35\AA of the reaction product can possibly be related to the ionicity of the fluorine. In carbon fluoride the bonding is covalent, whereas in the presence of the alkali metal the fluorine will be predominantly ionic with its associated larger size. Further evidence for the formation of a nonstoichiometric ternary phase is the shape of

the open circuit voltage curve observed on discharge (5), which is typical of that expected for such phase formation (12). A reaction where graphite and lithium fluoride are in equilibrium with carbon fluoride would yield a curve whose potential is independent of state of discharge.

The observed voltage is then the lithium partial molar free energy of the reaction



rather than for reaction [1]. The rate at which the lithium fluoride intercalated graphite decomposes to graphite and lithium fluoride, which is often observed in the x-ray pattern, is likely to be a complex function of the electrolyte used, the current density, and temperature. It is thus proposed that the formation of an intermediate ternary nonstoichiometric phase is one explanation for the lower than calculated voltages observed during the discharge of the fluorographite cathode. Such ternary phase formation, either as an intermediate or the final product of discharge, is probably more common than has heretofore been realized. Thus transition metal oxides such as V_2O_5 and MoO_3 react this way (13) and a number of ternary phases have been found in the high temperature Li-FeS_2 battery system (14).

Acknowledgment

The gift of the carbon fluorides from Dr. J. L. Margrave of Rice University is gratefully acknowledged.

Manuscript submitted Oct. 17, 1974; revised manuscript received Dec. 12, 1974.

Any discussion of this paper will appear in a Discussion Section to be published in the December 1975 JOURNAL. All discussions for the December 1975 Discussion Section should be submitted by Aug. 1, 1975.

Publication costs of this article were partially assisted by Exxon Research and Engineering Company.

REFERENCES

1. R. C. Croft, *Quart. Rev.*, **14**, 1 (1960).
2. L. Ebert, R. A. Huggins, and J. T. Braumann, *J. Am. Chem. Soc.*, **96**, 7841 (1974).
3. M. Fukuda and T. Iijima, Abstract 41, p. 100, Electrochemical Society Extended Abstracts, Fall Meeting, Cleveland, Ohio, October 3-7, 1971.
4. H. F. Hunger and G. J. Heymach, *This Journal*, **120**, 1161 (1973).
5. W. Tiedemann, *ibid.*, **121**, 1308 (1974).
6. N. Watanabe and M. Takashima, Paper P-19, 7th Int. Symp. on Fluorine Chemistry, Santa Cruz, California, July 15-20, 1973.
7. J. G. Gibson and J. L. Sudworth, "Specific Energies of Galvanic Reactions and Related Thermodynamic Data," Chapman and Hall, London (1973).
8. J. Wood, R. Bodachharpe, R. Lagow, and J. Margrave, *J. Phys. Chem.*, **73**, 3139 (1969).
9. O. Ruff and O. Bretschneider, *Z. Anorg. Allgem. Chem.*, **217**, 1 (1934).
10. J. G. Hooley, *Chemistry and Physics of Carbon*, **5**, 321 (1969).
11. M. B. Armand, in "Fast Ion Transport in Solids," W. van Gool, Editor, p. 665, North-Holland Publishing Co., Amsterdam (1973).
12. B. C. H. Steele, *ibid.*, p. 103.
13. M. S. Whittingham, Paper 160 presented at Electrochemical Society Meeting, San Francisco, California, May 12-17, 1974.
14. A. E. Martin, R. K. Steunenberg, and Z. Tomczuk, *This Journal*, **121**, 274C (1974).



Conductivity of Boules of Single-Crystal Sodium Beta-Alumina

William L. Fielder, Harold E. Kautz, J. Stuart Fordyce,* and Joseph Singer

NASA, Lewis Research Center, Cleveland, Ohio 44135

ABSTRACT

The two- and four-probe conductivities of single-crystal sodium beta-alumina ($\text{Na}_2\text{O} \cdot 8\text{Al}_2\text{O}_3$) were investigated over the range of 25°–300°C. After pretreating with liquid sodium at 300°C, the two-probe conductivity, above 140°C, was given by $KT = 3300 \exp(-3650/RT)$. The conductivity at 180°C remained essentially constant up to about 140 mA/cm².

To date, conductivity measurements on sodium beta-alumina single crystals have been restricted to a-c measurements on relatively small samples since large specimens have not been available. Conductivities have been reported for crystals occurring naturally in Monofrax-H fire brick (1) and for crystals ($\text{NaO} \cdot 9.5\text{Al}_2\text{O}_3$) obtained from the Carborundum Company (2).

Recently, two cylindrical boules of single-crystal sodium beta-alumina (nominal composition of $\text{Na}_2\text{O} \cdot 8\text{Al}_2\text{O}_3$) of about 2 cm diameter were prepared and made available to NASA-Lewis Research Center by the Crystal Products Department of Union Carbide Corporation. The present study provides the first a-c and d-c conductivity measurements made on such large, single-crystal material.

Experimental

The two boules of sodium beta-alumina, each obtained from separate single-crystal growths, were colorless. One boule was opaque and cleaved readily into many fragments while attempts were made to cut it with a diamond string saw using an organic coolant. The other boule, however, was relatively clear and remained uncleaved during cutting, producing samples A, B, and C. After cleaning with benzene and acetone, samples A and B were dried in a vacuum oven at 125°C and then maintained under an argon atmosphere. Sample C, being representative of this boule, was then analyzed in duplicate. The results were as follows: Na, 5.31 and 5.11%; Al, 49.15 and 49.15%; in agreement with the composition $\text{Na}_2\text{O} \cdot 8\text{Al}_2\text{O}_3$. Five parts per million of lithium was also found.

Conductivity measurements were made using both ion-blocking and reversible electrodes. Ion-blocking contacts of platinum were sputtered on the faces of sample A and a three-lead coaxial probe was connected to the contacts with conducting silver epoxy cement. Capacitance and conductance measurements were made over the range of –170°–250°C using a commercial automatic balancing bridge which provided frequencies of 10³, 10⁴, 10⁵, and 10⁶ Hz, as described previously (3).

Reversible electrodes of sodium were used on sample B by placing it between two stainless steel blocks

which contained sodium electrode reservoirs and positioned so that proper contact was maintained between the sample and the sodium during preheating and during subsequent conductivity measurements. Spring tension against the steel blocks pressing on the sample were adequate to maintain a leak-proof seal for the liquid sodium. The surfaces of both faces of the sample were pretreated with the sodium electrodes in place by preheating to 300°C for about 1 hr. After pretreating, two-probe conductances were measured at three frequencies (10², 10³, and 10⁴ Hz) over the temperature range of 35°–300°C using an impedance comparator bridge with standard resistors and capacitors.

Using the same apparatus, two-probe d-c conductances were obtained over the same temperature range. A current density of about 30 $\mu\text{A}/\text{cm}^2$ was maintained by means of a variable standard resistor in series with the sample. In addition, at 180°C, two probe d-c conductances were measured at larger current densities ranging between 1 and 140 mA/cm². To minimize localized heating at these higher currents, the conductances were determined within 10 sec of initiation of current flow. Finally, a four-probe d-c conductance was obtained at 40°C. For this measurement, a current density of about 5 mA/cm² was maintained and the measurements were made after about 1 min. The conductances for both the two- and four-probe measurements were calculated from the corresponding voltages across the sample and the standard resistors in series.

Results and Discussion

The a-c conductivities of sample A, using ion-blocking platinum electrodes, are shown in Fig. 1. The condition of resonance, assumed to be due to polarization of the sodium ions at the ion-blocking electrodes, occurs when $\omega\tau$ is equal to unity and is a function of both frequency and temperature given by the relation

$$\omega\tau = (\epsilon_s - \epsilon_\infty)\omega/\kappa \quad [1]$$

where ω is the angular frequency (sec⁻¹); κ is the conductivity (ohm⁻¹·cm⁻¹); ϵ_s is the low frequency limit of the real part of the dielectric constant; and ϵ_∞ is the high frequency limit (3–5). For 10³ and 10⁴ Hz, the conductivities started to deviate from the straight line due to the onset of sodium ion polarization at about –70° and –50°C, respectively. For 10⁵

* Electrochemical Society Active Member.

Key words: beta-alumina, solid electrolyte, sodium transport.

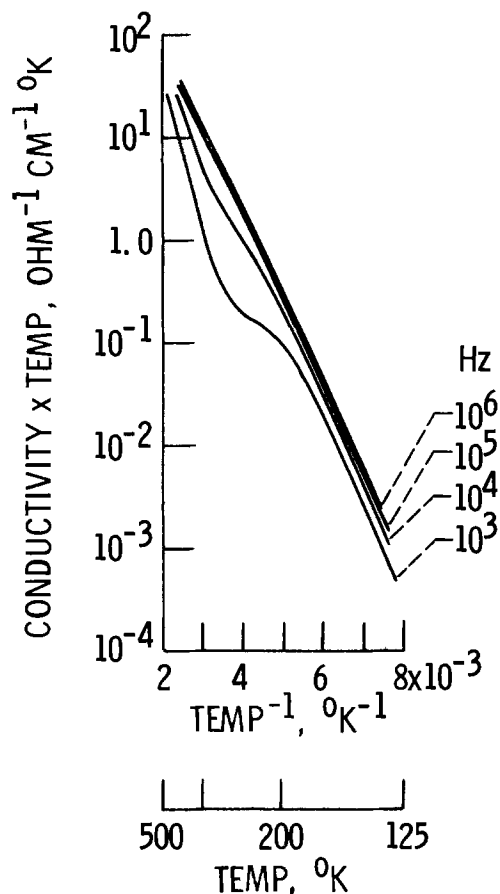


Fig. 1. A-C conductivities of sodium beta-alumina sample A using Pt electrodes.

and 10^6 Hz, resonance was not observed at the highest temperatures investigated. The conductivity of sample A at 10^6 Hz, therefore, was assumed to be polarization-free and could be fitted by a straight line over the temperature range -150°C – 125°C given by

$$KT = 4000 \exp(-3790/RT) \text{ ohm}^{-1}\text{-cm}^{-1} \text{ }^{\circ}\text{K} \quad [2]$$

At 25°C , this conductivity at 10^6 Hz is about $3 \times 10^{-2} \text{ ohm}^{-1}\text{-cm}^{-1}$ (cf. Table I).

The reversible electrode results on sample B for the two-probe a-c measurements at 10^4 Hz are shown in Fig. 2 and are compared with the four-probe d-c conductivity at 40°C . An extrapolation of this two-probe data to 40°C from the temperature region above 140°C , where the sodium is liquid, is in good agreement with the four-probe d-c value at 40°C of $2.8 \times 10^{-2} \text{ ohm}^{-1}\text{-cm}^{-1}$ (cf. Table I). This suggests that the higher temperature region and its extrapolation represent the polarization-free conductivity for the single crystal. The following results support this assumption: (i) the a-c conductances for the higher temperature region were essentially independent of frequency and (ii) the d-c conductances were essentially independent of time and also were in good agreement with the correspond-

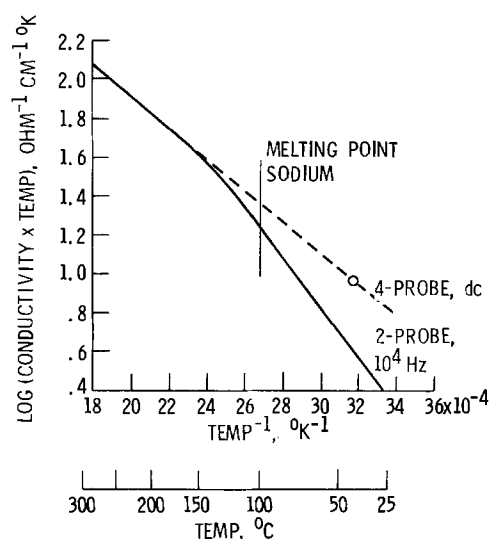


Fig. 2. Conductivities of sodium beta-alumina sample B using Na electrodes.

ing a-c values. The polarization-free conductivity for sample B can be expressed by

$$KT = 3300 \exp(-3650/RT) \text{ ohm}^{-1}\text{-cm}^{-1} \text{ }^{\circ}\text{K} \quad [3]$$

This activation energy of 3.65 kcal/mole and the conductivity at 25°C of $2.4 \times 10^{-2} \text{ ohm}^{-1}\text{-cm}^{-1}$ (cf. Table I) for sample B are in reasonable agreement with the data obtained for sample A using the platinum ion-blocking electrodes where an activation energy of 3.79 kcal/mole and a conductivity of $3 \times 10^{-2} \text{ ohm}^{-1}\text{-cm}^{-1}$ was obtained. Furthermore, these results for sample B show good agreement with published values. For example, an activation energy of 3.8 kcal/mole was reported for crystals obtained from Monofrax-H (1) and 3.79 kcal/mole for crystals obtained from the Carborundum Company (2). The respective conductivities were about 3×10^{-2} and $1.4 \times 10^{-2} \text{ ohm}^{-1}\text{-cm}^{-1}$ (cf. Table I).

Pretreating the surfaces of sample B by preheating in contact with liquid sodium at 300°C did reduce most of the interfacial polarization. However, even after pretreating, some interfacial polarization was still present in the two-probe data for temperatures where the sodium is solid. This is shown by a comparison of the two-probe data at 10^4 Hz with the extrapolated four-probe data (cf. Fig. 2 and Table I), by a decrease in the a-c conductivity with decreasing frequency, and by a decrease in d-c conductivity with increasing time. For example, at 25°C , the interfacial resistance at 10^4 Hz was about twice the resistance of the polarization-free single crystal.

Finally, to study the behavior of single-crystal material at current densities of practical interest, two-probe d-c measurements were made on sample B up to 140 mA/cm^2 at 180°C . As shown in Fig. 3, the conductivity remained essentially constant at about $0.127 \text{ ohm}^{-1}\text{-cm}^{-1}$. This shows that with liquid sodium electrodes, the conductivity (after pretreating with liquid

Table I. Conductivities of sodium beta-alumina crystals

Sample	Temperature ($^{\circ}\text{C}$)	Electrode	2-Probe a-c conductivity at 10^6 Hz, ($\text{ohm}^{-1}\text{-cm}^{-1}$)	2-Probe a-c conductivity at 10^4 Hz, ($\text{ohm}^{-1}\text{-cm}^{-1}$)	4-Probe d-c conductivity ($\text{ohm}^{-1}\text{-cm}^{-1}$)
A	25	Pt	3×10^{-2}	—	—
B	25	Na	—	8.1×10^{-3}	$2.4 \times 10^{-2(a)}$
B	40	Na	—	—	2.8×10^{-2}
Crystals obtained from Monofrax-H (1)	25	In	$3 \times 10^{-2(b)}$	—	—
Crystals obtained from Carborundum Co. (2)	25	Na_2WO_3	—	1.4×10^{-2}	—

(a) Extrapolated to 25°C .

(b) Average of 6 crystals at 5×10^6 Hz.

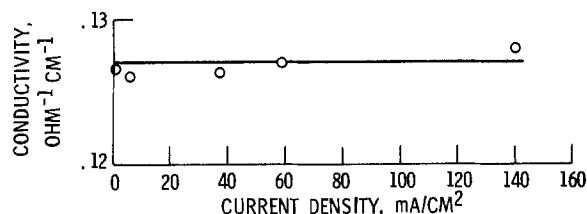


Fig. 3. D-C conductivities of sodium beta-alumina sample B at 180°C with current density.

sodium at 300°C) was essentially ohmic even up to these relatively large current densities.

The results suggest that similar (or improved) large, synthetic boules of this type of sodium beta-alumina might be developed as a suitable sodium ion solid electrolyte operating at current densities of practical interest. The material is potentially important for lower temperature applications. However, the polarization noted in this work with sodium as it solidifies suggests that liquid electrodes may be preferred. Below 100°C, sodium amalgams may be applicable for this purpose (6, 7). The main limitation of this material in practical application as exemplified by one of the boules appears to be its relative ease of cleavage. Further develop-

ment of the crystal growth technique might be expected to improve this situation.

Manuscript submitted June 24, 1974; revised manuscript received Oct. 1, 1974. This was Paper 157 presented at the San Francisco, California, Meeting of the Society, May 12-17, 1974.

Any discussion of this paper will appear in a Discussion Section to be published in the December 1975 JOURNAL. All discussions for the December 1975 Discussion Section should be submitted by Aug. 1, 1975.

Publication costs of this article were partially assisted by the National Aeronautics and Space Administration.

REFERENCES

1. Y. Y. Yao and J. T. Kummer, *J. Inorg. Nucl. Chem.*, **29**, 2453 (1967).
2. M. S. Whittingham and R. A. Huggins, *J. Chem. Phys.*, **54**, 414 (1971).
3. H. E. Kautz, J. Singer, W. L. Fielder, and J. S. Fordyce, NASA TN D-7146 (1973).
4. R. H. Radzilowski *et al.*, *J. Appl. Phys.*, **40**, 4716 (1969).
5. V. V. Daniel, "Dielectric Relaxation," p. 203, Academic Press, New York (1967).
6. F. G. Will and S. P. Mitoff, *This Journal*, **120**, 227C (1973).
7. F. G. Will, R. R. Dubin, and H. J. Hess, *ibid.*, **120**, 227C (1973).

The Lattice Misfit and Its Compensation in the Si-Epitaxial Layer by Doping with Germanium and Carbon

Yao Ting Lee, Nobuo Miyamoto, and Jun-ichi Nishizawa

Research Institute of Electrical Communication, Tohoku University, Sendai, Japan

ABSTRACT

When germanium and carbon are doped into silicon, the silicon lattice is expanded or contracted depending on the tetrahedral covalent radius of germanium or carbon, respectively. But this effect of electrically nonactive elements can be of considerable use for compensating the lattice strain caused by other impurities, which are electrically active elements in silicon. From the investigation of the electrical characteristics and lattice defects of epitaxial layers doped with germanium, it was found that doping of germanium in silicon up to 1×10^{20} atoms/cm³ does not change the electrical characteristics of silicon and also that germanium is an element suitable for strain compensation in silicon. By the single doping of carbon over its solubility, many defects were generated. However, when carbon and antimony are simultaneously doped into the epitaxial layers, the layers become free from lattice defects and the saturation solubility of carbon in silicon changes from a solubility concentration of 3×10^{18} atoms/cm³ to 7.6×10^{18} atoms/cm³ with an increase in the concentration of antimony. These results show that the saturation solubility of carbon depends largely on the lattice strain or the existence of an impurity.

Dislocations and other defects in silicon crystal generated by heavy doping of impurity have been reported by a number of authors (1-9). When impurities such as boron, phosphorus, and antimony, having different covalent radii from that of silicon, are doped into silicon, the lattice constant of the doped layer shows a value different from that of intrinsic silicon. The lattice expansion or contraction of silicon causes strain in the crystal and also in some cases results in defects such as dislocations (10, 11), which have a great influence on the characteristics of semiconductor devices. In order to avoid the generation of strains or defects due to this effect, a method, called the compensation of strain, has been used. For ex-

ample, a simultaneous doping of more than two impurities such as phosphorus and tin having different covalent radii has been performed and the strain compensation in epitaxial growth of silicon has been achieved (10). Because germanium is highly soluble in silicon, the compensation of the lattice strain by germanium can be effected over a wide range of concentration of some other impurity. On the other hand, the solid solubility of carbon (18-20) is so low that addition of carbon above the concentration of 3×10^{18} atom/cm³ results in precipitation in silicon. Germanium and carbon not only belong to the same column of the Group IV in the periodic table as tin and silicon, but also have better semiconductor characteristics than tin. Consequently, they are considered as the elements appropriate to compensate the lattice strain. In this paper, the physical properties of germanium and the

Key words: effect lattice constant of silicon, doping of carbon and germanium, strain compensation, silicon vapor epitaxy, change of saturation solubility by lattice stress.

behavior of carbon doped in silicon during epitaxial growth are investigated.

Experimental Procedure

The epitaxial layers were grown by vapor deposition through the hydrogen reduction of SiCl_4 . Germanium and carbon were doped using GeCl_4 and CCl_4 vaporized in a usual manner. Purities of GeCl_4 and CCl_4 were 99.99999% for GeCl_4 and 99.99% for CCl_4 . The growth condition was as follows. The mole fraction of SiCl_4 in H_2 , 1.5%; the line velocity of the gas mixture, 5 cm/sec in the reactor heated by the resistance furnace; the growth temperature, 1200°C; and the growth rate, about 0.7 μ /min. The concentrations of the dopant germanium and carbon were controlled by varying the flow rate of hydrogen gas carrying doping sources.

The substrates used were dislocation-free silicon crystals grown by the F.Z. method, which contain less carbon impurities than those grown by the C.Z. method, and were doped with phosphorus with a concentration of about 3.5×10^{13} atom/cm³; the impurity concentration was about 3.5×10^{13} atom/cm³. The impurity concentration of the substrates is so low that the lattice constant is almost the same as that of pure silicon ($a = 5.43018\text{\AA}$). Substrates were cut in parallel to the (111) plane. The shape of the substrates was rectangular with a size of 5×10 mm; their directions being $\langle 112 \rangle$ for the short side and $\langle 110 \rangle$ for the long side.

Substrate surfaces were cleaned and then etched chemically to a thickness of about 3-5 μ under a H_2 -HBr gas mixture at 1200°C in order to remove damaged surface layers and contaminants.

Measurements and Results

Lattice strain vs. impurity content.—The doping of impurities in silicon causes a lattice expansion or contraction. When the lattice constant of the epitaxial layer doped with impurity is different from that of the silicon substrate, the Bragg angles of x-ray reflected from the substrate and the epitaxial layer will differ by a small angle of $\Delta\theta$. The difference in the lattice constant Δa_0 can be obtained from $\Delta\theta$, i.e., the lattice strain ϵ , ϵ is expressed by the equation

$$\epsilon = \frac{\Delta a_0}{a_0} = \beta C = -\cot \theta_B \cdot \Delta\theta \quad [1]$$

where a_0 is the lattice constant for silicon, β is the solute lattice expansion (—) or the contraction (+) coefficient, C is the concentration of an impurity doped in silicon, θ_B is the Bragg reflection angle for the substrate of pure silicon (13). To measure $\Delta\theta$, an x-ray double crystal spectrometer was used, where the x-ray source was $\text{CuK}\alpha_1$ radiation. The diffractometer was arranged as $\{(511)^v, -(333)^s\}$ (14), that is, x-ray diffraction was first made upon a perfect and pure silicon crystal fixed to the low glancing angle position of $(511)^v$ for the incident beam to obtain a nondivergent monochromatic beam and then diffracted by the sample crystal fixed to the symmetric position of $(333)^s$. The rocking curves of the diffraction lines were recorded at a scanning speed of 1/256°/min. Since the Bragg angle θ_B is 47.482° for the silicon (333) plane, Eq. [1] yields

$$\epsilon = \beta C = 4.445 \times 10^{-6} \Delta\theta_{333} \quad [2]$$

For example, Fig. 1 shows the rocking curve for germanium-doped silicon epitaxial layers. The peak designated "epi" is separated from the main silicon substrate peak. If the impurity atoms occupy the substitutional sites in the silicon lattice, the solute lattice expansion (contraction) coefficient (12) is derived as

$$\beta = \frac{1}{3} \left[1 - \left(\frac{R_{\text{sol}}}{R_{\text{Si}}} \right)^3 \right] N^{-1} \quad [3]$$

where R_{Si} is the covalent radius of silicon, R_{sol} is the covalent radius of the solute atom, and N is the con-

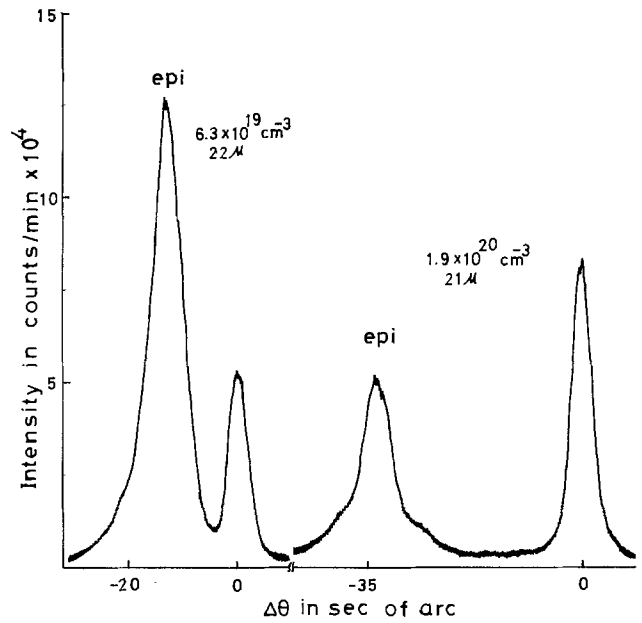


Fig. 1. X-ray rocking curve for germanium diffused layer in silicon.

centration of silicon atom sites (5×10^{22} atom/cm³). The covalent radii of some other elements are Ge = 1.22 \AA , C = 0.77 \AA , B = 0.88 \AA , P = 1.10 \AA , Si = 1.17 \AA , and Sb = 1.36 \AA . The values of β of those impurities doped in silicon are given as follows: $\beta_{\text{Ge}} = -8.91 \times 10^{-25}$ cm³/atom, $\beta_{\text{C}} = 4.77 \times 10^{-24}$ cm³/atom, $\beta_{\text{P}} = 1.13 \times 10^{-24}$ cm³/atom, $\beta_{\text{B}} = 3.83 \times 10^{-24}$ cm³/atom, $\beta_{\text{Sb}} = -3.8 \times 10^{-24}$ cm³/atom.

Using these coefficients of β , the relation between the change in lattice constant and the concentration of dopant impurities in silicon were calculated as shown in Fig. 2. Hence, one can determine the concentration of the dopant germanium necessary to compensate the lattice strain introduced by a certain amount of impurities such as boron and phosphorus. Similarly, this

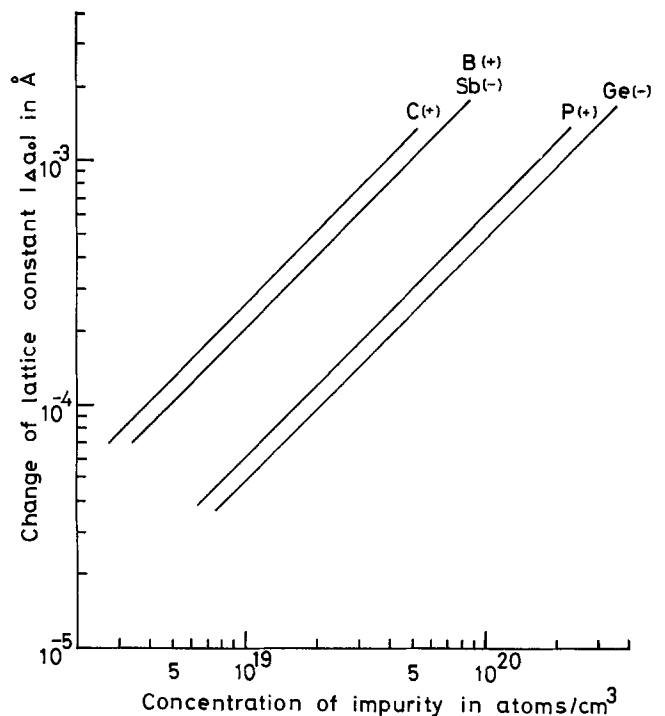
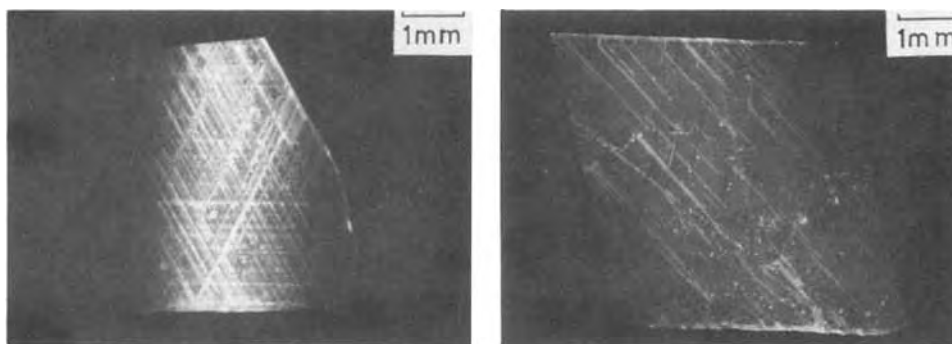


Fig. 2. Curves of lattice constant of concentration of impurity vs. (C, Sb, B, P, Ge)-doped silicon.

Fig. 3. X-ray projection topographs of (111) oriented specimens [MoK α_1 (220) reflection]. The impurity concentration of Ge-doped Si and the thickness of epitaxial grown layers are: (a, left) 1.6×10^{20} atom/cm 3 , 22 μ and (b, right) 6.3×10^{19} atom/cm 3 , 21 μ .



can be applied to carbon to compensate the strain induced by antimony.

Germanium doping.—As detailed above, the concentration of germanium in epitaxial silicon films was measured by using the x-ray double crystal method. It is shown in Fig. 1. X-ray projection topography (15, 16) was used to investigate misfit dislocations and other defects caused in epitaxial films, where MoK α_1 was applied as the x-ray source.

The x-ray projection topographs are shown in Fig. 3. Misfit dislocations are generated in the crystal when the impurity concentration exceeds a certain value in the epitaxial layer of a pure silicon substrate, and the critical concentration level also depends on the thickness of the epitaxially grown layer which contains the impurity. In this experiment, the critical level is found to be 5×10^{19} atom/cm 3 for germanium when the thickness of the film is about 20 μ .

Van der Pauw's method (17) was used to measure Hall coefficients and the bandgap of the epitaxial silicon film doped with germanium.

The measured carrier concentrations were about 5×10^{14} cm $^{-3}$ for 35–50 μ n-type films deposited on p-type substrates of 100 ohm-cm. The source of electrons of 5×10^{14} cm $^{-3}$ is believed to be impurities in GeCl $_4$, because the epitaxial layers of $\sim 10^{13}$ electrons/cm 3 can be grown from nondoped SiCl $_4$.

Table I shows the measured values of the electron Hall mobility and the bandgap for the epitaxial layers doped with about 0.02–0.2 atomic per cent (a/o) germanium. The values are not different from those of nondoped epitaxial layers. It is shown that the epitaxial silicon will not undergo any changes in its electrical properties even if germanium of 1×10^{20} atom/cm 3 is doped into silicon.

Carbon doping.—The concentration of carbon doped into epitaxial layers was measured by the same method as that for silicon doped with germanium. Figure 4 shows the rocking curve and Fig. 5 shows the observed surfaces of the epitaxial layer doped with carbon. When the concentration of the dopant carbon is below 3×10^{18} atom/cm 3 , silicon layers free from defects can be obtained as shown in Fig. 5a. At a higher concentration of carbon (3×10^{18} atom/cm 3), hexagonal defects are observed in the layers as shown in Fig. 5b. An electron microscope was used to examine these de-

fects and it was found that those hexagonal defects are of polycrystalline structure, where the lattice constant of these defects is 4.378 \AA within an error of 0.5% and is nearly consistent with that for β -SiC. Figure 6 shows a cross-sectional view of one of defects cleaved at its center. The defects are formed both at the epitaxial-substrate interface and in the epitaxial layer as seen from the different sizes of the hexagonal defects. From the above considerations, it seems likely that the mechanism of formation of the hexagonal pits is as follows. The presence of grown SiC polycrystals inhibits further growth of silicon; this causes SiC to locate at the bottom of the pits. An x-ray projection topograph of the epitaxial layer doped with carbon is

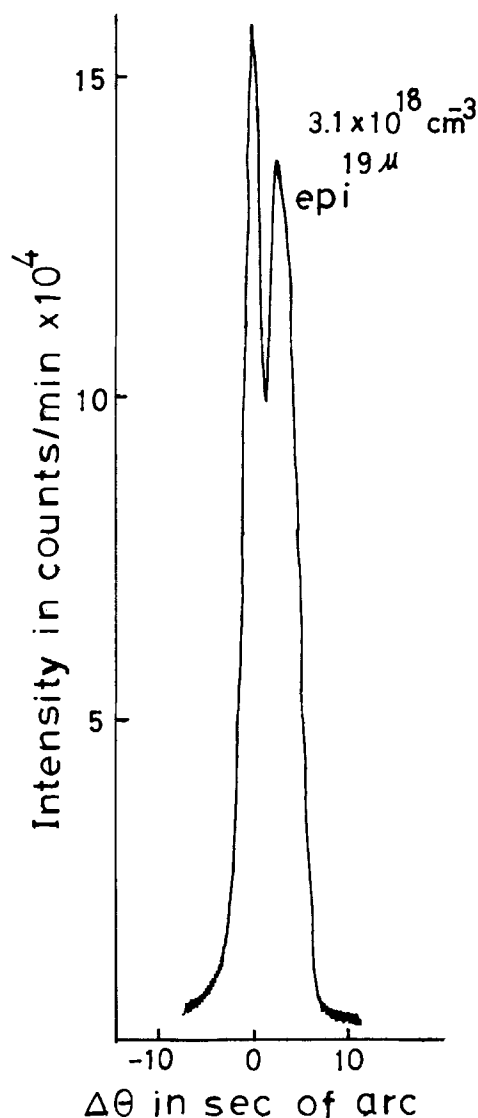


Fig. 4. X-ray rocking curve of the carbon diffused layer in silicon.

Table I. Hall mobility and energy gap of silicon epitaxial layers doped with germanium

Sample Ge a/o in Si	Electron Hall mobility (μ n)	Energy gap (eV)
1×10^{19} Ge/cm 3 0.02% in Si	1440	1.12
6×10^{19} Ge/cm 3 0.12% in Si	1365	1.14
1×10^{20} Ge/cm 3 0.2% in Si	1390	1.09
Ge 0% in Si	1400*	1.11*

* These values are taken from data of Wolf (23). For measuring the Hall effects 5×10^{14} atom/cm 3 n-type was doped into the epitaxial layers. Hall mobility was measured at 25°C.

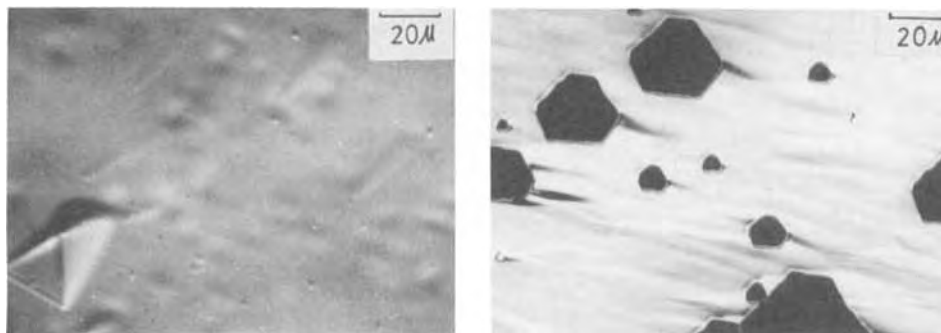


Fig. 5. Morphology of epitaxial layers doped with carbon. (a, left) Carbon concentration is below 3×10^{18} atom/cm³. (b, right) Carbon concentration is over 3×10^{18} atom/cm³.

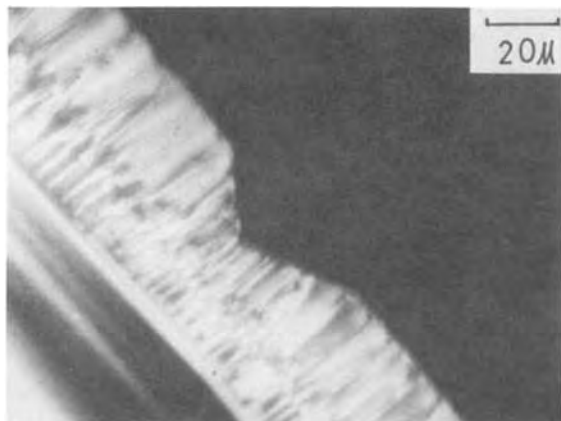


Fig. 6. The side-view of a cleaved tripyramid

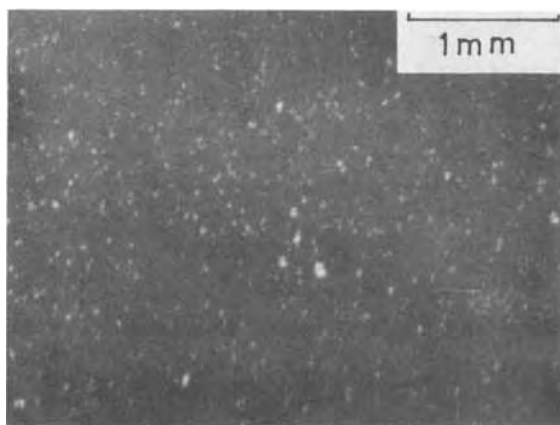


Fig. 7. X-ray projection topograph of an epitaxial layer doped with carbon.

shown in Fig. 7. The bright points correspond to these defects formed in the layer.

It was found that the solid solubility of carbon in silicon, when carbon alone is doped into silicon, is too

low to expect effective compensation of lattice strain caused by other dopants such as antimony. However, when carbon and antimony were simultaneously doped into silicon, a nearly perfect crystal was obtained even if the concentration of carbon exceeded its saturation solubility limit, and at the same time, the compensation of the lattice strain induced by antimony was successfully achieved. Antimony was doped into the silicon epitaxial layer by a conventional method using SbCl_5 . In order to check the effect of lattice strain compensation on an epitaxial layer, the results obtained when carbon and antimony were together doped into an epitaxial layer were compared with those obtained when either carbon or antimony were singly doped into an epitaxial layer. The antimony concentration was checked by measuring its resistivity and by the x-ray double crystal method.

The surface of epitaxial film shown in Fig. 8a was the one doped with carbon of higher concentration than its solid solubility at 1200°C . It appears that the rough surface of silicon was caused by the formation of many β -SiC polycrystals, the carbon concentration cannot be measured by the x-ray double crystal method. When antimony was doped simultaneously with carbon, however, the epitaxial films had fine surfaces as shown in Fig. 8b, indicating that the crystallinity is much better than the epitaxial layer in Fig. 8a. An x-ray projection topograph of this sample of Fig. 8b is shown in Fig. 9b. The presence of β -SiC polycrystals is scarce in the topograph, as distinct from the singularly carbon-doped film in Fig. 7; no dislocations result. These results indicate that the doping of carbon will not generate defects in epitaxial layers even if the carbon concentration is higher than the solid solubility of carbon in silicon when doped simultaneously with antimony. In Fig. 9a, the x-ray topograph of the antimony-doped sample is shown in comparison with that in Fig. 9b and confirmed that the dislocation defects generated by antimony are eliminated by the simultaneous doping of antimony and carbon.

Rocking curves are shown in Fig. 10a for the sample doped only with antimony. This suggests that the doping with antimony has the effect of increasing the lattice constant of silicon and is effective in compensating the strain induced by the doping of phosphorus as an n-type impurity. Figure 10b and c show the rocking of the specimens doped simultaneously with antimony

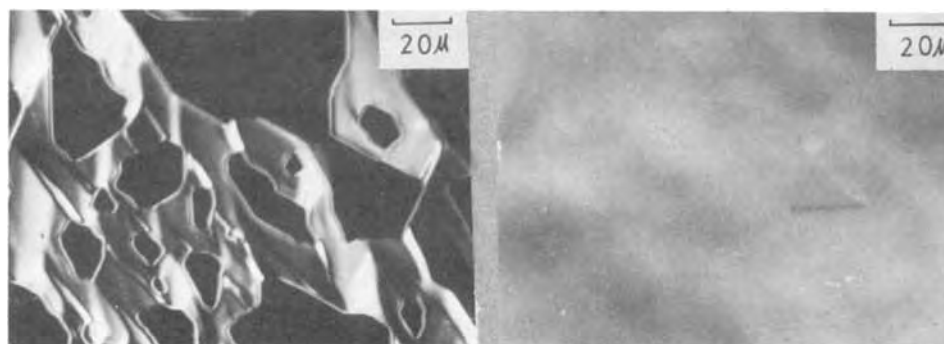
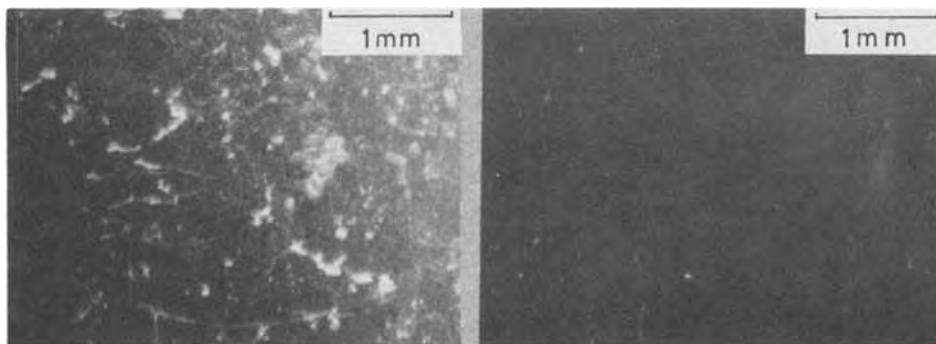


Fig. 8. (a, left) The morphology of an epitaxial layer doped with carbon, 7.6×10^{18} atom/cm³. (b, right) The morphology of an epitaxial layer doped simultaneously with carbon (7.6×10^{18} atom/cm³) and antimony (9.5×10^{18} atom/cm³).

Fig. 9. (a, left) X-ray transmitted topograph of a Si epitaxial layer doped with antimony, 9.5×10^{18} atom/cm³. MoK α_1 (220) reflection. (b, right) X-ray projection topograph of a Si epitaxial layer. This sample is the same as used in Fig. 8b.



and carbon; the former represents the case where the lattice constants of the substrate and the epitaxial layer are equal, and the latter indicates the case where the two are not completely equal. In these samples, the antimony concentration was controlled to be 9.5×10^{18} atom/cm³. Therefore, the carbon concentration can be estimated from the result of Fig. 2 to be about 7.6×10^{18} atom/cm³ as shown in Fig. 10b. This value is about 2.5 times as much as the saturation solubility of carbon in silicon at 1200°C.

Conclusion

From the results obtained in this work, the use of germanium for the compensation of the lattice strain appears to be feasible as is the case with tin. It should be noted that the epitaxial growth can be more readily achieved by doping of germanium than that of tin. The solid solubility of tin is about 5×10^{19} atom/cm³ in silicon (1200°C). This value can concentrate the strain induced by doping of phosphorus of about 1.6×10^{20} atom/cm³ or boron of 6×10^{19} in silicon. Above the concentration of phosphorus or boron impurity, it is not preferable to use tin for strain compensation, although a phenomenon similar to the simultaneous doping of carbon and antimony can be expected. In contrast to tin, germanium can be used for a higher impurity level. Braunstein (21, 22) has shown that nearly perfect single crystals containing as high as 5 a/o germanium in silicon can be obtained (about 2.5×10^{21} atom/cm³ germanium). According to their experi-

mental data, the characteristics of silicon doped with 5 a/o germanium are not changed.

The results of the present study show that the use of germanium is more effective than tin for performing the compensation of lattice strain induced by the doping of boron and phosphorus into silicon. Electronic properties of silicon doped with germanium, a higher concentration of germanium, need to be investigated further.

Carbon is the only element having a smaller covalent radius than that of silicon in IV-group of the periodic table and also carbon is the only element that can be used for the compensation of the lattice strain introduced by doping of the impurities such as antimony which have larger covalent radii than silicon. Although the saturation solubility of carbon in silicon is known to be low, carbon of higher concentration (for example 7.6×10^{18} atom/cm³ in this experiment) are soluble in silicon in the presence of antimony. Thus, it appears that the solubility of carbon and antimony depends on the internal stress of crystals and effective lattice spacing of the bulk crystal. The highest concentration of antimony doped simultaneously with carbon in this experiment is 9.5×10^{18} atom/cm³. Antimony of higher concentration than the value in this experiment may be soluble in silicon. The solubility phenomena mentioned above would be very interesting in the field of solid-state physics and technology.

Acknowledgment

The authors wish to thank Mr. Takeshi Terasaki, Mr. Jiro Shibata, and Mr. Masabumi Shimbo of Semiconductor Research Institute for their technical assistance.

Manuscript submitted June 19, 1973; revised manuscript received Sept. 30, 1974.

Any discussion of this paper will appear in a Discussion Section to be published in the December 1975 JOURNAL. All discussions for the December 1975 Discussion Section should be submitted by Aug. 1, 1975.

Publication costs of this article were partially assisted by Tohoku University.

REFERENCES

1. J. Nishizawa *et al.*, *Record of Electrical and Communication Engineering Conversation, Tohoku Univ.*, **21**, 101 (1952).
2. H. J. Queisser, *J. Appl. Phys.*, **32**, 1776 (1961).
3. S. Frussin, *ibid.*, **32**, 1876 (1961).
4. G. H. Schwuttke and H. J. Queisser, *ibid.*, **33**, 1540 (1962).
5. R. J. Jacobin, *Appl. Phys. Letters*, **4**, 114 (1964).
6. Y. Sato and H. Arata, *Japan. J. Appl. Phys.*, **3**, 511 (1964).
7. J. E. Lawrence, *J. Appl. Phys.*, **37**, 4106 (1966).
8. T. H. Yeh, S. M. Hu, and R. H. Kastl, *ibid.*, **39**, 4266 (1968).
9. Y. Sugita and M. Tamura, *ibid.*, **40**, 3089 (1969).
10. J. Nishizawa *et al.*, Seoul International Conference on IEEE (1970).
11. T. H. Yeh and H. L. Joshi, *This Journal*, **116**, 73 (1969).
12. K. Yagi, N. Miyamoto, and J. Nishizawa, *Japan. J. Appl. Phys.*, **9**, 246 (1970).
13. B. G. Cohen, *Solid-State Electron.*, **10**, 33 (1967).
14. M. Renninger, *Advan. X-Ray Anal.*, **10**, 32 (1967).
15. A. R. Lang, *J. Appl. Phys.*, **30**, 1748 (1959).

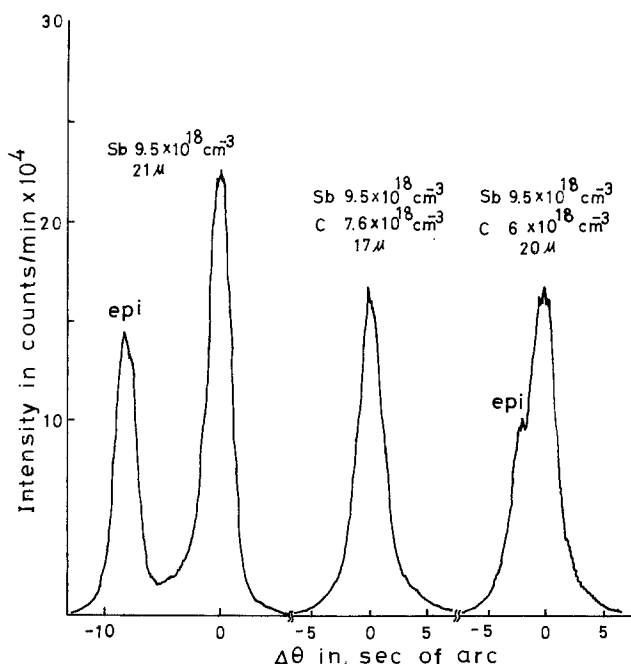


Fig. 10. X-ray rocking curves of Si epitaxial layers doped with (a) Sb- 9.5×10^{18} atom/cm³, (b) Sb- 9.5×10^{18} atom/cm³ and C- 7.6×10^{18} atom/cm³, (c) Sb- 9.5×10^{18} atom/cm³ and C- 6×10^{18} atom/cm³.

16. T. O. Baldwin and J. E. Thomas, *ibid.*, **39**, 4391 (1968).
17. L. J. Van de Pauw, *Philips Res. Rept.*, **13**, 1 (1958).
18. R. C. Newman and J. Wakefield, *J. Appl. Chem. Solids*, **19**, 230 (1961).
19. T. Nozaki, *This Journal*, **117**, 1567 (1970).
20. N. Schink, *Solid-State Electron.*, **8**, 767 (1965).
21. R. Braunstein, *Phys. Rev.*, **130**, 871, 879 (1958).
22. R. Braunstein, R. Moore, and F. Herman, *ibid.*, **109**, 695 (1958).
23. H. Wolf, "Silicon Semiconductor Data," chap. 1, Pergamon Press Inc., New York (1969).

Epitaxial Growth and Structure of CdSe Evaporated in Vacuum onto Ge

F. H. Gejji and D. B. Holt

Department of Metallurgy and Materials Science, Imperial College of Science and Technology, London, England

ABSTRACT

Films of CdSe were grown by focused electron beam evaporation *in vacuo* in the 10^{-6} Torr range on the three singular faces of Ge. The structures of the films were examined by transmission electron microscopy. On (100) oriented substrates, epitaxy was obtained throughout the range of substrate temperatures from 350° to 450°C, and the films had the sphalerite structure in parallel alignment with the Ge. The diffraction patterns contained no satellite spots but $\langle 111 \rangle$ streaks were present. On (110) oriented substrates the epitaxial growth range of temperatures was 300°–450°C. The films again had basically the sphalerite structure in (110) orientation but the domain-form faulted structure was found in all the films. On (111) Ge surfaces, CdSe grew epitaxially at all temperatures from 350° to 450°C and had the sphalerite structure in (111) orientation. Streaks but no satellite spots were observed in the electron diffraction patterns. Well-defined rosettes of Moire spots were observed in the transmission electron diffraction patterns of areas where comparable thicknesses of CdSe and Ge were present in the cases of both (100) and (111) substrates. These Moire diffraction patterns confirmed the parallel alignment of the films on (100) substrates but showed that on (111) substrates the films were azimuthally rotated through a small angle from the parallel orientation.

This work forms part of a program of study of the epitaxial growth of films of the Cd and Zn chalcogenides (II-VI compounds) evaporated in vacuum on to diamond-structure semiconductor substrates. Previous work in this program has dealt with the growth and structure of films of CdS on Ge (1, 2), ZnTe on Ge (3), and CdTe on Ge (4). It was found that on the (100) and (110) faces of Ge these compounds all grew with the sphalerite structure (5). A domain-form {111} faulted structure was found in the CdTe films grown on (110) surfaces (2, 4). The films were grown with relatively high levels of structural perfection. In this work and in all the other published work in the literature only two epitaxial orientation relationships were reported. These were the parallel orientation relation for sphalerite structure films grown on any face of diamond or sphalerite or NaCl structure substrates and the relationship (0001) film parallel to (111) substrate with $[11\bar{2}0]$ film parallel to $[\bar{1}\bar{1}0]$ substrate for wurtzite structure films grown on diamond or sphalerite-structure substrates (6). The significance of these facts in relation to nucleation theory and misfit dislocation theories of the heterojunction interface between II-VI films and semiconductor substrates was discussed in a recent review (6).

This paper reports the results of an investigation of the epitaxial growth and structure of films of CdSe evaporated in vacuum onto (100), (110), and (111) faces of Ge and discusses them in relation to the general conclusions that have emerged from similar previous work.

Experimental Techniques

The films were grown by evaporation in a conventional, oil-pumped high vacuum system using a fo-

cused electron beam furnace as described previously (1). Depositions were carried out in pressures of a few times 10^{-6} Torr.

The CdSe employed was in powder form. It was obtained from Koch-Light Laboratories Limited and stated by them to be of 99.999% purity. The germanium was obtained in the form of (100), (110), and (111) oriented p-type slices from the Electronic Materials Unit of the Royal Radar Establishment. The substrates were 3 mm diameter disks ultrasonically cut from the slices, to fit the specimen holders of the AEI EM6G transmission electron microscope which was used to examine the film structures. The substrate surfaces were mechanically and then chemically polished in a reagent consisting of 50 cm³ of 70% nitric acid, 30 cm³ of 99% glacial acetic acid, 30 cm³ of 40% hydrofluoric acid plus a drop of 79.92% bromine at about 60°C (2). After film growth, the Ge disks were thinned by jet electropolishing for transmission electron microscopy as in the previous studies (1).

The following points were found vital in order to obtain reproducible epitaxial growth of films of high structural perfection: (i) The substrate surfaces must be free of pits, scratches, or other roughness on a transmission electron microscope scale. (ii) The substrate holder and heater assembly must be outgassed by heating to about 900°C in vacuum between successive growth runs to prevent contamination of the substrates by material deposited in previous evaporations. (iii) The CdSe source material must be long and carefully outgassed using the defocused electron beam furnace to heat the whole volume of CdSe powder. Completion of this process can be detected by monitoring the pressure in the vacuum chamber. (iv) The substrates must be thermally cleaned by heating to 600°C and allowed to cool to the growth temperature when deposition is immediately commenced. The results re-

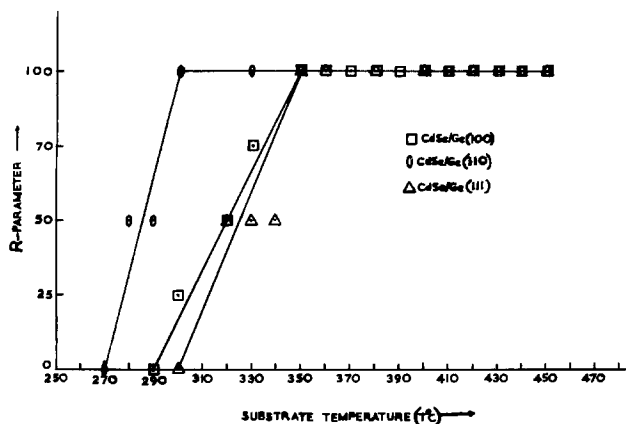


Fig. 1. The variation with substrate temperature of the degree of orientation R of films of CdSe evaporated on to Ge surfaces $R = 100$ indicates epitaxy \square : (100), \diamond : (110), and \triangle : (111) oriented substrates.

ported in this paper were only attainable when all these requirements were satisfied.

The electron beam evaporator was focused each time to produce a 2 mm diameter hot spot on the CdSe charge during evaporation. The evaporator input power was kept constant and continuously monitored. All the films were deposited for 1½ min. The film thicknesses were measured using a Nomarski interferometer attachment on a Reichert metallographic microscope. The values were found to range from 1200 to 2000 Å. Thus the combined effect of any variations in evaporation rate and sticking coefficient was a variation of only $\pm 25\%$ in film thickness.

Results

Epitaxial ranges of growth temperature.—Films of CdSe were deposited *in vacua* in the 10^{-5} to 10^{-6} Torr range of Ge substrates with (100), (110), and (111) orientations with the results shown in Fig. 1. The film structures are represented in this figure by means of the degree of orientation parameter R which has the values 100 for epitaxial films giving well-oriented electron diffraction spot patterns, $R = 0$ for randomly oriented polycrystalline films giving ring patterns and intermediate values for partially oriented films giving superposed spot and ring patterns (7, 8). These results show that epitaxial growth was invariably obtained for all substrate temperatures from 350° to 450°C on (100) and (111) oriented surfaces of Ge. On (110) surfaces the minimum epitaxial growth temperature was 50°C lower than on the other two singular surfaces. In this case the epitaxial growth range of substrate temperatures was 300°–450°C.

The maximum possible growth temperature, 450°C in all three surface orientations, was limited by the cessation of deposition. Similar deposition cut-off temperatures were observed to occur in all previously investigated II-VI/IV combinations (1-4, 6). In the present case as in those previously reported, the deposition cut-off temperature appeared to be set by the commencement of some form of chemical attack. Substrates which were held at temperatures above 450°C while CdSe was evaporated had etched surfaces.

Structure of CdSe films deposited on (100) Ge substrates.—Films deposited on (100) surfaces of Ge held at all temperatures in the epitaxial range, 350°–450°C, grew with the cubic sphalerite (i.e., zincblende) structure in (100) orientation as shown in Fig. 2(a) and (b). When the epitaxial (100) films were tilted slightly away from the exact (100) orientation in the electron microscope the diffraction patterns changed to the form shown in Fig. 2(c). Similar patterns have been observed in a number of other cases of II-VI films grown on (100) surfaces of cubic system crystal substrates. The sets of four intensity maxima occur-

ring around the positions of the CdSe spots occur where the Ewald sphere intersects $\langle 111 \rangle$ streaks in reciprocal space (9). That this was the correct interpretation was established by tilting the films and observing that the pseudo spots move in and out relative to the CdSe crystal diffraction spot positions and by noting that the pseudo spots have the characteristic elliptical form arising from the intersection of the approximately planar Ewald sphere with the right-circular-cylindrical $\langle 111 \rangle$ streaks. No satellite spots were ever seen in the diffraction patterns of the (100) CdSe films. Satellite spots would arise if any three-dimensional defects such as twins or included grains of CdSe with the hexagonal wurtzite structure were present. It may therefore be deduced that such three-dimensional defects were absent. The $\langle 111 \rangle$ streaks arise from $\{111\}$ planar defects present in high densities. The observation of the satellite pseudo spots therefore shows that numerous $\{111\}$ planar defects were present in the films. At these high densities the planar defects can be seen in dark field electron micrographs (1, 9), but are not sufficiently large or well separated for diffraction contrast analysis to be possible.

The best method to determine the epitaxial orientation relationship between the films and substrates is to observe the superimposed diffraction patterns that arise in areas of specimen in which both CdSe and Ge are present in comparable thicknesses. The patterns reported in Fig. 2 are those that arise from the CdSe alone, i.e., in areas of the specimen whence the thinning process has removed all the Ge. The diffraction patterns arising in overlapping CdSe and Ge will be referred to as Moire patterns since they arise from the diffraction effects which give rise to Moire fringes in the transmission electron micrographs.

The Moire electron diffraction pattern arising from overlapping epitaxial CdSe on (100) Ge is shown in Fig. 3(a). The neighboring pairs of spots arising from 220 type reflections in CdSe and Ge, give rise to additional spots by double diffraction. The result of double-diffraction replication of the 022 Ge spots round each of the CdSe spots is the square "Moire arrays" of spots shown in Fig. 3(b). These are the arrays seen in practice as shown in Fig. 3(a) and as previously reported in the case of CdTe grown on (100) Ge (4). The diffraction vectors involved in producing these Moire diffraction patterns lie in the (100) plane in reciprocal space. These diffraction conditions therefore are exactly satisfied without taking the effects of the buckling of the specimen into account and these arrays are readily obtained.

The Moire fringes resulting from the overlapping of crystals of differing lattice parameter but in parallel alignment are known as parallel Moire fringes. Their spacing is given (10) by

$$D_{\text{parallel}} = \frac{d_1 d_2}{d_1 - d_2} \quad [1]$$

where d_1 and d_2 are the spacings of the Bragg reflecting planes in the two crystals which give rise to the interfering Moire beams. Substituting for d_1 and d_2 the spacings of the 022 planes in CdSe and Ge we obtain as the calculated value: $D_{\text{parallel}} = 29.1 \text{ \AA}$. The measured value for the Moire fringes in CdSe/(100) Ge specimens was 29.2 Å. This excellent agreement confirms the interpretation given above for the diffraction patterns of the form shown in Fig. 3(a).

Structure of CdSe films grown on (110) Ge surfaces.—The diffraction patterns obtained from areas from which the Ge had been removed, when the film was tilted to the exact (110) orientation, were as shown in Fig. 4(a). These patterns were indexed and found to arise from the sphalerite structure in (110) orientation as shown in Fig. 4(b). When the films were tilted slightly off the exact (110) orientation, the spots appeared to split into pairs separated along the [002] direction as shown in Fig. 5(a). The characteristic

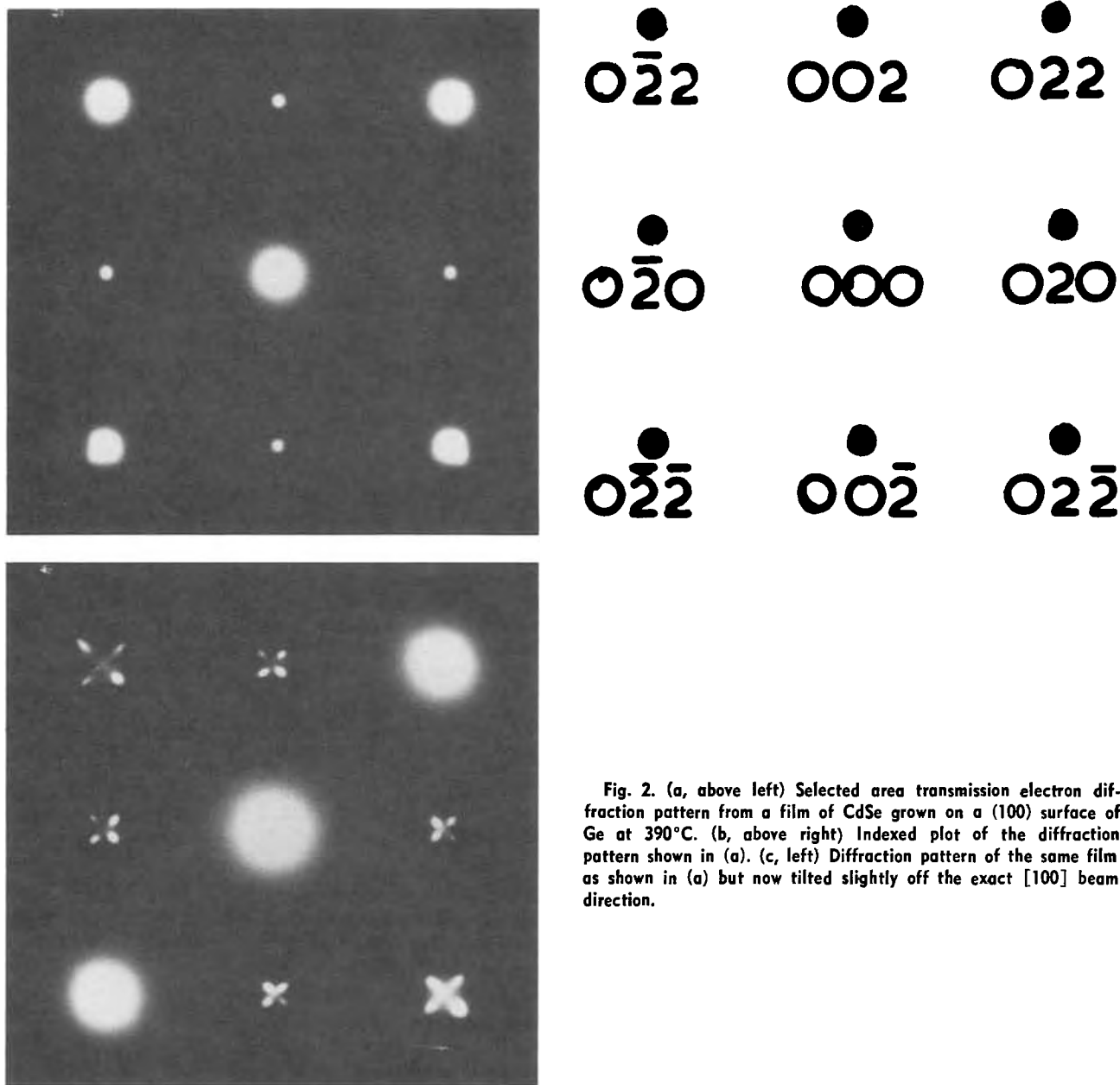


Fig. 2. (a, above left) Selected area transmission electron diffraction pattern from a film of CdSe grown on a (100) surface of Ge at 390°C. (b, above right) Indexed plot of the diffraction pattern shown in (a). (c, left) Diffraction pattern of the same film as shown in (a) but now tilted slightly off the exact [100] beam direction.

appearance of the micrographs of the (110) epitaxial films is shown in Fig. 5(b). This form of contrast in dark and bright areas of jig-saw-puzzle shape, led to this type of structure being termed a domain-form faulted structure in previous cases (2, 4). The structure arises from faulting on the two {111} planes inclined $35^{\circ}16'$ on either side of the normal to the films. One type of domain faults or transforms on the one plane and the second type of domain on the other plane. The two faulted planes give rise to streaks in reciprocal space in the $\langle 111 \rangle$ directions normal to the faults. The two types of streak run through every reciprocal lattice point and give rise to the pairs of "split" pseudo spots. The contrast shown in Fig. 5(b) arises because the one type of domain diffracts into the one pseudo spot of each pair while the second type of domain diffracts into the other pseudo spot and these are generally unequal in intensity.

The domain-form faulted structure was found in the CdSe films grown on (110) surfaces of Ge substrates at all temperatures throughout the epitaxial range, 300°-450°C.

Structure of CdSe films grown on (111) Ge surfaces.

—The diffraction patterns of epitaxial films of CdSe grown on (111) oriented Ge substrates showed the

films to have the sphalerite structure in (111) orientation. This was confirmed by the form of the Moire diffraction pattern shown in Fig. 6(a) which were obtained in areas of comparable thicknesses of overlapping CdSe and Ge. The diffraction patterns of the diamond structure of Ge and of the sphalerite structure in the (111) orientation contain the same set of permitted reflections. The pairs of spots with the same indices arising from the two structures are closely spaced. Double diffraction results in the production of hexagonal arrays of Moire spots at each permitted reflection site. If the CdSe however, had the other structure that is likely when epitaxially grown on (111) surfaces, namely the hexagonal wurtzite structure in (0001) orientation, the situation would be strikingly different. There is a set of six spots of the form $10\bar{1}0$ in the (0001) diffraction pattern of wurtzite which occur at only half the distance from the undeviated beam (center spot, 000) of the first hexagon of spots in the (111) diamond pattern, the 220 spots. The inner hexagon of $10\bar{1}0$ spots therefore have no near neighbors and no strong array of Moire spots occurs at such positions. The occurrence of arrays of Moire spots at the innermost set of spots in Fig. 7(a) indicates that

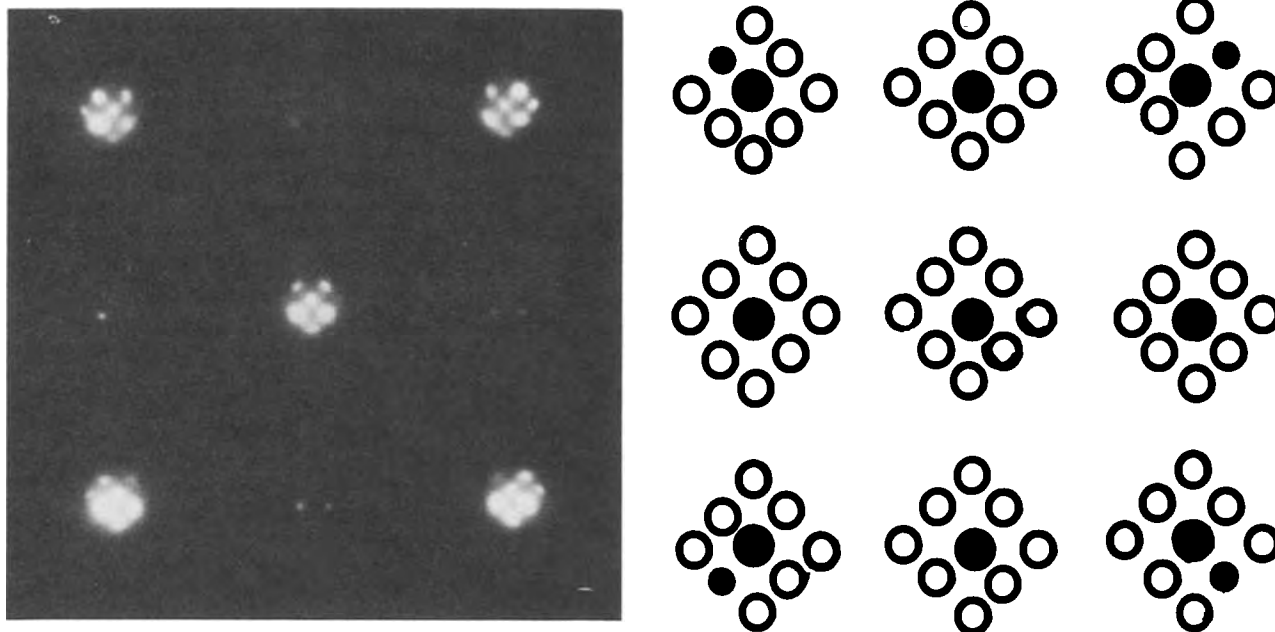


Fig. 3. (a, above left) Transmission electron diffraction pattern from an area in which the CdSe and Ge were of comparable thickness. The CdSe was epitaxially grown at 370°C on (100) Ge. (b, above right) The complete arrays of double diffraction Moire spots (open circles) about the CdSe spots (large solid circles) and Ge spots (small solid circles) in the (100) reciprocal lattice plane. This is the explanation of the experimental transmission electron diffraction pattern shown in (a).

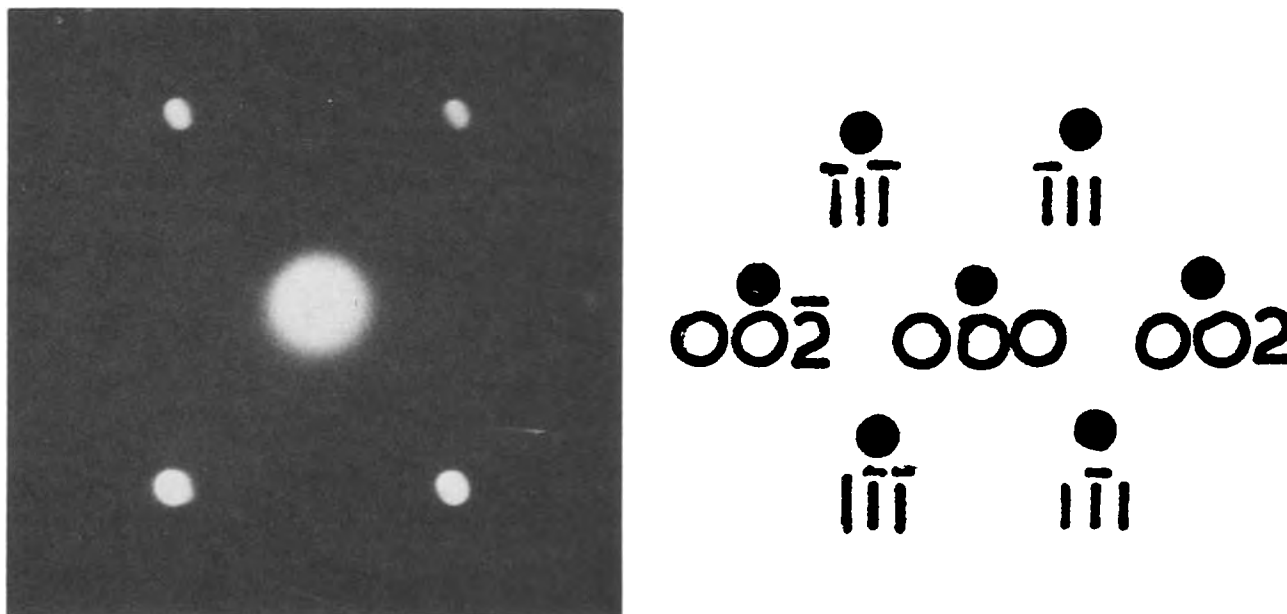


Fig. 4. (a, above left) Diffraction pattern of a CdSe film grown on a (110) oriented Ge substrate. This is the pattern obtained with the electron beam incident on the film in the exact [110] direction. (b, above right) The pattern in (a) is that of the spherulite structure in (110) orientation and indexes as shown.

these films have the sphalerite structure in (111) orientation.

The detailed form of the Moire pattern of Fig. 6(a) was unexpected. In all previous cases the epitaxial orientation relation between sphalerite structure films of II-VI compounds and cubic structure substrates had been that of parallel alignment (6). The Moire diffraction pattern in such cases for (111) substrates would have the form shown in Fig. 6(b). The actual form however, is that of Fig. 6(c), which will be referred to as the nearly parallel, rotation pattern for reasons that are more fully explained in Fig. 7. In the present case this type of pattern arises from the naturally occurring epitaxial orientation relation. No previous observation of this type of orientation relation is known to us. Previous instances of patterns of this type were

artifacts produced by attempts to lay one film on another in parallel orientation (11).

The reciprocal lattice "diffraction" vector g from the center spot to any particular diffraction spot has a length $1/d_{hkl}$ where d_{hkl} is the spacing of the hkl Bragg reflecting planes giving rise to the spot. The spacings of the Moire fringes which are produced in the micrographs by the interference between electron beams arising from the closely spaced spots are given by the reciprocals of the vectors joining the spots in reciprocal space. This leads (10, 11) to the Moire fringe spacing of Eq. [1]. When in addition to a difference in lattice parameter and hence interplanar spacings, d_{hkl} , between the overlapping crystals, there is an azimuthal rotation of the one crystal relative to the other through an angle α as shown in Fig. 6(c) and 7 and we have the



Fig. 5. (a, above left) Diffraction pattern of a film of CdSe grown on (110) Ge at 440°C. This is the pattern obtained when the film is tilted slightly off the exact (110) orientation. (b, above right) Bright field transmission electron micrograph of the same film.

nearly parallel, rotation pattern. Inspection of the actual Moire diffraction pattern of Fig. 6(a) together with the diagrams of Fig. 6(b) and (c) shows that the

azimuthal rotation α is such as to rotate the hexagonal array of Moire spots around each CdSe spot through 30° relative to their positions in the parallel Moire

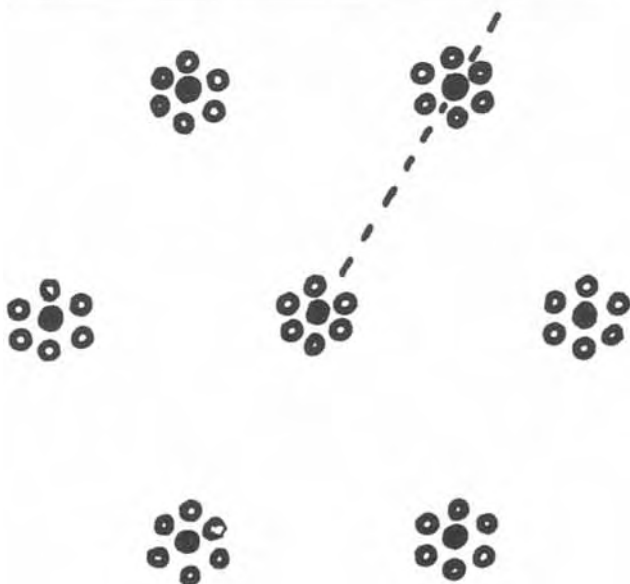
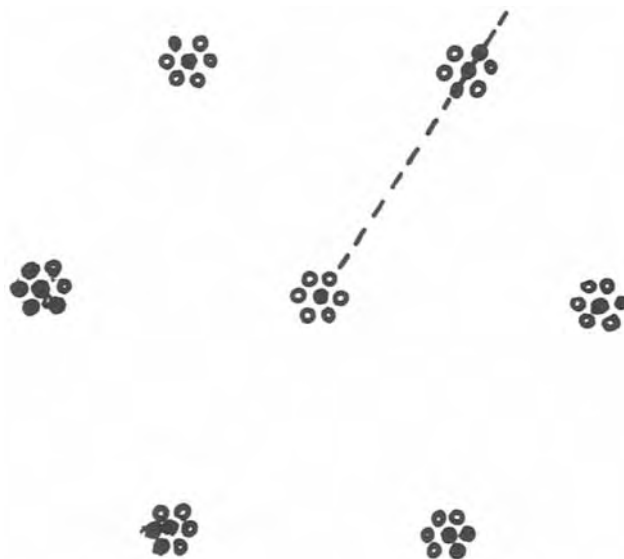
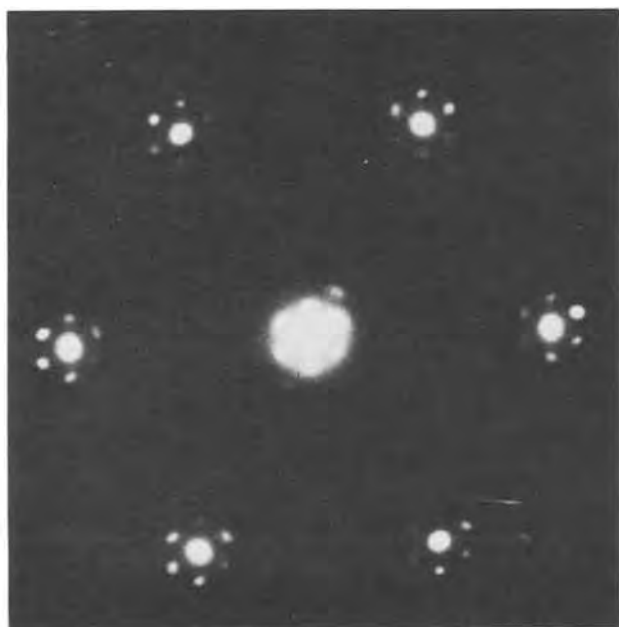


Fig. 6. (a, above left) Moire diffraction pattern obtained from an area of overlapping CdSe and Ge in (111) orientation. The film was grown at 400°C. (b, above right) The parallel Moire pattern for the (111) orientation. The CdSe and Ge single diffraction spots represented by large and small solid circles lie along common directions (radii) from the center 000 spot. (c, left) The nearly parallel, rotation Moire pattern for the (111) orientation. The diffraction vectors g to the corresponding CdSe and Ge spots are not parallel as in (b) (see the enlargements of a portion of these diffraction patterns in Fig. 7). The open circles represent double diffraction spots. The actual diffraction pattern in (a) is of the form (c) and not of the parallel form (b).

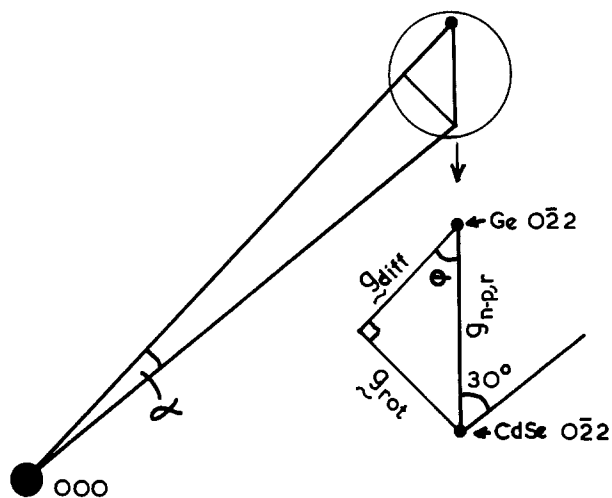


Fig. 7. In the nearly parallel, rotation Moiré diffraction pattern the $\bar{0}22$ diffraction vectors for CdSe and Ge differ in direction by an angle, α . The enlarged drawing shows the triangle, two of the apices of which are the CdSe and Ge $\bar{0}22$ diffraction spots.

array, as indicated in Fig. 7. The spacing of the Moiré fringes arising from the $\bar{0}22$ type of CdSe and Ge single diffraction beams in the nearly parallel, rotation case can be found as follows (see Fig. 7)

$$|\mathbf{g}_{n-p,r}|^2 = |\mathbf{g}_{diff}|^2 + |\mathbf{g}_{rot}|^2 \quad [2]$$

or, since α is small, (see Fig. 7)

$$|\mathbf{g}_{n-p,r}|^2 = \frac{(d_1 - d_2)^2 + \alpha^2 d_1 d_2}{d_1^2 d_2^2} \quad [3]$$

Therefore the nearly parallel, rotation Moiré fringe spacing is given by

$$D_{n-p,r} = \frac{1}{|\mathbf{g}_{n-p,r}|} = \frac{d_1 d_2}{\{(d_1 - d_2)^2 + \alpha^2 d_1 d_2\}^{1/2}} \quad [4]$$

This is the expression quoted in Ref. (10) but not that originally quoted by Bassett *et al.* (11). In the present case this type of pattern arises from the naturally occurring epitaxial orientation relation whereas previously such patterns were only known from laying films one on top of the other in nearly parallel orientation.

The azimuthal rotation, α , can be obtained for the general case as follows

$$\tan \theta = \frac{|\mathbf{g}_{rot}|}{|\mathbf{g}_{diff}|}$$

i.e.

$$\frac{\sin \alpha}{d_1} = |\mathbf{g}_{diff}| \tan \theta$$

or

$$\sin \alpha = \left(\frac{d_1 - d_2}{d_2} \right) \tan \theta \quad [5]$$

In the present case within experimental error, $\theta = 30^\circ$. Calculating the spacings of the $\bar{0}22$ planes in CdSe and Ge using the expression $d_{hkl} = a/(h^2 + k^2 + l^2)^{1/2}$ where the lattice parameters, a , for CdSe and Ge are 6.077 Å and 5.658 Å, respectively, and substituting into Eq. [5] gives $\alpha = 2^\circ 24'$. This angle does not appear to have any simple crystallographic significance, despite the crystallographic appearance of the $\sim 30^\circ$ angle of rotation of the Moiré spot arrays from their positions in a parallel epitaxial alignment pattern.

Recently Matthews (12) pointed out that in many cases misfit at epitaxial interfaces could be accommodated by arrays of misfit dislocations of screw type as well as by the conventionally considered edge type

networks. He gave expressions for the energy of the arrays which indicated that in some cases the minimum energy occurred for epitaxial orientation relationships azimuthally rotated from parallel alignment. This may be the explanation of the "nearly parallel, rotation" orientation relationship found here. Similarly small deviations from a quasi-parallel orientation which occurs between wurtzite structure films of CdS epitaxially grown on substrates of cubic system crystals were found by Igarashi (13). This too was quantitatively accounted for by a misfit dislocation model (13). This phenomenon of small deviations from parallel alignment therefore may occur frequently and be explicable in general in terms of misfit dislocations. Detailed studies of the actual misfit dislocations in the CdSe/(111)Ge interfaces will have to be carried out to test this hypothesis. Work on this problem is continuing. The small spacings of the misfit dislocations and the considerable densities of other defects present experimental difficulties.

Discussion

Similarities to previous observations.—As mentioned in the introduction, three general features had been found in all previous detailed studies of the epitaxial growth of vacuum evaporated films of II-VI compounds on Ge: These were: (i) the universal occurrence of the parallel epitaxial orientation relationship, (ii) the fact that only the sphalerite structure was found in films grown on (100) and (110) substrate surfaces, and (iii) the occurrence in the films of all the compounds when grown on (110) surfaces of the characteristic domain-form, faulted structure. A first objective of the work reported here was to discover whether the same structures and orientation relationships also occur in the case of CdSe grown on Ge. The results reported above show that generalizations (ii) and (iii) still hold good for all the materials so far examined. The parallel epitaxial orientation relationships are however, not accurately of universal occurrence. On (111) Ge, CdSe grows with a small azimuthal rotation, $\alpha = 2^\circ 24'$, from the exact parallel alignment. The reason for this deviation from parallel alignment may be that rotations minimize the energy of arrays of screw-type misfit dislocations (12).

The epitaxial growth ranges of temperature.—The epitaxial growth ranges of substrate temperature for the (100), (110), and (111) surfaces of Ge have a common upper limit, 450°C. This is a deposition cut-off temperature above which no CdSe can be made to deposit by evaporation in a pressure of a few times 10^{-6} Torr. This limit appears to be set by the onset of some vapor phase chemical attack reaction. The similarities in the deposition cut-offs in all cases investigated (6) were that (i) the cut-off temperature was well defined to within the accuracy of measurement of substrate temperatures ($\pm 5^\circ$ to 10°C), (ii) it was unaffected by growth conditions such as contamination, rate of evaporation of the II-VI compound (or only slightly affected by the latter), substrate surface orientation, etc., (iii) above the cut-off temperature evidence of chemical attack on the substrate surfaces in the form of pitting or tarnishing was observed.

The minimum epitaxial growth temperatures in contrast to the cut-off temperatures are strongly affected by the growth conditions. The minimum epitaxial growth temperatures are reduced as contamination from all sources is reduced. The minimum epitaxial growth temperature is sometimes dependent on substrate surface orientation. In the case of ZnTe on Ge the minimum growth temperature was 300°C for both (111) and (100) substrates, and it was 300°C for CdS grown on (100), (110), and (111) surfaces of Ge. For CdTe on Ge the minimum epitaxial growth temperature was 250°C for (100) substrates but only 200°C for (110) and (111) substrates and in the present case it was found to be 350°C on (100) and (111) substrates, but only 300°C on (110) surfaces. Thus in the four

combinations of materials studied thus far, two, namely ZnTe/Ge and CdS/Ge, showed no orientation dependence of the minimum epitaxial growth temperature, while the other two did show an orientation dependence but the form of the dependence in the two cases was different. For CdTe/Ge the minimum epitaxial growth temperature was higher for (100) than for the other two singular surfaces whereas for CdSe/Ge, it was lower for (110) than for the other two singular surfaces.

The structural perfection of the CdSe films.—Little work has been published on the epitaxial growth of CdSe films. Early Russian work concerned CdSe films evaporated on to ionic crystal substrates. Electron diffraction showed the best films to be polycrystalline or to contain both wurtzite- and sphalerite-structure material (14, 15). Epitaxial films were grown on mica but their structural perfection was not determined (16). A study of the nucleation and growth of CdSe films evaporated onto cleavage surfaces of NaCl also provided little information on the perfection of the best films produced (17).

The present paper thus is the first report of CdSe films grown free of both twins and wurtzite-structure material so that the films gave rise to diffraction patterns that were free of satellite or irrational spots. The level of perfection of these films is similar to that of the other II-VI compound films studied previously in this laboratory (1-4, 6, 8, 9). It is also similar to the best levels reported for other heteroepitaxial films. The structure of the films is sufficiently good to justify the use of epitaxial CdSe/Ge heterojunctions prepared by the present methods for physical property measurements.

Acknowledgments

Thanks are due to Professor J. G. Ball for the provision of research facilities and to the Science Research Council for financial support of the work on II-VI epitaxy in this laboratory. One of us (F. H. G.) wishes to

thank the Governments of India and of Karnataka State for the provision of a study grant. We are grateful to Mr. B. H. Barter for his help in the development of the vacuum evaporation and thinning techniques used in this work.

Manuscript submitted Sept. 6, 1974; revised manuscript received Dec. 2, 1974.

Any discussion of this paper will appear in a Discussion Section to be published in the December 1975 JOURNAL. All discussions for the December 1975 Discussion Section should be submitted by Aug. 1, 1975.

REFERENCES

1. D. B. Holt and D. M. Wilcox, *J. Cryst. Growth*, **9**, 193 (1971).
2. M. I. Abdalla, D. B. Holt, and D. M. Wilcox, *J. Mater. Sci.*, **8**, 590 (1973).
3. A. R. Mufti and D. B. Holt, *ibid.*, **7**, 694 (1972).
4. M. I. Abdalla and D. B. Holt, *Phys. Status Solidi*, **a17**, 267 (1973).
5. D. B. Holt and D. M. Wilcox, *Thin Solid Films*, **10**, 141 (1972).
6. D. B. Holt, *ibid.*, **24**, 1 (1974).
7. S. Ino, D. Watanabe, and S. Ogawa, *J. Phys. Soc. Japan*, **19**, 881 (1964).
8. D. B. Holt, *Brit. J. Appl. Phys.*, **17**, 1395 (1966).
9. D. B. Holt and J. M. Woodcock, *J. Mater. Sci.*, **5**, 275 (1970).
10. P. B. Hirsch, A. Howie, R. B. Nicholson, D. W. Pashley, and M. J. Whelan, "Electron Microscopy of Thin Crystals," p. 358, Butterworths, London (1965).
11. G. A. Bassett, J. W. Menter, and D. W. Pashley, *Proc. Roy. Soc.*, **A246**, 345 (1958).
12. J. W. Matthews, *Phil. Mag.*, **29**, 797 (1974).
13. O. Igarashi, *J. Appl. Phys.*, **42**, 4035 (1971).
14. I. P. Kalinkin, L. A. Sergeeva, V. B. Aleskovskii, and L. P. Strakhov, *Sov. Phys.-Sol. State*, **3**, 1922 (1962).
15. I. P. Kalinkin, L. A. Sergeeva, V. B. Aleskovskii, and L. P. Strakhov, *ibid.*, **5**, 86 (1963).
16. A. Brunnschwiler, *Nature*, **209**, 493 (1966).
17. Y. Yasuda, *Japan. J. Appl. Phys.*, **7**, 1171 (1968).

The Preparation and Characterization of a New, Highly Sensitive, Crosslinking Electron Resist

J. L. Bartelt and E. D. Feit

Bell Laboratories, Murray Hill, New Jersey 07974

ABSTRACT

The feasibility of current proposals for electron beam exposure systems depends heavily on the availability of electron resists of high sensitivity (greater than 100 m²/coulomb) in which relief images with submicron features can be made. An acrylate-based polymer system (a terpolymer of glycidyl methacrylate, ethyl acrylate, and methyl methacrylate partially esterified with methacrylic acid) containing epoxy and vinyl reactive sites has been found to be a promising negative electron resist system, called CER, whose characteristics include high sensitivity (125 m²/coulomb), good adhesion to SiO₂ and metals, and good chemical resistance to etchants for these materials. The composition, characteristics, and processing of CER are presented here in detail.

Electron Sensitive Polymers and E-Beam Microfabrication

The fabrication of microelectronic devices by means of electron exposure of specially prepared resists has several advantages over conventional photoresist technology. These advantages include higher theoretical resolution, larger depth of field, and the conveniences and economies of direct "on the wafer" exposures us-

ing automatic computer controlled pattern generation systems. The technology currently available for such exposure systems, however, places a great demand on the sensitivity of resists (1). For scanning systems with submicron beam sizes high sensitivity is required to allow rapid deflection of beams with relatively low current density. Deflection and blanking systems can operate at rates of about 10⁷ bits/sec so that with a raster of 2000 lines/mm (0.5 μm spot size) an area of 25 cm² can be covered in about 17 min. In order to

operate at these rates with the currents available for $0.1 \mu\text{m}$ beam sizes ($2.5 \times 10^{-8}\text{A}$ for a tungsten filament) resist sensitivities must be in excess of $100 \text{ m}^2/\text{coulomb}$.¹

While sensitivity is of critical importance, contrast, adhesion, etch resistance, and defect density are equally vital characteristics that influence electron resist selection. Molecular weight distribution and glass transition temperature are significant resist properties also (4), but we have concentrated on sensitivity and processing in this work. The adhesion, etch resistance, and resolution capabilities of this material will be presented in detail elsewhere (5).

In Fig. 1 we show the sensitivities of a number of electron sensitive crosslinking materials which have been reported in the literature (6), all of which have the potential of being negative electron resists. The three epoxy-based polymers [epoxidized-polybutadiene, epoxidized-polyisoprene, and polyglycidylmethacrylate (7)] and the polymer system marked CER which we have formulated are sufficiently sensitive to meet the criterion established above. As a practical matter, however, note that sensitivity can only be determined relative to the specific processing or end use for which it is intended. Factors such as film thickness, accelerating voltage, chemical developers, baking temperatures, etc. have an effect on sensitivity and thus one must be particularly careful in the use and comparison of these literature values. We have not been able to reproduce the exact sensitivity, for example, that was originally reported for the three epoxy-based polymers (5, 7). Moreover, we have found that CER responds more sharply to changes in dose (has higher contrast) than do the epoxy rubbers [see Fig. 4 and Ref. (5)].

Our approach to the development of a sensitive electron resist was an extension of the work on epoxy-

¹ There have been alternate proposals (2, 3) in which the resist is simultaneously exposed over an entire pattern and the beam is shaped by masks or patterned cathodes. Since much more current can be produced in such a beam, sensitivity is no longer a critical factor. The successful development of these systems will probably take several more years.

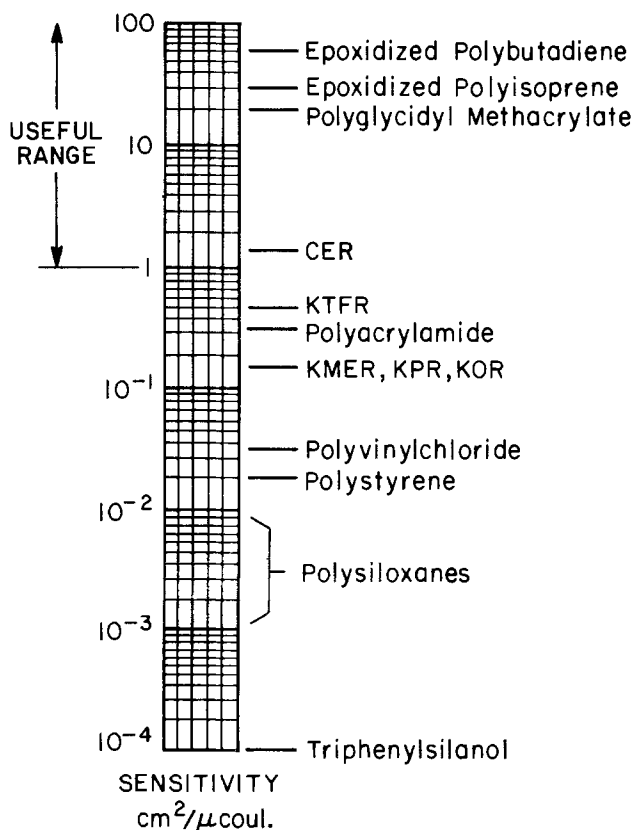


Fig. 1. Electron sensitivity of crosslinking polymers

based resists (7) in a direction already taken by Schoenthaler (8). In the latter's work, the epoxy groups of the polymer are esterified with acrylic and methacrylic acid. Some commercial photoresists in the Riston (du Pont) family are believed to have reactive binders based on this type of polymer (9).

The polymer system that we call CER is a material described by Burlant and Taylor as a radiation sensitive binder (10, 11). This material is a terpolymer of glycidyl methacrylate, methyl methacrylate, and ethyl acrylate. The epoxy groups in this terpolymer, provided by the glycidyl methacrylate, are partially esterified with methacrylic acid to introduce unsaturation. Figure 2 outlines this process and shows a composite of final components of CER.

Preparation and Characterization of CER

Synthesis.—CER was prepared according to the procedure of Burlant and Taylor (10). Benzoyl peroxide (1.00g, 4.1 mmol) was dissolved in a mixture of methyl methacrylate (26.0g, 260 mmol), ethyl acrylate (50.0g, 500 mmol), and glycidyl methacrylate (23.7g, 167 mmol). The vinyl monomers were used as supplied, without removal of stabilizers. This mixture was added over a 3 hr period with stirring to refluxing xylene (250 ml) in a nitrogen atmosphere. The mixture was refluxed for an additional 3 hr, cooled at 50°C , and stabilized with hydroquinone (0.0203g, 0.18 mmol). Methacrylic acid (14.7g, 171 mmol) was added. The reaction mixture was then gradually warmed to reflux and held at that temperature until the concentration of methacrylic acid was decreased to 30.8% of its original value as measured by titration of 2 ml aliquots of the reaction mixture with 0.05N KOH.

We purified the CER by solvent precipitation before use to eliminate low molecular weight material which affects the rate at which developer swells the film. Samples of crude, oily CER were diluted to about 2% solids with xylene and precipitated in an ice-cooled, 10:2:1 mixture of petroleum ether, isopropanol, and water. The resulting white, solid precipitate was filtered and dried.

Film preparation.—Films used to characterize CER were produced by spin coating on a Headway Research EC-101 Spinner from a 4% solution in xylene. For the metal and oxide substrates (Si, SiO_2 , W, Cr) that were used in this study good adhesion was obtained without the need for surface adhesion promoters or treatments. The film thickness depends on the spinning speed and on the concentration or viscosity of the resist. A convenient relation between thickness (T) in microns and spinning speed (S) in rpm for the 4% solution described above is

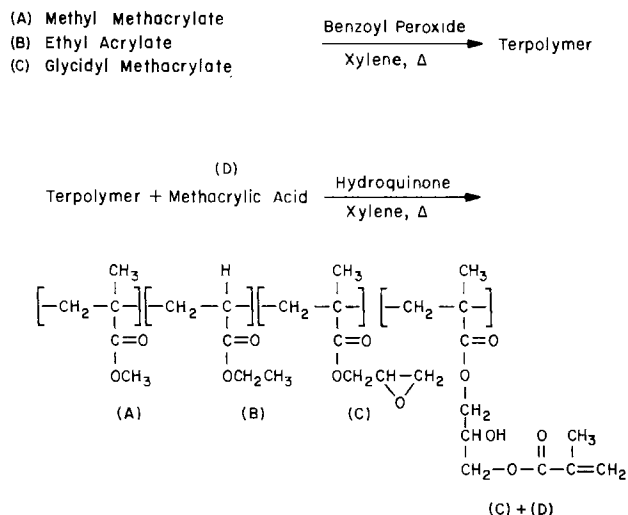


Fig. 2. Synthesis of CER

$$T = 13.4S^{-1/2}$$

We typically used the film in the range 0.2-0.4 μm , the thicker films being preferred to minimize pinhole problems. About 40 pinholes/cm² are found in 0.2 μm films of CER while 0.4 μm films have about 15 pinholes/cm².

Prior to use the films were prebaked in a vacuum oven at 90°C for 15 min. This serves to remove the solvent and by raising the CER above its glass transition temperature, to anneal any coating strain. After cooling, the material was exposed as soon as possible. If the material stood for long periods in a thin film after baking, it tended to spontaneously crosslink. The lifetime of the prepared films was on the order of 12-18 hr in room light. If the solution is kept cool and dark, its shelf life exceeds nine months.

Exposure and sensitivity.—Films of CER which were prepared according to the preceding steps were first tested for sensitivity to electron crosslinking by exposure in a flood gun system. A stationary beam is projected through a metal screen which forms a mask in contact with the sample. The beam voltage, current, and exposure time are controlled independently. Figure 3 shows a developed pattern in CER from just such an exposure. The exposure was made with an accelerating voltage of 10 kV and the dose was 3×10^{-7} coulomb/cm². It was later found that this exposure was less than optimum, but sufficient to define an image of the mask.

The technique which we prefer to use to measure the sensitivity of CER is one which can be used for any electron sensitive material: Using an SEM, 1 mm squares are exposed with a raster scan of at least 2500 lines at the required voltage, adjusting the current and exposure time so as to vary the dose over the required range. After developing and baking the thickness of

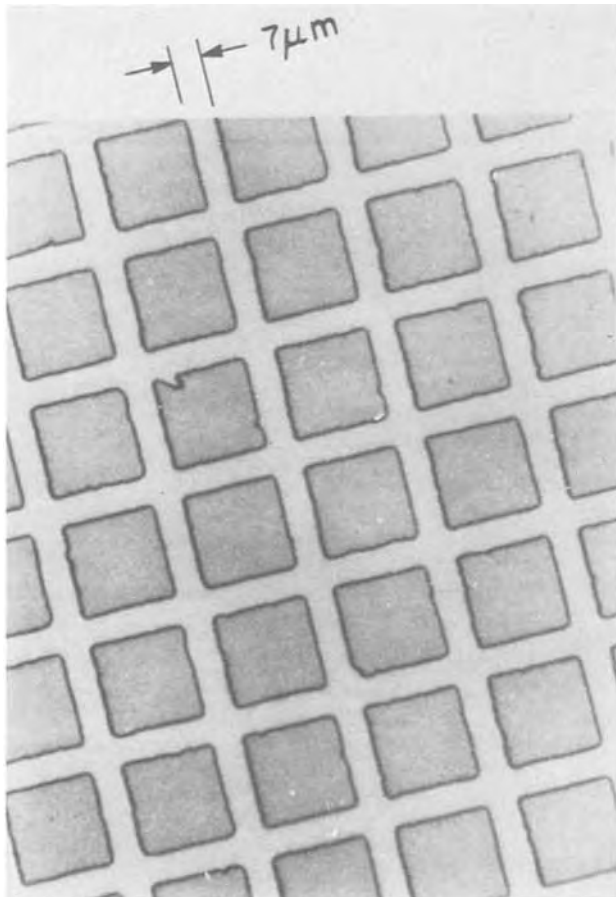


Fig. 3. Mesh pattern in CER produced by flood gun exposure

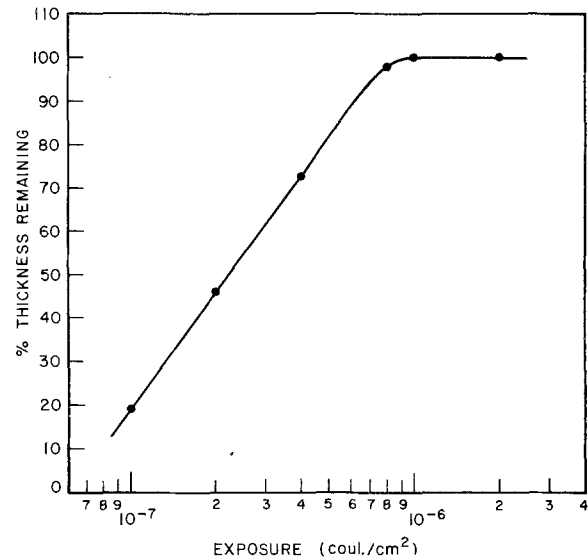


Fig. 4. Sensitivity of CER (thickness = 0.35 μm , accelerating voltage = 10 kV).

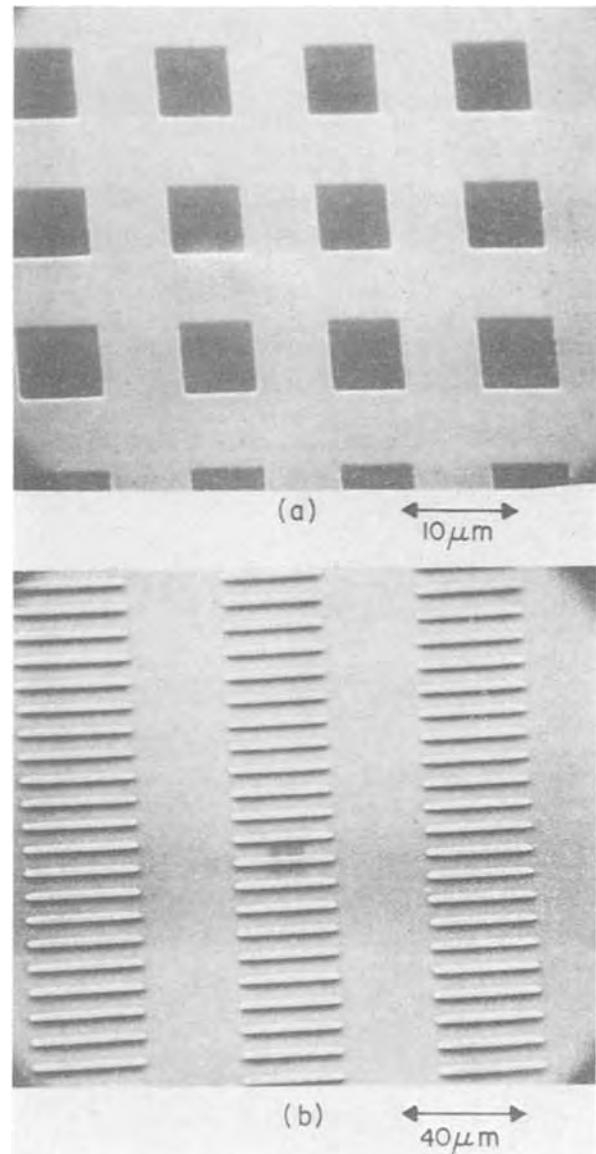


Fig. 5. (a) 6 μm windows etched into 0.2 μm of SiO₂ using CER as a mask, (b) 4 μm line and space patterns etched into W using CER as a mask.

each exposure square is measured with a calibrated stylus profilometer (Dektak, Sloan Technology Corporation). The per cent thickness remaining after development is then plotted as a function of dosage. Figure 4 shows a typical plot for 0.35 μm of CER exposed at 5 kV.

Development, postbaking, and stripping.—Initially the development for CER consisted of a 60 sec soak in xylene followed by a 30 sec spray of xylene and then blowing dry with air. While many of our initial patterns were developed in this manner, it was decided to switch to a spray development technique which has been successfully used with photoresists to improve edge acuity and resolution and to decrease pinholing due to extraction by progressively changing from solvent to nonsolvent as development proceeds. We also used an automatic spray developer (K & S Model 693 Photo Resist Spray Developer) to improve uniformity and reproducibility. A spray sequence of 7.5 sec of methyl ethyl ketone (MEK), 20 sec of 1:1 MEK:2-propanol, 15 sec of 2-propanol, and 30 sec of dry nitrogen was found to be quite effective.

After development a 20 min bake at 120°C is recommended before etching.

CER, patterned according to the process given above, has been used successfully to etch SiO_2 in buffered HF and to etch W in an alkaline ferricyanide solution (5). Features in the size range 4-6 μ are shown in Fig. 5. The ultimate resolution with this material can only be obtained with careful selection of film thickness, voltage, contrast, and exposure as detailed in Ref. (5).

Exposed CER is most conveniently removed by a dichromate-sulfuric acid cleaning solution, but ozone or plasma stripping as well as other strong oxidizing agents have also been used successfully.

Conclusions

The electron resist which we have documented here represents a significant improvement over many of the electron resists previously described in the literature (Fig. 1) and is a viable alternative to the others (7) with respect to the sensitivity, contrast, and reso-

lution required for electron beam fabrication of semiconductor devices. In addition we have demonstrated the patternability of CER and its usefulness as an etch mask for SiO_2 and W.

Acknowledgments

The authors would like to thank R. G. Brandes for making his exposure apparatus available, L. F. Thompson for Fig. 5, and R. D. Heidenreich, R. E. Kerwin and R. F. W. Pease for their helpful comments and advice.

Manuscript submitted March 28, 1973; revised manuscript received Oct. 10, 1974.

Any discussion of this paper will appear in a Discussion Section to be published in the December 1975 JOURNAL. All discussions for the December 1975 Discussion Section should be submitted by Aug. 1, 1975.

Publication costs of this article were partially assisted by Bell Laboratories.

REFERENCES

1. A. N. Broers and M. Hatzakis, *Sci. Am.*, **227**, 34 (1972).
2. H. Koops, G. Möllenstedt, and R. Speidel, *Optik*, **28**, 518 (1968/1969).
3. T. W. O'Keeffe, J. Vine, and R. M. Handy, *Solid-State Electron.*, **12**, 841 (1969).
4. H. Y. Ku and L. C. Scala, *This Journal*, **116**, 980 (1969).
5. L. F. Thompson, E. D. Feit, C. M. Melliar-Smith, and R. D. Heidenreich, *J. Appl. Phys.*, **44**, 4048 (1973).
6. This data has been extracted from a large number of references which have been compiled by A. R. Pierce, "Bibliography on Electron Beam Fabrication of Microcircuits (1960-1970)," Bell Laboratories LISC Bibliography No. 180, Holmdel, N. J. (1971).
7. T. Hirai, Y. Hatano, and S. Nonogaki, *This Journal*, **118**, 669 (1971).
8. A. C. Schoenthaler, U.S. Pat. 3,418,295 (Dec. 24, 1968).
9. J. R. Celeste, U.S. Pat. 3,469,982 (Sept. 30, 1969).
10. W. J. Burlant and C. R. Taylor, U.S. Pat. 3,528,844 (Sept. 15, 1970).
11. S. S. Labana and E. O. McLaughlin, *J. Elastoplastics*, **2**, 3 (1970).

Optimization of the Hydrazine-Water Solution for Anisotropic Etching of Silicon in Integrated Circuit Technology

Michel J. Declercq,¹ Levy Gerzberg,* and James D. Meindl**

Stanford Electronics Laboratories, Stanford University, Stanford, California 94305

ABSTRACT

Anisotropic etching of silicon with the hydrazine-water mixture is studied and characterized for its practical use in integrated circuit technology. The solution is applied to {100} wafers where the etch presents a v-shaped cross section limited at the side-walls by {111} planes and at the bottom by a {100} plane. The etching process is evaluated in terms of the etch rate of the {100} plane, quality of side-walls and bottom surface, and corner rounding. It is shown that the results are both concentration and temperature dependent. The optimal temperature for the etching process is found to be 100°C for both simple temperature control and high quality etching. It is also shown that the optimal mixture concentration must be chosen according to the particular use of the anisotropic etching. The optimal volume concentrations of hydrazine for the various applications are: 65% for VMOS devices and for v-groove isolation rings, 70-80% for two-level structures with flat bottom surface, and for electrode and sensor fabrication.

The anisotropic etching of silicon has been studied with increased interest in recent years (1-7) and is on the way to becoming a standard processing step in silicon technology (8-12).

Anisotropic etchants are usually 3-component solutions. They contain a base such as hydrazine, ethylene diamine, or potassium hydroxide, a complexing agent such as isopropyl alcohol or catechol, and water. The etching reaction involves the formation of hydrous silica which is dissolved through the formation of a complex (1). Some compounds such as hydrazine can act both as oxidant and complexing agent (2) and can therefore be mixed with water only. Another etching method based on an electrochemical displacement reaction has also been proposed recently (5).

All these solutions have the common property that they etch the silicon crystal with a higher rate along the <100> direction than along the <111> direction. When used on {100} oriented slices covered by an oxide mask, these etchants produce a pyramidal-shaped etch, limited at the side-walls by {111} surfaces and at the bottom by a {100} plane (Fig. 1). An interesting property of the anisotropic etching of {100} surfaces is that the etch is "self-stopping" at the point where the {111} planes intersect and the {100} bottom surface reduces to zero.

Among the most significant applications published for the anisotropic etching of the silicon are the v-groove or dielectric isolation of integrated circuits

(8-10), the VMOS structures (11-14), and the etching of microelectrodes and sensors (15, 16). Each of these applications has been concerned mainly with the quality of the groove side-walls, since the {100} bottom surface has completely disappeared either due to the "self-stopping" property or to the complete etching through of the entire wafer thickness. However, no optimization of the etching parameters has been reported for these applications.

On the other hand, many new applications may be anticipated if the etch is terminated before reaching its "self-stopping" point. For example, the resulting {100} bottom surface may be used for two-level structures, for direct contact to a lower layer of an integrated circuit, for the fabrication of pressure sensors and other devices for which a flat surface is required, etc. The anisotropic etch offers a unique possibility for two-level structures by its clean cut, nonvertical walls, which avoid breaking the photoresist or the metal strips on the step between the two levels.

The purpose of this study is to characterize the hydrazine-water mixture and to find the optimum etching parameters according to the particular application.

* Electrochemical Society Student Member.
** Electrochemical Society Active Member.
¹ Present address: Louvain University, Electronics Labs., Maxwell Building, B-1348 Louvain-la-Neuve, Belgium.
Key words: semiconductor technology, preferential etching, hydrazine-water solution, undercutting of corners, flat surfaces.

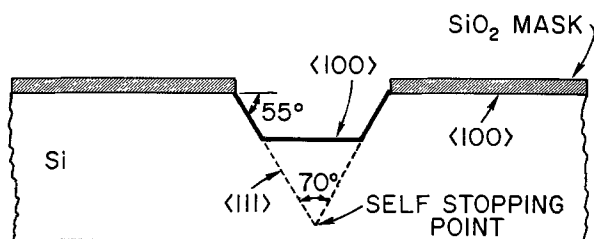


Fig. 1. Anisotropic etching of a {100} slice

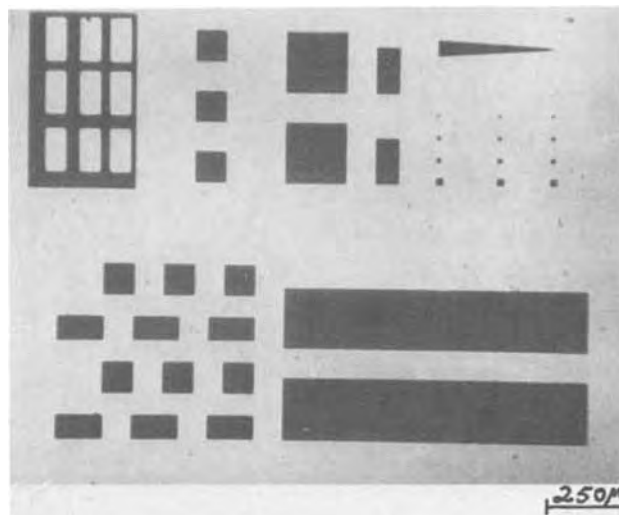


Fig. 2. The mask used for the evaluation of the anisotropic etching.

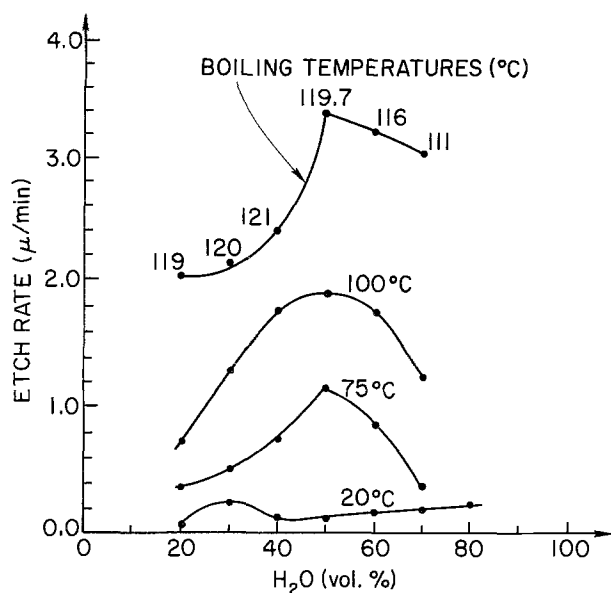


Fig. 3. Etch rate in the {100} plane as a function of water percentage for various temperatures.

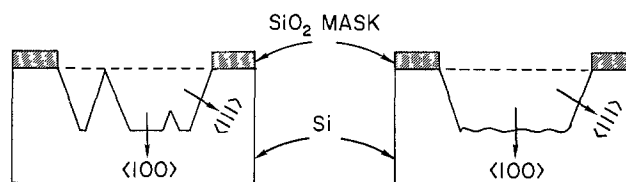


Fig. 4. Typical defects of the {100} bottom surface; left, pyramidal hillocks and right, waveshaped surface.

Experimental Procedure

A glass refluxing system was used to prevent composition change by loss of volatile matter. The temperature was controlled within $\pm 1^\circ\text{C}$ by a constant temperature bath. N-type {100} wafers of 3-5 ohm-cm resistivity were used throughout the experiment. An oxide layer of about 2000Å was grown on the wafers at a temperature of 1000°C. The mask was aligned on the <110> wafer flat with a precision of $\pm 1^\circ$ or better, in order to get straight side-wall lines as explained later. A standard cleaning procedure (17) was performed just before etching. The results of the anisotropic etching were evaluated in terms of the etch rate of the {100} plane, quality of side-walls and corners,

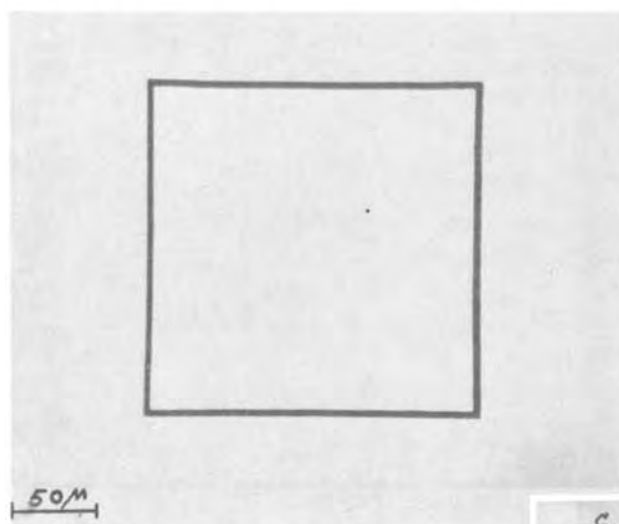
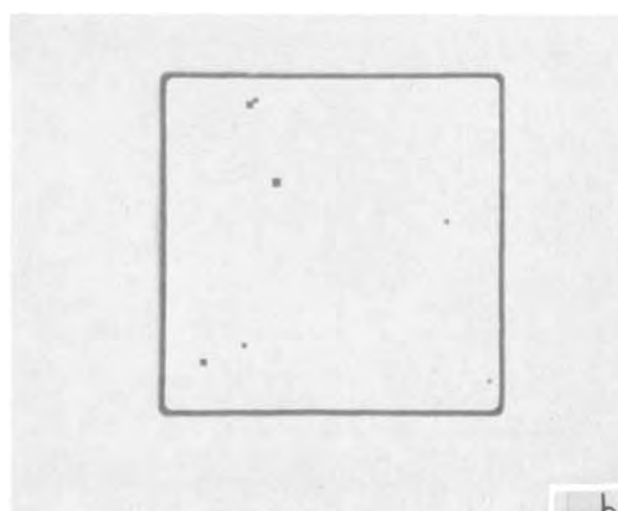
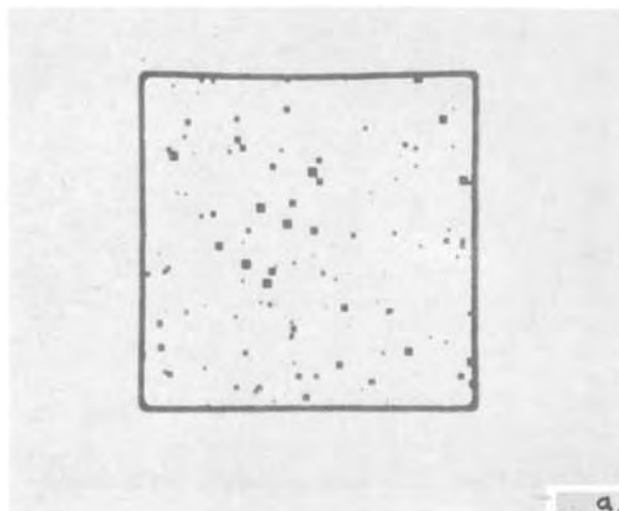


Fig. 5. 200 \times 200 (μm)² squares etched 5 μ deep at 100°C in solutions of various concentrations. a, above left H₂O/N₂H₄ = 50/50 (volume ratio); b, above right H₂O/N₂H₄ = 40/60 (volume ratio); c, left H₂O/N₂H₄ = 20/80 (volume ratio).

and quality of bottom surface. These parameters were examined for several concentrations of water and hydrazine at 20°, 75°, 100°C and at the boiling temperatures of the solutions. All the proportions of hydrazine and water were measured in volume per cent. The etched bottom surface was examined across both small area (~16 mil²) and large area (~400 mil²) structures. The side-walls were checked around these etched areas and in v-groove isolation type structures. A triangular area with a top angle of 7° was placed on the mask in order to evaluate the effect of a $\pm 3.5^\circ$ misalignment on the quality of the side-walls (Fig. 2). The depth of the groove was measured microscopically using a focusing stage calibrated to one micron per scale division. Each experiment was repeated several times on different samples in order to eliminate angle and depth measurement errors.

Results

Etch rate.—The etch rate of the {100} plane as a function of water percentage in the solution is shown in Fig. 3 for several temperatures. These results are in good agreement with the results reported by Lee (2). It is obvious from Fig. 3 that the etch rate can be temperature or concentration controlled. The etch rate increases with temperature, and in the high tempera-

ture range it reaches its maximum value when an equivolume solution of water and hydrazine is used. At 20°C, the etch rate has a minimum value which occurs for a 40% water-60% hydrazine solution.

Quality of bottom surface and side-walls.—It has been observed that the quality of the bottom surface may be affected in two ways: by the formation of pyramidal hillocks and by the formation of wave-shaped structures (Fig. 4).

The quality of the bottom surface was found to be dependent on both the temperature and the solution concentration as demonstrated in Fig. 5 and Fig. 6. For an equivolume solution of water and hydrazine, both pyramids and a wavelike bottom appear at any temperature. At 100°C less water gives higher bottom surface quality, and for 30% water or less there are no pyramids or waves on the bottom at all. The effect of temperature on the bottom surface quality is seen in Fig. 6 in which a solution of 20% water and 80% hydrazine was used at various temperatures. Etching at temperatures below or above 100°C caused a wave-shaped bottom surface. At room temperature, pyramids also appeared.

The quality of the bottom surface was measured in terms of the percentage of etched $100 \times 100 (\mu\text{m})^2$

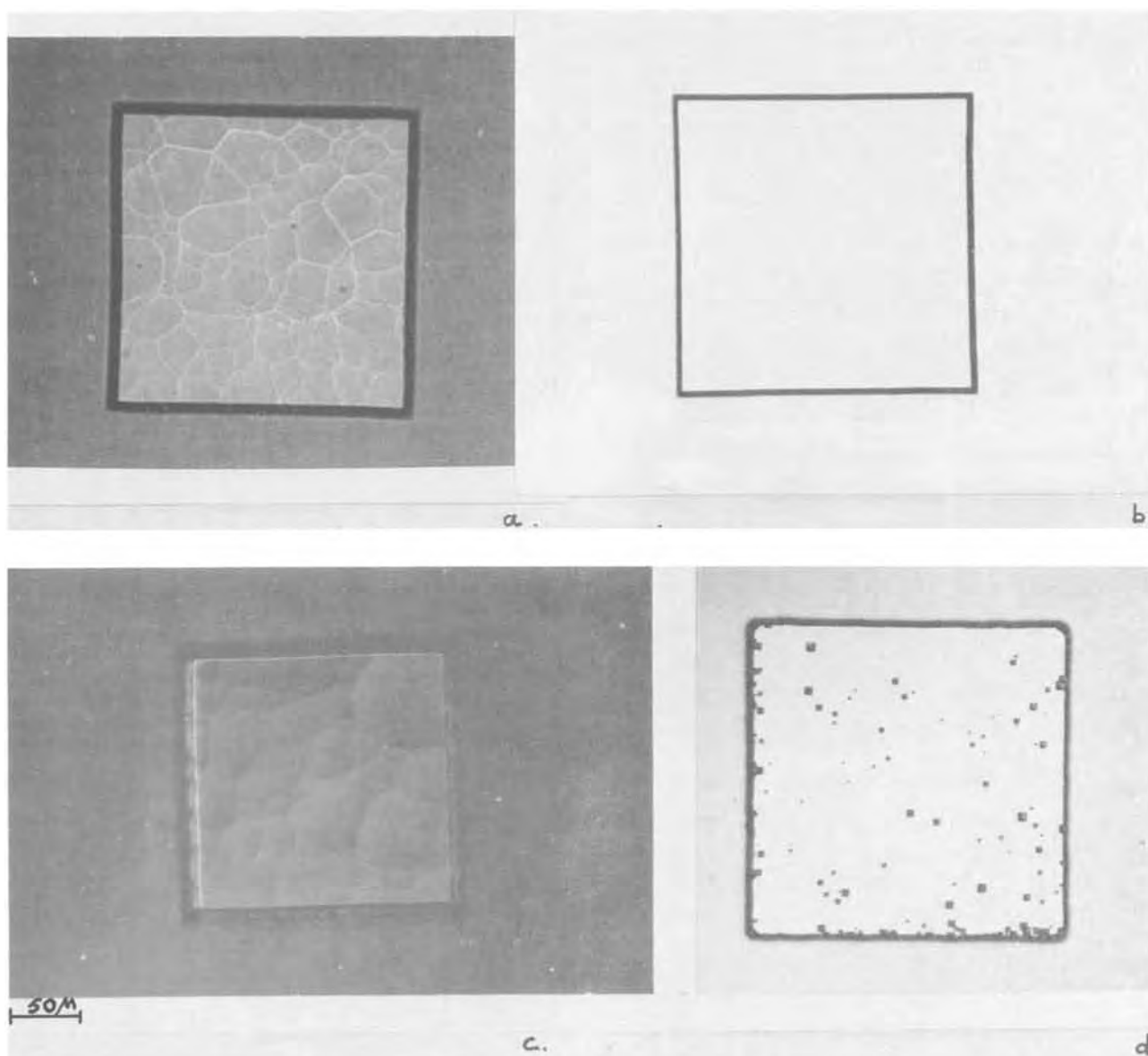


Fig. 6. $200 \times 200 (\mu\text{m})^2$ squares etched 5μ deep in solutions of 20% H_2O -80% N_2H_4 at various temperatures. a, 119°C; b, 100°C; c, 75°C; d, 20°C.

areas, free of waves or pyramids, which can be used for device fabrication. The measured quality function is plotted in Fig. 7. The quality of the side-walls was measured in terms of the side-wall edge formed by the intersection of the {100} and {111} planes. Walls with straight edges were considered to be of high quality. The best side-wall edges were obtained at 100°C. It has been observed that for this temperature, the side-wall lines become more straight as the percentage of water in the solution is increased. The observed quality of the side-wall edges for various temperatures as a function of the solution concentration is given in Fig. 7. An example of poor side-wall quality is given in Fig. 6c for etching with a solution of 20% water-80% hydrazine at 75°C.

From these results it can be inferred that straight walls can be obtained at 100°C and with 20-50% of water in the solution. However, the usable range of concentration for v-groove etching has to be limited by a maximum of 40% water, due to the pyramidal defects that may appear in the groove when higher percentage of water is used. When high quality of bottom surface is also required, the amount of water should not exceed 30%.

Quality of corners.—The quality of corners was examined in concave (90°) and convex (270°) corners. Concave corners, similar to those in rectangular etched surfaces, had very little corner rounding (Fig. 5, 6). Convex corners, like those existing in v-groove isolated structures, have more significant beveling (undercutting) due to etching in other crystallographic directions. The mean value measured for the angle made on the (100) surface by the bevel line and the trace of the {111} plane was 18° 41'. This confirms the observations made by Lee (2) and indicates that the planes being etched are the {112} planes which generate the theoretical angle of 18° 26' on the top surface. To get a quantitative estimate of this convex corner undercutting, let U be a normalized factor defined by

$$U = \frac{\delta}{H} \quad [1]$$

with δ , the distance between a {112} plane intersection line and a parallel line traced from the corner of the oxide limit (Fig. 8) and H , the groove depth.

With a constant temperature of 100°C, the undercutting factor decreases uniformly for an increased amount of water in the solution, as shown in Fig. 9a. At 20°C, the undercutting factor has a minimum at 30% H₂O-70% N₂H₄ and increases sharply for higher amounts of water in the solution. It is therefore obvious that U is also temperature dependent for a given concentration. This effect is illustrated in Fig. 9b for a solution of 20% H₂O-80% N₂H₄.

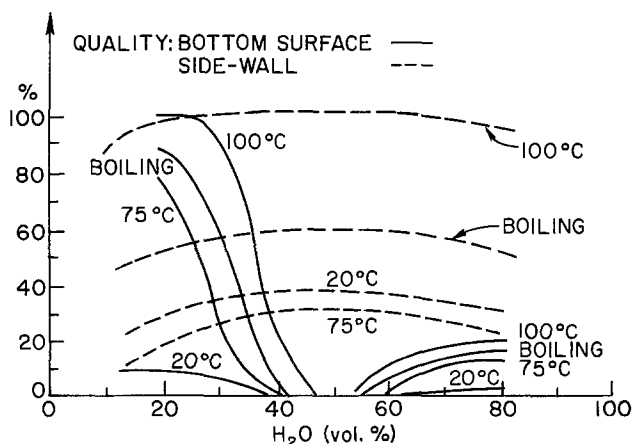


Fig. 7. Bottom surface quality (in per cent of usable 16 mil² squares) and side-wall quality (estimated value in per cent).

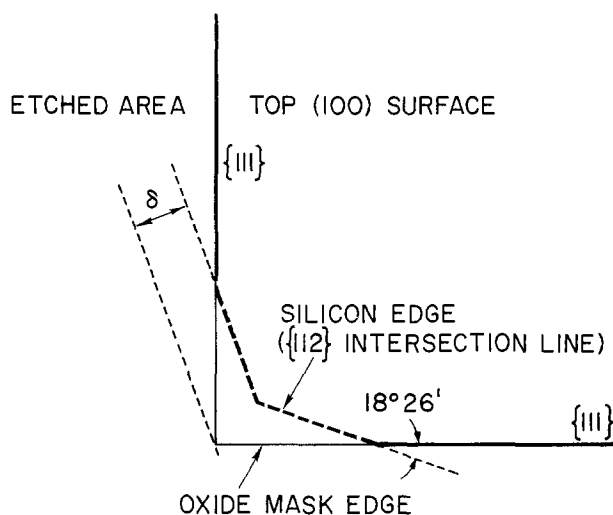


Fig. 8. Underetching of a convex corner under the SiO₂ mask along the {112} plane (top view).

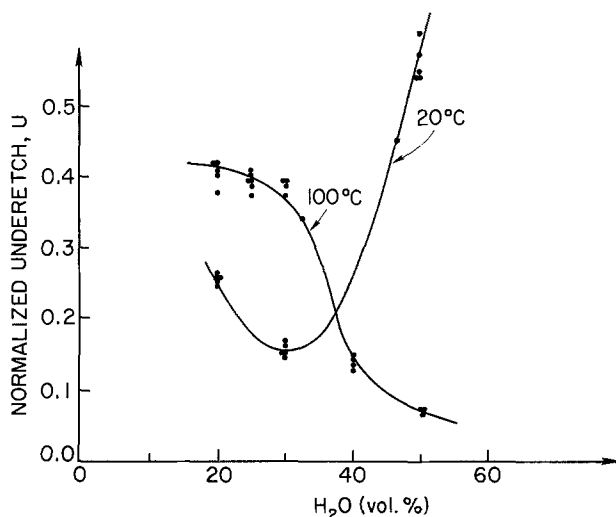


Fig. 9a. Variation of the undercutting factor U with the solution concentration.

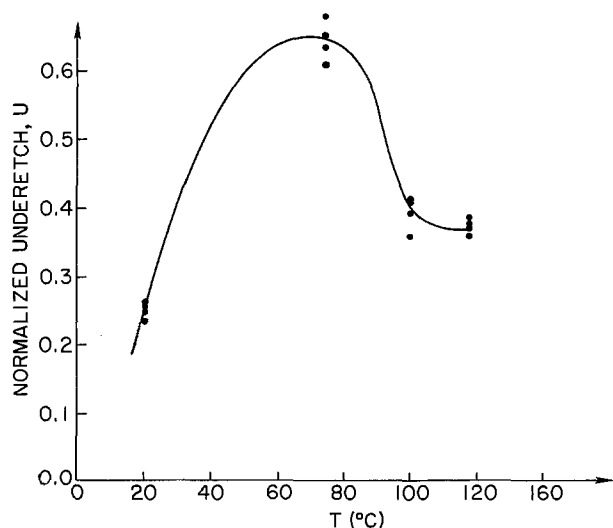


Fig. 9b. Variation of the undercutting factor U with the temperature for a solution of 20% H₂O-80% N₂H₄.

An example of the effect of the solution concentration on the corner underetch at 100°C is given in Fig. 10a, b. Both grooves have the same depth of 15 μ , but the groove of Fig. 10a was etched with a 20% H₂O-80% N₂H₄ mixture, while the groove of Fig. 10b was etched with a 50% H₂O-50% N₂H₄ mixture. This effect plays an important role in the design of a v-groove isolated bipolar transistor since it can reduce drastically the original surface. Underetching can be minimized by carefully choosing the parameters of the etching solution.

Self-correction of unstraight lines.—An interesting property due to the selectivity of the hydrazine-water solution is the fact that side-wall edges will come out straight after etching, even with small ripples in the oxide mask (Fig. 11). On the other hand, a large misalignment of the mask will give as a result a sawtooth-shaped line, even for straight mask edges (Fig. 12).

Discussion of the Results

In the experimental results previously described, two kinds of defects have been observed: pyramids and waves on the bottom surface. The appearance of pyramids is explained by the following reasons:

1. Square pyramidal hillocks may be formed from defects on the surface of the starting material or at deeper points in the bulk (Fig. 4 and Fig. 5).

2. The chemical reaction of the etching process is involved with the formation and dissolution of hydrous silica. In some cases, this oxide is locally not dissolved fast enough and gives rise to the development of new pyramids.

The effect of the formation of a large number of pyramids can easily be seen when using room temperature solutions. An example of the result obtained after 3 hr in a solution of 30% water and 70% hydrazine at 20°C is shown in Fig. 13.

It has been reported that the presence of an alcohol

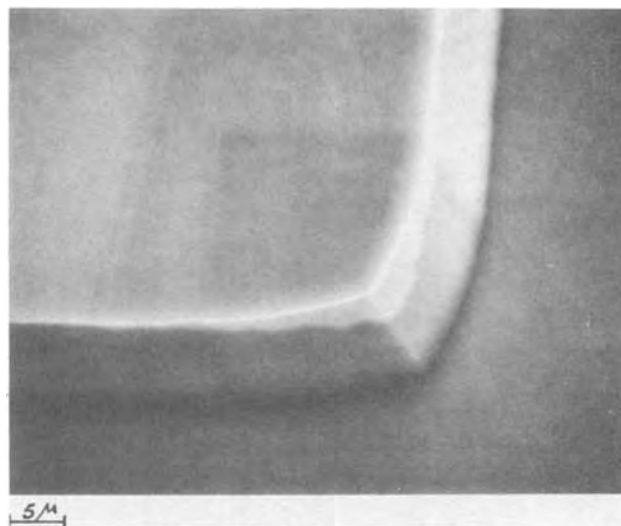


Fig. 11. Straightening out of silicon edges covered with a ragged oxide mask.

in the etching solution helps in the dissolution of the oxide, appearing during the reaction, by the formation of a complex (1,2). Although hydrazine itself is able to act both as oxidant and complexing agent (2), an attempt was made to add catechol in the solution to help the reaction. The result of this test compared to the result obtained with a solution containing water and hydrazine only is presented in Fig. 14. It can be seen that the opposite effect is obtained, and that many new pyramids were grown on the surface in the presence of alcohol. A suggested explanation for this behavior is the strong effect of alcohol on the relative etch rate along the different crystallographic direc-

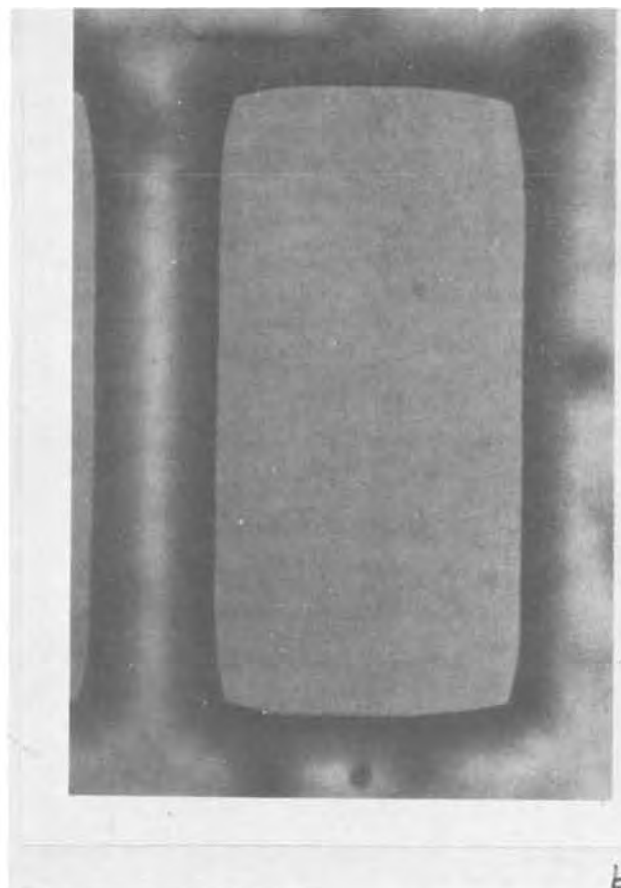
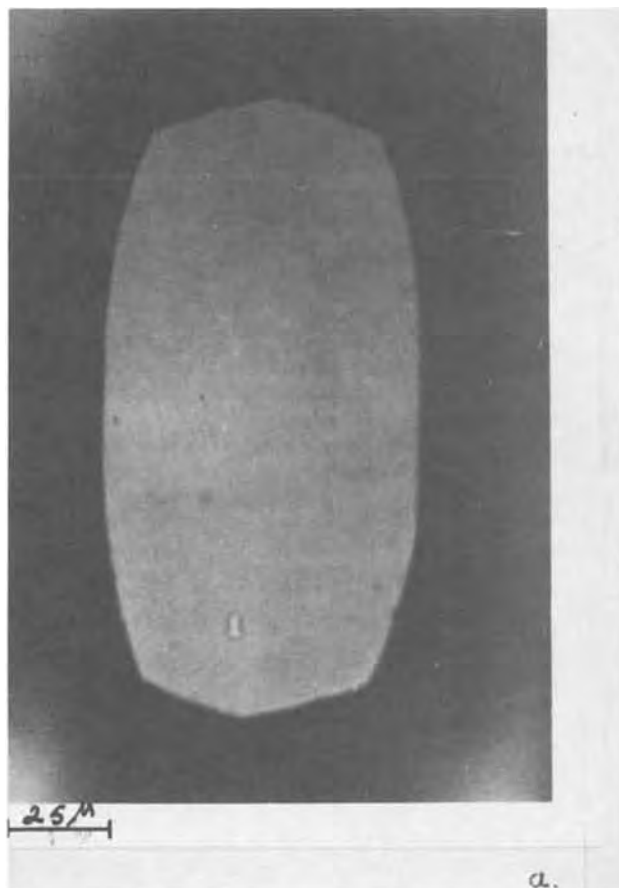


Fig. 10. Effect of the solution concentration on the corner underetching at 100°C (15 μ depth). a, Solution of 80% hydrazine; b, solution of 50% hydrazine.

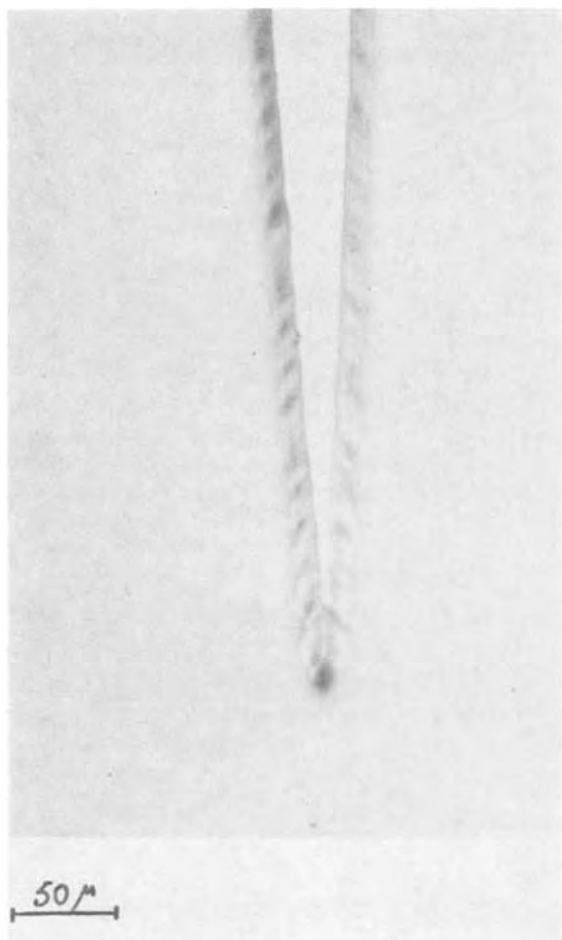


Fig. 12. Effect of the anisotropic etch on misaligned lines. The side-lines of the triangle are $\pm 3.5^\circ$ out of alignment with the $\langle 110 \rangle$ flat.

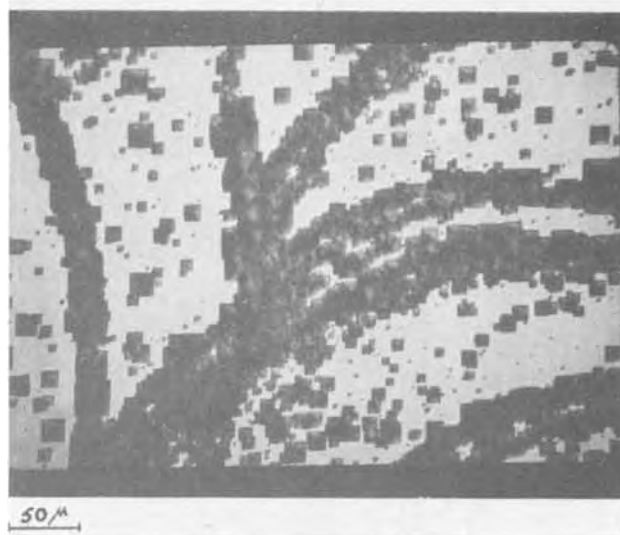


Fig. 13. Appearance of pyramids on the surface during a long etching at low temperature.

tions (2,6) which will affect the surface quality as explained later.

3. The fact that the quality of the bottom surface and side-walls is affected by temperature, solution concentration or the presence of an alcohol is also related to the selectivity of the etching solution.

When the selectivity of the solution is high (i.e., high etch rate along $\langle 100 \rangle$ and low along the other directions), every defect or contamination may be the origin of a pyramid. The side-walls, however, will be very well defined in this case by $\{111\}$ planes, and therefore will be very straight.

In solutions with low selectivity, pyramids that start growing are etched from the sides in the $\langle 111 \rangle$ and $\langle 112 \rangle$ directions and therefore will not exist at

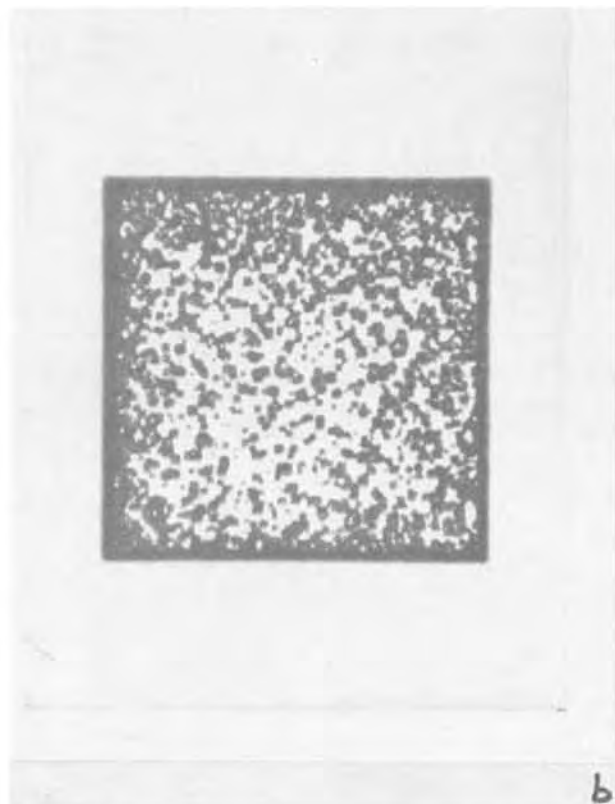
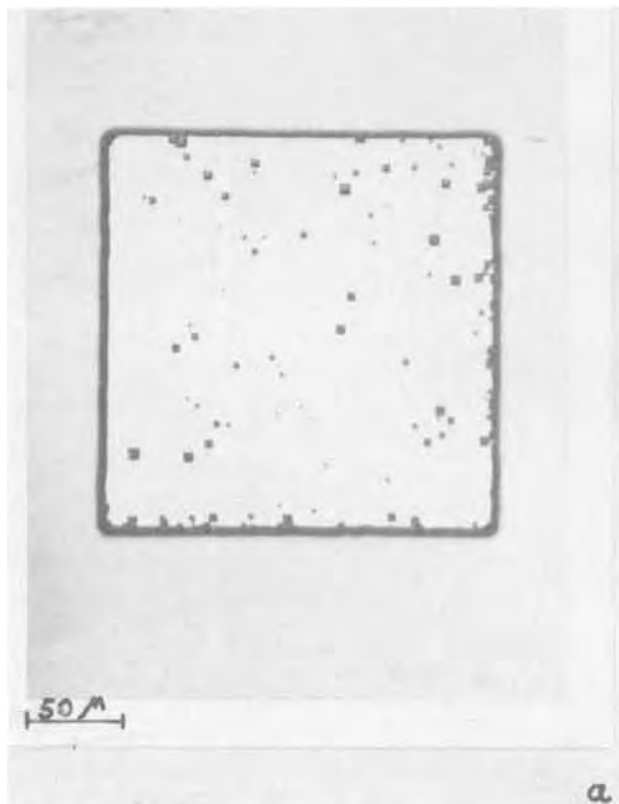


Fig. 14. Effect of the presence of an alcohol in the etching solution. a, Room temperature etch (20°C) with 20% water, 80% hydrazine, 5μ deep. b, Room temperature etch when 12g of catechol is added to 150 ml of the solution of Fig. 14a. The depth is 5μ .

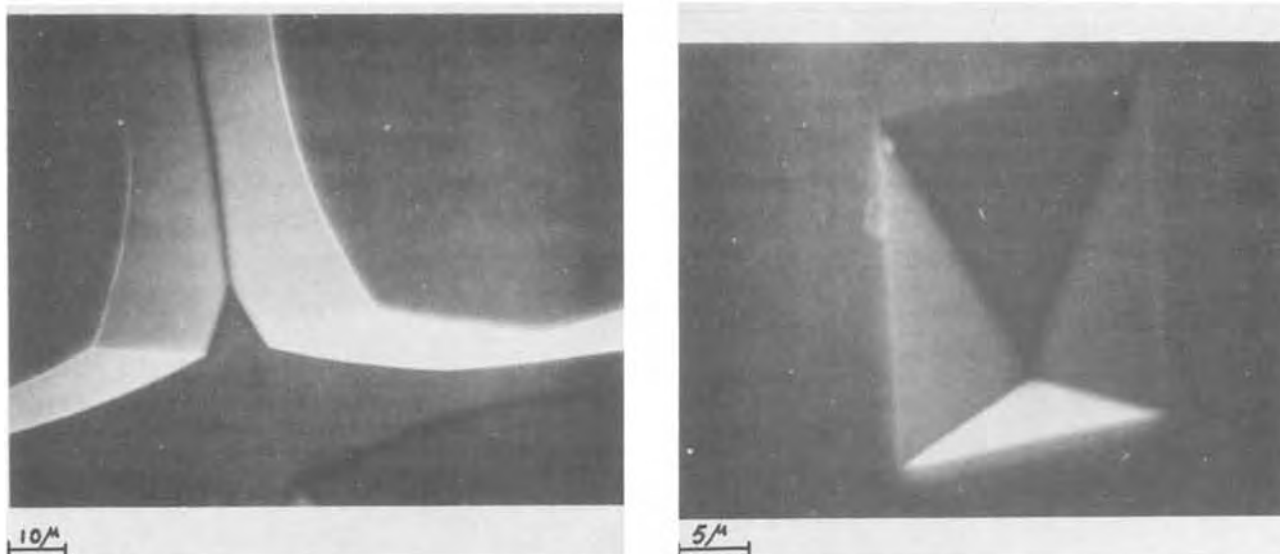


Fig. 15. Scanning electron microscope views of v-groove etches obtained with a solution of 30% H_2O -70% N_2H_4 at 100°C (15μ deep). a (above left), V-groove isolation ring (magnification $1000\times$) and b (above right), V-MOS structure (magnification $2000\times$).

the end of the etching process. For the same reason, the property of the self-correction of the mask edges (Fig. 11) is reduced, and therefore more wall defects may appear. Wave-type disturbances on the bottom surface may appear if care is not taken to avoid local nonuniformities in the etching solution. This effect usually happens when the wafer is not carefully dried before immersed in the etching solution, or when the solution is not well stirred. However, even with such care, some unexplained waviness appeared for particular temperatures and concentrations (Fig. 6).

Conclusions

The hydrazine-water mixture etches the silicon crystal anisotropically with a higher etch rate along the $\langle 100 \rangle$ direction than along the $\langle 111 \rangle$ direction.

It has been shown that temperature and solution concentration strongly influence the results. Besides the etch rate measurements, the etch quality has been examined in terms of wall and bottom surface quality, corner undercutting, and self-correction of unstraight mask edges. The conclusions may be summarized as follows:

1. The optimal temperature for the hydrazine-water anisotropic etch is found to be 100°C , for both simple temperature control and high quality etching.

2. The percentage of water in the mixture must be chosen according to the particular use of the anisotropic etching: (i) For v-groove rings like those used for bipolar transistor isolation, the solution which gives the best wall quality, low undercutting, and an acceptable yield at the same time should contain about 65% hydrazine (Fig. 15a). For these concentrations, typical values of the underetching factor U are around 0.25. The same range of concentration can be used for VMOS devices where $\{111\}$ wall quality is the only important parameter (11) (see Fig. 15b). (ii) For use in two-level structures where both good walls and high quality bottom surface are required, the best concentration range is between 70 and 80% hydrazine. The same ratio is recommended for the etching of electrodes and sensors where a large etched area with a high degree of smoothness is required. An example of the results obtained in this range of concentration is shown in Fig. 16.

3. The wafer should be carefully cleaned and dried just before etching.

4. In order to ensure constant solution concentration, the solution, while in use, should be kept in a reflux system to avoid excessive evaporation.

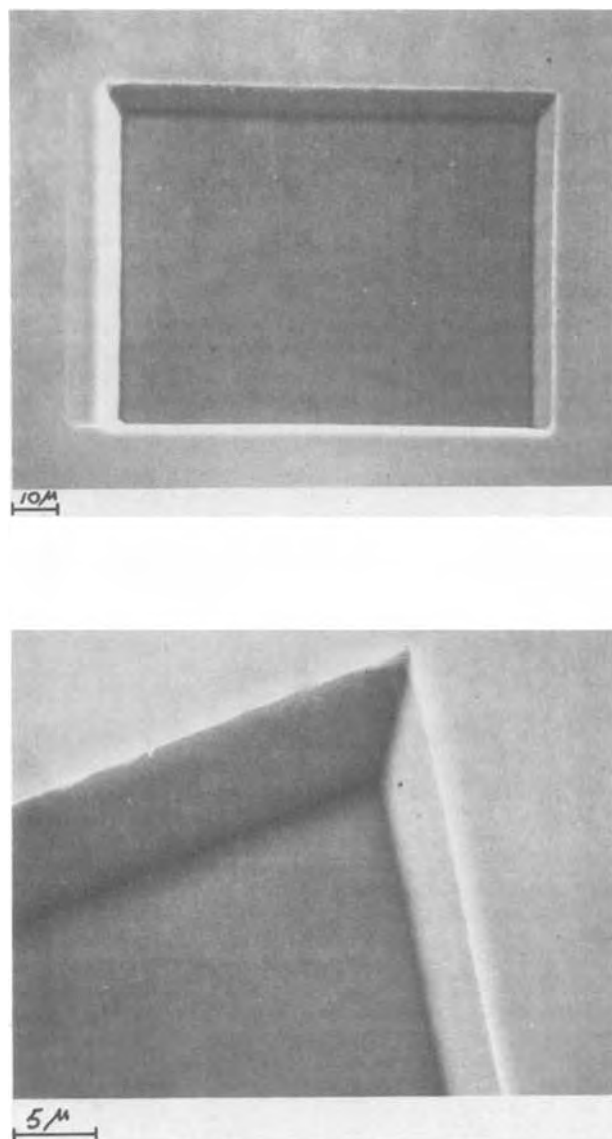


Fig. 16. Scanning electron microscope views of a 100×100 (μm)² square etched in a solution of 20% H_2O -80% N_2H_4 at 100°C . a (upper), Complete square and b (lower) a corner view.

Acknowledgments

The authors are grateful to T. J. Rodgers for helpful discussions and for the review of the manuscript. They wish to thank L. J. Anderson and C. R. Zercher for the scanning electron photomicrographs.

Manuscript submitted July 15, 1974; revised manuscript received Nov. 20, 1974. This was Paper 219 presented at the New York, New York, Meeting of the Society, Oct. 13-17, 1974.

Any discussion of this paper will appear in a Discussion Section to be published in the December 1975 JOURNAL. All discussions for the December 1975 Discussion Section should be submitted by Aug. 1, 1975.

Publication costs of this article were partially assisted by the Stanford Electronics Laboratories.

LIST OF SYMBOLS

H	groove depth, micrometer
U	normalized undercut
δ	distance between the {112} plane intersection line and a parallel line traced from the corner of the oxide limit, micrometer

REFERENCES

1. R. M. Finne, and D. L. Klein, *This Journal*, **114**, 965 (1967).
2. D. B. Lee, *J. Appl. Phys.*, **40**, 4569 (1969).
3. J. C. Greenwood, *This Journal*, **116**, 1325 (1969).
4. A. Bohg, *ibid.*, **118**, 401 (1971).

5. W. K. Zwicker, and S. K. Kurtz, in "Semiconductor Silicon 1973," Howard R. Huff and Ronald R. Burgess, Editors, pp. 315-326, The Electrochemical Society Softbound Symposium Series, Princeton, N. J. (1973).
6. J. B. Price, in "Semiconductor Silicon 1973," Howard R. Huff and Ronald R. Burgess, Editors, pp. 339-353, The Electrochemical Society Softbound Symposium Series, Princeton, N. J. (1973).
7. K. E. Bean, R. L. Yeakley, and T. K. Powell, Abstract No. 23, p. 68, The Electrochemical Society Extended Abstracts, Spring Meeting, San Francisco, California, May 12-17, 1974.
8. D. F. Allison, A. P. Youmans, and T. H. Wong, *Electronics*, **42**, 112 (1969).
9. J. M. Mudge, and K. Taft, *ibid.*, p. 65 (July 17, 1972).
10. T. J. Rodgers and J. D. Meindl, *IEEE Trans. Electron. Dev.*, **ED-20**, 226 (1973).
11. T. J. Rodgers and J. D. Meindl, ISSCC Conference, Philadelphia, Feb. 1974.
12. *Electronics*, **46**, 31 (1973).
13. F. E. Holmes, and C. A. T. Salama, *Electronics Letters*, **9**, 457 (1973).
14. C. M. Parks and C. A. T. Salama, *ibid.*, **9**, 593 (1973).
15. K. Wise, Ph.D. Dissertation, Stanford University (1969).
16. Samaun, Ph.D. Dissertation, Stanford University (1971).
17. W. Kern and D. A. Puotinen, *RCA Rev.*, **31**, 187 (1970).

Accurate Theoretical Arsenic Diffusion Profiles in Silicon from Processing Data

R. K. Jain and R. J. Van Overstraeten

Departement Elektrotechniek, Laboratorium Fysica en Elektronica van de Halfgeleiders,

Katholieke Universiteit Leuven, Kardinaal Mercierlaan 94, 3030 Heverlee, Belgium

ABSTRACT

An accurate knowledge of the impurity distribution in a semiconductor device is essential for its proper characterization. This task can be made simpler if one knows properly the concentration dependent impurity diffusion coefficient. In recent years various arsenic diffusion models were developed to explain the experimental results, but it seems that a better physical model is required. The present work gives the arsenic concentration dependent diffusivity in silicon considering different mechanisms involved during the diffusion process. The effects of heavy doping and high temperature have been successfully included in the present work. Attempts are made to calculate theoretical arsenic diffusion profiles only from the knowledge of the processing data. It is found that our physical model gives quite good results which are in reasonable agreement with the experimental profiles.

Accurate knowledge of the impurity distribution into a semiconductor device is essential for its proper characterization. The calculation of a distribution can be made if one knows the concentration dependent impurity diffusion coefficient. The present work is an attempt to calculate the arsenic concentration dependent diffusivity. Use of these results is to calculate numerically the arsenic diffusion profiles from the knowledge of the processing data.

It is now well known that the diffusion coefficient of the impurities in semiconductors is not only a function of the temperature but also depends on the impurity concentration. There are various phenomena which are responsible for this impurity concentration dependent diffusivity. In recent years various workers (1-6) have presented different models of arsenic diffusion in silicon. The first three models (1-3) explain the concentration dependent arsenic diffusivity in terms of the change in the electron concentration due to the impurity concentration. The mathematical approach by Kennedy and Murley (4) makes use of the

Boltzmann-Matano analysis on several experimentally determined arsenic profiles into silicon, to give a concentration dependent diffusion coefficient. The arsenic diffusion model developed by Chiu and Ghosh (5) is an improvement over Hu's (2) model and defines the concentration dependent diffusion coefficient taking into account the effects of two vacancy acceptor levels, effects of the internal electric field, and effects of arsenic clustering. Recently Fair and Weber (6) published an arsenic diffusion model based on an arsenic complex formation phenomena, which differs from the model of Chiu and Ghosh (5). The arsenic complex considered by Fair and Weber consists of two arsenic atoms; the model of Chiu and Ghosh assumes that each cluster consists of four arsenic atoms, after Hu (7).

Recently Van Overstraeten, De Man, and Mertens (8) have developed a new transport theory in heavily doped silicon and more recently Jain and Van Overstraeten (9) have extended this theory to high temperatures. In the present paper use of these results is made to calculate the concentration dependence of the arsenic diffusion coefficient by considering quantitatively the various mechanisms affecting the diffusion mechanism. Based on our data we also present some

Key words: arsenic diffusion profiles, silicon, heavy doping and high temperature effects, concentration dependent diffusion coefficient, processing data.

arsenic diffusion profiles. It is found that our numerically calculated arsenic profiles are in better agreement with the experimental arsenic profiles than the earlier theoretical results. In the present work we consider the diffusion of arsenic into a boron doped silicon crystal.

Brief Summary of the Basic Approach

The purpose of this section is to describe physically and mathematically the high doping and high temperature effects. More details are found in recent references (8, 9) and are omitted here for brevity.

Heavy doping effects.—Heavy doping effects are mainly characterized by the formation of band tails and of an impurity band as illustrated in Fig. 1. The scheme presented in Fig. 1 shows the density of states vs. electron energy for a heavily arsenic and lightly boron doped silicon. According to classical theory two parabolic density of states functions exist with well-defined band edges (E_{CI} for the conduction band and E_{VI} for the valence band); E_G is the intrinsic silicon bandgap energy. In the lightly arsenic (donor) and boron (acceptor) doped material there also exists a discrete arsenic (donor) energy level, E_{As} , and a boron (acceptor) energy level, E_B . However, when the doping level increases, the classically predicted picture is no longer valid because of the following two facts.

(i) Kane (10) has shown that the statistical distribution of the impurity atoms results in the formation of a Gaussian band tail, instead of a well-defined band edge and that this tail can be described mathematically by (10, 8)

$$\rho_{\text{cond}}(E) = m_e^{*3/2} (\sigma^2)^{3/2} \pi^{-1/2} \exp(-2\pi^{-2} \hbar^{-3} y(E/\sigma\sqrt{2})) \quad [1]$$

where

$$y(E/\sigma\sqrt{2}) = \frac{1}{\pi^{1/2}} \int_{-\infty}^{E/\sigma\sqrt{2}} (E/\sigma\sqrt{2} - m)^{1/2} \exp(-m^2) dm$$

Similarly an expression for $\rho_{\text{vale}}(E)$ can also be written.

(ii) Morgan (11) has shown that the impurity-impurity interaction causes the overlapping of the electron wave functions, so that the discrete impurity level splits into a continuous Gaussian impurity band, which is centered around the nondegenerate impurity level and can be described mathematically as (8, 11, 12)

$$\rho_{As}(E) = 2N_{As} (2\pi)^{-1/2} \sigma_{\text{eff}}^{-1} \exp\left[-\frac{(E - E_{As})^2}{2\sigma_{\text{eff}}^2}\right] \quad [2]$$

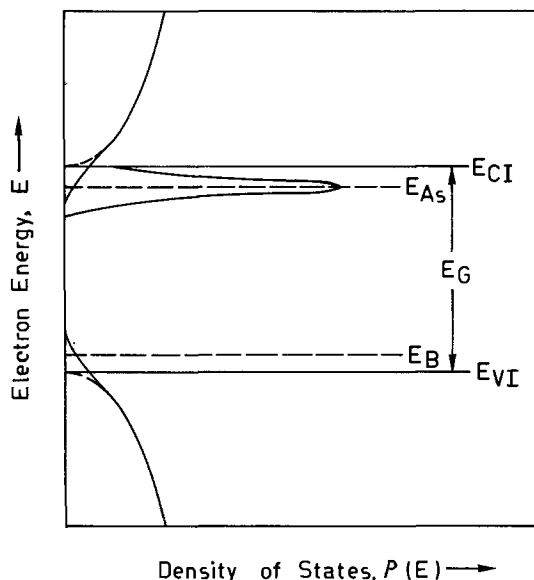


Fig. 1. Illustration of the heavy doping effects. Plots of the density of states functions vs. electron energy for a heavily arsenic doped silicon.

High temperature effects.—To perform theoretical calculations at diffusion temperatures (which are normally in the range 900°-1200°C for silicon) it is also necessary to incorporate the temperature dependence of the various physical parameters encountered in the calculations. Figure 2 illustrates quantitatively the high temperature effects. In Fig. 2a we have shown, respectively, the temperature dependence of the intrinsic silicon energy bandgap and of the various impurity and defect levels. The change in the position of the various impurity and defect levels from the middle of the bandgap has been assumed to be proportional to the change in the silicon bandgap. The mathematical equations in Fig. 2a describe the position of the various impurity and defect levels from the band edges. In Fig. 2b we have shown, respectively, the temperature dependence of the electron and of the hole density-of-states effective mass after a semi-empirical approach proposed by the authors (9).

Calculation of the Fermi level.—The Fermi energy, E_F , is the most important basic parameter which occurs in the various definitions explained in semiconductor physics. To develop a physical model for the impurity diffusion an accurate knowledge of the Fermi level as a function of the concentration is necessary. The detailed calculation of E_F taking into account a position dependent band structure and high temperature effects has been performed recently (8, 9) and is not considered here. The Fermi energy, E_F , is calculated numerically by solving the usual charge balance equation considering the effects mentioned earlier. Here it must be remarked that in the present analysis we have considered σ_{eff} for σ appearing in Eq. [1] because of the fact that the same physical effect (fluctuations in the crystal potential) is responsible for band tailing as well as for the impurity band formation. It must also be noted that in the present work we do not consider the numerical factor 2 [due to spin degeneracy (15)] appearing in Eq. [2], because of the fact that the donor states become part of the conduction band. It should be emphasized that the exact value of some heavy doping parameters is still questioned.

Calculation of the Total Arsenic Diffusion Coefficient in Silicon

For characterizing the impurity diffusion process quantitatively, the knowledge of the impurity diffusion coefficient is a necessity. This parameter essentially gives an idea about the motion of the impurity atoms into the semiconductor material and is a function of the temperature as well as of the impurity concentration. There are various physical mechanisms which play an important role during the diffusion process. For arsenic diffusion into silicon mainly the effects of the built-in electric field, excess vacancy generation, and cluster formation are important and are discussed here separately, taking the high doping and high temperature effects into account.

Effect of the built-in electric field.—It is now well known that the arsenic atoms diffuse into the silicon crystal lattice substitutionally which means that they move into the semiconductor material in the ionized state. It is also pointed out and considered by various authors that the diffusion of the charged atoms sets up an impurity gradient into the semiconductor material, which results in the generation of the internal electric field which enhances the motion of the impurity atoms at high concentrations. This effect can be accounted for quantitatively by defining a "built-in electric field diffusion enhancement factor," D_{ef} , defined by (13)

$$D_{\text{ef}} = 1 + \frac{N_{As}}{kT} \frac{dE_F}{dN_{As}} \quad [3]$$

From the knowledge of the Fermi level as a function of the impurity concentration for a desired diffusion temperature (9), D_{ef} can be evaluated accurately.

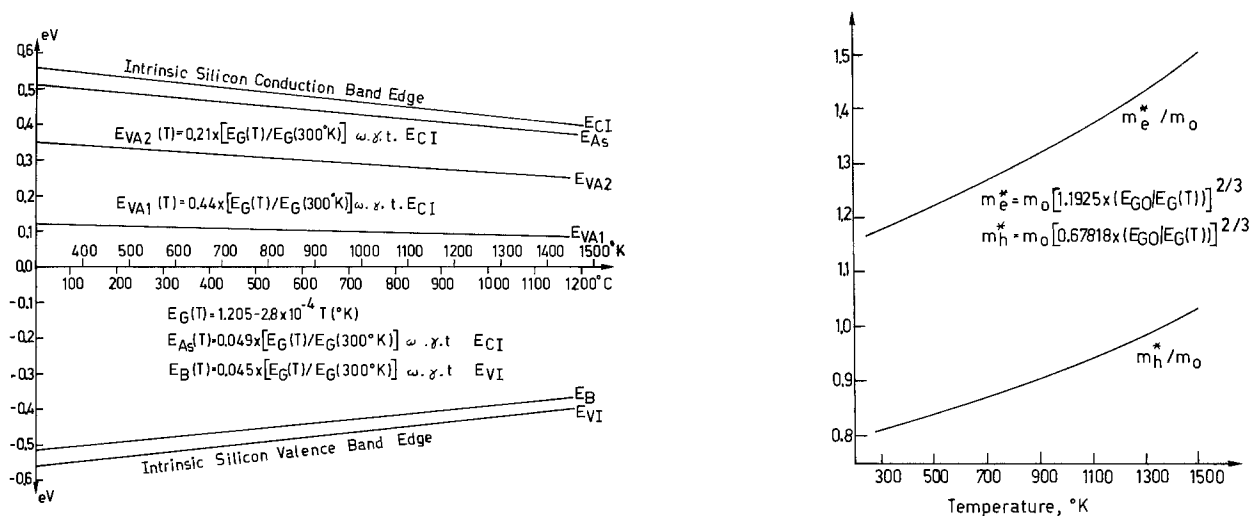


Fig. 2. Illustration of the high temperature effects. a, Temperature dependence of the various impurity and defect levels situated in the forbidden energy bandgap. b, Temperature dependence of the electron and hole density of states effective masses in terms of free electron rest mass.

Effect of the excess vacancy generation.—Since the diffusion of arsenic atoms into the silicon crystal lattice proceeds dominantly by the vacancy mechanism, any excess generation in the concentration of the vacancies will give rise to an increase in the motion of the impurity atoms into the semiconductor material. The arsenic diffusion induced vacancies produce two vacancy acceptor levels which lie in the upper half of the silicon bandgap. The effect of the extra vacancies generated on the diffusion mechanism can be accounted for quantitatively by defining an “excess vacancy diffusion enhancement factor,” D_{ev} . D_{ev} is nothing else than the ratio of the concentration of the total number of vacancies in the doped and in the intrinsic silicon crystal. This factor in terms of the Fermi and defect energies can be written after (14, 15) as

$$D_{ev} = \frac{1 + g_1 \exp \frac{E_F - E_{VA1}}{kT} + g_2 \exp \frac{2E_F - E_{VA1} - E_{VA2}}{kT}}{1 + g_1 \exp \frac{E_{FI} - E_{VA1}}{kT} + g_2 \exp \frac{2E_{FI} - E_{VA1} - E_{VA2}}{kT}} \quad [4]$$

$$D_{cf} = \frac{1}{1 + 4M \exp \left(\frac{\Delta H}{kT} \right) \left\{ \frac{1}{1 + 0.5 \exp \frac{E_{As} - E_F}{kT}} \right\}^4 \left\{ \frac{N_{As}}{N_{Si}} \right\}^3} \quad [5]$$

Effect of the arsenic clustering.—It has been shown that at very high arsenic concentrations, arsenic cluster formation takes place; but due to their small size ($\leq 25\text{\AA}$) attempts made to find their structure by using electron or x-ray diffraction techniques have not been successful (16). Hu (7) has developed a model of arsenic clustering into silicon which is largely based on the vapor pressure data of Sandhu and Reuter (17). Hu's proposed arsenic cluster consists of four arsenic atoms forming a tetrahedron either with a normal interstitial site or with a silicon atom at its center. Alternately the recent arsenic complex proposed by Fair and Weber (6) consists of two arsenic atoms situated on the second nearest neighbor sites around a

normal silicon vacancy. For chemical reasons only one complex structure dominates in a certain temperature range (17), therefore the tetratomic arsenic cluster (SiAs_4) (7) will exist in the vapor phase. On the other hand the formation energy (≈ 1.8 eV) of the diatomic arsenic cluster (SiAs_2) (6) is larger than the formation energy (1.3 eV) of the tetratomic arsenic cluster (SiAs_4) (7), which suggests that the probability of formation of the latter complex is larger. At the moment the validity of these arguments can be questioned because of the uncertainties existing in the arsenic cluster models. It seems that further fundamental research about impurity clustering is required to make sure about the number of impurity atoms involved and about their configuration. Anyhow it is certain that the effect of the cluster formation will be to retard the motion of the impurity atoms into the semiconductor material. Hu (7) has claimed that his model is strongly supported by its good fit with the vapor pressure data. The effect of the arsenic clustering on the diffusion mechanism can be accounted for quantitatively by defining a “cluster diffusion retardation factor,” D_{cf} , after (7) as

The factor D_{cf} can be evaluated accurately if we know the various cluster formation parameters and the Fermi energy.

Total arsenic diffusion coefficient and its concentration dependence.—The diffusion coefficient is the basic parameter in a diffusion process and its knowledge is highly essential for characterizing quantitatively the diffusion mechanism. As discussed earlier in this section various mechanisms affect the diffusion coefficient and must be considered simultaneously for defining the total diffusion coefficient. The diffusion coefficient can be written as

$$D_{As} = D_{iAs} \cdot D_{ef} \cdot D_{ev} \cdot D_{cf} \quad [6]$$

where D_{ef} , D_{ev} , and D_{cf} are discussed earlier and are given by Eq. [3], [4], and [5], respectively. D_{As} is the total arsenic diffusion coefficient and D_{iAs} is the arsenic diffusion coefficient in the intrinsic silicon. Various (3-5) empirical relations have been given for the temperature dependence of the intrinsic arsenic diffusivity, D_{iAs} , but we will consider the recent results (5) which can be described by

$$D_{iAs} = 24 \exp \left(- \frac{94070 \times 4.1868}{8.3143T} \right) \quad [7]$$

where T is the diffusion temperature in degrees Kelvin. Equation [7] is plotted in Fig. 3 for simplicity.

For determining the concentration dependence of the total arsenic diffusion coefficient, D_{As} , for a desired diffusion temperature, Eq. [6] must be solved by evaluating Eq. [3], [4], [5], and [7]. Figure 4 shows such results for various typical diffusion temperatures taking into account the high doping and high temperature effects. From Fig. 4 it is quite clear that D_{As} approaches D_{iAs} for low arsenic concentrations due to the fact that the last three terms in Eq. [6] are unity, i.e., the diffusion is normal. Now as the arsenic concentration increases, D_{As} also starts increasing (up to certain arsenic concentration) because the effects due to the built-in electric field and due to the excess vacancy generation are dominant as compared to the effects due to cluster formation. At higher arsenic concentrations D_{As} starts decreasing, because cluster formation becomes dominant.

Calculation of the Arsenic Profiles and Comparison with Experimental Results

The purpose of the present section is to calculate the total arsenic diffusion profiles using the approach described in the earlier sections. Figures 5 and 6 show such profiles after present work from the knowledge of the diffusion temperature and time for a given surface concentration. These profiles have been computed using a computer program DASI¹ specially

¹DASI (diffusion of arsenic in silicon) is a special computer program written in Fortran IV for calculating arsenic diffusion profiles in silicon which makes use of the physical diffusion model developed.

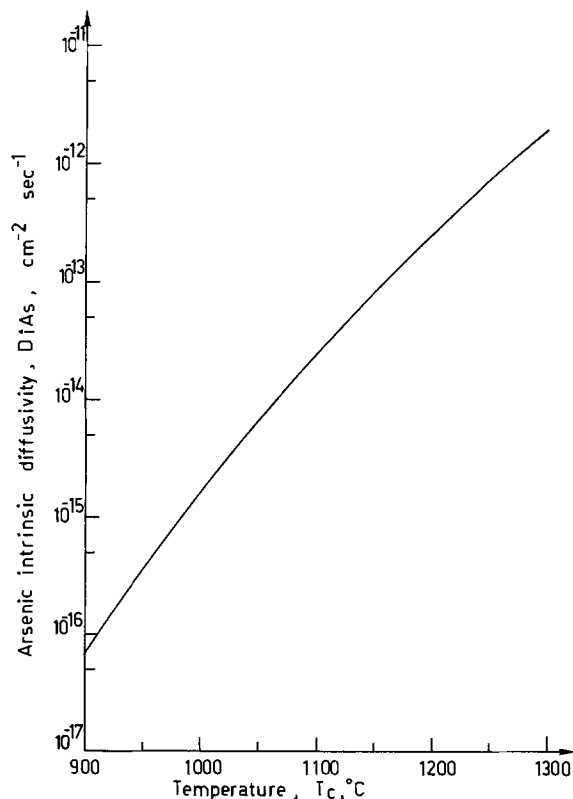


Fig. 3. Temperature dependence of the intrinsic arsenic diffusivity in silicon after Chiu and Ghosh (5).

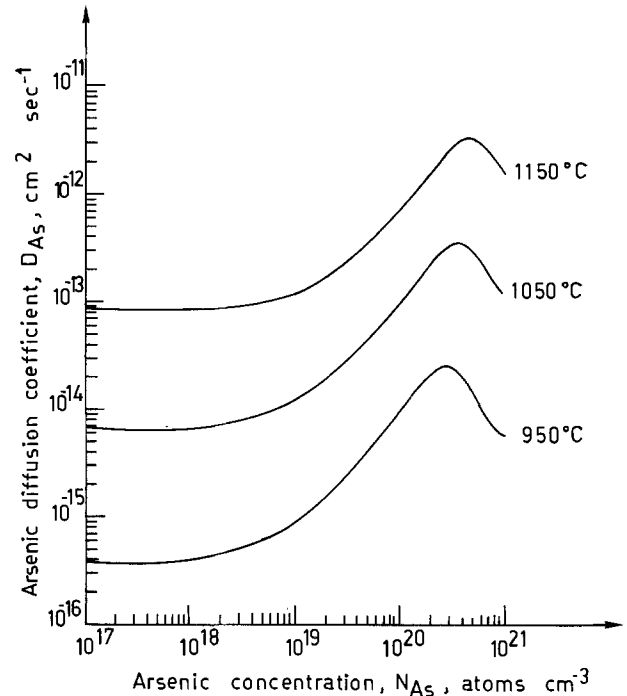


Fig. 4. Theoretical plot of the total arsenic diffusion coefficient vs. arsenic concentration for various typical diffusion temperatures taking high doping and high temperature effects into account. $N_B = 10^{17}$ atoms cm^{-3} .

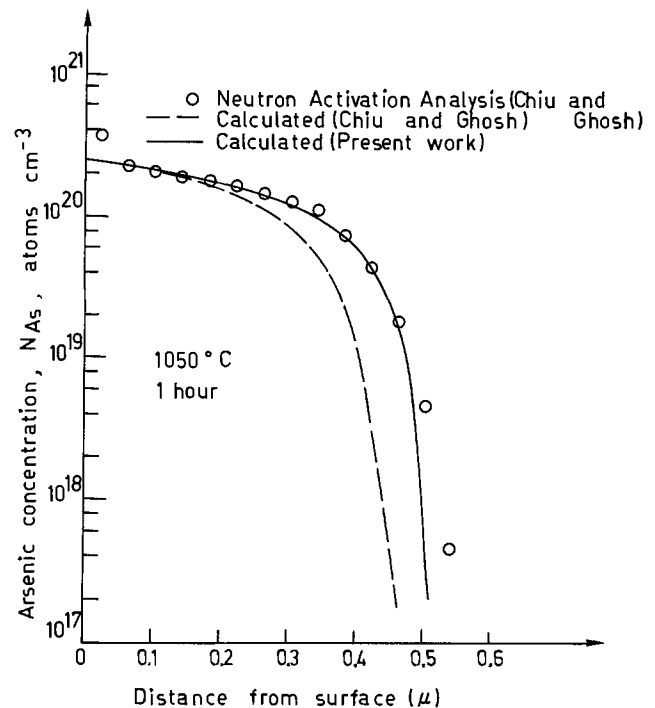


Fig. 5. Plots of the experimental and theoretical arsenic diffusion profiles. Diffusion temperature = 1050°C; diffusion time = 1 hr.

written for the calculation of arsenic profiles, by means of solving the diffusion equation. This program requires only processing data as its input information and does the rest by taking the high doping and high temperature effects into account. For comparison we also consider the experimental arsenic profiles measured by neutron activation analysis after Chiu and Ghosh (5) and Fig. 5 and 6. Further we also consider the theoretical arsenic profiles calculated by Chiu and Ghosh (5) after their empirical model in Fig. 5 and 6. Chiu and Ghosh (5) obtained their theoretical arsenic profiles by using four empirical constants. They found

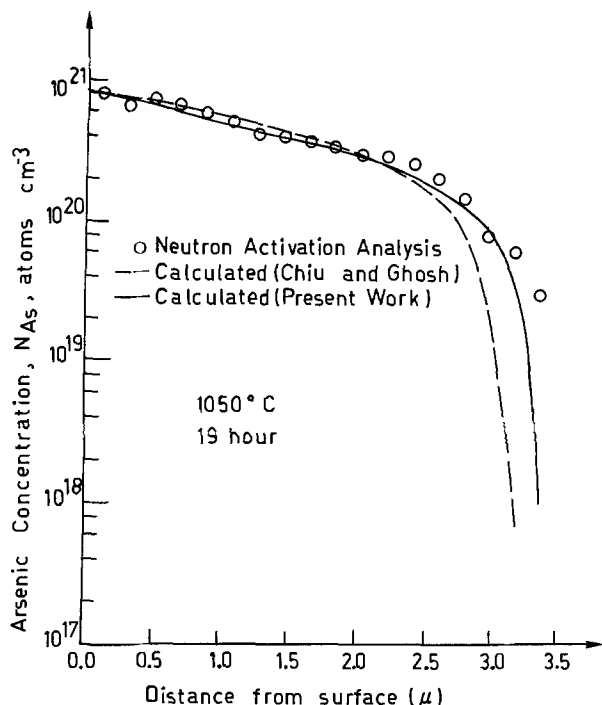


Fig. 6. Plots of the experimental and theoretical arsenic diffusion profiles. Diffusion temperature = 1050°C; diffusion time = 19 hr.

these four empirical constants by matching the theoretical results with various experimental profiles in a wide range of temperature and surface concentrations and are independent of the diffusion temperature. Now if we look to Fig. 5 and 6 we observe that our calculated profiles are in very good agreement with the experimental profiles which strongly supports the accuracy of our physical model based on high doping and high temperature calculations. Figures 5 and 6 are, respectively, for shorter and longer diffusion times, and for both cases the agreement is improved which suggests the validity of our results in general. Anyhow, slight disagreement at lower concentrations may be viewed as the consequence of the approximations involved in the theoretical calculations as well as in the measured results. However, our model gives quite good results and we hope that it will be possible for a device designer to know the impurity distribution before performing all the experiments. Here it must be remarked that the use of the arsenic cluster model by Fair and Weber (6) along with heavy doping and high temperature effects may also yield better results and this work must also be carried out. It must also be remembered here that the accuracy of the present work is limited because of the uncertainties involved in the use of heavy doping effects at high temperatures and also in the present knowledge about the effects of the electric field, vacancy generation, and clustering. It is felt that more rigorous research is needed so that the discrepancies among different models can be understood and minimized.

Conclusions

By incorporating the high doping and high temperature effects a quantitative theoretical model of the arsenic diffusion into silicon has been developed by considering the various important mechanisms occurring during the diffusion process. The total arsenic diffusion coefficient has been calculated as a function of the impurity concentration for typical common diffusion temperatures. Attempts have been made to calculate the arsenic diffusion profiles in silicon from processing data by using a computer program DASI based on our model. Good agreement has been found with the available experimental results. It is hoped that further research along these lines will be useful to understand

some mechanisms not at present clearly understood and known.

Acknowledgments

The authors are thankful to Dr. R. Mertens for his help in the computer programming at the early stages of the present work. Correspondence with Dr. S. M. Hu of IBM Systems Product Division, East Fishkill Laboratory, Hopewell Junction, New York, also helped in clearing some questions about the arsenic clustering mechanism. Helpful suggestions from Dr. R. B. Fair of Bell Laboratories, Reading, Pennsylvania, are also acknowledged. We also wish to express our thanks to the Computer Center of our university for running the computer programs. One of us (R. K. Jain) extends his special thanks to the Katholieke Universiteit te Leuven for granting him a research fellowship.

Manuscript submitted April 23, 1974; revised manuscript received Nov. 25, 1974. This was Paper 191 presented at the New York, New York, Meeting of the Society, Oct. 13-17, 1974.

Any discussion of this paper will appear in a Discussion Section to be published in the December 1975 JOURNAL. All discussions for the December 1975 Discussion Section should be submitted by Aug. 1, 1975.

Publication costs of this article were partially assisted by the Katholieke Universiteit Leuven.

LIST OF SYMBOLS

D_{As}	total arsenic diffusion coefficient
D_{iAs}	intrinsic arsenic diffusion coefficient
D_{ef}	cluster diffusion retardation factor
D_{ef}	built-in electric field diffusion enhancement factor
D_{ev}	excess vacancy diffusion enhancement factor
E	general energy
E_{As}	arsenic energy level
E_B	boron energy level
E_{CI}	intrinsic silicon conduction band edge
E_F	Fermi level
E_{FI}	intrinsic Fermi level
E_G	intrinsic silicon forbidden energy bandgap
E_{GO}	intrinsic silicon forbidden energy bandgap at 0°K
E_{VA1}	first arsenic vacancy acceptor level
E_{VA2}	second arsenic vacancy acceptor level
E_{VI}	intrinsic silicon valence band edge
\hbar	Planck's constant divided by 2π
k	Boltzmann's constant
M	configuration multiplicity of the arsenic complex
m_o	free electron rest mass
m_e^*	electron density of states effective mass
m_h^*	hole density of states effective mass
N_{As}	arsenic concentration
N_B	boron concentration
N_{Si}	concentration of the silicon lattice sites
T	absolute temperature
ΔH	energy of formation of the arsenic complex
σ_{eff}	effective value of σ
σ	standard deviation of the impurity band
ρ_{As}	arsenic impurity band density of states
ρ_{cond}	conduction band density of states
ρ_{vale}	valence band density of states
g_1	spin degeneracy weighting factor of the first vacancy acceptor level
g_2	spin degeneracy weighting factor of the second vacancy acceptor level

APPENDIX

Following is the list of numerical values of various quantities used in the calculations:

E_{As}	0.049 eV from E_{CI} at 300°K
E_B	0.045 eV from E_{VI} at 300°K
E_G	1.121 eV at 300°K
E_{GO}	1.205 eV
E_{VA1}	0.44 eV from E_{CI} at 300°K
E_{VA2}	0.21 eV from E_{CI} at 300°K
M	24
m_e^*/m_o	1.18 at 300°K
m_h^*/m_o	0.81 at 300°K
N_{Si}	$5 \times 10^{22} \text{ cm}^{-3}$
ΔH	1.3 eV

REFERENCES

1. S. M. Hu and S. Schmidt, *J. Appl. Phys.*, **39**, 4272 (1968).
2. S. M. Hu, *Phys. Rev.*, **180**, 773 (1969).
3. B. J. Masters and J. M. Fairfield, *J. Appl. Phys.*, **40**, 2390 (1969).
4. D. P. Kennedy and P. C. Murley, *Proc. IEEE*, **59**, 335 (1971).
5. T. L. Chiu and H. N. Ghosh, *IBM J. Res. Dev.*, **15**, 472 (1971).
6. R. B. Fair and G. R. Weber, *J. Appl. Phys.*, **44**, 273 (1973).
7. S. M. Hu, in "Atomic Diffusion in Semiconductors," D. Shaw, Editor, Chap. 5, Plenum Press, London (1973).
8. R. Van Overstraeten, H. De Man, and R. Mertens, *IEEE Trans. Electron Devices*, **ED-20**, 290 (1973).
9. R. K. Jain and R. Van Overstraeten, *ibid.*, **ED-21**, 155 (1974).
10. E. O. Kane, *Phys. Rev.*, **131**, 79 (1963).
11. T. N. Morgan, *ibid.*, **139**, A343 (1965).
12. D. D. Kleppinger and F. A. Lindholm, *Solid-State Electron.*, **14**, 407 (1971).
13. R. K. Jain and R. Van Overstraeten, To be published.
14. R. L. Longini and R. F. Greene, *Phys. Rev.*, **102**, 992 (1956).
15. W. Shockley and J. T. Last, *ibid.*, **107**, 392 (1957).
16. R. O. Schwenker, E. S. Pan, and R. F. Lever, *J. Appl. Phys.*, **42**, 3195 (1971).
17. J. S. Sandhu and J. L. Reuter, *IBM J. Res. Dev.*, **15**, 464 (1971).

Characteristics of Si-SiO₂ Interfaces Beneath Thin Silicon Films Defined by Electrochemical Etching

T. I. Kamins¹ and B. E. Deal*

Research and Development Laboratory, Fairchild Camera and Instrument Corporation, Palo Alto, California 94304

ABSTRACT

Capacitance-voltage measurements on thin silicon films defined by electrochemical etching have indicated that fixed surface charge (Q_{ss}) and fast surface states (N_{st}) located at the Si-SiO₂ interface beneath the silicon film can be affected by oxygen, nitrogen, or hydrogen heat-treatments. Both Q_{ss} and N_{st} can be minimized by annealing in hydrogen at high temperatures (900°-1200°C) while nitrogen or oxygen annealing in this same temperature range tends to increase Q_{ss} . At low temperatures (450°C) the conventional hydrogen anneal is not sufficient to eliminate fast surface states, probably because of masking of the hydrogen by the 7 μm thick films used in this study.

During previous measurements of the Hall mobility in thin silicon films defined by electrochemical etching (1), evidence of an accumulation layer near the bottom silicon-silicon dioxide interface was found on n-type samples (Fig. 1). Such an accumulation layer is not unexpected since the fixed charge Q_{ss} tends to accumulate the surfaces of n-type samples, and n-type dopant impurities tend to segregate into the silicon during oxidation (2), especially during the low-temperature, wet oxidation used in these experiments. Since the presence and magnitude of a surface layer will directly affect the characteristics of devices fabricated in the silicon films, the properties of the bottom Si-SiO₂ interface were investigated in more detail. MOS capacitors were fabricated with the field plate beneath the oxide which was covered by the silicon film (Fig. 2). The MOS capacitance-voltage characteristics were measured after various heat-treatments. It will be shown that the charges at the back Si-SiO₂ interface of these silicon-on-insulator structures can be controlled and minimized by hydrogen annealing at elevated temperatures.

Experimental Structure and Measurements

In order to investigate the properties of the Si-SiO₂ interface beneath the thin silicon film, a field plate was needed under the oxide that separates the thin film from the polycrystalline support in the normal structure (1) (Fig. 1). Since the field-plate material must be compatible with subsequent high-temperature processing, a highly doped layer of polycrystalline silicon was used. The fabrication of the experimental structure is described below, and the completed device is shown in Fig. 2.

After deposition of the initial p-type epitaxial layer ($N_A = 1-2 \times 10^{15} \text{ cm}^{-3}$), which becomes the thin film,

the sample was oxidized at 920°C in the following sequence: 5 min dry nitrogen preheat, 5 min dry oxygen, 75 min wet oxygen, and 5 min dry nitrogen. The oxide thickness was approximately 3000 Å for the (111)-oriented wafers normally used in these experiments. A 0.6 μm thick layer of polycrystalline silicon was then deposited in an rf-heated reactor at 950°C in a hydrogen ambient.² Arsenic dopant impurities were

* All temperatures cited are corrected for the emissivity of silicon and absorption by the walls of the reaction chamber when the rf-heated reactor was used.

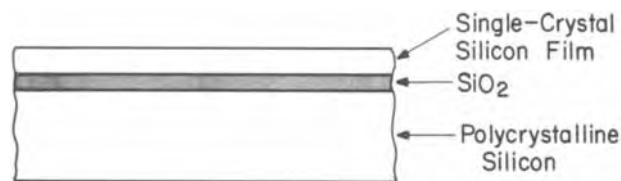


Fig. 1. Thin-film structure used for monolithic dielectrically isolated integrated circuits.

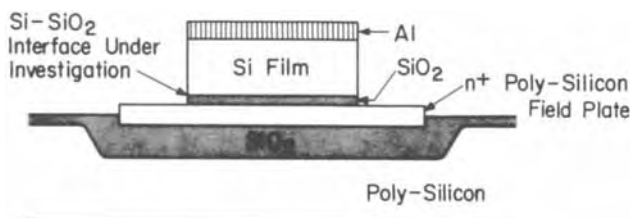


Fig. 2. Experimental structure used for capacitance-voltage measurements in this study.

* Electrochemical Society Active Member.

¹ Present address: Hewlett-Packard Laboratories, Palo Alto, California 94304.

Key words: silicon films, oxide charge, Si-SiO₂ interface.

added by ion implantation; the dose of $2 \times 10^{15} \text{ cm}^{-2}$ produced a sheet resistance of about 225 ohms/ \square after activation. The polycrystalline silicon was then oxidized to form a thin layer of thermal oxide for masking, and a grid pattern was defined so that the polycrystalline silicon remained only in squares 1 mm on a side. The structure was covered with 1 μm of vapor-deposited oxide, and a 250 μm thick layer of polycrystalline silicon was deposited by the decomposition of dichlorosilane at 1100°C. Since this is the same supporting layer that is used in the normal structure of Fig. 1, the experimental structure differed from the normal structure only by the addition of the thin, field-plate electrode. The heavily doped substrate wafer was then removed by electrochemical etching, and the sample was vapor etched in an HBr-H₂ ambient for 5 min at 1200°C to remove any residual n-type layer above the p-type thin film. The sample was cooled below 400°C in hydrogen after the vapor etch in order to insure reproducible starting conditions for all annealing experiments. The final film thickness was about 7 μm .

Each wafer was then subjected to the desired annealing cycle in a nitrogen, oxygen, or hydrogen ambient at a temperature between 920° and 1200°C. The samples were cooled slowly by withdrawing them from the furnaces over a specified time period: 2 min at 920°C, 6 min at 1100° and 1200°C. Any oxide grown on the exposed silicon surface during these heat-treatments was subsequently removed in HF, and the wafer was then covered with 1 μm of aluminum. The aluminum was deposited from a filament in most cases to avoid radiation damage. One experiment utilized electron-beam evaporated aluminum in order to study the effects of low-temperature annealing on the radiation damage. After the aluminum was defined by photomasking, it was used as an etch mask while the silicon film and underlying oxide were removed from the remainder of the area, exposing the underlying polycrystalline-silicon field plate. A final low-temperature (450°C) anneal in a hydrogen-nitrogen ambient completed the fabrication process. The finished experimental structure is shown in Fig. 2.

Capacitance-voltage characteristics were then measured at a frequency of 1 MHz. All samples were initially biased in inversion, and the voltage was changed toward accumulation to avoid effects of the slow generation of carriers in the inversion layer. The ratio of the minimum to maximum capacitance and the oxide thickness were used to determine the capacitance under flatband conditions, and the corresponding flatband voltage was then found from the experimental data. An effective value of Q_{ss} was determined by correcting for the work function difference between the p-type silicon film and the n⁺ field-plate electrode and multiplying by the oxide capacitance in the conventional manner (3). If the sample indicated any drift during a 300°C bias-temperature test, the flatband voltage was determined after a moderate negative bias ($-25 \text{ V}/\mu\text{m}$) was applied on the field plate at 300°C. This bias moved the mobile ions to the oxide-field plate interface where they would not influence the measured results.

Experimental Results and Discussion

The effective values of Q_{ss} found after various annealing treatments are shown in Fig. 3 and 4 and are discussed below. Control samples were included in each series of experiments. These control samples employed the same thin-film structure shown in Fig. 2 but received no heat-treatment between the 1200°C hydrogen cycle during the vapor etch and the aluminum deposition. They indicated a consistently low value of Q_{ss}/q of about $1.5 \times 10^{11} \text{ cm}^{-2}$.

Annealing ambient.—Figure 3 shows that an 1100°C anneal in either nitrogen or oxygen increases the effective value of Q_{ss} . The charge appears to approach its equilibrium value within 30 min, the shortest time in-

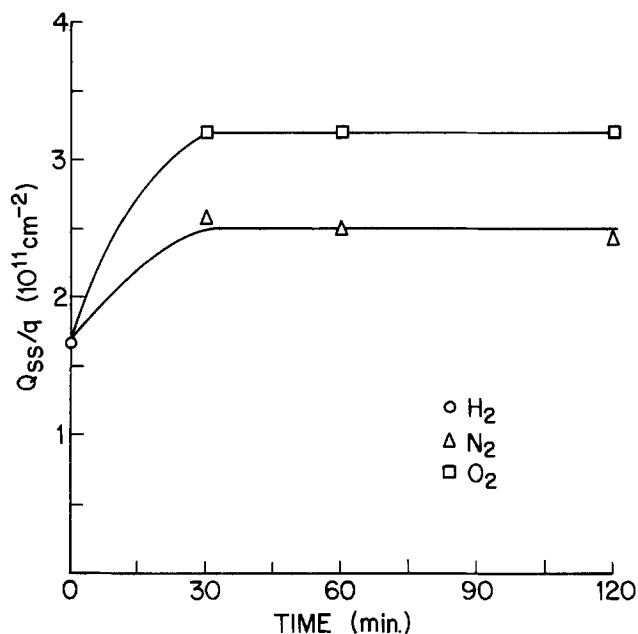


Fig. 3. Effective Q_{ss} as a function of annealing time in an oxygen or nitrogen ambient at 1100°C. The wafers were removed from the furnace in 6 min. Corresponding values for a conventional MOS structure are $7-8 \times 10^{11} \text{ cm}^{-2}$ after an oxygen anneal and $2 \times 10^{11} \text{ cm}^{-2}$ after a nitrogen anneal.

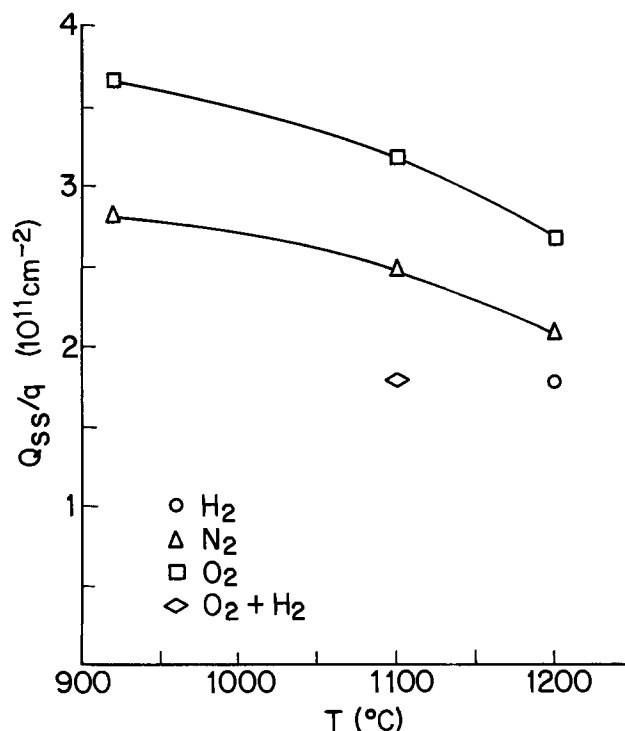


Fig. 4. Effective Q_{ss} as a function of annealing temperature in an oxygen or nitrogen ambient for 1 hr.

vestigated. The effective Q_{ss} is consistently higher after the oxygen anneal than after the anneal in nitrogen. This greater increase of Q_{ss} in oxygen was observed in all experiments and is consistent with results found in conventional MOS structures for slow pulls in oxygen (4). However, the values obtained in the conventional structures are normally about $7-8 \times 10^{11} \text{ cm}^{-2}$ for (111) silicon, approximately twice the values observed in the present study, where the Si-SiO₂ interface is covered by a silicon film. The film apparently

provides a shielding effect against the oxygen. A similar phenomenon has also been observed in these laboratories for thermally oxidized silicon structures covered by a polycrystalline-silicon film (5).

The value of Q_{ss} shown in Fig. 3 for the nitrogen anneal is slightly higher than for conventional structures, the latter being about $2 \times 10^{11} \text{ cm}^{-2}$ (4). However, the present results agree quite closely with data obtained in these laboratories for oxide structures covered by polycrystalline-silicon films. The low value of Q_{ss} obtained after a high-temperature hydrogen anneal is consistent with results obtained on conventional structures, where Q_{ss} values were found to be in the $1 \times 10^{11} \text{ cm}^{-2}$ range after high-temperature (1000°C) hydrogen anneals (5).

Annealing temperature.—The influence of the annealing temperature is indicated in Fig. 4. The effective Q_{ss} is raised substantially from its initial value by annealing in oxygen or nitrogen at any temperature in the 920°–1200°C range. The increase is greatest at the lower temperatures, although the difference between 920° and 1200°C is not large. The effective Q_{ss} is again appreciably higher after an oxygen anneal than after a nitrogen anneal at every temperature investigated. An important difference is seen when the data of Fig. 4 are compared with results from conventional structures. Conventional structures slow-pulled in oxygen indicate significantly higher Q_{ss} values for lower annealing temperatures (4). This trend is similar to that seen in the present investigation, although the Q_{ss} values obtained with the thin-film structure are markedly lower. In the case of nitrogen, Q_{ss} is not a function of annealing temperature in conventional structures, with values of $1.5\text{--}2 \times 10^{11} \text{ cm}^{-2}$ being obtained in all temperatures for (111)-oriented silicon. However, the value of Q_{ss} obtained after annealing the thin-film structure in nitrogen was a function of annealing temperature and was somewhat higher than that seen on conventional structures, especially at lower annealing temperatures.

One thin-film sample was given an 1100°C oxygen anneal to increase the effective Q_{ss} followed by an 1100°C hydrogen anneal for 1 hr. The final value of Q_{ss} was reduced to approximately that found on the control sample, indicating that the charges induced during annealing are reversible if the ambient can penetrate to the Si-SiO₂ interface of interest, which is shielded by about 7 μm of silicon in the present structure.

The time required for this reduction of the effective Q_{ss} in a high-temperature hydrogen ambient was briefly investigated. After the surface layers were removed from a set of silicon films by the H₂-HBr vapor etch, which lowered the effective value of Q_{ss} , the samples were given a 2-hr, oxygen anneal at 920°C to increase Q_{ss} . A control sample that received this oxygen anneal indicated an effective Q_{ss}/q of about $3.2 \times 10^{11} \text{ cm}^{-2}$. Each remaining sample was heated to 1100°C in an rf-heated reactor in a hydrogen ambient, held at 1100°C for a specified time, and then cooled in hydrogen. The holding time at 1100°C was varied from 3 min to 4 hr in order to study the effect of a wide range of times. In all cases the final value of Q_{ss}/q was found to be in the range of $1.4\text{--}1.8 \times 10^{11} \text{ cm}^{-2}$, indicating that the hydrogen ambient reduced the effective Q_{ss} during the shortest cycle and probably even while the wafers were being heated and cooled.

Cooling rate.—In conventional MOS structures the rate of removal from the furnace in an oxygen ambient can substantially influence the final value of Q_{ss} since a wafer which is removed from the furnace slowly spends an appreciable time at intermediate temperatures. Because higher values of Q_{ss} are induced at lower temperatures in oxygen, the effective Q_{ss} may be increased by slow removal from the furnace. In one experiment during the present study, wafers were cooled from 1200°C in an oxygen ambient

both slowly and rapidly. The difference in the effective value of Q_{ss}/q was only $0.2 \times 10^{11} \text{ cm}^{-2}$, which is within the experimental uncertainty of the measurements. Other experiments that compared different cooling rates indicate that the difference between slow and rapid cooling is not marked. For both cooling rates, the effective value of Q_{ss} is lower for higher annealing temperatures.

Radiation-induced states.—Electron-beam evaporation, rather than filament evaporation, was used to deposit the aluminum on one set of wafers. Electron-beam evaporation induces appreciable charge and fast states in the structure; the charge and radiation-induced fast states are generally removed from conventional MOS structures by a subsequent low-temperature anneal near 450°C in nitrogen with aluminum present or in hydrogen. In the present structure the penetration of hydrogen or other active species through the 7 μm thick silicon film at 450°C is questionable; if the presence of an active species is necessary, annealing may occur by lateral movement of the active species from the side of the pattern. The possibility of lateral nonuniformity in the final structure arising from lateral diffusion of the annealing species was investigated by defining the pattern on the silicon film before the low-temperature (450°C) hydrogen anneal on some wafers and after annealing on other wafers. The silicon films that were annealed at 450°C before being defined produced C-V curves more characteristic of uniform unannealed structures while the wafers defined before annealing indicated very nonuniform annealing of the radiation-induced states by the 450°C cycle. The C-V curve from the nonuniform samples could almost be divided into two regions, each with a different flatband voltage. The initially uniform wafers also exhibited the nonuniform characteristic after a second low-temperature hydrogen anneal subsequent to silicon definition and the initial C-V measurements. These results indicate that hydrogen or another active species is necessary for adequate annealing of the radiation-induced states in the present structure and that this species is not able to penetrate through the 7 μm thick silicon film at 450°C to affect the interface. The annealing is effective in reducing the radiation-induced states only near the edges of the pattern where lateral diffusion is possible. A similar masking effect observed in silicon nitride passivated MOS structures also indicates that the presence of an active species is necessary for the reduction of the radiation-induced states (6).

Fast states.—Figure 5 shows a set of C-V characteristics for a control wafer and several different oxygen-annealed samples, which were metallized with aluminum evaporated from a filament. In addition to the shift in the flatband voltage, the distortion of the curves increases with increasing Q_{ss} or decreasing annealing temperature. If we assume that the measurement frequency is high enough so that surface states do not contribute to the capacitance, then the dispersion in the curve must be attributed either to states which are charged or discharged as the Fermi level is swept through the bandgap at the surface or to lateral nonuniformities in the sample. In order to investigate the latter effect, measurements were taken on several wafers both before and after the low-temperature (450°C) hydrogen anneal. In each case the shape of the curve was similar before and after the low-temperature anneal, although the flatband voltage was somewhat different. In addition, the shape of the C-V curve for samples with filament-evaporated aluminum was markedly different from that seen on the nonuniform samples with electron-beam aluminum discussed above. During the high-temperature anneal, the silicon film was not defined into the final dot structure so lateral diffusion during this step cannot have led to the distortion in the C-V curves. These observations indicate that the dispersion seen in sam-

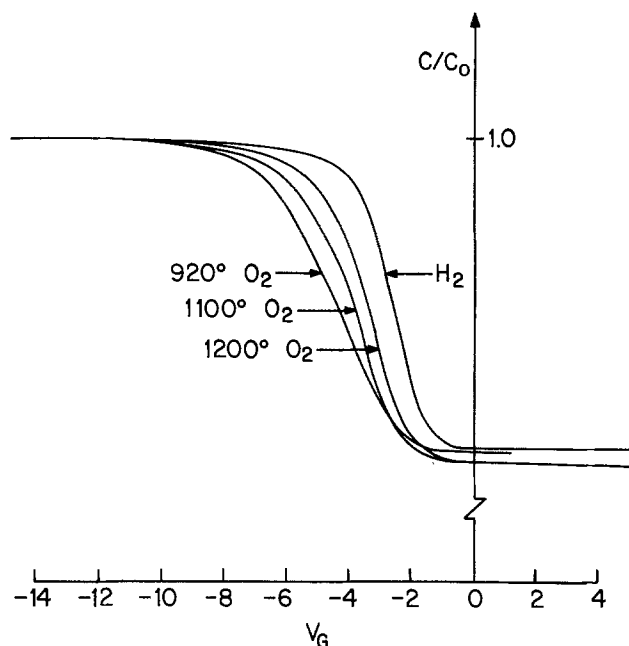


Fig. 5. Capacitance-voltage characteristics after hydrogen anneal and subsequent 1-hr, oxygen heat-treatments at three different temperatures. The (111)-oriented, p-type silicon films had a dopant concentration of $1.1\text{--}1.6 \times 10^{15} \text{ cm}^{-3}$, and the oxide thickness was approximately 3000Å.

ples given nitrogen or oxygen heat-treatments is not related to macroscopic nonuniformities near the edges of the samples. The possibility of microscopic nonuniformities which are consistent across the entire wafer cannot be eliminated. However, the presence of surface states with energies in the bandgap is more likely. This relationship between Q_{ss} and N_{st} , with both increasing and decreasing oxygen annealing temperatures, has been noted previously in these laboratories for conventional MOS structures, as well as by Werner (7).

Summary

Capacitance-voltage measurements on thin silicon films defined by electrochemical etching have indicated that fixed surface charge (Q_{ss}) and surface states at the Si-SiO₂ interface beneath the silicon film can be affected by various high-temperature heat-treatments. Both oxygen and nitrogen heat-treatments increase the effective value of Q_{ss} and probably the surface

state density. While the increase is greater for oxygen than for nitrogen, it is not as great as in conventional MOS structures after similar oxygen annealing. The increase is greatest at the lowest annealing temperatures for both ambients. The effective value of Q_{ss} is minimized by a high-temperature hydrogen heat-treatment after the initial film preparation. A high-temperature hydrogen anneal also reduces the effective value of Q_{ss} after it has been increased by a heat-treatment in oxygen. The low-temperature (450°C) hydrogen heat-treatment is insufficient to reduce the fast state density N_{st} . Radiation-induced states are reduced at 450°C by lateral diffusion of an active species beneath the silicon film although the active species does not penetrate through the 7 μm-thick silicon films used in this investigation.

It may be concluded that charges at the back Si-SiO₂ interface of silicon-on-insulator structures can be controlled and minimized by hydrogen annealing at elevated temperatures. On the other hand, the thick silicon film retards the action of oxygen or nitrogen on Q_{ss} at elevated temperatures as well as the reduction of N_{st} by hydrogen at low temperatures.

Acknowledgment

The authors would like to thank L. Field and S. Sekigahama for their assistance with the experimental investigation.

Manuscript submitted Aug. 1, 1974; revised manuscript received Nov. 5, 1974.

Any discussion of this paper will appear in a Discussion Section to be published in the December 1975 JOURNAL. All discussions for the December 1975 Discussion Section should be submitted by Aug. 1, 1975.

Publication costs of this article were partially assisted by Fairchild Camera and Instrument Corporation.

REFERENCES

1. T. I. Kamins, *Solid-State Electron.*, **17**, 675 (1974).
2. A. S. Grove, "Physics and Technology of Semiconductor Devices," pp. 69, 342, John Wiley & Sons, Inc., New York (1967).
3. A. S. Grove, *ibid.*, p. 271.
4. B. E. Deal, M. Sklar, A. S. Grove, and E. H. Snow, *This Journal*, **114**, 266 (1967).
5. M. Sklar and B. E. Deal, Private communication.
6. J. J. Tentor, Paper 233 RNP presented at the Detroit, Michigan, Meeting of the Society, Oct. 5-9, 1969.
7. W. M. Werner, Paper 24 presented at the San Francisco, California, Meeting of the Society, May 12-17, 1974.

Parameters Controlling the Reactive Sputter Deposition of the Hafnium Tantalum Nitride Resistive Sea

W. R. Knolle and W. C. Ballamy*

Bell Laboratories, Reading, Pennsylvania 19604

ABSTRACT

This paper presents a detailed discussion of the reactive sputtering of the hafnium tantalum nitride resistive sea for the silicon diode-array camera tube target. The importance of precise control of the sputtering parameters is emphasized by analyzing their effect on performance of the diode-array target. The resistivity of the film is shown to be controlled by both the hafnium/tantalum ratio and the metal/nitrogen ratio. These ratios in turn are controlled by the sputtering parameters. The properties of the film are shown to be sensitive to impurities incorporated in the film. Techniques used to keep these below an acceptable level are discussed. The precautions necessary to prevent degradation of the Si-SiO₂ interface during sputtering are also considered.

A reactively sputtered thin film of hafnium tantalum nitride has been developed as a resistive sea for coating the silicon diode-array camera tube target (1-3). The sea is deposited over the entire target by rf plus d-c reactive sputtering from a hafnium-tantalum composite cathode. During development work on this sea it was observed that the electrical properties of the diode-array target depend critically on the conditions prior to and during sputtering. The silicon target is therefore a sensitive probe for delineating the parameters of the reactive sputtering process that must be controlled for reproducible deposition of the hafnium tantalum nitride film. This paper presents a detailed discussion of the reactive sputtering of hafnium tantalum nitride for the resistive sea. The importance of precise control of the sputtering parameters is emphasized by analyzing their effect on the performance of the diode-array target.

Diode-Array Target

The operation of the silicon diode-array target has already been described (1). Briefly, the target consists of an array of diodes on a thin silicon membrane. A thin resistive film or resistive sea is deposited over the whole target to provide a controlled discharge path which prevents charge buildup on the oxide surface from the scanning electron beam. Without this film the silicon dioxide potential would charge below cathode potential and thus prevent the electron beam from landing on the diodes. For targets where the electron beam can recharge the diode junction capacitance to the full reverse bias voltage, the maximum output signal (saturation current or I_{sat}) for a given beam current is a function of the resistivity of the sea and will generally increase with decreasing resistivity. The dependence of I_{sat} on resistive sea sheet resistance is shown in Fig. 1 (4).

The target exhibits a background current or dark current which is independent of illumination level. This dark current is due primarily to surface-state regeneration of carriers at the silicon-silicon dioxide interface and to bulk generation of carriers in the depletion region. The magnitude of the dark current depends on the surface-state density at the Si-SiO₂ interface and so variations in the dark current are a sensitive indicator of changes in the Si-SiO₂ interface.

Sputtering Equipment

Sputtering was carried out in a rapid cycle station with provisions for both ion pumping and turbomolecular pumping. Gas composition in the system

was analyzed during sputtering by means of a quadrupole mass analyzer.

The sputtering apparatus was of the conventional diode type having two planar electrodes. The sputtering source was a hot pressed cathode with a composition of 47 atom per cent (a/o) hafnium and 53 a/o tantalum. The perimeter of the cathode was surrounded by a ground shield placed within the dark space of the glow discharge at a separation of about 0.5 cm. Cathode bias was d.c. plus rf after the technique of Vratny *et al.* (3). A copper anode plate was used to hold the diode-array targets during sputtering. The anode plate had raised pedestals which fit into the recessed back of the targets to insure good thermal contact. The anode plate in turn rested on the water-cooled anode of the sputtering system. The anode plate and electrodes are shown in Fig. 2. Prior to its use the entire copper plate was coated with hafnium tantalum to reduce the chance of contaminating the resistive sea with copper.

To conduct a typical sputtering run the anode plate was loaded with targets and the system evacuated to less than 5×10^{-8} Torr using the ion pump. Then the system was switched to the turbomolecular pump, the presputter gas introduced, and presputtering was initiated on the closed shutter. Typical sputtering pressure was $\sim 60 \times 10^{-3}$ Torr at a nitrogen throughput of ~ 400 cm³/min STP. Presputtering is described in some detail in the next section.

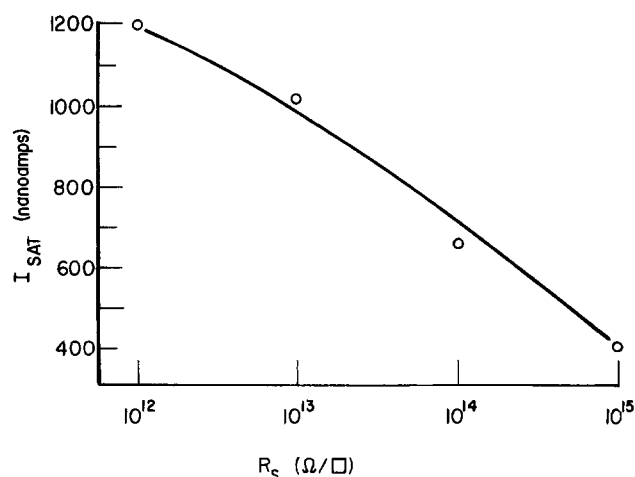


Fig. 1. Calculated dependence of saturation current on sea resistance. Material resistivity is 10 ohm-cm.

* Electrochemical Society Active Member.

Key words: silicon diode-array target, rf sputter, d-c sputter.

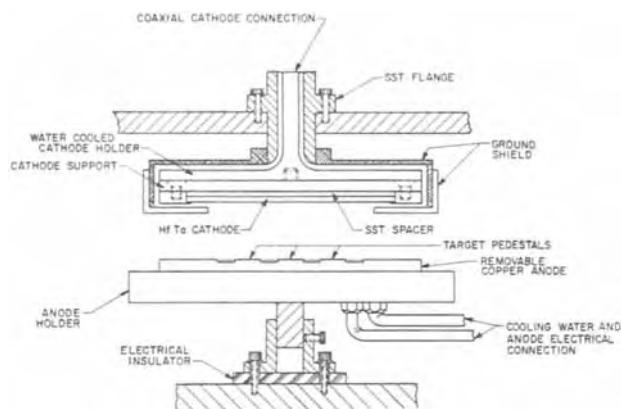


Fig. 2. Details of the diode sputtering system

When presputtering was completed the shutter was opened, the targets exposed to the plasma, and the hafnium-tantalum nitride film deposited. After deposition the system was backfilled very slowly with nitrogen and the targets were removed. To help insure cleanliness the interior of the system was exposed to the room ambient for as short a time as possible during loading and unloading.

Cathode Contamination

Early experiments showed that targets with reproducible saturation currents from run to run were not obtained until a presputter (sputtering above the closed shutters) of 45 min in argon followed by 30 min in nitrogen was used. Without an argon presputter a nitrogen presputter time of an hour or less yielded a sea whose resistivity was not repeatable from run to run. This was reflected in the electrical behavior of the sputtering system. When presputtering was initiated the d-c cathode bias voltage showed an initial rapid decrease followed by a slow increase to a final voltage which did not vary significantly during the remainder of the presputter. The magnitude of the fluctuation and the time to achieve system stabilization was dependent on the time that the system was under high vacuum prior to plasma initiation, as shown in Fig. 3. No pressure change was observed which accounts for the voltage change so the voltage fluctuation is interpreted to be a consequence of conditions at the hafnium-tantalum cathode. The behavior of the system suggests that the cathode is contaminated with gases which are adsorbed when the system is exposed to the room ambient and are

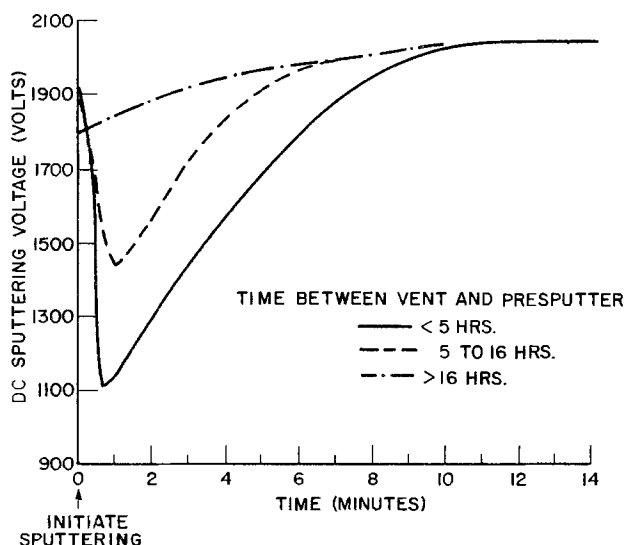


Fig. 3. Sputtering voltage vs. time from initiation of sputtering

slowly desorbed when the system is under vacuum. Alternatively, the gases are removed by presputtering.

This variation of ion current and d-c voltage at constant d-c power agrees with other work (5) where the stabilization of d-c current was used as a criterion for termination of presputtering and the commencement of sputtering. However, our results indicate that although the current may stabilize in a short time, all contaminants are not necessarily removed at that time. A shorter presputter cycle (15 min in argon followed by 30 min in nitrogen) yielded an increasing film resistivity (decreasing target saturation current) from run to run. In these runs the d-c sputtering voltage stabilized within 10 min, but it is apparent that the entire system did not.

The nature of the contaminant which is adsorbed on or absorbed in the hot-pressed cathode has not been determined. The resistivity of the film has been shown to be very sensitive to the presence of small amounts of impurities, particularly oxygen. An increase in resistivity with increasing oxygen content for sputtered tantalum thin films is well known (6). The efficiency of an argon presputter instead of a nitrogen presputter of similar duration in removing the contaminants is related to the more rapid sputtering rate in the argon ambient. This is in part due to the fact that in an argon atmosphere no nitride may build up on the cathode whereas in a nitrogen atmosphere the cathode is continuously being bombarded with reactive nitrogen. The rate of material removal from the cathode in an argon ambient is about an order of magnitude greater than the rate in the nitrogen ambient.

It has been postulated that significant amounts of gas may be trapped in the pores of hot-pressed cathodes (7). The density of hot-pressed cathodes is generally 75-85% of the theoretical density (8). We have observed that without an argon presputter of at least 45 min an insufficient amount of cathode will be sputtered and hence trapped gases (*i.e.*, O_2) may be released during sputtering and affect the resistivity of the deposited sea. Evidently ambient gas penetration into the cathode is several micrometers.

Electrical Properties of the Sea as a Function of Sputtering Variables

Presented in this section are data which relate the sputtering variables to the electrical characteristics of the resistive sea. The measurement of I_{sat} was made on the silicon target (not sealed in a camera tube) in a multiple position demountable tube system in a vacuum of 10^{-7} Torr or less. The error in an I_{sat} measurement is typically ± 20 nA.

D-C voltage, d-c current, and nitrogen pressure.—Figure 4 shows the relationship between d-c sputtering voltage and current obtained at various nitrogen pressures at a constant rf power level of 150W. The saturation current of the target as a function of d-c sputtering current is presented in Fig. 5. At lower pressures sea resistivity and consequently the saturation current depends strongly on d-c sputtering current. The constant power lines and isobars suggest that virtually any value of saturation current (film resistivity) is attainable by simply changing nitrogen pressure and d-c sputtering parameters.

RF power.—The effect of rf power was investigated at 150, 200, and 250W at a constant d-c power of 225W. No significant difference was found between the mean values of saturation current at 150 and 200W rf. A small decrease in the mean at 250W rf (647 ± 58 nA compared to 729 ± 64 nA at 150W rf) was observed. Referring to Fig. 4 and 5, this decrease may be explained by the somewhat lower d-c voltage (2100V) obtained at 250W rf power due to the increased plasma density at the higher power level.

The sputtering rate due to rf power alone is extremely low. Addition of the d-c bias at the levels used

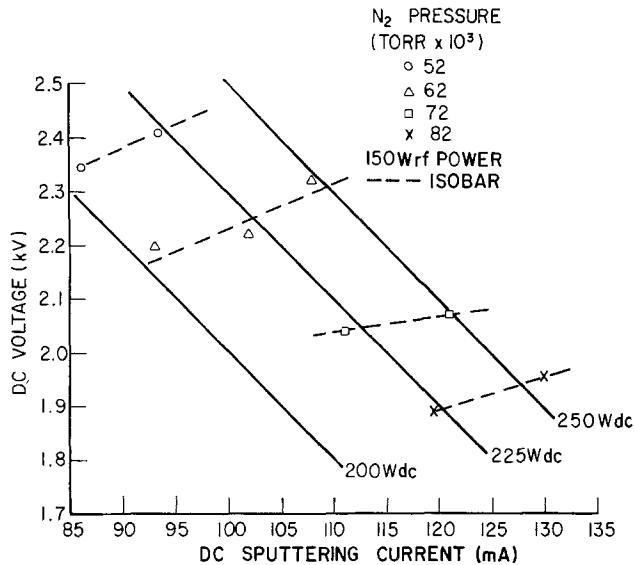


Fig. 4. D-C sputtering voltage vs. d-c sputtering current at various nitrogen pressures. Each point represents the average of two or more runs (6 to 8 targets) except 52×10^{-3} Torr at 225 and 250 W which were only run once.

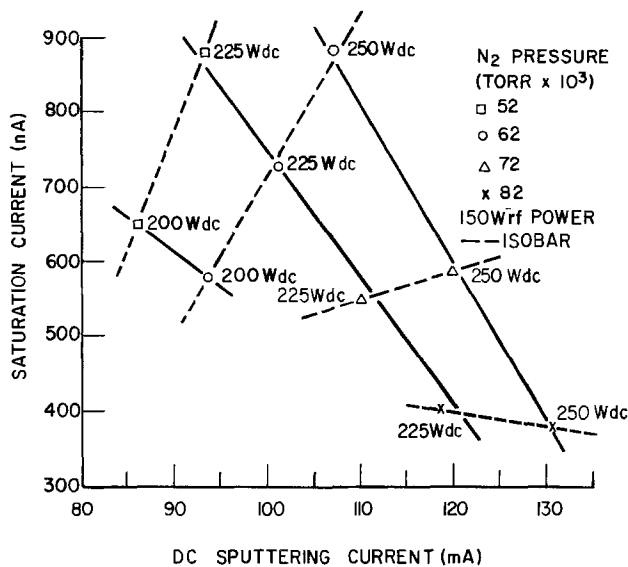


Fig. 5. Target saturation current as a function of d-c sputtering current at various nitrogen pressures.

in this work results in about an order of magnitude increase in deposition rate. The d-c sputtering alone cannot be used because a semi-insulating nitride layer builds up on the cathode, eventually reaching a thickness where the potential between the cathode and the plasma is reduced to the point where sputtering cannot take place. A minimum of 150W rf power is necessary to prevent the nitride buildup.

Nitrogen throughput and background contamination.—The nitrogen throughput of the system was reduced by about one-half for one run at 225W d.c. The targets produced in this run exhibited $I_{sat} \sim 150$ nA lower than that usually obtained at this power level. The decrease in I_{sat} is partially explainable in terms of a slight decrease in sputtering voltage 2165V instead of the normal value of 2223V. However, this only accounts for about 70 nA. The remainder of the decrease is due to an increase in sea resistivity caused by oxygen contamination. The nitrogen throughput was reduced by throttling the turbo pump. This resulted in an increased background contamination level and consequently in contamination of the film.

Early experiments indicated that the resistivity of the films is sensitive to oxygen contamination. Films

produced in a diffusion-pumped system, which was not capable of the low background pressure and high throughput of the turbomolecular-pumped system at the sputtering pressure, contained between 7 and 20 a/o oxygen as analyzed by the electron microprobe. Films with 50 a/o oxygen were produced on one occasion. Typical background water and oxygen levels for that system were at least 10^{-6} Torr during sputtering. The resistivity of films produced in that system varied uncontrollably and many were so highly resistive that the targets with these films charged during operation.

Typical background pressures in the turbo-pumped system were on the order of 10^{-9} Torr. The films produced in this system reproducibly contained about 7 a/o oxygen. See Table I for the electron microprobe analysis of diode-array targets with different saturation currents. However, since the electron microprobe samples to a depth of about a micrometer and therefore samples the underlying SiO₂ as well as the nitride film, it is probable that the bulk oxygen level in the film is much lower than that shown in the analysis.

Clearly, reactive sputtering must be done in a system capable of very low background pressure. This can be attained with good system bakeout procedures and sufficient pumping capacity to provide adequate throughput during sputtering.

Composition of the Sputtered Resistive Sea

The composition of the hafnium tantalum nitride resistive sea on three targets with different saturation currents (different resistivities) was determined by electron microprobe analysis, see Table I. The composition of the film is Hf_{0.45}Ta_{0.55}N_{1.20} or, to the nearest whole numbers, HfTaN₂. Minor amounts of carbon and oxygen were detected in each sample which did not correlate with the electrical properties of the targets and are considered to be surface contaminants of the sea for the most part. The metal-to-nitrogen ratio increased from 0.798 for a target that charged (high resistivity film) to 0.834 for a target with a saturation current of 820 nA (low resistivity). The resistivity of the HfTaN₂ film should decrease at higher metal-to-nitrogen ratios since the higher ratio favors formation of TaN which is known to have a low resistivity. A lower resistivity sea means that the saturation current of the target will be higher.

The Ta-to-Hf ratio increased from 1.16 for the target that charged to 1.21 for the target with the high saturation current. These results follow previous work (3) where resistivity of the film decreased as the Ta-to-Hf ratio increased; however, the observed shift in saturation current is much larger than would have been expected for the small change in Ta-to-Hf ratio. For our results the metal-to-nitrogen ratio is the controlling factor.

Interpretation of the Sputtering Results

The sputtering variables, namely, d-c current, d-c voltage, and nitrogen pressure, are interdependent for the diode sputtering system and at a constant rf power level cannot be varied independently. Figure 4 shows the relationship among d-c voltage, current, and nitrogen pressure for the sputtering module used in this work.

Table I. Electron microprobe analysis of HfTaN₂ resistive sea

Element	Target A	Target B	Target C
	Atomic per cent composition		
Ta	20.85	21.83	21.78
Hf	18.02	18.66	18.07
Zr	0.84	0.91	0.88
N	48.71	49.20	47.82
O	7.22	7.08	7.38
C	4.37	2.32	4.06
	Charged-Low	230	825
I_{sat}	I_{sat}	Nanoamperes	Nanoamperes
Ta/Hf	1.158	1.170	1.205
HfTa/N	0.798	0.824	0.834

Figures 6 and 7 illustrate the effect of d-c sputtering parameters on deposition rate. Varying the d-c voltage and current affects the deposition rate of the film by altering the conditions at the sputtering cathode. The d-c sputtering current reflects the rate at which ions strike the cathode and hence the rate at which material is sputtered. This is clearly shown in Fig. 6 which is a plot of deposition rate vs. d-c sputtering current at various d-c powers and nitrogen pressures. At constant pressure a higher d-c current yields a greater deposition rate of HfTaN₂.

The d-c voltage affects the sputtering yield and hence, at a constant ion current, an increase in voltage results in an increase in deposition rate. At lower nitrogen pressures (therefore higher d-c voltages; recall Fig. 4) and constant d-c power, the film deposition rate increased very linearly from about 2000 Å/hr at 82×10^{-3} Torr to 2400 Å/hr at 52×10^{-3} Torr.

With a fixed hafnium to tantalum ratio the film resistivity is controlled by the metal-to-nitrogen ratio and the metal-to-nitrogen ratio is controlled by the deposition rate of the film. Increasing the deposition rate at constant pressure increases the metal-to-nitrogen ratio in the film and therefore reduces the resistiv-

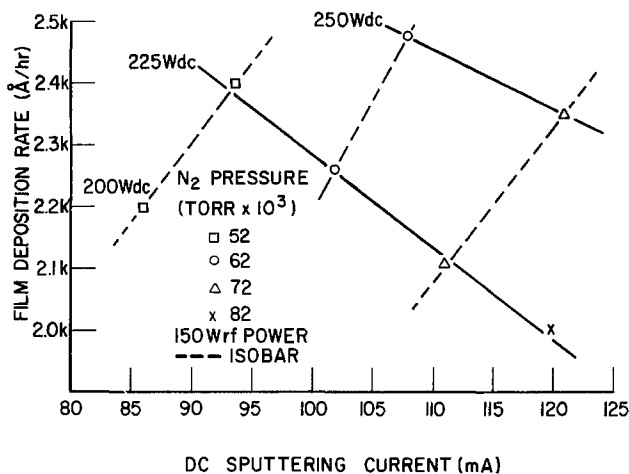


Fig. 6. Film deposition rate vs. d-c sputtering current at various nitrogen pressures.

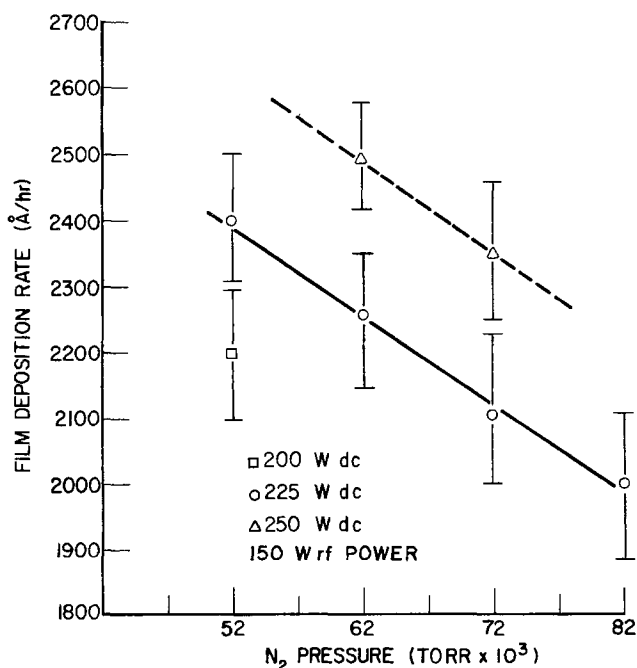


Fig. 7. Film deposition rate vs. nitrogen pressure at various d-c powers.

ity. This explains the results shown in Fig. 5, and accounts for most of the previously described effects of sputtering parameters. The effect is most pronounced at 52×10^{-3} Torr where a 10% increase in d-c sputtering current yielded a 250 nA increase in saturation current. At 82×10^{-3} Torr the effect is nonexistent. Evidently at sufficiently high nitrogen pressures, the increase in deposition rate is matched by the nitrogen available for incorporation into the film. Therefore the saturation current does not change as drastically. This is in agreement with previous work in which the resistivity of the film was varied by varying substrate temperature (3). The effect of substrate temperature is to vary the sticking coefficients of the various components of the sea. In particular, decreasing resistivity with increasing substrate temperature can be explained by a relative decrease in the sticking coefficient for nitrogen.

Dark Current

The diode-array target dark current-voltage characteristics are sensitive to interface state densities in the high 10^{10} cm^{-2} range and oxide charge in the $1 \times 10^{11} \text{ cm}^{-2}$ range.

Sputter deposition of the films described above had no effect on the dark current or flatband voltage exhibited by the targets. This was confirmed by measuring the "dark" I-V characteristics of targets with antimony trisulfide resistive seas (Sb_2S_3 is evaporated onto the target surface), then stripping the seas and depositing the hafnium tantalum nitride resistive sea on the same targets. The I-V characteristics with the hafnium tantalum nitride sea were identical to those with the antimony trisulfide sea.

During early experiments in which films heavily contaminated with oxygen were produced a second-order effect was found. In one run films were so highly resistive that their surface charged during testing and they could not be characterized. Subsequently, several runs were made to produce films of normal composition. The targets produced in these runs were found to have extremely high dark currents. The cause of the high dark current was found to be the insulating film which had been deposited over the surface of the copper anode plate as well as the targets. Evidently the presence of the insulating film on the anode resulted in an abnormally high concentration of electron current through the targets and a consequent deterioration of the oxide interface. Etching the anode plate to remove the insulating film resulted in normal dark currents for subsequent runs.

These experiments show that rf plus d-c sputtering can be utilized to deposit the hafnium-tantalum nitride resistive sea without affecting high quality Si-SiO₂ interfaces provided a high ratio of conducting anode to substrate area is maintained.

Conclusions

The influence of sea resistivity on the performance of the silicon diode-array target has been utilized to study the effect of sputtering parameters on the properties of the hafnium tantalum nitride resistive sea. The principal effect of varying the sputtering parameters is to vary the metal arrival rate at the substrate and perhaps the substrate processes and thus the metal-nitrogen ratio in the film.

The sensitivity of the film resistivity to impurities, particularly oxygen, demands that the vacuum system used have a low background contamination level. For reproducible results when reactively sputtering thin resistive films from a hafnium-tantalum cathode a system capable of attaining background pressures of 10^{-8} Torr or lower is necessary. This requirement together with high pumping speed to maintain an adequate throughput necessitates a pump with high speed and a low background pressure capability at the sputtering pressure such as a turbomolecular pump.

Even with good bakeout procedures and adequate pumping the presputter conditions are critical for reproducible resistive films. A presputter in argon was found necessary to prepare the cathode; nitrogen alone was not sufficient. Several micrometers of cathode must be sputtered away in order to be certain that gases adsorbed in the porous hot-pressed cathode are removed during presputter.

With the aforementioned precautions taken into account then the reactive sputtering gas pressure and d-c current must be controlled precisely. Evidently sputter rate and sputter yield are important with sputter deposition rate being more important at low nitrogen pressures where the d-c voltage is higher and sputter yield is greatest. At higher nitrogen pressures most large resistivity changes in the film with small changes in d-c current and d-c voltage disappear.

For easily achieved reproducible results when reactively sputtering hafnium tantalum nitride, the nitrogen pressure should be as high as possible. The metal-to-nitrogen ratio in the film is then less responsive to slight variations in d-c current and voltage.

Acknowledgments

Helpful discussions with J. R. Mathews are gratefully acknowledged. The authors thank S. M. Forst for

technical assistance and D. R. Wonsidler for the electron microprobe analyses.

Manuscript submitted May 23, 1974; revised manuscript received Oct. 21, 1974. This was Paper 37 presented at the San Francisco, California, Meeting of the Society, May 12-17, 1974.

Any discussion of this paper will appear in a Discussion Section to be published in the December 1975 JOURNAL. All discussions for the December 1975 Discussion Section should be submitted by Aug. 1, 1975.

Publication costs of this article were partially assisted by Bell Laboratories.

REFERENCES

1. W. C. Ballamy, W. R. Knolle, and L. D. Locker, *IEEE Trans. Electron Devices*, **ED-20**, 1147 (1973).
2. F. Vratny, U.S. Pat. 3,574,143 (April 6, 1971).
3. L. D. Locker, C. L. Naegele, and F. Vratny, *This Journal*, **118**, 1856 (1971).
4. W. E. Beadle and A. J. Schorr, *Bell System Tech. J.*, **49**, 921 (1970).
5. D. M. Mattox, *J. Vacuum Sci. Technol.*, **10**, 47 (1973).
6. See for example, C. A. Steidel and D. Gerstenberg, *J. Appl. Phys.*, **40**, 3828 (1969).
7. J. L. Vossen, *J. Vacuum Sci. Technol.*, **8**, 751 (1971).
8. L. D. Locker and D. L. Malm, *Rev. Sci. Instr.*, **42**, 1696 (1971).

Interface Effects in the Dissolution of Silicon into Thin Gold Films

H. Sankur* and J. O. McCaldin**

California Institute of Technology, Pasadena, California 91109

ABSTRACT

The dissolution of crystalline Si and amorphous Si substrates into thin films of evaporated Au was studied with an electron microprobe and scanning electron microscopy. The dissolution pattern was found to be nonuniform along the plane of the surface and dependent on the crystalline orientation of the Si substrate. The dissolution is greatly facilitated when a very thin layer of Pd is evaporated between the Si substrate and the Au film.

Gold is extensively used in microwave power device metallizations and in beam lead technology (1), because of its high conductivity, resistance to corrosion, and low failure rate due to electromigration. In these systems the current carrying Au metallization is separated from Si by various metallic layers. These intermediate layers perform the function of providing low-resistivity ohmic contact to the device, good adhesion to the substrate SiO₂, and also serve as diffusion barriers between various layers. The occurrence of mechanical damage during handling or thermal excursions in device manufacture or chemical interactions (2) in intermediate layers can cause direct contacting of Au and Si; this latter situation is a possible source of catastrophic failure of the device due to liquid phase alloying, given the remarkably low eutectic temperature of the Si-Au system (3), or due to excessive dissolution of Si into Au. In fact Si has been found to dissolve and diffuse rapidly into thin Au films at temperatures considerably below the eutectic temperature of the Si-Au binary system (4).

Hiraki *et al.* had shown that considerable transport of Si through thin (~1000Å) Au films vacuum deposited on Si substrates and growth of a SiO₂ layer on the Au surface occurred when the specimens were

annealed in an oxidizing ambient at temperatures as low as 150°C. Although nonuniformity of the SiO₂ layer was inferred from the backscattering analysis and the importance of the interface was pointed out (5, 6) by the same investigators, no detailed work to understand the effect of the interface was done. In the present investigation, the dissolution reaction of Si in Au has been studied by means of the electron microprobe and SEM. The importance of the Si-Au interface in causing varied dissolution patterns is clearly demonstrated.

An important aspect of the present work is the observation and analysis of the nonuniform nature of the interaction of the Si-Au system. The importance stems from the fact that other thin film systems may exhibit such nonuniform behavior and that investigations of these with methods like x-ray diffraction, He⁺ backscattering, Auger or mass spectrographic analysis coupled with sputter etching that average signal from a relatively large area will lead to invalid conclusions. Therefore, it is imperative to obtain information about uniformity of the interaction on a micron scale. Recent developments in the above-mentioned methods can make such an analysis possible.

Experimental

The electron microprobe has been used to detect the amount and the location of Si in thin films (7).

* Electrochemical Society Student Member.
 ** Electrochemical Society Active Member.
 Key words: Au thin films, interface effects, Si-Au, dissolution.

In this analysis a 10 keV, 0.1 μ A electron beam, focused to less than 1 μ diameter is directed perpendicular to the surface, to induce x-ray emission. At these energies, the penetration of the beam is only a fraction of the Au film thickness, and hence does not excite the Si substrate (Fig. 1). With the detector system tuned for SiK α line radiation, either qualitative or quantitative analysis of Si can be performed.

In this investigation, the microprobe was used in scanning mode, where the electron beam scanned the surface like a raster sampling an area, dimensions of which can be controlled. The information was displayed on a screen, by intensity modulation of the CRT with signal coming from the microprobe detection system. In this mode of operation, information about the local distribution of various elements can be quickly obtained (8).

Quantitative microprobe analysis showed that levels of SiK α radiation of Si dissolved into Au was very small due to low solubility of Si in Au and relatively high noise level of the Au matrix. In this case 1 μ thick Au was evaporated onto polished Si substrates. These specimens were heat-treated for various lengths of time at various temperatures between 200°-300°C, and then subjected to a brief dip in dilute HF solution just prior to microprobe analysis. This latter precaution was taken in order to eliminate any SiO $_2$ film that could have formed on the Au surface during heat-treatment or while the specimens were kept at room temperature after heat-treatment (9). The microprobe analysis that was performed with a broad defocused electron beam, showed that solubility of Si in Au was below the detection limit of the microprobe (200 ppm). Hence it was concluded that an accurate investigation could not be done by probing Si dissolved into Au. Therefore for purposes of this investigation, a thin Pd layer was deposited on the Au film as a sink material for Si. Si atoms that migrated through the Au film, reacted with Pd to form stable Pd $_2$ Si (10). Thus compound clusters formed at the Au-Pd interface, the amount of which was proportional to the amount of Si transported through Au, since no detectable Si was retained in the Au film; the location of these clusters corresponded to locations where Si dissolved into and migrated through the Au film to reach Pd or Pd $_2$ Si (Fig. 1), as is explained later in detail.

The preparation of typical specimens was as follows: Chemically polished Si wafers (p-type, 1-10 ohm-cm)¹ with <100>, <110>, <111> orientations were used as substrates. Amorphous Si was obtained by evapora-

¹ The Si substrates were block polished with Monsanto patented Syton. The reported etch pit density was 400/cm 2 . No surface features could be detected with optical microscope or SEM on these substrates.

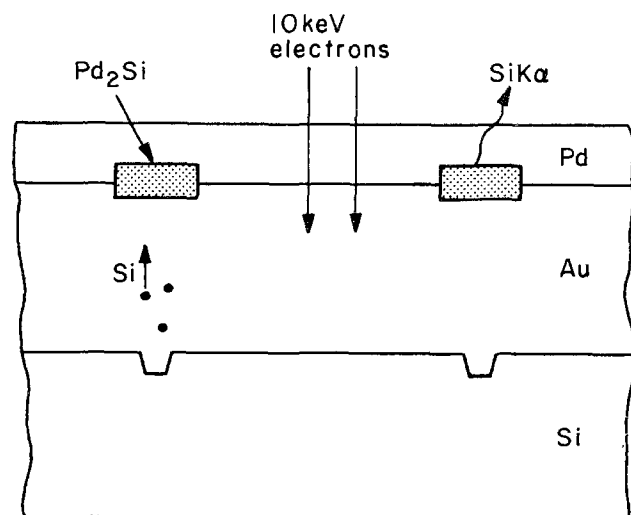


Fig. 1. Cross section of a specimen schematized to illustrate the experiment. Note that the vertical dimensions are not to scale.

tion of Si on thermally oxidized Si wafer substrates. The crystalline substrates were cleaned with organic solvents, rinsed with deionized water, dipped in dilute HF solution, rinsed thoroughly for 4-5 min, dried, and placed in the vacuum evaporation system. The depositions were done sequentially in a 3 crucible e-gun system, at pressures $\sim 5 \times 10^{-7}$ Torr. Au was evaporated from a 99.999% purity source to a thickness of 1 μ . The Pd film thickness was 600Å and was deposited from 99.9% purity source.

In a limited number of experiments a 200Å thick Pd underlay was evaporated before the Au and sink Pd layer at the top, with the intention of altering the Si-Au interface conditions.

The specimens were thereafter either immediately heat-treated in a tube furnace under a pressure of less than 10^{-5} Torr at 220°C or briefly stored in a desiccator under vacuum.

A limited number of specimens that consisted solely of evaporated Au on Si substrates were annealed in a tube furnace through which water vapor laden nitrogen flowed gently. The purpose of these latter experiments was to use a different sink material for Si, than Pd overlay (5).

The annealing times were ordinarily close to 1 hr, although longer annealing times were also tried.

Another parameter that was varied in some experiments, was the thickness of the Au film. Au films 3 and 10 μ thick were evaporated in addition to the majority of the specimens which had 1 μ thick Au film.

In one case Au films evaporated on Si were annealed in vacuo before the Pd evaporation, with the intention of causing change in the microstructure of the Au films.

After the microprobe analysis the Pd and Pd $_2$ Si layers were removed in boiling (HNO $_3$ + H $_2$ SO $_4$) solution in order to study the Au surface under SEM. Subsequently Au was removed in (KI + I $_2$) solution for the SEM study of the Si surface.

Results

He $^+$ backscattering studies² showed that at the temperature the specimens were heat-treated, the Au-Pd interdiffusion was negligible (11) and that all Si resided at the Au-Pd interface in the form of compound.

In the present investigation it was in general found that Si migrated through the Au film and reacted with Pd, only in random spots and along lines, 1-5 μ wide, that form closed curves from the top view. The regions between these were found to contain no silicide by quantitative microprobe measurements. However the degree of nonuniformity or the density of locations where Si dissolution took place depends on the orientation of the Si substrate as well as Si-Au interface conditions and surface preparation. Microprobe studies (Fig. 2a, 3-5) clearly show that Pd $_2$ Si is detected only in some line or band shaped boundaries and that regions between these do not contain any Si. However the distance between these boundaries measure 30-100 μ in the case of <111>-Si, whereas the areas formed by these lines have diameters 5-10 μ on <100>-Si (Fig. 4). The average diameter is slightly larger on <110>-Si (Fig. 5). In the case of amorphous Si, Si dissolution is also localized and the pattern of silicide growth bears a resemblance to the case of <100>-Si.

The <111>-Si substrate showed a host of features. Figure 3 shows part of a jagged boundary, while others run smooth. Occasionally short broken lines within an area enclosed by long lines were seen. A rare feature was formation of very dense pointlike growth of silicide in a certain area, whereas neighboring regions separated by lines showed no silicide in them.

The dissolution behavior of <111> substrate changed drastically upon introduction of a Pd underlay between Si and Au. A Pd film of 100-200Å thickness

² This part of the study was done by D. Sigurd and H. Sankur.

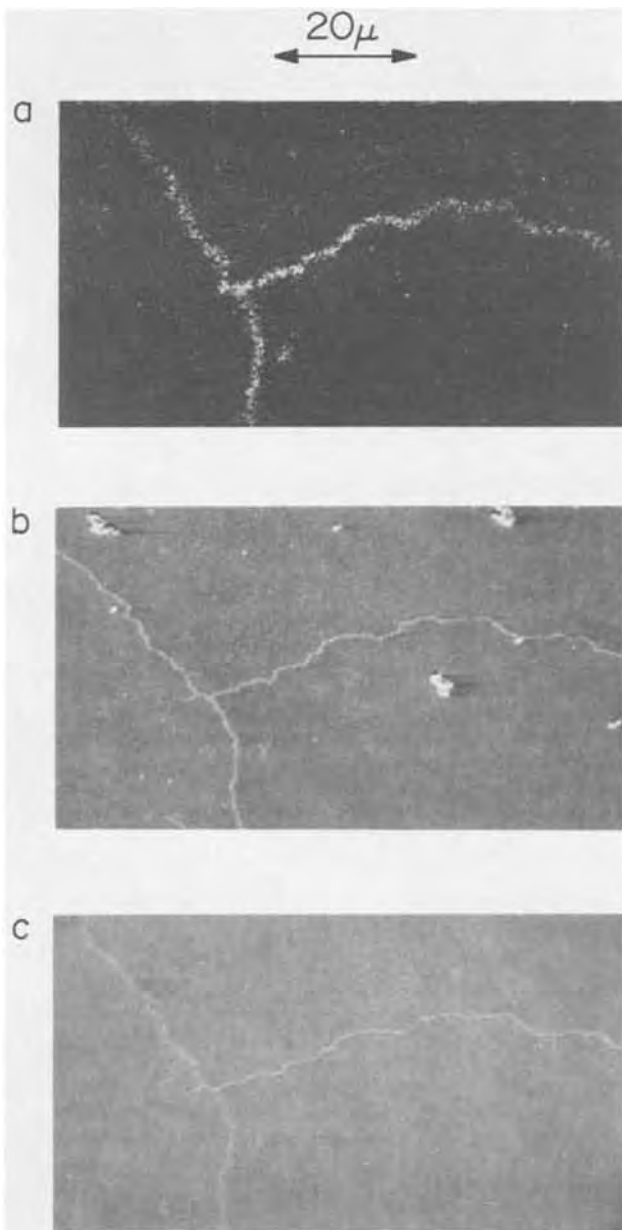


Fig. 2. A section of the complete specimen (a) as exhibited by the electron microprobe tuned to SiK fluorescence. Si in the Pd₂Si layer appears as white in this photograph. (b) SEM photo of the same section of the specimen after the microprobe analysis. (c) SEM photograph of the Si surface of the same area after removal of all metal and silicide. The substrate was <111>-Si.

evaporated on Si, before the Au and sink-Pd deposition caused upon annealing an increase in the density of silicide-rich boundaries at the Au-Pd interface or equivalently the density of dissolution locations at the Si surface, as is clarified later in this part. Figure 6 shows an electron microprobe micrograph of such a specimen. The silicide growth pattern although bearing some resemblance to the case of <100>, has a higher density of compound clusters.

The above-mentioned point or linelike regions of Pd-Si reaction become evident under optical microscopic investigation or SEM analysis (Fig. 2b), after about the first hour of heat-treatment for reasons that are explained in the Discussion section. After prolonged heat-treatment, the lines could be identified as brown-colored Pd₂Si, with respect to the white Pd overlay, implying that almost all Pd along these regions was consumed in the compound layer. In general a one to one correspondence was found between



Fig. 3. Microprobe photograph of another location of specimen in Fig. 2 where again white areas represent silicide within the metallization.

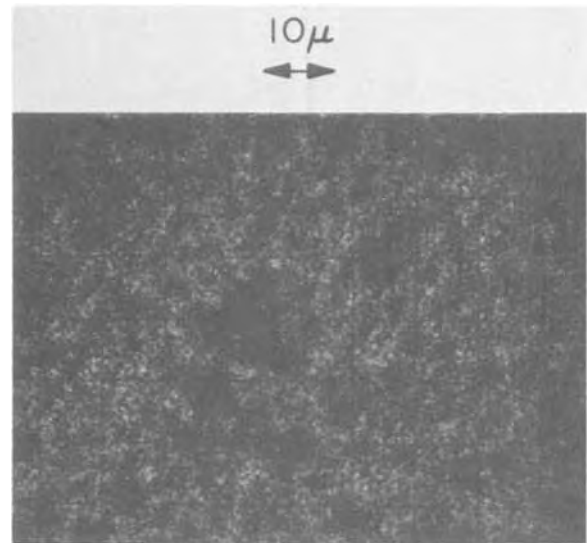


Fig. 4. Microprobe photograph of a specimen with <100>-Si substrate. Heat-treatment time, 1 hr.

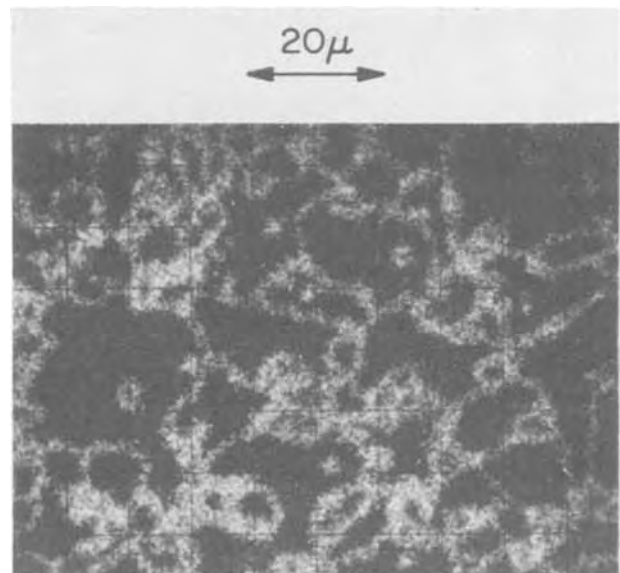


Fig. 5. Same as in Fig. 4, except the substrate is <110>-Si

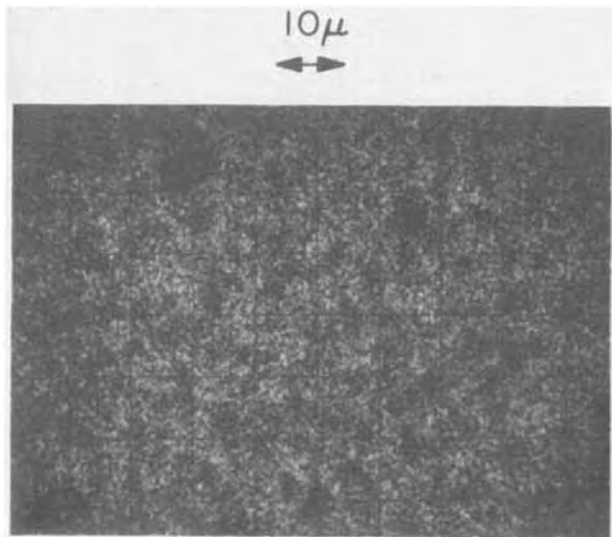


Fig. 6. Microprobe photograph of a specimen with $\langle 111 \rangle$ -Si substrate and a very thin layer of Pd between Au and Si. Note the increased density of silicide clusters compared to Fig. 2.

visible surface features and compound regions as revealed with the microprobe analysis.

The amount of Si in or the thickness of the silicide in the prementioned regions of Pd_2Si formation, as well as the width of the latter, increased with annealing time. This caused coalescence of boundaries to form continuous areas or bands of silicide growth when heat-treatment times were as long as 9 hr.

A replica of the above-mentioned geometrical features is seen in Au, after removal of the overlying Pd and Pd_2Si layers. However, a closer look with SEM reveals depressions in Au film, where Pd_2Si previously existed, attesting to the displacement of Au during Pd_2Si formation.

Figures 2c and 7 show the Si surface after removal of the Au layer. The previously described pattern is replicated in the form of canyonlike trenches or a series of elongated depressions in Si. These are regions where Si dissolved into Au and migrated

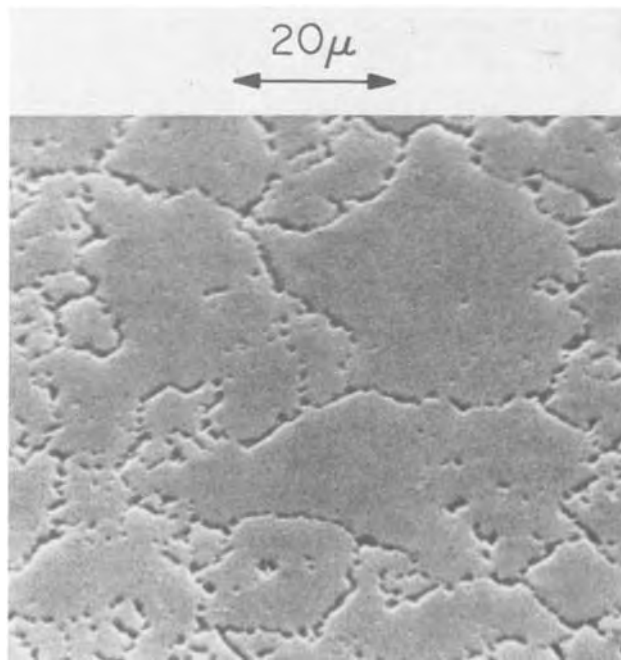


Fig. 7. SEM photograph of the Si surface after removal of Au, Pd, and compound layers. The substrate was $\langle 100 \rangle$ -Si. The areas enclosed by trenches are somewhat larger than average size, in this particular section.

through, to react with the Pd overlay. The trenches are 0.1-0.3 μ deep and 1-5 μ wide. The flat regions between these correspond to areas where no silicide was detected in microprobe analysis and hence contain no dissolution features. SEM analysis showed that a 1-5 μ wide depression formed in the middle of the 10-20 μ wide silicide-rich band, in specimens annealed at temperatures as high as 360°C. This and the fact that raised features were seen on the back side of Au-Pd metallic film, after etch-removing Si substrate (Fig. 8) led to the conclusion that Au moved in and possibly filled the trenches as Si dissolved and diffused out into Au.

The dissolution cavities on $\langle 100 \rangle$ (Fig. 7) and $\langle 110 \rangle$ surfaces do not form a continuous trench but are rather in the form of separated square or elongated rectangular cavities. These often show an alignment that reflects the crystalline orientation of the substrate.

The specimens that consisted solely of Au films on Si, and that were annealed in an oxidizing ambient, showed formation of a SiO_2 layer on Au which was laterally nonuniform. In fact the geometrical pattern of SiO_2 formation and its dependence on crystalline orientation resembled the silicide growth pattern mentioned in the first part of this section.

These results were also generally reproduced when the Au film thickness and annealing temperatures were varied. Specimens with 3 and 10 μ thick Au films showed identical behavior at 220°C and annealing time of 1 hr as specimens with 1 μ thick Au film. Higher temperature anneals at temperatures between 220° and 360°C of specimens with 1 μ thick Au film and Pd overlays exhibited a more rapid growth of the compound structure. The effect of the latter was to cause blending of silicide lines or points into an almost continuous compound layer in the case of $\langle 100 \rangle$ and $\langle 110 \rangle$ -Si substrate, after brief annealing times. However, the specimens with $\langle 111 \rangle$ -Si substrate showed only widening of compound boundaries and no blending due to much larger separation of the boundaries.

Discussion

The results show that migration of Si through thin evaporated Au films occurs along lines or occasionally in some spots, the density of which depends on the substrate Si surface condition or crystalline orientation. The relationship between these transport routes of Si and grain boundaries of the Au film are at present unknown. Microscopic analysis showed that Au grains were on the average 1-2 μ in diameter. Similarly the effect of thermal stresses is not yet known. However, annealing of Au at 250°C for 3 hr during which



Fig. 8. The back side of the metallization after removal of the Si substrate. The raised features correspond to trenches in the substrate $\langle 111 \rangle$ -Si, and reflect the crystalline nature of the substrate.

substantial grain growth and recrystallization might be expected (12) before Pd overlay deposition did not make any noticeable change in Si dissolution pattern.

The fact that silicide boundaries can be seen optically, before all the Pd layer is consumed in the compound and the boundaries assume a brownish color, can be attributed to the deformation of Au-Pd metal layer due to volumetric changes accompanying the compound formation and due to "sinking" of metal layers in the dissolution trenches on the Si substrate.

The increase in thickness and width of Pd₂Si-rich lines with time is probably due to Si diffusion in the Pd₂Si cluster after Si atoms reach the Au-Pd₂Si interface. This is also borne out by the fact that Si can diffuse through the Pd₂Si layer that forms at Si-Au interface when a thin Pd underlayer is evaporated on Si before Au deposition. However some "fanning" or diffusion of Si away from the plane of assumed Si migration also occurs, as evidenced by the larger size of silicide boundary width compared to that of trenches on the Si surface even for small annealing times. In fact given the vertical dimension of Pd overlay (600Å), the fact that growth of 1-5μ wide silicide region occurs before compound front arrives at the top surface, strongly suggests Si fanning out as well as migrating directly perpendicular to the surface.

Although the cause of localized dissolution reaction is at present unknown, it can be stated that difference of dissolution behavior for substrates of different orientations is neither due to Pd-sink layer nor to Au film. In fact cleaning, metal film depositions, annealing of specimens with <111>, <110>, <100> Si substrates were done simultaneously in a batch.

The localized dissolution behavior is predominantly an interface effect. Likely causes of this nonuniform behavior are discussed below. Chemical residues from polishing or cleaning of Si substrates, from absorbed species, or from native oxide can prevent Au from coming in intimate contact with Si, and hence allow Si to migrate in through few locations where coherency of the oxide or absorbed layer is disrupted. A similar behavior was observed in the case of the reaction of thin W-films evaporated onto Si surfaces (13). The difference between <111>-Si and substrates with other orientations can be explained on this basis also. The higher density of atoms on the <111> surface may bring about a more impervious oxide (14) or a layer of adsorbed chemicals that has sparser faults.

The thin oxide layer that forms on the Si surface by boiling the wafer in HNO₃ or H₂O₂ or exposing to air for a few days suppressed the reaction totally. It was also observed that allowing methanol, which is one of the organic cleaning agents used, to dry on Si wafer before deposition had a similar effect as native oxide in suppressing the reaction.

The effect of the intermediate Pd layer may be to disrupt this surface "dirt" layer, thanks to its higher reactivity with Si, thus paving way for Si to come in contact with Au at a larger number of locations. This result bears analogy to facts observed by Hiraki *et al.*

(6), where migration of Si in Au/Ag sandwiches was seen at low temperatures only when Au was in contact with Si, and not when Ag was in contact with Si.

Conclusion

Interaction of crystalline and amorphous Si with thin Au films was studied with SEM and electron microprobe. Si was found to migrate through the Au film at temperatures 190°-360°C in isolated lines or points. Variation of the separation of these lines was seen to depend on the substrate crystalline orientation and was attributed to surface adsorbed impurity or oxide layer. A drastic change in the dissolution behavior of <111>-Si substrates especially, was brought about by evaporation of a very thin layer of Pd before the Au deposition. Likely causes of these results will be the subject of further detailed investigations.

Acknowledgment

The efforts of R. Cunningham in microprobe analysis, of K. Evans in SEM analysis are deeply appreciated. The cooperation of D. Sigurd in backscattering analysis is also appreciated.

The work was partly supported by NASA through Jet Propulsion Laboratory and partly by Office of Naval Research.

Manuscript submitted March 19, 1974; revised manuscript received Sept. 19, 1974.

Any discussion of this paper will appear in a Discussion Section to be published in the December 1975 JOURNAL. All discussions for the December 1975 Discussion Section should be submitted by Aug. 1, 1975.

Publication costs of this article were partially assisted by California Institute of Technology.

REFERENCES

1. For example, M. P. Lepselter, *Bell System Tech. J.*, **45**, 233 (1966).
2. H. Day, A. Christou, and D. J. Bressman, To be published.
3. Max Hansen, "Constitution of Binary Alloys," p. 232, McGraw Hill Book Co., New York (1958).
4. A. Hiraki, M. A. Nicolet, and J. W. Mayer, *Appl. Phys. Letters*, **18**, 178 (1971).
5. A. Hiraki, E. Lugujo, and J. W. Mayer, *J. Appl. Phys.*, **43**, 3643 (1972).
6. A. Hiraki, E. Lugujo, J. W. Mayer, and M. A. Nicolet, *Phys. Status Solidi (a)*, **7**, 401 (1971).
7. J. O. McCaldin and H. Sankur, *Appl. Phys. Letters*, **19**, 524 (1971).
8. For example see J. O. McCaldin and H. Sankur, *ibid.*, **20**, 171 (1972).
9. Akira Yamagisawa and Mitsu Namba, *Japan. J. Appl. Phys.*, **12**, 748 (1973).
10. R. W. Bower and J. W. Mayer, *Appl. Phys. Letters*, **20**, 359 (1972).
11. Also see, S. S. Lau and R. C. Sun, *Thin Solid Films*, **10**, 273 (1972).
12. J. P. Chauvineau, P. Croce, G. Devant, and M. F. Verhaeghe, *J. Vacuum Sci. Tech.*, **6**, 776 (1969).
13. L. D. Locker and C. D. Capio, *J. Appl. Phys.*, **44**, 4366 (1973).
14. V. J. van der Meulen, *This Journal*, **119**, 530 (1972).

The Diffusion of Iron in Impurity Controlled Single Crystalline Nickel Oxide Between 1061° and 1241°C

William D. Stewart, Jr.¹ and J. Bruce Wagner, Jr.*

Department of Materials Science and Materials Research Center, Northwestern University, Evanston, Illinois 60201

ABSTRACT

The capability of an x-ray dispersive microanalyzer attachment on a scanning electron microscope to determine concentration profiles of iron in single crystalline NiO was studied. The technique is less precise but much less time consuming than radiotracer methods. The data support a model involving diffusion of iron via vacant nickel sites. The activation energies varied between 18 and 26 kcal/mole for diffusion under constant oxygen pressures between 0.011 and 1 atm. The diffusion was impurity controlled.

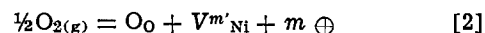
The purpose of this research was to study the rate and mechanism of diffusion of iron in nickel oxide. The x-ray wavelength dispersive analyzer of the JEOL-SMU-3 scanning electron microscope was used to detect the concentration of iron and thus provide a test for the capability of this instrument for studies of impurity diffusion in oxides. This study is part of a program to study impurity diffusion in oxides with special reference to high temperature corrosion problems.

Experimental

Single crystals of NiO were obtained from Dr. W. Clark of the Oak Ridge National Laboratory, Oak Ridge, Tennessee. The chemical analysis of an as-received crystal is shown in Table I. The boule was cleaved into rectangular parallelepipeds bounded by (100) crystal planes. Most crystals were first given a prediffusion anneal at the specified temperature ($\pm 2^\circ\text{C}$) under an oxygen, air, or argon-oxygen gas mixture flowing past the sample at a linear flow velocity of about 0.9 cm/sec. The chemical diffusivity data of Price and Wagner (1) were used to determine the time for equilibration. Several crystals were heated in preevacuated, closed tubes containing excess nickel so the partial pressure of oxygen corresponded to the Ni-NiO phase boundary (2, 3). The samples were quenched by withdrawing from the hot zone to room temperature in approximately 10 sec for crystals under a flowing gas atmosphere and 30 sec for the crystal in closed, quartz ampuls. The crystals were mounted in a JEOL evaporator and approximately 300Å of iron was deposited onto one face of the crystal so as to act as a thin source of iron into a semi-infinite NiO crystal. The crystals were then given a diffusion anneal for times from 5 to 9 days under the same conditions (temperature and oxygen pressure) as the prediffusion anneal. The crystals were then quenched as described previously and cleaved parallel to a (100) plane along the diffusion axes. The crystals were mounted on a stub, coated with carbon (about 100Å thick), and placed in a specimen stage. This assembly was introduced into the JEOL-SMU-3 SEM. A LiF crystal was used for the detection of iron. A typical concentration gradient is shown in Fig. 1 and the log of the concentration *vs.* distance squared is shown in Fig. 2. The error bars denote the errors due to the instrument, counting statistics, geometry, and sample preparation. The results were calculated using the thin source solution to Fick's second law

$$\frac{\partial \log C}{\partial x^2} = - \frac{1}{9.21 Dt} \quad [1]$$

where *C* is the activity in counts per minute observed at a penetration distance *x* (cm), *t* is the diffusion anneal time (sec), and *D* is the impurity diffusion coefficient of iron in NiO (cm²/sec). A large number of determinations (a minimum of five) of penetration *vs.* distance were made on a single cleaved surface. The diffusion coefficients determined from repeated sets of measurements on the same cleaved crystal were generally within 5% of each other using the line of best fit to the data for each experimental determination. Figure 3 shows Arrhenius plots for constant oxygen pressures. The higher the oxygen pressure, the more rapid the diffusivity of iron. This suggests that iron migrates via a vacancy mechanism inasmuch as the deviations from stoichiometry in NiO are due to cation vacancies according to



where the notation of Kröger and Vink (4) is used and the *m* denotes the degree of ionization of the vacancies. In very pure NiO, *m* = 2. The crystals used in the present studies were previously shown (5) to contain predominantly singly ionized vacancies, *m* = 1. This may be understood in view of the large concentration of aliovalent impurities as has been shown,

Table I. Impurity concentrations in nickel oxide (in parts per million atomic)

Element ^(a)	Detection limit (NiO)	NiO ^(b)
Li	0.01	0.03
B	—	—
C	1	420
N	0.1	7.2
F	0.1	42
Na	0.01	26
Mg	0.2	13
Al	0.3	42
Si	3	140
S	10	820
Cl	0.07	1.7
K	0.01	3.1
Ca	7	19
V	0.3	N.D.
Cr	0.3	11
Mn	0.3	N.D.
Fe	0.3	420
Ni	—	—
Cu	1	2
Zn	2	N.D.
Ga	0.7	36
Ge	3	N.D.
Se	3	N.D.
Y	—	—
Ar	1	54
Ag	1	26

^(a) No analysis was made for hydrogen. Analyses for tantalum and gold are not given since tantalum slits are used in the mass spectrometer and the samples were sparked against high purity gold. Analyses were by the Bell and Howell Research Laboratories, Pasadena, California.

^(b) The nickelous oxide crystal was obtained courtesy of Dr. W. Clark of the Oak Ridge National Laboratory, Oak Ridge, Tennessee.

* Electrochemical Society Active Member.

¹ Present address: Siemens Corporation, Iselin, New Jersey 08830.

Key words: scanning electron microscope.

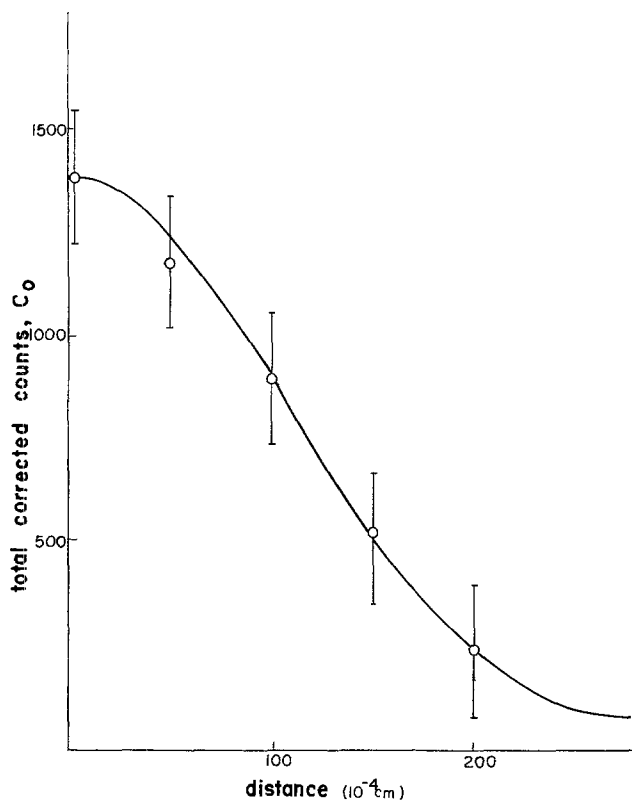


Fig. 1. Typical plot of the intensity (in terms of the corrected counts per minute) vs. penetration distance for a nickel oxide crystal heated at 1241°C under 1 atm oxygen for 5.21×10^5 sec.

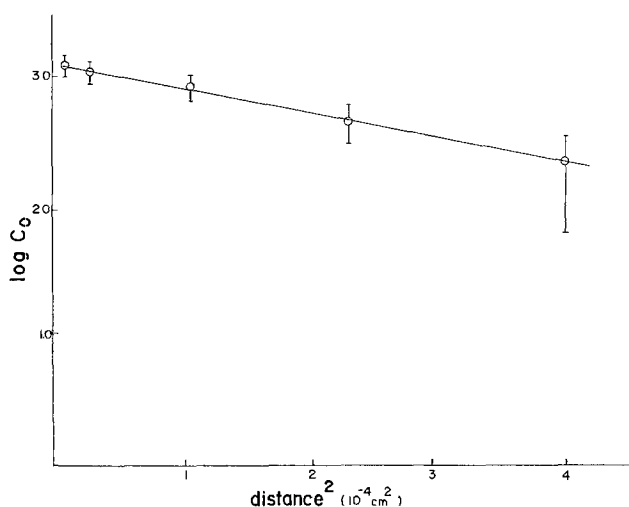


Fig. 2. Plot of the data shown in Fig. 1 as $\log C$ vs. x^2 in accord with Eq. [1].

e.g., by Tretyakov and Rapp (6). If iron migrates via singly ionized vacancies

$$D(\text{Fe} \rightarrow \text{NiO}) \propto V_{\text{Ni}} \quad [3]$$

then one should expect the diffusivity to be proportional to the one-quarter power of the oxygen pressure. Figure 4 shows the data plotted as $\log D$ vs. $\log p_{\text{O}_2}$ at 1060° and 1241°C. Based on only three data points, the slopes are 0.19 and 0.23, respectively. Because of the high concentration of impurities, the slopes are less than would be predicted as also has been observed by Crow (7).

The temperature dependences are given in Table II. The activation energies represent primarily the migration energy (enthalpy).

In the case of the Arrhenius plot for crystals heated under oxygen pressures corresponding to the phase

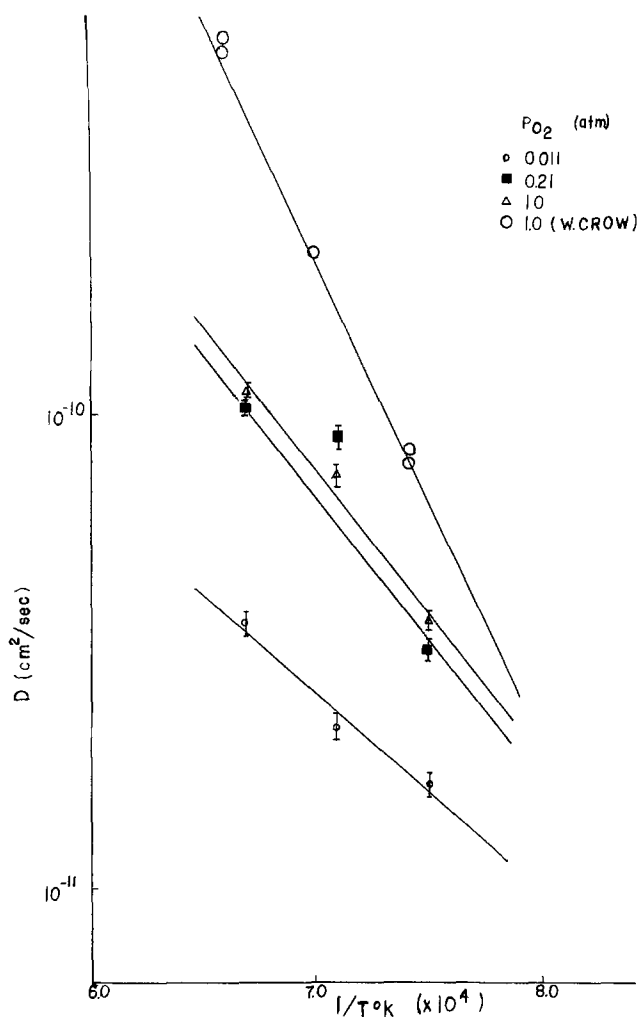


Fig. 3. Temperature dependence for the diffusion of iron in single crystalline NiO. The data of Crow (7) was obtained using radio-tracers.

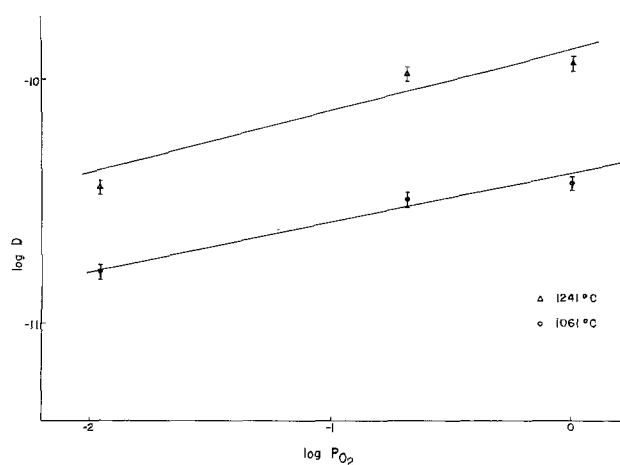


Fig. 4. Dependence of diffusivity of iron on oxygen partial pressure coexisting with single crystalline NiO.

boundary, Ni/NiO, the results are: $D(\text{Fe} \rightarrow \text{NiO coex. with Ni}) = 1.67 \times 10^{-5} \exp(-38,040/RT)$. The data obtained for these crystals presumably equilibrated at the Ni/NiO phase boundary were not consistent with the data obtained at the higher pressures and were orders of magnitude larger. It may have happened that the crystals did not equilibrate. The available data for comparison at the higher pressures has been carried out by Crow (7). His data for crystals

Table II. Temperature dependences

p_{O_2} (atm)	D_0 (cm ² /sec)	Activation energy Q , kcal/mole
0.011	1.6×10^{-9}	18.24
0.21	5.92×10^{-7}	25.90
1.0	6.74×10^{-7}	25.83

heated under 1 atm of oxygen are shown in Fig. 3. In order to make a direct comparison, Crow kindly furnished us with a single crystal used in his study (7). We carried out a pre-diffusion and diffusion anneal followed by a probe trace as described above. The result was $D = 5.4 \times 10^{-11}$ cm²/sec at 1050°C and $p_{O_2} = 0.21$ atm. This value, obtained on Crow's crystal, is almost identical to that obtained on our crystals. Crow's datum on his crystal amounted to about 9×10^{-11} cm²/sec at 1100°C. The data from both these studies are consistent at this one pressure and approximately the same temperature. Moreover, arguments advanced to the effect that our study may have involved interdiffusion owing to the thick layer of iron² (300 Å) or that sulfur (S₀'), as well as the metallic impurities, acts as a dopant, all suggest our diffusion coefficients should be larger than those of Crow. The converse was found. But the values of our activation energies, although consistent, were low. As a comparison, the diffusion of nickel in nickel oxide has been studied by a number of workers. The results for crystals heated in air are

$$D(\text{Ni} \rightarrow \text{NiO}) = 4.4 \times 10^{-4} \exp(-44,200/RT) \quad [5]$$

from Ref. (8)

$$D(\text{Ni} \rightarrow \text{NiO}) = 1.83 \times 10^{-3} \exp(-45,600/RT) \quad [6]$$

from Ref. (9)

$$D(\text{Ni} \rightarrow \text{NiO}) = 1.72 \times 10^{-3} \exp(-56,000/RT) \quad [7]$$

from Ref. (10)

and in 1 atm of oxygen

$$D(\text{Ni} \rightarrow \text{NiO}) = 4.77 \times 10^{-2} \exp(60,800/RT) \quad [8]$$

from Ref. (11)

The data expressed by Eq. [8] were repeated by Volpe, Peterson, and Reddy (12). Chen and Peterson (13) found for cobalt diffusing into NiO heated in air

$$D(\text{Co} \rightarrow \text{NiO}) = 9.12 \times 10^{-3} \exp(-54,160/RT) \quad [9]$$

Richards and Wagstaff (14) reported for diffusion of iron in nickel oxide heated in air

$$D(\text{Fe} \rightarrow \text{NiO}) = 1.81 \times 10^{-3} \exp(-44,500/RT) \quad [10]$$

Crow (7) studied the diffusion of iron in nickel oxide crystals cut from the same boule as that of Richards and Wagstaff. Crow found

$$D(\text{Fe} \rightarrow \text{NiO}) = 2.2 \times 10^{-3} \exp(46,200/RT) \quad [11]$$

for crystals heated under 1 atm of oxygen. All these data show much higher activation energies than we find. Crow's crystals contained about 275 ppm weight and he analyzed his diffusivity data in terms of impurity control. The crystals used in the present investigation contained orders of magnitude more impurities (see Table I). Therefore the data reported here are also impurity controlled and the activation energy is smaller than those of Crow (7) or of Richards and Wagstaff (14). Because the ionic radii of ferrous iron and nickel are approximately the same, one would expect similar activation energies for the

² For each square centimeter of area, 300Å of iron would amount to 2.5×10^{17} atoms of iron. This amount of iron should be less than the concentration of lattice defects initially present in an undoped NiO crystal. However, the concentration of impurities was much greater than this and hence the diffusion was impurity controlled (see later text).

diffusion of iron and of nickel in NiO provided both migrated via the same mechanism. Both appear to migrate via cation vacancies. We have no explanation at this time for our unusually low activation energies for iron diffusion except to note the very high concentration of impurities in the crystals.³

Final remarks concerning the use of the JSM-U-3 SEM with the x-ray wavelength dispersive analyzer are as follows. The peak to background ratio for the iron K α line is the major limitation of the SEM microprobe. The JSM-U-3 fully focusing wavelength dispersive spectrometer has a 670:1 peak to background ratio, which would result in a minimum detectable limit of 80 ppm for the background encountered. However, the precision of the analysis is a function of both the peak intensity and the background intensity, and, as shown in Fig. 2 the high background signal results in a relative error as great as 80% at the tail end of the diffusion profile.

The beam stability is very critical when long counting times are used. The SEM is not specifically designed for microprobe analysis, and the beam intensity will not remain constant for long periods of time. Counting periods in excess of 200 sec resulted in an error greater than the experimental error determined by multiple 10 sec counts, followed by beam alignment. The beam instability was particularly noticeable when returning to a previously counted area and re-counting without having continuously realigned the beam. An SEM equipped with a beam stabilizer would reduce the problem of beam intensity, as would using a conventional microprobe, where long term stability is a design feature. Our results suggest that the technique is much more rapid than the use of radiotracers but the scatter in the data inherent in this type of microprobe (see, e.g., Fig. 1) is much larger than that usually encountered in radiotracer determinations.

³ Note added in proof: The iron in the NiO may be trivalent under the high oxygen pressures. G. W. Weber (Ph.D. Thesis, The Pennsylvania State University (March 1975)) found for chromium diffusing into MgO, the activation energy under constant p_{O_2} is reduced from 70 (undoped) to 29.8 kcal/mole for Cu-doped MgO.

Acknowledgment

This work was supported by the Army Research Office, Durham, under Contract DAHC 04 70 C 0062.

Manuscript submitted June 21, 1973; revised manuscript received Oct. 7, 1974.

Any discussion of this paper will appear in a Discussion Section to be published in the December 1975 JOURNAL. All discussions for the December 1975 Discussion Section should be submitted by Aug. 1, 1975.

Publication costs of this article were partially assisted by Northwestern University.

REFERENCES

- J. B. Price and J. B. Wagner, Jr., *Z. Physik. Chem. N.F.*, **49**, 257 (1966).
- R. T. Grimely, R. P. Burns, and M. G. Inghram, *J. Chem. Phys.*, **35**, 551 (1961).
- W. C. Hahn, Jr. and A. Maun, *J. Phys. Chem. Solids*, **19**, 338 (1961).
- F. A. Kröger and H. J. Vink, "Solid State Physics," p. 307, Academic Press, New York (1956).
- N. G. Eror and J. B. Wagner, Jr., *Phys. Status Solidi*, **35**, 641 (1969).
- Y. D. Tretyakov and R. A. Rapp, *Trans. Met. Soc. AIME*, **245**, 1235 (1969).
- W. Crow, Ph.D. Thesis, Ohio State University (1969).
- M. T. Shim and W. J. Moore, *J. Chem. Phys.*, **26**, 802 (1957).
- J. S. Choi and W. J. Moore, *J. Phys. Chem.*, **66**, 1308 (1962).
- R. Lindner and A. Akerstrom, *Discussions Faraday Soc.*, **23**, 133 (1957).
- M. L. Volpe and J. Reddy, *J. Chem. Phys.*, **53**, 1117 (1970).
- M. L. Volpe, W. L. Peterson, and J. Reddy, *Phys. Rev.*, **B-4**, 1417 (1971).
- W. Chen and N. Peterson, *J. Phys. Chem. Solids*, **33**, 881 (1972).
- K. J. Richards and F. E. Wagstaff, *J. Phys. Chem.*, **70**, 1553 (1966).

Formation of Silica Films on Silicon Using Silane and Carbon Dioxide

William J. Kroll, Jr.* and Russell L. Titus*

Teletype Corporation, Subsidiary of Western Electric, Skokie, Illinois 60076

and J. B. Wagner, Jr.*

Department of Materials Science and Materials Research Center, Northwestern University, Evanston, Illinois 60201

ABSTRACT

The reaction of silane with carbon dioxide to form silica on silicon in the temperature range 700°-1100°C has been studied. The results of surface charge density (Q_{ss}) and breakdown voltage (E_{BD}) measurements on the silica film are discussed. Etch rates, weight density, and infrared spectra obtained for these films are compared with those exhibited by oxide films thermally grown with steam. The dependence of the reaction yield on reactor design is briefly discussed.

In the manufacture of planar semiconductor devices, silicon crystals with homogeneous and uniformly thick oxide layers are utilized. These layers are usually produced by oxidizing the silicon either in a moist oxygen or in a pure water vapor (steam) atmosphere at temperatures between 1000° and 1200°C (1). The substrate is a high purity, polished semiconductor crystal wafer approximately 0.014 in. thick, doped to the desired conductivity and carrier type. After production of the semiconductor crystal or dielectric layers (e.g., epitaxial silicon, polycrystalline silicon, silicon nitride, or alumina), it is desirable to deposit the oxide layer on the surface immediately, thereby avoiding the lengthy and expensive etching and purifying processes which precede conventional oxidation techniques. The advantages of this method have been demonstrated for reactions involving a metal halide such as silicon tetrachloride (2, 3).

Standard methods do not permit deposition of the silicon dioxide layer immediately following silane epitaxial growth, vapor phase etching, or dielectric film growth. When utilizing oxygen-containing gases, a lengthy, intermediate flushing with inert gas is required in order to purge the system and eliminate unwanted reactions. When gases containing water vapor are employed, reactions with the silicon halide or hydride residues remaining in the gas chamber or adsorbed on the apparatus walls are difficult to avoid even after prolonged flushing. The solid hydrolysis products of such reactions, primarily silicic acid, are carried by the gas current as a fine dust and settle on the blank silicon surfaces. It is impossible to produce an undisturbed oxide layer under such conditions. Therefore, the silica deposition is generally carried out in a separate reactor. Consequently, the silicon wafers must be chemically cleaned prior to insertion into the deposition apparatus; the complications associated with this two-step process are well known.

In contrast to experiments carried out in other types of reactors (4), the deposition method in the vertical "Pancake" production reactor shown in Fig. 1 permits deposition of silicon dioxide immediately after epitaxial growth, polycrystalline growth, silicon removal through a gaseous phase etch, or sequential dielectric film depositions. It is unnecessary to change the reactor or to carry out the cumbersome intermediate purging of the carrier gas since neither gas-forming materials nor materials hydrolyzing outside the high temperature zone are present. The immediate deposition of the silica on freshly formed, clean surfaces re-

sults in a very homogeneous, nonporous film of silicon dioxide. A silica layer thusly formed is very compatible with planar processing techniques.

At low temperatures, the carbon dioxide-silane mixture which initiates the deposition process is a dry, nonoxidizing gas. It is only in the high temperature zone of the chamber that the mixture reacts to form silica, which is in turn deposited on the substrate; the CO_2-SiH_4 mixture does not contribute to the direct oxidation of the silicon or to reaction of the silicon with the carrier gas. Because it eliminates the intermediate steps, this method is well suited to the production of semiconductor devices, e.g., silicon planar transistors, diodes, and integrated circuits, particularly where electrical properties must be controlled within close tolerances. The same method can be applied to the production of semiconductor structural components where the p-n junctions, which have been exposed through gaseous phase etching, are provided with a protective oxide layer to stabilize their characteristic

CHEMICAL VAPOR DEPOSITION EPITAXIAL GROWTH

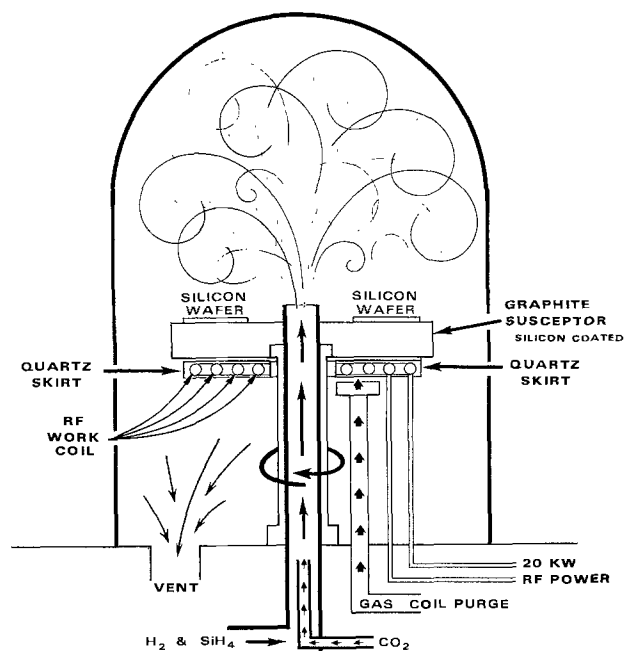


Fig. 1. Schematic drawing of the vertical reactor

* Electrochemical Society Active Member.

Key words: density, etching, breakdown voltage, chemical vapor deposition.

parameters, e.g., in the production of semiconductor structural components with mesa structures. The purpose of the present work was to study the formation of silica using silane and carbon dioxide and to compare the properties of the CVD silica with those of thermally grown silica.

Experimental

An Applied Materials Technology AMV 500 vertical epitaxial reactor was employed for the deposition. It holds six 1½ in. diameter silicon wafers on a silicon carbide coated graphite susceptor which rotates at 9 rpm and is inductively heated (Fig. 1); a 20 kW 450 kHz power supply provided the rf power. Substrate temperatures were measured with an infrared thermometer mounted at 45° with respect to the plane of the substrates. All temperatures cited are based on an emissivity correction factor of 0.70. The materials utilized inside the reactor head were either quartz, Teflon, or 316 stainless steel.

The silicon substrates were <111> oriented and doped with phosphorus to produce a resistivity of 3.5–7.0 ohm-cm. Following degreasing, the wafers were etched in hydrofluoric acid, scrubbed in a nonionic detergent, rinsed with 18 megohm water, and dried in a nitrogen stream. They were then loaded into the reactor and the temperature raised to 1100°C in a hydrogen atmosphere to remove contaminants remaining on the surface. After 5 min, the temperature was lowered to that desired for deposition and the silane and carbon dioxide introduced in a hydrogen carrier. All the gases were 4N purity or better. Flow rates were measured with mass flow meters. The gases were piped to the reactor head in 316 stainless steel lines. The hydrogen was purified and dried, and all gases were filtered through 0.45μ line filters prior to injection into the reactor. The carbon dioxide was injected concentrically with the silane-hydrogen mainstream (Fig. 1).

The oxide thicknesses on the silicon were measured by two methods: (i) ultraviolet-visible interference using a spectrophotometer with a specular reflectance attachment (5), and (ii) ellipsometry. The instrument used in the latter case also measured the index of refraction.

Results

Deposition rates.—The deposition rate of silica was studied as a function of the percentage of silane in the silane-hydrogen mixture, substrate temperature, reactor configuration, and carbon dioxide concentration. The first objective was to determine the flow rate at which the reaction ceased to be gas transport controlled. This flow rate was then used in all subsequent experiments. Figure 2 shows the results of these initial experiments at 900°C in which the carbon dioxide to silane ratio was maintained at 100:1. At low total flow

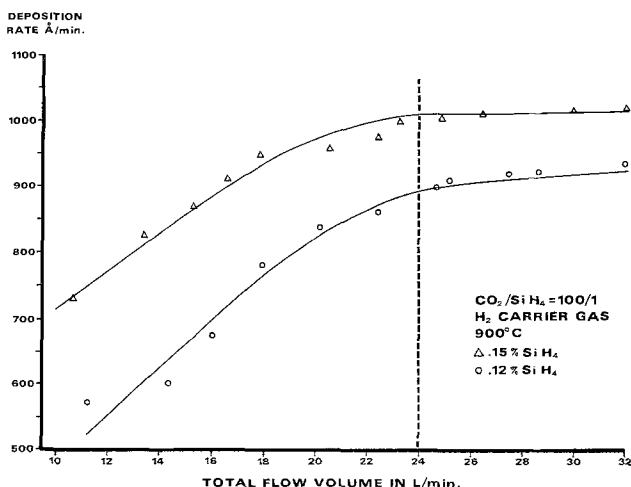


Fig. 2. Deposition rate of silica ($\text{\AA}/\text{m}$) vs. total flow

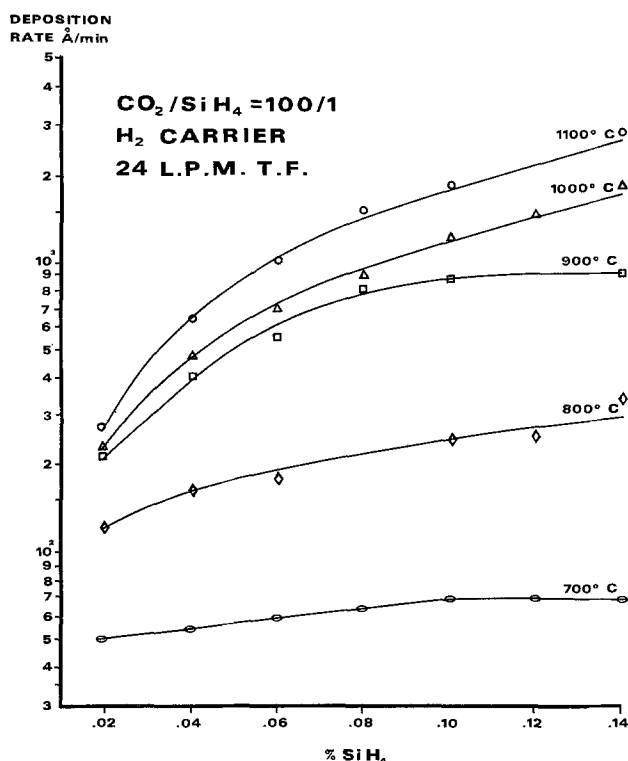


Fig. 3. Deposition rate of silica ($\text{\AA}/\text{min}$) vs. silane percentage in the gas phase. The total gas flow in liters per minute (LPM) amounted to 24.

rates, the deposition rate is a function of the flow rate, while at flow rates ≥ 22 liters/min the reaction is independent of flow rate (Fig. 3). A total flow rate of 24 liters/min was therefore chosen for all subsequent experiments¹ to insure that the reaction was not gas transport limited. A family of curves was then generated for deposition rate as a function of silane percentage. With the carbon dioxide to silane ratio fixed at 100:1, the temperature was varied from 700° to 1100°C, and deposition rates ranging from 50 to 3000 $\text{\AA}/\text{min}$ were observed. While the deposition rate was markedly dependent on temperature in the range between 700° and 900°C, considerably less dependence was observed between 900° and 1000°C. These data appear to agree quite well with those of Swann and Pyne (4), but if deposition rate is plotted as a function of $1/T$, differences between the two sets of data become apparent, as is discussed later.

The deposition rate was also determined as a function of carbon dioxide to silane ratio. At a given temperature with the percentage of silane constant, increasing amounts of carbon dioxide were added without achieving saturation with respect to the deposition rate. This is the same effect observed by Swann and Pyne, and our data are in good agreement with theirs.

Infrared spectra.—In order to investigate the densification effects reported by Pliskin and Lehman (6), the Si-O stretching bond at 1090 cm^{-1} was observed for various values of temperature and silane percentage using a blank silicon wafer from the same ingot as the sample in the reference beam. The intensity of this absorption band is a function of the bonding character, stoichiometry, density, and porosity of the films, whereas the band position is a function of porosity (density) and strain. The wave numbers are shifted to lower values for films of higher porosity and strain. The normalized bandwidth at half-maximum for the Si-O stretching band at various silane percentages as a function of temperature is shown in Fig. 4. Higher

¹ With the vertical "Pancake" reactor a calculation of the linear flow rate over the sample was not possible.

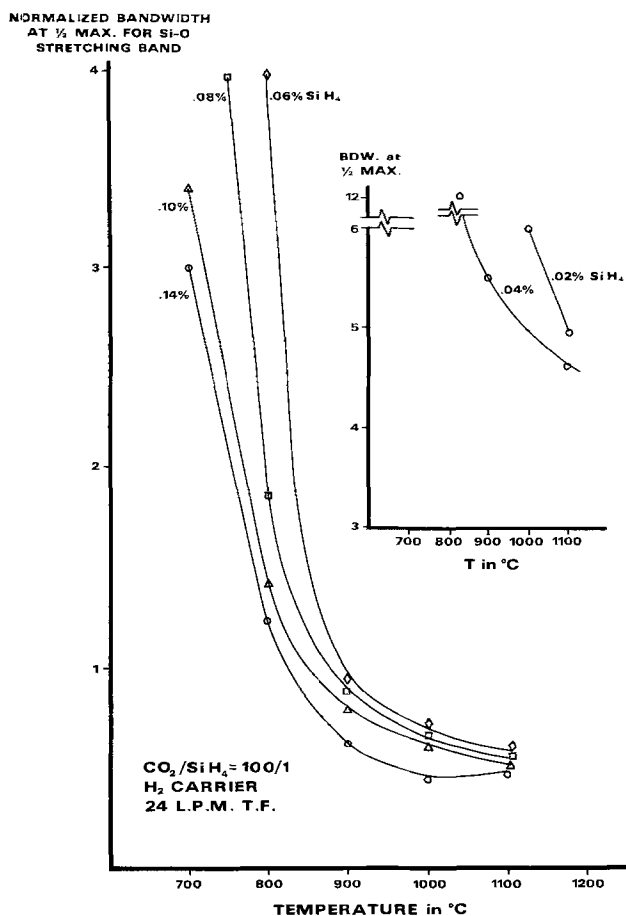


Fig. 4. Normalized bandwidth at one-half maximum of the Si-O stretching band as determined by infrared spectra vs. temperature of deposition. The insert shows similar data for the smaller concentrations of silane.

deposition temperatures consistently yielded narrower bandwidths implying the formation of denser and more stoichiometric films. Furthermore, as the silane percentage is increased, the silica film appears to become denser. For depositions carried out at the higher temperatures the normalized bandwidths at 1100°C are almost identical to those of a steam-grown thermal oxide sample measured at the same time (Fig. 5). Not only does the absorption band for Si-O stretching become more pronounced as the deposition temperature is increased, but it is also shifted to larger wave numbers. These data confirm the existence of the densification effects reported by Pliskin and Lehman (6).

Density.—Since the data obtained by infrared spectral analysis only permit qualitative determinations of the densification and stoichiometric effects, density was determined gravimetrically so that it could be correlated with deposition parameters. A second objective of this aspect of the work was to correlate the gravimetric results with those obtained from the infrared studies in the hope of quantifying the latter results since the infrared method is more readily applicable to semiconductor production processing. Both the gravimetric density and the infrared studies were performed on the same wafers, the gravimetric studies being carried out first. The diameters of the wafers were measured to a thousandth of an inch with a micrometer. The wafers were then cleaned as previously described and immediately weighed on an electrobalance situated in a dry box. They were then loaded into the reactor for deposition. Following the deposition process, the wafers were again weighed. An average weight change of approximately 37 mg was observed following deposition of a 16,000Å thick film, the weight change being measured to within 1%. The thickness of the film was measured to within 1% by a

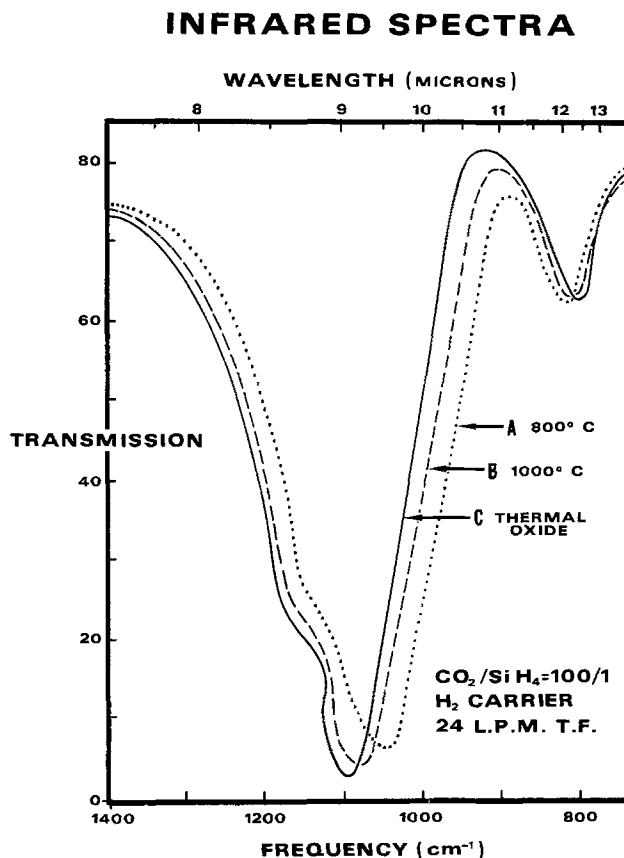


Fig. 5. Comparison of the infrared spectra for the silica deposited from silane and carbon dioxide (curves A and B) compared to that for a thermally grown oxide (1000°C in steam).

u.v. spectrophotometer. The density values should be accurate to within 2%. No allowance has been made for back side deposition which could conceivably result in an error on the order of 10-20%. Such back side oxidation of the wafer can occur because the contact between the wafer and the susceptor (holder) is not gastight; this has been observed by many investigators. However, in the present work adequate precautions were taken, and careful examination revealed no back side deposition. Some density values reported by other workers for thermally grown steam oxide are 11.5% higher than that for bulk silica. This increase may in part be attributed to this effect. Figure 6 shows the density as a function of the silane percentage at various temperatures. The values for fused silica (approximately 2.27 g/cm³) and thermally grown steam oxide have been inserted to permit direct comparison with those of the CVD oxides. As was predicted qualitatively by the infrared spectral data, the density increases as both deposition temperature and silane percentage are increased. Note that the slopes change at higher silane percentages and converge toward the bulk values. This effect is similar to that observed with the infrared data, in which the graph of the normalized bandwidth at half maximum vs. silane percentage exhibited nearly zero slope at high temperature and silane values. Densities of the deposited silica which are greater than the bulk density may be due to the presence of free silicon in the film. Infrared spectral studies revealed absorption peaks that could be attributed to the presence either of silicon or of water vapor. Free silicon could conceivably be present since polycrystalline or epitaxial silicon depositions can occur as low as 500°C (9). Electron microprobe studies on the film were attempted to determine if there were indeed traces of carbon or silicon; however, they were unsuccessful owing to the low concentrations and poor signal to noise ratio in such thin layers.

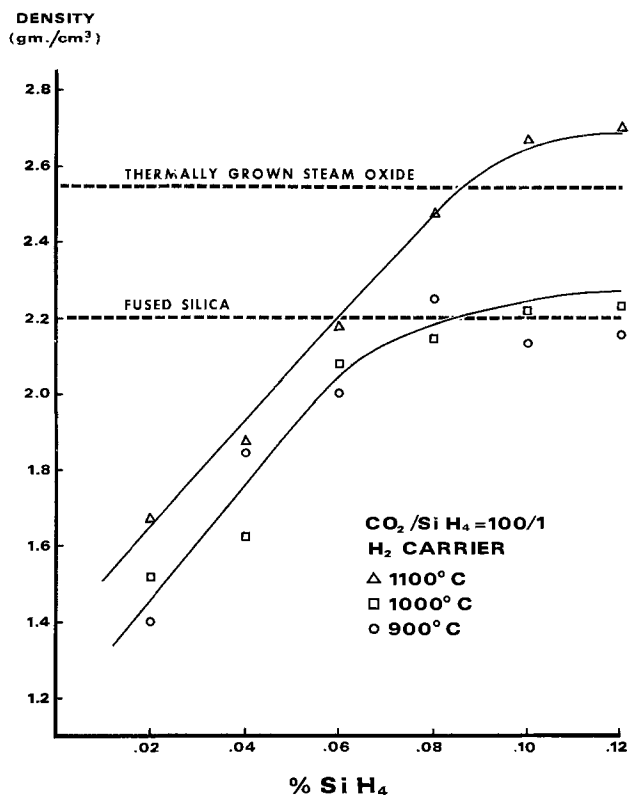


Fig. 6. Density of deposited silica films as a function of silane percentage as determined in the present study compared to values reported for thermally grown silica on silicon (1000°C in steam) by this laboratory and for fused silica. The higher values observed in the films may be due to the presence of free silicon. See text.

Etch rates.—The deposited silica used in deposition rate studies was subsequently used for the determination of etch rates. Etching was carried out in a polypropylene beaker with a 10:1 buffered hydrofluoric acid solution. The solution was maintained at 23°C, and the wafers were held in Teflon carriers. The etch rate vs. silane percentage (with the CO₂-SiH₄ ratio fixed at 100:1) was studied for various deposition temperatures. Some of these data are presented in Fig. 7. The data for 700°C were not plotted because they exhibited considerable scatter, and most of the etch rates were above 25 Å/sec.

For the higher temperatures and silane percentages, the etching characteristics of the CVD oxide approach

those of thermally grown steam oxides [the etch rate of the thermally grown oxide is 12.5 Å/sec (7) in buffered HF]. The etch rates are slightly shifted from the values given for thermal oxide just as the density data was shifted. The slower etch rates observed for CVD silica may be attributed to the presence of small amounts of free silicon in the vapor phase deposited silica, as was previously noted in the infrared observations. In the etch rate experiments, the oxide was considered to be completely removed when the wafer surface became completely hydrophobic. Our etching results do not agree with those published by Swann and Pyne (4). Their CVD etch rates are all greater than those of thermally grown oxide, with the maximum etch rate occurring for films deposited at 900°C. This discrepancy may be a result of their reactor design since upstream decomposition of the gases may have occurred and/or their films may have been less dense. Our reactor with its concentric injection was specifically designed to prevent premature reaction and decomposition.

Electrical properties.—The electrical properties of the CVD silica which were measured were breakdown voltage (E_{BD}) and surface-state charge density (Q_{SS}). These two parameters were chosen in preference to others because they yield important initial information concerning the electrical properties of a given dielectric material (8). The method used to obtain Q_{SS} was the conventional capacitance-voltage plot of a metal-oxide-semiconductor structure (MOS) (9, 10). Silica on the order of 1800Å was deposited on the test wafers and the film thickness measured. The wafers were masked with a metal mask containing 0.025 in. diameter holes and a 15,000Å layer of aluminum deposited utilizing an electron beam gun. After deposition of the aluminum, the wafers were annealed in a nitrogen atmosphere at 460°C to minimize damage due to the electron beam (11) and the diameters of the Al dots were measured. Capacitance as a function of voltage was then determined; these data are presented in Table I. It is interesting that 63% of the values of Q_{SS} lie below $2 \times 10^{11}/\text{cm}^2$; this compares favorably with the average value of $2.5 \times 10^{11}/\text{cm}^2$ determined at the same time for thermally grown steam oxides. Q_{SS} never exceeded $4.35 \times 10^{11}/\text{cm}^2$, nor did the wafers exhibit any room temperature hysteresis when biased from +50 to -50 VDC. Values of Q_{SS} were also plotted as a function of silane percentage to determine whether Q_{SS} changes with deposition temperature and silane percentage (CO₂/SiH₄ = 100/1). No trend was discerned.

ETCH RATE vs. % SiH₄

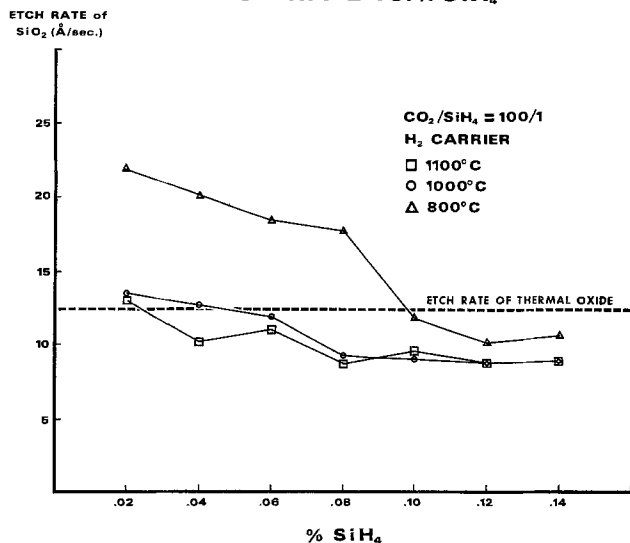


Fig. 7. Etch rate of SiO₂ (Å/sec) vs. silane percentage for the deposited films.

Table I. Frequency distribution of Q_{SS} *

From	Up to but not including	F	Per cent frequency
1.0×10^{10}	1.50×10^{10}	0	0
1.5×10^{10}	3.50×10^{10}	3	6.52
3.50×10^{10}	6.00×10^{10}	1	2.17
6.00×10^{10}	8.50×10^{10}	5	10.87
8.50×10^{10}	1.10×10^{11}	11	23.91
1.10×10^{11}	1.35×10^{11}	6	13.04
1.35×10^{11}	1.60×10^{11}	4	8.70
1.60×10^{11}	1.85×10^{11}	3	6.52
1.85×10^{11}	2.10×10^{11}	0	0
2.10×10^{11}	2.35×10^{11}	2	4.35
2.35×10^{11}	2.60×10^{11}	2	4.35
2.60×10^{11}	2.85×10^{11}	0	0
2.85×10^{11}	3.10×10^{11}	4	8.70
3.10×10^{11}	3.35×10^{11}	2	4.35
3.35×10^{11}	3.60×10^{11}	2	4.35
3.60×10^{11}	3.85×10^{11}	0	0
3.85×10^{11}	4.10×10^{11}	0	0
4.10×10^{11}	4.35×10^{11}	1	2.17
4.35×10^{11}	4.60×10^{11}	0	0
Number of variates		46	
Arithmetic mean of Q_{SS}		1.576×10^{11}	
Standard deviation		0.994	

* Q_{SS} is defined as the charge per square centimeter. It is the number of coulombs per square centimeter divided by the electronic charge per particle.

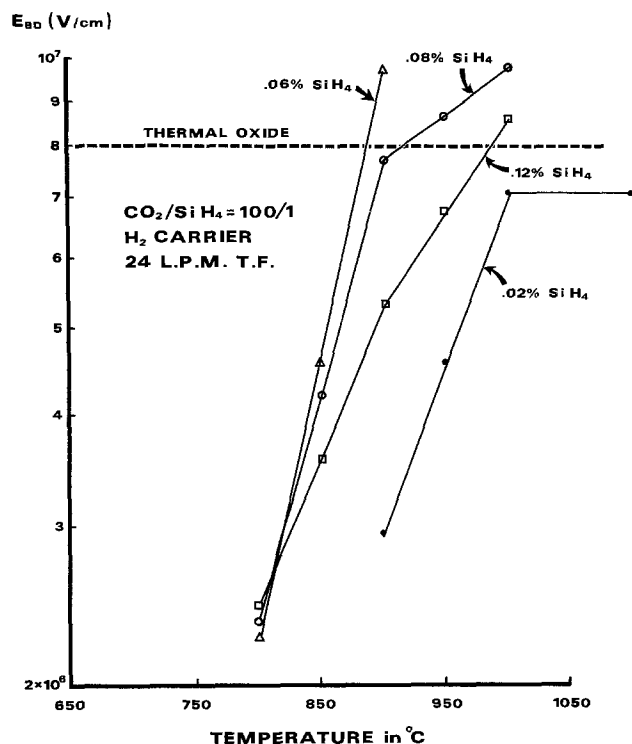


Fig. 8. Plot of breakdown voltage (E_{BD}) vs. temperature for deposited films. Also shown are average values for thermally grown silica films determined in the present study.

The breakdown voltage, E_{BD} , for the CVD grown silica wafers was measured next along with that of the thermally grown steam oxides (Fig. 8). E_{BD} is very sensitive to the deposition temperature; as the temperature increases, the breakdown voltage approaches that of the thermal oxide. When this effect is correlated with the density increase observed with increasing deposition temperature, one can predict that if the infrared spectra is intense and skewed toward 1090 cm^{-1} and the etch rate is low, the film will have good breakdown properties (i.e., large values of E_{BD}). Breakdown voltages greater than 10^7 V/cm could not be measured because of power supply limitations; however, results indicate that most of the films deposited at temperatures above 1000°C and silane percentages greater than 0.06% could have $E_{BD} > 10^7\text{ V/cm}$.

Mechanical properties.—All silica films deposited showed good adhesion with little or no surface irregularity. The films deposited from the reaction of carbon dioxide and silane showed no cracking in the 20,000–40,000Å thickness range, whereas films prepared using oxygen and silane crack quite badly at thicknesses approaching 20,000Å (12).

The silica films CVD deposited from carbon dioxide were also heat cycled at temperatures up to 1200°C without snapping the silicon substrate; many of the silica films prepared from oxygen and silane crack under these conditions. These slices were also subjected to scratch tests and demonstrated good film adhesion without cracking.

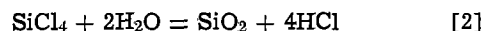
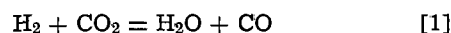
The pinhole density in oxide films with thicknesses of 1500–2000Å was also measured for silica films deposited at silane percentages from 0.02 to 0.14% and temperatures ranging from 700°C to 1100°C . These measurements utilized the electrophoresis effect in which copper deposits at the pinholes. These deposits can be counted and a defect density calculated. In practice, the defect density was measured by counting the sites where hydrogen bubbles were liberated from the plating reaction. No meaningful relationships between defect density and silane percentage or temperature could be ascertained. It is conjectured that defect

density is a function of deposition thickness rather than of the deposition parameters. For a given set of deposition parameters, a total of thirty wafers was deposited with varying thicknesses of silica and the resultant data curve fitted by computer to yield the following equation: $Y = A + (B/X)$, where $Y = \text{defects/cm}^2$, $X = \text{silica thickness in angstroms}$, $A = 0.571548$, and $B = 13,377.6$. Typical values of the defect density range from 24–30 defects/cm² for a film of 500Å thickness to 2–3 defects/cm² for CVD films measuring 5000–6000Å. This compares with defect densities for the thermal oxide films ranging from 30 defects/cm² for a 500Å film to 4–5 defects/cm² for films of 5000–6000Å thickness.

The refractive index of the CVD silica films was found to be 1.450 ± 0.005 . Thermally grown and silane-oxygen deposited silica films exhibited refractive indexes of 1.460 and 1.450, respectively.

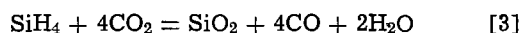
Thermodynamics and Reactor Design

The reaction of CO_2 , SiCl_4 , and H_2 to form silica has been proposed by Tung and Caffrey (2), Steinmaier and Bloem (3), and others as proceeding in two steps



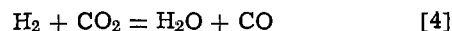
The silica is therefore formed by hydrolysis of the halide. These authors realized that intermediate reaction steps must exist.

From thermodynamic considerations (13), CO_2 and silane should react to form SiO_2 and CO according to the reaction

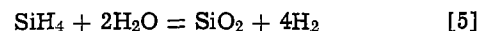


$$\Delta F^\circ = -115.019\text{ kcal/mole (13)}$$

The water formed during the reaction may hydrolyze further silane and thus speed deposition rates. Tests conducted with monocrystalline silicon, however, indicate that in a hydrogen carrier the reaction may proceed in two steps, i.e.



and



Swann and Pyne (4) used argon as a carrier gas to demonstrate that the reaction does not proceed by the water-gas reaction alone. Their results showed an even greater deposition rate with argon as the carrier gas rather than hydrogen. The higher deposition rates in argon may be due to the fact that the hydrogen carrier may act to inhibit either decomposition or hydrolysis of the silane as would be expected from mass action principles. This suggestion is consistent with the observation that the films formed by Swann and Pyne in an argon carrier gas contained free silicon which affected the dielectric loss and etch rates of the film. It may therefore be advantageous to use hydrogen despite the slower deposition rates achievable in order to minimize the decomposition of silane and subsequent formation of free silicon. The one-step reaction of silane and carbon dioxide is thought to be reasonable by Swann and Pyne; however, future studies should be carried out with silane and steam to determine the rate of hydrolysis of the silane.

In the present reactor design, it is desirable for the carrier gas and oxidizing agent to flow in an umbrella-type circular flow as shown in Fig. 1. Concentric injection of the oxidizing agent into the carrier gas flow is also important for control of both film uniformity and deposition rate. Typically, film thickness was uniform to $\pm 5\%$ from wafer to wafer and $\pm 7\%$ from run to run. When the injection nozzle was changed in either orifice size or in height, the deposition rate changed drastically; therefore, the nozzle was set for the maximum deposition rate in all experiments. Reducing the orifice size minimized bell jar deposition

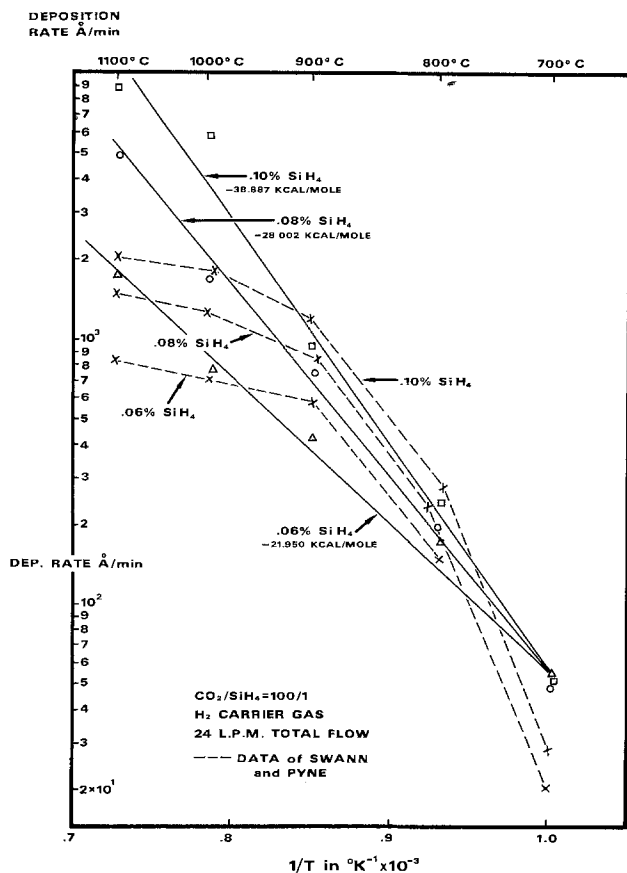


Fig. 9. Arrhenius plot of deposition rates vs. $1/T$ for data obtained both in the present study and by Swann and Pyne (4).

but also reduced the deposition rate at the substrates. Concentric injection of the gas was employed to minimize the upstream decomposition encountered by previous authors; the results shown in Fig. 9 reflect the success of this technique. The dashed lines in Fig. 9 represent the data of Swann and Pyne (4), and the solid lines represent data taken on films deposited in the vertical reactor previously described. The reactions in the concentric injection reactor yield normal Arrhenius plots from which meaningful activation energies can be calculated. The deposition rates obtained with the concentric injection converge at low temperatures. These results indicate that there may be more than one rate-determining step in the reaction, all of which are temperature dependent. However, this question has not yet been resolved. The data of Swann and Pyne which yield curved lines on the Arrhenius plot may be attributed to their reactor design because the gases were free to mix at a considerable distance from the substrates and to travel in almost laminar fashion past the heated substrates. This long path length probably enhances the upstream decomposition effects those authors observed.

Summary and Conclusions

The rate-determining step for the reaction between silane and carbon dioxide depends on temperature. The reactor design is important in controlling the reaction rate and deposition characteristics of the films. The deposited films exhibit excellent adhesive and mechanical properties, much the same as thermally grown steam oxides.

The MOS capacitance-voltage plots for all cases studied indicate that the films have properties adequate for gate passivation or deposited field oxide usage.

The surface charge density, Q_{ss} , was equal to or less than $1.0 \times 10^{11} \text{ cm}^{-2}$; therefore, the oxide may be used in composite deposited gate structures for MOS. Furthermore, there are strong correlations between the increased E_{BD} and the deposition temperature, silane percentage, and film density.

Oxides deposited by this reaction exhibit etch rates, indices of refraction, and densities almost identical to those of thermally grown steam oxide. Therefore, an oxide deposited by this technique can be substituted for thermally grown steam oxide without compromising the properties. In addition, the technique achieves a significant saving in processing time due to the high deposition rate of 1000 Å/min obtainable with the reaction of silane and carbon dioxide. Thus, the time required to deposit a 15,000 Å MOS field oxide by this technique would be 7-15 min while that required for thermal oxidation in steam at 1100°C would be 7-8 hr.

The chemical compatibility of this reaction with polycrystalline silicon depositions, silane-ammonia reactions, epitaxial silicon deposition, and aluminum trichloride-carbon dioxide reactions permits sequential depositions in one reactor without the tedious intermediate cleaning and purging steps, thus eliminating the chance of contamination occurring between layers. These sequential depositions could be utilized to obtain film combinations for device applications, e.g., silicon dioxide on silicon nitride (or vice versa), silicon dioxide on polycrystalline silicon for use as an etch mask or protective layer, silicon dioxide on epitaxial silicon for use as a diffusion mask, and silicon dioxide on alumina for use as an etch mask or composite gate structure.

Acknowledgment

This paper is based, in part, on the Master's Thesis of William J. Kroll, Jr., Northwestern University, Evanston, Illinois, 1971.

Manuscript submitted May 31, 1974; revised manuscript received Sept. 23, 1974. This was Paper 13 presented at the Houston, Texas, Meeting of the Society, May 7-11, 1972.

Any discussion of this paper will appear in a Discussion Section to be published in the December 1975 JOURNAL. All discussions for the December 1975 Discussion Section should be submitted by Aug. 1, 1975.

Publication costs of this article were partially assisted by Teletype Corporation.

REFERENCES

- R. M. Burger and R. P. Donovan, "Silicon Integrated Device Technology," Vol. 1, Prentice-Hall, Inc., Englewood Cliffs, N. J. (1967).
- S. K. Tung and R. E. Caffrey, *Trans. Met. Soc. AIME*, **233**, 572 (1965).
- W. Steinmaier and J. Bloem, *This Journal*, **111**, 206 (1964).
- R. C. Swann and A. E. Pyne, *ibid.*, **116**, 1014 (1969).
- R. Reizman and W. Van Gelder, *Solid State Electron.*, **10**, 625 (1967).
- W. A. Pliskin and H. S. Lehman, *This Journal*, **112**, 1013 (1965).
- D. A. Eaton, Teletype Corporation, Technical Report, Aug. 28, 1970.
- A. S. Grove, "Physics and Technology of Semiconductor Devices," John Wiley & Sons, Inc., New York (1967).
- A. S. Grove, B. E. Deal, E. H. Snow, and C. T. Sah, *Solid State Electron.*, **8**, 145 (1965).
- K. H. Zaininger and F. P. Heiman, *Solid State Technol.*, **13**, 49 (1970).
- D. A. Eaton, Teletype Corporation, Technical Report, Aug. 28, 1970.
- C. F. Covington, Teletype Corporation, Private communication, August 1970.
- JANEF Thermochemical Tables, Dow Chemical Co., Midland, Mich. (1965).

Kinetics of the Thermal Oxidation of Silicon in O₂/N₂ Mixtures at 1200°C

D. W. Hess* and B. E. Deal*

Research and Development Laboratory, Fairchild Camera and Instrument Corporation, Palo Alto, California 94304

ABSTRACT

The thermal oxidation kinetics of (100) and (111) oriented silicon in several oxygen/nitrogen mixtures ranging in oxygen partial pressure from 0.02 to 1.0 at 1200°C have been investigated. The parabolic rate constant B and the linear rate constant B/A varied linearly with respect to the oxygen partial pressure, while τ , a factor which accounts for an initial accelerated oxidation rate during dry oxidation of silicon, varied inversely with the oxygen partial pressure.

During the past ten years, numerous investigations have been reported concerning the thermal oxidation of silicon under dry oxidation conditions (1-9). However, only three of these studies have dealt with oxidation in oxygen/nitrogen mixtures under flow conditions (6-8), and none of these three have utilized a temperature above 1000°C, where the silicon oxidation kinetics should be primarily a diffusion-controlled reaction. Consequently, this study was undertaken to investigate the thermal oxidation of silicon in several oxygen/nitrogen mixtures at 1200°C.

According to the theory of silicon oxidation as developed by Deal and Grove (1), the thermal oxidation kinetics may be expressed in the general form

$$x_0^2 + Ax_0 = B(t + \tau) \quad [1]$$

where x_0 = oxide thickness in μ , A = constant in μ , B = parabolic rate constant in μ^2/hr , B/A = linear rate constant in μ/hr , t = oxidation time in hr, τ = correction factor which accounts for an observed initial accelerated growth rate in dry oxygen, in hr. B is further defined by Ref (1)

$$B \equiv 2D_{\text{eff}}C^*/N_1$$

where D_{eff} = effective diffusion coefficient of the oxidizing species in the oxide, C^* = equilibrium concentration of oxidant in the oxide, which, according to Henry's law, is directly proportional to the oxidant partial pressure, N_1 = number of oxidant molecules incorporated into a unit volume of the oxide, and τ by

$$\tau \equiv (x_i^2 + Ax_i)/B$$

where x_i is the effective oxide thickness initially present on the silicon surface. From these definitions, it can be seen that B should vary directly, and τ inversely, with the oxygen partial pressure, *i.e.*

$$B \propto P \text{ and } \tau \propto \frac{1}{B} \propto \frac{1}{P}$$

Also, the constant A should be independent of oxygen partial pressure, since it depends only on the diffusion coefficient of the oxidizing species and the rate constants of the reactions occurring at the gas-oxide and oxide-silicon interfaces (1).

Experimental Procedure

The silicon wafers used in this investigation were 4-6 ohm-cm, phosphorus doped, with (100) and (111) orientation. They were cleaned using sulfuric-peroxide, aqua regia, a hydrofluoric acid dip, and several de-ionized water rinses. Oxidations were carried out at 1200°C in a resistance-heated furnace containing an ultrahigh purity Mullite liner and a fused quartz tube. The wafers were pushed into the furnace in the oxy-

gen-nitrogen atmosphere and after various times were slow pulled (2 min) out of the furnace where they were allowed to cool in the O₂/N₂ mixture in which they had been oxidized. It should be noted that this procedure differs from the one utilized in Ref. (1), where the oxidations were stopped after the allotted oxidation time by pulling the samples very rapidly from the oxidation furnace tube.

The flow meters utilized in this study were calibrated using a Matheson Electronic Mass Flowmeter and a Porter-Vol-U-Meter. The total flow rate was 1 liter/min, which corresponded to a gas velocity of ~ 1 cm/sec. The oxygen and nitrogen used were from a liquid source and were further dried and filtered by passage through a Matheson Model 451 gas purifier.

The oxide thicknesses were measured with an Applied Materials (AME-500) ellipsometer. The reproducibility of the oxide thicknesses over the range investigated was $\pm 4\%$.

The contamination level present was determined for each oxidation by fabrication of MOS capacitors, and bias-temperature stressing them under a field of $\pm 5 \times 10^5$ V/cm at 300°C for 3 min. The mobile ion concentration ranged from less than 3×10^{10} cm⁻² for short (under 4 hr) oxidation times to 8×10^{10} cm⁻² for 16 hr oxidation in the various O₂/N₂ mixtures.

Results and Discussion

A log-log plot of thickness *vs.* time for the thermal oxidation of silicon in several O₂/N₂ mixtures at 1200°C is shown in Fig. 1. The 100% curve agrees well with that reported in Ref. (1), except for the shortest oxidation times, where the present oxide thicknesses are approximately 50Å greater than the previous work (1). This discrepancy is probably due to the different techniques utilized to remove the samples from the furnace after oxidation, *i.e.*, slow pulling in the oxidation ambient *vs.* rapid cooling. The plots in Fig. 1 are for (100) orientation, however, the thickness of the oxides grown on (100) and (111) silicon wafers differed by less than 2% over all oxidation times and mixtures. This, along with the fact that the slopes of the lines for the thicker oxides in Fig. 1 are very close to 0.5, indicates that dry oxidation of silicon is controlled mainly by diffusion of the oxidant across the oxide. It should be noted that the 2% mixture shows some scatter due to the fact that it was difficult to maintain the exact flow settings for such a small flow rate over long periods of time.

As indicated previously, an initial increased oxidation rate is observed during the dry oxidation of silicon. To obtain the correction factor τ , which accounts for this initial oxidation, a linear plot was made of oxide thicknesses *vs.* time, and the curves extrapolated back to zero oxide thickness (1). The extrapolated curves crossed the oxide thickness axis at $150 \pm 30\text{Å}$ for each oxidation mixture investigated.

* Electrochemical Society Active Member.

Key words: oxidation, silicon kinetics, oxygen partial pressure.

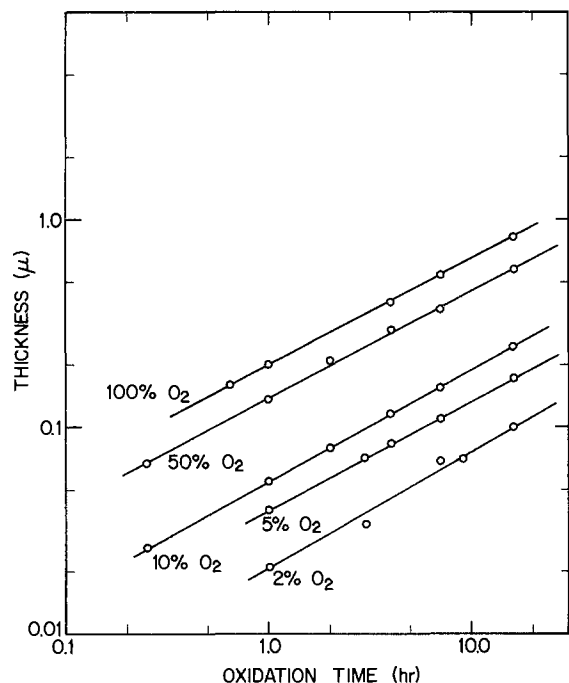


Fig. 1. Oxide thickness vs. time for the oxidation of (100) and (111) oriented n-type silicon in O_2/N_2 mixtures at $1200^\circ C$.

The resulting τ values are shown in Table I, along with the values obtained by using the numbers given by Deal and Grove (1) for 100% O_2 oxidation, and assuming that $\tau \propto 1/P$. The agreement is quite good with the possible exception of the 2% value, which, as stated previously, is probably due to a variation in the composition of the 2% mixture.

If x_0 is plotted vs. $(t + \tau)/x_0$ for each oxygen partial pressure, the slope and intercept of the resulting lines give B and $-A$, respectively (1). These values, obtained from a least squares analysis of the present data, are given in Table I. Each of the measured values of B agrees quite closely with the values predicted by the theory. The values of A should be independent of the oxygen partial pressure, and indeed, no trend is observed, although there is a reasonable amount of scatter. The largest deviation from the value of 0.04μ obtained from the theory (other than the 2% mixture) is observed for O_2 partial pressures of 0.50 and 1.0. This is probably due to the fact that the present oxidations were pushed (1 min) and pulled (2 min) in the oxidizing mixture, rather than quenched after oxidation as in Ref. (1). The present procedure would cause the shorter oxidation times to yield thicker oxides than if the oxidation was terminated immediately after the allotted oxidation time by rapid cooling. This effect would be most important for large O_2/N_2 ratios. In order to determine the effect a small decrease in oxide thickness would have on the value of A , a 5% change in the oxide thickness obtained after 15 min oxidation in 50% O_2/N_2 was incorporated into the least squares data in place of the previous

Table I. Comparison of calculated and measured values of constants τ , B , and A from oxidation at $1200^\circ C$ in O_2/N_2 mixtures

Oxygen partial pressure	τ (hr)		B (μ^2/hr)		A (μ)	
	Calc*	Mea-sured	Calc*	Mea-sured	Calc*	Mea-sured
1	0.027	0.03	0.045	0.043	0.04	0.025
0.50	0.054	0.06	0.0225	0.0213	0.04	0.019
0.10	0.27	0.29	0.0045	0.0045	0.04	0.049
0.05	0.54	0.51	0.00225	0.0022	0.04	0.038
0.02	1.35	1.09	0.0009	0.0010	0.04	0.076

* These values were calculated by assuming $\tau \propto 1/P$, $B \propto P$, and $A \neq f(P)$, and using the values of τ , B , and A obtained from Ref. (1) for an oxygen partial pressure of 1 (100% O_2) at $1200^\circ C$.

value. This generated values for A and B of 0.024μ and $0.0216 \mu^2/hr$, respectively. Thus a small change in the oxide thickness has little effect on B , but a substantial effect on A for short oxidation times and thin oxides.

A log-log plot of B and τ vs. oxygen partial pressure is shown in Fig. 2. The slopes of the lines for B and τ are 1 and -1 , respectively, which is in agreement with the theoretical oxygen partial pressure dependence of these quantities. The values of B determined in this investigation agree quite closely with those reported by Flint (10), who determined the oxygen partial pressure dependence of B at $1200^\circ C$ above a partial pressure of 0.25, using oxygen/argon mixtures. Also, it should be mentioned that since the linear rate constant is defined as B/A , it is apparent that it will show the same pressure dependence as B . There is some scatter observed, however, due to the variation in A .

Summary

The thermal oxidation kinetics of silicon in several O_2/N_2 mixtures at $1200^\circ C$ has been investigated. Little or no difference in oxidation rate was observed between (100) and (111) oriented silicon wafers, indicating that the oxidation of silicon at $1200^\circ C$ under various oxygen partial pressures is primarily a diffusion controlled reaction. It was also observed that the parabolic rate constant B and the linear rate constant B/A , vary proportionately with the oxygen partial pressure, while τ , a factor which accounts for an initial accelerated oxidation rate during dry oxidation of silicon, varies inversely with the oxygen pressure. These results agree with the pressure dependence predicted by the theory of silicon oxidation as reported by Deal and Grove.

Acknowledgments

The authors wish to acknowledge the assistance of Julia Bien in the experimental portion of this work.

Manuscript submitted Sept. 24, 1974; revised manuscript received Nov. 15, 1974.

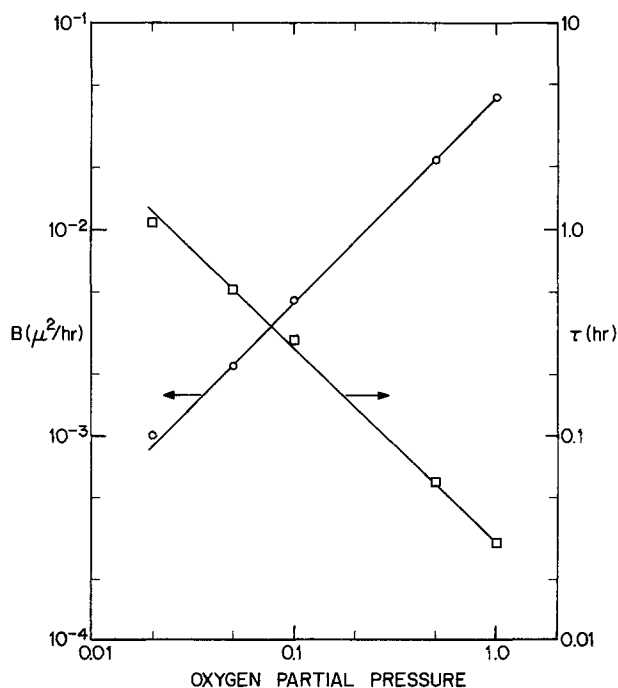


Fig. 2. Dependence of the parabolic rate constant B and the factor τ , introduced into the general oxidation equation to account for an initial accelerated oxidation rate in dry oxygen, on the oxygen partial pressure.

Any discussion of this paper will appear in a Discussion Section to be published in the December 1975 JOURNAL. All discussions for the December 1975 Discussion Section should be submitted by Aug. 1, 1975.

Publication costs of this article were partially assisted by the Fairchild Camera and Instrument Corporation.

REFERENCES

1. B. E. Deal and A. S. Grove, *J. Appl. Phys.*, **36**, 3770 (1965).
2. P. J. Burkhardt and L. V. Gregor, *Trans. Metl. Soc. AIME*, **236**, 299 (1966).
3. E. A. Gulbransen, K. F. Andrew, and F. A. Brasart, *This Journal*, **113**, 834 (1966).
4. A. G. Revesz and R. J. Evans, *J. Phys. Chem. Solids*, **30**, 551 (1969).
5. A. M. Goodman and J. M. Breece, *This Journal*, **117**, 982 (1970).
6. J. A. Aboaf, *ibid.*, **118**, 1370 (1971).
7. Y. J. van der Meulen, *ibid.*, **119**, 530 (1972).
8. T. Smith and A. J. Carlan, *J. Appl. Phys.*, **43**, 2455 (1972).
9. F. P. Fehlner, *This Journal*, **119**, 1723 (1972).
10. P. S. Flint, Paper No. 94 presented at Electrochemical Society Meeting, Los Angeles, California, May 6-10, 1962.

Technical Notes



A Comparative Study of Microwave and Radiofrequency Plasma Polymerization of Benzene

M. Duval* and A. Théorêt*

Hydro-Quebec Institute of Research, Varennes, Quebec, Canada

Chemical reactions in electrical discharges have been studied extensively over the past 15 years. The very thin polymer films that can thus be prepared have been given a number of new applications. For example, such films have been used as optical light guides (1). Several books and review articles covering all or part of the subject have been published recently (2-5). They contain many references to earlier work, which is abundant, particularly that concerning the reaction of aromatic hydrocarbons. However, the specific influence of the various reaction parameters, particularly discharge frequency, is not yet quite elucidated. In the case of aromatic hydrocarbons, some authors have tried to differentiate between radiofrequency and microwave discharges, by comparing published results obtained in radiofrequency discharges to those obtained in microwave discharges (6-9). The conclusions thus given are uncertain because reactor designs were not the same in the compared systems. For instance, in a work where the same reactor design was used with toluene as monomer, pressure was not kept constant, and no clear differences between radiofrequency and microwave could be evidenced (10). In another work with the same reactor design and benzene, the formation of diphenyl was shown to be more important in radiofrequency discharges than in microwave discharges, but the formation of the other reaction products, including polymers, was not studied (11).

In the present work, the same reactor design and controlled values of the other reaction parameters (pressure, flow rate, and power), have been used with benzene as monomer. Attention has been given to the formation of oligomers and polymers rather than to the formation of smaller molecular weight compounds, which is generally much less important and reproducible (12). And in order to understand the mechanism of the chemical reactions leading to polymer formation, the nature and the amount of the reactive

species formed in the discharge have been investigated. Such information has been obtained so far mainly from indirect identification methods, such as those relating electrical discharge reactions to the more well-known radiolysis or photochemical reactions (6, 13), or those deducing the nature of the intermediate species from the composition of the final products (7-9). Direct identification methods such as ESR, mass, or emission spectroscopy, are more reliable. However, only small plasma radicals have been studied by ESR spectroscopy (14), and the identification of some plasma species may be difficult with mass spectroscopy because of fragmentation processes (5). Emission spectroscopy has therefore been chosen in the present study.

Experimental

A schematic representation of the experimental setup used is shown in Fig. 1. Monomer vapor was admitted at regulated pressure and flow rate in the small, vertically mounted (9 mm inner diameter) quartz tube. Plasma was maintained in the upper end of the tube by means of a microwave cavity or radiofrequency fed copper sleeve electrodes. The Raytheon microwave generator and the Tracerlab radiofrequency generator used operated at 2540 and 13.56 MHz, respectively. Plasma emission spectra were observed through a quartz window and recorded from 7000 to 2000Å by means of a Cary 17 spectrophotometer equipped with a RCA 1P28 photomultiplier. Rearrangement products of the monomer molecules were deposited on a fixed circular target placed above the discharge zone and the films thus obtained were characterized by the ATR technique, with a Perkin Elmer Model 180 infrared spectrophotometer. Infrared and emission spectra obtained with similar reaction conditions were quite reproducible. Films soluble in tetrahydrofuran solvent were analyzed by gel permeation chromatography with a set of low porosity styragel columns, as described before (12). Products in the cold traps were analyzed by gas chromatography on SE 30 columns.

* Electrochemical Society Active Member.
Key words: thin films, electrical discharge, plasma emission, fragmentation.

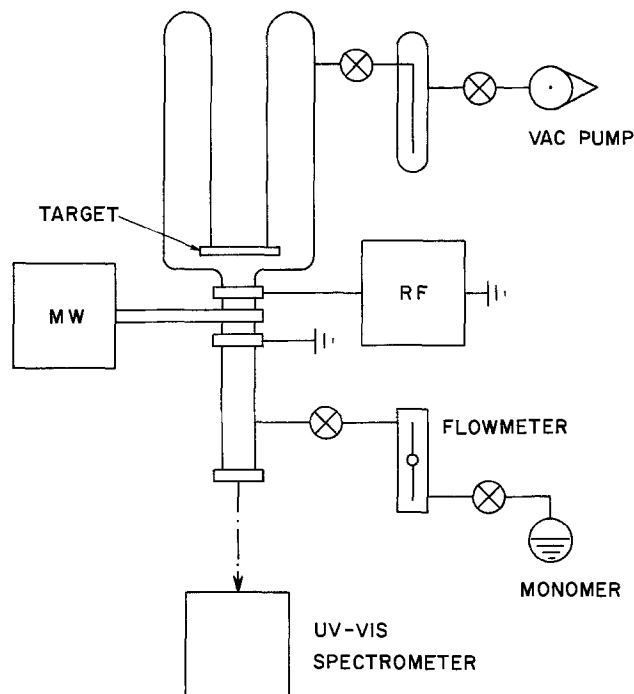


Fig. 1. Schematic representation of glow discharge reaction system. RF, radiofrequency; MW, microwave.

Several combinations of pressure and power were studied, from those below which the discharges cannot be sustained up to those above which carbonization of films occurs. Typical values of pressure and power range were from 0.2 to 2.0 Torr and from 15 to 100W, respectively. It was found convenient, as is usually done in plasma chemistry, to combine the values of monomer pressure P and power W supplied by the generators, and to consider the power-to-pressure ratio (W/P) as an indication of the energy given to the plasma. The greater the value of the W/P ratio, the more energetic is the plasma.

Results and Discussion

Films obtained with values of the W/P ratio larger than 200 are insoluble in most solvents, indicating a high degree of cross-linking. The compounds contained in soluble films cover a broad range of molecular weights, the amount of high molecular weight materials and compounds with sizes related to those of terphenyl and substituted benzenes being more important in the case of microwave discharges, as shown in Fig. 2. Large quantities of unreacted benzene and only small quantities of biphenyl, toluene, phenyl acetylene, indene, and styrene were found in the cold traps. The relative amounts of the cold-trapped products change only slightly with the W/P ratio, and biphenyl is the main cold-trapped product in the case of radiofrequency discharges.

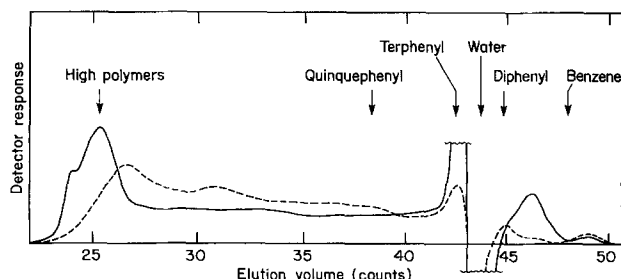


Fig. 2. GPC spectra of plasma produced polymers: —, MW; ---, RF; $W/P = 100$; concentration, 0.2% THF. The elution volumes of model compounds have been given as a reference of molecular size.

The infrared spectra represented in Fig. 3 are typical spectra of plasma-produced polymer films, containing the prominent features of all the obtained spectra. There are several differences among these spectra. The main one is the variable intensity of the main aromatic bands at 3020, 1600, and 1460 cm^{-1} and of the main aliphatic bands at 2920, 1450, and 1370 cm^{-1} . The ratios of the heights of these aromatic and aliphatic bands are independent of film thickness, and are a semiquantitative indication of the aromatic character of the polymers. Such ratios have been represented in Fig. 4, in the case of the bands at 3020 and

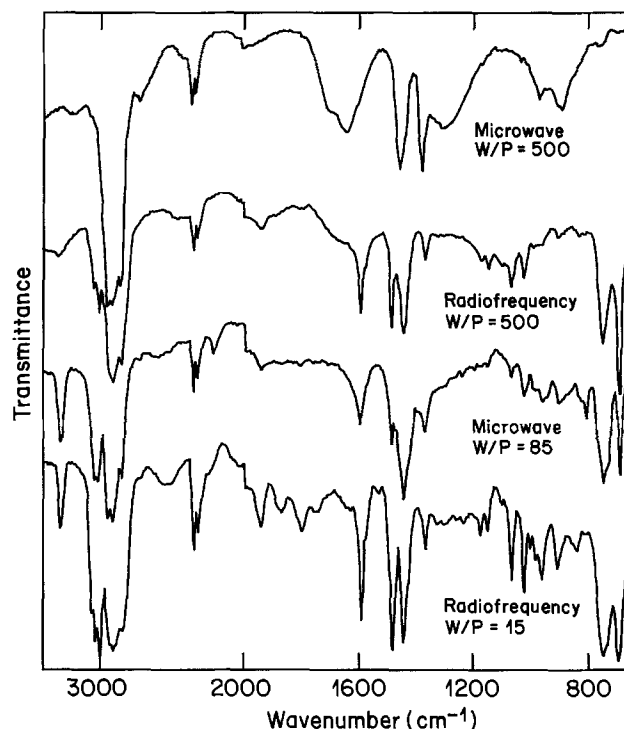


Fig. 3. Infrared spectra of polymer films produced in radiofrequency and microwave discharges with typical values of the W/P ratio.

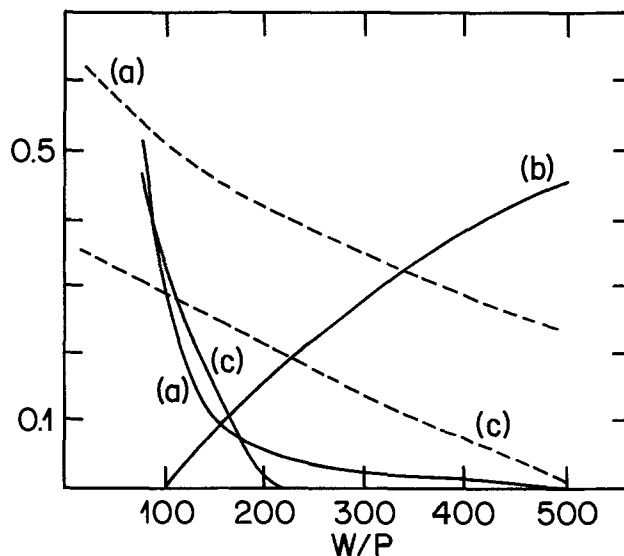


Fig. 4. Infrared band height ratio as a function of the W/P ratio: —, MW; --- RF. (a), 3020/2920 cm^{-1} ; (b), 1640/2920 cm^{-1} ; (c), 3300/2920 cm^{-1} . These ratios are independent of film thickness and indicative of the relative amounts of carbon-carbon aromatic bonds (a), double bonds (b), and triple bonds (c) in the polymer structure.

2920 cm^{-1} , as a function of the W/P ratio. Curves obtained in the case of the bands at 1600 and 1370 cm^{-1} are quite similar and have not been represented in the figure. It can be seen that the aromatic character of plasma-produced polymer is closely related to reaction conditions used and, more precisely, that it decreases continuously as the discharges become more energetic, and that it is lower in microwave than in radiofrequency discharges. The aromatic character of polymers obtained in low-energy radiofrequency discharges is close to that of conventional polystyrene. Previous authors had already reported a gas-phase formation of aromatic polymers in radiofrequency discharges (16, 9) and of aliphatic polymers in microwave discharges (15). The present results show that polymers with large differences of aromatic character may be obtained in microwave and radiofrequency discharges, simply by using different W/P ratios.

When the main aromatic bands are present, strong bands at 690 and 750 cm^{-1} are present, indicating that the aromatic rings are mostly monosubstituted, i.e., are pendant from an aliphatic or alicyclic polymer chain (17, 18). There are also weaker bands at 690, 1020, and 1071 cm^{-1} , which had been assigned once to a poly-benzyl cyclopentene structure (18), but could indicate a polystyrene structure as well. At last, especially in low-energy discharges, there are relatively strong bands at 3300 cm^{-1} , which had previously been observed in a-c discharges (17). They are indicative of a carbon-carbon triple bond structure. The relative intensity of these bands, as can be seen in Fig. 4, decreases as discharges become more energetic.

When the main aromatic bands are weak or missing, i.e., mainly in the case of high-energy microwave discharges, there are moderately strong bands in the 1620-1660 cm^{-1} region, and weaker ones in the 1300, 1150, and 960 cm^{-1} regions, indicating a carbon-carbon double bond structure, which had previously been observed in a-c (19) and microwave (15) discharges. The relative intensity of these bands decreases as discharges become more energetic, as can be seen in Fig. 4. Bands in the 1700-1750 cm^{-1} region are weak or missing in all the spectra. Oxygen contamination of the films, if any, is therefore very small. This was not the case in a-c discharges (19).

Plasma emission spectra represented in Fig. 5 are typical spectra which contain the prominent features of all the obtained spectra. Only limited parts of these spectra have been reported in previous plasma chemistry studies with aromatic hydrocarbons (7, 15-17, 20). Mono-, di-, and polyatomic radicals or ions, and excited molecules, are responsible for these emission spectra. They are gas-phase, unstable species, and should not be confused with the more stable radicals which may be trapped in the polymer films and that have been detected in some cases by ESR spectroscopy (9, 21). A number of these species have been identified in the present spectra. For instance, the bands at 4350, 4860, and 6580 Å are the main Balmer lines of the hydrogen atom. The bands at 3900 and 4310 Å are due to the ($A^2\Delta \rightarrow \chi^2\pi$) and ($B^2\Sigma^- \rightarrow \chi^2\pi$) transitions of the CH radical. The bands at 4310, 5160, and 5630 Å are the Swan bands due to the ($A^3\Pi_g \rightarrow \chi^3\Pi_u$) transition of the C_2 radical (22). The band system in the 2400-3300 Å region is due to the (${}^1B_{2u} \rightarrow {}^1A_{1g}$) transition of the benzene molecule (23). Schüler's "T spectrum," which can be observed in the 4673-6500 Å region, is due to the emission of $C_4H_2^+$ or of the C_2H radical (24). Schüler's "V spectrum" in the 4456-5900 Å region, and "W spectrum" in the 3400-4400 Å region, when present, are weak. They were assigned to the emission of the $C_6H_5CH_2$ and C_6H_4 radicals (25). Some bands in the 3300-4400 Å could not be identified, although emission in this region has once been attributed to the C_6H_5CH radical (26). The part of the continuum background which is located in the 2400-3300 Å region is due to the fluorescence resonance spectrum of the benzene mole-

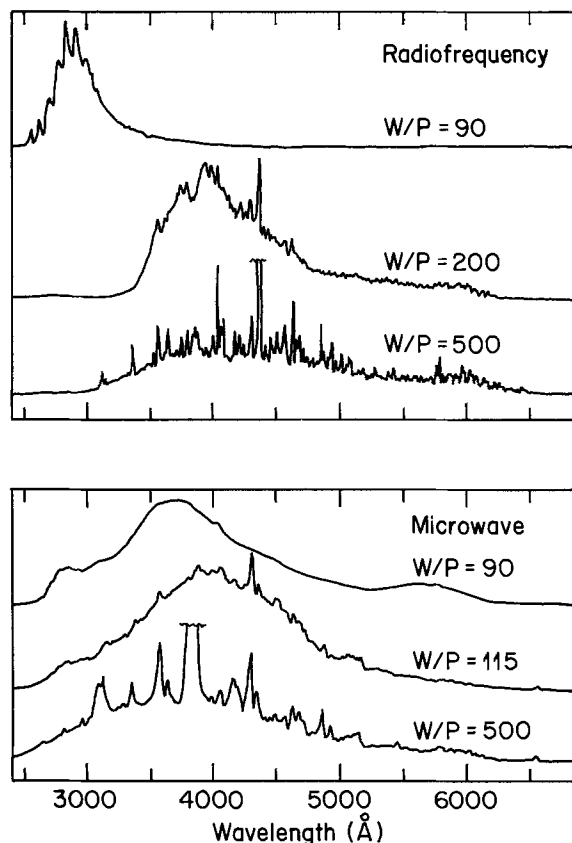
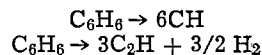


Fig. 5. Emission spectra of radiofrequency and microwave discharges for several typical values of the W/P ratio.

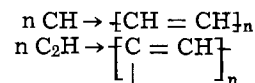
cule (27). That in the 3400-4400 Å region had been assigned to the C_6H_4 radical (25), or the C_6H_5C radical (26), but this is controversial (28). We believe that the large continuum between 3400 and 6500 Å could rather be due to the fluorescence resonance spectra of aromatic molecules larger than benzene (29, 30), possibly some of the reaction products themselves.

The following mechanisms of polymer formation, accounting for the observed polymer structures and plasma compositions, may therefore be postulated.

(i) In the case of high-energy microwave discharges, the main emission comes from CH radicals and, to a lower extent, from C_2 and C_2H radicals. These radicals are formed from breakdown reactions of the benzene molecule, such as for example

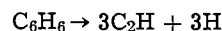


The formation of the observed olefinic polymers could therefore be explained by recombination reactions of these radicals, such as for example

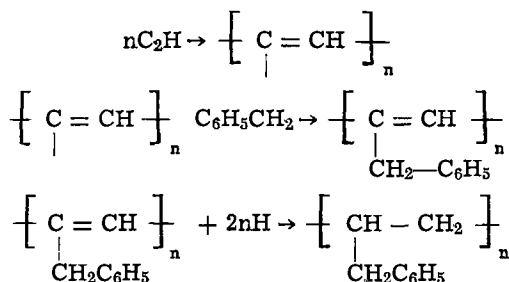


Polymer cross-linking would then be brought about by combination of free valences on neighboring chains.

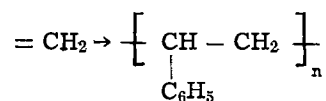
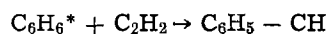
(ii) In the case of high-energy radiofrequency discharges, the main reactive species are H, C_2H , and to a lower extent C_6H_5 , CH_2 and C_6H_4 radicals. They are also formed from breakdown reactions of benzene, such as for example



Again the formation of the observed, partly aromatic, monosubstituted, saturated polymers would be consistent with recombination reactions of these radicals, such as for example



(iii) In the case of low-energy discharges, in agreement with previous observations (31, 32), ring fragmentation is replaced by ring excitation, particularly in the case of radiofrequency discharges, where the spectrum simply consists of the 2600Å system of benzene. However, the formation of polymers with mono-substituted aromatic ring structures cannot be explained by condensation reactions of these excited molecules. A possible mechanism, which has already been proposed (9), could involve the intermediate formation of acetylene, which actually forms from benzene in electrical discharges (6, 18) and would give no emission spectrum, followed by its reaction with excited benzene molecules to form styrene, and then by formation of polystyrene



The same mechanism, or a similar one involving the reaction of acetylene with excited molecules other than benzene, would apply to the case of low-energy microwave discharges. The formation of carbon-carbon triple bond structures could not be explained satisfactorily.

(iv) In the case of discharges of intermediate energy, there is a continuous variation, as a function of the W/P ratio, of the amount of CH and H radicals formed in the discharges, as can be seen in Fig. 6. This was also the case for the relative amounts of aromatic, olefinic, and acetylenic structures in the polymers (Fig. 5). Therefore it may be assumed realistically that the reaction mechanism which applies to discharges of intermediate energy is a combination of those which apply to high-energy and to low-energy discharges. In addition, the results we have obtained with toluene, ethylbenzene, and styrene suggest that the reaction mechanisms which apply to these monomers are not very different from those which apply to benzene.

Summary

The polymerization of benzene in microwave and radiofrequency discharges has been investigated with pressure and power as variable parameters. The infrared structures of the obtained polymers could be related satisfactorily to the degree and nature of fragmentation of benzene, as detected by plasma emission spectra. Polymer structures and plasma composition are significantly influenced by plasma energy level and discharge frequency. The influence of discharge frequency is particularly significant at high energy levels.

Acknowledgment

The authors wish to thank Mr. Y. Giguère for his valuable technical assistance and Dr. J. Castonguay for many helpful discussions.

Manuscript submitted July 13, 1973; revised manuscript received Dec. 17, 1974. This was Paper 12 presented at the Chicago, Illinois, Meeting of the Society, May 13-18, 1973.

Any discussion of this paper will appear in a Discussion Section to be published in the December 1975 JOURNAL. All discussions for the December 1975 Discussion Section should be submitted by Aug. 1, 1975.

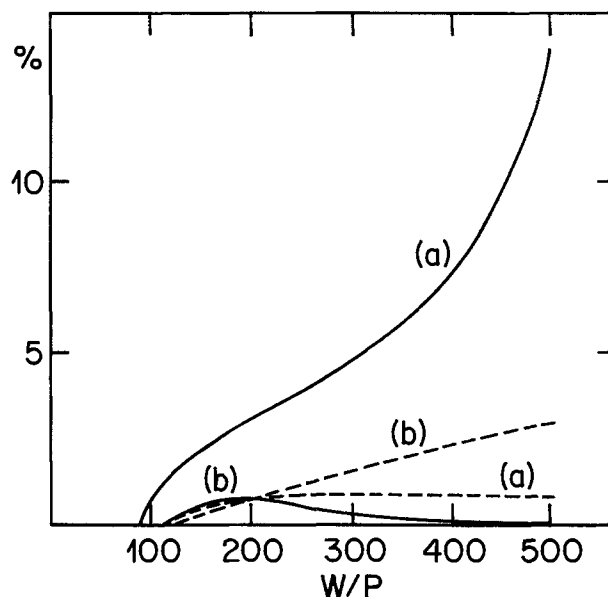


Fig. 6. Percentage of CH radicals (a) and H radicals (b) in plasma emission spectra, as a function of the W/P ratio; —, MW; ---, RF.

Publication costs of this article were partially assisted by the Hydro-Quebec Institute of Research, Canada.

REFERENCES

1. P. K. Tien, G. Smolinsky, and R. J. Martin, *Appl. Opt.*, **11**, 637 (1972).
2. P. L. Spedding, *Chem. Eng. (London)*, **225**, CE17 (1969).
3. M. Venugopalan, Editor, "Chemical Reactions under Plasma Conditions," Wiley Interscience, New York (1971).
4. B. D. Blaustein and Y. C. Fu, in "Techniques of Chemistry," Vol. I, Part IIB, A. Weissberger and B. W. Rossiter, Editors, pp. 91-207, Wiley Interscience, New York (1971).
5. J. P. Wightman, *Proc. IEEE*, **62**, 4 (1974).
6. B. W. Brooks and R. M. Sambrook, *J. Appl. Chem. Biotechnol.*, **22**, 9 (1972).
7. F. Le Goff, Ph.D. Thesis, University of Rennes, France (1971).
8. H. Suhr, *Z. Naturforsch.*, **23b**, 1559 (1968).
9. D. D. Neiswender, *Adv. Chem. Ser.*, **80**, 338 (1969).
10. K. Taki, *Sci. Papers Inst. Phys. Chem. Res. (Tokyo)*, **65**, 51 (1971); *ibid.*, **65**, 61 (1971).
11. R. Weisbeck, *Chem. Ing. Techn.*, **43**, 721 (1971).
12. M. Duval and A. Théorêt, *J. Appl. Polymer Sci.*, **17**, 527 (1973).
13. J. R. Hollahan, *Makromol. Chem.*, **154**, 303 (1972).
14. E. G. Janzen, T. Kasai, and K. Kuwata, *Bull. Chem. Soc. Japan*, **46**, 2061 (1973).
15. F. J. Vastola and J. P. Wightman, *J. Appl. Chem.*, **14**, 69 (1964).
16. J. K. Stille, R. L. Sung, and J. Vander Kooi, *J. Org. Chem.*, **30**, 3116 (1965).
17. P. L. Kronick, K. F. Jesch, and J. E. Bloor, *J. Polymer Sci., Part A1*, **7**, 767 (1969).
18. M. W. Ranney and W. F. O'Connor, *Adv. Chem. Ser.*, **80**, 297 (1969).
19. K. F. Jesch, J. E. Bloor, and P. L. Kronick, *J. Polymer Sci., Part A1*, **4**, 1487 (1966).
20. F. J. Dinan, S. Fridmann, and P. J. Schirmann, *Adv. Chem. Ser.*, **80**, 289 (1969).
21. S. Morita, T. Mizutani, and M. Ieda, *Jap. J. Appl. Phys.*, **10**, 1275 (1971).
22. A. G. Gaydon, "The Spectroscopy of Flames," Chapman and Hall, London (1957).
23. H. J. DeJong, *Chem. Phys. Letters*, **15**, 414 (1972).
24. H. Schüler and L. Reinebeck, *Z. Naturforsch.*, **9a**, 350 (1954).
25. H. Schüler and E. Lutz, *Spectrochim. Acta*, **10**, 61 (1957).
26. H. Schüler and A. Michel, *Z. Naturforsch.*, **10a**, 459 (1955).

27. H. F. Kemper and M. Stockburger, *J. Chem. Phys.*, **53**, 268 (1970).
 28. T. F. Bindley and S. Walker, *Trans. Faraday Soc.*, **58**, 217 (1962).
 29. J. M. Blondeau and M. Stockburger, *Ber. Bunsen. Gesellschaft*, **75**, 450 (1971).
 30. H. H. Jaffe and M. Orchin, "Theory and Applications of Ultraviolet Spectroscopy," John Wiley and Sons, Inc., New York (1962).
 31. S. Walker and R. F. Barrow, *Trans. Faraday Soc.*, **50**, 541 (1954).
 32. H. Schüler, *Spectrochim. Acta*, **4**, 85 (1950).

Chemical Vapor Deposition at Low Temperatures

J. C. Vigiú and J. Spitz

Commissariat à l'Energie Atomique-DMG-LEMM CENG, 38041 Grenoble, Cedex, France

Because of the potential industrial importance of chemical vapor deposition (CVD) at atmospheric pressure and at temperatures below 500°C, deposition of metals and oxides from the acetylacetonates was studied. The best way of transporting the materials is to expose the substrate to an aerosol of the chelate in a solvent. A distinction is made between true vapor deposition and splashing of droplets on the surface followed by condensed-phase reaction. With aerosol droplets small enough to ensure true vapor deposition, 500-5000Å films are of the same optical quality as those obtained by vacuum techniques. Suitable conditions have been defined for deposition of ferric oxide on glass.

Although the spraying of two or more liquids which react on mixing (e.g., to form epoxy resins) has been used in painting, the investigation of the pyrolysis of solution droplets has been limited (1). However, the method is of great practical interest, since, in certain cases, coatings can be formed on large surfaces (2, 3) without cumbersome protection against air, and at temperatures generally below 500°C where a great variety of substrates may be used.

Basic Considerations

When the operation takes place in air, the method is limited to compounds that are as stable or more stable than oxides (4). The salient feature of the process is that the metallic starting compound is transported in solution; droplets are carried at or near room temperature to within a few millimeters of the substrate surface.

Whether or not the process may be classified as chemical vapor deposition (CVD) depends upon two factors. (i, chemical) Only those compounds that vaporize without decomposition will undergo true CVD. Among the useful compounds, few react below 500°C, e.g., some chlorides and chelates. (ii, physical) The most important physical factor is the temperature of the environment which relates to the substrate temperature and gas temperature.

For clarity, we propose the classification of processes that occur with increasing temperature as shown in Fig. 1.

In process A, Fig. 1, the droplet splashes on the substrate, vaporizes, and leaves a dry precipitate in which decomposition occurs.

In process B, the solvent evaporates before the droplet reaches the surface and the precipitate impinges upon the surface where decomposition occurs.

In process C, the solvent vaporizes as the droplet approaches the substrate, then the solid melts and vaporizes (or sublimates) and the vapor diffuses to the substrate to undergo a heterogeneous reaction there. This is true CVD.

In process D, at the highest temperatures, the metallic compound vaporizes before it reaches the substrate and the chemical reaction takes place in the vapor phase.

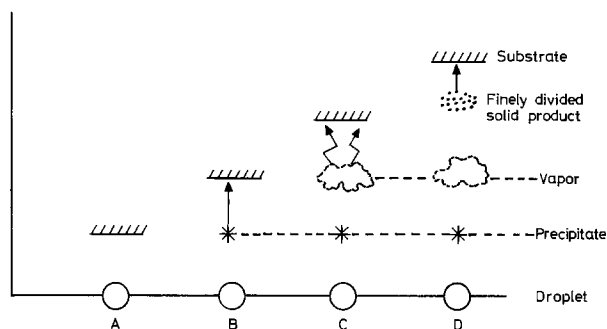


Fig. 1. Description of the deposition processes initiated with increasing substrate temperature.

Experimental

A chemical spray deposition process can be described with six parameters as depicted in Fig. 2. Typical values for these are listed in Table I.

For the purpose of relating our observations to continuous processes, we provide for substrate translation and describe the motion of the substrate inside the heated volume by velocity, v .

Records of temperature, T_s , during transit of the substrate through the heated zone were taken from a thermocouple set behind the substrate, as shown in Fig. 3.

The coatings were deposited on glass substrates, 50 × 50 mm, from solutions of chlorides and acetylac-

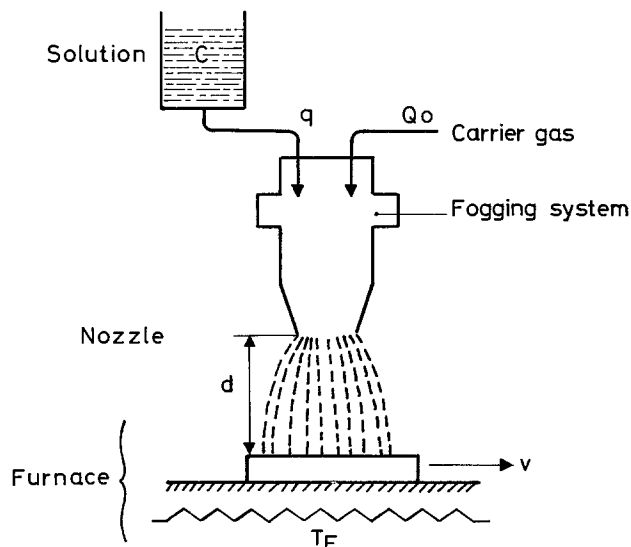


Fig. 2. Schematic diagram of equipment for chemical spray deposition.

Table I. Parameters of chemical spray deposition

Solution flow	Symbol	Piezo-electric transducer	Pneumatic transducer	Units
Temperature of the gaseous environment	T_E	400-550	500-550	$^{\circ}\text{C}$
Flow of carrier gas	Q_0	3-6	3-6	liter/min
Distance between nozzle and substrate	d	3-15	40	mm
Droplet radius	r	1-4	5-50	microns
Solution concentration	C	0.1-0.4	0.1-0.4	moles/liter
Solution flow	q	30-60	500-800	cm^3/hr
Speed of substrate through the furnace	v	10-40	10-40	mm/min

tonates. Solvents were water, butylacetate, butanol, and toluene.

The fogging system can be of different types (6, 7): pneumatic atomizer, resonant cavity, or piezoelectric transducer. We favor the last which has the following advantages: the carrier gas flow can be set at very low values, thus minimizing the cooling effect on the substrate; moreover, at a frequency of 1 MHz, the droplet diameter lies between 2 and 8μ (8). Table I gives typical values of the parameters for a pneumatic and a piezoelectric generator.

Results and Discussion

Adherent layers of both metals and oxides were obtained by chemical spray deposition. As shown in Table II, the only metals that can be prepared are the precious metals that do not form oxides. Their quality, as evaluated by reflectance, is at least equal to that of a film prepared by a vacuum technique, as shown in Fig. 4.

The deposition of ferric oxide from a solution of ferric acetylacetonate was investigated most thoroughly. The values of the experimental parameters listed in Table I lead to layers 1800-2600Å thick.

Because of the extreme temperature gradient in the vicinity of the substrate (estimated as $50^{\circ}\text{C}/\text{mm}$), it is difficult to know the temperature which truly characterizes the layer growth. An additional difficulty arises from the motion of the substrate, which destroys its equilibrium with the environment.

Three temperatures are available from the measurements (Fig. 3): (i) the temperature T_E of the gaseous environment which is close to the regulation temperature of the furnace; (ii) the temperature of the substrate facing the spray, T_s ; (iii) the temperature of the substrate out of the spray. With the assumption

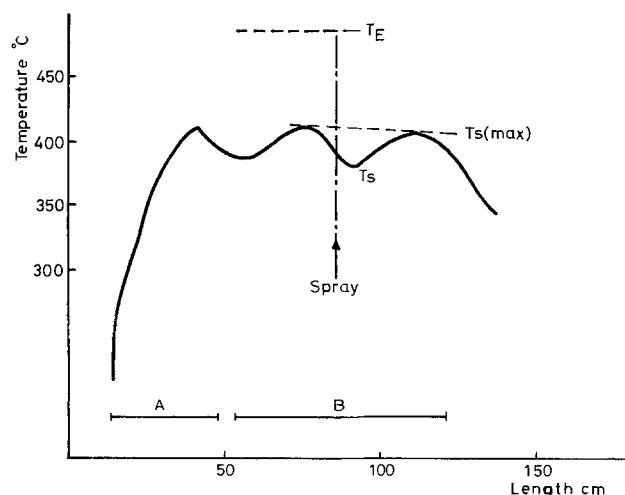


Fig. 3. Temperature of substrate passing through the heated zone. Speed 30 mm/min. A, Infrared heated zone; B, electric furnace at temperature T_E .

Table II. Chemical conditions of deposition

Layer	Starting compound	Solvent	Temperature T_E , $^{\circ}\text{C}$	Carrier gas
Fe_2O_3	$(\text{AA})_3\text{Fe}$	Butanol	400-550	Air
SnO_2	SnCl_4	$\text{H}_2\text{O} + \text{HCl}$	480-500	Air
In_2O_3	$(\text{AA})_3\text{In}$	Acetylacetonate	470-520	Air
Cr_2O_3	$(\text{AA})_3\text{Cr}$	Butanol	520-560	Argon
V_2O_5	$(\text{AA})_3\text{V}$	Butanol	450-510	Oxygen
Pd	$(\text{AA})_2\text{Pd}$	Butanol	300-350	$\text{N}_2 + \text{H}_2$
Ru	$(\text{AA})_3\text{Ru}$	Butanol	380-400	$\text{N}_2 + \text{H}_2$

AA = acetylacetonate.

that these values are generally proportional to each other, we decided to observe the layer structure as a function of the temperature of the substrate facing the nozzle, which constitutes a convenient reference for characterizing the coating behavior during heat-treatment.

The linear variation of growth rate with solution concentration (Fig. 5) suggests that the process is diffusion controlled rather than kinetically controlled. Growth rate, G , is related to the other parameters by

$$G = \frac{ev}{\alpha}$$

where e is the layer thickness, v is the translational velocity of the substrate, and α is the effective width of the spray in the direction of motion; under our conditions $\alpha = 3$ cm.

In Fig. 6, the layer thickness is plotted against v^{-1} (proportional to the dwell time of the substrate in the spray), which gives a line of slope G . Except for the points corresponding to higher substrate velocity, for which the temperature is lower, the growth rate is independent of layer thickness.

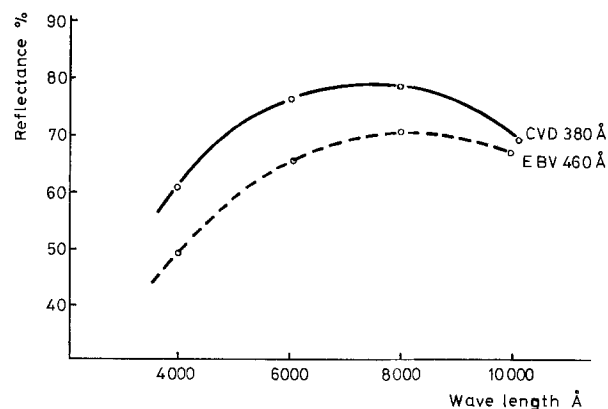


Fig. 4. Reflectance of palladium films prepared by CVD and by electron beam vaporization.

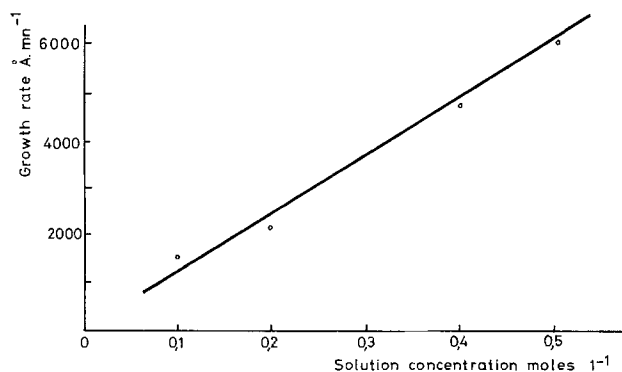


Fig. 5. Growth rate of Fe_2O_3 layers as a function of concentration of ferric acetylacetonate in toluene.

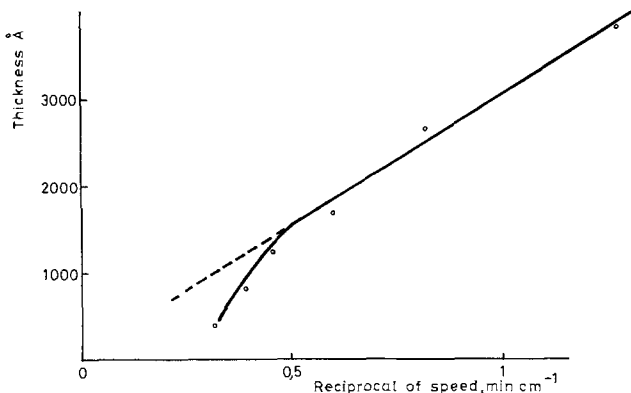


Fig. 6. Thickness of Fe_2O_3 as a function of translational velocity

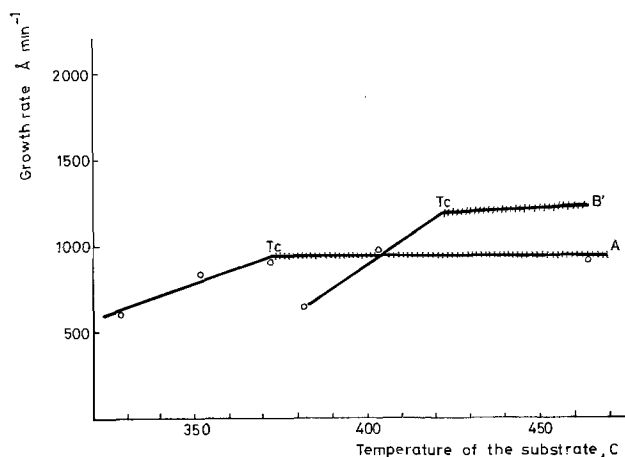


Fig. 7. Growth rate of Fe_2O_3 layers as a function of temperature. A, 0.1 mole/liter ferric acetylacetonate in butanol; B', 0.1 mole/liter ferric acetylacetonate in toluene.

The layer structure and the growth rate were observed as functions of the temperature of the substrate when facing the spray nozzle. As shown in Fig. 7, the growth rate reaches a point at T_c beyond which the dependence of growth rate on temperature decreases markedly. At the same time the deposit develops a crystalline structure beyond T_c . These factors suggest the operation of different mechanisms above and below T_c .

On the other hand, we found that the oven temperature T_E has a stronger influence on the structure of the coating than do temperatures measured on the substrates. The difference in T_c 's with toluene and butanol suggests that evaporation of the solvent is involved in one or both mechanisms.

As expected, the physical properties of the coating change rapidly in the neighborhood of the transition temperature T_c . In the case of a 1800Å ferric oxide film, grown from ferric acetylacetonate in butanol, transmission increases with a decrease in temperature, whereas resistance to abrasion rapidly decreases as the crystalline structure vanishes.

We observed that the size of crystallites obtained from sprayed solution of ferric chloride is independent of solution concentration. On the other hand, the average crystallite size can be increased by raising the temperature from 400° to 800°C. This supports the idea of formation from the vapor phase via process C, Fig. 1.

Explaining the growth of an amorphous layer is more of a problem. Some authors describe adherent, noncrystallized layers obtained from the acetates (9). The noncrystallized state appears to correlate with the lack of volatility of the starting compound, suggesting that process B is operative.

The photographs of Fig. 8 show films prepared under conditions suggestive of operation of the different processes. Processes A and D are believed to be of little practical interest because they lead to rough or non-adherent layers.

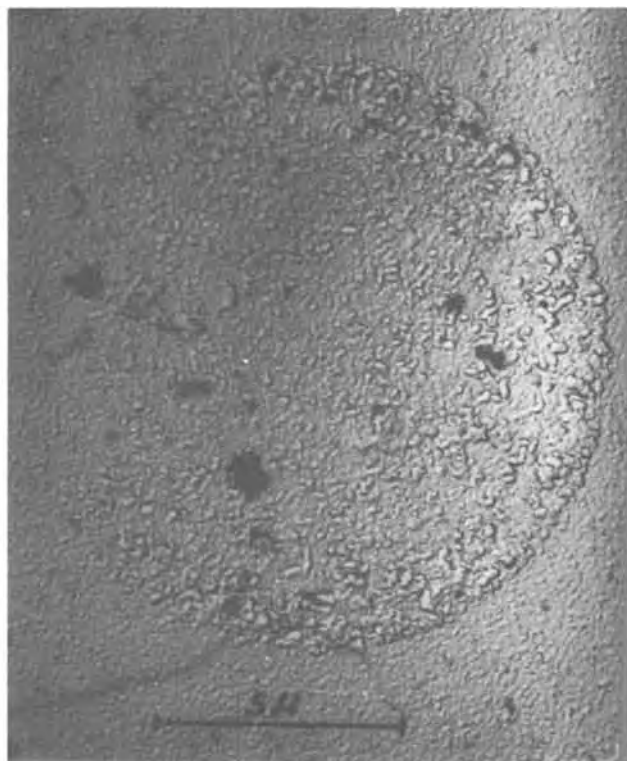
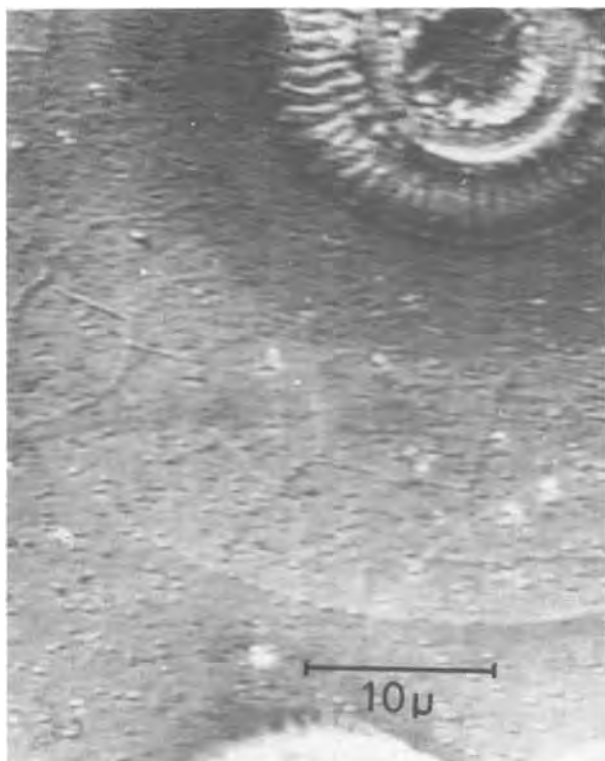


Fig. 8. Surface of Fe_2O_3 deposited from hydrochloric solution of FeCl_3 . (a, left), Low temperature processes, A and B; (b, right), high temperature process, C.

Conclusions

The different processes in chemical spray deposition depend not only on temperature; the coating morphology is influenced also by flow of carrier gas, distance between substrate and nozzle, droplet radius, solution concentration, and solution flow rate.

When droplets of different sizes are present in the aerosol, two of the possible processes can proceed concurrently. Use of piezoelectric transducers which produce droplets of a rather narrow size range facilitated identification of the processes.

These observations were valuable in choosing optimum conditions for the preparation of semitransparent photomasks.

Manuscript submitted Oct. 19, 1973; revised manuscript received Sept. 25, 1974. This was Paper 306RNP presented at the Boston, Massachusetts, Meeting of the Society, Oct. 7-11, 1973.

Any discussion of this paper will appear in a Discussion Section to be published in the December 1975 JOURNAL. All discussions for the December 1975 Discussion Section should be submitted by Aug. 1, 1975.

Publication costs of this article were partially assisted by the Commissariat à l'Energie Atomique, France.

REFERENCES

1. J. C. Withers and L. C. McCandless, in "Proceedings of the Second International Conference on Chemical Vapor Deposition," J. C. Withers and J. M. Blocher, Jr., Editors, p. 393, The Electrochemical Society Softbound Symposium Series, Princeton, N. J. (1970).
2. O. V. Vorob'eva and T. F. Polurotova, *Izv. Akad. Nauk SSSR Neorgan. Materialy*, **7**, 266 (1971).
3. O. V. Vorob'eva and E. S. Bessonova, *Steklo i Keram.*, **21**, 9 (1964).
4. R. R. Chamberlin and J. S. Skarman, *This Journal*, **113**, 86 (1966).
5. B. Franck and R. Groth, *Thin Solid Films*, **3**, 35 (1969).
6. M. N. Topp and P. Eisenklam, *Ultrasonics*, **12**, 7 (1972).
7. D. Ensminger, "Ultrasonics, the Low and the High Intensities Applications," pp. 467-471, Marcel Dekker, Inc., New York (1973).
8. J. Spitz and J. C. Viguié, French Pat. 2,110,622.
9. J. W. Gilliland and M. S. Hall, *Electrochem. Technol.*, **5**, 303 (1967).



A Critical Review of Solderability Testing

Joseph B. Long

Tin Research Institute, Incorporated, Columbus, Ohio 43201

Joining by soldering is essentially the penetration and filling of a particular clearance between two components with solder to provide for integrity, electrical continuity, or heat transfer in the assembly. In addition, solder joints form liquid and gas tight seals and provide some strength to the assembly at a variety of service temperatures. To fulfill the functions of a soldered joint, molten solder must wet mating surfaces at a temperature usually below 800°F (427°C), and the solder alloy must be distributed to all joint spaces by capillary action. Fluxes are normally required to aid the wetting and penetration of the solder by chemical dissolution of oxides and similar films on the component surfaces and on the advancing solder meniscus. Even though the physical geometry of a solder joint is satisfactory, there are wide differences in the ease with which a joint is made, and these differences are within the realm of solderability testing, which seeks to determine the facility with which a solder can wet surfaces. Secondly, solderability tests are designed to provide information on the soldering characteristics of the solder in relation to the chemical and physical nature of the surfaces being joined. The composition and the efficacy of both solder and flux systems and temperature-time cycles employed during the soldering operation can also be ascertained by appropriate solderability tests.

Many investigators have developed different procedures and equipment to assess solderability. Determination of solderability falls into one or more of the following categories, (i) capillary penetration tests, (ii) spreading tests, (iii) dip tests, and (iv) wetting time tests. A critical evaluation of the various testing methods and the significance of data derived from solderability testing programs will permit users of soldered joints to select materials to provide reliability and to evaluate optimum production schedules for the soldering process (Table I).

Capillary Penetration Tests

Capillary penetration tests are used to evaluate the effects of joint clearance, flux activity, or solder composition (1). In testing by this method, a capillary space is provided between two flat metal sheets (Fig. 1). The joint surfaces of the sheets are fluxed, preheated, and brought into contact with a molten solder

Key words: solders, fluxes, coatings, joints, reliability.

Table I. Tests for solderability

Materials tested	Tests commonly used			
	Capillary penetration	Spread	Dip	Wetting time
Solders	X	X	X	X
Fluxes	X	X	X	X
Base metals	X	X	X	X
Coatings	X	X	X	X
Printed circuit conductors			X	X
Plated through holes	X		X	X
Wire and component leads		X	X	X

bath for a specific time interval (2). After the sheets are removed from the solder and cooled, the capillary rise is measured on the wetted surfaces. Data from this type of test often show anomalous results due to non-uniform oxidation of metal surfaces or changes in the activity of fluxes during preheating.

Despite the anomalies associated with the capillary penetration tests, one of the quality control tests for electrolytic tinplate (Fig. 2) is made with samples of tinplate which are folded over to form a capillary space (3). The test samples are at ambient temperature, and after fluxing, are immersed vertically in the bath for 1 min. The sample is then removed, cooled, and the folded edge is sheared off. The sample is peeled apart and the height of the solder rise in the joint is measured. The sensitivity of this quality control check is low since it has been demonstrated that the difference in capillary rise between "good" and "poor" tinplate may be only 0.1-0.2 in. in a total capillary rise of 1 in.

The measurement of capillary rise of solders has also been made with electroformed metal tubes (Fig. 3), twisted wires, and interlocked joints (Fig. 4) (4-6).

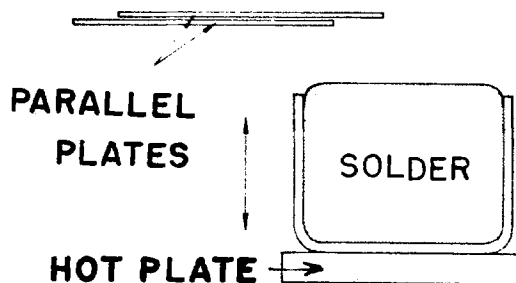


Fig. 1. Capillary penetration test using flat metal surfaces

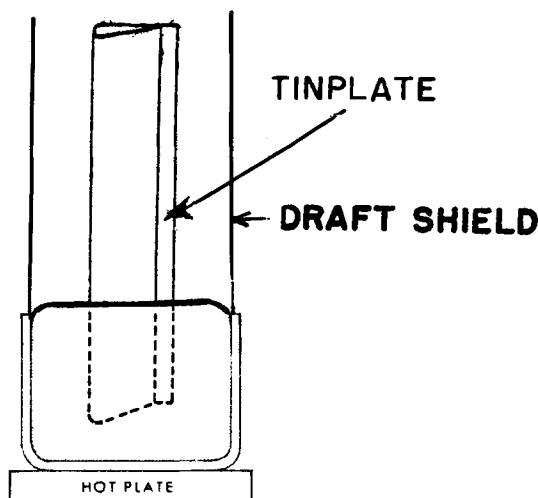


Fig. 2. Testing tinplate for solderability

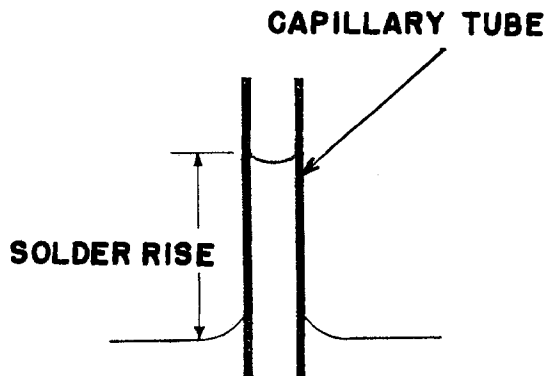


Fig. 3. Solder penetration test using an electroformed metal tube



Fig. 4. Interlocked metal joints used in the solder penetration test.

In the case of twisted wire samples, it was shown that the expansion of the wires when dipped in the molten solder bath, caused an uncontrollable change in the dimensions of the capillary clearances. It should be pointed out that in all capillary penetration tests using binary tin-lead solders, the amount of rise of the solder will greatly depend upon the availability of eutectic in the solder alloy. In solders where there is a high percentage of eutectic, capillary rise will be at a higher level than when solders of lower eutectic content are used.

It is recognized that capillary action will not occur in solder joints unless the molten solder is in contact with the capillary space. Therefore, it is necessary for solder to spread over surfaces to be in the best position to fill capillary spaces. The area of spread tests were developed to meet this requirement.

Area of Spread Tests

The area of spread tests have been used by both researchers and production personnel to compare solderability of coated surfaces (7) and evaluate the effectiveness of fluxes (8) and solders (9). In testing by this method, fixed volumes of solder and flux are placed on test coupons which are heated to a specific temperature. Various means are employed to heat the samples and electrical resistance heating or hot plates have been used. Some investigators have floated test coupons on a liquid solder or flux bath or employed oven heating as a heat source. However, oven heating is not recommended since the time required to bring a sample to temperature is often too long, and without a protective, nonoxidizing atmosphere, the sample surface can be oxidized sufficiently to affect test results. In addition, oven heating for long heat cycles is not representative of the conditions for the majority of soldering operations.

During heating of the test coupons, the solder melts and spreads over the surface. The extent of the solder spread pattern is influenced by the type of flux, metal surface condition, and solder composition. Variables such as the volume of either flux or solder are controlled by using flux cored solder wire of a specific diameter and core size. Alternately, solder preforms or constant size pellets are punched from solder sheet of known thickness and accurate quantities of flux are applied to the test specimens, usually with a graduated pipette or hypodermic syringe.¹

After the melted solder spreads over the surface to be tested, the sample is cooled and the area of spread can be measured with a planimeter. Alternately, the spots are photographed and enlargement is made for

direct measurement with a planimeter gauge. Often the solder spread is displayed on the screen of a projection microscope and standard charts are used to determine the spread area.

Figure 5 shows the relative spread of a 60 tin-40 lead solder on various coatings fluxed with a mixture of rosin and alcohol. The coating thickness in each case is 0.0003 in. (7.5 μm) thick, and it is clear that hot dipped tin, and electrodeposited alloys of tin-zinc provide high levels of solderability. Stannate tin, tin-cadmium alloy, and cadmium show intermediate solderability. Tin-nickel and silver are inferior, but nevertheless may be soldered satisfactorily under industrial conditions. Chromium is nonsolderable.

If the area of spread is determined and the volume of solder is known, the value of the theoretical contact angle of the solder drop with the basis metal can be determined by the equation

$$\theta = 7.12 \left(\frac{V}{\text{square root } A^3} \right)$$

where θ is the contact angle in degrees, V is the volume of solder in cubic centimeters, and A is the area of spread in square centimeters. This equation assumes that the volume of solder is small and therefore, gravitational effects are minimized. The value provided by the equation gives a numerical value for solderability, and small values of θ indicate good solderability.

Variations of the area of spread test were made by other investigators. In one test the maximum height of the melted solder above the test coupon surface was regarded as an index of solderability. However, this test is usually only appropriate for areas of spread which are approximately circular. Solder spread is more often irregular due to the chemical and physical properties of the test surfaces. In order to minimize the difficulties of testing associated with the shape of the solder spot, a solderability test was devised which employs solder wire samples with a diameter of 0.0625 in. For each solder sample, a three inch portion of wire solder is bent into the form of a figure 4. The vertical part of the 4 is about 1 in. long and is crossed by the horizontal portion of the wire sample in the middle. The end of the horizontal portion is looped under and then over the vertical portion and the loop pulled tight. The edges of the loop are then cut away. Thus, solder pellets of consistent weight are formed. The test is performed similarly as the spread test and both the height and area of spread are measured after the solder pellets are melted. Spread factors for a particular test surface are calculated by using the equation

$$\text{Spread factor} = \frac{D - H}{D} \times 100$$

where D equals the diameter of the sphere having a volume equal to that of the solder used, and H is the height of the solder spot. If there were no effect from gravity, surface tension or wetting (alloying) of the solder, the solder drop would assume the shape of a sphere where D would equal H and the spread factor would be zero. This would indicate nonsolderability of the surfaces tested. As solderability increases, the height of the solder spot decreases and the value of the spread factor increases. A percentage rating of the solderability of surfaces is thereby established and coatings are rated as follows:

Spread factor	Solderability	Approximate contact angle calculated from area of spread
60	Very poor	50°-
60-70	Poor to fair	50°-34°
70-80	Fair to good	34°-12°
80-90	Good to very good	12°- 3°
90	Excellent	3°-

A.S.T.M. tests were concerned with the effect of a variety of thicknesses of tin on brass and copper and

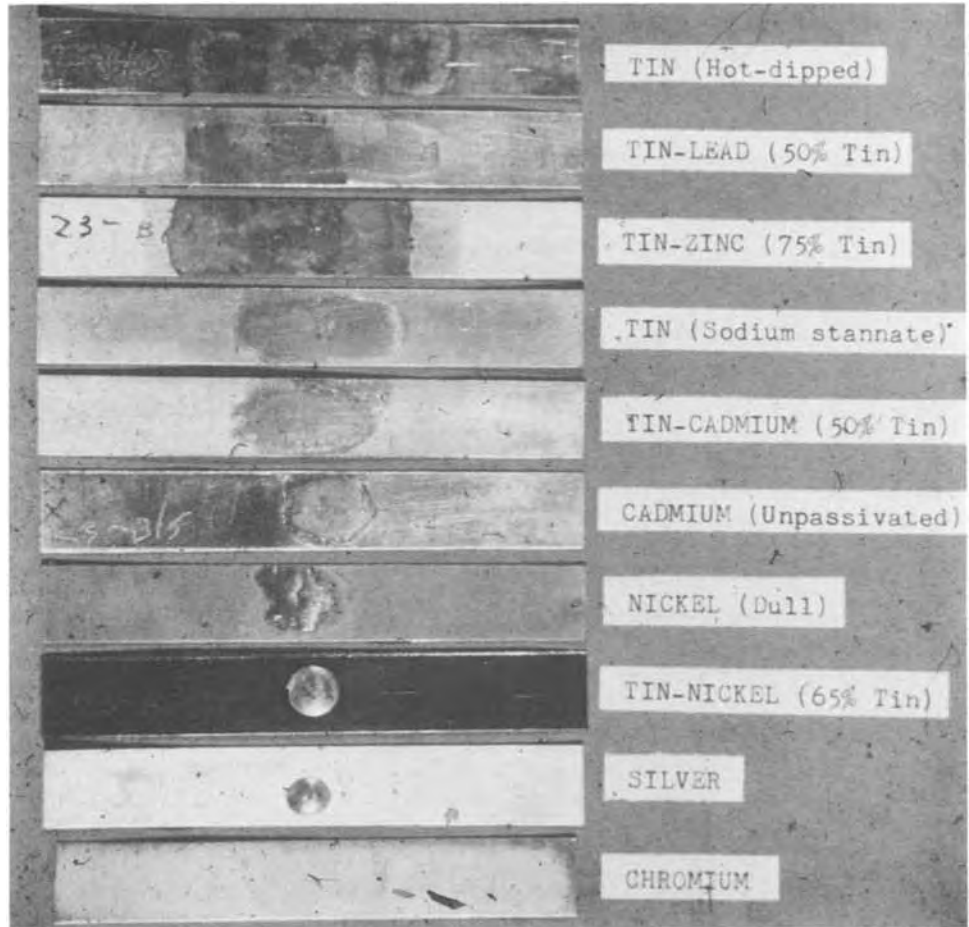


Fig. 5. Relative solder spread on various coatings, 0.0003 in. thick.

the spread factor was employed as a measure of solderability (11, 12). Samples were tested in the as-plated condition and after exposure of up to 1 yr at 100°F (38°C) and 85% humidity. Under prolonged temperature and high humidity conditions, substantial oxide films developed on the tin coatings and it was shown that the solder broke through and flowed under the oxide films on some of the test disks. This type of rupturing of surface films is more likely to occur where the film is least supported when the underlying coating melts, that is, on the thickest tin coatings. It would appear from these test results, that the area of spread test is not appropriate when aged, thick coatings are tested.

Reflection of incident light from the surface of a spreading solder drop has been used to study solderability of surfaces (13). The contact angle that a solder drop makes with the basis metal was measured by taking motion pictures of the solder as it spreads (Fig. 6). The advancing solder was illuminated from directly above and the camera was mounted at a known angle to the vertical light source. As the solder spread, the reflected light moved out from the surface to the edge of the drop and finally disappeared when the contact angle reached a value which was one-half the angle of separation of the light and camera. The method is probably best for testing the rate of spreading of a solder which has a low contact angle, but a dip test would be simpler to use. Dip tests are discussed later in this paper.

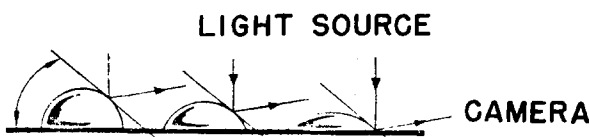


Fig. 6. Reflection of incident light from surface of spreading solder as an index of solderability.

Another spread test is part of Military Specification MIL-P-55110 (14). This test has been named the Meniscus Test and utilizes a test pattern on a printed circuit board which has a series of parallel conductor paths. The test board is placed in a test fixture which has three holes at its center and counter weights are used to hold the board to the fixture. When the test fixture and board are pressed into the solder bath, the solder rises through the holes in the fixture and forms meniscuses (Fig. 7). Since the printed wiring board is held at a measured distance above the holes, only the solder meniscuses contact the test board.

Three circular spots of solder are produced on the specially designed test pattern. After the sample is removed from the fixture, the spots are measured diagonally to the nearest hundredth of an inch. The average of 12 such spots made on two double-sided test boards is a measure of the board solderability. In addition, if any of the spots show unwetted or dewetted areas exceeding 25% of the total area of the board, the board is considered to have unsatisfactory solderability.

The test has shown little acceptance by the printed circuit manufacturing industry because the test equipment is unwieldy, and sensitivity of the test is not adequate. The over-all range of solder spots was shown to be 0.60-0.99 in. for a full range of nonsolderable surfaces. Natural aging data showed that a minimum

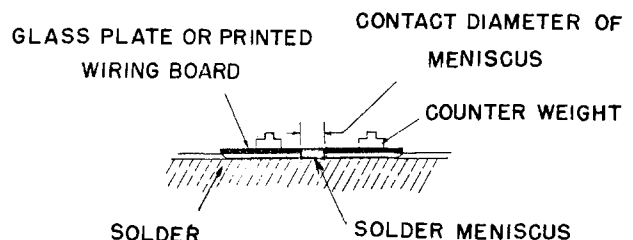


Fig. 7. Schematic of the Meniscus Test

value of 0.84 in. in the diagonal measurement of the wetted test paths was the point at which boards could be rejected for lack of solderability. It would appear that a spread difference of only 0.15 in. is too narrow to be an acceptable criterion for determination of good solderability.

Dip Tests

Dip tests are probably one of the easiest forms of solderability test to apply since the specimen to be tested is immersed in solder and the degree of coverage by the solder is noted as an index of solderability. One of the dip tests involves the use of unfluxed leads onto which is wound a loop of solid wire solder (15). After making the solder loop around the lead to be tested, the solder ends are cut away and the specimen is immersed into a bath of polyethylene glycol which is heated to about 392°F (200°C) above the melting point of the solder. The lead is held in the glycol bath 2 sec after the solder melts, then removed from the bath, cooled, and cleaned with alcohol. Examination of the lead is made and an even, continuous distribution of solder along the length of the lead demonstrates excellent solderability of the surface, but formation of solder globules with high contact angles is indicative of poor solderability (Fig. 8).

Military Standard 202C, Method 208 defines a solderability test for component lead materials (16). This test was also published by the Electronic Industries Association as their Standard RS178A (17). A lead is dipped into a rosin-alcohol flux and attached to an arm of a device which lowers the lead into a solder bath heated to 450°F (232°C). The arm of the apparatus is actuated by a motor driven cam and the entry into the bath, dwell time, and exit time from the solder are accurately controlled (Fig. 9). After the solder dip, the solder-coated lead is cooled, and flux residues are removed with isopropyl alcohol. The lead is considered to have acceptable solderability if surfaces are 95% covered with a continuous solder coating. The remaining 5% of the surface may contain pinholes or voids provided they are not concentrated in any one area. Evaluation of test results are difficult since the test does not readily distinguish between smooth and rough coatings. It has been suggested that a Microcard Viewer be used to determine surface imperfections, but this technique is slow and cumbersome.

The Institute of Printed Circuits utilizes an edge dip test in their standard IPC-S-801 (18) to determine solderability of printed circuit boards, laminated stock, and similar flat materials. The equipment and procedures are similar to the Military Standard 202C. Tested pieces are compared against standard samples or photographs showing various degrees of wetting of solder on copper coupons. The test has proven its importance to the manufacturers of printed circuit boards since they are able to determine the effectiveness of their board preparation steps and any processed boards which are found to be unsatisfactory by this solder-



Fig. 8. Wire samples showing solder spread

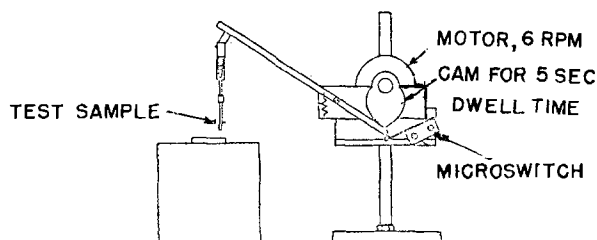


Fig. 9. Edge dip testing for solderability

ability test, can be corrected prior to assembly and final soldering.

The float test is considered a modification of the dip test and is used to check the soldering quality of plated through-holes (19). The boards are fluxed and then floated on a solder bath for about 5 sec. They are removed from the bath and the holes are examined visually. Uniform wetting along the sides of the holes as well as the lands is indicative of acceptable solderability.

In this age of complicated electronic circuitry, there is an increasing demand for optimum reliability. In addition, production requirements are such that several hundred joints may be made simultaneously on circuit assemblies by mass soldering methods. The time of contact of any given joint with molten solder is often as little as 2 sec and therefore, the time and perfection of wetting of the surfaces of components by solder is of primary importance to producers of electronic packages. It was this philosophy that led researchers and production engineers to design solderability tests which would demonstrate the effects of surface preparation techniques, compare the solderability of different coatings, and also indicate the merits of different fluxes for a given surface.

Wetting Time Tests

Wetting time tests for solderability have the virtues of simulating fairly closely mass soldering processes as well as simplicity of operation. The tests can be used to determine the soldering quality of component terminations or flat laminates as used in printed circuitry applications.

Solderability of pigtail leads is difficult to ascertain visually, and even though these lead materials may exhibit good solderability when new, experience has shown that coatings can become unsatisfactory after storage for extended periods. Gradual diffusion of copper into tin or solder plated coatings produces intermetallic compounds which, if reaching the surface of a joint to be soldered, can be cause for unwet or dewet conditions. It is therefore desirable for manufacturers and users of these components to check the solderability of surfaces at all stages of manufacture and storage to ensure maximum productivity and reliability during soldering operations.

A test has been devised for checking lead materials (20, 21). This test is commonly known as the Globule Test. A specific volume of solder (depending on the gauge of the wire tested) is melted on a heated mandrel and prefluxed wire is lowered horizontally into the solder globule, splitting it in two (Fig. 10, 11). The time for the solder to flow around and finally cover the top of the wire is a measure of the wetting time. In order to detect any tendency for dewetting, it is necessary to remove the wire from the solder globule, wipe off the excess solder, and retest in the same position. Artificial aging of wires for 16 hr at 311°F (155°C) in air can be used to simulate prolonged natural storage conditions. Figure 12 shows the results of solderability tests on copper wires plated with 0.0001 in. of 30 tin-70 lead alloy. The wires were tested using Sn60 solder and a 25% rosin-isopropanol flux mixture. The aging test was used to simulate industrial storage before soldering. However, the correlation of such aging treatments with natural storage is a subject under active discussion.

It is difficult to apply the Globule Test to very short terminations and only round wires can be tested. In spite of these difficulties, the test has been included in IEC Standard 68-2-20, Part 2T, British Standard 2011, and the German and Swedish Standards.

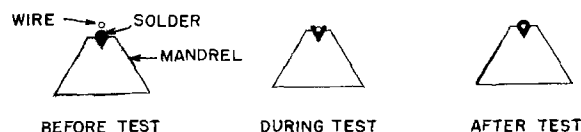


Fig. 10. Globule testing round wire leads

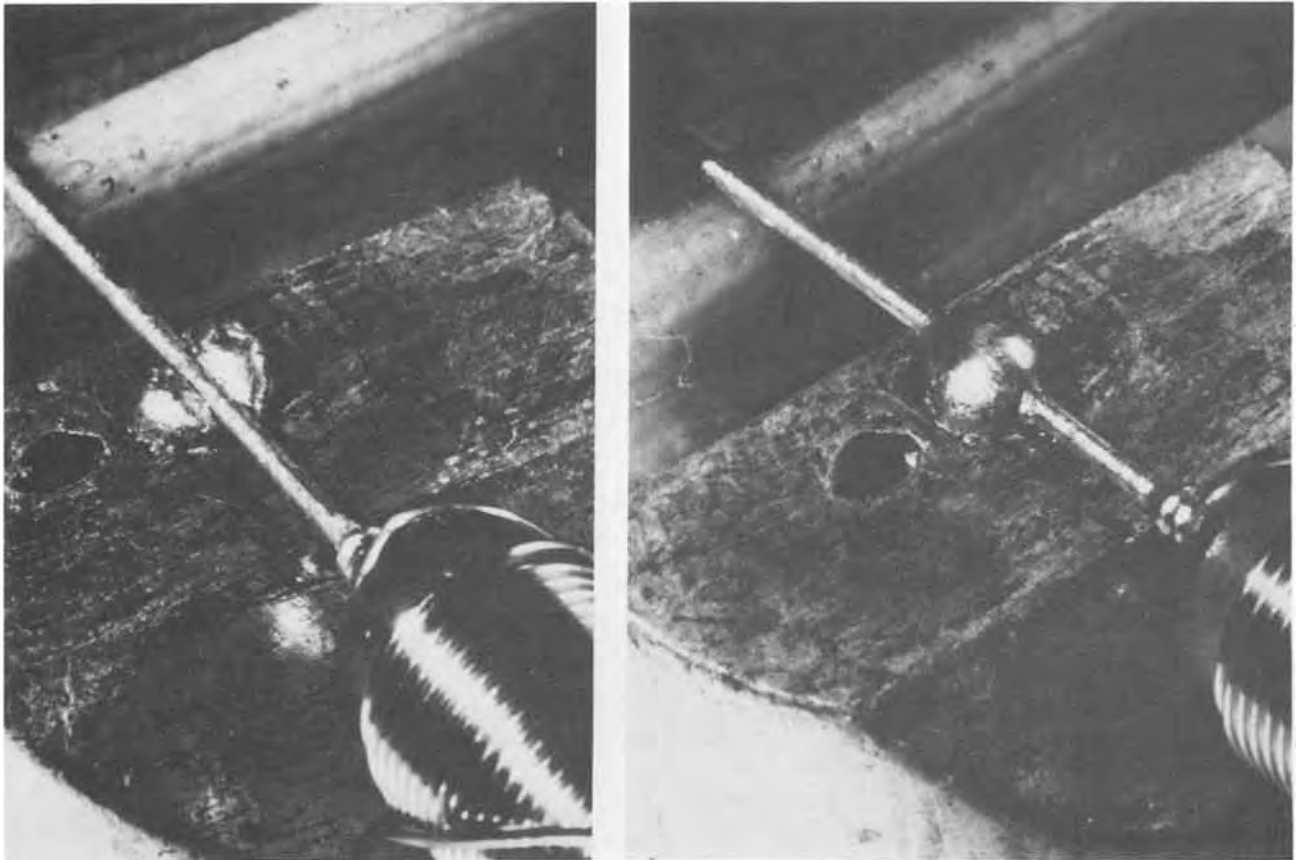


Fig. 11. Testing wire terminations for solderability

Wetting of a surface by molten solder involves the progressive reduction in the contact angle as well as a change in surface tension forces due to interaction of tin in the solder and the base metal. Thus, monitoring of surface tension may be considered to be a fundamental approach to the measurement of solderability (22, 23). Commercial apparatus is available for making such tests and standards have been prepared to provide for a quantitative evaluation of solders, fluxes, and surface solderability.

The apparatus for performing the test has three basic parts: a load-measuring system and readout circuit, a motor drive for moving the solder bath vertically, and a solder heating and temperature control system (Fig. 13, 14). A test piece is suspended from a transducer-monitored spring system, and the solder bath is raised until the specimen is immersed to a predetermined depth. Buoyancy from the displaced solder provides a transducer generated signal which is fed to an oscilloscope or high speed pen recorder. This condition is maintained until the solder wets the test specimen. The solder meniscus then rises, producing a downward

force on the specimen, and a signal of opposite polarity is developed by the transducer. These first and second stages permit measurement of the time to start wetting

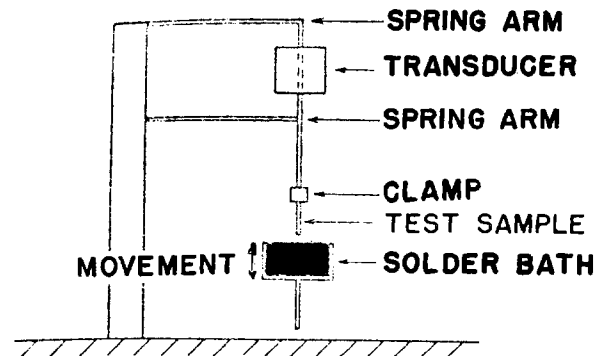


Fig. 13. Schematic of the surface tension apparatus

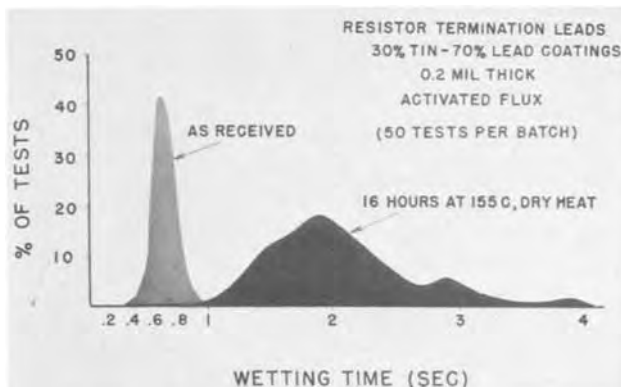


Fig. 12. The effect of artificial aging on solderability



Fig. 14. Commercial apparatus for determination of the wetting time of materials.

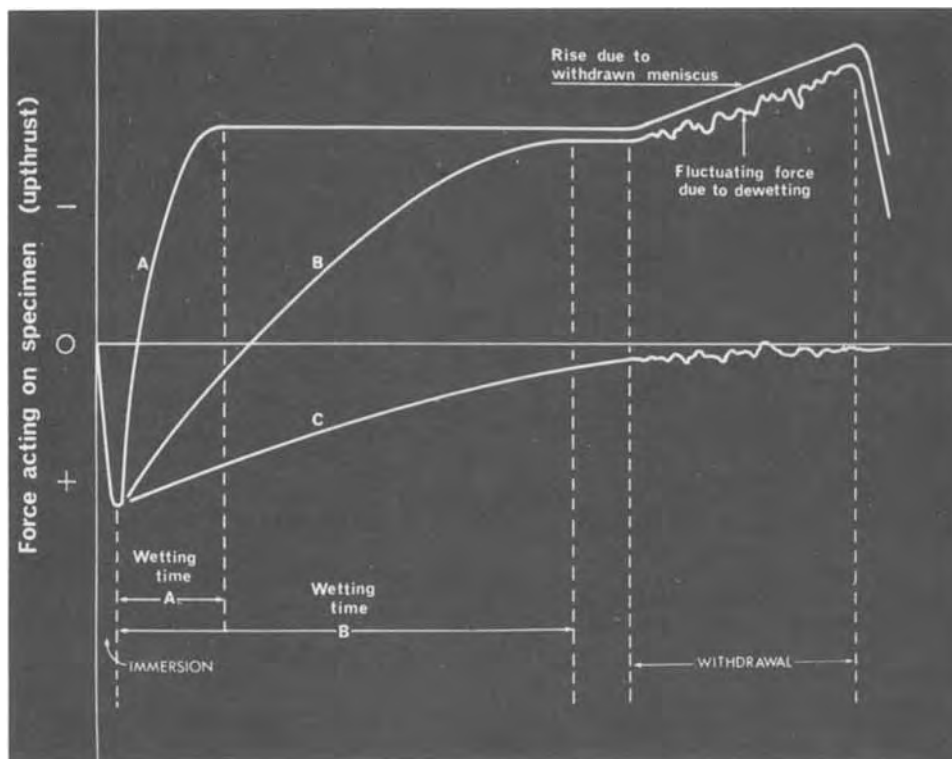


Fig. 15. Typical recorder traces from the surface tension apparatus.

and the rate at which wetting occurs. Eventually equilibrium is reached and the magnitude of the signal measures the ultimate extent of wetting. Figure 15 shows a typical recorder trace obtained from a solderability test using the surface tension apparatus. Curve A represents a material of high solderability while B has a much slower rate of wetting. Curve C represents material where there was no wetting by the solder. The fluctuating withdrawal force shown at the end of the curves is due to dewetting and the breakdown of the solder meniscus.

The interpretation of the wetting force curve is not understood fully. Maximum wetting force relates loosely with solderability in practice. Wetting time (*viz.*, time to cross the zero force axis) often gives anomalous results on certain materials.

It has been demonstrated that deviations from the normal curve shape can occur with very small components of good solderability. These components usually have low thermal capacity and their surfaces may begin to wet before a full upthrust signal has developed, resulting in a loss of the initial stages of the curve.

A dip tester has been developed to provide for solderability inspection of materials before assembly and soldering (24). This equipment has an adjustable frame mounted above a solder bath. The frame holds the test piece in such a way that it is dipped into the solder for a predetermined depth. A microscope mounted on a micrometer head allows the gauge to be set at zero, which corresponds to the level of the solder surface. The test piece is fluxed, warmed, and dipped into the solder. Solder wets and rises along the exposed side of the test piece, and the micrometer is adjusted to measure the height of the solder flow to the top of the meniscus. Solderability is determined by the height of the meniscus and the contact angle on the wetted surfaces in a given time of immersion can be derived. This test appears to be a combination of the spread test and the dip test and it can be used to make quantitative determination of the effects of different soldering parameters on the degree of wetting.

Equipment for assessing the minimum wetting time has been made available to industry (Fig. 16). The apparatus consists of a radial arm which carries the test piece over the solder bath surface and is driven in a circular path through the solder by a motor and gear

box (Fig. 17). The test technique involves a succession of test pieces which are exposed to progressively longer times of contact with the solder bath (25, 26). By visual examination, it is possible to ascertain the minimum time at which wetting is achieved and also the time at which dewetting may start to occur.



Fig. 16. The minimum wetting time apparatus

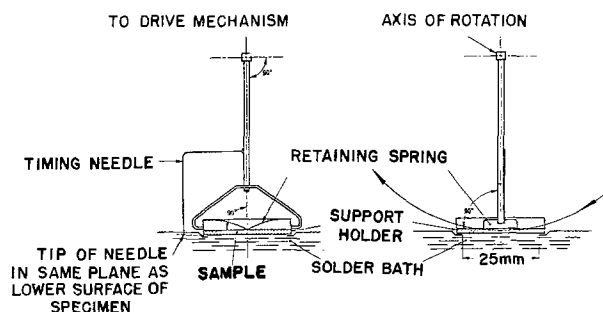


Fig. 17. Sketch of the rotary dip solderability tester. Right: front view; left: side view.

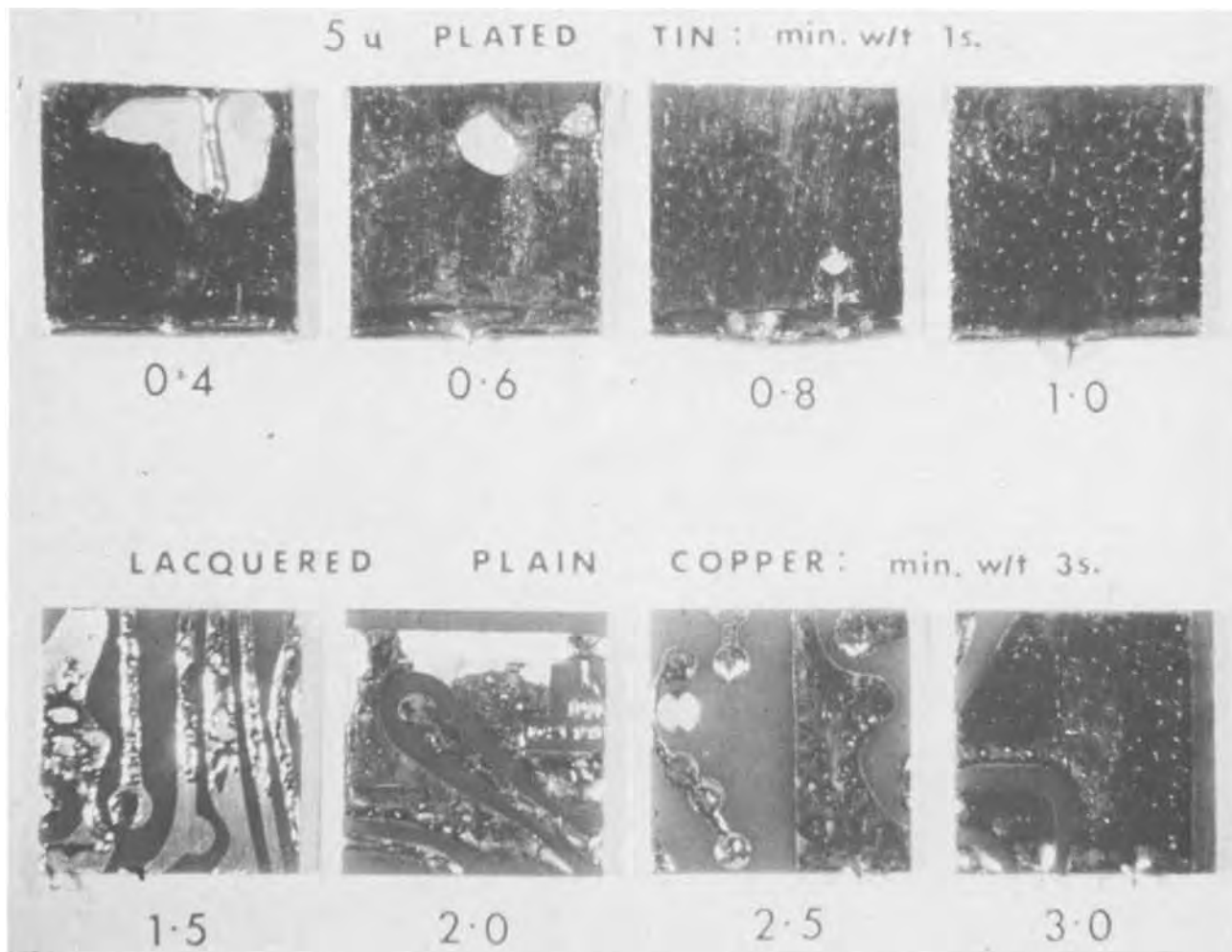


Fig 18. Progressive wetting of solder on test pieces

A typical series of test pieces is seen in Fig. 18. It may be seen that there is increasing coverage by the solder as contact time increases. The last specimens on the right in each series represents the wetting time for the specific material tested. Usually there is a narrow range in time at which wetting occurs. Shorter periods give rise to nonwetted surfaces. After full wetting is achieved, longer immersion times result in progressively poorer distribution of the solder. Often this latter effect is noted on test samples of copper clad laminates which have received inadequate or incorrect surface treatments.

The rotary dip solderability test is probably the simplest and most versatile method for quickly and inexpensively assessing solderability of printed circuit boards as well as plated-through holes in boards. With materials of good solderability there is little difficulty in obtaining capillary rise of solder plated through holes when the lower face of board samples is brought into contact with molten solder. Usually, solderability of the holes in circuit boards is based on the time and distribution of the solder rise to the top of the holes.

The rotary method of testing can be employed to check the suitability of different coatings and the optimum flux-solder-basis metal parameters for mass soldering operations. This wetting time test has been accepted by the International Electrotechnical Commission and published as their recommendation 68-2-20C, Part 2, Test T. The Rotary dip test is also in BS 4025 and the Swedish Production Engineering Standard. Tests conducted for the Institute of Printed Circuits have shown that this minimum wetting time test appears to be more sensitive to time in the bath than the edge dip test (27).

Summary

It would appear that soldering requirements for the future will be even more complex than for today's electronic circuitry. Consideration must be given to the mass joining of thousands of connections and soldering has proven to be a reliable and economical means for achieving this end. Solderability tests allow for a precise and objective method for assessing the ability of components to be soldered satisfactorily in the time and at the temperature appropriate to the assembly.

For the majority of quality assurance work, it is convenient to employ the rotary dip solderability test to evaluate solder-flux-metal systems and minimum wetting time of solders on coatings and basis metals. In addition, the Globule Test has shown to be a valuable tool in assessing the solderability of round termination wires. The use of these two tests will assure that all components and assemblies presented to the production line will have the highest solderability and ensure a minimum of repair work after soldering.

Manuscript submitted April 19, 1974; revised manuscript received July 29, 1974. This was Paper 111 presented at the New York, New York, Meeting of the Society, Oct. 13-17, 1974.

Any discussion of this paper will appear in a Discussion Section to be published in the December 1975 JOURNAL. All discussions for the December 1975 Discussion Section should be submitted by Aug. 1, 1975.

LIST OF SYMBOLS

θ	contact angle in degrees
V	volume in cubic centimeters
A	area in square centimeters

D diameter of sphere
H height of solder spot

REFERENCES

1. C. J. Thwaites, *Brit. Welding J.*, 543 (1965).
2. A. Latin, *J. Inst. Metals*, 72, 265 (1946).
3. H. Morimoto and I. Tanaka, *Tech. Rept., Toyo Kohan Co., Ltd.*, 4, 7 (1955).
4. E. J. Daniels and D. J. MacNaughtan, Tin Research Institute Publication No. B-6 (1937).
5. E. E. Schumacher, G. M. Bouton and G. S. Phipps, *Mater. Methods*, 22, 1407 (1945).
6. G. L. J. Bailey, *Sheet Metal Ind.*, 32, 47 (1955).
7. C. J. Thwaites, *Trans. Inst. Met. Finishing*, 36, 203, (1959).
8. G. L. J. Bailey and H. C. Watkins, *Metal Ind.*, 75, 551 (1949).
9. V. R. Miller, A. E. Schwaneke, and J. W. Jensen, Bureau of Mines, Report of Investigations 6963, 18 (1967).
10. L. Pessel, ASTM Special Technical Publication 189, Symposium on Solder, p. 159 (1965).
11. Anon., *Plating*, 52, 315 (1965).
12. *Ibid.*, 56, 819 (1969).
13. C. M. Adams, Jr., Tech. Rep. WAL TR 650/1 Contract No. DA-19-020-505-ORD-4917 Army Materials Research Agency, Watertown Arsenal, Watertown, Massachusetts, July, 1962.
14. Military Specification MIL-P-55110 (1968).
15. L. Pessel, *IEEE Trans. Prod. Eng. Prod.*, 28 (1963).
16. Military Standard, MIL-STD-202C, Method 208.
17. Electronic Industries Association Standard, EIA RS 178A.
18. Institute of Printed Circuits Standard, IPC-S-801.
19. H. H. Manko, *Evaluation Engineering*, 6, 20 (1967).
20. J. A. ten Duis and E. Van de Meulen, *Philips Tech. Rev.*, 28, 362 (1967).
21. J. A. ten Duis, *ibid.*, 20, 158 (1958/59).
22. D. MacKay, Proc. Inter/NEPCON, Ind. and Sci. Conf. Man. Inc., Brighton, 1970, 26 pp.
23. A. J. Mayhew and K. S. Monger, Proc. Inter/NEPCON, Ind. and Sci. Man., Inc., Brighton, 1970, 26 pp.
24. D. R. Wallis, *The Metallurgist and Materials Technologist*, 15 (1974).
25. C. J. Thwaites, *Elec. Mf.*, 8, 18 (1964).
26. C. J. Thwaites, *Welding J.*, 702 (1972).
27. A. T. Faro, Paper presented at Institute of Printed Circuits Spring Meeting, Miami (1974).



EST

The Effect of Low-Temperature Aging on Corrosion Resistance of 18Cr-2Mo Titanium-Stabilized Ferritic Stainless Steel

E. A. Lizlovs* and A. P. Bond*

Research Laboratory, Climax Molybdenum Company of Michigan, a Subsidiary of AMAX, Incorporated, Ann Arbor, Michigan 48106

ABSTRACT

Corrosion tests were conducted on 18Cr-2Mo titanium-stabilized ferritic stainless steel aged at 620°C for various time periods. Sensitivity to intergranular corrosion was detected in the Streicher test but not in the Strauss or Warren tests. The corrosion resistance in 45% boiling formic acid and in dilute chloride solution (600 ppm Cl⁻ + 20 ppm Cu⁺⁺, 90°C) was unaffected by aging at 620°C. Pitting potentials in molars NaCl at 25°C were also unaffected by the 620°C heat-treatment. Corrosion tests were also performed with the same 18Cr-2MoTi stainless steel aged at 475°C for 240, 2400, and 4800 hr (18Cr-2MoTi steel is embrittled after 240 hr at 475°C). The 475°C heat-treatment affected corrosion resistance to boiling formic acid. Corrosion resistance started to deteriorate after 2400 hr aging and was seriously impaired after 4800 hr aging. Pitting potentials were rendered less noble by the 475°C treatment. The 475°C embrittlement did not result in sensitization to intergranular corrosion in any environment as contrasted to the 620°C treatment which did sensitize the steel to intergranular corrosion in the Streicher test.

The ferritic stainless steels, even at high purity levels, are known to be sensitized to intergranular corrosion by exposure to temperatures in the range 600°-650°C (1-2). This type of sensitization generally has been detected either in Streicher or Huey tests, both of which involve highly oxidizing conditions. The mechanism invoked to explain the low-temperature sensitization usually is chromium carbide precipitation at the grain boundaries with resulting chromium depletion along the grain boundaries. However, a preliminary investigation disclosed that, while titanium-stabilized 18Cr-2Mo stainless steel was sensitized to intergranular corrosion in the Streicher test, the pitting potential of the steel was not affected by the 600°-650°C exposure, a finding inconsistent with the chromium depletion theory.

Prolonged exposure of ferritic stainless steel to still lower temperatures, near 475°C, causes a loss of ductility at room temperature. While the 475°C embrittlement phenomenon is well known, there is a definite lack of published information concerning the corrosion resistance of the embrittled ferritic stainless steels.

* Electrochemical Society Active Member.

Key words: intergranular corrosion, pitting potential, embrittlement, formic acid, chloride resistance.

Similarly, very little is known of the over-all corrosion resistance of ferritic stainless steel sensitized by low-temperature exposure. Therefore, an investigation was undertaken at Climax Laboratory to study the effect of low temperature aging on the over-all corrosion resistance of ferritic stainless steel.

Experimental Procedures

Materials and heat-treatment.—The material selected for this study was commercially produced, titanium-stabilized 18Cr-2Mo steel. Chemical composition of the stainless steel is given in Table I. The steel was exposed to the following heat-treatments: (i) 2 hr at 870°C, water quenched; (ii) 1 hr at 785°C, water quenched; (iii) 1 hr at 785°C, followed by 4 hr at 705°C and water quenched; (iv) 1 hr at 815°C, water quenched; (v) 1 hr at 815°C, water quenched, followed by 240 hr at 475°C, water quenched; (vi) 1 hr at 815°C, water quenched, followed by 2400 hr at 475°C, water quenched; (vii) 1 hr at 815°C, water quenched, followed by 4800 hr at 475°C, water quenched.

Samples from each of the base heat-treatments (i)-(iii) were further subjected to ¼, ½, 1, 4, and 10 hr exposures at 620°C. The 620°C temperature was known from preliminary experiments to cause the

Table I. Chemical composition of 18Cr-2MoTi ferritic stainless steel

Chemical composition, weight per cent															
C	Si	Mn	S	P	Cr	Mo	Ti	N	Cu	Ni	Sn	Pb	Ag	Al	O
0.007	0.37	0.40	0.007	0.008	18.95	2.00	0.17	0.010	<0.01	<0.01	0.02	0.002	0.0002	0.02	0.0059

most severe sensitization to intergranular corrosion in the Streicher test. Some samples from heat-treatment (iii) were also subjected to 64 hr aging at 620°C.

Immersion tests.—Intergranular corrosion resistance of the sensitized samples was determined by the Strauss, Streicher, and Warren tests (ASTM Designation A262-70) and of embrittled materials by the Strauss and Streicher tests. The Strauss test consists of exposing a sample for 24 hr in contact with metallic copper in boiling 16% sulfuric acid containing 6% copper sulfate. After the exposure, the test samples are bent to determine whether or not they will open at grain boundaries. The Streicher test consists of determining the corrosion rate over a 5 day period in boiling 50% sulfuric acid containing 25g of ferric sulfate per 600 ml of solution. The Warren test consists of exposing the test specimen to a solution containing 10% nitric and 3% hydrofluoric acid for 2 hr at 70°C. In view of high corrosion rates sustained by ferritic stainless steels in the Warren test, only one exposure period was employed.

The over-all corrosion resistance was evaluated in boiling formic acid and in dilute chloride solution. Formic acid tests were run for 24 hr and samples were activated by touching them with a magnesium rod immediately after immersion in acid. The tests were performed in 45 and 10% acid for embrittled materials and in 45% acid only for sensitized materials.

The dilute chloride test consisted of exposing test coupons from 1 to 2 weeks to an oxygenated solution containing 600 ppm Cl^- and 20 ppm Cu^{++} at 90°C. Corrosion coupons for all immersion tests, with the exception of the samples embrittled for 2400 and 4800 hr, were approximately 2.5 by 1.5 by 0.2 cm. Samples for 2400 and 4800 hr aging were prepared from tensile specimens and were 2.7 by 1 by 0.4 cm. All corrosion coupons were polished through No. 600 SiC paper. Prior to exposure, the corrosion coupons were washed with soap and water and rinsed in distilled water. After the exposure, the samples were rinsed and cleaned in an ultrasonic cleaner.

Pitting potentials.—Pitting potentials were determined in molar NaCl at 25°C using the potentiodynamic polarization technique. Potential scanning rate was 260 mV/hr. Electrode surfaces were polished through No. 600 SiC paper. Electrodes were masked with Glyptal to prevent interference by crevice corrosion (3). All potentials were measured against SCE and reported as volts vs. SCE.

Results

The results from the Streicher tests for the 18Cr-2MoTi steel exposed to the sensitizing heat-treatment at 620°C are summarized in Table II. The corrosion rates for the three basic heat-treatments [(i)-(iii)] were approximately the same. Metallographic examination indicated some intergranular attack for each of the three basic conditions. Each increment in sensitization time increased corrosion rates for each of the three basic heat-treatments. Increases in corrosion

Table II. Corrosion rates for 18Cr-2MoTi ferritic stainless steel in the Streicher test

Holding time at 620°C, hr	Corrosion rate, mg·dm ⁻² /day		
	Basic heat-treatment		
	870°C 2 hr, WQ	785°C 1 hr, WQ	785°C, 1 hr 705°C, 4 hr, WQ
0	327	358	337
¼	508	579	723
½	520	849	911
1	958	1282	1270
4	2075	3024	2580
10	3740	4860	3430
64	—	—	4380 ^a

^a Two-day exposure (all other samples exposed for 5 days).

rates were already evident after 15 min of sensitizing heat-treatment, especially for the 785°-705°C basic heat-treatment. After 4 hr of sensitizing treatment, corrosion rates were high for all three conditions. Metallographic examination showed extensive intergranular corrosion. No reductions in corrosion rates were observed after 10 hr of sensitization, nor after 64 hr. If anything, corrosion rates continued to increase with increased sensitization time. After sensitization for 64 hr, the corrosion rate was so high that tests could be run for 2 days instead of the normal 5 days.

The results from the Strauss test were completely different from those of the Streicher test. None of the sensitized samples, including the one sensitized for 64 hr, showed any intergranular corrosion. There was no visual evidence of any corrosion, and all samples could be bent without cracking. Hence, the low-temperature sensitization was not detectable by the Strauss test.

Corrosion rates in the Warren tests were high (Table III). The sensitization heat-treatment, however, did not increase these rates. Metallographic investigation showed that no significant intergranular corrosion occurred in this test for any samples sensitized up to 10 hr. After a sensitizing heat-treatment of 64 hr, some preferential grain boundary attack occurred; however, no grain dropping was observed. Thus, the Warren test did not reveal the low-temperature sensitization to intergranular corrosion, at least not up to 10 hr of sensitizing treatment.

The results from the formic acid exposure are shown in Table IV. While there were differences in corrosion rates, there was no definite pattern. It can be concluded that a sensitizing heat-treatment of up to 10 hr at 620°C had no effect on corrosion rates in boiling 45% formic acid. The differences in corrosion rates presumably resulted from differences in repassivation times. After activation, the sample will corrode for a given period of time; it then repassivates and no further corrosion takes place. If 18Cr-2MoTi steel continued to corrode actively, corrosion rates would be expected to be around 30,000 mg·dm⁻²/day (Table VII). Experiments involving an exposure for 1 week of a specimen sensitized for 10 hr at 620°C following a preliminary heat-treatment of 1 hr at 785°C plus 4 hr at 705°C confirmed that the specimen indeed repassivates after some corrosion following the activation. The corrosion rate after an exposure time of 1 week was 130 mg·dm⁻²/day. If all of the weight loss had been sustained within the first 24 hr, the corrosion rate then would be $130 \times 7 = 910$ mg·dm⁻²/day, which is within the range of corrosion rates obtained after 24 hr.

Table III. Corrosion rates for 18Cr-2MoTi stainless steel in 10% HNO₃ + 3% HF at 70°C (Warren test)

Holding time at 620°C, hr	Corrosion rate, mg·cm ⁻² /day		
	Basic heat-treatment		
	870°C 2 hr, WQ	785°C 1 hr, WQ	785°C, 1 hr 705°C, 4 hr, WQ
0	40,500	34,000	19,800
10	22,000	21,800	19,000
64	—	—	23,300

Table IV. Corrosion rates for 18Cr-2MoTi stainless steel in 45% boiling formic acid (24 hr exposure)

Holding time at 620°C, hr	Corrosion rate, mg·dm ⁻² /day		
	Basic heat-treatment		
	870°C 2 hr, WQ	785°C 1 hr, WQ	785°C, 1 hr 705°C, 4 hr, WQ
0	1245	891	979
¼	394	745	1161
½	1100	622	991
1	826	942	503
4	724	813	883
10	937	690	498

Table V. Corrosion rates for 18Cr-2MoTi ferritic and T304 and T316 austenitic stainless steels in 600 ppm Cl⁻ + 20 ppm Cu⁺⁺ at 90°C (1 week exposure)

Holding time at 620°C, hr	Ferritic stainless steels			Austenitic stainless steels	
	Corrosion rate, mg·dm ⁻² /day			T304	T316
	Basic heat-treatment				
	870°C, 2 hr, WQ	785°C, 1 hr, WQ	785°C, 1 hr, WQ 705°C, 4 hr, WQ		
0	0.7 1.1	0.4 0.4	0 1.7	31.5	21.7
¼	0.7 0	1.8 0.5	1.2 5.1		
½	3.0 0.9	1.6 0.3	0 1.9		
1	0.2 6.0	4.2 0.7	3.5 0.3		
4	0.4 0	0.5 4.1	0.6 0.9		
10	0.5 0.1	1.5 1.3	2.0 0.4		
64	0.1 5.9	1.2 0.3	1.7 0.4		
	0	2.7	1.5		
	0.4	1.2	0.7		
	0	0.3	0.1		
		0.8	—		
			1.0		
			0.8		

Table VI. Pitting potentials in molar NaCl at 25°C for 18Cr-2MoTi stainless steel

Basic heat-treatment	Holding time at 620°C, hr	Pitting potential, V vs. SCE
2 hr, 870°C, WQ	0	+0.400 +0.450
	¼	+0.430
	1	+0.465
1 hr, 785°C, WQ	10	+0.425
	0	+0.370
	1	+0.440
1 hr, 785°C 4 hr, 705°C, WQ	10	+0.455
	0	+0.420
	1	+0.410
	10	+0.460
	64	+0.430

Corrosion rates at 90°C in an oxygen-saturated solution containing 600 ppm Cl⁻ and 20 ppm Cu⁺⁺ are shown in Table V. Corrosion attack in this medium was localized in the form of small pits. Corrosion rates varied from 0 to 6 mdd, but no correlation with various heat-treatments was evident. Hence, the low temperature sensitization did not affect the corrosion resistance of 18Cr-2MoTi stainless steel to dilute chlorides. For comparison, the corrosion rates for solution-annealed samples of T304 and T316 stainless steel are also included in the table. Both of these standard austenitic grades of stainless steel suffered considerably more extensive corrosion damage than any of the 18Cr-2MoTi samples. Pitting potentials for the samples from the three basic heat-treatments and for the sensitized samples are given in Table VI. Pitting potentials for the samples from the 870° and 785°-705°C

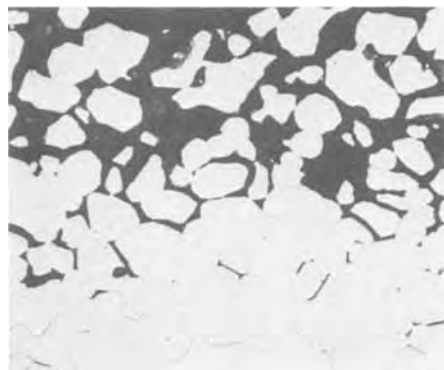


Fig. 1. Microstructure of 18Cr-2MoTi specimen after Streicher test (prior to test sample treated for 2 hr at 870°C, then sensitized for 10 hr at 620°C). Magnification 250X.

basic heat-treatments were of comparable magnitude, while the sample from the 785°C treatment had slightly lower pitting potential. The 620°C sensitizing heat-treatment did not result in any deterioration of pitting potentials; if anything, pitting potentials for sensitized samples tended to be somewhat more noble than for the basic heat-treatment. The pitting potentials for all sensitized samples were of comparable magnitude.

Results from the tests with samples aged at 475°C from 240 to 4800 hr were quite different from the results for samples exposed to 620°C sensitizing heat-treatment. It should be noted here that a marked drop of impact strength is already noticeable after 240 hr of exposure. Results from various corrosion tests are summarized in Table VII. The 18Cr-2MoTi steel passed the Strauss test after 240 hr of aging at 475°C, and the corrosion rates in the Streicher test were the same as for the basic heat-treatment (*iv*) above. After 2400 hr at 475°C, corrosion rates in the Streicher test were about an order of magnitude higher than for the basic heat-treatment. However, the mode of attack in the Streicher test was different for the embrittled sample than for the sample sensitized at 620°C. Metallographic investigation showed that while the sample exposed to 620°C suffered severe intergranular attack in the Streicher test, the sample aged for 2400 hr at 475°C suffered general corrosion (Fig. 1 and 2). Thus the embrittled samples were not sensitive to intergranular corrosion either in the Strauss or the Streicher tests.

Corrosion rates in boiling formic acid were quite sensitive to 475°C aging. The samples embrittled for 240 hr failed to repassivate in most cases in boiling 45% acid, and consequently much higher corrosion rates were obtained with embrittled than with standard specimens. In 10% acid, samples embrittled for 240 hr did repassivate and corrode at a negligible rate, but after 2400 hr of aging the samples failed to repassivate.

The deterioration of corrosion resistance in dilute chlorides was less dramatic than in formic acid. After

Table VII. Corrosion rates for 18Cr-2MoTi ferritic stainless steel after prior 475°C aging (2 week exposure)

Type of test	Sample No.	Corrosion rate, mg·dm ⁻² /day after indicated thermal treatment			
		1 hr, 815°C, WQ	240 hr, 475°C, WQ	2400 hr, 475°C, WQ	4800 hr, 475°C, WQ
Strauss test	1	Pass	Pass	Not tested	Not tested
Streicher test	1	324	335	2,800	Not tested
	2	366	434	3,610	Not tested
Formic acid: 10% (boiling)	1	3.2	2.7	23,000	Not tested
	2	nil	nil		
45%	1	873	33,100	Not tested	Not tested
	2	123	808		
	3	957	30,300		
600 ppm Cl ⁻ 20 ppm Cu ⁺⁺ 90°C, O ₂	1	0.2	0.1	1.7	55.6 ^a
	2	nil	0.7	1.5	99.6 ^a
	3			2.7 ^a	
	4			4.2 ^a	

^a Samples exposed for 1 week only.

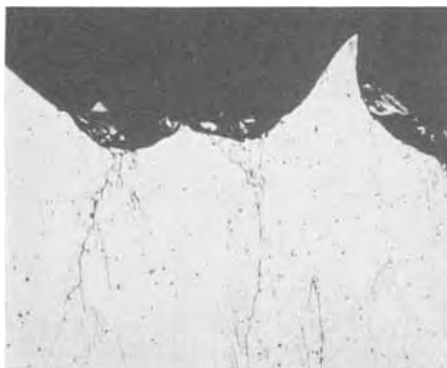


Fig. 2. Microstructure of 18Cr-2MoTi specimen after Streicher test (prior to test sample heated for 1 hr at 815°C, then embrittled for 2400 hr at 475°C). Magnification 500X.

240 hr of aging, there was no evidence of any loss of corrosion resistance. Some tendency of the corrosion rate to increase was first manifested after aging for 2400 hr. However, after aging for 4800 hr, severe loss of corrosion resistance in dilute chlorides was observable.

The pitting potentials for the standard heat-treatment and after 240 and 2400 hr aging at 475°C are summarized in Table VIII. As can be seen from the data in this table, the pitting potentials became more active as the aging time at 475°C increased. Comparison of pitting potentials in Tables VI and VIII discloses that the basic heat-treatment which resulted in the lowest pitting potential, 0.338V, SCE average, was 815°C. The differences in pitting potentials for various basic heat-treatments, however, are relatively small.

Discussion

The 620°C aging and the 475°C aging evidently affect the corrosion properties of 18Cr-2MoTi ferritic stainless steel by different mechanisms. The effect of aging at 475°C on the corrosion behavior can be rationalized considering the α' precipitation reaction. The embrittlement, as established by the work of Fisher, Dulis, and Carroll (5) is caused by the precipitation of α' phase, which has been identified as an Fe-Cr phase with 60-80% Cr. According to an earlier investigation (4) the α' precipitate becomes just visible, primarily at dislocations, after 240 hr at 900°F (480°C) exposure. After a 2400 hr exposure, α' particles are not only larger in size but are also present on grain boundaries and in the matrix. Since α' phase is rich in chromium, some depletion of Cr from the matrix accompanies the precipitation reaction. Lowering of chromium in the matrix would lead to a failure to repassivate in formic acid and to the loss of passivity in the Streicher test. Since the Streicher test involves highly oxidizing conditions, loss of passivity requires more severe chromium depletion than is achieved after a 240 hr heat-treatment. Since α' precipitation involves rather mild chromium depletion, especially in the initial stages, no

intergranular attack is observable in the Streicher test for samples treated for only 240 hr. After 2400 hr, chromium depletion apparently is sufficient to cause general loss of passivity. The depletion of chromium from the matrix also would lead to a shift of pitting potentials to more active values.

The effects of the 620°C aging are more difficult to rationalize. It is known that the maximum temperature for the occurrence of α' precipitation in 18Cr-2Mo steels is less than 540°C (4). On the other hand, the results of this investigation are not in accord with the carbide precipitation and chromium depletion theory proposed to explain the mechanism of low-temperature sensitization of ferritic stainless steels. Since the corrosion resistance in formic acid and in the Strauss test and the pitting potential were unaffected, most probably chromium depletion is not the main factor in low-temperature sensitization. It has been demonstrated that pitting potentials are greatly affected by sensitization of unstabilized ferritic stainless steels to intergranular corrosion (6,7). It is possible that some precursor of a chromium-rich intermetallic phase is formed along grain boundaries during heat-treatment around 620°C and is preferentially attacked in highly oxidizing media. A similar phenomena is thought to occur in T316L austenitic stainless steel which can suffer intergranular attack in nitric acid because of submicroscopic sigma phase (8). This hypothesis is further strengthened by the observation that the attack is more severe in the Streicher solution after a holding time of 64 hr at 620°C than after short holding times. If chromium depletion occurred because of precipitation of chromium carbonitrides, chromium back-diffusion from the matrix would be expected after long sensitization times, and consequently, in the Streicher test there would be a reduction in corrosion rate.

Another indication that chromium carbonitride precipitation at 620°C was not the only cause of loss of corrosion resistance is given by the lack of significant differences in aging behavior after the three different initial treatments. It was intended that these initial treatments would modify the amounts of carbon and nitrogen in solid solution and available for precipitation during aging. In particular, it was thought that a 4 hr hold at 705°C would cause a greater amount of the carbon and nitrogen to be precipitated as titanium carbonitride than would be the case for material quenched from 870°C. Unfortunately, quantitative information on the solubility of titanium carbides or nitrides at these temperatures is not available.

Failure to find evidence of chromium carbonitride precipitation leading to chromium depletion in this titanium-stabilized steel does not imply that chromium depletion may not occur in unstabilized steels. In fact, Rarey and Aronson (6) have reported work on sensitization at 620°C of unstabilized 25% Cr alloys containing 0-3% Mo that is consistent with the occurrence of chromium depletion because of chromium carbonitride precipitation. They found that the maximum loss in resistance to pitting and intergranular corrosion occurred after 15-60 min at 620°C and that corrosion resistance equivalent to that of the unaged alloy was recovered after about 4 hr at 620°C.

Another possible explanation of the effect of aging involves direct attack of highly oxidizing media on titanium carbonitrides. Bäuml (9) has demonstrated that bulk titanium carbide is attacked at highly oxidizing potentials and direct attack on titanium carbonitrides is thought to occur in boiling 65% HNO₃ in some titanium stabilized steels (10, 11). However, for this sort of attack to explain the intergranular corrosion observed in boiling Fe₂(SO₄)₃-50% H₂SO₄ a continuous or nearly continuous grain boundary film of titanium carbonitride would be required. Since most of the available carbon and nitrogen are thought to be precipitated as massive titanium carbonitrides during the initial anneal it is not clear how such continuous films

Table VIII. Pitting potential in molar NaCl at 25°C for 18Cr-2MoTi stainless steel

Heat-treatment	Pitting potential, V vs. SCE
1 hr at 815°C, WQ	+0.355
	+0.320
240 hr at 475°C, WQ	+0.338 Avg
	+0.263
	+0.305
	+0.265
	+0.278 Avg
2400 hr at 475°C, WQ	+0.155
	+0.150
	+0.153 Avg
	+0.153 Avg

could form on aging. It also seems likely that the different initial heat-treatments would have had a larger effect on the subsequent formation of titanium carbide films than was observed. Finally, no metallographic evidence of such a grain boundary film was obtained.

The results of this investigation clearly demonstrate that the low-temperature sensitization of 18Cr-2Mo titanium-stabilized ferritic stainless steel affects corrosion resistance only under highly oxidizing conditions, such as the Streicher test and the Huey test (1). Other corrosion properties, such as resistance to boiling organic acids, resistance to chlorides, and resistance to intergranular corrosion under moderate oxidizing conditions (Strauss test) are not adversely affected, and therefore, the exposure to temperatures around 600°C should not, for most cases, be detrimental to corrosion resistance of 18Cr-2MoTi stainless steel. Further work with both stabilized and unstabilized high-purity ferritic stainless steels is needed to demonstrate to what extent the above conclusions can be generalized or if they apply specifically to 18Cr-2MoTi steel.

Conclusions

1. The corrosion resistance of 18Cr-2MoTi ferritic stainless steel in most environments in unaffected by aging at 620°C for up to 10 hr. Low-temperature sensitization to intergranular corrosion is revealed only under highly oxidizing conditions, such as the Streicher or Huey tests. No sensitivity to intergranular corrosion is revealed either in Strauss or Warren (HNO₃-HF) tests.

2. The 475°C embrittlement treatment affects the corrosion resistance of 18Cr-2MoTi stainless steel in all

test media. While detrimental effects on corrosion properties were evident after a 240 hr treatment at 475°C, further gradual deterioration of corrosion resistance was observable after a 2400 and 4800 hr exposure. Corrosion properties adversely affected were resistance to boiling formic acid, pitting potential, and resistance to chlorides. The 475°C treatment does not lead to intergranular corrosion in the Streicher test.

Manuscript submitted July 8, 1974; revised manuscript received Jan. 10, 1975. This was Paper 114 presented at the Boston, Massachusetts, Meeting of the Society, Oct. 7-11, 1973.

Any discussion of this paper will appear in a Discussion Section to be published in the December 1975 JOURNAL. All discussions for the December 1975 Discussion Section should be submitted by Aug. 1, 1975.

Publication costs of this article were partially assisted by the Climax Molybdenum Company of Michigan.

REFERENCES

1. R. J. Hodges, *Corrosion*, **27**, 119 (1971).
2. R. J. Hodges, *ibid.*, **27**, 164 (1971).
3. E. A. Lizlovs and A. P. Bond, *This Journal*, **118**, 22 (1971).
4. P. J. Grobner, *Met. Trans.*, **4**, 251 (1973).
5. R. M. Fisher, E. J. Dulis, and K. G. Carroll, *Trans. AIME*, **197**, 690 (1953).
6. C. R. Rarey and A. H. Aronson, *Corrosion*, **28**, 255 (1972).
7. A. P. Bond, *This Journal*, **120**, 603 (1973).
8. D. Warren, *Corrosion*, **15**, 221t (1959).
9. A. Bäuml, *Stahl Eisen*, **84**, 798 (1964).
10. A. P. Bond and E. A. Lizlovs, *This Journal*, **116**, 1305 (1969).
11. A. P. Bond, *Trans. Met. Soc. AIME*, **245**, 2127 (1969).

Initial Anodic Growth of Oxide Film on Platinum in 2N H₂SO₄ under Galvanostatic, Potentiostatic, and Potentiodynamic Conditions: The Question of Mechanism

Lee B. Harris* and A. Damjanovic

Xerox Corporation, Webster Research Center, Webster, New York 14580

ABSTRACT

Potentiodynamic, galvanostatic, and hybrid galvanopotentiostatic experiments were conducted in O₂ saturated 2N H₂SO₄ on a polished platinum disk electrode. The results show conclusively that for coverage between one and three monolayers the law of anodic growth of oxide film on platinum is precisely the same regardless of the mode of growth (i.e., potentiostatic, galvanostatic, or potentiodynamic). A correspondence is analytically established between galvanostatic and potentiodynamic data, and this correspondence is verified experimentally. Galvanostatic and potentiodynamic data both show that the growth of the oxide film cannot be explained by any mechanism for which $(\partial V/\partial q)_i$ is independent of i (e.g., adsorption). The high-field ionic conduction model accounts for the major features of all the data. A comparison of galvanostatic and hybrid galvanopotentiostatic experiments shows that there is no aging of the film over a time interval, Δt , comparable to the duration of the experiments (20 sec $\leq \Delta t \leq$ 150 sec). The effect of "holding" (i.e., interrupting the potential sweep and maintaining a constant potential for a time) during potentiodynamic experiments is explained entirely in terms of the potentiostatic growth of the oxide film during the holding period.

It has been suggested by Ord and Ho (1) and others (2, 3) that the formation of anodic oxide film on platinum is controlled by high-field ionic conduction even in the earliest stages of growth. This model is controversial, however, and to settle the controversy one

must answer the following two questions: (a) Is the growth rate (i.e., the current density, i , associated with oxide growth) uniquely determined by the potential, V , and the thickness of the oxide film already formed (i.e., the charge $q = \int_0^t i dt$)? and (b) If so, what is the dependence of i on V and q , and is this dependence more satisfactorily explained by the high-field conduction model than by other proposed mechanisms?

* Electrochemical Society Active Member.

Key words: platinum, anodization, potentiodynamic, galvanopotentiostatic, mechanism.

The growth of the anodic film on platinum has been investigated by galvanostatic (1-3), potentiostatic (4, 5), and potentiodynamic (*i.e.*, potential sweep) experiments (6-8) with conflicting results and conclusions.

Experimental galvanostatic charging curves can be fitted (2, 3) by an equation of the form

$$\ln i = a + (V - V')/b(q) \quad [1]$$

where a and V' are constants, $b(q)$ is a linear function of q , and V is the anode potential with respect to a reference electrode. If the q -scale is shifted so that $b(q)$ becomes cq , and if V' is associated with electric fields outside the oxide film (*e.g.*, in the double layer) then Eq. [1] may be interpreted in terms of the Cabrera-Mott model of oxide growth in which metal ions are assumed to be injected and to migrate by field-assisted thermal hopping over a potential barrier. (The electric field pertaining to this process is $(V - V')/cq$.)

Equation [1] implies that under potentiostatic conditions $\ln i$ is inversely proportional to q ; but this relationship has not been satisfactorily established in potentiostatic experiments with platinum. For example, Gilman's potentiostatic measurements (4) appear to show that near monolayer coverage

$$\ln i = A - q/B \quad [2]$$

where A and B are constants at any particular potential. Integration of Eq. [2] yields

$$i = B/(t + t_0) \quad [3]$$

and

$$q = q' + B \ln(t + t_0) \quad [4]$$

where q' is a constant of integration and t_0 is determined by A and B . The results of potentiostatic experiments by Vetter and Schultze (5) fit Eq. [3] and [4], which imply [2] rather than [1]. Potentiostatic data on platinum oxidation has not provided evidence for the Cabrera-Mott model.

The potentiodynamic method has been used by Böld and Breiter (6), and more recently by Conway and co-workers (7, 8), among others. However, the usefulness of potentiodynamic data has been limited to some extent by the lack of a quantitative analysis relating it to galvanostatic and potentiostatic data, which are more easily interpreted than potentiodynamic data.

We initiated a series of experiments designed specifically to determine whether under otherwise identical conditions galvanostatic and potentiostatic data yield the same results, and to relate the results to potentiodynamic experiments conducted under the same conditions. Potentiodynamic, galvanostatic, and "hybrid" experiments were performed. The latter are initiated galvanostatically and continued potentiostatically at a preselected potential without interruption.

An especially important objective of this study is a better understanding of the results of the potentiodynamic experiments and their connection with galvanostatic and potentiostatic experiments on the growth of the oxide film.

Experimental

The all-Pyrex electrochemical cell is of conventional design. It has three compartments with separate gas bubblers in the main compartment and the compartment containing the counterelectrode (Pt foil, 2 cm²). A stopcock connects the reference electrode (saturated calomel, SCE) compartment to the main compartment containing the working electrode.

The working electrode, which is diamond-polished to a mirror finish, is the disk portion of a platinum ring-disk electrode. The disk diameter is 5 mm, the ring outer diameter is 7 mm, and the ring-disk spacing is approximately 0.2 mm. The electrode enters the cell from above through a closefitting, stationary Teflon washer that protects the interior of the cell from laboratory atmosphere.

In order to insure nearly cylindrical electrode geometry, the electrical path from the counterelectrode compartment is constrained by a glass tube (~1 cm diam) the open end of which faces the disk at a distance of about 1 cm. To reduce the fringe field at the edge of the disk, the ring is maintained at the same potential as the disk.

Control of potential or current at the disk is effected by conventional circuitry. The disk is kept at virtual ground potential by means of a chopper-stabilized current-to-voltage converter, and the ring is hard-grounded. For potential measurements a Luggin capillary (about 1 mm diam) is centered below the ring about ¼ mm from it.

For some experiments the circuitry is comprised of operational amplifiers (Analog Devices Inc. Models 234J or 184K). For other experiments a commercial potentiostat (Princeton Applied Research (PAR) Model 173) is used, but the circuitry functions in essentially the same way in both cases. A PAR Model 175 Universal Programmer was used for potentiodynamic experiments. All measurements were made using a Tektronix Model 7623 storage oscilloscope in the X-Y mode.

Solutions were prepared from Baker Reagent Grade sulfuric acid and triply distilled water. The cell and all glassware used in preparing the solutions were washed with a hot mixture of concentrated nitric and sulfuric acids and thoroughly rinsed with distilled water. Prior to each series of experiments the electrode was anodically oxidized and cathodically reduced several times and the solution then replaced. For all experiments the 2N H₂SO₄ solution was saturated with oxygen (Linde Ultra High Purity Grade). Except for about 1 in. of Tygon, only glass, metal, and Teflon are used in the gas line.

Results and Discussion

Potentiostatic vs. galvanostatic experiments.—Figure 1 shows a reproduction of the oscilloscope storage screen¹ after recording galvanostatic transients at four different current densities,² starting with 5 mA/cm² and decreasing by an order of magnitude for each subsequent test. Just prior to each test, any oxide film on the electrode was cathodically reduced. The electrode was then held for a few seconds at a potential just short of hydrogen evolution (~0.0V vs. SCE) and then allowed to drift at zero current to its "rest potential,"

¹ This and subsequent figures are carefully traced from the original photographs. All features, including the width of the trace and any noise on it are reproduced.

² Current densities are based on the geometrical area of the working electrode (0.20 cm²) and are not corrected for roughness factor.

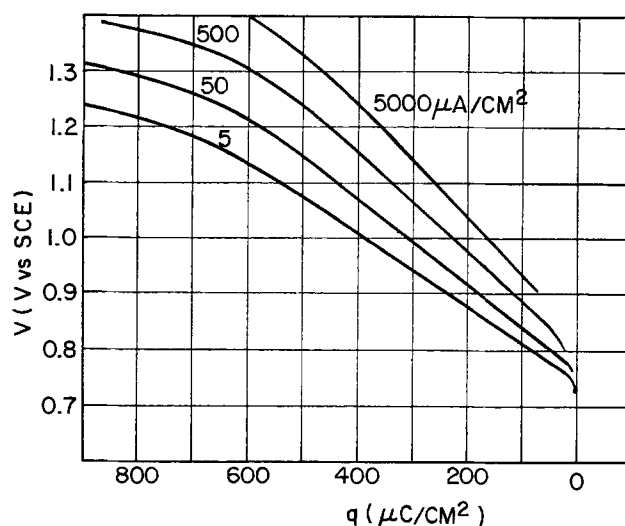


Fig. 1. Galvanostatic charging curves. Conditions are described in text.

in this case $+0.735V$ vs. SCE. The oscilloscope beam intensity was then turned up, an electronic integrator (connected to the output of the current-to-voltage converter) was started (by disconnecting with a toggle switch a small resistor across the integrating capacitor), and the current control then immediately switched³ from zero to a preset value. The potential of the working electrode is recorded in the vertical direction. For the sake of resolution a portion of the potential is (very precisely) suppressed. The output of the integrator is recorded horizontally. Following each run the electron beam was turned off and the integrating capacitor was discharged through a small resistor. The results shown in Fig. 1 are highly reproducible; two sets of tests conducted a week apart agree to within the width of the oscilloscope trace. Curves similar to those shown in Fig. 1 have been reported before and have recently been quantitatively analyzed to elucidate the mechanism of film growth (2, 3). In the present study, the curves in Fig. 1 may be considered to represent the relationship between potential (V), current density (i), and charge density (q), the latter being a measure of the thickness of the film formed during the experiment (assuming that no current is taken by any competitive reaction such as metal dissolution or oxygen evolution). If a unique relationship exists between these three variables; i.e., if

$$i = i(V, q) \quad [5]$$

then each point of the V, q diagram, no matter how it is reached, should correspond to a particular value of i . Conversely, if the current at each point (V, q) is independent of the manner in which the point is reached, this is evidence in support of Eq. [5].

Each measured point in Fig. 1 is reached along a path for which the current is constant. A particularly simple alternative to this is a hybrid "galvano-potentiostatic" path such as that shown in Fig. 2. The hybrid experiment shown in Fig. 2 was started galvanostatically (at 5 mA/cm^2) and switched from the galvanostatic mode to the potentiostatic mode at a particular potential. The switching⁴ is accomplished by a relay that closes when the potential reaches the desired value; e.g., $1.2V$ (SCE) in Fig. 2. The broken trace in Fig. 2 is a record of the current, the break being the point at which scope sensitivity is increased by a factor of twenty. The potential overshoots the mark by about 20 mV , probably due to an overload during the switch-

³ This switching was sometimes done electronically (when using the PAR potentiostat) but a manually operated toggle switch is satisfactory and was used for the tests shown in Fig. 1.

⁴ The circuitry for this is described by Bruckenstein and Miller (10). In the present experiments the switch S-1 [in Fig. 1 of Ref. (10)] is a mercury-wetted relay driven by a comparator.

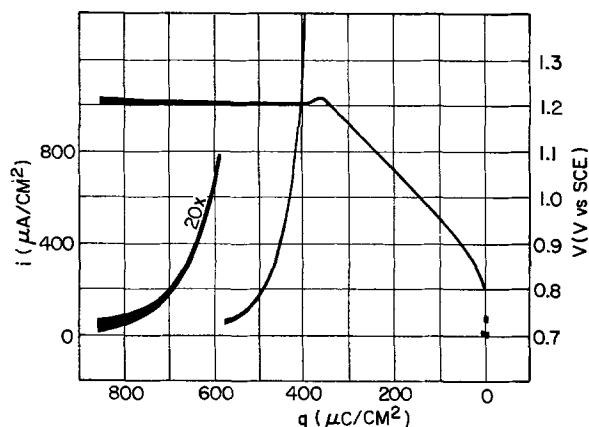


Fig. 2. Hybrid experiment. Continuous trace is potential. Current trace is broken where scope sensitivity was increased. Galvanostatic segment: 5 mA/cm^2 . Potentiostatic segment: $1.2V$. Other conditions described in text. Dots at lower right are starting positions of the two traces.

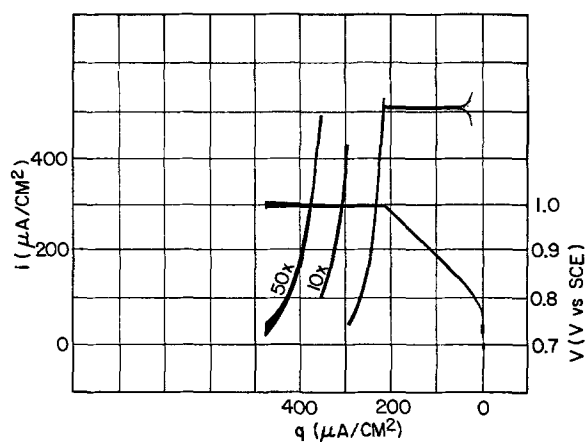


Fig. 3. Hybrid experiment. Galvanostatic segment: 500 μA/cm^2 . Potentiostatic segment: $1.0V$. See caption Fig. 2.

ing transient. This overshoot does not occur at lower currents, as shown in Fig. 3, which is a record of an experiment that was started at 500 μA/cm^2 and was switched to constant potential at $1.0V$. In Fig. 2 the current sensitivity is initially set at the highest value that will permit a record of the current just after the switching transient; for this reason the initial, constant current is not seen as it is in Fig. 3. Figure 2 represents the first of a series of galvano-potentiostatic experiments starting at 5 mA/cm^2 and switching to constant potential at $1.2, 1.1, 1.0,$ and $0.9V$ (SCE). In Fig. 4 the potentiostatic portions of these hybrid experiments are compared with the galvanostatic data of Fig. 1 by plotting the logarithm of the current density vs. the charge density at each potential for both sets of data (see caption, Fig. 4). The good agreement of the gal-

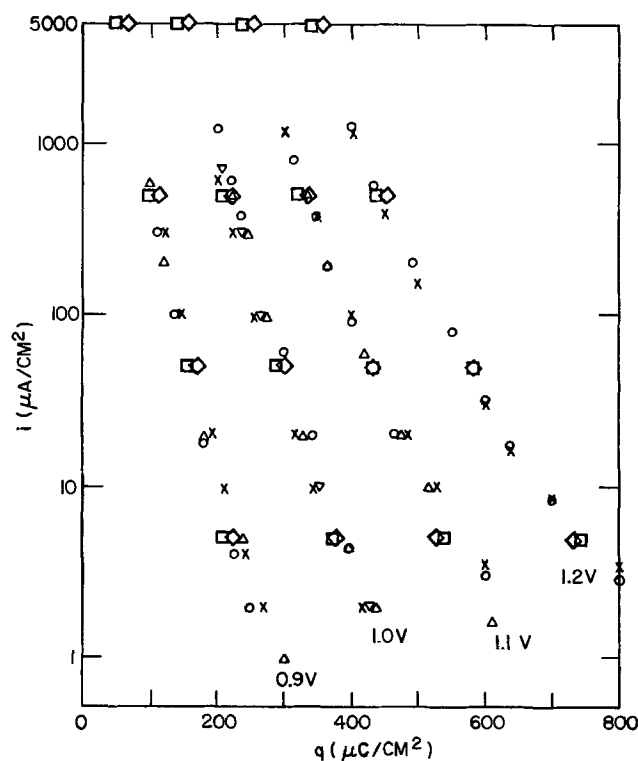


Fig. 4. Comparison of results of galvanostatic and hybrid experiments. Boldface symbols (\square, \diamond) are galvanostatic data; each horizontal row of symbols represents data from two repetitions at the same current. \square and \diamond are two weeks apart. Smaller symbols are from potentiostatic portion of hybrid experiments starting at 5 mA/cm^2 and continuing at the potential indicated at the bottom of each of the four strings of points (vs. SCE).

vanostatic and the hybrid data shows that Eq. [5] holds for both experimental modes. This further indicates that those properties of the film that affect film growth (e.g., the injection and transport of metal ions) do not change over a time period comparable to the duration of these experiments. For example, referring to Fig. 2, the time required to transfer 750 $\mu\text{coulombs/cm}^2$ (at which point $i = 5 \mu\text{A/cm}^2$) is about 19 sec as can be calculated from the formula $t = \int_0^q dq/i$. The same charge is transferred in 150 sec galvanostatically at 5 $\mu\text{A/cm}^2$; yet in both cases the potential corresponding to $i = 5 \mu\text{A/cm}^2$ and $q = 750 \mu\text{coulombs/cm}^2$ is 1.20V (SCE). This is strong evidence against any aging effects in these experiments.

Potentiodynamic vs. galvanostatic experiments.—The potentiodynamic method is not as simple conceptually as either the galvanostatic or potentiostatic method, and when applied to a system governed by an equation such as [1] the following analysis is helpful in understanding the behavior of the system.

Figure 5 shows a schematic representation of galvanostatic curves (labeled i_1, i_2, i_3) for a system governed by Eq. [5]. The heavy curve T that crosses the galvanostatic curve i_2 at (V_0, q_0) represents the locus of successive states (V, q) traversed by the system (in the direction of the arrow) during a hypothetical anodic potential sweep. In an anodic potential sweep experiment

$$\frac{dV}{dt} = \text{const.} \equiv S > 0 \quad [6]$$

and the slope at each point (V, q) on curve T is

$$\frac{dV}{dq} \equiv \frac{dV}{dt} \bigg/ \frac{dq}{dt} \equiv S/i(V, q) \quad [7]$$

If at any point on T its slope dV/dq is not equal to the slope of the galvanostatic curve passing through the same point, then the current is changing as the system passes through that point. For example, at (V_0, q_0) the slope of T is greater than that of the galvanostatic curve i_2 ; so T crosses i_2 and in passing through (V_0, q_0) in the direction of the arrow the system therefore moves from currents less than i_2 to currents greater than i_2 . Likewise if at any point on T its slope is less than that of the galvanostatic curve passing through that point, the current is decreasing. To formalize this argument, take V as the independent variable and, using Eq. [5], write

$$\frac{di}{dV} = \left(\frac{\partial i}{\partial V} \right)_q + \left(\frac{\partial i}{\partial q} \right)_V \frac{dq}{dV} \quad [8]$$

Using the identity

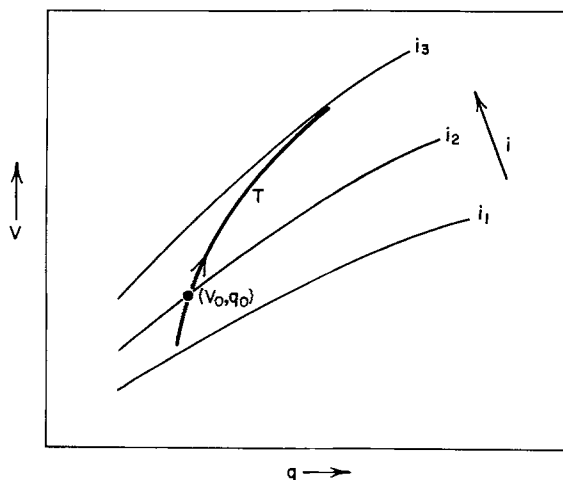


Fig. 5. Schematic diagram showing potentiodynamic response of a system governed by Eq. [5].

$$\left(\frac{\partial i}{\partial q} \right)_V \equiv - \left(\frac{\partial i}{\partial V} \right)_q \left(\frac{\partial V}{\partial q} \right)_i \quad [9]$$

Eq. [8] can be rewritten

$$\frac{di}{dV} = \left(\frac{\partial i}{\partial V} \right)_q \left[1 - \left(\frac{\partial V}{\partial q} \right)_i \bigg/ \frac{dV}{dq} \right] \quad [10]$$

Equation [10] shows that as the potential increases, the current will increase or decrease depending on whether the ratio $(\partial V/\partial q)_i/dV/dq$ is less than or greater than one [since $(\partial i/\partial V)_q, (\partial V/\partial q)_i > 0$ for usual electrochemical systems].

Returning to the discussion of curve T in Fig. 5, as the current increases, its rate of increase diminishes (cf. Eq. [10]) because dV/dq becomes smaller due to the relationship [7]. Thus, the current changes less and less rapidly and the system approaches a "steady state" in which dV/dq is equal to $(\partial V/\partial q)_i$; i.e., curve T becomes parallel to a galvanostatic curve. By substituting Eq. [7] into [10] we obtain

$$\frac{di}{dV} = \left(\frac{\partial i}{\partial V} \right)_q \left[1 - i \left(\frac{\partial V}{\partial q} \right)_i \bigg/ S \right] \quad [11]$$

from which it is clear that the steady-state current, i_s (i.e., the current such that its rate of change is zero) satisfies the condition

$$S/i_s = \left(\frac{\partial V}{\partial q} \right)_i \quad [12]$$

If the transient process shown in Fig. 5 takes place very quickly, it will be completed early in the potentiodynamic experiment, which then rapidly becomes nearly indistinguishable from a galvanostatic experiment. This is true of the potentiodynamic experiments to be discussed in this section. Before going on to these experiments, however, let us briefly examine (within the framework of the preceding discussion) the differences between steady-state potentiodynamic oxidation and adsorption.

Equation [5] sometimes has the special form

$$i = f(q, \eta) \quad [13]$$

where

$$\eta = V - V_e(q) \quad [14]$$

$V_e(q)$ may be called the "adsorption isotherm" (e.g., for the Temkin isotherm, $V_e(q) \equiv \text{const.} \times q$). Using Eq. [9], it can then easily be shown that

$$\left(\frac{dV}{dq} \right)_i = - \frac{\partial f}{\partial q} \bigg/ \frac{\partial f}{\partial \eta} + \frac{dV_e}{dq} \quad [15]$$

A particular special case, one that is often used in the literature (6, 7, 11), is that for which $f \equiv l(q) \exp(\eta/E)$ where $l(q)$ is a linear function of q and E is constant. For this case

$$\left(\frac{\partial V}{\partial q} \right)_i = \text{const.} \times E/l(q) + \frac{dV_e}{dq} \quad [16]$$

which does not depend on V and hence is independent of i .⁵ It follows from Eq. [12] that in this case the steady-state potentiodynamic current would be strictly proportional to S .

In contrast to this case, for the anodic oxidation of platinum (below $\sim 1.3\text{V}$ vs. SCE), $(\partial V/\partial q)_i$ increases with i (cf., Fig. 1). Therefore, according to Eq. [12] i_s must increase less rapidly with S than would be required by strict proportionality.

From Fig. 1 it can be determined that $(\partial V/\partial q)_i$ increases (linearly with $\log i$) by 50% as i increases from 5 $\mu\text{A/cm}^2$ to 5 mA/cm^2 ; this is shown graphically in Fig. 6. Using these data and Eq. [12] one may determine for various values of S , the steady-state cur-

⁵ Another somewhat more general case of interest is that for which the current depends much more strongly on η than on q ; i.e., $\partial f/\partial \eta \ll \partial f/\partial q$ (or, more precisely, $(\partial \eta/\partial q)_i \ll dV_e/dq$). In this case, $(\partial V/\partial q)_i \approx dV_e/dq$, which is also independent of i .

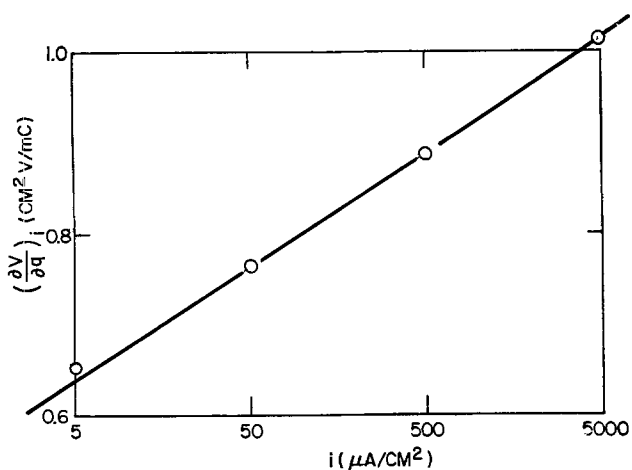


Fig. 6. Slopes of galvanostatic charging curves in Fig. 1, plotted vs. current density.

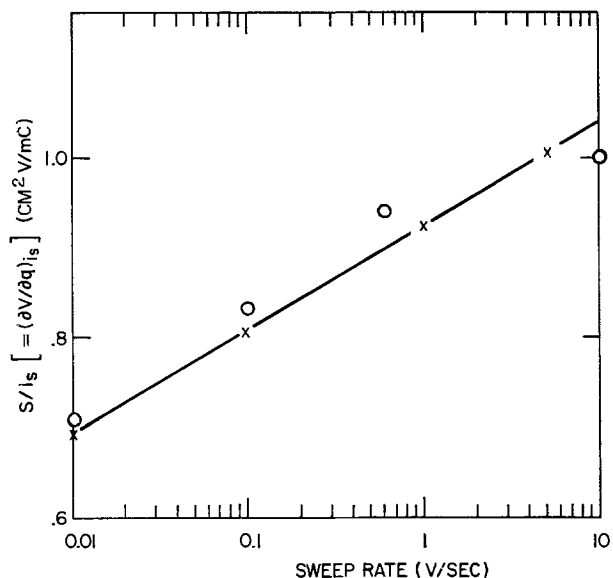


Fig. 7. Ratio of sweep rate S to steady-state potentiodynamic current i_s . X, calculated from galvanostatic data using Eq. [12]; O, measured.

rent i_s and the quantity $S/i_s \equiv (\partial V/\partial q)_i$ (which would have to be constant if i_s were proportional to S). In Fig. 7, values of S/i_s determined in this way are plotted (points marked X) as a function of S . Also plotted in the figure are values of S/i_s (points marked O) from potentiodynamic experiments (*vide infra*). The agreement between the potentiodynamic data and the results derived from galvanostatic data is good, the largest discrepancy being less than 5%. This verifies the validity of Eq. [12] and shows that the deviation from linearity (*i.e.*, about 50%) as measured by the variation of S/i_s is very close to the prediction based on the variation of $(\partial V/\partial q)_i$ in the galvanostatic experiments. Thus, the potentiodynamic and the galvanostatic data both show that the formation of the oxide film cannot be explained by any mechanism (*e.g.*, adsorption) for which $(\partial V/\partial q)_i$ is independent of i .

Examples of potentiodynamic experiments at 10^{-2} , 10^{-1} , and 10 V/sec are shown in Fig. 8, 9, and 10, respectively. The conditions are the same as for the galvanostatic experiments shown in Fig. 1. Figures 8 and 9 each also include traces showing i and V vs. q for a galvanostatic experiment conducted at a current density chosen to be approximately the same as the steady-state current in the potentiodynamic experiment. The V, q traces for the potentiodynamic and the

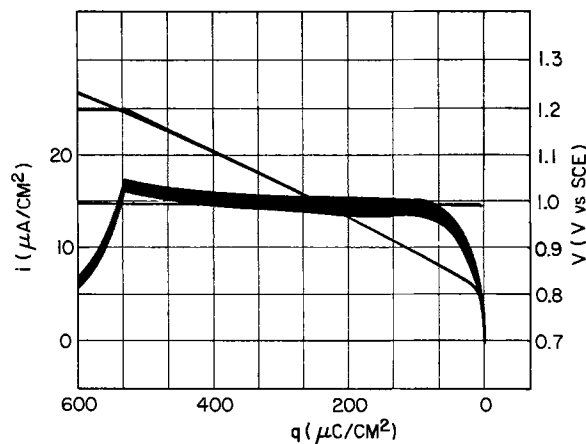


Fig. 8. Potentiodynamic and galvanostatic experiments. Noisy trace is current during potential sweep at 10 mV sec^{-1} . Horizontal trace is current during galvanostatic experiment. Other two traces show potential. Sweep arrested at 1.2V. Conditions given in text.

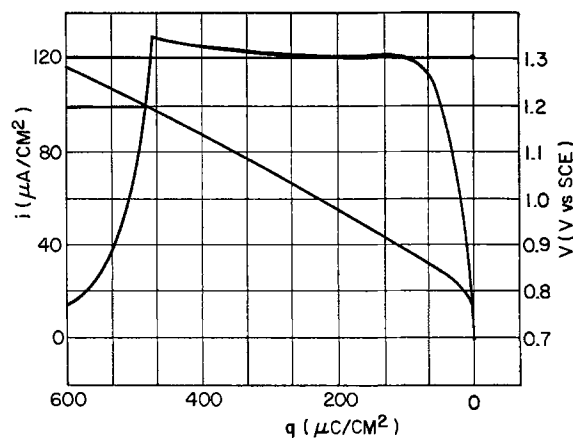


Fig. 9. Potentiodynamic and galvanostatic experiments. Sweep rate: 100 mV sec^{-1} . See caption Fig. 8.

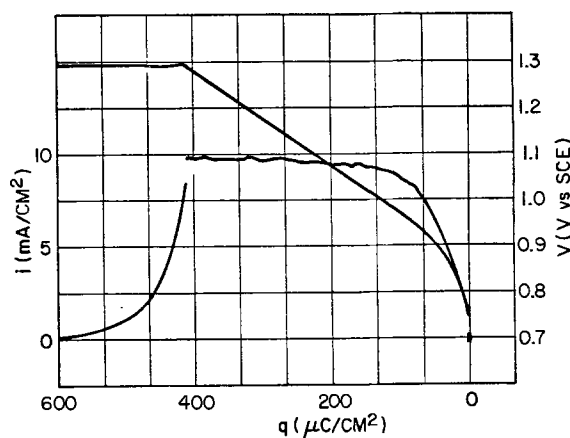


Fig. 10. Potentiodynamic experiment. Sweep rate: 10 V sec^{-1} . Noisy trace is current. Sweep arrested at $\sim 1.3\text{V}$. Slight switching transient on the potential may have caused break in current trace. Conditions same as Fig. 8 and 9. See text.

galvanostatic experiments are indistinguishable except at the end, when the potential sweep is arbitrarily arrested at 1.2V. These data show very graphically the connection between the galvanostatic and potentiodynamic experiments; namely, that the potentiodynamic steady-state current is given by Eq. [12] and varies only if $(\partial V/\partial q)_i$ varies with q . In Fig. 8-10 this variation is quite small.

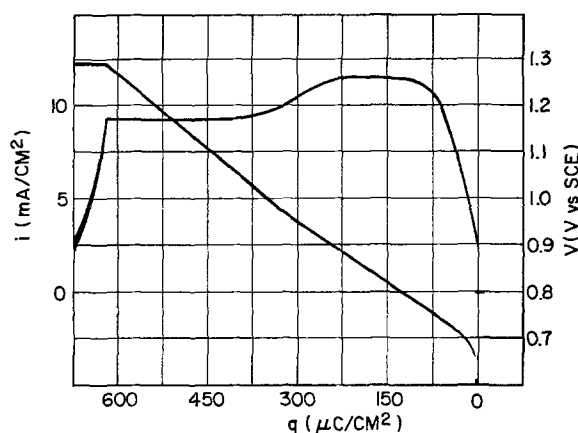


Fig. 11. Potentiodynamic experiment starting at 0.6V. Other conditions same as Fig. 10.

After the sweep is arrested (at 1.2V in Fig. 8 and 9, and 1.3V in Fig. 10) the current falls in the same way as in the hybrid experiments of Fig. 2 and 3. Plots of i vs. q during the potentiostatic segments of these experiments are indistinguishable from the other data of Fig. 4. This illustrates that the arrested potential sweep is essentially the same as hybrid experiment, and that the fall in current is due to the growth of the oxide at constant potential.⁶

Figure 11 is the record of an experiment similar to those previously described except that the electrode is held at 0.6V (SCE) prior to starting the sweep at 10 V/sec. Because of the lower starting potential the oxygen coverage is less to begin with; so subsequent buildup of the oxygen film⁷ at first takes place with a smaller value of $\partial V/\partial q$ than in Fig. 8-10. The easily perceptible change in slope has been observed before (7), and by comparison with hydrogen adsorption (7) it was associated with monolayer coverage during the formation of the oxygen film. We emphasize here that this change in slope is quantitatively related through Eq. [12] to the concurrent step in the potentiodynamic i, V profile.

The constant current "plateaus" seen in Fig. 8-11 are frequently observed during the potentiodynamic anodic oxidation of platinum in acid solution. Because of Eq. [12] we can see that the flatness of these plateaus is equivalent to the straightness of galvanostatic charging curves such as are shown in Fig. 1. In exactly the same sense, the nonlinear sweep rate dependence of plateau height is equivalent to the dependence on current of the slopes of the galvanostatic charging curves. Any model for the growth of the oxide film that satisfactorily explains the galvanostatic characteristics will automatically explain the equivalent potentiodynamic characteristics and vice versa. Therefore, in choosing a model one may use either potentiodynamic or galvanostatic data as a basis. Historically, the interpretation of potentiodynamic data has usually been based on some variant of the adsorption isotherm which is considerably more complex [e.g., see Ref. (11)] than the model used to explain galvanostatic data (i.e., Eq. [1]). As we have seen, simple adsorption models cannot explain the nonlinear sweep rate dependence of the plateau current. Therefore, it appears that Eq. [1] is the preferable alternative and that high-field ionic transport (e.g., the Cabrera-Mott model) is the simplest and in fact the only model that presently explains the data.

Potentiodynamic approach to steady state.—A potentiodynamic characteristic of any system such as that illustrated schematically in Fig. 5 is the asymptotic approach to steady state. For the oxidation of platinum, it is possible to analyze this characteristic in a

⁶ Again, there is no evidence for aging.
⁷ As yet not necessarily an "oxide" film.

simple quantitative manner and to compare the analytical results with experimental data. Consider a relatively small disturbance that changes the potentiodynamic steady-state current. Such a disturbance would be caused, for instance, by a small discontinuity in $(\partial V/\partial q)_i$; (i.e., a more abrupt version of what occurs in Fig. 11) or by an abrupt change in sweep rate. Immediately after the disturbance, the new steady-state current is different from the actual current, which will then approach the new steady-state value required by Eq. [12]. Using [7], Eq. [8] can be rewritten

$$\frac{di}{dV} = \left(\frac{\partial i}{\partial V} \right)_q + i \left(\frac{\partial i}{\partial q} \right)_v \Big| S \quad [17]$$

If we restrict ourselves to a relatively small deviation from the steady-state current and a limited excursion of q , then both the partial derivatives in [17] can be approximated by constants representing their average values. The approximate solution to [17] is then an exponential approach to the new steady-state current, i.e.

$$\Delta i / (\Delta i)_0 = \exp(-\Delta V/v) \quad [18]$$

where Δi is the deviation of the current from the new steady-state value; $(\Delta i)_0$ is the initial value of this deviation; ΔV is the change in V from its initial value; and the "time constant" for the approach to steady state is equal to S/v , where

$$v \equiv \left| S \right| \left(\frac{\partial i}{\partial q} \right)_v \Big| \quad [19]$$

An experimental test of Eq. [18] and [19] is shown in Fig. 12, which was obtained under the same conditions as Fig. 9 except that the sweep was momentarily interrupted and then resumed. Following the resumption of the sweep, the current returns toward the steady state from which it had fallen during the interruption. Examining the later part of this return ("a" in Fig. 12) we see, for example, that the current rises from 91 to 112 $\mu\text{A}/\text{cm}^2$ as the potential changes by about 33 mV. Since the steady-state current is about 122 $\mu\text{A}/\text{cm}^2$, (cf. Fig. 9), this represents a decrease of the deviation from steady state to about 32% of the initial deviation. Using these data (i.e., $\Delta i / (\Delta i)_0 = 0.32$, $\Delta V = 33$ mV), the experimental value of v , calculated from Eq. [18], is 30 mV. From Fig. 1, for $i \sim 125 \mu\text{A}/\text{cm}^2$, $q \sim 250 \mu\text{C}/\text{cm}^2$, $(\partial i/\partial q)_v \sim 3.4 \text{ sec}^{-1}$; so for $S = 0.1 \text{ V}/\text{sec}$, Eq. [19] yields $v \approx 30 \text{ mV}$ which agrees with the value estimated from Fig. 12.

The later part of the initial transient ("b") in Fig. 12 is similar to the subsequent recovery ("a") from the interruption of the sweep. Since both transients are governed by Eq. [18] this is understandable. However, in view of the fact that S appears explicitly in

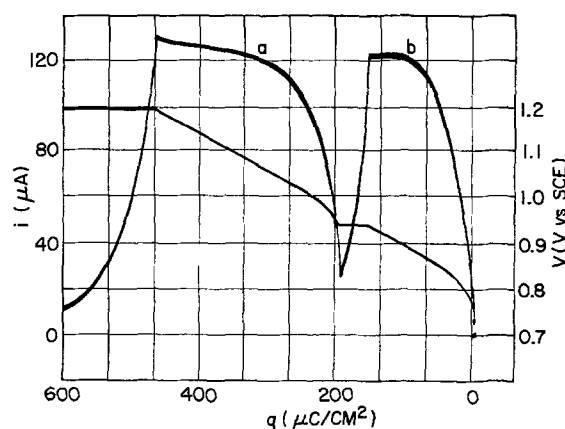


Fig. 12. Interrupted potential sweep. Same as Fig. 9 except for interruption.

Eq. [19], one may wonder why the initial transients in Fig. 8 and 9 are so similar in spite of the tenfold ratio of sweep rates. To investigate this point, Eq. [19] can be rewritten (with the help of Eq. [9] and [12]) in the form

$$v = i_s \left| \left(\frac{\partial i}{\partial V} \right)_q \right| \quad [20]$$

which brings out an interesting feature of the potentiodynamic growth of oxide on platinum. Since i depends exponentially on V (cf. Eq. [1]), $(\partial i/\partial V)_q/i$ depends only on q ; so from Eq. [20], as i approaches i_s , v depends only on q . Furthermore, from the lowest to the highest coverage in Fig. 1, the ratio of i to $(\partial i/\partial V)_q$ increases only by a factor of two; so that the value of v calculated from Eq. [20] increases by a factor of two over this wide range of coverage. This implies that in potentiodynamic recovery from small perturbations, the growth rate of oxide film on platinum returns to its steady-state value during a sweep excursion of 20-40 mV depending on coverage, but practically independent of sweep rate.

Relationship of potentiodynamic transients to a-c impedance.—A-C impedance measurements are sometimes carried out during potential sweep experiments.⁸ Here we analyze the relationship between the a-c impedance and the potentiodynamic transient response of the rate of oxide growth.

Suppose that a small periodic variation in potential, $\Delta V = (\Delta V)_0 e^{j\omega t}$ is superimposed on the potential sweep. Changing the independent variable from V to t in Eq. [8], and adding the periodic variation of V , we get

$$\frac{di}{dt} - i \left(\frac{\partial i}{\partial q} \right)_v = \left(\frac{\partial i}{\partial V} \right)_q [S + j\omega \Delta V] \quad [21]$$

The solution to this equation can be separated into two parts corresponding to the two terms in the bracket. The solution corresponding to the first term, S , is what we have already discussed. The solution corresponding to the second term is the component of the current due to the superimposed a-c potential. The steady-state a-c component of the current is

$$\Delta i = \frac{j\omega \Delta V}{j\omega \left(\frac{\partial V}{\partial i} \right)_q + \left(\frac{\partial V}{\partial q} \right)_i} \quad [22]$$

From Eq. [22] (using Eq. [9]) it can be shown that if $\omega \ll \omega_\tau$, where

$$\omega_\tau \equiv 1/\tau \equiv S/v = \left(\frac{\partial i}{\partial q} \right)_v \quad [23]$$

(cf. Eq. [19]) then the a-c response is exactly the same as the steady-state potentiodynamic response discussed previously. In other words, if the period of the superimposed a-c potential is long compared to the potentiodynamic "time constant," $\tau \equiv v/S$, its effect is merely to cause a slight periodic change in the sweep rate and hence a corresponding periodic change in the potentiodynamic steady-state current. However, if $\omega \gg \omega_\tau$ (i.e., the period of the superimposed a-c potential is short compared to v/S), then the conductance obtained from Eq. [22] is

$$\frac{\Delta i}{\Delta V} \approx \left(\frac{\partial i}{\partial V} \right)_q \quad [24]$$

Equation [24] is expected intuitively when the period of the a-c disturbance is much shorter than τ . The approach to potentiodynamic steady state involves the growth of the oxide film, and if as the potential fluctuates there is not sufficient time for growth to occur, the response is the same as it would be at constant coverage. Using the data of Fig. 1 to calculate

$(\partial i/\partial q)_v$ it can be shown that for current densities less than $150 \mu\text{A}/\text{cm}^2$ and intermediate values of coverage (i.e., $q > 200 \mu\text{coulombs}/\text{cm}^2$), ω_τ is less than $2\pi \text{ sec}^{-1}$. Therefore the a-c response at superimposed frequencies of several cycles per second is essentially at constant coverage.

These results can now be applied to data of Conway and Gottesfeld (8), who measured (at 32.5 Hz) the a-c conductance of the platinum oxide system during potential sweep at 26 and 104 mV/sec. For each of these sweep rates the current density can be calculated from Fig. 7, and since at this frequency $\omega \gg \omega_\tau$ the conductance can be calculated using [24] and the data of Fig. 1. The results of such calculations are shown in Table I. At the top of the table the calculated current density is shown for each sweep rate, and in the body of the table are shown the four conductances calculated for each sweep rate at each of the two potentials shown at the left. Since $(\partial i/\partial V)_q$ is proportional to i and varies slowly with q , Eq. [24] predicts a fourfold ratio of the a-c conductances corresponding to the fourfold ratio of the two sweep rates, and predicts a diminution by roughly a factor of two as the potential rises from 0.85 to 1.15V (vs. SCE). The data of Conway and Gottesfeld deviate significantly from the data in Table I. Their measured values of conductance are higher than the calculated values (by factors of five and two at 26 and 104 mV/sec, respectively) and, more significantly, the measured conductances differ by only about 20% at the two sweep rates rather than by a factor of four as predicted by Eq. [24]. The dependence of measured conductance on potential is comparable to that shown in the table, but this is probably fortuitous in view of the other discrepancies. Their data therefore indicate that the a-c conductance does not reflect Eq. [24]. Rather, it is likely that even at this relatively low frequency (32.5 Hz) the resistance of the oxide film is shorted by its capacitance and the measured a-c conductance reflects the lower effective resistance of other steps in the oxidation process; i.e., steps other than ion transport across the oxide film (e.g., charge transfer processes in the double layer).

Summary

The present experiments and analysis show conclusively that for the range of coverage between one and three monolayers the law of anodic growth of oxide film on platinum is precisely the same whether the film is grown potentiostatically, galvanostatically, or potentiodynamically.

A comparison of galvanostatic and hybrid galvanopotentiostatic experiments shows that there is no aging of the film over a time interval, Δt , comparable to the duration of the experiments ($20 \text{ sec} \leq \Delta t \leq 150 \text{ sec}$). The effect of "holding" (i.e., interrupting the potential sweep and maintaining a constant potential for a time) during potentiodynamic experiments is explained entirely in terms of the potentiostatic growth of the oxide film during the holding period.

A correspondence is analytically established between galvanostatic and potentiodynamic data, and this correspondence is verified experimentally. Galvanostatic and potentiodynamic data both show that the growth of the oxide film cannot be explained by any mechanism for which $(\partial V/\partial q)_i$ is independent of i (e.g., adsorption). The high-field ionic conduction model accounts for the major features of all the data.

Table I

	S (mV sec ⁻¹)	26	104
	i ($\mu\text{A}/\text{cm}^2$)	33	130
Potential	0.85V (SCE)	2	8
	1.15V (SCE)	1	4

The four entries in lower right section of table show the conductances (mmho cm⁻²) (calculated from Eq. [24]) for the conditions shown above and to the left.

⁸ See, e.g., Ref. (8).

Transient deviations from the potentiodynamic "steady state" are analyzed in terms of a "time constant" that can be calculated from galvanostatic data. The calculation is verified by experimental potentiodynamic transient measurements, and it is shown that the interpretation of a-c conductance measurements depends on whether the period of the a-c excitation is larger or smaller than the potentiodynamic time constant.

Acknowledgment

We are grateful to Drs. Wilhelmina Visscher, Anthony Ward, and James Kuder for discussions and helpful suggestions. Special thanks are due to Ms. Carol Troy for perfect typing and to Mr. Harry Wado for careful reproduction of the oscillographs.

Manuscript submitted Aug. 28, 1974; revised manuscript received Dec. 16, 1974.

Any discussion of this paper will appear in a Discussion Section to be published in the December 1975 JOURNAL. All discussions for the December 1975 Discussion Section should be submitted by Aug. 1, 1975.

Publication costs of this article were partially assisted by Xerox Corporation.

REFERENCES

1. J. L. Ord and F. C. Ho, *This Journal*, **118**, 46 (1971).
2. K. J. Vetter and J. W. Schultze, *J. Electroanal. Chem.*, **34**, 141 (1972).
3. A. Damjanovic, A. T. Ward, B. Ulrick, and M. O'Jea, To be published in *This Journal*.
4. S. Gilman, *Electrochim. Acta*, **9**, 1025 (1964).
5. K. J. Vetter and J. W. Schultze, *J. Electroanal. Chem.*, **34**, 131 (1972).
6. W. Böld and M. Breiter, *Electrochim. Acta*, **5**, 145 (1961).
7. H. Angerstein-Kozłowska, B. E. Conway, and W. B. A. Sharp, *J. Electroanal. Chem.*, **43**, 9 (1973).
8. B. E. Conway and S. Gottesfeld, *J. Chem. Soc. Faraday Trans. I*, **69**, 1090 (1973).
9. N. Cabrera, and N. F. Mott, *Rept. Prog. Phys.*, **12**, 163 (1948-1949).
10. S. Bruckenstein and B. Miller, *This Journal*, **117**, 1040 (1970).
11. B. V. Tilak, B. E. Conway, and H. Angerstein-Kozłowska, *J. Electroanal. Chem.*, **48**, 1 (1973).

The Electrochemical Oxidation of N,N,N',N'-Tetramethylbenzidine in Molten Sodium Tetrachloroaluminate

D. E. Bartak* and R. A. Osteryoung*

Department of Chemistry, Colorado State University, Fort Collins, Colorado 80523

ABSTRACT

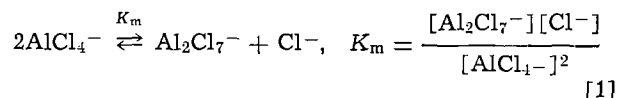
The electrochemical oxidation of N,N,N',N'-tetramethylbenzidine (TMB) in molten sodium tetrachloroaluminate at 175° was investigated as a function of pCl^- . The predominant species in these media was identified by ultraviolet spectroscopic and potentiometric techniques to be an aluminum chloride-TMB dicomplex in the pCl^- range of one to four. A chemical transformation of the dicomplexed amine to a monocomplexed amine precedes electron transfer. A $k_f'k_1$ value of 5×10^6 liters mole⁻¹ sec⁻¹ for the reaction $TMB(AlCl_3)_2 + Cl^- \rightleftharpoons TMB(AlCl_3) + AlCl_4^-$ with $K_1 = \frac{k_f'}{k_b'}$ was found using normal pulse voltammetric and chronoamperometric techniques. The dicomplexed amine is electroactive at more positive potentials. The product of both electron transfer processes is the orange dication of TMB. Cyclic voltammetric and constant potential coulometric techniques were used in obtaining diagnostic criteria for the elucidation of the above reaction pathways.

While the electrochemistry of a large number of organic compounds has been studied in a variety of aprotic and protonic solvents, very little organic electrochemistry has been reported in molten salt media. Aluminum chloride-alkali metal chloride melts have properties which should make electrochemical studies of organic compounds both feasible and interesting, namely: (i) low liquidus temperature, (ii) easily prepared and purified, (iii) aprotic, ionic characteristics, (iv) complete absence of water, and (v) acid-base properties which are readily manipulated. These melts also have possible applications in battery and fuel cell systems (1, 2).

Four papers, to date, have been published concerning organic electrode reactions in molten aluminum chloride-alkali metal chloride mixtures. Fleischmann and Pletcher (3) studied the oxidation of a series of aromatic hydrocarbons in 50-36-14 mole per cent (m/o) $AlCl_3$ - $NaCl$ - KCl at 150°C. Jones, Boxall, and Osteryoung (4, 5) examined the oxidation of triphenylamine and N,N-dimethylaniline in 50:50 m/o $AlCl_3$ - $NaCl$ at

175°C. They found unusual stabilization of the amine radical cations, via cyclic voltammetric data, relative to amine cation radical behavior in acetonitrile. Fung, Chambers, and Mamantov (6) have recently reported on the electrochemical oxidation of tetrathioethylene and thianthrene in molten $AlCl_3$ - $NaCl$ mixtures. The corresponding dications were also more stable in molten chloroaluminates at 150° than in "dry" acetonitrile at 25°C.

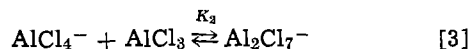
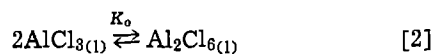
The sodium tetrachloroaluminate (50:50 m/o $AlCl_3$ - $NaCl$) melt can be considered as a Lewis acid-base system by the following equilibrium



in which the heptachloroaluminate ion and the chloride ion are the Lewis acid and base, respectively. The equilibrium recently has been studied by a number of workers. Tremillion and Letisse (7) obtained a K_m value of 13.3×10^{-3} . Torsi and Mamantov (8) studied various aluminum chloride-alkali metal chloride mixtures and found a K_m value of 8.8×10^{-3} for sodium

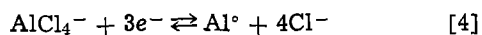
* Electrochemical Society Active Member.
Key words: oxidation of tetramethylbenzidine, fused salts, aluminum chloride melts, pulse polarography.

tetrachloroaluminate at 175°C. Boxall *et al* (9) recently reported on the above equilibrium in relation to two additional equilibrium reactions pertinent to tetrachloroaluminate media (Eq. [2] and [3])



By using these three reactions to describe the AlCl_3 - NaCl system and a concentration-dependent AlCl_4^- activity coefficient, Boxall and co-workers obtained a K_m value of 10.6×10^{-8} at 175°C.

The electrode reaction on an aluminum surface in these melts can be written as



with the electrode potential given by

$$E_{\text{AlCl}_4^-/\text{Al}^0} = E^\circ - \frac{RT}{3F} \ln \frac{(a_{\text{Cl}^-})^4}{a_{\text{AlCl}_4^-}} \quad [5]$$

Since the activity of AlCl_4^- ion remains approximately constant in the 50:50 m/o AlCl_3 - NaCl region (7), the aluminum electrode can act as a chloride ion indicator electrode in these melts.

In this paper, we summarize the results of our investigation of the electrochemical oxidation of N,N,N',N' -tetramethylbenzidine (TMB) in molten sodium tetrachloroaluminate. The acid-base behavior of the melt in relation to that of the amine determines the electroactive species and the chemical reactions that are important in electron transfer processes involving organic compounds in such media.

Results and Discussion

Cyclic voltammetry.—The cyclic voltammetric behavior of N,N,N',N' -tetramethylbenzidine (TMB) in sodium tetrachloroaluminate melt at 175°C with $p\text{Cl}^- = 1.1$ (i.e., most basic condition possible, as the melt is saturated with sodium chloride) is shown in Fig. 1. Since $i_{p,c} = i_{p,a}$, the electrochemistry of TMB comprises a chemically reversible couple at this $p\text{Cl}^-$ and scan rate. At a scan rate of 0.05 V/sec, $E_{p,a} - E_{p,c}$ is approximately 55 mV, which is significantly less than that expected for a reversible one-electron process (86 mV/n at 175°C) (10) and more consistent with a quasireversible, two-electron process to form the TMB dication.

The electrochemical oxidation of TMB was studied as a function of increasing $p\text{Cl}^-$ of the melt (Fig. 2).

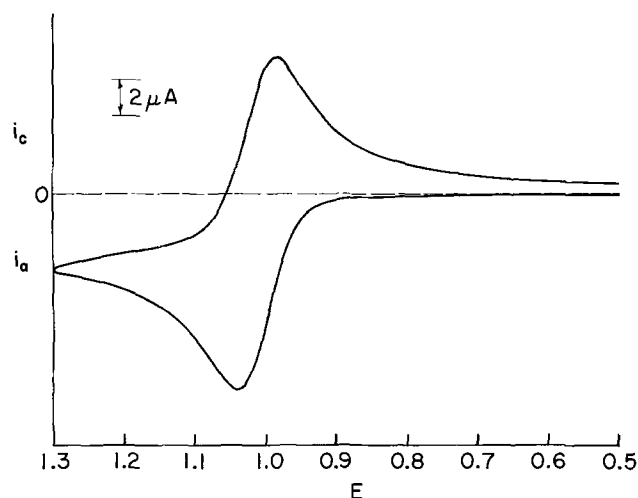


Fig. 1. Cyclic voltammogram of $5.2 \times 10^{-3}\text{M}$ N,N,N',N' -tetramethylbenzidine (TMB) in NaAlCl_4 melt at 175°C and $p\text{Cl}^- = 1.1$. Scan rate, 0.1 V/sec; tungsten planar electrode ($A = 0.01 \text{ cm}^2$).

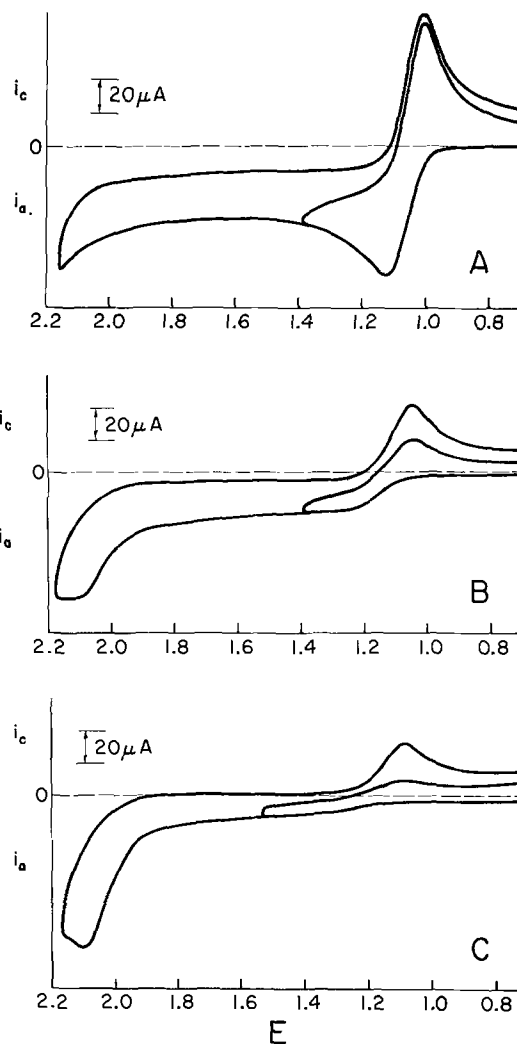


Fig. 2. Cyclic voltammograms of $3.6 \times 10^{-3}\text{M}$ TMB in NaAlCl_4 melt at a scan rate of 0.25 V/sec on a tungsten planar electrode ($A = 0.07 \text{ cm}^2$). (A) $p\text{Cl}^- = 1.5$; (B) $p\text{Cl}^- = 2.5$; (C) $p\text{Cl}^- = 3.5$.

At a constant scan rate of 0.25 V/sec, the oxidation wave near 1.1V shifts positively as the $p\text{Cl}^-$ is increased. At a $p\text{Cl}^-$ of 2.5, a second wave emerges at more positive potentials ($\sim 2.1\text{V}$). As the $p\text{Cl}^-$ is increased to 3.5, the second wave becomes even more predominant. In order to determine the processes responsible for the two oxidation waves, the scan rate was varied at a constant $p\text{Cl}^-$. With increasing scan rate at acidic $p\text{Cl}^-$'s, $i_p/v^{1/2}$ for the first wave decreased, while $i_p/v^{1/2}$ for the second wave increased. These results indicate that both oxidations are kinetically controlled and the equilibrium, which characterizes the two electroactive species, is $p\text{Cl}^-$ dependent.

The peak current of the single reduction wave is dependent on whether the scan rate is reversed after the first oxidation wave ($E_\lambda = 1.6\text{V}$) or after both oxidation waves ($E_\lambda = 2.2\text{V}$) (Fig. 3). Since the reduction peak current is increased when $E_\lambda = 2.2\text{V}$ vs. $E_\lambda = 1.6\text{V}$, the cathodic wave near 1.1V includes the reduction of a product of both oxidation reactions. Furthermore, when $E_\lambda = 1.6\text{V}$ and $p\text{Cl}^- > 2.0$, the ratio of the peak cathodic to peak anodic current, determined by Nicholson's empirical method (11), was found to exceed one. This suggests that a chemical reaction precedes electron transfer for the first oxidation wave.

The peak potential of the single reduction wave is scan rate and $p\text{Cl}^-$ dependent. At constant, acidic $p\text{Cl}^-$'s, the reduction peak potential shifts in a negative direction with increasing scan rate. The reduction

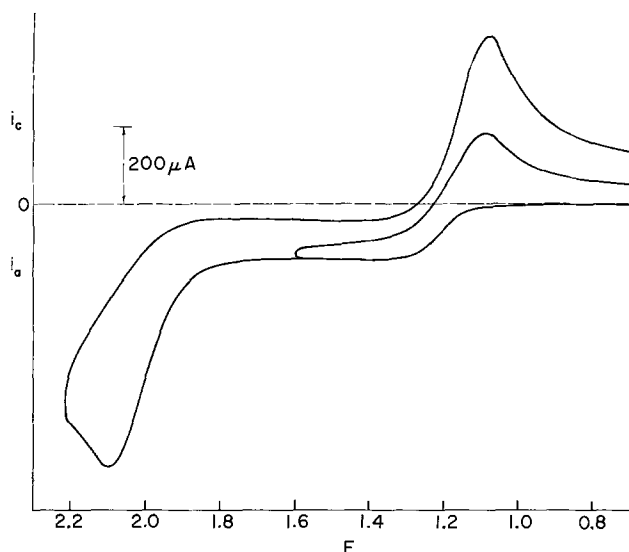


Fig. 3. Cyclic voltammograms of 29×10^{-3} M TMB in NaAlCl_4 melt at $p\text{Cl}^- = 3.4$ and at a scan rate of 0.5 V/sec on a vitreous carbon planar electrode ($A = 0.08$ cm 2).

peak potential shifts positively with increasing $p\text{Cl}^-$, at a constant scan rate. These results are consistent with the theoretical model which involves electron transfer, followed by a $p\text{Cl}^-$ dependent chemical reaction.

Coulometry.—Exhaustive, controlled-potential electrolysis of TMB in basic ($p\text{Cl}^- = 1.1$), tetrachloroaluminate melt at a potential of 1.5 V gave an n value of 2 ($n_{\text{expt}} = 1.85$). The melt turned from almost colorless to bright orange during the course of the electrolysis. Cyclic voltammetric examination of the exhaustively electrolyzed amine indicated the presence of a reducible species in the melt with $E_{p,c} = 1.0$ V (i.e., the dication of TMB). The bright orange color disappeared after approximately 1 hr with a resultant decrease in the height of the reduction wave. Thus the dication of TMB in the tetrachloroaluminate melt at $p\text{Cl}^- = 1.1$ is unstable for long times.

Normal pulse voltammetry (12, 13).—Normal pulse voltammetry was used to elucidate the electrode reaction for TMB in the sodium tetrachloroaluminate melt. Figure 4A is a normal pulse voltammogram at a $p\text{Cl}^-$ of 1.1 . At this basic $p\text{Cl}^-$, one well-defined, anodic wave is observed and a plot of $\log(i_d - i)/i$ vs. E (Fig. 4B) is linear with a slope of 48 mV and $E_{1/2} = 1.012$ V. As the theoretical slope is $89/n$ mV for reversible electron transfer at 175°C , the voltammogram represents a quasireversible, two-electron process.

The normal pulse voltammetric behavior of TMB was also studied as a function of $p\text{Cl}^-$ of the melt. The $E_{1/2}$ for the oxidation wave shifts in a positive direction as the $p\text{Cl}^-$ is increased. A plot of $E_{1/2}$ vs. $p\text{Cl}^-$ for the initial oxidation wave is shown in Fig. 5. The slope of 94 mV suggests that the ratio of chloride ions to electrons involved in the electrode reaction is unity (14, 15). Concurrently, as the $p\text{Cl}^-$ is increased, a second wave emerges at more positive potentials. The limiting current of the second oxidation wave, at a constant pulse width, increases as the $p\text{Cl}^-$ is increased. Simultaneously, the amplitude of the first wave decreases as the acidity of the melt is increased. The sum of the two waves at acidic $p\text{Cl}^-$'s is approximately equal to the height of the single wave at the most basic $p\text{Cl}^-$ (Fig. 6). The ratio of the limiting current for the first wave to that of the limiting current for the second wave is a function of the pulse width (Fig. 7). These results again indicate that both oxidation waves are kinetically controlled in an acidic

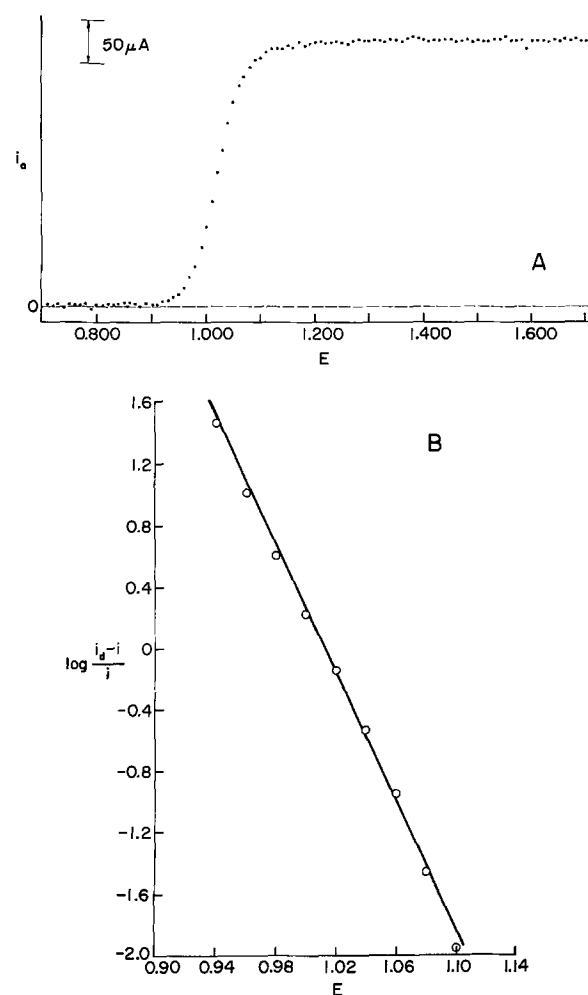


Fig. 4. (A) Normal pulse voltammogram of 5×10^{-3} M TMB in NaAlCl_4 melt at 175°C and $p\text{Cl}^- = 1.1$. Pulse width, 50 msec; delay time, 0.5 sec; tungsten planar electrode ($A = 0.07$ cm 2). (B) Plot of $\log(i_d - i)/i$ vs. E from normal pulse voltammogram of 5×10^{-3} M TMB. Pulse width, 500 msec; delay time, 0.5 sec; tungsten planar electrode ($A = 0.07$ cm 2).

medium and that the species responsible for the waves are in equilibrium with one another.

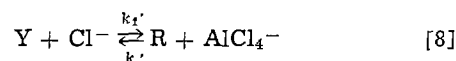
The first oxidation wave is diffusion controlled for pulse widths of 10 msec to 1 sec and when $p\text{Cl}^-$ is less than 1.5 ($i_{\text{lim}}t^{1/2}$ is constant, where $t =$ pulse width). At $p\text{Cl}^-$'s greater than 1.5 , the limiting current for the first wave is kinetically controlled and $p\text{Cl}^-$ dependent (Table I). The cyclic voltammetric and pulse voltammetric data suggest that the first wave includes a chemical reaction, which precedes electron transfer. Rate constants for the preceding chemical reaction were calculated from the pulse voltammetric data using the following equation (16)

$$\frac{i_k}{i_d} = \pi^{1/2} \lambda \exp(\lambda^2) \operatorname{erfc} \lambda \quad [6]$$

where $\lambda = (k_f K t)^{1/2}$ and $i_k =$ kinetic current, $i_d =$ diffusion controlled current. The above equation is based on the model



with $K = [R]/[Y]$ and $t =$ pulse width. Consistent values of $k_f K_1$ (Table I) were obtained as a function of $p\text{Cl}^-$ and pulse width by defining the present system with the reactions



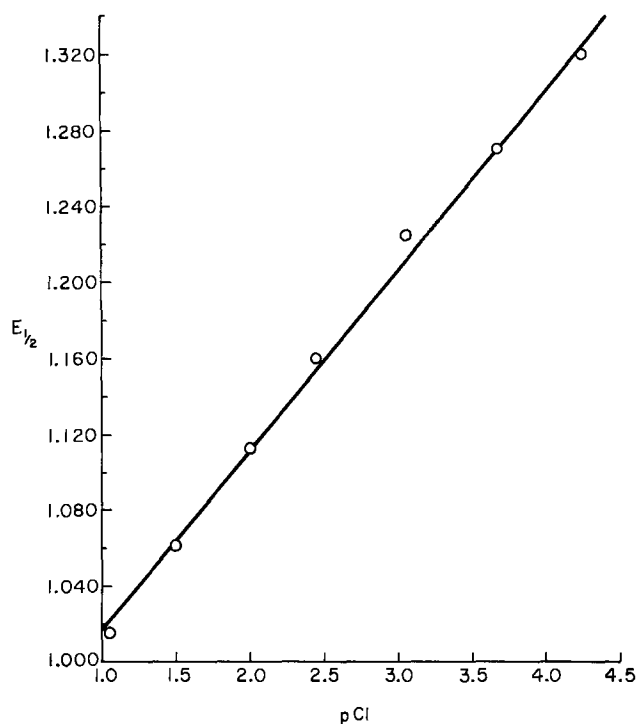


Fig. 5. Plot of $E_{1/2}$ vs. pCl^- for $5.1 \times 10^{-3}M$ TMB in $NaAlCl_4$ melt at $175^\circ C$. The slope is 94 mV. Pulse width, 100 msec; delay time, 1.0 sec; tungsten planar electrode ($A = 0.07 \text{ cm}^2$).

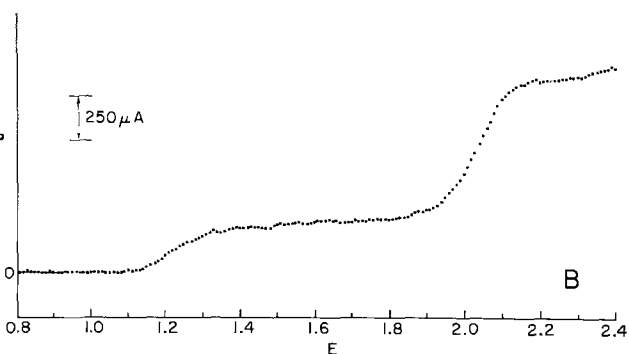
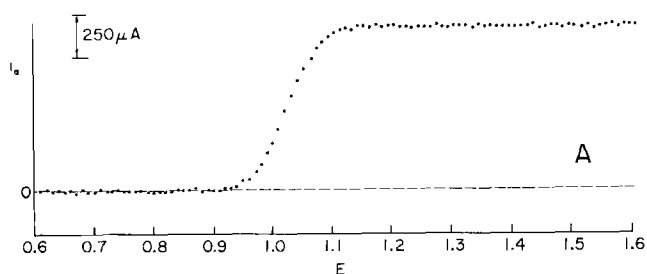


Fig. 6. Normal pulse voltammograms of $29 \times 10^{-3}M$ TMB in $NaAlCl_4$ melt at a pulse width of 100 msec and delay time of 1.0 sec. (A) $pCl^- = 1.1$; (B) $pCl^- = 3.4$. Vitreous carbon planar electrode ($A = 0.08 \text{ cm}^2$).



with $K_1 = k_f'/k_b'.1$

Chronoamperometry.—Single potential step chronoamperometry was also used to study the kinetics of the preceding chemical reaction, which is associated

¹ Since $K_1 = \frac{[R][AlCl_4^-]}{[Y][Cl^-]}$ and $k_f' = \frac{k_f}{[Cl^-]}$, then $k_f'K_1 = k_f'K_1[Cl^-]^2/[AlCl_4^-]$ with $[AlCl_4^-] = 8.8M$ in the 50:50 m/o $AlCl_3$: $NaCl$ melt.

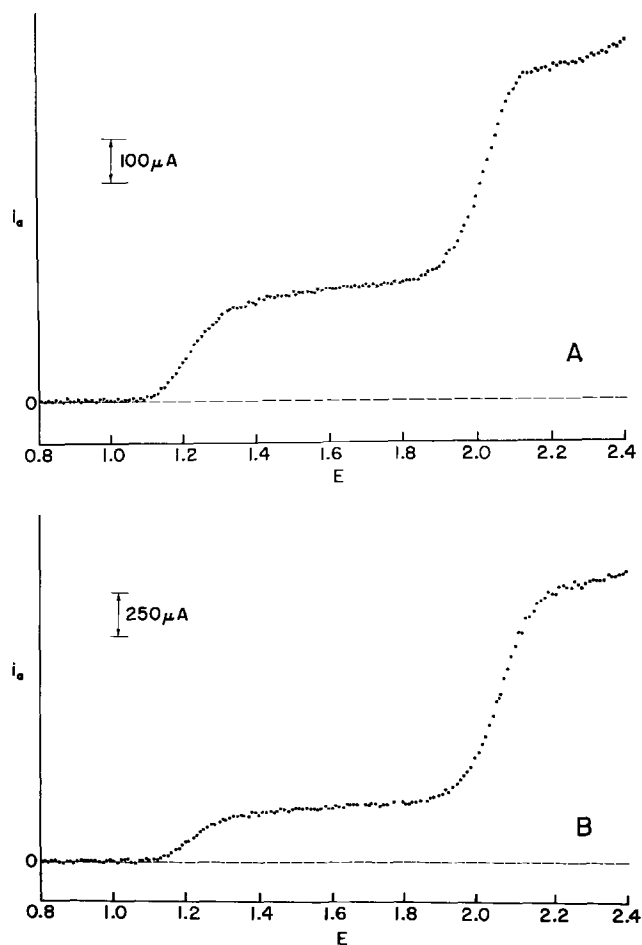


Fig. 7. Normal pulse voltammograms of $29 \times 10^{-3}M$ TMB in $NaAlCl_4$ melt at $pCl^- = 3.4$. (A) Pulse width, 200 msec; delay time, 2 sec; (B) pulse width, 50 msec; delay time, 0.5 sec. Vitreous carbon planar electrode ($A = 0.08 \text{ cm}^2$).

with electron transfer for the first oxidation wave of TMB. In this technique the potential is stepped from a potential where no electrochemical reaction takes place

Table I. Summary of pulse voltammetric data for N,N,N',N' -tetramethylbenzidine^(a) as a function of pCl^- and pulse width

pCl^-	$i_k^{(c)}$	i_k/i_d	$k_f'K_1$ ($\times 10^6$) ^(d)
A. Pulse width = 10 msec ^(b)			
2.0	450	0.69	5.5
2.5	220	0.34	5.5
B. Pulse width = 100 msec ^(e)			
2.0	190	0.91	3.7
2.5	122	0.58	2.7
3.0	66	0.31	4.2
C. Pulse width = 200 msec ^(f)			
2.0	140	0.95	3.8
2.5	102	0.69	2.1
D. Pulse width = 500 msec ^(g)			
2.5	70	0.78	2.1
3.0	51	0.56	4.7
E. Pulse width = 1 sec ^(h)			
2.5	53	0.81	1.4
3.0	43	0.65	4.3

^(a) Concentration of TMB is $5.1 \times 10^{-3}M$; area of tungsten electrode is 0.07 cm^2 .

^(b) Diffusion limiting current at 10 msec pulse width is $650 \mu A$ ($pCl^- = 1.1$).

^(c) All values for current expressed in microamperes.

^(d) Liter mole⁻¹ sec⁻¹.

^(e) Diffusion limiting current at 100 msec pulse width is $210 \mu A$ ($pCl^- = 1.1, 1.5$).

^(f) Diffusion limiting current at 500 msec pulse width is $90.5 \mu A$ ($pCl^- = 1.1, 2.0$).

^(g) Diffusion limiting current at 1.0 sec pulse width is $66 \mu A$ ($pCl^- = 1.1, 2.0$).

(0.7V) to a potential beyond the first wave (1.5V), but not into the second wave. The resulting constant $it^{1/2}$ values indicate diffusion-control ($5 \text{ msec} < t < 2 \text{ sec}$) at $p\text{Cl}^-$'s of 1.1 and 1.5. However, the $it^{1/2}$ values decrease as a function of time at $p\text{Cl}^-$'s greater than 1.5. The finite rate of the dissociation reaction for the amine-aluminum chloride complex is responsible for the decrease in $it^{1/2}$ values with decreasing time. As the $p\text{Cl}^-$ is increased to more acidic values, the equilibrium, which governs the dissociation of the complex, is shifted to the left (i.e., lower bulk concentration of electroactive species).

Figure 8 is a plot of n_{app} where

$$n_{\text{app}} = \left(\frac{(it^{1/2})_{\text{kinetic}}}{(it^{1/2})_{\text{diffusion}}} \right) n \quad [10]$$

as a function of time at $p\text{Cl}^-$'s from 1.1 to 3.7. Good agreement between the experimental data and a theoretical curve, obtained by computer simulating a CE mechanism (17, 18), is found at $p\text{Cl}^-$ of 2.0 ($k_f'K_1 = 4 \times 10^6 \text{ liters mole}^{-1} \text{ sec}^{-1}$), $p\text{Cl}^-$ of 2.5 ($k_f'K_1 = 4 \times 10^6 \text{ liters mole}^{-1} \text{ sec}^{-1}$), $p\text{Cl}^-$ of 3.0 ($k_f'K_1 = 3 \times 10^6 \text{ liters mole}^{-1} \text{ sec}^{-1}$), and $p\text{Cl}^-$ of 3.6 ($k_f'K_1 = 5 \times 10^6 \text{ liters mole}^{-1} \text{ sec}^{-1}$) for reaction [8].² Thus the data are consistent with a CE model in which the formation of electroactive species is first order in chloride ion concentration.

Spectroscopy.—Spectrophotometric techniques were employed to determine, if possible, the values for the amine-complex equilibrium constants. The sodium tetrachloroaluminate melt at 175° has an excellent optical window with a 200 nm cutoff. Since amines have been shown to absorb in the ultraviolet region, the u.v. spectrum of TMB was studied as a function of $p\text{Cl}^-$. N,N,N',N'-tetramethylbenzidine in the NaAlCl₄ melt revealed a λ_{max} at 256 nm with an extinction coefficient of greater than 10^3 . However, the TMB spectrum was $p\text{Cl}^-$ independent over the $p\text{Cl}^-$ range of

² Computer simulation of CE mechanism was based on the model: $Y \xrightleftharpoons[k_b]{k_f} R \xrightarrow{-ne} O$, where $[Y] \gg [R]$. Values of $k_f'K_1$ for reaction [8] were calculated from $k_f'K_1 = k_f K[\text{AlCl}_4^-]/(\text{Cl}^-)^2$.

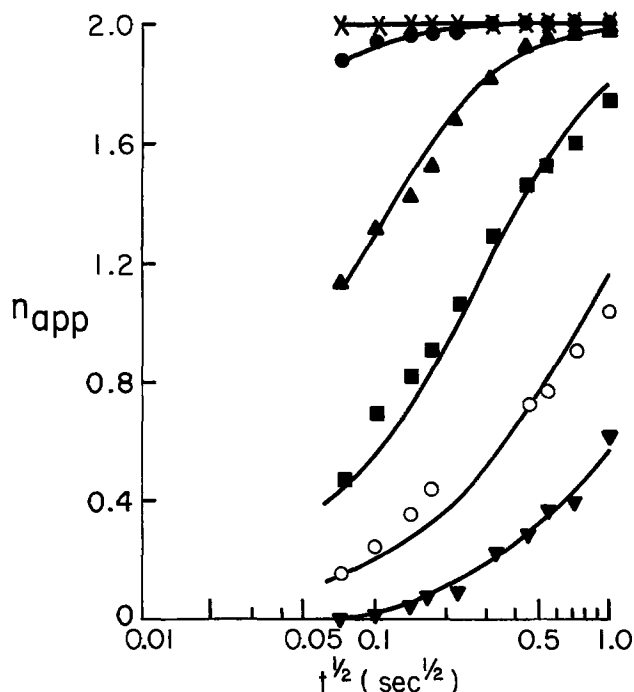
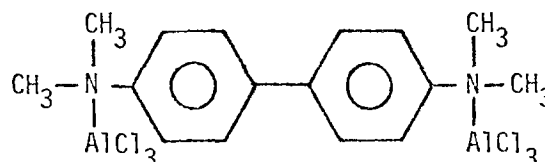


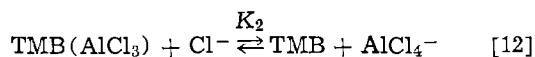
Fig. 8. Single potential step chronoamperometric data for $5.2 \times 10^{-3} \text{ M}$ TMB as a function of $p\text{Cl}^-$. (x) $p\text{Cl}^- = 1.1$; (●) $p\text{Cl}^- = 1.5$; (▲) $p\text{Cl}^- = 2.0$; (■) $p\text{Cl}^- = 2.5$; (○) $p\text{Cl}^- = 3.0$; (▼) $p\text{Cl}^- = 3.6$. The solid line was obtained by digital simulation of Eq. [7] with $Y \gg R$.

1-4. Diprotonated TMB (via perchloric acid) in acetonitrile has been shown by Saget and Plichon (19) to have a λ_{max} of 250 nm, while the monoprotated and the unprotonated form of the diamine exhibit λ_{max} values of 320 and 310 nm, respectively. The u.v. spectrum of biphenyl was also obtained in the NaAlCl₄ melt at 175°C and exhibited a λ_{max} at 253 nm with an extinction coefficient greater than 10^3 . The literature λ_{max} value for the $\pi \rightarrow \pi^*$ transition of biphenyl in a solvent such as cyclohexane is 252 nm with an extinction coefficient of 19,000 (20). An interesting analogy is the case of benzene ($\lambda_{\text{max}} = 255 \text{ nm}$, $\epsilon = 230$) and aniline ($\lambda_{\text{max}} = 280 \text{ nm}$, $\epsilon = 1430$), the latter of which has $\pi \rightarrow \pi^*$ transition energy requirements reduced due to $n-\pi$ conjugation. However, the anilinium ion, which does not have any nonbonding electrons for $n-\pi$ conjugation shows λ_{max} of 254 nm with $\epsilon = 160$ (20).

Since the apparent $\pi \rightarrow \pi^*$ transition for TMB in NaAlCl₄ is independent of $p\text{Cl}^-$ and resembles that for biphenyl in the same medium the predominant TMB species in even the most basic melt is thought to be an acid-base adduct³ with the nonbonding electrons on the amino group being shared with a Lewis acid, in this case, aluminum chloride, i.e.



Electrode reaction pathways.—The spectroscopic and potentiometric evidence indicates that N,N,N',N'-tetramethylbenzidine forms a Lewis acid-base complex in the sodium tetrachloroaluminate melt. The predominant species present in the melt at the most basic $p\text{Cl}^-$ is the aluminum chloride dcomplex of the amine, i.e., TMB(AlCl₃)₂. The equilibria which best describe this chemical system can be written as

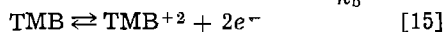
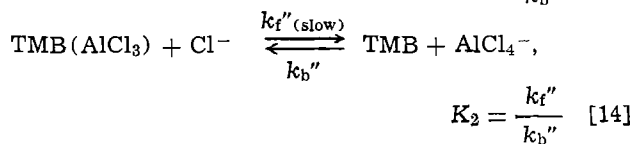
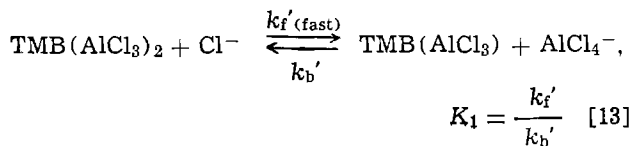


Since the electrochemical data indicate the presence of a precursor chemical reaction accompanying electron transfer, the first anodic wave at $E_{1/2} = + (0.922 + 0.094 p\text{Cl}^-) \text{ V}$ includes the two-electron oxidation of either the uncomplexed or monocomplexed species to a dication. Furthermore the $E_{1/2}$ vs. $p\text{Cl}^-$ plot for the first wave indicates that the ratio of chloride ions to electrons involved in the total electrode reaction is unity. Since the exhaustive electrolysis data demonstrate unequivocally that the first anodic wave involves two electrons, the stoichiometry of chloride ions in the electrode reaction must also be two.

Three reaction schemes can readily be postulated to account for the oxidation of a diamine (either free or monocomplexed) and which includes the same number of chloride ions and electrons (two) in the total electrode reaction. In the first scheme the dcomplex dissociates via two discrete reactions to the free diamine, which is then oxidized to its dication

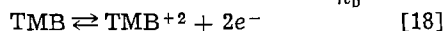
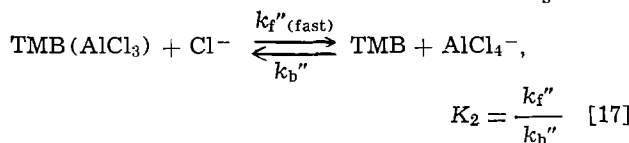
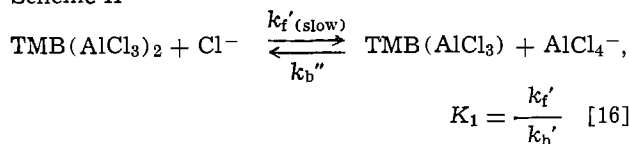
Scheme I

³ Potentiometric studies, whereby Al³⁺ (via Al⁰ anodization) was added to a basic melt containing the amine, also indicated that the amine was completely complexed at $p\text{Cl}^- = 1.1$, since the titration curve shows no break other than that for the solvent tetrachloroaluminate equilibrium (9). Addition of TMB to a basic melt ($p\text{Cl}^- = 1.1$) precipitates sodium chloride from such a melt. Potentiometric titration of TMB with solid AlCl₃ indicated stoichiometry for dcomplex formation. In this experiment, the $p\text{Cl}^-$ of the melt is initially adjusted to 2.5 (least buffered $p\text{Cl}^-$ region). Aluminum chloride (127 mg) is then added to the melt (~10 milliliters), with a resultant increase in $p\text{Cl}^-$ to values greater than 4. The amine (TMB) is then added slowly with stirring until the $p\text{Cl}^-$ is adjusted back to 2.5. From the weight of the amine added (112 mg) the ratio of AlCl₃ to TMB is 2:1.



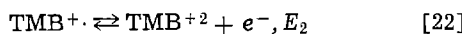
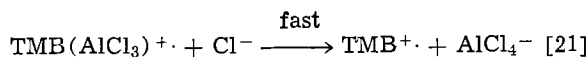
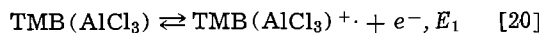
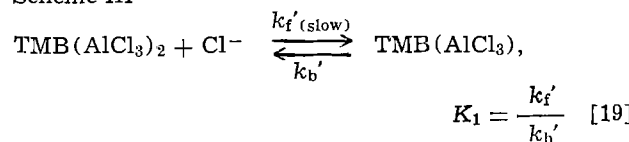
Formation of the electroactive diamine in scheme I would be second order in chloride ion concentration. In the second scheme, the free diamine is again the electroactive species, however, its formation is first order in chloride ion concentration

Scheme II



In scheme III the electroactive species is the mono-complexed diamine and its formation is first order in chloride ion concentration

Scheme III

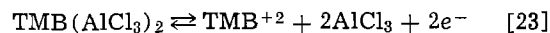


where $E_1 > E_2$.

The normal pulse voltammetric and chronoamperometric data indicate that the electroactive species for the first wave is formed by a chemical reaction which is kinetically first order in chloride ion concentration. Thus, both schemes II and III are valid possibilities that could represent the total electrode process describing the anodic wave at $E_{1/2} = +(0.922 + 0.094 \text{ pCl}^-) \text{ V}$. In scheme II, k_f' is less than k_f'' . If one assumes that $k_b' \approx k_b''$ (diffusion controlled), then K_1 is less than K_2 . The acid dissociation constants for common diprotic acids are usually such that K_1 is greater than K_2 (e.g., dissociation of protonated TMB in acetonitrile (19)). Therefore, scheme III is the more acceptable model and the total electrode reaction for the initial anodic wave includes the oxidation of the monocomplex of the diamine with $K_1 k_f' = 5 \times 10^6$ liters mole⁻¹ sec⁻¹. Since the value for K_1 must be less than 10, (at $\text{pCl}^- = 1.1$, predominant species is di-complexed amine) a k_f' value of 5×10^5 liters mole⁻¹ sec⁻¹ represents a lower limit for this second order reaction.

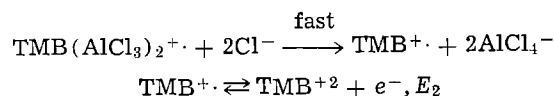
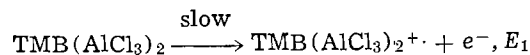
The di-complexed form of the amine can be assumed to be difficult to oxidize, because both unshared pairs of electrons on the amino groups are no longer available for electron transfer. One might expect, therefore, the oxidation potential of the di-complex ($\text{TMB}(\text{AlCl}_3)_2$) to be similar to that of biphenyl. The electrochemical oxidation of biphenyl was investigated briefly in the sodium tetrachloroaluminate melt at 175°C. Cyclic

voltammetric evidence indicates that biphenyl is oxidizable in this medium with $E_{p/2} = 1.8$ and 2.0V on a vitreous carbon electrode *vs.* the saturated sodium tetrachloroaluminate-aluminum reference electrode. Fleischmann and Pletcher (6) have reported $E_{p/2}$ values for the oxidation of biphenyl in 50:36:14 m/o $\text{AlCl}_3:\text{NaCl}:\text{KCl}$ melt at 150°. The two waves observed for the oxidation of biphenyl were at $E_{p/2} = 1.66$ and 2.03V on a pyrolytic graphite electrode *vs.* an aluminum reference electrode. Thus, as the predominant species in the melt is a di-complex and the less positive anodic wave involves the oxidation of a mono-complex, we have concluded that the wave at $E_{1/2} = 1.95\text{V}$ involves the oxidation of a di-complex of the amine, e.g., $\text{TMB}(\text{AlCl}_3)_2$. Furthermore, the cyclic voltammetric data at an acidic pCl^- (Fig. 3) reveal that the product of the more positive wave ($E_{1/2} = 1.95\text{V}$) is identical to the oxidation product of the less positive wave ($E_{1/2} = (0.922 + 0.094 \text{ pCl}^-) \text{ V}$). The reaction for the second oxidation wave can be written



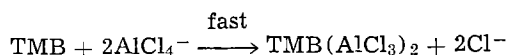
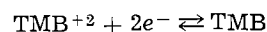
The normal pulse voltammetric data indicate that the limiting current for the more positive wave is pCl^- and pulse width dependent, however the $E_{1/2}$ value for this wave is pCl^- independent. The oxidation of a di-complex as written in Eq. [23] would be expected to be pCl^- dependent if electron transfer were reversible (*i.e.*, Nernstian). If, however, electron transfer is slow or irreversible, the $E_{1/2}$ values are determined solely by the kinetics of the charge-transfer process.

A plot of $\log(i_d - i)/i$ *vs.* E for the second anodic wave at a pCl^- of 4.0 reveals a slope of 105 ± 5 mV over a tenfold increase in concentration, and using either a tungsten or vitreous carbon electrode. Since the Nernstian value for a reversible two-electron process at 175°C is 45 mV, the second wave is clearly not reversible. The cyclic voltammetry data indicate the presence of an EC mechanism since no reverse current for the reduction of the product of the second anodic wave is observed on the cathodic sweep until one reaches potentials at which the product of the first oxidation wave is reduced (*i.e.*, the dication of TMB). An EC mechanism, in which reversible electron transfer precedes a rapid follow-up reaction, requires that $E_{p,a} - E_{p/2,a} = 72/n$ mV and that E_p shifts anodically $45/n$ mV for each tenfold increase in scan rate (at 175°C) (10). We observe $E_{p,a} - E_{p/2,a}$ for the second wave to vary from 80 to 90 mV depending on scan rate for TMB in acidic melts (*i.e.*, $\text{pCl}^- > 3.5$). Furthermore, $E_{1/2}$ (as determined from normal pulse voltammetry) shifts anodically approximately 79 mV for every tenfold decrease in the pulse width. Thus, we conclude that electron transfer, even though relatively rapid, must be slow relative to the rates of the follow-up reactions (10, 21) (*i.e.*, loss of AlCl_3 from the oxidized form of the di-complex). Therefore, the probable electrode reaction for the second wave can be written as



where $E_1 > E_2$.

Cyclic voltammetric data indicate that the peak potential for the single cathodic wave is scan rate and pCl^- dependent. The reduction peak potential shifts positively with increasing pCl^- and decreasing scan rate. As these results are consistent with an EC model, one can write the reactions for the reduction wave as



Lithium tetrachloroaluminate system.—A 50:50 m/o LiCl-AlCl₃ melt system was also used in the study of these amine-aluminum chloride complexes. It was initially hoped that since the pK_m' for the LiCl-AlCl₃ system was 2.46 (22) as compared to 5.08 for the NaCl-AlCl₃ system,⁴ one could obtain melts of lower acidity with the lithium tetrachloroaluminate system and thus obtain accurate equilibrium constants via spectroscopic methods for the amine-aluminum chloride complexes. However, due to the limited solubility of LiCl in LiAlCl₄ at 175°C the pCl^- of a saturated LiCl melt at 175° is 0.3. Figure 9A is a cyclic voltammogram of TMB in the LiAlCl₄ melt (saturated with LiCl) (i.e., $pAl_2Cl_7^- = 2.2$), while Fig. 9B is a cyclic voltammogram of TMB in a NaAlCl₄ melt adjusted by Al anodization to a pCl^- of 2.2 (i.e., $pAl_2Cl_7^- = 2.9$). The general shape of the wave and the ΔE_p value are qualitatively the same for the TMB in the two melt systems. Since the electrochemistry of TMB in the two melt systems is heptachloroaluminate ion concentration dependent in the same qualitative relationship, it is reasonable to assume that the amine is complexed with the Al₂Cl₇⁻ or AlCl₃ species. The formation of aluminum chloride-amine complexes in organic solvents have been previously reported in the literature (23, 24). Eley and co-workers (25-27) have reported heats of reaction for several aliphatic and aromatic amine-aluminum chloride complexes. They found that the greater the electron density on the nitrogen atom, the higher the heat of mixing or the stronger the bond formed between the donor-acceptor moieties.

Drahowzhal (28) found that complexes of aromatic tertiary amines with aluminum chloride, such as C₆H₅N(CH₃)₂-AlCl₃ are useful catalysts for the alkylation of aromatics with alkyl halides.

⁴ K_m' is defined: $K_m' = [Al_2Cl_7^-][Cl^-] = K_m[AlCl_4^-]^2$ where $[AlCl_4^-] = 8.8M$ in NaAlCl₄ and $[AlCl_4^-] = 9.3M$ in LiAlCl₄.

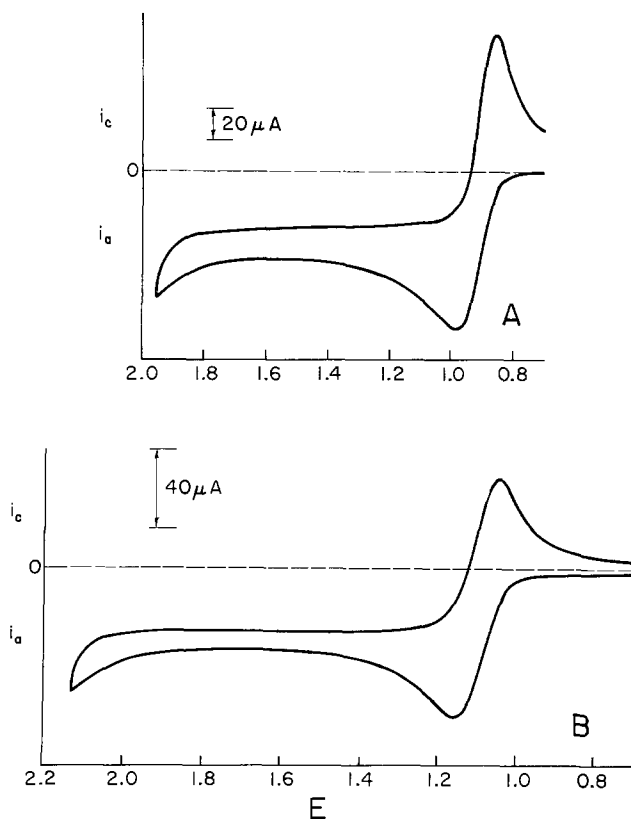


Fig. 9. (A) Cyclic voltammogram of $7 \times 10^{-3}M$ TMB in lithium tetrachloroaluminate at 175°C and $pCl^- = 0.3$. Scan rate, 0.1 V/sec; tungsten planar electrode ($A = 0.07 \text{ cm}^2$). (B) Cyclic voltammogram of $5.2 \times 10^{-3}M$ TMB in sodium tetrachloroaluminate at 175°C and $pCl^- = 2.2$. Scan rate, 0.1 V/sec; tungsten planar electrode (0.07 cm^2).

Experimental Section

Electrochemical instrumentation.—The cyclic voltammetric, chronoamperometric, and pulse voltammetric studies were performed on a multipurpose instrument utilizing operational amplifier circuitry described previously (29). The above instrument was interfaced (30) to Digital Equipment Corporation Models PDP-12 and PDP-8/e computers for the pulse voltammetric and chronoamperometric studies. Read-out of the data was by either Houston Model 2000 X-Y recorder or a Hewlett-Packard Model 7030-Am X-Y recorder with point plotting capabilities.

Potentiometric studies were performed using a Leeds and Northrup Student Potentiometer and a Keithley Model 160 Multimeter. A Sargent Coulometric Constant Current Source was used during melt composition determinations, and to adjust the acidity of the melt to the required pCl^- .

Melt preparation and purification.—All of the experimental work was carried out under a purified argon atmosphere in a Vacuum Atmospheres Company dry box equipped with a Model HE-493 Dri-Train for constant recirculation of the argon gas through a column consisting of activated copper and molecular sieves. In an attempt to qualitatively assess the oxygen content of the dry box atmosphere (31), 25W light bulb filaments using line voltage were burned inside the box. Satisfactory results were obtained in that the filaments' lifetime was from 7-10 days. To insure that the water content of the box atmosphere was low, P₂O₅ in evaporating dishes was also placed inside the box. Melt preparation and purification was carried out in a cell which has been previously described (32). The fusion of 2 moles of aluminum chloride (Fluka, A. G., iron-free) and 2 moles of sodium chloride (Fisher, certified ACS grade) produced a faintly yellow colored melt at 175°C. Purification of the molten mixture was accomplished by means of pre-electrolysis with an aluminum rod anode (Johnson Matthey Specpure grade), coiled aluminum wire cathode (Alfa Inorganics, m5N), and the Sargent Coulometric Constant Current Source. After ten days of electrolysis at a current density of about 0.5 mA cm⁻², the resultant melt was clear and colorless.

Electrodes.—Two planar working electrodes were used in pulse voltammetric and chronoamperometric studies: (i) a 1/8 in. diameter tungsten rod (Alfa Inorganics, m3N8) and (ii) 3 mm diameter vitreous carbon rod electrode (Atomergic Chemetals, V25). The tungsten rod was sealed into Pyrex using a bead of uranium glass, ground flat on an emery wheel, and polished, successively, with 600 grit silicon carbide powder and Type B alumina powder (Fisher) to a mirror-like finish. The vitreous carbon electrode was sealed in a Pyrex glass tube using the procedure described by Gupta (33) and polished in the same manner as the planar tungsten electrode.

The reference electrode was isolated for all experiments from the bulk of the melt with a fine glass frit. The reference electrode was a coiled aluminum wire in the sodium tetrachloroaluminate melt saturated with sodium chloride at 175°C. The potential of this stable reference electrode system was 175 mV negative of the aluminum electrode in a 50:50 m/o AlCl₃-NaCl melt.

The auxiliary electrode for all experiments was a coiled aluminum wire, which was isolated by means of a fine glass frit for the controlled potential electrolysis experiments. The working electrode for the controlled potential coulometry experiments was a tungsten gauze basket, fabricated from 100 mesh tungsten wire cloth (Research Inorganics). A Pyrex glass stirring bar was used to facilitate mass transfer for the exhaustive electrolysis experiments.

Spectrophotometric studies.—Spectra were recorded with a Cary Model 17 Spectrophotometer equipped with a water-cooled sample compartment to protect the rest of the optics during high temperature experiments.

The furnace was an aluminum block (10 × 10 × 10 cm), fitted directly into the Cary sample compartment. The furnace was heated by four Chromalox cartridge heaters, placed symmetrically about the cell holder (12.7 × 12.7 mm) and controlled with a Thermo Electric Model 32422 temperature controller, which was also used for electrochemical studies. The cells used were 10 mm pathlength Suprasil (12.5 × 12.5 × 45 mm) rectangular type fitted with an air-tight Teflon cover.

The melt, to which the organic compound had been added, was transferred directly in the dry box to the heated optical cell with a heated pipette. The portable furnace containing the closed cell and its contents was then taken directly out of the dry box and placed in the sample compartment of the spectrophotometer. To further insure that water or air would not enter into the closed cell, the sample compartment of the spectrophotometer was purged with purified nitrogen.

Acknowledgment

Acknowledgment is made to the donors of the Petroleum Research Fund, administered by the American Chemical Society, for partial support of this research. Partial support by the Air Force Office of Scientific Research (Grant No. AFOSR 71-1995) is also acknowledged. The authors would like to thank Dr. Roger Abel for the computer simulation of the model CE mechanism. Helpful discussions were held with Dr. H. Lloyd Jones.

Manuscript submitted Nov. 11, 1974; revised manuscript received Dec. 17, 1974. This was Paper 335 presented at the San Francisco, California, Meeting of the Society, May 12-17, 1974.

Any discussion of this paper will appear in a Discussion Section to be published in the December 1975 JOURNAL. All discussions for the December 1975 Discussion Section should be submitted by Aug. 1, 1975.

Publication costs of this article were partially assisted by Colorado State University.

REFERENCES

1. A. A. Fannin, L. A. King, and D. W. Seegmiller, *This Journal*, **119**, 801 (1972).
2. G. L. Holleck and J. Giner, *ibid.*, **119**, 1161 (1972).
3. M. Fleischmann and D. Pletcher, *J. Electroanal. Chem.*, **25**, 449 (1970).
4. H. L. Jones, L. G. Boxall, and R. A. Osteryoung, *ibid.*, **38**, 476 (1972).
5. H. L. Jones and R. A. Osteryoung, *ibid.*, **49**, 281 (1974).
6. K. W. Kung, J. Q. Chambers, and G. Mamantov, *ibid.*, **47**, 81 (1973).
7. B. Tremillion and G. Letisse, *ibid.*, **17**, 371 (1968).
8. G. Torsi and G. Mamantov, *Inorg. Chem.*, **10**, 1900 (1971).
9. L. G. Boxall, H. L. Jones, and R. A. Osteryoung, *This Journal*, **120**, 223 (1973).
10. R. S. Nicholson and I. Shain, *Anal. Chem.*, **36**, 706 (1964).
11. R. S. Nicholson, *ibid.*, **38**, 1406 (1966).
12. E. P. Parry and R. A. Osteryoung, *ibid.*, **37**, 1634 (1965).
13. K. B. Oldham and E. P. Parry, *ibid.*, **38**, 867 (1966).
14. M. Heyrovsky and S. V. Vavrička, *J. Electroanal. Chem.*, **36**, 203 (1972).
15. P. J. Elving, *Pure Appl. Chem.*, **7**, 432 (1963).
16. P. Delahay, "New Instrumental Methods of Electrochemistry," p. 90, Interscience Publishers, Inc., New York (1954).
17. S. W. Feldberg, "Electroanalytical Chemistry," A. J. Bard, Editor, Vol. 3, pp. 199-296, Marcel Dekker, New York (1969).
18. I. Ruzić and S. W. Feldberg, *J. Electroanal. Chem.*, **50**, 153 (1974).
19. J. P. Saget and V. Plichon, *Bull. Soc. Chim. Fr.*, **1969**, 1395.
20. H. H. Jaffe and M. Orchin, "Theory and Applications of Ultraviolet Spectroscopy," pp. 242-286, John Wiley & Sons, Inc., New York (1962).
21. D. H. Evans, *J. Phys. Chem.*, **76**, 1160 (1972).
22. G. Torsi and G. Mamantov, *Inorg. Chem.*, **11**, 1439 (1972).
23. N. N. Greenwood and K. Wade, "Friedel-Crafts and Related Reactions," G. A. Olah, Editor, Vol. 1, pp. 569-606, Interscience Publishers, Inc., New York (1963).
24. J. K. Ruff, "Developments in Inorganic Nitrogen Chemistry," C. B. Colburn, Editor, Vol. 1, pp. 494-497, Elsevier Publishing Co., Amsterdam (1966).
25. M. H. Dilke, D. D. Eley, and M. G. Sheppard, *Trans. Faraday Soc.*, **46**, 261 (1950).
26. D. D. Eley and H. Watts, *J. Chem. Soc.*, (1952), 1914.
27. D. D. Eley and H. Watts, *ibid.*, (1954), 1319.
28. F. Drahowzahl, *Monatsh.*, **88**, 842 (1957).
29. G. Lauer, H. Schlein, and R. A. Osteryoung, *Anal. Chem.*, **35**, 1789 (1963).
30. J. Christie, Ph.D. Thesis, Colorado State University, Fort Collins, Colorado, 1974.
31. I. D. Eubanks and F. J. Abbott, *Anal. Chem.*, **41**, 1708 (1969).
32. L. G. Boxall, H. L. Jones, and R. A. Osteryoung, *This Journal*, **121**, 212 (1974).
33. N. K. Gupta, *Rev. Sci. Instr.*, **42**, 1368 (1971).

Electrochemistry of Multisulfur Heterocycles: Trithiocarbonates and Trithiocarbenium Ions

P. R. Moses and J. Q. Chambers

Department of Chemistry, University of Tennessee, Knoxville, Tennessee 37916

and J. O. Sutherland and D. R. Williams

Department of Chemistry, University of Colorado, Denver, Colorado 80202

ABSTRACT

The electrochemistry of trithiocarbonates and trithiocarbenium ions has been studied in nonaqueous solvents, mainly in acetonitrile. Trithiocarbonates are reduced to the corresponding radical anions which undergo further chemical reactions. Anodic oxidation of trithiocarbonates leads to coupling products, but does not provide synthetic entry into the tetrathioethylenes. The latter class of compounds is available by a procedure which involves reductive coupling of trithiocarbenium cations, followed by pyrolysis of the resulting orthothiooxalates. The mechanism of the dimerization reaction appears to involve a simple radical-radical coupling (DIMI mechanism). Details of the synthetic procedure are given along with voltammetric data for six trithiocarbonates and eighteen trithiocarbenium ions.

As part of a continuing study on the electrochemistry of multisulfur heterocycles (1-4), a series of trithiocarbonates and their monoalkylated derivatives have been studied in nonaqueous solvents. The investigation was directed to the possibility of a convenient synthetic entry into tetrathioethylenes and, specifically, into derivatives of the highly interesting tetrathiofulvalenes.

The electrical properties of charge transfer complexes formed from acceptor molecules such as tetracyanoquinodimethane (TCNQ) and donor molecules such as tetrathiofulvalene (TTF) are currently of considerable interest (5, 6). The crystalline charge transfer complex, $\text{TTF}^+ \cdot \text{TCNQ}^-$, exhibits extremely high electronic conductivity which also has a negative temperature coefficient. The conductivity of this compound has been attributed to a metallic chain in which electron delocalization occurs through an infinite stack of TTF radical cations (7). These properties are characteristic of metals and the salts have been termed "organic metals" or "unidimensional metals" in the literature.

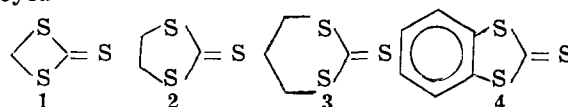
Recently, structural modifications of one of the partners in the charge-transfer complexes have been achieved in an effort to discover more highly conducting materials. The tetramethyl (8) and tetrathiomethoxy tetrathiofulvalenes (4) have been reported. TCNQ salts of the former donor molecule are insulators at low temperature, but electronic conductors at room temperature. The tetraselenofulvalene (TSeF) has been synthesized and preliminary results indicate that $\text{TSeF}^+ \cdot \text{TCNQ}^-$ complexes have greater electronic conductivity than the TTF^+ salt (9).

A need exists for synthetic methods for the preparation of good electron donor molecules which can be used to form new charge transfer complexes. Previous synthetic pathways to tetrathioethylenes involve oxidative elimination of sulfur from the appropriate trithiocarbonate followed by coupling of the 1,3-dithiolium ion with base (10, 11) or by treatment of the thione with a phosphorous(III) compound (12-14). During the course of this study anodic elimination of the thiocarbonyl sulfur was observed in acetonitrile (2), but no evidence for the formation of a tetrathioethylene was noted. However, entry into the tetrathioethylenes was achieved under relatively mild electrolysis conditions by reduction of monoalkylated trithio-

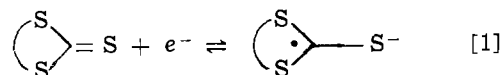
carbenium ions (15, 16) followed by pyrolysis of the resulting dimer (17). The electrochemical route is attractive for the formation of substituted TTF derivatives since the stringent oxidizing conditions of the above methods are avoided.

Results and Discussion

Trithiocarbonates, reduction.—Trithiocarbonates are readily reduced at mercury and platinum electrodes in nonaqueous solvents. Voltammetric data for compounds 1-3 are given in Table I. At the fastest sweep rates employed



in this study (ca. 200 V/sec) compounds 2-4 gave reversible one-electron cyclic voltammograms which indicate formation of the respective radical anions.



This conclusion is supported by the weak electron spin resonance (ESR) signals which were obtained by cathodic electrolysis of compounds 2, 3, and 4 in the cavity of an ESR spectrometer. The signals which were presumably due to the respective radical anions exhibited no hyperfine structure.

At slower sweep rates the ratio of anodic to cathodic peak currents decreased to zero and the cathodic current function increased to a value roughly twice the

Table I. Voltammetric properties of trithiocarbonates, reduction at a hanging mercury drop electrode (area = 0.0628 cm²); CH₃CN, 0.1M TEAP

Compound	ν (V/sec)	E_p (V) ^(a)	$E_{p/2} - E_p$ (mV)	CF ^(b)	i_p^2/i_p^c
1	0.06	-1.5 ^(c)	10 ^(c)	1.34 ^(c)	0
	32.9	-1.72	80	1.04	0
2	0.06	-1.73	52	2.39	0.21
	77.4	-1.76	81	1.44	0.93
3	0.06	-1.59	49	2.20	0.08
	58.4	-1.61	62	1.31	0.63

^(a) V vs. SCE.

^(b) Current function; units: A cm⁻² M⁻¹ (V/sec)^{-1/2}.

^(c) Wave distorted by a sharp current maximum; see text.

Key words: cyclic voltammetry, radical anions, radical cations, electrodimmerization.

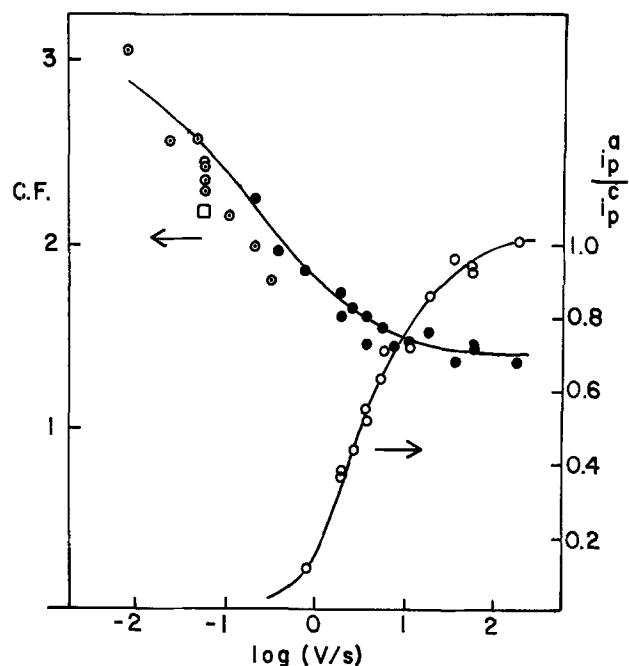


Fig. 1. Variation of the cathodic current function (CF) and the ratio of anodic to cathodic peak currents (i_p^a/i_p^c) of **2** with sweep rate $CF = i_p/AC\sqrt{v}$, units: $A\text{ cm}^{-2} M^{-1} V^{-1/2} \text{ sec}^{1/2}$. Hanging mercury drop electrode. Dotted circles: $1.78 \times 10^{-3}M$, solid circles: $1.17 \times 10^{-3}M$, square: platinum electrode.

fast sweep rate value. This behavior is shown in Fig. 1 for **2** in wet acetonitrile, 0.1M TEAP solution. These variations and the ESR results are characteristic of an ECE mechanism although the quality of the data did not allow a distinction between various ECE pathways to be made. The peak potential data were also consistent with an ECE mechanism. For **2** the plot of E_p vs. \log (sweep rate) exhibited two straight-line segments which intersected at $v_1 \approx 0.2$ V/sec.

Addition of the proton donors phenol or additional water to the solution had only minimal effect on the cyclic voltammograms of **2**. Thus protonation of the radical anion is probably not the rate-determining chemical step in the ECE mechanism. Other reactions of the radical anion, e.g., dimerization or disproportionation, are possible, but the present results do not permit further mechanistic analysis.

Cyclic voltammograms of **1** at hanging mercury drop electrodes featured a large maximum in the region of the peak potential. The data reported in Table I are approximations of the diffusion controlled current after the spike was subtracted from the voltammograms. Chronoamperometric experiments in which the potential was stepped into the region of the maximum re-

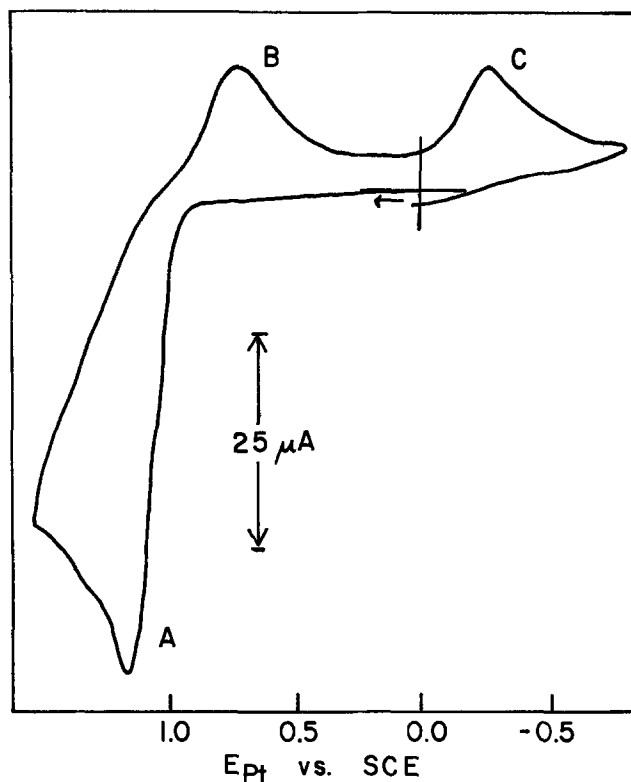


Fig. 2. Cyclic voltammogram of **2** in acetonitrile. Conditions: $1.0 \times 10^{-3}M$ **2**, 0.1M TEAP, 0.080 V/sec, Pt electrode.

sulted in a constant current instead of the usual Cottrell $it^{1/2}$ decay. For a 0.063 cm^2 Hg drop electrode, the current was $64\ \mu A$ at $-1.60V$ vs. SCE and $190\ \mu A$ at $-1.70V$ vs. SCE. At $-1.80V$ vs. SCE, which was more negative than the spike potential region, a normal $it^{1/2}$ decay was observed. Cyclic voltammograms of **1** at platinum electrodes did not exhibit the current maximum on the reduction waves.

Trithiocarbonates, oxidation.—Extensive cyclic voltammetric experiments were carried out on the oxidation of the trithiocarbonates. An oxidation wave at ca. $1.0V$ vs. SCE was present for all of the trithiocarbonates studied. Figure 2 shows a cyclic voltammogram of **2** which exhibits this oxidation wave (A) and two cathodic waves (B and C) due to the reduction of oxidation products. The two product reduction waves, B and C, were not present to the same extent for all of the trithiocarbonates. Wave B was absent at sweep rates less than 5 V/sec for **4** and was absent at all sweep rates for **1**. Also wave A in the voltammograms of **1** was split into two peaks. The voltammetric parameters for the oxidation of trithiocarbonates **1-6** are given in Table II.

Table II. Cyclic voltammetric parameters for the oxidation of trithiocarbonates in acetonitrile, 0.1M TEAP: Pt electrode, sweep rate = 0.060 V/sec

Compound	Wave A			Wave B		Wave C	
	$E_{p,oxld}$	$E_p - E_{p/2}$	CF	$E_{p,redn}$	CF	$E_{p,redn}$	CF
1	1.165 ^(a)	80 ^(b)	(c)	(d)	(d)	-0.3 ^(a)	0.2 ^(e)
2	1.075	89	1.03 ^(e)	0.78 ^(a)	0.27 ^(e)	-0.30	0.2
3	0.992	86	0.98	0.61	0.37	-0.15	0.1
4	1.157	106	0.61	(d)	(d)	-0.25	0.20
5	0.948	62	1.08	0.79	0.47	-0.20	0.2
6	1.21	108	1.34	0.97	0.46	-0.24 ^(f)	—

(a) Volts vs. SCE.

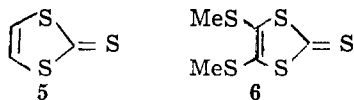
(b) Millivolts.

(c) Double peak.

(d) Absent.

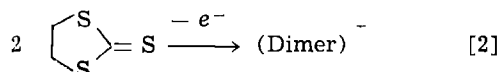
(e) $A\text{ cm}^{-2} M^{-1} (V/\text{sec})^{-1/2}$; current function.

(f) Absent on first cycle, present in multicycle voltammograms.



The cyclic voltammetric parameters were dependent on the choice of solvent and supporting electrolyte. In addition to acetonitrile, which was the main solvent used in this study, voltammograms were obtained for solutions in benzonitrile, methylene chloride, and nitromethane. In methylene chloride at platinum electrodes, wave B showed maxima which are characteristic of adsorption of the electroactive species (18), while in nitromethane solutions wave B was absent at all sweep rates for all of the trithiocarbonates studied.

The current functions, $i_p/AC\sqrt{v}$, where i_p is the peak current, A is the electrode area, C is the concentration, and v is the sweep rate (19), of waves A, B, and C for **2** in acetonitrile are given in Fig. 3 as a function of sweep rate. The current function of wave A decreases as the sweep rate increases and approaches a value of $0.6 \text{ A cm}^{-2} \text{ M}^{-1} \text{ V}^{-1/2} \text{ sec}^{1/2}$ which is one-half the slow sweep rate value. This current function is less than half of the reversible one-electron value ($1.4 \text{ A cm}^{-2} \text{ M}^{-1} \text{ V}^{-1/2} \text{ sec}^{1/2}$) which is found for the formation of the radical anion, Fig. 1. The slow sweep rate current function for wave A ($1.1 \text{ A cm}^{-2} \text{ M}^{-1} \text{ V}^{-1/2} \text{ sec}^{1/2}$) is consistent with an irreversible one-electron oxidation process and a diffusion coefficient of $2.7 \times 10^{-5} \text{ cm}^2 \text{ sec}^{-1}$. The results are consistent with a mechanism in which a dimer radical cation is formed in the initial oxidation process, Eq. [2]. This would result in an n -value of 0.5 at times less than the lifetime of the dimer radical cation.



Concurrent with the decrease in the current function of wave A, the current function of wave C decreases to zero at fast sweep rates, Fig. 3. Assignment of wave C to the reduction of a decomposition product of the dimer cation radical would account for this behavior. Similar behavior was observed for the other trithiocarbonates investigated.

The variations of the current functions of waves A, B, and C for **2** with concentration are shown in Fig. 4 and 5. At sweep rates greater than ca. 2 V/sec^{-1} the current function of wave A became almost independent of the concentration of **2**. Similarly, the ratio of the peak currents of waves B and A was only slightly dependent on the concentration (Fig. 5). These results suggest the rapid formation of the dimer cation radical in an electrochemically irreversible step, Eq. [2], followed by a first-order decomposition of the dimer cation radical.

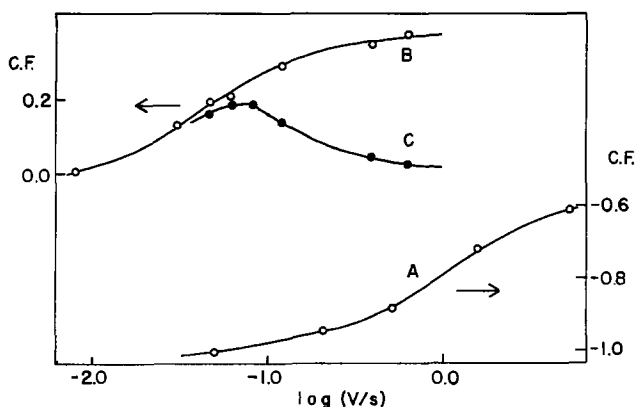


Fig. 3. Variation of the current functions for waves A, B, and C in the cyclic voltammograms of **2** with sweep rate. Units: see Fig. 1. Platinum electrode.

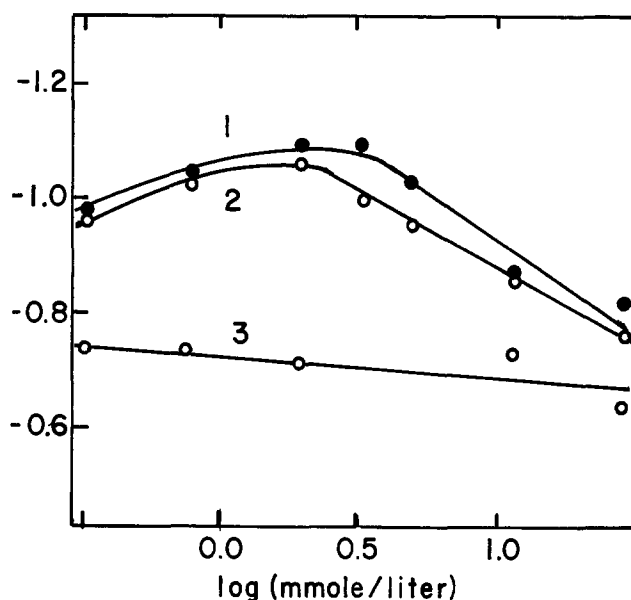


Fig. 4. Variation of the anodic current function of wave A for **2** with concentration. Units: see Fig. 1. Platinum electrode. Curve 1, 0.056 V/sec ; curve 2, 0.199 V/sec ; curve 3, 1.99 V/sec .

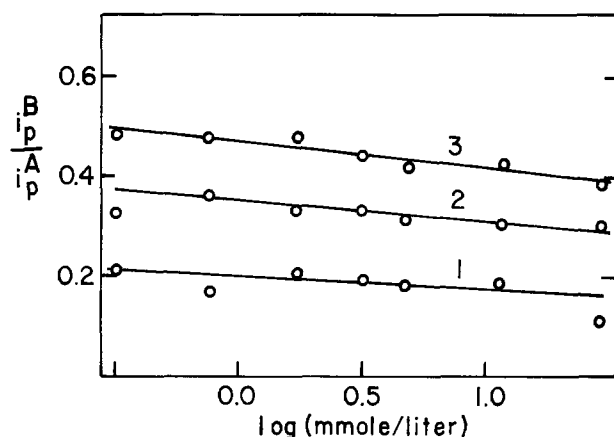
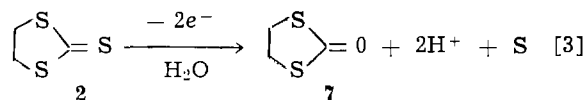


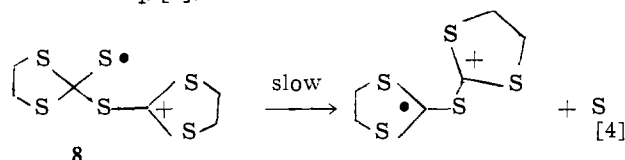
Fig. 5. Variation of the peak current ratio for wave B to wave A with concentration of compound **2**. Curve 1, 0.056 V/sec ; curve 2, 0.199 V/sec ; curve 3, 1.99 V/sec .

Exhaustive electrolysis of the trithiocarbonate **2** in wet acetonitrile gave a coulometric n -value of 1.9 ± 0.3 . Isolation and identification of the dithiocarbonate **7** from the electrolysis solutions has been described previously (2). In addition a gummy yellow precipitate of elemental sulfur, which was not fully characterized, was obtained.



Exhaustive electrolysis in very dry acetonitrile took place very slowly and did not lead to tractable products in our hands. Addition of water to the solutions greatly increased the rate of electrolysis.

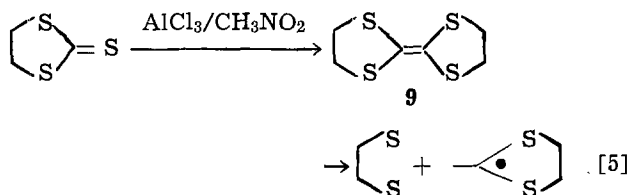
A possible structure for the dimer cation radical is shown in Eq. [4].



This proposed structure is consistent with the known nucleophilic properties of trithiocarbenium ions (20, 21). Wave B could arise from the one-electron reduction of **8**; however, these results do not permit a distinction to be made between structure **8** and others such as a disulfide radical cation.

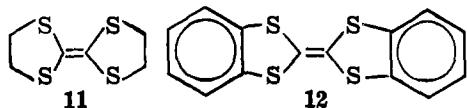
Several attempts were made to detect traces of tetrathioethylene in the cyclic voltammograms of **2**. The tetrathioethylene which corresponds to **2** gives characteristic reversible one-electron waves at 0.68 and 1.12V vs. SCE (1) which could readily be detected in the cyclic voltammograms. Square wave electrolyses were carried out between potentials positive of wave A and less than wave B. No trace of any waves which could be assigned to a tetrathioethylene wave were detected.

This electrochemical behavior can be contrasted with the oxidation of trithiocarbonates in AlCl_3 -nitromethane solutions which leads to radical cations of tetrathioethylenes. Oxidation of **2** under these conditions produced a nine-line ESR spectrum which had a splitting pattern consistent with eight equivalent protons ($a_H = 2.41 \pm 0.03$ gauss, g -value = 2.0079 ± 0.0005).



The spectrum closely resembled the one obtained by electrochemical oxidation of the parent tetrathioethylene in acetonitrile (1) and was identical to the spectrum produced by AlCl_3 oxidation of **9**. This conclusion was corroborated by thin layer chromatographic (TLC) isolation of the tetrathioethylene **9** from the reaction mixture. The reaction mixture and an authentic sample of **9** were seen to yield identical spots on a TLC plate.

The trithiocarbonates **1**, **3**, and **4** were investigated in the same manner and similar results were obtained for **3** and **4**. For **1** no ESR signal was detectable in the AlCl_3 oxidation mixture. This, together with the absence of any coloration, indicates that **1** does not yield a stable odd-electron species under these conditions. Compound **3**, on the other hand, yielded an ESR spectrum which consisted of nine lines ($a_H = 3.16 \pm 0.02$ gauss, $g = 2.0097 \pm 0.0005$) and was identical with that obtained by AlCl_3 oxidation of the tetrathioethylene **11**. The splitting pattern suggests that only the protons on carbon atoms adjacent to sulfur cause hyperfine splitting.



Oxidation of **4** under the same conditions gives a green solution which on standing turns bright orange. The ESR spectrum recorded with the green solution consisted of a narrow unresolved line (line width = 1.4 gauss, $g = 2.0078 \pm 0.0005$) which was also identical with that obtained from **12**.

Quenching of the colored solutions produced by AlCl_3 oxidation with water followed by methylene chloride extraction gives back mostly the starting materials as determined by TLC analysis. Evidently, the amount of material oxidized is quite small in these experiments. In the TLC analysis of the products from the quenched reaction of **4**, the presence of the tetrathioethylene **11** was established by comparison with authentic material.

The view which emerges from these studies is that both chemical and electrochemical oxidation of trithiocarbonates leads to elimination of sulfur and dimerization products. The electrochemical reaction appears to be more selective than the chemical procedures with AlCl_3 or trivalent phosphorous (12-14) in that con-

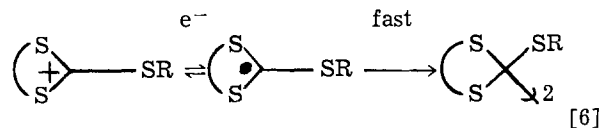
densation to the tetrathioethylenes does not occur. However, an electrochemical pathway to the tetrathioethylenes is afforded by reduction of alkylated trithiocarbonates.

Trithiocarbenium ions, reduction.—Derivatives of the trithiocarbonates **1-6** are readily alkylated (see Experimental Section) to give the corresponding carbenium cations. These species may be easily electrodimersized under very mild electrochemical conditions.

Cyclic voltammograms of all of the cations studied exhibited a single irreversible reduction wave at ca. -0.4V vs. SCE. On the reverse scan a single oxidation wave was generally observed at ca. 1.0V vs. SCE. Figure 6 shows a cyclic voltammogram of **25**, a carbenium ion derived from **4**. Table III contains the voltammetric parameters and the structures of the carbenium ions examined in this study. Tetrafluoroborate, fluorosulfonate, hexafluorophosphate, and perchlorate anions were the counterions. There was no appreciable dependence of the voltammetric parameters on the counterion.

A reverse wave was never observed for the initial reduction wave under the conditions of this study. These included voltage sweep rates up to ca. 100-200 V/sec and several low temperature studies (-24°C). Since analysis of the wave shape, concentration, and sweep rate dependence of the reduction wave indicated Nernstian one-electron transfer, this suggests that the radical species has a lifetime much less than the time scale of these electrochemical measurements which was ca. 1 msec at the fast limit.

An extensive sweep rate and concentration study was undertaken to determine the mechanism of the electrode process. The results are given in Table IV. The results are consistent with a rapid dimerization of the radical species, the DIM1 mechanism of Saveant and co-workers (22), Eq. [6].



The electrodimersation product, an orthothiooxalate, is electroactive and oxidation waves for these species are seen at ca. $0.9\text{-}1.4\text{V}$ vs. SCE in the cyclic voltammograms.

The experimental diagnostic parameters in Table IV also support a dimerization mechanism in which the orthothiooxalate is formed by a rate-determining electron transfer reaction between the dimer radical cation and the parent carbenium ion in the diffusion layer.

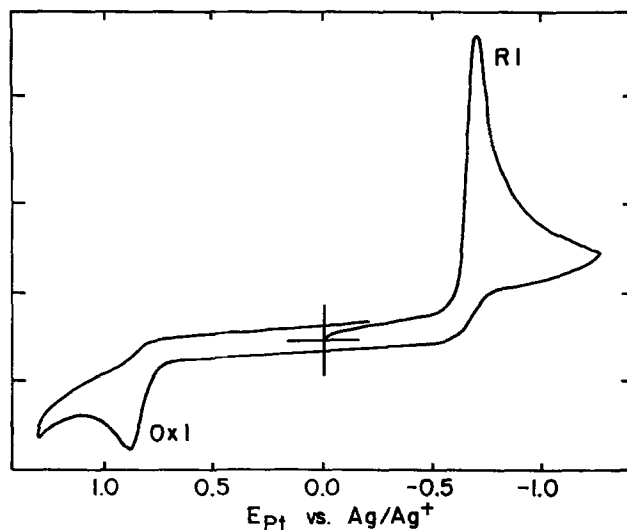
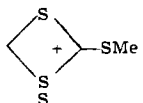
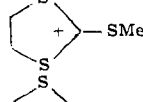
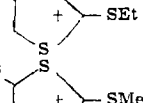
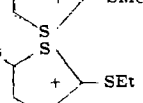
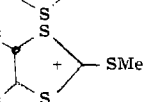
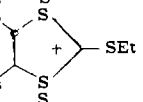
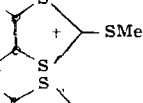
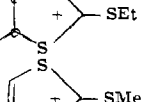
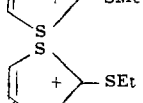
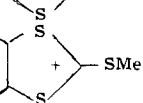
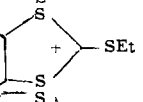
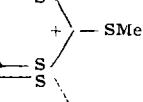
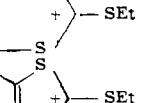
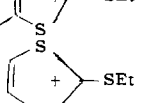
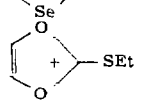
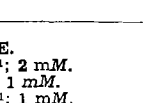
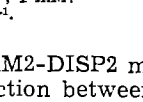
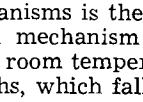


Fig. 6. Cyclic voltammogram of **25** in acetonitrile. Conditions: $1.0 \times 10^{-3}\text{M}$ **25**, 0.1M TEAP, 0.1 V/sec , Pt electrode.

Table III. Voltammetric peak potentials of trithiocarbenium ions in acetonitrile, 0.1M TEAP, Pt electrode

Cation	R1 ^(a)	OX1 ^(a)	OX2 ^(a)	
18		-0.57 ^(b)	1.37	1.57
14		-0.52 ^(c)	1.44	—
15		-0.50 ^(c)	0.90	1.39
16		-0.53 ^(c)	1.37	—
17		-0.49 ^(b)	1.37	—
18		-0.41 ^(b)	1.52	—
19		-0.39 ^(c)	1.46	—
20		-0.40 ^(b)	1.42	—
21		-0.43 ^(b)	1.35	1.46
22		-0.56 ^(b)	0.90	—
23		-0.55 ^(b)	0.94	—
24		-0.44 ^(c)	1.09	—
25		-0.43 ^(c)	1.11	—
26		-0.41 ^(c)	0.81	1.29
27		-0.50 ^(c)	1.30	—
28		-0.47 ^(c)	1.06	1.80
29		-0.52 ^(d)	0.99	—
30		-0.51 ^(e)	—	—

^(a) Volts vs. SCE.

^(b) 100 mV sec⁻¹; 2 mM.

^(c) 1 Volt sec⁻¹; 1 mM.

^(d) 100 mV sec⁻¹; 1 mM.

^(e) 256 mV sec⁻¹.

This is the DIM2-DISP2 mechanism (22). The experimental distinction between the diagnostic criteria for the two mechanisms is the peak width which is 39 mV for the DIM1 mechanism and 45 mV for the latter mechanism at room temperature. Since the experimental peak widths, which fall between these values, may

be increased either by uncompensated resistance or by rate-determining heterogeneous electron transfer, the radical-radical coupling shown in Eq. [6] is indicated.

Coulometric *n*-values were 1.00 ± 0.05 for cations 13 to 28. (Coulometric and product isolation studies were not carried out on 29 and 30.) The electrolyses at a platinum cathode proceeded rapidly with no indication of electrode filming. Isolation of the reduction products confirmed the formation of orthothiooxalates in all cases except the reduction of 15. The orthothiooxalates were obtained in nearly quantitative yields in most cases. After isolation, the orthothiooxalates were pyrolyzed under mild conditions (ca. 100°C, sealed tube or refluxing bromobenzene) to yield the expected tetrathioethylene and dialkyldisulfides (17) in moderate yields, up to 60-70%. The ease of the elimination reaction was evident by the detection of the characteristic oxidation waves of tetrathioethylenes in cyclic voltammograms of room temperature electrolysis solutions of many of the five-membered ring cations.

An orthothiooxalate was not isolated from the electrolysis solutions of 15. Only the corresponding tetrathioethylene and diethyldisulfide were recovered from the solutions. Comparison of room temperature and low temperature cyclic voltammograms of 15 suggests that the orthothiooxalate is formed initially, but undergoes further chemical reactions. Cyclic voltammograms recorded at room temperature and slow sweep rates (see Fig. 7) show several poorly defined product oxidation waves at ca. 1.0V vs. SCE. At faster sweep rates (e.g., 30 V/sec⁻¹) or at lower temperatures (see Fig. 7) the product oxidation waves sharpen considerably and two reversible waves appear after the product oxidation wave is passed. These reversible waves can be assigned to the tetrathioethylene, 9, and this behavior is characteristic of orthothiooxalate oxidation (3, 23).

In addition, cyclic voltammograms of electrolysis solutions carried out at -25°C showed a single product oxidation wave which corresponded to the orthothiooxalate. When the solution was worked up at room temperature only tetrathioethylene and disulfide were recovered. Other unidentified products were also present. No explanation is readily apparent for the relative instability of the dimer derived from 15 at room temperature.

Trithiocarbenium ions, oxidation.—The unsaturated trithiocarbenium ions, 22-25 and 28, could be oxidized at platinum in acetonitrile solutions. Table V lists the peak potentials of the oxidation waves and the reduction waves which result from oxidation products. No well-defined product waves were present when the scan was reversed.

Comparison of the peak currents of the oxidation waves at slow sweep rates to the corresponding one-electron reduction waves indicates that two electrons are involved in the oxidation process. Cation 28 gave the most straightforward behavior. At slow sweep rates two irreversible oxidation waves were present in the

Table IV. Linear sweep parameters for the reduction of some trithiocarbenium ions

Cation	$\frac{\partial E_p}{\partial \log v}$	$\frac{\partial E_p}{\partial \log c}$	CF	ΔE
14	-19.5 ± 1.9 ^(a)	18.0 ± 4.0 ^(a)	0.84 ^(b)	41 ^(c)
15	-15.4 ± 1.9	21.2 ± 2.7	1.23	46
16	-21.5 ± 2.0	19.8 ± 2.3	0.94	44
23	-17.9 ± 2.1	23.8 ± 1.5	1.26	41
24	-23.5 ± 1.6	15.0 ± 2.8	1.25	44
25	-28 ± 2		1.39	42
26	-17.0 ± 0.5	28.4 ± 4.0	1.23	41
27	-18.7 ± 0.9	24.7 ± 2.0	1.15	43
28	-19.8 ± 1.1	17.8 ± 5.2	1.11	44
29			1.10	46

^(a) Millivolts/decade.

^(b) A cm⁻² M⁻¹ (V/sec)^{-1/2}.

^(c) Millivolts.

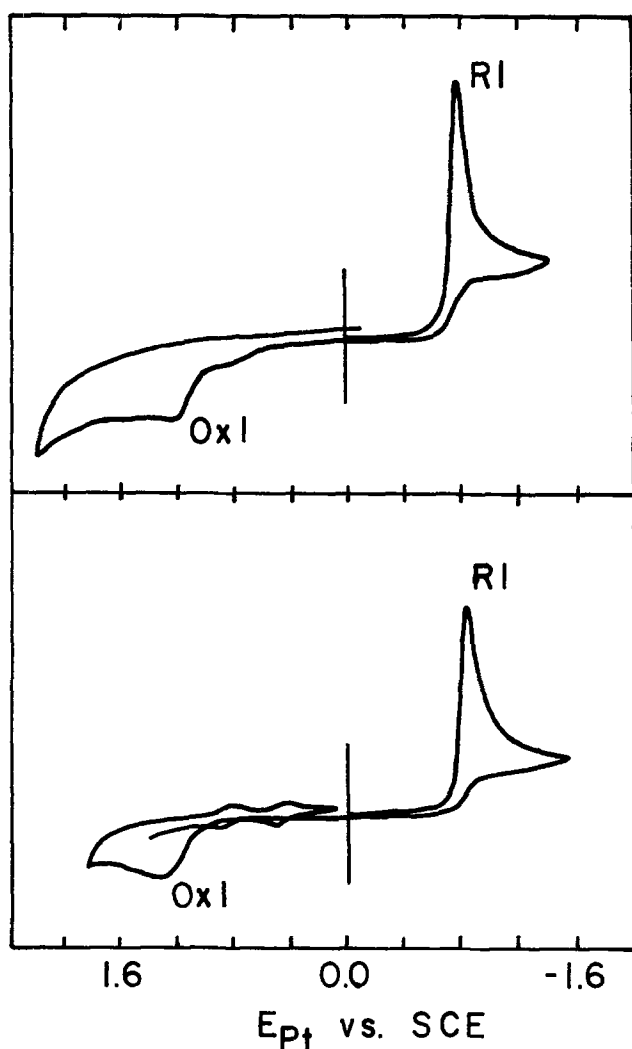


Fig. 7. Cyclic voltammograms of 15 in acetonitrile. Conditions: $2.0 \times 10^{-3}M$ 15, 0.1M TEAP, 0.104 V/sec, Pt electrode. Upper, room temperature; lower, $-24^\circ C$.

cyclic voltammograms. As the sweep rate was increased, the first wave split into two waves, the first of which appeared to be a reversible couple. Figure 8 shows this behavior. Final products are probably derived from fragmentation of the highly reactive dication and trication species. An unsuccessful attempt was made to observe an ESR signal for 28^{2+} by anodic electrolysis in the cavity of an ESR spectrometer.

Summary

Anodic oxidation of trithiocarbonates is not a viable synthetic entry into tetrathioethylenes. Anodic elimination of sulfur and condensation does occur in nonaqueous solvents, but the dimer radical cation which is formed does not yield the tetrathioethylene.

Cathodic reduction of trithiocarbenium cations, on the other hand, does provide a convenient method of synthesizing orthothiooxalates which can be readily

Table V. Voltammetric peak potentials of oxidation waves of some trithiocarbenium cations^(a)

Cation	OX1 ^(b)	OX2 ^(b)	RI ^(b)
22	2.3 ^(c)	—	-0.4
23	2.49	—	-0.2
24	1.83	—	—
25	1.71	—	—
28	1.70	2.03	—

^(a) Concentration = ca. 1 mM. Sweep rate = ca. 100 mV/sec.

^(b) Volts vs. SCE.

^(c) Shoulder on background.

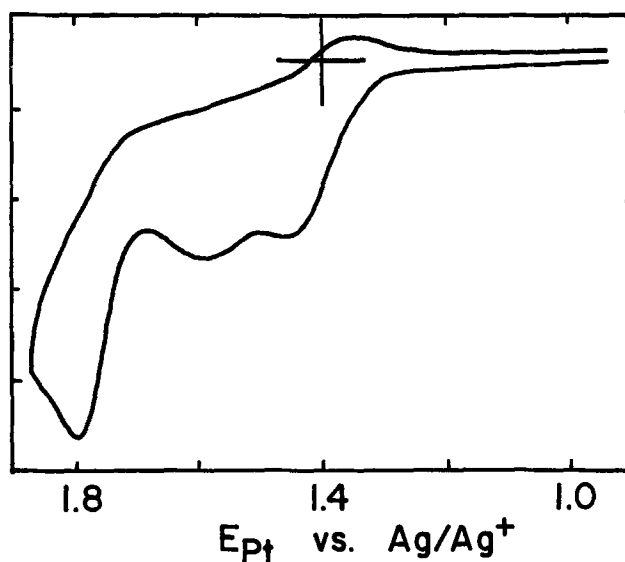


Fig. 8. Cyclic voltammogram of 28 in acetonitrile. Conditions: $0.3 \times 10^{-3}M$ 28, 0.1M TEAP, 30 V/sec, Pt electrode, Ag/Ag^+ reference electrode, 0.1 mA/div.

pyrolyzed to tetrathioethylenes. This preparation of orthothiooxalates takes place under milder conditions and higher yields than the free radical addition reactions or organo-lithium complex dimerizations carried out by Uneyama *et al.* (24) and Seebach and co-workers (25-27). The stringent nonaqueous and oxygen free conditions necessary for these chemical methods are not required for the cathodic reduction of the cations which occurs between -0.40 and $-0.60V$ vs. SCE. The method also seems to be more general than the action of diazomethane on trithiocarbonates as used by Coffen and co-workers (1) and Runge and co-workers (28) to prepare cyclic orthothiooxalates.

Experimental Section

Instrumentation.—Electrochemical experiments were performed with conventional three-electrode potentiostats. The instrument used for the sweep rate and concentration studies was equipped with positive feedback to minimize uncompensated iR drop between the tip of the reference electrode and the working electrode (29).

A Digital Equipment Corporation PDP-12 twelve bit minicomputer was used to record and evaluate cyclic voltammetric data. An assembly language program was written which recorded a voltammogram into core by converting fifteen current data points and then one potential data point. Linear interpolation between potential data points was performed to complete the current-potential voltammogram. The voltammogram in core could be displayed and the data manipulated and evaluated by operator controlled cursors. Sweep rates up to $75 V/sec^{-1}$ were accessible with this program.

Electrochemical experiments were carried out in a Vacuum Atmospheres Company Model HE-43-2 inert atmosphere enclosure filled with nitrogen except in the cases where "wet" acetonitrile is specified. The inert atmosphere was continuously regenerated by an HE-493 Dri-Train (Vacuum Atmospheres Company) which kept oxygen and water at ca. 1 ppm. No oxygen reduction wave was observed in the cyclic voltammograms of solvent-supporting electrolyte using $0.22 cm^2$ platinum electrodes.

Nonaqueous reference electrodes were constructed by dipping a cleaned silver wire into a solution which was 0.01M in $AgNO_3$ and 0.1M in supporting electrolyte in acetonitrile. The potential of these electrodes were ca. $0.30V$ vs. SCE. The potential of the reference electrode was measured prior to each days work and potentials in this paper are referred to aqueous SCE unless specified otherwise.

Procedures.—Large scale electrolyses were carried out in a three-compartment cell in which the counter-electrode was separated from the working electrode by two 20 mm fine porosity glass frits. Electrolysis solutions were ca. 0.03M in electroactive compound and nearly saturated with supporting electrolyte. The cell current was integrated electronically. Products were extracted from the electrolysis solution by evaporating the solution nearly to dryness and extracting with either ether or chloroform.

ESR spectra of radical cations in $\text{AlCl}_3\text{-CH}_3\text{NO}_2$ solutions were obtained following the procedure of Forbes and Sullivan (30).

Chemicals.—Acetonitrile, the principal solvent used in this investigation, was purified by the abbreviated method of O'Donnell, Ayres, and Mann (31, 32). The final distillate was collected over nitrogen and immediately transferred into the inert atmosphere enclosure. Methylene chloride was distilled once from calcium hydride and stored in an inert atmosphere. N,N-dimethylformamide (DMF) was purified by the procedure of Faulkner and Bard (33).

Supporting electrolytes were prepared by standard methods (34), recrystallized at least three times from water-alcohol solutions, and dried at elevated temperatures in vacuum.

Ethylenetrithiocarbonate was purchased from Aldrich Chemical Company and recrystallized from acetonitrile. All of the remaining trithiocarbonates were prepared by literature methods: 1,3-dithiole-2-thione (35), 5; 1,3-dithiane-2-thione (36), 3; 1,3-dithietane-2-thione (37), 1; benzo-1,3-dithiole-2-thione (38), 4; 4,5-thiomethoxy-1,3-dithiole-2-thione (4, 39), 6; 4-phenyl-1,3-dithiolane-2-thione (40); *cis*-4,5-diphenyl-1,3-dithiolane-2-thione (40); *trans*-4,5-diphenyl-1,3-dithiolane-2-thione (41, 42).

All of the trithiocarbonium cations studied are simple alkylated derivatives of trithiocarbonates. They were synthesized by the action of either triethyloxonium ion, dimethylsulfate, or methyl fluorosulfonic acid on the appropriate thione in methylene chloride solution (15, 16). A slight excess of trithiocarbonate was used in the reaction. The solid products were moderately sensitive to atmospheric moisture and oxygen and were handled in the inert atmosphere enclosure whenever possible. The solid products were generally washed with dry carbon tetrachloride until the washings were colorless, dried in vacuum at room temperature, and stored under nitrogen. Yields were nearly quantitative in all cases.

2-thiomethyl-1,3-dithietanium fluorosulfonate, **13**; oil; NMR: $\delta = 4.13$ (s) 2H, 2.00 (s) 3H.

2-thiomethyl-1,3-dithiolanium perchlorate, **14**; mp: 101°-103°; NMR: $\delta = 4.31$ (s) 4H, 3.18 (s) 3H.

2-thioethyl-1,3-dithiolanium hexafluorophosphate, **15**; mp: 46.5°-48.5°; NMR: $\delta = 4.30$ (s) 4H, 3.7 (q) 2H, 1.54 (t) 3H.

2-thiomethyl-4-phenyl-1,3-dithiolanium fluorosulfonate, **16**; mp: 100.5°-103.0°; NMR 4.6 (d) 2H, 7.6 (m) 5H, 6.2 (m) 1H, 3.17 (s) 3H.

2-thioethyl-4-phenyl-1,3-dithiolanium hexafluorophosphate, **17**; oil; NMR: 4.6 (d) 2H, 7.6 (m) 5H, 6.2 (m) 1H, 3.70 (q) 2H, 1.55 (t) 3H.

trans-4,5-diphenyl-2-thioethyl-1,3-dithiolanium fluorosulfonate, **18**; mp: 48°-55°; NMR: 6.36 (d) 2H, 7.53 (s) 10H, 3.18 (s) 3H.

trans-4,5-diphenyl-2-thioethyl-1,3-dithiolanium hexafluorophosphate, **19**; mp 55°-58°; NMR: 6.38 (d) 2H, 7.55 (s) 10H, 3.71 (q) 2H, 1.58 (t) 3H.

cis-4,5-diphenyl-2-thiomethyl-1,3-dithiolanium fluorosulfonate, **20**; mp: 159°-168°; NMR: 6.42 (d) 2H, 7.55 (s) 10H, 3.30 (s) 3H.

cis-4,5-diphenyl-2-thioethyl-1,3-dithiolanium hexafluorophosphate, **21**; oil; NMR: 6.32 (d) 2H, 7.3 (m) 10H, 3.7 (q) 2H, 1.62 (t) 3H.

2-thiomethyl-1,3-dithiolium fluorosulfonate, **22**; mp: 165°-176°; NMR: 8.66 (s) 2H, 3.18 (s) 3H.

2-thioethyl-1,3-dithiolium hexafluorophosphate, **23**; mp: 99°-102°; NMR: 8.62 (s) 2H, 3.6 (q) 2H, 1.60 (t) 3H.

2-thiomethylbenzo-1,3-dithiolium fluorosulfonate, **24**; mp: 165°-176°; NMR: 7.8 (m) 4H, 2.90 (s) 3H.

2-thioethylbenzo-1,3-dithiolium hexafluorophosphate, **25**; mp: 112°-116°; NMR: 8.2 (m) 4H, 2.7 (q) 2H, 1.63 (t) 3H.

2-thiomethyl-1,3-dithianium perchlorate, **26**; mp: 91.0°-92.0°; NMR: 2.5 (m) 2H, 3.7 (m) 4H, 3.0 (s) 3H.

2-thioethyl-1,3-dithianium hexafluorophosphate, **27**; mp: 81.4°-83.0°; NMR: 3.7 (m) 4H, 2.5 (m) 2H, 3.0 (q) 2H, 1.50 (t) 3H.

Compounds **29** and **30** were prepared from the respective thiones (43) which were obtained as gifts from E. M. Engler and V. V. Patel.

Acknowledgment

This work was supported by a grant from the National Science Foundation (GP 31884) and the University of Tennessee Faculty Research Fund. The mini-computer facilities were purchased in part by funds from the NSF as well. Dennis Green carried out the voltammetric experiments on compounds **29** and **30**.

Manuscript submitted Oct. 25, 1974; revised manuscript received Jan. 6, 1975.

Any discussion of this paper will appear in a Discussion Section to be published in the December 1975 JOURNAL. All discussions for the December 1975 Discussion Section should be submitted by Aug. 1, 1975.

REFERENCES

- D. L. Coffen, J. Q. Chambers, D. R. Williams, P. E. Garrett, and N. D. Canfield, *J. Am. Chem. Soc.*, **93**, 2258 (1971).
- J. Q. Chambers, P. R. Moses, and R. N. Shelton, *J. Electroanal. Chem.*, **38**, 245 (1972).
- P. R. Moses and J. Q. Chambers, *ibid.*, **49**, 105 (1974).
- P. R. Moses and J. Q. Chambers, *J. Am. Chem. Soc.*, **96**, 945 (1974).
- J. Ferraris, D. Cowan, V. Walatka, and A. J. Perlestein, *ibid.*, **95**, 948 (1973).
- A. F. Garito and A. J. Heegar, *Accounts Chem. Res.*, **7**, 232 (1974).
- Y. Tomkiewicz, B. A. Scott, L. J. Tao, and R. S. Title, *Phys. Rev. Letters*, **32**, 1363 (1974).
- S. P. Ferraris, T. O. Poehler, A. N. Bolch, and D. O. Cowan, *Tetrahedron Letters*, 2553 (1973).
- E. M. Engler and V. V. Patel, Private communication.
- D. L. Coffen, *Tetrahedron Letters*, 2633 (1970).
- S. Hünig, G. Kiesslich, H. Quast, and D. Scheut-zow, *Liebigs Ann. Chem.*, 310 (1973).
- H. D. Hartzler, *J. Am. Chem. Soc.*, **95**, 4379 (1973).
- E. J. Corey, F. A. Carey, and R. A. E. Winter, *ibid.*, **87**, 934 (1965).
- F. Wudl, G. M. Smith, and E. J. Hufnagel, *Chem. Commun.*, 1435 (1970).
- T. Nakai and M. Okawara, *Bull. Chem. Soc. Japan*, **43**, 3882 (1970).
- K. Gomper and E. Kutter, *Chem. Ber.*, **98**, 1365 (1964).
- P. B. Shevlin and J. L. Greene, *J. Am. Chem. Soc.*, **94**, 8447 (1972).
- R. H. Wopshall and I. Shain, *Anal. Chem.*, **39**, 1514 (1967).
- R. S. Nicholson and I. Shain, *ibid.*, **36**, 706 (1964).
- T. Nakai and M. Okawara, *Bull. Chem. Soc. Japan*, **34**, 1864, 3882 (1970).
- W. P. Tucker and G. L. Roof, *Tetrahedron Letters*, 2747 (1967).
- C. P. Andrieux, L. Nadjó, and J. M. Saveant, *J. Electroanal. Chem.*, **26**, 147 (1970).
- N. D. Canfield, J. Q. Chambers, and D. L. Coffen, *ibid.*, **24**, A7 (1970).
- K. Uneyama, T. Sadakage, and S. Oae, *Tetrahedron Letters*, 5193 (1969).
- D. Seebach, H. B. Stegmann, K. Scheffler, A. K. Beck, and K.-H. Geiss, *Chem. Ber.*, **105**, 3905 (1972).
- D. Seebach and A. K. Beck, *ibid.*, **105**, 3892 (1972).
- D. Seebach, H. B. Stegmann, and A. K. Beck, *Angew. Chem. Internat. Ed.*, **10**, 500 (1971).

28. E. Taeger, Z. El-Hewehi, and F. Runge, *J. Prakt. Chem.*, **18**, 269 (1962).
29. E. R. Brown, T. G. McCord, D. E. Smith, and D. D. DeFord, *Anal. Chem.*, **38**, 1119 (1966).
30. W. F. Forbes and P. D. Sullivan, *J. Am. Chem. Soc.*, **88**, 2862 (1966).
31. J. F. O'Donnell, S. T. Ayers, and C. K. Mann, *Anal. Chem.*, **37**, 1161 (1965).
32. J. A. Lanning and J. Q. Chambers, *ibid.*, **45**, 1010 (1973).
33. L. R. Faulkner and A. J. Bard, *J. Am. Chem. Soc.*, **90**, 6284 (1968).
34. H. O. House, E. Feng, and N. Peet, *J. Org. Chem.*, **36**, 2371 (1971).
35. R. Mayer and B. Gebhardt, *Chem. Ber.*, **97**, 1998 (1964).
36. W. H. Mills and B. C. Saunders, *J. Chem. Soc.*, 537 (1931).
37. P. E. Garrett, Ph.D. Thesis, University of Colorado, Boulder, Colo. (1969).
38. E. Fleckenstein and S. Hünig, *Liebigs Ann. Chem.*, **738**, 192 (1970).
39. S. Wawzonek and S. M. Heilmann, *J. Org. Chem.*, **39**, 511 (1974).
40. C. G. Overberger and C. Drucker, *ibid.*, **29**, 360 (1964).
41. G. Braun, *Org. Syn.*, Coll. Vol. 1, 431 (1941).
42. B. M. Lynch and K. H. Pausacker, *J. Chem. Soc.*, 1525 (1955).
43. E. M. Engler and V. V. Patel, Submitted for publication.

Rotating Ring-Disk Electrode Studies of the Electrochemistry of Aromatic Carbonyl Compounds in the Solvent Sulfolane

Neal R. Armstrong¹ and Nicholas E. Vanderborgh

Department of Chemistry, University of New Mexico, Albuquerque, New Mexico 87131

and Rod K. Quinn*

Sandia Laboratories, Albuquerque, New Mexico 87115

ABSTRACT

The method of rotating ring-disk voltammetry has been applied to the study of the reduction of benzaldehyde and *para*-substituted benzaldehydes in sulfolane. Benzaldehyde undergoes an EC reduction mechanism with an anion dimerization as the following reaction. Digital simulation techniques give values of the second order rate coefficients of $k_2 = 2.4 \times 10^3$ liters/mole-sec. *Para*-cyanobenzaldehyde undergoes a mixed reduction mechanism. At low disk currents the reduction intermediate is proposed to be a parent-anion complex. At higher fluxes, dimerization becomes the significant following process; $k_2 = 45$ liters/mole-sec. A single electroactive intermediate is observed for the first one-electron reduction of *p*-nitrobenzaldehyde. The single, chemically, reversible redox mechanism for this compound in sulfolane agrees with our spectroelectrochemical results.

The cyclic voltammetric behavior of *para*-substituted benzaldehydes and nitrobenzene in the solvent sulfolane has been described in a recent communication (1). These data show an enhanced lifetime of the one-electron-carbonyl adduct from that found in protic solutions. It was of interest to explore these chemical systems using the technique of ring-disk electrochemistry.

Benzaldehyde reductions have been thoroughly investigated in aqueous solutions (2-12). Saveant and co-workers have used linear sweep and cyclic voltammetry techniques for this purpose (2-6). They propose a mechanism that involves protonation and coupling of the reduction intermediate to form the pinacol dimer. This does not disagree with our cyclic voltammetric studies in sulfolane (1). However, *in situ* spectrophotometric observations for the reduction process suggest that additional radical-anion reactions, besides dimerization and protonation, are important in these systems (13).

The method of ring-disk voltammetry has been used with success in studying organic electrode processes (8-12, 14, 15). Nekrasov and Korsun have used this technique to study benzaldehyde and other carbonyl reductions in aqueous-ethanol media over a wide pH range (8-11). Their results demonstrate the presence of a short-lived radical anion intermediate. They also

show the existence of a second ring electrode oxidation wave at potentials several hundred millivolts anodic of the oxidation of the radical anion. This second process was attributed to the oxidation of a charge transfer complex formed between the radical anion and the parent molecule.

Ring-disk kinetic studies originally were done using current transients at the disk electrode (16-23). This approach is limited in applicability to the study of first order homogeneous following reactions. More recently digital simulation techniques have been applied to determine rate parameters for more complicated processes (14, 15, 24). Puglisi and Bard have shown that digital simulations allow the discrimination between second order EC and ECE reactions as well as other mixed coupling reactions (14, 15). In this paper we make use of digital simulation techniques to determine the magnitude of second order kinetic parameters of the following chemical reactions undergone by the one-electron product of these aromatic carbonyl reductions.

Experimental

The electrochemical cell design has been reported previously (1). The reference electrode used in this work was a large silver plate (Ag pseudoreference electrode) immersed into the electrolysis solution. Drift in the potential of this electrode was negligible. The working electrode (RRDE) was a platinum ring-disk electrode (Pine Instrument Corporation, Model TB 18). The significant dimensions are disk radius = 0.239 cm, ring inner radius = 0.270 cm, ring outer

* Electrochemical Society Active Member.

¹ Present address: Department of Chemistry, The Ohio State University, Columbus, Ohio 43210.

Key words: benzaldehyde reductions, EC reduction mechanism, digital simulation, dimerization.

radius = 0.320 cm. This electrode was modified to extend the ring electrode contact up the electrode shaft and outside the electrolysis cell. Two spring-pressured, graphite brushes were used to make independent electrical contact to the ring and disk. Contact resistance in this configuration was less than 5 ohms. The electrode was coupled to a controlled d-c motor (Motomatic Model 550) using a chuck constructed in these laboratories. Less than 1% eccentricity was noted in rotation rates up to 500 radians/sec.

The three-electrode potentiostat was one described previously (1). The ring-disk experiment requires simultaneous, independent potential control of the ring and disk electrodes. The potentiostat was modified using the design of Miller (25) and Napp *et al.* (26). A Chemtrix Potentiostatic Waveform Source was used as the potential source for the ring electrode; a Burr-Brown 3312-12C operational amplifier was used as the ring control amplifier. Current at the two electrodes can be measured simultaneously. Periodic calibration of the ring current-to-voltage converter (Burr-Brown 3308-12C operational amplifier) was necessary.

Purification procedures have been described previously (1). The benzaldehyde was chromatographed on an activated alumina column before use. Residual oxygen was removed by extensive deaeration with a purified argon stream. Electrolysis using a massive platinum cathode poised at a potential corresponding to the foot of the benzaldehyde reduction wave was used to pretreat the solution before beginning an experiment. Residual currents after this step permitted a potential scan of greater than 4V. This cathodic pretreatment eliminated the reduction prewave described previously (1).

The theoretical collection efficiency for this electrode was estimated using the procedure of Alberly *et al.* (18) as $N_0 = 0.3075$. This was checked using a chemical model system, the ferrocene oxidation. The disk electrode was poised at a potential to cause the oxidation of a ferrocene solution while the ring was poised at the reduction potential of the species produced at the disk. The ratio of the ring to disk currents ($i_{r,1}/i_{d,1} = N_0$) was evaluated at a variety of angular velocities. The collection efficiency was unaffected by rotation velocity and found to be $N_0 = 0.305$.

The procedure for generating ring-disk voltammograms was to first determine the rotating disk voltammogram for a particular compound at a fixed rotation rate. The potential of the disk electrode was then poised near the foot of the carbonyl reduction and the ring electrode potential was scanned positively from this point. This trace determined the residual current at the ring. Then the disk potential was set to correspond to the diffusion limited plateau ($i_d = i_{d,1}$) and the ring electrode again scanned positively. The difference in current corresponds to the ring current reported here.

Data used for the determination of the homogeneous kinetic parameters were taken at constant potentials by measuring the steady-state currents at various applied potentials along the voltammogram. The current parameter used in the digital simulation (see below), CONI ($i_d/i_{d,1}$), was computed at each of these potentials. Ring currents were measured at each value of CONI and then values of the collection efficiency were determined. This technique is similar to that described by Puglisi and Bard (14, 15) although procedures of constant potential are described here.

Results and Discussion

A ring-disk voltammogram for the benzaldehyde reduction is shown in Fig. 1. The supporting electrolyte here was 0.1M tetrabutylammonium perchlorate. When the disk is poised at a potential corresponding to the limiting current plateau (point A) the ring voltammogram shows two anodic waves. The half-wave potential of the first ring wave (point 1) occurs at

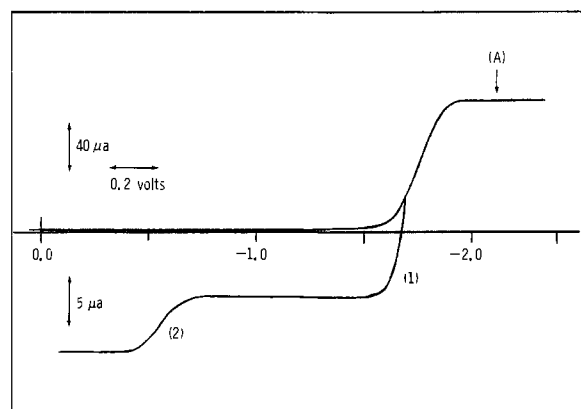


Fig. 1. Rotating ring-disk voltammogram of 5.02 mM benzaldehyde in 0.1M TBAP/sulfolane solution. $\omega = 105$ radians/sec. Upper curve is the disk trace. Lower trace is the anodic behavior shown by the ring electrode while the disk electrode is maintained at potential shown by (A). Note different current sensitivities for cathodic (disk) and anodic (ring) trace.

potentials that represent a reoxidation of the one-electron product produced at the disk (1). The second oxidation wave (point 2) occurs at potentials nearly 1.0V positive of the first wave. A second anodic wave was also seen by Nekrasov *et al.* (8). It was of interest to determine the nature of this wave.

The benzaldehyde reduction wave occurs at potentials close to the cathodic limit in this solvent system. Experiments were performed to explore the nature of the more positive ring wave and see if it involves reactivity of the carbonyl compounds. A solution of TBAP in sulfolane was prepared and was electrolyzed by maintaining the disk at a potential corresponding to the potential of the limiting current for the aldehyde reduction. Scanning the ring electrode anodically produced a ring wave even though no carbonyl compound was present. This wave occurred at potentials similar to those for the second wave (point 2) shown in Fig. 1. This behavior could also be observed by maintaining the ring electrode at a fixed potential (on the limiting current plateau of the second wave) and then scanning the disk to more negative potentials. The ring current increased as the disk approached the potential of solvent decomposition. We conclude that the second ring wave results from the oxidation of an electrode product formed during the steps of the cathodic solvent electrolysis. There appears no way that this can be assigned to a reaction involving the carbonyl compound.

The collection efficiency of the carbonyl reduction process was found to vary as a function of angular velocity. As ω increased, N_k also increased suggesting a chemical reaction which consumes the disk product to form a product that is not electroactive at the ring. The collection efficiency at fixed rotation rates decreases with increasing bulk concentration of the aldehyde. These data are consistent with a second order following chemical reaction such as the dimerization of the one-electron adduct suggested previously from cyclic voltammetric studies (1, 2).

The collection efficiency was studied as a function of applied potential. Therefore the currents are obtained under constant potential conditions for various bulk concentrations. Plots of collection efficiency, N_k , vs. the disk current function, $(1 - i_d/i_{d,1} = 1 - \text{CONI})$ (14, 15) are shown in Fig. 2 for the benzaldehyde reduction. The collection efficiency for the oxidation process increases with decreasing disk current. The flux of the intermediate decreases with decreasing disk current and appears to slow the over-all rate of the following chemical reaction. Puglisi and Bard (14, 15) and Nekrasov and co-workers (8-12) have shown that this type of behavior results from the dimerization of the reduction intermediate

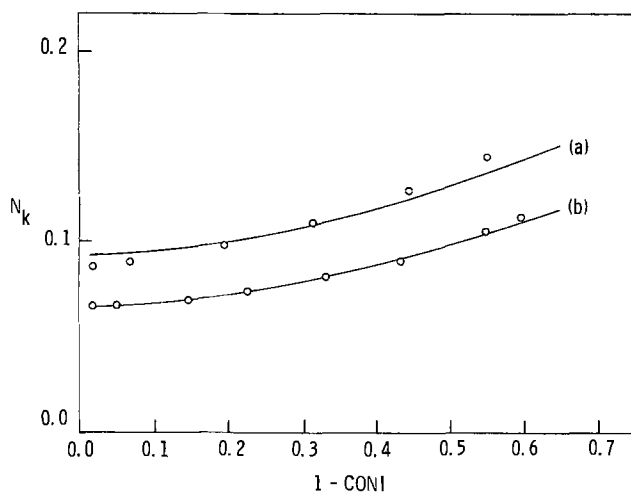


Fig. 2. Collection efficiency, N_k , vs. $1 - \text{CONI}$ for the first ring wave of the benzaldehyde reduction in 0.1M TBAP/sulfolane solution. $\omega = 105$ radians/sec. (a) $C_{\phi\text{-CHO}}^b = 2.51$ mM and (b) $C_{\phi\text{-CHO}}^b = 5.02$ mM. Solid lines are theoretical curves for (a) $\text{XKTC} = 2.6$ and (b) $\text{XKTC} = 4.7$.



Figure 3 shows the results of the addition of millimolar amounts of water to the solvent system. Water can be considered as a proton source in this solvent. Adding water decreases the lifetime of the disk product and suggests that protonation or perhaps solvation promotes the following reaction. These data depict a linear decrease in N_k with the square root of added water concentration. This suggests a 2:1 stoichiometry for the reaction, although one must consider that the mechanism might change as the proton activity of the solvent increases.

Experimental ring-disk data were interpreted using working curves of N_k vs. $(1 - \text{CONI})$ generated using digital simulation techniques (14, 15, 24). The simulations require dimensionless parameters for the ring and disk radii, the diffusion coefficients for the parent molecule (A) and the intermediate (B), the disk current function, CONI , and the rate parameter, XKTC . For the electrode system used here, the radii are $\text{IR}_1 =$

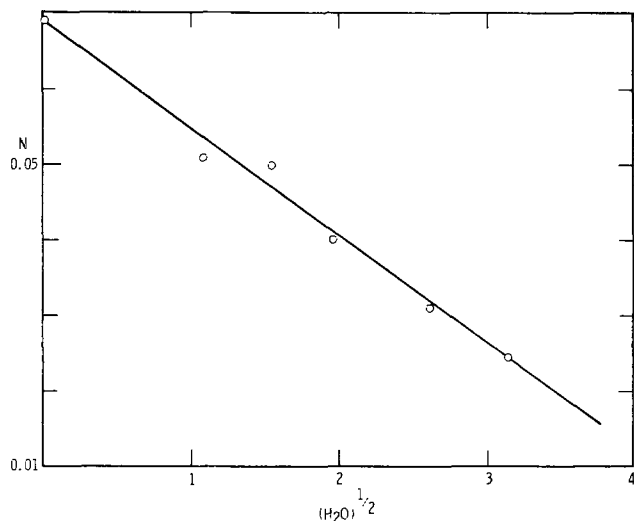


Fig. 3. Collection efficiency, N_k , vs. added water concentration, $[\text{H}_2\text{O}]^{1/2}$ in units of $(\text{mM})^{1/2}$ for the first ring oxidation wave of benzaldehyde in 0.1M TBAP/sulfolane solution. $\omega = 105$ radians/sec and $C_{\phi\text{-CHO}}^{\text{bulk}} = 7.53$ mM.

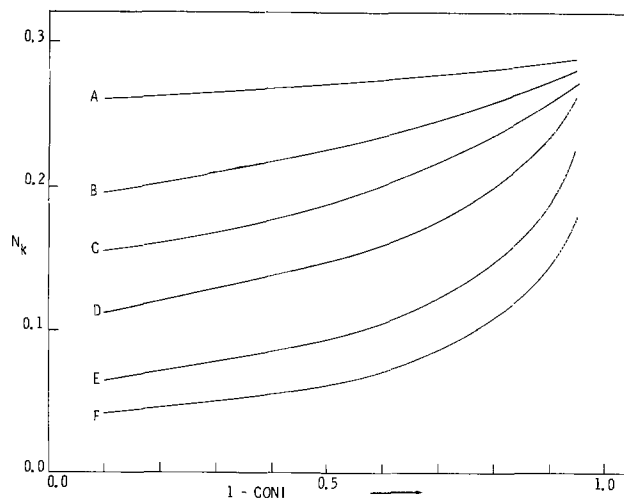


Fig. 4. Simulated plots of collection efficiency, N_k , vs. $1 - \text{CONI}$ for a dimerization reaction following electronation at various values of XKTC , (A) 0.1, (B) 0.5, (C) 1.0, (D) 2.0, (E) 5.0, and (F) 10.0. The parameter XKTC is equal to $(0.51)^{2/3} \nu^{1/3} D^{-1/3} \omega^{-1} k_2 C^b$.

120, $\text{IR}_2 = 136$, $\text{IR}_3 = 161$ (24). The dimensionless diffusion coefficients for species A, DMA, and species B, DMB, were both chosen as $\text{DMA} = \text{DMB} = 0.45$. XKTC is selected to represent a dimensionless form of the rate parameters: $\text{XKTC} = (0.51)^{-3/2} \nu^{1/3} D^{-1/3} \omega^{-1} k_2 C^b$ where ν is the kinematic viscosity of sulfolane at 50°C [$= 4.9$ centistokes (27)], D is the diffusion coefficient of the parent molecule ($= 1.29 \times 10^{-6}$ cm^2/sec) (1), ω is the radial velocity (rad/sec), k_2 is the second order rate coefficient (liters/mole-sec), and C^b the bulk concentration.

Sets of working curves are shown in Fig. 4 for several values of XKTC . These were computer simulated curves calculated for a dimerization reaction. The experimentally determined data, N_k vs. $(1 - \text{CONI})$, were fit to these simulated working curves. From the simulated values of XKTC which most closely represented the experimental cases, values for the second order (dimerization) rate coefficient, k_2 , were estimated. These are given in Table I.

Data is also included for *p*-cyanobenzaldehyde. This compound shows a single anodic ring wave when the disk electrode is poised at the limiting current of the aldehyde reduction. The absence of the second wave correlates well with the reduction potential being considerably less negative than that of benzaldehyde (1). The collection efficiency, N_k , was larger at the same rotation rate and bulk concentration than that found for the benzaldehyde system.

Plots of N_k vs. $(1 - \text{CONI})$ for the *p*-cyanobenzaldehyde system show two regions of interest (Fig. 5). At high values of disk current, N_k decreases as ex-

Table I. Values of k_2 determined by digital simulation methods for benzaldehyde and *p*-cyanobenzaldehyde

a. Benzaldehyde ($\phi\text{-CHO}$) $\omega = 105$ radians/sec		
$C_{\phi\text{-CHO}}^{\text{bulk}}$ (mM)	XKTC	k_2 (liters/mole-sec)
2.51	2.6	2.07×10^8
2.51	4.8	3.80×10^8
3.52	4.0*	2.28×10^8
5.02	4.7	1.79×10^8
Average = 2.40×10^8		
* Fit up to $1 - \text{CONI} = 0.350$.		
b. <i>p</i> -Cyanobenzaldehyde (PCNB) $\omega = 105$ radians/sec		
$C_{\text{PCNB}}^{\text{bulk}}$ (mM)	XKTC	k_2 (liters/mole-sec)
5.50	0.14	48.6
8.10	0.18	42.4
Average = 45.2		

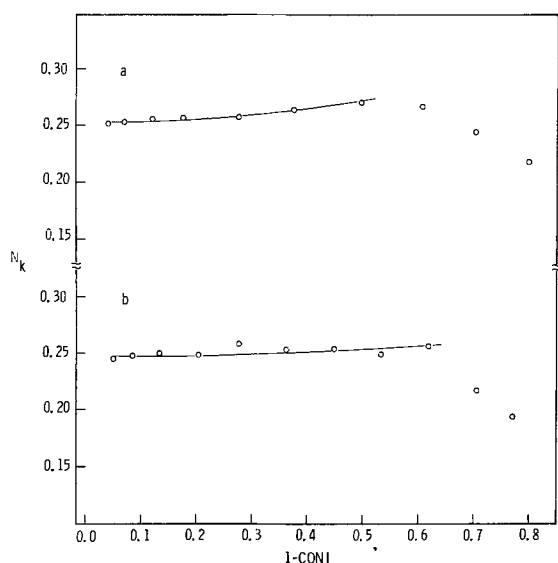


Fig. 5. Collection efficiency, N_k , vs. $1 - \text{CONI}$ for the *p*-cyanobenzaldehyde reduction in 0.1M TBAP/sulfolane solution with $\omega = 105$ radians/sec. (a) $C_{\text{PCNB}}^{\text{bulk}} = 5.50$ mM and (b) $C_{\text{PCNB}}^{\text{bulk}} = 8.81$ mM. Solid lines are theoretical curves for (a) $\text{XKTC} = 0.14$ and (b) $\text{XKTC} = 0.18$.

pected for the dimerization of the reduction intermediate. At lower values of current, however, values of N_k become constant or decrease with increasing $(1 - \text{CONI})$. Constant values of N_k with increasing $(1 - \text{CONI})$ are consistent with a first order following reaction. Decreasing values of N_k with increasing $(1 - \text{CONI})$ suggests a second-order ECE mechanism (16)



where C is electroactive at potentials which produce B



Simulated data for the dimerization model fit the experimental N_k vs. $(1 - \text{CONI})$ data up to values of $(1 - \text{CONI}) = 0.600$. Values are shown in Table I for dimerization rates obtained from this region.

These *p*-cyanobenzaldehyde data show that two types of reaction consume the reduction intermediate. At small fluxes, the intermediate is present at relatively low concentration. Here a pseudo first order mechanism predominates. This reaction may be with solvent impurities or complexation with the parent (scheme 4). At higher fluxes and corresponding higher concentrations of the radical anion, dimerization becomes the significant following process. The data suggest a mixed mechanism, one that favors the first order process at low fluxes and then switches to anion dimerization as the concentration increases. This mechanism explains much of the data we have seen in these systems (1, 13).

Data were also taken for the one-electron reduction of *p*-nitrobenzaldehyde. The reduction process produces a single electroactive intermediate at the disk electrode that can be oxidized at the ring. This species shows a collection efficiency that remains constant as the velocity of the electrode is varied and has a value (0.306) close to that predicted by theory. This represents behavior of a single chemically reversible redox system.

Conclusions

Ring-disk electrode investigations indicate an EC mechanism for the reduction of benzaldehyde in sulfolane. Digital simulation methods allow the evaluation

of second order rate coefficients for the dimerization following reactions. These values agree well with previously determined values in this solvent (1, 13). The data again show the higher stability of the aldehyde reduction, one-electron intermediates in this solvent.

The study of the reduction of benzaldehyde is complicated since the solvent reduces at potentials close to the carbonyl reduction energy. Recent work suggests that the cathodic limit in sulfolane might be due to reduction of trace quantities of water (28). This interpretation may apply to this study. The second anodic wave seen during the benzaldehyde reduction appears to be the result of this process. The resulting disk current due to this coreduction process would contribute a small positive error in the determination of the dimerization reaction rate coefficient, k_2 .

The data for *p*-cyanobenzaldehyde show a mixed reduction mechanism. Preliminary spectroelectrochemical studies have indicated two reduction intermediates (13). One of these compounds is the expected one-electron adduct while the second was identified as a complex of the one-electron adduct with other species, perhaps with the parent molecule. Ring-disk voltammograms do not show unique electrochemical behavior for this complex species. Evidence presented here for EC behavior at low concentrations of the reduction intermediate corroborates the spectroelectrochemical information.

Acknowledgments

The authors are grateful to Prof. A. J. Bard for supplying the computer program used to generate the digitally simulated working curves of N_k vs. $1 - \text{CONI}$. One of us (N.R.A.) acknowledges the Associated Western Universities for financial support through an AWU/AEC Graduate Fellowship at Sandia Laboratories.

This work was supported by the U.S. Atomic Energy Commission.

Manuscript submitted Oct. 23, 1974; revised manuscript received Dec. 20, 1974.

Any discussion of this paper will appear in a Discussion Section to be published in the December 1975 JOURNAL. All discussions for the December 1975 Discussion Section should be submitted by Aug. 1, 1975.

Publication costs of this article were partially assisted by Sandia Laboratories.

REFERENCES

- N. R. Armstrong, R. K. Quinn, and N. E. Vanderborgh, *Anal. Chem.*, **46**, 1759 (1974).
- J. Saveant and E. Vianello, *Electrochim. Acta*, **12**, 1545 (1967).
- C. P. Andrieux, L. Nadjo, and J. M. Saveant, *J. Electroanal. Chem.*, **26**, 147 (1970).
- L. Nadjo and J. M. Saveant, *ibid.*, **33**, 419 (1971).
- F. Ammar, L. Nadjo, and J. M. Saveant, *ibid.*, **47**, 146 (1973).
- C. P. Andrieux, L. Nadjo, and J. M. Saveant, *ibid.*, **42**, 223 (1973).
- J. W. Hayes, I. Ruzic, D. E. Smith, G. L. Booman, and J. R. Delmastro, *ibid.*, **51**, 269 (1974).
- L. N. Nekrasov and A. D. Korsun, *Elektrokhimiya*, **4**, 489 (1968).
- L. N. Nekrasov and A. D. Korsun, *ibid.*, **4**, 539 (1968).
- L. N. Nekrasov and A. D. Korsun, *ibid.*, **4**, 996 (1968).
- A. D. Korsun and L. N. Nekrasov, *ibid.*, **5**, 212 (1969).
- L. N. Nekrasov, D. N. Soshchin, and V. N. Gramenitskaya, *ibid.*, **6**, 1577 (1970).
- N. R. Armstrong, Ph.D. Dissertation, The University of New Mexico, 1974.
- V. J. Puglisi and A. J. Bard, *This Journal*, **119**, 829 (1972).
- V. J. Puglisi and A. J. Bard, *ibid.*, **119**, 833 (1972).
- W. J. Albery, *Trans. Faraday Soc.*, **62**, 1915 (1966).
- W. J. Albery and S. Bruckenstein, *ibid.*, **62**, 1920 (1966).
- W. J. Albery, S. Bruckenstein, and D. T. Napp, *ibid.*, **62**, 1932 (1966).

19. W. J. Albery, S. Bruckenstein, and D. C. Johnson, *ibid.*, **62**, 1938 (1966).
 20. W. J. Albery and S. Bruckenstein, *ibid.*, **62**, 1946 (1966).
 21. W. J. Albery and S. Bruckenstein, *ibid.*, **62**, 2584 (1966).
 22. W. J. Albery and S. Bruckenstein, *ibid.*, **62**, 2596 (1966).
 23. W. J. Albery, *ibid.*, **63**, 1771 (1967).
 24. K. B. Prater, Ph.D. Dissertation, University of Texas, 1969; and K. B. Prater and A. J. Bard, *This Journal*, **117**, 207 (1970).
 25. B. Miller, *This Journal*, **116**, 1117 (1969).
 26. D. T. Napp, D. C. Johnson, and S. Bruckenstein, *Anal. Chem.*, **39**, 481 (1967).
 27. Shell Development Co., Emeryville, California, Technical Bulletin IC-63-13 R (1963); J. W. Vaughn, and C. F. Hawkins, *J. Chem. Eng. Data*, **9**, 140 (1964).
 28. B. Gosse, *J. Electroanal. Chem.*, **55**, 119 (1974).

A Correlation Between the Quantum Efficiency of Electrogenerated Chemiluminescence and the Redox Potentials of Rubrene in Various Solvents

A. Pighin

Bell-Northern Research, Ottawa, Ontario, Canada

and B. E. Conway

Chemistry Department, University of Ottawa, Ottawa, Ontario, Canada

ABSTRACT

The effect of solvent on the quantum efficiency of electrogenerated chemiluminescence (EGCL) was studied by measuring the coulombic efficiency (ϕ_{coul}) of rubrene EGCL in eleven different solvents. ϕ_{coul} was found to vary significantly amongst the solvents employed. Various attempts were made to correlate ϕ_{coul} with some property of the solutions. A correlation between ϕ_{coul} and the difference between the oxidation and reduction potential was obtained, ϕ_{coul} increasing with increasing potential difference. The correlation is explained in terms of changes in solvation with the solvent affecting the degree of ion radical quenching of the lowest excited triplet state through which rubrene EGCL is produced.

Rubrene has been widely studied as an electrochemiluminescent material in aprotic solvents (1-3). Its electrogenerated chemiluminescence (EGCL) has useful potential applications in display devices (4). The quantum efficiency of the light-producing process is both of fundamental interest in regard to energy transfer mechanisms and of practical concern in device applications.

The emitting species of rubrene EGCL is the lowest excited singlet state. Recent investigations of rubrene EGCL have established that the fluorescence is indirectly produced via triplet-triplet annihilation in each of the several solvents studied: (i) Bezman and Faulkner (5) concluded from Feldberg plots of the EGCL intensity *vs.* time that the luminescence arose from the triplet route, (ii) Tachikawa and Bard (6) observed a magnetic field enhancement of the intensity of the EGCL and suggested that this was an indication of an important involvement of triplets in the reaction pathway, and (iii) Pighin (7) calculated from experimental thermodynamic data that the change in enthalpy of the anion-cation-radical charge neutralization re-

action was less than the energy of the lowest excited singlet state. Thus, the singlet state must be produced through triplet-triplet annihilation.

The mechanism for rubrene EGCL is, therefore, as shown in Table I. The products of the reactions are produced in the proportions shown because of statistical factors, assuming that these reactions are not influenced by the solvent (8). It can be calculated from this mechanism that the theoretical maximum quantum efficiency of rubrene EGCL is 0.075 photons/electron.

Although "quantum efficiency" is simple to define, e.g.

quantum efficiency =

$$\frac{\text{No. of photons of EGCL generated sec}^{-1}}{\text{faradaic current (in electrons sec}^{-1}) \text{ transferred}} \quad [1]$$

its actual measurement is not trivial. The most difficult problem in this measurement arises from the low light intensities which originate from EGCL. Other obstacles to be overcome with the light measurements are the uncertainties inherent in such factors as reflection losses at the electrode, absorption losses in the solu-

Key words: electrogenerated chemiluminescence, rubrene, quantum efficiency.

Table I. Rubrene EGCL mechanism

(R = rubrene)

Formula	Mechanism	Equation No.
$R \rightarrow \cdot R^+ + e$	(Oxidation of rubrene at electrode)	[2]
$R + e \rightarrow \cdot R^-$	(Reduction of rubrene at electrode)	[3]
$\cdot R^+ + \cdot R^- \rightarrow 3/4 \cdot R^* + 5/4 R$	(Homogeneous electron transfer/triplet formation)	[4]
$\cdot R^* + \cdot R^* \rightarrow 1/4 \cdot R^* + 3/4 \cdot R^* + R$	(Triplet-triplet annihilation/singlet formation)	[5]
$\cdot R^* \rightarrow R + h\nu$	(Radiative decay of excited singlet)	[6]

tion, collection efficiency of the detector, and spectral response of the detector.

The electrolytic current consists of faradaic and capacitive components. Only the faradaic component of the total current is used to produce light, the capacitive component being involved in charging and discharging the double layer at the electrode. Consequently, in order to obtain true quantum efficiency data, it is necessary to separate the electrolytic current into its faradaic and capacitive components. Of the ion radicals produced, some could diffuse away from the reaction zone without being neutralized while others can be lost to side reactions. The faradaic current employed to calculate the quantum efficiency should not include these losses since they do not contribute to the generation of electronically excited molecules.

The presence of all of these factors limits the accuracy with which the quantum efficiency of EGCL can be determined.

The light from EGCL has been measured using calibrated photon detectors (9), actinometry (10), and integrating spheres (11), while the electrical current was, or was assumed, to be entirely faradaic. Previous results in the literature for the quantum efficiency of the same system (rubrene in tetra-*n*-butylammonium perchlorate in benzonitrile) range from a low value of 0.1% (corrected for both photon and current losses) to a high one of 8.7% (without any corrections) (12). These variations in the values of the published quantum efficiency of the same EGCL system have led us to develop another independent method for evaluating the quantum efficiency which has been described recently (7). This method provides the basis for the experiments reported in the present paper.

Bezman and Faulkner (5) measured the quantum efficiency of rubrene EGCL in both DMF and benzonitrile and found it to be twice as large in benzonitrile in comparison with DMF. They estimated higher triplet yields in the solvent in which the EGCL was more efficient. Tachikawa and Bard (6) reported that the magnetic field enhancement of the intensity of rubrene EGCL decreased with decreasing dielectric constant of the solvent. This was explained by suggesting that the degree of direct singlet formation increased with decreasing dielectric constant of the solvent. In our previous work (7), it was shown in a preliminary way that the quantum efficiency of rubrene EGCL was solvent dependent although the EGCL was produced exclusively by the triplet route in both solutions studied, decreased with increasing frequency of the a-c potential used to electrolyze the fluorescor solutions, and was independent of the electrolyte (tetra-*n*-butylammonium perchlorate) concentration. The absence of an electrolyte effect was interpreted as an indication of the lack of importance of ion pairing in the solvents studied (DMF and equivolume benzene-DMF) while the frequency dependence was explained by suggesting that the triplets could be quenched by the electrode. It was speculated that the effect of solvents on the coulombic efficiency (ϕ_{coul}) of rubrene EGCL could result from preferential solvation of the ion radicals by the polar, aprotic component of the mixed solvent while the nonpolar, aromatic component of the mixed solvent preferentially solvated the neutral rubrene, including that in the excited triplet state. The different solvation shells hindered (kinetically) the quenching of the excited triplets by the parent ion radicals, a well-known process (13).

In the present paper, further evaluation of the effect of the solvent on ϕ_{coul} of rubrene EGCL is reported. The results presented here corroborate the tentative explanation proposed earlier.

Method for Determination of Quantum Efficiency

In the method developed (7) for measuring the quantum efficiency of EGCL, the EGCL solution is electrolyzed at a pair of equal-area electrodes with a moderately high frequency (20-1000 Hz) symmetrical

square wave voltage. This stimulus, because of its relatively high frequency, provides a periodic EGCL signal of constant amplitude and reproducible waveform for at least the duration of the measurements, about 15 min. Cyclic voltammetric inspection of the electrolyzed solutions did not indicate any compositional changes as a result of the electrolysis. Therefore, it was concluded that the quantum efficiency of the EGCL was being determined in the absence of side reactions.

The average rectified a-c electrolysis current and average photon "current" are measured at selected voltages. From a plot of the average electrolysis current vs. applied voltage, the current-voltage line prior to the appearance of EGCL (a linear relationship caused by the purely capacitive nature of this current) is extrapolated into the voltage region which produces EGCL and subtracted from the total current to obtain the faradaic component of the total current at that voltage. An example of this procedure is shown in Fig. 1.

The measured photon current was multiplied by 1.7 to obtain the actual, corrected photon current which emerged from the electrolysis cell. The correction factor employed compensates only for the spectral response of the solar cell material (0.7 electrons/photon) and the collection efficiency of the solar cell box (5 electrons/6 photons). The corrected photon current is then plotted against the faradaic current from which twice the quantum efficiency can be obtained from the slope of the plot. This plot yields twice the quantum efficiency because both electrodes emit the same amount of light and the total light output was measured. Figure 2 illustrates a typical plot of corrected photon current vs. faradaic current.

This method for determining the quantum efficiency of EGCL yields the apparent coulombic efficiency, ϕ_{coul} .

Experimental

All of the solutions studied contained rubrene as the fluorescor and tetra-*n*-butylammonium perchlorate (TBAP) as the electrolyte. Both of these solutes were purified first by repeated recrystallization and then by vacuum drying. The rubrene (obtained from Aldrich)

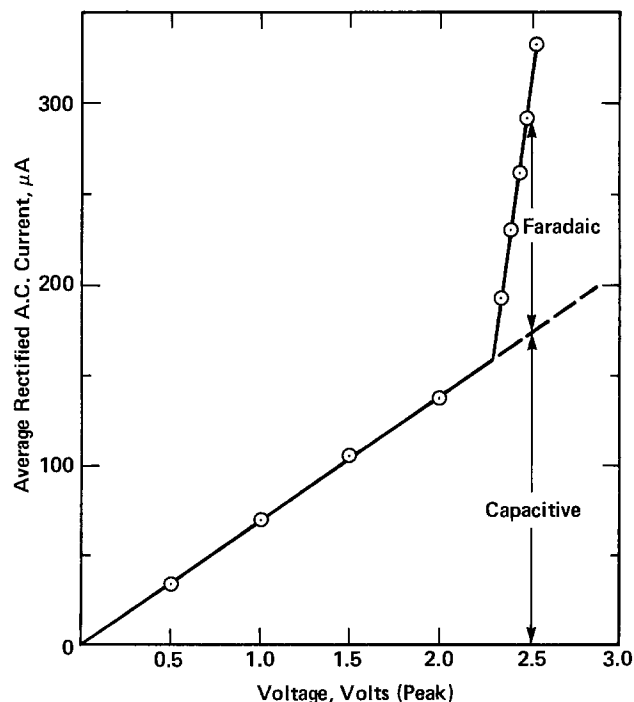


Fig. 1. Typical current-voltage plot used to calculate the faradaic component of the total electrolysis current. Solution: 1.00 mM rubrene in 0.100M TBAP in equivolume benzene-DMF.

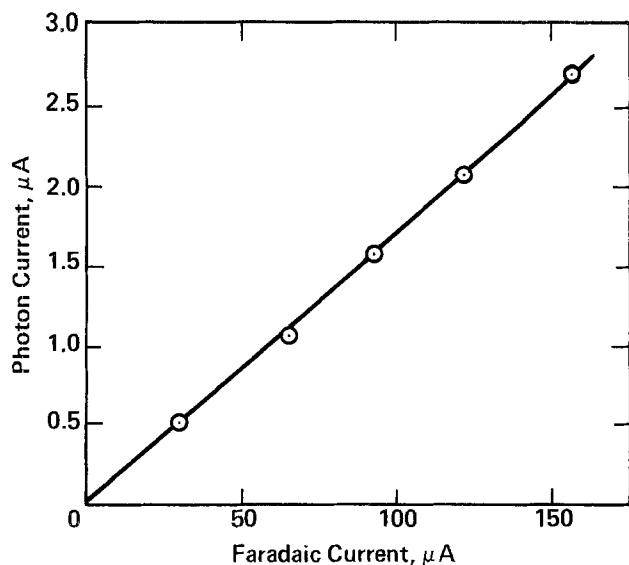


Fig. 2. Typical plot of photon current vs. faradaic current from whose slope ϕ_{coul} can be calculated. Solution: 1.05 mM rubrene in 0.100M TBAP in equivolume benzene-acetonitrile.

was recrystallized from xylene-methanol and the TBAP [obtained from Matheson, Coleman and Bell (MC&B)] from ethanol.

In this investigation, N,N-dimethylformamide (DMF), benzonitrile (PhCN), acetonitrile (ACN), and propylene carbonate (PC) were employed as aprotic solvents and benzene was added to each to produce solvents of mixed polarity. Fisher D-133 DMF was found to be sufficiently pure to require only drying with Linde Type 5A molecular sieves for its solutions to exhibit constant EGCL intensity with time on continuous generation. The purity of the solvents was ascertained with a Hewlett-Packard 5754B Research Gas Chromatograph, using suitable chromatographic columns. Spectroquality grade PhCN was obtained from MC&B and it too had only to be dried with the sieves for the required electrochemical stabilities of rubrene to be achieved in its solutions. Commercial ACN was found to contain troublesome impurities which were difficult to remove. It was possible, however, to purify some lots of MC&B and Aldrich ACN by passing them through an activated alumina column followed by vacuum distillation of the eluent. The Eastman No. 7050 PC had first to be vacuum distilled and then pre-electrolyzed (with TBAP as the electrolyte). The distillate from the electrolyzed solution was found to be sufficiently pure for the EGCL experiments. The benzene, Fisher B-414, did not contain significant quantities of undesirable impurities but was nevertheless dried with sieves before being used in the preparation of solutions for EGCL experiments.

All of the solutions studied were prepared from purified components in a dry box filled with nitrogen. The electrolysis cell used for the quantum efficiency measurements and the three-electrode electrochemical cell were charged with solution and all measurements were carried out in the dry box. The temperature in the dry box was $25 \pm 2^\circ\text{C}$.

A Princeton Applied Research Model 170 Electrochemistry System and a three-electrode electrochemical cell were used to record cyclic voltammograms of the oxidation and reduction of the rubrene in each solution studied. A silver wire immersed in the test solution was used as the reference electrode (14); it was contained inside a compartment whose Luggin tip extended to within 2 mm of the platinum bead working electrode. In taking the recordings, iR compensation was employed to eliminate the fanning out of the voltammetric waves due to the electrolytic resistance of the solutions. It was estimated that the residual, un-

compensated iR drop was at the most several millivolts (7). The cyclic voltammograms were obtained at a scan rate of 100 mV sec^{-1} . At lower scan rates, the oxidation of the rubrene began to exhibit irreversibility while at higher scan rates the recorder response became a limitation.

Results and Discussion

In the previous work, it was found that ϕ_{coul} of rubrene EGCL decreased with increasing frequency of the electrolysis voltage used to generate the EGCL. Consequently, in these experiments, the frequency employed was always 100 Hz, square wave.

Since it was found that ϕ_{coul} also decreased with increasing fluorescor concentration (Fig. 3), a fluorescor concentration of 1 mM was used in all cases so that the individual values of ϕ_{coul} could be compared. Bezman and Faulkner (5) did not obtain a concentration dependence of ϕ_{coul} of rubrene EGCL in both DMF and benzonitrile. Fleet *et al.* (15), in studying the analytical usefulness of EGCL, found that the maximum intensity from rubrene EGCL was directly proportional to the rubrene concentration. This indicates that the quantum efficiency was independent of concentration. A notable difference exists between our work and that of Bezman and Faulkner and Fleet *et al.* Relatively more concentrated solutions were employed in the present work. Other EGCL systems investigated by Fleet *et al.* exhibited deviations from nonlinearity at high concentrations which were ascribed to quenching. It is interesting to note that the present ϕ_{coul} results decrease linearly with \log (rubrene concentration). Such a variation in ϕ_{coul} with rubrene concentration could be explained by the self-absorption of rubrene EGCL.

The reproducibility of the ϕ_{coul} data was such that the results for the same system, using solutions prepared nine months apart, were within 10% of each other. A number of equivalent solutions prepared simultaneously yielded ϕ_{coul} values which had a standard deviation of better than 5%.

In Table II are shown the values of ϕ_{coul} of rubrene EGCL in the various solutions studied. These results are the average of several determinations using the same and equivalent solutions and have a precision of $\pm 5\%$. Bard *et al.* have made a tabulation of the available quantum efficiencies of EGCL (12). In that summary, values of the quantum efficiency of EGCL of 1 mM rubrene in 0.1M TBAP in DMF and benzonitrile solvents are given. Our results, in these solvents, when compared with those reported by others, agree best with the values obtained by Bezman and Faulkner. Their results are consistently lower than ours but we both obtained greater efficiency in benzonitrile than in DMF. Bezman and Faulkner generated their EGCL with triple-potential steps, each step 1 sec in duration,

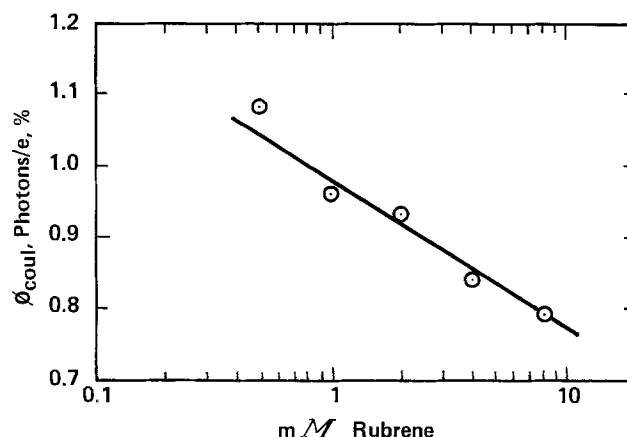


Fig. 3. Decrease in ϕ_{coul} with increasing rubrene concentration in 0.100M TBAP in equivolume benzene-DMF.

Table II. ϕ_{coul} of 1 mM rubrene EGCL in the 0.100M TBAP solutions studied at 25°C

Solution No.	Solvent	ϕ_{coul} , %
1	1:1* benzene:ACN	0.91
2	PhCN	0.90
3	1:1 benzene:PhCN	1.02
4	DMF	0.65
5	1:99 benzene:DMF	0.70
6	1:19 benzene:DMF	0.69
7	1:4 benzene:DMF	0.80
8	1:1 benzene:DMF	0.96
9	3:1 benzene:DMF	1.01
10	1:1 benzene:DMF	0.68
11	DMF (0.020M TBAP)	0.64

* For the mixed solvents, the volume ratios are shown.

while we employed a symmetrical 100 Hz square wave voltage to produce our EGCL. In our preliminary report of this work (7), we showed that ϕ_{coul} increased with decreasing frequency. The triple-potential step used by Bezman and Faulkner to generate the EGCL is equivalent to a relatively lower frequency than ours. If we were to extrapolate our frequency dependence of ϕ_{coul} of rubrene EGCL down to the equivalent frequency of their triple-potential step, then on the basis of our results, Bezman and Faulkner should have measured relatively greater efficiencies. Since, in fact, their ϕ_{coul} values are lower than ours, then it must be concluded that the near agreement with the magnitudes of our results was accidental.

It is clearly evident from the data in Table II that ϕ_{coul} of rubrene EGCL is dependent on the solvent. Various attempts were made to correlate the data in Table II with some property of the solution and the procedures used are reported below.

Since different solvents containing the same electrolyte concentration (0.100M TBAP) were used to prepare the solutions for the present study, then the solution conductivity was a potentially significant variable in this work. The importance of iR effects was evaluated by also measuring ϕ_{coul} of 1 mM rubrene EGCL in 0.020M TBAP in DMF. Reducing the electrolyte concentration in DMF solvent from 0.100 to 0.020M TBAP had no measurable effect on ϕ_{coul} of rubrene (Table II). Consequently, iR effects are unimportant in the interpretation of the ϕ_{coul} data in Table II.

It is already known from earlier work that the changes in enthalpies of the anion-cation-radical charge neutralization reactions in DMF and equi-volume benzene-DMF are nearly the same and are significantly less than the energy of the emitting state, i.e., the lowest excited singlet state of rubrene. The emitting state has the same energy in both of these solutions and the fluorescence efficiencies are also the same in both solutions. Despite the similar thermodynamic and spectroscopic properties of rubrene in these solutions, the ϕ_{coul} of rubrene in the mixed solvent solution is, however, nearly 50% greater than that of the purely polar solvent. Therefore, the solvent dependence of ϕ_{coul} of rubrene EGCL cannot be explained by significant solvent effects on either the type of EGCL mechanism or on the fluorescence efficiency of the rubrene. Tachikawa and Bard (6) have suggested an alternative explanation for the effect of solvent on the quantum efficiency of rubrene EGCL which is in conflict with our above conclusion of a solvent-independent rubrene EGCL mechanism. They assume that rubrene excited singlets are produced both directly by the ion-radical charge neutralization reaction and indirectly via the triplet route. According to their explanation, the degree of direct singlet formation increases with decreasing dielectric constant of the solvent. It will be shown later in the discussion that our values of ϕ_{coul} do increase with decreasing dielectric constant of the solvent. However, from our thermodynamic measurements in DMF and equi-volume benzene-DMF, rubrene EGCL is produced exclusively via

the triplet route in both solutions and yet ϕ_{coul} in the mixed solvent is 150% that in DMF alone.

The triplet-triplet annihilation reaction and both the homogeneous and heterogeneous electron transfer reactions are essentially diffusion controlled (16, 17). Addition of benzene [$\eta = 0.61$ centipoise (cp) (18)] to DMF [$\eta = 0.80$ cp (19)] decreased the solution viscosity and, in this case, ϕ_{coul} increased with decreasing solution viscosity. However, the viscosity of benzonitrile [$\eta = 1.24$ (18)] is much greater than that of DMF and yet ϕ_{coul} is much greater in the more viscous solution. Thus, the ϕ_{coul} data in Table II do not show a consistent trend with solution viscosity (regardless of the composition of the solvent). It therefore appears that ϕ_{coul} of rubrene EGCL is independent of the rates of these diffusion-controlled reactions.

Although the exact dielectric constants of the solutions used in this ϕ_{coul} study are not known, it is nevertheless possible to conclude that ϕ_{coul} increases with decreasing dielectric constant of the solution. As the fraction of benzene [$\epsilon = 2$ (18)] added to DMF [$\epsilon = 37$ (19)] is increased, ϕ_{coul} increases. Similarly, addition of benzene to benzonitrile [$\epsilon = 26$ (6)] also results in an increase in ϕ_{coul} . Hoytink (13) has shown from theoretical considerations that the rate of transfer of an electron from an anion to a cation radical should increase with decreasing dielectric constant. A larger homogeneous rate constant in a medium of lower dielectric could affect the extent of quenching of the excited triplets by the parent ion radicals. However, the effective dielectric constant at a molecular level can be significantly different from the bulk dielectric constant so that the former should be preferentially employed in establishing a correlation with ϕ_{coul} , especially for mixed solvent solutions as employed in this study, where preferential solvation can prevail. Besides assuming a dielectric continuum, the Hoytink model also pertains to spherical particles, a condition which is not realized with rubrene which has a flat ring structure for a backbone. It is to be appreciated, then, that it is both difficult and risky to attempt to correlate ϕ_{coul} data with the dielectric constant of the solution. Hence, it was decided to attempt to correlate ϕ_{coul} with a more readily determinable property of the solution, the relative change in solvation energy with solvent, which is related to the dielectric constant of the solution by the Born equation (16).

It was not possible to dissolve the rubrene in either conducting ACN or PC to the extent of 1 mM and only slightly more than 1 mM rubrene could be dissolved in conducting DMF. The solubility of rubrene in conducting benzonitrile solution was about 2 mM. By adding benzene to all of the polar, aprotic solvents, the solubility of rubrene in the resultant mixed solvent solutions was, in each case, much greater than in the polar solvent alone. For example, 8 mM rubrene could be dissolved in conducting equi-volume benzene-DMF.

Inspection of the ϕ_{coul} data in Table II reveals that addition of benzene to both PhCN and DMF caused an increase in ϕ_{coul} . Furthermore, with reference to the DMF data, it is noted that ϕ_{coul} increased as the benzene fraction of the mixed solvent solution was increased. Thus, the addition of an aromatic solvent to the polar solvents not only increased the solubility of the fluoroscor but it also increased ϕ_{coul} .

The solvation of rubrene must follow its saturation solubility in the various solvents. It therefore became apparent that ϕ_{coul} increases with increasing solvation of the neutral rubrene. In order to establish this correlation, it was necessary to determine differences in the solvation energy of rubrene in the various solutions.

The half-wave potential of a redox process is given by the following equation in which the symbols have their usual significance (16)

$$E_{1/2} = E^\circ - \frac{RT}{nF} \ln \frac{f_{\text{red}}}{f_{\text{ox}}} + \frac{RT}{nF} \ln \left(\frac{D_{\text{red}}}{D_{\text{ox}}} \right)^{1/2} \quad [7]$$

For an oxidation

$$E^{\circ}_{\text{ox}} = I + \Delta G^{\circ}_{\text{sol},\text{R}^+} - \Delta G^{\circ}_{\text{sol},\text{R}} + C \quad [8]$$

and for a reduction

$$E^{\circ}_{\text{red}} = A + \Delta G^{\circ}_{\text{sol},\text{R}^-} - \Delta G^{\circ}_{\text{sol},\text{R}^+} + C \quad [9]$$

where I and A are the gas-phase ionization potential and electron affinity, respectively, of the substance being electrolyzed, G°_{sol} are the standard free energies of solvation, and C is a constant. Since the solvation terms are the only contributions to the electrochemical potentials which are dependent on the solvent, then the electrochemical potentials of rubrene in the various solutions can be used as a measure of the relative energies of solvation of the rubrene.

It is known from the rubrene solubility data in these solutions that the solvation of rubrene increases with increasing benzene fraction in all mixed solvent solutions. The solutions actually studied each contained about 1 mM of rubrene. Since benzene is a nonpolar solvent while the aprotic solvents are all polar, then the addition of benzene to the aprotic solvent lowers the dielectric constant of the resulting solution. The Born theory predicts that the solvation of the ion radicals would become more difficult (less negative) with decreasing dielectric constant. Thus, the addition of benzene to an aprotic solvent would normally tend to increase $\Delta G^{\circ}_{\text{sol},\text{R}}$ and decrease both $\Delta G^{\circ}_{\text{sol},\text{R}^+}$ and $\Delta G^{\circ}_{\text{sol},\text{R}^-}$. Consequently, since the changes in solvation energies of the neutral and charged species of the redox couple are reinforcing, E°_{ox} will become more positive and E°_{red} more negative with the addition of benzene.

When benzene was added to an aprotic solvent there always remained a large excess of polar component in the solvent relative to the rubrene concentration. Hence, the probability that the radical ions are, in fact, preferentially solvated by the polar component of the mixed solvent must be recognized; then the solvation energy of the ion radicals would not be expected to significantly change relative to the change in solvation energy of the neutral rubrene, when benzene was added to the aprotic solvent. This leaves changes of $\Delta G^{\circ}_{\text{sol},\text{R}}$ as the main contribution to changes of E° which are found to be solvent dependent (for a given polar solvent with various amounts of benzene).

The peak oxidation and reduction potentials ($E_{\text{p,ox}}$ and $E_{\text{p,red}}$, respectively) of rubrene in various solutions were determined by means of cyclic voltammetry. A typical cyclic voltammogram is shown in Fig. 4. The voltammograms were recorded on a potential scale of 0.2V in.⁻¹. This allowed ($E_{\text{p,ox}} - E_{\text{p,red}}$) to be resolved within ± 5 mV. The measured values of ($E_{\text{p,ox}} - E_{\text{p,red}}$) are given in Table III together with the corresponding differences between the forward and reverse peak potentials for the cathodic processes. At 25°C, the latter difference should be 58 mV (21). Any measured excess was assumed to have resulted from residual uncompensated iR drops and was subtracted from the measured ($E_{\text{p,ox}} - E_{\text{p,red}}$) to obtain the correct (ed) ($E_{\text{p,ox}} - E_{\text{p,red}}$). The largest correction made, 20 mV, was to the data for the 0.020M TBAP in DMF solution.

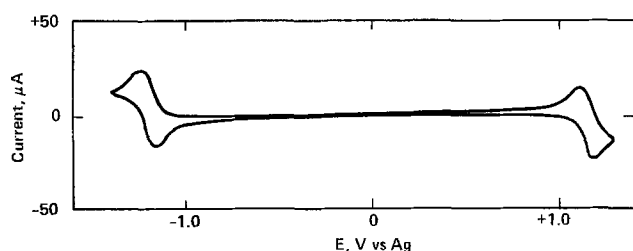


Fig. 4. Cyclic voltammogram of 1.01 mM rubrene in 0.100M TBAP in benzonitrile.

Table III. Electrochemical data for redox processes involving rubrene

Solution No.	Measured ($E_{\text{p,ox}} - E_{\text{p,red}}$), V	($E_{\text{p,R}^+/\text{R}^-} - E_{\text{p,R}^+/\text{R}}$), mV	Corrected ($E_{\text{p,ox}} - E_{\text{p,red}}$), V
1	2.450	70	2.440
2	2.405	65	2.400
3	2.510	65	2.505
4	2.380	70	2.370
5	2.380	65	2.375
6	2.385	65	2.380
7	2.400	65	2.395
8	2.455	65	2.450
9	2.540	70	2.530
10	2.400	70	2.390
11	2.395	80	2.375

Figure 5 shows the plot of ϕ_{coul} vs. the corresponding value of ($E_{\text{p,ox}} - E_{\text{p,red}}$). The variation in the difference between the redox potentials of rubrene with change in solvent is twice the magnitude of the change in solvation energy of the neutral rubrene for the reasons previously discussed. A clear correlation between ϕ_{coul} and ($E_{\text{p,ox}} - E_{\text{p,red}}$) is obtained, ϕ_{coul} being found to increase with increasing ($E_{\text{p,ox}} - E_{\text{p,red}}$). Since the increases in ($E_{\text{p,ox}} - E_{\text{p,red}}$) result from relatively greater solvation of the neutral rubrene than of the conjugate ion radicals, then the correlation between ϕ_{coul} and ($E_{\text{p,ox}} - E_{\text{p,red}}$) can be interpreted as an indication that the increase of ϕ_{coul} is mainly due to increasing solvation of the neutral rubrene.

The excited triplets which lead to the emission of light are also neutral species of rubrene. It is thus reasonable to assume that the solvation of the excited triplets also increases with increasing ($E_{\text{p,ox}} - E_{\text{p,red}}$). The excited triplets are susceptible to quenching by the parent ion radicals (13). A more strongly solvated triplet is, however, less likely to be quenched by the rubrene ion radicals because the solvation cage will tend to shield (kinetically) the triplets from energy exchange with the radical ions. In a solvent of mixed polarity, it is assumed that the triplets will be preferentially solvated by the less polar component, i.e., benzene, and the ion radicals by the more polar component, the aprotic solvent, thereby further reducing the efficiency of the quenching mechanism.

The rate of increase in ϕ_{coul} with increasing ($E_{\text{p,ox}} - E_{\text{p,red}}$) decreases with increasing ($E_{\text{p,ox}} - E_{\text{p,red}}$). This is to be expected because the solvent component

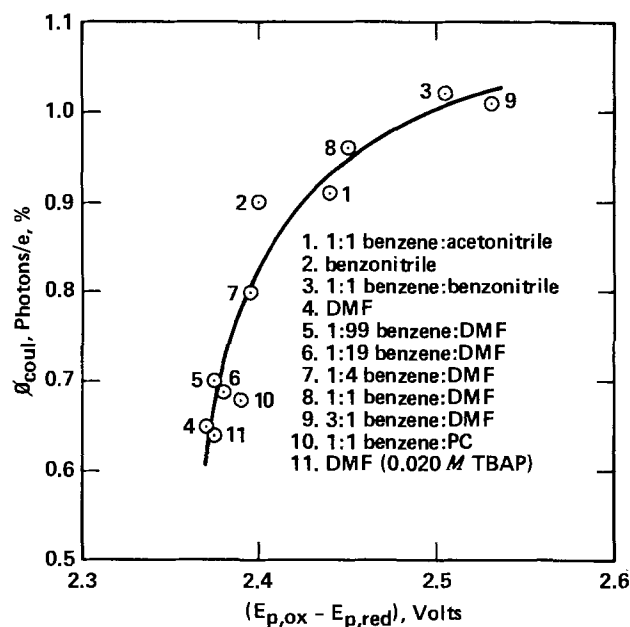


Fig. 5. Correlation between ϕ_{coul} and ($E_{\text{p,ox}} - E_{\text{p,red}}$) of 1 mM rubrene in various solvents containing 0.100M TBAP. The EGCL was generated with a symmetrical, 100 Hz square wave voltage.

(benzene) which tends to produce relatively high ($E_{p,ox} - E_{p,red}$) will also then tend to solvate the radical ions. When both the rubrene in its excited triplet state and its ion radical form are similarly solvated, the identical solvation shells will tend to offer less resistance to the quenching process than if they were different.

The four aprotic solvents employed, viz., DMF, PhCN, ACN, and PC, are physically very different and yet ϕ_{coul} of rubrene EGCL in their solutions correlates very well with ($E_{p,ox} - E_{p,red}$). It is therefore concluded that the degree of solvation of the neutral rubrene is the dominant factor in determining ϕ_{coul} of its EGCL.

Acknowledgments

This work was supported in part by the National Research Council of Canada through its Industrial Research Assistance Program and by assistance to one of us (B.E.C.) at the University of Ottawa. We also wish to express our gratitude to R. M. van Dyk and D. P. Malanka for help received in preparing these experiments.

Manuscript submitted May 29, 1974; revised manuscript received Dec. 28, 1974. This was Paper 291 presented at the San Francisco, California, Meeting of the Society, May 12-17, 1974.

Any discussion of this paper will appear in a Discussion Section to be published in the December 1975 JOURNAL. All discussions for the December 1975 Discussion Section should be submitted by Aug. 1, 1975.

Publication costs of this article were partially assisted by Bell-Northern Research.

REFERENCES

1. D. M. Hercules, *Science*, **145**, 808 (1964).
2. R. E. Visco and E. A. Chandross, *Electrochim. Acta*, **13**, 1187 (1968).
3. S. A. Cruzer and A. J. Bard, *J. Am. Chem. Soc.*, **91**, 267 (1969).
4. M. A. Kabayama, A. Pighin, and W. M. Coderre, Paper presented at Symposium of Soc. for Info. Displays, New York, May 1973.
5. R. Bezman and L. R. Faulkner, *J. Am. Chem. Soc.*, **94**, 6324 (1972); **95**, 3083 (1973).
6. H. Tachikawa and A. J. Bard, *Chem. Phys. Letters*, **26**, 246 (1974).
7. A. Pighin, *Can. J. Chem.*, **51**, 3567 (1973).
8. B. Brocklehurst, *Chem. Phys.*, **2**, 6 (1973).
9. R. Bezman and L. R. Faulkner, *Anal. Chem.*, **43**, 1749 (1971).
10. J. T. Maloy and A. J. Bard, *J. Am. Chem. Soc.*, **93**, 5968 (1971).
11. P. M. Schwartz, R. A. Blakeley, and B. B. Robinson, *J. Phys. Chem.*, **76**, 1868 (1972).
12. A. J. Bard, C. P. Keszthelyi, H. Tachikawa, and N. E. Tokel, in "Chemiluminescence and Bioluminescence," M. J. Cormier, D. M. Hercules, and J. Lee, Editors, p. 193, Plenum Press, New York (1973).
13. G. J. Hoytink, *ibid.*, p. 147.
14. D. J. Fisher, W. L. Belew, and M. T. Kelley, in "Polarography 1964," G. J. Hills, Editor, Vol. 2, p. 1043, Interscience Publishers, Inc., New York (1966).
15. B. Fleet, P. N. Keliher, G. F. Kirkbright, and C. J. Pickford, *Analyst*, **94**, 847 (1969).
16. M. E. Peover, in "Electroanalytical Chemistry," A. J. Bard, Editor, Vol. 2, p. 1, Marcel Dekker, New York (1967).
17. C. A. Parker, "Photoluminescence of Solutions," Elsevier, Amsterdam (1968).
18. "Handbook of Chemistry and Physics," 49th ed., R. C. Weast, Editor, The Chemical Rubber Co., Cleveland, Ohio (1968-1969).
19. Du Pont DMF Technical Information Bull., A-655I0 E.I. Du Pont de Nemours and Co., Wilmington, Delaware.
20. R. S. Nicholson and I. Shain, *Anal. Chem.*, **36**, 706 (1964).

Thermodynamic Properties of the Alkali Metals in Aluminum Chloride-Propylene Carbonate Solution

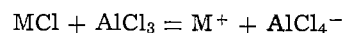
Jacob Jorné*¹ and Charles W. Tobias*

Inorganic Materials Research Division, Lawrence Berkeley Laboratory and Department of Chemical Engineering, University of California, Berkeley, California 94720

ABSTRACT

EMF measurements were performed at 25° and 35°C on the general cell M(s)/MCl [solution in AlCl₃ (1m) in PC]/TlCl(s)/Tl(Hg), where M represents Li, Na, K, Rb, and Cs. The standard electrode potentials of the alkali metals in AlCl₃ (1m) - PC solution evaluated by extrapolation to infinite dilution follow the order: Cs < Rb < K < Li < Na which is different than the order in water. Activity coefficients of the alkali metal chlorides were calculated for a wide range of molalities. The partial molal Gibbs free energies, entropies, and enthalpies of the cell reactions have been evaluated and compared to those in other solvents.

The feasibility of the deposition of all the alkali metals from their chlorides in AlCl₃-propylene carbonate solution has been demonstrated (1). Lithium, sodium, potassium, rubidium, and cesium were deposited at ambient temperature showing stable and reversible behavior. The alkali metal chlorides are practically insoluble in PC, however in the presence of AlCl₃ a complex is formed between the chloride and AlCl₃ according to the reaction



This reaction proceeds for all the alkali metals and is the only combination that gives high solubility and conductivity for all the alkali metals. The electrodeposition of the alkali metals from their chloride solutions in AlCl₃-PC is proposed as a new process for the electrodeposition and refining of the alkali metals at ambient temperature (2). In order to characterize such a process, thermodynamic, kinetic, and transport data are needed. With this goal in mind, emf measurements of the alkali metals in their chloride solutions in AlCl₃(1m)-PC were performed on the cell

* Electrochemical Society Active Member.

¹ Present address: Department of Chemical Engineering and Material Sciences, Wayne State University, Detroit, Michigan 48202.

Key words: alkali metals, propylene carbonate, aluminum chloride, standard potentials.

M(s)/MCl(m), AlCl₃(1m) in PC/TlCl(s)/Tl(Hg)

The measurements were performed in order to establish a scale of standard electrode potentials in AlCl₃(1m)-PC solution, and to obtain activity coefficients data; both are needed for the design of an electrorefining cell, and for the prediction of the separation and purification of the alkali metals in such a cell (2). In addition, kinetic (3), conductance, and specific volume measurements (4) are reported elsewhere.

The thermodynamics of some of the alkali metals in various solutions in PC were investigated by Salomon (5-7) using the emf method. The thermodynamics of LiCl and LiBr (5), NaI (6), LiI and KI (7), were measured using the cell-type

M/MX in PC/TlX(s)/Tl(Hg)

where M represents Li, Na, and K, and X represents Cl⁻, Br⁻, and I⁻. In the case of the potassium system, potassium amalgam replaced the metallic potassium, and the data were corrected for the free energy of formation of the amalgam. The standard potentials were obtained by extrapolation to infinite dilution following the Guggenheim equation (8). The thermodynamics of single ion solvation in PC and water is summarized by Salomon (9).

The extensive work of Salomon did not include rubidium and cesium and in addition, iodide was the only common anion which shows high solubility for Li, Na, and K. With the exception of lithium, the chlorides of the alkali metals are highly insoluble in pure PC. In the present work, emf measurements were performed for all the alkali metals, and the fact that the same common anion was used enabled the establishment of a scale of standard potentials for the alkali metals series.

Experimental

Solvent purification.—Propylene carbonate (Jefferson Chemical Company, Houston, Texas) was distilled at 0.5 mm Hg in a commercially available distillation column (Semi-CAL Series 3650, Podbielniak, Franklin Park, Illinois) packed with stainless steel helices. The reflux ratio was 60 to 100 and the head temperature 65°C. The first 10% and last 25% of the solvent were discarded. Argon gas was bubbled through the solvent during distillation. The collection vessel was not detached from the column; the solvent was discharged directly into the dispensing vessel. The transfer was done under an argon atmosphere. The dispensing vessel was evacuated on the vacuum line to approximately 50 μ Hg, closed tightly and transferred into the glove box.

The "as received" solvent contains a few tenths of a per cent of the following impurities: water, propylene glycol, propion aldehyde, propylene oxide (10). Gas chromatographic analysis of the product performed in this laboratory showed the water content to be always below 50 ppm. The presence of a second impurity at a very low concentration was identified as propylene oxide; its concentration was estimated below 1 ppm (1). Molecular sieves (Linde 4A) were ineffective in removing propylene oxide from PC.

The glove box (Lawrence Livermore Laboratory design) was maintained under dry and oxygen-free argon (1). The water content of the inlet argon stream was measured by a moisture monitor (Consolidated Electrochemicals Corporation, Model 26-303 ME) and was always below 1 ppm.

Electrolytic solutions.—All solutions of the alkali metal chlorides in AlCl₃(1m)-PC were prepared by weighing the salts and the solvent inside the glove box. The 1.0 molal (m) solutions of AlCl₃ in PC were made by adding the salt very slowly to the solvent, since the heat of solution is very high. The AlCl₃ in PC solutions were prepared inside the box under argon and were cooled with chloroform-carbon tetrachloride-dry ice bath mixture. Careless addition of AlCl₃ to PC resulted

in a brown solution; this occurred particularly when the salt was not a fine powder, but rather in small granules, which upon addition to PC resulted in local heating and darkening of the solution.

The alkali metal chlorides were dried inside a vacuum oven (Hotpack, Philadelphia) at 200°C and approximately 50 μ Hg for at least 24 hr. The amounts needed for the specific molalities were calculated each time from the weights of the solvent. Stirring for a few hours was required in order to achieve complete dissolution of the alkali metal chlorides. The final solutions were treated with molecular sieves (Linde 4A) in order to remove traces of water introduced by the salts. The molecular sieves were treated before use by heating (300°C), high vacuum, and several flashes with argon. This procedure was found effective in further removing traces of water and therefore increased the stability of the alkali metals during the potential measurements.

Reference electrode.—Earlier investigations in this laboratory revealed the excellent nature of thallium amalgam-thallos halide electrodes in PC (11) and DMSO (12, 13). Thallos chloride was found to be only slightly soluble in PC and does not dissolve in excess of chloride. This reference electrode has been applied to the cell Li/LiX(DMSO)/TlX(s)/Tl(Hg) in order to determine the standard potential of the cell and the activity coefficients of LiX in DMSO. Salomon (5-7) used this reference electrode to measure standard potentials and activity coefficients of alkali metal halides in PC. The Tl(Hg) solidus TlCl electrode was found to be stable and reversible in DMF (12).

The performance of Tl(Hg)/TlCl electrode in PC was reversible with good stability. The solubility product of TlCl in PC is $K_{sp} = 10^{-12.4}$ (11), extremely low even when compared with other aprotic solvents (e.g., for DMSO $K_{sp} = 10^{-6.26}$) (14).

The thallium wire used for preparation of the amalgam was 99.999% pure (United Mineral and Chemical Corporation, New York). The oxide coating on the metal was removed by successive washing with oxygen-free distilled water under argon atmosphere. The shining Tl was transferred directly into the glove box without exposure to air. The resulting silvery white metal dissolved readily in mercury. The mercury used was triple distilled. The amalgam concentration was prepared by weight. The thallium amalgam was then placed inside the electrode cups containing about 5 ml of the amalgam, exposing around 1 cm² of shiny surface (see Fig. 1). The amalgam surface was then covered with a thin adherent layer of fine TlCl. The electrode was gently shaken in order to get a complete and uniform coverage of the surface.

The electrical connection to the amalgam was through a platinum lead which was connected to a tungsten wire. All the connections and leads were overlaid with uranium glass for a vacuum-tight seal. The platinum tip was immersed well beneath the surface of the amalgam to prevent creeping of the solvent between the amalgam and the glass.

Cell for potential measurements.—The cell used for potential measurements, shown in Fig. 1, was developed earlier by Smyrl (13, 15). In this six-compartment cell each compartment is connected to the central one by a narrow pipe. The cup electrode for the thallium amalgam-thallos chloride reference electrode is shown in Fig. 1. A detailed description of the cell is given by Smyrl and Tobias (15). The electrode holder for the solid alkali metals (Li, Na, K) is shown in Fig. 1. The alkali metal wire was attached to the platinum wire by a stainless steel connector. Alkali metal amalgam electrodes were prepared by pouring the amalgams into cup electrodes similar to those used for the reference electrodes.

Rubidium and cesium electrodes were prepared by heating the capsules in which these metals had been received, and the electrode's cups, and then pouring the

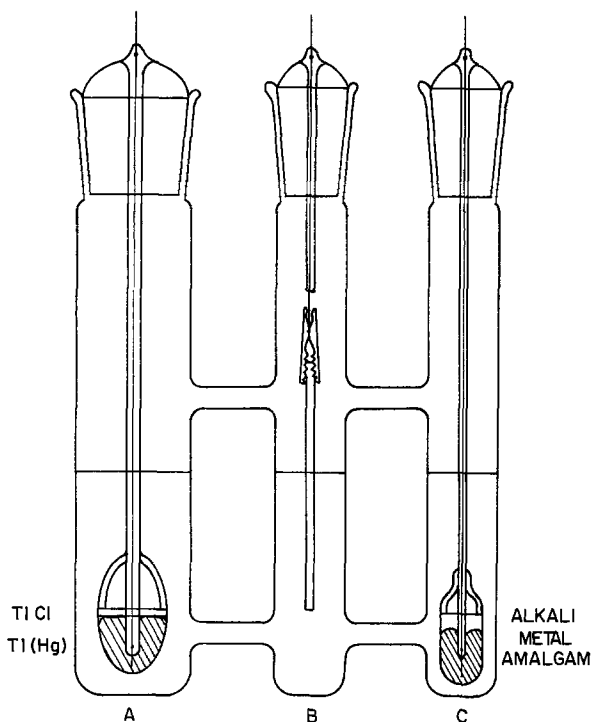


Fig. 1. Six-compartment cell for potential measurements (only three compartments are shown). A, Reference electrode; B, alkali metal electrode; C, alkali metal amalgam electrode.

liquid metals into the cups well above the platinum leads. Lithium was obtained as $\frac{1}{8}$ in. wire and was rinsed with the pure solvent. Sodium and potassium obtained in the form of ribbons were extruded through a stainless steel extruder of 1.13 cm diameter, and then were washed with the pure solvent. All the alkali metal electrodes kept their shining surfaces during the measurements. Electrodes which turned gray or black after being immersed in the solution, consequently giving erratic potentials, were discarded.

The arrangement of the electrodes was the following: For every measurement there were two reference electrodes, two alkali metal electrodes, and two alkali metal amalgam electrodes of identical composition. The cell, the electrode holders, and the cup electrode, besides all volumetric flasks and glassware, were cleaned prior to each experiment by concentrated nitric acid and were rinsed several times with distilled water. Periodically the cells were cleaned with concentrated sodium hydroxide, dilute sulfuric acid, and distilled water. Occasionally the cells and the cup electrodes were cleaned with an ultrasonic vibrator to remove solids from the glass. All glassware was dried in a vacuum oven at 50μ and 200°C for at least 24 hr and then transferred quickly into the glove box.

Assembly of cell.—The six-compartment cell was filled with approximately 100 cm^3 solution of a specific concentration of the alkali metal chloride in AlCl_3 (1m)-PC. Thallium amalgam was dispensed into the cup of each of the two reference electrodes, a small amount of TlCl was spread on the surface, the ground joints were lubricated, and the reference electrodes were inserted into the cell. The alkali metal amalgam was then dispensed into the cups of each of the two-cup electrodes and was inserted into the cell. The alkali metal wire was cut, connected to the stainless steel holders, and inserted into the cell. The cell was then closed and removed from the glove box. The cell was next suspended in a constant temperature water bath for equilibrium and micropolarization measurements (3). The measurements were done at 25° and 35°C , $\pm 0.01^\circ\text{C}$.

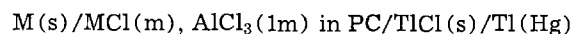
Cell potential measurements.—Measurements of the cell potentials were taken with a John Fluke Model 887—A differential voltmeter (accuracy $\pm 0.005\text{ mV}$) which was calibrated against an Eppley Laboratory, low temperature coefficient standard cell.

The measurements began 15 min after the suspension of the cell in the bath. Measurements included: (i) Cell potentials between the alkali metal electrodes and the reference electrodes. (ii) Cell potentials between the alkali metal amalgam electrodes and the reference electrodes. (iii) Potentials between the alkali metals and their amalgams. (iv) Bias potentials between the two alkali metal electrodes, the two alkali metal amalgam electrodes, and the two Tl(Hg)/TlCl reference electrodes. The potential measurements were repeated each 30 min for the first few hours and then were recorded several times each day for at least one week. The cell was then transferred to the 35°C bath and identical measurements were taken. The cell then was transferred back to the 25°C bath and the first series repeated.

Micropolarization measurements were conducted during the potential measurement period. The alkali metal electrodes were polarized in both cathodic and anodic directions and the reversibility of the electrodes was checked.

Results

Tables I-V contain the results of the experimental measurements of the general cell



at 25° and 35°C , where M represents Li, Na, K, Rb, and Cs. The measurements were repeated for each metal at different alkali metal chloride molalities. The concentration of the thallium amalgam, the same in all experiments, was 4.749% by weight.

The first column in each table gives the concentration of the alkali metal chloride in molality units (moles of MCl per 1000g of pure PC). The measured cell potential in volts is listed in the second column.

Table I. Results of cell potential measurements, lithium system

m	E	25°C E_1	E_2	E	35°C E_1	E_2
1.0	2.3571	2.2621	2.2621	2.3594	2.2614	2.2614
0.5	2.3848	2.2838	2.2542	2.3891	2.2911	2.2543
0.25	2.4044	2.3094	2.2382	2.4075	2.3095	2.2359
0.25	2.4179	2.3229	2.2517	2.4210	2.3230	2.2494
0.10	2.4160	2.3210	2.2027	2.4193	2.3213	2.1991
0.10	2.4090	2.3140	2.1957	2.4123	2.3153	2.1931
0.10	2.4199	2.3249	2.2066	2.4233	2.3253	2.2031
0.05	2.4371	2.3421	2.1882	2.4404	2.3424	2.1833
0.01	2.4601	2.3651	2.1255	2.4641	2.3661	2.1216
0.005	2.4707	2.3757	2.1035	2.4769	2.3789	2.0976
0.005	2.4740	2.3790	2.1068	2.4800	2.3820	2.1007
0.002	2.4591	2.3641	2.0449	2.4693	2.3713	2.0413

Table II. Results of cell potential measurements, sodium system

m	E	25°C E_1	E_2	E	35°C E_1	E_2
0.5	2.1790	2.0840	2.0484	2.1874	2.0894	2.0526
0.25	2.1875	2.0925	2.0213	2.1986	2.1006	2.0270
0.10	2.1863	2.0913	1.9730	2.2037	2.1057	1.9834
0.01	2.2440	2.1490	1.9124	2.2621	2.1641	1.9196
0.01	2.2446	2.1496	1.9130	2.2607	2.1627	1.9182

Table III. Results of cell potential measurements, potassium system

m	E	25°C E_1	E_2	E	35°C E_1	E_2
1.0	2.404	2.309	2.309	2.422	2.324	2.324
1.0	2.413	2.318	2.318	2.430	2.332	2.332
0.5	2.436	2.341	2.306	2.452	2.354	2.317
0.5	2.433	2.338	2.303	2.449	2.351	2.314
0.25	2.473	2.378	2.306	2.516	2.418	2.344
0.25	2.468	2.373	2.302	2.511	2.413	2.340
0.1	2.507	2.412	2.294	2.526	2.428	2.306
0.01	2.511	2.416	2.179	2.536	2.438	2.193
0.0025	2.551	2.456	2.148	2.572	2.474	2.156

Table IV. Results of cell potential measurements, rubidium system

<i>m</i>	<i>E</i>	25°C <i>E</i> ₁	<i>E</i> ₂	<i>E</i>	35°C <i>E</i> ₁	<i>E</i> ₂
1.0	2.353	2.258	2.258	2.354	2.256	2.256
0.5	2.432	2.357	2.321	—	—	—
0.25	2.487	2.392	2.320	—	—	—
0.10	2.479	2.384	2.266	2.489	2.391	2.269
0.10	2.476	2.381	2.263	2.487	2.389	2.267
0.05	2.475	2.380	2.226	2.491	2.394	2.234
0.01	2.497	2.402	2.165	2.524	2.426	2.181
0.0025	2.540	2.445	2.137	2.595	2.497	2.179

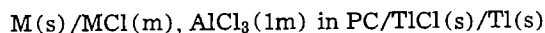
Table V. Results of cell potential measurements, cesium system

<i>m</i>	<i>E</i>	25°C <i>E</i> ₁	<i>E</i> ₂	<i>E</i>	35°C <i>E</i> ₁	<i>E</i> ₂
1.0	2.403	2.308	2.308	2.416	2.318	2.318
1.0	2.403	2.308	2.308	2.414	2.316	2.316
1.0	2.397	2.302	2.302	2.412	2.314	2.314
0.5	2.475	2.380	2.345	2.496	2.398	2.361
0.25	2.508	2.413	2.342	2.539	2.441	2.368
0.10	2.490	2.395	2.277	2.526	2.428	2.305
0.10	2.505	2.410	2.291	2.537	2.439	2.316
0.01	2.515	2.420	2.183	2.556	2.458	2.213
0.01	2.510	2.415	2.178	2.551	2.453	2.209
0.0025	2.555	2.460	2.152	2.606	2.508	2.189
0.0010	2.529	2.435	2.080	2.581	2.483	2.116

This value for each concentration is the average value of the potential of the two alkali metal electrodes *vs.* the two reference electrodes. The potential difference between two thallium amalgam-thallos chloride reference electrodes was always smaller than 1 mV. The bias potential between the two alkali metal electrodes was different for the various metals. The bias potential was smaller than 1, 1, 10, 5, 5 mV for the Li, Na, K, Rb, and Cs systems, respectively.

The potential *E*₁ is tabulated in the third column and represents the corrected value of *E* for the thallium amalgam concentration. The correction was taken from the work of Richards, and Daniels (16), who measured the potentials between different thallium amalgam concentrations and pure thallium.

The function *E*₂ is listed in the fourth column and the method used to obtain this function is given below. The potential of the cell



is given by

$$E_1 = E^{\circ}_1 - RT/F \ln(m_{Cl^-} \gamma_{Cl^-} / m_M \gamma_M) \quad [1]$$

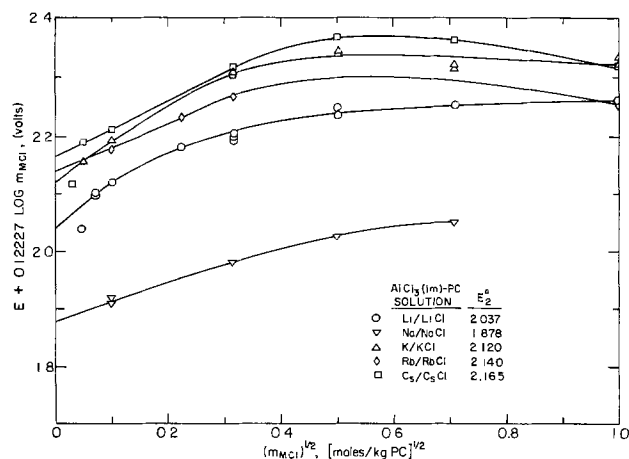
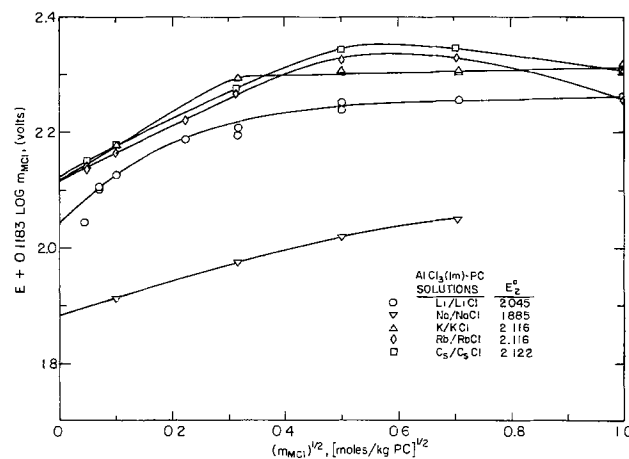
where *m* is the molality and γ the activity coefficient of a particular ion. Since the molality of AlCl₃ is held constant, it is convenient to choose the reference state as AlCl₃(1m) in PC. By this convention, the solvent is considered to be a unit molality solution of AlCl₃ in PC and not pure PC as usual. The cell potential according to this convention is given by

$$E_1 = E^{\circ}_2 - 2RT/F \ln(m_{MCl} \gamma_{MCl}) \quad [2]$$

where *E*₂^o is the standard oxidation potential of the cell in AlCl₃(1m)-PC solution. The standard state of the solute is taken at infinite dilution of the alkali metal chloride in AlCl₃(1m)-PC solution where the activity coefficient of the alkali metal chloride approaches unity. The problem of determining *E*₂^o and thus the activity coefficients at different concentrations of MCl involves extrapolation to infinite dilution. The method of extrapolation to infinite dilution using the Guggenheim equation (8) cannot be employed here since the ionic strength is very high. Instead, rearranging Eq. [2] gives

$$E_2 = (E_1 + 2RT/F \ln m_{MCl}) = E^{\circ}_2 - 2RT/F \ln \gamma_{MCl} \quad [3]$$

Following the method presented by Lewis, Randall, Pitzer, and Brewer (17) (pp. 315-316), if we plot the left-hand side of Eq. [3] as ordinate against some function of *m*_{MCl} as abscissa, the limit approached by the ordinate at infinite dilution is equal to *E*₂^o. It is

Fig. 2. EMF measurements of the cell: M/MCl(m), AlCl₃(1m)-PC/TlCl(s), Tl(s) at 25°C.Fig. 3. EMF measurements of the cell: M/MCl(m), AlCl₃(1m)-PC/TlCl(s), Tl(s) at 35°C.

common to extrapolate with (*m*_{MCl})^{1/2} as abscissa since such a choice should give a curve approximating linearity at high dilution following the Debye-Hückel limiting law. However, here this dependence is used to expand the low concentration range. Figures 2 and 3 show the plot of *E*₂ *vs.* (*m*_{MCl})^{1/2} for all the alkali metals at 25° and 35°C, respectively. The intercepts at zero molalities give *E*₂^o, the standard potentials at AlCl₃(1m)-PC solution. The difference between the extrapolated values at 25° and 35°C gives the temperature dependence of the standard potential at constant pressure. The results of the extrapolations are given in Table VI.

From the standard cell potentials and their variation with temperature, the standard free energy ΔG°_2 , entropy ΔS°_2 , and enthalpy ΔH°_2 can be calculated

$$\Delta G^{\circ}_2 = -n F E^{\circ}_2 \quad [4]$$

$$\Delta S^{\circ}_2 = n F (\partial E^{\circ}_2 / \partial T)_p \quad [5]$$

$$\Delta H^{\circ}_2 = -n F (E^{\circ}_2 - T (\partial E^{\circ}_2 / \partial T)_p) \quad [6]$$

These functions are related to the following cell reaction

Table VI. Standard cell potentials at 25° and 35°C

Metal	<i>E</i> ₂ ^o , 25°C	<i>E</i> ₂ ^o , 35°C	($\partial E^{\circ}_2 / \partial T$) _p
Li	2.045 ± 0.010	2.037 ± 0.010	-0.8 10 ⁻³
Na	1.885 ± 0.010	1.878 ± 0.010	-0.7 10 ⁻³
K	2.116 ± 0.020	2.120 ± 0.020	+0.4 10 ⁻³
Rb	2.116 ± 0.020	2.140 ± 0.020	+2.4 10 ⁻³
Cs	2.122 ± 0.020	2.165 ± 0.020	+4.3 10 ⁻³

Table VII. Standard free energies, entropies, and enthalpies for reaction [7] for all the alkali metals

Metal	ΔG°_2 , kcal/mol		ΔS°_2 , e.u.	ΔH°_2 , kcal/mol	
	25°C	35°C		25°C	35°C
Li	-47.2	-47.0	-18.4	-52.7	-52.7
Na	-43.5	-43.3	-16.1	-48.3	-48.3
K	-48.8	-48.9	+9.2	-46.0	-46.1
Rb	-48.8	-49.3	+55.3	-32.3	-32.3
Cs	-48.9	-49.9	+64.7	-29.6	-29.6

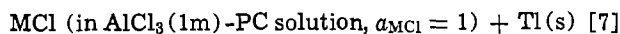
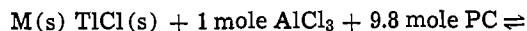


Table VII presents ΔG°_2 , ΔS°_2 , and ΔH°_2 on the molal scale for the above cell reaction at 25° and 35°C. The uncertainty in ΔS°_2 and ΔH°_2 is quite high because they were calculated from the difference between extrapolated values.

EMF of the alkali metal-alkali metal amalgam cells.—In addition, emf's of the cell $M(s)/MCl(m)$, $\text{AlCl}_3(1m)$, $\text{PC}/M(\text{Hg})$ were also measured. The concentrations of the Na, K, and Rb amalgams were adjusted to the exact concentrations of the amalgams used by Lewis and his co-workers (18-21). This was done in order to be able to make comparison with emf data for the single amalgam concentrations listed in the literature. In the case of lithium amalgam, the activity coefficient data of lithium was obtained from the work of Cogley and Butler (22). The cesium amalgam concentration did not match the concentration used by Bent *et al.* (23). The agreement between the present measurements and those in the literature is in all cases better than 4.2 mV.

Activity coefficients of the alkali metal chlorides in $\text{AlCl}_3(1m)$ -PC solution.—Mean molal activity coefficients of the alkali metal chlorides in $\text{AlCl}_3(1m)$ solution in PC were calculated from

$$\ln \gamma_{MCl} (F/2RT) (E^{\circ}_2 - E_2) - \ln m_{MCl} \quad [8]$$

where E°_2 is the extrapolated value of the standard cell potential given in Table VI. The calculated activity coefficients at 25°C are given in Table VIII. Figure 4 presents the plots of $\ln \gamma_{MCl}$ vs. $(m_{MCl})^{1/2}$ for all the alkali metal chlorides. It should be mentioned again that the reference state is $\text{AlCl}_3(1m)$ in PC and not the pure solvent.

Discussion

EMF measurements of the cell without transference: $M(s)/MCl(m)$, $\text{AlCl}_3(1m)$ -PC/ $\text{TiCl}(s)/\text{Ti}(\text{Hg})$ gave reproducible results. Potential measurements involving the lithium and sodium systems were especially reproducible. The greatest scattering of data points was experienced with the potassium system. Potassium electrodes were less stable in PC and in some cases turned purple after a few days of repeated measurements. This was probably due to the high sensitivity of K electrodes to small traces of water. Lithium and sodium gave reproducible results within ± 1 mV, while rubidium and cesium were somewhat less reproducible, and their bias potentials varied within ± 5 mV, probably because of difficulties ex-

Table VIII. Activity coefficients of the alkali metal chlorides in $\text{AlCl}_3(1m)$ -PC solution at 25°C

m	LiCl	NaCl	$-\ln \gamma_{MCl}$ KCl	RbCl	CsCl
1.0	4.051		3.808	2.768	3.738
0.5	3.892	3.181	3.623	3.990	4.455
0.25	3.719	2.652	3.626	3.970	4.398
0.10	2.863	1.713	3.423	2.885	3.273
0.05	2.604			2.143	
0.01	1.427	0.442	1.193	0.961	1.263
0.005	0.962				
0.0025	0.989		0.631	0.412	0.872

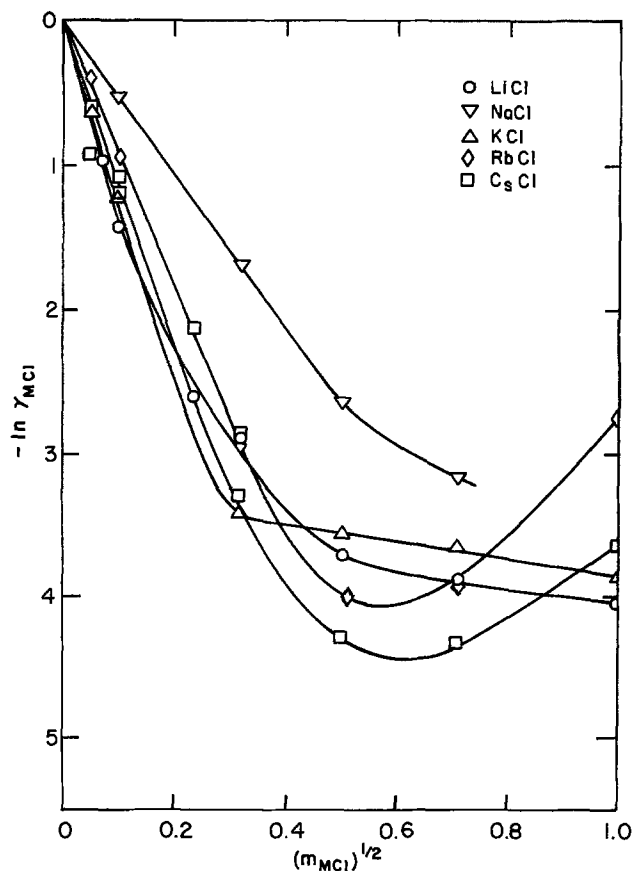


Fig. 4. Activity coefficients of the alkali metal chlorides in $\text{AlCl}_3(1m)$ -PC solution at 25°C.

perienced in preparing the electrodes in the molten state.

The change in cell potential with time was followed by measuring the potentials every 30 min for the first few hours. The potentials were measured then for at least one week before the cell was disassembled. For the first half-hour, especially for solutions having a low concentration of alkali metal chloride, changes in potentials were observed. The potential was then steady within ± 5 mV for a few hours, followed by a steady decrease in the cell potential, during the next day. In every case the potential drifted toward the discharge of the cell. The decrease in potential was faster for low alkali metal chloride concentrations, and was minimal when the molality of MCl approached unity or 1:1 ratio with respect to AlCl_3 molality in PC. Figure 5 presents the time dependence of the potential for two lithium cells. The lower curve represents the change in potential of a cell containing $\text{LiCl}(1.0m)$ in $\text{AlCl}_3(1m)$ -PC. The upper curve shows the behavior of a cell containing $\text{LiCl}(0.01m)$ in $\text{AlCl}_3(1m)$ -PC.

Similar behavior of cell discharge was observed by Salomon (5) for the alkali metal halides in PC. A steady decrease in cell potentials was observed for lithium halides in DMSO (24, 25), dimethylformamide (12), and N-methylformamide (26). A strong decrease of cell potential with time was observed in the cell $\text{Pt}, \text{H}_2/\text{HCl}(m)/\text{AgCl}, \text{Ag}$ in formamide (27-29); the true cell potentials were obtained by extrapolating the observed potentials to zero time. Here a decrease of approximately 20 mV was observed during a period of 2 hr (27-29).

The reasons for the steady decrease in cell potentials have been attributed to either solubility and diffusion of the thallos halide and subsequent reaction with the alkali metal (24, 25), or the reaction of the alkali metal with the solvent or with solvent impurities such as water (5). Salomon attributed the phenomena to the reactivity of the alkali metals with impurities rather

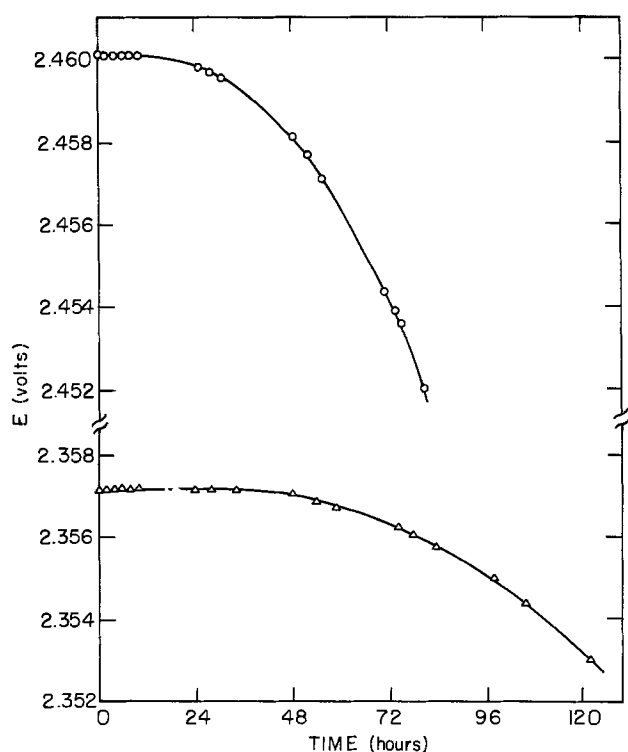
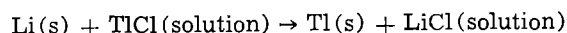


Fig. 5. Time dependence of lithium cell potential at 25°C. \circ , $m_{\text{LiCl}} = 1.0$ and \triangle , $m_{\text{LiCl}} = 0.01$.

than to TlCl diffusion across the cell, because the solubility of TlCl in pure PC is extremely low ($K_{\text{sp}} = 10^{-12.4}$). In addition, fritted glass was used to slow the diffusion of the thallium species across the cell. However in the present work TlCl is probably somewhat more soluble in the presence of an excess of AlCl_3 . The behavior of the cell potentials in the present work was similar to the one reported by Smyrl and Tobias for LiCl in DMSO (13), where, after a period of several hours of relatively constant potential, the potential started to decrease steadily due to the reaction

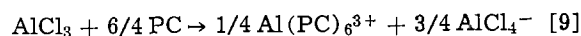


The standard cell potentials of the alkali metals in $\text{AlCl}_3(1\text{m})$ -PC solution, relative to Tl/TlCl, are presented in Table VI along with the cell potential temperature coefficients. These results were obtained by extrapolation to infinite dilution with respect to the alkali metal chloride molalities. The order of the standard potentials in the alkali metal series does not follow that in aqueous solution, where lithium has the highest standard potential. The standard potentials of the alkali metals in water and in several other solvents are presented in Table IX, along with the present results. The present results, as well as Salomon's data assign a noticeably higher standard potential to potassium than to lithium. Since the work of Salomon does

not include measurements of the rubidium and cesium cells, further comparison cannot be made. Cesium, followed by rubidium shows the highest oxidation potentials in $\text{AlCl}_3(1\text{m})$ -PC. This is not the case in acetonitrile, N-MF, and water, where lithium has the highest oxidation potential (see Table IX). It may be proper to quote the prediction made by Lewis and Argo in 1915 (21) concerning the peculiarity of the order of the standard potentials in the alkali metal series: "The potentials of the alkali metals follow a curious order, namely, lithium, rubidium, potassium, and sodium. It is interesting, however, to observe that this is the order of the heats of formation of the several ions in aqueous solution. In order to illustrate this fact, the heat of formation of the chlorides of the four metals in aqueous solution are: 102, 101, 101, 96 kcal/mole for LiCl, RbCl, KCl, and NaCl, respectively. The heat of formation of aqueous cesium chloride is given as 105 kcal/mole, and if this figure is correct, we might predict the potential of cesium to be higher than any of the other alkali metals" (21). However, this prediction did not materialize when 14 years later Bent, Forbes, and Forziani (23) obtained the normal electrode potential of cesium, $E^\circ = 2.923$ volts, "...very close to the corresponding value for rubidium, but still 34 millivolts below that for lithium."

Figures 2 and 3 present the potential measurements and the extrapolation to infinite dilution. The fact that almost linear behavior is obtained by plotting the potential E_2 vs. $(m_{\text{MCl}})^{1/2}$ is very helpful in obtaining the standard potentials, although it should be remembered that this behavior is not well described by the Debye-Hückel limiting law, because the reference solvent was a solution of AlCl_3 in PC, in which the ionic strength is very high. The plotting of the results vs. the square root of the molality was adopted to expand the dilute region and to obtain a better accuracy in the extrapolation.

The extrapolation procedure of the emf measurements does not involve any assumption concerning the nature of the complexes and ionic species in solution. The predominant ions in a solution of MCl in AlCl_3 -PC solution are M^+ , $\text{Al}(\text{PC})_n^{3+}$, and AlCl_4^- . Keller *et al.* (30) studied directly the ionic equilibria of AlCl_3 in PC using NMR technique. From the ^{27}Al spectra it was concluded that the main species are $\text{Al}(\text{PC})_n^{3+}$ and AlCl_4^- , similar to the species present in acetonitrile. High resolution ^1H spectra of 1M AlCl_3 in PC indicates peaks due to coordinated PC as well as bulk PC. From the ^1H and the ^{27}Al spectra, Keller *et al.* (30) showed that the Al^{3+} coordination number (n) is six. Therefore the dissociation of AlCl_3 in PC proceeds according to

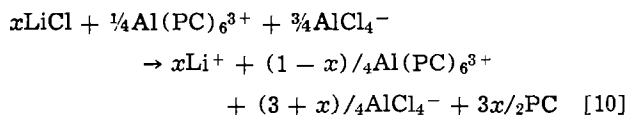


Furthermore it was observed that the addition of LiCl to an AlCl_3 -PC solution reduces the concentration of the coordinated Al species, and at the saturation point where the LiCl: AlCl_3 ratio is 1:1 the coordinated Al species disappears. Such observation can be explained by the reaction between LiCl and $\text{Al}(\text{PC})_6^{3+}$ to give mainly AlCl_4^-

Table IX. Standard oxidation potentials in nonaqueous solvents

	Aceto- nitrile	N-MF	Formamide	Ethylene glycol	Propylene carbonate			PC- $\text{AlCl}_3(1\text{m})$	H_2O
Li	3.23	3.124	—	2.996	1.85080*	1.84223*	1.8452	2.045	3.045
Na	2.87	2.807	—	2.686	—	—	1.6188	1.885	2.714
K	3.16	3.021	2.872	2.897	—	—	1.934	2.116	2.925
Rb	3.17	—	2.855	—	—	—	—	2.116	2.925
Cs	3.16	2.987	—	—	—	—	—	2.122	2.923
Ref. elec.	H_2/H^+	Ag/AgCl	H_2/H^+	Ag/AgBr	Tl/TlCl	Tl/TlBr	Tl/TH	Tl/TlCl	H_2/H^+
Reference	(33, 34)	(35)	(36)	(38)	(5)	(5)	(6, 7)	(present work)	(37)

* Salomon made an error in the thallium amalgam corrections in his work with LiCl and LiBr in PC. The corrections at 25°C for thallium amalgam compositions of 3.147 and 7.76% wt are 112.5 and 78.6 mV, respectively, as is evident from the work of Richards and Daniels (16), and not 135.34 and 94.6 mV as reported by Salomon (5). The results obtained for the other systems studied by Salomon cannot be checked, as detailed data are not available (6, 7).



At the saturation point where $x = 1$, all the coordinated $\text{Al}(\text{PC})_6^{3+}$ converted to AlCl_4^- and the predominant species present are Li^+ and AlCl_4^- . Keller *et al.* (30) summarizes the results for solutions of AlCl_3 in DMF, AN, and PC. The complexing strength of Al^{3+} toward Cl^- is stronger than toward PC, AN, and water, but weaker than toward DMF where the dominant species are $\text{Al}[\text{DMF}]_6^{3+}$ and Cl^- . Movius and Matwiyoff (31) report PMR data for aluminum halides (AlX_3) in DMF which can be interpreted in terms of second coordination sphere interaction between a well-defined $\text{Al}(\text{DMF})_6^{3+}$ ion and X^- .

The potentials for lithium cells in which the molality of LiCl was less than 0.005m showed a substantial drift to lower values. This can be observed in Fig. 2 and 3 by the tailing off at the very low LiCl concentration. The potential at 0.002m LiCl was not included in the extrapolation. Tailing off at low concentration was observed by others, especially for lithium cells in DMSO (13, 24), N-methyl formamide (26), and in dimethyl formamide (12). Deviations were not observed in LiI solution in PC (7), nor in LiI solution in DMSO (32). Deviations were not observed in sodium and potassium cells in PC (6, 7), nor in sodium, potassium, and rubidium cells in N-methyl formamide (26).

The standard potentials in the present work are given on a molal basis. The molal basis has been chosen because the molecular weight of PC is more than 5 times larger than that of water. Since many authors present their results on a molar basis, it should be remembered that the standard potential, on a molal basis, can be converted into a molar basis, according to the following relation

$$E^\circ_c = E^\circ_m + \frac{2RT}{F} \ln \rho_0 \quad [11]$$

where E°_c and E°_m are the standard potentials on a molar and molal basis, respectively, and ρ_0 is the density of the solvent. The solvent in the present case is an $\text{AlCl}_3(1\text{m})$ -PC solution, and its density is reported as 1.2628 and 1.2530 g/cm^3 at 25° and 35°C, respectively (1). The standard potentials of the alkali metals, on a molar basis are presented in Table X. In addition, the standard potentials on a mole fraction basis are presented as well. The mole fraction basis is probably the most suitable way to present thermodynamic data, where the solute mole fraction is comparable with the solvent mole fraction. The standard potential on a mole fraction basis can be obtained from the following equation

$$E^\circ_N = E^\circ_m + \frac{2RT}{F} \ln \left(\frac{1000}{\text{M.W.}} + 1 \right) \quad [12]$$

where E°_N is the standard potential on a mole fraction basis, and M.W. is the molecular weight of the solvent. In the present case, the reference state is a 1m solution of AlCl_3 in PC.

The behavior of the sodium curves in Fig. 2 and 3 is different from the rest of the alkali metals. The solubility of NaCl in $\text{AlCl}_3(1\text{m})$ -PC solution was around 0.5m, in contrast to the rest of the alkali metal chlorides,

which dissolved corresponding to a 1:1 ratio with respect to AlCl_3 . There is no explanation for this unexpected behavior, although there are indications that the solubilities of RbCl and CsCl in $\text{AlCl}_3(1\text{m})$ -PC are not exactly 1.0m but drop slightly upon standing. The decrease in the potentials at high concentrations for the rubidium and cesium systems, given in Fig. 2, indicates probable solvate formation.

The activity coefficients of the alkali metal chlorides in AlCl_3 -PC solution are shown in Fig. 4. The sharp decrease in the activity coefficients at low concentrations is due to the reaction between the chloride ions and Al^{3+} species yielding AlCl_4^- . Since AlCl_3 is part of the solvent, this decrease in the activity coefficients is equivalent to systems where the solute reacts with the solvent, e.g., NH_3 in water or hydrate formation in aqueous solution.

Estimation of the standard potentials of the alkali metals in pure PC.—The standard potentials obtained were calculated with respect to the cell $\text{M}(\text{s})/\text{MCl}, \text{AlCl}_3(1\text{m})\text{-PC}/\text{TlCl}(\text{s}), \text{Tl}(\text{s})$ where the standard state was chosen as infinite dilution of MCl in $\text{AlCl}_3(1\text{m})$ -PC solution. The standard potentials of the alkali metals in pure PC can be measured from the cell $\text{M}(\text{s})/\text{MCl}, \text{PC}/\text{TlCl}(\text{s}), \text{Tl}(\text{s})$. However, the solubilities of the alkali metal chlorides in PC are very low, and only LiCl is soluble enough to permit accurate potential measurements. Salomon measured the standard potential of lithium in LiCl solution in PC; however, in order to establish a scale of standard potentials in PC for the rest of the alkali metals, he switched to the alkali metal iodides which are soluble in PC. Salomon did not measure the standard potentials of rubidium and cesium.

An estimation of the standard potentials of cells of the alkali metal chlorides in pure PC can be made on the basis of the results of the present work and the standard potential of the LiCl cell as reported by Salomon (5). The standard potential of the cell $\text{Li}(\text{s})/\text{LiCl}(\text{m}), \text{AlCl}_3(1\text{m}), \text{PC}/\text{TlCl}(\text{s}), \text{Tl}(\text{s})$ is given by

$$E_1 = E^\circ_1 - \frac{RT}{F} \ln (m_{\text{Li}^+} \gamma_{\text{Li}^+} m_{\text{Cl}^-} \gamma_{\text{Cl}^-}) \quad [13]$$

where E°_1 is the standard potential at infinite dilution. The cell potential on the basis of $\text{AlCl}_3(1\text{m})$ -PC as a reference state is given by

$$E_1 = E^\circ_2 - \frac{2RT}{F} \ln (m_{\text{LiCl}} \gamma_{\text{LiCl}}) \quad [14]$$

As $m_{\text{LiCl}} \rightarrow 0$

$$E^\circ_2 - E^\circ_1 = - \frac{RT}{F} \ln (m_{\text{Li}^+} \gamma_{\text{Li}^+} m_{\text{Cl}^-} \gamma_{\text{Cl}^-}) \quad [15]$$

The left-hand side of Eq. [13] can be calculated, since E°_2 was measured in the present work, and E°_1 for lithium is reported by Salomon as, $E^\circ_1 = 1.85080\text{V}$. (This value is the corrected one, since Salomon made an error in the thallium amalgam correction, see Table IX)

$$- \frac{RT}{F} \ln (m_{\text{Li}^+} \gamma_{\text{Li}^+} m_{\text{Cl}^-} \gamma_{\text{Cl}^-})_{m_{\text{LiCl}} \rightarrow 0} = \\ 2.045 - 1.851 = 0.194\text{V}$$

If we assume that this value does not change much going through the alkali metal series, we can estimate the standard potentials E°_1 for the rest of the alkali metals

$$E^\circ_1 = E^\circ_2 - 0.194$$

Table XI summarizes the approximated standard potentials of the cell $\text{M}(\text{s})/\text{MCl}, \text{PC}/\text{TlCl}(\text{s}), \text{Tl}(\text{s})$.

On the basis of these estimated standard oxidation potentials, it is expected that even in pure PC the standard oxidation potential of Cs will be the highest, followed by Rb, K, Li and Na.

Table X. Standard oxidation potentials on a molar and a mole fraction basis for $\text{AlCl}_3(1\text{m})$ -PC cells

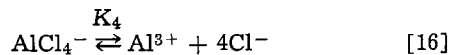
	$E^\circ_{2,c}$		$E^\circ_{2,N}$	
	25°C	35°C	25°C	35°C
Li	2.054	2.046	2.162	2.158
Na	1.894	1.887	2.002	1.998
K	2.125	2.127	2.233	2.241
Rb	2.125	2.149	2.116	2.261
Cs	2.131	2.174	2.239	2.286

Table XI. Estimated standard oxidation potentials for the alkali metals in pure PC

Cell	E° , volt	ΔG° , kcal/mole
Li/LiCl,PC/TiCl,Tl	1.85080*	-42.9*
Na/NaCl,PC/TiCl,Tl	1.691	-39.0
K/KCl,PC/TiCl,Tl	1.922	-44.3
Rb/RbCl,PC/TiCl,Tl	1.922	-44.3
Cs/CsCl,PC/TiCl,Tl	1.928	-44.5

* Measured by Salomon (5).

Ionic equilibria considerations.—The predominant ions in a solution of MCl in AlCl_3 -PC solution are M^+ , $\text{Al}(\text{PC})_6^{3+}$, and AlCl_4^- . A rough calculation was made of the equilibrium constant of the reaction



on the assumption that this equilibrium accounts for all the difference between the activity of MCl and that of a typical univalent salt. The calculations were performed only in the case of LiCl because its standard potential on the pure solvent basis was obtained by Salomon (5)

The fourth ionization constant K_4 is given by

$$K_4 = \frac{(\text{Al}^{3+})(\text{Cl}^-)^4}{(\text{AlCl}_4^-)} \quad [17]$$

Multiplying and dividing by (Li^+) results in

$$K_4 = \frac{\gamma_{\text{Al}^{3+}}^4 [\text{Al}^{3+}] [\text{Cl}^-]^3 a_{\text{LiCl}}}{\gamma_{\text{AlCl}_4^-} [\text{AlCl}_4^-] [\text{Li}^+]} \quad [18]$$

where brackets indicate molality and parentheses activity.

For a constant ionic strength we can define a new constant

$$K_4' = \frac{\gamma_{\text{Al}^{3+}}^2}{\gamma_{\text{AlCl}_4^-}} K_4 = \frac{(1-m)a_{\text{LiCl}}}{(3+m)m} [\text{Cl}^-]^3 \quad [19]$$

where m is the molality of the added LiCl. The activity of LiCl based on pure PC as a standard state, a_{LiCl} , can be estimated from the present emf measurements and the standard potential $E^{\circ} = 1.8508\text{V}$ obtained by Salomon (5) for the cell: Li/LiCl in PC/TiCl/Tl

$$E = 1.8508 - (RT/F) \ln a_{\text{LiCl}} \quad [20]$$

The ionic strength is fairly constant over most of the experimental range and can be evaluated for the general case of adding m moles of LiCl to 1m solution of AlCl_3 in PC (see Eq. [10]) according to

$$I = \frac{1}{2} \sum_i m_i z_i^2 = \frac{1}{2} \left[\frac{(3+m)}{4} (-1)^2 + \frac{(1-m)}{4} (+3)^2 + m(+1)^2 \right] = \frac{(12-4m)}{8} \quad [21]$$

When $m = 0$ the ionic strength is $I = 1.5$ and drops to $I = 1.0$ when $m = 1.0$. The ionic strength is fairly constant up to $m = 0.25$ and over this range we can assume the ratio $\gamma_{\text{Al}^{3+}}^2/\gamma_{\text{AlCl}_4^-}$ is fairly constant.

Table XII presents the calculations of $K_4'/[\text{Cl}^-]^3$ as a function of the added molality of LiCl, m , and the total ionic strength, I . As can be seen from Table XII the chloride concentration $[\text{Cl}^-]$ increases very slightly as we add LiCl. Although we increase the LiCl concentration up to 50 times, the free chloride concentration increases by a factor of merely 1.8. Also, it should be kept in mind that K_4' depends on the ionic strength since it includes the ratio of the activity coefficients. However, as has been mentioned earlier, the ionic strength remains fairly constant up to 0.25m of added LiCl.

Table XII. Instability constant K_4' and free chloride molality

m	$10^3 \times a_{\text{LiCl}}$	$I^{1/2}$	$10^3 \times (K_4'/[\text{Cl}^-]^3)$	$[\text{Cl}^-]$
0.005	1.1	1.223	7.29	$239.4 \times (K_4')^{1/3}$
0.01	1.8	1.222	5.92	256.6
0.05	4.6	1.219	2.87	326.6
0.10	11.1	1.204	3.22	314.3
0.25	13.1	1.173	1.21	435.6
0.50	17.8	1.118	1.02	461.1
1.00	105.3	1.000	—	—

Acknowledgment

This work was conducted under the auspices of the U.S. Atomic Energy Commission.

Manuscript submitted Jan. 14, 1974; revised manuscript received Jan. 7, 1975. This was Paper 278 presented at the Chicago, Illinois, Meeting of the Society, May 13-18, 1973.

Any discussion of this paper will appear in a Discussion Section to be published in the December 1975 JOURNAL. All discussions for the December 1975 Discussion Section should be submitted by Aug. 1, 1975.

Publication costs of this article were partially assisted by the University of California.

REFERENCES

- J. Journé, Thesis, University of California, Berkeley (1972).
- C. W. Tobias and J. Journé, U. S. Pat. 3,791,945 (1974).
- J. Journé and C. W. Tobias, *This Journal*, **121**, 994 (1974).
- J. Journé and C. W. Tobias, *J. Phys. Chem.*, **78**, 2521 (1974).
- M. Salomon, *ibid.*, **73**, 3299 (1969).
- M. Salomon, *J. Electroanal. Chem.*, **25**, 1 (1970).
- M. Salomon, *ibid.*, **26**, 319 (1970).
- E. A. Guggenheim, "Thermodynamics," 4th edition, North-Holland, (1959).
- M. Salomon, *J. Phys. Chem.*, **74**, 2519 (1970).
- R. Jasinski, in "Advances in Electrochemistry and Electrochemical Engineering," P. Delahay and C. W. Tobias, Editors, Vol. 8, Interscience, New York (1971).
- F. G. K. Baucke and C. W. Tobias, *This Journal*, **116**, 34 (1969).
- J. N. Butler and J. C. Synnott, *J. Am. Chem. Soc.*, **92**, 2602 (1970).
- W. H. Smyrl and C. W. Tobias, *This Journal*, **115**, 33 (1968).
- J. N. Butler, in "Advances in Electrochemistry and Electrochemical Engineering," P. Delahay and C. W. Tobias, Editors, Vol. 7, Interscience, New York (1970).
- W. H. Smyrl and C. W. Tobias, *This Journal*, **113**, 754 (1966).
- T. W. Richards and F. Daniels, *J. Am. Chem. Soc.*, **41**, 1732 (1919).
- G. N. Lewis, M. Randall, K. S. Pitzer, and L. Brewer, "Thermodynamics," 2nd edition, McGraw-Hill Book Co., New York (1961).
- G. N. Lewis and C. A. Kraus, *J. Am. Chem. Soc.*, **32**, 1459 (1910).
- G. N. Lewis and F. G. Keyes, *ibid.*, **35**, 340 (1913).
- G. N. Lewis and F. G. Keyes, *ibid.*, **34**, 119 (1912).
- G. N. Lewis and W. L. Argo, *ibid.*, **37**, 1983 (1915).
- D. R. Cogley and J. N. Butler, *J. Phys. Chem.*, **72**, 1017 (1968).
- H. E. Bent, G. S. Forbes, and A. F. Forziati, *J. Am. Chem. Soc.*, **61**, 709 (1939).
- W. H. Smyrl and C. W. Tobias, *Electrochim. Acta*, **13**, 1581 (1968).
- G. Holleck, D. R. Cogley, and J. N. Butler, *This Journal*, **116**, 952 (1969).
- E. Luksha and C. M. Criss, *J. Phys. Chem.*, **70**, 1496 (1966).
- R. K. Agarwall and B. Nayak, *ibid.*, **70**, 2568 (1966).
- R. K. Agarwall and B. Nayak, *ibid.*, **71**, 2062 (1967).
- M. Mandel and P. Decroly, *Nature*, **182**, 794 (1958).
- R. Keller, J. N. Foster, D. C. Hanson, J. F. Hon, and J. S. Muirhead, Final Report, Contract NAS 3-8521, Dec. 1969.
- W. G. Movijs and N. A. Matwiyoff, *J. Phys. Chem.*, **72**, 3063 (1968).

32. M. Salomon, *This Journal*, **117**, 325 (1970).
 33. V. A. Pleskov, *Usp. Khim.*, **16**, 254 (1947).
 34. V. A. Pleskov, *Zh. Fiz. Khim.*, **22**, 351 (1948); *Chem. Abstr.*, **42**, 6249.
 35. H. Lund, *Acta Chem. Scand.*, **11**, 491 (1957).
 36. T. Pavlopoulos and H. Strehlow, *Z. Physik. Chem. (Frankfurt)* **2**, 89 (1954).
 37. W. M. Latimer, "Oxidation Potentials," Prentice-Hall, Englewood Cliffs, N. J. (1952).
 38. K. K. Kundu, A. K. Rakshit, and M. N. Das, *Electrochim. Acta*, **17**, 1921 (1972).

Electrogenerated Chemiluminescence

XXIII. On the Operation and Lifetime of ECL Devices

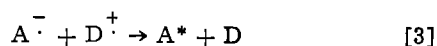
Daniel Laser and Allen J. Bard*

Department of Chemistry, The University of Texas at Austin, Austin, Texas 78712

ABSTRACT

Factors affecting the lifetime of ECL devices, including decomposition of starting materials, formation of side products which react with radical ions or quench excited states, and filming of the electrodes are discussed. The mode of operation of the ECL device is shown to be important in determining its behavior and lifetime; operation of: (i) three-electrode pulsed potentiostatic, (ii) two-electrode pulsed voltage, (iii) two-electrode pulsed constant current, and (iv) thin-layer cells is discussed and illustrated, in studies of the Ru(bip)₃²⁺ system in acetonitrile and the rubrene system in benzonitrile.

Electrogenerated chemiluminescence (ECL) involves the production of excited state species and ultimately light from the reaction of electrogenerated oxidants and reductants (1-7). Since several ECL systems are capable of producing fairly bright light at reasonable electrical efficiencies, several applications of practical devices based on the ECL phenomenon, e.g., lasers, display devices, image converters, etc. (8-12), have been suggested. For these devices to be practical, however, good lifetimes of the systems are required. In principle an ideal ECL system involving stable electrogenerated reactants (e.g., a radical anion, A⁻, and radical cation, D⁺) should show a very long lifetime, since the ECL cycle (e.g., Eq. [1]-[4]) involve no net chemical change in the system. In fact most ECL systems show a decay in emission with



time (minutes to hundreds of hours) under continuous electrical excitation. The rate of this decay depends on the nature and purity of the ECL system as well as the design of the ECL cell and the form of the electrical excitation. It is the purpose of this paper to discuss the factors affecting the lifetime of ECL cells and give examples of the behavior of these devices under different experimental conditions.

Experimental

Purification of the solvents, acetonitrile (ACN) and benzonitrile (BZN), the supporting electrolyte, tetrabutylammonium perchlorate (TBAP), and the reactants followed previous practice (7, 11). All experiments were conducted in a Vacuum Atmospheres (Los Angeles, California) Glove Box equipped with a Model MO 40-1 Dri-Train.

* Electrochemical Society Active Member.
 Key words: electrochemiluminescence, nonaqueous solvents, thin-layer electrochemistry, radical ions, cyclic voltammetry.

The macro-cell had a solution volume of 30 mliters with an optically flat Pyrex glass window. The working electrode was a polished platinum disk (0.25 cm²) sealed flush into soft glass and aligned parallel to, and about 1 cm away from, the window. The large auxiliary electrode was a platinum foil (ca. 5 × 2 cm) surrounding the working electrode and immersed directly in the test solution. The reference electrode was a silver wire immersed in 10⁻²M AgNO₃ in ACN, contained in a 6 mm glass tube closed at the bottom by a plug of porous Vycor (Corning Type 7930 "thirsty glass"), which was held to the glass tube by a piece of shrinkable Teflon tubing. For experiments with working and auxiliary electrodes of equal size, two matched Pt wires were employed.

The thin-layer ECL cells were constructed with two pieces of transparent Cu-doped SnO₂ glass (Corning), ca. 20 ohm/square, spaced apart by a thin Teflon spacer, and clamped by spring clamps. The active electrode area in these cells was ca. 0.5 cm².

All electrochemical measurements were made with a Princeton Applied Research Corporation Model 176 instrument, with a Wavetek Model 114 function generator, a Mosley Model 7005A XY recorder, and a Tektronix Model 564 dual beam oscilloscope. Relative light intensities were measured with a Centralab Semiconductor solar cell attached to the ECL cell window.

Results and Discussion

Failure modes.—There are several modes by which an ECL system will undergo changes which will ultimately cause a substantial decrease in light emission. These are:

1. Loss of the electroactive substances A and/or D, leading to a decrease in the concentration of the reacting ions A⁻ and D⁺, and thus of the emitting species.

This frequently occurs when the radical ion species A⁻ or D⁺ decay by reaction with solvent or impurities; in this case the rate of decay of intensity is related to the kinetics of the decomposition reaction (13, 14). In several systems, e.g., A = D = rubrene (in BZN or DMF), A = D = tris-bipyridylruthenium(II) (in ACN), A = 9,10-diphenylanthracene (DPA), D = thianthrene (in ACN), the radical ion species are very stable, and ECL

systems which have failed show no or only a very small change in the A and D concentrations as determined by cyclic voltammetry or spectroscopy before and after the ECL experiment. However if the electrode potential is not closely controlled and is allowed to move to regions where later waves (e.g., production of A^{2-} or D^{2+}) or electrolysis of solvent or supporting electrolyte occurs, then loss of A and D can be significant. This occurs because of instability of the dianion and dication of most organic species employed in ECL. This can happen even in three-electrode potentiostatic experiments if the reference electrode potential drifts during the lifetime test or if the system goes into large oscillations during adjustment of the positive feedback iR -compensation circuit. When this occurs the solution often turns a brownish color and it cannot be restored to a light-emitting condition.

2. Production of small amounts of side products from slow reactions of $A^{\cdot -}$ or $D^{\cdot +}$ with other system components or impurities; these side products can react with $A^{\cdot -}$ or $D^{\cdot +}$ decreasing their life or they may act as quenchers of the excited states. These decomposition reactions could involve reactions of A^{2-} (formed on disproportionation of $A^{\cdot -}$) or D^{2+} (formed on disproportionation of $D^{\cdot +}$). Although the equilibrium constants for these disproportionation reactions are small (e.g., 10^{-8} for a ca. 0.5V separation between E° values of radical ion and doubly charged ion half-reaction), the dianions and dications are usually very reactive species; this disproportionation decay of radical ions, in connection with much faster reactions, however, has been discussed extensively (15-17). A useful estimate of the maximum rate of buildup of side-product (or rate of loss of reactant) can be derived as follows: Assuming that the electrolysis of the reacting component (e.g., A) is diffusion controlled, the moles of species A electrolyzed per pulse is

$$\begin{aligned} \text{moles electrolyzed per pulse} &= \int_0^{t_f} i dt / F \\ &= 2AC (Dt_f/\pi)^{1/2} \quad [5] \end{aligned}$$

where C and D are the concentration and diffusion coefficient of A, t_f is the pulse length, and A the electrode area. If $A^{\cdot -}$ decomposes by a first-order or a pseudo-first-order reaction with a rate constant, k, the fraction of $A^{\cdot -}$ converted to product, Q, is $1 - e^{-kt_f}$. Thus the maximum number of moles of Q produced per pulse is moles Q produced per pulse

$$= 2(1 - e^{-kt_f})AC (Dt_f/\pi)^{1/2} \quad [6]$$

The concentration of Q produced in the total solution volume, V, after N pulses is

$$[Q] = 2(1 - e^{-kt_f})C N(A/V) (Dt_f/\pi)^{1/2} \quad [7]$$

The total system lifetime, T, is $2Nt_f$. Moreover, in any practical system kt_f is small, so that $1 - \exp(-kt_f)$ is essentially kt_f . With these substitutions the lifetime can be approximated by

$$T = ([Q]/C) (V/A) (\pi/Dt_f)^{1/2} / k \quad [8]$$

The time required to build up a significant concentration of side product for a given k, depends on the pulse length and V/A ratio. For example, for the typical values, $D = 5 \times 10^{-6}$ cm²/sec and $t_f = 0.01$ sec, and assuming the device lifetime is attained when the impurity level builds up to 1% of starting substance ($[Q]/C = 0.01$), the lifetime expression is

$$T(\text{hr}) \approx 0.02 (V/A) (\text{cm}) / k (\text{sec}^{-1}) \quad [9]$$

Thus a 1000 hr lifetime requires $k < 2 \times 10^{-3}$ sec⁻¹ for a V/A ratio of 100 cm, characteristic of a large scale cell, while a $k < 2 \times 10^{-7}$ sec⁻¹ is required for a V/A ratio of 10⁻² cm, typical of a thin-layer cell.

The decreased lifetime of the radical ion species is signaled by decreased reversal currents in cyclic voltammetry over those originally observed. These side products can also behave as quenchers of the generated excited states. The radiative lifetime of singlet states is short (about 10⁻⁸ sec) so that small concentrations of generated quenchers should not be of importance in ECL systems where singlet excited states are produced

directly on reaction of $A^{\cdot -}$ and $D^{\cdot +}$ [i.e., S-route systems, e.g., DPA(-)/DPA(+) in DMF]. However triplet states have longer radiative lifetimes (10⁻³ to several seconds) and can be quenched by low concentrations of side products. Thus systems which involve direct formation of triplets followed by triplet-triplet annihilation to produce emitting singlets [T-route systems, e.g., rubrene(-)/rubrene(+) in DMF and many energy deficient mixed systems] may be susceptible to this decay mode. In certain special cases photochemical-type reactions of the excited state species (rearrangements, cycloadditions, etc.) could also occur.

The applied excitation signal also affects this decay mode. The assumption has been made that the anodic and cathodic coulombs were equal, so that no excess

of either $A^{\cdot -}$ or $D^{\cdot +}$ is produced over long, repeated pulsing. However this condition is only obtained by careful control and appropriate relative electrode areas. In the absence of this condition one of the reactants builds up in the bulk solution and can show more extensive decomposition to side products.

3. Production of side products from the electrolysis of impurities in the solvent, supporting electrolyte, or radical ion precursors, which can react with $A^{\cdot -}$ and/or $D^{\cdot +}$ or quench the excited states. For example traces of water, which are difficult to remove from solvents such as DMF and ACN, could be oxidized on anodic pulses to oxygen, which in turn could be reduced to $O_2^{\cdot -}$

on cathodic pulses. Electrogenerated $O_2^{\cdot -}$ has been shown to react as a nucleophile and as a base (18). In the process free radicals such as HO_2^{\cdot} and HO^{\cdot} are produced, which may initiate chain reaction decomposition of system components. Since 2 ppm water represents 0.1 mM water, or 1-10% of the A and D species, very high purities of system components are required. If electrolysis of the solvent or supporting electrolyte occurs, either because of lack of control of the applied signal or because the radical ion generation processes occur on the foot of background discharge, deleterious substances can also be generated. For example, it is known that the light level of the DPA(-)/DPA(+) in the DMF system decreases sharply when the potential of the Pt generating electrode reaches those where cathodic background currents become appreciable (19).

4. Filming of the electrode by production of insoluble products (e.g., polymers) from side reactions of the radical ions, or by electrolysis of impurities, solvent, or supporting electrolyte. These films can cause progressive blockage of the electrode or by buildup of a layer which can catalyze side reactions. When this form of decay is important, removing and polishing the electrode and returning it to the ECL system will at least partially restore the emission. This behavior was

noticed upon generation of DPA⁻ in ACN (19); other examples of filming are discussed below.

Electrical excitation of ECL.—The discussion of failure modes points to the importance of the mode of electrical excitation to long term stability. In general a desirable mode of excitation will (a) maintain the electrode potentials of both working and auxiliary electrodes in regions where only $A^{\cdot -}$ and $D^{\cdot +}$ can be produced; (b) be coulometrically symmetric, i.e., have equal anodic and cathodic (faradaic) coulombs on alternate pulses; (c) maximize reaction between $A^{\cdot -}$

and D^+ , i.e., cause the direct oxidation of A^- and reduction of D^+ at the electrode to be minimal. For example the square wave potentiostatic mode causes very little loss of the radical ions by direct electrolysis, while appreciable losses occur with the sinusoidal or triangular wave potentiostatic or constant current modes.

Potentiostatic (three-electrode) pulsed mode.—This method is that employed in most recent experimental ECL studies and has been treated theoretically (13, 14, 20). With regard to operation of a long-duration cell the design of the reference and auxiliary electrodes becomes important. The reference electrodes frequently employed in ECL are silver or platinum wire quasi-reference electrodes which show reasonable stability over experiments of a few hours duration but which show much too large drifts in potential with continuous pulsing over long time periods to be reliable. Other, more poised, reference electrodes, like the aqueous saturated calomel electrode (SCE) can leak undesirable amounts of water or alkali metal ion into the ECL solution on prolonged immersion, even when separated with double sintered-disk salt bridges. We have found that the Ag/Ag^+ (ACN) contained in a porous Vycor tube, as described in the Experimental section, maintained a reproducible and constant potential, and showed no detectable leakage of Ag^+ into the main body of solution after many tens of hours of use. The auxiliary electrode design is also of importance, since uncontrolled electrochemical processes occur there and these may lead to solution contamination. The usual electrochemical technique of isolating the auxiliary electrode in a separate chamber separated from the working electrode chamber by sintered glass disks, salt bridges, etc., is not desirable in ECL since this greatly increases the power necessary to drive the cell, and may prevent potentiostatic control of the working electrode in the early stages of pulse reversal when large currents flow. An auxiliary electrode which is somewhat larger than the working electrode and immersed directly into the ECL solution compartment in a geometry where the current density across its surface is fairly uniform can be employed. The current density at its surface will be smaller than that at the working electrode, and hence it will attain less negative and less positive potentials (with respect to the adjacent solution) than those of the working electrode. Certainly a small auxiliary electrode is to be avoided, since it will be forced to more negative and positive potentials causing undesired electrode reactions to supply the current required for potentiostatic control of the working electrode. The role of the auxiliary electrode is illustrated in a discussion of two-electrode cells in the next section.

To illustrate the necessity of potential control and the behavior of an ECL system under continuous long-term pulsing we consider the *tris*-bipyridylruthenium(II) ($Ru(bip)_3^{2+}$) system in ACN. The electrochemistry and ECL of this system have been described (21, 22). Briefly, $Ru(bip)_3^{2+}$ undergoes three reversible reduction steps (to the +1, 0, and -1 species) and a reversible oxidation (to the +3 species) in dry, deoxygenated ACN (Fig. 1). Controlled potential coulometry experiments have demonstrated that the +3 species is very stable, but that the +1 species, although apparently stable on the cyclic voltammetric time scale, undergoes a very slow decomposition reaction (22). ECL results from reaction of the +3 species with either the +1, 0, or -1 generated on the cathodic cycle. The application of alternate potential steps between +1.200 and -1.900V vs. Ag/Ag^+ with 95% *iR* compensation, i.e., from oxidation to second reduction wave, with a frequency of 100 Hz (i.e., $t_f = 5$ msec) in a cell with $V = 20$ cm³ and $A = 0.25$ cm² produced intense ECL with a half-life, $T_{1/2}$, (the time for the ECL intensity to decrease to one-half its initial value), of about 5 hr.

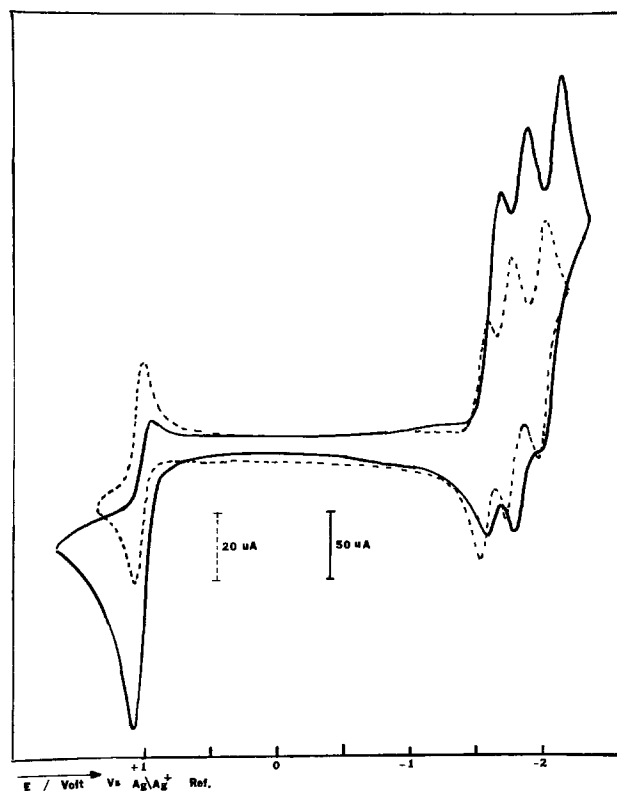


Fig. 1. Cyclic voltammetry of 0.6 mM $Ru(bip)_3(CIO_4)_2/0.1M$ TBAP/ACN solution at Pt electrode with a scan rate of 100 mV/sec. ---, Original solution; —, the same solution after 5 hr of ECL production by pulsing between +1.20 and -1.90V at 100 Hz after which no further ECL emission is observed.

The cyclic voltammogram at this time taken at the same working electrode in the ECL cell is noticeably different than the original one (Fig. 1). The height of the reduction peaks (+2 \rightarrow +1, +1 \rightarrow 0, 0 \rightarrow -1) depend on the positive potential the electrode has attained during the anodic scan; they are larger (and anomalous) when the anodic scan includes the +2/+3 wave than when the scan stops at the foot of this wave. Similarly the +2/+3 wave is anomalous when the cathodic scan includes the +2/+1 wave. This behavior is evidence of surface changes at the electrode causing changes in electrochemical reaction. Furthermore a yellow-brown precipitate covers the electrode surface. If the electrode is removed from the ECL cell in an inert atmosphere box, polished with 0.03 μ alumina and replaced, both the original cyclic voltammetric behavior and the original ECL intensity is restored.

The nature of the interfering precipitate was elucidated by some experiments at the RRDE. As shown previously (22) when the disk potential is held at the second reduction wave (production of $Ru(bip)_3^0$) and the ring potential held at the foot of the first reduction (corresponding to oxidation 0 \rightarrow +2), the disk current, after a short time of constancy equal to twice the current of the first reduction wave, begins to increase with time (up to a one order of magnitude increase) without a corresponding increase in the ring current. This lack of increase in the ring current demonstrates that the increasing disk current cannot be attributed to formation of soluble $Ru(bip)_3^0$. If the disk potential is scanned back toward more positive potentials a large oxidation disk current peak is observed at potentials corresponding to the +1 \rightarrow +2 wave. A similar large oxidation current peak is seen at the ring at this time ($E_R = 0.0V$). These results can be explained by the formation of a deposit on the disk electrode. This deposit catalyzes the reduction of solvent or electrolyte (giving rise to the enhanced disk current) and is oxidatively stripped off during the positive potential

sweep. The nature of the deposit has not been established. It could be some form of $\text{Ru}(\text{bip})_3^0$ itself or Ru-metal formed by its decomposition. Attempts to reproduce this effect on a stationary Pt electrode by electro-deposition of finely divided Ru-metal were unsuccessful. A deposit of a zero-valent Ru-species would explain the stripping experiment, if the disk oxidation peak represented the oxidation of this deposit to the +1 species while the ring current represented the further oxidation of +1 \rightarrow +2. An alternate explanation would require falling away of some of the zero-valent species during the oxidation scan producing +1 species (upon reaction with +2 in the gap region) which is oxidized at the ring. Thus for the long duration ECL with the $\text{Ru}(\text{bip})_3^{2+}$ system the second reduction wave must be avoided; pulsing to the second reduction wave is also undesirable, because of lack of coulombic symmetry and the consequent slow buildup of reduced species in the bulk solution. Since the first and second reduction waves are separated by only about 200 mV, close potential control (better than ± 50 mV) is required, with the negative potential limit adjusted between $E_{p/2}$ and E_p of the first reduction wave. The positive potential limit was at or beyond that peak for the oxidation to the +3 species. Under these conditions, with pulsing between -1.650 and $+1.100$ V at 100 Hz for a 2.5 mM $\text{Ru}(\text{bip})_3^{2+}$, 0.1M TBAP solution in ACN, the ECL emission increased slightly from its initial value and maintained this level for 50 hr. The intensity-time behavior in this system is shown in Fig. 2; the experiment was terminated at 112 hr. Cyclic voltammetry after this period shows no change in $\text{Ru}(\text{bip})_3^{2+}$ concentration, but evidence for production of a small amount of an unidentified electroactive species is found (Fig. 3).

Voltage (two-electrode) pulsed mode.—Practical ECL devices will probably be based on two-electrode systems. The way in which the potentials of the working electrode and the counterelectrode vary during pulsing with a low impedance function generator depend on the cell geometry and relative electrode areas. In this mode the technique of applying a symmetrical square wave to the cell and increasing the voltage until maximum emission is observed or alternatively applying a signal of $\pm \Delta E_p$ (the peak potential separation) can result in overdriving the cell and degraded device life.

Before the system is perturbed both electrodes are at their open-circuit or rest potentials, which will be essentially identical, if both electrodes are composed of

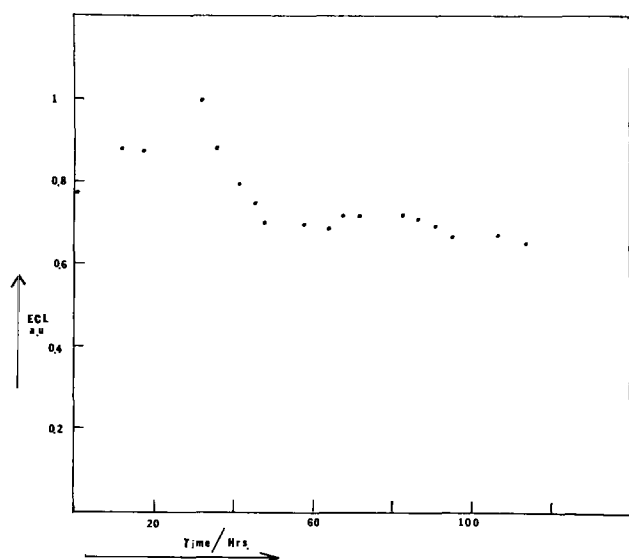


Fig. 2. ECL intensity vs. time behavior for a 2.5 mM $\text{Ru}(\text{bip})_3(\text{ClO}_4)_2/0.1\text{M}$ TBAP/ACN solution with pulsing between $+1.200$ and -1.650 V vs. Ag/Ag^+ (ACN) electrode at 100 Hz.

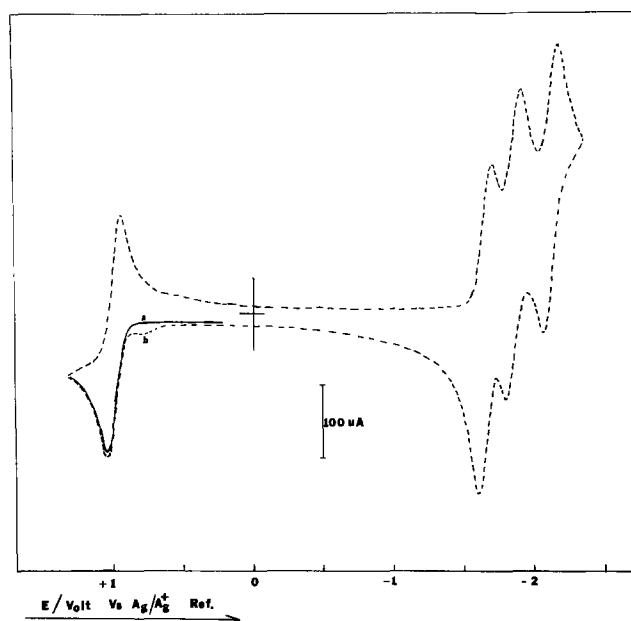


Fig. 3. Cyclic voltammetry of the system of Fig. 2 at a scan rate of 100 mV/sec. (a) Original solution; (b) after 120 hr of ECL production.

the same material and have been subjected to similar pretreatments; this rest potential will generally be

somewhere between the A/A^- and D/D^+ half-reaction potentials. When the voltage step, V , is applied between the working and counterelectrodes the potentials of the electrodes move in opposite directions such that their difference plus the solution iR -drop equals V , with the current in one electrode being equal in magnitude and opposite in direction from that in the other. When the pulse is reversed the electrode potentials switch to new values which again satisfy the aforementioned conditions, but in general they do not simply interchange the potentials observed during the first pulse. Let us consider two possible cases when (a) the auxiliary electrode is much larger than the working electrode and (b) both electrodes are the same size and the rest potential lies about midway between the peaks.

In case (a) the current at the auxiliary electrode during the pulse will be largely (or even completely) nonfaradaic and will be consumed in charging the electrical double layer (dl) *i.e.*, most of the current will be consumed in moving the electrode potential of the auxiliary from its rest potential, but the potential of this electrode will not attain a value where a faradaic reaction can occur. The shift in the auxiliary electrode potential is thus inversely proportional to its dl capacity and hence its area; if the area is large enough (compared to the coulombs passed during the pulse), its potential will only shift very slightly from the rest potential. For the small area working electrode however, the electrode rapidly charges its dl and then carries out a faradaic oxidation or reduction. Under these conditions the small working electrode shifts by almost the total of the applied pulse, V . For example, if the working electrode moved immediately to the diffusion-limited plateau region, the faradaic current in the system would be governed by the Cottrell equation and the total coulombs passed during the pulse would be given by [5] plus the coulombs needed to charge the working electrode Q_{dlw} . The large auxiliary electrode, of area A_{aux} , will only shift by an amount ΔE_{aux} , given by

$$\Delta E_{aux} = \frac{2A_w F(Dt_f)^{1/2} \pi^{-1/2} + Q_{dlw}}{A_{aux} C_{dl}} \quad [10]$$

where C_{dl} is the dl capacity per unit area of the auxilli-

ary electrode. For example, for $A_w/A_{aux} \approx 100$, concentrations in the mM range, and C_{dl} of $10 \mu\text{f}/\text{cm}^2$, ΔE_{aux} will be about 100 mV for a 100 msec pulse. To illustrate this effect, we describe an ECL experiment with a solution of 2 mM rubrene and 0.1M TBAP in benzonitrile, with two platinum electrodes of ratio 80:1. An Ag/Ag⁺ reference electrode was employed to monitor the potentials of both electrodes as a voltage pulse of $\pm 2.1\text{V}$ was applied across the Pt electrodes at a frequency of 10 Hz. The results, shown in Fig. 4, demonstrate that the large auxiliary electrode stays within ± 100 mV of its rest potential ($+0.6\text{V}$ vs. reference electrode), while the small electrode moves $\pm 2\text{V}$, from its rest potential to potential regions where secondary electrode reactions occur. (The slightly larger shift of the auxiliary electrode potential immediately after pulse reversal is caused by the large iR -drop at this time which is included mainly in the measured auxiliary electrode potential, because the reference electrode was located near the small working electrode). Thus, for this configuration, the large auxiliary electrode behaves as a practical reference electrode and the proper potential program can only be achieved by knowing the system rest potential and applying an unsymmetrical voltage program derived from the cyclic voltammetry of the system. If the rest potential does not lie exactly midway between the redox potentials for reduction and

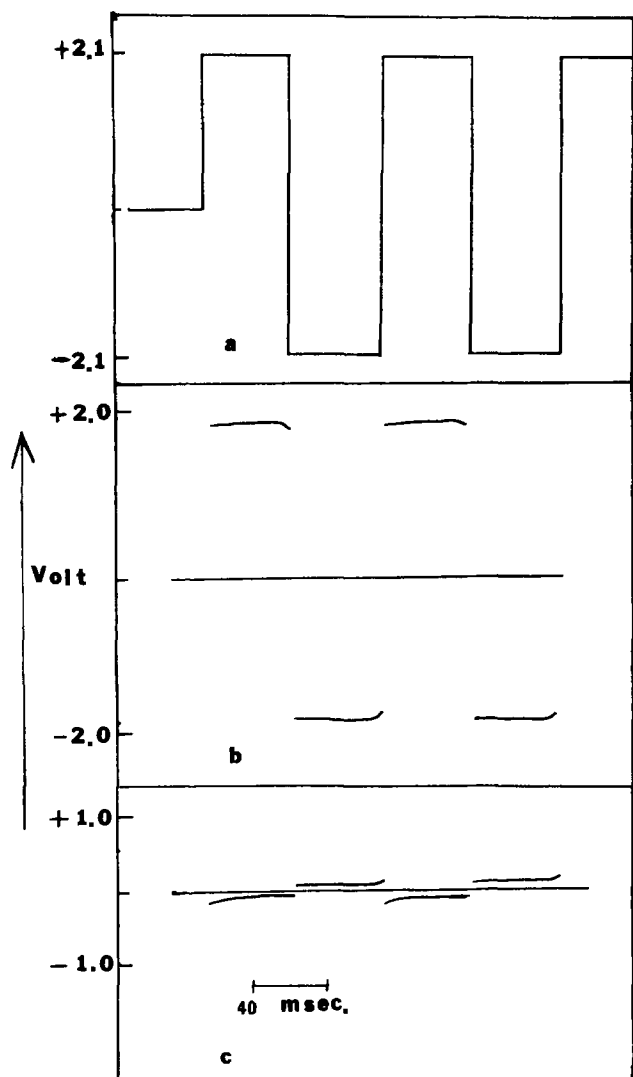


Fig. 4. Potentials of working and auxiliary electrodes (area ratio ca. 1:80) in the two-electrode voltage pulsed mode of operation. The solution was 2 mM rubrene/0.1M TBAP/BZN. (a) Applied voltage; (b) potential displacement of small electrode; (c) potential displacement of large electrode.

oxidation, an applied symmetrical (square) wave equal to one-half the peak separation either may not produce efficient ECL or may lead to "overpulsing" and shortened lifetime. Certainly a square wave of amplitude equal to the peak separation will lead to rapid system deterioration.

Case (b) involves two electrodes of the same size with the rest potential lying approximately midway between the peak potentials. In this case both electrodes will shift about the same amount in potential in opposite directions from the rest potential, i.e., the applied potential is shared between the electrodes. This effect is illustrated in Fig. 5, where the conditions are the same as case (a) (Fig. 4), except that the electrodes are of equal size. Here both of the working electrodes shift by about $\pm 1\text{V}$ vs. the reference electrode for the $\pm 2.1\text{V}$ applied; the slight asymmetry in the shifts is caused by the rest potential not lying exactly midway between the peak potentials, but, in fact, lying about 50 mV toward E_{pa} . Thus the desired potential program for two equal size electrodes involves applied voltages essentially twice as large as for the very small-very large case, but both electrodes produce light. If the rest potential does not lie midway between the peaks, the general behavior will be the same, but the unequal extent of charging of the two electrodes will make behavior more complicated when the amount of nonfaradaic charge per pulse is appreciable.

For the general case of two electrodes of unequal, but not very disproportionate, size, the behavior will be intermediate to cases (a) and (b) above, and a carefully selected and controlled potential program is required; a symmetrical square wave will, in general, not be suitable.

Constant current pulsed mode.—A two-electrode mode in which alternate anodic and cathodic constant current pulses are applied has been suggested (23). This mode has the advantage of precise coulombic symmetry with simple control circuitry. However, the coulombic ECL efficiency is smaller in this mode and the applied current density, i_0 , and pulse duration, t_f , must be maintained in a rather narrow range to obtain ECL yet prevent overdriving. The applied current again is distributed between dl charging and the faradaic process; in this case the rate of dl charging is controlled by i_0 , with appreciable charging occurring before any faradaic process begins. Thus $i_0 t_f$ must be larger than the

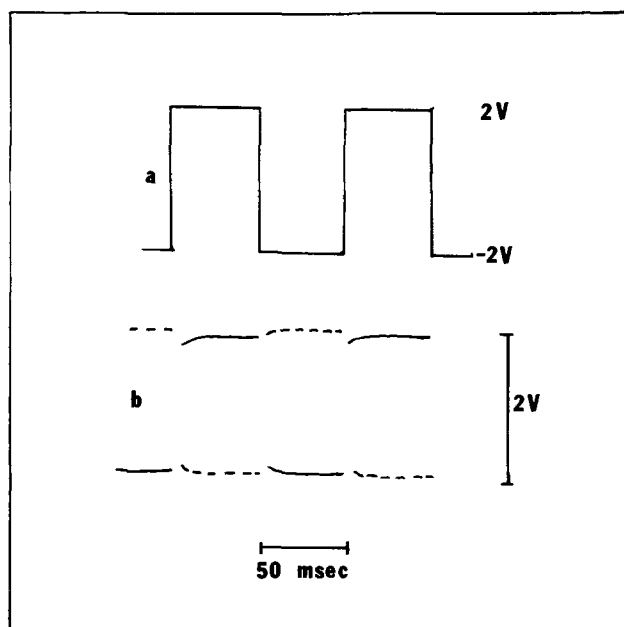


Fig. 5. Potentials of working and auxiliary electrodes (area ratio 1:1) in the two-electrode voltage pulsed mode. Solution as in Fig. 4. (a) Applied voltage; (b) potential displacement of electrodes.

number of coulombs required to charge the dl, approximately $C_{dl}\Delta E$ (i.e., about 2×10^{-5} coulombs/cm² for 10 $\mu\text{f/cm}^2$ dl capacity and 2V step). However $i_0 t_f^{1/2}$ must be maintained below $i_0 \tau^{1/2}$, where τ , the chronopotentiometric transition time, is given by (24)

$$i_0 \tau^{1/2} = \pi^{1/2} F n D^{1/2} C / 2 = 85.5 n D^{1/2} C \text{ (mA-sec}^{1/2}\text{)} \quad [11]$$

if the electrode potential is to be maintained at values where secondary electrode reactions do not occur. Actually Eq. [11] pertains to a single constant current step; the transition time under constant pulsing conditions with continuous regeneration of parent will be close to this value. The useful working range of i_0 and t_f in ECL based on these criteria is shown in Fig. 6, under the simplified assumption that dl charging is separable from the faradaic process.

With constant current ECL, upon reversal, the current first is consumed totally in reversing the process of the preceding pulse, without generation of a reacting species required for light emission. For example, if the first current pulse was cathodic and led to production of A^- (Eq. [1]), then during the time period up to $(1/3)t_f$, the next anodic pulse would totally involve

the oxidation of A^- to A , as is usual for reversal chronopotentiometry (25). After this time the potential jumps in a positive direction, at a rate primarily determined by dl charging, to values where oxidation of D occurs (Eq. [3]). During this transition period oxidation of A^- to A continues. However once D^+ production begins at the electrode, direct electrode oxidation

of A^- becomes negligible and ECL commences. The observed experimental behavior (Fig. 7) shows the delay in emission intensity on reversal, followed by a sharp increase, a maximum, and slow decay, in agreement with the results obtained by a digital simulation for this mode of operation.

The maximum steady-state ECL efficiency under these conditions, neglecting dl charging, is 0.62 that for the potential-step mode. The simulation results also predict an intensity proportional to the current, independent of cycling frequency. Moreover the total number of photons emitted per pulse is proportional to i_0 at fixed frequency, is proportional to t_f at fixed i_0 , and is inversely proportional to i_0 at fixed $i_0 t_f^{1/2}$. In practice,

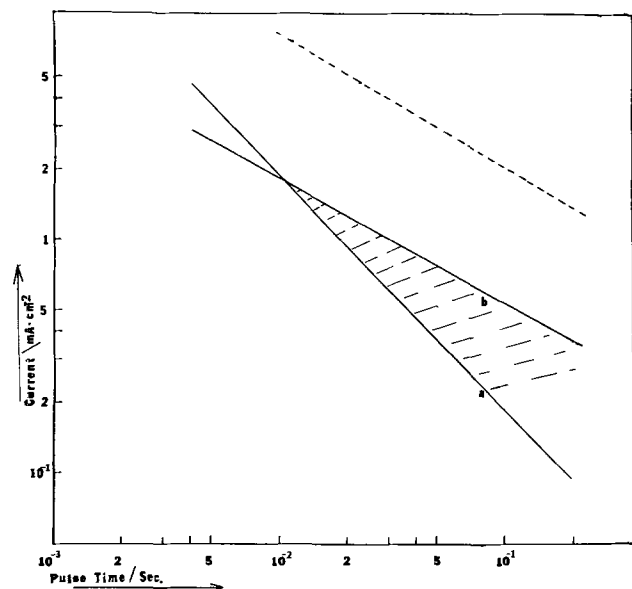


Fig. 6. Useful working region for pulsed constant current ECL. (a) Double layer charging limit, assuming $it_p = 20 \mu\text{coulombs/cm}^2$; (b) upper (transition time) limit for $i\tau^{1/2} = 0.2 \text{ mA} \cdot \text{sec/cm}^2$ (i.e., for $n = 1$, $D = 5 \times 10^{-6} \text{ cm}^2/\text{sec}$ and $C = 1 \text{ mM}$); - - -, upper limit for i as in (b), except for $C = 2 \text{ mM}$.

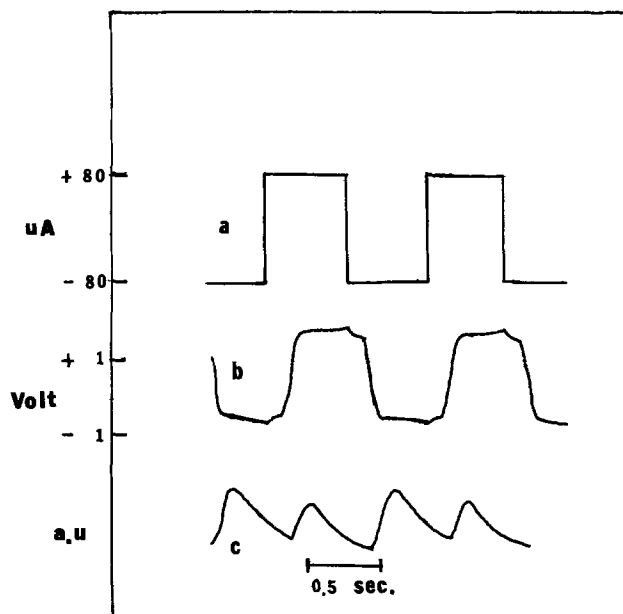


Fig. 7. Pulsed constant current ECL for a 2 mM rubrene/0.1M TBAP/BZN solution. (a) Applied current; (b) working electrode potential; (c) light intensity.

however, dl charging is not negligible, so that although the proportionality to i_0 at fixed t_f is observed (Fig. 8A), the intensity is relatively smaller at higher frequencies because of the relatively greater importance of the nonfaradaic processes at small t_f values (Fig. 8B). Within the limitations of the method, however, this operation mode may be preferred to a controlled voltage mode for long lifetime operation.

Special controlled current modes which conserve the desirable features of constant current operation but overcome some of its problems, are also possible at the expense of greater driver complexity. For example a double pulse current mode, similar to that used in galvanostatic studies of fast electrode reactions (26) could be employed. This would involve a short, very large current pulse to charge the dl and, in ECL, also rapidly drive the electrode potential into the region where ECL begins, followed by a lower current of magnitude sufficient to maintain ECL (if the second

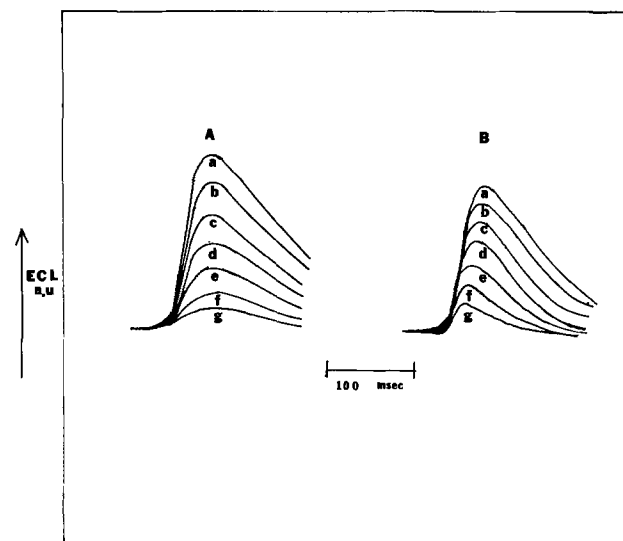


Fig. 8. Light intensity profiles in pulsed constant current ECL (conditions as in Fig. 7) with (a) pulsing at 1 Hz for currents of a-g 100, 90, 80, 70, 60, 50, 40 μA ; (b) constant current of 100 μA for pulsing at 1, 1.2, 1.4, 1.6, 1.8, 2.0, 2.2 Hz, respectively.

current were too low the potential would drop back to the region where only reversal, e.g., $A^- \rightarrow A$, occurred). This double pulse, constant current mode would require very careful adjustment and control to prevent overdriving, however.

Thin-layer cell, d-c mode.—Thin-layer ECL involves the use of two closely spaced electrodes (at least one of which is transparent) in which, during d-c electrolysis, the oxidized and reduced forms produced at the different electrodes diffuse (and migrate) together, near the middle of the interelectrode spacing, to annihilate, and produce light, and regenerate starting materials. The basic principles of thin-layer electrochemistry have been reviewed (27-29) and some thin-layer ECL experiments have been attempted (30-32). Thin-layer ECL has the advantage of producing a continuous and steady-state light with a low voltage d-c excitation. Only the rotating ring-disk electrode (RRDE) has been capable of producing true steady-state ECL previously (19). Moreover the close spacing minimizes the iR drop between the electrodes and the d-c operation eliminates charging current contributions, except during the initial switching on of the cell. However the very small cell volume places severe requirements on solution purity and reactant stability if long-life operation is to be attained.

The behavior of a thin-layer ECL cell follows that of the usual twin-electrode thin-layer cell (27-29), except that the concentration profiles of the electrogenerated

reactants (A^- and D^+) are such that, assuming equal diffusion coefficients and equal concentrations of A and D, both will have zero concentration in the middle of the cell at steady state. Thus, the limiting steady-state current will be

$$i_{ss}^{lim} = nFADC/0.5l \quad [12]$$

where l is the interelectrode spacing (cavity thickness); the concentration profiles of A^- and D^+ will be linear. The steady-state current-applied voltage behavior of the cell, assuming reversible electrode reactions, will be given by

$$\Delta V = \Delta E_{1/2} + \frac{2RT}{nF} \ln \left(\frac{i_{ss}^{lim}}{i_{ss}} - 1 \right) + i_{ss} R_{cell} \quad [13]$$

where ΔV is the applied cell voltage, $\Delta E_{1/2}$ is the difference in half-wave potentials between the A/A^- and D/D^+ reactions, and i_{ss}^{lim} is the limiting steady-state current which obtains when the parent concentrations at the electrode surface are essentially zero. The ECL intensity, I , is proportional to the flux of A^- and D^+ at the middle of the cavity and hence is proportional to the current

$$I = \phi_{ECL} i_{ss}/nF \quad [14]$$

just as in RRDE experiments (19).

The behavior of thin-layer ECL cells was tested using the rubrene in benzonitrile and $Ru(bip)_3^{2+}$ in ACN systems. Satisfactory lifetimes could only be obtained when no supporting electrolyte (TBAP) was added to the cell solution. For the $Ru(bip)_3^{2+}$ system this cation and the ClO_4^- counterion served as electrolyte. For the rubrene system, small amounts of impurities, perhaps introduced in the drying stages, probably served as electrolyte until the concentration of electrogenerated ions built up to aid in the conduction. The results, shown in Fig. 9 and 10, fit the predicted behavior quite well. The lack of proportionality of I and i_{ss} at low i_{ss} values shown in Fig. 10, is reminiscent of the "foot" observed in I vs. disk current in RRDE ECL studies (19), ascribed there to reaction of low levels of impurities with the excited states.

The rise time in a thin-layer ECL cell depends upon the time required for A^- and D^+ to diffuse together

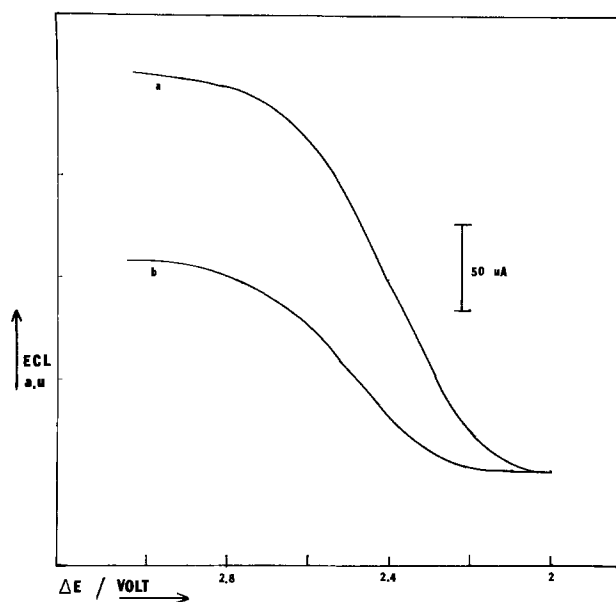


Fig. 9. Thin-layer ECL for 4 mM rubrene/BZN for 50μ spacing and scan rate of 2 mV/sec. (a) Current vs. applied voltage; (b) light intensity vs. applied voltage.

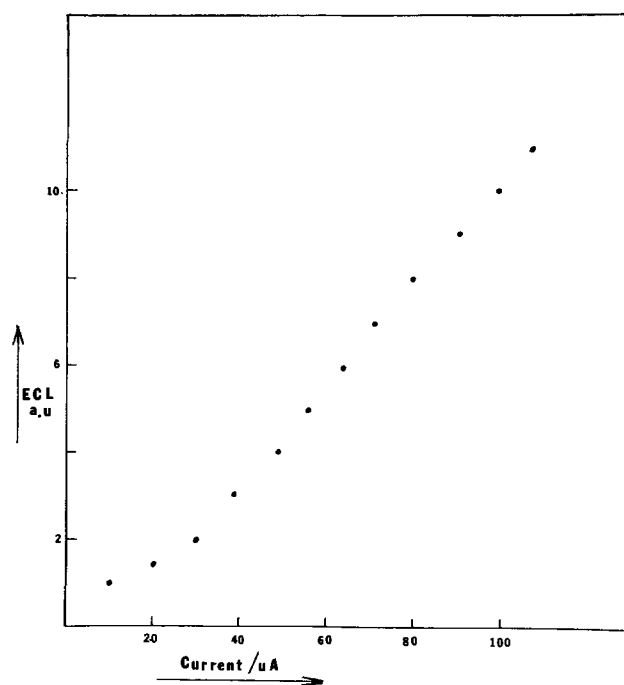


Fig. 10. Light intensity vs. applied d.c. in thin-layer ECL (conditions as in Fig. 9).

after the current flow commences and for the current to decay to its limiting value. To a first approximation then, light emission should commence at $t_s = l^2/16D$, (or for $l = 100$ and $20\mu m$, t_s is of the order of one and 0.04 sec, respectively). A more sluggish response suggests the occurrence of some slow chemical step or quenching of the excited state species. In the absence of complications the intensity should then level off at the value given by Eq. [14] (Fig. 11). In all cases we have observed a decay in signal level with time, probably indicative of the processes which limit the lifetime of the large cells but which are greatly accelerated because of the small cell volume. We should note that while half-lifetimes of about 10 min can be obtained in cells that contain no added TBAP, those that contain the usual 0.1M levels of TBAP have considerably

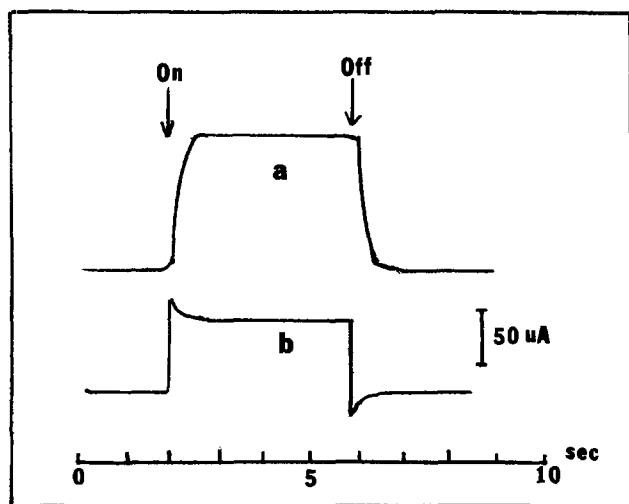


Fig. 11. Transients in thin-layer ECL. (a) Light intensity; (b) current cell. Spacing, 30μ (other conditions as in Fig. 9).

shorter lifetimes (maximum of about 3 min), suggesting that the supporting electrolyte may be an important source of impurities or quencher progenitors in ECL systems.

The thin-layer cell can also be operated in the pulsed cyclic mode. For pulse lengths small with respect to the time to diffuse half the cell thickness, the previous two-electrode treatments apply. For pulse lengths of the order of t_s , when the electrode polarity is reversed a sharp light spike is observed, because of the new annihilation reactions occurring near the electrodes; the light then decays until the mid-cell reaction becomes important and the light increases again toward its steady-state value (Fig. 12). In both the d.c. and pulsed mode thin-layer ECL cells will be useful in studying decay mechanisms in ECL cells and in accelerated life testing.

The small interelectrode spacing of the thin layer ECL cell makes possible the use of solvent systems which would be too resistive for conventional electrochemical cells. For example a solution of 10^5 ohm-cm specific resistance will only produce a 50 mV iR drop

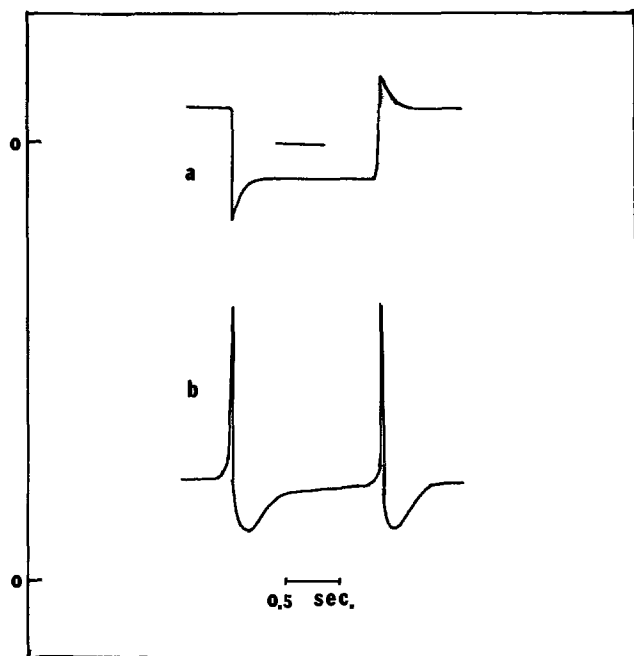


Fig. 12. Effect of reversal of electrode polarity in thin-layer cell. (a) Current; (b) light intensity (cell and solution as in Fig. 11).

for $l = 20 \mu\text{m}$ and a current density of $250 \mu\text{A}/\text{cm}^2$. In the presence of low electrolyte concentrations very high fields can be produced inside the cell by using external high voltage sources. These would lead to appreciable migration of the electrogenerated species, i.e.,

in effect the D^+ and A^- would be "fired" at one another by the large field gradient. The study of ECL and electrochemical reactions under these conditions is potentially of interest and is currently under study.

Steady-state efficiency of ECL cells.—The measurement and kinds of efficiency in ECL have been discussed (14, 19, 33). What is of interest in ECL devices is $\bar{\phi}_{\text{coul}}^{\text{ss}}$, the number of photons emitted per number of faradaic electrons passed, per pulse, after sufficient repetitive cycles that steady-state electrochemical behavior is observed

$$\bar{\phi}_{\text{coul}}^{\text{ss}} = \frac{\int_0^{t_r} I dt_N}{\int_0^{t_r} i dt_N} \quad [15]$$

The maximum value of this parameter, which applies when $\phi_{\text{ECL}} = 1$, i.e., when every radical ion encounter produces an emitted photon, depends on the mode of electrical excitation and cell geometry. This can be estimated by digital simulation (13, 14, 20) of repetitive pulses with the appropriate boundary conditions. The efficiencies quoted here are based on simulations in which only a single species (e.g., species A) is the par-

ent of both radical ions (A^- and A^+) and all species have equal diffusion coefficients. It is assumed that the radical annihilation reaction is diffusion controlled and leads directly to an emitting species which emits with unit efficiency (luminescence quantum yield of one). The simulation employed 2000 simulation time units (L) per pulse.

For the pulse potentiostatic (three-electrode) mode, assuming that only the working electrode emits, the following values of $\bar{\phi}_{\text{coul}}$, obtained by counting the total number of annihilations per pulse and dividing by the total electric charge required in that pulse, were ob-

tained beginning with pulse 1 (production of A^+): pulse 1, 0; 2, 0.549; 3, 0.462; 4, 0.507; 5, 0.484; 6, 0.494; 7, 0.491; 8, 0.489. Thus the limiting value of $\bar{\phi}_{\text{coul}} \cong 0.49$. For example, during a cathodic pulse, N , 49% of the current produces A^- which reacts with the A^+ produced during the previous pulse ($N - 1$) and the remainder

produces excess A^- which will react with A^+ in the pulse $N + 1$. Only about 2% of the current is consumed by direct reduction of A^+ (in the two-electron reaction

to form A^-) at the electrode and very little of the A^- produced in this pulse will eventually diffuse into bulk solution. Steady state is attained after about 7 or 8 pulses, and at steady state the concentration profiles of

the electrogenerated species (A^- in pulse N) and the reacting previously generated species (A^+ in pulse $N - 1$) are essentially the same from pulse to pulse except for a small diminishing tail of the species first produced

(A^+ in the example) spreading out into the bulk solution. The value $\bar{\phi}_{\text{coul}}^{\text{ss}} = 0.49$ implies that under ideal conditions, the coulombic efficiency approaches the maximum possible value for pulsed ECL efficiency (0.50) and that few faradaic electrons are lost in the process. For two-electrode cells in the voltage pulsed mode, for case (a) (large auxiliary electrode), the maximum value of $\bar{\phi}_{\text{coul}}^{\text{ss}}$ is the same as in the potentiostatic case. For case (b) (electrodes of equal size), both electrodes will emit, so the over-all cell efficiency can

approach a maximum value of 98%. In the constant current mode, because of the greater extent of non-radiative radical ion loss by direct electrode reaction, the maximum efficiency per electrode is only 30% (or 60% for emission at both electrodes). The thin-layer d-c cell will show a maximum efficiency of 100%, since every radical ion produced should ultimately annihilate in the middle of the cell. The practical efficiencies of cells will depend on the actual value of ϕ_{ECL} (for the most efficient systems, this lies in the range of 0.01 to 0.1), the magnitude of the nonfaradaic current and the cell resistance.

Acknowledgment

The support of this research by the U.S. Army Research Office-Durham is gratefully acknowledged.

Manuscript submitted Oct. 29, 1974; revised manuscript received Dec. 24, 1974.

Any discussion of this paper will appear in a Discussion Section to be published in the December 1975 JOURNAL. All discussions for the December 1975 Discussion Section should be submitted by Aug. 1, 1975.

Publication costs of this article were partially assisted by The University of Texas at Austin.

REFERENCES

1. T. Kuwana, in "Electroanalytical Chemistry," A. J. Bard, Editor, Vol. 1, Chap. 3, Marcel Dekker, New York (1966).
2. A. J. Bard, K. S. V. Santhanam, S. A. Cruser, and L. R. Faulkner, in "Fluorescence," G. G. Guilbault, Editor, Chap. 14, Marcel Dekker, New York (1967).
3. A. Zweig, *Advan. Photochem.*, **6**, 425 (1968).
4. E. A. Chandross, *Trans. N. Y. Acad. Sci. Ser. 2*, **31**, 571 (1969).
5. D. M. Hercules, *Accounts Chem. Res.*, **2**, 301 (1969).
6. D. M. Hercules, in "Physical Methods of Organic Chemistry," A. Weissberger and B. Rossiter, Editors, 4th Ed., Part II, Academic Press, New York (1971).
7. A. J. Bard and L. R. Faulkner, in "Creation and Detection of the Excited State," W. R. Ware, Editor, Vol. 3, Marcel Dekker, New York (In press).
8. J. T. Bowman and A. J. Bard, Unpublished results; see J. T. Bowman, Ph.D. Dissertation, The University of Texas at Austin (1971).
9. C. P. Keszthelyi and A. J. Bard, Unpublished results; see C. P. Keszthelyi, Ph.D. Dissertation, The University of Texas at Austin (1973).
10. R. M. Measures, *Appl. Optics*, **13**, 1121 (1974).
11. C. P. Keszthelyi and A. J. Bard, *This Journal*, **120**, 241 (1973).
12. M. M. Nicholson, *ibid.*, **119**, 461 (1972).
13. S. A. Cruser and A. J. Bard, *J. Am. Chem. Soc.*, **91**, 267 (1969).
14. R. Bezman and L. R. Faulkner, *ibid.*, **94**, 3699 (1972).
15. Y. Murata and H. J. Shine, *J. Org. Chem.*, **34**, 3368 (1969).
16. L. S. Marcoux, *J. Am. Chem. Soc.*, **93**, 537 (1971).
17. V. D. Parker, *J. Electroanal. Chem.*, **36**, App. 8, (1972).
18. R. Dietz, A. E. J. Forno, B. E. Lacombe, and M. E. Peover, *J. Chem. Soc., (B)*, (1970), 141.
19. J. T. Maloy and A. J. Bard, *J. Am. Chem. Soc.*, **93**, 5968 (1971).
20. S. W. Feldberg, *ibid.*, **88**, 390 (1966).
21. N. E. Tokel and A. J. Bard, *ibid.*, **94**, 2862 (1962).
22. N. E. Tokel-Takvoryan, R. E. Hemingway, and A. J. Bard, *ibid.*, **95**, 6582 (1973).
23. J. A. Seckel, T. M. Huret, and J. T. Maloy, Abstract No. 63, 24th Pittsburgh Conference on Analytical Chemistry and Applied Spectroscopy, March 5-9, 1973.
24. H. J. S. Sand, *Phil Mag.*, **1**, 45 (1901).
25. T. Berzins and P. Delahay, *J. Am. Chem. Soc.*, **75**, 4205 (1953).
26. H. Gerischer and M. Krause, *Z. Physik Chem. (N.F.)*, **10**, 264 (1957); **14**, 184 (1958).
27. A. T. Hubbard and F. C. Anson, "Electroanalytical Chemistry," A. J. Bard, Editor, p. 129, Marcel Dekker, New York (1971).
28. A. T. Hubbard, *CRC Crit. Rev. Anal. Chem.*, L. Meites, Editor, p. 201, Chemical Rubber Co., Cleveland, Ohio (1973).
29. C. N. Reilly, *Rev. Pure Appl. Chem.*, **18**, 137 (1968).
30. P. T. Kissinger, (Michigan State Univ.), Private communication.
31. J. S. Dunnett and M. Voinev, (Battelle-Geneva), Private communication.
32. J. Murphy, (Westinghouse Corp.), Private communication.
33. A. J. Bard, C. P. Keszthelyi, H. Tachikawa, and N. E. Tokel, "Chemiluminescence and Bioluminescence," M. J. Cormier, D. M. Hercules, and J. Lee, Editors, Plenum Press, New York (1973).

Technical Notes



Penetration of Hydrogen into Aluminum on Exposure to Water

Henry Leidheiser, Jr.* and Narayan Das

Center for Surface and Coatings Research, Lehigh University, Bethlehem, Pennsylvania 18015

Data in the literature indicate that hydrogen has limited solubility in aluminum (1, 2) equilibrated with gaseous hydrogen. For example, the solubility of hydrogen in pure aluminum at 300°C is reported to be of the order of 0.001 ml/100g. The solubility increases to approximately 0.04 ml/100g at 660°C. Our immediate interest was to determine the amount of hydrogen that penetrates into aluminum as a consequence of exposure of the metal to water.

Aluminum samples were in the form of flat plates, approximately 12 × 1 × 0.1 cm. The composition was 99.994% aluminum, 0.003% copper, 0.002% iron, and 0.001% silicon. The samples were metallographically polished, washed with ethanol and acetone, dried in vacuum for 6 hr, and annealed at 600°C for 4 hr at a pressure of 10⁻⁶ Torr. The samples were then cooled in vacuum and exposed to liquid water at 60°-100°C for varying periods of time. After exposure to water, the corrosion product was removed by heating in a mixture of 2% CrO₃ and 5% H₃PO₄ at 95°C for 60 min.

* Electrochemical Society Active Member.

Key words: hydrogen, aluminum, aqueous corrosion.

Table I. Hydrogen extracted from pure aluminum after exposure to liquid water

Temperature of water, °C	Exposure time	Penetrated hydrogen in ml at STP/100 of aluminum				Average value	Penetrated hydrogen in terms of ml at STP/cm ² of aluminum
		Individual expt. values					
60	24 hr	0.146, 0.090, 0.132, 0.105, 0.097, 0.150				0.12	0.00018
100	10 min	0.159, 0.155, 0.138, 0.136, 0.201, 0.148				0.156	0.00023
100	30 min	0.156, 0.167, 0.201, 0.135, 0.140, 0.161				0.160	0.00023
100	6 hr	0.130, 0.144, 0.192, 0.202, 0.168, 0.154				0.165	0.00024
100	24 hr	0.172, 0.155, 0.162, 0.156, 0.170, 0.205				0.170	0.00025
100 (3.5% NaCl)	24 hr	0.442, 0.378, 0.540, 0.480, 0.385, 0.315				0.42	0.00062
100 (99.8% D ₂ O)	24 hr	0.056 (H ₂ + D ₂) (8)					0.00008

Information generated by Lewis and Plumb (3) indicates that this medium dissolves the oxide on the surface and reacts very slowly with the metal. The sample was again washed in ethanol and acetone, dried in vacuum, and inserted into the gas extraction system. After extraction of the hydrogen, the degassed sample was again immersed in the CrO₃-H₃PO₄ electrolyte for 60 min at 95°C, washed in ethanol and acetone, and the extraction process repeated. The penetrated hydrogen introduced by exposure to water was taken to be the difference between the hydrogen values obtained in these two experiments.

The extraction apparatus consisted of a Vycor reaction vessel, a palladium thimble maintained at 400°C through which the hydrogen diffused, an automatic Toepler pump, and associated valves and auxiliary diffusion pumps. After pumping the system to 10⁻⁶ Torr, the sample was heated to 150°C and maintained at this temperature for 1 hr under vacuum conditions. Any gas evolved in this step was pumped to waste and was not collected. The purpose of this intermediate temperature treatment was to remove the majority of water from the sample surface to minimize the amount of hydrogen formed in the reactor as a consequence of the reaction, Al + H₂O = Al₂O₃ + H₂. The aluminum was heated rapidly to 600°C and maintained at this temperature for 3 hr. The evolved gas was collected and its volume measured. In selected experiments, portions of the gas were removed for mass spectrometric analysis. In all cases it was found to be essentially pure hydrogen with traces of oxygen, water, and nitrogen.

As a test of the method, degassed samples were removed from the extraction vessel, exposed to room air for 5 min, and reinserted into the extraction vessel. No hydrogen was extracted under the same experimental conditions normally used.

The data summarized in Table I indicate that the amount of hydrogen penetrated into aluminum approaches a saturation value in less than 10 min. Corrosion rate data at 100°C are given in Fig. 1, along with three data points taken from the paper by Vedder and

Vermilyea (4). It will be noted that the reaction rate is very rapid in the first 10 min. The weight gain data are in accord with the visual observation that gas evolves copiously during the first 30-60 sec, suggestive of an initially high rate of reaction involving hydrogen as a product, and then decreases to the point where the surface is only mildly active in catalyzing the formation of vapor bubbles.

The values shown in Table I are not inconsistent with the observations of Draley and Ruther (5) that samples of 1100 aluminum exposed to water at 290°C for 2 days contained 0.304 ml of hydrogen/100g of aluminum.

It is likely that the observed hydrogen is confined to the region close to the surface since etching the samples in the CrO₃-H₃PO₄ electrolyte for times longer than 2 hr resulted in a decrease in the amount of hydrogen obtained upon extraction. Proton-proton scattering experiments (6) kindly carried out on our samples by Professor B. L. Cohen of the University of Pittsburgh provided additional confirmation that the hydrogen is concentrated near the surface. It is recognized that aluminum of this purity is subject to intergranular attack (7). In fact, such intergranular attack was observed on samples exposed repeatedly or exposed for very long periods of time. It is not felt that hydrogen trapped at the grain boundaries or oxide unremoved at the grain boundaries by the CrO₃-H₃PO₄ electrolyte is responsible for a major portion of the experimentally determined hydrogen. The evidence for this viewpoint is that samples used for the first time, where intergranular attack was insignificant, yielded similar values for penetrated hydrogen as samples used many times previously.

Acknowledgment

Appreciation is expressed to D. Iyengar who provided assistance in the early stages of this work and to Professor B. L. Cohen for carrying out the proton-proton scattering experiments.

Manuscript submitted Oct. 28, 1974; revised manuscript received Jan. 13, 1975.

Any discussion of this paper will appear in a Discussion Section to be published in the December 1975 JOURNAL. All discussions for the December 1975 Discussion Section should be submitted by Aug. 1, 1975.

Publication costs of this article were partially assisted by Lehigh University.

REFERENCES

1. C. Ransley and H. Neufeld, *J. Inst. Metals*, **74**, 599 (1948).
2. W. Baukloh and F. Osterlen, *Z. Metallk.*, **11**, 386 (1938).
3. J. E. Lewis and R. C. Plumb, *This Journal*, **105**, 496 (1958).
4. W. Vedder and D. A. Vermilyea, *Trans. Faraday Soc.*, **65**, 561 (1969).
5. J. E. Draley and W. E. Ruther, Argonne Natl. Lab. Rept. ANL-5658, 26 pp. (1957).
6. B. L. Cohen, C. L. Fink, and J. H. Degnan, *J. Appl. Phys.*, **43**, 19 (1972).
7. M. J. Lavigne, *Corrosion*, **14**, 226t (1958).
8. H. Leidheiser, Jr. and N. Das, *J. Colloid Interface Sci.*, **38**, 665 (1972).

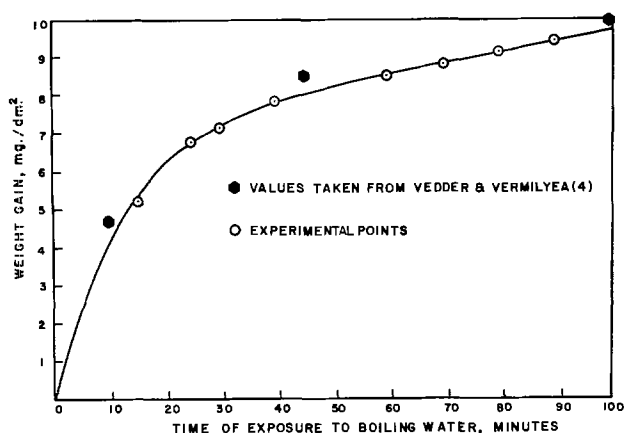


Fig. 1. The rate of corrosion of aluminum in boiling water as determined gravimetrically.

Thermal Oxidation and Electrolytic Etching of Silicon Carbide

W. von Münch and I. Pfaffeneder

Institut A für Werkstoffkunde, Technische Universität, D-3 Hannover, Germany

Silicon carbide can be oxidized in a manner similar to that used for the growth of silicon dioxide layers on silicon (1, 2). The oxide layers on silicon carbide may be utilized for various purposes in the technology of SiC devices, including junction delineation, masking for preferential etching by Cl_2/O_2 , passivation of p-n junctions, and identification of the surface polarity (3). Junction delineation is also accomplished by electrolytic etching in HF solution, since this etch is specific for p-type material (4). It is the purpose of this communication to point out that the oxidation and electrolytic etching techniques are also most useful for the discrimination of the polytypes of SiC and the detection of doping inhomogeneities in SiC.

Silicon carbide exists in several different modifications (polytypes). These polytypes can be described in terms of different stacking orders of the Si-C double layers. Among the most abundant types of silicon carbide are the 6 H crystals with a unit cell of six Si-C layers and hexagonal symmetry and the 15 R crystals (unit cell with fifteen layers and trigonal symmetry). For technical applications of silicon carbide, therefore, it is desirable to have a simple method to discriminate between these polytypes.

A series of oxidation experiments has been carried out with the following experimental conditions: temperature, 1070°C; time, 6 hr; gas stream, 45 liter/hr O_2 , saturated with H_2O at 90°C.

Silicon carbide crystals of the 6 H and 15 R polytypes of both conduction types and different doping levels were oxidized on the following faces: (0001), (1120), (1100), and (0001). The position of the low index faces of silicon carbide crystals is shown in Fig. 1. These faces were polished with diamond powder in three steps (15, 6, and 1 μm grain size) prior to the oxidation. The surface quality was checked by electron diffraction (pattern of Kikuchilines).

Table I gives the averaged results of about 15 measurements taken on each face of the n-type crystals. The oxide thickness was measured with an interferometer after a step-etching and metallization process. By comparison with the interference of nonmetallized oxide steps it was found that the refractive index of the oxide on silicon carbide is slightly higher than that of silicon dioxide; the etch rate is lower by a factor of 0.6, as compared with silicon dioxide on silicon.

Key words: polytypes, junction delineation, doping inhomogeneities.

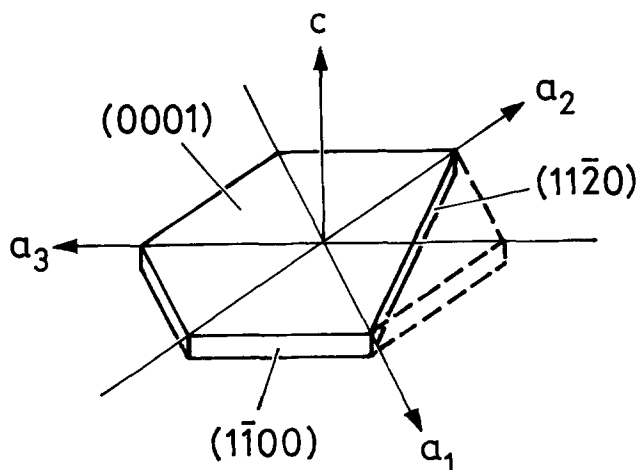


Fig. 1. Low index faces of silicon carbide crystals

Table I. Oxide thickness (in Å) on different faces of n-type SiC

	(0001)	(1120)	(1100)	(0001)
6 H, n-type	2680 ± 80	1940 ± 130	1620 ± 210	310 ± 30
15 R, n-type	2810 ± 160	1550 ± 420	1590 ± 440	350 ± 60
All n-type crystals	2740 ± 150	1750 ± 370	1600 ± 350	330 ± 50

Table II. Oxide thickness (in Å) on different faces of p-type SiC

	(0001)	(1120)	(1100)	(0001)
6 H, p-type	2420	1100	1000	450
15 R, p-type	2200	1360	1270	420

Table I confirms the well-known fact that the oxidation rate on the carbon (0001) face is about 10 times higher than on the opposite basal plane (silicon face). An intermediate oxidation rate is found for the (1120) and (1100) planes, as may be expected from the even distribution of silicon and carbon atoms on such faces. There are slight differences of the oxidation behavior for 6 H and 15 R material: the oxidation of the 15 R polytype is faster on the <0001> planes but slower on the other two planes. It has to be pointed out that the large spread of the experimental values in Table I is not entirely due to experimental errors, but also reflects the influence of the doping level of the crystals used in this investigation.

A different oxidation behavior has been found for p-type material (Table II): for 15 R crystals the oxidation rate is higher (with respect to 6 H) on the (1120) and (1100) faces, but lower on the {0001} faces. Except for the (0001) faces, all SiO_2 layers on p-type material were thinner than those on corresponding crystal faces of n-type material.

Figure 2 gives an example of polytype discrimination by the oxidation technique. The (1100) face of a p-type crystal was cut and polished prior to an oxidation treatment as described above. Under these circumstances the interference color of the oxide on the 15 R part of the crystal is light blue, whereas a deep blue is seen on the 6 H part. This interpretation was confirmed by electron diffraction studies.

The influence of the donor concentration on the oxidation rate of 6 H silicon carbide is seen from Table III.

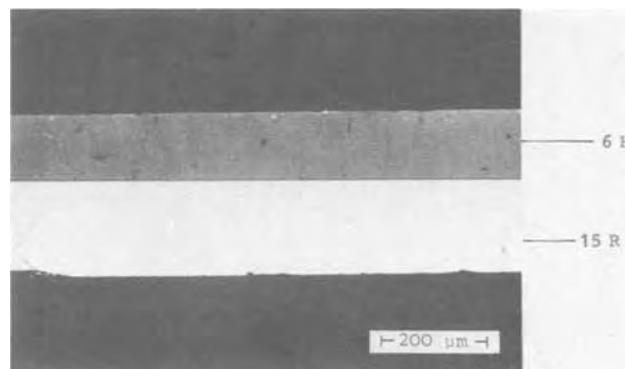


Fig. 2. Oxidized (1100) face of a p-type silicon carbide crystal containing 6 H and 15 R regions.

Table III. Oxide thickness (in Å) on different faces of n- and p-type SiC

	(0001)	(1120)	(1100)	(0001)
6 H, n-type, heavily doped	2730	1980	1720	310
6 H, n-type, lightly doped	2560	1830	1330	300
6 H, p-type	2420	1000	1000	450

A high donor concentration ($n > 10^{18} \text{ cm}^{-3}$) obviously enhances the thermal oxidation. The p-type SiC oxidation data are added in Table III for comparison.

Electrolytic etching in a 2:1 mixture of alcohol and 40% HF is mainly used for the delineation of p⁺p- and n⁺n-junctions and for those p-n junctions where both sides are very lightly doped. The delineation which is accomplished partly by surface attack and partly by staining may be markedly enhanced by a subsequent oxidation. Thus, the combination of electrolytic etching and oxidation has been found to be successful for the delineation of all junctions of practical interest. Furthermore, the existence of doping inhomogeneities can be revealed by this technique. Figure 3 shows an angle lap of an n-type epitaxial SiC layer on an n-type substrate. It is clearly seen that there are impurity striations in the substrate whereas the doping of the epitaxial layer is uniform.

In conclusion, it can be stated that the thermal oxidation of silicon carbide is a useful tool for polytype discrimination. An unambiguous determination of the polytype (6 H or 15 R), however, is possible only in those cases where the dependence of the oxidation rate on the conductivity type and the doping level is negligible or can be taken into account properly. The electrolytic etching technique serves for the delineation of impurity concentration gradients. A combination of both methods often provides an enhanced contrast.

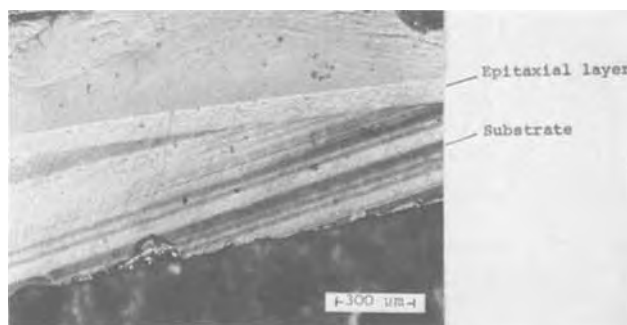


Fig. 3. Angle lap of n-type epitaxial layer on n-type substrate (etched and oxidized).

Manuscript submitted Sept. 16, 1974; revised manuscript received Dec. 23, 1974.

Any discussion of this paper will appear in a Discussion Section to be published in the December 1975 JOURNAL. All discussions for the December 1975 Discussion Section should be submitted by Aug. 1, 1975.

Publication costs of this article were partially assisted by the Technische Universität Hannover.

REFERENCES

1. J. A. Dillon, in "Silicon Carbide," p. 235, Pergamon Press, New York (1960).
2. P. J. Jorgensen, M. E. Wadsworth, and I. B. Cutler, *ibid.*, p. 241.
3. R. B. Campbell and H.-C. Chang, in "Semiconductors and Semimetals," R. K. Willardson and A. C. Beer, Editors, Vol. 7B, p. 625, Academic Press, New York and London (1971).
4. R. W. Brander and A. L. Boughey, *Brit. J. Appl. Phys.*, **18**, 905 (1967).

Mass Transfer to a Continuous Moving Sheet Electrode

Der-Tau Chin*¹

Electrochemistry Department, Research Laboratories, General Motors Corporation, Warren, Michigan 48090

This article presents a theoretical study of mass transfer to a continuous flat sheet moving at high speed. Such a system has long been used in the electroplating of steel sheets (1) and copper wires (2). It is also widely used in other manufacturing industries. Typical examples are continuous cooling in the fabrication of sheet glass (3) and steel plates (4), and the drying process in the paper (5) and the polymer film (6) manufacturing industries.

Despite its wide applications, few studies have been reported on this geometry. Sakiadis (7-9) and Koldenhof (10) calculated the laminar and the turbulent flow boundary layers on continuous flat and cylindrical surfaces. Experimental investigations of the flow field were made by Tsou, Sparrow, and Goldstein (11) and by Griffith (12). Numerical solutions of the thermal boundary layers on the continuous flat surface have been obtained by Tsou *et al.* (11), Erickson, Cha, and Fan (13), and Rhodes and Kammer (14). Erickson *et al.* also derived an approximate solution for heat transfer at larger Prandtl numbers. Griffin and Throne (15) reported an experimental study of heat transfer from a continuous moving belt to air.

In this study, an asymptotic solution is derived for mass transfer to the continuous moving flat sheet under

laminar conditions. A curve fitting of Sakiadis's flow results is used in the analysis. The solution covers a range $0.7 \leq Sc < \infty$; within this range, the maximum error which occurs at $Sc = 0.7$ is less than 1%.

Analysis

Consider a continuous semi-infinite flat sheet electrode moving with a constant velocity, U_s , through a stationary electrochemical cell. The sheet enters the cell through a watertight slot at one end of the cell and leaves the cell at the opposite side through a second slot as shown in Fig. 1. The motion of the solid surface induces a flow of the adjacent electrolyte along the di-

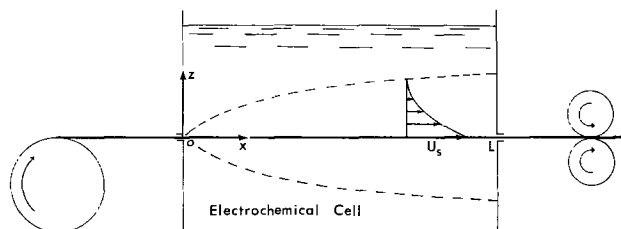


Fig. 1. The continuous moving sheet electrode and the fixed space coordinates x and z . The electrode is moving through a cell of length L with a constant velocity U_s . The induced flow boundary layers are designated by the dashed curves.

* Electrochemical Society Active Member.

¹ Present address: Department of Chemical Engineering, Clarkson College of Technology, Potsdam, New York 13676.

Key words: asymptotic theory of convective diffusion, limiting current.

rection of the sheet movement. This creates a flow boundary layer that originates at the inlet slot and grows in thickness along the direction of the sheet movement. To analyze mass transfer in such a system, we shall make the following assumptions: (i) the sheet is moving at a sufficiently high speed to permit application of the boundary layer solutions; (ii) the electrolyte flow in the vicinity of the moving sheet electrode is laminar in nature; (iii) the cell is long and deep enough so that the effect of the cell wall on the flow boundary layer is negligible; (iv) sufficient inert salt is present in the electrolyte so that the migration flux of the diffusing ion in the electric field can be neglected (this assumption also applies to binary electrolytes); (v) physical properties of the electrolyte are constant; (vi) the effect of gravitational force on the diffusion field is negligible. Under the steady-state conditions, the system can be described with a set of fixed coordinates, x and z . Here x is the linear distance from the inlet slot and points toward the direction of the sheet movement; z is the perpendicular distance from the sheet surface. The equation of convective diffusion to the moving electrode then takes the form

$$u \frac{\partial C}{\partial x} + v \frac{\partial C}{\partial z} = D \frac{\partial^2 C}{\partial z^2} \quad [1]$$

Here u and v are the velocity components of the electrolyte along the x - and the z -directions, respectively; C and D are the concentration and the diffusivity of the diffusing ion. The boundary conditions are

$$\left. \begin{array}{l} \text{at } z = 0, \quad C = C_0 \\ \text{at } z \rightarrow \infty, \quad C = C_\infty \\ \text{at } x = 0, \quad C = C_x \end{array} \right\} \quad [2]$$

Equations [1] and [2] imply that under the steady-state conditions, the diffusion layer in the electrolyte can be regarded as a function of fixed-space coordinates only, even though it is adjacent to a moving solid boundary. An observer fixed in space would note that the concentration of the diffusing ion at every point in the surrounding electrolyte is not changing with time regardless of an ever-changing electrolyte/electrode interface because of the sheet movement. This condition is analogous to those occurring on a rotating disk (16) and rotating sphere (17).

Introducing a similarity transformation, η , and a stream function, $f(\eta)$, defined as (9)

$$\eta = z \sqrt{\frac{U_s}{\nu x}} \quad [3]$$

$$u = U_s f'(\eta) \quad [4]$$

$$v = \frac{1}{2} \sqrt{\frac{\nu U_s}{x}} [\eta f'(\eta) - f(\eta)] \quad [5]$$

the equation of convective diffusion may be reduced to a linear second-order ordinary differential equation

$$\frac{d^2 \Phi}{d\eta^2} + \frac{1}{2} Sc f \frac{d\Phi}{d\eta} = 0 \quad [6]$$

where Φ is a dimensionless concentration defined as

$$\Phi = \frac{C - C_\infty}{C_0 - C_\infty} \quad [7]$$

and Sc is the Schmidt number defined as the ratio of the kinematic viscosity of the electrolyte, ν , to the diffusivity of the diffusing ion, D . The boundary conditions are now changed to

$$\left. \begin{array}{l} \text{at } \eta = 0, \quad \Phi = 1 \\ \text{at } \eta \rightarrow \infty, \quad \Phi = 0 \end{array} \right\} \quad [8]$$

Curve fitting for the stream function.—To solve Eq. [6] analytically, one needs a mathematical expression for the stream function, $f(\eta)$. The flow boundary layer on a continuous moving flat surface has been calculated numerically by Sakiadis (9). In this analysis we have found that his tabulated values of the stream function can be represented by the following relation

$$f = 1.61605[1 - e^{-\eta}(1 + 0.381207\eta + 0.0185019\eta^2 - 0.00543507\eta^3)] \quad [9]$$

Figure 2 shows the close agreement between Eq. [9] and Sakiadis's calculations. In the next section, Eq. [9] is used in the integration of Eq. [6].

Asymptotic solutions.—To find a simple solution for the convective diffusion equation, we follow the procedures illustrated by Chin (18-20), and assume that Φ can be represented by an asymptotic series in the descending powers of Sc

$$\Phi = \phi_0 + \frac{1}{Sc^{1/2}} \phi_1 + \frac{1}{Sc} \phi_2 + \frac{1}{Sc^{3/2}} \phi_3 + \dots; \quad (\text{for } Sc \gg 1) \quad [10]$$

Here ϕ_0 , ϕ_1 , ϕ_2 , and ϕ_3 are called the zeroth, the first, the second, and the third order solutions, respectively, of the convective diffusion equation. They are functions of a stretched coordinate, ξ , defined as

$$\xi = Sc^{1/2} \eta = z \sqrt{\frac{U_s}{Dx}} \quad [11]$$

Substituting Eq. [9]-[11] into Eq. [6], expanding the exponential function in the stream function, f , into a power series of Sc , and then equating the terms having the like powers of Sc in the resulting equation, we have

$$\frac{d^2 \phi_0}{d\xi^2} + \frac{1}{2} \xi \frac{d\phi_0}{d\xi} = 0 \quad [12]$$

$$\frac{d^2 \phi_1}{d\xi^2} + \frac{1}{2} \xi \frac{d\phi_1}{d\xi} = 0.110937 \xi^2 \frac{d\phi_0}{d\xi} \quad [13]$$

$$\frac{d^2 \phi_2}{d\xi^2} + \frac{1}{2} \xi \frac{d\phi_2}{d\xi} = 0.110937 \xi^2 \frac{d\phi_1}{d\xi} \quad [14]$$

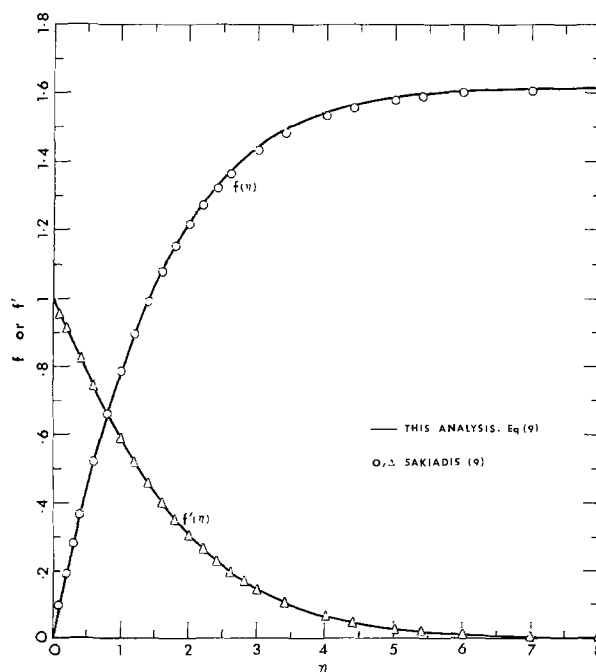


Fig. 2. The stream function f and its derivative f'

$$\frac{d^2\phi_3}{d\xi^2} + \frac{1}{2}\xi \frac{d\phi_3}{d\xi} = 0.110937 \xi^2 \frac{d\phi_2}{d\xi} - 0.00580312 \xi^4 \frac{d\phi_0}{d\xi} \quad [15]$$

Equations [12]-[15] are subject to the following boundary conditions in accordance with Eq. [8]

$$\left. \begin{aligned} \text{at } \xi = 0, \quad \phi_0 = 1 \\ \phi_1 = \phi_2 = \phi_3 = 0 \\ \xi \rightarrow \infty, \quad \phi_0 = \phi_1 = \phi_2 = \phi_3 = 0 \end{aligned} \right\} \quad [16]$$

Equations [12]-[16] can be integrated analytically to give the following solutions

$$\phi_0 = \operatorname{erfc} \left(\frac{\xi}{2} \right) \quad [17]$$

$$\phi_1 = 0.166906 \left[\left(1 + \frac{\xi^2}{4} \right) e^{-\frac{\xi^2}{4}} - \operatorname{erfc} \left(\frac{\xi}{2} \right) \right] \quad [18]$$

$$\begin{aligned} \phi_2 = 0.0278576 \operatorname{erfc} \left(\frac{\xi}{2} \right) \\ - e^{-\frac{\xi^2}{4}} (0.0278576 - 0.0462903\xi + 0.00696441\xi^2 \\ - 0.00771505\xi^3 - 0.000771505\xi^5) \quad [19] \end{aligned}$$

$$\begin{aligned} \phi_3 = -0.00747613 \operatorname{erfc} \left(\frac{\xi}{2} \right) \\ + e^{-\frac{\xi^2}{4}} (0.00747613 - 0.00772613\xi + 0.00186903\xi^2 \\ - 0.00128769\xi^3 + 0.000516273\xi^4 \\ - 0.000128769\xi^5 + 0.000152158\xi^6 + 0.00000950988\xi^8) \quad [20] \end{aligned}$$

Here erfc designates the complementary error function; its numerical values and related properties are tabulated in Abramowitz and Stegun (21). Thus the concentration profile in the diffusion layer can be calculated for systems with $Sc \gg 1$.

The local mass flux at the electrode surface is related to the concentration gradient by

$$j = -D \left(\frac{\partial C}{\partial z} \right)_{z=0} = k(C_0 - C_s) \quad [21]$$

where k is the local mass transfer coefficient. The concentration gradient at the surface can be obtained by differentiating Eq. [10] and Eq. [17]-[20]. The local Sherwood number, Sh_x , defined as kx/D , can now be calculated from the following equation

$$\begin{aligned} Sh_x = \left(\frac{kx}{D} \right) = Re^{1/2} Sc^{1/2} \left(0.56419 - \frac{0.094167}{Sc^{1/2}} \right. \\ \left. - \frac{0.030573}{Sc} + \frac{0.0035082}{Sc^{3/2}} + \dots \right) \quad [22] \end{aligned}$$

where Re is the local Reynolds number defined as $U_s x / \nu$. For a cell of length L , the average Sherwood number can be obtained by integrating k over the electrode surface. The result is

$$\begin{aligned} Sh = \left(\frac{KL}{D} \right) = Re^{1/2} Sc^{1/2} \left(1.12838 - \frac{0.18833}{Sc^{1/2}} \right. \\ \left. - \frac{0.061147}{Sc} + \frac{0.070164}{Sc^{3/2}} + \dots \right) \quad [23] \end{aligned}$$

Here K is the geometrical average of k , and Re is the Reynolds number defined as $U_s L / \nu$.

Discussion

For a uniform surface temperature, Tsou, Sparrow, and Goldstein (11) have made numerical calculations

Table I. Comparison of the present analysis with previous numerical solutions

Sc	$Sh_x / \sqrt{Re Sc}$		
	Present result, Eq. [22]	Tsou <i>et al.</i> , numerical solution	Erickson <i>et al.</i> , approximate solution
0.7	0.4140	0.4174	
1.0	0.4430	0.4438	
10	0.5315	0.5314	
100	0.5545	0.5545	
∞	0.5642		0.53

at several Prandtl numbers for the rate of heat transfer from a continuous moving flat surface. An approximate solution was derived by Erickson, Cha, and Fan for large Prandtl numbers. Since the Prandtl number is equivalent to the Schmidt number used in mass transfer, we may use these point solutions to estimate the accuracy of the present analysis. The comparison is given in Table I, where values of $Sh_x / \sqrt{Re Sc}$ obtained from the three analyses are tabulated for Sc (or Pr) at 0.7, 1, 10, 100, and ∞ . It is seen that for $Sc \cong 10$, there is essentially no difference between the present results and those of Tsou *et al.* The present asymptotic solution is based on $Sc \gg 1$; however, at $Sc = 0.7$, the value computed from Eq. [22] agrees with the numerical calculation to within 0.8%. At $Sc = 1$, the agreement between the two sets of values is within 0.2%. Thus, we may say the rate expressions given in the forms of Eq. [22] and [23] are valid for the Schmidt number greater than 0.7; within this range the accuracy is better than 99%. For large Schmidt numbers, the approximate solution of Erickson *et al.* is about 5% smaller than the asymptotic results.

At large Schmidt numbers, Eq. [22] can be simplified to

$$Sh_x = 0.5642 Re^{1/2} Sc^{1/2} \quad [24]$$

This equation states that the local Sherwood number is proportional to the square root of the Schmidt number. This is the most significant result in the present analysis. For most other known flowing systems, such as pipe flow, flat plate, or rotating disk, the rate of laminar mass transfer is invariably proportional to the cube root of the Schmidt number. The square root relation gives the continuous moving sheet an advantage on the transfer rate at high Schmidt numbers. Although there has been little experimental investigation of the continuous moving sheet electrode, this advantage in the mass transfer rate shows a great promise for potential applications in electrochemical as well as other industrial processes.

Conclusions

In conclusion, we have obtained an asymptotic theory for mass transfer on a continuous moving sheet electrode. The theory is valid for $Sc \cong 0.7$; within this range the accuracy is better than 99%. It is shown that at large Schmidt numbers, the Sherwood number is proportional to the square root of the Schmidt number, rather than the usual cube root relations.

Manuscript submitted July 11, 1974; revised manuscript received Sept. 16, 1974.

Any discussion of this paper will appear in a Discussion Section to be published in the December 1975 JOURNAL. All discussions for the December 1975 Discussion Section should be submitted by Aug. 1, 1975.

Publication costs of this article were partially assisted by General Motors Corporation.

LIST OF SYMBOLS

- C concentration of the diffusing ion, g-mole/cm³
- C_0 concentration of the diffusing ion at the electrode surface, g-mole/cm³
- C_s bulk concentration of the diffusing ion, g-mole/cm³
- D diffusivity of the diffusing ion, cm²/sec

- f dimensionless stream function defined in Eq. [4] and [5]
- j local rate of mass flux at the electrode surface, g-mole/cm² sec
- k local mass transfer coefficient defined in Eq. [21], cm/sec
- K geometric average mass transfer coefficient, cm/sec
- L length of the continuous moving sheet exposed to the electrolyte in the cell, cm
- R_x local Reynolds number based upon the surface distance measured from the leading edge of the flow boundary layer. For the continuous moving sheet electrode, it is defined as $U_s x/\nu$, dimensionless
- Re Reynolds number based upon the electrode length L , $U_s L/\nu$, dimensionless
- Sc Schmidt number defined as ν/D , dimensionless
- Sh average Sherwood number defined as KL/D , dimensionless
- Sh_x local Sherwood number based upon the surface distance measured from the leading edge of the flow boundary layer. For the continuous moving sheet electrode, it is defined as kx/D , dimensionless
- u velocity component of the electrolyte along the direction of the sheet movement, x , cm/sec
- U_s velocity of the continuous sheet moving through the electrolyte, cm/sec
- v velocity component of the electrolyte normal to the electrode surface, cm/sec
- x a fixed space coordinate measured from the point where the continuous sheet electrode enters the electrolyte, and points toward the direction of the sheet movement, cm
- z a fixed space coordinate measured perpendicular to the surface of the continuous sheet electrode
- η a similarity coordinate defined as $z\sqrt{U_s/\nu x}$, dimensionless
- ν kinematic viscosity of the electrolyte, cm²/sec
- ξ a stretched coordinate for the diffusion boundary layer defined as $Sc^{1/2}\eta$ or $z\sqrt{U_s/Dx}$, dimensionless
- Φ dimensionless concentration defined as $(C - C_\infty)/(C_0 - C_\infty)$
- $\phi_0, \phi_1, \phi_2, \phi_3$ the zeroth, the 1st, the 2nd, and the 3rd order solutions of Φ , as defined in Eq. [10], dimensionless differentiation with respect to η

REFERENCES

- W. E. Hoare and E. S. Hedges, "Tinplate," Edward Arnold, London (1945).
- A. Tvarusko, *This Journal*, **119**, 43 (1972).
- R. Persson, "Flat Glass Technology," Butterworths, London (1969).
- Bethlehem Steel Company, "Steel Plates," Bethlehem, Pa. (1935).
- J. P. Casey, "Pulp and Paper. Vol. II. Papermaking," Interscience Publishers, Inc., New York (1960).
- O. J. Sweeting, Editor, "The Science and Technology of Polymer Films," Wiley-Interscience, New York (1971).
- B. C. Sakiadis, *A.I.Ch.E. J.*, **7**, 26 (1961).
- B. C. Sakiadis, *ibid.*, **7**, 221 (1961).
- B. C. Sakiadis, *ibid.*, **7**, 467 (1961).
- E. A. Koldenhof, *ibid.*, **9**, 411 (1963).
- F. K. Tsou, E. M. Sparrow, and R. J. Goldstein, *Intern. J. Heat Mass Transfer*, **10**, 219 (1967).
- R. M. Griffith, *I&EC Fundamentals*, **3**, 245 (1964).
- L. E. Erickson, L. C. Cha, and L. T. Fan, *Chem. Eng. Progr. Symp. Ser.*, **62**, 157 (1966).
- C. A. Rhodes and H. Kaminer, Jr., *A.I.A.A. J.*, **10**, 331 (1972).
- J. F. Griffin and J. L. Throne, *A.I.Ch.E. J.*, **13**, 1210 (1967).
- V. G. Levich, "Physicochemical Hydrodynamics," Prentice-Hall, Englewood Cliffs, N. J. (1962).
- D-T. Chin, *This Journal*, **118**, 1434 (1971).
- D-T. Chin, *ibid.*, **119**, 1049 (1972).
- D-T. Chin, *ibid.*, **120**, 628 (1973).
- D-T. Chin and M. Litt, *ibid.*, **119**, 1338 (1972).
- M. Abramowitz and I. A. Stegun, Editors, "Handbook of Mathematical Functions," Dover, New York (1965).

Brief Communications



An Investigation of a Nickel-Tin Electroplating Solution by Laser-Raman Spectroscopy

B. E. Wynne,¹ J. M. Sykes,² and G. P. Rothwell

Cambridge University, Department of Metallurgy and Materials Science, Cambridge, England

Nickel-tin alloys can be electrodeposited from solutions containing nickel chloride, stannous chloride, and ammonium bifluoride (1). These solutions are unusual in that over a wide range of solution compositions and plating conditions, the deposit contains approximately equiatomic proportions of nickel and tin. Unlike cast alloys, which at equiatomic composition contain equal mole fractions of Ni₃Sn₂ and Ni₃Sn₄, the electrodeposited alloy is composed of a single intermetallic compound NiSn (2). Anomalous behavior is also observed in the deposition process: the alloy is deposited at low

overpotential and with very high current efficiency, whereas Ni and Sn deposited alone show quite different behavior.

Because the nickel and tin ions tend to deposit in a 1:1 ratio, it has been suggested (3) that they might be associated in the plating solution, possibly as an uncharged complex species NiSnF₄. Brook, Davies, and Price (4) have found very low transport numbers for nickel ions in this solution and suggest that this result supports such an idea.

Rau and Bailar (5) measured the refractive index of solutions containing Ni⁺⁺ and Sn⁺⁺, using the method of continuous variations, and found a maximum deviation from ideal behavior at a Ni⁺⁺:Sn⁺⁺ ratio of 1:1 provided that at least one fluoride ion per Ni⁺⁺-Sn⁺⁺ pair was present. They suggest that the Ni⁺⁺

¹ Present address: Lancaster University, Department of Sociology, Lancaster, England.

² Present address: Sunderland Polytechnic, Sunderland, County Durham, England.

Key words: alloy deposition, nickel-tin, solution analysis, mechanism, complex ions.

and Sn^{++} ions are associated by means of at least one fluoride bridge. However, measurements of absorption by the Ni^{++} ions at 2500 cm^{-1} in similar solutions, using a Pye-Unicam SP800 ultraviolet spectrophotometer failed to detect any such deviation or any shift in the absorption peak (6).

In solutions containing SnCl_2 and excess chloride, the complex ions SnCl_3^- (and possibly $\text{SnCl}_4^{=}$) are produced. These have been shown to be powerful ligands, which form stable complexes with organometallic compounds and with platinum, iridium, rhodium, and rhenium (7-9). The platinum-tin complexes have been isolated in the solid state and the crystals are believed to contain platinum-tin bonding. If, as might be expected, similar complexes were formed with Ni^{++} ions, this would radically alter the electrodeposition process and could well explain the abnormal stability of the 1:1 intermetallic compound.

Experimental

In laser-Raman spectroscopy the solutions are irradiated with a coherent monochromatic light beam which will excite vibrations or rotations in the bonds between the atoms or ions in solution. Energy is lost from the quanta of incident radiation and new quanta of lower frequency are found in the scattered radiation. The frequency shift is a characteristic of the vibrational mode which is absorbing energy.

For the present tests, solutions were prepared containing nickel, tin, or mixtures of both, together with 40 g/liter of ammonium bifluoride (Table I). pH was adjusted in all cases to 2.5 by the addition of small quantities of concentrated hydrochloric acid. The solutions were irradiated in an 8 cm capillary with an argon-ion laser (wavelength 5145 \AA), and Raman spectra plotted at least 6 times on a Cary Laser-Raman Spectrophotometer at a scan rate of $50\text{ cm}^{-1}/\text{min}$.

The frequencies of the characteristic peaks observed for solutions of Ni^{++} or Sn^{++} alone were found to shift in solutions containing mixtures of Ni and Sn (Table II). The peaks at 270 and 390 cm^{-1} due to variations in the bonds between Ni^{2+} and H_2O in the hexaquo-cation were shifted by about 25 cm^{-1} when tin was added (although this was masked with an excess of nickel present). Similarly the peaks due to $\text{Sn}^{++}\text{-F}^-$ bonding were shifted by $10\text{-}25\text{ cm}^{-1}$ by the addition of Ni^{2+} . However, no new peaks were observed.

Table I. Solutions for laser-Raman spectroscopy

Solution No.	Concentrations	
	SnCl_2 (M)	NiCl_2 (M)
1	0	2
2	2	0
3	0.5	2
4	0.5	0.5

Table II. Characteristic peaks observed by laser-Raman spectroscopy

Solution No.	Frequency (cm^{-1})					
	1	2	3	4	5	6
1	270	390	—	—	—	—
2	—	—	310	260	140	120
3	275	390	320	—	145	—
4	295	415	325	285	150	140

$\text{Ni}^{++}\text{-H}_2\text{O}$ bonding

$\text{Sn}^{++}\text{-F}^-$ bonding

Discussion

From the absence of new peaks characteristic of metal-metal bonding in the Raman spectra for Ni-Sn solutions, we infer that such bonding is absent in these solutions. The shifts in frequencies associated with metal-ligand bonding suggest that there is some interaction between the nickel and fluostannite ions, possibly by the type of fluoride bridging discussed above (5). Had strong metal-metal bonding been observed, this would have provided an attractive explanation for the formation of the equiatomic NiSn intermetallic compound; however, it seems improbable that the observed weak metal-ligand association would be an overriding factor in controlling the electrodeposition process.

Acknowledgments

We are grateful to Dr. M. J. Mays of the University Chemical Laboratory, Cambridge, for helpful discussion, and to the Department of Chemistry, Imperial College, London, for the use of their laser-Raman spectrophotometer. We are also glad to acknowledge financial support provided for B.E.W. and J.M.S. by the Science Research Council.

Manuscript received Nov. 6, 1974.

Any discussion of this paper will appear in a Discussion Section to be published in the December 1975 JOURNAL. All discussions for the December 1975 Discussion Section should be submitted by Aug. 1, 1975.

REFERENCES

1. A. E. Davies, *Trans. Inst. Metal Finishing*, **31**, 401 (1954).
2. P. K. Dutta and M. Clarke, *ibid.*, **46**, 20 (1968).
3. J. W. Cuthbertson, N. Parkinson, and H. P. Rooksby, *This Journal*, **100**, 107 (1953).
4. P. A. Brook, A. E. Davies, and J. W. Price, *J. Appl. Chem.*, **5**, 81 (1955).
5. R. L. Rau and J. C. Bailar, *This Journal*, **107**, 745 (1960).
6. J. M. Sykes, Unpublished work.
7. M. J. Mays and S. M. Pearson, *J. Chem. Soc. (A)*, **136** (1969).
8. J. F. Young, R. D. Gillard, and G. Wilkinson, *J. Chem. Soc.*, 5176 (1964).
9. R. D. Cramer, R. V. Lindsey, C. E. Prescott, and V. G. Stolberg, *J. Am. Chem. Soc.*, **87**, 658 (1965).

Electrochemical Current Balance with the Hydrogen-Palladium System

M. A. Fullenwider*

R.K.P. Industries, Incorporated, Allentown, Pennsylvania 18103

The hydrogen-palladium system has attracted much attention in the past because of its unique properties. Palladium diffuses larger quantities of hydrogen than any other metal and when hydrogen loaded has a rest potential 50 mV anodic to the reversible hydrogen potential. The system was the subject of the first application of the bi-electrode technique (1). The present paper describes novel, current balance experiments with the system allowing a rigorous check on some of the assumptions and conclusions of previous investigators. Previously it was assumed, for one thing, that the diffusion coefficient was independent of concentration. Nanis and Nambodhiri (2) recently reported the dependence of the diffusion coefficient upon concentration for the hydrogen-iron system where such behavior had previously been unsuspected. This paper describes a new technique for the detection of this type of behavior and its use with the hydrogen-palladium system. The method also allows a direct determination of surface coverage to be made. Until now, surface coverage with the hydrogen-palladium system was only accessible through anodic stripping, and it was never certain whether or how much the equilibrium between adsorbed and absorbed hydrogen was affected during the anodic stripping time interval.

Experimental Technique

The method employed was the bi-electrode technique, which has been described elsewhere (1). Previous to the present study, current balance had not been attained, that is, the cathodic steady-state current was always larger than the anodic current. Current balance was obtained here by simply modifying the gasket holding the palladium membrane so that there was a line seal about the aperture on the two sides of the membrane. All membranes were annealed at 900°C in an atmosphere of purified argon for 2 hr prior to experiment and were 7×10^{-3} cm in thickness. Potential control was effected with two de Ford type electronic potentiostats.

Analysis

The rationale of the method can be understood by referring to Fig. 1-3. In Fig. 1 and 2 typical anodic and cathodic traces are shown. Prior to $t = 0$ both sides of the membrane are at 300 mV anodic to the reversible hydrogen potential, and no hydrogen is present; at $t = 0$ the cathodic side of the membrane is brought to, in this case, a potential of 136 mV, introducing hydrogen at this side; at t_1 , some time after equilibrium has been established, the anodic side is raised to the same potential as the cathodic side, producing a uniform concentration profile; and at t_2 both sides are again taken to 300 mV, extracting all of the hydrogen.

Now assuming a steady-state profile at t_1 of the type shown in Fig. 3, in the event that material balance is attained, it is possible to define some quantities. Again referring to Fig. 1 and 2 we have

$$\int_0^{t_1} J_{Cd} dt - \int_0^{t_1} J_{Ad} dt = \Delta_1 = \Gamma + C_0 \delta' + C_0 \delta / 2 \quad [1]$$

and

$$\int_0^{t_2} J_{Cd} dt - \int_0^{t_2} J_{Ad} dt = \Delta_2 = 2\Gamma + C_0(\delta' + \delta) \quad [2]$$

* Electrochemical Society Active Member.

Key words: hydrogen diffusion, concentration dependent diffusion, rate limitation.

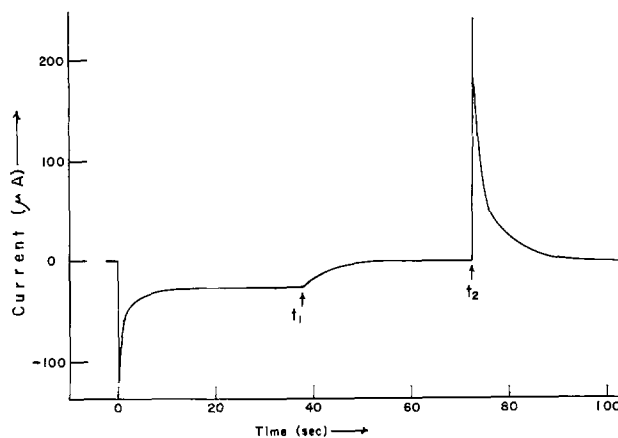


Fig. 1. Typical cathodic trace

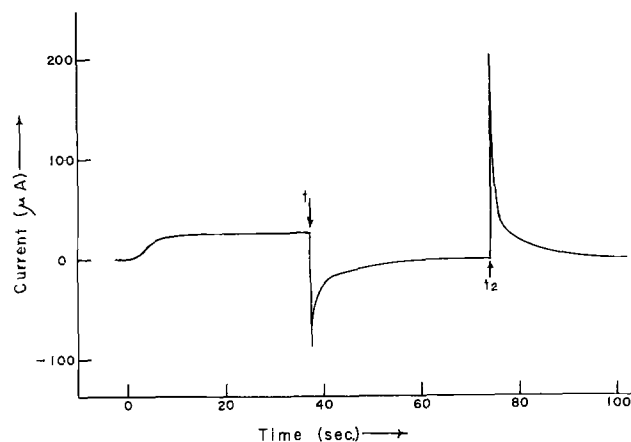


Fig. 2. Anodic trace corresponding to Fig. 1

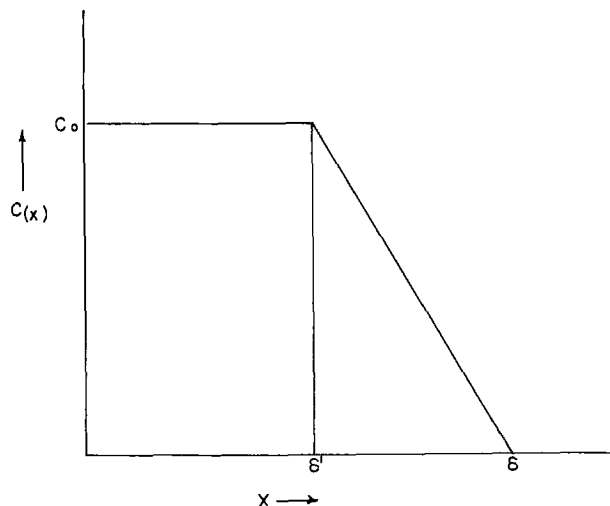


Fig. 3. Hypothetical concentration profile

or

$$\Delta_2 - 2\Delta_1 = -C_0\delta' \quad [3]$$

where δ' is some undefined distance into the membrane, δ is the thickness of the membrane, J_C is the cathodic current, J_A is the anodic current, Γ is the surface coverage, and C_0 is the maximum hydrogen concentration within the membrane. Also we have a quantity

$$\Delta_3 = \int_{t_2}^{\infty} J_C dt + \int_{t_2}^{\infty} J_A dt \quad [4]$$

which should be equal to Δ_2 , the total amount of hydrogen in the membrane at saturation.

If the quantity $\Delta_2 - 2\Delta_1$ is negative the profile is of the type shown in Fig. 3 (D increases with increasing concentration), if it is zero the profile is linear (D is independent of concentration), and if it is positive the profile is concave upward (D decreases with increasing concentration).

In the case that the diffusion coefficient is independent of concentration the following relation holds for $t < t_1$ (4)

$$\int_0^t J_C dt - \int_0^t J_A dt = \Gamma + \delta^2 J_A / 2! D + (\delta^4 / 4! D^2) dJ_A / dt + (\delta^6 / 6! D^3) d^2 J_A / dt^2 + \dots \quad [5]$$

or at t_1

$$\int_0^{t_1} J_C dt - \int_0^{t_1} J_A dt = \Gamma + \delta^2 J_A / 2D \quad [6]$$

where D is to be determined from the shape of the anodic transient by suitable mathematical analysis. There are two possibilities for the quantity J_t/J_∞ , the fractional attainment of steady-state anodic current. If it is the case that there is no rate limitation at the cathodic surface, that is, that there is a step function in concentration at this side at $t = 0$, the result is (3, 4)

$$J_t/J_\infty = \theta_0(0, Dt/\delta^2) \quad [7]$$

or

$$J_t/J_\infty = [2\delta/(\pi Dt)^{1/2}] \sum_{m=0}^{\infty} (-1)^m \exp[-(2m+1)^2 \delta^2 / 4Dt] \quad [8]$$

where θ_0 is one of the theta functions listed by Doetsch (5). If, on the other hand, there is rate limitation at this surface, then there will be a flux step function at $t = 0$, and we will have for the same quantity (4)

$$J_t/J_\infty = 1 - \int_0^1 \theta_1(u/2, Dt/\delta^2) du \quad [9]$$

or

$$J_t/J_\infty = 1 - (4/\pi) \sum_{m=0}^{\infty} [(-1)^m / (2m+1)] \exp[-\pi^2 (2m+1)^2 Dt / 4\delta^2] \quad [10]$$

The two expressions can best be compared according to the value of Dt/δ^2 corresponding to $J_t/J_\infty = 0.5$. We will call this quantity $Dt_{1/2}/\delta^2$, and we have from Eq. [8]

$$Dt_{1/2}/\delta^2 = 0.14 \quad [11]$$

and from Eq. [10]

$$Dt_{1/2}/\delta^2 = 0.38 \quad [12]$$

Results and Discussion

Figure 4 shows plots of Eq. [8] and [10], normalized about $t_{1/2}$, together with a typical experimental anodic transient. The experimental data can be seen to fit Eq. [10]. Equation [10] predicts a slower diffusion rate than Eq. [8], the equation normally used, and this implies the presence of a "rate limitation" at the cathodic surface of a slightly different nature but in the same

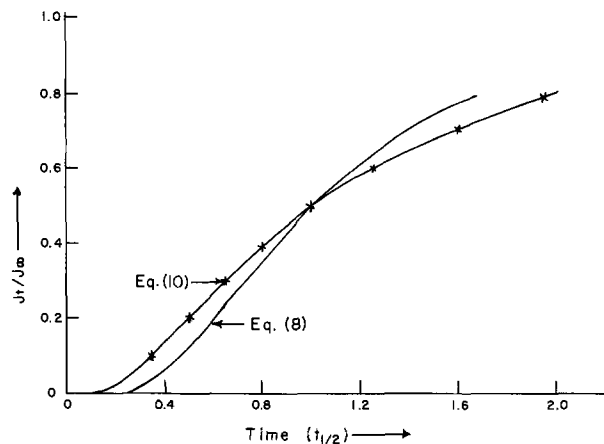


Fig. 4. Fractional attainment of steady-state current as a function of half rise time (J_t/J_∞ vs. time).

sense as Smits (7). On the other hand, previous investigators (1, 6) used a concentration step function model in the analysis of their data. This would result in an underestimation of the value of the diffusion coefficient.

In Table I are listed a typical set of values of the quantities Δ_1 , Δ_2 , and Δ_3 at various potentials. The difference $\Delta_2 - 2\Delta_1$ is positive for all but the most anodic of potentials where it is zero, i.e., the diffusion coefficient decreases with increasing concentration. Also Δ_2 agrees fairly well with Δ_3 . The decrease of the diffusion coefficient can easily be rationalized as being due to the blocking of diffusional pathways at higher concentrations. It is interesting that the results of Nanis and Namboodhiri (2) showed an increase of the diffusion coefficient of hydrogen in iron with concentration.

Also listed in Table I are values of Γ calculated from the relation, following from Eq. [1] and [6]

$$\Gamma = \Delta_1 - \delta^2 J_A / 2D \quad [13]$$

where the difference $\Delta_2 - 2\Delta_1$ is zero and the relations hold. It is not possible to obtain Γ by simple analysis at more cathodic potentials. Γ can be seen to be approaching a monolayer at about 210 mV. Previously (6), a much lower value for Γ was reported in this potential region, and thus it would appear that the value of the anodic stripping time used here was not long enough, i.e., a large part of the hydrogen on the surface at this potential was missed.

The diffusion coefficient in the linear region was calculated from Eq. [12] to be 4.5×10^{-7} cm² sec⁻¹, slightly larger than values previously reported which were in the range $(1.3-3.1) \times 10^{-7}$ cm² sec⁻¹. We can only conclude that all previous determinations of the diffusion coefficient were either made in the concentration dependent region, or involved an incorrect mathematical model.

Table I. Various integrals and surface coverages at different potentials

E, mV, RHE	Δ_1 , coulombs cm ⁻²	Δ_2 , coulombs cm ⁻²	Δ_3 , coulombs cm ⁻²	Γ , coulombs cm ⁻²
74	1.8×10^{-2}	6.8×10^{-3}	7.4×10^{-3}	
93	7.5×10^{-3}	2.9×10^{-2}	3.5×10^{-2}	
117	4.0×10^{-3}	1.1×10^{-2}	1.3×10^{-2}	
133	2.4×10^{-3}	7.6×10^{-3}	7.7×10^{-3}	
154	1.6×10^{-3}	3.5×10^{-3}	3.4×10^{-3}	
174	8.9×10^{-4}	1.9×10^{-3}	1.7×10^{-3}	
197	4.7×10^{-4}	9.7×10^{-4}	8.0×10^{-4}	
212	2.1×10^{-4}	4.2×10^{-4}	5.0×10^{-4}	1.3×10^{-4}
237	8.5×10^{-5}	1.9×10^{-4}	1.8×10^{-4}	6.0×10^{-5}

Acknowledgments

The author would like to thank Professor E. Schmidt for helpful discussions during the course of the work and Dr. H. Siegenthaler for help with the electronic arrangements.

Manuscript submitted July 26, 1974; revised manuscript received Dec. 16, 1974.

Any discussion of this paper will appear in a Discussion Section to be published in the December 1975 JOURNAL. All discussions for the December 1975 Discussion Section should be submitted by Aug. 1, 1975.

Publication costs of this article were partially assisted by R.K.P. Industries, Incorporated.

REFERENCES

1. M. A. V. Devanathan and Z. Stachursky, *Proc. Roy. Soc.*, **A270**, 90 (1962).
2. L. Nanis and T. K. G. Nambodhiri, *This Journal*, **119**, 691 (1972).
3. J. McBreen, L. Nanis, and W. Beck, *ibid.*, **113**, 1218 (1966).
4. E. Schmidt and H. Siegenthaler, *Helv. Chim. Acta*, **53**, 321 (1970).
5. G. Doetsch, "Tabllen zur Laplace-Transformation," Springer Verlag, Berlin (1947).
6. V. Breger and E. Gileadi, *Electrochim. Acta*, **16**, 177 (1971).
7. F. M. Smits, *Proc. I.R.E.*, **46**, 1049 (1958).

Erratum

In the paper "Germanium-Doped GaAs for P-Type Ohmic Contacts" by D. R. Ketchow which appeared on pp. 1237-1239 in the September 1974 JOURNAL, Vol. 121, No. 9, Ketchow has published data on the hole concentration p in degenerate Ge-doped LPE GaAs ($p < 5 \times 10^{19} \text{ cm}^{-3}$). D. L. Rode, R. L. Brown, and D. R. Ketchow have redetermined p for similar growth conditions (800°C, 6°C/hr) to study the apparent variation with orientation of the distribution coefficient between (100) and (111)B substrates. The larger values of hole concentration reported earlier (see sample No. B113 and B115 of Ketchow in the article mentioned above) for degenerate (111)B substrates compared to (100) substrates are in error due to inaccurate determination of the Hall coefficient. At the liquidus concentration 44.5 a/o Ge, Rode, Brown, and Ketchow obtain $p = 5.09 (\pm 0.27) \times 10^{19} \text{ cm}^{-3}$ for (111)B GaAs ($p =$

$8.2 \times 10^{19} \text{ cm}^{-3}$ reported previously by Ketchow in the above-mentioned article). Previous values for Hall mobility remain unaffected within experimental error (see Table I). The present values of hole concentration for (111)B substrates are essentially equal to those for (100) substrates within experimental error.

Table I. Composition and electrical data of semi-insulating substrate samples

Sample No.	Orientation	Ge concentration in solution (a/o)	Hole concentration at 25°C (cm^{-3})	Hall mobility at 25°C ($\text{cm}^2/\text{V sec}$)	Layer thickness (μm)
B114	(111)	44.5	5.33×10^{19}	16.8	1.00
B115	(111)	44.5	5.12×10^{19}	16.6	1.25
B117	(111)	44.5	4.82×10^{19}	16.9	1.43



Anodic Oxidation of GaAs as a Technique to Evaluate Electrical Carrier Concentration Profiles

H. Müller,^{*1} F. H. Eisen,² and J. W. Mayer*

California Institute of Technology, Pasadena, California 91109

ABSTRACT

An anodic oxidation process of p- and n-type GaAs, using a constant current source, is described. Homogeneous and reproducible oxide layers were obtained using N-methylacetamide adjusted to a pH value of 8.3 by NH₄OH. For chemically polished and etched surfaces, oxide growth was found to be 20.2 Å/V and the amount of GaAs consumed in the oxide was 13.4 Å/V. This technique has been successfully applied to differential sheet resistivity and Hall measurements on ion-implanted semi-insulating GaAs.

The anodic oxidation of GaAs offers several interesting applications with respect to planar device technology, e.g., masking, surface passivation, and removal of surface damage. Successive, controlled layer removal can be applied to the determination of electrical carrier concentration profiles in either thin epitaxial layers or in ion-implanted GaAs. Recently several publications have reported the possibility of native oxide growth on n- and p-type GaAs. Logan *et al.* (1) used a concentrated (30%) H₂O₂ electrolyte, which was adjusted to a pH value of 2 using H₃PO₄. A constant voltage source applied for a time period of 10 min produced oxide thicknesses proportional to the applied voltage. Composition analysis by Feldman *et al.* (2) combining He backscattering and He-induced x-rays showed the films to be deficient in As within 200 Å of the surface and with a Ga:As of approximately 1:1 for the rest of the oxide.

Dell'Oca *et al.* (3) reported on anodic oxidation in a dilute aqueous ammonium pentaborate solution using a constant current source. They found that oxide formation at constant voltage will in general lead to films of nonuniform thickness. Revesz and Zaininger (4) reported on anodization in acetic anhydride saturated with KNO₃ and observed severe pitting owing to simultaneous dissolution of the films. Simultaneous growth and dissolution of anodic oxide films were found by Harvey and Kruger (5) in their studies of the mechanism of layer formation. Dissolution of the anodic oxide film was shown to be rapid in strongly acidic solutions. However, to use anodic oxidation for reproducible layer removal, it is necessary to minimize oxide film dissolution during the anodization process. This is important, for example, in determining electrical profiles in diffused or implanted GaAs samples.

The application of a constant voltage source in an anodization process in general has some disadvantages. Since the cell voltage is used as a reference for the oxide thickness, voltage drops across the electrolyte and contact resistance have to be small compared to

the voltage drop across the oxide layer. This will be satisfied if the final current flowing through the layer is small enough not to cause significant voltage drops. The resistivity of the electrolyte can be determined independently, but contact resistance may depend on substrate doping and may not be reproducible from sample to sample for a particular alloy process. As a second parameter either the anodization time, in Ref. (1), 10 min, or the final current has to be used to define a cutoff condition. These difficulties do not arise with a constant current source, since the initial voltage is a measure both for voltage drops across the electrolyte and contact resistance and the difference between initial voltage and cell voltage can be directly used as a reference for the oxide thickness.

In this paper we describe a procedure, which allows the use of a constant current source. N-methylacetamide, which is a common electrolyte for silicon (6-8) was found to be applicable to GaAs. Details of the anodization process are given. The influence of various adjusted pH values of the solution on oxide growth or etching will be described. The main emphasis in developing the anodic oxidation technique was put on the application to successive layer removal on ion implanted GaAs. Sheet resistivity and Hall-effect measurements and layer removal were performed *in situ* and will be demonstrated for sulfur-implanted semi-insulating GaAs.

Experimental Techniques

The material used for evaluation of the anodic oxidation process was generally <111> oriented, n-type GaAs, silicon doped with a net donor concentration of 10¹⁸ cm⁻³. Usually the anodizations were carried out on a chemically polished A face. Other samples were etched in a solution of 3H₂SO₄:1H₂O₂:2H₂O at 0°C (etch rate ~ 1000 Å/sec) and about 1 μm was removed. Growth rates were compared on a few samples of p-type material of <100> orientation with a net acceptor concentration of 3 × 10¹⁷ cm⁻³.

The anodizations were carried out in a Teflon beaker, described in detail elsewhere (9). Its main features are a vinyl plate with a 5 mm in diameter opening which exposes part of the sample surface to the solution and acts as a seal between the sample and the Teflon

* Electrochemical Society Active Member.

¹ Permanent address: Lehrstuhl Fuer Integrierte Schaltungen Technische Universitaet, Munich, Germany.

² Science Center, Rockwell International, Thousand Oaks, California, 91360.

Key words: gallium arsenide, anodic oxidation, implanted carrier concentration profiles.

beaker. A platinum cathode was used, and anode contact was achieved by a gold plate underneath the sample. Generally the backside of the samples were only lapped and no effort was taken with respect to back-contact preparation. For large area anodizations, samples were held by a stainless steel clamp and dipped into the solution close to the clamp. In these cases, both sides of the samples could be anodized.

The solution was N-methylacetamide ($\text{CH}_3\text{CONHCH}_3$ —J. T. Baker Chemical Company) adjusted to various pH values as described below in detail. A constant current source with a maximum open-circuit voltage of 300V was applied. The voltage increase as a function of time was monitored on a recorder. Generally the cell voltage was used as a thickness reference and corrections were made by subtracting initial voltage drops.

Determination of the oxide thickness as a function of the forming voltage (*i.e.*, cell voltage minus initial voltage drop) was done by ellipsometry, interferometry, and by use of a Talystep. The amount of GaAs consumed in the oxide layer was determined by interferometry, Talystep measurements, and He backscattering. In the latter case a Te implant was used as a marker (10), and the shift of the peak of the profile towards higher energies was used for calibration of the amount of GaAs removed.

Successive anodization and layer removal were used to evaluate electrical carrier concentration profiles by sheet resistivity and Hall measurements. Semi-insulating, Cr-doped material was implanted with sulfur and tellurium, with implantation energies of 100 and 400 keV, respectively. The sample preparation for *in situ* stripping and electrical measurements was done by the following procedure. First, four Au-Ge-Ni contacts were evaporated (diameter ~ 1.5 mm) and alloyed at 450°C for 45 sec in forming gas. In a photoresist step (KMER) a van der Pauw type pattern was defined and mesa etched to 3.3 μm . A sample holder described elsewhere in detail (11) was used to both perform Hall and sheet resistivity measurements and anodization of the exposed area. The main feature of this sample holder is a spring-loaded Teflon insert which seals the mesa pattern along the dashed line shown in the schematic of Fig. 1 and protects the electrical contacts against the solution. A platinum wire was used as cathode, and connection of the four contacts served as the anode during oxide growth. After each anodization the oxide was removed in diluted H_3PO_4 (1:1 with H_2O), and the sample was rinsed in deionized H_2O and methanol and then dried in dry N_2 flow.

Results and Discussion

Oxide growth in N-methylacetamide.—Several aspects were considered when using N-methylacetamide

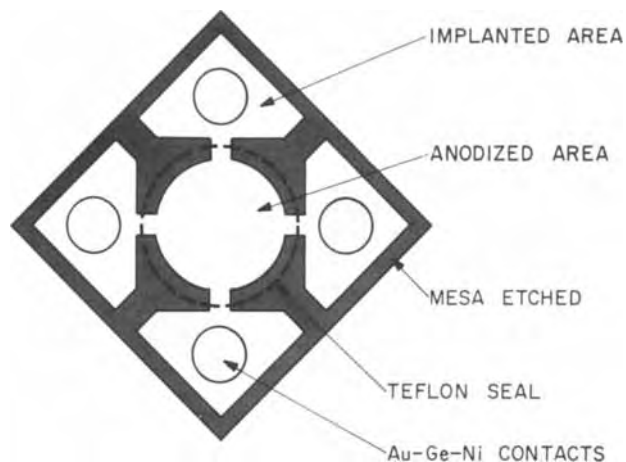


Fig. 1. Schematics of mesa-etched van der Pauw pattern employed for layer removal by anodic oxidation.

(NMA) as an electrolyte for anodization. A pure solution has a melting point of 27°C, and it is common practice (7) to add small amounts of H_2O (5-10%) to lower the melting point. The specific resistance is also known to be high (6). Therefore, in silicon anodization, oxygen-containing electrolytes such as KNO_3 are added to increase the conductivity. It was found that these compounds are not involved in the mechanism of oxide growth (6).

On the other hand, it is known (1) that in contrast to silicon, native oxides on GaAs are soluble in all common acids (like H_3PO_4 , HCl , H_2SO_4) and that the oxide growth in case of H_2O_2 is sensitive to the pH value of the solution; a similar behavior may be anticipated for N-methylacetamide. Therefore, in our application of N-methylacetamide to the anodization of GaAs, the pH value of the solution was considered as an additional parameter when trying to obtain a proper low resistivity solution.

In Fig. 2 the influence of H_2O on the bath resistance for a given geometry, and on the pH value are shown. For small amounts of H_2O (sufficient to prevent crystallization) the pH value is close to neutral and the resistance was found to be 23.8 kohm. Resistance values were measured using two platinum electrodes with ~ 20 mm² each separated by ~ 1.5 cm. With increasing content of H_2O the resistance can be lowered by almost a factor of two but simultaneously the pH value of the solution decreases to an acidic character. Anodizations carried out on n-type GaAs at a current density of 0.5 mA/cm² resulted in an oxide growth for a ratio of H_2O to NMA less than one but showed severe pitting. Worm-like craters about 50 μm deep were formed; areas between these showed homogeneous oxide growth. No relation to crystal orientation (preferential oxidation) or surface preparation of the samples could be found. The density of the defects increased with increasing amounts of H_2O . For H_2O to NMA ratios above one the anodization turned into an etching process.

The results of Fig. 2 indicate that two competing mechanisms are involved at pH values below 7. Oxide growth and thickness for a given reference voltage were found to be enhanced at increased current densities, but simultaneous dissolution, presumably due to the acidic character of the solution, could not be suppressed. No reproducible thickness *vs.* voltage relationship could be achieved.

Further experiments were performed at pH values above 7. Figure 3 shows the bath resistance as a function of pH value adjusted by NH_4OH .³ A decrease in resistance by a factor of 6 is observed when the pH is

³ Because of the hygroscopic nature of NMA, unknown initial amounts of H_2O can cause significant changes in resistance values. In some cases of as-purchased NMA up to 20% H_2O had to be added before adjustments with NH_4OH .

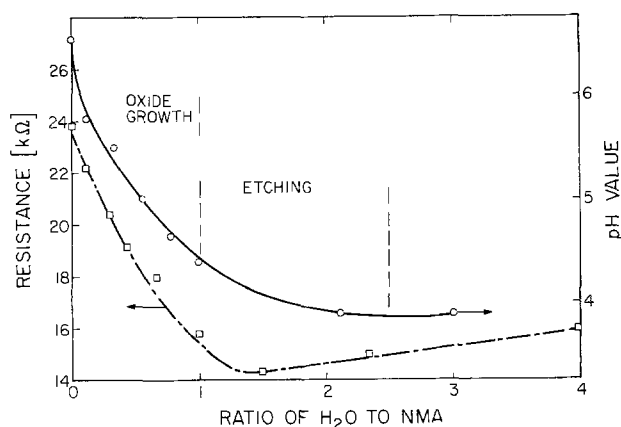


Fig. 2. Resistance and pH dependence of NMA solution on H_2O content.

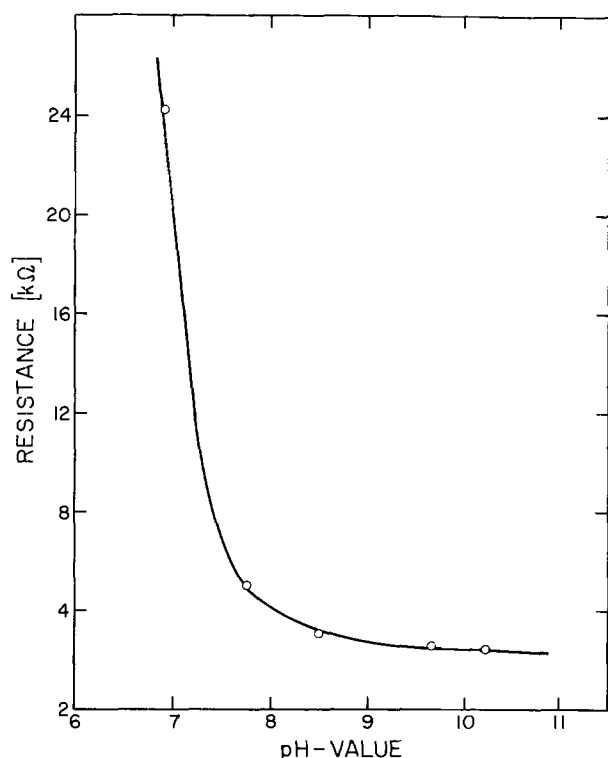


Fig. 3. NMA bath resistance vs. pH value adjusted by NH_4OH

adjusted to 8.3. At this value very homogeneous layers could be obtained and no further influence of oxide thickness on current density was found, which suggests that dissolution of the oxide was suppressed to a very small amount. At pH values above 10 a slight dependence of oxide thickness on current density was found due to the fact that the layers are soluble in NH_4OH .

Conditions for oxide growth.—For a pH value of 8.3 the current density was chosen to be 0.5 mA/cm^2 which results in a cell voltage increase of 9.5 V/min . A typical cell voltage vs. time plot is shown in Fig. 4. The initial voltage drop is 3.5 V and represents the total voltage drop across electrolyte, semiconductor bulk, and back contact. Generally, for the first anodization of a polished surface, a slightly higher voltage drop was observed than for following anodizations after layer removal. A light source was found not to be necessary for voltages up to 40 V . In order to reproducibly approach a certain voltage, the reference voltage was chosen to be larger than the desired voltage and as soon as the desired voltage was reached, the current source was switched off. This determined the applied current density, which should allow a reasonably slow approach to a desired voltage value. For voltages above 40 V , a slight nonlinearity in the voltage-time plot is observed, as can be seen in Fig. 4. The nature of this effect was not carefully investigated; however, it was found that using a light source and increasing the current density by a factor of 3, the deviation from a linear cell voltage vs. time relationship occurs at about 80 V . Since the main emphasis of this paper is to demonstrate a technique which allows successive removal of thin layers ($100\text{--}300 \text{ \AA}$) the voltage range above 40 V was not investigated in detail.

Oxide thickness and amount of GaAs consumed.—A series of oxides were prepared on chemically polished n-type surfaces, the cell voltage was used as a reference, and the voltages were chosen between 20 and 60 V . In all cases, an initial voltage drop of about 3 V was observed and subtracted from the cell voltage to give the forming voltage which defines the x-axis in Fig. 5. The solid line in Fig. 5 represents the average oxide thickness vs. forming voltage for different tech-

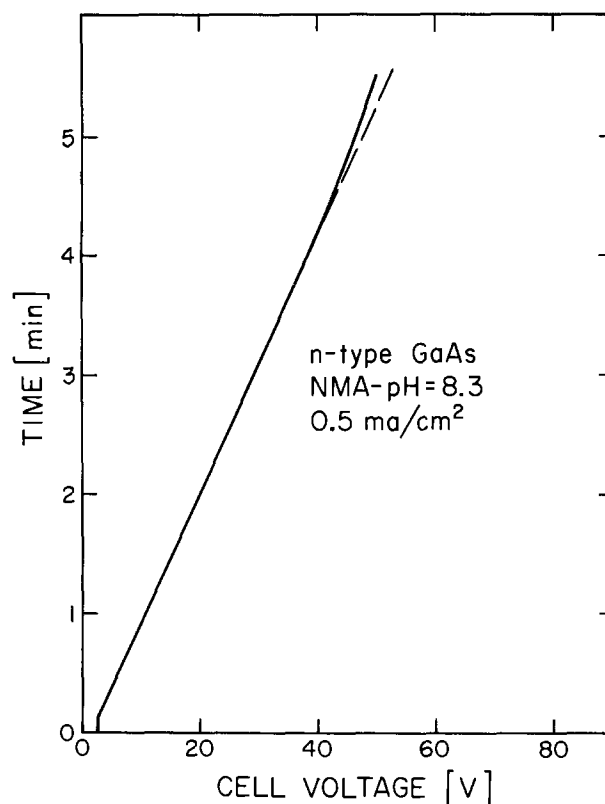


Fig. 4. Cell voltage vs. time plot for anodization in NMA adjusted to $\text{pH} = 8.3$.

niques. The open circles were obtained from ellipsometry measurements. The refractive index of the oxide layers was found to be $n = 1.815 \pm 0.005$ over the entire voltage range similar to what Dell'Oca *et al.* (3) found. From the slope an oxide growth rate of 20.2 \AA/V was obtained. For comparison, Talystep and interferometer measurements were performed on some of the samples. Photoresist processing was used to remove part of the oxide and to create a well-defined step. In the case of interferometer measurements, Al was evaporated on the samples to create a highly reflecting surface. The observed growth rate agrees very well with results by Logan *et al.* (1) obtained on abrasively polished surfaces. For comparison, p-type material with a carrier concentration of $3 \times 10^{17} \text{ cm}^{-3}$ was anodized. In a first approach the colors of the oxide layers appeared identical to the colors obtained on n-type material. Ellipsometry measurement confirmed an identical 20.2 \AA/V thickness to voltage relationship. The refractive index also turned out to be identical.

Identical growth rates were obtained for both chemically polished and etched surfaces on n- and p-type material. Generally for the first anodization a somewhat higher initial voltage was found compared to following anodizations. This difference may be indicative of changes in surface appearance. Since the nature of this difference is not known, it is difficult to deduce a change in growth rates. Using the forming voltage as a reference for the oxide thickness, no change in growth rate was found on successively anodized samples. No preferential oxidation either due to surface roughness or changes in surface homogeneity was found for as many as 27 successive anodizations ($\sim 0.7 \text{ \mu m}$ of GaAs removed).

The amount of GaAs consumed in the oxide layer was primarily measured by Talystep. For comparison interferometer measurements were taken. In order to develop a step in the material which corresponds to the amount of GaAs consumed in the oxide, a first oxide was grown; then part of this oxide was removed by photomasking, and a second oxide was grown on this

area. The oxide thickness was measured on both areas after first and second anodization by ellipsometry in order to ensure that no further growth took place on the original first oxide. Thus, the difference in oxide heights corresponds to the amount of GaAs consumed. From the dotted line in Fig. 5 the average amount of GaAs consumed in the oxide layer corresponds to 13.4 Å/V.

A slightly lower amount of material consumed was found by backscattering measurements as indicated in Fig. 5. A dose of $2 \times 10^{15} \text{ cm}^{-2}$ Te was implanted at 350°C into n-type GaAs at an energy of 400 keV. 2.5 MeV He⁺ backscattering was used to determine the implanted Te profile. Energy-to-depth conversion (12) of the backscattered spectrum allows the determination of the mean projected range of Te. After anodization and layer removal the Te peak is closer to the surface, and the shift corresponds to the amount of GaAs consumed in the oxide. It was found that the Te profile is not changed by the oxide growth, which is a basic assumption for electrical profile determination by successive layer removal.

Application of anodic oxidation to profile determination in ion-implanted GaAs.—To demonstrate the application of anodic oxidation a typical profile of sulfur implanted into semi-insulating GaAs is shown in Fig. 6. The energy of the implantation was 100 keV at 350°C target temperature and the dose was 10^{14} cm^{-2} . Reactively sputtered (13) Si₃N₄ was used as an encapsulation for annealing at 850°C, for 10 min in H₂ atmosphere. Anodization was carried out at 20V (which corresponds to 268Å removal of GaAs) and after each layer removal sheet resistivity and Hall measurements were performed. From these data the profile of electrical carriers was evaluated using equations described for example in Ref. (14). The electrical activity of the implant was found to be 13%. The arrow in Fig. 6 indicates the mean projected range according to LSS theory (15). A strong deviation from the predicted gaussian distribution is apparent. The circles and tri-

angles in Fig. 6 show results obtained on two different samples treated under identical conditions, but anodized at different voltages. There is significant scatter in the data close to the surface (linear plot), but in the tail region excellent reproducibility is observed. Hall mobility data are also included in Fig. 6. Detailed results on sulfur and Te implants with respect to electrical activity of the implanted species and carrier mobilities will be presented in Ref. (16).

From a series of profile measurements a lower limit of this technique with our experimental setup was found when sheet resistivity values approached 100 kohm/□. These sheet resistivity values correspond to carrier concentrations between 2×10^{16} and $8 \times 10^{16} \text{ cm}^{-3}$ depending on the mobility and the gradient of the profile. In order to obtain information on the continuation of the profiles towards lower concentration values, Schottky-barrier C-V techniques were employed.

Summary

An anodic oxidation technique for both p- and n-type GaAs (net carrier concentration 10^{17} - 10^{18} cm^{-3}) was developed which allows the use of a constant current source. The electrolyte was N-methylacetamide adjusted to a pH value of 8.3 by NH₄OH. The current density was 0.5 mA/cm² which resulted in a forming voltage increase of 9.5 V/min. Large areas could be homogeneously and reproducibly anodized. A linear dependence between forming voltage and anodization time was found up to 40V; using a light source and increased current density this linear dependence could be extended to 80V.

Measurements of oxide thicknesses and the amount of GaAs consumed in the oxide were done by ellipsometry, Talystep, and interferometry. An oxide growth rate of 20.2 Å/V was found and the amount of GaAs consumed in the oxide was 13.4 Å/V.

The application of this technique to evaluate electrical carrier concentrations in ion-implanted semi-insulating GaAs was demonstrated in case of a 100 keV sulfur implant successively anodized and analyzed by differential Hall effect and sheet resistivity measurements.

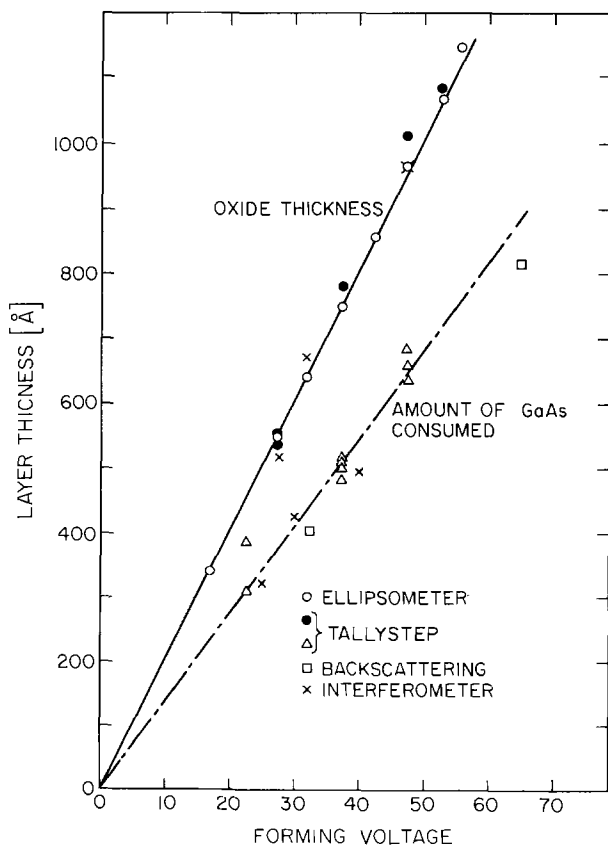


Fig. 5. Oxide thickness and amount of GaAs consumed vs. forming voltage.

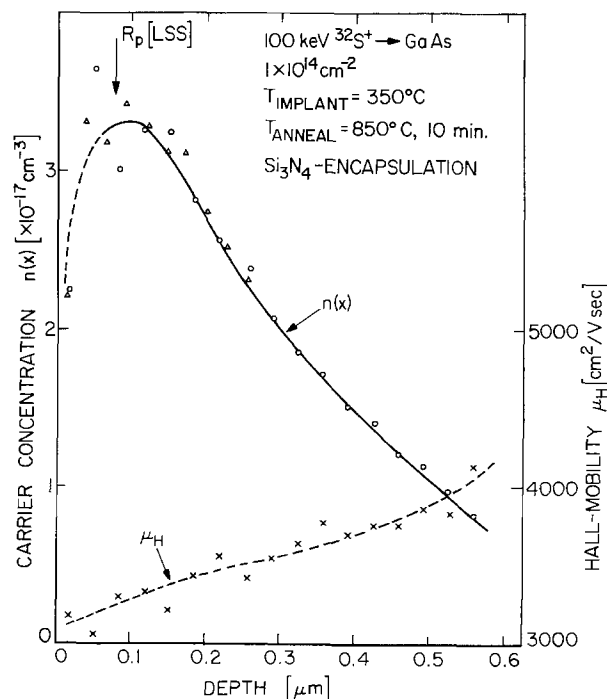


Fig. 6. Electrical carrier concentration profile for sulfur-implanted semi-insulating GaAs obtained by differential Hall and sheet resistivity measurements.

The anodization technique is presently used for a detailed study of sulfur and tellurium implanted profiles in semi-insulating and p-type GaAs with respect to implant and anneal conditions (16). Oxide layers will be investigated with respect to their application of MOS structures.

Acknowledgments

The authors wish to thank Tom Sigmon of Hewlett-Packard for providing Talystep measurements and B. Welch of the Rockwell International Science Center for performing the implantations.

This research was supported by the Defense Advanced Research Projects Agency, the Department of Defense, and was monitored by Air Force Cambridge Research Laboratories, under Contract No. F19628-74-C-0038.

Manuscript received Aug. 5, 1974.

Any discussion of this paper will appear in a Discussion Section to be published in the December 1975 JOURNAL. All discussions for the December 1975 Discussion Section should be submitted by Aug. 1, 1975.

Publication costs of this article were partially assisted by the California Institute of Technology.

REFERENCES

1. R. A. Logan, B. Schwartz, and W. J. Sundburg, *This Journal*, **120**, 1385 (1973).
2. L. C. Feldman, J. M. Poate, F. Ermanis, and B. Schwartz, *Thin Solid Films*, **19**, 81 (1973).
3. C. J. Dell'Oca, G. Yan, and L. Young, *This Journal*, **118**, 89 (1971).
4. A. G. Revesz and K. H. Zaininger, *J. Am. Ceram. Soc.*, **46**, 606 (1963).
5. W. W. Harvey and J. Kruger, *Electrochim. Acta*, **16**, 2017 (1971).
6. E. F. Duffek, C. Mylroie, and E. A. Benjamin, *This Journal*, **111**, 1042 (1964).
7. R. L. Pertritz, *Phys. Rev.*, **110**, 1254 (1958).
8. H. Ryssel, H. Müller, and K. Schmid, *Appl. Phys.*, **3**, 321 (1974).
9. N. G. E. Johansson, J. W. Mayer, and O. J. Marsh, *Solid State Electron.*, **13**, 317 (1970).
10. W. K. Chu, H. Kräutle, J. W. Mayer, H. Müller, M-A. Nicolet and K. N. Tu, To be published.
11. H. Ryssel, K. Schmid, and H. Müller, *J. Phys.*, **E**, **6**, 402 (1973).
12. J. F. Ziegler and W. K. Chu, *Thin Solid Films*, **19**, 281 (1973).
13. R. D. Pashley, H. Müller, J. W. Mayer, F. Eisen, and B. Welch, Paper 137 presented at Electrochemical Society Meeting, San Francisco, California, May 12-17, 1974.
14. J. W. Mayer, L. Eriksson, and J. A. Davies, "Ion Implantation in Semiconductors." Academic Press, New York (1970).
15. W. S. Johnson and J. F. Gibbons, "Projected Range Statistics in Semiconductors," Stanford University Bookstore, Stanford (1969).
16. H. Müller, J. Gyulai, J. W. Mayer, F. Eisen, and B. Welch, "Proc. of 1V Intl. Conference on Ion Implantation Osaka (1974)," To be published.

Use of a ZnS:Er,Cu Cathodoluminescent Phosphor with Spectral Filtering for Contrast Enhancement

E. Schlam, J. J. Pucilowski, and I. Reingold

United States Army Electronics Technology and Devices Laboratory,
United States Army Electronics Command, Fort Monmouth, New Jersey 07703

ABSTRACT

It is shown that the contrast of a narrow-line emitting cathodoluminescent ZnS:Er,Cu phosphor may be considerably improved through the use of a spectral filter whose bandpass is coincident with the phosphor emission spectrum. Such enhancement is due to the selective exclusion of ambient light not in the spectral region of the phosphor emission. The erbium-activated zinc sulfide phosphor reported here has a primary emission from the ${}^2H_{11/2} \rightarrow {}^4I_{15/2}$ transition. The contrast enhancement of the rare earth phosphor achieved through the utilization of this method is reported. It is compared with the contrast enhancement of P-2, a broadband emitting phosphor. It is shown that the efficiency requirement for the rare earth phosphor is considerably less than that of the broadband emitting phosphor, for the same degree of viewability.

The need for displays which are effective in high-ambient lighting is becoming more widespread. Simultaneous with this need is the reluctance to accept displays which must be heavily shielded from intense ambient light in order to be readable. This reluctance stems from the need for more mobile, versatile, and useful displays and the expectation that the present level of technology should be able to provide a solution to this problem. The most important information display, the cathode-ray tube (CRT), in its elementary form has severe problems with regard to viewability in high ambient because of the high degree of reflectivity of its phosphor surface. There are two general approaches which attempt to alleviate this problem. The first approach involves increasing the intensity of the phosphor emission in order to overcome the effect of the ambient light. To get an effective result requires

large increases in phosphor output and is accomplished by means of a direct view storage tube (DVST) or by a CRT incorporating a thick phosphor screen and high beam power density, such as a projection-type tube. However, these tubes suffer from systems oriented disadvantages such as a lack of selective erase in the former and a short operating life in the latter.

More elegant means to increase the viewability of CRT's in high ambient light involve the increase of contrast by reducing the amount of ambient light reflected into the viewer's eyes. This may be accomplished by incorporating a transparent phosphor screen, thereby reducing its reflectivity, or by the use of filtering. The former approach can be made particularly effective through the use of high efficiency transparent phosphors (1) and by the use of a black absorbing layer on the back of the phosphor screen (2). Unfortunately, at present, CRT's incorporating these features require special processing techniques

which are costly and limit their use. The filtering approaches are generally external to the CRT and therefore do not require special CRT manufacturing techniques. The simplest filtering approach utilizes a neutral density filter over the phosphor screen. This enhances contrast since the ambient light passes through the filter twice and is therefore attenuated more than the CRT emission which passes through the filter once. A more effective approach will utilize a spectral filter which takes advantage of the spectral emission of the phosphor. In this case, ideally, the filter has a band-pass which passes all of the phosphor emission and absorbs the ambient in the remaining portion of the visible spectrum (3). In essence such a filter has the advantages of a neutral density filter in doubly attenuating the ambient light, but completely passing the phosphor emission. Clearly such a technique is most effective when two conditions are present: (i) the phosphor emission must be as spectrally narrow as possible with the filter providing maximum transmission limited to the phosphor spectral range; (ii) the remaining portion of the ambient light must be effectively eliminated. This is a particular problem with an interference filter because of its high reflectivity. One way consideration (ii) may be effected is by the use of circular polarizers, and this technique was recently successfully applied to red and green light-emitting diodes (4). Consideration (i) is the subject of this paper which describes the application of spectral filtering for contrast enhancement of a rare earth activated cathodoluminescent phosphor.

Experimental

In this study, phosphors were synthesized by activation of a pure, presynthesized commercially available ZnS host material. Proper amounts of ErCl_3 and CuCl_2 are mixed with water and NH_4OH , respectively. The ErCl_3 solution is added to the ZnS host material to form a slurry, and the CuCl_2 solution is added to the slurry and agitated. This mixture is then oven-dried resulting in a fine powder which is ground with mortar and pestle. The mixture is placed in a graphite crucible which in turn is placed in a quartz tube. The crucible is plugged with quartz wool to prevent loss of sample by thermal agitation. H_2S is introduced to the sample through a quartz tube, and the gas is exhausted through an absorbent material. Firing temperature is carefully controlled as the sample is fired in a saturated atmosphere of H_2S . The entire assembly is rapidly removed from the oven in order that the wurtzite phase be preserved. The sample is then allowed to cool in the H_2S atmosphere. A detailed study and description of the phosphor synthesis has previously been reported (5).

In order to obtain its photoluminescent spectrum, a small amount of the phosphor is mixed with amyloacetate and placed on an aluminum slide suitable for introduction into a spectrophotofluorometer with corrected spectra attachment. The sample is illuminated by radiation of proper wavelength to afford peak photoluminescent output, and that output spectrum is recorded on an x-y recorder.

To obtain the cathodoluminescent data, a portion of the sample is deposited on a glass slide using standard settling techniques with suitable binders. This slide is affixed in a specially designed demountable cathode-ray tube which is capable of holding nine such samples. Cathodoluminescent output is measured at various anode voltages (5-30 kV) and beam currents (1-5 μA). Spot size is variable from 10 to over 100 mils but is usually adjusted to yield no greater than 3 W/cm^2 of electron beam energy impinging on the phosphor surface. This is due to the fact that the samples were not aluminumized and higher power densities would burn the phosphors. During the phosphor development stages all samples were screened using the photoluminescent equipment described. Samples which exhibited little or no rare earth emission under photoluminescent ex-

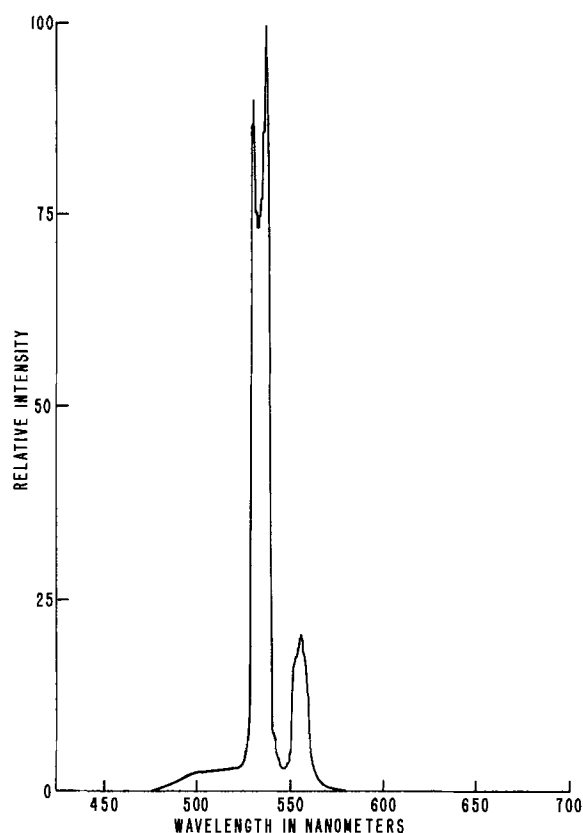


Fig. 1. Emission spectrum of ZnS:Er,Cu phosphor

citation did not exhibit this emission under cathodoluminescent excitation. Unfortunately however, high rare earth photoluminescent output does not guarantee such emission under cathodoluminescence.

The final developed phosphor exhibits both efficient photoluminescent and cathodoluminescent rare earth emission. These samples are placed in the demountable CRT. The anode voltage is raised from 10 to 30 kV in steps of 5 kV. Current is varied from 1 to 5 μA for each anode voltage level, and the corresponding cathodoluminescent data is taken. A predetermined spot size is held constant throughout. Spectral output was taken on a Jarrell-Ash $\frac{1}{2}$ -meter monochromator, while luminance levels were measured with a Photo Research Spectra Spot Brightness Meter. A sun gun was used to illuminate the samples to the required ambient light levels. A narrow band optical filter chosen for its spectral overlap with the rare earth emission of ZnS:Er,Cu was employed during this study.¹ Measurements were made with and without the filter so that the degree of contrast enhancement achieved could be determined.

Results

A typical cathodoluminescent spectrum of the ZnS:Er,Cu phosphor as seen in Fig. 1, is basically identical to that of the photoluminescent spectrum. The primary rare earth transition is that of the $^2\text{H}_{11/2}$ excited state to the $^4\text{I}_{15/2}$ ground state of the triply ionized erbium ion. It is noted that a slight broadband component peaking at a wavelength somewhat shorter than that of the rare earth line is present. The nature of this broadband has been previously discussed (5). It may be seen graphically in Fig. 2 where the amplitude ratio of the primary rare earth peak and the broadband peak are plotted as a function of electron beam energy. The ratio of the amplitudes is relatively insensitive to electron beam current variation as may be seen in Fig. 3. The over-all radiant efficiency of this

¹ Filter was obtained from Barr Associates, West Concord, Massachusetts.

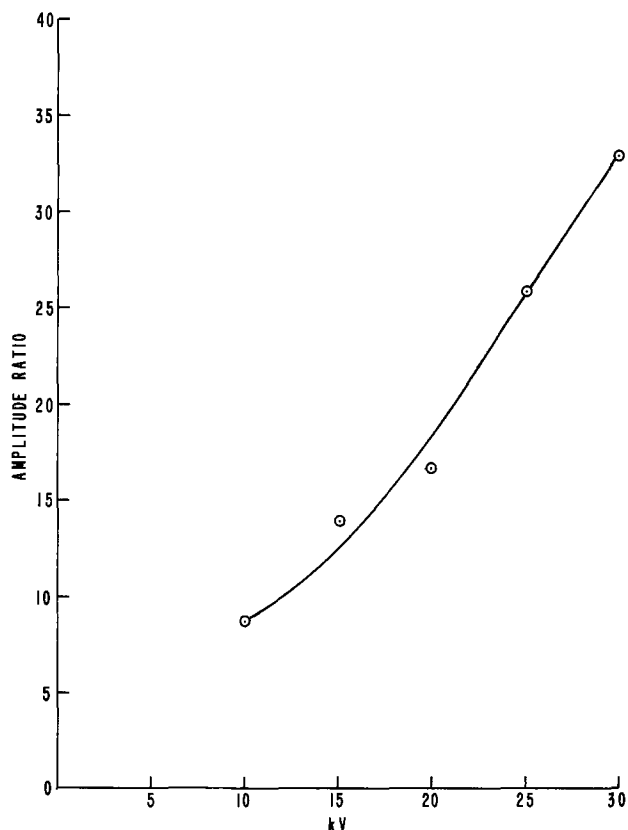


Fig. 2. Ratio of the amplitude of the primary narrow-line emission of ZnS:Er,Cu phosphor to the broadband emission of that phosphor as a function of electron beam energy.

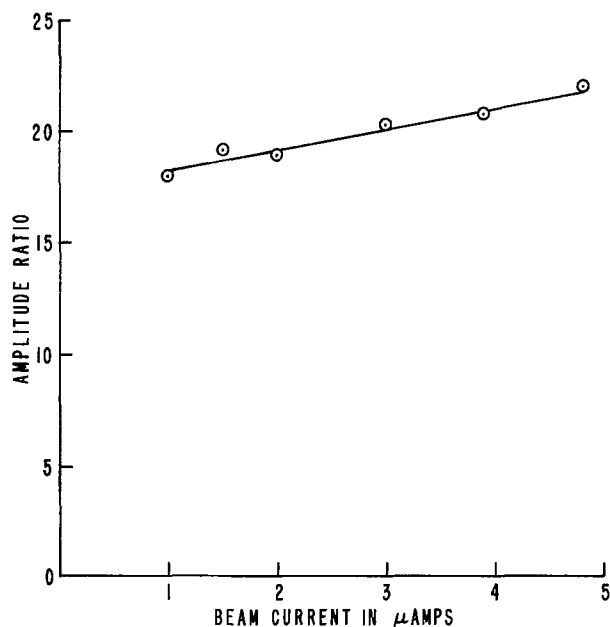


Fig. 3. Ratio of the amplitude of the primary narrow-line emission of ZnS:Er,Cu phosphor to the broadband emission of that phosphor as a function of beam current, at 20 kV.

phosphor is 0.25 times that of the Sylvania Electric Products Incorporated P-2 sample used in this experiment as a control. P-2 is a high efficiency broadband emitting phosphor of the ZnS family. The luminous efficiency of the rare earth phosphor is 0.32 times that of the P-2 phosphor since the rare earth emission has more of its energy concentrated closer to the peak of the spectral photopic response. Figure 4 is a

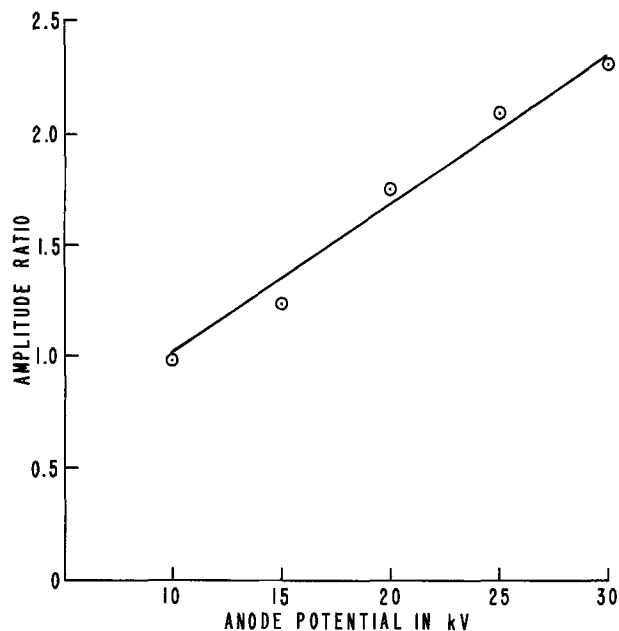


Fig. 4. Ratio of the amplitude of the primary narrow-line emission of ZnS:Er,Cu to the amplitude of the P-2 emission as a function of electron beam energy.

plot of the ratio of the peak amplitude of the rare earth emission to the peak amplitude of P-2 emission as a function of anode potential. As may be seen, the plot is linear and the ratio reaches a value of 2.3 at 30 kV. This value of anode potential was used for all the contrast determinations.

The transmission spectrum of the narrow band filter and the rare earth emission spectrum are shown in Fig. 5. The half-width of the filter is 8.6 nm. The corresponding spectra for P-2 and a Wratten 55 filter chosen for overlap with the P-2 emission spectrum, are shown in Fig. 6.

The contrast of the phosphor emission is defined as

$$C = \frac{L_1}{L_2} \quad [1]$$

and with the appropriate spectral filter, this contrast becomes

$$C_F = \frac{T_p L_1}{T_b L_2} \quad [2]$$

where L_1 is the luminance of the excited phosphor with no ambient and L_2 is the luminance of the unexcited phosphor due to reflection of the ambient. T_p is the per cent transmission of the filter to the phosphor emission and T_b is the per cent transmission of the filter to ambient light which passes through the filter and is reflected from the phosphor surface. When the filter is placed over the phosphor, contrast is increased since T_p is greater than T_b and the luminance seen by the viewer is decreased since T_p is less than unity. To properly analyze the effect of the contrast enhancement, the output luminance should be specified. Figure 7 depicts a family of curves representing the contrast C_F as a function of phosphor luminance L_1 according to Eq. [2], for an assumed ambient illuminance of 4500 ft-c which results in a reflected ambient luminance of 2500 ft-L for the 55% reflectivity of the faceplate-phosphor configuration in the demountable system used in this experiment. The parameter determining the different curves is an assumed set of different peak filter transmissions, T , for the filters used in this experiment. Loci of points corresponding to a net output luminance through the filter of 20 ft-L is shown in the figure. These loci represent the best filtering that can be performed for

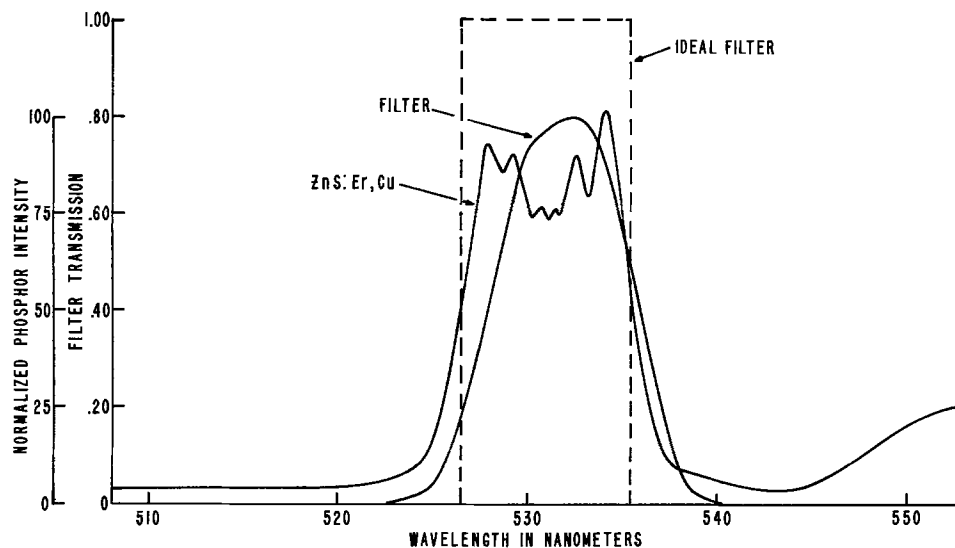


Fig. 5. The normalized emission spectrum of ZnS:Er,Cu and the Barr filter transmission spectrum.

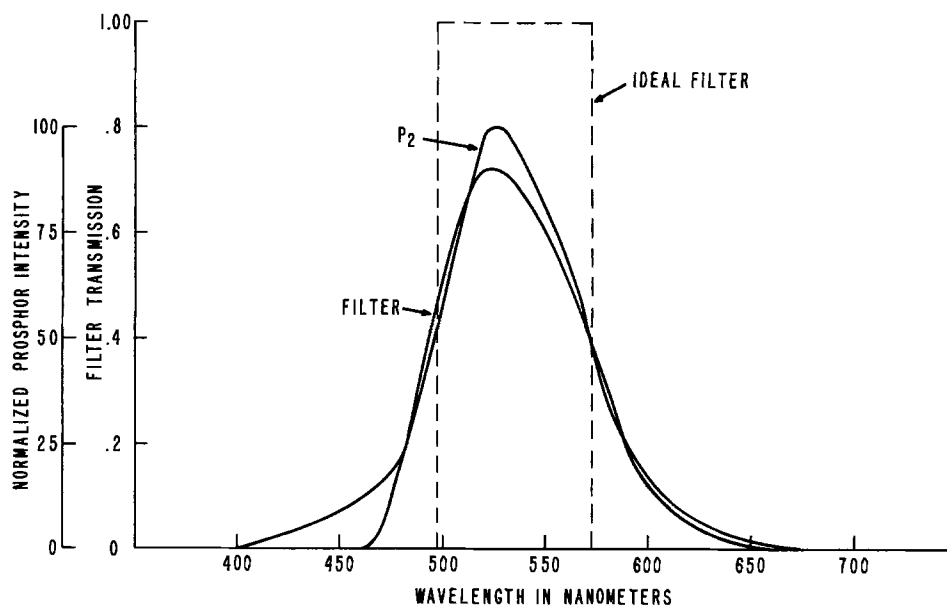


Fig. 6. Normalized emission spectrum of P-2 and transmission spectrum of the Wratten 55 filter.

the specified output luminance. In the absence of filters, the contrasts would vary from 0.04 at 100 ft-L phosphor output to 0.2 at 500 ft-L phosphor output, neglecting front surface reflections.

Discussion

In referring to Fig. 7 it is seen that at a phosphor luminance of approximately 400 ft-L, the contrast of the rare earth activated phosphor is enhanced from 0.16 to 12.6 with the use of a 0.105 peak transmission filter at a 4500 ft-c incident illumination. This is an enhancement of 78 times. The P-2 contrast is enhanced to 3.4 with a 0.072 peak transmission filter for an enhancement of 21 times. Although the contrast of the rare earth phosphor is enhanced 3.7 times more than that of the wide banded P-2, it should be realized that the rare earth phosphor is being driven with a higher input power to achieve the 400 ft-L starting luminance due to the fact that P-2 has approximately 3 times the luminous efficiency of this experimental ZnS:Er,Cu phosphor at its present stage of development. Therefore if one were to choose a desired contrast ratio, it could be achieved with 1/3 less power with the use of P-2 as compared to the present rare earth phosphor. Using this consideration as a quality determination, it is seen that with the filter used in this experiment an equivalent rare earth phosphor

with an efficiency only greater than 1/2 that of P-2 would be preferable to P-2.

The effect of a neutral density filter in enhancing the contrast of these phosphors may be compared to the spectral filter results by choosing an imaginary neutral density filter of a density such that the luminance of the phosphor through the filter would be identical to the luminance through the spectral filter. The contrast with a neutral density filter is

$$C = \frac{T_N L_1}{T_N^2 L_2} = \frac{L_1}{T_N L_2} \quad [3]$$

where T_N is the transmission of the filter. To achieve the same luminance through the neutral density filter as with the spectral filter used here, a transmission of 36% is required. Using this value of T_N for the 4500 ft-c ambient and 400 ft-L phosphor output gives an expected contrast of 0.44. It is seen therefore, that in the case at hand, the use of the 0.8 peak transmission spectral filter results in a 3.6 times contrast enhancement as compared to the use of a neutral density filter. The spectral filter itself results in a 10 times contrast enhancement over no filter at all under these conditions. It is clear from Fig. 5 that the particular spectral filter used does not have a perfect overlap with the emission spectrum of the rare earth phosphor, and if

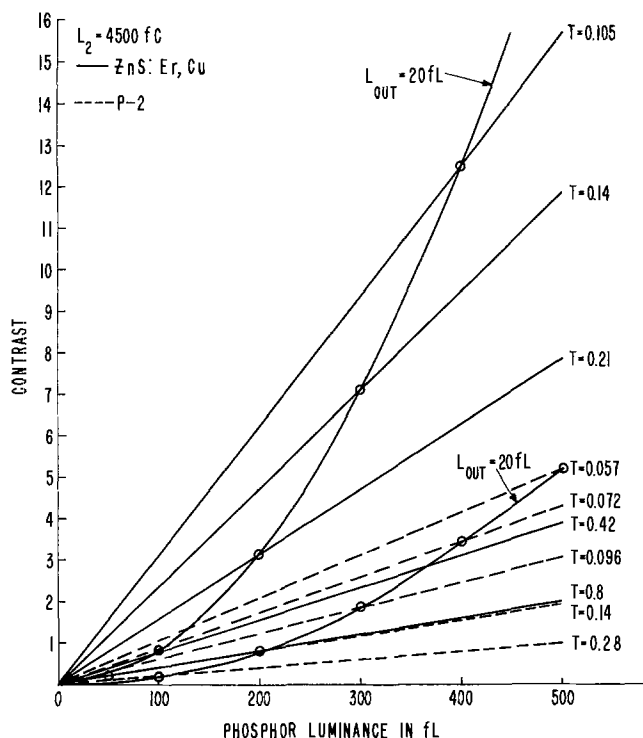


Fig. 7. Contrast of ZnS:Er,Cu and P-2 as a function of phosphor luminance. Peak transmission of the appropriate spectral filter T , is a parameter. The locus of points representing luminance through the filter of 20 ft-L is depicted. Ambient intensity is 4500 ft-c.

such an overlap were approached, the contrast enhancement would be further improved, and luminous efficiency less than $\frac{1}{2}$ that of P-2 would result in contrast ratios higher than those achievable with P-2.

Conclusions

It has been demonstrated that expected contrast enhancement from spectral filtering is achievable in actual phosphors. The particular experiments in this paper indicate that the greatest improvement in contrast for the combination of phosphor and filters studied occurs at voltages in the 20-30 kV region. It is a straightforward engineering procedure to design and utilize the necessary equipment for the operation of CRT's at these voltage levels.

In particular, the narrow-line emitting ZnS:Er,Cu phosphor developed here shows a 10 times contrast enhancement with the use of a commercially available spectral filter with a peak transmission of 0.8 which is essentially matched to the spectral output of this rare earth phosphor. Even in this case, the filter does not provide a perfect overlap to the phosphor emission and

therefore further improvement is achievable. Such contrast enhancement is superior to that achieved by neutral density filtering. One particular disadvantage of such narrow filtering is the need for an interference filter to achieve the desired spectral properties. Such filters are by nature highly reflecting in their non-bandpass region; however, these reflections can be eliminated, for example, through the use of circular polarizers.

Clearly, the narrower the emission band of the phosphor, the better the expected contrast enhancement. Further consideration in regard to phosphor spectral bandwidth, luminous efficiency and spectral region and in regard to filter spectral match, transmission, and absorption properties can undoubtedly result in greater contrast enhancement than reported here. It is recognized that the results of this study are largely empirical, and for a specific phosphor. However, the concept can provide a stimulus to others to carry on further work which will result in a better understanding of the phosphor physics involved; and in the synthesis of new phosphors, and the application of rare earth phosphors with narrow-line width and controlled characteristics. The technique discussed in this paper, in conjunction with proper attention to phosphor characteristics such as spectral bandwidth, luminous efficiency, and spectral region, can result in the design of CRT's with significantly enhanced luminance and contrast ratios, features that are most important where high ambient illumination levels are present.

Acknowledgment

The authors wish to express their appreciation to Lt. R. Schuman for his capable collection of data and calculation of overlap integrals.

Manuscript submitted Aug. 29, 1974; revised manuscript received Dec. 26, 1974.

Any discussion of this paper will appear in a Discussion Section to be published in the December 1975 JOURNAL. All discussions for the December 1975 Discussion Section should be submitted by Aug. 1, 1975.

The publication costs of this article were partially assisted by the Department of the Army.

REFERENCES

1. R. V. Alves, R. A. Buchanan, W. I. Dobrov, T. G. Maple, L. E. Sobon, and H. Bailey, "Luminescent Applications of Rare Earth Materials," Contract Report LMSC-D246757 January 1972 (ARPA Contract DAHC 15-71-C-0138).
2. E. Schlam, *Proc. IEEE*, **61**, 894 (1974).
3. W. D. Partlow, *Appl. Opt.*, **11**, 1491 (1972).
4. J. Pucilowski, R. Schuman, and J. Velasquez, *ibid.*, **13**, 2248 (1974).
5. E. Schlam and J. Pucilowski, "Proceedings of the 1970 IEEE Conference on Electron Device Techniques," pp. 143-147 (1970).

On the Efficiency of Yb³⁺-Er³⁺ Activated Up-Conversion Phosphors

A. Bril, J. L. Sommerdijk, and A. W. de Jager

Philips Research Laboratories, Eindhoven, Netherlands

ABSTRACT

Efficiencies of Yb³⁺-Er³⁺ activated up-conversion phosphors are determined by the efficiency of the excitation process and by that of the final emission process in the Er³⁺ ion. The former process is dependent on the infrared excitation density. We measured the efficiency of the emission process by excitation to selected Er³⁺ levels for various host lattices and as a function of Yb³⁺ and Er³⁺ concentrations. For one of the best up-conversion phosphors known at present, α -NaYF₄-0.20 Yb-0.03 Er, the efficiency of the green emission, is about 6%.

The light output of infrared-to-visible up-conversion phosphors activated with trivalent rare earth ions was very much increased as a consequence of the observation of Auzeil (1) and of Ovsyankin and Feofilov (2) that coactivation with a large amount of Yb³⁺ was very effective due to its relatively strong absorption of the infrared radiation and its efficient transfer of the absorbed energy to the other rare earth ions like Er³⁺, Tm³⁺, and Ho³⁺ in various host lattices. Hewes and Sarver (3) found that LaF₃-Yb-Er was a good phosphor of this type, giving green emission with infrared excitation. Other good Yb-Er activated fluorides subsequently found were YF₃ (4), BaYF₅ (5), and α -NaYF₄ (6).

Nevertheless rather low values were obtained for the infrared-to-green conversion efficiency even for the brightest phosphors mentioned above. This efficiency is dependent on the excitation density of the infrared radiation. Since two infrared quanta are involved in the excitation, the light output increases as the square of the excitation density. For about 1 mW/cm² absorbed exciting radiation at a wavelength $\lambda = 0.97 \mu\text{m}$ a quantum efficiency between 10⁻⁴ and 10⁻³ is found for the best phosphors [see, e.g., Ref. (7) and below].

In the mechanism of the infrared-to-visible conversion we can distinguish between an excitation process in which infrared energy absorbed by the Yb³⁺ ions excites the Er³⁺ ions to the visible-emitting levels, and an emission process in which the excited Er³⁺ ions luminesce. The latter is independent of the excitation density.

To understand the infrared-to-visible conversion it is important to know how efficient this emission process is and whether it limits the total efficiency of the infrared-to-visible conversion. Up to now the efficiency of the luminescence process has not been determined in a direct way. Part of the energy level scheme of Er³⁺ is given in Fig. 1. In the following we describe experiments designed to determine the efficiencies of both Er³⁺ and Yb³⁺-Er³⁺ activated phosphors when excited in the characteristic ⁴F_{5/2}, ⁴F_{3/2} levels which are located just above the ⁴S_{3/2} level from which the green emission takes place. The experiments were carried out for various host lattices, both fluorides and oxides.

Experimental

The method of measurement used for determining the efficiency of the Er³⁺ luminescence with excitation in the characteristic ⁴F_{5/2}, ⁴F_{3/2} levels of the Er³⁺ ion is similar to that described earlier by Bril, Blasse, and Bertens (8) for the Eu³⁺ luminescence. A schematic diagram of the setup is given in Fig. 2. The phosphor was irradiated monochromatically through a grating monochromator. The instrument used is a modified Perkin-Elmer Model 13 spectrophotometer, equipped with a Bausch and Lomb grating with 600 grooves/mm blazed at 500 nm. The Nernst source with mirror was

replaced by an exchangeable tungsten-halogen and a deuterium radiation source, respectively, in combination with a quartz lens.

Two measurements were carried out for the selected Er³⁺ absorption region: (i) The excitation spectrum of the green Er³⁺ emission was measured, i.e., the luminescent radiation collected by a photomultiplier (EMI 9558QA with S20 photocathode) was determined

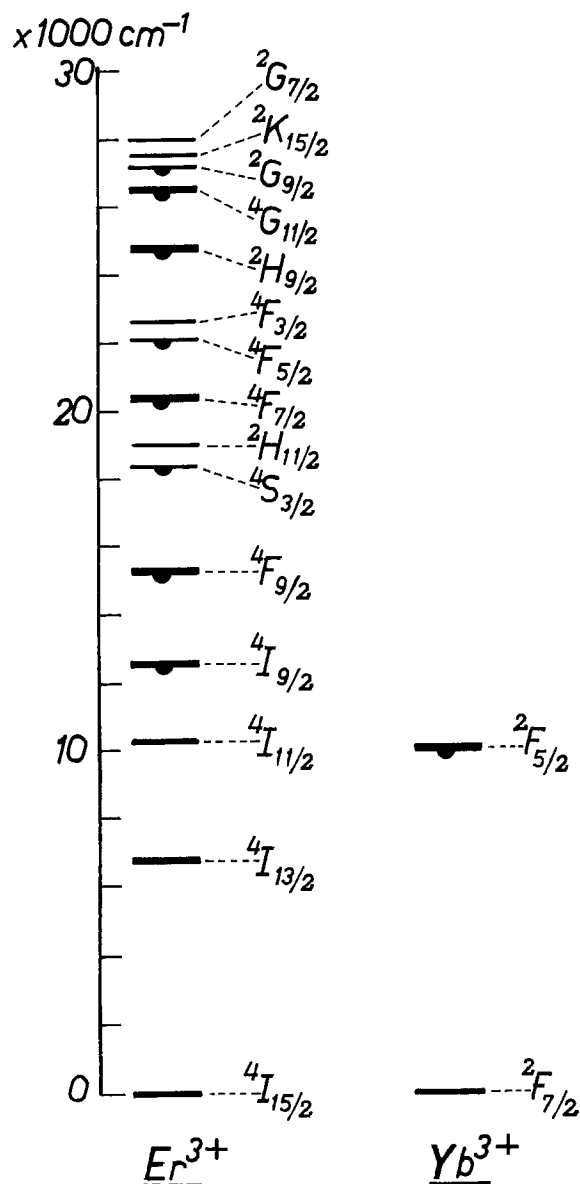


Fig. 1. Part of the energy level diagrams of Er³⁺ and Yb³⁺

Key words: luminescence, quantum efficiency, infrared phosphors, NaYF₄-Yb-Er.

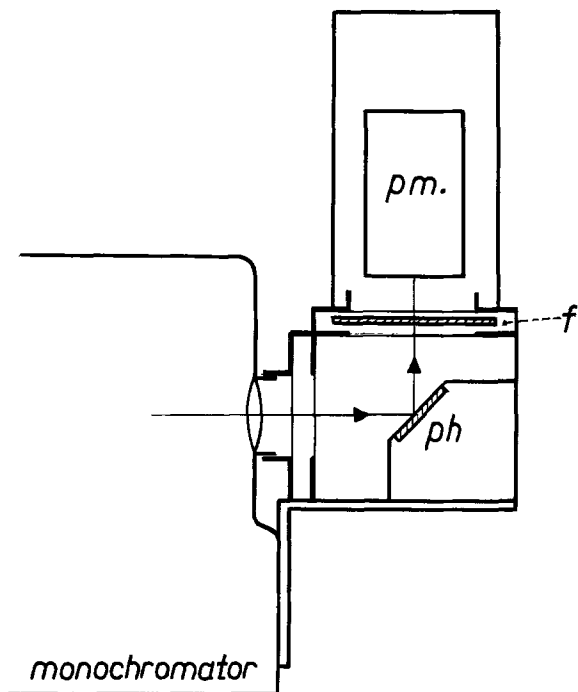


Fig. 2. Schematic diagram of the experimental setup: ph = phosphor sample, f = filter combination, pm = photomultiplier.

as a function of wavelength. In front of the photomultiplier a filter combination Schott BG 18 (2 mm) and GG 14 (2 mm) was used to pass only the luminescence. (ii) The diffuse reflection spectrum was measured. The only difference from the previous measurement was that the filter combination was replaced by a BG12 (2 mm), transmitting only the exciting radiation ($\lambda \approx 450$ nm). As has been discussed in Ref. (8), the quantum efficiency can easily be calculated from the ratio of the peaks found in the two measurements. Examples of the measurements are given in Fig. 3 for $\text{LaNbO}_4\text{-3\% Er}$ and in Fig. 4 for $\alpha\text{-NaYF}_4\text{-3\% Er}$. The calculation of the efficiencies from these two measurements is summarized in the following. The radiant efficiency is the ratio of the emitted power E to the absorbed exciting power A . The latter is determined by the area under the absorption curve of a certain peak with correction for the transmission τ_A of the filter used and for the photomultiplier response $G(\lambda_A)$ in the absorption region. The emitted power E is determined by the corresponding area under the excitation curve with correction for the transmission τ_E of the filter used in this case and the response $G(\lambda_E)$ in the emission region.

For single narrow peaks we can take the ratio of the ordinate maxima in the absorption and excitation spectra U_A and U_E , respectively, instead of the area. We find then for the emitted power

$$E = U_E \frac{\int_{em} p(\lambda) d\lambda}{\int_{em} p(\lambda) G(\lambda_E) \tau_E(\lambda) d\lambda}$$

where $p(\lambda) d\lambda$ is the relative emitted power in a region $d\lambda$ (integration extended over the total spectral region of the emission). The absorbed power is given by

$$A = \frac{U_A}{G(\lambda_A) \tau_A}$$

Then the radiant efficiency η is

$$\eta = \frac{E}{A} = \frac{U_E \tau_A G(\lambda_A) \int_{em} p(\lambda) d\lambda}{U_A \int_{em} p(\lambda_E) G(\lambda) \tau_E(\lambda) d\lambda}$$

The quantum efficiency q is derived from the radiant efficiency by

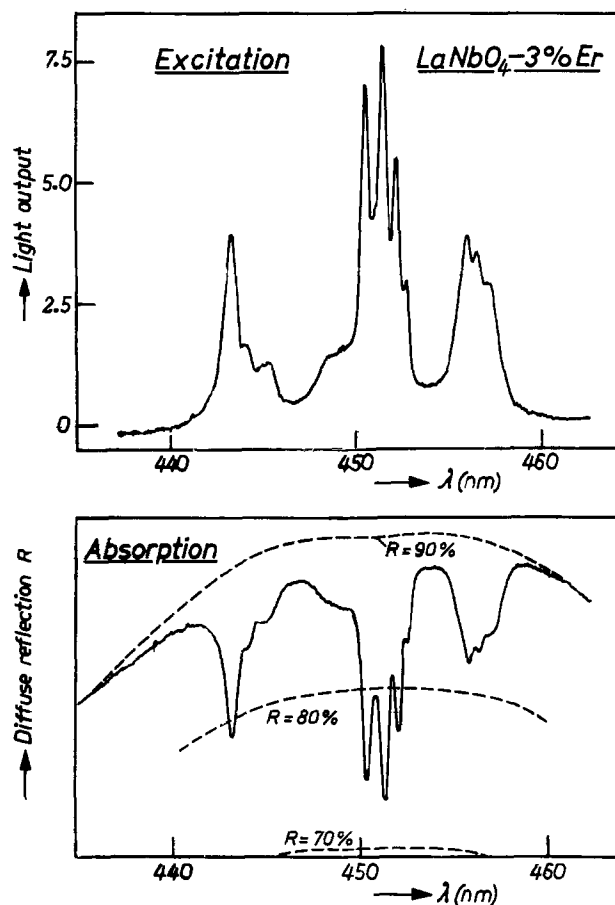


Fig. 3. The excitation spectrum of the green Er^{3+} emission and the diffuse reflection spectrum of $\text{LaNbO}_4\text{-3\% Er}$ in the $\lambda \approx 450$ nm region. The ordinate scale of the excitation curve is magnified $25\times$ with respect to that of the diffuse reflection curve. The dashed lines are lines of constant reflection.

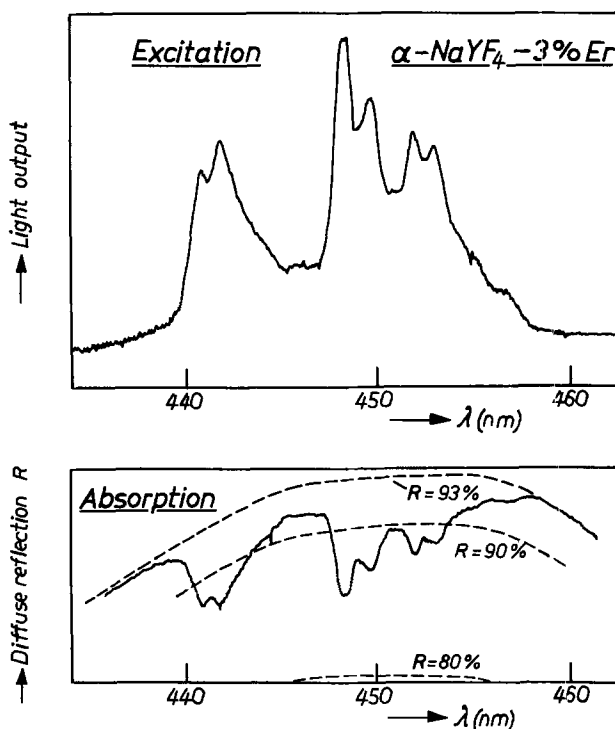


Fig. 4. Similar curves as in Fig. 3 for $\alpha\text{-NaYF}_4\text{-3\% Er}$. The ordinate scale of the excitation curve is magnified $25\times$ with respect to that of the diffuse reflection curve. For the dashed lines see Fig. 3.

$$q = \eta \frac{\int_{em} \lambda p(\lambda) d\lambda}{\lambda_A \int_{em} p(\lambda) d\lambda}$$

The error in this type of measurement will be of the order of 10-25% depending on the value of the absorption. This large error is caused by the low value of the absorption in the Er^{3+} -ion.

For the infrared-to-visible up-conversion process the radiant efficiency of the green luminescence of $\alpha\text{-NaYF}_4\text{-Yb-Er}$ was determined with excitation in the infrared region near $\lambda = 0.97 \mu\text{m}$. This was done in the following way: The phosphor was irradiated via a monochromator at $\lambda = 0.97 \mu\text{m}$ with a bandwidth of $\Delta\lambda = 5 \text{ nm}$. As a detector a Philips photomultiplier 150 CVP (Cs-O-Ag photocathode) was used, the response of which was determined in amperes/watt for both the green and the infrared regions with the aid of a photocell (150 CV). This photocell had been calibrated by the National Physical Laboratory in Teddington (Great Britain). The green luminescence was measured with a 4 mm Schott BG18 filter in front of the photomultiplier, and the exciting infrared power was measured without filter via barium sulfate under exactly the same conditions.

The ratio of the two values gives the radiant efficiency after correction for the response of the photomultiplier and the transmission of the filter. The irradiation density of the exciting infrared radiation was determined directly at the exit slit of the monochromator with the aid of the calibrated photocell.

All optical measurements were performed at room temperature.

The samples were prepared as described previously (9, 10). Their light output was not optimized except for $\alpha\text{-NaYF}_4\text{-Yb-Er}$.

Results and Discussion

We start with the efficiency of an up-conversion phosphor when excited with infrared radiation. It was measured for $\alpha\text{-NaYF}_4\text{-Yb-Er}$, which is known to be the best system for up-conversion at the moment (6). For excitation at $\lambda = 0.97 \mu\text{m}$ with a bandwidth of 5 nm in the maximum of the excitation peak the radiant efficiency was found to be 3×10^{-4} for $\approx 1 \text{ mW/cm}^2$ absorbed irradiation density of the infrared. This figure is of the same order of magnitude as Auzel and Pecile found for some phosphors (7).

Now we direct our attention to what can be called the emission process within the Er^{3+} ion. The quantum efficiency q of the green luminescence of $\alpha\text{-NaYF}_4\text{-Er}$ was measured as a function of the Er-concentration C_{Er} for excitation in the ${}^4\text{F}_{5/2,3/2}$ levels ($\lambda_{\text{exc}} \approx 450 \text{ nm}$). The results are given in Fig. 5. We see that very strong concentration quenching is present, which is due

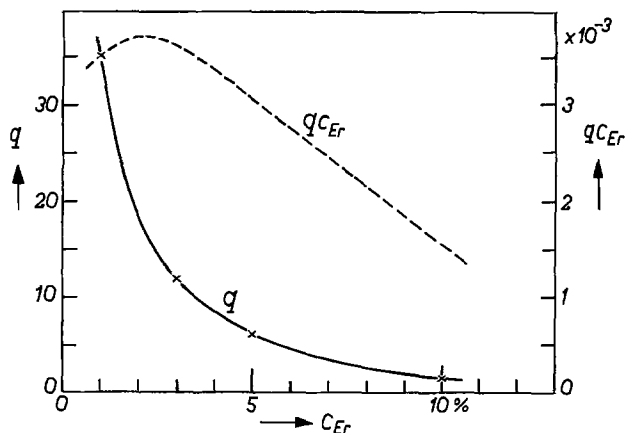


Fig. 5. Curve 1, quantum efficiency q of the green emission of $\alpha\text{-NaYF}_4\text{-Er}$ as a function of the Er concentration C_{Er} . Curve 2, qC_{Er} as a function of C_{Er} .

to interaction between neighboring Er^{3+} ions. We see also that for low Er concentrations a reasonably high quantum efficiency ($q = 35\%$) is found. When both Yb^{3+} and Er^{3+} are present in the lattice, as they are in the up-conversion phosphors normally used, the infrared excitation energy is transferred from the Yb^{3+} to the Er^{3+} ions. The number of excited Er^{3+} ions is proportional to C_{Er} . Therefore the light output from infrared excitation of the $\text{Yb}^{3+}\text{-Er}^{3+}$ activated phosphors is proportional to qC_{Er} . In Fig. 5 the dependence of qC_{Er} on C_{Er} is also given. We see that the optimum light output is reached at $C_{\text{Er}} \approx 1\text{-}3\%$. This concentration is in good agreement with the Er concentration used in practice in order to obtain the highest output of the green luminescence (6).

We found that the quantum efficiency of $\alpha\text{-NaYF}_4\text{-}3\% \text{ Er}$ is 12% for excitation in the ${}^4\text{F}_{5/2}$ level. When Yb^{3+} is added as coactivator, the efficiency decreases. For $\alpha\text{-NaYF}_4\text{-}20\% \text{ Yb-}3\% \text{ Er}$ the efficiency is only 6%. This decrease is due to interaction between neighboring Er^{3+} and Yb^{3+} ions, resulting in an increase of nonradiative transitions from the ${}^4\text{S}_{3/2}$ level (11). The addition of Yb is nevertheless necessary for the infrared-to-visible conversion in order to obtain sufficient absorption of infrared radiation, as has already been mentioned in the introduction. The oscillator strength of the transition involved in Yb^{3+} is about ten times stronger than that of Er^{3+} . Moreover up about 20% Yb can be built into the lattice before the $\text{Er}^{3+}\text{-Yb}^{3+}$ interaction limits further increase of the light output (6). In fact $\alpha\text{-NaYF}_4\text{-}20\% \text{ Yb-}3\% \text{ Er}$ is one of the best systems for up-conversion known at the moment (6, 9).

Concentration quenching of the Er^{3+} emission is also observed in YF_3 , the efficiencies being comparable to those for $\alpha\text{-NaYF}_4$. The intensity of the green emission upon infrared excitation of $\text{YF}_3\text{-Yb,Er}$ is also relatively high (4), although not as high as for $\alpha\text{-NaYF}_4\text{-Yb,Er}$ (6, 9).

The quantum efficiency of $\beta\text{-NaYF}_4\text{-Er}$ is comparable to that of $\alpha\text{-NaYF}_4\text{-Er}$ and $\text{YF}_3\text{-Er}$. On the other hand, the green light output of $\beta\text{-NaYF}_4\text{-Yb-Er}$ as an up-conversion phosphor is relatively low (9). This is to some extent also reflected in the present measurement on the $\text{Yb}^{3+}\text{-Er}^{3+}$ activated sample.

For the oxidic lattices LaGaO_3 and LaNbO_4 quenching of the green emission is also found with increasing Er concentration and/or at addition of Yb. The quantum efficiencies of these systems are quite comparable to those for $\alpha\text{-NaYF}_4$ and YF_3 . However, at infrared excitation of the Yb-Er doped compounds the green light output is much weaker in oxides than in these fluorides by a factor of at least ten (10). This loss in efficiency is a consequence of the difference in properties of the O^{2-} and the F^- ion, the former being much less stable than the latter. Therefore part of the charge of the O^{2-} ions is more readily transferred to neighboring ions. Interaction between the activator and the host lattice is therefore much stronger in oxides than in fluorides, introducing a high probability of radiationless transitions from the infrared-emitting levels and thus a loss in light output (10).

Oxides are therefore generally less suitable as up-conversion phosphors. This is contrary to the case of phosphors used for ultraviolet excitation or cathode-ray excitation (12). In the latter applications strong interaction with the lattice is favorable for the excitation of the activator ions.

The green Er^{3+} emission of the $\text{NaYO}_2\text{-Er}$ phosphor shows a low quantum efficiency. The $\text{Yb}^{3+}\text{-Er}^{3+}$ activated lattice, when excited with infrared radiation, shows a green emission which is about a thousand times weaker than that of $\alpha\text{-NaYF}_4\text{-Yb-Er}$ (10). Part of the weakening can be ascribed to losses from the infrared-emitting levels, as is the case with the other oxides. Another part, however, must be ascribed to the lower quantum efficiency of the green emission in the

Table I. Quantum efficiencies of the green Er^{3+} luminescence for $\lambda_{\text{exc}} \approx 450 \text{ nm}$

Phosphor	q (%)
$\alpha\text{-NaYF}_4$ — 1% Er	35
— 3% Er	12
— 5% Er	6
— 10% Er	2
— 20% Yb-3% Er	6
$\beta\text{-NaYF}_4$ — 3% Er	9
— 20% Yb-3% Er	≈ 1
YF_3 — 1% Er	23
— 3% Er	6
LaGaO_3 — 1% Er	43
— 20% Yb-1% Er	4
— 3% Er	18
LaNbO_4 — 3% Er	6
— 20% Yb-3% Er	2
NaYO_2 — 3% Er	<0.2

luminescence process, which is smaller than 0.2% for $C_{\text{Er}} = 3\%$ (see Table I).

It is interesting to compare these efficiency measurements with decay measurements of the green luminescence. As is well known, the quantum efficiency is equal to the ratio of the radiative probability A_r to the sum of the probabilities of all transitions from the excited level $A_r + A_{\text{nr}}$ (radiative and the competitive nonradiative transitions mentioned earlier). Weber (13) calculated that the probability of the green emission ($^4\text{S}_{3/2} \rightarrow ^4\text{I}_{15/2}$) in $\text{LaF}_3\text{-Er}$ had a value of $A_r = 662 \text{ sec}^{-1}$. Chamberlain, Paxman, and Page (14) found for this probability in $\text{Y}_3\text{Ga}_5\text{O}_{12}\text{-Er}$ a value of around 850 sec^{-1} at room temperature. The value of A_r for Er^{3+} in $\alpha\text{-NaYF}_4$ will not differ much from that in LaF_3 , so that $A_r \approx 700 \text{ sec}^{-1}$ seems to be a reasonable estimate. We found for the decay time of $\alpha\text{-NaYF}_4\text{-20\% Yb-3\% Er}$ with cathode-ray excitation (15 kV) a value of about $100 \mu\text{sec}$, corresponding to a total transition probability $A_r + A_{\text{nr}} \approx 10^4 \text{ sec}^{-1}$ [see also Ref. (11)]. We then find for the quantum efficiency a value of $q \approx 700/10^4 = 7\%$, which agrees reasonably with the value obtained from direct measurement (see Table I).

Acknowledgment

The authors are indebted to Mr. J. A. de Poorter, Mr. R. E. Breemer, and Mr. P. Vries for some of the optical measurements, and to Miss F. Strik for preparing part of the samples.

Manuscript submitted Sept. 9, 1974; revised manuscript received Nov. 20, 1974. This was Paper 100 presented at the San Francisco, California, Meeting of the Society, May 12-17, 1974.

Any discussion of this paper will appear in a Discussion Section to be published in the December 1975 JOURNAL. All discussions for the December 1975 Discussion Section should be submitted by Aug. 1, 1975.

Publication costs of this article were partially assisted by Philips Research Laboratories.

REFERENCES

1. F. E. Auzel, *Compt. Rend.*, **262B**, 1016, (1966).
2. V. V. Ovsyankin and P. P. Feofilov, *JETP. Letters*, **4**, 317, (1966).
3. R. A. Hewes and J. R. Sarver, Paper 339RNP presented at Electrochemical Society Meeting, Boston, Mass., May 5-9, 1968; R. A. Hewes and J. R. Sarver, *Phys. Rev.*, **182**, 427 (1969).
4. L. G. Van Uitert, L. Pictroski, and W. H. Grodkiewicz, *Mater. Res. Bull.*, **4**, 777 (1969).
5. H. J. Guggenheim and L. F. Johnson, *Appl. Phys. Letters*, **15**, 51 (1969).
6. G. Blasse and A. D. M. de Pauw, French Patent Specification nr. 2107248 (1970); The phosphor was improved by M.G.A. Tak and O. J. van Klinken (Private communication).
The $\alpha\text{-NaYF}_4\text{-Yb-Er}$ phosphor has also been described by: N. Menyuk, K. Dwight, and J. W. Pierce, *Appl. Phys. Letters*, **21**, 159 (1972) and by: T. Kano, H. Yamamoto, and Y. Otomo, *This Journal*, **119**, 1561 (1972).
7. F. E. Auzel and D. Pecile, *J. Luminescence*, **8**, 32 (1973).
8. A. Bril, G. Blasse, and J. A. A. Bertens, *This Journal*, **115**, 395 (1968).
9. J. L. Sommerdijk, *J. Luminescence*, **6**, 61 (1973).
10. J. L. Sommerdijk, W. L. Wanmaker, and J. G. Verriet, *ibid.*, **4**, 404 (1971) and **5**, 297 (1972).
11. J. L. Sommerdijk, A. Bril, J. A. de Poorter, and R. E. Breemer, *Philips Res. Repts.*, **29**, 13 (1974).
12. See, e.g., G. Blasse and A. Bril, *Philips Tech. Rev.*, **31**, 304 (1970) and J. L. Sommerdijk and A. Bril, *ibid.*, **34**, 24 (1974).
13. M. J. Weber, *Phys. Rev.*, **157**, 262 (1967).
14. J. R. Chamberlain, D. H. Paxman, and J. L. Page, *Proc. Phys. Soc.*, **89**, 143 (1966).

Perfect Crystal Growth of Silicon by Vapor Deposition

Jun-ichi Nishizawa

Research Institute of Electrical Communication, Tohoku University, Sendai, Japan

Takeshi Terasaki

Semiconductor Research Institute, Sendai, Japan

and Kunihiko Yagi and Nobuo Miyamoto

Research Institute of Electrical Communication, Tohoku University, Sendai, Japan

ABSTRACT

Investigations have been made of the compensation effect of lattice strain on silicon epitaxially grown by the simultaneous doping of tin and phosphorus. The stress induced by doping of phosphorus with a concentration of 4.0×10^{19} atom/cm³ is compensated by the simultaneous doping of phosphorus and tin (2×10^{19} atom/cm³). The generation of misfit dislocations is also restrained by the simultaneous doping of phosphorus and tin. The difference in the effective lattice constants of epitaxial films and substrates is measured by an x-ray double crystal spectrometer using the asymmetric Bragg reflection. The difference can be eliminated by proper doping of tin and nearly perfect, highly doped crystal films can be grown on high-resistivity silicon.

Perfect silicon crystal is of great importance in increasing the reliability, reproducibility, and packing density, because crystal defects affect the characteristics of semiconductor devices, anomalous diffusion, device yield, etc. In 1953 we reported that doping of Group IV elements was effective in producing perfect crystals (1). Later, Dash (2) obtained perfect silicon crystals by the floating zone method using a rapid growth technique.

More recently it has been observed that wafers bend after epitaxial deposition, forming heterojunctions or homojunctions (3-9), and that misfit dislocations frequently appear near the heterojunctions or homojunctions. These phenomena have been attributed to the differences in lattice constant and thermal expansion coefficient between the substrates and the grown films. Schwuttke (7) and Sugita (8) reported the bending phenomena and the generation of interfacial misfit dislocations in homojunctions of the silicon-boron doped silicon system. In this system, the difference in thermal expansion coefficient between the epitaxially grown film and the substrate can be ignored; instead, the lattice misfit between the film and the substrate should be taken into consideration. The generation of dislocations has also been observed (9-11) in the case of diffusion of impurity such as boron or phosphorus into silicon.

In a previous paper (12), lattice strains induced by diffusions of phosphorus, arsenic, antimony, and tin into silicon were measured. The amounts of lattice stress induced by the diffusion of those impurities were considered to be dependent on both the size of impurity atoms diffused into silicon and the impurity concentration. It was also established that the lattice stress induced by phosphorus diffusion was compensated by prediffusion of tin or a simultaneous diffusion of tin and some other impurity into silicon.

The purpose of this paper is to investigate the compensation effect of lattice stress in the case of the epitaxially grown silicon.

In the case of phosphorus- or boron-doped epitaxial growth, the bending of the specimens is concave toward the epitaxially grown surface. On the contrary, the bending of the tin- or antimony-doped one is convex. On the basis of these results, the simultaneous doping of tin and phosphorus, tin and boron, or antimony and phosphorus is applied to epitaxial growth.

Key words: epitaxial growth free from misfit dislocation, compensation of lattice strain, control of lattice constant.

Experimental Procedures

Preparation of specimens.—Wafers used in this experiment were lightly boron-doped silicon single crystals grown by the pulling method. They were cut into slices in the (111) plane. Since the concentration of the dopant boron in the wafers was about 1.7×10^{15} atom/cm³, the lattice constants of the wafers were almost equal to that of pure silicon crystal. The original etch pit density of the wafers was of the order of less than 500 pit/cm². The wafers were lapped and chemically etched to remove completely the surface damage. They were then cut into a rectangular shape 1 cm long and 0.5 cm wide, the direction of the long side of the rectangular specimens lying on $\langle 110 \rangle$. The final thickness of the specimens was about 200 μ .

Epitaxial growth procedure.—Prior to chemical deposition, the surface of the specimen was etched to a depth of 5 μ using a gas mixture of H₂ and HBr at 1200°C.

The apparatus of epitaxial deposition used for the compensation of lattice strain is schematically shown in Fig. 1. The experimental condition of epitaxial deposition was as follows: growth temperature, 1200°C; flow velocity of gas, 0.5 m/sec through the reactor tube; and mole fraction, SiCl₄/H₂ = 0.005 ~ 0.02. Impurity dopants used in the experiment were liquidus halide such as PCl₃, BBr₃, SnCl₄, and AsCl₃ being kept in vessels at constant temperature, and only PCl₃ and BBr₃ were diluted into solution with SiCl₄ for the close control of the doping levels of phosphorus and boron impurities in the silicon layers.

X-ray measurement of bending and x-ray projection topography.—Bending of specimens resulting from the lattice misfit between the epitaxial films and substrates were measured using the Lang camera. The x-ray beam was collimated through a receiving vertical slit 0.05 mm wide. The MoK α_1 (220) reflection was used in this experiment. The variation in the angle of the Bragg reflection with the position of the curved specimens was obtained. From these results the curvature of the specimen was calculated. Prior to the bending measurement of the epitaxially deposited specimens, it was found that bending did not occur either in the original substrate or in the specimen subjected to the same heat-treatment as that undertaken for the epitaxial growth.

Misfit dislocations and other crystalline defects were observed by x-ray projection topography.

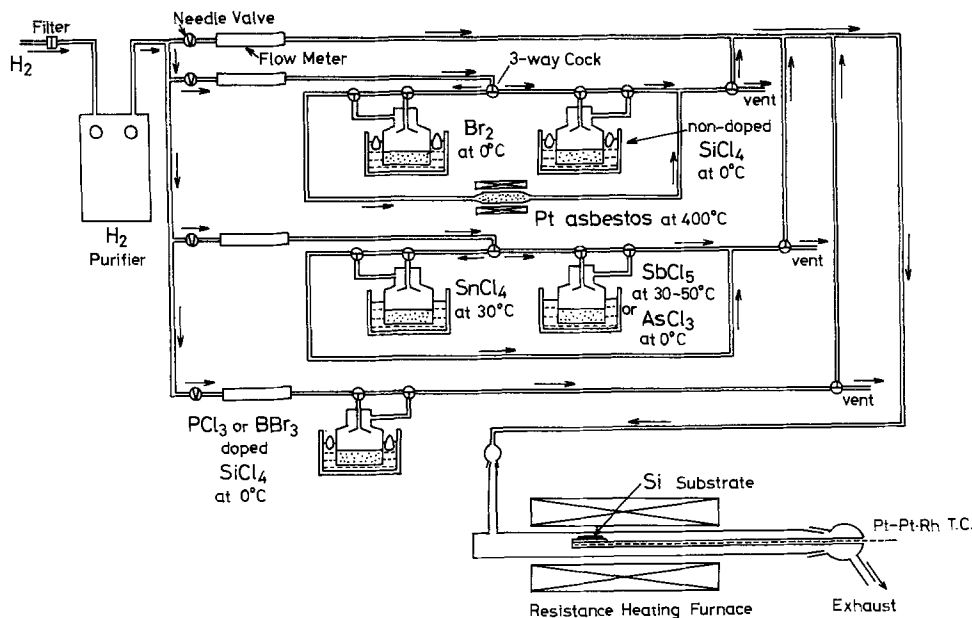


Fig. 1. Schematic representation of apparatus for vapor deposition.

Measurement of the change in lattice constant.—In order to measure the effective difference between the lattice constants of the epitaxial film and the substrate, an x-ray double-crystal spectrometer was used and the asymmetric Bragg reflection (13, 14) was applied to the first crystal. $\text{CuK}\alpha_1$ radiation was used throughout the present experiment. As the first crystal, a dislocation-free single crystal of silicon cut parallel to the (111) plane was used. This crystal was positioned to the (511) reflection. The specimen to be measured as the second crystal was arranged in a (333) symmetric reflection. According to Renninger (13), this "parallel" double-crystal spectrometer arrangement is described as $\{(511)^v, -(333)^s\}$. To record the rocking curve, the speed of rotation of the second crystal was fixed at $1/256^\circ/\text{min}$.

When the pure silicon substrate was positioned as the second crystal, the width at half of the maximum intensity (half-width) of the rocking curve was measured to be 3.0 sec of arc.

Results and Discussion

Simple theoretical analysis of the bending and the lattice strain.—If there is difference between the lattice constants of the substrate and the layer, such phenomena as bending, lattice strain, and misfit dislocations can be observed and calculated under the condition where the impurity atoms have different sizes from that of silicon atoms and occupy the substitutional sites in the silicon lattice.

Applying the well-known relationship between the curvature of the specimens and the film thickness of bimetallic strip with respect to the elastic bending of bicrystals (16), the difference in the thermal expansion $\Delta\alpha\Delta T$ is replaced by the lattice misfit f . Hence, we obtain

$$\frac{1}{R} = \frac{6t_f \cdot t_s \cdot f}{(t_s + t_f)^3} \quad [1]$$

where R is the radius of curvature, t_f and t_s are the thickness of the epitaxial film and the substrate, respectively, and f is equal to ϵ as is demonstrated later. The relationship between the curvature resulting from the elastic bending and the thickness of the epitaxial films is considered to satisfy Eq. [1]. Therefore, the convexity or concavity in the epitaxial surface side due to the bending depends on the lattice contraction or expansion in the epitaxial layer.

The difference between the lattice constant of the layer and the substrate was measured from the rocking curve by an x-ray double-crystal spectrometer. In

this case, the rocking curve has a main peak and a secondary peak; these correspond to the diffraction lines satisfying the Bragg condition for the substrate and the epitaxial layer, respectively.¹ The average lattice strain ϵ is obtained from angular difference between the two peaks, $\Delta\theta$

$$\epsilon = \frac{\Delta a}{a} = -\cot \theta_B \cdot \Delta\theta \quad [2]$$

where a is the lattice constant for silicon (5.43018\AA) and θ_B is the Bragg angle [47.476° for the (333) reflection in silicon using $\text{CuK}\alpha_1$]. The change in the lattice crystal Δa is evaluated from Eq. [2].

A simple model for the lattice strain due to the difference in atomic size has been proposed in the previous paper (12): When impurity atoms having an atomic size different from that of silicon occupy substitutional sites in silicon, the lattice stress is induced around the impurity atoms. The amount of the stress depends on the degree of the lattice misfit, R_i/R_{Si} (the ratio of the covalent radius of the impurity atom to that of the silicon atom) and the concentration of the dopant impurity in silicon. It is assumed that the solute lattice contraction (expansion) coefficient, β , is given by a relation of the form

$$\beta \equiv \frac{1}{3} [1 - (R_i/R_{\text{Si}})^3] N^{-1} \quad [3]$$

where N is the atomic density for silicon (5×10^{23} atom/cm³). The calculated values of β for some impurity atoms are listed in Table I. For the epitaxially grown film within the limit of elasticity and of the dopant impurity concentration of N_i , the lattice strain ϵ is given by

$$\epsilon = \beta N_i \quad [4]$$

Since ϵ is $\Delta a/a$, the values of Δa are calculated from the above equation.

¹ Effective lattice constant by the strain varies gradually and not abruptly, so that it cannot be considered to be established in simple form. Further details concerning this implication will be reported in a separate article.

Table I. Calculated β values for some impurity atoms

Doped impurity	Atomic radius, A	R_i/R_{Si}	β , cm ³ /atom
P	1.10	0.94	$+1.03 \times 10^{-24}$
Sn	1.40	1.193	-4.7×10^{-24}
Sb	1.36	1.162	-3.8×10^{-24}
Si	1.17	—	—

Bending of the phosphorus-doped epitaxially grown wafer.—The bending of the phosphorus-doped silicon deposited on the lightly boron-doped substrate, was concave toward the epitaxially grown side. Figure 2 shows a plot of the values of the experimentally determined curvature of the specimens having different phosphorus doping levels as a function of the thickness of the epitaxial film. These results indicate that the amount of bending depends on the doping concentration of phosphorus and the thickness of the epitaxial film. In this experiment, the curvature of bending increases with an increase in phosphorus concentration and also increases almost linearly with an increase in epitaxial layer thickness and in the concentration of phosphorus. Figure 3 shows x-ray projection topographs of specimens different in the thickness of epitaxial films (concentration of the dopant phosphorus was fixed at 4×10^{19} atom/cm³). Misfit dislocations along the $\langle 110 \rangle$ direction can be seen clearly in Fig. 3(b) and (c). It can be considered that these misfit dislocations generate when the lattice stress exceeds a certain critical value at high temperatures of $700^\circ \sim 800^\circ\text{C}$, and increases with an increase in the concentration of the dopant impurity and in the thickness of the grown layer.

The x-ray projection topographs for the various impurities and layer thicknesses show that the critical value of the curvature required to induce dislocations by misfit is $1/R = 10 \times 10^{-4} \text{ cm}^{-1}$, which agrees well with Sugita's result (8). Some examples of the rocking curves are shown in Fig. 4. The diffraction intensity of the secondary peak which appeared on the high angle side of the main peak increased with increasing thickness of the epitaxial film. The fact that the main peak corresponded to the reflection from the substrate and the secondary peak to the reflection from the epitaxial film was also confirmed experimentally by gradually etching the epitaxial film from its surface. The difference in the angle between this secondary peak and the main peak, $\Delta\theta$, increases almost linearly with increasing concentration of the dopant phosphorus; it also increases with increasing epitaxial layer thickness at a constant doping level of the impurity. In the present measurements, the density of dislocations is zero or less than 10^2 cm^{-2} as observed in the x-ray projection topographs and the change of the lattice constant due to bending is within $\pm 10^{-5} \text{ \AA}$ of the true value. Therefore, among the effects of dislocations, other defects, and the bending of bicrystals due to lattice

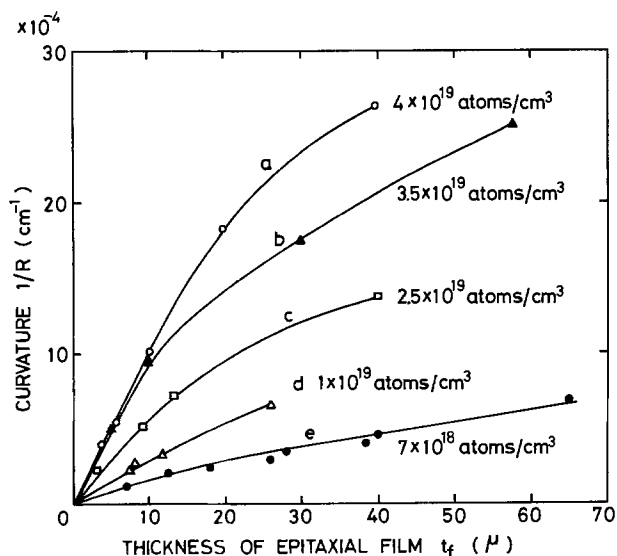


Fig. 2. Curvature vs. thickness of the phosphorus-doped epitaxial film. Curve a, concentration of phosphorus $N_i = 4 \times 10^{19}$ atom/cm³; curve b, $N_i = 3.5 \times 10^{19}$ atom/cm³; curve c, $N_i = 2.5 \times 10^{19}$ atom/cm³; curve d, $N_i = 1 \times 10^{19}$ atom/cm³; curve e, $N_i = 7 \times 10^{18}$ atom/cm³.

strain, it appears that the lattice strain affects most strongly the lattice constant due to the doping of phosphorus. These considerations are also applicable to other impurities. The change in the lattice constant of the Sn-, P-, Sb-, and B-doped epitaxial films, Δa , is plotted against the concentration of each dopant in Fig. 5 using the experimental data on $\Delta\theta$ defined by Eq. [2]. The lattice constant of the phosphorus-doped

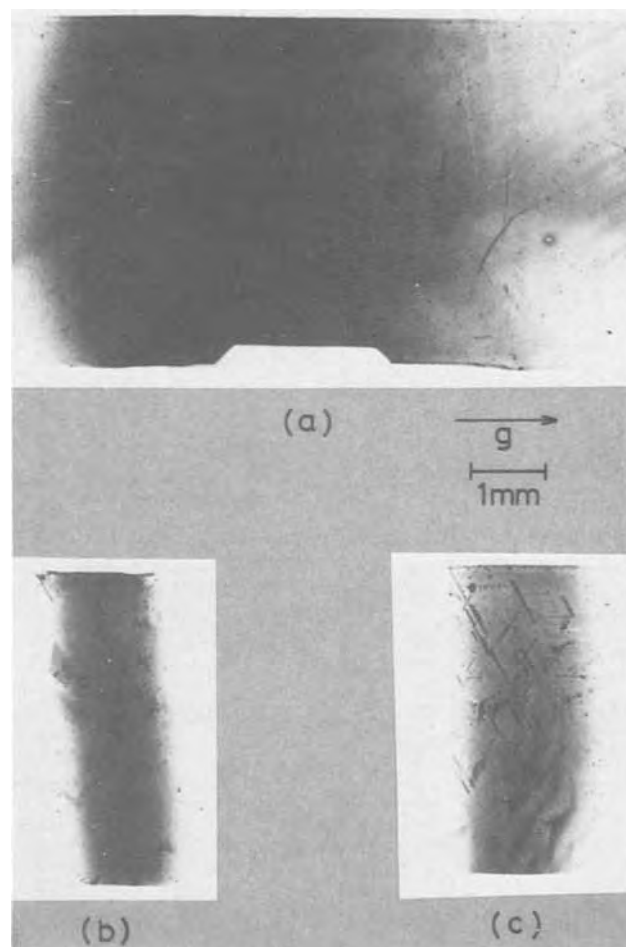


Fig. 3. X-ray projection topographs of phosphorus-doped specimens having various thicknesses. (Concentration of phosphorus: 4×10^{19} atom/cm³). (a) $t_f = 4 \mu$. (b) $t_f = 10.5 \mu$. (c) $t_f = 14 \mu$.

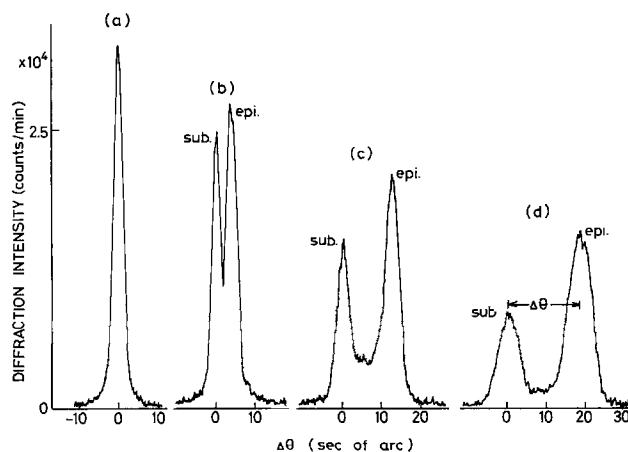


Fig. 4. X-ray rocking curves of $\{(511)^v, - (333)^s\}$ reflection for various concentrations of the dopant phosphorus. (a) Silicon substrate. (b) Concentration of the dopant phosphorus $N_i = 7 \times 10^{18}$ atom/cm³, thickness of the epitaxial film $t_f = 13 \mu$. (c) $N_i = 2.2 \times 10^{19}$ atom/cm³, $t_f = 13 \mu$. (d) $N_i = 3.5 \times 10^{19}$ atom/cm³, $t_f = 15 \mu$.

epitaxial film is smaller than that of the substrate silicon crystal, and increases linearly with increasing concentration of the dopant phosphorus impurity. The values of Δa calculated from Eq. [3] and [4] are also plotted by solid lines in Fig. 5. The experimental values coincide with the calculated line of our model, but shifts slightly from the line on the higher side of $|\Delta a|$.

The value of about 6×10^{-5} for the misfit f can be obtained from Eq. [1] using the experimental curve b of Fig. 2. This value is in approximate agreement with the value of 7.3×10^{-5} obtained at the same phosphorus concentration of 3.5×10^{19} atom/cm³ in Fig. 5. This result also indicates that the bending of the specimens depends on the lattice misfit between the epitaxially grown film and the substrate silicon crystal.

Bending of the tin-doped epitaxially grown wafer.—The bending of epitaxial slices having layers doped only with tin on lightly boron-doped silicon substrates was completely opposite to that of phosphorus-doped ones. Namely, the bending of these specimens was convex toward the epitaxially grown side. The values of curvature obtained are minus, which are plotted in Fig. 6. In this figure, the curves b and e are obtained by changing the amount of gas flow of SnCl₄ mixed with SiCl₄. For determination of the concentration of tin as a neutral impurity in the epitaxial film, only the x-ray double-crystal spectrometer was used. Some examples of the rocking curves of these tin-doped specimens are shown in Fig. 7. The secondary peak designated "epi" appeared on the low angle side of the main peak, which is opposite to that of the phosphorus-doped ones. The calculation of Δa for tin was performed in a way similar to phosphorus. Calculated values are also shown in Fig. 5. The maximum concentration of tin obtained in the present work was 3×10^{19} atom/cm³. Dislocations caused by the lattice misfit were also observed in the tin-doped epitaxially grown specimens as shown in Fig. 8; the dislocations increase also with increasing concentration of tin and epitaxial thickness. The phenomena of tin doping was almost similar to that of phosphorus doping.

Doping of other impurities in the epitaxially grown film.—Other impurities such as boron, arsenic, and antimony were also added to the epitaxially grown films and the changes in the lattice constants of these specimens were measured. The values obtained are

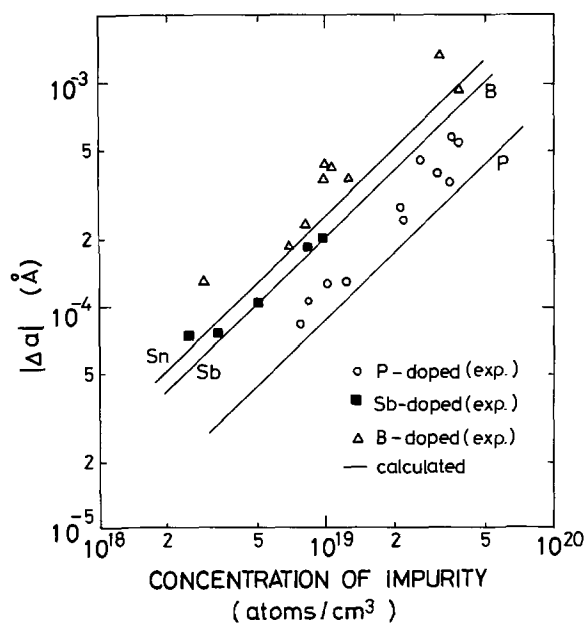


Fig. 5. Lattice constant of impurity-doped epitaxially grown silicon vs. concentration of the dopant impurity curves.

plotted against the impurity concentration as shown in Fig. 5. The lattice constant of the boron-doped epitaxially grown film is smaller than that of the substrate silicon crystal, whereas that of the antimony-doped film is larger than the substrate. The lattice contraction or expansion by impurity doping can be expected and calculated from the covalent radius of the impurity atoms. The change in the lattice constant of the arsenic-doped epitaxially grown films was barely detectable even at its concentration of 4×10^{19} atom/cm³, because the covalent radius of arsenic (1.18Å) was nearly identical with that of Si (1.17Å). In the

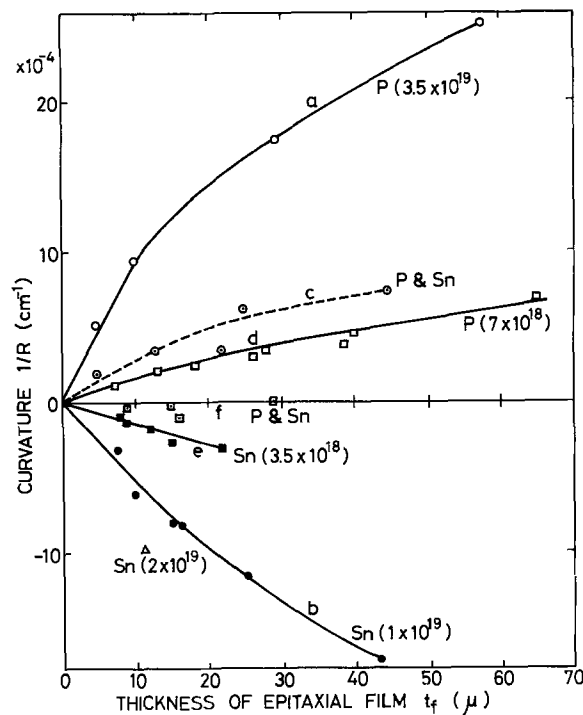


Fig. 6. Curvature vs. thickness of epitaxial film. Curve a, for phosphorus doping; concentration of the dopant phosphorus $N_i = 3.5 \times 10^{19}$ atom/cm³. Curve b, for tin doping; concentration of tin $N_i = 1 \times 10^{19}$ atom/cm³. Curve c, for simultaneous doping of tin and phosphorus; concentrations of phosphorus and tin are 3.5×10^{19} atom/cm³ and 1×10^{19} atom/cm³, respectively. Curve d, for phosphorus doping; $N_i = 7 \times 10^{18}$ atom/cm³. Curve e, for tin doping; $N_i = 3.5 \times 10^{18}$ atom/cm³. Curve f, for simultaneous doping of tin and phosphorus; concentrations of phosphorus and tin are 7×10^{18} atom/cm³ and 3.5×10^{18} atom/cm³, respectively.

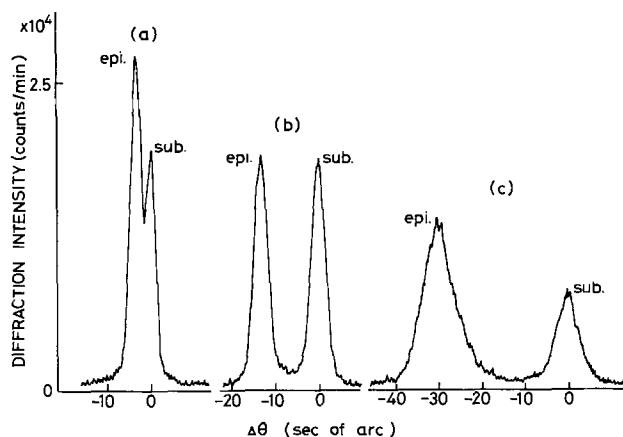


Fig. 7. X-ray rocking curves of $\{511\}^v - \{333\}^s$ refraction for tin-doped specimens. (a) Concentration of tin $N_i = 3.5 \times 10^{18}$ atom/cm³; $t_f = 15\mu$. (b) $N_i = 1 \times 10^{19}$ atom/cm³; $t_f = 12\mu$. (c) $N_i = 2 \times 10^{19}$ atom/cm³; $t_f = 17\mu$.



Fig. 8. X-ray projection topograph of tin-doped specimen: concentration of tin 1×10^{19} atom/cm³; $t_f = 43\mu$.

case of diffusion of arsenic into silicon by the sealed, evacuated capsule method using metallic arsenic as the diffusion source, the lattice constant of the diffused layer with a surface concentration of $5 \sim 10 \times 10^{20}$ atom/cm³ was found to be slightly smaller ($1 \times 10^{-4}\text{\AA}$) than that of the substrate silicon crystal after quenching from its diffusion temperature (1200°C). It was interesting to note that the lattice constant became much larger than that of the substrate after subsequent low temperature heat-treatment of the arsenic-diffused specimen (17).

Compensation of lattice strain in epitaxial growth.— On the basis of the experiments under consideration, the simultaneous doping of tin and phosphorus was applied to the epitaxial growth. In Fig. 6, curve c was obtained from a combination of curves a and b and the curve f, which coincides with the abscissa (namely, no bending occurs), and from a combination of curves d and e. It is apparent from Fig. 6 that simultaneous doping of tin and phosphorus reduces the bending strain. This was confirmed by measurement of the change in lattice constant between the epitaxial film and the substrate silicon crystal. Some examples of the rocking curves of the simultaneously doped specimens are shown in Fig. 9 and 10. It is evident from Fig. 9 and 10 that one of the two peaks present in the case of doping with a single impurity such as tin or phosphorus disappears and the half-width of the rocking curve approaches the value obtained in the substrate silicon crystal (3 sec of arc). It is ascertained from these results that the difference in lattice constants between the epitaxially grown film and the substrate is small or zero.

Figure 11 shows x-ray projection topographs of the phosphorus-doped specimens and the tin- and phosphorus-doped ones. In the phosphorus-doped specimens (concentration $3.5 \sim 4 \times 10^{19}$ atom/cm³) misfit dislocations are observed in epitaxial films for the thickness over 15μ . On the contrary, misfit dislocations are hardly observable in the specimens doped simultaneously with tin and phosphorus at approximately the same concentration and even with a film thickness of 43μ . Since the maximum concentration of tin in the present work was 3×10^{19} atom/cm³, the lattice strain induced by doping of phosphorus of which concentration is 8×10^{19} atom/cm³ can be compensated by the simultaneous doping of tin and phosphorus.

Lattice strain compensation was also achieved by the simultaneous doping of tin and boron whose concentrations were 3×10^{19} atom/cm³ and 2×10^{19} atom/cm³, respectively. In the case of the simultaneous doping of antimony and phosphorus, the maximum concentration of antimony in the epitaxial silicon film obtained in the present work was less 1×10^{19} atom/cm³, indicating that the lattice strain compensation was less effective than the simultaneous doping of tin and phosphorus. Germanium can also be applied to the compensation of lattice strain.

Conclusions

It has been established experimentally that in the case of simultaneous doping of tin and phosphorus, tin and boron, or antimony and phosphorus, the strain compensation can be made in the epitaxially deposited silicon on silicon substrates. The magnitude of bend-

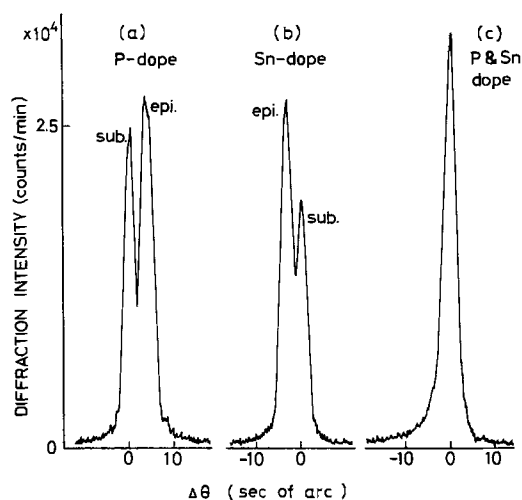


Fig. 9. X-ray rocking curves of $\{(511)^v, -(333)^s\}$ for compensated specimens by simultaneous doping of tin and phosphorus. (a) Phosphorus doping; $N_i = 7 \times 10^{18}$ atom/cm³; $t_f = 13\mu$. (b) Tin doping; $N_i = 3.5 \times 10^{18}$ atom/cm³; $t_f = 15\mu$. (c) Simultaneous doping of tin and phosphorus; concentrations of phosphorus and tin are 7×10^{18} atom/cm³ and 3.5×10^{18} atom/cm³, respectively; $t_f = 15\mu$.

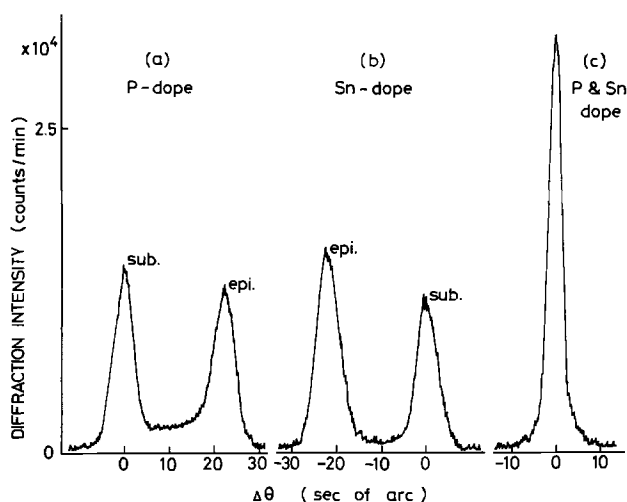


Fig. 10. X-ray rocking curves of $\{(511)^v, -(333)^s\}$ for compensated specimens by simultaneous doping of tin and phosphorus. (a) Phosphorus doping; $N_i = 4 \times 10^{19}$ atom/cm³; $t_f = 10\mu$. (b) Tin doping; $N_i = 2 \times 10^{19}$ atom/cm³; $t_f = 11.5\mu$. (c) Simultaneous doping of tin with phosphorus, concentrations of phosphorus and tin are 4×10^{19} atom/cm³ and 2×10^{19} atom/cm³, respectively; $t_f = 16\mu$.

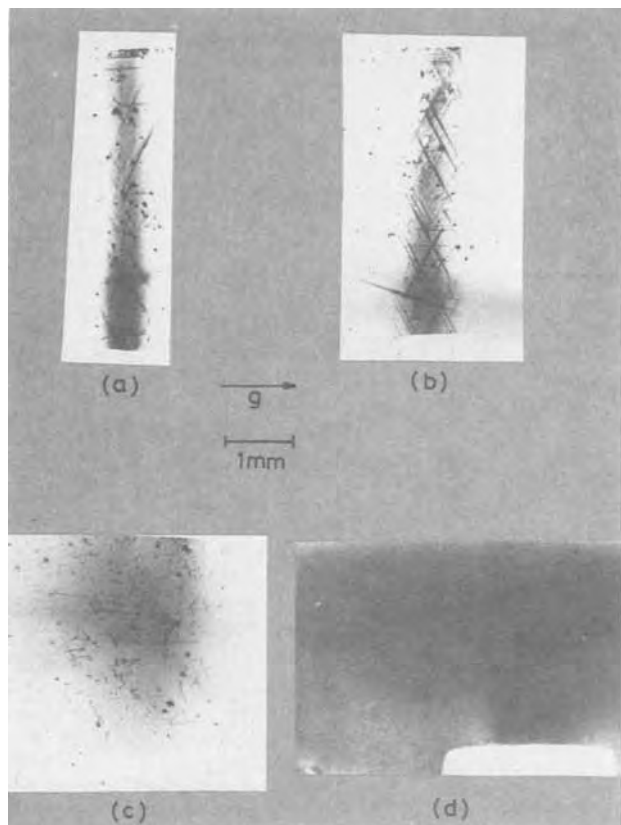


Fig. 11. X-ray transmitted diffraction topographs. (a) Phosphorus doping; $N_i = 3.5 \times 10^{19}$ atom/cm³; $t_f = 16\mu$. (b) Phosphorus doping; $N_i = 3.5 \times 10^{19}$ atom/cm³; $t_f = 40\mu$. (c) Simultaneous doping of tin with phosphorus; concentrations of phosphorus and tin are 3.5×10^{19} atom/cm³ and 1×10^{19} atom/cm³, respectively; $t_f = 43\mu$. (d) Simultaneous doping of tin with phosphorus; concentrations of phosphorus and tin are 4×10^{19} atom/cm³ and 2×10^{19} atom/cm³, respectively; $t_f = 20\mu$.

ing or the amount of lattice strain induced by the doped impurities are affected remarkably by the size of impurity atoms and the concentration of impurity atoms which occupy the substitutional lattice sites of silicon. Using the technique of the simultaneous doping of the impurity atoms which are smaller and larger in atomic radius than the silicon atoms, the

lattice constant of the epitaxially grown film can be fitted to that of the substrate silicon crystal and thick epitaxial films can be deposited on the substrate without generation of misfit dislocations.

Acknowledgment

The authors wish to thank Mr. Jiro Shibata for his technical assistance.

Manuscript submitted Jan. 2, 1973; revised manuscript received Nov. 1, 1974.

Any discussion of this paper will appear in a Discussion Section to be published in the December 1975 JOURNAL. All discussions for the December 1975 Discussion Section should be submitted by Aug. 1, 1975.

Publication costs of this article were partially assisted by Tohoku University.

REFERENCES

1. Y. Watanabe, J. Nishizawa, H. Kon, T. Ikegami, and T. Matsushima, *Record of Electrical and Communication Engineering Conversation, Tohoku Univ.* **21**, No. 4, 101 (1953).
2. W. C. Dash, *J. Appl. Phys.*, **30**, 459 (1959).
3. T. B. Light, M. Berkenblit, and A. Reisman, *This Journal*, **115**, 969 (1968).
4. R. S. Mrozkowski, A. F. Witt, and H. C. Gatos, *ibid.* **115**, 750 (1968).
5. R. H. Saul, *J. Appl. Phys.*, **40**, 3273 (1969).
6. M. S. Abrahams, *ibid.*, **40**, 3754 (1969).
7. G. H. Schwuttke, "Advances in Vacuum Science and Technology," p. 301, Pergamon Press Ltd., Oxford (1965).
8. Y. Sugita, M. Tamura, and K. Sugawara, *J. Appl. Phys.*, **40**, 3089 (1969).
9. S. Prussin, *ibid.*, **32**, 1876 (1961).
10. W. Czaja, *ibid.*, **37**, 3441 (1966).
11. J. Washburn, G. Thomas, and H. J. Queisser, *ibid.*, **35**, 1909 (1964).
12. K. Yagi, N. Miyamoto, and J. Nishizawa, *Japan. J. Appl. Phys.*, **9**, 246 (1970).
13. M. Renninger, *Advanc. X-Ray Anal.*, **10**, 32 (1967).
14. K. Kohra, *J. Phys. Soc. Japan*, **17**, 589 (1967).
15. Y. Sugita and M. Tamura, Technical Group on Semiconductors and Semiconductor Devices, IECE of Japan, No. SSD69-13 (1969).
16. J. S. Vermaak and J. H. Van der Merwe, *Phil. Mag.*, **10**, 785 (1964); **12**, 453 (1965).
17. N. Miyamoto, E. Kuroda, and S. Yoshida, Proceedings 5th International Conference on Solid State Devices, Tokyo (1973); *Japan. J. Appl. Phys.*, **43**, 408 (1974).

Effects of Illumination on Preferential Etching of N-Type GaAs in a CrO₃-HF-AgNO₃ Solution

Tadashi Saitoh, Sunao Matsubara, and Shigekazu Minagawa*

Central Research Laboratory, Hitachi Limited, Kokubunji, Tokyo, Japan

ABSTRACT

Photoetching using a CrO₃-HF-AgNO₃ aqueous solution was studied in an attempt to reveal inhomogeneities of n-type GaAs. This method enabled us to obtain etch patterns of striations and dislocations with high resolution. In addition, an etch depth for revealing dislocations was only about 0.1 μm and striations were delineated with an etch depth of about 0.6 μm. The method was applied to the examination of defects in-depth, and it was possible to identify independent dislocations and dislocation networks. The activation energy for etching in the dark was 7.5 kcal/mol, which is for the diffusion controlled process. The etch rate increased linearly with illumination intensity and the increases of etch rate under illumination were almost independent of etch temperatures and the concentrations of Ag⁺ ions. Photoetched patterns were ridged at defects, in contrast to recessed patterns revealed in the dark. This result suggests that the distribution of charges on the surface, including minority carriers (holes) and/or light-induced electron-hole pairs, plays an important role in revealing defects.

The inhomogeneities in semiconductor crystals have been characterized using chemical etching techniques because of their simplicity and their high resolution. For GaAs crystals, Schell (1) used a nitric acid solution and White and Roth (2) a dilute aqua regia to reveal crystal defects. However, their etchants produced etch pits only on the {111}A face of GaAs. By using a dilute nitric acid containing a silver ion, Richard and Crocker (3) were able to produce etch pits on both the {111}A and {111}B faces. An ordinary etchant containing CrO₃, AgNO₃, and HF was applied by Abrahams and Buiocchi (4) to the low index faces of {111}A, {111}B, {110}, and {100}. However, the depth of etching in the case of the etchant reported by Abrahams and Buiocchi (AB etchant) was about 100 μm in order to obtain etch patterns with high resolution. Hence, conventional etching techniques were not suitable for examining crystal defects in thin layers as prepared by a vapor-phase or liquid-phase epitaxial growth.

Recently, Kuhn-Kuhnenfeld (5) reported that etching in a H₂SO₄-H₂O₂ aqueous solution under intense illumination revealed striations and dislocation lines on the low index faces of Czochralski-grown GaAs. A photoetching using a modified AB etchant, as described in this paper, is also useful for obtaining highly resolved patterns relating to the inhomogeneities, *viz.* striations and dislocations. It, however, has the advantage of a shallow etch depth less than 1 μm.

Experimental

Sample preparation.—Samples used in this study were n-type GaAs with carrier concentrations in the range of 10¹⁷-10¹⁸ cm⁻³, grown by the horizontal Bridgmann technique. The crystal surfaces were {100}, {110}, {111}A and {111}B in the case of Si-doped GaAs and {100} in the case of Te-doped or Cr-doped GaAs. The samples were mechanically polished using Al₂O₃ abrasives with a particle size of 0.2 μm and chemically etch-polished in a 4H₂SO₄-1H₂O₂-1H₂O solution at 65°C for 10 min prior to preferential etching.

Etching procedure.—The etchant used was a modified AB solution as the etching was performed at 300°K or at lower temperatures. The etchant was prepared by dissolving 80 mg AgNO₃, 10g CrO₃, and 10 ml HF in 20 ml H₂O, successively. Then, the solution was decanted to obtain a transparent solution free of any precipitates such as Ag₂CrO₄ or CrO₃. The concentrations of Ag⁺

ions and CrO₄²⁻ ions in the clear etchant analyzed by atomic absorption spectroscopy were 2.0 × 10⁻³ g-ion/liter and 2.7 g-ion/liter, respectively. In addition, this etchant, diluted 8 to 1, was also used for revealing defects in a very shallow depth of etching.

In the photoetching, the illumination was provided by an ordinary tungsten lamp. The light intensity was about 5000 ft-c measured by a 50 A Opto-Meter (United Detector Technology). The etchant was protected from heat by locating a water vessel between the etchant containing the sample and the lamp. This held the temperature rise of the etchant within 1°C during etching time. Etch patterns were examined using the Nomarski technique.

Photoetched Patterns

In typical etch patterns revealed under illumination, dot-like defects, irregular linear defects, and growth striations are observed. The patterns have excellent resolution and are ridged as opposed to the recessed patterns produced by the Abraham's method or the etching in the dark. Photoetched patterns were also found to vary in shape or length with orientation, dopant, and etch depth.

Effect of illumination on etch patterns.—In order to examine the effect of illumination on preferential etching, {111}B surfaces were etched under illumination or in the dark. In the photoetched patterns of {111}B surfaces, one can see dot-like defects, linear defects, and growth striations. The dot-like defects denoted by arrows D in Fig. 1 consist of an elevated pyramidal structure. The pyramidal defects are more abundant than the linear defects denoted by arrows L on the {111}B surfaces. Growth striations indicated by arrows S in Fig. 1(a), which were difficult to observe in the other etching method performed under room light, were delineated. Also shown in Fig. 1(b) are minute irregularities with very shallow etch depths, which could not be observed using the usual microscopy except for the Nomarski technique. However, the origin of this type of defects is uncertain.

On the other hand, etch patterns produced in the dark consisted of independent etch pits, chains of smaller etch pits, and striations, as shown in Fig. 2. Independent etch pits correspond to the pyramidal etch hillocks indicated in Fig. 1(b), and chained pits to the dislocation lines in Fig. 1(a). Furthermore, the recessed lines of striations in Fig. 2 correspond to the ridged lines in Fig. 1. The etch patterns revealed in the dark closely resemble those in the conventional

* Electrochemical Society Active Member.

Key words: photoetching, striations, dislocations, defects in-depth, etching rates.

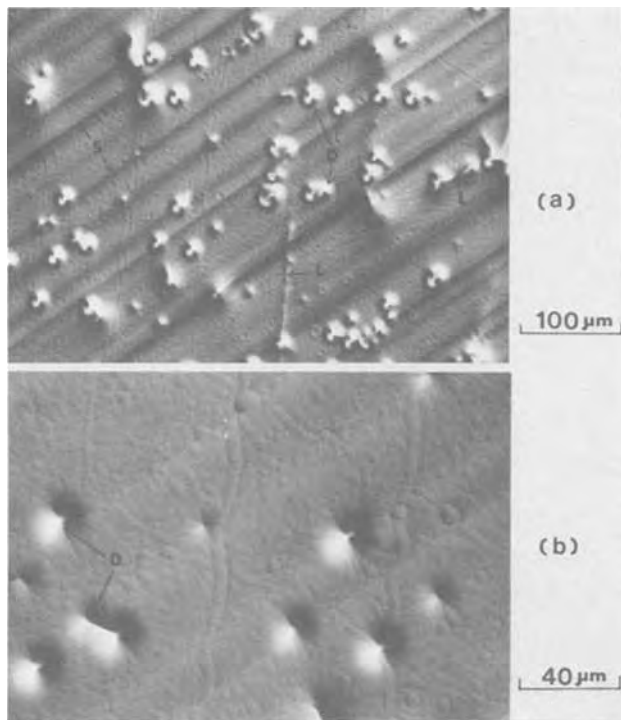


Fig. 1. Photoetched patterns of Si-doped GaAs. (a) $\{111\}$ surface ($n = 5 \times 10^{17} \text{ cm}^{-3}$); (b), magnification of (a). The etch depth is about $6 \mu\text{m}$ at etch temperature of 23°C and etch time of 2 min.

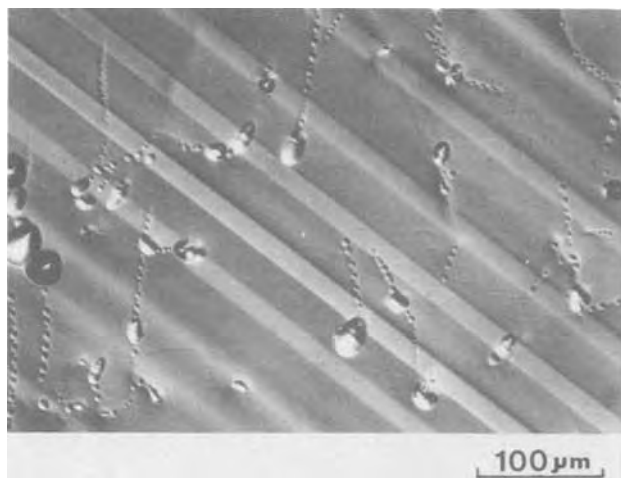


Fig. 2. $\{111\}$ B surface of Si-doped GaAs ($n = 5 \times 10^{17} \text{ cm}^{-3}$) etched in the dark. The etch depth is $14 \mu\text{m}$ at etch temperature of 23°C and etch time of 7 min.

method under room light, although the former are clearer than the latter. However, the photoetching method is superior to other etching methods, including the etching in the dark, especially for obtaining etch patterns of $\{100\}$ and $\{110\}$ surfaces. The density of dot-like and linear defects in the photoetched patterns was found to be in the ranges of $8\text{--}11 \times 10^3 \text{ cm}^{-2}$.

Thus, inverse patterns can be obtained by etching under illumination or in the dark. This result suggests that the distribution of charges on the GaAs surface, including minority carriers (holes), ionized donors, surface states and/or light-induced carriers, plays an important role in obtaining etch patterns with high resolution.

Effect of surface orientation.—As for $\{100\}$ surfaces and $\{110\}$ cleaved faces, linear defects and dot-like

defects were found to exist as shown in Fig. 3, although linear defects were more abundant than dot-like defects. The linear defects are considered to be dislocation lines because they develop with etching time as shown later in Fig. 4. Furthermore, these linear defects are quite similar to the lines reported by Huber and Champier (6), who indicated that the lines are dislocation lines due to the correlation between the etch patterns and the x-ray topograph. This is in contrast with the aforementioned patterns of $\{111\}$ B surfaces on which dot-like defects mainly existed. This is considered to be due to the existence of dislocations comparatively normal to $\{111\}$ B surfaces and inclined to $\{100\}$ or $\{110\}$ faces.

Growth striations were delineated on $\{111\}$ B surfaces as well as $\{111\}$ A, $\{100\}$, and $\{110\}$ surfaces, although striations on $\{110\}$ faces with low resolution are also observed. Striations, especially for $\{100\}$ and $\{110\}$ of GaAs crystals, have been difficult to observe and so, this photoetching method is superior to other etching methods in revealing them. This is quite similar to the result that intense illumination is essential for revealing growth striations in the ease of selective etching using a $\text{H}_2\text{SO}_4\text{--H}_2\text{O}_2$ aqueous solution (5). As shown in Fig. 2, however, one can see striations in the etch pattern revealed in the dark, which are more highly resolved than that produced in an etching under room light using the same AB etchant. Therefore, the distribution of charges on the surface is considered to play an important part in revealing striations.

It is possible to examine defects in-depth by comparing two photomicrographs of adjacent regions on the $\{100\}$ surface and $\{110\}$ cleaved face. Note that dislocation lines, designated by arrows A in Fig. 3, are observed on both the $\{100\}$ and $\{110\}$ surfaces. This result suggests that dislocation lines are connected. On the other hand, arrows B and C are revealed on either the $\{110\}$ face or the $\{100\}$ surface. The dislocation line shown by arrow B appeared on the $\{100\}$ surface during further etching. On the other hand, the dislocation line shown by C was a "memory" of dissolved dislocation because no pattern relating to C, is observed on the $\{110\}$ face.

Variation of etch patterns with etch depth.—This photoetching technique is also effective in observing how etch patterns vary with etch depth because the technique requires a shallow etch depth to obtain highly resolved patterns. A typical variation of etch patterns for $\{100\}$ surfaces of GaAs is shown in Fig. 4, in which arrows E to G are typical examples of defects. Arrow E is a dot-like defect in Fig. 4(a). Then, it changes into a linear defect as indicated in Fig. 4(b). In Fig. 4(c), the length of the linear defect remains constant during prolonged etching. Therefore, this defect is a short one independent of other defects, and

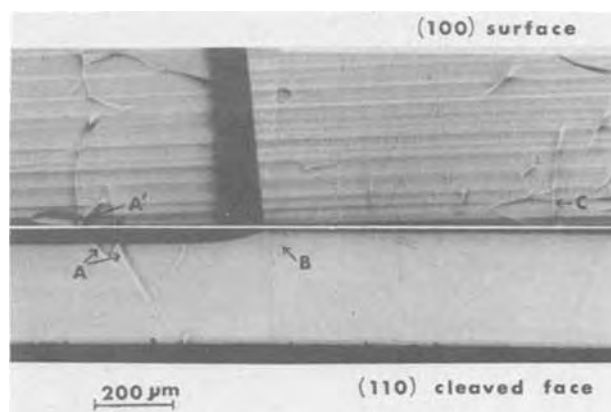


Fig. 3. Photoetched surfaces of adjacent $\{100\}$ surface and $\{110\}$ cleaved face for Si-doped GaAs ($n = 2 \times 10^{18} \text{ cm}^{-3}$).

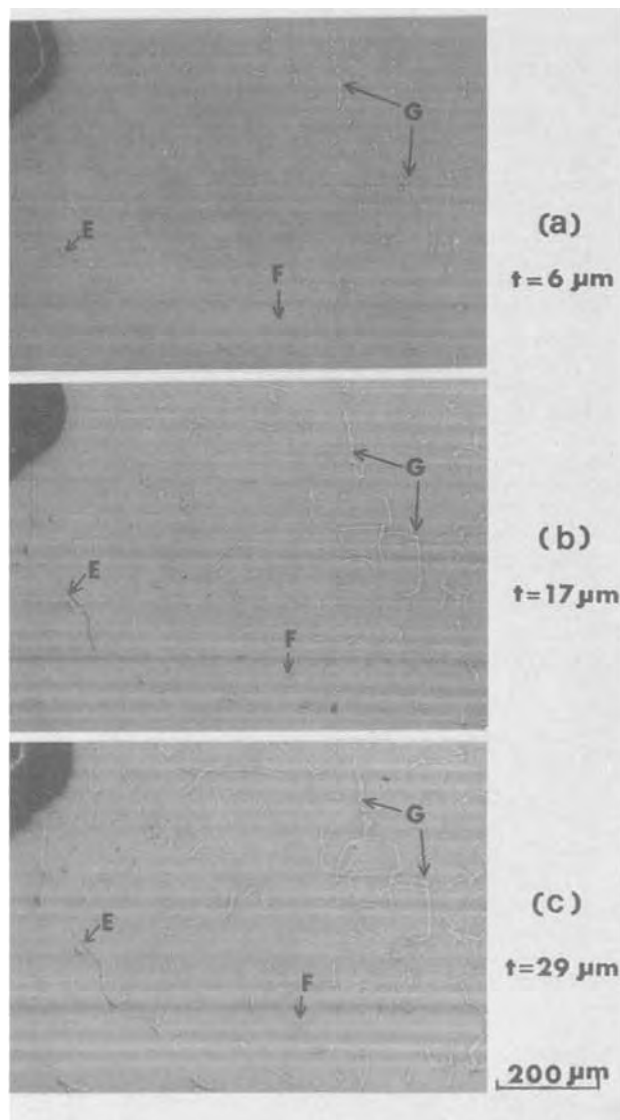


Fig. 4. Variation of photoetched {100} surfaces with the depth of etching for Si-doped GaAs ($n = 2 \times 10^{18} \text{ cm}^{-3}$).

it also exists more or less on the {100} surface.

The shape of the dot-like defect denoted by arrow F does not vary with etch depth. Hence, this defect is considered to be a dislocation lying in the $\langle 100 \rangle$ direction.

Also observable in Fig. 4 is a defect which exists three-dimensionally in GaAs as depicted by arrows G. Arrows G shown in Fig. 4(a) consist of independent linear defects. As the depth of the etching increases, the defects are connected to form a network, as shown in Fig. 4(b) and (c).

The etch depth in the decanted AB solution is about $6 \mu\text{m}$ for maximum resolution at an etch temperature of 23°C and light intensity of 4000 ft-c. However, the defects should be revealed with an etch depth less than $1 \mu\text{m}$ when the etching was performed at lower temperatures or when more intense lights were used. Consequently, {100} surfaces of GaAs were photoetched at 7°C for 15 sec, so that the inhomogeneities such as striations and etch hillocks were revealed in an etch depth of about $0.6 \mu\text{m}$. Furthermore, the etchant diluted 8 to 1 was also used at 23°C to decrease etch rates and to increase light intensity as the CrO_4^{2-} -containing solution absorbs lights. As a result, striations as well as dot-like and linear defects were delineated in an etch depth of about $0.7 \mu\text{m}$ and an etch depth for revealing dot-like and linear defects was only about $0.1 \mu\text{m}$, as shown in Fig. 5. These values

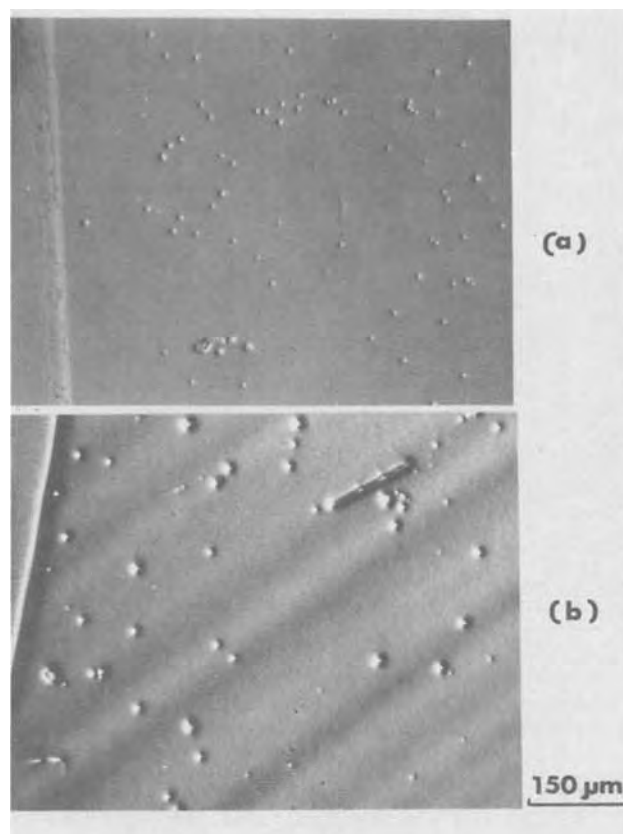


Fig. 5. Photoetched {100} surfaces of Si-doped GaAs using the etchant diluted 8 to 1. Etch depths in (a) and (b) are $0.1 \mu\text{m}$ and $0.7 \mu\text{m}$, respectively.

were remarkably lower than those obtained by conventional preferential etching.

Effect of dopant.—Photoetched patterns of Si-doped GaAs have already been shown in Fig. 1-3. As for the Te-doped GaAs indicated in Fig. 6(a), striations, as well as dislocation lines surrounded by slightly concave and rugged regions were observed. These regions were not observed in Si-doped or Cr-doped GaAs. The regions were examined using cathodoluminescence so that they were found to be brighter in the cathodoluminescent image than the dislocation lines or the regions where no dislocation lines existed. This result is consistent with that reported by Casey (7) who said that the precipitation of a Te-rich solid solution may account for the inhomogeneous cathodoluminescent images associated with dislocations.

Photoetched patterns of Cr-doped GaAs shown in Fig. 6(b) consist of ridged dislocation lines surrounded by slightly hollowed regions and defects with a peculiar cell structure. However, striations were difficult to observe in Cr-doped semi-insulating GaAs, in contrast to photoetched patterns of Si-doped and Te-doped GaAs. The cell structure observed in the peripheral region of melt-grown GaAs wafers is considered to relate to precipitates due to the low solubility of Cr in GaAs.

In order to examine the effect of carrier concentrations on the photoetched patterns, Si-doped GaAs with carrier concentrations of $4 \times 10^{17} \text{ cm}^{-3}$ and $2 \times 10^{18} \text{ cm}^{-3}$ were etched simultaneously. Photoetched patterns were similar in spite of the difference of carrier concentrations. However, an etch rate of GaAs with the carrier concentration of $4 \times 10^{17} \text{ cm}^{-3}$ was about 10% higher than that of GaAs with $2 \times 10^{18} \text{ cm}^{-3}$. This result seems to indicate that ridged lines correspond to higher carrier concentrations than recessed bands in the striations.

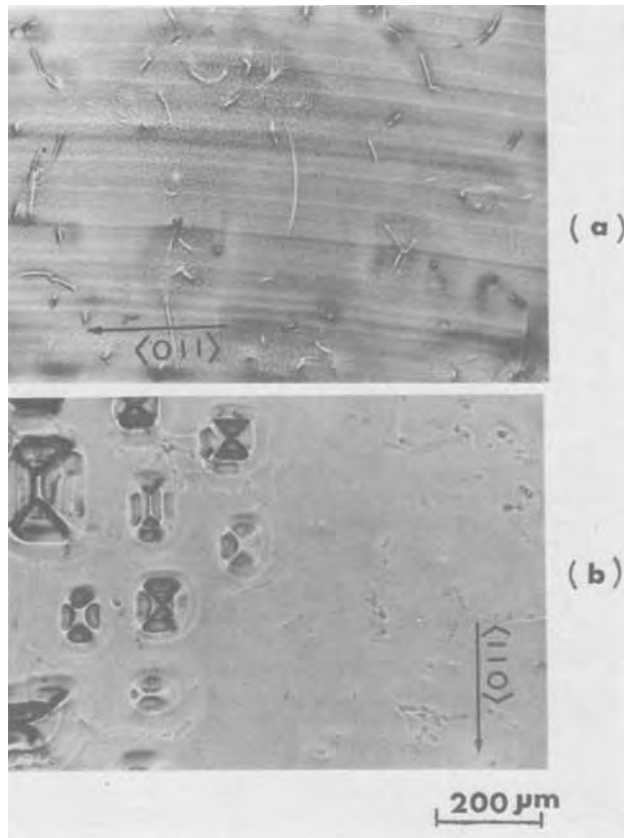


Fig. 6. Photoetched $\{100\}$ surfaces. (a), Te-doped GaAs; (b), Cr-doped GaAs. The etch depths are about $6 \mu\text{m}$.

Etching Rates

In photoetching using the modified AB solution, etching rates depended mainly on concentrations of CrO_3 and HF, light intensity, and etching temperature. This paper describes only the effects of light intensity and etching temperature on etching rates of GaAs. First, we examined the relationship between etch depth and etch time as a function of etch temperature. The etch depth was found to be proportional to the etch time. This linear relationship differs from the result reported by Abrahams *et al.* (4) who indicated that the etch rate shows a saturation with time. It was considered to be due to the formation of Ag_2CrO_4 precipitate during etching which occurred more easily at the high etch temperature of 65°C .

Figure 7 shows the Arrhenius plot of etch rates for illuminated or dark condition. Etch rate decreases linearly with the increase of the reciprocal temperature for etching in the dark condition but nonlinearly for etching under illumination. Furthermore, the differences of etch rates for illuminated and dark conditions are almost equal irrespective of etch temperatures. Therefore, photoetching rates (V) should be depicted as the following equation

$$V = A \exp\left(-\frac{\Delta E}{RT}\right) + BL \quad [1]$$

where A is a constant relating to the concentrations of reagents in the etchant and ΔE is an activation energy for etching in the dark. B is a constant and L is an incident light flux. From Fig. 7, one can obtain $A = 7.1 \times 10^5 \mu\text{m}/\text{min}$ and $\Delta E = 7.5 \text{ kcal/mol}$, typical for the diffusion controlled process. In order to obtain the value of B , we examined the relationship between the etch rate and the light intensity. Figure 8 shows the relationship from which we obtained the value of $B = 1.5 \times 10^{-4} \mu\text{m}/\text{min}\cdot\text{ft}\cdot\text{c}$.

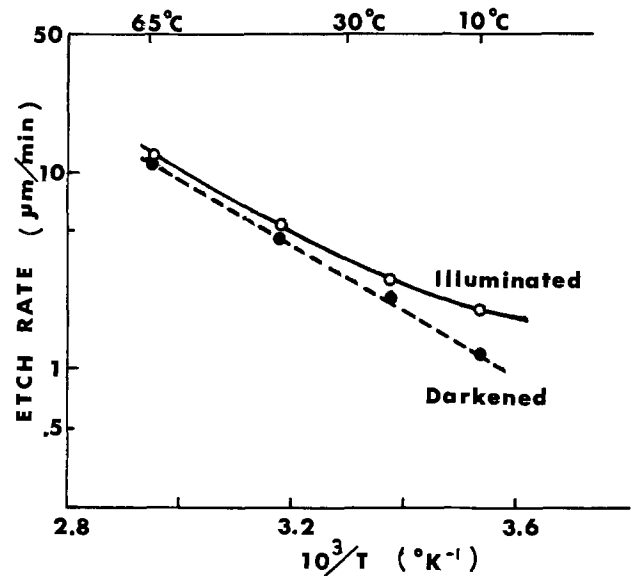


Fig. 7. Effect of illumination on the etching rate of $\{100\}$ surface of Si-doped GaAs as a function of temperature. The light intensity is $4 \times 10^3 \text{ ft}\cdot\text{c}$.

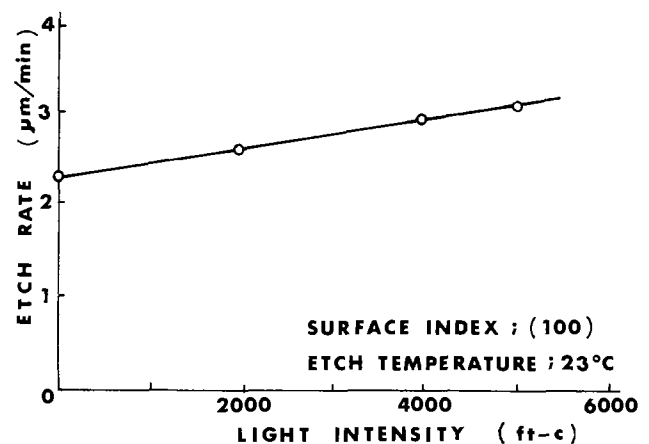


Fig. 8. Etching rate of $\{100\}$ surface as a function of light intensity for Si-doped GaAs etched at 23°C for 10 min.

The effect of Ag^+ ion concentrations up to $2 \times 10^{-3} \text{ g-ion/liter}$ on the etch rates was examined for $\{100\}$ surfaces of Si-doped GaAs ($n = 2 \times 10^{18} \text{ cm}^{-3}$) at 23°C and $4 \times 10^3 \text{ ft}\cdot\text{c}$. However, Ag^+ ions were found not to influence the etch rate of n-type GaAs, although effective in obtaining etch patterns with a little higher resolution. The reason positive ions such as Ag^+ do not effect etch rates is considered to be due to the anodic behavior of n-type GaAs surfaces in the etching solution.

Discussion

At the interface between an n-type semiconductor and an etchant, there exists a space-charge layer on the semiconductor surface near the etchant as well as a Helmholtz layer and a Gouy layer in the electrolyte close to the semiconductor (8). It has been shown that interfacial holes are required for anodic reactions at an n-type semiconductor surface (9, 10).

Generally, the preferential etching of defects has been attributed to the differences of chemical energies of the dislocation cores, or the local strain field around a dislocation. So, the higher concentration of holes, trapped at the dislocation combined with chemical energies or with the local strain field, increases the etch rate, causing etch pits. This explains why in the case of $\{111\}$ B face, etch patterns revealed in the dark

have a higher resolution than those produced by etching under room light.

Next, consider the effect of illumination for the chemical etching of n-type GaAs. The concentration of positive charges on the surface generated by photon absorption increases with the illumination, causing an increase of the etching rate as indicated in Fig. 7. Although Kuhn-Kuhnenfeld (5) has applied photoetching techniques in revealing defects of GaAs, no explanation was included in his paper on why the defects have ridged structures. The following is a possible model, based on the difference of positive charge distribution between the dislocation sites and the regions without dislocations. Defects, such as dislocations, are generally expected to be an effective recombination site of light-induced electron-hole pairs due to potential deformation. In photoetching, both electrons and holes generated by light recombine instantaneously at the dislocation rather than separate in the built-in electric field in the surface space charge layer. Thus, the concentrations of positive charges at dislocation sites become lower than those in the regions without dislocations. As a result, the etching rate at a dislocation decreases relatively so that an etch hillock is formed at the dislocation. This mechanism is consistent with the result of Ellis (11) who showed that the anodic etching of Ge is not uniform if dislocations are present at the surface and that this is presumably related to the trapping of electron-hole pairs at the dislocations.

In addition to the formation of etch hillocks, it should be pointed out that the built-in electric field decreases due to the generation of photovoltage in the photoetching. This decrease causes a relative increase in the deformation potential of the dislocation. Consequently, a dislocation becomes a more effective site to recombine light-induced carriers in contrast to the etching in the dark.

After an etch hillock has appeared under illumination, whether the hillock will remain or not depends on etch rates of various planes around the hillock.

Let us call the etch rate for a side of the hillock V_s and that for a surface plane V_p . The condition for the stability of the hillock is $V_p \cong V_s$. If the condition is not fulfilled, the hillock etches away faster than the surface plane and disappears. On the other hand, the

condition for developing etch pits revealed in the dark is $V_p < V_s$.

As shown in Fig. 7, the etching rate for the modified AB solution near room temperature is diffusion-controlled and the concentrations of light-induced carriers on various planes are expected to be independent of orientation. This suggests that the etch rates do not vary with orientation. In fact, the photoetching rate of a {100} surface was only about 10% larger than that of a {111}B surface. Therefore, the "memory" effect of etching patterns becomes more noticeable in photoetching than with other etching methods.

Acknowledgment

The authors would like to thank Dr. S. Kishino for his discussion, Dr. E. Maruyama for his critical reading of this manuscript, and Dr. Y. Ohtomo for his encouragement throughout this work.

Manuscript submitted July 12, 1974; revised manuscript received Dec. 18, 1974.

Any discussion of this paper will appear in a Discussion Section to be published in the December 1975 JOURNAL. All discussions for the December 1975 Discussion Section should be submitted by Aug. 1, 1975.

Publication costs of this article were partially assisted by Hitachi, Limited.

REFERENCES

1. H. A. Schell, *Z. Metallk.*, **48**, 158 (1957).
2. J. G. White and W. C. Roth, *J. Appl. Phys.*, **30**, 946 (1959).
3. J. L. Richards and A. J. Crocker, *ibid.*, **31**, 611 (1960).
4. M. S. Abrahams and C. J. Buiocchi, *ibid.*, **36**, 2855 (1965).
5. F. Kuhn-Kuhnenfeld, *This Journal*, **119**, 1063 (1972).
6. A. M. Huber and G. Champier, "Proc. 3rd Int. Symp. on GaAs and related Compds.," p. 118 (1970).
7. H. C. Casey, Jr., *This Journal*, **114**, 153 (1967).
8. J. F. Dewald, "The Surface Chemistry of Metals and Semiconductors," p. 205, John Wiley & Sons Inc., New York (1959).
9. W. H. Brattain and C. G. B. Garrett, *Bell System Tech. J.*, **34**, 129 (1955).
10. D. R. Turner, *This Journal*, **103**, 252 (1956).
11. S. G. Ellis, *Phys. Rev.*, **100**, 1140 (1955).

Auger Electron Spectroscopy of Cleanup-Related Contamination on Silicon Surfaces

Michael G. Yang¹ and K. M. Koliwad

Semiconductor Research and Development Laboratory, Texas Instruments Incorporated, Dallas, Texas 75222

and G. E. McGuire

Central Research Laboratory, Texas Instruments Incorporated, Dallas, Texas 75222

ABSTRACT

Auger electron spectroscopy has been used to evaluate the chemical state of silicon (111) surfaces cleaned by various liquid reagents, ion sputtering, and plasma treatment. The two most common impurities observed were carbon and oxygen. Results indicated that liquid reagent cleaning produced surfaces which were heavily contaminated with carbon, and that when oxidizing reagents were used, carbon contamination could be kept to a minimum. Sputtering was found to be an unsatisfactory method of cleaning because slices became activated after sputtering and adsorbed impurities from the atmosphere when removed from the vacuum system. Plasma treatment was the most effective of the three types of cleanups used, producing surfaces with the lowest carbon concentrations. One exception was CF_4 plasma which was shown to deposit carbon on the surface.

A large number of processes are used by the semiconductor industry for the cleaning of silicon prior to process steps such as oxidation, diffusion, and metal deposition. The chemical state of the surface after cleanup has not been systematically investigated, resulting in wasteful consumption of chemicals and the use of "overkill" in slice cleanup. We have investigated the effect of eight liquid reagent cleaning sequences, six plasma cleanups, argon sputtering, and deionized water rinsing on silicon surfaces.

Auger electron spectroscopy (AES) has been shown to be a useful and highly sensitive tool for the study of etched silicon (1) and chemically cleaned germanium surfaces (2), particularly for the determination of the effects of carbon contamination (3), and has been chosen for this study. The principles of AES have been described in the literature (4-6).

In this work carbon was found to be one of the major contaminants, along with oxygen, on chemically cleaned silicon surfaces and the effectiveness of various chemicals, plasma, and sputtering for the removal of carbon have been examined.

Experimental

The samples used were 0.76 mm thick mechanically polished 10 ohm-cm boron-doped silicon (111) slices. The slices were cut from the same boule in order to minimize the effect of the bulk material on the surface contamination. Strips from the slices were then subjected to liquid cleaning, argon ion bombardment, or plasma cleaning. All reagents used were (ACS) Low Mobile Ion Grade and the deionized water used for rinsing had a resistivity of 18 megohms. Details of the process sequences used to prepare the samples are given in Tables I (liquid reagent), II (argon ion sputter), and III (plasma).

Argon ion bombardment was performed with a Varian ion gun (Model 981-1045) at 5×10^{-5} Torr argon (Matheson, Research Grade) pressure, which produced a 12 mm diameter ion beam at 600 eV energy. Samples could be heated inside the Varian Cylindrical Mirror Analyzer system (Model 981-2607) by conduction from radiatively heated stainless steel blocks on which they were mounted for analysis. Chromel-Alumel thermocouples, spot welded on stainless steel retaining strips used to press the samples to

the heated blocks, were used to measure the temperature of the samples.

To minimize contamination due to post-cleanup handling, all treated samples were transported in clean, covered Pyrex containers and loaded into the

Table I. Liquid reagent cleanup sequences^(a)

A	Trichloroethylene Methyl alcohol Deionized water rinse Piranha ^(b) Deionized water rinse HF, concentrated, dip Deionized water rinse, 100°C Deionized water rinse Spin dry
B	Piranha Deionized water rinse HF, 10%, ^(c) dip Deionized water rinse Isopropanol Freon vapor dry
C	Piranha Deionized water rinse, 100°C HF, concentrated, dip Deionized water rinse HNO ₃ , concentrated, 90°C Deionized water rinse Spin dry
D	Deionized water rinse Piranha Deionized water rinse HF, 10%, dip Deionized water rinse Spin dry
E	Piranha Deionized water rinse HF, concentrated, dip Deionized water rinse HNO ₃ , concentrated, 90°C Deionized water rinse Spin dry
F	Trichloroethylene Methyl alcohol Deionized water rinse Spin dry
G	HF, concentrated Deionized water rinse Blow dry with nitrogen
H	H ₂ SO ₄ 60%-HNO ₃ 40% solution Deionized water rinse Bell No. 2 ^(d) Deionized water rinse Blow dry with nitrogen

^(a) All liquid treatments are 1 min in duration with reagents at room temperature unless otherwise stated. All deionized water rinses are 10 min in duration, unless specified as a dip.

^(b) The composition of Piranha is as follows: 70% H₂SO₄, 30% H₂O₂.

^(c) All percentages indicated are volume per cent.

^(d) Bell No. 2 is formulated as follows: 200 ml H₂O, 200g NH₄F, 45 ml HF.

¹ Present address: Republic Steel Corporation, Research and Development Center, Independence, Ohio 44131.

Key words: Auger, surface, electron spectroscopy, cleanup.

Table II. Argon ion bombardment sequences

A1	Ar ⁺ sputtered for 45 min
A2	Ar ⁺ sputtered for 45 min Annealed at 770°K for 30 min, examined at temperature
A3	Ar ⁺ sputtered for 45 min Annealed at 770°K for 30 min Cooled to room temperature and examined
A4	Ar ⁺ sputtered for 45 min Removed from vacuum system and exposed to room air for 20 min Reintroduced into vacuum system and examined after standard pumpdown
A5	Ar ⁺ sputtered for 45 min Removed from vacuum system and exposed to room air for 24 hr Reintroduced into vacuum system and examined after standard pumpdown
A6	Ar ⁺ sputtered for 45 min Annealed at 770°K for 30 min Cooled to room temperature Removed from vacuum system and exposed to room air for 30 min Reintroduced into vacuum system and examined after standard pumpdown

Table III. Plasma cleaning sequences^(a)

B1	O ₂ plasma treatment, 10 min
B2	N ₂ plasma treatment 10 min
B3	Ar plasma treatment, 10 min
B4	CF ₄ plasma treatment, 10 min
B5	CF ₄ plasma treatment, 5 min followed by O ₂ plasma treatment, 5 min
B6	O ₂ plasma treatment, 5 min followed by N ₂ plasma treatment, 5 min

^(a) Typical operating conditions are as follows: gas pressure = 1 Torr, flow rate = 100 cm³/min, RF power = 300W, substrate temperature = 373°K.

vacuum system after a maximum of 90 min storage. A base pressure of 10⁻⁹ Torr was attained without bake-out, after overnight pumping, before Auger analysis was performed.

Results

Due to the large number of AES spectra ($dN(E)/d(E)$ vs. E) obtained, it is cumbersome to present the actual data. Instead, relative surface coverage values, obtained by a normalization method explained below are given.

The per cent coverage was computed using the following equation

$$\text{Per cent coverage} = \left(\frac{a_i/a_i^0}{\sum_j a_j/a_j^0} \right) \times 100$$

where a_i is the Auger peak-to-peak intensity from the i th element and a_i^0 is the "standard" peak-to-peak intensity obtained from the pure element. The "standard" peak-to-peak intensities were taken from the "Handbook of Auger Spectroscopy" (7). In the case of a compound standard, the measured standard peak-to-peak intensity was first divided by the mole fraction of the element of interest in the compound. The AES spectra shown in the Handbook were of course taken under fixed conditions.

The a_i^0 for the Si (78 eV) transition, which is characteristic of clean SiO₂ surfaces but does not appear in the Handbook (7), was calculated in the following manner. Auger spectra were obtained from a 1000Å thick thermally grown SiO₂ film using our Auger system. The ratio of the peak-to-peak intensities of the O (510 eV) transition (from the MgO sample) obtained from Ref. (7) to that of the O (510 eV) transition of the SiO₂ sample was then multiplied by the peak-to-peak intensity of the Si (78 eV) transition from the SiO₂ sample and corrected for the mole fraction to yield the required a_i^0 .

The reduced data for each type of cleanup are tabulated in Tables IV, V, and VI. It should be noted that the numbers shown in the tables are for comparison of the effects of the different surface treatments only and do not represent accurate surface coverages.

Liquid reagent cleanup.—Table IV summarizes the Auger data obtained for slices subjected to various liquid chemical treatments.

Table IV. Per cent surface coverage, liquid reagent cleanup

Cleanup	Si (78 eV) ^(a)	Si (91 eV)	B/Cl ^(b)	S	C	N	O	Fe	Ni
Untreated	17.2	11.3	Tr ^(c)	0.14	55.4	1.2	14.7		
A	37.4	32.1	Tr		10.5		20.0		
B		75.4			21.3		3.3		
C	35.4	16.2			15.3	2.4	24.0	1.9	4.9
D	36.4	17.1			14.3	2.4	25.6	1.0	3.3
E	22.5	22.6			37.4	1.6	16.0		
F	27.0	17.6			34.1	1.9	19.3		
G		25.7			72.0	0.5	1.8		
H		51.5		0.12	45.1	0.4	2.9		
D.I. rinse	37.4	32.1			10.5		20.0		

^(a) In the change of chemical state from Si to SiO₂ a shift in the energy of the Si peak from 91 to 78 eV in the low energy Auger spectrum occurs. The 78 and 91 eV transitions may be easily distinguished even when present in the same spectrum and the ratio of the two peaks may be used to estimate the Si/SiO₂ content of the surface.

^(b) The Auger transitions of boron (179 eV) and chlorine (181 eV) occur within the same narrow energy range so that for practical purposes they are indistinguishable by AES. However, one may use the Auger apparatus to distinguish boron from chlorine by an electron loss technique. The high energy Cl (2400 eV) transition could not be observed using our system since the electron gun had a maximum energy of 2000 eV.

^(c) Trace level.

A salient feature is the presence of carbon in relatively high concentrations on every sample analyzed. In conjunction with this observation, it is of interest that the degree of oxidation of the surface apparently has an effect on the surface carbon contamination, i.e., the higher the oxygen concentration at the surface, the lower is the carbon concentration observed. This is not surprising since an oxidized surface is expected to be much more stable chemically than a bare silicon surface. Furthermore we have observed that an oxidized silicon surface that has been sputtered with positive argon ions to produce an atomically clean surface adsorbs only an insignificant amount of carbonaceous material when exposed to room air. This result is quite different from that found after exposing a sputtered silicon surface to air whereupon, as will be shown below, the surface acts as a very effective getter of carbon-bearing species from the ambient.

The cleanups which produced the surfaces with the highest carbon contents are G and H. Cleanup G was a concentrated HF dip followed by deionized water rinsing and in cleanup H, the last reagent used, was Bell No. 2 which consists of an HF-NH₄F solution (see footnote in Table I). The indication is that concentrated hydrofluoric acid treatment increases the propensity of the silicon surface for adsorption of hydrocarbons. This effect, which has also been observed by Henderson (9), is due to the fact that HF removes the native oxide from the surface and leaves behind a very active bare surface as described above.

Cleanup D, which consisted of a 10 volume per cent HF dip followed by deionized water rinsing, was not expected to produce a completely oxide-free surface since in the presence of water a steady state is attained such that removal of oxide and reoxidation in the aqueous medium occur simultaneously. Thus when the slice was transferred (through air) into the water rinse it presented an oxidized surface unfavorable for adsorption of carbon-containing gaseous species. The results shown in Table IV bear this out.

With the exception of cleanups C and D, no metal contamination was found on the samples examined. Since the same techniques and chemical sources were used in preparing all the chemically cleaned samples, it appears that the traces of Ni and Fe found in samples C and D were introduced by accident either into the solutions or directly onto the slices by the operator rather than from an inherent defect in the cleaning processes.

Ion bombardment cleanup and contamination by air.—The effect of positive argon ion bombardment, annealing in ultra-high vacuum, and exposure to room air are presented in Table V. Extremely clean

Table V. Per cent surface coverage, argon ion bombarded

Cleanup	Si (78 eV)	Si (91 eV)	B/Cl	Ar ^(a)	S	C	N	O
Untreated	17.2	11.3	Tr ^(b)	Tr	0.1	55.4	1.2	14.7
A1		94.3		Tr		5.7		
A2		88.9	Tr			10.8		0.1
A3		75.9		Tr		22.5		1.5
A4	2.5	12.0		Tr	Tr	72.5	2.4	10.6
A5	7.8			Tr		78.6	3.0	10.6
A8		6.2		Tr		89.0	0.3	4.4

^(a) The effect of low energy (600 eV) argon ion bombardment of a surface is the removal of material with a small amount of the bombarding gas being implanted in the first several monolayers. Argon has a distinct Auger transition and does not interfere with the identification of other species. It does occupy a fraction of the detectable volume and must be considered when determining the number of detected atoms for each element when present in significant quantities.

^(b) Trace level.

silicon surfaces can be generated by this technique, as shown by the AES data, and the same technique has been used by Farnsworth *et al.* (10) and by Schlier and Farnsworth (11) to produce atomically clean silicon surfaces for adsorption studies.

Annealing of the sputtered samples at 770°K for 30 min resulted in an increase in the carbon concentration at the surface. This may have been caused by either out-diffusion from the bulk or by beam assisted decomposition of adsorbed carbon compounds. The former mechanism is believed to be the one which was operative since carbon segregation to the surface during annealing was also found when the vacuum conditions were such that the time for a monolayer of carbon compounds to adsorb on the surface was much greater than the total time of the AES experiment.

In order for sputter cleaning to be a useful process for integrated circuit manufacture, it is necessary to be able to anneal out the surface damage (and simultaneously to eliminate the active adsorbent layer). The annealing time and temperature sufficient to restore surface order on silicon was found to be (10) a few minutes at 1170°K. An alternative to annealing out damage would be to perform the next process step without exposing the slice to contaminating atmospheres, such as is possible in some metal sputter-deposition machines.

Plasma cleaning.—The silicon samples subjected to plasma cleaning were by far the least contaminated of those prepared by standard processing methods (see Table VI). All of the surfaces cleaned by this technique showed very low carbon levels, the only exception being the sample treated for 10 min in a CF₄ plasma. The latter is due to deposition of carbon from plasma-decomposed source gas (12). It is interesting to note that the surfaces are all (excepting the CF₄ case) heavily oxidized and thus reduce the degree of hydrocarbon adsorption when exposed to the atmosphere. The presence of fluorine is believed to have resulted from the decomposition of CF₄ which is used to clean the plasma system and is expected to be heavily adsorbed on the system walls. The presence of nitrogen in the Auger spectra has not yet been fully understood.

Table VI. Per cent surface coverage, plasma treated

Cleanup	Si (78 eV)	Si (91 eV)	B/Cl	S	C	N	O	F
Untreated	17.2	11.3	Tr ^(a)	0.1	55.4	1.2	14.7	
B1	55.5	6.4	0.46		2.1	0.3	33.8	1.4
B2	54.4	3.8			2.2	Tr	38.2	1.0
B3	64.7	4.8			6.6	0.3	24.3	0.3
B4	3.0	16.9			76.1	0.6	3.4	0.8
B5	57.0				3.2		34.9	1.4
B6	50.0		0.23	0.2	2.9	1.3	44.8	

^(a) Trace level.

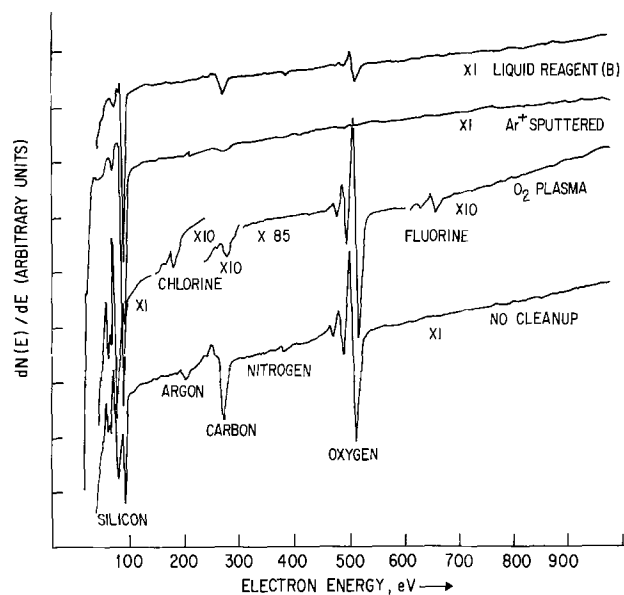


Fig. 1. Typical Auger spectra after various surface cleaning procedures.

Summary

The effects of liquid reagent, sputtering, and plasma cleaning on the chemical state of bare silicon (111) surfaces have been characterized and significant differences in carbon and oxygen contamination have been found. The Auger spectra for three of the most effectively cleaned samples (one from each group of cleanups) are shown in Fig. 1, together with the spectrum from an uncleaned sample for comparison. Liquid methods were found least effective in removing surface carbon. In particular, hydrofluoric acid formulations appeared to enhance hydrocarbon adsorption and actually increased the degree of carbon contamination. Rinsing in deionized water was an effective method for removing much of the carbonaceous material from the starting (untreated) material. Sputtering with argon ions can result in atomically clean surfaces but has the major drawback of leaving an active (for adsorption) and damaged surface. Plasma methods constituted the most encouraging techniques both in terms of surface cleanliness and practicability.

Acknowledgment

This work was supported by the Air Force Materials Laboratory, Wright-Patterson Air Force Base, Ohio 45433 under contract F33615-73-C-5-47. The help of Margaret Jarvis in the preparation of samples is gratefully acknowledged. We would also like to express our appreciation to Dan Stallings for his assistance in taking some of the data and to Dr. David Lam for preparing the plasma cleaned samples.

Manuscript submitted July 29, 1974; revised manuscript received Dec. 20, 1974.

Any discussion of this paper will appear in a Discussion Section to be published in the December 1975 JOURNAL. All discussions for the December 1975 Discussion Section should be submitted by Aug. 1, 1975.

Publication costs of this article were partially assisted by Texas Instruments Incorporated.

REFERENCES

- C. C. Chang, *Surface Sci.*, **23**, 293 (1970).
- D. A. Kiewit, I. J. D'Haenens, and J. A. Roth, *This Journal*, **121**, 310 (1974).
- B. A. Joyce, J. H. Neave, and B. E. Watts, *Surface Sci.*, **23**, 283 (1970).
- P. Auger, *Phys. Radium*, **6**, 205 (1925).
- J. J. Lander, *Phys. Rev.*, **91**, 1382 (1953).

6. L. A. Harris, *J. Appl. Phys.*, **39**, 1419 (1968).
7. P. W. Palmberg, G. E. Riach, R. E. Weber, and N. C. MacDonald, "Handbook of Auger Spectroscopy," Physical Electronics Industries, Inc., Edina, Minn. (1972).
8. M. G. Yang and G. E. McGuire, Unpublished data.
9. R. C. Henderson, *This Journal*, **119**, 772 (1972).
10. H. E. Farnsworth, R. E. Schlier, and J. A. Dillon, *J. Phys. Chem. Solids*, **8**, 116 (1959).
11. R. E. Schlier and H. E. Farnsworth, *J. Chem. Phys.*, **30**, 917 (1959).
12. D. K. Lam, Private communication.

Effect of Substrate Microdefects Due to Thermal Etching on the Near-Junction Properties of GaP:Zn,O Grown by Liquid Phase Epitaxy

C. Michel

Philips Laboratories, Briarcliff Manor, New York 10510

ABSTRACT

The effect of individual interfacial microdefects due to thermal etching on the cathodoluminescence (CL) and minority carrier diffusion length (L_e) have been investigated with a scanning electron microscope for p-type GaP:Zn,O layers grown by liquid phase epitaxy (LPE) on n-type GaP substrates. For layers grown by conventional tilting or sliding techniques, both CL and L_e are significantly reduced in the vicinity of a defect, probably because of the strong growth anisotropy generated there. However no degradation was observed for layers grown by an LPE technique that employs controlled substrate meltback and a Te-compensated growth solution. This difference may account for the improvement of about 15% in electroluminescent efficiency that has been reported for light-emitting diodes prepared from layers grown by a meltback technique.

Efficient GaP light-emitting diodes (LED's) can be obtained (1, 2) by liquid-phase epitaxy (LPE). Since the layer-substrate interface in these devices is close to the active region, the quality of the substrate surface is expected to influence their performance. However the electrical and optical effects associated with individual interfacial microdefects have not been clearly demonstrated. The difficulty is usually of an experimental nature in that the microscopic interaction between a particular defect and the near-junction characteristic cannot be observed directly by any of the conventional low-resolution techniques, e.g., x-ray topography.

In this investigation, a scanning electron microscope (SEM) operated in the cathodoluminescence (CL) and beam-induced current (BIC) modes has been used to study the near-junction properties of diode structures prepared by growing LPE layers of p-type GaP:Zn,O on n-type GaP substrates cut from crystals grown by the liquid-encapsulated Czochralski (LEC) technique. Three different LPE growth procedures, based on the tilting, sliding, and dipping techniques, were used. In all cases, interfacial microdefects resulted from the thermal etching of the substrates that occurred prior to LPE growth. The SEM measurements showed that the cathodoluminescence and minority-carrier diffusion lengths were reduced in the vicinity of these microdefects for layers grown by the tilting and sliding procedures, but not for those prepared by the dipping method.

Thermal Etching of GaP Substrates

The GaP substrates used in this investigation were (111)B wafers cut from LEC crystals doped with Te or S ($N_D - N_A = 2-5 \times 10^{17} \text{ cm}^{-3}$). P-type GaP:Zn,O layers were grown on these substrates by three different LPE processes described in the next section. In each process the LPE growth temperature is 1040°C, which yields (3) the maximum concentration of the Zn,O centers responsible for red emission, and the sub-

strate is kept at this temperature for 5-10 min prior to LPE growth. Even during this short time a considerable amount of P is lost from the substrate by preferential evaporation, since the P pressure over GaP at 1040°C is about 0.2 Torr, much higher than the Ga pressure.

To investigate the surface defects resulting from P evaporation, an SEM was used to examine (111)B GaP wafers that had been thermally etched under conditions similar to those encountered prior to LPE growth. Such wafers typically exhibit a roughly uniform distribution of deep etch pits a few micrometers in size, as shown in Fig. 1. In some cases, triangular etch pits, shown in Fig. 2, with well-defined edges aligned along preferential crystallographic directions

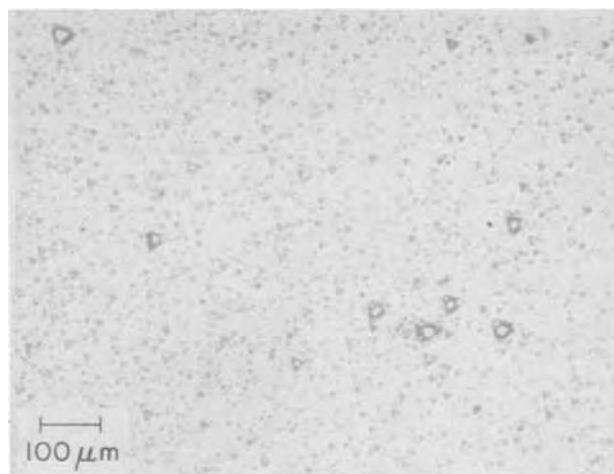


Fig. 1. SEM photomicrograph of thermal etch pits on the surface of a (111)B GaP substrate. The experiment was performed at 1020°C for 3 hr in a sealed ampul.

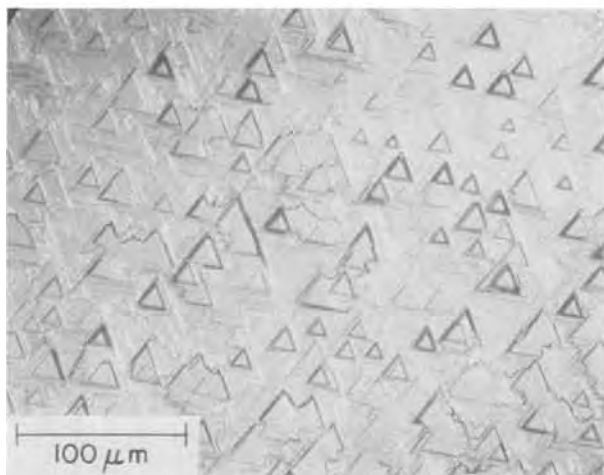


Fig. 2. SEM photomicrograph of triangular etch pits on the surface of a thermally etched GaP substrate (same experimental conditions as Fig. 1).



Fig. 4. SEM photomicrograph of Ga droplets located at the bottom of a typical conical etch pit.

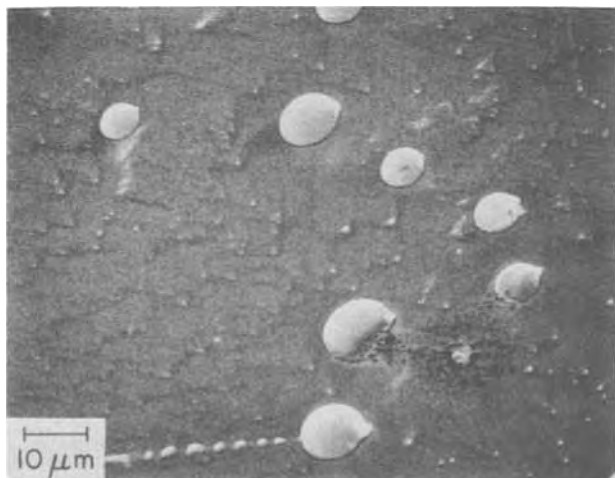


Fig. 3. SEM photomicrograph of typical Ga droplets on the surface of a thermally etched GaP substrate (same experimental conditions as Fig. 1).

are also obtained. In addition, droplets of Ga are frequently observed on the etched surfaces, as shown in Fig. 3 and 4. It can be seen in these figures that the droplets are generally located at the bottom of etch pits, consistent with the conclusion of Solomon and DeFevre (2) that the thermal etching is due to straightforward thermal decomposition.

The P evaporation rate was found to be strongly dependent on the quality of the substrates, particularly on their dislocation densities. Table I gives the evaporation rate at 1040°C measured for one LPE and two LEC samples that were sealed in evacuated fused quartz ampuls. Furthermore, a strong difference was observed in the etch pattern and the thermal etch-pit density, depending on the type of material. This difference is well illustrated in Fig. 5, a photomicrograph taken along a metallurgical junction of an LPE layer grown on an LEC crystal.

Our experiments showed that in an open-tube system the thermal etch rate is independent of the carrier gas (N, He, Ar) but strongly dependent on the gas flow rate. It is also known (5) that changes in surface morphology are markedly dependent on the degree of undersaturation maintained during heating, on the temperature range, and on the crystal orientation.

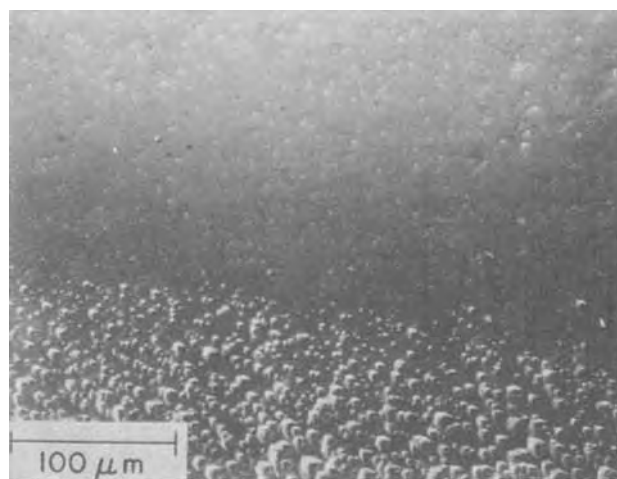


Fig. 5. SEM photomicrograph of a junction composed of a p-type LPE layer (low density of thermal etch pits) on an n-type LEC substrate (high density of thermal etch pits).

Procedures for LPE Growth and SEM Characterization

P-type, GaP:Zn,O layers were grown at 1040°C from saturated Ga-rich solutions on various n-type substrates. The growth solutions were also saturated with oxygen (from Ga₂O₃) and doped with Zn to give carrier concentrations in the layers of $3-4 \times 10^{17} \text{ cm}^{-3}$. Three different LPE techniques were used: (i) A tilting, closed-tube system similar to the one described by Saul, Armstrong, and Hackett (1). (ii) A horizontal, open-tube system with a modified sliding boat based on the design of Panish, Sumski, and Hayashi (6). (iii) A vertical, open-tube dipping system (5) similar to the one reported by Solomon and DeFevre (2), that is designed to minimize thermal etching of the substrate.

The growth conditions for techniques (i) and (ii) were such that substrate meltback did not occur at

Table I. Thermal etch rate for various GaP crystals at 1040°C

Type of crystal	Net carrier concentration/cm ³	Dislocation count/cm ²	Thermal etch rate, mg/cm ² -sec
LEC	Te 5×10^{17}	1.5×10^5	9×10^{-4}
LEC	Te 4×10^{17}	2×10^4	$3-5 \times 10^{-4}$
LPE	Zn $3-5 \times 10^{17}$		$1-7 \times 10^{-4}$

the beginning of LPE growth. (With these techniques, the edge of the substrate where the LPE layer did not grow was taken as a reference.) With technique (iii), however, the substrate was strongly solution-etched prior to LPE growth. The growth solution used for technique (iii) contains an excess of Zn dopant, which is largely compensated by adding Te. The LPE layers grown by this technique therefore have a Zn concentration exceeding 10^{18} cm^{-3} , but the measured carrier concentration is still about $3\text{-}4 \times 10^{17} \text{ cm}^{-3}$.

Measurements of the near-junction properties of red-emitting p-n junction structures grown by LPE were made with an AMR-900 scanning electron microscope (SEM), using the secondary-emission (SE), cathodoluminescence (CL), deflection-modulation (DM), beam-induced-current (BIC), and voltage contrast (VC) modes of detection (7). A lens and light pipe were inserted to transmit the CL recombination radiation through the exit port of the specimen chamber for detection with an S20 photomultiplier. Details of the electron beam excitation system and emission detection system have been given previously (7).

The position of the p-n junction on a cleaved section of the sample was observed on the CRT screen using the BIC or the VC mode. Simultaneously, the spatial distribution of the CL intensity in the p-region was also displayed.

Effect of Thermal Etching on Near-Junction Properties

The SEM measurements performed on cleaved p-n junction structures show that thermal etching has a detrimental effect on the near-junction properties of samples prepared by the LPE techniques (i) and (ii) listed above. Typical results for such a sample in the vicinity of a thermal etch pit are shown in Fig. 6, which consists of four SEM photomicrographs of the cleaved surface that were obtained by using (from top to bottom) the direct CL, DM, VC, and BIC modes of detection. The lower portion of each photomicrograph corresponds to the GaP substrate, and the upper portion to the LPE layer. The location of the electronic p-n junction is shown by the BIC (bottom) pattern. The etch pit has a flat bottom parallel to the original substrate surface [i.e., to the (111) plane] and sharp, well-defined edges. All the pits examined have this

shape, although their size and spacing vary considerably. The CL (top) pattern shows that cathodoluminescence is emitted only by the LPE layer and that a dark ring of decreased intensity is formed around the etch pit. Such a decrease in CL intensity around etch pits and microsteps was observed for all samples that had been grown by LPE techniques (i) and (ii).

To obtain quantitative data on the variation of BIC and CL in the vicinity of a thermal etch pit, SEM line scans using these two detection modes were made across the p-n junction of the sample of Fig. 6 at the three positions indicated by arrows in that figure. Scan a, taken outside of the thermal etch pit, is shown in Fig. 7 with a CL profile that is the complementary function of the BIC profile normally characteristic of a p-n junction behavior with no "dead layers" (8, 9). For the scans made at the edge (scan b) and center (scan c) of the etch pit, the CL intensity has a minimum at the position of the dark ring shown in Fig. 6.

For each scan of Fig. 7, the minority carrier diffusion lengths were calculated from the logarithmic plot of the BIC intensity vs. the distance from the junction as shown in Fig. 8. The hole diffusion length (L_n) on the n-type side of the junction is about $0.5 \mu\text{m}$ for all three scans, but the electron diffusion length (L_e) is significantly reduced for the scans that pass through the etch pit. Thus the values of L_e for scans a, b, and c are 1.0 , 0.75 , and $0.65 \mu\text{m}$, respectively. Similar measurements made on other thermally etched substrates show a systematic degradation of the CL intensity around an etch pit or microstep. This effect is visualized by a typical "dark" ring on the CL display as shown in Fig. 6. In addition, an appreciable decrease of L_e in the p-region was measured in all these samples at the edge of the pit.

Recent studies of the vapor-phase epitaxial growth of GaAs within chemically etched windows on GaAs(111)B substrates suggest a possible explanation for the effect of thermal etch pits on the near-junction properties of GaP LPE layers. A strong growth anisotropy in the vicinity of the window edges has been clearly demonstrated by impurity striation (10, 11) and Peltier-effect (12) studies. A similar growth perturbation could take place during the initial stage of LPE growth at a thermal etch pit on the GaP sub-

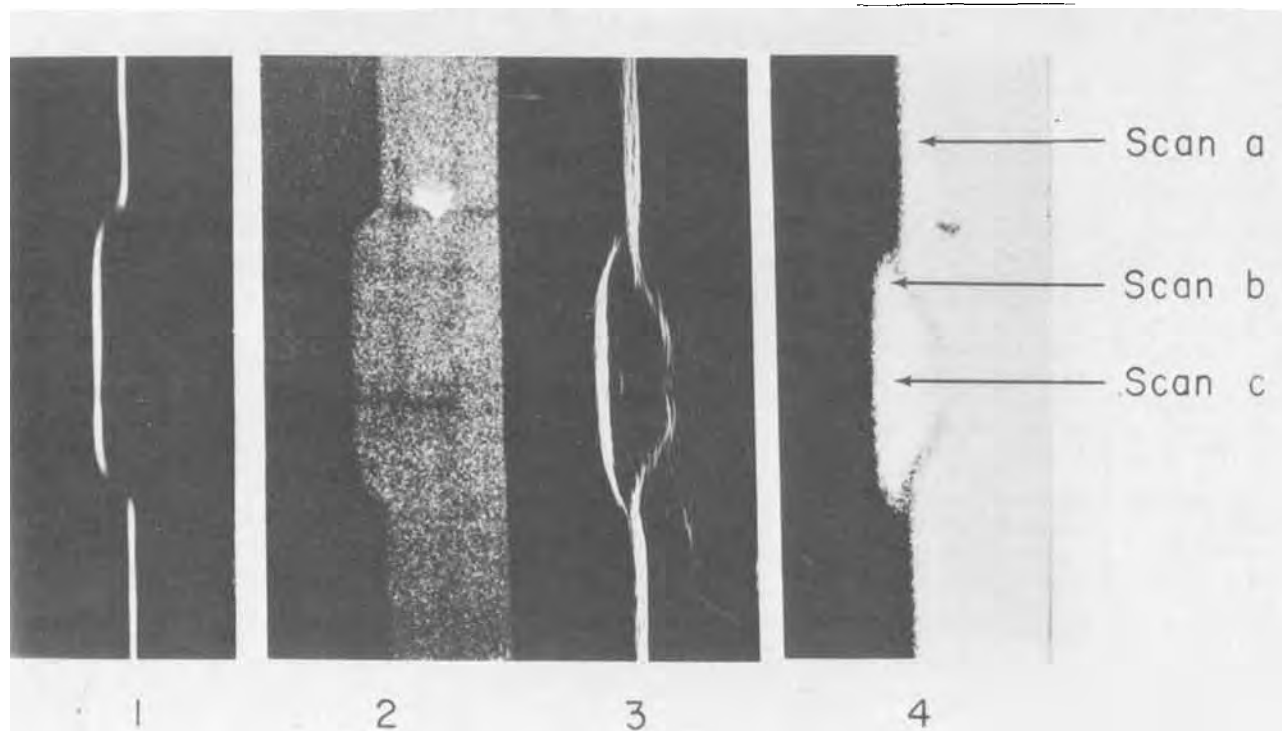


Fig. 6. SEM photomicrograph of the p-n junction of a cleaved GaP wafer in the vicinity of a thermal etch pit, generated in different modes of detection: 1, BIC mode; 2, VC mode; 3, CL intensity in deflection modulation mode; 4, CL intensity.

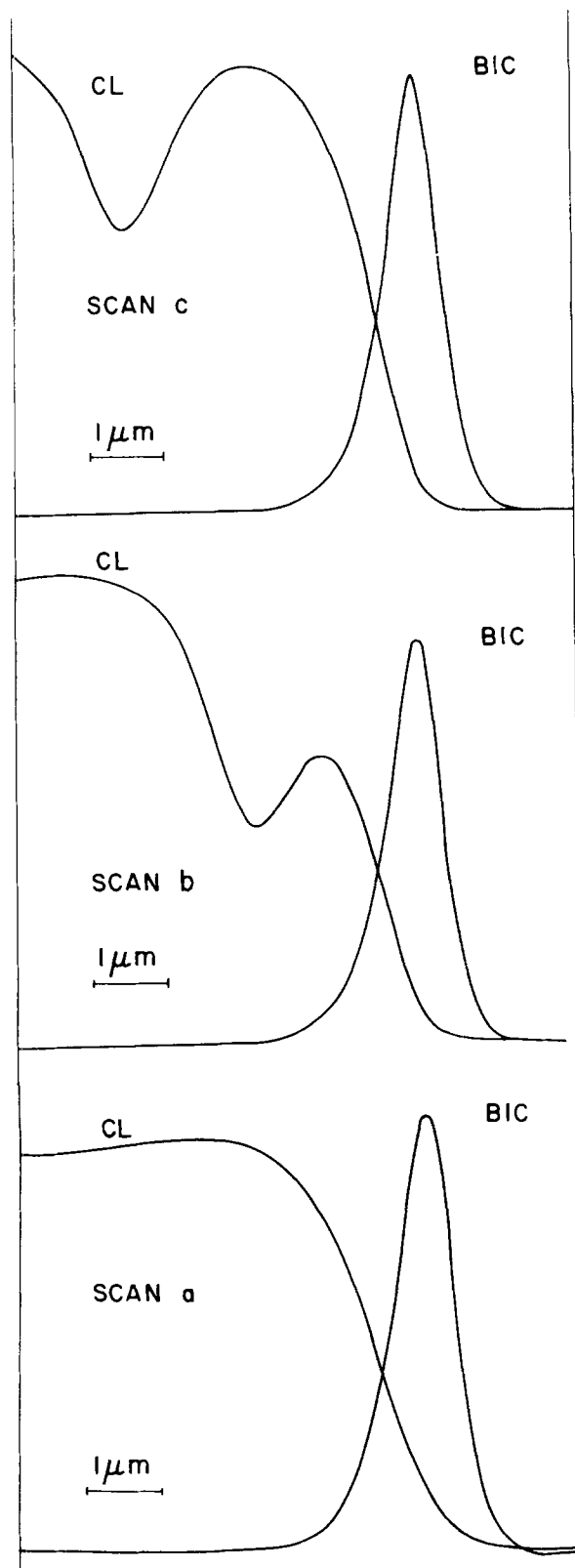


Fig. 7. Line scans of CL intensity and BIC signal taken across the p-n junction of the sample of Fig. 6. Scan (a) was taken outside the thermal etch pit, scan (b) at the corner edge of the pit, and scan (c) at the center of the pit.

strate surface. Hence, a growth direction different from the substrate orientation would be favored at the corner edge of the pit, causing a variation in the growth rate and dopant incorporation along the junction. Furthermore, such a local growth perturbation can induce a highly stressed region (13). In our case, the sharp corner edge of a thermal etch pit could be a

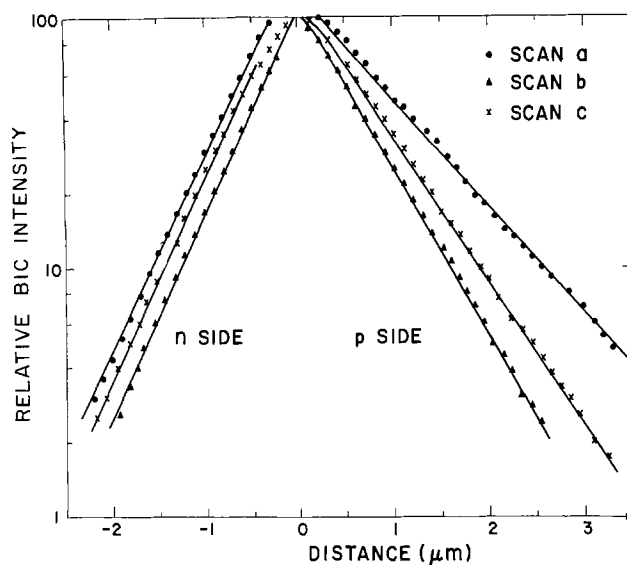


Fig. 8. BIC signal as a function of distance from the p-n junction, evaluated from the scans of Fig. 7. Scan (a) is off the pit, scan (b) is at the corner, and scan (c) at the center of the pit.

region of high density of dislocations, thereby acting (14-16) as a sink for nonradiative "killer" centers that could decrease the CL efficiency and degrade the minority-carrier lifetime.

In GaP LED's with p-n junction structures like those studied in this investigation, radiative recombination of injected carriers occurs within a few micrometers of the junction. Therefore a reduction in the electroluminescence (EL) efficiency of these devices can be expected to occur when there is a degradation in CL efficiency and L_e in the active region due to thermal etch pits. Since the reduction in EL efficiency should increase as the density of these pits increases, our observation that this density depends on substrate quality and growth conditions could account for the broadened distribution of LED efficiencies reported by Solomon and DeFevere (2) as resulting from thermal etching. However, any direct correlation between the near-junction properties and LED device performance should be treated with caution. It is quite clear that the growth conditions also have to be examined in order to determine, unambiguously, the validity of such correlations; for materials grown with a tilting or sliding system, the substrate is in the hot zone during the entire LPE cycle. Hence, thermal etching of the substrate prior to the LPE growth inevitably occurs (but in various degrees) at these high temperatures. It should be noted that an intentional or non-intentional solution-etch during the initial stage of the epitaxy tends to reduce the surface roughness of the substrate. In this case, a wavy but smooth interface is observed by conventional etching, VC or BIC modes of detection.

The dipping technique differs from techniques (i) and (ii) namely, minimum exposure of the substrate to the thermal etch action

meltback of the substrate prior to the final LPE p-type Zn,O doped layer.

Furthermore, in this particular technique the variation of the doping concentration due to the dissolution of the n-type substrate in the p-type growth solution should be minimized because the solution is already highly counterdoped with Te.

In general, meltback prior to the epitaxial growth tends to smooth out the substrate roughness and reduce considerably the influence of the surface microdefects induced by thermal etching. Under these conditions, a microstep as shown in Fig. 9 apparently does not influence the near-junction properties. A close

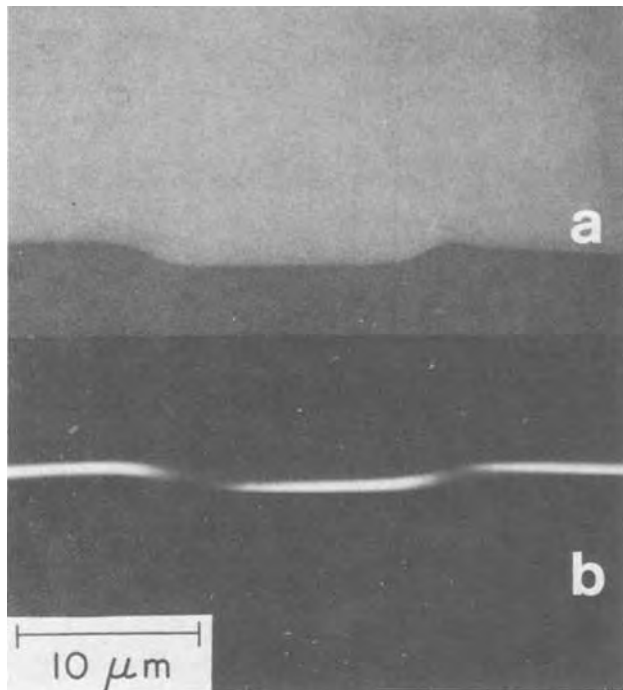


Fig. 9. SEM photomicrograph of the p-n junction of a cleaved GaP sample in which the LPE layer was grown by dipping with substrate meltback (technique *iii*). (a) CL mode, (b) BIC mode.

examination of these compensated materials showed no measurable degradation of either CL or L_e , suggesting that the meltback process has eliminated the local degradation observed in LPE layers grown by techniques (i) and (ii).

It has previously been found (17) that GaP layers grown by the meltback technique lead to diodes with better electroluminescence efficiency. An increase of about 15% in average EL efficiency of red GaP diodes due to meltback has also been recently reported (18). This improvement is consistent with our SEM study.

Conclusions

In the fabrication of GaP:ZnO red-emitting LED's by LPE, thermal etching at the optimum growth temperature seriously degrades the smoothness of the substrate surface. Imperfections present at the surface of the substrate, such as thermal etch pits or microsteps, affect the near-junction properties of the materials.

For p-n junctions obtained by using conventional tipping and sliding LPE techniques without substrate meltback, SEM examination shows that the CL efficiency and L_e in the p-type layers are reduced in the vicinity of each thermal etch pit. This reduction is probably due to the strong anisotropy of the initial

LPE growth at the corners of the pits. Since the etch pit density depends on the quality of the substrate and on the growth conditions, this degradation of near-junction properties could account for the increased variation in EL efficiency that has been reported for LED's prepared by growth on thermally etched substrates. No such degradation was observed when LPE layers were grown by a dipping technique that employs a Te-compensated growth solution and substrate meltback. This difference may account for the improvement in EL efficiency that has been observed for LED's prepared by meltback techniques.

Acknowledgments

The author would like to thank Drs. G. Blom, R. N. Bhargava, and E. Fabre for helpful discussions regarding this work and Messrs. M. Fucci and A. Sicignano for capable technical assistance.

Manuscript submitted May 17, 1974; revised manuscript received Nov. 22, 1974.

Any discussion of this paper will appear in a Discussion Section to be published in the December 1975 JOURNAL. All discussions for the December 1975 Discussion Section should be submitted by Aug. 1, 1975.

Publication costs of this article were partially assisted by North American Philips Corporation.

REFERENCES

1. R. H. Saul, J. Armstrong, and W. H. Hackett, *Appl. Phys. Letters*, **15**, 229 (1969).
2. R. Solomon and D. DeFevre, *J. Electron. Materials*, **1**, 26 (1972).
3. R. H. Saul and W. H. Hackett, *This Journal*, **119**, 542 (1972).
4. G. J. Russell and D. Haneman, *ibid.*, **114**, 398 (1967).
5. P. Murau and R. N. Bhargava, Paper 326 RNP presented at Electrochemical Society Meeting, Chicago, Illinois, May 13-18, 1973.
6. M. B. Panish, S. Sumski, and I. Hayashi, *Met. Trans.*, **2**, 795 (1971).
7. G. Lidgard, *Solid-State Electron.*, **15**, 159 (1972).
8. W. H. Hackett, R. H. Saul, R. W. Dixon, and G. W. Kammlott, *J. Appl. Phys.*, **43**, 2857 (1972).
9. A. Calverley and D. R. Wight, *Solid-State Electron.*, **13**, 382 (1970).
10. J. P. Chane, L. Hollan, and C. Schiller, *J. Crystal Growth*, **13/14**, 325 (1972).
11. S. Iida and K. Ito, *ibid.*, **13/14**, 336 (1972).
12. A. F. Witt and G. M. Blom, Private communication.
13. A. G. Lapierre, R. G. Wolfson, and E. M. Juleff, "Proc. International Conference on Crystal Growth," Boston, Mass., June 1966.
14. H. C. Casey, *This Journal*, **114**, 153 (1967).
15. D. A. Shaw and P. R. Thornton, *J. Mater. Sci.*, **3**, 507 (1968).
16. G. A. Rozgonyi and M. A. Afromowitz, *Appl. Phys. Letters*, **19**, 153 (1971).
17. R. N. Bhargava and P. C. Murau, Private communication.
18. R. C. Vehse and D. D. Manchon, Jr., Abstract 230, p. 572, Electrochemical Society Extended Abstracts, Fall Meeting, Miami Beach, Florida, Oct. 8-13, 1972.

Growth and Properties of Heteroepitaxial GaInAs Alloys on GaAs Substrates Using Trimethylgallium, Triethylindium, and Arsine

B. Jayant Baliga^{*1} and Sorab K. Ghandhi

Electrophysics and Electronic Engineering Division, Rensselaer Polytechnic Institute, Troy, New York 12181

ABSTRACT

Heteroepitaxial films of GaInAs have been grown on GaAs substrates by the reaction of triethylindium and trimethylgallium with arsine gas. Specular films have been obtained over the entire composition range at a substrate temperature of 600°C. The observed mobilities of 1-2 μm thick films are about one-third of the reported bulk values in literature and show a minimum at a composition of approximately 20 mole per cent InAs. The mobility of such films decreases sharply with decreasing temperature.

Interest has been focused on GaInAs alloys because of promising applications in coherent light emission in the wavelength range extending from 0.84 to 3.1 μm . Lasers have been fabricated with spontaneous emission at 2.07 and 1.77 μm with a half-width of 500Å at a current of 600 A/cm² (1). Another potential application of these alloys is for negative electron affinity photocathodes. GaInAs photocathodes have been shown to be ideal for detecting radiation from GaAs LED's and lasers (2, 3), and represent an increase in sensitivity by two to three orders of magnitude over S-1 and S-20 phosphors. Interest in these materials has also arisen from their potential applications in high frequency devices (4). The alloys can be designed to have much larger bandgaps than InAs and higher mobilities than GaAs. This makes them better suited for high frequency, field effect transistors.

Epitaxial layers of GaInAs alloys have been grown by liquid phase epitaxy (5, 6), by chloride transport (3, 7), and by using organometallic sources of gallium and indium (8). Synthesis by liquid phase epitaxy, with either InAs (5) or GaAs (6) as sources of arsenic, have yielded alloy films with only up to 23 mole per cent (m/o) InAs. Further, these films have been observed to have terraced surfaces at best. Mobilities of between 4000 and 5000 cm²/V-sec have been reported for alloys in this range of composition. Better results have been reported for alloys grown by chloride transport of gallium and indium from elemental sources (3, 7). In this case, alloys were obtained over the entire composition range. When elemental arsenic was used as a source, carrier concentrations of 1×10^{16} cm⁻³ were achieved in the alloys deposited on GaAs substrates. Mobilities of 20,000 cm²/V-sec were observed in InAs layers and 7000 cm²/V-sec in GaAs layers. Alloys with compositions of 60 m/o GaAs exhibited lower mobilities of 3000 cm²/V-sec. Vapor phase epitaxial growth of GaInAs alloys using organometallic sources of gallium and indium was achieved by Manasevit and Simpson on GaAs and Al₂O₃ substrates (8), but their work was confined to alloys of composition midway between GaAs and InAs.

In this paper we describe the growth and electrical properties of GaInAs alloys, grown on {100} gallium arsenide substrates, using organometallic sources of gallium and indium. It is demonstrated that organometallic source transport can be used to obtain alloys over the entire composition range, $0 \leq x \leq 1$. Further, electrical properties of thin epitaxial layers, ranging from 1 to 2 μm in thickness, which are particularly suited for device applications, are reported on for the

first time. The mobility of these films is found to follow the same composition dependence as in bulk single-crystal alloys. Temperature dependence of mobility in the alloys is found to follow a T^n law with n close to unity, in contradiction to Brooks' theory of disorder scattering (9).

Experimental Conditions

The growth of InAs, GaAs, and their alloys was carried out in a horizontal tube epitaxial reactor whose schematic is shown in Fig. 1. The system consists of a 50 mm ID quartz tube, 45 cm long, containing a molybdenum susceptor heated by infrared radiation from a set of eight, 500W quartz-halogen lamps. Vapors of triethylindium² (TEI) and trimethylgallium² (TMG) were transported to the substrate by bubbling hydrogen through the liquids. TEI was maintained at room temperature (25°C), and TMG at 0°C. Arsine gas, diluted to 2% in hydrogen,³ was mixed with the organometallic vapors just before entering the quartz tube. Due to the reaction between the organometallic compounds and arsine at room temperature, they were not premixed before entry to the hot zone. In addition, a separate source of ultra high purity hydrogen at a flow rate of 10 liters/min was used as a carrier gas in all the experiments. This carrier gas flow served to transport the reactants down the quartz tube and to minimize the formation of reaction products upstream from the susceptor. Stainless-steel tubing was used throughout in order to minimize system contamination.

Substrate.—Epitaxial growth was carried out on {100} chromium-doped semi-insulating GaAs sub-

² Alfa Products Division, Beverly, Massachusetts 01915.

³ Matheson Gas Products, East Rutherford, New Jersey 07073. All arsine flows given in the paper refer to actual arsine content.

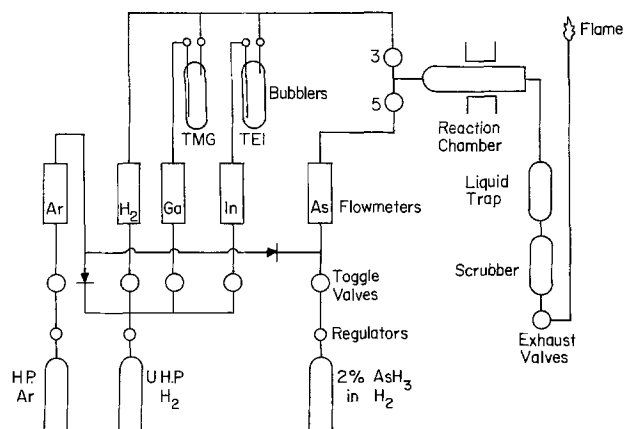


Fig. 1. Schematic diagram of epitaxial reactor

* Electrochemical Society Active Member.

¹ Present address: Corporate Research and Development Center, General Electric Company, Schenectady, New York 12301.

Key words: heteroepitaxy, chemical vapor deposition, organometallic compounds, indium arsenide, gallium arsenide, alloy semiconductors.

strates to facilitate subsequent electrical evaluation. The substrates were obtained commercially with one face polished.⁴ No further attempts were made to polish the wafers. Before epitaxy, however, the substrates were cleaned in methanol⁵ and checked to ensure the absence of dust particles. Substrates were placed perpendicular to the gas flow to obtain uniform growth over the entire surface.

Procedure.—Substrates were heated to 500°C in hydrogen, at which point arsine was introduced into the reaction tube. Arsine flows greater than 0.5 mliters/min were sufficient to prevent substrate dissociation from occurring up to temperatures of 750°C. After stabilizing the arsine flow for 2 min, the substrate temperature was raised to 600°C, and maintained for an additional 2 min before the introduction of the organometallic compounds.

Growth rate determination.—It was established that no loss in weight of the substrate took place up to substrate temperatures of 750°C, in the presence of more than 0.5 mliters/min arsine flow rate. Since the reactions involved in the system do not generate any etchant species, the thickness of the layers could be directly measured from the increase in mass after epitaxy. Angle lapping and staining techniques were initially used to measure the thickness of the epitaxial layers. However, etching of the surface by the staining and plating solutions and the presence of large depletion layer widths at the interface resulted in considerable error in determining layer thickness.

In the gravimetric measurements, the density used to determine the epitaxial layer thickness was calculated as

$$D_x = 6.68(145 + 45x)/(5.654 + 0.404x)^3$$

where x is the mole fraction InAs in the alloy. This equation was obtained by using Vegard's law and the zinc blende structure of these alloys (10).

Growth Characteristics

In order to study the growth of GaInAs alloys it is helpful to independently grow both the end components, GaAs and InAs. In addition, it is useful to achieve comparable growth rates for both these components under identical reactor conditions (substrate temperature, arsine concentration, and carrier gas flow rate). It was found that high quality GaAs films (11, 12) could be grown over a wide range of substrate temperatures (600°–800°C) whereas InAs films of comparable quality were restricted to substrate temperatures of 580°–620°C (13, 14). It was also found that, at a substrate temperature of 600°C, good quality GaAs and InAs films could be grown with arsine flows in excess of 1 and 1.4 mliters/min, respectively. Finally, low hydrogen carrier gas flows (1 liter/min) through the reactor resulted in InAs film growth rates of less than 0.01 $\mu\text{m}/\text{min}$. Increasing the hydrogen carrier gas flow to 10 liters/min increased the growth rate to 0.1 $\mu\text{m}/\text{min}$, indicating that significant depletion of the TEI occurred due to reaction upstream of the susceptor for low carrier gas flows. For GaAs, growth rates⁶ in excess of 1 $\mu\text{m}/\text{min}$ were obtained at hydrogen carrier gas flows of 1 liter/min, decreasing to 0.1 $\mu\text{m}/\text{min}$ when the carrier gas flow was raised to 10 liters/min, indicating that the dilution effect of the higher carrier gas flow was dominant in this case. As a consequence of these observations, we were able to achieve high quality films of GaAs and InAs with comparable growth rates under the following reactor conditions: (a) substrate temperature of 600°C, (b) arsine flow of 2 mliters/min, and (c) hydrogen carrier gas flow of 10 liters/min.

Under the above conditions, the growth of InAs could be controlled by varying the hydrogen flow through the TEI bubbler, as shown in Fig. 2. Growth rate was found to increase linearly with increasing hydrogen flow through the TEI bubbler, over the range of 0.02–0.07 $\mu\text{m}/\text{min}$. Under the same reactor conditions, the growth rate of GaAs films could be controlled by varying the hydrogen flow through the TMG bubbler, as shown in Fig. 3. Again, a linear dependence of growth rate on the hydrogen flow through the bubbler was observed.

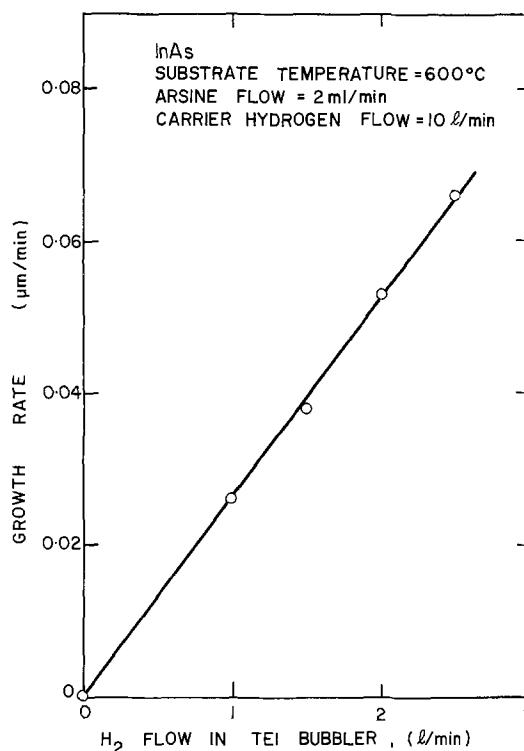


Fig. 2. Variation of InAs growth rate with hydrogen flow through the TEI bubbler.

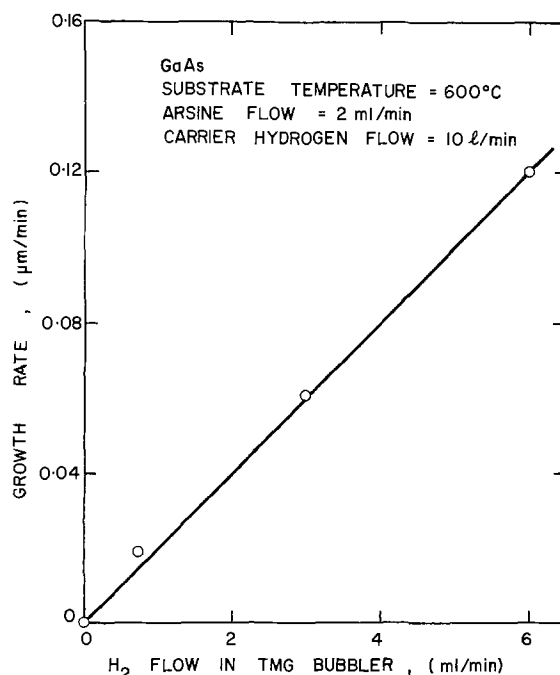


Fig. 3. Variation of GaAs growth rate with hydrogen flow through the TMG bubbler.

⁴ Electronic Materials Corporation, Pasadena, California 91107.

⁵ Substitution of methanol with more sophisticated cleaning solutions and procedures did not produce any significant change in the growth rate or surface quality of the epitaxial films.

⁶ These growth rates correspond to a hydrogen flow of 6 mliters/min through the TMG bubbler.

Having achieved comparable growth rates for the end components under identical reactor condition, growth of the alloys could now be achieved by simultaneous introduction of TEI and TMG into the reactor. Further, the growth rate of either component could be independently controlled by adjusting the hydrogen flow through the respective source liquids, thus allowing the growth of the alloys over the entire composition range.

The effect of varying the TEI and TMG flows on the alloy composition was examined by keeping one component fixed and changing the other. Arsine flow was maintained at 2 mliters/min in all these experiments. The alloy composition was measured by x-ray energy dispersal analysis in a scanning electron microscope. Figure 4 shows the variation of the InAs mole fraction in the epitaxial layers as the mole fraction of TEI in the gas phase ($TEI/(TEI + TMG)$) is changed. This fraction was determined using a vapor pressure of 66 mm Hg at 0°C for TMG, and 0.4 mm Hg at 25°C for TEI, and assuming saturated conditions. A strong one-to-one correlation between the mole fraction of InAs in the layers and TEI in the gas phase is observed when the TMG flow is kept constant and the TEI flow is varied. A somewhat weaker correlation is observed when the TEI flow is kept constant and the TMG flow is varied. This is due to the extremely small hydrogen flows through the TMG bubbler, required to obtain the low growth rates of GaAs necessary for the growth of the alloys. The one-to-one correlation between the mole fraction of InAs in the layers and of TEI in the gas phase indicates that indium and gallium are independently incorporated into the lattice and that the reactions between TEI and arsine and between TMG and arsine occur without significant interaction.

We have also observed that arsine flow has only a small effect on the composition of the alloys. Figure 5 shows the extent of this effect for layers grown at 600°C using a hydrogen flow of 6 mliters/min through the TMG bubbler and 2.5 liters/min through the TEI bubbler. Changes in arsine flow of one order of magnitude produced only small changes in composition. Thus, good control over the concentrations of TEI and TMG in the reactor was adequate for controlling the composition of the layers.

GaAs layers grown under the conditions described in this paper had featureless surfaces under Nomarski interference phase contrast microscopy up to magnifications of 400 \times . On the addition of 4 m/o InAs to the layers, a cross-hatched pattern appeared on the epitaxial layer, as shown in Fig. 6a. Such patterns have been observed in the growth of heteroepitaxial layers by other workers when the composition of the epitaxial layer is nearly that of the substrate or when the composition of the epitaxial layer is graded (3, 15),

and has been ascribed to grading dislocations. With the addition of larger amounts of InAs, the large difference in lattice constant between the layer and the substrate (InAs has a lattice constant of 6.058Å while GaAs has

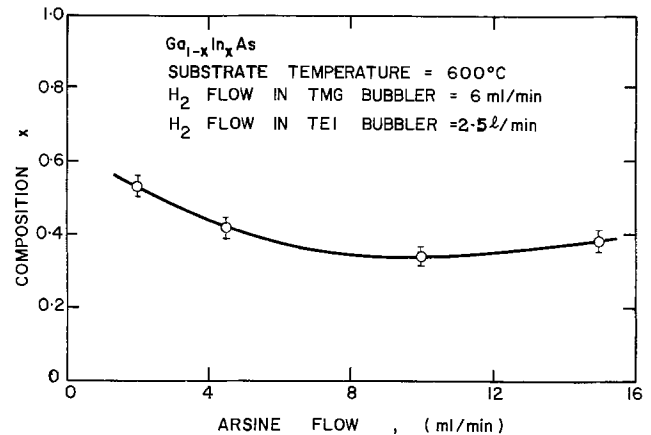


Fig. 5. Effect of changes in arsine flow on composition of GaInAs alloys.

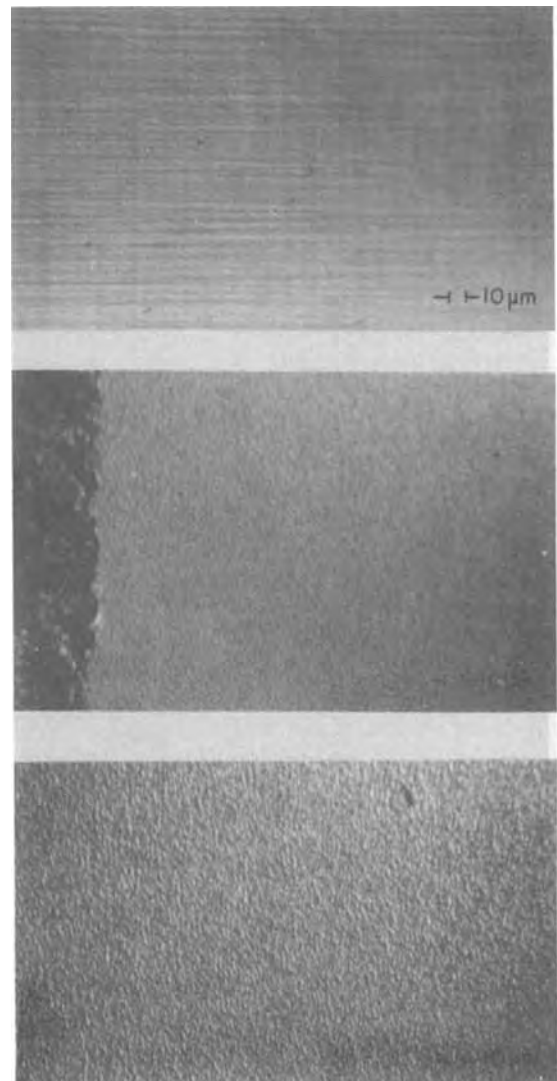


Fig. 6. Nomarski interference phase contrast photomicrographs of surfaces of 1 to 2 μ m thick GaInAs layers grown on GaAs substrates. (a, top) $Ga_{0.96}In_{0.04}As$, (b, center) $Ga_{0.48}In_{0.52}As$, (c, bottom) InAs.

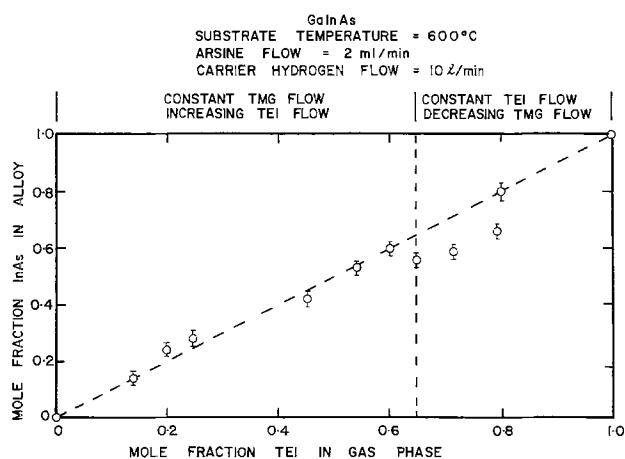


Fig. 4. Variation of composition of the GaInAs layers with change of TEI mole fraction in the gas phase.

a lattice constant of 5.654Å) results in terraced surfaces as shown in Fig. 6b and c. All these surfaces have a specular appearance to the unaided eye.

Electrical Properties

Hall measurements were used to determine the carrier concentration and the mobility of alloy films grown on semi-insulating GaAs substrates. Conventional bridge-shaped samples were delineated in the epitaxial layers, and ohmic contacts made to the arms of the sample by alloying indium spheres at 400°C for 30 sec in a reducing gas ambient.

Mobility variation with composition.—The effect of composition on the Hall mobility of the alloys was examined for layers of between 1 and 2 μm in thickness. The carrier concentration in the layers was in the lower 10^{16} cm^{-3} range.

The observed variation in mobility with composition is shown in Fig. 7, and compared with results of other workers (7, 16-18). The mobility of our thin films (1-2 μm) were generally one-third of the observed bulk values. Published data on thick films ($> 15 \mu\text{m}$) have been correspondingly scaled for comparison. The mobility was found to exhibit a minimum at a composition of approximately 20 m/o InAs in layers grown in this study. In bulk material the minimum in mobility has been observed at x between 0.1 and 0.2 (17, 18); for epitaxial layers grown on GaAs by chloride transport, the minimum has been observed at x between 0.4 and 0.5 (7). One author (16) has claimed to have observed a monotonic variation in mobility with composition. However, his work did not involve any measurement on layers in the composition range $0 < x < 0.7$ where the minimum occurs.

The observed shape of the mobility *vs.* composition characteristic follows Brooks' theory (9) for materials in which disorder (alloy) scattering is the dominant limitation on mobility. Using this theory and a linear variation of electron effective mass between InAs and GaAs (19, 20) results in a mobility minimum for approximately 30 m/o InAs (10). Actual values of mobility, calculated on the basis of this theory, were found to be several orders of magnitude greater than the measured values in our films, as well as those of other workers.

Hall mobility variation with sample temperature.—Hall measurements were conducted to determine the variation in the mobility of the layers over a temperature range from 300° to 77°K. The mobility variation with temperature of GaAs films of 7 μm and greater in thickness was found to be the same as that for polar

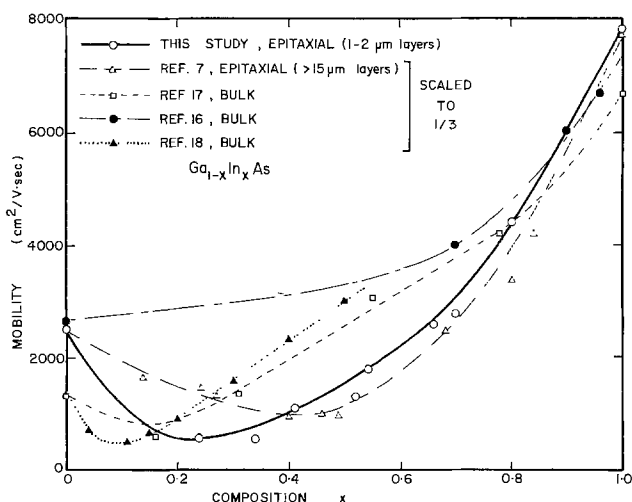


Fig. 7. Variation of room temperature mobility of GaInAs layers with composition.

optical scattering in bulk crystals. The variation of mobility with temperature for InAs layers is shown in Fig. 8 for samples with different thicknesses. The mobility of the thicker films (e.g., 7.2 μm) is seen to increase with decreasing temperature, consistent with the behavior of bulk InAs where the dominant scattering mechanism in this temperature range is polar optical scattering. However, the mobility of thin samples ($\leq 1.5 \mu\text{m}$) decreased with decreasing temperature, with the slope of this curve becoming steeper with decreasing layer thickness. It is proposed that the dominant scattering in these layers is dislocation scattering. Although there is no established theory for dislocation scattering in polar semiconductors, this mechanism has been analyzed (21) for nonpolar semiconductors using the deformation potential approach. It has been shown that mobility dominated by dislocation scattering should vary as T^{+1} , and that this scattering effect becomes comparable to lattice scattering at room temperature when the dislocation density exceeds 10^{11} cm^{-2} . The calculated dislocation density (22) at the InAs-GaAs interface is $4 (a_{\text{GaAs}}^{-2} - a_{\text{InAs}}^{-2}) = 1.61 \times 10^{14} \text{ cm}^{-2}$ for {100} surfaces, if an abrupt transition is assumed. Thus, dislocation scattering is expected to be significant in thin layers and can produce the observed flattening in the temperature dependence of the mobility characteristic.

The detailed nature of the variation in mobility of GaInAs alloys with temperature has not been reported in the literature. This variation was measured for alloy films with thicknesses between 1 and 2 μm , over a temperature range of 300°-77°K. In every alloy layer (see Fig. 9), for $0.41 \leq x \leq 0.8$, the mobility fell sharply with decreasing temperature. The mobility is observed to decrease according to a T^{+n} law, with n close to unity. Other authors (7, 17, 18), who have observed the temperature variation of mobility for GaInAs alloys in bulk and epitaxial form have also reported that mobility decreases with decreasing temperature. These results for alloy layers are in variance with Brooks' theory, which predicts an increase in mobility due to disorder scattering when the temperature decreases, with a coefficient $n = 1/2$. This disagreement again points to the inadequacy of the pres-

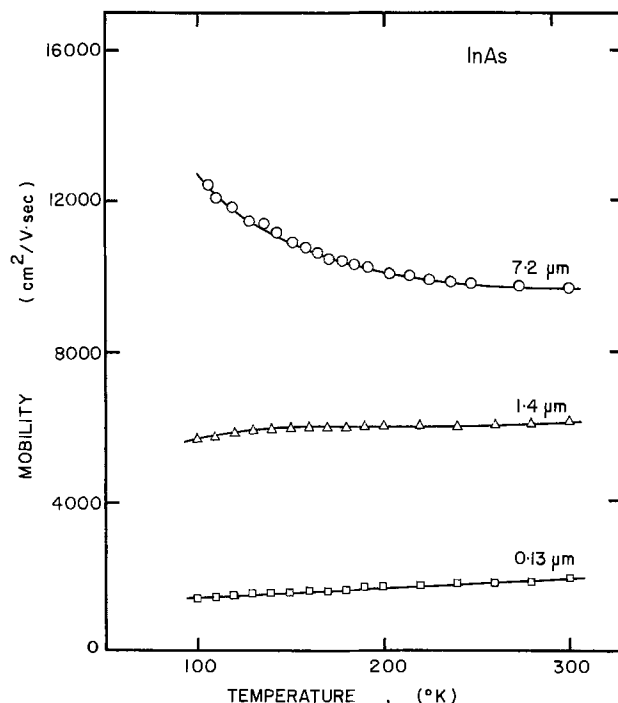


Fig. 8. Variation of Hall mobility with sample temperature for epitaxial InAs films on GaAs substrates, with layer thickness as parameter.

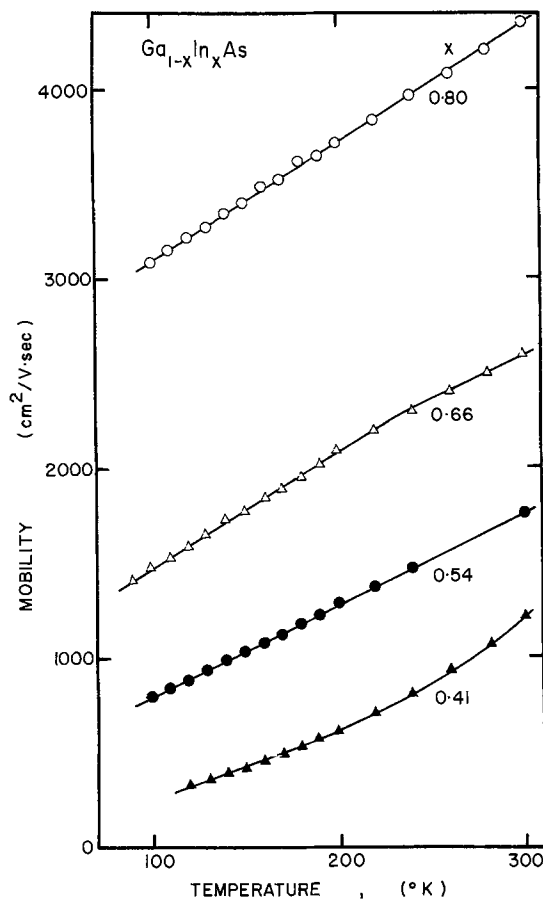


Fig. 9. Variation of Hall mobility with sample temperature for epitaxial GaInAs layers on GaAs substrates, with composition as parameter.

ent theory. A theory of disorder scattering which does explain all the observed effects is yet to be developed.

Conclusions

Epitaxial layers of GaInAs alloys can be grown using organometallic sources of indium and gallium in combination with arsine gas to obtain specular films over the entire composition range at a substrate temperature of 600°C. The composition of the alloys can be controlled by adjusting the relative flows of TEI and TMG in the reactor and is relatively insensitive to arsine flow.

The mobility of layers with thicknesses between 1 and 2 μm shows a minimum at an alloy composition of approximately 20 m/o InAs. Mobilities of these thin films are found to be about a third of that measured in bulk single-crystal material. Although the mobility of layers of pure InAs and GaAs in this thickness range increases on cooling to 100°K, the mobility of the alloys decreases sharply with a temperature de-

pendence of T^{-n} , $n \simeq 1$. This is in variance with Brooks' theory but in agreement with observations on bulk samples by other workers. This points to the need to develop an improved disorder scattering theory.

Acknowledgments

The authors wish to acknowledge the assistance received from R. Bhat in the composition measurements, Dr. J. Pankove in obtaining bulk GaInAs calibration samples for the x-ray energy dispersal analysis, and R. Rafun for manuscript preparation. This work was supported by Grant No. GK-31332 from the National Science Foundation.

Manuscript submitted Oct. 2, 1974; revised manuscript received Dec. 13, 1974.

Any discussion of this paper will appear in a Discussion Section to be published in the December 1975 JOURNAL. All discussions for the December 1975 Discussion Section should be submitted by Aug. 1, 1975.

Publication costs of this article were partially assisted by Rensselaer Polytechnic Institute.

REFERENCES

1. I. Melngailis, A. J. Strauss, and R. H. Rediker, *Proc. IEEE (Corr)*, **51**, 1154 (1963).
2. B. F. Williams and J. J. Tietjen, *Proc. IEEE*, **59**, 1489 (1971).
3. R. E. Enstrom, D. Richman, M. S. Abrahams, J. R. Appert, D. G. Fisher, A. H. Sommers, and B. F. Williams, 1970 Symposium on GaAs, Paper 3, p. 30 (1970).
4. W. Fawcett, C. Hilsum, and H. D. Rees, *Electron. Letters*, **5**, 313 (1969).
5. G. A. Antypas, *This Journal*, **117**, 1393 (1970).
6. K. Takahashi, T. Moriizumi, and S. Hirose, *ibid.*, **118**, 1639 (1971).
7. R. W. Conrad, P. L. Hoyt, and D. D. Martin, *ibid.*, **114**, 164 (1967).
8. H. M. Manasevit and W. I. Simpson, *ibid.*, **120**, 135 (1973).
9. L. Makowski and M. Glicksman, *J. Phys. Chem. Solids*, **34**, 487 (1973).
10. B. J. Baliga, Ph.D. Thesis, Rensselaer Polytechnic Institute, Troy, New York (1974).
11. M. Inoue and K. Asahi, *Japan. J. Appl. Phys.*, **11**, 919 (1972).
12. P. Smith, Ph.D. Thesis, Rensselaer Polytechnic Institute, Troy, New York (1973).
13. H. M. Manasevit and W. I. Simpson, *This Journal*, **116**, 1725 (1969).
14. B. J. Baliga and S. K. Ghandhi, *ibid.*, **121**, 1646 (1974).
15. M. S. Abrahams, L. R. Weisberg, C. J. Buiocchi, and J. Blanc, *J. Mater. Sci.*, **4**, 223 (1969).
16. J. W. Wagner, *This Journal*, **117**, 1193 (1970).
17. M. S. Abrahams, R. Braunstein, and F. D. Rosi, *J. Phys. Chem. Solids*, **10**, 204 (1959).
18. T. V. Dzhakhutashvili, A. A. Mirtskhulava, L. G. Sakvarelidze, A. L. Shkol'nik, and M. S. Matinova, *Sov. Phys.-Semicond.*, **5**, 190 (1971).
19. M. B. Thomas and J. C. Woolley, *Can. J. Phys.*, **49**, 2052 (1971).
20. Yu. M. Burdukov *et al.*, *Sov. Phys.-Semicond.*, **4**, 1184 (1971).
21. D. L. Dexter and F. Seitz, *Phys. Rev.*, **86**, 964 (1952).
22. D. B. Holt, *J. Phys. Chem. Solids*, **27**, 1053 (1966).

The Direct Bonding of Metals to Ceramics by the Gas-Metal Eutectic Method

J. F. Burgess* and C. A. Neugebauer

General Electric Corporate Research and Development, Schenectady, New York 12301

and G. Flanagan

General Electric Company, Heavy Military Electronic Systems Product Department, Syracuse, New York 13201

ABSTRACT

The direct bonding of metals to ceramics is possible utilizing a gas-metal eutectic. The mechanism of direct bonding of copper foil to ceramics in a slightly oxidizing atmosphere is presented. It involves the formation of eutectic melt between copper and oxygen at a temperature slightly below the melting point of copper, which serves to bring the foil into intimate contact with the substrate. A brief review of other metal-ceramic bonding techniques is given for comparison. Metals to which this technique is applicable include Cu, Fe, Ni, Co, Ag, Cr, Mo, and Al.

Strong bonding of metals to ceramics generally does not take place unless an intermediary layer is present, or forms due to diffusion or reaction. The adhesion of the metal to this intermediary layer is better than to the ceramic directly. However, an intermediary layer is undesirable in many applications. This is true, for instance, where high heat conductivity is required. The presence of an intermediary layer generally reduces heat conductivity, especially if the layer is non-metallic. Further, in high frequency applications, where the current flows in a thin skin at the metal-ceramic boundary, intermediary layers are undesirable because they are generally more resistive than the metal to be bonded. Finally, intermediary layers are often less corrosion resistant and lead to premature failure.

Unfortunately, strong direct metal to ceramic bonds are not common, either because the bond is inherently weak, or because of the difficulty of bringing the metal into intimate contact with the ceramic. In this paper, a new method of direct bonding of metals to ceramics is given. For a better perspective, a short summary of the mechanisms of presently used metal-ceramic bonding techniques is also included.

Bonding Mechanisms Involving Intermediary Layers

Some of the more pertinent literature in this area has been reviewed by Helgesson (1), and a short review was recently given by Loasby *et al.* (2). Commonly used intermediary layers are glass layers, where the glass is intentionally added or is originally present in the ceramic itself, or polycrystalline semi-conducting compounds formed by the reaction between the metal or metal oxide and the ceramic itself.

Glassy intermediary layers.—Glassy phases are usually present in the grain boundaries of impure (<99.8%) ceramics. Thus, Al_2O_3 or BeO ceramics usually contain glassy mixtures of MgO , SiO_2 , and CaO concentrated in the grain boundaries. When a metallizing mixture is applied to such a ceramic, and the temperature is raised to sintering temperatures, the glass from the ceramic penetrates into the (porous) metal layer and locks it to the ceramic after cooling by mechanical forces.

More commonly, glass is intentionally added to the metallizing mixture to form the intermediate layer. This is particularly true if the ceramic is pure. For example, to take advantage of the high thermal conductivity of BeO ceramic, glass must be kept out of the grain boundaries. Therefore, the common metallizing mixtures, such as Mo-Mn, when used on beryl-

lia, contain up to 20% SiO_2 . Thus the composition of a typical mixture is 71.5% Mo, 10.7% Mn, and 17.8% SiO_2 , fired on BeO at 1300°C . There is an interdiffusion of manganese cations with other cations in the glass.

Another commonly practiced method of bonding through an intermediary glass phase involves glass frit additions to the finely divided metal in the metallizing mixture. Thus, the majority of the so-called "thick film" conductor pastes contain a glass frit, generally chosen for low melting point and thermal expansion match, in addition to dispersed metal (normally noble metals) in an organic carrier. After screening the paste on the ceramic, it is fired in air. The glass frit melts and reacts with the ceramic (usually Al_2O_3), and it also forms a network within the metal conductor. Thus, the bond between the metal and the ceramic is due to mechanical locking by the reacted glass, although some chemical bonding undoubtedly also occurs.

Polycrystalline intermediary layers.—Such layers are usually compounds formed between the metallizing mixture and the ceramic. In one method, the metal oxide is applied to the ceramic and sintered with the ceramic to form a mixed oxide compound. For instance, such a compound is formed between copper oxide and alumina, possibly CuAlO_2 , when they are sintered together at 1150°C in air. Subsequent reduction gives an adherent metal layer bonded on the mixed oxide phase. This method is also applicable to cobalt, nickel, iron, and silver.

The widely used moly-manganese process also falls into this category. In this process, a mixture of molybdenum and manganese oxide is fired on alumina (not beryllia) at 1400°C in an atmosphere of wet hydrogen. The manganese oxide reacts with the alumina to form the intermediate layer compound $\text{MnO}\cdot\text{Al}_2\text{O}_3$. Molybdenum ions, which have been formed by the partial oxidation of the metal, are unable to diffuse deeply into pure Al_2O_3 , but will diffuse readily into the manganese aluminate spinel. This leads to good adhesion of the Mo layer. When MoO_3 alone is used, some penetration of alumina by MoO_3 occurs, especially in hydrogen atmospheres at high humidities. A compound between Mo and Al_2O_3 , perhaps $\text{Al}_2(\text{MoO}_4)_3$ (3, 4), is formed to provide the intermediary bonding layer.

Direct Bonding

Direct bonding here implies the absence of a readily identifiable intermediate phase between the metal and the ceramic. It does not exclude, however, the presence of a transition layer one or two monolayers thick, such as perhaps oxygen bridges between the metal and ceramic.

* Electrochemical Society Active Member.
Key words: copper, ceramics, joining, eutectic.

A method of direct bonding which does not depend on any kind of intimate bond between metal and ceramic is that involving mechanical locking or keying.

In this process the metal is screened on the ceramic in the form of an organometallic paste. The paste decomposes on heating in air, with the result that metal particles are now locked in pores in the ceramic surface to give a mechanical bond. Films of noble metals, such as platinum, are typically applied in this way. However, poor adhesion is obtained in the mechanical locking process. Clearly, in order to get good adhesion by direct bonding it is required that (i) the metal must be brought into intimate contact with the ceramic over the entire area on an atom to atom basis, and (ii) the metal must form a strong bond with the ceramic, be it by Van der Waal's or chemical bonding, without extensive reaction or diffusion of the two phases into each other.

To get intimate contact between metal and a ceramic surface, the metal could be brought into the liquid state by melting. The liquid will replicate the ceramic surface where it wets it, and if a strong bond is formed, good adhesion is obtained after cool-down. For instance, when copper is melted in hydrogen on an alumina substrate, a molten droplet is formed with a melting angle of approximately 120° , which after cool-down to room temperature adheres strongly to the ceramic. The problem with simply melting the metal, of course, is that one or more droplets are formed, and the metal member to be bonded entirely loses its shape. This can be avoided by the gas-metal eutectic method.

Direct bonding by the gas-metal eutectic method.—The basic idea here is to form a liquid skin around the metallic member to be bonded. The liquid must wet both the metallic member and the ceramic and form a strong bond after cool-down. The melting point of this liquid should be near the melting point of the metal member itself, say within 50° , so that the metal member becomes soft and pliant and conforms easily to the shape of the substrate surface. Further, the predominant constituent of this liquid should be the same element as makes up the metallic member, and any additional constituent should be present in only small amounts or be easily removable after bonding. The thickness of the molten skin must be kept small in comparison to the thickness of the member to be bonded.

Ideal for use as the skin material are eutectics formed by the flow gas in a bonding system with the metal member itself. Such a eutectic exists, for instance, between copper and oxygen, at 0.39 weight per cent (w/o) oxygen (5). The melting point of this eutectic is 1065°C , as compared to 1083°C for pure copper. Thus, if the oxidizing conditions in the flow gas are chosen properly, one may have the molten copper-oxygen eutectic mixture and solid copper (containing a small amount of dissolved oxygen) coexist together, in the temperature interval $1065^\circ < T < 1083^\circ\text{C}$. It is this copper-oxygen eutectic skin which is in effect used as a glue to bond the solid copper member to the ceramic, without the Cu member losing its shape. Thus, in order to bond copper foil to ceramic, the process is as follows.

The Cu foil is laid on top of the ceramic in a furnace containing a flow gas atmosphere consisting primarily of an inert gas, such as argon or nitrogen, with a small addition of oxygen, typically of the order of a few hundredth of a per cent. Copper initially reacts during the heat-up period with the oxygen in the flow gas. A small amount of oxygen dissolves in the copper, but most of it reacts to form Cu_2O around the foil. When 1065°C or above is reached, a liquid phase of or near the eutectic composition forms a skin around the copper. The thickness of this molten skin depends on the O_2 partial pressure and the oxidation time. If the partial O_2 pressure in the flow gas is less

than $1.5 \cdot 10^{-6}$ atm (the equilibrium partial pressure over Cu_2O at 1065°C), Cu_2O will not form and the eutectic phase also will not form. The formation of a molten layer between the Cu foil and the substrate serves to bring the copper in intimate contact with the ceramic by wetting it over the entire interface. Once in intimate contact with the ceramic, copper forms a strong bond with it. The temperature must remain below 1083° , the melting point of copper, since otherwise the foil loses its structural integrity and liquid drops are formed. Similarly, if the partial pressure of oxygen is too high, all copper present is converted into eutectic melt. Thus, an intermediate O_2 partial pressure is required where both phases are present simultaneously. On cool-down below 1065° , the eutectic segregates into Cu and Cu_2O . Evidence of this is shown in Fig. 1, which is a micrograph through a section of bonded copper foil, and indicates the presence of a second phase. This oxide phase may now be reduced in hydrogen at low temperature without loss of adhesion. The bonding process is schematically illustrated in Fig. 2.

The possibility exists, of course, that one or more monolayers of copper oxide still exist at the copper-ceramic interface, even after reduction, perhaps combined with alumina to give a spinel such as CuAlO_2 . This has recently been suggested by O'Brien and Chaklader (6). However, removal of the copper by etching in nitric acid or ferric chloride solution leaves no copper-containing residues, thus ruling out intermediate layers consisting of copper compounds insoluble in these etchants.

Copper has been bonded successfully by the gas-metal eutectic methods on alumina, beryllia, silica, various other spinels, other metals, and to itself. It does not bond, however, to boron nitride or carbon. The bond strength to oxygen-containing ceramics can be in excess of 20,000 psi. Since the copper itself does not melt during bonding, precut or stamped foils of copper of the desired shapes can be bonded. In addition, holes previously cut into ceramic substrates can be covered hermetically, and the copper can overhang the ceramic. Bonds between copper and other metals, and between two copper members, can also be made by this method. A photograph of various direct bonded copper structures prepared in this laboratory are shown in Fig. 3.

Application to other metal-ceramic systems.—For the direct bonding of metal by the gas-metal eutectic method, the following prerequisites must be fulfilled: (a) a eutectic must exist between the metal and the flow gas, (b) the percentage of the gas component in the eutectic must be low and/or easily removable after bonding, (c) the eutectic temperature must be at least

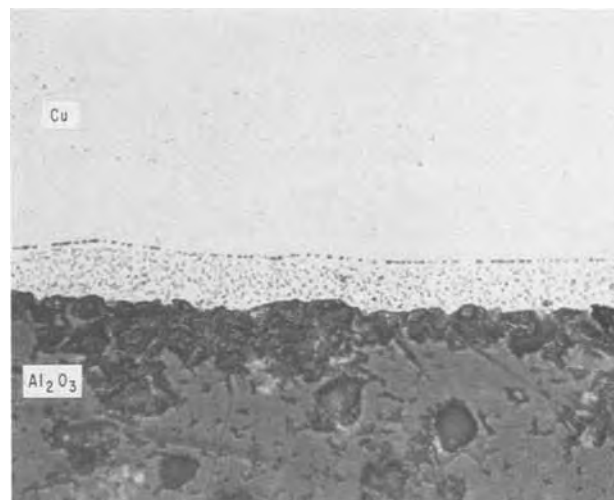


Fig. 1. Micrograph of section through direct copper bond to alumina, showing precipitated Cu_2O from the eutectic.

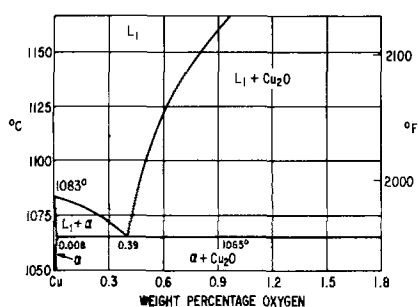


Fig. 2. Eutectic phase diagram and schematic of bonding process.

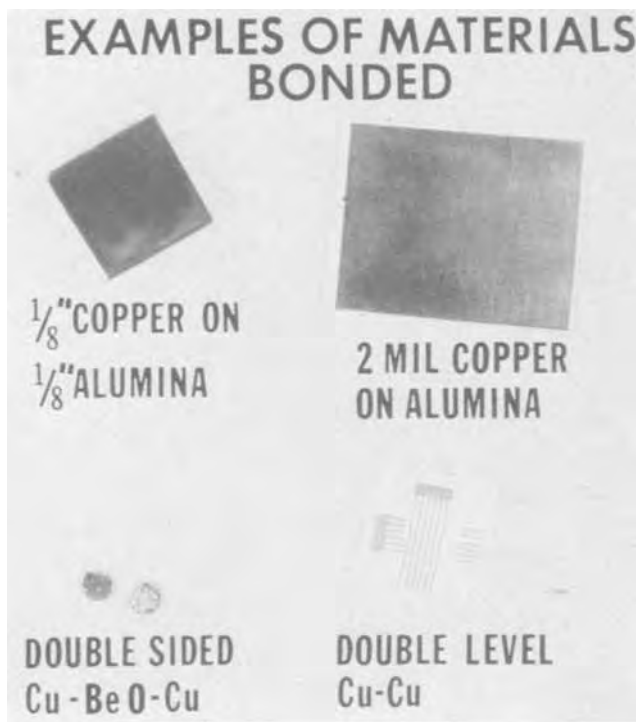
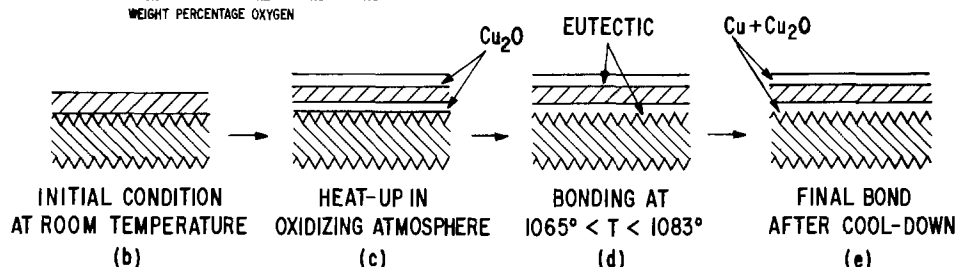


Fig. 3. Direct bonded copper structures

10° or so below the melting point of the metal to give a realistic temperature range for bonding, and (d) the metal must be pliant at the bonding temperature so that it conforms to the substrate shape.

Inspection of phase diagrams of metals with the more common gases reveals a number of possibilities. In particular, oxygen, sulfur, and phosphorous form eutectics with several metals. These are listed in Table I, in addition to the eutectic temperature, the melting point of the metal, and the percentage of the gas component in the eutectic.

Table I. Metal-gas eutectics for direct bonding

Eutectic	Eutectic temperature, °C	Weight per cent of nonmetal	Melting point of metal, °C
Copper-oxygen	1065	0.39	1083
Iron-oxygen	1523	0.16	1535
Nickel-oxygen	1438	0.24	1452
Cobalt-oxygen	1451	0.23	1480
Copper-sulfur	1067	0.77	1083
Silver-sulfur	906	1.8	960
Chromium-sulfur	1550	2.2	1615
Silver-phosphorous	878	1.0	960
Nickel-phosphorous	880	11.0	1452
Copper-phosphorous	714	8.4	1083
Molybdenum-silicon	2070	5.5	2625
Aluminum-silicon	577	11.7	660

The flow gas would contain small amounts of oxygen, hydrogen disulfide, phosphine, or silane, as appropriate. However, silicon would not be easily removable, and the bond in such a case could not, strictly speaking, be called "direct."

Manuscript submitted June 24, 1974; revised manuscript received Sept. 23, 1974. This was Paper 38 presented at the San Francisco, California, Meeting of the Society, May 12-17, 1974.

Any discussion of this paper will appear in a Discussion Section to be published in the December 1975 JOURNAL. All discussions for the December 1975 Discussion Section should be submitted by Aug. 1, 1975.

Publication costs of this article were partially assisted by General Electric Company.

REFERENCES

- C. I. Helgesson, "Ceramic to Metal Bonding," Bost Tech. Publ., Cambridge, Mass. (1969).
- R. G. Loasby, N. Davey, and H. Barlow, *Sol. State Tech.*, p. 46 (May 1972).
- A. G. Pincus, *Ceram. Age*, **63**, 16 (1954).
- A. G. Pincus, *ibid.*, **63**, 30 (1954).
- A. Butts, "Copper, The Science and Technology of the Metal, Its Alloys and Compounds," p. 475, Reinhold Publishing Corp., New York (1954).
- T. E. O'Brien and A. C. D. Chakiader, *J. Am. Ceram. Soc.*, **57**, 329 (1974).

Interaction Parameters in the Zn-Pb-Sn System at Low Zinc Concentration

Z. Moser*¹ and W. Zakulski

Institute for Metal Research, Polish Academy of Sciences, Kraków, Poland

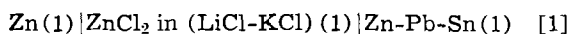
ABSTRACT

The thermodynamic properties of liquid dilute zinc solutions at a lead concentration of $X_{Pb} = 0.01-0.7$ molar fraction were determined by means of emf measurements of concentration cells. These investigations combined with previous analogical experiments at a tin concentration of $X_{Sn} = 0.01-0.1$ molar fraction enabled the calculation of ternary interaction parameters ϵ_{Zn}^{Pb} and ϵ_{Zn}^{Sn} from plots $(\ln \gamma_{Zn})_{X_{Zn} \rightarrow 0}$ vs. X_{Pb} . For the binary end-points on the plots $\ln \gamma_{Zn}$ vs. X_{Pb} and $(\ln \gamma_{Zn})_{X_{Zn} \rightarrow 0}$ vs. X_{Pb} separate measurements were carried out for Zn-Sn and Zn-Pb systems at concentrations up to 0.1 molar fraction of zinc. Experimental results were interpreted by means of Krupkowski's formalism and attempts were made to calculate ϵ_{Zn}^{Pb} and ϵ_{Zn}^{Sn} on the basis of limiting values of activity coefficients of components of binary systems Zn-Sn, Zn-Pb, and Pb-Sn.

Initiated several years ago, experimental investigations on dilute binary and ternary liquid metal solutions by the emf method of concentration cells have several aims. First of all, from the experimental point of view it was necessary to adjust the concentration range where the emf method of concentration cells gives satisfactory results. It was shown that experiments on zinc alloys at a concentration of $X_{Zn} = 0.01-0.1$ molar fraction give results associated with considerable error, in the case of alloys like Zn-Cd (1), Zn-In (2), and Zn-Ga (3) with components which are close in position to zinc in the electromotive series. This is the result of side reactions between $ZnCl_2$ from the electrolyte and cadmium, indium, gallium from the alloy electrode, respectively. As a result, when composite binaries show side reactions, experiments in the ternary systems (4) were not carried out at the lowest concentration, $X_{Zn} = 0.01$ mole fraction. The binary systems influence the thermodynamic behavior in ternary systems, especially when they show considerable deviations from Raoult's law. For example the Zn-Pb system with marked positive deviations, plays a decisive role in investigations on ternary systems when small amounts of a third component (Bi, Sb, In, and Cd) are added (4). The present measurements on the Zn-Pb-Sn ternary system fit this pattern. The analysis of the plots $(\ln \gamma_{Zn})_{X_{Zn} \rightarrow 0}$ vs. X_i (where i is component 2 or 3 of the investigated ternary) have shown that the direction and magnitude of deviation from linear dependence is directly connected with properties of the 2-3 system without zinc (4). The aim of the present paper is the determination of ternary interaction parameters ϵ_{Zn}^{Pb} and ϵ_{Zn}^{Sn} from experimental data from plots $(\ln \gamma_{Zn})_{X_{Zn} \rightarrow 0}$ vs. X_{Pb} . These plots were obtained by combining the results from a previous paper (5) at $X_{Sn} = 0.01-0.1$ with the data presented in this paper at $X_{Pb} = 0.01-0.7$ mole fraction. Some attempts were carried out also to calculate both ϵ_{Zn}^{Pb} and ϵ_{Zn}^{Sn} from the limiting values of the activity coefficients of the composite binaries.

Experimental

Experiments were carried out over the temperature range 714°-877°K by means of concentration cells with liquid electrodes and liquid electrolyte according to the following scheme



* Electrochemical Society Active Member.

¹ Present address: Iowa State University, Ames Laboratory, USAEC, Ames, Iowa 50010.

Key words: interaction parameter, concentration cells, dilute zinc solution, Krupkowski's formalism, Wagner's linear equations.

The details of experimental arrangements were given in preceding papers (6) and (7). Emf measurements were carried out at concentrations $0.03 \leq X_{Zn} \leq 0.1$ and when $0.01 \leq X_{Pb} \leq 0.7$ mole fraction. Emfs were measured against a zinc reference electrode and simultaneously against binary solutions of Zn-Sn or Zn-Pb of the same zinc concentration as for the ternary alloys. Such a procedure has been carried out to test whether the results for binary alloys are similar to those previously obtained in separate measurements for Zn-Sn (1) and Zn-Pb (7) systems with $0.01 \leq X_{Zn} \leq 0.1$ mole fraction.

At the temperature range 714°-877°K both for binary and ternary alloys a linear dependence of emf vs. temperature was obtained. In Fig. 1, for example, the emf data at $X_{Zn} = 0.05$ are given. It is clear from this plot that the measurements for some alloys were repeated as shown by open and filled points. The least squares fit was applied to average the data and resultant linear equations of the type $E_{mV} = a + bT^\circ K$ for $X_{Zn} = 0.05$ are presented in Table I. The data at $0.01 \leq X_{Sn} \leq 0.1$ as well as for other zinc concentrations are taken from previous measurements (5). This table also contains the values of correlation coefficients and standard deviations of slopes and emf data. Next, from linear equations the emf data at chosen temperatures 714°, 757°, 805°, 842°, and 877°K were obtained and recalculated into $\ln \gamma_{Zn}$ according to the relation

$$\gamma_{Zn} = \frac{1}{X_{Zn}} e^{-nEF/RT} \quad [2]$$

where γ_{Zn} , X_{Zn} are zinc activity coefficients and its concentration in mole fraction; F is Faraday's constant 23,062 cal·V⁻¹; R , gas constant 1987 cal·deg⁻¹; E , measured emf value in volts, n , valence of zinc equal 2.

The very small solubility of zinc in the liquid electrolyte does not change the composition of the tested alloys as was shown by chemical analysis after the prolonged time of measurements. The last column of Table I shows the errors in $\ln \gamma_{Zn}$ at 805°K. They are more pronounced at the range of low lead content as the high emf data are recalculated into small values of $\ln \gamma_{Zn}$. The errors in $\ln \gamma_{Zn}$ are especially important as they are used for evaluating the interaction parameters, and it may be assumed that similar errors will be associated with both interaction parameters ϵ_{Zn}^{Pb} and ϵ_{Zn}^{Sn} .

The interaction parameters in dilute solutions were introduced by Wagner (8). For ternary alloys the relation of $\ln \gamma_i$, excluding the higher terms in Taylor's series, is as follows

$$\ln \gamma_i / \ln \text{solvent } k / = \ln \gamma_i^0 + \epsilon_i^i X_i + X_j \epsilon_i^j \quad [3]$$

where γ_i^0 is the limiting value of activity coefficient of component i when $X_i = X_j = 0$ and $\epsilon_i^i, \epsilon_i^j$ are defined as

$$\epsilon_i^i = \left(\frac{\ln \gamma_i}{\partial X_i} \right)_{X_i=0} \quad \text{self-interaction parameter in the binary system } i-k$$

and

$$\epsilon_i^j = \left(\frac{\partial \ln \gamma_i}{\partial X_j} \right)_{\substack{X_i=0 \\ X_j=0}} \quad \text{ternary interaction parameter in the ternary system } i-j-k$$

The range of applicability of Eq. [3] is normally experimentally determined and generally this relation is valid up to the concentration $X_i = X_j = 0.1$ molar fraction.

Values of $\ln \gamma_{\text{Zn(Pb)}}$, $\ln \gamma_{\text{Zn(Sn)}}$ and both self-interaction parameters $\epsilon_{\text{Zn}^{\text{Zn}}}$ in binary systems Zn-Pb and Zn-Sn were obtained from Fig. 2 and 3. In Fig. 2 the relation of $\ln \gamma_{\text{Zn}}$ vs. X_{Zn} in liquid Zn-Sn solutions is plotted. It is seen from this plot that the slopes of the curves drawn through the data are zero, or $\epsilon_{\text{Zn}^{\text{Zn}}} = 0$, however, the data for 842° and 877°K show appreciable scatter. A zero slope or $\epsilon_{\text{Zn}^{\text{Zn}}} = 0$ was assumed for these two temperatures because similar results were obtained from previous separate measurements for this system. Besides $\epsilon_{\text{Zn}^{\text{Zn}}} = 0$ satisfies Eq. [3] in the calculation of $\ln \gamma_{\text{Zn}}$ at high tin concentrations. The obtained deviations in Fig. 2 may be influenced by the proximity of tin and zinc in the electromotive series. The calculated difference between standard free energy of formation, $\Delta G_{\text{ZnCl}_2}^0 - \Delta G_{\text{SnCl}_2}^0$ equals nearly -7000 cal in which case according to Wagner and Werner (9) the possibility of side reactions may be expected. Extrapolated values of $\ln \gamma_{\text{Zn}}$ to $X_{\text{Zn}} \rightarrow 0$ enabled the obtaining of the relation of $\ln \gamma_{\text{Zn}}^0$ vs. temperature in the form

$$\ln \gamma_{\text{Zn(Sn)}}^0 = \left(\frac{1039}{T} - 0.74 \right) \quad [4]$$

In Fig. 3, the experimental data of $\ln \gamma_{\text{Zn}}$ vs. X_{Zn} in the system Zn-Pb are plotted. They result in negative values of $\epsilon_{\text{Zn}^{\text{Zn}}}$ and in the relation of $\ln \gamma_{\text{Zn}}^0$ vs. temperature of the form

$$\ln \gamma_{\text{Zn(Pb)}}^0 = \left(\frac{2924}{T} - 0.965 \right) \quad [5]$$

In Fig. 3, deviations from linear dependence are observed at $X_{\text{Zn}} = 0.1$. These may result from the proximity of the immiscibility gap in the liquid state. The dashed line extrapolation for the temperatures of 714° and 757°K refers to this immiscibility region.

The results obtained from both Fig. 2 and 3 for both systems Zn-Pb and Zn-Sn examined simultaneously with ternary alloys Zn-Pb-Sn are similar to previous separate measurements (1, 7). In Table II the data from both sets of measurements for $\epsilon_{\text{Zn}^{\text{Zn}}}$ are summarized. Some slight differences in $\epsilon_{\text{Zn}^{\text{Zn}}}$ for the Zn-Pb system appear at the higher temperatures. Both relations for limiting activity coefficients from Ref. (1) and (7) are very similar to Eq. [4] and [5], namely $\ln \gamma_{\text{Zn(Sn)}}^0 = (1119/T - 0.84)$ and $\ln \gamma_{\text{Zn(Pb)}}^0 = (2798/T - 0.96)$.

The interaction parameters $\epsilon_{\text{Zn}^{\text{Pb}}}$ and $\epsilon_{\text{Zn}^{\text{Sn}}}$ were obtained in the following manner. The data of $\ln \gamma_{\text{Zn}}$ vs. X_{Pb} for ternary alloys were plotted in Fig. 4-7. From these figures the values of $\ln \gamma_{\text{Zn}}$ at constant $X_{\text{Pb}}/X_{\text{Sn}}$ ratios were considered. The thirteen ratios chosen as shown in Table III approximately correspond to the concentrations of the particular alloys as given in Table I. The values obtained at zinc concentrations $X_{\text{Zn}} = 0.03-0.1$ were used for plots $\ln \gamma_{\text{Zn}}$ vs. X_{Zn} at constant ratio $X_{\text{Pb}}/X_{\text{Sn}}$, and then the respective curves were extrapolated to $X_{\text{Zn}} \rightarrow 0$. In Table III the values of $(\ln \gamma_{\text{Zn}})_{X_{\text{Zn}} \rightarrow 0}$ obtained in this manner are reported, and were used to plot $(\ln \gamma_{\text{Zn}})_{X_{\text{Zn}} \rightarrow 0}$ vs. X_{Pb} in Fig. 8. From Fig. 8 both data of $\epsilon_{\text{Zn}^{\text{Pb}}}$ and $\epsilon_{\text{Zn}^{\text{Sn}}}$ were determined as the slopes of the respective lines over the range up to 0.1 mole fraction of both tin and lead.

In Table II the values of both ternary interaction parameters are given. In the case of $\epsilon_{\text{Zn}^{\text{Sn}}}$ the data from a previous paper (5) are also included showing nearly

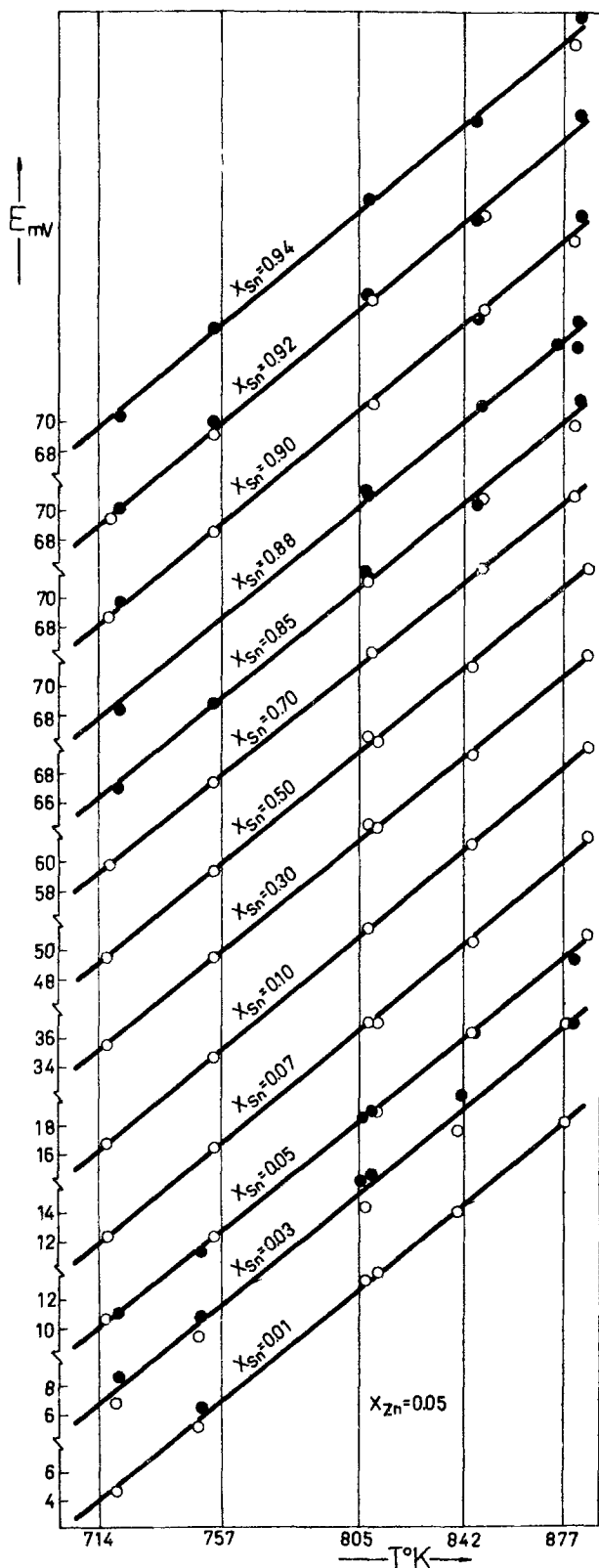


Fig. 1. Relation of E_{mV} vs. $T^{\circ}\text{K}$ in liquid Zn-Pb-Sn system at $X_{\text{Zn}} = 0.05$.

Table I. Experimental data for $X_{Zn} = 0.05$ in the Zn-Sn-Pb liquid alloys

X_{Sn}	X_{Pb}	$E_{mV} = a + bT^{\circ}K$	714°K	$\ln \gamma_{Zn}$ 805°K	877°K	r	$s(b)$	$s(\bar{y})$	Per cent error of $\ln \gamma_{Zn}$ at 805°K*
0.0100	0.9400	$E_{mV} = -109.84 + 0.1595T$	2.863	2.459	2.199	0.9989	0.00333	0.1744	±0.50
0.0300	0.9200	$= -107.22 + 0.1595T$	2.779	2.385	2.131	0.9957	0.00492	0.2737	±0.75
0.0500	0.8999	$= -100.78 + 0.1552T$	2.667	2.296	2.058	0.9994	0.00179	0.1032	±0.29
0.0700	0.8799	$= -102.45 + 0.1600T$	2.609	2.233	1.990	0.9995	0.00261	0.1450	±0.48
0.1000	0.8500	$= -97.83 + 0.1598T$	2.466	2.107	1.875	0.9999	0.00082	0.0561	±0.18
0.3000	0.6500	$= -76.00 + 0.1558T$	1.850	1.570	1.390	0.9994	0.00263	0.1463	±0.69
0.5000	0.4499	$= -62.92 + 0.1569T$	1.397	1.166	1.017	0.9994	0.00263	0.1461	±0.93
0.7000	0.2499	$= -51.96 + 0.1556T$	1.070	0.879	0.756	0.9999	0.00121	0.0717	±0.66
0.8500	0.1000	$= -45.31 + 0.1563T$	0.839	0.673	0.565	0.9994	0.00274	0.1559	±1.72
0.8800	0.0700	$= -45.31 + 0.1583T$	0.792	0.625	0.518	0.9972	0.00533	0.2901	±3.28
0.9000	0.0500	$= -46.36 + 0.1603T$	0.780	0.610	0.500	0.9993	0.00243	0.1553	±1.73
0.9280	0.0300	$= -46.69 + 0.1618T$	0.756	0.584	0.474	0.9987	0.00312	0.1753	±1.99
0.9399	0.0100	$= -45.69 + 0.1614T$	0.732	0.564	0.456	0.9985	0.00445	0.2734	±3.60

* Errors were calculated for 95% confidence range of emf values as obtained from least squares fit.

a, intercept in the linear equation.

b, slope of the line E_{mV} vs. temperature, mV/K°.

r, the correlation coefficient.

s(b), standard deviation of the slope.

s(y), standard deviation of the electromotive force.

X_{Zn} , X_{Pb} , X_{Sn} , mole fractions weighed-in basis. For repeated measurements, the mean values of all alloys for the same composition.

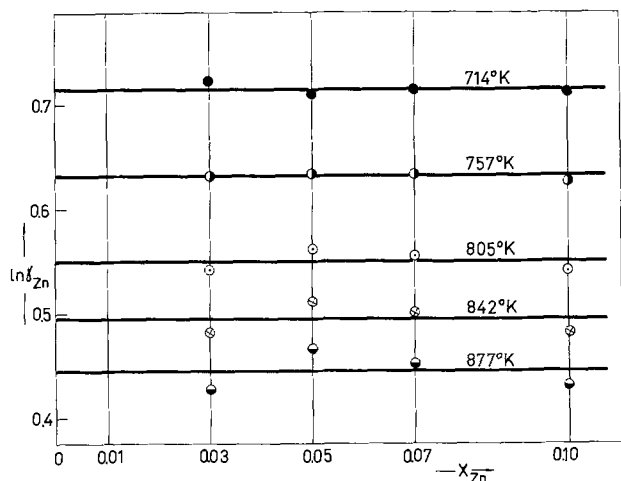


Fig. 2. $\ln \gamma_{Zn}$ vs. X_{Zn} in the Zn-Sn liquid solutions at temperatures 714°-877°K.

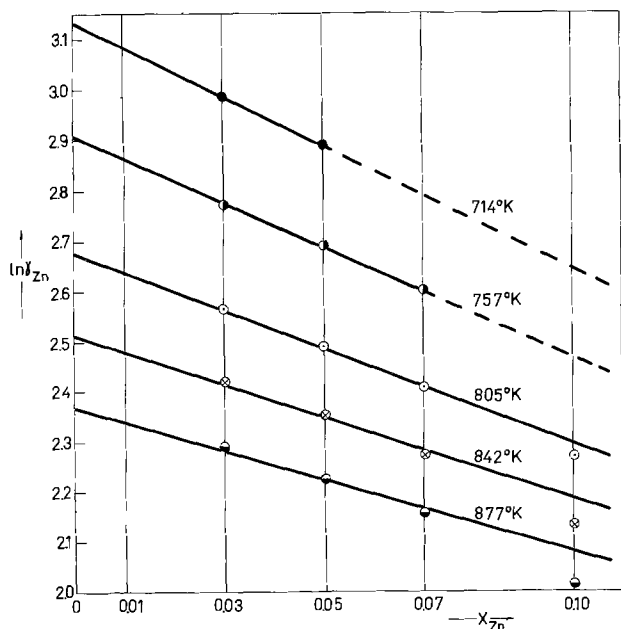


Fig. 3. $\ln \gamma_{Zn}$ vs. X_{Zn} in the Zn-Pb liquid solutions at temperatures 714°-877°K.

identical values. In Ref. (5) the values of ϵ_{Zn}^{Sn} were obtained from the plots of $\ln \gamma_{Zn}$ vs. X_{Sn} and $[(\partial \ln \gamma_{Zn}) / (\partial X_{Sn})]_{X_{Zn}=\text{const}}$ vs. X_{Zn} using the results only at $X_{Sn}=0$.

$0.01 \leq X_{Sn} \leq 0.1$ mole fraction.

The binary end points in Fig. 4-8 were taken from Fig. 2 and 3 for Zn-Pb and Zn-Sn systems, respectively. In general, it may be assumed that the extrapolation from ternary data is in good agreement with the binary data. Some differences appear when $X_{Zn} = 0.07$ and 0.1 when $X_{Sn} = 0$ as a result of deviations from linearity in Fig. 3, when $X_{Zn} = 0.1$ mole fraction.

Application of Krupkowski's Method in the Thermodynamic Analysis of Binary and Ternary Systems

For binary solutions Krupkowski (10) presented relations of the form

$$\ln \gamma_j = \omega_{jk}(T) \left[(1 - X_k)^{m_{jk}} - \frac{m_{jk}}{m_{jk} - 1} (1 - X_k)^{m_{jk}-1} + \frac{1}{m_{jk} - 1} \right] \quad [6]$$

$$\ln \gamma_k = \omega_{jk}(T) (1 - X_k)^{m_{jk}} \quad [7]$$

Equation [6] is derived from Eq. [7] using the Gibbs-Duhem equation. As results from Eq. [6] and [7] the function $\omega(T)$ and m should be determined from experimental results. Usually for this purpose the data at concentrations $X_k = 0.1-0.9$ mole fraction are used. Analysis of such a procedure has been demonstrated in Ref. (11).

From previous papers Eq. [6] and [7] in the binary systems take the following forms: from Ref. (12) in the Zn-Sn liquid solutions

$$\ln \gamma_{Zn} = \left[\frac{2489}{T} + 1.824(\ln T - 1) - 12.929 \right] (1 - X_{Zn})^{1.1} \quad [8]$$

$$\ln \gamma_{Sn} = \left[\frac{2489}{T} + 1.824(\ln T - 1) - 12.929 \right] [(1 - X_{Zn})^{1.1} - 11(1 - X_{Zn})^{0.1} + 10] \quad [9]$$

from Ref. (4) in the Zn-Pb liquid solutions

$$\ln \gamma_{Zn} = \left(\frac{3000}{T} - 1.059 \right) (1 - X_{Zn})^{1.53} \quad [10]$$

Table II. Experimental values of binary and ternary interaction parameters at temperatures 714°-877°K

T °K	Ref. (5)	$\epsilon_{Zn^{Sn}}$	$\epsilon_{Zn^{Pb}}$	$\epsilon_{Zn^{Zn}}$ system Zn-Sn		$\epsilon_{Zn^{Zn}}$ system Zn-Pb	
		This study from Fig. 8	this study from Fig. 8	Fig. 2	Ref. (1)	Fig. 3	from Ref. (7)
714	-4.65	-4.65	1.27	0	0	-4.95	-4.87
757	-4.47	-4.47	1.25	0	0	-4.33	-4.16
805	-4.21	-4.20	1.20	0	0	-3.71	-3.51
842	-3.93	-3.92	1.15	0	0	-3.29	-3.09
877	-3.60	-3.62	1.07	0	0	-2.92	-2.68

$$\ln \gamma_{Pb} = \left(\frac{3000}{T} - 1.059 \right) [(1 - X_{Zn})^{1.53} - 2.887(1 - X_{Zn})^{0.53} + 1.887] \quad [11]$$

and finally for the Pb-Sn liquid solutions, Ref. (13)

$$\ln \gamma_{Pb} = \frac{638}{T} (1 - X_{Pb})^{1.9} \quad [12]$$

$$\ln \gamma_{Sn} = \frac{638}{T} [(1 - X_{Pb})^{1.9} - 2.111(1 - X_{Pb})^{0.9} + 1.111] \quad [13]$$

From Eq. [7] it is clear that when $X_k \rightarrow 0$, $\ln \gamma_k = \omega_{jk}(T)$, and from Eq. 6, when $X_j \rightarrow 0$, $\ln \gamma_j = \omega_{jk}(T) \times [1/(m_{jk} - 1)]$. In the case of Zn-Pb, Zn-Sn, and Pb-Sn binary systems Eq. [7] has been used for zinc and lead, respectively. As a result $\ln \gamma_{Zn(Sn)}$ and $\ln \gamma_{Zn(Pb)}$ are equal directly to respective $\omega(T)$ functions in Zn-Pb and Zn-Sn systems. In this manner determination of the $\omega(T)$ function from concentrations $X_k = 0.1-0.9$ may be additionally tested by means of experiments in dilute solutions. It is interesting to note that the numerical results from Eq. [4] and [5]

and as $\omega(T)$ from relations [8]-[9] and [10]-[11] at considered temperatures 714°-877°K are very similar. It is also true in the case of the Zn-Sn system when the form of the $\omega(T)$ relation is different in comparison with Eq. [4]. The limiting activity coefficients are readily calculated from Eq. [6] and [7] for both components and will be used in the next part of the paper in calculations of $\epsilon_{Zn^{Pb}}$ and $\epsilon_{Zn^{Sn}}$.

Krupkowski's method for obtaining the relations of activity coefficients in multicomponent systems requires only the data of composite binary systems in the form of Eq. [6] and [7]. The details of such procedure were given in a previous paper, Ref. (14). Assuming this procedure and Eq. [8]-[13] the $\ln \gamma_{Zn}$ in Zn-Pb-Sn system has the following form

$$\begin{aligned} \ln \gamma_{Zn} = & -\omega_{ZnPb}(1 - X_{Zn})^{m_{ZnPb}-2} X_{Zn} X_{Pb} \\ & + \omega_{ZnPb}(1 - X_{Zn})^{m_{ZnPb}-2} X_{Pb} \\ & - \omega_{ZnSn}(1 - X_{Zn})^{m_{ZnSn}-2} X_{Zn} X_{Sn} \\ & + \omega_{ZnSn}(1 - X_{Zn})^{m_{ZnSn}-2} X_{Sn} \\ & - \omega_{PbSn}(1 - X_{Pb})^{m_{PbSn}-2} X_{Pb} X_{Sn} \quad [14] \end{aligned}$$

From Eq. [14] when $X_{Zn} \rightarrow 0$, $\ln \gamma_{Zn}$ takes the form

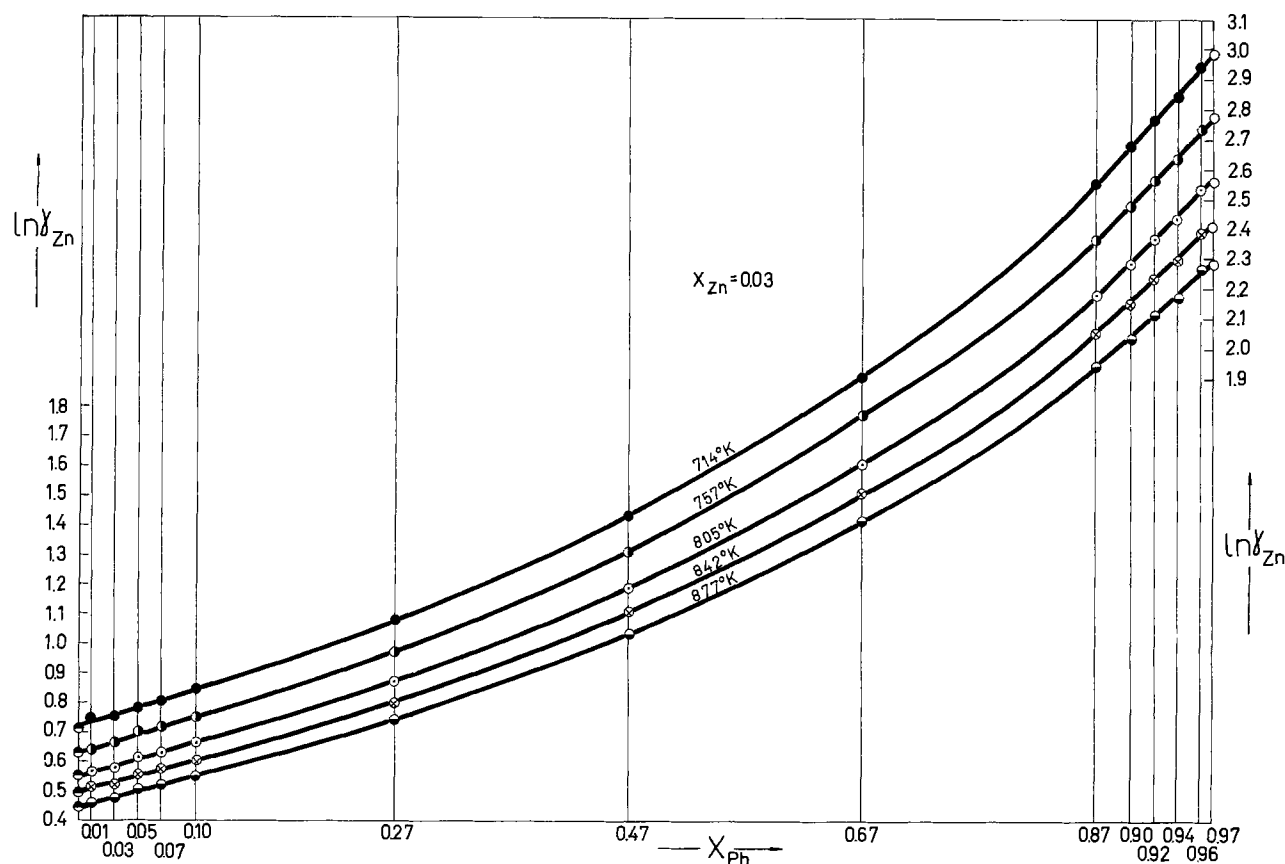


Fig. 4. $\ln \gamma_{Zn}$ vs. X_{Pb} in the Zn-Pb-Sn liquid solutions at temperatures 714°-877°K when $X_{Zn} = 0.03$. \bullet , Obtained from Fig. 2 and \circ , obtained from Fig. 3.

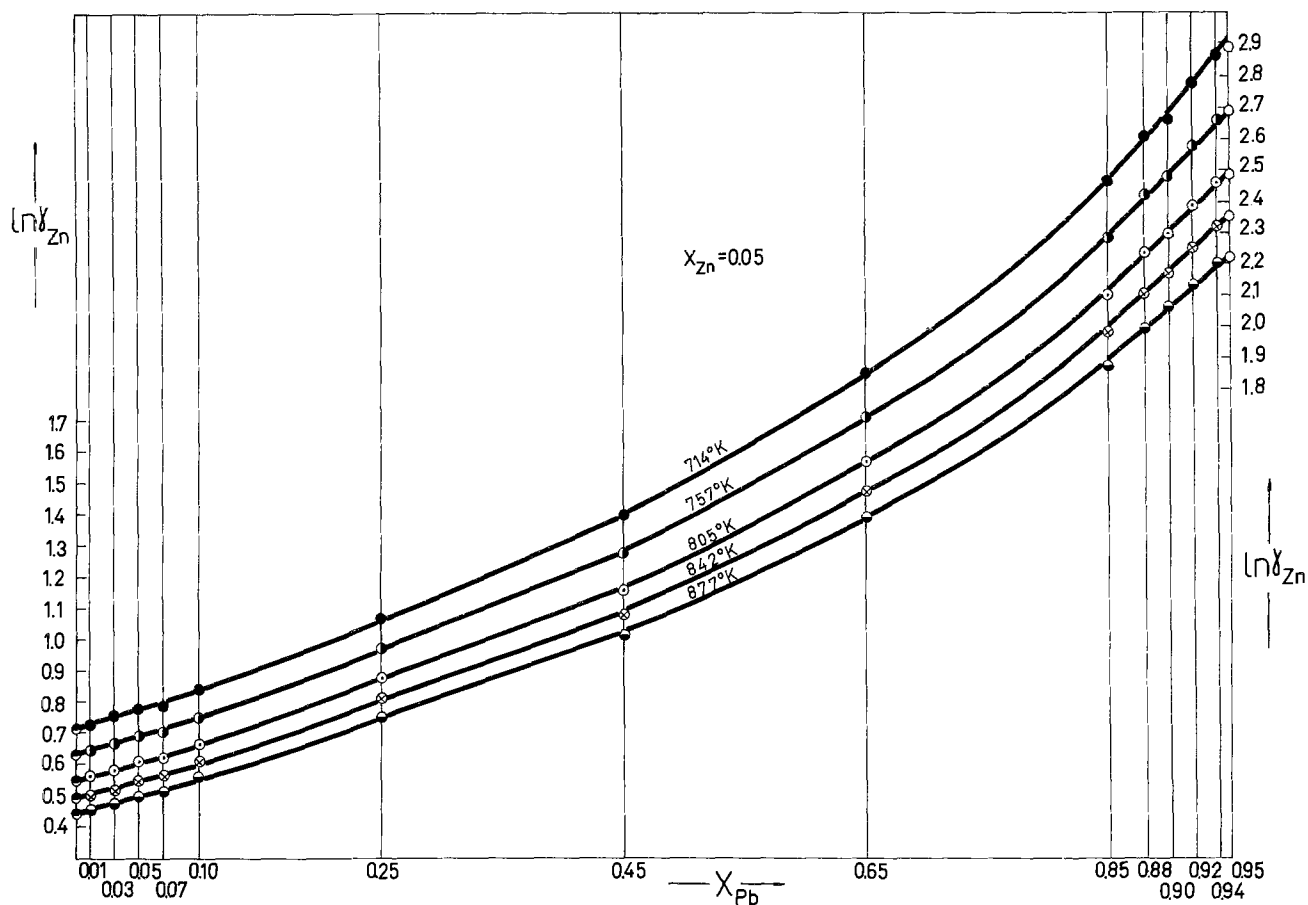


Fig. 5. $\ln \gamma_{Zn}$ vs. X_{Pb} in the Zn-Pb-Sn liquid solutions at temperatures 714°-877°K when $X_{Zn} = 0.05$. ●, Obtained from Fig. 2 and ○, obtained from Fig. 3.

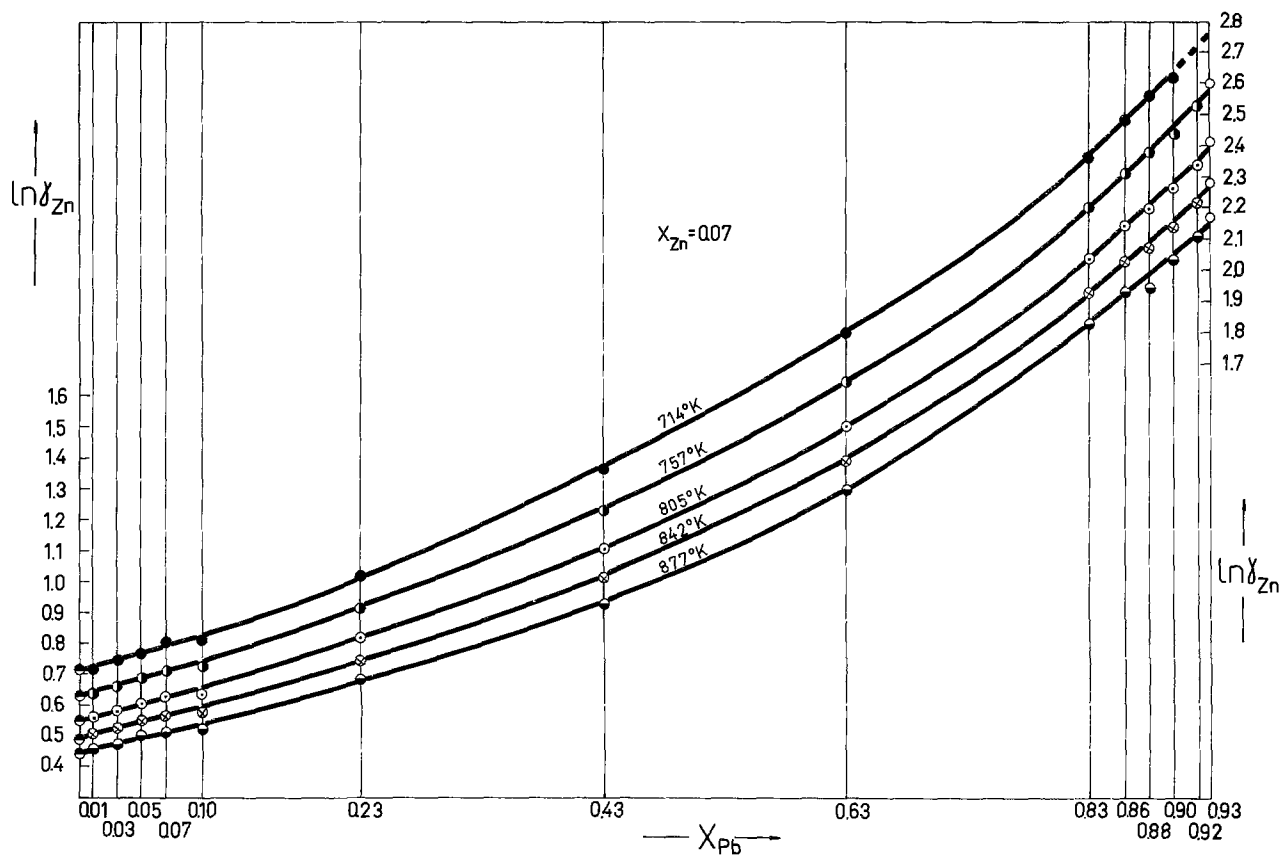


Fig. 6. $\ln \gamma_{Zn}$ vs. X_{Pb} in the Zn-Pb-Sn liquid solutions at temperatures 714°-877°K when $X_{Zn} = 0.07$. ●, Obtained from Fig. 2 and ○, obtained from Fig. 3.

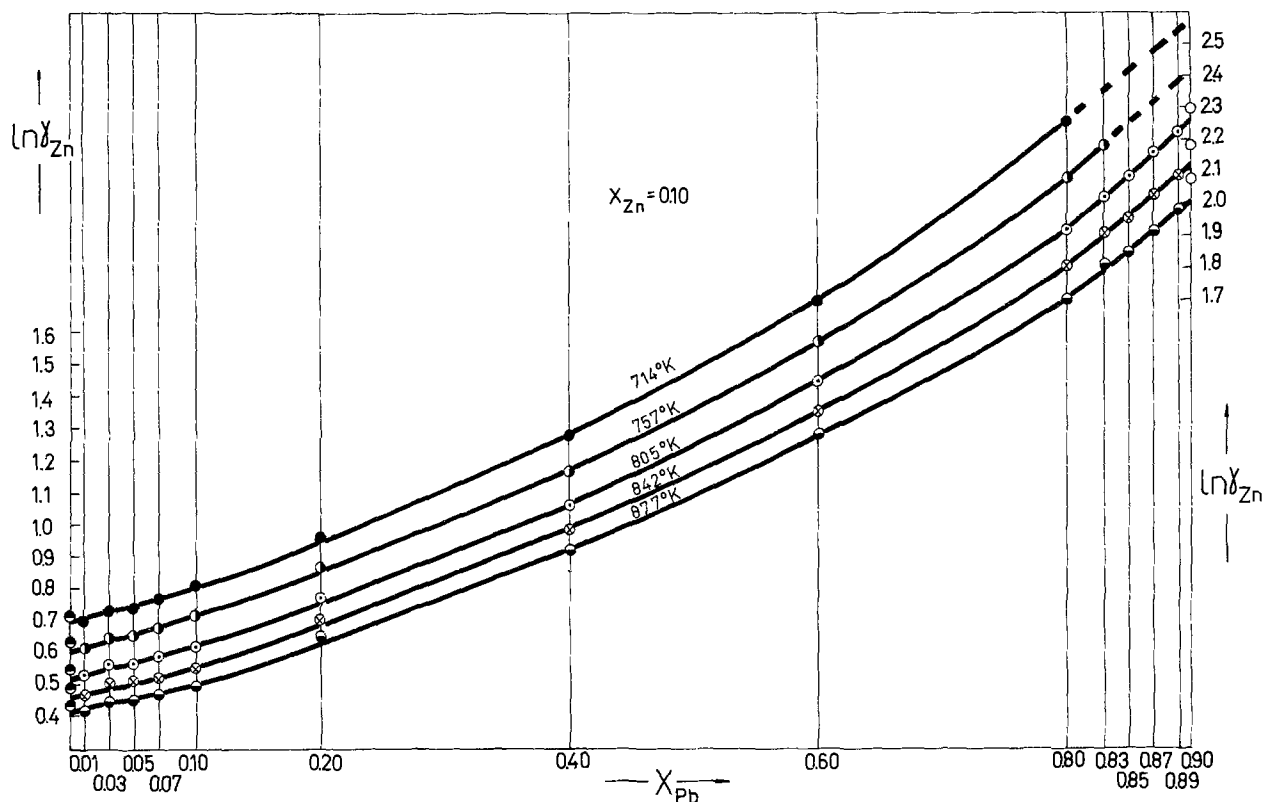


Fig. 7. $\ln \gamma_{Zn}$ vs. X_{Pb} in the Zn-Pb-Sn liquid solutions at temperatures 714°-877°K when $X_{Zn} = 0.1$. ●, Obtained from Fig. 2, and ○, obtained from Fig. 3.

$$(\ln \gamma_{Zn})_{X_{Zn} \rightarrow 0} = \omega_{ZnPb} X_{Pb} + \omega_{ZnSn} X_{Sn} - \omega_{PbSn} (1 - X_{Pb})^{m_{PbSn}} - 2X_{Pb}X_{Sn} \quad [15]$$

In both Eq. [14] and [15] the last term corresponds to the thermodynamic properties of the Pb-Sn system. Values of $\ln \gamma_{Zn}$ at $X_{Zn} = 0.05$ were calculated from Eq. [14] and values of $(\ln \gamma_{Zn})_{X_{Zn} \rightarrow 0}$ were calculated from Eq. [15], in both cases at 714°, 805°, and 877°K. It is seen when comparing these calculated values summarized in Table III, with experimental values in Tables I and III that the agreement is satisfactory, except for the central region where the concentration of lead is $0.3 \leq X_{Pb} \leq 0.7$. It is probably the result of inaccurate determination of $\omega(T)$ and m in the Pb-Sn system.

It is interesting to note that by differentiating Eq. [14] it is possible to obtain formulas for calculation of both ϵ_{Zn}^{Pb} and ϵ_{Zn}^{Sn} in which the $\omega(T)$ functions for binary systems appear. Similar formulas with the

relations for limiting activity coefficients were proposed by Alcock and Richardson (15, 16) and by Lupis and Elliott (17, 18) assuming a random distribution of atoms in solution

$$\epsilon_{Zn}^{Pb} = \ln \gamma_{Zn(Pb)} - \ln \gamma_{Zn(Sn)} - \ln \gamma_{Pb(Sn)} \quad [16]$$

$$\epsilon_{Zn}^{Sn} = \ln \gamma_{Zn(Sn)} - \ln \gamma_{Zn(Pb)} - \ln \gamma_{Sn(Pb)} \quad [17]$$

By application of Eq. [6] and [7] the limiting activity coefficients may be easily calculated from $\omega(T)$ and m of binary systems as was previously mentioned. Therefore, substituting appropriate $\omega(T)$ and m from Eq. [8]-[13] into Eq. [16] the values of ϵ_{Zn}^{Pb} at temperatures 714°, 805°, and 877°K were calculated with numerical values of 1.53, 1.43, and 1.33. Analogically from Eq. [17] at the same temperatures the resulting values of ϵ_{Zn}^{Sn} are -3.42, -3.21, and -3.00. The values of both ternary interaction parameters differ slightly from those obtained from experiments, but they exhibit the same sign and dependence upon temperature.

Table III. Experimental and calculated values of $\ln \gamma_{Zn}$ when $X_{Zn} \rightarrow 0$ and $\ln \gamma_{Zn}$ at temperatures 714°, 805°, and 877°K

$\frac{X_{Pb}}{X_{Sn}}$	Experimental data ($\ln \gamma_{Zn}$) $_{X_{Zn} \rightarrow 0}$			Calculated from Eq. [15] ($\ln \gamma_{Zn}$) $_{X_{Zn} \rightarrow 0}$			Calculated from Eq. [14] $\ln \gamma_{Zn}^*$ at $X_{Zn} = 0.05$		
	714°K	805°K	877°K	714°K	805°K	877°K	714°K	805°K	877°K
94.000	3.067	2.632	2.297	3.103	2.633	2.330	2.870	2.435	2.155
30.687	2.967	2.540	2.217	3.032	2.570	2.273	2.802	2.376	2.101
18.000	2.870	2.452	2.140	2.963	2.510	2.218	2.736	2.318	2.048
12.571	2.772	2.365	2.065	2.896	2.451	2.165	2.672	2.261	1.997
8.500	2.627	2.235	1.952	2.798	2.365	2.087	2.578	2.179	1.922
2.800	1.967	1.675	1.462	2.314	1.940	1.702	2.008	1.677	1.468
1.111	1.462	1.240	1.050	1.762	1.455	1.265	1.519	1.248	1.081
0.461	1.122	0.952	0.800	1.291	1.043	0.893	1.103	0.884	0.753
0.118	0.852	0.675	0.560	0.895	0.697	0.583	0.836	0.650	0.543
0.079	0.810	0.635	0.525	0.828	0.639	0.531	0.787	0.607	0.505
0.055	0.785	0.610	0.505	0.796	0.611	0.506	0.755	0.579	0.480
0.033	0.760	0.585	0.480	0.764	0.583	0.481	0.724	0.552	0.456
0.011	0.735	0.560	0.460	0.733	0.556	0.456	0.693	0.525	0.432

* Values of $\ln \gamma_{Zn}$ at $X_{Zn} = 0.05$ were calculated for the same concentrations as alloys from Table I.

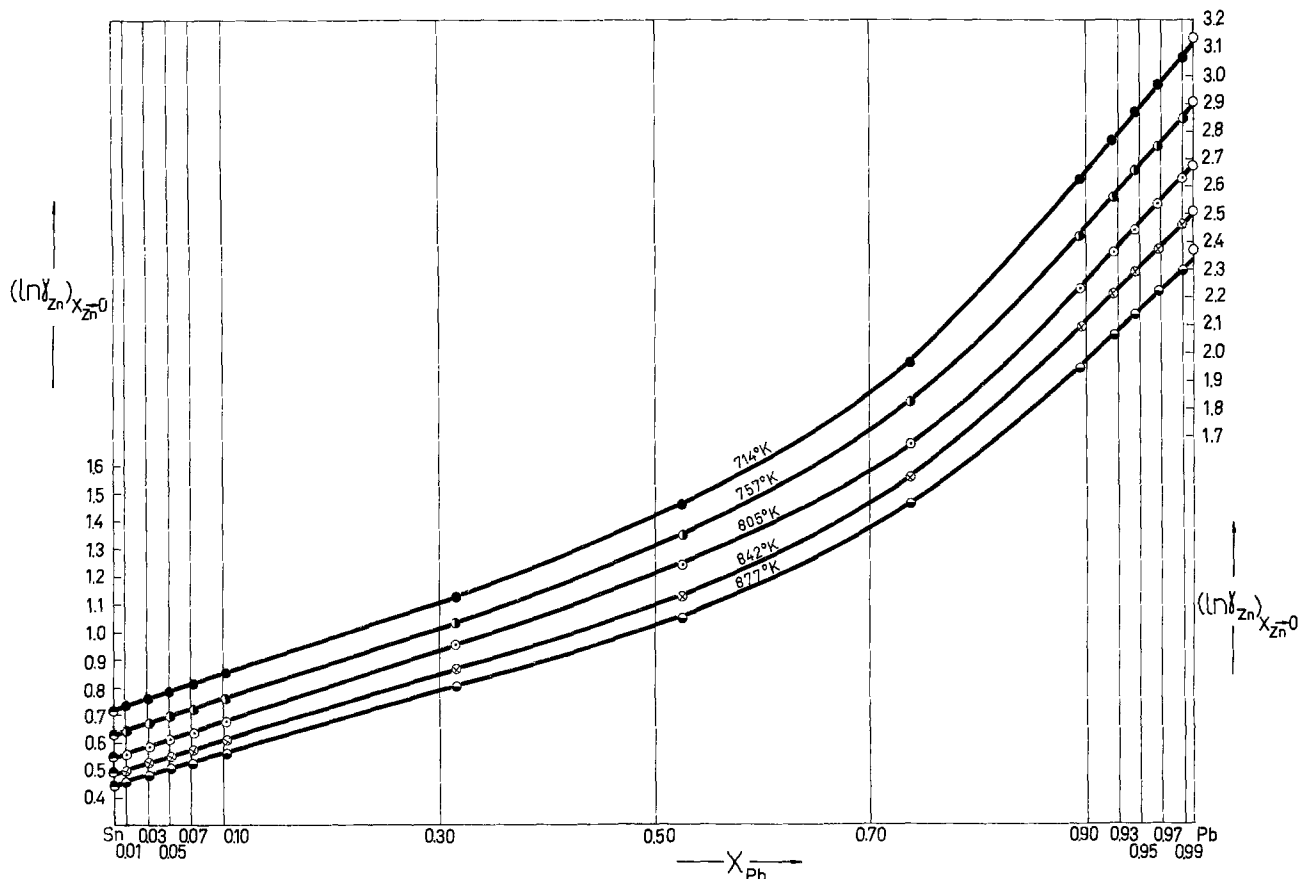


Fig. 8. $\ln \gamma_{Zn}$ vs. X_{Pb} obtained from the experimental data for $X_{Zn} \rightarrow 0$ at temperatures 714°-877°K in the Zn-Pb-Sn liquid solutions. ●, Obtained from Fig. 2 and ○, obtained from Fig. 3.

Discussion

The experimental data permitted the determination of both ternary interaction parameters ϵ_{Zn}^{Pb} and ϵ_{Zn}^{Sn} from plots $(\ln \gamma_{Zn})_{X_{Zn} \rightarrow 0}$ vs. X_{Pb} . Both values of ϵ_{Zn}^{Pb} and ϵ_{Zn}^{Sn} were also compared with calculated data on the basis of limiting activity coefficients obtained from $\omega(T)$ and m of respective binary systems interpreted by Krupkowski's method.

Okajima and Pehlke (19) as well as Cleveland, Okajima, and Pehlke (20) also reported from emf measurements the data of ϵ_{Zn}^{Pb} and ϵ_{Zn}^{Sn} but they limited the experiments only to 0.1 mole fraction of tin and lead, respectively. At the temperature of 823°K they found $\epsilon_{Zn}^{Pb} = 2.2$ and $\epsilon_{Zn}^{Sn} = -3.6$ which compare with values of about 1.17 and -4.0 , respectively, as interpolated from our data in Table II. In the next reference, Gluck and Pehlke (21) also presented the plot of $(\ln \gamma_{Zn})_{X_{Zn} \rightarrow 0}$ vs. X_{Pb} for Zn-Sn-Pb system combining their results for dilute solutions to $X_{Pb} = X_{Sn} = 0.1$ mole fraction with extrapolated data for the central region. However, their plots using literature data (22) differ from the results presented in Fig. 8. This disagreement is believed to be the result of their less precise extrapolation of $\ln \gamma_{Zn}$ to $X_{Zn} \rightarrow 0$ for $X_{Zn} \cong 0.1$.

The magnitude of the deviation from a straight line obtained by connecting $\ln \gamma_{Zn}^{(Sn)}$ and $\ln \gamma_{Zn}^{(Pb)}$ in Fig. 8 is influenced by the thermodynamic properties of the Pb-Sn system. Positive departure from Raoult's law in this system results in negative deviations from linearity (23). The data in Fig. 8 at $X_{Pb} = 0.53$ and $X_{Sn} = 0.47$ result in the experimental deviation in $\ln \gamma_{Zn}$ at temperatures 714°, 805°, and 877°K of the magnitude 0.54, 0.41, and 0.38. These data may be compared using Eq. [15] and assuming that deviation from linearity is governed by the term $-\omega_{PbSn}(1 - X_{Pb})^{m_{PbSn}} - 2X_{Pb}X_{Sn}$. However, such calculations exhibit

the deviations of the order 0.24, 0.21, and 0.19 at the mentioned temperatures. It is probably the result of inaccuracy in the $\omega(T)$ and m in Eq. [12] and [13] for the Pb-Sn system. These parameters were calculated by Ptak (13) using the Pb-Sn phase diagram and probably are subject to appreciable uncertainty. The close position of lead and tin in the electromotive series excludes however the use of concentration cells and obtaining more precise data.

The deviation from linearity may also be calculated according to Richardson (24) and is characterized approximately by the term $-\Delta G^*_{PbSn}/RT$ where ΔG^*_{PbSn} is the molar excess free energy in the Pb-Sn system. Using the data for ΔG^*_{PbSn} from the Hultgren *et al.* monograph, (25) at 823°K, $X_{Pb} = X_{Sn}$ the value of 0.32 for the deviation was obtained which corresponds to some extent to the results shown in Fig. 8.

Error analysis of the experimental data at the chosen concentration $X_{Zn} = 0.05$ molar fraction results in maximal errors in $\ln \gamma_{Zn}$ of about $\pm 4\%$. Next, the $\ln \gamma_{Zn}$ data are the starting point for determination of both ϵ_{Zn}^{Sn} and ϵ_{Zn}^{Pb} , and therefore one may assume that ternary interaction parameters will be associated with similar errors.

It is assumed that in investigations on dilute liquid solutions the most important phenomena are connected with reciprocal interactions of a respective group of atoms. The simpler cases are those in which the composite binary alloys show positive deviations from Raoult's law. Then, the attractive forces between the same species of atoms are greater than those between different species of atoms. In such a case the ternary interaction parameters of the type ϵ_1^2 and ϵ_1^3 from Eq. [16] and [17] result in comparatively good agreement with experimental data. When one of the binaries shows marked deviations from Raoult's law, as for instance Zn-Pb, in comparison to other systems such as Zn-Sn and Pb-Sn in the investigated Zn-Pb-

Sn ternary system, then the properties of such a binary system play a decisive role. This system has a rather dominant value of $\ln \gamma_{\text{Zn(Pb)}}^{\circ}$ in relation to $\ln \gamma_{\text{Zn(Sn)}}^{\circ}$ and $\ln \gamma_{\text{Pb(Sn)}}^{\circ}$ which strongly influences both $\epsilon_{\text{Zn}^{\text{Pb}}}$ and $\epsilon_{\text{Zn}^{\text{Sn}}}$ when calculated from Eq. [16] and [17]. Future experimental research in ternary systems in dilute solutions will be directed toward verification of Eq. [16] and [17] and also to the combinations of the interaction parameters thus obtained with the energy of interaction of respective groups of different atoms.

Acknowledgments

The authors are greatly indebted to Professor P. Chiotti from Iowa State University, Ames Laboratory, USAEC for helpful advice and having revised the English text.

Manuscript submitted Feb. 5, 1974 revised manuscript received Oct. 2, 1974.

Any discussion of this paper will appear in a Discussion Section to be published in the December 1975 JOURNAL. All discussions for the December 1975 Discussion Section should be submitted by Aug. 1, 1975.

REFERENCES

- Z. Moser, *Bull. Acad. Polon. Sci. Ser. Sci. Tech.*, **17**, 27 (1969).
- Z. Moser, *ibid.*, **18**, 51 (1970).
- Z. Moser, *Met. Trans.*, **4**, 2399 (1973).
- Z. Moser, *ibid.*, **2**, 2175 (1971).
- Z. Moser and W. Zakulski, *Arch. Hutnictwa*, **19**, 87 (1974).
- W. Ptak and Z. Moser, *Trans. Met. Soc. AIME*, **242**, 558 (1968).
- Z. Moser, *Arch. Hutnictwa*, **14**, 371 (1969).
- C. Wagner, "Thermodynamics of Alloys," Addison-Wesley Publishing Co., Cambridge, Mass. (1952).
- C. Wagner and A. Werner, *This Journal*, **110**, 326 (1963).
- A. Krupkowski, *Bull. Acad. Polon. Sci. Lett.*, **1**, 15 (1951).
- Z. Moser, *Rev. Roumaine Chim.*, **16**, 327 (1971).
- W. Ptak, *Arch. Hutnictwa*, **5**, 169 (1960).
- W. Ptak, "Księga Jubileuszowa dla uczczenia zasług naukowych Aleksandra Krupkowskiego" (in Polish), (Jubilee book to celebrate the scientific achievements of Alexander Krupkowski), Warszawa, p. 413 (1965).
- W. Ptak and Z. Moser, *Arch. Hutnictwa*, **11**, 289 (1966).
- C. B. Alcock and F. D. Richardson, *Acta Met.*, **6**, 385 (1958).
- C. B. Alcock and F. D. Richardson, *ibid.*, **8**, 882 (1960).
- C. H. P. Lupis and J. F. Elliott, *ibid.*, **14**, 529 (1966).
- C. H. P. Lupis and J. F. Elliott, *ibid.*, **14**, 1019 (1966).
- K. Okajima and R. D. Pehlke, *J. Japan Inst. Metals (Sendai)*, **29**, 961 (1965).
- S. Cleveland, K. Okajima, and R. D. Pehlke, *J. Phys. Chem.*, **69**, 4085 (1965).
- J. V. Gluck and R. D. Pehlke, *Trans. Met. Soc. AIME*, **245**, 711 (1969).
- L. Oleari and M. Fiorani, *Ric. Sci.*, **29**, 2349 (1959).
- Z. Moser, *Z. Metallk.*, **65**, 106 (1974).
- F. D. Richardson, *Trans. Met. Soc. AIME*, **230**, 1215 (1964).
- "Selected Values of the Thermodynamic Properties of the Binary Systems," prepared by R. Hultgren, P. Desai, D. Hawkins, M. Gleisler, and K. Kelley," Edited by American Society for Metals, Metals Park, Ohio (1973).

Micro Weighing Study of Iodinations of Thin Metal Films with Quartz Crystal Oscillators

M. Shiojiri

Department of Physics, Kyoto Technical University, Matsugasaki, Sakyo-ku, Kyoto 606, Japan

ABSTRACT

The reactions of iodine vapor with vacuum-deposited copper and lead films have been investigated in the temperature range 25°-300°C. Below 150°C, the iodination of copper films obeys the parabolic rate relationship, and its activation energy is estimated to be 3.9 kcal/mole. Above 150°C, the iodination obeys the linear rate relationship, and the iodination rate decreases with increasing temperature. The chemisorption of iodine gas is the rate-determining factor of the linear reaction and leads to the observed temperature dependence of the reaction. The iodination of lead films approximately obeys the parabolic rate relationship, and its activation energy is 13.9 kcal/mole.

Tammann and Köster (1, 2) found in the early studies of the reactions of various gases with metals that the reaction rates for the iodination of silver, copper, and lead were independent of temperature. There have been very few studies of the halogenation of such metals since (3-6), and such peculiar reactions which do not obey an Arrhenius equation are still unclear (7) and await explanation (8). The method for measuring the film thickness based on interference colors as used in their experiments was not very accurate, and much more accurate experimentation is required for a clear understanding of the halogenation mechanism.

Weight gains due to the reaction of iodine vapor with vacuum-deposited copper films were previously measured in the temperature range from 25° to 300°C with quartz crystal oscillators (9). It is the object of

the present paper to discuss in detail the iodination of copper films. The results are also given of investigations concerning the reaction of iodine vapor with vacuum-deposited lead films in the temperature range 25°-300°C. The reactions of iodine vapor with silver films have been discussed in previous papers (10-12).

Experimental

The weight gains due to the iodination of copper and lead films were continuously measured by using a quartz crystal oscillator microbalance with a counting ratemeter and a pen recorder (13). Quartz plates with 3.58 MHz resonance frequency, whose sensitivity for mass determination is 2.89×10^7 Hz/(g/cm²), were used. The quartz plates were vibrated at an exciting power of about 5 mW, and the vibration had no appreciable influence on the reactions of iodine with the metal films (14).

About 5000Å thick copper (99.999%) films were prepared by vacuum-deposition onto one of the gold electrodes of the water-cooled quartz plates in a vacuum of 5×10^{-7} Torr. The quartz plate was placed in a reaction chamber for the iodination. Specimen lead (99.99%) was vacuum-deposited onto the quartz plate in the reaction chamber evacuated to a pressure of 2×10^{-7} Torr or less, so as to minimize the surface oxidation. The iodine vapor was immediately introduced into the chamber, without exposing the specimen to the air. The gold electrodes, when in contact and alloyed with copper or lead, were appreciably attacked by iodine vapor at higher temperatures. Therefore, in the experiments at temperatures above 150°C, the specimen films were directly deposited onto one side of the plates and were simultaneously used as one of the electrodes. Both of copper and lead films were polycrystalline, preferably oriented with the (111) planes parallel to their surfaces. The steps in the experimental procedure were the same as described in the previous papers (10, 12).

Results

Iodination of copper films.—Various experiments were repeated at a given temperature and pressure, and the reproducibility was usually good. Some rate curves are presented in Fig. 1. The iodination was performed at an iodine pressure of 0.032 Torr. The reaction product was the γ -form (zinc blende type) of cuprous iodide crystals. The mean thickness of the grown cuprous iodide layer can be estimated by assuming that the film was uniformly attacked by iodine and the product was the stoichiometric compound. The scales of micrometers for the mean thickness of the cuprous iodide layer, and of milligrams per square centimeter for the weight gain, are also presented. The results showed a clear temperature dependence of the iodination of copper which is in disagreement with the conclusion of Tammann and Köster (2); between 25° and 150°C the reaction rate increases with increasing temperature, but above 150°C it decreases with temperature. Squares of the weight gains plotted against time fell on straight lines below 150°C. This shows that the reaction of iodine with copper between 25° and 150°C approximately obeys the parabolic rate relationship. However, square plots of the data above 150°C did not lie on straight lines; rather, the curves shown in Fig. 1 lie on straight lines after about 10 sec. Therefore, the reaction above 150°C seems to obey the linear rate relationship rather than parabolic rate relationship.

The logarithms of the reaction rates at a reaction time of 30 sec are plotted against the inverse of reaction temperature in Fig. 2. Black and white circles show the corresponding reaction rates for the para-

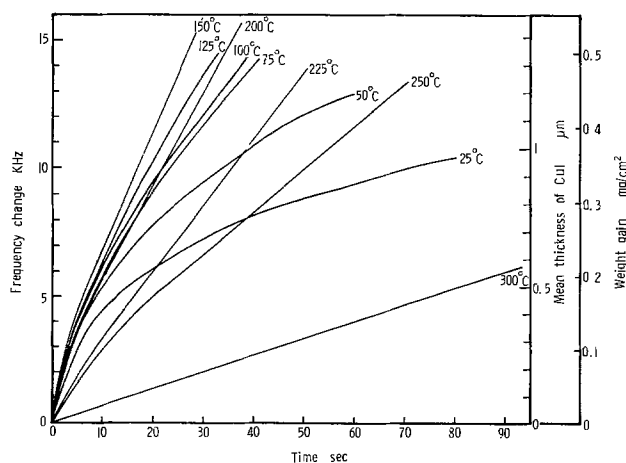


Fig. 1. Weight gain data for iodination of copper films at iodine pressure of 0.032 Torr.

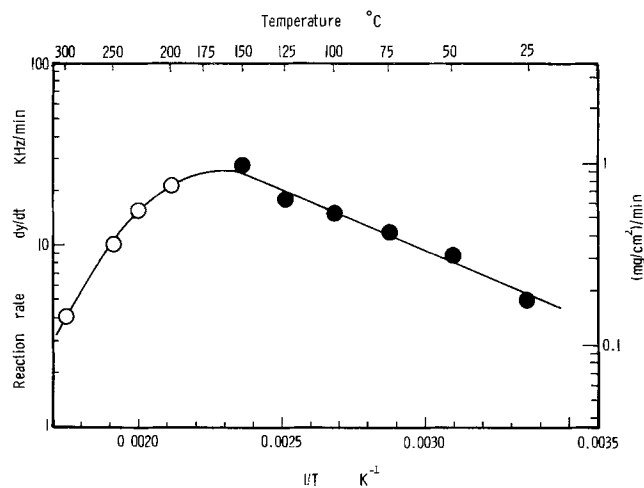


Fig. 2. Temperature dependence of parabolic (black) and linear reaction rates (white) at a reaction time of 30 sec, at iodine pressure of 0.032 Torr.

bolic and linear iodinations, respectively. The diameter of the circles is almost equal to the probable error of the reaction rates. It is clear that the rates are at a maximum near 150°C. The rate constant k_p was determined for each rate curve represented by the parabolic relationship $(df)^2 = k_p t$, where df is frequency change and t is time. Arrhenius plots of k_p lie on a straight line, like the reaction rates below 150°C lie on a straight line in Fig. 2. Thus, the activation energy for the parabolic reaction has been estimated to be 3.9 kcal/mole, and k_p for the reaction at an iodine pressure of 0.032 Torr is represented as

$$k_p = 7.1 \times 10^4 \exp(-3900/RT) \text{ kHz}^2/\text{min} \\ = 85.5 \exp(-3900/RT) (\text{mg}/\text{cm}^2)^2/\text{min}$$

where R is the gas constant and T is absolute temperature.

Iodination of lead films.—Double logarithmic plots of weight gain data for the iodinations of lead films are presented in Fig. 3. The reproducibility was usually good under the experimental condition that the specimen lead surface was never exposed to the air and the residual gas pressure was less than 2×10^{-7} Torr during the deposition of lead and the iodination. Lead iodide (PbI_2 , hexagonal) crystals were formed. Since the data fall on straight lines with a gradient of about $\frac{1}{2}$, the reaction of iodine with lead films approximately obeys the parabolic relationship, which has been reported by Tammann and Köster (2). The reaction rate evidently increases with increase of temperature, in disagreement with their conclusion that the reaction rate was independent of temperature. The experiments were performed at iodine pressures of 0.08, 0.13, 0.21, and 0.41 Torr, and a definite difference could not be recognized among the data for the reactions at the same temperature.

The reactions below 100°C were complicated. The reproducibility of experiments was not very good. The reaction rates slowed down, especially for an initial few minutes, and thus the reaction could not be represented by a simple equation. The reaction rate was apt to decrease with decreasing iodine pressure. Dotted curves in Fig. 3 are the data for the reaction of the lead films, which were once exposed to the air for a short time, with iodine at 300°, 200°, and 150°C. The curves show that the retardation of reaction by a surface oxidation was larger with decreasing temperature. Thus, it is reasonable to assume that the iodination below 100°C was influenced by a little surface oxidation owing to the residual gas and showed the poor reproducibility.

Fig. 3. Double logarithmic plots of weight gain data for iodination of lead films at iodine pressure of 0.21 Torr.

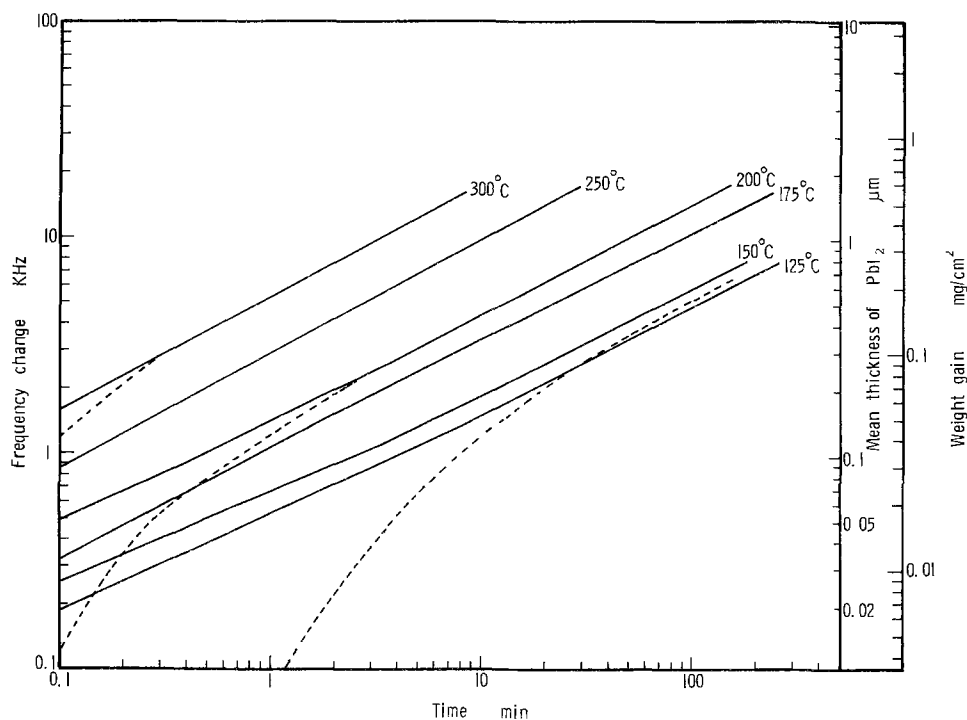


Figure 4 shows an Arrhenius plot that applies to this reaction. The probable errors of the rate constants are equal to or less than the diameter of the circles. The rate constant k_p for this parabolic iodination is represented as

$$k_p = 6.4 \times 10^6 \exp(-13,900/RT) \text{ kHz}^2/\text{min} \\ = 77 \times 10^2 \exp(-13,900/RT) (\text{mg}/\text{cm}^2)^2/\text{min}$$

Discussion

The present results for the iodination of copper are not in agreement with the early measurements of Tammann and Köster (2), who reported the independence of reaction rate from temperature, as described above. Nagel and Wagner (5) reported that a tarnish constant of copper in iodine vapor is 3.4×10^{-10} equivalents $\text{cm}^{-1} \text{sec}^{-1}$ at 195°C and at 46 Torr. Weiss (6) also reported the tarnish constants in the temperature range $105^\circ\text{--}440^\circ\text{C}$ at pressure of 1-500 Torr. The constants increase with increase of temperature or pressure. He concluded from his results that in the α - and β -CuI phase region above 420°C , the electron defect conduction was rate determining and in the γ -CuI phase region, ionic conduction was rate determining. The present results for the reactions below 150°C are not contradictory to his conclusion, although our experiments were performed at lower pressure than his experiments, and our accurate weight measurements through the course of the reaction with time confirm the applicability of the parabolic rate relationship.

A very small activation energy of 3.9 kcal/mole was observed for the parabolic iodination of copper below 150°C . According to Wagner theory (5, 6), the absorption of iodine causes cuprous ions and electrons to migrate to the surface and the CuI lattice to extend, leaving the vacancies in the cuprous ion lattice and a defect of electrons. The weight changes due to the absorption of iodine were estimated for the CuI films, which were produced from the 5000\AA thick Cu films, by using the results of Maurer (15) who measured the concentration of absorbed iodine by CuI. The weight changes are 1.235 and $0.080 \mu\text{g}/\text{cm}^2$ at 25° and 150°C , respectively, when the iodine pressure is 0.032 Torr. The concentration of vacancies of the cuprous ions, whose diffusion is rate determining for the parabolic reaction, definitely decreases with increasing temperature. Thus, the decrease of the vacancy concentration

acts on the reaction rate to slow down with increase of temperature and may lead to the very small activation energy.

The decrease of reaction rate with increasing temperature above 150°C cannot be ascribed to the decrease of the vacancy concentration because the parabolic reaction no longer prevails in this temperature range. A phase boundary reaction can be assumed to

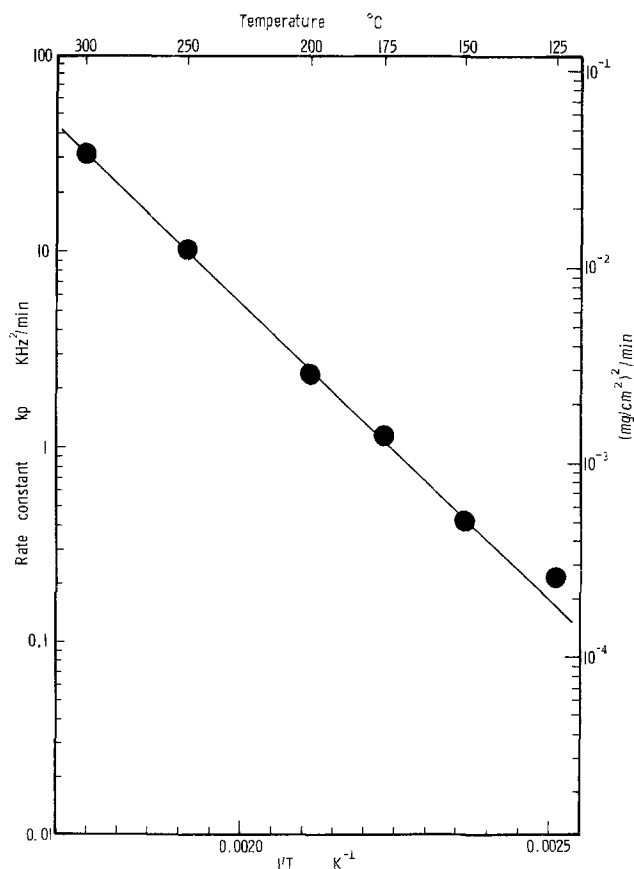


Fig. 4. Temperature dependence of rate constant for iodination of lead films.

be the rate-determining factor in the linear reaction. The most probable mechanism is the chemisorption of iodine atoms and the introduction of chemisorbed ions in the gas/iodide interface. The number of adsorbed iodine atoms staying at the interface is proportional to the number of impinging iodine molecules on the surface and the time of adsorption during which the adsorbed molecules stay at the surface before reevaporation (20). If we assume a heat of adsorption of 9 kcal/mole which is a possible value for the gas consisting of heavy molecules, then the decrease of the adsorbed atoms is about 5-fold between 200° and 300°C, and is in good agreement with the observed decrease of the reaction rate. The effect of adsorption on the linear reaction has been observed between the reactions performed at different iodine pressures. That is, the reaction rate changed from 2.32 to 28.8 ($\mu\text{g}/\text{cm}^2$)/sec as the iodine pressure was raised from 0.032 to 0.16 Torr at 300°C, while it was little changed at 25°C in the parabolic reaction, as shown in a previous note (9). The increase of the reaction rate, however, is much larger in comparison with the increase of the impinging molecules, which is 5 times between pressures of 0.032 and 0.16 Torr. The result may be ascribed to the increase of a condensation coefficient (the probability that an impinging molecule is adsorbed at the surface) with increasing temperature; the coefficient may increase about 2.5 times between 0.032 and 0.16 Torr.

Since the diffusion rate decreases with increasing layer thickness, the linear rate is applicable only to the point where the diffusion rate becomes comparable with the rate of the phase boundary reaction. With further growth of the protective layer, the diffusion rate becomes the rate-determining factor (12, 16-19), and the parabolic rate relationship prevails. The tarnish constants above 150°C, which were shown by Nagel and Wagner (5) Weiss (6), can be assumed to be those corresponding to this parabolic reaction.

The iodination of lead films followed the parabolic relationship, although in the experiments below 100°C the definite parabolic relationship was not observed because of the tarnishing of the surface by the residual gas. The conduction mechanism of the lead iodide is very complicated because both lead and iodine ions participate in conduction (21). Since the ionic conduction is predominant in any case and since parabolic

rate behavior was observed, it can be concluded that electronic conduction through the lead iodide layers is the rate-determining step of the iodination process.

Manuscript submitted March 19, 1974; revised manuscript received Oct. 7, 1974.

Any discussion of this paper will appear in a Discussion Section to be published in the December 1975 JOURNAL. All discussions for the December 1975 Discussion Section should be submitted by Aug. 1, 1975.

REFERENCES

1. G. Tammann, *Z. Anorg. Chem.*, **111**, 78 (1920).
2. G. Tammann and W. Köster, *ibid.*, **123**, 196 (1922).
3. U. R. Evans and L. C. Bannister, *Proc. Roy. Soc. London*, **A125**, 370 (1929).
4. H. Reinhold and H. Seidel, *Z. Electrochem.*, **41**, 499 (1935).
5. K. Nagel and C. Wagner, *Z. Phys. Chem.*, **B25**, 71 (1934).
6. K. Weiss, *Z. Phys. Chem. N. F.*, **B12**, 68 (1957).
7. K. Hauff, "Oxidation of Metals," p. 155, Plenum Press, New York (1965).
8. O. Kubaschewski and B. E. Hopkins, "Oxidation of Metals and Alloys," p. 49, Butterworths, London (1967).
9. M. Shiojiri, Y. Hasegawa, K. Konishi, and Y. Tsujikura, *Japan. J. Appl. Phys.*, **12**, 1279 (1973).
10. M. Shiojiri, Y. Hasegawa, and K. Konishi, *J. Appl. Phys.*, **44**, 2996 (1973).
11. M. Shiojiri, Y. Hasegawa, K. Konishi, and Y. Tsujikura, *ibid.*, **44**, 3370 (1973).
12. M. Shiojiri, Y. Hasegawa, K. Konishi, and Y. Tsujikura, *Japan. J. Appl. Phys.*, **12**, 1670 (1973).
13. M. Shiojiri, Y. Hasegawa, Y. Murata, and S. Matsumura, *ibid.*, **8**, 783 (1969).
14. M. Shiojiri, Y. Hasegawa, and Y. Tsujikura, *ibid.*, **10**, 143 (1971).
15. R. J. Maurer, *J. Chem. Phys.*, **13**, 321 (1945).
16. K. Fischbeck, L. Neundeubel, and F. Salzer, *Z. Electrochem.*, **40**, 517 (1934).
17. K. Hauffe and H. Preiffer, *Z. Metallk.*, **44**, 27 (1953).
18. U. R. Evans, *Trans. Electrochem. Soc.*, **91**, 547 (1947).
19. H. Nöldge, *Physik. Z.*, **39**, 546 (1938).
20. J. H. deBoer, "The Dynamical Character of Adsorption," p. 20, Oxford University Press, Oxford, England (1953).
21. O. Kubaschewski and B. E. Hopkins, "Oxidation of Metals and Alloys," p. 26, Butterworths, London (1967).

Deposition of Polycrystalline Silicon by Pyrolysis of Silane in Argon

John Y. W. Seto

Electronics Department, General Motors Research Laboratories, Warren, Michigan 48090

ABSTRACT

Deposition of silicon on thermally grown silicon dioxide substrates by pyrolysis of silane in argon is postulated as a three-step process involving adsorption and decomposition of silane on, and desorption of hydrogen from the substrate surface. This postulate was verified by experimental data. The morphology of the polysilicon films was strongly affected by the cleaning process employed before the silicon dioxide was grown. To obtain an optically smooth surface, it was mandatory that the silicon substrate be cleaned by a strong oxidizing agent. The grains of the polysilicon film were randomly oriented and the grain size increased as the deposition temperature was increased.

Polycrystalline silicon (polysilicon) is extensively used in silicon technology. Polysilicon films have been used in silicon gate MOS devices (1), as dielectric

Key words: polycrystalline silicon, chemical vapor deposition, chemical kinetics, thin films, silane.

isolation in high power integrated circuits (2,3), in stacking gate nonvolatile memory devices (4), and in charge couple devices (5). In some of these applications, it is desirable to be able to deposit polysilicon at a low temperature so as to preserve the doping pro-

files. In other applications the surface texture of the polysilicon has a detrimental effect on the device performance. Therefore, it is desirable to be able to deposit optically smooth polysilicon films at low temperatures. Deposition of polysilicon by thermal decomposition of silane in argon was reported by Yasuda *et al.* (6). They showed that the polysilicon deposition rate was higher and the grain size was smaller if argon rather than hydrogen was used as the carrier gas. We report here the study of the kinetics of the polysilicon growth rate as a function of silane concentration in argon and temperature of deposition, and the morphological and crystallographical structure of the polysilicon films prepared.

Film Preparation

The polysilicon films were deposited in a radiant heated horizontal reactor. The walls of the quartz reactor tube were cooled by a flow of 14,000 SLM of air. Both polysilicon-coated and silicon carbide-coated susceptors were used in this study. The susceptor was supported by a horizontal quartz sled. The temperature of the susceptor was measured using a Type S (Pt/Pt + 10% Rh) thermocouple fitted in a hole in the susceptor such that the thermocouple was in thermal contact with the center of the susceptor. The output of the thermocouple controlled the power supplied to the quartzline heating lamps to maintain a preset temperature. The substrates were in thermal contact with the susceptor, therefore, the temperature of the substrates was approximated to be that measured by the thermocouple. The actual substrate temperature could be as much as 30°C cooler than that measured by the thermocouple. This approximation was taken because the reactor was radiant heated and a direct measurement of the substrate temperature by a pyrometer was difficult. However, by making sure that the substrates were in good thermal contact this error could be reduced. Argon was used as the carrier gas. The argon gas source was nominally 99.99% pure; it was passed through a 0.45 μm particle filter and a three-stage (titanium, copper oxide, and molecular sieve) rare gas purifier. The silane used for this work came from a 100% silane source. The carrier gas and silane were mixed before entering the reactor tube. All the gas lines were helium leak checked to ensure no gas contamination due to leakage. The argon flow rate was usually 12.6 SLM (2.7 cm/sec). Deposition temperatures of 650°-800°C and silane flow rates ranging from 0.1 to 1.2% of the total flow rate were studied.

The substrates were 10 ohm-cm, boron-doped, <111> oriented, polished silicon wafers. These wafers were cleaned in a boiling 1:1:1 mixture of methyl alcohol, acetone, and trichloroethylene with ultrasonic agitation. The wafers were then cleaned in acetone and rinsed with deionized water. They were finally cleaned in hot (75°C) HNO_3 for 10 min, spin rinsed, and dried in hot nitrogen. The wafers were immediately transferred to a dry or wet oxygen atmosphere oxidation furnace to grow a silicon dioxide layer of about 1500 or 3000 Å thick. Immediately after the oxidation step and as soon as the wafers were cooled down to room temperature, the wafers were transferred to the reactor and polysilicon was deposited to a thickness in the range of 0.5-3 μm . The thickness of the polysilicon films was measured by an infrared interference technique (7); the accuracy of the measurement was periodically checked with a surface profiler.

Growth Rate

In Fig. 1 the growth rate of polysilicon is plotted as a function of $1/T^\circ\text{K}$ for various silane flow rates. The deposition rate could be varied from 0.01 $\mu\text{m}/\text{min}$ at 650°C for 0.1% silane to about 0.5 $\mu\text{m}/\text{min}$ at 800°C for a flow of 1.2% silane. It was observed that a straight line could be drawn to pass through points at temperatures higher than 700°C. However, if such a

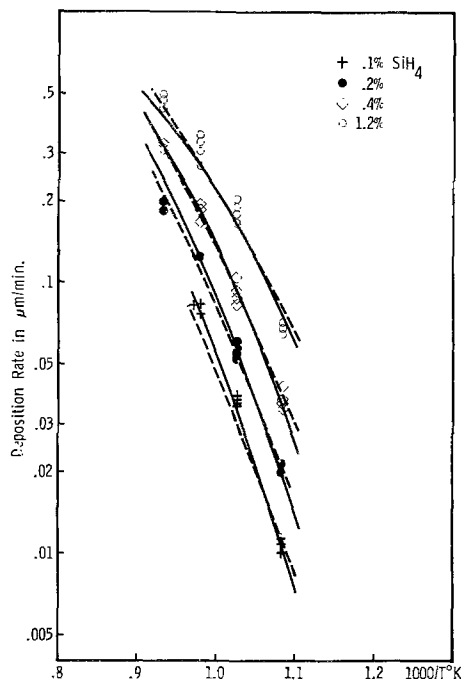
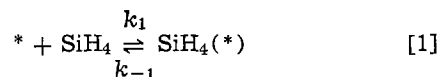


Fig. 1. Experimental and calculated deposition rates vs. $1/T^\circ\text{K}$. Dashed line was calculated using all data points. Solid line was calculated by neglecting data points at 800°C.

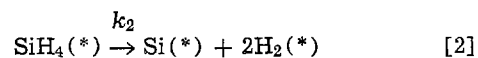
straight line was drawn it would not pass through the data point at 650°C. The same result was apparently obtained by Yasuda *et al.*, although those authors assumed a straight line and obtained an activation energy of 1.0-1.1 eV. If the same process was done to our data, the slope gave a value of about 1.02 eV.

The kinetics of the decomposition of silane in an inert gas at temperatures lower than 850°C has not been reported. It was shown in the deposition of single crystalline silicon that the decomposition of silane in hydrogen at 1050°C was a diffusion limited process (8). Our experimental results cannot be satisfactorily explained by such a reaction process. We propose an alternative reaction process consisting of the following steps:

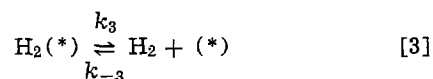
- (a) chemisorption of silane on the nucleation sites, *, on the surface of the substrate



- (b) decomposition of silane into silicon and hydrogen, assuming this process to be the rate-controlling step



- (c) desorption of hydrogen gas formed by the decomposition of silane over the substrate surface



Solving Eq. [1] to [3] by chemical kinetic analysis, for a substrate of finite surface, the deposition rate of silicon is given as

$$\frac{dx}{dt} = \frac{M_{\text{Si}}}{\delta_{\text{Si}}} \frac{k_2 K_1 [\text{SiH}_4]}{\left(\frac{[\text{H}_2]}{K_3} + K_1 [\text{SiH}_4] + 1 \right)} \quad [4]$$

where

$$k_2 = k_{20} e^{-E/RT} \quad [5]$$

$$K_1 = k_1/k_{-1} = K_{10}e^{-\Delta H/RT} \quad [6]$$

$$K_3 = k_3/k_{-3} = K_{30}e^{-\Delta H_H/RT} \quad [7]$$

In Eq. [4], dx/dt is the growth rate of silicon in cm/sec, and M_{Si} , δ_{Si} are the molecular weight and the density of silicon, respectively. $[SiH_4]$ and $[H_2]$ are the silane and hydrogen concentrations in the gas phase in moles/cm³. E , ΔH , ΔH_H , R , and T have the usual meanings and definitions. There was no hydrogen present in our incoming gas. If the silane conversion efficiency is low, we can assume that the hydrogen gas produced by the decomposition of silane is immediately carried away by the gas stream, and the hydrogen concentration at the substrate surface is essentially zero. Then Eq. [4] can be approximated by

$$\frac{dx}{dt} = \frac{M_{Si}}{\delta_{Si}} \frac{k_2 K_1 [SiH_4]}{(K_1 [SiH_4] + 1)} \quad [8]$$

The consequence of Eq. [8] is that if $K_1 [SiH_4] \gg 1$ the growth rate is independent of the silane concentration and the reaction is zero-order. The deposition rate is an exponential function of $1/T$. Under this condition all the available surface sites on the substrate are saturated by silane so that any further increase in silane concentration will not change the rate by which silane molecules are absorbed on the substrate surface. On the other hand, when $K_1 [SiH_4] \ll 1$ the deposition rate is proportional to the silane concentration and the decomposition is a first-order reaction. Equation [8] shows that if the reciprocal of the deposition rate at a fixed temperature is plotted as a function of the reciprocal of silane concentration, a straight line should be obtained. The slope of such a plot yields $1/(K_1 k_2)$ and the intercept gives $1/k_2$. If k_2 and K_1 are determined over a range of temperatures, ΔH , E , k_{20} , and K_{10} can be obtained and the deposition rate can be determined theoretically for all temperatures and silane concentrations.

This theory is a steady-state calculation so that the theory is applicable only after a monolayer of polysilicon has grown on the substrate and the deposition rate is not a function of time. Our deposition rates were derived from polysilicon films deposited for a sufficiently long time such that the above condition was satisfied. If the reaction step (b) is to be the rate-controlling step, as postulated, the reaction rate must not be a mass transport limited process. The flow rate of the gases should be so high that the deposition rate is not a function of the flow rate. This condition was verified in our experiment by doubling the flow rate and the deposition rate was found to be increased by less than 10%. Since the reactor had a run-to-run reproducibility of $\pm 10\%$, it was concluded that the reaction was not mass transport limited.

In Fig. 2, the experimental data are plotted for $1/(\text{deposition rate})$ vs. $1/(\text{silane concentration})$ at constant temperatures. The averages of the experimental values in Fig. 1 were taken as the deposition rates. Straight lines are obtained for all the temperatures studied in our experiments. This implies that Eq. [8] can be used to describe the reaction and that the hydrogen produced in the decomposition of silane is not affecting the decomposition rate. The hydrogen gas resulting from the decomposition changed by a factor of at least four between the minimum and maximum silane concentration used in our experiments. If the hydrogen concentration is high enough to affect the deposition rate, Fig. 2 would not yield straight lines. Using the data in Fig. 2, a linear regression is performed by a computer to find the slopes and intercepts of the curves. From the slopes and intercepts, K_1 and k_2 at each temperature are found. From Eq. [5] and [6], if $\ln K_1$ and $\ln k_2$ are plotted as a function of $1/T^\circ K$, straight lines should be obtained and the slopes give $\Delta H/R$ and E/R . The intercepts yield K_{10} and k_{20} , respectively. The values of $\ln K_1$ and $\ln k_2$ are plotted as a function of $1/T$ in Fig. 3. All

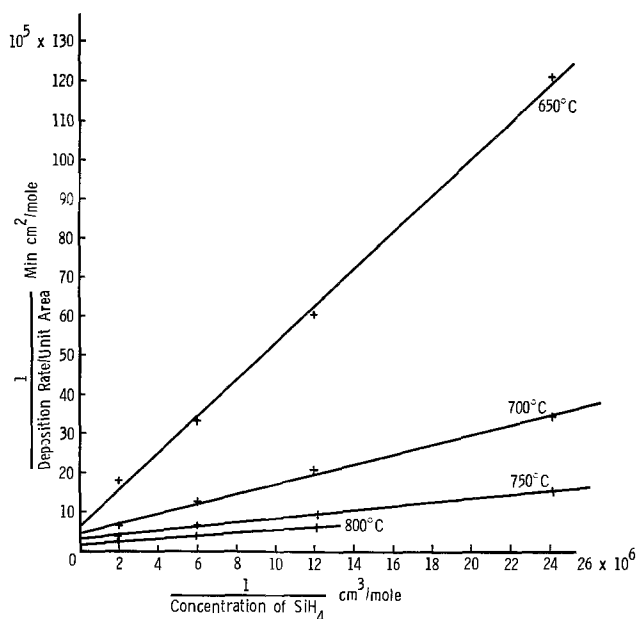


Fig. 2. Reciprocal of deposition rates vs. reciprocal of silane concentration at constant temperature.

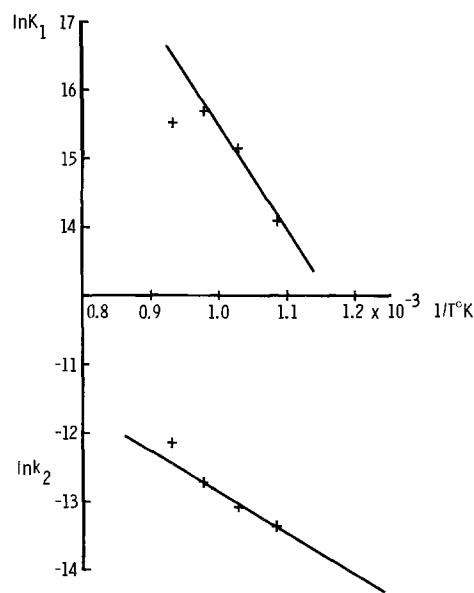


Fig. 3. $\ln K_1$ and $\ln k_2$ vs. $1/T^\circ K$

the points fall into two straight lines with the exception of the 800°C values. With the values in Fig. 3 linear regression is again performed to find K_{10} , k_{20} , E/R , and $\Delta H/R$. The values obtained for E and ΔH are 15.32 and 19.45 kcal/mole, respectively. The deposition rate as a function of $1/T^\circ K$ for different silane concentrations calculated using the values of K_{10} , k_{20} , E , and ΔH derived is shown as the dashed curve in Fig. 1.

It was observed that for 0.2 and 0.4% silane at 800°C the deposition rate was higher at the incoming gas stream end of the susceptor than the exhaust end. We concluded that for those deposition conditions the gas stream might have a lower concentration of silane when it reached the substrates. Therefore, the deposition rates measured did not represent the true deposition rates for the silane concentrations calculated from the flow rates. A more accurate value of E , ΔH and, consequently, the prediction of the deposition rate could be obtained by neglecting the points at 800°C. When the slopes and intercepts were found by

linear regression, E and ΔH were given as 11.86 and 30.28 kcal/mole, respectively. The deposition rates calculated using the K_{10} , k_{20} , E , and ΔH obtained are plotted as the solid lines in Fig. 1. The agreement between experimental and theoretical values is extremely good. This activation energy is only about half of that obtained by fitting a straight line to the data points in Fig. 1. The activation energy for the decomposition of silane in reduced pressure ranged from 10.1 to 37.1 kcal/mole (9-11) was reported. Our activation energy of 11.86 kcal/mole is in close agreement with the value of 10.1 kcal/mole obtained by Farrow and Filby (9).

Morphological and Crystallographical Structures

If the deposition temperature was kept at 650°C or below, the surface of the polysilicon film was always shiny as long as the surface of the substrate was degreased and cleaned. However, when the substrate was cleaned in hot HNO_3 a better microscopic surface was obtained. As the deposition temperature was raised above 700°C, the surface texture of the polysilicon film was strongly affected by the cleaning process before the silicon wafer was oxidized. Figure 4 shows examples of polysilicon films deposited in identical conditions on properly and improperly cleaned substrates. The film grown on the improperly cleaned substrate has a very rough and nonuniform surface; and many hillocks are as high as 1 μm . The surface of the film grown on the substrate cleaned in hot HNO_3 is optically smooth and shiny. The cleaning steps become more critical as the temperature is raised. Cowher and Sedgwick (12) also found that the substrate cleaning was critical to obtaining smooth polysilicon surfaces using hydrogen as carrier gas in the deposition of polysilicon. They employed an "aqueous oxidation" step, using a mixture of H_2O_2 and H_2O at 90°C. This cleaning step was tested and no improvement over that of hot nitric acid was observed. A combination of nitric acid and "aqueous oxidation" steps did not produce any higher quality polysilicon films. Both H_2O_2 and hot nitric acid are strong oxidizing agents. It is then concluded that to obtain a smooth polysilicon surface the last cleaning step in substrate preparation should be in a strong oxidizing agent. It was shown that silicon dioxide grown on a dirty silicon surface has many imperfections and small crystallites (13, 14). By heating silicon wafers in hot nitric acid the surface of the silicon becomes uniformly hydrophilic and silicon dioxide can be grown with fewer imperfections (15). It appears that either imperfections or small crystallites of silicon dioxide or both can nucleate

polysilicon growth more effectively than an amorphous silicon dioxide surface. Once silicon is deposited on a nucleation site, the growth of silicon is accelerated, possibly by autocatalytic effect. Since the growth rate of silicon is higher at higher temperature, the difference in the amount of silicon deposited on sites nucleated at different times is larger, so that for the same amount of imperfection on the silicon dioxide substrate, the hillock size increases as the temperature of deposition increases. Another possible explanation is that the difference in the nucleation rates between the imperfections and the amorphous substrate becomes larger as the temperature of deposition is increased. We believe that the former explanation is more plausible in this study. In either case, one obvious way to minimize the hillock growth is to provide as uniform a substrate surface as possible so that nucleation occurs uniformly on the substrate and a uniform growth is obtained. This is accomplished by cleaning the silicon substrate in a strong oxidizing agent to grow a more perfect silicon dioxide film. For substrates prepared this way the polysilicon films were obtained with an optically shiny surface. The results are consistently reproducible. Figure 5 is a transmission electron microscope picture of a tungsten oxide shadowed replica of a typical surface of polysilicon film approximately 1 μm thick. The surface was very smooth.

There was no evidence that the silane concentration affects the surface structure of the polysilicon film as long as the concentration was high enough to prevent premature decomposition. When argon is used as the carrier gas in the thermal decomposition of silane, premature decomposition can take place resulting in a blackish gray deposit of amorphous silicon (12). Premature decomposition occurs when the gas mixture is hot enough for homogeneous decomposition to take place before it reaches the substrate surface. The amorphous silicon rains down onto the substrate in the form of small particles. The temperature at which premature decomposition takes place depends on the concentration of silane in the gas and the experimental apparatus. For the apparatus used in this study a silane concentration of 0.1% gave premature decomposition when the susceptor was at about 750°C. As the silane concentration was increased to 0.2% or higher, no premature decomposition occurred up to 800°C. No at-

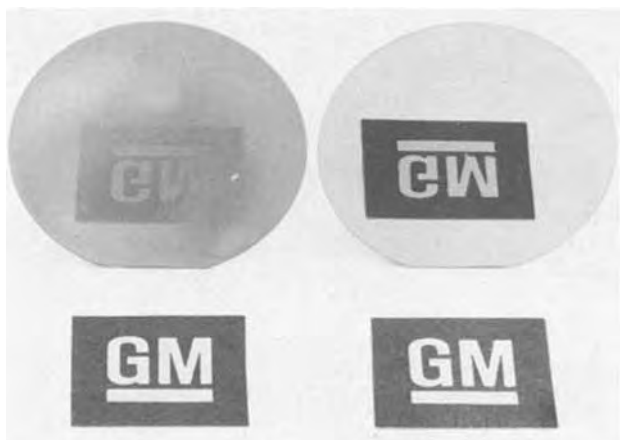


Fig. 4. Polysilicon films deposited on properly and improperly cleaned substrates.

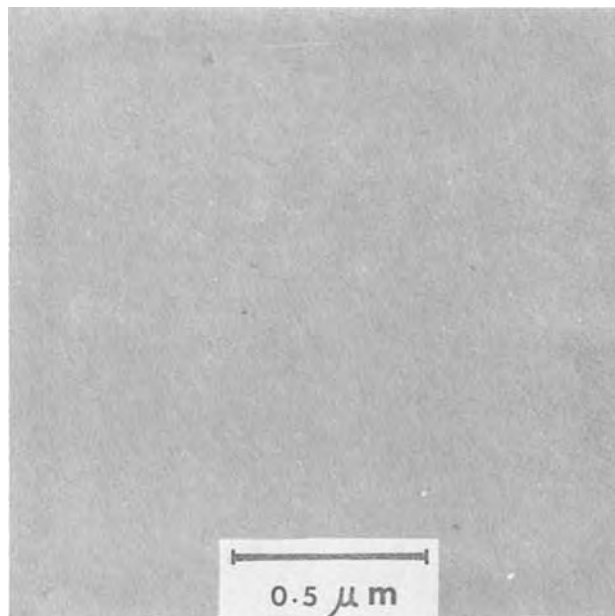


Fig. 5. Tungsten oxide shadowed replica picture of polysilicon deposited at 650°C.

tempts were made to find the temperatures at which premature decomposition occurred for different silane concentrations.

It is interesting to note that our result is in contrast to that of Eversteign (17) who made a detailed study of the gas phase decomposition of silane in hydrogen. He found that as the temperature is increased the gas phase decomposition started at a lower silane concentration. We do not know the cause of this discrepancy, although one might suspect that the causes might be related to the difference in the carrier gas used and the difference in the gas dynamics in the reactor systems.

Transmission electron microscope (TEM) was used to study the grain structure of the polysilicon films. The samples for TEM study were prepared by the following method. An oxide of about 3000Å thick was grown on the polysilicon film. The silicon dioxide on the single-crystal silicon substrate surface was removed by an oxide etch and then the single-crystal silicon substrate was etched away by chlorine gas at 800°C. Since chlorine does not etch silicon dioxide the polysilicon was left behind with a silicon dioxide coating. The silicon dioxide was removed by an oxide etch. The polysilicon was further thinned by floating the polysilicon film on a potassium hydroxide solution, until a film of a few thousand angstroms thick was obtained. There was some question if the oxidation and the high temperature etch could have changed the crystal structure of the films. Samples prepared by other etchants and without the oxidation step did not show any change in the results observed. The TEM study consisted of electron diffractions and TEM micrographs. Figures 6a and b are the electron diffraction patterns for polysilicon films deposited at 650° and 750°C, respectively. From the diffraction pattern it can be seen that both films consist of polycrystalline materials with randomly oriented grains (18). Figures 7a and b are the bright field TEM micrographs of the same films. The micrographs were analyzed by image analysis, yielding an average grain size of 183 and 700Å, respectively, for the films deposited at 650° and 750°C. At high magnification, it was observed that there were structures inside the small crystallites. Most of these structures were lines and it was assumed that these were dislocation lines. Numerous dislocations are to be expected since the films were grown on amorphous substrates.

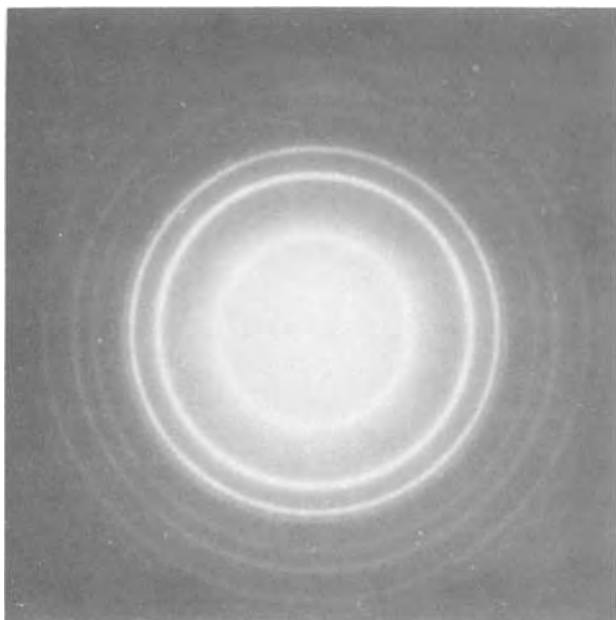


Fig. 6a. Electron diffraction pattern of a 650°C deposited polysilicon film.

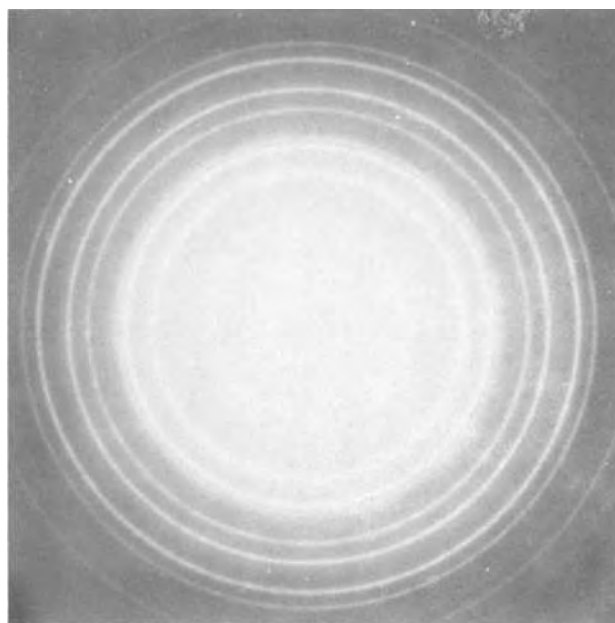


Fig. 6b. Electron diffraction pattern of a 750°C deposited polysilicon film.

The vertical growth of the polysilicon films was studied by breaking the substrate. The edge of the substrate with polysilicon film was observed with a scanning electron microscope, Fig. 8. There was no columnar growth visible.

Conclusion

The deposition rate of polysilicon films on silicon dioxide substrates by thermal decomposition of silane in an argon atmosphere can be varied from less than 0.01 to about 0.5 $\mu\text{m}/\text{min}$ by changing the concentration of silane between 0.1 and 1.2%, and the deposition temperature from 650° to 800°C. It is proposed that the deposition process consists of three steps: chemisorption and decomposition of silane on and desorption of hydrogen from the substrate surface. The deposition rate equation was derived based on a kinetic analysis of the postulated reaction sequence. The experimental results confirmed the postulated mechanism.

It was found that optically smooth polysilicon films could be obtained without any special cleaning process if the deposition temperature was about 650°C and lower. However, if the deposition temperature was above 700°C, the surface texture of the polysilicon film depended strongly on the substrate preparation procedure. To obtain optically smooth surfaces, it was necessary to clean the silicon substrate in a strong oxidizing solution such as hot HNO_3 or H_2O_2 . It was important that the silane concentration and the deposition temperature be adjusted so that no gas phase premature decomposition of silane occurred. With the proper substrate preparation, optically smooth surfaces were obtained consistently. The grain size of the polysilicon films was a function of the deposition temperature and increased from about 200Å at 650°C to 700Å at 750°C. The grains were found to be randomly oriented in the range of the deposition temperatures investigated.

Acknowledgments

The author would like to thank Dr. M. C. Steele and Mr. J. W. Hile for many fruitful discussions. Thank are also due to Dr. L. Hegedus for proposing the chemical kinetic model and the calculations. The technical support of Mrs. B. Vannoy and Mr. A. Fritz is appreciated. The author is grateful for the assistance provided by Dr. H. Bendler in the TEM study, Mr. J. Homaday in image analysis, and Mr. T. Schreiber in taking the SEM micrograph.

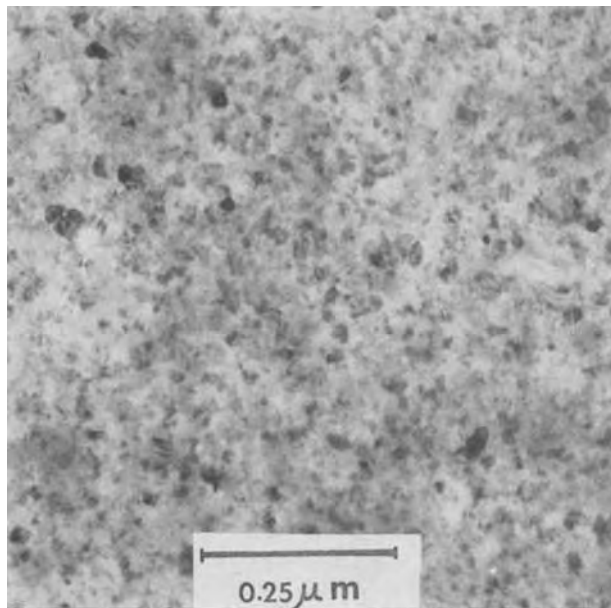


Fig. 7a. Bright field electron micrograph of a 650°C deposited polysilicon film.

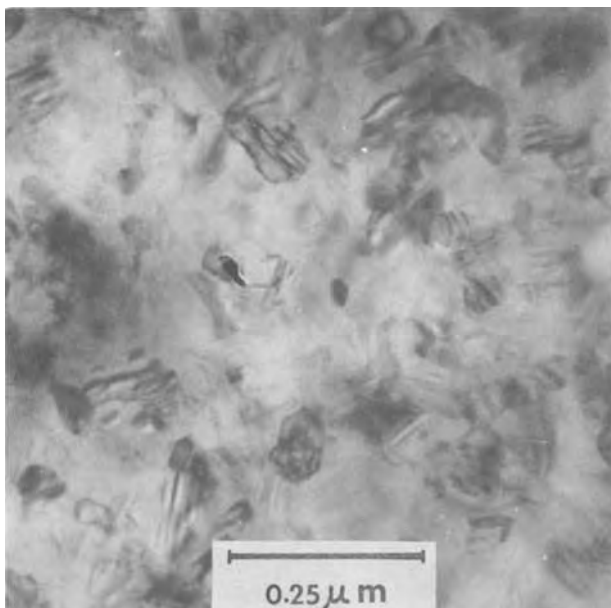


Fig. 7b. Electron micrograph of a 750°C deposited polysilicon film

Manuscript submitted March 4, 1974; revised manuscript received Dec. 19, 1974.

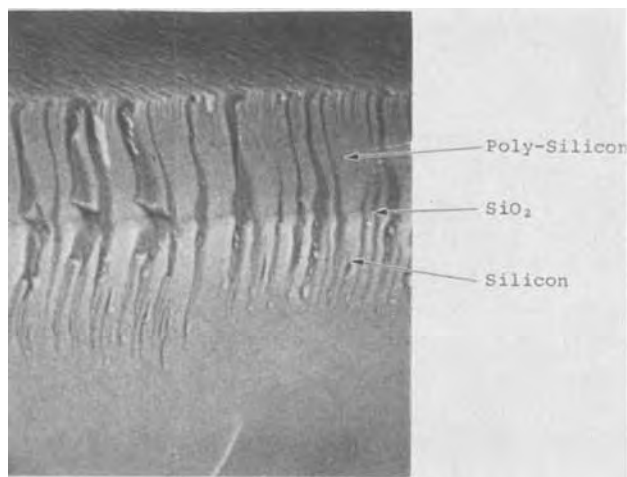


Fig. 8. Section of broken polysilicon film on silicon substrate with a layer of SiO_2 . Polysilicon film was about $3 \mu\text{m}$ thick.

Any discussion of this paper will appear in a Discussion Section to be published in the December 1975 JOURNAL. All discussions for the December 1975 Discussion Section should be submitted by Aug. 1, 1975.

Publication costs of this article were partially assisted by General Motors Corporation.

REFERENCES

1. F. Faggin and T. Klein, *Solid-State Electron.*, **13**, 1125 (1970).
2. I. Kobayashi, *IEEE Trans. Electron Devices*, **ED-18**, 45 (1971).
3. I. Kobayashi, *ibid.*, **ED-20**, 399 (1973).
4. H. Iizuka, F. Masuoka, and T. Sato, *J. Japan Soc. Appl. Phys. Supplement*, **42**, 158 (1973).
5. L. J. M. Esser, M. G. Collet, and J. G. Van Santen, Paper presented at International Electron Device Meeting, Washington, D.C., December 1973.
6. Y. Yasuda, M. Yamanaka, T. Moriya, and T. Yoshii, Paper 23 presented at Electrochemical Society Meeting, Houston, Texas, May 7-11, 1972.
7. C. J. Dell'Oca, *This Journal*, **119**, 108 (1972).
8. F. C. Eversteyn, P. J. W. Severin, C. H. J. v. d. Brekel, and H. L. Peek, *ibid.*, **117**, 925 (1970).
9. R. F. C. Farrow and J. D. Filby, *ibid.*, **118**, 149 (1971).
10. B. A. Joyce and R. R. Bradley, *ibid.*, **110**, 1235 (1963).
11. R. C. Henderson and R. F. Helm, *Surface Sci.*, **30**, 310 (1972).
12. M. E. Cowher and T. O. Sedgwick, *This Journal*, **119**, 1565 (1972).
13. B. E. Deal, *ibid.*, **110**, 527 (1963).
14. R. Stickler and J. W. Faust, Jr., *ibid.*, **111**, 298 (1964).
15. M. M. Atalla, E. Tannenbaum, and E. J. Scheibner, *Bell System Tech. J.*, **38**, 749 (1959).
16. T. R. Hogness et al., *Am. Chem. Soc.*, **58**, 108 (1936).
17. F. C. Eversteyn, *Philips Res. Rept.*, **26**, 134 (1971).
18. R. D. Heidenreich, "Fundamentals of Transmission Electron Microscope," Interscience Publishers, New York (1964).

Determination of Oxygen Chemical Diffusion Coefficients in Single Crystal SrTiO₃ by Capacitance Manometry

D. B. Schwarz¹ and H. U. Anderson*

Department of Ceramic Engineering, University of Missouri-Rolla, Rolla, Missouri 65401

ABSTRACT

The oxidation kinetics of a single crystal of SrTiO₃ were measured with a tensivolometric system over the temperature range 700°-975° at 0.03 atm oxygen pressure. The oxidation was found to be oxygen diffusion limited with an activation energy of 14.9 ± 1.3 kcal/mole. Combining the kinetic data with relative defect concentration data yielded an activation energy for oxygen self-diffusion of 57 ± 16 kcal/mole. The enthalpy of formation of doubly ionized oxygen vacancies was calculated to be 126 ± 13 kcal/mol.

Recently, BaTiO₃ was investigated in the temperature range of 300°-1000°C and at oxygen partial pressures as low as 10^{-6} atm with a capacitance manometer (1, 2). Calibration shows the sensitivity of this instrument to be 10-100 times greater than that of a microbalance. As has been reported, changes in oxygen stoichiometry as small as 10^{-8} moles were easily detected on approximately 10g BaTiO₃ samples.

The limit of sensitivity of this particular system was about 3×10^{-9} moles oxygen gas or a 10^{-7} g change in total sample weight. On a smaller volume system, Turcotte *et al.* (3, 4) report an even higher sensitivity of 2×10^{-9} g.

In another study, Greskovich and Schmalzried (5) investigated nonstoichiometry in Co₂SiO₄ and in CoAl₂O₄-MgAl₂O₄ crystalline solutions and determined changes in cobalt vacancy concentrations as low as 10^{-2} atom per cent (a/o).

In addition to being useful in determining changes in stoichiometry, the initial work on BaTiO₃ and that of Greskovich and Schmalzried indicates that the kinetics of oxygen exchange are easily measurable so chemical diffusion coefficients can be calculated by solving Fick's second law for the appropriate boundary conditions of the system (6).

The tensivolometric technique of measuring the gaseous exchange with a solid is both very rapid and sensitive, so an evaluation of this technique for the determination of chemical diffusion coefficients is of practical value. Since both the oxygen diffusion coefficients and the limit of oxygen nonstoichiometry of SrTiO₃ have been measured (7-10), this oxide was chosen to make this evaluation.

In previous experiments with 0.1 μm crystallite-size BaTiO₃ and SrTiO₃ (1), attempts to use the exchange kinetics to calculate chemical diffusion coefficients were not successful. Evidently, the exchange was not entirely diffusion limited. As a result of the small particle size, the exchange can be expected to be dependent upon the surface exchange reaction as well as upon diffusion (11). Thus, to limit control by the surface exchange reaction in this study, oxygen exchange with large single crystal SrTiO₃ was measured.

Experimental

The apparatus used is similar to that described by Conger (1) and Meurer (12). It consists of two symmetrical chambers, separate and vacuum-tight, but with provision for interconnection. The oxide sample is sealed into one side with the other being left empty as a reference. An atmosphere of known oxygen pressure is admitted to both sides and allowed to equilibrate.

After rapidly changing both the sample and reference sides to a new value of oxygen pressure, the two sides are separated. The attainment of a new equilibrium with the sample is followed with a sensor head by monitoring the pressure change (caused by an oxygen loss or uptake) in the sample side of the system relative to the reference side.

The sensor head is an open loop, taut metal membrane capacitance manometer² with a range of 1.3×10^{-8} to 1.3×10^{-3} atm.

The sample and reference tubes were heated in a wire-wound furnace whose maximum temperature was 1000°C. At temperatures up to 1000°C, the furnace temperature was controlled to approximately $\pm 3^\circ\text{C}$ with both linear and radial gradients of less than 2°C in the region where the sample was contained.

If the temperature of the entire apparatus is maintained at constant temperature, the measured pressure change, Δp due to evolution or uptake of gas is related to the change in the number of moles of gas, Δn by the relation $\Delta p = \Delta n RT/V$ where V is the volume of the sample side, R is the gas constant, and T is the temperature.

In actual practice, the expression for the observed pressure change is not so simple since the temperature of the system is not uniform (that is, the gauge and the sample chamber are at different temperatures). The expression will, instead, involve a correction factor arising from temperature gradient effects.

The measured pressure change is thus described as $\Delta p = K(T) \Delta n$ where Δp is the sample-induced pressure change and $K(T)$ is a temperature dependent correction factor containing the gas constant R , the sample side volume V , and some function of gauge and furnace temperatures.

An empirical calibration was necessary in order to relate measured pressure changes to oxygen concentration changes in a sample. This was accomplished by measuring the pressure changes occurring for known changes in gas concentration at a series of furnace temperatures (20°-950°C). The correction factor was found to be independent of oxygen pressure and to be only a function of furnace and gauge temperature. With the system thermostated at $38^\circ \pm 0.01^\circ\text{C}$ and the head temperature constant, the calibration constant varied from 31.0 ± 0.20 atm/mole to 33.8 ± 0.28 atm/mole with the furnace at 20° and 950°C, respectively.

For the minimum detectable pressure change of 1.3×10^{-8} atm, the maximum sensitivity attainable is $\Delta n = 4 \times 10^{-10}$ moles which corresponds to a weight change of 1.3×10^{-8} g of oxygen. Interaction between the gas and the system was found to place a practical limit on detectability of 4×10^{-9} moles oxygen.

* Electrochemical Society Active Member.

¹ Present address: Dow Chemical Company, Midland, Michigan 48640.

Key words: oxidation, oxygen vacancy concentration, oxygen self-diffusion.

² MKS Instruments, Incorporated, Burlington, Massachusetts 01803.

Due to the limited range of nonstoichiometry of SrTiO₃, it was found that the apparatus could not detect the exchange kinetics by stepping the oxygen pressure in the range 10⁻⁶-1 atm at temperatures below 1000°C. To achieve a detectable pressure change within the temperature and pressure range of the apparatus it was necessary to reduce the sample in either forming gas (8% H₂ in N₂) or CO. The oxidation kinetics were then measured when the reducing gas was replaced by O₂.

The crystal was cut from 99.9 weight per cent (w/o) pure SrTiO₃ boule.³ Prior to use, the crystal was polished and annealed to remove surface roughness and internal strain. The final dimensions of the rectangularly shaped crystal were 1.24 cm × 1.33 cm × 2.04 cm ± 0.02 cm. The weight of the crystal was determined to be 16.9903 ± 0.0002g, with a density of 5.121 ± 0.001 g/cm³. No attempt was made to orient the crystal so any effects of crystallographic directions could not be observed.

Mathematical Analysis

Diffusion coefficient.—When a sample re-equilibrates from an initially homogeneous nonstoichiometric condition, diffusion occurs under the influence of a chemical potential or concentration gradient. This type of diffusion is commonly referred to as chemical diffusion and the diffusion coefficient resulting from it is termed as the chemical diffusion coefficient, \tilde{D} . The relationship between the chemical diffusion coefficient and self-diffusion coefficient have been extensively treated elsewhere, so will not be discussed here (11, 13, 14).

For a brick-shaped geometry, the solution to Fick's second law which applied to the change in stoichiometry resulting from the oxide crystal re-establishing thermodynamic equilibrium due to changes in oxygen activity was originally derived by Newman (15). Later it was used by Price and Wagner (16) in determining chemical diffusion coefficients for single crystals of NiO and CoO by electrical conductivity techniques. The format presented here is similar to that of Price and Wagner, with the exception of incorporating the measurable parameters of the tensivolumetric technique.

For long times the relative defect concentration, (1 - Q), is given by

$$1 - Q = 1 - \frac{\Delta w_t}{\Delta w_x} \simeq \frac{512}{\pi^6} \exp \left[-\frac{\pi^2 \tilde{D} t}{4} \left(\frac{1}{a^2} + \frac{1}{b^2} + \frac{1}{c^2} \right) \right] \quad [1]$$

where Δw_t is the weight change at time t , Δw_x is the total weight change measured between the initial and final equilibrium states, \tilde{D} is the chemical diffusion coefficient and $2a$, $2b$, and $2c$ are the sample dimensions. This solution assumes as boundary conditions that the crystal is initially in equilibrium with a certain partial pressure of oxygen, and at time $t = 0$, the surface of the crystal is in immediate equilibrium with another oxygen partial pressure. The re-equilibration is assumed to be limited by diffusion rather than surface reaction and the observed weight change is then just an integrated measure of the adjustment of the defect concentration to the new equilibrium state.

The changes in defect concentration may be expressed either as weight changes in the sample or as changes in the pressure in the tensivolumetric apparatus. Therefore, from Eq. [1], weight changes may be equated to the induced pressure changes as follows

$$1 - Q = 1 - \frac{\Delta w_t}{\Delta w_x} = \frac{\Delta w_x - \Delta w_t}{\Delta w_x} = \frac{\Delta P_x' - \Delta P_t'}{\Delta P_x'} \quad [2]$$

where the total induced pressure change, $\Delta P_x'$ equals $\Delta P_x + \Delta P_t$ and the total induced pressure change at time t , $\Delta P_t'$ equals $\Delta P_t + \Delta P_t$. The terms ΔP_t and ΔP_x represent, respectively, the measured differential oxygen pressure as a function of time, and the final measured differential oxygen pressure. The quantity ΔP_t is a correction factor that would be zero if the measurement of ΔP_t began at the instant that the system pressure was changed (that is at $t = 0$, exchange = 0). Since this cannot be the case, ΔP_t will always be greater than zero.

Therefore for use with the tensivolumetric system, Eq. [1] is rearranged to read

$$1 - Q = (\Delta P_x - \Delta P_t) / (\Delta P_x + \Delta P_t) \simeq 512 / \pi^6 \exp \left[-\pi^2 \tilde{D} t / 4 (1/a^2 + 1/b^2 + 1/c^2) \right] \quad [3]$$

or

$$\log (\Delta P_x - \Delta P_t) \simeq \log (\Delta P_x + \Delta P_t) + \log (512 / \pi^6) - (\tilde{D} t \pi^2 / 9.21) \times (1/a^2 + 1/b^2 + 1/c^2) \quad [4]$$

Defect concentration.—As previously described, the calibration factor $K(T)$ relates the defect-associated change in the number of moles of oxygen in the sample, to the change in pressure in the system. From this relationship and the total induced pressure change, $\Delta P_x'$, changes in stoichiometry can be investigated.

The oxidation (or reduction) kinetics for this type of experiment will be determined by the most rapid diffusing cation-hole or anion-electron complex. If the material is predominantly an electronic conductor, then the diffusivity of the ionic defects will control the kinetics. For a binary compound, the most rapid diffusing ionic defect is the majority defect. Due to the additional component in a ternary compound, this is not necessarily true. However, for the case of nonstoichiometric SrTiO_{3- δ} , the majority defect and the fast diffusing ionic defect are the same and have been shown to be oxygen vacancies (7-10). Thus, for SrTiO_{3- δ} , this experiment can determine both the concentration of oxygen vacancies, δ , and the chemical diffusion

coefficient, \tilde{D} . Changes in the parameter δ , ($\Delta\delta$) can be related to changes in the gas concentration, Δn by

$$\Delta\delta = 2\Delta n M / m = 2\Delta P_x' M / K(T) m \quad [5]$$

where M is the molecular weight of stoichiometric SrTiO₃, m is the mass of the sample.

The defect concentration can be related to the parameter δ by

$$[\text{defect}] = \delta \rho / M \quad [6]$$

where [defect] represents the mole concentration (moles/cm³) of some atomic defect and ρ is the density of SrTiO₃. Changes in defect concentration can be represented as

$$\Delta[\text{defect}] = \Delta\delta \rho / M \quad [7]$$

or

$$\Delta[\text{defect}] = [2\rho/m][\Delta P_x' / K(T)] \quad [8]$$

Results and Discussion

An illustration of a typical oxidation curve is shown in Fig. 1. If a plot of $\log \Delta P_t$ vs. $\log t$ of the initial part of these data is made, a slope of $1/2$ is obtained which indicates bulk diffusion controls the process (11). Such a plot is not included since it is essentially redundant.

From the oxidation data, ΔP_t vs. time, and Eq. [4], a plot of $-\log (\Delta P_x - \Delta P_t)$ vs. time can be generated. Figure 2 is an example of this relationship. From the intercept of these curves ΔP_t can be obtained which allows the relative defect concentration (1 - Q) to be calculated. If the assumptions leading to Eq. [4] are correct, then a plot of $-\log (1 - Q)$ vs. time will be linear. Figure 3 is an example of such a plot for five different isothermal exchanges from 700° to 975°C. The excellent adaptability of the experimental data to Eq.

³ NL Industries, South Amboy, New Jersey 08879.

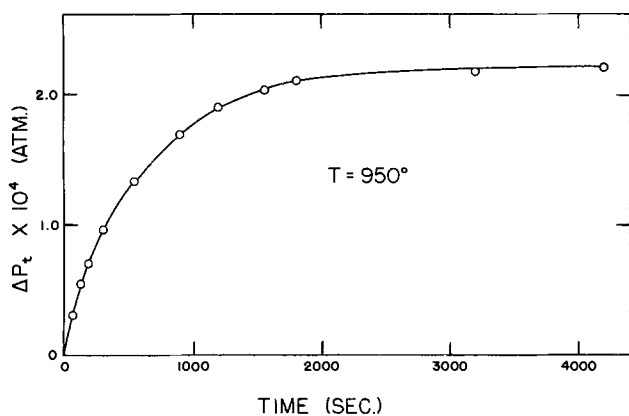


Fig. 1. Typical curve obtained for a sample initially reduced in CO and then oxidized in 0.03 atm O₂. T = 950°C.

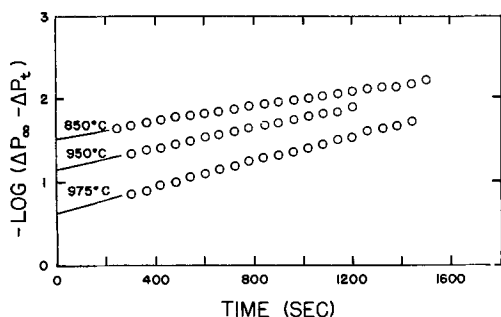


Fig. 2. Plot of Eq. [4] to obtain chemical diffusion coefficients

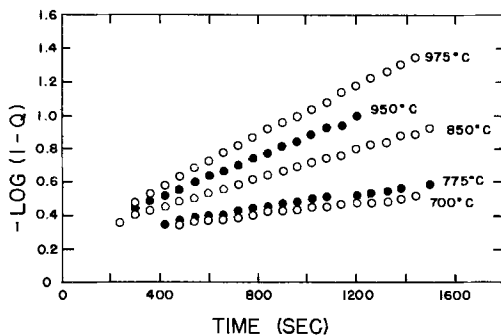


Fig. 3. Plot of log of relative defect concentration vs. time

[4] suggests that the sample oxidation proceeds by a process of homogeneous volume diffusion. The oxygen chemical diffusion coefficient obtained from the slopes of the plots of Eq. [4] can be represented by

$$\tilde{D} = 10^{-1.3 \pm 0.2} \exp\left(-\frac{14,900 \pm 1,300}{RT} \text{ cal/mole}\right) \text{ cm}^2/\text{sec} \quad [9]$$

in the temperature range 700°–975°C at an oxygen pressure of 0.03 atm.

Figure 4 compares the results of this study with previous investigators. The two points at the lower right-hand side of this figure are diffusion coefficients calculated from vacancy mobility data of Blanc and Staebler (17) using the Einstein relation (18).

Paladino (7) measured oxidation kinetics of reduced single crystal SrTiO₃ by a thermogravimetric technique. The calculated oxygen chemical diffusion coefficients in the temperature range 850° and 1460°C, can be represented by

$$\tilde{D} = 0.33 \exp\left(-\frac{22,500 \pm 5,000 \text{ cal/mole}}{RT}\right)$$

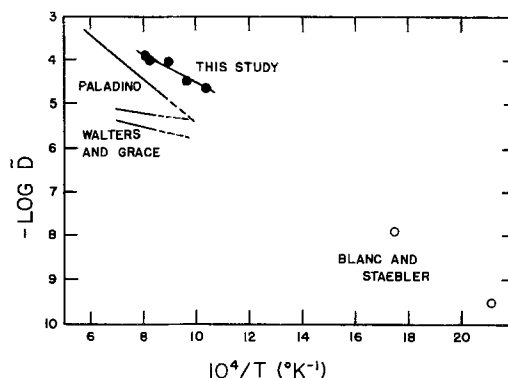


Fig. 4. Compilation of oxygen chemical diffusion data for SrTiO₃.

cm²/sec. The calculated diffusion coefficients of this study are close to those obtained by Paladino. This is an important point since both studies measured oxidation kinetics of reduced single crystal SrTiO₃, so the results of the two techniques should correspond. The enthalpy of motion term also compares reasonably well.

An extrapolation of Blanc and Staebler data into the higher temperature region correlates favorably with both this study and the work of Paladino.

The measurements of Walters and Grace (9) were made by an electrical conductivity technique. They observed an activation energy of only about 6 kcal/mole which is much less than either the results of this study or of Paladino. The reasons for this difference are not understood. However, they did note a difference between samples (as shown by the two lines) which possibly could account for some of the observed differences.

The difference in defect concentrations existing in the crystal in equilibrium with the reducing atmosphere and at 0.03 atm oxygen pressure can be calculated from the values of ΔP_i obtained from Eq. [4]. Table I lists the average change in defect concentrations. The large deviations were due to interactions between the gas and the system. These interactions resulted from the use of reducing gases and are much larger than the detectability limit of the system (4 × 10⁻⁹ moles oxygen).

The results obtained from making exchanges with no sample in the apparatus showed that the pressure change occurring with the system alone amounted to as much as 20% of that occurring with the sample; however, this interaction ceased in less than 15 min which is short compared to the total exchange times of 2–24 hr. Since only the latter part of the exchange data was used to make diffusion coefficient calculations, this interaction did not influence diffusion measurements. However, since the defect concentration calculation is dependent upon the total induced pressure change, it is greatly influenced by any gas-system interaction. In fact at the lowest temperature, 700°C, measurements could not be made. At the higher temperatures the interaction places about a 50% scatter in the data. This interaction is a systematic problem which will have to be corrected before precise defect concentration determinations can be made if reducing gases need to be used.

Table I. Oxygen vacancy concentrations in SrTiO₃ single crystal after reduction in CO

Temperature (°C)	Vacancy concentration (cm ⁻³)
775	3.5 ± 2.0 × 10 ¹⁷
850	7.8 ± 1.5 × 10 ¹⁷
950	5.6 ± 4.5 × 10 ¹⁸
975	7.6 ± 3.5 × 10 ¹⁸

The determination of the chemical diffusion coefficient \tilde{D} , and the oxygen vacancy concentration $[V_{O\cdot\cdot}]$, makes it possible to calculate the oxygen self-diffusion coefficient from the relation (19)

$$D_{O \rightarrow SrTiO_3} = \frac{[V_{O\cdot\cdot}]D_{V_{O\cdot\cdot}}}{N} \quad [10]$$

where N is the total number of oxygen ions in the lattice per cubic centimeter. The oxygen vacancy diffusion coefficient, $D_{V_{O\cdot\cdot}}$, can be calculated directly from the oxygen chemical diffusion coefficient by the relation (11,14)

$$D = (1 + |z|)D_{V_{O\cdot\cdot}} \quad [11]$$

where z is the charge on the diffusing ion which in this case is two. This relationship is valid only when electronic conductivity predominates which is the case for $SrTiO_3$ (10).

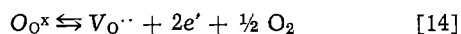
The resulting calculated oxygen self-diffusion coefficient is given by

$$D_{O \rightarrow SrTiO_3} = 60 \exp \left(- \frac{57,000 \pm 16,000}{RT} \text{ cal/mole} \right) \text{ cm}^2/\text{sec} \quad [12]$$

If the assumption is made that the diffusion is via intrinsic defects rather than impurity generated defects, then the activation energy is composed of two separate enthalpy terms according to the relation

$$D_{O \rightarrow SrTiO_3} = D_0 \exp \left(- \frac{\Delta H_m + \Delta H_{V_{O\cdot\cdot}}/3}{RT} \right) \quad [13]$$

where ΔH_m is the enthalpy of motion of a doubly ionized oxygen vacancy plus two electrons, and $\Delta H_{V_{O\cdot\cdot}}$ is the enthalpy of formation of this defect. From the above relation, the energy of formation of doubly ionized oxygen vacancies resulting from the reaction



under the condition

$$[e'] = 2[V_{O\cdot\cdot}] \quad [15]$$

can be calculated to be 126 ± 13 kcal/mole. Within the range of the experimental error, this value is comparable to 133 kcal/mole which was found by Yamada and Miller (10).

The validity of such a calculation is questionable since it requires that the acceptor impurity content be low enough that it does not exceed the native defect concentration. For the specimen used in this study, the total acceptor impurity concentration is reported to be less than 10^{18} atoms/cm³. The measured oxygen vacancy concentrations exceed this level at temperatures above 900°C, however the values obtained at temperatures as low as 775°C did not show any systematic variation which would suggest a shift to extrinsic behavior. Thus, perhaps the actual acceptor impurity might be less than that reported by chemical analysis.

Summary

The correlation between the oxygen vacancy diffusion coefficients obtained in this study and those found in previous determinations adequately demonstrates the applicability of the capacitance manometer system to the measurement of the diffusion coefficient of the rate controlling species. Interactions of the reducing

gas with the system caused a rather large variation in the calculated defect concentration. Even with this difficulty, the calculated enthalpy of formation for the oxygen vacancy was very close to the best value in the literature. This suggests that when this systematic problem has been removed from the system, it should be possible to obtain defect concentration data which are compatible to those obtained by other techniques.

It should also be noted that the apparatus, even when operating in a very insensitive manner as was done here, is capable of determining changes in oxygen content of less than 10^{-5} moles which corresponds to weight changes of less than 10 μ g.

Acknowledgment

This work was supported in part by the Tetronix Foundation and by the National Science Foundation Grant No. GH42915. This paper is based on part of a thesis submitted by one of the authors (D.B.S.) for a M.S. degree at the University of Missouri Rolla (1974).

Manuscript submitted July 10, 1974; revised manuscript received Nov. 11, 1974.

Any discussion of this paper will appear in a Discussion Section to be published in the December 1975 JOURNAL. All discussions for the December 1975 Discussion Section should be submitted by Aug. 1, 1975.

Publication costs of this article were partially assisted by the University of Missouri-Rolla.

REFERENCES

- G. J. Conger, M. S. Thesis, University of Missouri, Rolla, Missouri (1972).
- G. J. Conger and H. U. Anderson, *J. Am. Ceram. Soc.*, **55**, 539 (1972).
- R. P. Turcotte, T. D. Chikalla, and L. Eyring, *Anal. Chem.*, **43**, 958 (1971).
- R. P. Turcotte, T. D. Chikalla, and L. Eyring, *Inorg. Nucl. Chem.*, **33**, 3749 (1971).
- C. Greskovich and H. Schmalzried, *J. Phys. Chem.*, **31**, 639 (1969).
- W. Jost, "Diffusion," Academic Press, New York (1960).
- A. E. Paladino, *J. Am. Ceram. Soc.*, **48**, 476 (1965).
- A. E. Paladino, L. G. Rubin, and J. S. Waugh, *J. Phys. Chem. Solids*, **26**, 391 (1965).
- L. C. Waiters and R. E. Grace, *ibid.*, **28**, 245 (1967).
- H. Yamada and G. R. Miller, *J. Solid State Chem.*, **6**, 1969 (1973).
- P. E. Childs and J. B. Wagner, Jr., "Heterogeneous Kinetics at Elevated Temperatures," W. E. Worrell and Belton, Editors, pp. 269-342, Plenum Press, New York (1969).
- H. Meurer, Doctoral Dissertation, University of Clausthal, 1969.
- J. B. Wagner, Jr., "Mass Transport in Oxides," Nat. Bur. Std. Special Publication No. 296, 65 (1968).
- M. O'Keefe, "Proc. Int'l Conf., Sintering and Related Phenomena," G. C. Kuczynski, Editor, p. 57, Gordon and Breach, New York (1967).
- A. B. Newman, *Trans. Am. Inst. Chem. Engr.*, **27**, 203 (1931).
- J. B. Price and J. B. Wagner, Jr., *Z. Phys. Chem. Neue Folge*, **49**, 257 (1966).
- J. Blanc and D. L. Staebler, *Phys. Rev.*, **B**, **4**, 3548 (1971).
- P. G. Shewmon, "Diffusion in Solids," p. 61, McGraw-Hill Book Co., New York (1963).
- N. F. Mott and R. W. Gurney, "Electronic Processes in Ionic Crystals," p. 34, Dover Publications, Inc., New York (1964).



On the Interpretation of Mott-Schottky Plots Determined at Semiconductor/Electrolyte Systems

R. De Gryse, W. P. Gomes, F. Cardon, and J. Vennik

*Rijksuniversiteit Gent, Laboratorium voor Kristallografie en Studie van de Vaste Stof,
Krijgslaan 271, B-9000 Gent, Belgium*

In this note we want to comment on the interpretation which has to be given, in semiconductor electrochemistry, to the relationship between C^{-2} and V , measured under circumstances where a depletion layer exists at the semiconductor surface. Here, C represents the differential capacitance of the electrochemical cell which contains a semiconductor electrode and a metal counterelectrode, the surface area of the latter being sufficiently large to make its contribution to the capacitance negligible (C is expressed per cm^2 of semiconductor/electrolyte contact area); V represents the voltage, applied to the semiconductor electrode and expressed with respect to a reference electrode. From an observed linear relationship between C^{-2} and V , it is often concluded [see, e.g., the references (1,2) dealing with highly doped SnO_2] that the following inequalities hold

$$C_S \ll C_H \quad [1]$$

$$|\phi_S| \gg |\phi_H| \quad [2]$$

in which C_S and C_H are the differential capacitances per square centimeter of the depletion layer of the semiconductor and of the Helmholtz layer at the semiconductor surface, respectively, ϕ_S is the potential drop over the depletion layer, and ϕ_H the change in Helmholtz potential drop caused by the applied voltage (it is assumed here that the electrolyte solution is sufficiently concentrated so that the Gouy layer can be left out of consideration). Assuming the inequalities [1] and [2] to be valid, and considering, e.g., an n-type semiconductor, the donor density N_D and the flatband potential V_{fb} are then deduced from the experimental C^{-2} vs. V plots by using the Mott-Schottky relationship

$$C^{-2} = (8\pi/\epsilon q N_D) (V - V_{fb} - kT/q) \quad [3]$$

which describes the behavior of the depletion region (ϵ is the dielectric constant of the semiconductor, q the absolute value of the elementary charge, and the other symbols have their usual meaning).

Reversing the argument, C^{-2} vs. V data which are in disagreement with Eq. [3] are not seldom ascribed to effects of the Helmholtz layer. It has been, e.g., suggested (3) that a discrepancy between predicted and observed Mott-Schottky slopes in the case of NiO might follow from the invalidity of inequality [2]. Deviations from linearity of the C^{-2} vs. V plots measured at TiO_2 electrodes have been interpreted (4) by assuming that inequality [1] does not hold in the given case. On the other hand, with NiO and in a voltage range where calculation shows that inequality [2] is not valid, a linear C^{-2} vs. V relationship was found experimentally, a result which was felt to be a discrepancy (5).

It should be noted that in all cases mentioned, semiconductor electrodes are involved in which the con-

Key words: semiconductor electrochemistry, Mott-Schottky plots, Helmholtz layer.

centration of ionized donors or acceptors is high (typically several times 10^{18} to several times 10^{20} cm^{-3}), so that in principle the possibility must be considered that inequalities [1] and [2] do not hold. It is our purpose here to derive the relationship between C^{-2} and V for this case. The derivation will be made for an n-type semiconductor. Our reasoning is analogous to that used in Ref. (6) for the case of an MOS system.

The applied voltage (with respect to the flatband situation) divides itself partly over the depletion region, partly over the Helmholtz layer at the semiconductor/electrolyte interface

$$V - V_{fb} = \phi_S + \phi_H \quad [4]$$

In the case considered, one has $V > V_{fb}$, $\phi_S > 0$, and $\phi_H > 0$. The measured capacitance can be written as

$$C^{-1} = C_S^{-1} + C_H^{-1} \quad [5]$$

We will assume that the variation of C_H as a function of ϕ_H is negligible. This is reasonable if the ionic part of the double layer at the semiconductor/electrolyte interface is located in the outer Helmholtz plane exclusively, which, in the case of concentrated electrolyte solutions, implies the absence of ion adsorption (7). It has been suggested that adsorption on semiconductor electrodes is mainly restricted to radical species (8). Experimental data, such as ion-insensitive values of the flatband potential (9, 10), and electron-transfer rates being first order in the solved ionic reactant over a large concentration range (11), indeed indicate that ion adsorption on compound semiconductor electrodes is rather uncommon. Under the above assumption, the potential change ϕ_H can be expressed as

$$\phi_H = Q_S/C_H \quad [6]$$

where Q_S is the space charge in the semiconductor (for simplicity, it will be assumed that no charge is present in surface states). Solving the Poisson equation for a depletion layer in an n-type semiconductor by using the Mott-Schottky approximation, the following relationship is found between Q_S and ϕ_S

$$Q_S = (\epsilon q N_D / 2\pi)^{1/2} (\phi_S - kT/q)^{1/2} \quad [7]$$

From Eq. [6] and [7], the following relationship is deduced between ϕ_H and ϕ_S

$$\phi_H = 2a(\phi_S - kT/q)^{1/2} \quad [8]$$

where

$$a = (\epsilon q N_D / 8\pi C_H^2)^{1/2} \quad [9]$$

Equation [8] is analogous to the expression, used in Ref. (5) to calculate the contributions of the depletion region and of the Helmholtz layer to the potential drop at the semiconductor/electrolyte interface. Inserting Eq. [8] into Eq. [4] and subtracting kT/q from

both terms, the following quadratic equation in $(\phi_S - kT/q)^{1/2}$ is obtained

$$V - V_{fb} - kT/q = (\phi_S - kT/q) + 2a(\phi_S - kT/q)^{1/2}$$

Hence

$$(\phi_S - kT/q)^{1/2} = -a + [a^2 + (V - V_{fb} - kT/q)]^{1/2} \quad [10]$$

By differentiation of Eq. [7] with respect to ϕ_S , the well-known expression for C_S is obtained

$$C_S = (\epsilon q N_D / 8\pi)^{1/2} (\phi_S - kT/q)^{-1/2} \quad [11]$$

From Eq. [9], [10], and [11], it follows then that

$$C_H/C_S = -1 + [1 + (V - V_{fb} - kT/q) \cdot a^{-2}]^{1/2}$$

Hence, taking into account Eq. [5]

$$(C_H/C_S) + 1 = C_H/C = [1 + (V - V_{fb} - kT/q) \cdot a^{-2}]^{1/2}$$

and, substituting a by its value (Eq. [9])

$$C^{-2} = C_H^{-2} [1 + (8\pi C_H^2 / \epsilon q N_D) (V - V_{fb} - kT/q)] \quad [12]$$

As can be seen from Eq. [12], the relationship between C^{-2} and V is linear, the slope $\Delta(C^{-2})/\Delta V = 8\pi/\epsilon q N_D$ being the same as in the simple Mott-Schottky relationship (Eq. [3]). However, the intersection with the V axis which follows from Eq. [12] corresponds to a voltage V_0 equal to

$$V_0 = V_{fb} + kT/q - \epsilon q N_D / 8\pi C_H^2 \quad [13]$$

and is thus characterized by a shift of $-\epsilon q N_D / 8\pi C_H^2$ with respect to the value deduced from Eq. [3]. For instance, for the (001) face of a TiO_2 electrode ($\epsilon = 173$) with $N_D = 10^{19} \text{ cm}^{-3}$, assuming $C_H = 10^{-5} \text{ f}\cdot\text{cm}^{-2}$, this shift would be approximately $-0.12V$.

Several conclusions can be drawn from the above calculation:

(i) It does not necessarily follow from an experimentally found linear relationship between C^{-2} and V that inequalities [1] and [2] hold. Therefore, one can hardly decide unambiguously from the observed C^{-2} vs. V dependence whether or not the energy levels at the semiconductor surface can be considered as being fixed, when the applied voltage is varied, with respect to the energy level in the reference electrode and hence to the levels of a redox system in the electrolyte. In the experiments with highly doped SnO_2 , e.g., Ref. (2), the potential dependence of the anodic current in the presence of certain reducing agents may be at least partly due to a change of ϕ_H with applied voltage. Therefore also, the determination of V_{fb} by extrapolation of C^{-2} vs. V plots in the case of semiconductor electrodes characterized by a relatively high density of ionized donors or acceptors is subject to a certain error, since the denominator in the last term of the expression for V_0 (Eq. [13]) contains the square of C_H , a quantity the value of which is not known exactly in most cases.

(ii) Since the slope $\Delta(C^{-2})/\Delta V$ has the same value whether inequalities [1] and [2] are valid or not, a discrepancy between predicted and measured slopes, such as, e.g., the one mentioned in Ref. (3), cannot be attributed to a shift in the Helmholtz potential with applied voltage. The confusion apparently originates here from the fact that the effect of the Helmholtz layer was considered on the depletion layer capacitance C_S only, and not on the total capacitance C . The same reasoning is presumably followed in Ref. (12) where it is claimed to be necessary in order to have C^{-2} varying linearly with V , the Helmholtz potential being voltage-dependent, that the change in the Helmholtz potential is a constant fraction of $V - V_{fb}$.

(iii) According to our derivation, nonlinearity of the C^{-2} vs. V plot is not attributable to the fact that the conditions [1] and [2] are not fulfilled. Therefore, we think that alternative reasons have to be sought for the observed curvatures in Ref. (4), such as inhomogeneous donor distribution, e.g. Therefore also, we see no contradiction between the linearity of the C^{-2} vs. V plots and the fact that a considerable fraction of the applied voltage changes occur over the Helmholtz layer, as was observed at the NiO electrode (5).

For future research in the field of semiconductor electrochemistry, it seems important in connection with the above remarks to collect more detailed information concerning the structure and properties of the Helmholtz layer at the semiconductor/electrolyte interface.

Manuscript received July 24, 1974.

Any discussion of this paper will appear in a Discussion Section to be published in the December 1975 JOURNAL. All discussions for the December 1975 Discussion Section should be submitted by Aug. 1, 1975.

Publication costs of this article were partially assisted by Rijksuniversiteit Gent.

REFERENCES

1. F. Möllers and R. Memming, *Ber. Bunsenges. Physik. Chem.*, **76**, 469 (1972).
2. R. Memming and F. Möllers, *ibid.*, **76**, 475 (1972).
3. T. O. Rouse and J. L. Weininger, *This Journal*, **113**, 184 (1966).
4. A. Fujishima, A. Sakamoto, and K. Honda, *Seisan-Kenkyu*, **21**, 450 (1969).
5. D. M. Tench and E. Yeager, *This Journal*, **120**, 164 (1973).
6. A. Goetzberger and E. H. Nicollian, *Appl. Phys. Letters*, **9**, 444 (1966).
7. J. O'M. Bockris and A. K. N. Reddy, "Modern Electrochemistry," Vol. 2, p. 753-756, Plenum Press, New York (1970).
8. H. Gerischer and H. Rösler, *Chem. Ing.-Tech.*, **42**, 176 (1970).
9. S. R. Morrison, *Surface Sci.*, **15**, 363 (1969).
10. R. A. L. Vanden Berghe and W. P. Gomes, *Ber. Bunsenges. Physik. Chem.*, **76**, 481 (1972).
11. T. Freund and S. R. Morrison, *Surface Sci.*, **9**, 119 (1968).
12. V. A. Tyagai, *Izv. Akad. Nauk. SSSR Ser. Khim.*, **34** (1964).

Free Energy of Formation of Sodium Tungsten Bronzes, Na_xWO_3

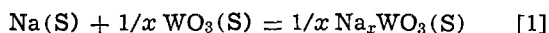
M. Stanley Whittingham*

Corporate Research Laboratories, Exxon Research and Engineering Company, Linden, New Jersey 07036

The sodium tungsten bronzes, Na_xWO_3 , are highly nonstoichiometric compounds which are metallic conductors (1) and have therefore been used as electrodes for both fuel cells (2) and conductivity cells (3); yet until recently nothing quantitative was known about their thermodynamic properties. This paper reports some electrochemical studies of the sodium activity in these materials for $0.3 < x < 0.8$ at ambient temperatures.

Single crystal samples were prepared by the electrolytic decomposition of sodium polytungstates (4) and powder samples by the solid-state reaction of Na_2WO_4 , WO_3 , and W in the appropriate proportions (5). Analysis of phase and composition was performed by x-ray diffractometry, the lattice constant of the cubic perovskite phase being a linear function of composition (6). The partial molar free energy of sodium was measured using an electrochemical cell comprising a sodium electrode and a tungsten bronze electrode, and as electrolyte a solution of sodium iodide in propylene carbonate. The use of sodium hexafluorophosphate as the electrolyte salt gave consistently high emf's (e.g., 2.78V at $x = 0.4$) presumably due to reaction with the oxide matrix giving an oxyfluoride salt. The tungsten bronze crystal was held in the end of a glass tube by epoxy cement, electrical contact being made through a mercury pool (7). Powders were packed into a capillary tube around a platinum wire.

The emf results are shown in Table I; these were stable over several weeks to within ± 5 mV. The variation between different compositions was confirmed by measuring the potential difference between two bronzes immersed in the above electrolyte and in an aqueous sodium chloride solution. The sodium partial molar free energy, $\overline{\Delta G}_{\text{Na}}$, and the free energy of reaction [1], ΔG , calculated using the graphical technique (8), are also listed in Table I



In Fig. 1 the free energy of formation per mole of sodium tungsten bronze obtained here is compared with the enthalpy of formation measured by Dickens

* Electrochemical Society Active Member.

Key words: thermodynamics, tungsten bronzes, battery cathode, oxides.

Table I. Thermodynamic properties of Na_xWO_3

x	E, volts	$-\overline{\Delta G}_{\text{Na}}$, kJ/mole	$-\Delta G$, kJ/mole	$-\log [\text{O}_2]$ atmos.
0.273 p	2.600	250.9	250.9	12.0
0.400 c	2.598	250.7	250.8	13.7
0.597 c	2.570	248.0	250.6	17.9
0.695 p	2.500	241.2	249.8	19.0
0.755 p	2.470	238.4	249.2	20.9
0.790 c	2.430	234.5	248.4	22.8

c = single crystal; p = powder sample.

and Nield (9) using solution calorimetry. The error introduced by using the enthalpy rather than the free energy in this comparison is about 5 kJ/mole, assuming a partial molar entropy change of 23.0 J/K mole as calculated (9) from the data of Gerstein, Klein, and Shanks (10) for $x = 0.68$. These data compare well with the emf's obtained by Steele (11) using beta-alumina as the electrolyte. It should be noted, however, that the sodium activity will be a function of the oxygen activity, and may therefore vary from sample to sample; the oxygen activities of the specimens used here have been determined (4, 12), and are given in Table I.

At all but the highest sodium concentrations the integral molar free energy of solution, ΔG , of sodium into the WO_3 matrix is almost independent of sodium content indicating that interactions between the sodium ions only become significant at high x values. In addition ΔG is independent of the phase, the 0.4 sample being a pure single crystal of the complex tetragonal II tunnel structure (1), all higher x values having the perovskite structure, and the $x = 0.3$ speci-

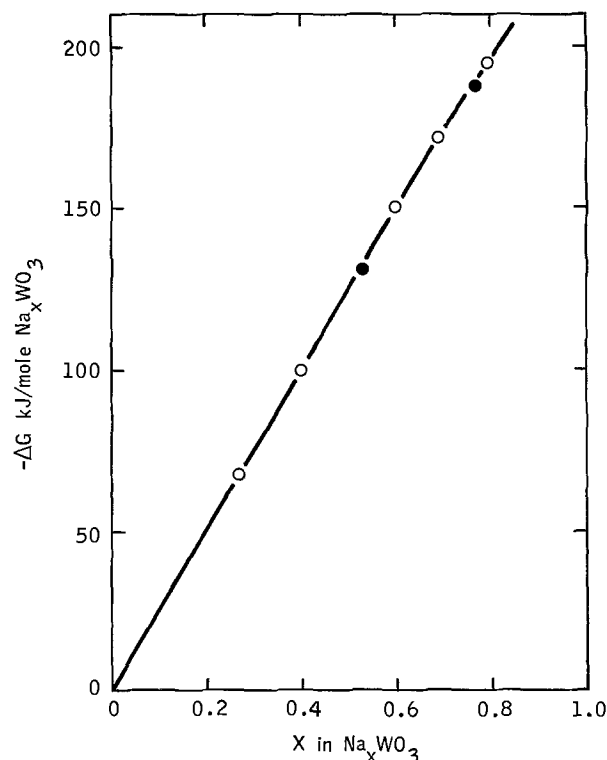


Fig. 1. Free energy of formation per mole of sodium tungsten bronze. ○, This work; ●, calorimetric enthalpies of formation of Ref. (9).

men is a mixture of the two. This is in agreement with the measurements of oxygen activity (12) which, although they showed a marked composition dependence, exhibited no measurable phase dependence. This explains why it has been easy to obtain the cubic phase at very low sodium concentrations (13) in the domain of the tetragonal phases.

Diffusion of the sodium ions in the cubic structure is very low (14), $\sim 10^{-15}$ cm²/sec for the cubic perovskite phase, $\sim 10^{-9}$ cm²/sec for the ammonium ion in the hexagonal tunnel structure, and intermediate for the tetragonal tunnel structure. Although these values in the tungsten bronzes are insufficient for their use as cathodes in battery systems at ambient temperatures, such is not the case for the layer-like compounds of V₂O₅ and MoO₃ which have been successfully used (15, 16). The potentials, measured as above, are shown in Fig. 2; they compare well with previous data (15-17). As expected from the increase in stability of the highest oxidation states in going down the periodic table the emf is higher for V₂O₅ than for either MoO₃ or WO₃. In these cases alkali metal ions, in particular lithium, can be readily intercalated within the oxide matrices without any appreciable change in their structures forming a ternary phase, Li_xV₂O₅ or

Li_xMoO₃. It is this ternary phase formation that is responsible for the voltage found being higher than that expected for the simple disproportionation reaction, i.e., to Li₂O and VO₂ or MoO₂. The importance of this insertion-type reaction in determining the cathodic properties of materials will be discussed in detail in a future paper. For contrast the emf characteristics of the potassium intercalation compounds of graphite (18) are also shown in Fig. 2; these are much more akin to metallic alloys than to the salt-like oxide phases discussed above and could conceivably be used as the anode of a battery system.

Manuscript submitted Oct. 7, 1974; revised manuscript received Dec. 11, 1974. This was Paper 160 presented at the San Francisco, California, Meeting of the Society, May 12-17, 1974.

Any discussion of this paper will appear in a Discussion Section to be published in the December 1975 JOURNAL. All discussions for the December 1975 Discussion Section should be submitted by Aug. 1, 1975.

Publication costs of this article were partially assisted by Exxon Research and Engineering Company.

REFERENCES

1. P. G. Dickens and M. S. Whittingham, *Quart. Rev. Chem. Soc.*, **22**, 30 (1968).
2. J. P. Randin, A. K. Vijh, and A. B. Chughtai, *This Journal*, **120**, 1174 (1973).
3. M. S. Whittingham and R. A. Huggins, *J. Chem. Phys.*, **54**, 414 (1971).
4. M. S. Whittingham and R. A. Huggins, in "Solid State Chemistry," R. S. Roth and S. J. Schneider, Editors, Nat. Bur. Std. Special Publication 364, p. 51 (1972).
5. P. G. Dickens and M. S. Whittingham, *Trans. Faraday Soc.*, **61**, 1226 (1965).
6. B. W. Brown and E. Banks, *J. Am. Chem. Soc.*, **76**, 963 (1954).
7. R. S. Alwitt and A. K. Vijh, *This Journal*, **117**, 413 (1970).
8. R. A. Swalin, "Thermodynamics of Solids," John Wiley and Sons, Inc., New York (1962).
9. P. G. Dickens and D. J. Neild, *J. Chem. Soc. Dalton*, 1074 (1973).
10. B. C. Gerstein, A. H. Klein, and H. R. Shanks, *J. Phys. Chem. Solids*, **25**, 177 (1964).
11. B. C. H. Steele, Personal communication.
12. M. S. Whittingham and P. G. Dickens, in "Reactivity of Solids," J. S. Anderson, M. W. Roberts, and F. S. Stone, Editors, p. 642, Chapman and Hall, London (1972).
13. W. McNeill and L. E. Conroy, *J. Chem. Phys.*, **36**, 87 (1962).
14. M. S. Whittingham and R. A. Huggins, in "Fast Ion Transport in Solids," W. Van Gool, Editor, North-Holland Publishing Co., Amsterdam (1973).
15. A. N. Dey, *This Journal*, **120**, 228C (1973); Abstract 54, p. 132, Electrochemical Society Extended Abstracts, Fall Meeting, Boston, Massachusetts, Oct. 7-11, 1973.
16. L. Campanella and G. Pistoia, *This Journal*, **118**, 1905 (1971).
17. P. G. Dickens, M. Jewess, D. J. Neild, and J. C. W. Rose, *J. Chem. Soc. Dalton*, 30 (1973).
18. S. Aronson, F. J. Salzano, and D. Bellafiore, *J. Chem. Phys.*, **49**, 434 (1968).

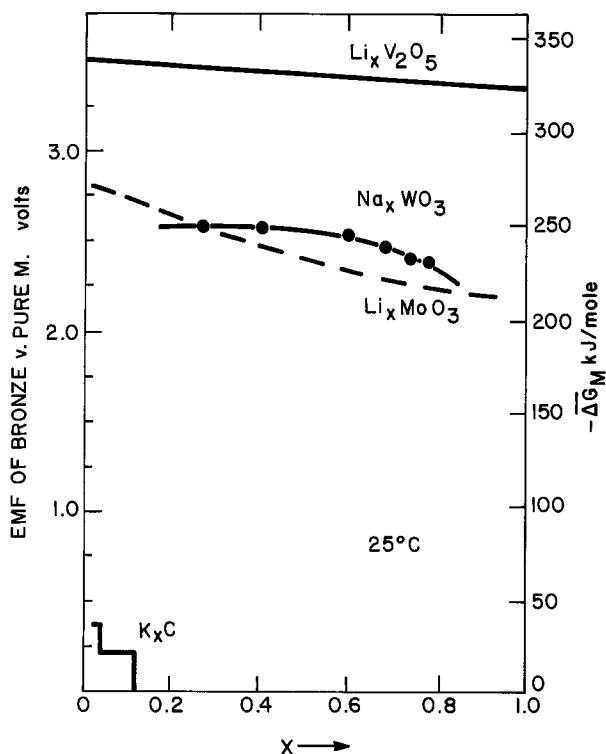
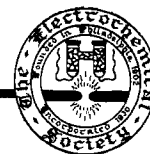


Fig. 2. Thermodynamics of sodium tungsten bronze compared with the ternary phases Li_xV₂O₅ and Li_xMoO₃ and the graphite intercalation compound C_xK (18).



The Effect of Heat-Up on the Performance of Magnesium Batteries

L. F. Urry

Union Carbide Corporation, Battery Products Division, Cleveland, Ohio 44101

ABSTRACT

The heat produced as a result of the inefficiency of magnesium MnO_2 dry cells can be an advantage on high rate application in that it results in a higher cell temperature. The higher the temperature the better the cell performs. Multicell batteries magnify this effect. Experimental BA-4840 military batteries discharged in a 70°F room show internal temperatures of over 130°F and yield 33 W-hr/lb. Insulation can be employed to enhance this effect.

A well-known characteristic of the magnesium- MnO_2 dry cell is the large amount of heat formed upon discharge, resulting from a low operating voltage relative to the theoretical and a high wasteful corrosion of the magnesium anode on discharge. For example, with a 70% anode efficiency and on moderate loads, 1.60 kcal of heat are produced per ampere hour of useful discharge of the cell. This is over 3 times that produced by other conventional dry cell systems such as the Leclanché or alkaline MnO_2 . This high heat-to-output ratio is usually just accepted as an undesirable shortcoming of the system with the liabilities of wasted energy, the need to design additional water and magnesium into the cell to compensate for discharge corrosion loss, and the need for special closures to vent the considerable quantities of hydrogen gas resulting from the corrosion.

In this paper we have attempted to show that the high heat output of the magnesium cell can be utilized to render the system an excellent high rate performer superior to most of the presently available aqueous systems, especially at low temperatures. It also illustrates that magnesium cell heat-up should be taken into account when testing to consider new battery applications.

Discussion

The magnesium MnO_2 dry cell system has three physical properties that render it especially efficient when used in multicell batteries on high rate discharge. They are:

(i) It is sensitive to temperature over a broad range. The higher the temperature the better the performance.

(ii) For every ampere hour of output there is a significant quantity of heat produced. For example, with a 70% anode efficiency, and on moderate to heavy loads, 1.60 kcal of heat are produced per ampere hour of output.

(iii) The system will function well at temperatures higher than can be tolerated with most conventional, aqueous, dry cell, systems.

These three properties are demonstrated as follows.

Sensitivity to heat.—Single, long "C" size, magnesium, round cells were cycled on loads representative

Key words: magnesium cells, battery heat-up, insulated batteries.

of the transmit-receive cycling of cells in a BA-4386 magnesium military battery, on the PRC-25 transceiver application, at various temperatures.

The voltage at the end of each heavy drain pulse (the transmit portion) *vs.* time on test are shown in Fig. 1. It can be seen that the higher the temperature, the more the hours service and the higher the average voltage.

The cells at 130°F gave over 3 times the service of the cells at 40°F. The efficiency of the utilization of the available manganese dioxide assuming a reduction from MnO_2 to Mn_2O_3 *vs.* temperature is shown in Fig. 2.

There is a steady increase in efficiency with temperature, going from 20% at 40°F to 73% at 130°F. The cutoff of these cells is 1.28V and the average current per cell on the transmit load is over 400 mA on a cell smaller in volume than the standard "D" size cell. This is a high efficiency for such conditions.

Another experiment demonstrates the quantity of heat formed on discharge, and also the effect of the temperature rise, resulting from this heat, on the performance of the magnesium MnO_2 dry cell. Cells were tested on short circuit, noting the temperature and the current of the cell *vs.* time. Cells were tested in open

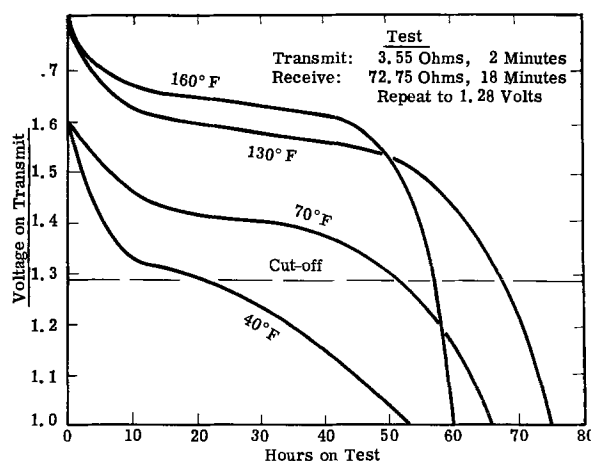


Fig. 1. Effect of temperature on the hours service of single "C" size magnesium cells.

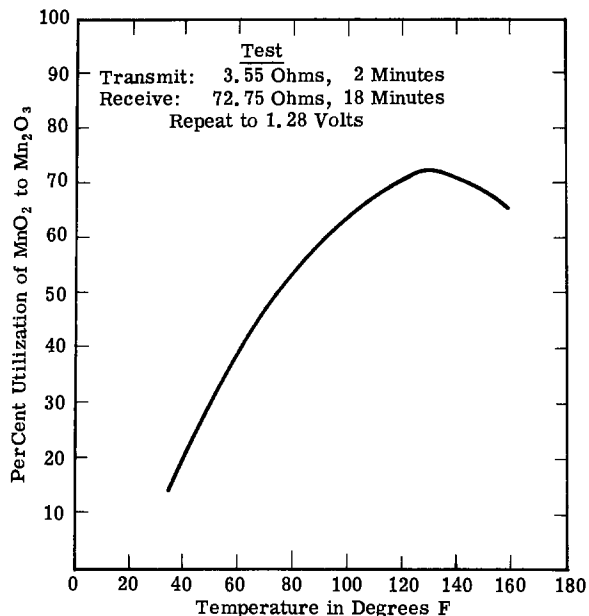


Fig. 2. Effect of temperature on the MnO_2 utilization of single "C" size magnesium cells.

air and compared with cells where the temperature rise was minimized by holding them in a 70°F water bath during testing.

As shown in Fig. 3, the cell shorted in the air and exhibited a steady rise in the temperature of the can to a high of 224°F, where apparently the heat loss matches the heat gained and the temperature peaks. The current at first dropped as is the conventional behavior of cells on a short circuit, but it soon rose to a value higher than the initial amperage. Eventually both the temperature and the current fell off, but by the time the current had dropped to 1A the output in ampere hours was 45% of the theoretical based on MnO_2 to Mn_2O_3 . This is a high efficiency for a short circuit drain to such a high amperage cutoff.

The temperature rise of the cell, shorted while in the 70°F waterbath was low and the amperage did not increase after the initial drop. The ampere hour output to the 1A cutoff was only 21% of that of the cell shorted in the air. The conclusion is that much heat was produced on short circuit, and the difference in temperature resulted in a significant improvement in output.

Relationship of heat produced to output.—The heat which is produced during discharge of the magnesium MnO_2 dry cell is from two causes: (i) the difference between the operating voltage and the theoretical voltage, and (ii) the wasteful corrosion of the magnesium which always accompanies discharge.

The former is essentially calculated by converting to heat the power obtained by multiplying the voltage

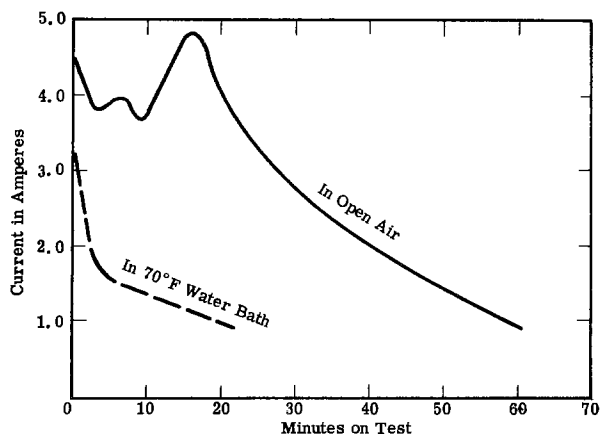


Table I. Calculations, heat produced per cell per ampere hour of output

$$1 \text{ A-hr} \times (2.7 - 1.6\text{V}) \times 860 \text{ cal/W-hr} = 946 \text{ cal}$$

Corrosion at anode = $\text{Mg} + 2\text{H}_2\text{O} \rightarrow \text{Mg}(\text{OH})_2 + \text{H}_2 + 82.1 \text{ kcal/g}$ (4)

Heat of corrosion per ampere hour of cell output for a 70% magnesium efficiency is

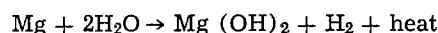
$$1 \text{ A-hr} \times \frac{0.30}{0.70} \times 82.1 \text{ kcal/g-mole} \times \frac{1}{2 \times 26.8 \text{ A-hr/g-mole}} = 656 \text{ cal}$$

Total heat/cell/ampere hour = $946 + 656 \text{ cal} = 1,602 \text{ kcal}$
Heat of corrosion = 41%; heat of inefficiency = 59%

difference times the current. The magnesium cell on moderate drains operates at an average voltage of 1.6V vs. a theoretical voltage of approximately 2.7V (1, 2). The heat produced when 1 A-hr is withdrawn from the cell is therefore 946 cal as shown in Table I.

The magnesium anode suffers very little corrosion on storage because of the effectiveness of the inhibitor system. However, on discharge the protective film must be broken down in order for the cell to function. Corrosion of the anode can then occur. The corrosion on discharge seems to be directly proportional to the discharge current. The corrosion rate, or to express it another way, the efficiency of the magnesium for a given set of physical conditions in a cell, seems to be constant over a wide range of temperature and load conditions. The magnesium MnO_2 round cell using a magnesium perchlorate electrolyte and AZ21X1F magnesium alloy has an anode efficiency of approximately 70% (3).

The corrosion reaction appears to be



The heat produced is 82.1 kcal/g-mole of magnesium corroded, which for a 70% magnesium efficiency works out to be 656 cal/A-hr output per cell (4).

The total heat output per cell at a 70% anode efficiency is $946 + 656 \text{ cal} = 1.60 \text{ kcal/A-hr/cell}$.

With a 70% magnesium efficiency, therefore, approximately 59% of the heat formed on discharge is due to the low operating voltage of the cell and 41% is due to the wasteful corrosion of the anode which occurs simultaneously with discharge.

The relationship of heat output, with magnesium efficiency for the magnesium MnO_2 dry cell is shown in Fig. 4.

An increase in the anode efficiency from the 70% level will not result in a major change in the amount of heat formed on discharge per ampere hour of output, however, a lower anode efficiency will. This is the principle used in high altitude meteorological batteries (6). A low efficiency magnesium alloy is used to increase the heat of discharge corrosion, and thus offset the extreme cold of the high altitudes. In addition the inhibition is reduced, thereby further increasing the corrosion on discharge, and also causing significant corrosion on open circuit stand. The latter results in

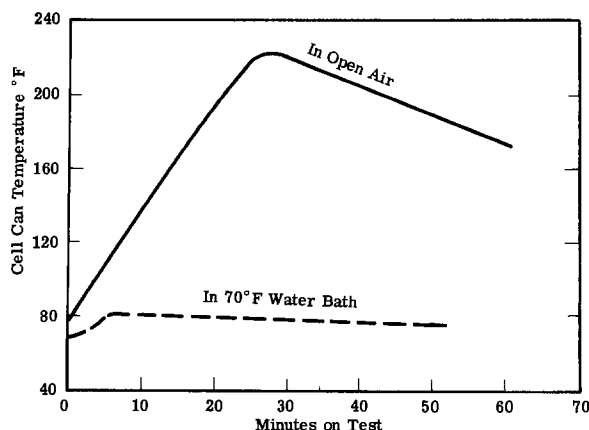


Fig. 3. Effect of temperature upon the short circuit current of long "C" magnesium cells.

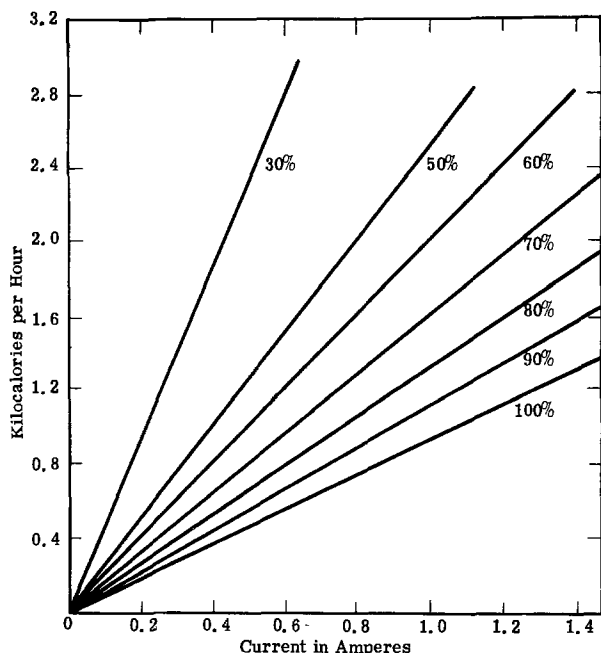


Fig. 4. Heat produced by the magnesium cell at different anode efficiencies (6).

cell heat-up immediately upon activation. Because of the poor shelf life of such batteries in the activated state, they are usually made as reserve batteries.

Other conventional systems such as the alkaline MnO_2 and the Leclanché have practically no wasteful corrosion of the anode associated with discharge, and the operating voltages are much closer to the theoretical so that the heat per ampere hour with these systems is less than one-third of that of the magnesium MnO_2 for moderate drains (3). The magnesium cell will therefore have a greater heat-up on discharge.

The behavior of the BA-4840 magnesium battery, a high rate battery developed for the U.S. Army Electronics Command under a Research and Development contract, demonstrates the practical use of this heat-up effect. The BA-4840 battery contains 64 long "C" round cells made up of 16 strings of four paralleled cells connected in series. The light load, heavy load cycling application (receive-transmit), averages 578 mA.

The specific heat of a magnesium battery has been calculated to be approximately 0.30 cal/°C/g. The BA-4840 battery weighs 10 lb. The temperature rise in 1 hr of test if there is no heat loss should be

$$0.578 \text{ A-hr} \times 1610 \text{ cal/A-hr} \times 16 \text{ cells in series}$$

$$\frac{10 \text{ lb} \times 453.6 \text{ g/lb} \times 0.3 \text{ cal/g}}{10 \text{ lb} \times 453.6 \text{ g/lb} \times 0.3 \text{ cal/g}}$$

$$= 10.9^\circ\text{C} \text{ or } 19.7^\circ\text{F}$$

The rise in temperature at the center of a BA-4840 battery is shown in Fig. 5. The temperature rise in the early part of the discharge is approximately 20°F/hr with a gradual fall off in rate as the heat loss approaches the rate of heat generation. The MnO_2 efficiency vs. voltage discharge curve is shown in Fig. 6. The MnO_2 efficiency to 1.25V/cell is 65% which is high for a test where the high rate (transmit) drain is 1.16A for a cell which is approximately the same volume as a standard "D" size cell. The output is 33 W-hr/lb of complete battery. It is unlikely that such a high energy density could have been achieved without the heat-up effect. Single cells discharge on the same loads per cell had less temperature rise due to a higher rate of heat loss, and the output per cell to cutoff was lower.

Ability of the magnesium cell to withstand high temperatures.—The high heat in relationship to output characteristic of the magnesium MnO_2 dry cell could

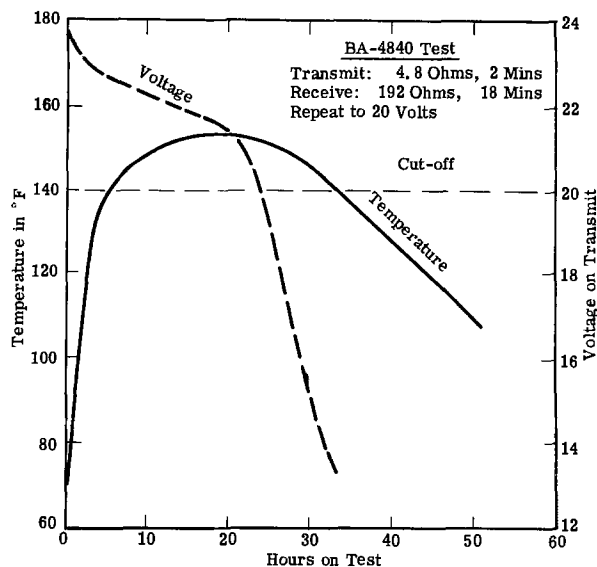


Fig. 5. Temperature in center of battery and voltage on transmit for BA-4840 battery tested in 75°F room.

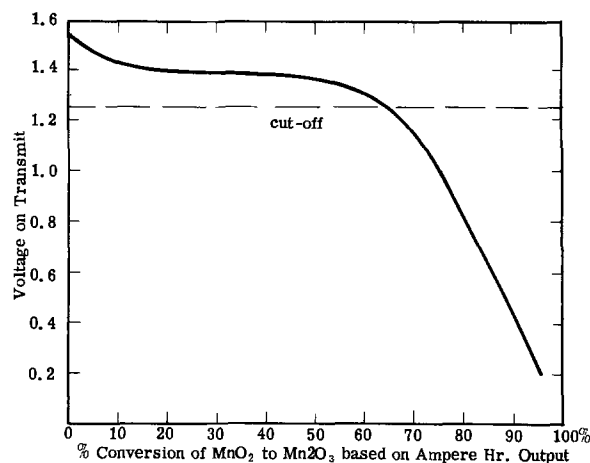


Fig. 6. Efficiency of utilization of available MnO_2 of BA-4840 battery tested in 75°F room.

be a detriment under certain conditions if the system were unstable at high temperatures. Situations where such high internal temperatures might occur in batteries are: when discharging on high rate drains in high environmental temperature or under extremely high rate discharge, especially if insulated.

Fortunately, the magnesium MnO_2 dry cell, as now generally made, will withstand temperatures much higher than those that are detrimental to other conventional aqueous dry cell systems. A major factor is that the magnesium cell uses plain paper as the separator instead of decomposable gels.

As an example of this ability to perform well at high temperatures, short "A" size magnesium cells were made with special closures that would remain stable at high temperatures. These cells were discharged on a 20 mA constant current load while held immersed in oil at 240°F. The results are shown in Fig. 7. The voltage on load was exceptionally high averaging 1.8V and the efficiency of utilization of the MnO_2 was 73% to a 1.7V cutoff with an energy density of 47 W-hr/lb of cell.

Since the magnesium cell (i) does produce a significant amount of heat on discharge, (ii) improves in performance with increasing temperature, and (iii) can withstand high temperatures, special provisions to minimize the heat loss, thus increasing still farther the battery internal temperature, should yield additional improvement. Insulated batteries have shown significant improvement over uninsulated batteries (7).

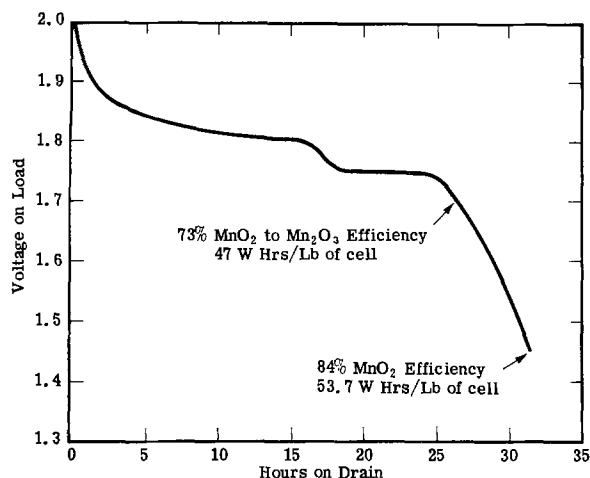


Fig. 7. Short "A" size magnesium cells on 20 mA, 8 hr/day while in oil at 240°F.

The BA-4840 battery mentioned earlier would not even rise to cutoff when tested at 20°F but when encased in styrofoam, the hours service at 20°F equaled that of the uninsulated battery at 70°F. The advantage was not just at low temperature. Smaller cells in the same size battery, but also including insulation, resulted in the same service at room temperature as had been obtained with larger cells in the uninsulated version of the battery.

This response of the magnesium cell to temperature has implications beyond just service application in that it must also be taken into account in testing. Cells tested individually, but in close proximity in a confined space, will give much better service than cells spread out in circulating air, especially on heavy continuous drains. This could lead to false conclusions, if the variable being considered was something other than test conditions, for instance if one lot was tested individually and the other as part of a clustered group.

Also, in predicting the service of a proposed battery involving the combination of many cells, it is often the practice, for convenience, to do the actual testing on single cells. In the case of magnesium cells this could lead to false conclusions and the rejection of a combination which might actually meet the require-

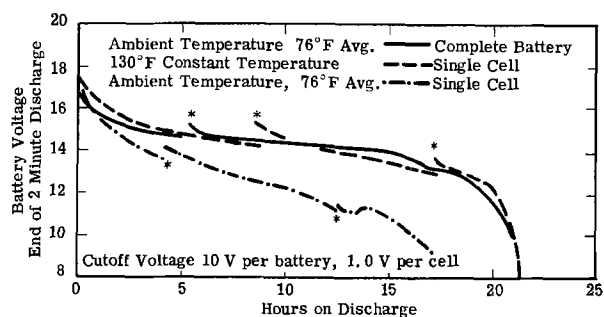


Fig. 8. Single cells at elevated temperature to simulate conditions in a multicell battery. *, Rest on open circuit overnight.

ment when tested as a complete battery. This is demonstrated in Fig. 8.

While working under a USAECOM Research and Development contract, to develop a high rate battery to power an experimental transceiver, an attempt was made to predict battery service from the results of testing single cells. The load per cell was approximately the same as on the cells of the aforementioned BA-4840 battery. The single cells tested at room temperature (approx. 76°F) gave only 16 hr, whereas the complete battery in the same room gave 21 hr. The average internal temperature of the battery during discharge was found to be 130°F. So single cells were then tested in a 130°F oven. The service then equaled that of the battery. Single cell testing at 130°F was then used to evaluate a group of design variables, and the best combination was selected while keeping the number of cells manufactured to a minimum. The results of the single cell testing were then validated by building and testing actual batteries (8).

The conclusion here is that if single cell testing is desirable to predict the performance of a multicell battery, a way to accomplish this is to determine the average internal temperature of the battery and test individual cells at this temperature.

In summary, the magnesium MnO_2 dry cell is somewhat unique among aqueous primary cells in the amount of heat which accompanies discharge, the improvement with high temperatures, and the stability at high temperatures. These properties can be exploited to advantage, in high rate multicell batteries, can be abetted by insulation, and should be taken into account in testing.

Manuscript received Dec. 20, 1974. This was Paper 7 presented at the New York, New York, Meeting of the Society, Oct. 13-17, 1974.

Any discussion of this paper will appear in a Discussion Section to be published in the December 1975 JOURNAL. All discussions for the December 1975 Discussion Section should be submitted by Aug. 1, 1975.

Publication costs of this article were partially assisted by Union Carbide Corporation.

REFERENCES

1. Selected Values of Chemical Thermodynamic Properties, National Bureau of Standards, Circular 500, Washington, D.C. (1952).
2. G. W. Heise and N. C. Cahoon, Editors, "The Primary Battery," Vol. 1, p. 163, John Wiley and Sons, Inc., New York (1971).
3. P. F. King and J. L. Robinson, 2nd Quarterly Report, USAECOM DA 36-039-SC-88912, Dow Chemical Company, Midland, Mich. Jan. 1962.
4. O. A. Hougen and K. M. Watson, "Chemical Process Principles," John Wiley and Sons, Inc., New York (1943).
5. D. B. Wood, in "Batteries, Vol. 1 Manganese Dioxide," K. V. Kordesch, Editor, Chap. 4, p. 521, Marcel Dekker, Inc., New York (1974).
6. G. W. Vinal, "Primary Batteries," p. 277, John Wiley and Sons, Inc., New York (1950).
7. D. B. Wood, "Improved Utilization of the Mg/ MnO_2 Dry Cell System," 26th Power Sources Symposium, April, 1974.
8. L. F. Urry, USAECOM DA-28-043-AMC-02586(E), Union Carbide Corp., Cleveland, Ohio Sept. 1968.

Anodic Polarization Behavior of High-Purity 13 and 18% Cr Stainless Steels

E. A. Lizlovs* and A. P. Bond*

Research Laboratory Climax Molybdenum Company of Michigan, Ann Arbor, Michigan 48106

ABSTRACT

Potentiodynamic polarization curves were obtained in N H_2SO_4 and in N HCl for 13 and 18% Cr ferritic stainless steels containing 0-5% Mo. The critical current density for passivation was decreased by molybdenum additions in both acids, the decrease being more pronounced for the 18% Cr steels than for the 13% Cr steels. No complete passivity was obtained for the 13% Cr steels, even with the 5% Mo addition, in N HCl . The addition of 1% Mo to 18% Cr steels resulted in complete passivity in N HCl . Pitting potentials in M $NaCl$ at 25°C increased linearly with molybdenum content. Pitting potentials increased more rapidly for the 18% Cr steels than for the 13% Cr steels. All alloys suffered pitting corrosion in 10% $FeCl_3$; however, alloys of higher Cr-Mo content were the least pitted and showed the smallest weight losses.

Earlier work at the Climax Laboratory and other laboratories has clearly demonstrated the excellent corrosion resistance of high-purity ferritic stainless steels (1-6). However, more information is needed to establish the effect of molybdenum on polarization behavior at various chromium levels. In continuation of previous work with 25% Cr steels, the investigations were carried out with 13 and 18% Cr steels alloyed with up to 5% Mo.

Experimental Procedures

Materials.—The experimental ferritic stainless steels were produced by induction melting and casting in vacuum. The compositions are given in Table I. The ingots were hot forged at 2000°F (1080°C) to $\frac{3}{4}$ in. (1.90 cm) thick plates, which were then hot rolled to 0.30 in. (0.76 cm) thick plate and then cold rolled to 0.15 in. (0.38 cm) thickness. Materials containing 0, 1, and 2% Mo were heat-treated for 1 hr at 1500°F (815°C), followed by water quenching. Materials containing 3.5 and 5% Mo were heat-treated for 1 hr at 1800°F (980°C), followed by water quenching. Metallographic examinations did not show the presence of intermetallic phases in any of the materials. The composition and heat-treatment of alloys were such that they were immune to intergranular corrosion.

Polarization experiments.—Potentiodynamic polarization experiments were performed in nitrogen-saturated N H_2SO_4 and N HCl at $29.8^\circ \pm 0.1^\circ C$ using standard equipment and techniques. The potential scanning rate was 520 mV·hr⁻¹. The electrodes were mounted in epoxy, the exposed surface, approximately 0.6 by 0.5 cm, always being a longitudinal section parallel to the rolled surface. Electrodes were mechanically polished, using standard metallographic techniques; the final polish was with 0.3 μ alumina.

Pitting potentials were determined for all experimental stainless steels in M $NaCl$ at $25^\circ \pm 0.1^\circ C$. Electrodes for the determination of pitting potentials were the same as described above, except that polishing was only through 600-grit SiC metallographic paper. Furthermore, the fine crevices between the epoxy mount and the stainless steel sample were masked with Glyptal to prevent crevice corrosion of the electrode. The "scratch" technique, introduced by Pessall and Liu (7), was employed for the determination of pitting potentials. The electrode was first polarized potentiostatically to some potential well below the expected pitting potential. The polarization current and potential were continuously recorded by a two-pen strip-chart recorder. The polarization current was allowed

to stabilize and then the electrode surface was scratched with a sharp silicon-carbide crystal mounted on the end of a glass tube. The scratching of the electrode surface resulted in a sharp polarization current "blip." The electrode potential was manually adjusted by 20 mV steps to more and more noble potential values, until the scratch failed to repassivate, a failure which was indicated by a gradual current rise after the electrode was scratched. The pit was allowed to develop for 10 min, and then the electrode was examined visually. Only those results were considered to be valid where pits actually developed at the scratched site.

Some potentiostatic experiments with selected alloys were also performed in N HCl . In these experiments, a preset potential, corresponding to the minimum current in the passive state in hydrochloric acid, was immediately applied after the masked electrode was immersed in acid. The electrode was kept at this potential for several hours and current was recorded as a function of time. These experiments were designed to determine whether a particular alloy would suffer general corrosion in hydrochloric acid at passive potentials.

All potentials were measured and reported with respect to the saturated calomel electrode.

Immersion tests.—All of the alloys were tested in acidified 0.33M $FeCl_3$ (pH 1). Test duration was 24 hr. Selected alloys were also tested in N H_2SO_4 , saturated with oxygen at 25°C, and in N HCl , saturated with nitrogen, also at 25°C. Test duration, unless otherwise noted, was 24 hr. Test coupons were 2.5 by 2 cm, polished through No. 600 SiC paper. In all immersion tests, except for the ferric chloride test, samples were activated by touching with a magnesium rod immediately after immersion in acid.

Results

Polarization experiments.—Characteristic potentiodynamic polarization curves for the 13% Cr ferritic

Table I. Chemical composition of the alloys studied

Stainless steel type	Element, %			
	C	Cr	Mo	N
13Cr	0.003	13.68	0.08	0.004
13Cr-1Mo	0.005	13.14	1.04	0.0035
13Cr-2Mo	0.002	13.60	1.88	0.004
13Cr-3.5Mo	0.003	12.94	3.48	0.0039
13Cr-5Mo	0.003	13.04	4.77	0.0032
18Cr	0.002	17.35	<0.01	0.003
18Cr-1Mo	0.003	17.53	1.14	0.0036
18Cr-2Mo	0.004	17.61	2.02	0.004
18Cr-3.5Mo	0.005	17.58	3.52	0.0034
18Cr-5Mo	0.004	17.38	4.75	0.0037

* Electrochemical Society Active Member.
Key words: corrosion, potentiodynamic polarization, molybdenum, pitting, sulfuric acid, hydrochloric acid.

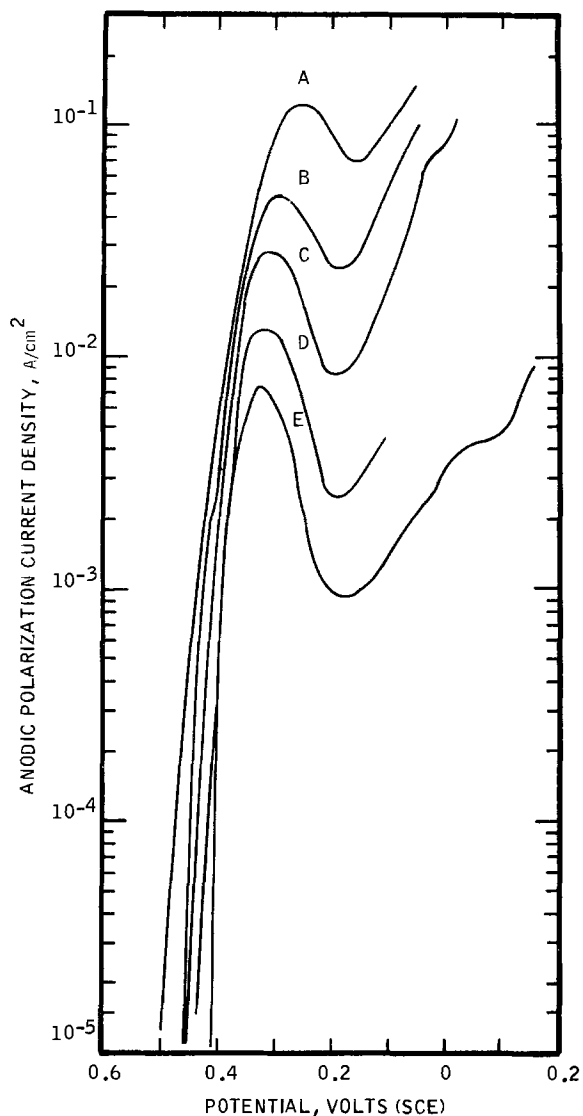


Fig. 1. Anodic potentiodynamic polarization curves for 13% Cr high-purity stainless steels in *N* HCl at 29.8°C. A, 0% Mo; B, 1% Mo; C, 2% Mo; D, 3.5% Mo; E, 5% Mo

stainless steels in *N* HCl are shown in Fig. 1. A similar set of curves, except for much more pronounced critical peaks, was also obtained for 18% Cr steels in *N* HCl. Critical current density decreased with an increase in molybdenum content for all materials (Fig. 2). Beyond the critical peak, current for unmasked electrodes fell to some minimum value and then increased again, so that no well-defined passive region was obtained for any of the materials. In general, the relatively high and increasing polarization current beyond the critical peak for the unmasked electrodes in hydrochloric acid is caused either by crevice corrosion along the metal-epoxy mount boundary or by general corrosion because of incomplete passivation. Visual inspection of the 13Cr-5Mo electrode after the potentiostatic exposure to *N* HCl (29.8°C) at -0.220V for approximately $1\frac{1}{2}$ hr showed that the electrode surface was uniformly etched. Furthermore, the polarization current density remained constant, after the rapid initial rise, at about 0.9 mA/cm^2 , which was approximately the same current density as recorded under potentiodynamic conditions at -0.220V (Fig. 1). In view of the fact that all of the other 13% Cr alloys exhibited higher minimum current densities, it can be assumed that all of the 13% Cr ferritic stainless steels suffered general corrosion at potentials beyond the critical peak.

The masked 18Cr-1Mo and 18Cr-2Mo alloys were exposed to *N* HCl at -0.080 and -0.100V , respectively. The current density, at first, was of the order of 10^{-6}

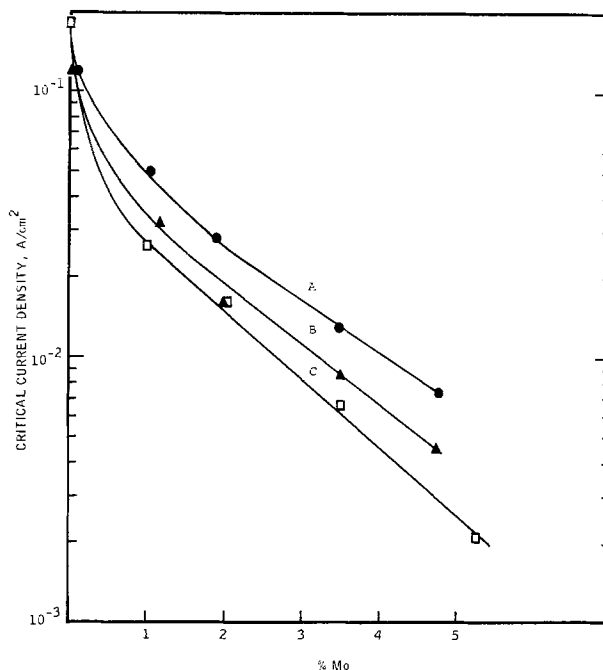


Fig. 2. Dependence of critical current density on molybdenum content for high-purity ferritic stainless steels in *N* HCl at 29.8°C. A, 13% Cr; B, 18% Cr; C, 25% Cr [data from Ref. (4)].

A/cm^2 , as expected for complete passivity; however, it increased in an irregular manner to the order of 10^{-5} A/cm^2 . Examination of the electrode surface showed no general corrosion. The corrosion damage was localized at places along and under the Glyptal masking. Hence, these materials did passivate completely in 1*N* HCl, but were very sensitive to crevice corrosion, which could be initiated quite readily at the Glyptal-metal boundary. The 18% Cr steel was not investigated in these experiments, but 18 and 25% Cr steels have been previously shown to sustain general corrosion at passive potentials (3, 4). Besides, current density at the minimum is more than 10^{-3} A/cm^2 , which also indicates that this material should suffer general corrosion in *N* HCl at passive potentials.

Polarization curves in *N* H₂SO₄ were normal; that is, they showed a critical peak and a complete passive region up to normal transpassive transition potentials with passive current densities in the order of 10^{-6} A/cm^2 . Critical current densities decreased with an increase in molybdenum content (Fig. 3). Results on 25Cr alloys are included from a previous study (4).

In contrast to a strong and well-pronounced effect on critical current densities the effect of molybdenum on primary passivation potential was only slight and possibly without practical significance. Nevertheless some trends were observable. Primary passivation potentials in hydrochloric acid became more active as the molybdenum was increased, and 18% Cr steels had more active primary passivation potentials than corresponding 13% Cr steels (Table II). In sulfuric

Table II. Primary passivation potentials for the 13 and 18% Cr ferritic stainless steels

Steel type	Primary passivation potential, V (SCE)	
	<i>N</i> H ₂ SO ₄	<i>N</i> HCl
13Cr	-0.383	-0.250
13Cr-1Mo	-0.413	-0.295
13Cr-2Mo	-0.450	-0.305
13Cr-3.5Mo	-0.413	-0.318
13Cr-5Mo	-0.445	-0.322
18Cr	-0.433	-0.310
18Cr-1Mo	-0.452	-0.320
18Cr-2Mo	-0.461	-0.345
18Cr-3.5Mo	-0.445	-0.353
18Cr-5Mo	-0.442	-0.351

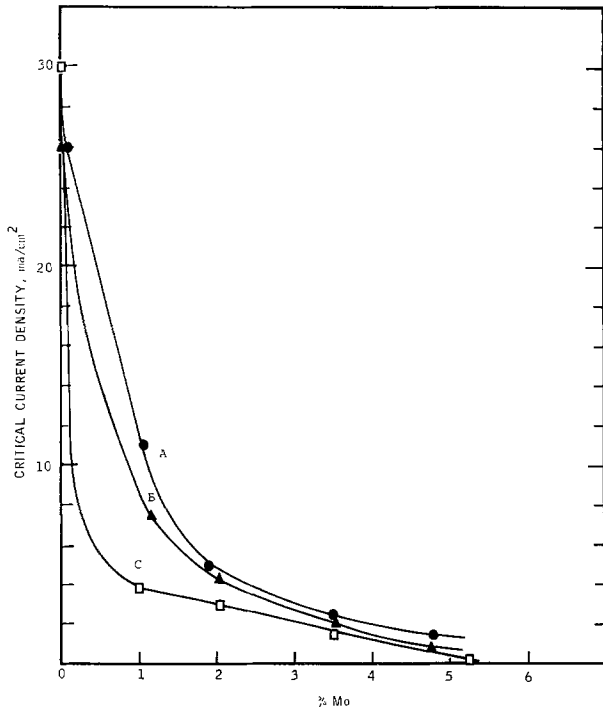


Fig. 3. Dependence of critical current density on molybdenum content for the high-purity ferritic stainless steels in $N H_2SO_4$ at $29.8^\circ C$. A, 13% Cr; B, 18% Cr; C, 25% Cr [data from Ref. (4)].

acid primary passivation potentials first became more active then tended to become more noble as the molybdenum content was increased. The 18% Cr steels in sulfuric acid showed a tendency to have somewhat more active primary passivation potentials than corresponding 13% Cr steels.

Pitting potentials became more noble for both series of stainless steels with an increase in molybdenum content, the increase being more pronounced for the 18% Cr series (Fig. 4). In both cases, the relationship between the pitting potential and molybdenum content appeared to be linear. Pitting potentials for the 13Cr-

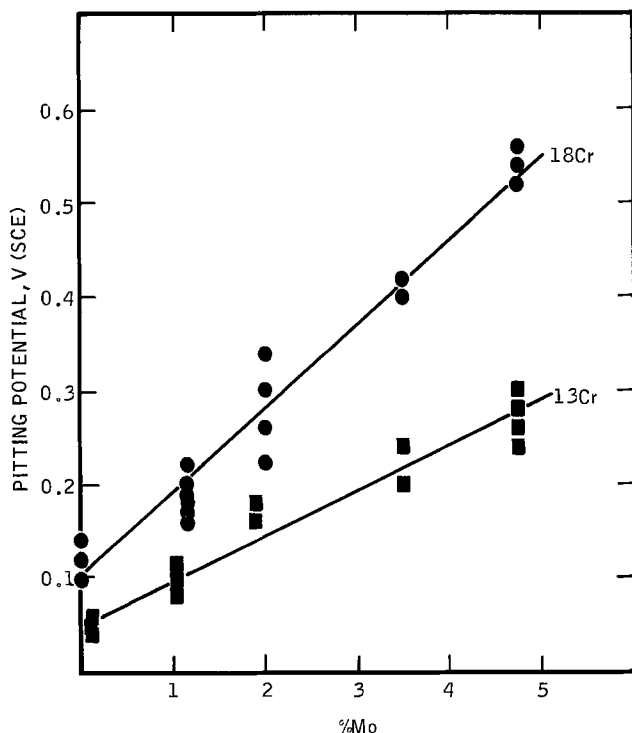


Fig. 4. Pitting potentials for the 13 and 18% Cr ferritic stainless steels in $M NaCl$ at $25^\circ C$.

2Mo alloy were approximately 20-40 mV more noble than predicted by the linear relationship. The chromium content, however, for this alloy was 13.60% (Table I), as compared to an average close to 13% for other molybdenum-containing steels in the series, and this higher chromium content probably accounts for most of the deviation.

Immersion tests.—Corrosion rates in acidified 0.33M $FeCl_3$ (pH 1) are given in Table III. The 13Cr- and 1Mo steels suffered severe general corrosion in ferric chloride, while the remaining materials were pitted. No beneficial effect of molybdenum on the rate of pitting corrosion was evident for the 13% Cr steels. On the 18% Cr base, higher molybdenum concentrations do result in a decrease in pitting rate; however, the effect becomes evident above a molybdenum content of 1%.

Corrosion rates in oxygen-saturated $N H_2SO_4$ and nitrogen-saturated $N HCl$, both at $25^\circ C$, are given in Table IV. Data for the 25% Cr ferritic stainless steels from a previous investigation (4) are also included in Table IV for comparison.

Discussion

The effect of molybdenum on the active-passive transition and on the ability to develop a passive film under severe experimental conditions is dramatically illustrated by families of polarization curves in $N HCl$ (Fig. 1); at the 13% Cr level, no complete passivity (characterized by current densities on the order of $10^{-6} A/cm^2$ or less for masked electrodes and absence of general corrosion) in 1N HCl was achieved even at 5% Mo content. The current maxima were displayed for all 13% Cr materials at potentials where the critical current density peaks were expected, and, therefore, these peaks were considered to be critical current densities, even if no complete and pronounced passive region was present. Beyond the critical peak, the current dropped to some minimum value and then rose again sharply. The critical current densities and cur-

Table III. Corrosion rates in 0.33M $FeCl_3$ solution (pH 1) at $25^\circ C$, 24-hr exposure

Steel type	Corrosion rate, $mg \cdot dm^{-2}/day$
13Cr	1,260 (general corrosion)
13Cr-1Mo	3,690 (general corrosion)
13Cr-2Mo	119
13Cr-3.5Mo	228
13Cr-5Mo	197
18Cr	214
18Cr-1Mo	352
18Cr-2Mo	177
18Cr-3.5Mo	78
18Cr-5Mo	41

Table IV. Corrosion rates of high-purity alloys at $25^\circ C$

Steel type	Run	Corrosion rate, $mg \cdot dm^{-2}/day$, after 24 hr exposure	
		Oxygen-saturated 1N H_2SO_4 at $25^\circ C$	Nitrogen-saturated 1N HCl at $25^\circ C$
13Cr	1	1,820	227
	2	1,280	106
13Cr-2Mo	1	1,010	231
	2	1,160	104
13Cr-5Mo	1	1,730	113
	2	1,300	110
18Cr	1	4,600	1,020
	2	4,060	645
18Cr-2Mo	1	1,400	281
	2	1,400	253
18Cr-5Mo	1	1,280	145
	2	1,770	130
25Cr*	1	20,000	39,000
25Cr-2Mo*	1	2,450	1,260
25Cr-3.5Mo*	1	nil	556
25Cr-5Mo*	1	nil	307

* Data from Ref. (4).

rent density minima decreased and became more pronounced as the molybdenum content increased. This can be interpreted as a decrease in active and passive dissolution rates with an increase in molybdenum content. Especially interesting is the sharp decrease in dissolution rate beyond the primary passivation potential. It can be assumed that a decrease in dissolution rate of a metal beyond its primary passivation potential results from the hindering effect of the formation of the passive film; instead of direct dissolution, the alloy forms a passive film first, which then dissolves. Apparently, as molybdenum content increases, the film formation reaction is greatly enhanced resulting in more pronounced current minima for alloys of higher molybdenum content.

The effect of molybdenum additions to 18% Cr steels is similar to that for 13% Cr steels. At the 18% Cr level, however, the addition of 1% Mo is enough to permit development of complete passivity, as evidenced by decreased values of current minima; however, even at 5% Mo content, materials still remain quite sensitive to crevice corrosion in *N* HCl. As shown in earlier work, increasing the chromium content to 25% does allow molybdenum-bearing alloys to develop a passive film that completely resists crevice corrosion in *N* HCl (4, 6, 8).

In a less-severe medium, *N* H₂SO₄, all materials developed complete passivity and a full passive range. Active corrosion rates decreased and ease of active-passive transition was enhanced by the increase in molybdenum content, as evidenced by decreasing critical current densities with increasing molybdenum content (Fig. 3).

The analysis of the critical current density data showed an interesting correlation with the molybdenum content. The plots of the critical current density vs. molybdenum content at 13, 18, and 25% Cr in *N* H₂SO₄ and *N* HCl acid are shown in Fig. 2 and 3. Data for 25% Cr steels are taken from previous work (4), supplemented by the results from trial experiments with 26Cr-1Mo alloy in *N* H₂SO₄. As shown in Fig. 2 and 3, the increase in molybdenum content from 0 to 1% results in a sharp decrease in critical current density peak in *N* H₂SO₄ and *N* HCl. This decrease becomes more pronounced with an increase in chromium level. At 25% Cr level even small additions of molybdenum should result in a very sharp decrease in critical current density. Further increases in molybdenum content from 1 to 5% for 18 and 25% Cr steels and from 2 to 5% for 13% Cr steels were semilogarithmic (exponential) for HCl. Again, the effect of molybdenum on the critical current density became more pronounced with an increase in chromium level.

Families of curves given in Fig. 2 and 3 should be very useful in predicting the magnitude of critical current densities for 13-25% Cr steels in *N* H₂SO₄ and *N* HCl. These curves should also allow predictions of relative critical behavior in other media.

The effects of molybdenum on pitting potentials were strongly dependent on the chromium level of ferritic stainless steels. The pitting potentials for 18% Cr steels were more noble than for corresponding 13% Cr steels. Furthermore, the shift of pitting potentials to more noble values with increasing molybdenum content was more pronounced at 18% Cr than at the 13% Cr level. Previous work has shown that at the 25% Cr level molybdenum-containing steels are not only highly resistant to pitting but are also resistant to crevice corrosion, even under severe oxidizing conditions (4, 6, 8).

According to pitting potentials, the 18% Cr ferritic stainless steels containing 2% or more molybdenum

and 13% Cr steels containing over 3% Mo should be quite resistant to pitting corrosion in chloride environments under moderately oxidizing conditions. None of these materials, however, is expected to be resistant under strong oxidizing conditions, and, indeed, all alloys are subject to pitting corrosion in ferric chloride at room temperature.

While crevice corrosion was not specifically studied for 13 and 18% Cr steels, they are all expected to be very sensitive to this type of corrosion, as predicted by polarization curves in 1*N* HCl. Also, in general, any materials that are subject to pitting corrosion will be subject to crevice corrosion.

Data presented in Table IV show some interesting correlations between corrosion rates and chromium and molybdenum contents. The steels of lower chromium content corroded at lesser active rates in sulfuric and hydrochloric acid than corresponding steels of higher chromium content. An increase in molybdenum content from 0 to 5% at the 13% Cr level had no significant effect on active corrosion rates in sulfuric and hydrochloric acids; at the 18% Cr level there was a pronounced decrease, while at 25% Cr there was a very sharp decrease. The 25% Cr-3.5% Mo and 25% Cr-5% Mo steels actually repassivated after being activated in oxygenated *N* H₂SO₄ (4).

Summary

The effect of molybdenum on the decrease of critical current density in *N* H₂SO₄ and *N* HCl acids is dependent on the chromium level; the higher the chromium level, the more pronounced was the effect of molybdenum, especially in the 0-2% range. The effect of molybdenum on the formation and stability of the passive film is also dependent on the chromium level; no complete passivity was attained for any of the 13% Cr steels in *N* HCl; at the 18% Cr level the addition of 1% Mo allowed achievement of complete passivity in *N* HCl.

Pitting potentials in *M* NaCl at 25°C increased linearly with an increase in molybdenum content. The pitting potentials increased more rapidly for the 18% Cr steels than for the 13% Cr steels. All alloys suffered pitting corrosion in 10% FeCl₃ solution; however, steels of higher Cr-Mo content were the least pitted and showed the smallest weight losses.

Manuscript submitted Oct. 24, 1974; revised manuscript received Jan. 20, 1975. This was Paper 80 presented at the Miami Beach, Florida, Meeting of the Society, Oct. 8-13, 1972.

Any discussion of this paper will appear in a Discussion Section to be published in the December 1975 JOURNAL. All discussions for the December 1975 Discussion Section should be submitted by Aug. 1, 1975.

Publication costs of this article were partially assisted by the Molybdenum Company of Michigan.

REFERENCES

1. G. P. Chernova and N. D. Tomashov, *Korroziya Metallov i Splavov*, Sb. 2 (Moscow), 7 (1965).
2. C. D. Schwartz, I. D. Franson, and R. J. Hodges, *Chem. Eng.*, **000**, 164 (1970).
3. E. A. Lizlovs and A. P. Bond, *This Journal*, **116**, 574 (1969).
4. E. A. Lizlovs and A. P. Bond, *ibid.*, **118**, 22 (1971).
5. A. P. Bond and E. A. Lizlovs, *Werkstoffe Korrosion*, **21**, 336 (1970).
6. E. A. Lizlovs, *ASTM STP 516*, 201 (1972).
7. N. Pessall and C. Liu, *Electrochim. Acta*, **16**, 1987 (1971).
8. E. A. Lizlovs, *This Journal*, **117**, 1335 (1970).

Effect of Arsenic on the Composition and Optical Constants of Iron Passive Film Reduced at 100% Current Efficiency

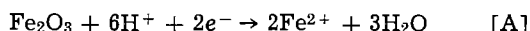
B. Agius* and J. Siejka*

Groupe de Physique des Solides de l'Ecole Normale Supérieure, Tour 23, 11 Quai Saint-Bernard, 75005 Paris, France

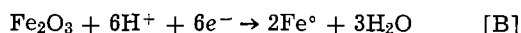
ABSTRACT

Nuclear reaction microanalysis, Rutherford backscattering of 1.8 MeV $^4\text{He}^+$ ions, and ellipsometric techniques have been used to investigate cathodic reduction of iron passivated in O^{18} enriched neutral solutions containing arsenic. Arsenic inhibition allows the reduction to take place at -3°C with 100% current efficiency. Thus reduction of iron from Fe^{3+} to Fe^0 and of hydrogen was completely inhibited. It was found that arsenic could only adsorb if the surface was oxide free. During cathodic reduction, the composition and optical constants of the film remain constant ($n_{\text{ox}}^* = 1.47 - 0.80i$ for a layer with initial thickness of 30Å), but during passivation of the film they vary with the oxidation potential.

The cathodic reduction of iron passivated in a solution of 0.15N sodium borate and 0.15N boric acid is reported to take place following either the mechanism



which associates an electronic charge of $n = 2e/3$ with each oxygen ion passing into the solution, or the mechanism



which yields a value of $n = 2e$. Previous work on this subject has used a wide variety of measurement techniques: coulometry (1), ellipsometry (2, 3), spectrophotometry (1-3), and nuclear microanalysis (4). More specifically, the current efficiency of the cathodic reduction assuming mechanism [A] was measured by Sato and Kudo (2) to be 50% and by Nagayama and Cohen (1) to be 70%. With most methods n can only be deduced from changes of electrical or optical parameters of the oxide film. Nuclear microanalysis of stable oxygen isotopes, permits direct measurement of the quantity of oxygen fixed at the sample surface thus providing direct calculation of the electronic charge n associated with each oxygen atom going into the solution. In a previous work (4) determinations of oxygen loss gave a current efficiency of the cathodic reduction of 48% at 23°C , calculated according to mechanism [A]. The current efficiency varies with the temperature and reaches 64% at -3°C and 35% at 50°C (4). This difference in faradaic yield might be attributed to hydrogen evolution, to the reduction of Fe^{3+} to Fe^0 (1), or to the presence of Fe^{6+} cations (1). All these assumptions are both possible and probable, and they demonstrate the difficulty of delineating passivation phenomena.

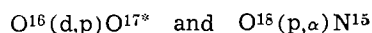
To clear up this problem, we have sought a system in which the cathodic reduction would take place only according to mechanism [A], where 2/3 electronic charge would be associated with each oxygen atom going into solution. In fact, given such a system we can be certain of its stoichiometry (Fe_2O_3), of its structure (compact and homogeneous), and of the absence of any parasitic reaction. Use of ellipsometry together with our method of oxygen analysis would permit determining the optical parameters of the film.

We have therefore worked in this direction, taking account of our previous work at low temperature (4) as well as of Sato's conclusions from his study of corrosion inhibition (5). The present article is the first

in a series of general discussions of passivation; previous articles (6, 7) were devoted to nickel passivation. Here we will deal with iron passivated in a buffered solution of 0.15N sodium borate and 0.15N boric acid in O^{18} enriched water in the presence of 4×10^{-4} M/liter of As_2O_3 and maintained at -3°C . For such a system there is in fact excellent agreement between the theoretical mechanism [A] of cathodic reduction and the experimental results obtained by nuclear microanalysis.

Experimental

Measurement of O^{16} and O^{18} .—The nuclear microanalysis method used for this study is based on the determination of the number of particles resulting from the following nuclear reactions



It yields a number $N_{\text{O}^{16}}$ or $N_{\text{O}^{18}}$ of oxygen atoms per square centimeter fixed on the specimen surface. The general technical principles of this method have been described elsewhere by members of our laboratory (8, 9), and the general principles of its application to various fields are described by Amsel *et al.* (10-12). The number of oxygen atoms coming from the solution, $\hat{N}_{\text{O}^{18}}$, can be obtained by dividing $N_{\text{O}^{18}}$ by the solution enrichment (ratio of O^{18} to the total oxygen in the solution), i.e., by normalizing the results.

Measurement of arsenic.—When a sample is bombarded with charged particles of mass m and energy E_0 , the energy E of the particles backscattered by nuclei of mass M is given, at an angle of 180° , by the Rutherford formula

$$E = E_0 \left(\frac{M - m}{M + m} \right)^2$$

The energy spectrum of the backscattered particles depends on the masses of the nuclei present in the target. This analysis method, described elsewhere (12), is of special interest when traces as low as 1/1000 of a monatomic layer of high-Z elements are observed on a low-Z matrix (13). A 1.8 MeV $^4\text{He}^+$ beam was used in the present experiments to determine the inclusion of arsenic inhibitor in passive films.

Preparation of solutions and specimens.—The specimen used was a pure iron electrode (99.99% pure, obtained from the National Research Corporation) with a surface area of 10×10 mm; an iron wire electrode welded to the specimen provided electrical contact.

* Electrochemical Society Active Member.

Key words: current efficiency, arsenic, inhibitor, iron, O^{18} tracing, cathodic polarization, nuclear microanalysis, ellipsometry.

Polishing and preparation of the specimen surface were the same as described in Ref. (4).

A buffered solution ($\text{pH} = 8.42$) of 0.15N sodium borate and 0.15N boric acid in deaerated water, 10% enriched¹ in O^{18} , was used. Owing to the high cost of the enriched solution, a special small-capacity cell was used, with the volume of the electrolyte being 10 cm^3 . For the inhibitor study, As_2O_3 was added at 4×10^{-4} M/liter. The isotopic exchange of oxygen between BO_3^{3-} , AsO_2^- , and H_2O was found to be fast (14).

All potentials are expressed with respect to the standard hydrogen scale. Most of the experiments were carried out at $-3^\circ \pm 1^\circ\text{C}$.

Ellipsometric measurements.—A commercially manufactured manual ellipsometer measuring angles to within 0.01° was used. The light source was a 250W tungsten lamp with a photomultiplier as the detector. The measurements were made in a dark room to prevent stray light from producing spurious signals in the detector. All ellipsometric measurements were made at 5461\AA , at an angle of incidence $\phi = 70^\circ 54'$, with a quarter-wave plate as compensator. The ellipsometer was aligned with respect to the iron specimen by the procedure described by McCrackin *et al.* (15), and the relative phase retardation (Δ) and relative amplitude reduction ($\tan \psi$) caused by reflection of light from the specimen were determined for the components of the electric vector parallel and normal to the plane of incidence.

All our measurements were made *in situ*, generally on samples passivated in O^{18} enriched solutions. As noted previously, we used a low-volume oxidation cell (10 cm^3) (16). The light beam entered and left through two optically flat glass windows. Measurements on the same specimen, dry inside and outside the cell, gave agreeing results: the cell does not influence the polarization state of the light.

A computer program developed by McCrackin (17) was used to compute values of the real (n) and imaginary ($-ik$) parts of the complex index of refraction n^* of the specimen itself which was assumed to be bare or covered by a film of given thickness grown on its surface.

Experimental procedure.—The experimental procedure is essentially the same as that used previously (4). First the sample was cathodically cleaned, then the ellipsometer was set at its extinction point. Optical parameters of the bare surface were measured. After this cathodic pretreatment the polarization was stopped for 5 min; the potential increased from $\phi_c = -650$ mV to a final value of stabilization of $\phi_{s2} = -510$ mV.

There is a very small change in P and A during this step of sample pretreatment. This change is only observable when the measurement is very sensitive ($\Delta P = \Delta A = 0.03^\circ$). This effect will be discussed further in another article (18) and related to the nuclear method (4).

After the pretreatment (and change in P and A), the anodic films were formed in the same solution by potentiostatic oxidation at $+940$ mV. As with our previous work, we stopped the oxidation at a constant final current ($5 \mu\text{A}/\text{cm}^2$) and at this time remeasured P and A . The film was then reduced cathodically, again in the same solution, at a constant current density of $10 \mu\text{A}/\text{cm}^2$.

Measurements of O^{18} losses were carried out by nuclear microanalysis on a series of six samples; each point of the curve $\hat{N}_{\text{O}^{18}} = f(Q_{\text{mcoulombs}/\text{cm}^2})$ was obtained on a new sample. Two kinds of ellipsometric experiments were made: the first on the same series of samples used to study O^{18} losses and the second on a single sample from the beginning to the final reduction state.

Ferrous ion concentration.—Since each step of our experimental procedure can place a certain number of

ferrous ions in the electrolyte solution, which could conceivably interfere with the measurements of film growth, we have calculated the maximum possible number of ions which might be released by (i) cathodic pretreatment, (ii) the active-passive transition, and (iii) cathodic reduction of the passive film.

(i) **Cathodic pretreatment.**—After electropolishing, the specimen surface was covered by a natural oxide which contains 10^{16} oxygen atoms per square centimeter (4). During cathodic pretreatment, ferrous ions from the reduction of this oxide go into solution. Assuming a Fe_2O_3 oxide, at most 1.3×10^{16} ferrous ions should be found in the solution.

(ii) **Active-passive transition.**—An iron electrode passivated from its initial bare surface condition must pass through the active state. During this transition, some Fe^{2+} ions are released into the electrolyte. Their concentration (upper limit) can be estimated from the charge passed through the circuit during the formation of the passive film at its lower potential, *i.e.*, -260 mV. This charge is equivalent to about 3 mcoulombs, or 1.5 mcoulombs/ cm^2 . This value is of the same order of magnitude (1.8 mcoulombs/ cm^2) as that found by Nagayama and Cohen (1) in the absence of arsenic and at 27°C . This quantity of charge corresponds to the oxidation ($\text{Fe} \rightarrow \text{Fe}^{2+}$) of 10^{16} iron atoms. Thus, at the time the sample is passivated, the concentration of iron ions in the electrolyte is no greater than 3.6×10^{-6} M/liter, *i.e.*, 2.3×10^{16} ions in all.

(iii) **Cathodic reduction.**—During cathodic reduction the number of ferrous ions in the solution will increase if the cathodic reduction takes place according to mechanism [A]. In this case the concentration of the ferrous ions added to the electrolyte for the total reduction of a film passivated at $+940$ mV, is directly proportional to the total charge passed through the circuit. In Fig. 1 the total charge is 4 mcoulombs, equivalent to 2.5×10^{16} Fe^{2+} ions ($\text{Fe}^{3+} \rightarrow \text{Fe}^{2+}$).

The total quantity of ferrous ions placed in solution by all three experimental procedures is at most 4.8×10^{16} atoms, or 7×10^{-6} M/liter. According to the literature (19, 20), the current densities and optical constants of the passive film are not affected by the presence of iron ions in the solution when their concentration does not exceed 5×10^{-5} M/liter. Hence, seven successive oxidation-reduction cycles of passive films formed at $+940$ mV could be performed in the same solution without exceeding a ferrous-ion concentration of 5×10^{-5} M/liter. Moreover, to minimize the possible influence of a deposition of iron oxide resulting from the oxidation of ferrous ions from the solution, some experiments were carried out with the solution being changed after each oxidation-reduction cycle. Essential ellipsometric measurements were performed in these conditions. No difference was detected when the concentration of ferrous ions did not exceed 5×10^{-5} M/liter.

We have also noted that the formation time of the passive film was rather short, 150 sec at $+940$ mV (4) rather than the 3600 sec usual in other studies (1, 2, 19). This minimizes the possible formation of a deposited oxide film.

Finally, we checked the concentration of iron in the solution by observing the decrease in current density during the potentiostatic oxidation of the iron. It is well known (19) that the final current density increases as a function of the iron concentration in the electrolyte.

All these observations permit the conclusion that the possible deposition of an iron oxide film from the oxidation of ions in solution is not important in the present work. Therefore in subsequent experiments the electrolyte was not changed after the cathodic pretreatment. It should be noted that in our apparatus it is very difficult to change the O^{18} -enriched solution without exposing the sample to the atmosphere.

¹ Normalized O^{18} enriched water produced at the Weizmann Institute, Rehovot, Israel. The natural abundance of O^{18} is 0.204%.

Evaluation of the optical parameters from ellipsometric and nuclear microanalysis.—Nuclear microanalysis yields the number N_0 of oxygen atoms per square centimeter fixed on the specimen surface. From N_0 an equivalent geometric thickness L_{nucl} can be deduced if the roughness of the metal-oxide interface and the density of the layer covering the sample surface are known or approximated. Ellipsometry is very sensitive to changes of state [adsorption of quantities equal to or less than a monolayer (21)]; it is nevertheless purely qualitative. From the two measurements ψ and Δ it is not possible to deduce the three physical parameters (the equivalent thickness d , the refraction index n , and the coefficient of adsorption k) characterizing the film which changes the state of the surface of the sample. Clearly, only in the case of a very flat surface, should the variation of the angle of incidence permit the ellipsometry to be self-consistent. Variation in the wavelength would only resolve this problem of quantitativity if n and k were independent of λ which is hardly the case with passive films (22). For homogeneous growth of a film (n and k constant), measurements made at two different thicknesses could make ellipsometry quantitative if one were sure of this homogeneity of the film within a tolerable limit of error.

It seems rather imprudent, particularly in the case of absorbing films, to assume a value for either the refractive index or the absorption coefficient when the study involves thicknesses equivalent to several monolayers which in the study of iron passivity corresponds to something less than 15Å. Furthermore, for a film of well-determined stoichiometry, a change in structure from compact to porous or vice versa involves a variation in optical index [related, for the case $k = 0$, to the density of the film by Clausius Mosotti's equation (23)]. Variation in the index observed by ellipsometry, particularly in the study of thin absorbing films, should be interpreted physically as a change either in stoichiometry or in electron structure of the film studied, or a combination of the two. The association with ellipsometry of another method just as sensitive, but more quantitative, permits resolution for the third unknown quantity. In nuclear microanalysis, if L_{nucl} is known precisely, then the simultaneous use of the two methods would permit choosing the pair n , k which fits the values of d and L_{nucl} . Only under these conditions can the measurements be free of the specific indetermination of ellipsometry (two experimental measurements to determine three unknowns).

Results and Interpretation

Cathodic reduction behavior.— O^{18} content in passive layers formed and reduced in O^{18} labeled solutions containing As_2O_3 .—Figure 1 shows the number of oxygen-18 atoms fixed on the sample surface and the corresponding drop in potential as a function of the charge Q which has passed through the circuit during the cathodic reduction. All these samples were oxidized potentiostatically at +940 mV and then reduced at $I = 10 \mu A/cm^2$ for various times. The oxidation-reduction cycles were run at constant temperatures: +23° and -3°C. Let us notice immediately that this oxidation potential (+940 mV) is higher than the oxidation potential $As^{3+} \rightarrow As^{5+}$ ($\phi = +330$ mV in our solution). Thus we assume that, if there is some incorporation of arsenic into the film during the oxidation of the sample, that arsenic is included as As^{5+} . The solid lines are the curves calculated for the reductive dissolution of ferric oxide at 100% current efficiency according to reactions [A] and [B]. However, for a borate system in the presence of arsenic pentoxide the over-all theoretical slope

$$\left(\frac{\Delta Q_{\text{mcoulombs/cm}^2}}{\Delta \hat{N}_{O^{18}}} \right)$$
 according to the mechanism [A] can vary from 0.66e for pure Fe_2O_3 to 0.8e corresponding to the reduction of the film containing only

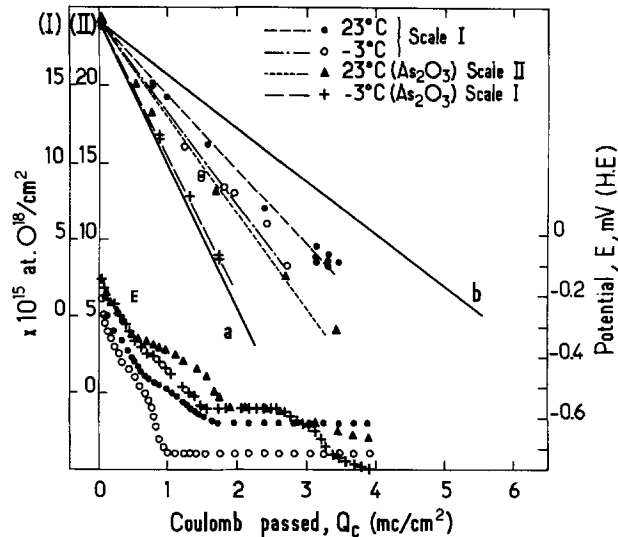
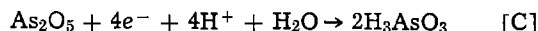


Fig. 1. Change of $\hat{N}_{O^{18}}$ and in potential (E) of iron during galvanostatic cathodic reduction at $10 \mu A/cm^2$ of passive films formed potentiostatically at +940 mV in 0.15N boric-borate buffer solution at pH 8.42, with and without 4×10^{-4} M/liter As_2O_3 .

a, $n = 2/3e$ (theoretical value).

b, $n = 2e$ (theoretical value).

As_2O_5



Experimentally, from the reciprocal of the slope of $\hat{N}_{O^{18}} = f(Q_{\text{mcoulombs/cm}^2})$ we have found $n = 0.70 \pm 0.07e$ for -3°C in presence of arsenic. Thus to determine the stoichiometry of the film we have measured the quantity of arsenic incorporated in the layer.

Determination of the stoichiometry of the passive film.—For incident $^4He^+$ ions at 1.8 MeV, Fig. 2 shows typical backscattering amplitude spectra obtained from iron passivated at +940 mV in the presence or absence of arsenic. The neatly resolved peak at 1.46 MeV confirms the presence of arsenic. Calculations based on the Rutherford formula for elastic scattering cross sections lead to the value of 2×10^{15} arsenic atoms/square centimeter with an accuracy of 10%. As shown on Fig. 1, this film contains 19×10^{15} oxygen atoms/square centimeter. With the quantities of oxygen and arsenic present in the film known, the stoichiometry of this oxide can be calculated. At this passive potential most

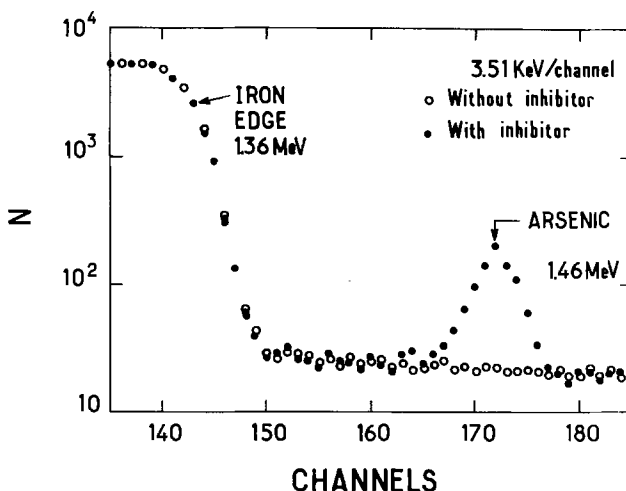


Fig. 2. Backscattering signal amplitude spectra for $^4He^+$ ions at 1.8 MeV obtained on iron passivated at +940 mV in 0.15N boric-borate buffer solution of pH 8.42 with and without 4×10^{-4} M/liter As_2O_3 .

authors agree on the γ -ferric oxide structure. For the compound formed at $\phi = +940$ mV this implies the over-all stoichiometry $(As_2O_5) \cdot (Fe_2O_3)_{4.66}$.

During oxidation, arsenic might become localized at the interface between the passive film and the solution, be distributed in the passive film, or be placed at the metal-oxide interface. Figure 3 shows the arsenic loss during cathodic reduction of the film as a function of time, i.e., as a function of the number of O^{18} atoms. This indicates that all arsenic atoms fixed during the oxidation of the film are embedded in the bulk of the oxide and, in particular, the arsenic resulting from the oxidation can be assumed to be distributed homogeneously in the film rather than being accumulated at the metal-passive film interface.

Let us now calculate the elementary charge associated with each oxygen atom going into solution during reduction of the system $(As_2O_5) \cdot (Fe_2O_3)_{4.66}$. We have shown that for each arsenic atom there are nine oxygen atoms present in the oxide. But, according to mechanism [C], 0.8 elementary charge is associated with each oxygen atom going into solution from the As_2O_5 reduction. On the other hand, 0.66 electronic charge is required for each oxygen atom from the Fe_2O_3 reduction. The average total charge associated with each oxygen atom going into solution would be

$$\frac{0.8 \times 5 + 0.66 \times 14}{19} = 0.7 \text{ electronic charge}$$

This is represented by curve "A" on Figures 4, 5, and 6a.

This theoretical value, available only after a determination of the arsenic in the film, agrees very well with the experimental value. We therefore conclude that the cathodic reduction of iron passivated in neutral solution containing 5×10^{-4} M/liter of arsenic and maintained at -3°C proceeds at a current efficiency of 100%, according to mechanism [A].

Equivalent film thickness L_{nucl} .—The thickness equivalent to the number of oxygen atoms has been calculated as a function of the charge Q passed during the cathodic reduction. The density of the passive film, whose stoichiometry has been determined [$(As_2O_5) \cdot (Fe_2O_3)_{4.66}$], the roughness coefficient of the metal-oxide interface, and its structure (which is compact, as we shall show later) must be known. We assume for

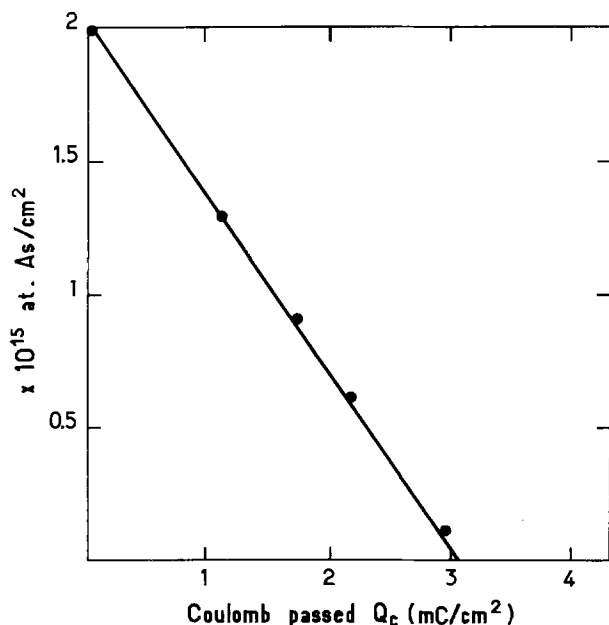


Fig. 3. Change of arsenic content during galvanostatic cathodic reduction at $10 \mu\text{A}/\text{cm}^2$ for the passive films formed potentiostatically at -3°C and $+940$ mV in $0.15N$ boric-borate buffer solution of pH 8.42 containing 4×10^{-4} M/liter As_2O_3 as inhibitor.

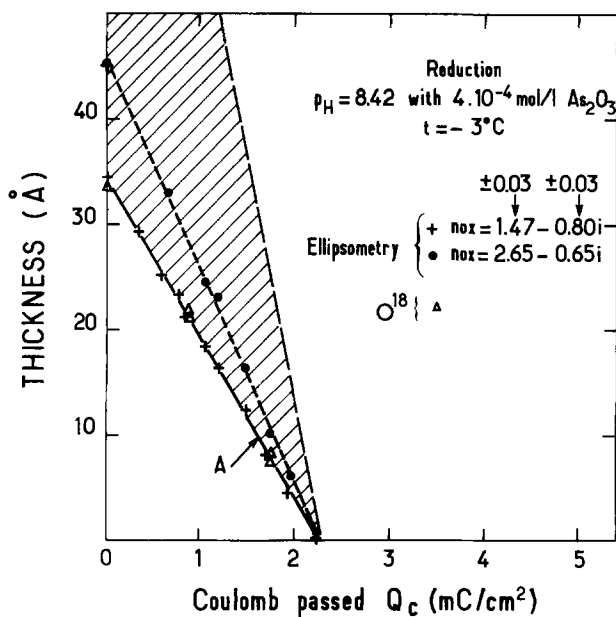


Fig. 4. Shaded zone, film thicknesses calculated from ellipsometric data obtained during galvanostatic cathodic reduction assuming the optical constant of the oxide ($n_{ox} - k_{ox}$) to be in the ranges 1-3.5 and 0-1, respectively. Film formation and reduction conditions are the same as for Fig. 3. A, theoretical curve calculated for reduction of $(Fe_2O_3)_{4.66} \cdot As_2O_5$ with 100% current efficiency, $n = 0.7e$.

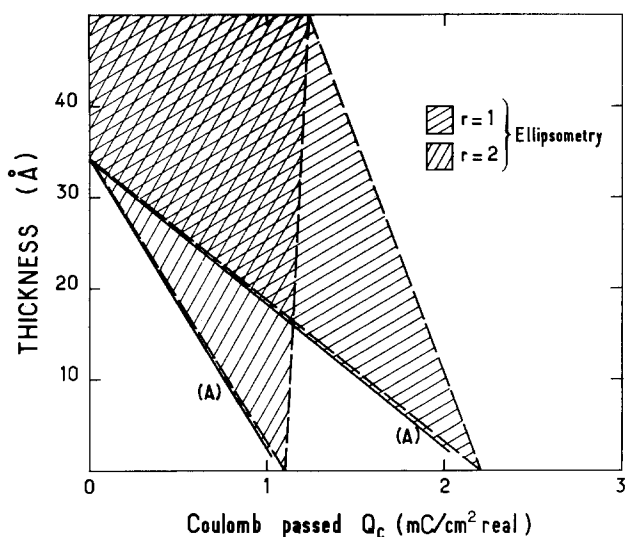


Fig. 5. Effect of the roughness factor (r) on the ellipsometric data from Fig. 4.

the sake of the calculation that the density of the passive film follows a simple additive law and that the densities are $5.24 \text{ g}/\text{cm}^3$ for Fe_2O_3 and $4.32 \text{ g}/\text{cm}^3$ for As_2O_5 (24). The result is a density $\rho = 5.0 \text{ g}/\text{cm}^3$. For this density, the thickness of a layer containing 10^{15} oxygen atoms/ cm^2 is equivalent to 1.7Å . It is clear that, whatever the roughness value of the sample being studied, the slope giving the elementary charge associated with each oxygen atom going into solution is always $n = 0.7e$. This is important for understanding what follows.

Determination of the optical constant of pure iron.—In ellipsometric determination of surface films, the bare metal surface is used as optical reference. The iron sample is given cathodic pretreatment before being anodized. We showed previously (4) that our specimen under cathodic polarization was free of oxygen coming from the solution. We thus assume that the cathodically cleaned sample is free of any oxygen, and the optical constants of the bare iron sample are

Table I. Comparison of the optical constants n and k of iron obtained in the present study with values in the literature ($\lambda = 5461\text{\AA}$)

	n	k
MacBee and Kruger (1969) (22)	3.35	3.84
Sato and Kudo (1971) (2)	3.18	3.85
Bockris et al. (1971) (23)	3.24 ± 0.16	3.98 ± 0.28
Present work	3.30 ± 0.2	3.70 ± 0.2

measured in terms of Δ and ψ . From the measured values of Δ and ψ we calculated the refractive index n^*_s of iron applying the theory to film free surfaces. The result is

$$n^*_s = n_s - ik_s = (3.3 \pm 0.2) - (3.7 \pm 0.2)i$$

the mean of 20 measurements. Owing to spread among the samples, the measurements vary within 5% for both n and k . As shown in Table I, our values are fairly close to the complex refractive index for iron reported in the literature.

Estimation of the film parameters from ellipsometric results.—Determination of the film parameters.—For each pair of experimentally measured values P and A , we can calculate many different values of the refractive index and thickness of the passive film, provided that the refractive indexes of the iron substrate ($n_s = 3.30-3.70i$) and solution ($n = 1.332$) are known.

Following a customarily used procedure, we calculate the thickness and the optical constants

$$n^*_{ox} = n_{ox} - ik_{ox}$$

of the film assuming n_{ox} to be in the range 1-3.5 and k_{ox} in the range 0-1. For a given pair of experimental values P and A , calculation produces a number of values of n^*_{ox} and d , all of which fit the measured P and A within a given error limit (0.05°). It should be emphasized that the sensitivity of our measurements corresponds to uncertainties of 0.03° for P and A , which induce errors of 0.008 for n and 0.004 for k . Besides, the variation among samples would produce a deviation no greater than 0.03 of n and k . Therefore all points whose optical constants differ by less than 0.06 would represent a homogeneous growth of the film. All optical-constant values given hereafter are understood to be subject to these error limits.

We have represented all our ellipsometric results in the shaded zone of Fig. 4. From among the wide range of possible solutions, we have shown in the figure the variation in thickness corresponding to an optical in-

dex close to that generally used in the literature² for pure compact Fe_2O_3 : $n^*_{ox} = 2.65 - 0.65i$. These results have been drawn as functions of the number of coulombs per unit of apparent surface (i.e., for $r = 1$). The results for $r = 2$ are also shown (Fig. 5), considering the assumptions generally accepted in the literature (3, 25) of the independence of the ellipsometric parameters ψ and Δ with respect to roughness. This is discussed in the next section.

Note that the roughness variation alters the slopes of the various curves $d = f(Q_{\text{mcoulombs/cm}^2})$. To characterize the reduction of the passive film and understand its mechanism we must know at least one other magnitude characterizing this film, for example, its thickness.

Ellipsometric results with a known film thickness.—

We have transformed the number of oxygen-18 atoms, directly measured, into equivalent nuclear thickness (see Fig. 1). This is not possible except when the stoichiometry of the film is known [$(\text{Fe}_2\text{O}_3)_{4.66}(\text{As}_2\text{O}_5)$]. We have simply assumed a roughness factor of 1 for the initial calculation. In thus combining the ellipsometric and nuclear studies, we can then choose among all the possible ellipsometric solutions whose pairs n_{ox} and k_{ox} give the same thickness as equivalent nuclear thickness. We have thus obtained the following values of n^*_{ox} for the optical constant of this film

$$n^*_{ox} = (1.47 \pm 0.03) - (0.80 \pm 0.03)i \quad [1]$$

This differs from the value generally given for the ferrous oxide $\gamma\text{-Fe}_2\text{O}_3$ ($n^*_{ox} = 2.55 - 0.4i$). To explain this low value of the index of refraction, we can consider two hypotheses. The first involves the formation of a deposited film; the second, the presence of arsenic in the passive film. Using an ellipsometric method, Ord and De Smet (20) studied deposited films of iron oxide on different substrates and found a real refractive index of 1.7 at a wavelength of 6328 \AA and an angle of incidence of 60° . To avoid the formation of such a deposited film, we chose experimental conditions: 3.6×10^{-6} M/liter (see experimental procedure). The first hypothesis can therefore be discarded. One might then imagine that the presence of arsenic inside the film could influence this optical constant. This will be discussed later, but meanwhile let us study the effect of roughness on the optical index of the film. Figure 6a summarizes the preceding discussion of

² $\gamma\text{-Fe}_2\text{O}_3$: $n_{ox} = 2.55-0.4i$.

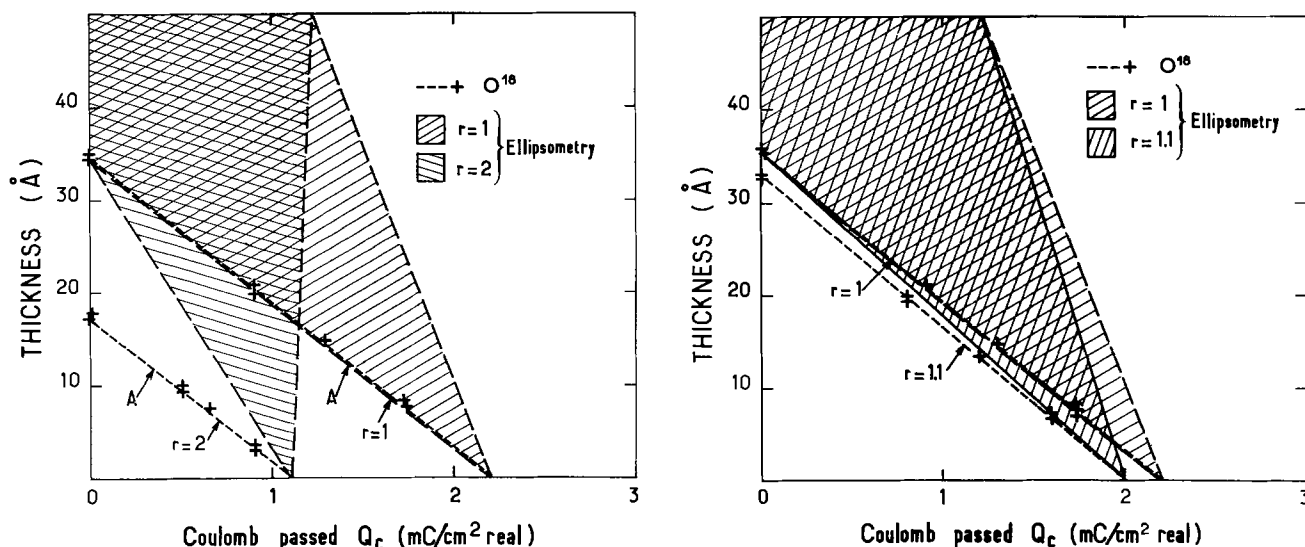


Fig. 6. Effect of the roughness factor (r) on the nuclear and ellipsometric data obtained under conditions described for Fig. 3. Ellipsometric data from Fig. 4 and nuclear data from Fig. 1.

(a, left) Calculations for $r = 1$ and $r = 2$.

(b, right) Calculations for $r = 1$ and $r = 1.1$.

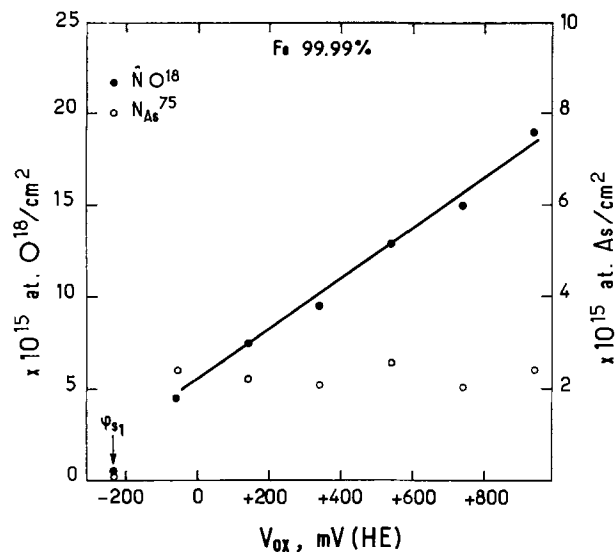


Fig. 7. Quantities of oxygen and arsenic atoms fixed on iron oxidized potentiostatically ($i_{\text{final}} = 5 \mu\text{A}/\text{cm}^2$) as a function of potential. Solution the same as for Fig. 3.

the influence of the roughness factor on all the nuclear and ellipsometric data. Let us recall that the slope of the reduction curve $\hat{N}O^{18} = f(Q)$ (Fig. 1), which gives the value of the elementary charge associated with each oxygen atom going into solution, was independent of the roughness coefficient. Thus, if Δ and ψ are supposed to be independent of roughness (3, 25), clearly the optical and nuclear-thickness data are inconsistent for all values of τ , except for a roughness of 1. This inconsistency is marked for a roughness of 2 (Fig. 6a) but exists all the same for a roughness $\tau = 1.1$ very close to the ideal surface (Fig. 6b). So the fact that there is inconsistency (except for $\tau = 1$) between optical and nuclear thickness seems to indicate that Δ and ψ vary with roughness. How could this happen? For the moment a precise answer would be difficult. However, if their variation is linear, as in coulometry, which appears to be plausible, then nothing would be changed in our deductions, since the opti-

cal thickness would diminish in the same proportion as τ would increase. We are currently trying to verify this by studying the influence of the incident angle ϕ on such a system, ϕ being the only parameter capable of carrying this information.

If ellipsometry does depend on roughness but differently than coulometry does, the presence of arsenic would still influence the value of the optical index. The curves obtained for $n^*_{\text{ox}} (\gamma\text{-Fe}_2\text{O}_3) = 2.55 - 0.4i$ never coincide with the theoretical curve A assuming the cathodic reduction mechanism of the $(\text{As}_2\text{O}_5) \cdot (\text{Fe}_2\text{O}_3)_{4.66}$ system with a current efficiency of 100%. At the worst, if ellipsometry does not vary with roughness as coulometry does, it would mean a slight variation of n_{ox} around $n^*_{\text{ox}} = 1.47 - 0.80i$. In what follows, as a working assumption, we assume that $\tau = 1$.

We previously hypothesized that the presence of arsenic in the passive film might explain the value which was suggested for its optical index and which is small compared to that generally accepted for a pure stoichiometric film of Fe_2O_3 . To verify this hypothesis, we have studied the passive film prepared in the same solution but by another procedure, namely, at different oxidation potentials.

Anodic oxidation.—After the cathodic pretreatment the iron surface was oxidized potentiostatically as previously described above. Figure 7 shows the number of oxygen-18 atoms fixed on the sample surface as a function of the potential and the corresponding arsenic content of the passive films. Note that the quantity of arsenic is constant whatever the thickness of the film considered. This means that the stoichiometry of the film varies from $(\text{As}_2\text{O}_5) \cdot (\text{Fe}_2\text{O}_3)_{4.66}$ for $\phi = +940$ mV to $(\text{As}_2\text{O}_5) \cdot (\text{Fe}_2\text{O}_3)$ at $+140$ mV. However, even though the stoichiometry varies with potential, the thickness equivalent to the number of oxygen atoms is always 1.7\AA per 10^{15} atoms of measured oxygen-18, no matter what oxidation potential is used, assuming the additivity of densities (see above). We have thus translated the preceding results into equivalent nuclear thickness and have also shown (Fig. 8a, b) on the same figure the ellipsometric measurements made under the same conditions. Among the ellipsometric thicknesses possible, the one which would agree with the equivalent nuclear thickness would have for its index (Fig. 8b)

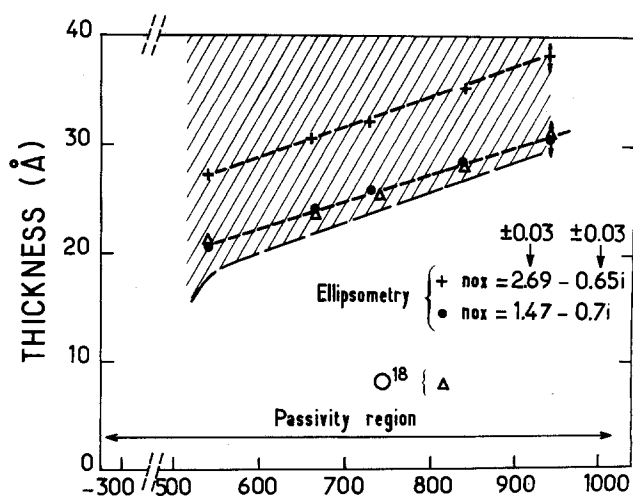
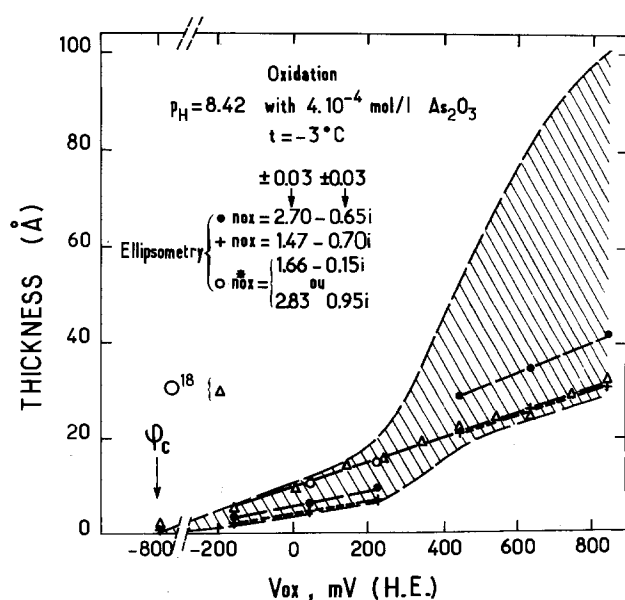


Fig. 8. Δ , Equivalent nuclear thicknesses of passive films deduced from O^{18} and As contents; shaded zone, film thicknesses calculated from the ellipsometric data obtained during passive film formation with the optical constant n_{ox} and k_{ox} assumed to be in the ranges 1-3.5 and 0-1. Solution the same as for Fig. 3.

(a, left) For the whole passive region.

(b, right) Between $+550$ mV and $+950$ mV/S.H.E.

$$n^*_{\text{ox}} = (1.47 \pm 0.03) - (0.7 \pm 0.03)i$$

and this in a potential region between + 550 and + 950 mV/HE, that is, for thicknesses greater than 20Å. For "nuclear thicknesses" thinner than 20Å, there is no agreement between these thicknesses and the ellipsometric thicknesses chosen for the same index. This could be explained by a structural change directly related to a variation in optical index of the film. However, taking the nuclear measurements as references independent of the applied passivation potential, the ellipsometric thickness agrees with the nuclear thickness for the indexes whose values are

$$n^*_{\text{ox}} = 1.66 - 0.15i$$

or

$$n^*_{\text{ox}} = 2.83 - 0.95i$$

rather than

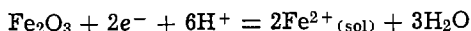
$$n^*_{\text{ox}} = 1.47 - 0.70i$$

for thicknesses greater than 20Å.

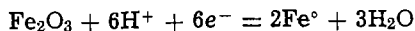
The second value of the index should not be accepted, for if the variation of n^* is related to the presence of arsenic in the film, this increase would mean a diminution of the quantity of arsenic with the thickness of the passive film. But we have seen that there is nothing of the sort. In contrast, if $n^*_{\text{ox}} = 1.66 - 0.15i$ effectively defines the optical properties of the film for thicknesses less than 20Å, this would mean that for these thicknesses the conductivity is much lower, that is, that the structure of the layer is not yet perfect and that only for films thicker than 20Å will it tend towards a spinel structure and be a good conductor ($k = 0.7$).

Discussion

Mechanism of cathodic reduction.—From previous and present results, it is now possible to establish in detail the mechanism of the cathodic reduction of a passive film formed on iron in a sodium borate-boric acid solution of pH 8.42 containing 4×10^{-4} M/liter arsenic trioxide as inhibitor and maintained at about -3°C . Detailed study of the cathodic reduction was made for the film $(\text{As}_2\text{O}_5) \cdot (\text{Fe}_2\text{O}_3)_{4.66}$ but the resulting conclusions can reasonably be considered as possible to generalize to any stoichiometry. Thus, in these experimental conditions the reductive dissolution of the film takes place at 100% current efficiency, following the mechanism corresponding to iron reduction



This would then (in the presence of arsenic) exclude the possibility that iron would return to its metallic state



and also excludes the possibility that protons would be transformed into H^0 by capturing an electron from the metal.

During the passive-film reduction, the reduction of protons is blocked either at the oxide-solution interface or at the metal-oxide interface if hydrogen is transported across the passive film. The fact that arsenic inhibits the entry of hydrogen has recently been observed by McCright and Staehle (26). None of these conclusions contradicts the curve of potential variation which shows a plateau at -510 mV corresponding to the electrochemical reaction mechanism [A]. After the reduction of Fe_2O_3 is complete, a potential characteristic of hydrogen evolution on iron (a second plateau) is reached which can be expected at about -750 mV at the pH used.

In addition, the fact that the faradaic yield of cathodic reduction equals 100% means that the number of coulombs of current passed during the cathodic reduction is exactly equal to the theoretical quantity required for the production of Fe^{2+} from Fe_2O_3 . If there had been an excess difference between experimental and theoretical charges, that difference would be at-

tributed to the presence of some cation-vacant (high-iron-valence) oxide. This is not the case, which contradicts the findings of Nagayama and Cohen (1)—under admittedly different experimental conditions, particularly the absence of arsenic—who proposed a different mechanism for the reduction of Fe_2O_3 formed in neutral sodium borate-boric acid solutions.

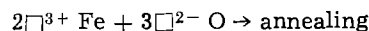
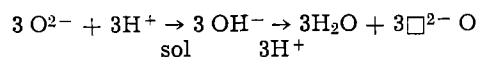
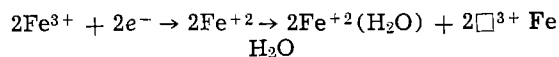
Finally, while it is not possible by direct passivation to obtain homogeneous layers of 5-20Å, it is possible, by cathodic reduction starting with a thickness of 40Å, to attain these homogeneous layers by step dissolutions of 5Å.

The data in the literature (27) permits us to consider that the iron oxide constituent of the passive film formed at high potential (+ 940 mV) has a γ -ferric oxide structure, i.e., a structure formed by a rearrangement of oxygen and iron ions in which the oxygen forms a face-centered cubic lattice with iron atoms fitted into octahedral and tetrahedral sites. What place has arsenic in such a structure? We have determined the presence of one atom of arsenic per six atoms of iron and nine of oxygen at $\phi = +940$ mV, but in the spinel structure there is one free octahedral position for each oxygen atom. Thus, for nine oxygen atoms there are nine octahedral spaces available, and these would be occupied by six iron atoms and one arsenic. In the spinel structure arsenic atoms could occupy the free substitution positions that exist, and without deforming the structure, since the ionic radii of Fe^{3+} ($R = 0.64\text{\AA}$), As^{3+} ($R = 0.58\text{\AA}$), and As^{5+} ($R = 0.46\text{\AA}$) are close enough to one another. Note that the order of magnitude of the ionic radii of As^{3+} and As^{5+} make it unlikely that these cations take tetrahedral positions, since this requires radii of 0.22-0.41Å, smaller than the ionic radii corresponding to the two possible arsenic valences.

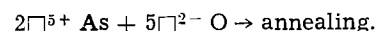
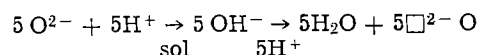
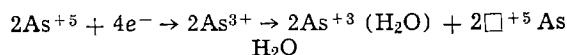
In which oxidizing form should the arsenic be found? If we recall that the cation in the octahedral position should have an ionic radius between 0.41 and 0.73Å, both oxidizing forms are allowed. To differentiate between them, we must take account of the potential of the reaction $\text{As}^{3+} \rightarrow \text{As}^{5+}$ which is 580 mV at pH zero and becomes 330 mV/HE under our experimental conditions. This means, then, that arsenic incorporated in the form As^{3+} is immediately oxidized to As^{5+} and takes an octahedral position inside the Fe_2O_3 structure which we already suggested in determining the average charge associated with each oxygen atom in the system $(\text{As}_2\text{O}_5) \cdot (\text{Fe}_2\text{O}_3)_{4.66}$ cathodically reduced.

What is the microscopic role of arsenic? It should be observed that the adsorption of arsenic takes place on a metal devoid of oxide and solely on such a metal, and otherwise that even in the presence of arsenic when the temperature is increased, the faradaic yield on cathodic reduction diminishes though arsenic has an inhibiting effect. This will be discussed further in another article.

We can now propose a cathodic reduction mechanism by which γ - Fe_2O_3 may be reduced to form a cation vacancy (\square) structure which is still in the cubic system by the reactions



Whereas for arsenic it is possible to envisage the following reduction mechanism



Acknowledgments

The authors wish to thank Dr. G. Amsel for his numerous comments and suggestions during this work. The technical assistance of Messrs E. Girard, A. Laurient, and J. Moulin was much appreciated. This work was supported by the Centre National de la Recherche Scientifique (RCP No. 157), the DRME, and the DGRST.

Manuscript submitted Oct. 23, 1974; revised manuscript received Feb. 7, 1975.

Any discussion of this paper will appear in a Discussion Section to be published in the December 1975 JOURNAL. All discussions for the December 1975 Discussion Section should be submitted by Aug. 1, 1975.

Publication costs of this article were partially assisted by Groupe de Physique des Solides de l'Ecole Normale Supérieure.

REFERENCES

- M. Nagayama and M. Cohen, *This Journal*, **109**, 781 (1962); **110**, 670 (1963).
- N. Sato and K. Kudo *Electrochim. Acta*, **16**, 447 (1971).
- N. Sato and T. Noda, 5th European Corrosion Congress, Paris, September 1974.
- B. Agius and J. Siejka, *This Journal*, **120**, 1019 (1973).
- N. Sato, K. Kudo, and T. Noda, 3rd Intern. Congr. Metallic Corrosion, Cambridge, England, July 1970.
- J. Siejka, C. Cherki, and J. Yahalom, *Electrochim. Acta*, **17**, 2371 (1972).
- J. Siejka, C. Cherki, and J. Yahalom, *This Journal*, **119**, 991 (1972).
- G. Amsel and D. Samuel, *Anal. Chem.*, **39**, 1689 (1967).
- G. Amsel, J. P. Nadai, E. D'Artemare, D. David, E. Girard, and J. Moulin, *Nucl. Instr. Methods*, **92**, 481 (1971).
- G. Amsel, in "Physics of Electrolytes," Vol. 1, J. Hladik, Editor, p. 127, Academic Press, London (1972).
- F. Abel, G. Amsel, E. D'Artemare, M. Bruneaux, C. Cohen, B. Maurel, C. Ortega, S. Rigo, J. Siejka, M. Croset, and D. Dieumegard, *J. Radioanal. Chem.*, **16**, 567 (1973).
- W. K. Chu, J. W. Mayer, M. A. Nicolet, T. M. Buck, G. Amsel, and F. Eisen, *Thin Solid Films*, **17**, 1 (1973).
- F. Abel, G. Amsel, M. Bruneaux, C. Cohen, B. Maurel, S. Rigo, and J. Roussel, *J. Radioanal. Chem.*, **16**, 587 (1973).
- D. Samuel, Private communication.
- F. L. McCrackin, E. Passaglia, R. R. Stromberg, and K. L. Steinberg, *J. Res. Natl. Bur. Std.*, **67A**, 363 (1963).
- B. Agius and J. Moulin, In publication.
- F. L. McCrackin, *Natl. Bur. Std. Tech. Note* 479 (1969).
- B. Agius and J. Siejka, To be published.
- V. Markovac and M. Cohen, *This Journal*, **114**, 674 (1967); **114**, 678 (1967).
- J. L. Ord and D. J. De Smet, *ibid.*, **118**, 206 (1971).
- A. J. Melmed and J. J. Carroll, *J. Vacuum Sci. Technol.*, **10**, 164 (1973).
- C. L. McBee and J. Kruger, *Surface Sci.*, **16**, 340 (1969).
- J. O'M. Bockris, M. A. Genshaw, V. Brusica, and H. Wroblowa, *Electrochim. Acta*, **16**, 1859 (1971).
- "Handbook of Chemistry and Physics", 48th ed., pp. 155-185, Chemical Rubber Publishing Co., Cleveland, Ohio (1967-1968).
- J. Kruger and J. P. Calvert, *This Journal*, **114**, 43 (1967).
- R. D. McCright and R. W. Staehle, *ibid.*, **121**, 609 (1974).
- C. L. Foley, J. Kruger, and C. J. Bechtoldt, *ibid.*, **114**, 994 (1967).

A Study of the Anodization of Niobium Using the Method of Open-Circuit Transients in Aqueous and Nonaqueous Solutions

C. M. Daly and R. G. Keil*

Department of Chemistry, University of Dayton, Dayton, Ohio 45469

ABSTRACT

The anodic oxidation of niobium in glacial acetic acid-sodium tetraborate solution and in aqueous boric acid-sodium tetraborate solution has been studied over a potential range of 74V using the open-circuit transient analysis technique. The results indicate that the relationship between the formation current density, i , and the formation potential, V , is of the form $i = i_0 \exp(V/V_0)$ where i_0 and V_0 are parameters resulting from data analysis. V_0 was found to be a linear function of the formation voltage. The quantity, θ , was found to be essentially equal to zero, a result which agrees with results previously reported for vanadium and molybdenum. Attempts were made to correlate the results with film structure.

It is known that the analytical chemistry of niobium in aqueous solutions is complicated by the tendency of niobium(V) to hydrolyze and by the instability of the lower oxidation states of the element (1). Previous studies (2-4) have shown that anodic oxide films may be grown successfully on valve metals if a nonaqueous solution is employed. The intention of the present study was to utilize the open-circuit transient method

in a comparative study to determine the electrical properties of niobium oxide films in aqueous and nonaqueous solutions.

In an earlier work on niobium, Young (5) determined certain electrical properties of the niobium oxide by specular reflectivity studies. In that work he concluded that the evidence is consistent with a uniform film apart from the preexisting film. In 1960, Young (6) also reported experimental results on the oxidation of tantalum which showed that the relation between $\ln i$ and E was not linear and that a better fit

* Electrochemical Society Active Member.

Key words: anodic oxidation, niobium, transients, aqueous, nonaqueous.

of the data could be obtained by replacing the term qaE by $a(\alpha - \beta E)E$. This result was confirmed by the results of Young and Zobel (7) who, in addition, showed the necessity for including the nonlinear term in the fit of data for niobium oxide.

Recently, using *in situ* ellipsometric measurements on niobium, tantalum, and tungsten, Ord *et al.* (8) have found that the thicknesses of all three metals were found to increase linearly with the electric field. They also showed that the inclusion of the linear dependence of the dielectric constant upon the field into an effective model of the ionic conduction process to be a possible explanation of the curvature in the plot of $\ln i$ vs. E for the anodic oxidation process. These results have been disputed, more recently, by Cornish and Young (9) who in an ellipsometric study of tantalum found that anodic tantalum oxide films are optically isotropic and homogeneous in the absence of an applied field and that the dependence of both the index and thickness upon the field is quadratic.

To date, several theories (6, 10-14) and methods of study of anodic oxidation have been proposed. Open-circuit transient analysis has been used in the study of the anodic oxidation of several metals (3, 14-17). Its use in the study of the anodic niobium oxide film under these conditions and comparison with previous results (6-9) may help establish the nature of the anodic niobium oxide film and the general mechanism of film growth.

Experimental

Anodizations were performed (i) in a glacial acetic acid solution 2.0M in water and 0.02M in sodium tetraborate and (ii) in an aqueous solution 0.1M in H_3BO_3 and 0.018M in sodium tetraborate. High-purity (99.99%) niobium rods, 0.314 cm^2 in surface area purchased from Materials Research Corporation were used for this work. The electrode was mounted and prepared for anodization by methods previously described (2). Film growth was accomplished both potentiostatically and galvanostatically. The acetic acid-borax-water solution had a conductivity of 79 micro-(ohm-cm) $^{-1}$. These studies were all performed at 25°C. An inert ambient of nitrogen was maintained in the reaction flask and the anodizing solutions were degassed prior to use.

Under galvanostatic conditions current densities not less than 15.9 $\mu A/cm^2$ were used. For the open-circuit transient studies a pair of Philbrick SP102 operational amplifiers were used for galvanostat and voltage follower. The potentials and open-circuit transients were recorded on an oscillographic recorder (Sanborn 7701 B). All potentials were recorded relative to the saturated calomel reference electrode. Overpotentials were calculated from observed voltages by subtracting the value of the open-circuit potential. Apparent current densities were obtained by dividing the applied current by the macroscopic surface area of the niobium anode.

Results

The oxide film on the niobium surface may be considered to be equivalent to a capacitor with a dielectric medium located between the capacitor plates (substrate metal and anodizing solution). The differential equation describing this circuit is given by

$$i + C \frac{dV}{dt} = i_e \quad [1]$$

where i is the current density through the film, i_e is the externally applied current density, V is the overpotential, and C is the capacitance per unit area of film.

For niobium, the experimental voltage transients fit an expression of the form

$$V = k - V_0 \ln(t + \theta) \quad [2]$$

Here V_0 , k , and θ are parameters which depend on the particular transient and its initial conditions. It follows, by differentiating Eq. [2] and substituting into

Eq. [1], with $i_e = 0$, that the expression for the current density through the film becomes

$$i = i_0 \exp(V/V_0) \quad [3]$$

This expression includes certain assumptions which have been discussed previously (3). For niobium, the voltage-time transients fit an equation of the form of Eq. [2]. Analysis of the voltage-time transients were performed with the aid of a UNIVAC series 70/7 digital computer. The computer was fed voltage vs. time data in increments no larger than one-hundredth volt. The following functions were then performed (i) the computer chose from a large selection the value of θ which produced a minimum standard deviation of all data points when the data were subjected to a linear least squares analysis, and (ii) a print-out of the values k , θ , V_0 , and standard deviation was obtained. The parameter i_0 is equivalent to

$$i_0 = C V_0 \exp(-k/V_0) \quad [4]$$

An equation of this form is the mathematical consequence of the differential equation describing the system and the experimental voltage-time profile. Here i_0 and V_0 are experimentally determined parameters whose dimensions are the same as i and V , respectively. If time zero equals the commencement of the transient, the transients fit Eq. [2] for times corresponding to 80% of the potential decay at a current density of 159 $\mu A/cm^2$ and 60% of the potential decay at 79.5 and 15.9 $\mu A/cm^2$. Figures 1 and 2 show the relationship between the parameter V_0 and the formation potential in aqueous and acetic acid solutions, respectively. For a given formation current density V_0 is a linear function of the formation potential and all lines nearly pass through the origin. The slope of each line is obviously a function of the formation current density and decreases with increasing current density.

From data analysis, we learned that the value of θ required to fit the transient data to Eq. [2] is quite small, with values ranging from essentially zero to 0.05. Small values are not unexpected because of the relatively large initial formation current densities and

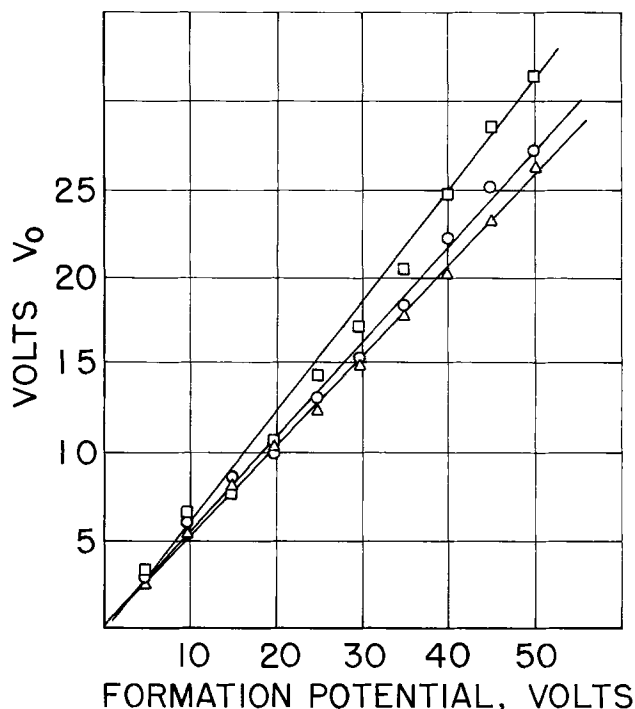


Fig. 1. Dependence of V_0 on formation potential for niobium in boric acid-borax-water solution. The formation current density was 15.9 $\mu A/cm^2$ for the data represented by \square , 79.5 $\mu A/cm^2$ for the data represented by \circ , and 159 $\mu A/cm^2$ for the data represented by \triangle .

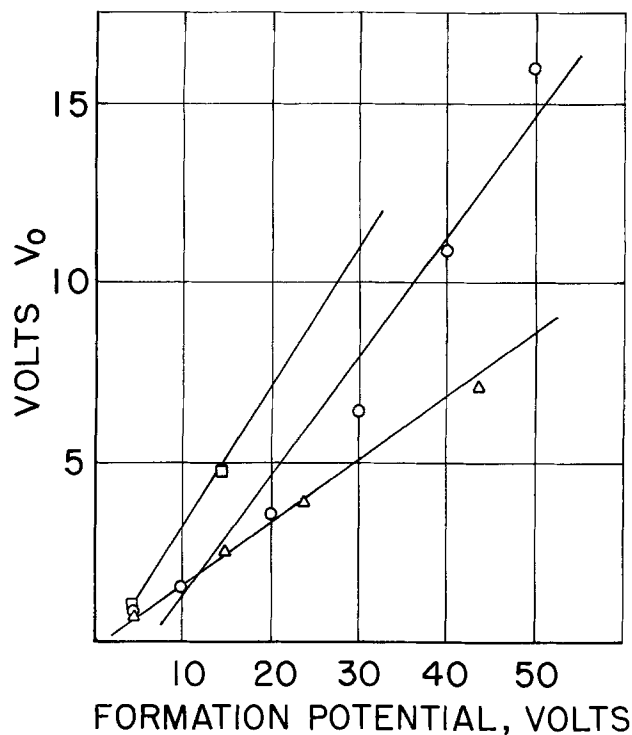


Fig. 2. Dependence of V_0 on formation potential for niobium in acetic acid-borax-water solution. The formation current density was $15.9 \mu\text{A}/\text{cm}^2$ for the data represented by \square , $79.5 \mu\text{A}/\text{cm}^2$ for the data represented by \circ , and $159 \mu\text{A}/\text{cm}^2$ for the data represented by \triangle .

$\theta = C V_0 / i_0$. A typical value in both aqueous and non-aqueous anodizing solutions at $159 \mu\text{A}/\text{cm}^2$ is 0.001. Generally, θ increased both with increasing current densities and formation potentials of the film. Tables I and II show the relationship between the reciprocal capacitance and the formation potential. The reciprocal capacitance is related to θ by the equation $1/C = V_0 / i_0 \theta$. Evidence of the variation of reciprocal capacitance with V_0 and θ can be demonstrated by Tables I and II and also by Fig. 3 and 4. It will be noted that at high current density ($159 \mu\text{A}/\text{cm}^2$) a linear relationship is definitely established. The apparent shifts in slopes as shown in Table I and Fig. 3 indicate that the initial film on the niobium is chemically different from the anodic film. A similar conclusion was drawn by

Table I. Relationship between reciprocal capacitance and formation potentials in $0.1M \text{H}_3\text{BO}_3$ -borax- H_2O anodizing solution

V_f (V)	C.D. ($\mu\text{A}/\text{cm}^2$)	θ	$1/C$ ($\mu\text{F}^{-1} \text{cm}^2$)
15	15.9	0.06	1.65
15	79.5	0.001	21.55
15	159.0	0.001	10.29
30	15.9	0.059	3.69
30	79.5	0.001	38.57
30	159.0	0.001	18.86
45	15.9	0.082	4.38
45	79.5	0.001	63.19
45	159.0	0.001	29.34

Table II. Relationship between reciprocal capacitance and formation potentials in HOAc-borax- H_2O solution

V_f (V)	C.D. ($\mu\text{A}/\text{cm}^2$)	θ	$1/C$ ($\mu\text{F}^{-1} \text{cm}^2$)
15	15.9	0.044	1.92
15	79.5	0.008	2.95
15	159.0	0.001	12.15
30	79.5	0.016	3.85
30	159.0	0.001	25.19
45	79.5	0.026	5.07
45	159.0	0.001	35.36

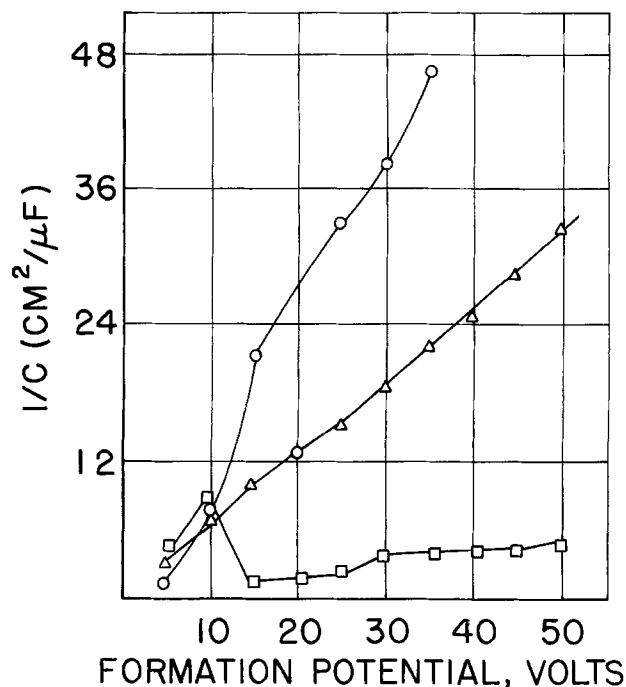


Fig. 3. Dependence of the reciprocal capacitance on formation potential in boric acid-borax-water solution. The formation current density was $15.9 \mu\text{A}/\text{cm}^2$ for the data represented by \square , $79.5 \mu\text{A}/\text{cm}^2$ for the data represented by \circ , and $159 \mu\text{A}/\text{cm}^2$ for the data represented by \triangle .

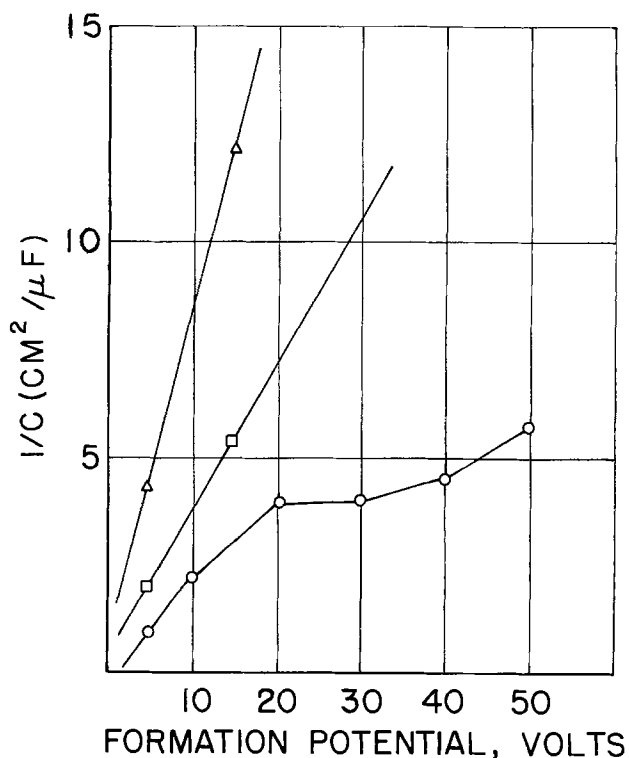


Fig. 4. Dependence of the reciprocal capacitance on formation potential in acetic acid-borax-water solution. The formation current density was $15.9 \mu\text{A}/\text{cm}^2$ for the data represented by \square , $79.5 \mu\text{A}/\text{cm}^2$ for the data represented by \circ , and $159 \mu\text{A}/\text{cm}^2$ for the data represented by \triangle .

Young (18) in explaining the shift in intercept for his work on tantalum, a metal quite similar to niobium.

Discussion

An exponential dependence of the current density through the oxide film on the overpotential can be interpreted in terms of an activation-energy-controlled process (18). The theoretical description for such a

process, in the high-field case, is given in its simplest form by

$$i = 2an\nu \exp - (U/kT) \exp (qaE/kT) \quad [5]$$

where a is the half-jump distance, n is the density of the charge carriers, ν is the frequency of the oscillating ions, U is the activation energy for the process, q is the effective charge on the mobile ions, and E is the electric field at the activation barrier. The other symbols have their usual meanings. Ord *et al.* have concluded (8) that an effective field model merits serious consideration when examining the ionic conduction process for niobium. These workers found that the thickness change depends linearly on the field change, the thickness increasing with increasing field. It has been shown in previous studies (3, 14) that if an assumption is made that the field at the activation barrier is equal to the average electric field, a comparison of Eq. [3] and [5] yields the relationship

$$V_0 = (kT/qa)D \quad [6]$$

Thus, V_0 is proportional to the thickness of oxide layer, D .

The experimental data verified a model of this type. Figure 1 (aqueous solution) shows that the values of V_0 are linearly proportional to the formation potential for a given formation current density over a wide range of values and that the lines intersect the origin. In Fig. 2 which is a plot of V_0 vs. formation potential in a nonaqueous anodizing solution, we again see a linear relationship and the lines nearly intersect the origin. These results indicate that a high-field conduction process limits the current through the layer. Lee *et al.* reported (19) results for the plasma anodization of niobium, demonstrating that the most acceptable model is one in which ionic conduction is controlled by an effective field, e.g., the Lorentz field $1/3 (\epsilon_r + 2)E$. Earlier studies (20) used the Lorentz field as the effective field, which was able to obtain reasonable estimates of jump distance and was independent of temperature, at least up to 70°C.

Data taken for different formation current densities fall on lines of differing slopes. In buffer solution (Fig. 1) at a current density of 15.9 $\mu\text{A}/\text{cm}^2$ the slope is 0.127, at 79.5 $\mu\text{A}/\text{cm}^2$ the slope is 0.107, and at 159 $\mu\text{A}/\text{cm}^2$ the slope is 0.101. These varying slopes indicate that the field in the layer and i_0 may both depend on the formation current density. An analogous situation occurs in Fig. 2, the slope at 79.5 $\mu\text{A}/\text{cm}^2$ is 0.26 and the slope at 159 $\mu\text{A}/\text{cm}^2$ is 0.14. The field in the dielectric may increase with increasing formation current densities because of an increase in the ion jump distance at higher formation current densities.

The values of θ required to linearize Eq. [3] are unusually small. It will also be noted that the θ values for films formed in glacial acetic acid solutions containing 0.02M $\text{Na}_2\text{B}_4\text{O}_7$ and 2.0M H_2O are lower than for films formed in aqueous 0.1M H_3BO_3 containing 0.018M $\text{Na}_2\text{B}_4\text{O}_7$. We interpret low values of θ in either case to indicate that niobium films formed in acetic acid are relatively porous compared to those formed in aqueous solution. The film is relatively porous compared to tantalum. This hypothesis is further supported by the relatively large value of the final leakage current on niobium. Lilienfeld and Miller (21) used boric acid plus borate electrolyte in forming films on aluminum. The buffer used gave comparatively high leakage currents so that the possibility of cracks and pores cannot be ruled out as an explanation for their results or for ours. We have reported this porosity effect on vanadium (3) and also on molybdenum (22) films formed in acetic acid. In addition, inspection of the reciprocal capacitance plots, Fig. 3 and 4, suggests the existence of a channel-type "porous" film structure. The changes in slope at 15.9 and 79.2 $\mu\text{A}/\text{cm}^2$ may

be accounted for by field effects. At 159 and 79.5 $\mu\text{A}/\text{cm}^2$ a linear relationship is observed. At the lowest current density the fluctuations in $1/C$ values with formation potential are most likely due to the raising of the oxidation state of the layer (23).

The results of this investigation on niobium are similar to those obtained in earlier works on vanadium (3) and molybdenum (22). The three metals when subjected to anodic polarization in the acetic acid-water-sodium tetraborate solution do form films exhibiting intense interference colors. A number of ellipsometer studies to determine the nature of anodic oxide films formed in a plasma (8, 19, 24, 25) have not as yet shown definitively whether a single or multilayer anodic film is formed. The understanding of the nature of wet films is consistent with several (26-28) authors reporting two layers being formed. The behavior of niobium in nonaqueous anodizing solutions leads us to the conclusion that the films are probably a mixture of barrier and porous layers. The similarities of our results with molybdenum (22), vanadium (3), and niobium as well as those of others (5-8) lead us to agree with Ord and Ho (29) that any meaningful theory of anodic oxidation must not be overly sensitive to either the chemistry of the metal or the structure of the oxide.

Manuscript submitted Aug. 12, 1974; revised manuscript received Jan. 14, 1975.

Any discussion of this paper will appear in a Discussion Section to be published in the December 1975 JOURNAL. All discussions for the December 1975 Discussion Section should be submitted by Aug. 1, 1975.

Publication costs of this article were partially assisted by the University of Dayton.

REFERENCES

1. I. M. Kolthoff and P. J. Elving, Editors, "Treatise on Analytical Chemistry," Part II, Vol. 6, Interscience Publishers, New York (1964).
2. R. G. Keil and R. E. Salomon, *This Journal*, **115**, 628 (1968).
3. R. G. Keil and K. Ludwig, *ibid.*, **118**, 864 (1971).
4. R. W. Santway and R. S. Alwitt, *ibid.*, **117**, 1282 (1970).
5. L. Young, *Can. J. Chem.*, **38**, 1141 (1960).
6. L. Young, *Proc. Roy. Soc. (London)*, **A258**, 496 (1960).
7. L. Young and F. G. R. Zobel, *This Journal*, **113**, 277 (1966).
8. J. L. Ord, M. A. Hopper, and W. P. Wang, *ibid.*, **119**, 439 (1972).
9. W. D. Cornish and L. Young, *Proc. Roy. Soc. (London)*, **A335**, 39 (1973).
10. C. P. Bean, J. C. Fisher, and D. A. Vermilyea, *Phys. Rev.*, **101**, 551 (1956).
11. J. F. Dewald, *J. Phys. Chem. Solids*, **2**, 55 (1957).
12. M. J. Dignam, *This Journal*, **112**, 722 (1965).
13. M. J. Dignam, *ibid.*, **112**, 729 (1965).
14. D. J. DeSmet and M. A. Hopper, *ibid.*, **116**, 1184 (1969).
15. J. L. Ord and J. H. Bartlett, *ibid.*, **112**, 160 (1965).
16. J. L. Ord, *ibid.*, **113**, 213 (1966).
17. B. H. Ellis, M. A. Hopper, and D. J. DeSmet, *ibid.*, **118**, 860 (1971).
18. L. Young, "Anodic Oxide Films," Academic Press, New York (1961).
19. W. L. Lee, G. Olive, D. L. Pulfrey, and L. Young, *This Journal*, **117**, 1172 (1970).
20. R. J. Maurer, *J. Chem. Phys.*, **9**, 579 (1941).
21. J. E. Lilienfeld and C. Miller, *This Journal*, **100**, 222 (1953).
22. C. M. Daly and R. G. Keil, *ibid.*, In press.
23. J. L. Ord and F. C. Ho, *ibid.*, **118**, 46 (1971).
24. K. Knorr and J. D. Leslie, *ibid.*, **121**, 805 (1974).
25. C. J. Dell'Oca, G. Yan, and L. Young, *ibid.*, **118**, 89 (1971).
26. R. S. Alwitt and W. J. Bernard, *ibid.*, **121**, 1019 (1974).
27. A. W. Smith, *ibid.*, **120**, 1068 (1973).
28. C. J. Dell'Oca and L. Young, *ibid.*, **117**, 1545 (1970).
29. J. L. Ord and F. C. Ho, *ibid.*, **117**, 1229 (1970).

Factors Influencing the Lifetime of Pure Beta-Alumina Electrolyte

Y. Lazennec, C. Lasne, P. Margotin, and J. Fally

Laboratoires de Marcoussis, Centre de Recherches de la Compagnie Générale d'Electricité, Marcoussis, France

ABSTRACT

The influence of some impurities on the aging and the lifetime of sodium-sulfur and sodium-sodium experimental cells is studied. The aging mechanism involves an ion exchange between impurities of the reactants and the sodium ions of the β -alumina lattice. In particular, introduction of potassium changes lattice parameters of β -alumina and Na^+ mobility. An important conclusion of this work is that pure β -alumina does allow the transfer of large amounts of total charge (*i.e.*, of sodium ions) before failure. The present figures are in excess of 1700 A-hr/cm². These results have enabled the authors to construct Na-S cells which have given in excess of 4,000 cycles or 16,000 hr of continuous operation.

The sodium-sulfur battery, based on the sodium β -alumina electrolyte, was first described by Weber and Kummer (1) and is to date the most promising high-temperature, high-energy density battery. The reasons for this developmental success depend on the use of the solid sodium-conducting β -alumina between the molten sodium anode and molten sulfide-polysulfide electrolyte in contact with the sulfur cathode. This solves immediately the self-discharge and constructional problems involving the use of matrix or pastes to retain molten components (either liquid alkali, metal, or molten salt electrolyte) in all-liquid high-temperature systems (2).

Development of the system so that a wide range of practical applications will result requires the solution of two major difficulties, both economic. The first is clearly one of initial investment cost per kW-hr of capacity or kW of power. This depends on many factors, the most important being:

(i) The cost of the β -alumina used, which depends not only on precise conditions of manufacture and sintering, but also on the purity of the α -alumina used.

(ii) The cost of the current collector material at the sulfur electrode (graphite or carbon felt).

(iii) The total cost of manufacture, which depends on the development of efficient sealing techniques.

The second factor is battery lifetime. Economic considerations dictate that a minimum lifetime of 2-3 years should be aimed at for urban electric vehicles, and of about 5 years for urban mass transit (buses). On the off-peak power storage application, for which the sodium-sulfur system seems eminently suitable provided that its cost-lifetime ratio is sufficiently low, a lifetime at the order of 10 years should be aimed at.

In the present paper, some factors influencing cell lifetime will be discussed.

Lifetime of β -Alumina Electrolyte

In an earlier paper (2) we demonstrated that magnesia additives used as stabilizers for certain β -alumina compositions had a detrimental influence on electrolyte lifetime in sodium-sulfur experimental cells. At the same time, it was shown that impurities present in the reactants could enter the β -alumina lattice during electrochemical cycling (2, 3). Because of this knowledge of impurities, work carried out in this laboratory has concentrated on two aspects of the aging problem, namely (i) the effect of the initial purity of the β -alumina used; (ii) the effect of introduction of impurities into the lattice of pure β -alumina during electrochemical cycling. The present publication considers

Key words: sodium-sulfur cells, beta-alumina, high-temperature cells, beta-alumina aging, effect of impurities.

the latter effect on lifetime of the ceramic under electrochemical conditions and represents an updating of work previously described (2, 3).

Na-S Cells

Na-S cells used in our experiments generally have a glass or stainless steel outer envelope (S-Na polysulfide reservoir) and a glass sodium reservoir. Sodium filling is effected by electrolysis of molten NaNO_3 through a membrane. In consequence, the major source of impurities is corrosion of the reservoirs by the cell reactants.

We have in general detected two types of impurity: (i) transition metals (Fe, Ni, Co, Cr) which result from attack of steels or alloys used, and (ii) alkali metals (in particular potassium) released by etching of glass reservoirs by molten sodium.

Experimental

In the present work, experiments were conducted using sodium-sodium and polysulfide-polysulfide cells, similar to the sodium-sulfur cells used normally for life-testing. Their construction is shown in Fig. 1.

The solid electrolyte membranes used were a pure β -alumina of two-block composition containing no additives or stabilizers (3, 4), in the form of closed-end tubes 45 mm long and 8 mm external diameter, and wall thickness 0.6 mm. The reservoirs were constructed of Sovirel¹ S 74701 glass.

Cells were either electrically cycled between Na_2S_3 and Na_2S_5 or left on open circuit. In general, for cycled cells, the current density was 0.2 A/cm² at a temperature of 330°C.

Aging of the cells was checked by (i) internal resistance measurements as a function of time; (ii) chemical analysis of β -alumina before and after operation, using spark source mass spectrometry for purity control and atomic absorption spectrometry for Na^+ and K^+ ion determination; and (iii) electrolyte resistivity was measured using a standard four-probe a-c method at 1000 Hz.

Results and Discussion

Sodium-sodium and sodium-sulfur experiments.—Figure 2 indicates the aging characteristics of sodium-sodium cells at various temperatures as a function of time, in terms of internal resistance changes. The lifetime is closely temperature dependent: cells operating at 250° and 200°C invariably function beyond 14,000 hr, whereas only 300 hr is observed at 330°C. A steep rise in resistance is noted before failure.

Comparable results are observed with Na-S cells, at longer lifetimes (see Fig. 3).

¹ Sovirel, 92-Levallois-Perret, France.

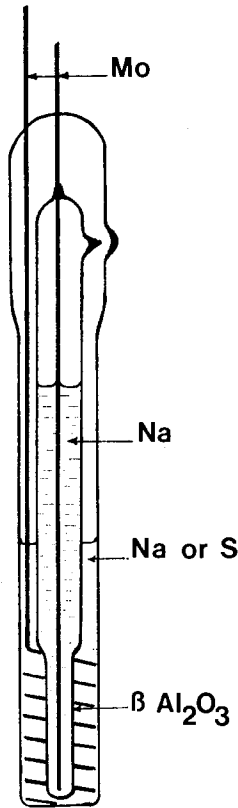


Fig. 1. Schematic of an experimental cell

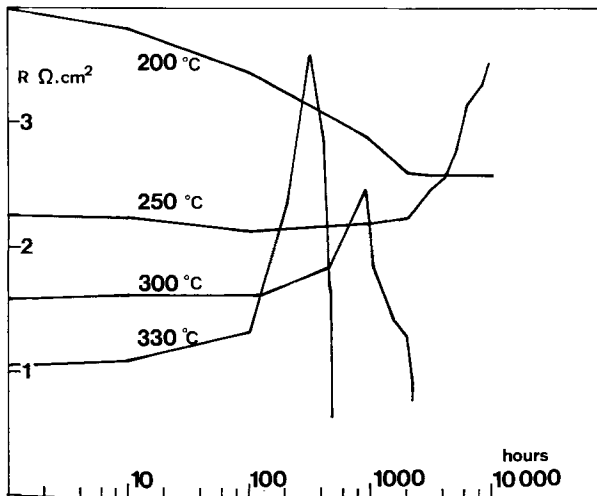


Fig. 2. Time dependence of the resistance of Na-Na cells operating at various temperatures.

The results of chemical analysis are indicated in Table I for Na-Na and Na-S cells before and after operation. The most important result is a considerable contamination by potassium, with the presence of smaller quantities of silicon.

The potassium is accounted for by attack of the glass reservoirs of the cells by molten sodium; presumably by ion exchange. The potassium enters the β -alumina lattice and is immobilized at Na-free sites.

Table I

Elements, wt ppm	Mg	Si	K	Ca	Cr	Fe	Ni	Ga
Initial	1.5	20	12	1	1.5	7	2	3
After Na-Na*	1	390	8.10 ³	2	3	6	0.5	7
After Na-S**	8	190	2.10 ³	1	2	9	1	4

* 7500 hr at 250°C.
 ** 5600 hr at 300°C.

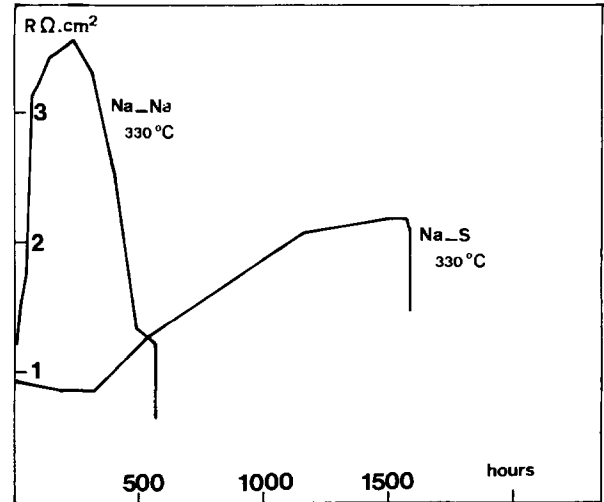


Fig. 3. Comparison of the evolution of the resistance of Na-Na and Na-S cells.

Both the rate of dissolution of potassium, and its rate of entry into the β -alumina lattice, are strongly temperature dependent. Introduction of potassium into the lattice would be expected to be manifested by changes in its physical properties, due to the larger ionic radius (1.33Å for K⁺, 0.95Å for Na⁺). In particular, site blockage, changes in lattice parameters, and changes in Na⁺ mobility (hence resistivity) would be expected. The resistivity of β -alumina before and after electrochemical operation in Na-Na cells is plotted in Fig. 4. A marked increase is shown at each temperature, corresponding to the changes noted in Fig. 2. In our view, the most probable explanation of this phenomenon is the incorporation of K⁺ ion into the lattice. We have established that, for example, incorporation of 0.5 weight per cent (w/o) K⁺ ion into the β -alumina lattice increases resistivity from 15 to 39 ohm-cm at 330°C. This deterioration mechanism also receives confirmation from measurements of β -alumina lattice parameters after K⁺ ion contamination. We have determined that the c parameter increases substantially when the β -alumina lattice is contaminated with potassium, the corresponding figures being 22.76Å (potas-

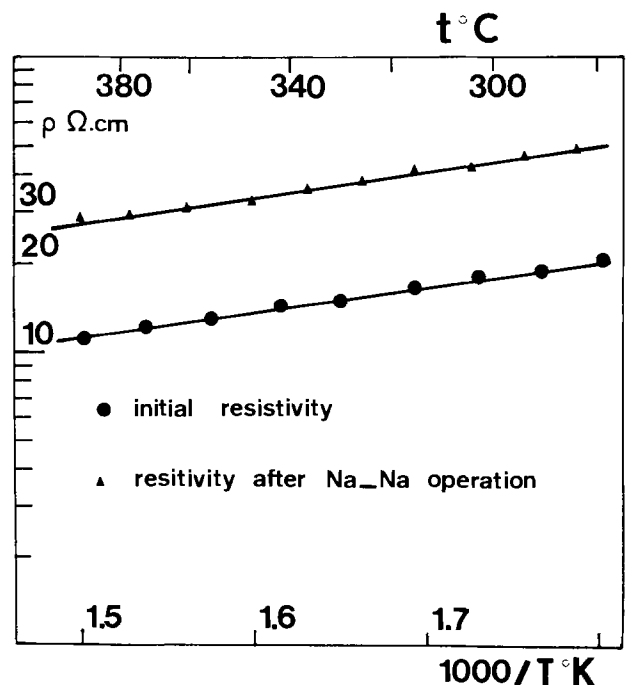


Fig. 4. Resistivity of a β -alumina electrolyte before and after operation in a Na-Na cell at 330°C.

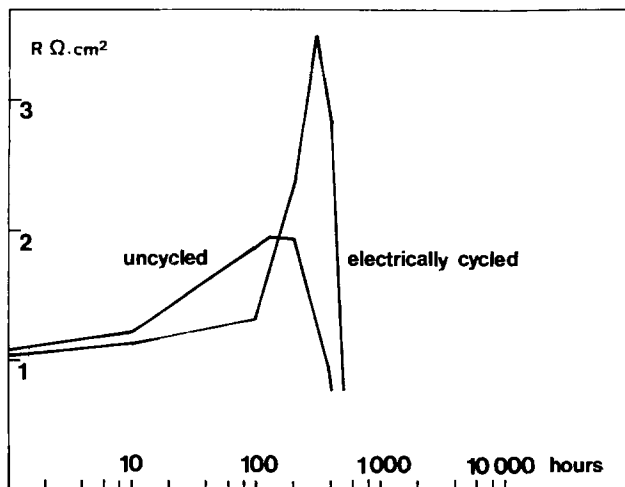


Fig. 5. Analysis of β -alumina tubes after Na-Na and Na-S operation.

sium-contaminated) and 22.16Å (pure β -alumina). The a parameter of the lattice is, however, not affected. This ion exchange property of β -alumina has been studied by Yao and Kummer (6).

An interesting phenomenon is shown in Fig. 5; it appears that potassium contamination of the electrolyte (as indicated by resistance changes) is not wholly dependent on the total charge passed through the β -alumina. The lifetime before catastrophic breakdown of the electrolyte membrane at 330°C is of the same order for electrochemically cycled and uncycled cells. In the particular case reported, the magnitude of the resistance change is different for the cycled and uncycled cells, but this shows considerable dispersion and is related to the total glass area wetted by the molten sodium.

No interpretation can be done today to explain how Si enters the crystal.

Polysulfide-polysulfide cells.—It is evident that one possible method of avoiding contamination of β -alumina by K^+ ion would be to use potassium-free glasses as battery reservoirs. Practically, however, all-glass systems seem out of the question for nonstationary applications especially in transportation, hence metal reservoirs will be required. Corrosion will be a continual problem, especially at the polysulfide-metal interface.

In view of the above results concerning physical property changes in β -alumina after contamination with K^+ , eventually leading to failure, we decided to examine the effect of transition metal ions. Five weight per cent (w/o) of Fe, Ni, Co, and Cr were dissolved in molten sodium polysulfide of commercial purity ($> 99\%$ Na_2S_4) which was then subsequently used in Na polysulfide- β -alumina-Na polysulfide cells. Even at this very high concentration these metals were completely dissolved in polysulfide. The cells were electrochemically cycled at 330°C at 0.150 A/cm² so that the polysulfide compositions varied continuously between Na_2S_3 and Na_2S_5 . After operation for 300 hr, the β -alumina tubes were analyzed.

In addition, tubes that had been simply immersed in molten Na_2S_4 containing the same quantities of transition metal contaminants, under the same time and temperature conditions, were also analyzed. Results are given in Table II. It is apparent that no contamination of the solid electrolyte has occurred, under either cycled or uncycled conditions. It would be interesting to explain why metal ions do not enter the β -alumina lattice in these conditions.

Conclusions

In this paper, we have studied the influence of impurities introduced in the reactants on the behavior of

Table II

Elements, wt ppm	Cr	Fe	Ni	Co
Initial	1.5	7	2	0.5
After cycling*	3	13	2.5	0.4
Without cycling**	0.4	3	0.4	—

* Between Na_2S_3 and Na_2S_5 .

** In Na_2S_4 .

initially pure β -alumina electrolytes of two-block composition, under the conditions of operation of sodium-sulfur cells.

The addition of potassium has a marked influence on the aging and ultimate lifetime of the β -alumina, whereas by contrast, transition metal ions are not incorporated into the lattice and appear to have no influence on aging.

In previous work we have shown the effect of ceramic thickness, as well as of operating temperature and ultimate purity, on lifetime (3). As we have pointed out above, operation at a somewhat lower temperature reduces attack on glass hardware. Similarly, tubes of slightly greater thickness show the effect of K^+ contamination to a lesser degree as they contain a greater amount of material.

These results have enabled us to construct Na-S cells, using 1 mm thick electrolyte, which have given in excess of 4,000 cycles or 16,000 hr of continuous operation at 285°C in all-glass hardware (0.067 A/cm² charge, 0.2 A/cm² discharge). These cells are still operating.

In addition, we have also shown that, at higher operating temperatures, stable resistances and long lifetimes may be obtained by using ceramic or metal hardware (Fig. 6 for Na-Na cells).

An important conclusion of this work is that pure β -alumina does allow the transfer of large amounts of total charge (*i.e.*, of sodium ion) before failure. The present figures are in excess of 1700 A-hr/cm². As far as our work is concerned, lifetime and aging seem only to be related to incorporation of impurities, especially K^+ . The work is at present being extended toward the influence of the initial purity of β -alumina on lifetime.

We are confident that with our present β -alumina, cells of very long lifetimes will be obtainable (i) by the use of corrosion-resistant reservoirs, and (ii) by the use of efficient ceramic or glass-to-metal seals (of minimum area and low potassium content) between β -alumina and the anodic reservoir, and between the anodic and cathodic compartments.

We think that such additive-free ceramics can be economically interesting, especially for use in offpeak power storage batteries and even for the electric car if their wall thickness is 1 mm or less.

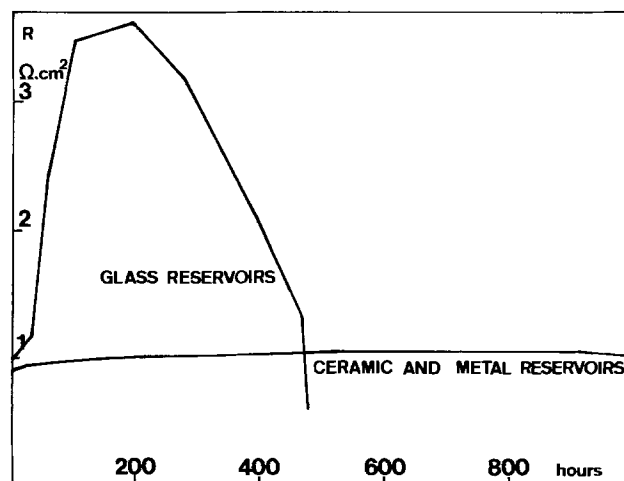


Fig. 6. Aging of Na-Na cells at 330°C

In general, β -alumina compositions containing stabilizing additives are used that are optimized for conductivity rather than lifetime. In addition, commercial or reagent-grade sodium, containing metallic impurities, are employed in Na-S cells. Reported lifetimes are generally much shorter than those indicated here.

In view of our previous work (3) on the effect of magnesia additives on lifetime, we feel that the β -aluminas used in Ref. (4) and (5) have intrinsically weakened surfaces and show a tendency to easy Griffith crack propagation, due to the microscopically uneven distribution of additive, and consequent local stressing of the material. This occurs in pure β -alumina to a significant degree only after sufficient K^+ ion has been incorporated. The surface condition of our electrophoretically formed material may also be different.

The K^+ ion, incorporated mainly (due to diffusion limitations) at the surface of the β -alumina, stresses, the material locally by changing its \bar{c} parameter. Incorporation mainly at the β -alumina surface is indicated by the similarity of lifetime under cycled and uncycled conditions as shown in Fig. 5. When crack propagation following the mechanism outlined in Ref. (4) and (5) progresses, resistance suddenly falls just before failure, as indicated in Fig. 2. It would therefore appear that long lifetimes can be expected, if β -alumina containing only sodium ions are used in sodium-sulfur cells.

The above results were obtained using hexagonal two-block β -alumina free of additives. Recent results obtained at Ford (7) indicate that long lifetime can be obtained with three-block β' -alumina type ceramic containing Li_2O , as additive, but free of MgO . Similar lifetime seems also obtained at the Electricity Council with ceramics containing β - and β' -alumina. It could be interesting to compare the behavior of such elec-

trolytes, in respect to their composition, with the introduction of impurities in their lattice.

Acknowledgment

The authors thank J.-Y. Barraud, J. Bouthegourd, J. Leboucq, and F. Grivon for their participation in this study. They are grateful to Dr. John Appleby for useful discussion of this work and for the help in the writing of this paper.

A part of this work was sponsored by the "Délégation à la Recherche Scientifique et Technique."

This paper was presented at the 24th Meeting of I.S.E., Eindhoven, Netherlands, September 10-14, 1973.

Manuscript submitted March 15, 1974; revised manuscript received Dec. 24, 1974.

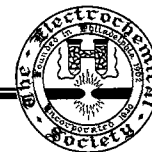
Any discussion of this paper will appear in a Discussion Section to be published in the December 1975 JOURNAL. All discussions for the December 1975 Discussion Section should be submitted by Aug. 1, 1975.

Publication costs of this article were partially assisted by the *Compagnie Générale d'Electricité*.

REFERENCES

1. J. T. Kummer and N. Weber, *S.A.E.*, **670**, 179 (1967).
2. J. Fally, C. Lasne, Y. Lazenec, and P. Margotin, *This Journal*, **120**, 1292 (1973).
3. J. Fally, C. Lasne, Y. Lazenec, Y. Le Cars, and P. Margotin, *ibid.*, **120**, 1296 (1973).
4. R. H. Richman, G. J. Tennenhouse, and R. C. Ku, Paper presented at Am. Ceram. Soc. Meeting, Cincinnati, Ohio, May 1973.
5. R. Armstrong, T. Dickinson, and J. Turner, Paper presented at the Soc. for Electrochem. Intern. Conf. on Electrolytes for Power Sources, Brighton, England, December 1973.
6. Yung-Yang Yu Yao and J. T. Kummer, *J. Inorg. Nucl. Chem.*, **29**, 2453 (1967).
7. NSF, Rann annual report (1974).

Brief Communications



The Total Reduction of Carbon Tetrachloride at the Glassy Carbon Electrode

Frank L. Lambert, Bruce L. Hasslinger, and Robert N. Franz, III

Department of Chemistry, Occidental College, Los Angeles, California 90041

In their classic polarographic study Kolthoff and co-workers (1) a quarter century ago showed that carbon tetrachloride gave two waves when it was reduced at the dropping mercury electrode (DME) in methanol-water solution with tetramethylammonium bromide as the supporting electrolyte. The first wave involved the reduction of carbon tetrachloride to chloroform because the second wave was shown to be identical to that given by pure chloroform. Von Stackelberg and Stracke published similar results, using dioxane-water, in a survey of the voltammetry of organic compounds at the DME (2).¹

Key words: polarography, chloroform, methylene chloride, methyl chloride.

¹ In butanol-water, when methylene chloride and methyl chloride were mixed with carbon tetrachloride and chloroform (during an experiment to prove the utility of quantitatively determining CCl_4 and $CHCl_3$ in such a four-component mixture), von Stackelberg and Stracke (2) detected three waves, with the third wave corresponding to the combined methylene and methyl chlorides.

As reported some 10 years later, Wawzonek and Duty (3) in their thorough investigation of the mechanism of the carbon tetrachloride reduction used *N,N*-dimethylformamide (DMF) as a solvent and were able to demonstrate three waves in the reduction at the DME: the third wave, not present in earlier work in methanol- or dioxane-water, was attributed to the reduction of methylene chloride, presumably to methyl chloride.

After our discovery that alkyl monochlorides, a class generally found to be irreducible at the dropping mercury electrode (with the exception of methyl or activated alkyl chlorides such as allyl), could all be readily reduced at the glassy carbon electrode (GCE) in DMF (4) we were led to look at the behavior of carbon tetrachloride at the GCE. We are reporting our results now because of the possible practical and theoretical implications of the behavior of many polyhalo-

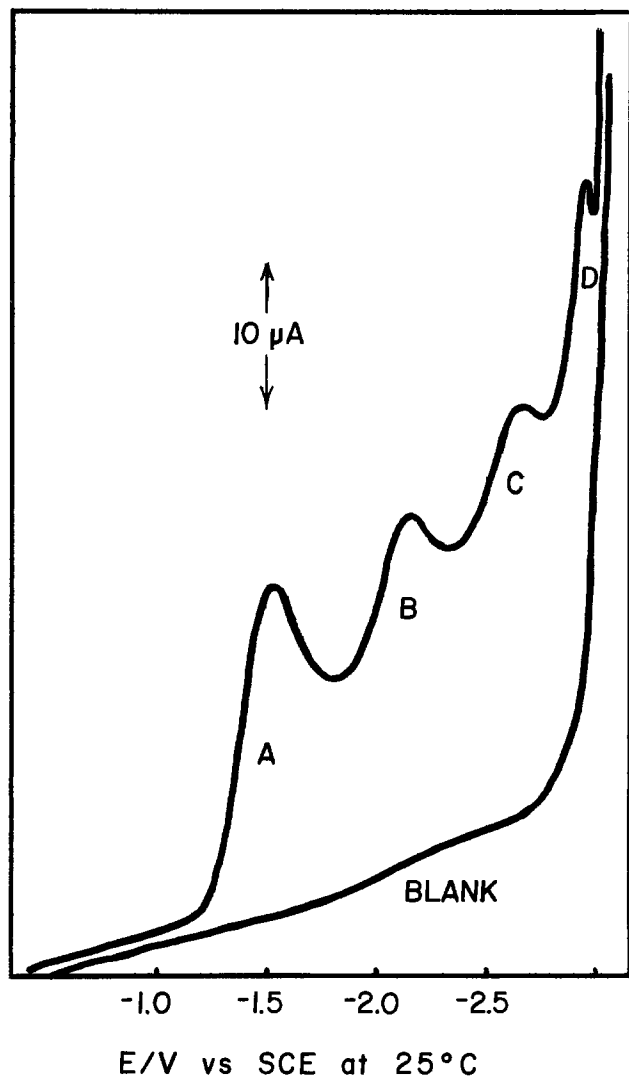


Fig. 1. Voltammogram of CCl_4 in DMF at the GCE²

compounds at the GCE and because we do not intend to proceed further with work involving such polyhalo substances.

In DMF with tetraethylammonium perchlorate as the supporting electrolyte,² carbon tetrachloride at the GCE yields the rather remarkable voltammetric curve shown in Fig. 1, where four waves delineate the total reduction of carbon tetrachloride to methane: first, A, the reduction of CCl_4 itself; then, B, of chloroform; C, of methylene chloride; and finally, D, of methyl chloride.³ The half-peak potentials, $E_{p/2}$ correspond to those of the individual pure substances in independent experiments at the GCE, as shown in Table I, and are "rational" in the sense that the differences between the succeeding half-peak potentials in the series are of comparable magnitude, *ca.* $0.44 \pm 0.14\text{V}$ with the $E_{p/2}$ of CCl_4 at -1.33V vs. the saturated calomel electrode. At the DME, the half-wave potentials of chloroform and methylene chloride increase by -0.12 and -0.08V , respectively, when water is added to the DMF (3). This is not the case at the glassy carbon electrode; the half-peak values do not change by more than 0.02V in 10% aqueous DMF.⁴

² All experimental conditions as described in Table I, except that in Fig. 1 and 2 the voltage was applied at the rate of 50 mV/sec over a chart span of 500 mV/in. (rather than $1/5$ those values) for more compact visual presentation.

³ The source of hydrogen in the reduction of an alkyl halide when tetraethylammonium salts are used as supporting electrolytes has been thought to be the $\beta\text{-H}$ of an ethyl group in the $(\text{CH}_3\text{CH}_2)_4\text{N}^+$ [see, for example, the works of Fry and Reed (5)]. However, the work of Jensen and Parker (6) indicates that Et_3N^+ is a less effective protonation agent for aromatic anions than are traces of water.

⁴ The DMF was dry as that used by Wawzonek and Duty (3), but not dried as was that of Jensen and Parker (6).

Table I. Half-peak potentials, $E_{p/2}$,^a at the glassy carbon electrode (GCE)

Compound	1st wave	2nd wave	3rd wave	4th wave
In N,N-dimethylformamide (DMF)				
CCl_4	-1.33	-1.91	-2.43	-2.77
CHCl_3	-1.90	-2.42	-2.78	
CH_2Cl_2	-2.44	-2.78		
CH_3Cl	-2.76			
In acetonitrile				
CCl_4	-1.40	-1.93	-2.41	
CHCl_3	-1.91	-2.43		
CH_2Cl_2	-2.44			

^a In volts vs. the saturated calomel electrode. Halide concentrations of $1\text{-}3 \times 10^{-3}\text{M}$ in purified anhydrous N,N-dimethylformamide (9) with 0.01M tetraethylammonium perchlorate as supporting electrolyte. Curves recorded on a Beckman Electroscan 30 with saturated calomel electrode (SCE) as reference, platinum wire as auxiliary, and glassy carbon disk of 7.9 mm^2 area (Tokai Electrode Manufacturing Company, Tokyo, Japan) as working electrode at 25°C . Light polishing of the working electrode surface with Linde 0.05μ alumina, wet with DMF, between runs was essential for reproducibility of (typically) 3 mV standard deviation. Rate of scan was 10 mV/sec and normal voltage span of an experiment was 1V .

Wawzonek and Duty also discovered that methylene chloride could not be reduced in acetonitrile at the DME. Here, too, the glassy carbon electrode is usefully different from the DME: carbon tetrachloride gives three waves in acetonitrile at the GCE and the third wave is that of methylene chloride as shown by its coincidence with the wave for pure methylene chloride in separate experiments (Fig. 2 and Table I).

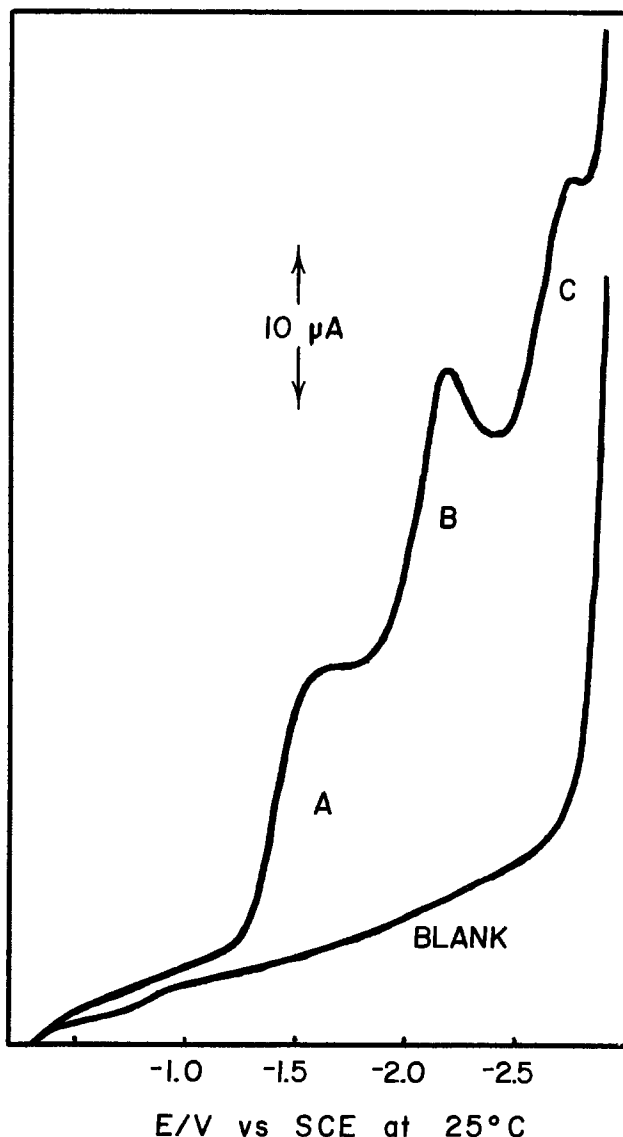


Fig. 2. Voltammogram of CCl_4 in acetonitrile at the GCE²

In view of the often-repeated (and generally true) statement about the easier reduction of polyhalides than monohalides (7), the original report of von Stackelberg and Stracke (2) that methylene chloride, CH_2Cl_2 , at the DME in dioxane-water is reduced at -2.33V whereas methyl chloride, CH_3Cl , with its single chlorine is easier to reduce, at -2.23V , is somewhat surprising. We have found that this unusual order of reduction is also true in anhydrous DMF at the DME.⁵ Considering the order of the half-wave potentials of CH_3Cl and CH_2Cl_2 at the DME, and the clearly discrete reduction of methylene chloride prior to methyl chloride that we have discovered at the carbon electrode, it seems highly possible that mercury is chemically involved before or during the potential-determining step at the DME in the electroreduction of methyl and methylene chlorides. This suggestion is in accord with a number of reports of chemical interaction of mercury with organic bromides (8).

Acknowledgment

We wish to thank the Research Corporation for a Cottrell College Science Grant which made this research possible.

This is the fifth paper in the series "The Voltammetry of Organic Halogen Compounds;" parts IV and III were published previously (4, 9).

Manuscript submitted Aug. 15, 1974; revised manuscript received Nov. 27, 1974.

⁵ The $E_{1/2}$ of CH_2Cl_2 is -2.17V and that of CH_3Cl , -2.10V (both vs. Hg pool) with a supporting electrolyte of 0.01M tetraethylammonium perchlorate in anhydrous DMF.

Any discussion of this paper will appear in a Discussion Section to be published in the December 1975 JOURNAL. All discussions for the December 1975 Discussion Section should be submitted by Aug. 1, 1975.

Publication costs of this article were partially assisted by the Research Corporation.

REFERENCES

1. I. M. Kolthoff, R. S. Lee, D. Stocesova, and E. P. Parry, *Anal. Chem.*, **22**, 521 (1950).
2. M. von Stackelberg and W. Stracke, *Z. Elektrochem.*, **53**, 118 (1949).
3. S. Wawzonek and R. C. Duty, *This Journal*, **108**, 1135 (1961).
4. F. L. Lambert and G. B. Ingall, *Tetrahedron Letters*, 3231 (1974).
5. A. J. Fry and R. G. Reed, *J. Am. Chem. Soc.*, **93**, 553 (1971); *ibid.*, **94**, 8475 (1972).
6. B. S. Jensen and V. D. Parker, *Chem. Soc. Chem. Commun.*, 367 (1974).
7. For example, M. Brezina and P. Zuman, "Polarography in Medicine, Biochemistry and Pharmacy," p. 206, Interscience Publishers, Inc., New York (1958); D. R. Crow and J. B. Westwood, "Polarography," p. 97, Methuen and Co., Ltd., London (1968); C. K. Mann and K. K. Barnes, "Electrochemical Reactions in Non-Aqueous Systems," p. 212, Marcel Dekker, Inc., New York (1970).
8. J. Casanova and H. R. Rogers, *J. Am. Chem. Soc.*, **96**, 1944 (1974). Other examples are cited by J. Casanova and L. Ebersson, in "The Chemistry of the Carbon-Halogen Bond," S. Patai, Editor, pp. 1034-1036, Wiley-Interscience, New York (1974).
9. F. L. Lambert, *J. Org. Chem.*, **31**, 4184 (1966).

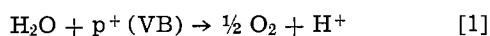
Semiconductor Electrodes

I. The Chemical Vapor Deposition and Application of Polycrystalline N-Type Titanium Dioxide Electrodes to the Photosensitized Electrolysis of Water

Kenneth L. Hardee* and Allen J. Bard**

Department of Chemistry, The University of Texas at Austin, Austin, Texas 78712

A number of investigations on photoeffects on semiconductor electrodes have been reported (1, 2). Most studies have been concerned with single crystal semiconductor materials, although some polycrystalline semiconductors, e.g., SnO_2 (3-6), have also been used. Recently the photosensitized electrolytic oxidation of water on n-type TiO_2 single crystal electrodes has been described (7-9). In the absence of illumination the hole concentration in the valence band of n-type TiO_2 is very small, so that no appreciable anodic current flows for the oxidation of water, even at very positive potentials (9). When the electrode is irradiated with light with energy greater than the bandgap energy (ca. 3.2 eV), holes are formed in the valence band (VB) by excitation of electrons to the conduction band (CB). Under anodic polarization the bands in the semiconductor are bent in such a direction that the CB electrons migrate in the external circuit to the counterelectrode while the VB holes move to the surface where they combine with water molecules producing oxygen



* Electrochemical Society Student Member.

** Electrochemical Society Active Member.

Key words: semiconductor electrodes, oxygen evolution, photoelectrochemistry.

Unlike many other semiconductor materials (e.g., ZnO, GaAs), TiO_2 is stable with respect to dissolution under these conditions. These photoassisted electrolytic processes are obviously of interest with respect to the conversion of light to chemical and electrical energy. For practical applications, however, low cost polycrystalline electrode materials will probably be required for large area electrodes. Moreover, variation of the composition of the semiconductor (e.g., to change the bandgap or the donor or acceptor levels or to alter the surface states) leading to changes in spectral sensitivity or electrochemical behavior, can be accomplished more easily during the preparation of such polycrystalline materials. Mollers, Tolle, and Memming (10) have recently reported measurements of photocatalytic deposition on polycrystalline TiO_2 in 1M H_2SO_4 solutions. We report here details of the preparation of n-type TiO_2 electrodes by chemical vapor deposition (CVD) onto titanium metal substrates and a comparison of the photoassisted anodic oxidation of water on CVD and single crystal n-type TiO_2 .

The CVD technique employed was based on the method of Fitzgibbons, Sladek, and Hartwig (11), who studied dielectric thin films of TiO_2 for solid-state devices and integrated circuit applications. This technique involves the reaction of a titanium alkoxide and

water to produce TiO_2 and an alcohol. By utilizing vapors generated in a flask and delivered to the reaction site by a carrier gas, the reaction can be controlled in both rate and location. An alkoxide that produces a low boiling alcohol permits a low temperature of deposition; the only requirement is that the temperature is sufficient to boil off the resulting alcohol so that it will not be incorporated into the film. The reaction can be directed toward any suitable substrate simply by positioning the delivery tubes.

Experimental

The n-type TiO_2 on a Ti substrate was produced in the following manner (Fig. 1). Tetra-isopropyl orthotitanate from Eastman Organic Chemicals was heated in a flask in a water bath maintained at $80^\circ\text{--}85^\circ\text{C}$. Dry nitrogen (passed through CaCl_2 and molecular sieves) was used as a carrier gas; it was passed over the titanate and then through a delivery tube to the substrate. The tip of the delivery tube was located about 2.5 cm above the Ti substrate. Pure Ti was used as the substrate and was heated to about 150°C on a hot plate. The water vapor source also used nitrogen as the carrier gas. The water vapor was carried to the substrate through a tube parallel to the titanate delivery tube. Similar results could be obtained employing only water vapor from the air; however, an auxiliary water vapor source allowed shielding of the substrate from air currents which disrupt uniform film growth. To allow the development of a full space charge region in the semiconductor electrode, which can be as large as $10,000\text{\AA}$, depending upon carrier density, fairly thick TiO_2 films are required. Fitzgibbons *et al.* (11) reported that attempts to use continuous CVD to produce films thicker than $4000\text{--}5000\text{\AA}$ resulted in cracking of the films, but that heating the films between deposition allowed thicker films to be produced. The following CVD procedure was thus adopted.

The Ti substrate was cut into 1×1 cm squares, polished using very fine emery paper, and finally buffed to a mirror finish with a polishing wheel and rouge. This step was necessary to achieve good adherence of the TiO_2 and to promote growth of thicker layers. Unbuffed Ti (although polished with emery paper or etched in HF) gave films that were dull and nonuniform in appearance and which yielded much lower photocurrents. It was also difficult to achieve thicker films on unpolished material since flaking or formation of white powdered TiO_2 occurred when repeated depositions were attempted. A convenient film growth rate was established by adjusting the flow rates of the nitrogen over the titanium isopropoxide and water while watching the growth of interference rings on glass with white light. The polished Ti substrate was then placed under the nozzles and growth allowed for a given time period (typically about 2 min for the formation of two complete sets of interference rings). The substrate was then held in a bunsen burner flame for 3-4 min during which time the Ti turned red hot, the interference rings disappeared, and the surface took on a uniform, shiny, blue-gray appearance. After the flame treatment, the substrate was cooled in air briefly, then returned to the deposition apparatus for

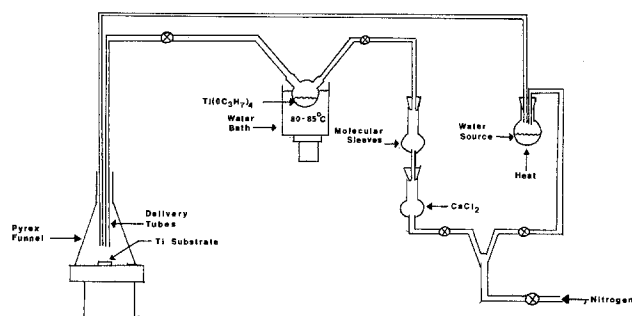


Fig. 1. Diagram of deposition apparatus

further CVD. Electrodes with between two and nine 2-min coatings were produced. The TiO_2 film thicknesses for these electrodes ranged from about 1.4 to 7μ , respectively.

The electrodes obtained by the above procedure showed a high resistance. They were placed in 10^{-5} Torr vacuum at 600°C for $1\frac{1}{2}$ hr. This treatment causes oxygen vacancies in the TiO_2 structure and produces n-type material with a much lower resistance. A copper wire was attached to the cleaned back of the Ti piece with silver epoxy cement (Epoxy Products Company), and the piece was mounted in a glass tube with silicone rubber cement (Dow Corning Corporation) so that only the surface covered by the TiO_2 was exposed to the solution.

The single crystal n-type TiO_2 was produced by National Lead Company and was given a similar vacuum-treatment. Ohmic contact was made with indium by ultrasonic welding, and it was mounted in glass using silicone rubber cement.

Some experiments were also attempted with TiO_2 produced anodically by oxidation of Ti substrates in 15% H_2SO_4 , 2% Na_3PO_4 , 5% Na_2HPO_4 , saturated H_3BO_3 , or 50:50 ethylene glycol saturated oxalic acid solutions (12). A 1×1 cm Ti piece was anodized for several hours in the electrolyte with greater than 10V applied. A metallic blue coating appeared immediately, but it changed little with time. These deposits are probably very thin, since production of the insulating TiO_2 film slows down or stops the anodization process.

All electrochemical measurements were performed with a multipurpose instrument constructed from solid-state operational amplifiers previously described (13-15). Current-potential curves were recorded with a Moseley Model 7005A X-Y Recorder. The electrode was illuminated through a quartz window in the cell wall. The counterelectrode was Pt and the reference electrode was a saturated calomel electrode (SCE).

Illumination was accomplished with a 200W mercury lamp (PEK-Illumination Industries). Either the full polychromatic output of the lamp was used, or the light was passed through a circular graded filter.

Results and Discussion

Current-potential curves for both single crystal and CVD TiO_2 (n-type) in the dark and under illumination in a 0.5M potassium chloride solution buffered at pH 6 are shown in Fig. 2. Curves at other pH's, from 1N NaOH to 1N H_2SO_4 are very similar to these on both the single crystal and CVD material, but are shifted in the negative direction 58 mV per unit increase in pH. The anodic region in the dark is characterized by a very low current until a certain breakdown potential when a marked current rise occurs. For the CVD TiO_2 this current rise occurs at potentials of about 2V vs. SCE and probably represents tunneling or film break-

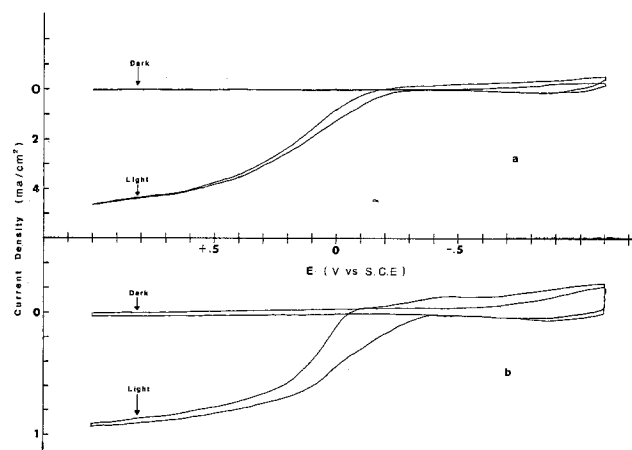


Fig. 2. Current density vs. potential for (a) single crystal TiO_2 , and (b) CVD TiO_2 in 0.5M KCl solution buffered to pH 6.

down; this region was not investigated further. A similar current rise, at somewhat less positive potentials, was noted by Möllers *et al.* (10). This effect appears similar to that observed when Ti is anodized, where the TiO_2 formation and passivation region is followed by breakdown. The single crystal TiO_2 shows no such current rise until potentials beyond 10V. On the reverse scan, or a cathodic scan from the open-circuit potential, in the dark, the potential rise occurs when hydrogen evolution commences, as evidenced by the appearance of gas bubbles on the electrode.

When the electrodes are illuminated with either polychromatic light or wavelengths corresponding to energies greater than the bandgap (e.g., 370 nm), anodic current and bubble formation on the electrodes is observed. The saturation oxidation current density under illumination is a function of light intensity and is somewhat smaller for the CVD TiO_2 than for the single crystal material. The higher C.D. observed with the single crystal material probably reflects the differences in structure between the CVD TiO_2 , which is a mixture of polycrystalline anatase and rutile (11), and the rutile single crystal. Thus, there may be better efficiency in light absorption, and hence generation of holes, as well as fewer hole-electron recombinations in the single crystal material. On the reverse scan into the negative potential region following oxidation under illumination a cathodic current larger than that observed in the dark is observed. This is attributed to the reduction of oxygen formed during the anodic scan, and is absent in scans into the cathodic region alone in the presence of light in deaerated solutions. In solutions containing dissolved air, a small cathodic wave is observed in this region on an initial cathodic scan. The wave observed on reversal from a photosensitized oxidation is about 4 times larger, suggesting that some of the oxygen produced anodically is adsorbed at the TiO_2 surface or that a saturated solution of oxygen is formed near the electrode surface.

The shift in the location of the photosensitized oxidation wave with pH is the same for both single crystal and CVD TiO_2 . A plot of E_L , the potential where the photocurrent commences *vs.* pH (Fig. 3), shows that both electrode materials fit the same linear correlation, with $\Delta E_L/\Delta \text{pH} = 58 \text{ mV/pH}$ unit. The spectral sensitivities of both materials, shown by photocurrent *vs.* wavelength plots (Fig. 4), are also virtually identical.

The CVD TiO_2 is very stable at open circuit, to solutions ranging in pH from 0 to 14 (1N H_2SO_4 to 1N NaOH), as is the single crystal material; no noticeable decreases in saturation current densities occurred with prolonged immersion. The CVD TiO_2 is also mechanically stable, and withstands gentle polishing with very fine emery paper, although scraping the surface will destroy the film. Prolonged exposure of the CVD TiO_2 to positive potentials, with and without light, showed no noticeable changes in the appearance of the coating or maximum current density. Prolonged cathodic evolution of hydrogen occasionally produced small

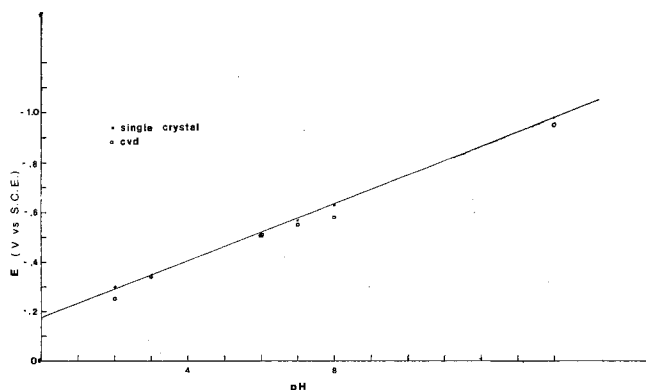


Fig. 3. E_L vs. pH for single crystal and CVD TiO_2

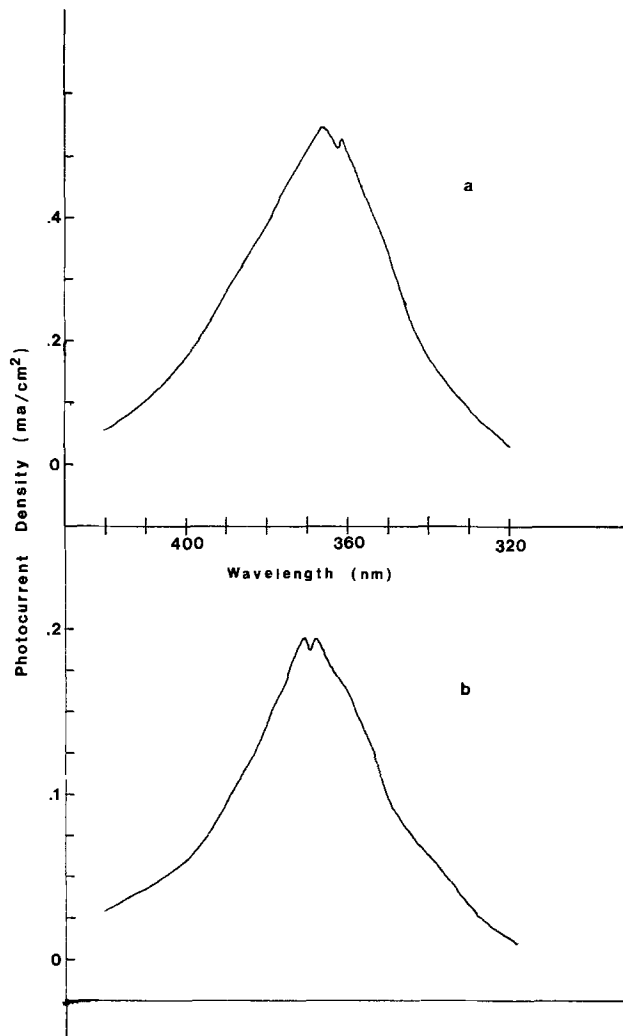


Fig. 4. Photocurrent vs. wavelength at potential of $+0.775\text{V}$ (vs. SCE) for (a) single crystal TiO_2 , and (b) CVD TiO_2 . Curves are uncorrected for mercury lamp emission and transmittance variations of circular graded filter.

blisters or flakes on scattered portions of the surface. This may indicate poor adhesion of the TiO_2 film to the Ti substrate in these areas, perhaps because of some contaminant on the substrate prior to deposition.

A brief study of the photosensitized oxidation of water on a TiO_2 film produced by anodization of Ti was undertaken to compare its behavior to that of the CVD material. Small photocurrents were observed on the anodized Ti, but the current densities were about 30-40 times lower than that of CVD TiO_2 . The shift in potential of the anodized Ti at open circuit upon exposure to light (ca. -0.10V in 1M KCl) was also smaller than that observed for CVD or single crystal TiO_2 (ca. -0.50V in 1M KCl). This behavior suggests that the TiO_2 film formed on anodization of Ti is of insufficient thickness to support a full space charge, and it may also differ structurally from that of CVD TiO_2 .

The CVD deposition technique can also be used to deposit TiO_2 upon glass [see also Ref. (10)], suggesting possible applications as a transparent electrode material, particularly in the region of negative potentials where SnO_2 electrodes sometimes are not useful. Moreover, the good stability of these CVD TiO_2 electrodes may make them useful in other electrolytic processes, for example, for photoassisted oxidations or reductions of organic materials in nonaqueous solvents. These applications are currently under investigation.

Acknowledgment

The support of this research by the National Science Foundation and the Army Research Office, Durham, is

gratefully acknowledged. We are indebted to Professor D. Tchernev for the sample of single crystal TiO_2 and for his helpful suggestions.

Manuscript submitted Nov. 7, 1974; revised manuscript received Feb. 13, 1975.

Any discussion of this paper will appear in a Discussion Section to be published in the December 1975 JOURNAL. All discussions for the December 1975 Discussion Section should be submitted by Aug. 1, 1975.

Publication costs of this article were partially assisted by The University of Texas at Austin.

REFERENCES

1. V. A. Myamlin and Yu. V. Pleskov, "Electrochemistry of Semiconductors," Plenum Press, New York (1967).
2. H. Gerischer, in "Physical Chemistry," H. Eyring, D. Henderson, and W. Jost, Editors Vol. IXA, Chap. 5, Academic Press, New York (1970).
3. F. Möllers and R. Memming, *Ber. Bunsenges. Physik. Chem.*, **76**, 469 (1972).

4. R. Memming and F. Möllers, *ibid.*, **76**, 475 (1972).
5. H. A. Laitinen, C. A. Vincent, and T. M. Bednarski, *This Journal*, **115**, 1024 (1968).
6. O. Elliot, D. L. Zellmer, and H. A. Laitinen, *ibid.*, **117**, 1343 (1970).
7. A. Fujishima, K. Honda, and S. Kikuchi, *J. Chem. Soc. Japan (Ind. Chem. Sec.)*, **72**, 108 (1969).
8. A. Fujishima and K. Honda, *ibid.*, **74**, 355 (1971).
9. P. J. Boddy, *This Journal*, **115**, 199 (1968).
10. F. Möllers, N. J. Tolle, and R. Memming, *ibid.*, **121**, 1160 (1974).
11. E. T. Fitzgibbons, K. J. Sladek, and W. H. Hartwig, *ibid.*, **119**, 735 (1972).
12. W. J. James and M. E. Straumanis, in "Encyclopedia of Electrochemistry of the Elements," A. J. Bard, Editor, Marcel Dekker, Inc., New York, in press.
13. F. E. Anson and D. A. Payne, *J. Electroanal. Chem.*, **13**, 35 (1967).
14. D. A. Payne, Ph.D. Dissertation, The University of Texas at Austin (1970).
15. D. A. Payne and A. J. Bard, *This Journal*, **119**, 1665 (1972).

DISCUSSION SECTION



This Discussion Section includes discussion of papers appearing in the *Journal of The Electrochemical Society*, Vol. 121, No. 8 and 12; August and December 1974.

The Electroreduction of Oxygen and Hydrogen Peroxide on Sodium-Tungsten Bronzes

J.-P. Randin (pp. 1029-1033, Vol. 121, No. 8)

J. McHardy:¹ The paper under discussion largely bears out the findings of earlier workers² but two observations do call for comment. The first is that the presence of platinum in a bronze crystal did not increase its electrocatalytic activity for oxygen reduction and the second is that the $\log i$ vs. E curve for hydrogen peroxide reduction passed through a maximum.

In the 8 years since Sepa *et al.*³ first reported sodium tungsten bronze to be an electrocatalyst for oxygen reduction, many publications have appeared on this and related subjects.² Several workers⁴⁻⁷ were able to reproduce Sepa's results, but only by incorporating platinum in the bronze crystals. Other papers also reported beneficial effects of platinum upon electrocatalysis although Randin cites two of them^{8,9} as evidence that platinum had no effect. Detection of the electrocatalysis is not a simple matter because the limiting current density for oxygen reduction is quite low (10-100 times lower than the diffusion controlled current observed at large overpotentials) and can easily be masked, *e.g.*, by corrosion currents.

Comparison of Randin's data with those of workers who did reproduce Sepa's results reveals differences both in condition and technique. Most significantly, Randin used more concentrated acid (tending to ag-

gravate corrosion problems) and limited his measurements to relatively high current densities ($\geq 10^{-5}$ A/cm²). In my own work,⁷ platinum-induced electrocatalytic activity was observed only after reducing corrosion currents to 10^{-8} A/cm² or less and even then it was confined to current densities below 10^{-5} A/cm².

Turning to the second point, I would draw attention to the work of Voinov and Tannenberger¹⁰ who also examined the reduction of hydrogen peroxide on tungsten bronzes. Despite differences in the interstitial element (they used Ce_xWO_3 and Yb_xWO_3) kinetic data at the rotating electrode were quite similar. Unlike Randin, however, Voinov and Tannenberger reported no maximum in the $\log i$ - E curve. The disagreement casts some doubt on Randin's interpretation of the maximum and raises the possibility that it may have been an experimental artifact.

J.-P. Randin:¹¹ Among the various published investigations in which oxygen reduction reaction on sodium-tungsten bronzes was studied, only McHardy's work⁷ and the paper under discussion include a detailed quantitative evaluation of the effect of platinum incorporated by using a platinum anode (or crucible) during the preparation of the bronzes by electrolysis of a polytungstate melt. Other workers also reported various effects of platinum incorporated by extended potential cycling in acid solutions containing Pt metal ions⁸ or by electrodeposition from chloroplatinic acid.¹² The latter methods gave relatively high surface concentrations of Pt as compared to the low bulk concentrations (in the ppm range) involved in the study under discussion. These studies^{8,12} are therefore not relevant to the specific criticisms of McHardy.

It is evident from both McHardy's work¹³ and from our own¹⁴ that a significant corrosion current is ex-

¹ Pratt & Whitney Aircraft, Materials Engineering and Research Laboratory, Middletown, Connecticut 06457.

² For a review of the relevant literature through 1973 see J. McHardy and P. Stonehart, in "M.T.P. International Review of Science, Physical Chemistry," Series 2, Butterworths, London (In Press).

³ D. B. Sepa, A. Damjanovic, and J. O'M. Bockris, *Electrochim. Acta*, **12**, 746 (1967).

⁴ A. J. Appleby and N. Van Drunen. To be published.

⁵ L. W. Niedrach and G. J. Haworth, in "Hydrocarbon-Air Fuel Cells," Report No. 12, July-December 1967, Contract DAAK 02-67-C-0080, U.S. Army Mobility Equipment R&D Center, Ft. Belvoir, Va.

⁶ R. A. Fredlein, Personal communication.

⁷ J. O'M. Bockris and J. McHardy, *This Journal*, **120**, 61 (1973).

⁸ J. M. Fishman, J. F. Henry, and S. Tessore, *Electrochim. Acta*, **14**, 1314 (1969).

⁹ B. Broyle, *J. Catalysis*, **10**, 13 (1968).

¹⁰ M. Voinov and H. Tannenberger, in "From Electrocatalysis to Fuel Cells," G. Sandstedt, Editor, p. 101, University of Washington Press, Seattle, Washington (1972).

¹¹ Present address: Ebauches S.A., Département Technique, CH 2001 Neuchâtel, Switzerland.

¹² J. Heffer and H. Böhm, *Metalloberfläche-Angew. Electrochem.*, **27**, 77 (1973).

¹³ J. McHardy and J. O'M. Bockris, *This Journal*, **120**, 53 (1973).

¹⁴ J.-P. Randin, A. K. Vijh, and A. E. Chughtai, *ibid.*, **120**, 1174 (1973).

hibited by the bronze electrode. The background current in helium saturated solutions was determined in a previous publication¹⁴ and found to be in the range 10^{-6} - 10^{-5} A/cm². McHardy has presented no figure on this point and hence his claim that he could "reduce" the corrosion current down to 10^{-6} A/cm² is not supported by actual data. Steady-state current-potential curves for the oxygen reduction will be influenced by parasitic current as long as the applied current density is not significantly higher than the corrosion current. It is our experience that reproducible results for the oxygen reduction reaction, i.e., current-potential curves free of hysteresis between the ascending (potential acquiring more negative values) and descending curves, were obtained only by working at current densities higher than about 10^{-5} A/cm². In our experiments (see Fig. 1), the concentration of sulfuric acid from 1 down to 0.01N did not significantly influence the shape of the current-potential curve nor the current density at a given potential (except in the hydrogen evolution region). It is therefore unlikely that the acid concentration might be the cause of the discrepancy between McHardy's results and ours.

Figure 1 also shows that the limiting current density is much higher than that reported by McHardy.⁷ The range of potential of the limiting current increases as the pH and, consequently, the hydrogen overvoltage increases. This behavior enables us to study the dependence of the current density on the rotation rate of the electrode in the limiting current region without interference from the hydrogen evolution reaction. At pH 2.7, the linear plot $1/i$ vs. $f^{-1/2}$ (f = rotation rate of the electrode) given in Fig. 2 indicates that the oxygen reduction reaction is first order with respect to dissolved oxygen and is purely diffusion controlled at $E = -0.4V$ since the extrapolation to $f^{-1/2} = 0$ yields a zero intercept. The diffusion limiting current is obtained at $i = 10^{-2.7}$ A/cm² as is also found at noble metal electrodes, whereas Brockris and McHardy found a value of about 10^{-5} A/cm².⁷ Furthermore, the data in Fig. 1 indicate roughly a zero-order reaction with respect to hydrogen ion concentration, as compared to a reaction order of $-1/2$ found by Brockris and McHardy.⁷

The data reported in Fig. 2 show that the rotation of the electrode raised the limiting current as expected for a diffusion-controlled current. Brockris and McHardy⁷ took their low limiting currents as evidence that only a small fraction of the surface actively catalyzed oxygen reduction. The latter authors did not report on the effect of the rotation of the electrode on the limiting current and therefore did not support their claim by actual data.

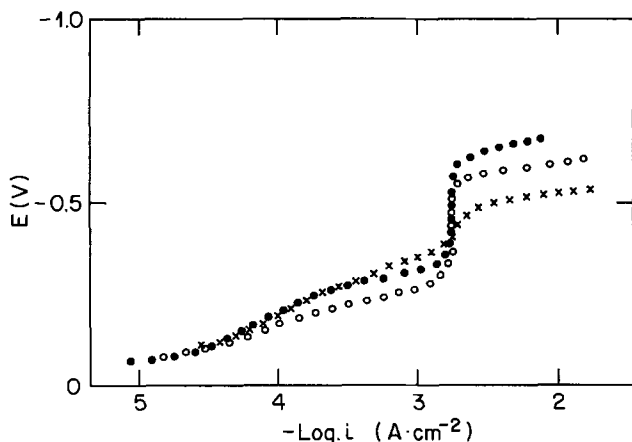


Fig. 1. Steady-state current-potential relationship on $\text{Na}_{0.65}\text{WO}_3$ (1 ppm Pt) in O_2 -saturated 1N H_2SO_4 [$\text{pH} \approx 0.3$, (X)], 0.1N $\text{H}_2\text{SO}_4 + 0.45\text{M Na}_2\text{SO}_4$ [$\text{pH} \approx 1.7$, (O)], and 0.01N $\text{H}_2\text{SO}_4 + 0.495\text{M Na}_2\text{SO}_4$ [$\text{pH} \approx 2.8$, (●)] at 900 rpm. Measurements performed with potentials increasing in the cathodic direction.

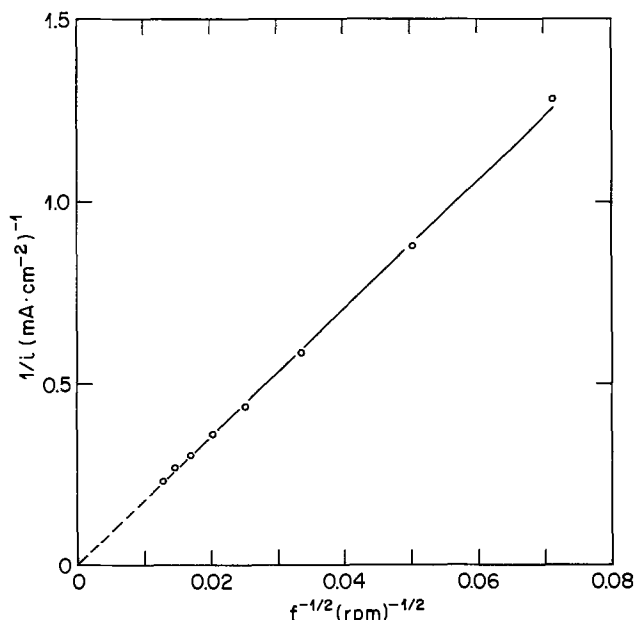


Fig. 2. A plot of $1/i$ vs. $f^{-1/2}$ (f = rotation rate of the electrode) for the reduction of oxygen on $\text{Na}_{0.65}\text{WO}_3$ in O_2 -saturated 0.01N $\text{H}_2\text{SO}_4 + 0.495\text{M Na}_2\text{SO}_4$ ($\text{pH} = 2.8$) at $E = -0.4V$.

Another serious objection concerning the electrocatalytic effect ascribed to traces of platinum is the kinetics of hydrogen evolution and dissolution reactions at tungsten bronzes. If platinum can participate in a process of spillover of adsorbed intermediates to the bronze in the oxygen reduction reaction, the same enhancing effect would also be expected for the hydrogen evolution and dissolution reactions. Such an effect has not been observed, however.^{15,16}

Concerning the second point of McHardy's discussion, i.e., the maximum in the steady-state current-potential curve for hydrogen peroxide reduction, I would refer to a recent publication¹⁷ in which the electrocatalytic activities of Na_xWO_3 , Ni_xWO_3 , Co_xWO_3 , and WO_3 were studied and compared to that of Ce_xWO_3 and Yb_xWO_3 examined by Voinov and Tannenberger.¹⁰ The linear part of the current-potential curve for hydrogen peroxide reduction, from about 0.5 to 0.2V, was not found to depend significantly on the nature of the electrode material for $\text{Na}_{0.58}\text{WO}_3$ - $\text{Na}_{0.59}\text{WO}_3$, $\text{Co}_{0.03}\text{WO}_3$, $\text{Ni}_{0.03}\text{WO}_3$, and WO_3 ,¹⁷ as well as for $\text{Ce}_{0.1}\text{WO}_3$ and $\text{Yb}_{0.1}\text{WO}_3$.¹⁰ At potentials more cathodic than about 0.2V, however, the current-potential curves differ from one material to the other.¹⁷

The current-potential curves reported by Voinov and Tannenberger¹⁰ were restricted to potentials less cathodic than 0V. In the potential range 0.5-0V, Na_xWO_3 is the only electrode which exhibited an inhibition inflexion. The other electrodes studied by Voinov and Tannenberger¹⁰ as well as by us¹⁷ exhibited a change in the slope of the current-potential curve around 0.15V. A closer comparison of the inhibition region, i.e., the second part of the curve between 0.2 and 0V, for Co_xWO_3 , Ni_xWO_3 , Ce_xWO_3 , and Yb_xWO_3 , under the same experimental conditions, indicates a very similar behavior for the four electrodes.

The results obtained by Voinov and Tannenberger¹⁰ for the hydrogen peroxide reduction on Ce_xWO_3 and Yb_xWO_3 are, consequently, in good agreement with our own results on Ni_xWO_3 and Co_xWO_3 . The different behavior of Na_xWO_3 for hydrogen peroxide reduction in the inhibition region, as compared to other tungsten bronzes, may be due to the different charge of the interstitial cation and/or crystallographic differences.¹⁷

¹⁵ D. B. Sepa, D. S. Ovcin, and M. V. Vojnovic, *ibid.*, 119, 1285 (1972).

¹⁶ J.-P. Randin and A.-K. Vijn, *Electrochim. Acta*, 20, 37 (1975).

¹⁷ J.-P. Randin, *J. Electroanal. Chem.*, 51, 471 (1974).

Effect of Gaseous Pretreatment on Oxidation of Iron

A. W. Swanson and H. H. Uhlig (pp. 1551-1554, Vol. 121, No. 12)

D. Chatterjee:¹⁸ The importance of surface-state charge in Uhlig's theory for the so-called first stage of logarithmic oxidation¹⁹ has been emphasized in recent works.²⁰⁻²² The theory has been modified^{21,22} for p-type oxide formation by using Bardeen's concept on the rectifier theory of the metal/semiconductor junction.²³ The modified theory has been successfully applied to elucidate the logarithmic oxidation behavior of polycrystalline metals.²² We would like to apply this theory to the present case of iron and also to the recent results on a single crystal of copper.²⁴

The modified theory²² applies to p-type oxide containing a uniform density space charge layer. The various estimated data are given in Tables I and II for iron (at 250°C) and copper (at 200°C), respectively. The energy (eV_s) and density (n_s) due to the surface-state charge of the oxide are considered to be confined within the metal/oxide interfacial layer, and is equivalent to the average length of individual surface dipole (about 3Å).²² The estimated values for ferrous are thus 2.34 eV and $6 \times 10^{14} \text{ cm}^{-2}$ for eV_s and n_s , respectively. These are calculated using the

¹⁸ The British Aluminum Company, Ltd., Chalfont Park, Gerrards Cross, Buckinghamshire SL9 0QB, England.

¹⁹ H. H. Uhlig, *Acta Met.*, **4**, 541 (1956).

²⁰ A. T. Fromhold, *This Journal*, **115**, 883 (1968).

²¹ B. Chattopadhyay, Ph.D. Thesis, London University (1967).

²² B. Chattopadhyay, *Thin Solid Films*, **16**, 117 (1973).

²³ J. Bardeen, *Phys. Rev.*, **71**, 717 (1947).

²⁴ A. W. Swanson and H. H. Uhlig, *This Journal*, **118**, 1325 (1971).

Table I. Some critical parameters of ferrous oxide at 250°C

Pretreatment condition at 800°C*	Rate constant* (Å)	Space charge density, n_v^{**} ($\text{cm}^{-3} \times 10^{15}$)	Maximum thickness* (Å)	Energy due to space charge, eV_p^{**} (eV)
pco/pco ₂ = 2.3	103	11.29	265	0.184
N ₂ , H ₂ or Ar	129	9.01	297	0.164
pH ₂ O/pH ₂ = 10 ^{-0.5}	140	8.3	360	0.184
pH ₂ O/pH ₂ = 10 ⁻¹	175	6.6	380	0.155

* From the paper under discussion.

** As estimated.

Table II. Some estimated critical parameters of cuprous oxide at 200°C

Plane	Surface-state charge		Space charge	
	Energy, eV_s (eV)	Density, n_s (cm^{-2})	Energy, eV_p (eV)	Density, n_v (cm^{-3})
(100)	0.012	2.32×10^{12}	0.06	8.67×10^{17}
(110)	0.083	1.60×10^{13}	0.09	3.94×10^{18}

work function (ϕ_m) of iron as 4.7 eV,²⁵ 2.2 eV as the electron affinity of oxygen (V_a),²⁶ 0.155 eV as the activation energy of oxidation (ΔE) of iron,²⁷ and 14 as the dielectric constant of ferrous oxide.²⁸ The various parameters of Table II have been estimated by using the data given by Swanson and Uhlig²⁴ for the first stage of logarithmic oxidation of a single crystal of copper.

The different pretreatment conditions of iron altered the rate constant as well as the space charge density (n_v) with little effect on the energy increase (eV_p) due to the space charge (Table I). The estimated n_v -values of Table I and II are reasonable figures for the density of trapping centers in the oxide.^{21,22} It is noted that there is negligible difference in n_v -values of the cuprous oxide formed on the single crystal (Table II) and the polycrystal²² ($n_v = 3 \times 10^{18} \text{ cm}^{-3}$). However, eV_p of the oxide formed on the single crystal is much lower than that on a polycrystalline copper²² ($eV_p = 0.15 \text{ eV}$ using Uhlig's data¹⁹) or iron (Table I). The results showing $eV_s \gg eV_p$ for polycrystalline iron with any pretreatment (Table I) and copper²² obviously indicate the importance and predominant contribution of surface-state charge over the space charge to the potential across the oxide. This kind of behavior is expected.²⁰⁻²² However, in the case of oxidation of a single crystal of copper there is no definite relation between eV_s and eV_p of cuprous oxide formed on the various crystal faces (Table II). Furthermore, a negative eV_s -value is obtained for the oxide on the (111) face when the derived relation²² $eV_s = (e\phi_m - eV_a) - \Delta E$ is used. It is believed that the work function of the (111) face of the metal in contact with oxide, given by Swanson and Uhlig,²⁴ is somewhat lower than expected.

The effect of metal properties on the double layer of surface-state charge and space charge, has been ignored in our theory²² by assuming a high n_s -value. According to Bardeen,²³ there will be no effect of the metal on the double layer of the semiconductor if n_s is sufficiently high, e.g., $n_s > 10^{13} \text{ cm}^{-2}$. The high n_s -values of oxides on polycrystalline iron (as shown here to be $6 \times 10^{14} \text{ cm}^{-2}$) and copper²² ($3.8 \times 10^{14} \text{ cm}^{-2}$) point out the justification of adopting the modified theory^{21,22} in these cases to explain the logarithmic oxidation kinetics. However, the value of n_s is less than or just about equal to 10^{13} cm^{-2} for oxide formed on a single crystal (Table II). Thus the kinetic results of the first stage of logarithmic oxidation of polycrystalline metals cannot be compared with those of single crystals; the latter would involve a different mechanism with low n_s and anomalous relation between eV_s and eV_p of the oxide formed on the various crystal faces.

²⁵ A. B. Cardwell, *Phys. Rev.*, **92**, 554 (1953).

²⁶ N. Cabrera and N. F. Mott, *Rept. Progr. Phys.*, **12**, 163 (1949).

²⁷ P. B. Needham, H. W. Leavenworth, and T. J. Driscoll, *This Journal*, **120**, 778 (1973).

²⁸ "Handbook of Chemistry and Physics," 49th ed., Chemical Rubber Co., Cleveland, Ohio (1968-69).



Oxygen Permeability of Stabilized Zirconia Solid Electrolytes

S. F. Palguy, V. K. Gilderman, and A. D. Neujmin

Institute of Electrochemistry, Urals Scientific Center of the Academy of Sciences, Sverdlovsk, USSR

ABSTRACT

The oxygen permeability of solid electrolytes 85.0 mole per cent (m/o) $ZrO_2 + 15.0$ m/o CaO (I), 90.0 m/o $ZrO_2 + 10.0$ m/o Y_2O_3 (II), 89.0 m/o $ZrO_2 + 8.0$ m/o $Y_2O_3 + 3.0$ m/o Al_2O_3 (III), 90.0 m/o $ZrO_2 + 10.0$ m/o Sc_2O_3 (IV) is investigated at temperature range 900°-1250°C and partial pressures of oxygen 0.01-1.0 atm. The oxygen permeability in this range of oxygen pressures is proportional to $P_{O_2}^{1/4}$. It is shown that the diffusion coefficient of oxygen does not depend on its pressure in a gas atmosphere. Transport numbers of electron holes, which were found to be in limits $1.7 \cdot 10^{-3} + 5 \cdot 10^{-5}$, were determined from the experimental data. The parameter $P_{\ominus}^{1/4}$ ($H_{\ominus} = H_{O_2^-}$) is also calculated.

The oxygen permeability of solid electrolytes with zirconia base, play a big role in the functioning of certain electrochemical devices. However, there are only few investigations on this subject (1-4), and permeability of yttria- and scandia-stabilized zirconia is still not investigated.

We investigated the permeability to oxygen of several solid electrolytes: 85.0 mole per cent (m/o) $ZrO_2 + 15.0$ m/o CaO (I), 90.0 m/o $ZrO_2 + 10.0$ m/o Y_2O_3 (II), 89.0 m/o $ZrO_2 + 8.0$ m/o $Y_2O_3 + 3.0$ m/o Al_2O_3 (III), and 90.0 m/o $ZrO_2 + 10.0$ m/o Sc_2O_3 (IV).

The measurements were made by using a cell schematically shown in Fig. 1. We use the principle that the rate J of penetration of gas through a plate diaphragm of area S cm² is connected directly with a rate of pressure rise ($\Delta P/t$) in a calibrated volume (5). The expression which shows this principle is

$$J = \frac{V\mu}{RTS\rho} \cdot \frac{\Delta P}{t} \frac{\text{cm}}{\text{sec}} \quad [1]$$

Where μ , V , ρ , R , and T are molecular weight, volume, and density of gas at the standard conditions, universal gas constant, and working temperature in °K, respectively.

The permeability constant (η) is given by

$$\eta = \frac{V\mu l}{RTS\rho\Delta P_{O_2}^{1/4}} \cdot \frac{\Delta P}{t} \frac{\text{cm}^2}{\text{sec} \cdot \text{atm}^{1/4}} \quad [2]$$

where l is the thickness of diaphragm and ΔP_{O_2} is the difference of oxygen pressures on the opposite sides of the diaphragm.

The specimens were of oxide solid electrolyte tubes closed at one end. They were placed in an electric resistance furnace in which temperature was precisely controlled and was constant (with accuracy $\pm 2^\circ$) along the working length. The tubes were prepared by common technology (a slicker method). They were 200 mm long, with 9.6 mm outside diameter and about 8.0 mm inside diameter. Porosity was about 5%. Water

absorption of the ceramics was close to zero, and permitted us to consider the porosity to be essentially closed. Chemical analysis of the specimens is given in Table I.

Before every measurement, the tubes were outgassed for a period of 8 or 10 times the time for the gas flow to establish a stationary state. The experimental data are processed by the least squares method. Permeability of the tubes to hydrogen, nitrogen, and argon at a gas pressure difference on the diaphragm equal to 1 atm

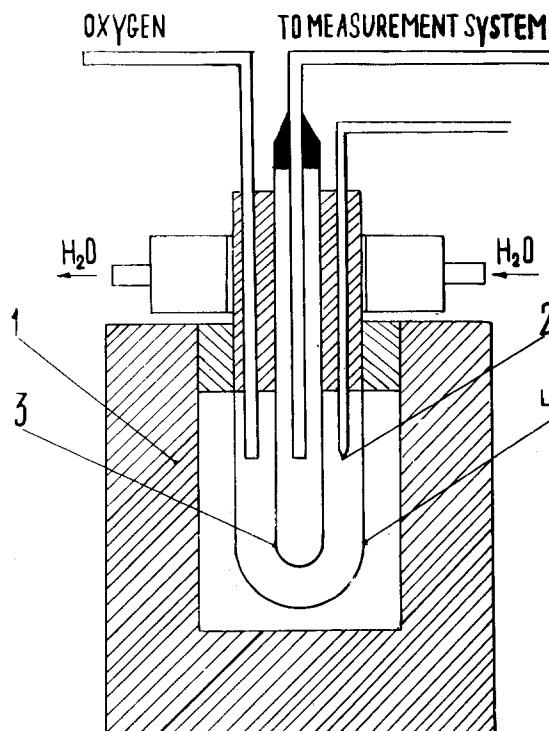


Fig. 1. Scheme of the measuring cell: 1, electric resistance furnace; 2, thermocouple; 3, specimen; 4, quartz tube.

Key words: stabilized zirconia, oxygen permeability, solid electrolyte.

Table I

Sample	Impurity content (w/o)								
	SiO ₂	Fe ₂ O ₃	Al ₂ O ₃	Cr ₂ O ₃	TiO ₂	MnO ₂	Ni ₂ O ₃	MgO	CaO
I	0.23	0.18	0.10	0.03	0.048	0.010	0.009	0.075	—
II	0.65	0.17	0.007	—	0.095	—	—	0.08	0.07
III	1.0	0.6	—	—	0.01	—	—	0.002	0.05
IV	0.26	0.21	0.45	0.01	0.033	0.019	—	0.53	—

was preliminarily investigated. The permeabilities to these gases were lower than the lowest limit of accuracy of our experimental cell ($3 \cdot 10^{-9}$ cm²/atm · sec), that is, the permeation to hydrogen, nitrogen and argon was practically negligible. This shows that pores did not extend through the tube.

Figure 2 shows the curve of the typical oxygen pressure change in calibrated volume in the period of time after the oxygen was admitted into the evacuated solid electrolyte tube. The section BC on the curve corresponds to the establishment of stationary gas flow. The section OA which is cut off by the BC curve on the abscissa, determines the time of diffusion process delay. After Barrer (6) this value, L , is equal to

$$L = \frac{b^2}{6D} \quad [3]$$

The dependencies of the oxygen permeability constant of the investigated specimens upon temperature are shown in Fig. 3. They are given below in units of cm²/sec · atm for the temperature range 900°-1250°C.

$$\eta(\text{I}) = 3.82 \cdot 10^{-1} \exp\left(-\frac{37,200 \pm 400}{RT}\right)$$

$$\eta(\text{II}) = 1.55 \exp\left(-\frac{43,100 \pm 300}{RT}\right)$$

$$\eta(\text{III}) = 1.52 \exp\left(-\frac{42,700 \pm 500}{RT}\right)$$

$$\eta(\text{IV}) = 1.93 \exp\left(-\frac{38,900 \pm 600}{RT}\right)$$

The obtained values of the activation energy and pre-exponent factors of the permeability constant lie within the values, which were obtained for other compositions of zirconia-based solid electrolytes (2, 4, 7-9). The values of permeability are different, whereas the activation energy differ negligibly since they are mainly determined by diffusion process.

The process of oxygen permeation through a dense diaphragm with oxygen ion conductivity and a small part of electronic conductivity consists of several stages.

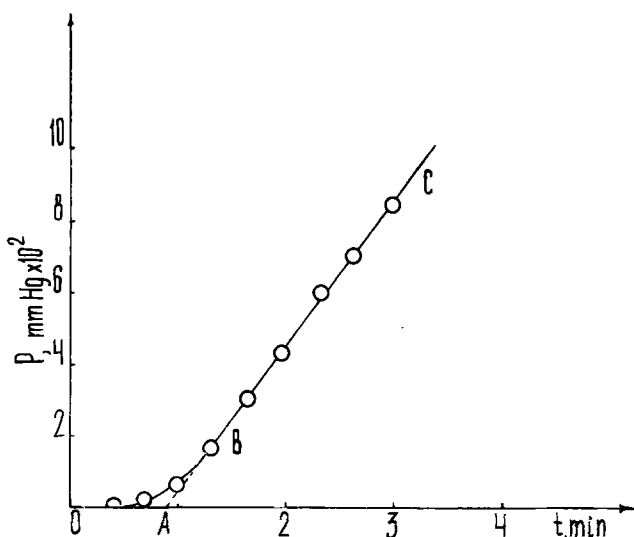


Fig. 2. The curve of oxygen pressure change in the calibrated volume (specimen III at temperature 1240°C).

Oxygen diffuses from gaseous phase to a surface of the diaphragm, adsorbs and dissolves there. Oxygen ions diffuse through the crystal lattice of an oxide electrolyte. Simultaneously electron holes move in the opposite direction. At the other side of the diaphragm oxygen ions turn into atoms and, after forming into molecules, desorb to diffuse into a gas phase.

Gas permeation is determined by two processes: diffusion of oxygen through ceramics and of oxygen solubility in it. If the values of the diffusion coefficients in different electrolytes are close to each other, the greater oxygen permeability may be explained by a greater solubility of oxygen.

As is seen in Fig. 4, permeation is proportional to $P_{O_2}^{1/4}$ for all the specimens in the investigated range of oxygen pressure (0.01-1.0 atm). The same dependence is reported by others (2, 4). That fact is an evidence of controlling the oxygen permeability by diffu-

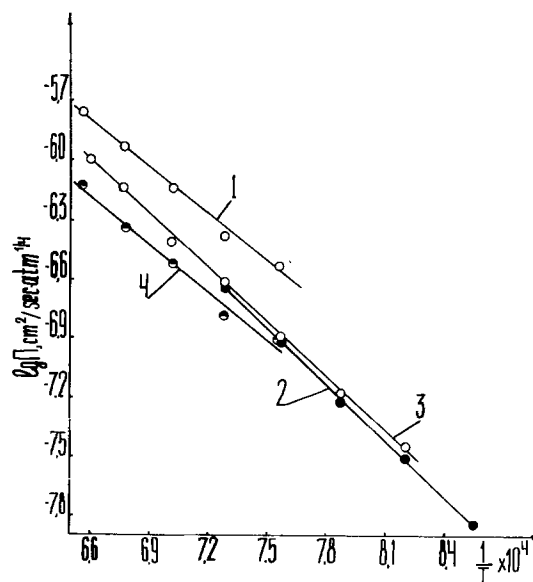


Fig. 3. The temperature dependence of oxygen permeability constant. Specimens: 1, I; 2, II; 3, III; 4, IV.

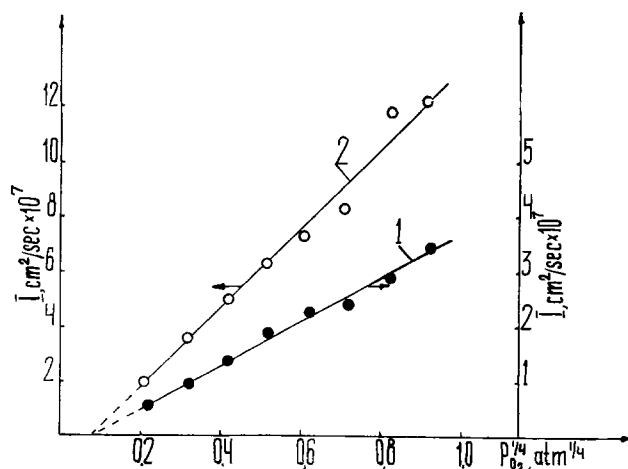


Fig. 4. The dependence of oxygen permeability upon oxygen pressure in a gas phase for specimens: 1, IV at 1150°C and 2, I at 1200°C.

sion of the electron holes. But in our case at the small values of oxygen pressures, the dependence changes.

If a diaphragm is thick enough, the rate of adsorption and desorption of oxygen on the surface of oxide is faster than the rate of diffusion, therefore surface layers of the oxygen electrolyte must be in a state near to an equilibrium with the gas phase. Probably the rate of oxygen adsorption and desorption processes at small pressures ($P_{O_2} \ll 4.10^{-5}$ atm) becomes comparable with diffusion rate, and the process of permeability begins to be controlled by the adsorption and desorption processes.

Diffusion coefficients of oxygen were calculated from the experimental data. Values L were determined by graphic method from the curves of type shown in Fig. 2. Then using Eq. [3] the diffusion coefficients were calculated. Temperature dependences of diffusion coefficients for some electrolytes are shown in Fig. 5. They are given in terms of square centimeters per second by the expressions

$$D(I) = 1.07 \exp \left(\frac{36,400 \pm 800}{RT} \right)$$

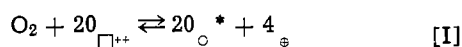
$$D(II) = 1.29 \exp \left(\frac{34,100 \pm 500}{RT} \right)$$

$$D(IV) = 0.76 \exp \left(\frac{35,800 \pm 700}{RT} \right)$$

Values of the pre-exponent factor and activation energy lie close to each other, so that the dependence upon the kind of stabilizing addition used is slight.

Dependence of diffusion coefficients upon oxygen pressure is also shown in Fig. 5. It is seen that the diffusion coefficient does not depend on oxygen pressure. Therefore the mobility of electron holes in the investigated electrolytes practically does not depend on their concentration (in a range oxygen pressures 0.01-1.0 atm). But at the same time, the data obtained for the permeability and diffusion coefficients, show that the hole concentration depends on partial oxygen pressure in power 1/4.

Since for our solid electrolytes, $D_{\oplus} C_{\oplus}$ is much smaller than $D_{\ominus} C_{\ominus}$, diffusion coefficient of oxygen will be determined by flow of holes (10). The hole concentration in a surface layer of the diaphragm is determined by an oxygen exchange reaction between the gas phase and the solid electrolyte



Here $O_{\square^{++}}$ is the oxygen vacancy, O_{\circ}^* , the oxygen atom in a normal position of a crystal lattice.

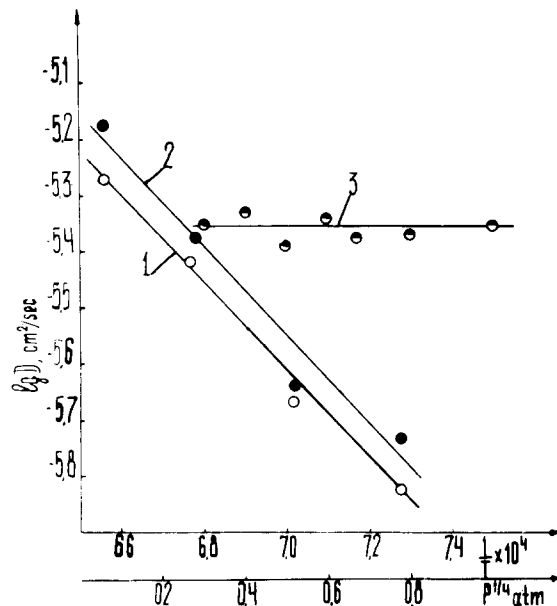


Fig. 5. The temperature dependence of diffusion coefficient for specimens: 1, IV; 2, 1; 3, dependence of diffusion coefficient upon oxygen pressure for specimen IV at temperature 1200°C.

Using the law of mass action to reaction (I) the dependence of the hole concentration in surface layer on the oxygen pressure is derived.

$$C_{\oplus} = K_s \cdot P_{O_2}^{1/4} \quad [4]$$

Where the solubility constant, K_s , is equal to the hole concentration at 1 atm oxygen pressure.

Using the Nernst-Einstein equation, the electric conductivity value, caused by migration of holes (H_{\oplus}) in an electrolyte, can be obtained

$$H_{\oplus} \cdot (P_{O_2} = 1 \text{ atm}) = \frac{4F^2 \eta_0}{RT} \exp \left(- \frac{E_n}{RT} \right) \quad [5]$$

Here E_n is the activation energy of oxygen permeability, η_0 is the pre-exponential factor, and F , Faraday's constant.

Transference number of the electron holes at $P_{O_2} = 1$ atm is equal to

$$t_{\oplus} = \frac{4F^2 \eta_0}{RTH_0} \exp \left(- \frac{E_n - E_0}{RT} \right) \quad [6]$$

where E_0 is the activation energy of oxygen conductivity and H_0 is the pre-exponential factor.

Table II. Ionic and electronic parts of conductivity and transference numbers of electron holes in some electrolytes on the zirconia basis

T°C	85.0 m/o ZrO ₂ + 15.0 m/o CaO			90.0 m/o ZrO ₂ + 10.0 m/o Y ₂ O ₃		
	H _⊕ (ohm ⁻¹ ·cm ⁻¹)	H _⊖ (ohm ⁻¹ ·cm ⁻¹) (11)	t _⊕	H _⊕ (ohm ⁻¹ ·cm ⁻¹)	H _⊖ (ohm ⁻¹ ·cm ⁻¹) (12)	t _⊕
1050	4.0·10 ⁻⁵	3·10 ⁻²	1.4·10 ⁻³	1.9·10 ⁻⁵	1.8·10 ⁻¹	1.0·10 ⁻⁴
1100	6.4·10 ⁻⁵	4.5·10 ⁻²	1.4·10 ⁻³	3.3·10 ⁻⁵	2.4·10 ⁻¹	1.4·10 ⁻⁴
1150	1.0·10 ⁻⁴	6.8·10 ⁻²	1.5·10 ⁻³	5.5·10 ⁻⁵	3.1·10 ⁻¹	1.8·10 ⁻⁴
1200	1.6·10 ⁻⁴	9.6·10 ⁻²	1.6·10 ⁻³	8.9·10 ⁻⁵	3.9·10 ⁻¹	2.3·10 ⁻⁴
1250	2.3·10 ⁻⁴	1.3·10 ⁻¹	1.7·10 ⁻³	1.4·10 ⁻⁴	4.9·10 ⁻¹	2.8·10 ⁻⁴
T°C	89.0 m/o ZrO ₂ + 8.0 m/o Y ₂ O ₃ + 3.0 m/o Al ₂ O ₃			90.0 m/o ZrO ₂ + 10.0 m/o Sc ₂ O ₃		
	H _⊕ (ohm ⁻¹ ·cm ⁻¹)	H _⊖ (ohm ⁻¹ ·cm ⁻¹) (13)	t _⊕	H _⊕ (ohm ⁻¹ ·cm ⁻¹)	H _⊖ (ohm ⁻¹ ·cm ⁻¹) (14)	t _⊕
1050	2.0·10 ⁻⁵	1.4·10 ⁻¹	1.5·10 ⁻⁴	1.6·10 ⁻⁵	3.2·10 ⁻¹	5.1·10 ⁻⁵
1100	3.5·10 ⁻⁵	1.8·10 ⁻¹	1.9·10 ⁻⁴	2.6·10 ⁻⁵	3.7·10 ⁻¹	7.2·10 ⁻⁵
1150	5.9·10 ⁻⁵	2.4·10 ⁻¹	2.4·10 ⁻⁴	4.2·10 ⁻⁵	4.3·10 ⁻¹	9.8·10 ⁻⁵
1200	9.6·10 ⁻⁵	3.1·10 ⁻¹	3.1·10 ⁻⁴	6.3·10 ⁻⁵	4.9·10 ⁻¹	1.3·10 ⁻⁴
1250	1.5·10 ⁻⁴	4.0·10 ⁻¹	3.7·10 ⁻⁴	9.3·10 ⁻⁵	5.5·10 ⁻¹	1.7·10 ⁻⁴

Table III. Parameter $P_{\oplus}^{1/4}$ for solid electrolytes on the zirconia basis in temperature range 1050°-1250°C

Electrolyte	H_{\oplus} (ohm ⁻¹ ·cm ⁻¹)	$H_{O^{--}}$ (ohm ⁻¹ ·cm ⁻¹)	$P_{\oplus}^{1/4} (H_{\oplus} = H_{O^{--}})$ (atm)
85.0 m/o ZrO ₂ + 15.0 m/o CaO	$\frac{7.64 \cdot 10^4}{T} \cdot \exp\left(-\frac{37,200}{RT}\right) \cdot P_{O_2}^{1/4}$	$8.32 \cdot 10^2 \cdot \exp\left(-\frac{27,000}{RT}\right)$	$1.09 \cdot 10^{-2} \cdot T \cdot \exp\left(\frac{10,200}{RT}\right)$
90.0 m/o ZrO ₂ + 10.0 m/o Y ₂ O ₃	$\frac{3.1 \cdot 10^5}{T} \cdot \exp\left(-\frac{43,100}{RT}\right) \cdot P_{O_2}^{1/4}$	$3.89 \cdot 10^2 \cdot \exp\left(-\frac{20,200}{RT}\right)$	$1.25 \cdot 10^{-3} \cdot T \cdot \exp\left(\frac{22,900}{RT}\right)$
89.0 m/o ZrO ₂ + 8.0 m/o Y ₂ O ₃ + 3.0 m/o Al ₂ O ₃	$\frac{3.04 \cdot 10^5}{T} \cdot \exp\left(-\frac{42,700}{RT}\right) \cdot P_{O_2}^{1/4}$	$4.9 \cdot 10^2 \cdot \exp\left(-\frac{21,600}{RT}\right)$	$1.61 \cdot 10^{-3} \cdot T \cdot \exp\left(\frac{21,100}{RT}\right)$
90.0 m/o ZrO ₂ + 10.0 m/o Sc ₂ O ₃	$\frac{3.86 \cdot 10^4}{T} \cdot \exp\left(-\frac{38,900}{RT}\right) \cdot P_{O_2}^{1/4}$	$1.98 \cdot 10 \cdot \exp\left(-\frac{19,900}{RT}\right)$	$5.12 \cdot 10^{-4} \cdot T \cdot \exp\left(\frac{20,000}{RT}\right)$

Table II gives the results of calculations of the transference numbers of electron holes in investigated electrolytes at the oxygen pressure 1 atm. The temperature dependence of electrical conductivity used in calculations was taken from literature (11-14). It can be seen that the transference numbers of holes are within the limits $5 \cdot 10^{-5}$ - $1.7 \cdot 10^{-3}$. It is seen that the electrolyte with a scandia addition has the smallest part of electronic conductivity.

The dependence of hole conductivity upon the pressure of oxygen in a gas phase and analytical expressions for the temperature dependence of parameter $P_{\oplus}^{1/4}$ (the oxygen pressure in a gas phase, when the values of electronic p-type and ionic conductivities are equal) are also calculated. The results are given in Table III.

Manuscript submitted May 30, 1974; revised manuscript received Dec. 24, 1975.

Any discussion of this paper will appear in a Discussion Section to be published in the December 1975 JOURNAL. All discussions for the December 1975 Discussion Section should be submitted by Aug. 1, 1975.

REFERENCES

1. Yu. M. Ovchinnikov, S. V. Karpachov, A. D. Neumin, and S. F. Palguyev, *Ogneupory*, **30**, 40 (1965).
2. A. W. Smith, F. W. Meszares, and C. D. Amata, *J. Am. Ceram. Soc.*, **49**, 240 (1966).
3. R. Hartung and H. H. Moebius, *Z. Phys. Chem. (Leipzig)*, **243**, 133 (1970).
4. W. A. Fischer, in "Fast Ion Transport in Solids. Solid State Batteries and Devices" W. Van Gool, Editor, pp. 503-512, North-Holland Publishing Company, Amsterdam (1972).
5. V. E. Volkov, R. A. Ryabov, P. V. Geld, and G. D. Fedorov, *Izv. Vysshikh Uchebn. Zavedenii Fiz.*, **15**, 127 (1972).
6. R. Barrer, "Diffusion in Solids" (Russian translation) (1948).
7. H. Ullmann, *Z. Phys. Chem. (Leipzig)*, **237**, 71 (1968).
8. H. H. Moebius and R. Hartung, *Silikat Techn.*, **55**, 363 (1951).
9. H. H. Moebius and R. Hartung, *ibid.*, **16**, 276 (1965).
10. F. A. Kroger, "The Chemistry of Imperfect Crystals," North-Holland Publishing Company, Amsterdam (1964).
11. A. D. Neumin, S. F. Palguyev, V. N. Strekalovskii, and G. V. Burov, *Tr. Inst. Elektrochim. Akad. Nauk SSSR Ural'sk Filial*, **4**, 83 (1963).
12. A. G. Kotlyar, A. D. Neumin, S. F. Palguyev, and V. N. Strekalovskii, *Izv. Akad. Nauk USSR. Neorg. Mater.*, **6**, 532 (1970).
13. A. G. Kotlyar, Thesis, Institute of Electrochemistry, Sverdlovsk, USSR (1969).
14. A. D. Neumin, Ju. N. Karavaev, and S. F. Palguyev, *Tr. Inst. Elektrochim. Akad. Nauk SSSR*, **21**, (1975).

Heterogeneous Halide-Silica Phosphors

Willi Lehmann*

Westinghouse Research Laboratories, Pittsburgh, Pennsylvania 15235

ABSTRACT

Efficient photoluminescence in phosphors containing about 90% SiO₂ and 10% CaCl₂ or other halides is observed after activation with Eu²⁺ (violet to blue colors) or Eu²⁺ plus Mn²⁺ (yellow to red). The materials are heterogeneous, consisting of luminescent halides dispersed in small segregations inside of bigger and nonluminescent SiO₂ particles. The phosphors are stable in water and acids (except HF) because the hygroscopic halides are protected by surrounding SiO₂.

Quartz containers used to prepare red emitting CaS:Eu²⁺ phosphors frequently show blue luminescence which is easily excited by irradiation with ultraviolet. The optical properties of the luminescence and the absence of a corresponding effect on quartz containers used to prepare CaS-phosphors with any of the many other impurities active in CaS (1) clearly indicate that Eu²⁺ is the responsible activator. The blue luminescence appears to be a property of

the solid quartz container, i.e., it cannot be mechanically removed without destroying the quartz and the only chemical means to remove it is strong hydrofluoric acid. An investigation was started to find the origin of this very striking luminescence, and we discovered a peculiar class of heterogeneous materials which appear not to be reported before.

SiO₂ obviously is involved since the blue luminescence is restricted to the walls of the containers and does not appear in its content of CaS:Eu²⁺. Attempts to reproduce it in calcium silicates were not successful; Eu²⁺ does not show this blue luminescence in

* Electrochemical Society Active Member.
Key words: luminescence, phosphors, halide, silica, europium, manganese.

any of the known calcium silicates (2). However, the blue luminescence does appear in preparations containing also CaCl_2 besides CaO and SiO_2 . Since several calcium and strontium halo-silicates have been reported already (3, 4), a calcium halo-silicate, perhaps of a still unknown composition, became suspect and the investigation was broadened to include various ratios of $\text{CaO}:\text{CaCl}_2:\text{SiO}_2$. Surprisingly, the optimum ratio turned out to be about 90 mole per cent (m/o) SiO_2 and 10 m/o CaCl_2 with little or no CaO at all (Fig. 1). The following describes preparational details and results of the investigation.

Preparation

Heterogeneous phosphors of this kind are easily prepared by firing a uniform mixture of silicic acid, CaO , Eu_2O_3 , and an excess of NH_4Cl at about $950^\circ\text{--}1000^\circ\text{C}$ in slightly reducing atmosphere (e.g., $\text{N}_2 + 1\% \text{H}_2$). The preferred molar ratio of $\text{SiO}_2:\text{CaO}:\text{Eu}_2\text{O}_3$ is about 95:4.5:0.5 to 80:19.5:0.5. The NH_4Cl reacts with CaO and Eu_2O_3 to form the halides *in situ*, all excess of NH_4Cl not used in this conversion sublimates out of the container during firing. After firing and cooling, the phosphors are washed in water to remove any free halide. When dry, they are free flowing powders, stable in air, water, alkaline solutions, and acids with the only exception of strong hydrofluoric acid.

Calcium in the above formation may be replaced by Sr, Li, or La (but not by Mg, Ba, Na, K, Zn, Cd, Y). The chloride may be replaced by bromide or by iodide (but not by fluoride). Europium may not be replaced by any other activator but can be combined with manganese in which case the emission of Eu^{2+} sensitizes Mn^{2+} for excitation by ultraviolet. Depending on composition, emission ranging from violet to blue (for Eu^{2+}) and from yellow to red and infrared (for Mn^{2+}) may thus be obtained.

Results

Chemical analysis of a sample $(\text{CaCl}_2\text{-SiO}_2):\text{Eu}^{2+}$, Mn^{2+} made with the addition of 1% EuCl_2 , 1% MnCl_2 , and 8% CaCl_2 (rest SiO_2) showed approximately half of the added amounts of Eu, Mn, and Ca still present after firing and washing, the other half mainly lost into the washing water.

X-ray diffraction spectra of the phosphor samples normally show only lines corresponding to the α -cristobalite modification of SiO_2 . Whatever else is present must be either amorphous or in amounts too small to be detected by routine x-ray analysis (detectability limit: several %).

Microscopic examination shows mainly irregularly shaped particles roughly 5-20 μm in size. Some are relatively clear. Others contain so many small in-

clusions (0.1-0.3 μ) that the particles appear almost opaque against white background illumination. Only these inclusions are visibly luminescent under ultraviolet irradiation, the clear parts of the inclusion carrying particles and all of the completely clear particles remain dead (Fig. 2). Particles with many luminescent inclusions dominate in a material made to optimum performance, fired at about $950^\circ\text{--}1000^\circ\text{C}$. Too low ($\sim 800^\circ\text{C}$) and too high ($\sim 1200^\circ\text{C}$) firing temperatures result mainly, or only, in clear particles (Fig. 3) and correspondingly poor luminescence.

Emission spectra of phosphors made with various halides and activated with Eu^{2+} and Mn^{2+} are shown in Fig. 4-6. Approximate peak positions of the emission bands, at room temperature, are given in Table I. Eu^{2+} produces violet to blue emissions; it responds to near-ultraviolet because of its strong and broad optical absorption next to the emission (Fig. 7). Mn^{2+} emission does not appear in the strontium halides (Fig. 5). In the other halides, it can optically be excited if Eu^{2+} is present as a sensitizer. The efficiency of the energy transfer $\text{Eu}^{2+} \rightarrow \text{Mn}^{2+}$ depends on the concentrations of both; it may be fairly high (approaching unity) but is never complete. Several per cent of the Eu^{2+} emission usually are left unconverted even in phosphors designed to have strong Mn^{2+} emission.

The over-all quantum efficiency (Eu^{2+} plus Mn^{2+}) is surprisingly high (80-90% have repeatedly been measured) if one considers the fact that most of the materials consist of nonluminescent SiO_2 .

Figure 8 compares the emission of heterogeneous $(\text{CaCl}_2\text{-SiO}_2):\text{Eu}^{2+}$ to that of plain $\text{CaCl}_2:\text{Eu}^{2+}$ with-

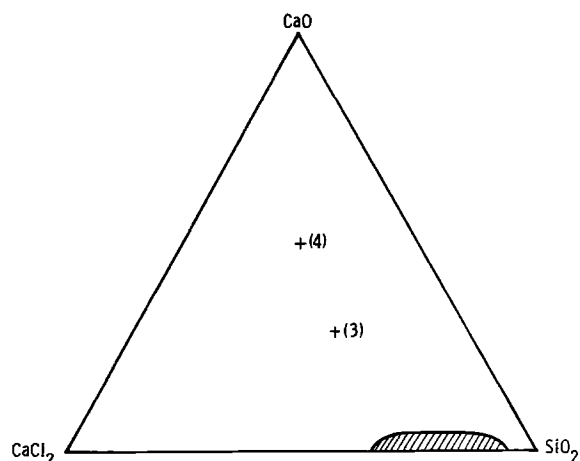


Fig. 1. Optimum compositions of blue-violet Eu^{2+} -emission in the ternary system $\text{CaO-CaCl}_2\text{-SiO}_2$ (shaded areas). Points (3) and (4) correspond to the halo-silicates reported in Ref. (3) and (4).

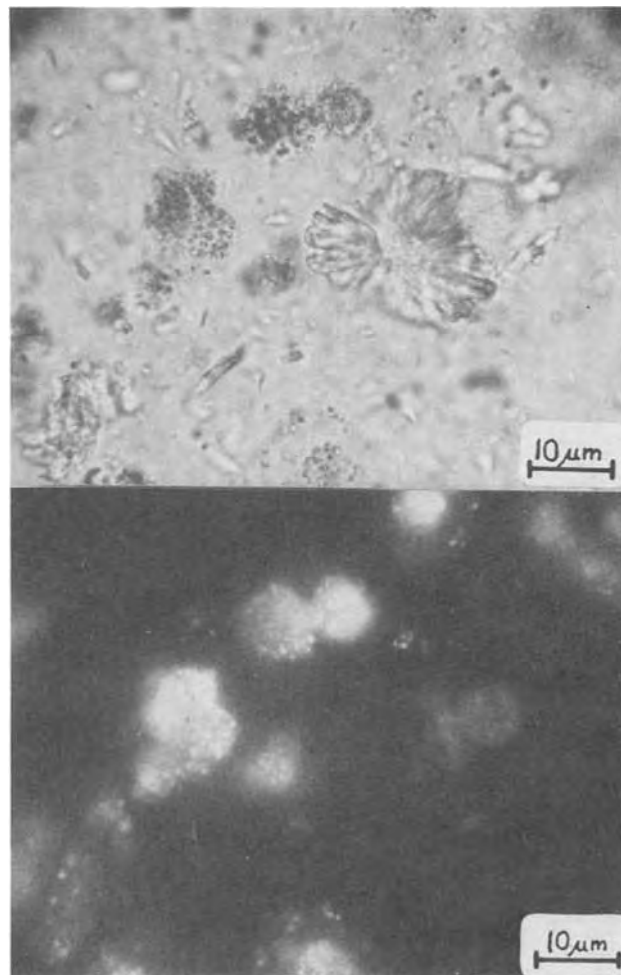


Fig. 2. Photomicrograph of $\text{CaCl}_2:\text{Eu}^{2+}, \text{Mn}^{2+}\text{-SiO}_2$ particles (92% SiO_2) illuminated by white light from the rear (top) and in their own luminescence excited by ultraviolet irradiation.

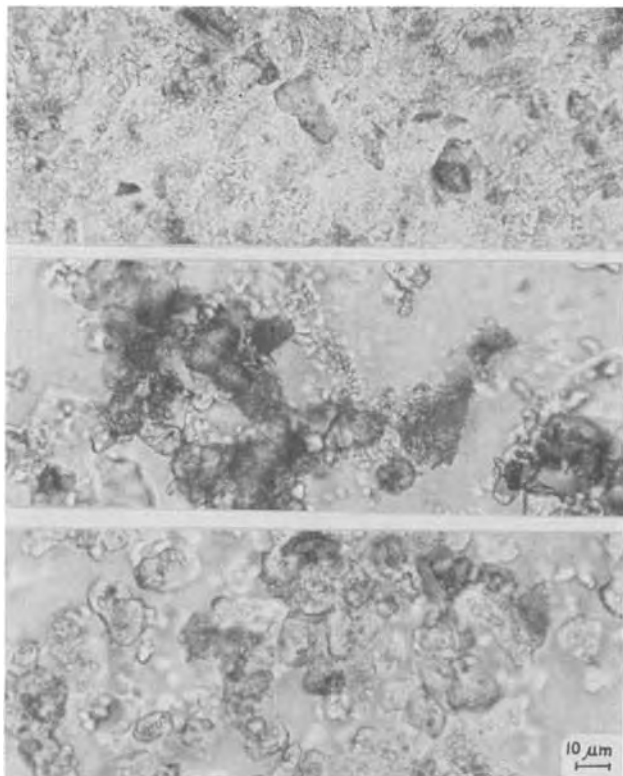


Fig. 3. Photomicrograph of heterogeneous $\text{CaCl}_2:\text{Eu}^{2+}-\text{SiO}_2$ (92%) after firing 1 hr at (top to bottom) 800° , 1000° , and 1200°C .

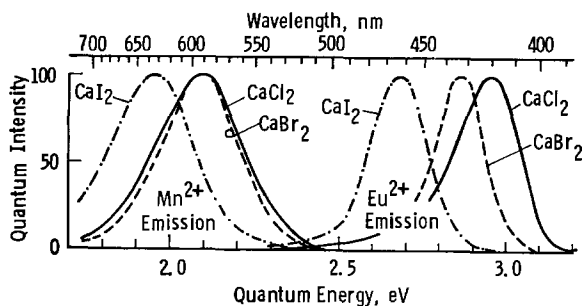


Fig. 4. Emission spectra of Eu^{2+} and Mn^{2+} in CaCl_2 , CaBr_2 , and CaI_2 .

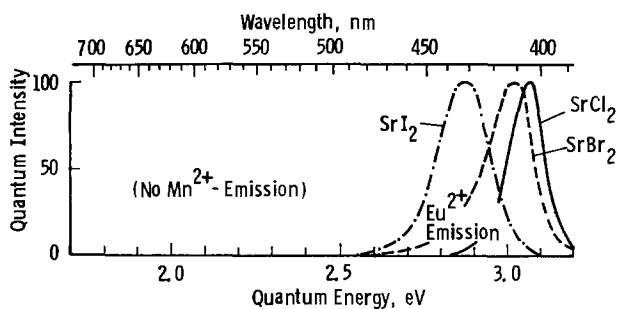


Fig. 5. Emission spectra of Eu^{2+} in SrCl_2 , SrBr_2 , and SrI_2

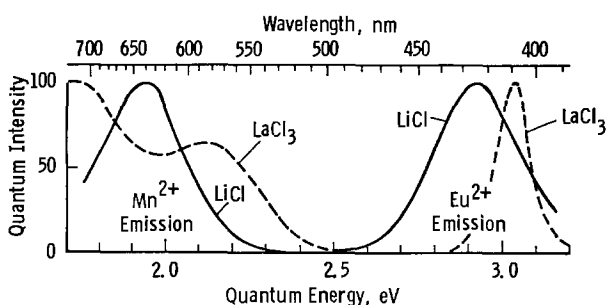


Fig. 6. Emission spectra of Eu^{2+} and Mn^{2+} in LiCl and LaCl_3

Table I. Emission peak positions (in nm) of halides dispersed in SiO_2

	Eu^{2+}	Mn^{2+}
CaCl_2	426	590
CaBr_2	433	590
CaI_2	463	634
SrCl_2	405	—
SrBr_2	411	—
SrI_2	431	—
LiCl	424	639
LaCl_3	409	581 + 717

out addition of any oxide. Except for the low-energy tail (frequently observed in heterogeneous phosphors) of the former, the spectra are sufficiently alike to indicate common origin. Emission spectra of Mn^{2+} are given in Fig. 9 of heterogeneous $(\text{CaCl}_2-\text{SiO}_2)\text{Eu}^{2+}$, Mn^{2+} , of several similar preparations where SiO_2 was replaced by MgO , Al_2O_3 , or Y_2O_3 , and of plain $\text{CaCl}_2:\text{Eu}^{2+}$, Mn^{2+} made without addition of an oxide. Again, the spectra are alike enough to indicate com-

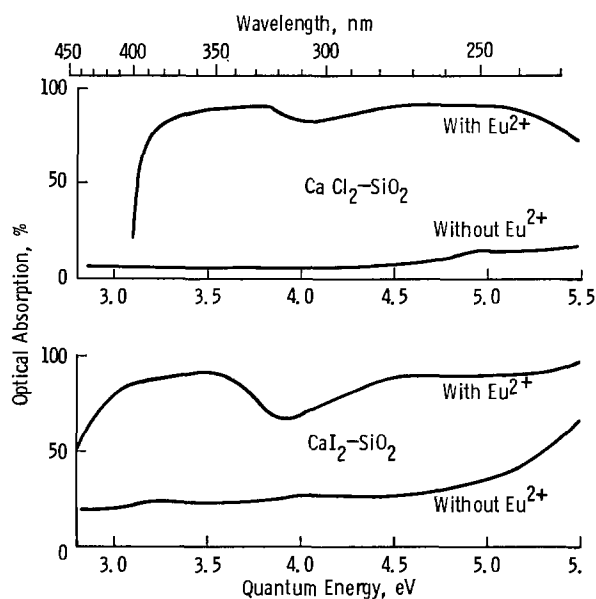


Fig. 7. Optical absorption spectra of CaCl_2 (top) and CaI_2 (bottom) in SiO_2 with or without Eu^{2+} .

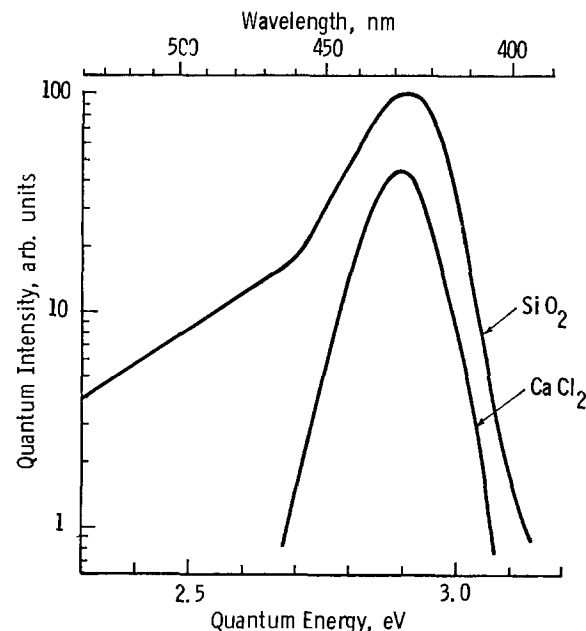


Fig. 8. Eu^{2+} emission of $\text{CaCl}_2-\text{SiO}_2$ (top) and of plain CaCl_2 (bottom curve). Logarithmically calibrated ordinate. Spectra are arbitrarily moved up and down to avoid confusion.

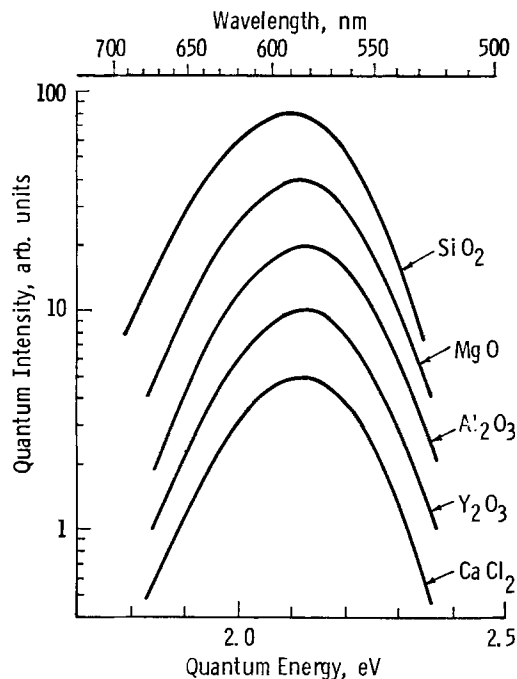


Fig. 9. Mn^{2+} emission of $CaCl_2$ condensed in or on (top to bottom) SiO_2 , MgO , Al_2O_3 , Y_2O_3 , and of plain $CaCl_2$. Logarithmically calibrated ordinate. Spectra are arbitrarily moved up and down to avoid confusion.

mon origin. The main difference between all these materials is the chemical stability. Heterogeneous SiO_2 -containing phosphors are insensitive to water; all others are hygroscopic and their luminescence is immediately destroyed if they come into contact with water. This observation is trivial for the case of $CaCl_2$ (no SiO_2) which is well known to be hygroscopic and soluble in water. Microscopic inspection of the particles of materials made with addition of MgO , Al_2O_3 , or Y_2O_3 does not reveal the sort of luminescent inclusions as they are observed in SiO_2 . Obviously, the luminescent $CaCl_2$ phase in these materials is present not in, but outside of, the oxide particles where it easily can all be removed by washing in water.

Figures 9 and 10 show the temperature dependence of the luminescence of several materials (plaques, excited by 365 nm u.v.). The data represent quantum densities, arbitrarily normalized to 100 units at room temperature. Simultaneously with a decreasing efficiency, the emission of Mn^{2+} shifts appreciably to shorter wavelengths with increasing temperature. A

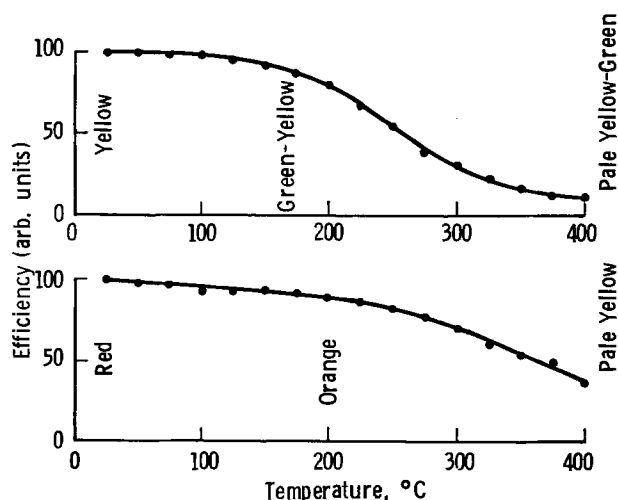


Fig. 10. Temperature dependence of luminescent efficiency and color shift of yellow $CaCl_2:Eu^{2+}, Mn^{2+}$ (top) and of red $CaCl_2:Eu^{2+}, Mn^{2+}$ (bottom), both in SiO_2 .

similar shift of the emission of Eu^{2+} is much less pronounced.

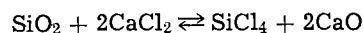
Discussion

In view of the inability of pure SiO_2 (without halides) to show the observed luminescence in presence of Eu^{2+} or Mn^{2+} , of all other observations described above, and of the known blue luminescence of $SrCl_2:Eu^{2+}$ reported before (3), we conclude heterogeneous halide-silica phosphors to consist of two separate phases. One phase (roughly 9/10 of the entire material) is SiO_2 either present as α -cristobalite or amorphous. It is not visibly luminescent, but it is very transparent for ultraviolet or visible radiation. The other, smaller phase is luminescent metal halide containing Eu^{2+} or $Eu^{2+} + Mn^{2+}$. After firing, but before washing the phosphor, part of the halide is present in small segregations inside, another part apparently is condensed on the surfaces outside, of bigger SiO_2 particles. Washing in water dissolves the latter but not the former. The luminescent segregations inside of the particles are protected by surrounding SiO_2 against about anything but strong hydrofluoric acid. This permits studying and utilizing the luminescence of metal halides which otherwise would be too hygroscopic to be handled unprotected in open air.

A somewhat similar heterogeneous phosphor system has been reported by Wachtel (5) for the composition $x \cdot SiO_2 - (1 - x) \cdot Al_2O_3:Eu^{2+}$ where $x = 0.9-0.95$. Wachtel attributes the luminescence of this material to $3Al_2O_3 \cdot 2SiO_2:Eu^{2+}$ dispersed in SiO_2 . The luminescent halides dispersed in SiO_2 described above appear to be another example of the same phenomenon.

Heterogeneous halide-silica phosphors made by reaction of La_2O_3 with NH_4Cl in presence of an excess of SiO_2 might be open to dispute whether the luminescent phase is $LaOCl$ or $LaCl_3$. We believe it to be the latter since $LaOCl:Eu$, even if especially prepared in reducing atmosphere, invariably shows the typical red line emission of Eu^{3+} which is completely absent in the heterogeneous phosphors described here (Fig. 6).

The question comes up how the halide segregations end up inside of solid SiO_2 particles during preparation. Obviously, this must involve a transport of matter. We suggest a reversible reaction of the kind



to be involved. The equilibrium of this reaction during firing apparently is heavily, but not entirely, on the left side. Little or no formation of $SiCl_4 + 2CaO$ as intermediate products could not explain the growth of SiO_2 particles, with or without inclusions, at the

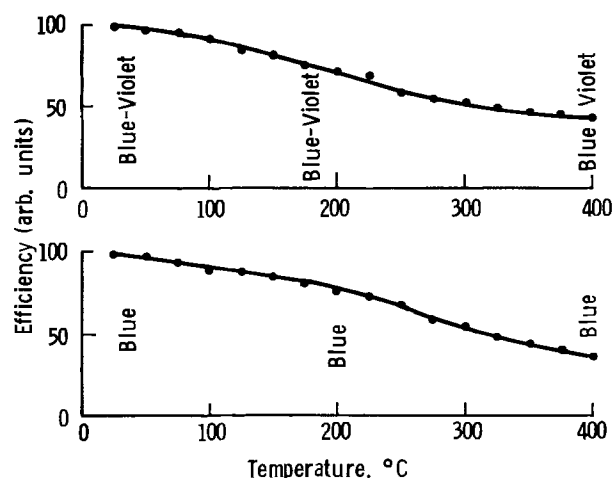


Fig. 11. Temperature dependence of luminescent efficiency of blue-violet $CaCl_2:Eu^{2+}$ (top) and of blue $CaCl_2:Eu^{2+}$ (bottom), both in SiO_2 .

relatively low temperature of 950°-1000°C. On the other hand, if the equilibrium would be heavily on the right side, volatile SiCl_4 should escape and CaO should remain either as a separate phase or reacted with the rest of the SiO_2 as calcium silicate. Neither is actually observed. This necessary balance of the reaction equation favoring the left side without entire exclusion of the right, may not be present if CaCl_2 is replaced by a halide of Mg, Ba, Na, etc., and this appears to be the reason why these combinations do not work to form heterogeneous silica phosphors of the described sort.

Systems analogous to heterogeneous silica phosphors appear to be possible also with other glass-forming oxides like GeO_2 , P_2O_5 , and B_2O_3 although the conditions of preparation are somewhat different from those involving SiO_2 . Details of these cases are not yet available. Such materials containing luminescent halides suspended in optically inert glass-forming oxides may easily be mistaken by superficial examina-

tion as uniform phosphor compounds. We warn against this misinterpretation.

Manuscript submitted Nov. 15, 1974; revised manuscript received Feb. 7, 1975. This was Paper 197 presented at the Toronto, Canada, Meeting of the Society, May 11-16, 1975.

Any discussion of this paper will appear in a Discussion Section to be published in the December 1975 JOURNAL. All discussions for the December 1975 Discussion Section should be submitted by Aug. 1, 1975.

Publication costs of this article were partially assisted by Westinghouse Electric Corporation.

REFERENCES

1. W. Lehmann, *J. Luminescence*, **5**, 87 (1972).
2. B. Phillips and A. Muan, *J. Am. Ceram. Soc.*, **42**, 414 (1959).
3. H. L. Burrus, K. P. Nicholson, and H. P. Rooksby, *J. Luminescence*, **3**, 467 (1971).
4. W. L. Wanmaker and J. G. Verriet, *Philips Res. Rept.*, **28**, 80 (1973).
5. A. Wachtel, *This Journal*, **116**, 61 (1969).

The Interaction of Color Centers and Cd^{+2} and Sb^{+3} Ions in Calcium Fluorophosphate

R. W. Warren, F. M. Ryan,* and R. H. Hopkins

Westinghouse Research Laboratories, Pittsburgh, Pennsylvania 15235

and J. Van Broekhoven*

Westinghouse Electric Corporation, Fluorescent and Vapor Lamp Division, Bloomfield, New Jersey 07003

ABSTRACT

Calcium fluorophosphate powders containing various amounts of cadmium and antimony and single crystals containing antimony were subjected to u.v. irradiation and thermal annealing treatments. The color centers formed by the irradiations were studied by electron spin resonance and by optical techniques. Two previously unreported color centers were observed, one associated with the presence of antimony and the other with the presence of cadmium. Growth dynamics and models for these two centers are given and their importance in phosphors is discussed. A simple model for phosphor depreciation is proposed in which these centers play crucial roles.

Calcium fluorophosphate $\text{Ca}_{10}(\text{PO}_4)_6\text{F}_2$ is a common mineral called apatite which has attracted scientific interest in three widely diverse fields. Powdered calcium fluorophosphate modified by the substitution of chlorine and cadmium and activated by the addition of manganese and antimony is used as the phosphor in most fluorescent lamps. Single crystals of calcium fluorophosphate and many chemically modified forms of this prototype may be activated with neodymium to provide an excellent laser material (1). Irradiated samples of calcium fluorophosphate and its modifications provide a host of color centers whose relationships and interactions can be observed (2, 3) with unusual clarity.

In each of these fields of interest a major effort has been exerted to obtain information on an atomic scale of the site at which the substituted ion or color center sits, as well as a description of its surroundings, for instance, whether or not a charge-compensating defect is nearby. The major tools used have been optical spectroscopy and both electron and nuclear resonance spectroscopy. If the defect to be studied is paramagnetic, and particularly if single crystals are available, the resonance techniques have several advantages over the

optical measurements. These include the ability to positively identify the spectra with a particular atom because of its distinctive hyperfine structure, the ease with which the symmetry of the center may be determined, and the high resolution attainable which may be a crucial factor in unraveling complicated spectra to which several different centers are contributing. Optical spectroscopy on the other hand is the only tool available with nonmagnetic defects and can be useful in combination with resonance spectroscopy, particularly when samples are available only in powder form.

Accordingly, in reviewing our knowledge of defects in calcium fluorophosphate, we find that highly specific information is available about paramagnetic color centers formed by irradiation, but that much less is known about the much more numerous nonmagnetic defects from which the color centers were formed. In the same way, detailed information is only available about paramagnetic impurities. For example, we know of at least four different ways in which Mn^{+2} can enter fluorophosphate samples (4-5), but little is known about diamagnetic antimony or cadmium. The information which is available is derived from optical measurements and often depends upon questionable assumptions, for example that the atom in question is present in the crystal at only one kind of site. Measurements show that this is often not the case, for instance, the

* Electrochemical Society Active Member.
Key words: halophosphate, depreciation, color centers, antimony, cadmium.

measurements made on manganese that are referred to above and unpublished measurements of our own which show that Nd can occupy at least nine different sites in apatite.

Recently optical and ESR measurements have been made before and after u.v. irradiation on samples of single crystal and powdered calcium fluorophosphate containing antimony or cadmium. New resonances and optical spectra were observed which are caused by complex centers which include both an impurity ion and a color center. These spectra and a description of the centers involved are of normal interest in themselves, but they are important for two other reasons: the detailed information we can infer about the state of the impurity ions before the irradiation, and the implication which the description of the new centers has with regard to the deterioration of phosphors during the u.v. irradiation which normally occurs in fluorescent lamps. The purpose of this paper is to present the optical and ESR measurements made of the new centers and to discuss their structures and their implications.

Experimental Procedures

Sample preparation.—Powdered samples were prepared in a manner consistent with techniques used for lamp phosphors, i.e., raw materials were weighed out, mixed, and fired to about 1175°C for 1 hr in a nitrogen atmosphere in covered ceramic trays. The resulting material, sintered into a loosely bound cake, was then broken apart into a powder whose individual particles averaged about 7 μ m in diameter. The composition of the starting material for samples containing cadmium was as follows

CaHPO ₄	3.00 mole
CaCO ₃	1.35-2.30 mole
CaF ₂	0.45 mole
CdCO ₃	0-0.05 mole

These mixtures deviate slightly from stoichiometry and therefore contain small amounts of second phases. While highly efficient halophosphate phosphors may be prepared from a stoichiometric mix of starting materials, the preparation is very critical. A slight excess of CaCO₃ will lower the efficiency disastrously while a slight deficiency of CaCO₃ has only a small effect on the efficiency. This bias occurs because the formation of X centers (3) (and thus color centers) is enhanced by any excess oxygen in the starting mix. The easiest way to insure that no excess of oxygen is present is to deliberately create a deficiency by using a less than stoichiometric amount of CaCO₃. A slight deficiency of CaF₂ content produces a less vitreous cake which can be more easily broken up into a powder. No complications were observed in the ESR or optical spectra due to the presence of the small amounts of second phases.

Powdered samples containing antimony were also prepared but are not reported here because single crystal samples were also available. These were prepared by conventional Czochralski crystal growing methods (1) except that heroic measures were taken to insure that some antimony was maintained in the melt at the elevated growth temperature (~1600°C) in spite of its high vapor pressure. Measures that were tried included the addition of grossly excessive amounts of antimony to the original charge, the continuous addition of antimony to the melt during growth, very fast growth, and Bridgman growth inside an iridium "bomb." Using these techniques a crystal could occasionally be grown which contained a useful amount of antimony. Such samples appeared to behave optically in exactly the same way as powdered samples, i.e., the same absorption and emission spectra. Similar techniques were applied to the growth of crystals containing cadmium but no success was achieved presumably because of the even higher vapor pressure of the evaporating cadmium compounds.

Sample irradiation and annealing.—In most cases color centers were produced in the samples by u.v. irradiation in flowing nitrogen at room temperature using the unfiltered emission from a low pressure mercury discharge in a "Suprasil" quartz envelope. To achieve a more uniform irradiation, the single crystal samples containing antimony were cut in the form of thin slabs, ~0.1 mm thick, and were irradiated equally from both sides. The absorption of these slabs before irradiation, shown in Fig. 1, was so high at 185 nm, the important wavelength, that the u.v. dose still varied about 10% within the slab. The powder samples were irradiated uniformly by being dusted into a layer about one particle (7 μ m) thick on a quartz plate and by being irradiated from both sides. After irradiation the powder was collected and packed into a small plastic cup for ESR and optical measurements. Samples were sometimes irradiated at low temperatures and measured without warming. Special ESR and optical cells were available for this purpose.

Color centers can be converted into different kinds of centers or be destroyed by irradiation with light of special wavelengths and by annealing at a sufficiently high temperature (2). This conversion is sometimes achieved by the transfer of an electron, other times by the diffusion of a vacancy or other defect, and occasionally by both processes occurring together. These optical and thermal conversion techniques can be very useful experimentally for a variety of purposes such as the following: (i) to destroy most of the centers when a spectrum is a superposition of many parts, so that the remaining ones display spectra simple enough to be understood; (ii) to relate ESR and optical spectra to the same center by showing that they disappear under the same optical or thermal treatment; and (iii) to relate two different centers by showing that one grows at the expense of the other under some particular treatment. Annealing, in particular, has been used extensively for these purposes in the work to be described.

ESR procedures.—The X band apparatus used is largely conventional. Most of the measurements were carried out at 77°K although runs at 4.2°K were also sometimes made to increase resolution when necessary to resolve closely spaced lines. An important part of the apparatus was a device which allowed rotations of the crystal sample in the external field to allow a precise determination of the symmetry of each defect site.

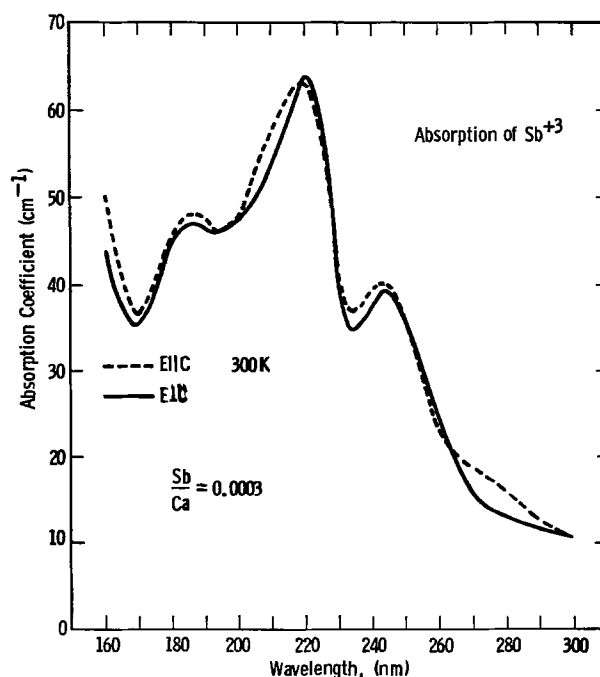


Fig. 1. The optical absorption of a single crystal of calcium fluorophosphate containing 0.03 atomic per cent antimony.

Optical procedures.—Two different optical techniques were used to investigate samples. With single crystal samples, polarized transmission measurements were made using a Cary 14 spectrometer throughout the visible and near IR regions and a McPherson Model 218 spectrometer in the u.v. out to 150 nm. Diffuse reflectance measurements were made on powder samples using a Cary 14 spectrometer and an integrating sphere attachment covering the range 250–2000 nm. Diffuse reflectance measurements for wavelengths shorter than 250 nm were performed with the McPherson spectrometer. An integrating sphere was not used for these measurements. Instead, the reflectance was measured at an angle of 45 degrees relative to the incident beam. An Eastman Kodak barium sulfate white reflectance standard was used. No published data could be found on the reflectance of Eastman Kodak barium sulfate at wavelengths shorter than 200 nm. We found its reflectance to be considerably higher than high purity lithium fluoride and undoped calcium fluorophosphate over the range of 150–200 nm. As a result, we used the Eastman Kodak reflectance standard down to 150 nm with some introduction of error due to a lack of knowledge of its absorption in this range.

Results

ESR spectra of samples containing Sb.—ESR measurements of undoped unirradiated crystal or powder samples usually show only the spectra of the HII center, identified (2) as a paramagnetic O^- center substituted at an F^- site. Optical spectra of such samples usually show a strong absorption due to the X center, identified (3) as the defect $(VOV)^+$ substituted on three adjacent fluorine sites. The nomenclature used in this paper to discuss the color centers follows the conventions presented in Ref. (3). The symbol V represents a vacancy, O an O^{-2} ion, and the + sign signifies that the complex composed of these adjacent parts has a positive charge compared to the three F^- ions it replaces. These defects, the HII and X centers, are closely related to each other and are both normally present because of the loss of fluorine and its replacement by oxygen during crystal growth. Unirradiated samples grown with antimony doping show a strong reduction in the X center absorption and a reduction in the HII center concentration. A scavenging of oxygen by antimony appears to be occurring, and the existence of an Sb-O center in the crystal appears to be likely. The existence of such a center has been discussed by Davis *et al.* (6). We have noticed that the same kind of coupling with oxygen appears to occur for another trivalent ion, Nd^{+3} , substituted in this host. No interaction of this kind between Cd^{+2} and oxygen has been noticed.

Irradiation produces several kinds of E centers (2, 3) in undoped crystals all involving a fluorine vacancy and an extra electron. The irradiated samples containing antimony show unusual E center ESR spectra. An example of this is shown in Fig. 2, where the

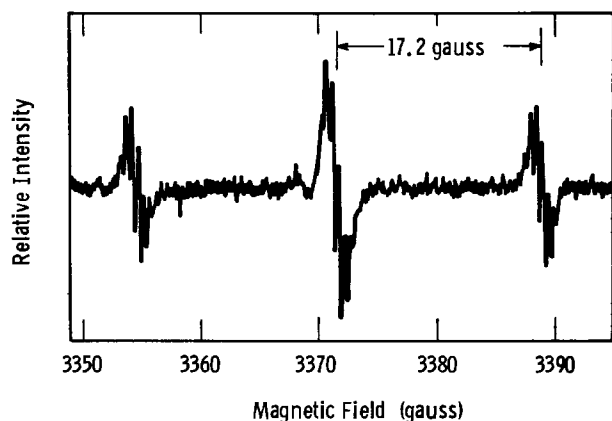


Fig. 2. The ESR derivative spectrum of an irradiated crystal of calcium fluorophosphate containing antimony.

temperature is 77°K, the crystal has an antimony concentration $Sb/Ca = 0.03\%$, it is oriented with its crystalline c axis perpendicular to the magnetic field, and the derivative of the ESR absorption is shown. The ESR spectrum normally observed in undoped but irradiated samples of fluorophosphate is three narrow lines of intensities 1:2:1 separated from each other by about 17g. It is caused by the EII center, and is identified (2) as a fluorine vacancy containing one electron. This center has two neighboring fluorine ions which contribute a local magnetic field which splits the resonance into three hyperfine lines. Additional couplings to more remote fluorine ions and to other magnetic ions contribute to the line width of about one gauss. The new spectrum, shown in Fig. 2, satisfies all of these descriptions, but in addition, each line is further split into several components. If ESR measurements are made at other orientations of the crystal relative to the external magnetic field, the new structure rapidly washes out and the spectrum becomes indistinguishable from that of an ordinary EII center. To deduce the symmetry of the new center, measurements of the spectrum were made as the crystal was rotated while keeping its c axis perpendicular to the external field. As expected the threefold crystalline symmetry was evident in the spectrum, *i.e.*, the clear splitting shown in Fig. 2 was most evident at six symmetrical positions but disappeared in between these positions. As a result of the symmetry of the crystal, the spectrum observed must be either the superposition of three spectra from equivalent centers with reflection symmetry or the superposition of six spectra from equivalent centers with no symmetry. The blurring and sharpening with rotation is a result of the variable overlap of their individual spectra. In an attempt to distinguish between these possibilities, a "rocking" measurement was performed in which the crystal was slowly rotated so that the magnetic field moved away from the plane perpendicular to the crystalline c axis. The spectrum of a center with reflection symmetry behaves differently under these conditions than one without this symmetry. The splitting was observable over a considerable range ($\sim 40^\circ$) away from this plane, but unfortunately it was too small, and the over-all resolution was inadequate to realize our aims. To show how small the splitting effect is, a powdered sample was made by crushing a crystal which contained antimony and only the modified EII center. The ESR powder spectrum showed what appeared to be a normal EII spectrum with no evidence of the new fine lines. Thus the new fine structure is barely observable in a single crystal, and then only when the field is aligned in one of a few special directions.

The new E center is identical to the EII center except that it has been very slightly modified by the presence of an Sb ion. We will call this new center the EII (Sb) center. Its concentration, $EII(Sb)/Ca = 0.003\%$. Figure 3A shows an enlargement of the central "line" of Fig. 2 and also shows our analysis of this line in terms of the hyperfine splitting of the EII spectrum which would occur if an antimony ion with its characteristic nuclear moment were near each EII center. The theoretical curve was calculated by taking into account the relative abundance of the two antimony isotopes and the relative values of their nuclear magnetic moments (shown in Table I). The contribution from all three

Table I

Isotope	Abundance, %	Spin	NMR freq. $\times 10^6$ Hz
Sb^{121}	57.25	5/2	10.2
Sb^{123}	42.75	7/2	5.5
Cd^{111}	12.9	1/2	9.03
Cd^{113}	74.8	0	—
Cd^{113}	12.3	1/2	9.44
F^{19}	100	1/2	40.1

Properties of the various magnetic isotopes which cause a splitting of the EII center.

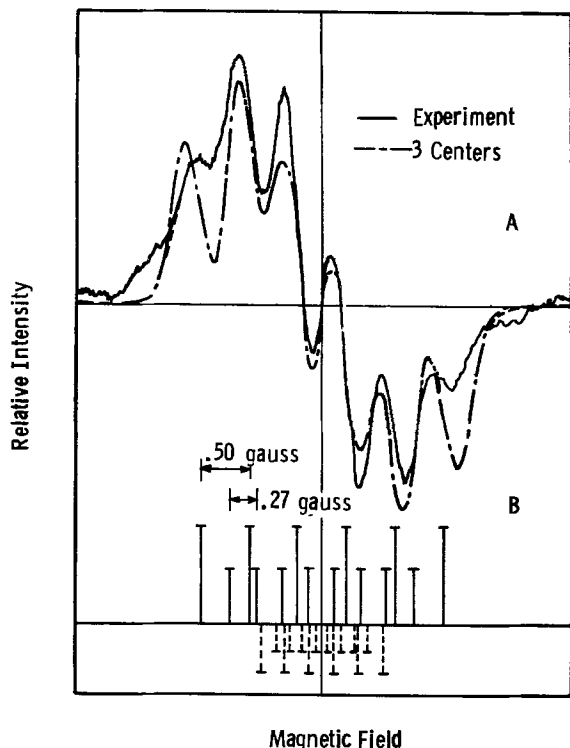


Fig. 3. Features of the central "line" in the ESR derivative spectrum of an irradiated crystal of calcium fluorophosphate containing antimony. Analysis of the "line" is given in terms of the expected hyperfine splitting of the direct EII spectrum by a nearby antimony ion.

(or six) equivalent centers was included and reasonable assumptions were made about the alignment of these centers with the magnetic field, the relative strengths of their coupling to the EII center and their line widths. In particular, we assumed that the angle which gives the best resolution of the fine structure shown in Fig. 2 and 3A corresponds to the crystal orientation which gives the hyperfine splitting of two of the equivalent centers the same value. To fit the data we picked the magnitude of the coupling for these two centers so that they alone would produce the spectrum shown by the solid line diagram in Fig. 3B. The remaining center was assigned the spectrum shown by the dotted line diagram in Fig. 3B. It necessarily has one-half the intensity of the solid line diagram and, for fitting purposes, about one-half its coupling strength. The number of lines resolved in the theoretical curve agrees with the experimental curve, and its over-all shape is approximately correct. An even better agreement between experiment and theory could be attained by further adjusting the many parameters which are at our disposal. We have not done this because the resolution of the spectra is not sufficient to make the fit unique, because the new information would not be very useful to us, and because the main purpose of the fit, to show that the cause of the perturbation to the EII center is a nearby Sb³⁺ ion, has been clearly demonstrated. In some cases various amounts of unaltered EII center (*i.e.*, the EII center with no nearby Sb ion) must also be included in the calculation to achieve a reasonable fit. For long irradiation times, essentially no unaltered EII center is required in this way. Thus in these samples essentially all of the EII centers are near antimony ions.

Some samples were irradiated and observed at low temperatures. The production of the EII and EII (Sb) centers was very low. In accordance with our understanding of the dynamics of color center growth (3), E centers are produced from a precursor center which traps an electron. If a particular E center is produced at room temperature but not at low temperatures, this means that the precursor for that center was not

formed at low temperatures. Applied specifically to the EII (Sb) center, this implies that the vacancy from which this E center was produced was not present near the antimony ion before irradiation but moved up to it during the irradiation at room temperature.

ESR spectra of samples containing Cd.—The powdered samples containing Cd were all irradiated at room temperature and measured at 77°K. No samples were irradiated at 77°K because the complicated powder-handling steps could not easily be accomplished at low temperatures. Figure 4B is an example of the resonance pattern obtained on a sample with Cd/Ca = 1%. Figure 4C shows the resonance spectrum of the normal EII center in a powder. Clearly the addition of cadmium has caused the generation of another new E center. Its concentration relative to calcium is about 0.01%. From the negative value of the *g* shift

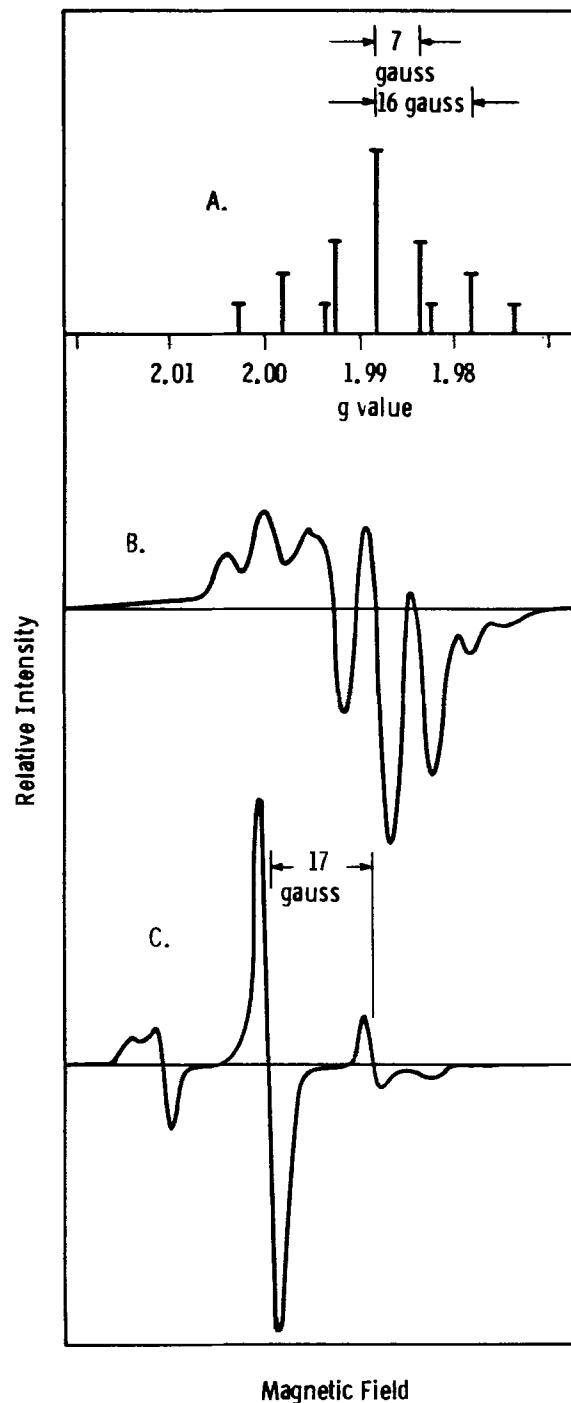


Fig. 4. A schematic direct spectrum for an EII center perturbed by a nearby cadmium ion (4A), the ESR derivative spectrum of irradiated calcium fluorophosphate powders containing cadmium (4B), and the derivative spectrum of the normal EII center (4C).

for this center we identify it as an E-type center and note that the shift is unusually large. The structure on this resonance can have several causes. Like that of the EII center, it may contain components due to the nuclear moment of nearby fluorine ions. In addition the various isotopes of Cd, some of which have nuclear moments, may contribute. Finally the spectrum will be changed from that of the EII center by the crystalline fields and the lowered point symmetry caused by the presence of Cd. It is difficult to unravel these different contributions from a powder pattern; the existence of a single crystal specimen would have been very helpful. Before we discuss our analysis of this spectrum, we should point out that this center, which we call the EII (Cd) center, shows a much greater difference from the EII center than the EII (Sb) center does. In particular the shift and splitting and broadening are of the order of 10g rather than 1g. A reasonable explanation for this is that the Cd ion is much closer to the EII center than the Sb ion is.

The most obvious structure in the EII (Cd) line is the three largest lines in the center whose heights are roughly in the ratio 1:2:1. The EII center is the only known E center which has this same structure. It is because of this similarity that we identify this center as basically an EII-type center. Following this line of reasoning, the other structure shown in Fig. 4B must be due to the hyperfine splitting caused by the magnetic nuclei of Cd. We show in Fig. 4A the simplest kind of spectrum which can be assigned to an EII center which is interacting with the nuclear field of a cadmium ion. We have assumed that the couplings to the cadmium and fluorine nuclei are isotropic, have included the effect of all isotopic components of cadmium in their observed abundance, and have picked values for the couplings of the EII center to the F^- and Cd^{+2} ions which best fit the experimental curve. The resulting structure, if sufficiently broadened by other kinds of magnetic coupling, agrees reasonably well with the observed spectra both in the approximate strengths of the individual lines and their number and relative spacing. We have so far ignored the fact that hyperfine coupling is generally not isotropic and that this lack of symmetry greatly alters the spectrum. An example of this is the simple EII center shown in Fig. 4C where the shape of the powder spectrum differs considerably from the expected three lines, and their strengths from the expected 1:2:1 ratio. The better agreement found for the EII (Cd) center is puzzling. Either the coupling is more isotropic for this center or our identification of the structure is incorrect and part of it is due to the nonisotropic nature of the coupling or g value.

Following this alternative approach we can achieve a reasonable fit by ignoring the hyperfine coupling to Cd and emphasizing the contribution of an anisotropic g value. Accordingly, if we assume that the EII (Cd) site is approximately axial and that the g shift for orientations where the magnetic field is perpendicular to the axis of symmetry is much greater than for the parallel orientation (which is a likely situation and is observed to hold for all of the H centers), we would expect a spectrum crudely like Fig. 4B. In particular, the three dominant lines are caused by the F hyperfine splitting and are generated by those powder particles oriented with their axes perpendicular to the field. The three smaller peaks to the left are produced by the particles with parallel orientation. The other minor peaks to the right side of Fig. 4B must be explained by other perturbations such as deviations from our approximation of axial symmetry.

We have been able to generate two different models which approximately fit the observed spectrum. Working solely with powdered specimens we have little hope of choosing between them. Their most important features, however, the proximity of cadmium and the reduced coupling to the fluorine ions, are common to both models.

Further observations were made on the annealing behavior of the EII (Cd) center. It was much more tolerant of high temperatures than the EII center. A 100°C anneal for 1 hr destroys the EII center completely (2) while even a 300°C anneal fails to completely destroy the EII (Cd) center. After irradiation at room temperature a mixture of different E centers is present but for sufficiently long irradiations the EII (Cd) center dominates the others by roughly an order of magnitude. The spectrum shown in Fig. 4B was made on a sample annealed to 200°C for an hour to eliminate the other E centers.

Optical measurements on crystals containing Sb.—Figure 1 shows a measurement of the optical absorption of a fluorophosphate crystal made with polarized light on a crystal about 0.03 cm thick containing Sb ions at a measured Sb/Ca concentration of 0.03%. Excitation within these absorption bands leads to the typical blue fluorescence which is essentially unpolarized and indistinguishable from the emission from powder samples. This and other similar samples were irradiated with u.v. light and the absorption and fluorescence examined for evidence of the presence of a new color center which could be identified with the EII (Sb) center. No optical evidence for a new center of this sort could be found between 150 and 700 nm. The usual absorption bands near 360 and 450 nm ascribed to the EII and EIII centers were seen and an accompanying reduction in the fluorescent intensity was easily observable as shown on Fig. 8. These observations are not conclusive evidence against the existence of a new E center, however, for the EII and EIII bands are sufficiently broad and featureless to hide small changes which might have been brought about by the presence of a nearby Sb ion.

Optical measurements on powders containing cadmium.—Measurements were made of the diffuse reflectance of powdered samples of fluorophosphate containing various amounts of cadmium. Strong absorption was found in the ultraviolet region which is in general agreement with that presented previously by Apple (7). After u.v. irradiation, new bands were seen by Apple and by us. We call these the EII (Cd) bands. These are shown in Fig. 5 for a sample containing cadmium whose concentration relative to Ca is 1%. No polarization information could be obtained from these powder measurements. A similar sample with $Cd/Ca = 0.1\%$ developed both the EII (Cd) bands and the normal E bands, and in approximately the same strength. Under this same u.v. exposure, a powder sample containing Cd and an appreciable concentration of antimony develops no observable color center band of any kind. This low growth rate is probably caused by the strong absorption of Sb at 185 nm and the shielding it affords to the X center, preventing the conversion of X centers to color centers (3).

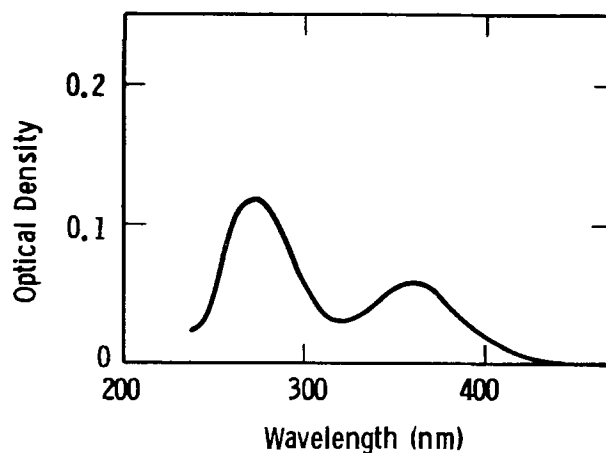


Fig. 5. Optical absorption bands produced by u.v. irradiation in calcium fluorophosphate powders containing cadmium.

Interpretation of Results

A model of the EII (Cd) center.—Our model of the EII (Cd) center is shown in Fig. 6, and a description of its formation is given below. Figure 6 shows schematically the part of the crystal exposed by a cut made through the a-c plane and the chains of fluorine ions. The Ca and PO_4 ions have been left out for clarity. The threefold c axes are arranged vertically and pass through the chains of F^- ions and a fluorine vacancy (represented by the square symbol). One of the three CaII ions next to the vacancy has been replaced by a Cd ion. A reflection plane passes through the Cd ion and the vacancy and the two unmodified CaII ions (not shown) on the right side of the vacancy. An electron is bound to this complex. This center is identical to the EII center except that the Cd ion has replaced a Ca ion.

Energetically the substitution of Cd for Ca is reasonable, for Cd^{+2} has the same charge as Ca^{+2} and has almost the same ionic size. It can substitute for calcium at either the CaI or CaII site and should perturb the normal lattice hardly at all. When color centers are produced, however, the special properties of Cd becomes more important. This can be seen by examining a model of the EII center used by Piper, Kravitz, and Swank (2) to calculate g values. It involves a $\text{Ca}_3\text{F}_2^{+4}$ molecular ion with an attached electron and fluorine vacancy. In this model, the electron can be bound to any of the Ca^{+2} ions with an energy of roughly 12 eV, i.e., the second ionization potential of calcium. Our model of the EII (Cd) center can be described by the same kind of molecular model, but one of the Ca^{+2} ions in the $\text{Ca}_3\text{F}_2^{+4}$ molecular ion is replaced by Cd^{+2} . The electron in the new center will be preferentially bound to the Cd^{+2} ion by 17 eV, its second ionization potential. This increase in binding energy of 5 eV is a driving force which causes the EII center [which readily migrates at room temperature in the dark (3)] to preferentially sit next to one of those Cd^{+2} ions which has replaced Ca^{+2} at a Ca(II) site. Since the electron is more strongly bound to the Cd^{+2} ion than the Ca^{+2} ion it replaces, the electronic wave function will concentrate there and will overlap the fluorine ions less. This will cause less F^- hyperfine coupling in agreement with our analysis of the observed spectra. Being largely centered on the Cd^{+2} ion, the electron's coupling to the Cd nucleus may

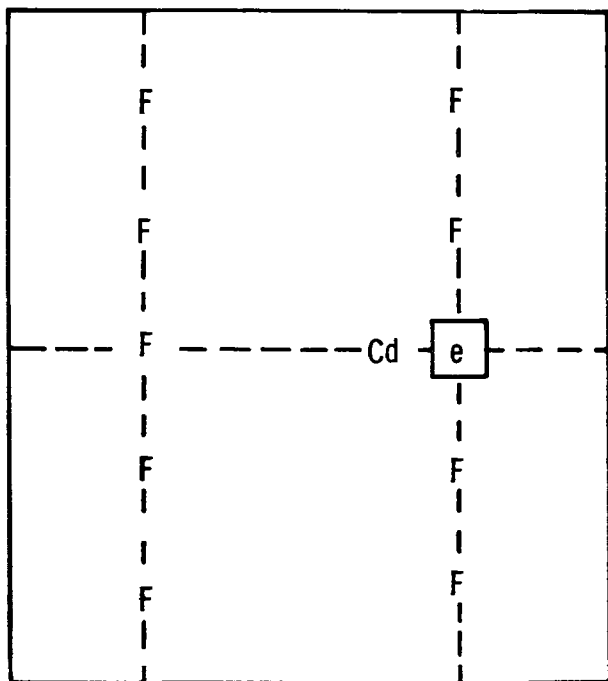


Fig. 6. Proposed model for the configuration of the EII (Cd) center.

involve mainly a contact term and display a nearly isotropic splitting. This could help to explain the relatively sharp unblurred powder pattern. An explanation of the relatively isotropic coupling to the fluorine ions also depends upon the importance of the contact term. The arguments are more speculative and will not be dealt with here.

The g shift observed for the EII (Cd) center ($\Delta g \cong -0.01$) is much larger than is observed for any of the common E centers (2). This must be caused (8) either by the stronger spin orbit coupling of the cadmium ion or by the existence of excited states of Cd^{+1} of the right character which have particularly low energy. The spin orbit coupling parameter of Cd^{+1} can be estimated from the splitting of its excited states (9) and is found to be much larger (~ 10 times) than that of Ca^{+1} explaining this g shift and lending support to our model.

Other models for the EII (Cd) center can be proposed which satisfy the observed data reasonably well. The special virtues of the one proposed are that it is simple and it is consistent with our understanding of the energetic and dynamic properties of the fluorophosphate lattice and color centers.

A model of the EII (Sb) center.—A most striking observation about the EII (Sb) center is the small change that the presence of antimony has had on the normal EII center. If the Sb^{+3} ions were sitting right next to a normal EII center, however, as in our model for EII (Cd), a highly perturbed E center should result. The important conclusion is that the Sb and the EII center must be separated farther than Cd and EII are, and yet the only possible reason for this is that the Sb and EII parts are somehow blocked from assuming their closest and lowest energy configuration. A logical explanation is that the Sb^{+3} ion is located at the CaII site and is indeed blocked, being charge-compensated with an O^{-2} ion substituted at the nearest fluorine site. Assuming that this compensation still holds as an EII center approaches, the possible arrangements of the three parts of this complex center can rapidly be narrowed down. Figure 7 shows those that we have considered. Figures 7 and 6 have been prepared in the same way except in Fig. 7 the F ions

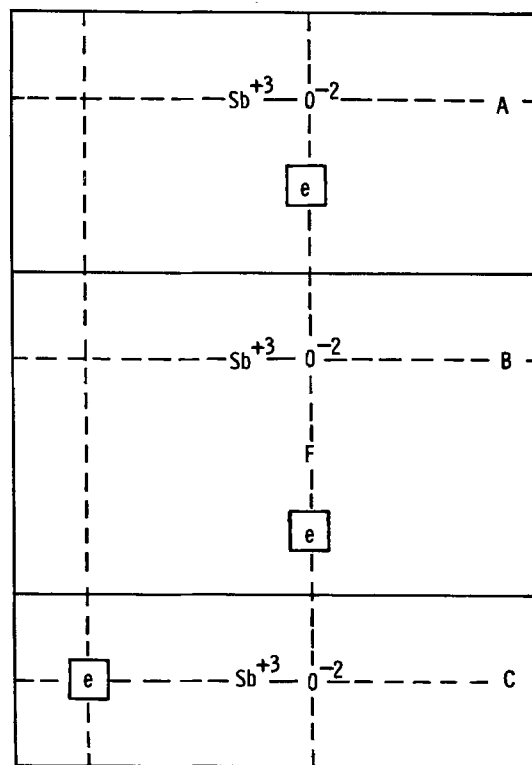


Fig. 7. Possible models for the configuration of the EII (Sb) center. Model 7C is the favored model as discussed in the text.

have been left out for clarity. In Fig. 7 the crystalline *c* axes are aligned vertically, the Sb^{+3} ion has been substituted at a CaII site, and a horizontal line through the Sb^{+3} ion is in a reflection plane unless the nearby E center has destroyed this symmetry as in Fig. 7A and 7B. The vertical column containing fluorine and oxygen ions is on the *c* axis. It normally contains only fluorine ions and is the channel along which color centers readily migrate. An arrangement like that shown in Fig. 6 with no blocking O^{-2} ion, has already been ruled out because it would radically perturb the EII center and its spectra. Figure 7A, representing the closest spacing of the E center and the Sb-O complex, is ruled out because this E center is like the EI (not EII) center and should show only a two-line ESR spectra (and be thermally unstable at room temperature). Figure 7B represents the next larger Sb^{+3} -E center spacing. This configuration should also be rejected, for the ESR spectra of the EII center will display the inequivalence of its two neighboring fluorine ions by a splitting of the central line. We expect this effect to be observable but it could not be detected in our measurements. The Sb-vacancy spacing for this configuration is about 7Å; if the E center is moved away along the fluorine chain one more step the spacing is about 11Å. Other more likely arrangements can be found with spacings less than this. For example, as shown in Fig. 7C, the EII center can be moved to the nearest spot on one of the next fluorine chains. There are six different ways to do this corresponding to the six nearest chains. That with the closest spacing gives a Sb-vacancy spacing of about 7Å. An even closer (~6Å) but less likely arrangement involves an Sb^{+3} ion located on a nearest CaI site. Some of these possibilities could be ruled out if the symmetry of the EII (Sb) center could be extracted from the ESR data, but unfortunately the resolution is insufficient to allow this.

We have considered which of the arrangements should have the lowest electrostatic energy. There is no difference on a point charge model because the E center has a net charge of -1 which equals that of the F^- ion it has replaced. On the next level of approximation, that which considers the dipole moment of the E center, we find differences. The $\text{Sb}^{+3}\text{-O}^{-2}$ couple generates a dipole field which polarizes the E center and lowers its energy. We expect that the polarizability of the E center is much smaller parallel to the *c* axis than perpendicular to it. Comparing models 7B and 7C, the arrangement shown in 7C generates a stronger dipole field at the E center, and the direction of the field is such as to polarize the E center in the favorable direction, perpendicular to the *c* axis. Thus, our choice for the most likely model of the EII (Sb) center is one of the six described by Fig. 7C which has the smallest Sb-vacancy spacing. The experiments clearly show that essentially all of the E centers are bound to antimony and that their thermal stability is essentially the same as that of the normal EII center, supporting this choice and ruling out, for example, model 7A. We have ruled out a model involving the Sb ion at the CaI site because existing calculations (10) and measurements indicate that this is unlikely.

The optical measurements made on the two new kinds of E centers are in general agreement with the models that we have chosen. The EII (Sb) absorption bands are indistinguishable from the EII bands because these centers differ so little. The EII (Cd) center has quite different bands because the center is strongly perturbed by the nearby Cd^{+2} ion. The annealing results are also in agreement with our model. The EII (Sb) center is destroyed at the same low (~100°C) temperature as the normal EII center that allows it to migrate to and be annihilated by an oppositely charged H center. The EII (Cd) center, on the other hand, can tolerate a much higher anneal temperature which implies that the strong binding of the EII center to the Cd^{+2} ion restricts its wanderings and

keeps it separated from the relatively immobile H centers.

Models for the Sb and Cd centers as they exist before u.v. irradiation.—Evidence has been presented previously (3) that EII centers are produced in undoped samples largely by an indirect process. Complex precursor defect centers, X or Y, bind a free electron to produce, respectively, an EI or EIV center. These E centers are thermally unstable at room temperature and decompose by the separation and migration of the EII center away from the oxygen-containing residue. ESR measurements were made on samples containing antimony which had been irradiated at low temperatures. These measurements show that this indirect phenomenon is also occurring in this doped crystal, *i.e.*, most of the E centers produced at low temperatures are other than EII or EII (Sb) centers while those produced at room temperature are essentially all EII (Sb) centers. If a complex including Sb-O and a nearby vacancy existed before irradiation, we would expect, in contrast, that the EII (Sb) center would be generated in large concentrations by the low temperature irradiation. Our conclusion from these observations is as follows: before irradiation the Sb-O complex is well separated from other defects. The irradiation produces remotely situated EI and EIV centers which decompose as usual into EII centers. The EII centers migrate to the Sb-O complexes and are bound there in the special configuration we call an EII (Sb) center.

We have no experimental evidence supporting the same conclusions for the Cd center. It appears unlikely, however, that a Cd-vacancy complex would be stable, and more likely that the vacancy would prefer energetically to be bound to oxygen ions in an X or Y center. Thus we propose that an isolated Cd center exists before irradiation and that the EII (Cd) center is produced by a remotely formed EII center which migrates to the Cd ion and is bound there.

Depreciation of Phosphors

The result of this work is of two different kinds. First, we have presented models and supporting arguments for two new color centers in fluorophosphate and have made inferences which lead to information about the Sb^{+3} and Cd^{+2} ions which are present in the samples before becoming associated with color centers. On a different level, we can use the results of this work to help our understanding of the depreciation of fluorophosphate phosphors and the role played in depreciation by color centers and antimony and cadmium ions. We will discuss this aspect of depreciation below.

Role of antimony.—Depreciation of antimony-activated halophosphate phosphors has always been loosely associated with the generation of color centers for it has long been recognized that both the degree of depreciation and the concentration of color centers depend upon irradiation and other treatments in roughly the same way. For example, both grow with 185 nm u.v. irradiation, fall with 254 nm irradiation, and fall with thermal annealing (11). No clear picture has been formed, however, of the details of the interaction between the color centers and the antimony center which causes the reduction in the intensity of its fluorescence. A likely model involves energy transfer from antimony through its emission band centered at 480 nm. This transfer can occur by several different mechanisms. Experiments with our single crystal samples containing antimony illustrate one form, direct absorption of the emission by the two EII absorption bands. This is evident in Fig. 8 where 8A is the fluorescent envelope measured before u.v. irradiation and 8C afterwards. Curve 8B is the same as 8A except that it has been reduced in amplitude by about 20% so as to coincide with curve 8C at long wavelengths. Curve 8C shows a characteristically distorted antimony emission band, *i.e.*, two "holes" have been "dug" in the normal Sb band at the two EII center wavelengths, 360 and 450 nm, by a direct absorption process.

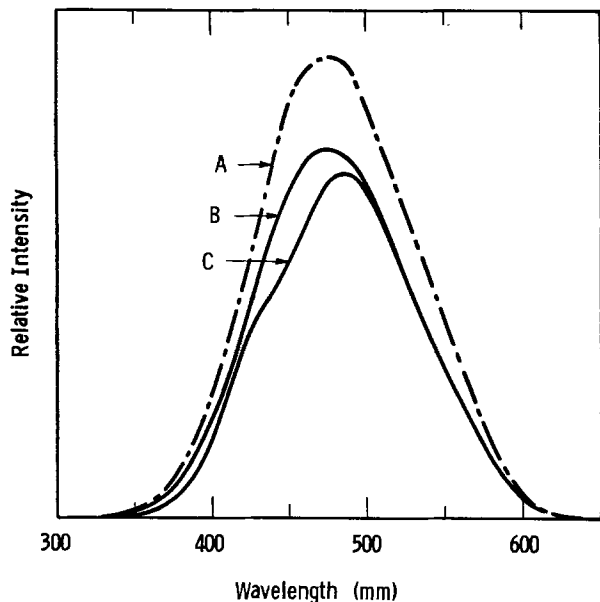


Fig. 8. The fluorescent envelope of a single crystal of calcium fluorophosphate containing antimony before (A) and after (C) u.v. irradiation. Absorptions due to the EII and EIII centers are evident by the dips in curve C at 360 and 450 nm.

Now the same distorted emission is not observed in normal phosphors. This is because the much lower ratio of color center to antimony concentrations makes the direct absorption of the color centers much less important. How then do we explain the depreciation in normal phosphors and the 20% or so of the depreciation shown in Fig. 8 not associated with the direct absorption by the EII center? We would like to invoke an energy transfer and quench process, but we need some reason to expect an unusually close spacing between the color centers and the antimony ions. A conclusion of the present work, stated above, is that this close coupling indeed occurs. Because of this our interpretation of the dynamics of the depreciation process is easy. As the EII centers are produced they diffuse through the crystal until they find an antimony ion to which they stick, stopping perhaps 7Å away. The 7Å separation of the EII center and Sb is sufficiently small that the energy of antimony in its excited state is preferentially transferred to the EII center before normal radiation occurs. The EII center is then quenched and transmits the energy directly to the lattice, for its fluorescent efficiency is known to be low (2). This transfer process will not cause a distorted antimony emission line shape but will reduce its intensity. For the sample that we have examined, ESR measurements show that about 10% of the antimony ions have EII centers nearby. This is in crude agreement with the observed 20% drop in efficiency not explained by direct absorption. The lifetime of the excited antimony will probably not be shortened to a measurable degree as the time scale for the transfer to the EII center would be $\sim 10^{-10}$ sec while the radiative lifetime of Sb is $\sim 10^{-6}$ sec.

Discussions and calculations can be found in the literature (12) which confirms the statement made above about the speed of energy transfer from antimony to the EII center. This transfer over about 7Å is not restricted by selection rules. It is most likely to occur by a dipole-dipole process although dipole-quadrupole and exchange process are also strong enough to dominate over fluorescence. Soules *et al.* (13) have investigated the analogous situation where an Sb³⁺ ion in apatite transfers to a Mn²⁺ ion. Although dipole-dipole transitions are not allowed in this system due to the forbidden nature of the Mn transition, exchange transitions are still stronger than fluorescent for separations up to about 13Å.

The model described above for the transfer and quenching of the energy originally absorbed by the

antimony ion is in agreement with many other observations made on this system. Most important of these, perhaps are the beneficial effects of heat and 254 nm irradiation on depreciated samples. Both can be explained by the destruction of the EII center. As described elsewhere (2) heating the EII centers above about 100°C either destroys it or causes its migration to other sites. On our model this should restore the original efficiency of a phosphor. Similarly it has been shown (3) that 254 nm irradiation is absorbed by the HII center and frees a hole which, in turn, recombines with the electron contained in the EII center. The resulting centers are not expected to interfere with the Sb ion in its normal emission process, thus much of the original efficiency of the phosphor should be restored.

In deriving this model we have assumed that mechanisms active in a crystal containing 0.03% antimony are important in commercial phosphors where the antimony concentration is over an order of magnitude greater. While this is felt to be the case, we can offer no proof of the validity of this assumption.

Role of cadmium.—Cadmium reduces depreciation in phosphors, but how it accomplishes this has not been clear. One way has been described by Apple (7) and has been confirmed by the measurements of this paper, *i.e.*, the Cd²⁺ center in fluorophosphate absorbs u.v. light at 185 nm and so reduces the intensity of this damaging mercury radiation in the phosphor. Since this radiation is also needed to produce fluorescence, only a moderate amount of cadmium can be added to the phosphor before the initial brightness of the phosphor suffers.

The results of this paper imply a second mode of protection by cadmium, *i.e.*, while the EII center produced by u.v. irradiation wanders through the crystal looking for an antimony ion to damage, the cadmium ion acts as a scavenger. If the EII center finds the cadmium ion before the antimony ion, it sticks to the cadmium ion and the antimony is spared. For the samples examined in this paper about 1% of the Cd ions are modified in this way. Since the cadmium ion concentration is normally larger than that of the antimony ion and since its binding energy for the EII center is larger, the protection afforded by cadmium by this mode is probably important.

Acknowledgment

The authors would like to thank W. Kramer for growing one of the crystals described in this paper and Dr. J. Murphy for helpful discussions concerning g values.

Manuscript submitted Nov. 7, 1974; revised manuscript received Feb. 10, 1975. This was Paper 97 presented at the San Francisco, California, Meeting of the Society, May 12-17, 1974.

Any discussion of this paper will appear in a Discussion Section to be published in the December 1975 JOURNAL. All discussions for the December 1975 Discussion Section should be submitted by Aug. 1, 1975.

Publication costs of this article were partially assisted by Westinghouse Electric Corporation.

REFERENCES

1. R. Mazelsky, R. H. Hopkins, and W. E. Kramer, *J. Crystal Growth*, **7**, 260 (1968); R. Mazelsky, R. C. Ohlmann, and K. B. Steinbruegge, *This Journal*, **115**, 68 (1968); R. C. Ohlmann, K. B. Steinbruegge, and R. Mazelsky, *Appl. Optics*, **7**, 905 (1968).
2. R. K. Swank, *Phys. Rev.*, **135**, A266 (1964); W. W. Piper, L. C. Kravitz, and R. K. Swank, *ibid.*, **138**, A1802 (1965).
3. R. W. Warren, *ibid.*, **B6**, 4679 (1972).
4. R. W. Warren, *ibid.*, **B2**, 4383 (1970).
5. R. W. Warren and R. Mazelsky, *ibid.*, To be published.
6. T. S. Davis, E. R. Kreidler, J. A. Parodi, and T. F. Soules, *Luminescence*, **4**, 48 (1971).

7. E. F. Apple, *This Journal*, **110**, 374 (1963).
8. William Low, "Parametric Resonance in Solids," p. 120, Academic Press, New York and London (1960).
9. "Atomic Energy Levels," C. E. Moore, Editor, *Nat. Bur. Std.* #467, Vol. I, p. 245, Vol. III, p. 58.
10. T. F. Soules, T. S. Davis and E. R. Kreidler, *J. Chem. Phys.*, **55**, 1056 (1971).
11. J. H. Singleton and L. Suchow, *This Journal*, **110**, 36 (1963).
12. D. L. Dexter, *J. Chem. Phys.*, **21**, 836 (1953).
13. T. F. Soules, R. L. Bateman, R. A. Hewes, and E. R. Kreidler, *Phys. Rev.*, **B7**, 1657 (1973).
14. J. G. Rabatin, G. R. Gillooly, and J. W. Hunter, *This Journal*, **114**, 956 (1967).
15. S. Kamiya *et al.*, U.S. Pat. 3,549,550 (1970).

Growth of Epitaxial GaAs Structures for High Efficiency IMPATT's

L. C. Luther and J. V. DiLorenzo*

Bell Laboratories, Murray Hill, New Jersey, 07974

ABSTRACT

The development of the modified Read Lo-Hi-Lo high efficiency GaAs IMPATT requires special growth techniques permitting controlled growth of thin (100-1000Å) layers containing specified amounts of n-type impurities with high accuracy. To meet this need a gas dopant injection system compatible with standard CVD apparatus was constructed. An accurately measured total amount of H₂S for doping the n⁺ layer is instantaneously released into the gas stream passing over the growing epitaxial layer and is partially incorporated in that layer. The control exercised over parameters of the n⁺ layers was: the width, ±8%; the position, ±10%; and the impurity content, ±18%. It is shown that the width of a sulfur-doped layer is determined by (i) the experimental geometry, (ii) gas flow rates, (iii) gaseous diffusion, and (iv) growth rate. The incorporation of sulfur is shown to be proportional to the number of moles of H₂S injected and varies as the (growth rate)^{1.6}. Studies of postgrowth diffusion in the solid indicate that the widths of the high-doped layers broaden by amounts consistent with a value for the diffusion coefficient of sulfur in GaAs of

$$D_{\text{S}_{\text{GaAs}}}^{S} (750^{\circ}\text{C}) = 2 \times 10^{-15} \text{ cm}^2/\text{sec}$$

The doping technique has yielded the first experimental measurement of a distribution coefficient of sulfur between the gas and the solid phases. This distribution coefficient is defined as

$$k = \frac{[S^+] P_{\text{H}_2}}{N_{\text{S}} P_{\text{H}_2\text{S}}}$$

and has a value ranging between 13 and 26 for our experimental conditions. This study has shown that the injection doping system allows control of the concentration of impurities via the ideal gas law in layers as thin as 150Å. It has furthermore been demonstrated that growth rate control is of primary importance for doping control and that future studies to improve doping control should focus on the variables affecting growth rates.

Recent experimental and theoretical work toward high efficiency, high power GaAs Schottky barrier IMPATT microwave diodes has established the superior performance of Read-profile structures over uniformly doped layers (1-4). As a result the demands on reproducibility and control of the crystal growth process have increased steeply. There have been two Read-profile structures which have received the greatest attention: the Lo-Hi-Lo doping profile and the Hi-Lo doping profile. This report is concerned with the Lo-Hi-Lo structure which consists of a uniformly low-doped layer on top of which a very narrow, high-doped layer is grown, followed in turn by another low-doped layer. Salmer *et al.* (5) in discussing this structure have described the critical dependence of the device efficiency on the parameters of the n⁺ layer. In our initial efforts, the material grown for device development was grown in a standard vapor phase reactor which accomplished the doping of the n⁺ layer by temporarily opening a fine valve, which admitted a flow of dilute H₂S (1000 ppm H₂S in H₂) at flow rates on the

order of 0.1 mliter/min. Since the valve operation requires about 30 sec, the desired control could not be achieved. The idea was advanced that in order to improve doping control a reproducible amount of gas should be discharged into the carrier gas stream at the exact time required. The injected gas would be carried to the deposition site within a predictable time span (~ 1 min). While the injected gas "cloud" was traveling from the injection site to the substrate, gaseous diffusion would spread the cloud sufficiently to allow growth of a layer of requisite thickness (100-500Å) during its passage over the substrate. The experimental realization of this idea was aided by the availability of high quality injection valves used in gas chromatography and available commercially. Using this type of valve in a standard AsCl₃ vapor deposition reactor we have grown about 50 GaAs structures, some of which have yielded IMPATT diodes of high efficiency and power.

This report describes the experimental apparatus and procedures used to grow GaAs epitaxial layers containing narrow doping spikes with characteristics designed to yield IMPATT diodes operating between 5 and 11 GHz. The experimental section is followed by a discus-

* Electrochemical Society Active Member.
Key words: GaAs CVD, sulfur-doped GaAs, diffusion (S in GaAs), distribution coefficient.

Table I.

Bore of reactor	40-41 mm
Total gas flow	650-700 milliters/min
Gas velocity in deposition zone	55 cm/min at RT 190 cm/min at 800°C
Mole fraction AsCl ₃ (p^1 AsCl ₃ , atm)	$2-7 \times 10^{-3}$
Ga surface area (3.3×7.5 cm)	25 cm
Ga source temperature	760°-810°C
Substrate temperature	725°-755°C
Substrate temperature gradient	1.5°-3°C/cm
Dopant gas (H ₂ S in H ₂)	100-1000 ppm

sion of doping profile measurements and their interpretation. Typical Lo-Hi-Lo doping profiles are described and the characteristics of the narrow doping spike or Hi-layer are explained in terms of growth conditions. Sulfur incorporation is correlated with growth rates and the implications of this result for doping control and future work are discussed. Device results will be reported separately (6).

Experimental Crystal Growth

General.—The Ga/AsCl₃/H₂ vapor deposition reactor used in this study was similar to one described by DiLorenzo (7). The dimensions of the reactor were scaled up to accommodate 1 in. square wafers in upright position. For convenience the various experimental conditions which can easily be identified by the reader familiar with similar reactors are described in Table I. The epitaxial deposition is preceded by an *in situ* etch in AsCl₃/He (8) and growth of a 4 μ thick n⁺ buffer layer. Depletion of the As content of the large area (see Table I) Ga source was often observed, especially at low (760°C) source temperature and is discussed in more detail further on. To avoid the uncontrolled growth condition associated with As depletion (incomplete GaAs crust) each run was preceded by a source saturation cycle, the end of which was identified by the appearance of elemental As at the exit of the furnace tube. After each deposition run the furnace was moved downstream to vapor etch the substrate region of the furnace. All substrates were Br₂/MeOH polished (9) on a plane 3½° off a (100) plane. Substrate cleaning included boiling in organic solvents, etching in 5:1:1 H₂SO₄:H₂O₂:H₂O followed by DI H₂O rinses, soaking in conc HCl, and centrifuge spin-off from MeOH.

Injection doping system.—The injection valve (Varian Aerograph) has 8 ports for two exchangeable sample loops, Fig. 1. The carrier gas (solid line) is passed through one loop (A) into the system while the doping gas (broken line) passes through the other loop (B) into the exhaust as shown for position I. Turning the valve handle results in an interchange of

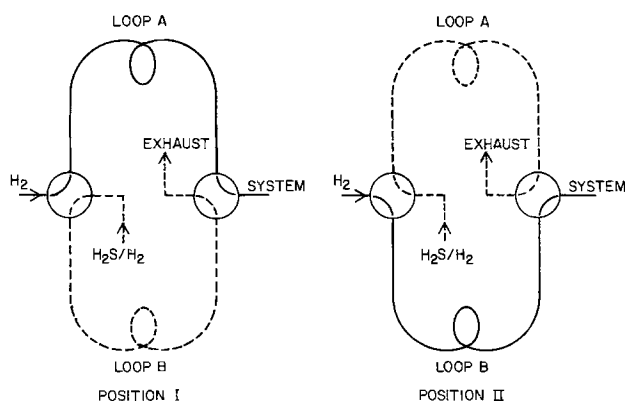


Fig. 1. Gas flow diagram for the dopant injection valve. In order to show the gas flow paths more clearly the 8-port cylinder has been separated into two levels with 4 ports each. Operation of the valve rotates both levels simultaneously by 90° in the same direction. The path of the carrier (solid line) and the dopant gas (broken line) are shown before (position I) and after operation (position II) of the valve.

the two loops, position II. The volume of dopant gas trapped in loop B, which is now in the system line, is flushed out by the carrier gas into the system. A few seconds are needed to replace the H₂ by doping gas in loop A, which now is in the exhaust line. After this time the valve may be operated again. We have injected up to six volumes at 10 sec intervals without loss of doping control.

Source saturation.—Shaw (10) has called attention to the necessity of establishing an unbroken GaAs crust over the Ga source in a H₂/Ga/AsCl₃ reactor. The primary effect on the gas composition in chemical equilibrium with a crusted Ga source is the maintenance of the high As partial pressure. The presence of free Ga reduces the As partial pressure by orders of magnitude (10). It is, therefore, not surprising that a correlation can be established between the deposition of elemental As at the furnace exit and effective control of growth rates and doping levels. When no special precautions were taken it was often observed that part or all of the growth cycle proceeded without any deposition of elemental As at the furnace exit. In some of the runs the As appeared during growth of the first layer, the n⁺ buffer. In these cases the time of appearance of the first As was noted and correlated with the position of an etch line in the buffer layer as seen on a cleaved and stained (110) plane. It was found that the first part of the buffer layer, deposited before excess As appeared, grew at a rate about 2-3 times the rate observed later in the process when excess As was present. The first grown part of the buffer layer was doped about 4 times higher than the second part. Likewise, active layers grown without excess As showed prominent doping ramps, always with a decreasing doping level with time. By deliberately growing from a 75% saturated Ga source, growth rates as high as 0.7 μ /min were obtained. Upon completion of the saturation process the rates fell to 0.2 μ /min. A source with exposed free Ga is expected to react more completely with HCl than a GaAs crusted source on the basis of equilibrium thermodynamics (10). Thus in the absence of a GaAs crust the partial pressure of HCl downstream from the source is lower than it is under normal, controlled growth conditions. Since HCl favors the dissolution reaction of GaAs we have a mechanism for increased growth rates in the presence of free Ga. However, the As pressure also decreases under these circumstances and this would be expected to reduce the rate of the deposition reaction. The resultant growth rate is a balance of opposing tendencies, the details of which we cannot predict. Nevertheless, the experimental conditions for ensuring a high As₄ partial pressure are readily and reproducibly established with the presaturation cycle.

Experimental Measurement

Growth rates.—The thickness of the epitaxial layer was measured by taking photographs of cleaved and stained sample at 640 \times using a phase contrast microscope. The etchant used is alkaline K₃Fe(CN)₆ (11) which delineates abrupt concentration changes in 5-10 sec at room temperature. The precision of this method is equivalent to fringe count methods on angle lapped and stained sample with a resolution of 0.3 μ . This was established by direction comparison before adopting the cleave and stain method, which was considered to be faster and easier. Average growth rates were then obtained by dividing layer thickness by growth time. Since two layers were always grown, this yields two measurements. In each sample the very narrow high-doped layer served as a marker permitting an additional independent measurement of growth rate at the time of dopant introduction. The distance of the center of this layer from the surface (0.5-1.5 μ) was measured using a capacitance profiler. This distance was divided by the time between dopant injection and termination of growth by withdrawal from the furnace. A small correction amounting to 0.7 min was made to allow for the time of passage of the dopant gas from injec-

tion site to the substrate. In most instances this growth rate established for the last 5-10 min of growth was in good agreement with the average growth rate. Exceptions were noted in cases where the Ga source was significantly depleted and growth rates decreased rapidly.

C-V profiles.—The doping profile of the layers, that is the doping level as a function of distance from the surface of the crystal, was measured by means of a feedback profiler designed by Miller (12). This profiler processes differential capacitance measurements and plots doping level *vs.* distance from the surface. Schottky barrier diodes are formed by depositing 10 and 20 mil Au dots on a step-etched sample. Step etching is accomplished by dipping a sample strip into a stirred mixture of 5:1:1 H₂SO₄:H₂O₂:H₂O at room temperature. Several steps are usually needed to establish a complete profile. Occasionally "punch through" devices were obtained which allowed depletion and hence profiling of the entire active layer. As a check on possible fringe field effects on the capacitance voltage profiles, mesa Schottky diodes were prepared by ion milling through an evaporated 3000Å gold layer and about 1μ of one GaAs epitaxial layer. The mesas were defined with Photoresist. The n⁺ layer was located at a depth of 0.4μ, *i.e.*, within the mesa. No difference was seen between the profiles of the n⁺ layer as obtained from the planar and the mesa Schottky diodes.

The interpretation of differential capacitance (C-V) profiles containing abrupt transitions in impurity concentration requires some care. A distinction must be made between the impurity profile, $N(x)$, and the majority carrier profile, $n(x)$. Electrons in n-type material with large concentration gradients diffuse away from the impurity donor atoms. Balance is restored by drift currents in the resulting field. The situation is similar to that prevailing near a p-n junction. To first order the C-V profiler measures the majority carrier profile and all the abrupt features of the underlying impurity profile are washed out. A step function impurity profile is "rounded off" with shoulders extending several Debye lengths to either side of the function (13).

An additional correction must be made for the influence of the electrical measurement (application of d-c bias) on the thermal equilibrium of the majority carriers. Johnson and Panousis (14) have obtained estimates for this effect from computer simulation studies. They showed how the differential capacitance profile, $N^*(x)$, differs from the equilibrium majority carrier profile, $n(x)$, and how the deviation depends upon the geometry of measurement. The C-V profile of a step function is an S-curve intersecting the vertical branch of the step function at about one-third of its height and reaching full height only after 3-4 Debye lengths. We have synthesized a two-step function impurity distribution from two step functions of opposite sign and approximated the corresponding C-V profile from the computer simulation curves, Fig. 2. The asymmetry is due to the experimental geometry: the contact is either on the high- or the low-doped side of the step function. We considered on Fig. 2 two limiting cases. The width of the two-step function is expressed in units of Debye lengths appropriate to the high doping level. If the two-step function is equal to or more than 7 Debye lengths (λ_D) the peak of the C-V profile, N^*_{max} , is nearly equal to the impurity doping level, N_{max} . The width at the $0.6 N_{max}$ level, which is the 2σ level if the profile is approximated by a Gaussian curve, is about $2\lambda_D$ narrower than the width of the impurity distribution. If, on the other hand, the two-step function is only two λ_D wide, the C-V profile peak will approach two-thirds of the impurity doping peak while the 2σ width is nearly equal to the true width. This second case is the delta function model intuitively applied to Hi-layers. As we shall see, our Hi-layers are typically $3-5\lambda_D$ wide at the 2σ level, or somewhere between the two extremes considered. Their C-V profiles are

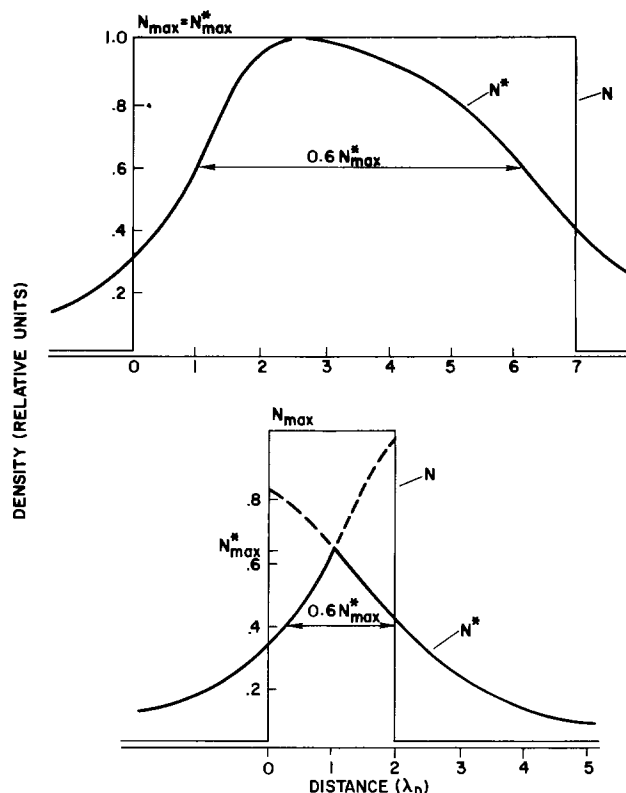


Fig. 2. Simple models of Hi-layer impurity distributions, $N(x)$, and the corresponding C-V profile, $N^*(x)$. The models were constructed using the computer simulation studies of step functions described by Johnson and Panousis (14).

probably 1-2 Debye lengths narrower than the width of the impurity profile. Although the above considerations are of a qualitative nature only they will be helpful in the discussion of dopant incorporation.

Impurity content of Hi-layers.—We have used two different methods to estimate the amount of impurity in Hi-layers. One method, profile integration, yields the amount of charge per unit surface area by integrating the Miller profile $N^*(x)$ over the distance, where $N^*(x)$ is significantly above the background. This assumes that $N^*(x) = n(x)$, which is a reasonable approximation. According to the Johnson-Panousis analysis $N^*(x) < n(x)$ at the edge of a step function profiled from the low doping side, and $N^*(x) > n(x)$ if profiled from the high doping side. The deviations are small and in opposite directions and so tend to cancel.

The other method (15) utilizes

$$C = \frac{\Delta Q}{\Delta V} \quad \text{and} \quad \Delta Q = qN(x) dx$$

to obtain

$$Q = q \int_{\Delta x} N(x) dx = \int_{\Delta V} C(V) dV$$

The capacitance as a function of voltage for a typical doping "spike" is shown in Fig. 3. Integration was done numerically or by use of a planimeter. The voltage differential was established by noting the d-c bias on the C-V profiler before and after passing the depletion zone through the high-doped region. Alternatively a separate $N(V)$ plot was made using the profiler to define $N(V)$. The agreement between the two methods of estimating impurity content was checked on a uniformly doped layer. For such a layer the gross distortions of the profile associated with abrupt changes in doping level do not exist, and agreement was within $\pm 10\%$. The same level of precision was observed on 200Å wide n⁺ layers.

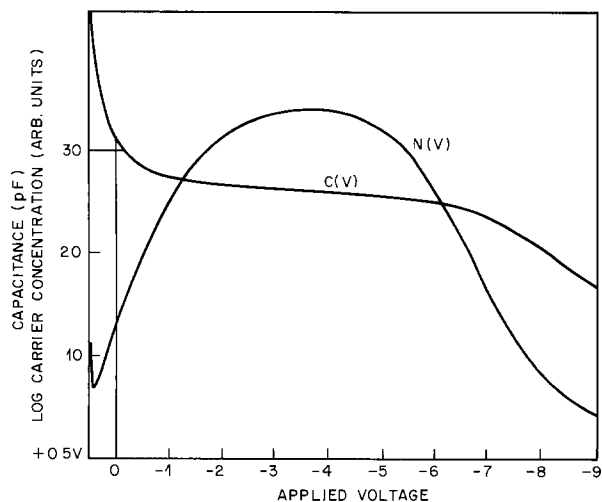


Fig. 3. $C(V)$ and $N(V)$ profiles of an impurity spike from which the impurity density is obtained by integration.

Results

Profiles.—Typical differential capacitance ($C-V$) profiles of Lo-Hi-Lo structures grown by injection doping are reproduced on Fig. 4 and 5. Often these profiles exhibit a more or less pronounced decrease in apparent doping after the high region. This “dip” we believe to be an artifact of the measurement technique for the following reasons. Empirically, it has been established that the following conditions favor the appearance of dips: (i) large amounts of charge in the high-doped layer, (ii) low background doping, and (iii) small distance from the surface of the crystal.

In Fig. 5 the top profile shows no dip in an experimental profile with a Hi-layer containing an integrated impurity concentration of $0.6 \times 10^{12} \text{ cm}^{-2}$. The second

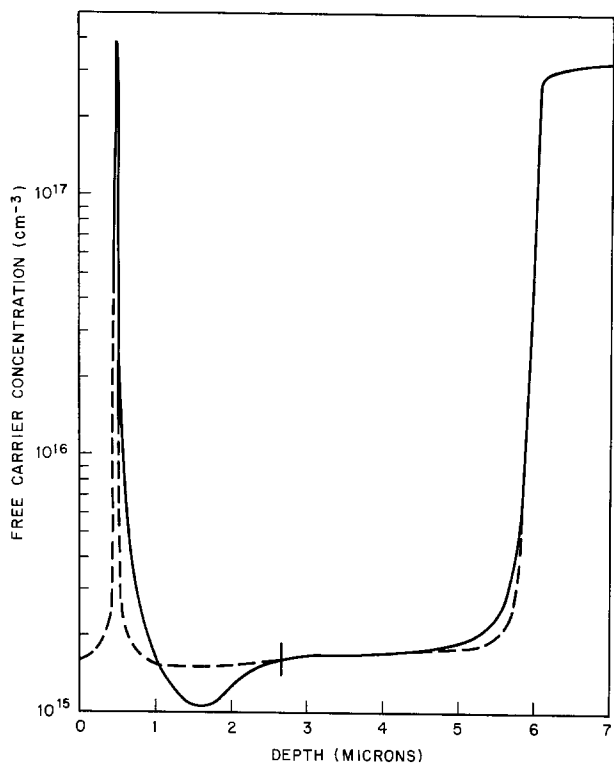


Fig. 4. $C-V$ profile of a Lo-Hi-Lo structure (full line). The broken line is believed to be representative of the underlying impurity distribution. The dip in the background doping is probably an artifact; its depth is a function of the position of the spike relative to the surface. The marker at 2.6μ indicates the depth at which the Schottky diode on the unetched surface broke down and where the profile was patched together using a second diode on the taper-etched portion of the test strip.

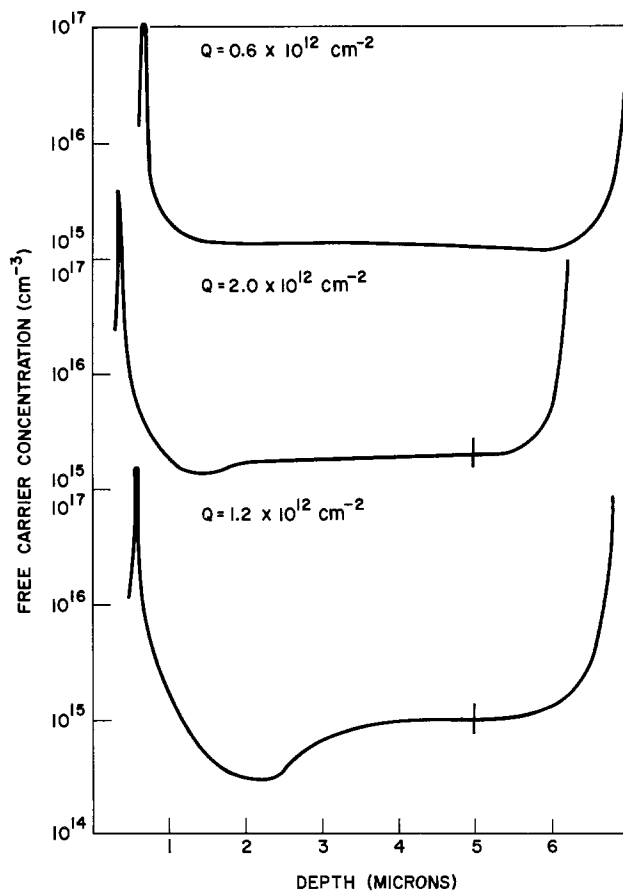


Fig. 5. Three $C-V$ profiles of Lo-Hi-Lo structures with varying impurity densities, Q , and background doping levels. The profile undershoot or dip near the Hi-layer appears to be a function of both Q and background doping level. Breakdown of unetched surface Schottky diodes is indicated by the vertical markers.

profile shows a pronounced dip for a total impurity concentration of $2 \times 10^{12} \text{ cm}^{-2}$ in the Hi-layer. The bottom profile illustrates how the dip dominates the profile if the background doping level falls to $1 \times 10^{15} \text{ cm}^{-3}$. Figure 6 illustrates the effect of distance from the surface of the crystal on the severity of the dip. The test strip was step etched to remove material above

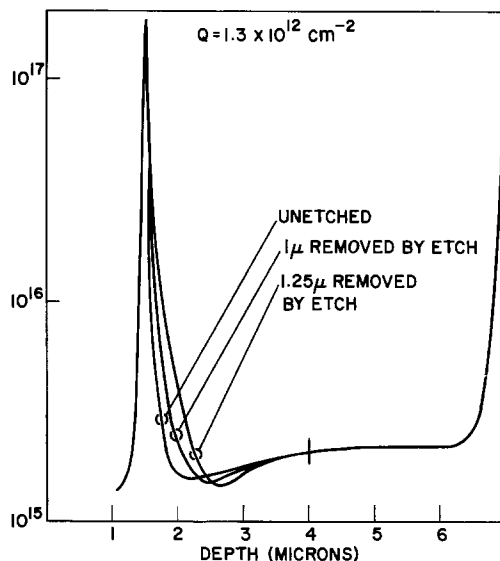


Fig. 6. $C-V$ profile of a “deep” Hi-layer as measured with and without step etching. Material above the Hi-layer is removed in two steps. The three profiles obtained show how the dip in the background doping level is intensified with decreasing distance from the surface. Breakdown of the unetched surface Schottky diode is marked at 4μ .

the Hi-layer. As the Hi-layer moves to the surface the dip becomes more pronounced. The accumulated indirect evidence together with the geometrical asymmetry (the dip appears only on the far side of a Hi-layer as seen from the Schottky barrier) supports the view that the dip is a profiling artifact and does not reflect either a sudden drop in a background doping level or an impurity segregation caused by the larger concentration gradient near a Hi-layer.

In Fig. 7 we show a high resolution C-V profile of a Hi-layer and compare the thickness at high and low concentration levels with the corresponding Debye lengths which provide a measure of the distortion of the impurity profile. A curve of the form $N^*_{\max} \exp(x^2/2\sigma)$ was found to approximate the free carrier concentration reasonably well, except that the decay of the latter is less rapid than the Gaussian below 0.3 N^*_{\max} . Identification of the carrier distribution with a Gaussian distribution simplifies the discussion of the Hi-layers by providing a standard measure of the width of Hi-layers. This width will be defined as the width at 0.607 times the peak height, N^*_{\max} . The Gaussian approximation should not be used to estimate the impurity content of a Hi-layer. The area under a Gaussian distribution is given by $\sigma N^*_{\max} \sqrt{2\pi}$. This formula was found to underestimate the impurity content by ~40%.

Width of Hi-layers.—The widths of Hi-layers grown under different conditions and annealed for varying times after growth exhibit regularities which indicate that both growth rate and solid-state diffusion after growth must be considered in an analysis. Figure 8 shows the variation of the square of the Hi-layer width (2σ) with growth rate squared. Only Hi-layers with postgrowth anneal times between 4 and 5 min are included. These samples have undergone a minimum of diffusion broadening (having been held at temperature for only 5 min) while still yielding Hi-layers that can

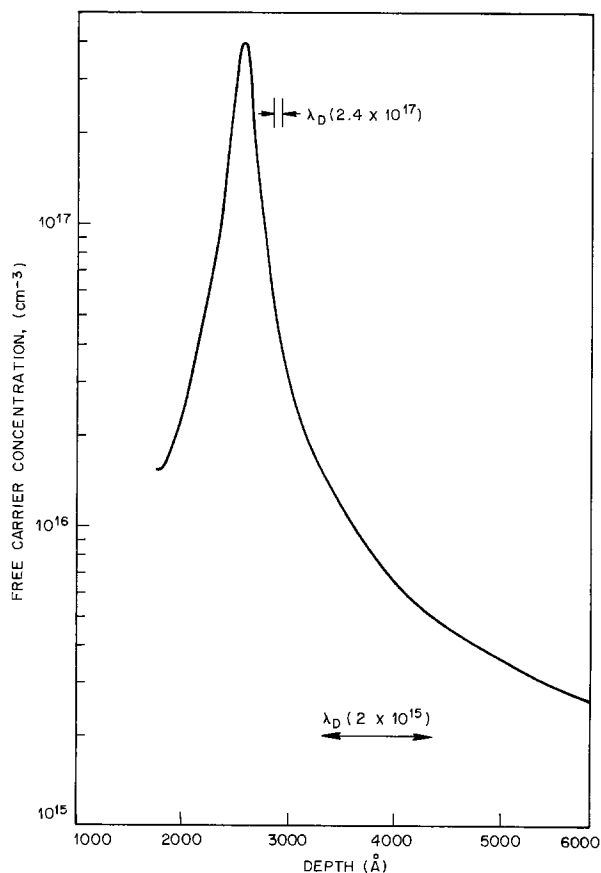


Fig. 7. High resolution C-V profile of a Hi-layer. The width of the Hi-layer is compared with the Debye length, λ_D , at background doping level and with the Debye length, at the 2σ level (~ half-height).

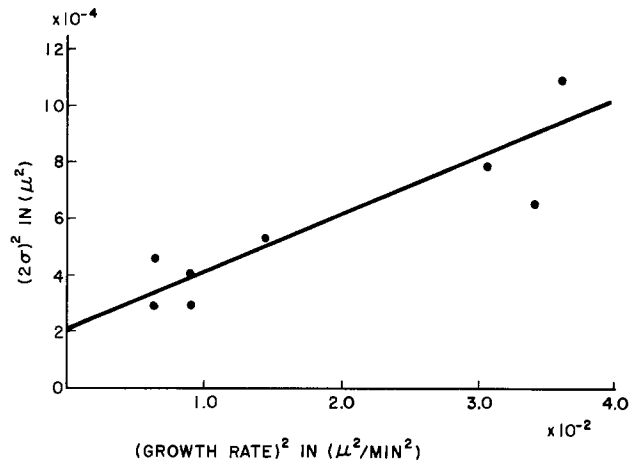


Fig. 8. Correlation between width (2σ) of short term (4-5 min) annealed Hi-layers and epitaxial growth rate. The squares of both variables are plotted for reasons explained in the text.

be fully profiled. A correlation between the width and the growth rate is inferred from the data. If the widths were dominated by diffusion broadening no dependence on growth rate would have been observed. The reason for plotting the squares of the variables are discussed in the following. Diffusion broadening is best studied on structures exposed to long postgrowth anneals. Several deeply buried Hi-layers were grown and evaluated. In addition, one wafer was returned to the furnace and annealed for 16 hr at growth temperature after removal of a test piece. Following the discussion of a model for the growth process we show that the final width of long time annealed structures as well as the diffusion broadening of minimally annealed layers is in accord with the ideal diffusion law.

In the following a simple model for the growth of Hi-layers is developed. Figure 9 is a schematic diagram of the experimental situation during layer growth. The dopant gas is injected into the reactor tube from a small bore quartz tube passing over the Ga source. We disregard any mixing that may occur due to interdiffusion and turbulence between carrier gas and dopant gas during the travel from the injection valve to the injection point in the reactor. After injection the dopant gas cloud travels a distance, d , until it passes over the substrate. During this passage it diffuses rapidly and

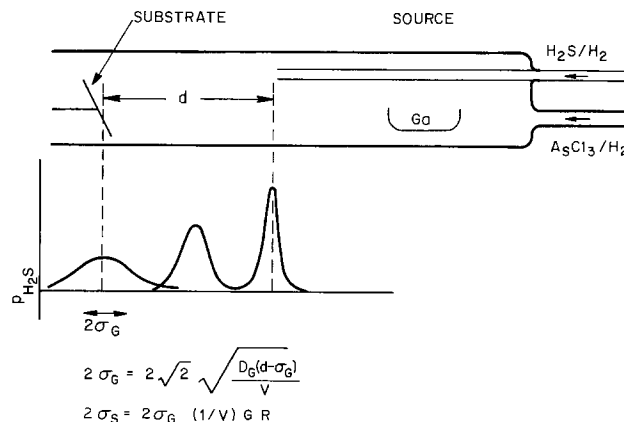


Fig. 9. Diagram of the sulfur injection tube and the sulfur cloud as it travels toward the substrate. The sulfur cloud is modeled by a plane source

$$P_{H_2S}(x,t) = \frac{P_0}{2\sqrt{\pi D_G t}} e^{-\frac{(x-vt)^2}{4D_G t}}$$

where x is the distance from the injection point and t is the time since injection. The original partial pressure, P_0 , falls as the cloud spreads by gaseous interdiffusion characterized by a diffusion coefficient D_G .

we will assume that the concentration of dopant in the carrier gas is given by a plane source model

$$C(x, t) = \frac{C_0}{2\sqrt{\pi D_G t}} \exp - \frac{(x - vt)^2}{4D_G t}$$

where x is the distance measured from the injection point, D_G is the gaseous interdiffusion coefficient, and t the time elapsed since the injection.

It is important to take into account the fact that the carrier gas velocity, v , at growth temperatures is much higher than the room temperature velocity obtained by dividing the flow rate by the cross-section area. Due to thermal expansion of the gas volume the velocity increases by a factor given by the ratio of the initial and final temperatures

$$\frac{1050}{300}, \text{ or } 3.5$$

The progress of the doping gas cloud is drawn schematically in Fig. 9. When the dopant gas cloud passes over the substrate its width is given by

$$2\sigma_G = 2\sqrt{\frac{2D_G(d - \sigma_G)}{v}} \quad [1]$$

We assume that the doping level in the growing layer is directly proportional to the dopant gas concentration which results in an impurity concentration profile of width $2\sigma_S$, given by

$$2\sigma_S = \frac{2\sigma_G}{v} \text{ G.R.} \quad [2]$$

where G.R. is the growth rate. Subsequently, a layer of low-doped material is grown over a time span t_D . Alternately, the grown layer may be annealed without additional growth. During such periods solid-state diffusion of the incorporated impurity will broaden the Hi-layer. The theoretical amount of diffusion broadening can be obtained from the well-known delta function solution of the ideal diffusion equation (16) by simply adding an imaginary prediffusion process in the mathematical model. If the diffusion broadening is denoted by $2\sigma_D$

$$2\sigma_D = 2\sqrt{2D(t + t_0)} - 2\sqrt{2Dt_0}$$

where t_0 is the time required to broaden a delta function (in the imaginary prediffusion process) to the width of the initial (as grown) Gaussian distribution and t is the time of the actual diffusion. With the initial width as given by Eq. [2]

$$2\sqrt{2Dt_0} = \frac{2\sigma_G}{v} \text{ G.R.}$$

We find that the total width 2σ of the n^+ layer after diffusion broadening is

$$2\sigma = 2\sqrt{2D(t + t_0)} = 2\sqrt{2Dt + \frac{\sigma_G^2}{v^2} (\text{G.R.})^2}$$

which gives us the rationale for plotting the data $(2\sigma)^2$ vs. $(\text{G.R.})^2$ as was done on Fig. 8. Extrapolation to zero growth rate yields

$$8Dt = 2 \times 10^{-4} \mu^2$$

from which with $t = 240$ sec, we find a value for the diffusion coefficient, $D = 1 \times 10^{-15}$ cm²/sec.

Table II shows pertinent data for a number of representative Hi-layers grown under different conditions and annealed for different lengths of time. The gaseous interdiffusion coefficient was estimated from

$$D_G(1100^\circ\text{K}) = D_G(300^\circ\text{K}) \left(\frac{1100}{300} \right)^{1.5}$$

using $D_G(300^\circ\text{K}) = 0.7$ cm²/sec (17). To obtain agreement for the long term diffusions a diffusion coefficient of 2×10^{-15} cm²/sec was used. This value is intermediate between that obtained by extrapolation of published data (18) to the growth temperature (750°C): 5×10^{-15} cm²/sec, and the value obtained by extrapolation to zero growth rate. With some exceptions for very narrow Hi-layers the agreement between estimate and experiment is within one Debye length. The qualitative considerations of the free carrier diffusion and the distortions of the C-V profile discussed earlier may be applicable and explain the tendency of the profile widths to be narrower than the estimated widths. Alternatively, various shortcomings of the model may be responsible for the discrepancies. The assumption of a plane source gaseous dopant is clearly an oversimplification. The dopant gas is injected from a small bore tube (0.4 mm ID) with a nozzle velocity about 10-20 times the carrier gas velocity. It is possible that gas mixing takes place closer to the substrate and is due to turbulence rather than diffusion. A more serious difficulty is the assumption that the solid-state diffusion after growth can be adequately described by a concentration independent diffusion process.

We have found that for steady-state S-doping in GaAs grown by CVD, saturation of free carriers occurs at $4-5 \times 10^{18}$ cm⁻³. This limit agrees well with that obtained by Mil'vidskii and Pelevin (19) for melt growth of GaAs. According to their data the difference between the total amount of S and the electrically ac-

Table II.

Run No.	Growth rate, μ/min	$t_D^{(a)}$, min	$Q^{C-V, (b)}$, $\times 10^{12}$	$N_{Hi}^{(c)}$, $\times 10^{17}$	$2\sigma_S^{(e)}$, Å	$2\sigma_D^{(d)}$, Å	Theor. width, $^{(e)}$ Å	Profile width, $^{(f)}$ Å	$\lambda_D^{(g)}$ Å
A	0.070	4.3	2.1	8	55	160	215	160	65
B	0.10	4.3	1.5	4	80	140	220	200	85
C	0.12	5.3	1.8	5	100	145	245	230	77
R	0.17	4.3	3.0	7	135	110	245	250	70
K	0.083	10.3	2.4	6	65	260	325	200	55
U	0.065	30	1.1	1.1	50	500	550	470	170
T	0.10	70	0.7	0.6	80	800	880	1150	350
T _A	0.10	960	—	0.07	80	3000	3100	3000	700

^(a) t_D = time after growth of Hi-layer during which the epitaxial layer was held at 730°-750°C.

^(b) Q = total amount of impurity in the Hi-layer (atoms/cm²).

^(c) $2\sigma_S$ = width of the impurity distribution at $0.6 \times$ peak doping level prior to solid-state diffusion.

$$= \frac{2\sigma_G}{v} \text{ G.R.}$$

where $2\sigma_G$ = width of sulfur distribution in the carrier gas

$$= 2\sqrt{\frac{2D_G(d - \sigma_G)}{v}}$$

where v = carrier gas velocity at growth temperature, 190 cm/min; D_G = diffusion coefficient in gas phase at 800°C, 5 cm²/sec; and d = distance traveled by dopant between injection site and substrate, 25 cm.

^(d) $2\sigma_D$ = diffusion broadening of Hi-layer.

^(e) Theoretical width: $2\sigma_S + 2\sigma_D$.

^(f) Profile width: width of free carrier distribution as given by C-V profiles.

^(g) λ_D = Debye length at $0.6 N_{Hi}$.

tive S becomes significant when the free carrier concentration exceeds $2 \times 10^{18} \text{ cm}^{-3}$. We conclude from this comparison that for CVD GaAs the component of neutral S will probably also become significant when the free carrier concentration exceeds $2 \times 10^{18} \text{ cm}^{-3}$.

For an impurity density of $2 \times 10^{12} \text{ cm}^{-2}$ in a typical n^+ layer this limit is exceeded when $2\sigma < 100 \text{ \AA}$. If the layer were narrower than 100 \AA the initial stage of the diffusion process, lasting until the peak concentration is reduced to $2 \times 10^{18} \text{ cm}^{-3}$, is complicated by the presence of at least two species. The serious discrepancy seen for sample K which is representative of several similar layers, may be due to such an effect.

Sulfur incorporation.—The distribution coefficient for an impurity incorporated into a solid in equilibrium with the gas phase is

$$k = \frac{x_s}{x_g}$$

This is the definition for dilute solutions ($k = x_s/x_L$) given by Thurmond and Struthers (20), where the mole fraction in the liquid (x_L) is replaced by the mole fraction in the gas phase. We shall apply this definition to the case of sulfur-doped GaAs. The mole fraction of the almost completely ionized sulfur in the solid (for low doping levels) is given by

$$x_s = \frac{[S^+]}{N_s} = \frac{[S^+]}{L \frac{d}{\text{F.W.}}}$$

where $[S^+]$ is the number of ionized sulfur atoms/cm³, N_s is the number of available lattice sites, L is Avogadro's number, d is the density of GaAs (5.35 g/cm^3), and F.W. is the formula weight of GaAs (144 g/mole). For the dilute case we have

$$x_g = \frac{P_{\text{H}_2\text{S}}}{P_{\text{H}_2}}, \quad k = \frac{[S^+]P_{\text{H}_2}}{N_s P_{\text{H}_2\text{S}}} \quad [3]$$

Simple estimates using JANAF (21) data show that H₂S is by far the most stable sulfur species at 1100°K with $P_{\text{H}_2} = 1 \text{ atm}$ and very low total sulfur concentration. Since we cannot measure the instantaneous sulfur doping level corresponding to an instantaneous sulfur partial pressure we integrate over the time interval, Δt , needed to grow the Hi-layer

$$\int_{\Delta t} k dt = \frac{\text{F.W.} P_{\text{H}_2}}{Ld} \int_{\Delta t} \frac{[S^+]}{P_{\text{H}_2\text{S}}} dt$$

It is known from the diffusion studies of Young and Pearson (18) that the solid solubility of sulfur in GaAs is a linear function of the sulfur vapor density. Depending on the diffusivity of the dopant the equilibrium incorporation behavior may or may not be reflected in the doping level of a crystal grown at finite growth rates. For S-doped GaAs linearity between dopant gas (H₂S) concentrations and doping level was observed by Goldsmith and Oshinsky (22) in the range 4×10^{17} – $4 \times 10^{13} \text{ cm}^{-3}$ at growth rates comparable to ours.

The first-order doping dependence allows us to integrate over the two sulfur concentrations separately

$$\frac{1}{\Delta t} \int_{\Delta t} k dt = k = \frac{\text{F.W.} P_{\text{H}_2}}{Ld} \frac{\int_{\Delta t} [S^+] dt}{\int_{\Delta t} P_{\text{H}_2\text{S}} dt}$$

The upper integral is

$$\int_{\Delta t} [S^+] dt = \int_{\Delta t} [S^+] \frac{\partial t}{\partial x} dx = \frac{1}{\text{G.R.}} Q$$

where G.R. is the growth rate and Q is the charge density/cm² of the Hi-layers. For the gas phase we have

$$\int_{\Delta t} P_{\text{H}_2\text{S}} dt = \frac{RT}{F} \int_{\Delta t} \frac{F P_{\text{H}_2\text{S}}}{RT} dt = \frac{RT}{F} n$$

where n is the total number of moles of hydrogen sulfide injected, R is the gas constant, T the temperature at which the flow rate, F , in the reactor is measured. The distribution coefficient is now given by

$$k = \frac{\text{F.W.} P_{\text{H}_2}}{RT d} \frac{F}{\text{G.R.}} \frac{Q}{N}$$

where we have converted the number of moles of H₂S injected to atoms: $L n = N$. If the growth rate, G.R., is expressed in cm/min, and F , the flow rate, in liters/min at room temperature we find for typical experimental growth conditions

$$k = 0.75 \frac{Q/N}{\text{G.R.}} \quad [4]$$

The amount of H₂S injected during epitaxial growth to produce the high-doped layer of the Lo-Hi-Lo structure can be varied by changes in the pressure, and the concentration of the gas flowing through the injection loop and by changing the volume of the loop. All three parameters have been varied in the course of the study. Additionally the number of injections can be varied to increase the volume. The amount of dopant gas is conveniently measured in moles according to

$$n = \frac{m \cdot V \cdot C \cdot P}{RT}$$

where m is the number of injections, V , C , and P the volume, concentration, and pressure of the injected gas. The gas constant R is $0.082 \text{ liter atm/}^\circ\text{K}$ and T the room temperature is in $^\circ\text{K}$.

Typically, a volume of 0.7 mliter at a concentration of 300 ppm and 2 atm pressure was injected ($m = 1$) corresponding to $n = 1.7 \times 10^{-8}$ moles and containing 1×10^{16} S atoms. At a growth rate of $0.08 \mu/\text{min}$ this amount of H₂S yielded a Hi-layer containing $2 \times 10^{12} \text{ cm}^{-2}$. Inserting these numbers into Eq. [3] gives

$$\frac{Q/N}{k} = 2 \times 10^{-4} \\ k = 20$$

The doping efficiency, Q/N , was found to be independent of the total amount of sulfur injected, N , for a fixed growth rate. For 13 layers grown at rates between 0.65 and $0.75 \mu/\text{min}$ the ratio Q/N remained constant with an average value of 2.05×10^{-4} and a standard deviation of 19% as N was varied by a factor of 4. This result supports the assumption discussed earlier that sulfur doping in the 10^{17} – 10^{13} cm^{-3} range is linear with H₂S partial pressure.

On Fig. 10 we show similar data obtained for other growth rates. The growth rate was varied intentionally by changing the source and the substrate temperatures and also unintentionally by depletion of the Ga source. Thus for a source temperature of 765°C and substrate temperature of 725°C the growth rates fell from 0.11 to $0.04 \mu/\text{min}$ as the source was depleted. The reason for this decrease is presumably that the HCl to GaCl conversion efficiency decreased. By increasing the source temperature to 805°C and by varying the substrate temperature between 750° and 735°C the growth rate could be varied from 0.04 to $0.18 \mu/\text{min}$. The straight line drawn through the combined data on Fig. 11 using least squares fitting has a slope of 1.6 rather than unity as given by Eq. [4]. This implies that the experimentally measured distribution coefficient is not an equilibrium value as required by theory. It is reasonable to propose that the departure is due to kinetic effects. If this is true, then the slowest experimentally realized growth rates would yield the best estimate of k . The lowest value of k obtained in this study is

$$k_{\text{min}} = 13$$

A value of k larger than unity does not imply depletion of the gas phase dopant concentration which would invalidate the simple model used to estimate Hi-layer widths. This is readily seen from the experimental

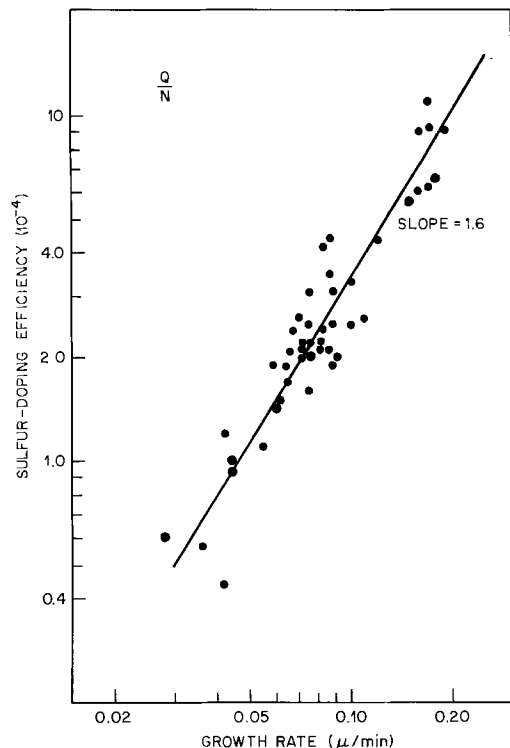


Fig. 10. Sulfur incorporation efficiency Q/N as a function of growth rate. The impurity content of a Hi-layer, Q , is divided by the number of S-atoms, N , injected into the gas stream. The quotient, Q/N , is related to a concentration averaged distribution coefficient k by $k = 0.75 Q/N (\text{G.R.})^{-1}$, Eq. [4].

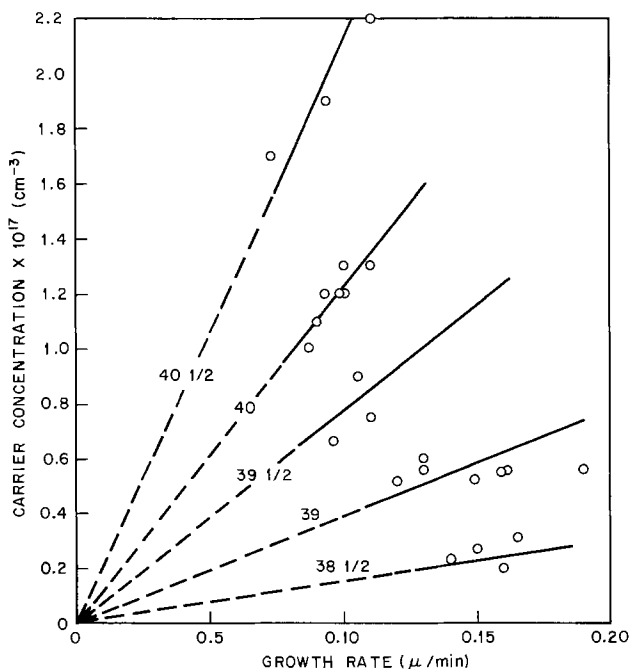


Fig. 11. Free carrier concentration vs. growth rate for steady-state S-doping. The numbers indicate the settings of the variable leak (Granville Phillips) used. Calibration of the leak indicates that leak flow rates increase linearly with the leak settings at a rate of a factor of 5 per integral number in the range covered here.

ratio Q/N , which is of the order 10^{-4} - 10^{-3} . The wafer area is 4 cm^2 and there is no wall nucleation near the substrate. Thus at most 2.5% of the injected sulfur is taken up by the solid.

It is realized that the experimental values for the distribution coefficient obtained in this study are probably influenced by factors not recognized specifically, i.e., they are probably system dependent. System de-

pendent data should not be modeled, but summarized as simply as possible, e.g., as a coefficient of linearity. The relatively complex approach taken here is not a model and attempts only to remove the time dependence of the growth process to isolate a coefficient of linearity which may be compared to more conventional steady-state doping coefficients obtained with other crystal growth systems.

The S-doping data given by Goldsmith and Oshinsky (22) can be applied to the formula given in Eq. [3] to yield an experimental distribution coefficient for their system

$$k = 140$$

This value represents an order of magnitude more efficient sulfur incorporation. Among major differences between the two systems compared is the nature of the Ga and As sources. Goldsmith and Oshinsky used GaCl_3 and As. The gas flow data and source temperatures given in their report lead to the estimate that the Ga/As ratio in their system was ~ 1 , taking into account that GaCl_3 vapor is dimeric. For a typical Ga/As Cl_3 system the Ga/As ratio is ~ 2 (23). In conflict with experimental results, the more As-rich system would be expected to incorporate the As-substituting impurity less efficiently. Another effect is to be expected from the partial pressure of free HCl which must be higher in the GaCl_3/As system. However, the range of Si-background doping governed by P_{HCl} is negligible compared with 10^{17} - 10^{18} cm^{-3} S-doping levels.

Steady-State S-Doping

The observation that the experimentally determined distribution coefficients vary superlinearly with growth rate suggests that steady-state doping might show growth rate dependence too. For this case the analysis would not involve the time integration required for a transient phenomenon and, therefore, no growth rate dependence would be predicted. But the additional fractional (0.6) growth rate dependence suggested by the data on Fig. 10 may be expected to be reflected in the steady-state case too. Experimentally (10) this is indeed observed. We used the standard method of doping with dilute (1000 ppm) H_2S admitted through a variable leak. Figure 11 shows that doping data for a limited range of growth rates are qualitatively in agreement with the transient doping data. The straight lines drawn through the data points suggest a linear relationship, i.e., larger than the 0.6 power dependence suggested by the transient experiments. However, the data cover too narrow a range to allow discrimination between a 0.6 and a unity power dependence. The scatter is probably due to the difficulty of setting the leak reproducibly to a given opening.

Returning to the definition of k we can calculate the partial pressure of H_2S in equilibrium with a given doping level in the solid, e.g., $2 \times 10^{17} \text{ cm}^{-3}$. With $k = 20$ we obtain

$$P_{\text{H}_2\text{S}} = \frac{P_{\text{H}_2}}{20} \frac{2 \times 10^{17}}{2 \times 10^{22}} = 5 \times 10^{-7} \text{ atm}$$

Thus for steady-state doping using 1000 ppm H_2S with a carrier gas velocity of 0.7 liter/min we find that the leak flow rate of dopant should be 0.35 mliter/min. This estimate agrees well with leak doping experience and with extrapolation of leak flow rates measured at higher leak settings.

The positive growth rate dependence of steady-state S-doping can be compared with the results obtained by Wolfe *et al.* on Sn-doping of GaAs (24). For this system at low growth rates comparable to ours, a negative growth rate dependence was found. For growth rates higher than $0.2 \mu/\text{min}$ the dependence changed sign and became first order. The explanation advanced by Wolfe *et al.* was based on the suggestion that higher growth rates lead to increasing roughness of the growing surface, thereby creating more surface area available for dopant adsorption. But since at all growth rates there

Table III. Reproducibility of sulfur doping and n^+ -layer width

Run No.	$n \times 10^{-18}$ mole	Growth rate, μ/min	$Q^0 - V_{\text{avg}}$	ΔQ	Width, \AA
E	1.54	0.064	1.7	-0.8	150
F	1.54	0.078	2.5	—	150
G	1.85	0.096	2.8	+0.3	170
H	1.46	0.065	1.7	-0.8	180
K	1.89	0.082	2.4	-0.1	200
L	1.93	0.077	2.5	—	160
M	1.89	0.086	2.4	-0.1	150
N	1.93	0.074	2.7	+0.2	140
P	1.89	0.064	2.0	-0.5	150
$\sigma = 0.46$					165 \pm 20

$$Q - \text{Target } 2.5 \times 10^{23}$$

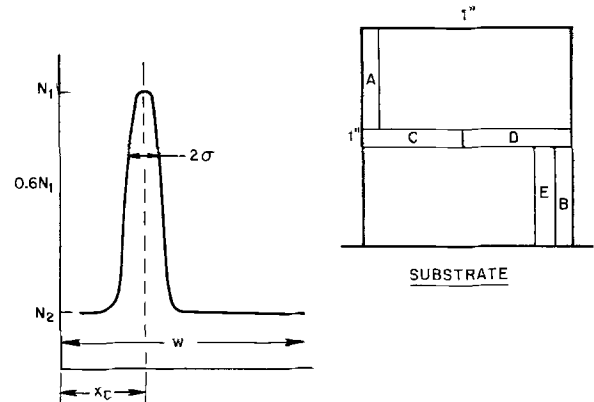
$$\frac{0.46}{2.5} = 18\%$$

Note: The standard deviation is here taken with respect to the target, 2.5×10^{23} , rather than the experimental mean of 2.3×10^{23} . Using the latter, σ becomes 0.4×10^{23} or 17%.

is competition between dopant and host atoms for sites, this mechanism seems unlikely to produce the observed effects unless the proportion of surface area of different facets changes with growth rate. If so, the growth rate dependence of the sulfur incorporation would actually be due to an orientation effect. We found no correlation between surface roughness, growth rate, and doping. One layer grown at the rate of $0.04 \mu/\text{min}$ had a fish scale pattern with features registering between 500 and 1500\AA high on the Talysurf. Another grew at a rate of $0.18 \mu/\text{min}$ and exhibited features less than 300\AA high.

The observed growth rate dependence of the sulfur incorporation is undesirable as it magnifies the difficulties of doping control. The inherent dependence might be eliminated by changing to a different dopant or by increasing the growth rate. If a dopant were found with a higher distribution coefficient, the basic idea of injection doping would offer better control than was realized with sulfur. Alternatively, a dopant with a negative inherent growth rate dependence should be employed. For such a dopant the two observed growth rate dependences would cancel. The results of Wolfe *et al.* suggest the use of tin which, however, for application in the present system would have to be available in gaseous form (metalloorganic).

As a result of the strong growth rate dependence (1.6 power) of the sulfur incorporation the reproducibility of doping was not improved by employing injection doping. Using the manually operated valve in a series of consecutive runs we aimed at a target impurity density of $1.25 \times 10^{12} \text{ cm}^{-2}$. The slice-averaged impurity density ranged from 0.95 to $1.56 \times 10^{12} \text{ cm}^{-2}$ with a standard deviation of $0.20 \times 10^{12} \text{ cm}^{-2}$, or 16%. In a similar series of 9 injection doping runs the target of $2.5 \times 10^{12} \text{ cm}^{-2}$ was obtained with a standard deviation of $0.45 \times 10^{12} \text{ cm}^{-2}$, or 18%, and a range of 1.7 - $2.8 \times 10^{12} \text{ cm}^{-2}$, Table III. These results show that improving the control over the amount of dopant added does not solve the problem. An idea of the uniformity across a 1×1 in. wafer grown by S-injection may be obtained by referring to Fig. 12. The level of uniformity is comparable to that of wafers produced by conventional steady-state doping. The table also contains data on the reproducibility of the width of the Hi-layers. Additional data on reproducibility and uniformity will be published as a separate report (6). Two useful results have been obtained using injection doping. The minimum practicable width of Hi-layers has been reduced by a factor of five. Using the manually operated variable leak the narrowest Hi-layers achieved were about 700\AA wide. With the injection valve Hi-layers only 150\AA wide (uncorrected C-V profile) could be reproducibly grown. Although no improvements in the performance of 6-11 GHz devices have been attributable to the reduction in layer width, it is possible that such improvements may be realized for higher frequency devices. This suggestion is based on the fact that higher frequency devices have $x_c \leq 1000 \text{\AA}$ and



POINT	x_c (μ)	Q (10^{12} cm^{-2})	$N_2 (2\mu)$ (10^{15} cm^{-3})	2σ (μ)	N_1 (10^{17} cm^{-3})
A	0.65	2.1	2.0	0.016	6.9
B	0.85	1.8	1.2	0.016	5.0
C	0.83	2.4	1.7	0.014	9.0
D	0.74	1.8	2.2	0.014	6.5
E	0.86	1.8	1.7	0.015	7.5
AVERAGE $\pm \sigma$	0.78 ± 0.05	2.1 ± 0.3	1.8 ± 0.4	0.015 ± 0.001	7.0 ± 1.1

Fig. 12. Doping parameters at various points on a 1×1 in. Lo-Hi-Lo wafer.

therefore, layers of widths approaching 1000\AA are not feasible for this type of device.

Secondly, the injection doping technique has been useful in demonstrating that doping control is primarily dependent on growth rate control. Future work will have to aim at improvements in the reproducibility of growth rates.

Conclusions

An experimental approach to investigate the reproducibility of growing 100 - 200\AA thin epitaxial layers with a predictable impurity content is described. This system has been utilized to grow Lo-Hi-Lo (modified Read profile) structures for GaAs IMPATT diodes. The dopant system is very flexible, allowing control of the amount of dopant through three easily manipulated variables: pressure, volume, and concentration of the doping gas. The position, width, and impurity density of the Hi-layers could be explained in terms of the experimental conditions and known material parameters. A distribution coefficient of ~ 20 for S-doping from the gas phase was extracted from the data. A strong growth rate dependence of the total amount of incorporated impurity was observed. It is, in part, due to the transient nature of the doping procedure. In addition there appears to be a positive, inherent growth rate dependence of sulfur incorporation. As a result of the growth rate dependence no improvement in doping control was achieved compared with previously used methods. The value of injection doping lies in the achievement of sufficient precision in the control of amount of dopant added to obtain reliable data on sulfur incorporation. These data justify the conclusion that improved growth rate control will lead to improved doping control.

Acknowledgments

The authors gratefully acknowledge the technical assistance of D. T. Lassota. Numerous stimulating discussions with W. C. Niehaus and J. D. Wiley helped to shape our ideas. In addition, discussions with A. S. Jordan, F. A. Trumbore, C. D. Thurmond, and H. C. Cox were most helpful.

Manuscript submitted Aug. 14, 1974; revised manuscript received Dec. 26, 1974.

Any discussion of this paper will appear in a Discussion Section to be published in the December 1975 JOURNAL. All discussions for the December 1975 Discussion Section should be submitted by Aug. 1, 1975.

Publication costs of this article were partially assisted by Bell Laboratories.

REFERENCES

- W. G. Matthei, *Microwave J.*, **16**, 29 (1973).
- J. C. Irvin, in Proc. Fourth Biennial Cornell Electrical Engineering Conference (Aug. 1973), p. 287, Cornell University Press, Ithaca, N. Y.
- C. K. Kim, W. G. Matthei, and R. Steele, *ibid.*, p. 299.
- W. R. Wisseman, D. W. Shaw, R. L. Adams, and T. E. Hasty, *IEEE Trans. Electron Devices*, **ED-21**, 317 (1974).
- G. Salmer, J. Pribetich, A. Farrayre, and B. Kramer, *J. Appl. Phys.*, **44**, 314 (1973).
- W. C. Niehaus, L. C. Luther, J. C. Irvin, and D. E. Iglesias, *IEEE Trans. Electron Devices*, To be published.
- J. V. DiLorenzo, *J. Crystal Growth*, **17**, 189 (1972).
- J. V. DiLorenzo, in Proc. 5th International Symposium on GaAs and Related Compounds, Deauville, France, 1974, To be published.
- M. V. Sullivan and G. A. Kolb, *This Journal*, **110**, 585 (1963).
- D. W. Shaw, *J. Crystal Growth*, **8**, 117 (1971).
- W. Riessler, *Z. Angew. Phys.*, **12**, 433 (1960).
- G. L. Miller, *IEEE Trans. Electron Devices*, **ED-19**, 1103 (1972).
- D. P. Kennedy, P. C. Murley, and W. Kleinfelder, *IBM J. Res. Develop.*, **12**, 399 (1968).
- W. C. Johnson and P. T. Panousis, *IEEE Trans. Electron Devices*, **ED-18**, 965 (1971).
- P. L. Hower *et al.*, in "Semiconductors and Semimetals," R. K. Willardson and A. C. Beer, Editors, Vol. 7, Part A, Chap. 3, p. 167, Academic Press, New York (1971).
- H. S. Carslaw and J. C. Jaeger, in "Conduction of Heat in Solids," 2nd Edition, p. 50, Clarendon Press, Oxford (1959).
- J. O. Hirschfelder, C. F. Curtiss, and R. B. Bird, "The Molecular Theory of Gases and Liquids," John Wiley & Sons, Inc., New York (1954).
- A. B. Y. Young and G. L. Pearson, *J. Phys. Chem. Solids*, **31**, 517 (1970).
- M. G. Mil'vidskii and O. V. Pelevin, *Inorg. Mater.*, **3**, 1024 (1967), translated from *Izv. Akad. Nauk SSSR, Neorgan. Materialy*, **3**, 1159 (1967).
- C. D. Thurmond and J. D. Struthers, *J. Phys. Chem.*, **57**, 831 (1953).
- JANAF Interim Thermochemical Tables, Dow Chemical Co. (1965).
- N. Goldsmith and W. Oshinsky, *RCA Rev.*, **24**, 546 (1963).
- J. V. DiLorenzo and G. E. Moore, *This Journal*, **118**, 1823 (1971).
- C. M. Wolfe, G. E. Stillman, and W. T. Lindley, in Proc. 2nd International Symposium on GaAs, Dallas (1968), p. 43, Institute of Physics and the Physical Society (1969).

Reactions Between the Ta-Pt-Ta-Au Metallization and PtSi Ohmic Contacts

H. M. Day,* A. Christou, W. H. Weisenberger, and J. K. Hirvonen

Naval Research Laboratory, Washington, D.C. 20375

ABSTRACT

The purpose of this work was to determine processing and/or operating limitations of the proposed microwave power transistor metallization scheme consisting of Si/PtSi-Ta-Pt-Ta-Au. Typical Si-PtSi ohmic contacts were processed and metallized along with larger area wafers and annealed at temperatures from 400° to 785°C. Small area contacts were checked for variation of contact resistivity and the large area metallizations were examined by Auger electron spectroscopy (AES), Rutherford backscatter (RBS) analysis, and x-ray diffraction at a 5° glancing angle. Evidence of significant interdiffusion and chemical interaction at 400°C was absent. Above 600°C tantalum was found to react with gold and PtSi to form various compounds. Consumption of silicon from the substrate accompanied the formation of TaSi₂ with the formation of PtSi as an intermediate step. These thermochemical reactions with the accompanying diffusions which take place at temperatures in the range sometimes used for device processing could significantly alter device geometry and, therefore, device performance. At normal operating temperatures and temperatures up to 400°C the PtSi-Ta-Pt-Ta-Au system appears to be adequately stable.

Gold has been found to be less susceptible than aluminum to electromigration (1) and metal restructuring effects (2). It is, therefore, a strong candidate for a more reliable metallization system for microwave power transistors. However, due to the lower eutectic temperature of the Au-Si system (377°C) a diffusion barrier between gold and silicon is necessary to prevent alloying and shorting of the device. Several refractory metals have been used for this purpose as well as for better adhesion. In previous work (3, 4) the authors found that a Ta-Pt-Ta sandwich is an effective barrier to the interdiffusion of gold and silicon and provides satisfactory adhesion to the PtSi coated silicon substrate as well as to SiO₂ coated areas.

The reliability of composite contact metallizations is expected to be affected by diffusion controlled processes which take place at the various interfaces. Previous investigations (5-7) have indicated that while providing satisfactory adhesion in most cases the refractory metals tend to form silicides themselves. More

recent work (8) indicates that the presence of PtSi between tungsten and silicon actually enhanced the rate of WSi₂ formation. In the case of a Si-PtSi-Al contact a reaction between Al and PtSi was also observed to take place, significantly altering the characteristics of the contact (9).

Thus, an evaluation of tantalum films on PtSi is necessary in order to determine processing and/or operating limitations of the proposed microwave power transistor metallization scheme consisting of Si/PtSi-Ta-Pt-Ta-Au.

The present investigation concentrates upon the stability and contact resistance of the Si/PtSi-Ta-Pt-Ta-Au metallization system in which interfacial reactions and diffusion under extreme conditions can result in the formation of a number of additional compounds such as Ta₅Si₃, TaSi₂, TaPt, and TaAu. We report on the interdiffusion of the various constituents of the system, the various compounds actually formed as a function of annealing temperatures up to 785°C, and the variation or stability of the contact resistance at annealing temperatures up to 400°C. The tech-

* Electrochemical Society Active Member.

Key words: contacts, metallizations, reliability, transistors.

niques and procedures used in the formation of small area contacts are presented along with the methods used to obtain compositional data. These methods include Auger electron spectroscopy (AES), Rutherford backscattering (RBS) analysis, and 5° glancing angle x-ray diffraction.

Experimental Techniques

Ohmic contact processing.—The substrate used for ohmic contact processing and evaluation consisted of an n-type single-crystal silicon wafer with localized (oxide window, boron diffused) regions of p-type material of approximately 0.05 ohm-cm resistivity or 180 ohms per square sheet resistance. This resistivity was selected as being typical of the npn L-band microwave power transistor base region. The test pattern consisted of six parallel contacts $125 \times 10 \mu$ defined by oxide windows spaced 35μ on center within the base area diffusion window. Contacting pads were extended onto the surrounding oxide which was typically 5000 Å thick. The contact resistivity was measured according to the method outlined by Terry and Wilson (10).

Platinum silicide was formed in the contact windows by sputter deposition of 600 Å of Pt at a substrate temperature of 110°C followed by a 10 min sinter in vacuum at 475°C. The excess Pt was removed by etching in aqua regia or by sputter etching. For many applications, sputter etching produces excessive ion bombardment damage to the surrounding oxide. Platinum silicide exposed to aqua regia is also etched and left with a very roughened texture. To avoid the above problems, the PtSi reaction was driven to completion by further sintering in air at 475°C for 10 min. A layer of SiO₂, grown during sintering effectively masked the PtSi from attack by aqua regia during the removal of the excess platinum (11). The SiO₂ was subsequently removed by etching in buffered hydrofluoric acid before metal deposition.

Thin film deposition.—Layers of Ta, Pt, Ta, and Au were sputter deposited in sequence to thicknesses of approximately 1000, 300, 1000, and 3000 Å, respectively, at 200 W rf power, 5 μm argon pressure, and 110–112°C substrate temperature. Conventional photolithographic techniques were used to define the resistivity test pattern in the Au. Using the Au layer as a mask, the top layer of Ta was etched away in a solution of 9 parts saturated KOH (heated in a boiling water bath) and one part H₂O₂, added just before etching (12). The top layer of Ta was removed within 20 to 30 sec, whereupon the Pt layer prevented further etching. Further etching of the Ta was accomplished only after the Pt layer was removed by sputter etching at 100 W rf power and 5 μm argon pressure. An alternative to the above procedure is to use low power reactive plasma etching techniques, followed by a chemical etch for the final Ta layer.

Two centimeter diameter wafers of silicon and PtSi coated silicon were metallized simultaneously with the small area contact substrates. The larger wafers were used for compositional analysis and profile studies. The sputtered films were annealed in vacuum at pressures less than 10^{-4} Torr.

Compositional analysis.—Metallization diffusion profiles were obtained by AES (13) analysis as a function of argon ion sputter etching times and by RBS analysis (14, 15). Compositional data after the various heat-treatments were obtained by x-ray diffraction (16).

The AES profiles were made in a Physical Electronics, Model 1300 Auger electron spectrometer. Multiplexing and a peak-to-peak detection capability were used permitting variations in Auger signal amplitudes to be read out directly while sputter etching. The AES data were taken with a 50 μA beam current at a 3 kV beam voltage. A 2 kV, 30 mA argon ion beam was used for sputter etching. The AES depth-composition profiles are normalized so that the amplitude of the Auger signal for each element is compared to the signal amplitude obtained for 100% surface coverage by that element. The normalized peak amplitude corre-

sponds to the per cent coverage of a particular element assuming that the signal is unaffected by the presence of other elements or compounds on the surface. However, ion bombardment during sputter etching is known to produce chemical and topographical changes (13). Therefore, the correspondence of the depth composition profile to actual atomic per cent distribution of the elements in the samples can only be approximately determined. Robinson and Jarvis (17) have estimated that, at a given depth, in the specific case of a gold metallization on gallium arsenide, the per cent composition for any of the constituents is correct to within 15%.

With RBS analysis (18) ⁴He⁺ ions which penetrate the sample are backscattered from within the sample to give information on interdiffusion without the conventional sectioning by sputter etching during AES profile analysis. RBS analysis in this case was performed on the metallization specimens Si-PtSi and Si-PtSi-Ta-Pt after a sequence of annealing treatments up to 785°C. These measurements were performed using a 2.0 or 4.0 MeV ⁴He⁺ beam from the NRL 5 MV Van de Graaff accelerator. The backscattered ions were detected at an angle of 165° in a silicon surface barrier detector with a system resolution of approximately 12 keV FWHM.

Results and Discussion

Preanneal film structure and contact resistivity.—The grain size of the sputter deposited tantalum and gold films measured by electron diffraction was 100–300 and 300–600 Å, respectively. Likewise, the grain size of the platinum film was 200–400 Å. The gold was strongly (111) textured while the tantalum and platinum did not show any observable texture. The electrical resistivity of the gold films after deposition was measured to be 1.25 times the bulk resistivity. The sputtered tantalum films had a resistivity of 2.1 times that of bulk tantalum. The tantalum films were deposited as β-Ta as verified by electron diffraction examination (19).

The contact resistivity before annealing was found to be typically less than 8 μohm-cm² and did not vary with annealing temperatures up to 400°C for 24 hr. As a result of the particular measurement technique used, this value contains a component of resistance due to nonuniform fields and, therefore, represents an upper limit. In comparison, an average value computed from the Terry and Wilson data (10) for PtSi contacts on approximately equal resistivity material was 110 μohm-cm². This is an average of contact resistivity values for Al, Mo, Ni, Cr, and Ti on PtSi with a substrate resistivity of 0.04 ohm-cm. However, the PtSi-Al contact resistivity was consistently an order of magnitude below the average value. A value of approximately 15 μohm-cm² for a PtSi-W contact on p-type material doped to 2×10^{19} /cm³ (or 0.05 ohm-cm) was obtained by Sinha (7).

Metallurgical stability.—Figure 1 compares the Auger depth-composition profiles of the Ta-Pt-Ta-Au metallizations on silicon substrates as-deposited and after annealing at 550°C and 10^{-7} Torr. The fact that the interfaces in general appear slightly diffused initially may be attributed to differential sputtering (17). After annealing at 550°C interdiffusion is evident by a slight decrease in the slope of each peak with extensive tailing at each interface. Tantalum has diffused completely through the thin platinum layer while gold has not completely penetrated the thicker tantalum layer. A comparison of the RBS spectra of the Si-PtSi-Ta-Pt metallization taken on samples as-deposited and after being annealed at 785°C is shown in Fig. 2. The verticle arrows indicate the energy of the backscattered ⁴He⁺ ions which would be obtained for a particular species if it were on the outer surface. The width of a peak is a measure of the thickness of that particular layer, while the slope of the edge of a particular peak after taking energy straggling into account is a measure of the diffusion at that particular

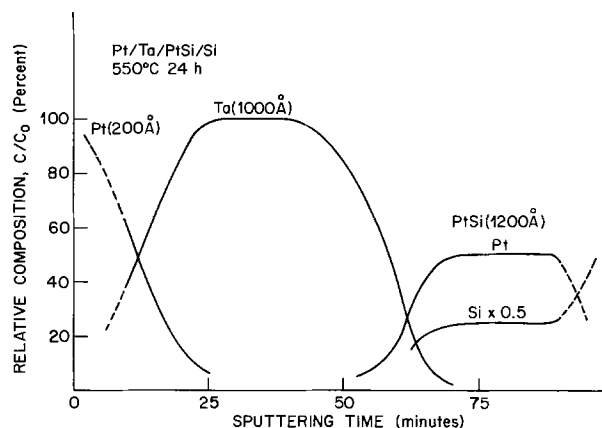
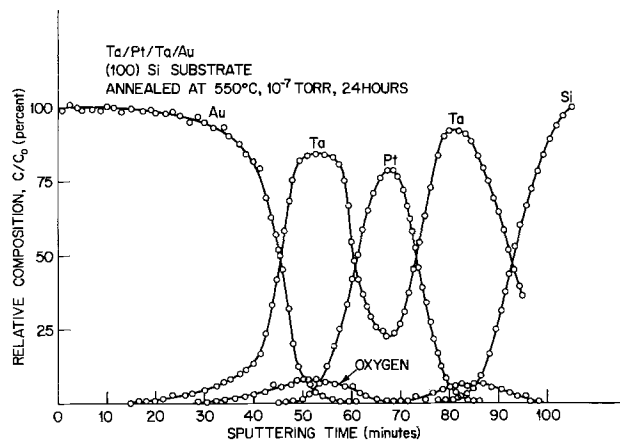
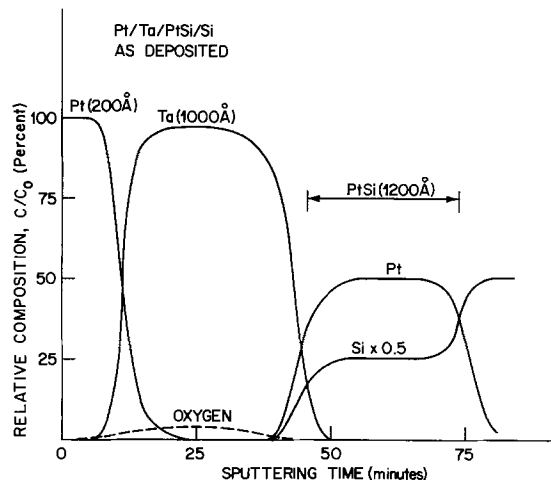
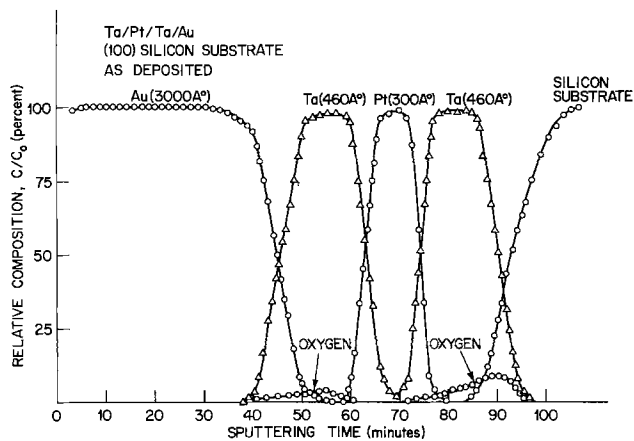


Fig. 1. Ta-Pt-Ta-Au metallization on (100) silicon substrate; as-deposited and as annealed at 550°C, 10⁻⁷ Torr for 24 hr.

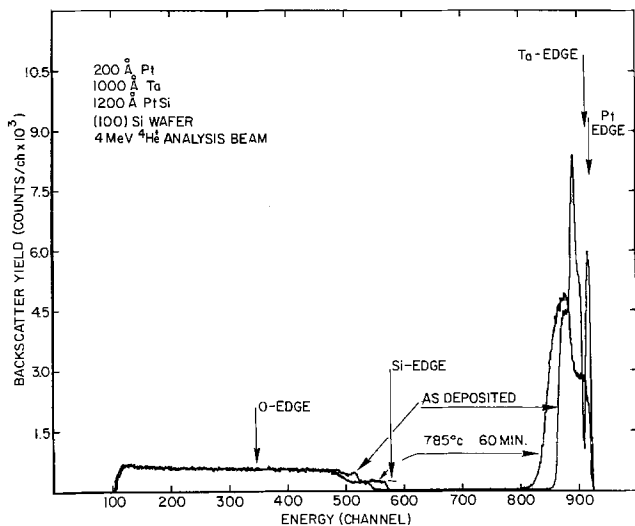


Fig. 2. RBS spectra of a PtSi-Ta-Pt metallization on (100) Si wafer; as-deposited and after annealing at 785°C for 60 min.

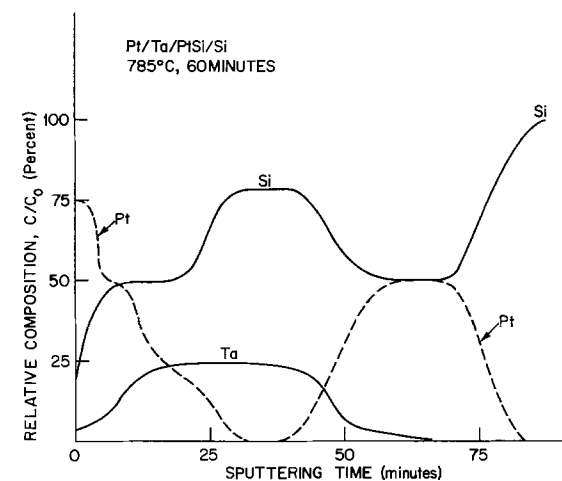


Fig. 3. Auger electron spectra of the PtSi-Ta-Pt metallization on (100) Si wafer; as-deposited and after annealing at 550°C for 24 hr and 785°C for 60 min.

interface. The increase in signal at the silicon edge and the decrease in the low energy edge of the Ta-Pt mixture after annealing at 785°C indicates that considerable intermixing and movement of the Si-PtSi interface has taken place with silicon penetrating to the outer surface. This is further corroborated by Auger spectra of identical specimens shown in Fig. 3 along with the spectrum of another specimen annealed at 550°C. The spectrum of the 550°C specimen shows significantly less interdiffusion or reaction of Pt-Ta as compared to the spectrum of the 785°C specimen. The latter clearly indicates that TaSi₂ has formed while the PtSi layer between the TaSi₂ and the silicon substrate remains essentially unchanged. Similar spectra (Fig. 1) of the Ta-Pt-Ta system directly on silicon

likewise show less interdiffusion or reaction of Ta and Si when annealed at 550°C. Finally, x-ray diffraction data on three Si-PtSi-Ta-Pt specimens (the control and specimens annealed at 600° and 785°C) are shown in Fig. 4. After annealing at 600°C, tantalum-rich silicides are predominant though the Auger spectra showed little interdiffusion at 550°C. After annealing at 785°C the x-ray spectra, in agreement with the Auger spectra, show that TaSi₂ is dominant with the (112) PtSi line increasing in intensity.

The reaction of tantalum with PtSi in this case is exactly analogous to the reaction of tungsten with PtSi to form the more stable WSi₂ as observed by Sinha (6). Similar observations have been made for other refractory metals according to reports by Tu and Mayer (18). In the case of the Si-PtSi-Ta reaction, movement of the Si-PtSi interface at temperatures above approximately 600°C takes place by a complex

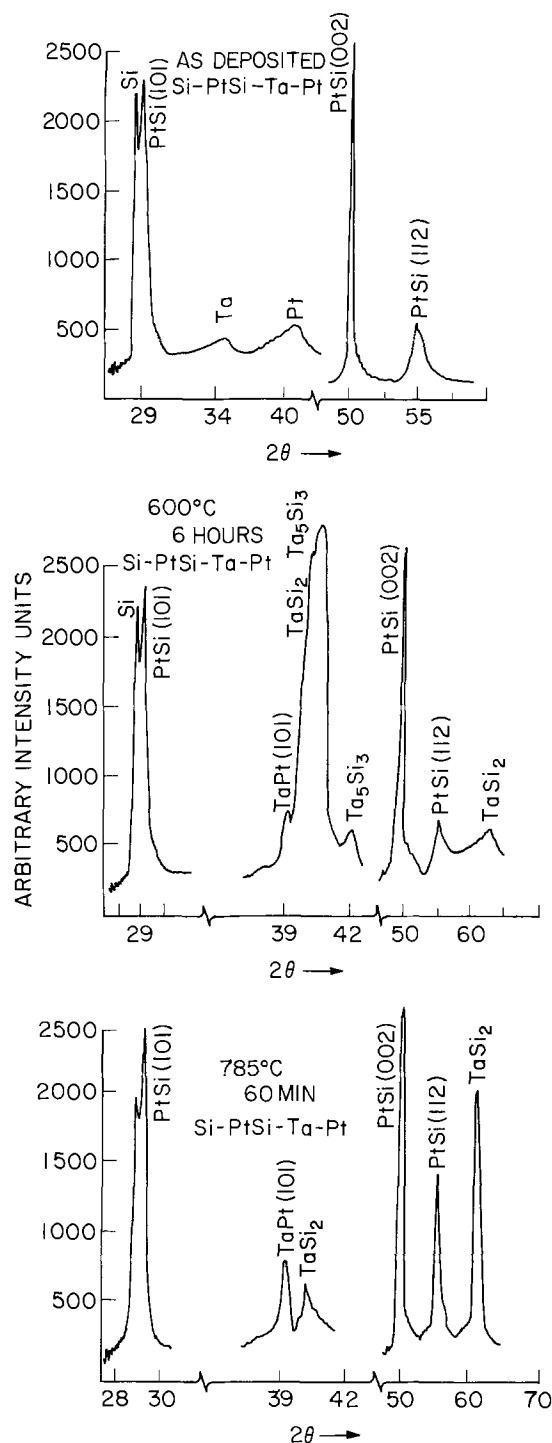


Fig. 4. X-ray diffraction spectra of the PtSi-Ta-Pt metallization on (100) Si wafer; as-deposited and after annealing at 600°C for 6 hr and 785°C for 60 min.

reaction (between PtSi and tantalum) in which silicon is the diffusing species. Thus, from a combination of the data it can be inferred that at excessively high temperatures tantalum displaces silicon from PtSi to form the various tantalum silicides until the most stable one, TaSi₂, is formed. As platinum is displaced it is free to react further with the silicon substrate to form more platinum silicide. During and upon completion of these reactions, silicon diffuses through the

resulting films or layers at a rate which depends on the temperature and the particular layer.

Conclusions

Reactions between silicon substrates and a stabilized tantalum gold metallization with and without an intervening PtSi layer have been studied as a function of annealing temperatures up to 785°C. A complex reaction between PtSi and tantalum results in the formation of TaSi₂ at excessively high temperatures resulting further in the uptake or consumption of silicon of the substrate at the higher temperatures. The contact resistance of small area PtSi ohmic contacts with geometries representative of microwave power transistors overlaid with the Ta-Pt-Ta-Au system remained constant during anneals up to 400°C for 24 hr. This indicates that thermochemical reactions and diffusion observed to take place at higher temperatures are probably not significant at normal operating temperatures but could be significant at some processing temperatures.

In view of the fact that enhanced reactions take place in this system at elevated temperatures, additional work should be done in order to completely characterize the system. The energies of formation of the compounds Ta₅Si₃ and TaSi₂ should be determined along with those of the intermetallic compounds TaPt, Ta₂Pt, and TaAu.

Manuscript submitted Sept. 30, 1974; revised manuscript received Jan. 2, 1975. This Paper 75 presented at the San Francisco, California, Meeting of the Society, May 12-17, 1974.

Any discussion of this paper will appear in a Discussion Section to be published in the December 1975 JOURNAL. All discussions for the December 1975 Discussion Section should be submitted by Aug. 1, 1975.

Publication costs of this article were partially assisted by the Naval Research Laboratory.

REFERENCES

1. J. C. Blair, C. R. Fuller, P. B. Ghate, and C. T. Haywood, *J. Appl. Phys.*, **43**, 307 (1972).
2. E. Philofsky, K. Ravi, E. Hall, and J. Black, Ninth Annual Proceedings Reliability Physics, 1971.
3. A. Christou and H. M. Day, *J. Elect. Mat.*, **3**, 25 (1974).
4. A. Christou and H. M. Day, *This Journal*, **121**, 1076 (1974).
5. A. Christou and H. M. Day, *J. Appl. Phys.*, **44**, 3386 (1973).
6. A. K. Sinha and T. E. Smith, *ibid.*, **44**, 3465 (1973).
7. A. K. Sinha, *This Journal*, **120**, 1767 (1973).
8. A. K. Sinha, M. H. Read, and T. E. Smith, *ibid.*, **120**, 1775 (1973).
9. H. H. Hosack, *J. Appl. Phys.*, **44**, 3476 (1973).
10. L. E. Terry and R. W. Wilson, *Proc. IEEE*, **57**, 1580 (1969).
11. M. J. Rand and J. F. Roberts, *Appl. Phys. Letters*, **24**, 49 (1974).
12. J. Grossman and D. S. Herman, *This Journal*, **116**, 674 (1969).
13. P. W. Palmberg, *J. Vacuum Sci. Technol.*, **9**, 160 (1972).
14. M. A. Nicolet, J. W. Mayer, and I. V. Mitchell, *Science*, **177**, 841 (1972).
15. W. K. Chu, J. W. Mayer, M. A. Nicolet, T. M. Buck, G. Amsel, and F. H. Eisen, *Thin Solid Films*, **17**, 1 (1973).
16. R. Feder and B. S. Berry, *J. Appl. Cryst.*, **3**, 372 (1970).
17. G. Y. Robinson and N. L. Jarvis, *Appl. Phys. Letters*, **21**, 507 (1972).
18. J. W. Mayer and K. N. Tu, *J. Vacuum Sci. Technol.*, **11**, 86 (1974).
19. M. H. Read and C. Altman, *Appl. Phys. Letters*, **7**, 51 (1965).

The Characterization of GaAs Surfaces

David R. Wood and D. Vernon Morgan

Electrical and Electronic Engineering, The University of Leeds, Leeds LS2 9JT, England

ABSTRACT

In this paper, we discuss the preparation of GaAs crystal surfaces by mechanical and chemical techniques. A comparative study of the surface in the course of consecutive polishing by various chemical etchants is made. The surface is assessed qualitatively by microscopy and quantitatively by the Rutherford backscattering/channelling technique. The concentration of gallium and arsenic at the surface is reported, and it is found that the surface is generally arsenic rich, the excess depending on the chemical polish used. Low concentrations of surface impurities (e.g., $\text{Te} \gtrsim 2.10^{13}$ atoms cm^{-2}) are measured and the variation monitored between the chemical polishing stages. No systematic behavior in the variation of impurity concentrations is observed.

The advent of GaAs as a new material for fabricating semiconductor devices has demanded a new technology different from that used for silicon devices. An important part of this technology is the fabrication of electrical contacts to the completed device. Transferred electron devices, for example, are thought to require two low resistance ohmic contacts whereas Barritt diodes need high quality Schottky barriers. A prerequisite for fabricating reproducible electrical contacts, is the development of analytical techniques to study the semiconductor surface prior to the deposition of the metal contacts. In this way it should be possible to relate any variations in the electrical behavior of the contact to the physical nature of the crystal surface. In this paper, we consider the physical characteristics of GaAs surfaces resulting from a wide variety of surface preparations.

The techniques which we used to study GaAs surfaces fall into two groups, qualitative and quantitative. In the first group we have the techniques of optical and scanning electron microscopy which give information about the topography of the surface. However, microscopy when combined with surface decoration techniques can yield quantitative information on the dislocation density and hence the surface damage present. Optical interferometry was also used to investigate surface irregularities. The second group comprises the technique of Rutherford scattering and channelling. This technique is now well established as a versatile tool suitable for lattice site location (1), thin film analysis (2), impurity detection (3), and more recently for surface studies (4). The latter technique has been described in detail in an earlier paper (5).

Surface Preparation

For the majority of the work described in this paper, the material used was Czochralski grown, Te-doped n-type gallium arsenide. The samples were approximately $8 \times 8 \text{ mm}^2$ in area, and in order to obtain the best channelling results, the (110) orientation was used. The surface preparation consists of two stages; (i) mechanical lapping/polishing to obtain a flat smooth surface and (ii) a chemical polish to remove the surface damage left by the mechanical polish.

The mechanical preparation was carried out in two stages, mechanical lapping followed by vibratory polishing, (Table I). First, the samples were lapped with diamond abrasive to remove the gross damage and produce an optically flat surface. In order to minimize damage, two grades of abrasive were used; 1.0-5.0 μm grit followed by 0.5-2.0 μm grit. After washing in trichloroethylene to remove contamination due to the abrasive, the samples were vibratory polished (6). Four samples were polished simultaneously in the

polisher bowl in order to encourage the samples to spin around and hence reduce directional polishing. The abrasive was alumina dispersed in water and again two grit sizes were used, 1.0 followed by 0.05 μm .

The samples were then cleaned using "Analar" grade organic solvents in an ultrasonic bath. Particular attention was paid to this cleaning procedure since the presence of grease, dirt, or any impurity can drastically affect any subsequent chemical etching (11). The chemical etchants examined in this paper are described in Table II and were chosen because of their extensive use in the preparation of GaAs crystals. Most of the work concentrated on the first four, polishes A-D, since these are the ones most commonly used.

Polish E was included so that our results could be compared with those of Hvalgård *et al.* (3) who used Rutherford backscattering to study changes in surface impurity concentration on GaAs caused by chemical etching.

The mechanical/chemical etching procedure, used with polish D, was carried out on an apparatus similar to that described by Dymont and Rozgonyi (12). Here, the sample was mounted onto the bottom of a small stainless steel holder which was then placed on the turn table which was covered with a microcloth. The microcloth was initially soaked in 0.1% bromine-methanol and then while the table rotated at 60 rpm fresh

Table I

Initial preparation	Thickness removed, μm	Removed rate, $\mu\text{m}/\text{min}$	Comments
Mechanical lapping			
1-5 μm	9.0	0.6	Damaged caused by abrasive and especially loose material. Optically flat surface.
0.5-2 μm	2.5	0.06	
Vibratory polishing			
1.0 μm	16.0	0.04	Smooth featureless surface with rounding of sample edges.
0.05 μm	4.0	0.01	

Table II

Etchant	Composition*	Rate,** $\mu\text{m}/\text{min}$	Comments and references
Polish A	HF:HNO ₃ :H ₂ O 1:3:2	24	Polish, fast reaction producing rough surface. (7)
Polish B	Br ₂ :CH ₃ OH 4:100	9	Polish (8)
Polish C	H ₂ SO ₄ :H ₂ O ₂ :H ₂ O 3:1:1	20	Polish, controllable reaction. (9)
Polish D	Br ₂ :CH ₃ OH 0.1:100	0.3	Chemical/mechanical polish. (8)
Polish E	HF:HNO ₃ :H ₂ O 1:9:5	—	Polish, very fast reaction producing rough surface. (3)

Key words: gallium arsenide polishing, Rutherford backscattering/channelling.

* Reagent assays: HF(40%), HNO₃(63%), H₂SO₄(98%), H₂O₂(40%).
** Measured on (110) Te-doped GaAs.

etchant was dripped onto the cloth at about 15 ml/min. In every case, the etchant was freshly made up from Analar grade reagents which were mixed together in the same order. The polishing was carried out under normal illumination with slight agitation and at room temperature. The etchants had been previously calibrated for similar material, so that the thickness of material removed by the etchants was known to within $\pm 1 \mu\text{m}$.

Results and Discussion

Mechanical polishing.—After lapping with the 1-5 μm diamond grit, there are numerous straight shallow scratches across the surface caused by the abrasive. More serious is the presence of jagged and deeper scratches and areas of damage caused by material chipped from the sample edges scoring the surface. The use of interference microscopy ($\lambda = 547 \text{ nm}$) confirms that the surface is optically flat. When a further 4 μm is removed by the 0.5-2.0 μm abrasive, there is a marked improvement in the condition of the surface. Some scratches from the abrasive are present but in general these are less than 2 μ deep. In addition, some of the severe damage of the previous lapping remains.

After vibratory polishing in 1.0 μm alumina, no linear damage from the lapping process is visible, although there are some curved scratches caused by this polishing. In contrast with the even polishing produced by the planetary motion of the previous lapping, a tendency for directional polishing is seen. This is caused by the shape of the sample having a preferred orientation to the direction of travel as it moves across the microcloth.

Furthermore, since the holder is not rigidly held parallel to the plane of the abrasive surface during polishing, the surface becomes less flat especially near the edges. It should be noted that, although the abrasive particles used in this vibratory polish are similar in size to those used in the previous lapping stage, the rate of removal and, hence, the depth of damage, is considerably less. After the final mechanical polish with 0.05 μm abrasive, the crystal surface is very smooth. This is confirmed by optical and scanning electron microscopy, which reveals no visible surface damage. Interferometry patterns show a slight degradation in flatness, with a variation of 1% across the surface.

Consider now the results obtained by the Rutherford scattering/channelling technique. A typical energy spectrum is illustrated in Fig. 1(a) which shows the scattering yield as a function of the energy of the backscattered alpha particles. The energy axis can be converted into either a mass scale or a depth scale (5, 13). The depth resolution for the experimental configuration used is also shown in Fig. 1(a).

This energy spectrum is obtained when a 2.2 MeV beam of alpha particles is scattered through 135° from a (110) GaAs crystal which has been vibratory polished. The inset shows the surface peak after the random line-shape background correction (5) (shown as a dotted line in the figure). This correction procedure is used throughout the results presented in this paper. For a good quality crystal, two surface peaks are observed corresponding to the Ga and As sublattices. However, because of the surface damage resulting from the vibratory polishing, two peaks cannot be resolved. This is a result of multiple scattering by unscreened Ga and As atoms in the thick disordered layer which causes the two surface peaks to overlap. From the area, A , under this surface peak, the total concentration of atoms, N_T , is calculated using the expression

$$N_T = \frac{t}{l} \cdot N_{(110)} \quad [1]$$

In this expression, l is the monolayer separation; $N_{(110)} = 1.77 \cdot 10^{15} \text{ atoms} \cdot \text{cm}^{-2}$ is the concentration of atoms in one monolayer of GaAs(110); and t is the disordered layer thickness obtained from [Eq. 7, Ref. (5)]

$$t = \frac{A}{Y[k^2 S(E_0) - S(E_1)/\cos\theta]} \quad [2]$$

where Y is the random yield; k^2 is the kinematic factor; $S(E_0)$ and $S(E_1)$ are the stopping powers of the ion in GaAs at the energies E_0 and E_1 , respectively; and θ is the scattering angle. For the vibratory polished surface shown in Fig. 1(a), $N_T = (3.51 \pm 0.5)10^{16} \text{ atoms} \cdot \text{cm}^{-2}$. By comparing N_T with $N_{(110)}$, the extent of the surface disorder can be assessed.

An alternative qualitative measure of the perfection of the crystal at the surface is the minimum yield, χ_{min} , where

$$\chi_{\text{min}} = \frac{\text{Aligned Yield}}{\text{Random Yield}} \quad [3]$$

measured just behind the surface peak [i.e., at X in Fig. 1(a)]. For a high quality damage free crystal, at room temperature $\chi_{\text{min}} \simeq 0.03$ while for the vibratory polished crystal $\chi_{\text{min}} = 0.13$, indicating that there is a large amount of damage present at the surface.

The peak beyond the leading edge of the host spectrum corresponds to the impurity tellurium. By comparing the area of this impurity peak, with the yield from the host crystal the concentration is calculated to be $(3.4 \pm 0.5)10^{14} \text{ atoms} \cdot \text{cm}^{-2}$. Although it is convenient to express impurity concentrations as $(\text{atoms} \cdot \text{cm}^{-2})$, it must be remembered that this is the total concentration of unscreened impurity atoms

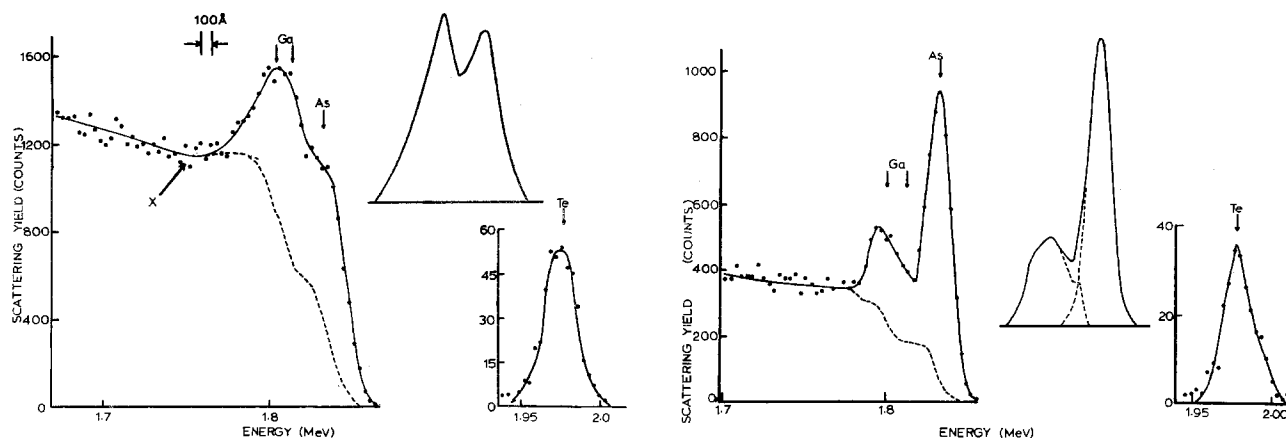


Fig. 1. The energy spectra for 2.2 MeV alpha particles scattered through 135° by (110) GaAs. (a, left) For the surface vibratory polished in 0.05 μm alumina. The inset shows the surface peaks after the removal of the background (broken line). Also shown in (a) is the detection resolution and at X, the position of the measurement of χ_{min} . (b, right) The same crystal after 10 μm has been removed by polish A. The reduction in damage enables the contributions to the surface peak of the Ga and As atoms to be separated as shown by the dashed line in the inset. In (a) and (b), small peaks produced by surface tellurium are seen beyond the leading edge of the host spectra.

distributed throughout the whole of the disordered layer.

Chemical polishing.—The effect of subsequent chemical polishing is illustrated in Fig. 2. There is a loss of surface flatness as polishing continues due to a variation in the rate of attack over the crystal surface. The nature of the surface also varies with the actual etchant used and the crystal face being polished, e.g., the production of etch pits on the (111) Ga face of GaAs by the bromine-methanol etchant (7). After the first etch, which removes 5 μm , the surface becomes uneven, and as further polishing is carried out, this irregularity increases. In the worst case, polish A, the surface is covered with hillocks. In Fig. 2, we show typical areas of the sample surfaces after the removal of 20 μm by the various etchants. The rough surface produced by polish A is caused by the adhesion of gas bubbles which passivate varying areas on the surface. The optical micrograph shows that after the removal of all the damage (i.e. $\geq 10 \mu\text{m}$ of material), polish A produces no preferential etch pits.

Similar changes in appearance are observed for polishes B and C, although both these etchants produce smoother surfaces than polish A. Before using polish C, it is important to ensure that the surface is completely scratch free, since any areas of localized damage are attacked preferentially, and are not removed by the etchants. It was because of the degradation in surface flatness that the mechanical/chemical technique was developed. In Fig. 2(d), we illustrate the improvement in flatness obtained by this procedure. Furthermore, the surface retains its flatness even after a short "free" etch in polish B, necessary to ensure a damage free surface.

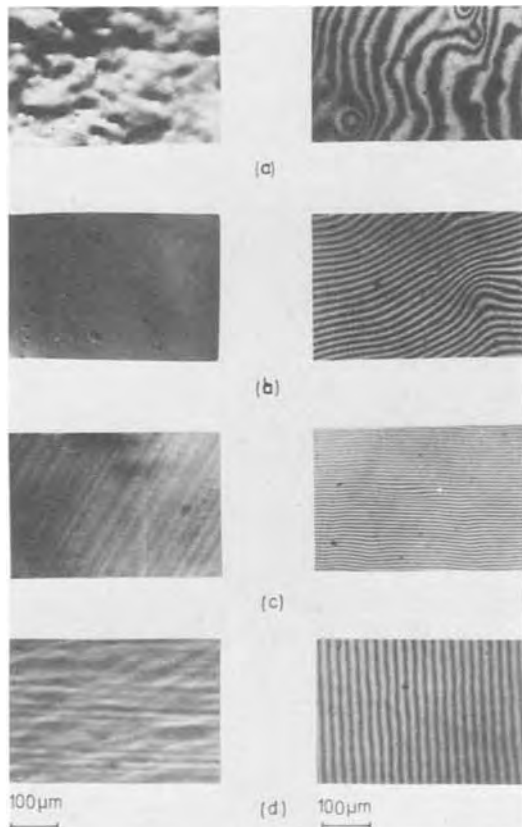


Fig. 2. Optical micrographs (left) and interference micrographs (right) of n-type (110) GaAs. The photographs show typical random areas of the surface after removal of 20 μm by (a) polish A, (b) polish B, (c) polish C, and (d) polish D. ($\lambda = 547 \text{ nm}$ for the interference pictures).

With the removal of 5 μm of damaged material, the Ga and As surface peaks of the Rutherford scattering spectrum, are resolved. From the areas of these individual Ga and As peaks, we can calculate the absolute concentration of unscreened Ga and As and hence the surface stoichiometry (5). In this case the values obtained are $N_{\text{As}} = (1.2 \pm 0.2) \cdot 10^{16} \text{ atoms cm}^{-2}$, $N_{\text{Ga}} = (7.3 \pm 0.1) \cdot 10^{15} \text{ atoms cm}^{-2}$ and hence $N_{\text{As}}/N_{\text{Ga}} = 1.7$. It should be noted that this ratio is for the surface region only ($\sim 4 \text{ nm}$) and that any departure from bulk stoichiometry is caused entirely by the selective action of the chemical etchant. The removal of 5 μm of damaged material also produces a corresponding decrease in χ_{min} to ~ 0.057 . A tellurium surface impurity peak is visible again but in this case it corresponds to a concentration of $(7.4 \pm 1.0) \cdot 10^{12} \text{ atoms cm}^{-2}$.

When a further 5 μm of material is removed, χ_{min} decreases to 0.030 and the surface peaks are more clearly resolved [Fig. 1(b)], and their separation depends only on the resolution of the detector. Etching of the crystal by polish A is continued in stages until a total of 60 μm is removed. Two energy spectra from the final surface are taken with beam energies of 2.2 and 4.0 MeV. The results from the 4.0 MeV analysis are more accurate (5) and are used as a check on the 2.2 MeV results.¹

Similar measurements are made on identical material but with the crystals etched in polishes B and C, until a total of 45 and 30 μm , respectively, had been removed. A summary of the results obtained at the various stages of chemical treatment is given in Table III. The variation of χ_{min} with thickness removed is similar for all three polishes and illustrates that in order to obtain a damage-free surface it is necessary to remove $> 10 \mu\text{m}$ of GaAs. Although the theoretical value of χ_{min} is 0.01 for a perfect crystal surface, this ignores the effect of oxides and hydrocarbons on the surface so that $\chi_{\text{min}} \sim 0.03$ (with a liquid nitrogen cold shield) is typical of a good quality crystal surface (14). The ratio, χ_{min} , is extremely sensitive to disorder and Table III shows that although N_{T} for the vibratory polished surface indicates a disordered surface of only $\sim 9 \text{ nm}$, the crystal structure immediately below the surface is badly strained and $\sim 10 \mu\text{m}$ has to be removed before a damage free crystal is obtained. This is confirmed by the use of the Abrahams and Buiocchi dislocation etch (10) which reveals a steady dislocation density of $\sim 10^4 \text{ cm}^{-2}$ for all the surfaces after 10 μm has been removed.

In Table III, we see that, initially, the total concentration of unscreened atoms, constituting the disordered surface region, N_{T} , shows the same variation as χ_{min} . However, after 10 μm is removed, N_{T} depends

¹ All the results presented in this paper were obtained with an incident energy of 2.2 MeV which is the limit of the Aarhus and Salford Van de Graaff accelerators.

Table III

	Polishing solution	Thickness removed by polishing solution (μm)				
		0	5	10	20	45
χ_{min}	Polish A	0.128	0.057	0.030	0.021	0.023
	Polish B	0.090	0.050	0.020	0.033	0.036
	Polish C	0.116	—	0.045	0.041	0.028*
$N_{\text{T}} \cdot 10^{15} \text{ atoms cm}^{-2}$	A	26.9	18.9	10.3	7.2	8.0
	B	45.6	15.5	5.9	10.4	9.8
	C	34.0	—	9.75	7.7	8.3*
$N_{\text{As}}/N_{\text{Ga}}$	A	—	1.6	1.7	1.5	1.7
	B	—	1.1	1.1	1.1	1.3
	C	—	—	1.0	1.2	1.4*
$N_{\text{Te}} \cdot 10^{12} \text{ atoms cm}^{-2}$	A	33.7	17.0	14.4	1.6	25.6
	B	27.6	1.3	0.29	1.2	0.68
	C	47.6	—	0.58	2.6	2.45*
$N_{\text{B}} \cdot 10^{13} \text{ atoms cm}^{-2}$	B	—	20.3	8.57	21.6	35.1

* After 30 μm has been removed by polish C.

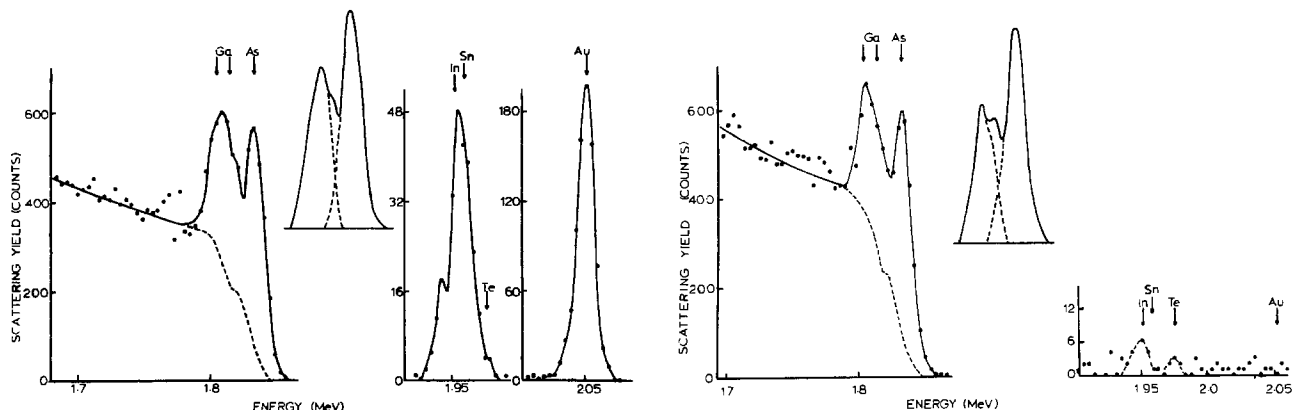


Fig. 3. The energy spectra for 2.2 MeV alpha particles scattered through 135° by (110) GaAs. (a, left) After the removal of $10 \mu\text{m}$ by polish D and (b, right) the same sample after a further $2 \mu\text{m}$ has been removed by polish B. The insets show the surface peaks after the background correction. In (b), the impurity symbols are used to indicate where the peaks would occur if those impurities were detectable.

only on the chemical nature of the surface produced by the etchant and is the result of natural oxides and other impurities at the surface.² The values of N_{As} and N_{Ga} , and their ratio (Table III) are closely dependent on the actual etchant used. All the etchants produce arsenic-rich surfaces and the excess arsenic varies with polish as

$$[N_{\text{As}}/N_{\text{Ga}}]_{\text{A}} > [N_{\text{As}}/N_{\text{Ga}}]_{\text{C}} > [N_{\text{As}}/N_{\text{Ga}}]_{\text{B(or D)}} \quad [4]$$

In order to investigate the consistency of the ratio ($N_{\text{As}}/N_{\text{Ga}}$) across the surface of a sample, three energy spectra were taken from different positions on the same surface for samples in polishes A and B. For both of these polishes, there is no variation in stoichiometry within experimental error. However, this does not rule out microscopic variations since these results are averaged over the area of the analyzing beam (i.e., 1.0 mm^2).

The variation of the main surface impurities with etching is presented in Table III. The amount of Te present on the surface at all stages is larger than would correspond to the bulk doping, $8 \times 10^{10} \text{ atoms cm}^{-2} \text{ monolayer}^{-1}$. Furthermore, although there are large variations, the concentration of Te is generally larger for polish A than for polish B with the effects of polish C somewhere in between. We also note the presence of impurities deposited from the etchant such as bromine and gold from polishes B and D (Fig. 3) and occasionally zinc from polish C. In Fig. 3(a), the energy spectrum for the sample prepared by the removal of $10 \mu\text{m}$ by polish D is shown. This energy spectrum has two interesting features:

(i). The large impurity peak corresponding to In or Sn on the surface. The samples used to obtain the results presented here were cleaved from the same (110), GaAs wafer, and the presence of small concentrations ($\sim 10^{13} \text{ atoms cm}^{-2}$) of Sn or In is occasionally observed in all of them. However, the large concentration, $(2.0 \pm 0.2) \cdot 10^{14} \text{ atoms cm}^{-2}$, seen here appears to be a direct result of the dilute solution (0.1%) of bromine in methanol used to prepare this crystal.

(ii) The large gold peak corresponding to $(1.9 \pm 0.2) \cdot 10^{14} \text{ atoms cm}^{-2}$. Small concentrations ($\sim 2 \cdot 10^{12} \text{ atoms cm}^{-2}$) of gold have been observed (4) occasionally after using polish B and are thought to arise from the organic solvent, methanol. Thus, the large gold peak present after the etch in polish D is consistent with the large volume of methanol used during the polishing. However, after a short free etch in polish B to ensure a damage free surface [Fig. 3(b)], no gold peak is observed

indicating that the bromine concentration is also important in determining the gold impurity concentration. This second chemical polish also reduces the Sn or In concentration to $(2.3 \pm 1.0) \cdot 10^{13} \text{ atoms cm}^{-2}$. (Because of the poor statistics of the impurity counts, dashed lines are used to position the peaks.) The effect of polish D on the host lattice of Ga and As, is similar to that of polish B and the above qualitative remarks concerning polish B apply equally to polish D.

It is clear from these results, that it is impossible to make exact predictions about the behavior of a dopant impurity in a particular etchant with time. The tellurium concentration shows no consistent behavior with etching time but varies randomly with consecutive etches. This is in contrast with the results of Hvalgård *et al.* (3) who observed, with polish E, a definite increase in dopant concentration with time. Now polish A acts very rapidly removing $0.4 \mu\text{m sec}^{-1}$ and leaves a rough finish (see Fig. 2). For these reasons, attempts were made to produce a more controllable etchant and at the same time repeat the work of Hvalgård *et al.* Thus, the ratios of $\text{HF}:\text{HNO}_3:\text{H}_2\text{O}$ listed in Table IV, together with their effects, were investigated. The main problem with polish A, is the release of a gas which together with the fast rate of attack produces a rough finished surface. The 1:3:5 etchant is slow and controllable but produces a poor dull surface covered with a white reaction product. As the nitric acid concentration is increased, the reaction rate increases correspondingly and produces a finished surface similar to that of polish A. The final etchant, polish E, is even less controllable than polish A and produces a rougher surface. As seen in Table IV, the Te concentration at the surface actually decreases with the consecutive polishes. These results conform to the unpredictable nature of chemical polishing discussed above.

The effect of the chemical etchants on other crystal planes and with different impurity dopants was investigated. In particular results were obtained for the (111)Ga and the (111)As faces etched in polishes A, B, and C. From these we conclude that there are no measurable differences between the two faces. There are two reasons for this result: (i) The surface peaks are produced by unscreened atoms, and there are equal Ga and As atoms visible to the analyzing beam even for a perfect (111) or (111) crystal surface. (ii) The

Table IV

Etchant composition HF:HNO ₃ :H ₂ O	$N_{\text{As}}/N_{\text{Ga}}$	$N_{\text{T}} \times 10^{10}$ atoms $\cdot \text{cm}^{-2}$	$N_{\text{Te}} \times 10^{14}$ atoms $\cdot \text{cm}^{-2}$	Polishing time, sec
1:3:5	3.3	2.92	1.5	40
1:6:5	3.4	2.16	7.1	40
1:9:5	1.4	2.05	1.3	15
1:9:5	1.1	7.15	0.54	30

² Because of the dependence of the collision cross section for Rutherford scattering on the (atomic number) (Z) and the large background from the GaAs, it is not possible to detect small concentrations of the light elements, especially carbon and oxygen that are known to be there from Auger electron spectroscopy measurements (15).

rearrangement of the surface atoms caused by oxidation and absorption of impurities results in a loss of the original Ga and As surface structure. The results obtained are consistent with those obtained for the (110) planes, i.e., arsenic-rich surfaces were produced in all cases, and the degree of nonstoichiometry increased in the order B, C, A.

The effect of using material with different doping species was examined by studying the surfaces of Zn-doped (p-type) and semi-insulating Cr-doped material. These results are in agreement with those from the n-type material. The p-type GaAs has arsenic rich surfaces, $N_{As}/N_{Ga} = 1.23$ and 2.53 after 30 and 90 sec in polish A, respectively.

However, because the Zn is lighter than the host material, it is much more difficult to detect than a heavier dopant such as Te and, in fact, none is detected (indicating an upper limit of $\sim 5 \cdot 10^{14}$ zinc atoms \cdot cm $^{-2}$). Similarly, no chromium impurity peak is observed for the semi-insulating case. However, the familiar excess arsenic surfaces are produced by both etchants, the values being $N_{As}/N_{Ga} = 2.3$ and 1.1 and $N_{As} = 9.9 \cdot 10^{15}$ and $5.3 \cdot 10^{15}$ atoms \cdot cm $^{-2}$ for polish A and polish B, respectively. For all these etchants, there is no measurable difference in etch rate for the different materials, and it is probable that the reactions are diffusion limited with photogeneration providing sufficient carriers for the reaction (11).

Conclusions

In this paper, we have tried to characterize the quality and the chemical state of the surface of GaAs. We have shown that great care must be exercised during the mechanical handling of the material, in order to minimize the extent of damage at the crystal surface. For the procedure described above, at least $10 \mu\text{m}$ of material had to be removed chemically in order to ensure a damage free surface.

The chemically prepared surface was investigated qualitatively using microscopy techniques and quantitatively using the Rutherford backscattering/channeling technique for a variety of chemical etchants. It was found that the surface consisted of a disordered layer of GaAs ~ 3 nm thick and that its stoichiometry could vary appreciably from the equality of the bulk. Absolute measurements of the concentrations of gallium and arsenic showed that the surface was always arsenic rich, the degree of nonstoichiometry increasing in the order polish B (polish D), polish C, and polish A. In all cases, the impurity dopant tellurium accumu-

lated at the surface although no predictable behavior with etching time was observed.

Acknowledgments

We wish to thank our colleagues Dr. E. Bøgh (Aarhus), Professor G. Dearnaley (A.E.R.E., Harwell), Professor G. Carter (Salford) for the use of their Van de Graaff accelerators; Drs. J. Whitton (Chalk River), D. Colliver (R.R.E. Malvern), and M. J. Howes (Leeds) for many useful discussions. We also wish to thank Dr. T. Gallon and Mr. D. Smith (York) for assistance with the Auger measurements made at their laboratory. The work was supported by the S.R.C. who provided finance for accelerator time; N.A.T.O. and C.V.D. who awarded research grants. Finally, one of us (D.R.W.) would like to thank the S.R.C. for the award of a studentship.

Manuscript submitted Aug. 27, 1974; revised manuscript received Jan. 22, 1975.

Any discussion of this paper will appear in a Discussion Section to be published in the December 1975 JOURNAL. All discussions for the December 1975 Discussion Section should be submitted by Aug. 1, 1975.

REFERENCES

1. J. W. Mayer, L. Eriksson, and J. A. Davies, "Ion Implantation in Semi-Conductors," Academic Press, New York and London (1970).
2. I. V. Mitchell, M. Kamoshida, and J. W. Mayer, *J. Appl. Phys.*, **42**, 4378 (1971).
3. J. O. Hvalgård, S. L. Andersen, and T. Olsen, *Phys. Status Solidi (a)*, **5**, K83 (1971).
4. D. V. Morgan and E. Bøgh, *Surface Sci.*, **32**, 278 (1972).
5. D. V. Morgan and D. R. Wood, *Proc. Roy. Soc. (London)*, **A335**, 509 (1973).
6. J. L. Whitton, *J. Appl. Phys.*, **36**, 3917 (1965).
7. J. L. Richards and A. J. Crocker, *ibid.*, **31**, 611 (1960).
8. C. S. Fuller and H. W. Allison, *This Journal*, **109**, 880 (1962).
9. F. A. Cunnell, J. T. Edmond, and W. R. Hardin, *Solid-State Electron.*, **1**, 97 (1960).
10. M. S. Abrahams and C. J. Buiochi, *J. Appl. Phys.*, **36**, 2855 (1965).
11. H. C. Gatos, *Progr. in Semicond.*, **9**, 1 (1965).
12. J. C. Dymant and G. A. Rozgonyi, *This Journal*, **118**, 1346 (1971).
13. E. Bøgh, *Proc. Roy. Soc.*, **A311**, 35 (1969).
14. D. R. Wood and D. V. Morgan, *Phys. Status Solidi (a)*, **17**, K143 (1973).
15. D. R. Wood, Ph.D. Thesis, Leeds (1975).

Thermochemical Analyses and Optimum Conditions for Vapor Epitaxy of GaAs_{1-x}P_x (0.7 < x < 0.9)

Tao Yuan Wu^{*,1}

Research Laboratories, General Motors Corporation, Warren, Michigan 48090

ABSTRACT

The gas-solid relationships for the vapor phase epitaxy of GaAs_{1-x}P_x (0.7 < x < 0.9) at a temperature of 840°C have been established. The GaCl-AsH₃-PH₃-H₂ process and <100> oriented GaP substrates were employed. Experimental data were obtained and then a semiempirical calculation was carried out to give accurate relationships between gas concentrations and solid composition. Furthermore, effects of vapor pressures on surface morphology have been investigated and certain optimum conditions were determined. Such conclusions, together with the above relationships, have been used to determine optimum flow rates for specific growth compositions.

In recent years, the observation of efficient radiative processes in indirect-gap GaAs_{1-x}P_x due to nitrogen isoelectronic traps (1-3) has made such materials attractive for use in amber and yellow light-emitting diodes. Compositions with GaP content between 70 and 90% are of particular interest. However, accurate and detailed relationships between the input gas concentrations and the resulting crystal composition for the vapor epitaxy process, as well as the optimum growth conditions, have not been available in the literature. Previous papers (4-6) by the author have reported such relationships and conditions in the composition range of 0.3 < x < 0.5, which is particularly important for applications in red emission, microwave switching (7), high speed current limiting (8), and superlattice structures (9). The present report extends such results to the composition range of 0.7 < x < 0.9.

Experimental

Figure 1 shows a schematic diagram of the epitaxial reactor, together with the temperature profile. The apparatus is the same as that used previously in this study for 0.3 < x < 0.5 (4), except that GaP was used as the substrate, and higher temperatures were used in the reactor. A total flow rate of 1000 ml/min was always maintained during the growth process. Similar designs have been adopted by other people (10-12). Preliminary experiments here established that such conditions yielded good growth for 0.7 < x < 0.9.

The experimental procedure described in (4) was also used here except that GaP was grown initially, and the taper layer was produced by increasing AsH₃

flow and decreasing PH₃ flow. Under such growth conditions, the input HCl is almost completely converted into GaCl and no deposition occurs upstream of the substrates. This allows one to accurately relate the input flow rates to the gas concentrations in the substrate region. The input flow rates were varied from run to run to determine the effect of the growth atmosphere and the gas-solid relationships.

The same effects of the growth atmosphere observed previously for 0.3 < x < 0.5 were found to be true in the present case. The gas-solid relationships were determined by measuring the flow rates with precision flowmeters and the crystal composition with electron microprobe analysis.

The results are listed in Table I as a function of the input flow rate ratios, $f^{\circ}_{\text{HCl}}/f^{\circ}_{\text{H}_2}$, $f^{\circ}_{\text{AsH}_3}/f^{\circ}_{\text{H}_2}$, and $f^{\circ}_{\text{PH}_3}/f^{\circ}_{\text{H}_2}$. All these data were found to be reproducible. It was estimated that x_0 is accurate to ± 0.01 and various flow rate ratios to be within $\pm 5\%$.

Semiempirical Calculations

The same model used for 0.3 < x < 0.5 (4) was adopted in the present case. With this model, one can calculate the crystal composition together with all the partial pressures at any given incoming gas concentrations, once all the equilibrium constants and the interaction parameter are evaluated.

Using Kirwan's results (13), all the equilibrium constants were evaluated, and are given in Table II, at the

Table I. Relationships between the input flow rates and the grown crystal composition obtained in the present experiments

$f^{\circ}_{\text{HCl}}/f^{\circ}_{\text{H}_2}$	$f^{\circ}_{\text{AsH}_3}/f^{\circ}_{\text{H}_2}$	$f^{\circ}_{\text{PH}_3}/f^{\circ}_{\text{H}_2}$	$f^{\circ}_{\text{PH}_3}/f^{\circ}_{\text{AsH}_3}$	x
1.0 × 10 ⁻²	0.5 × 10 ⁻²	0.5 × 10 ⁻²	1	72 × 10 ⁻²
2.0	1.0	1.0	1	71
1.0	2.0	2.0	1	81
2.0	2.0	2.0	1	78
3.0	2.0	2.0	1	75
2.5	3.0	3.0	1	80
1.5	0.5	1.0	2	82
2.0	0.5	1.0	2	80
3.0	0.5	1.0	2	75
1.5	1.0	2.0	2	85
3.0	1.0	2.0	2	81
3.3	2.0	4.0	2	85
1.0	0.1	0.3	3	80
3.0	0.1	0.3	3	74
1.0	0.3	0.9	3	85
1.0	0.5	1.5	3	87
2.0	0.5	1.5	3	86
2.8	0.6	1.8	3	85
3.0	1.0	3.0	3	87
1.0	0.1	0.4	4	85
3.0	0.1	0.4	4	80
2.9	0.3	1.2	4	85
1.3	0.5	2.0	4	89
2.0	0.5	2.0	4	88
4.0	0.5	2.0	4	85
3.0	1.0	4.0	4	89
3.0	0.1	0.5	5	84
1.8	0.5	2.5	5	90
3.0	0.5	2.5	5	89

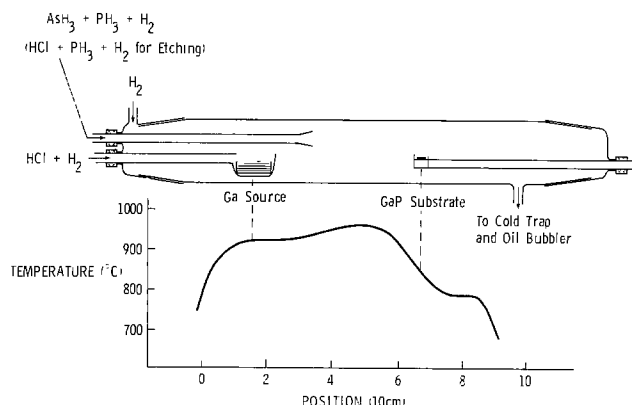


Fig. 1. Schematic diagram of the epitaxial reactor with the temperature profile used in this study.

Table II. Thermochemical constants used in the present calculation

$K_1 = 4 \times 10^8$	(a)
$K_2 = 40$	(a)
$K_3 = 2.4 \times 10^{-4}$	(a)
$K_4 = 1.4 \times 10^{-8}$ (atm units)	(a)
$K_5 = 9.6 \times 10^{16}$	(a)
$K_6 = 9.9 \times 10^2$	(a)
$\alpha = -1.9 + 4.8x$ kcal/mole	(b)

(a) After Kirwan.
(b) By fitting the experimental data to the theoretical equations.

temperature of interest here, 840°C. Also given in the table is the interaction parameter, which was evaluated by fitting some of the measured data in Table I into the above equations with the above constants. Finally, a computer calculation based on all the equations and constants was carried out and the following results for the crystal composition as a function of the input flow rates were obtained.

Results and Discussions

Figures 2 and 3 give the calculated x as a function of $f^{\circ} \text{PH}_3/f^{\circ} \text{AsH}_3$, $f^{\circ} \text{AsH}_3/f^{\circ} \text{H}_2$, and $f^{\circ} \text{HCl}/f^{\circ} \text{H}_2$, together with the measured data. The solid lines are calculated results. They agree with all the experimental data to a precision in x of ± 0.02 . Based on these two figures, the flow relationships to achieve $x = 0.85$ at 840°C were obtained as is shown in Fig. 4. Similar figures can be plotted for any other $0.7 < x < 0.9$. Although wide ranges of flow rates can be used to achieve a specific x , only one set of flow rates will yield optimum crystal morphology.

As mentioned above, the optimum flow rate condition obtained previously for $0.3 < x < 0.5$ (5, 6) was found to be valid in the present case, i.e., $f^{\circ} \text{HCl}/f^{\circ} \text{H}_2 = (f^{\circ} \text{PH}_3 + f^{\circ} \text{AsH}_3)/f^{\circ} \text{H}_2 = 0.02$. This means the growth atmosphere must be stoichiometric. If it is rich in Ga, pyramids were developed; if rich in P+As, pits were al-

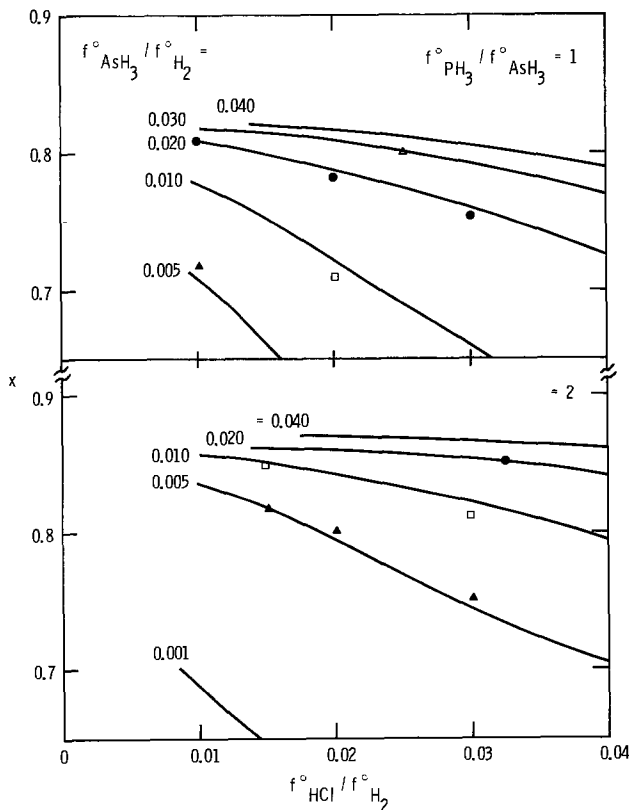


Fig. 2. Crystal composition x as a function of input flow rate ratios $f^{\circ} \text{HCl}/f^{\circ} \text{H}_2$, $f^{\circ} \text{AsH}_3/f^{\circ} \text{H}_2$, and $f^{\circ} \text{PH}_3/f^{\circ} \text{AsH}_3$ ($= 1$ and 2) at a growth temperature of 840°C. Solid lines are calculated results. The values of $f^{\circ} \text{AsH}_3/f^{\circ} \text{H}_2$ for various measured data are: 0.005 (\blacktriangle), 0.010 (\square), 0.020 (\bullet), and 0.030 (\blacktriangledown).

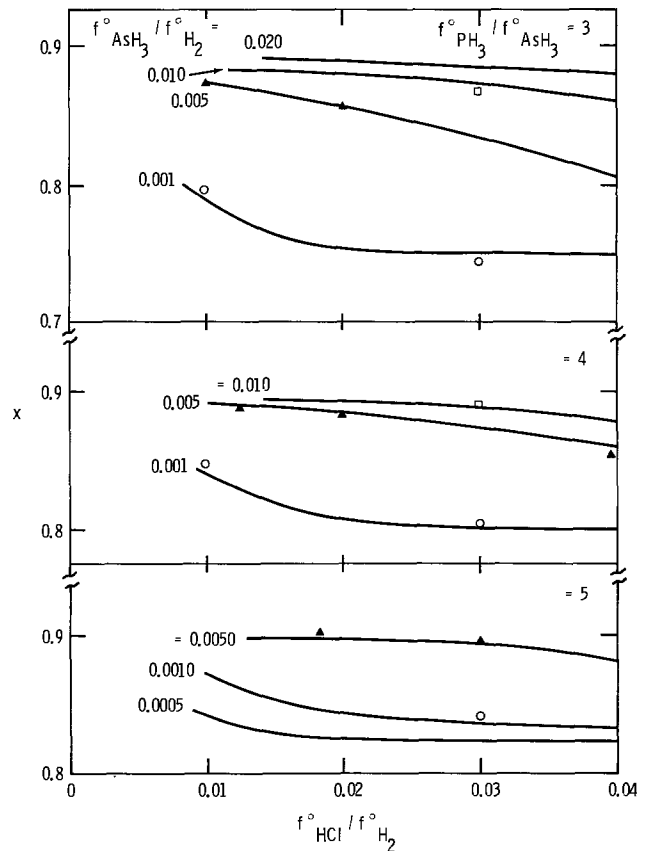


Fig. 3. Crystal composition x as a function of input flow rate ratios $f^{\circ} \text{HCl}/f^{\circ} \text{H}_2$, $f^{\circ} \text{AsH}_3/f^{\circ} \text{H}_2$, and $f^{\circ} \text{PH}_3/f^{\circ} \text{AsH}_3$ ($= 3, 4,$ and 5) at a growth temperature of 840°C. Solid lines are calculated results. The values of $f^{\circ} \text{AsH}_3/f^{\circ} \text{H}_2$ for various measured data are: 0.001 (\circ), 0.005 (\blacktriangle), and 0.010 (\square).

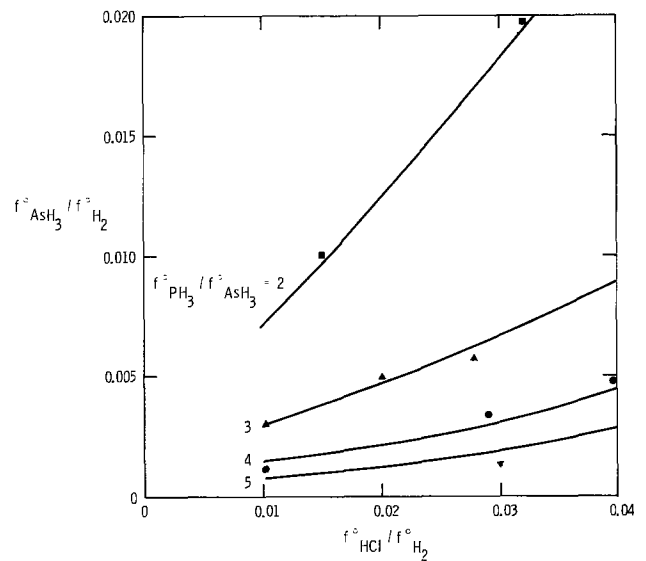


Fig. 4. Input flow rate ratio $f^{\circ} \text{AsH}_3/f^{\circ} \text{H}_2$ required to achieve $x = 0.85 \pm 0.02$ with various fixed $f^{\circ} \text{HCl}/f^{\circ} \text{H}_2$ and $f^{\circ} \text{PH}_3/f^{\circ} \text{AsH}_3$ at 840°C. All the lines are calculated results. The values of $f^{\circ} \text{PH}_3/f^{\circ} \text{AsH}_3$ for various measured data are: 2 (\blacksquare), 3 (\blacktriangle), 4 (\bullet), and 5 (\blacktriangledown).

ways observed. A model has been proposed to explain such behavior in this study (5). Now, applying such a condition to Fig. 4, one can obtain an optimum flow rate condition to grow $x = 0.85$ at 840°C, namely, $f^{\circ} \text{HCl}/f^{\circ} \text{H}_2 = 0.02$, $f^{\circ} \text{AsH}_3/f^{\circ} \text{H}_2 = 0.005$, and $f^{\circ} \text{PH}_3/f^{\circ} \text{H}_2 = 0.015$. Similar conditions, of course, can be obtained for other values of x .

In a previous paper (4), the author explained the variation in x due to $f^{\circ} \text{HCl}/f^{\circ} \text{H}_2$ or $f^{\circ} \text{AsH}_3/f^{\circ} \text{H}_2$, while

keeping the other two flow rate ratios constant, in terms of the combined effects of pressure and reactivities. Such an explanation is also valid in the present case. Furthermore, the same argument can be used to explain the increase in x and decrease in $|dx/d(f^{\circ}_{\text{HCl}}/f^{\circ}_{\text{H}_2})|$ as $f^{\circ}_{\text{PH}_3}/f^{\circ}_{\text{AsH}_3}$ increases, while keeping $f^{\circ}_{\text{HCl}}/f^{\circ}_{\text{H}_2}$ and $f^{\circ}_{\text{AsH}_3}/f^{\circ}_{\text{H}_2}$ constant in the range of interest here.

The semiempirical approach used here has been found to be a good technique to determine accurate phase relationships in a relatively simple way (4, 14). The present results further confirm such observations. Since the objective here is to establish accurate and practical gas-solid relationships rather than a theoretical model, the empirical adjustment is necessary. Shaw (12, 13) has reported, after all, that kinetic effects cannot be ignored in actual cases.

In conclusion, accurate relationships between input flow rate conditions and the grown crystal composition have been obtained for $0.7 < x < 0.9$ at a satisfactory growth temperature of 840°C . In addition, flow rate conditions which yield optimum growth morphology have also been determined. Such relationships and conditions can be applied to any systems satisfying the present, practical design criteria.

Acknowledgments

The author would like to acknowledge the competent and enthusiastic technical assistance of L. Green, and that of J. C. Price who provided the computer program.

Manuscript submitted Aug. 19, 1974; revised manuscript received Feb. 1, 1975. This was Paper 145 presented at the San Francisco, California, Meeting of the Society, May 12-17, 1974.

Any discussion of this paper will appear in a Discussion Section to be published in the December 1975 JOURNAL. All discussions for the December 1975 Discussion Section should be submitted by Aug. 1, 1975.

Publication costs of this article were partially assisted by the General Motors Corporation.

REFERENCES

1. W. O. Groves, A. H. Herzog, and M. G. Craford, *Appl. Phys. Letters*, **19**, 184 (1971).
2. N. Holonyak, Jr., D. R. Scifres, M. G. Craford, W. O. Groves, and D. L. Keune, *ibid.*, **19**, 256 (1971).
3. N. Holonyak, Jr., D. R. Scifres, H. M. Macksey, R. D. Dupuis, Y. S. Moroz, C. B. Duke, G. G. Kleiman, and F. V. Williams, *Phys. Rev. Letters*, **28**, 230 (1972).
4. T. Y. Wu, *This Journal*, **121**, 1357 (1974).
5. T. Y. Wu, *J. Crystal Growth*, **21**, 85 (1974).
6. T. Y. Wu, *ibid.*, **23**, 348 (1974).
7. G. A. Foggato and G. L. Pearson, *Proc. IEEE*, **60**, 456 (1972).
8. A. Majerfeld and G. L. Pearson, *IEEE Trans. Electron Devices*, **ED-14**, 632 (1967).
9. A. E. Blakeslee, *This Journal*, **118**, 1459 (1971).
10. J. J. Tietjen and J. A. Amick, *ibid.*, **113**, 724 (1966).
11. J. W. Burd, *Trans. AIME*, **245**, 571 (1969).
12. R. A. Burmeister, Jr., G. P. Pighini, and P. E. Greene, *ibid.*, **245**, 587 (1969).
13. D. J. Kirwan, *This Journal*, **117**, 1572 (1970).
14. T. Y. Wu and G. L. Pearson, *J. Phys. Chem. Solids*, **33**, 409 (1972).
15. D. W. Shaw, *This Journal*, **117**, 683 (1970).
16. D. W. Shaw, *J. Crystal Growth*, **8**, 117 (1971).

Abnormal Impurity Distributions in High-Purity Epitaxial Silicon Layers

H. Nihira and T. Shirasu¹

Research Institute of Electrical Communication, Tohoku University, Sendai, Japan

T. Terasaki

Semiconductor Research Institute, Sendai, Japan

and J. Nishizawa*

Research Institute of Electrical Communication, Tohoku University, Sendai, Japan

ABSTRACT

High-resistivity epitaxial layers with carrier concentrations of the order of 10^{12} - 10^{13} atoms/cm³ have been reproducibly grown on heavily Sb- or B-doped substrates. The epitaxial layers so obtained have been used to observe the behavior of impurities during epitaxial growth. When the epitaxial growth is performed using an as-grown surface as the substrate, an abnormal peak in the impurity distribution appears near the substrate-epitaxial interface. The resistivity of the layers is found to increase by heat-treatment in a hydrogen atmosphere, which is probably due to the effect of defects. Similar epitaxial layers have also been obtained by pyrolysis of SiH₄ and the carrier concentrations of these layers are found to have a considerably larger temperature dependence than the layers from SiCl₄. It has been established that the carrier concentration of the epitaxial layer is a function of the contamination from the substrate and the experimental apparatus. However, from the results of the present investigation, it appears that the impurities adsorbed on the substrate surface and defects introduced during epitaxial growth also play a role in determining the impurity distribution of such a high-purity epitaxial layer.

High power silicon devices and high frequency silicon devices have required high-purity epitaxial layers deposited on heavily doped substrates. The method for the vapor growth of silicon epitaxial layers by hydrogen reduction of SiCl₄ and pyrolysis of SiH₄ has been the subject of many studies. Some phenomena relating to the behavior of impurities such as the autodoping process, have been reported only for epitaxial layers containing carrier concentrations higher than 10^{14} - 10^{15} atoms/cm³ (1-10).

In the present investigation, reproducible, highly pure epitaxial layers with carrier concentrations as low as 10^{12} - 10^{13} atoms/cm³ have been grown successfully on heavily Sb-doped substrates, and the use of these epitaxial layers has been instrumental to a better understanding of impurity behavior during epitaxial growth. This paper deals mainly with abnormal impurity profiles observed at the interface between the high-resistivity layers. The difference between the temperature dependences of the impurity distribution by hydrogen reduction of SiCl₄ and pyrolysis of SiH₄ is also briefly discussed.

Experimental

The epitaxial growth was carried out by means of hydrogen reduction of SiCl₄ and pyrolysis of SiH₄ in a conventional horizontal reactor. In fabricating the epitaxial deposition system, however, scrupulous precautions were taken to minimize background contamination, and the susceptor was made of high-purity quartz. Commercially available nondoped SiCl₄ was used without further purification.

Silicon substrate wafers were prepared by either the floating zone or Czochralski techniques and doped with impurities such as P, As, Sb, or B in the concen-

tration range of 10^{13} - 10^{19} atoms/cm³. The wafer orientation was (111). Dislocation densities of wafers were in the range of 0 - 10^4 cm⁻². The substrates were mechanically or chemically mirror polished and cleaned by the usual semiconductor process before loading into the reactor.

Normally, the growth conditions were as follows: The growth temperature was $1200^\circ \pm 5^\circ\text{C}$ in resistance heating; the ratio of mole fraction SiCl₄/H₂, 0.01-0.015; the gas flow rate in the reactor, 5-10 cm/sec; the growth rate, in the range of 0.2-1.5 μ /min; and HBr vapor etching was performed at the same temperature as the growth temperature just before the epitaxial growth.

Impurity profiles of the epitaxial layers were calculated from capacitance measurements of mesa diodes formed on the grown surface by shallow diffusion of B or P at 1000°C for 10 min. Surface carrier concentrations after the diffusion were 10^{19} - 10^{20} atoms/cm³, and the junction depth was about 0.3 μ . The thickness of the epitaxial layer was determined from the size of stacking faults on the as-grown surface. The error in the measurements was less than 0.5 μ .

The conduction types of the epitaxial layers were detected by hot probe methods and *I-V* characteristics of the diodes made after B or P diffusion. In the case of p⁻ substrates, Hall effect measurements were made to determine the carrier concentration and conductivity of the epitaxial layers.

Results and Discussion

The epitaxial layers deposited on various substrates.—The conduction types and the carrier concentrations of the epitaxial layers on various substrates by resistance heating are listed in Table I. Using high-resistivity n⁻ (P-doped) or p⁻ (B-doped) substrates with carrier concentrations less than 10^{14} atoms/cm³, the epitaxial layers are always of the n-

* Electrochemical Society Active Member.

¹ Present address: Semiconductor Research Integrated Circuit Division, Hitachi, Ltd., Kodaira, Tokyo, Japan.

Key words: high-purity epitaxial growth, silicon abnormal distribution, interface, temperature dependence.

Table I. The conduction type and the carrier concentration of nondoped epitaxial layers on various substrates. Thickness of the layer about 15μ

Substrate {111}	Conduction type	Carrier concentration (atom/cm ³) (5μ away from the substrate layer interface)
n^- 0.01 ohm-cm P-doped	n	$8 \times 10^{14} \sim 4 \times 10^{15}$
n^- 0.015 ohm-cm As-doped	n	$5 \times 10^{13} \sim 1 \times 10^{15}$
n^- 0.01 ohm-cm Sb-doped	n	$4 \times 10^{12} \sim 3 \times 10^{13}$
p^+ 0.015 ohm-cm B-doped	p	$3 \times 10^{12} \sim 3 \times 10^{13}$
n^- 300 ohm-cm P-doped	n	$3 \times 10^{12} \sim 6 \times 10^{13}$
p^+ 3000 ohm-cm B-doped	n^*	4×10^{12}

* Determined by Hall effect measurements.

type in conductivity and are less than 10^{13} atoms/cm³ in carrier concentration. From this, it is obvious that the obtained high resistivity is not caused by the contamination of p-type impurities. In the Hall effect measurements from liquid nitrogen temperature to room temperature, no deep impurity levels were observed.

As can be seen from Table I, carrier concentrations in the range of 10^{12} – 10^{13} atoms/cm³ were reproducibly obtained on heavily Sb-doped substrates. However, in the case of P- and As-doped substrates, the concentrations in the layers were higher.

In general, the carrier concentration and the conduction type depend strongly on the characteristics of the substrate impurity and are significantly affected by the back surface of the substrate (6–8). It must be noted that the effect of the substrate on the epitaxial layer can be clearly seen only if the intrinsic system contamination is low. Since the concentration in the epitaxial layer due to the deposition system has been as low as 10^{12} atoms/cm³, the influence of the substrate would be detectable with high sensitivity. It is well known that in a multislice system the epitaxial layer concentration far from the interface, or the impurity doping level as it is generally termed, of samples which are placed downstream on the susceptor is much higher than that of samples placed upstream (8). This effect has also been ascertained and is discussed below.

The n^- (P-doped, 300 ohm-cm) substrates and the n^+ (0.01 ohm-cm) substrates were alternately placed on the susceptor along the gas stream. The epitaxial growth was performed without vapor etching. These results are shown in Fig. 2 and 3 for Sb-doped n^+ substrates, and in Fig. 4 for As-doped n^+ substrates. Figure 1 illustrates the experimental conditions presented in Fig. 2 and 3. In Fig. 2 and 3, the horizontal axis is the growing time. In Fig. 4, curves (a) and (b) are the impurity profiles when only a single n^- (P-doped) substrate and a single n^+ (As-doped) substrate, respectively, were used at position 1.

It should be noticed that the growth rate is a function of the position and decreases in the downstream portion of a reactor (11, 12). However, the increase of the carrier concentration of the epitaxial layer in the downstream portion cannot be explained by the decrease of the growth rate. This is because the carrier concentration of the layer deposited only on the n^- substrate was in the order of 10^{12} atoms/cm³ for growth rates in the range 0.2–1.5 μ /min as depicted in Table I.

From these experiments, it was confirmed that the transfer ratio of Sb is very small in comparison with that of P and As (8, 13), and that the autodoping effect is more pronounced in the case of As and P than Sb (7, 8). It is generally believed that the impurities are evaporated out of the n^+ substrates, and are transferred along the gas stream to make the gas impurity-rich in the downstream portion. Cave *et al.* (8) have reported that the increase in downstream doping is caused by the reaction of the quartz with silicon which

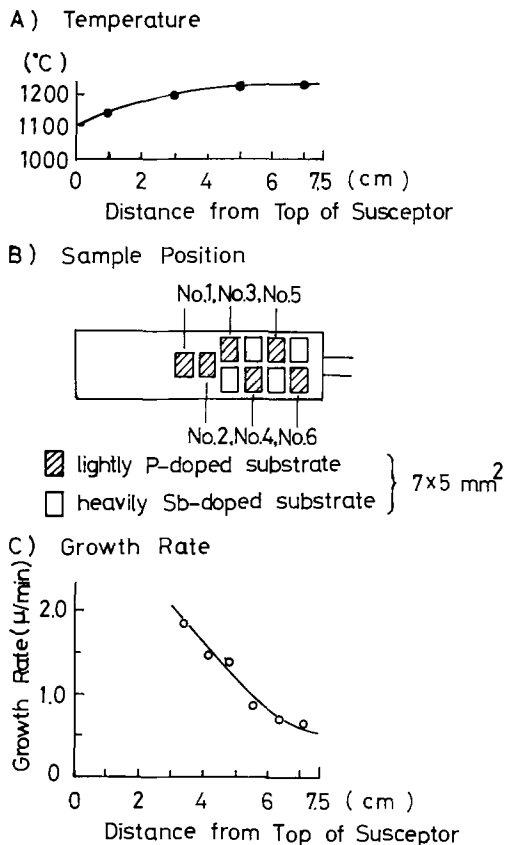


Fig. 1. The experimental conditions. Before the epitaxial growth, heat-treatment at the growth temperature was performed for 20 min. Growth time 40 min.

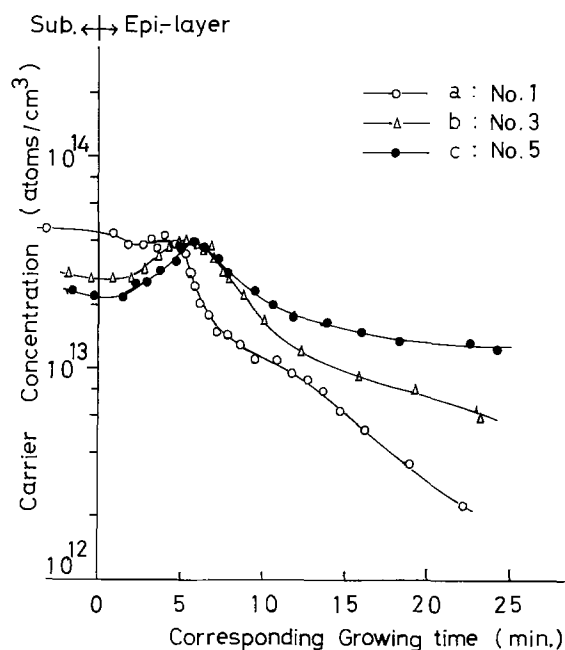


Fig. 2. The impurity profile of the epitaxial layers deposited on the n^- substrates in the experimental conditions presented in Fig. 1. (a) No. 1, (b) No. 3, (c) No. 5.

liberates the substrate dopant. On the other hand, Shepherd (4) proposed an autodoping model based on impurity liberation from the back surface. However, this model is not adequate when the growth rate is a function of the position for a large substrate.

It appears that the impurity liberated out of the back surface of the substrate by means of the etch back mechanism and etching reaction with HCl is a dominant factor in the present high-purity epitaxial growth. Hence, a model based on a detailed analysis of

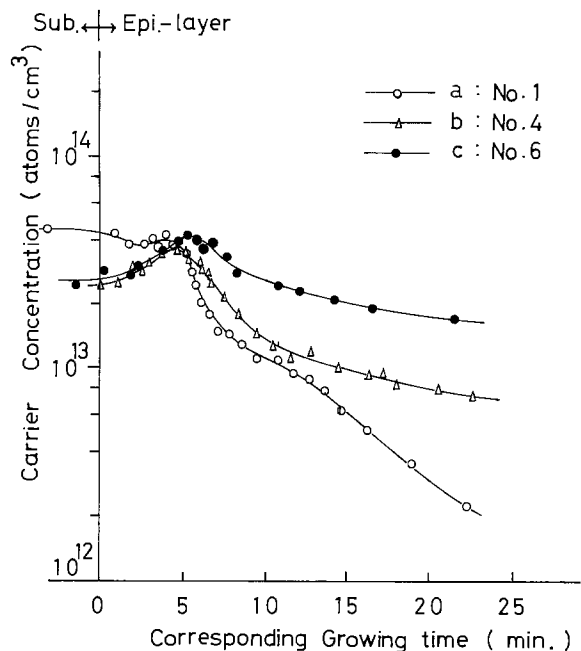


Fig. 3. The impurity profile of the epitaxial layers deposited on the n^- substrates in the experimental conditions presented in Fig. 1. (a) No. 1, (b) No. 4, (c) No. 6.

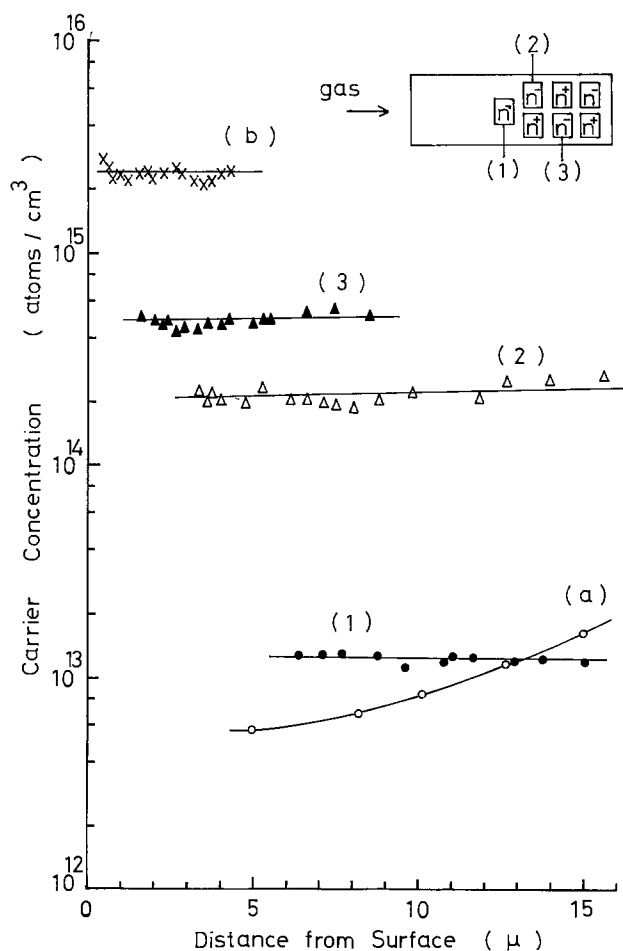


Fig. 4. The impurity profile of the epitaxial layers. Curves 1, 2, and 3 represent the carrier concentrations corresponding to the experimental conditions shown in Fig. 1, but n^+ substrates are As-doped (0.01 ohm-cm). (a) and (b) are the carrier concentrations when the growth was performed individually using the n^- (P-doped, 300 ohm-cm) substrate and the n^+ (As-doped, 0.01 ohm-cm) substrate, respectively.

Abnormal impurity distribution phenomena.—In investigation of the mechanism of the impurity distribution and the autodoping phenomena during the epitaxial growth using the high-purity epitaxial growth technique, an abnormal impurity distribution has been observed at or near the interface between the high-purity epitaxial layers. To specifically understand the origin of this abnormal impurity distribution, the following experiments were performed.

After the epitaxial growth of the high-resistivity layer from the n^+ (Sb-doped, 0.01 ohm-cm, 10^4 cm^{-2} in dislocation density) substrate (it is called hereafter the first epitaxial layer), the sample is taken out of the reactor and exposed to the atmosphere for a varying time in the as-grown surface condition, loaded into the reactor again, and the epitaxial growth is performed under the same growing conditions without pre-etching (this layer is called hereafter the second epitaxial layer). In this case an abnormal peak of the carrier concentration can always be observed at or near the interface between the first epitaxial layer and the second epitaxial layer. The peak value of the abnormal impurity profile is in the range of 10^{13} - 10^{15} atoms/cm³. A typical impurity profile thus obtained is shown in Fig. 5.

The phenomenon does not depend on the growth conditions such as the mole fraction SiCl_4/H_2 , the flow rate, and growth rate. The abnormal impurity distribution can be observed to have the same order of the carrier concentration even on the n^- (P-doped) substrates with a carrier concentration of 10^{13} atoms/cm³ and a dislocation density of 10^4 cm^{-2} . Moreover, there is no significant difference in the peak value of the abnormal impurity profile between the n^- substrates with and without dislocations as shown in Fig. 6.

The peak is not observed when light chemical etching is applied to remove the surface layer of the first epitaxial layer before the second growth. The absence

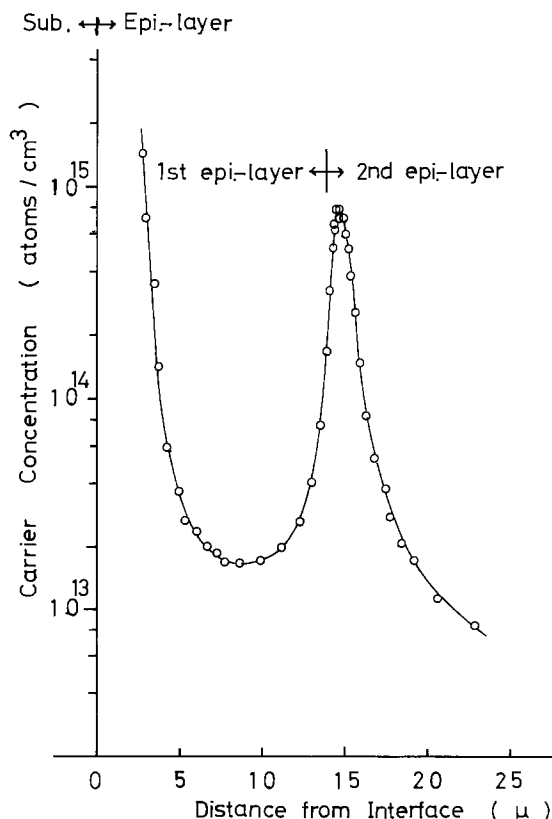


Fig. 5. The impurity distribution of the epitaxial layer deposited on the n^+ (Sb-doped) substrate. After the first epitaxial growth, the sample was exposed to the atmosphere for 24 hr. The first epitaxial layer is deposited to a thickness of 14.8μ for 20 min, and the second epitaxial layer to 18.2μ for 30 min.

the gas composition in the reactor is necessary to fully explain the impurity liberation from the substrate.

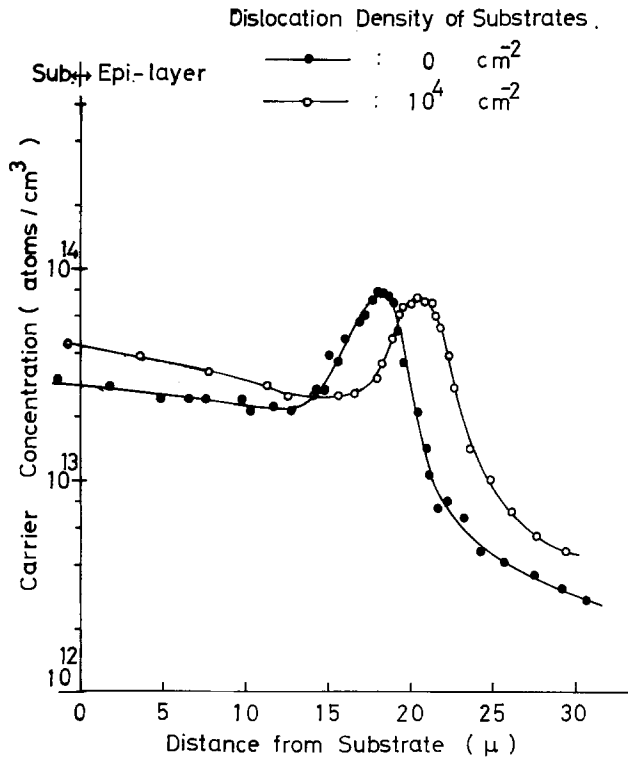


Fig. 6. The impurity profile of the epitaxial layer deposited on the n^- substrate of dislocation density 10^4 cm^{-2} and zero. The first growth for 20 min and the second for 20 min. Growth rate ca. $0.8 \mu/\text{min}$. After the first epitaxial growth, the samples were exposed to the atmosphere for 24 hr.

of the peak is also observed when vapor etching is performed before the second growth in the case of a n^- substrate. Further, the peak is not present when a n^- substrate exposed to the atmosphere is used for epitaxial growth.

The phenomenon is not due to the transient behavior at the initial stages of the second epitaxial growth. To ascertain this, the following experiment was performed. First, after the first epitaxial layer is deposited on the n^+ (Sb-doped) substrate, the sample is kept in the low temperature region of the reactor for about 10 min, the second epitaxial growth is performed. In this case, the abnormal peak of the impurity distribution cannot be observed as shown in Fig. 7.

From these observations, the abnormal impurity distribution is caused by the interaction between the as-grown surface and the atmosphere. The abnormal peak is not related to the dislocation density of the substrate, but it seems to appear depending on the surface conditions of the first epitaxial layer, such as the existence of defects on the surface.

By heat-treating in a hydrogen atmosphere at the same temperature as the growth temperature, a variation of the carrier concentration of the high-resistivity layer occurs in the n^+ (Sb-doped) substrate as shown in Fig. 8. The deviation of the impurity profile near the interface by heat-treatment can be explained by the normal diffusion of impurity from the substrate. On the other hand, the variation of the impurity doping level cannot be explained by such a diffusion process. Further, a similar variation is also observed for the epitaxial layer deposited on a n^- substrate. From these results, the variation of this type seems to be caused mainly by defects involved in the layer and activated by heat-treatment.

It is very likely that the as-grown surface of the epitaxial layer is activated and exists in an unstable condition, because the surface is extremely clean and appears to have many steps and kinks. Therefore, during its exposure to the atmosphere, impurities, oxides, and other contaminants would be adsorbed on the

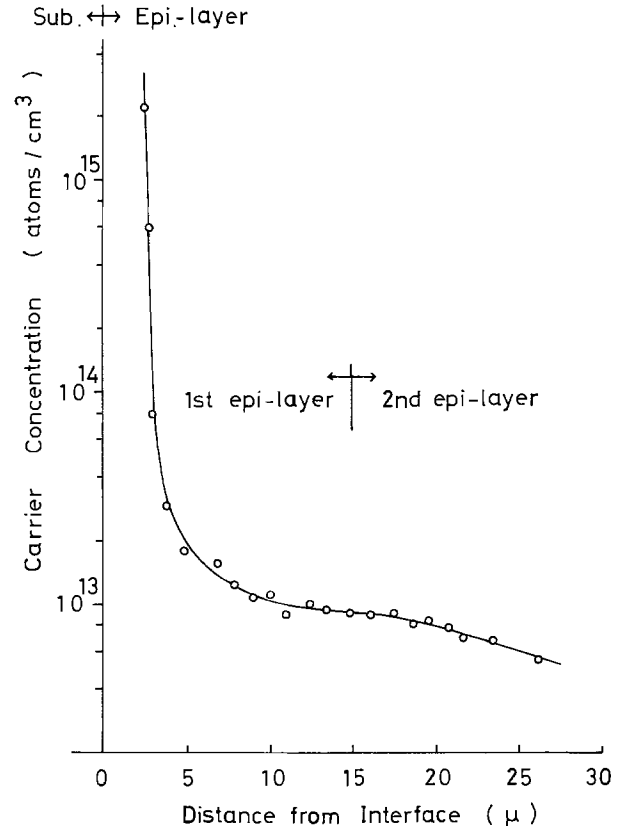


Fig. 7. The impurity profile of the epitaxial layer deposited on the n^+ substrate (Sb-doped, 0.01 ohm-cm). After the epitaxial growth was suspended, the sample was not exposed to the atmosphere and the second epitaxial growth was started. Growth rate $0.75 \mu/\text{min}$. Total growth time 40 min.

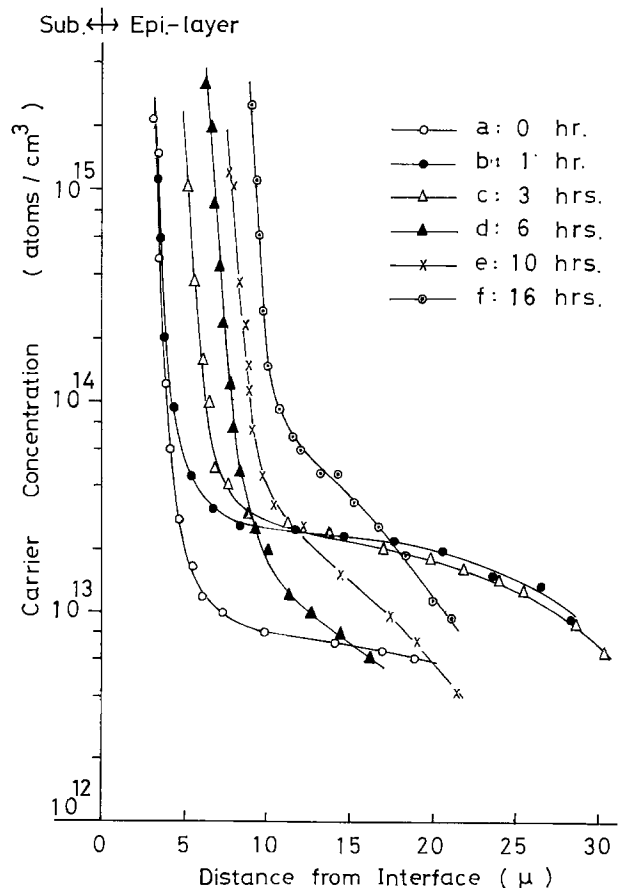


Fig. 8. The variation of the impurity profile by the heat-treatment at 1200°C in hydrogen atmosphere. Epitaxial layers, about 35μ . Growth time 30 min. (a) The sample without heat-treatment. Heat-treating times: (b) 1 hr, (c) 3 hr, (d) 6 hr, (e) 10 hr, (f) 16 hr.

active as-grown surface. These adsorbents are expected to induce defects at the interface between the first and second epitaxial layers and consequently to increase n-type carrier concentrations. However, the mechanism remains unresolved.

Temperature dependence of impurity distribution.—In these experiments, the same rf heated deposition system was used to obtain the epitaxial layers from SiCl_4 and SiH_4 . The susceptor was a heavily Sb-doped silicon which was coated sufficiently with the high-purity epitaxial layer grown by the hydrogen reduction of SiCl_4 .

The impurity profiles of high-resistivity layers, grown at 1200°, 1100°, and 1000°C by the hydrogen reduction of SiCl_4 , are shown in Fig. 9. No significant difference between the impurity doping levels can be observed for the different growth temperatures for a substrate size of 1×1 cm. But, for a relatively large substrate, the carrier concentration grown at 1000°C is about one order lower than that grown at 1200°C (3, 5).

Experiments were also performed by the pyrolysis of SiH_4 to compare with the results from SiCl_4 on small substrates. The temperature dependence of impurity doping levels is observed clearly as shown in Fig. 10. To ascertain this, the epitaxial growth is performed in steps at different temperatures (1200°, 1100°, 1000°C) on the small substrate. The experimental conditions of the growth temperature and the growing time and results are shown in Fig. 11, from which it is evident that the impurity doping level decreases with increasing temperature as in the case of Fig. 10, and that the temperature dependence cannot be explained in terms of outdiffusion of the impurity of the substrate.

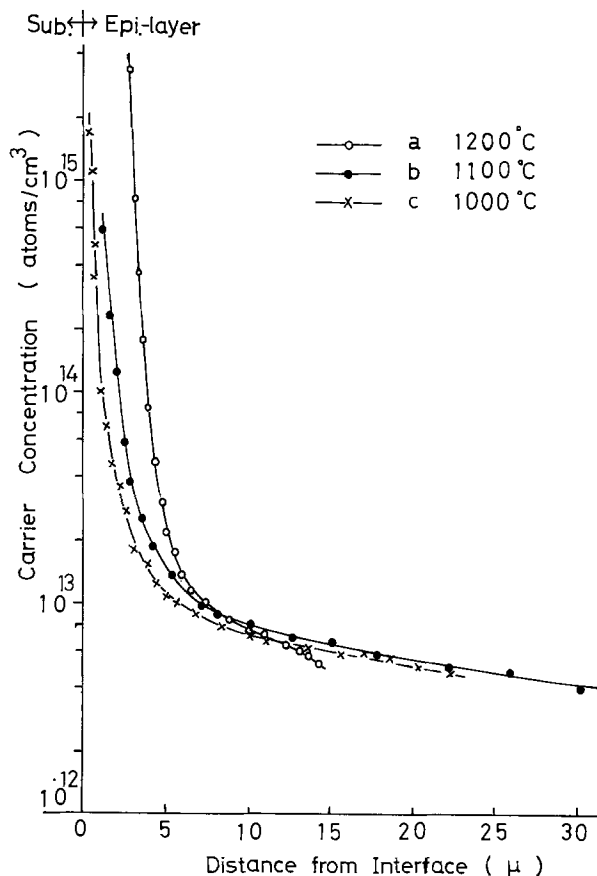


Fig. 9. The growth temperature dependence of impurity distribution of the epitaxial layer by the hydrogen reduction of SiCl_4 in rf heating. Growth time 50 min. Growth temperature: (a) 1200°C, (b) 1100°C, (c) 1000°C. Growth rates of the same position for growth temperature: (a) 0.43 μ/min , (b) 0.99 μ/min , (c) 0.62 μ/min .

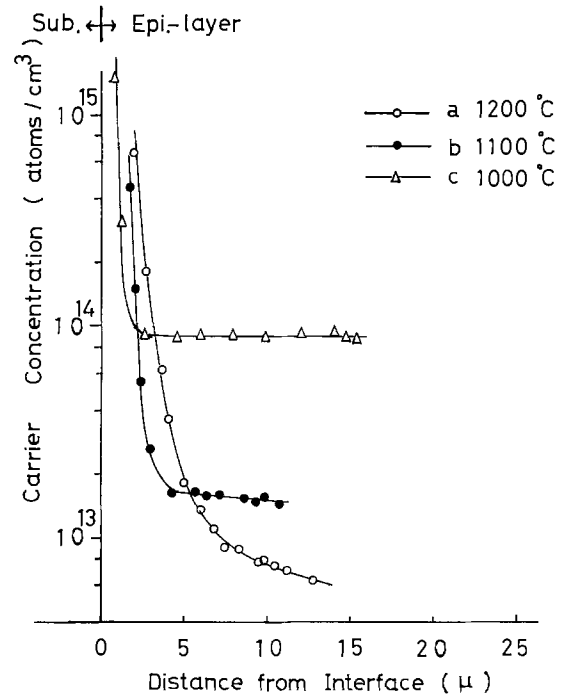


Fig. 10. The temperature dependence of impurity distribution of the epitaxial layer by the pyrolysis of SiH_4 in rf heating. The growth temperature is the same as that in Fig. 10. Growth rates ca. 0.34 μ/min .

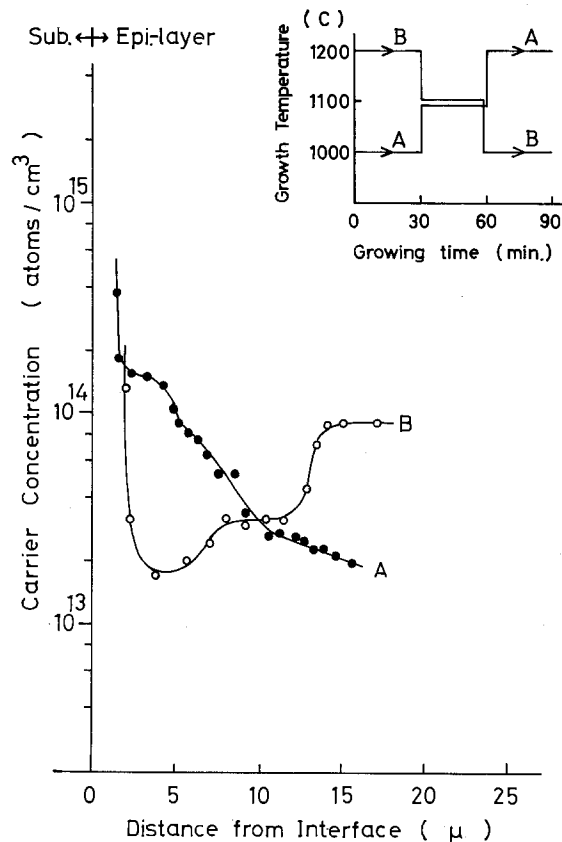


Fig. 11. Growth temperature vs. growing time and carrier concentrations as a function of distance from the interface.

These results show the epitaxial layer grown by the pyrolysis of SiH_4 seems to be independent of the surface condition of the pregrown layer or the substrate, and is influenced by defects introduced during the epitaxial growth, or by the growth mechanism where obviously no chlorine can be present (14-16). In the case of the hydrogen reduction of SiCl_4 , the incorpora-

tion of the dopant in the epitaxial layer of the small substrate does not change with temperature. Further, the number of defects in the epitaxial layer and the surface morphology influencing the carrier concentration, if present, would not vary significantly with temperature.

Conclusions

In the epitaxial growth of high-resistivity layers (10^{12} - 10^{13} atoms/cm³ concentration) it has been found that the intrinsic impurities in the deposition system are n-type and give rise to a concentration of about 10^{12} atoms/cm³ in the epitaxial layers. An abnormal peak in the impurity distribution is found to appear when the active as-grown surface exposed to the atmosphere is used as the substrate.

The carrier concentration of high-resistivity epitaxial layers obtained varies within the range of 10^{13} atoms/cm³ by heat-treatment at 1200°C in a hydrogen atmosphere. The epitaxial layer concentration obtained by the hydrogen reduction of SiCl₄ does not depend on the growth temperature for a small substrate, but that obtained from SiH₄ strongly depends on the temperature.

It has been considered that defects involved in such a high-purity epitaxial layer influencing the carrier concentration originate from defects to be induced by materials adsorbed on the active silicon surface.

Acknowledgment

The authors wish to thank Mr. S. Tagami for carrying out the pyrolysis of SiH₄.

Manuscript submitted April 26, 1973; revised manuscript received Nov. 25, 1974.

Any discussion of this paper will appear in a Discussion Section to be published in the December 1975 JOURNAL. All discussions for the December 1975 Discussion Section should be submitted by Aug. 1, 1975.

Publication costs of this article were partially assisted by Tohoku University.

REFERENCES

1. D. Kahng, C. O. Thomas, and R. C. Manz, *This Journal*, **109**, 1106 (1962).
2. C. O. Thomas, D. Kahng, and R. C. Manz, *ibid.*, **109**, 1055 (1962).
3. W. H. Shepherd, *ibid.*, **115**, 541 (1968).
4. W. H. Shepherd, *ibid.*, **115**, 652 (1968).
5. B. A. Joyce, J. C. Weaver, and D. J. Maule, *ibid.*, **112**, 1100 (1965).
6. H. Basseches, S. K. Tung, R. C. Manz, and C. O. Thomas, *Met. Semicond. Mater.*, **15**, 69 (1962).
7. A. S. Grove, A. Roder, and C. T. Sah, *J. Appl. Phys.*, **36**, 802 (1965).
8. E. F. Cave and B. R. Czorny, *RCA Rev.*, **24**, 523 (1963).
9. G. Skelly and A. C. Adams, *This Journal*, **120**, 116 (1973).
10. P. H. Langer and J. I. Goldstein, *ibid.*, **121**, 563 (1974).
11. P. C. Rundle, *Int. J. Electronics*, **24**, 405 (1968).
12. E. Fujii, H. Nakamura, K. Haruma, and Y. Koga, *This Journal*, **119**, 1106 (1972).
13. R. Nuttall, *ibid.*, **111**, 317 (1964).
14. D. C. Gupta, *Solid State Technol.*, **14**, 33 (1971).
15. F. C. Everstein, *Philips Res. Rept.*, **26**, 134 (1971).
16. J. Bloem, *J. Crystal Growth*, **18**, 70 (1973).

Diffusion Gettering of Au and Cu in Silicon

R. L. Meek,* T. E. Seidel, and A. G. Cullis*

Bell Laboratories, Murray Hill, New Jersey 07974

ABSTRACT

The gettering of Au and Cu by phosphorus diffused from PBr₃ and POCl₃ sources and by boron diffused from a BBr₃ source has been studied. Samples were intentionally contaminated with moderate to large amounts of Au and Cu to obtain impurity levels above the background level, then gettered and finally examined by ion backscattering. The solubilities of Au and Cu were experimentally measured for phosphorus diffusions at various temperatures. The gettering, using either phosphorus source, was found to take place in the silicon and not in the source glass and the Cu and Au atoms were on lattice sites. Differences in the shapes of the profiles of gettered Au for POCl₃ and PBr₃ diffused sources were found and these are discussed in terms of vacancy enhancement effects. In general, phosphorus diffusion gettering appears to operate by solubility enhancement and ion pairing of substitutional metal acceptors. Boron diffusion gettering is less effective than phosphorus, a result which is consistent with solubility calculations and physical arguments. When the solubility is exceeded new phases are formed. The formation of precipitates for boron diffusions has been studied by electron microscopy.

Recent studies of diffusion (1, 2) and ion damage (1, 3) gettering have greatly increased our understanding of gettering. However, when the recent diffusion results are compared with older studies (4-6) many unanswered questions remain. For example, recently it was shown by the use of backscattering that phosphorus (PBr₃) diffusion gettering of Au takes place entirely in the phosphorus-diffused layer (1) (900°-1100°C), while Lambert and Reese (5) reported a non-negligible fraction of the gettered Au to be in the diffusion-source glass. Hence the conditions under which a significant amount of Au will be in the glass appears to be an open question. In this paper we show that the

gettering takes place in the silicon for PBr₃, POCl₃, as well as BBr₃ diffusions, all of which have different glass compositions. In all our samples, the Au impurity content of the glass is, at most, a few per cent of that of the silicon and, as shown with control samples, this can always be attributed to furnace contamination.

Another question concerns the nature of the gettering mechanism. Recently it was shown that Cu and Au were gettered onto substitutional sites by phosphorus diffusion, while these impurities were gettered onto nonsubstitutional sites by boron diffusion (1). This pointed to an association mechanism: namely that Cu and Au, which are acceptors on substitutional sites, are paired with phosphorus donors (1, 2). However, in the case of boron diffusion, which produces a high density of acceptors, the solubility of Cu and Au donors would

* Electrochemical Society Active Member.

Key words: gettering, diffusion, solubility enhancement, ion pairing, ion scattering.

be enhanced so that Cu and Au would be on nonsubstitutional sites. This complementary behavior involving Cu and Au on substitutional sites under a diffused donor profile and on nonsubstitutional sites under a diffused acceptor profile was experimentally verified (1). These results gave a qualitative understanding and formed the basis for detailed solubility calculations (2). More experimental results are reported here which supplement the earlier work (1, 7). The principal concern is to obtain meaningful experimental values for the saturated solubility of Au and Cu by phosphorus diffusions. Solubilities of Cu and Au in P- or B-doped silicon have previously been studied, mainly for low P and B concentrations (8, 9). In the present work, the impurity content in the samples is progressively increased until precipitation is observed in the gettering layer. The procedure for this is described in the experimental section on determination of solubility limit below. Our earlier work (1) used only a fixed impurity content.

Another question regarding the mechanism is the role of vacancies in the gettering process. Differences in the Au profile under POCl_3 and PBr_3 diffusions have been observed in this study. The peak concentration of Au is buried for POCl_3 diffusion and is at the surface for PBr_3 diffusion. This result is interpreted in terms of a vacancy assisted gettering for the POCl_3 process. The PBr_3 and POCl_3 diffusion processes have different gas flow conditions. Hence the different physical effects observed and reported here are not necessarily due to the different chemical species in the bubbler. Our early work (1, 3) was done with PBr_3 sources, and we found a qualitatively different dislocation structure with TEM than that found by Dash and Joshi (10), who used a POCl_3 source. This led us to suspect that PBr_3 and POCl_3 diffusions result in different dislocation configurations and to make comparisons of gettering behavior.

The solubility calculations (2) for Au and Cu in the case of boron diffusion led to the conclusion that if interstitial donor Au and Cu were ion paired to the boron atoms then the Au and Cu would be very well gettered, which is contrary to experience and leads to a several order of magnitude discrepancy with existing solubility data. This led to physical arguments for the absence of ion pairing between interstitial Au and Cu and substitutional boron (2). The experiments presented here show that boron diffusion getters Au by the formation of precipitates at moderate to heavy Au contamination levels. It may well be that dislocations extract Cu and Au into their cores thereby promoting the formation of small precipitates (11). These precipitates are not found for more dilute Au contamination levels. Transmission and scanning electron microscopy were used to study the precipitates in the boron-diffused layers.

Experimental

Sample preparation.—Sample wafers, approximately 10 mils thick, were prepared from 10 ohm-cm, $\langle 111 \rangle$, n-type, low dislocation silicon. One side of the sample was covered by evaporation of 1000Å of Au or Cu, equilibrated with the metal at temperatures typically $\sim 1100^\circ\text{C}$ in a nitrogen ambient and quenched to $\sim 100^\circ\text{C}$ in ~ 3 sec. The wafers were lapped and etched so that ~ 1 mil of each surface was removed. It has been shown that this is more than sufficient to remove metal pile-up at the surface and that all surface damage is removed. The samples were diffusion gettered and examined by Rutherford backscattering.

Backscattering.—Rutherford backscattering of 1.8-2.0 MeV He ions, which has been reviewed by others in detail elsewhere (12, 13), was used to determine the number, distribution, and lattice location of the gettered impurities. The details of the technique as utilized in this laboratory may be found in Ref. (7) and (14); here we only give a brief summary. The energy of the backscattered ion identifies the mass of the atom from which it is scattered, and the number of backscattered

ions determines the number of scattering atoms. For scattering from target atoms of a given mass, the scattered ion energy scale may be converted to a substrate depth scale through knowledge of the kinematics and the stopping power. The channeling effect is used to determine impurity atom lattice location (13).

Electron microscopy and x-ray microanalysis.—Certain samples were examined in the scanning electron microscope (SEM) and, in addition, x-rays excited by the electron beam were monitored using an energy dispersive spectrometer to provide elemental analyses. Furthermore, samples were thinned from the side opposite the diffused layer of interest (3) so that the region adjacent to the diffusion gettered surface could be examined using the transmission electron microscope (TEM).

Determination of solubility limit.—We have calculated the solubility of Cu and Au in silicon for heavy dopings and high temperatures taking into account solubility enhancement (Fermi level effect) and pairing of metal and dopant ions (2). It is possible to obtain concentrations of impurities in excess of the solubility limit by sample preparation with infinite sources. For this reason an effort has been made to carry out experiments with both "limited" and "infinite" sources of impurities. Quantitative effects are rather difficult to assess unless some intentional contamination is introduced. The background Au and Cu levels can vary by a factor of ten, but with added Au and Cu the total impurity levels can always be controlled at a level which is well above the background variations (1). Hence the generic study of PBr_3 and POCl_3 diffusions and solubility is best carried out using moderate impurity levels.

The metal-Si-dopant ternary phase diagram is doubtless very complex. A qualitative cross section, for constant Si/P ratio, for the M-P-Si system might appear as in Fig. 1. In region 1 one has the metal in solution in phosphorus-doped silicon. Line a-b represents the metal solubility and line c-d a new phase, which, as we will show, is generally a metal-dopant compound or the metal itself which precipitates out of solid solution. In zone 2, then, one has a two-phase equilibrium. For comparison with the above-mentioned calculations (2), it is necessary to determine the point B along A-B-C. This is done experimentally by providing various amounts of metal in the wafer, by equilibrating at different temperatures, and then gettering at the same temperature and for the same time, and by eventually going to an "infinite" source of metal.

Infinite source samples are prepared by providing a diffused layer in an uncontaminated sample, evaporating metal onto the opposite side, and diffusing the metal across the wafer to the diffused layer (15). The occurrence of new phases is determined by backscattering, SEM and TEM. In this way we obtain an estimate of the point B on the phase diagram for comparison to the calculated values.

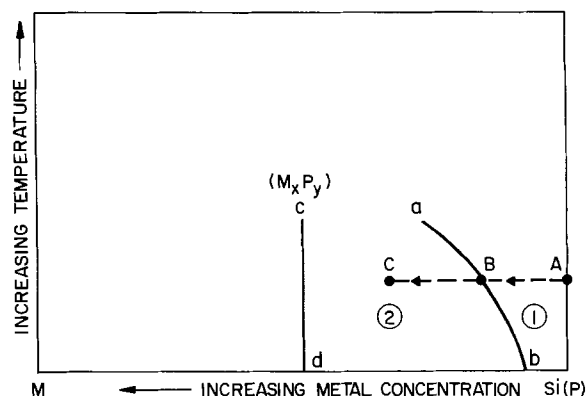


Fig. 1. Cross section of qualitative phase diagram for the system metal-phosphorus-silicon along a constant P/Si ratio surface.

Results

PBr₃ diffusion.—Figure 2 is a typical backscattered ion spectrum obtained from a Au-equilibrated and PBr₃-gettered sample. The phosphosilicate glass remained on the sample during measurement. Note that most (~90%) of the Au is found in the phosphorus-diffused silicon layer. In fact, simultaneous phosphorus diffusion of a control sample, containing no Au, yielded the same amount of Au in the glass (see Fig. 2) so it is clear that the Au in the glass came from furnace contamination. Generally, when precautions were taken to preserve furnace cleanliness, no Au (or Cu) was detected in the glass on either intentionally contaminated or control samples. The detection limit was $\sim 10^{13}$ cm⁻² for Cu and $\sim 10^{12}$ cm⁻² for Au (14).

Figure 3 shows random <110> axial channeled spectra for a similar sample after the glass had been removed. The large reduction in yield in the channeling direction shows essentially all of the Au (~90%) to be substitutional. Similar results are obtained for Cu in agreement with earlier results (1). Also, it is apparent that the Au profile is at its maximum at the surface and decreases with increasing depth into the silicon as the phosphorus concentration decreases.

Figures 4 and 5 are detailed angular scans across the <110> axis for gettered Au and Cu, respectively. The energy windows were set so that counts from the metal or Si from 200 to 3000Å below the surface were accepted. This eliminates counts corresponding to metal or Si at the surface so that the results are representative of the diffused layer in the silicon. For undiffused silicon we typically find that the silicon minimum yield is 0.03 and the channeling angle $2\psi_{1/2}(\text{Si})$ is 1.0 degrees. Here we see that the silicon minimum yield is ~ 0.05 and that $2\psi_{1/2}(\text{Si})$ is ~ 0.8 degrees. This indicates the presence of a small amount of lattice disorder or strain. The channeling angle for the metal atoms is approximately equal to that for silicon, the minimum yield is somewhat greater and no structure is observed in the angular scan. From Fig. 4 the Au is found to be 90% substitutional and from Fig. 5 the Cu is found to be 80% substitutional for these particular samples. In general, substitutional fractions of from 75 to 100% are observed. In summary, most of the Au and Cu atoms reside on substitutional sites, a result that is accounted for by enhanced solubility and ion pairing considerations (2). The fact that $\sim 20\%$ of the atoms are not substitutional suggests an occasional clustering of impurities or the formation of small pre-

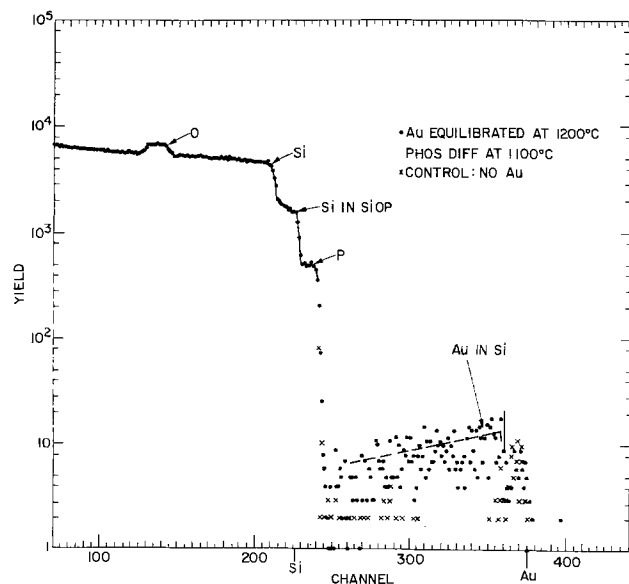


Fig. 2. Typical backscattered ion spectrum (scattered ion yield as counts per channel vs. scattered ion energy as channel number) from a phosphorus-gettered, Au-contaminated sample. Diffusion source glass is on.

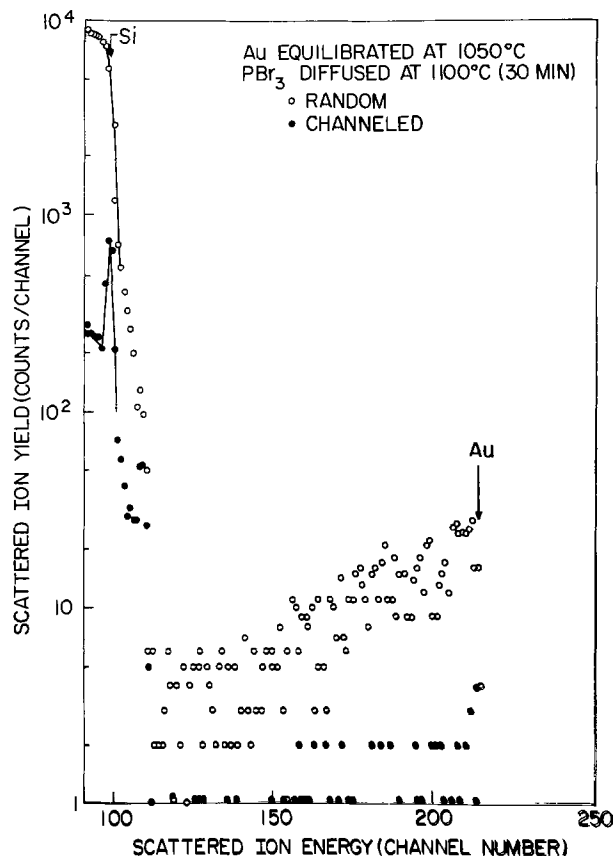


Fig. 3. Backscattered ion spectrum for phosphorus-gettered, Au-contaminated sample with glass removed. The arrows labeled Si and Au denote the scattered ion energies for scattering from Si and Au at the sample surface.

cipitates. The solubility at saturation is essentially the maximum value that appears substitutionally (2). The nonsubstitutional component is further discussed below.

Figure 6 illustrates the result of increasing the diffusion time. For 900°C, 30 min diffusion and this Au equilibration level, not all the Au is gettered (4), so we expect that increasing the diffusion time will cause more gettering of the Au. Figure 6 shows that increasing the gettering time by a factor of four does not change the Au concentration at the surface but does increase the depth of the gold profile by a factor of two in agreement with the factor of two increase in phosphorus diffusion length. The lack of change in the peak Au concentration indicates near saturation of the profile with Au. The total amount of Au gettered is, of course, a factor of two greater for the 2 hr than for the $\frac{1}{2}$ hr diffusion.

Figures 7 and 8 for Au and Cu respectively, show the result of increasing the contamination level by raising the metal equilibration temperature in the case of 1000°C, 30 min P diffusion. In each case, metal is gettered from the sample and it remains mainly substitutional in the diffused layer. There is no evidence of the appearance of a second phase. The increased Au concentration for the higher equilibration temperature suggests the higher Au concentration is closer to saturation, while the constant Cu concentration suggests that saturation has been reached. At the surface, for the higher temperature equilibration, the Au concentration is 10^{19} cm⁻³ and the copper concentration is $5(10)^{20}$ cm⁻³.

Figure 9 shows the quite different result when an "infinite" source of Cu is provided. The annealing time was 30 min. During this time, Cu atoms are diffused from a 1000Å thick evaporated Cu film across the sample to the already phosphorus diffused layer. Clearly the copper concentration at and near the surface has increased significantly and is found to be completely off

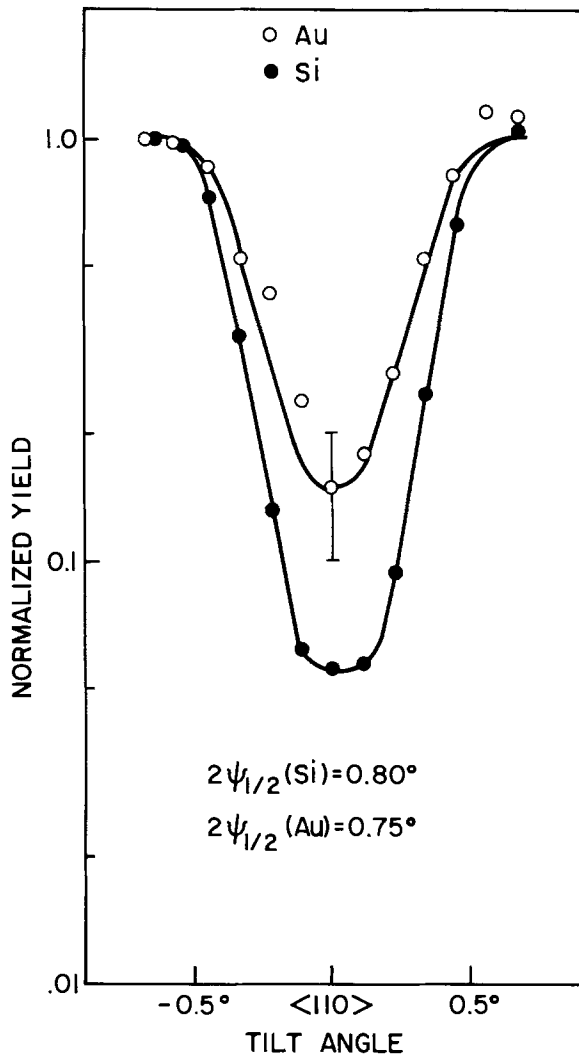


Fig. 4. Angular scan across $\langle 110 \rangle$ axis for a Au-contaminated (1200°C), phosphorus-gettered (PBr_3 , 1000°C , 30 min) sample.

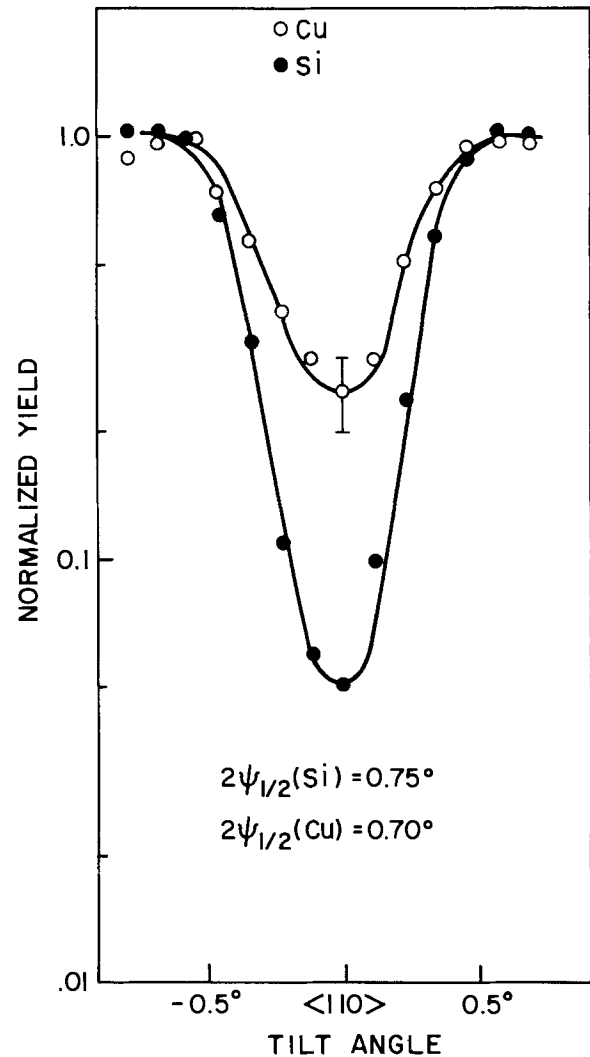


Fig. 5. Angular scan across $\langle 110 \rangle$ axis for a Cu-contaminated (1200°C), phosphorus-gettered (PBr_3 , 1000°C , 30 min) sample.

lattice sites. Furthermore, at and near the surface the phosphorus is also completely off lattice sites, and it is possible that a second phase has precipitated. Comparing off lattice site phosphorus and Cu indicates that there is an over-all Cu to P ratio of approximately 2:3 and a volume concentration of $\sim 10^{21} \text{ cm}^{-3}$. Note that much of the Cu is substitutional at a depth ~ 0.4 - 0.5μ (corresponding to channel 120-140). The phase Au_2P_3 is found (16) when the Au solubility is exceeded in heavily P doped silicon.

POCl_3 diffusion.— POCl_3 diffusions yield silicon lattice defects which are significantly different, as determined by both backscattering and by TEM, from those associated with PBr_3 diffusions. (As noted above, the flow rates are different as well as the phosphorus sources.) Briefly, when examined using the TEM, PBr_3 diffusions produce only relatively few very small dislocation loops, whereas the POCl_3 diffusions produce larger loops together with a more deep and dense network of dislocations. In backscattering, the aligned ion beam is dechanneled at a greater rate in passing through a POCl_3 diffused zone than in passing through a PBr_3 diffused one.

Figure 10 shows a typical spectrum from a Au-contaminated sample gettered by POCl_3 diffusion. Comparison to Fig. 3 shows that the shape of the Au distribution in the diffused layer is considerably different from that obtained after a PBr_3 diffusion. That this is, in fact, an Au distribution has been confirmed by etching off $\sim 500 \text{ \AA}$ of silicon and redetermining the spectrum. We emphasize, however, that the Au is almost all (in this case 95%) substitutional. Different parts of the

same Au-equilibrated sample have been PBr_3 and POCl_3 diffused. The observed Au profiles are shown in Fig. 11. The curves are the predictions of theoretical calculations (2) to which we shall return in the next section. The total amount of Au gettered by PBr_3 and POCl_3 is the same within experimental error.

BBr_3 diffusions.—It is a rather general observation that boron diffusion provides a relatively poor gettering system. We have attempted to explain (2) this in terms of the enhanced solubility and ion pairing theory of metal solubility. Essentially, the argument relies upon configurational and vibrational entropy effects which indicate that ion pairing of interstitial metal donors and substitutional acceptors is not important at these temperatures and doping levels, so that the total metal solubility in a heavily doped p-type region is much less than that in a similar n-type region.

Figure 12 is a typical spectrum obtained when a Au-contaminated wafer is boron diffused. The only gold detected is a surface peak. Similar surface peaks are often obtained when an Au-contaminated sample is prepared in the usual manner and then annealed, but not gettered. This is simply another type of control, see e.g., Fig. 4 of Ref. (1). Similar results are obtained for Cu. Again, it should be mentioned that boron glasses are impurity free if the furnace is not contaminated.

If the metal contamination level is increased by raising the initial equilibration temperature, the experimental observations change in a characteristic manner, as shown in Fig. 13 for Au. Now a large amount of Au is present and $\langle 110 \rangle$ and $\langle 111 \rangle$ axial channeled spectra show the same yield from Au atoms as does the

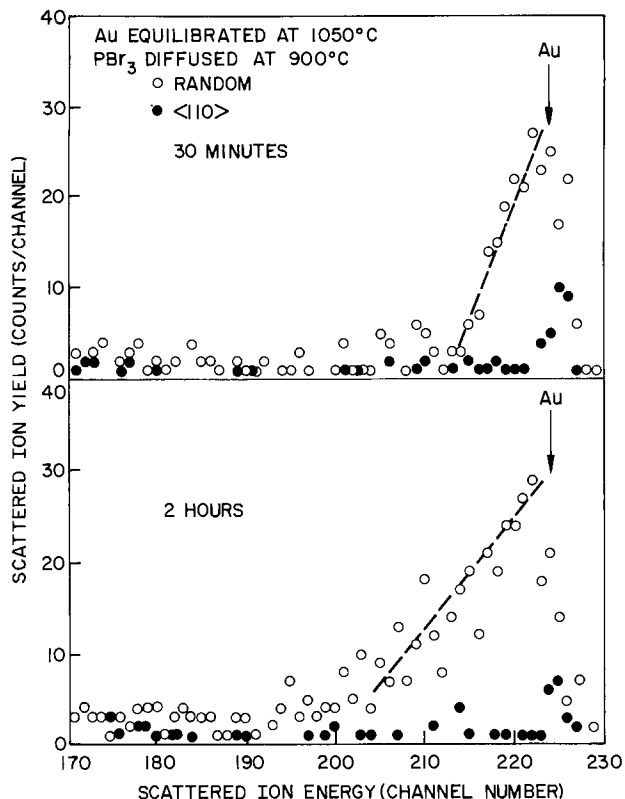


Fig. 6. Au spectra from Au-equilibrated, phosphorus-diffused samples at 900°C.

random spectrum, showing that the Au is distinctly off matrix lattice sites. Figure 14 is an angular scan across the $\langle 110 \rangle$ axis. Note that for silicon the minimum yield and channeling angle are those of undiffused silicon; thus any precipitates formed do not appear to introduce significant strain or disorder into the silicon

matrix. For scattering from Au, no structure is apparent in the angular scan for the $\langle 110 \rangle$ or $\langle 111 \rangle$ axes. (The $\langle 111 \rangle$ scan is not shown.) This latter observation suggests the presence of precipitates rather than interstitial metal atoms because of the absence of any flux-peaking effects.

We have used the boron (p, α) nuclear resonance (17) in an attempt to detect differences in, on, and off lattice site boron fraction for layers which either did or did not contain precipitates. However, $15 \pm 5\%$ of the boron is found off lattice sites in all cases, including a boron diffused, uncontaminated sample.

Electron microscopy.—In order to resolve this problem, the surfaces of boron-diffused samples were examined using the SEM. The sample which had been equilibrated with Au at the highest temperature was observed to have many precipitate-like islands distributed over its surface. These varied in size over a range, the largest being present in number densities of $\sim 10^6 \text{ cm}^{-2}$ and often having triangular shapes with edge dimensions of $\sim 5000 \text{ \AA}$ (Fig. 15a). Correlation of images with crystallographically oriented electron channeling contours showed that the edges of such features were sometimes aligned near $\langle 110 \rangle$ type matrix directions. Furthermore, the triangular islands were often located in shallow depressions in the matrix surface.

In order to determine whether the islands contained an impurity element they were subjected to electron probe x-ray microanalysis. Selected regions of the specimen surface were scanned with a $3000 \text{ \AA} \times 3000 \text{ \AA}$ electron raster and the x-rays produced showed that the islands alone contained substantial quantities of Au. To confirm that the Au impurity was contained within the island structures, scanning x-ray images were generated using only x-ray photons which contributed to one of the Au x-ray peaks (2.14 keV). Such an image is given in Fig. 15b, which shows the same specimen area as the electron image of Fig. 15a, and it is clearly seen that Au-produced x-rays have emanated from the regularly shaped island. Photon counts regis-

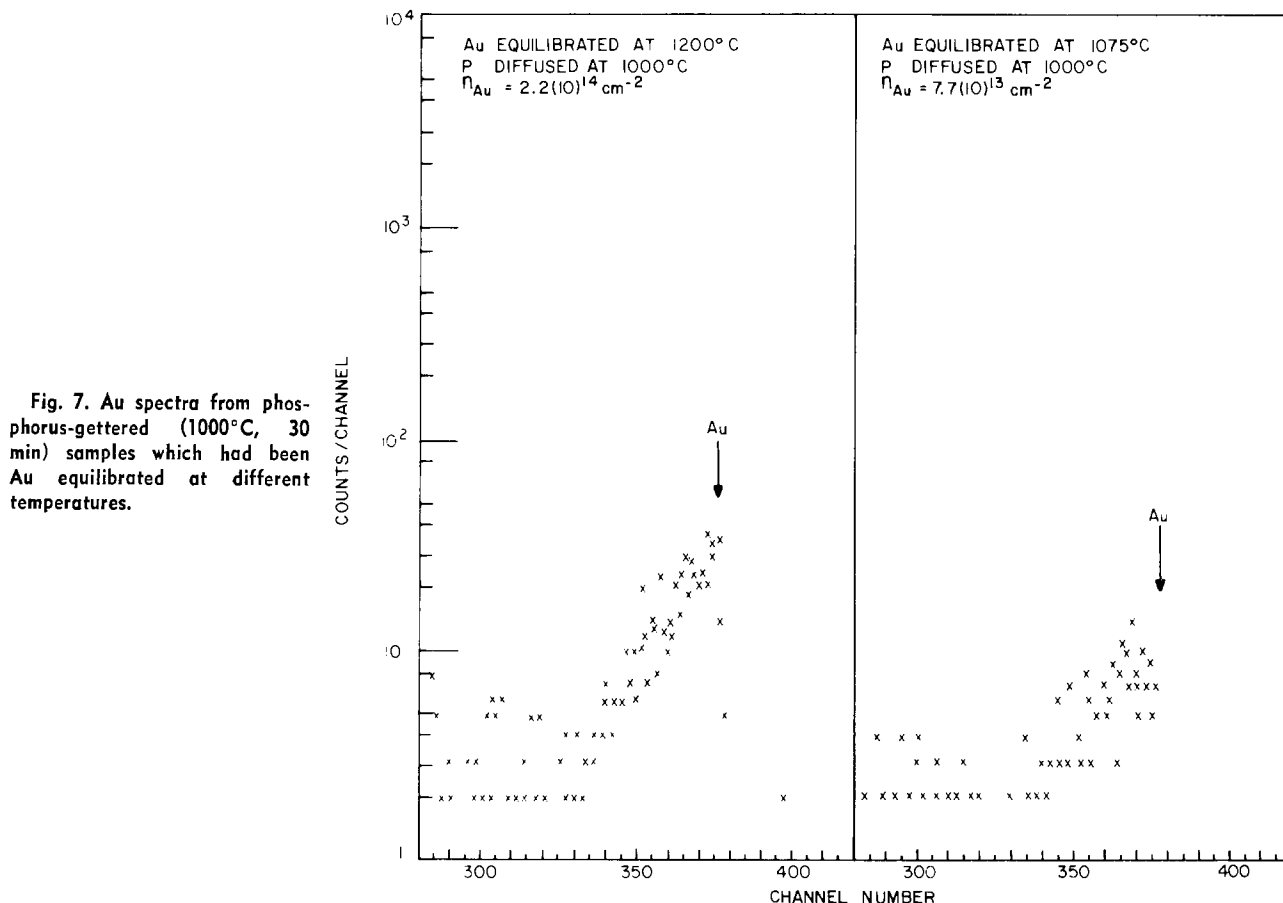


Fig. 7. Au spectra from phosphorus-gettered (1000°C, 30 min) samples which had been Au equilibrated at different temperatures.

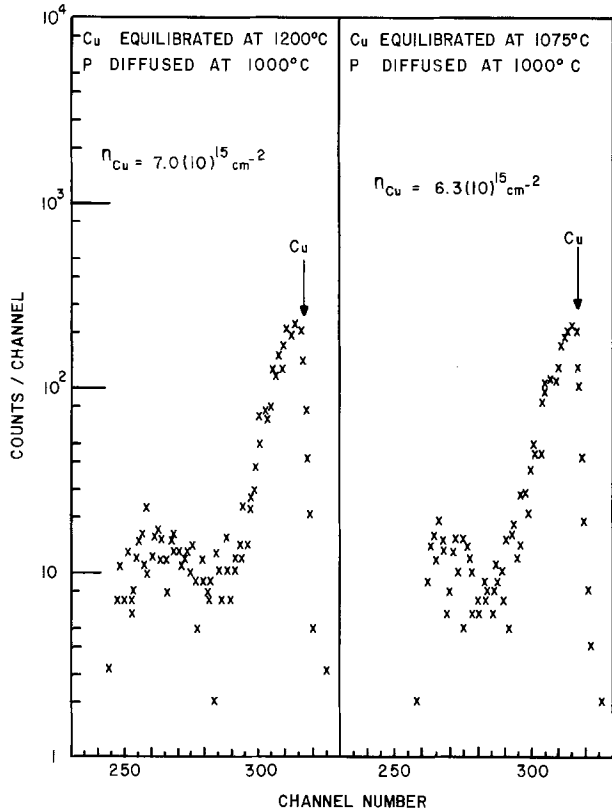


Fig. 8. Cu spectra from phosphorus-gettered (PBr_3 , 1000°C, 30 min) samples which had been Cu equilibrated at different temperatures.

tered from the surrounding matrix were contributions from the random x-ray background and do not indicate

the presence of a detectable Au concentration. A typical impurity x-ray spectrum is given in Fig. 16 where it will be seen that the Au peak at 2.14 keV has an amplitude $\sim 25\%$ of that of the matrix Si peak at 1.74 keV.

The Au-containing precipitates described above were also studied using the TEM. A typical island is shown in Fig. 17, and the depression in which it is situated is clearly evident. Such islands were composed of a well-defined precipitate phase, and by analysis of transmission electron diffraction patterns containing precipitate Bragg reflections it has been found that the phase was elemental Au (18). The islands did not appear to have a unique orientation relationship with the Si matrix and they often showed evidence for the presence of internal defect structures. The linear features within the precipitate of Fig. 17 may be dislocations or micro-twin lamellae.

For comparison with the above observations, the surfaces of other boron-diffused Si samples which had originally contained the lower Au impurity concentrations were also studied. In such cases, no Au-containing precipitates were found to be present and Au impurity levels were below the limit of detection. It should also be noted that the presence of the boron diffused layer is apparently necessary for formation of the precipitates, since an Au contaminated sample which was annealed but not diffused, did not yield precipitates.

Concluding Discussion

Our results clearly show that metal impurities are gettered into the diffused layer in the Si, not into the diffusion source glass. This result is contrary to some previous results (5, 6), but we emphasize that the backscattering measurement plus the use of control samples gives a clearly unambiguous result. Others (19, 20) have arrived at similar conclusions, using somewhat different experimental methods, but there still exists considerable confusion in the literature (21).

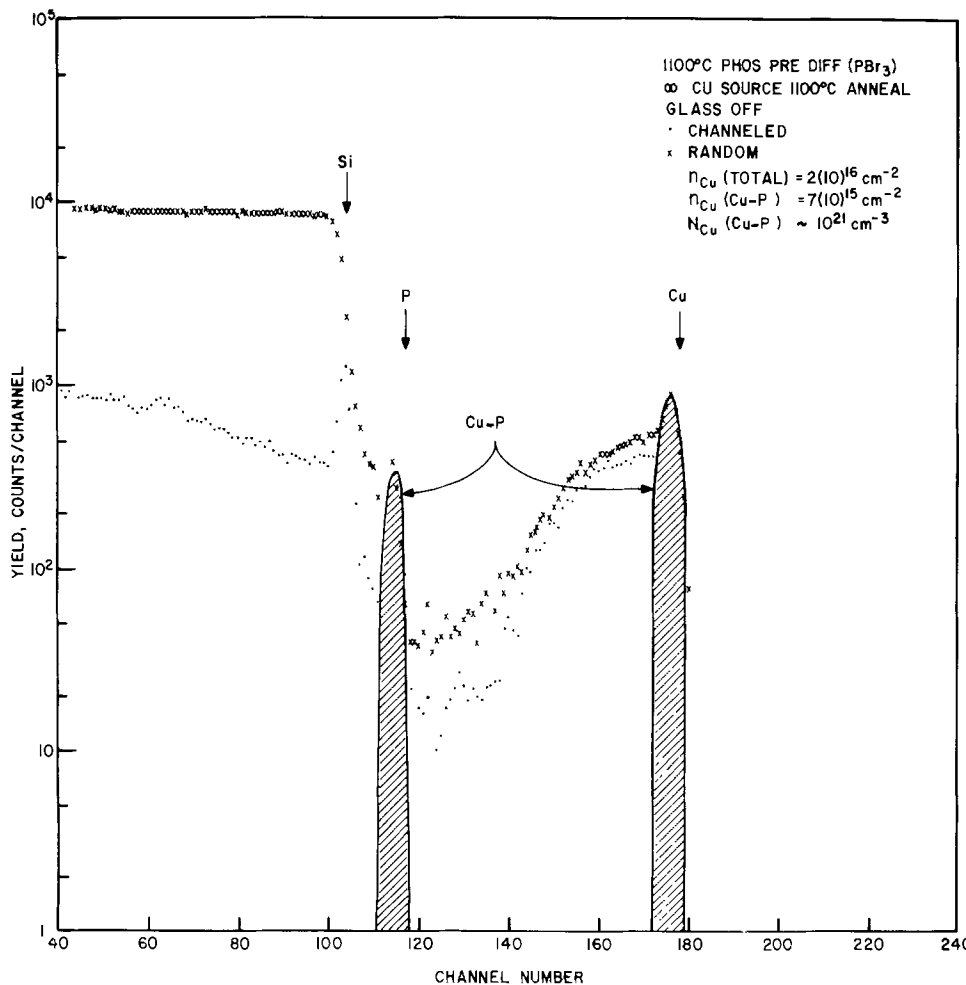


Fig. 9. Spectra from "infinite" Cu source sample (30 min anneal).

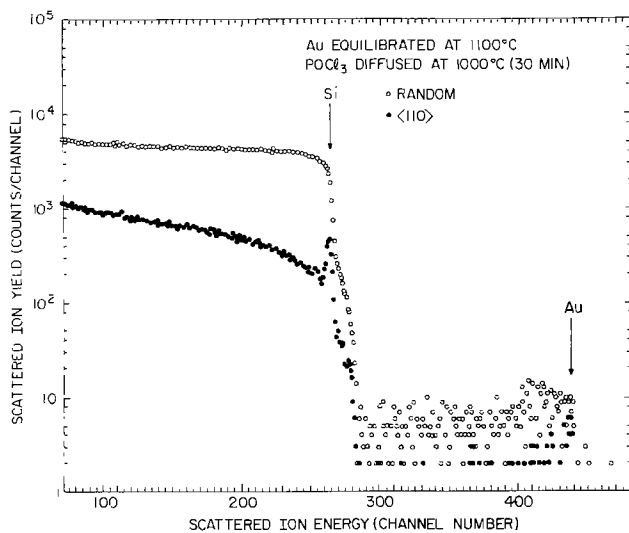


Fig. 10. Spectra from POCl_3 -diffused, Au-contaminated sample

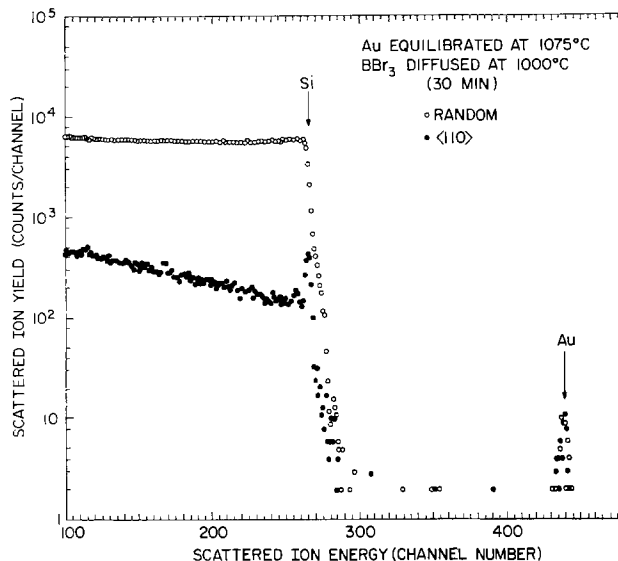


Fig. 12. Spectra from B-diffused sample, originally Au equilibrated at 1075°C .

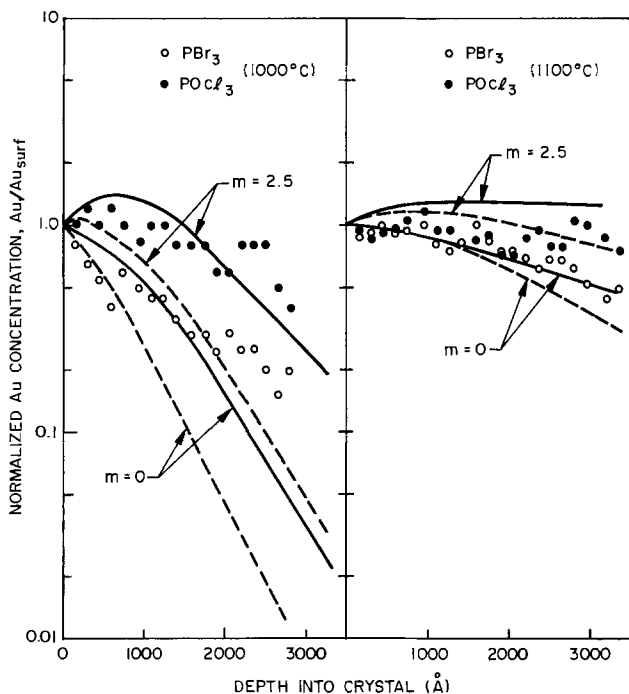


Fig. 11. Au concentration profiles from different parts of the same sample which were PBr_3 - and POCl_3 -diffused (30 min diffusion, 1000°C and 1100°C). Samples originally equilibrated with Au at 1200°C .

For phosphorus diffused layers, the gettered metal atoms are found to be on lattice sites. In general, Cu and Au can exist in silicon as a substitutional acceptor and as an interstitial donor [see Ref. (2) and references quoted therein]. We propose that the gettering mecha-

nism for P diffusion is solubility enhancement and ion pairing (22) of the substitutional metal acceptor. This is especially convincing for the case of Cu, where at 1000°C the intrinsic interstitial solubility is $\sim 10^{17}\text{ cm}^{-3}$ and the intrinsic substitutional solubility is $\sim 10^{13}\text{ cm}^{-3}$, but yet one finds up to $5(10)^{20}\text{ cm}^{-3}$ Cu on substitutional sites in heavily doped n layers. The experiments [see also Ref. (1)] show 75-100% substitutional character while the calculations (2) predict 100% substitutional at the highest P concentrations. However, we note that as the sample is cooled from the diffusion temperature, it becomes supersaturated at some lower temperature, so that some of the dissolved metal may be able to redistribute slightly or cluster to appear off lattice sites.

POCl_3 diffusion yields a somewhat different Au or Cu profile than does PBr_3 diffusion (see Fig. 11). Although the dislocation structure is more closely spaced and extends deeper into the matrix for the POCl_3 diffusion, the fact that the impurity is still essentially all substitutional throughout the diffused layer implies that the impurity atoms are not directly associated with the dislocation network.

Rather, we postulate that the POCl_3 result is caused by vacancy enhancement due to the climbing dislocation network as proposed by Hu and Yeh (23) for an explanation of the emitter push effect. In Fig. 11 the calculated curves are: $m = 0$, no vacancy enhancement; $m = 2.5$, vacancy enhancement predicted by the quasi-static approximation to Hu and Yeh's (23) theory. The solid and dashed lines are for two different values of the activity coefficient for electrons [see Ref. (2)]. The data for PBr_3 diffusions [and other data in Ref. (2)] indicate little or no vacancy enhancement. For POCl_3 diffusions, however, the Au profile is much flatter, and in fact peaks at a significant distance from the surface in fairly good agreement with the vacancy enhancement predictions.

In the linearized approximation (2) to Hu and Yeh's (23) quasi-steady-state theory, the vacancy enhancement is given by

Table I. Solubility of Cu and Au in heavily doped Si

Dopant	Temperature ($^\circ\text{C}$)	Dopant surface concentration (cm^{-3})	Cu solubility (cm^{-3})		Au solubility (cm^{-3})	
			Exp.	Theory	Exp.	Theory
P	900	$6(10)^{20}$	$2.5 \pm 1(10)^{20}$	$2 \pm 0.5(10)^{20}$	$9 \pm 3(10)^{18}$	$5 \pm 2(10)^{18}$
P	1000	$1.1(10)^{21}$	$5 \pm 2(10)^{20}$	$5 \pm 2(10)^{20}$	$1.5 \pm 0.5(10)^{19}$	$3 \pm 2(10)^{19}$
B	1000	$4(10)^{20}$	$<10^{19}$	$9 \pm 3(10)^{18}$	$<10^{18}$	$7.5 \pm 2.5(10)^{18}$

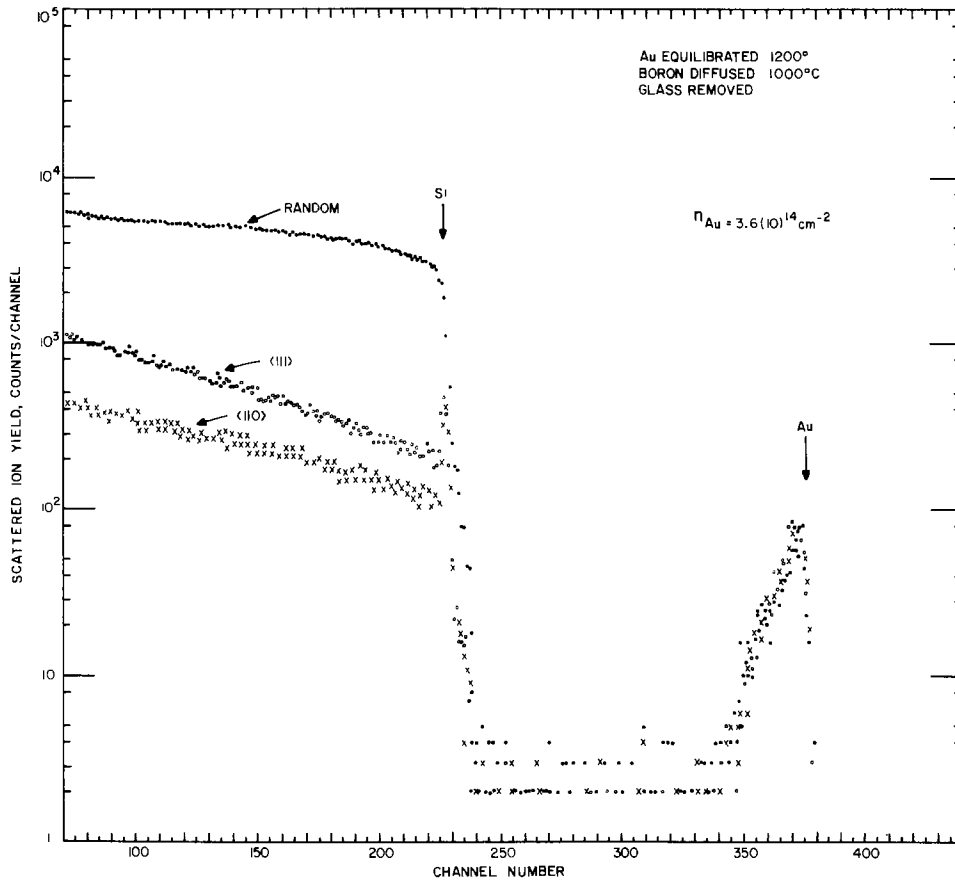


Fig. 13. Spectra from B-diffused sample (30 min), originally Au equilibrated at 1200°C.

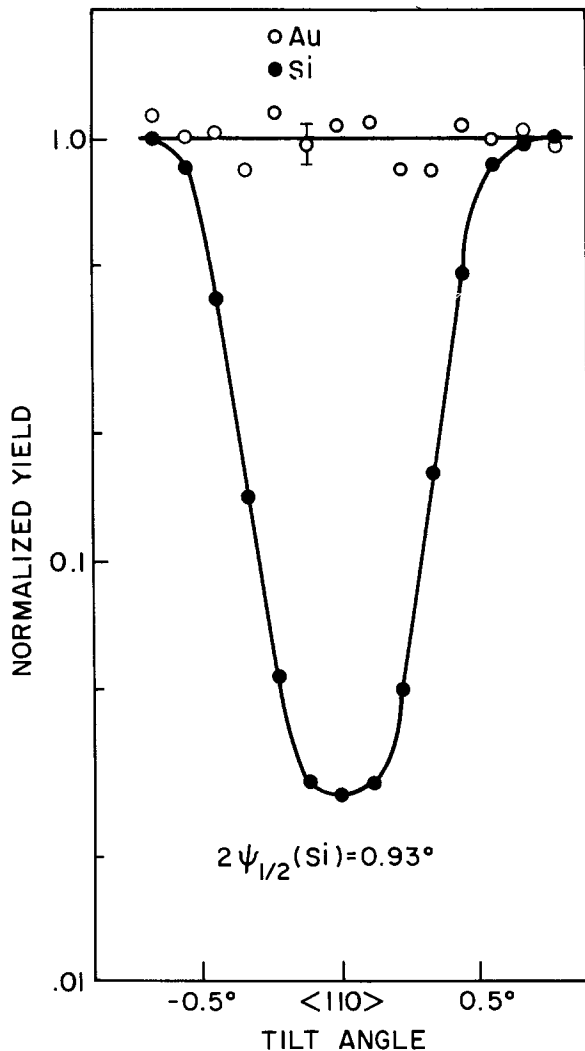


Fig. 14. Angular scan across <110> axis for sample from Fig. 13.

$$\frac{V}{V_{eq}} = 1 + mx/(Dt)^{1/2}$$

for $x \leq 2(Dt)^{1/2}$, where

$$m = 2\langle R \rangle tD/N_0D^*$$

In the above formulas, x is distance into the crystal, t is diffusion time, D is the effective phosphorus diffusivity, $\langle R \rangle$ is the mean rate of vacancy generation per unit volume, D^* is the intrinsic silicon self-diffusivity, and N_0 is the number of lattice sites per unit volume. Using our TEM results to estimate $\langle R \rangle$, we find that for $POCl_3$ diffusions $m \sim 1$ and for PBr_3 diffusions $m \leq 0.1$. Thus theory and experiment are in agreement with the hypothesis that vacancy enhancement is significant for $POCl_3$ but not for PBr_3 diffusions. However, it should also be pointed out that the shape of the P profile itself may be quite different for the two diffusion sources.

Our estimates of the saturation solubilities are given in Table I. We compare theory and experiment near the surface where the dopant should be at its solubility limit (24) and where vacancy enhancement should not be significant (23). Detailed examination of the leading edge of the Si spectrum shows a small shoulder corresponding to scattering from ^{31}P at the surface which is separated from the 3.12% abundant ^{30}Si isotope by about 20 keV. The magnitude of this shoulder indicates that assuming the surface phosphorus concentration to be equal to the solubility is reasonable, and the channeled spectrum indicates that $\sim 10\%$ of the phosphorus atoms are off lattice sites at the surface. Similarly, the boron (p, α) nuclear resonance experiment indicates that it is reasonable to take the boron surface concentration to be equal to the boron solubility. In Table I, the range of experimental values is due to the fact that we cannot determine that we have passed point B on Fig. 1 until a detectable amount of the new phase has formed. The range of theoretical values is due to the range of possible electron activity coefficients (2). The agreement between theory and experiment is within the uncertainty in either value.

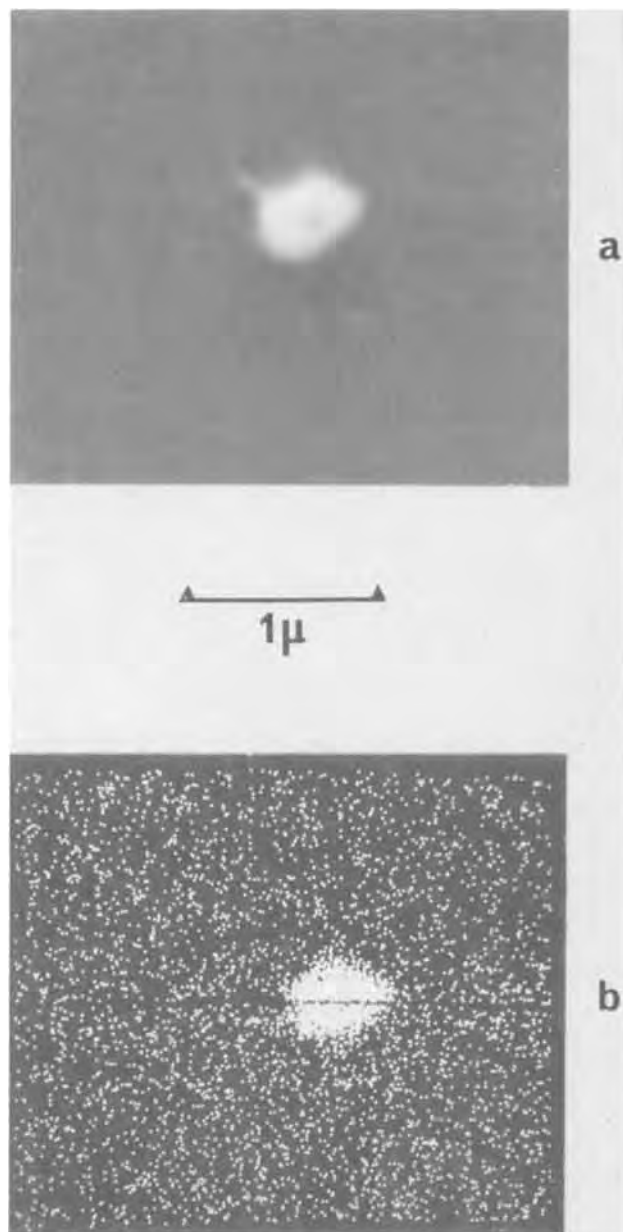


Fig. 15. (a) Scanning electron micrograph of partially truncated triangular island in boron diffused sample. (b) Scanning x-ray micrograph obtained using photons with energies near to 2.14 keV. Same specimen area as shown in part (a).

In the case of B diffusion, except for a surface peak already discussed, the gettered Cu or Au is at or near the detection limit until the solubility limit has been exceeded, and a new phase precipitates. We conclude, therefore, that the solubility is less than or nearly equal to the detection sensitivity of our measurements which is $\sim 10^{18} \text{ cm}^{-3}$ for Au and $\sim (10)^{19} \text{ cm}^{-3}$ for Cu. Again this conclusion is in agreement with solubility calculations (2).

Acknowledgments

We would like to thank J. M. Poate for his participation in the early angular scan experiments, W. M. Augustyniak for his invaluable assistance in the (p, α) resonance experiment, and F. L. Worthing for his capable sample preparation.

Manuscript submitted Aug. 1, 1974; revised manuscript received Jan. 17, 1975.

Any discussion of this paper will appear in a Discussion Section to be published in the December 1975 JOURNAL. All discussions for the December 1975 Discussion Section should be submitted by Aug. 1, 1975.

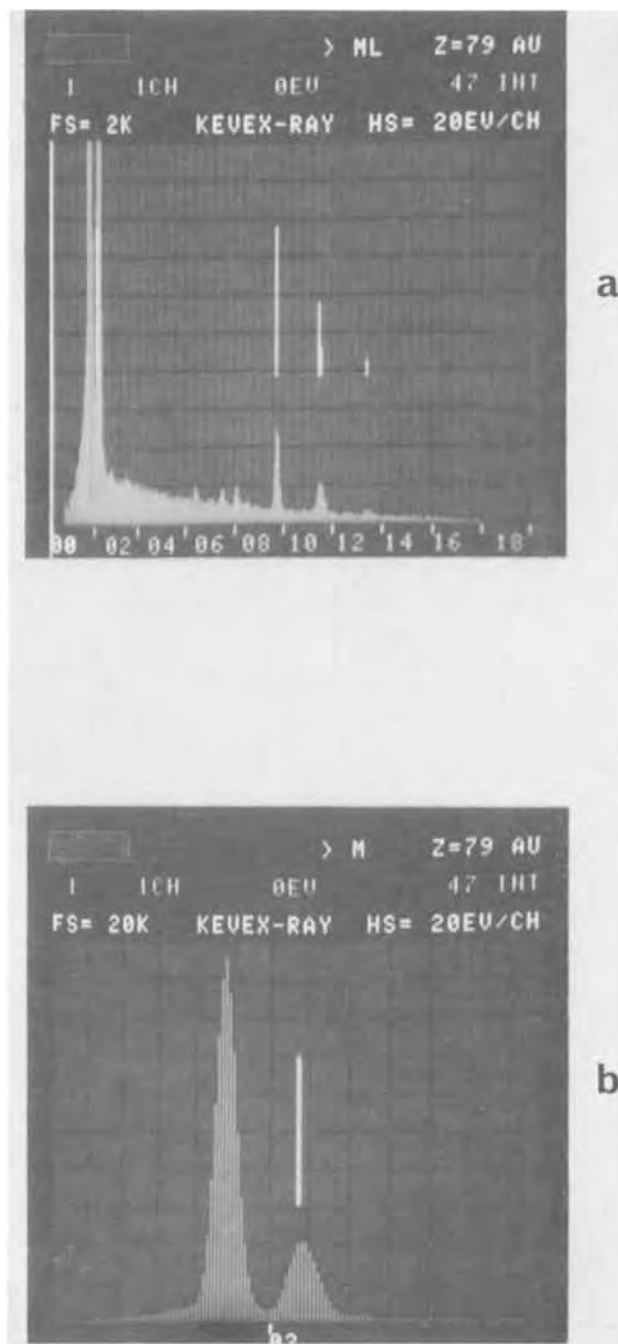


Fig. 16. X-ray spectrum given by island (a) general spectrum showing M and L Au peaks, (b) expanded spectrum showing Au peak at 2.14 keV for comparison with matrix Si peak at 1.74 keV.

Publication costs of this article were partially assisted by Bell Laboratories.

APPENDIX

The equilibrium solubilities for Cu and Au in silicon have been calculated for high temperatures (900°-1100°C) and heavy dopings (10^{19} - $10^{21}/\text{cm}^3$). For strongly n-type material a large solubility enhancement is calculated (about 10^3 times the intrinsic solubility) due to ion pairing of substitutional metal acceptors with substitutional donors. The equilibrium pairing is described by

$$MD = K_{\text{pair}} M^s D^+ \quad [\text{A-1}]$$

where MD is the metal-donor pair density, M^s is the substitutional concentration of the metal in the presence of donors, D^+ is the ionized donor concentration. M^s is given by $M^s = M_i^s \gamma_e n / n_i$ where M_i^s is for the undoped-intrinsic case, γ_e is the activity coefficient depending on doping degeneracy, n the free electron concentration, and n_i the intrinsic electron concentration.

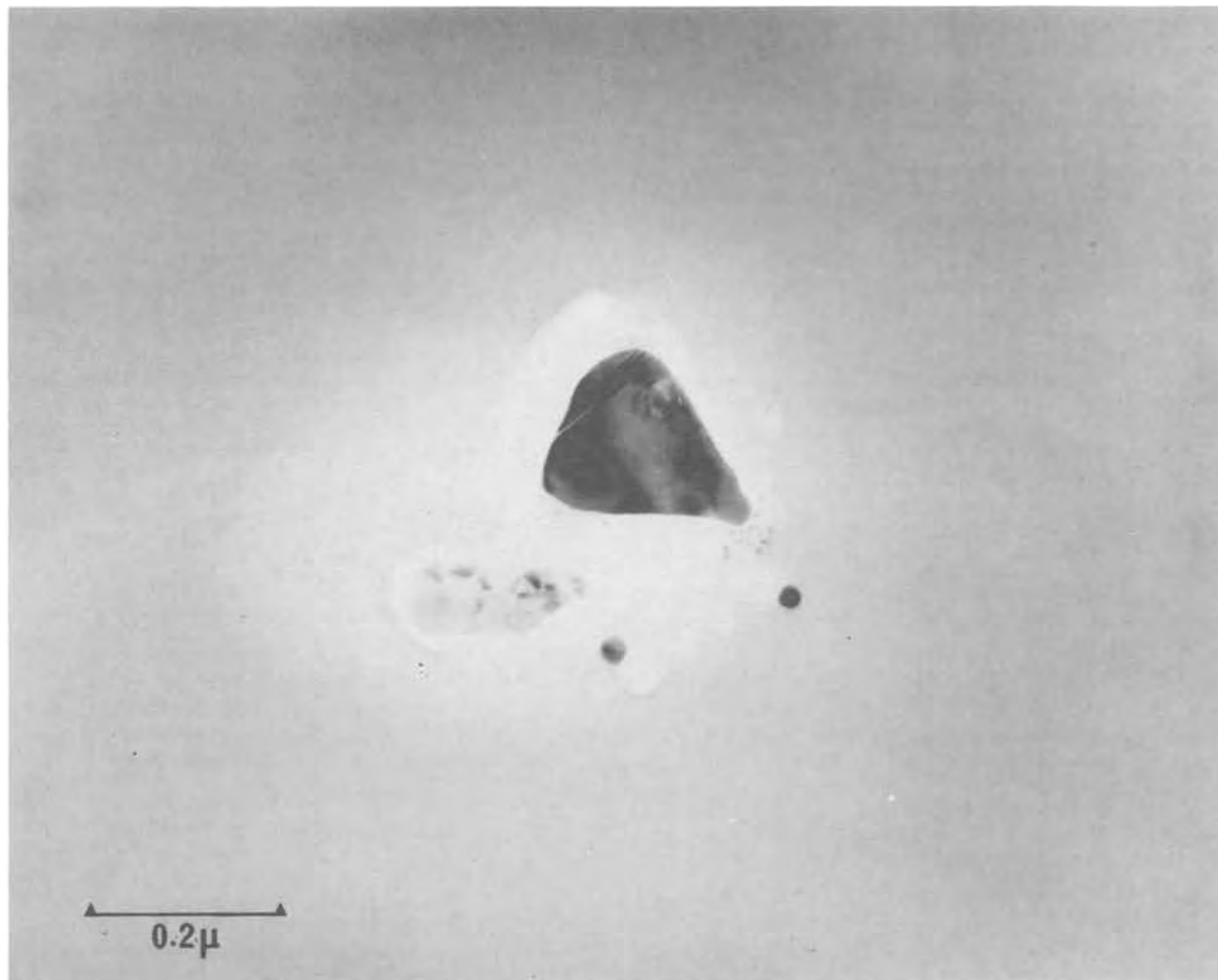


Fig. 17. Transmission electron micrograph (bright-field) showing geometrically shaped precipitate island situated in matrix surface depression.

The pairing constant is estimated from Coulomb considerations (25, 26)

$$K_{\text{pair}} = (Z/N) \exp(nq^2/\epsilon akT) \quad [A-2]$$

where (Z/N) is the ratio of nearest neighbor sites to the atom lattice site density and n is the charge on the substitutional metal atom, ϵ is the bulk dielectric constant, and a is the nearest neighbor distance of the pair. Typically the coulomb energy is 0.4 eV ($n = 1$) so for multiply charged acceptors like Cu ($n = 3$) the coulomb energy is ~ 1.2 eV and the pairing constant is $\sim 10^4$ more than for Au with phosphorus donors. Hence the pairing model predicts that the gettering is more thermally stable for Cu than for Au.

When considering the pairing probability for interstitial donors (metal) and substitutional acceptors such as boron, the influence of the changed vibrational frequencies and configurational possibilities on entropy must be taken into account. The effect is to decrease the pairing constant. This argument has been used to explain the relatively weak solubility enhancement of metal donors under boron diffused layers.

REFERENCES

1. T. E. Seidel and R. L. Meek, in "Ion Implantation in Semiconductors and Other Materials," B. L. Crowder, Editor, pp. 305-316, Plenum Press, New York (1973).
2. R. L. Meek and T. E. Seidel, *J. Phys. Chem. Solids*, To be published (1975). See the Appendix for a summary.
3. T. E. Seidel, R. L. Meek, and A. G. Cullis, *J. Appl. Phys.*, **46**, 600 (1975).
4. A. Goetzberger and W. Shockley, *ibid.*, **31**, 1821 (1960).
5. J. L. Lambert and M. Reese, *Solid-State Electron.*, **11**, 1055 (1968).
6. V. Vakamura, T. Kato, and N. Oi, *Jap. J. Appl. Phys.*, **7**, 512 (1968).
7. R. L. Meek and C. F. Gibbon, *This Journal*, **121**, 444 (1974).
8. R. N. Hall and J. H. Racette, *J. Appl. Phys.*, **34**, 379 (1964).
9. W. M. Bullis and J. R. Streiter, *ibid.*, **39**, 314 (1964).
10. S. Dash and M. L. Joshi, "Silicon Device Processing," Nat. Bur. Std. Special Publication 337, C. P. Marsden, Editor, p. 202 (1970).
11. M. R. Poponiak, W. A. Keenan, and R. D. Schwenker, in "Semiconductor Silicon/1973," H. R. Huff and R. R. Burgess, Editors, p. 701 The Electrochemical Society Softbound Symposium Series, Princeton, N. J. (1973).
12. M. A. Nicolet, J. W. Mayer, and I. V. Mitchell, *Science*, **177**, 841 (1972).
13. W. K. Chu, J. W. Mayer, M. A. Nicolet, T. M. Buck, G. Amsel, and F. Eisen, *Thin Solid Films*, **17**, 1 (1973).
14. R. L. Meek, T. M. Buck, and C. F. Gibbon, *This Journal*, **120**, 1241 (1973).
15. T. M. Buck, K. A. Pickar, J. M. Poate, and C. M. Hsieh, *Appl. Phys. Letters*, **21**, 485 (1972).
16. E. D. Wolley and R. Stickler, *This Journal*, **114**, 1287 (1967).
17. J. M. North and W. M. Gibson, *Appl. Phys. Letters*, **16**, 126 (1970).
18. A. G. Cullis, 32nd Ann. Proc. Electron Microscopy Soc. Amer., St. Louis, Missouri, 1974, C. J. Arceneaux, Editor, p. 496.
19. T. A. O'Shaughnessy, H. D. Barber, D. L. Thompson, and E. L. Heasell, in "Semiconductor Silicon/1973," H. R. Huff and R. S. Burgess, Editors, p.

- 683, The Electrochemical Society Softbound Symposium Series, Princeton, N. J. (1973).
20. S. Dash, in "Semiconductor Silicon/1973," H. R. Huff and R. R. Burgess, Editors, p. 626, The Electrochemical Society Softbound Symposium Series, Princeton, N. J. (1973).
21. E. L. MacKenna, Abstract 216, p. 531, The Electrochemical Society Extended Abstracts, Fall Meeting, New York, New York, Oct. 13-17, 1974.
22. H. Reiss, C. S. Fuller, and F. J. Morin, *Bell Syst. Tech. J.*, **35**, 535 (1956).
23. S. M. Hu and T. H. Yeh, *J. Appl. Phys.*, **40**, 4615 (1969).
24. F. A. Trumbore, *Bell Syst. Tech. J.*, **39**, 205 (1960).
25. A. B. Lidiard, *Phys. Rev.*, **94**, 29 (1954).
26. J. D. Wiley, *J. Phys. Chem. Solids*, **32**, 2053 (1971).

Rotating Scan for Ion Implantation

G. I. Robertson

Western Electric Company, Engineering Research Center, Princeton, New Jersey 08540

ABSTRACT

With the development of 1-2 mA beam current ion sources, production implantation systems became limited by scanning techniques. In particular, high beam currents could not be used efficiently for low and moderate dose implants. To overcome this deficiency, a multiwafer rotating mechanical scan technique was developed. Combining the high speed advantage of low current electrical scan and the high current capability of mechanical scan, the rotating scan technique can achieve implantation times of less than 1 sec per 2 in. wafer at full beam current with better than 99% uniformity.

The rotating mechanical scan described in this paper is a mechanism that permits the implant time of high current ion implantation machines to be reduced by up to two orders of magnitude. Although ion sources can produce over 1 mA of analyzed beam, the scanning system often limits the usable current, especially for low or medium dose implants. A production implantation system must make full use of the available beam current: a reduced beam current directly affects the throughput of the system, thereby increasing the cost of the implant. Rotating mechanical scan enables a wide range of ion doses to be implanted using the full available beam current.

The two principal methods of uniformly implanting an ion beam into a wafer are electrical scanning of the beam and mechanical scanning of the wafer through the beam. Electrical scanning has been in general use since the start of ion implantation technology as it is simple and effective. However, with the advent of analyzed beam currents of 1-2 mA, space charge spreading in the drift space between the deflection plates and target increase the beam to unacceptable dimensions. The beam diameter must be kept small to avoid large overscan losses, and this limits the usable current to a few hundred microamperes. Mechanical scanning techniques overcome this disadvantage. Since the beam is stationary, a shorter machine is possible, minimizing space charge effects at high currents. Moreover, there are additional advantages to mechanical scanning. By moving the wafer parallel to its surface, the angle of the beam with respect to the crystal-line lattice remains constant, so there is no channeling nonuniformity across the wafer. Also, neutralized particles are scanned with ions, thus avoiding a hot spot, but instead causing a small dose measuring error. Finally, mechanical scan is conducive to batch implantation and the number of wafers handled in one batch is limited only by the mechanical requirements of the target chamber.

Conventional X-Y mechanical scanning systems suffer from one disadvantage which has outweighed all their advantages in most cases; they are slow. To achieve the required uniformity of implant, many overlapping scans must be made. Taking the Harwell-Lintott X-Y mechanical scan as an example, the minimum time required to implant at 1% uniformity is about 1 min per wafer (1). The X-Y mechanical scan is thus only efficient when the implant time is 1 min

or more per wafer: that is, at high doses or low beam currents. In other cases the system is scan limited.

There have been several attempts to combine electrical and mechanical scans into a system in which the fast axis is scanned electrically and the slow axis mechanically (2). This technique permits large batches to be implanted and improves the throughput over a purely electrical scan system. The principle disadvantage of electrical scan remains however, so hybrid scan is classified with electrical scan for the purpose of this paper.

Considering the relative limitations of the two types of scan, it is apparent that the single advantage of electrical scan is the ability to scan the beam rapidly. This is not possible in the case of X-Y mechanical scanning because of inertia.

The rotating mechanical scan described in this paper is not limited by inertia, so rapid scanning is possible. The uniformity limited minimum implant time is about 1 sec per wafer, depending on dose, and high beam currents may be used. The rapid throughput of rotating scan makes it a suitable technique for high capacity production line machines.

Concept of Rotating Scan

The wafers to be implanted are mounted on a disk which is rotated about an axis parallel to the ion beam at approximately 1000 rpm, providing the first direction, or rapid scan. Typically the disk is 50 cm diameter, and holds 50-60 wafers. The disk is slightly dished, which holds the wafers in position centrifugally thereby avoiding hold-down clips. The second direction of scan is provided by translating the entire rotating disk back and forth in the plane of the disk and perpendicular to the beam as is depicted in Fig. 1. The speed of the fast scan is about two orders of magnitude higher than is possible with an X-Y mechanical scan, so the minimum implant time is similarly reduced.

The dose uniformity is controlled only by the lateral translation velocity of the disk. This velocity must vary inversely with the radial position of the beam on the disk, and directly with the beam current, as is shown below.

Comparison of Rotary and X-Y Scans

The uniformity of a mechanical scan system is determined largely by the step size y of the slow speed scan. If the beam is assumed to have a pillbox intensity profile for the present purpose, and its width in the direction of the slow scan is a , then the uniformity

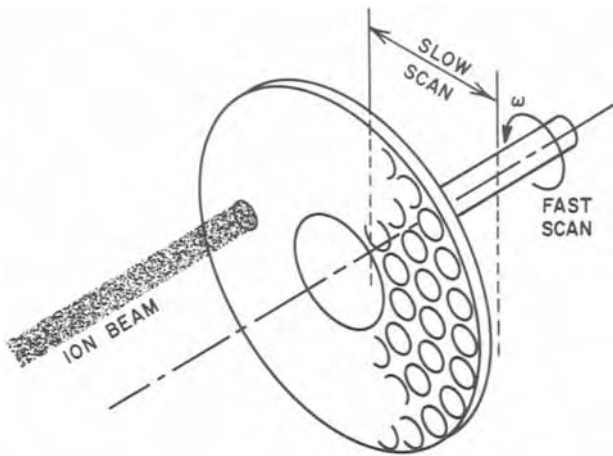


Fig. 1. Fast and slow scan motions of the rotating scan target

may be written as

$$\pm \frac{\Delta D}{D} = \frac{y}{2na} \quad [1]$$

where D represents the dose, y is the increment in the slow scan direction, and n is the number of passes made for one implant. This is a crude representation of the uniformity and assumes the worst case when the beam is extinguished during a constant speed scan. In practice, the speed of the scan may be made dependent on the beam current as will be shown later, but Eq. [1] is suitable for the present comparison.

The maximum speed at which the slow scan may be incremented is determined by the time taken for a fast scan. The minimum time for a complete pass of the wafer holder is then

$$t_{\min} = \frac{Y}{y} \cdot \frac{X}{V_x} \quad [2]$$

where X and Y are the dimensions of the plate in the fast and slow scan directions respectively, and V_x is the maximum x -velocity. Combining [1] and [2] gives

$$t_{\min} = \frac{XY}{V_x \cdot 2na \frac{\Delta D}{D}} \quad [3]$$

If there are N wafers on the holder the minimum implant time per wafer t'_{\min} is

$$t'_{\min} = \frac{XY}{V_x \cdot 2na \frac{\Delta D}{D} N} \quad [4]$$

But since N is roughly proportional to the wafer holder area XY

$$t'_{\min} \propto \frac{1}{V_x} \quad [5]$$

for a given uniformity.

If the velocity limited implantation time for a required uniformity occurs at a high beam current and dose, then the only way to achieve lower doses is to lower the beam current.

In Fig. 2 the relationship between dose, implantation time, and beam current is plotted. The diagonal lines are lines of constant scanned beam current, and are common to all scanning methods. For reference, the maximum practical beam current for electrical scanning is shown as the solid diagonal line at $200 \mu\text{A}$. This limit is appropriate for present day implantation equipment.

The Harwell-Lintott system is again taken as the example of a typical X-Y scan. For a $\pm 1\%$ uniformity using a beam 1 in. high, the minimum implant time is 50 sec/2 in. wafer. This is shown as the upper solid line in Fig. 2. In contrast, for the same uniformity and

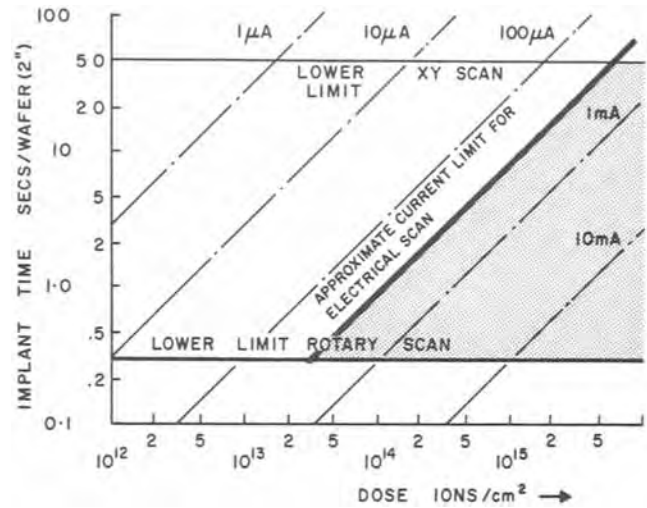


Fig. 2. Implant time for 1% uniformity as a function of ion dose. The limits for the three scan methods are shown.

beam size, the minimum implant time for a rotating scan of the type described is 0.3 sec/2 in. wafer, due solely to the increased velocity V_x of the fast scan (Eq. [5]). This limit is shown as the lower solid line in Fig. 2. The shaded area enclosed by these three solid lines is that region particularly suited to rotating mechanical scan. It can be seen that it includes doses of $2 \cdot 10^{13}$ ions/cm² and over, using ion beams of $200 \mu\text{A}$ and over.

The principal benefit of rotating scan over X-Y mechanical scan is the ability to use high beam currents efficiently for low or moderate dose implants, as well as for high dose implants. There are two other benefits of lesser importance. Firstly, the current loss due to overscan is reduced. The ion beam should be overscanned by at least one radius in each direction to assure edge uniformity. In the case of a typical X-Y scan, the loss is approximately 15%. With rotating scan, overscan occurs only in the radial direction and many more wafers are implanted in each batch, so a typical overscan loss is 5%. Secondly, the average power applied to each wafer by the ion beam is reduced because of the increased batch size. Present machines are capable of beam currents of up to 1 mA at 300 kV acceleration, which represents a beam power of 300W. The instantaneous heating of the surface of the wafer is a complex subject (3), but to first order it is a function of the number of wafers in each batch. To dissipate 300W, the six wafers of the Harwell-Lintott X-Y scan must dissipate an average of 50W each, whereas the 60 wafers on a rotating scan disk need dissipate only 5W each. In this context it should be noted that a pure electrical scanning system cannot put 300W into a single wafer for more than 1 sec or so, although the AI hybrid scan (2) can absorb this power.

Dose Uniformity

The circumferential uniformity of the implanted dose is guaranteed if the rotation of the disk is sufficiently rapid to average out all the beam fluctuations. The possibility of stroboscopic effects can be avoided by rotating the disk at a speed not synchronous with harmonics of the line frequency. Radial uniformity, however, requires a precise control of the radial velocity which must vary as a function of disk position and beam current. The theoretical translational velocity is derived below, first for a small dimension ion beam and then for the general case.

Initially it is assumed that the beam has a small, rectangular cross section $L_1 \times L_2$ as shown in Fig. 3. The center of the disk is R from the beam, and the disk is translating at a velocity $V(t, R)$. The current density of the beam is $j(t)$, so the average current density seen by the annulus that passes through the beam is

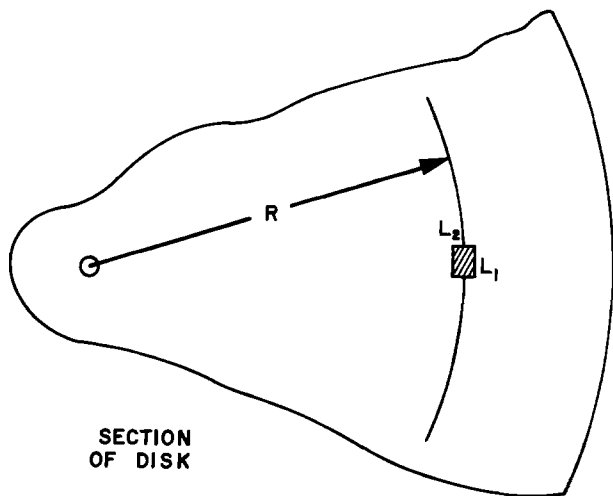


Fig. 3. Section of the target disk showing the small ion beam approximation.

$$\frac{j(t)L_1}{2\pi R} \tag{6}$$

The average current density is received on this annulus for a time $L_2/V(t, R)$ before it has passed through the beam, so the total ion dose D at a point R from the disk center is

$$D = \frac{L_1 L_2 j(t)}{2\pi R q V(t, R)} \tag{7}$$

where q is the ion charge. But $L_1 L_2 \cdot j(t)$ is the total beam current $I(t)$. Therefore the dose is

$$D = \frac{I(t)}{2\pi R q V(t, R)} \tag{8}$$

and to achieve a uniform dose over the target disk, the velocity $V(t, R)$ must be

$$V(t, R) = \frac{1}{2\pi D q} \cdot \frac{I(t)}{R} \tag{9}$$

Now consider the case shown in Fig. 4. An ion beam with irregular current distribution is shown divided into n annuli of constant width δr . The total current in each annulus is $I_1, I_2, \dots, I_n, (t)$. An arc passes through the current weighted average of the ion beam, at radius R from the center of the disk, such that the distance to each annulus of the ion beam is d_1, d_2, \dots, d_n , and

$$\sum_{j=1}^n I_j(t) d_j = 0.$$

To determine the total dose implanted, consider the annulus on the disk, at radius R_a , which is just about to enter the ion beam. Assuming that it spends times $\delta t_1, \delta t_2, \dots, \delta t_n$ in each section of the ion beam, the total dose received by the annulus will be

$$D_a = \frac{1}{q 2\pi R_a \delta r} \sum_{j=1}^n I_j(t) \delta t_j \tag{10}$$

We now show that the same translation velocity derived for the small beam case in Eq. [9] will make D_a constant, independent of the radius R_a . From Eq. [9]

$$V(t, R) = \frac{\delta r}{\delta t_j} = \frac{1}{2\pi D q} \cdot \frac{I(t)}{R} \tag{11}$$

But

$$R = R_a + d_j$$

so

$$\delta t_j = \frac{q 2\pi D (R_a + d_j) \delta r}{I(t)}$$

Combining with [10]

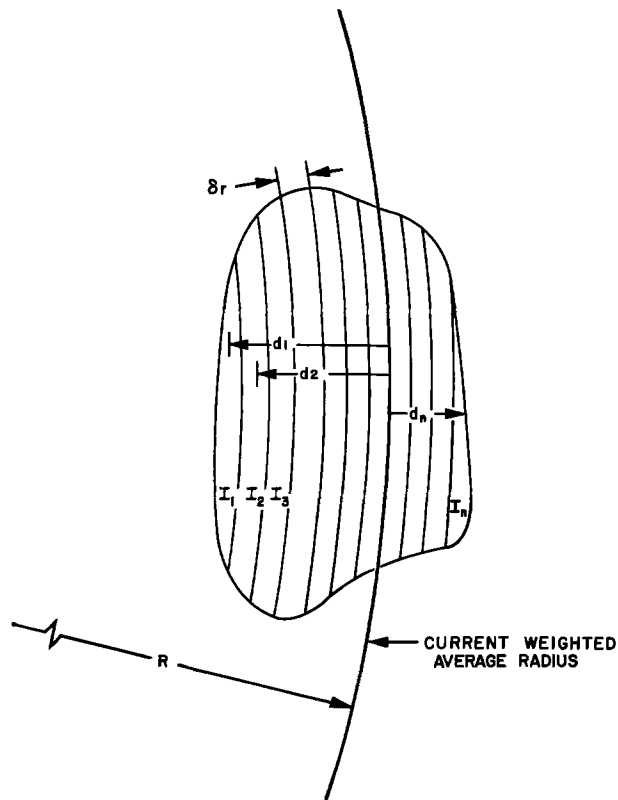


Fig. 4. Diagram of large ion beam divided into n sections

$$D_a = \frac{D}{I(t) R_a} \sum_{j=1}^n I_j(t) (R_a + d_j)$$

or

$$D_a = \frac{D}{I(t)} \sum_{j=1}^n I_j(t) \left(1 + \frac{d_j}{R_a} \right)$$

$$D_a = D \left[1 + \frac{I}{R_a I(t)} \sum_{j=1}^n I_j d_j \right] \tag{12}$$

But by definition $\sum_{j=1}^n I_j d_j = 0$, so $D_a = D = \text{constant}$.

Thus a finite size beam may be treated as a small beam if its effective radius R is the radius to the weighted current average point.

The above derivation neglects the changing curvature of the annuli, and breaks down if the beam is comparable in size with its radial position R . However, for all reasonable beam sizes and radii, the results are accurate to better than 0.5%.

Control Methods

Equation [9] shows that the lateral translation velocity of the disk should be an inverse function of the distance R between the disk center and beam, and a direct function of the beam current I . The ion dose will then be uniform across the disk. Unfortunately it is not easy to generate an exact drive velocity, and any errors will be accumulated. A more suitable form of the control equation can be derived.

From Eq. [9], V and I may be rewritten

$$\frac{dR}{dt} = \frac{1}{2\pi D q} \frac{dQ}{R} \tag{13}$$

Integrating

$$Q = \pi D q R^2 + C \tag{14}$$

where Q is the total charge received since some time t_0 . The constant of integration is found by assuming that $Q = 0$ when the beam is at the starting radius R_0 .

Equation [14] is now in a more suitable form for control. The total charge received may conveniently be measured by a current integrator, and the value of R can be found either by using a linear potentiometer attached to the disk carriage, or by counting the steps of a digital stepping motor. Of course, Eq. [14] refers only to a single pass of the disk through the beam. While it is possible to obtain the correct dose in this manner, it is preferable to make several more rapid passes. Travel in the reverse direction is readily accomplished by treating each unit of charge as a negative quantity, instead of a positive quantity.

The control system may be either analog or digital. Each has advantages, and the principles of each are outlined below. In general analog control is simpler to construct, but it is not as flexible as digital control.

Figure 5 shows a block diagram of an analog control system. The ion current is measured by a current integrator, which generates a pulse every time a certain charge is accumulated. The pulses are summed in a counter, which is connected to a d/a converter (dac). The voltage output from the dac is then a measure of the accumulated charge. The required dose per sweep is set on the potentiometer at the output of the dac, and in turn is connected to one input of the servo amplifier.

The second input to the servo amplifier is taken from a precision square-law potentiometer attached to the disk carriage. The servo motor drives the carriage and satisfies Eq. [14] by keeping the two amplifier inputs balanced.

When the limits of the scan are reached, a micro-switch triggers a bistable latch. The latch is connected to the count-up/count-down input of the counter, and causes it to change the direction of its count on receipt of each integrator pulse. In this manner, the incoming current causes an increase in the dac output if the motor is to move forward, and a reduction in the dac output if the motor is to move in reverse. The limit switch at one end of the scan also increments a second counter which terminates the implant when the correct number of scans has been completed.

This type of analog control is easy and relatively cheap to construct. Its main disadvantage lies in its accuracy, which is affected by two potentiometers and one digital to analog converter. It is suitable for dose reproducibilities of approximately 2%.

A higher degree of precision may be obtained at the expense of increased complexity by using digital control. The ion beam current is measured using a current

integrator as before, but the disk translation is by a stepping, rather than a servo motor. A stepping motor eliminates the requirement for a feedback potentiometer, since the position of the carriage is known at all times by counting the stepping motor pulses. A small computer is programmed to solve Eq. [14] in real time as the integrator pulses are received. A disadvantage of using a stepping motor is that it must either be run slowly, or provision must be made to accelerate and decelerate it at the ends of each sweep.

A significant advantage of a digital system is that the control computer may be used to perform many peripheral tasks. Prior to the implant, the various parameters that determine the dose may be calculated. Printers may be used to provide a log of all implants, and the system can be made self-monitoring to some degree. In a complex system like a high energy implantation machine, there are sequences of events to be followed, and emergency conditions to be recognized and acted upon. All of these are easily implemented once there is a small computer on line.

Conclusion

A rotating mechanical scan is particularly suited to production line equipment, since it combines the high speed of electrical scan with a high current handling capacity. Uniformity limited minimum implant times are about 1 sec per wafer at 1% uniformity.

The prototype system uses digital control with a small computer controlling the implant, although an analog system could also be used. Sixty wafers may be implanted in 1 or 2 min, excluding pumpdown time, so currents as high as 1 mA may be used to implant doses of 1×10^{15} ions/cm².

Figure 6 is a histogram of the dose nonuniformity within each batch of 60 wafers, measured using the van der Pauw technique. Each point in the histogram represents the mean dose on one wafer, and the percent dose deviations have been calculated relative to the average dose of all wafers implanted during a run. The uniformity across the target disk is better than 0.9% (1σ). When different runs are included the absolute dose accuracy and batch to batch reproducibility together are measured as 1.5% (1σ).

Manuscript submitted May 16, 1974; revised manuscript received Feb. 5, 1975. This was Paper 223 presented at the San Francisco, California, Meeting of the Society, May 12-17, 1974.

Any discussion of this paper will appear in a Discussion Section to be published in the December 1975

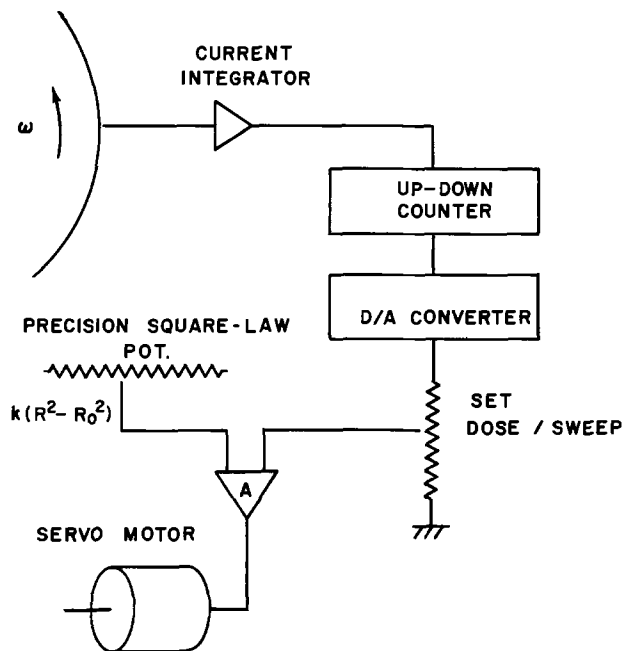


Fig. 5. Simple circuit block diagram suitable for analog control of rotating scan.

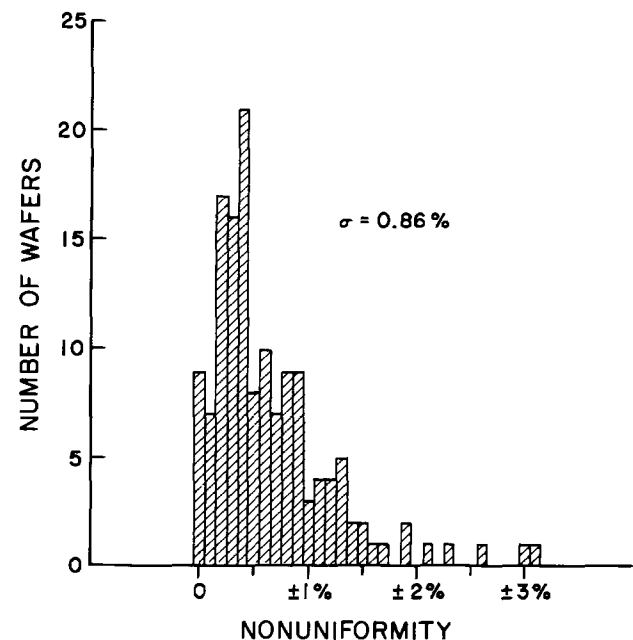


Fig. 6. Percentage nonuniformity of wafers within a batch, referred to the batch mean.

JOURNAL. All discussions for the December 1975 Discussion Section should be submitted by Aug. 1, 1975.

Publication costs of this article were partially assisted by Western Electric Company.

LIST OF SYMBOLS

a	width of pill-box ion beam
D	ion dose ions/cm ²
d	distance from beam center to beam element, cm
I	ion beam current, A
j	ion beam current density, A/cm ²
L_1, L_2	dimensions of small ion beam, cm
n	number of passes made per implant
N	number of wafers implanted together
q	ion charge, cb
Q	total charge received since time 0, cb

R	radius between ion beam and disk center, cm
t	time required for implant, sec
V	scanning velocity, cm/sec
X	dimension of scan, cm
y	scanning increment in the slow direction, cm
Y	dimension of scan, cm

REFERENCES

1. J. H. Freeman, L. R. Caldecort, K. C. W. Done, and R. J. Francis, "An Industrial Scale Ion Implantation Facility," AERE-R6496, 1970, Harwell, England.
2. Accelerators Inc., Austin, Texas.
3. P. D. Parry and R. Leiby, "Silicon Water Heating During Ion Implantation," 1973 IEEE International Electron Devices Meeting in Washington, D.C., December 5, 1973.

Boron Diffusion in Silicon-Concentration and Orientation Dependence, Background Effects, and Profile Estimation

Richard B. Fair*

Bell Laboratories, Reading, Pennsylvania 19603

ABSTRACT

Boron is almost universally used as a p-type dopant in Si devices. Since this dopant is introduced into the Si lattice under a wide range of diffusion conditions, effects are often observed which appear anomalous because the mechanism of B diffusion is not completely understood. Anomalous effects that have been observed include a concentration-dependent diffusion coefficient, orientation-dependent diffusion under oxidizing conditions, and retarded or accelerated diffusion in the presence of n-type impurities. This paper discusses a model of B diffusion which can be used to explain these observed effects. Data and arguments are presented which show that B diffuses via a monovacancy mechanism when the diffusion is performed in a non-oxidizing ambient. A donor-type vacancy is responsible which has a presumed energy level of $\sim E_v + 0.37$ eV as suggested from the quenching experiments of Elstner and Kamprath. High concentration ($>2 \times 10^{19}$ cm⁻³) B diffusions into Si over a 550°C temperature range in neutral ambients result in profile data that fit a normalized universal curve which is a polynomial approximation to the solution of the diffusion equation with concentration-dependent diffusivity. From this result, useful curves of surface concentration vs. resistivity and junction depth are presented.

For high concentration ($>10^{19}$ cm⁻³) single component diffusions of Group III and V dopants in silicon (Si) it is known that simple complementary error functions and gaussian functions do not correctly describe the resulting diffusion profiles. At lower concentrations ($<10^{19}$ cm⁻³) the diffusivity is essentially constant, and these simplified analytical expressions can be used. However, at high doping densities or when multiple component diffusions are performed, the diffusion coefficients of these elements in Si exhibit a dependence on the local concentrations of the diffusing species. For the case of boron (B) in Si it has been suggested that the cause of this dependence is either related to plastic deformation and degeneracy of the highly doped Si (1, 2) or to interactions of the B⁻ ions with positively charged defects (3-6). It is the purpose of this paper to present data and arguments which give support to the model that B generally diffuses by interacting with donor-type monovacancies with an electronic energy level at $\sim E_v + 0.37$ eV. Support for the existence of this level comes from the quenching experiments of Elstner and Kamprath (7) and the thermodynamic arguments of Van Vechten and Thurmond (8). It will be shown that

this model predicts the linear dependence of B diffusivity on B concentration, and also explains why the diffusion of B is retarded in a heavily As-doped substrate.

In the first section, data will be presented which describe the concentration-dependence of B diffusivity and the general shape of high concentration B diffusion profiles in Si when diffusions are performed in nonoxidizing ambients. Then it will be shown that the profile data fit a normalized universal curve which is not an exact solution to the diffusion equation. However, an approximate result is used to generate useful curves of surface concentration vs. resistivity and junction depth. Following a discussion of the monovacancy diffusion model for B, the diffusion of B in an oxidizing ambient will be discussed.

Experimental Results

Concentration-dependent diffusivity.—In order to obtain information on the concentration-dependence of B diffusivity, Boltzmann-Matano analysis was performed on several B diffusion profiles obtained by Tsai(9) using the differential conductivity method. Tsai's data, which represent BN disk and B₂O₃ box source diffusions into (111) oriented Si in N₂ ambients, were combined with previously reported results (10, 11), and are shown plotted in Fig. 1a and b. In Fig.

* Electrochemical Society Active Member.
Key words: ion implantation, vacancies, cooperative diffusion.

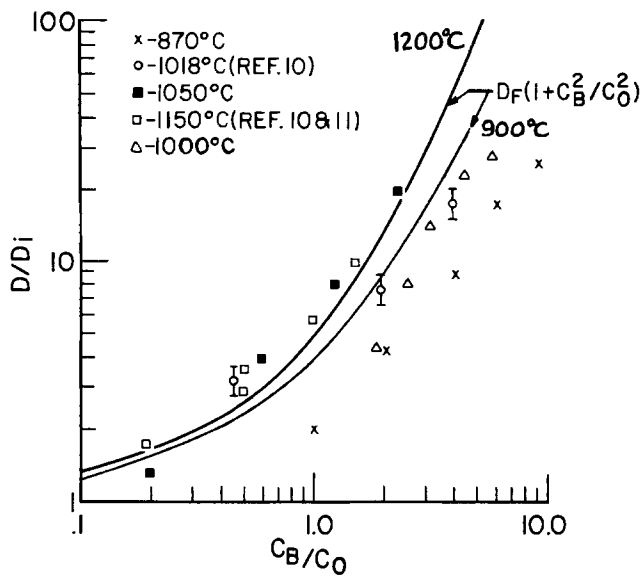


Fig. 1a. Normalized B diffusivity vs. B concentration normalized to Thai's "anomalous diffusion" parameter (1, 2, 11).

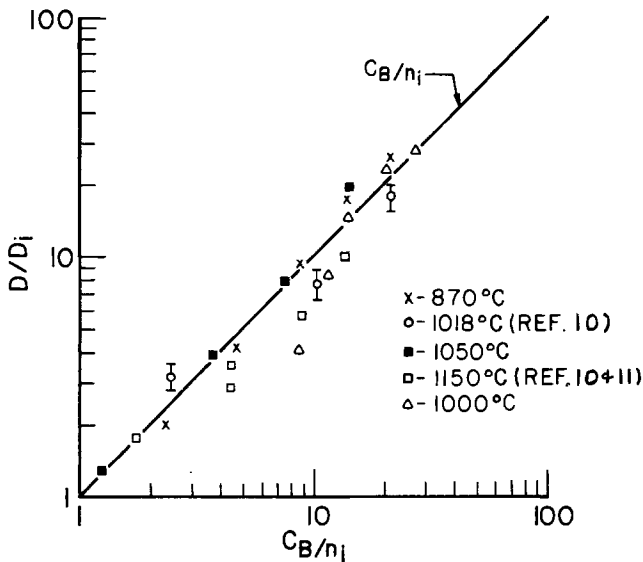


Fig. 1b. Normalized B diffusivity vs. B concentration normalized to the intrinsic electron concentration at the diffusion temperature.

1a normalized diffusivity is plotted vs. normalized B concentration, where D_i is the intrinsic diffusivity and C_0 is Thai's characteristic concentration parameter (1, 2) which gives the solute density necessary to cause anomalous diffusion to occur. The C_0 values used are those corrected values reported by Jain and Van Overstraeten (11), and it is assumed that $p \approx C_B$, where C_B is the B concentration.

It can be seen that for diffusions performed at temperatures greater than $\sim 1050^\circ\text{C}$, the data approximately agree with Thai's theoretical curve which is the equation

$$D = D_F(1 + (C_B/C_0)^2) \quad [1]$$

where D_F is a factor that carries the effects of electric-field enhancement and degeneracy. Since Eq. [1] cannot be completely normalized with respect to temperature, two curves are shown, one for 1200° and one for 900°C .

The data obtained from lower temperature diffusion profiles do not agree with Thai's theory. In Fig. 1b these same data are plotted with C_B normalized to n_i (intrinsic electron concentration at the diffusion temperatures). Heavy doping effects on n_i are neglected

here, but may be important for large values of C_{SB} . Values of n_i used in Fig. 1b are shown in Fig. 2 along with the D_i vs. temperature curve. From Fig. 1b it can be seen that the diffusion data are approximately described by the equation

$$\frac{D}{D_i} = \frac{C_B}{n_i} \quad [2]$$

over the entire temperature range studied. This result agrees with previous observations (3).

Profile shape.—In Fig. 3, B concentration profiles normalized with respect to surface concentration, C_{SB} , and junction depth, x_j , are plotted. All of the diffusions, which had $C_{SB} > 2 \times 10^{19} \text{ cm}^{-3}$, were performed in nonoxidizing ambients, and the junction depth was measured at $\sim 0.01 C_{SB}$ (typically $\sim 10^{18} \text{ cm}^{-3}$). Also shown are the erfc curve and two curves of the general form

$$\frac{C_B}{C_{SB}} = 1 - Y^n, \quad 0 \leq Y \leq 1 \quad [3]$$

where

$$Y = Y(x, t, T) \quad [4]$$

The polynomial approximation to the solution of the diffusion equation that describes the arsenic profile shape in Si^{12} is also shown. It can be seen that over a 550°C temperature range the high concentration profile data follow neither the erfc curve nor the As profile curve. However, the profile data do follow approximately a universal curve of the form

$$\frac{C_B}{C_{SB}} = 1 - Y^{2/3} \quad [5]$$

In the next section the functional form of Y will be determined for the general Eq. [3] so that an expression for junction depth as a function of C_{SB} , D_i , and t can be determined for $n = 2/3$.

Analysis

Diffusion equation solution.—In order to find the functional form of Y in Eq. [3] for concentration-dependent B diffusion expressed by Eq. [2], Eq. [2] and

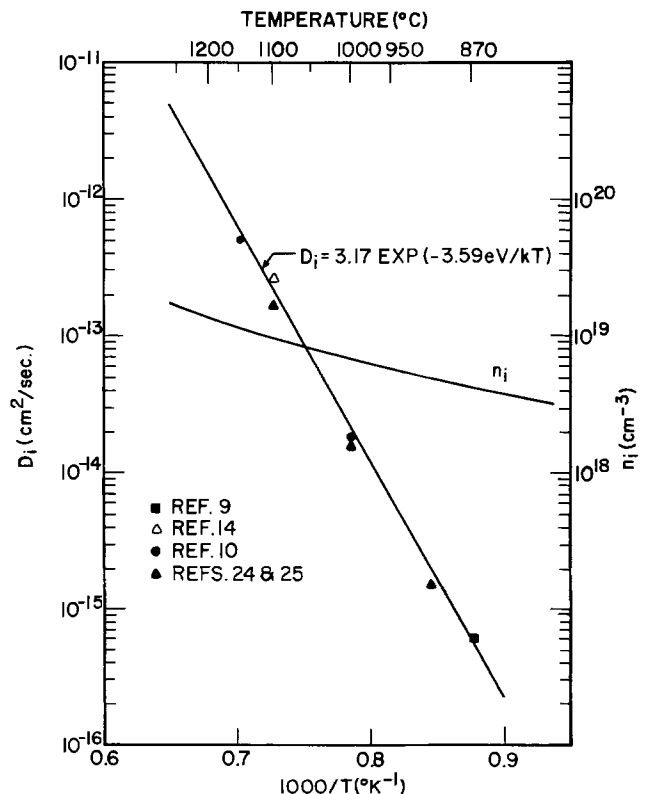


Fig. 2. Intrinsic B diffusivity, D_i and intrinsic electron concentration, n_i vs. temperature.

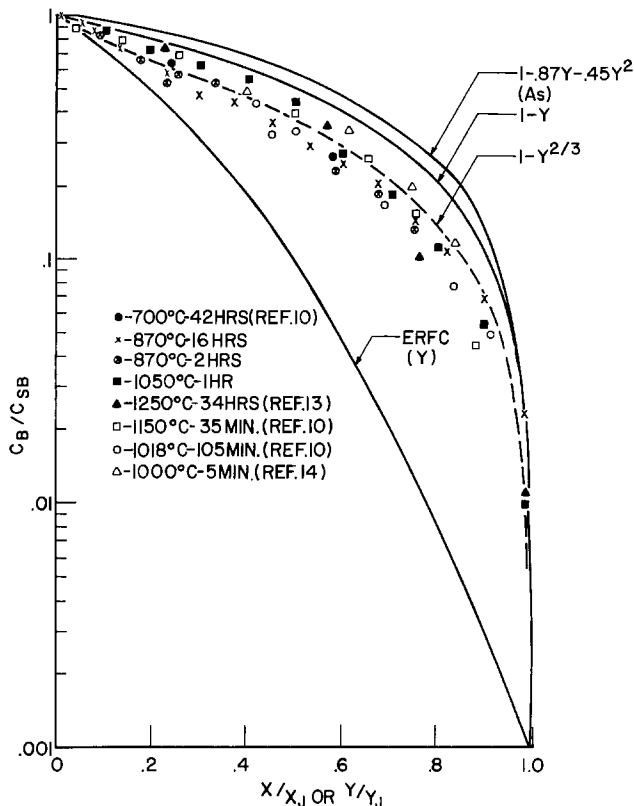


Fig. 3. B diffusion profiles normalized with surface concentration and junction depth. All data have $C_{SB} > 2 \times 10^{19} \text{ cm}^{-3}$ and x_J is taken at $C_B \approx 0.01 C_{SB}$.

[3] will be substituted into the diffusion equation given by

$$\frac{\partial C_B}{\partial t} = D_s \frac{\partial}{\partial x} \left(\frac{C_B}{C_{SB}} \frac{\partial C_B}{\partial x} \right) \quad [6]$$

where

$$D_s = \frac{C_{SB}}{n_i} D_i \quad [7]$$

Thus

$$-\frac{\partial Y}{\partial t} = D_s \left(\frac{\partial Y}{\partial x} \right)^2 Y^{-1} [Y^n(2n-1) + 1 - n] - D_s (1 - Y^n) \frac{\partial^2 Y}{\partial x^2} \quad [8]$$

Since Y is dimensionless it will have the general form (12)

$$Y = \left(\frac{x^2}{K_1 D_s t} \right)^{1/m} \quad [9]$$

where K_1 is a dimensionless constant that must be determined. Substitution of Eq. [9] into Eq. [8] yields

$$Y = \left[\frac{\frac{x^2}{2D_s t} + \left(\frac{2n-1}{m} \right)}{\frac{4n}{m} - 1} \right]^{\frac{1}{n}} \quad [10]$$

In order for Eq. [10] to have a similar functional form in x and t as Eq. [9], then $n = m$ and

$$Y = \left[\frac{x^2}{6D_s t} + \frac{1}{3} \right]^{\frac{1}{m}} \quad [11]$$

Equation [11] is not a valid form for Y since at the surface ($x = 0$), Y must equal zero according to Eq. [3]. This result indicates that the empirical Eq. [3] (or [5]) with Y defined as it is in Eq. [9] is not an

exact solution to the diffusion equation, since no functional form of Y can be derived from it that satisfies all the requirements on Y . However, near the junction as $x \rightarrow x_J$, the first term on the right hand side of Eq. [11] becomes ~ 10 times larger than the $1/3$ term, and Eq. [11] approximates Eq. [9] with $K_1 = 6$. Setting $Y = 1$, Eq. [11] becomes at the junction

$$x_J = 2.45 \left(\frac{C_{SB} D_i t}{n_i} \right)^{1/2} \quad [12]$$

or

$$\frac{x_J}{2\sqrt{D_i t}} = 1.225 \sqrt{C_{SB}/n_i} \quad [13]$$

Equation [13] is shown plotted in Fig. 4a along with data of normalized surface concentration vs. normalized junction depth. All of the data referenced on the figure were taken from measured diffusion profiles (usually obtained by the differential conductivity method), and the junction depths were taken as the distance from the surface at which C_B had fallen to $\sim 10^{18} \text{ cm}^{-3}$. Good agreement between data and the theoretical curve is obtained. These same data are shown plotted in Fig. 4b with C_{SB} normalized to $C_B = 1 \times 10^{18} \text{ cm}^{-3}$. By comparing these data with the complementary error function curve plotted in the figure, the significance of neglecting the concentration dependence of B diffusivity can be seen.

Resistivity vs. surface concentration.—The sheet resistance of a diffused layer is given by the equation

$$R_s = \frac{1}{q\bar{\mu} \int_0^{x_J} C_B dx} \quad [14]$$

where $\bar{\mu}$ is the effective bulk carrier mobility (cm^2/Vsec). For $C_B > 5 \times 10^{19} \text{ cm}^{-3}$, the hole mobility in silicon becomes approximately independent of C_B ($\mu \approx 55 \text{ cm}^2/\text{Vsec}$) (15). If it is assumed that $\bar{\mu}$ is essentially that value of μ corresponding to the doping near the surface, and if Eq. [5] is integrated to give

$$Q = \int_0^{x_J} C_B dx = 0.4 C_{SB} x_J \quad [15]$$

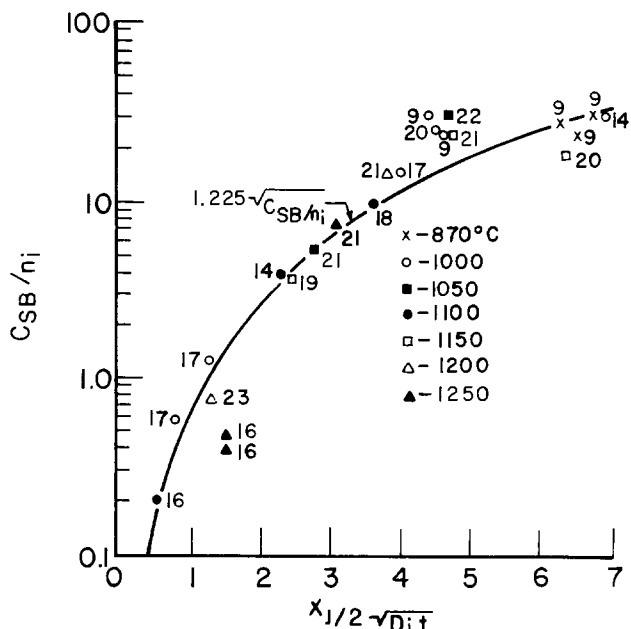


Fig. 4a. B diffusion profile surface doping normalized to n_i vs. normalized junction depth ($x_J \rightarrow C_B \approx 10^{18} \text{ cm}^{-3}$). The solid curve is Eq. [13].

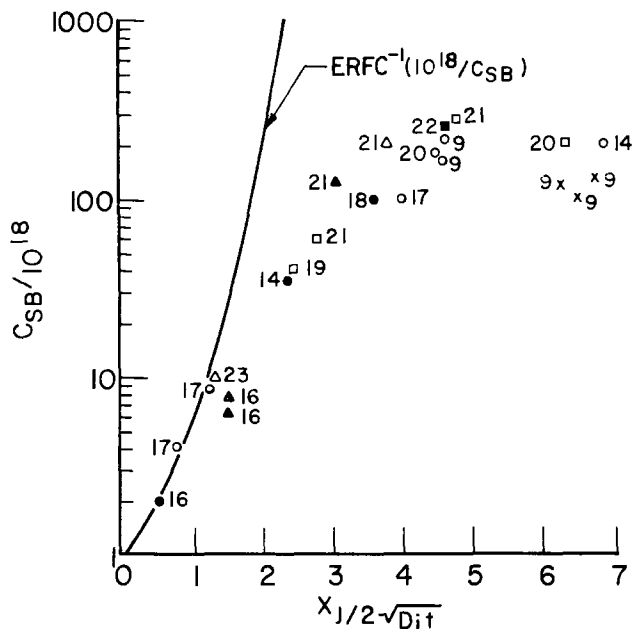


Fig. 4b. B diffusion profile surface doping normalized to $C_B = 10^{18} \text{ cm}^{-3}$. The solid curve is an erfc curve.

then Eq. [14] becomes

$$C_{SB} = \frac{2.78 \times 10^{17}}{R_S x_J} \quad [16]$$

An estimate of the accuracy of Eq. [16] can be obtained by referring to Fig. 5 where $C_{SB}(x_J, R_S)$ data are plotted along with Eq. [16]. All of the data shown fall within 20% of the theoretical curve for $C_{SB} > n_i$.

Again, x_J corresponds to the distance from the surface at which C_B falls to $\sim 10^{18} \text{ cm}^{-3}$.

Discussion

Boron diffusion model.—The linear relationship between the apparent diffusivity of boron in silicon and the boron concentration suggests several possible dif-

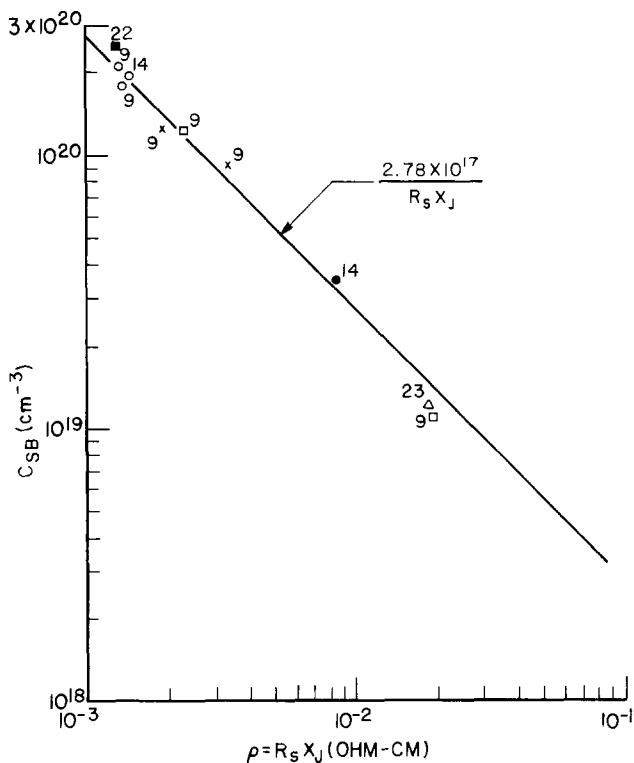


Fig. 5. B surface concentration vs. diffused layer resistivity

fusion mechanisms: the interstitialcy mechanism, the vacancy mechanism, and the divacancy mechanism. In the interstitialcy mode of diffusion, it would be necessary for Si self-interstitials to have a donor level in the lower half of the bandgap. Thus, the donor-type Si interstitial concentration would be enhanced by the Fermi-level lowering effect of the B dopant. It seems plausible that some form of the interstitialcy mode of diffusion will occur when there exists an extrinsic source of interstitial Si atoms (such as during oxidation, see later discussion). However, the donor properties of Si interstitials have not been confirmed, since it has not yet been possible to identify intrinsic interstitials definitely. Recently, Van Vechten (26) has presented experimental and theoretical arguments which show that the enthalpy of formation of the interstitial component of a Frenkel pair is $\approx 8 \text{ eV}$ in Si (as compared to 2.8 eV for the vacancy). Thus, the ratio of the concentration of interstitials to vacancies in equilibrium in Si near the melting point would be of the order of 10^{-15} or less.

With regard to the divacancy mechanism of impurity diffusion discussed by Kendall and DeVries (6), Hu (4) has pointed out that since the monovacancy concentrations are $< 10^{16} \text{ cm}^{-3}$ in Si at high temperatures, thermal equilibrium should favor the formation of monovacancies, and divacancies will dissociate rapidly after their creation. In addition, it is apparent that monovacancies rather than divacancies are involved in the extrinsically created vacancy transients described in the present cooperative diffusion theories (27, 28), since the activation energy of monovacancy migration is much lower than that of divacancies.¹

Watkins (5) discussed the coulombic interactions between positively charged monovacancies and ionized acceptor-type dopants in Si. Crowder *et al.* (3) showed that a positively charged defect model could be used to explain the diffusion results of B in Si. It is known from the experiments of Elstner and Kamprath (7) that an energy level exists at $E_v + 0.37 \text{ eV}$ associated with donor-type complexes in quenched p-type Si samples. Van Vechten (26) and Thurmond (8) have argued that these complexes will contain vacancies of the dominant charge state that existed at the temperature from which the quenching occurred. While the observed ionization spectrum of the complexes is not necessarily the same as that for the individual vacancies,² Van Vechten and Thurmond have shown that by assigning the $E_v + 0.37 \text{ eV}$ level to donor-type vacancies yields reasonable estimates of the entropy and enthalpy of vacancy formation at low temperature.

Assigning the $E_v + 0.37 \text{ eV}$ level to a V^+ vacancy means that above 800°K , V^+ is the dominant charge state of the monovacancy in p-type Si. Consequently, the hypothesis that B⁻ ions diffuse by interacting with V^+ vacancies becomes very reasonable, and will, therefore, form the basis of the B diffusion model presented here.

The ionization reaction of a neutral vacancy is given by



and the equilibrium relation is

$$K_1(T) = \frac{[V^+]}{[V^0]} n \quad [18]$$

where n is the electron concentration. Evaluating [18] under intrinsic conditions and using the electron-hole mass-action relation gives

¹ For more complete arguments against the formation of divacancies at high temperatures, see Van Vechten [Ref. (26)] and A. Seeger and K. P. Chik, *Phys. Status Solidi*, 29, 455 (1968).

² In quenching experiments it is likely that most vacancies have associated with oxygen or other impurities by the time the sample has cooled. However, the effect of association is only to shift the ionization energy of the donor level by a small amount [see H. J. Stein in "Radiation Effects in Semiconductors," J. W. Corbett and G. D. Watkins, Editors, p. 125, Gordon and Breach, London (1971)].

$$\frac{[V^+]}{[V_i^+]} = \frac{p}{n_i} \quad [19]$$

where $[V_i^+]$ is the ionized monovacancy concentration under intrinsic conditions. The diffusing B will be an ionized acceptor and will control the hole concentration, p . If the diffusivity of B in intrinsic Si is D_i and is proportional to the ionized vacancy concentration, then at high B concentrations $[V^+]$ is enhanced and the diffusivity is given by

$$\frac{D}{D_i} = \frac{p}{n_i} \quad [20]$$

which is just Eq. [2]. In a similar manner, if the $[V^+]$ concentration is decreased below $[V_i^+]$ which would occur if B were diffusing in heavily doped n-type Si, then the diffusivity would decrease accordingly. In terms of the Fermi level, E_F , and V^+ energy level, E_{v^+} , Eq. [19] can be written as

$$\frac{[V^+]}{[V_i^+]} = \frac{1 + \exp[(E_{F_i} - E_{v^+})/kT]}{1 + \exp[(E_{v^+} - E_{F_i})/kT]} \cdot \frac{1 + \exp[(E_{v^+} - E_F)/kT]}{1 + \exp[(E_F - E_{v^+})/kT]} \quad [21]$$

where spin-degeneracy factors have been neglected. Equation [21] is shown plotted in Fig. 6 as a function of the Fermi level. Also shown are values of $D/D_i = [V^+]/[V_i^+]$ for several values of donor concentrations with $C_B = 5 \times 10^{19} \text{ cm}^{-3}$ boron calculated from the curves of Jain and Van Overstraeten (29) in which heavy doping effects on band structure are taken into account. For $E_F < E_{F_i}$ it can be seen that values of $D/D_i > 10$ can be obtained at high B concentration at 1000°C, in agreement with the data of Fig. 1b. For $E_F > E_{F_i}$, values of $D/D_i < 0.1$ are possible.

As an example of a profile calculation using Eq. [21], the results of Crowder *et al.* (3) will be simulated. They implanted B into intrinsic Si and into Si doped with $\approx 1-2 \times 10^{20} \text{ cm}^{-3}$ As (assumed to be the electrically active As concentration). Both kinds of samples were subsequently diffused at 1000°-1100°C for 30-120 min. The resulting profile data are shown in Fig. 7 for a 40 keV, $1.15 \times 10^{15} \text{ cm}^{-2}$ implant (30). It can be seen from Fig. 7 that the B diffusion was retarded in the As-doped sample. This retardation

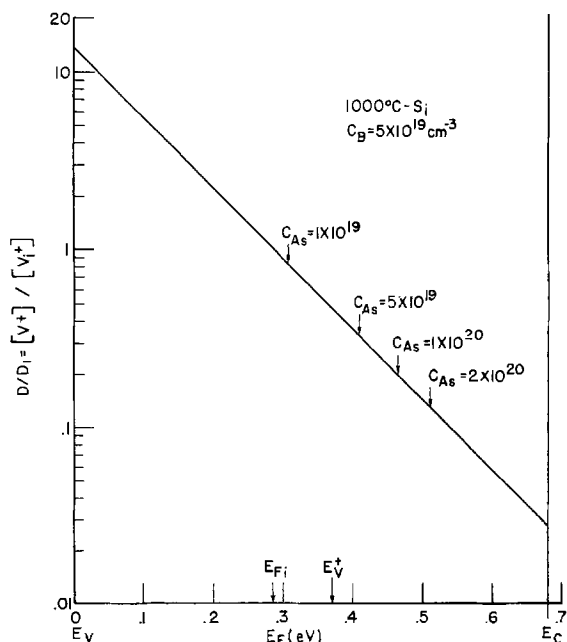


Fig. 6. Normalized concentration of positively charged vacancies vs. Fermi energy.

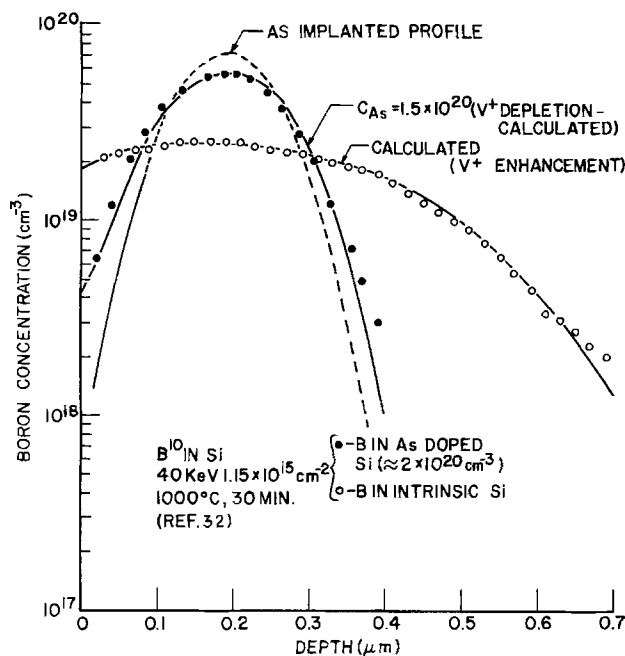


Fig. 7. Calculated B profiles in heavily As-doped Si and in intrinsic Si. The data are from Ziegler *et al.* (30).

cannot be attributed to As-vacancy complexing since a diffusion source for As was not used during the B drive-in (31) (As⁺-complex equilibrium probably had been established already). Therefore, in order to determine whether the B retardation was due to a depletion of positively charged vacancies as described by Eq. [21], the diffusion equation for B in the presence of As was solved with values of D determined from Fig. 2 and 6. Thus

$$\frac{\partial C_B}{\partial t} = D \frac{\partial}{\partial x} \left[h_1 \frac{\partial C_B}{\partial x} \right] \quad [22]$$

where $\partial C/\partial x$ (As) ≈ 0 (uniformly As-doped Si) and h_1 is the field enhancement factor described in Ref. (28). Since no data was published on the as-implanted B profile, the straggle and range were extrapolated from a 50 keV, $1 \times 10^{15} \text{ cm}^{-2}$ B implantation profile obtained by Tsai (9) using the secondary ion mass spectrometry technique (SIMS). The parameters used for 40 keV B in Si were $R_p = 0.19 \text{ }\mu\text{m}$ and $\Delta R_p = 0.062 \text{ }\mu\text{m}$. Excellent agreement between the calculated and measured profiles resulted with $D = 3.7 \times 10^{-15} \text{ cm}^2/\text{sec}$, [compares to $2 \times 10^{-15} \text{ cm}^2/\text{sec}$ as determined by Crowder *et al.* (3)] corresponding to a background As doping of $\approx 1.5 \times 10^{20} \text{ cm}^{-3}$ ($E_F = -0.19 \text{ eV}$). The B redistribution in intrinsic Si was calculated with $D_i = 2.1 \times 10^{-14} \text{ cm}^2/\text{sec}$, and the concentration dependence of D was accounted for by using Eq. [21] and the calculated local Fermi level. Good agreement with the data also is obtained. Additional data and calculations are published elsewhere in support of the vacancy model (32).

Orientation-dependent diffusion during oxidation.—Up to this point, consideration in this study has been given only to the diffusion of B in nonoxidizing ambients. However, a considerable amount of information has been reported on the enhanced diffusion of B during oxidation and the orientation dependence of this enhancement. Recently, Hu (33) presented a quantitative model of B diffusion during oxidation in which he combined the observations of stacking fault growth and B diffusion characteristics. Briefly, it is known that the rate of growth of stacking faults is dependent upon the crystal orientation of surface planes, and increases in the order (111), (110), and (100). The B

diffusivity is also dependent upon orientation, and increases in the same order.

Sanders and Dobson (34) have pointed out that mass transfer in Si is responsible for oxidation-induced fault growth which could result from the flow of Si self-interstitials from the interface into the Si substrate bulk. Hu's model for the formation of faults is based upon this observation.

In order to correlate enhanced B diffusivity with enhanced Si interstitial density, Hu assumed that B diffused (at least partially) by the interstitialcy mechanism. This observation is consistent with the fact that the Si interstitial prefers to replace Group I, II, and III substitutional impurities (but not Group V substitutional impurities) (35, 36). Thus, one can envisage the oxidation-induced flux of Si interstitials interchanging with B atoms and creating B interstitials which migrate through the lattice until they interact with a vacancy, and then continue to diffuse via a vacancy mechanism. The fact that Si interstitials do not readily replace Group V substitutional impurities (presumably because the enthalpy of Group V interstitial formation is larger) explains why the enhanced diffusion of As (but sometimes P) during oxidation is not observed (37, 38).

Summary and Conclusions

The apparent diffusion coefficient of B in Si increases linearly with ionized B concentration for $C_B > n_i$. Consequently, the erfc impurity distribution function may only be used with confidence when C_{SB} is $< 10^{19}$

cm^{-3} . When B diffuses into heavily As-doped Si, the diffusion is retarded. In this paper the model invoked to explain these results assumes that in p-type Si the dominant charge state of monovacancies is V^+ at typical diffusion temperatures. The concentration of V^+ increases linearly with ionized boron concentration from $[V_i^+]$, where $[V_i^+]$ is the concentration of V^+ in intrinsic Si. For the situation in which the background n-type doping is greater than the local B concentration, $[V^+]$ decreases as the background doping increases, thus affecting a decrease in the B diffusivity. It should be pointed out that the V^+ depletion effect is a "local" effect, and does not contribute significantly to the "long-range" interactions that have been observed between B and in-diffusing P and As regions in Si. These interactions have been attributed to extrinsic vacancy transients (27, 28).

The diffusivity of B can also be enhanced by Si self-interstitials which are known to replace the substitutional B atoms, making them interstitial B atoms. These B atoms then migrate to a vacancy wherein normal diffusion (monovacancy mechanism) continues until interaction with another Si self-interstitial occurs. Since the concentration of Si interstitials is extremely small under equilibrium conditions, this type of diffusion enhancement will only occur when Si interstitials are extrinsically generated (such as during oxidation). Since during oxidation the concentration of Si interstitials is so much greater in (100) oriented Si than in (111) Si, enhanced B diffusivity and stacking fault growth in (100) Si should be, and are, observed.

Acknowledgments

The author would like to thank Dr. J. C. Tsai for making his B profile data available for this work.

Discussions with Dr. L. E. Katz are also gratefully acknowledged.

Manuscript submitted July 19, 1974; revised manuscript received Feb. 16, 1975.

Any discussion of this paper will appear in a Discussion Section to be published in the December 1975 JOURNAL. All discussions for the December 1975 Discussion Section should be submitted by Aug. 1, 1975.

Publication costs of this article were partially assisted by Bell Laboratories.

REFERENCES

1. N. D. Thai, *J. Appl. Phys.*, **41**, 2859 (1970).
2. N. D. Thai, *Solid-State Electron.*, **13**, 165 (1970).
3. B. L. Crowder, J. F. Ziegler, F. F. Morehead, and G. W. Cole, in "Ion Implantation in Semiconductors and Other Materials," B. L. Crowder, Editor, p. 267, Plenum, New York (1973).
4. S. M. Hu, in "Atomic Diffusion in Semiconductors," D. Shaw, Editor, Chap. 5, Plenum, London (1972).
5. G. D. Watkins, *Phys. Rev.*, **155**, 802 (1967).
6. D. L. Kendall and D. B. DeVries, in "Semiconductor Silicon," R. R. Haberecht and E. L. Kern, Editors, p. 358, The Electrochemical Society Softbound Series, New York (1969).
7. L. Elstner and W. Kamparth, *Phys. Status Solidi*, **22**, 541 (1967).
8. J. A. Van Vechten and C. D. Thurmond, To be published.
9. J. C. Tsai, Unpublished results.
10. G. L. Vick and K. M. Whittle, *This Journal*, **116**, 1142 (1969).
11. R. K. Jain and R. Van Overstraeten, *J. Appl. Phys.*, **44**, 2437 (1973).
12. R. B. Fair, *ibid.*, **43**, 1278 (1972).
13. M. Okamura, *Jap. J. Appl. Phys.*, **8**, 1440 (1969).
14. G. Masetti, P. Negrini, S. Solmi, and G. Sancini, *Alta Freq.*, **42**, 346 (1973).
15. E. M. Conwell, *Proc. IRE*, **46**, 1281 (1958).
16. R. N. Ghoshtagore, *Phys. Rev. B*, **3**, 389 (1971).
17. K. Sato, Ayav Miyazaki, and T. Abe, Unpublished.
18. J. F. Ziegler, G. W. Cole, and J. E. E. Baglin, *Appl. Phys. Letters*, **21**, 177 (1972).
19. J. W. Colby and C. L. Paulnack, Unpublished.
20. K. M. Whittle and G. L. Vick, *This Journal*, **116**, 645 (1969).
21. M. Okamura, *Jap. J. Appl. Phys.*, **8**, 1440 (1969).
22. P. A. Iles and B. Leibenhaut, *Solid-State Electron.*, **5**, 331 (1962).
23. K. H. Nicholas, *ibid.*, **9**, 35 (1966).
24. A. D. Kurtz and R. Yee, *J. Appl. Phys.*, **31**, 303 (1960).
25. S. Wagner, *This Journal*, **119**, 1570 (1972).
26. J. A. Van Vechten, *Phys. Rev. B*, **10**, 1482 (1974).
27. S. M. Hu and T. A. Yeh, *J. Appl. Phys.*, **40**, 4615 (1969).
28. R. B. Fair, *ibid.*, **44**, 283 (1973).
29. R. K. Jain and R. J. Van Overstraeten, *IEEE Trans. Electron Dev.*, **ED-21**, 155 (1974).
30. J. F. Ziegler, G. W. Cole, and J. E. E. Baglin, *J. Appl. Phys.*, **43**, 3809 (1972).
31. R. B. Fair, *Solid-State Electron.*, **17**, 17 (1974).
32. R. B. Fair and P. N. Pappas, To be published.
33. S. M. Hu, *J. Appl. Phys.*, **45**, 1567 (1974).
34. I. R. Sanders and P. S. Dobson, *Phil Mag.*, **20**, 881 (1969).
35. E. E. Klontz and J. W. Mac Kay, *J. Appl. Phys.*, **30**, 1269 (1959).
36. G. D. Watkins, in "Effects Des Rayonnements Sur Les Semiconductors," p. 97, Dunod, Paris (1965).
37. T. C. Chan and C. C. Mai, *Proc. IEEE*, **58**, 588 (1970).
38. H. Higuchi, M. Maki, and Y. Takano, Unpublished.

The Synthesis of Boron Carbide in an RF Plasma

I. M. MacKinnon

Borax Consolidated Limited, Borax Research Centre, Chessington, Surrey KT9 1SJ, England

and B. G. Reuben

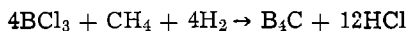
Department of Chemistry, University of Surrey, Guildford, Surrey GU2 5XH, England

ABSTRACT

The increasing demand for finely powdered boron carbide together with the rapidly rising cost of this material has stimulated research into alternative methods for its production. When boron trichloride is reacted with methane-hydrogen mixtures in a radio frequency argon plasma, boron carbides of variable B/C ratios are obtained as submicron powders, the product stoichiometry depending on the reactant composition. This reaction has been studied over a range of reactant compositions and flow rates to obtain information about the reaction mechanism involved and the growth of particles from the gas phase. The amount of reaction taking place and the product stoichiometry have been determined as functions of the reactant stoichiometry and flow rate using a factorial experimental design. The products obtained were studied by x-ray diffraction analysis to determine any changes in crystal structure with composition. It was found that the B/C molar ratio of the products varied linearly with the B/C molar ratio of the reactants, was unaffected by the H₂/BCl₃ molar ratio (for H₂/BCl₃ > 1) and decreased as the reactant flow rate increased. X-ray diffraction analysis of the products revealed that the lattice parameters of the crystalline material decreased linearly as the carbon content increased up to the composition B₄C. Samples containing excess carbon over the composition B₄C showed the presence of free graphite, while most of the samples with a carbon content of less than 13.6% (corresponding to B₇C) also showed the presence of β-rhombohedral boron, the product obtained in the absence of methane. Line broadening measurements suggest that the crystallite sizes of both the boron carbide and β-rhombohedral boron lie in the 200-300Å range.

Boron carbide has a combination of physical, electrical, mechanical, and nuclear properties which have resulted in its being used in such diverse applications as control rods for nuclear reactors, armor plating, electrodes, and shot-blast nozzles. In most cases the boron carbide is fabricated by being hot-pressed in a mold. The process requires careful control over the particle size range in the powder. Where the maximum density, hardness, and surface finish are important, the use of fine powder (< 5 μm) reduces processing costs and improves product quality. Because boron carbide is so hard, its comminution by conventional techniques *e.g.*, ball-milling, is expensive and usually leads to a product contaminated with iron from the grinding process. Figure 1 shows how the cost of commercially available boron carbide varies with particle size.

An rf plasma torch has recently been used in this laboratory to produce pure boron (1, 2) and the technique has now been extended to boron carbide. The results of some early experiments have already been published (3). In this paper we describe further work on the reaction between boron trichloride, methane, and hydrogen and the nature of the product obtained. The reaction, represented by the equation



has been studied over a range of reactant compositions and flow rates in order to obtain information about the reaction mechanism and the growth of particles from the gas phase.

The production of boron carbide by reaction of boron trichloride with a hydrocarbon or hydrogen/hydrocarbon mixture is well known. Where the interest has been in the preparation of protective coatings, chemical vapor deposition techniques have been used to produce boron carbide films on a variety of substrates including graphite, tungsten, tantalum, mullite, silica, molybdenum, and boron nitride.

Key words: boron, carbide, plasma, mechanism, structure.

Boron carbide films have been produced by the reaction between boron trichloride and methane on an induction-heated graphite substrate (4) and by the reaction between BCl₃/H₂ (1:1) mixtures containing 2 volume per cent (v/o) toluene (5). The use of BCl₃/CH₄/H₂ mixtures has been widely investigated (6-10) and BBr₃/CH₄/H₂ mixtures have been used to deposit B₁₃C₂ crystals onto a boron nitride substrate (11). Patents have been issued covering the deposition of boron carbide films from BCl₃/C₃H₈ mixtures in an electrical discharge (12), BCl₃/CH₄ mixtures (13) and BCl₃/CH₄/H₂ mixtures (14, 15). The preparation of boron carbide powder by reaction of BCl₃/CH₄ mixtures in a hydrogen plasma jet is covered by one patent (16). The product formed is said to have a mean particle diameter of 0.02 μm.

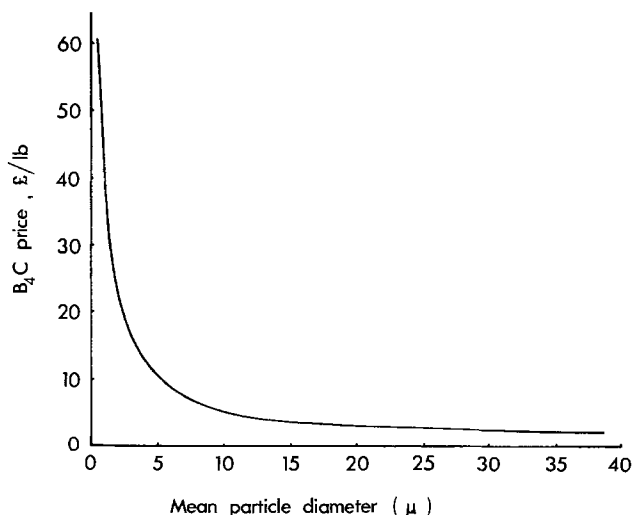


Fig. 1. Boron carbide selling price as a function of particle size (U.K. prices, 1974).

Apparatus and Procedure

A diagram of the apparatus is shown in Fig. 2. The plasma torch consisted of a water-jacketed silica tube 50 mm ID \times 70 mm OD \times 200 mm long fitted with a tangential inlet at one end for the plasma-forming gas. The torch was sealed to a water-cooled brass tail ring through which reactants were introduced to the plasma tail-flame. The products were passed down a water-cooled brass quench tube 50 mm ID \times 1500 mm long and through a glass-fiber bag-filter which retained the boron carbide powder. The waste gases were passed up a scrubbing tower to remove acid by-products before being released to the atmosphere. Power for the plasma was supplied by a Radyne RD 300 0-30 kW rf generator operating at a frequency of 2-5 MHz.

Boron trichloride was produced on site by the interaction of chlorine with commercial grade boron carbide, its purity being determined by IR spectroscopy and observations of its color. The main impurity detected spectroscopically was hydrogen chloride [< 0.5 weight per cent (w/o)]; the absence of any color in the liquid indicated that it was free from iron and lower boron chlorides. Methane (C.P. grade) was supplied by British Oxygen Limited, argon and hydrogen (commercial grades) were supplied by Air Products Limited.

The plasma was initiated in argon but could be run on boron trichloride or argon/boron trichloride mixtures as required. To maintain the maximum coupling efficiency of the generator to the plasma adjustments to the size of the inductance coils were made to match the resistive load of the different plasma gases used. Boron trichloride (bp 12.5°C) was vaporized in a simple coil heat exchanger immersed in a water bath at 80°C before being mixed with the other reactants.

After each run a sample of the product formed was degassed *in vacuo* to remove adsorbed BCl_3 which would otherwise have hydrolyzed on exposure to the atmosphere and contaminated the product with boric acid. The upgraded products were analyzed for total boron, carbon, and water-soluble boric oxide contents. The x-ray diffraction pattern of each sample was determined on a Philips 1050 goniometer using $\text{CuK } \alpha$ radiation.

Experimental Results

The reaction between boron trichloride and methane was carried out in the absence of argon and hydrogen by addition of methane to the tail-flame of a boron trichloride plasma. A plasma power of 28 kW with a boron trichloride flow rate of 100 g/min was used

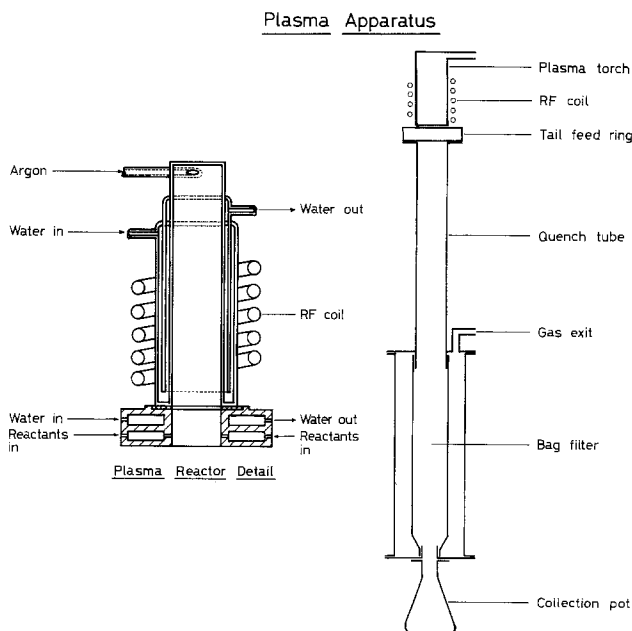
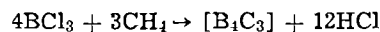


Figure 2

throughout this section of the work, with methane being added in amounts giving CH_4/BCl_3 molar ratios of 0.125-0.750. In all cases it was found that the product contained a higher proportion of carbon than indicated by the equation



the stoichiometry of which predicts a carbon content of 45.4 w/o. Equations of other stoichiometries predict the formation as by-products of either chlorinated hydrocarbons or chloroboranes for products that are boron-rich or carbon-rich respectively relative to $[\text{B}_4\text{C}_3]$. The gaseous reaction products were analyzed by IR spectroscopy and gas chromatography and found to contain appreciable amounts of hydrogen and dichloroborane, BHCl_2 , in addition to hydrogen chloride and unreacted boron trichloride. When boron trichloride was reduced with hydrogen alone, *i.e.*, in the absence of methane, dichloroborane was not formed.

In Fig. 3 and 4 the conversions of boron trichloride and methane respectively to solid product are plotted as functions of the reactant composition. It was found that the boron trichloride conversion was proportional

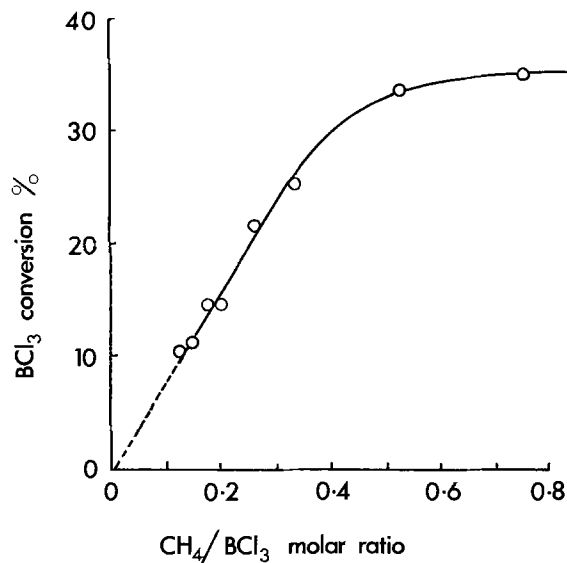


Fig. 3. BCl_3 conversion vs. $(\text{CH}_4/\text{BCl}_3)$ molar ratio. Reaction carried out in the absence of argon and hydrogen. Plasma power, 28 kW; BCl_3 flow rate, 100 g/min.

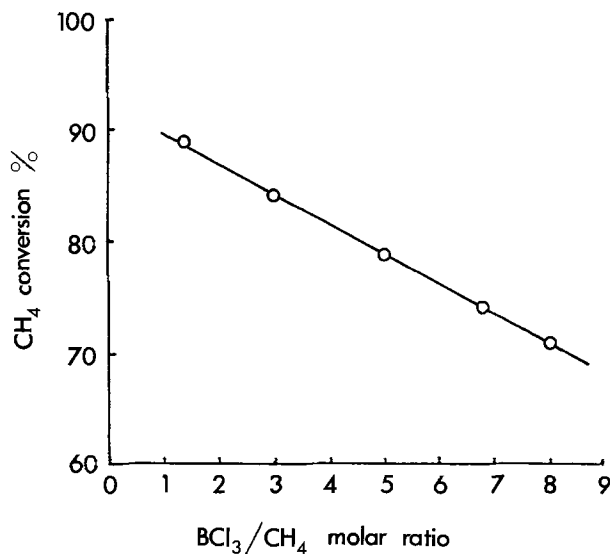


Fig. 4. CH_4 conversion vs. $(\text{BCl}_3/\text{CH}_4)$ molar ratio. Reaction carried out in the absence of argon and hydrogen. Plasma power 28 kW, BCl_3 flow rate 100 g/min.

to the CH_4/BCl_3 molar ratio for $\text{CH}_4/\text{BCl}_3 < 0.35$ and tended to a maximum of about 35% at higher methane concentrations. The methane conversion decreased linearly with the BCl_3/CH_4 molar ratio over the range of experimental conditions investigated.

The reduction of boron trichloride by CH_4/H_2 mixtures was carried out under constant reactor conditions by feeding a mixture of the reactants into the tail-flame of a 20 kW argon plasma (argon flow rate 40 liters/min). The effect of varying the composition and throughput of the reactants was investigated by means of a $3 \times 3 \times 6$ factorial experiment in which the three variables and their values were:

BCl_3 flow rate (g/min) : 20, 60, 100
 H_2/BCl_3 molar ratio : 1, 4, 8
 CH_4/BCl_3 molar ratio : 0, 0.05, 0.063, 0.083, 0.125, 0.25

Thus eighteen different compositions were each reacted at three different flow rates. The upper limit to the CH_4/BCl_3 molar ratio was chosen as that value which yielded a product containing carbon in excess of B_4C ; x-ray analysis showed that such products usually contained free graphite.

The product from each run appeared as a light fluffy powder containing small compacted flakes. These flakes broke up readily on passage through a coarse mesh sieve (250 μm aperture) to give a free-flowing powder. The products ranged in color from brown for plasma boron through gray to black for products with a high carbon content. The product was usually found to contain a small amount (1-2 w/o) of boric oxide. This was believed to be due either to hydrolysis of boron trichloride which the upgrading process had failed to remove, or to the presence of air remaining after the apparatus had been flushed with argon before each run. The boron carbides prepared by the reaction of boron trichloride and methane alone also contained boric oxide, indicating that the argon and hydrogen were not sources of oxygen. The amount of boron present as boric oxide was subtracted from the total boron content before calculation of product stoichiometry.

In Fig. 5 the boron-to-carbon ratio in the product, $(\text{B}/\text{C})_P$ is shown as a function of the boron-to-carbon ratio of the reactants, $(\text{B}/\text{C})_R$. Over the range of experimental conditions investigated, a linear dependence was observed except when the reactant flow rates, BCl_3/H_2 ratios and $(\text{B}/\text{C})_R$ ratios were all high. Under these conditions the products contained a substantial excess of carbon over B_4C . Provided hydrogen was present in excess, the $(\text{B}/\text{C})_P$ ratio was largely independent of the H_2/BCl_3 ratio. The $(\text{B}/\text{C})_P$ ratio increased as the reactant flow rate decreased, i.e., as the residence time increased.

The experimental data on the conversions of boron trichloride and methane to boron carbide show considerable scatter when plotted against reactant composition. This scatter is probably due to inefficient retention of the product by the bag-filter during the early stages of each run. This would cause the calculated conversions of boron trichloride and methane to appear too low. A finer grade of filter tended to block

causing premature termination of the run. Significant effects were identified by a Yates analysis of the original data (17). Yates analyses were carried out for the conversions of boron trichloride and methane separately and also the $(\text{B}/\text{C})_P$ ratio. The significant effects are listed below in terms of the H_2/BCl_3 ratio (a), the boron trichloride flow rate (i.e., total reactant flow rate) (b) and the CH_4/BCl_3 molar ratio (c), in order of significance:

1. BCl_3 conversion : -b, -ab, a
2. CH_4 conversion : -ab, -bc, -ib
3. $(\text{B}/\text{C})_P$: -c, a, -b

The negative sign indicates that the measured quantity decreases as that factor or interaction increases. Variations in H_2/BCl_3 molar ratio had as much effect on the residence time of the reaction as had variations in total flow rate. This leads to possible ambiguities in interpretation of the results.

In general terms it was found that at high boron trichloride flow rates (100 g/min) the boron trichloride conversion remained approximately constant at about 25% over the whole range of reactant compositions, while the methane conversion decreased both with increasing methane concentration and increasing hydrogen concentrations. At low boron trichloride flow rates (20 g/min), however, the reverse effect occurred with both the boron trichloride and methane conversions increasing as both the methane and hydrogen concentrations increased (Fig. 6).

When the flow rates of each reactant composition were varied, it was found that for hydrogen-deficient compositions ($\text{H}_2/\text{BCl}_3 = 1$) the amount of reaction taking place was approximately independent of the residence time. When the hydrogen was present in excess, the amount of reaction increased with time, the increase becoming more pronounced as both the CH_4/BCl_3 and H_2/BCl_3 ratios increased.

Production rates varied with reaction conditions and no attempt has yet been made to optimize this process for the production of boron carbide. Production rates of about 250 g/hr were achieved during the course of this experimental work.

Crystallographic Results

When boron trichloride is reduced with hydrogen in a thermal rf plasma, β -rhombohedral boron (the high temperature form) is obtained (18, 19). The addition of small amounts of methane to the system yielded a product shown by x-ray diffraction analysis to contain both β -rhombohedral boron and boron carbide (α -rhombohedral boron structure). The presence of β -rhombohedral boron was detected in all samples with carbon contents from 6.2 w/o (the lowest prepared) to 10.9 w/o and in some other samples with carbon contents up to 13.9 w/o. Free graphite was detected in all but one of the samples with carbon contents in excess of 21.5 w/o.

The position of the boron carbide peak corresponding to the (021) reflection was determined as a function of the carbon content of each product (Fig. 7). During

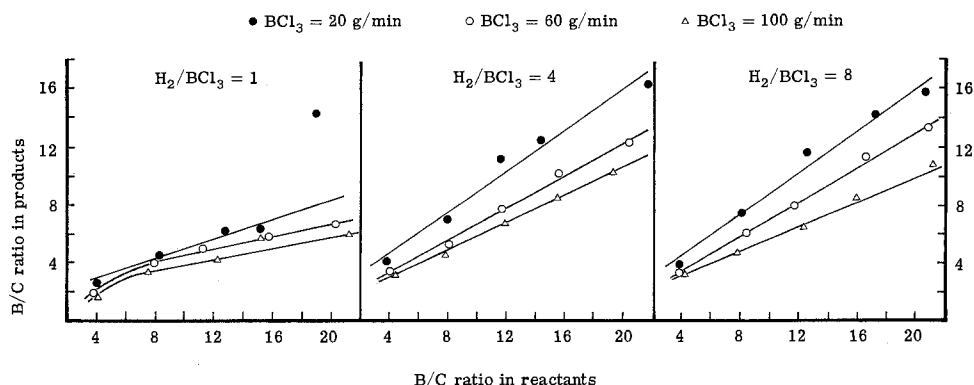


Fig. 5. B/C molar ratio in products vs. B/C molar ratio in reactants. Argon flow rate, 40 liters/min; plasma power, 20 kW.

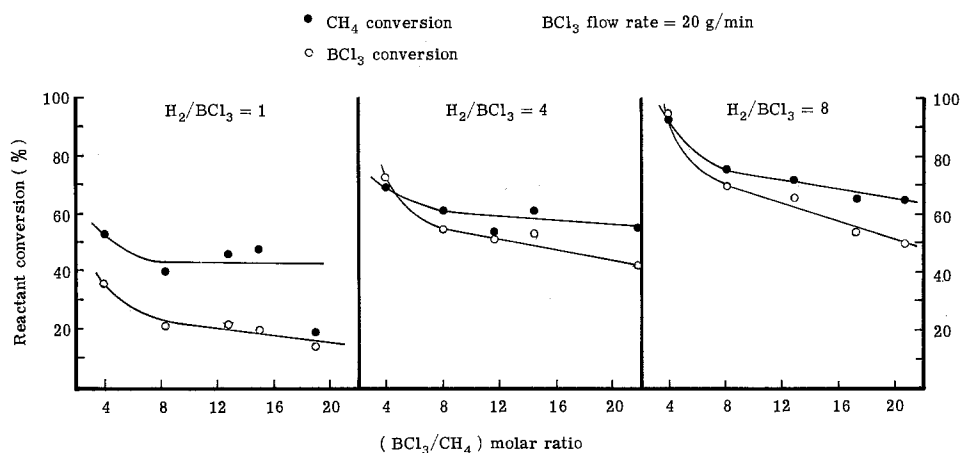


Fig. 6. Reactant conversion vs. (BCl₃/CH₄) molar ratio. Argon flow rate, 40 liters/min; plasma power, 20 kW.

these measurements it was found that, for thick layer samples of each product (~ 1.5 mm), the diffraction peak was distorted and the apparent peak position was too low. This was explained (20) as being due to absorption and multiple reflection of the incident radiation by elements of low atomic number in samples thicker than about $50 \mu\text{m}$. The boron carbide peak position was remeasured using thin layer samples obtained by painting a slurry of each product in acetone onto a glass slide. This method led to greatly reduced sensitivity, but produced symmetrical peaks whose position could be measured with an accuracy of $\pm 0.02^\circ 2\theta$.

The displacement of the boron carbide peak position in samples with low carbon contents towards higher values of the diffraction angle is consistent with the evidence that these samples also show the presence of free boron. Thus the boron carbide peak in these samples will have arisen from crystallites with a higher carbon content than the sample as a whole.

Line broadening measurements carried out on five samples indicated that the crystallite sizes of both boron carbide and β -rhombohedral boron lay in the range 200-300 Å.

Figure 8 shows an electron micrograph of a typical product with the composition B₄C.

Discussion of Plasma Results

At this stage in the work, any mechanism for this reaction would be speculative. A number of interesting features, however, deserve comment.

1. Work on the BCl₃/H₂ reaction (1) has suggested that boron trichloride dissociates completely and reversibly under plasma conditions yielding mainly BCl and chlorine but also BCl₂ and B atoms. Hydrogen, in contrast, is known not to dissociate more than a few per cent in the plasma. Methane is assumed to give CH₃· as a primary product (21) which then combines to give C₂ compounds. These lose hydrogen, and the main product is acetylene formed via C₂H·.

2. The thermal dissociation of methane is inhibited by hydrogen (22) and the effect is said to be proportional to [H]². Presumably it acts by displacing to the left the equilibria involved in the hydrogen loss processes. If the thermal decomposition of methane and the formation of such species as C₂H· were important in the reaction, then addition of hydrogen to the CH₄/BCl₃ reaction mixture should suppress C₂H· formation and hence increase the (B/C)_P ratio. Figure 5 shows that this is qualitatively true at low proportions of hydrogen, although the effect is not as large as one would

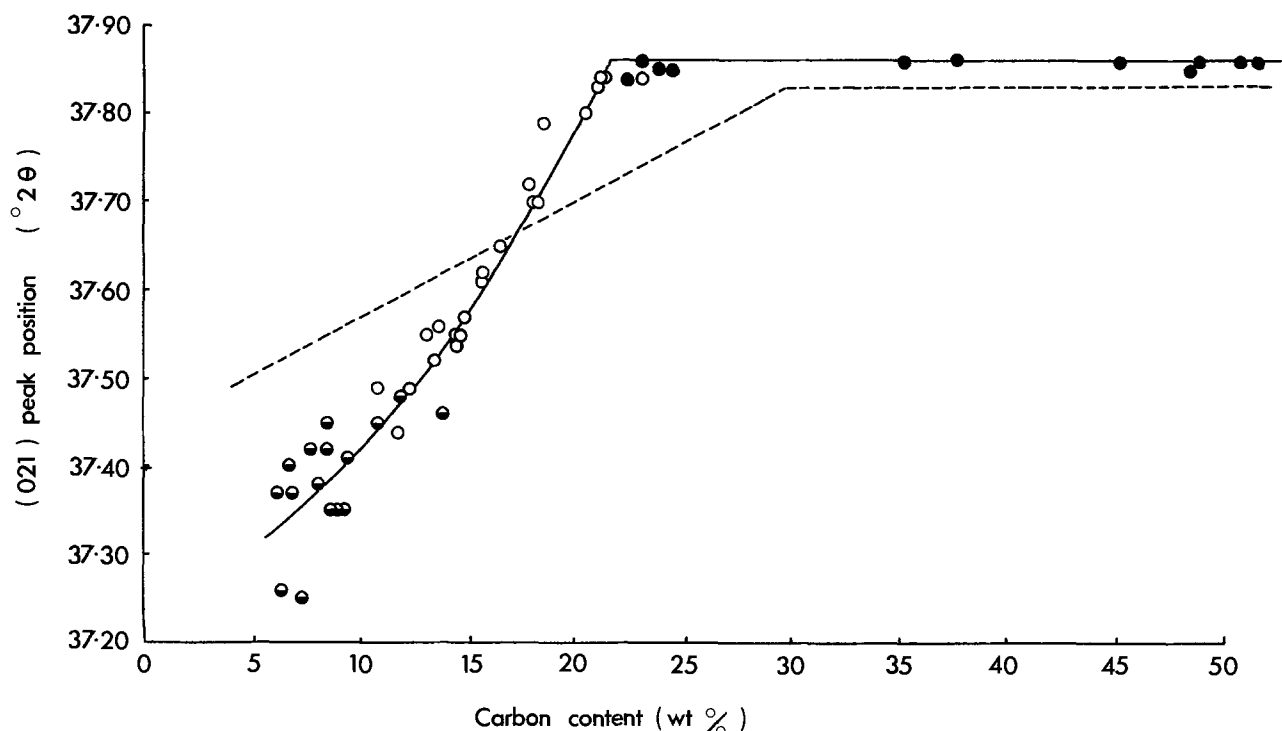


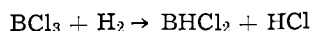
Fig. 7. XRD study of plasma B₄C. 2θ values of the (021) reflection vs. carbon content. ○ Boron carbide, ● boron carbide containing free graphite, ◐ boron carbide containing free boron, --- Ref. (23).



Fig. 8. Electron micrograph of B_4C . (X40,000).

expect, and that in the presence of excess hydrogen additional hydrogen has virtually no effect. It is possible that removal of C_2H by a reaction to give a boron carbide might swing the equilibria back to the right, but it is unlikely that this would balance the contrary effect of hydrogen. Examination of the reaction by-products for traces of acetylene etc. should provide a crude test of this.

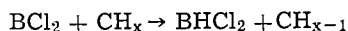
3. The formation of dichloroborane is difficult to explain simply. The reaction



is attractive but does not explain why dichloroborane is formed in BCl_3/CH_4 plasmas and in $BCl_3/CH_4/H_2$ plasmas but not in BCl_3/H_2 plasmas. As the chlorination of methane would require several steps, it is reasonable to suppose that dichloroborane is formed from a boron compound which already contains two atoms of chlorine, i.e., BCl_3 or BCl_2 . Exchange reactions of the type



are *prima facie* unlikely and would lead to chlorinated hydrocarbons in the reaction products which we have been unable to detect. However, processes of the type



are much more likely. Hamblyn *et al.* (18) considered that BCl_2 was only a minor product of the dissociation of boron trichloride, but this view was based on the intensity of BCl_2 lines in the emission spectrum. The formation of ground-state BCl_2 would have been overlooked by this technique.

4. The greatest conversion of boron trichloride to boron carbide (93%) was obtained at a low boron trichloride flow rate (20 g/min), a high H_2/BCl_3 ratio (8:1), and stoichiometric CH_4/BCl_3 ratio (1:4). In general the amount of reaction taking place increased with residence time except under hydrogen-deficient conditions. In the BCl_3/H_2 work, it appeared that after the boron trichloride has dissociated, the hydrogen acted merely as a scavenger for the chlorine. It is possible that in the present work, hydrogen is again scavenging chlorine and the B, BCl , and BCl_2 fragments are reacting with the CH_x species. The idea is supported by the observation (Fig. 5) that as the residence time of any given reaction mixture increases, so does the $(B/C)_P$ ratio of the product obtained. This implies that an initial boron-carbon compound is formed which subse-

quently reacts slowly with further boron-containing species. It may well be the reverse of the process by which, when boron carbide is heated, boron evaporates from the lattice.

Discussion of Crystallographic Results

The results of the x-ray work are in qualitative agreement with the results of Glaser, Moskowitz, and Post (23) who found that the lattice constant of the boron carbide unit cell decreased as the carbon content increased. However, the amount of variation was greater than they found, and the limiting carbon content was found to be 21.6 w/o as compared with their figure of 30 w/o. We attribute the discrepancy to differences in experimental technique mentioned in the results section. The change in the d spacing of the lattice corresponded to a change in the b axis from 5.43 to 5.35 Å and in the c axis from 12.31 to 12.12 Å as the carbon content increased from 6.2 to 21.6 w/o.

The figure of 21.6 w/o is significant because it implies a compound of formula B_4C (carbon content 21.7 w/o). The structure of this compound was originally determined by x-ray diffraction analysis (24, 25) and was reported to consist of B_{12} icosahedra and linear C-C-C chains. It was subsequently shown by nmr investigations (26) that the central atom of the triatomic chain was in fact a boron atom, and two distinct phases have since been identified; $B_{13}C_2$, otherwise $B_{12}(CBC)$ and $B_{12}C_3$, in which one icosahedral boron atom is replaced by a carbon atom to give $B_{11}C$ (CBC). Of these two, $B_{13}C_2$ is the more thermally stable and is the only congruently melting phase.

It has recently been suggested (27) that the phase $B_{11}C$ (CBC) is not formed at temperatures below 1800°C, and possibly below 2500°C, but that a phase of composition $B_{13}C_3$, i.e., $(B_{12}(CBC)C)$, containing one interstitial carbon atom per unit cell is formed instead. This composition has a carbon content of 20.4 w/o, and it was stated that all samples with carbon contents > 21.0 w/o contained free graphite. Our results do not support this conclusion. Figure 7 includes five points obtained from samples containing more than 20.4 w/o carbon (four of them containing more than 21.0 w/o carbon) none of which show the presence of free graphite. The point of intersection between the rising curve and the horizontal line in Fig. 7 represents the point at which the lattice ceases to change. It appears to come at a carbon content of 21.7 w/o corresponding to B_4C , and to move this point to a carbon content of 20.4% would not fit so well with the experimental data. The difference between 21.7 w/o carbon and 20.4 w/o carbon is not large but we feel that the balance of probability in this work favors the more conventional formula B_4C .

Acknowledgments

The authors thank Dr. R. Koenigsberger (University of Surrey) for gas chromatographic analyses, Mr. R. Hockham (University of Surrey) and the Structural Studies Unit (University of Surrey) for electron micrographs and Mrs. P. M. Bills (University of Surrey) and Mr. C. L. Peers (Borax Consolidated Limited) for advice and assistance with x-ray diffraction work. The authors also thank Dr. A. J. Wickens (Borax Consolidated Limited) and Dr. R. H. Biddulph (Borax Consolidated Limited) for helpful discussions and Dr. R. Thompson (Borax Consolidated Limited) for permission to publish this work.

Manuscript submitted July 22, 1974; revised manuscript received Jan. 7, 1975.

Any discussion of this paper will appear in a Discussion Section to be published in the December 1975 JOURNAL. All discussions for the December 1975 Discussion Section should be submitted by Aug. 1, 1975.

Publication costs of this article were partially assisted by Borax Consolidated Limited.

REFERENCES

1. S. M. Hamblin and B. G. Reuben, "Advances in Inorganic and Radiochemistry," In press.
2. S. M. L. Hamblin, B. G. Reuben, and R. Thompson, "Special Ceramics 5," P. Popper, Editor, The British Ceramic Research Association, Stoke-on-Trent (1972).
3. I. M. MacKinnon and A. J. Wickens, *Chemistry in Industry*, 800-1 (1973).
4. S. Marinkovic, C. Synznjevic, and I. Dezarov, *Carbon*, **7**, 185 (1968).
5. C. F. Powell, J. H. Oxley, and J. M. Blocher, "Vapour Deposition," p. 359, John Wiley and Sons, London (1966).
6. J. B. Higgins, A. Gatti, and J. J. Gebhardt, *This Journal*, **116**, 137 (1969).
7. E. Fitzer and M. Rohm, *ibid.*, **120**, 245C (1973).
8. J. G. Donaldson, J. B. Stephenson, and A. A. Cochran, U.S. Mines Rept. Invest., No. 7150 (1968).
9. R. L. Heestand, J. I. Federer, and C. F. Leitten, *Met. Soc. Am. Inst. Mining, Met. Petrol. Engrs., Inst. Metals Div., Spec. Rept. Ser.*, **10**, 539 (1964).
10. A. W. Moore and H. F. Volk, *U.S. Govt. R. and D. Repts.*, **69**, 95 (1969).
11. K. Ploog, *J. Less-Common Metals*, **31**, 177 (1973).
12. Compagnie de St. Gobain, U.S. Pat. 2,952,598 (1958).
13. Union Carbide Corp., U.S. Pat. 3,334,967 (1965).
14. G. E. C. Ltd., Brit. Pat. 1,148,325 (1969).
15. G. E. C. Ltd., Fr. Pat. 1,445,856 (1966).
16. CIBA Ltd., Brit. Pat. 1,069,748 (1967).
17. F. Yates, "Design and Analysis of Factorial Experiments," Imperial Bureau of Soil Sciences, London (1937).
18. S. M. L. Hamblin, B. G. Reuben, and I. M. MacKinnon, To be published.
19. J. Cueilleron and B. Cruiziat, *Bull. Soc. Chem. France*, **4**, 1207 (1973).
20. P. M. Bills, University of Surrey, Private communication.
21. I. A. Schneider, *Z. Physik Chem. (Leipzig)*, **220**, 199 (1962).
22. L. Bogdandy, W. Rutsch, and I. N. Stranski, *Z. Elektrochem*, **66**, 661 (1962).
23. F. W. Glaser, D. Moskowitz, and B. Post, *J. Appl. Phys.*, **24**, 731 (1953).
24. G. S. Zhdanov and N. G. Sevast'yanov, *Dokl. Akad. Nauk. SSSR*, **32**, 432 (1941).
25. H. K. Clark and J. L. Hoard, *J. Am. Chem. Soc.*, **65**, 2115 (1943).
26. A. H. Silver and P. H. Bray, *J. Chem. Phys.*, **31**, 247 (1959).
27. K. Ploog, *J. Less-Common Metals*, **35**, 131 (1974).

I-V Characteristics of PtSi-Si Contacts Made from CVD Platinum

Myron J. Rand*

Bell Laboratories, Allentown, Pennsylvania 18103

ABSTRACT

Small amounts of phosphorus codeposit during the chemical vapor deposition of thin-film platinum from $\text{Pt}(\text{PF}_3)_4$. Because of the possibility that the P may dope a narrow zone of adjacent Si during silicide formation, the room temperature I-V characteristics of such PtSi contacts made at 450°-700°C to various Si types were investigated. CVD Pt readily forms PtSi in a few minutes at temperatures as low as 450°C. Contacts to n^+ or p^+ Si made at 450°-700°C are ohmic. Contacts formed at 450°C to lightly doped n-Si are good quality Schottky barrier diodes with a barrier height of 0.84 eV and an "ideality factor" $n = 1.02$. At higher sintering temperatures the reverse current increases, and with sintering at 650°-700°C the contact becomes ohmic. In the case of lightly doped p-Si, PtSi contacts made at 450°C from CVD Pt have an ohmic room-temperature characteristic, as expected. If the silicide is made at 700°C, a p-n junction is created in the p-Si. PtSi contacts made from CVD Pt at 450°C are thus electrically equivalent to those made from sputtered Pt at ~ 600°C. At higher formation temperatures, deviations from expected behavior are observed, all of which are consistent with diffusion of phosphorus from the PtSi into the Si to a depth in the range 10-100Å.

The chemical vapor deposition (CVD) of thin-film platinum by $\text{Pt}(\text{PF}_3)_4$ pyrolysis was developed to provide a simple and radiation-free Pt deposition for high-reliability PtSi contacts to silicon and for beam-lead metallization (1). It was soon discovered that small amounts of phosphorus codeposit with the platinum, and that this phosphorus is not uniformly distributed in depth but instead concentrates at interfaces (2). Depending on what happens when Pt on Si is heated to form the silicide, the phosphorus, if it has any detectable effect at all, might be either helpful, e.g., in gettering impurities or harmful, e.g., by changing Si doping levels and therefore current-voltage characteristics. It was the purpose of the work reported here to see in at least a preliminary way if there are any restrictions on the use of CVD Pt in contacting

Si, or any phenomena different from those seen with sputtered or e-gun Pt.

Some aspects of the interdiffusion of CVD Pt and single-crystal Si have already been reported (2, 3). With the usual Pt thicknesses of 500-1000Å the reaction to PtSi is complete in 10 min at 450°C. The PtSi grain size, as seen by transmission electron microscopy, is about 600Å, or about 900Å if formed at 625°C in 10 min. A low-voltage-sputtered Pt sample diffused at the same time gave PtSi grain sizes about twice these values. The phosphorus profiles have been investigated by sputtering-Auger and ion-probe methods. At present these cannot give accurate quantitative analyses, but the situation is believed to be as shown schematically in Fig. 1. After Pt deposition at 225°C there is a high P concentration in the outer ~ 50Å of the Pt, perhaps ~ 0.1 atom per cent P in the bulk of the film, and a broad peak of 1% or so coincident with the Pt-Si interdiffusion zone. When PtSi is formed,

* Electrochemical Society Active Member.

Key words: chemical vapor deposition, platinum, platinum silicide, contacts to Si, Schottky barrier diodes.

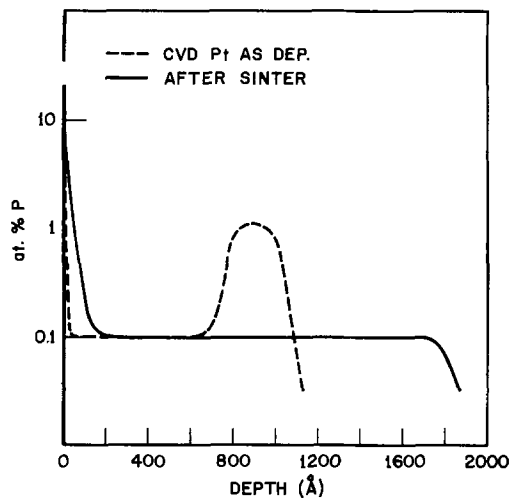


Fig. 1. Phosphorus profiles in 900Å CVD Pt on 4 ohm-cm As-doped $\langle 100 \rangle$ Si, as deposited and after sintering to 1800Å PtSi. %P is approximate only. Note that the ordinate scale is logarithmic.

this latter P moves to the outer surface, and no accumulation can then be detected at the PtSi-Si interface.

This behavior would seem to be harmless to the electrical properties of PtSi contacts, but the analytical methods lack both adequate sensitivity and depth resolution to assure that there is no phosphorus doping of the Si. The contacts themselves are the best tool for this. We report here room-temperature current-voltage characteristics and other diagnostic experiments on both Schottky barrier and ohmic PtSi contacts to various Si types where the PtSi was formed from CVD Pt at varying temperatures.

Both conventional and guard-ringed structures were studied. In the latter a diffused diode, *e.g.*, p^+ Si in n -Si, underlies the periphery of the silicide and blocks leakage caused by edge effects such as diffusion spikes, stress concentrations, small radii of curvature, etc. Results using guard rings characterize the best attainable contact interfaces. Those from unguarded contacts have practical usefulness because integrated circuit designers may choose to avoid the extra processing and chip space guard rings require if some leakage can be tolerated.

Experimental

Test arrays were fabricated in 3μ thick epitaxial Si, 2-6 ohm-cm As or B doped, on heavily doped $\langle 100 \rangle$ or $\langle 111 \rangle$ substrates, in order to minimize series resistance which would mask the contact characteristics. Square windows ranging in size from 0.5 to 20 mils were opened in 6000Å thermal SiO_2 . Some windows were enclosed by heavily diffused rings of the opposite type and some left unguarded. (The SiO_2 mask extended to the middle of the guard ring.) In each array a heavily diffused (P or B) ohmic contact was included, and also a heavily diffused contact of opposite conductivity type, to provide a p - n diode. The latter was made in the same diffusion step as the guard rings and thus served as a control for their characteristics. With the processing sequence used, diffusions were $\sim 1\mu$ deep.

Test slices were given a 45 sec dip in 3% HF before loading into the CVD apparatus, but no other cleaning or surface treatment. Platinum was deposited in 1 atm hydrogen at 225°-250°C at 40-80 Å/min to a thickness of 500-800Å. Sintering was done in ultrahigh-purity grade (99.999%) hydrogen (Matheson Gas Products) in a tube furnace, temperatures and times as given. Some samples received an additional air-bake to increase resistance to aqua regia (3). Platinum was stripped in 50% 7:1 HCl:HNO₃ at 85°C; the clearing time was 1-2 min. After 1 min in 3% HF the patterns were metallized with 0.7-1.0 μ filament-evaporated Al, con-

tact pads for the probes being provided some distance removed from the silicide contacts. The Al was not further sintered, since here it serves only to contact PtSi and not to form contacts to Si.

Current-voltage curves were displayed using a Tektronix 576 Curve Tracer, and currents were measured by standard electrometer techniques. The diffused ohmic contact, rather than the back of the slice, was always used as one contact. The result of probing two ohmic contacts was checked in several locations on each slice. In the case of Schottky barrier contacts, the effect of contact dimension was observed by measuring reverse currents of 1, 3, 8, and 20 mil contacts and plotting current *vs.* dimension on a log-log scale. On all occasions the slope of this plot was 2, showing leakage current proportional to contact area. If leakage were occurring chiefly at edges the slope would have been close to unity.

An additional test of ohmic contact integrity was provided by a test pattern devised by Bindell (4), which contains arrays of 600 contacts series-connected alternately by p^+ diffusions and by metallization. A single high-resistance or rectifying contact in the entire chain is easily detected. Statistics are provided by four window sizes and 55 chips per wafer.

One determination was made of the resistivity of the PtSi, a quantity for which most existing reports are estimates only. For this purpose Pt was deposited on a $\frac{1}{4} \times \frac{1}{2}$ in. strip of 50 ohm-cm B-doped $\langle 111 \rangle$ Si and sintered at 525°C, 30 min. After sheet-resistance measurement by four-point probe, part of the silicide was wax-masked and the exposed remainder removed by etching in buffered HF, 1 min, followed by 85° aqua regia and then another BHF treatment (3). The step height, after wax removal and Al evaporation, was determined by multiple-beam interferometry, thereby establishing the silicide thickness.

Results

PtSi Resistivity.—A $2000 \pm 50\text{Å}$ thick PtSi film gave a sheet resistance of 1.87 ohm/ \square or a resistivity of 37 $\mu\text{ohm-cm}$. Using the product of electron density (5) = $1.5 \times 10^{22}/\text{cm}^3$, mobility = 13 $\text{cm}^2 \text{V}^{-1} \text{sec}^{-1}$, and electronic charge = 1.60×10^{-19} coulomb, a conductivity of $3.1 \times 10^4 \text{cm}^{-1} \text{ohm}^{-1}$ may be calculated, or a resistivity of 32 $\mu\text{ohm-cm}$. For single-crystal PtSi a value of 27 $\mu\text{ohm-cm}$ has been reported (6).

Ohmic contact.—The work reported here involved examination of several hundred PtSi contacts made from CVD Pt and single-crystal Si at temperatures from 450° to 700°C. No case of failure to silicide was seen. Reaction invariably occurred over the entire window area and produced a smooth, characteristically pearl-gray contact. When two ohmic contacts were probed using the curve tracer the I - V curve was linear, on either side of the origin, to current densities beyond 400 A/cm². Observed resistances were within less than a factor of 2 of those calculated from a knowledge of the test structure geometry and epitaxial layer resistivity.

Table I gives results of a test employing the arrays of 600 series-connected contacts. Here the CVD Pt

Table I. Test of ohmic contact to 10^{19} B-doped Si

Percentage of 600-contact strings testing < 30 kohms
(55 strings measured in each case)

Silicide source	Window size			
	10 × 7 μ	7 × 7 μ	7 × 5 μ	5 × 5 μ
500Å CVD Pt sintered 525°C, 30 min, H ₂	100	100	98	84
500Å e-gun Pt sintered 525°C, 30 min, H ₂	89	82	75	80
1000Å filament-evaporated Pd sintered 450°C, 10 min, forming gas	100	98	98	80

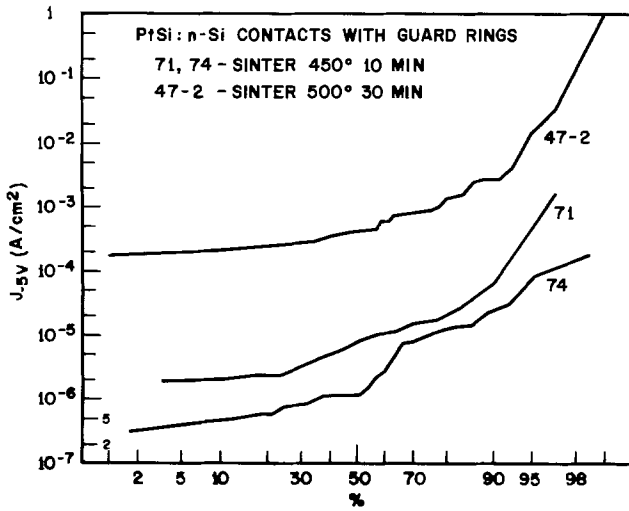


Fig. 2. Log-normal probability plot of reverse leakage current densities of guard-ringed Schottky barrier PtSi:n-Si contacts.

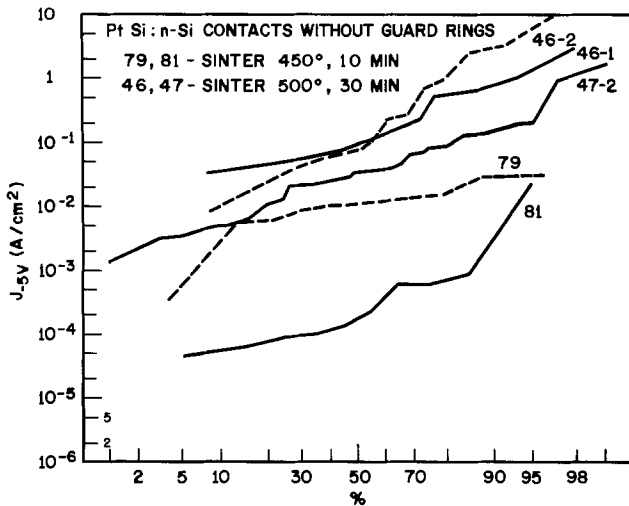


Fig. 3. Log-normal probability plot of reverse leakage current densities of unguarded Schottky barrier PtSi:n-Si contacts.

emerges superior to e-gun Pt sintered in identical fashion, and at least the equal of typical Pd₂Si contacts.

Schottky barrier contacts.—Figures 2 and 3 show results of reverse leakage current measurements at 5V, for guard-ringed (Fig. 2) and unguarded (Fig. 3) Schottky barrier contacts. Sinter temperatures, as shown, are in the range 450°-500°C. Most of the data are from 1 to 8 mil square contacts. Different sizes have been normalized by plotting current densities. In these log-normal probability plots, showing the distribution of the results, no data have been arbitrarily discarded. Table II summarizes the conditions and median values of J_{-5V} . Two other numbers included in

Table II. Reverse leakage currents of Schottky barrier contacts

Run	Guard ring	Sinter		Number tested	Median value $J_{(-5V)}$ A/cm ²
		°C	Min		
71	Yes	450	10	15	8×10^{-9}
74	Yes	450	10	31	1.2×10^{-9}
79	No	450	10	12	1.0×10^{-2}
81	No	450	10	10	1.8×10^{-4}
46-1	No	500	30	24	8×10^{-2}
46-2	No	500	30	17	6.3×10^{-2}
47-2	Yes	500	30	48	4.0×10^{-4}
47-2	No	500	30	50	2.9×10^{-2}
Theoretical*					1×10^{-7}
Useful, allowing $1 \mu\text{A}/\text{mil}^2$					1.5×10^{-1}

* See Ref. (5).

the table represent the leakage of an ideal theoretical Schottky barrier and the leakage at which the contact becomes of marginal usefulness in circuit design. For this latter criterion a $1 \mu\text{A}/\text{mil}^2$ rule of thumb has been chosen.

The guard-ringed contacts made at 450°C are very good, approaching within one or two orders of magnitude of ideality. Contacts made at 500°C are about two orders of magnitude more leaky; this is still quite acceptable.

Without guard rings the leakage increases roughly another two orders of magnitude in each case. The 450°C contacts are still safely below the $1 \mu\text{A}/\text{mil}^2$ limit but the 500°C contacts are now within one order of magnitude of it.

After measurement, the contacts of run 71 (Fig. 2) including their Al metallization, were baked in air at 325°C for 8 hr. Leakage currents changed less than 10% in all cases, and most decreased.

A representative guard-ringed contact made at 450°C (run 74) has also been characterized by its room-temperature forward-bias characteristic, as shown in Fig. 4. A voltage change of 61 mV changes the current one decade; the 100 A/cm² turn-on voltage is 0.56V. These results are in close accord with the prediction of the standard forward-bias diode equation with $T = 300^\circ\text{K}$ if ϕ_B , the barrier height, = 0.843 eV. ϕ_B is determined most simply by extrapolating to zero voltage to obtain the "saturation" current density

$$J_s = A^{**}T^2 e^{-q\phi_B/kT}$$

where A^{**} is the Richardson constant. Our "ideality parameter"

$$n = \frac{q}{kT} \frac{\partial V_F}{\partial (\ln I_F)}$$

is 1.02. Barrier heights for PtSi:n-Si have been reported (5, 7) in the range 0.83-0.85 eV.

Thus PtSi contacts made by interdiffusing CVD Pt and Si at 450°C are of good quality and have all the expected properties; there is no hint of the presence of electrically active phosphorus. There is no obvious reason for higher leakage in Schottky barrier contacts made at 500°C unless a narrow diffusion zone of more

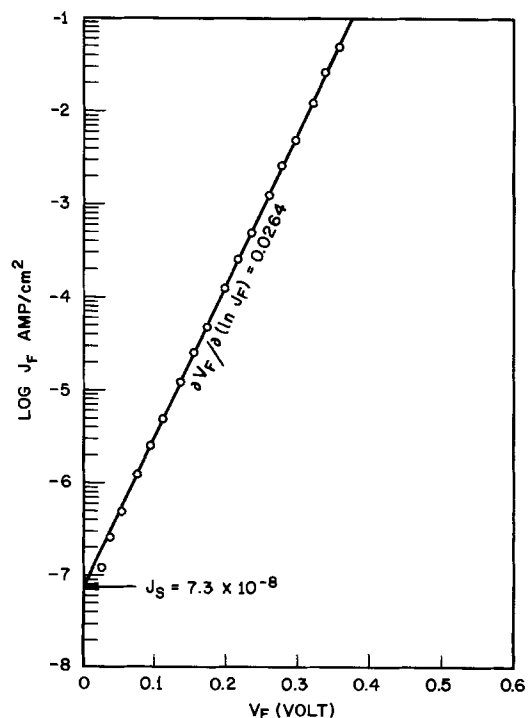


Fig. 4. Room temperature forward-bias characteristic of PtSi:n-Si Schottky barrier contact (run 74).

heavily doped Si has formed at the PtSi-Si interface. If this occurs, sintering at yet higher temperatures should have an even greater effect. This is indeed the case. In the formation range 500°-625°C the contacts become progressively more leaky, and a gamut of soft rectifying characteristics has been seen. Figure 5, showing the I-V curve for a contact to 3 ohm-cm n-Si made at 525°C for 60 min, is typical.

Finally, at formation temperatures of 650°-700°C the process reaches its logical conclusion: ohmic contact is made to lightly doped n-Si without a separate n⁺ diffusion step. Such a contact, made at 700°C, 10 min, to 5 ohm-cm n-Si, is shown in Fig. 6, along with the conventionally diffused ohmic contact. (A factor of 2 in apparent contact resistance results from difference in contact size and a greater diffusion depth for the n⁺ contact, leaving a shorter current path in the epi layer. The change in slope at +1V in curve B is a contribution from the forward current of the guard-ring diode.) An ohmic contact made this way in device processing cuts out one photolithography step and one diffusion step. Requirements for practical use would appear to be that the device be able to tolerate 650°-700°C at this stage, that a larger n⁺ area than contact area is not required, and that one cannot make ohmic and Schottky contacts in the same siliciding step.

If the phosphorus in CVD Pt can dope Si, the consequences should be evident in working with p-type material also. With heavily boron-diffused Si the contact characteristic is unaffected (see Table I). It re-

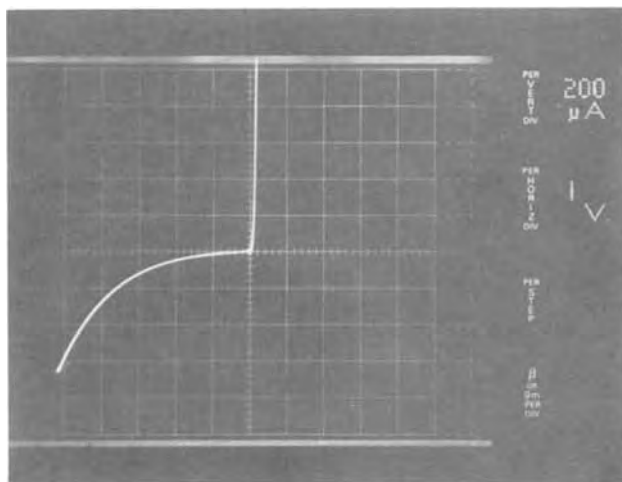


Fig. 5. Soft rectifying contact to 3 ohm-cm n-Si produced by sintering CVD Pt at 525°C, 60 min.

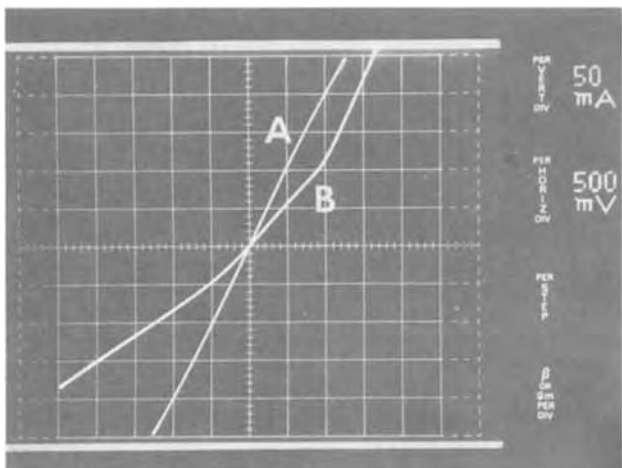


Fig. 6. Ohmic contact to 5 ohm-cm n-Si produced by sintering CVD Pt at 700°C, 10 min (curve B). The diffused (n⁺) contacts (curve A) are 50% larger in area than the test contacts. Above +1V there is a contribution from the forward current of the guard-ring diode in curve B.

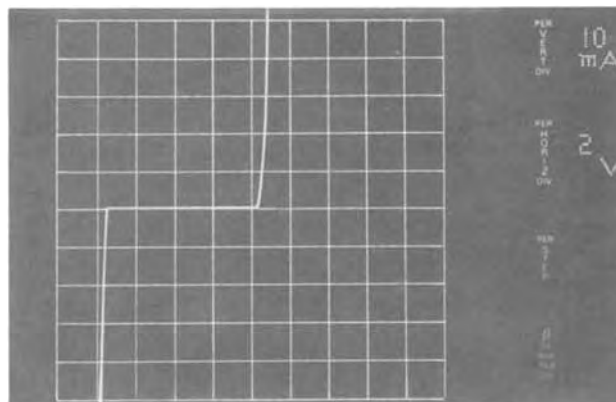


Fig. 7. p-n diode created in 3 ohm-cm p-Si produced by sintering CVD Pt at 700°C, 10 min.

mains so even at 700°C, since in the n-type test slice described in the preceding paragraph the forward current of the diffused p-n diode was normal when contacted with PtSi. If the series structure PtSi/n/p/n had been developed, the I-V characteristics would have been those of back-to-back diodes.

With lightly doped p-Si contacted by PtSi made at 450°C, the room-temperature I-V plot appears strictly ohmic, and essentially indistinguishable from that for the p⁺ diffused contact. This is what would be expected for PtSi:p-Si, where the barrier height is only 0.25 eV (5). Thus no phosphorus impurity effect is evident, just as in the case of 450°C PtSi:n-Si. Judging by what happens with 700°C PtSi:n-Si, however, there should be more than enough phosphorus diffusion to convert 10¹⁶/cm³ p-Si and produce an n-type layer at the PtSi-Si interface at this temperature. In other words, a p-n diode could be created in the p-Si. Figure 7 shows a rectifying characteristic for CVD Pt sintered with 3 ohm-cm B-doped Si at 700°C, 10 min. (We have not yet thoroughly analyzed this characteristic.)

Even though we have not been able to detect by analytical techniques $\cong 0.1\%$ P in the vicinity of the PtSi-Si interface, all the effects we have described are consistent with phosphorus doping of the Si adjacent to the "interface," wherever that might be. If the high-temperature diffusion constant for phosphorus in single-crystal Si is accepted for $\sim 600^\circ\text{C}$, it may be calculated that in 15 min, movement of the order of 10 \AA could occur. Of course, the Si near PtSi is highly stressed, and the crystal structure is undoubtedly highly disturbed also. Since 10¹⁹ B-doped Si was not compensated by the phosphorus, an upper limit of 10¹⁸/cm³ P can be assigned. It may then be calculated that a p-n junction to 3 ohm-cm p-Si would require of the order of 30 \AA phosphorus diffusion depth. Thus it appears entirely reasonable that diffusion of phosphorus into lightly doped silicon at $> 500^\circ\text{C}$ could be detectable in the I-V characteristics of what was intended to be a Schottky barrier contact.

A qualitative summary of the results of using CVD Pt to make PtSi contacts appears in Table III. In brief, with heavily doped Si and sintering at 450°-700°C no electrical anomalies appear. The contacts behave like those from the vacuum-deposited Pt that represents present practice. With light doping, there still is no problem provided a relatively low ($\sim 450^\circ\text{C}$) inter-

Table III. PtSi-Si room temperature I-V characteristics

	n ⁺	10 ¹⁵ -10 ¹⁹ /cm ³		
		n	p	p ⁺
Sputtered Pt, sinter 600°C	Ohmic	Schottky	Ohmic	Ohmic
CVD Pt, sinter 450°C	Ohmic	Schottky	Ohmic	Ohmic
CVD Pt, sinter 700°C	Ohmic	Ohmic	p-n diode	Ohmic

diffusion temperature is used. CVD Pt reliably forms PtSi at this temperature. With higher contact formation temperature, changes in the *I-V* characteristics set in; these effects apparently result from phosphorus out-diffusion from the PtSi. At PtSi formation temperature $\sim 700^\circ\text{C}$ contact behavior is altered to such a degree that PtSi formation from CVD Pt may be considered as contacting and phosphorus-doping in a single operation.

Acknowledgments

The author is indebted to James F. Roberts and Charles K. Sells, who performed most of the electrical measurements. The tests summarized in Table I were provided by J. B. Bindell. There were numerous helpful discussions with John M. Andrews.

Manuscript submitted July 26, 1974; revised manuscript received Jan. 16, 1975. This was Paper 17RNP presented at the San Francisco, California, Meeting of the Society, May 12-17, 1974.

Any discussion of this paper will appear in a Discussion Section to be published in the December 1975

JOURNAL. All discussions for the December 1975 Discussion Section should be submitted by Aug. 1, 1975.

Publication costs of this article were partially assisted by Bell Laboratories.

REFERENCES

1. M. J. Rand, *This Journal*, **120**, 686 (1973).
2. J. M. Morabito and M. J. Rand, *Thin Solid Films*, **22**, 293 (1974).
3. M. J. Rand and J. F. Roberts, *Appl. Phys. Letters*, **24**, 49 (1974).
4. J. B. Bindell, Bell Laboratories, Private communication.
5. M. P. Lepselter and J. M. Andrews, in "Ohmic Contacts to Semiconductors," B. Schwartz, Editor, p. 167, The Electrochemical Society Softbound Symposium Series, New York (1969); J. M. Andrews and M. P. Lepselter, *Solid State Electron.*, **13**, 1011 (1970).
6. R. J. Baughman and R. K. Quinn, *Mat. Res. Bull.*, **7**, 1035 (1972).
7. H. Jager and W. Kosak, *Solid State Electron.*, **12**, 511 (1969); N. G. Anantha and K. G. Ashar, *IBM J. Res. Dev.*, **15**, 442 (1971); P. Guteknecht and M. J. O. Strutt, *Appl. Phys. Letters*, **21**, 405 (1972).

Effect of Reactant Nitrogen Pressure on the Microstructure and Properties of Reactively Sputtered Silicon Nitride Films

C. J. Mogab, P. M. Petroff,* and T. T. Sheng

Bell Laboratories, Murray Hill, New Jersey 07974

ABSTRACT

The quality of silicon nitride films deposited by rf reactive sputtering of silicon in a nitrogen discharge is found to be strongly dependent on the discharge nitrogen pressure. For a given substrate to target spacing there is a "critical" sputtering pressure which, if exceeded, results in deposition of films with noticeably inferior properties. The properties of silicon nitride films deposited both above and below this critical pressure are compared. The degradation of film properties accompanying an increase in the nitrogen discharge pressure is correlated with the presence of microvoids ($\sim 50\text{\AA}$), revealed by transmission electron microscopy. It is suggested that the microvoids result from a reduction in the reemission of deposited material as the discharge pressure is increased.

Amorphous silicon nitride films have found widespread use in silicon integrated circuit processing, primarily as a junction seal against penetration by undesirable contaminants. Certain processing schemes require that the nitride film be deposited at low temperature ($\lesssim 350^\circ\text{C}$) thus making sputtering a potentially useful deposition technique. In the course of evaluating rf reactively sputtered silicon nitride films for integrated circuit applications we have found that the nitrogen pressure used during sputtering has a pronounced effect on film properties. Hu and Gregor (1) observed a similar effect, although they offered no explanation for it.

This paper describes some of the observed effects and correlates them with changes in film microstructure determined by transmission electron microscopy.

Experimental

Silicon nitride films were formed by the rf reactive sputtering of an 8 in. diameter silicon (99.999%) target in a research grade (<1 ppm total impurities) nitrogen discharge. A Varian sputtering module (Model No. 980-2097) and matching network mounted on an all

metal, turbomolecular pumped vacuum chamber were used for deposition. Gas pressure was measured with a capacitance manometer and controlled with a servo-driven leak valve.

Substrates for deposition were Si or thermally oxidized Si wafers which were supported on a grounded, stainless steel, water-cooled anode. Film thickness and refractive index were measured by ellipsometry at 5461\AA . In certain cases, film thickness was determined by Talystep measurement on a step created by etching in 7:1 buffered HF (BHF) solution. Infrared spectra were obtained with a Perkin-Elmer Model 621 spectrophotometer. Film stresses were determined by comparing wafer curvature before and after deposition. The curvature was measured by an optically levered laser technique.

Sodium penetration was measured by standard ^{22}Na tracer techniques. This involved deposition of a NaCl film containing ^{22}Na on nitride coated, thermally oxidized silicon wafers followed by annealing at 400°C for 22 hr in forming gas. ^{22}Na profiling was then done by repetitive etching and counting of the coincident 0.51 MeV gamma rays emitted at 180° to each other upon positron decay. BHF was used for etching except near the nitride-oxide interface where refluxed boiling phosphoric acid was employed to selectively etch the

* Electrochemical Society Active Member.

Key words: insulator films, transmission electron microscopy, ion bombardment.

nitride film. Autoradiographs were also made, using fast x-ray film, after various etch steps to reveal the spatial distribution of the remaining ^{22}Na .

Current-voltage and breakdown characteristics were measured using 10, 15, and 25 mil diameter aluminum field plates over nitride films deposited on 0.1 ohm-cm N-type wafers.

The microstructure of the silicon nitride films deposited on SiO_2 and Si substrates was investigated by transmission electron microscopy (TEM). Samples suitable for TEM observations were prepared by chemical etching of the substrate in a standard Si etch solution; the nitride film was protected by a wax coating during the thinning of the substrate. Carbon surface replicas were also made on several films which had been etched in BHF for various times. The thinned specimens and the carbon replicas were examined by TEM with a microscope operated at 200 keV in an attempt to correlate the film etching rate with its microstructure. In addition to the silicon nitride films deposited by sputtering, a few films deposited by chemical vapor deposition (CVD) using SiH_4 and NH_3 at 720°C were examined for comparison purposes.

Results

For a target to substrate spacing of 5 cm, the deposition rate for sputtering in pure N_2 was found to be nearly independent of pressure over the range 2-40 mTorr N_2 . The deposition rate increased nearly linearly with power density from 65 Å/min at 1 W/cm 2 to 215 Å/min at 4.8 W/cm 2 . In addition, the infrared spectra for films deposited within this pressure range were indistinguishable. An example of one such spectrum is shown in Fig. 1 for a 6400 Å thick film deposited at 8 mTorr and at a power density of 4.8 W/cm 2 . Figure 1 exhibits the prominent Si-N bands at ≈ 11.5 and 21 μm (2) and is representative of all sputtered films. No additional bands were observed in the range 2.5-50 μm .

In contrast to the relative insensitivity of infrared spectra to N_2 pressure, the BHF etch rate showed a marked dependence on pressure as seen in Fig. 2. These data are similar, although not identical, to those presented by Hu and Gregor (1) for rf reactively sputtered silicon nitride films. Hu and Gregor found an etch rate nearly independent of pressure between ≈ 2 -13 mTorr with a sudden step rise beginning at about 20 mTorr. They also noted that film density decreased by about 7% over the range of deposition pressure from 5 to 30 mTorr. However, they suggested that the increased etch rate could not be attributed solely to a lowering of the film density and proposed that the change might be due to an increase in the content of

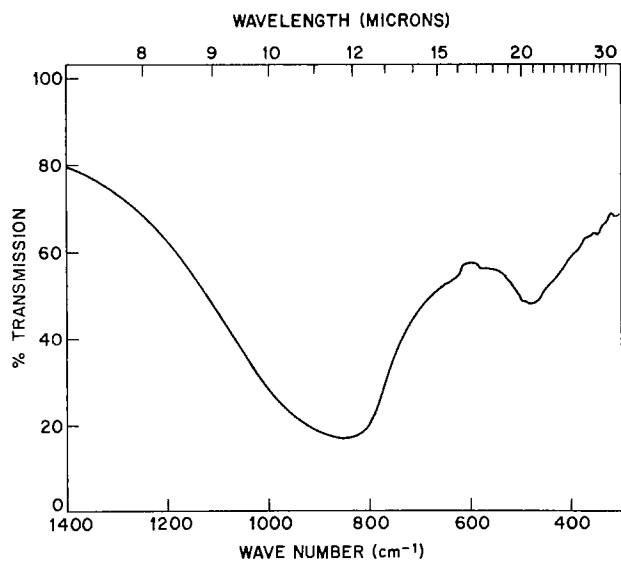


Fig. 1. Infrared spectrum of typical sputtered silicon nitride film. No additional peaks were observed between 2.5 and 8 μ .

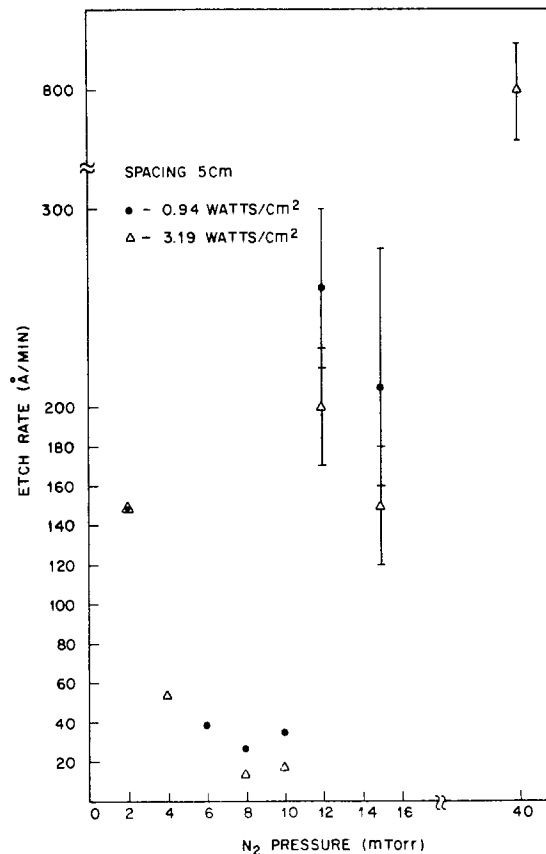


Fig. 2. Variation of film etch rate in 7:1 buffered HF solution with deposition pressure. (Si substrate.)

trapped impurities in the films formed at higher pressure. As will be shown, the increased etch rate and reduced density are both explainable in terms of the marked change in film microstructure which occurs above a certain "critical" deposition pressure whose magnitude depends on the substrate-target spacing.

It will be convenient to refer to films formed at pressures below this critical pressure as "good" films and those formed above it as "bad" films. The dependence of critical pressure on substrate-target spacing is shown in Fig. 3. The dashed line in Fig. 3 cor-

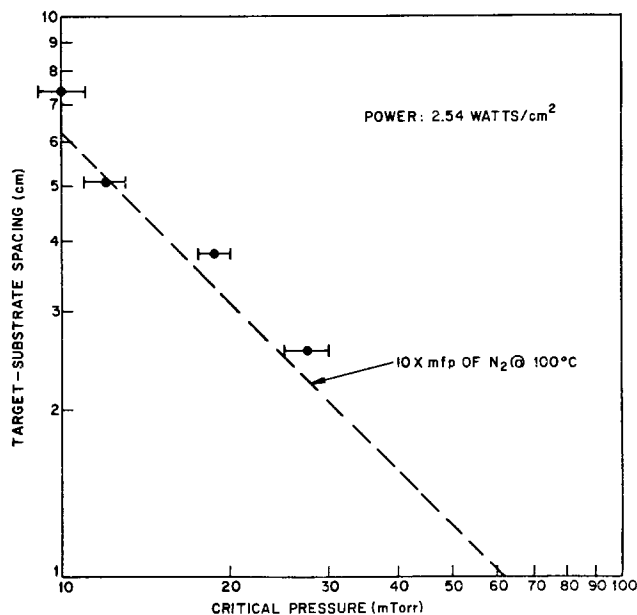


Fig. 3. The dependence of critical pressure on the substrate-target spacing. The dashed line corresponds to ten mean free paths for N_2 at 100°C .

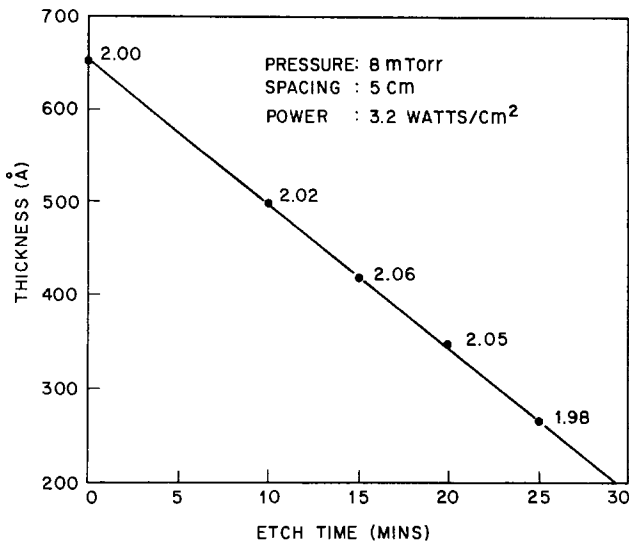


Fig. 4. Variation of film thickness with etch time in 7:1 BHF etchant. The numbers next to the data points correspond to refractive index values measured after each etch step. (Si substrate.)

responds to ten mean free paths for N_2 at $100^\circ C$. Its significance is discussed later. The critical pressure at a fixed spacing is relatively insensitive to power density although films formed at low power ($<2.5 W/cm^2$) and just below the critical pressure often exhibit some features of bad films. That is, the demarcation pressure separating good and bad films is somewhat more diffuse than is implied by stating a single value for the critical pressure. In any case, films deposited at 1 mTorr or more in excess of the critical pressure are reproducibly bad. Films deposited by sputtering in mixtures of argon and nitrogen exhibit the same microstructural dependence on total pressure as those deposited in pure N_2 . In this case the N_2 content of the mixture must exceed $\approx 10\%$ in order to produce a nitride film.

It is worthwhile to present some differences in properties between good and bad films before considering their microstructures. Figure 4 indicates the BHF etch behavior of a good film, and shows that the etch rate and refractive index are constant through the film thickness, within the accuracy of the measurements. In contrast, bad films etch at a nonuniform rate and have an apparent refractive index which varies erratically through the film. An example of the results of etching a bad film are given in Table I. Note that the refractive index and thickness as determined by ellipsometry show inconsistencies. The ellipsometric measurements were made after removal of the film from the etchant followed by a DI H_2O rinse and spin drying. Measurement of etch rate and refractive index has proved to be a reasonably sensitive method of distinguishing good and bad films.

Figure 5 illustrates typical $I-V$ characteristics for good and bad films. Good films always exhibit linear

Table I. Etch behavior of a bad film; etchant, 7:1 buffered HF solution

Etch time, min	Ellipsometric parameters		Apparent refractive index	Apparent thickness, Å
	Δ	ψ		
0	187.85	12.35	—	1750*
1	226.20	12.46	2.60	986
2	258.50	16.40	2.26	1082
3	286.88	28.26	1.84	1238
4	305.79	62.00	1.64	1120
5	74.18	45.25	1.54	846
6	81.58	21.81	2.06	360
7	94.14	27.74	1.48	456
8	109.22	19.29	1.51	299

* Actual as-deposited thickness as measured on an etched step using a Talystep.

$\ln I$ vs. $V^{1/2}$ plots indicative of a Poole-Frenkel conduction mechanism,¹ whereas $I-V$ data for bad films

¹ Other conduction mechanisms can yield the same functional dependence of current on voltage. The slope of the straight line in Fig. 5 yields a dielectric constant for silicon nitride films of 4 when the Poole-Frenkel mechanism is assumed.

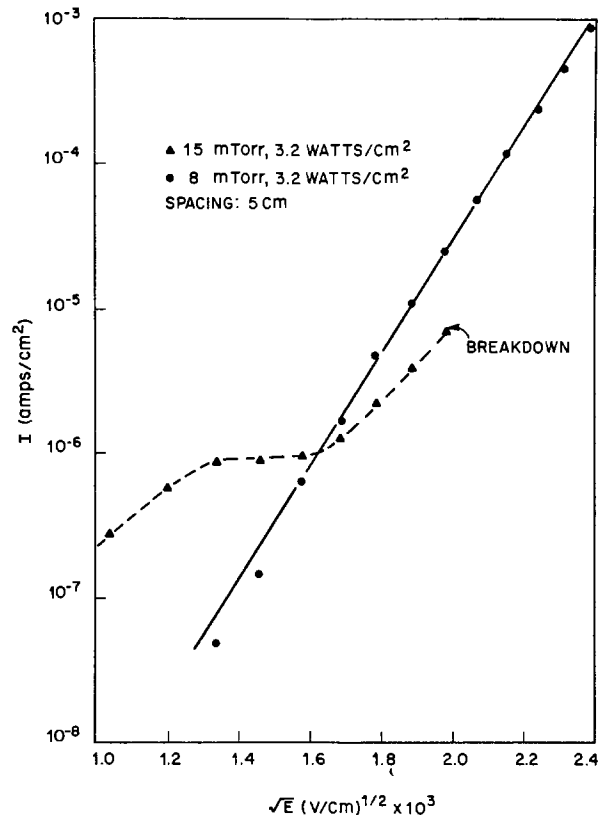


Fig. 5. Current voltage characteristics of good (8 mTorr deposition pressure) and bad (15 mTorr deposition pressure) films.

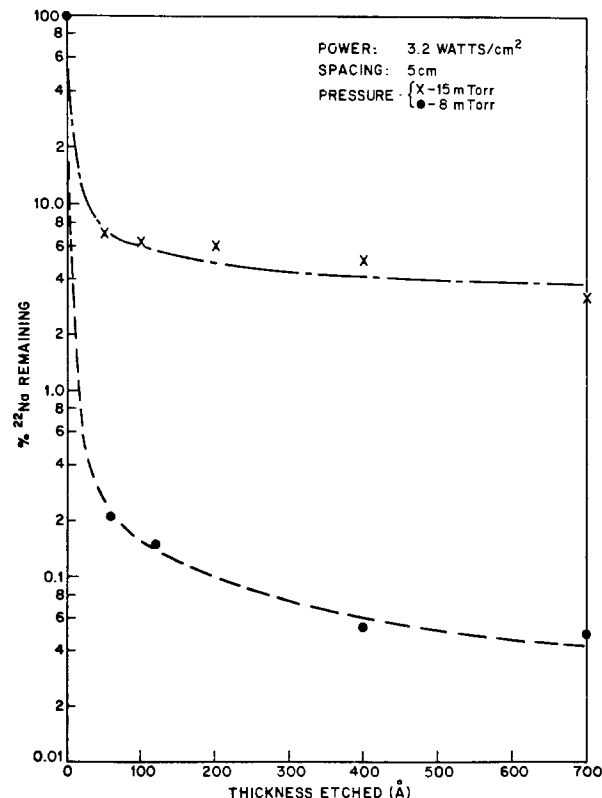


Fig. 6. Penetration profiles for ^{22}Na in good (8 mTorr deposition pressure) and bad (15 mTorr deposition pressure) films following a 22 hr, $400^\circ C$ drive-in. Both films were 1400Å thick as-deposited.

invariably exhibit curvature when plotted in the same manner. Moreover, bad films break down on the average at approximately half the field needed to cause breakdown in good films.

Figure 6 shows Na penetration profiles for good and bad films following a 400°C, 22 hr anneal. Autoradiographs taken at selected depths indicate that penetration is nearly uniform over the bad film and not just a result of a few large, isolated defects in the film. In contrast, for good films, penetration occurs only at isolated defects (e.g., pinholes).

Stress measurements indicate little or no difference in the stresses in good and bad films deposited at the same power density. For example, films deposited at 3 W/cm² exhibit a compressive stress of about 8×10^9 dynes/cm² independent of the discharge N₂ pressure.

TEM analysis of the films shows them to be completely amorphous. A phase contrast technique (3) was used to image possible microdefects which might be present in the bad films. A series of electron micrographs of the films taken under "overfocused," "in

focus," and "underfocused" conditions indicate the presence of microcavities in the bad films. As shown in Fig. 7, the contrast of the cavities is reversed when imaged in under- or overfocused conditions. No cavity contrast is visible in the "in focus" condition indicating that the strain field of these defects is small. The density and size of the cavities is dependent on the pressure and power of deposition. As seen in Fig. 8, the density of cavities as a function of pressure (at a power density of 2.54 W/cm²) varies from 0 to $10^{12} \times \text{cm}^{-2}$. The size of the cavities (see Fig. 7) ranges from ≈ 10 to $\approx 50 \text{ \AA}$. From stereoelectron micrograph pairs the cavities are found to be more numerous at the side of the silicon nitride film close to the substrate. The good films and CVD films imaged with the same contrast technique do not show any cavities.

The etched silicon nitride surfaces are also different for the good and bad films. The TEM micrographs of carbon surface replicas for the bad films show that a very irregular and rough surface develops near the film-substrate interface subsequent to etching (see Fig.

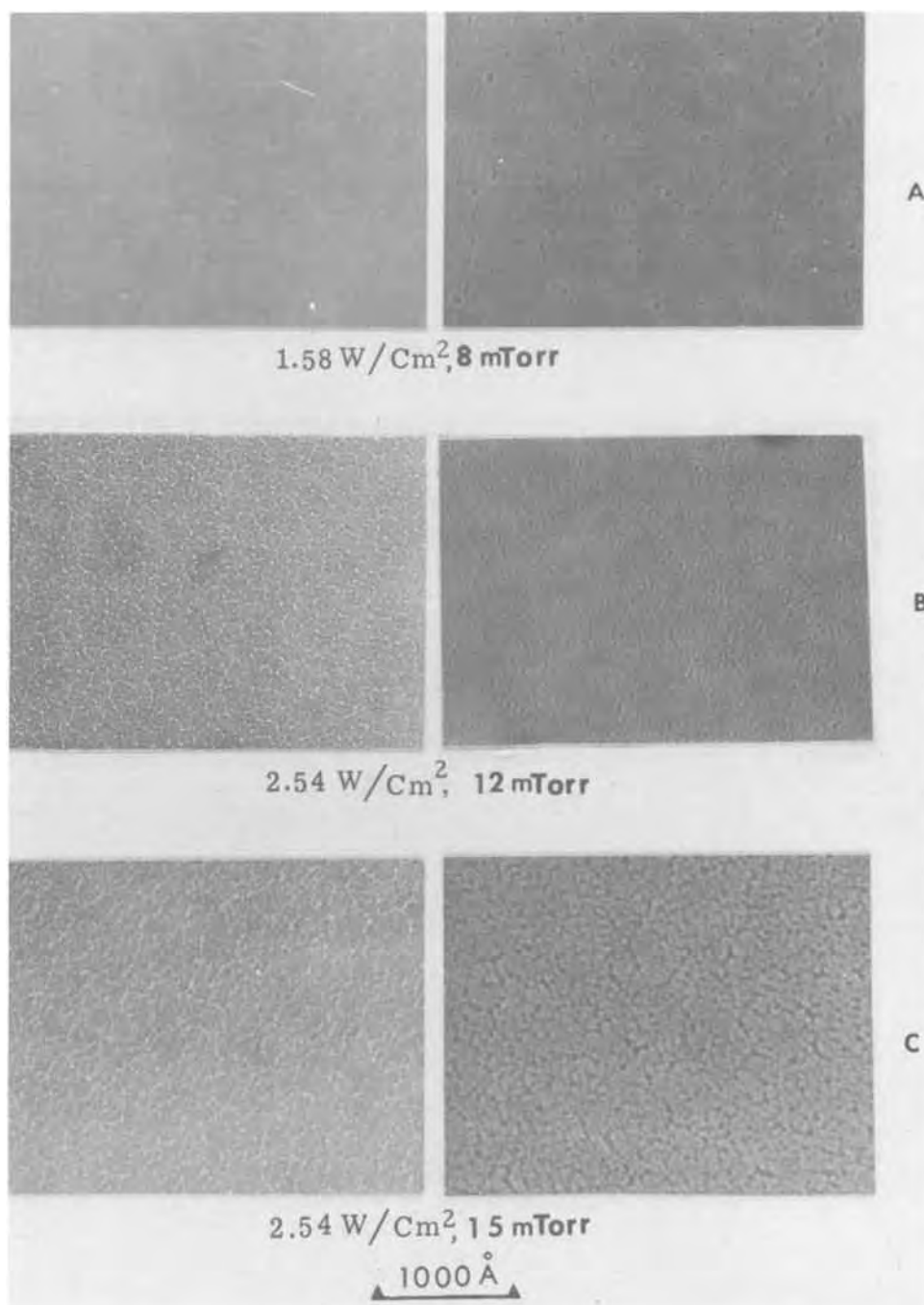


Fig. 7. Bright field transmission electron micrographs of sputtered silicon nitride films deposited under various power and N₂ pressure conditions. The micrographs in the left and right columns correspond, respectively, to underfocused and overfocused imaging conditions.

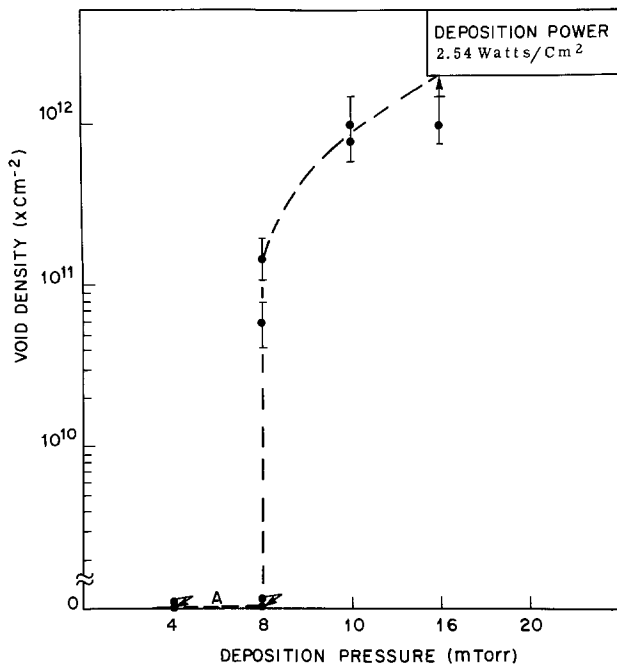


Fig. 8. Void density as a function of deposition pressure for silicon nitride films deposited at 2.54 W/cm².

9). The etched surface of a good film is smooth and regular through the entire film thickness, as shown in Fig. 10.

Discussion

The TEM structural analyses strongly suggest that the marked increase in etch rate and sodium penetration in films formed above the critical pressure arises from the large amount of internal surface area associated with the microvoids present in these films. It should be pointed out that good and bad films (of equivalent thickness) are indistinguishable by visual inspection. The microvoids are too small to produce detectable scattering of visible light and thus as-deposited bad films are quite specular and uniform in appearance. Extended etching of bad films generally leads to a less specular, nonuniform appearance due to surface roughening (see Fig. 9), whereas good films remain specular and uniform on etching (Fig. 10). Surface roughening evidently results from penetration of the etchant into the microvoids. The roughened surface and the possibility of trapped etchant or rinse in the voids probably account for the anomalous variation of measured refractive index following step etching (see Table I).

The extent and uniformity of sodium penetration over the entire slice in the case of bad films would indicate that the microvoids are distributed throughout the film and form an interconnected network. As noted before, however, there is evidence from TEM stereo pairs and surface replicas of etched films (see Fig. 9) that the microvoids are more concentrated near the substrate-film interface.² In the presence of a void network sodium can migrate by surface diffu-

² When pressure is changed in the middle of a run from less than to greater than the critical pressure films containing microvoids result indicating that these defects are not due to some nucleation phenomenon.

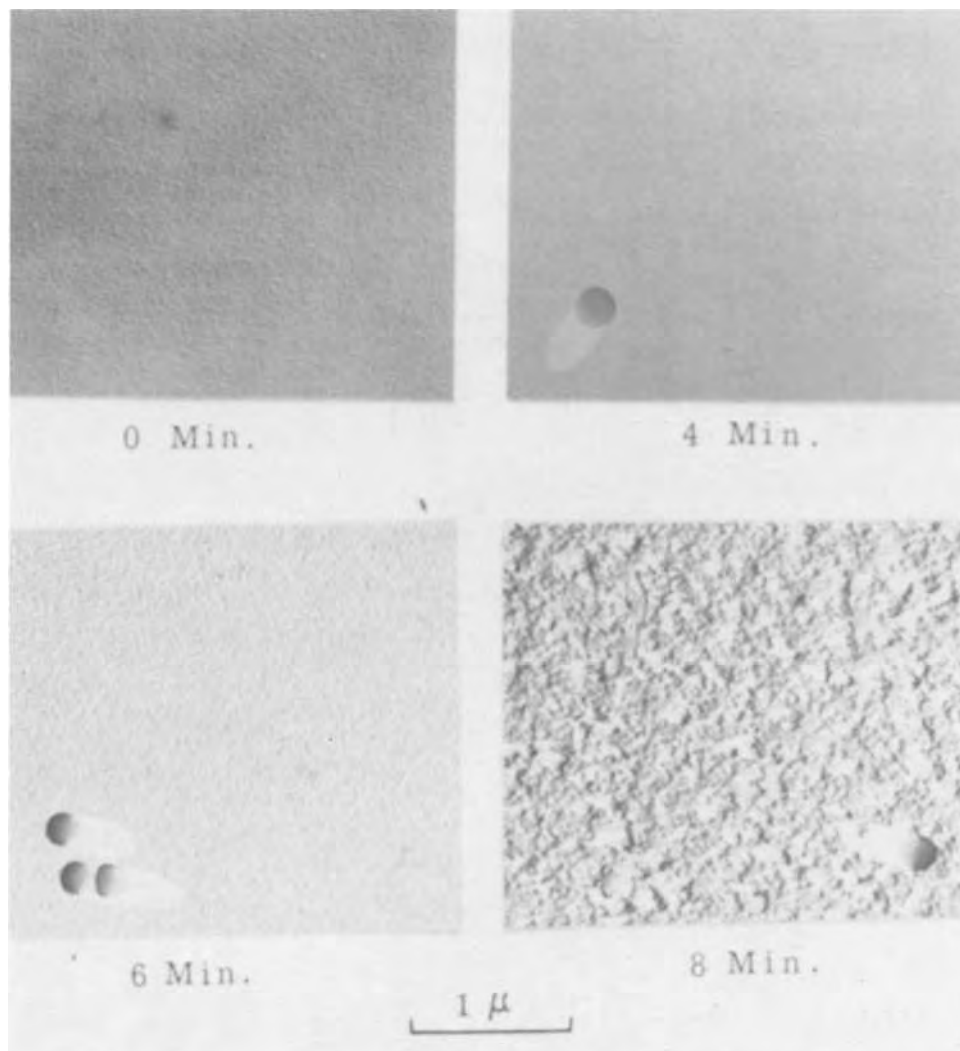


Fig. 9. Transmission electron micrographs of surface carbon replicas of a bad silicon nitride film as a function of increasing etching time.

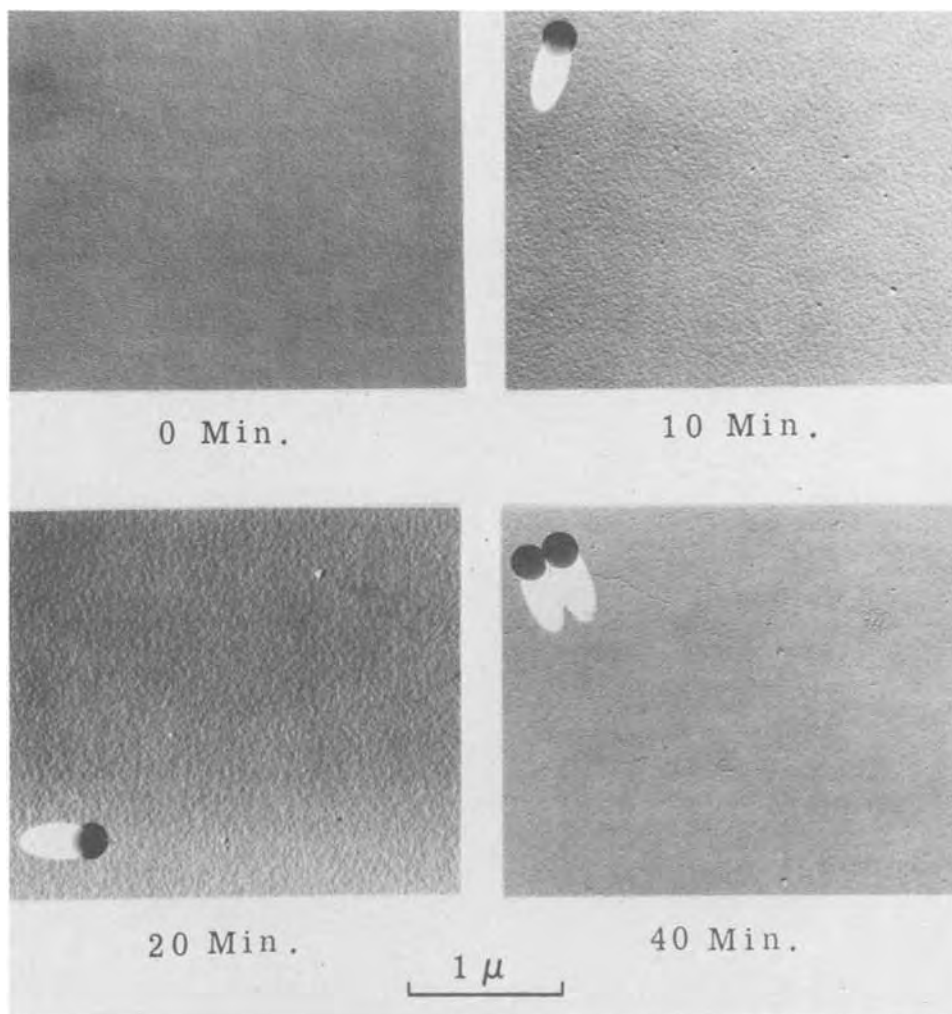


Fig. 10. Transmission electron micrographs of surface replicas of a good silicon nitride film as a function of increasing etching time.

sion which is expected to be considerably faster than diffusion through bulk regions of a dense nitride film. Pinhole-free regions of good films exhibit excellent resistance to the penetration of sodium and are comparable in this respect to high temperature CVD silicon nitride films.

Whereas, the microvoids are clearly responsible for the marked differences between good and bad films, the reason for the existence of the voids is less evident. Possible explanations include impurity effects, change in reaction site, gas trapping, and the effects of energetic particle bombardment on film growth.

Impurity effects should be considered since an increase in pressure which produces the transition from good to bad films can result in an increased impurity content of the film. This can occur as a result of an increased partial pressure of impurity gases introduced with the sputtering gas or because of an increase in discharge-induced heating and outgassing effects. Accordingly, the impurity content of good and bad films was compared, semiquantitatively, by ion scattering and by combining ion milling with Auger spectroscopy. No pronounced differences in impurity content of good vs. bad films were found. For both types of films oxygen was the only detectable impurity (<1%); the oxy-

gen content was highest at the free surface of the films and decreased rapidly with depth. On the average, bad films had a higher oxygen content than good films but never by more than a factor of two. It seems likely that the enhanced oxygen content of bad films is a result of adsorption, both during and after deposition, within microvoids rather than their cause. This conclusion is supported by the fact that oxynitride films intentionally "doped" with substantial amounts of oxygen do not contain microvoids. Thus, impurity effects

do not provide a reasonable explanation for void formation.

Mixtures of argon and nitrogen wherein the nitrogen pressure is held below the critical value but the total pressure is above the critical value also result in microvoids. This observation would seem to rule out any void formation mechanism dependent on a change in reaction site from substrate to cathode as the N_2 pressure is increased. Additional evidence in support of this contention comes from the invariance of deposition rate and film stress as nitrogen pressure is increased. Both of these parameters might reasonably be expected to change if the reaction site shifted within a small range of pressure.

Trapping of the discharge gas in the film can also be considered as a possible mechanism for microvoid generation. Gas entrapment presumably must occur in conjunction with sorption of the gas at or near the surface of a growing film. Molecular nitrogen (N_2) in the ground state, which is the predominant species impinging on the film during growth,³ is not chemisorbed (4) and thus, cannot be trapped. There are several species in the discharge, however, which presumably bombard the film and can be chemisorbed. In this regard the work of Shahin (5) is of interest. He studied the ions present in the cathode region of a nitrogen discharge and found that N_2^+ and N^+ were the dominant species, with N^+ being formed primarily in the dark space according to $N_2^+ + N_2 \rightarrow N^+ + N + N_2$. Thus, N_2^+ , N^+ , and N are present in the discharge. Atomic nitrogen impacting the film should be readily chemisorbed. Since the insulating nitride film probably floats at a negative potential with respect to the

³ According to Winters and Kay (4) the ratio of excited to ground-state species in a typical sputtering discharge is less than 10^{-3} .

plasma during deposition some bombardment by N_2^+ and N^+ must also occur. Either of these species can be sorbed; the N^+ being highly active and the energetic N_2^+ (>8 eV) having a high probability of dissociation upon impact with the film surface (4, 6). Therefore, the sorbed species in every case is atomic nitrogen. It is reasonable to assume that these sorbed atoms are converted to silicon nitride "molecules," i.e., that the reaction between silicon and nitrogen occurs at the substrate via these sorption events (7). Such a highly active sorbate would be unlikely to revert to N_2 and become trapped in the film. There is, of course, the possibility that energetic neutral N_2 molecules are driven into film and trapped as suggested by Cordes (8). [Trapping of energetic Ar in sputtered Ni films has been observed by Winters and Kay (6).] However, this effect should be reduced by an increase in pressure [as is the case for Ar entrapment (6)] and would thus not explain the formation of microvoids at higher pressure. In short, gas entrapment does not seem to afford a viable explanation.

In an attempt to confirm this expectation several samples of good and bad films deposited under identical conditions (5 cm spacing, 3.2 W/cm²) except for the discharge pressure were analyzed by Rutherford backscattering (9) of 1.8 MeV $^4He^+$ ions. From these measurements one can determine the ratio of silicon to nitrogen atoms at a particular depth in the film, with a depth resolution of the order of 200 Å. Films deposited below the critical pressure had a silicon to nitrogen ratio of ≈ 0.6 while those deposited above it had a ratio of ≈ 0.76 . In both cases this ratio was constant with depth into the film. Thus, good films are nitrogen rich (based on a comparison to the compound Si_3N_4) while bad films are more nearly stoichiometric. This result is obviously inconsistent with the hypothesis of gas entrapment being the cause of microvoid formation. Moreover, as already mentioned, films formed in mixtures of argon and nitrogen, such that the nitrogen partial pressure was well below the critical pressure but the total pressure was just above it, still contained microvoids. The probability for trapping argon is much smaller than for nitrogen (4); thus, suggesting again that gas entrapment is not responsible for microvoid formation.

A more plausible mechanism for microvoid generation can be inferred from the functional form of the dependence of critical pressure on substrate-cathode spacing. Figure 3 shows that the critical pressure is raised in inverse proportion to the spacing. An identical relationship exists between the N_2 molecular mean free path and pressure as indicated by the dashed line in Fig. 3. This suggests that the existence of micro-

voids is related to the extent to which energetic particle (atoms, ions, molecules) bombardment of the growing film is suppressed. For a given substrate-cathode spacing the number of energy dissipative collisions suffered by the average particle (ion, atom, molecule) increases rapidly with pressure so that the energy of the particle at the instant of impact with the growing film is strongly dependent on pressure. The higher the pressure the less the energy, on the average, of the particles bombarding the film. Energetic particle bombardment can lead to densification in at least two ways: (i) enhancement of surface mobility of depositing atoms and (ii) reemission of weakly bound atoms or clusters which are in unfavorable positions for achieving optimum density. Both of these effects will be attenuated due to scattering collisions as pressure is increased.

Reemission of deposited material has been shown to be necessary for obtaining high quality rf sputtered SiO_2 films (10-12), formed by sputtering of an SiO_2 target. The work on SiO_2 films can be summarized as follows. The reemission coefficient (a measure of the fraction of deposited material reemitted from the film surface during deposition) decreases when either pressure or cathode to substrate spacing is increased (10-11). For a fixed spacing and pressure the reemission coefficient is increased by an increase in negative bias at the surface of the growing film, indicating that energetic positive ion bombardment is a major contributor to reemission. However, reemission can still occur at zero bias due to bombardment by energetic neutrals (11, 12).

Assuming that a high reemission coefficient is necessary to the attainment of defect-free films, one would expect that the onset of microvoid generation would be dependent on power (or cathode self-bias) as well as pressure since the former parameter determines the energy spectrum of excited species in the discharge. This is consistent with our observations. Deposition at lower power (<2.5 W/cm²) can result in microvoids even at pressures slightly below the critical pressure for higher power deposition. We had also anticipated, on the basis of the reemission model and consideration of the results on sputtering of SiO_2 (10-12), that deposition in the presence of an rf bias on the substrate would lead to high quality, void-free films even at pressures somewhat above the critical pressure. This follows from the fact that use of an rf bias results in a d-c self-bias on the depositing film which is negative with respect to the plasma and should therefore promote positive ion bombardment. To our surprise, the application of rf biases resulting in d-c self-bias values ranging from -150 to $-300V$ yielded films having

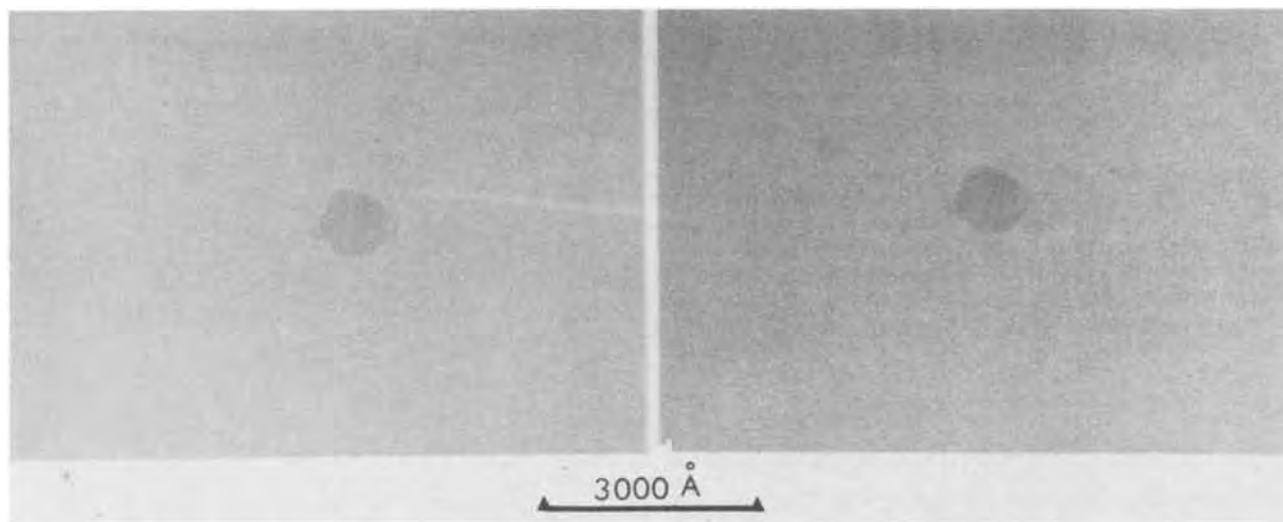


Fig. 11. Transmission electron micrographs of an rf bias sputtered silicon nitride film. The micrographs in A (left) and B (right) correspond, respectively, to underfocused and overfocused imaging conditions.

BHF etch rates from 300-600 Å/min. This was true even at total discharge pressures well below the critical pressure for a given spacing. TEM examination revealed that films formed under rf bias, both above and below the nominal critical pressure, did not contain microvoids. However, as shown in Fig. 11 for a film deposited with a 10% rf bias, the microstructure of these films was different than that for good films formed in the absence of applied bias. In addition, Rutherford backscattering studies revealed that bias-sputtered films were substantially more nitrogen-rich than films deposited without bias. The silicon to nitrogen ratio for rf bias sputtered films was ≈ 0.5 . The higher nitrogen content is consistent with an increased positive ion bombardment as expected.

The absence of voids at pressures greater than the critical value in the bias sputtered case is consistent with the reemission model. The change in microstructure and marked increase in etch rate of bias sputtered films suggest that the reaction does, in fact, occur at the substrate and that these parameters may be very sensitive to the film stoichiometry in the nitrogen-rich regime. More work is needed to clarify this.

Conclusions

The microstructure of silicon nitride films deposited on electrically grounded or isolated substrates and formed by rf sputtering of a silicon target in a nitrogen discharge is strongly influenced by the nitrogen pressure. An increase of pressure beyond a certain critical value results in the incorporation of microscopic ($\sim 50\text{Å}$) void-like defects which can be observed directly by a through-focus TEM technique and which are responsible for marked degradation of film properties. The interdependence of critical pressure and the substrate-target separation has a functional form which suggests that the voids arise from the reduction of energetic particle bombardment of the growing film at higher pressure. This results in a reduction in the mobility of adsorbed atoms or molecules at the surface

of the film and/or a decrease in the reemission of condensed material.

Acknowledgments

The authors wish to thank H. J. Levinstein and R. S. Wagner for helpful advice pertaining to this work. We are indebted to J. M. Poate for the Rutherford backscattering studies and to C. C. Chang for Auger analysis.

Manuscript submitted Oct. 21, 1974; revised manuscript received Dec. 30, 1974.

Any discussion of this paper will appear in a Discussion Section to be published in the December 1975 JOURNAL. All discussions for the December 1975 Discussion Section should be submitted by Aug. 1, 1975.

Publication costs of this article were partially assisted by Bell Laboratories.

REFERENCES

1. S. M. Hu and L. V. Gregor, *This Journal*, **114**, 826 (1967).
2. E. A. Taft, *ibid.*, **118**, 1341 (1971).
3. M. Rühle, in "Radiation Induced Voids in Metals," J. W. Corbett and L. C. Ianniello, Editors, Vol. 26, p. 255, USAEC Symposium Series (1972).
4. H. F. Winters and Eric Kay, *J. Appl. Phys.*, **43**, 794 (1972).
5. M. M. Shahin, *J. Chem. Phys.*, **43**, 1798 (1965).
6. H. F. Winters and Eric Kay, *J. Appl. Phys.*, **38**, 3928 (1967).
7. E. Hollands and D. S. Campbell, *J. Mater. Sci.*, **3**, 544 (1968).
8. L. F. Cordes, *Appl. Phys. Letters*, **11**, 383 (1967).
9. W. K. Chu, J. W. Mayer, M. A. Nicolet, T. M. Buck, G. Amsel, and F. Eisen, *Thin Solid Films*, **17**, 1 (1973).
10. L. I. Maissel, R. E. Jones, and C. L. Standley, *IBM J. Res. Develop.*, **14**, 176 (1970).
11. R. E. Jones, C. L. Standley, and L. I. Maissel, *J. Appl. Phys.*, **38**, 4656 (1967).
12. J. S. Logan, *IBM J. Res. Develop.*, **14**, 172 (1970).

Technical Note



The Relative Dielectric Constant of Two Semiconductor Passivation Glasses

Alvin M. Goodman, Kenneth W. Hang, and James M. Brece

RCA Laboratories, Princeton, New Jersey 08540

A variety of glasses is commercially available for hermetically sealing and thereby passivating silicon devices against the effects of hostile ambient environments. The glass is often used in direct contact with the silicon at or near p-n junctions. The operating characteristics of the devices may for this reason depend strongly upon the relative dielectric constant K of the glass. This is particularly true when large reverse bias is applied to the junctions. This note describes the measurement of K for two widely used commercial glasses, Innotech IP760 and IP820.¹ To our knowledge, no previous measurement of K for these glasses has been reported.

Key words: glass properties, silicon-passivation glass, dielectric measurement.

¹ Further information available from Innotech Corporation, Norwalk, Connecticut 06851.

The usual methods of forming layers of this type of glass (1)¹ may, under some conditions of preparation, lead to bubble formation thereby rendering the material unsuitable for a measurement of K . We chose to circumvent this problem by using a long glass fusion time to allow bubble dissipation. This is treated below wherein we describe the preparation of "bubble-free" glass samples and appropriate electrode structures. The electrical measurements and results are also presented.

Sample Preparation

Glass fusion.—The glass samples were prepared by powder fusion of the commercial glass. Due to the high fraction of glass particles in a size range below 2μ , a long fusion time was necessary to remove the small bubbles. A covered platinum + 40% rhodium

crucible of 80 cm³ capacity was used to fuse the powder in an air ambient for 20 hr at 1200°C. The crucible was then quickly cooled in air to facilitate removal of the solidified glass from the crucible. The IP820 glass was annealed at 650°C for 1 hr and slow-cooled in the furnace. The IP760 glass was annealed at 540°C for 1 hr and slow-cooled in the furnace.

Glass analysis.—By physical property and wet chemical analysis the glasses were found to have the composition shown in Table I.

Shaping and polishing.—A disk (right-circular cylinder) with nominal dimensions of 2.1 cm diameter and 0.1 cm thick was cut from each fused boule. The two large faces of the disk were made flat, parallel, and smooth by polishing with progressively finer abrasive, finishing with 0.5 μ diamond paste. The surfaces were flat to better than $\lambda/4$ of the green line of mercury and parallel within 25 sec of arc. A microscopic examination of the disk showed that it was "bubble-free." That is, the bubble volume was less than one part in 10⁶ of the volume of the glass.

Electrodes.—Evaporated aluminum was used to produce a "three-electrode system" (2) on the faces of each disk. A single solid layer (unguarded electrode) was used on one side while the pattern on the other side consisted of a center area (guarded electrode) of circular geometry surrounded by an annular layer (guard electrode).

Dimensions.—Multiple observation measurements were carried out to determine the average values and probable errors of the diameter, $2r_1$, of the guarded electrode, the gap, g , between the guarded and guard electrodes, and, t , the thickness of the disk. An optical comparator (Nikon Shadowgraph) was used for the measurements of $2r_1$ and g ; a dial-indicator-type mechanical height comparator was used for the t measurements. The accuracy of each comparator was checked against gauge blocks (dimensions certified to 5×10^{-6} in.). The resultant values and their probable errors (3) are given in Table II.

Electrical Measurements and Results

Three terminal grounded-guard capacitance measurements were carried out in the frequency range 10²-10⁶ Hz. Three capacitance bridges were used to cover this range: a General Radio Model 1615A (10²-10⁵ Hz), a Boonton Electronics Model 75C (5×10^3 to 5×10^5 Hz) and a Boonton Electronics Model 75B-S8 (10⁶ Hz). All of the measurements were performed with the sample at room temperature. The results are shown for IP760 in Fig. 1 and for IP820 in Fig. 2. The agreement between the results obtained using different bridges is excellent and well within the maximum expected inaccuracy for any data point (0.25%). There is a small but clearly observable decrease in capacitance with increasing frequency for each sample. Within the frequency range measured this decrease is approximately linear with the logarithm of frequency.

Table I. Composition in mole per cent of major constituents of IP760 and IP820

	PbO	SiO ₂	B ₂ O ₃	Al ₂ O ₃
IP760	18.3	65.3	14.0	2.4
IP820	23.7	69.8	—	6.5

Table II. The average values and probable errors of the sample dimensions

	\bar{r}_1 , cm	\bar{t} , cm	\bar{g} , cm
IP760	0.40495 \pm 0.00083	0.09223 \pm 0.00004	0.04222 \pm 0.00122
IP820	0.40423 \pm 0.00094	0.10127 \pm 0.00049	0.04353 \pm 0.00133

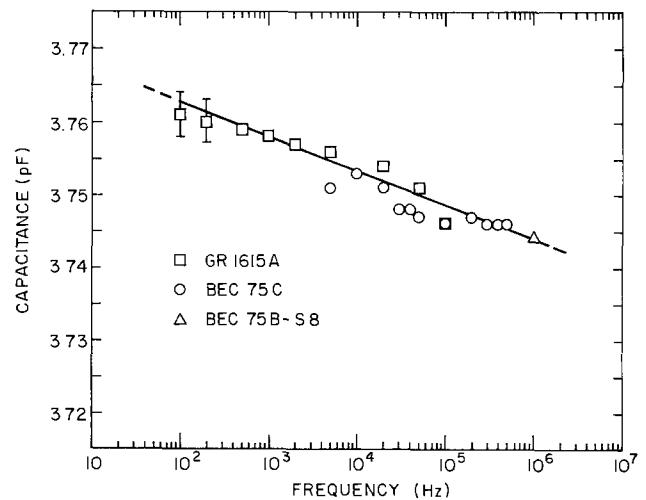


Fig. 1. Capacitance vs. frequency of a sample of IP-760 glass using a three-electrode, grounded-guard system. The data symbols indicate the manufacturer and model of the capacitance bridge used for each measurement (see text). The flags on the data points at 100 and 200 Hz indicate the approximate width of the null point determinations; at higher frequencies the null points could be determined within ± 0.001 pF.

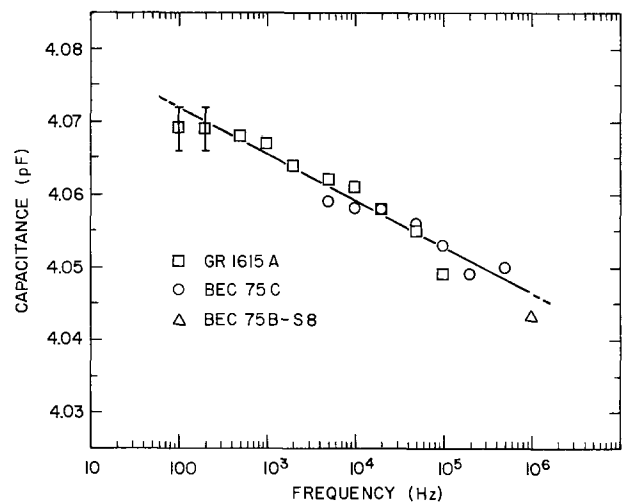


Fig. 2. Capacitance vs. frequency of a sample of IP-820 glass using a three-electrode, grounded-guard system. The data symbols indicate the manufacturer and model of the capacitance bridge used for each measurement (see text). The flags on the data points at 100 and 200 Hz indicate the approximate width of the null point determinations; at higher frequencies the null points could be determined within ± 0.001 pF.

The capacitance C and the relative dielectric constant K are linearly related by the formula

$$K \equiv SC = \frac{t}{\pi r^2 \epsilon_0} C \quad [1]$$

where S is a constant that is determined by the structure (geometry) of the sample and r is the effective radius of the guarded electrode. The value of r is given by (2, 4)

$$r = r_1 + g/2 - \frac{2t}{\pi} \ln \cosh \left(\frac{\pi g}{4t} \right) \quad [2]$$

The value of S and its probable error limits (3) have been computed from the sample dimensions

$$\begin{aligned} S(\text{IP760}) &= (1.859 \pm 0.004) \times 10^{12} \text{F}^{-1} \\ S(\text{IP820}) &= (2.040 \pm 0.011) \times 10^{12} \text{F}^{-1} \end{aligned}$$

Since the capacitance varies with frequency, K is, in fact, not a constant. As a practical matter, however,

we can say that in the range 10^2 - 10^6 Hz, $K(\text{IP760}) = 6.98$ and $K(\text{IP820}) = 8.28$ within 1%.

Acknowledgment

The assistance of Carl Bjorling with the sample preparation is gratefully acknowledged.

Manuscript submitted Dec. 4, 1974; revised manuscript received Feb. 6, 1975.

Any discussion of this paper will appear in a Discussion Section to be published in the December 1975 JOURNAL. All discussions for the December 1975 Discussion Section should be submitted by Aug. 1, 1975.

Publication costs of this article were partially assisted by RCA Corporation.

REFERENCES

1. W. A. Pliskin and E. E. Conrad, *Electrochem. Technol.*, **2**, 196 (1964).
2. R. F. Field, in "Dielectric Materials and Applications," A. R. von Hippel, Editor, The Technology Press of MIT and John Wiley and Sons, Inc., New York (1954).
3. H. Margenau and G. M. Murphy, "The Mathematics of Physics and Chemistry," Ch. 13, D. Van Nostrand Co., New York (1963).
4. W. G. Amey and F. Hamburger, Jr., *Proc. Am. Soc. Testing Materials*, **49**, 1079 (1949).

Selective Removal of BP from Si Substrate

M. Takigawa, T. Satoh, and K. Shohno

Department of Electronics, Sophia University, Chiyoda-ku, Tokyo, Japan

Boron monophosphide (BP) can be epitaxially grown on Si substrates by the thermal reaction of B_2H_6 and PH_3 in the presence of H_2 (1-3). The crystallographic orientation of the BP is the same as that of the Si substrate. BP is chemically stable and is not attacked by normal chemical etchants. BP has a forbidden energy gap of 2.0 eV (4) and may be useful as an optoelectronic material. For optoelectronic applications a technique must be found for removing the BP selectively from the Si substrate.

The experimental apparatus for epitaxial growth of BP has been reported in a previous paper (3). A BP thin film of n-type with a thickness of 0.5 - $5 \mu\text{m}$ was grown at a substrate temperature of 950°C . The Si (100) substrates used had a thickness of $180 \mu\text{m}$ and a resistivity of 5 - 8 ohm-cm (p-type). The BP obtained had an electron concentration of $5 \times 10^{18} \text{ cm}^{-3}$ and a Hall mobility of 40 - $60 \text{ cm}^2/\text{V-sec}$. When the thickness of the BP grown on the Si (100) substrate was less than $7 \mu\text{m}$, the surface of the BP was as smooth as the Si substrate, and no bending of the wafers could be detected. However, when the thickness of the BP film was more than $7 \mu\text{m}$, crack lines along $\langle 011 \rangle$ directions in the BP, and bending of the wafers were observed.

After the epitaxial growth of the BP on the Si substrates, the water was spin-coated with liquid photoresist and then baked to drive off the resist solvents. It was then exposed with a standard test mask. The resists used in this experiment were of positive type (AZ 1350) and negative type (KTFR). The mask pattern was oriented to the flat edge of the wafer, which is parallel to a $\langle 011 \rangle$ direction. Subsequent development of the photoresist removed the resist from the unnecessary areas. After a second bake to complete the polymerization of the photoresist, the wafer was ready for electrolytic removal.

The experimental apparatus for removing the BP, shown schematically in Fig. 1, is the same as that used for anodic oxidation of Si wafers. The solution consisted of 4N aqueous sodium hydroxide. The Si wafer was placed at the anode side, and a platinum plate was used as the cathode. A d-c pulse voltage was repeatedly impressed. The duration of the d-c pulse voltage was adjusted to 1 sec in this experiment. After all the BP was removed from those areas that were free of photoresist, the remaining photoresist was removed in a suitable stripping solution.

When the first voltage pulse of 30 - 50V was applied, crack lines in the BP film along the edge of the resist were clearly visible with an optical microscope. This is

an initial change observed in the BP. After a few more pulses, the BP areas free from resist changed to a yellowish color. At this stage, exposure to ultrasonic vibrations in an organic solvent was found to be the easiest way to remove the BP from the Si substrate. The bare Si surface areas were not oxidized. An example of the process, using a resist of the positive type and one of the negative type is shown in Fig. 2 (a) and (b). Minimum BP line-widths and spacing are $4 \mu\text{m}$ for AZ 1350 and $2 \mu\text{m}$ for KTFR. The limiting dimensions are determined by the size limitation of the photoresist.

By repeating the voltage pulse, the BP can also be removed from the Si substrate without the use of ultrasonic agitation. The BP film removed floated on the solution and the bare Si surfaces were anodically oxidized. When a voltage pulse of more than 50V was applied, the BP could be removed from the Si substrate with only one or two pulses.

When a constant d-c voltage was applied, the resist curled up at the edges and eventually came off.

Several alkaline and acid solutions were used, but almost any kind of ionic solution can be used successfully for this purpose. The number of voltage pulse repetitions needed for the complete removal of the BP did not depend on the solution used.

However, the total number of voltage pulse repetitions needed for the complete removal of the BP depended on the thickness of the BP. For a thin BP film ($0.5 \mu\text{m}$), two or three voltage pulses of 30V were sufficient. On the other hand, for a thick BP film (5

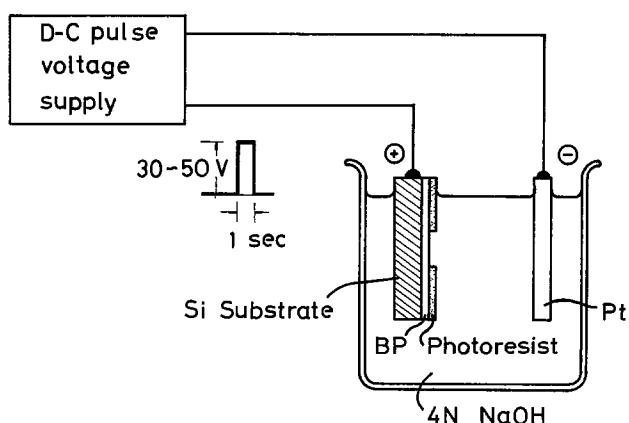


Fig. 1. Schematic diagram of the experimental apparatus for the selective removal of BP from Si substrates by the electrolytic process.

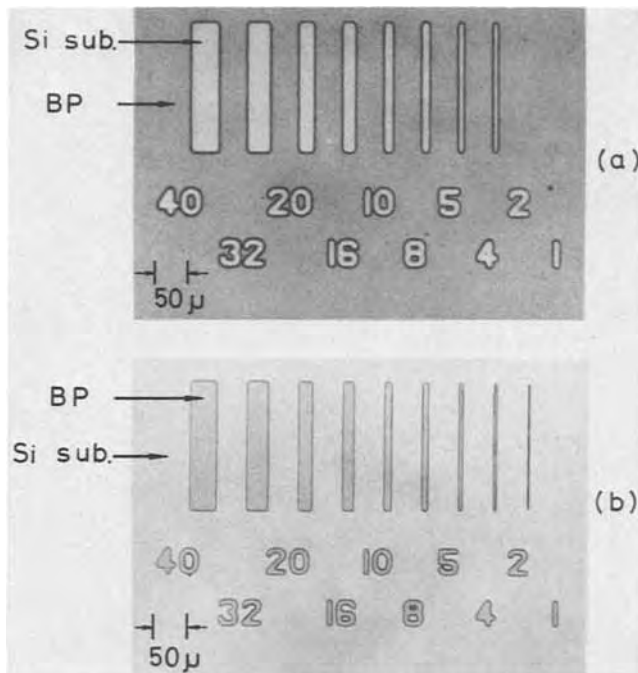


Fig. 2. Microscopic photographs of selectively removed BP by the electrolytic process. (a) BP areas removed using positive type resist (AZ 1350). (b) BP areas remained using negative type resist (KTFR). The thickness of the BP is $0.85 \mu\text{m}$.

μm), 7 or 8 pulses of 50V were necessary for complete removal.

The BP films obtained by removal of the Si substrate by chemical etching with HF-HNO₃ solution were smooth and flat. However, the BP films removed electrolytically had many small cracks. This difference can be seen in Fig. 3 (a) and (b). The cracked features of the BP films depend on the conditions of the electrolytic process, mainly on the voltage applied between the cathode and the anode. These differences in the BP films suggest that strong forces are applied to the BP

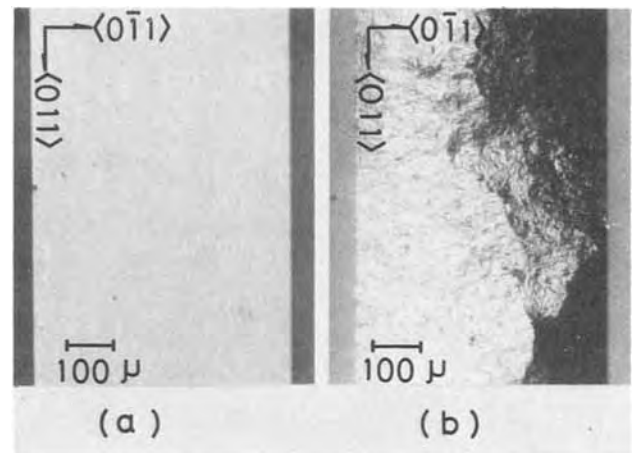


Fig. 3. Microscopic photographs of BP films with thicknesses of $5.0 \mu\text{m}$. (a) BP film obtained by chemical etching of the Si substrate. (b) BP film obtained by the electrolytic process; it has many small cracks.

when removed from the Si substrates by the electrolytic process.

Manuscript submitted Nov. 4, 1974; revised manuscript received Feb. 24, 1975.

Any discussion of this paper will appear in a Discussion Section to be published in the December 1975 JOURNAL. All discussions for the December 1975 Discussion Section should be submitted by Aug. 1, 1975.

Publication costs of this article were partially assisted by Sophia University.

REFERENCES

1. T. Nishinaga, H. Ogawa, H. Watanabe, and T. Arizumi, *J. Crystal Growth*, **13/14**, 346 (1970).
2. T. L. Chu, J. M. Jackson, A. F. Hyslop, and S. C. Chu, *J. Appl. Phys.*, **42**, 420 (1971).
3. M. Takigawa, M. Hirayama, and K. Shohno, *Japan. J. Appl. Phys.*, **13**, 411 (1974).
4. C. C. Wang, M. Cardona, and A. G. Fisher, *RCA Rev.*, **25**, 159 (1964).

Beveling Aluminum in Multilayer Metal Circuitry

T. Agatsuma,* A. Kikuchi, K. Nakada, and A. Tomozawa

Semiconductor and Integrated Circuits Division, Hitachi Limited, Kodaira, Tokyo, Japan

Fabrication of semiconductor multilayer metal IC's and LSI's involves a number of photoengraving steps, and the surface topography becomes increasingly more complex as the processing proceeds. The exact processing conditions and materials used determine the contour of the edge of photolithographically delineated structures. If the device structure involves steep steps, sharp corners, or multilevel metals, improper coverage of the surface topography can lead to a variety of reliability and yield problems.

Two processing techniques have been developed for improving multilayer metallization. The first involves optimizing substrate topography by application of beveling techniques; conventional deposition techniques serve to cover the modified topography. The second involves improvement of the quality of deposited oxide contours, taking advantage of several types of specialized film deposition techniques.

Regarding oxide deposition, effects of rates of gas flow in the system (1), rate of deposition of the oxide, and ratio of oxide/metal layer thickness (2) on oxide

contours have been shown to be significant; however, when a thick metal layer is used, its step becomes steep and optimization of its step coverage by oxide will be limited. A technique for producing good oxide coverage over steep metal steps is to deposit phosphosilicate glass (PSG) or borosilicate glass (BSG) at temperatures of 700°C or more (3), or to fuse the glass at a temperature above its softening point (4) which depends on the phosphorus content of the glass. However, applicability of these methods is limited to devices such as Si Gate MOSLSI's, where higher melting point materials are used as gate electrodes or first level conductors.

In the case of two level aluminum metallization, such as bipolar IC's or LSI's, higher temperature deposition or oxide fusion cannot be used. The quality of step coverage by a CVD oxide layer over an aluminum pattern can be almost entirely determined by the contour of the aluminum; hence the importance of beveling the edge of the first level aluminum.

Two approaches to beveling aluminum have been studied. The first is photoresist undercutting (5) which achieves lateral attack at the polymer/aluminum inter-

* Electrochemical Society Active Member.

Key words: multilayer circuit, aluminum, anodic oxidation.

face, using a suitable etchant so as to produce undercutting of the photoresist due to loss of its adhesion during photoetching. However, practical use will be difficult because of lack of reproducibility as a result of the many process parameters involved.

The second is to deposit or form an additional faster etching layer over the aluminum prior to coating with photoresists. In this technique, formation of the upper layer and composition of the etchant become predominant factors in determining bevel angle. The use of phosphosilicate glass (6) or an anodic oxide film (7) have already been presented as means for beveling aluminum. This paper discusses a beveling technique for aluminum using an anodic oxide film of aluminum as a bevel control layer, and discusses the effects of process variables on reproducibility of the results.

Experiments

Silicon dioxide layers were grown on Si slices by thermal oxidation, and the aluminum of $1.0 \sim 1.2 \mu$ thickness was evaporated by a resistance-heated filament or electron beam. Subsequently, anodic oxidation of the aluminum was performed in diluted oxalic acid, forming a porous anodic oxide film on the evaporated aluminum.

Anodizing current was observed to rise rapidly just after applying voltage, and then decrease slowly until it was saturated (8). The saturated value of current for anodization of 1.0V and 25°C in 5% oxalic acid was 0.14 mA/cm^2 . Oxide film thickness was determined by etching the oxide film selectively in chromic acid and measuring the steps with a talystep. Dividing step height by the time required for anodization, growth rate of the oxide film per unit voltage was estimated as $33 \sim 38 \text{ \AA/min}$ for 5% oxalic acid at 25°C in the range 0.5 to 3.0V.

Photoresist coating followed a precoating bake of the anodized wafer at 200°C for 20 min in N_2 ambient. Negative-type resists used were OMR81-PL, OMR83, and KTFR. After defining the patterns, the photoetching was performed using a conventional aluminum etchant (H_3PO_4 : 76, CH_3COOH : 15, HNO_3 : 3, H_2O : 5 by volume) containing a small amount of ammonium fluoride, NH_4F .

To express the degree of bevel or taper angle preferentially, the bevel etch factor was defined in Eq. [1], which is the reciprocal of the usual definition of etch factor. In this way the value of bevel etch factor better expresses the degree of beveling aluminum at its edge during etching

$$\text{Bevel etch factor} = d/t \quad [1]$$

where t is the thickness of evaporated aluminum and d is the extent of beveling measured from the bottom edge of the aluminum.

Bevel etch factor was measured by a microscope at 400X magnification. When the bevel etch factor is smaller than unity, light reflected from the bevel surface will be scattered and not reach the microscope field of view. In this case the measured bevel etch factor is smaller than its actual value. As a correction for the effect of light in this case, a value of $t/2$ (t is the aluminum thickness in micrometers) must be added to the measured value of bevel etch factor, because the actual value of bevel etch factor measured at zero or near zero was observed equal to $t/2$.

Results and Discussion

Figure 1 shows how the bevel etch factor varies when changing oxide film thickness with anodizing time for a fixed value of anodizing voltage at 1.0V. Etchant used was 3/100 or 4/100; these are the volume ratios of ammonium fluoride to the aluminum etchant. This figure may be roughly divided into two regions on either side of a 1000Å film thickness. When the oxide film is in the range 0-400Å, both the value of bevel etch factor and its variability were extremely large; they both decreased sharply with increasing oxide film thickness, reaching minimum values at a thickness near

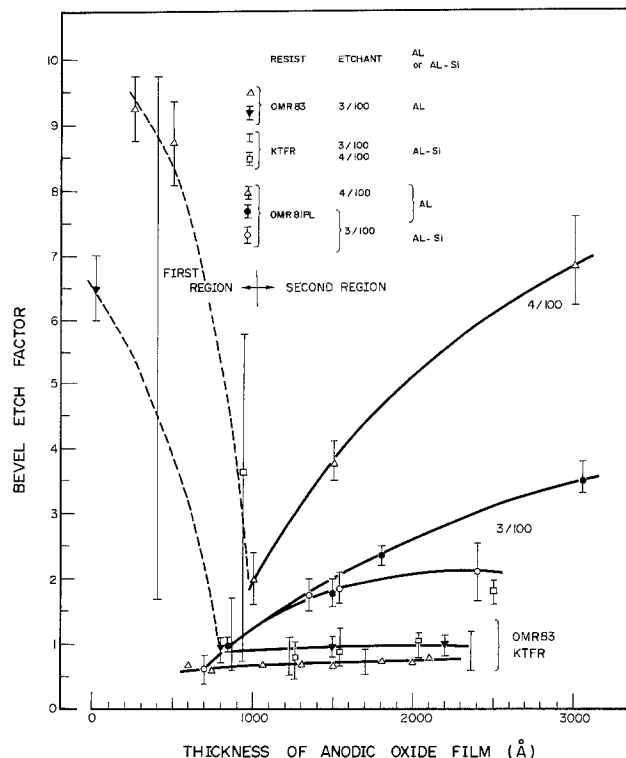


Fig. 1. Variations of bevel etch factor with thickness of anodic oxide film formed at an anodizing voltage of 1.0V. Content of ammonium fluoride in aluminum etchant and types of photoresist are taken as parameters.

1000Å. The first region is defined by a thickness range 0 to near 1000Å, where the bevel etch factor decreased from its initial value to a minimum. Oxide film thickness in the region of the minimum was in the range 500-1000Å, depending on type of resist and composition of the etchant.

The second region, as seen in Fig. 1, defines a range of oxide film thickness in which the bevel etch factor tends to increase gradually from its minimum value; the rate of increase differs with type of resist and composition of the etchant. With OMR81PL resists, the rate of increase in the bevel etch factor with thickness was extremely large, and varies appreciably with composition of the etchant. Bevel etch factor for OMR83 and KTFR resists maintained almost constant values of $0.5 \sim 1.5$ over the range 700-2500Å. The bevel profile of aluminum obtained using the conventional aluminum etchant without forming the anodic oxide film exhibited a near vertical slope at the top edge and curved cylindrically towards the bottom edge. In this case, the value of bevel etch factor was measured at zero or near zero.

Figure 2(a) top shows beveled aluminum patterns for the first and second regions of Fig. 1. In the first region, partial etch undercut is seen to occur, thereby resulting in large values of bevel etch factor. This may be caused by preferential attack at the photoresist/oxide film interface due to loss of adhesion between photoresist and the oxide film during etching. In this region, controlled beveling could not be attained.

A bevel with constant slope was obtained in the second region, as seen in the bottom of Fig. 2(a), and Fig. 2(b), where SiO_2 was deposited to delineate the beveled aluminum surface. Bevel etch factor depends on etch rates of the interface layer which relates to adhesion between photoresist and the oxide film, the oxide film and the aluminum itself. It will be impossible to control etch rates of the interface layer and the oxide film separately. Thus, bevel etch factor is considered to be determined by etch rates of the composite layer consisting of the interface layer and the oxide film, as shown in Fig. 3, and the aluminum.



Fig. 2(a) Beveled aluminum patterns for the first and second regions shown in Fig. 1.

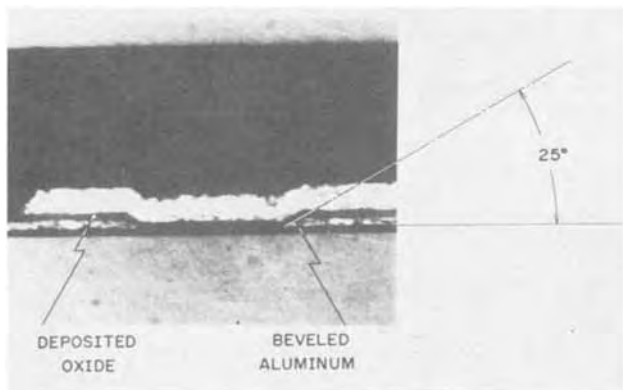


Fig. 2(b). Beveled aluminum for the second region showing a constant slope of $\theta = 25^\circ$ at the beveled surface.

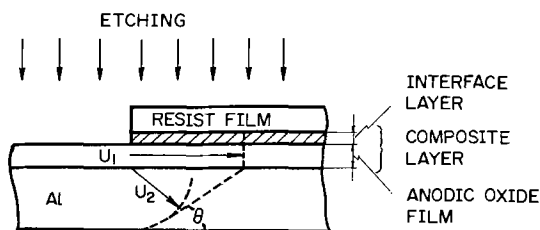


Fig. 3. Schematic illustration of etching for a composite layer consisting of interface layer and anodic oxide film.

Expressing etch rate of the composite layer and the aluminum as U_1 and U_2 respectively, the angle θ of the etched edge slope of aluminum is given by Eq. [2], as shown in Fig. 3

$$\theta = \arcsin (U_2/U_1) \quad [2]$$

Here, it is assumed that etch rate of the composite layer is that of lateral attack, and etching in aluminum proceeds isotropically. The cross section in Fig. 2(b) corresponds to the case of $U_1/U_2 = 2 \sim 2.4$, giving $\theta = 30 \sim 25^\circ$ from Eq. [2].

Figure 4 shows how etch rates for OMR81PL resist of the composite layer U_1 and aluminum U_2 change with content of ammonium fluoride in the aluminum etchant; a 1500Å oxide film and an anodizing voltage of 1.0V are used. Etch rate of the aluminum decreased gradually with increasing ammonium fluoride, and became constant at an ammonium fluoride content exceeding 3/100. On the other hand, etch rate of the composite layer is smaller than that of the aluminum when the content of ammonium fluoride is low, and increases with NH_4F content. Etch rate of the composite layer is seen to be identical with that of the aluminum at an NH_4F content of near 1.7/100, where U_1 and U_2 curves in Fig. 4 intersect. Under this condition, bevel etch factor becomes unity for an aluminum thickness of 1.0μ from Eq. [1] because θ becomes 45° by putting $U_2/U_1 = 1$ into Eq. [2]. When the content of ammonium fluoride exceeds 1.7/100, etch rate of the composite layer becomes larger than that of the aluminum. This results in an increase in the bevel etch factor, as shown in the second region for OMR81PL of Fig. 1.

Figure 5 illustrates how the film thickness of OMR81PL resist and its corresponding bevel etch factor vary with oxide film thickness, when exposure time to light was varied from 2 to 16 sec at a constant value of light intensity. Resist film thickness is a slowly decreasing function of oxide film thickness, with exposure time as a parameter. But, its corresponding bevel etch factor shows different behavior in the first and second regions. In the first region, bevel etch factor decreases appreciably with oxide film thickness, and displays a larger value for shorter exposure time corresponding to thin resist film. That is, the value of bevel etch factor is seen to be related to resist film thickness as a function of exposure time. This may indicate that etch rate of the interface layer, which depends on adhesion between photoresist and the oxide film, becomes an influencing factor in determining bevel etch factor.

In the second region bevel etch factor increases with oxide film thickness, although resist film thickness varies according to exposure time and decreased slowly with film thickness as in the first region. This is a re-

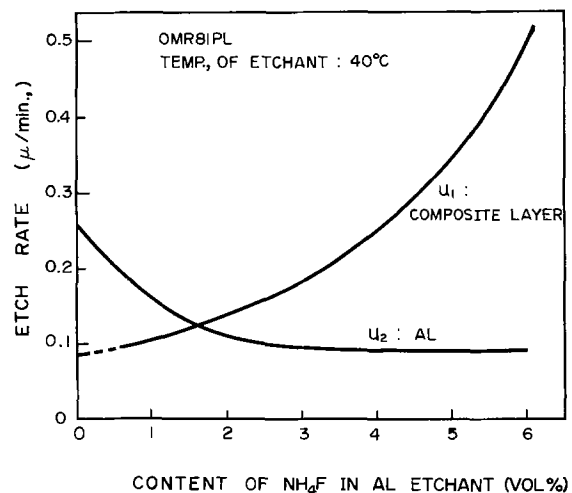


Fig. 4. Changes in etch rate of composite layer U_1 and that of aluminum U_2 with content of ammonium fluoride, OMR81 resist.

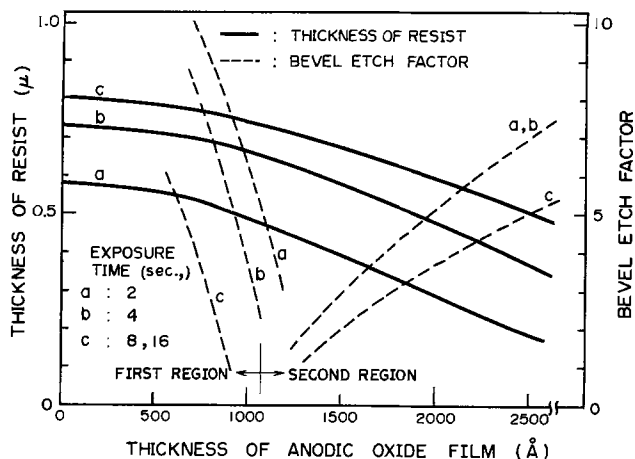


Fig. 5. Variations of film thickness of OMR81PL resist and corresponding bevel etch factor with anodic oxide film thickness. Exposure time to light is taken as a parameter.

verse tendency to that of the first region. Thus, behavior of bevel etch factor in the second region cannot be explained in terms of the etch rate of the interface layer *vs.* the resist film thickness which is controlled by exposure time.

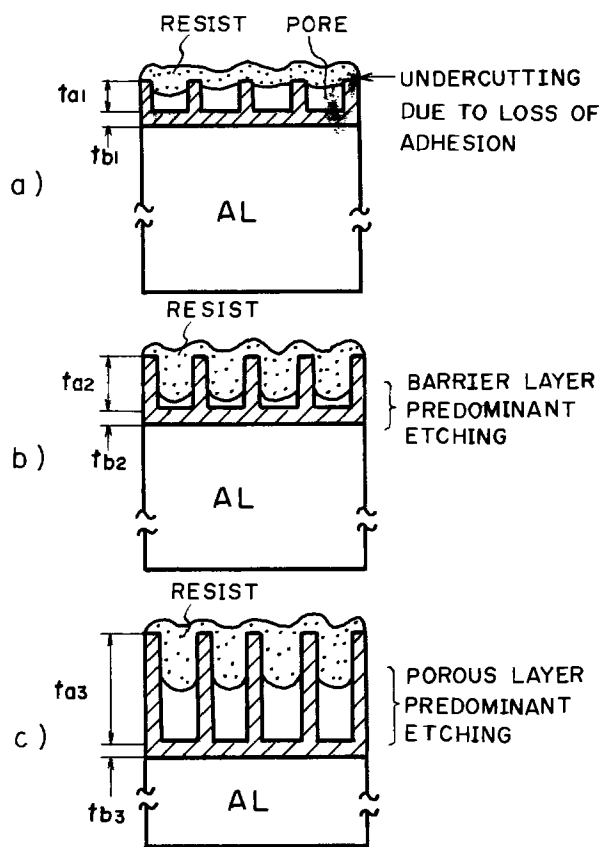
The anodic oxide film consists of a porous layer which grows with anodizing time, and a barrier layer determined by the anodizing voltage (10). Variations of the composite layer structure with oxide film thickness are shown schematically in Fig. 6(a), (b), and (c). When oxide film thickness is far below 1000Å, the porous layer is also so thin that adhesion between photoresist and the oxide film will be poor. This will result in a large value of bevel etch factor as in the first region. At around 1000Å, the porous layer becomes thicker and photoresist adhesion will be enhanced giving a slow etch rate of the interface layer. Thus, etch rate of the composite layer will be determined by the barrier layer with a slow etch rate, resulting in a smaller value of the bevel etch factor.

When oxide film thickness is further increased beyond 1000Å, porous layer thickness will be increased although the barrier layer does not change with oxide film thickness. As a result, the porous layer will exert a predominant influence on etching characteristics, and etch rate of the composite layer will be increased, giving rise to a larger value of bevel etch factor. Thus, as shown in Fig. 1, there appears a minimum value of bevel etch factor at a thickness near 1000Å.

In the case of OMR83 and KTRF resist, as shown in Fig. 1, bevel etch factor in the second region is not largely altered by oxide film thickness. This cannot be explained by the processes as stated above, but differences in chemical composition of photoresist materials may be involved in connection with the anodic oxide structure as illustrated in Fig. 7(a) and (b).

Since the polymeric composition of OMR81PL is natural cisrubber, it is believed that the high polymers such as proteins and similar types are included in the rubber (9). The size of the polymer molecule after polymerization is, therefore, considered to be of the same order of magnitude as the diameter of the pore of the porous layer, $\sim 170\text{Å}$ (10). Thus, the resist may not flow completely into the pores, but covers the pores as seen in Fig. 7(a). Then, the etch rate of the composite layer for OMR81PL will be determined predominantly by the etch rate of the porous layer which increases with oxide layer thickness as stated previously.

In the case of OMR83 and KTRF resist, on the other hand, the polymer molecule will be sufficiently small compared to the pore diameter because these resist are said to be synthetic rubber (9), and the pores will be completely filled with resist as seen in Fig. 7(b), eliminating effects of the porous layer on etch rate. Thus, etch rate of the composite layer asso-



t_a ; THICKNESS OF POROUS LAYER

$$t_{a1} < 1000\text{Å}$$

$$t_{a2} \approx 1000\text{Å}$$

$$t_{a3} > 1000\text{Å}$$

t_b ; THICKNESS OF BARRIER LAYER

$$t_{b1} = t_{b2} = t_{b3}$$

Fig. 6. Schematic illustration of changes in structure of composite layer and its associated etch rate limiting factor with anodic oxide film thickness.

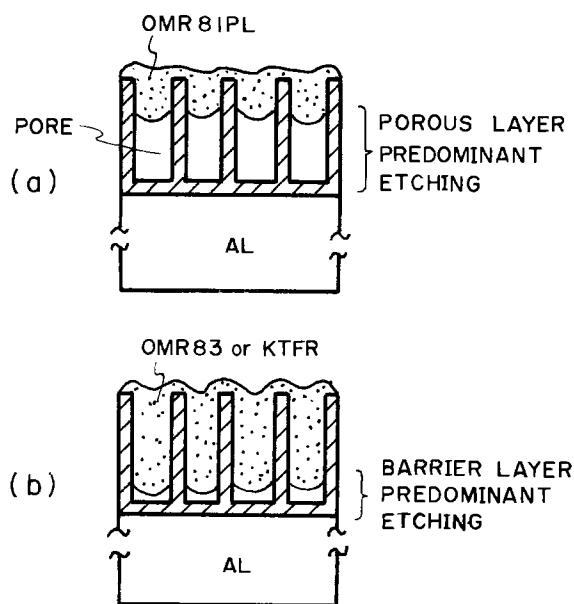


Fig. 7(a), (b). Schematic illustration of difference in etch rate limiting factor of composite layer with OMR81PL and OMR83 resist.

ciated with OMR83 or KTFR resist will not be predominantly influenced by the etch rate of the porous layer, although it increases with oxide film thickness, but by that of the barrier layer determined by the anodizing voltage. This will explain the small dependence of bevel etch factor for OMR83 or KTFR in the second region on the oxide film thickness for an anodizing voltage of 1.0V as shown in Fig. 1. But, when the anodizing voltage becomes lower, it was observed that etch rate of the porous layer, rather than the barrier layer limited over-all etch rate.

Figure 8 shows the variation of bevel etch factor for OMR83 resist when changing the anodizing voltage from 0.5 to 3.0V with oxide film thickness as a parameter. When the anodizing voltage is above 1.0V, the thickness dependence of bevel etch factor and its variation with anodizing voltage are seen to be small. On the other hand, when the anodizing voltage drops below 1.0V, the bevel etch factor increases with decreasing voltage, and its dependence on thickness of the oxide film becomes pronounced particularly for increasing oxide film thickness. When comparing oxide films having the same film thickness but different anodizing voltages, the film anodized at a lower voltage has a larger porous layer thickness than the film produced with a higher anodizing voltage. This may be explained by considering that with decreasing anodizing voltage, etch rate of the porous layer becomes a limiting factor for the composite layer rather than etch rate of the barrier layer.

Summary

Beveling of an aluminum edge for multilayer metal circuitry was performed by forming a porous anodic oxide film on aluminum during conventional photoresist and aluminum etch processing. The aluminum etchant employed contained a small amount of ammonium fluoride. The bevel etch factor was found to vary largely with anodic oxide film thickness, content of ammonium fluoride, and type of photoresist.

Bevel etch factor vs. oxide film thickness curves were divided into two regions on either side of a thickness near 1000Å. In the first region, with the oxide thickness in the range 0 to near 1000Å, the value of bevel etch factor and its variation were so large that the controlled beveling could not be attained. This may be due to partial undercut at the interface between photo-

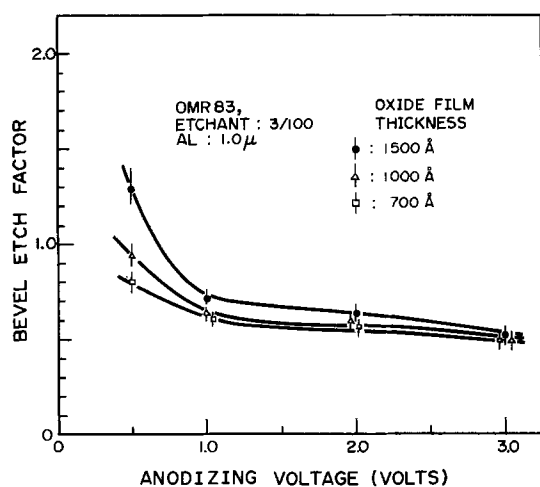


Fig. 8. Variations of bevel etch factor for OMR83 resist with anodizing voltage with anodic oxide film thickness as a parameter.

resist and the oxide film. As the oxide film approached 1000Å in thickness, the bevel etch factor declined to a minimum value.

In the second region above 1000Å, the bevel etch factor tended to increase from its minimum value with oxide film thickness; the rate of increase differed with types of resist and composition of etchant. The beveled surface in this region varied linearly at a constant slope determined by etch rate of the composite layer U_1 and that of the aluminum U_2 . Etch rates were found to be controlled by the content of ammonium fluoride.

The increase in bevel etch factor with oxide film thickness was observed predominantly for OMR81PL resist. This can be explained by assuming that the limiting factor of etch rate of the composite layer U_1 changes from etch rate of the barrier layer to that of the porous layer with increasing oxide layer thickness at a constant anodizing voltage. For OMR83 and KTFR resists, however, the variation of bevel etch factor with oxide film thickness was not so pronounced. The results were explained by assuming that etch rate of the composite layer may be influenced by its structure, which is determined by the chemical composition of resists and the pore diameter of the anodic oxide film.

Acknowledgments

The authors wish to thank Mr. H. Nakane, Manager of Tokyo Ohka Kogyo Company, for many fruitful discussions and are grateful to Dr. I. A. Lesk of Motorola for reading an earlier manuscript and suggestions that improved its content. Thanks are also due to S. Nishida and K. Terada for their support of this study.

Manuscript submitted Sept. 4, 1973; revised manuscript received Nov. 15, 1974. This was Paper 87 presented at the Chicago, Illinois, Meeting of the Society, May 13-18, 1973.

Any discussion of this paper will appear in a Discussion Section to be published in the December 1975 JOURNAL. All discussions for the December 1975 Discussion Section should be submitted by Aug. 1, 1975.

Publication costs of this article were partially assisted by Hitachi, Limited.

REFERENCES

1. W. Kern, J. L. Vossen, and G. L. Schnable, 11th Annual Proceedings, Reliability Physics, IEEE, 214 (1973).
2. D. L. Tolliver and C. J. Santoro, *Solid State Technol.*, **14**, 32 (1971).
3. I. Matsushima, T. Enomoto, and H. Fukuwatari, Abstract 92, p. 230, Electrochemical Society Extended Abstracts, Spring Meeting, Chicago, Illinois, May 13-18, 1973.
4. C. T. Naber, *This Journal*, **119**, 301C (1972).
5. J. Dey, M. Lundgren, and S. Harrell, "Kodak Photoresist Seminar Proceedings," Vol. II, p. 4, Eastman Kodak Co., Rochester, N. Y. (1968).
6. G. L. Schnable and R. S. Keen, in "Advances in Electronics and Electron Physics," Vol. 30, L. Marton, Editor, p. 79, Academic Press, New York (1971).
7. T. Agatsuma, A. Kikuchi, and K. Nakada, Abstract 87, p. 220, Electrochemical Society Extended Abstracts, Spring Meeting, Chicago, Illinois, May 13-18, 1973.
8. M. Nagayama and K. Tamura, *Denki Kagaku*, **36**, 34 (1968).
9. H. Nakane, Private communication.
10. F. Keller, M. S. Hunter, and D. L. Robinson, *This Journal*, **100**, 411 (1953); J. P. O'Sullivan and G. C. Wood, *Proc. Roy. Soc. (London)*, **A317**, 511 (1970).

Adaption of Ion Implantation for Integrated Circuits

S. Prussin*

TRW Semiconductor Division, Lawndale, California 90260

and Anthony M. Fern*

TRW Systems, Lawndale, California 90260

Ion implantation has become established as a useful process for MOS device manufacture. In this use the implantation process determines the positioning of the electrically active atoms. Further processing consists of low temperature annealing whose primary function is to return the implanted atoms to full electrical activity.

For processing bipolar IC's, ion implantation is used primarily as a means of obtaining the uniform and reproducible deposition of electrically active impurity atoms. This is usually followed by high temperature heat-treatments which result in the redistribution of these deposited atoms. Such heat-treatments include the oxidation of the surface silicon as well as the indiffusion of additional chemical species. The interaction of these heat-treatments with the radiation defects introduced by the prior ion implantation has been shown to result in the generation of stacking faults and dislocation loops capable of affecting device performance (1).

Uniformity of Ion-Implanted Impurity Deposition

The interest in applying ion implantation as a deposition technique in the processing of bipolar integrated circuits stems from two sources, the inherent uniformity obtainable over an entire wafer surface and the reproducibility from wafer to wafer. This uniformity was evaluated by measuring the resistance of identical 10Ω resistors for 82 IC's which fitted over a 2 in. diameter wafer. The resistors were generated by implanting a fluence of $2.5 \times 10^{13} \text{ p}^{31} \text{ cm}^{-2}$ at an energy of 100 keV. The background was a p-well similar to that used in CMOS construction. Implantation was carried out at room temperature using commercially available equipment. The coefficient of variation, i.e., the standard deviation divided by the average resistor value was 1.0%. This uniformity is reflected in the uniformity of electrical parameters when ion implantation is used as a processing technique.

Experimental Study

This study was based on a specific IC design which had been successfully produced for several years by a triple diffusion technique for which a detailed performance record was available. The three chemical diffusions begin with an arsine collector deposition and drive. The base is formed by a BN deposition and a two-stage drive, first in wet N_2 and then in dry N_2 . A PH_3 emitter diffusion completes the diffusions. Test diodes permitted easy evaluation of all the following pn junctions: the $\text{n}^- \text{p}^-$ collector-substrate junction, the $\text{p}^+ \text{n}^-$ base collector junction, the $\text{n}^+ \text{p}^+$ emitter-base junction and the $\text{n}^+ \text{p}^-$ emitter substrate junction.

Experience indicated that the base deposition was the most critical diffusion operation and it was chosen for replacement with an implantation of $1.2 \times 10^{15} \text{ B}^{11} \text{ cm}^{-2}$ at 30 keV. The chemical emitter diffusion and other steps were maintained without change with one exception. Unless special precautions were taken with the base drive, heavy stacking fault concentrations resulted. These were found to correlate with excess leakage in the $\text{n}^+ \text{p}^+$ junctions.

* Electrochemical Society Active Member.

Key words: ternary defects, stacking faults, leakage currents.

Ternary Defect Generation

Annealing processes which result in complete return of implanted ions to electrically active substitutional positions usually leave a concentration of microdefects of a size requiring transmission electron microscopy for their individual distinction (2). These have been referred to as secondary defects (3). Initial studies have shown that the thermal oxidation of silicon surfaces containing B atoms implanted at room temperature causes the small extrinsic dislocation loops to expand by several orders of magnitude into dislocation loops large enough to be easily detected by chemical etching and optical microscopy (1). These are referred to as ternary defects.

The combination of wet oxidation for 1 hr at 1100°C with Sirtl etching was found to result in easily discernible ternary defects when applied to ion implanted surfaces. Figures 1 and 2 illustrate the defects found for implantations of 10^{14} and $10^{15} \text{ B cm}^{-2}$. The upper left-hand corner of the illustration was shielded from implantation by the retaining chip which held the silicon wafer in position during the implantation. The ternary defects associated with the $10^{14} \text{ B cm}^{-2}$ implantation appear to be an array of individual stacking faults, those associated with the $10^{15} \text{ B cm}^{-2}$ implantation contain stacking faults superimposed over a background of fine substructures. This is illustrated in Fig. 3, where the fine substructure appears to consist of short defects, 0.5-1 μ in length, grouped in radial arrays. High temperature annealing treatments in dry N_2 were found effective in preventing the generation of ternary defects (1).

Diffusion into Ion Implanted Surfaces

The all-chemically diffused process utilized a BN deposition followed by a two-step drive consisting of 15 min wet N_2 followed by 30 min dry N_2 , both at 1140°C . Windows were opened in the oxide and the emitters were indiffused with PH_3 . When ion implantation of B was substituted for BN deposition, the test diodes for the $\text{n}^- \text{p}^-$, $\text{p}^+ \text{n}^-$, $\text{n}^+ \text{p}^-$, and $\text{n}^+ \text{p}^+$ junctions

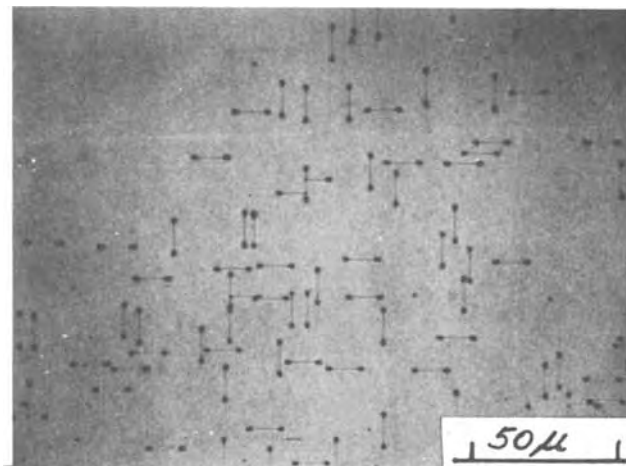


Fig. 1. Ion implant boundary, $10^{14} \text{ B cm}^{-2}$, 30 keV, (100) wet oxidized at 1100°C for 1 hr, Sirtl etched 30 sec. Magnification 405X.

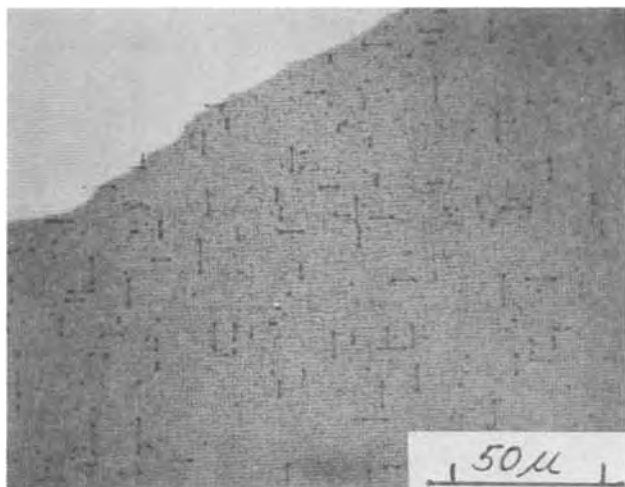


Fig. 2. Ion implant boundary, 10^{15} B cm^{-2} , 30 keV, (100) wet oxidized at 1100°C for 1 hr Sirtl etched 15 sec. Magnification 405X.

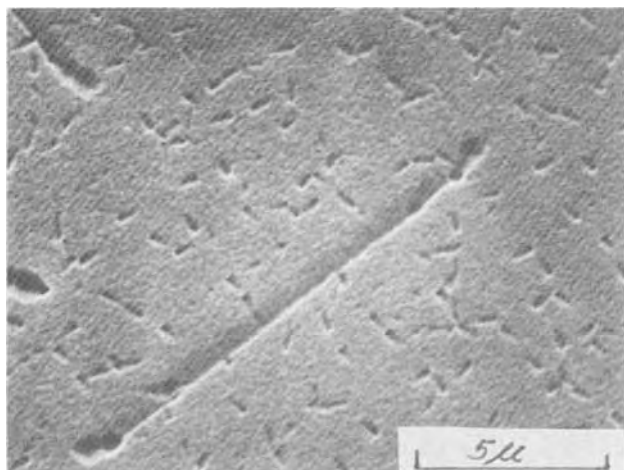


Fig. 3. Scanning electron micrograph, 10^{15} B cm^{-2} , 30 keV (100) wet oxidized at 1100°C for 1 hr, Sirtl etched 15 sec. Magnification 6000X.

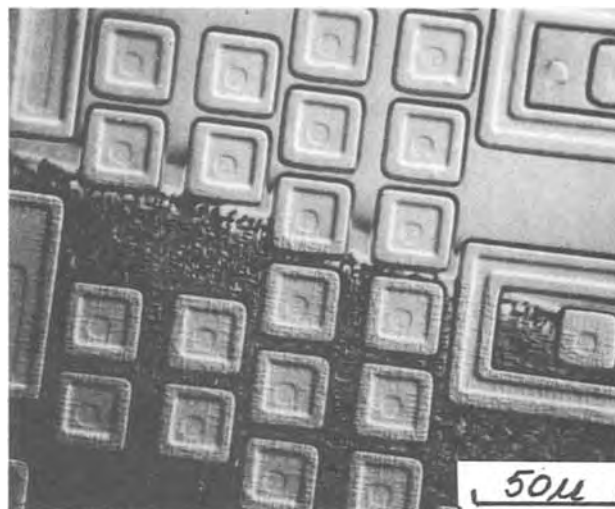


Fig. 4. Ion implant boundary, base deposition 1.2×10^{15} B cm^{-2} , 30 keV, base drive 15 min wet N_2 , 30 min dry N_2 , both at 1140°C , standard PH_3 emitter, Sirtl etched 15 sec, Nomarski phase contrast. Magnification 476X.

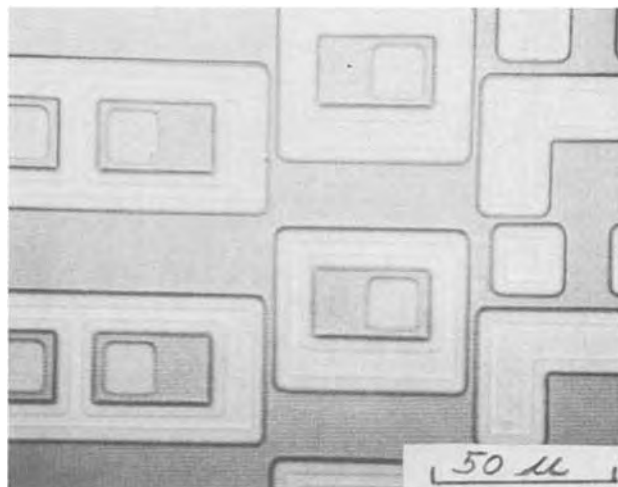


Fig. 5. IC surface, base deposition 1.2×10^{15} B cm^{-2} , 30 keV, base drive 15 min dry N_2 , 15 min wet N_2 , 15 min dry N_2 , all at 1140°C , standard PH_3 emitter, Sirtl etched 15 sec. Magnification 405X.

were evaluated. Similar characteristics were found for chemically deposited and ion implanted bases except for the n^+p^+ diodes. Here the leakage at reverse bias was much greater for the ion implanted diodes.

To reduce the generation of ternary defects without substantially changing the processing procedure, the base drive was changed from 15 min wet, 30 min dry, to a 15 min dry, 15 min wet, and 15 min dry sequence. The leakage current for three sizes of n^+p^+ test diodes for these two driving conditions is given in Table I. The introduction of a dry N_2 anneal at the beginning of the drive results in a leakage that is kept at, or below, the level associated with the all-chemical process.

Figures 4 and 5 illustrate emitter and base areas subjected to Sirtl etching to bring out defect structures. They represent structures that are identical except for being subject to different annealing cycles. The difference in their electrical properties is described

in Table I. The upper area in Fig. 4 was shielded from ion implantation. The darkened cross-hatched areas, characteristic of structural defects appear in the emitter areas only where they are superimposed over the ion implanted base areas. For Fig. 5, where the base drive included an initial anneal in dry N_2 , no such structural defects appeared in any of the diffused emitter areas.

The presence of stacking faults and edge dislocations has been associated with soft junctions and emitter-collector pipes in all-chemically diffused npn structures (4, 5). Such pipes were found only under the phosphorus-diffused emitter areas and not in the remainder of the base area. This suggested a model that the pipes are a result of enhanced phosphorus diffusion along crystalline defects (4). The addition of gold increases the junction leakage suggesting that the precipitation of gold or other fast diffusers on the defects passing through the collector-base junction may also play a significant role (5).

Parameter Control Comparison

Table II compares the parameter distribution found for a lot of wafers processed with chemical diffusion

Table I. Correlation of base drive with leakage

	Average leakage current in pA, $V_R = 3V$		
Drive treatment	0.1 sq. mils	0.5 sq. mils	2.0 sq. mils
15 min wet N_2 30 min dry N_2 at 1140°C	2.3×10^3	10×10^3	47×10^3
15 min dry N_2 15 min wet N_2 15 min dry N_2 at 1140°C	1.1	2.1	7.0

Table II. Parameter control comparison of typical lots
(Approximately 640 devices of each type represented)

Parameter	Average value		Coefficient of variation % wafer to wafer array 8 wafers within lot		Average coefficient of variation % within a wafer 80 samples per wafer	
	Chem	Ion	Chem	Ion	Chem	Ion
Pinched resistor (K)	4.64	5.83	14	7.9	14.5	7.5
NPN transistor						
Beta	26.9	34.0	18.8	10.2	25.5	15.3
$V_{BE(mV)}$	692	774	0.6	0.5	0.9	0.7
$V_{SAT(mV)}$	22.6	43.8	20.7	2.9	26.0	8.2
PNP transistor						
Beta	15.4	15.0	16.9	6.9	8.5	4.1
$V_{BE(mV)}$	713	723	0.2	0.4	0.25	0.3

Points outside of computed 3σ have been deleted in final calculation.

only with the parameter distribution found when an ion-implanted base is substituted for BN deposition. The average electrical parameters for both production techniques were very close with the exception of the V_{SAT} values. This is attributed to the fact that the Q value for the collector deposition was chosen to be substantially less for the case where the base was ion implanted than for the case where the base was chemi-

cally deposited. It is noted that the ion-implanted group exhibits significantly greater uniformity over individual wafers and greater reproducibility from lot to lot.

Acknowledgments

The authors thank Dr. Arthur Hochberg and Ralph Miller for their support and useful discussions, and Leonard Braun and Jay Levine for preparing the ion-implanted specimens.

Manuscript submitted Aug. 15, 1974; revised manuscript received March 3, 1975. This was Paper 85 presented at the San Francisco, California, Meeting of the Society, May 12-17, 1974.

Any discussion of this paper will appear in a Discussion Section to be published in the December 1975 JOURNAL. All discussions for the December 1975 Discussion Section should be submitted by Aug. 1, 1975.

Publication costs of this article were partially assisted by TRW Incorporated.

REFERENCES

1. S. Prussin, *J. Appl. Phys.*, **45**, 1635 (1974).
2. J. F. Gibbons, *Proc. IEEE*, **9**, 1062 (1972).
3. Masao Tamura, *Appl. Phys. Letters*, **23**, 651 (1973).
4. F. Barson, M. S. Hess, and M. M. Roy, *This Journal*, **116**, 304 (1969).
5. P. C. Parekh, *Solid-State Electron.*, **14**, 273 (1971).

A Nondestructive Method for Examining Compositional and Doping Variations in GaAs-GaAlAs Heterostructure Material Using a Scanning Electron Microscope

R. A. Linnell

Bell Laboratories, Murray Hill, New Jersey 07974

Presently, layer thickness measurements of multi-layered GaAs-GaAlAs material are usually made by optically viewing samples that have been mechanically lapped at a shallow angle and etched to reveal the interfaces of thin layers. This technique suffers from two major defects: (i) it is inherently destructive and wastes material; and (ii) polishing-induced scratches obscure micron-size defects. An alternate method of layer thickness measurement requires cleaving a facet perpendicular to the epitaxial layers, etching to achieve topographic distinction among the layers, and then observing with a scanning electron microscope (SEM). This method also has drawbacks which are often important: (i) the etching (partial destruction) of the laser mirror surface makes the method unsuitable for studying a device which is subsequently to be used; (ii) cleaving faults, often produced in as-grown wafers, can parallel and be indistinguishable from the etch-revealed layer interfaces; (iii) "highlights" and shadows associated with etch-revealed edges can often make the thickness determination of thin layers somewhat uncertain; and (iv) some etchants have the effect of producing sloping facets at interfaces so that subsequent viewing with the SEM can misleadingly reveal additional layers (1).

This paper discusses a third method of layer thickness measurement which allows a sample without prior treatment to be measured quickly using the SEM. Since no etching of the cleaved face is required, this technique is appropriate for observations of micron-size defects, for layer thickness or taper determina-

tions, etc., in devices that are to be subsequently used. An acronym which serves as a convenient shorthand notation and which describes our technique is ACABOB (Adjustment of Contrast, Amplifier type, Brightness, Orientation and Beam current). The enhanced contrast in our case is related to signal processing and should be distinguished from what is commonly known (2) as the voltage-contrast technique. In the latter case, contrast at a p-n junction is achieved by applying an external d-c voltage across the specimen; this is unnecessary in our case. It should be noted that scanning electron micrographs somewhat similar to our Fig. 2-4 have appeared in the literature (3) but no discussion of the techniques employed has been given.

When one attempts to accurately measure the spatial variations in thicknesses of epitaxially grown layers of GaAs-GaAlAs laser material, it is convenient to view these layers in an end-on fashion. If a smooth and clean surface, as would be obtained by properly cleaving this material, is oriented normally to the primary beam, the variations in the image formed by Secondary Electron Emission (SEE) can be attributed entirely to changes in work function caused by changes in impurity doping and material composition of the various layers. Under normal operating conditions, these variations are extremely small compared with the over-all image intensity and meaningful determinations are difficult to make. The purpose of this paper is to describe a technique for greatly enhancing these variations and to illustrate the application of this technique for characterization of epitaxially grown GaAs-GaAlAs laser material.

A major component of the image formed by SEE is noise. Noise can be detected as backscattered electrons (those electrons emerging from deeper regions of the primary beam interaction volume and hence from a larger region of surface area) or as unwanted, self-generated signals in the electron detection and imaging system. Unfortunately, under normal operating conditions the noise fluctuations are often larger than the variations due to the specimen's compositional differences. In an effort to improve the signal-to-noise ratio it has been found that the number of electrons reaching the sample can be increased by decreasing the current in the first condenser lens. This results in an increased primary beam diameter at the sample surface and thus decreases the resolution of SEE. The majority of SEM's presently in use have an absolute resolution of 100Å in the SEE mode. Since the layer thicknesses of interest are usually greater than 0.1 μ , we can tolerate some degradation in resolution. In practice we find the improvement in signal-to-noise (which is primarily a function of the beam area) is greater than the loss of resolution (which is primarily a function of the beam diameter), and we can usually find a point at which both parameters are satisfactory. The resulting improvement in the discrimination of intensity variations of the image formed by SEE is still often insufficient to allow easy identification of layer interfaces. Therefore, several additional electronic image processing techniques are employed to maximize these variations.

The image from SEE (or any other mode) is typically amplified, electronically processed, and then dis-

played on a cathode ray tube (CRT). Since the CRT phosphor has a limited dynamic range, the image produced by SEE must be confined within that range through video image processing. The a-c (contrast) and the d-c (dark level) portions of the video signal can be separately controlled. Small variations in amplitude in an image can be maximized by increasing the contrast until the maximum signal variations are as large as the useful range of the CRT and then by decreasing the dark level until the signal variations fall within that range of the CRT (4). In addition, it has also been suggested (4) that the use of a logarithmic circuit element (γ -control) will reduce the contrast variation when one region of the image has a much greater amplitude than the remainder of the image. Without the γ -control, contrast would be limited by the need to keep the largest amplitude within the range of the CRT. Figure 1 illustrates these techniques.

Figure 1a is a schematic of double heterostructure gallium arsenide laser material and the other figures are single line waveforms of SEE from this material. Figure 1b displays the waveform which would result from the use of the linear video amplifier and the "normal" setting of the dark level for our SEM. The useful range of the CRT is bracketed at the left. The amplitude of the image from SEE for the metal contact is much greater than the amplitude of the image from SEE for GaAs and appears above the useful range of the CRT. Figure 1c shows the result when a logarithmic video amplifier is introduced. The signal from the metal contact is now within the range of the CRT but notice that the contrast differences of the

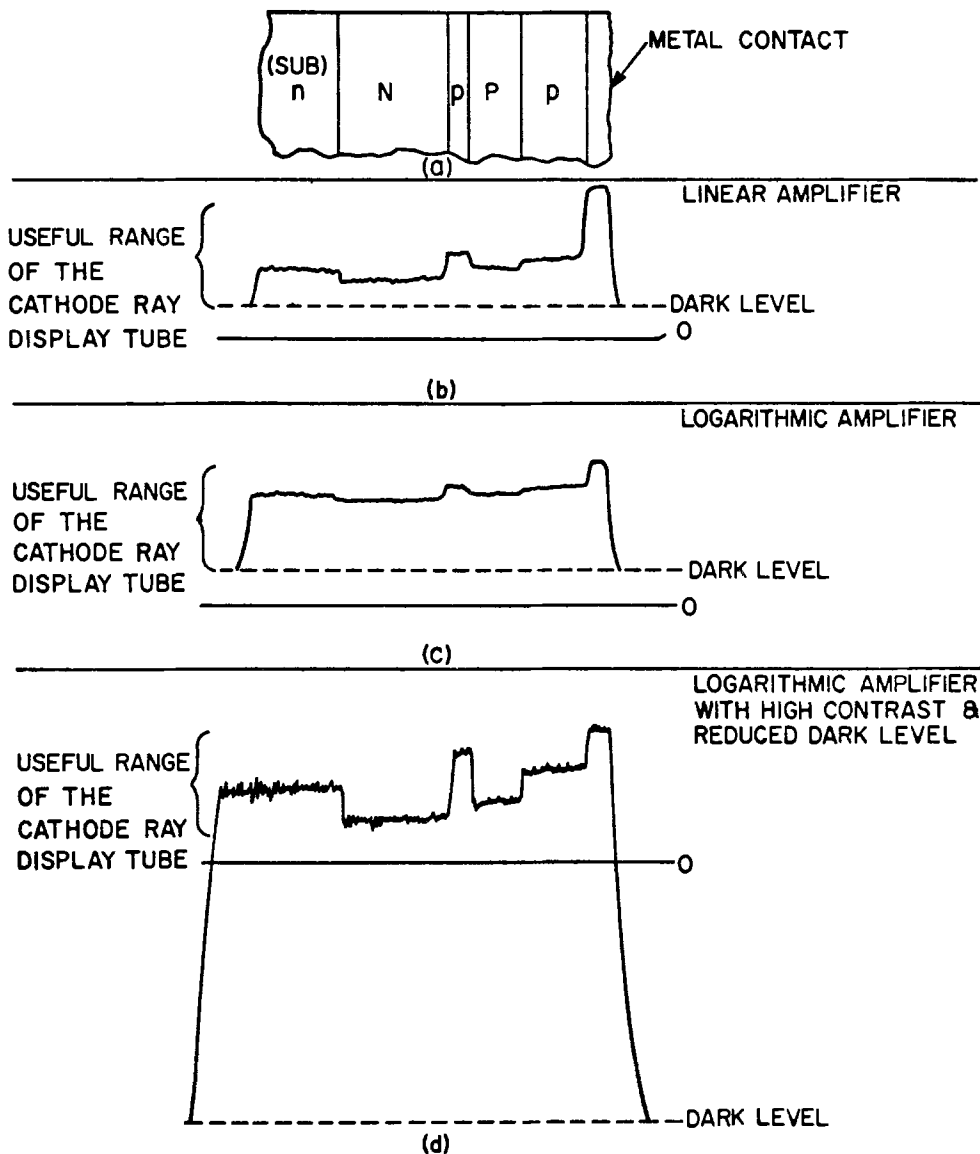


Fig. 1. (a) A schematic of double heterostructure GaAs-GaAlAs laser material with an n-type GaAs substrate, an N-type GaAlAs ternary layer, a p-type GaAs active layer, a P-type GaAlAs ternary layer, a p-type GaAs cap layer and a metal contact. (b) A single line scan of secondary electron emission (SEE) of the material in (a). Normal settings of dark level and contrast, and linear amplification are used. (c) Same line scan as (b) with the same settings of dark level and contrast, but using logarithmic amplification. (d) Same line scan as (c) with the dark level reduced and the contrast increased to utilize the maximum dynamic range of the cathode ray display tube.

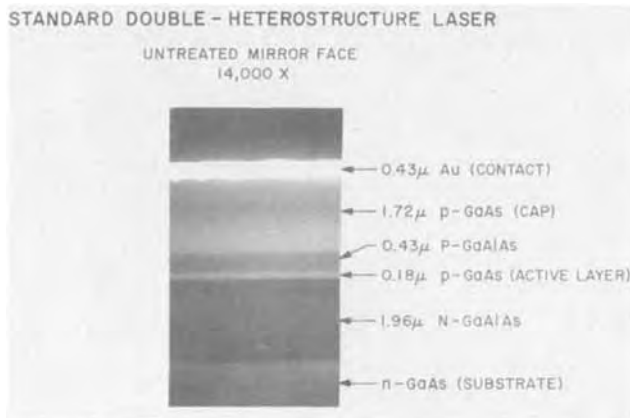


Fig. 2. Scanning electron micrograph of an untreated, cleaved mirror face of a double-heterostructure laser with a metal contact.

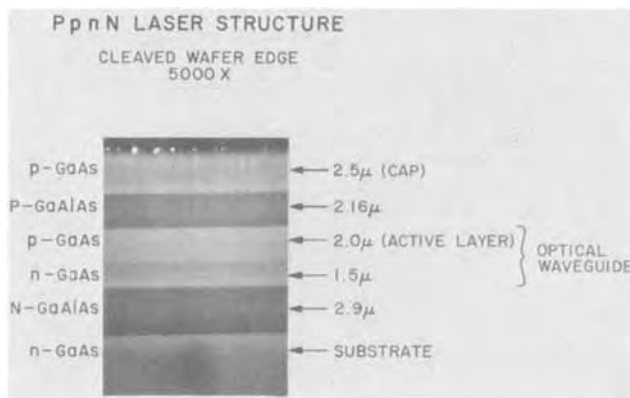


Fig. 3. Scanning electron micrograph of an untreated, cleaved face of a thick optical cavity laser without metallization.

layers have been reduced to a small portion of the useful CRT dynamic range. Figure 1d utilizes the entire dynamic range of the CRT to display information from layer differences. As shown, the contrast has been increased and the dark level decreased to place the signal within the useful range of the CRT. These techniques were employed to make the scanning electron micrograph of a metallized double heterostructure laser (5) shown in Fig. 2.

One further technique proved useful when examining layers of material with no metallization, such as

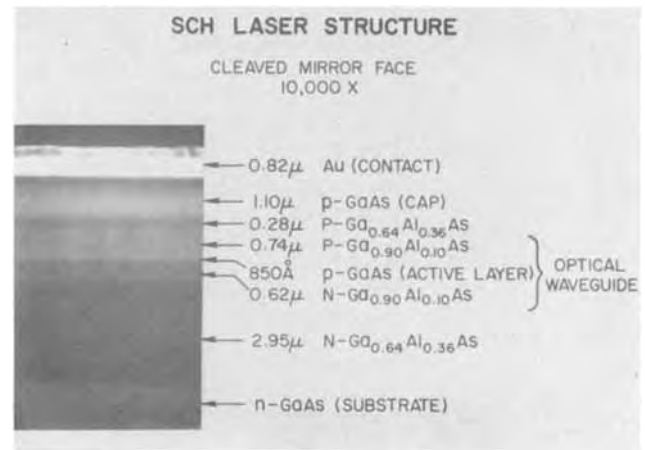


Fig. 4. Scanning electron micrograph of an untreated, cleaved mirror face of a separate confinement heterostructure laser with adjacent ternary layers and a thin active layer.

portions of as-grown wafers. When a primary beam strikes a sharply curving surface such as the edge of a specimen, more secondary electrons are generated. In order to prevent the edge from appearing overly bright and "washing out" the interface between the first two layers, the normal to the sample face is placed at a slight angle with respect to the primary beam axis with the troublesome edge farthest from the detector. This puts the edge in "shadow" and eliminates interfering "highlights". With no metallization, a linear amplifier, rather than a logarithmic amplifier can be employed. Figure 3 illustrates this technique. Shown is a scanning electron micrograph of an unmetallized thick optical cavity laser (6). The bright spots along the edge are dirt particles extending over the cleaved face.

A severe test of the resolution of the ACABOB technique is the separate confinement heterostructure laser (7) shown in Fig. 4. This configuration differs from the double heterostructure configuration in that the GaAs active layer is sandwiched between four GaAlAs layers rather than just two. The two ternary layers on each side have differing aluminum concentrations: the outer layer has 36 atom per cent (a/o) Al; and the inner layer has only 10 a/o Al. In addition, the active layer is only 850 Å thick. While all interfaces can be seen, the interfaces between the 10 a/o ternary layers and the active layer are less clear than the interfaces in the first two micrographs. The variance in mea-

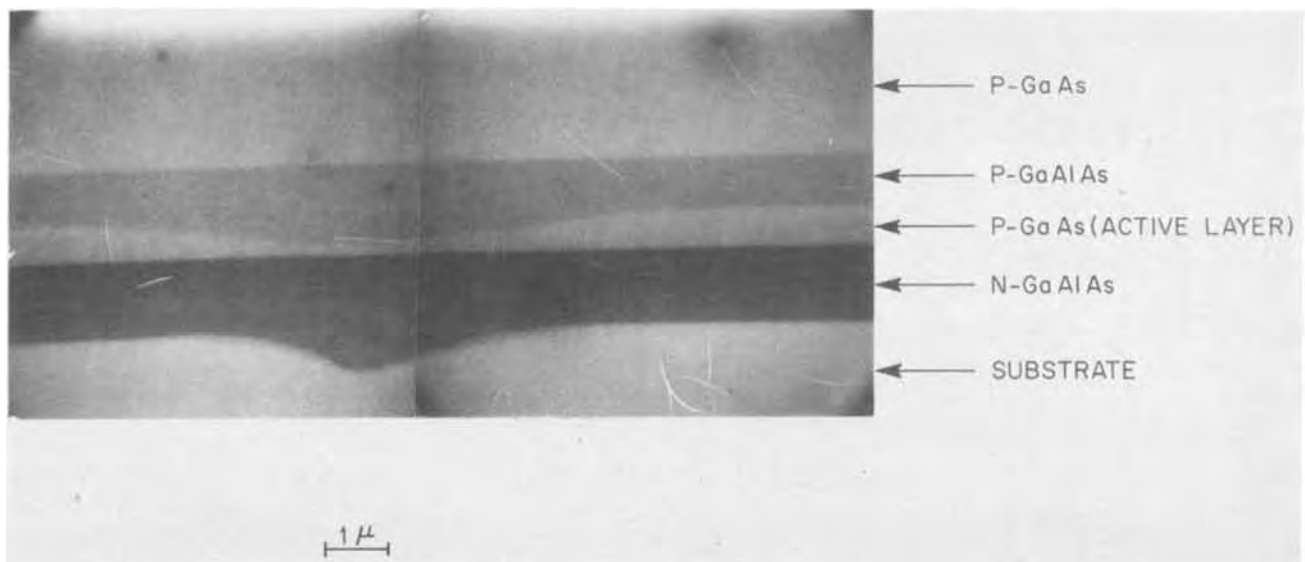


Fig. 5. Scanning electron micrograph of an untreated, cleaved face of double-heterostructure laser material, revealing two defects in the layers.

measurements of the thin active layer using this and other micrographs of the same sample is $\pm 250\text{\AA}$, suggesting an ability to detect layers as thin as 500\AA .

The ACABOB technique can also be used to examine micron-size defects appearing at the cleaved surface. Figure 5 is a scanning electron micrograph of a DH structure showing defects in the layers which would adversely affect laser operation. These defects are three dimensional, and the cleaved face is a cross section in one plane. It appears that the bottom defect has been cleaved near its diameter, while the upper defect center is either into or out of the paper. The locations of the cleave must be known to properly analyze the nature of the revealed defects. No lapping procedure could reveal defects of this magnitude.

Sample contamination due to the presence of hydrocarbons in the vacuum space of the specimen chamber is inherent in all scanning electron microscopes using a hydrocarbon-based diffusion pump fluid. Such contamination will act as a mask if the sample is subsequently exposed to one of the standard etchants (8). The increase in rate of contamination with increasing primary electron beam current might seem to be a drawback of the ACABOB technique. We do not find this to be the case since the contamination can be removed by cleaning and no evidence of permanent specimen damage can be found.

Acknowledgment

The author would like to thank R. W. Dixon and F. R. Nash for their guidance and helpful discussions.

Manuscript submitted Oct. 28, 1974; revised manuscript received March 5, 1975.

Any discussion of this paper will appear in a Discussion Section to be published in the December 1975 JOURNAL. All discussions for the December 1975 Discussion Section should be submitted by Aug. 1, 1975.

Publication costs of this article were partially assisted by Bell Laboratories.

REFERENCES

1. D. J. Stirland *et al.*, "Characterization of Sub-Micron Semiconductor Layers, Annual Research Report, April-October 1973," Appendix I, The Plessey Co., Ltd., (1973).
2. J. W. S. Hearle, J. T. Sparrow, and P. M. Cross, "The Use of the Scanning Electron Microscope," p. 37, Pergamon Press, New York (1972).
3. I. Hayashi, M. B. Panish, and F. K. Reinhart, *J. Appl. Phys.*, **42**, 1929 (1971); B. I. Miller, E. Pinkas, I. Hayashi, and R. J. Capik, *ibid.*, **43**, 2817 (1972); B. Schwartz, J. C. Dymont, and S. E. Haszko, Proc. of the International IPPS Symposium on GaAs, 1972, p. 187.
4. P. R. Thornton, "Scanning Electron Microscopy," pp. 22-23, Chapman & Hall, Ltd., London (1968).
5. R. L. Hartman, J. C. Dymont, C. J. Hwang, and M. Kuhn, *Appl. Phys. Letters*, **23**, 181 (1973).
6. T. L. Paoli, B. W. Hakki, and B. I. Miller, *J. Appl. Phys.*, **44**, 1276 (1973).
7. M. B. Panish, H. C. Casey, Jr., S. Sumski, and P. W. Foy, *Appl. Phys. Letters*, **22**, 590 (1973).
8. C. H. Gooch, "Gallium Arsenide Lasers," p. 166, Wiley-Interscience, London (1969).

DISCUSSION SECTION



This Discussion Section includes discussion of papers appearing in the *Journal of The Electrochemical Society*, Vol. 121, No. 8, 9, 10, and 12; August, September, October, and December 1974.

Thermodynamics and Kinetics of Pack Aluminide Coating Formation on IN-100

S. R. Levine and R. M. Caves (pp. 1051-1064, Vol. 121, No. 8)

J. M. Trenouth:¹ In the paper under discussion, the authors reported that the variation in coating weights and thicknesses of specimens within a pack was generally small whereas there was more variation in these measurements between packs. It was noted that this latter variation influenced coating composition and microstructure but no satisfactory explanation for its occurrence could be found.

Such behavior has been observed in some of the experimental coating work conducted in this laboratory (and also noted in other coating results reported in the literature). While a number of coating variables such as activator carry-over and pack permeability as well as those mentioned by Levine and Caves in the paper under discussion were considered, it was concluded that, in our coating experiments, the primary variable responsible for such coating variation was pack temperature. In these experiments it was calculated that a 10°C variation in coating temperature would result in a 10% change in coating weight during deposition of a chromium-titanium alloy coating using processing times of 2, 4, or 8 hr at 1300°C . Based on their reported level of temperature control for the box furnace used for coating formation ($\pm 15^\circ\text{C}$) and their subsequently determined temperature dependence of coat-

ing formation (a $+15^\circ\text{C}$ variation in temperature giving an 18% increase in coating thickness), it is suggested that pack temperature variability may adequately explain the variation in coating weights and thicknesses between packs noted in the paper being discussed.

S. R. Levine and R. M. Caves: We agree that temperature control was primarily responsible for the variability between packs run under the same nominal conditions.

Hall Effect, Schottky Barrier Capacitance, and Photoluminescence Spectra Measurements for GaAs Epitaxial Layer and Their Correlation

T. Katoda and T. Sugano (pp. 1066-1073, Vol. 121, No. 8)

R. Bhat:² With regards to the paper under discussion we wish to point out that when the Fermi level goes below the donor level (Fig. 7 of that paper) the donors will be positively ionized but the acceptors will remain neutral. This can be seen from the following expression obtained using detailed balance

$$\frac{Na^-}{Na} = \frac{1}{1 + 2 \exp(E_A - E_F)/kT}$$

where Na^- is the number of ionized acceptors and Na is the total number of acceptors. Since $(E_A - E_F)$ is positive for the case being considered, it follows that (Na^-/Na) is very small, i.e., most of the acceptors are un-ionized.

¹ National Research Council of Canada, Structures and Materials Laboratory, Ottawa, Ontario, Canada K1A 0R6.

² Rensselaer Polytechnic Institute, School of Engineering, Troy, New York 12181.

The difference they obtain between the variation of the number of mobile carriers with temperature and the variation of the number of ionized impurities with temperature is probably due to inaccuracies in their theory rather than the presence of impurities which are undetectable by Schottky barrier capacitance and photoluminescence methods.

T. Katoda and T. Sugano: We thank the above author for his discussion of our work. Here we would like to direct his attention to the change of the shape of the distribution function as well as to the shift of the Fermi level with increase of temperature, with regards to the change of ionized acceptor density as shown in Fig. 7 in the paper being discussed.

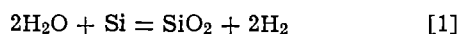
For example, assuming that the acceptor level is located 0.07 eV above the Fermi level, that is $E_A - E_F = 0.07$ eV at 118°K, where the carrier density of the sample No. 213 begins to increase abruptly as shown in Fig. 5 of the paper under discussion, we find out that electrons trapped at the acceptor level increase by more than a factor of 50 even if the Fermi level goes down by 0.01 eV, i.e., $E_A - E_F = 0.08$ eV, with an increase of temperature to 300°K.

Figure 7, of the paper under present consideration, which shows the shift of Fermi level to a value lower than that of the donor level, rather exaggerates the shift of Fermi level, but the above numerical example indicates that acceptors can be negatively ionized at room temperature even if the Fermi level is below the acceptor level.

Reexamination of Some Aspects of Thermal Oxidation of Silicon

Y. Ota and S. R. Butler (pp 1107-1111, Vol. 121, No. 8)

R. H. Doremus:³ The authors of the paper under discussion have concluded that "there is no acceptable model for the processes going on at the gas-oxide interface." However, their experiments do not measure processes at the gas-oxide interface, but rather the rate of transport of water through the silica film. A model of molecular diffusion of water through the oxide film⁴ can explain their results and those of Deal and Grove.⁵ In this model water molecules diffuse through the film to the silicon-oxide interface, where they react to form more oxide

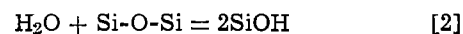


The hydrogen formed in this reaction diffuses rapidly out of the film.

Gas molecules dissolve and diffuse in the open structure of amorphous silica.⁶ Molecules as large as krypton and xenon dissolve and diffuse in silica, as well as argon, oxygen, water, and smaller molecules. The diffusion coefficient of water molecules in amorphous silica is about $3(10)^{-9}$ cm²/sec at 1000°C, so the measured rates of oxidation of silica by water can readily be explained by molecular diffusion of water.

In this model the parabolic rate coefficient B in the paper under discussion should be directly proportional to the water vapor pressure, as found in the above-mentioned work and by Deal and Grove,⁵ since the molecular solubility of water is proportional to the gas pressure. There is no conflict with the results of Moulson and Roberts,⁷ since they measured the concentration of water that had reacted with the silicon-oxygen lattice to form SiOH groups, not the concen-

tration of molecularly dissolved water. The concentration of reacted water should be proportional to the square root of the water vapor pressure, as found by Moulson and Roberts, because of the reaction



The hydrogen formed in reaction [1] diffuses rapidly from the oxide because of the small size of the hydrogen molecule. Addition of external hydrogen pressure does not affect the rate of water diffusion or oxidation because these molecules diffuse independently in the silica lattice.⁶ Only if the hydrogen pressure is high enough to suppress reaction [1] and make its rate the controlling step in the oxidation process would one expect to find an influence of hydrogen. Thus the similarity of oxidation rates with and without hydrogen, as found in the paper being discussed, is consistent with the molecular diffusion model.

Y. Ota and S. R. Butler: We are grateful to Doremus for pointing out his molecular diffusion model for H₂O transport in SiO₂.⁶ This model is consistent with the linear pressure dependence for the oxidation rate equation coefficient B ⁵ as he asserts. Further, he supplies a logical rationale for the inapplicability of the data of Moulson and Roberts⁷ to the analysis of silicon oxidation rates of Deal and Grove.⁵ Doremus also asserts that the diffusion coefficient of 3×10^{-9} cm²/sec⁶ will account for the observed oxidation rates.

However, if we take this value for the concentration of dissolved H₂O, 2.9×10^{-7} moles/cm³⁶ (which converts to 1.7×10^{17} cm⁻³) and calculate the coefficient B we obtain $\sim 2 \times 10^{-14}$ cm²/sec, which is nearly 2 orders of magnitude less than the measured value of Deal and Grove⁵ at 1000°C. We cannot therefore agree that the oxidation rates can be "readily" explained by the molecular solution and diffusion model. In addition, if we apply the model of diffusion with chemical reaction which Doremus has proposed for H₂O transport in SiO₂,⁶ we obtain a further reduction in the effective diffusion coefficient by two orders of magnitude. We must still conclude that there is no adequate model of the process of silicon oxidation.

The Temperature and Oxygen Pressure Dependence of the Ionic Transference Number of Nonstoichiometric CeO_{2-x}

G. J. VanHandel and R. N. Blumenthal
(pp. 1198-1202, Vol. 121, No. 9)

H. L. Tuller⁸ and A. S. Nowick:⁹ In the paper under discussion VanHandel and Blumenthal reported results for the ionic transference number, t_i , of "pure" CeO_{2-x} as a function of p_{O_2} and temperature. Because these results showed maxima in the plot of t_i vs. p_{O_2} at 590° and 702°C, they concluded that electron holes become the dominant charge carriers at high p_{O_2} and low T .

The question of electronic contributions to the conductivity of ceria has become particularly important of late because of interest in ceria doped with lower valent cations (e.g., Ca²⁺ and Y³⁺ ions) as a possible solid oxide-ion electrolyte for application in fuel cells.¹⁰⁻¹² In recent papers,^{13,14} the present authors presented results for the system CeO₂:5% Y₂O₃ from

³ Department of Physics, Technion, Haifa, Israel.

⁴ Henry Krumb School of Mines, Columbia University, New York, New York 10027.

⁵ T. Takahashi, K. Ito, and H. Iwahara, in "Proc. Journees Int. d'Etude des Piles a Combustible III," p. 42, S.E.R.A.I., Bruxelles (1965).

⁶ M. V. Perflav and S. F. Paluev, in "Electrochemistry of Molten and Solid Electrolytes," Vol. 4, p. 153, Consultants Bureau, N.Y. (1967).

⁷ T. Takahashi, in "Physics of Electrolytes," Vol. 2, J. Hladik, Editor, p. 989, Academic Press, London (1972).

⁸ H. L. Tuller and A. S. Nowick, *This Journal*, 122, 255 (1975).

⁹ H. L. Tuller and A. S. Nowick, in "Proc. 9th University Conf. on Ceramic Science," Plenum Press, To be published.

³ Materials Division, Rensselaer Polytechnic Institute, Troy, New York 12181.

⁴ R. H. Doremus, in "Reactivity of Solids," Mitchell, DeVries, Roberts, and Cannon, Editors, p. 667, John Wiley and Sons, Inc., New York (1969).

⁵ B. E. Deal and A. S. Grove, *J. Appl. Phys.*, 36, 3770 (1965).

⁶ R. H. Doremus, "Glass Science," p. 121 ff, John Wiley and Sons, Inc., New York (1973).

⁷ A. M. Moulson and J. P. Roberts, *Trans. Faraday Soc.*, 57, 1208 (1961).

which the electrolytic domain (T - p_{O_2} region for which $t_1 \cong 0.99$) was determined. It was concluded that doped ceria looked particularly attractive as a solid oxide electrolyte at temperatures below 800°C. In such applications it is important that electronic contributions be kept very small. Accordingly, it is essential that all sources of electronic carriers be established in this range of prospective application.

In this discussion, we will demonstrate that the maximum in t_1 reported in the paper under discussion which led VanHandel and Blumenthal to propose an electron hole contribution, is inconsistent with electrical conductivity measurements which we have made,¹⁵ and we will attempt to explain the discrepancy.

Since the reported maximum in t_1 is a value whose magnitude is ~ 0.5 , and since the mobility of the oxygen-ion vacancies V''_O is much smaller than that of electrons and holes, it follows that the maximum must occur in the range where $[V''_O] \gg n, p$ and therefore where the vacancies are primarily compensated by impurities (mainly Ca''_{Ce}) so that

$$[Ca''_{Ce}] = [V''_O] \quad [1]$$

In this range, the total conductivity may be expressed the form¹⁶

$$\sigma_{total} = C_i \mu_i + C_h \mu_h p_{O_2}^{1/4} + C_e \mu_e p_{O_2}^{-1/4} \quad [2]$$

where the μ 's are mobilities and the C 's are constants, the subscripts $i, h,$ and e referring to ions (i.e., vacancies), holes, and electrons, respectively. The ionic transference number is then

$$t_1 = C_i \mu_i / \sigma_{total} \quad [3]$$

since $C_i \mu_i \equiv \sigma_i$ is the ionic conductivity.

One can therefore investigate the question of a hole contribution in this range of p_{O_2} by observing the p_{O_2} dependence of either σ or t_1 . If the hole contribution is significant, Eq. [2] predicts a minimum in σ as a function of p_{O_2} while Eq. [3] predicts a maximum in t_1 , such as reported in the paper being discussed. On the other hand, if the hole contribution is negligible, σ should decrease with increasing p_{O_2} until a plateau in σ is reached, the magnitude of which is determined by the constant contribution of σ_i . In that case, t_1 should increase toward a saturation value close to unity without passing through any maximum.

A dependence of conductivity of the second sort has in fact been observed by the present authors¹⁵ in single crystal CeO_2 at 635°C. Figure 1 shows a plot of σ_{total} (normalized with respect to the constant σ_i term) as a function of p_{O_2} both for the experimentally obtained values at 635°C and for values derived from the t_1 data in the work under consideration at 590°C.¹⁷ While the increase in σ_{total} at low p_{O_2} has been widely observed (and is known to be due to the electronic contribution which appears when CeO_2 is reduced to CeO_{2-x}), there is no evidence for the increase in σ_{total} for $p > 10^{-4}$ atm predicted from the data for t_1 in VanHandel's and Blumenthal's paper. Rather the conductivity shows a slow decrease toward a p_{O_2} -independent saturation value. Such a discrepancy between the two sets of data would be explained if our sample were substantially less pure than that in the paper being discussed. However, from the absolute conductivity values as well as the analysis published by Blumenthal *et al.*¹⁸ in comparison with an analysis of our own material, it appears that, if anything, the aliovalent cation impurity content of the material in the paper under discussion is slightly higher than that of ours.

¹⁵ H. L. Tuller and A. S. Nowick, To be published.

¹⁶ R. A. Rapp and D. A. Shores, in "Techniques of Metals Research," Vol. 4, Book 2, John Wiley and Sons, Inc., New York (1970).

¹⁷ A correction for the temperature difference would make the rise in the curve of Fig. 1 from the paper under discussion slightly less steep, but nevertheless it would be clearly present.

¹⁸ R. N. Blumenthal, F. S. Brugner, and J. E. Garnier, *This Journal*, 130, 1230 (1973).

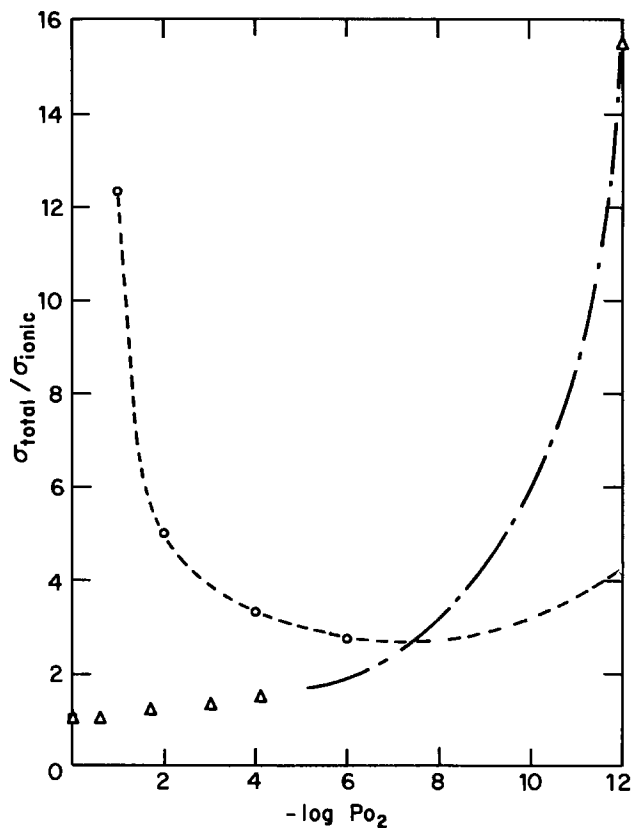


Fig. 1. Isothermal plots of σ_{total}/σ_i vs. $\log p_{O_2}$ from direct measurements and as calculated from t_1 data in paper under discussion by VanHandel and Blumenthal. \circ , Calculated from the work of VanHandel and Blumenthal at 590°C; Δ , measured by Tuller and Nowick¹⁵ at 635°C.

In seeking the cause of this discrepancy, we wish to note the possibility that the experimental apparatus used in the work being discussed is subject to errors in the determination of t_1 due to possible leakage and mixing of gases between the cathodic and anodic chambers. From the equation relating the measured emf of the cell to t_1

$$E_{meas} = (RT/4F) t_1 \ln(p_{O_2}'/p_{O_2}) \quad [4]$$

it is clear that any unaccounted-for mixing of gases between the two chambers will always result in a calculated value of t_1 which is less than the true value. Such leakage would be expected to be a more serious problem at the lower temperatures of this experiment due to a decrease in viscosity of the Pyrex "O"-ring used. This, in addition to possible polarization problems at these lower temperatures, could explain the apparent maxima obtained in the paper being discussed. In fact, preliminary cell measurements in our laboratories, in which a calcia-stabilized zirconia reference electrolyte was employed to avoid the problem of gas leakage, do not indicate the appearance of a maximum in t_1 at low temperature and high p_{O_2} .

In summary, it can be said that the suggestion that the electron hole is a significant contributor to the conductivity in the range close to stoichiometry is not supported by the observed partial pressure dependence of the conductivity in this range. Rather, a model involving impurity compensating oxygen vacancies, which give rise primarily to ionic conductivity, appears to be consistent with the results. Such positively charged vacancies also serve to explain the "p-type" thermoelectric power observed in this range.¹⁹ It appears that the decreasing values of t_1 at high p_{O_2} and low temperatures reported in the paper under con-

¹⁹ Y. Wilbert, J. J. Oehlig, and A. Duquesnoy, *C.R. Acad. Sci. Paris*, C272, 1960 (1971).

sideration may be explained by the occurrence of gas mixing and/or polarization effects.

Acknowledgment

This work was supported in part by the National Science Foundation.

G. J. VanHandel and R. N. Blumenthal: In the paper under discussion we reported the results of a study employing an electrochemical cell technique to measure the ionic transference number, t_i , of sintered specimens of "pure" CeO_{2-x} as a function of P_{O_2} and temperature. The results were described in terms of a high and low oxygen pressure region. At high oxygen pressures t_i is controlled by impurities. In this region the electronic conductivity was p-type at lower temperatures and n-type at higher temperatures. No attempt was made to quantitatively analyze the data in this P_{O_2} region, because the electrical conductivity has been reported to be influenced by impurities.²⁰ In the low oxygen pressure region $t_i \sim 0.05$ when both the electronic and ionic conduction is controlled by the nonstoichiometric defects.

The above comments by Tuller and Nowick suggest that the electron hole conduction in "pure" CeO_{2-x} is negligible. They base their argument on the use of the following expression (i.e., Eq. [2] in the above discussion) for the total electrical conductivity

$$\sigma_{\text{total}} = C_i \mu_i + C_{\text{h}\mu_{\text{h}}} P_{\text{O}_2}^{1/4} + C_{\text{e}\mu_{\text{e}}} P_{\text{O}_2}^{-1/4} \quad [1]$$

and the P_{O_2} dependence of a single crystal of CeO_2 at 635°C.

It is difficult to compare directly the transference numbers calculated by the above-mentioned authors with the t_i data we obtained using an electrochemical cell technique at high P_{O_2} and low temperatures, because the departure from stoichiometry²¹ is small in this region and thus the electrical conductivity is very sensitive to impurities. We have found, for example, the dependence of σ on P_{O_2} is different for sintered CeO_2 specimens prepared from the same grade of CeO_2 powder.

Since we cannot make a direct comparison of the results of these two studies, we will demonstrate some of the problems associated with calculation of ionic transference numbers from Eq. [1] and the P_{O_2} dependence of the electrical conductivity of "pure" CeO_{2-x} .

As an example consider the results of Tuller and Nowick (see their Fig. 1 above) where the plot of $1/t_i$ vs. $\log P_{\text{O}_2}$ would suggest that t_i approaches zero asymptotically with decreasing P_{O_2} below approximately 10^{-12} atm. In contrast to their results, our direct measurements of t_i at low oxygen pressures (in the work being discussed) show that t_i approaches a value of approximately 0.05 over a wide range of oxygen pressures and temperatures and thus the nonstoichiometric defects (i.e., V_{O} and Ce'_{Ce} ²¹) control both the ionic and electronic conduction. Using the value of $t_i \approx 0.05$ an estimate of the diffusion coefficient for doubly ionized oxygen vacancies, $D_{V_{\text{O}}} \approx 3.5 \times 10^{-5}$ cm²/sec, at 1000°C was calculated by combining recently obtained thermodynamic $x = x(P_{\text{O}_2}, T)$ and conductivity $\sigma = \sigma(P_{\text{O}_2}, T)$ data with the Nernst-Einstein relation. Within experimental error the result was in good agreement with $D_{V_{\text{O}}} \approx 1.1 \times 10^{-5}$ cm²/sec calculated at 1000°C from the expression for $D_{V_{\text{O}}}$ obtained from a recent electrical conductivity study¹⁵ on CaO-doped CeO_2 . Information of this type could not be obtained from the analysis used by Tuller and Nowick above. In fact at low oxygen pressures (i.e., $10^{-3} < x < 10^{-2}$) the electronic conductivity is proportional to $P_{\text{O}_2}^{-1/5}$ and Eq. [1] would not be applicable.^{20,21}

²⁰ R. N. Blumenthal, P. W. Lee, and R. J. Panlener, *This Journal*, 118, 123 (1971).

²¹ R. J. Panlener, R. N. Blumenthal, and J. E. Garnier, *J. Phys. Chem. Solids*, To be published.

At high oxygen pressures Tuller and Nowick report that σ approaches a plateau with increasing P_{O_2} and as shown in Fig. 1 above, $t_i = 1$ at $P_{\text{O}_2} = 1$ atm. Thus according to these authors there is no evidence from their study to suggest the presence of any p-type conduction. In contrast to these results of Tuller and Nowick an investigation of ionic transference of CaO-doped CeO_2 [i.e., $t_i = t_i(\text{CaO}, P_{\text{O}_2}, T)$] using an oxygen concentration type cell²²⁻²⁴ shows that $t_i \approx 0.9$ (the exact value depending on T , P_{O_2} , and CaO content) at high oxygen pressures (i.e., $1 < P_{\text{O}_2} < 10^{-4}$ atm). The absolute value of the t_i measurements has also been confirmed in this laboratory using a novel new method based on a coulometric type titration technique. The $t_i = t_i(\text{CaO}, P_{\text{O}_2}, T)$ data was combined with recently reported electrical conductivity data $\sigma = \sigma(\text{CaO}, P_{\text{O}_2}, T)$ ^{18,22-24} and thermodynamic data $x = x(\text{CaO}, P_{\text{O}_2}, T)$ ²⁵ to determine the dependence of the ionic and electronic conductivities on CaO content, oxygen nonstoichiometry, and temperature. The results of this study show that the electronic conductivity at high oxygen pressures (i.e., $1 < P_{\text{O}_2} < 10^{-4}$ atm) is much larger in magnitude than would be expected assuming n-type electronic conduction only (i.e., $\sigma_e \propto P_{\text{O}_2}^{-1/4}$). These observations can be more easily explained by assuming the presence of some p-type conduction. It is interesting to note that σ is essentially independent of P_{O_2} in this oxygen pressure region¹⁸ and thus according to Eq. [1], the calculated value of t_i should be equal to unity. This calculated value of t_i , however, is inconsistent with the above experimentally measured value of t_i .

There may be some question about the presence of some p-type conduction in "pure" CeO_2 at high oxygen pressures because of (i) the influence of impurities in the region near stoichiometry and (ii) the effect of possible leaks in the Pyrex seal at lower temperatures on the oxygen concentration t_i measurements. However, in CaO-doped CeO_{2-x} there appears to be some evidence for the presence of p-type conduction.

In summary it is the authors' opinion that analysis of the electronic and ionic conduction based only on the dependence of σ on P_{O_2} provides information only about the predominant type of conduction mechanisms. A more reliable determination of the ionic and electronic conductivities requires a combined analysis of data obtained from measurements of t_i , σ , and departures from stoichiometry over a wide range of P_{O_2} and temperature.

A Simplified Method of Measuring Lifetime Using Steady-State Back Illumination of an MOS Capacitor

C. St. L. Rhodes and C. A. T. Salama
(pp. 1219-1222, Vol. 121, No. 9)

W. Zechall:²⁶ In the above-cited work the authors reported about a simplified method for determining minority carrier lifetime from the transient response of a back-illuminated MOS capacitor.

If this method is applied for measuring lifetime on thin silicon slices, the measured lifetime values usually are very small and there is but little scatter in their spatial distribution. This result does not agree with results obtained by the frequently used pulsed MOS capacitance method without back illumination. In this case the measured lifetime values usually are

²² G. J. VanHandel, Ph.D. Dissertation, Marquette University, Milwaukee, Wisconsin (1972).

²³ R. N. Blumenthal, S. Reddy, and G. J. VanHandel, Paper 161 presented at Electrochemical Society Meeting, San Francisco, Calif., May 12-17, 1974.

²⁴ S. Reddy and R. N. Blumenthal, *This Journal*, To be published.

²⁵ J. E. Garnier, R. N. Blumenthal, R. J. Panlener and R. K. Sharma, *J. Phys. Chem. Solids*, To be published.

²⁶ Institut für Theoretische Elektrotechnik, Technische Hochschule Aachen, 51 Aachen, West Germany.

much larger and there is a large scatter in their spatial distribution.²⁷⁻²⁹

In order to understand the reason of this disagreement, a numerical analysis of the transient response of a back-illuminated MOS capacitor on n-type substrate was carried out by solving the following differential equation

$$j_{\text{gen}} = q \int_0^{w(t)} \frac{pn - n_i^2}{\tau_{n0}(p + n_i) + \tau_{p0}(n + n_i)} dx + q \sqrt{\frac{D_p}{\tau_{p0}}} (p_w - 2C_1) \quad [1]$$

where

$$C_1 = \frac{p_w \sqrt{\frac{D_p}{\tau_{p0}}} \exp\left(\frac{d}{l_d}\right) - g}{2 \sqrt{\frac{D_p}{\tau_{p0}}} \cosh\left(\frac{d}{l_d}\right)} \quad [2]$$

j_{gen} is the current flowing normal to the interface of the MOS system, D_p the diffusion coefficient of holes, n and p the concentrations of electrons and holes, $w(t)$ the width of the space charge region, τ_{n0} and τ_{p0} the low-level lifetimes of electrons and holes, l_d the diffusion length of holes, d the thickness of the silicon slice, g the optical generation rate, and p_w the hole concentration at the edge of the space charge region.

The differential equation consists of a first term which considers thermal carrier generation in the space charge region according to Shockley, Read, and Hall^{30,31} and a diffusion term which considers diffusion of carriers optically generated on the back of the specimen. This current component causes the interface charge in the MOS-system to increase much faster than in the case of thermal generation only.

From the numerical solution of this equation we calculated capacitance-time plots for an n-type substrate impurity concentration of $3 \times 10^{15} \text{ cm}^{-3}$, a slice thickness of 0.2 mm, a gate voltage step from 0 to -20V, an oxide thickness of 0.12 μ , an optical generation rate of $10^{14} \text{ cm}^{-2} \text{ sec}^{-1}$ and various values of generation lifetime $\tau_{\text{gen}} = \tau_{n0} + \tau_{p0}$. From these theoretical plots we determined lifetime τ_{Ph} by applying Eq. [2], [5], [6], and [7] of the paper under discussion. The result of this evaluation is plotted in our Fig. 1.

²⁷ G. H. Schwuttke, IBM System Product Div., East Fishkill Laboratories, Tech. Rept. No. 1, (Jan. 1973).

²⁸ D. R. Young and C. M. Osburn, *This Journal*, 120, 1578 (1973).

²⁹ W. Zechall, Paper 61 presented at Electrochemical Society Meeting, Chicago, Ill. May 13-18, 1973.

³⁰ W. Shockley and W. T. Read, *Phys. Rev.*, 87, 835 (1952).

³¹ R. N. Hall, *ibid.*, 87, 387 (1952).

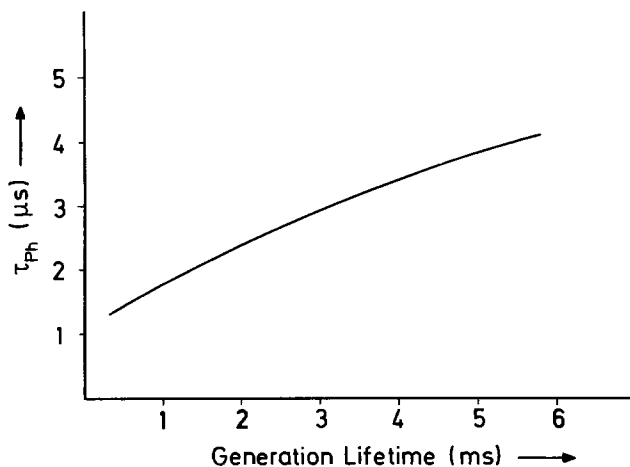


Fig. 1. Lifetime values τ_{Ph} as dependence on generation lifetime.

Firstly, the plot shows that lifetime values τ_{Ph} are much smaller than generation lifetime τ_{gen} . Secondly, a change of generation lifetime does not cause a change of lifetime τ_{Ph} by the same percentage. For instance, a variation of generation lifetime from 5.5×10^{-4} to 5.5×10^{-3} sec only yields a change of lifetime τ_{Ph} from 1.4 to 4.0 μsec . Therefore we can conclude that lifetime values τ_{Ph} are mainly controlled by diffusion of carriers optically generated on the back of the specimen. This effect causes the values τ_{Ph} to be much less dependent on the actual values τ_{n0} and τ_{p0} of low-level lifetime in the thin silicon slice. Therefore the method described in the paper under discussion cannot be applied for material characterization on thin silicon slices.

C. St. L. Rhodes and C. A. T. Salama: Zechall's comments on the back illumination method³² of measuring lifetime imply a misinterpretation on his part of the basic principles underlying the method of measurement. Zechall claims that the values of lifetime measured using our method are usually very small (and exhibit but little scatter in their spatial distribution) as compared to the measured values using Zerbst's method.³³ Our experimental data,³² however, indicate that when properly implemented the back illumination method and Zerbst's method yield almost identical values of lifetime. Zerbst's method, as commonly implemented without taking into account the position of the trapping level in the energy gap, yields large values of lifetime particularly if the dominant trap is not at midgap.³²

Equations [1] and [2] in Zechall's comments above do not represent the physical situation during proper implementation of the back illumination method.³² These equations appear (Zechall, above, has not clarified his boundary conditions) to represent the case of back illumination using short wavelength light which does not significantly penetrate the silicon, thus causing most of the generation to occur at the back surface. For proper implementation of the back illumination method, a red or near infrared, light-emitting diode source must be used to ensure that light penetrates deeply into the silicon. The back illumination method requires that, under steady-state conditions, the diffusion flux be sufficiently large to ensure that the excess carrier density r at the edge of the space charge region in the semiconductor is much larger than the minority carrier density under thermal equilibrium conditions. The back illumination method derives the lifetime from an indirect measurement of the steady-state recombination rate in the space charge region and from a measurement of the excess carrier density in the space charge region. The lifetime is not obtained from measurement of the diffusion parameters of the silicon slice.

Furthermore, the experimental implementation of the back illumination method requires that the device be initially biased in the inversion region. Zechall's calculations, above, assume an initial bias of 0V; as well as assuming an optical generation rate which is insufficient to meet the requirement on r mentioned above. Thus, his use of Eq. [2], [5], [6], and [7] in our paper under discussion is not justified.

One final comment should be made on the order of magnitude of the generation lifetime quoted by Zechall. These values appear to be at least one order of magnitude larger than values commonly referred to in the literature³⁴ for high quality silicon slices.

³² C. St. L. Rhodes and C. A. T. Salama, *J. Phys. D: Appl. Phys.*, 6, 1798 (1973).

³³ D. K. Schroeder and H. C. Nathanson, *Solid State Electron.*, 13, 577 (1970).

³⁴ D. K. Schroeder and J. Guldberg, *ibid.*, 14, 1285 (1971).

The Incorporation of Phosphorus in Silicon Epitaxial Layer Growth

J. Bloem, L. J. Gilling, and M. W. M. Graef
(pp. 1354-1357, Vol. 121, No. 10)

S. E. Craig, Jr.³⁵ In the paper under discussion J. Bloem *et al.* present informative data on the electrically active phosphorus concentration in silicon deposited from a feed gas mixture of H₂, SiH₄, and PH₃. In addition they present an original and correct concept of how the intrinsic-extrinsic behavior of silicon influences the chemical equilibrium. However, their analysis of the results is misleading because it is based upon an assumption which logically contradicts itself, i.e., "It is assumed, because of the low growth rate which is being used, that equilibrium in the gas phase is attained near the silicon surface, and that the transport effects are of minor importance."

In reality, if equilibrium is obtained at the solid-gas interface, then the rate of reaction must be mass transfer controlled. The logic is that for equilibrium to be obtained, the rates of the various chemical reactions must be extremely fast compared to other possible rate-limiting steps and the only other possible rate-limiting step is mass transfer in the gas phase.

In this experiment, the argument that mass transfer is unimportant because the rate is small cannot be accepted. The true fact is that the rate is small because the feed gas concentrations are very small. Concentration gradients must exist in the gas phase to cause the active species to migrate to the solid where the major deposition reactions occur. Since the feed gas concentrations are so small, it is necessary that the concentration gradients be exceedingly small. Therefore, the rate of reaction must be small even for a mass transfer controlled reaction.

In the work under present consideration the authors also err in the use of this assumption. That is, equilibrium involving phosphorus in the solid phase was not included in the calculations. Rather, it appears that Bloem *et al.* assumed equilibrium between the solid silicon and the gas phase species containing silicon but then assumed that the various phosphorus species in the gas phase were in equilibrium with each other, but not with the phosphorus in the solid phase. [Bloem's *et al.*'s unnumbered chemical equation representing this equilibrium, P(g) \rightleftharpoons P(Si), was not included in the equilibrium calculations.] Bloem *et al.* treated the phosphorus as if its rate of incorporation into the solid was limited by some step other than mass transfer control. The only remaining possibility is that the rate of incorporation is limited by some activated chemical step. If this were true we would have an equation of the form

$$J_D = k_{a1}[P] + 2k_{a2}[P_2] + k_{a3}[PH_3] + \dots$$

where J_D is the flux of dope being incorporated into the solid and the bracketed quantities would represent the chemical activities or partial pressures of the indicated gas phase species as given by the authors' calculations. The various k_a 's are reaction velocity constants for the chemical reactions. An equation of this form seems to fit their results until it is noted that these k_a 's are strong exponential functions of temperature (i.e., they must fit the Arrhenius equation). Therefore, if this model were correct, the rate of incorporation of dope at 1600°K would be much greater than the rate at 1400°K. Since this is contrary to the experiment we must reject this model. It appears that Bloem *et al.* assigned no rate-limiting step to the incorporation of phosphorus into the solid.

In the following paragraphs, we shall show that gas phase mass transfer controlled kinetics fully explains the results in the paper being discussed pro-

vided that the solid-gas equilibrium calculations are complete.

To simplify the analysis, we shall neglect the following minor points: (i) the increase in number of gas phase moles caused by the reaction; (ii) the change in hydrogen partial pressure caused by the reaction; and (iii) differences between the mole ratio and mole fraction of phosphorus in the solid. We shall also neglect differences in the gas phase mass transfer coefficients for the various chemical species. This assumption greatly simplifies the mathematical development and the errors that it causes should be less than $\pm 20\%$.

The model we propose consists of three steps. (i) Diffusion of the gas phase species from the bulk gas phase to the solid-gas interface. (ii) Very rapid kinetics for the inclusion of the silicon and phosphorus into the solid at the solid-gas interface. Step (iii) is a direct result of these very rapid reactions. (iii) Chemical equilibrium between all gas phase species and the solid at the solid-gas interface.

Bloem has identified the important gas phase species. Each of these species containing phosphorus will diffuse toward the solid-gas surface because of concentration gradients. The total flux of phosphorus toward the surface is

$$-J_P = \frac{D_1}{RT} \frac{\partial [P]}{\partial z} + \frac{D_2}{RT} \frac{\partial [PH]}{\partial z} + \frac{D_3}{RT} \frac{\partial [PH_2]}{\partial z} + \frac{D_4}{RT} \frac{\partial [PH_3]}{\partial z} + 2 \frac{D_5}{RT} \frac{\partial [P_2]}{\partial z} + 4 \frac{D_6}{RT} \frac{\partial [P_4]}{\partial z}$$

where z is the direction normal to the surface, R is the ideal gas constant, T the absolute temperature, and D_i 's are the gas phase diffusion coefficients. The bracketed quantities are the chemical activities or partial pressures of the indicated species. When all the D_i 's have the same value the equation reduces to

$$J_D = -\frac{D}{RT} \frac{\partial [D]}{\partial z} \quad [1]$$

where $[D]$ is the pseudo total chemical activity of phosphorus in the gas phase defined by the equation

$$[D] = [P] + [PH] + [PH_2] + [PH_3] + 2[P_2] + 4[P_4] \quad [2]$$

An important consideration concerning Eq. [1] and [2] is that the gas phase chemical reactions given by Bloem *et al.* in their Eq. [1] through [6] in the paper under discussion cannot change the value of $[D]$ and therefore cannot affect the rate of mass transfer in the bulk gas phase. In other words, to a first approximation, it makes no difference whether or not chemical equilibrium is obtained in the bulk gas phase.

The only way $[D]$ can be changed is by adding or removing phosphorus atoms from the gas phase. This is accomplished at the feed point where phosphorus is added and at the solid-gas interface where it is removed.

At the feed, or in the bulk gas phase, the total phosphorus activity is $[D^*] = [PH_3^*]$. At the solid-gas interface, phosphorus is removed from the gas phase so that the total phosphorus activity is reduced to $[D^*]$. The phosphorus atoms are transported from the feed to the gas-solid interface by flow and by diffusion. The effective gas phase diffusion length is approximately the same for each species. Therefore, Eq. [1] integrates into

$$J_D = k_m([D^*] - [D^*]) \quad [3]$$

where k_m is the mass transport coefficient and includes the combined effects of flow, diffusivity, and effective diffusion length.

In all cases, $[D^*]$ is equal to or greater than the value given by chemical equilibrium at the surface.

³⁵ Department of Chemical Engineering, Arizona State University, Tempe, Arizona, 85281.

For mass transfer controlled kinetics, $[D^*]$ is equal to the equilibrium value. Hereafter, all quantities followed by "*" will indicate the value at equilibrium at the solid-gas interface.

A similar treatment³⁶ gives the flux of silicon as

$$J_{Si} = k_m ([Si^\circ] - [Si^*]) \quad [4]$$

The ratio of the flux of phosphorus to the flux of silicon gives the atomic fraction of phosphorus in the solid. For silicon, this is the concentration of phosphorus atoms, N_p^+ , divided by $5(10^{22})$

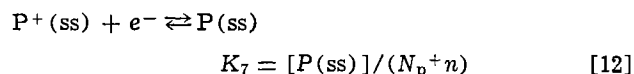
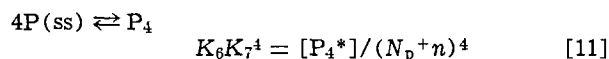
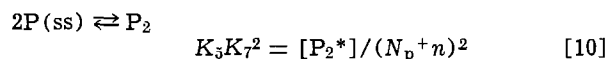
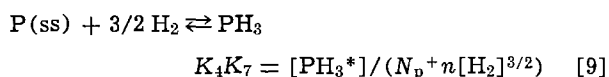
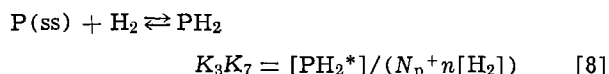
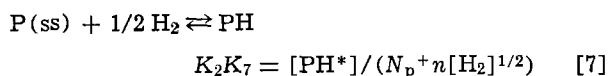
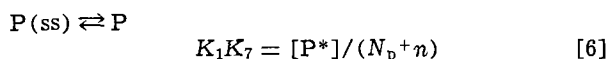
$$\frac{N_p^+}{5(10^{22})} = \frac{[D^\circ] - [D^*]}{[Si^\circ] - [Si^*]} \quad [5]$$

Again we have neglected the minor differences in mass transport coefficients between the various species.

Figure 2 in the paper under discussion shows that the equilibrium activity of silicon in the gas at the solid interface is much smaller than the feed gas activity of silicon, $[Si^\circ]$. Therefore

$$[Si^\circ] - [Si^*] = [Si^\circ] = 2.2(10^{-3})$$

The chemical reaction and equilibrium equations which dictate the value of $[D^*]$ are



Electron hole generation in solid silicon

$$k_1 = np \quad [13]$$

where $P(ss)$ is neutral phosphorus in solid solution and $[P(ss)]$ is its chemical activity. n , p , and N_p^+ are the concentrations of electrons, holes, and ionized phosphorus in the solid silicon, respectively.

Equation [12] is necessary because at the reaction temperature essentially all the phosphorus in the solid is ionized. However, the available thermodynamic data for solids pertains only to neutral solid silicon.

The values of the equilibrium constants K_1 through K_6 reported in Table I were computed from the JANAF Tables³⁷ using a hypothetical standard state of pure, solid red phosphorus at the reaction tempera-

³⁶ S. E. Craig, Jr., *This Journal*, **112**, 1257 (1965).

³⁷ JANAF Thermochemical Tables, 2nd ed., NSRDS-NBS 37 (1971).

Table I.

T, °K	1400	1500	1600
log K_1	-5.312	-4.407	-3.797
log K_2	-3.980	-3.401	-2.898
log K_3	-2.208	-1.938	-1.706
log K_4	-2.123	-2.113	-2.107
log K_5	1.704	2.082	2.402
log K_6	4.023	4.237	4.400
log $\sqrt{k_1}$	19.278	19.491	19.683
log K_7	-42.389	-42.292	-42.248

tures. The values of k_1 were obtained from Morin's equation.³⁸

The total electron concentration within the silicon is equal to that from the ionized phosphorus plus that from the silicon lattice, $n = N_p^+ + p$. When this is combined with Eq. [13], the electron concentration is found to be

$$n = (N_p^+ + \sqrt{(N_p^+)^2 + 4k_1})/2 \quad [14]$$

The solutions to Eq. [14] are plotted in Fig. 1. Three features of these solutions should be noted. First, for $N_p^+ < 10^{18}$ the silicon is intrinsic and n is a constant. Next, in this intrinsic range, n increases sharply with temperature. Finally, for $N_p^+ > 10^{20}$, the silicon becomes extrinsic and $n = N_p^+$. In this region there is no temperature effect upon n .

The value of K_7 is not directly known. However, the N_p^+ vs. $[PH_3^\circ]$ data in the work being discussed for the intrinsic region was used in Eq. [2], [4], and [6] through [13] to calculate the values of K_7 for each temperature. This is the only parameter in the analysis that must be determined from the experimental data. Now that it has been determined, it can be used for any other Si-P system.

The equilibrium concentrations shown in Fig. 1 were calculated from Eq. [6] through [14] and the values in Table I. These equilibrium values are far below those calculated by Bloem *et al.* in the paper under consideration because these values include the effect of the phosphorus in the solid. A unique feature of these equilibrium curves is the manner in which they all deflect upward near $N_p = 10^{19} \text{ cm}^{-3}$. This is a direct result of the increase in the number of electrons as the silicon shifts toward extrinsic. These additional electrons force all the chemical reactions toward the right. The value of $[D^*]$ computed from Eq. [2] is also included in Fig. 1.

These values of $[D^*]$ were used in Eq. [5] to compute the theoretical N_p^+ vs. $[PH_3^\circ]$ curves shown in Fig. 2. At low values of N_p^+ , the silicon is intrinsic, n is a constant, PH_2 and PH_3 are the major gas phase species, and $[D^*]$ is a linear function of N_p^+ . This

³⁸ F. J. Morin and J. P. Maita, *Phys. Rev.*, **96**, 28 (1954).

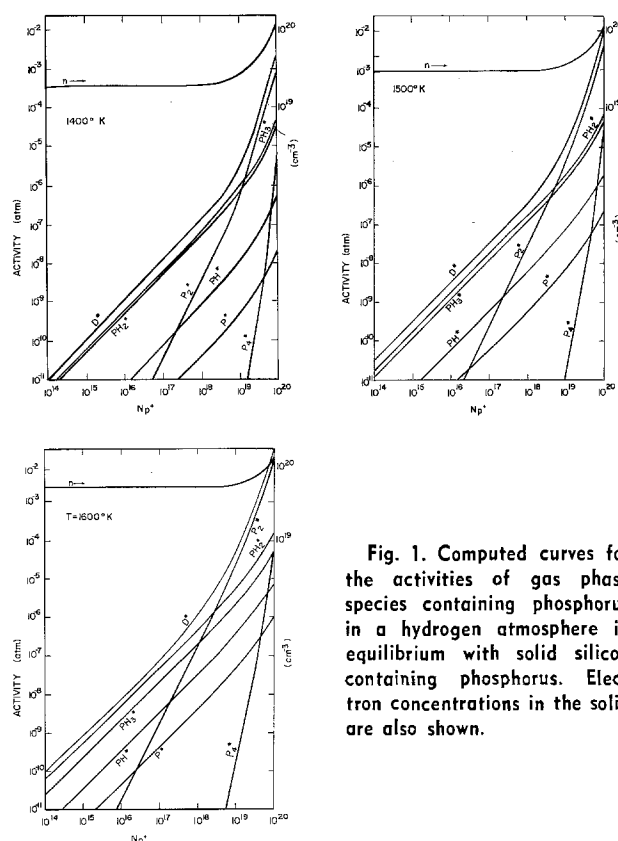


Fig. 1. Computed curves for the activities of gas phase species containing phosphorus in a hydrogen atmosphere in equilibrium with solid silicon containing phosphorus. Electron concentrations in the solid are also shown.

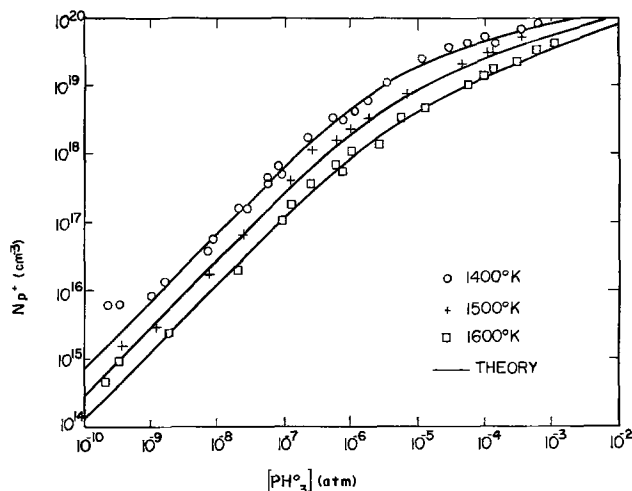


Fig. 2. A comparison of the theoretically and experimentally determined concentration of phosphorus donor centers in silicon as a function of the partial pressure of phosphine in the feed gas. The reaction gas mixture is $\text{SiH}_4\text{-PH}_3\text{-H}_2$.

led to N_p^+ being directly proportional to $[\text{PH}_3^o]$. At very high values of N_p^+ , the silicon is extrinsic and n is equal to N_p^+ . Also P_2 is the major gas phase species. These two facts cause N_p^+ to be proportional to $[\text{PH}_3^o]^{1/4}$ at high values.

The decrease in N_p^+ with increasing temperature is caused by two phenomena. First, silicon is more volatile at higher temperatures as shown by the increases in K_1 to K_8 with temperature. Secondly, the concentration of intrinsic electrons increases with temperature. Both of these phenomena cause $[D^*]$ to increase with temperature and this reduces the rate at which phosphorus is transported to the solid-gas interface.

The experimental data from the paper under discussion are also shown on Fig. 2. The excellent fit between theory and data attests to the validity of the theory as well as to the accuracy of the data.

In summation, the data of Bloem *et al.* in the work being discussed not only fit a kinetic model based on gas phase mass transport, but in addition, their data allow the determination of thermodynamic data not previously available.

The analysis presented here is totally general and can be applied to all epitaxial, chemical vapor deposition systems now in use.

J. Bloem, L. J. Giling, and M. W. M. Graef: In the above discussion by Craig three points emerge: (i) the model, based on gas-phase diffusion; (ii) inclusion of electron concentration and ionized P in the solid; and (iii) determination of equilibrium constant for the ionization of P.

As regards point (i) the discussion given by Craig above on the incorporation of P in Si is interesting but the suggestion that the amount of P incorporated in the growing Si is mass transfer controlled is not applicable in our case.

Mass transfer control is evidently present for the growth of silicon itself, but not for P. This is shown by the experimental evidence that the concentration of P in the layer is independent of the Si growth rate, as already indicated in Ref. (7) of the original article.

Equation [5] in the above discussion shows that following his assumption of mass transfer control an increase in silicon growth rate (with constant input of PH_3) would give a decrease in the amount of P incorporated in the silicon. This is not the case; the use of much higher growth rates than the one used here firstly gives an increase and later a decrease in the donor concentration. This shows that at low growth rates the transfer of P to the surface is not rate limiting, that only a small part of the P present is in-

corporated in the growing layer, and that a direct relation exists between the phosphorus concentration in the gas phase and in the solid, described by the equilibrium segregation coefficient.

Concerning point (ii) the ionization of P in the solid and the intrinsic or extrinsic origin of electron concentration is adequately covered in the article under discussion and no new points emerge from Craig's analysis above.

It is interesting that in the paper being discussed the gas phase equilibria and the equilibrium in the solid are kept separated, in order to be able to discuss the segregation of P between gas and solid in a subsequent article. This link has been laid by Craig in combining the equilibria in gas and solid by the introduction of a segregation coefficient k_1 in which it is implicitly assumed that the evaporation of P from the silicon matrix is equal to the evaporation of P from a hypothetical solid P source at the same temperature. This, of course, is an oversimplification and an analysis based on the work of Thurmond and Struthers³⁹ and Weiser⁴⁰ using the experimental data then can give more information on the energy of incorporation of P in solid silicon.

As regards point (iii), according to Craig, the ionization of P in the solid is the only unknown in the series of equilibria; the equilibrium constant, k_7 in the above discussion, however, is readily calculated.

For the ionization of P

$$\text{P} \rightleftharpoons \text{P}^+ + e^-$$

$$\frac{1}{k_7} = \frac{[\text{P}^+] \cdot n}{[\text{P}]} = N_c \exp(-E_D/kT)$$

where N_c is the density of states in the conduction band of silicon, equal to $2(2\pi mkT/h^2)^{3/2}$ and E_D is the distance of the donor level from the conduction band (≈ 0.04 eV). The value of $1/k_7$ is of the order of $10^{20}\text{-}10^{21}$ cm^{-3} in the range of temperatures considered.

The real unknown is the segregation coefficient of phosphorus between gas phase and solid, (k_1); knowing the value of k_7 , k_1 can then be determined from the experimental data giving information on the incorporation of P in Si as indicated in our comments here on point (ii).

It is interesting to note how the use of the simplified value of k_1 leads to such a good correlation between theory and experiment. In the theory of Craig above the difference in input ($p_{\text{PH}_3^o} = D^o$) and the weighted sum of the resulting equilibrium values of the phosphorus components (D^*) has to be great in order to conclude to a mass transfer controlled reaction. As this is not the case ($D^o \approx D^*$) the model of Craig converts to the equilibrium model with $D^o = D^*$ proposed in the article under discussion.

A New Generation of "Deluxe" Fluorescent Lamps, Combining an Efficacy of 80 Lumens/W or More with a Color Rendering Index of Approximately 85

J. M. P. J. Versteegen, D. Radielović, and L. E. Vrenken
(pp. 1627-1631, Vol. 121, No. 12)

W. A. Thornton:⁴¹ In the tradition of "the mouse that roared," the United States is being invaded by one of her small friends from across the water, who lays claim to a most interesting and unexpected development in practical illuminants. But this development occurred on the home ground of *This Journal*. The prime reference⁴² includes the results of a conference in 1966 in New Jersey at which sixty experts witnessed the remarkable properties of the new illuminant. The

³⁹ C. D. Thurmond and J. D. Struthers, *J. Phys. Chem.*, **57**, 831, (1953).

⁴⁰ K. Weiser, *J. Phys. Chem. Solids*, **7**, 118 (1958).

⁴¹ Westinghouse Electric Corporation, Bloomfield, New Jersey 07003.

⁴² W. A. Thornton, *J. Opt. Soc. Am.*, **61**, 1155 (1971).

new fluorescent lamps were demonstrated and discussed in 1972 at the Tulsa conference of the Illuminating Engineering Society,⁴³ and the general phenomenon was the keynote of the May 1972 Electrochemical Society Meeting in Houston, Texas (luminescence). The essential discovery⁴² was that both luminous efficiency and color rendering capability are astonishingly high when the white light is composed predominantly of three very specific colors, near 450, 540, and 610 nm, since called the prime colors; the luminous efficiency-color rendering index, in combination, excels all other possible spectral power distributions.⁴² It has become clearer that both characteristics are due to strongly peaked visual response at these three wavelengths.⁴⁴

What the authors of the paper under discussion call the "Koedam-Opstelten principle" is in itself impractical, since lamps of considerably higher color rendering index have long been commercially available. Only when it is shown that efficacy is also high, or that color preference⁴⁵ is pronounced, are three-spectral color illuminants recognized to be of profound interest. In regard to color preference, I think that the above authors will find that the new lamps have an appeal far beyond that indicated by the color rendering index. Two-hundred observers preferred daylight-color prime-color lamps well above real daylight itself for illuminating foods,⁴⁶ and the standard daylight lamp was much lower still in preference.

Possibly the performance of the new aluminate phosphors will in the long run justify their cost, but at present the performance improvement over more familiar phosphors appears to be marginal. Prior use of blue-emitting Eu^{2+} phosphors, green-emitting Tb^{3+} phosphors, and red-emitting Eu^{3+} phosphors, all in lamps, might well have been referenced.

The proposed new high-efficacy fluorescent lamps,⁴⁷

⁴³ H. H. Haft and W. A. Thornton, *J. Illum. Eng. Soc.*, 2, 29 (1972).

⁴⁴ W. A. Thornton, *J. Opt. Soc. Am.*, 62, 457 (1972); *J. Illum. Eng. Soc.*, 3, 99 (1973); *J. Color Appearance*, 11, 23 (1973).

⁴⁵ W. A. Thornton, *Lighting Design Appl.*, 2, 51 (1972).

⁴⁶ W. A. Thornton, *J. Illum. Eng. Soc.*, 4, 48 (1974).

⁴⁷ H. F. Ivey, *J. Opt. Soc. Am.*, 53, 1185 (1963).

with essentially only blue and yellow emission, certainly do have disastrously poor color rendering. We use these lamps in demonstrations to show how bad color rendering can get without changing the white color of the lamplight. Their commercial promise we consider to be negligible.

Some additional background references dealing with optimization of the spectral power distributions of lamps include Ivey,⁴⁷ the Einhorn,⁴⁸ and Walter.⁴⁹

J. M. P. J. Verstegen, D. Radielović, and L. E. Vrenken: It is unfortunate if a technical discussion is clouded by arguments of essentially nontechnical nature. We will refrain from that and stay with the paper under discussion.

Dr. Thornton's claim that our three-spectral color lamp has an appeal far beyond that of the color rendering index, is irrelevant as long as the CRI is the unit agreed upon internationally.

Apart from that, his claim has proven to be basically untrue. Comparison of our conventional "deluxe" lamp of 4000 K with the new aluminate lamp, does not result in overwhelming preference for the latter. Comparison of the standard halophosphate 4000 K lamp and the aluminate lamp, however, does but this is to be expected from the higher CRI of the latter.

We were and are unaware of any efficient green-emitting Tb^{3+} phosphor with acceptable lamp performance before our aluminate was developed. However, we referred to the use of (Sr, Eu) chloroapatite [our Ref. (6) in the paper under discussion].

The performance improvement of the aluminates might be marginal in the eyes of a United States citizen, but the 10 lm/W increase over the Haft and Thornton lamp is a respectable gain for a "small friend."

The proposed new high-efficacy fluorescent lamp with 100 lm/W would certainly outgrow Dr. Thornton's demonstration kit and develop into a useful outdoor illuminant.

⁴⁸ H. D. Einhorn and F. D. Einhorn, *Illum. Eng.*, 62, 154 (1967).

⁴⁹ W. Walter, *Appl. Opt.*, 10, 1108 (1971).



Low-Rate Cathodic Linear Sweep Voltammetry (LSV) Studies on Anodized Lead

Thomas F. Sharpe*

Electrochemistry Department, Research Laboratories, General Motors Corporation, Warren, Michigan 48090

ABSTRACT

Low-rate (~ 0.5 mV/sec) cathodic linear sweep voltammetry (LSV) experiments were conducted on preanodized antimonial and nonantimonial lead. The sweeps were supplemented by current-time traces obtained during the short term (≤ 1 hr) anodic treatment above the $\text{PbO}_2/\text{PbSO}_4$ reversible potential in H_2SO_4 electrolytes. Despite complications from additional substrate corrosion during the sweeps, semiquantitative observations were possible and the cathodic discharge could be resolved into α - and β - PbO_2 components. A major finding was that antimony in the lead retards the formation of β - PbO_2 in the preliminary anodic treatment. Implications from the results with regard to the behavior of the Pb-acid battery positive plate are briefly discussed.

In view of the fundamental information gained in recent years on the behavior of PbO_2 through the use of linear sweep voltammetry (LSV) (1-3), it would appear that such a technique might be useful for studying the differences in behavior of specific lead alloys used as grids for lead-acid battery positive plates. Although Panesar (4) has reported anodic and cathodic LSV studies on both antimonial and nonantimonial lead, many details concerning the PbO_2 reduction step were not considered. In his studies, anodization was effected by a low-rate (0.5 mV/sec) sweep extending from the potential for hydrogen evolution up to that for oxygen evolution. Under these conditions, the time above the $\text{PbO}_2/\text{PbSO}_4$ reversible potential was very short and the value of the potential was continuously changing, thereby making it impossible to relate the PbO_2 discharge phenomena to the potential of anodic treatment.

For Panesar's anodic treatment, only one cathodic current peak was resolved that could be ascribed to PbO_2 reduction in the subsequent cathodic scan. It is known, however, that two polymorphs of PbO_2 (α and β) exist, and that each may exhibit a different discharge overpotential (5-7). Depending upon the time and potential of anodic treatment, both polymorphs may be present in the corrosion film (8, 9). From x-ray diffraction, it has been established that β - PbO_2 resides primarily in the outer portion of the film and that α - PbO_2 exists, along with tetragonal PbO (PbO_1) in the inner portion of the film closer to the metal. The latter species are thermodynamically unstable in acid medium, but it is believed that they are formed in a localized high pH environment that is protected from the bulk acid by a PbSO_4 layer highly impermeable to H_2SO_4 (10).

In the present work, attempts are made to resolve in greater detail the PbO_2 discharge products using low-rate cathodic LSV following specified conditions of anodization. The sweeps were supplemented by current-time transients that were obtained during the

anodization at constant potentials above the $\text{PbO}_2/\text{PbSO}_4$ reversible potential. It was of particular interest to compare antimonial and nonantimonial lead because of the well-known fact that antimonial grids prolong positive plate cycle life.

Experimental

The alloys chosen for this study were Pb/4.5% Sb and Pb/0.05% Ca. Both alloys contained the same level of concentration of Sn (0.6%) and were essentially free of other alloying constituents; therefore, the difference in behavior between the alloys in this study is ascribed to the effect of antimony. Test electrodes were current collector tabs cut from battery grids and the portion exposed to the electrolyte had a geometric area of 5 cm^2 . The test electrodes were wiped with cotton wet with acetone, air-dried, and then given a 1 mA/cm^2 cathodic treatment for 5 min in the test cell prior to anodic treatment. The counter-electrode was sheet lead of 99.99+ % purity and the reference electrode was $\text{Hg}/\text{Hg}_2\text{SO}_4$. The electrolyte was either 1.16 (2.7M) or 1.26 sp gr (4.5M) H_2SO_4 prepared from reagent grade chemical and distilled water. All experiments were conducted at ambient temperature ($\sim 25^\circ\text{C}$).

The $\text{PbO}_2/\text{PbSO}_4$ reversible potential values in each acid were determined by measuring (with a high-impedance electrometer) the steady-state rest potentials of anodic films formed on Pb/Ca alloy for 2 hr at oxygen evolution potentials. These were 1142 ± 5 mV in 1.26 sp gr H_2SO_4 and 1067 ± 5 mV in 1.16 sp gr H_2SO_4 .

For the potential sweeps, the 10 turn potentiometer of a commercial potentiostat was driven by an electric motor whose speed could be changed to give the desired linear sweep rate. All currents and potentials were continuously monitored with a strip chart recorder. Following preliminary work, greater sensitivity on the potential scale was achieved by synchronizing the speed of the recorder to the chosen sweep rate so that each major division (2.54 cm) of the strip chart corresponded to 12 mV.

* Electrochemical Society Active Member.
 Key words: lead electrode, lead dioxide electrode, lead corrosion, lead-acid battery.

Results and Discussion

Lead preanodized at constant current.—In preliminary work, cathodic potential sweeps were obtained on test electrodes after they were anodized at constant current, and typical results are shown in Fig. 1. The sweeps were started immediately after switching off the current and covered a potential range of about 200 mV on each side of the $\text{PbO}_2/\text{PbSO}_4$ reversible potential. The cathodic current peaks, just below that potential, correspond to the reduction of PbO_2 to PbSO_4 . Two peaks were observed; a major peak b and a minor peak b'. For the Pb/Sb alloy the minor peak became well defined after anodization at the higher current.

Just following the reduction of PbO_2 , Panesar (4) reported an anodic current peak which he correlated to a cathodic current peak appearing at more negative potentials. From thermodynamic considerations these must be assigned¹ respectively, to the formation and reduction of PbO_2 in the interior of the corrosion

¹ See the discussion of Panesar's paper in Ref. (10).

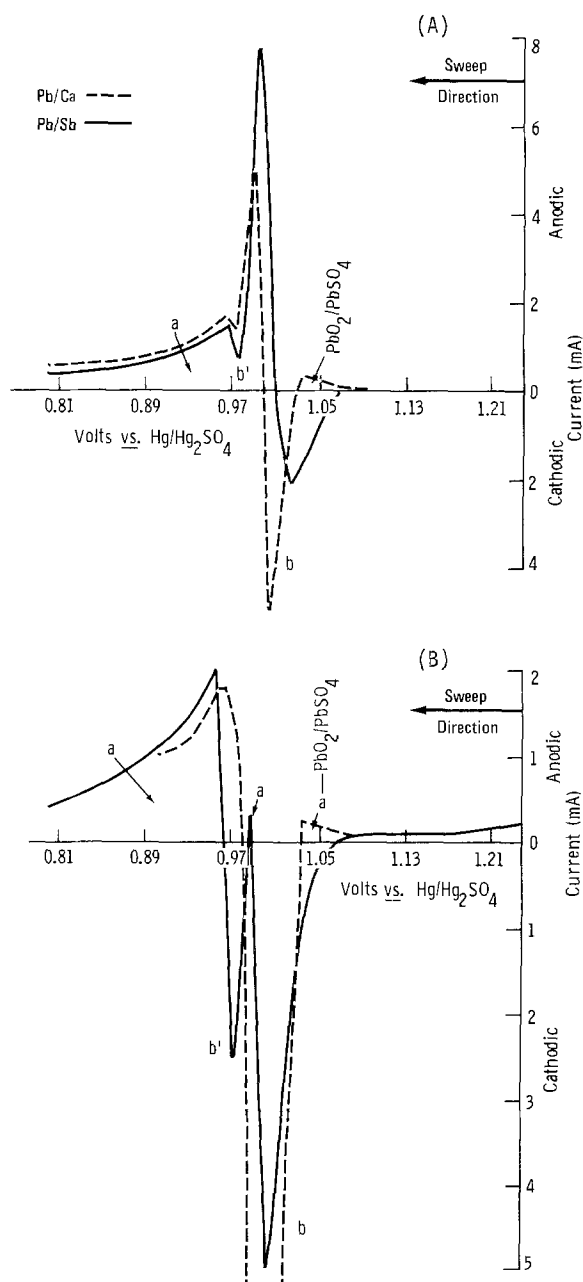


Fig. 1. Cathodic sweeps on Pb electrodes that were preanodized at (A) 5 mA and (B) 25 mA for 3 hr. Electrode area = 5 cm^2 ; $\text{H}_2\text{SO}_4 = 1.16 \text{ sp gr}$; sweep rate = 0.28 mV/sec .

film. In the present work, a number of anodic current constituents were present in the scans, and it is shown subsequently that these are portions of an anodic current peak that extends throughout much of the PbO_2 discharge potential range. It has been demonstrated (6, 10) that in the vicinity of the $\text{PbO}_2/\text{PbSO}_4$ reversible potential, oxidation and reduction processes can occur at nearly the same potential. As a result, if the oxidation process gives rise to sufficient anodic current, the net current will exhibit anodic values, even though a reduction (cathodic) reaction (e.g., $\text{PbO}_2 \rightarrow \text{PbSO}_4$) is occurring. This is believed to account for the rather peculiar voltammetric behavior observed in Fig. 1 and subsequent figures.

Lead preanodized at constant potential.—To gain greater insight, the shape of the sweeps was followed as a function of preanodization potential in increments at least as small as 50 mV above the $\text{PbO}_2/\text{PbSO}_4$ reversible value. During potentiostatic control, a continuous current-time (*i-t*) trace was obtained. The *i-t* traces for Pb/Ca alloy are similar to those previously reported by Ruetschi and Angstadt (11). Current-time traces at constant potential for Pb/Sb alloys have not been reported previously.

Results for Pb/Ca alloy.—Current-time traces obtained from 1150 to 1400 mV and corresponding selected cathodic sweeps in 1.26 sp gr H_2SO_4 are given in Fig. 2. After the 1 hr potentiostatic treatment, the potentials of the test electrodes were immediately de-

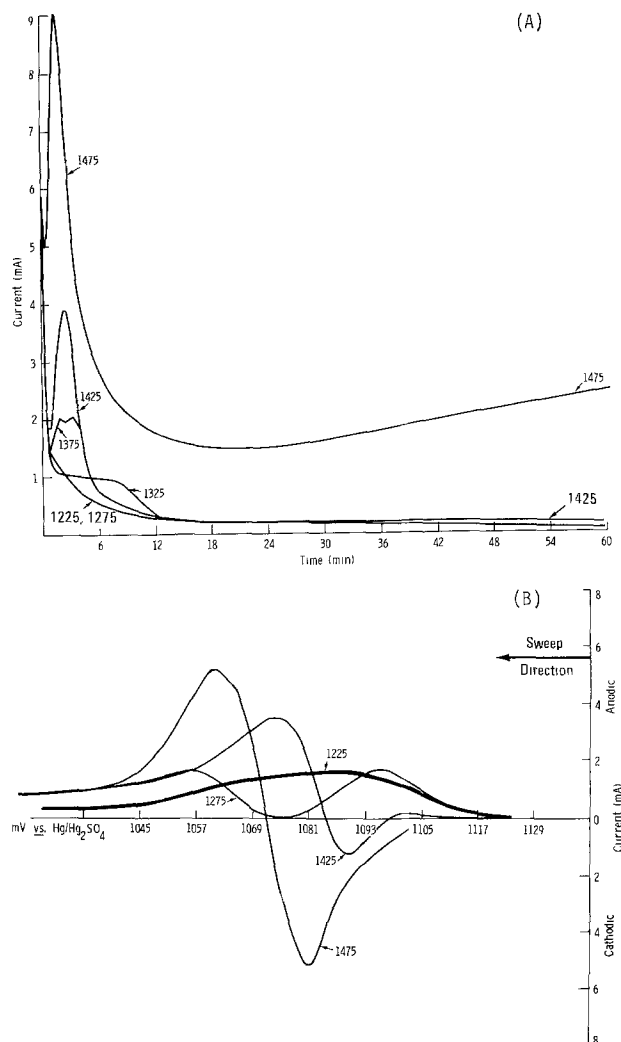


Fig. 2. Current-time curves (A) and subsequent cathodic sweeps (B) for Pb/Ca electrodes in 1.26 sp gr H_2SO_4 . Numbers on curves indicate potential of anodic treatment. Electrode area = 5 cm^2 ; sweep rate = 0.42 mV/sec .

creased to the $\text{PbO}_2/\text{PbSO}_4$ reversible potential, and then the sweeps were started.

Following control at 1225 mV (about 75 mV above $\text{PbO}_2/\text{PbSO}_4$) the current in the scans was entirely anodic, as emphasized by the heavy line in Fig. 2B. At 1275 mV a current peak in the cathodic direction emerged, indicating the reduction of some tetravalent Pb compound. Up to that potential, the $i-t$ traces indicated only the formation of PbSO_4 (11). It is assumed that the tetravalent compound corresponds to $\alpha\text{-PbO}_2$ that formed by the oxidation of PbO_t beneath the partially passivating PbSO_4 layer.

After control at successively higher potentials, the onset of the cathodic current peak shifted to higher potentials along the anodic current profile and increased substantially in capacity. This trend is illustrated in greater detail in Fig. 3 after control at 50 mV increments and at a slower sweep rate. The shift and buildup in capacity can be correlated to the buildup of a pronounced peak in the $i-t$ transients (Fig. 2A) that has been ascribed (11) to the oxidation of PbSO_4 to $\beta\text{-PbO}_2$ in the outer part of the corrosion layer. It appears, therefore, that the 1325-1375 mV interval marks the transition at which the cathodic peak in the scans becomes affected primarily by the discharge of $\beta\text{-PbO}_2$.

At or above 1475 mV, the current increase in the $i-t$ transient, after the first few minutes (Fig. 2A and Fig. 4A) signifies the onset of oxygen evolution and pronounced base metal corrosion. The corresponding sweeps (Fig. 4B) indicate a shoulder emerging on the negative-potential side of the growing $\beta\text{-PbO}_2$ discharge peak. This is ascribed to the buildup of additional dischargeable $\alpha\text{-PbO}_2$ that is expected to form by the direct oxidation of base metal at these high potentials.

A complicating issue in the cathodic scans is a background anodic current that extends throughout much of the $\text{PbO}_2/\text{PbSO}_4$ reversible potential region. As a result, net currents are involved and as mentioned above, despite the presence of dischargeable PbO_2 , the net current may show an anodic value. This is especially exemplified in Fig. 5 where the effect of increasing time at high potential (1575 mV) is considered. At first, the current is slightly anodic which may be due to the further formation of PbSO_4 . As the alkalinity beneath the PbSO_4 film becomes established (and as the electrode becomes progressively roughened by further anodic treatment), the anodic current would be expected to increase through the further anodic generation of Pb^{2+} to form PbO_t . At the same time, the buildup of PbO_2 also occurs (as confirmed on replicate electrodes by increasing time arrests at the $\text{PbO}_2/\text{PbSO}_4$ reversible potential after 30 sec anodic treatment) but not in sufficient quantity

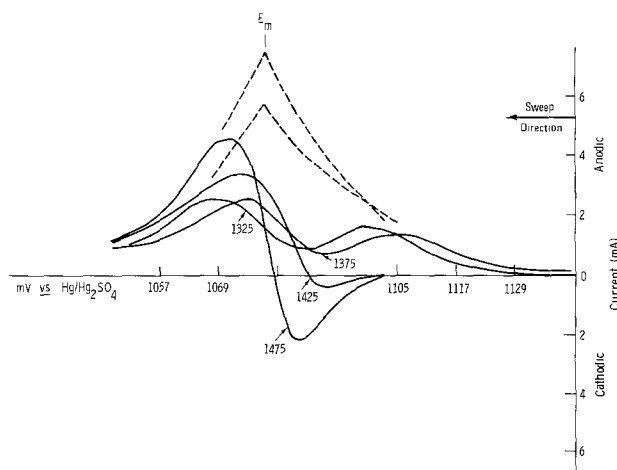


Fig. 3. Cathodic sweeps for Pb/Ca electrodes following 1 hr control at potential values indicated on sweeps. $\text{H}_2\text{SO}_4 = 1.26$ sp gr; electrode area = 5 cm^2 ; sweep rate = 0.21 mV/sec .

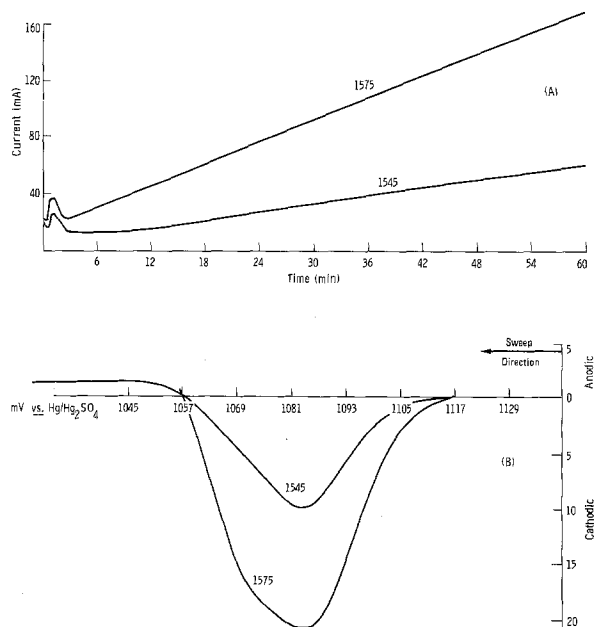


Fig. 4. Current-time curves at 1545 and 1575 mV (A) and subsequent cathodic sweeps (B) for Pb/Ca electrodes in 1.26 sp gr H_2SO_4 . Electrode area 5 cm^2 ; sweep rate 0.42 mV/sec .

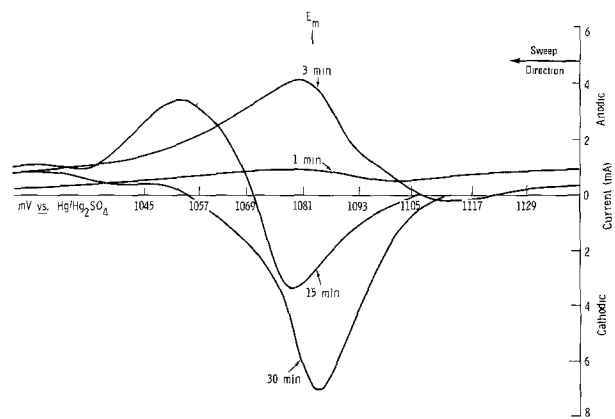


Fig. 5. Cathodic sweeps for Pb/Ca electrodes after control at 1575 mV for various times in 1.26 sp gr H_2SO_4 . Electrode area = 5 cm^2 ; sweep rate = 0.42 mV/sec .

to compensate for that effect so the net current increases in the anodic direction. However, as the amount (and therefore the discharge capacity) of the PbO_2 increases, the net current builds in the cathodic direction.

Although the exact anodic current profile is always obscured by dischargeable PbO_2 , there is seen in Fig. 5 a tendency toward a peak value at about 1.08V. This is in agreement with results obtained after control at lower potentials, where ascending and descending portions of the anodic current profile are well defined and can be extrapolated (cf., broken lines, Fig. 3). Similar maxima (E_m) have been observed based on steady-state corrosion current (11) and weight loss (12, 13) measurements. Lander (12) established that the E_m (on the $\text{Hg}/\text{Hg}_2\text{SO}_4$ scale) is a function of acid concentration, and the value interpolated from his data is in good agreement with the present observations.

It is also observed from Fig. 5 that the peak ascribed to $\beta\text{-PbO}_2$ reduction continues to grow beyond the time observed for PbSO_4 oxidation in the $i-t$ curve. X-ray diffraction has indicated (9) that the amount of $\beta\text{-PbO}_2$ in the corrosion film is substantially larger than that provided by the oxidized PbSO_4 . This has been ascribed (9) to an ionic current of Pb^{4+} passing through the corrosion film at high potentials to give

additional β -PbO₂ at the solution/corrosion film interface.

Selected *i-t* transients and subsequent cathodic sweeps obtained in 1.16 sp gr H₂SO₄ are shown in Fig. 6, and the buildup of dischargeable PbO₂ as a function of time at high potentials (1515 mV) are shown in Fig. 7. The discharge occurs \sim 75 mV below that observed in 1.26 sp gr which is, of course, expected from the difference in PbO₂/PbSO₄ rest potential values. The shape of the sweeps, however, is

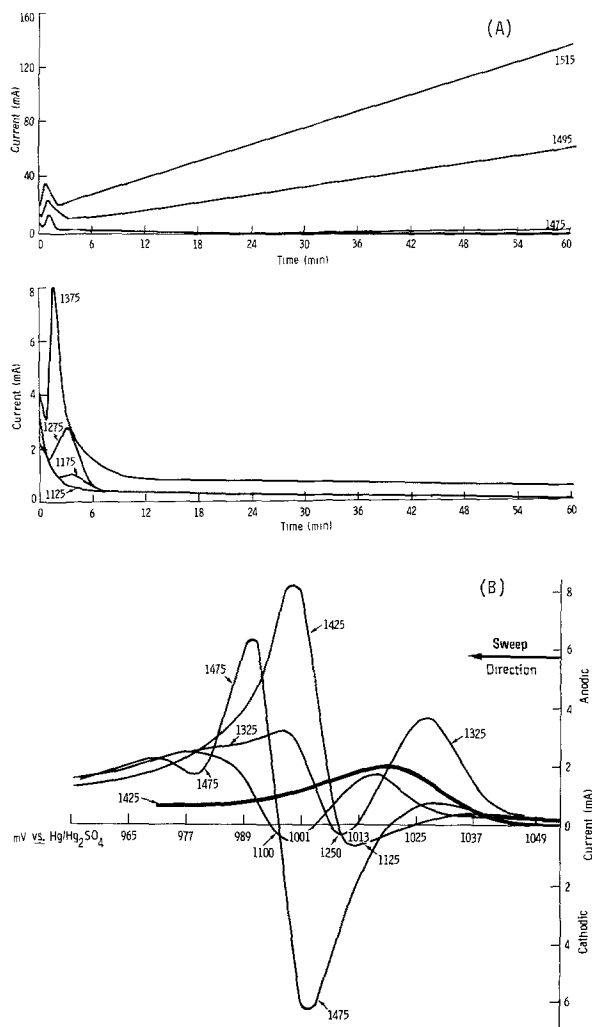


Fig. 6. Current-time curves (A) and subsequent cathodic sweeps (B) for Pb/Ca electrodes in 1.16 sp gr H₂SO₄. Numbers on curves indicate potential of anodic treatment. Electrode area = 5 cm²; sweep rate = 0.42 mV/sec.

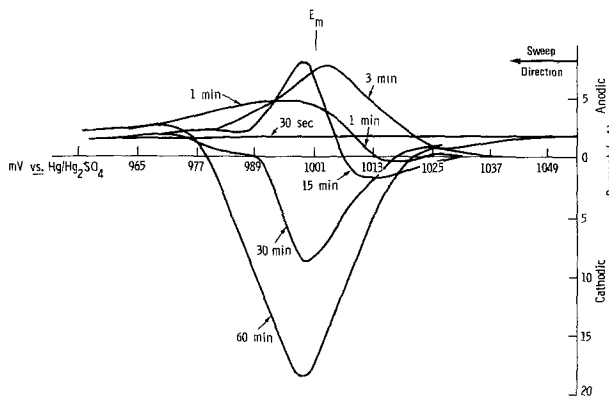


Fig. 7. Cathodic sweeps for Pb/Ca electrodes after control at 1515 mV for various times in 1.16 sp gr H₂SO₄. Electrode area = 5 cm²; sweep rate = 0.42 mV/sec.

somewhat different, which can be explained primarily on the basis of increased substrate corrosion during the sweeps. A comparison between the sweeps in Fig. 7 and Fig. 5, obtained after the earliest stages of anodization under conditions where the *i-t* curves can be superimposed, indicates a greater tendency in the more dilute acid toward net currents in the anodic direction. Although this could be the result of a kinetic limitation on the PbO₂ discharge brought about by decreasing the acid strength, such an effect is not expected to be significant at these slow sweep rates. However, by decreasing the bulk concentration of acid, the pH in the interior of the film would be further increased, thereby favoring a greater anodic current flow. This is in agreement with Lander's observation (12) that weight loss at the potential of maximum anodic current increases with decrease in acid concentration.

Results for Pb/Sb alloy.—Current-time traces and corresponding cathodic sweeps in 1.26 sp gr H₂SO₄ are shown in Fig. 8. A notable feature is that the current peak for PbSO₄ oxidation to β -PbO₂ does not occur below 1375 mV, a significantly higher overvoltage than required to effect that reaction on Pb/Ca alloy. After control at or below that potential, the current is only slightly anodic in the sweeps. Above that potential an anodic current profile develops which gradually becomes masked after control at successively higher potentials by the buildup of two cathodic current peaks. The buildup of the cathodic peaks along the ascending and descending branches of the anodic current profile is also shown in Fig. 9, which gives the effect of anodization time at high potential (1575 mV).

The same experiments were repeated in 1.16 sp gr H₂SO₄, but for brevity only that series showing the effect of time at a high potential (1515 mV) is shown (Fig. 10). As in the case for the Pb/Ca alloy, the difference in sweep profiles as the acid strength is decreased appears to be the result of increased substrate corrosion during the sweeps. From the results in Fig. 9 and 10, a reasonable estimation of the peak

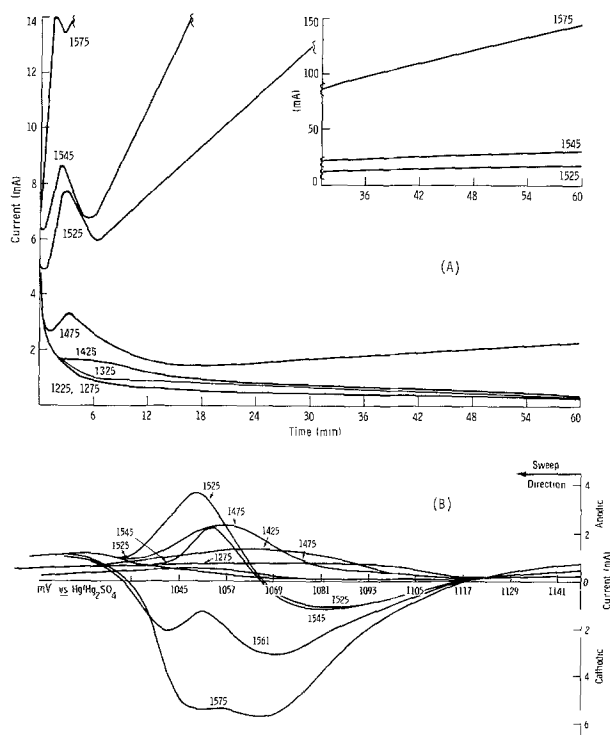


Fig. 8. Current-time curves (A) and subsequent cathodic sweeps (B) for Pb/Sb electrodes in 1.26 sp gr H₂SO₄. Numbers indicate potential of anodic treatment. Electrode area = 5 cm²; sweep rate = 0.42 mV/sec.

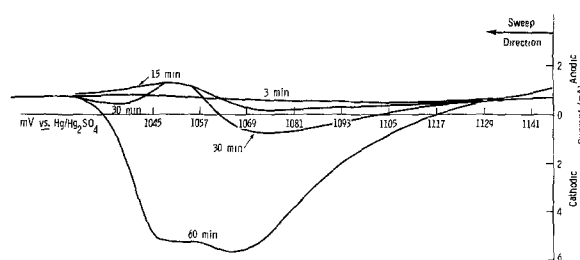


Fig. 9. Cathodic sweeps for Pb/Sb electrodes after control at 1575 mV for various times in 1.26 sp gr H_2SO_4 . Electrode area = 5 cm^2 ; sweep rate = 0.42 mV/sec .

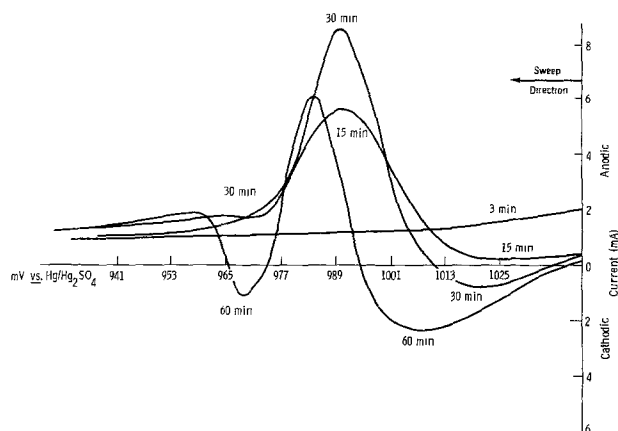


Fig. 10. Cathodic sweeps for Pb/Sb electrodes after control at 1515 mV for various times in 1.16 sp gr H_2SO_4 . Electrode area = 5 cm^2 ; sweep rate = 0.42 mV/sec .

anodic current potentials (E_m 's) are 1050 and 990 mV, respectively. These are slightly lower than the corresponding indications on Pb/Ca alloy (1075 and 1003 mV).

The two cathodic discharge peaks emerging after control at high potentials, as well as the peaks observed after constant current anodic treatment (Fig. 1) appear to correspond to the two plateaus observed by Ruetschi (6) during the constant current discharge of Pb/Sb alloy that had been anodized at constant current. In that work, however, an unambiguous assignment of each plateau to a specific PbO_2 polymorph could not be made. By analogy to the results for Pb/Ca alloy in the present work, the peak discharging at the higher potential would be assigned to β - PbO_2 . A further indication that this is the correct choice is shown in Fig. 11, where an electrode that was discharged in the course of anodic treatment exhibited a growth of the peak at the higher potential. Such an intermittent discharge would provide additional $PbSO_4$ for oxidation, thereby enhancing the β - PbO_2 discharge peak.

Summary and Conclusions

Cathodic potential sweeps were obtained on an antimonial (Pb/4.5% Sb) and a nonantimonial (Pb/0.05% Ca) alloy after specific conditions of short-term anodization above the PbO_2 - $PbSO_4$ reversible potential. The situation is complicated by additional substrate corrosion during the sweeps which gives rise to a substantial background anodic current that extends throughout much of the PbO_2 discharge potential range. As a result, net currents are always obtained, and the sweep profiles may exhibit the extremes shown schematically by the solid lines in Fig. 12. After control near the PbO_2 / $PbSO_4$ reversible potential, or at higher potentials for very short periods of time, the current may be entirely anodic (a). It is believed that at the low-sweep rates employed the maximum anodic current in the scans (observed

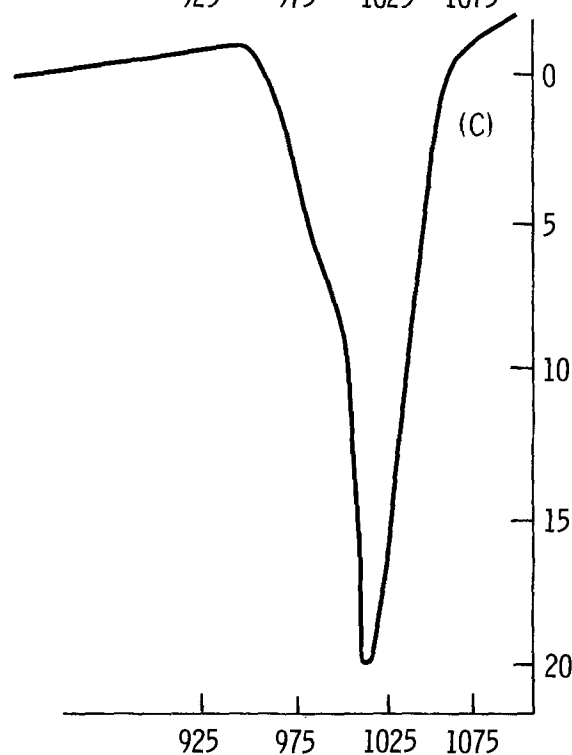
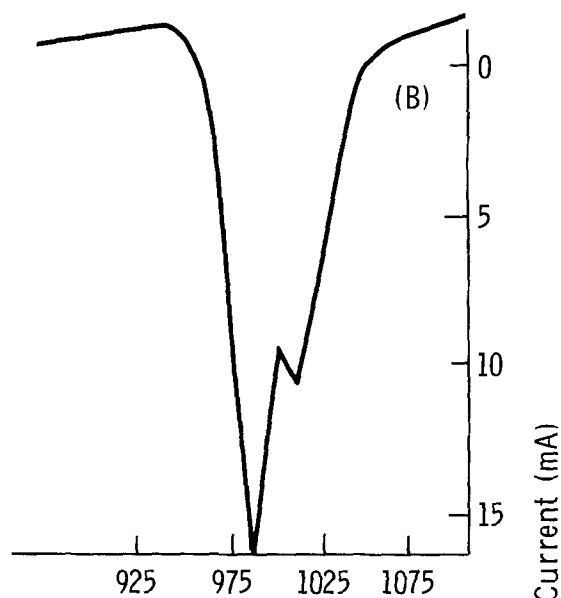
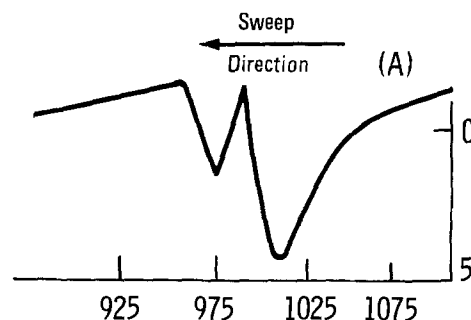


Fig. 11. Cathodic sweeps for Pb/Sb electrodes in 1.16 sp gr H_2SO_4 after control at 1525 mV for (A) 1.5 hr, (B) and (C) 3 hr. In (C), electrode was given intermittent discharge to 925 mV after 1.5 hr. Electrode area = 5 cm^2 ; sweep rate = 0.28 mV/sec .

prior to the buildup of appreciable discharge product) can be related reasonably well to the potential at which maximum corrosion would occur (E_m) under steady-state conditions near the PbO_2 / $PbSO_4$ reversible potential.

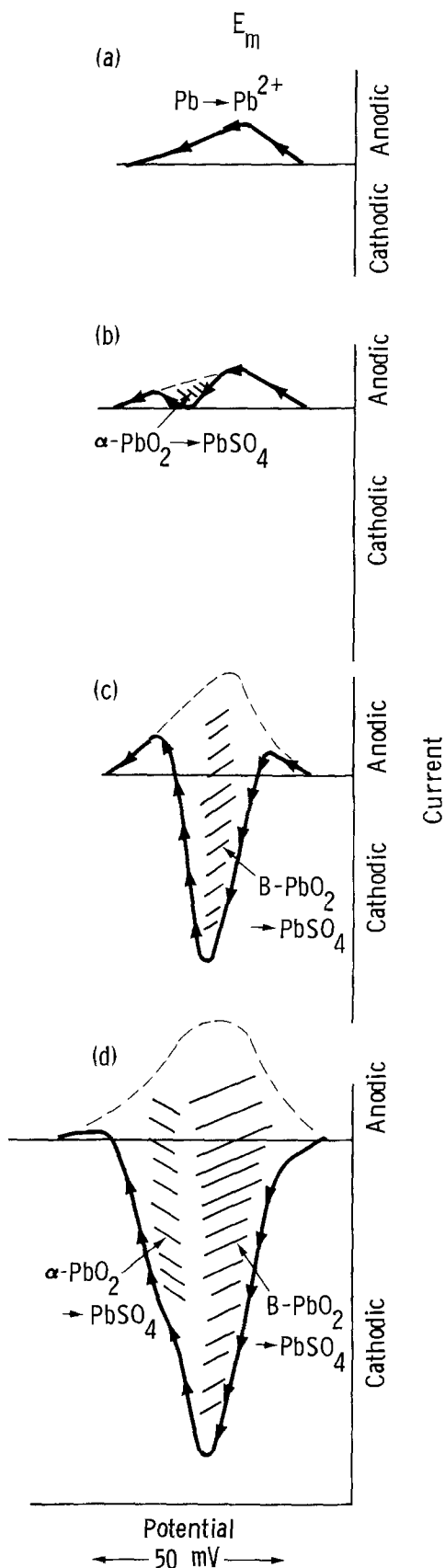


Fig. 12. Schematic showing possible cathodic sweeps for pre-anodized lead (see text).

As dischargeable PbO_2 is built up, the anodic current (broken lines, Fig. 12) may become partially or totally obscured. The sweep profile may then be influenced primarily by the discharge of $\alpha\text{-PbO}_2$ (Fig. 12b), $\beta\text{-PbO}_2$ (Fig. 12c) or a composite of the two (Fig. 12d). The cathodic current peak intensities de-

pend upon potential and time of anodic treatment and are strongly influenced by antimony in the lead.

Comparisons between nonantimonial and antimonial lead.—For nonantimonial (Pb/Ca) lead, the cathodic sweeps essentially follow the series of profiles in Fig. 12 after anodic control at progressively higher overvoltages. From the i - t curves obtained during the anodic treatment, the conversion of PbSO_4 to $\beta\text{-PbO}_2$ became evident at overvoltages of no more than 175 mV (vs. $\text{PbO}_2/\text{PbSO}_4$).

A striking feature of the Pb/Sb alloy was that substantially higher overvoltages ($\eta = 375$ mV) were required before effects due to oxidation of PbSO_4 to $\beta\text{-PbO}_2$ were observed in the i - t curves. A low rate of buildup of $\beta\text{-PbO}_2$ on antimonial alloy has also been observed by x-ray diffraction following anodic treatment at constant current (14). This may stem from parasitic oxidation of the antimony, occurring preferentially to the oxidation of PbSO_4 in the corrosion film. The difficulty in forming PbO_2 on antimonial lead has also been recognized in cathodic protection applications (15).

After control at high potentials ($\eta = 425$ mV) the concomitant growth of α - and $\beta\text{-PbO}_2$ discharge peaks was observed, but the $\beta\text{-PbO}_2$ discharge peak was substantially lower in capacity than that observed on the nonantimonial lead after comparable anodic treatment.

Antimony in positive plate grids.—Proposals as to why antimony prolongs positive plate cycle life have been based primarily on the observed effects of antimony on morphology and other properties of the PbO_2 active material (16). Antimony has also been shown to affect grid growth (17). An estimation of the importance of the numerous factors involved would indeed be a formidable task. However, it has been generally observed that corrosion films on nonantimonial lead, which, in view of the present work, contain substantial quantities of $\beta\text{-PbO}_2$, are more powdery and loosely adherent than those found on antimonial lead. The desirable effect from antimony, therefore, may be to inhibit the buildup of excess $\beta\text{-PbO}_2$ during the formation step, thereby providing a thinner, and presumably more tenacious film on which the active material of the plate can be formed. If this mechanism is operable, then it would appear that other effects that have been observed after formation and cycling would be of a secondary nature.

At the rather modest level of antimony concentration considered here (4.5%), there was also an indication that Sb shifts the E_m to more negative values. Although the trend was marginal, it was in a direction that would extend positive plate cycle life. It may be of interest to examine that trend, as well as the other findings of this study, as a function of antimony concentration in the alloy.

Manuscript submitted Nov. 6, 1974; revised manuscript received March 6, 1975.

Any discussion of this paper will appear in a Discussion Section to be published in the June 1976 JOURNAL. All discussions for the June 1976 Discussion Section should be submitted by Feb. 1, 1976.

Publication costs of this article were partially assisted by General Motors Corporation.

REFERENCES

1. J. P. Carr and N. A. Hampson, *This Journal*, **118**, 1262 (1971).
2. J. P. Carr, N. A. Hampson, and R. Taylor, *J. Electroanal. Chem.*, **33**, 109 (1971).
3. For a comprehensive summary, see J. P. Carr and N. A. Hampson, *Chem. Rev.*, **72**, 679 (1972).
4. H. S. Panesar, in "Power Sources 3," D. H. Collins, Editor, p. 79, Oriel Press, Newcastle-Upon-Tyne (1971).
5. H. B. Mark, *This Journal*, **109**, 634 (1962).
6. P. Reutschi and B. D. Cahan, *ibid.*, **105**, 369 (1958).
7. E. Voss and J. Freundlich, in "Batteries," D. H.

- Collins, Editor, p. 73, Pergamon Press, New York (1963).
8. D. Pavlov, C. N. Poulieff, E. Klaja, and N. Iordanov, *This Journal*, **116**, 316 (1969).
 9. D. Pavlov and N. Iordanov, *ibid.*, **117**, 1103 (1970).
 10. P. Ruetschi, *ibid.*, **120**, 331 (1973).
 11. P. Ruetschi and R. Angstadt, *ibid.*, **111**, 1323 (1964).
 12. J. J. Lander, *ibid.*, **103**, 1 (1956).
 13. E. Voss, "Trans. Second Int. Symp. Batteries, Interdepartmental Committee on Batteries, Bourne-mouth, Oct. 1960," Sydenham and Co., Ltd., Oxford Road, Bournemouth, England.
 14. T. F. Sharpe, Abstract No. 347, p. 828 Electrochemical Society Extended Abstracts Spring Meeting, San Francisco, California, May 12-17, 1974.
 15. J. H. Morgan, *Corrosion Technol.*, **5**, 347 (1948).
 16. E. J. Ritchie and J. Burbank, *This Journal*, **117**, 299 (1970).
 17. A. C. Cannone, D. O. Feder, and R. V. Biagetti, *Bell System Tech. J.*, **49**, 1279 (1970).

Anodic Passivation by "CdO" Studied by ESR

E. J. Casey* and C. L. Gardner

Defence Research Establishment Ottawa, Ottawa, Ontario, Canada K1A 0Z4

ABSTRACT

The appearance of superoxide O_2^- and ozonide O_3^- ions in strong KOH electrolyte at temperatures 25° to -40°C during the anodic oxidation of cadmium and oxygen evolution has been investigated using the electron spin resonance technique. The fact that O_2^- forms at the higher temperatures and O_3^- predominates at -40°C correlates with the appearance of β -Cd(OH)₂ at higher and γ -Cd(OH)₂ at lower temperatures, but it is argued that this correlation is coincidental and that it is the character of the surface states of the elusive and dynamic "CdO" underlayer beneath the Cd(OH)₂ that determines which paramagnetic species is produced. These new facts and the interpretation are discussed within the framework of the solid state/solution-precipitation mechanism.

In this paper the evidence for a form of cadmium oxide as the instrument of anodic passivation of cadmium in aqueous KOH from 33° to -40°C is reviewed, and some new evidence obtained via ESR is added and interpreted. The mechanism by which the metal ceases to be anodically oxidizable after a period of active oxidation is one important element of the information needed if more efficient utilization of the metal in negative plates of alkaline batteries is to be achieved. Other important elements, such as those related to surface exposed and to pore structure (1), are not reviewed here.

Review of Evidence for CdO as an Intermediate Product

Since 1950, Epelboin (2) has written extensively about the probability of the existence of monovalent intermediates such as Cd⁺ resulting from anodic, one-electron charge-transfer steps, especially during electropolishing of metals. The evidence is still equivocal, direct proof still lacking in the case of cadmium. By 1950 Huber (3) and Ershler *et al.* (4) had found CdO by x-ray diffraction of samples taken from the surface of Cd anodized at high potentials. Lake and Casey (5) studied the electrical behavior of cadmium before, during, and after passivation, and inferred that a solid-film intermediate, "CdO," must be a substantial intermediate in the reactions which eventually lead to Cd(OH)₂ in KOH and to CdCO₃ in K₂CO₃ solutions, and which ultimately causes the passivation.

Many workers have sought CdO, without finding it, in the passivating layer. Falk (6a) found none at room temperature in Sweden (20°C). Sanghi *et al.* (6b) found none at room temperature in India (33°C!). Nor did Croft (6c), nor Thirsk *et al.* (6d). Nor did others (7). The hexagonal platelets of β -Cd(OH)₂ are usually identified as the product, either by x-ray diffraction of moist or dry particulate samples, or by electron diffraction of dried, anodically formed, very thin films. However, Breiter and Vedder (8), and later Okinaka and Whitehurst (9a), found the more recently identified (10) needlelike monoclinic γ -Cd(OH)₂ as the major product: the former authors during experiments at

room temperature and the latter group during experiments at low temperatures. The γ -Cd(OH)₂ seems to be more readily reducible to metallic cadmium than is the β -form, especially at low temperatures, during the electrochemical charging reaction (9a). More recently (9b), the needles have been shown by the scanning electron microscope technique at 25° and possibly [note the authors' uncertainty, Ref. (9b)] up to 40°C in porous electrodes.

No attempts were made by the authors of any of the quoted work to freeze-dry, or otherwise to stop any hydrolysis, hydration, or protonation of CdO which could occur after anodic treatment ceases and during manipulation of the wet sample.

Yoshizawa and Takehara (11a), however, did find CdO by x-ray diffraction of samples buried within thick plates. Ohse found it also (11b), and concluded that it formed underneath the Cd(OH)₂. The results found by Devanathan *et al.* (11c) suggested to those workers that the CdO and Cd(OH)₂ form at the same time. Okinaka (12) also found CdO, following a period of vigorous oxygen evolution in solutions of low KOH concentration [conditions much like Huber's (3)]. Galushko *et al.* (13) recently reported further experimental conditions (low concentration of KOH, mild anodic treatment) under which CdO could accumulate, be identified, and its electrochemical reduction studied.

Indirect evidence also exists that CdO forms as an intermediate. Thus Breiter and Weininger (8b), using triangular voltage sweeps for anodic oxidation and cathodic reduction, found a reduction peak just about where one would expect the polarized Cd/CdO potential on an electrode which had not been heavily passivated anodically; they concluded that CdO was indeed formed and then remained stable long enough to be electrochemically reduced. Okinaka (12) showed that the CdO reduction peak occurs also following anodic oxidation during ring-disk experiments.

On Mechanisms

Throughout the past fifteen years there have been several papers containing discussion of the relative merits of and the role of two proposed mechanisms of the anodic oxidation: (i) the "solid-state mechanism"

* Electrochemical Society Active Member.

Key words: CdO, cadmium, anodic passivation, ozonide O_3^- .

(Cd^{++} penetrating an underlayer [CdO ? $\text{Cd}(\text{OH})_2$?] to the solid/solution interface and reacting with electrolyte there); (ii) the "solution-precipitation mechanism" (Cd^{++} ions dissolving directly from Cd metal, as $\text{Cd}(\text{OH})_3^-$, perhaps, to precipitate as $\text{Cd}(\text{OH})_2$).

Either one offers a good first approximation (6a, 6b) over a narrow range of experimental conditions. Neither, however, can describe polarization data taken on cadmium over a wide range of current density, temperature, and electrolyte composition, both before and after passivation, but especially during passivation. As far as we are aware, only the combined solid-phase/solution-precipitation mechanism (see Fig. 1) has the flexibility needed. Thus an underlayer which is difficult to detect is pictured as being covered by the x-ray-detectable final reaction product: cadmium ions penetrate the nonstoichiometric "CdO," the outer surface of which is continually dissolving (i.e., complexing) and precipitating out again as the final product, $\text{Cd}(\text{OH})_2$. At passivation this dynamically self-refurbishing glassy underlayer seals over, dissolves only slowly, and is continuously being replaced.

A mechanism for the escape of the soluble complexes from the "CdO" surface has been proposed (15). It has already been shown that when this part of the process is significantly slowed down by conducting the experiments at -40° , the total anodic film need be only about 6 CdO-layers thick to effect passivation (15). It was early argued [see Fig. 5, Ref. (5b)] that the underlayer must be nonstoichiometric everywhere except at one interior plane: rich in O^\ominus near the CdO/electrolyte interface, rich in Cd^{++} near the Cd/CdO interface; thin and glassy, nonstoichiometric, continuous; of the variable composition so elegantly demonstrated directly by Hoar quite recently on iron-tin using Auger techniques (16).

No direct physical identification of CdO as an intermediate during active oxidation of cadmium or even after passivation of cadmium at low oxygen overpotentials, has been acquired, presumably because it is (a) buried beneath the final hydrolysis product, and (b) rapidly converted to final product under all but exceptional conditions. The final reaction products may be formed through soluble intermediates such as $\text{Cd}(\text{OH})_3^-$ or $\text{Cd}(\text{OH})_4^{2-}$ in KOH, $\text{Cd}_3(\text{CO}_3)_4^{2-}$ in K_2CO_3 , or through poorly characterized hydroxy-carbonates in mixed electrolytes (14a and b). The question

of what soluble complexes exist in high concentrations of KOH has not been conclusively answered, some evidence favoring $\text{Cd}(\text{OH})_3^-$ and other favoring $\text{Cd}(\text{OH})_4^{2-}$. Gilman and Sangermano (17a) recently wrestled with this difficulty, as had others earlier (17b, 17c).

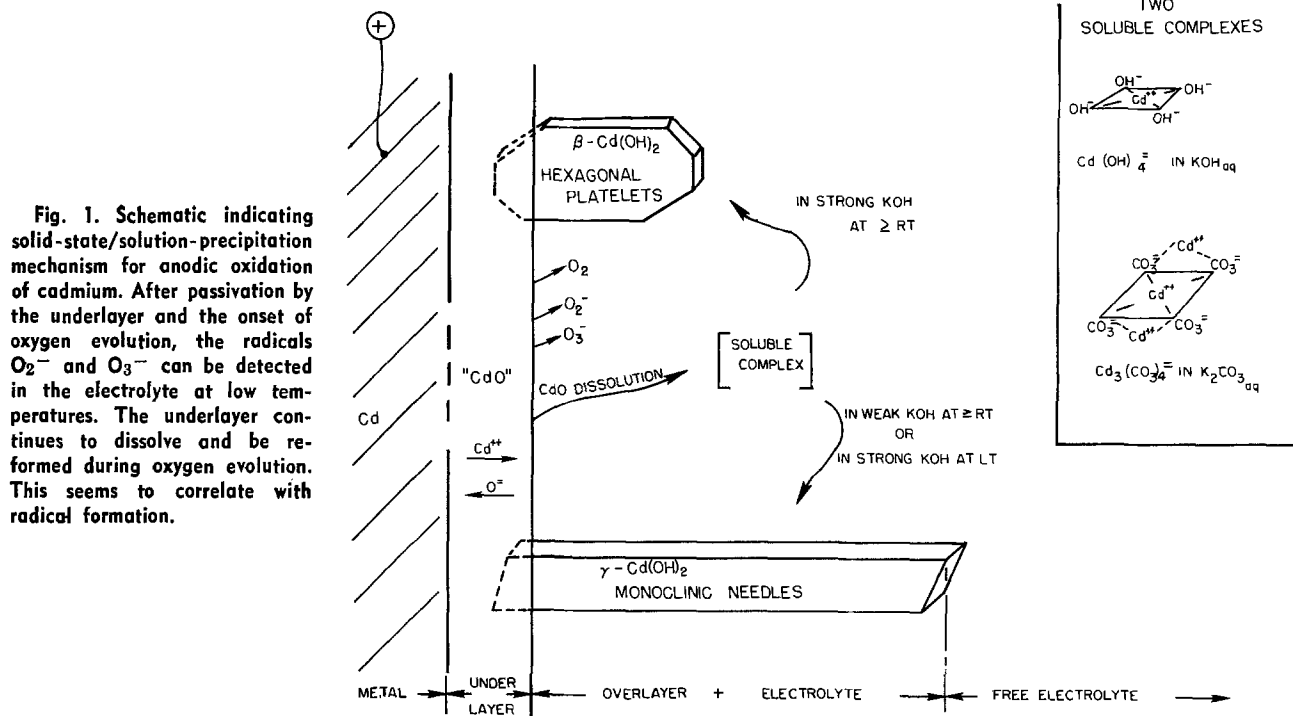
Such investigations have elaborated the complexity of the anodic oxidation of cadmium. The search continues for new evidence.

Detection of Anodically formed O_3^- and O_2^-

By the late 1960s, we were applying ESR techniques to the anodic oxidation of cadmium and silver, and to other similar basic problems. It was found (18) that O_3^- and other paramagnetic species such as O_2^- , and CuO_2^\ominus , produced anodically on some metals in aqueous KOH, at temperatures well below 0°C , were stable enough to be identified, and that their concentrations could be measured. Concerning cadmium we have reported (18a) that O_2^- is the detectable product of anodic oxidation in aqueous KOH at the higher temperatures (-10° to -20°C), while O_3^- is the observable product at the really low temperatures (down to -40°). Temperature inversion from one species to the other was sought but not observed (18b). The technique has been improved, and O_2^- has been detected in the anolyte during oxygen evolution off Cd even at room temperature, both in this work and elsewhere (18c).

Figure 2 shows the distinctly different spectra of O_2^- and O_3^- . The O_2^- was produced chemically by the decomposition of H_2O_2 in KOH solutions. The O_3^- was produced electrochemically during O_2 evolution on oxidized silver, as before (19). In each case electrolyte samples were quick-frozen in liquid nitrogen and spectra recorded on the frozen samples at 77°K , as described in Ref. (19). Characteristic g -values are given for each. The g_z for O_2^- shifts much more with the electrostatic environment to which it is bound than do g_x and g_y . [See Lunsford's Table 2 (20).]

Measurements taken with an electrochemical cell placed directly in the microwave cavity were insensitive, as the cavity was detuned by gas bubbles. After anodic oxidation for ~ 5 min at ~ 100 mA/cm² at the temperature shown, samples of electrolyte from near the cadmium anode were withdrawn into thin quartz tubes and quick-frozen in liquid nitrogen. Spectra of



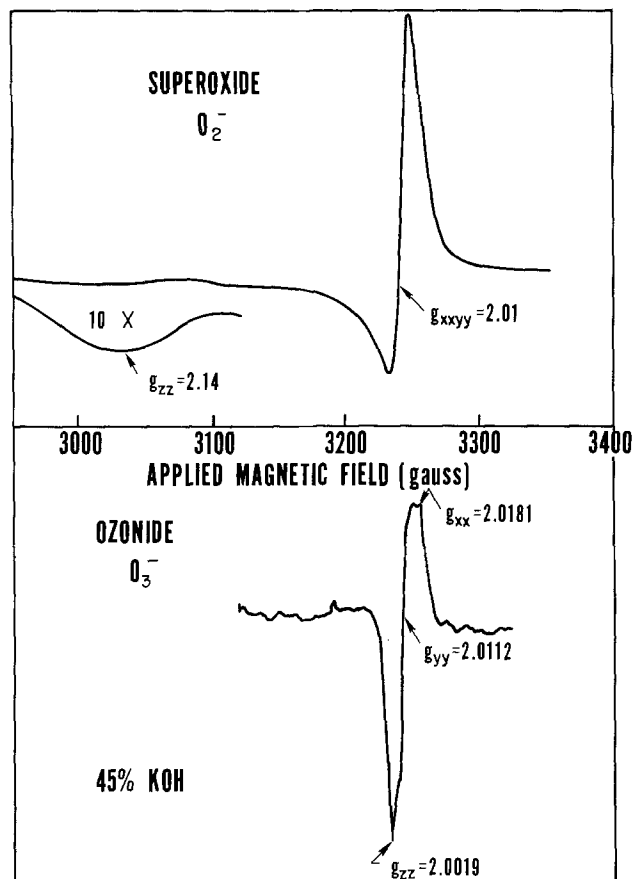


Fig. 2. ESR spectra taken at 77°K of O_2^- and O_3^- . Note distinctly different line shapes as expressed by the g -values. The g_{zz} peak of O_2^- is shown amplified 10 \times for clarity.

these samples were then taken at 77°K. From Fig. 3 it can be seen that the superoxide ion O_2^- is the main paramagnetic product detected from +25° to -25°C, while at -35° the O_3^- predominates. At -40° in 45% KOH the spectrum is that of O_3^- only, there being no evidence at all for O_2^- . Careful inspection reveals that the absorption by species "X," at $g = 2.00$, which will be discussed below, appears from under that of O_2^- as the spectrum of O_2^- fades out at lower temperatures.

So far no evidence has been obtained with the ESR technique for the anodic formation of free-radical intermediates from Cd except during oxygen evolution, i.e., after passivation. The question of whether any free-radical intermediates which might be formed before and/or during passivation can somehow be detected by this method is still an open one: it will be necessary to find conditions under which the intermediates can desorb into the electrolyte, accumulate there, and then be stable while a sample of the anolyte is being quick-frozen and examined in the ESR cavity. The following discussion, therefore, refers only to the situation after passivation, after completion of the "CdO" underlayer.

Discussion

Of the several metals studied so far cadmium is the only one from which both O_2^- and O_3^- have been detected having been produced during anodic oxygen evolution. From the fact that O_2^- is formed at the higher temperatures investigated and O_3^- at the lower, one can infer that the passivating glassy underlayer is different at different temperatures. Perhaps it is more highly protonated at -10° than at -40°, and the primary product of the discharge of OH_{ads}^- , namely O_{ads}^- , is more weakly bound at -10° than at -40°. The mechanism could change as follows. Since the second discharge event produces O_{ads} in both cases, the O_{ads}^- can rapidly combine with one O_{ads} to evolve O_2^- from the surface of the underlayer at -10°, while at

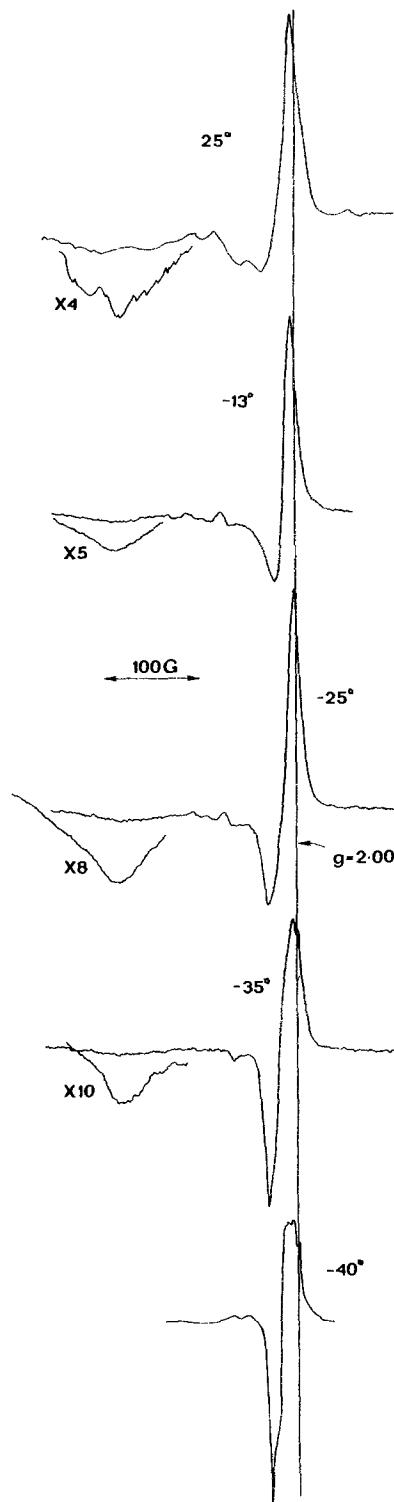
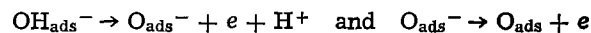
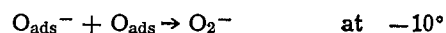


Fig. 3. Spectra of strong KOH anolyte samples extracted in a capillary and quick-frozen to 77°K, following anodic oxygen evolution off cadmium at temperatures shown. Clear spectra of O_2^- for 25° and O_3^- for -40°C. "X" is just perceptible near $g = 2$ at -35° and -40°.

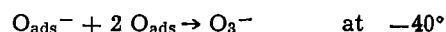
-40° it gets away more slowly and then only by combining with two O_{ads} to evolve O_3^- . In summary, the discharge reactions



followed by

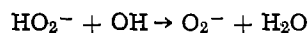
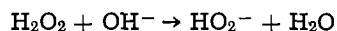
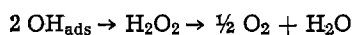


and

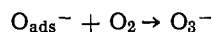


produce the paramagnetic species detected.

These mechanisms seem simpler than those proposed in our earlier work (18, 19), namely



and



although there is no experimental reason to favor one over the other at this juncture.

A cautionary note is introduced by the possibility that O_3^- is not observed at the higher temperatures from Cd simply because it decays too fast (in the cadmium-saturated electrolyte) and not that it never was formed in the first place, as we have implied above. This will be a hard point to prove experimentally.

In addition to the oxygen species the elusive species "X" which gives a sharp ESR absorption peak at $g = 2.0023$, is produced as a second anodic reaction product of cadmium [and several other metals (18)] in strong KOH at low temperatures. The nature of species X is still uncertain. Its decay rate varies markedly (minutes to less than seconds) (19). In the case of cadmium oxidation this sharp absorption line (Fig. 2, -35° and -40°) could be due to conduction electrons in colloidal metal which has been undermined during anodic dissolution, a manifestation of the classical "chunk effect" (21). Or, it might be due to complexed electrons arising from oxidation of Cd^+ by electrolyte. Although it is unlikely to be due to Cd^+ itself [whose magnetic parameters (22) are $g = 1.992$ to 2.001 , and a large hyperfine splitting for the isotope 114, none for the more abundant isotope 112], it could be due to the electron which has just been ejected from anodically formed Cd^+ and which is temporarily resting in the metal-ion/hydroxyl-ion/water complex, $\text{M}(\text{OH})_n^{2-n} \cdot x\text{H}_2\text{O}$. The analogy with Epelboin's recent work (23) on Be^+ produced anodically in an aprotic solvent elicits further thought along these lines. However, since the absorption peak at 2.0023 is devoid of fine structure, ESR work to date cannot distinguish unambiguously between colloidal metal or complexed electron.

The elements of the solid-phase/solution-precipitation mechanism given in this paper seem able to accommodate the new facts obtained by ESR as well as many seemingly incompatible observations earlier reported. New techniques which can permit *in situ* examination of composition, structure, and electrical properties are still needed, however, as is a quantitative theory which can describe the discontinuities of the passivation process. To delay the onset of passivation during anodic oxidation of the metal remains the primary practical objective of work of this kind.

The ESR results reported in this paper can be considered as relevant to the mechanisms operating at the cadmium electrode of a cadmium-alkali cell which has been driven into cell reversal (*i.e.*, forced discharge) at low temperatures. Attack of cell components by anodically produced free radicals, which are mobile in the electrolyte, can be anticipated.

Acknowledgment

This was issued as DREO Report No. 721.

Manuscript submitted Sept. 3, 1974; revised manuscript received Feb. 13, 1975.

Any discussion of this paper will appear in a Discussion Section to be published in the June 1976 JOURNAL.

All discussions for the June 1976 Discussion Section should be submitted by Feb. 1, 1976.

Publication costs of this article were partially assisted by Defense Research Establishment Ottawa.

REFERENCES

1. E. S. Carr, "Proceedings of 25th Power Sources Symposium," p. 57, PSC, Red Bank, N. J. (1972); E. J. Casey and B. E. Vergette, *Electrochim. Acta*, **14**, 897 (1970), and reference there in.
2. I. Epelboin, *Métaux*, **32**, 55 (1975); *Z. Electrochem.*, **59**, 689 (1955), *e.g.*
3. K. Huber, *This Journal*, **100**, 376 (1953); *Z. Physikal.*, **62**, 675 (1958); K. Huber and S. Stucki, *Helv. Chim. Acta*, **51**, 1343 (1968).
4. S. A. Rozentsveig, B. V. Ershler, E. L. Shtrum, and M. M. Ostanina, *Tr. Soveshch. Elektrokhim. Akad. Nauk SSSR*, 1950, p. 571 (1953).
- 5a. P. E. Lake and E. J. Casey, *This Journal*, **105**, 52 (1958); b. P. E. Lake and E. J. Casey, *ibid.*, **106**, 913 (1959).
- 6a. S. U. Falk, *ibid.*, **107**, 661 (1960); b. I. Sanghi, S. Visvanathan, and S. Ananthanarayanan, *Elektrochim. Acta*, **3**, 65 (1960); c. G. T. Croft, *This Journal*, **106**, 278 (1959); G. T. Croft and D. Tuomi, *ibid.*, **108**, 915 (1961); d. R. D. Armstrong, E. H. Boulton, D. F. Porter, and H. R. Thirsk, *Electrochim. Acta*, **12**, 1245 (1967).
- 7a. J. P. G. Farr and N. A. Hampson, *Electrochem. Technol.*, **6**, 10 (1969); b. H. Y. Kang, *This Journal*, **118**, 462 (1970).
- 8a. M. Breiter and W. Vedder, *Trans. Faraday Soc.*, **63**, 1042 (1967); b. M. Breiter and J. L. Weininger, *This Journal*, **113**, 651 (1966); M. Breiter and J. L. Weininger, in "Power Sources 1966," D. H. Collins, Editor, p. 269, Pergamon Press, London (1967).
- 9a. Y. Okinaka and C. M. Whitehurst, *This Journal*, **117**, 583 (1970); b. D. Chua and R. J. Diefendorf, "Proceedings 25th Power Sources Conf. 1972," p. 52.
- 10a. P. M. de Wolff, *Acta Cryst.*, **21**, 432 (1966); b. O. Glemser, U. Hauschild, and H. Reichert, *Z. Anorg. Allgem. Chem.*, **290**, 58 (1957). See however Feitknecht *et al.*, *Helv. Chim. Acta*, **34**, 2266 (1951) and *Chimia*, **11**, 166 (1957) concerning stabilization by Cl^- .
- 11a. S. Yoshizawa and Z. Takehara, *Electrochim. Acta*, **5**, 240 (1961); b. R. W. Ohse, *Z. Electrochim.*, **64**, 1171 (1960); c. M. A. V. Devanathan and S. Lakshmann, *Electrochim. Acta*, **13**, 667 (1968).
12. Y. Okinaka, *This Journal*, **117**, 289 (1970).
13. V. P. Galushko, E. F. Zavgorodnyaya, R. V. Podolskaya, and Yu. P. Rodak, *Elektrokhim.*, **8**, 1216 (1972).
- 14a. E. J. Casey, A. R. Dubois, P. E. Lake, and W. J. Moroz, *This Journal*, **112**, 371 (1965); b. W. Feitknecht, *Fortschr. Chem. Forsch.*, **2**, 670 (1953), AERE Harwell Translation, p. 622.
15. E. J. Casey, *Chem. Can.*, **12**, 49 (1960).
16. T. P. Hoar, M. Talerman, and E. Trad, *Nature*, **244**, 41 (1973).
- 17a. S. Gilman and L. D. Sangermano, *This Journal*, **118**, 1953 (1971); b. P. C. Milner and U. B. Thomas, *Advan. Electrochem. Electrochem. Eng.*, **5**, 1 (1967); c. W. Feitknecht and P. Schindler, *Pure Appl. Chem.*, **6**, 130 (1963).
- 18a. C. L. Gardner and E. J. Casey, *Can. J. Chem.*, **49**, 1782 (1971); b. C. L. Gardner and E. J. Casey, *Faraday Discussions No. 56*, Sept. 1973; c. R. L. Deming, Private communication, 1974.
19. C. L. Gardner and E. J. Casey, *Can. J. Chem.*, **52**, 930 (1974).
20. J. H. Lunsford, *Catalysis Rev.*, **8**, 135 (1973).
21. W. J. James and M. E. Straumanis, *This Journal*, **118**, 1960 (1971), *e.g.*
22. R. S. Eachus, M. C. R. Symons, and J. K. Yandell, *Chem. Comm.* 1969, p. 979.
23. H. Aida, I. Epelboin, and M. Garreau, *This Journal*, **118**, 1961 (1973).

Behavior of Salicylaldoxime and 8-Hydroxyquinoline at a Copper Electrode

Katsumi Niki,^{*1} Frank M. Delnick,^{**} and Norman Hackerman[†]

Department of Chemistry, Rice University, Houston, Texas 77001

ABSTRACT

Effects of salicylaldoxime (SAO) and of 8-hydroxyquinoline (HQ) on the anodic dissolution of copper were studied by using a potentiokinetic polarization method and phase-selective a-c polarography at a rotating copper disk electrode at various pH values. At pH 1.5, where cupric ions do not precipitate as the chelates of SAO and HQ, the anodic dissolution of copper was retarded slightly by these additives. At pH 2.8 and 5.0, where SAO precipitates cupric ions quantitatively, the anodic dissolution of copper was markedly retarded by SAO, especially from the rotating disk electrode. The anodic polarization curves of copper in the SAO solutions were similar to those obtained in the passivation of iron. A thin protective chelate film was formed on the copper electrode. At very positive potentials, the chelate film ruptured and the anodic dissolution of copper started. On the other hand, HQ chemisorbed strongly on the copper electrode from pH 2.8-5.0, where HQ also precipitates cupric ions, and the copper dissolution was retarded markedly. The Cu-HQ chelate did not act as a barrier for the copper dissolution in this pH range.

Numerous studies have been made to elucidate the mechanism of corrosion inhibition by organic substances. Inhibitors of the first class are physically adsorbed on the metal surfaces. This adsorption is nonspecific and reversible. On the other hand, for inhibitors of the second class the adsorption is chemical in nature and is specific to the metal. For instance, as a general rule, organic inhibitors are more effective with ferrous metals than with nonferrous metals. It can be predicted that for a given inhibitor the order of increasing effectiveness is likely to be: $Zn < Cu < Ni < Fe$. It is interesting, also, that the series cited above is a familiar one in terms of the stability of chelate complexes.

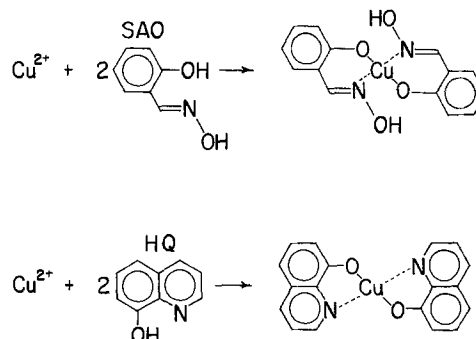
Hayakawa and Ida (1) estimated the stability constants for a series of hydroxyazo compounds of aluminum and they suggested that inhibition of aluminum corrosion in alkaline solutions by these compounds should be increasingly effective with increasing stability of the complex. These chelating agents were considered to form protective films of aluminum chelates on the aluminum surface.

Benzotriazole forms a water-insoluble precipitate with both cuprous and cupric ions and has been used as an efficient corrosion inhibitor for copper in a wide variety of environments (2-7). Cotton (2-4) concluded that benzotriazole inhibits the corrosion of copper by forming a Cu(I)-benzotriazole compound on the copper surface. Poling (8) showed from infrared reflectance spectra that the protective film was highly inert Cu(I)-benzotriazole complex polymer.² Wall and Davis (9) suggested that benzotriazole reacts to form an invisible insoluble chelate on the copper surface. On the other hand, Mansfeld *et al.* (7) suggested, on the basis of ellipsometric studies, that benzotriazole is chemisorbed on the copper surface.

Ushenina and Klyuchnikov (10) studied the influence of various chelating agents on the corrosion rates of iron, cobalt, zinc, and copper. Both benzotriazole and 8-hydroxyquinoline retarded the corrosion of copper considerably in ammoniacal buffer. Inhibitor efficiencies of these chelating agents were 90.2 and 44.3%, respectively. On the other hand, the inhibitor efficiency of salicylaldoxime in ammoniacal

buffer was only 6.2%. They stated that when the chelate is formed directly on the surface as a compact film having good adhesion to the metal (discharge and nucleation mechanism), it retards corrosion. When the chelate is formed in the bulk of the solution and is then deposited (dissolution-precipitation mechanism), the film has only a slight retarding effect on corrosion.

In the present work we have investigated the anodic dissolution of copper in the presence of salicylaldoxime (SAO) and 8-hydroxyquinoline (HQ). Cu^{2+} is precipitated quantitatively by SAO at pH values higher than 2.6 (12), and by HQ at pH values between 5.3 and 14.5 (incomplete precipitation begins at pH 3.5) (11), according to the following reactions:



Solutions of pH 1.5, 2.8, and 5.0 were chosen so that the relation between the stability and/or solubility of the chelates and the inhibition efficiency could be studied.

Experimental

All chemicals except SAO (Eastman) were analytical grade and were used without further purification. All solutions were prepared using doubly distilled water (deionized and then distilled). The composition of the buffer solutions was as follows: pH 1.5, 0.05M H_2SO_4 ; pH 2.8, 0.2M monochloroacetic acid, 0.1M NaOH; and, pH 5.0, 0.1M sodium acetate, 0.033M acetic acid.

The ionic strength of these solutions was adjusted to 0.5 by the addition of sodium sulfate. All solutions were deaerated using purified nitrogen. A single-crystal copper rod (6.0 mm in diameter) with the

² Benzotriazole (BTA) forms a water-insoluble stoichiometric compound Cu(I) (BTA) with cuprous ions, whereas it precipitates a nonstoichiometric Cu(II) (BTA)_x ($x = 1.4-2.0$) with cupric ions.

* Electrochemical Society Active Member.

** Electrochemical Society Student Member.

† Electrochemical Society Honorary Member.

¹ Present address: Department of Electrochemistry, Yokohama National University, Yokohama, Japan.

Key words: chemisorption, chelate, inhibition.

(100) plane as the electrode surface was sheathed in a Teflon cylinder. The electrode surface was polished mechanically with No. 600 emery paper and then electropolished in concentrated phosphoric acid. After washing with distilled water, the electrode was attached to a Beckman rotating electrode assembly with variable drive. A potentiostat with a linear-sweep voltage source (constructed locally with Teledyne-Philbrick operational amplifiers) was used. The phase-selective a-c polarograph was built according to the circuit given by Matsuda *et al.* (13). Unless otherwise stated, all polarization curves were obtained potentiokinetically with a sweep rate of 50 mV/min, after polarizing the rotating copper electrode to a pre-determined potential in the region of hydrogen evolution. All measurements were carried out at $25^\circ \pm 1^\circ\text{C}$, and potentials were measured against a saturated calomel electrode.

Results

pH 1.5.—The polarization curves for the rotating copper disk electrode in the solutions of pH 1.5 containing the chelating agents are shown in Fig. 1a and 1b. Both SAO and HQ retarded the dissolution rate of copper. The Tafel slope for the copper dissolution was not altered by the addition of either SAO or HQ. The polarization curve shifted to more cathodic potentials with an increase in the rate of rotation. At high anodic polarizations the current tends to be diffusion controlled, as reported by Leckie (14). The effect of additives on the polarization of copper at high anodic polarization was significantly decreased but did not disappear. However, the effect of rotation disappeared.

Salicylaldoxime.—The polarization curves in the presence of SAO at pH 2.8 are shown in Fig. 2a and

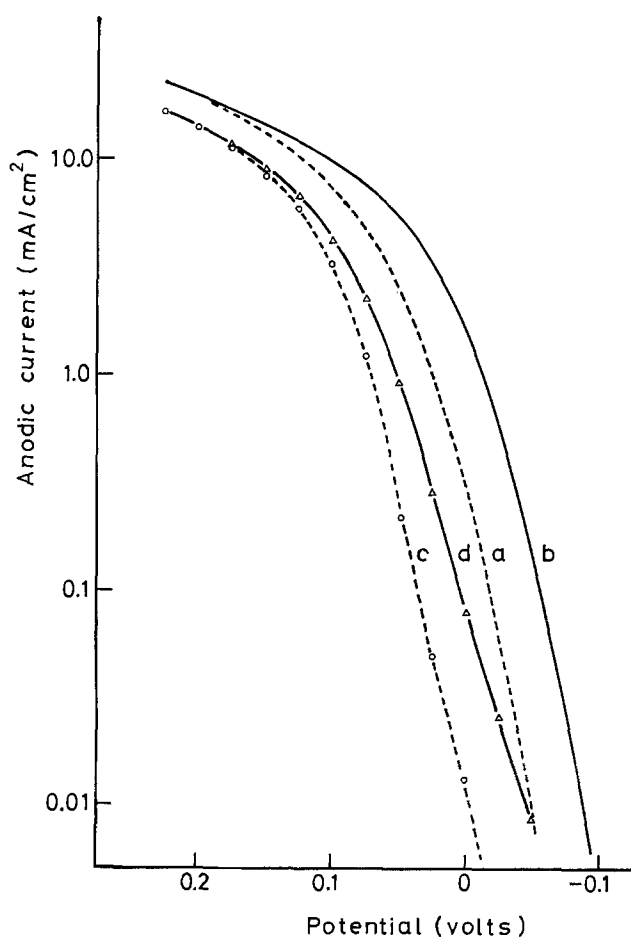


Fig. 1a. Tafel plots in SAO solution at pH 1.5. In the base solution with stationary disk electrode (SDE) (curve a), and with rotating disk electrode (6000 rpm) (RDE) (curve b). In 5.0 mM SAO solution with SDE (curve c), and with RDE (6000 rpm) (curve d).

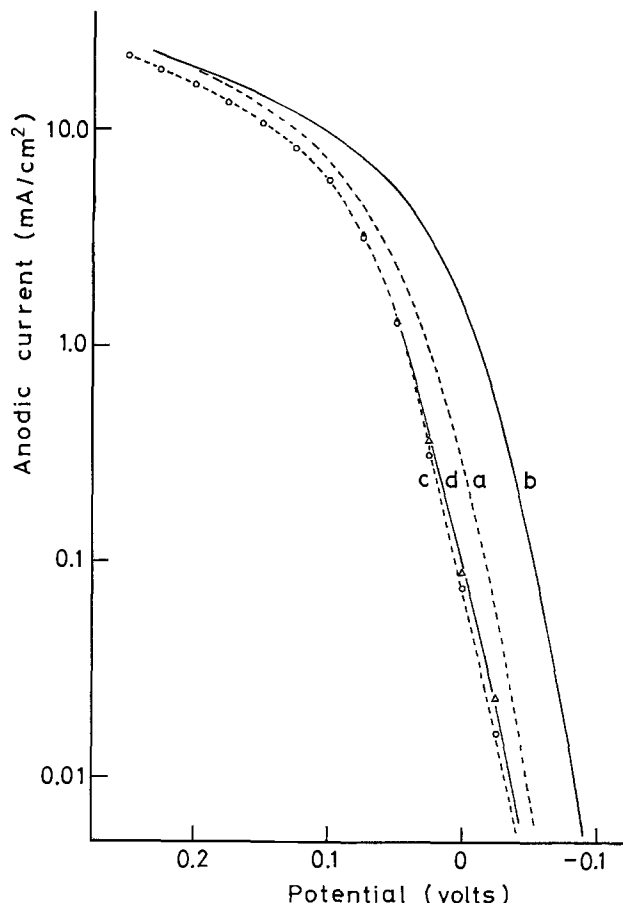


Fig. 1b. Tafel plots in HQ solution at pH 1.5. In the base solution with SDE (curve a), and with RDE (6000 rpm) (curve b). In 5.0 mM HQ solution with SDE (curve c), and with RDE (6000 rpm) (curve d).

2b: A current maximum and minimum were observed, followed by a current increase at more anodic potentials. The polarization curves shifted slightly toward cathodic potentials as the rate of rotation was increased at lower current densities (in the potential region of the current peak). The peak current was higher and the peak potential more anodic at the lower concentration of SAO and lower rotation rate. The current in the passive region which followed the current peak decreased with increasing concentration of SAO. At higher anodic polarizations (trans-passive potential, region), a white precipitate of $\text{Cu}(\text{SAO})_2$ was seen to fall from the stationary disk electrode. The curves corresponding to increasing and decreasing polarization did not coincide. The current at decreasing polarization was higher than that observed during increasing polarization in the passive region and the current peak was not observed, as shown in Fig. 2a.

In the steady-state potentiostatic polarization curves from cathodic to anodic direction, the current peak was not observed.

In the acetate buffer solution at pH 5.0 (Fig. 3a and b), the effect of SAO on the copper dissolution was qualitatively similar to that at lower pH values, but was more pronounced. The current peak occurred at about -0.05V , which is more cathodic than at pH 2.8. The current peak was also observed with the stationary electrode when the concentration of SAO was more than 10 mM at pH 5.0 and 20 mM at pH 2.8, respectively. The polarization curves in the trans-passive region were not influenced significantly by the rotation rate (600-6000 rpm) (Fig. 3a), and depended slightly on the concentration of SAO (Fig. 3b); the electrode surface showed local corrosion on a shiny background after polarization in this region. However, it remained shiny when the anodic

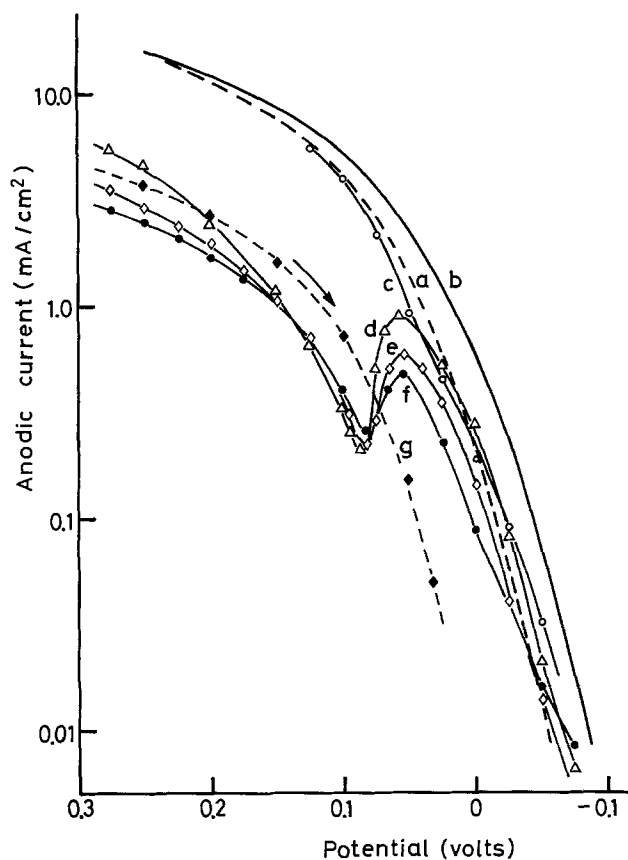


Fig. 2a. Tafel plots in 5 mM SAO solution at pH 2.8 with various rotation rates. In the base solution with SDE (curve a), and RDE (6000 rpm) (curve b). In 5 mM SAO solution with SDE (curve c), 600 rpm (curve d), 1200 rpm (curve e), 3000 rpm (curve f), and with RDE (1200 rpm) polarized from anodic to cathodic direction (curve g).

polarization was stopped at potentials more cathodic than the second increase in current rise.

Cyclic voltammetry at the copper electrode in the SAO solution (Fig. 4) showed that the surface film formation was irreversible. The chelate film was partially reduced at potentials more cathodic than about $-0.6V$. Successive anodic sweeps started from potentials more cathodic than $-0.6V$ gave a larger anodic current peak at $-0.1V$; the chelate film formed during the anodic process was almost completely reduced at $-1.0V$.

The total amount of electrical charge involved in the Cu-SAO chelate film formation in the potential region of the current peak depended on the pH of the solution, the concentration of SAO, and the rate of rotation of the electrode (Table I). With increase in the rotation rate, the amount of electrical charge involved in the chelate film formation decreased slightly.

The impedance of the copper electrode in the presence of SAO at pH 5.0 was measured by using the phase-selective a-c polarograph and was represented

Table I. Effect of concentration

The amount of charge (mcoulomb/cm²) required to form the protective film by salicylaldoxime

Concentration, mM	pH 2.8	pH 5.0
2.5	—	18.1
5.0	30.8	11.4
10.0	28.5	7.3
20.0	17.2	1

Rotation speed 3000 rpm.

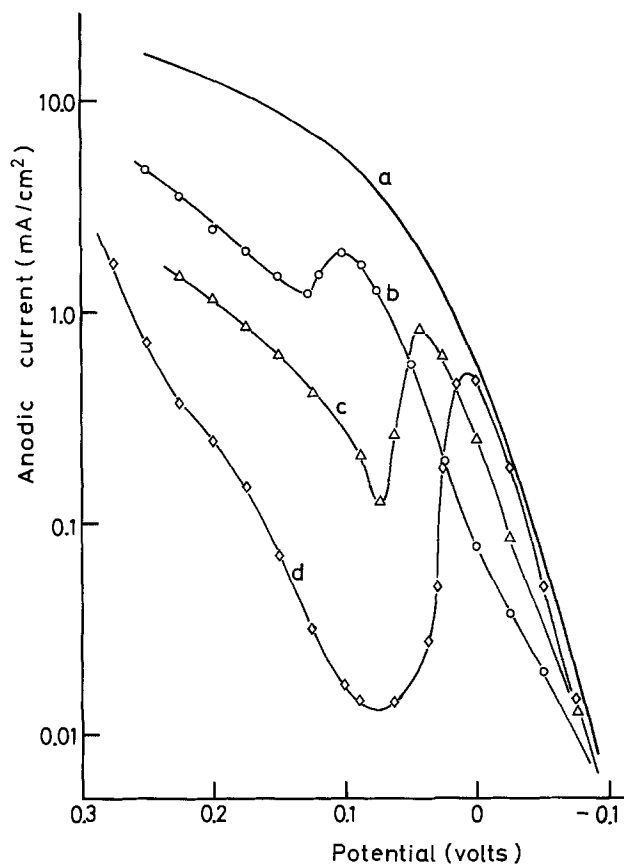


Fig. 2b. Tafel plots in SAO solutions at pH 2.8 with RDE (3000 rpm). In the base solution (curve a), 2.5 mM SAO (curve b), 5.0 mM SAO (curve c), and 10 mM SAO (curve d).

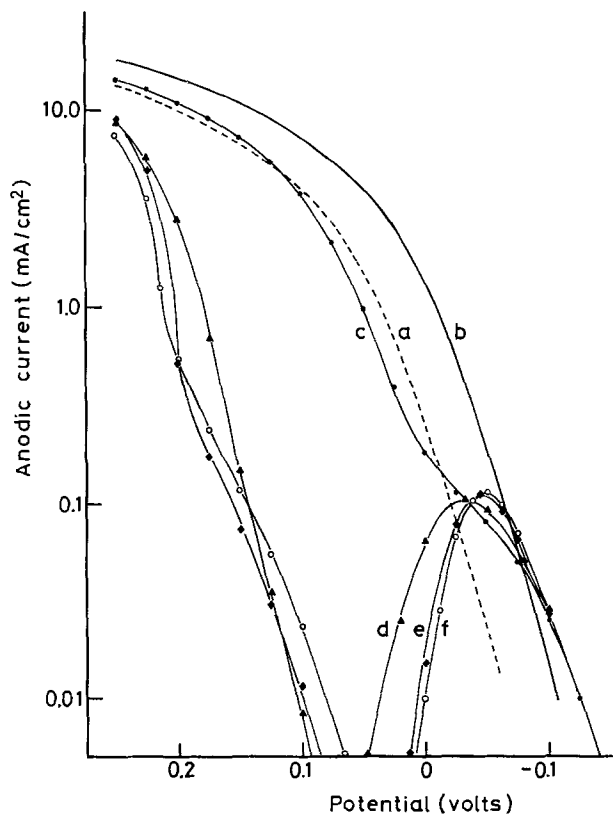


Fig. 3a. Tafel plots in 5 mM SAO solution at pH 5.0 with various rotation rates. In the base solution with SDE (curve a), and with RDE (6000 rpm) (curve b). In 5 mM SAO solution with SDE (curve c), 600 rpm (curve d), 1200 rpm (curve e), and 3000 rpm (curve f).

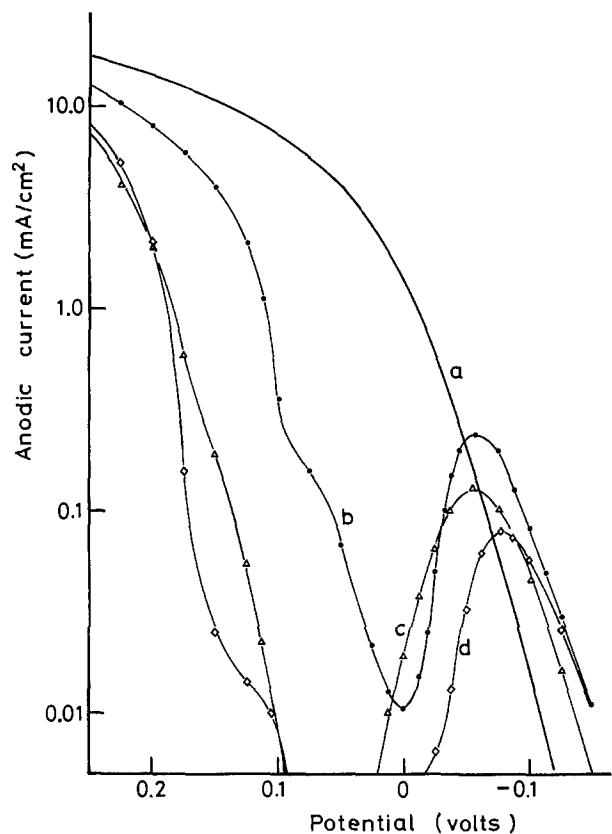


Fig. 3b. Tafel plots in SAO solution at pH 5.0 with RDE (3000 rpm). In the base solution (curve a), 2.5 mM SAO (curve b), 5.0 mM SAO (curve c), and 10 mM SAO (curve d).

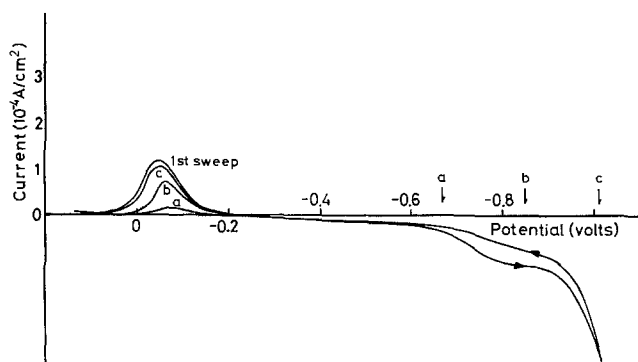


Fig. 4. Cyclic voltammograms of RDE (3000 rpm) in 5.0 mM SAO solution at pH 5.0. The first sweep started at -0.4V toward anodic. Arrows indicate the points where the direction of potential scan was reversed. The peaks are labeled with respect to the corresponding reversal of potential. Scan rate is 0.5 V/min .

as a series combined of a capacitance, C_s , and a resistance, R_s (Fig. 5). In the double layer region, C_s decreased markedly on addition of SAO. On the other hand, R_s remained constant regardless of the concentration of SAO. In the region of the d-c peak, C_s increased slightly, and then decreased to a very small value in the passive region, whereas R_s increased steeply to a very large value.

8-Hydroxyquinoline.—In a solution of 5.0 mM HQ at pH 2.8 (Fig. 6), the dissolution rate increased monotonically as the potential became more anodic, and no current peak was observed. With the rotating disk electrode, a shoulder was observed in the anodic polarization curves at about $2 \times 10^{-4}\text{ A/cm}^2$. At current densities smaller than $2 \times 10^{-4}\text{ A/cm}^2$, the polarization curve shifted slightly to the more cathodic region and above this current density it shifted toward the anodic side on rotating the electrode. The

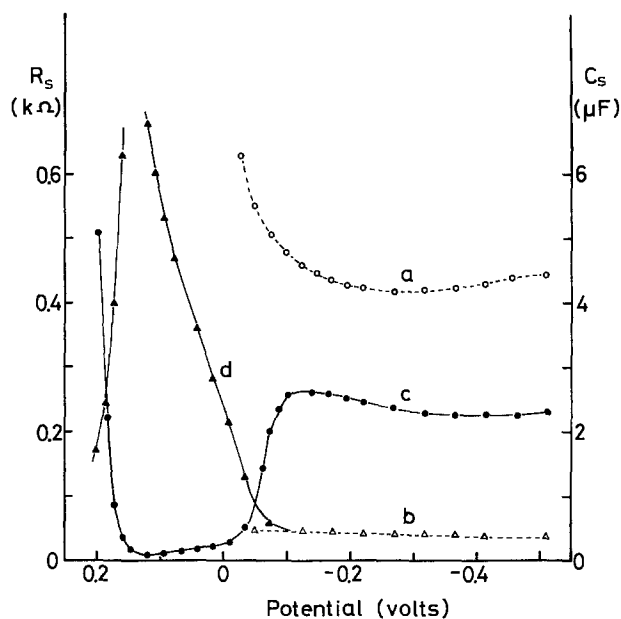


Fig. 5. The resistive and capacitive components (R_s and C_s are in series) of the copper electrode in 5.0 mM SAO solution at pH 5.0. In the base solution (curve a) C_s and (curve b) R_s . In the SAO solution (curve c) C_s and (curve d) R_s .

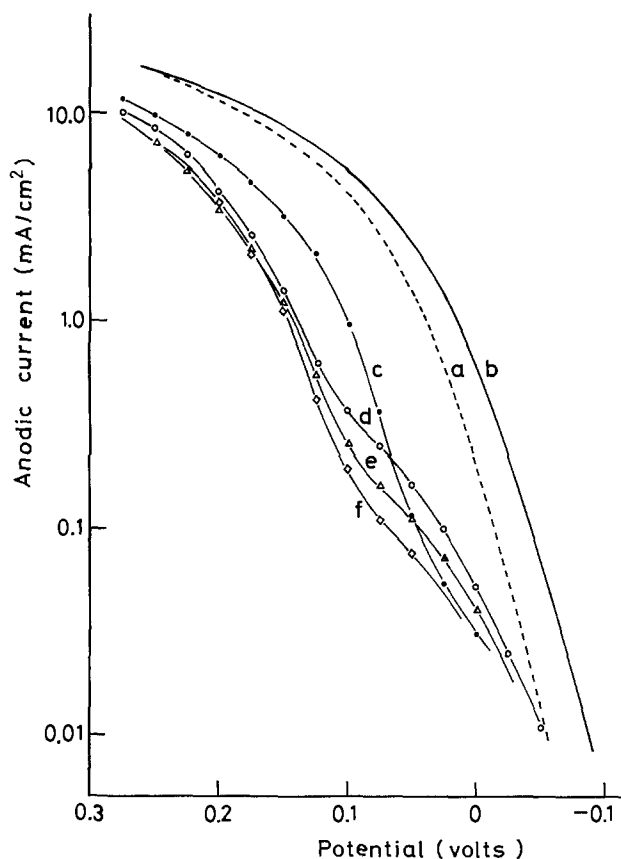


Fig. 6. Tafel plots in 5 mM HQ solution at pH 2.8 with various rotation rates. In the base solution with SDE (curve a) and with RDE (6000 rpm) (curve b). In 5.0 mM HQ solution with SDE (curve c), 600 rpm (curve d), 1200 rpm (curve e) and 3000 rpm (curve f).

effect of rotation rate on the polarization curve was small in a 5 mM HQ solution at pH 5.0 (Fig. 7). With an increase in the rotation rate the polarization curve shifted slightly to more anodic potentials.

Figure 8 shows C_s and R_s for the copper electrode in a 5 mM HQ solution (pH 5). HQ depressed C_s markedly in the double layer region as in the case of the SAO solution and C_s showed a considerable increase

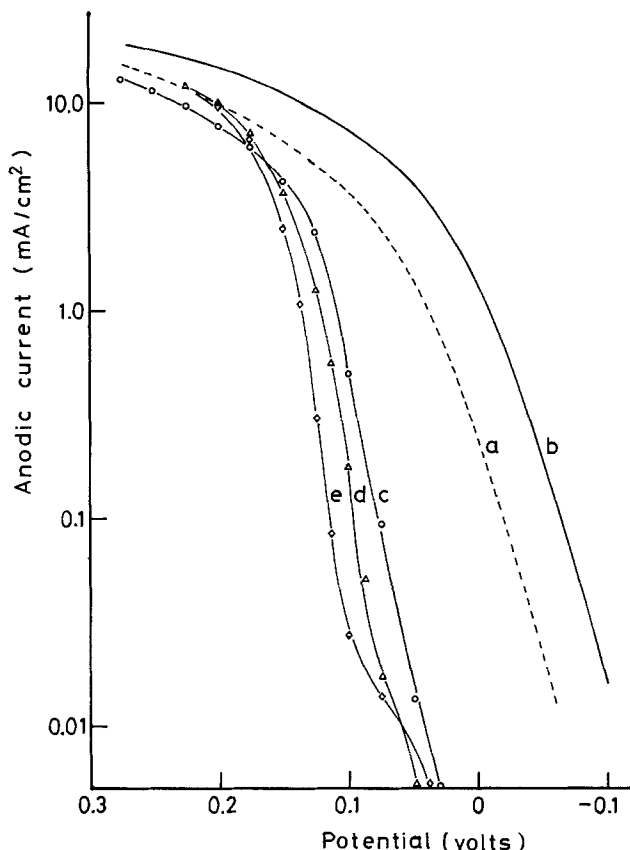


Fig. 7. Tafel plots at pH 5.0 in the presence of HQ. In the base solution with SDE (curve a) and with RDE (6000 rpm) (curve b). In 5.0 mM HQ solution with SDE (curve c), 3000 rpm (curve d), and 6000 rpm (curve e).

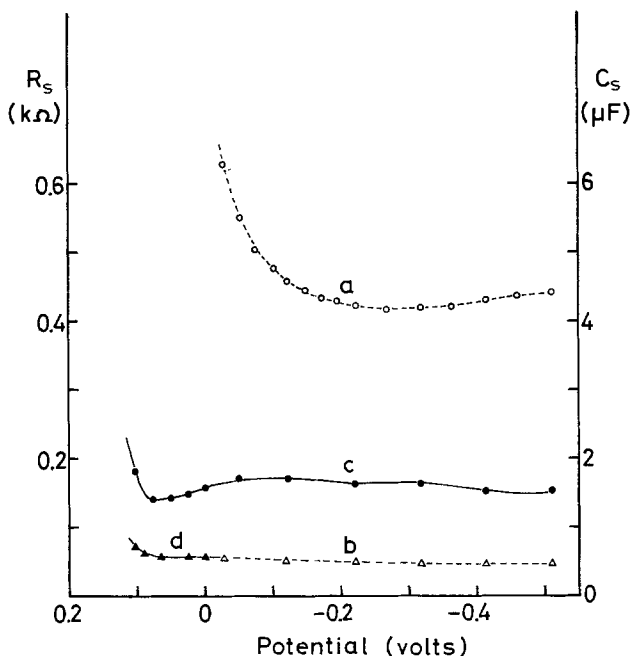


Fig. 8. The resistive and capacitive components (R_s and C_s are in series) of the copper electrode in the 5.0 mM HQ solution at pH 5.0. In the base solution (curve a) C_s and (curve b) R_s . In the HQ solution (curve c) C_s and (curve d) R_s .

in the potential region where the d.c. started to increase.

Discussion

At pH 1.5.—About one-half of SAO and most of HQ molecules are protonated in the solution at pH 1.5 (15, 16). According to earlier work (17, 18), SAO

would therefore be expected to be a better corrosion inhibitor. If we assume that the deceleration of the copper dissolution is only due to a blocking effect and that the surface coverage is independent of the electrode potential, the Tafel slope should not be affected by organic additives because the mass transport to or from the electrode is not disturbed by the additives (19). The shift of the Tafel plots with rotation in the absence of SAO was comparable with that in the presence of SAO; this suggests that the adsorption of SAO did not disturb the diffusion of products from the electrode. Capacity measurements indicated that the potential dependence of the SAO adsorption was very small in this potential region. Although the solubility of HQ is smaller than that of SAO at pH 1.5, the inhibitor efficiency of SAO was slightly better than that of HQ. The adsorption of SAO on the copper electrode is probably chemical in nature.

Salicylaldoxime.—In the pH range where Cu^{++} precipitates as a chelate with SAO, the polarization curves are similar in shape to those observed for the passivation of iron. In this case, however, the current peak corresponds to the faradaic process for the formation of an insoluble Cu-SAO chelate film at the electrode surface. After the copper electrode surface was covered by the insoluble film the dissolution of copper was completely inhibited. The protective film of Cu-SAO chelate may be very similar to that formed by benzotriazole which reacts at the copper surface to form benzotriazole complexes. Poling (8) identified these complexes as a near stoichiometric Cu(I)-benzotriazole polymer. With increasing anodic polarization beyond the potential of the current peak, the anodic current reached a minimum (which corresponds to the passivation region of iron) and then started to increase again. The current increase in the transpassive potential region was caused by a rupture of the protective chelate film. This is evidenced by a visible localized corrosion of the copper surface.

Hysteresis of the polarization curve also suggests chelate film formation and rupture of the film at very anodic potentials, as in the case of passivation of iron.

In the pH range where SAO precipitates Cu^{2+} as Cu-SAO chelate, the formation of Cu-SAO chelate at the copper electrode is thermodynamically more favorable than the dissolution of copper as Cu^{2+} . At pH 2.8, however, the rate of chelate film formation at the copper electrode is slow, and the SAO film chemisorbed on the copper electrode, suggested by the data of Fig. 5, inhibited the dissolution of copper. With increase in the electrode potential, the faradaic process took place for the formation of Cu-SAO chelate as a first step. The chelate film formation is probably due to the reaction between the chemisorbed SAO and copper at the copper electrode surface. This mechanism was supported by the fact that the effect of rotation of the electrode on the polarization curves was insignificant at lower current densities. The mass transport of SAO to the electrode surface was so slow with the stationary electrode that the dissolution of copper as Cu^{2+} became predominant at higher current densities and the effect of SAO disappeared at very positive potentials.

With the rotating disk electrode the mass transport of SAO to the electrode was sufficient to form the chelate film on the electrode and the chelate film formation was a predominant reaction at the copper electrode in the current peak region. With increase in the rotation rate of the electrode the mass transport of SAO to the electrode was enhanced and the height of the current peak became smaller because the dissolution of copper was completely inhibited and the peak potential shifted cathodically. This behavior was very similar to the dependency of the polarization curves on the concentration of SAO as shown in Fig. 2b.

At pH 5.0, SAO also accelerates the faradaic process for formation of the chelate film on the electrode in the potential region of the current peak. The polarization curves shifted toward the cathodic region with increase in pH values of the solution. This is due to the formation of a more stable chelate film at pH 5.0 than that at pH 2.8.

The anodic process for the chelate film formation on the copper electrode in the presence of SAO can be considered to be due to: (i) the chelate film formation taking place at the electrode covered by the chemisorbed SAO, θ_{ad} ($1 - \theta_{film}$), where θ_{ad} is the fraction of the electrode surface covered by the chemisorbed SAO and θ_{film} is the fraction of the electrode surface covered by the chelate film; $Cu + 2(SAO)_{ad} \rightarrow Cu(SAO)_2$, and (ii) copper dissolution taking place at the uncovered electrode surface and Cu^{2+} formed by the anodic process reacting with SAO in the diffusion layer at the electrode interface and this Cu-chelate diffusing away from the electrode.

The mathematical solution of this process was very complicated and hence impractical for the analysis of the experimental data.

We made the further simplification that the electrode surface covered by the chemisorbed SAO was considered to be appreciably high on the basis of the differential capacity measurements so that the dissolution of copper as Cu^{2+} from the uncovered surface was ignored. The fraction of the electrode surface covered by SAO, θ_{ad} , was assumed to be a constant because the peak currents shown in Fig. 3a were far less than the flux of the limiting diffusion of SAO to the electrode surface under the present condition. The current-potential relation in the potentiokinetic measurement can be easily calculated by using Eq. [1] and [2]

$$i = 2Fk\theta_{ad}^2(1 - \theta_{film})\exp(2\beta FE/RT) \quad [1]$$

$$i = Sd\theta_{film}/dt \quad [2]$$

$$E = E_i + vt \quad [3]$$

where i (A/cm²) is the faradaic current for the chelate film formation; k the rate constant for the chelate formation at $E = 0$, β the anodic transfer coefficient; θ_{film} and θ_{ad} (%) the fraction of the electrode surface covered by the chelate film and chemisorbed SAO, respectively; S (coulombs/cm²) the amount charge required to cover the electrode surface by the chelate film; v (V/sec) the scan rate, and t (sec) time. A solution of Eq. [1] is easily obtained as follows: (i) Substitute i and E into Eq. [1], and then integrate Eq. [1] to get θ_{film} as a function of time. (ii) Substitute $\theta_{film}(t)$ into Eq. [1] and then set its time derivative equal to zero to get t_{max} , the time required to reach the current peak potential from $E = E_i$.

One can obtain

$$t_{max} = \frac{\bar{K}_1}{v} - \frac{\bar{K}_2}{v} \ln \theta_{ad} \quad [4]$$

where

$$\bar{K}_1 = \frac{RT}{2\beta Fv} \ln \left(\frac{S\beta v}{RTk} \right) - \frac{E_i}{v}$$

and

$$\bar{K}_2 = RT/\beta Fv$$

Then one can easily obtain the peak current

$$i_{max} = \ln(2\beta Fv/RT) - 1 + (RTk\theta_{ad}^2/S\beta v) \times \exp(2\beta FE_i/RT) = \bar{K}_3 + \bar{K}_4 \theta_{ad}^2 \quad [5]$$

The peak potential shifts linearly toward cathodic values with $\log \theta_{ad}$ and the peak height increases linearly with θ_{ad}^2 .

The shift of the peak potential with respect to the SAO concentration is shown in Fig. 9. Since θ_{ad} is a function of concentration of SAO, the steeper the slope of plots, the stronger is the adsorption of SAO on the copper electrode. Qualitatively, the adsorption of SAO onto the copper electrode becomes stronger with in-

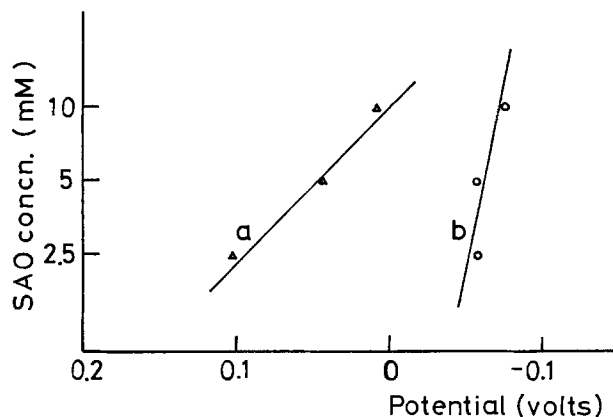


Fig. 9. Shift of peak potential with the concentration of SAO at pH 2.8 (curve a) and pH 5.0 (curve b).

creasing pH of the solution. Similar behavior was observed with EDTA, adsorbed on a mercury electrode (20).

The marked decrease in the capacitive component, C_s , of the copper electrode in the presence of SAO (Fig. 5) suggested that SAO adsorbed strongly on the electrode in the pH range where the Cu-SAO chelate is stable. In the current peak region of the above condition, the capacitive component became very small and the resistive component reached several thousands ohms. These changes strongly suggested the chelate film formation on the electrode surface. With the stationary disk electrode in the 5 mM SAO solution at pH 5.0, both C_s and R_s started to increase from the values in the double layer region at about +0.05V which is 75 mV more anodic than those in the base solution. This is probably due to the dissolution of copper as Cu^{2+} because of the insufficient supply of SAO onto the electrode to form a compact chelate film.

If we assume that the chelate film is formed through the dissolution-precipitation mechanism (21) the peak current in the cyclic voltammogram with a rotating disk electrode should increase with increasing rotation rate such as in the passive film formation on copper (22). In the present case, however, the peak current decreased with an increase in the rotation rate. This behavior indicates a discharge-nucleation mechanism for the formation of the Cu-SAO chelate on the copper electrode (21).

Assuming the density to be 2 g/cm³, the thickness of the surface film calculated from the amount of charge required for its formation ranged from 100Å, in 20 mM SAO solution at pH 5.0, to 1000Å, in 5.0 mM SAO solution at pH 5.0. These thicknesses are comparable with those reported by Poling (8) for the Cu-benzotriazole film on copper electrode.

8-Hydroxyquinoline.—In the HQ solution at pH 2.8, a shoulder was observed in the polarization curves with the rotating disk electrode (Fig. 6). The cathodic shift of the polarization curve at lower current densities (2×10^{-4} A/cm²) would be explained from the analogy of the copper electrode in the HQ solution to that in the SAO solution. The effect of HQ in the pH 5.0 solution is more pronounced than that in the pH 2.8 solution and the polarization curves were not influenced by the rotation rate (Fig. 7).

A strong adsorption of HQ on the copper electrode in the pH range where HQ precipitates cupric ions was evidenced by the capacitance curve in the double layer region (Fig. 8). Both capacitive and resistive components of the copper electrode in the pH 5.0 solution remained at almost the same value up to about +0.1V which corresponded to the potential at which the anodic dissolution of copper started. No decrease of the capacitive component was observed in the HQ solution. This result suggests that the inhibition of copper dissolution by HQ is not due to the chelate film on the

electrode but mainly to the chemisorbed film. This mechanism is also supported by the evidence that the rotation rate did not show any significant influence on the anodic polarization curves. The formation of a Cu-HQ chelate film on the electrode was evidenced by the result that the decreasing polarization curve (from anodic to cathodic) was higher than that of the increasing ones. However, the adhesion of the film on the electrode was not so strong as to decrease the capacitive component of the electrode, in contrast to the case of the SAO solution.

Conclusion

It was shown that the adsorption of both SAO and HQ on the copper electrode became stronger with increase in pH of the solution. This tendency is parallel to the stability of the copper chelates of SAO and HQ. In the pH range where SAO and HQ precipitate cupric ions as a chelate, the adsorbability of these chelating agents increased markedly and the anodic dissolution rate of copper was retarded to a considerable extent. In the SAO solutions the anodic polarization curves of copper were similar in shape to those for the passivation of iron. The Cu-SAO chelate film was formed in the active-to-passive transition region and the copper electrode became passive after the surface was covered by the chelate film. In the HQ solutions, on the other hand, the chemisorbed film retarded the dissolution of copper. The Cu-HQ chelate did not adhere to the copper electrode.

Acknowledgment

The authors express their appreciation to the Robert A. Welch Foundation, Houston, Texas, for its support of this research. One of the authors (K.N.) also expresses his appreciation to Dr. Reita Tamamushi and Mr. Kiyoshi Matsuda, Institute of Physical and Chemical Laboratory, Japan, for the phase-selective polarographic work, and to Dr. H. H. Bauer, University of Kentucky, for his helpful discussions and suggestions in the course of preparing this manuscript.

Manuscript submitted Feb. 5, 1973; revised manuscript received Feb. 20, 1975. This was Paper 79 presented at the Miami Beach, Florida, Meeting of the Society, Oct. 8-13, 1972.

Any discussion of this paper will appear in a Discussion Section to be published in the June 1976 JOURNAL.

All discussions for the June 1976 Discussion Section should be submitted by Feb. 1, 1976.

Publication costs of this article were partially assisted by Rice University.

REFERENCES

1. Y. Hayakawa and I. Ida, *Denki Kagaku (J. Electrochem. Soc. Japan)*, **26**, 643 (1958).
2. J. B. Cotton, *Trans. Inst. Marine Eng.*, **77**, 165 (1965).
3. J. B. Cotton, "Proceedings 2nd International Congress on Metallic Corrosion," p. 590, NACE, New York (1963).
4. I. Dugdale and J. B. Cotton, *Corrosion Sci.*, **3**, 69 (1963).
5. J. B. Cotton and I. R. Scholes, *Brit. Corrosion J.*, **2**, 1 (1967).
6. P. L. Bonora, G. P. Bolognesi, P. A. Borea, G. L. Zucchini, and G. Brunoro, "3rd European Symposium on Corrosion Inhibitors," p. 685, Ferrara (1971).
7. F. Mansfeld, T. Smith, and E. P. Parry, *Corrosion*, **27**, 289 (1971).
8. G. W. Poling, *Corrosion Sci.*, **10**, 359 (1970).
9. K. H. Wall and I. Davies, *J. Appl. Chem.*, **15**, 389 (1965).
10. U. F. Ushenina and N. G. Klyuchnikov, *Zhur. Prikl. Khim.*, **44**, 191 (1971).
11. H. R. Fleck and A. M. Ward, *Analyst*, **58**, 388 (1933).
12. N. Furman and F. J. Flagg, *Ind. Eng. Chem., Anal. Ed.*, **12**, 738 (1940).
13. K. Matsuda, K. Takahashi, and R. Tamamushi, *Sci. Papers Inst. Phys. Chem. Res.*, **64**, 62 (1970).
14. H. P. Leckie, *This Journal*, **117**, 1478 (1970).
15. K. E. Jabalpurwala, K. A. Venkamachalam, and M. B. Kabadi, *J. Inorg. Nucl. Chem.*, **26**, 1011, 1027 (1964).
16. R. Nasanen, P. Lumme, and A. L. Mukula, *Acta Chem. Scand.*, **5**, 1199 (1951).
17. N. Hackerman, R. M. Hurd, and R. R. Annand, *Corrosion*, **18**, 371 (1962).
18. N. Hackerman and A. C. Makrides, *Ind. Eng. Chem.*, **46**, 523 (1954).
19. K. K. Niki and N. Hackerman, *J. Phys. Chem.*, **73**, 1023 (1969).
20. K. Niki, K. Suzuki, G. P. Sato, and N. Mori, *J. Electroanal. Chem.*, **49**, 27 (1974).
21. A. K. N. Reddy, *ibid.*, **28**, 217 (1970).
22. T. Yoshimura, Y. Imanaka, and M. Yamashita, *Sci. Eng. Rev., Doshisha Univ.*, **14**, 43 (1974).

The Mechanism of Metallic Chromium Electrodeposition in the Cathodic Dichromate Treatment of Tinplate

Ph. Aubrun and P. Rocquet

Centre de Recherches du Fer Blanc, B. P. 135, 57100 Thionville, France

ABSTRACT

The passivation film deposited on tinplate by a cathodic treatment in a dichromate solution partly consists of metallic chromium. In order to clarify this rather surprising electrodeposition of metallic chromium, the successive reactions taking place were characterized. As a consequence, it is explained why the metallic chromium electrodeposition is made possible, and for what reason the deposit is of limited amount. The role played by the high hydrogen overvoltage on tin is emphasized.

At the end of its manufacturing process, electrolyte tinplate is subjected to a passivation treatment which improves its properties. Generally, this treatment consists of making the strip cathodic in a low-acid, sodium

Key words: tinplate passivation films, mechanism of chromium electrodeposition.

dichromate solution (CDC treatment). Tinplate is thus coated with a thin film containing metallic chromium (1, 2). This has been established by means of anodic dissolutions of the film, part of which involves six electrons per atom-gram of chromium. One cannot fail to be surprised by the following two items: First, how

Table I. Conditions of metallic chromium deposition

	CDC treatment	Conventional chromium plating
Electrolyte: concentration	0.09M $\text{Na}_2\text{Cr}_2\text{O}_7 \cdot 2\text{H}_2\text{O}$	0.5M CrO_3
Acidity	pH 3-8	pH 1
Catalyzer	None	Yes
Current density	1 A/dm ²	20 A/dm ²

can metallic chromium be deposited under conditions so different from those under which this metal is generally deposited (Table I)? Second, why does the amount of metallic chromium obtained through tinplate CDC treatment rapidly reach a limit, dependent on the experimental factors, whereas it increases proportionally to the time with conventional chromium plating of iron (Fig. 1)?

A good understanding of the mechanism of metallic chromium electrodeposition during CDC treatment is required to explain these two facts. This is the subject of the first part of the present paper; then the two characteristics of this electrodeposition are explained in the last parts.

Successive Steps Leading to the Metallic Chromium Electrodeposition during CDC Treatment

In the case of conventional chromium plating of iron, the potentiokinetic cathodic polarization curve indicates the reaching of successive reactions (3). Prior to metallic chromium deposition, the building up of two films of chromium oxides and hydrogen evolution are noted (Fig. 2). It is noteworthy that if one substitutes the conventional chromium electrolyte with a dilute sodium dichromate solution, the successive waves of Fig. 2 disappear; at the same time, there is no metallic chromium electrodeposition.

Now, if we plot a curve of the same type, but relating to a tin electrode and a dilute sodium dichromate solution, we note (Fig. 3) the same features as those shown in Fig. 2, but only if we have used rolled tin or hot-dipped tinplate, cathodically cleaned in a Na_2CO_3

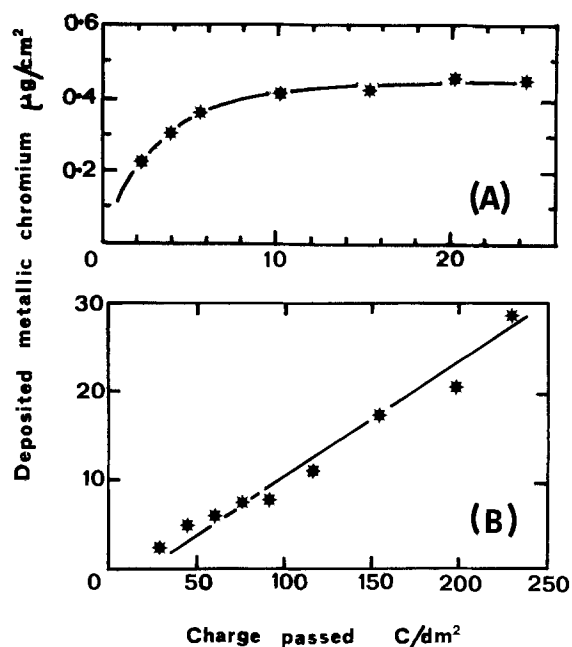


Fig. 1. Comparison between the rates of metallic chromium electrodeposition in the CDC treatment (A) and the conventional chromium plating of iron (B). (A) Cathode of electrolytic tinplate flow-melted and alkaline-cleaned. $\text{Na}_2\text{Cr}_2\text{O}_7 \cdot 2\text{H}_2\text{O}$ 25 g/liter (0.083M); pH 5.1; temperature 47°-49°C; 2 A/dm². (B) Cathode of mild steel cold-rolled, annealed, and alkaline-cleaned. CrO_3 50 g/liter (0.5M); H_2SO_4 0.5 g/liter; 20 A/dm².

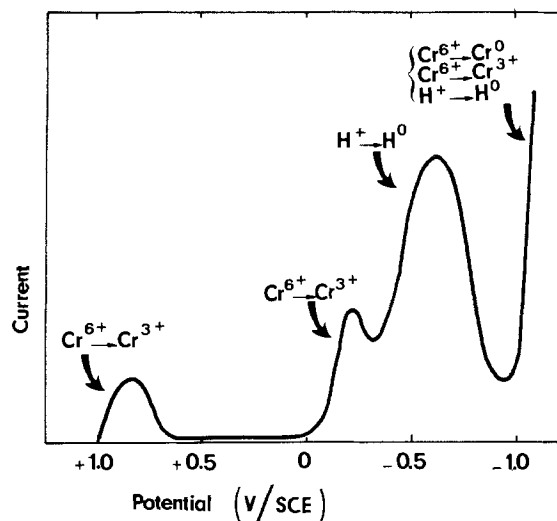


Fig. 2. Cathodic polarization curve of iron in a chromium plating bath ($\text{CrO}_3\text{-H}_2\text{SO}_4$) plotted potentiokinetically. Published by A. T. Yagryan and D. N. Usachev, *Zhur. Fiz. Khim.*, 32, 1900 (1958); after (3).

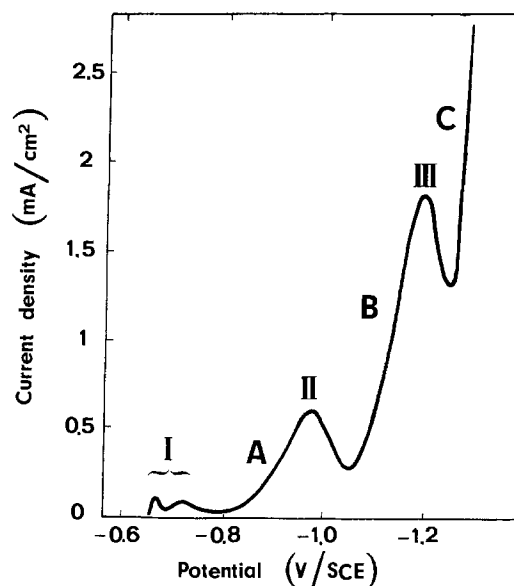


Fig. 3. Cathodic polarization curve plotted potentiokinetically with pure tin in an aqueous solution of $\text{Na}_2\text{Cr}_2\text{O}_7 \cdot 2\text{H}_2\text{O}$, 0.085M; pH 5.2; temperature 55°C; sweep rate 6 V/hr. Curve shape remains unchanged in the range of: $\text{Na}_2\text{Cr}_2\text{O}_7 \cdot 2\text{H}_2\text{O}$, 0.02-0.25M; temperature 25°-70°C; sweep rate 0.166-60 V/hr.

aqueous solution (5 g/liter). Under the same conditions, peak II does not appear with electrolytic tinplate as flow-melted, although we still notice the final deposition of metallic chromium. This particular behavior of electrolytic tinplate is probably due to an absorption of phenolsulfonic acid in the tin coating, as revealed by experiments which are not reported in this paper.

Comparison between Fig. 2 and 3 provides information on the studied mechanism. Thus, peak I (or the group of peaks I) would correspond to the building up of a primary chromium oxide film after the reduction of the tin oxides, peak II to the building up of a secondary chromium oxide film which changes at peak III. The final slope C results from a visible hydrogen evolution and from a chromium deposit under the metallic and oxide forms as indicated by chemical analysis.

The above propositions were investigated by repetitive potentiokinetic oxidation and reduction to specific potentials.

Electrochemical oxidations and reductions which do not reach the A slope (Fig. 3) show how the shape of

the group of peaks I depends on the potential of the oxidation taking place prior to the reduction. When this oxidation potential is increased, the group first consists of a single peak I, to which a second peak with a more cathodic potential is added, then again a single peak but with an even more cathodic potential (Fig. 4). Additional experiments (4) allow us to assign the reductions of Sn(II), Sn(IV), and SnO_x (1) to these successive peaks. Prior to peak I, the electrode was already coated with chromium due to immersion in the electrolyte, as a subsequent oxidation (around + 0.8 V/SCE) reveals the peak where oxidation of metallic chromium and chromium oxide generally takes place (4-6). Chemical analysis (1) allows us to specify that only chromium oxide is present. However, it is to be noted that tin oxide reduction at peak I increases this deposit of chromium oxide (which will be qualified as primary) as it raises the height of the oxidation peak which is located at + 0.8 V/SCE.

Peak II very likely corresponds to a film of chromium oxide as, after the dissolution of the primary chromium oxide through electrochemical oxidation at + 0.8 V/SCE, a tin polarization up to the A slope is sufficient to recover subsequently an oxidation peak at + 0.8 V/SCE (Fig. 5). Therefore, this new film will be called "secondary." The reaction which originates it is apparently reversible as indicated in Fig. 6. It is thought that chromium oxide may have valency III in the secondary film.

As long as the cathodic scanning end remains in the B slope, the secondary film of chromium oxide retains its solubility and the originating reaction retains its reversibility (Fig. 7). As soon as the maximum of peak III has been passed, peak II disappears whatever the scanning direction may be. This disappearance is progressive as long as the cathodic end remains between

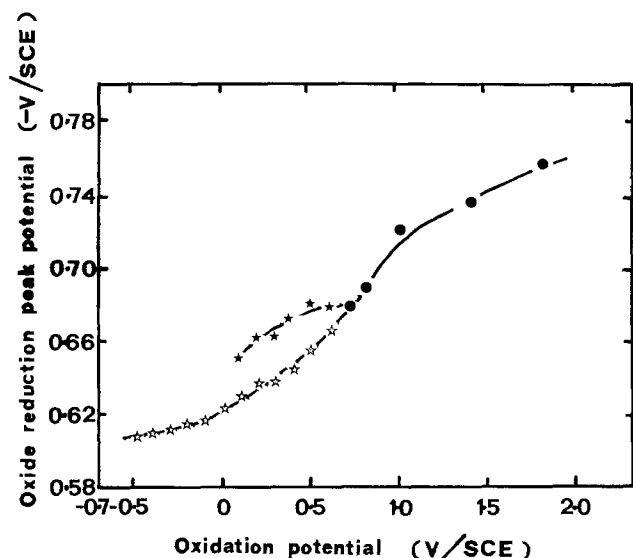


Fig. 4. Reduction potential(s) of tin oxide(s) vs. potential of oxidation done before. ☆☆☆ SnO; ★★ SnO₂; ●● what we have called SnO_x (1). Solution of Na₂Cr₂O₇ · 2H₂O, 0.085M de-aerated by nitrogen bubbling; pH 5.2; temperature 55°C; sweep rate 6 V/hr.

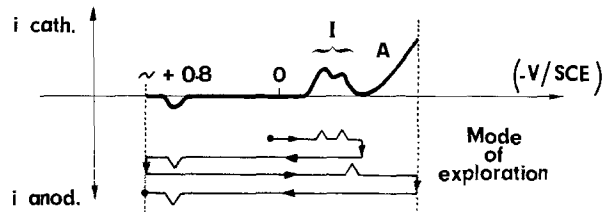


Fig. 5. Repetitive potentiokinetic oxidation and reduction to specific potentials. See text.

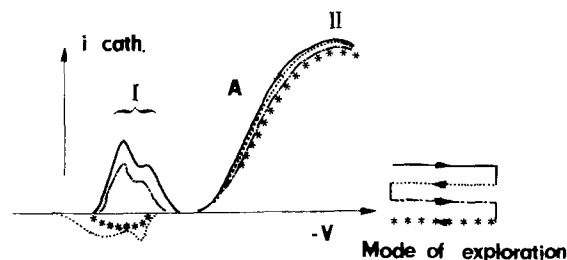


Fig. 6. Repetitive potentiokinetic oxidation and reduction to specific potentials. See text.

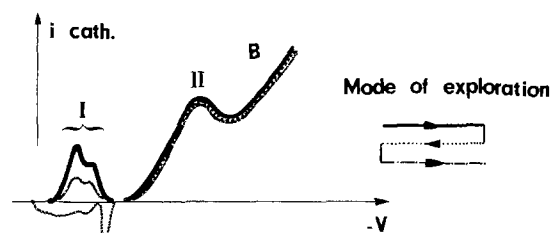


Fig. 7. Repetitive potentiokinetic oxidation and reduction to specific potentials. See text.

peak III and the valley which separates it from the C slope (Fig. 8); it occurs suddenly when the cathodic end is in the C slope (Fig. 9). Peak III corresponds to a change in chromium oxide film, but not to its destruction: in fact, oxidation of the sample at + 0.8 V/SCE is sufficient to obtain the peak of chromium oxidation (Fig. 9) and to regenerate the electrode as a subsequent reduction will reveal the peak II again. (In order to avoid any possible interference of the primary chromium oxide film, the sample was oxidized at + 0.8 V/SCE prior to the first scanning in the cathodic direction of Fig. 8.)

As previously indicated, deposits of metallic chromium and of trivalent chromium oxide build up and a hydrogen evolution occurs in the C slope. It is noteworthy that we regenerate the electrode which reaches the C slope through a simple oxidation at + 0.8 V/SCE: a subsequent cathodic polarization restores peaks I, II, and III (Fig. 10).

The reaction sequence of tin CDC treatment is reminiscent of the one of conventional chromium plating of iron. Using tin, we have pointed out the successive

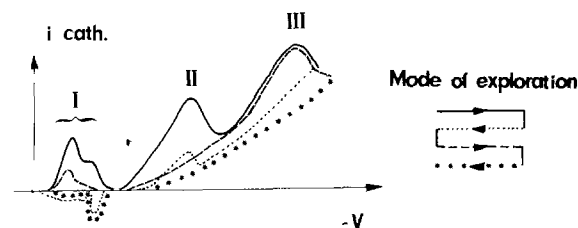


Fig. 8. Repetitive potentiokinetic oxidation and reduction to specific potentials. See text.

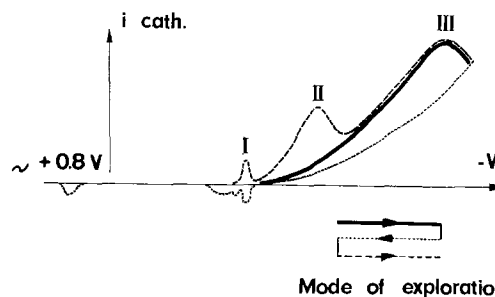


Fig. 9. Repetitive potentiokinetic oxidation and reduction. See text. The first sweep begins after the last one drawn in Fig. 8.

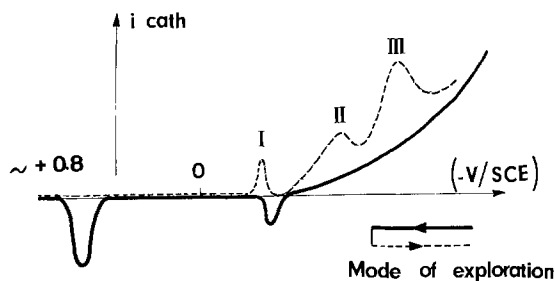


Fig. 10. Repetitive potentiokinetic oxidation and reduction. See text. The start point is in the slope C.

steps: (i) building up of a chromium oxide primary film; (ii) reduction of tin oxides and strengthening of the primary film; (iii) building up of a secondary film of chromium oxide; (iv) alteration of this film at the time of a hydrogen evolution; and (v) hydrogen evolution, deposition of metallic chromium and chromium oxide.

Limited Amount of Metallic Chromium Deposition

As stated above, the amount of metallic chromium deposited through CDC treatment reaches a limit (4, 8) (see first diagram of Fig. 1).

It has been shown that this limited amount can be deposited at several times as long as the surface film is not damaged by water rinsing. This is clearly reflected in a galvanokinetic cathodic polarization experiment (Fig. 11, in which the various features of Fig. 3 are easily traced), the results of which are shown in Table II.

This limited amount of metallic chromium which may be deposited depends on experimental factors (8) (temperature, acidity, foreign ion content of the electrolyte) which also alter the magnitude of peaks II and III on the potentiokinetic curve of the cathodic polarization. Comparison of the effects of these factors on the limited metallic chromium deposition and on the polarization curve (Table III) shows that an intensification of peaks II and III increases the limited amount of metallic chromium. We can say that the limited amount of metallic chromium is directly dependent on the amount of chromium oxide of the secondary film (and possibly the primary film) which is modified by the reaction of peak III.

Consequently, the maximum amount of metallic chromium to be deposited is determined when the electrode reaches the C slope.

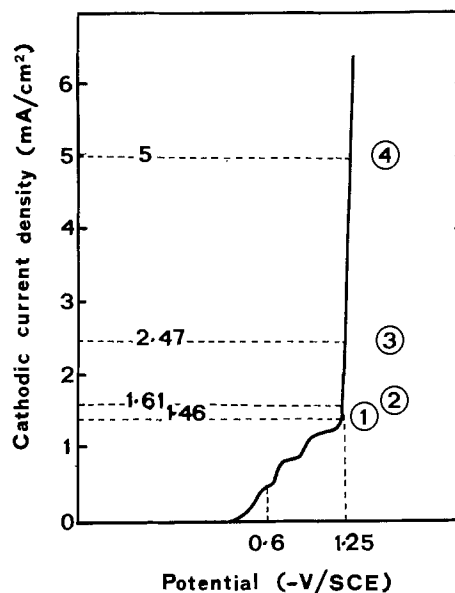


Fig. 11. Cathodic polarization curve plotted galvanokinetically. Pure tin. $\text{Na}_2\text{Cr}_2\text{O}_7 \cdot 2\text{H}_2\text{O}$, 0.085M; pH 5.2; temperature 55°C; sweep rate 0.25 A/cm²/mn. Encircled numbers refer to the text and to Table II.

Let us now consider the shape of the C slope when increasing amounts of metallic chromium are deposited through CDC treatment on a tin electrode. Figure 12 shows that it rises progressively, moves toward less cathodic potentials, and finally stabilizes. This matches the cathodic polarization curve of a chromium electrode dipped in this dichromate electrolyte.

To conclude, metallic chromium which is deposited on tin during CDC treatment originates from the film or films of chromium oxides built up during the previous steps and its amount is limited. After deposition, the electrode changes and becomes a chromium electrode.

Reason for Metallic Chromium Deposition during CDC Treatment

We have shown in the previous part that dichromate solution is unable to continue the metallic chromium deposition once the electrode becomes a chromium electrode. We can therefore assume that this deposition is due to the nature of the tin electrode.

Table II. Possibility for a two-step deposition of the limited amount of metallic chromium

Cathode reduction up to ^(a)	→	Metallic chromium level ^(b)	Cathodic reduction up to ^(a)	+	Water rinsing	+	Cathodic reduction up to ^(a)	→	Metallic chromium level ^(b)
1		0.23	1		No		4		2.7
1		0.23	1		Yes		4		1.6
2		0.29	2		No		4		2.4
3		1.31	3		No		4		2.6
4		2.5	4		No		4		2.5

^(a) Numbers in this column refer to circled numbers in Fig. 11.

^(b) Metallic chromium levels are given for guidance and are expressed in $\mu\text{g}/\text{cm}^2$.

Table III.

Factor	Influence on the peaks of the polarization curve	Influence on the maximum amount of metallic chromium deposited during full-scale or laboratory passivation trials
Dichromate concentration	None between 13 and 74 g/liter $\text{Na}_2\text{Cr}_2\text{O}_7 \cdot 2\text{H}_2\text{O}$	None
pH increase	Reduces peaks II and III	Decrease
Rise in temperature	Intensifies peaks II and III	Increase
Additions of Cl^- or SO_4^{2-}	At high content levels, lightly reduce peaks II and III	Not obvious at low industrial contents
Phosphate addition	Little effect on peak II, but lessens peak III	Delays the deposition
Increase of the amount of tin oxide	Little influence on peaks II and III from which peak I element has been subtracted	Negligible if any

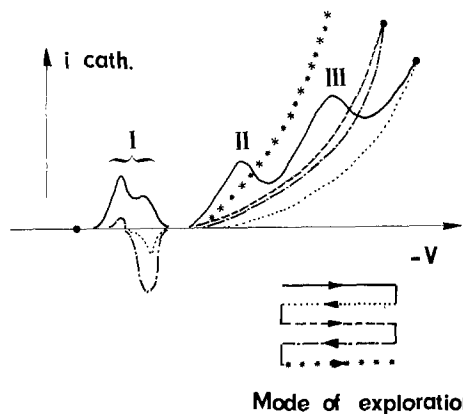


Fig. 12. Repetitive potentiokinetic oxidation and reduction. See text. *** refers to the cathodic polarization curve plotted in the same conditions but with a metallic chromium electrode.

As one of the properties of tin is a very high hydrogen overvoltage, which is not true for metallic chromium, we may ask ourselves if this is actually the determinative factor.

In order to answer this question, we have studied the potentiokinetic curve of cathodic polarization of some other common metals. Lead is the only metal to present the same peaks as those of tin (Fig. 13). The other metals (platinum, iron, copper, nickel, cadmium, chro-

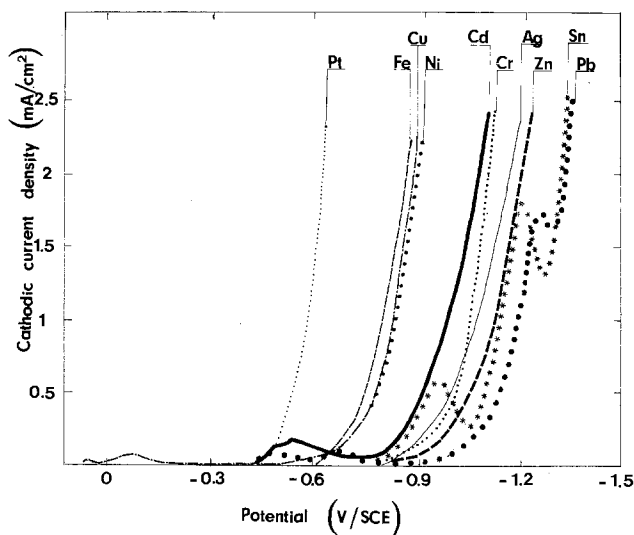


Fig. 13. Cathodic polarization curves plotted potentiokinetically with many metals; $\text{Na}_2\text{Cr}_2\text{O}_7 \cdot 2\text{H}_2\text{O}$, 0.085M; pH 5.2; temperature 55°C ; sweep rate 6 V/hr.

mium, silver, and zinc) present normal curve sections. Among the metals investigated, tin and lead are the only two to possess the higher hydrogen overvoltage in their final curve sections.

As a result, CDC treatment deposits metallic chromium due to the high hydrogen overvoltage on tin. We are thus in compliance with the result given in the last part: Deposition is only possible when tin is not coated with a metallic chromium film, the thickness of which has therefore to be very uniform.

Conclusions

The points developed in this report allow us to state that:

1. CDC treatment includes the following successive reactions: (i) building up of a chromium oxide primary film; (ii) reduction of tin oxides and strengthening of the primary film; (iii) building up of a chromium oxide secondary film; (iv) alteration of this film (or films) at the time of hydrogen evolution; and (v) hydrogen evolution, deposition of metallic chromium and chromium oxide.
2. Metallic chromium deposition, under conditions very different compared with those of conventional chromium plating of iron, is made possible by the high overvoltage of hydrogen on tin.
3. Metallic chromium deposition stops when the electrode changes to become a metallic chromium electrode. The amount which can be deposited is limited by the amount of chromium oxide which has built up during the previous steps: It is therefore dependent on the experimental conditions.

Manuscript submitted Dec. 28, 1973; revised manuscript received Feb. 12, 1975. This was Paper 76 presented at the Boston, Massachusetts, Meeting of the Society, Oct. 7-11, 1973.

Any discussion of this paper will appear in a Discussion Section to be published in the June 1976 JOURNAL. All discussions for the June 1976 Discussion Section should be submitted by Feb. 1, 1976.

Publication costs of this article were partially assisted by Centre de Recherches du Fer Blanc.

REFERENCES

1. P. Rocquet and Ph. Aubrun, *Corrosion (Fr.)*, **5**, 229 (1968).
2. S. E. Rauch, Jr. and R. N. Steinbicker, *This Journal*, **120**, 735 (1973).
3. H. Okada and K. Yamamoto, *Electrochem. Technol.*, **6**, 389 (1968).
4. P. Rocquet and Ph. Aubrun, Unpublished results.
5. S. C. Britton, *Brit. Corrosion J.*, **1**, 91 (1966).
6. D. Salm, *BHP Tech. Bull.*, **16**, 2 (1972).
7. H. Okada, Thesis, University of Hokkaido, p. 139 (1962).
8. P. R. Carter, *This Journal*, **108**, 782 (1961).
9. P. Rocquet and Ph. Aubrun, *Brit. Corrosion J.*, **5**, 113 (1970).

On the Structure and Electrical Properties of Electroless Ni-B Films

N. Hedgecock, P. Tung, and M. Schlesinger*

Department of Physics, University of Windsor, Windsor, Ontario, Canada N9B 3P4

ABSTRACT

An electron microscope study and measurements of electrical resistivity have been performed on electrolessly deposited Ni-B thin films. In contrast to Ni-P films, the islands of Ni-B films show a marked internal structure. Ni-B films have higher electrical resistivity than equally thick Ni-P films.

Electroless deposition of the nickel-boron system is possible using either alkali borohydrides or amine boranes as reducing agents. A survey of early work has been given by Goldie (1). More recent studies have been made by Fléchon *et al.* (2-4), Petrov *et al.* (5), and Gorbunova *et al.* (6, 7).

The as-deposited state of both Ni-P and Ni-B is highly disordered, and metastable in that heat-treatment irreversibly induces a state of higher crystallinity. In both systems, the initial state is a solid solution of phosphorus (8) or boron (4, 6) in nickel. For the deposits studied in this work the phosphorus and boron contents were about 20 and 25 per cent atomic, respectively.

Heat-treatment of Ni-P above 325°C produces two components, fcc nickel and tetragonal Ni₃P. The latter in bulk form has an electrical conductivity close to that of nickel, and indeed has an electronic band structure remarkably similar to that of nickel (9).

X-ray and thermal studies of Ni-B (3-7) have revealed analogous formation of nickel borides after annealing in vacuum. The formation of Ni₃B occurs around 300°C, accompanied by an abrupt change in

electrical properties (3, 4). Above 400°C, Ni₂B and possibly other borides are formed.

The present work describes further studies of electroless Ni-B films, involving electron microscopy and measurements of electrical resistivity. Results are presented for both freshly deposited and heat-treated films prepared under different conditions. Some results are also compared with those obtained from our earlier work on the nickel-phosphorus system (8).

Experimental

Electron microscopy.—A Hitachi HU-12 electron microscope operated at 100 kV was employed for obtaining transmission micrographs and selected area diffraction patterns. An aluminum foil standard was used to calibrate measurements of diffraction patterns. In many cases, the diffraction rings obtained were broad, indicating small crystallite size, and limiting the accuracy of measurement to about 1%.

The Ni-B films were grown on glass microscope slides coated with Formvar (4g polyvinyl formal in 1 liter ethylene dichloride). The Formvar layer was subsequently floated off in distilled water, and samples were deposited on copper grids for insertion into the microscope.

* Electrochemical Society Active Member.
Key words: electroless, thin film, nickel-boron.

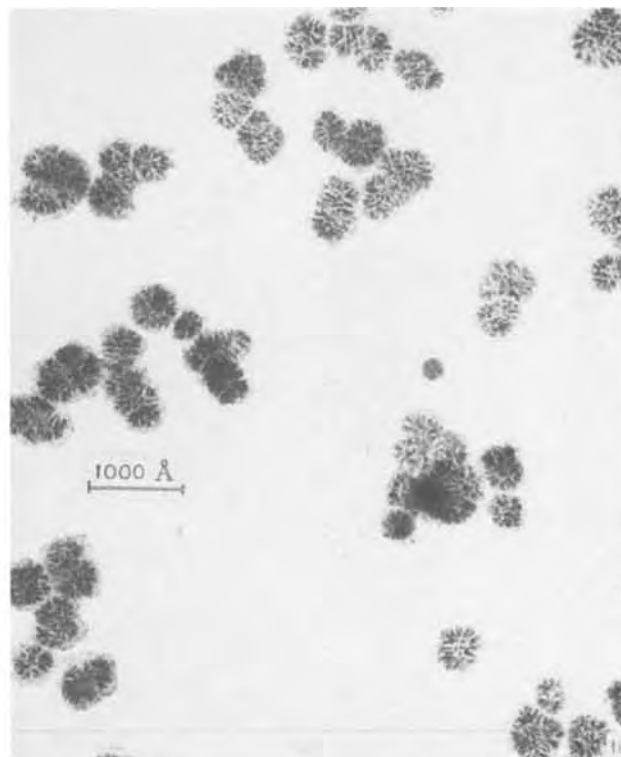
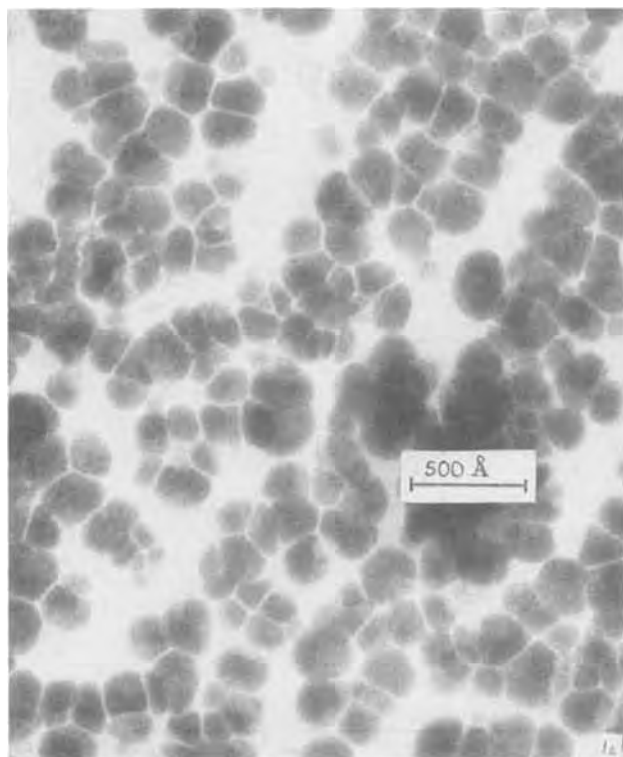


Fig 1. Transmission electron micrographs of thin films of (a, left) Ni-P deposited at room temperature from acidic (pH = 5.3) solution, (b, right) Ni-B deposited at 60°C using conventional SnCl₂/HCl sensitizer.

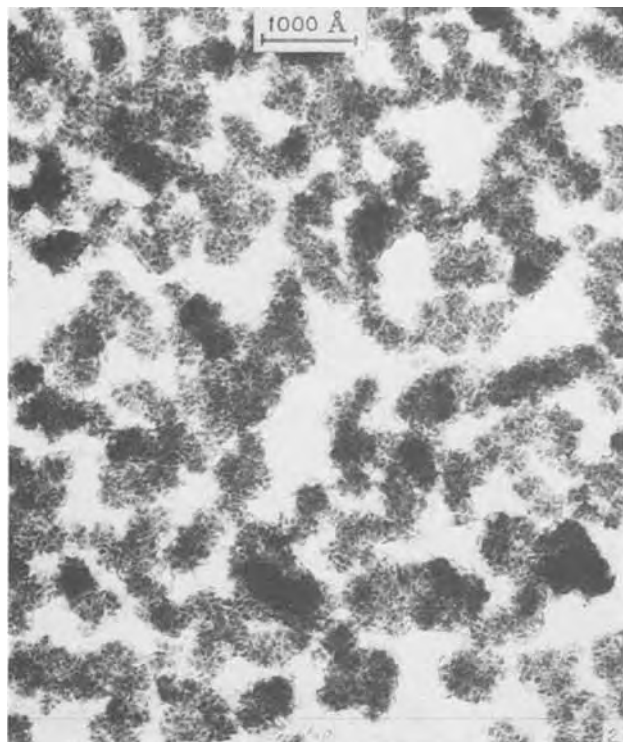


Fig. 2. Transmission electron micrograph of a thin film of Ni-B deposited at 60°C using improved (SnCl_2/HCl with additional aged SnCl_4) sensitizer.

Three different sensitizers were employed in preparing the substrates for deposition: fresh SnCl_2/HCl with and without additional aged SnCl_4 , and aged (4-6 days) SnCl_2/HCl . All were used in conjunction with the usual PdCl_2/HCl activator. The properties of these solutions have been investigated previously (10) and (11). The metallizing bath was that given as "B" by Gorbunova *et al.* (7). It employs borohydride as the reducing agent, has a pH of 14, and contains no stabilizer. This solution was maintained at 60°C; depo-

sition times ranged from 40 sec for the thin samples prepared for electron microscopy to 100 sec for the thickest samples used in the electrical measurements.

Samples were examined in the electron microscope before and after heat-treatment at 400°C. The heating was carried out in an evacuated glass tube which was flushed with dry nitrogen prior to evacuation. The pressure in the tube during heating was about 10^{-5} Torr. The heating sequence was as follows: 45 min heating from room temperature to 400°C; 45 min at 400°C; 45 min cooling back to room temperature.

Electrical resistivity.—The four-probe method of van de Pauw (12) was used to determine the resistivity of films of various thicknesses. For these measurements, deposition was made directly onto microscope slide glasses. Circular samples of 1 in. diameter were subsequently made by placing the deposited glasses in a Teflon mask, and etching away the unwanted Ni-B with a solution of HCl and HNO_3 . Spring-loaded stainless steel contacts were located symmetrically on the periphery of the circular samples for the measurements. The resistivity was determined both before and after the same heat-treatment as described above. The current in the samples was restricted to 100 μA during the measurements. For comparison, similar samples of Ni-P films of various thicknesses were made and their resistivity measured before and after the heat-treatment. For both Ni-B and Ni-P samples, the improved sensitizer was used. Film thicknesses were determined using the Tolansky interferometric method.

Results and Discussion

Electron microscopy.—Electron micrographs reveal both similarities and differences between Ni-P and Ni-B deposits. Figure 1 shows (a) Ni-P deposited at room temperature from acidic (pH = 5.3) solution and (b) Ni-B deposited at 60°C using conventional sensitizer. In both cases the deposit is composed of islands, typical of the initial stage of thin film growth in general. Moreover the islands are circular in shape and of rather uniform size. For Ni-P, these islands resemble liquid drops and have no discernible internal features. In contrast, the Ni-B islands usually show a characteristic "flowerlike" internal structure. The diffraction

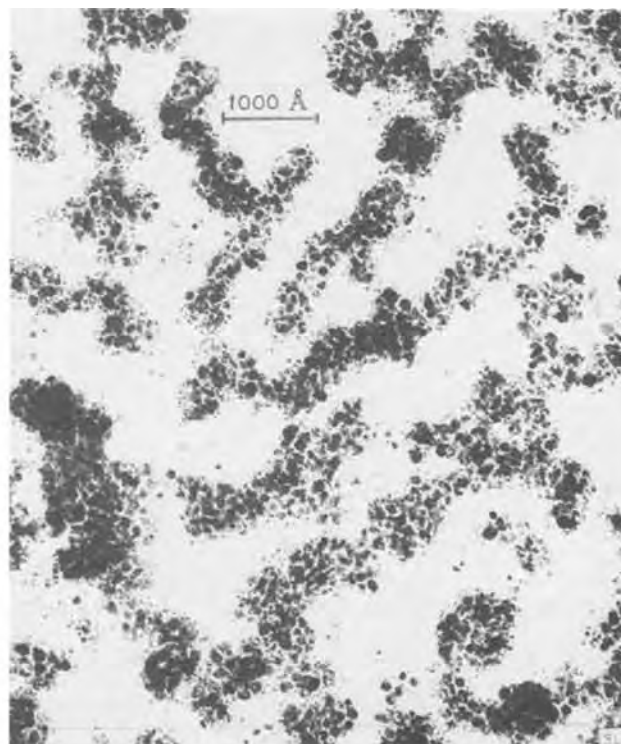
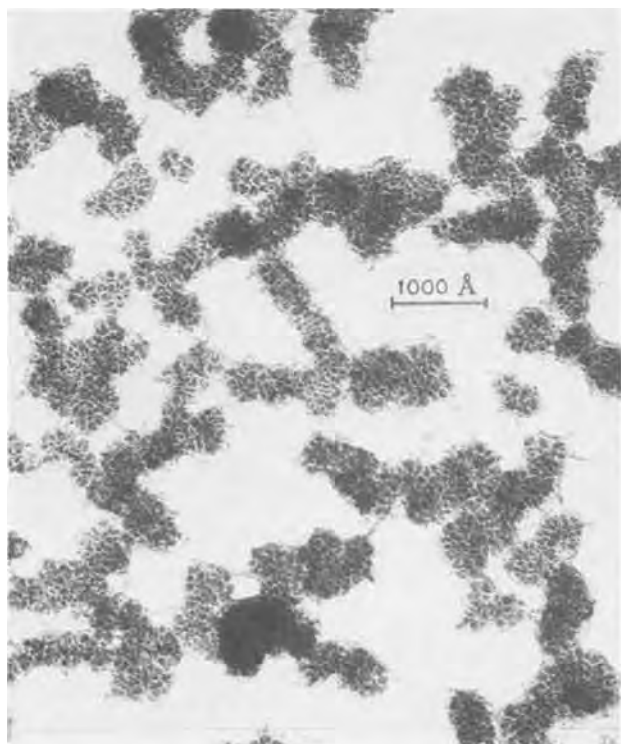


Fig. 3. Transmission electron micrographs of a thin film of Ni-B (a, left) freshly deposited (b, right) after heat-treatment at 400°C

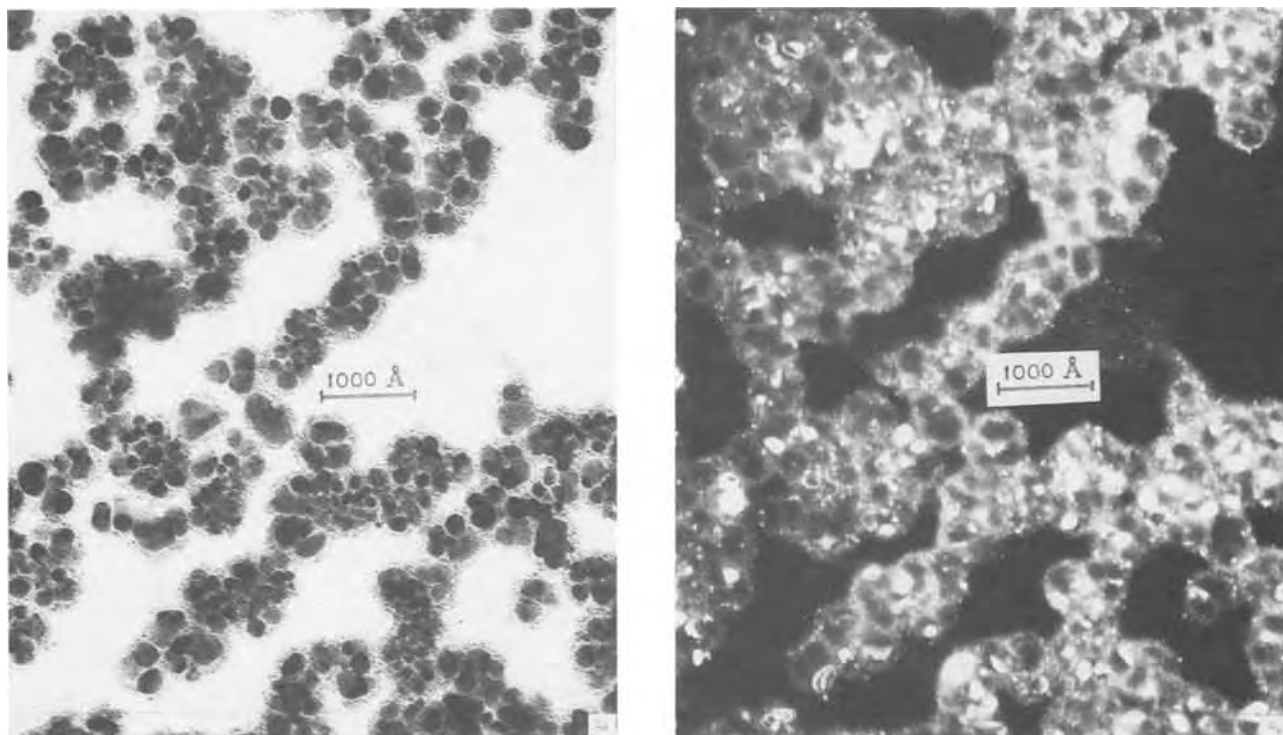


Fig. 4. Transmission electron micrograph of a thin film of Ni-B after heat-treatment at 400°C in (a, left) bright field mode (b, right) dark field (111) mode.

patterns obtained in the two cases are indistinguishable; they consist of a few very broad rings, characteristic of liquidlike or fine polycrystalline structures having essentially no long-range order.

A typical result obtained with improved sensitizer is shown in Fig. 2. The higher island density and uniformity of the deposit is evident, as is the tendency of the islands to join in clusters (10). The diffraction pattern obtained in this case shows sharper rings, some of which can be identified with a face-centered cubic structure.

The result of heat-treatment of Ni-B is a deposit consisting of small crystals. Diffraction patterns reveal clearly fcc structure with a lattice constant matching that of bulk nickel within our experimental error. No conclusive evidence for the presence of Ni₃B was found. This is presumably due to the fact that the diffraction intensity of the fcc nickel component is much greater than that of the small amount of boride formed in our annealing procedure. Electron diffraction studies of heat-treated Ni-P only revealed Ni₃P after annealing above 500°C (13), although the phosphide starts to form at 325°C. Figure 3 shows (a) freshly deposited Ni-B and (b) the same sample after heat-treatment. It appears that the cells within the islands have been replaced by crystallites of approximately the same size (typically 50Å) as the original cells. This trend has been seen in many other samples. Dark field microscopy shows even more clearly the presence of crystals ranging in size from 30 to 300Å. This can be readily seen by comparison of the bright and dark field micrographs shown in Fig. 4.

Electrical resistivity.—The results of measurements of the electrical resistivity of Ni-B and Ni-P films of various thicknesses are shown in Fig. 5. They are in general agreement with previous work on Ni-B (4) and Ni-P (14). The following observations can be made: (i) Within each system, the effect of heat-treatment appears to be a shift in resistivity which roughly preserves the shape of a curve drawn through the experimental points. This shift amounts to about 2 orders of magnitude for Ni-B over the thickness range studied, and 3-4 orders of magnitude for Ni-P. For thicknesses greater than 600Å, the resistivity of a Ni-B

film is about one order of magnitude greater than that of an equally thick Ni-P film. (ii) The transition from continuous films, indicated by the sharp rise in resistivity with decreasing thickness, occurs at about 500Å for Ni-B compared with about 250Å for Ni-P (14). The island size is comparable in the two systems under the same sensitization conditions, and it seems therefore likely that this effect is attributable to the internal structure of the Ni-B islands. If the islands are fragmented into cells, then a larger number of contacts between cells would be required to produce a drop in resistivity.

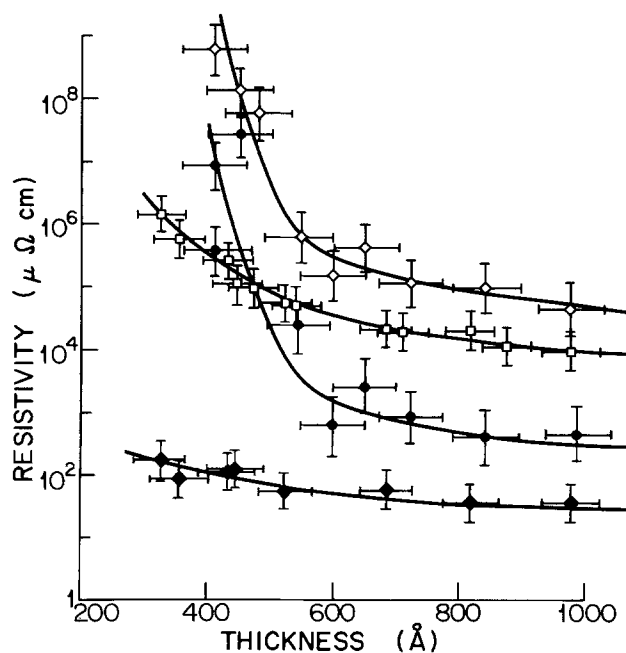


Fig. 5. Resistivity of films as a function of thickness: Ni-B \diamond freshly deposited; \bullet heat-treated at 400°C; Ni-P \square freshly deposited; \blacklozenge heat-treated at 400°C.

Acknowledgment

This work has been supported by the National Research Council of Canada. The research constitutes part of a M.Sc. thesis submitted by one of us (P.T.) to the University of Windsor.

Manuscript submitted June 24, 1974; revised manuscript received Jan. 29, 1975.

Any discussion of this paper will appear in a Discussion Section to be published in the June 1976 JOURNAL. All discussions for the June 1976 Discussion Section should be submitted by Feb. 1, 1976.

Publication costs of this article were partially assisted by the University of Windsor.

REFERENCES

1. W. Goldie, "Metallic Coating of Plastics," Vol. 1, Electrochemical Publications Ltd., London (1968).
2. J. Fléchon and F. Voiriot, *Bull. Soc. Chim. France*, **3**, 509 (1963).
3. J. Fléchon and F. Voiriot, *J. Phys.*, **24**, 767 (1963).
4. J. Fléchon and F. A. Kuhnast, *J. Chim. Phys.*, **69**, 1136 (1972).
5. Yu. N. Petrov, V. V. Kovalev, and M. M. Marcus, *Dokl. Akad. Nauk SSSR (Chem.)*, **198**, 389 (1971).
6. M. V. Ivanov, V. P. Moiseev, and K. M. Gorbunova, *Dokl. Akad. Nauk SSSR (Physical Chem.)*, **194**, 719 (1970).
7. K. M. Gorbunova, M. V. Ivanov, and V. P. Moiseev, *This Journal*, **20**, 613 (1973).
8. J. P. Marton and M. Schlesinger, *ibid.*, **115**, 16 (1968), and references therein.
9. J. Drake and M. Schlesinger, *Solid State Comm.*, **11**, 1597 (1972).
10. N. Feldstein, S. L. Chow, and M. Schlesinger, *This Journal*, **120**, 875 (1973).
11. N. Feldstein, M. Schlesinger, N. E. Hedgecock, and S. L. Chow, *ibid.*, **121**, 738 (1974).
12. L. J. van der Pauw, *Philips Res. Rept.*, **13**, 1 (1958); *Philips Tech. Rev.*, **20**, 220 (1968).
13. S. T. Pai, J. P. Marton, and J. Brown, *J. Appl. Phys.*, **43**, 282 (1972).
14. M. Schlesinger and J. P. Marton, *ibid.*, **40**, 507 (1969).

Catalytic Decomposition of Nitric Oxide on Zirconia by Electrolytic Removal of Oxygen

S. Pancharatnam, R. A. Huggins,* and D. M. Mason

Department of Chemical Engineering and Department of Material Sciences, Stanford University, Stanford, California 94305

ABSTRACT

Zirconia stabilized with 8 mole per cent of scandia has a very high oxygen ion conductivity and can "pump" oxygen from oxygen-bearing gases thus decomposing them. In this study the rate of decomposition of the air-pollutant species, nitric oxide, to harmless species (via the reaction: $2\text{NO} \rightarrow \text{N}_2 + \text{O}_2$) was found to be markedly catalyzed when a potential above 1V was applied across a zirconia disk coated with either a porous platinum or porous gold electrode. It is known that platinum can both form oxides and catalyze the decomposition of NO; whereas, gold does neither. The catalytic decomposition of NO on platinum metal is inhibited by O_2 , such behavior being attributed to preferential chemisorption of O_2 over NO as well as the possible formation of an inhibiting platinum oxide surface. The original rationale for this investigation was the possibility that the decomposition of NO might be enhanced if O_2 were electrolytically "pumped" away from a platinum electrode deposited on zirconia, keeping the platinum oxygen-free. However it was not anticipated that at high potentials dissociation rates a thousandfold that on nonporous platinum electrodes occur in the presence of either a platinum or gold porous electrode. No reactivity at all was observed on a nonporous gold electrode. These results suggest that catalysis occurs mainly on a surface other than the platinum or gold, namely, on the zirconia surface itself. It is proposed that F-centers on the zirconia surface formed by the applied potential are primarily responsible for the observed enhanced catalysis.

A number of studies (1-4) have shown that the catalytic decomposition of nitric oxide (NO) on platinum is markedly inhibited by oxygen. This behavior has been attributed to preferential chemisorption of O_2 over NO as well as possible formation of a surface oxide (3, 4). Recent development of solid oxide electrolytes possessing high oxygen ion mobility and relatively low electronic conductivity has made it possible to "pump" oxygen at very low concentrations ($<10^{-20}$ atm) by the application of an electrical potential. Therefore it was suggested and tested in a preliminary measurement (5), that by using platinum as the electrode material deposited on stabilized zirconia, O_2 might be removed electrochemically from the Pt surface leading to substantial enhancement of the rate of

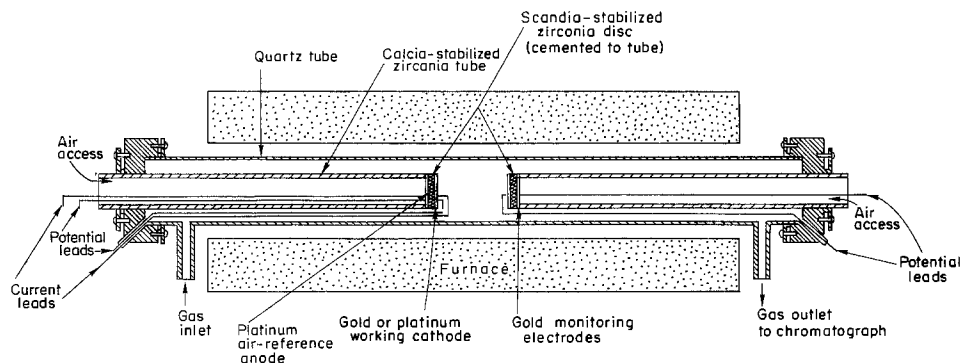
NO decomposition. The purpose of this paper is to present the results of more extensive experiments (6, 7) confirming the pumping of oxygen from NO along with some postulated reaction mechanisms. The wealth of information concerning the preparation, properties, and applications of solid electrolytes has been reviewed in numerous places (8, 9). Although the zirconia pump has been previously employed for the decomposition of oxygen-bearing gaseous compounds such as CO, CO_2 , and H_2O (11-13) it is believed that the present application relating to the enhancement of the catalytic activity of the zirconia itself by imposing an electrical potential and forming F-centers as active sites has not been reported.

Experimental Procedures

The apparatus used consisted of a high vacuum source (10^{-6} Torr) for purification of NO by distil-

* Electrochemical Society Active Member.
Key words: nitric oxide, solid electrolyte zirconia, air pollution, catalytic muffler.

Fig. 1. Zirconia reactor assembly.



lation with subsequent condensation and storage. The reactor-gas distribution system contained a gas-phase chromatograph for analyzing the product nitrogen formed by the decomposition of NO and details of design of this system are given elsewhere (7). The chromatograph used was a single column Varian Model A90-P3 with a thermal conductivity detector. The column was made of 1/4 in. OD \times 8 ft long stainless steel tubing hand-packed with 60-80 mesh Linde molecular sieve 13 \times . The column was preactivated at 250°C for 5 min with a rapid purge of helium at a flow rate of 120 ml/min and the optimal operating conditions were found to be as follows: the carrier gas helium was introduced at a flow rate of 30 ml/min while the reference flow rate was 6 ml/min; the filament current was maintained at 180 mA; the volume of samples was 0.75 ml; the temperatures of the distillation column, injector, and detector were 75°, 55°, and 100°C, respectively. A resolution of 50 ppm N₂ in 100% NO was possible, which set the lower acceptable limit on the conversion of NO, viz., 0.01% for pure NO and 1% for a mixture of 1% NO in helium.

The experimental observations consisted of measuring current-voltage characteristics at 600°-800°C for various concentrations of NO in the feed and for various gas flow rates. All electrical measurements were made on a Fluke 8200A digital voltmeter with an input impedance of 10¹⁴ ohm.

The reactor assembly is shown in Fig. 1. The working electrode consisted of a zirconia disk electrolyte with either platinum or gold deposited as electrode material. The monitor electrode system consisted of another zirconia disk with gold electrodes for measuring oxygen formed at the working electrode. The disks consisted of 8 mole per cent (m/o) scandia-stabilized zirconia of dimensions: 1 mm thick \times 12 mm diameter with a superficial area of 0.713 cm². The disk was cemented to one end of a calcia-stabilized zirconia supporting tube of dimensions 12.5 mm OD \times 300 mm long. This disk construction permitted easy application of electrode materials and facilitated inspection and characterization of the surface morphology by photomicrography prior to and after the experimental runs. Also by approaching the conditions of a continuous-flow differential reactor with uniform accessibility of reactants to the surface with negligible resistance to gas-phase mass transport, this disk-configuration allowed unambiguous chemical rate data to be obtained directly. In a practical system however such a configuration consisting of a series of ring-shaped electrode-electrolyte cells deposited on the outside of a porous zirconia tube with electrical interconnectors might more appropriately be employed. This design has been used for solid-state fuel cells for "burning" coal gases (14). Simplified kinetics and diffusion models for such tubular reactor systems under both laminar and turbulent flow regimes are available (7).

The extent of decomposition of NO on the cathode surface was determined coulometrically as well as by measuring the concentration of N₂ in the exit gas by chromatographic techniques. The polarization studies were restricted to currents less than 50 mA/

cm² and overpotentials less than 2V to avoid irreversible electrolysis of the zirconia. The influence on the over-all current-voltage characteristics of rate processes at the anode, with air being used as the reference oxygen-bearing gas, was negligible under the conditions of these experiments (7, 11).

Results

Nonporous platinum film cathode.—The cathodic polarization behavior for a 0.4 μ m thick nonporous sputtered platinum film electrode is shown in Fig. 2 for 700°C where current vs. overpotential, ($E-E^\circ$), is plotted. (E° is the open-circuit voltage, E the closed-circuit voltage.) The behavior at 600° and 800°C was qualitatively similar and complete experimental data are presented elsewhere (7). The straight thin line through the origin represents the measured ohmic cell resistance of 11 ohms at an alternating current frequency of 1000 Hz.

The current is simply related to the reaction rate by the relationship

$$I = 2A\rho Fr \quad [1]$$

where A = superficial electrode area, ρ = roughness

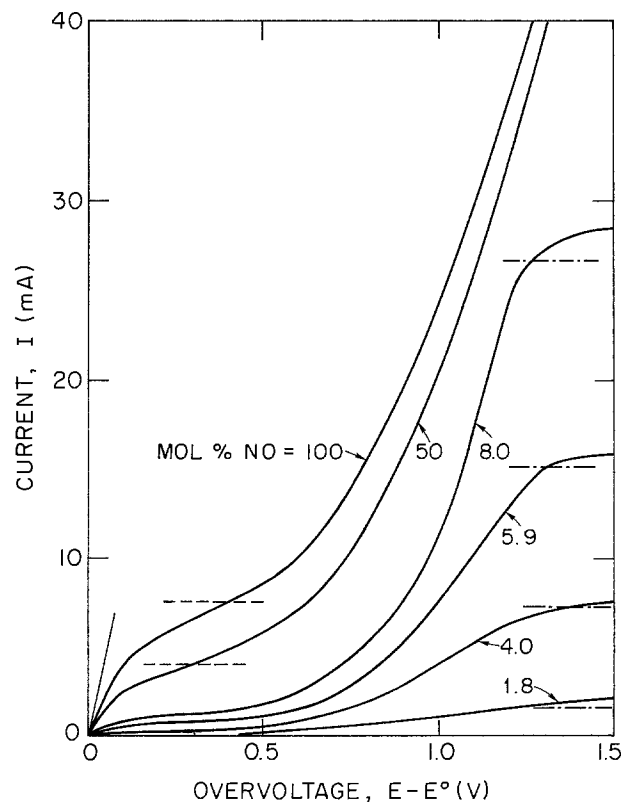


Fig. 2. NO decomposition on zirconia with a nonporous platinum cathode at 700°C. — 100 Hz (a.c.), - - - current equivalent based on nitrogen produced at open circuit, - · - · - current equivalent based on maximum constant nitrogen produced at overvoltages greater than 1.5V.

factor, and F = Faraday's constant. The number two is the equivalence for oxygen ion formation. The reaction rate (r) is given in mols NO/sec-cm².

Two sets of horizontal lines intersecting the curves have been included in Fig. 2. The left-hand set of lines intersecting the curves near the point of inflection represents the current calculated from Eq. [1] from the chromatographically measured rate of nitrogen produced by NO decomposition at open circuit. The right-hand set of horizontal lines represents the current equivalent to the observed rate of N₂ generated for overpotentials around 1.5V. It should be noted that these latter lines are below the plateaus of current observed in Fig. 2. It is evident that there are two reaction-rate limiting processes represented by the two sets of lines. The limiting current at the lower overpotentials and high NO concentration was generally ill-defined resulting in a point of inflection, though definite plateaus occurred at lower NO concentrations. Plateaus at the higher overpotentials are evident for all concentrations. The fractional conversion of NO was generally less than 1% and the influence of gas flow rate (50-100 ml/min) on the I vs. $E-E^\circ$ behavior was inappreciable, demonstrating that the process is not affected by gas phase mass-transfer rates. The O₂ concentration measured by the downstream gold electrodes varied between 10⁻³-10⁻⁴ atm at zero current and 10⁻⁵-10⁻⁶ atm at potentials greater than 1V.

The relationship between the measured N₂ production rate and the measured electrical current (or its equivalent in terms of O₂ pumped) calculated from Eq. [1] for the data in Fig. 2 is shown in Fig. 3, which is typical of all runs. The line of unit slope represents the equivalence, in accordance with Eq. [1] between coulombs passing through the electrolyte and O₂ (or N₂) produced at the surface. The deviations to the left of this line which can be seen at low currents (and potentials) and high NO concentrations indicate a condition where not all of the O₂ formed by the decomposition of NO is electrochemically removed. The rate of production of O₂ (or N₂) rises slightly in approaching the equivalence line. This behavior is depicted in a different fashion by the left-hand set of horizontal lines in Fig. 2.

The deviations to the right of the equivalence line in Fig. 3 occur at the lower NO concentrations with

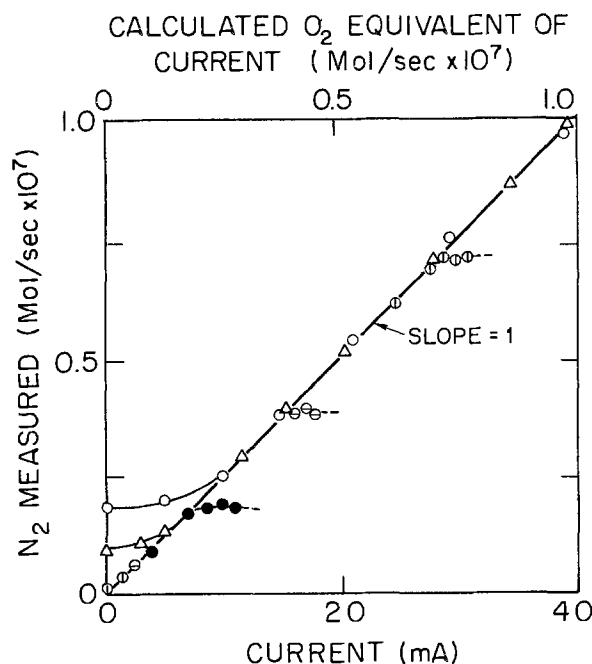


Fig. 3. Test of the equivalence of N₂ produced on nonporous platinum on zirconia vs. current at 700°C. Mole per cent NO in feed: ○, 100; △, 51; ⊙, 8; ⊖, 6; and ●, 4.

high currents (and potentials). This behavior is probably due to the contribution of a measurable amount of electronic current added to the O₂-pumping current. In Fig. 2 this behavior is seen in the deviation of the right-hand set of horizontal lines from the plateaus. These lines represent a process limited by the maximum inherent rate of reaction of NO decomposition on oxygen-free platinum. These two current limiting phenomena will now be further analyzed.

Behavior at low overpotentials.—Since the low voltage saturation current shows a good correlation with the rate of NO decomposition at zero potential (and current), the rate has been plotted in Fig. 4 vs. the concentration of NO in the feed. Owing to the insensitivity of the chromatographic analysis of N₂, the rate of decomposition could be precisely determined only for NO concentrations of the order of 10 m/o or greater. The straight lines drawn through the origin in Fig. 4 represent the reaction rate calculated from the rate expression given in (3) with $P_{O_2} \rightarrow 0$

$$r_1 = \frac{k[\text{NO}]}{1 + KP_{O_2}} \quad [2]$$

where

$$k = 8.1 \exp\left(\frac{-17,100}{RT}\right) \text{ cm sec}^{-1} \quad [2a]$$

and

$$K = 13.9 \exp\left(\frac{6600}{RT}\right) \text{ atm}^{-1} \quad [2b]$$

The points represent the open-circuit decomposition rates determined by the chromatographic measured rate of formation of N₂.

Because of the small superficial area of the disk electrodes it was impossible to determine the surface area by any conventional means such as BET adsorption measurements. Thus the NO rate data from (3) with known surface areas were used for the oxygen saturated electrodes in this study. The surface roughness factor (ρ) for the present data was used as an adjustable parameter to give agreement with (3) and a value of $\rho \cong 3$ fits the data well.

Behavior at high overvoltages.—The high overvoltage limiting current plateaus displayed in Fig. 2 are represented on a log-log scale in Fig. 5 where limiting current, I_1 is plotted vs. NO concentration in the exit gas which was approximately equal to that in feed gas owing to the low conversions that occurred. The data are well approximated by straight lines of slope 2 which indicates that the rate-determining step has a second order dependence on NO. Except for the deviations from this behavior at high concentrations of NO, a rate expression of the form

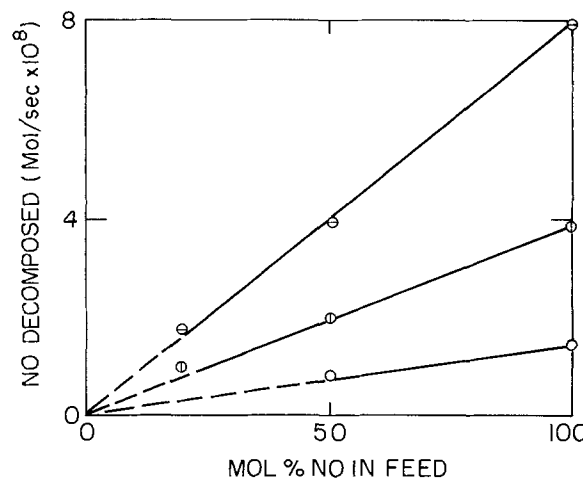


Fig. 4. Rate of decomposition of NO on nonporous platinum-coated zirconia for open circuit, ○ 600°C; ⊙ 700°C; ⊖ 800°C (roughness factor of 3 assumed). -- Data from Ref. (3).

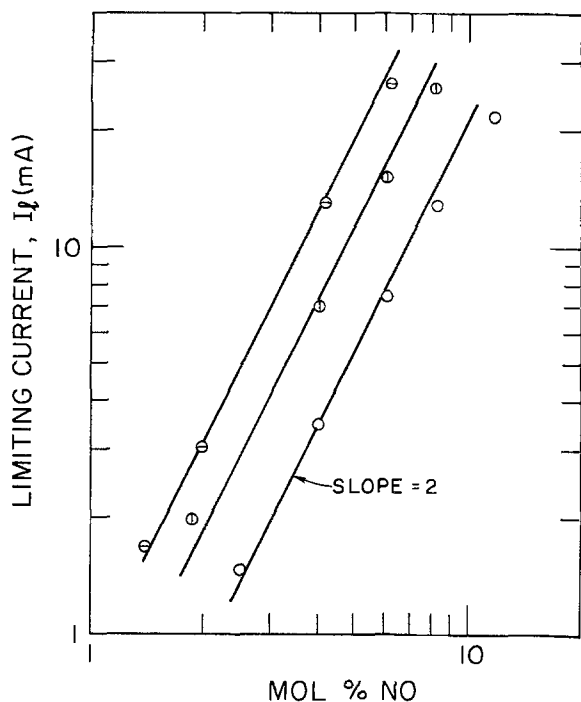


Fig. 5. Limiting current equivalent to maximum N_2 produced on zirconia with nonporous platinum electrode at overpotential $> 1.5V$. \circ $600^\circ C$; \odot $700^\circ C$; \ominus $800^\circ C$.

$$\tau_{II} = k_2[NO]^2 \quad [3]$$

may be used. An Arrhenius plot of $\log k_2$ vs. $1/T$ shown in Fig. 6 yields the following expression for k_2

$$k_2 \left(\frac{cm^4}{mol \cdot sec} \right) = 5.05 \times 10^8 \exp \left(\frac{-17,000}{RT} \right) \quad [4]$$

Since diffusion of oxygen through platinum has been shown to have an activation energy of 35-60 kcal/mol (14), the low activation energy for k_2 rules out a diffusion-controlling mechanism. It will be shown subsequently that the high voltage behavior corresponds to the dissociation of NO on oxygen-free platinum.

Porous platinum electrodes.—The cathodic current overvoltage characteristics shown in Fig. 7 were typical for temperatures of $700^\circ C$ and greater. The limiting current shown as the left-hand set of horizontal dashed lines are equivalent to the open current N_2 production rate. As was the case of the nonporous film electrode data (Fig. 2), the low-potential current saturation is again noticeable either as points of inflection at high NO concentrations or as plateaus at low NO concentrations. However (as seen by com-

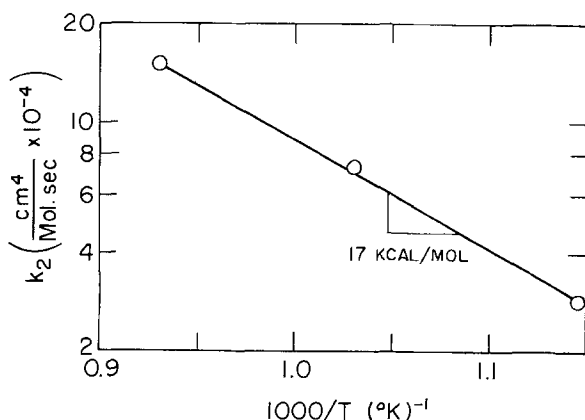


Fig. 6. Second order NO decomposition rate coefficient on zirconia with nonporous Pt electrode vs. $1/T$. (Roughness factor $\cong 3$.)

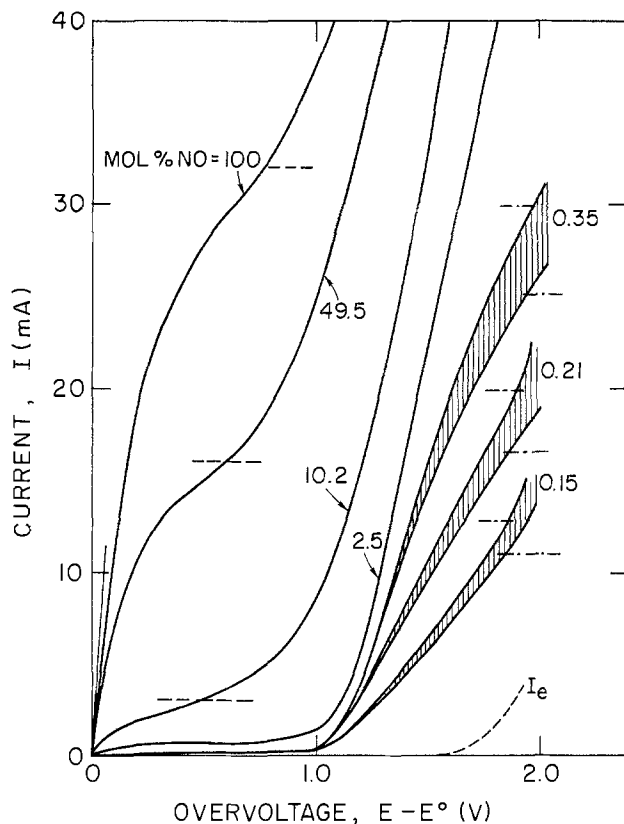


Fig. 7. NO decomposition on zirconia coated with porous platinum at $800^\circ C$. (Shaded area represents influence of flow rate, 80-100 ml/min.) — (1000 Hz a.c.), - - - current equivalent based on nitrogen produced at open circuit, — — — current equivalent based on nitrogen produced at high overvoltages.

paring Fig. 2 and 7) in contrast with the case of the nonporous platinum electrode, the current at high overvoltages increases continuously with increasing overvoltage and merges with the electronic transport curve I_e without exhibiting a plateau. From the measured rate of N_2 generation, the current equivalents for high overpotentials are shown in the right-hand set of horizontal lines in Fig. 7. The striking feature of the porous electrode is the extremely low concentration of NO in the feed gas at which extremely high decomposition rates have been observed. The effect of gas flow rate (80-100 ml/min) evidenced in Fig. 7 is predominantly due to the high rates of decomposition and high conversions of NO ranging from 40-70%. It is believed that under these conditions the cathode no longer behaves as a differential reactor and also mass transfer in the gas phase may be influencing the process, resulting in the observed increase in current with increasing flow rate.

Porous Pt electrode at low overpotentials.—The low potential limiting behavior was analyzed by comparing the zero-current rate of decomposition of NO with the rate expression given in Eq. [2]. As in the case of nonporous Pt, the agreement was found to be satisfactory when a roughness factor of about 6 was employed.

Porous Pt electrode at high potentials.—A plot of the equivalent high potential limiting current vs. concentration of NO in exit gas is shown in Fig. 8. Despite the scatter in the data, a first order dependence of I_l on $[NO]$ is indicated over the experimental range of NO concentrations. The corresponding value of the first order rate constant k , has been shown in Fig. 9 as a function of $1/T$ which gives an approximate expression for k_1

$$k_1 (cm \cdot sec^{-1}) \cong 4.7 \times 10^5 \exp \left(\frac{-25,500}{RT} \right) \quad [5]$$

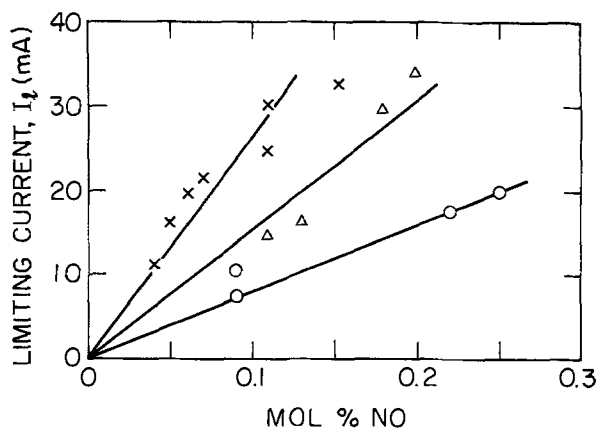


Fig. 8. Limiting current equivalent to maximum N_2 produced on zirconia with porous platinum electrode at high overvoltages (Δ 1.5V). \circ , 700°C; Δ , 750°C; \times , 800°C.

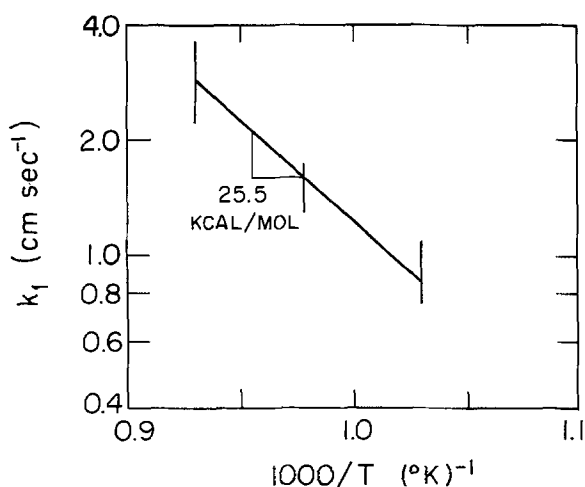


Fig. 9. k_1 , first order NO decomposition rate coefficient on zirconia with porous platinum electrode vs. $1/T$ (roughness factor \approx 6).

The experimental difficulties associated with the relatively high rates of reaction and poor sensitivity of chromatographic analysis for low concentrations of NO and N_2 have resulted in a rather small operating range of temperatures and NO concentration.

Nonporous and porous gold electrodes.—The cathodic behavior of porous gold at 800°C is shown in Fig. 10. No limiting current or limiting decomposition rates were observed in the whole range of overpotentials investigated. The current was found to be essentially ionic over the range shown and decomposition of NO at open circuit was negligible, indicating neither the gold nor zirconia is catalytic. No ionic current or NO decomposition was observed at any potential for a nonporous gold electrode, confirming the noncatalytic nature of gold with respect to NO decomposition. Appreciable ionic current was, however, obtained when the originally nonporous electrode surface was scored to expose the zirconia, thus strongly supporting the hypothesis that an enhanced catalytic decomposition of NO occurs on the zirconia surface itself.

Discussion of Results

NO decomposition on nonporous Pt.—It is speculated that the high potential limiting process represents the decomposition of NO on a clean platinum surface, uncontaminated with oxygen, obeying the following Rideal-Eiley mechanism found to apply to nonelectrochemical catalysis (4)

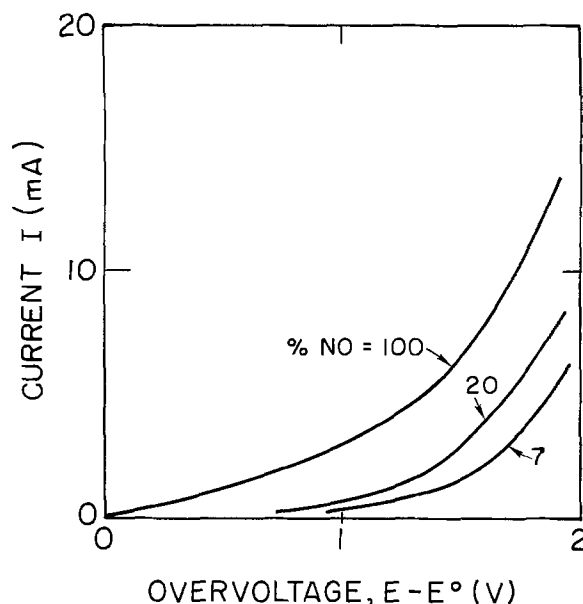
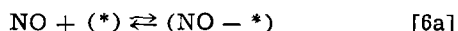
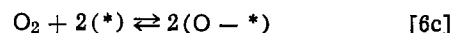


Fig. 10. NO decomposition on zirconia with a porous gold electrode. (Flow rates varied between 40 and 80 ml/min.)

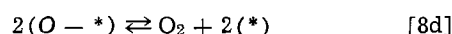
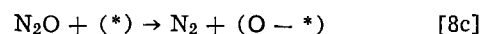
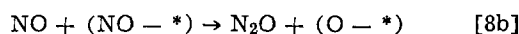
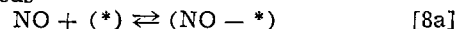


where (*) denotes an adsorption site on the Pt surface and $(NO - *)$ and $(O - *)$ represent respective species adsorbed on a site. Steps [6a] and [6c] are assumed to be at equilibrium and step [6b] is rate determining. The exact nature of all the processes involved in step [6b] cannot be determined from these experiments, but some speculation will be subsequently made. The rate expression for the above reaction scheme with a constant number of total sites [$* + (NO - *) + (O - *)$] is

$$r_{II} = \frac{k_2[NO]^2}{1 + K_1[NO] + K_2[O_2]^{1/2}} \quad [7]$$

Equation [7] reduces to Eq. [3] for low fractional coverage of active sites by NO, i.e., ($K_1[NO] \ll 1$) and for $[O_2] \rightarrow 0$.

The rates of decomposition of NO on Pt observed by various techniques are compared in Fig. 11 in terms of "turnover number," (molecules of NO reacting per surface site per second) based on a nominal value of 10^{15} sites/cm². For comparison with Ref. (3) the data of various batch studies have been extrapolated to 48 Torr using first order kinetics. This assumption is reasonable because at the high concentrations of NO actually used in the batch studies (400-2000 Torr) first order kinetics were closely obeyed (e.g., $1 \ll K_1[NO]$ in Eq. [7]). Two sets of results were reported in Ref. (3); the lower rates (curve 6 with rate expression Eq. [2]) were observed when O_2 was fed along with NO, and the higher rates (curve 7) correspond to O_2 -free gas feeds, but with 0.1-0.3% O_2 generated by the decomposition of NO. Both of these rates had been extrapolated to zero O_2 concentration. The following mechanism was proposed in Ref. (3) for the case of O_2 -free gas feeds



Steps [8a] and [8d] were assumed to be in equilibrium; step [8b] was assumed to be rate determining. For total sites equal to [$* + (NO - *) + (O - *)$] this mechanism leads to a rate expression identical to

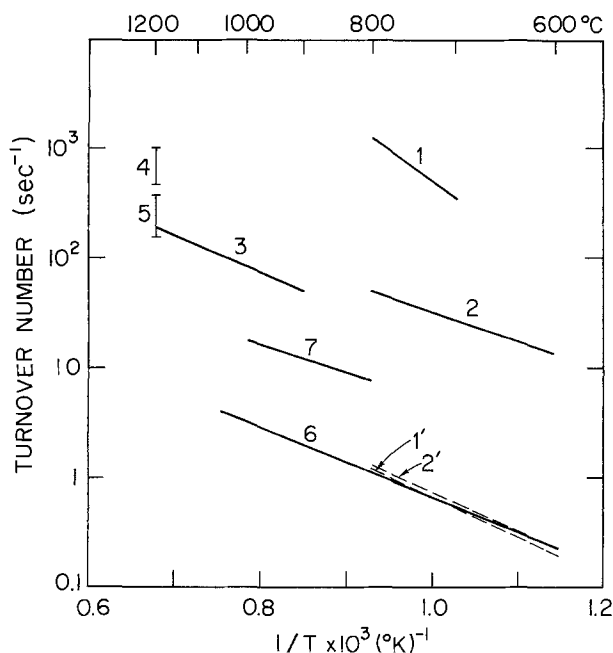


Fig. 11. Summary of data on turnover for NO decomposition on platinum at 48 Torr. 1', porous Pt, open circuit; 2', nonporous Pt, open circuit. Curve 1, porous Pt maximum rate of N₂ formation corresponding to clean platinum and F-center catalysis. Curve 2, nonporous Pt maximum rate N₂ formation corresponding to clean platinum surface. Curve 3, heated Pt wire [Ref. (4)]. Curve 4, heated Pt wire [Ref. (2)]. Curve 5, Heated Pt wire [Ref. (1)]. Curve 6, [Ref. (3)] Pt foil with O₂ in feed extrapolated to zero (O₂). Curve 7, [Ref. (3)] Pt foil without O₂ in feed extrapolated to zero (O₂).

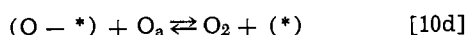
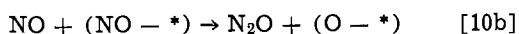
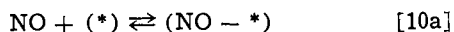
Eq. [7]. If the assumption is made that (NO - *), (O - *) >> (*) or the total sites are equal to (NO - *) + (O - *), the resulting rate expression is

$$r_{II} = \frac{k[\text{NO}]}{1 + K[\text{O}_2]^{1/2}/[\text{NO}]} \quad [9]$$

For (O₂) → 0 this rate expression leads to first order kinetics with respect to NO. The agreement between the results of electrochemical studies with Pt and the various batch studies is quite good. The lower rates observed in the study of Ref. (3) even for O₂-free gas feeds may be attributed to appreciable coverage of the active sites by oxygen owing to the relatively large conversion of NO to O₂ in the region of the catalyst. This hypothesis is supported by the reported nature of chemisorption of O₂ on Pt (16-18).

NO decomposition with porous Pt.—The high rate of decomposition of NO observed at high overpotential which characterizes porous Pt leads one to believe that an entirely different mechanism of NO decomposition occurs than in the case of nonporous Pt.

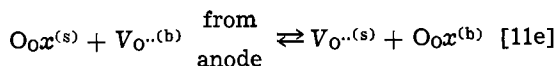
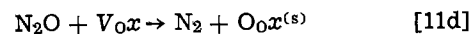
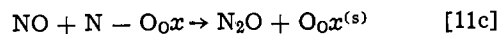
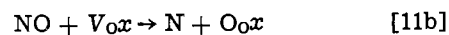
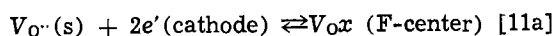
The decomposition of NO on metal oxides has been studied extensively (3) and a catalytic sequence of five steps with similarity to Eq. [8a]-[8d] for oxygen free feed can be speculated



where O_a represents a mobile surface-O atom. The rate expression found experimentally was unimolecular in NO, identical to Eq. [2], which may be obtained from the above reaction sequence along with the assumptions that: step [10a] is irreversible; step [10d] is in

quasi-equilibrium; the concentration of mobile oxygen O_a is constant; and [*], [O - *] >> [NO - *], or the total site concentration equals [*] + [O - *]. The activation energy for *k* (Eq. [2]) ranged from 20 to 30 kcal/mol with a value of 28 kcal/mol being reported for pure zirconia, which was also reported by Fraser and Daniels (18). From the dissociation energies of NO (151 kcal/mol) and NO⁻ (112 kcal/mol) it was argued (3) that the active site (*) is probably an oxygen ion vacancy with at least one trapped electron, i.e., an "F-center."

Taking into consideration the injection of electrons from the cathode and transport of vacancies from the anode, the following modified electrocatalytic sequence is proposed



where V_O· = a vacant oxygen ion; e' = an electron; V_{Ox} = an oxygen ion vacancy with two trapped electrons; O₀x = a normal oxygen ion; and the superscripts (s) and (b) denote lattice positions in the surface and in the bulk of the electrolyte, respectively. Under the influence of an impressed potential, the exchange step [11e] would be driven toward the right, thus leading to an acceleration of the steps [11c] and [11d]. Hence as in the case of a nonelectrochemical reaction, step [11b] would be the rate-determining step for the over-all decomposition. Assuming a high concentration of F-centers sustained by an applied potential, the surface average concentration of (NO) and (O) may be neglected with total sites equal to V_{Ox} and the following rate expression resulting

$$r_{III} = k'[\text{V}_{\text{Ox}}][\text{NO}] = k''[\text{NO}] \quad [12]$$

The rate is proportional to the surface concentration of F-centers which would increase with increasing cathodic applied overpotential. From Eq. [1] and [12] one would expect a continuous increase of current with overpotential until all of the NO in the feed has been decomposed. In reality migration of electrons and F-centers to the anode can occur before this limit is reached and thus set an apparent upper limit on the value of *k*'. The activation energy for *k*' observed in the current experiments (25.5 ± 5 kcal/mol) shows a fair agreement with that found in (3) supporting the belief that the nature of active sites and the rate-controlling step are probably the same in both the studies.

An interesting study of the nonstationary state behavior of metal oxides was made in (3). In the absence of oxygen presaturation, initial decomposition rates 6-10 times greater than the steady-state values were reported. This behavior was explained by postulating higher concentration of F-centers generated on the surface when the catalyst was flushed with pure helium. In other words a partially reduced surface seems to result at very low concentration of O₂ in the gas. The turnover numbers (Fig. 12) reported in (3) for zirconia at 400-1000°C seem to be lower than the values in the current study by 6-8 orders of magnitude. The reaction rates observed in the electrochemical experiments can be satisfactorily explained by assuming that only 1% of the surface sites have been converted to F-centers and the sticking probability for the adsorption of NO on an F-center is about 0.01. Association of catalytic activity with surface defects has been confirmed in recent studies on ZnO (20) and d-band perovskites (21). The hypothesis that the surface of zirconia can be made active to NO decomposition by applying an electrical potential is also confirmed quali-

tatively by the studies on a gold cathode. The results of the gold experiments, however, could not directly be compared quantitatively with those on porous Pt because of the lack of identical electrode morphology and due to the catalytic action of Pt which dominates the current-potential behavior at high NO concentrations and low potentials.

Conclusion

Decomposition of NO on nonporous Pt with electrolytic removal of O₂ reinforces the previous observation that the presence of O₂ not only inhibits the decomposition of NO but also alters the kinetic behavior. A second order rate mechanism observed in the present study is in agreement with the previous findings from batch as well as continuous flow experiments.

The feasibility of altering the catalytic activity by controlling the oxygen concentration has been established in another way. The tremendous enhancement of the rate of NO decomposition in the case of either porous platinum or gold demonstrates a convenient and powerful technique of reducing oxygen bearing species, *viz.*, the injection of F-centers on the surface of the electrolyte at sufficiently high overpotentials. This mechanism is supported by the following facts: (i) catalytic enhancement for zirconia covered with a nonporous layer of platinum is that typical for pure platinum in a nonelectrolytic system and (ii) with nonporous gold electrodes no decomposition occurs at all, typical of gold in a nonelectrolytic system. From these observations it may be concluded that any non-noble metal porous electrode could be chosen for dissociating NO on zirconia in the presence of F-centers.

A summary of the general behavior of the zirconia electrochemical system is as follows:

1. For low potentials (0-0.5V) the rate of decomposition of NO with both porous and nonporous platinum electrodes is found to be first order with respect to NO consistent with the reported rate data for "O₂-saturated" platinum metal catalysts.

2. For nonporous Pt films the limiting current at higher potentials (1.3-1.6V) corresponds to the second order rate of decomposition of NO mixtures containing 5-10 m/o NO reported for O₂-free platinum. These rates are about fiftyfold higher than on oxygen saturated platinum surfaces.

3. On either porous platinum or porous gold surfaces, at potentials around 1.5V, first order rates of the order of a thousandfold that in case 1. are obtained, owing to the presence of highly catalytic F-centers on the zirconia surface.

Remaining to be studied systematically is the porous electrode configuration with carefully controlled electrode morphology and surface areas. Also to permit unambiguous kinetics data the disk electrode system should be redesigned so that reactant gases strike the electrode surface head-on, thus increasing mass-transfer rates and insuring at high reaction rates that the reactor behaves differentially with uniform accessibility to reactant species.

Acknowledgment

The authors are grateful for the support of the Environmental Protection Agency (Grant No. 5R01 801337) which made this investigation financially feasible.

Manuscript submitted July 30, 1974; revised manuscript received Feb. 26, 1975. This was Paper 334 presented at the San Francisco, California, Meeting of the Society, May 12-17, 1974.

Any discussion of this paper will appear in a Discussion Section to be published in the June 1976 JOURNAL. All discussions for the June 1976 Discussion Section should be submitted by Feb. 1, 1976.

Publication costs of this article were partially assisted by Stanford University.

REFERENCES

1. T. E. Green and C. N. Hinshelwood, *J. Chem. Soc.*, **129**, 1709 (1926).
2. P. W. Bachman and G. B. Taylor, *J. Phys. Chem.*, **33**, 447 (1929).
3. A. Amirnazmi, Ph.D. Thesis, Stanford University (1973). Also A. Amirnazmi, J. E. Benson, and M. Boudart, *J. Catal.*, **30**, 55 (1973).
4. S. Pancharatnam, K. Lim, and D. M. Mason, *Chem. Eng. Sci.*, Accepted for publication (1975).
5. S. Wittingham and R. A. Huggins, Private communication.
6. S. Pancharatnam and D. M. Mason, Paper presented at the 39th Annual Chemical Engineering Symp. of Am. Chem. Soc., Chicago, Illinois (Jan. 1973).
7. S. Pancharatnam, Ph.D. Thesis, Stanford University (1974).
8. T. H. Etsell, and S. M. Flengas, *Chem. Rev.*, **70**, 339 (1970).
9. Per Kofstad, "Non-Stoichiometry, Diffusion and Electrical Conductivity in Binary Metal Oxides," Wiley-Interscience, New York (1972).
10. S. Wittingham and R. A. Huggins, Paper presented at the 5th Materials Research Symp., N.B.S., Gaithersburg, Md. (Oct. 1971).
11. T. H. Etsell and S. M. Flengas, *This Journal*, **118**, 1890 (1971).
12. J. Weissbart, W. H. Smart, and T. Wydeven, *Aerospace Med.*, **40**, 136 (1969).
13. J. Weissbart and W. H. Smart, Abstract 37, p. 92, The Electrochemical Society Extended Abstracts, Fall Meeting, Atlantic City, N. J., Oct. 4-8, 1970; W. H. Smart and J. Weissbart, Abstract 38, p. 99, *ibid.*
14. E. F. Sverdrup, C. J. Warde, and R. L. Eback, *Energy Conversion*, **13**, 129 (1973).
15. J. E. Bauerle, *J. Phys. Chem. Solids*, **30**, 2657 (1969).
16. H. L. Grüber, *J. Chem. Phys.*, **66**, 48 (1972).
17. V. S. Boronin, V. S. Nikulina, and O. M. Poltorak, *Russ. J. Phys. Chem.*, **41**, 1443 (1967).
18. G. R. Wilson and W. K. Hall, *J. Catal.*, **24**, 306 (1972).
19. J. M. Fraser and F. Daniels, *J. Phys. Chem.*, **62**, 215 (1958).
20. J. D. Levine, A. Willis, W. R. Bottoms, and P. Mark, *Surface Sci.*, **29**, 144 (1972).
21. F. J. Morin and T. Wolfram, *Phys. Rev. Letters*, **30**, 1214 (1973).

Electrochemical and Spectroscopic Properties of Cation Radicals

III. Reaction Pathways of Carbazolium Radical Ions

James F. Ambrose,^{*1} Lawrence L. Carpenter,² and Robert F. Nelson
Department of Chemistry, University of Georgia, Athens, Georgia 30602

ABSTRACT

Previous work had elucidated the anodic oxidation pathways of carbazole and several N-substituted derivatives. These studies have now been extended to seventy-six ring-substituted carbazoles using electrochemical and spectroscopic techniques to study the reactivity of the various substituted carbazole cation radicals. Generally, it was found that 3, 6, and 9 (N) positions are extremely reactive; if these sites are not blocked by inert substituents the cation radicals generated by electrolytic oxidation react rapidly via coupling-deprotonation. In some cases, substituents are eliminated from the 3 and 6 positions in the cation radicals followed by coupling to form substituted bicarbazyls. In other cases, relatively stable cation radicals were obtained and their EPR and visible absorption spectra were recorded. It was found that the reactivities of substituted carbazole cation radicals are considerably greater than those of analogous di- and triphenylammonium ions due to the planarity of the carbazole aromatic rings.

Carbazole, a relatively unimportant molecule in the past, is of considerable interest at present due to the uses of substituted carbazoles in polymerization studies and as inhibitors of zoxazolamine-induced paralysis (1). In addition, polycyclic carbazoles have been established as carcinogenic agents by a number of workers (2-4) and methyl-substituted carbazoles have been isolated from cigarette smoke (5, 6). Since the carcinogenic activity of these molecules may be associated with their redox properties, and considering that present and future studies may verify the presence of other substituted carbazoles in our environment, it was deemed desirable to carry out a broad survey of the anodic oxidation pathways of a number of variously substituted carbazoles. Due to solubility problems, these studies were limited to nonaqueous media, namely acetonitrile. This work is also designed to serve as a basis for investigating the oxidation behavior of simple and biologically important indoles. Preliminary work has shown that indole and its derivatives are extremely reactive upon anodic oxidation, so it was hoped that a good deal of background knowledge could be obtained from studies of the less reactive carbazoles. Due to the large number of compounds involved, substitution patterns as well as substituent effects upon the reaction pathways of the carbazole cation radicals were generally elucidated; however, several compounds have been incompletely characterized and so full disclosure must await further, more detailed investigations. Because of this survey nature, considerable license has been taken with regard to speculation on the mechanisms and products involved; on-going studies will hopefully refute or verify these speculations but in any case it is felt that the ideas forwarded are at least plausible and often likely.

Previous work had established that carbazole, upon anodic oxidation, forms a very unstable cation radical that reacts via coupling-deprotonation to 9,9'- and 3,3'-bicarbazyls;³ higher polymers were thought to form

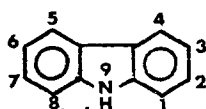
^{*} Electrochemical Society Student Member.

¹ Present address: Department of Chemistry, University of Kansas, Lawrence, Kansas 66044.

² Undergraduate Research Fellow, Sacramento State College, Sacramento, California 95819.

Key words: carbazole, anodic oxidation, electrosynthesis, cation radicals.

³ We are employing the traditional carbazole nomenclature where the nitrogen is numbered "9" as opposed to the standard heterocyclic numbering where N is "1". The ring carbons are numbered clockwise, with the bridge-head carbons omitted.



upon prolonged electrolysis (8). When alkyl or phenyl groups were placed on the carbazole nitrogen only the corresponding 3,3'-bicarbazyls formed, in quantitative yields, and they appeared to be quite stable under electrolytic conditions. These findings were in agreement with previous work on the chemical oxidations of carbazole and its derivatives (8-13).

There is a paucity of data available in the literature on the chemical oxidation pathways of ring-substituted carbazoles; however, chemical substitution reactions indicate that the active ring sites are the two positions *para* to the nitrogen (3 and 6) and, to a lesser extent, those *ortho* to it (1 and 8). It was anticipated that by blocking the 3, 6, and 9 positions relatively stable cation radicals would be formed; these could then be studied using EPR as a probe to elucidate the electron distribution in the cation radicals. It was found that the carbazole nucleus is so reactive, in fact, that upon oxidation normally inert substituents undergo unusual decomposition reactions in several cases. Some success was achieved in the EPR and visible absorption spectral studies of the primary cation radicals, however, and the preliminary results are reported herein, along with the electrochemical data on these interesting and sometimes piquant molecules.

Experimental

All of the electrochemical studies were carried out in acetonitrile (MeCN) using tetraethylammonium perchlorate (TEAP) as supporting electrolyte. Purifications of these materials, as well as the general instrumentation employed, have been previously described (7).

Throughout this paper radical stabilities are cited as half-lives; these are estimates from cyclic voltammograms taking into account voltage sweep rates and cathodic to anodic peak current ratios. The uncertainty in the values is estimated at ± 10 -20%.

Rotating disk studies were performed with a 10,000 rpm Motomatic E-550 motor and E-550M master control unit using the rotoamperometric technique for rapid data collection (14). Evaluation of coupling rate constants were carried out at low concentrations (10^{-4} to 10^{-5} F), so all rotoamperograms were corrected for background currents. A previously published working curve was employed for the determination of numerical values for the coupling rate constants (15).

Electrochemical n values were obtained using a Wenking 61RH potentiostat and a digital coulometry assembly employing two counters, one for gating, and one for totalizing (16). The gating counter was found

to be very useful for following the course of the decaying electrolysis current; chemical complications in the electrochemical processes were immediately apparent using this sensitive technique. Most of the n -value determinations were carried out at parent concentrations of 10^{-3} to 10^{-5} F. At these levels the electrolyses were found to be extremely sensitive to impurities in the MeCN and TEAP. Therefore, both solvent and supporting electrolyte were freshly prepared before coulometry experiments. If these precautions were not taken, n values that were found to be about 2.0 under proper conditions varied up to values as high as 5 to 7 and even then low steady-state currents were often obtained.

Preparative electrolyses.—Preparative electrolyses were effected using a home-built potentiostat designed to deliver ± 70 V, ± 3 A. Typically, 100 mg of the carbazole derivative was dissolved in 150 ml MeCN/0.1F TEAP and exhaustively electrolyzed at a large platinum gauze at a potential 200 mV past the anodic peak current voltage. The reference electrode was a SCE and the auxiliary was a carbon rod contained within a porous ceramic cup. The solution was then rereduced at -0.7 V to convert any products to the neutral form and reduce off protons liberated in the coupling reactions. Electrolysis solutions were then taken to dryness by evaporation of the solvent (ambient conditions) and the residue was partitioned with benzene/hot water mixtures. The benzene layer was concentrated by evaporation and chromatographed on Woelm neutral alumina. The products were then recrystallized from the appropriate solvent mixture.

Electrolyses were carried out on compounds from each major group where radical reaction pathways were detected. For the 3- and 3,6-disubstituted carbazoles intractable mixtures were obtained following electrolysis in unbuffered MeCN, but in the presence of the organic base 2,4,6-trimethylpyridine good yields of the corresponding N,N'-coupled products could be isolated. Pertinent data are given below for the various classes of compounds.

3-Methylcarbazole.—100 mg was oxidized in the presence of 2,4,6-trimethylpyridine (threefold molar excess) at 1.3V to 3,3'-dimethyl-9,9'-bicarbazyl (87% yield), recrystallized from benzene/EtOH as off-white crystals, mp 176° - 178° . Calculated for $C_{26}H_{20}N_2$: C, 86.7; H, 5.55; N, 7.78. Found: C, 86.5; H, 5.62; N, 7.74.

3-Fluoro-N-Ethylcarbazole.—100 mg was oxidized in MeCN/0.1F TEAP at 1.4V to 3,3'-difluoro-N,N'-diethyl-6,6'-bicarbazyl (86% yield), recrystallized from benzene/EtOH as pale yellow flakes, mp 201° - 203° . Calculated for $C_{28}H_{22}N_2F_2$: C, 79.2; H, 5.24; N, 6.60. Found: C, 79.2; H, 5.26; N, 6.63.

3,6-Dibromocarbazole.—100 mg was oxidized in the presence of a threefold molar excess of 2,4,6-trimethylpyridine in MeCN/TEAP at 1.5V to 3,3',6,6'-tetrabromo-N,N'-bicarbazyl (93% yield), recrystallized from benzene/EtOH as small white cubes, mp 248° - 250° [Ref. (9) 248° - 250°].

N-(p-Methoxyphenyl)carbazole.—100 mg was oxidized in MeCN/TEAP at 1.4V to N,N'-bis (p-methoxyphenyl)-3,3'-bicarbazyl (88% yield), recrystallized from benzene/hexane as a cream colored amorphous solid, mp $> 275^{\circ}$. Calculated for $C_{38}H_{28}N_2O_2$: C, 83.7; H, 5.17; N, 5.14. Found: C, 83.5; H, 5.15; N, 5.09.

N-(p-nitrophenyl)carbazole.—100 mg was oxidized in MeCN/TEAP at 1.6V to N,N'-bis (p-nitrophenyl)-3,3'-bicarbazyl (72% yield), recrystallized from benzene/hexane as a yellow amorphous solid, mp 240° - 245° (decomp.). Calculated for $C_{36}H_{22}N_4O_4$: C, 75.2; H, 3.86; N, 9.74. Found: C, 75.3; H, 3.82; N, 9.77.

Preparation and characterization of carbazole derivatives.—Many of the compounds studied have been previously reported in the literature. These synthetic routes were followed with some modifications in work-

ups; structures were verified by comparison of melting points with literature values, where possible, and by spectroscopic data in all cases. New compounds were verified by their CHN analyses.

Infrared spectra, obtained on a Perkin-Elmer 621 spectrometer, proved very useful in structure and purity determinations. Carbazoles substituted at the nitrogen atom do not show the strong N-H stretching peak at about 3400 cm^{-1} present in carbazole and its ring-substituted derivatives. The disappearance of this peak was used to chart the progress of Ullmann reactions when a carbazole was reacted with a *para*-substituted iodobenzene to produce substituted N-phenylcarbazoles. Carbazoles with either one or both rings unsubstituted show two strong out-of-plane bending (*ortho*-disubstituted ring) peaks at about 725 and 750 cm^{-1} ; these peaks were used to ascertain the completeness of 3,6-disubstitution reactions. N-phenylcarbazole, N-*p*-biphenylcarbazole, and ring-substituted N-phenylcarbazoles show a weak out-of-plane bending (monosubstituted ring) peak at 760 cm^{-1} . If the compound has an unsubstituted carbazole ring the 760 cm^{-1} peak will appear as a shoulder on the 750 cm^{-1} peak. The *para*-substituted N-phenylcarbazoles show a strong out-of-plane bending (*para*-disubstituted ring) peak between 825 and 850 cm^{-1} , the position depending upon the electron-donating ability of the *para*-substituent. A rough Hammett-type correlation was obtained whereby the peak frequency was found to shift to lower values with increasing electron-donating ability. Carbazoles substituted at the 3-position show a strong out-of-plane bending peak around 810 cm^{-1} and a medium intensity peak between 840 and 905 cm^{-1} , both indicative of a 1,2,4-trisubstituted aryl ring.

The position of this latter peak was found to depend upon the electron-donating effect of the substituent in much the same way as does the 725 - 750 cm^{-1} peak found in *para*-substituted N-phenylcarbazoles.

Carbazoles disubstituted at the 3 and 6 positions also show both the 1,2,4-trisubstitution peaks but the medium intensity peak is usually 5 - 15 cm^{-1} lower than in the corresponding 3-substituted carbazoles. The fact that this lowering occurs for substituents such as NH_2 and NMe_2 is reasonable but why it also is observed with electron-withdrawing groups is not understood at present. This latter peak was found to be well suited for determining the extent of synthetic reactions such as halogenations and acylations where both 3- and 3,6-substituted products could be formed. For mixtures, two peaks are readily discernable.

The purity and structure of some of the 3,6-disubstituted N-ethyl- and N-phenylcarbazoles were confirmed by nmr spectroscopy using a Perkin-Elmer R20 spectrometer; an ABX splitting pattern in the aromatic region is readily observed. Many others could not be analyzed via nmr due to either limited solubility or spectral complexity.

Column chromatography using benzene, hexane, or heptane as the solvent and either basic or neutral alumina (Woelm) as the support was invaluable in purification of all but the carboxyl-substituted carbazoles. Also, the 3,6-dinitro-substituted carbazoles were chromatographed with acetone or nitrobenzene on neutral alumina.

The carbazole-3-carboxylic acids were purified by sublimation and the carbazole-3,6-dicarboxylic acids by repeated formation of the salt in aqueous base and reprecipitation of the free acid with strongly acidic solutions.

In halogenation and acylation reactions, separation of the mono- and di-substituted products was often a problem. In these cases, recrystallization from refrigerated methanol solutions was used to separate the mixtures. In the cold solutions the disubstituted carbazoles precipitated first and were collected before recrystallization of the monosubstituted derivatives began.

Brief descriptions of the compound preparations are given below. Although some of it is repetitive of litera-

ture methods, modifications in work-up were effected in every case.

3-Substituted carbazoles.—3-Aminocarbazole was obtained from Aldrich Chemical Company and was purified by recrystallization three times from ethanol, mp 255°–258° [Ref. (17) 254°]. Methylation with trimethylphosphate gave 3-dimethylaminocarbazole, which was recrystallized twice from heptane, mp 114°–115° [Ref. (18) 114°–116°]. Diazotization of the hydrochloride salt of 3-aminocarbazole, followed by treatment with sodium tetrafluoroborate, heating in xylene and extraction with benzene gave 3-fluorocarbazole. The crude material was chromatographed on neutral alumina and recrystallized twice from benzene/hexane, mp 208°–209° [Ref. (19) 202°–203°]. 3-Chlorocarbazole was prepared by treating carbazole with an equimolar amount of sulfuryl chloride in chloroform, followed by chromatography with benzene on basic alumina. Two recrystallizations from cold methanol and one from ethanol (charcoal) yielded the product, mp 197°–198° [Ref. (20) 196°–197°]. 3-Bromocarbazole was prepared by reacting carbazole with an equimolar amount of N-bromosuccinimide in carbon tetrachloride containing a small amount of benzoyl peroxide. Chromatography with benzene on basic alumina, followed by two recrystallizations from cold methanol and one from ethanol (charcoal) yielded white flakes, mp 195°–197° [Ref. (21) 194°–196°]. Heating of 3-bromocarbazole with cuprous cyanide in pyridine at 215°–225° for 24 hr produced a solid reaction mass which was chromatographed twice with benzene on basic alumina; recrystallization from ethanol/heptane yielded 3-cyanocarbazole, mp 183°–184° [Ref. (22) 184°–185°]. Treatment of carbazole with an equimolar iodide-iodate solution (23) yielded 3-iodocarbazole, which was purified by chromatography on basic alumina with benzene and two recrystallizations from cold methanol and one from ethanol (charcoal) to yield the product, mp 195°–196° [Ref. (23) 192°–194°]. 3-Nitrocarbazole was prepared by nitration of N-nitrosocarbazole and subsequent removal of the nitroso group (24). Chromatography with benzene on neutral alumina and recrystallization from benzene yielded a yellow powder, mp 213°–214° [Ref. (21) 212°–213°]. 3-Methylcarbazole was synthesized by formylation of carbazole followed by a Wolff-Kishner reduction (25); the product was chromatographed twice on neutral alumina with benzene and recrystallized from methanol, mp 205°–207° [Ref. (26) 206°–207°]. N-Benzoylcarbazole was obtained commercially and converted to 3-benzoylcarbazole by a Fries rearrangement, mp 206° [Ref. (27) 206°].

3-Substituted-N-ethylcarbazoles.—3-Nitro-N-ethylcarbazole and 3-amino-N-ethylcarbazole were donated by Southern Dyestuffs Company and were purified by chromatography with benzene on basic alumina. Recrystallizations from benzene/ethanol yielded the products, mp 128°–129° [Ref. (28) 128°] and 111°–112° [Ref. (28) 113°–114°], respectively. Methylation analogous to that for 3-aminocarbazole yielded 3-dimethylamino-N-ethylcarbazole, which was recrystallized once from heptane, mp 62°. Calculated for $C_{16}H_{18}N_2$: C, 80.7; H, 7.60; N, 11.7. Found: C, 80.8; H, 7.67; N, 11.7. Acetylation of the amino derivative yielded, after recrystallization from ethanol, 3-acetamido-N-ethylcarbazole, mp 194°–196° [Ref. (29) 203°–204°]. Diazotization of the 3-amino-N-ethylcarbazole hydrochloride salt and work-up similar to that for 3-fluorocarbazole yielded 3-fluoro-N-ethylcarbazole, which was chromatographed on basic alumina to yield a colorless oil which solidified after several months' standing, mp 44°–48°. Calculated for $C_{14}H_{12}NF$: C, 78.9; H, 5.67; N, 6.57. Found: C, 79.2; H, 5.63; N, 6.52. 3-Formyl-N-ethylcarbazole was obtained from Aldrich Chemical Company and purified by benzene chromatography on basic alumina followed by recrystallization from benzene/hexane, mp 88°–89° [Ref. (30) 92°–93°]. Wolff-Kishner reduction (25) and two recrystallizations from methanol yielded 3-methyl-N-ethylcarbazole, mp 43°–44° [Ref. (25) 45°]. Methods

similar to those described for the 3-substituted carbazoles were employed to obtain 3-chloro-N-ethylcarbazole, mp 66°–67° from cold methanol [Ref. (31) 81°–82°]; 3-bromo-N-ethylcarbazole, mp 78°–80° from ethanol [Ref. (30) 81°–82°]; 3-iodo-N-ethylcarbazole, mp 78°–80° from methanol [Ref. (30) 82°–83°]. Treatment of the bromo derivative with cuprous cyanide in pyridine produced 3-cyano-N-ethylcarbazole which was purified in the same fashion as the 3-cyanocarbazole to yield the product mp 113°–115° from benzene/hexane. Calculated for $C_{15}H_{12}N_2$: C, 81.8; H, 5.49; N, 12.7. Found: C, 81.8; H, 5.55; N, 12.7. 3-Acetyl-N-ethylcarbazole was prepared by Friedel-Crafts acylation of N-ethylcarbazole; the product was recrystallized twice from ethanol, mp 112°–114° [Ref. (31) 115°]. Similarly, 3-benzoyl-N-ethylcarbazole was synthesized from N-ethylcarbazole and benzoyl chloride and chromatographed with benzene on basic alumina, followed by recrystallization twice from ethanol to yield mp 90°–92°. Calculated for $C_{21}H_{17}NO$: C, 84.3; H, 5.72; N, 4.68. Found: C, 84.2; H, 5.72; N, 4.59. The N-ethylcarbazole-3-carboxylic acid was prepared by lithiation of the 3-bromo derivative followed by addition of CO_2 to yield the product, mp 232°–234° [Ref. (32) 224°–226°]. Esterification of the latter product with ethanol gave ethyl-N-ethylcarbazole-3-carboxylate, which was purified by benzene chromatography on basic alumina to yield a colorless, viscous oil. Calculated for $C_{17}H_{17}NO_2$: C, 76.4; H, 6.40; N, 5.24. Found: C, 76.3; H, 6.38; N, 5.25.

3,6-Disubstituted carbazoles.—3,6-Dinitrocarbazole was donated by Southern Dyestuffs Company mixed with the 1,6 isomer. They were separated by selective solubilities of the potassium salts (33) followed by chromatography with acetone on neutral alumina and recrystallization from acetone, mp > 350° [Ref. (33) 386°–387°]. 3,6-Dichlorocarbazole, mp 204°–205° from methanol [Ref. (31) 201°–203°], 3,6-dibromocarbazole, mp 211°–212° from methanol [Ref. (9) 211°–213°], and 3,6-diiodocarbazole, mp 205°–206° from methanol [Ref. (9) 204°–206°] were synthesized in manners similar to the monohalogenated derivatives except that two moles of halogenating reagent was used per mole of carbazole. Purification methods were identical. 3,6-Diacetylcarbazole was prepared by Friedel-Crafts acylation and recrystallization twice from ethanol, mp 236°–238° [Ref. (32) 233°]. The 3,6-dicyanocarbazole was synthesized by heating 3,6-dibromocarbazole with an excess of cuprous cyanide in pyridine at 220°–230° for 48 hr. The product was extracted from the hot reaction mass with benzene and chromatographed on neutral alumina; recrystallization was effected from benzene, mp > 300° [Ref. (22) > 360°]. Photolysis of bis (*p*-anisylamine) in cyclohexane at 300 nm for 24 hr yielded 3,6-dimethoxycarbazole. The crude product was purified by benzene chromatography twice on basic alumina followed by recrystallization from benzene/ethanol, mp 175°–177°. Due to the presence of large amounts of unreacted parent, great care must be taken in the chromatographic separation; the carbazole comes off the column after the parent diphenylamine. Calculated for $C_{14}H_{13}NO_2$: C, 74.0; H, 5.94; N, 6.16. Found: C, 74.2, H, 5.89; N, 6.13.

Several *t*-butylated carbazoles were kindly donated by F. A. Neugebauer of the Max-Planck Institute, Heidelberg, Germany, namely the 3,6-di-*t*-butylcarbazole, 1,8-di-*t*-butylcarbazole, 1,3,6-tri-*t*-butylcarbazole, 1,3,8-tri-*t*-butylcarbazole, and 1,3,6,8-tetra-*t*-butylcarbazole.

3,6-Disubstituted-N-ethylcarbazoles.—Treatment of 3-nitro-N-ethylcarbazole with 1.2 equivalents of nitric acid in refluxing acetic acid produced 3,6-dinitro-N-ethylcarbazole as a precipitate. The crude material was chromatographed on neutral alumina with acetone and recrystallized twice from nitrobenzene, mp > 300°. Calculated for $C_{14}H_{11}N_3O_4$: C, 59.0; H, 3.90; N, 14.7. Found: C, 58.8; H, 3.86; N, 14.7. Reduction of this compound with tin/HCl in ethanol, followed by neutralization gave 3,6-diamino-N-ethylcarbazole which was

purified by repeated acid-base recrystallization, mp 188°-189°. This compound air oxidizes very readily and darkens rapidly upon standing. Calculated for $C_{14}H_{15}N_3$: C, 74.6; H, 6.71; N, 18.7. Found: C, 74.5; H, 6.75; N, 18.6. Methylation of the diamino derivative with trimethylphosphate, followed by benzene/basic alumina chromatography (twice) and recrystallization from benzene/heptane yielded 3,6-bis(dimethylamino)-*N*-ethylcarbazole, mp 120°-122°. Calculated for $C_{18}H_{23}N_3$: C, 76.8; H, 8.23; N, 14.9. Found: C, 76.5; H, 8.27; N, 15.0. Photolysis of *N*-ethylbis-(*p*-anisyl)amine in cyclohexane at 300 nm for 24 hr, followed by chromatography with benzene on basic alumina and recrystallization from ethanol produced 3,6-dimethoxy-*N*-ethylcarbazole, mp 178°-180°. Calculated for $C_{16}H_{17}NO_2$: C, 75.3; H, 6.71; N, 5.49. Found: C, 75.1; H, 6.58; N, 5.62. 3,6-Dichloro-*N*-ethylcarbazole, mp 117°-118° from methanol [Ref. (31) 113°], 3,6-dibromo-*N*-ethylcarbazole, mp 137°-138° from ethanol [Ref. (31) 136°], 3,6-diiodo-*N*-ethylcarbazole, mp 152°-153° from ethanol [Ref. (32) 154°], 3,6-dimethyl-*N*-ethylcarbazole, mp 62°-63° from benzene/heptane [Ref. (25) 67°] and 3,6-diacetyl-*N*-ethylcarbazole, mp 182°-183° from benzene [Ref. (31) 182°] were all prepared in manners similar to those for the monosubstituted analogs with the exception that the substituting reagents were doubled in concentration (or, in the case of the methyl derivative the substitution reaction was carried out twice). 3,6-Dipropionyl-*N*-ethylcarbazole was prepared similarly to the diacetyl compound to yield mp 133° [Ref. (31) 132°]. Wolff-Kishner reduction of the diacetyl derivative followed by chromatography with benzene twice on basic alumina generated the 3,6,*N*-triethylcarbazole. Recrystallization twice from cold methanol yielded the pure product, mp 81°-85° [Ref. (29) oil]. 3,6-Di-*t*-butyl-*N*-ethylcarbazole was prepared by a Friedel-Crafts alkylation of *N*-ethylcarbazole with *t*-butylchloride. Chromatography with benzene on basic alumina and recrystallization from benzene/heptane yielded the product, mp 151°-153°. Calculated for $C_{22}H_{29}N$: C, 85.9; H, 9.53; N, 4.55. Found: C, 85.5; H, 9.47; N, 4.56. *N*-Ethylcarbazole-3,6-dicarboxylic acid was prepared by a hypobromite oxidation of 3,6-diacetyl-*N*-ethylcarbazole according to the method of Buu-Hoi (29), mp > 300° [Ref. (29) > 300°]. Dimethyl-*N*-ethylcarbazole-3,6-dicarboxylate was synthesized by esterification of the diacid with methanol and was purified by recrystallization twice from methanol/benzene/pet. ether, mp 187°-188° [Ref. (36) 187°]. Treatment of 3,6-dibromo-*N*-ethylcarbazole with excess cuprous cyanide according to the previously mentioned procedure for cyanations, followed by benzene extraction, chromatography on neutral alumina and recrystallization from benzene gave 3,6-dicyano-*N*-ethylcarbazole, mp 230°-231°. Calculated for $C_{16}H_{11}N_3$: C, 78.3; H, 4.54; N, 17.1. Found: C, 78.1; H, 4.52; N, 17.1. 3-Acetyl-6-methyl-*N*-ethylcarbazole and 3-acetyl-6,*N*-diethylcarbazole were obtained from N. P. Buu-Hoi and were used without further purification.

Substituted *N*-phenylcarbazoles.—The purification of *N*-phenylcarbazole has been previously described (7). *N*-(*p*-nitrophenyl)carbazole was prepared from carbazole and nitrobenzene by the method of de Montmolin (37) and was recrystallized once from toluene and then once from benzene, mp 211°-213° [Ref. (37) 212°]. Reduction of this compound with tin/HCl in ethanol produced *N*-(*p*-aminophenyl)carbazole, which precipitated out after several hours' refluxing as the hydrochloride salt. The free base can be obtained from the salt by neutralization but it is difficult to purify, apparently forming a matrix with many solvents. Chromatography using benzene on a basic alumina column followed by evaporation of the solvent from the eluent gave an oil [Ref. (38) resin]. After several hours' heating *in vacuo* a brown, glass-like solid was obtained which possessed a large variable melting point range. Methylation of the amino derivative with trimethylphosphate (careful heating required!), followed by

chromatography with benzene on basic alumina and recrystallization from benzene/hexane yielded *N*-(*p*-dimethylaminophenyl)carbazole, mp 213°-215° [Ref. (39) 210°-212°]. Acetylation of the amino derivative gave *N*-(*p*-acetamidophenyl)carbazole; recrystallization twice from ethanol yielded the desired compound, mp 258°-260° [Ref. (38) 260°]. Several of these *N*-*para* substituted phenylcarbazoles were obtained using a modified Ullmann reaction in which an appropriately *para*-substituted iodobenzene is allowed to react mole-per-mole with carbazole in the presence of copper powder and potassium carbonate. The mixture is heated for 12-24 hr at about 200° without solvent (the iodobenzenes melt and serve as the solvent; in some cases a few ml of xylene was added to keep the mixture fluid). The hot reaction mixture is extracted with benzene (in which unreacted carbazole is almost totally insoluble), and the benzene solution is chromatographed on basic alumina. The first fraction contains the substituted phenylcarbazole; all were then recrystallized from benzene/hexane or benzene/ethanol. Pertinent data on these compounds, many of which are believed to be new, are given below:

N-(*p*-anisyl)carbazole, from benzene/ethanol, mp 154°-155° [Ref. (40) 149°-150°].

N-(*p*-methylthiophenyl)carbazole, from benzene/ethanol, mp 153°-155°. Calculated for $C_{15}H_{15}NS$: C, 78.9; H, 5.22; N, 4.84. Found: C, 78.7; H, 5.18; N, 4.76.

N-(*p*-biphenyl)carbazole, from benzene/ethanol, mp 225°-227° [Ref. (42) 224°-226°].

N-(*p*-tolyl)carbazole, from benzene/ethanol, mp 106°-108° [Ref. (42) 105°-107°].

N-(*p*-*t*-butylphenyl)carbazole, from benzene/ethanol, mp 191°-192°. Calculated for $C_{22}H_{21}N$: C, 88.2; H, 7.06; N, 4.68. Found: C, 88.2; H, 7.12; N, 4.62.

N-(*p*-fluorophenyl)carbazole, from benzene/ethanol, mp 120°-122°. Calculated for $C_{18}H_{12}NF$: C, 82.7; H, 4.63; N, 5.36. Found: C, 82.6; H, 4.69; N, 5.29.

N-(*p*-chlorophenyl)carbazole, from benzene/ethanol (charcoal), mp 141°-143° [Ref. (37) 146°].

N-(*p*-bromophenyl)carbazole, from benzene/ethanol, mp 142°-143° [Ref. (43) 146°-147°].

N-(*p*-iodophenyl)carbazole, from benzene/ethanol then benzene/hexane, mp 139°-140°. Calculated for $C_{18}H_{12}NI$: C, 58.6; H, 3.28; N, 3.80. Found: C, 59.0; H, 3.30; N, 3.74.

N-(*p*-carbomethoxyphenyl)carbazole, from benzene/ethanol, mp 116°-118°. Calculated for $C_{20}H_{15}NO_2$: C, 79.7; H, 5.01; N, 4.65. Found: C, 79.5; H, 5.03; N, 4.57.

N-(*p*-cyanophenyl)carbazole, from benzene/ethanol, mp 180°-183° [Ref. (37) 165°].

Several other 3,6-disubstituted *N*-phenylcarbazoles were synthesized by methods similar to the *N*-ethyl analogs; below the crystallization media and physical data are given for these compounds:

3,6-Di-*t*-butyl-*N*-phenylcarbazole, from benzene/heptane (twice), mp 144°-146°. Calculated for $C_{26}H_{29}N$: C, 87.8; H, 8.21; N, 3.94. Found: C, 87.7; H, 8.24; N, 3.95.

3,6-Diiodo-*N*-phenylcarbazole, from heptane (twice), mp 179°-182°. Calculated for $C_{18}H_{11}NI_2$: C, 43.7; H, 2.24; N, 2.83. Found: C, 43.9; H, 2.30; N, 2.79.

3,6-Dibromo-*N*-phenylcarbazole, from benzene, mp 159°-160°. Calculated for $C_{18}H_{11}NBr_2$: C, 53.9; H, 2.76; N, 3.49. Found: C, 53.9; H, 2.75; N, 3.53.

3,6-Dichloro-*N*-phenylcarbazole, from benzene/heptane, mp 140°-141°. Calculated for $C_{18}H_{11}Cl_2$: C, 69.2; H, 3.55; N, 4.49. Found: 69.4; H, 3.59; N, 4.43.

3,6-Dichloro-*N*-(*p*-chlorophenyl)carbazole was prepared via an Ullmann reaction involving 3,6-dichlorocarbazole and *p*-chloriodobenzene. It was twice chromatographed with benzene on basic alumina and recrystallized from benzene/ethanol, mp 174°-175°. Calculated for $C_{18}H_{10}NCl_3$: C, 62.4; H, 2.91; N, 4.04. Found: C, 62.8; H, 3.02; N, 3.93. Photolysis of tris(*p*-tolyl)amine at 300 nm in cyclohexane for 24 hr, followed by chromatography with benzene on neutral alumina and recrystallization from benzene/heptane yielded 3,6-dimethyl-*N*-(*p*-tolyl)carbazole, mp 105°-107°. Calculated

for $C_{21}H_{19}N$: C, 88.4; H, 6.71; N, 4.91. Found: C, 88.2; H, 6.72; N, 4.90.

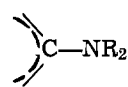
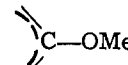
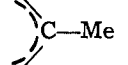
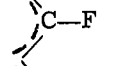
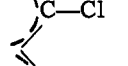



Spectroscopic studies.—Visible absorption spectra were obtained on a Cary 14 spectrometer by external electrolysis of the carbazole solution and immediate transfer to a standard cuvette. Only those carbazoles whose cation radicals were known from electrochemical data to be quite stable were studied in this manner.

The EPR spectra were recorded on a Varian E-3 spectrometer using either external electrolytic generation or by chemical oxidation with iodine/propylene carbonate. Although interpretations are incomplete at present, we are confident that the spectra obtained are those of the primary carbazole cation radicals, based on the stabilities of the compounds as determined by electrochemical methods.

HMO calculations.—HMO calculations were carried out using a simple Hückel program modified for cation radical systems; the heteroatom parameters were those shown below:

carbazole nitrogen: $h_N = 1.0$ $k_{C-N} = 0.8$

(same for N—H or N—Et)

	$h_N = 1.0$	$k_{C-N} = 0.8$
R = H, Me		
	$h_C = 2.0$	$k_{C-C} = 0.8$
(methyl carbon neglected)		
	$h_C = -0.3$	(inductive model, neglecting methyl carbon)
	$h_F = 3.0$	$k_{C-F} = 0.7$
	$h_{Cl} = 2.0$	$k_{C-Cl} = 0.4$
	$h_{Br} = 1.5$	$k_{C-Br} = 0.3$
	$h_{C(\text{cyano})} = 0.0,$ $h_N = 1.0,$	$k_{C-C} = 0.9,$ $k_{C≡N} = 2.0$
	$h_N = 2.2,$ $h_{N-O} = 1.67$	$k_{C-N} = 1.2,$ $h_O = 1.4,$

The "frontier orbital" approach was employed, in which one assumes that the reactivity of the cation radical is best described by the c^2 coefficients in the highest filled orbital (HFMO).

Results and Discussion

Due to the large number of compounds studied, the electrochemical data are broken down into compound classes according to the mode of substitution. It was found that there are characteristic reaction pathways for the cation radicals in each group but there are also variations and so each substitution group is discussed in some detail.

Since spectral data have only been obtained on those molecules possessing stable radicals all compound classes are considered together in these sections.

Electrochemical Data

Carbazoles and N-substituted derivatives.—Although the electrochemistry of these molecules has been presented in detail previously (7), a brief review at this point will serve as a useful basis for discussing the ring-substituted derivatives.

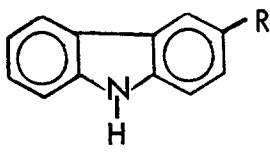
When carbazole is oxidized in MeCN/TEAP at platinum, the initial step is a (proposed) removal of one electron to form a very unstable cation radical. This cation radical reacts by deprotonation-coupling (the sequence is not known) to form the 9,9'- and 3,3'-bicarbazyls. Both bicarbazyls were chemically synthesized and were thus available for comparison. The 3,3'-bicarbazyl is more easily oxidized than carbazole itself and so the former loses two electrons in two reversible one-electron steps to yield a moderately stable dication with extensive conjugation. The 9,9'-bicarbazyl is only formed initially under cyclic voltammetric conditions and could not be isolated from controlled-potential electrolyses in unbuffered MeCN; the 3,3'-bicarbazyl was isolated in moderate yields. The 9,9'-bicarbazyl was found to form quantitatively, however, when electrolyses were carried out in the presence of an organic base such as pyridine. This fact led to the conclusion that the carbazole cation radical forms the 9,9'-bicarbazyl by diffusing out into solution, followed by deprotonation of the central nitrogen and subsequent coupling of the resultant free radicals in solution before they can diffuse back to the electrode to be further oxidized.

Interestingly, the 9,9'-bicarbazyl was found to oxidize considerably more anodic than carbazole (E_p 's of 1.85 and 1.20V, respectively) in a multielectron, irreversible process accompanied by severe filming to form unknown products.

In accordance with this scheme, N-alkyl- and N-phenylcarbazoles were found to form only the corresponding 9,9'-disubstituted-3,3'-bicarbazyls cleanly in quantitative yields. Due to the steric hindrance afforded by the alkyl and phenyl groups no 1,1'- or 3,1'-coupling products were detected.

3-Substituted carbazoles.—The electrochemical data for these compounds are presented in Table I. In general, the electrochemistry of this class is similar to that

Table I. Electrochemical data for 3-substituted carbazoles

No.		$E_{p/2}^a$	$it^{1/2}/C$	n value	Product(s) (% yield), comments
I	R = NH ₂	0.47	44	0.99	Irreversible one-electron oxidation, coupled product appears to form
II	NMe ₂	0.38	46	0.98	Stable cation radical, second reversible process at $E_{p/2} = 1.00V$, moderately stable dication, no bicarbazyls appear to form
III	Me	1.12	133	2.6 ^b	Bicarbazyl ^c forms in poor yield
IV	F	1.23	132	3.4 ^b	Bicarbazyl ^c forms in poor yield
V	Cl	1.27	115-121 ^d	3.4 ^b	Bicarbazyl ^c forms in poor yield
VI	Br	1.26	107-115 ^d	3.2 ^b	Bicarbazyl ^c forms in poor yield
VII	I	1.25	102	3.0 ^b	Bicarbazyl ^c forms in poor yield
VIII	COPh	1.36	100	2.8 ^b	Bicarbazyl ^c forms in poor yield
IX	CN	1.43	106-123 ^d	4.0	Bicarbazyl ^c forms in poor yield
X	NO ₂	1.51	113-122 ^d	4.0	Product(s) unknown

^a In volts vs. SCE, taken from linear scan voltammograms; values shift anodic with increasing scan rate.

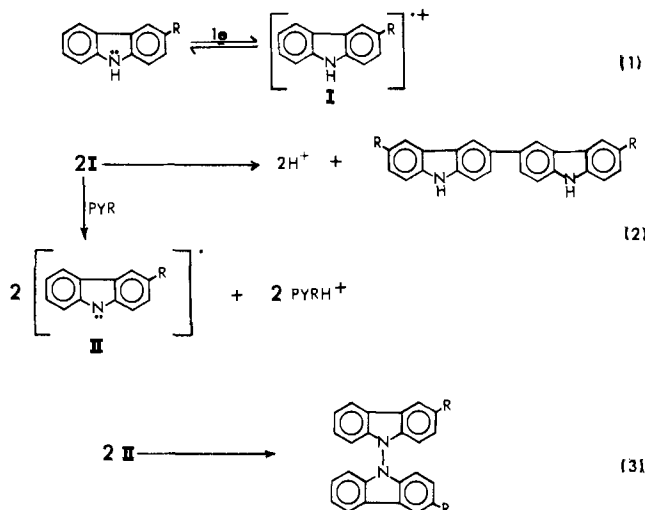
^b Low steady-state currents are observed at these n values; the cut-off point is not uniform for all compounds and so only the trend in the n values is meaningful.

^c From controlled-potential electrolyses in MeCN/TEAP; in all cases the bicarbazyl is the 3,3'-disubstituted-6,6'-bicarbazyl in yields of 20-40%.

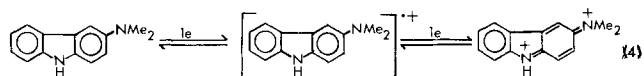
^d Chronoamperometric value increases with increasing electrolysis time (1-8 sec).

of carbazole itself. Since both the N(9) and 6 sites are open in these molecules one has the possibility for N-N, N-ring, and ring-ring couplings. Cyclic voltammograms show the presence of 6,6'- and N,N'-disubstituted bicarbazyls as in the case of carbazole with the exception of the fluoro derivative, which shows only 6,6'-bicarbazyl formed. However, controlled-potential electrolyses in MeCN/TEAP yield only the 3,3'-disubstituted-6,6'-bicarbazyls in poor yields; this has also been reported for carbazole (7). In addition, when the electrolyses are conducted with 2,4,6-trimethylpyridine added to the solution one obtains only N-N coupling; this is observed on both cyclic voltammograms and in controlled-potential electrolyses. This was also reported for carbazole and seems to point to a general rule that N-N coupling can only occur if the cation radical is deprotonated (7). This is shown graphically in Fig. 1 for 3-methylcarbazole; the curves are not well defined, but it is apparent that addition of the pyridine derivative wipes out formation of the ring-ring coupled product and gives essentially a quantitative yield of the 9,9'-bicarbazyl. In accordance with this, the peak current of the initial oxidation wave on curve B is about half that in curve A and the 3,3'-disubstituted-6,6'-bicarbazyl couple seen on curve A is absent in the presence of the relatively strong pyridine base on curve B. The oxidation process for the substituted 9,9'-bicarbazyl is a multielectron process (7) and so the bicarbazyl wave height on curve B is quite large relative to the primary oxidation wave. Formation of the 9,9'-bicarbazyl was verified by carrying out a preparative-scale electrolysis after which it was isolated in high yield (see Experimental section).

This reactivity pattern was found to be general for all of the 3-substituted carbazoles except for the amino and dimethylamino derivatives and is identical to the scheme presented previously for carbazole itself (7); the R group denotes all the substituents shown in Table I except amino and dimethylamino



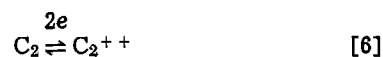
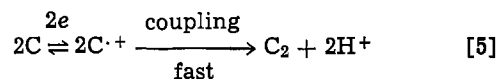
The rather high n values observed as one goes to more electron-withdrawing substituents is indicative of significant secondary chemical reactions in these systems. The dimethylamino derivative is completely different in that it has a stable cation radical, as verified by a complicated but well-resolved EPR spectrum (*vide infra*). Further one-electron oxidation to the dication quinonedimine occurs and this couple is also reversible. This is to be anticipated due to the highly conjugated species that can be generated by loss of two electrons



The dication does react slowly, and the cation radical more slowly still (half-lives of about 30-40 sec and 20-30 min, respectively), but neither appears to form a

bicarbazyl in either the 6 or 9(N) positions. This is not surprising, since the charge density at the open 6-ring position is very low in this molecule. Simple HMO calculations show that the 6-position will not be a center of reactivity and thus the 6,6'-bicarbazyl is not likely to form. The reactive site is instead predicted by HMO calculations to be the dimethylamino group and its *ortho* ring carbons and so the reaction pathway may be similar to that for N,N-dimethylaniline, where coupling has been shown to take place through the N-methyl groups and, possibly, the ring positions *ortho* to it (44).

3-Aminocarbazole undergoes a different oxidation pathway in that the first step, also a one-electron process, is irreversible. The cyclic voltammograms and n value of unity suggest formation of a product generated by intermolecular coupling and subsequent oxidation with concomitant protonation of parent material (thus rendering it electroinactive at the parent oxidation potential) according to the general mechanism

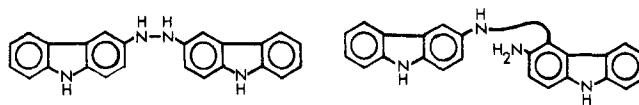


Thus, a total of four electrons is taken up and four parent molecules are removed from the system either by electrolysis or protonation. From known reactivities of aniline derivatives and the observed instability of the 3-aminocarbazole cation radical compared to that of the dimethylamino derivative, one would anticipate that the NH_2 group is directly involved in the coupling reaction; however, it is not certain at this time whether N-N or N-ring compounds are being generated.

Considering all the potential active sites, a large number of coupled products are possible. Although the 6-position is open, simple HMO calculations again predict a reactivity pattern characteristic of a substituted aniline, analogous to the dimethylamino derivative; thus, 6,6' coupling is not likely. The numbers shown below are c^2 values⁴ for the highest filled orbitals occupied by a single electron for carbazole and 3-aminocarbazole (the picture for the dimethylamino compound would be very close to the latter); one sees that these crude calculations predict a drastic change in reactivity, a change that is qualitatively confirmed by the experimental data



In the 3-amino compound, the charge density is very low in the unsubstituted ring and is largely restricted to the amino group and the ring positions *ortho* and *para* to it. Of all the possible coupled products, the two shown below seem most likely based on these calculations

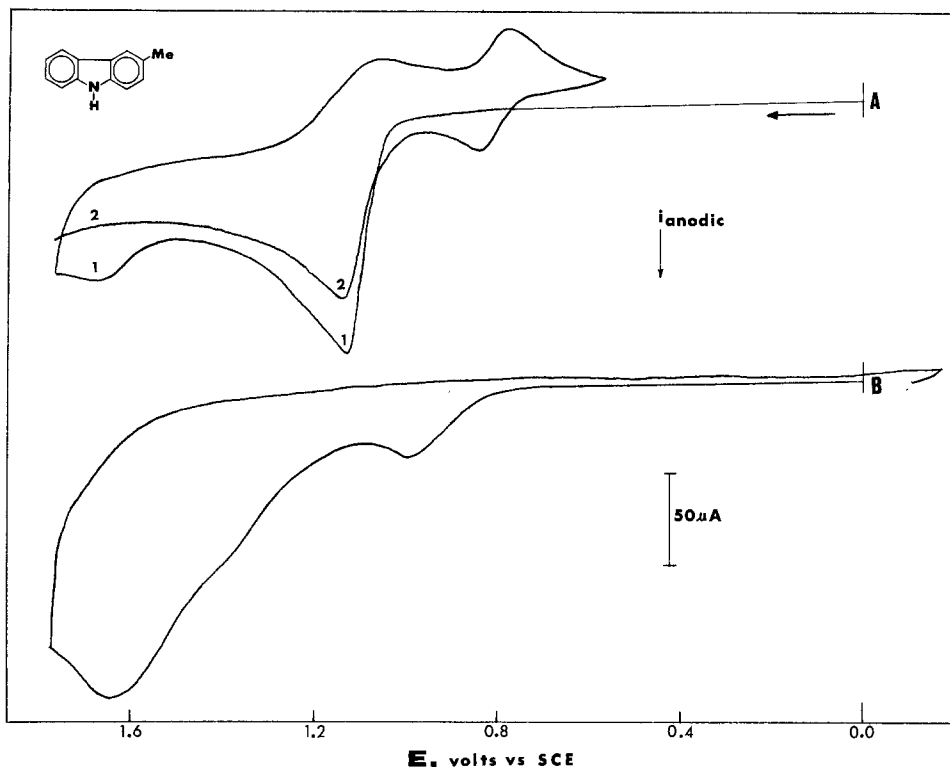


Studies are now under way to determine the structure(s) of the coupled product(s) derived from both 3-amino- and 3-amino-N-ethylcarbazole.

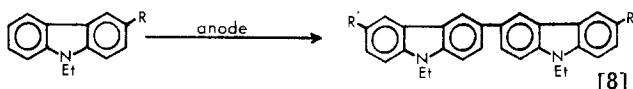
3-Substituted-N-ethylcarbazoles.—It was anticipated that blocking of the carbazole nitrogen with an ethyl

⁴ The c^2 values (squares of atomic orbital coefficients) are roughly proportional to the unpaired electron densities, and it has been empirically observed that the values for each atom taken only from the highest filled orbital, rather than summing the values for all the occupied orbitals, give reliable reactivity patterns for aromatic cation radicals.

Fig. 1. Curve A: Cyclic voltammogram of $1.2 \times 10^{-3}F$ 3-methylcarbazole in MeCN/TEAP, sweep rate = 150 mV/sec. Curve B: Cyclic voltammogram of the same solution with excess 2,4,6-trimethylpyridine added, sweep rate = 50 mV/sec.



group would render the previous systems somewhat less complicated, in a similar fashion to the previous studies on carbazole and N-ethylcarbazole (7). With the nitrogen blocked, N-N and N-ring coupling cannot occur and one should obtain only the 3,3'-disubstituted-N,N'-diethyl-6,6'-bicarbazyls by bond formation through the only available active site (excluding the amino and dimethylamino derivatives)



This is observed for most of these compounds, as shown in Table II and Fig. 2. By and large, the bicarbazyls are the major products in these systems, but most of the coupled products are somewhat unstable and react further, particularly in the presence of impurities in

the solvent or supporting electrolyte. As for the 3-substituted carbazoles, the n values cited in Table II were taken at parent concentrations of 10^{-3} to $10^{-4}F$ and the amounts of bicarbazyl cited were estimated from peak currents on cyclic voltammograms of exhaustively electrolyzed $10^{-3}F$ solutions. Very good product yields were only obtained at low concentrations and in very pure solvent, so the numbers cited in Table II are probably near the optimum values to be expected. At higher concentrations further reactions ensue in many cases and telomers or other unidentified products are obtained. As with the 3-substituted carbazoles, low steady-state currents were encountered in exhaustive electrolyses, but they were generally quite a bit lower, indicating that the 3-substituted-N-ethylcarbazoles are considerably "cleaner." Cyclic voltammograms of exhaustively electrolyzed solutions suggest that prepara-

Table II. Electrochemical data for 3-substituted-N-ethylcarbazoles

No.	R	$E_{p/2}$	$it^{1/2}/C$	n value	Product(s) (% yield), comments
XI	$R = NH_2$	0.48	45	0.75	Unstable cation radical, coupled product appears to form
XII	NMe_2	0.36	47	0.96	Stable cation radical, second reversible process at $E_{p/2} = 0.98V$, stable dication, no dicarbazyls appear to form
XIII	$NHCOMe$	0.96	48-52 ^a	2.12 ^b	6,6'-bicarbazyl, ^c other products
XIV	Me	1.09	103-110 ^a	2.08 ^b	6,6'-bicarbazyl (40), other products
XV	F	1.20	95	2.03	6,6'-bicarbazyl (100)
XVI	Cl	1.28	93	1.93 ^{b,c}	6,6'-bicarbazyl (60) ^d
XVII	Br	1.25	91	2.13 ^{b,c}	6,6'-bicarbazyl (50) ^d
XVIII	I	1.24	88	2.20 ^{b,c}	6,6'-bicarbazyl (60)
XIX	CHO	1.34	103-89 ^e	2.09 ^{b,c}	6,6'-bicarbazyl; films badly and is largely insoluble
XX	COMe	1.30	87	2.12 ^b	6,6'-bicarbazyl (90)
XXI	COPh	1.30	91	2.12 ^b	6,6'-bicarbazyl (85)
XXII	COOH	1.32	74-81 ^e	2.11 ^b	6,6'-bicarbazyl (90) totally insoluble
XXIII	COOEt	1.35	93	2.22 ^b	6,6'-bicarbazyl (70) ^d
XXIV	CN	1.44	94-118 ^a	2.24 ^{b,c}	6,6'-bicarbazyl (60)
XXV	NO_2	1.46	102-110 ^a	2.26 ^{b,c}	6,6'-bicarbazyl (50)

^a Chronoamperometric value increases with increasing electrolysis time (1-8 sec).

^b Low steady-state currents are observed at these n values; however, they are considerably lower than in the case of the 3-substituted carbazoles (see text).

^c n value is very sensitive to solvent/supporting electrolyte impurities.

^d Yields are lower at higher carbazole concentrations.

^e Current-time curves are distorted due to severe filming.

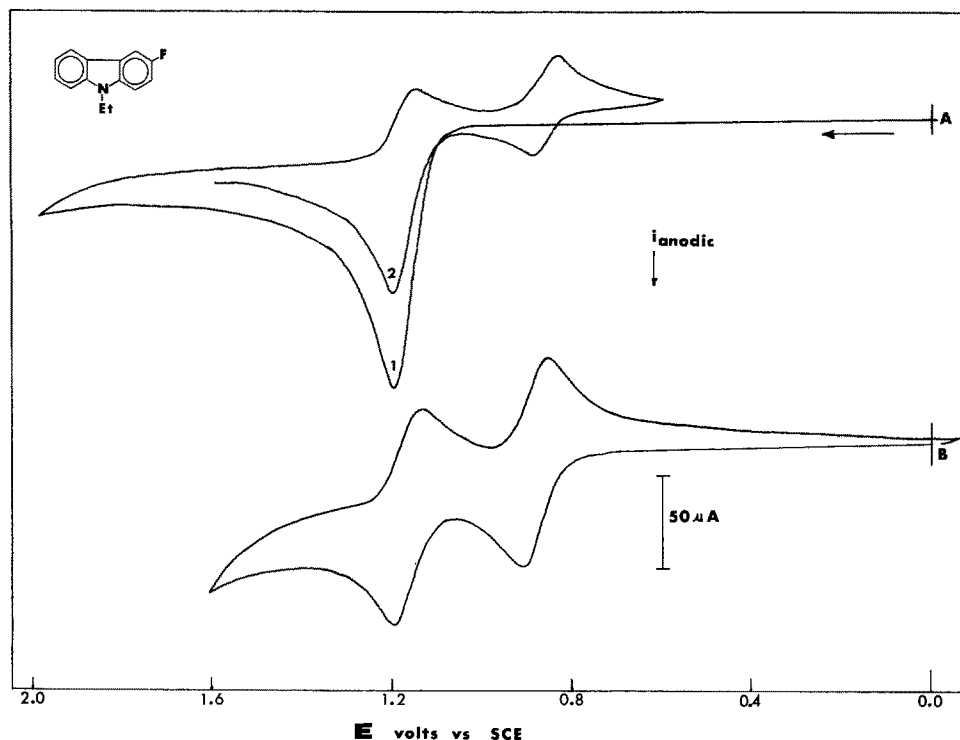


Fig. 2. Curve A: Cyclic voltammogram of $9.6 \times 10^{-4}F$ 3-fluoro-N-ethylcarbazole in MeCN/TEAP, sweep rate = 100 mV/sec. Curve B: Cyclic voltammogram of the same solution following exhaustive electrolysis at 1.4V, sweep rate = 67 mV/sec.

tive studies on these systems would be difficult at best. However, several derivatives can be electrolyzed on a preparative scale ($\sim 0.5g$) to give moderate yields of bicarbazyls, among them the fluoro, iodo, acetyl, benzoyl, ethylcarboxylate, cyano, and nitro compounds (see Experimental section).

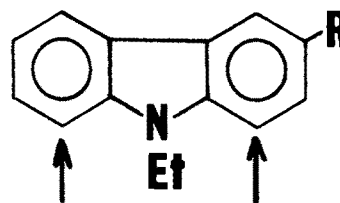
At short electrolysis times, these systems are model two-electron over-all ECE processes and so several attempts were made to measure the coupling rate constants for bicarbazyl formation using rotating disk voltammetry and digital simulation methods (14). In all cases, the coupling rates were too fast to measure, which indicates that a lower limit for the second-order k 's would be a value of about $10^8 \text{ mole}^{-1} \text{ sec}^{-1}$. This is not surprising since the carbazole ring system is planar and thus the charge densities at the 6-positions are quite high for the molecules in this series compared to, say, 4-substituted triphenylamines, which have second-order coupling rate constants ranging from 0.6 to $10^4 \text{ mole}^{-1} \text{ sec}^{-1}$ (45). Thus, the primary reaction pathway of these cation radicals is intermolecular coupling to form the corresponding bicarbazyls; these latter species then further decompose in a variety of secondary follow-up reactions.

In some cases, these secondary reactions following bicarbazyl formation can be speculated upon. The acetamido derivative yielded an appreciable amount of bicarbazyl but also a second product that appears to be a hydrazine-type derivative formed by deacetylation of the acetamido group and coupling through the 3-amino substituents. The methyl derivative also exhibited secondary reactions and cyclic voltammograms of exhaustively electrolyzed solutions indicated that further coupling through the methyl groups might be taking place in a similar fashion to the behavior previously reported for N,N-dimethyl-*p*-toluidine (46).

In several instances, the bicarbazyls formed were found to be only sparingly soluble and tended to film the electrode severely. In these cases, the product was collected by filtration of the electrolysis solution; the IR spectra indicated that these were perchlorate salts, probably of the bicarbazyl dication. This phenomenon was very marked for the aldehyde and carboxylic acid derivatives, although the ethyl ester was relatively uncomplicated and exhibited no filming.

In other cases, the nature of the secondary reactions could not be ascertained but previous chemical oxidation studies have shown that the 1 and 8 ring positions,

denoted by arrows below, are active and can be readily substituted in the absence of steric inhibition. These



ring sites could also be susceptible to attack in the bicarbazyls and so further couplings past the latter cannot be ruled out. This is also consistent with the observed fact that the stabilities of the bicarbazyls increase markedly as the carbazole nitrogen is substituted with first ethyl and then phenyl groups (*vide infra*). However, whereas further couplings past the bicarbazyl may be occurring, it should be pointed out that these reactions would never yield an n value greater than two, since the formation of successive telomers introduces increasingly greater possibilities for more conjugated systems generated by removal of electrons, but at the same time involves the consumption of more parent molecules. Thus, the secondary reactions leading to higher n values are more likely degradation of the bicarbazyl skeleton or the attached substituents. If further coupling reactions were involved, they would have to be intramolecular in nature.

Again, different behavior is observed for the amino and dimethylamino derivatives, these being quite similar to the 3-substituted analogs in not undergoing the standard bicarbazyl couplings. The major exception is that the N-ethyl compounds have more stable cation radical and diimine forms; in fact, 3-dimethylamino-N-ethylcarbazole exhibits two nicely reversible redox steps, as shown in Fig. 3. Comparison of the current-voltage curves for compounds I, II, XI, and XII confirms a general characteristic of *p*-phenylenediamine-type molecules in that protection of the nitrogen with alkyl or phenyl groups lends considerable stability to both the cation radical and diimine species. As with compound II, however, both the cation radical and diimine of compound XII slowly react to form unknown products.

When the 3-amino group is not methylated (No. XI) the cation radical is much less stable, although reversi-

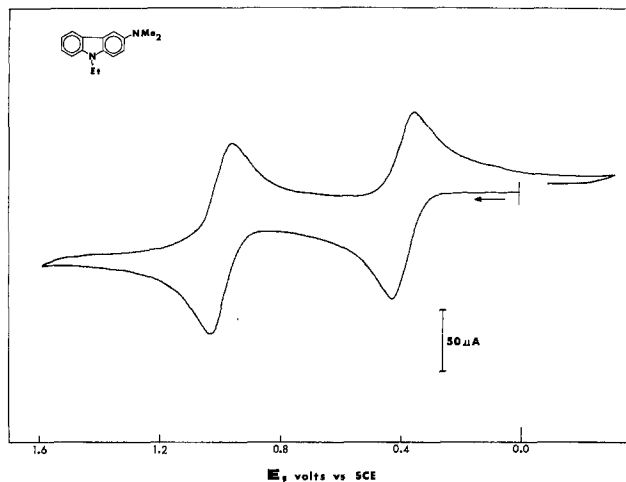


Fig. 3. Cyclic voltammogram of $1.0 \times 10^{-3} M$ 3-dimethylamino-N-ethylcarbazole in MeCN/TEAP, sweep rate = 150 mV/sec.

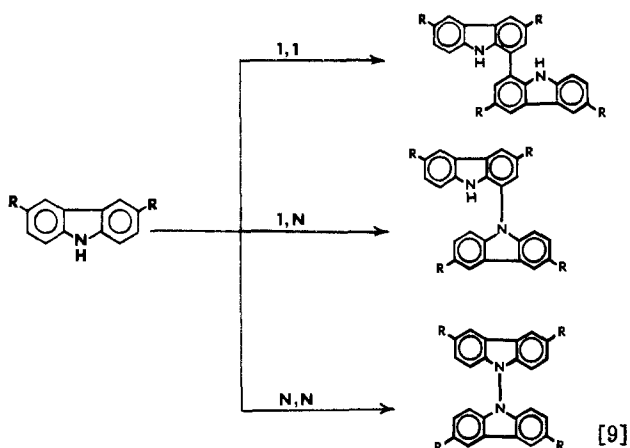
bility can still be observed on both the first and second anodic waves even at sweep rates as low as 200 mV/sec. At sweep rates of about 2 V/sec and above the first process is completely reversible, and a half-life of about 0.5 sec for the primary cation radical can be estimated. As with compound I, however, little is known about the process taking place and the n value of 0.7-0.8 (average value = 0.75), which was obtained repeatedly and appears to be genuine, is quite perplexing. This is, of course, different than for 3-aminocarbazole, which had an n value of unity. It is difficult to propose a mechanism involving 0.75 electrons per molecule with simple coupling as the only pathway. If the oxidized form of the bicarbazyl were to lose one or two protons this would generate n values of 0.80 or 0.67, respectively; it is conceivable that a mixture of these two processes is taking place, but it seems more likely that a completely different mechanistic pathway yet to be considered is operative here.

It is interesting to note that the primary radical of the acetamido derivative, No. XIII, is moderately stable, having a half-life of about 30 sec. As mentioned above, the reaction pathways of this radical are complex but again they are different than for No. XI and XII and are more characteristic of the other derivatives in this series in that an appreciable amount of the 6,6'-bicarbazyl is formed. It appears that the acetamido group is withdrawing electron density from the unsubstituted ring, but not to the extent that the $-NH_2$ and $-NMe_2$ groups do; these latter substituents stabilize the primary radicals by markedly decreasing electron density at the reactive 6-position. The result is that for these two compounds the electrochemistry is more characteristic of *p*-phenylenediamine-type molecules. There is probably also a steric factor for the acetamido derivative in that any coupling reactions involving the 3-substituent will be hindered by the acetyl group.

In all of the other compounds, No. XIV-XXV, simple HMO calculations indicate that the 3-substituents either have little effect on the 6-position electron density or actually increase it (relative to N-ethylcarbazole) making coupling more likely. The result is that in all cases the primary cation radicals are extremely short lived.

Thus, radical stabilities in this series can be interpreted in terms of the electron density at the reactive 6-position. Substituents such as $-NH_2$, $-NMe_2$, and $-NHCOMe$ (and presumably $-OR$ and $-SR$) can accommodate the unpaired electron density in the cation radicals and thus remove electron (and charge) density from the open ring. The others from $-Me$ through $-NO_2$ do not and in fact enhance coupling at the 6-position.

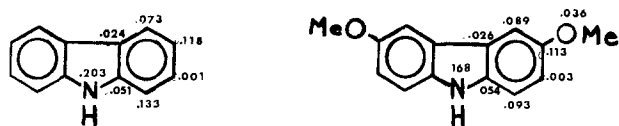
3,6-Disubstituted carbazoles.—For this series, it is apparent that barring substituent elimination, the only likely coupling sites would be the 1, 8, and 9 (N) positions. Thus, only the 1,1-1-N, and N-N coupled products should, in principle, be possible



As with the other systems previously mentioned, the feasibility of these products forming depends upon the status of the carbazole nitrogen (protonated or unprotonated) and the electron densities at the remaining reactive coupling sites. In addition, since all of the above reactions would be expected to be rapid and the carbazole nitrogen and 1 and 8 ring positions are unprotected cation radicals in this series would be predicted to be quite unstable.

Cyclic voltammetric data for these compounds are varied, as is seen in Fig. 4, and the electroanalytical data in Table III further indicate the diverse and generally poorly defined behavior in MeCN/TEAP. Current-voltage and current-time curves for a number of the derivatives in this series were markedly affected by adsorption of either parent material or electrolysis products and cyclic voltammograms run after exhaustive electrolyses were very poorly defined and showed little in the way of discernable products.

Only the methoxy derivative, No. XXVI, shows reversibility at low sweep rates and in fact the cation radical is quite stable, having a half-life ($t_{1/2}$) of several minutes. The primary radicals for the other compounds in this group are quite unstable, having $t_{1/2}$'s of 0.1-1.0 sec, but all of these radicals are much more stable than those of previously mentioned compounds with open 3 or 6 positions, with the exception of the aminocarbazoles. This marked stabilizing effect of methoxy groups has been noted previously (45, 47, 48) and is due to delocalization of charge and electron density out onto the methoxy's, with a resultant decrease at reactive sites in the carbazole nucleus. This is shown below, where electron densities are again represented by c^2 values for the HFMO; with the 3 and 6 positions blocked activity would be expected to shift to the 1, 8, and 9 sites, but as can be seen the latter are considerably deactivated



Of the other functional groups, only the *t*-butyl is predicted to have a similar effect, but to a much lesser extent. The others actually increase the electron density at the active sites and so further destabilize the primary cation radicals in a regular fashion, the stability decreasing from chloro to nitro.

It is interesting to note that the HMO calculations show an appreciable enhancement in electron density at the 4 and 5 ring carbons *ortho* to the methoxy groups (similar to the 3-aminocarbazole systems) to a point where these positions must be considered as possible coupling sites. Since methoxy is classically an *ortho-para* director this is not totally unexpected, but it will

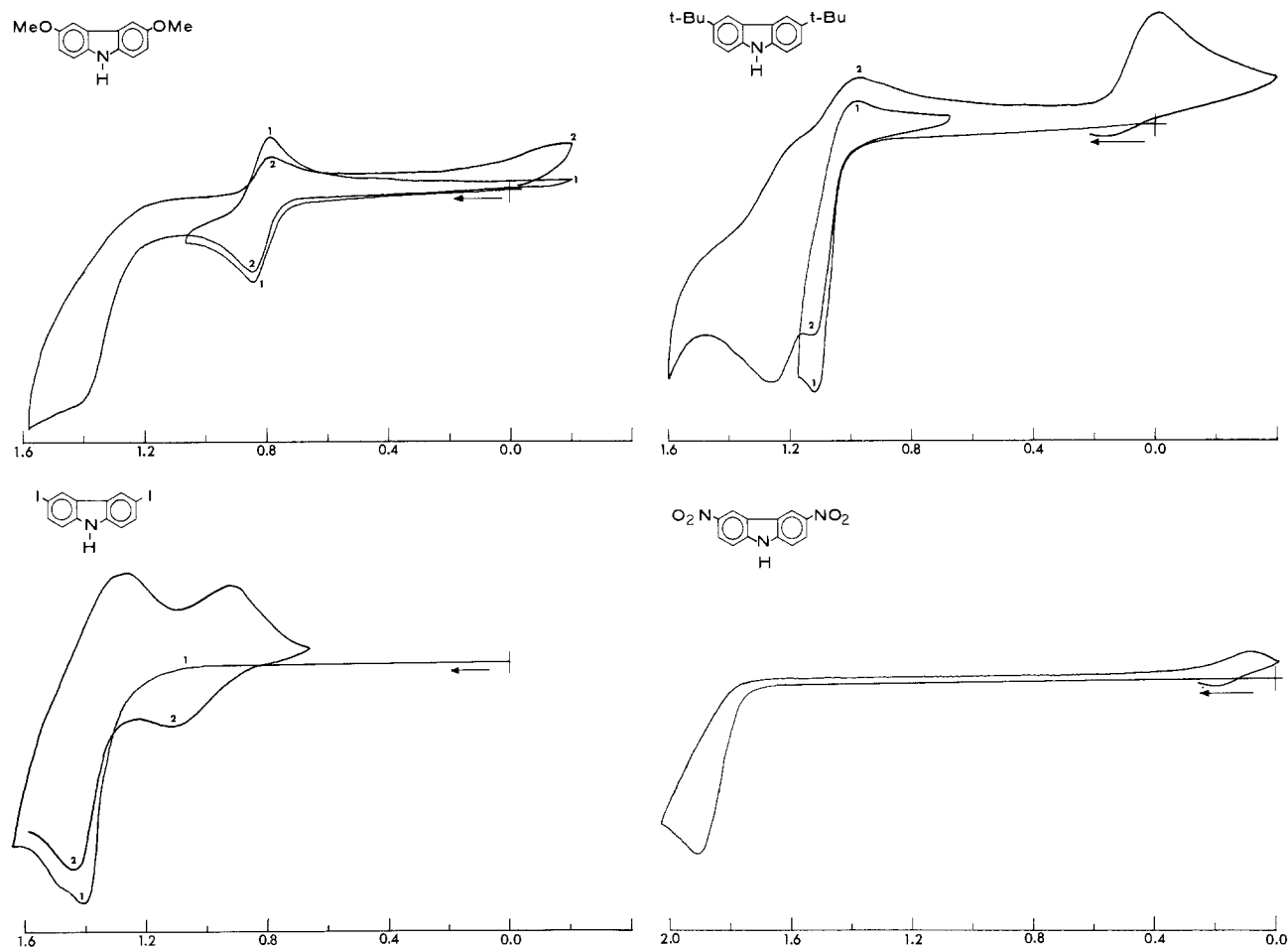


Fig. 4. Cyclic voltammograms of 3,6-disubstituted carbazoles in MeCN/TEAP. Abscissa is in volts vs. SCE and for all curves the solutions were $1.0 \times 10^{-3}F$ in the carbazoles and the sweep rate was 150 mV/sec. In some cases, scans are numbered sequentially.

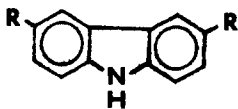
be indeed interesting if further work on the reaction pathways of these molecules verifies the HMO prediction. It is particularly germane, since EPR studies have indicated that the spin density at the 4 and 5 positions is quite low in some substituted carbazoles (*vide infra*) (49).

Little has actually been determined concerning the reactivity routes of No. XXVII-XXXIII in MeCN/TEAP. Some substituent elimination does occur for the halogen derivatives, leading to 6,6'-disubstituted-3,3'-bicarbazyls; this can readily be seen in Fig. 4 for 3,6-diiodocarbazole. The follow-up peaks in the region between 1.0 and 1.4V match perfectly with those for the 6,6'-bicarbazyl formed from 3-iodocarbazole. Of the other derivatives, it has only been determined that the

primary cation radicals are very unstable ($t_{1/2} \approx 1$ sec) and the decay pathways do not appear to involve substituent elimination.

In the presence of 2,4,6-trimethylpyridine, a strong organic base, electrolysis again produces only the substituted 9,9'-bicarbazyls in near quantitative yields. They are easily isolated, since they are in some cases insoluble and can be filtered off following electrolysis; alternatively, they are easily separated from the solvent and supporting electrolyte by column chromatography (see Experimental section). Such electrolyses in basic medium exactly parallel similar chemical work involving permanganate oxidations in acetone of the bromo (9) and *t*-butyl (49) derivatives, and it appears that near quantitative yields of the 9,9'-bicarbazyls

Table III. Electrochemical characteristics of 3,6-disubstituted carbazoles

No.		$E_{p/2}$	$it_{1/2}/C$	n value	Product(s) (% yield)
XXVI	R = OMe	0.78	48-53	1.76 ^d	Stable cation radical, decomposition pathway unknown
XXVII	<i>t</i> -Bu	1.07	106-115	2.91, 1.87 ^a	Corresponding 9,9'-bicarbazyl ^a (90-100)
XXVIII	Cl	1.38	120-148	3.60	3,3'- and 9,9'-bicarbazyls ^c
XXIX	Br	1.37	120-143 ^b	2.87, 1.93 ^a	9,9'-bicarbazyl ^a (90-100)
XXX	I	1.34	104	1.88	3,3'- and 9,9'-bicarbazyls ^c
XXXI	COMe	1.50	170-217 ^e	3.10	Unknown
XXXII	CN	1.71	120-136 ^b	3.04	Unknown
XXXIII	NO ₂	1.84	134-170	2.68	Unknown

^a Electrolyses in MeCN/TEAP with added excess 2,4,6-trimethylpyridine.

^b Data are distorted by strong adsorption of parent material or electrolysis product.

^c Observed on cyclic voltammograms in MeCN/TEAP, no 2,4,6-trimethylpyridine added. The 3,3'-bicarbazyls are formed by substituent elimination and subsequent coupling.

^d Current decays rapidly to about $n = 1$ where a low steady-state current ensues, the latter slowly dropping further to near zero.

^e Primary oxidation wave overlaps substantially with a second wave which is also included in the potential step.

Table IV. Radical stabilities of *t*-butylated carbazoles

No.	Compound	$E_{p/2}$	Radical half-life	Decomposition product
XXVII		1.07	~1 sec	1,1'-bicarbazyl ?
XXXIV		1.17	<<1 sec	3,3'-bicarbazyl
XXXV		1.15	<<1 sec	3,3'-bicarbazyl*
XXXVI		1.08	~1 min	1,1'-bicarbazyl ?
XXXVII		1.09	~30 min	?

* Verified with an authentic 3,3'-bicarbazyl sample.

from any of the 3,6-disubstituted derivatives can be readily obtained by either chemical or electrochemical means.

In the case of 3,6-di-*t*-butylcarbazole, authentic samples of the corresponding 1,9'- and 9,9'-bicarbazyls were available to aid in product identification. Cyclic voltammetric and optical spectra indicate that these are not the major product(s) in MeCN/TEAP electrolyses, however, and so it appears by a process of elimination that the most likely reaction pathway is ring-ring coupling-deprotonation to form the 1,1'-bicarbazyl.

In the pathways above, it appears that there is a reaction selectivity order that is highly contingent upon the acidity of the solution near the electrode similar to the diphenylamine system previously reported by Cauquis (50). That is, in acid solution, which is the case in unbuffered MeCN after coupling is initiated and protons are released into solution, only C-C coupling occurs, while the presence of a weak base would be expected to promote mixed C-C and C-N coupling. Strong bases in solution then lead exclusively to formation of the N-N coupled products.

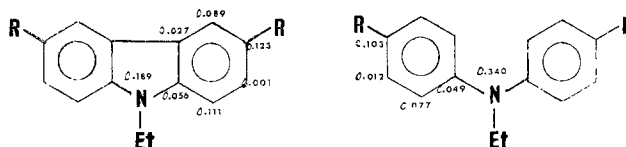
The series of *t*-butylated carbazoles shown in Table IV provide further valuable information on the possibilities of various coupling modes and the importance of steric factors in stabilizing the primary cation radicals. It is apparent from the radical stabilities shown that the 3 and 6 positions are far more reactive than the 1, 8, and 9 sites. Steric blocking of the 8 and 9 positions by a 1-*t*-butyl group (No. XXXVI) stabilizes the primary cation radical substantially compared to No. XXVII and introduction of another *t*-butyl substituent on the 8-carbon leads to a very stable cation radical for No. XXXVII. Stabilization through electronic effects would be minimal with *t*-butyl groups and so this is clearly an example of hindering reaction pathways by blocking reactive ring positions with inert functional groups.

The information provided by the molecules in this series is that simple blockage of the highly reactive 3 and 6 carbons does stabilize the primary cation radicals to a substantial degree, but the half-lives are still in the 0.1-1.0 sec region. An exception is the methoxy derivative which stabilizes by a delocalization mechanism similar to that operative for No. I, II and XI-XIII. When a reaction does take place, it appears to occur through the nitrogen in the presence of a strong organic

base and through the 1 and 8 ring carbons in unbuffered MeCN; this last assertion is speculative at present. Introduction of blocking groups at these latter sites leads to substantially more stable primary cation radicals.

3,6-Disubstituted-*N*-ethylcarbazoles.—With the nitrogen alkylated (and the 1 and 8 ring positions thus somewhat sterically hindered) and both the 3 and 6 ring carbons substituted, one might anticipate that the primary cation radicals of such molecules would be quite stable. To some degree this was found to be true and as a result the electrochemistry of this series of molecules is centered about detectably stable cation radicals with $t_{1/2}$ values ranging from about 1 sec up to several days; the electroanalytical data are given in Table V.

Even at that, the lifetimes of these radicals are less than what might have been expected, since previous studies have shown that structurally similar 4,4'-disubstituted-*N*-alkyldiphenylamines possess very stable primary cation radical species (51, 52). In general, the carbazole radicals are at least two orders of magnitude less stable than the correspondingly substituted diphenylamines; this phenomenon appears to be largely due to the fact that the carbazoles have a very planar pi system whereas the diphenylamine rings are skewed. This leads to marked differences in electron distributions, as shown below for the alkyl derivatives (these calculations do not include the alkyl substituents, all of which are considered equivalent, but their electron densities will be proportional to the ring carbons to which they are attached)

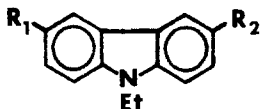


The major change is that electron density in the carbazole system is, relative to the diphenylamine skeleton, distributed more into the aromatic rings and less on the central nitrogen; this assertion has been quantitatively substantiated by EPR data (49). It is normally the case that increased delocalization leads to enhanced cation radical stability, but it appears at first glance that here the opposite is the case, i.e., the more highly delocalized carbazoles are the less stable radicals. The alternate viewpoint however, is that at the same time decreased localization takes place in the carbazoles relative to the diphenylamines at the unreactive central nitrogen with an attendant increase in electron density in the more reactive aromatic rings. Interestingly, the same result can be qualitatively achieved in the HMO calculations by increasing the pi overlap between the central nitrogen and the aromatic rings in the diphenylamine systems by increasing the value for the resonance integrals for the central nitrogen and the adjacent ring carbons. The net effect is to generate a more planar diphenylamine. As expected, electron density is drained away from the central nitrogen into the aromatic rings more and more as the k_{CN} value is increased.

The same effect is seen in a comparison of the calculated orbital energies with the experimentally obtained oxidation potentials. The calculations indicate that the carbazole HOMO's are lower (more positive) in energy than the correspondingly substituted diphenylamines and in accordance with this the oxidation potentials of the carbazoles are consistently more anodic by 0.2-0.3V. This is reasonable if one considers that the carbazoles are more "hydrocarbon-like" than "amine-like" relative to the diphenylamines (because of enhanced delocalization into the aromatic rings) and thus would be more difficult to oxidize.

The net result of all this is that the ring positions in the carbazoles are more reactive, particularly the 3 and 6 carbons, and so even though the rings are heavily substituted and sterically protected radical stability is

Table V. Electrochemical characteristics of 3,6-disubstituted-N-ethylcarbazoles

No.		$E_{p/2}$	$t_{1/2}/C$	n value	Product(s) (% yield), comments
XXXVIII	$R_1 = R_2 = \text{NH}_2$	0.32	47	1.09	Unstable cation radical, structure of coupled product is unknown
XXXIX	NMe_2	0.22	45	1.03	Highly stable cation radical, stable dication formed at $E_{p/2} = 0.60\text{V}$, unstable trication radical generated at $E_{p/2} = 1.41\text{V}$
XL	OMe	0.80	48	1.01 ^a	Stable cation radical, unstable dication; mode of decomposition appears to be hydrolysis
XLI	Me	1.04	59-103 ^b	2.2 ^a	Moderately stable cation radical, decomposition appears to be via coupling through methyl groups
XLII	Et	1.06	119-184 ^b	3.1 ^a	Unstable cation radical, decomposition appears to be via coupling through ethyl groups
XLIII	<i>t</i> -Bu	1.04	43	1.07 ^a	Stable cation radical, slowly decomposes probably via 1,1'-coupling
XLIV	Cl	1.48	53-67 ^b	1.3 ^a	Moderately stable cation radical, decomposition pathway unknown
XLV	Br	1.40	43-48 ^b	1.2 ^a	Moderately stable cation radical, decomposition pathway unknown
XLVI	I	1.34	78-88 ^b	2.0 ^a	Unstable cation radical, eliminates iodine, forms corresponding 3,3'-bicarbazyl (60-70) ^c
XLVII	COMe	1.50	79-136 ^b	3.2 ^a	Unstable cation radical, some deacetylation occurs to form the corresponding 3,3'-bicarbazyl
XLVIII	COEt	1.50	86-144 ^b	3.4 ^a	Unstable cation radical, eliminates propionyl group, forms corresponding 3,3'-bicarbazyl
XLIX	COPh	1.49	76-105 ^b	2.9 ^a	Unstable cation radical, eliminates benzoyl group, forms corresponding 3,3'-bicarbazyl
L	COOMe	1.56	— ^c	— ^c	Unstable cation radical, products unknown
LI	CN	1.74	81-133 ^{b,d}	3.4 ^a	Moderately stable cation radical, products unknown
LII	NO ₂	1.81	116-211 ^{b,d}	3.8 ^{a,d}	Moderately stable cation radical, products unknown
LIII	$R_1 = \text{Me}, R_2 = \text{COMe}$	1.26	124-165	2.7	Unstable cation radical, alkyl coupling predominates, small amount of deacetylation
LIV	$R_1 = \text{Et}, R_2 = \text{COMe}$	1.25	166-188	2.9	Unstable cation radical, alkyl coupling predominates, small amount of deacetylation

^a n value at the onset of low steady-state current.

^b Taken from $t = 1-8$ sec; value increases with increasing time.

^c Primary wave is very obscure, merges with more anodic waves; meaningful data could not be obtained.

^d Data are affected by proximity to background; residual currents are quite high.

diminished relative to systems such as the diphenylamines. Of course, the cation radicals in this series are enormously more stable than those previously discussed herein, but even so very few could be called truly stable (half-life of 30-60 min). Interestingly, it was generally found that protecting the area around the carbazole nitrogen (with N-alkyl or N-phenyl substitution) shielded the moderately reactive 1- and 8-carbons and led to greatly enhanced activity at the nominally blocked 3 and 6 ring sites; the decay reactions of the less stable radicals in this series were thus found to take place at these latter positions.

In all cases in this series, the initial process involves removal of one electron to generate the cation radical. Of those which are reasonably stable, the dimethylamino derivative, No. XXXIX, is by far the longest lived. Not only is the primary radical stable for days, but the dication quinonediimine also appears to have a negligible decomposition rate. In fact, a third redox process can be observed which is reversible even at moderately low voltage scan rates, as shown in Fig. 5. One readily sees that switching past the first two waves (dotted lines) yields substantial reverse current and a lesser amount is observed on the third anodic wave; however, oscilloscope traces show that this latter process is completely reversible above sweep rates of about 2 V/sec. Chronoamperometric data yield constant $it_{1/2}/C$ quotients for the first two anodic processes (45 and 91, respectively) and coulometric measurements indicate n values of 1.03 past the first wave and 2.05 past the second. This third anodic wave, then, is apparently due to further oxidation of the stable dication and so the reversibility seen at high sweep rates indicates that this molecule has a moderately stable trication radical with $t_{1/2} \approx 1$ sec. This is an extremely rare species, of which few examples are available (53); it offers the very exciting possibility of matching of spectral data for the cation and and trication radicals of a single species.

The amino derivative exhibits behavior similar to the previously discussed 3-aminocarbazoles except that the

electrolysis product is much more in evidence on cyclic voltammograms. Since this same general electrochemical behavior was noted for 3-amino- and 3-amino-N-ethylcarbazole this would imply that the carbazole nitrogen is not implicated and the common reaction pathway, if it is indeed common, is N-N or N-ring coupling involving the amino groups and the 1, 4, 5, or 8 ring carbons. Again, the primary cation radical is short-lived ($t_{1/2} \approx 1$ sec), but its existence was verified by rapid-sweep cyclic voltammetry.

Of the other derivatives in this series, both the methoxy and *t*-butyl compounds were found to have stable primary radicals with half-lives of 1 hr or more. The 3,6-dimethoxy-N-ethylcarbazole cation radical is exceptionally stable, probably due to the low charge density at the 1 and 8 ring sites and the blocking action

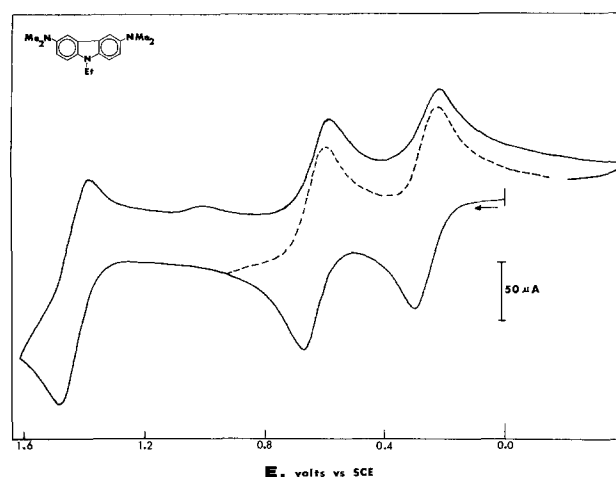
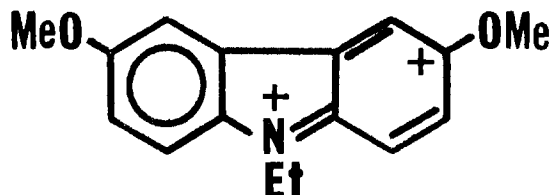


Fig. 5. Cyclic voltammogram of $1.0 \times 10^{-3} \text{M}$ 3,6-bis(dimethylamino)-N-ethylcarbazole in MeCN/TEAP, sweep rate = 667 mV/sec.

of the N-ethyl group. The cation radical is oxidized to the dication in a second anodic process at $E_{p/2} = 1.36\text{V}$; no reverse current was observed even at a sweep rate of 10 V/sec . The dication of this molecule would have



several resonance forms but the one shown above would be very susceptible to nucleophilic attack by trace amounts of water in the MeCN to generate the corresponding hydroxy derivative, 3-hydroxy-6-methoxy-N-ethylcarbazole. This is suggested by the cyclic voltammograms for this compound which are very similar in shape to other aromatic amine systems where a similar hydrolysis mechanism has been shown to occur (54, 55). The primary cation radical probably reacts via this same route, but at a markedly slower rate.

The 3,6-di-*t*-butyl-N-ethylcarbazole cation radical was also found to be quite stable, but slow decomposition was evident. Reaction probably occurs via 1-1 ring coupling, as was speculated for the *t*-butylated carbazoles No. XXVII and XXXIV-XXXVII. Nevertheless, a half-life of 30-40 min (stability for this compound, as for many of the others, is dependent upon concentration and solvent purity) ensures that this radical can be easily studied.

The methyl and ethyl derivatives, No. XLI and XLII, have cation radicals that are considerably more reactive than the *t*-butyl analog and beyond this the ethyl is much less stable than the methyl. This assertion is graphically illustrated in Fig. 6, where cyclic voltammograms for the three alkyl derivatives are shown. The *t*-butyl curve is seen to be perfectly reversible with no sign of decomposition products (however, holding the potential at the anodic limit for about 1 min and then sweeping back to more cathodic potentials yields a ratio of cathodic to anodic peak currents of about 0.92, indicating that the primary radical is in fact reacting very slowly). The methyl compound also shows considerable reverse current, but a small cathodic wave near -0.2V corresponding to reduction of protons indicates that the cation radical is not exceptionally stable ($t_{1/2} = 1-2\text{ min}$); the ethyl curve shows extensive reaction and reversal just past the primary wave (dotted line) shows very limited stability for the cation radical ($t_{1/2} \approx 0.8\text{ sec}$).

These data are consistent with a mechanism whereby the electrogenerated cation radical diffuses away from the electrode surface and a proton is lost from the alkyl carbon alpha to the carbazole skeleton, thus generating a benzylic-type free radical. Coupling of the resulting free radicals out in solution would ensue to generate a bridged bicarbazyl in a fashion similar to that proposed for No. XIV and previously published systems (46, 56). The relative stabilities of the methyl, ethyl and *t*-butyl compounds are thus explained by ring alkyl proton loss from the cation radical; a proton will eliminate more readily from a secondary carbon (ethyl) than from a primary (methyl) and when no alpha hydrogens are present (*t*-butyl) elimination cannot occur and enhanced stability is to be anticipated, as well as slow reaction via a different pathway. These relative stabilities are also nicely mirrored in the chronoamperometric data in Table V, which show the *t*-butyl derivative having a fairly constant one-electron value, and the others having much higher, and rapidly increasing, $it^{1/2}/C$ quotients. The n value data also point up the same disparity. The general mechanism is shown below for No. XLI but would also apply to No. XLII

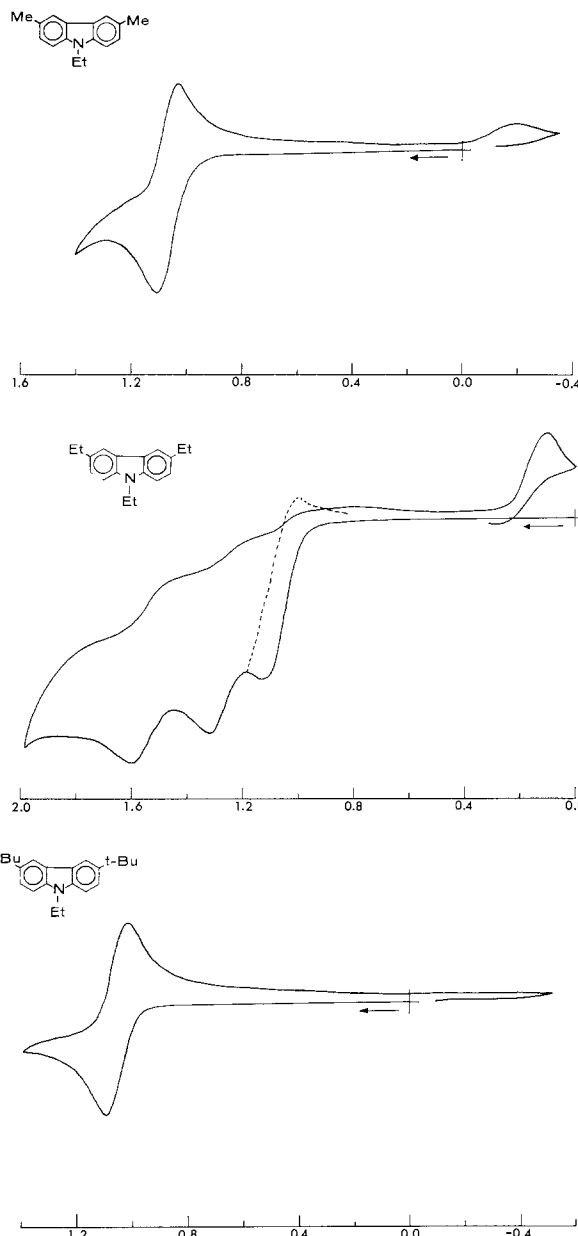
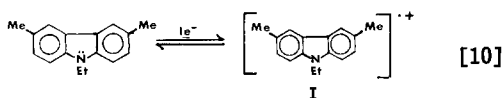
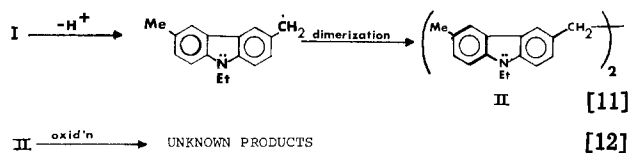


Fig. 6. Cyclic voltammograms of 3,6-dialkyl-N-ethylcarbazoles in MeCN/TEAP. Abscissa is in volts vs. SCE and for all curves the solutions were $1.0 \times 10^{-3}F$ and the sweep rate was 150 mV/sec .



The halogen derivatives, No. XLIV-XLVI, offer an interesting contrast in that the iodo compound eliminates iodine from the primary cation radical quite rapidly ($t_{1/2} \approx 0.5\text{ sec}$) with subsequent coupling to form 6,6'-diiodo-N,N'-diethyl-3,3'-bicarbazyl, the same compound that is generated by oxidation of 3-iodo-N-ethylcarbazole. The products from electrolysis of the mono- and diiodo-N-ethylcarbazoles were found to be identical by matching of cyclic voltammograms and visible absorption spectra run on exhaustively electrolyzed solutions; in both cases the match-up is perfect.

The bromo and chloro analogs (No. XLIV and XLV), however, have reasonably stable primary cation radicals with half-lives of several minutes. In addition, it does not appear in our as yet cursory studies of these

latter two compounds that the radicals decompose by halogen elimination and subsequent coupling; the primary reaction route may instead be some form of ring-ring coupling. This observation is also in marked contrast to the data on the 3,6-dihalocarbazoles, No. XXVIII and XXIX, for which appreciable halogen elimination and subsequent 3,3'-coupling was noted, even though the cation radicals were much less stable than for the N-ethyl analogs and the 1, 8, and 9 positions are less protected.

As a group, No. XLVII-XLIX are characterized by unstable cation radicals which appear to react via elimination and subsequent 3,3'-coupling as the dominant, but not exclusive, pathway. Acetyl and benzoyl group eliminations are indicated by the fact that as with the 3-iodo- and 3,6-diiodo-N-ethylcarbazoles above identical cyclic voltammograms and visible absorption spectra were obtained from exhaustively electrolyzed solutions of the mono- and diacetyl-N-ethylcarbazoles (No. XX and XLVII) and the mono- and dibenzoyl-N-ethylcarbazoles. Of the cation radicals here, the acetyl derivative is least stable ($t_{1/2} \approx 0.6$ sec), followed by the propionyl ($t_{1/2} \approx 0.9$ sec) and the benzoyl ($t_{1/2} \approx 1.5$ sec) compounds. The enhanced stability of the latter compound may be due in small part to increased delocalization afforded by the phenyl rings of the benzoyl groups by a mechanism other than direct conjugation, since this cannot be invoked here. This mode of cation radical reaction is quite unique and so we are at present pursuing kinetic and mechanistic studies of this novel pathway.

Little has been determined for No. L, the methyl ester, beyond the facts that the primary cation radical is unstable ($t_{1/2} \approx 0.5$ sec) but detectable and it appears to react by direct ring coupling rather than by elimination and subsequent 3,3'-coupling; cyclic voltammograms of electrolyzed solutions show no 3,3'-bicarbazyl present.

The carboxylic acid derivative, N-ethylcarbazole-3,6-dicarboxylic acid, was prepared but its electrochemistry could not be investigated due to its complete lack of solubility in MeCN/TEAP.

The nitro and cyano derivatives, No. LII and LI, respectively, were also only lightly studied, but it appears here that ring coupling is the mode of cation radical reaction. In addition, the primary radicals have surprisingly long half-lives; $t_{1/2}$ for the cyano compound is 5-7 sec and that for the nitro derivative is 2-3 sec.

Compounds LIII and LIV offer a fascinating comparison between alkyl coupling and acetyl group elimination as competitive pathways. Cyclic voltammograms indicate that alkyl coupling is the dominant pathway, with a small amount of acetyl elimination observed. Thus, the radical for No. LIII is considerably more stable ($t_{1/2} \approx 1$ sec) than for No. LIV ($t_{1/2} \approx 0.1$ sec) but both are much shorter lived than their dialkyl analogs due to the destabilizing influence of the acetyl group. This is indicative of a fairly drastic change in electron distribution which makes the alkyl groups much more acidic in No. LIII and LIV than in No. XLI and XLII.

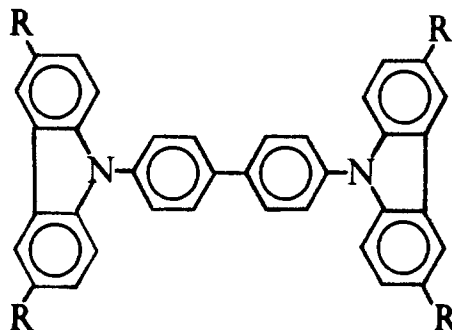
Whereas in the previous section we saw that blockage of the highly reactive 3 and 6 ring carbons largely forced the radical reactions to the area around the carbazole nitrogen, the data presented in this section indicate that N-alkyl substitution in many cases shifts the center of reactivity back to the 3 and 6 sites. The primary radicals are much more stable than if either of these positions is open and so in all cases they can be readily detected. These data clearly show that relatively few substituents can be considered "inert" as possible agents for blocking reactive sites in cation radicals. For intrinsic inertness to reactivity and for having the additional property of affecting as little as possible the electron distribution in the molecular skeleton, the *t*-butyl group seems to be most satisfactory,

a view previously forwarded by Neugebauer in his EPR spectral work on carbazole derivatives (49).

Substituted N-phenylcarbazoles.—Substitution of a phenyl group on the carbazole nitrogen would be expected to have at least two beneficial effects with regard to radical stability. The phenyl ring extends the pi system of the carbazole skeleton and thus contributes to radical stabilization through enhanced delocalization. In addition, the bulky phenyl group acts as an efficient blocking agent for the 1 and 8 ring sites, more so than an N-alkyl group. On the other hand, the phenyl ring introduces the possibility of another coupling site, namely the phenyl carbon *para* to the carbazole nitrogen. Since these molecules are structurally quite similar to triphenylamines such a reaction is not unlikely, but it was not detected in the previous study on the anodic oxidation of N-phenylcarbazole (7).

With the above stabilizing factors in mind, we might expect that 3,6-disubstituted N-phenylcarbazoles such as No. LXXI-LXXIV should have primary radicals more stable than their N-ethyl analogs, No. XLIII-XLVI. In fact, this was found to be the case, although it is not apparent in the chronoamperometric or n value data. The iodo derivatives are probably the easiest to compare, since for these there is rapid reaction via iodine elimination, a reaction contingent upon the electron density at the 3 and 6 ring positions. Whereas the 3,6-diiodo-N-ethylcarbazole cation radical was observed to have a half-life of roughly 0.5 sec, the phenyl analog has $t_{1/2} \approx 1$ sec. This twofold gain in stability appears to be due to the extended delocalizing influence of the N-phenyl ring.

The other three compounds in this series (No. LXXI-LXXIII) appear to have a common mode of radical reaction that is different from the N-ethyl analogs. All exhibit a quasi-reversible (anodic to cathodic peak separation of about 250 mV) redox couple about 0.2-0.4V less anodic than the primary oxidation waves. It is not altogether unlikely that these radicals may slowly undergo a triphenylamine-type coupling to generate something akin to a tetraphenylbenzidine, as shown below.



This species would be more easily oxidized than the parent carbazole and the twisted nature of the N-ring-ring-N portion would lead to irreversible redox behavior (57, 58). Further support for this view is afforded by the observation that no such follow-up couple is seen in the current-voltage curves for No. LXXV and LXXVI, compounds in which the *para* position of the N-phenyl group is substituted. In addition, the cation radical for No. LXXV was qualitatively observed to be more stable than that for No. LXXII by about a factor of three.

The major factor mitigating against this mode of reaction is the rather low electron density that would be predicted for the potential coupling site assuming a moderate amount of twisting of the N-phenyl ring due to steric interaction with the 1 and 8 ring protons. HMO calculations show that as the twist angle is increased from a nominal value of about 45° (that assumed for a freely rotating triphenylamine-type system) the electron density at the *para* site on the N-phenyl ring drops dramatically. Unfortunately, we have no data on the twist angles in cation radicals of

this type, but molecular models show that such twisting would be expected to be substantial. Obviously, the question can best be answered by isolation and characterization of the electrolysis product; we are at present attempting to carry this out.

Stabilization through enhanced delocalization is also indicated by the somewhat greater stability of No. LXXVI as compared to No. XLI, N-substituted-3,6-dimethylcarbazoles. Though both radicals appear to react by alkyl coupling through the 3 or 6 methyl groups, the radical half-life of the N-phenyl derivative is 4-5 min, as compared to 1-2 min for the N-ethyl analog. The disparity is seen even more clearly in the chronoamperometry and n value data in Tables V and VI.

Other effects of the N-phenyl group upon the carbazole skeleton were detected in the electrochemical behavior of No. LV-LXX. These are all N-(*p*-substituted) phenylcarbazoles with both the 3 and 6 carbazole ring positions open for coupling. Not surprisingly, then, it was found that the 3,3'-coupling mode dominates this series, as can be seen in Table VI; the bicarbazyls are generated in high yields and can be readily isolated following controlled-potential preparative-scale electrolyses (see Experimental section).

Two exceptions to this are the amino and dimethylamino derivatives, No. LV and LVI, whose anodic oxidation pathways are more characteristic of *para*-substituted anilines and N,N-dimethylanilines, respectively. In both cases, the carbazole skeleton functions as a rather inert substituent and HMO calculations show most of the electron density residing in the aminophenyl rings; thus, it is not surprising that 3,3'-coupling is not observed. The electrochemical behavior for these compounds appears to be similar to that discussed previously for carbazole derivatives with an amino or dimethylamino group *para* to the carbazole nitrogen, i.e., the N-(*p*-dimethylaminophenyl) carbazole shows two reversible one-electron redox processes; the first leads to a stable cation radical and the second to a moderately stable quinonediimine form that slowly de-

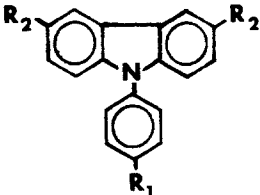
composes to a product other than a 3,3'-bicarbazyl. The amino derivative has an irreversible one-electron wave (the cation radical was, however, detected by rapid-sweep cyclic voltammetry), and it appears that again some sort of N-ring or N-N (amino nitrogen) coupled product is generated in a fashion similar to the other amino-substituted carbazoles.

Interestingly, if the amino group is deactivated by acetylation (No. LVIII) the redistribution of electron density is such that the radical reacts predominately via the 3,3'-coupling-deprotonation route.

Another exception to the 3,3'-coupling mode is the methylthio derivative, No. LVIX. This compound has a very unstable cation radical that decomposes to an unknown product, probably involving oxidation of the methylthio substituent. As can be seen in Table VI, the over-all process involves a one-electron transfer, but no radical species could be detected using EPR spectroscopy with *intra muros* electrochemical generation.

All of the other compounds in this series undergo an initial one-electron oxidation to generate a very reactive cation radical ($t_{1/2} \ll 1$ msec); two of these then couple at the 3 positions to yield a N,N'-bis(*p*-substituted phenyl)-3,3'-bicarbazyl. This species is then oxidized more easily than the corresponding carbazole to a stable dication, so over-all one has a classic two-electron ECE mechanism identical to that previously characterized for *para*-substituted triphenylamines (45). The reaction is quantitative and these systems are extremely "clean," as is seen in Fig. 7 for the *t*-butyl derivative. On the time scale of chronoamperometry or rotating disk experiments this reaction appears to be quantitative for all the derivatives studied with the exceptions mentioned above. This group thus constitutes an unusual series of organic molecules in that one has a single, quantitative homogeneous chemical reaction following the initial electron transfer process in a classic ECE pathway for a wide variety of substituents.

Table VI. Electrochemical characteristics of substituted N-phenylcarbazoles

No.		$E_{p/2}$	$it^{1/2}/C$	n value	Product(s) (% yield), comments
LV	$R_2 = H, R_1 = NH_2$	0.84	46	1.01	Unstable cation radical, product unknown
LVI	$R_2 = H, R_1 = NMe_2$	0.71	49-50 ^a	1.03 ^b	Stable cation radical, second reversible wave at $E_{p/2} = 1.18V$, forms moderately stable quinonediimine
LVII	OMe	1.19	84	1.98	Bicarbazyl (100) ^{c,e}
LVIII	NHCOMe	1.19	68 ^d	1.93	Bicarbazyl, ^e insoluble, forms black perchlorate salt
LVIX	SMe	1.13	50	1.05	No bicarbazyl formed, product unknown
LX	Ph	1.24	85	2.11	Bicarbazyl (80-90) ^{c,e}
LXI	Me	1.24	89	1.98	Bicarbazyl (100) ^{c,e}
LXII	<i>t</i> -Bu	1.22	92	2.04	Bicarbazyl (100) ^{c,e}
LXIII	F	1.26	90-93 ^a	2.08	Bicarbazyl (90-100) ^{c,e}
LXIV	Cl	1.28	91-93 ^a	2.14	Bicarbazyl (80-90) ^{c,e}
LXV	Br	1.30	90-95 ^a	2.12	Bicarbazyl (80-90) ^{c,e}
LXVI	I	1.31	89	2.04	Bicarbazyl (90-100) ^{c,e}
LXVII	COOMe	1.31	84-66 ^d	1.96	Bicarbazyl, ^e insoluble, forms black perchlorate salt
LXVIII	CN	1.33	88-92 ^a	2.05	Bicarbazyl (90-100) ^{c,e}
LXIX	NO ₂	1.36	86-94 ^a	2.36	Bicarbazyl (60-70) ^{c,e}
LXX	H	1.24	88	2.03	Bicarbazyl (100) ^{c,e}
LXXI	$R_1 = H, R_2 = t-Bu$	1.12	47-49 ^a	1.10 ^f	Stable cation radical, slowly decomposes to an unknown product
LXXII	Cl	1.38	47-53 ^a	1.07 ^f	Stable cation radical, slowly decomposes to an unknown product
LXXIII	Br	1.38	52-58 ^a	1.10 ^f	Stable cation radical, slowly decomposes to an unknown product
LXXIV	I	1.40	76-111 ^a	1.94	Unstable cation radical, eliminates iodine to form 6,6'-diiodo-N,N'-diphenyl-3,3'-bicarbazyl
LXXV	$R_1 = R_2 = Cl$	1.42	48-50 ^a	1.06 ^f	Stable cation radical, slowly decomposes to an unknown product
LXXVI	Me	1.08	56-61 ^a	1.09 ^f	Stable cation radical, slowly decomposes to an unknown product

^a Taken from $t = 1-8$ sec; value increases with increasing time.

^b Low steady-state current at the end of the electrolysis.

^c Estimated from peak currents of cyclic voltammograms run on exhaustively electrolyzed solutions.

^d Data are distorted by strong filming of the electrode surface.

^e Cation radicals are very unstable ($t_{1/2} < 1$ msec); 6,6'-disubstituted-N,N'-diphenyl-3,3'-bicarbazyls are formed in all cases.

^f Drifts slowly to $n = 2$.

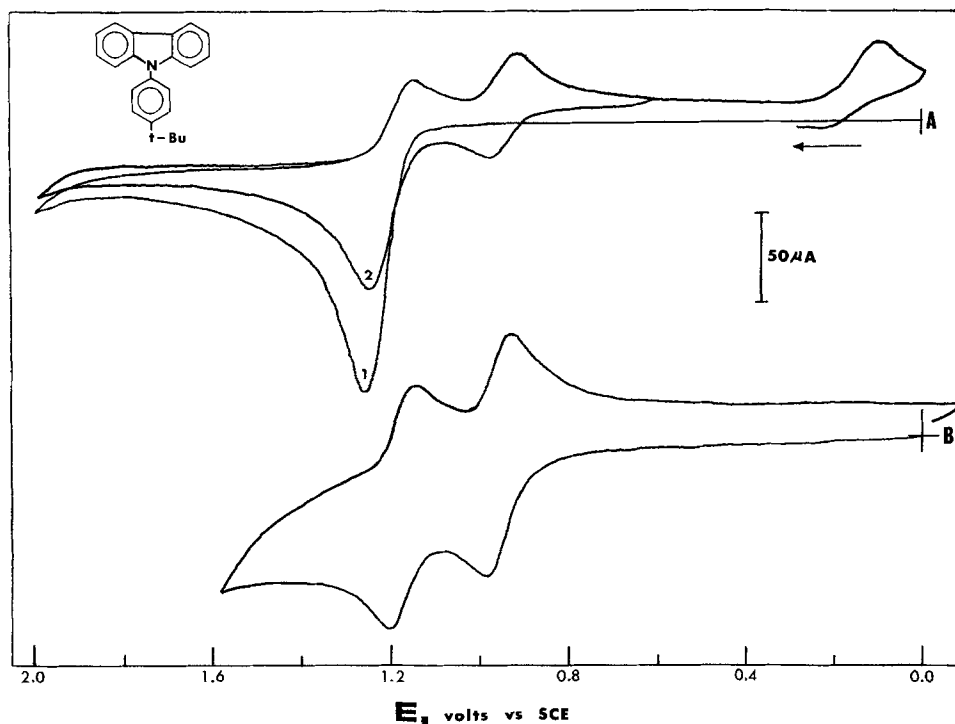
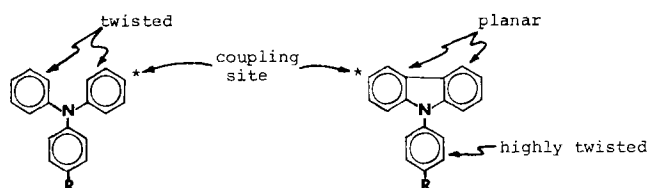


Fig. 7. Curve A: Cyclic voltammogram of $8.0 \times 10^{-4} F$ N-(p-t-butylphenyl)carbazole in MeCN/TEAP, sweep rate = 100 mV/sec. Curve B: Cyclic voltammogram of the same solution following exhaustive electrolysis at 1.4V, sweep rate = 67 mV/sec.

Unfortunately, the rate constants for the coupling reactions are extremely rapid and as such are difficult to measure. However, some preliminary data have been obtained from rotating disk experiments at very low (10^{-4} to $10^{-5} F$) parent concentrations and these numbers are presented in Table VII, along with similar data for a series of correspondingly substituted triphenylamines; these data provide some interesting comparisons concerning the reactivities of organic cation radicals as a function of geometry.

The basic difference between these compounds is that the carbazoles are planar across two rings while the triphenylamines have all three rings at angles to one another. Also, as mentioned, the substituted ring in the carbazole is highly twisted because of steric interaction with the 1 and 8 ring hydrogens



Thus, two effects are to be anticipated, namely that due to the planarity of the carbazole system and the attendant high electron density at the reactive sites (cf. the comparison of diphenylamine and carbazole HMO calculations) the coupling rates will be much faster than for the triphenylamines. Also, there will be a dimin-

Table VII. Comparative electrochemical and kinetic data for triphenylamine and carbazole derivatives

R	Triphenylamine		Carbazole	
	$E_{p/2}, V$	k^a	$E_{p/2}, V$	k^a
OMe	0.76	$6 \pm 2 \times 10^{-1}$	1.19	$7 \pm 4 \times 10^5$
Me	0.87	$9.0 \pm 1.0 \times 10^1$	1.24	$8 \pm 4 \times 10^6$
C ₆ H ₅	0.89	$6.0 \pm 0.6 \times 10^1$	1.24	
H	0.97	$1.2 \pm 0.4 \times 10^2$	1.24	$9 \pm 6 \times 10^7$
Cl	1.02	$6.5 \pm 1.3 \times 10^2$	1.28	
Br	1.02	$1.4 \pm 0.3 \times 10^3$	1.30	
NO ₂	1.22	$1.4 \pm 0.4 \times 10^4$	1.36	

^a Bimolecular coupling rate constant in mol⁻¹ sec⁻¹.

ished substituent effect on the coupling rate constants for the carbazoles due to the lesser interaction of the substituted rings with the rest of the system. The much enhanced carbazole coupling rate constants can readily be seen even in the rough data in Table VII; greater reactivity for the carbazole systems relative to the corresponding triphenylamines is also predicted by HMO calculations.

The lessened substituent effects cannot be clearly seen in the rate constant data due to their uncertainties, but it is evident in the half-peak potential data; the change in $E_{p/2}$ going from OMe to NO₂ is considerably greater for the triphenylamines (0.46V) than for the carbazoles (0.17V). These data must be tempered with the facts that the triphenylamine values were taken from rotating disk curves and are for reversible processes, i.e., there is no shift in the half-peak potentials with variation of the time gate due to associated homogeneous chemical reactions, whereas the carbazole data were obtained from linear scan voltammograms and the $E_{p/2}$ values are markedly affected by the associated chemical reactions and their attendant peak potential shifts. Still, it is felt that the data are qualitatively valid in indicating a substantial difference in substituent effects for the two series.

Conclusions.—The foregoing data allow us to formulate a series of "selection rules" for the various radical reaction pathways. It appears that in many organic systems there is a series of possible reaction pathways for the electrogenerated cation radicals, one being most favorable with the others then occurring in a given sequence as the molecular structure is changed by introduction of various substituents at different sites. The following selection rules apply to carbazole derivatives:

1. The cation radical of the parent molecule, carbazole, reacts by both 3,3'- and 9,9'-couplings, the former taking place in acidic unbuffered MeCN and the latter dominating in basic solution; the same applies for 3-substituted carbazoles with the exception of the amino and dimethylamino derivatives.

2. Blockage of the 9-nitrogen with alkyl or phenyl groups results in exclusive formation of 3,3'-bicarbazyls; the same holds true if the 3 position is substituted but the 6 carbon left open, as in the 3-substituted-N-ethylcarbazoles, again with the exception of the amino and dimethylamino compounds.

3. Substitution of the 3 and 6 sites with the 9 nitrogen left open results in unstable, but detectable, cation radicals which decompose by substituent elimination (I, Br, Cl) or (presumably) ring-ring coupling (OMe, *t*-Bu, OAc, CN, NO₂); the systems are poorly behaved. Electrolysis in basic MeCN leads smoothly in all cases to the 9,9'-bicarbazyls. Further substitution of the 1 and 8 ring positions protects the 9 nitrogen and leads to considerably more stable cation radicals.

4. Blockage of the 3, 6, and 9 sites, as in the 3,6-disubstituted-N-ethylcarbazoles, predictably yields quite stable cation radicals (relative to the other series of substituted carbazoles) since all the active coupling positions are substituted. Many of the derivatives react relatively slowly by as yet undetermined ring-ring coupling modes. A number of compounds in this series show unusual reactions through the 3 and 6 substituents such as alkyl coupling (Me, Et) and group elimination (I, COMe, COEt, CPh). Analogous N-phenyl derivatives appear to have more stable cation radicals because of enhanced delocalization and more efficient blockage of the 1 and 8 ring sites; an additional complication, however, is the possibility of coupling through the N-phenyl rings.

5. Compounds with NH₂ or NMe₂ groups (and presumably OR-type substituents) *para* to the carbazole nitrogen behave very much like *p*-phenylenediamine derivatives. The electron distributions in these compounds are changed so much that they no longer are characteristic of carbazole systems; thus, the cation radicals are quite stable relative to others in the same series and in the cases of the dimethylamino-substituted molecules reasonably stable dication diimines are generated by a second one-electron process. In all cases, the reaction pathways appear to be more representative of aniline-type molecules than of carbazoles.

Spectroscopic Studies

The spectroscopic studies were undertaken in order to obtain information concerning electron distributions in carbazole cation radicals and correlate these data with the chemical reactivities monitored electrochemically. In addition, it was deemed desirable to provide some basic spectral data on these types of radicals since little is available in the literature. It was hoped that optical spectra would provide an idea of the degree of delocalization of the unpaired electron in the cation radicals and the EPR spectra would give a concrete picture of electron distributions from coupling constant data. The data collected thus far, along with those from other sources, are generally consistent with the electrochemical studies in the previous sections.

Optical spectra.—Ledwith first reported optical data on the carbazole and N-methylcarbazole cation radicals (59), which were proposed to arise through charge-transfer interaction with tropylium tetrafluoroborate and exhibited absorption maxima at 506 and 520 nm, respectively. N-isopropylcarbazole was also shown to form charge-transfer complexes with a number of acceptors (60), and it was subsequently claimed that the optical spectrum of the N-isopropylcarbazole cation radical had been obtained by electrolytic oxidation in MeCN (61). However, for the latter two studies the data reported correspond quite closely to optical and EPR spectra previously published for similar carbazole systems where assignments were made to oxidized forms of the corresponding 3,3'-bicarbazyls (7, 62), the optical spectra having two broad maxima positioned at roughly 400 and 800 nm. More recently, cation radical optical spectra for carbazole (63) and N-vinylcarbazole (64) have been reported, the former having an absorption maximum of 610 nm, the latter a series of bands ranging from 508-780 nm.

From this array of conflicting data and the electrochemical data in the previous sections of this paper, it is obvious that optical spectra of carbazole and its N-alkyl derivatives must be considered with caution. Although we have not as yet measured rate constants

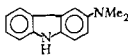
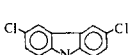
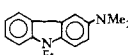
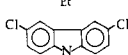
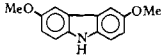
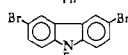
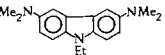
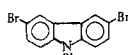
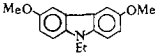
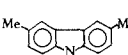
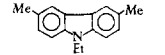
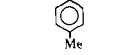
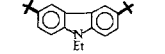
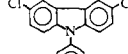
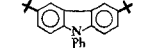
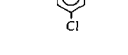
for the decomposition reactions of these radicals, it is clear from the electrochemical studies that their half-lives are, at best, in the microsecond region. As we have seen, though, by proper substitution these radicals can be stabilized and more reliable spectral data should then be obtainable. Thus, Neugebauer has reported λ_{\max} values for 1,3,6,8-tetra-*t*-butylcarbazole cation radical with the primary absorption band being at 925 nm and lesser peaks at 583 and 547 nm (49). We have also obtained spectral data for a number of carbazole derivatives and these data, as shown in Table VIII, verify the fact that carbazole cation radicals have primary absorption bands in the 750-850 nm region, with the exception of the dimethylamino derivatives, which have absorption spectra more characteristic of *p*-substituted-N,N-dimethylanilines (65). It is noteworthy that these primary electronic transitions are at quite long wavelengths compared to other known cation radicals. Such facile transitions are suggestive of a very "loose" pi system in which there is extensive delocalization of the unpaired electron, assuming that these primary bands correspond to a transition of the unpaired electron from the highest filled to the lowest unfilled molecular orbitals.

In addition, these data cast considerable doubt on many of the previously reported λ_{\max} values for the carbazole and N-alkylcarbazole cation radicals. From the absorption maxima shown in Table VIII for the series of 3,6-disubstituted-N-ethylcarbazoles, we feel that we can safely predict that the carbazole and N-alkylcarbazole cation radicals will have absorption maxima for the longest wavelength primary electronic transitions in the 750-790 nm region (58). This assertion will be expanded upon and reported in full in the near future.

EPR studies.—The degree of delocalization can be more quantitatively ascertained from EPR coupling constants, since these latter parameters are generally analogous to unpaired electron densities at the various atoms in a cation radical.

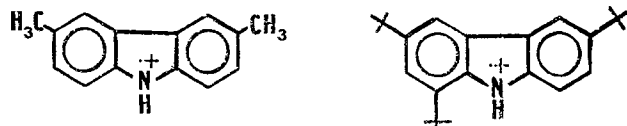
We have obtained moderately well-resolved EPR spectra for all of the radicals shown in Table VIII, but interpretations at this time have not been realized. Neugebauer has, however, obtained interpreted EPR spectra for the substituted carbazole radicals shown below (49, 66), and these can be used as indicators of the degree and direction of delocalization in the carbazole nucleus. These molecules are particularly well suited, since the alkyl substituents will not perturb the

Table VIII. Wavelengths of principal absorption bands of carbazole cation radicals

Compound	λ_{\max} , nm	Compound	λ_{\max} , nm
	611		800 (780) ^a
	625		794 (722) ^a
	758 (684) ^a		823 (775) ^a
	715, 664		811 (738) ^a
	758 (682) ^a		787 ^a
	787 (707) ^a		787 ^a
	798 (716) ^a		860 ^a
	809 (728) ^a		

^a Principal band is at left; a broad shoulder to the blue is present, with a secondary peak in parentheses in some cases.

electron distribution greatly relative to the parent carbazole nucleus



$a_N = 6.89G$	$a_{H(NH)} = 8.09G$	$a_N = 6.6G$
$a_{H1} = 3.84G$	$a_{H2} = 0.80G$	$a_{H(NH)} = 7.8G$
$a_{H4} = 0.80G$	$a_{H(CH3)} = 6.57G$	$a_{H1} = 3.4G$

These coupling constants correlate nicely with the qualitative reactivity data determined electrochemically in showing that large spin densities exist at the central nitrogen and the ring positions *ortho* and *para* to it (the 1,3,6,8 sites). Thus, these are shown quantitatively to be the centers of reactivity in these molecules and so the relatively short radical lifetimes encountered are not unexpected with so many active sites.

The rather large coupling constant for the methyl groups in 3,6-dimethylcarbazole is also consistent with the proposal of alkyl coupling through the substituent groups in No. XIV, XLI, and XLII, since the alkyl group deprotonation is contingent upon a high unpaired electron spin density at the benzylic position.

The spectra of the 3-dimethylamino derivatives (No. II and XII) have not been fully interpreted, but it is apparent that the coupling constant pattern is much more like that of *p*-substituted-*N,N*-dimethylanilines than substituted carbazoles in showing large spin densities on the dimethylamino group and the ring positions *ortho* and *para* to it and virtually none in the unsubstituted ring. Again, this is compatible with the electrochemical data.

Acknowledgments

We are indebted to the Petroleum Research Fund (Grant No. 1039-G3) and the National Science Foundation (Grant No. GP-20606) for financial support of this work. A substantial portion of this study was done at Sacramento State College, and we are grateful for the use of facilities there. Samples of various carbazoles were kindly donated by Southern Dyestuffs Company, Charlotte, North Carolina, Dr. N. P. Buu-Hoi of the Institute for the Chemistry of Natural Substances in Gif-sur-Yvette, France, and Dr. Franz Neugebauer of the Max-Planck Institute in Heidelberg, Germany. Technical assistance by Larry Line, Sam Creason, and Kurtz Carpenter proved to be invaluable. Special thanks are also due to Drs. R. N. Adams and D. E. Smith for their support and encouragement.

This work was extracted in part from the M.S. thesis of one of the authors (J.F.A.) at Sacramento State College (1968).

Manuscript submitted Aug. 22, 1974; revised manuscript received March 17, 1975. This was Paper 145, presented at the New York, New York, Meeting of the Society, May 4-9, 1969.

Any discussion of this paper will appear in a Discussion Section to be published in the June 1976 JOURNAL. All discussions for the June 1976 Discussion Section should be submitted by Feb. 1, 1976.

Publication costs of this article were partially assisted by the Petroleum Research Fund.

REFERENCES

- N. P. Buu-Hoi and Do-Phuoc Hien, *Biochem. Pharmacol.*, **17**, 1227 (1968).
- J. I. Fernandez-Alonso, L. Carbonell-Vila, and R. Domingo, *J. Am. Chem. Soc.*, **79**, 5839 (1957).
- N. P. Buu-Hoi, *Cancer Res.*, **24**, 1511 (1964).
- H. Hoellinger, N. P. Buu-Hoi, and Ph. Mabile, *J. Chem. Soc. (C)*, **1968**, 2209.
- D. Hoffman, G. Rathkamp, and S. Nesnow, *Anal. Chem.*, **41**, 1256 (1969).
- D. Hoffman, G. Rathkamp, and H. Wozowodski, *Beitr. Tabakforsch.*, **4**, 253 (1968); *Chem. Abstr.*, **71**, 19643z (1969).
- J. F. Ambrose and R. F. Nelson, *This Journal*, **115**, 1159 (1968).
- S. H. Tucker, *J. Chem. Soc.*, **1926**, 3033.
- J. McLintock and S. H. Tucker, *ibid.*, **1927**, 1214.
- M. Kuroki, *Y. Gosei Kagaku Kyokai Shi*, **23**, 447 (1965); *Chem. Abstr.*, **63**, 4238d (1965).
- P. Maitland and S. H. Tucker, *J. Chem. Soc.*, **1927**, 1368.
- W. H. Perkin, Jr. and S. H. Tucker, *ibid.*, **1921**, 216.
- G. K. Branch and W. H. Hall, *J. Am. Chem. Soc.*, **46**, 438 (1924).
- S. C. Creason and R. F. Nelson, *J. Electroanal. Chem.*, **27**, 189 (1970).
- L. S. Marcoux, R. N. Adams, and S. W. Feldberg, *J. Phys. Chem.*, **73**, 2611 (1969).
- A. J. Bard and E. Solon, *Anal. Chem.*, **34**, 1181 (1962).
- T. C. Whitner, Jr., *J. Am. Chem. Soc.*, **46**, 2326 (1924).
- J. A. Miller and E. C. Miller, *J. Exptl. Med.*, **87**, 139 (1948).
- F. L. Allen and H. Suschitzky, *J. Chem. Soc.*, **1953**, 3845.
- P. A. Smith, J. M. Clegg, and J. H. Hall, *J. Org. Chem.*, **23**, 524 (1958).
- P. A. S. Smith and B. B. Brown, *J. Am. Chem. Soc.*, **73**, 2435 (1951).
- R. Preston, S. H. Tucker, and J. Cameron, *J. Chem. Soc.*, **1942**, 500.
- S. H. Tucker, *ibid.*, **1926**, 546.
- V. Shishkina, S. Omel'chenko, and W. Soshin, *Tr. Ural'sk Politekhn. Inst.*, **19** (1960); *Chem. Abstr.*, **55**, 24715c (1961).
- N. P. Buu-Hoi and N. Hoan, *J. Org. Chem.*, **16**, 1327 (1951).
- D. P. Chakraborty, K. C. Das, and S. P. Basak, *J. Indian Chem. Soc.*, **45**, 84 (1968).
- S. G. Plant and M. L. Tomlinson, *J. Chem. Soc.*, **1932**, 2188.
- H. Lindemann, *Ber.*, **57B**, 555 (1924).
- N. P. Buu-Hoi and R. Royer, *J. Org. Chem.*, **15**, 123 (1950).
- P. Bruck, A. Ledwith, and A. White, *J. Chem. Soc. (B)*, **1969**, 205.
- N. P. Buu-Hoi and R. Royer, *Rec. Trav. Chim.*, **66**, 533 (1947).
- H. Gilman and S. Spatz, *J. Am. Chem. Soc.*, **63**, 1553 (1941).
- H. M. Grotta, C. J. Riggle, and A. E. Bearse, *J. Org. Chem.*, **29**, 2474 (1964).
- D. Mitchell and S. G. Plant, *J. Chem. Soc.*, **1936**, 1295.
- R. F. Nystrom and C. R. A. Berger, *J. Am. Chem. Soc.*, **80**, 2896 (1958).
- H. Gilman and R. Kirby, *J. Org. Chem.*, **1**, 146 (1936).
- G. deMontmollin and M. deMontmollin, *Helv. Chim. Acta*, **6**, 94 (1923).
- M. Nemes and S. H. Tucker, *J. Chem. Soc.*, **1933**, 1523.
- O. Neuenhoffer and P. Heitmann, *Chem. Ber.*, **94**, 2511 (1961).
- M. Kuroki, *Nippon Kagaku Zasshi*, **88**, 463 (1967); *Chem. Abstr.*, **68**, 95187g (1968).
- H. Gilman and J. Honeycutt, *J. Org. Chem.*, **22**, 226 (1957).
- H. G. Dunlop and S. H. Tucker, *J. Chem. Soc.*, **1939**, 1945.
- C. Buchanan and S. H. Tucker, *ibid.*, **1953**, 2750.
- R. Hand and R. F. Nelson, *This Journal*, **117**, 1353 (1970).
- S. C. Creason, J. Wheeler, and R. F. Nelson, *J. Org. Chem.*, **37**, 4440 (1972).
- M. Melicharek and R. F. Nelson, *J. Electroanal. Chem.*, **26**, 201 (1970).
- E. T. Seo, R. F. Nelson, J. M. Fritsch, L. S. Marcoux, D. W. Leedy, and R. N. Adams, *J. Am. Chem. Soc.*, **88**, 3498 (1966).
- R. F. Nelson and R. N. Adams, *ibid.*, **90**, 3925 (1968).
- F. A. Neugebauer, H. Fischer, S. Bamberger, and H. O. Smith, *Chem. Ber.*, **105**, 2694 (1972).
- G. Cauquis, H. Delhomme, and D. Serve, *Tetrahedron Letters*, 4645 (1971).
- P. Berkenkotter and R. F. Nelson, Unpublished data.
- R. F. Nelson, Ph.D. Thesis, University of Kansas (1966).
- K. Bechgaard and V. D. Parker, *J. Am. Chem. Soc.*, **94**, 4749 (1972).

54. R. Hand, M. Melicharek, D. I. Scoggin, R. Stotz, A. K. Carpenter, and R. F. Nelson, *Collection Czech. Chem. Commun.*, **36**, 842 (1971).
55. L. Line, R. Reynolds, and R. F. Nelson, *J. Am. Chem. Soc.*, **96**, 1087 (1974).
56. V. D. Parker, *Chem. Commun.*, 848 (1969).
57. F. T. Eggertsen and F. T. Weiss, *Anal. Chem.*, **28**, 1008 (1956).
58. R. F. Nelson, Unpublished data.
59. A. Ledwith and M. Sambhi, *Chem. Commun.*, 64 (1965).
60. J. H. Sharp, *J. Phys. Chem.*, **70**, 584 (1966).
61. W. Klopfer, *Z. Naturforsch.*, **24a**, 1923 (1969).
62. D. H. Iles and A. Ledwith, *Chem. Commun.*, 498 (1968).
63. V. E. Sahini, M. Dobrescu, and C. Bendic, *Rev. Roum. Chim.*, **16**, 1131 (1971).
64. Y. Shirota, K. Kawai, N. Yamamoto, K. Tada, H. Mikawa, and H. Tsubomura, *Chem. Letters*, 145 (1972).
65. J. Wheeler and R. F. Nelson, Submitted for publication.
66. F. A. Neugebauer, Private communication.

Electrohydrodimerization Reactions

V. Liquid Ammonia as a Solvent for Reductive Coupling of Diethyl Fumarate, Cinnamitrile, and Acrylonitrile

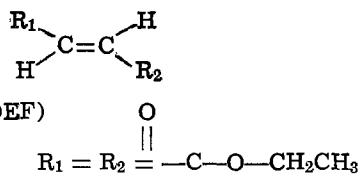
Iuliana Vartires,¹ Wayne H. Smith, and Allen J. Bard*

Department of Chemistry, The University of Texas at Austin, Austin, Texas 78712

ABSTRACT

Cyclic voltammetric (CV) and controlled potential coulometric investigations of the reduction of several activated olefins in anhydrous liquid ammonia containing either 0.1M methyl-tri-n-butylammonium iodide or 0.1M potassium iodide as supporting electrolytes are reported. For diethyl fumarate and cinnamitrile the studies provide evidence for formation of a radical anion, which undergoes dimerization and polymerization reactions, and of dianion formation at more negative potentials. The effect of adding isopropanol and glacial acetic acid was also investigated.

The reduction of activated olefins in aprotic media has been the subject of numerous investigations [see (1, 2) and references therein]. Diactivated olefins (R) react via formation of the radical anion and produce, depending upon the acidity of the medium, hydrodimer (R₂H₂), reduced monomer (RH₂), and polymer. At more negative potentials, where dianion is produced, extensive polymerization apparently occurs, so that the second reduction waves observed in voltammetry are frequently much smaller than the first waves. We have previously shown that anhydrous liquid ammonia is a useful medium for studies of the electroreduction of organic compounds (3, 4) and that stable dianions of benzophenone and nitrobenzene could be prepared in this solvent. This stability of radical anions and dianions in ammonia can be attributed to the low acidity of the solvent, the possibility of preparing highly pure solutions through the use of vacuum line techniques and solvent treatment with sodium, and the fact that these studies are carried out at low temperatures, decreasing the rate of homogeneous chemical reactions following the electron transfer steps. Previous studies of amalgam reductions leading to hydrodimerization in liquid ammonia have also been described (5). In this paper we describe preliminary cyclic voltammetric and coulometric experiments on the reduction of several activated olefins in liquid ammonia; the structures of the substances studied are shown below



Cinnamitrile (CN) $\text{R}_1 = \text{---C}_6\text{H}_5$ $\text{R}_2 = \text{---CN}$

Acrylonitrile $\text{R}_1 = \text{H}$ $\text{R}_2 = \text{---CN}$

* Electrochemical Society Active Member.

¹ Permanent address: Research Center for Physical Chemistry, Bucharest, Roumania.

Key words: cyclic voltammetry, coulometry, electrochemical dimerizations, organic electrochemistry.

Experimental

General experimental techniques were the same as those reported previously (2-4); a detailed description is available (6). The four-compartment cell, containing separate chambers for the working, reference, and auxiliary electrodes, and an intermediate chamber between the working and auxiliary compartments was employed. A gold working microelectrode, polished with AB ALPHA polishing alumina (Buehler Limited, Evanston, Illinois) before each experiment, was employed in cyclic voltammetric experiments and a 3 cm by 8 cm platinum electrode was used in coulometry. A silver wire (Ag. R.E.) isolated in a separate compartment closed with a sintered-glass disk was used as reference electrode. All experiments were carried out with a Princeton Applied Research Corporation Model 170 electrochemistry system using positive feedback resistance compensation. All experiments were conducted on a high vacuum line (10⁻⁵ Torr) at -43°C.

Results and Discussion

Diethyl fumarate.—The cyclic voltammetric (CV) reduction of DEF in DMF solution shows a fairly reversible first reduction wave at fast scan rates and has been characterized by reversible reduction to the radical anion followed by a coupling reaction (2). The second reduction wave is very small or even characterized by a current decrease in polarography or RDE voltammetry, which has been ascribed to production of the dianion which initiates a rapid polymerization reaction removing parent from the vicinity of the electrode. In liquid ammonia, the CV reduction occurs in two reversible waves at fast scan rates (Fig. 1a) with the reversal wave heights decreasing at slower scan rates (Fig. 1b) indicating decomposition reactions of the electrogenerated species. Typical data for CV experiments for DEF are shown in Table I. The theory of CV for electrode reactions with following dimerization reactions has been presented (7, 8); application of this theory in estimating the rate constant for the dimerization step from the variation of i_{pa}/i_{pc} for the first reduction wave yields a value of about 0.1 M⁻¹ sec⁻¹.

Table I. Cyclic voltammetric data for reduction of diethyl fumarate in liquid ammonia^a

Concentration, C (mM)	Scan rate, ν (mV/sec)	First wave			Second wave		
		i_{pc} (μ A)	i_{pa}/i_{pc}	$-E_{pc}^b$ (V)	i_{pc} (μ A)	i_{pa}/i_{pc}	$-E_{pc}^b$ (V)
A. 0.1M Methyl-tri-butylammonium iodide							
1.5	50	28	0.41	0.87	10	0.42	1.40
	100	36	0.48	0.88	16	0.87	1.41
	200	49	0.64	0.89	24	0.86	1.42
	500	71	0.87	0.91	52	0.96	1.45
	20,000	620	1.0	0.94	450	1.0	1.50
$i_{pc}(1)/\nu^{1/2}C = 1.95$							
3	50	49	0.64	0.87	13	0.66	1.40
	100	63	0.54	0.88	24	0.33	1.41
	200	84	0.60	0.90	41	0.68	1.44
	500	123	0.78	0.92	82	0.9	1.48
	$i_{pc}(1)/\nu^{1/2}C = 2.0$						
4.6	50	65	0.50	0.85	15	0.46	1.42
	100	90	0.53	0.86	29	0.43	1.39
	200	128	0.53	0.87	56	0.70	1.40
	500	200	0.67	0.88	120	0.80	1.42
	$i_{pc}(1)/\nu^{1/2}C = 2.4$						
B. 0.1M KI ^c							
2.3	50	12.5		0.74			1.33
	100	22.5		0.75			1.34
	200	29		0.76			1.35
	500	38		0.77			1.37
	$i_{pc}(1)/\nu^{1/2}C = 0.98$						

^a Solution contained indicated supporting electrolyte in anhydrous liquid ammonia.

^b vs. Ag-wire reference electrode.

^c Second reduction wave and reversal waves were to ill-defined for precise current measurements.

The addition of alkali metal ions has been shown to increase the rate of the coupling reaction in DMF, probably by formation of ion pairs with the radical anions (2). The CV reduction of DEF is similarly affected by the addition of KI in liquid ammonia (Fig.

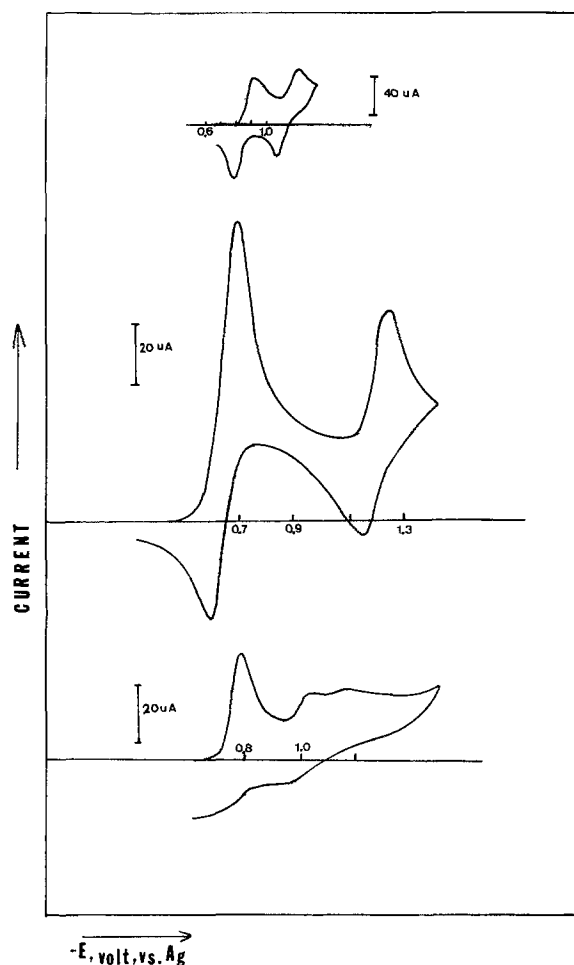


Fig. 1. Cyclic voltammograms of diethyl fumarate in liquid ammonia: (a) 1.75 mM DEF, 0.1M MTBAI, $\nu = 20$ V/sec; (b) 3 mM DEF, 0.1M MTBAI, $\nu = 0.2$ V/sec; (c) 3.5 mM DEF, 0.1M KI, $\nu = 0.2$ V/sec.

1c), although the kinetics of the reactions were not studied in this case. The addition of a threefold excess of a proton donor, either the weak acid, isopropanol (i-PrOH), or the strong acid, acetic acid (HOAc) to the DEF/MTBAI/ NH_3 system has essentially no effect on the first reduction wave, but decreases the reversal current of the second wave and shifts the second wave to more positive potentials. The extent of the shift increases linearly with the log of the proton donor concentration; for acetic acid $\Delta E_p/\Delta \log[HOAc] = 39$ mV; and for i-PrOH, $\Delta E_p/\Delta \log[i-PrOH] = 57$ mV. These results suggest that protonation of the radical anion species does not occur, even with the strong acid HOAc, while the dianion reacts with acid. This scheme is reminiscent of that found with benzophenone (3), and the CV reaction order treatment of Savéant and Vianello (8) probably applies here as well. From the limiting slopes of the peak shift with log proton donor concentration we find a reaction order of dianion (m_z) and proton donor (m_z) of 0.5 and 1.9, respectively, for i-PrOH and 0.4 and 1.2 for HOAc. This half-order dependence on dianion is the same as that observed for benzophenone dianion and probably indicates kinetic complications in the electron transfer reaction or interferences due to the dianion polymerization reaction.

Controlled potential coulometry of DEF in the presence of either MTBAI or KI as supporting electrolyte (Table II) at potentials beyond the first reduction peak show n_{app} values less than one, even in the presence of proton donor. This result suggests, as do the similarly low values of n_{app} in DMF, that a slow polymerization reaction of the radical anion occurs on the coulometric time scale. CV experiments after coulo-

Table II. Controlled potential coulometry results

Compound	Concentration (mM)	Conditions	n_{app}
DEF	4.3	0.1M MTBAI	0.6
	10	0.1M MTBAI	0.5
	20	0.1M MTBAI + 40 mM i-PrOH	0.5
DEF	7	0.1M KI	0.4
	3	0.1M KI + 14 mM HOAc	0.5
CN	10.4	0.1M MTBAI	0.16
	13.6	0.1M MTBAI + 40 mM i-PrOH	0.04
AN	20	0.1M MTBAI + 40 mM i-PrOH	0.27
	3	0.1M MTBAI	0.05
AN	14	0.1M MTBAI	0.17
	10	0.1M KI + 10 mM i-PrOH	0.96
AN	20	0.1M KI + 20 mM i-PrOH	0.88
	20	0.1M KI + 10 mM HOAc	2

metric reduction showed no reduction or oxidation peaks.

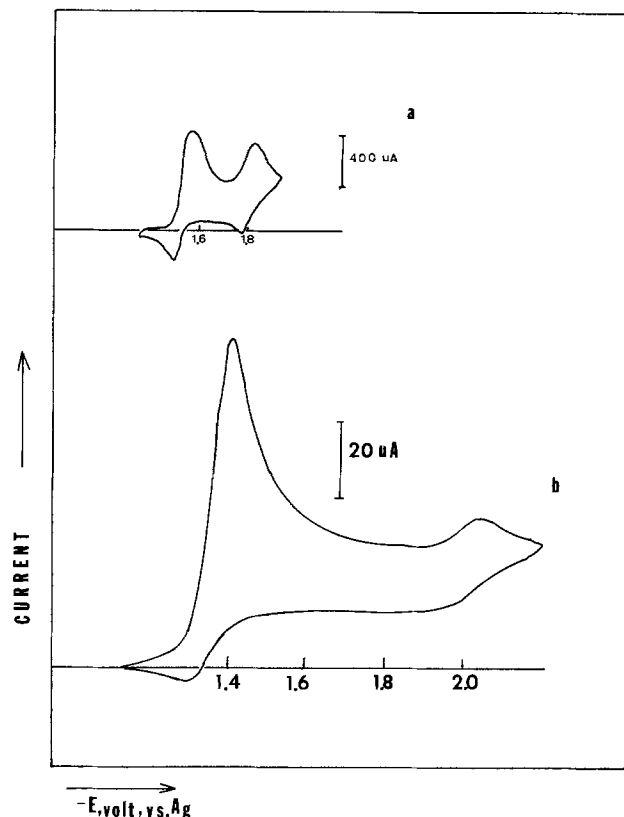


Fig. 2. Cyclic voltammograms of 3.2 mM cinnamionitrile in liquid ammonia containing 0.1M MTBAI with a v of (a) 20 and (b) 0.2 V/sec.

Cinnamionitrile.—The CV reduction of CN at high scan rates (Fig. 2) also shows two reduction waves with appreciable anodic currents on reversal. Typical CV data for CN are shown in Table III. At slower scan rates the second reduction peak decreases in size and the reversal currents decrease. For CN, as opposed to DEF, the value of $i_p/v^{1/2}C$ decreases significantly with

Table III. Cyclic voltammetric data for reduction of cinnamionitrile in liquid ammonia^a

Concentration, C (mM)	Scan rate, v (mV/sec)	i_{pc} (μA)	$-E_{pc}^b$ (V)	$-E_{pc}^c$ (2) (V)
1.6	50	38	1.27	1.90
	100	55	1.28	1.88
	200	73	1.28	1.88
	500	105	1.33	1.90
$i_{pc}/v^{1/2}C = 3.3$				
3.2	50	52	1.26	1.90
	100	88	1.27	1.90
	200	120	1.28	1.90
	500	140	1.36	1.88
$i_{pc}/v^{1/2}C = 3.1$				
7.2	50	82	1.27	
	100	133	1.27	
	200	195	1.28	
	500	260	1.33	
$i_{pc}/v^{1/2}C = 2.2$				
10	50	127	1.25	
	100	175	1.27	
	200	240	1.28	
	500	300	1.34	
$i_{pc}/v^{1/2}C = 1.6$				
20	50	170	1.24	
	100	212	1.25	
	200	280	1.27	
	500	395	1.35	
$i_{pc}/v^{1/2}C = 0.8$				

^a Solution contained 0.1M MTBAI.

^b First wave, V vs. Ag-wire reference electrode.

^c Second wave. Peak too ill-defined at higher concentrations for precise measurement.

increasing concentration of CN, suggesting that the polymerization reaction of the radical anion is important, even on the CV time scale. Treatment of the i_{pa}/i_{pc} data for the first reduction wave, assuming a following coupling reaction of the radical anion, yields a dimerization rate constant of about $5.7 M^{-1} sec^{-1}$. The CV behavior in the presence of proton donor resembles that of DEF: the first wave is unaffected by additions of *i*-PrOH or HOAc, while the second wave is shifted to more positive potentials. The limiting E_p vs. log proton donor concentration plots for the second wave yield reaction orders m and m_z of 0.4 and 2, respectively, for *i*-PrOH and 0.7 and 1 for HOAc. Controlled potential coulometry of CN (Table II) in the absence of proton donor or with *i*-PrOH showed very low n_{app} values suggesting abundant polymerization.

Acrylonitrile.—The CV reduction of AN at all scan rates up to 20 V/sec in both MTBAI and KI electrolytes occurs in a single irreversible wave (Fig. 3); typical CV data are shown in Table IV. The very low $i_p/v^{1/2}C$ values observed with MTBAI as electrolyte are evidence of a very rapid polymerization of AN, as is also observed in aprotic solvents in the absence of proton donor. In the KI electrolyte however the $i_p/v^{1/2}C$ values are larger and closer to those of DEF and CN. Controlled potential coulometric reduction of AN (Table II) also shows evidence of polymerization in MTBAI. In a KI + *i*-PrOH medium, however, n_{app} values close to one are obtained, suggesting significant formation of the hydrodimer product. Product analysis

Table IV. Cyclic voltammetric data for reduction of acrylonitrile in liquid ammonia

Concentration, C (mM)	Scan rate, v (mV/sec)	i_{pc} (μA)	$-E_{pc}$ (V vs. Ag R.E.)
A. 0.1M Methyl-tributyl ammonium iodide			
4.3	50	12	1.86
	100	20	1.86
	200	24	1.91
	500	27	1.96
$i_{pc}/v^{1/2}C = 0.55$			
5.8	50	5	1.78
	100	9	1.83
	200	15	1.86
	500	23	1.98
$i_{pc}/v^{1/2}C = 0.25$			
8.6	50	10	1.84
	100	12	1.86
	200	16	1.86
	500	19	1.96
$i_{pc}/v^{1/2}C = 0.07$			
11.5	50	6	1.86
	100	10	1.86
	200	15	1.90
	500	20	2.05
$i_{pc}/v^{1/2}C = 0.13$			
14.6	50	18	1.91
	100	20	1.90
	200	24	1.91
	500	37	1.96
$i_{pc}/v^{1/2}C = 0.06$			
23.2	50	16	1.93
	100	21	1.99
	200	28	2.00
	500	49	2.06
$i_{pc}/v^{1/2}C = 0.11$			
B. 0.1M Potassium iodide			
5.8	50	85	1.61
	100	120	1.62
	200	205	1.64
	500	285	1.67
$i_{pc}/v^{1/2}C = 1.7$			
10.3	50	70	1.62
	100	130	1.64
	200	220	1.68
	500	340	1.70
$i_{pc}/v^{1/2}C = 1.8$			
11.5	50	55	1.62
	100	93	1.64
	200	225	1.68
	500	430	1.70
$i_{pc}/v^{1/2}C = 2.1$			
20.12	50	95	1.62
	100	135	1.63
	200	195	1.64
	500	335	1.67
$i_{pc}/v^{1/2}C = 1$			

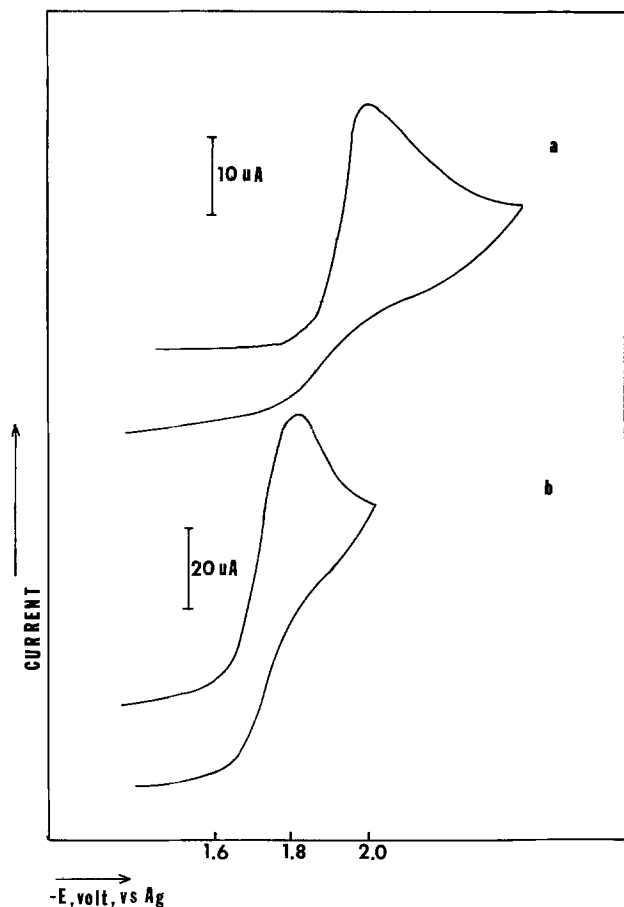


Fig. 3. Cyclic voltammograms of acrylonitrile in liquid ammonia; (a) 5.75 mM acrylonitrile, 0.1M MTBAI, $\nu = 0.2$ V/sec; (b) 5.16 mM acrylonitrile, 0.1M KI, $\nu = 0.2$ V/sec. Curves are of same form at higher scan rates.

of these solutions by gas chromatography was attempted, but unambiguous analyses were not obtained. The addition of HOAc yields n_{app} values near 2, probably signalling the production of some of the two-electron protonated product, propionitrile, in the presence of strong acid.

The preliminary results show the formation of radical anions and dianions of the deactivated olefins DEF and CN and suggest that with the addition of suitable amounts of proton donor, hydrodimerization reactions can be carried out in liquid ammonia. After this paper was submitted, a communication by Chiba *et al.* (9) appeared, in which the electrolytic reduction of acrylonitrile in liquid ammonia containing ammonium perchlorate as supporting electrolyte at a mercury cathode was described. These authors found a high yield of adiponitrile with some formation of propionitrile under these conditions with constant current electrolysis.

Acknowledgment

The support of the National Science Foundation (GP 31414X) and fellowship support to Iuliana Vartires by the International Research and Exchanges Board is gratefully acknowledged.

Manuscript submitted Jan. 20, 1975; revised manuscript received March 20, 1975.

Any discussion of this paper will appear in a Discussion Section to be published in the June 1976 JOURNAL. All discussions for the June 1976 Discussion Section should be submitted by Feb. 1, 1976.

Publication costs of this article were partially assisted by The University of Texas at Austin.

REFERENCES

1. M. M. Baizer in "Organic Electrochemistry," M. M. Baizer, Editor, Chap. XIX, Marcel Dekker, Inc., New York (1973).
2. M. J. Hazelrigg, Jr. and A. J. Bard, *This Journal*, **122**, 211 (1975).
3. A. Demortier and A. J. Bard, *J. Am. Chem. Soc.*, **95**, 3495 (1973).
4. W. H. Smith and A. J. Bard, *ibid.*, In press.
5. Y. Arad, M. Levy, H. Rosen, and D. Vofsi, *J. Polymer Sci., Pt. B*, **7**, 197 (1969).
6. W. H. Smith, Ph.D. Dissertation, The University of Texas at Austin (1974).
7. M. L. Olmstead, R. G. Hamilton, and R. S. Nicholson, *Anal. Chem.*, **41**, 260 (1969).
8. J. M. Savéant and E. Vianello, *Electrochim. Acta*, **12**, 629 (1967).
9. T. Chiba, Y. Takata, and A. Suzuki, *Chem. Letters*, **1974**, 1241

Electrochemical Oxidation of Iminobibenzyl and Related Compounds

S. N. Frank* and Allen J. Bard*

Department of Chemistry, University of Texas at Austin, Austin, Texas 78712

and Anthony Ledwith

Donnan Laboratories, University of Liverpool, Liverpool L693BX, England

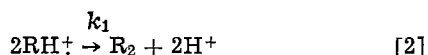
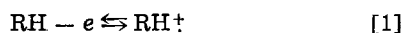
ABSTRACT

Electrochemical oxidation of iminobibenzyl and several related compounds has been investigated in acetonitrile. The mechanism of the oxidation is best described by an ECE process with coupling of the product of an initial one-electron oxidation in a subsequent but very fast reaction to form a dimeric compound that is further oxidized by an over-all two-electron process at potentials more negative than those required for oxidation of the parent compounds. The electrochemistry of these compounds is complicated by the release of protons during the oxidation which protonate the starting materials and the neutral dimerized products rendering them electrochemically inactive. Differences in the electrochemistries of the various coupled products are discussed in terms of structural variations.

In recent years considerable effort has been expended in elucidating the mechanisms of electrolytic oxidation of heterocyclic nitrogen and amine compounds as well as other nitrogen containing species. [See Ref. (1) and (2) for reviews of the work in this area.] One of the prominent characteristics of aromatic amines is oxidative coupling to form a variety of dimerized derivatives of the original parent compounds. Certain heterocyclic nitrogen compounds such as carbazole which may be considered as being derived from diphenylamine also undergo a similar coupling process on oxidation (3).

The present investigation was initially undertaken to compare the electrochemistry of imipramine hydrochloride, a widely prescribed antidepressant drug, with the electrochemical behavior of the structurally similar but physiologically less active iminobibenzyl and 5-methyliminobibenzyl. We also felt it worthwhile to compare the electrochemistry of these compounds with that of the related carbazoles (I) whose primary structural difference with the above compounds is the nature of the biphenyl linkage.

The homogeneous oxidation of most of the present compounds along with a number of carbazoles with chemical oxidants (e.g., 2,3-dichloro-5,6-dicyano-p-benzoquinone) has shown recently (4) that all of the compounds undergo oxidative coupling with ultimate formation of the cation radical salt of the coupled product. The electrochemical coupling of the carbazoles has been previously investigated by Ambrose and Nelson (3) who showed that the neutral coupled products can be oxidized to corresponding cation radicals and dications at potentials negative of those for the oxidation of the parent compounds. The electrochemical behavior of the carbazoles was consistent with an ECE mechanism with oxidative peak heights of the potential sweep voltammograms being twice those expected for a 1-electron process (3). Controlled potential electrolysis also gave an n value of 2. Ambrose and Nelson (3) proposed the following mechanism for the oxidative coupling of the carbazoles (3).

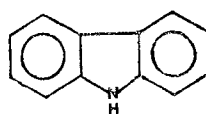


* Electrochemical Society Active Member.

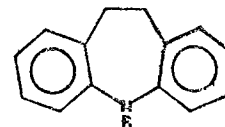
Key words: cyclic voltammetry, coulometry, oxidative coupling, imipramine, 5-methyliminostilbene.

The chemical reaction in Eq. [2] is undoubtedly very rapid, since under no circumstances was it possible to observe the reduction of the radical cation of the oxidized parent (RH^{\dagger}). In neither study (3,4) were the investigators able to determine if the protons are lost before or after coupling.

We report here the electrochemical oxidation of iminobibenzyl (II), 5-methyliminobibenzyl (III), imipramine·HClO₄ (IV) and 5-methyliminostilbene (V), and the electrochemical behavior of the products of the oxidation

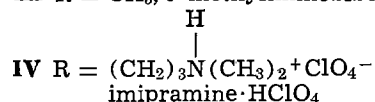


I Carbazole

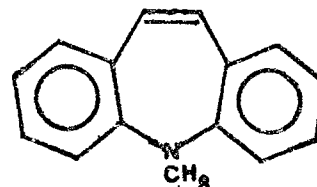


II R = H, iminobibenzyl

III R = CH₃, 5-methyliminobibenzyl



IV R = (CH₂)₃N(CH₃)₂⁺ ClO₄⁻
imipramine·HClO₄



V 5-methyliminostilbene

Experimental

The preparation of the compounds used in this study has been described (4). Tetrabutylammonium perchlorate (TBAP), the supporting electrolyte in all experiments, was of polarographic grade and purchased from Southwestern Analytical Chemicals. The TBAP which is contaminated with water was dried under vacuum at about 100°C for 24 hr. All other chemicals were of reagent grade quality and used without further purification.

Acetonitrile used as the solvent in these experiments was prepared from spectrograde acetonitrile by vacuum distillation from P₂O₅ at room temperature. The distillation was repeated at least three times with periodic freeze-pump-thawing to remove air.

Table I. $i_p/Cv^{1/2}$ ratios and oxidation and reduction peak potentials for parent and product of the oxidation of parent

Compound	$i_p/Cv^{1/2}$ ^a Parent	E_p ox ^b	E_p ox ^b Product	E_p red ^b
Carbazole ^c		+0.86	0.86, 0.56	0.8, 0.5
Iminobibenzyl	17.9	+0.48	0.42, 0.24	0.36, 0.18
5-Methyliminobibenzyl	18.3	+0.61	0.48	0.40
Imipramine HClO ₄ ^e	17.7	+0.75	0.61	0.55
5-Methyliminostilbene	17.9	+0.58	-0.27	-0.30
10-Methylphenothiazene ^d	16.1			

^a i_p in μA , C in mM, v in V/sec. Within experimental error the $i_p/Cv^{1/2}$ values were independent of sweep rate between 0.2 and 10 V/sec.

^b Sweep rate = 0.2 V/sec. E_p vs. Ag/0.1M AgNO₃.

^c Imipramine hydrochloride was converted to the perchlorate by passing an aqueous solution through an anion exchange column in the perchlorate form and freeze drying the eluent.

^d A standard one-electron oxidant of similar geometric size to the compounds under investigation. Due to the similarity in size the diffusion coefficients should be nearly the same for all compounds.

The cell used in this study for coulometric and electrochemical characterizations was of conventional design (5). The working electrode for coulometry was a platinum gauze. The working electrode for cyclic voltammetry was a small platinum disk electrode sealed in glass ($\sim 0.013 \text{ cm}^2$) and was polished before each use with 0.5μ alumina polishing powder. The auxiliary electrode was a platinum wire and the reference electrode a silver wire which for certain experiments was in contact with a solution of 0.1M AgNO₃ in acetonitrile; the potential of this electrode was +0.333V vs. an aqueous SCE. All potentials are reported vs. this Ag/Ag⁺ electrode.

All electrochemical experiments were carried out under an inert helium atmosphere in a Vacuum/Atmospheres Corporation (Hawthorne, California) dry box. A PAR Model 170 electrochemical system (Princeton Applied Research Corporation, Princeton, New Jersey) was used for the electrochemical experiments.

Infrared measurements were made with a Beckman Model IR5A spectrophotometer (KBr pellets). Mass spectra were obtained on a Bell & Howell Model 21-491 low resolution mass spectrometer.

Results

Iminobibenzyl.—At a voltammetric sweep rate of 0.2 V/sec iminobibenzyl shows an oxidation wave with E_{pa} at +0.48V vs. the Ag/0.1M Ag⁺ electrode. The height of this peak corresponded to that for a one-electron process by calibration against the peak height for the known one-electron oxidation of 10-methylphenothiazene (Table I). This result contrasts with the two-electron peak height previously observed for the carbazoles (3). On sweep reversal two reduction peaks were observed with E_{pc} 's at +0.36 and +0.18V (Fig. 1). Upon repeated cycling two new oxidation peaks were evident at +0.42 and +0.24V. The peak potentials for iminobibenzyl and the other compounds in this study are summarized in Table I.

Table II. Coulometric n_{app} values for parent compounds and the products of a controlled potential oxidation of the parent compounds

Compound ^a	n_{app} OX Parent	n_{app} Red Product	n_{app} OX of red product	n_{app} red of H ⁺
Iminobibenzyl	2.02	0.96	0.94	0.95
5-Methyliminobibenzyl ^b	1.0	0.5	0.5	0.5
	2.2	0.93	0.9	0.98
Imipramine HClO ₄	0.92	0.45	0.44	1.5
5-Methyliminostilbene	0.95	0.45	0.43	0.47

^a The concentration of compound ~ 1 mM in all coulometric experiments.

^b The two values listed correspond to the two breaks observed in the Q-t curve.

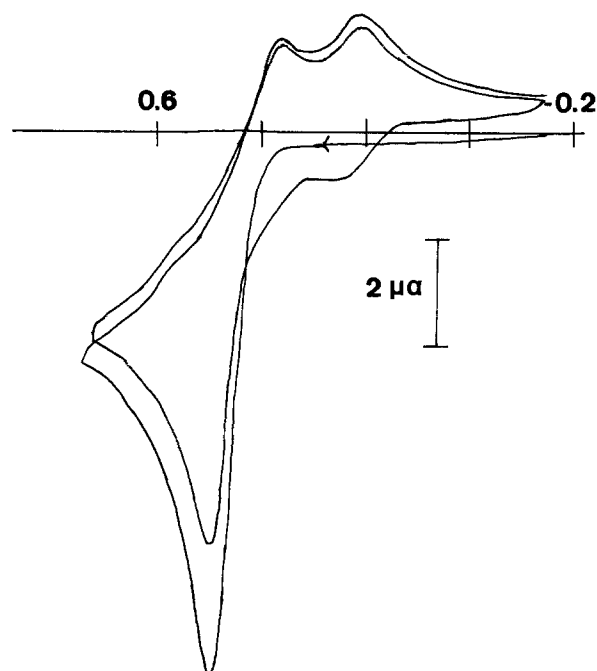


Fig. 1. Cyclic voltammogram of 1.25 mM iminobibenzyl. Conditions: sweep rate = 0.2 V/sec; 0.1M TBAP supporting electrolyte; X-axis is E, V, vs. Ag/0.1M Ag⁺ reference electrode.

Controlled potential electrolysis at +0.85V gave an n_{app} value of 2 (where n_{app} represents the coulombs of electricity per mole of electroactive compound) (Table II) which is twice the value indicated by the voltammetry results. The oxidized solution had an intense blue color. Cyclic voltammetry of the solution following oxidation showed a redox couple centered at about +0.5V (Fig. 2) and a hydrogen ion reduction wave commencing at about -0.5V. Controlled potential coulometry of this solution indicated that the product of the initial oxidation could be reduced (at $E = +0.2V$) and then reoxidized again (at $E = +0.85V$) with an $n_{app} = 1$. Controlled potential reduction at -1.3V (following the oxidation at +0.85V) showed the release of one H⁺ per parent molecule oxidized (i.e., $n_{app} = 1.0$) during the initial oxidation at +0.85V. After the reduction of the protons only the two redox couples observed after repeated cycling of a solution of unoxidized parent were present (Fig. 3). There was no evidence of any

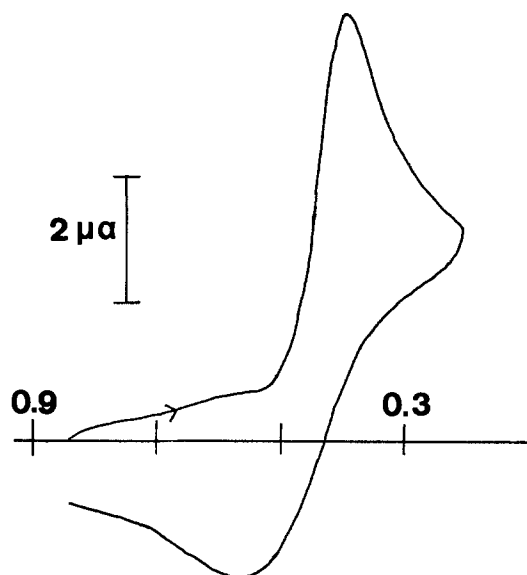


Fig. 2. Cyclic voltammogram of 1.25 mM iminobibenzyl after oxidative electrolysis at +0.85V. Conditions: Same as Fig. 1.

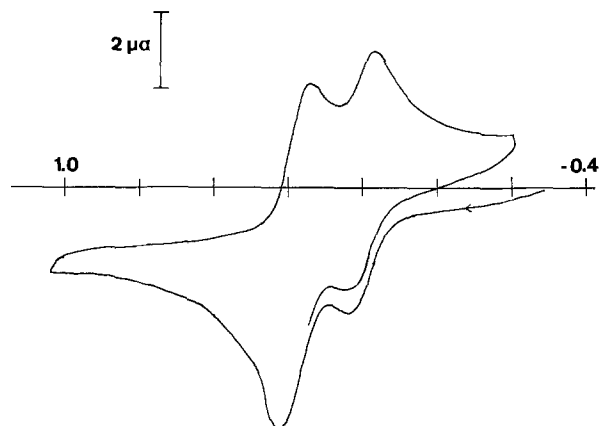
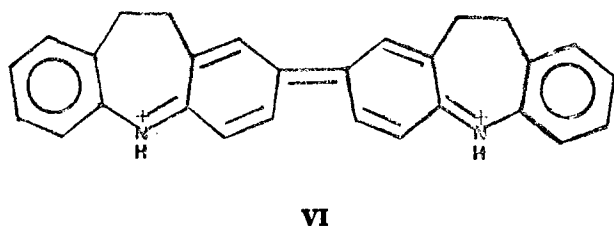


Fig. 3. Cyclic voltammogram of 1.25 mM iminobibenzyl following electrolysis at +0.85 and at -1.3V. Conditions: Same as Fig. 1.

remaining parent or the couple observed at +0.5V following the initial oxidation at +0.85V. The separation between E_{pa} and E_{pc} for each couple was 60 mV and indicates that each couple corresponds to a one-electron process. Coulometry demonstrated that a total of one electron was necessary to oxidize and then reduce both couples. In the absence of protons the product of the oxidation of parent at +0.85V behaved electrochemically in an entirely analogous manner to the carbazole products where two one-electron couples were also seen. In fact, except for the anomalous voltammetric peak height observed for the parent and the electrochemical behavior of the product of the oxidation of iminobibenzyl in the presence of protons, the electrochemistry is similar to that for the carbazoles. It seems likely therefore that a similar mechanism is operative in the case of iminobibenzyl with ultimate formation of a product (VI) which, by analogy with homogenous studies (4), probably arises by coupling at the 2-position



The rate of the coupling reaction is fast because no evidence was obtained for reduction of the parent radical cation during the voltammetry experiments.

In order to confirm that VI is indeed the major product of the oxidation at +0.85V, an attempt was made to isolate the neutral analog of VI prepared by a controlled potential reduction of a solution of VI. At the relatively high solution concentrations necessary to isolate a reasonable quantity of material ($\cong 20$ mM), the electrochemistry of iminobibenzyl was not as clean as observed at lower concentrations (~ 1 mM). This is probably because of precipitation of the electrolysis products onto the working electrode. At these concentrations it was not possible to carry the oxidations or reductions to theoretical completion before the electrolysis currents decayed to very small values. The solutions that resulted upon reduction of an oxidized solution of iminobibenzyl contained significant quantities of unreduced material as indicated by an intense bluish-green color. Removing the acetonitrile solvent after reduction on a vacuum line followed by dissolution of the solid in benzene to separate the neutral from most of the charged products and extraction of the benzene solution with water to remove most of the remaining charged species re-

sulted on freeze-drying in a brown solid with a slight violet tinge. Infrared spectra of this material showed a strong absorption at 805 cm^{-1} . This is the same absorption expected for the iminobibenzyl dimer with coupling at the 2-position (4). The parent peak of a mass spectrum of this compound occurred at a molecular weight of 388 the same as the bibenzyl dimer. The mass spectrum also indicated the presence of minor amounts of higher molecular weight materials.

Possible complications due to the presence of H^+ that may explain the anomalous behavior of the coupled product and one electron peak height of the parent will be discussed later.

5-Methyliminobibenzyl.—Investigations of the homogeneous oxidation of 5-methyliminobibenzyl have demonstrated a similar coupling process as was found for iminobibenzyl with coupling also taking place at the 2-position (4). In view of this and the strong supporting evidence presented above demonstrating that the homogeneous and electrochemical oxidations of iminobibenzyl result in the same reaction product, it is assumed that the product of the electrolytic oxidation of 5-methyliminobibenzyl is structurally similar to VI.

5-Methyliminobibenzyl also had a voltammetric peak height on oxidation the same as that expected for a 1-electron process (See Table I). On sweep reversal, a reduction peak approximately one-half the height of the oxidation peak was observed (Fig. 4). The ratio of the two peak heights was independent of sweep rate up to 10 V/sec. At a sweep rate of 0.2 V/sec E_{pa} and E_{pc} were 0.61 and 0.40V, respectively. If cycling was continued, a new oxidation peak develops at about +0.48V.

A number of controlled potential electrolysis experiments were performed with 5-methyliminobibenzyl. $Q-t$ curves for electrolysis at +0.8V showed a sharp break at an n_{app} value of 1. The oxidized solutions were an intense blue color. The slope of the $Q-t$ curves after this break was small but definitely larger than the slope usually found after complete electrolysis. On continuing the electrolysis, another break in the $Q-t$ curves was observed at an n_{app} value of 2-2.2. If the electrolysis was stopped after the first break ($n = 1$) and a cyclic voltammogram obtained, a redox couple was seen centered at +0.44V (Fig. 5). There was no evidence for the original peak at +0.61V. When the scan was continued to negative enough potentials, a number of irreversible and distorted peaks corresponding to proton reduction was seen between -0.3 and -1.2V. When the electrolysis was continued until $n_{app} = 2$, cyclic voltammetry (with the initial potential at the potential of the electrolysis) showed only the reduction peak at +0.4V. There were no oxidation peaks at +0.48 or 0.61V. Stopping the electrolysis at +0.8V at any stage and electrolyzing at

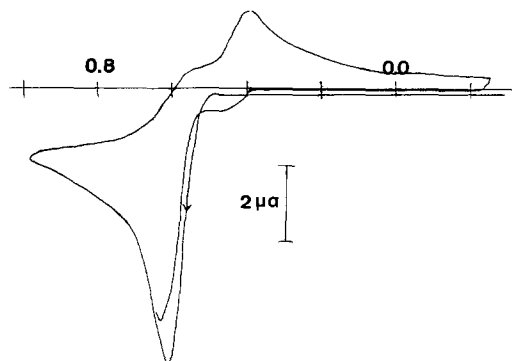


Fig. 4. Cyclic voltammogram of 0.85 mM 5-methyliminobibenzyl. Conditions: Same as in Fig. 1.

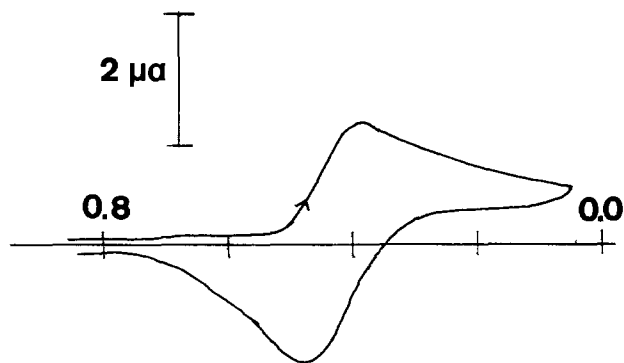
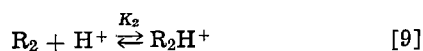
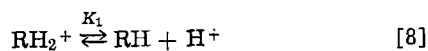
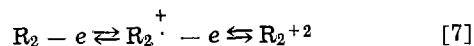
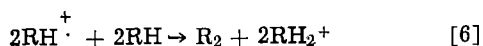
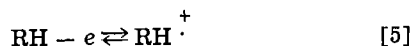


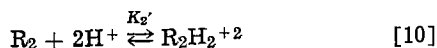
Fig. 5. Cyclic voltammogram of 0.85 mM 5-methyliminobibenzyl after one electron of electrolysis at +0.8V. After two electrons of electrolysis the oxidation peak is not observed. Conditions: Same as in Fig. 1.

+0.2V always resulted in half of the number of coulombs for reduction as had been passed during oxidation at +0.8V. The number of electrons obtained in reduction at -1.3V after electrolysis at +0.2V was the same as the number that had been obtained at +0.2V. Cyclic voltammetry following this reduction at -1.3V showed oxidation waves at +0.48 and +0.61V (Fig. 6), unless a complete electrolysis had been carried out at +0.8V ($n_{app} = 2$) at which time the +0.61V peak was absent.

A mechanism consistent with the above results is



and/or



Equation [6] above implies no mechanistic interpretation since it cannot be ascertained whether coupling occurs before or after loss of a proton from the

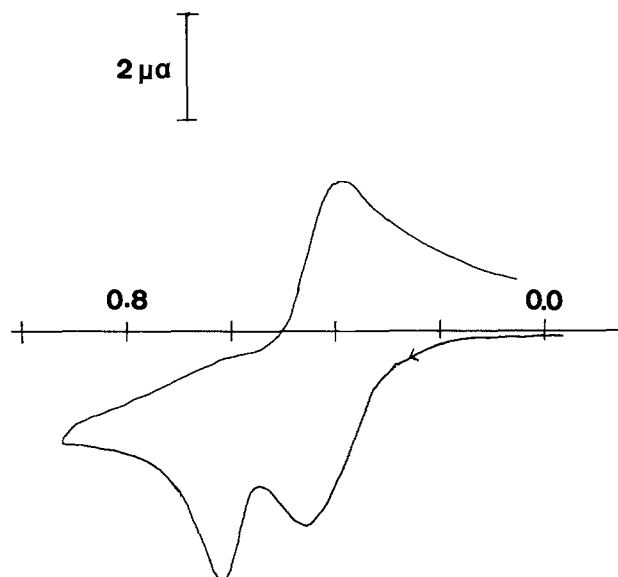


Fig. 6. Cyclic voltammogram of 0.85 mM 5-methyliminobibenzyl after one electron of electrolysis at +0.8V followed by electrolysis at -1.3V. After two electrons of electrolysis, the oxidation peak at 0.61V is not observed. Conditions: Same as in Fig. 1.

cation radical. The proposed mechanism is the same as that for carbazole except for the protonations of the neutral parent and coupled product. The chemical reactions in Eq. [6] are undoubtedly very rapid as demonstrated by the absence of a reverse reduction peak accompanying the oxidation peak at +0.61V. The reduction peak at +0.40V and the oxidation peak at +0.48V correspond to the redox processes of Eq. [7]. Both redox processes occur at similar potentials since only one peak is observed. The apparent total one-electron oxidation of the 5-methyl parent plus coupled product; whereas two would be expected by analogy to carbazole, comes about because of the protonation of the parent molecule in Eq. [6] which renders the parent molecule electrochemically inactive. By the time half the parent has become oxidized the remaining parent is protonated. The small residual slope of the $Q-t$ curves after one electron of oxidation is due to the oxidation of the small amount of parent that can remain in equilibrium with protons and protonated parent, Eq. [8]. If the resulting dication is now reduced, the neutral dimer itself can be protonated and rendered inactive to oxidation, Eq. [9]. This mechanism is consistent with the fact that 5-methyliminobibenzyl is a stronger base than the related carbazoles (*vide infra*) where protonation of parent introduced no complications.

In an attempt to verify the role of protons, several experiments were carried out in the presence of the nucleophile pyridine in the hope of scavenging protons. When a large excess of pyridine was present (>10:1), cyclic voltammograms indicated that two electrons were transferred. Controlled potential electrolysis, however, showed that eventually in excess of four electrons were transferred. Pyridine apparently attacks the dication dimer forming a species that is oxidized further. The rate of the attack cannot be too rapid or else the voltammetry and electrolysis would have indicated the same number of electrons. Cyclic voltammetry showed no evidence of the couple at +0.44 following an oxidation with a large excess of pyridine. Also, the solution did not attain the intense blue color found after electrolysis performed without pyridine. If the electrolysis was carried out until the first break in the $Q-t$ curves with a somewhat less than stoichiometric amount of pyridine followed by a reductive electrolysis at +0.2, the yield of the neutral dimerized product was 30% greater than was found in the absence of pyridine ($n_{app} = 0.65$ vs. 0.5, the time of the oxidative electrolysis was about the same). Some proton scavenging is apparently taking place. Interestingly, pyridine acted only as a proton scavenger in the electrolysis of carbazoles (3).

Experiments were also performed with added acid. According to the proposed mechanism, the acid should protonate the parent and no oxidation should be observed. Addition of equivalent amounts of acetic acid resulted in no change in the electrochemical behavior. However, when acetic acid was in large excess (100:1), the peak height of the +0.61V oxidation was somewhat diminished. At these concentrations of acetic acid a new smaller peak approximately 100 mV positive of the main oxidation appeared. With equivalent amounts of H_2SO_4 , the +0.61V peak was absent and the new peak at $\sim +0.7V$ attained its maximum development, about one-third the peak height of the original oxidation. Further addition of H_2SO_4 resulted in the disappearance of this peak also. The results suggest that acetic acid is too weak an acid to protonate the 5-methyliminobibenzyl parent. Blank experiments where only supporting electrolyte and acid were present showed oxidative currents in the region of the peak observed above at +0.7V. These currents are probably due to added impurities such as water which undergoes a pH dependent oxidation in this region.

Imipramine · $HClO_4$.—A number of electrochemical experiments were also performed on the $HClO_4$ salt of

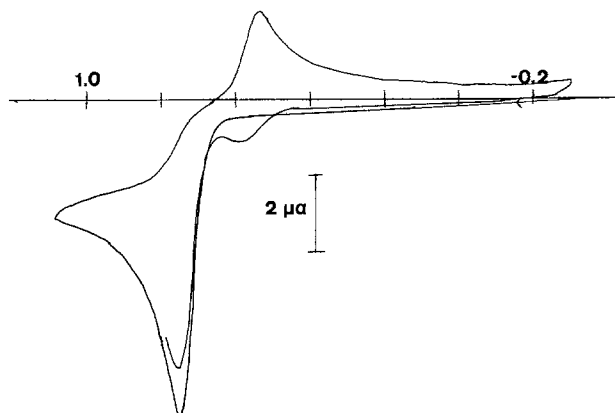


Fig. 7. Cyclic voltammogram of 1.0 mM imipramine HClO_4 . Conditions: Same as in Fig. 1.

imipramine. After reduction of the proton of the tertiary amine group, the tertiary amine probably serves as a base for scavenging protons. The electrochemistry of the protonated imipramine was in all ways similar to 5-methyliminobibenzyl. An apparent one-electron oxidation was observed at +0.75V and an apparent one-half electron reduction at +0.55V (Fig. 7). These ratios and numbers were confirmed with controlled potential oxidations and reductions. Reduction of the amine proton (-1.2V) apparently activated the amine group which was oxidized before 0.75V. Controlled potential electrolysis at +0.9V indicated that considerably more than two electrons were necessary for complete oxidation. The mechanism, however, appeared to be complicated and was not pursued further.

5-Methyliminostilbene.—Homogeneous oxidations of 5-methyliminostilbene (4) have shown that the coupling process may be more complicated than with the related bibenzyl compounds. A possibility of coupling at both the 2 and 10 positions was postulated (4). Electrochemical oxidation might then be expected to result in a more complex product distribution than was observed with the above compounds.

Cyclic voltammograms of 5-methyliminostilbene were characterized by two oxidation peaks at +0.58 and +1.0V at 0.2 V/sec (Fig. 8). The height of the 0.58V peak corresponded to 1 electron (Table I). The peak at +1.0V was more rounded and corresponded to about 0.2 electrons. On sweep reversal a new redox couple was observed at -0.28V (peak separation = 30 mV). There was no evidence for reduction of the oxidized parent (radical cation). Coulometry at +0.7V resulted in an initial $n_{\text{app}} = 1$. The oxidized solution (with a yellow color) had a reduction peak at -0.30 and an accompanying oxidation peak at -0.27 (Fig. 9). No evidence was seen of the original oxidation peaks at +0.58 and +1.0V suggesting that the +1.0V peak may be oxidation of the parent or a species formed at

+0.58V. Close inspection of the region around -0.28V showed evidence of another redox couple at somewhat more positive potentials suggesting that at least two products may result from the oxidation at +0.7V. Controlled potential reductions and oxidations of the couples in the -0.28V region showed that one-half the number of electrons are required as are initially consumed at +0.7V. Reduction of protons at -1.3 suggest that one proton is liberated per parent molecule oxidized. Reduction of protons results in the reappearance of the +0.58 and +1.0V peaks (Fig. 10) which are about one-half of their original height. The mechanism of oxidative coupling of 5-methyliminostilbene at +0.7V appears similar to 5-methyliminobibenzyl except more coupling positions are available.

An apparent change in mechanism occurs when the oxidation is performed at a potential positive of the +1.0V peak. Performing such an electrolysis resulted in an n_{app} of about 1.85 and the product distribution appears to be much more complicated. The resulting products are reduced with one-half of the number of electrons required for the oxidation. Electrolysis at -1.3V requires the same number of electrons as required for reduction of the products of the oxidation.

Discussion

The general oxidative behavior of all of the above compounds is probably similar. The likely initial step in the oxidation is the formation of a cation radical of the parent compound. In a very fast follow-up reaction the cation radicals couple at the 2-position (except possibly for iminostilbene where more coupling modes are possible) with the loss of one proton per parent. The proposed mechanism now deviates from the carbazole mechanism in that the parent and neutral coupled product may be protonated by the protons released during coupling and become electrochemically inactivated. A similar inactivation by released protons has been proposed for the anodic oxidation of N-alkylanilines (6).

Differences in electrochemical behavior between the compounds may in part be explained by differences in basicity of the parents. A relatively minor decrease in basicity of iminobibenzyl as compared to 5-methyliminobibenzyl would probably not increase the concentration of unprotonated parent that can remain in equilibrium with protons enough to have an easily measurable effect on the height of the oxidation wave. Because of the difference in time scale between potential sweep and coulometric experiments, this relatively small increase in unprotonated parent could have a significant effect on the shape of the $Q-t$ curve. What might be expected would be a more drawn out $Q-t$ curve with a less well-defined break. This is in fact the case with iminobibenzyl and supports the contention that iminobibenzyl is less basic than the 5-methyl analogue. Protonation of the neutral iminobibenzyl dimer might well be responsible for the merging and shifting of the two product couples observed in cyclic

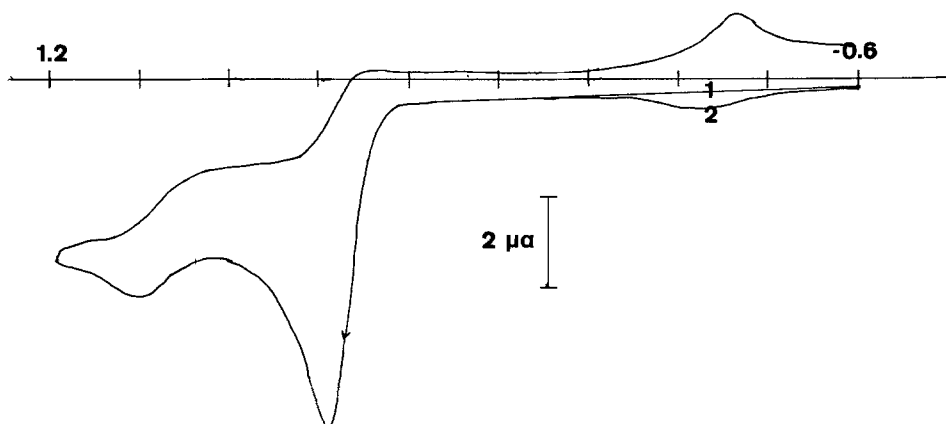


Fig. 8. Cyclic voltammogram of 1.0 mM 5-methyliminostilbene. 1, 1st sweep; 2, 2nd sweep. Conditions: Same as in Fig. 1.

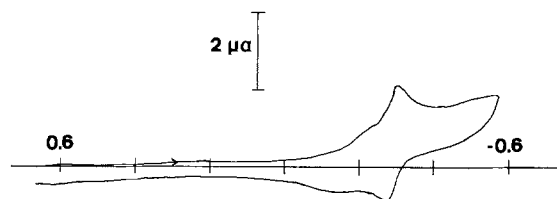


Fig. 9. Cyclic voltammogram of 1.0 mM 5-methyliminostilbene after electrolysis at +0.7V. Conditions: Same as in Fig. 1.

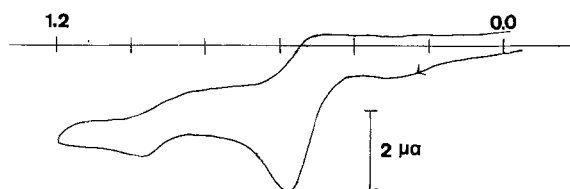


Fig. 10. Cyclic voltammogram of 1.0 mM 5-methyliminostilbene after electrolysis at +0.7V followed by electrolysis at -1.3V.

voltammetry of the parent compound as indicated by the reappearance of these couples upon reduction of protons.

The difference in basicities between the present compounds and the carbazoles can be explained in terms of structural considerations. The planar structure of the carbazoles permits the interaction of the lone pair of electrons on the nitrogen with the pi-electrons of the benzene rings making the lone pair less nucleophilic and very much less basic. X-ray structures of iminobenzyl-type compounds of interest in this study have not been obtained. However, x-ray studies of related compounds (7) and other considerations (8) indicate that the ethylene bridge of iminobenzyl, 5-methyliminobenzyl, and imipramine prevents easy attainment of a planar structure thus making the nitrogen lone pair more available. Although some increase in planarity is expected for 5-methyliminostilbene due to the unsaturated nature of the ethylene linkage, consideration of molecular models indicates that this bridge is highly strained and some rotation out of the plane is expected with a subsequent increase in basicity as compared to carbazole.

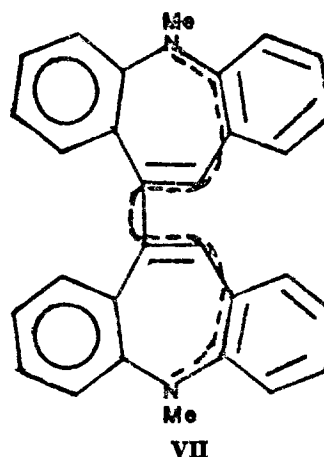
The subtle variation in basicities among the studied compounds is not as easily explained. The greater basicities of the N-substituted iminobenzyls may partly result from the electron-donating properties of the aliphatic substituents on the nitrogens. Comparisons of the changes in basicity that result from substituting an aliphatic chain for hydrogen in a variety of amine compounds [e.g., pK_a 's for anilinium and N,N-dimethylanilinium are 4.63 and 5.15, respectively (9)] indicate that the effect may not be large.¹ However, it may be that only small effects are necessary to explain the observed differences. An attractive aspect of this explanation is that it may explain why 5-methyliminostilbene is apparently a stronger base than iminobenzyl even though it should be more planar. Arguments are presented below that suggest that iminobenzyl is more planar, and therefore less basic, than 5-methyliminobenzyl, perhaps because of some nonbonding interaction between the nitrogen methyl group and the benzene rings (9). Steric hindrance around the nitrogen atom of iminobenzyl is well established from N-alkylation studies (10). Several attempts were made at determining the pK_a 's for these compounds by titration of the base-forms in acetonitrile with perchloric acid (made anhydrous by addition of an excess of acetic anhydride). However, the basicity of these compounds (less than that of acetate

¹ Most pK_a 's determined are for aqueous solutions where as pK_a 's for nonaqueous solvents would be more appropriate. For certain nonaqueous solvents such as acetonitrile pK_a 's and the differences between pK_a 's may well be much larger than found in aqueous systems.

ion) was too small to show glass electrode responses larger than the drifts we observed for this electrode in changing from one calibration solution to another (up to 100 mV). Moreover, to account quantitatively for the differences in these compounds, differences in the acidity of the very unstable radical cations would also have to be considered.

Differences in planarity should also have some effect on the redox potentials of these compounds. Unfortunately, the irreversible nature of the following chemical reaction prevents using peak potentials as a reliable guide as to the ease of oxidation of the parent compounds although where known the differences in potentials correlate with the differences in ionization potentials (11). For the most part the redox processes of the coupled products are reversible or nearly so. Inspection of Table I shows that no real trend exists for the redox potentials of the coupled products, and it is likely that a number of effects such as the relative stabilization of reduced and oxidized forms by delocalization and conformational effects may play important roles. Related substituent effects are apparent in the anodic oxidation of N-alkyl anilines (6).

Deserving special note, though, is the unusual ease with which the 5-methyliminostilbene dimer may be oxidized. A reasonable explanation is that the major product of the 5-methyliminostilbene oxidation is a dimer coupled at the 10-position rather than the 2-position as is the case for the other compounds. A structure VII reminiscent of a



diamiminobutadiene results (dotted line outlines the butadiene backbone). Compounds such as this are known to be exceedingly easy to oxidize (12). One might also consider VII to be related to the dihydro forms of bipyridylum dication which are very easily oxidized (13). VII cannot be isolated in the presence of atmospheric oxygen because of its low oxidation potential. Attempts at isolating the dication salt of VII after bulk electrolysis were unsuccessful.

If the parent molecules are sufficiently nonplanar, the two parent moieties of the dimers are effectively electronically decoupled. Removing an electron results in most of the positive charge residing on one of the parent moieties. Removing the second electron should then not be much more difficult than the first. The oxidation peaks for the two processes would then appear close together. This appears to be the case for 5-methyliminobenzyl and imipramine. The two oxidation peaks observed for iminobenzyl suggests on the basis of the above argument that iminobenzyl is more planar than the 5-methyl analogue.

Since the coupled 5-methyliminostilbene also has only one oxidation peak, one might be tempted to suggest that a reaction scheme analogous to that of 5-methyliminobenzyl was occurring. However, the peak separation between the oxidation is 30 mV and it is, therefore, not possible to ascertain whether these peaks correspond to two 1-electron processes occurring at the same potential or one 2-electron process.

A nuance of the 300 mV separation between the two oxidations of bicarbazoles is that any neutral bicarbazole formed as a transient in the oxidation of carbazole can react with dication to yield the radical cation. A measurable ESR signal might be expected during electrolysis. Such an ESR signal was observed for carbazole (3). The closeness of the two oxidations for the dimeric 5-methyliminobibenzyl make the driving force for such a reaction sequence much smaller. Accordingly, the probability of producing a sufficient number of free radicals to observe during an electrolysis in an ESR cavity is much less. In line with this reasoning, an *in situ* electrolysis of 5-methyliminobibenzyl in an ESR (14) cavity resulted in no ESR signal.

Acknowledgment

The support of this research by the National Science Foundation (GP-31414X) and the Robert A. Welch Foundation is gratefully acknowledged. The cooperative Texas-Liverpool effort was made possible by a grant from NATO (Research Grant No. 668).

Manuscript submitted Oct. 21, 1974; revised manuscript received Feb. 17, 1975.

Any discussion of this paper will appear in a Discussion Section to be published in the December 1976 JOURNAL. All discussions for the June, 1976 Discussion Section should be submitted by Feb. 1, 1976.

Publication costs of this article were partially assisted by the University of Texas at Austin.

REFERENCES

1. "Organic Electrochemistry: An Introduction and Guide," M. M. Baizer, Editor, Marcel Dekker, Inc., New York (1973).
2. C. K. Mann and K. K. Barnes, "Electrochemical Reactions in Nonaqueous Systems," Marcel Dekker, Inc., New York (1970).
3. J. F. Ambrose and R. F. Nelson, *This Journal*, **115**, 1159 (1968).
4. P. Beresford, D. H. Iles, L. J. Kricka, and A. Ledwith, *J. Chem. Soc. Perkin I*, 276 (1974).
5. W. V. Childs, J. T. Maloy, C. P. Keszthelyi, and A. J. Bard, *This Journal*, **118**, 874 (1971).
6. R. L. Hand and R. F. Nelson, *J. Am. Chem. Soc.*, **96**, 850 (1974).
7. L. J. Kricka and A. Ledwith, *Chem. Rev.*, **1**, 101 (1974).
8. J. R. Huber and J. E. Adams, *Ber. Bunsenges. Phys. Chem.*, **78**, 217 (1974); R. J. Abraham, L. J. Kricka, and A. Ledwith, *J. Chem. Soc. Perkin II*, In press.
9. Handbook of Chemistry and Physics, 51st ed., The Chemical Rubber Co., P D120, (1970); "Determination of Organic Structures by Physical Methods," E. H. Braude and F. C. Nachod, Editors, p. 567, Academic Press, New York (1955).
10. L. J. Kricka and A. Ledwith, *J. Chem. Soc. Perkin I*, 2292 (1972).
11. H. J. Haink, J. E. Adams, and J. R. Huber, *Ber. Bunsenges. Phys. Chem.*, **78**, 436 (1974).
12. J. M. Fritsch, H. Weingarten, and J. D. Wilson, *J. Am. Chem. Soc.*, **92**, 4038 (1970).
13. E. Steckhan and T. Kuwana, *Ber. Bunsenges. Phys. Chem.*, **78**, 253 (1974).
14. I. B. Goldberg and A. J. Bard, *J. Phys. Chem.*, **75**, 3281 (1971).

Emf's across CdI_2 - Cd_2I_2 Electrolytes Using Electrodes of Bare W, Molten Cd, and Molten Au-Cd: Bare Electrode Effects, Use of $n \neq 2$, Premonitory Phenomena and Liquid Structure in Au-Cd, and the Cd- CdX_2 Phase Diagrams

David Nin-Kou Wang¹

Department of Mining, Metallurgical, and Fuels Engineering, University of Utah, Salt Lake City, Utah 84112

Guy R. B. Elliott^{*,2}

University of California, Los Alamos Scientific Laboratory, Los Alamos, New Mexico 87544

and Charles H. Pitt

Department of Mining, Metallurgical, and Fuels Engineering, University of Utah, Salt Lake City, Utah 84112

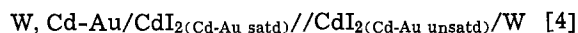
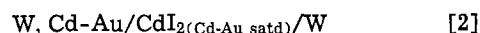
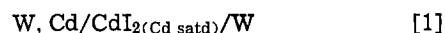
ABSTRACT

Emf measurements have been made on cells with CdI_2 - Cd_2I_2 mixed-valence electrolytes (a) to establish structural and thermodynamic properties for molten Au-Cd alloys and (b) to study the source and behavior of some unexpected voltages associated with bare W electrodes dipping into these electrolytes. Changes with temperature and composition of the partial molal entropies, enthalpies, and free energies of the Cd component in the Au-Cd melts point out the existence of premonitory changes a few degrees above the liquidus as well as of liquid structural changes far from the liquidus; these changes correlate with earlier studies by vapor pressure and by electrical conductivity in the Au-Cd system at higher temperatures. $n = 1.87 + 0.001(773T)$ is used to evaluate the effective valence for these electrolytes when saturated with Cd; this n appears in calculation of $\Delta\bar{F} = -nF\epsilon$. Apparently the mixed-valence electrolyte, plus probable oxide impurities, reacts with the bare electrode (in this case W) surfaces by direct chemical action to form surface films which protect the metal below against direct chemical attack. These films are in equilibrium with the electrolytes. When, however, electrochemical attack is permitted, as when an emf measurement is made, then the underlying metal becomes subject to attack and another reactant enters the reaction. This effect leads to anomalous voltages in electrodes which are normally considered to be inert in molten salts, e.g., W, Mo, and graphite. If these sources of voltage are recognized, then proper determinations of activities and phase boundaries can be made; some earlier measurements of this type which neglected these voltages, however, must be re-evaluated. Application of these proper techniques to the Cd- CdI_2 system is made.

In aqueous systems the usual "inert" electrodes are platinum, gold, silver, etc. These electrodes are unsatisfactory in many molten salt systems, however, because of their tendency to form alloys with many metals. Attack can occur either by direct contact with these metals or by secondary reaction with the products formed by dissolution of the metals in their molten salts. Thus platinum dipping into pure molten CdI_2 is stable, but if the CdI_2 is in contact with a molten Cd phase below, then the platinum is attacked by the CdI_2 - Cd_2I_2 mixture formed by the dissolution of Cd in CdI_2 , and a Pt-Cd alloy is formed.

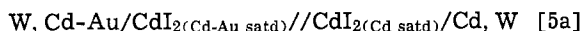
In order to avoid alloying attack in molten salt systems it is customary to turn to "inert" electrodes, i.e., tungsten, molybdenum, graphite, etc. It is the thesis of this paper that such electrodes are often not inert and that a number of apparent thermodynamic conflicts in the literature can be resolved if this fact is recognized. As corollary we offer a thermodynamically acceptable interpretation of these anomalies and of the electrode behavior.

To study this problem we have used cells of the types

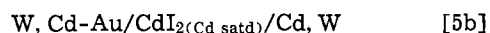


Here all phases are molten except W, and one must recognize that the shiny, cleaned W will be coated with traces of oxides. These cells have been studied as functions of composition, temperature, and time.

In addition usual [e.g., Ref. (1-3)] stirred H-cell measurements were made between molten Cd and molten Cd-Au alloy. There the cell is represented exactly as



but it can be represented to a close approximation by



as long as the Cd activity in Cd-Au is close to unity, thus making the CdI_2/Cd_2I_2 ratio essentially identical at both electrodes, as set by the equilibrium constant

$$K = (a_{Cd_2I_2}) / (a_{CdI_2}) (a_{Cd}) \quad [6]$$

* Electrochemical Society Active Member.

¹ Present address: IMRD, Lawrence Berkeley Laboratory, Berkeley, California 94720.

² Present address: CNC-2, LASL, Los Alamos, New Mexico 87544.

Key words: mixed valence electrolytes, alloy activities, surface reactions.

Experimental Chemicals, Apparatus, and Operations

Emf cells.—Two modifications of the usual stirred H-cells mentioned above were used. These cells allow for composition changes *in situ* by additions of pre-weighed solids in the sidearms, for stirring and long equilibrations to assure that phases are homogeneous and at equilibrium, and for initial cleanup operations such as the vacuum melting of CdI_2 before it is melted and poured or vaporized into the H-cell portion of the system. Temperatures are very uniform (to $< 0.01^\circ\text{K}$) because of the heat distribution and heat ballast from nesting copper cylinders.

Type I.—This version differs from the usual stirred H-cell only in that a second W lead in each cell leg is mounted on the stirrer so as to be exposed bare to the electrolyte. As is customary the exposed portion of the other lead was completely immersed in molten cadmium or alloy. (See Fig. 1.)

This cell type was used for almost all the data presented here.

Type II.—In this modification the bottoms of the H-cell legs were joined so that a single alloy touched the electrolyte in both legs. The electrolyte in each leg was essentially independent of that in the other, and stirring one side did not agitate the other. (See Fig. 2.)

Two types of electrodes dipped into the electrolyte, namely (a) large current collectors made by wrapping ~ 100 cm of 10 mil W wire around each stirrer but not touching the alloy, and (b) small potential sensors exposing ~ 3 cm of 10 mil rod to the CdI_2 , there being two of these in each cell leg.

Chemicals and their purification.—Commercial cadmium of purity reported as 99.999% was melted in

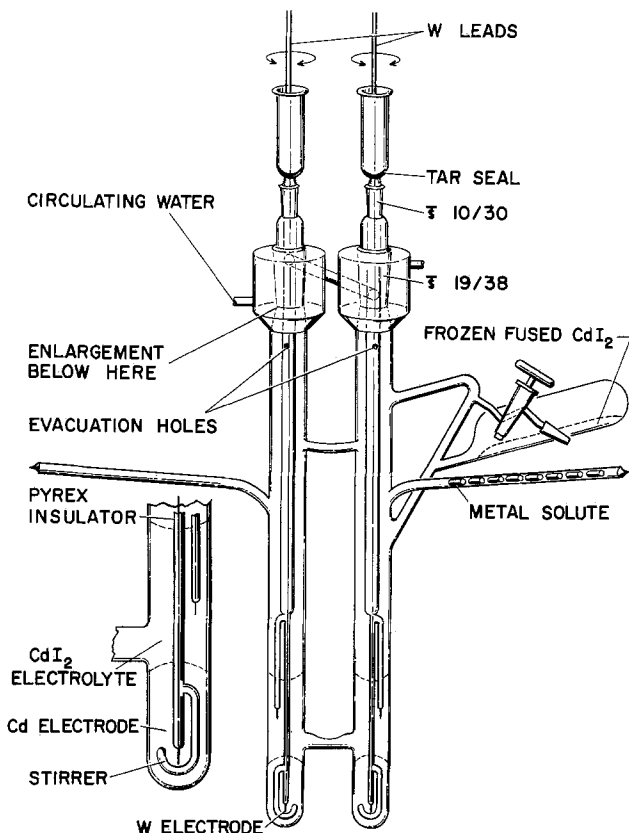


Fig. 1. Stirred H-cell for studying various usual reactions (e.g., reaction [5a]) as well as the bare electrode reactions (e.g., reactions [1]-[4]). Sometimes the metal solute sidearm included a standard taper joint which could be turned to make sequential solute additions more easily as they were needed. Only the lower sections of the legs are involved in the emf measurements; the upper portions are outside the furnace and are used during loading. This is the type I cell design.

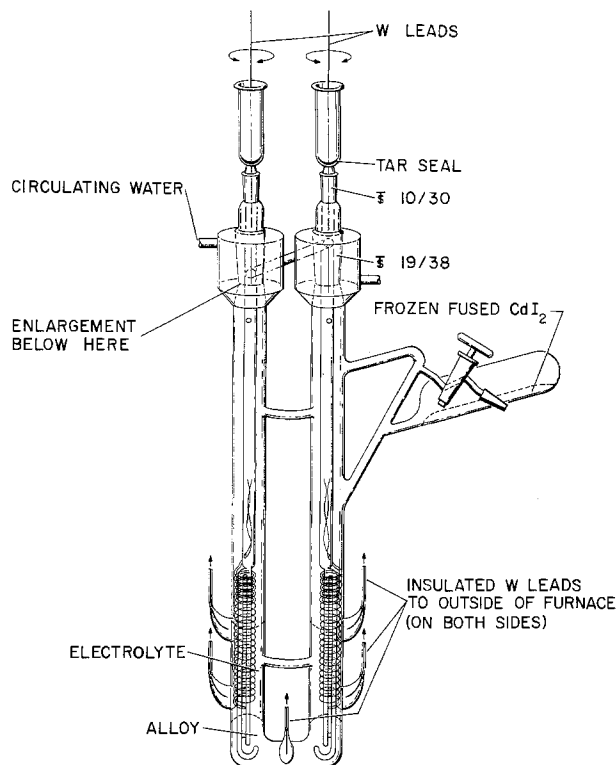


Fig. 2. Multiple electrode cell for checking reproducibility of bare electrode emf's (reaction [2]) with time, with stirring, with composition, and with different sources of tungsten having different levels of initial oxidation on their surfaces.

vacuum and washed with boiling, molten CdI_2 . Reagent grade CdI_2 was sometimes (cell type II) melted under vacuum and washed with molten Cd. Later this material or new reagent grade CdI_2 (cell type I) was loaded into the sidearm of the cell and remelted repeatedly under vacuum, the final melting being used to introduce the salt into the cell legs. Commercial argon was condensed at liquid nitrogen temperatures, flash frozen by evacuation to flush out the more volatile impurities, then gently warmed and distilled into the cells at ~ 0.5 atm.

For cells of type I the electrodes were cleaned by a-c electrolysis in NaOH solution, then were water washed and dried by touching tissue. With cells of type II the working electrodes on the stirrers were made from commercially cleaned and still shiny 10 mil W wire. Additional potential sensors were made from a different commercial tungsten; these electrodes were oxidized to a dark color during a Pyrex anneal and were not cleaned further. The electrodes represent two commercial sources and two levels of preliminary oxidation of the W surface.

Gases adsorbed on the Pyrex or chemicals were removed by evacuation at 10^{-5} - 10^{-6} Torr while the system was in the furnace, and then the purified argon was added.

Electrical equipment.—Usual measurements with potentiometers having no connection to house current were employed (Wenner, K-2, etc.). Pt/Pt-10% Rh thermocouples were used.

For further discussion of these various techniques, see our earlier papers, e.g., Ref. (1-3).

Cell operation.—Consistent with earlier observations (1), cadmium solutions required much stirring before equilibrium was reached, as compared with Sn-SnCl₂ solutions [e.g., (2)]. When a cell could be stirred with almost negligible effect on the voltage, and when it also returned in a few minutes to the original voltage, the system was accepted as being at equilibrium. (As must always be faced, a system can often be in equilibrium with regard to one type of reaction while it is

far off of equilibrium with regard to other reactions.) The equilibrium condition was achieved in about 2 hr after adding Cd to the CdI₂ electrolyte, if stirring had been frequent. For gold additions, equilibrium was achieved in 4 hr or more, and further stirring or long standing did not alter the emf except at the highest temperatures studied, where a small amount of Cd evaporated. For temperature changes at a single composition, some measurements were taken about one-half hour apart, but most were taken more quickly.

Solubility measurements.—The cell that had been used for the study of Au-Cd alloys was held in the furnace at 773°K with sufficient stirring to ensure that equilibrium had been achieved. The cell was then taken out of the furnace at 773°K and cooled rapidly, consistent with a technique that had been used earlier (1). The cadmium that had dissolved into the electrolyte over the reference electrode was determined by breaking open the cell, washing away the electrolyte, and establishing the weight loss of the cadmium electrode.

Results, Methods of Calculation, and Conclusions

The significant figures carried reflect the differences between compositions which can be identified. The absolute compositions vary slightly because of the dissolution of some Cd into CdI₂ to form the equilibrium concentration of Cd₂I₂ which is unstable as the pure condensed phase but can be present in solution in the salt melt.

The effect of this solubility on n in $\Delta\bar{F} = -nF\epsilon$ must be considered in the evaluation of thermodynamic properties from the emf data. (Contrary to popular assumption, the value of n is seldom whole-numbered for molten salt systems, and the effect of solubility equilibria such as for Eq. [6] must be considered even if an inert carrier solvent such as LiCl-KCl is being used.) For CdI₂ at 773°K the value of n has been recently determined by three independent experimental checks. First, and most directly, Houseman and Elliott (1) have shown that the value of the apparent n is markedly dependent on the charging rate, and Houseman (4) has carried out very slow conduction experiments which can be extrapolated to zero current. His value of effective n , reflecting both the concentrations and mobilities of the Cd₂⁺⁺ and Cd⁺⁺ species, is 1.87. Second, $n = 1.87$ is what agrees with the vapor pressure measurements for several systems as reported by Conant and Elliott (5). Third, $n = 1.87$ is what brings a number of dilute solutions into asymptotic approach to Raoult's law when activities are calculated from emf's, as shown by Conant (6), by Houseman and Conant (7), and by Conant and Elliott (5).

Because Houseman (4) has shown that the mobilities of Cd⁺⁺ and Cd₂⁺⁺ are nearly the same and that the solubility measurements by Topol and Landis (8) and by us here can be used for predicting n at 773°K, we will use the temperature dependence of solubility from Topol and Landis and will assume that equal mobilities continue to other temperatures in order to make our calculations of thermodynamic properties. These solubility values from Topol and Landis also agree with our solubility measurements at 713°K, as is discussed later.

By using the assumption and solubilities just discussed, we get the calculation of n by the equation

$$n = 1.87 + 0.001(773T) \quad [7]$$

(Although solubilities often follow a logarithmic dependence on T , Topol and Landis's values do not appear to require this form.)

To understand the calculations using Eq. [7], recognize that Topol and Landis's solubility of Cd at 773°K is 0.065 mole fraction, leading to 0.065 of the Cd having zero valence and 0.935 having a valence of 2. Our value for this solubility is 0.063 in this present paper. Doubling the 0.935 (or 0.937) leads to a value of $n =$

1.87. This calculation is independent of what species form as long as mobilities of the species and their charges are equal.

Results with Cell Type I

Measurements using cells as in Fig. 1 were made on two types of emf's: (a) between the cadmium reference electrode and the alloy whose composition could be varied, and (b) between cadmium or alloy and bare electrodes made of tungsten which dipped into molten CdI₂, the CdI₂ being partially or completely saturated with Cd. As will be developed, the former were of "thermodynamically" expected form, but the latter did not conform to usual expectations.

Metal vs. alloy studies.—The experimental emf values at 4 mole fractions of the solvent taken over a temperature range of 50°K are represented in Fig. 3-6.

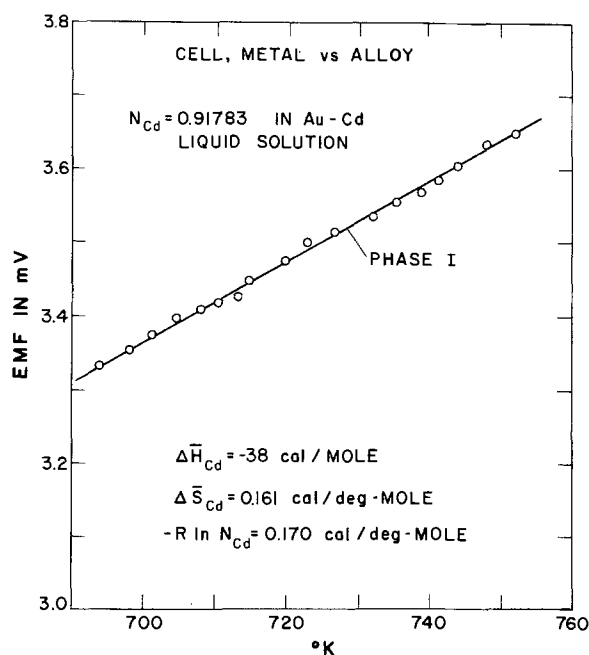


Fig. 3. Reaction [5a] for Cd vs. Au-Cd at $N_{Cd} = 0.91783$. No phase boundary for liquid Au-Cd solution is detected over the temperature range studied.

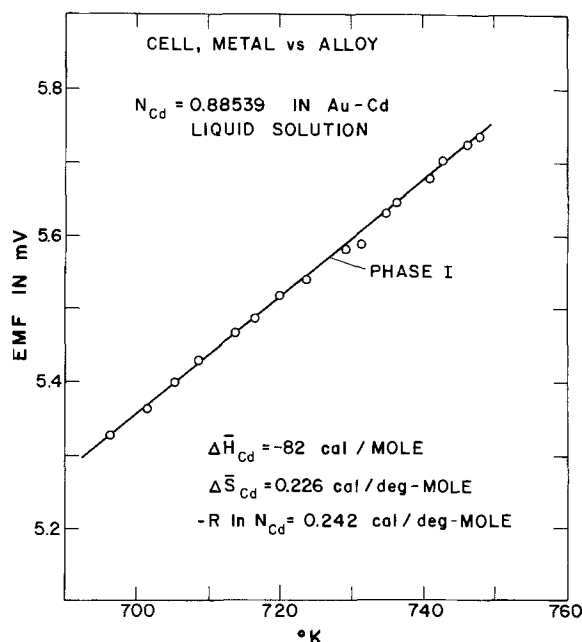


Fig. 4. Reaction [5a] for Cd vs. Au-Cd at $N_{Cd} = 0.88539$. No phase boundary for liquid Au-Cd solution is detected over the temperature range studied.

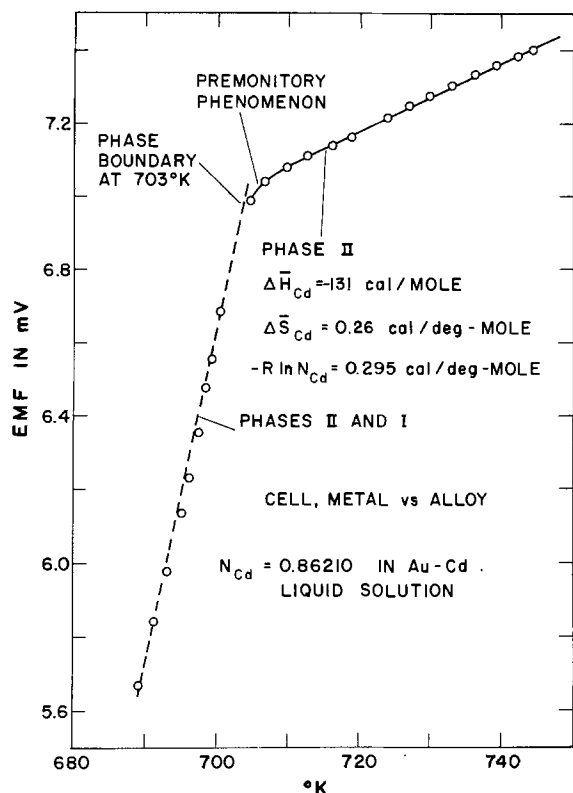


Fig. 5. Reaction [5a] for Cd vs. Au-Cd at $N_{Cd} = 0.86210$. The liquidus is detected at 703°K, and premonitory phenomena are detected about 4°K before the liquidus temperature is reached.

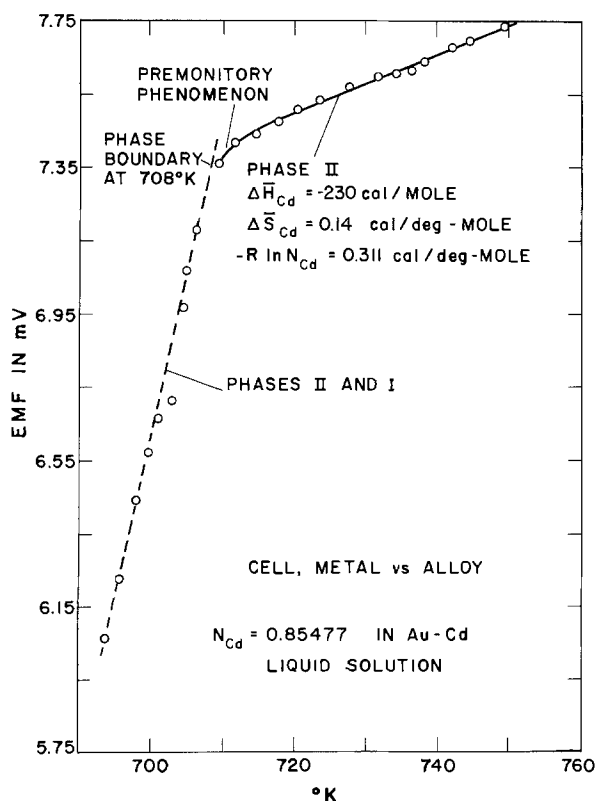


Fig. 6. Reaction [5a] for Cd vs. Au-Cd at $N_{Cd} = 0.85477$. The liquidus is detected at 708°K, and premonitory phenomena are detected for perhaps 4°K before the liquidus temperature is reached.

Pure single-phase region is observed at $N_{Cd} = 0.91783$ and 0.88539 (Fig. 3 and 4), but for $N_{Cd} = 0.86210$ and 0.85477 (Fig. 5 and 6) there are phase changes as indicated by the slope shift in the emf-

temperature data. In the transition region between pure single-phase region linearity and the two-phase region linearity there is in each case a transition region labeled "premonitory phenomena."

The thermodynamic quantities listed have been calculated using Eq. [7], but we have neglected the small changes of alloy composition as the solubility of Cd in CdI_2 changes with temperature.

Note that with correction of n off the usually accepted 2, the partial molal entropy of the Cd falls close to the ideal random solution value for the three higher concentrations. If n were accepted as 2, the apparent partial molal entropies would be about 50% larger than the ideal values.

Figure 7 and Table I give the variation of emf and activity with composition for a single temperature using $n = 1.93$ corresponding to the equation above. Table I indicates both the added alloy composition and the corrected composition due to Cd_2I_2 formation in the iodide.

Conclusions from the Cd vs. Au-Cd emf studies.—The liquidus is detected at two compositions (Fig. 5 and 6) and occurs at temperatures consistent with the accepted phase diagram (9).

Premonitory phenomena (depressions of the cell voltage) are observed slightly above the liquidus at these same compositions. In further support of this view, premonitory phenomena near phase boundaries (including the liquidus) have already been detected in this same system by vapor pressure-composition studies at constant, but higher, temperature (939°K) using an isopiestic balance (10).

Note that these premonitory phenomena show smaller voltages than extrapolation would predict. Of course, the total activity must drop for any such reaction to occur, so we conclude that the necessary component activity decrease and phase stabilization must occur for the nonvolatile component. This kind of activity behavior is not uncommon: For example, the

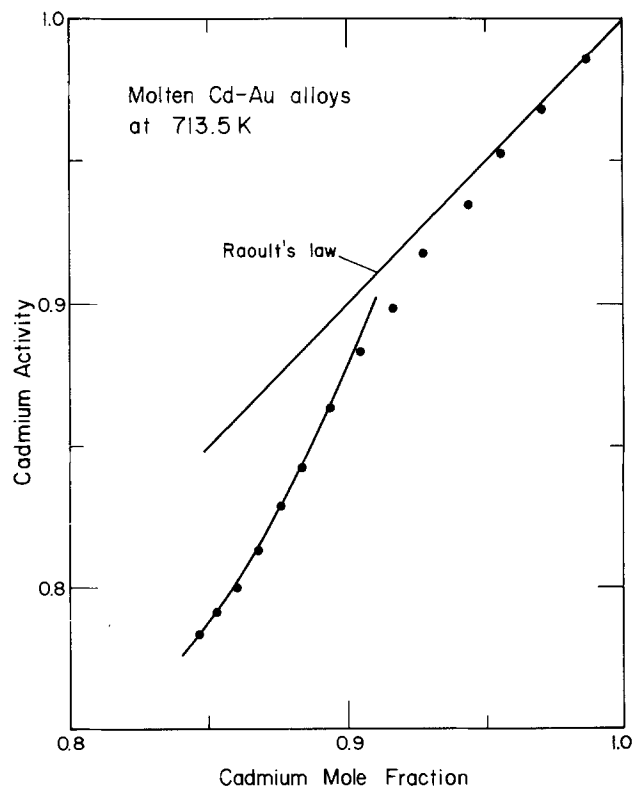


Fig. 7. Cadmium activity-mole fraction relations from emf's (reaction [5a]) for various molten Au-Cd alloys at 713.5°K. At least one liquid alloy structural change is probable at ~ 0.9 mole fraction of Cd, consistent with a change detected earlier at this composition by vapor pressure at 939°K.

Table I. Composition-emf data for the cell of:
W, Cd, Au (liquid solution)/CdI₂ (l)/Cd(l), W
at temperature 713.5°K

Gold added, total g	Cadmium mole fraction		Tem- perature (°K)	Emf ^(e) (mV)	a _{Cd} ^(d)
	Added ^(a)	Corrected ^(b)			
0	0	0	713.5	(0.0240)	
0.70255	0.98647	0.98624	713.2	0.4584 ^c	0.98570
1.55000	0.97055	0.97013	713.2	1.0400	0.96785
2.35210	0.95609	0.95536	713.6	1.5571	0.95228
3.02770	0.94418	0.94327	713.5	2.1572	0.93449
3.93975	0.92857	0.92742	713.3	2.7480	0.91729
4.58530	0.91783	0.91652	713.6	3.4178	0.89823
5.27025	0.90670	0.90477	713.5	3.9637	0.88295
5.97820	0.89547	0.89385	713.7	4.6829	0.86329
6.62940	0.88539	0.88364	713.6	5.4602	0.84246
7.13005	0.87780	0.87594	713.9	5.9759	0.82899
7.67010	0.86975	0.86779	713.7	6.5903	0.81312
8.19260	0.86210	0.86004	713.6	7.1122	0.79988
8.70165	0.85477	0.85263	714.0	7.4418	0.79175
9.14515	0.84849	0.84627	713.7	7.7597	0.78362

(a) The amount of Cd added was 29.2264g.

(b) Assumed solubility of Cd in CdI₂ from present investigation (same as Topol's and Landis's data): 713°K, N_{Cd} = 0.0348.

(c) Corrections have been added to the observed emf to give the listed readings. This correction, 0.0240 mV, was measured when no solute had been added to either cell leg. Those emf readings were taken after sufficient stirring and did not change after further stirring or long standing.

(d) Calculated for 1.93 electrons involved per cadmium atom transferred.

solid CeCd_{~4.5} microphases showed metastable extensions which include many examples of both too high and too low Cd component activity before the transformation took place (11).

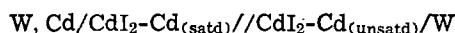
The change of activity-composition behavior at N_{Cd} ≈ 0.9 shown in Fig. 7 was noted also at higher temperatures in the earlier vapor pressure studies (10). Likewise, comparing Fig. 3-5 vs. 6, there is a sharp decrease of the $\Delta\bar{S}_{Cd}$ from that for ideal solutions as we pass from 0.86210 to 0.85477 mole fraction of Cd. It seems likely that this change of entropy behavior corresponds with the liquid-liquid transformation at 0.8620-0.8625 shown at 939°K in the isopiestic balance studies just mentioned.

Metal or alloy vs. bare electrode studies using cell type I and CdI₂-Cd₂I₂ electrolytes.—In the development of the stirred H-cell design (1, 2) it became clear that, if the W or Mo current leads to metal and alloys were not insulated as they passed through the electrolyte, then the cell behavior would be erratic in the μ V range. It was important sometime to learn the causes and implications of this behavior.

Preliminary studies (to be presented in part later under the heading cell type II) had indicated that W, Mo, and graphite all showed persistent voltages in the millivolt range when bare electrodes dipping in CdI₂ were compared against Cd or Au-Cd in contact with the bottom of the electrolyte. Furthermore, use of cell type I with Mo or W electrodes in SnCl₂-based electrolytes vs. Au-Sn molten alloy shows similar behavior. [This latter work was carried out along with the Au-Sn alloy liquid structure work (3) but was not included in the publication of that already complex paper.]

For the present studies measurements were made on both saturated and unsaturated solutions of Cd in CdI₂ (i.e., CdI₂-Cd₂I₂ solutions).

Unsaturated solutions.—Cells as in Fig. 1 were operated with initially no liquid Cd phase on the right side and with small solid Cd pieces in the sidearm. The emf-temperature relationships for reaction [4], i.e.



at unsaturated solution compositions are plotted in Fig. 8-11. The compositions, N_{Cd} = 0.0143 and 0.0348, do achieve saturation at the lower temperatures, however.

For the first few days the solutions in one leg of the H-cell were not allowed to become saturated. First, limited Cd was added to the CdI₂ to partially saturate it, and the solution was stirred periodically for a day while composition and temperature equilibrium was being achieved.

The next day more Cd was added and the solution was stirred periodically for 4 hr. Then the stirring was stopped, and the system was cooled slowly. The emf changes were systematic (Fig. 8) with the two electrodes agreeing to about 1 mV. The system was then reheated and again slowly cooled, this time over a two day period with cooling by increments rather than steadily (Fig. 9). By this time the two electrodes agreed within ~0.2 mV. A further heating and cooling cycle is shown on Fig. 10.

Because we do not know how to handle the mixed *n* values (the CdI₂/Cd₂I₂ ratios are different in the two cell legs), we have calculated apparent values of $\Delta\bar{H}_{Cd}$ and $\Delta\bar{S}_{Cd}$ as shown on Fig. 9 by using *n* = 2.

Although the solutions followed a single relationship during a heating or a cooling half-cycle, there were slower over-all changes in the apparent values of both the magnitude of the emf and of the slope of the emf-temperature relationships. The magnitudes of the emf values did not appear to be approaching zero, however. Considering the emf at 740°K, the emf dropped from 82.5 mV on the second day, to 64 on the third day, to 56 on the fifth day, to 55 on the sixth day. Likewise, the corresponding apparent $\Delta\bar{S}_{Cd}$ fell from 25 to 18 eu to 15 eu and remained 15 eu. After the initial changes, the major changes of emf and slope seemed to be associated with hysteresis following electrolyte phase changes such as freezing. (Does the electrode surface crack and strain?) For example, in Fig. 9 the freezing of CdI₂ is detected in the initial cooling, but the emf's are lowered for the higher temperatures as well (Fig. 10 vs. Fig. 9).

Comparing Fig. 10 and 11 will show the influence of electrolyte composition upon the emf. Likewise, these data pick off the Cd-CdI₂ phase boundary both on cooling and on heating. Finally, they show that shorting the two "inert" electrodes together allows an

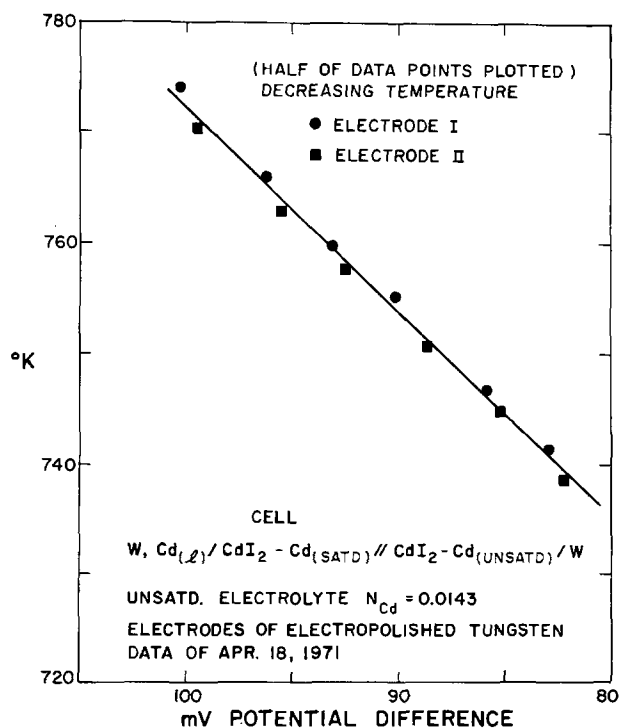


Fig. 8. Studies of the emf between a cadmium electrode in one leg of an H-cell and tungsten electrodes in an unsaturated Cd-CdI₂ solution in the other leg. (Electrode I was high in the solution and electrode II was low.)

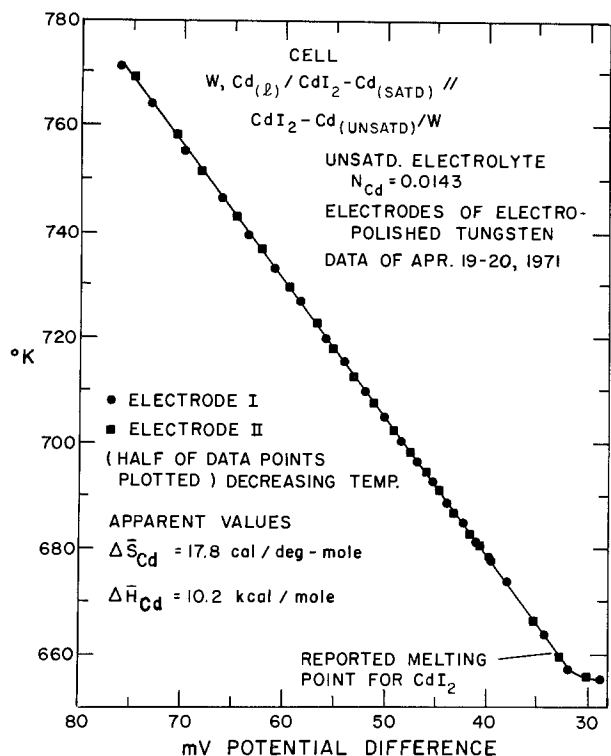


Fig. 9. Two-day cooling of the cell in Fig. 8. Cooling was not continuous. $\Delta \bar{H}_{Cd}$ and $\Delta \bar{S}_{Cd}$ calculated with $n = 2$, i.e., no correction for Cd_2^{++} was made here. See text.

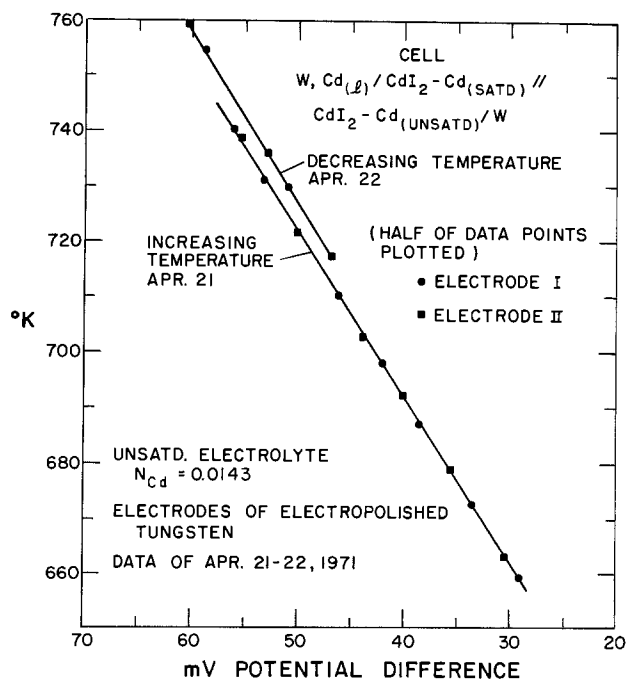


Fig. 10. Cell behavior for the cell in Fig. 8 and 9 as shown 3 and 4 days after freezing then remelting the electrolyte.

electrochemical drain which does change the electrode behavior temporarily.

Saturated solutions.—These measurements refer to the potentials observed in comparing a molten Cd reference electrode with a bare tungsten electrode dipping into molten $CdI_2-Cd_2I_2$ solution. The Cd_2I_2 concentration is set by equilibration with either molten Cd or molten Au-Cd.

Figure 12 shows tests of reaction [1]. Physically, referring to Fig. 1, the reference Cd was in the left leg and the bare electrodes were over a second Cd melt in the right side. Later, gold would be added to the right-

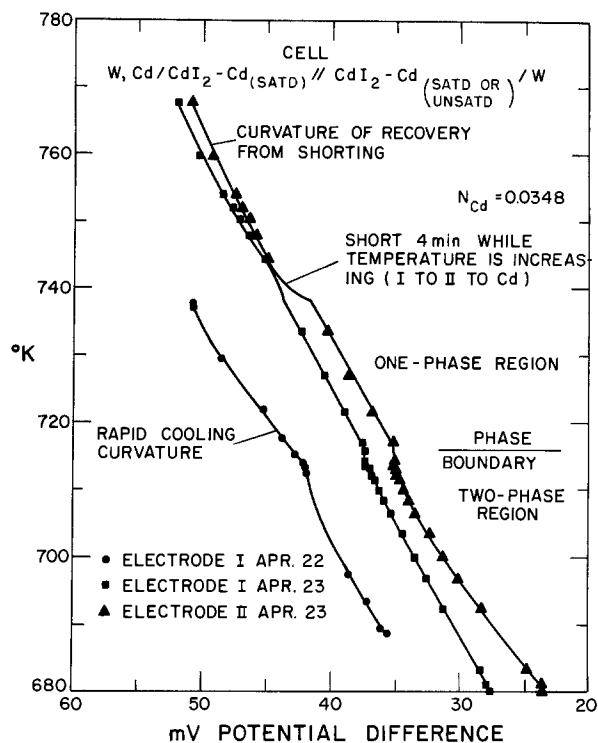


Fig. 11. Saturated and unsaturated electrolyte and effects of electrochemical drain at N_{Cd} in $CdI_2 = 0.0348$ on the emf of bare tungsten electrodes.

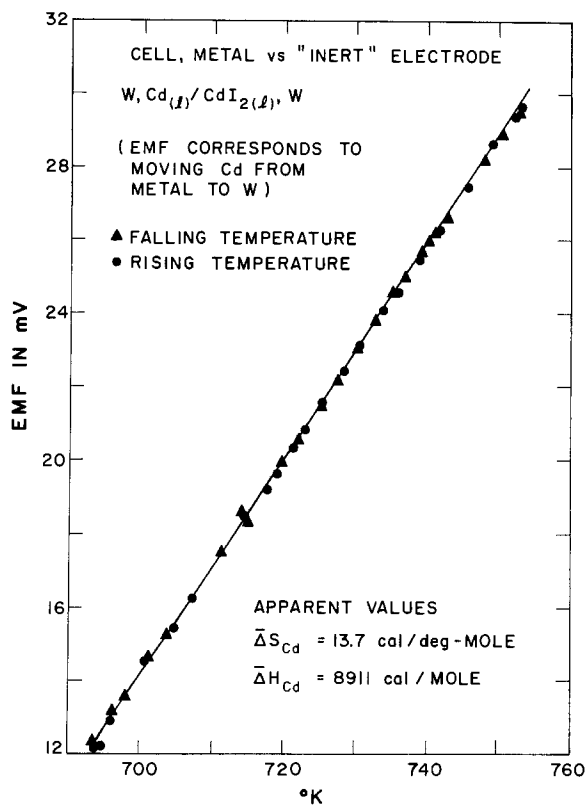


Fig. 12. The effect of temperature on the bare tungsten electrode emf in CdI_2 solutions saturated with Cd. The CdI_2 and Cd phases in contact were stirred intermittently during heating and cooling stages. Heating and cooling stages were separated by 3 days.

side melt to give the data in Fig. 13, again with reference to the same Cd in the left side.

With regard to Fig. 12 note that the heating and cooling half-cycles gave the same results even though the half-cycles were separated by three days. Similar

temperature coefficients of emf are shown by the W vs. Cd couples where Au-Cd alloys supplied the Cd_2I_2 to the electrolyte in the W region (Fig. 13).

These voltages were stable, reproducible, and (according to usual expectation) very large. The changes of voltage with alloy composition (~ 3 mV on Fig. 13) were smaller than would have been expected from the changes of alloy activity (~ 7.5 mV on Fig. 6) and the temperature coefficients were different. Part of the difference in temperature coefficient is a consequence of carrying out the measurements for Fig. 13 without stirring; the metal-electrolyte and the alloy-electrolyte interfaces adapt quickly to the changing n but the electrolyte CdI_2 - Cd_2I_2 mixture in the bulk of that phase readily supersaturates relative to metallic Cd. There are further differences, however, because the line for $N_{\text{Cd}} = 0.85477$ as the saturating solution does not follow the other trends of voltage. (Remember that the $\Delta\bar{S}_{\text{Cd}}$ at $N_{\text{Cd}} = 0.85477$ was also anomalous, Fig. 6.)

Apparently traces of impurity (probably CdO) do influence the voltage significantly, since the long-term stability was not achieved until after the cell had been at temperature with much stirring for a month. A few milligrams of material had then vaporized to form a brown condensate ring. (This could, for example, have been volatile tungsten oxydides whose vaporization removed $\text{O}^=$ from the electrolyte solution.)

In this case the effect of stirring was not large. The data for Fig. 12 were taken with stirring during heating and cooling while the alloy solutions were stirred extensively at the highest temperature before cooling but not during the cooling.

Conclusions from the unsaturated and saturated solution studies using type I cells.—These emf's are real, large, and roughly reproducible. They satisfy many usual tests of equilibrium. They vary with composition. They react to phase changes. They vary reproducibly with temperature during tests over several hours. They react to and recover from drains and imposed voltages.

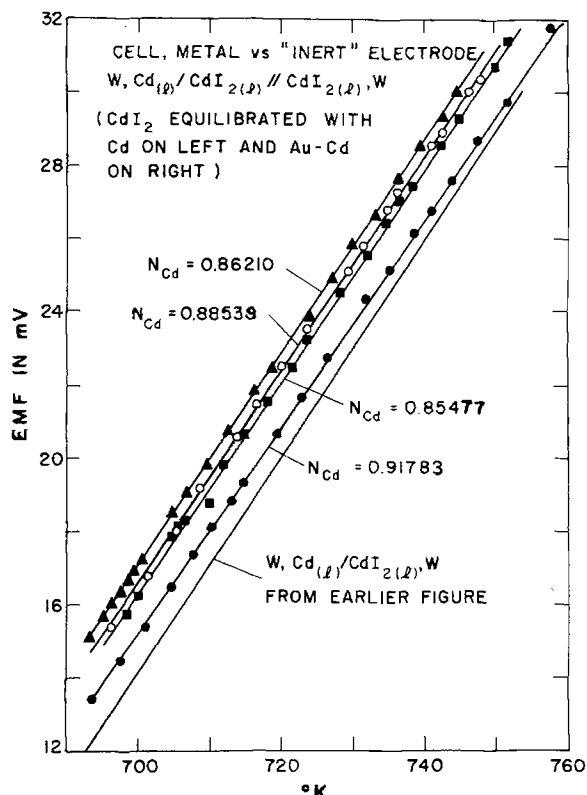


Fig. 13. The effects of temperature and composition on the emf of cells in which bare tungsten electrodes dip into CdI_2 equilibrated with Cd-Au alloys of various compositions.

Considering that (for Henry's law solutions) 30 mV would correspond to about one-fourth of the saturation concentration at these temperatures, it would be most difficult to write the voltages off as due to reproducible partial saturation of the CdI_2 by Cd. Furthermore, the electrolyte phase is at least nearly homogeneous as shown by comparison between different electrodes in different parts of the electrolyte. This homogeneity is much more strongly emphasized by results from the type II cells to be discussed later. Finally, including information from our unpublished work, different electrode materials do show different voltages in the same electrolyte solutions. Another aspect of this difference in behavior is discussed later during analysis of published phase diagrams and solution activity studies.

Likewise, these voltages cannot be written off as the "stray voltages which always occur when one dips metal into electrolyte." Here there is several per cent of Cd_2I_2 so that the activity of Cd as set by metal or alloy is well buffered even though metallic Cd is, of course, not an electrolyte species. This is not a case where a tiny concentration of a species varies tremendously during any attempt to measure it.

It is our interpretation that W (and at least most other potentially useful solid electrodes for these molten salt systems) will form a protective film (probably oxide) over the metal surface. The surface comes into equilibrium fairly rapidly with the electrolyte, and it reacts to changes in the electrolyte activity. Thus the chemical equilibria available involve electrolyte and surface.

But the electrochemical equilibrium permits attack on the base W because the surface passes ions and the metal passes electrons. Thus it can reflect very different reactions from those which have come into equilibrium during the long purely chemical equilibration.

Because unit activities of the base W and the surface film are not involved, we see no way to predict the magnitudes of the emf effects superimposed on the usually expected voltages.

Solubility of Cd in CdI_2 .—The cell which had been used for the unsaturated electrolyte studies was broken open after cooling rapidly from 773°K. The remaining metallic Cd was found to contain 2.07055g less than initially had been added, the loss being due to saturating 100g of CdI_2 . The corresponding solubility of Cd in CdI_2 at 773°K is 0.063 mole fraction.

The solubility from the temperature coefficient of emf (Fig. 11) is 0.0348 at 713°K.

Both of these solubilities are completely in agreement with Topol's and Landis's results (8).

Results with Cell Type II

This cell design is shown in Fig. 2. The cell was (a) loaded with 78.361g Cd, 18.573g Au, 183.5g CdI_2 , and ~ 0.5 atm Ar, (b) heated at 773°K for nearly 3 months, (c) stirred occasionally, (d) electrically drained periodically, and (e) monitored for open circuit at six tungsten vs. alloy couples.

The results of the emf measurements are indicated on Fig. 14. The following observations should be made.

1. The plots are offset on the ordinate to avoid overlap.

2. On any particular day all six W vs. Au-Cd couples showed nearly the same voltage.

3. The stirrer voltages (electrodes made from W wire) were consistently slightly larger, by 1-2 mV, than those of the potential sensors (made from W rod).

4. All voltages increased together with time. Apparently this change was associated with the change of alloy composition resulting from slow evaporation of Cd to cooler portions of the cell. Melting the evaporated Cd ($\sim 10\%$ of the Cd) back into the alloy decreased the voltage.

5. Electrically shorting the large stirrer leads together and to the alloy caused the voltage to drop.

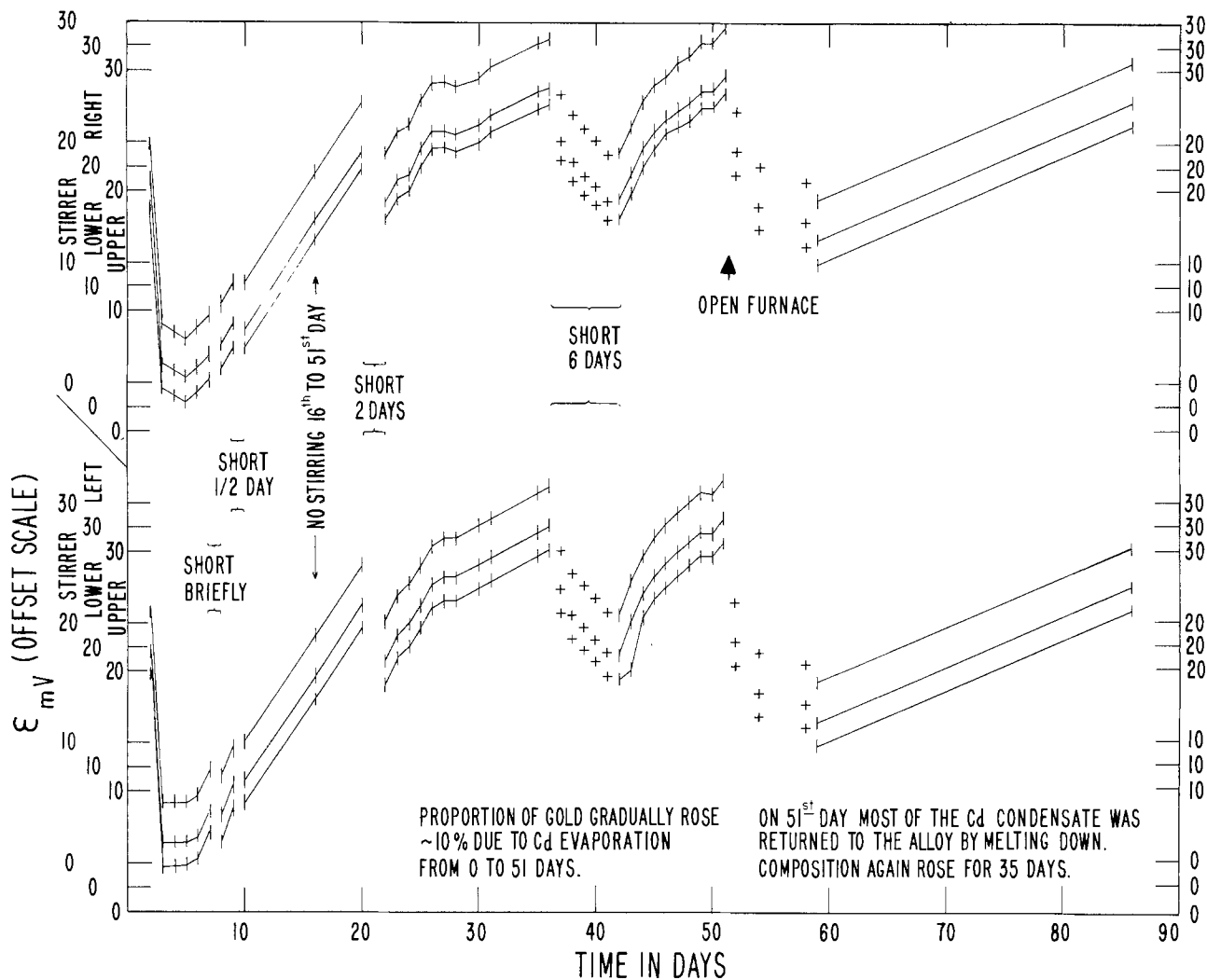


Fig. 14. Offset-scale plots for the open-circuit voltages of W vs. Cd-Au couples (reaction [2]) in a type II cell. Six electrodes vs. Cd-Au are represented as identified beside the ordinate: three in left leg, three in right; upper and lower are potential sensors; indicated shorting is via outside connections between the stirrer electrodes and the alloy. See text.

The potential sensors followed the drained electrodes.

6. Reaction of the alloy with the electrolyte appeared to create nearly identical conditions in the two electrolyte regions.

7. Reaction of the electrolyte with the oxidized potential sensors and with the unoxidized current collectors on the stirrers yielded nearly equivalent behavior in both (except for the 1-2 mV difference which we associate with compositional and strain differences between W wire and rod).

Conclusions from the type II cell measurements.—With adequate stirring and equilibration time, the metal or alloy sets the Cd_2I_2 concentration in the electrolyte following K in reaction [6]. The chemical reaction of the electrolyte with the electrode surfaces sets the surface activities. The electrochemical reaction can involve the base metal, not just its surface coat, and can be very different from the feasible purely chemical reactions. This difference can lead to anomalous voltages in what have been treated as inert electrodes in molten salts.

See also the conclusions regarding type I cells given earlier and the applications to published data to follow.

Applications of These Conclusions to Published Data

We have long believed that a major source of irreproducibility and scatter in the published data for molten salt emf cells lies with improper equilibration with the electrolyte and with failure to insulate the "inert" leads which pass through the electrolyte. These present measurements strongly support that belief.

A number of papers have been published in which the activities of dissolved species have supposedly been determined by measuring the voltages of bare W, Mo, or graphite "inert" electrodes dipping into unsaturated solutions as compared with saturated solutions. In principle these are cells with provision to carry out reactions like reaction [3], but many systems can be used. In physical design the cells can look much like cell type I.

As noted in this present paper, one can determine solubilities and activities as long as he corrects for the residual "inert" electrode voltage some way, e.g., note the correct determination of the solubility of Cd in CdI_2 at $713^\circ K$ by the change of emf-temperature pattern in Fig. 11. However, one would be incorrect to assume that zero voltage difference between bare electrode and reference metal gave the saturation composition.

Figures 15 and 16 show data where people have neglected the bare electrode voltage. In Fig. 15 Mashovets and Poddymov (12) and Crawford and Tomlinson (13) have attempted to establish the activity of Cd in $CdCl_2$ solutions by calculation from the emf's of bare Mo, W, or graphite vs. molten Cd, assuming the electrodes are inert. These voltages differ by as much as 5 mV, corresponding to a 15% difference in apparent activity. In Fig. 16 we see the Cd- $CdCl_2$ liquidus as established by standard techniques and as "established" by extrapolating to zero voltage by Mashovets and Poddymov.

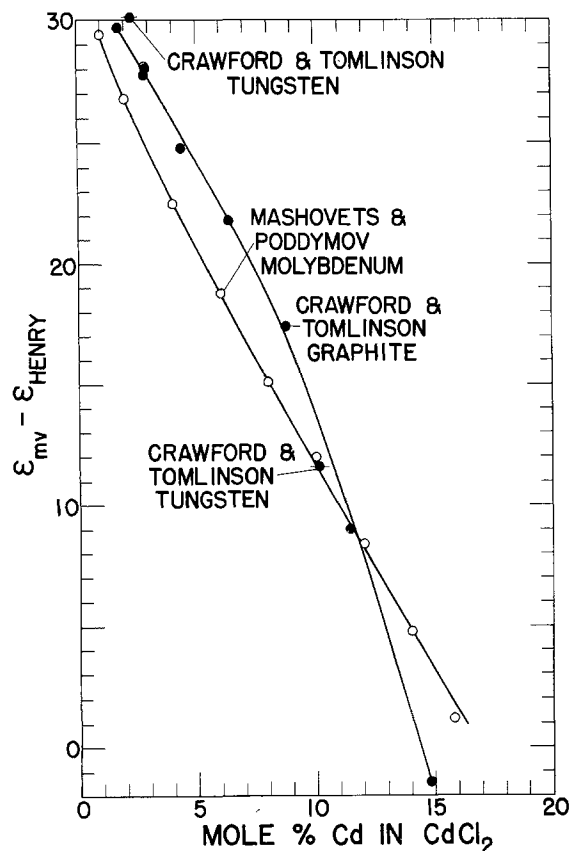


Fig. 15. Cd-CdCl₂ activity studies by emf using "inert" graphite, molybdenum, and tungsten electrodes at 873°K.

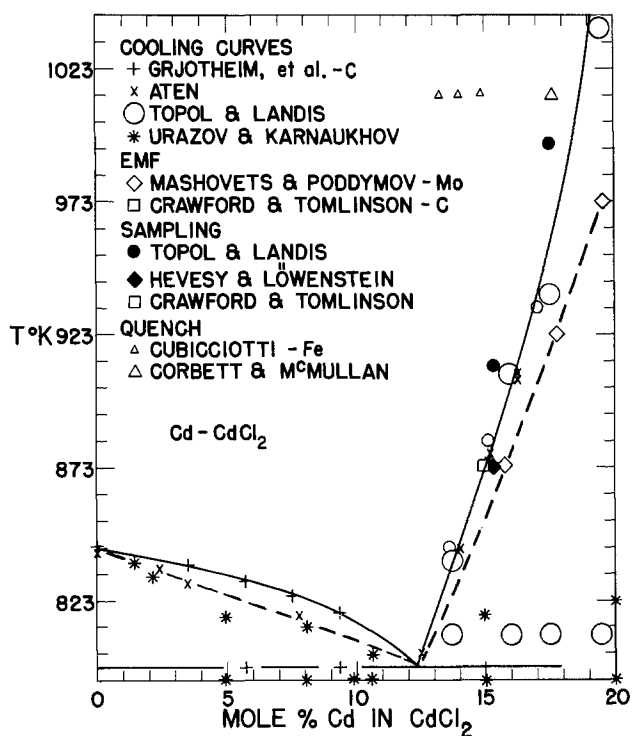


Fig. 16. Cd-CdCl₂ phase diagram measurements by different techniques with use of electrical conductors indicated. Hedger and Terry data are indicated by small circles.

Melting, Freezing, and Premonitory Phenomena

Both here in emf and earlier in vapor pressures (10), there has been evidence of unexpected variations of activity with composition near phase boundaries for molten Au-Cd alloys. Similar phenomena have often been reported in sensitive properties such as changes

of viscosity with temperature; thus the phenomena are detectable whether the phase boundary is approached with changing composition or with changing temperature.

Changes in property near a phase boundary are often called "premonitory phenomena," and we accept the term even though our measurements indicate that these deviations in the trends of properties reflect the true, equilibrium condition rather than some phenomenon akin to prescience. For molten alloys in this case, but also apparently for other kinds of solutions, e.g., molten salts, when a composition is close to the phase boundary there can sometimes exist significant quantities of atoms in atomic groupings which are similar to the atomic groupings which will be met when the adjacent phase becomes stable. These structures exist primarily because a large entropy of mixing overcomes an unfavorable enthalpy, thus they are often inherently dilute, but the fact of their existence indicates the solution free energy is decreased by their formation. In the case of metallic bonds in alloys, the shift of expected activities is particularly sharp; this sharpness reflects the fact that impurities weaken the metallic bond, and the new structures look like impurities to the resonance in the existing "metallic lattice."

Melting and freezing.—Premonitory phenomena and clustering similar to those we observe have been examined for pertinence to the relationship of solids to liquids, e.g., (14) and (15). This relationship has been subject to controversy. For example, Borelius (16) argues with experimental support that a continuous (but physically unattainable) curve joins the properties of a liquid metal to those of its solid, Danilov and Neimark [see Neimark in Ref. (17)] show x-ray correlations between solid and liquid mercury, and Saxton and Sherby (18) demonstrate good correlation between solid and liquid properties. Turnbull (19) presents the thermodynamic argument that melting occurs because of the crossing of the free energy-temperature curves, which for the solid and liquid, are "quite independent" of each other. He concludes that, "Therefore there should be no unusual changes in the properties of either the liquid or the crystal when they pass from their stable to their metastable condition." Also supercooling is sometimes used to conclude that the melting-freezing phenomena involve changes only in the solid, since the liquid may be unchanged at the melting point while the solid always does change. Assigning all the pretransformation effects to the solid leads to a further theoretical concern about the sharpness of the melting point and the absence of rapid changes in the solid properties close to the melting point as calculated by melting models related to that of Lennard-Jones and Devonshire.

In our view prenuclei similar to those discussed in the previous section would be important to certain solid-liquid equilibria. Where the solid and liquid structures were very different, there would be two possible liquid structures at the melting point: (i) One form would be a simple continuation of the usual liquid properties to lower temperatures; this structure would be metastable (though otherwise showing equilibrium behavior), supercoolable, and unable to exist in equilibrium with the solid. (ii) The second and stable liquid form would contain the solid precursors (prenuclei) at an equilibrium concentration. It is this latter form that might pass along a continuous but hypothetical curve relating solid and liquid properties as Borelius proposes. Stabilizing the liquid by the presence of prenuclei would remove part of the temperature region in which the solid was stable and would reduce the opportunity to observe premelting phenomena in such a system.

Once a prenucleus happened to form it would presumably act as a template for the formation of the equilibrium concentration of prenuclei. This is indicated in our systems by the absence of vapor pressure results intermediate between those for the presence or

absence of prenuclei, even in the prenuclei region the results are reproducible. Likewise, our second phases apparently form without difficulty once their equilibrium concentration has exceeded their solubility in the liquid, as indicated by the absence of metastable extensions (supersaturation) into two-phase regions by solutions containing prenuclei.

The pertinence of this work to the freezing of pure substances seems to be as follows: If the usual solid and liquid structures are rather different as emphasized by Turnbull, then the solid and liquid cannot be in equilibrium until the liquid becomes saturated with prenuclei. The freezing point is that point where the cooling liquid becomes saturated with prenuclei, i.e., where the equilibrium concentration or size of prenuclei becomes greater than the liquid can hold in solution. In this view the deviation in properties between the supercoolable and nonsupercoolable liquids occurs not at the freezing point but rather at some higher temperature.

If the solid and liquid metal structures are very simply related as emphasized by Borelius, then any supercooling would seem to result largely from the metallic resonance energy which would have to be overcome in the region where the solid first formed in the liquid phase. In this case there would be no particular reason to expect that a significant concentration of prenuclei would exist in the liquid at equilibrium with the solid.

Acknowledgment

The work reported in this paper was sponsored in part by the United States Atomic Energy Commission.

Manuscript submitted July 26, 1973; revised manuscript received Oct. 7, 1974. This work was presented in part as Paper 145 presented at the Houston, Texas, Meeting of the Society, May 7-11, 1972.

Any discussion of this paper will appear in a Discussion Section to be published in the June 1976 JOURNAL. All discussions for the June 1976 Discussion Section should be submitted by Feb. 1, 1976.

Publication costs of this article were partially assisted by Los Alamos Scientific Laboratory.

SYMBOLS

$\Delta\bar{F}_{\text{Cd}}$, $\Delta\bar{H}_{\text{Cd}}$, and $\Delta\bar{S}_{\text{Cd}}$ partial molal free energy, enthalpy, and entropy of the Cd component of solution

K	equilibrium constant
n	effective valence for the Cd_2^{++} - Cd^{++} mixture for use in calculation of activity and free energy from emf; the calculations involve both concentrations and mobilities of species where mixed valences are involved
F	Faraday constant (23,061 cal/V equiv)
e	cell potential
N_{Cd}	Cd mole fraction
a	activity
T	degrees Kelvin
X	Cl, Br, or I

REFERENCES

- B. L. Houseman and G. R. B. Elliott, *This Journal*, **116**, 1363 (1969).
- G. R. B. Elliott and J. F. Lemons, *ibid.*, **114**, 935 (1967).
- P. L. Robinson and G. R. B. Elliott, *High Temp. Sci.*, **4**, 1 (1972).
- B. L. Houseman, Submitted for publication.
- D. R. Conant and G. R. B. Elliott, Submitted for publication.
- D. R. Conant, *J. Chem. Eng. Data*, **16**, 430 (1971).
- B. L. Houseman and D. R. Conant, Submitted for publication.
- L. E. Topol and A. L. Landis, *J. Am. Chem. Soc.*, **82**, 6291 (1960).
- R. Hultgren, P. D. Desai, D. T. Hawkins, M. Gleiser, and K. K. Kelley, "Selected Values of the Thermodynamic Properties of Binary Alloys," p. 247, American Society for Metals, Metals Park, Ohio (1973).
- G. R. B. Elliott, C. C. Herrick, J. F. Lemons, and P. C. Nordine, *High Temp. Sci.*, **1**, 58 (1969).
- G. R. B. Elliott and J. F. Lemons, in "Nonstoichiometric Compounds," R. Ward, Editor, p. 153, American Chemical Society, Washington, D. C. (1963).
- V. P. Mashovets and V. P. Poddymov, *Zh. Prikl. Khim.* (English), **37**, 815 (1964).
- G. A. Crawford and J. W. Tomlinson, *Trans. Faraday Soc.*, **62**, 3046 (1966).
- A. R. Ubbelohde, *Angew. Chem. Intern. Ed. Engl.*, **4**, 587 (1965).
- K. Furukawa, B. R. Orton, J. Hamor, and G. I. Williams, *Phil. Mag.*, (8), 141 (1963).
- G. Borelius, *Arkiv Fysik*, **11**, 217 (1956).
- A. M. Samarin, Editor, "Structure and Properties of Liquid Metals." Academy of Sciences USSR, Moscow (1960). Translated as AEC-tr-4879, May 1962.
- H. J. Saxton and O. D. Sherby, *Am. Soc. Metals, Trans. Quart.*, **55**, 826 (1962).
- D. Turnbull, *Trans. AIME*, **221**, 422 (1961).

Sodium Phosphate Solubility and Phase Relations Basis for Invariant Point Chemistry Control

A. J. Panson, G. Economy, Chia-tsun Liu,
T. S. Bulischeck, and W. T. Lindsay, Jr.*

Westinghouse Research Laboratories, Pittsburgh, Pennsylvania 15235

ABSTRACT

A study of sodium phosphate solubility and phase relations was made in the temperature region of 300°C. A sharp retrograde temperature dependence of solubility was observed for disodium phosphate solutions. Solubility at constant temperature is strongly dependent on the composition of the solution. A low-Na/PO₄-ratio solid precipitates incongruently from solutions that have Na/PO₄ ratios from 2.13 to 1.6. A high-ratio solid phase precipitates incongruently from solutions with Na/PO₄ above 2.13, which corresponds to an invariant or "drying-up" point in the system. Both solid phases have a range of variable composition, indicating that they are solid solutions. The effects of concentration and dry-up in localized zones are discussed in terms of this new information. The work shows that chemistry variations can be controlled by maintaining solution composition above the invariant point in the phase diagram.

Sodium phosphate has been used in boiler applications to serve as a pH buffer for corrosion control and for prevention of scale by precipitation of hardness ions. Phosphate concentrations in the bulk solution usually are maintained at low levels, for example in the range of 10⁻⁴ M or about 10 ppm or less. However, boiling in regions of restricted flow can lead to concentration and precipitation of sodium phosphate salts. Thus, it is important to know the composition and concentration of the saturated solutions that can be produced and the effects of salt precipitation on the composition of saturated solutions as dry-up progresses.

The work of Ravich and Shcherbakova (1) has provided key information on solubility and phase relations of sodium phosphate salts in the 300°C region. These workers determined that, at 300°C, trisodium phosphate solutions show retrograde solubility, and solutions of Na/PO₄ mole ratio 2.85 precipitate a congruent solid solution phase, while solutions of greater than 2.85 mole ratio precipitate a solid solution phase of lower mole ratio. Thus, an increase in solution mole ratio results when precipitation occurs. Significantly, solutions of mole ratio greater than 3 can be produced in this manner so that a "free caustic" condition which may be detrimental to boiler materials can be produced. The work of Ravich and Shcherbakova thus provided a basis for controlling chemistry variations on precipitation to prevent formation of "free caustic." By maintaining boiler water solutions at a mole ratio less than the congruent ratio of 2.85, formation of high mole ratio solutions can be prevented. Precipitation from solutions of mole ratio less than the congruent ratio, 2.85, leads to a decrease in solution mole ratio since a solid solution of higher mole ratio precipitates. This operating strategy for sodium phosphate solutions is known as congruent control (2).

The work described in this paper was undertaken to provide more complete information on solubility and phase relations of sodium phosphate solutions.

This work has investigated solubility and phase relations in the system Na₂O-P₂O₅-H₂O at Na/PO₄ molar ratios primarily from 1.6 to 2.4 at 300°C (572°F). Some additional data have been obtained at 275°C and 324°C, and also at some compositions of higher molar ratios.

* Electrochemical Society Active Member.

Key words: sodium phosphate, solubility, phase, precipitates, invariant point.

Experimental

The experiments were carried out in two-liter autoclaves of stainless steel (A.I.S.I. Type 316) and Inconel Alloy 600 fitted with internal sampling tubes and filters. Three different experimental procedures were followed in obtaining the solubility results: nonisothermal procedures with slow, steady heating and continuous sampling of the autoclave contents; isothermal experiments with saturation approached from below by increasing the temperature, followed by equilibration for periods ranging from hours to many days; and experiments in which saturation was approached by evaporation at approximately isothermal conditions. Samples of solution were periodically removed from the autoclaves and analyzed by potentiometric acid-base titrations. The results from all three methods were essentially in agreement within experimental error.

The compositions of solids precipitated from the saturated solutions were calculated from differences between successive solution samples. In some instances it was possible to recover solids from the vessels for direct determination of sodium-to-phosphate ratios and comparison with calculated compositions. The agreement was satisfactory.

Results

Disodium phosphate solubility.—The solubility of Na₂HPO₄ hydrates has been shown to increase with temperature (3, 4). Above the 95°C temperature for transition from the dihydrate to anhydrous Na₂HPO₄, the solubility appears to be nearly independent of temperature up to about 240°C. The results of our work show that the solubility becomes sharply retrograde above 240°C. Figure 1 shows this information in the form of a binary melting point phase diagram. The diagram suggests that a new solid is the stable saturating phase above 220°C at pressures close to the vapor pressure of the saturated solution.

We have found that the solids which precipitate from disodium phosphate solutions are incongruent as evidenced by our observation of a decrease in solution Na/PO₄ mole ratio on precipitation. Thus, the solids precipitating from solution have Na/PO₄ mole ratios greater than 2. At 300°C, the precipitating solid phase has a mole ratio of 2.1.

The solubility of disodium phosphate solutions shown in Fig. 1 was obtained by slowly heating under-

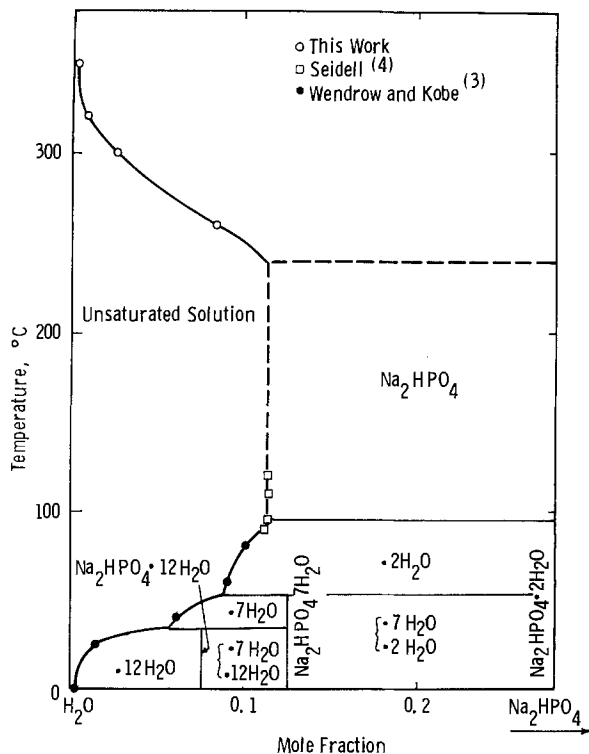


Fig. 1. Solubility of Na_2HPO_4 vs. temperature

saturated solutions in a Type 316 stainless steel autoclave and determining the temperature at which precipitation first occurred. Solution samples were withdrawn at temperatures by means of an internal sampling tube. The samples were conveniently checked for onset of precipitation by measuring their room temperature conductivity. Figure 2 presents these data. The solution compositions were determined by a potentiometric acid base titration. Tables I and II present the data of two experiments which show how the solution composition of disodium phosphate solutions pro-

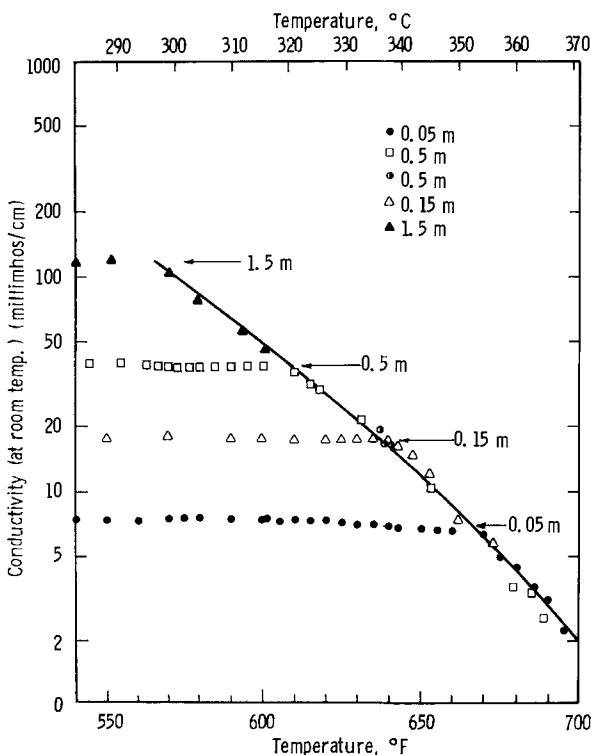


Fig. 2. Conductivity variations of disodium phosphate solutions on heating.

Table I. Precipitation from 0.5 molal solution initially $\text{Na}/\text{PO}_4 = 2$

Temp. on sampling (°F)	pH of sample diluted fivefold	m moles PO_4 in 5 ml	Na/PO_4 in soln (by titration)
100	9.08	2.41	2.00
205	9.02	2.43	2.00
310	9.00	2.43	2.00
400	8.88	2.45	1.98
495	8.46	2.42	1.97
555	8.23	2.38	1.95
600	7.98	1.29	1.86
640	7.80	0.76	1.83
645	7.73	0.54	1.87
660	7.51	0.20	1.75

Table II. Precipitation from 0.5 molal solution initially $\text{Na}/\text{PO}_4 = 2$

Temp. on sampling (°F)	pH of sample	m moles PO_4 in 5 ml	Na/PO_4 in soln (by titration)
Room temp.	9.06	2.41	2.01
510	8.55	2.41	2.01
617	8.25	1.61	1.93
648	7.83	0.57	1.86
677	7.3	0.16	1.69
679	7.3	0.16	1.63

ceed to lower mole ratio as precipitation proceeds on heating to higher temperatures. Mole ratios as low as 1.6 were obtained.

Retrograde solubility and formation of low ratio solutions on precipitation from disodium phosphate solutions were not anticipated and were considered to be undesirable in the steam generator since corrosive reactions could result from the changed composition of the solutions.

Invariant point determination.—Application of the phase rule provided a means to avoid solution composition changes on precipitation. We anticipated that if the disodium phosphate solubility curve intersection with the trisodium phosphate solubility curve could be found then, at the point of intersection, two solid phases would be present, and the three component system, Na_2O , P_2O_5 , H_2O , would be invariant. On evaporation, precipitation then would proceed with no solution composition changes as long as the two equilibrium solid phases were present.

A conceptual idea of the ternary phase diagram is provided in Fig. 3, which shows a solution invariant composition at the intersection of two solubility curves and a congruent composition. On this diagram, a solution of composition to the left of the congruent composition but to the right of the invariant composition will precipitate higher ratio solids and proceed in composition toward the invariant ratio at which point a second solid will precipitate and the system will be invariant.

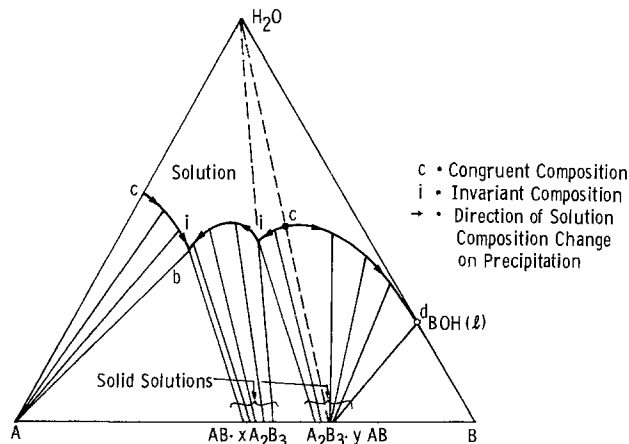


Fig. 3. Isothermal solubility diagram illustrating series of solid solutions between two compounds.

The solution composition is fixed and the over-all composition of the precipitating solid solutions will lie in the range covered in the gap between the two solids or in compositions between the solid solution composition limits. The final over-all composition depends on the initial solution composition.

A series of isothermal solubility determinations were made and the results are presented in Table III. The composition of the precipitating solids was determined by a mass balance and also, in some cases, by direct analysis of the solids as a check. Good agreement was found as shown in Table IV.

Figure 4 shows a plot of solution compositions in equilibrium with the various solid compositions formed at 300°C. The horizontal center section of the curve indicates that two solid phases coexist along with a

Table III. Results of isothermal solubility measurements and phase relationship studies

Run No.	Na/PO ₄ ratio in solution	Na/PO ₄ ratio in precipitated solid	Solubility, PO ₄ molality
275°C (527°F)			
56	2.0	—	>8.0
58	2.10	—	>2.5
82	2.15	2.13	3.79
85	2.15	2.23	3.26
30	2.24	2.87	1.29
31	2.25	2.86	0.64
44	2.32	2.73	0.74
57	2.57	2.84	0.42
75	2.69	2.76	0.41
72	3.24	2.83	0.26
300°C (572°F)			
25	1.58	1.62	5.73
39	1.60	1.60	5.68
42	1.65	1.65	6.95
23	1.75	1.84	2.94
76	1.81	1.91	0.94
56	1.92	1.99	1.06
18	1.97	2.04	0.85
52	2.00	2.22	0.51
90	2.10	2.37	0.64
19	2.11	2.23	0.68
91	2.13	2.56	0.33
88	2.13	2.63	0.44
26	2.14	2.28	0.47
28	2.14	2.44	0.55
21	2.14	2.35	0.66
30	2.16	2.33	0.67
44	2.18	2.55	0.38
31	2.19	2.58	0.43
57	2.46	2.82	0.25
70	2.89	2.75	0.14
324° (615°F)			
42	1.48	1.71	2.08
22	1.55	1.79	0.70
39	1.56	1.66	3.63
46	1.63	1.70	3.86
76	1.71	1.90	0.38
83	1.89	2.03	0.28
41	1.93	2.16	0.33
35	1.97	2.01	0.34
52	1.97	2.14	0.19
90	1.98	2.27	0.26
28	2.08	2.29	0.24
30	2.13	2.37	0.26
97	2.14	2.54	0.17
31	2.15	2.44	0.20
44	2.17	2.48	0.19
91	2.32	2.42	0.07
57	2.54	2.76	0.11
78	3.04	2.74	0.08
70	3.28	2.72	0.06

Table IV. Comparison between solid phase composition determinations

Run No.	Final temperature °C (°F)	Precipitate compositions	
		Direct analysis of recovered solids	Result of mass balance calculation
18	316 (600)	2.00	2.01
19	300 (572)	2.22	2.15
21	300 (572)	2.33	2.35
22	321 (610)	1.80	1.79
26	301 (574)	2.24	2.28
27	321 (610)	1.77	1.72
30	324 (615)	2.37	2.37

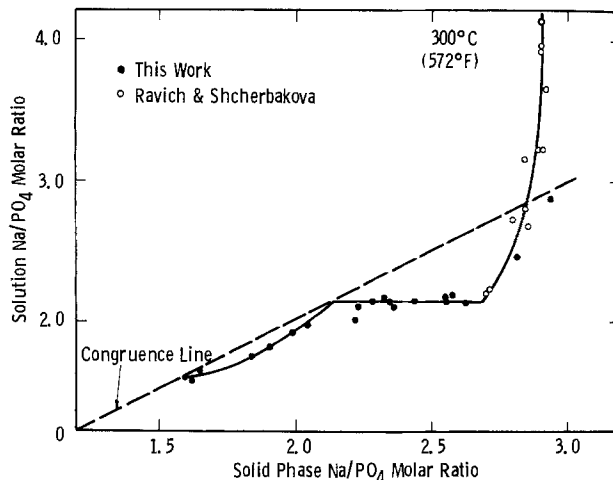


Fig. 4. Phase relationship in sodium phosphate precipitation equilibrium at 300°C.

solution of invariant composition at Na/PO₄ approximately 2.13. The other segments of the curve show variable composition for both solid and solution, indicating that the solids are solid solution phases. An upper congruent composition of 2.85 Na/PO₄ is indicated by the intersection with the dashed line. A lower congruent composition appears to occur at 1.6 Na/PO₄.

Solubility is plotted as a function of solution mole ratio and temperature in Fig. 5. The curves were drawn as an intersection of two solubility curves as indicated by the plateau or two-phase region in the phase relation plot. The intersection is the invariant point at which two solid phases precipitate. On both Fig. 4 and 5, the data of Ravich and Shcherbakova are seen to be consistent with this extension of their work to lower Na/PO₄ ratios.

A test of the invariant point could now be made by heating undersaturated solutions of composition greater than the invariant ratio to cause them to precipitate and proceed to the invariant composition. Table V shows the results of experiments in which solutions of initial ratio greater than the invariant ratio were heated to cause precipitation. No further compositional decrease was observed after an initial decrease to the invariant ratio. The result is in strong contrast to the behavior of disodium phosphate solutions in the experiments described earlier in which a significant ratio decrease below 2 was observed. These solutions were initially at a composition lower than the invariant ratio so that they proceeded to decrease in ratio on precipitation moving towards some lower invariant ratio.

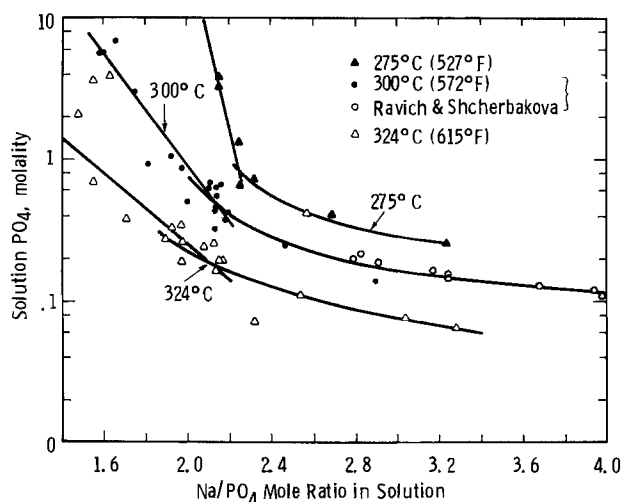


Fig. 5. Solubility of sodium phosphate solutions as a function of Na/PO₄ solution mole ratio.

Table V. Solution composition variation on precipitation of solids from solution initially close to and above invariant point

	Temperature range (°F)	Percent depletion of dissolved salt by precipitation	Solution Na/PO ₄ ratio
A.	<541	0	2.31
	570-582	18	2.22
	591-605	45	2.15
	608-625	63	2.20
	633-653	76	2.18
	657-664	85	2.21
B.	<532	0	2.21
	570-590	14	2.17
	595-607	29	2.16
	612-627	56	2.15
	630-640	75	2.14
	649-667	89	2.14
C.	<467	0	2.19
	478-518	1	2.18
	575-587	16	2.15
	593-594	36	2.13
	610-614	49	2.14
	628-636	65	2.13
	636-659	82	2.11

Thus, solution mole ratio decrease below 2 in an acid direction on precipitation can be prevented by using solutions of mole ratio above the invariant ratio.

Discussion

In this work, we have found that disodium phosphate solutions have a sharply retrograde solubility above 240°C. Incongruent solids of higher mole ratio than 2 precipitate so that precipitation causes the solution mole ratio to proceed to lower or more acid values. An invariant composition of 2.13 at 300°C was found. The solubility increases sharply with decreasing mole ratio from the invariant point of 2.13 to 1.6.

These results provide a rational basis for controlling the composition of sodium phosphate solutions in boilers. As previously recognized by Marcy and Halstead (2), the Na/PO₄ ratio should be maintained below the upper congruent composition to avoid excessive alkalinity caused by incongruent precipitation during evaporative concentration. This work indicates that the Na/PO₄ ratio should also be maintained above the invariant composition to avoid composition shifts toward the lower ratio compositions of very high solubility as evaporative concentration and dry-up proceed.

Manuscript submitted Oct. 17, 1974; revised manuscript received March 12, 1975. This was Paper 81 presented at the New York, New York, Meeting of the Society, Oct. 13-17, 1974.

Any discussion of this paper will appear in a Discussion Section to be published in the June 1976 JOURNAL. All discussions for the June 1976 Discussion Section should be submitted by Feb. 1, 1976.

Publication costs of this article were partially assisted by Westinghouse Electric Corporation.

REFERENCES

1. M. I. Ravich and L. G. Shcherbakova, *Izvest. Sek-tora Fiz-Khim Analiza, Inst. Obshch. Neorgan. Khim., Akad. Nauk SSSR*, **26**, 248 (1955).
2. V. M. Marcy and S. L. Halstead, *Combustion*, **35**, 45 (1964).
3. B. Wendrow and K. A. Kobe, *Ind. Eng. Chem.*, **44**, 1439 (1952).
4. A. Seidell and W. F. Linke, "Solubilities of Inorganic and Metal Organic Compounds," 4th ed., Vol. II, American Chemical Society, Washington, D.C. (1965).

Chemisorption on Powdery Indium Amalgams: Catalysis of the Oxygen Reduction

R. Barrue* and J. F. Rialland

Laboratoire de Génie Electrique (LGEP-LCIE), 92260 Fontenay-Aux-Roses, France

ABSTRACT

A number of works have described the catalytic properties of powdery indium amalgams in the electrochemical reduction of oxygen in basic media. X-ray diffraction studies of these powders exhibit that their surface mainly consists of the three following compounds: In(OH)₃, InOOH, and In₂O₃. The chemisorption isotherms, determined in the pressure range 0-1.5 atm, show that only In₂O₃ can take a predominant part in the catalytic properties of the powdery amalgams. Electrochemical measurements of oxygen cathodic reduction in aqueous basic solutions corroborate the previous result.

Indium amalgams are liquid at room temperature for indium concentrations lower than 69 atomic per cent (a/o). These liquid alloys may yield a powdery material through strong mechanical shaking under atmosphere. This phenomenon seems to be attributed to a superficial enrichment in indium and an adsorption of gases. X-ray diffraction studies have led us to suggest a grain model which consists in a liquid core surrounded with a quasi solid superficial layer (1).

A number of works (1-3) have described the catalytic properties of those powdery amalgams in the electrochemical reduction of oxygen in basic media. X-ray analyses have established that the superficial

layer of grains mainly consists of the three following compounds: indium oxide (In₂O₃), indium oxyhydrate (InOOH), and indium hydroxide (In(OH)₃).

In this paper, our purpose is to specify if the catalytic properties of the powdery indium amalgams may be specifically attributed to one of those three compounds.

Oxygen Chemisorption Isotherms

In heterogeneous catalysis, the adsorption of the reactive compounds is the first step of the catalytic process. This fact led us to determine the oxygen chemisorption isotherms on the powdery amalgams and on the three above-mentioned compounds. The isotherms have been plotted for usual pressures in heterogeneous catalysis and at room temperature.

* Electrochemical Society Active Member.

Key words: chemisorption, catalysis, indium amalgams, indium oxide.

Experimental

The powdery amalgam samples were obtained from a liquid alloy of 16 a/o In through mechanical shaking under atmosphere (1). Indium oxide and indium hydroxide were made and then analyzed by means of x-ray diffraction, in our laboratory. For InOOH, an ultrapure product (Ventron U.S.A.) was used. The powdery samples consisted of particles of about 50 μm diameter. Oxygen and nitrogen were high purity gases ($\text{O}_2 \geq 99.995\%$; $\text{N}_2 \geq 99.998\%$).

The diagram of the apparatus is shown in Fig. 1. The volume of the cell is about 500 cm^3 . In a first step, a 10g sample was put in the cell. After a 48 hr long desorption in a high vacuum (10^{-6} Torr), a mixture of oxygen and nitrogen (an unchemisorbed gas) was introduced into the cell. The number of moles for each of the two gases contained in the cell was determined by means of the gas-chromatography analysis of a 1 cm^3 gaseous sample. The change of the partial pressures of the two gases as a function of time was obtained in the same way.

As an example, Fig. 2 shows the superposition of two chromatograms obtained at the start (s) and the end (e) of adsorption on a powdery amalgam sample. The first peak is the one of oxygen, and the second peak is the one of nitrogen. The numbers of moles for each gas are in ratio to the corresponding peak areas. The examination of the chromatograms shows that the N_2 peak is unchanged, while the O_2 peak area is strongly reduced, exhibiting a large adsorption of this gas.

Results

No adsorption on $\text{In}(\text{OH})_3$ and InOOH could be detected, while oxygen adsorption on In_2O_3 and on the powdered amalgam was measurable by the experimental method.

The specific surface areas were determined from the BET transforms (4) of the nitrogen physical adsorption isotherms at 77°K. The values deduced from these measures are: 115 m^2/g for the powdery amalgam and 74 m^2/g for In_2O_3 .

The times for establishing the adsorption-desorption equilibrium were relatively long. The time constants were related mainly to diffusion phenomena through the powdery material. Thus in order to quicken the rate of reaction, the powdery samples were shaken by using a magnetic device. With this agitation, the equilibrium was reached after about 7 days for the powdery indium amalgam and after about 15 days for In_2O_3 . In Fig. 3 the amounts of adsorbed oxygen are plotted vs. time for the two adsorbents.

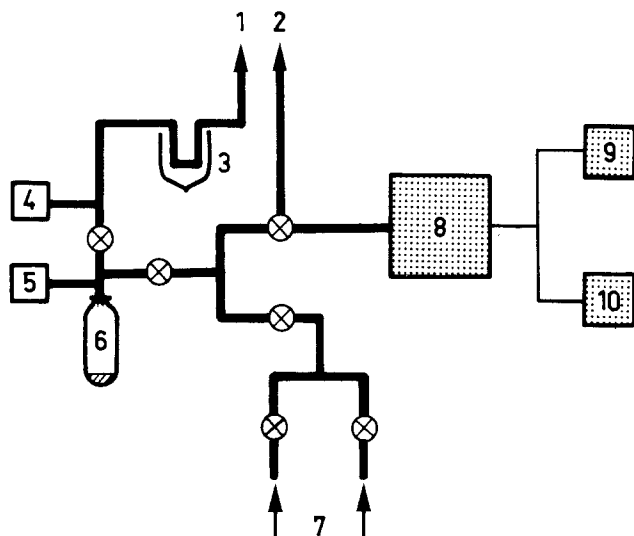


Fig. 1. Apparatus for chemisorption isotherms measurements. 1, To high vacuum; 2, to vacuum; 3, trap; 4, vacuum gauge; 5, pressure gauge; 6, adsorption cell; 7, gas supplies; 8, chromatograph; 9, recorder; 10, digital integrator.

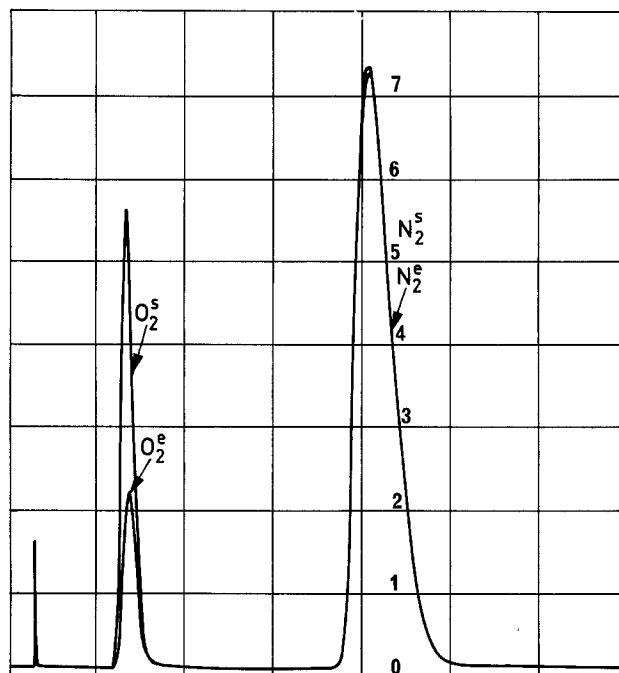


Fig. 2. Superposition of chromatograms. Adsorbent: powdery indium amalgams. Lasting of adsorption: 5 days; $T = 25^\circ\text{C}$. $P_{\text{O}_2}^s = 0.2$ atm; s = start; e = end.

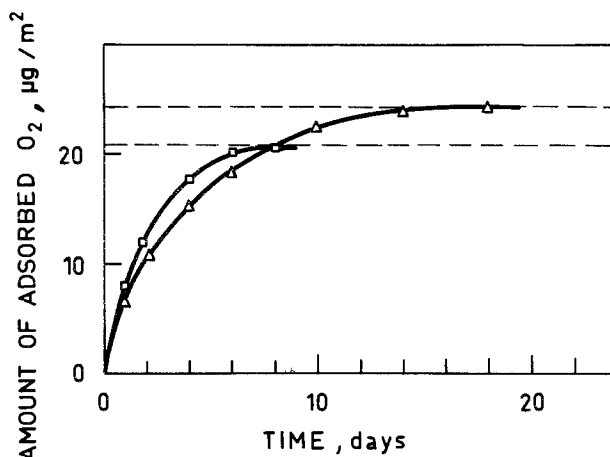


Fig. 3. Kinetics of oxygen adsorption referred to unit surface area. Temperature: $T = 25^\circ\text{C}$. Initial pressure: $P_{\text{O}_2}^s = 0.5$ atm. Square, on powdery amalgams; triangle, on indium oxide

The isotherms are plotted in Fig. 4. For the two curves, a saturation quickly occurs in terms of pressure. For oxygen partial pressures over 1 atm, the powdery amalgam isotherm increases again; in addition, the adsorbed oxygen could not be desorbed fully by the usual ways. This behavior may be attributed to the existence of a secondary chemical reaction, as in the oxidation of a metallic phase (mercury or indium).

Oxygen Reduction on an Indium Oxide Electrode

The catalytic effect of indium oxide in the electrochemical reduction of oxygen in basic media has been specified by electrochemical measurements.

Experimental

Gas porous electrodes were made with indium oxide. Two grams of indium oxide and 2g of powdered metallic indium were mixed and compressed in a cylindrical matrix. The binding material was sintered at 150°C for 24 hr. The powdered indium was included to ensure good cohesion and good electrical conductivity in the sintered material. The area of the electrode was about 1.5 cm^2 . Electrolyte was an aqueous solution of sodium hydroxide (1M NaOH); the temperature was 25°C . The

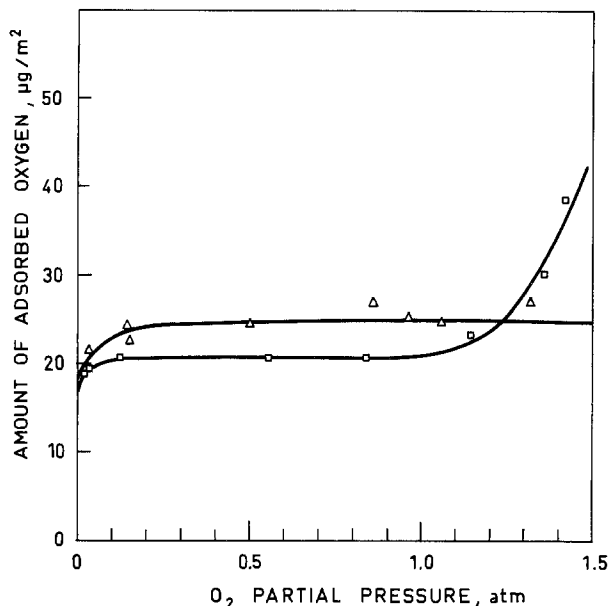
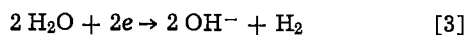
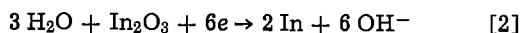
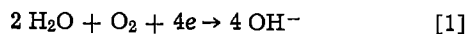


Fig. 4. Oxygen chemisorption isotherms referred to unit surface area. Temperature: $T = 25^\circ\text{C}$. Square, on powdery amalgams; triangle, on indium oxide.

cathodic potentials were recorded *vs.* the Hg/HgO potential.

Results

Three reactions were possible



Only reaction [1] was associated with the catalytic process. This reaction occurred with the reduction of oxide to metal (reaction [2]). In the studied current density range, reaction [3] was so slow that the current corresponding with the H_2 -release was negligible.

The current density potential curves are plotted for different pressures of oxygen in Fig. 5. The curves are typical of electrodes for which the oxide capacity is 4160 coulombs (2g of In_2O_3). Curve 1 is associated with the reduction of oxide. The differences between this curve and curves 2 and 3 show the effect of oxygen. Curve 4 was obtained with a powdered amalgam electrode studied under the same conditions (1).

Because of its slowness, the chemisorption of oxygen is probably the limiting step of reaction [1]. In Fig. 3, the maximum rate of adsorption is given by the slope at origin; this rate is too slow to explain the effect of oxygen in the electrochemical measurements. In fact, the time constants determined in chemisorption were mainly due to diffusion through the pores of the powdery bulk. In the electrochemical measurements there is forced convection of oxygen and thus an increase in adsorption rate. Thus the rate of adsorption cannot be determined from the curves of Fig. 3.

Conclusion

Oxygen chemisorption on $\text{In}(\text{OH})_3$ and InOOH cannot be detected by our experimental method. With re-

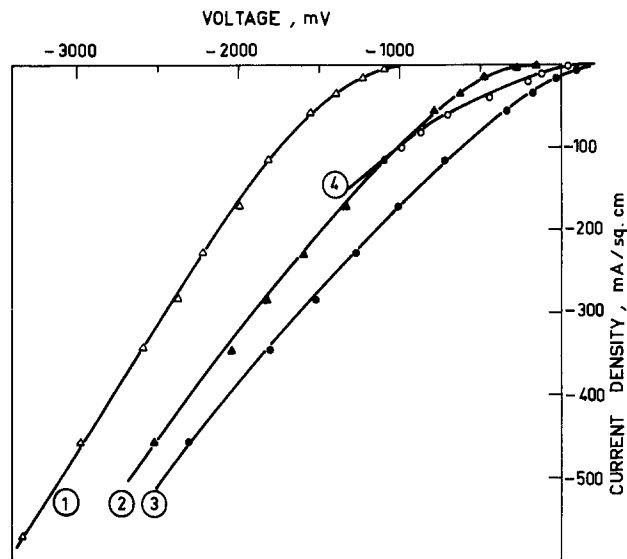


Fig. 5. Effect of O_2 pressure on polarization curves. 1, In_2O_3 - O_2 pressure = 0; 2, In_2O_3 - O_2 pressure = 1 atm; 3, In_2O_3 - O_2 pressure = 2 atm; 4, powdery indium amalgams- O_2 pressure = 2 atm. Temperature: $T = 25^\circ\text{C}$. Electrolyte: 1M NaOH. Reference: Hg/HgO · 1M NaOH.

gard to In_2O_3 and to the powdery indium amalgams, the amounts of adsorbed oxygen are about the same order of magnitude.

The electrochemical experiments exhibit the catalytic effect of In_2O_3 in oxygen reduction in basic media. The measured cathodic potentials are comparable with those obtained for a powdery indium amalgam electrode.

These results lead us to attribute the catalytic properties of the powdery amalgams to the presence of In_2O_3 in the surface layer of the individual grains.

At the present time, investigations on the powdery indium amalgams are being made to differentiate the kinetics of In_2O_3 reduction from that of catalytic oxygen reduction.

Manuscript submitted July 3, 1974; revised manuscript received Feb. 12, 1975. This was Paper 329 presented at the San Francisco, California, Meeting of the Society, May 12-17, 1974.

Any discussion of this paper will appear in a Discussion Section to be published in the June 1976 JOURNAL. All discussions for the June 1976 Discussion Section should be submitted by Feb. 1, 1976.

Publication costs of this article were partially assisted by the Laboratoire de Génie Electrique.

REFERENCES

1. J. F. Rialland and J. Robert, *J. Chim. Phys.*, **66**, 354 (1969).
2. J. F. Rialland, Thesis, University of Paris, 1968.
3. J. Deprez, J. Rabit, J. F. Rialland, and J. Robert, *J. Physique*, **32**, 805 (1971).
4. S. Brunauer, P. H. Emmett, and E. Teller, *J. Am. Chem. Soc.*, **60**, 309 (1938).

Undervoltage Deposition of Alkali Metal at Carbon Electrodes in the LiCl-KCl Eutectic Melt

S. D. James*

Electrochemistry Division, Naval Surface Weapons Center, White Oak, Maryland 20910

ABSTRACT

Voltammograms and charge-discharge curves are presented for carbon electrodes of varying graphitic crystallinity in LiCl-KCl eutectic melt at 703°K (430°C). For rods of glassy carbon, graphite, and pyrolytic graphite there is a very marked cathodic depolarization below about $-2.5V$ vs. a chlorine electrode. Chemical analysis of the cathodized carbons shows that this depolarization is caused by undervoltage deposition of alkali metal. The deposited metal normally consists entirely of Li but in two cases, during potentiostatic cathodizing, significant amounts of K were codeposited. Cathodized graphite rods disintegrate before reaching the Li potential but glassy carbon rods do not and can survive about 25 charge-discharge cycles before breaking up. The uninflected charging curves obtained for glassy carbon and graphite give no indication of distinct transitions between Li intercalation compounds of different stages. However, the relatively low Li contents of cathodized carbons, their x-ray diffraction patterns and the absence of acetylene in their reaction with water all favor the presence of intercalation compounds rather than a carbide. Lithium contents of glassy carbon rods cathodized toward the Li potential range up to about 7 weight per cent compared with 8.9% for C_6Li , the richest intercalation compound and 37% for Li_2C_2 . Even quite brief exposures of carbon electrodes in this melt to potentials below $-2.5V$ have lasting effects on electrode behavior; carbon loses its melt-repellency and the electrode suffers a 1-2V lowering of its open-circuit voltage.

Unexpectedly high cathodic currents were noticed when carbon electrodes were driven below $-2.5V$ vs. the chlorine electrode in LiCl-KCl melt at 703°K (430°C). This surprised us since it occurred more than a volt above the equilibrium potential of lithium in this melt, *viz.*, $-3.65V$ vs. the chlorine electrode (1). Since a literature search failed to unearth any explanation of this anomaly we made tests to elucidate its cause. The present paper describes these tests and the conclusions arrived at.

Experimental

Equipment.—The LiCl-KCl eutectic melt volume was 376 cm³, occupying a 115 mm depth in a 210 mm tall, 70 mm diameter Pyrex test tube. This inner test tube rested inside a 360 mm tall, 76 mm diameter, flange-topped Pyrex pot (flange assemblies were of 3 in. Conical Pipe System from the Corning Glass Company). A flanged Pyrex lid with Teflon O-ring gasket was bolted onto the pot. This lid has six short vertical glass tubes acting as ports through which a thermocouple, a 4 mm Pyrex gas-bubbling tube and various electrodes can be fed down into the melt. Sliding seals at these ports were made using modified Teflon Tube Fittings (Beckman Instrument Incorporated). A cylindrical electric furnace was used; its temperature was controlled to $\pm 1^\circ K$ ($1^\circ C$) by Versatherm Model 2157 (Cole Palmer Instrument Incorporated). A Chromel-Alumel thermocouple inside a 6 mm Pyrex tube thermowell dipped into the melt. At 703°K the 110 mm deep, normally unstirred melt was $1^\circ K$ hotter at the top than at the bottom.

The Tacussel fast-rise potentiostat PIT20-2X (plus GSTP2 function generator) was used in the potentiostatic or galvanostatic mode giving rise to linear scan voltammograms and constant current charge-discharge curves, respectively. The voltammograms were displayed on a Tektronix X-Y oscilloscope model 561A with two, 2A63 differential amplifier plug-ins. The two inputs of the Y-plate plug-in were connected across a standard resistor (normally one ohm) in the counter-

electrode lead, thus registering cell current. The other plug-in received the controlled voltage sweep (test electrode vs. reference) from a jack on the potentiostat. The voltammograms were photographed. In the constant current mode, the voltage-time curves were recorded on a strip chart recorder (Varian G-11A with B1 input chassis).

Materials.—Lithium chloride and potassium chloride powders were ACS certified reagents from Fisher Scientific Company. Chlorine gas (used both in the reference electrodes and for dehydrating the melt) was Electronic Grade, 99.98% pure, from Precision Gas Products, Rahway, New Jersey. The usual cell atmosphere was high purity argon (water pumped, 99.996%), passed through a drying train of Drierite (anhydrous calcium sulfate). Three types of carbon rods were used as electrode materials. Glassy carbon rods, 1.5 or 3 mm in diameter (grade V25-99.99% carbon) were obtained from the Carbone Company, of Boonton, New Jersey. Synthetic graphite rods of spectroscopic purity (99.999% carbon) came from Ultra Carbon Corporation, Bay City, Michigan. Both $\frac{1}{8}$ in. (3.0 mm) and $\frac{1}{4}$ in. (6.1 mm) diameter rods were used. In one experiment, graphite rods, 254 \times 6.3 mm, covered with a 0.1 mm thick coating of pyrolytic graphite were used. The graphite orientation is said to be such that the a-b planes are parallel to the coated surface at all points. These rods, designated EC-2, were bought from the General Electric Company, Detroit, Michigan.

Electrodes.—Working electrodes of glassy carbon used in getting the cyclic voltammetry data of Fig. 2 are illustrated in Fig. 1A. These were made as follows. Firstly a 25 mm length of 1.5 mm diameter glassy carbon rod was carbon-cemented 6 mm deep into the end of a 3 \times 600 mm spectroscopic graphite rod. The composite rod was then sealed into a Pyrex tube and sawn off at 45°. This angular cut allows any chlorine bubbles, anodically formed during use, to escape from the electrode. A final polish was given to the Pyrex-carbon sawn surface on a 180 grit diamond-coated wheel. The geometric area of the exposed glassy carbon ellipse was 2.43 mm². The Carbone Company's

* Electrochemical Society Active Member.

Key words: molten salts, carbon electrodes, intercalation compounds, cathode depolarization, high temperature electrochemistry.

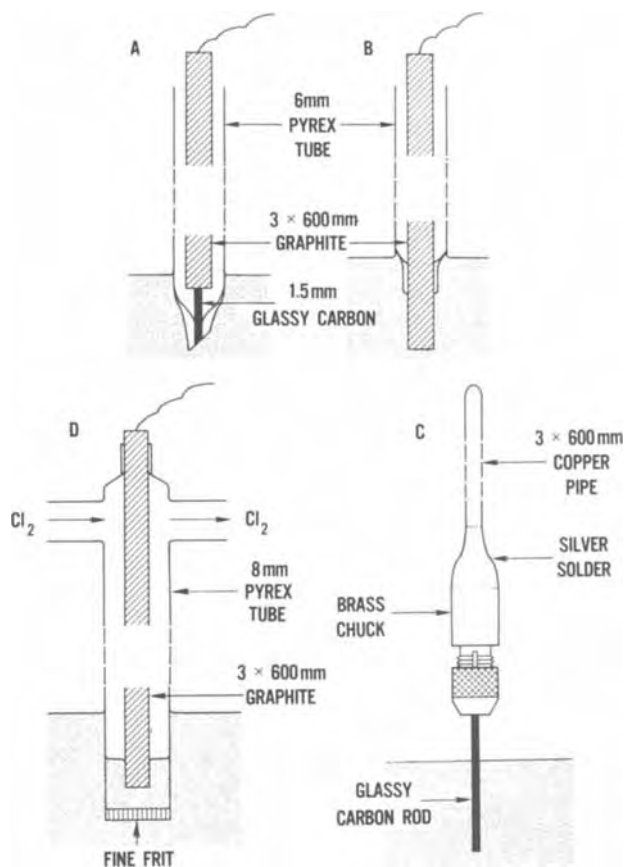


Fig. 1. Types of carbon electrode used: (A) working electrode of glassy carbon sealed in Pyrex, (B) working or counterelectrode of graphite sealed through Pyrex, (C) working electrode of glassy carbon held in chuck, (D) chlorine reference electrode.

glassy carbon has a thermal expansion coefficient of $3.2 \mu\text{m}/\text{m}\cdot\text{K}$ at 373°K . This is almost as big as that of the Pyrex glass (3.3 for Corning 7740) and thus the carbon-Pyrex seal of Fig. 1A has little or no tendency to leak. In the early experiments it was noticed that the Pyrex tips of working electrodes like those of Fig. 1A and B cracked and admitted melt after prolonged cathodic polarization (even at potentials well positive of the Li/Li^+ equilibrium). It became apparent later that this was caused by swelling of the carbon tip due to its absorption of alkali metal deposited at undervoltage. In subsequent work designed to examine this undervoltage deposition, the Pyrex envelopes were dispensed with and the bare carbon was dipped directly into the melt. A graphite working electrode used in the initial cyclic voltammetry is shown in Fig. 1B. The end of a 3 mm diameter graphite rod (Ultra's U7, a high density grade, $1.90 \text{ g}/\text{cm}^3$) protruded 20 mm from the sealed Pyrex tube. The geometric area of exposed graphite was 2.0 cm^2 . Electrode (C) of Fig. 1 was used when we wished to weigh the carbon before and after cathodic treatment. The carbon rod was gripped in a brass chuck (taken from an electrical test prod). The only carbon material studied in this way was glassy carbon. Rods 1.5 mm in diameter slipped easily into the chuck whereas 3 mm rods had to be tapered by filing.

The counterelectrode was a $6 \times 600 \text{ mm}$ graphite rod (Ultra, U7) dipping about 75 mm undermelt. When acting as a cathode in pure LiCl-KCl melt, graphite absorbs alkali metal plated onto it. In the anodic mode it reoxidizes this absorbed metal and/or gasses chlorine. None of these reactions significantly contaminates the melt. A graphite rod of these wetted dimensions can absorb at least 1500 coulombs of cathodic charge before there is any danger of its disinte-

grating under the stress of the absorbed alkali metal (see below)

The chlorine electrode was used as reference. It is illustrated in Fig. 1D. Ultra Carbon's U120 grade of spectroscopic graphite rod was normally used as the electrode substrate although other grades of pure graphite worked just as well. The chlorine flows by the carbon and over the melt rather than through the carbon and into the melt as is more customary (2). This flow-by electrode has the advantage of relative ease of construction and safety from the danger of the melt sucking back and freezing. It takes about 10-15 hr of chlorine flow to equilibrate the electrodes to within 1 mV of the reversible chlorine potential. We always used a pair of reference electrodes, regularly monitoring their interelectrode or bias potential. After the initial equilibration period the bias potential never exceeded 1 mV during weeks of continuous use. All quoted potentials are *vs.* this chlorine electrode.

Melt purification.—A charge of LiCl-KCl salt powders (mixed in the eutectic proportion) was outgassed at $2.66\text{-}6.65 \text{ N}\cdot\text{m}^{-2}$ ($20\text{-}50 \mu \text{ Hg}$) while being heated up to about 703°K (430°C). On melting, a brisk evolution of water vapor commenced and continued for 30-45 min. Residual water was then removed by bubbling chlorine through the melt for 60 min (3). It was then freed from platable impurities by preelectrolysis at an auxiliary aluminum cathode (*vs.* a graphite anode). The cathode was 80 cm^2 in area and held at -2.95 V to the chlorine electrode. Preelectrolysis was continued for 24 hr although the residual current density (at the cathode) fell to a steady value of $10 \mu\text{A}/\text{cm}^2$ after 4 hr. The Al cathode which had become dark gray was withdrawn from the melt at the end of the preelectrolysis.

X-ray examination of cathodized carbons.—After cathodizing in the melt at constant current down to the lithium potential (-3.65 V *vs.* the chlorine electrode), several different types of 3 mm carbon rod were x-rayed to see if any structural change had occurred. After filing free from adherent solidified melt the rods were laid in a Lucite x-ray sample holder and filed half round so as to expose a $10 \text{ mm} \times 22 \text{ mm}$ expanse of flat carbon surface. This was all done in an argon-filled glove bag. Then each holder was securely enveloped with one layer of cellulose acetate transparent adhesive tape (Magic Tape 3M Company) and placed in its own, argon filled, screw-cap bottle. The x-ray diffraction pattern was recorded in air without removing the tape, immediately after taking the holder from its bottle. The Standard Phillips x-ray powder diffractometer was used employing $\text{CuK}\alpha$ radiation.

Chemical analysis of cathodized carbons.—Cathodized carbon rods were ground up and extracted with water which was then analyzed for Li^+ , K^+ , Cl^- , and OH^- . The rods were first freed from solidified melt by a quick rinse with a jet of distilled water then dried, crushed in a press and ground in a mortar. The powders were then weighed; weights varied between 0.2 and 0.8g. After 4 hr of refluxing with distilled water, the extracts were filtered and analyzed for Li^+ and K^+ by atomic absorption spectroscopy and for Cl^- and OH^- by conventional titrimetry. In some cases, second extractions were done on the powder. The second extracts contained the sought ions at no more than background levels. In spite of this apparently complete removal of alkali metal, flame tests showed that most of the extracted carbons still contained appreciable amounts of Li. Hence the extracted powders were ashed to constant weight in silica crucibles at 1023°K (750°C) then digested in water which was analyzed to determine the residual alkali metal.

Results and Discussion

Voltammograms.—Figure 2 shows current-voltage curves obtained at a glassy carbon electrode of Fig. 1A

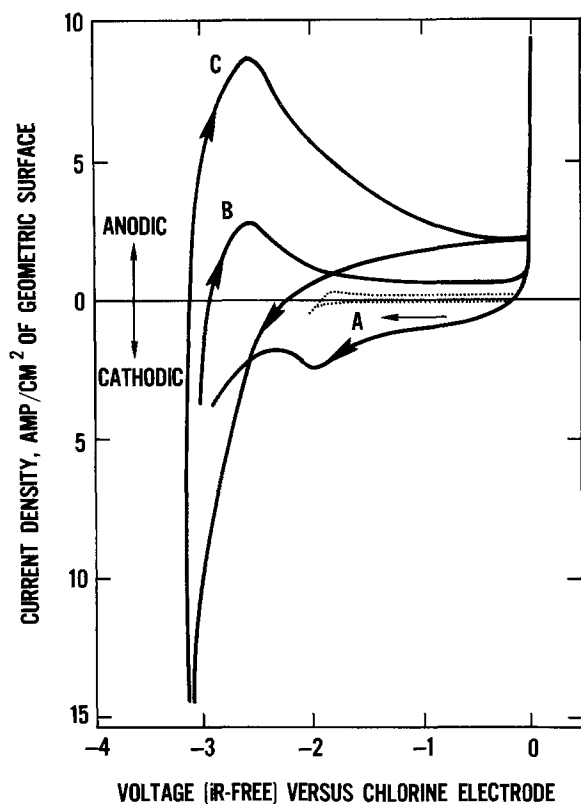


Fig. 2. Voltammograms at glassy carbon in LiCl-KCl at 430°C as a function of the range of applied voltage. Sweep cycle time was 0.2 sec.

type construction. The geometric area of the carbon ellipse was 0.0243 cm², and the electrode was dipping in a purified melt at 703°K (430°C). Basically similar curves were obtained using a 2.0 cm² graphite electrode (Fig. 1B type). The curves of Fig. 2 are the reproducible ones obtained after a train of five or more voltage triangles had been applied to the working electrode. The nominal voltage range of these triangles were: Curve A, -2.0 to 0.0V; B, -3.5 to +0.5V; C, -4.0 to 0.0V vs. the chlorine electrode. However, after correction for substantial *iR* drops the actual limits of voltage excursion were -3.2 and 0.0V. In the low amplitude sweeps of curve A the trace differs little from expected, except perhaps at -2V where cathodic current is starting followed by a small anodic peak after sweep reversal. These effects are much more marked in B which also has a pronounced cathodic peak at -2.1V. This latter peak is presumably due to reduction of chlorine generated at positive voltages since it vanishes if the positive excursion of applied voltage is restricted to 0.0V. In curve C the cathodic depolarization below -2.5V is very striking. Extremely large cathodic current densities are found and a big anodic peak appears after voltage sweep reversal as species produced in the cathodic sweep are reoxidized.

These results were unexpected; we did not look for significant cathodic current till below about -3.65V, the lithium potential in this melt (1). Such big cathodic currents (10 A/cm², at 0.7V above the Li potential) cannot arise from impurities at the level normally found in reagent grade salts. This is confirmed by the independence of the effect on the degree of melt purification employed. So it seems that carbon electrodes are far from inert in this metal. The rest of this paper shows that carbon rods of diverse types will, between -2.5 and -3.6V, absorb at undervoltage, large quantities of alkali metal (mainly Li). Due to a compound formation between carbon and deposited metal (probably a laminar or intercalation compound) deposition is energetically assisted, i.e., occurs at undervoltage.

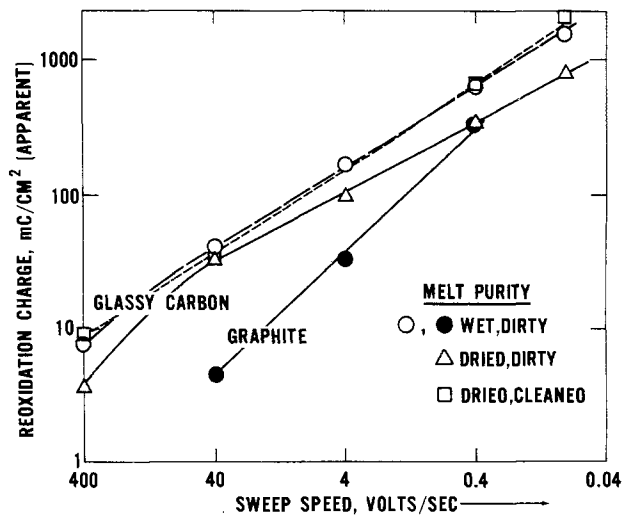


Fig. 3. Coulombic charge of anodic peaks in voltammograms at carbon electrodes. Applied voltage range: -3.5 to +0.5V, vs. chlorine electrode. LiCl-KCl at 430°C.

Figure 3 shows the electrical charge used to reoxidize the material plated out at undervoltage. The coulombic content of the anodic peaks in curves such as those of Fig. 2 is plotted against the voltage sweep rate. The glassy carbon was a Fig. 1A type and the graphite electrode a 1B type. There is no correlation of reoxidation charges with melt purity which, together with the very high values of the cathodic currents in Fig. 2 shows that these currents do not correspond to reduction of impurities in the melt. Thus these currents must arise from the cathodic reduction of the lithium or potassium cations. The deposited metal is obviously quitting the interface as fast as it is formed there, otherwise the cathode voltage would fall immediately to the potential range of Li or K deposition (<-3.6V). Thus the alkali metal is either soaking rapidly into the carbon rods or dissolving rapidly in the melt. Since an iron rod under the same conditions cannot sustain even 8 mA/cm² cathodic current without plunging at once to the Li potential (see Fig. 4) it seems the carbon must be soaking up the alkali metal in some way. Undervoltage deposition of a metallic monolayer on various substrates is well known in aqueous solution (4) and even recently in fused salts (5). However, the charges of Fig. 3 at slow sweeps correspond to many thousands of monolayers. Thus undervoltage deposition of a single superficial monolayer cannot explain our data. The alkali metal must be continuously soaking into the carbon. The slower the voltage sweep speed, the more time is available in the anodic sweep to reoxidize this metal as it diffuses back to the melt interface; hence the larger is the reoxidation charge.

Charge-discharge curves.—Figure 4 shows first-cycle charge-discharge curves at a 1.5 mm diameter rod of glassy carbon. The 76 mm long rod was carbon-cemented into the end of a 600 mm long, ¼ in. diameter graphite rod, serving as support and electrical lead. The glassy carbon protruded 70 mm from the graphite and dipped 25 mm undermelt such that its wetted area was 1.2 cm². On switching on cathodic current at A, carbon voltage falls sharply to about -2.7V then more gradually, leveling off when the wetted carbon whitens with a coating of tiny white Li droplets. On current reversal at B, the discharge curve after a small step due to *iR* drop, more or less mirrors the charging curve except that (i) the discharge time to chlorine evolution, τ_a , is only about 0.9 of the charging time, τ_c , (ii) on switching off the anodic current at C, carbon voltage falls almost to -3V, two volts lower than the original value of about -1V, the usual voltage of untreated carbon in these melts. The

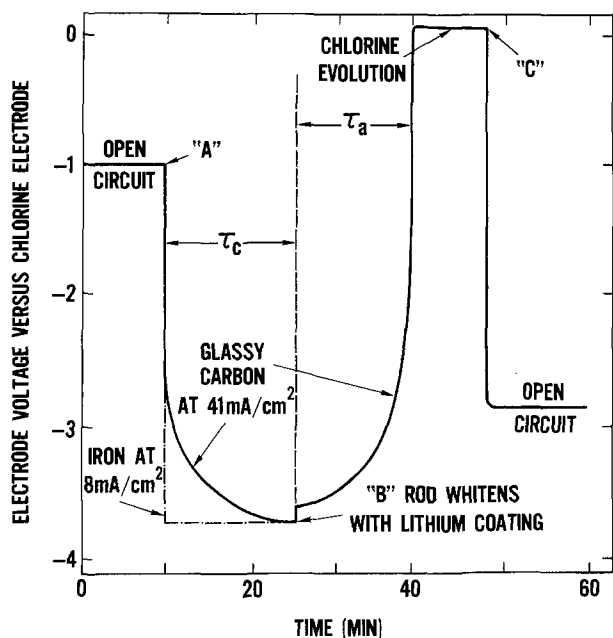


Fig. 4. Charge-discharge curves for 1.5 mm glassy carbon rod in LiCl-KCl at 430°C. Current switched on cathodically at A, reversed at B, and switched off at C.

dot-dash-dot curve depicts the behavior of a pure iron rod cathodized at 8 mA/cm²; it was driven to the Li potential in less than 3 sec. This shows that the depolarization exhibited by carbon arises on the carbon side rather than the melt side of the interface.

The data of Fig. 4 parallel those of Fig. 2 but they go further, showing the effects to be large ones rather than merely a transitory depolarization. Large amounts of charge are passing at undervoltage. Chemical analysis of various cathodized rods showed this charge to be wholly in the form of deposited Li absorbed in the carbon, to the extent of about 5 weight per cent (w/o) Li. The rod whose first charge-discharge cycle is illustrated in Fig. 4 was subjected to 24 additional similar cycles at four successively higher current densities (43, 83, 143, and 286 mA/cm²). It was found that the coulombic charges Q_c and Q_a corresponding to times τ_c and τ_a had no significant dependence on current density. Neither did the ratio Q_c/Q_a which remained at an average value of 0.90 ± 0.015 . The first observation shows that Li permeates the glassy carbon structure quite easily. If this were not so, high current densities would soon effect, in the skin of the carbon rod, such Li enrichment on charge and Li depletion on discharge as to polarize the electrode quickly to the Li and Cl₂ potentials, respectively. The Q 's would then depend sharply on current density which was not observed. The fact that $Q_a/Q_c = 0.90$ suggests either a low current efficiency for Li deposition or that some of the absorbed Li is bound too tightly to be reoxidized anodically. The lack of variation of Q_a/Q_c with current density favors the latter explanation.

Graphite rods gave very similar charging curves to that of Fig. 4. However, with graphite rods the charging curves could not be completed to the Li potential as the rods broke prior to this point. Sometimes they snapped cleanly at the melt meniscus but more often, towards the end of the charge, fine carbon powder began to fall from the meniscus area of the rod which soon necked down till the wetted part of the rod fell off. Presumably this is caused by high stresses arising at the demarcation between wetted carbon swollen with absorbed Li and relatively unaffected material above the meniscus. A few experiments with graphite rods coated with a 0.1 mm thick layer of pyrolytic graphite also gave charging curves similarly shaped to that of Fig. 4. According to the manufacturer, the graphitic planes in the pyrolytic graphite coating were

parallel to the coated substrate at all points. Thus either the Li atoms can permeate freely through the carbon hexagons of the pyrolytic coating or this coating is highly imperfect. We suspect the latter since Li, atomic radius 0.153 nm (1.53Å) would be grossly deformed in passing through a carbon hexagon (inner radius 0.071 nm). On the other hand, in intercalation compounds, the alkali metal atoms are believed to be substantially ionized (6). In this case the Li⁺ ionic radius of 0.068 nm, would permit it to pass through the sheets.

A series of well-defined Li graphite intercalation compounds has been made in other laboratories by reacting Li directly with crystals of natural graphite (6). These are: C_xLi where $x = 72, 36, 18, 12, 8, \text{ or } 6$. None of our charge-discharge curves ever showed any arrests in voltage corresponding to the formation of compounds successively richer in Li. Arrests would have been seen in the charging curve of Fig. 4 after about 2.5, 5, and 10 min corresponding to compounds with $x = 72, 36, \text{ and } 18$. On the contrary, the smooth curves of Fig. 4 suggest a continuous spectrum of interaction energies of Li with the carbon structure. Perhaps this difference is related to the relatively amorphous structure of glassy carbon and synthetic graphite used in this work as opposed to natural graphite which is much more highly crystalline.

Figure 5 shows data for five separate glassy carbon rods cathodized at different constant current densities between 9 and 144 mA/cm². The rods were 76 × 1.5 mm, held in a chuck as in Fig. 1C and dipped 60 mm undermelt. The original charging curves were replotted as voltage vs. amount of charge passed, to aid their comparison. The results show there is a small but significant concentration polarization effect. At the same stage of charge there is a 0.1V spread in voltage according to the charging rate. Thus at the higher current density there is a perceptible backup of the permeating Li. The curves merge close to the Li potential as all the rods approach saturation with Li.

Composition of cathodized carbon rods.—Glassy carbon.—Figure 6 shows the Li uptake of glassy carbon rods (determined by chemical analysis) as a function of potential. Seven, 3 mm rods, supported in chucks as in Fig. 1C were held for 60 min at various constant potentials. They were then removed from the melt and analyzed chemically for Li and K. Their Li contents rise smoothly with falling voltage with a sharp rise close to the reversible Li potential (though ostensibly from the same batch, the rod with the anomalously high Li content at -3.0V was also anomalously hard; it was very difficult filing its end tapered to enter the chuck). No study was made of Li uptake vs. time at constant potential so it is not certain that the data points of Fig. 6 represent true equilibrium values. However, in getting the constant current

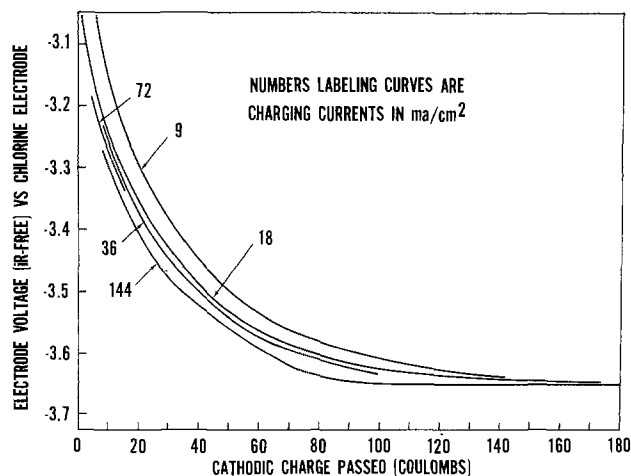


Fig. 5. Voltage vs. amount of charge passed for glassy carbon rods cathodized at various rates in LiCl-KCl at 430°C.

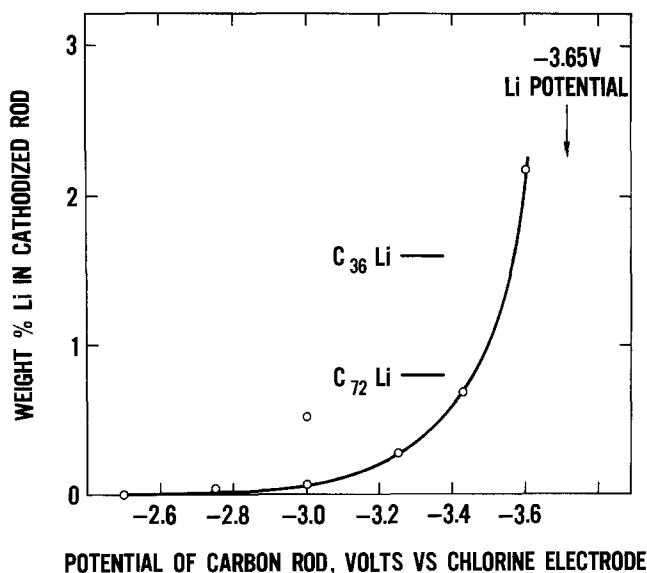


Fig. 6. Lithium uptake of glassy carbon rods as a function of potential in LiCl-KCl at 430°C. A separate rod was held at each potential for 60 min then removed from melt for Li determination by chemical analysis.

charging data of Fig. 7 we found that 1.5 mm diameter rods could be charged up to 3.6 w/o Li in only 8 min. Thus it is unlikely that the curve of Fig. 6 would be significantly altered by longer potentiostating. The smooth curve of Fig. 6 agrees with the smooth charging curves of Fig. 4 and 5. They both indicate continuous rise in Li content with falling voltage; there are no arrests in voltage as might occur during the transformation of one layer-compound to another richer in Li, e.g., $C_{12}Li$ to C_8Li . This contrasts with the preparation of layer compounds from single-crystal graphite. Here at 673°-773°K (400°-500°C), steps were obtained in curves of composition vs. alkali metal vapor pressure for both K and Cs (6, 7). The uninflected voltage-composition curves of the present work are probably associated with the relatively

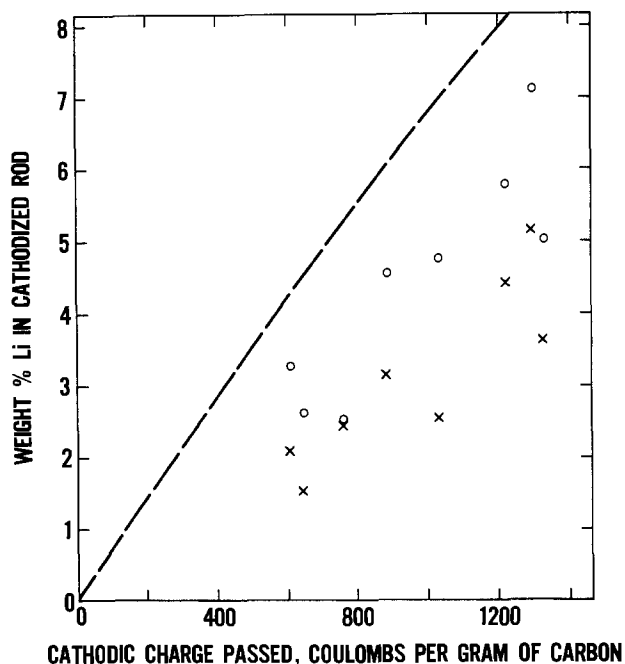


Fig. 7. Lithium uptake of glassy carbon rods cathodized at constant current toward the Li potential (LiCl-KCl, 430°C). Broken line: Assumes carbon absorbs Li, equivalent to the total charge passed. Circles: Observed per cent gain in weight. Crosses: Li contents from chemical analysis.

amorphous nature of the glassy carbon used. This agrees with the work of Herold *et al.* (8, 9). Using the same source and grade of glassy carbon as the present work (V25 from Carbone Company) they got uninflected isotherms for the absorption of K vapor at 873°K (600°C). Their richest material was 25.8 w/o K (C_8K contains 29.0 w/o K). They considered this material to be, at least partially, an intercalation compound. This work of Herold and a brief note by Halpin (10) seem to be the only published data on the action of alkali metals on glassy carbon and is restricted to potassium. Recently (11) steps were obtained in constant-current charging curves using cathodes of synthetic graphite foil. In these room-temperature experiments, Li, K, and NMe_4 were cathodically impregnated into the graphite from salt solutions in dimethyl sulfoxide. It would seem thus that high crystallinity of the carbon and low temperature of impregnation favor the observation of steps in charging curves.

In the intermediate potential range of Fig. 6, significant amounts of K were found in the glassy carbon. For the rod at -3.0V, anomalously rich in Li, K/(K + Li) was 0.39 mole fraction and at -3.25V the fraction was 0.16. No chloride was found in these rods so all their K came by electrodeposition rather than by uptake of melt. These two rods were the only cases in this work where K was found to be codeposited at undervoltage with Li. It is not clear why K deposition was restricted to this intermediate range of potential. At inert iron cathodes in LiCl-KCl eutectic, highly pure Li with less than 0.1%, K is deposited (12).

Figure 7 shows the Li uptake of eight glassy carbon rods cathodized at constant current toward the Li potential. The experimental setup was the same as in the constant potential work. The rods were 76 mm long, 1.5 mm diameter and dipped 60 mm undermelt. No K^+ or Cl^- were found in the extracts of these rods and within experimental error the extracts contained Li^+ and OH^- in equivalent amounts. Thus Li deposition was solely responsible for the observed depolarization in the charging curves, and no melt is absorbed by glassy carbon rods. In spite of the scatter of the data it can be seen that the rods absorb Li proportional to the cathodic charge passed. In Fig. 7 the Li contents determined by chemical analysis (X) are almost all higher than the -3.6V value of Fig. 7. This is consistent with the open-circuit voltages of the rods at the end of charging; these varied from -3.630 to -3.654V. The Li contents of Fig. 7 range up to about 7 w/o. These relatively low values plus the absence of acetylene on reacting cathodized carbons with water show no carbide is present (lithium carbide has 37 w/o Li). The observed Li contents tally much better with those of intercalation compounds, the richest of which, C_6Li , has 8.9% Li.

In Fig. 7 it is clear that Li contents obtained by chemically analyzing the carbon rods are systematically less than those derived from weight gains, which in turn are consistently below those calculated from the total cathodic charge passing. The analytical figures average 0.69 ± 0.09 of those from weight gain which themselves average 0.67 ± 0.10 of the calculated values. During the electrolyses, the melt was pale yellow from dissolved chlorine formed at the graphite counterelectrode. However, calculation based on chlorine's solubility and diffusivity in the melt (13) shows that, even in chlorine-saturated melt, the limiting current for chlorine reduction should be below 1 mA/cm². Parallel reduction of chlorine can thus not account for the discrepancies of Fig. 7 as these data were secured at 9-144 mA/cm². Furthermore, there was no correlation at all between current density and the magnitude of deviation of measured values below the broken line. Thus at this time we have no explanation for these deviations. More work is also needed to elucidate the systematically lower measured Li contents from chemical analysis as opposed to weight gain.

Graphite.—Much less work was done with graphite rods because charging curves could not be completed to the Li potential before the rods disintegrated at the melt meniscus level. Also, at these highly negative potentials, graphite rods wicked up significant amounts of the melt. This effect precluded determining weight gains and confused the results of chemical analysis by introducing into the graphite an unknown proportion of Li^+ and K^+ from the melt. Two grades of synthetic graphite were used, U7 and UF4S from Ultra Carbon Company, having densities of 1.90 and 1.76 g/cm^3 , respectively. The glassy carbon used, at 1.50 g/cm^3 was more porous than both graphites. Nevertheless glassy carbon approaches Pyrex glass in its resistance to gas flow while graphite is typically 5-10 orders of magnitude more permeable. Apparently glassy carbon's pore system is largely blind and inaccessible to the melt whereas graphite's is open and interconnected (13). Thus it is understandable that no chloride was found in any cathodized glassy carbon while significant amounts were found in each cathodized graphite rod. The wicking up of this melt into porous carbon at negative potentials was previously observed and utilized by Adams (15) with activated carbon.

Six 3 mm diameter graphite rods were cathodized to breakage in LiCl-KCl at 703°K (430°C). They averaged 590 ± 290 coulombs/g of carbon at the breaking point (glassy carbon rods were routinely charged without breaking to 1200 coulombs/g of carbon where Li droplets covered the carbon surface). Aqueous extracts of the cathodized graphite rods contained mainly Li^+ and OH^- with lesser amounts of K^+ and Cl^- . Extracts with higher K^+ contents had proportionately more Cl^- . This indicates that potassium was entering the rods via absorbed melt rather than by electrodeposition. So it seems that, with graphite also, the observed depolarizations are basically due to undervoltage deposition of Li. From the OH^- content of the most highly charged rod we derive a Li content of 4.1 w/o. This is in line with the Li contents of Fig. 7 for glassy carbon. Thus the limited amount of data secured using graphite indicates its behavior to be basically similar to that of glassy carbon with the added complication of uptake of melt into the more permeable graphite.

X-ray analysis of cathodized carbons.—Figures 8 and 9 compare the x-ray diagrams of carbon rods before and after cathodizing toward the Li potential in the melt at 700°K (427°C). Figure 8 refers to a 3 mm diameter glassy carbon rod whose Li content by chemical analysis was 4.4 w/o. Figure 9 refers to the 3 mm graphite rod which was analyzed as

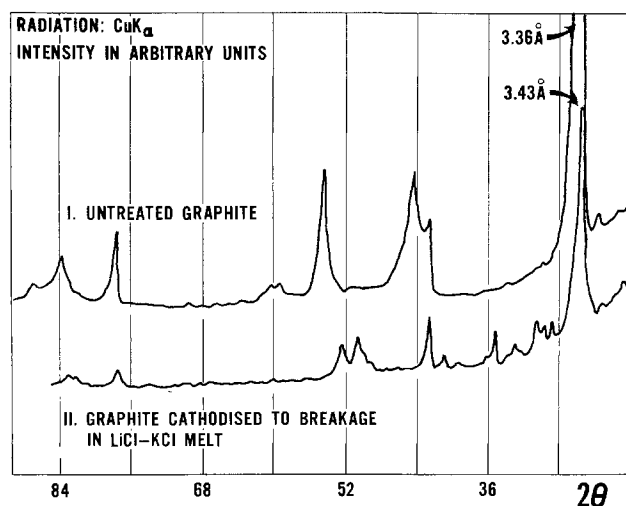


Fig. 8. X-ray diffractograms for glassy carbon rods before and after undervoltage deposition of Li in LiCl-KCl at 430°C.

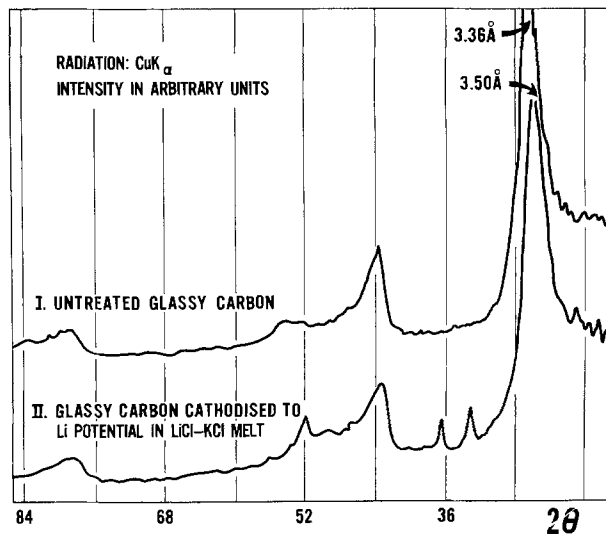


Fig. 9. X-ray diffractograms for synthetic graphite rods before and after undervoltage deposition of Li in LiCl-KCl at 430°C. (Graphite: Grade U7 from Ultra Carbon Company.)

4.1 w/o Li. The x-ray lines of glassy carbon are fewer and broader than those of graphite. This reflects the more disordered, amorphous structure of glassy carbon (14). For both types of carbon, electrolysis effected marked changes in the x-ray patterns; new lines appeared and old ones vanished or weakened. Although the data are not accurate enough to determine a- and c-spacings it is clear that the structure of the cathodized carbons is still basically graphitic. The intense reflection corresponding to the graphite hexagonal sheets is still present though the interplane distance has slightly expanded from the original 0.336 nm (3.36Å) to 0.343 nm for graphite and 0.350 nm for glassy carbon. No lines corresponding to potassium graphite or to lithium or potassium carbides are present. Thus the x-ray data are consistent with the formation of Li intercalation compounds.

Some implications of undervoltage deposition of alkali metal for the use of carbon electrodes.—Considering the very marked depolarizing effect that undervoltage deposition causes (Fig. 2 and 4) and the common use of carbon electrodes in alkali halide melts it is surprising that the phenomenon has not previously been studied. The most that is apparent in the literature is some fleeting references to the effect e.g., by Laitinen (1) at synthetic graphite in LiCl-KCl at 723°K (450°C), by Mamantov (16) for pyrolytic graphite in LiF-NaF-KF at 773°K (500°C), and by Thonstad (17) for Na deposition in pyrolytic graphite from cryolite-alumina melts at 1283°K (1010°C). It is virtually certain that undervoltage deposition of alkali metal vitiated the early measurements by Neumann of decomposition voltages of metal halides between graphite electrodes (18). For fused chlorides of Li, Na, K, and Ca at 1073°K (800°C), his values were 0.77, 0.59, 0.44, and 0.51V, respectively, less than those derived from modern thermochemical data (19). This was certainly due to some form of compound formation (alkali metal carbide or intercalation compound) at the graphite cathode.

In the present work it was found that carbon electrodes exposed to undervoltage Li deposition suffered a lasting negative bias to their open-circuit voltages which could be very misleading in their subsequent use as indicator electrodes. In one case, glassy carbon and graphite rods, after cycling for an hour between -3.1 and 0.0V, vs. chlorine electrode, were left overnight in Ar-saturated melt. When the melt was then saturated with chlorine for an hour, the carbon voltages varied erratically between -1.1 and -2.6V and showed no sign of approaching the chlorine potential. Unelectrolyzed carbons are normally within 10 mV of the chlorine potential by this time. Thus a

worker unaware of the easy entry of Li into carbon below about $-2.5V$ could seriously contaminate his carbon electrode without realizing it during even a brief excursion to negative potentials (such as when obtaining a background voltammogram of his melt). The electrode would then be unable for some time to function as an inert, indicator electrode.

Carbon is not normally wetted by purified chloride melts (20). However, lithiation of the carbon causes it to effectively contact the melt. This was shown in the present work where no chloride was found in graphite rods soaked in the melt for hours at open circuit whereas significant amounts had penetrated the rods after relatively brief contact at potentials close to the reversible Li value. This wetting effect was used by Adams (15) to flood activated carbon with fused LiCl-KCl and create a high-area carbon electrode. He did it by cycling the carbon between 0 and $-3V$ vs. chlorine electrode. The resultant wetting was stable even during prolonged exposure of the carbon to voltages well above $-2V$. This emphasizes again the important and lasting effects on the carbon-melt interface of quite brief exposure to negative potentials. While vital to the operation of a high-area electrode, the stable wetting induced by lithiation would be of course fatal to the performance of a porous carbon gas-cathode. Flooding of the porous carbon by melt causes severe cathode polarization.

The lasting effects of lithiation at potentials where Li is thermodynamically quite unstable may be due to the presence of a Li residue compound. Graphite intercalation compounds on extraction or evacuation are known to retain tenaciously a minor proportion of their adduct molecules forming the so-called residue compounds (21). There is evidence that this residual adduct is tightly bound at lattice imperfections as distinct from normal adduct which can move freely between the graphite sheets.

In recent years, undervoltage deposition of Li has been reported from organic solvents into a variety of metals at room temperature, e.g., Sn, Pb, Al, Au, Zn, Cd (22), and Pt (22, 23). Intermetallic Li compounds were formed. No such undervoltage deposition of the other alkali metals or of alkyl ammonium was obtained. In the paper mentioned earlier (11), Li, K, and tetramethylammonium were impregnated at undervoltage into graphite foil cathodes from dimethyl sulfoxide solutions at room temperature. Intercalation compounds resulted. However, cathodizing glassy carbon resulted in immediate deposition of free alkali metal at this relatively impermeable material. In these room temperature studies undervoltage deposition currents were limited to about 1 mA/cm^2 by the relative slowness of solid-state diffusion at this temperature. At the higher temperature of the present molten salt study much higher (hundreds

of milliamperes per square centimeter) undervoltage currents were possible.

Acknowledgment

This research was supported by the Independent Research Program of the Naval Surface Weapons Center, White Oak, Maryland.

Manuscript submitted Jan. 3, 1975; revised manuscript received Feb. 25, 1975.

Any discussion of this paper will appear in a Discussion Section to be published in the June 1976 JOURNAL. All discussion for the June 1976 Discussion Section should be submitted by Feb. 1, 1976.

Publication costs of this article were partially assisted by the Naval Surface Weapons Center.

REFERENCES

1. H. A. Laitinen and C. H. Liu, *J. Am. Chem. Soc.*, **80**, 1015 (1958).
2. S. Senderoff and G. W. Mellors, *Rev. Sci. Instr.*, **29**, 151 (1958).
3. D. L. Maricle and D. N. Hume, *This Journal*, **107**, 354 (1960).
4. D. P. Sandoz, R. M. Peekema, H. Freund, and C. F. Morrison, *J. Electroanal. Chem.*, **24**, 165 (1970).
5. W. K. Behl, *This Journal*, **120**, 1692 (1973).
6. Yu N. Novikov and M. E. Vol'pin, *Russ. Chem. Rev.*, **40**, 733 (1971).
7. J. G. Hooley, in "Chemistry and Physics of Carbon," P. L. Walker, Editor, Volume 5, Marcel Dekker, New York (1969).
8. A. Herold and B. Carton, *Compt. Rend.*, **269C**, 792 (1969).
9. A. Herold and B. Carton, *Bull. Soc. Chem.*, 4264 (1970).
10. M. K. Halpin and G. M. Jenkins, *Nature*, **218**, 950 (1968).
11. J. O. Bensenhard and H. P. Fritz, *J. Electroanal. Chem.*, **53**, 329 (1974).
12. G. T. Motock, *Electrochem. Technol.*, **1**, 122 (1963).
13. J. D. VanNorman and R. J. Tivers, in "Molten Salts. Characterization and Analysis," G. Mamantov, Editor, Marcel Dekker, New York (1969).
14. V. D. Chekanova and A. S. Fialkov, *Russ. Chem. Rev.*, **40**, 413 (1971).
15. H. A. Adams, U.S. Pat. 3,428,493 (1969).
16. G. Mamantov, in "Molten Salts. Characterization and Analysis," G. Mamantov, Editor, p. 535, Marcel Dekker, New York (1969).
17. J. Thonstad, *J. Appl. Electrochem.*, **2**, 315 (1973).
18. B. Neumann and H. Richter, *Z. Elektrochem.*, **31**, 287, 296, 481 (1925).
19. W. J. Hamer, M. S. Malmberg, and B. Rubin, *This Journal*, **103**, 8 (1956).
20. H. V. Wartenberg, *Angew. Chem.*, **69**, 258 (1957).
21. R. C. Croft, *Quart. Rev. Chem. Soc.*, **14**, 1 (1960).
22. A. N. Dey, *This Journal*, **118**, 1547 (1971).
23. I. Fried and H. Barak, *J. Electroanal. Chem.*, **30**, 279 (1971).

Mass Transfer to an Eccentric Rotating Disk Electrode

Charles M. Mohr, Jr.* and John Newman**

*Inorganic Materials Research Division, Lawrence Berkeley Laboratory, and
Department of Chemical Engineering, University of California, Berkeley, California 94720*

ABSTRACT

The mass transfer rate to a rotating disk electrode rotated about an off-center axis is calculated for eccentricities of from zero to 5 electrode radii. An asymptotic form for the transfer rate valid for large eccentricities is also derived and compared to two previous analyses. It is found that mass transfer is not affected until a critical eccentricity is reached and that the asymptotic expression provides a good approximation to the rate of mass transfer even at moderately small eccentricities. The analysis is supported by experimental data on the deposition of copper on several electrodes of eccentricities between 0.66 and 3.94.

When the active portion of a rotating disk electrode is offset from the axis of rotation, the Levich formula (1) for the mass transfer rate may no longer be applicable. Riddiford (2) implies that exact centering of the active portion is an important design consideration for such electrodes but does not estimate the change in mass transfer rate due to an eccentricity. More recently Chin and Litt (3) have treated the effect of large eccentricities, where the small active portion is located at least several diameters from the center of rotation. Also, Bardin and Dikumar (4) have attempted an analysis for moderate eccentricities (offsets slightly greater than the electrode radius).

Both of these works are limited in their applicability. Chin's paper is nearly correct for large eccentricities but is inappropriate for only slightly off-center electrodes. Bardin and Dikumar erred seriously in their simplifying assumptions, and their conclusions are incorrect for all eccentricities.

We hope to provide here a more rigorous formulation of the problem and, particularly, to describe the behavior at small eccentricities where the easily developed asymptotic form (for large eccentricities) is not applicable. The small eccentricity behavior should be found useful in assessing error limits due to machining tolerances in the manufacture of rotating disk electrodes. Attention is given to large eccentricities for the purpose of completeness only. It seems unlikely that disk electrodes would be operated in this fashion since the imbalance could be dangerous at high rotation rates.

A little contemplation suggests that the mass transfer rate is strictly constant until an eccentricity is reached where a fluid trajectory can spiral off the disk electrode and then back onto it. We have sought the value of the eccentricity at this limit as well as the behavior of the mass transfer rate for somewhat larger eccentricities.

Theory

The laminar flow pattern near a rotating disk has been described by Von Kármán with later improvement (in numerical constants) by Cochran (5). Basically, a fluid particle drawn toward the disk near its center spirals outward while approaching the disk and eventually leaves the region of interest. For Schmidt numbers typical of electrolytic solutions, the diffusion layer is very near the disk, and the radial and tangential velocities of the fluid relative to the disk may be adequately expressed as linear functions of the distance from the disk. Cochran found that these velocities are

$$\begin{aligned} v_r &= 0.510r(\omega^3/\nu)^{1/2}z \\ v_\theta - r\omega &= -0.616r(\omega^3/\nu)^{1/2}z \end{aligned} \quad [1]$$

where ν is the kinematic viscosity of the solution and ω is the rotation speed (sec^{-1}).

A fluid particle near the disk will be tracing a path $r(\theta)$, relative to the disk, described by

$$\frac{1}{r} \frac{dr}{d\theta} = \frac{v_r}{v_\theta - r\omega} = -0.828 \quad [2]$$

Note that this is independent of either r or z within the range of validity of the linear approximations in Eq. [1]. Thus the path followed by any fluid particle near the disk is such that its direction of travel is at an angle α to a ray drawn from the center of rotation (see Fig. 1) and

$$\alpha = \cot^{-1}(0.828) = 50.38^\circ \quad [3]$$

Equation [2] can be integrated to yield the equation for the trajectory passing through the point (r_1, θ_1)

$$r = r_1 \exp[(\theta_1 - \theta) \cot \alpha] \quad [4]$$

On the other hand, a point on the edge of the electrode is given by

$$r = r_0 \sqrt{\epsilon^2 + 1 - 2\epsilon \cos \theta'} \quad [5]$$

The condition of uniform accessibility, that is, uniform rate of mass transfer, will be maintained for nonzero eccentricities as long as fluid particles spiraling off the electrode never return to or pass over the electrode again. Fluid begins to return to the electrode for an eccentricity at which a trajectory first becomes tangent to the edge of the electrode. Tangency is given by $\alpha = \beta$, where β is the angle

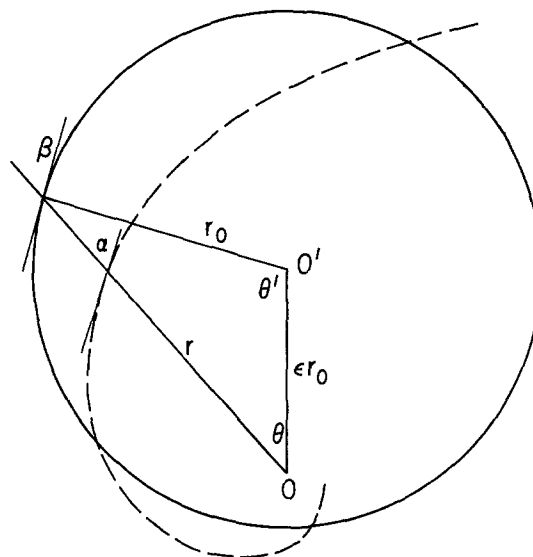


Fig. 1. Nomenclature for offset disk electrode

* Electrochemical Society Student Member.
** Electrochemical Society Active Member.
Key words: convective diffusion, diffusion coefficient measurement.

between the edge of the disk and the ray drawn from the center of rotation.

Geometrical considerations then lead to the relation

$$\alpha = \beta = \theta + \theta' - \frac{\pi}{2} \quad [6]$$

for a tangent point on the edge. Since the relationship between θ and θ' is

$$\theta = \tan^{-1} \left(\frac{\sin \theta'}{\epsilon - \cos \theta'} \right) \quad [7]$$

the condition for a tangent point reduces to

$$\theta' = \alpha + \cos^{-1} \left(\frac{\cos \alpha}{\epsilon} \right) \quad [8]$$

after rearrangement using trigonometric identities. This equation shows that no point of tangency exists for $\epsilon < \cos \alpha$. Thus, the critical eccentricity we seek is

$$\epsilon_c = \cos \alpha = 0.6377 \quad [9]$$

For $\epsilon > \cos \alpha$, Eq. [8] gives two tangent points

$$\theta'_{t1} = \alpha - \cos^{-1} \left(\frac{\cos \alpha}{\epsilon} \right)$$

and

$$\theta'_{t2} = \alpha + \cos^{-1} \left(\frac{\cos \alpha}{\epsilon} \right) \quad [10]$$

where the principal branch of \cos^{-1} is now to be used.

As $\epsilon \rightarrow 1.0$, it eventually becomes possible for the same trajectory to spiral off the disk, return, spiral off again, and then return once more. Since in this analysis we will not attempt to treat this case, we must determine at what eccentricity this effect begins. At the onset of this behavior, the critical trajectory is one that is tangent to the disk at two points, (r_1, θ'_{t1}) and (r_2, θ'_{t2}) , as shown in Fig. 2. To determine the eccentricity at which this occurs, we begin with 5 equations in 5 unknowns ($r_1, r_2, \theta'_{t1}, \theta'_{t2}, \epsilon$). Equation [10] gives two relations for the angles at the tangent points. Equation [5] gives two relations for points on the edge of the electrode. Since the two points must be on the same spiral, Eq. [4] can be written

$$r_2 = r_1 \exp \left\{ \left[\tan^{-1} \left(\frac{\sin \theta'_{t1}}{\epsilon - \cos \theta'_{t1}} \right) - \tan^{-1} \left(\frac{\sin \theta'_{t2}}{\epsilon - \cos \theta'_{t2}} \right) + 2\pi \right] \cot \alpha \right\} \quad [11]$$

where 2π appears since the trajectory completes a full spiral before the second tangent point is reached. These 5 equations can be reduced to one equation in ϵ

$$\epsilon^2 + 1 - 2\epsilon \cos \left[\alpha + \cos^{-1} \left(\frac{\cos \alpha}{\epsilon} \right) \right] = \left\{ \epsilon^2 + 1 - 2\epsilon \cos \left[\alpha - \cos^{-1} \left(\frac{\cos \alpha}{\epsilon} \right) \right] \right\} \exp \left\{ \left[\pi + \cos^{-1} \left(\frac{\cos \alpha}{\epsilon} \right) \right] 4 \cot \alpha \right\} \quad [12]$$

which has two solutions

$$\begin{aligned} \epsilon_1 &= 0.998476 \\ \epsilon_2 &= 1.001523 \end{aligned} \quad [13]$$

The second solution is significant for calculations with $\epsilon > 1$, since it gives the eccentricity at which fluid begins to pass over the disk only once. Eccentricities between these two critical values will not be treated in this analysis.

The mass transfer rate to the electrode may now be determined. It should be noted that for eccentricities $0.9985 > \epsilon > 0.6377$, some of the fluid experiences a situation similar to what would occur in a ring-disk system. That is, it spirals off the electrode, passes over an insulating surface, and then spirals over an active surface once more, after which it leaves the region of interest. It seems then that we may calculate the mass transfer rate for fluid following such a trajectory by determining the radii (r_1, r_2, r_3) at which this fluid (i) leaves the electrode initially, (ii) returns to the electrode, and (iii) leaves the electrode for the last time, and then use the appropriate formula (6, 7) for mass transfer to a ring-disk electrode which is operated at the limiting current for the same reaction on both the ring and disk. Similarly, for $\epsilon > 1.0015$ one could determine the radii at which a trajectory enters and leaves the electrode surface and use Levich's formula (1) for mass transfer to a ring electrode, with inner and outer dimensions identical to these, to determine the transfer rate along that trajectory. Since each trajectory would have a different ring-disk (or ring only, for $\epsilon > 1.0015$) analogue, it would be necessary to section the surface of the electrode into thin strips following the trajectories (shaded on Fig. 3) and determine, via the above method, the transfer rate to each. In the following discussion, details are presented only for the case $\epsilon > 1.0015$, which can be compared easily to previous treatments. The analysis for $0.6377 < \epsilon < 0.9985$ is similar except that the more complicated expression for mass transfer to a ring-disk system must be substituted for Levich's equation for transfer to a ring electrode only.

For a ring electrode with the active portion between r_1 and r_2 , the Levich formula for mass transfer to a segment of width $d\theta$ is

$$dj = \frac{(r_2^3 - r_1^3)^{2/3}}{\sqrt{\nu/\omega}} \frac{Dc_\infty}{2\Gamma(4/3)} \left(\frac{0.510\nu}{3\mathcal{D}} \right)^{1/3} d\theta \quad [14]$$

The total mass transfer to the disk will be given by this equation integrated between the two tangent points θ_{t1} and θ_{t2} . Upon changing the independent variable from θ to θ' and dividing by the rate of mass transfer to a centered disk electrode of equal area (j_{disk}), we find

$$j/j_{\text{disk}} = \frac{1}{2\pi} \int_{\theta'_{t1}}^{\theta'_{t2}} \left(\frac{r_2^3}{r_1^3} - 1 \right)^{2/3} \left[\epsilon \frac{\cos(\theta' - \alpha)}{\cos \alpha} - 1 \right] d\theta' \quad [15]$$

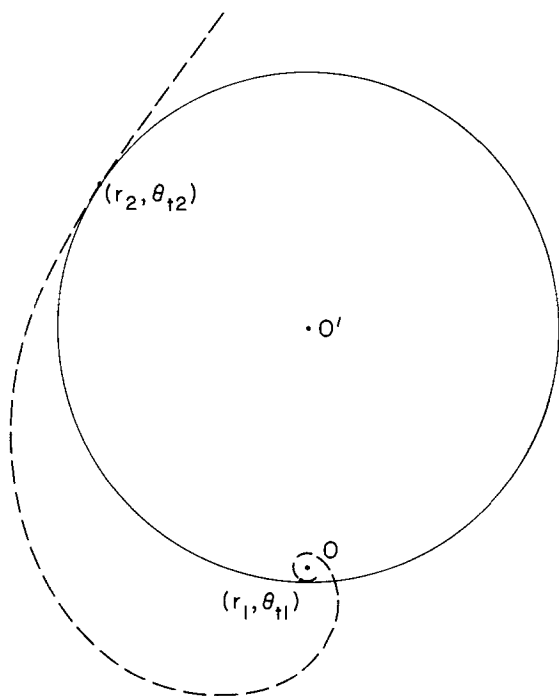


Fig. 2. Trajectory for eccentricity at which analysis fails

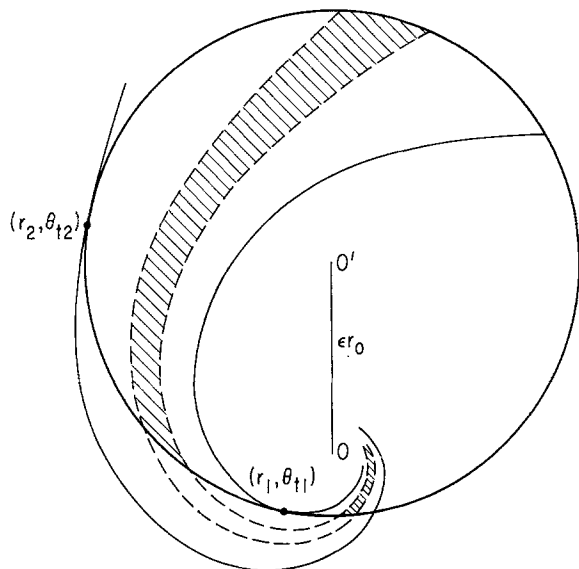


Fig. 3. Partitioning scheme for ring-disk analogy ($\epsilon < 1$)

Given θ_1 , the quantity r_2/r_1 can be determined by simultaneous solution of Eq. [4] and [5]. This must be done numerically due to the complexity of these equations. As a test of this numerical procedure, one can verify the identity

$$2\pi = \int_{\theta_{t1}}^{\theta_{t2}} \left(\frac{r_2^2}{r_1^2} - 1 \right) \left[\epsilon \frac{\cos(\theta' - \alpha)}{\cos \alpha} - 1 \right] d\theta' \quad [16]$$

which results from calculating the area of the electrode.

The asymptotic behavior as $\epsilon \rightarrow \infty$ is of some interest since it shows clearly the differences between this analysis and those of Chin and Litt and Bardin and Dikusar. As $\epsilon \rightarrow \infty$

$$\begin{aligned} \frac{r_1}{r_0} &\rightarrow \epsilon - \cos \theta' \\ \frac{r_2}{r_0} &\rightarrow \epsilon + \cos(\theta' - 2\alpha) \\ \theta_{t1} &\rightarrow \alpha - \frac{\pi}{2} \\ \theta_{t2} &\rightarrow \alpha + \frac{\pi}{2} \end{aligned} \quad [17]$$

and with $x = \sin(\theta' - \alpha)$, Eq. [15] becomes

$$\begin{aligned} j/j_{\text{disk}} &\rightarrow \frac{1}{\pi} \left(\frac{36\epsilon}{\cos \alpha} \right)^{1/3} \int_0^1 (1-x^2)^{1/3} dx \\ &= \frac{1}{\sqrt{\pi}} \left(\frac{9\epsilon}{2 \cos \alpha} \right)^{1/3} \frac{\Gamma(4/3)}{\Gamma(11/6)} = 1.027 \epsilon^{1/3} \end{aligned} \quad [18]$$

correct to the largest order in ϵ . The method of Bardin and Dikusar leads to

$$j/j_{\text{disk}} \rightarrow \frac{1}{\sqrt{\pi}} \left(\frac{9\epsilon}{2} \right)^{1/3} \frac{\Gamma(4/3)}{\Gamma(11/6)} = 0.884 \epsilon^{1/3} \quad [19]$$

while Chin and Litt obtained an expression equivalent to

$$j/j_{\text{disk}} \rightarrow \frac{3}{2\pi^{1/6}} \left(\frac{\epsilon}{3 \cos \alpha} \right)^{1/3} = 0.998 \epsilon^{1/3} \quad [20]$$

The differences arise from different schemes for segmenting the electrode before applying the ring analogy. Bardin and Dikusar took the streamlines to be radially outward from the center of rotation (Fig. 4). Chin and Litt approximate the circular electrode by a square of equal area, but with the proper angle given to the spiral streamlines. Thus we conclude that the shape approximation used by Chin and Litt introduces

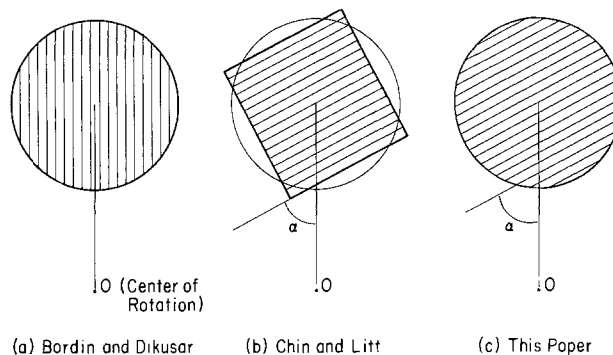


Fig. 4. Comparison of partitioning schemes ($\epsilon > 1$)

less than a 3% error in the asymptotic transfer rate, but the neglect of the fluid trajectory by Bardin and Dikusar yields a 14% error.

Experimental Technique

The mass transfer rates for centered and eccentric electrodes were determined for electrodeposition of copper onto copper electrodes. The solution used was 0.008M CuSO_4 in 1.5M H_2SO_4 . The rotating disk electrodes were fabricated from Plexiglas, drilled and fitted with short sections of 0.25 in. copper rod. The over-all diameters of the disks were 1.5 in., except for the electrode with an eccentricity of 3.94, for which a 2.0 in. disk was used. The electrodes were polished with emery paper and then wet crocus cloth prior to use. Limiting current curves were recorded at three rotation speeds, 405, 510, and 1590 rpm, at room temperature (22°C) for electrodes of eccentricities 0.00, 0.66, 0.88, 2.13, 2.94, and 3.94. The ratios j/j_{disk} were then calculated for each electrode and rotation speed by dividing the total current to the eccentric disk by that to the centered electrode at the same rotation speed. To minimize the effect of temperature variations, the centered electrode was used for every third run, and these results used to calculate the transfer ratios for the noncentered electrodes used in the immediately preceding and following runs.

Results

The experimental results are given in Fig. 5 along with the numerical results, the large eccentricity asymptote Eq. [18]), and the analytical and experimental results of Bardin and Dikusar. The data emphasize the importance of sectioning the electrodes along streamlines in order to use the Levich equation for ring electrodes to predict the mass transfer rate. Our data disagree significantly with those of Bardin and Dikusar, due, perhaps, to their use of quite small electrodes (~ 1 mm in diameter). This small size might make accurate determination of the eccentricity difficult and would tend to emphasize edge effects. The data gathered by Chin and Litt support this analysis also, since they correlated well with their theoretical analysis, which differs from the present analysis by only 3% at the large eccentricities at which their experimental work was conducted ($\epsilon > 9$).

Although, as previously noted, this analysis fails in a limited region about $\epsilon = 1$, the curves for the results for $\epsilon < 1$ and $\epsilon > 1$ can be joined with no apparent discontinuity at $\epsilon = 1$, as shown on Fig. 5.

The close agreement between the numerical and asymptotic (analytic) results is somewhat surprising in view of the fact that curvature of the trajectories was ignored in the asymptotic analysis and becomes pronounced as ϵ becomes small. It appears that the formula

$$\frac{j}{j_{\text{disk}}} = 1.027 \epsilon^{1/3} + 0.044 \epsilon^{-5/3} \quad [21]$$

will be accurate to within 1.0% for $\epsilon > 0.8$. The ex-

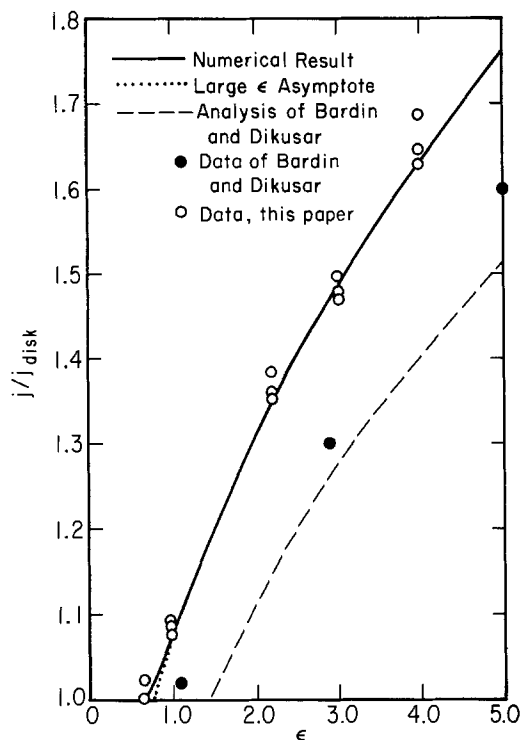


Fig. 5. Mass transfer ratio j/j_{disk} vs. eccentricity for an off-center rotating disk electrode.

ponent $-5/3$ is justified by an extension of the asymptotic analysis.

Acknowledgments

This work was supported by the United States Atomic Energy Commission.

Manuscript submitted May 17, 1974; revised manuscript received Jan. 27, 1975.

Any discussion of this paper will appear in a Discussion Section to be published in the June 1976 JOURNAL. All discussions for the June 1976 Discussion Section should be submitted by Feb. 1, 1976.

Publication costs of this article were partially assisted by the University of California.

LIST OF SYMBOLS

c_{∞}	bulk concentration of reactive species (g/cm ³)
D	diffusion coefficient of reactive species (cm ² /sec)
j	mass transfer rate to electrode (g/sec)
j_{disk}	mass transfer rate to a centered electrode (g/sec)
O	center of rotation
O'	center of electrode
r	radial coordinate from center of rotation (cm)
r_0	radius of electrode (cm)
v_r, v_{θ}	velocity components relative to the disk (cm/sec)
z	coordinate normal to disk (cm)
α	angle of fluid trajectories near disk
β	angle between edge of disk and ray from O
ϵ	offset of center of rotation
ϵ_c	critical offset for nonuniform accessibility
θ	angular coordinate from center of rotation
θ'	angular coordinate from center of disk
ν	kinematic viscosity of solution (cm ² /sec)
ω	rotation speed of disk (sec ⁻¹)

REFERENCES

1. V. Levich, "Physicochemical Hydrodynamics," Prentice-Hall, Englewood Cliffs, N. J. (1962).
2. A. Riddiford, in "Advances in Electrochemistry and Electrochemical Engineering," P. Delehay, Editor, Vol. 4, pp. 47-116, Interscience Publishers, Inc., New York (1966).
3. D. T. Chin and M. Litt, *This Journal*, **119**, 1338 (1972).
4. M. Bardin and A. Dikumar, *Elektrokhimiya*, **6**, 1147 (1970).
5. W. Cochran, *Proc. Cambridge Phil. Soc.*, **30**, 365 (1934).
6. W. Smyrl and J. Newman, *This Journal*, **119**, 212 (1972).
7. W. J. Alberry and S. Bruckenstein, *Trans. Faraday Soc.*, **62**, 1920 (1966).

An Electrochemical Study of Undercutting during Etching of Duplex Metal Films

J. J. Kelly and C. H. de Minjer

Philips Research Laboratories, Eindhoven, Netherlands

ABSTRACT

For various technological applications patterns are chemically etched in metal films partly covered with a nobler metal. As a result of the bimetallic contact, accelerated etching may occur, giving rise to considerable undercutting. From electrochemical considerations it was expected that the use of certain chemical polishing solutions would significantly reduce the degree of such undercutting. This was verified by studying the electrochemical properties of various polishing and nonpolishing etching agents. Suitable solutions were developed for the etching of Al, Mo, and Ni-P. These etching agents, when used to etch metal films partly covered by nobler metals, gave markedly less undercutting than nonpolishing etching agents.

In various technologies it is often necessary to etch fine patterns in metal films. Important factors determining the choice of a chemical etching agent are generally the etching rate, the degree of undercutting, the chemical aggressiveness of the solution to other materials present, and the definition of the etched patterns. One particular problem arises with duplex systems when patterns have to be etched in metal films

Key words: aluminum, chemical polishing, duplex metal films, electropolishing, etching of metals.

partly covered by a nobler metal. Because of galvanic action arising from the bimetallic contact, accelerated etching may occur, causing considerable undercutting at the interface between the two metals. This paper describes an electrochemical study of such undercutting and suggests how the effect may be avoided by a suitable choice of etching agent.

The increase in the rate of dissolution of a metal due to contact with a nobler metal may be explained by considering the partial polarization curves for the

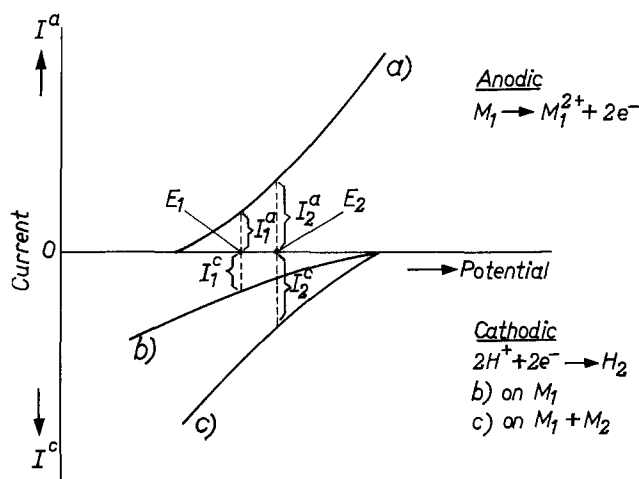


Fig. 1. Partial polarization curves for dissolution of metal M_1 in a nonpolishing solution.

process (1). An example is shown in Fig. 1 for a metal M_1 , of a given area, dissolving in acidic solution. Curves (a) and (b) are the partial anodic and cathodic polarization curves for metal dissolution and hydrogen evolution, respectively. Under open-circuit conditions (no external current) M_1 dissolves at a rest potential E_1 ($I_1^a = I_1^c$) and at a rate given by I_1^a . When M_1 is connected to a second metal M_2 , which does not dissolve in the potential region shown, only hydrogen evolution will occur at M_2 and the cathodic polarization curve for $M_1 + M_2$ may be represented by curve (c). The increase in the cathodic current depends, among other factors, on the area of M_2 . With this combined system, the rest potential is shifted to a more positive value E_2 ($I_2^a = I_2^c$). It is obvious that, with no external current, M_1 dissolves more rapidly when connected to M_2 ($I_2^a > I_1^a$). When the cathode area is further increased by increasing the area of M_2 , then M_1 should dissolve even more rapidly.

It seemed to us that such accelerated etching might be prevented by choosing a solution for which the anodic partial current does not increase as a function of potential in a suitable potential range. Electropolishing solutions generally give such current-potential characteristics (2, 3) and a typical polarization curve for such a system is shown in Fig. 2, curve (a). At lower potentials the current increases with increasing potential and etching of the metal is observed. At higher potentials a "polishing" film, consisting of either a viscous layer or an oxide or salt film, is present on the metal. No increase in current is obtained despite an appreciable increase in potential and, as a rule, polishing is observed in this range. When an oxidizing agent with a cathodic polarization, curve (b) as shown in Fig. 2, is added to the electropolishing solution, the metal M_1 is "chemically polished" at an

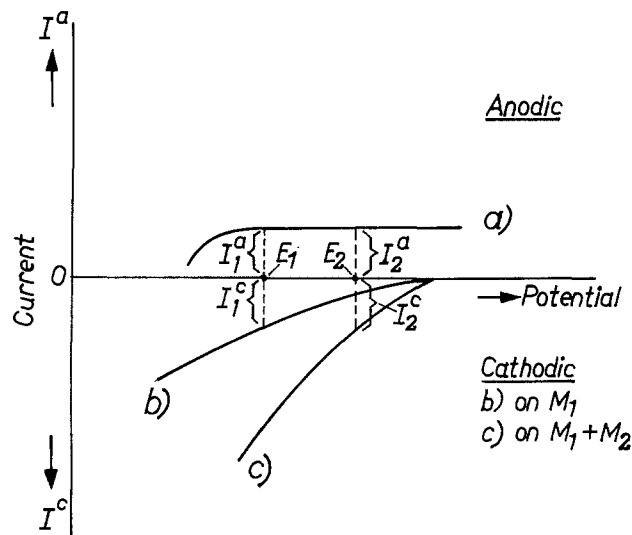


Fig. 2. Partial polarization curves for dissolution of metal M_1 in a polishing solution.

open-circuit potential E_1 and at a rate given by I_1^a . Enlarging the cathodic surface by combining M_1 with a noble metal M_2 leads to an increase in the cathodic current at a given potential (curve c, Fig. 2). Despite the fact that the rest potential increases to E_2 the rate of dissolution of the metal should remain the same ($I_1^a = I_2^a$). When such a solution is used as an etching agent for M_1 , the etching rate should not be affected by the presence of a noble metal. The purpose of this work was to determine experimentally if this assumption was correct and in this way to develop suitable etching agents for bimetallic systems.

Our investigations were directed mainly to the study of etching agents for Al and, to a lesser extent, for Mo and Ni-P.

Experimental

Electrode materials.—Aluminum metal (99.99%) was supplied by Rebag (Grevenbroich, West Germany) in the form of 8 mm thick plate and molybdenum (99.9%) by Philips N.V. (Maarheeze, Netherlands) as cylindrical rods with a diameter of 6 mm. Nickel-phosphorus electrodes, containing approximately 10% P by weight, were made by electroless deposition of a 100 μm thick layer onto Ni strips.

The electrodes for the polarization measurements were first mechanically machined and, after cleaning, were electropolished in the same solutions as used for the electrochemical experiments (Table I). Since current-voltage curves were measured in electropolishing solutions, generally under polishing conditions, essentially no roughening of the electrode surface occurred. The metal disks for the chemical dissolution experi-

Table I. Solutions used for etching metal films

Metal	Electropolishing solution	Corresponding chemical polishing solution	Nonpolishing Solution
Al	(i) 75g Na_2CO_3 35g $\text{Na}_3\text{PO}_4 \cdot 12\text{H}_2\text{O}$ 0.5 liter H_2O	75g Na_2CO_3 35g $\text{Na}_3\text{PO}_4 \cdot 12\text{H}_2\text{O}$ 16g $\text{K}_3\text{Fe}(\text{CN})_6$ 0.5 liter H_2O	0.25M NaOH
Al	(ii) 40 ml H_3PO_4 (85%) 40 ml CH_3COOH (100%) 20 ml H_2O	40 ml H_3PO_4 (85%) 40 ml CH_3COOH (100%) 10 ml HNO_3 (65%) 10 ml H_2O	
Mo	50 ml H_3PO_4 (85%) 50 ml H_2O	50 ml H_3PO_4 (85%) 30 ml HNO_3 (65%) 20 ml H_2O	22% (wt) $\text{Ce}(\text{NH}_4)_2(\text{NO}_3)_6$ in 1% HNO_3
Ni-P	90 ml H_3PO_4 (85%) 10 ml H_2O	(i) 90 ml H_3PO_4 (85%) 10 ml HNO_3 (65%) (ii) 30 ml H_2SO_4 (85%) 15 ml HNO_3 (65%) 4 ml HCl (37%) 1 ml H_2O	50 ml HNO_3 (65%) 50 ml H_2O

ments were either chemically or electrolytically polished, prior to use.

Metal films.—For the etching experiments metal films were prepared on glass microscope slides ($18 \times 18 \times 0.12 \text{ mm}^3$). Aluminum films ($0.4 \mu\text{m}$ thick) were made by evaporation, Mo films ($0.03 \mu\text{m}$ thick) by sputtering, and Ni-P films (10% P) ($0.3 \mu\text{m}$ thick) by electrodeless deposition. The metal films were then partly covered either with photoresist or noble metal patterns containing details of $5 \mu\text{m}$ and greater.

The Al was provided with a noble metal pattern by first sputter-etching the metal surface to remove the oxide film and then depositing a $0.1 \mu\text{m}$ Pt film on the clean Al in the same apparatus. Through the windows of a resist pattern a $2 \mu\text{m}$ thick Au film was electrodeposited on the Pt. After removal of the resist, the thin Pt film, not protected by the thick Au film, was removed by sputter-etching.

In a similar manner a thin Au film was sputtered onto the clean Mo film and a thicker Au film was electrodeposited through the windows of a photoresist pattern. After removal of the resist the thin Au film was chemically etched to expose the underlying Mo. The Ni-P films were also provided with a Au pattern by electrodeposition.

In all cases the area of the exposed metal film was kept small compared to the area covered by resist or noble metal.

Composition of etching solutions.—Table I gives a list of the solutions used for the electrochemical and chemical etching experiments with the different metals. All chemicals used in this work were of reagent grade.

Determination of dissolved Al.—Etching rates were measured by removing 1 ml samples from the etching solution at regular intervals and determining the concentration of dissolved Al spectrophotometrically using 8-hydroxyquinoline (4).

Measurements of the polarization curves.—Polarization curves were recorded at a scanning rate of 95 mV/min using a Wenking 61 TR potentiostat and a Philips PM 8100 recorder. Because both the dissolution of metals in a potential-independent current region and the electrolytic reduction of various oxidizing agents may be diffusion controlled, we used rotating disk electrodes (RDE) for the Al study. The metal electrode (Al or Pt) in the form of a cylinder with a face area of 1 cm^2 , was imbedded in a Teflon shaft, which was driven by a motor with an electronically regulated feedback system.

The cell consisted of a Pyrex vessel coated with a conducting tin oxide layer which acted as a heating element. The reference standard calomel electrode (SCE) was placed in a sidearm which was connected to the bottom of the main cell via an inlet fitted with a capillary extending to just below the center of the rotating disk. The counterelectrode was a Pt ring set at the bottom of the capillary inlet. For certain experiments a large area Pt strip was placed against the inner wall of the cell and connected to the rotating electrode via the mercury contact.

For experiments with Mo and Ni-P, only a stationary test electrode in the form of a flat metal strip was used with a Pt strip as counterelectrode. The SCE reference was placed in a second vessel containing the same solution and was connected to the test electrode in the working cell via a salt bridge and a Luggin capillary. The solutions were not stirred in this case.

All potentials quoted either in the text or in the figures of this paper are values with respect to SCE.

Results and Discussion

Aluminum

Numerous electropolishing agents for Al are described in the literature (2, 3). From the various solutions investigated by us, current-potential measurements indicated that two of these, an alkaline and

an acidic solution, had electrochemical properties suitable for our purposes.

Alkaline polishing solution.—**Anodic polarization measurements.**—The current-potential characteristics of a 1 cm^2 Al RDE at 24°C in an electropolishing solution containing Na_2CO_3 and Na_3PO_4 (cf. Table I) are shown in Fig. 3, curve (a). For potentials greater than -0.8V the anodic current is constant. In this potential range 3 faradays are required to dissolve 1 mole of Al in agreement with Faraday's law. No cathodic reaction occurs in this region. At potentials below -0.8V hydrogen is cathodically evolved at the Al electrode. The current voltage curves were reproducible to within approximately 5% for the scan rate shown. The difference between the limiting anodic current density measured potentiostatically and during scanning at 95 mV/min was $<10\%$.

The partial current for Al dissolution was calculated from the dissolution rate of the metal and is shown in Fig. 3, curve b. The difference between this partial current and the total current (curve a) at lower potentials is due to the cathodic reaction—hydrogen evolution.

The effect of a stationary 15 cm^2 Pt electrode in contact with the 1 cm^2 Al rotating electrode in the same solution at the same temperature and rotation rate is shown in Fig. 3, curve (c). The differences between the polarization curves (c) for Al + Pt and (a) for Al alone are due to a lower hydrogen overvoltage on Pt than on Al and to oxygen evolution at the Pt electrode as is shown in curve (d), the polarization curve for the Pt strip alone. It is obvious from Fig. 3 that a relatively wide potential region exists in which the anodic current of Al is not affected by the presence of the noble metal.

A plot of the limiting anodic current density as a function of the square root of the rotation rate gave a straight line. This indicates, that for the rotation range 100-1000 rpm, the reaction is diffusion controlled (5). The line did not pass through the origin (intercept 4 mA/cm^2).

Anodic current-potential measurements performed at temperatures between 25° and 60°C and at the same rotation rate showed in each case a well-defined constant current region. The activation energy for the electropolishing process, calculated from the limiting current densities, was $9.8 \pm 0.2 \text{ kcal/mole}$, a value which is in good agreement with that reported by Gabe (6) for a similar Brytal-type bath. This is higher than values reported for reactions in other diffusion-controlled electrochemical systems (5, 7, 8) ($\leq 4 \text{ kcal/mole}$). In the case of electropolishing a highly viscous film and/or an oxide layer may be

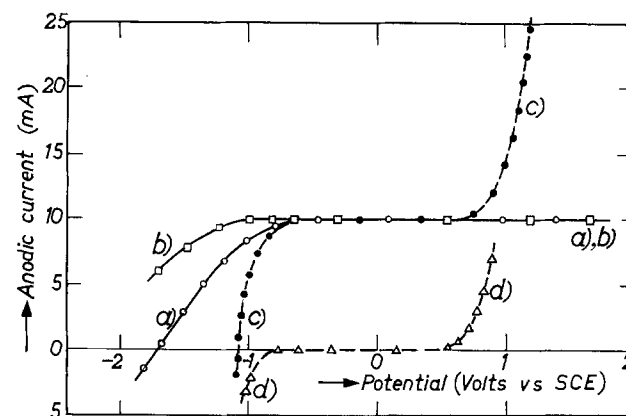


Fig. 3. Polarization curves measured in $\text{PO}_4^{3-}/\text{CO}_3^{2-}$ solution at 24°C . Curves (a), (c), and (d) are curves recorded using: (a) 1 cm^2 Al RDE, 550 rpm; (c) 1 cm^2 Al RDE + 15 cm^2 stationary Pt electrode; (d) 15 cm^2 stationary Pt electrode. Curve (b) is the partial anodic curve for case (a) calculated from Al dissolution rates.

present on the electrode and this may be responsible for the higher activation energy.

For comparison we also measured the polarization curve for an Al RDE in a nonpolishing solution, 0.25M NaOH. In this case the anodic current density increased significantly with increasing potential.

Chemical dissolution of Al.—As an oxidizing agent for the alkaline electropolishing solution we chose $\text{K}_3\text{Fe}(\text{CN})_6$ (0.092M). The solution shown in Table I had a pH of 12.6. The ferricyanide/ferrocyanide system in 0.01M NaOH has a standard potential of +0.22V (9) which is in the region of constant anodic current of Fig. 3.

Curve (a) of Fig. 4 shows the amount of Al chemically dissolved as a function of time at 24°C and 550 rpm for a 1 cm² Al RDE (circles) and for the same disk connected to a stationary Pt strip (15 cm²) in the same solution (squares). No increase in the Al dissolution rate due to the noble metal was observed. If the rate of Al dissolution is expressed as current density, then this value agrees well with the limiting anodic current density observed in Fig. 3.

Results are also shown in Fig. 4 for chemical dissolution of Al at 36°C (curve b) and at 48°C (curve c). For Al alone (circles) the current densities calculated from these rates are lower than those expected from the corresponding limiting anodic current densities. This effect will result when the cathodic process, the reduction of ferricyanide, is rate determining at the rest potential. When the Al disk was in contact with a large area Pt strip (squares), an increase in the rate of chemical dissolution was observed at these temperatures. In this case the measured chemical dissolution rates agreed with the values calculated from the limiting anodic current densities. This must mean that the anodic process is rate determining.

Cathodic polarization measurements.—In order to check the above explanation, polarization curves for the ferricyanide reduction in the $\text{PO}_4^{3-}/\text{CO}_3^{2-}$ solution were measured. Figure 5 shows such a curve for a Pt RDE at 24°C and 550 rpm. A well-defined diffusion-controlled cathodic current density (i_1^c) was observed. The limiting current density was directly proportional to the $\text{Fe}(\text{CN})_6^{3-}$ concentration as can be seen in Fig. 5 and to the square root of the rotation rate (5, 8).

The cathodic limiting current was determined as a function of temperature between 20° and 60°C and an activation energy of 3.9 kcal/mole was calculated from these results. This is in the region expected for a process controlled by laminar flow (5, 7, 8).

The anodic limiting current density for Al dissolution (curve a) and the cathodic limiting current density for the reduction of ferricyanide (curve b) are

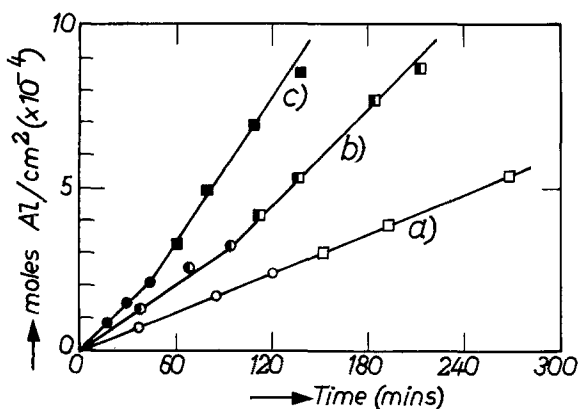


Fig. 4. Chemical dissolution of Al as a function of time for an Al RDE alone (circles) and in contact with a 15 cm² Pt strip (squares) in $\text{PO}_4^{3-}/\text{CO}_3^{2-}/\text{Fe}(\text{CN})_6^{3-}$ solution, 550 rpm at (a) 24°C, (b) 36°C, and (c) 48°C.

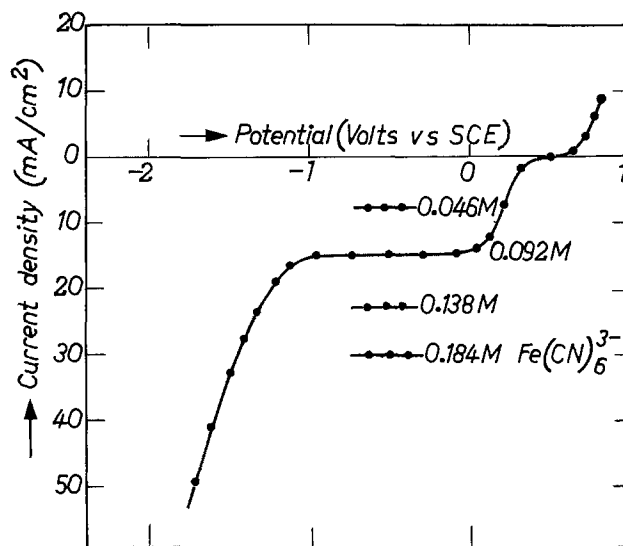


Fig. 5. Cathodic polarization curve for a 1 cm² Pt RDE in $\text{PO}_4^{3-}/\text{CO}_3^{2-}/\text{Fe}(\text{CN})_6^{3-}$ (0.092M) solution, 550 rpm, 24°C. Limiting current densities are also shown for other concentrations.

plotted as a function of temperature in Fig. 6. The measured chemical dissolution rates of Al, expressed as current densities, are also plotted in Fig. 6, circles for Al alone and crosses for Al in contact with a 15 cm² Pt strip. It is clear that for the case of Al alone at temperatures below 32°C, the limiting anodic current density is less than the cathodic ($i_1^a < i_1^c$) and in this range the chemical dissolution rate expected from i_1^a is obtained. For temperatures above 32°C, $i_1^c < i_1^a$ and the dissolution rate for Al alone is determined by the magnitude of i_1^c . Hence the circles fall on the cathodic line (curve b). Contacting the Al with Pt leads to an increase in cathodic current, therefore $\text{Fe}(\text{CN})_6^{3-}$ reduction is no longer rate determining and the crosses fall on the anodic curve. The chemical etching results shown in Fig. 4 can be explained in this way, using the partial polarization results.

It is obvious from the electrochemical results shown in Fig. 6 that the etching of bimetallic systems without the risk of undercutting in the $\text{PO}_4^{3-}/\text{CO}_3^{2-}/\text{Fe}(\text{CN})_6^{3-}$ solution (Table I) is only guaranteed at or below 32°C, i.e., where the etching rates of both Al alone and of Al in contact with Pt are under anodic control. For temperatures above 32°C the etch-

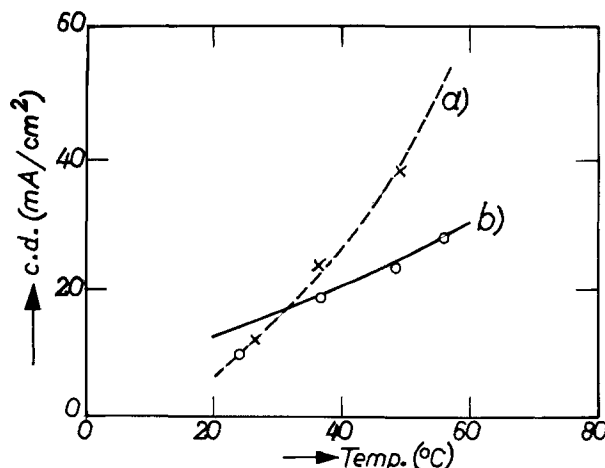


Fig. 6. Summary of electrochemical and chemical results: anodic (curve a) and cathodic (curve b) limiting current densities are plotted as a function of temperature; chemical dissolution rates of Al alone and of Al in contact with Pt are given by circles and crosses, respectively.

ant can be modified by increasing the ferricyanide concentration sufficiently (see Fig. 5) so that the etching is no longer under cathodic control.

Rest potential of Al.—The value of the rest potential of Al measured in the $\text{PO}_4^{3-}/\text{CO}_3^{2-}/\text{Fe}(\text{CN})_6^{3-}$ solution was -1.05V . From the partial anodic Al curve measured in $\text{PO}_4^{3-}/\text{CO}_3^{2-}$ solution (Fig. 3, curve b) and the cathodic curve measured on Pt in the $\text{PO}_4^{3-}/\text{CO}_3^{2-}/\text{Fe}(\text{CN})_6^{3-}$ solution (Fig. 5) a much higher value of the rest potential ($+0.16\text{V}$) was expected, i.e., 1.2V higher. The cathodic polarization curve for Al in aqueous $\text{Fe}(\text{CN})_6^{3-}$ solution, with no $\text{PO}_4^{3-}/\text{CO}_3^{2-}$ present, showed that ferricyanide was reduced only at potentials much more cathodic ($>1\text{V}$) than on Pt. This was also found to be the case for cathodic reduction of $\text{Fe}(\text{CN})_6^{3-}$ in $\text{PO}_4^{3-}/\text{CO}_3^{2-}$ solution. This considerable shift in the cathodic curve for Al with respect to that for Pt explains the discrepancy between measured and predicted values of rest potential. The value of the limiting cathodic current density was the same for both metals.

Petrocelli has reported similar effects for Al using $\text{Fe}(\text{CN})_6^{3-}/\text{Fe}(\text{CN})_6^{4-}$ in NaOH solution (10) and $\text{Ce}^{4+}/\text{Ce}^{3+}$ in H_2SO_4 solution (1). He suggests (1, 11) that a coherent oxide film, the thickness of which increases with increasing potential, exists on Al even at cathodic potentials. He attributes the shift in the cathodic reduction curves to the fact that Al ions may diffuse or migrate through the oxide film while electrons may only pass through by quantum mechanical tunneling.

Acidic polishing solution.—The acidic polishing solution was not as extensively studied as the alkaline solution. However the same general features were also observed in this case.

The anodic current-potential curve, measured using an Al RDE (1 cm^2) at 25°C in a solution containing H_3PO_4 and CH_3COOH (Table I), was similar in form to that found for the alkaline solution. At a rotation rate of 500 rpm, a rest potential of -0.9V and a limiting anodic current density of $3\text{ mA}/\text{cm}^2$ were observed. The limiting current density depended on the rotation rate. Over a broad potential range ($+0.2$ to $+0.8\text{V}$) the anodic polarization curve was essentially unaffected by contacting the Al electrode with a large area Pt strip.

Nitric acid (Table I) was a suitable oxidizing agent for this system. During chemical dissolution of Al in this solution a rest potential in the required plateau region was observed. The cathodic current was not a limiting factor for the Al dissolution rate at 25°C .

Application of polishing solutions for Al etching.—In order to test the applicability of these chemical polishing solutions as etching agents, Al films were etched through the windows of a photoresist or a noble metal pattern. Because it was more convenient to electrodeposit thick layers of gold instead of platinum, we used gold for the upper noble metal layer in these experiments. The electrochemical behavior of gold in these solutions was the same as that of platinum. During etching the solutions were stirred. The degree of undercutting was studied by observing the etched film through the glass substrate using a microscope.

Etching Al/resist films with the $\text{PO}_4^{3-}/\text{CO}_3^{2-}/\text{Fe}(\text{CN})_6^{3-}$ and $\text{H}_3\text{PO}_4/\text{CH}_3\text{COOH}/\text{HNO}_3$ solutions gave results similar to those obtained with 0.25M NaOH, i.e., a controlled etching rate, good definition, and negligible undercutting.

The etching rate of Al in 0.25M NaOH for the Al/noble metal films was much greater than for the corresponding Al/resist films. In Table II the times required to etch the two types of film are given. An increase in etching rate by a factor of 7 was observed. Figure 7a shows the results of 3 min etching of an Al film partly covered with Pt + Au. Considerable undercutting ($\sim 10\text{ }\mu\text{m}$) has occurred at the

Table II. Etching of Al films

Solution	Film	Etching time (min)
0.25M NaOH	Al/resist	7 ± 2
	Al/Pt + Au	1 ± 0.5
$\text{PO}_4^{3-}/\text{CO}_3^{2-}/\text{Fe}(\text{CN})_6^{3-}$	Al/resist	3 ± 1
	Al/Pt + Au	3 ± 1
$\text{H}_3\text{PO}_4/\text{CH}_3\text{COOH}/\text{HNO}_3$	Al/resist	12 ± 3
	Al/Pt + Au	11 ± 2

Al/Pt + Au interface. For comparison a photograph of an Al/resist interface is also included (Fig. 7b) in which the Al film has been etched for 7 min under the same conditions. Only slight undercutting was observed.

The Al tracks, not covered by either noble metal or resist, were approximately $200\text{ }\mu\text{m}$ wide. In the NaOH solution, etching of the Al covered by noble metal was considerably accelerated both at the contact area (Fig. 7a) and in the narrow tracks (Table II). In general the effect of the noble metal in such solutions will always be greater near the bimetallic contact. Although the resistances of the metals are low and the metals have the same potential, the resistance of the solution is higher and the current density will therefore decrease with increasing distance from the contact area. Besides this, complications may also arise due to inadequate refreshing of the etching electrolyte in narrow slits, local excessive stirring, or the formation of islands in the etching metal.

The data given in Table II show that no appreciable difference in etching time was found for the Al/resist and Al/Pt + Au films using the two polishing solutions. Figure 7c shows the results of 4 min etching of the Al/Pt + Au film in the alkaline polishing solution. Very little undercutting was observed. A similar result was also found for the acidic solution.

A higher etching rate in the alkaline solution can be obtained by either increasing the temperature and/or replacing Na_2CO_3 by NaOH with equally favorable results. In both cases the $\text{Fe}(\text{CN})_6^{3-}$ concentration must be increased to prevent the cathodic reaction from becoming rate determining.

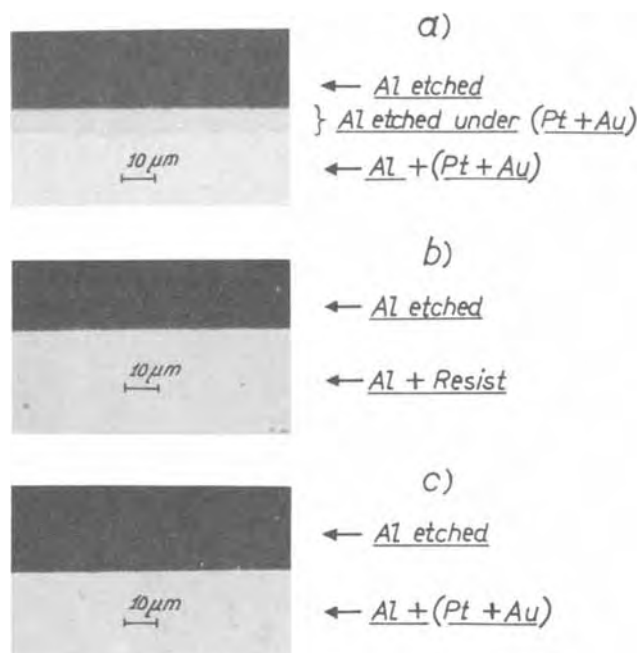


Fig. 7. Undercutting in Al films: (a) Al/(Pt + Au) film etched 3 min in 0.25M NaOH; (b) Al/resist film etched 7 min in 0.25M NaOH; (c) Al/(Pt + Au) film etched 4 min in $\text{PO}_4^{3-}/\text{CO}_3^{2-}/\text{Fe}(\text{CN})_6^{3-}$ solution.

Molybdenum

For etching Mo a solution of $\text{Ce}(\text{NH}_4)_2(\text{NO}_3)_6$ in HNO_3 is often used (Table I). With no noble metal present, this solution etches Mo at a rate of approximately $0.1 \mu\text{m}/\text{min}$. Thus a $0.03 \mu\text{m}$ Mo film partly covered by a photoresist film could be etched in 20-30 sec without significant undercutting. When the Mo film was etched through the windows of a gold pattern for 15 sec using the same solution, enormous undercutting ($80 \mu\text{m}$) was found (Fig. 8a). The etching rate of Mo under Au was more than three orders of magnitude greater than that of Mo under resist.

The polarization curve measured using a stationary Mo electrode in the same solution showed that the anodic current rose very steeply for very slight increases in potential. The corresponding curve for a stationary Pt electrode in this solution showed a limiting cathodic current due to reduction of Ce^{4+} , which in this case determined the etching rate. The fact that the anodic current rises so rapidly means that very large acceleration factors in etching rate are possible when the cathode area is large relative to the exposed Mo area.

Molybdenum may be electropolished in H_3PO_4 solution (2) (Table I). The polarization curve shows a wide potential region above $+0.6\text{V}$ with an essentially constant anodic current. Nitric acid is a suitable oxidizing agent giving a rest potential of approximately $+0.8\text{V}$. This chemical polishing etching agent gave very little undercutting (Fig. 8b), as expected from the electrochemical results.

Nickel-Phosphorus

An etching agent often used for Ni-P films is a diluted HNO_3 solution (Table I). The anodic polarization curve of Ni-P in this solution does not show a constant current region and accordingly the etching of Ni-P under a gold pattern with this solution gives rise to undercutting.

We did not succeed in finding an electropolishing solution for Ni-P. Various solutions which are used to electropolish pure Ni (2, 3) did not give favorable results with Ni-P. Our earlier experiments had shown that the anodic behavior of Ni-P is quite different from that of pure Ni. As an example Ni tends to passivate in H_2SO_4 solutions while Ni-P does not.

Although no polishing effect was observed a concentrated H_3PO_4 solution (Table I) gave polarization curves for Ni-P in which the anodic current did not increase appreciably between 0.8 and 1.7V.

Nitric acid was used as the oxidizing agent and the rest potential of Ni-P in this solution was 0.85V. Much less undercutting of Ni-P/Au films was observed with this solution than with the diluted HNO_3 solution. A solution containing HCl , HNO_3 , H_2SO_4 , and H_2O (Table I), which is widely used to etch Ni-P films in the presence of Cu, also gives rise to very little undercutting.

Summary

The aim of this work was to investigate whether it was possible from electrochemical considerations to develop etching agents with the property that the rate of dissolution of the metal in the solution remains unaffected by contact of the metal with a nobler metal. The procedure for a given metal was to choose a solution having a suitable potential range in which the anodic current is constant and to add an oxidizing agent with a standard potential in this range. Electropolishing solutions usually fulfill the requirement of a constant current range and addition of an oxidizing agent to such a solution gives a chemical polishing solution.

As electropolishing agent for Al, a $\text{Na}_3\text{PO}_4/\text{Na}_2\text{CO}_3$ solution was investigated. To obtain a corresponding chemical polishing solution, $\text{K}_3\text{Fe}(\text{CN})_6$ was added as oxidizing agent. Various aspects of the anodic and cathodic polarization curves for Al in these polishing solutions were studied, e.g., dependence of the limiting current density on temperature, concentration, and rotation rate. The rates of dissolution of an Al rotating disk alone and in contact with a Pt strip were measured in the chemical polishing solution. As expected from the electrochemical results no increase in the dissolution rate of Al at 24°C due to the presence of the nobler metal was observed. This etching solution gave very little undercutting of Al films partly covered by a Pt + Au film, whereas considerable undercutting was found with a nonpolishing solution.

An acidic polishing solution for Al gave equally favorable results.

Suitable etching agents for duplex metal systems with Mo or Ni-P films, in combination with Au films, were also found.

These results confirm the hypothesis that certain chemical polishing solutions, when used to etch metals in the presence of nobler metals, give much less undercutting than nonpolishing solutions.

Manuscript submitted Oct. 15, 1974; revised manuscript received Feb. 24, 1975.

Any discussion of this paper will appear in a Discussion Section to be published in the June 1976 JOURNAL. All discussions for the June 1976 Discussion Section should be submitted by Feb. 1, 1976.

Publication costs of this article were partially assisted by Philips Research Laboratories.

REFERENCES

1. J. V. Petrocelli, *This Journal*, **97**, 10 (1950).
2. P. V. Shchigolev, "Electrolytic and Chemical Polishing of Metals," Freund Publishing House, London (1970).
3. W. J. Mc. G. Tegart, "The Electrolytic and Chemical Polishing of Metals," Pergamon Press, London (1959).
4. A. Claassen, L. Bastings, and J. Visser, *Anal. Chim. Acta*, **10**, 373 (1954).
5. V. G. Levich, "Physicochemical Hydrodynamics," Prentice Hall, Englewood Cliffs, N. J. (1962).
6. D. R. Gabe, *Trans. Inst. Metal Finishing*, **51**, 32 (1973).
7. D. P. Gregory and A. C. Riddiford, *J. Chem. Soc.*, 3756 (1956).
8. Yu. M. Povarov and P. D. Lukovtsev, *Electrochim. Acta*, **18**, 13 (1973).
9. Handbook of Chemistry and Physics, 51st ed., p. D-111 (1970-1971).
10. J. V. Petrocelli, *This Journal*, **99**, 513 (1952).
11. J. V. Petrocelli, *ibid.*, **106**, 566 (1959).

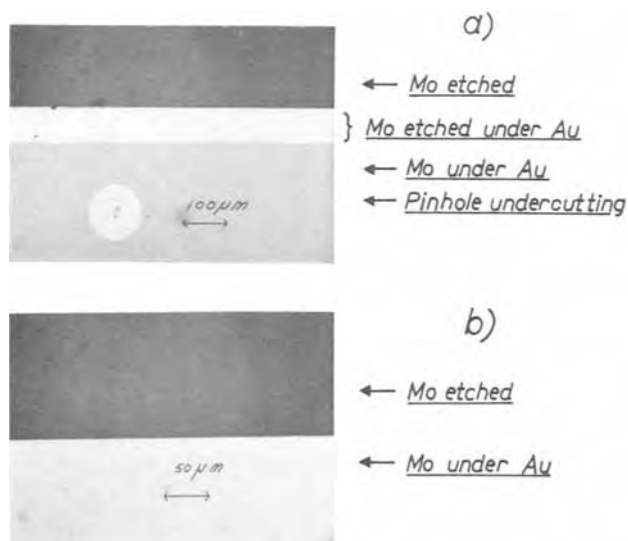


Fig. 8. Undercutting in Mo films: Mo/Au film etched using (a) $\text{Ce}(\text{NH}_4)_2(\text{NO}_3)_6/\text{HNO}_3$ solution, 15 sec, and (b) $\text{H}_3\text{PO}_4/\text{HNO}_3$ solution, 15 sec. In photo (a) the result of etching of the Mo at a pinhole in the Au is also shown.

Electrochemical Determination of Porosity in Nickel Electroplates on a Uranium Alloy

L. J. Weirick*

Metallurgy and Electroplating Division 8312, Sandia Laboratories, Livermore, California 94550

Typical chemical and electrographic test procedures for the determination of porosity in electroplates are usually destructive in nature and not generally applicable to process control procedures. Electrochemical techniques are preferable because they offer good sensitivity and rapid analysis and are relatively non-destructive. A quality control technique having these characteristics was needed to determine the porosity in nickel electroplates on a uranium-3/4 weight per cent titanium alloy.

Mansfeld (1) has derived general expressions for the corrosion potential ϕ_g of galvanic couples in terms of the anodic and cathodic areas. For the case of Tafel behavior or activation control, his expression is

$$\phi_g = \frac{b_a \phi_o^C + b_c \phi_o^A}{b_a + b_c} + \frac{b_a b_c}{b_a + b_c} \log \frac{i_o^C A^C}{i_o^A A^A} \quad [1]$$

If the influence of area variations is investigated while all other parameters are held constant and the cathodic and anodic area fractions (A_A , A_C) are introduced, Eq. [1] can be written in the form

$$\phi_g = k + \frac{b_c b_a}{b_a + b_c} \log \frac{A_C}{A_A} \quad [2]$$

For base metal specimens coated with noble metal electroplates of moderate to low porosity, $A_C \gg A_A$. In this case, A_C approaches unity, $(\log A_C)$ approaches zero, and Eq. [2] can be reduced to the form

$$\phi_g = k - \frac{b_a b_c}{b_a + b_c} \log A_A \quad [3]$$

Starting from a general expression by Stern (2) Morrissey (3) derived an equation identical to Eq. [3], for the case of only one metal undergoing corrosion in a binary galvanic couple controlled by activation polarization.

For a second case, Mansfeld (1) assumed that the corrosion rate of metal A is controlled by the diffusion rate of the oxidizer to the surface of metal A and that metal C is acting only as an oxygen electrode. In this case, after following arguments and simplifications similar to those used for the previous case, the expression for the corrosion potential is

$$\phi_g = \phi^A - b_a \log A_A \quad [4]$$

In summary, Eq. [3] and [4] are both linear in form, and a plot of corrosion potential vs. $\log A_A$ will yield a linear trace in either case. If the cathodic and anodic reactions are activation-controlled, the slope will be $(b_a b_c / b_a + b_c)$; if the cathodic reaction is diffusion-controlled, the slope will be b_a .

Luborsky, Breiter, and Drummond (4) investigated gold-copper couples in ammonium chloride solutions. They found that these couples were under activation control in 0.1M NH_4Cl , but under cathodic diffusion control in 1.0M NH_4Cl . Morrissey (3) also studied gold-copper couples in ammonium chloride solutions and found them to be activation-controlled in 0.1M NH_4Cl . He established techniques for determining calibration curves of corrosion potentials as a function of base metal area fraction of galvanically connected noble-base couples. These techniques were applied in the present study, the purpose of which was to determine the amount of porosity in nickel electroplates on a uranium alloy.

Experimental

Experiments were undertaken to determine the change in corrosion potential as a function of uranium alloy area fraction in galvanically connected nickel-uranium alloy couples. Figure 1 is a schematic of the experimental arrangement. Electroplated nickel sheet (stripped from a steel mandrel) was cut to form a 7.62 cm (3 in.) square having a geometric gross surface area of 116.13 cm^2 (18 in.^2). This square was used as the standard nickel specimen in all subsequent determinations and was suspended in the electrolyte by means of a platinum wire (the platinum wire caused no secondary effects in this particular arrangement).

For uranium alloy area fractions above 1%, coupons of uranium alloy were cut from a 25 mil sheet to the dimensions necessary to obtain the desired sur-

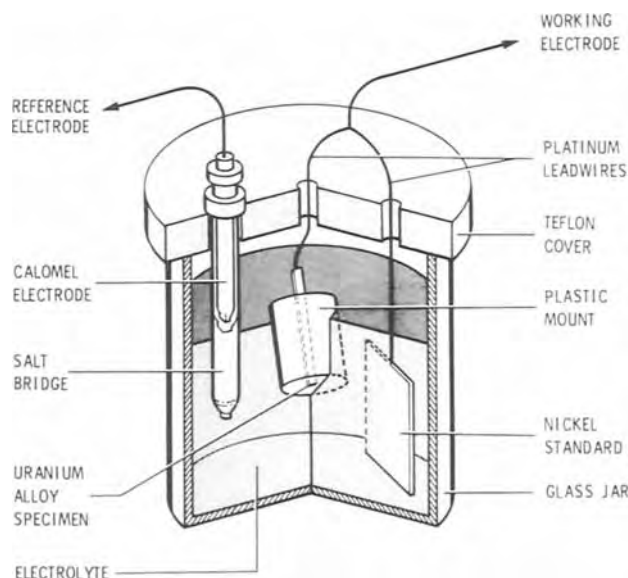


Fig. 1. Schematic of electrochemical cell

* Electrochemical Society Active Member.
Key words: galvanic couples, corrosion potentials, U-3/4 Ti.

face areas. These coupons were spot-welded to platinum wires for suspension in the electrolyte. For area fractions below 1%, wires of rectangular cross section were cut from the alloy sheet and mounted in plastic with the ends of the wires exposed. After these mounts had been polished, the cross-sectional area of the alloy was determined and the area fraction ratios were calculated. The potted wires were electrically connected on the back side of the mount to leads above the electrolyte surface.

A saturated calomel electrode (SCE) was used as the reference electrode. A 0.1M KCl solution was chosen as the electrolyte for the initial calibration curve determination. Subsequent curves were generated based on other concentrations of KCl and a 0.1M solution of KBr. Electrolytes of nitric, sulfuric, acetic, and oxalic acids and sodium carbonate, oxalate, and thiocyanate were also tried.

Corrosion potentials of uranium alloy specimens electroplated with various thicknesses of nickel were measured, and the area fraction of exposed alloy was determined from the calibration curves.

Results and Discussion

Plots of measured corrosion potential (*vs.* SCE) as a function of area fraction A_A of uranium alloy for nickel-uranium alloy couples in KCl solutions are shown in Fig. 2. Deviations from linearity can be observed in Fig. 2 at large values of area fraction A_A . This is in accordance with Eq. [2], for then $\log A_C$ can no longer be considered negligible. It can also be seen that the corrosion potential for a given area fraction becomes more positive in more dilute solutions, a point further expanded in the following. In addition, the slopes of the calibration curves in Fig. 2 decreased when the solutions were more dilute. As outlined previously, the analysis by Mansfeld suggests that the couple is under activation control if the slope is equal to $b_a b_c / b_a + b_c$ and under diffusion control if the slope is equal to b_a . From Fig. 2, the

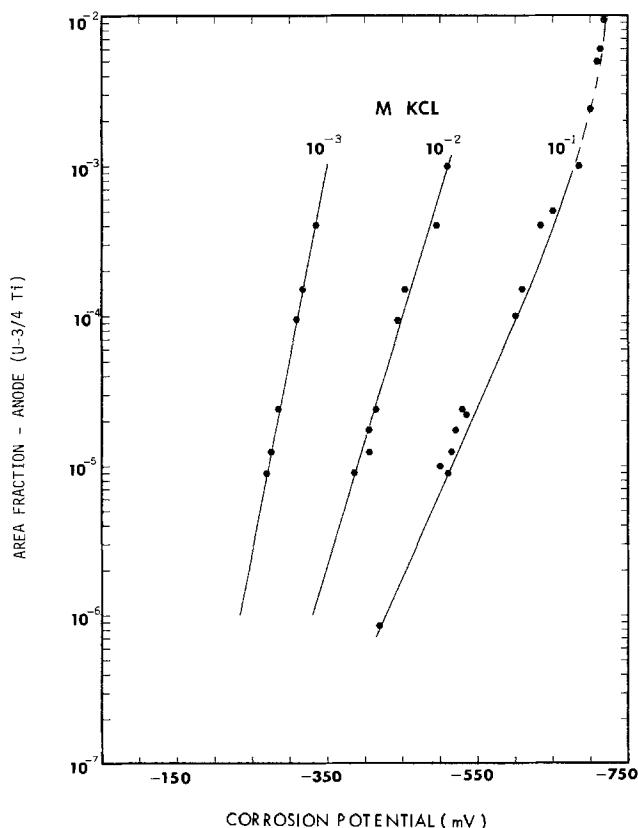


Fig. 2. Corrosion potential as a function of uranium alloy area fraction in potassium chloride.

slopes are approximately 90, 60, and 40 mV for 10^{-1} , 10^{-2} , and 10^{-3} KCl, respectively.

In order to compare these values for the slopes to the values calculated from the Tafel constants, thus determining whether the corrosion reaction was under activation or diffusion control, anodic and cathodic polarization curves were made for each solution, as shown in Fig. 3. However, the uranium alloy undergoes severe pitting in these KCl solutions, as indicated by the significant upturn in the anodic polarization curves. It was also observed that the pitting became more severe with increased chloride concentration. Thus the anodic polarization curves and the anodic Tafel slopes are significantly affected by, and perhaps determined by, this pitting reaction. The use of these anodic Tafel slopes to compare with the slopes of the calibration curves to determine whether the corrosion reaction is activation or diffusion controlled is thus not correct. However, indications of the type of control can be gotten from the intersections of the anodic and cathodic polarization curves in Fig. 3. These intersections occur in the diffusion-controlled region for all three electrolyte concentrations. The intersection for the most concentrated solution, however, is close to an activation-controlled region, that is, the discharge of water. Thus the resulting experimentally determined slopes are most likely a combination of both activation and diffusion control, with diffusion control the more dominant at dilute concentrations. The change in the slope of the calibration curves with concentration may be simply a reflection of a change in pitting severity with concentration.

Figure 3 also shows why the galvanic corrosion potential becomes more cathodic in more dilute solutions for a given area fraction. This is shown by the more positive values of potential at the intersection of the polarization curves (corrosion potential) for more dilute solutions.

Figure 4 is a plot of measured corrosion potential (*vs.* SCE) as a function of area fraction of uranium alloy in 0.1M KBr solution. It is observed that the corrosion potential for a given area fraction is smaller in this solution than it was in the comparable 0.1M KCl solution. Since the bromide ion Br^- is known to be less aggressive towards uranium alloys than the chloride ion Cl^- , this result is consistent with previous studies (5). The slope of the calibration curve measured in 0.1M KBr is very steep; in fact, steeper than that measured in 10^{-3} M KCl solution. Therefore, if this solution were used in process control to monitor porosity in nickel electroplates, the measurement would be less accurate than if the 0.1M KCl solution were used.

Solutions of 0.1M concentrations of nitric, sulfuric, acetic, and oxalic acids were tried as electrolytes to determine analogous calibration curves. In spite of

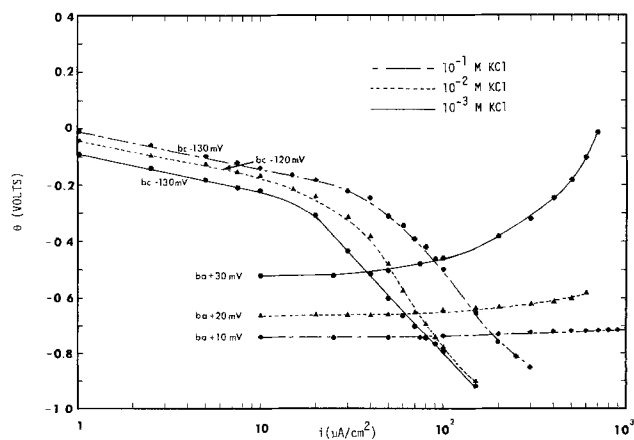


Fig. 3. Anodic (uranium alloy) and cathodic (nickel) polarization curves in potassium chloride.

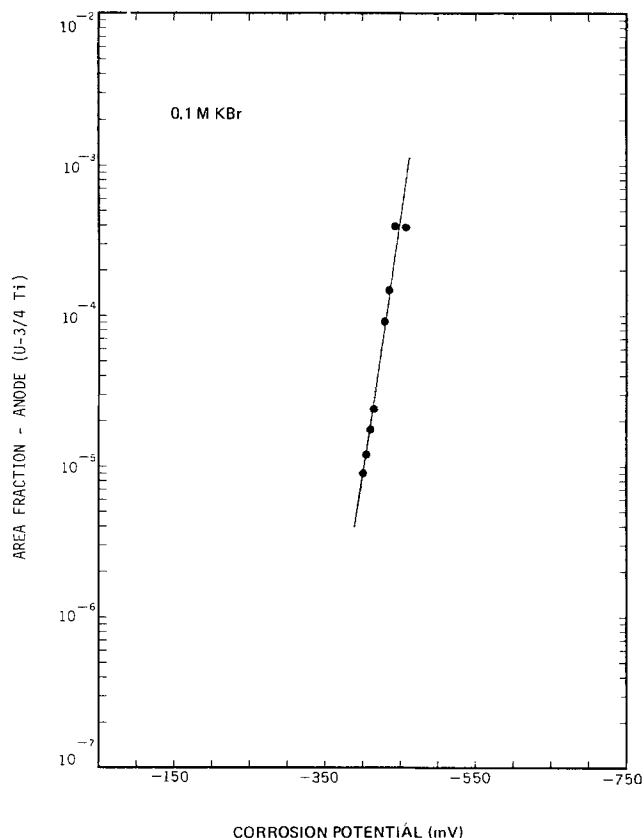


Fig. 4. Corrosion potential as a function of uranium alloy area fraction in potassium bromide.

reported ability of these acids to dissolve uranium (6), the corrosion potential did not change with varying area fractions. The apparent reason for this was that the exchange current density of nickel was high relative to the exchange current density of uranium in these solutions. Thus, as outlined by Mansfeld (7) in his case of an active metal imperfectly coated by a noble metal, when the ratio of the exchange current densities of the substrate to the coating is small, the reaction kinetics of the coating, and not the area relationships of the couple, fix the potential of the system.

Solutions of 0.1M concentrations of sodium carbonate, oxalate, and thiocyanate were also tried as possible electrolyte candidates. However, in oxalate and carbonate solutions, insoluble compounds which suppressed the corrosion reactions were formed. Only the thiocyanate ion produced any change in corrosion potential with varying area fractions of cathode, and these changes were very small.

The utility of this electrochemical technique for determining the amount of porosity in nickel electroplates on the uranium alloy was demonstrated in further experiments. Four coupons of U-3/4 Ti of dimensions $1.9 \times 2.5 \times 0.32$ cm ($3/4 \times 1 \times 1/8$ in.) were electroplated with nickel in a nickel sulfamate bath to thicknesses of 0.25, 0.50, 0.75, and 1.0 mil, respectively. Platinum wires were spot-welded to the specimens for electrical connection. The measured corrosion potentials of the four specimens as compared to the calibration curve generated in 10^{-3} M KCl solution are shown in Fig. 5. Progressive reductions in porosity with increasing plating thickness were observed. The total surface area of exposed uranium alloy in the specimen plated with 1 mil of nickel was extremely low, i.e., porosity below $10^{-3}\%$.

Summary

This study has shown that for uranium alloy specimens galvanically coupled to a nickel sheet in KCl electrolytes, the corrosion potential varies linearly

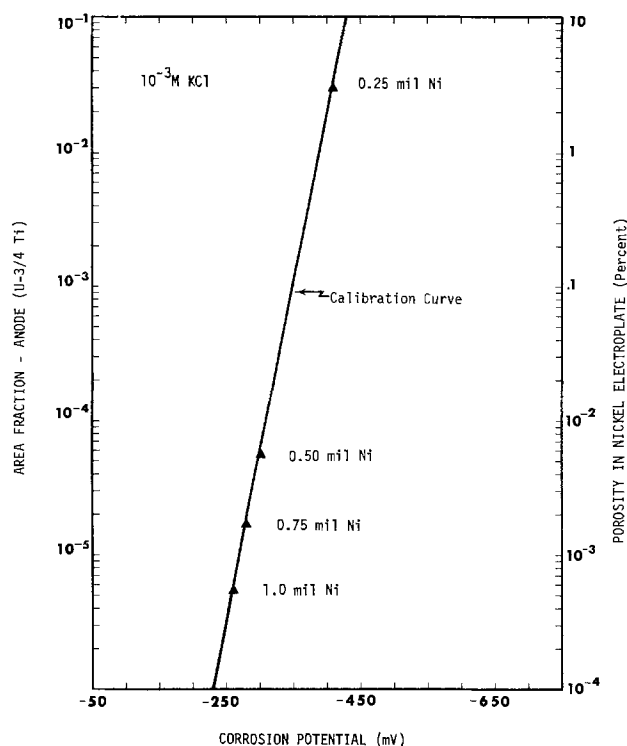


Fig. 5. Amount of porosity in nickel electroplates on a uranium alloy as a function of nickel thickness.

with the logarithm of the exposed area fraction of uranium alloy according to expressions derived by Mansfeld (1, 7). It was possible to calibrate the technique so that the exposed base metal area fractions of uranium alloy specimens plated with nickel could be estimated to a reasonable approximation. This technique is relatively nondestructive and offers the advantages of simplicity and high sensitivity, particularly at low porosities.

Acknowledgments

The author wishes to thank J. W. O'Connor of the Metallurgy and Electroplating Division at Sandia Laboratories, Livermore, for his experimental assistance during this study. The author also wishes to give special thanks to Dr. Florian Mansfeld, Science Center, Rockwell International, Thousand Oaks, California, for his assistance and instruction on the electrochemical theory of galvanic couples.

This work was supported by the United States Atomic Energy Commission, Contract Number AT (29-1)-789.

Manuscript submitted Nov. 19, 1973; revised manuscript received Feb. 20, 1975.

Any discussion of this paper will appear in a Discussion Section to be published in the June 1976 JOURNAL. All discussions for the June 1976 Discussion Section should be submitted by Feb. 1, 1976.

Publication costs of this article were partially assisted by Sandia Laboratories.

LIST OF SYMBOLS

ϕ_B	corrosion potential of galvanic couple
ϕ_o^C	reversible potential for oxidation/reduction reaction of oxidizer
ϕ_o^A	reversible potential for oxidation/reduction reaction of metal A
b_a	Tafel slope for anodic reaction on metal A
b_c	Tafel slope for cathodic reaction on metal B
i_o^C	exchange current density for oxidation/reduction reaction of oxidizer on metal C
i_o^A	exchange current density for oxidation/reduction of metal A
A^C	area of metal C

A^A area of metal A
 A_C cathodic area fraction = $A^C/A^C + A^A$
 A_A anodic area fraction = $A^A/A^A + A^C$

REFERENCES

1. F. Mansfeld, *Corrosion*, **27**, 436 (1971).
2. M. Stern, *ibid.*, **14**, 329 (1958).
3. R. J. Morrissey, *This Journal*, **117**, 742 (1970).
4. F. E. Luborsky, M. W. Breiter, and B. J. Drummond, *ibid.*, **119**, 92 (1972).
5. S. W. Zehr, *Corrosion*, **28**, 196 (1972).
6. R. C. Weast, "Handbook of Chemistry and Physics," 52nd ed., The Chemical Rubber Co., Cleveland, Ohio (1971).
7. F. Mansfeld, *J. Applied Electrochemistry*, **2**, 183 (1972).



The Effects of Lead on the Hot Corrosion of Nickel-Base Alloys

D. Chatterji,* D. W. McKee, G. Romeo,* and H. S. Spacil*

Corporate Research and Development, General Electric Company, Schenectady, New York 12301

ABSTRACT

Lead is often found as a trace impurity in fuels used in gas turbines. In addition, lead salts may form on hot superalloy parts during turbine operation in contaminated urban environments. An experimental and thermodynamic study of Na_2SO_4 -induced hot corrosion of nickel-base alloys at 900°C , in the presence of small concentrations of lead salts, has shown that these contaminants can be very deleterious to alloy corrosion resistance. PbO reduces the corrosion resistance of Ni-Cr and Ni-Al alloys by complexing normally protective scale to form PbCrO_4 and $\text{PbO}\cdot\text{Al}_2\text{O}_3$ which are soluble in the sulfate melt. PbO is a more aggressive contaminant than PbSO_4 , and PbO concentrations of 1 mole per cent in the salt condensate can result in catastrophic corrosion rates with Ni-Cr alloys.

Accelerated corrosion of high temperature superalloys in the presence of ingested sodium salts and residual sulfur is a problem of major concern in marine and industrial gas turbines and is the subject of an extensive literature (1). The increased use of crude oil and residual fuels in these applications has led to the recognition that severe corrosion effects can also be induced by traces of metallic impurities present in these low grade fuels. In particular, the deleterious effects of vanadium have been well documented (2). Lead impurities may arise from various sources. Industrial gas turbines may ingest particulate lead compounds during operation in contaminated urban atmospheres. Occasionally contamination of turbine fuels with lead tetraethyl from gasoline residues may occur in tankers and storage vessels. Lead compounds have been detected occasionally in crude oils in concentrations up to 2 ppm (3). However, in spite of these considerations, the effects of lead compounds on the hot corrosion behavior of superalloys have not been previously reported.

Thermodynamic calculations have shown (4) that a level of 1-2 ppm of lead in the fuel can be expected to produce a salt condensate containing up to 1 mole per cent (m/o) $\text{PbO} + \text{PbSO}_4$ in Na_2SO_4 at temperatures in the hot corrosion range of 850°C and above. Deposits on gas turbine blades formed during operation with aviation fuel containing lead have indeed been found to contain PbO (5), although the effects of lead on hot corrosion rates have not been studied. There are, however, reports that lead deposits on Ni-Cr-Fe alloy manifolds and afterburners in gasoline engines are associated with accelerated corrosion (6, 7).

This paper describes the results of an experimental investigation into the effects of low concentrations of lead salts on the Na_2SO_4 -induced hot corrosion of nickel-base alloys and an attempt to interpret the observed effects from an equilibrium thermodynamic standpoint.

* Electrochemical Society Active Member.

Key words: sulfidation, high temperature alloys, molten salt corrosion.

Experimental

Binary Ni-Cr and Ni-Al alloys used in the corrosion experiments were prepared by induction melting and casting in argon. From bars of 1-in. round stock, rectangular coupons of dimensions $5/8 \times 1/4 \times 1/16$ in. were cut and polished through 600-grit silicon carbide paper. The nominal and actual compositions of the alloy specimens are listed in Table I.

Salts used in the crucible experiments were anhydrous sodium sulfate (Mallinckrodt Analytical Reagent), lead oxide (Matheson, Coleman and Bell Reagent PbO), and lead sulfate (Fisher Certified Reagent).

Polished coupons of the alloys were placed in glazed porcelain crucibles containing 1g quantities of the powdered salt mixtures which had previously been ground in an agate mortar and blended in a Fisher Minimill. On heating the crucible and contents to 900°C , the salt melted and wetted the alloy coupon to form a thin liquid layer with the excess salt forming a pool at the bottom of the crucible. Weight changes of the crucibles and contents were measured thermogravimetrically in the Chevenard balance described previously (8). Corrosion experiments were carried out isothermally at 900°C in both air and a 0.1% SO_2 -76% O_2 -balance N_2 gas mixture, using a constant gas flow rate of 250 ml/min. Postexperimental examination of the corroded alloy specimens by means of conventional metallographic and electron microprobe techniques showed that the attack was generally fairly uniform throughout the length of the specimen and

Table I. Composition of alloys, weight per cent

Nominal composition	Actual composition
Ni	100 Ni
Ni-5 Cr	Ni-5.0 Cr
Ni-10 Cr	Ni-9.9 Cr
Ni-15 Cr	Ni-14.9 Cr
Ni-20 Cr	Ni-19.8 Cr
Ni-50 Cr	Ni-49.8 Cr
Ni-30 Al	Ni-29.3 Al

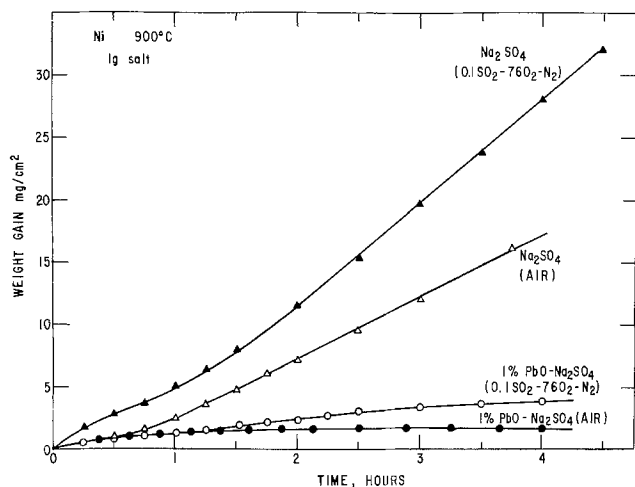


Fig. 1. Effect of 1 m/o PbO on the Na_2SO_4 -induced corrosion of nickel at 900°C . Weight changes vs. time in air and 0.1% SO_2 -76% O_2 - N_2 atmospheres.

therefore the total sample geometrical area was used to compute kinetic data. A blank experiment carried out in the absence of an alloy sample showed that the crucible gained less than 0.04 mg/cm^2 of internal surface after exposure to a melt of 1% PbO- Na_2SO_4 for 6 hr at 900°C . Weight changes resulting from attack on the crucible were therefore considered to be negligible under the conditions of the experiments.

Results

Nickel.—Thermogravimetric data for the corrosion of pure nickel specimens by Na_2SO_4 alone and by 1 m/o PbO- Na_2SO_4 mixtures in atmospheres of air and 0.1% SO_2 -76% O_2 -balance N_2 , are presented in Fig. 1. These experiments were all carried out at 900°C , using polished nickel coupons partially immersed in 1g of the powdered salt. In Fig. 1, weight gains of the crucibles and contents are plotted as functions of time, the extent of corrosion being computed as weight gain in milligrams per square centimeter of total alloy surface.

Corrosion of nickel by Na_2SO_4 alone took place at a rapid rate at 900°C in both gaseous atmospheres, weight gains being essentially linear with time for the duration of the experiments. The rate of attack in the 0.1% SO_2 -76% O_2 - N_2 environment was substantially greater than that in air, although in both cases the extent of the corrosion could be characterized as catastrophic,¹ with weight gains that exceeded 20 mg/cm^2 after a 5 hr exposure to the salt melt. By contrast, the experiments carried out with an initial 1% PbO- Na_2SO_4 salt mixture resulted in sharply reduced rates of corrosion, with weight gains of less than 4 mg/cm^2 during the 5 hr runs. Although weight increases were again larger in the SO_2 -containing atmosphere than in air, in both cases corrosion of the nickel specimens was minimal in the presence of the lead salt.

Postexperimental metallographic examination of the metal coupons showed marked differences in the morphology of the corrosion layers produced in the presence and absence of the lead additive. As shown in Fig. 2(a), corrosion experiments with the PbO- Na_2SO_4 salt mixture produced a protective oxide layer on the surface of the nickel, with no evidence of subscale sulfide formation. Electron microprobe examination of this sample, shown by the traverse in Fig. 2(b), indicated that the scale was dense NiO , the concentration of Pb being too low to be detectable. Corrosion of nickel by Na_2SO_4 alone produced a thick porous scale, shown in section in Fig. 3. In this case, x-ray images of Ni and S for an area at the base of the scale (Fig. 4) indicated that finely divided sulfides were distributed in a band beneath the outer oxide layer.

Additional experiments carried out with nickel specimens immersed in salt mixtures of composition 1 m/o PbSO_4 - Na_2SO_4 gave the same rapid weight gains and catastrophic corrosion rates as found with pure Na_2SO_4 , indicating that the inhibitory effect observed with PbO is not a general effect associated with the presence of lead salts. No appreciable corrosion of nickel was observed with PbSO_4 alone at 900°C .

Nickel-chromium alloys.—The most significant result found with binary Ni-Cr alloys was that the presence of PbO in the salt condensate caused a considerable

¹ Hot corrosion rates are generally regarded as "catastrophic" when they amount to 1-2 orders of magnitude greater than for normal oxidation (9).

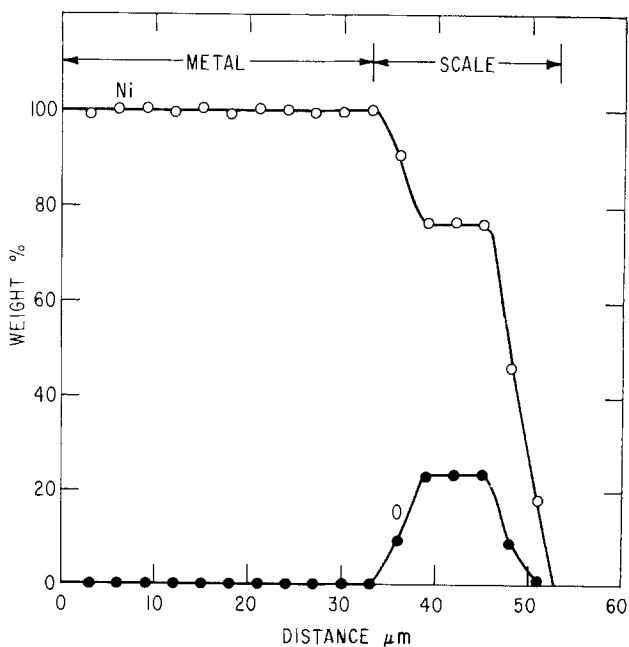
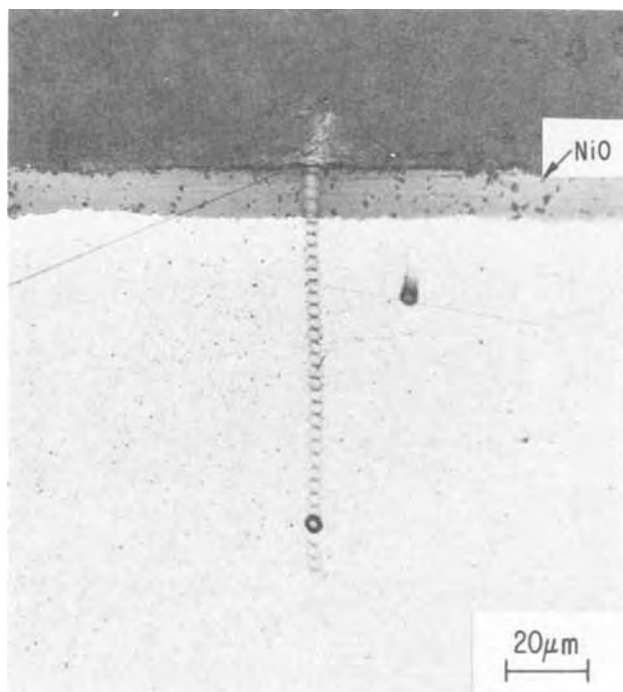


Fig. 2. Transverse section through Ni sample after 6 hr exposure to 1 m/o PbO- Na_2SO_4 at 900°C in air. (a, left) Optical micrograph showing uniform NiO scale. (b, right) Microprobe traverse along electron beam trace shown in (a).

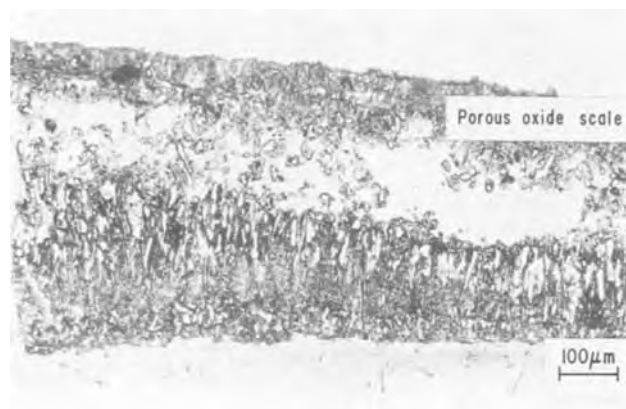


Fig. 3. Section of Ni sample after 5 hr exposure to 1g Na_2SO_4 at 900°C in 0.1% SO_2 -76% O_2 - N_2 atmosphere.

increase in the rate of Na_2SO_4 -induced hot corrosion at 900°C . The magnitude of the effect, however, depended to a large extent on the chromium content of the alloy.

Typical thermogravimetric results for Ni-15 Cr specimens are summarized in Fig. 5, which shows weight gain data obtained in crucible experiments with Na_2SO_4 and 1 m/o PbO- Na_2SO_4 salt mixtures in both air and 0.1% SO_2 -76% O_2 - N_2 atmospheres. When coupons of Ni-15 Cr were immersed in pure Na_2SO_4 and heated in flowing air at 900°C , a very small weight gain was observed ($<0.5 \text{ mg/cm}^2$) over a period of 5 hr and corrosion was very slight as the result of the formation of a protective Cr_2O_3 scale. Addition of 1 m/o PbO to the initial salt, however, resulted in a marked increase in corrosion rate and the specimen weight continued to increase during the course of the experiment. As with nickel, the corrosion rate in the PbO- Na_2SO_4 experiments was still further increased when 0.1% SO_2 was present in the ambient atmosphere, as shown in Fig. 5.

Metallographic examination of the corrosion layers produced on this alloy by the PbO- Na_2SO_4 salt melt showed (Fig. 6) a thick nonuniform Cr_2O_3 surface layer and dispersed chromium sulfide globules at depths of 40-50 μm into the bulk alloy, which are not clearly visible in the micrograph. This morphology is characteristic of sulfidation under conditions of high sulfur potential (8).

The results of an experiment on the interaction of Ni-15 Cr alloy with PbSO_4 alone are shown in Fig. 7. In this case the alloy specimen was partially immersed in 1g of the powdered salt and heated at 900°C in the 0.1% SO_2 -76% O_2 - N_2 gas mixture for a period of 5 hr. A moderate (3 mg/cm^2) weight gain was observed during this period and metallographic examination of a section of the specimen at the end of the experiment showed localized areas where sulfide particles had formed beneath the surface oxide scale. Although the extent of corrosion was greater with PbSO_4 than with Na_2SO_4 alone, the attack was much less intense and less uniform than with the 1% PbO- Na_2SO_4 salt mixture under the same conditions. As PbSO_4 is solid at 900°C , a direct comparison of corrosion rates is not possible.

A series of experiments was carried out with Ni-50 Cr alloy coupons, immersed in PbO- Na_2SO_4 mixtures of various compositions and heated at 900°C in the 0.1% SO_2 -76% O_2 - N_2 gas mixture. This alloy is very resistant to both oxidation and Na_2SO_4 -induced hot corrosion and weight changes in pure Na_2SO_4 amounted to less than 1 mg/cm^2 in a 5 hr period at 900°C . However, as shown in Fig. 8, immersion in a 1 m/o PbO- Na_2SO_4 mixture resulted in an initial rapid weight change, which amounted to 3.6 mg/cm^2 in the first hour of the experiment. The corrosion rate then diminished as the lead concentration in the salt melt

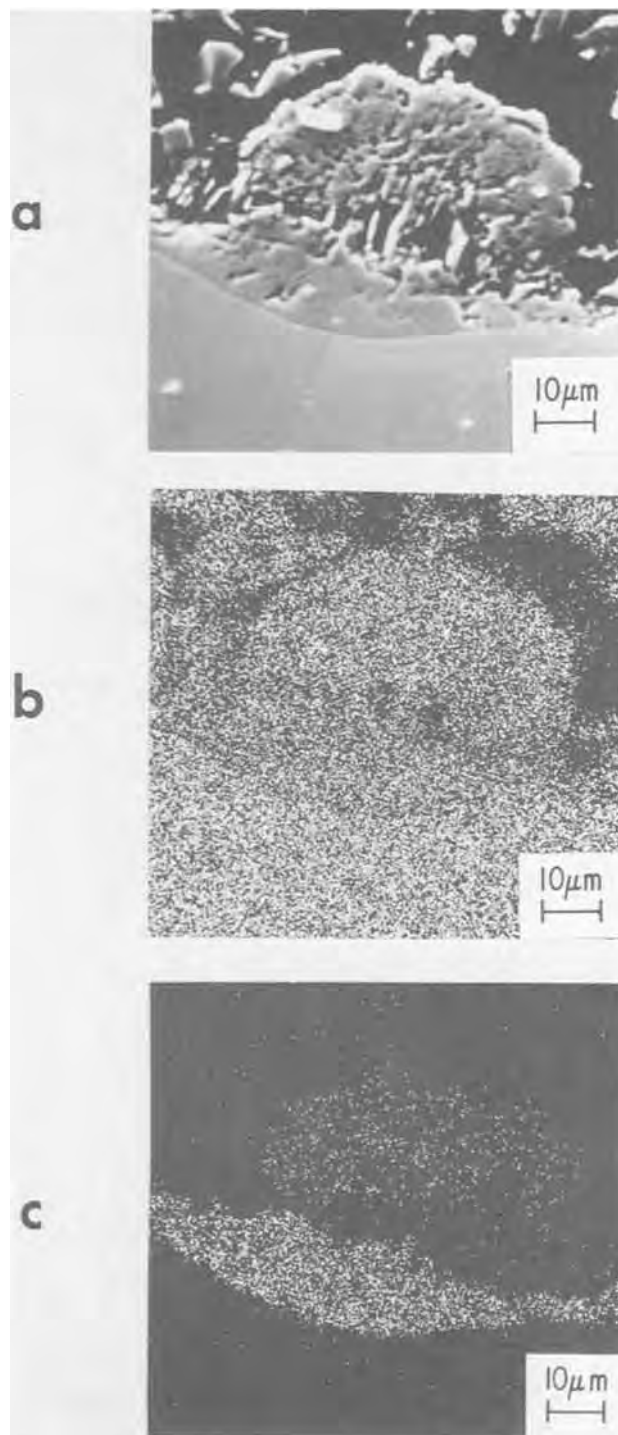


Fig. 4. X-ray images of base of corrosion layer on Ni following 5 hr exposure to 1g Na_2SO_4 at 900°C . (a) Back-scattered image, (b) $\text{NiK}\alpha$ scan, (c) $\text{SK}\alpha$ scan.

became depleted. The Nomarski interference contrast micrograph of the corrosion layer on this specimen, shown in Fig. 9, revealed a thick Cr_2O_3 scale on the surface, particles of chromium sulfide in the subscale region, and a zone about $20 \mu\text{m}$ thick near the surface which has become depleted in the chromium-rich eutectic, which is visible as irregular inclusions in the bulk alloy. As shown in Fig. 8, increasing initial PbO concentrations in the salt mixture resulted in marked increases in the corrosion rate of the Ni-50 Cr alloy, initial weight gains amounting to 5 and $10 \text{ mg/cm}^2\text{-hr}$ for initial 5 and 10% PbO- Na_2SO_4 salt compositions, respectively. (The morphology of the corrosion layer following exposure to the 5% PbO- Na_2SO_4 mixture is shown in Fig. 10. Penetration of sulfides into the bulk

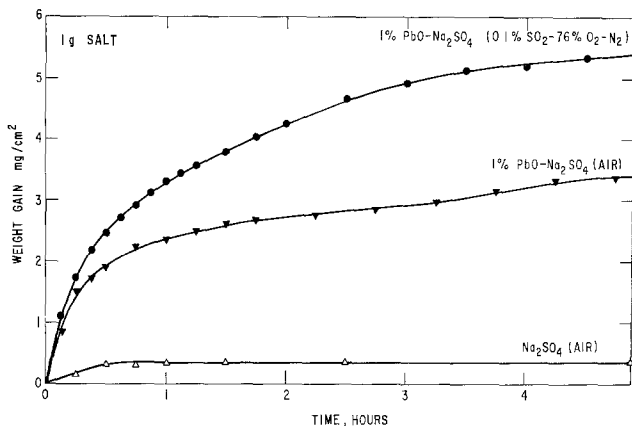


Fig. 5. Effect of 1 m/o PbO on Na₂SO₄-induced corrosion of Ni-15 Cr at 900°C. Weight changes vs. time in air and 0.1% SO₂-76% O₂-N₂ atmospheres.

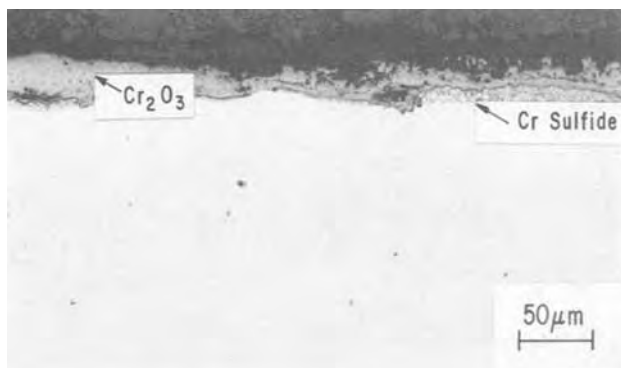


Fig. 6. Section of Ni-15 Cr sample showing corrosion morphology following exposure to 1 m/o PbO-Na₂SO₄ salt mixture for 6 hr in air at 900°C.

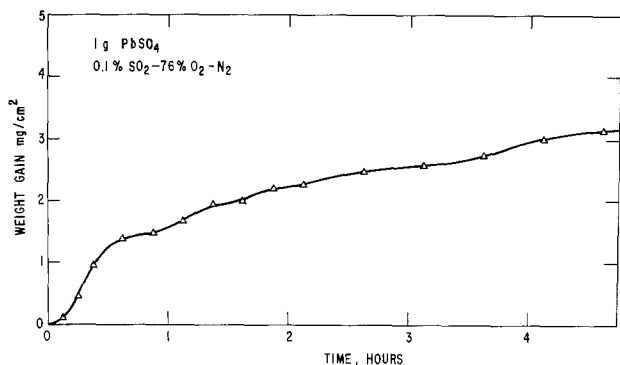
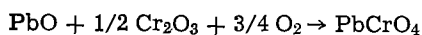


Fig. 7. Corrosion of Ni-15 Cr by PbSO₄ at 900°C. Weight changes vs. time in 0.1% SO₂-76% O₂-N₂ gas mixture.

alloy is obviously more marked than in the experiment with 1% PbO-Na₂SO₄.) In each case the salt residue at the end of the experiment was colored bright yellow, which chemical analysis showed to be due to the presence of chromate. For example, analysis of the residue from the experiment with 5 m/o PbO-Na₂SO₄ gave a CrO₄⁼ concentration of 0.22 and 2.17 weight per cent (w/o) in the case of the run with 10 m/o PbO-Na₂SO₄ initially. With Na₂SO₄ alone in contact with the Ni-50 Cr alloy, the concentration of residual chromate after the 5 hr experiment at 900°C was 0.098 w/o. Apparently the effect of PbO in the salt was to promote the formation of chromate as a result of the reaction



A combined TGA-DTA experiment with a 2:1 molar mixture of PbO and Cr₂O₃ heated at a rate of 10°C/min

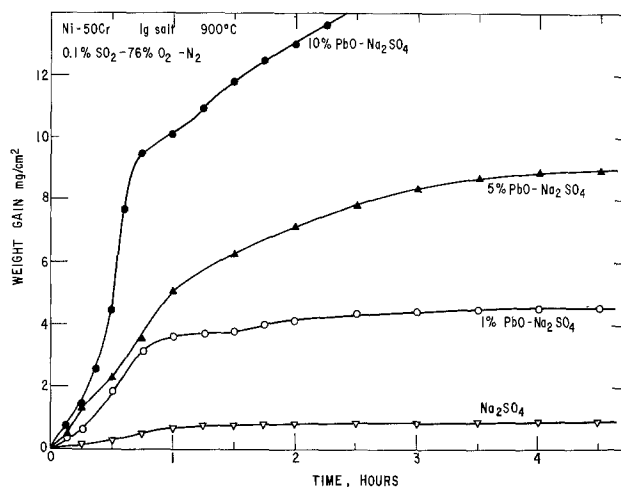


Fig. 8. Corrosion of Ni-50 Cr in PbO-Na₂SO₄ salt mixtures at 900°C. Weight changes vs. time for various initial PbO concentrations.

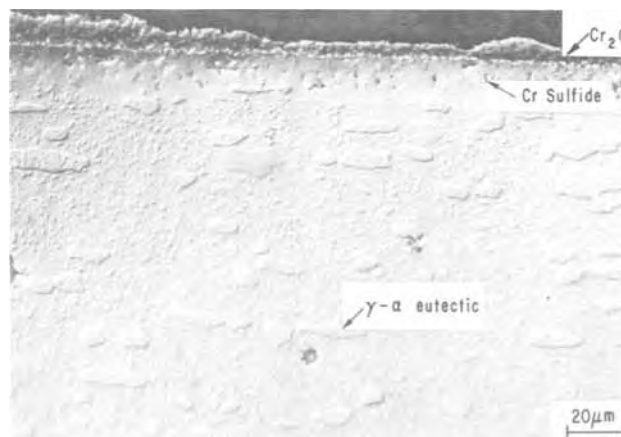


Fig. 9. Section of Ni-50 Cr sample showing corrosion morphology following exposure to 1 m/o PbO-Na₂SO₄ for 6 hr at 900°C in 0.1% SO₂-76% O₂-N₂ atmosphere.

in an atmosphere of flowing O₂ showed that this reaction began to occur at 400°C and was virtually complete at 750°C.

With the Ni-Cr binary alloys the corrosion rates were greatest during the first hour of the experiments, hence the measured weight gains for the initial 1 hr of exposure could be used as a basis for qualitative comparison of the corrosion behavior of the different alloy compositions. Figure 11 shows initial corrosion rates for the Ni-Cr alloy series computed in this manner; these are expressed in arbitrary units because the kinetics in general did not follow established rate laws. Postexperimental metallographic observations of the extent of corrosion confirmed the general trends shown in Fig. 11. The lower curve shows that the rate of corrosion by Na₂SO₄ alone decreased rapidly as chromium was added to nickel and became very low for Cr contents of 15 w/o or more, due to the formation of a protective Cr₂O₃ scale. By contrast, corrosion rates in the 1% PbO-Na₂SO₄ melt were low for pure nickel but increased rapidly as the Cr content of the alloy was increased and became very rapid for alloys containing 10-15 w/o Cr. In these cases, complexing of the surface Cr₂O₃ by the lead component of the salt melt produced a porous unprotected Cr-depleted matrix which was readily attacked by the Na₂SO₄ melt. Further increases in chromium content resulted in some decrease in the rate of corrosion because of the high residual content of Cr in the alloy matrix even after removal of the surface layer by lead complexing. However, even alloys containing 50 w/o Cr were more

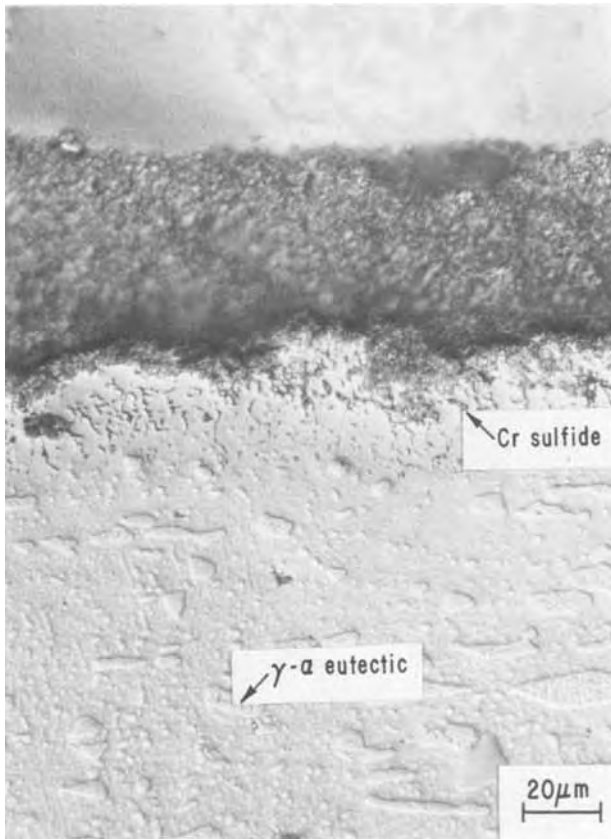


Fig. 10. Section of Ni-50 Cr sample showing corrosion morphology following exposure to 5 m/o PbO-Na₂SO₄ for 5 hr at 900°C in 0.1% SO₂-76% O₂-N₂ atmosphere.

readily attacked in the presence of PbO than by Na₂SO₄ alone. Typical catastrophic attack by PbO-Na₂SO₄ on Ni-Cr alloys in the intermediate Cr range is illustrated in Fig. 12 which shows the corrosion layer produced on a Ni-10 Cr specimen following exposure to 1% PbO-Na₂SO₄ for 5 hr at 900°C. The surface of the alloy is extensively degraded to form a porous oxide layer and widespread chromium sulfide globules within the alloy interior.

At higher chromium concentrations corrosion in the presence of PbO was less catastrophic, although sulfide particles were formed at considerable depths beneath the surface scale. Figure 13 shows a section of the corrosion layer formed on a Ni-20 Cr specimen after the same treatment as that described above. The extent of attack may be compared with that shown in

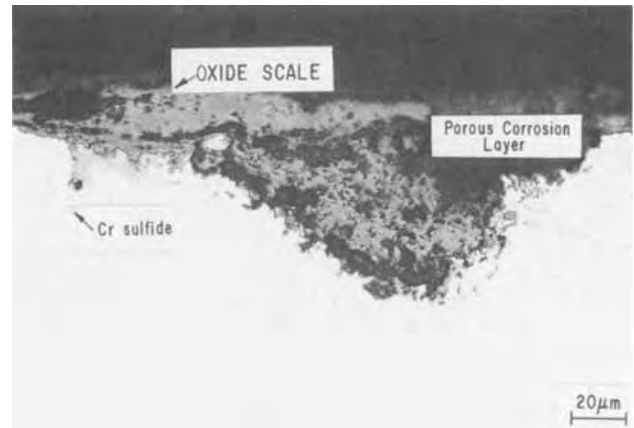


Fig. 12. Section of Ni-10 Cr sample following exposure to 1 m/o PbO-Na₂SO₄ for 5 hr at 900°C in 0.1% SO₂-76% O₂-N₂ atmosphere. Total salt concentration = 1g.

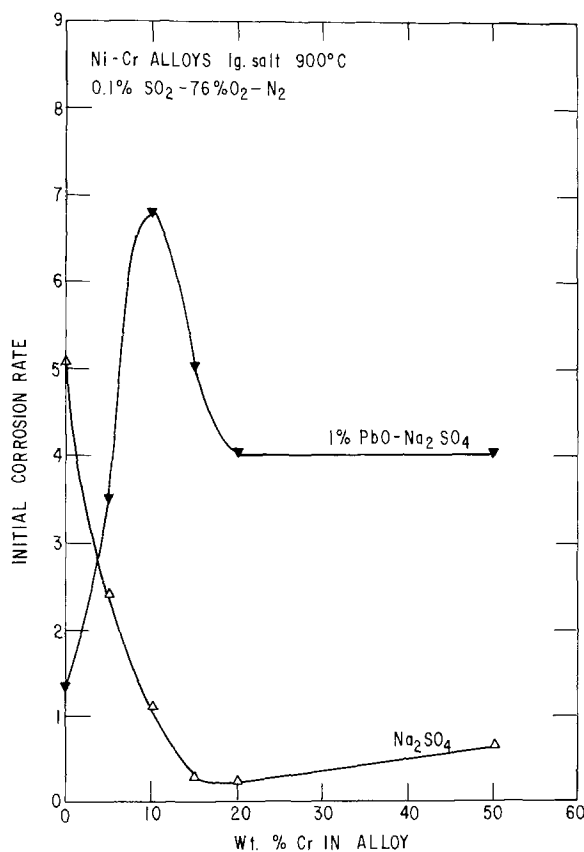


Fig. 11. Effect of PbO on initial corrosion rates of Ni-Cr alloys by Na₂SO₄. Corrosion rates after 1 hr (in arbitrary units) at 900°C in Na₂SO₄ and 1 m/o PbO-Na₂SO₄ as a function of Cr content.

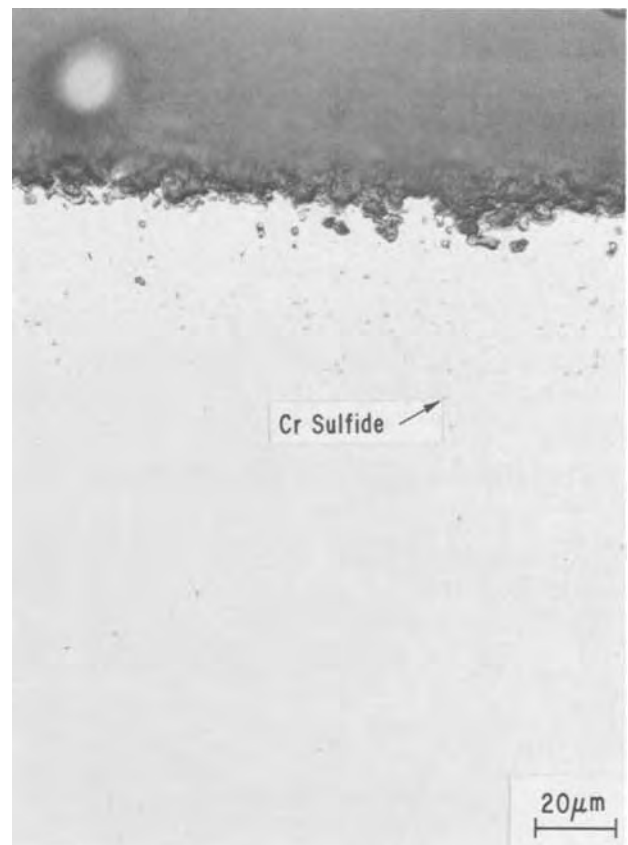


Fig. 13. Section of Ni-20 Cr sample following exposure to 1 m/o PbO-Na₂SO₄ for 5 hr at 900°C in 0.1% SO₂-76% O₂-N₂. Total salt concentration = 1g.

Fig. 6 for a Ni-15 Cr alloy and in Fig. 9 for a Ni-50 Cr alloy.

Nickel-aluminum alloys.—A series of crucible experiments was carried out with Ni-Al alloy specimens, of composition 5-30 w/o Al, which were partially immersed in 1g quantities of Na_2SO_4 and 1 m/o $\text{PbO-Na}_2\text{SO}_4$ salt mixtures and heated at 900°C in the 0.1% SO_2 -76% O_2 - N_2 gas mixture. Under these conditions, alloys with aluminum concentrations in the range 5-20 w/o were vigorously attacked by Na_2SO_4 alone, the corrosion becoming catastrophic at an alloy composition of Ni-13 Al (Ni_{13}Al). Alloy coupons of this composition were reduced to a gray porous mass after exposure to the molten salt for a period of only 2 hr (10). The presence of PbO exerted very little influence on the very high corrosion rates of these alloys. By contrast, an alloy of composition Ni-30 Al (the β -NiAl phase) was very resistant to corrosion by excess Na_2SO_4 because of the formation of a protective Al_2O_3 scale and gained only 0.5 mg/cm^2 during 4 hr contact with molten Na_2SO_4 at 900°C , as shown by the lower curve in Fig. 14. Addition of 1% PbO to the initial salt mixture resulted in a marked increase in the extent of corrosion of this alloy which gained weight in an almost linear manner during the course of the run, as shown by the upper curve of Fig. 14. Although the magnitude of the enhanced corrosion induced by the PbO was much less than with the Ni-Cr alloys, metallographic examination of the corroded specimen (Fig. 15) showed that a protective oxide scale was not formed in the presence of PbO , the thick corrosion layer showing a porous structure of finely dispersed particles identified by electron microprobe analysis as oxides and sulfides. Similar enhanced corrosion rates and morphology were found with a salt mixture of

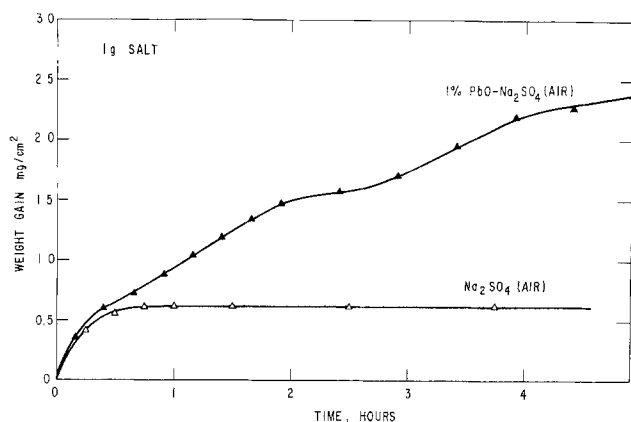


Fig. 14. Effect of 1 m/o PbO on the Na_2SO_4 -induced corrosion of Ni-30 Al at 900°C . Weight changes vs. time in air.

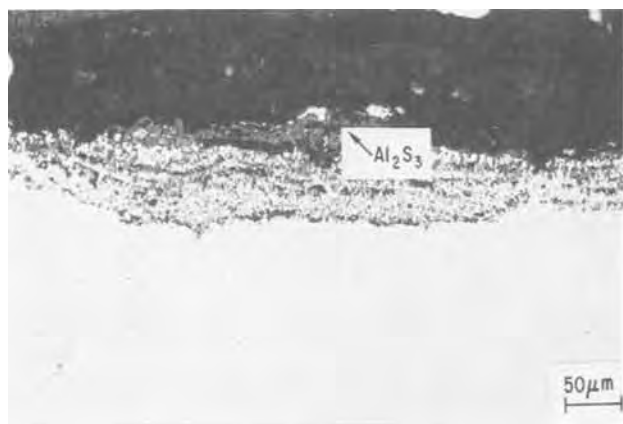


Fig. 15. Section of Ni-30 Al coupon after 6 hr exposure to 1 m/o $\text{PbO-Na}_2\text{SO}_4$ in air at 900°C . Total salt concentration = 1g.

composition 1 m/o $\text{PbSO}_4\text{-Na}_2\text{SO}_4$. An experiment in which a coupon of Ni-30 Al was immersed in 1g of powdered PbSO_4 and heated in the $\text{SO}_2\text{-O}_2\text{-N}_2$ mixture for 5 hr at 900°C resulted in localized attack of the alloy coupon at points of contact with the salt particles. Thick porous oxides were formed in these regions, as shown in Fig. 16, in which networks of oxide particles could be identified.

Discussion

As far as oxidation behavior is concerned, the alloys selected for the present study can be broadly classified as belonging to the following groups: (a) NiO formers (e.g., pure Ni), (b) Cr_2O_3 formers (e.g., Ni-50 Cr), (c) Al_2O_3 formers (e.g., Ni-30 Al), and (d) mixed oxide formers (e.g., Ni-15 Cr, Ni-5 Al). Unlike the first three classes of alloys where only one type of oxide is observed at steady state, the mixed oxide forming alloys may exhibit a complex, multiphase external scale plus extensive internal oxidation. For example, depending on temperature and time of oxidation and grain size, Ni-15 Cr can form a duplex NiO scale with a Cr_2O_3 subscale, a scale composed entirely of Cr_2O_3 only, or a scale containing islands of Cr_2O_3 or spinel surrounded by NiO (11-14).

Since the selected alloys depend mainly on NiO, Cr_2O_3 , or Al_2O_3 for protection in salt-free oxidizing environments, an understanding of the thermodynamic reactivity of these oxides to salt environments becomes essential in interpreting the salt-induced hot corrosion behavior of these alloys. Thermochemical stability diagrams (1, 15-18) are very helpful in identifying and predicting the products formed in reactions involving gases and condensed phases. Reactions likely to occur between Na_2SO_4 and oxide scales are, therefore, best discussed in terms of isothermal Na-S-O-M ($M = \text{Ni, Cr, or Al}$) stability diagrams (16) (Fig. 17a-d²). The solid lines in these diagrams outline the stability limits of individual condensed phases and represent equilibria between two coexisting compounds at unit activities and the gas phase. The shaded regions outline the stability limits of individual Na_2SO_4 /metal oxide reaction products, e.g., NaNiO_2 , Na_2CrO_4 , and NaAlO_2 .

It should be emphasized that the phase boundaries shown in Fig. 17a-d were calculated assuming unit activity for all condensed phases and neglecting mutual solubility among them. In reality, however, all these compounds exist over a range of stoichiometry and show finite mutual solubilities. Thus, for example, Na_2SO_4 has a finite Na_2O activity that is determined by the experimental variables, i.e., temperature, pressure, and oxygen and sulfur potentials in the gas phase.

Point A in Fig. 17 refers to the gas phase composition utilized in most of our experiments, viz., 0.1% SO_2 -76% O_2 - N_2 . Calculations by Spacil (16) indicate that this composition closely simulates, at least as far

² Note that the diagrams shown in Fig. 17 are for 1200°K whereas our experiments were done at 1173°K (900°C). This temperature difference does not affect our discussions to any significant extent.



Fig. 16. Section of Ni-30 Al coupon after 5 hr immersion in 1g PbSO_4 at 900°C in 0.1% SO_2 -76% O_2 - N_2 atmosphere.

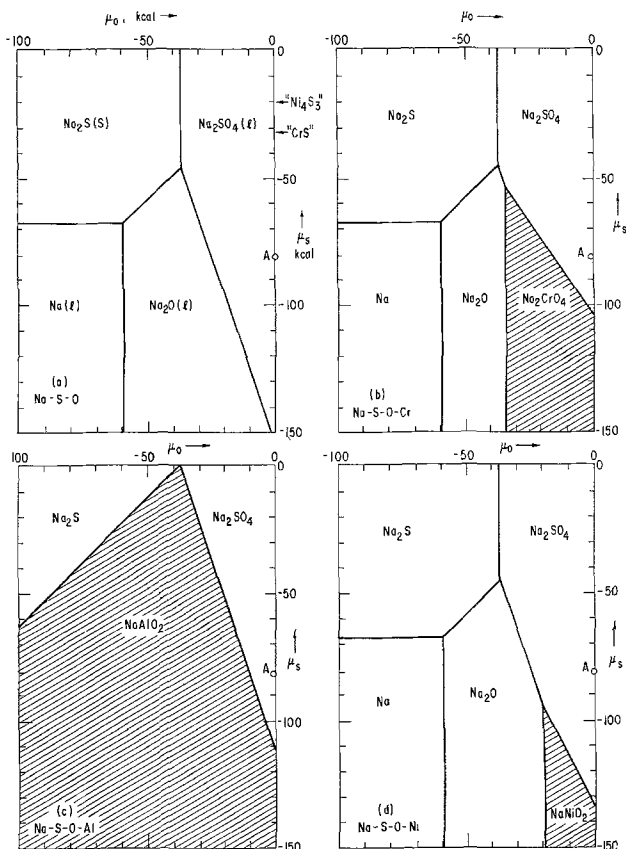
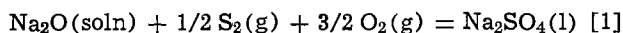


Fig. 17. Stability diagrams for (a) Na-S-O, (b) Na-S-O-Cr, (c) Na-S-O-Al, and (d) Na-S-O-Ni systems at 1200°K.

as oxygen and sulfur potentials are concerned, the nominal conditions prevailing in the first stage of a gas turbine operating at an average pressure of 5 atm with typical air/fuel ratios. The Na_2O activity in a Na_2SO_4 melt equilibrated in this environment can be calculated as follows



$$K_1 = \frac{a(\text{Na}_2\text{SO}_4)}{a(\text{Na}_2\text{O}) P_{\text{S}_2}^{1/2} \cdot P_{\text{O}_2}^{3/2}} = 1/[a(\text{Na}_2\text{O}) \cdot P_{\text{S}_2}^{1/2} P_{\text{O}_2}^{3/2}]$$

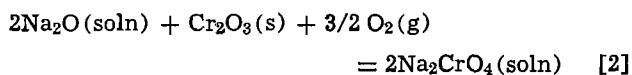
$$\Delta G^\circ_1 = -RT \ln K_1$$

$$= RT [\ln a(\text{Na}_2\text{O}) + \ln P_{\text{S}_2}^{1/2} + 3 \ln P_{\text{O}_2}^{1/2}]$$

$$= RT \ln a(\text{Na}_2\text{O}) + \mu_s + 3\mu_o$$

$$\ln a(\text{Na}_2\text{O}) = [\Delta G^\circ_1 - \mu_s - 3\mu_o]/(RT)$$

For 1200°K and $\mu_s = -81.4$ kcal/mole, $\mu_o = -0.33$ kcal/mole (point A in Fig. 17), $\Delta G^\circ_1 = -155.5$ kcal/mole, and $a(\text{Na}_2\text{O}) = 4.8 \times 10^{-14}$. The "reactivity" of such a melt to NiO, Cr_2O_3 , and Al_2O_3 scales can be estimated from considerations of the following type



$$K_2 = \frac{a^2(\text{Na}_2\text{CrO}_4)}{a(\text{Cr}_2\text{O}_3) \cdot a^2(\text{Na}_2\text{O}) \cdot P_{\text{O}_2}^{3/2}}$$

$$= \frac{a^2(\text{Na}_2\text{CrO}_4)}{a^2(\text{Na}_2\text{O}) \cdot P_{\text{O}_2}^{3/2}}$$

$$\ln a(\text{Na}_2\text{CrO}_4)$$

$$= [2RT \ln a(\text{Na}_2\text{O}) + 3\mu_o - \Delta G^\circ_2]/(2RT)$$

$$a(\text{Na}_2\text{CrO}_4) = 9.7 \times 10^{-5}$$

Results of similar calculations for Al_2O_3 and NiO are summarized in Table II.

Table II. Expected activity of Na-M-O reaction products, i , dissolved in Na_2SO_4 equilibrated with a 0.1% SO_2 -76% O_2 -balance N_2 atmosphere at 1200°K ($\mu_s = -81.4$ kcal, $\mu_o = 0.33$ kcal)

Oxide	ΔG° (a)	i	a_i	% i (b)
Cr_2O_3	-103,600	Na_2CrO_4	9.7×10^{-5}	0.0097
Al_2O_3	-42,800	NaAlO_2	1.8×10^{-3}	0.18
NiO	-19,900	NaNiO_2	1.3×10^{-5}	0.0013

(a) Refers to net ΔG° for dissolution reactions similar to reaction [2].

(b) Assuming % $i = 100 N_i \approx 100 a_i$.

It is obvious from Table II that among the oxides considered, only Al_2O_3 may be complexed to an appreciable extent by Na_2SO_4 ; Cr_2O_3 and NiO are expected to dissolve in Na_2SO_4 only to limited extents. Some caution must be exercised, however, in directly extending this conclusion about the relative thermodynamic reactivities of these oxides to the actual corrosion behavior of the alloys. The above analysis does not take into account kinetic, morphological, and other nonthermodynamic features of the corrosion phenomenon, and allows calculation of upper limits of activity provided all other factors are favorable. Sometimes the kinetics are slow, as in the case of Na_2SO_4 attack of Ni-30 Al (Fig. 14), and the actual corrosion rate is less than that expected from thermodynamic reasonings alone. In some cases, the morphology of the oxide is such that a number of side processes may occur and confuse the over-all picture. Thus, the scale forming on Ni, for example, is not very dense and cannot effectively isolate the alloy from the salt. The extent of corrosion as measured by weight change is consequently quite high (Fig. 1) although NiO is relatively inert under the experimental condition employed. Considerations of oxide stability in Na_2SO_4 , therefore, may play an important role in understanding the corrosion behavior of an alloy but must be supplemented by kinetic and morphological information on the system. Before proceeding to a detailed discussion of corrosion features of the various alloys, an attempt will be made to compare the corrosive capabilities of PbSO_4 as well as 1 m/o $\text{PbO-Na}_2\text{SO}_4$ following the thermodynamic framework presented earlier.

Figure 18 is a composite diagram showing the stability limits of relevant compounds in the Pb-S-O system at 1200°K as well as the products likely to be formed in presence of Cr_2O_3 and Al_2O_3 . Considerable controversy exists in the literature on the thermochemistry of the Pb-S-O system (19-21). Figure 18 is based on the data that are in the authors' opinion, most acceptable. These are listed in Table III. Thermodynamic data for PbCrO_4 are available (22) but the same cannot be said for $\text{PbO} \cdot \text{Al}_2\text{O}_3$ (23). In view of what is known about double oxides like $\text{PbO} \cdot \text{WO}_3$, $\text{PbO} \cdot \text{MoO}_3$,

Table III. Thermochemical data used in the present investigation (a)

Compound	State	ΔG° (1200°K), cal
Na_2O	l	-58,100
Na_2S	l	-67,400
Na_2SO_4	l	-213,600
Al_2O_3	s	-308,800
Cr_2O_3	s	-197,200
NiO	s	-32,000
NaAlO_2	l	-204,900
Na_2CrO_4	l	-208,500
NaNiO_2	l	-71,000
PbO	l	-24,400
PbS	s	-15,300
PbSO_4	s	-109,200
$\text{PbSO}_4 \cdot \text{PbO}$	s	-139,300
$\text{PbSO}_4 \cdot 2\text{PbO}$	s	-165,900
$\text{PbO} \cdot \text{Al}_2\text{O}_3$	s	$\approx (-343,000)$
PbCrO_4	l	-138,200
SO_2	g	-65,600

(a) Reference states: Na(g), S_2 (g), O_2 (g), Al(l), Cr(s), Ni(s), and Pb(l) at 1200°K.

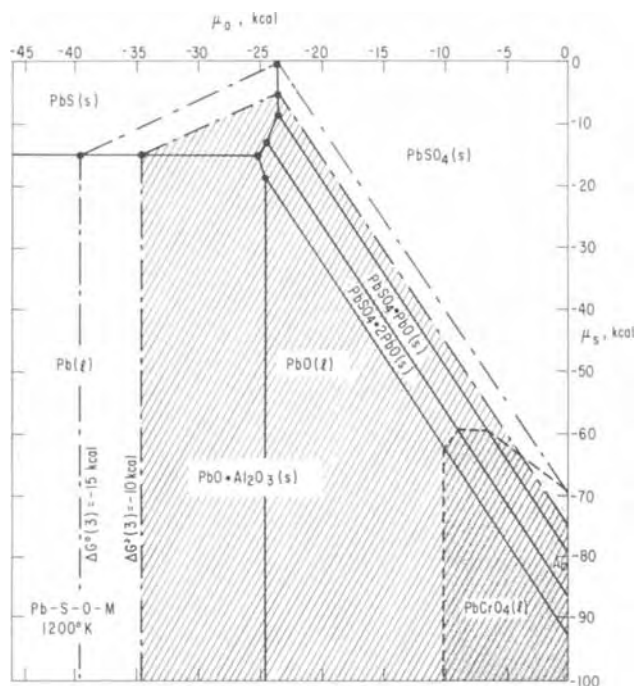
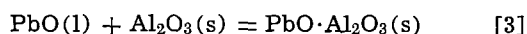


Fig. 18. Stability diagram for Pb-S-O-M system showing the regions of PbCrO_4 and $\text{PbO} \cdot \text{Al}_2\text{O}_3$ stability. Effect of assuming different ΔG° values for the reaction $\text{PbO} + \text{Al}_2\text{O}_3 = \text{PbO} \cdot \text{Al}_2\text{O}_3$ is indicated by dash-dot lines.

and the numerous spinels that form exclusively through condensed phase reactions, it is unlikely that ΔG° for the reaction



will be more negative than -10 kcal. The boundaries of the $\text{PbO} \cdot \text{Al}_2\text{O}_3$ stability region in Fig. 18 were calculated using the reasonable value of ΔG° ($\text{PbO} \cdot \text{Al}_2\text{O}_3$) of -343 kcal. Figure 18 also shows how the stability region for $\text{PbO} \cdot \text{Al}_2\text{O}_3$ would look if a value of -15 kcal were chosen for ΔG°_3 , i.e., -348 kcal for ΔG° ($\text{PbO} \cdot \text{Al}_2\text{O}_3$). It is clear that in going from $\Delta G^\circ_3 = -10$ to -15 kcal, only the over-all size of the stability region has increased; no major changes have occurred in the features of the diagram.

As no Pb-Ni-O compound apparently exists, the reactivity of NiO to PbSO_4 or PbO cannot be discussed in terms of a complexing capability of the lead salt. The behavior of NiO formers in the presence of lead salts can nevertheless be rationalized if all the chemical and physical processes occurring in the vicinity of the alloy surface are taken into consideration. Discussion of actual corrosion processes for the individual alloys will appear later in this section.

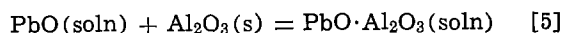
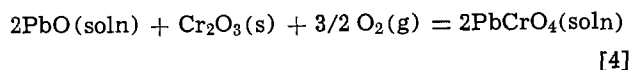
As before, point A on the stability diagram of the Pb-S-O-M system (Fig. 18) indicates the composition of the SO_2 - O_2 - N_2 gas phase used in the present experiments. The Pb-S-O phase that is stable in this environment is of the type $\text{PbSO}_4 \cdot n\text{PbO}$ (most likely $\text{PbSO}_4 \cdot \text{PbO}$). In other words, irrespective of whether PbO or PbSO_4 is used at the beginning of an experiment, the phase likely to be found at equilibrium is Pb-oxysulfate. It is obvious from Fig. 18 that both Cr_2O_3 and Al_2O_3 are unstable in the presence of $\text{PbSO}_4 \cdot n\text{PbO}$ and will react to form PbCrO_4 and $\text{PbO} \cdot \text{Al}_2\text{O}_3$, respectively. That PbCrO_4 is the only reaction product that is liquid under these conditions should be noted at this point. Since formation of liquid phases is usually detrimental to the corrosion resistance of an alloy, Cr_2O_3 formers are more likely to be attacked by a PbSO_4/PbO environment than Al_2O_3 formers.

Since the presence of a pure PbSO_4/PbO type condensate in actual turbine practice is ruled out, the be-

havior of the protective oxides in a Na_2SO_4 melt containing minor amounts of Pb compounds must be considered. Spacil (4), has carried out a preliminary thermochemical analysis of the most likely reactions in a turbine burning Pb-contaminated fuels, and has concluded that the combined PbSO_4 plus PbO content in a typical Na_2SO_4 -base condensate is not likely to exceed 1 m/o. Preliminary experiments showed that 1% PbO- Na_2SO_4 melt was more corrosive than 1% PbSO_4 - Na_2SO_4 . All subsequent work involved 1% PbO- Na_2SO_4 as the corrosive medium. It is believed that the results obtained provide an assessment of the effects of Pb contamination on hot corrosion that is somewhat over-pessimistic but nevertheless realistic.

A quantitative estimation of the reactivity of Cr_2O_3 and Al_2O_3 to the PbO- Na_2SO_4 melt is a rather difficult task. The system, in either case, contains as many as five components (Na, S, O, Pb, M) and involves multi-phase equilibria. Calculation of activities of individual reactive species in the melt therefore becomes a formidable problem. A simple approach may nevertheless provide qualitative information on the effect of PbO contamination on the complexing of protective scales.

Addition of 1% PbO to Na_2SO_4 is likely to produce a homogeneous melt free from second phases. The presence of PbO may or may not affect the activity of Na_2O in the melt; in view of the fact that no Na-Pb-O compound is known, it is unlikely that PbO will substantially affect the 10^{-14} value of $a(\text{Na}_2\text{O})$ in the melt. The initial activity of PbO may be approximately equated to the concentration of PbO on the melt; i.e., initial $a(\text{PbO}) \approx N(\text{PbO}) \approx 10^{-2}$. Although such an assumption is obviously speculative, as will be shown later, the qualitative conclusions to be derived here would remain unchanged even if $a(\text{PbO})$ were as low as 10^{-4} , i.e., even if substantial Na-Pb-O-S interactions took place. In any event, $a(\text{PbO}) \gg a(\text{Na}_2\text{O})$ and PbO is expected to be the most corrosive species in the melt. Exposure of Cr_2O_3 and Al_2O_3 to the PbO- Na_2SO_4 melt should then promote the following reactions



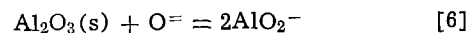
For these reactions, the activities of the complex compounds are related to $a(\text{PbO})$ through the following relations (valid for 1200°K)

$$a(\text{PbCrO}_4) = (587) \cdot a(\text{PbO})$$

$$a(\text{PbO} \cdot \text{Al}_2\text{O}_3) = (66) \cdot a(\text{PbO})$$

These relationships over a broad activity range are graphically illustrated in Fig. 19. It is obvious from this figure that even for $a(\text{PbO})$ in the range of 10^{-4} - 10^{-5} , $a(\text{PbCrO}_4)$ and $a(\text{PbO} \cdot \text{Al}_2\text{O}_3)$ would reach values as high as 10^{-2} . In pure Na_2SO_4 , on the other hand, the equilibrium activities of Na-chromate and Na-aluminate are only about 10^{-5} and 10^{-3} , respectively (Table II). The 1% PbO- Na_2SO_4 melt is, therefore, expected to complex Cr_2O_3 and Al_2O_3 to a greater extent than Na_2SO_4 alone.³

The above conclusion could also have been reached from an analysis of the type presented by Goebel, Pettit, and Goward (17, 18). In terms of their model, addition of PbO to Na_2SO_4 should increase oxide ion activity, $a(\text{O}^=)$, in the melt. This increase should in turn cause an increased fluxing (i.e., increased aluminate and chromate ion concentrations) of the protective scales



³ Compounds of the type PbCrO_4 -PbO are known to be volatile (24). Rapid volatilization of reaction products may occur for Cr_2O_3 -forming alloys in PbO- Na_2SO_4 melts leading to a further increase in corrosion. Although such vaporization processes might have influenced the observed weight gains in the corrosion experiments, corrections for such losses could not be applied owing to the lack of volatilization data for the complexes involved. In any case this effect will not invalidate the basic conclusions reached in this study.

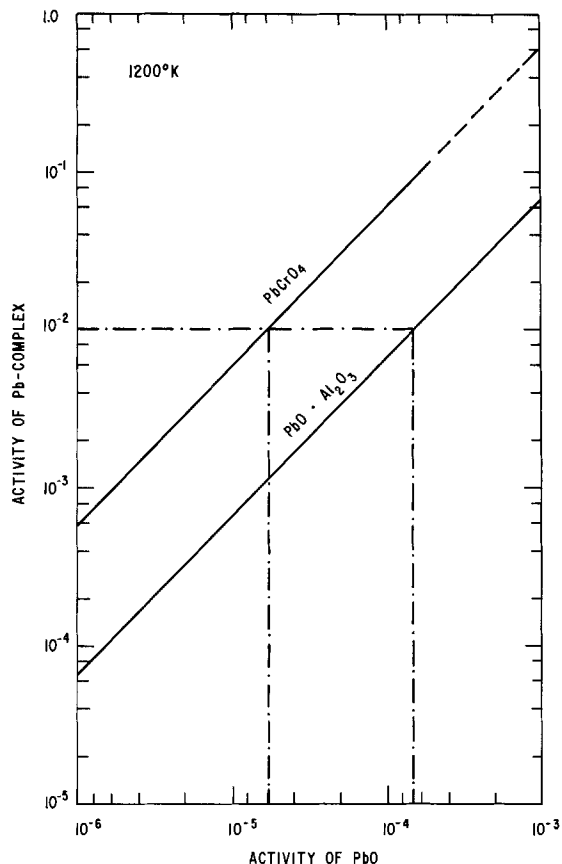
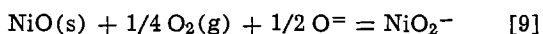


Fig. 19. Equilibrium Pb-chromate and Pb-aluminate activity in Na_2SO_4 -PbO for different $a(\text{PbO})$ values.



The situation in the presence of PbO then roughly corresponds to that referred to by Goebel *et al.* as "accelerated corrosion due to basic fluxing."

Although the model proposed by Goebel and co-workers explains the effect of PbO on the corrosion of Cr_2O_3 and Al_2O_3 , problems appear when NiO reactivity is considered. According to their fluxing model, increased O^- ion activity should lead to increased NiO dissolution through nickelate ion formation

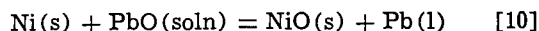


PbO should therefore induce accelerated corrosion of Ni. The present experiments (Fig. 1) indicate, however, that PbO causes a dramatic reduction in the hot corrosion of Ni. The complexing model, on the other hand, does not predict what the effect of PbO would be on corrosion of Ni. This dilemma demonstrates clearly that processes in addition to simple fluxing or complexing may become important in particular alloy systems. The physical and chemical processes which may occur simultaneously or concurrently in the immediate vicinity of the individual alloy surfaces will now be examined in some detail.

Nickel.—In view of the work done by Goebel and Pettit (17) and the kinetic and morphological results obtained during the present work, the important stages involved in the hot corrosion of Ni in pure Na_2SO_4 can be said to have been identified. When a specimen embedded in Na_2SO_4 is heated to the experimental temperature of 900°C , the salt melts almost instantaneously and screens the specimen from direct contact with oxygen in the gas phase. Consequently, the metal oxidizes by consuming oxygen from the melt in its immediate vicinity. This locally raises the sulfur potential to such high levels that liquid Ni-S phases begin to form at (or immediately underneath) the

metal surface. Occurrence of these two concurrent reactions and formation of a solid-liquid phase mixture results in the development of a porous nonprotective scale that does not prevent further Na_2SO_4 infiltration. In the presence of excess Na_2SO_4 (as in our experiments but not in Pettit's), the sequence of oxidation-sulfidation can repeat many times and accelerate the corrosion process. Figure 20(a) schematically outlines this model.

It seems likely that the presence of 1% PbO in Na_2SO_4 alters the corrosion mechanism for Ni in the following way. Following melting of the salt mixture and the formation of homogeneous solution, Ni oxidizes by reducing PbO



A large thermodynamic driving force exists for this reaction

$$\begin{aligned} \Delta G &= \Delta G^\circ + RT \ln a(\text{PbO}) \\ &= -7600 + RT \ln a(\text{PbO}) \\ &< -7600 \text{ cal} \end{aligned}$$

Since the oxygen needed for NiO formation is obtained from PbO in the melt, the stoichiometry of Na_2SO_4 (and the sulfur potential in it) remains virtually unchanged, and no sulfides can form. In the absence of sulfide formation, dense protective NiO scale can develop over the metal. The scale formed over Ni exposed to the 1% PbO- Na_2SO_4 melt (Fig. 2) is identical in appearance to the scale observed in ordinary oxidation in a salt-free environment [Fig. 3a in Ref. (17)]. Figure 20(b) schematically summarizes the processes responsible for the development of dense sulfide-free NiO scale on Ni in the 1% PbO- Na_2SO_4 melt.

Nickel-chromium alloys.—Corrosion processes occurring in Ni-Cr alloys are more complex than in Ni because the nature of the scale on these alloys depends on alloy composition, grain size, the surface condition, and time and temperature of oxidation (11-14). All Ni-Cr alloys pass through an initial transition stage during which nuclei of NiO and Cr_2O_3 form on the surface, the amounts of each mainly depending on

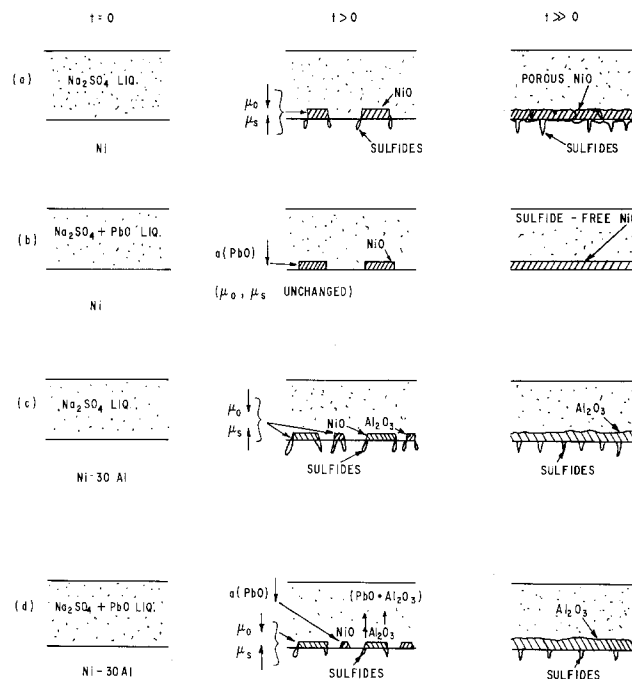


Fig. 20. Schematic summary of proposed reactions responsible for development of steady-state corrosion morphologies in (a) Ni in Na_2SO_4 , (b) Ni in $\text{Na}_2\text{SO}_4 + 1\%$ PbO, (c) Ni-30 Al in Na_2SO_4 , and (d) Ni-30 Al in $\text{Na}_2\text{SO}_4 + 1\%$ PbO.

the alloy composition (12). For alloys such as Ni-5 Cr, NiO rapidly covers the surface isolating and encapsulating the initially formed Cr_2O_3 particles. Some internal oxidation of Cr may also occur. Ni-Cr alloys containing 20% or more Cr, on the other hand, form Cr_2O_3 and NiO initially, the former process is more rapid however, so that the steady-state scale is essentially pure Cr_2O_3 . For alloys in the 10-15% Cr range, experimental and microstructural variables determine whether a duplex NiO scale will form over a Cr_2O_3 subscale, or a Cr_2O_3 scale will cover the entire surface, or an intermediate, mixed mode of oxidation will ensue (11, 12, 14). Since earlier discussion has established that Cr_2O_3 is susceptible to complexing by PbO, the extent of corrosion in Ni-Cr alloys is expected to be a function of Cr-concentration in the alloy. Figure 11 shows that indeed such a functional relationship exists. The presence of a peak in the initial corrosion rate at about 10-15% Cr indicates that simultaneous NiO and Cr_2O_3 formation on an alloy (i.e., a mixed mode of oxidation) makes it particularly vulnerable to PbO attack. It is interesting to note that attack by Na_2SO_4 alone monotonically decreases with increasing Cr-content and does not show any peak throughout the entire composition range.

Figure 21(a) schematically outlines the important stages in the morphological development of a reasonably dense NiO scale over Ni-5 Cr in pure Na_2SO_4 . Corrosion processes occurring here are not very different from those occurring in pure Ni [Fig. 20(a)] except that solid Cr-sulfides form in Ni-5 Cr instead of liquid Ni-sulfides. Prevention of liquid sulfide formation helps in forming a dense scale over Ni-5 Cr and in reducing the corrosion rate in Na_2SO_4 (Fig. 11).

Figure 21(b) schematically summarizes the processes occurring on Ni-5 Cr in 1% PbO- Na_2SO_4 . The processes are similar to those occurring on Ni-5 Cr in Na_2SO_4 alone except that the initially formed Cr_2O_3 is complexed away by PbO to form liquid (and possibly volatile) (24) PbCrO_4 . Formation of liquid or volatile reaction products tends to make the NiO scale developing on Ni-5 Cr porous, at least until no more Cr_2O_3 forms. These factors together are responsible for increasing the initial PbO- Na_2SO_4 corrosion rate of Ni when 5% Cr is added to it.

Unlike Ni-5 Cr where NiO is the sole constituent of the steady-state scale, both NiO and Cr_2O_3 may persist

at steady state on Ni-Cr alloys containing 10-15% Cr. NiO is generally seen to cover grains and forms the matrix, and Cr_2O_3 is found at sites where grain boundaries meet the external surface (11). Often Cr_2O_3 islands link up to form chainlike paths in the NiO matrix (11-13). Sometimes NiO and Cr_2O_3 react to form spinels within the scale, or a Cr_2O_3 subscale develops under a duplex NiO scale (13, 14). In any event, the presence of large amounts of Cr_2O_3 on Ni-(10-15%) Cr alloys makes them susceptible to PbO complexing for longer periods than with Ni-5 Cr. Removal of Cr from the alloy through Cr_2O_3 complexing as well as Cr-sulfide formation cause the Cr concentration at the scale/alloy interface to drop gradually. Ni-15 Cr and Ni-10 Cr, however, cannot sustain severe Cr depletion without becoming a virtual NiO former. After a finite time, therefore, these alloys begin to behave like Ni-5 Cr. But the scale developing at this late stage is not very protective because of all the surface irregularities already introduced by processes such as sulfidation and complexing. Figure 21(c) shows schematically how the scale may develop on Ni-15 Cr in 1% PbO- Na_2SO_4 . Ni-15 Cr in pure Na_2SO_4 will show a dense thin protective layer of Cr_2O_3 plus some internal sulfide particles because Cr_2O_3 does not dissolve appreciably in Pb-free Na_2SO_4 (Table II).

Ni-50 Cr withstands Na_2SO_4 attack very well (Fig. 8) because it is a strong Cr_2O_3 former. For the same reason, however, it is expected to be susceptible to attack by the PbO- Na_2SO_4 melt. However, Cr_2O_3 is the sole constituent of the scale in this case and the protective scale develops quite rapidly. Subsequent complexing of Cr_2O_3 must then proceed solely through dissolution at the scale/melt interface. This is quite unlike the irregular dissolution behavior occurring in the NiO/ Cr_2O_3 scale over Ni-15 Cr where porous scales are easy to form. Thus although Ni-50 Cr undergoes accelerated attack in 1% PbO- Na_2SO_4 in comparison to Na_2SO_4 alone (Fig. 11), the attack is not as severe as for Ni-15 Cr.

As discussed in the case of Ni-15 Cr, removal of Cr through sulfide and complex formation reduces the Cr-concentration at the scale/alloy interface in Ni-50 Cr. This appears as a band free from α -Cr particles in Fig. 9 and 10. In the case of Ni-50 Cr, however, the alloy is so rich in Cr initially that the Cr depletion cannot reduce it to a NiO former. In Na_2SO_4 alone, the processes are identical to those shown in Fig. 21(d) for Ni-50 Cr in 1% PbO- Na_2SO_4 , except that no PbCrO_4 forms in pure Na_2SO_4 and the corrosion is lower in magnitude.

An examination of the kinetic curve for Ni-50 Cr corrosion in 1% PbO- Na_2SO_4 (Fig. 8) reveals that the alloy undergoes a relatively rapid corrosion initially, but the corrosion rate becomes negligible within a short time. This suggests that the melt becomes fully complexed and loses its potency quite quickly. This is not surprising in view of the facts that the alloy is very rich in Cr and the melt initially contains only 1% PbO. The series of experiments with 5 and 10% PbO in Na_2SO_4 (Fig. 8) showed that with larger amounts of PbO added to the melt, longer times were necessary for melt saturation and assumption of "steady-state" corrosion. In fact, for the 10% PbO melt, steady state was not reached during the course of the 4 hr experiment. That the amount of Cr depletion and over-all corrosion of the alloy also increases with increasing PbO content of the melt is clear from Fig. 9 and 10.

Nickel-aluminum alloys.—Ni-30 (β -NiAl) is the only Ni-Al alloy studied in depth in the present investigations. Alloys containing lower amounts of Al generally contained the γ -Ni₃Al phase as well and were catastrophically attacked even in pure Na_2SO_4 . Experiments involving these alloys and Na_2SO_4 -PbO melts were, therefore, not attempted.

Figure 14 shows that PbO in the melt increases the hot corrosion of Ni-30 Al but not as significantly as in

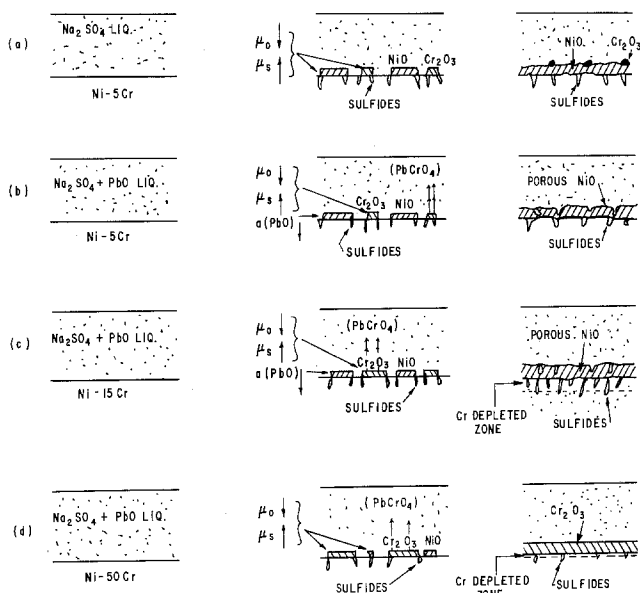
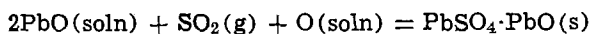


Fig. 21. Schematic summary of proposed reactions responsible for development of steady-state corrosion morphologies in (a) Ni-5 Cr in Na_2SO_4 , (b) Ni-5 Cr in $\text{Na}_2\text{SO}_4 + 1\%$ PbO, (c) Ni-15 Cr in $\text{Na}_2\text{SO}_4 + 1\%$ PbO, and (d) Ni-50 Cr in $\text{Na}_2\text{SO}_4 + 1\%$ PbO.

the case of Ni-Cr alloys (Fig. 5). (Note that the vertical scale in Fig. 14 is expanded by a factor of two from that in Fig. 5.) This observation is in general agreement with the thermochemical analysis presented earlier (Fig. 19). Kinetic factors may also be responsible for the relatively small effect of PbO in increasing corrosion of Ni-30 Al. For example, unlike PbCrO₄ which forms a liquid at 900°C, PbO·Al₂O₃ may first appear as a solid and then dissolve in the melt at this temperature. Processes such as these are likely to place kinetic restriction on a system.

Figure 20(c) and (d) attempt to describe schematically how the corrosion morphology may develop in Ni-30 Al exposed to Na₂SO₄ and 1% PbO-Na₂SO₄, respectively. Ni-30 Al is a strong Al₂O₃ former and the sequence of reactions occurring in Ni-30 Al in PbO-Na₂SO₄ [Fig. 20(d)] is analogous to that occurring in Ni-50 Cr [Fig. 21(d)] except for the obvious difference that Ni-50 Cr forms Cr₂O₃ on the surface. Both Ni-30 Al and Ni-50 Cr are very rich in the protective element, and the scale can continue to reform in both cases despite partial dissolution in the melt.

Before concluding the discussion, some incidental observations made during this study need to be examined briefly. One of these involves the effect of SO₂ in the environment and the other involves the relative complexing abilities of PbSO₄ and PbO. Corrosion experiments in SO₂-O₂-N₂ environments always produced more extensive material degradation (Fig. 1 and 5, for example) than in air. No simple explanation can be offered for this observation. If PbO complexing of oxide scales was the only reaction determining the extent of corrosion, air should have been the more aggressive environment for the equilibrium $\alpha(\text{PbO})$ would be higher under those conditions. Obviously the answer to this apparent contradiction must lie in the side reactions accompanying the complexing processes. One such reaction is the stabilization of PbO to Pb-oxysulfate in presence of SO₂



[11]

This reaction would consume $\underline{\text{O}}$ from the melt, increase the sulfur potential locally, and thereby enhance overall corrosion rates. In air, on the other hand, the extent of PbO stabilization is much less, and the net effect on Na₂SO₄ stoichiometry and over-all corrosion rates, etc., should be minimal. This line of reasoning appears to explain the experimental observation but is admittedly speculative at this stage.

No apparent contradiction arises in comparing experimental observations with thermochemical arguments as far as the relative complexing capabilities of Na₂SO₄-PbO and Na₂SO₄-PbSO₄ melts are concerned. If the thermochemical analysis leading to Fig. 19 were repeated with PbSO₄ replacing PbO in the proper manner, the calculated activities of PbCrO₄ and PbO·Al₂O₃ would be found to be smaller than those already derived (<10⁻³-10⁻²). This relatively low amount of corrosion observed in PbSO₄-Na₂SO₄ is therefore not difficult to understand. Moreover, reactions of type [11] are not expected to be important in the PbSO₄-Na₂SO₂ environment, and less amounts of sulfides are likely to form.

A few experiments were conducted in the course of the present work to determine the reactivity of Ni-Cr and Ni-Al alloys to PbSO₄ alone. Figure 7 shows the kinetics of PbSO₄-induced corrosion of Ni-15 Cr. A comparison with the data in Fig. 5 shows pure PbSO₄ to be more aggressive than pure Na₂SO₄ but less so than PbO-Na₂SO₄ (or PbSO₄-Na₂SO₄). Moreover, the corrosion morphology in pure PbSO₄ is quite irregular and is characterized by random localized attack. These features are probably due to the fact that pure PbSO₄ is solid at the experimental temperature whereas Na₂SO₄ and Na₂SO₄-base mixtures are liquid. As far as Al₂O₃ formers are concerned, the net corrosion in PbSO₄ was somewhat more than in Na₂SO₄, and the

attack was again localized. Figure 16 shows the morphological features of this localized corrosion. It is interesting to note that PbCrO₄ is liquid at 900°C but PbO·Al₂O₃ is solid. This fact may be partially responsible for the fact that Cr₂O₃ formers are generally more susceptible to pure PbSO₄ attack than Al₂O₃ formers.

Conclusions

1. Addition of 1 m/o PbO to the salt melt reduces sharply the rate of corrosion of pure nickel by Na₂SO₄ at 900°C.
2. With Ni-Cr alloys a large increase in the rate of Na₂SO₄ hot corrosion at 900°C results from addition of 1% PbO to the salt melt.
3. This effect, which is due to the formation of PbCrO₄ which is soluble in the molten Na₂SO₄, becomes more significant with increasing Cr content of the alloy and results in catastrophic corrosion rates with alloys containing 10-15% Cr.
4. The Na₂SO₄-induced hot corrosion of Ni-30 Al is also enhanced by the addition of PbO to the salt, probably as a result of the formation of the soluble complex PbO·Al₂O₃, although the effect is less dramatic than with Ni-Cr alloys.
5. PbO is a more deleterious condensate than PbSO₄, although both are likely to form together during turbine operation with lead-contaminated fuels.
6. In general, hot corrosion rates are higher in a simulated turbine environment (0.1% SO₂-76% O₂-N₂) than in air.

Acknowledgments

The authors are indebted to R. E. Hanneman and R. L. McCarron for many useful discussions, and to A. Ritzer and B. Beach for the metallography.

Manuscript submitted Nov. 18, 1974; revised manuscript received Feb. 10, 1975.

Any discussion of this paper will appear in a Discussion Section to be published in the June 1976 JOURNAL. All discussions for the June 1976 Discussion Section should be submitted by Feb. 1, 1976.

Publication costs of this article were partially assisted by General Electric Company.

SYMBOLS

a_i	activity of species i
c	condensed phase
ΔG	free energy of a reaction
ΔG°	standard free energy of a reaction
g	gas
K	equilibrium constant at a given temperature
l	liquid
μ_i	chemical potential of species i
N_i	mole fraction of species i
R	universal gas constant
s	solid
soln	solution
T	temperature

REFERENCES

1. E. L. Simons, G. V. Browning, and H. A. Liebhaftsky, *Corrosion*, **11**, 505t (1955); J. Stringer, Battelle Memorial Institute, MCIC Report 72-08 (1972).
2. P. I. Fontaine and E. G. Richards, in "Hot Corrosion Problems Associated with Gas Turbines," ASTM Pub. STP 421, p. 246 (1967).
3. P. A. Bergman, in "High Temperature Metallic Corrosion of Sulfur and Its Compounds," Z. A. Foroulis, Editor, p. 224, The Electrochemical Society Softbound Symposium Series, New York (1970).
4. H. S. Spacil, General Electric Company, Unpublished results (1973).
5. P. A. Bergman, General Electric Company, Unpublished observations (1973).
6. R. W. Ross, Jr. and R. C. Scarberry, *Corrosion*, **30**, 211 (1974).
7. J. W. Sjöberg and A. I. Rozmanith, *Mater. Prot. Perf.*, **10** (9), 31 (1971).

8. D. W. McKee and G. Romeo, *Met. Trans.*, **5**, 1127 (1974).
9. J. A. Goebel, E. J. Felten, and F. S. Pettit, Symposium on "Corrosion Problems in Energy Conversion and Generation," C. S. Tedmon, Editor, p. 102, The Electrochemical Society Softbound Symposium Series, Princeton, N. J. (1974).
10. G. Romeo and D. W. McKee, *This Journal*, **122**, 188 (1975).
11. C. S. Giggins and F. S. Pettit, *Trans. TMS-AIME*, **245**, 2495 (1969); **245**, 2509 (1969).
12. C. S. Giggins and F. S. Pettit, *This Journal*, **118**, 1782 (1971).
13. G. C. Wood and T. Hodgkiess, *ibid.*, **113**, 319 (1966).
14. D. Chatterji, H. C. Graham, and H. H. Davis, Paper No. 81-B-73 presented at 75th Annual Meeting of American Ceramic Society, Cincinnati, April 1973.
15. E. A. Gulbransen and S. A. Jansson, in "High Temperature Metallic Corrosion of Sulfur and Its Compounds," Z. A. Foroulis, Editor, p. 3, The Electrochemical Society Softbound Symposium Series, New York (1970).
16. H. S. Spacil, General Electric Company, Unpublished results (1972).
17. J. A. Goebel and F. S. Pettit, *Met. Trans.*, **1**, 1943 (1970).
18. J. A. Goebel, F. S. Pettit, and G. W. Goward, *ibid.*, **4**, 261 (1973).
19. H. H. Kellogg and S. K. Basu, *Trans. TMS-AIME*, **218**, 70 (1960).
20. E. Rosen and L. Wittung, *Acta Chem. Scand.*, **26**, 2427 (1972).
21. L. Wittung, *Scand. J. Met.*, **1**, 91 (1972).
22. M. Kh. Karapet'yants and M. L. Karapat'yants, "Thermodynamic Constants of Inorganic and Organic Compounds," Ann Arbor-Humphrey Science Publishers, Ann Arbor, Michigan (1970).
23. E. M. Levin, C. R. Robbins, and H. W. McMurdie, "Phase Diagrams for Ceramists," The American Ceramic Society, Columbus, Ohio (1964).
24. R. C. DeVries and J. F. Fleischer, *J. Am. Ceram. Soc.*, **49**, 782 (1970).

Efficiency of Dy³⁺-Activated Phosphors

J. L. Sommerdijk and A. Bril

Philips Research Laboratories, Eindhoven, Netherlands

ABSTRACT

The quantum efficiency of Dy³⁺-activated phosphors is reasonably high in lattices where a low activator concentration (< 1%) is already sufficient for effective energy transfer from the lattice to the activator ions. When more activator is needed for effective energy transfer, the quantum efficiency is limited due to concentration quenching of the Dy³⁺ emission. The results are compared with those of corresponding Eu³⁺- and Tb³⁺-activated phosphors.

The luminescence of Dy³⁺ is well known (1-9). Emission spectra of Dy³⁺ usually consist of narrow lines in the regions 470-500 nm and 570-600 nm together with some weak lines at longer wavelengths. Due to the location of the strong lines it is possible to get a near-white emission if the intensities of these lines in the two regions are of the same order. Its luminescence has therefore become of some interest in view of its possible application in low- and high-pressure mercury vapor discharge lamps (6, 7, 9). The Dy³⁺ ions cannot be excited effectively by these discharges which emit mainly at $\lambda > 250$ nm (corresponding to the wave number region $\kappa < 40,000$ cm⁻¹). The lowest charge transfer level of Dy³⁺ in oxides is situated at energies corresponding to $\kappa > 50,000$ cm⁻¹ (10) and the same applies to the lowest 5d level of Dy³⁺ (11). Excitation of Dy³⁺ can therefore occur only by 4f-4f transitions. These have a relatively low oscillator strength ($\approx 10^{-6}$) since they are in first order forbidden by the parity selection rule (12). The radiation of mercury discharges is therefore only weakly absorbed by the Dy³⁺ ions.

The problem of low absorption can be circumvented sometimes by using Dy³⁺-activated phosphors in which the lattice strongly absorbs the mercury radiation and can transfer the absorbed energy to the Dy³⁺ ions. Some examples of such phosphors reported in the literature are: YVO₄-Dy (2, 5, 7-9), Y₂WO₆-Dy (4), and Ga₂O₃-Dy (6). To our knowledge, the efficiency of these and other Dy³⁺-activated phosphors has not yet been systematically studied, as has been done, for example, for Eu³⁺- and Tb³⁺-activated phosphors (13, 14). It seemed, therefore, interesting to determine the quantum efficiencies of a number of Dy³⁺-activated phosphors. In this paper we discuss the efficiencies of

the lattice emission and that of the Dy³⁺ emission for various lattices and as a function of the Dy³⁺ concentration. We will compare our results with those reported in the literature (2, 4, 13-17) for corresponding Eu³⁺- and Tb³⁺-activated phosphors.

Experimental

Samples were prepared by the usual techniques as described, for example, in Ref. (2, 4, 13-17). Reaction products were checked by analysis of x-ray powder diagrams (Cu K α radiation). Quantum efficiencies of the Dy³⁺-activated phosphors were measured by comparison with the standard phosphors issued by the National Bureau of Standards as described in Ref. (18, 19). As excitation source, a high-pressure mercury discharge lamp with a Cl₂/NiSO₄/UG5 filter combination was used, emitting mainly in the 250-270 nm region. In view of the dependence on the sample preparation (the output of the samples was not optimized) and because of the limited accuracy of the optical measurements, only approximate values are given for the quantum efficiencies. All measurements were performed at room temperature.

Results and Discussion

Table I contains the results for Dy³⁺-activated YNbO₄, LaNbO₄, and CeMgAl₁₁O₁₉. In all cases the quantum efficiency of the Dy³⁺ emission is limited, both for low and high Dy³⁺ concentrations. This can be explained in the following way. For these phosphors, a large amount of Dy³⁺ is needed in order to have efficient energy transfer from the lattice to the Dy³⁺ ions. It is known that energy transfer through these lattices is not efficient (16, 20). For the niobates this is due to the poor overlap between the NbO₄³⁻ emission and absorption bands (20). For CeMgAl₁₁O₁₉ the overlap between the Ce³⁺ emission and absorption

Table I. Quantum efficiencies (*q*) of lattice emission and Dy³⁺ emission under 250-270 nm excitation of Dy³⁺-activated YNbO₄, LaNbO₄, and CeMgAl₁₁O₁₉

Composition	<i>q</i> , %	
	Lattice emission	Dy ³⁺ emission
YNbO ₄	45	—
YNbO ₄ -0.5% Dy	35	10
1.5	30	15
5	20	12
15	10	10
LaNbO ₄	40	—
LaNbO ₄ -0.5% Dy	30	10
1.5	25	15
5	10	15
15	<2	2
CeMgAl ₁₁ O ₁₉	60	—
CeMgAl ₁₁ O ₁₉ -10% Dy	20	10
20	15	15
35	5	10

band is also small (16) and furthermore the shortest Ce³⁺-Ce³⁺ distance is rather large (5.6Å). Since the energy transfer through the lattices is not effective, the transfer from excited lattice centers (NbO₄³⁻, Ce³⁺) to Dy³⁺ ions can occur only directly. The probability of this transfer decreases very strongly with increasing distance (21), so that this transfer in effect is restricted to short distances. This implies that a high Dy³⁺ concentration (> 10%) is needed for complete transfer from lattice to Dy³⁺. The required Dy³⁺ concentration is so high that considerable quenching of the Dy³⁺ emission occurs. This concentration quenching is due to mutual Dy³⁺-Dy³⁺ interactions (22) and starts generally at a concentration of a few atomic per cent. In conclusion, the quantum efficiency is limited at low Dy³⁺ concentrations by the ineffective energy transfer to Dy³⁺ and at high Dy³⁺ concentrations by the concentration quenching of the Dy³⁺ emission.

Table II contains the results for Dy³⁺-activated Y₂WO₆, Lu₂WO₆, CePO₄, and CaWO₄. In these phosphors, the probability of energy transfer through the lattice is somewhat higher than for the phosphors of Table I. This is mainly due to the stronger energy overlap of the lattice absorption and emission bands. In Ref. (23) the transfer probability in Y₂WO₆ has been compared quantitatively with that in YNbO₄. It appeared that the average transfer distance through the lattice is twice as great for the tungstate as for the niobate. This explains why quenching of the lattice emission by Dy³⁺ occurs more effectively (i.e., with less Dy³⁺) in Y₂WO₆ than in YNbO₄. Similar arguments have been used in Ref. (23) to explain the difference between YNbO₄-Eu and Y₂WO₆-Eu. The compound Lu₂WO₆ has the same crystal structure and about the same luminescence properties as Y₂WO₆ (24). The situation of Lu₂WO₆-Dy will therefore resemble that of Y₂WO₆-Dy. Also in CePO₄ energy transfer through the lattice occurs. This can be derived from the concentration quenching of the Ce³⁺ emission

Table II. Values of *q* (cf. Table I) for Dy³⁺-activated Y₂WO₆, Lu₂WO₆, CePO₄, and CaWO₄

Composition	<i>q</i> , %	
	Lattice emission	Dy ³⁺ emission
Y ₂ WO ₆	12	—
Y ₂ WO ₆ -1% Dy	10	15
3	5	20
10	<2	10
Lu ₂ WO ₆	12	—
Lu ₂ WO ₆ -1% Dy	10	15
3	5	15
10	<2	10
CePO ₄	35	—
CePO ₄ -1% Dy	15	15
3	5	10
10	<2	3
CaWO ₄	60	—
CaWO ₄ -1% Dy ^(a)	10	20
3	5	25
10	<2	7

^a Charge compensation with Na⁺ according to 2 Ca²⁺ → Na⁺ + Dy³⁺.

observed for La_{1-x}Ce_xPO₄ (17). This quenching is due to energy transfer from one Ce³⁺ ion to another until an energy sink is reached (17, 21). The efficiency of the Ce³⁺-Ce³⁺ transfer is only moderate, however, since the maximum quantum efficiency of CePO₄ is still 40% (17). This explains why still some 5-10% Dy³⁺ is necessary for complete quenching of the Ce³⁺ emission of CePO₄. Moderate energy transfer through the CaWO₄ lattice has been demonstrated in Ref. (25) where the phosphor CaWO₄-Sm was studied. Similarly, complete quenching of the CaWO₄ emission occurs at a Dy³⁺ concentration of about 5-10%. Since the amount of Dy³⁺ required for complete transfer from the lattice is lower than for the phosphors of Table I, the effect of concentration quenching of the Dy³⁺ emission is less detrimental. As a result somewhat higher quantum efficiencies can be obtained.

Table III contains the results for Dy³⁺-activated Ga₂O₃ and YVO₄. Here a small Dy³⁺ content (< 1%) is already sufficient for effective transfer from the lattice to Dy³⁺. We found that only a little amount of Dy³⁺ can be dissolved into Ga₂O₃. Efforts to dissolve more than 1% Dy³⁺ into Ga₂O₃ were not successful. Instead a second phase occurred which on analysis of the x-ray diffraction diagrams was found to have the composition Dy₃Ga₅O₁₂. This phase had the garnet structure with cubic cell parameter *a* = 12.35Å and it was nonluminescent. In Ref. (6) it was reported that the optimum Dy³⁺ concentration for Ga₂O₃-Dy was 5-10%. In our opinion, the actual Dy³⁺ concentration in the luminescent phase is much lower (< 1%). The x-ray diffraction diagrams of our samples doped with 5-10% Dy³⁺ indicated that nearly all the Dy³⁺ went into the nonluminescent Dy₃Ga₅O₁₂ phase. In spite of the slight solubility of Dy³⁺ in Ga₂O₃, the energy transfer from Ga₂O₃ to Dy³⁺ is nearly complete. This implies that this transfer is very efficient. In YVO₄ effective energy transfer occurs through the lattice (23). As a result the Dy³⁺ centers can be easily reached, cf. Ref. (2, 7), the lattice emission being completely quenched at a Dy³⁺ concentration as low as 0.3%. The required amount of Dy³⁺ is so low that concentration quenching of the Dy³⁺ emission is not yet important. As in other Dy³⁺-activated phosphors, concentration quenching of YVO₄-Dy sets in at about 1% Dy (Table III). By choosing the appropriate Dy³⁺ concentration (< 1%), the efficiency of this type of phosphors is therefore not limited by the effect of concentration quenching, so that reasonably high efficiencies can be obtained.

It is interesting to compare the efficiencies of the Dy³⁺-activated phosphors with those of the corresponding Eu³⁺- and Tb³⁺-activated phosphors. Table IV compares the maximum quantum efficiencies under 250-270 nm excitation of some phosphors. The data for the Eu³⁺- and Tb³⁺-activated phosphors have been taken partly from the literature (4, 14-17). Usually, lattices giving strong rare earth emissions when activated with Eu³⁺, do not do so when activated with Tb³⁺. Examples of this are YNbO₄, Y₂WO₆, and YVO₄ (4, 14, 15). This has been ascribed to formation of Tb⁴⁺-containing complexes, which is favored in these lattices and which causes radiationless relaxation to the ground state before Tb³⁺ emission can take place

Table III. Values of *q* (cf. Table I) for Dy³⁺-activated Ga₂O₃ and YVO₄

Composition	<i>q</i> , %	
	Lattice emission	Dy ³⁺ emission
Ga ₂ O ₃	40	—
Ga ₂ O ₃ -<1% Dy	4	30
YVO ₄	5	—
YVO ₄ -0.1% Dy	3	40
0.3	1	60
0.5	1	65
1.0	1	65
2	1	60
4	1	50
5	1	40

Table IV. Comparison between the maximum quantum efficiencies (q_m) of the rare earth emission under 250-270 nm excitation of Eu^{3+} -, Tb^{3+} -, and Dy^{3+} -activated lattices

Lattice	q_m , %		
	Eu^{3+} emission	Tb^{3+} emission	Dy^{3+} emission
YNbO_4	30	<5	15
$\text{CeMgAl}_{11}\text{O}_{19}$	<5	65	15
Y_2WO_6	40	<5	20
CePO_4	<5	40	15
Ga_2O_3	<5	<5	30
YVO_4	70	<5	65

(14, 20). Such a quenching process does not occur for the Eu^{3+} -activated phosphors since the fourth ionization potential of Eu is much higher than that of Tb. On the other hand, the compounds $\text{CeMgAl}_{11}\text{O}_{19}$ -Tb and CePO_4 -Tb show strong Tb^{3+} emission (16,17), whereas the Eu^{3+} emission of $\text{CeMgAl}_{11}\text{O}_{19}$ -Eu and CePO_4 -Eu is very weak (16, 17). The low efficiencies of Eu^{3+} -activated Ce^{3+} compounds have been ascribed to formation of Ce^{4+} - Eu^{2+} containing complexes causing radiationless losses instead of Eu^{3+} emission. This type of quenching does not occur for Tb^{3+} , since this ion has no tendency to become divalent.

Let us now consider the Dy^{3+} -activated phosphors. The tendency of Dy^{3+} to become tetravalent is much less than that of Tb^{3+} , and its tendency to become divalent is much less than that of Eu^{3+} . We can therefore expect that the formation of the type of killer complexes as formed with Tb^{4+} and Eu^{2+} is much less pronounced in the case of Dy^{3+} . In agreement with this, in none of the lattices studied was the efficiency of the Dy^{3+} emission very low. Dy^{3+} is at least the second best of the three activators due to the low efficiency of either the Eu^{3+} emission ($\text{CeMgAl}_{11}\text{O}_{19}$, CePO_4) or the Tb^{3+} emission (YNbO_4 , Y_2WO_6 , YVO_4) or of both (Ga_2O_3). On the other hand, the efficiency of the Dy^{3+} emission is limited in those phosphors where the required amount of Dy^{3+} is so high that considerable concentration quenching occurs (Tables I and II). For the Eu^{3+} and Tb^{3+} activated phosphors, concentration quenching usually occurs at much higher activator concentrations (26). This explains why the maximum efficiencies of YNbO_4 -Eu, $\text{CeMgAl}_{11}\text{O}_{19}$ -Tb, Y_2WO_6 -Eu, and CePO_4 -Tb are considerably higher than those of the corresponding Dy^{3+} -activated phosphors. For YVO_4 -Dy and Ga_2O_3 -Dy, the Dy^{3+} concentration can be held low enough to ensure that concentration quenching practically does not limit the efficiency. Correspondingly, the efficiency of YVO_4 -Dy is quite comparable to that of YVO_4 -Eu. The optimum Dy^{3+} concentration of YVO_4 -Dy ($\approx 0.5\%$) is considerably lower than that of Eu^{3+} in YVO_4 -Eu which amounts to 3-10% (2). This suggests that the transfer from the YVO_4 lattice occurs even more effectively to Dy^{3+} than to Eu^{3+} . Finally there remains Ga_2O_3 -Dy which shows Dy^{3+} emission of medium efficiency ($\approx 30\%$). On the contrary, neither Ga_2O_3 -Eu nor Ga_2O_3 -Tb showed any rare earth emission. At the moment we can offer no satisfactory explanation for the exceptional behavior of Ga_2O_3 -Dy. The luminescence mechanism of Ga_2O_3 itself is not known but is probably significantly different from that of the other lattices under consideration (27). It has been indicated

that the properties of Ga_2O_3 are similar to those of ZnS-type phosphors (27). Probably the Dy^{3+} luminescence of Ga_2O_3 -Dy resembles that of rare earth activated ZnS which has been studied by various authors (28).

Acknowledgments

The authors are indebted to Miss R. B. Engelen for the optical measurements and to Mrs. F. M. J. H. Hoex-Strik for the preparation of part of the samples.

Manuscript submitted Feb. 13, 1975; revised manuscript received March 3, 1975.

Any discussion of this paper will appear in a Discussion Section to be published in the June 1976 JOURNAL. All discussions for the June 1976 Discussion Section should be submitted by Feb. 1, 1976.

Publication costs of this article were partially assisted by Philips Research Laboratories.

REFERENCES

- G. H. Dieke and S. Singh, *J. Opt. Soc. Am.*, **46**, 495 (1956).
- F. C. Palilla, A. K. Levine, and M. Rinkevics, *This Journal*, **112**, 776 (1965).
- M. J. Taylor, *Proc. Phys. Soc.*, **87**, 281 (1966).
- G. Blasse and A. Bril, *J. Chem. Phys.*, **45**, 2350 (1966).
- R. C. Ropp, *J. Opt. Soc. Am.*, **57**, 1240 (1967).
- W. C. Herbert, H. B. Minnier, and J. J. Brown, *This Journal*, **115**, 104 (1968).
- S. Faria and D. T. Palumbo, *ibid.*, **116**, 157 (1969).
- G. W. Ludwig and J. D. Kingsley, *ibid.*, **117**, 348 (1970).
- J. J. Opstelten, D. Radielovic, and W. L. Wanmaker, *ibid.*, **120**, 1400 (1973).
- C. K. Jorgensen, R. Pappalardo, and E. Rittershaus, *Z. Naturforsch.*, **20a**, 54 (1965).
- E. Loh, *Phys. Rev.*, **147**, 332 (1966).
- B. G. Wybourne, "Spectroscopic Properties of Rare Earths," Interscience Publishers, Inc., New York (1965).
- G. Blasse, *J. Chem. Phys.*, **45**, 2356 (1966).
- G. Blasse and A. Bril, *Philips Res. Rept.*, **22**, 481 (1967).
- W. L. Wanmaker, A. Bril, J. W. ter Vrugt, and J. Broos, *ibid.*, **21**, 270 (1966).
- J. M. P. J. Versteegen, J. L. Sommerdijk, and J. G. Verriet, *J. Luminescence*, **6**, 425 (1973).
- G. Blasse and A. Bril, *J. Chem. Phys.*, **51**, 3252 (1969).
- A. Bril and W. Hoekstra, *Philips Res. Rept.*, **16**, 356 (1961).
- A. Bril and W. L. Wanmaker, *This Journal*, **111**, 1363 (1964).
- G. Blasse and A. Bril, *ibid.*, **115**, 1067 (1968).
- D. L. Dexter, *J. Chem. Phys.*, **21**, 836 (1953).
- L. G. van Uitert, in Proc. Int. Conf. Luminescence, Budapest, G. Szigeti, Editor, p. 1588, Akad. Kiadó, (1966).
- G. Blasse, *Philips Res. Rept.*, **24**, 131 (1969).
- H. J. Borchardt, *J. Chem. Phys.*, **39**, 504 (1963).
- T. P. J. Botden, *Philips Res. Rept.*, **6**, 425 (1951).
- L. G. van Uitert and L. F. Johnson, *J. Chem. Phys.*, **44**, 3514 (1966).
- G. Blasse and A. Bril, *J. Phys. Chem. Solids*, **31**, 707 (1970).
- See, for example, S. Larach, in Proc. Int. Conf. Luminescence, Budapest, G. Szigeti, Editor, p. 1549, Akad. Kiadó (1966).

Electrochemichromic Systems for Display Applications

I. F. Chang,* B. L. Gilbert, and T. I. Sun

IBM Thomas J. Watson Research Center, Yorktown Heights, New York 10598

ABSTRACT

Several electrochemical systems exhibit an intense color change when an electrochemical reaction is induced by an applied electrical field or current. The electrochemical and electro-optical properties of several such systems have been investigated. These systems are termed electrochemichromic and they can be classified into the following categories: (i) simple redox reaction; (ii) redox reaction coupled with an independent chemical reaction, resulting in variable color persistence; (iii) redox reaction coupled with a chemical reaction producing an insoluble colored species; (iv) redox reaction wherein a solid film deposited on one electrode is reduced and exhibits an intense color change. Analytical models which can describe the electrochemichromic behavior are presented for the different categories.

The spectrum of information display is very broad and fast growing. Functionally, display devices range from a simple status indicator, such as a traffic light, to a complex alphanumeric and graphic information presentation, such as a computer display with graphic and interactive capability. Physically, they vary from small electronic wrist watch displays for personal use to large screen displays for mass entertainment. Display devices are still finding new applications in the areas of automotive electronics, medical diagnosis, supermarket and department store retailing, banking terminals, etc. Not surprisingly, established display technologies cannot cope with the growth in applications, and certainly no single technology can serve all display needs and requirements. Thus new display technologies are constantly being pursued. For instance, liquid crystal displays, d-c plasma panels, and light emitting diodes have already made their entry in the low end (small number of characters) display market and there is some hint that plasma displays may very well penetrate some of the CRT strongholds in the near future (1).

Very recently, several new display devices have been introduced which are based on electrochemistry or some electrochemical effects (2-5). One such device is designated an electrophoretic (EP) display, indicating the phenomenon involved (2). The others, termed electrochromic (EC) [more properly electrochemichromic (ECC)¹] (3), electrochemiluminescent (ECL) (4), and fluorescence quenching (FQ) displays (5) are related to electrochemical redox reactions. The electrophoretic display employs a dye suspension which changes color as a result of electrophoretic migration of dye particles. The electrochemichromic effect is the direct result of a color change induced by an electrochemical redox reaction taking place at or near an electrode. Electrochemiluminescence is produced by a recombination of two species reduced and oxidized at a cathode or an anode, respectively, in a chemical solution. Fluorescence quenching occurs when a fluorescent ion or molecule is reduced or oxidized at an electrode to a nonfluorescent species. The latter two devices are active displays, that is, light is generated by the display medium whereas the former two are passive devices which modulate the reflected or transmitted ambient light. The EP display device has a very poor threshold characteristic, which would inhibit multiplexing, and requires high operating voltages (75-100V). Comparing the other three redox systems, all have low threshold voltages (0.5-2V) and generally similar electrical behavior. However, the ECC display

devices are more attractive because they have fewer chemical system constraints, simpler device operation, and better performance in terms of memory capability and high contrast under bright ambient. Therefore, it is technologically important to make a thorough investigation of various ECC systems, their electrochemical, electrical and electro-optical properties. It is also scientifically interesting to study their physical mechanisms, with the hope that such study can lead to an evaluation of the potential in display applications for ECC systems.

This paper presents a study of several ECC systems with display applications in mind. The systems which are described below in the section on electrochemichromic systems show a relatively efficient electrochemichromic effect. They are categorized into different types according to the electrochemistry involved. Their general characteristics are also presented. In the section on electrochemical and electro-optical properties of ECC systems, we describe the experimental investigation of the electrochemical, electrical, and electro-optical properties of these systems. Polarographic, voltammetric, and electro spectroscopic data are presented. In order to gain a better understanding of the ECC effect, we have devised some analytical models for describing various types of ECC systems. This is detailed in the section on the analytical model for electrochemichromic behavior. Although a different model is derived for each type of ECC system, the ECC response of all systems can be expressed in terms of a common function which represents an optimal ECC response and which, therefore, can be used to assess the ultimate potential of ECC systems for display application. The final section contains such an assessment, as well as a comparison of advantages and disadvantages, for different types of ECC systems.

Electrochemichromic Systems

Electrochromism, in the terminology of display technology, is broadly defined as the production of a color absorption band in a display medium by an applied electric field or current. A number of solid and liquid materials exhibit an EC effect, although the physical mechanisms involved may be different. For example, there are two mechanisms in solids that can lead to electrochromism, the well-known color center absorption due to trapping of an electron in an anion vacancy site in alkali halides (6) or other wide bandgap materials (7-9), and the absorption induced by charge transfer among impurity centers in insulators (10).

On the other hand, there are certain electrochemical effects (3, 11-13) occurring in liquids which also show a relatively efficient EC effect. The color change in these systems can be due to one of three different mechanisms: The first is electroplating, either of metals (12) or of nonmetallic elements (13). The sec-

* Electrochemical Society Active Member.

Key words: electrochromic, electrochemical, display, redox, electrochemichromic.

¹ Electrochromism is more broadly defined and also covers some solid-state phenomena such as color centers induced by an applied electrical field in an inorganic solid. For electrochemical electrochromic systems we propose the nomenclature electrochemichromic.

ond is based on a pH indicator effect, i.e., when the pH value near an electrode is changed by an electrochemical reaction, certain chemicals in an aqueous solution may either change color or fluoresce (11). A third mechanism depends upon the fact that an ion or molecule can be reduced or oxidized at an electrode, changing to a color absorbing species. The important point is that all these effects are governed by the basic electrochemical redox reaction. Thus, we designate all these liquids ECC systems.

The experimental ECC systems investigated here are, by definition, all based on an electrochemical redox reaction; however, some of these systems couple a chemical reaction with the redox reaction, or they involve a solid film in the redox reaction. Therefore, we may classify them into different types as follows:

Type I. Simple redox reaction. Ions or molecules in solution may be either reduced at the cathode or oxidized at the anode to become color absorbing species.

Type II. Redox reaction coupled with an independent chemical reaction, resulting in variable persistence. The chemical reaction controls the rate of reversal of the colored species back to its uncolored state.

Type III. Redox reaction coupled with a chemical reaction producing an insoluble colored species. The insoluble species exhibits excellent persistence and can only be erased electrochemically.

Type IV. Redox reaction in which a solid film deposited on one electrode is reduced and exhibits an intense color change. The color formation is confined to the solid film.

The experimental systems in the present work are listed in Table I according to the above classification. Abbreviations for these systems are listed in the last column and shall be used throughout the paper. All systems are aqueous, although some can be dissolved in a nonaqueous solvent such as dimethyl formamide. Generally the nonaqueous solutions show a relatively weak ECC sensitivity limited by solubility. The electrochemical reactions for these four different types can be described by the following formulas:

Type I. $A \pm ne \rightarrow B$ (colored species)

Type II. $A \pm ne \rightarrow B$ (colored species); $B + Z \rightarrow A + Z'$, $Z' \mp me \rightarrow Z$. The example listed in Table I is $A = \text{PTA}$, $Z = \text{H}_2\text{O}_2 + 2\text{H}^+$, $B + n/2 (\text{H}_2\text{O}_2 + 2\text{H}^+) \rightarrow A + n\text{H}_2\text{O}$, $n\text{H}_2\text{O} - ne \rightarrow n/2 (\text{H}_2\text{O}_2 + 2\text{H}^+)$. By varying the concentration of Z, the persistence of the color absorbing species can be controlled.

Type III. $A \pm ne \rightarrow B$; $B + C \rightarrow \text{BC} \downarrow$ where BC is an insoluble compound. The example listed in Table I is $A = \text{HV}^{++}$ (dihetyl viologen ion), $B = \text{HV}^+$ (one-electron reduction), $C = \text{Br}^-$ (bromine ion). In this case, the electrochemical reaction, $\text{HV}^{++} \pm e \rightarrow \text{HV}^+$, may very well contain another reaction as suggested by Schoot *et al.* (3), $\text{HV}^{++} + 2e \rightarrow \text{HV}$, $\text{HV}^{++} + \text{HV} \rightarrow 2\text{HV}^+$. However, so long as the reactions are fast, this series of reactions may be viewed as one step.

Type IV. $m\text{WO}_3 + 2n\text{H}^+ + 2ne \rightarrow \text{W}_m\text{O}_{3m-n}$ (blue color) $+ n\text{H}_2\text{O}$ where $\text{W}_m\text{O}_{3m-n}$ signifies that the ratio of oxygen *vs.* tungsten is reduced to allow color centers to be created. A similar equation applies to MoO_3 films.

Electrochemical and Electro-Optical Properties of ECC Systems

The general characteristics of an ECC system are outlined in Appendix I where we compare them with

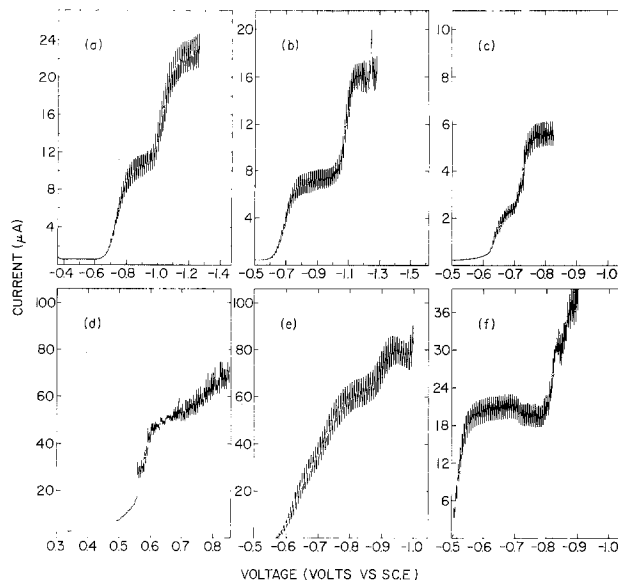


Fig. 1. Polarograph of ECC aqueous systems (a) DPDHC, 50 mg/100 cm³, pH 3.1, $E_{1/2} = -0.75, -1.05\text{V}$; (b) MVDC, 50 mg/100 cm³, pH 5.3, $E_{1/2} = -0.68, -1.07\text{V}$; (c) HVDB, 60 mg/100 cm³, pH 5.5, $E_{1/2} = -0.65, -0.725\text{V}$; (d) OTOL, 50 mg/100 cm³, pH 2.1, $E_{1/2} = +0.58\text{V}$; (e) PTA, $\text{Na}_2\text{WO}_4 \cdot 2\text{H}_2\text{O}$ 3 g/100 cm³, ClCH_2COOH 2 g/100 cm³, pH 3.1, cathodic wave; (f) HVDB-KBr, 0.02M HVDB, 0.02M KBr.

those of ECL, FQ, and EP systems. In this section we present electrochemical, electrical, and electro-optical properties of each type of ECC system. Polarography and cyclic voltammetry were used to investigate their threshold behavior. Electro spectroscopy was employed to obtain their ECC sensitivity and efficiency. These are the most significant performance parameters of an ECC display device.

Polarography.—A Sargent polarograph Model 21 was used to measure the polarographs of each ECC system. The results are shown in Fig. 1(a-f). One notes that the viologen family [Fig. 1(a-c)] all show two cathodic waves, (indicating a two-electron reduction process). The DPDHC, MVDC, and HVDB have their first half-wave potentials at $-0.75, -0.68,$ and -0.65V and second half-wave potentials at $-1.05, -1.075,$ and -0.725V , respectively. [All potentials are given with respect to a saturated calomel electrode (SCE).] The OTOL system with pH value of 2.1 [Fig. 1(d)] shows only one clear anodic wave (one-electron oxidation) with half-wave potential about 0.58V (*vs.* SCE). The polarograph for the PTA system [Fig. 1(e)] is rather poorly defined. There seems to be another wave at lower potential; however, this is not observed in cyclic voltammetry measurement. One does not see a clear one-electron reduction. This suggests that one may have more than one type of polytungsten anion in the solution. When H_2O_2 is added to the solution no significant change in polarographic behavior is observed. Figure 1f shows the polarograph of HVDB when KBr is added as an electrolyte. The half-wave potentials are shifted to -0.52 and -0.8V (*vs.* SCE).

Cyclic voltammetry.—Cyclic voltammetry measurements were performed using a circuit configuration de-

Table I. Electrochromic systems

Type	Sample	Formula	Electrolyte	Abbreviation
I	Polytungsten anion	$\text{Na}_2\text{WO}_4 + \text{ClCH}_2\text{COOH}$	—	PTA
	44' Dipyridinium dihydrochloride	$\text{N}_2\text{C}_{10}\text{H}_{10}\text{Cl}_2$	KCl	DPDHC
	Dimethyl viologen dichloride	$\text{N}_2\text{C}_{12}\text{H}_{14}\text{Cl}_2$	KCl	MVDC
II	O'Tolidine	$[\text{N}_2\text{C}_{14}\text{H}_{18}]$	KCl	OTOL
	PTA + H_2O_2	$\text{Na}_2\text{WO}_4 + \text{ClCH}_2\text{COOH} + \text{H}_2\text{O}_2$	—	PTA2
III	Dihetyl viologen dibromide	$\text{N}_2\text{C}_2\text{H}_8\text{Br}_2$	KBr or tetramethyl ammonium bromide	HVDB-KBr
IV	Tungsten trioxide	WO_3	H_2SO_4	WO_3
	Molybdenum	MoO_3	H_2SO_4	MoO_3
	Trioxide			

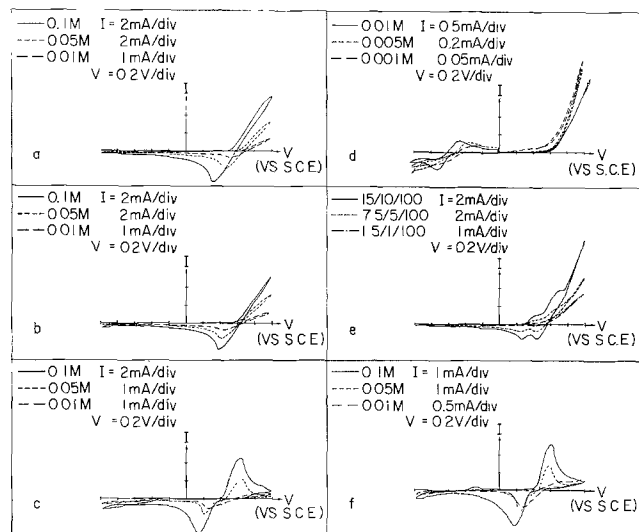


Fig. 2. Cyclic voltammety measurements of ECC aqueous systems with gold electrode. (a) DPDHC, (b) MVDC, (c) HVDB, (d) OTOL, (e) PTA, (f) HVDB-KBr.

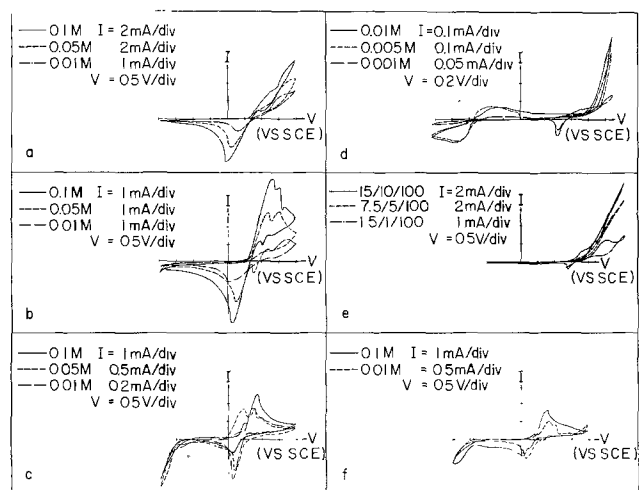


Fig. 3. Cyclic voltammety measurements of ECC aqueous systems with tin oxide coated glass electrode. (a) DPDHC, (b) MVDC, (c) HVDB, (d) OTOL, (e) PTA, (f) HVDB-KBr.

scribed by Schwarz and Shain (14). A low frequency (0.01 Hz) triangular wave was used in all measurements. The results are shown in Fig. 2(a-f) and Fig. 3(a-f), where the working electrodes were gold and a transparent conductor (tin-oxide-coated glass²), respectively. In these measurements high concentrations of ECC materials and electrolyte were used. This tends to wash out the distinction between successive electron reductions. However, we were interested in the current-voltage behavior with solution impedance levels more appropriate to real device operating conditions.

One notes that in Fig. 2(a-c) (data for the viologen family) one cannot distinguish the first electron reduction and the second electron reduction; however, the two reduction steps are more noticeable in Fig. 3(a-c) for the tin oxide electrode cases. Since these scans were taken at high current level with a rate about 80 mV/sec, it might be expected that the two-electron reductions would not be as clearly distinguished in these scans as they were in the polarographs. On the other hand, for the PTA sample, the reduction with the gold electrode [Fig. 2(e)] shows more structure in the I-V scan than is the case with the tin oxide electrode [Fig. 3(e)]. In fact, Fig. 2(e) shows distinctively two reduction steps which are not apparent in the polarograph shown in Fig. 1(e). The half-wave potentials for

these reductions may be approximately assigned as -0.37 and $-0.6V$ with respect to SCE potential. Figures 2(d) and 3(d) are the voltammety curves for OTOL. In both cases, for gold and tin oxide electrodes, the oxidation step is clearly exhibited, the half-wave potential being about $+0.6V$ (vs. SCE), which is in close agreement with the value from the polarograph ($+0.58V$ vs. SCE). However, one should point out that Kuwana and Strojek (15) have also observed one oxidation wave in their cyclic voltammety trace in a pH 2.0 solution but observed two oxidation waves in a solution of pH 4.0. This is consistent with results presented in Fig. 2(e) and 3(e) where the pH value is about 2. One recalls that when electrolyte (KBr) is added to the HVDB solution, the polarograms obtained show significant shifts of half-wave potentials; this is not observed in the cyclic voltammety curves [comparing Fig. 2(f) and 3(f) with Fig. 2(c) and 3(c)]. The high currents employed in the cyclic voltammety may have masked these shifts.

Electrospectroscopy.—Color and contrast are two important parameters for a display medium. Spectroscopic data for an ECC system in the colored state and noncolored state would be very useful for performance evaluation. Unfortunately, for most of the ECC systems discussed here, there is no spectroscopic data available; therefore, it was necessary to carry out such characterizations. However, in performing absorption measurements, one problem is encountered in the Type 1 and Type 2 samples. The problem is that the colored species electrochemically induced at the electrode tends to diffuse away from it. Due to this diffusion, a nonuniform optical density distribution and a short color persistence result. The reduced (or oxidized) absorbing ion species when meeting an oxidizing (or reducing) ion in the bulk solution will be restored to the uncolored original ion species. Because of this difficulty, among all ECC systems of Type 1 and Type 2 we have measured only the electrochemically induced absorption of the PTA system. Type 3 and Type 4 ECC systems can be measured relatively more easily.

A special optical cell was constructed for the absorption measurement. The cell is O-ring sealed with two windows, either of which can be a transparent electrode serving as a cathode, or working electrode. In the case of measurements of a WO_3 film, the film is deposited on one of the windows. The central vertical port is for a reference electrode such as a SCE. A tilted port next to the central port is for the counter-electrode, which was generally a gold wire. In this cell, one can use either a potentiostatic drive (three electrodes) or a two terminal drive to induce the electrochemical reaction. One also notes that two other side ports are provided for nitrogen flushing, to minimize the oxygen content in the cell.

The three terminal drive is more advantageous than the two terminal drive since it allows a convenient erasure procedure. However, one important fact should be pointed out here: When a colored layer is induced electrochemically on one electrode, an emf is also built up at that electrode. This emf tends to supply through the circuit a reverse current which reverses the redox reaction and erases the color layer. This is especially critical in a three terminal potentiostatic drive circuit, since the back-emf is amplified by the operational amplifier. One remedy for this situation is to use a high off-impedance ($\sim 10^{10}$ ohms) FET switch in the drive circuit, so that the reverse current may be minimized.

The absorption spectrum of the reduced PTA ions is shown in Fig. 4. This is derived from many repeated measurements. One notes a broad absorption band peaked at 710 nm. Considerable asymmetry suggests that a secondary absorption in the infrared around 1000-1200 nm is perhaps superimposed on the main absorption. The resulting color for the reduced PTA ions is a deep blue.

² Corning Glass Works.

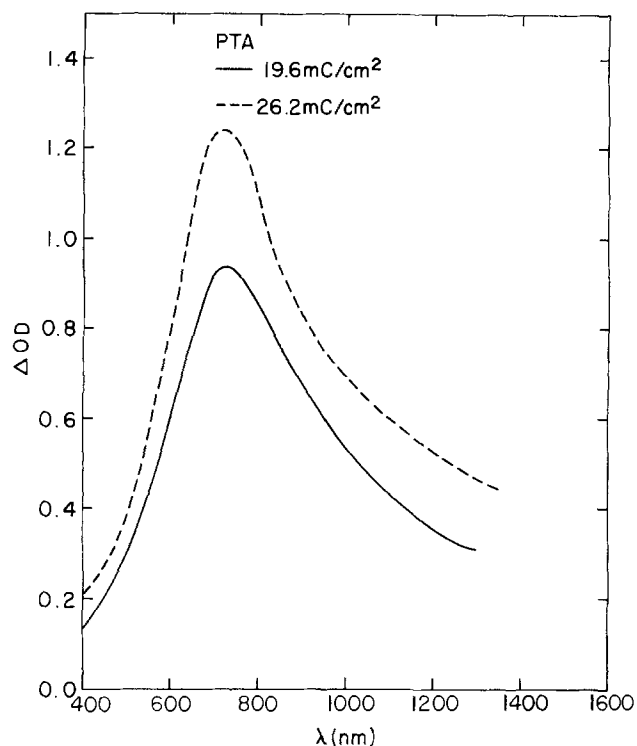


Fig. 4. Absorption spectrum for PTA

The absorption spectra for Type III and Type IV ECC systems are more reliable since there is no color drifting or diffusion in the bulk solution. Figure 5 shows the induced absorption for the HVDB-KBr system. The spectrum exhibits two absorption bands peaked around 515 and 550 nm. The reduced layer has a deep purple color. The induced absorption for a solid WO_3 film is shown in Fig. 6. A very broad absorption band centered around 980 nm is observed. The re-

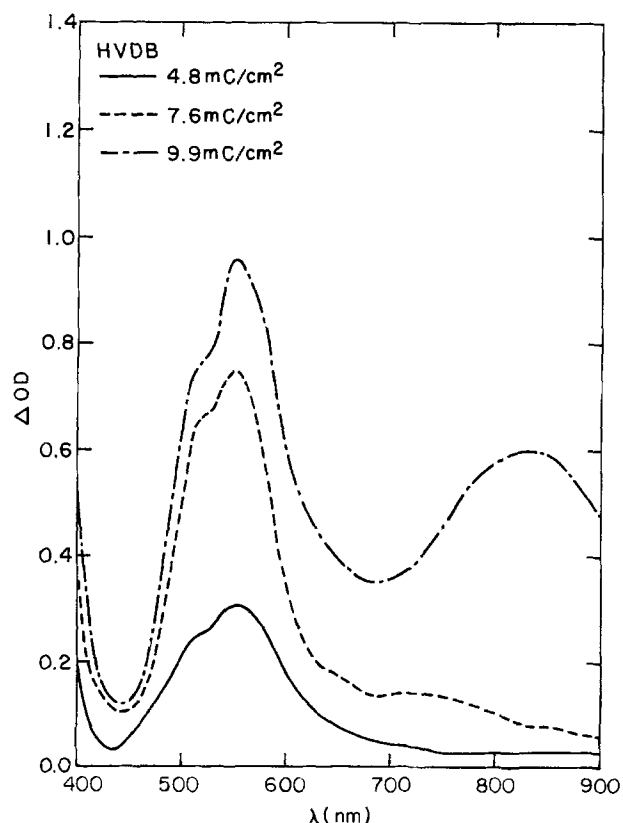


Fig. 5. Absorption spectrum for heptyl viologen bromide

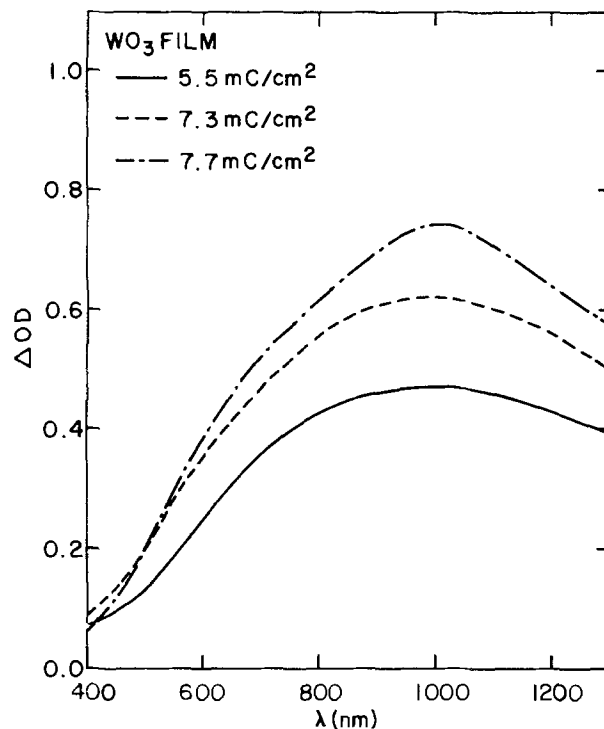


Fig. 6. Absorption spectrum for W_mO_{3m-n}

duced WO_3 also exhibits a deep blue color. In all cases (Fig. 4-6), the induced optical density is proportional to the applied charge density.

Analytical Model for Electrochromic Behavior

In order to assess the feasibility and ultimate potential of an ECC system for display device application, it is desirable to derive an analytical model for the ECC effect. The model should consider all first order physical mechanisms involved in the ECC effect and as a consequence should identify the physical parameters relevant to ECC behavior.

In analyzing the ECC effect, one finds that there are two major factors governing the ECC behavior, the electrochemical reaction and diffusion. Other mechanisms such as convection and ion migration can be neglected or minimized in a practical ECC solution. The first mechanism, the electrochemical redox reaction, can be characterized by two constants, the forward and backward reaction rates K_f and K_b (16). The second mechanism is the diffusion process which is characterized by the diffusion equation. The solution of the diffusion equation is governed by the boundary and initial conditions of the oxidant or reductant concentration, $C(x, y, z, t)$. The electrochemical reaction is coupled to the diffusion mechanism through the boundary conditions.

The complete solution to a three-dimensional diffusion equation is very complicated unless some simplifying approximations are made to the problem. Before we proceed to derive models for each different type of ECC system, the following assumptions are made: The first assumption is that the liquid solution is of large volume and is bounded by parallel plane electrodes having a separation much greater than a diffusion length for any species involved. The assumption is a realistic one for a typical experimental cell, although it is certainly possible to make practical cells which violate it. With this assumption one can describe the problem by a one-dimensional diffusion equation. Furthermore, one may consider that the liquid solution extends to infinity relative to the electrode under consideration, thus implying $C(x = \infty, y, z, t) = \text{constant}$ as one boundary condition. The second assumption which we make initially is that the speed of the ECC effect is not limited by the electrochemical reaction;

that is, one deals only with fast electrochemical reactions. Again, this assumption is a reasonable one, since for display application one naturally searches for an ECC with a fast reaction rate. Furthermore, in display device operation a sufficiently high voltage is always applied to the device [for instance, one may use $E = 2E_0$ or $3E_0$ in half-select or three-to-one matrix address schemes (17)] such that a fast reaction occurs. For such an operating condition, the most significant limiting mechanism governing the ECC behavior would be the diffusion process. Thus, the analytical model describing ECC systems of practical interest is just a linear diffusion model with appropriate boundary conditions. Analytical models for the four types of ECC systems are presented below.

Type I ECC systems.—Based on the initial and boundary conditions given in Appendix II, the functions C_0 and C_R can be determined by the use of Laplace transforms with the result

$$C_0(x, t) = C^0 [hS + \operatorname{erf}(x/2 D_0^{1/2} t^{1/2})] / (1 + hS) \quad [1]$$

$$C_R(x, t) = C^0 [h \operatorname{erfc}(x/2 D_R^{1/2} t^{1/2})] / (1 + hS) \quad [2]$$

where C^0 , D_0 , D_R , and S are defined in Appendix II, $h = (D_0/D_R)^{1/2}$, erf and erfc are error function and complementary error function, respectively. The current flowing through the cell is given by

$$i = nFA D_0 \left. \frac{\partial C_0}{\partial x} \right|_{x=0} = i_a / (1 + hS) \quad [3]$$

where F is Faraday's constant, A is the electrode area, and n is the number of electrons involved in the reduction. i_a is the limiting current when the electrochemical reaction rate is so high that the concentration of oxidant at the electrode surface is zero, *i.e.*

$$i_a = i(S = 0) = nFA D_0^{1/2} C^0 \pi^{-1/2} t^{-1/2} \quad [4]$$

The optical density change induced by the electrochemical reaction is proportional to the density of the colored species produced, which in turn is proportional to the charge supplied by the electrode. Thus, we have

$$OD = \frac{a}{2.3} \int_0^\infty C_R dx = \frac{a}{2.3} \frac{\int_0^t i dt}{nFA} = OD_a / (1 + hS) \quad [5]$$

where a is the absorptivity in terms of liters/M cm, and the numerical factor $1/2.3$ implies that the contrast ratio for a given optical density is 10^{OD} rather than e^{OD} , and

$$OD_a = OD(S = 0) = \frac{2}{2.3} a D_0^{1/2} C^0 \pi^{-1/2} t^{1/2} \quad [6]$$

Again the significance of $S = 0$ is that the reaction is very fast due to either K_f being very large or $E \ll E_0$. Under this condition, $C_0(0, t) = 0$, $C_R(0, t) = hC^0$, $i = i_a$, and $OD = OD_a$. This is the optimal condition for the ECC effect in Type I systems.

Type II ECC systems.—In this type of system, a catalytic chemical reaction is coupled with the electrochemical redox reaction. Therefore we have two coupled diffusion equations

$$\frac{\partial C_A}{\partial t} = D_A \frac{\partial^2 C_A}{\partial x^2} + k C_z C_B \quad [7]$$

$$\frac{\partial C_B}{\partial t} = D_B \frac{\partial^2 C_B}{\partial x^2} - k C_z C_B$$

where k is the rate of the catalytic chemical reaction and C_z is the concentration of the catalyst. The problem can be simplified considerably if we assume that C_z is constant throughout the solution cell at all times and the diffusion constants D_A and D_B are equal, say

D . Applying the same boundary conditions given by Eq. [A-2]-[A-4] and setting $S = 0$ [*i.e.*, $C_A(0, t) = 0$], one obtains the following solutions

$$C_B(x, t) = \frac{1}{2} e^{-x/(D\tau)^{1/2}} \operatorname{erfc}[x/2(Dt)^{1/2} - (t/\tau)^{1/2}] + \frac{1}{2} e^{x/(D\tau)^{1/2}} \operatorname{erfc}[x/2(Dt)^{1/2} + (t/\tau)^{1/2}] \quad [8]$$

$$OD = \frac{a}{2.3} \int_0^\infty C_B dx = \frac{a}{2.3} C_A^0 \sqrt{D\tau} \operatorname{erf}[(t/\tau)^{1/2}] = OD_a \left[1 - \frac{1}{3} (t/\tau) + \frac{1}{5 \cdot 2!} (t/\tau)^2 \dots \right] \quad [9]$$

$$i = nFA D^{1/2} C_A^0 \left\{ (1/\tau)^{1/2} \operatorname{erf}[(t/\tau)^{1/2}] + (\pi t)^{-1/2} \exp(-t/\tau) \right\} \quad [10]$$

where $\tau = 1/kC_z$ is the oxidizing time constant. The more oxidizing agent is added, the smaller the time constant. As $kC_z \rightarrow 0$, $\tau \rightarrow \infty$ (*i.e.*, no oxidizing agent added), $i \rightarrow i_a$ and $OD \rightarrow OD_a$. Equations [9] and [10] indicate that the ECC response is reduced from the optimal response due to the catalytic action. The reduction is directly related to the chemical reaction rate and the concentration of catalyst.

Type III ECC systems.—For this type of system, modeling of its ECC response is more complicated. It is particularly so if one considers all possible intermediate reactions involving both one-electron and two-electron reductions as well as the final chemical reaction. However, based on the assumption that we are only dealing with fast reactions, *i.e.*, if both electrochemical and chemical reaction rates are high, then the ECC response of such a system may still be regarded as diffusion limited. The system would then be equivalent to the straightforward electrolytic deposition of an insoluble substance on an electrode. This is certainly a reasonable assumption for the HVDB-KBr system which exhibits very fast reactions.

The corresponding boundary conditions for this case are similar to those of the Type I ECC system, but they are complicated by the fact that the activity of the deposit, f_{RCR} , is not known until the electrode is completely covered with at least one monolayer of deposit at which point it becomes equal to one. In view of the fact that the ECC system under consideration is a fast one, we neglect the initial uncertainty of the activity of the oxidant and assume that it is equal to one throughout the ECC response. The error introduced by this approximation is very small, and it applies only to the very early stage of the ECC reaction. With this approximation, the boundary condition of oxidant concentration at the electrode becomes

$$C_0(0, t) = S' = \frac{1}{f_0} \exp[nF(E - E_0)/RT] \quad [11]$$

The solution for this problem is then

$$C_0(x, t) = S' + (C^0 - S') \operatorname{erf}(x/2 D_0^{1/2} t^{1/2}) \quad [12]$$

$$i = nFA D_0 \left. \frac{\partial C}{\partial x} \right|_{x=0} = i_a (1 - S'/C^0) \quad [13]$$

$$OD = OD_a (1 - S'/C^0) \quad [14]$$

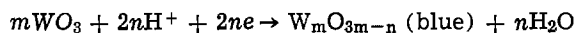
However, in Eq. [14], OD_a should be expressed as

$$OD_a = \alpha' \frac{\int i dt}{A} = 2 \alpha' nF C^0 D_0^{1/2} \pi^{-1/2} t^{1/2} \quad [15]$$

where $\alpha' = a/2.3nF$ with units of $(\text{coulomb/cm}^2)^{-1}$. In this case the absorbing species is insoluble in solution; thus, its absorptivity should be defined in terms of ion charge density rather than molar concentration. One should point out that the current and the optical den-

sity functions are both related to their optimal value by a common factor $(1 - S'/C^0)$.

Type IV ECC system.—The electrochemical reaction of this system is not the same as for the above redox reactions involving soluble species. The Type IV system is rather unique in the sense that it is the thin solid film (~ 0.2 – $1 \mu\text{m}$ thick) deposited on the electrode which undergoes a redox reaction. Since the film is an oxide, the reduction is facilitated by the presence of protons. This is borne out by the fact that the redox takes place easily in acidic solution. In fact, the electrochromic sensitivity is proportional to the concentration of hydrogen ions in the solution. Furthermore, we have performed cyclic voltammetry measurements on a WO_3 - H_2SO_4 system. The result is shown in Fig. 7 and indicates that the reduction does occur (blue color appears) near the hydrogen redox potential. This seems to support the hypothesis that the over-all electrochemical reaction is of the form



Although the involvement of protons is certain, exactly what occurs at the electrode or inside the oxide is not clear at all. One may speculate on several possible mechanisms. One possibility is that H^+ ions are reduced at the solid film surface (since WO_3 or MoO_3 films are semi-insulating and in fact become more conducting when reduced to colored film) becoming hydrogen atoms which then diffuse into the film and reduce it. The solid film is very likely porous which would promote the diffusion of the reduction product, H_2O , out to the solution. A second possibility is that H^+ ions diffuse into the film toward the electrode, an electrochemical reduction takes place within the film, and a chemical reduction reaction follows thereafter. A third possibility is that the oxide film is reduced by receiving electrons from the electrode, and oxygen ions diffuse out of the film to combine with hydrogen ions, which diffuse toward the electrode through the solution. No matter which mechanism prevails, the over-all electrochemical reaction seems to be the one given above.

Although we do not have evidence to support any one of the above described mechanisms, it is clear that in any case the diffusion of H^+ ions in the solution is a possible speed limiting mechanism in that the supply of H^+ ions to the electrode may govern. If one assumes that the electrochemical or chemical reaction taking place in the solid film is fast, then the analytical model for this case is just a diffusion-limited electrochemical reaction of H^+ . Since H^+ ions are reduced and combined with oxygen to form water which has an activity of 1, the boundary condition for this problem is the same as that for the HVDB-KBr system, as given by Eq. [A-2], [11], and [A-4]. Thus, the solutions given in

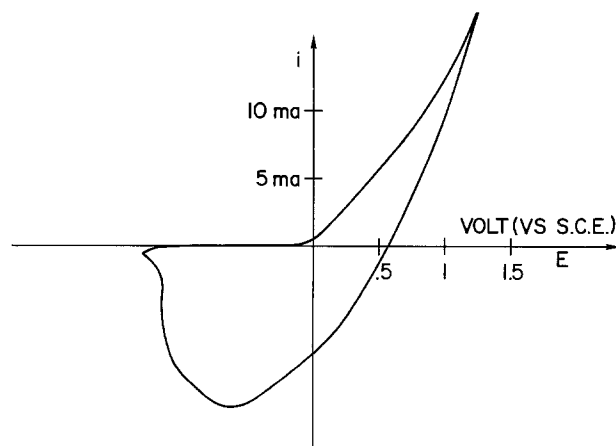


Fig. 7. Cyclic voltammetry measurement of tungsten trioxide film in sulfuric acid (0.3M).

Eq. [12], [13], and [14] apply here for the Type IV ECC system. In fact, electrical measurements made on the reduction of WO_3 films (18) indicate that the current is indeed a function of $t^{-1/2}$. This certainly supports the validity of this model.

Comparison with experimental data.—Current response, $i(t)$, and electro-optical response, $OD(t)$, of several ECC systems which belong to the four types discussed here have been performed and presented elsewhere (18). The experimental results (18) indicate that for Type I, III, and IV ECC systems, the current response is indeed a function of $t^{-1/2}$ and the optical density a function of $t^{1/2}$. This evidence certainly supports the validity of analytical models presented here. For Type II systems, the model is only confirmed for long persistence systems (*i.e.*, $\tau > 1$ sec). For systems having smaller τ (more oxidizing agent), more experimental work is required to confirm the validity of Eq. [9] and [10].

Discussion and Summary

The systems evaluated here are certainly only a small representation of all possible organic and inorganic ECC systems. The Table I ECC systems are the simplest from an electrochemical point of view. However, for display device applications, they are not practical due to the fact that the induced color species, being soluble, can diffuse or drift away from the electrode, thus causing smearing of an image. There are some possible remedies (19), such as using a gel (or semisolid) electrolyte, but such an approach appears to slow down the ECC response. The second type of ECC system eliminates the color drift problem by providing conversion back to the uncolored species. This feature is acceptable in a display device application where the information can be periodically refreshed. A refresh rate can be selected according to the type and amount of oxidizing chemical used. However, in this type of system, the ECC efficiency is reduced. This effect has been experimentally demonstrated with the PTA- H_2O_2 system (18). As one notes from Eq. [9], unless the oxidizing time constant τ is made much longer than the addressing time (or turn-on time) t , the optical density change is reduced from its optimal value. This condition (*i.e.*, $\tau \gg t$) would normally prevail for a multiline matrix display, since it is desirable in that case to select τ to be approximately equal to the refresh cycle time or frame time T .

The third type of ECC system has the advantage of having "memory" capability, since the colored layer is insoluble in the solution. It can only be removed electrochemically. However, because of the presence of this layer there is a back-emf associated with it. This back-emf tends to supply a reverse current through the system if a current path is provided. This leakage current makes matrix addressing complicated (18). However, if all leakage paths are eliminated, the insoluble layer tends to persist indefinitely. This feature offers the potential of saving power in certain applications such as displays for electronic calculators or electronic watches.

The ECC system of the fourth type, namely, a solid ECC film, has similar characteristics to those of Type III. However, the solid film allows the possibility of having such a film deposited on only one electrode, thereby producing an asymmetry not present in the other cases. Figure 8 shows an experimental device arranged in such a manner. When a negative voltage is applied to an electrode coated with an electrochromic solid film, an image is produced (as shown in Fig. 8); and upon reversal of the applied potential, the colored layer is erased without creating a similar colored layer at the opposite electrode. For the other categories of ECC systems an opaque or blocking medium may be required to shield the unwanted coloration created at the opposite electrode by the erasure voltage.

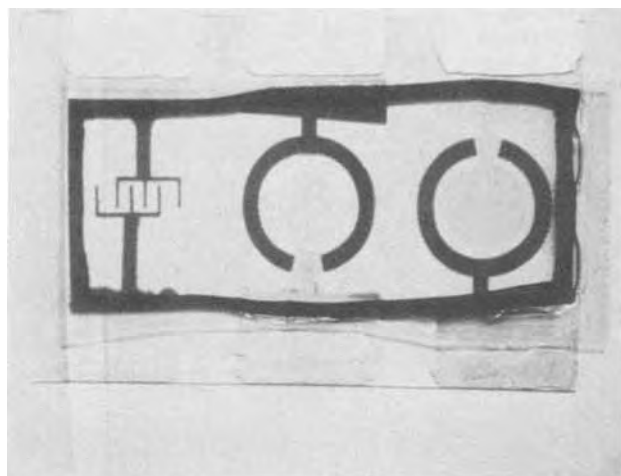


Fig. 8. A display image written on an experimental device containing $\text{WO}_3\text{-H}_2\text{SO}_4$ gel material.

We have argued that most ECC systems can be described by a diffusion model with appropriate boundary conditions. Solutions for each type of system are all related to an optimal ECC response function OD_a , given by Eq. [6]. One can use this optimal response function to assess the potential of ECC systems for display device applications. If one expresses OD_a as a function of addressing time (turn-on time) in a log-log plot one obtains a straight line with a slope of 1/2. Since OD_a is proportional to the concentration C^0 , the absorptivity α or α' and the square root of diffusion constant D , the straight line moves up and down according to the values of these constants. Figure 9 shows a plot for a typical set of constants, $C = 0.1 \text{ M/l}$, $D = 5 \times 10^{-6} \text{ cm}^2/\text{sec}$, $\alpha = 5 \times 10^4 \text{ liters/M cm}$. In a transmission mode, one would require a turn-on time ~ 30 msec to obtain an optical density change of 1 (10 to 1 contrast), whereas in a reflection mode (where the light passes through the absorption path twice), a turn-on time ~ 9 msec would be required for $OD = 0.5$ (10 to 1 contrast). Of course, the above example illustrates the ECC response of a typical system under optimal conditions. In practice, Eq. [A-7], [14], or [5] should be used to assess a particular system. ECC device characteristics measured on various ECC systems (18) do in fact indicate that the analytical models are valid and applicable in assessing their performance.

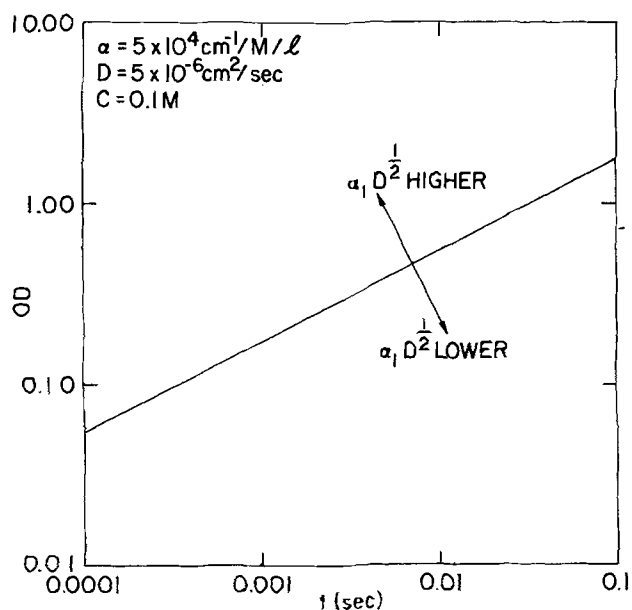


Fig. 9. Induced optical density change of a typical ECC system as a function of addressing time.

Another important question related to ECC device application is their operating life. Although, most examples discussed here were not given a life test, it is worthwhile pointing out that Schoot *et al.* (3) have demonstrated a 10^5 write-erase cycle with the HVDB-KBr system.

In summary, several ECC systems have been evaluated. They are classified into different categories according to the electrochemical reactions involved. The electrochemical, electrical, and electro-optical properties of these systems have been examined and compared. Analytical models which describe the ECC behavior have been derived for the various system types. Based on these models, a performance assessment of the ECC effect can be made. A typical efficient ECC system should have response time in the order of 10-100 msec for contrast of 10 to 1. This response, combined with characteristics such as low threshold voltage, memory capability, and wide viewing angle makes the ECC a strong candidate for direct-addressed segmented displays and small matrix-addressed displays.

Acknowledgment

We thank Drs. Jean W. Horkans, Webster E. Howard, and L. T. Romakiew for useful discussions. We also express our appreciation to Dr. B. Welber (spectroscopy laboratory) and to Dr. R. B. Laibowitz (thin film deposition laboratory) for making their equipment available to us and to W. C. Kateley for his valuable assistance in thin film preparations.

Manuscript submitted Dec. 26, 1974; revised manuscript received March 5, 1975. This was Paper 200 presented at the New York, New York, Meeting of the Society, Oct. 13-17, 1974.

Any discussion of this paper will appear in a Discussion Section to be published in the June 1976 JOURNAL. All discussions for the June 1976 Discussion Section should be submitted by Feb. 1, 1976.

Publication costs of this article were partially assisted by the IBM Corporation.

APPENDIX I

Comparison of Electrochemical Display Systems

	EP ²	ECC	ECL ⁴	FQ ⁵
Mode	Passive	Passive	Active	Active
Ultimate contrast	40:1	30:1	30:1	25:1
Memory	Yes	Yes	No	No
Operating voltage	75V	1-2V	5-10V	1-2V
	(d-c pulse)	(d-c pulse)	(a-c)	(d-c pulse)
Threshold	Poor	Yes	Yes	Yes
Power or energy	200 $\mu\text{W}/\text{cm}^2$	10 mJ/cm^2	40 mW/cm^2	28 mW/cm^2
Write speed	20 msec	10 msec	1 msec	10 msec
Erase speed	10 msec	10 msec	—	—
Gray scale	No	Yes	Yes	Yes

APPENDIX II

Initial and Boundary Conditions for Electrochemichromic Effect

The analytical models presented in this paper are given for a reduction process, thus, the initial conditions are

$$C_O(x, 0) = C^0 \quad [\text{A-1}]$$

$$C_R(x, 0) = 0$$

where subscript (or superscript) O and R signify oxidant and reductant, respectively. Equation [A-1] specifies that the ECC solution initially contains only oxidant having a constant concentration C^0 throughout the cell. In the case of oxidation reactions one simply interchanges subscript (or superscript) O to R and vice versa in all derivations.

Using the semi-infinite solutions approximation, the boundary conditions are

$$C_O(\infty, t) = C^0, C_R(\infty, t) = 0 \quad [\text{A-2}]$$

$$C_O(0, t)/C_R(0, t) = S = (f_R/f_O) \exp(nF(E - E_0)/RT) \quad [\text{A-3}]$$

and

$$D_O \frac{\partial C_O}{\partial x} \Big|_{x=0} + D_R \frac{\partial C_R}{\partial x} \Big|_{x=0} = 0 \quad [\text{A-4}]$$

Equation [A-3] essentially is the Nernst equation which describes the equilibrium situation at the electrode. f_R and f_O are activity coefficients of reductant and oxidant which may be assumed to be equal for the most redox pairs. The third equation indicates that the incoming flux of oxidant to the electrode is equal to the outgoing flux of reductant. D_O and D_R are diffusion constants, for the oxidant and reductant, respectively.

The above description is based on one fundamental assumption, specifically that the electrochemical reaction rate is fast. It is therefore interesting to see what results if this assumption is removed. Most importantly, one requires a different boundary condition at the cathode

$$D_O \frac{\partial C_O}{\partial x} \Big|_{x=0} = K_f C_O(0, t) - K_b C_R(0, t) \quad [\text{A-5}]$$

With this boundary condition, along with that given by Eq. [A-2] and [A-4], the solutions for the current flowing through the cell and the optical density induced are

$$i = nFA C^0 K_f \exp(Q^2 t) \operatorname{erfc}(Qt^{1/2}) \quad [\text{A-6}]$$

$$OD = \frac{1}{2.3} (\alpha C^0 K_f / Q^2) [\exp(Q^2 t) \operatorname{erfc}(Qt^{1/2}) + 2Q(t/\pi)^{1/2} - 1] \quad [\text{A-7}]$$

where $Q = K_f/D_O^{1/2} + K_b/D_R^{1/2}$. Since one deals with a reduction when the applied potential $E \ll E_0$, we should have $Q = K_f/D_O^{1/2}$ substituted in Eq. [A-6] and [A-7]. These solutions apply to slow ECC systems. They approach the results for diffusion-limited current i_a and optimal optical density change OD_a if $Qt^{1/2}$ is large, for instance greater than 5.

REFERENCES

1. E. I. Gordon and L. K. Anderson, *Proc. IEEE*, **61**, 807 (1973).
2. I. Ota, J. Ohnishi, and M. Yoshiyama, *ibid.*, **61**, 832 (1973).
3. C. J. Schoot, J. J. Ponjee, H. T. Van Dam, R. A. Van Doorn, and P. T. Bolwijn, *Appl. Phys. Letters*, **23**, 64 (1973).
4. M. A. Kabayama, A. Pighin, and W. M. Coderre, *SID Symposium Late News* (1973).
5. D. P. Hamblen and J. R. Clarke, *IEEE Trans. Electron Devices*, **ED-20**, 1028 (1973).
6. J. H. Schulman and W. D. Compton, "Color Centers in Solids," Pergamon Press, New York (1962).
7. I. F. Chang, *This Journal*, **121**, 815 (1974).
8. I. F. Chang and A. Onton, *J. Electronic Materials*, **2**, 17 (1973).
9. S. K. Deb, *Appl. Optics*, Supplement 3, 192 (1969).
10. B. W. Faughnam, D. L. Staebler, and Z. J. Kiss, "Applied Solid State Science," Vol. 2, Academic Press, New York (1971).
11. J. R. Alburger, *Electronic Industries and Tele-Tech. Feb.* 1957, 50-3.
12. S. Zaromb, *This Journal*, **109**, 903 (1962).
13. C. J. Sambucetti, U.S. Pat. 3,736,043 (1973).
14. W. M. Schwarz and I. Shain, *Anal. Chem.*, **35**, 1770 (1963).
15. T. Kuwana and J. W. Strojek, *Discussions Faraday Soc.*, **45**, 134 (1968).
16. P. Delahay, "New Instrumental Methods in Electrochemistry," Interscience, New York (1954).
17. T. Kilburn, G. R. Hoffman, and R. E. Hayes, *Proc. IEEE*, **105B**, 136 (1958).
18. I. F. Chang and W. E. Howard, *IEEE-SID Conf. on Display Devices and Systems*, New York, Oct. 9-10, 1974; *IEEE Trans. Electron Devices*, To be published.
19. I. F. Chang, B. L. Gilbert, and K. S. Pennington, Unpublished.

On the Correction to be Applied to the Thickness of an Epitaxial Layer Measured with Infrared Multiple Interference

P. J. Severin and F. C. Eversteyn

Philips Research Laboratories, Eindhoven, Netherlands

ABSTRACT

The extreme values of k plotted against the order of the extrema yield a straight line characterized by a slope d_s and an intercept $\delta_0/2\pi$. The thickness d_m of the deposited layer can be measured with a method described by Eversteyn and van den Heuvel. It turns out that $d_s - d_m$ depends linearly on $\delta_0/2\pi$, the relations being different for N^+ and N^{++} , but further independent of substrate resistivity or thickness. After calibration for a particular growth process the thickness can be determined with d_m as a standard reference from a conventional infrared multiple interference spectrum.

The thickness of a silicon layer grown epitaxially on a conductive substrate of resistivity ρ is an important parameter for integrated circuit technology. In this note fairly conclusive experimental evidence is presented for the validity of the method of interpreting infrared multiple interference spectra described earlier and practiced in this laboratory for several years. The introduction of a new experimentally accessible standard reference allows us now to also discuss the accuracy of the method.

It is well known that the wavenumber k of an extremum depends on the order l by the relation

$$2ndk = l - \frac{1}{2} + \frac{\delta(k, \rho)}{2\pi} \quad [1]$$

where n and d are the refractive index and the thickness of the layer, respectively. The phase shift $\delta(k, \rho)$ can be calculated from the optical parameters of the layer and the substrate. Over a limited wavenumber range, $\delta(k, \rho)$ may be approximated by a linear relationship

$$\frac{\delta}{2\pi} = \frac{\delta_0}{2\pi} - 2nk\Delta d \quad [2]$$

which yields, with Eq. [1] and after writing $d_s = d + \Delta d$

$$2nd_s k = l - \frac{1}{2} + \frac{\delta_0}{2\pi} \quad [3]$$

It has been shown earlier (1) that when k is plotted vs. l , a straight line is obtained from which the slope d_s and the intercept $\delta_0/2\pi$ can be easily determined. In a second paper (2) this formal solution, Eq. [2], has been suggested without actually specifying any experimental values of Δd and $\delta_0/2\pi$. In the absence of a well-defined and experimentally accessible reference for the thickness of an epitaxial layer, there was no point in discussing Δd and the accuracy of the infrared multiple interference method.

However, recently Everstejn and van den Heuvel (3) outlined a method of thickness measurement particularly suited for epitaxial layers. It is based on the use of the metallurgical thickness d_m , measured with a Taylor Hobson Talystep as a standard reference. It was found that d_m is related to the thickness $d_{m(\text{poly})}$ of polycrystalline silicon deposited simultaneously on an adjacent Si_3N_4 layer and measured in the same way, with accuracy to the second decimal, by

$$d_{m(\text{poly})} = d_m + 0.10 \mu\text{m} \quad [4a]$$

and that the same layer measured with infrared interference and interpreted as described above (1, 2) yields the same thickness also within $0.01 \mu\text{m}$

$$d_{s(\text{poly})} = d_{m(\text{poly})} \quad [4b]$$

In this paper, the thickness d_s and the constant phase shift $\delta_0/2\pi$ are shown to be correlated to this metallurgical thickness d_m . The experimental data are presented in the next section and possible interpretations are also discussed in this paper. In the last section the conclusions and recommendations are summarized.

Experimental Results

A large number of epitaxial layers was grown in SiH_4 at 1050°C corrected temperature, undoped, on Sb-doped N^+ substrates and As-doped N^{++} substrates. By plotting k vs. l the thickness d_s and the constant phase shift $\delta_0/2\pi$ are determined as in Eq. [3]. When d_m , as measured on an adjacent polycrystalline layer, is plotted against the thickness d_s , the latter does not present the appearance of a reliable parameter. However, when the difference $d_s - d_m$ is plotted against $\delta_0/2\pi$, the parameters show correlation. In Fig. 1 the N^{++} substrate data (1.3-2 mohm-cm) turn out to be clearly separated from the N^+ substrate data (8-15 mohm-cm). The experimental data show no systematic dependence when they are labeled with the appropriate substrate resistivity or thickness values.

For N^+ substrates, $d_s - d_m$ assumes any value between 0 and $0.6 \mu\text{m}$ correlated linearly with a value of $\delta_0/2\pi$ between 0 and 0.3, satisfying

$$d_s - d_m = 2 \frac{\delta_0}{2\pi} \mu\text{m} \quad [5a]$$

From Fig. 1 it is also clear that the N^{++} substrate data show a greater phase shift than any N^+ substrate does roughly satisfying

$$d_s - d_m = 2 \frac{\delta_0}{2\pi} - 0.45 \mu\text{m} \quad [5b]$$

The linear relationships are obeyed with a precision of about $0.05 \mu\text{m}$ which amounts to about 1% for $5 \mu\text{m}$ thick epitaxial layers. This error is due in the first place to the lack of precision in measuring k of the extrema for the epitaxial layer to determine d_s with Eq. [3], and for the polycrystalline layer to determine d_m with Eq. [4a] and [4b]. The error in the wavenumber depends slightly on the range but amounts to about $5 \cdot 10^{-3}$ with the instrument used.¹ Secondly, the refractive index n of silicon has been assumed, as usual, to be 3.42. Recently Villa (4) pub-

¹ Spectrophotometer, Model Epi-G3, Hitachi Ltd., Tokyo, Japan.

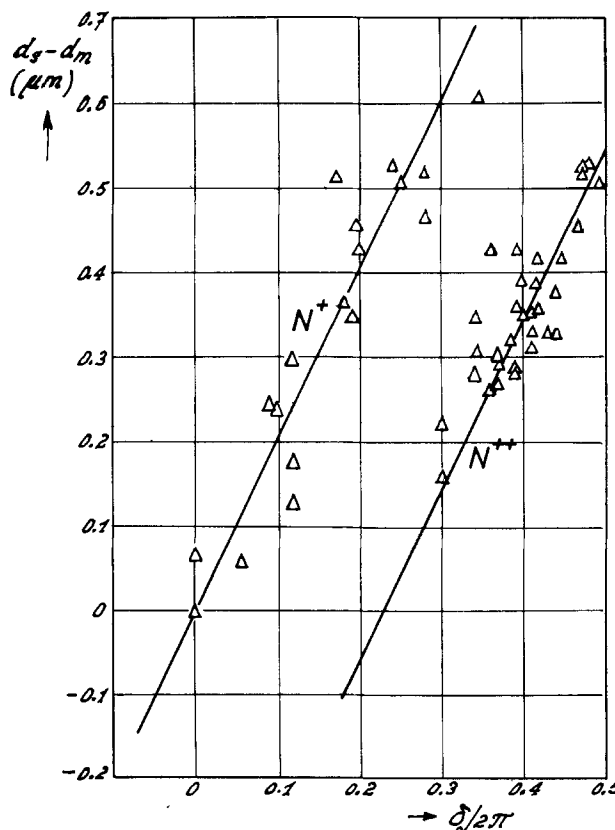


Fig. 1. The difference $d_s - d_m$ depends on the measured constant phase shift $\delta_0/2\pi$. The N^+ and N^{++} data are well separated and the lines are drawn according to Eq. [5a] and [5b].

lished measurement results, for which $2 \cdot 10^{-4}$ accuracy is claimed, in the range from 1.3 to $11 \mu\text{m}$ yielding 3.4371 and 3.4176 for the refractive index of two samples of silicon of nonspecified resistivity at $11 \mu\text{m}$. Thereupon, the refractive index was measured in the range from 8 to $25 \mu\text{m}$ by multiple interference between the polished sides of an 8 ohm-cm, n-type silicon slice. It was found that the slope of the line k vs. l is constant with a precision of $4 \cdot 10^{-3}$. The thickness of the slice was measured with a precision of $2 \cdot 10^{-3}$ and thus the refractive index was determined to be 3.4135 ± 0.0042 which is equal to 3.42, well within the relevant accuracy and precision of $5 \cdot 10^{-3}$ for k .

Interpretation

A classical derivation of the dependence of the phase shift δ on the wavenumber k and the substrate resistivity ρ has been given by Schumann *et al.* (5, 6). It was based on a model with an abrupt junction for dopant atoms and charge carriers with bulk material properties on both sides of the interface. The values of Δd and $\delta_0/2\pi$ have been cursorily calculated from linear approximations to these curves, $\delta(k, \rho)$, over a limited wavenumber range ($400\text{-}1200 \text{ cm}^{-1}$) and expediently plotted in Fig. 2. This is clearly different from Fig. 1.

For N^+ substrates, the range covered in $d_s - d_m$ and in $\delta_0/2\pi$ is larger than allowed by Fig. 2, where the classical substrate electron dispersion acts as the only cause of $\delta(k, \rho)$. Although it is difficult to speculate about this departure, it may be surmised that the particular state of this interface causes an additional and partly nonreproducible δ -dependence on k , for instance because the interface is not as strain-free as assumed.

The N^{++} substrate data are more concentrated around the values expected from Fig. 2

$$\delta_0/2\pi = 0.45 \text{ and } d_s - d_m = 0.35 \mu\text{m}$$

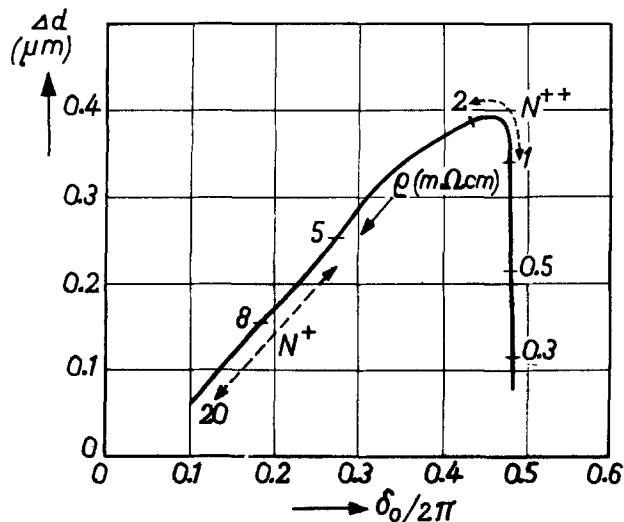


Fig. 2. The correction Δd and the constant phase shift $\delta_0/2\pi$ with the substrate resistivity ρ as a parameter, derived from Schumann's curve. The sections labeled N^+ and N^{++} cover the ranges studied.

Apparently here the phase shift is determined by the substrate resistivity more than by anything else.

It is worth stressing that there is no underlying theory to Eq. [5a] and [5b], but it is the authors' feeling that the nature of the interface conditioned by the growth parameters plays a vital role. This implies that for a range of growth conditions and substrate dopant levels relations similar to Eq. [5a] and [5b] have to be measured. Then the accuracy of the infrared multiple interference method can be established. It is important to note that, from the absence of any correlation between $\delta_0/2\pi$ and d_s or d_m , it follows that out-diffusion of substrate dopant atoms can be ruled out as a determining factor.

Summary and Conclusion

The procedure recommended (7) by the ASTM for determining the thickness of an epitaxial layer is based on the model of an abrupt interface. This definition of the thickness is used in the expression which describes the extreme values of k and in the correction formula used for $\delta(k, \rho)$. In fact, the result is defined by the procedure and cannot be verified otherwise. The precision is determined by the error with which the extreme values of k are reproduced by the instrument

and can be read from the spectrum. Accuracy is not claimed.

The procedure described in this paper envisages the production of precise and accurate numerical values of the thickness of the deposited layer by properly interpreting the infrared multiple interference spectrum. In the first place, the experimental observation (1, 2) has been used that, within the attainable precision, a plot of k vs. l yields a straight line characterized by the slope d_s and the intercept $\delta_0/2\pi$. Because it is physically clear that the phase shift at the interface must show dispersion and decrease with increasing k , this can only be combined by employing a linear approximation to $\delta(k)$ over a small range of k . In the second place, the experimentally verified procedure has been used, outlined by Eversteyn and van den Heuvel (3), by which the thickness d_m of the deposited layer is measured. It has been shown above that d_m can be found from d_s by subtracting an amount Δd linearly related to $\delta_0/2\pi$. The parameters of this linear relation probably depend on the growth conditions of the epitaxial layer. There is no dependence on the thickness.

It has been found experimentally that the correction Δd to be applied to the measured thickness d_s is different for N^+ and N^{++} substrates, but does not show any dependence on substrate resistivity beyond that. Therefore, any correction procedure based on the substrate resistivity as a criterion for $\delta(k)$ is unsound.

Manuscript submitted Nov. 20, 1972; revised manuscript received Sept. 4, 1973.

Any discussion of this paper will appear in a Discussion Section to be published in the June 1976 JOURNAL. All discussions for the June 1976 Discussion Section should be submitted by Feb. 1, 1976.

Publication costs of this article were partially assisted by Philips Research Laboratories.

REFERENCES

1. P. J. Severin, *Appl. Opt.*, **9**, 2381 (1970); Silicon Device Processing, NBS Special Publication 337, p. 224 (1970).
2. P. J. Severin, *Appl. Opt.*, **11**, 691 (1972).
3. F. C. Eversteyn and G. van den Heuvel, *This Journal*, **120**, 699 (1973).
4. J. J. Villa, *Appl. Opt.*, **11**, 2102 (1972).
5. P. A. Schumann, R. P. Phillips, and P. J. Olshefski, *This Journal*, **113**, 368 (1966).
6. P. A. Schumann, Silicon Device Processing, NBS Special Publication 337, p. 234 (1970).
7. Annual Book of ASTM Standards, F95-73, p. 406, (1974).

Penetration of Gold and Platinum Through Phosphorus-Doped n^+ Layers in Silicon

W. Mielke

AEG-Telefunken Forschungsinstitut, Frankfurt am Main, Germany

ABSTRACT

The penetration of gold and platinum through phosphorus-doped n^+ layers in silicon was studied by diode recovery measurements and by four-point measurements together with neutron activation analysis. A sudden breakthrough of gold in a small temperature range for a given n^+ layer and diffusion time is quantitatively observed for gold, while no important inhibition for platinum could be detected. Therefore platinum is proposed as an advantageous substitute for gold in silicon semiconductor device technology. The penetration of gold may be explained by compound formation of Au_2P_3 being in chemical equilibrium with gold and phosphorus in silicon.

Gold and platinum are widely used as contact materials and recombination centers in silicon semiconductor device technology. While gold is well known to control minority carrier lifetime it was only recently realized by Bailey and Mills (1, 2) that platinum possesses similar properties. In 1962, Cicconella, Forster, and Rulison (3) took into consideration a replacement of gold by platinum for providing a controlled reduction of minority carrier lifetime. Further properties of platinum in silicon were published by Carchano and Jund (4), Conti and Panchieri (5), and Charlot and Vapaille (6), while the properties of gold in silicon were reviewed by Bullis (7) in 1966. A general review about properties of deep impurities in silicon was presented by Schibli and Milnes (8, 9).

An intricate problem with gold in silicon is its affinity to phosphorus-doped n^+ layers. This property is positively used in gettering processes (10), while its negative aspects are manifested in its uncontrolled influence on the fabrication of fast switching devices (11). Indiffused gold profiles in phosphorus-doped n^+ layers in silicon were studied by Wilcox, La Chapelle, and Forbes (12) with radiotracer experiments. They stated that these layers greatly slow down gold diffusion and as a possible explanation offered a compound formation (Au_2P_3) between gold and phosphorus. Quantitative results for an enhanced solubility of gold in uniformly heavily doped silicon were presented by Cagnina (13) who emphasized that a solubility enhancement according to the Shockley-Moll model is much too small to explain his data and therefore again cited a possible compound formation.

To give a further insight into this technologically important problem the penetration of gold through phosphorus-doped n^+ layers has been studied and compared with the behavior of platinum.

Experimental Procedure

Silicon float-zone prepared, $\langle 111 \rangle$ -oriented single crystals were used as a starting material. Their further data were: 20 mm diameter, 10^{15} cm^{-3} boron doping, 10^4 cm^{-2} Sirtl etch pit density, and 230 μsec photoconductive decay minority carrier lifetime. Neutron activation analysis showed a gold concentration of $0.5\text{--}3.0 \cdot 10^{10} \text{ cm}^{-3}$ measured with a specimen of 250 mg Si. Platinum concentration was below the detection limit of $5 \cdot 10^{13} \text{ cm}^{-3}$.

A phosphorus indiffusion was then performed using an open tube configuration with a P_2O_5 source at 250°C and clean dry nitrogen as a carrier gas. Mirror etched slices of 500 μm thickness were treated for 2 hr at 1180°C with a subsequent cooling rate of 70°C/hr to 700°C . This diffusion step produced n^+ layers with a

phosphorus glass layer thickness of 0.5 μm (2.4 g/cm^3), a sheet resistance of 1 ohm/square, and a junction depth of 10 μm . The phosphorus glass layer was removed. Net donor surface concentration was checked by successive four-point measurements to be $5 \cdot 10^{20} \text{ cm}^{-3}$. No significant change in resistivity and etch pit density of the base material was observed. Gold concentration in the base material was measured to be $0.8\text{--}9.0 \cdot 10^{10} \text{ cm}^{-3}$ using 80 mg Si. Again no platinum was detectable. For a further evaluation of the phosphorus diffusion step, n^+p junctions 1.0 mm in diameter were produced by spraying 13 piceine varnish dots through a metal mask onto the n^+p slice, drying and melting the dots, and subsequently etching n^+p junctions to a depth of 20 μm and cleaning off the piceine dots. The thickness of the n^+p configuration was then 465 μm , because one n^+p side of the original 500 μm n^+pn^+ slice has been lapped away. Simple, adequate recombination contacts were applied by rubbing a gallium-wetted aluminum rod onto the silicon. Reverse currents were taken at 23°C and 1.0V and found to be from 1 to $8 \cdot 10^{-9}\text{A}$. Minority carrier lifetime was evaluated by diode recovery measurements. In this method a diode is switched from constant forward to constant reverse current and the delay time of the forward voltage to reach zero, the storage time, is measured and converted to minority carrier lifetime according to graphs for p^+n diodes with an arbitrary base width given by Grove and Sah (14). It is assumed that the p^+n graphs are approximately the same for n^+p diodes. Diode recovery measurements were performed at low injection levels by using forward currents from 1.0 to 20 mA (reverse currents from 0.1 to 2.0 mA), paying attention to junction capacitance and neglecting surface recombination velocity. Minority carrier lifetimes ranged from 6 to 15 μsec . The diodes showed sharp reverse characteristics and breakdown voltages about 200V were observed.

On manufactured n^+pn^+ and pn^+ structures gold was evaporated or platinum sputtered to a thickness of 0.1 μm , checked by weight. This resulted in Au n^+pn^+ , Au pn^+ , Pt n^+pn^+ , and Pt pn^+ structures. During this step the slice temperature remained below 300°C . Subsequently a number of heat-treatments, gold diffusions, and platinum diffusions were performed varying the parameter time from 10 sec to 6 hr, temperature from 800° to 1100°C , and junction depth from 4 to 10 μm . It should be noted that heat-treatments, gold diffusions, and platinum diffusions each had their own quartz tube and were all performed with an open tube configuration using dry clean nitrogen as a flow gas and a one tube diffusion furnace without ceramic protection tube. The slices were quickly put into or pulled from the constant temperature zone of the furnace, n^+pn^+ and pn^+ specimens were treated to-

Key words: diode recovery measurements, four-point measurements, neutron activation analysis.

gether. The treated slices were subjected to the same electrical measurements as before the heat-treatments, gold or platinum diffusions.

For neutron activation analysis a disk of 400 μm thickness and 10 mm diameter was symmetrically prepared out of the p zone by lapping, etching, and ultrasonically drilling. It should be emphasized that the same slice was evaluated by neutron activation analysis which has undergone the given electrical examinations.

Neutron activation analysis was performed by exposing the specimens to a thermal neutron flux of $10^{13} \text{ cm}^{-2}\text{-sec}^{-1}$ for 10 days. The specimens were then shortly etched with the following mixture: 25% fuming nitric acid, 10% hydrofluoric acid of 40%, 45% acetic acid, 20% nitric acid of 60%. The mixture was doped with inactive gold and platinum and the specimens were then checked in a multichannel counter to examine their cleanliness. After weighing they were dissolved in inactively doped etch, the solution cooked to dryness. The remaining gold and platinum were taken up with aqua regia and measured against a standard in a multichannel counter. Gold revealed by the 411 keV γ -radiation of Au 198 with a half-life of 65 hr while platinum gave a 158 and 208 keV γ -radiation of Au 199 with a half-life of 76 hr. It should be noted that platinum was roughly a factor 1000 less detectable than gold. The reached sensitivities were: $5 \cdot 10^{10} \text{ cm}^{-3}$ gold concentration and $5 \cdot 10^{13} \text{ cm}^{-3}$ platinum concentration with 50 mg of silicon and a measuring time of 10 min.

Experimental Results and Discussion

Results are given by drawing minority carrier lifetime τ , specific resistivity ρ , gold concentration C_{Au} , and platinum concentration C_{Pt} of the p region from n^+pn^+ (\circ , \bullet , \ominus) or pn^+ structured specimen (\square , \blacksquare , \boxminus) vs. heat-treatment or diffusion time t , four-point conductance $1/R$ of the n^+ layer or temperature T of the heat-treatment diffusions.

For each chosen set of parameters in a diffusion experiment a heat-treatment as a control experiment was performed to check whether the observed changes in experimental data were mainly due to the intended gold or platinum doping. In heat-treated slices no platinum could be detected. It should be noted that the presented results are not corrected for their control values. Slices supplied with gold or platinum were weighed before and after diffusion to check constancy of these metals. A qualitative difference was observed with the "gold slices," e.g., at 1000°C , 1 hr, the alloy at the p side of an Au pn^+ slice showed a "gold-like glimmering" while this could not be observed with Au n^+pn^+ slices, the gold has "disappeared" into the n^+ layer. Through phosphorus glass layers no penetration of gold during diffusion runs of 1 hr from 800° to 1000°C was observed. After diffusion the gold could be wiped off simply. No such experiments were performed with platinum.

According to Fig. 1 heat-treated n^+pn^+ structures exhibited lower gold concentrations than pn^+ structures, in accordance minority carrier lifetime was higher in n^+pn^+ structures. For gold diffusion a breakthrough of gold was observed, except for the 10 sec point for which the n^+pn^+ structure showed roughly a gold concentration three orders of magnitude lower than for the pn^+ structure. The increase of gold concentration with time is well known to be due to a "vacancy controlled" diffusion mechanism of gold in silicon (7, 15, 16). Furthermore it is well known that there is a steep increase of resistivity when the gold concentration reaches the boron concentration (10^{15} cm^{-3}) (7).

It should be noted that, because of the influence of junction capacitance of the diodes 1 mm in diameter, minority carrier lifetime could only be measured down to 0.1 μsec .

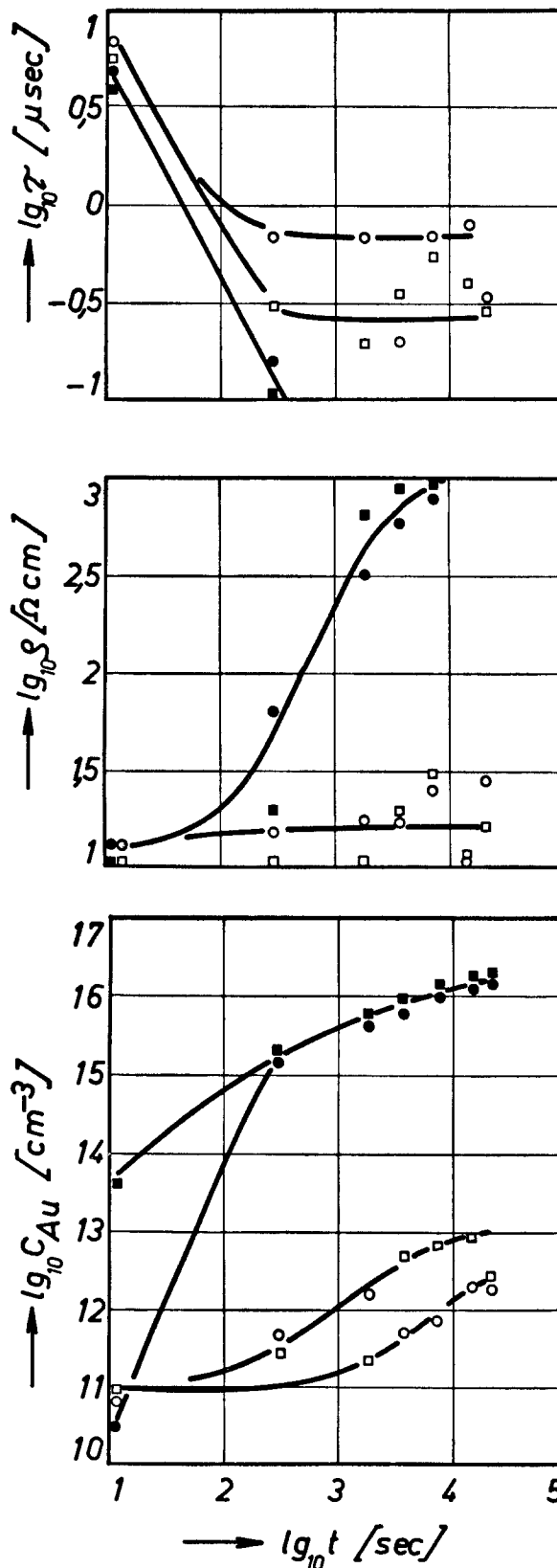


Fig. 1. Heat-treatments (\circ , \square) and gold diffusions (\bullet , \blacksquare) at 1100°C ; junction depth, 10 μm . Circles and squares represent n^+pn^+ and pn^+ samples, respectively.

In order to check the validity of the given gold concentration values, profiles of the central disks were taken with the 30 min and 6 hr gold-diffused slices by one side etching thereby dividing the disk 400 μm thick into 7 portions: $3 \times 30 + 220 + 3 \times 30 \mu\text{m}$. For the 30 min pn^+ slice an increase from 3 over a central value $5\text{--}7 \times 10^{15} \text{ cm}^{-3}$ gold concentration was measured with the high value at the p side where gold

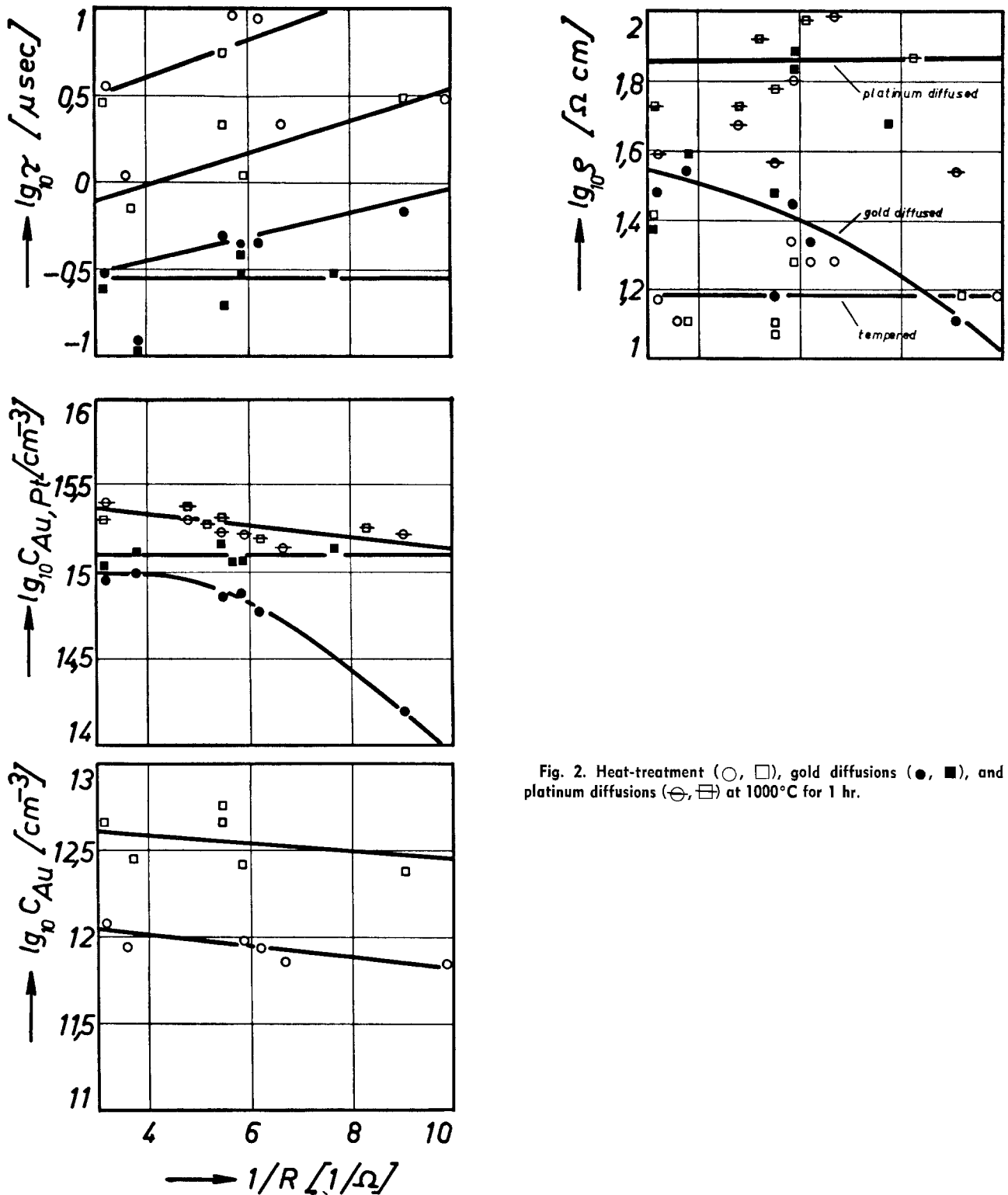


Fig. 2. Heat-treatment (\circ , \square), gold diffusions (\bullet , \blacksquare), and platinum diffusions (\oplus , $\opl�$) at 1000°C for 1 hr.

had been evaporated while, for the 6 hr n^+pn^+ and pn^+ slices, concave profiles were measured with a 30% rise at the edges (17). Therefore the given gold concentration values which were averaged for the whole central disk seem to be reasonable.

According to Fig. 2 various n^+ layer thicknesses which were obtained by modifying phosphorus diffusion times are given by their four-point conductance $1/R$ because these values are roughly proportional to the number of electrically active phosphorus atoms per cm^2 . A rough proportionality was checked for the $1/R$ values against the square root of phosphorus diffusion times. Lifetimes τ for platinum-diffused specimens were too low to be measured. It is interesting to note the decreasing gold content of gold-diffused n^+pn^+ slices with increasing $1/R$ (18). The scattering

in specific resistivity ρ may be due to variations in the resistivity of the starting material. Profile checks were taken for two n^+pn^+ and one pn^+ platinum-diffused slices leading to a decrease of roughly a factor 2 from the "platinum sputtered side" to the other side of the central disk.

According to Fig. 3 the gold concentration of n^+pn^+ slices steeply increased around 965°C ; this temperature being the breakthrough temperature for gold through this n^+pn^+ specimen for a 1 hr diffusion.

According to Fig. 4 no differences between n^+pn^+ and pn^+ structures diffused with platinum could be observed.

As mentioned earlier in this paper, Wilcox, La Chapelle, and Forbes (12) and Cagnina (13) in order to explain their results with the behavior of gold in

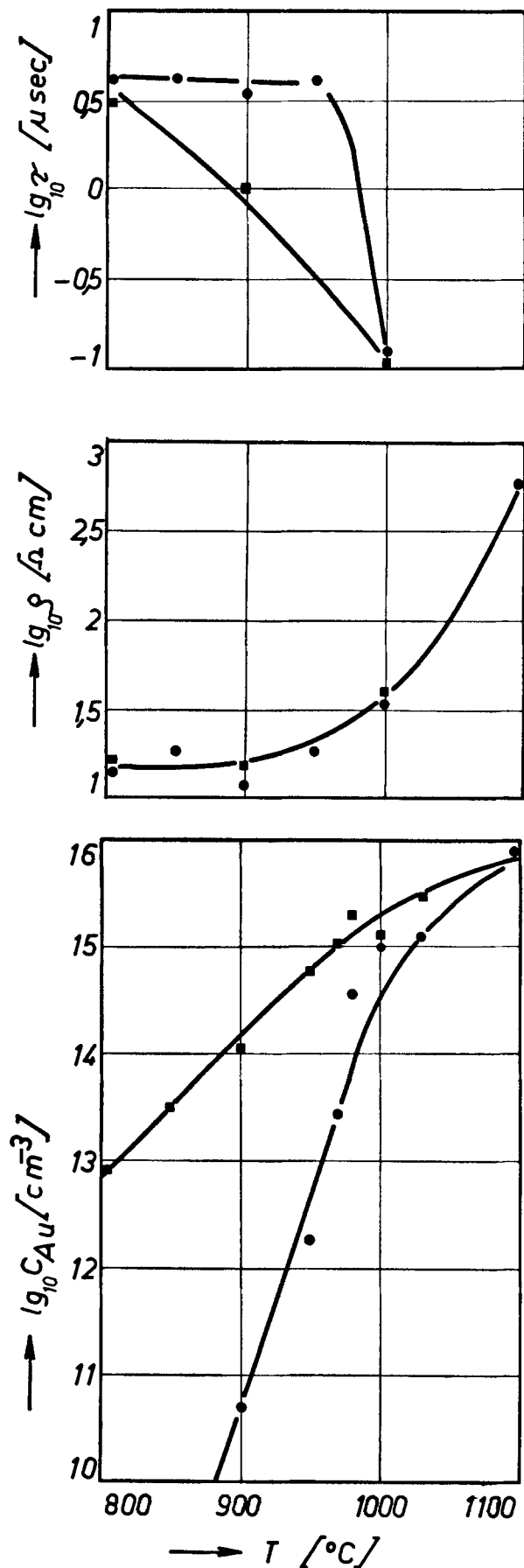


Fig. 3. Gold diffusions (●, ■) for 1 hr; junction depth, 10 μm

highly phosphorus-doped silicon assumed a compound formation of Au₂P₃, which of course is the most stable compound in the gold-phosphorus system (19), while in the gold-silicon system there is no compound forma-

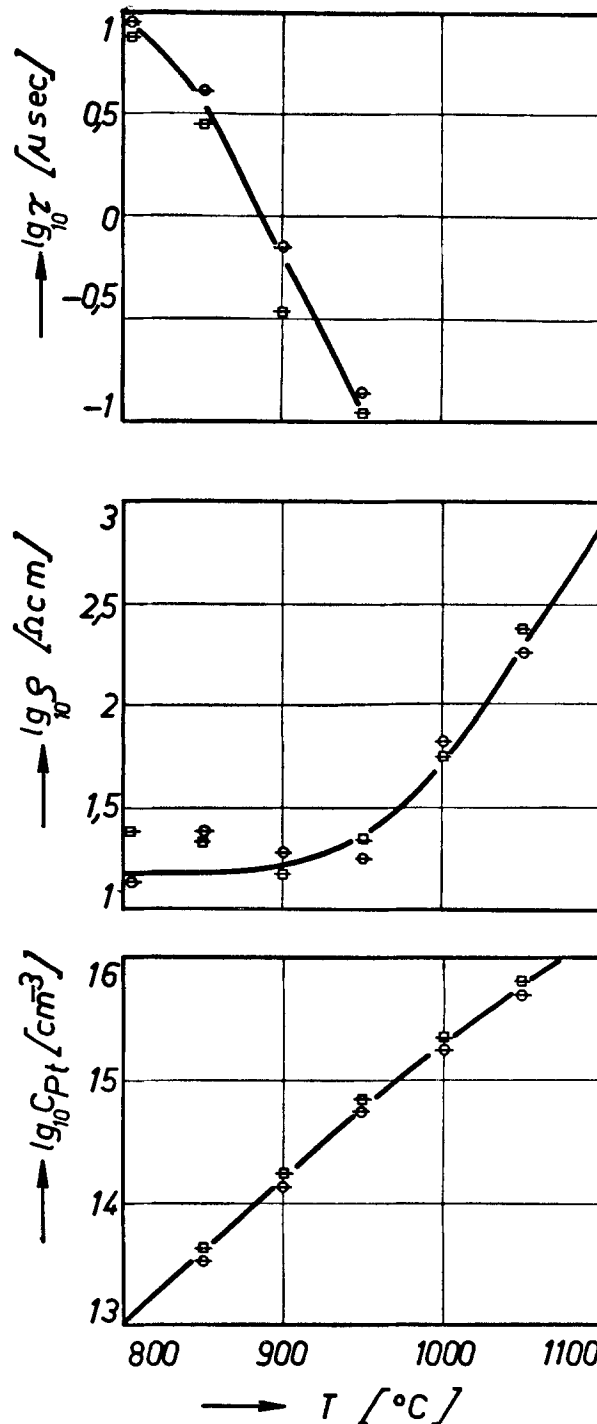


Fig. 4. Platinum diffusions (⊖, ⊕) for 1 hr; junction depth, 10 μm.

tion (19). For platinum there is a stable compound PtP₂ in the platinum-phosphorus system (20), but the same is true for the platinum-silicon system with Pt₂Si and PtSi (20). Using compound formation as a hypothetical assumption the given experimental arrangement would be describable as a reactive diffusion through thin layers as treated by Sah, Sello, and Tremere (21) for explaining masking properties of silicon dioxide films against phosphorus diffusion.

However while Au₂P₃ precipitates could be observed in gold-diffused silicon wafers (22), a similar observation of PtP₂ is not known. Together with the results of the given experiments which show no occurrence of masking or gettering of platinum by phosphorus-doped n⁺ layers in silicon (Fig. 4) one may suggest that, in spite of the existence of a stable platinum-phosphorus compound PtP₂, such a compound formation does not occur in phosphorus-doped silicon.

The breakthrough according to Fig. 3 may well occur, if the amount of gold in the n^+ layer reaches the amount of phosphorus, so that no further compound formation is possible.

Considering the actual experimental procedure a 0.1 μm thick gold layer was evaporated onto the specimen which corresponds to approximately 6×10^{17} gold atoms per cm^2 . Treated with temperature a gold-silicon alloy, 0.1-0.2 μm thick according to temperature, was formed. The junction depth was 10 μm with a surface concentration of $4 \times 10^{20} \text{ cm}^{-3}$ which roughly yields 10^{17} phosphorus atoms per cm^2 , indicating that a saturation of all phosphorus atoms is indeed possible.

Conclusion

In order to avoid the affinity of gold to phosphorus n^+ layers in silicon, platinum can be used as an advantageous substitute (23).

The measured penetration of gold through these layers may be explained by assuming a compound formation of Au_2P_3 , so that gold only can penetrate if all phosphorus has been saturated.

Acknowledgments

The author wishes to thank Dr. M. Reese, H. Pilz, and B. Struck, for devising and performing neutron activation analysis. Misses D. Löchel and G. Kehm prepared the samples while U. Gözinger from AEG-Telefunken, Heilbronn, provided the platinum sputtering. Drs. G. Köhl (†), H. Schlangenotto, K. Roy, and J. Hesse gave valuable comments.

Manuscript submitted Sept. 9, 1974; revised manuscript received Feb. 14, 1975.

Any discussion of this paper will appear in a Discussion Section to be published in the June 1976 JOURNAL. All discussions for the June 1976 Discussion Section should be submitted by Feb. 1, 1976.

Publication costs of this article were partially assisted by AEG-Telefunken Forschungsinstitut.

REFERENCES

1. R. F. Bailey and T. G. Mills, in "Semiconductor Silicon," R. R. Haberecht and E. L. Kern, Editors, pp. 481-489, The Electrochemical Society Soft-bound Symposium Series, New York (1969).
2. R. F. Bailey, U.S. Pat. 3,640,783 (1972).
3. D. F. Ciccolella, J. H. Forster, and R. L. Rulison, U.S. Pat. 3,067,485 (1962).
4. H. Carchano and C. Jund, *Solid-State Electron.*, **13**, 83 (1970).
5. M. Conti and A. Panchieri, *Alta Frequenza*, **40**, 544 (1971).
6. J.-J. Charlot and A. Vapaille, *Compt. Rend. B*, **273**, 1027 (1971).
7. W. M. Bullis, *Solid-State Electron.*, **9**, 143 (1966).
8. E. Schibli and A. G. Milnes, *Mat. Sci. Eng.*, **2**, 173, 229 (1967-1968).
9. A. G. Milnes, "Deep Impurities in Semiconductors," John Wiley & Sons, Inc., New York (1973).
10. A. Goetzberger and W. Schockley, *J. Appl. Phys.*, **31**, 1821 (1960).
11. J. M. Fairfield and G. H. Schwuttke, *ibid.*, **37** 1536 (1966).
12. W. R. Wilcox, T. J. La Chapelle, and D. H. Forbes, *This Journal*, **111**, 1377 (1964).
13. S. F. Cagnina, *ibid.*, **116**, 498 (1969).
14. A. S. Grove and C. T. Sah, *Solid-State Electron.*, **7**, 107 (1964).
15. F. A. Huntley and A. F. W. Willoughby, *ibid.*, **13**, 1231 (1970).
16. J. L. Lambert, *Phys. Status, Solidi (a)*, **4**, K33 (1971).
17. J. Martin, E. Haas, and K. Raithel, *Solid-State Electron.*, **9**, 83 (1966).
18. P. C. Parekh, *ibid.*, **13**, 1401 (1970).
19. Gmelins Handbuch der anorganischen Chemie, 8th ed., system number: 62-gold, p. 727, Verlag Chemie GmbH., Weinheim/Bergstrasse (1954).
20. Gmelins Handbuch der anorganischen Chemie, 8th ed., system number: 68-platinum, p. 128, Verlag Chemie GmbH., Weinheim/Bergstrasse (1940).
21. C. T. Sah, H. Sello, and D. A. Tremere, *J. Phys. Chem. Solids*, **11**, 288 (1959).
22. E. D. Wolley and R. Stickler, *This Journal*, **114**, 1287 (1967).
23. W. Mielke, *German Offenlegungsschrift*, **22**, (10), 200 (1973).

Developer Characteristics of Poly-(Methyl Methacrylate) Electron Resist

James S. Greeneich*

Electronics Department, General Motors Research Laboratories, Warren, Michigan 48090

ABSTRACT

We report on the solubility characteristics of poly-(methyl methacrylate) electron-resist for developer combinations of methyl isobutyl ketone (MIBK) and isopropyl alcohol (IPA). The solubility rate is determined in terms of the fragmented molecular weight which is a function of original molecular weight and the energy absorbed by the polymer in degrading to a lower molecular weight. An empirical formula for the solubility rate is $K = [R_0 + \beta/M_f^\alpha]e^{-E_a/kT}$, where M_f is the fragmented molecular weight, R_0 , β , and α are constants characteristic of a given developer. The temperature dependence is characterized by an activation energy, E_a , for a given developer. The solubility kinetics are discussed showing a rate limited process for most developer conditions. From the solubility rate and the characteristic energy absorption in the resist, the development time and contrast are defined and calculated for a variety of exposure parameters including beam energy, resist thickness, developer, developer temperature, and original molecular weight. Compared to the standard developer, 1:3 MIBK:IPA, an improved sensitivity of 10-50 times is obtained using MIBK at the expense of increased development time. For a given contrast level the development time is greatly reduced by increasing the developer temperature. A lower original molecular weight also reduces the required development time.

Electron-beam and x-ray lithography are important new technologies for fabricating semiconductor devices and circuits with submicron dimensions. The most widely used resist medium is the positive acting poly-(methyl methacrylate), PMMA (1). In addition to a resolution requirement, the performance of the resist is measured in terms of its sensitivity to the incident radiation. Typically the sensitivity is expressed in terms of the required incident charge per unit area to produce the desired resist pattern of the desired thickness. The final resist thickness is important in terms of the suitability of the resist as an etching mask and for the metal lift-off technique (1) for positive resists.

Using the standard developer, 1:3 methyl isobutyl ketone (MIBK):isopropyl alcohol (IPA), the reported sensitivity of PMMA is in the range 5×10^{-5} to 5×10^{-4} C/cm². The range in reported sensitivities is primarily due to varying exposure conditions such as beam energy, resist thickness, type of substrate, and geometry of the irradiated pattern (2, 3). For this solvent the development is nearly time independent. Consequently, the sensitivity has been expressed in terms of a critical absorbed energy density (3) which is independent of the exposure parameters. This model is not adequate for time-dependent developer systems described in this paper.

What is the influence of the developer solvent and temperature on the sensitivity and development time for positive electron-beam resists? In the case of PMMA this is an important question since its sensitivity is considered low and improving its sensitivity through the development process is important. Ethyl and methyl alcohol are also used as developers for PMMA with approximately the same sensitivity as the standard developer (4). Hatzakis and Broers (5) report the use of MIBK as a time-dependent developer with increased sensitivity, but the original resist thickness was rapidly reduced. Ting (6) reported on the MIBK developer in terms of a solubility rate as a function of an "effective" charge and Greeneich (7) has shown that high contrast exposures can be made using MIBK if a very high molecular weight polymer is used.

We report a method for evaluating the sensitivity of positive electron resists in which the solubility rate is

expressed in terms of the basic quantity which changes during electron radiation, namely the fragmented molecular weight. From the solubility rate the required development time and resulting contrast are defined and evaluated for many of the parameters affecting resist sensitivity.

We report on the solubility of PMMA in several developer combinations of MIBK and IPA at several temperatures. We report an empirical relationship between developer solubility rate and the fragmented molecular weight of the form $R = (R_0 + \beta/M_f^\alpha)e^{-E_a/kT}$, where R_0 , β , and α are constants and E_a is an activation energy. An improved sensitivity compared to the standard developer of from 10 to 50 times is obtained by using different developers.

The kinetics of the solubility process is found to be adequately described by a rate-limited process for most developer conditions. At high temperatures it is found that the standard developer has nonlinear solubility properties.

Relationship Between Fragmented Molecular Weight and Exposure Parameters

A positive electron resist is characterized by a reduction of molecular weight owing to chain scission of the original molecules. Since polymers with different molecular weights have different solubility characteristics in a given solvent, the resist developer is required to distinguish between the fragmented molecular weight, M_f , and the original molecular weight, M_n .

The relationship between M_f and M_n and the exposure parameters is expressed in terms of the absorbed energy density, ϵ , as (7, 8)

$$M_f = \frac{M_n}{1 + \frac{g\epsilon M_n}{\rho A_0}} \quad [1]$$

where ρ is the resist density, A_0 is Avogadro's number, and g is an efficiency factor proportional to the radiation chemical yield. For PMMA we take g to be 1.9×10^{-2} events/eV (9). It should be noted that [1] only applies as long as the resist degrades during electron bombardment. In the case of PMMA cross-linking events dominate at high doses of electron-beam radiation (1, 2).

* Electrochemical Society Active Member.

Key words: electron-beam lithography, electron-resist developers, contrast function, energy dissipation in resists.

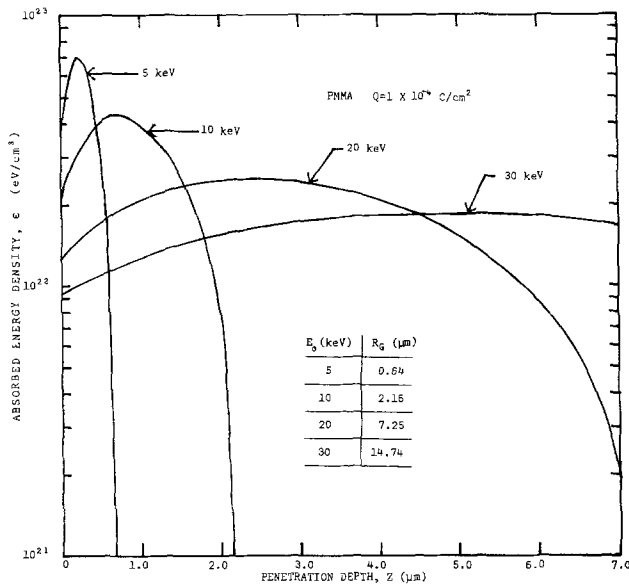


Fig. 1. Energy dissipation per unit volume for area exposures as a function of penetration depth for various incident energies. The table gives the Grun range (Eq. [4]).

The absorbed energy density is in general a complicated function of position within the resist film; the exact dependence being a function of the exposure parameters such as beam energy, resist thickness, type of substrate, and geometry of the irradiated pattern (2, 3). In the case of an area exposure on a low atomic number substrate such as silicon, ϵ is given by the depth-dose function (10) in terms of the depth, z , in the resist and the incident energy, E_0 . Specifically

$$\epsilon = \frac{Q E_0}{q R_G} \lambda(f) \quad [2]$$

where

$$\lambda(f) = 0.74 + 4.7f - 8.9f^2 + 3.5f^3 \quad [3]$$

In [2], Q is the incident charge per unit area, q is the electronic charge, $f = z/R_G$, where R_G is the Grun range given by

$$R_G = \frac{4.6 \times 10^{-6}}{\rho} E_0^{1.75} \quad [4]$$

when E_0 is in units of keV. The absorbed energy density in PMMA for an incident dose of 10^{-4} C/cm² is shown in Fig. 1 for several beam energies. Two important points are illustrated in Fig. 1. There is a range, R_G , (tabulated in Fig. 1) beyond which ϵ is small; consequently the resist thickness must be equal to or less than R_G . For the higher beam energies and thin resist films ($<3000\text{\AA}$), ϵ is approximately uniform and consequently, from Eq. [1], M_f is nearly independent of depth.

Experimental Results

Various molecular weight samples of PMMA were dissolved in trichlorethylene and spin coated onto silicon wafers, resulting in a typical resist thickness of $\sim 3000\text{\AA}$. The nature of the carrier solvent used in coating the resist and the pre-exposure baking play a role in the solubility characteristics of the resist. For example, Fig. 2 shows the resist thickness vs. time in the solvent MIBK for various prebaking conditions where MIBK and trichloroethylene were used as carrier solvents. After ~ 4 min in MIBK the trichlorethylene sample dissolves at about the same rate as the well-baked MIBK sample.

Similarly the solubility rate of degraded PMMA is influenced by remaining carrier solvent; we have observed ~ 2 times less Q is required for samples developed in the standard developer when MIBK remains. All samples used in this study were coated with trichlorethylene as the carrier solvent and baked for ≥ 90 min at 160°C .

Typical areas of 10^{-3} cm² were irradiated with 20 keV electrons using a Cambridge S4-10 scanning electron microscope (SEM) equipped with a beam blanking unit. The incident dose was varied by changing the frame scan time. Some variation in exposure was observed depending on whether or not the beam is

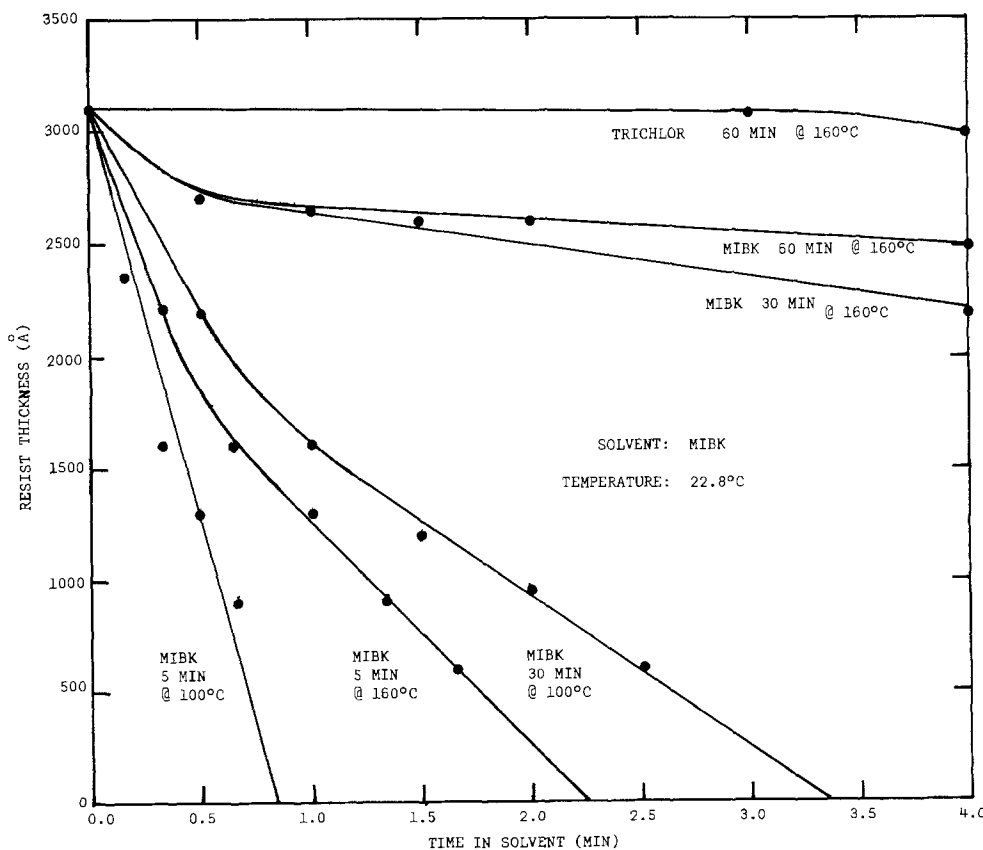


Fig. 2. The influence of the resist carrier solvent on solubility in MIBK for the indicated prebake conditions.

blanked during flyback; all results reported here are for the condition with beam blanking on.

After irradiation the samples were immersed in the developer solvent, which was not agitated. Periodically the samples were removed and the resist thickness determined by the interference color of the irradiated area. Ellipsometer measurements on non-irradiated samples established the refractive index to be 1.48 ± 0.02 and the accuracy of the interference method to be $\pm 150\text{\AA}$. Only a slight increase in re-

fractive index (≤ 0.04) was observed as a result of solvent migration into the film during prolonged soaking (30 min) in the developer solvents; this did not affect the measured solubility rates.

Several solvents were tested as developers; these consisted of MIBK, 1:1 MIBK:IPA and 1:3 MIBK:IPA. The temperature dependence of MIBK and 1:3 MIBK:IPA was also investigated.

Two different types of behavior were observed. Figures 3 and 4 show the results for 1:1 MIBK:IPA at

Fig. 3. A typical experimental result characteristic of a rate-limited process relating resist thickness as a function of developer time for various fragmented molecular weights.

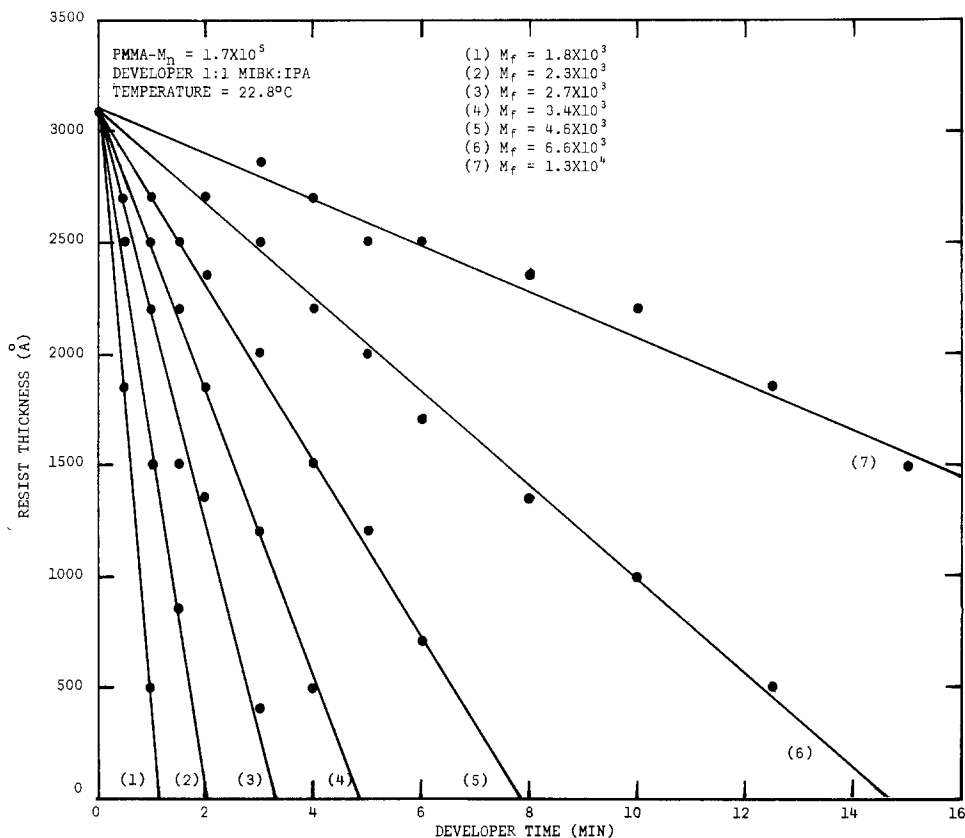
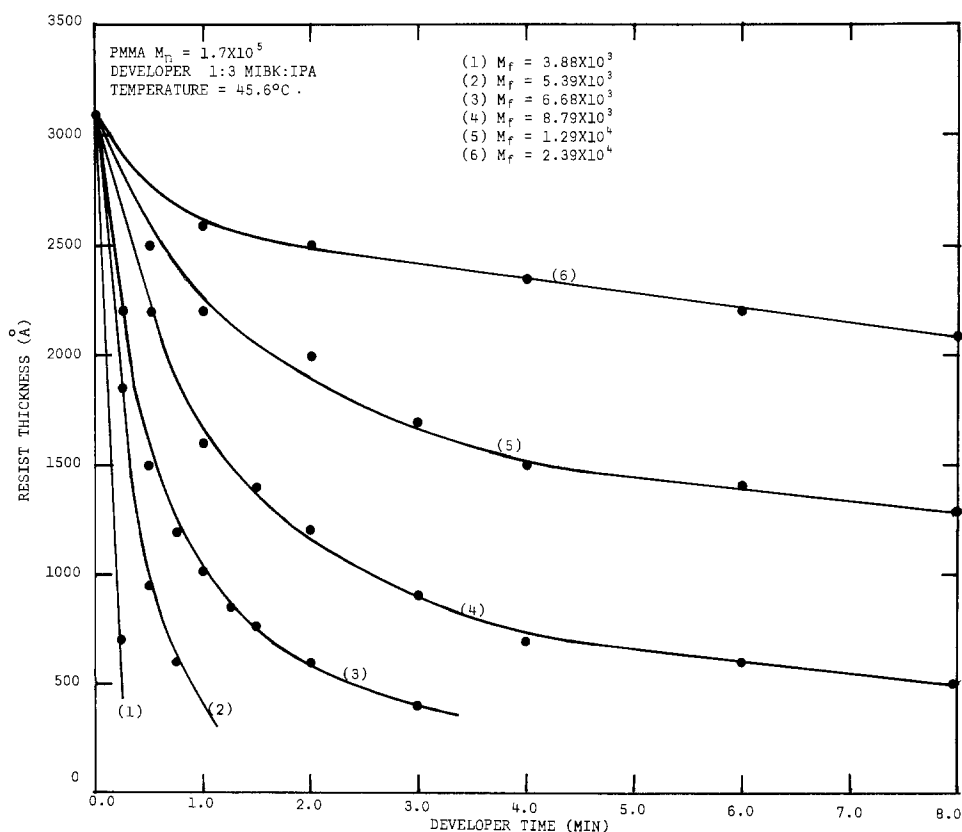


Fig. 4. Experimental results for 1:3 MIBK:IPA at 45.6°C showing the nonlinearity in the solubility rate.



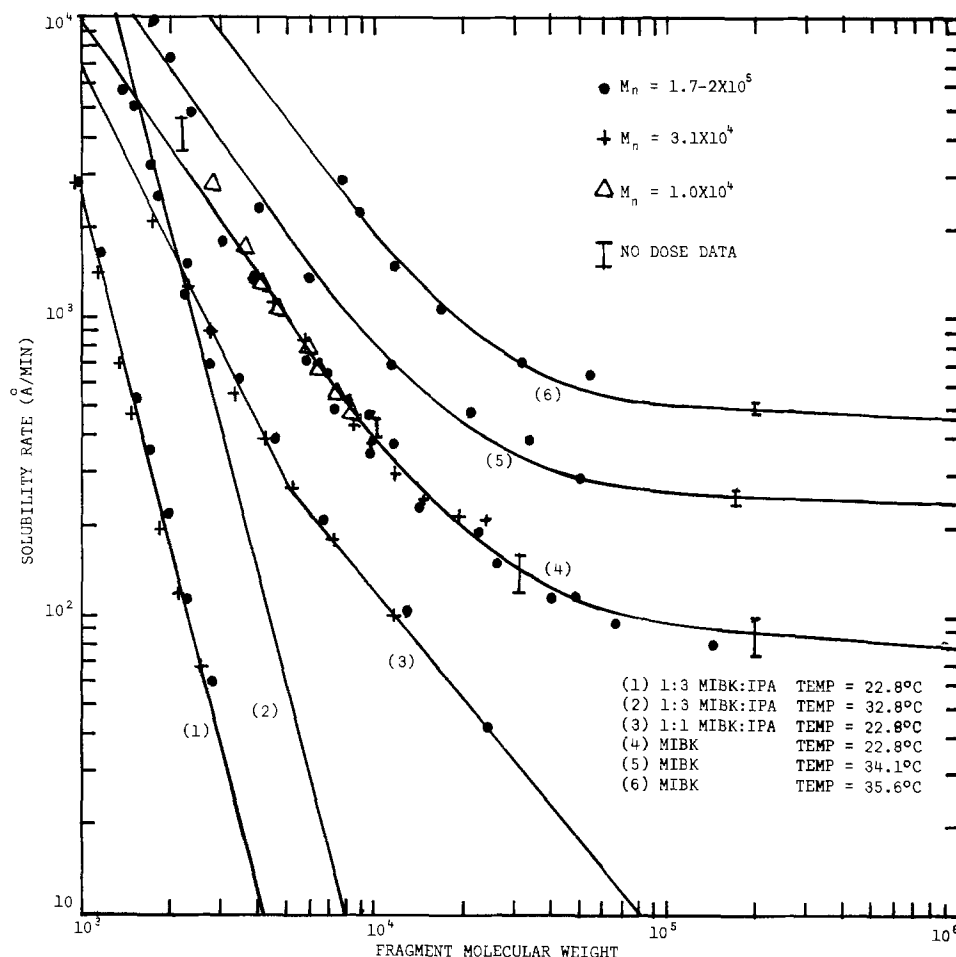


Fig. 5. The solubility rate vs. fragmented molecular weight for three different developers and for various temperatures. Data is for original molecular weights between 10^4 and 2×10^5 .

22.8°C and 1:3 MIBK:IPA at 45.6°C, respectively. Figure 3 is typical of most of the developer conditions studied and is indicative of a reaction rate process while the result shown in Fig. 4 is representative of a more complicated kinetics problem. The kinetics of the solubility process is discussed in more detail in a later section.

Solubility Rate

According to [1] the results of electron radiation on positive electron resists is expressed in terms of the fragmented molecular weight. Previously (7) we showed that the solubility rate for MIBK, defined as the slope of the thickness-developer time curve, is a function of fragment molecular weight as given by [1]. This result also applies to the other developer solvents reported here. In Fig. 5 we show the solubility rate vs. M_f for original molecular weights between 10^4 and 2×10^5 for the indicated developer conditions. In each case the solubility characteristics are of the rate limited type.

An empirical formula of the form

$$R = R_0 + \frac{\beta}{M_f^\alpha} \quad [5]$$

was fitted to the experimental data and is shown by the solid lines in Fig. 5. In Table I the values of R_0 , β , and α are given for R in angstroms per minute.

Kinetics of the Solubility Process

In this section we consider the two types of solubility characteristics illustrated in Fig. 3 and 4. We do not consider any solvent to remain in the polymer film although the increased solubility rate when solvent remains is expected on the basis of increased availability of the solvent at the plane of polymer-solvent interaction.

Ueberreiter has reviewed the solution process for polymers (11). According to the model a gel-like skin is formed between the pure solvent and the pure polymer after a short induction period.¹ For this model the solubility rate is given by

$$R = \frac{dz}{dt} = \frac{\bar{D}}{d} \quad [6]$$

where \bar{D} is a mutual diffusion coefficient of the polymer-solvent system and d is the skin thickness. Consequently, this model describes the linear decrease in resist thickness typical of most of the developer conditions reported.

According to the rate limited process the temperature dependent rate, R_T , is given in terms of an activation energy, E_a , as

¹ We have observed such an induction period for MIBK for very high molecular weight materials.

Table I. Parameters are tabulated for the solubility rate for various combinations of MIBK and IPA at several temperatures

Solvent	Temperature	R_0	β	α	Mol wt range
1:3 MIBK:IPA	22.8°C	0.0	9.332×10^{14}	3.86	—
1:3 MIBK:IPA	32.8°C	0.0	1.046×10^{16}	3.86	—
1:1 MIBK:IPA	22.8°C	0.0	6.700×10^9	2.00	—
1:1 MIBK:IPA	22.8°C	0.0	6.645×10^8	1.188	$> 5 \times 10^8$
MIBK	22.8°C	84.0	3.140×10^8	1.50	—
MIBK	34.1°C	241.9	5.669×10^8	1.50	—
MIBK	35.6°C	464.0	1.435×10^9	1.50	—

$$R_T = R e^{-E_a/kT} \quad [7]$$

where the functional dependence of R on M_f is given by [5]. Figure 6 shows a plot of $\ln R$ vs. $1/kT$ for MIBK for the indicated molecular weights. For the highest molecular weights, 2×10^5 , the straight line fit is excellent with an activation energy of 1.04 eV. For lower molecular weights the fit is somewhat worse.

The solubility rate of a polymer is determined by two factors: (i) the kinetic suitability of the solvent which determines \bar{D} , and (ii) the thermodynamic suitability of the polymer-solvent system is found in d which acts as a resistance to the penetrating solvent (11). In choosing a developer for positive electron resists, thermodynamic arguments are often used as commonly expressed in terms of a solubility parameter and an associated hydrogen bonding index (4, 12). For PMMA the result is a combination of a poor solvent (IPA) and a borderline solvent (MIBK). Many other solvent combinations with desirable thermodynamic properties are possible; a developer with a higher solubility rate results for solvents with high values of \bar{D} , and among molecules of similar chemical composition the rate depends mainly on the size of the molecule (11). This is an area for continued investigation.

As we show later it is desirable for the parameter α in [5] to be as large as possible for high contrast exposures. The temperature dependence of the developer 1:3 MIBK:IPA was investigated in hopes of increasing its solubility rate while maintaining its large value of α . Unfortunately, the solubility rate is nonlinear for temperatures $\geq 32.8^\circ\text{C}$; a typical result is shown in Fig. 4. This nonlinear time dependence is not well understood. Initially the solubility rate behaves in a manner consistent with lower temperature data. This is evidenced by an activation energy of 2.43 eV as shown in Fig. 7 where $\ln R$ vs. $1/kT$ is plotted. In Fig. 7 the initial solubility rate

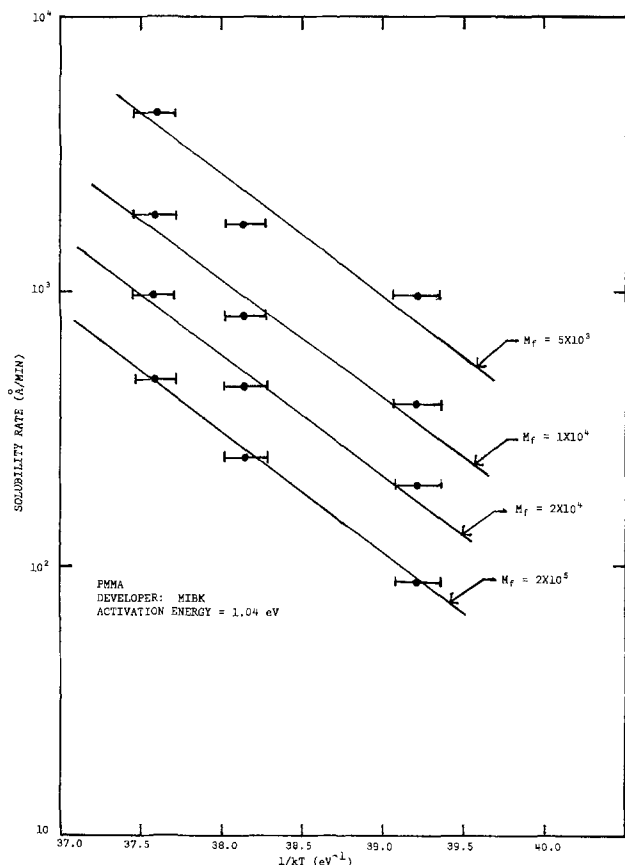


Fig. 6. Developer activation energy for MIBK

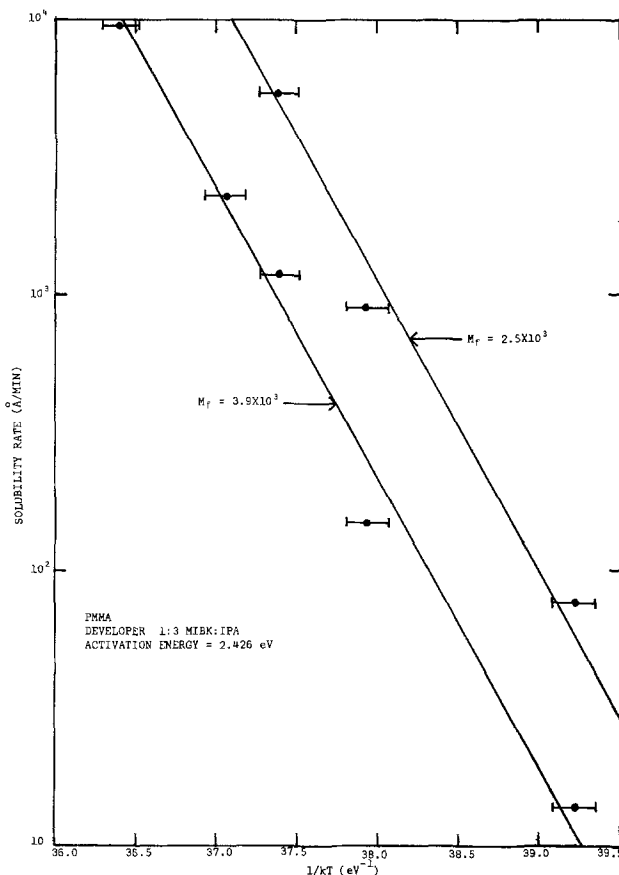


Fig. 7. Developer activation energy for 1:3 MIBK:IPA

was used for the higher temperature data. The higher activation energy of the standard developer compared to MIBK is perhaps indicative of the relatively poor thermodynamic solubility of the standard developer. From Fig. 4 it is apparent that the solubility rate saturates at a level independent of molecular weight. This behavior is found in the temperature range investigated, $37.2^\circ\text{--}54.4^\circ\text{C}$. The temperature dependence for the saturated solubility rate is difficult to determine; however, from the limited data available it appears to be nearly independent of temperature and molecular weight. This is perhaps indicative of a diffusion mechanism in which the transport across the boundary layer is the rate-limiting step.

Development Time and Contrast

In choosing a developer solvent and the electron-beam exposure parameters, a variety of objectives may be sought. For example, one may wish to obtain the highest resolution, minimize the incident charge per unit area, or minimize the developer time. There is a trade-off between these objectives. For the purposes of this section we will be concerned with area exposures and assume that the principal objective is to minimize the incident charge. As a secondary goal, the developer time should be minimized. The influence of developers on spatial resolution will be reported elsewhere (13).

To evaluate the relative merits of various exposure conditions we compute the developer time, τ , at a given temperature as

$$\tau = \int_0^{T_0} \frac{dz}{\left(R_0 + \frac{\beta}{M_f^\alpha} \right)} \quad [8]$$

where T_0 is the original resist thickness and the dependence of the solubility rate on z is found from [1]–[4]. For positive resists complete development to the resist-substrate interface is required. Consequently, the contrast, Γ , is found as (7)

$$\Gamma = 1 - \left(R_0 + \frac{\beta}{M_n^\alpha} \right) \frac{\tau}{T_0} \quad [9]$$

where M_n is the original molecular weight.

In the following we examine the influence of developer solvent, developer temperature, beam energy, resist thickness, and original molecular weight on the contrast and development time. We previously established (7) that for a given contrast level a larger M_n reduces the required Q at the expense of increased developer time.

Consider 5000Å of resist, molecular weight of 2×10^5 , subjected to 20 keV electrons. The required development time and contrast are shown in Fig. 8 and 9 as a function of Q for MIBK, 1:1 MIBK:IPA and 1:3 MIBK:IPA at 22.8°C and also MIBK at 35.6°C. The contrast for the 1:3 MIBK:IPA developer is taken as unity owing to the extremely small removal rate for the original molecular weight. According to [9] Γ should be independent of temperature; however, owing to the slight deviation from $\exp(-E_a/kT)$ in the experimental data, Γ varies slightly with temperature for MIBK as shown in Fig. 9.

It is apparent that a wide range of contrasts and developer times are obtained for the various developer conditions. For example, accepting a 50% contrast (2500Å of resist remains), the required charge

can be reduced by over an order of magnitude compared to the standard developer by using other developers. A penalty is paid in developer time. For example, the developer time for $\Gamma = 0.5$ for 1:1 MIBK:IPA would be 750 min, hardly a usable developer. More reasonable developer times are obtained for $\Gamma = 0.5$ for MIBK: 29 min at 22.8°C and 5.3 min at 35.6°C.

According to Fig. 1, for a given Q a lower beam energy results in a higher ϵ . This results in a smaller fragmented molecular weight and, hence, an increased solubility rate. The influence of beam energy on Γ is shown in Fig. 10 for E_0 between 10 and 30 keV. The development time (upper time axis) for a given Γ is shown as the dotted line; it is the same for each of these energies except for very small Γ .

For a given resist thickness there is a lower useful limit on the incident energy; the range R_G [4] defines the thickness and hence energy beyond which the energy absorption is negligible. For positive resists, narrow linewidths are easily obtained at higher incident energies (3) and consequently reducing the beam energy to increase energy absorption may not always be compatible with the desired resolution. Another practical aspect is, for a given SEM beam diameter a decrease in beam energy decreases the beam current, I_B . This decrease is approximately first order in beam energy. Since the increase in ϵ is also first order in energy, then as the beam energy is decreased the required resist exposure time per unit area, Q/I_B , would remain constant independent of energy. Scaling the results in Fig. 10 by the ratio of beam energies confirms this conclusion.

In using a developer such as MIBK which slowly removes high molecular weight PMMA, some reduction in the required Q is achieved by using thicker resist films and taking advantage of the increased ϵ with increasing penetration depth. In this situation the remaining resist thickness, T_r , is specified. In Fig. 11 the required Q is plotted as a function of T_0 for two values of T_r (solid lines) for $E_0 = 10$ keV, $M_n = 2 \times 10^5$ and MIBK at 22.8°C. The right-hand axis gives the required development time and is plotted vs. T_0 (dashed lines). Certainly a reduction in original Q is obtained as T_0 increases at the expense of increased developer time. Two values of T_0 might be considered as optimum. One is the thickness at which the peak in the energy dissipation occurs (0.76 μm at 10 keV) and the other is the thickness at which the energy dissipation equals that at the surface (1.6 μm at 10 keV). The former is preferred if narrow linewidths are required.

Given a desired T_r and choosing E_0 and T_0 , the development time is reduced by increasing the devel-

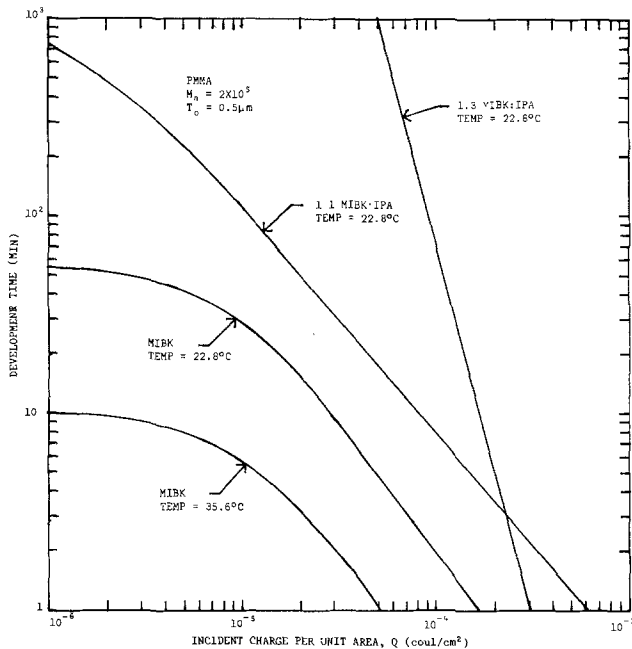


Fig. 8. The dependence of developer time on Q

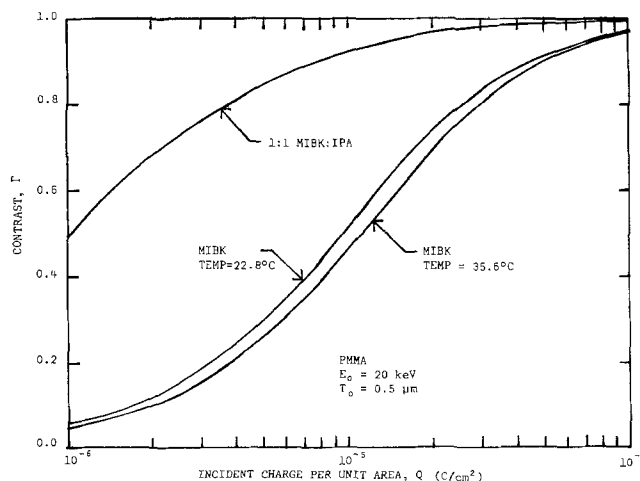


Fig. 9. The contrast as a function of Q

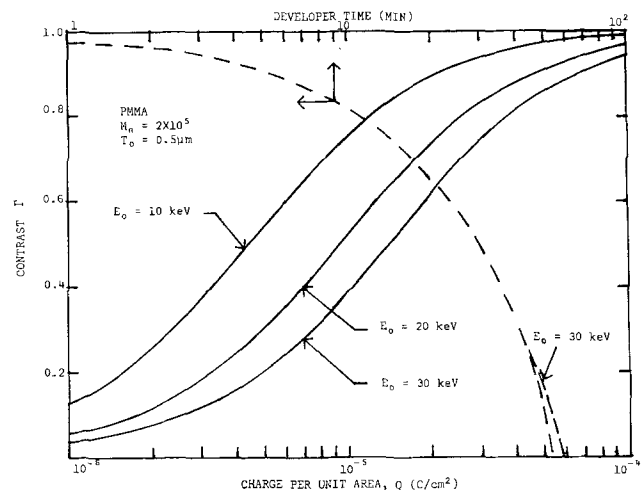


Fig. 10. Influence of beam energy on contrast. The dashed line gives the development time (upper time axis) for a given contrast level.

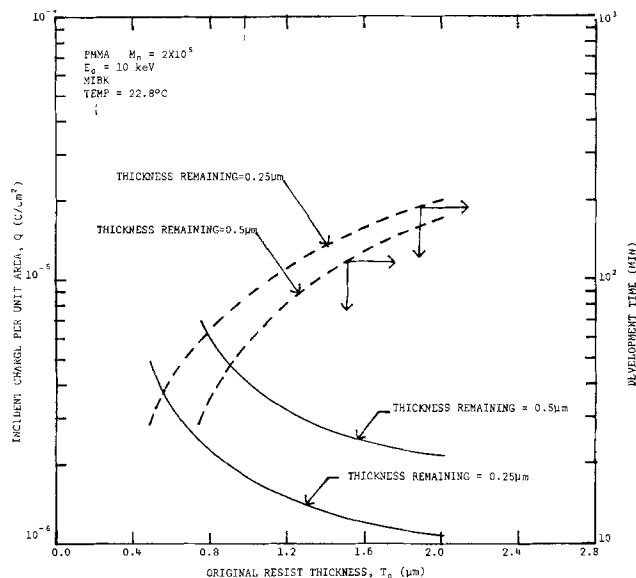


Fig. 11. The required charge per unit area as a function of the original resist thickness (solid lines) resulting in the two final resist thicknesses indicated. The corresponding development time (right axis) is shown as a function of Q by the dashed lines and indicated by the arrows.

oper temperature and/or reducing the original molecular weight. This is illustrated in Table II for $T_r = 0.25 \mu\text{m}$, $E_0 = 10$ keV, and $T_o = 0.76 \mu\text{m}$. The developer is MIBK at two temperatures, 22.8° and 35.6°C. Also given in Table II is the required incident charge to yield the desired resist thickness. For this situation the required incident dose is reduced by a factor of ~50 compared to the standard developer at 22.8°C.

Conclusions

The following results and conclusions are made for the combinations of MIBK and IPA used as developers for PMMA in this study.

1. A technique for predicting developer characteristics for positive electron resists has been developed in which the solubility rate is determined as a function of fragmented molecular weight.

2. An empirical formula for the solubility rate of the form $R = (R_0 + \beta/M_r^\alpha) e^{-E_a/kT}$ is found with the constants R_0 , β , and α dependent upon the developer solvent. Activation energies, E_a , for MIBK and 1:3

Table II. The influence of original molecular weight and developer temperature on development time is tabulated. Also shown is the required minimum Q to yield the final resist thickness, 0.25 μm.

Original molecular weight	MIBK Development time (min)		Required charge per unit area ($\mu\text{C}/\text{cm}^2$)	
	Temp = 22.8°C	Temp = 35.6°C	Temp = 22.8°C	Temp = 35.6°C
2.5×10^4	30.6	6.1	2.6	2.9
5.0×10^4	44.6	8.6	2.3	2.6
7.5×10^4	50.4	9.5	2.3	2.6
1.0×10^5	54.3	10.0	2.3	2.7
1.5×10^5	57.0	10.4	2.4	2.8
2.0×10^5	58.3	10.6	2.5	2.8

MIBK:IPA are found to be 1.04 and 2.43 eV, respectively.

3. The contrast and development times are functions of developer, developer temperature, beam energy, resist thickness, and original molecular weight.

4. An improved sensitivity compared to the standard developer for PMMA of from 10 to 50 times is obtained by using different developers and temperatures.

5. The solubility kinetics of PMMA is characterized by a rate-limited process for most developer conditions. At high temperatures 1:3 MIBK:IPA shows a combination of a rate-limited process and a diffusion process.

Acknowledgments

The author would like to thank M. C. Steele and J. W. Hile for helpful discussions of this material. Thanks are also due to L. L. Hegedus for discussions of the solubility kinetics, E. R. Cprek for use of the SEM, R. A. Ottovani for several samples of PMMA, A. M. Wims for molecular weight analysis, and B. J. Vannoy for substrate preparation.

Manuscript submitted July 17, 1974; revised manuscript received Nov. 18, 1974.

Any discussion of this paper will appear in a Discussion Section to be published in the June 1976 JOURNAL. All discussions for the June 1976 Discussion Section should be submitted by Feb. 1, 1976.

Publication costs of this article were partially assisted by General Motors Corporation.

REFERENCES

1. M. Hatzakis, *This Journal*, **116**, 1033 (1969).
2. J. S. Greeneich and T. Van Duzer, *J. Vacuum Sci. Technol.*, **10**, 1056 (1973).
3. J. S. Greeneich and T. Van Duzer, *IEEE Trans. Electron Devices*, **ED-21**, 286 (1974).
4. R. F. Herzog, J. S. Greeneich, T. E. Everhart, and T. Van Duzer, in "Record of 11th Symposium on Electron, Ion, and Laser Beam Technology," R. F. M. Thornley, Editor, San Francisco Press, San Francisco (1971). Also *IEEE Trans. Electron Devices*, **ED-19**, 635 (1972).
5. M. Hatzakis and A. N. Broers, in "Record of 10th Symposium on Electron, Ion, and Laser Beam Technology," L. Marton, Editor, pp. 107-114, San Francisco Press, San Francisco (1969).
6. C. H. Ting, in "Record of 11th Symposium on Electron, Ion, and Laser Beam Technology," R. F. M. Thornley, Editor, pp. 337-344, San Francisco Press, San Francisco (1971).
7. J. S. Greeneich, General Motors Research Publication, GMR-1547; *This Journal*, **121**, 1669 (1974).
8. J. S. Greeneich, Unpublished Ph.D. dissertation, University of California, Berkeley, California (1973). Also, Ref. (4) contains a similar expression.
9. A. Chapiro, "Radiation Chemistry of Polymeric Systems," Vol. 15, pp. 337-380, John Wiley and Sons, Inc., New York (1962).
10. T. E. Everhart and P. H. Hoff, *J. Appl. Phys.*, **42**, 5837 (1971).
11. K. Ueberreiter, in "Diffusion in Polymers," J. Crand and G. S. Park, Editors, pp. 219-257, Academic Press, London (1968).
12. M. J. Bowden and L. F. Thompson, "165th Meeting ACS—Organic Coatings and Plastics Chemistry," Dallas, Texas, April 8, 1973.
13. J. S. Greeneich, *J. Appl. Phys.*, To be published.

Cross-Slip Dislocations and Their Multiplication in (001)-Oriented Silicon Wafers

Junji Matsui

Nippon Electric Company, Limited, Central Research Laboratories, Kawasaki, 211 Japan

ABSTRACT

Dislocations consisting of a pair of half-loops are found to be characteristic of (001)-oriented silicon wafers, and they are also found to develop and multiply by a combination of cross-slipping of screw segments and their interaction with wafer surfaces. They originate from internal sources which seem to be precipitates formed during course of thermal oxidation.

Recently, silicon single crystals free from dislocations have been available for device fabrications. As is well known, however, several types of defects are often generated in dislocation-free silicon wafers during various device fabrication processes such as thermal oxidation, impurity diffusion, or application of an epitaxial layer. It has been reported that, from the device fabrication point of view, generation of these defects makes it less significant to use a dislocation-free crystal as a starting material. Among those defects, dislocations are especially harmful to the characteristics of fabricated devices, such as leakage current of diodes, whether they are complete dislocations with a Burgers vector of $a/2\langle 110 \rangle$ type or partial dislocations with that of either $a/6\langle 211 \rangle$ or $a/3\langle 111 \rangle$ type. Therefore, it becomes important to know mechanisms in which the dislocations of any type form and multiply in silicon crystals. Several mechanisms of the dislocation formation and multiplication in (111)-oriented silicon wafers have been proposed by many investigators (1-12). Sources of the dislocations have been associated with precipitates (1, 3-4), ruptures at wafer edges (2, 5-6), scratches (7-10), surface irregularities (1-2, 11), and some other defects (12).

It has also been reported that dislocation-free silicon wafers subjected to heat-treatments often reveal a number of circular stacking faults (13-14) and prismatic dislocation loops (14-16) either in the (111)- or (001)-oriented wafers. Particularly when float-zoned, dislocation-free silicon wafers containing grown-in defects along swirls were thermally oxidized, a number of circular stacking faults were also preferentially generated along swirls. On reheating to the subsequent oxidation, hexagonal half-loops of complete dislocation were found to be formed in addition to the stacking faults (17). The nature and structure of the circular stacking faults have been investigated previously (13) but not in detail for the hexagonal half-loops. Structure and dislocation velocities of similar half-loops in the case of (111)-oriented wafers have been determined by Patel and Freeland (8) and George *et al.* (10, 18) from the experimental results of intentional load application to the materials.

This paper describes detail features of the hexagonal half-loops and discusses the multiplication mechanism which may be characteristic of (001)-oriented wafers, from the observation of the dislocations by means of x-ray diffraction topography.

Experimental

Specimens used were (001)-oriented, n-type silicon wafers with a resistivity of about 10 ohm-cm, cut from a float-zoned, dislocation-free crystal rod with a diameter of about 30 mm. Some swirl patterns could be made visible by suitable etching on surfaces of the specimen wafers. They were thinned to about 200 μm by mechanical and chemical methods. Two sequential

Key words: dislocation multiplication, cross-slip, x-ray topography.

thermal oxidations were employed. First thermal oxidation for the generation of circular stacking faults along swirls was carried out at 1200°C for 22 hr in a dry oxygen atmosphere. A rapid cooling from the first oxidation was made by extracting the specimens from the center of a furnace to the edge of a quartz tube in less than 20 sec. Second thermal oxidation was carried out in such a manner that the specimens were inserted into the furnace from room temperature to around 600°C very rapidly and then moved to the center of the high temperature zone in about 20 sec and kept there at 1200°C for 3 hr in a wet oxygen atmosphere, which gave rise to the generation of prismatic dislocation loops or hexagonal half-loops. Formation of both the stacking faults and hexagonal half-loops described in this report did not appear to be essentially dependent on whether the oxygen is dry or wet.

In order to observe configurations of both the defects and to determine their Burgers vectors, x-ray diffraction topographs were taken after each oxidation using $\text{MoK}\alpha_1$ radiation. All the topographs were recorded on Fuji nuclear plates, ET-7B type, 50 or 100 μm thick emulsion.

Results

Figure 1 shows a topograph of a part of a wafer taken after the second thermal oxidation. Some contrasted ellipses designated as S have been found to correspond to circular stacking faults, each of them surrounded by a partial dislocation loop with a Burgers vector of $a/3\langle 111 \rangle$ Frank sessile type (13-14). These faulted loops were found to be formed in one of $\{111\}$ planes during the course of the first thermal oxidation.

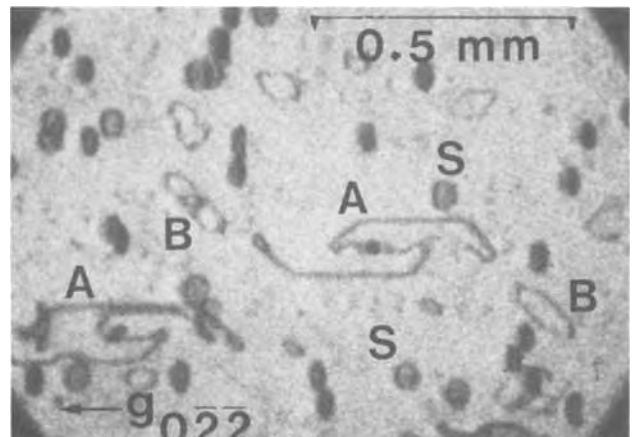
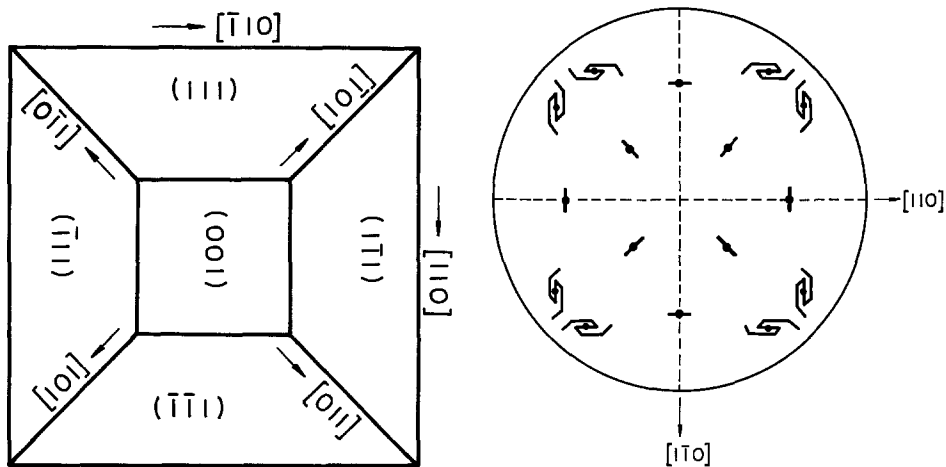


Fig. 1. Topograph of a specimen taken after double thermal oxidation. Besides a number of circular stacking faults, designated as S, which are generated after a first thermal oxidation, several dislocations consisting of a pair of half-loops are observed. The Burgers vectors of the dislocations A and B are parallel and inclined to the wafer surface, respectively.

Fig. 2. a (left), Orientations of dislocation lines and glide planes. b (right), Illustration showing a rough distribution and configuration difference of dislocations in a single wafer.



At the conclusion of the second thermal oxidation, other kinds of dislocations in addition to the above circular stacking faults are seen, designated as A and B in Fig. 1. From observation of stereotopographs and topographs reflected from various planes, it is found that the dislocations A in Fig. 1 are lying in two sets of $\{111\}$ planes inclined at the same angle of $54^{\circ}44'$ to the (001) surface plane, and that they have Burgers vectors of $a/2\langle 110 \rangle$ type parallel to the surface and consist of 60° and screw segments with $\langle 110 \rangle$ orientation.

Figure 2 presents a schematical rough distribution and configuration difference of dislocations in a single wafer. Pairs of half-loops are mostly symmetrical in shape with respect to two equivalent $\{110\}$ planes normal to the (001) surface. These dislocations appear to be located in the vicinity of the surfaces, and dislocations close to the upper and lower surfaces give a similar feature on a projected topograph, which may be due to the effect of external stresses during heat-treatments, as will be discussed later in detail.

A typical configuration of the dislocation on a certain stage of development as seen in Fig. 1 is schematically shown in Fig. 3 judged from stereotopographic observation. Since the Burgers vector of this dislocation is parallel to the $[110]$ direction, segment a (Fig. 3) emerging at the surface is a 60° dislocation with the $[101]$ orientation, segment b a screw dislocation parallel to the surface, segment c a 60° dislocation with the $[011]$ orientation, and segment d again a screw dislocation. [Hereafter, these will be abbreviated, respectively, as segments a(M, $[101]$), b(S, $[110]$), c(M, $[011]$), and d(S, $[110]$).] Thus, segments a, b, c, and d are lying in the inclined (111) plane, while segments l(S, $[110]$), m(M, $[011]$), n(S, $[110]$), and o(M, $[101]$) are in the $(\bar{1}\bar{1}\bar{1})$ plane. Segments e(M, $[011]$), f(S, $[110]$), and g(M, $[101]$) are parallel to segments m, n, and o, respectively, and segments i(M, $[101]$), j(S, $[110]$), and k(M, $[011]$) are parallel to segments a, b, and c, respectively. As this feature has not been observed in (111)-oriented wafers (8, 10), the dislocation configuration mentioned above seems to be characteristic of (001)-oriented wafers due to crystallographic orientation of the $\{111\}$ glide planes, i.e., a pair of inclined $\{111\}$ planes, as (111) and $(\bar{1}\bar{1}\bar{1})$ planes in this case, which always lie symmetrically and intersect at a line parallel to the (001) surface.

Besides the fact that the dislocations, as well as the stacking faults, appear preferentially along swirls in oxidized dislocation-free crystals, it is observed that the dislocations consisting of half-loops show dark contrast of a nucleation source lying mostly along a screw segment (as segment h in Fig. 3) which connects two half-loops lying in the different $\{111\}$ planes. These facts may suggest that the dislocations originate from some clustered defects such as precipitates of oxygen atoms (1, 3, 19), which seem to nucleate during

the course of the first thermal oxidation at the grown-in defects usually located along swirls in float-zoned, dislocation-free silicon crystals (20-21). Although the precipitate particles can be expected to nucleate not only near the wafer surfaces but also in the bulk, growth of the dislocation loops around the precipitates may be more intensive near the oxidizing surfaces than in the interior, as will be discussed later.

Discussion

Formation mechanism of dislocations.—It has been reported that oxidized, Czochralski-pulled, dislocation-free silicon crystals reveal both stacking faults surrounded by a Frank partial dislocation and prismatic

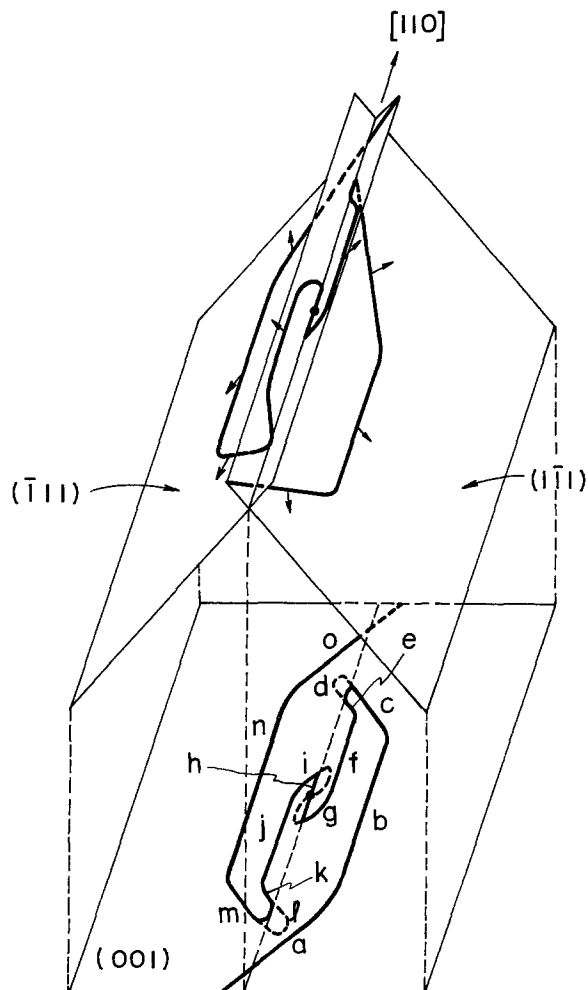


Fig. 3. Spatial illustration of a dislocation lying in two different $\{111\}$ planes with its projection onto (001) plane.

dislocation loops consisting of $a/2\langle 110 \rangle$ type complete dislocations (14-15). In case of float-zoned, dislocation-free crystals containing such grown-in defects along swirls as in the present experiment, however, extrinsic stacking faults surrounded by a Frank partial dislocation loop, i.e., faulted loops, rather than prismatic dislocation loops, are believed to be preferably generated after the first thermal oxidation. But, the fact that the density of the circular stacking faults in a singly oxidized wafer is always lower than that of the grown-in defects which can be seen by etching before oxidation seems to indicate that not all of the grown-in defects turn out to be nuclei of the extrinsic stacking faults. It can be expected, therefore, that the rest of the grown-in defects may provide requisite sites for the aggregates of oxygen atoms which are pre-existent in the specimen or also induced from the surfaces.

On rapid cooling after a first high temperature oxidation, considerably large thermal strains will arise around the precipitate particles since the precipitate particles, probably SiO_2 , form with larger specific volume than the silicon. It is speculated, therefore, that small prismatic loops of complete dislocation start to develop at the precipitate surfaces at the beginning of a second thermal oxidation so that the strains may be accommodated. Once the dislocation loops are formed, they will become more active emission sources of vacancies than are the stacking faults during a second thermal oxidation. These ideas seem to be supported by a previous report (22) describing the fact that cir-

cular stacking faults failed to be formed in dislocated crystals or in the vicinity of complete dislocations in low-dislocation-density crystals, and also by the fact that additional stacking faults were not observed at all after a second thermal oxidation while a number of prismatic dislocation loops and hexagonal half-loops were.

From the above consideration, the prismatic dislocation loops would be expected to be of interstitial type rather than of vacancy type and thus, as are the extrinsic stacking faults, the dislocation loops would be bulged by dislocation climb resulting from vacancy emission from the dislocation lines to the surfaces where the vacancies are consumed under oxidation conditions (23). Expansion of the loops should take place more markedly in the region close to the oxidizing surfaces for the above mechanism to be important, in order to be consistent with the present experimental result that the nucleation sources lying along the connecting screw segments are located at depths of less than $40 \mu\text{m}$ below the surfaces, which are known from the observation of the topographs.

Figures 4(a-f) reveal various configurations of the dislocations and indicate that they are on different stages of development and of multiplication probably due to the difference of magnitude of thermal stresses exerted on them during a second thermal oxidation. From the observation of those dislocations, development processes can be derived as schematically illustrated in Fig. 5 which presents successive views of dis-

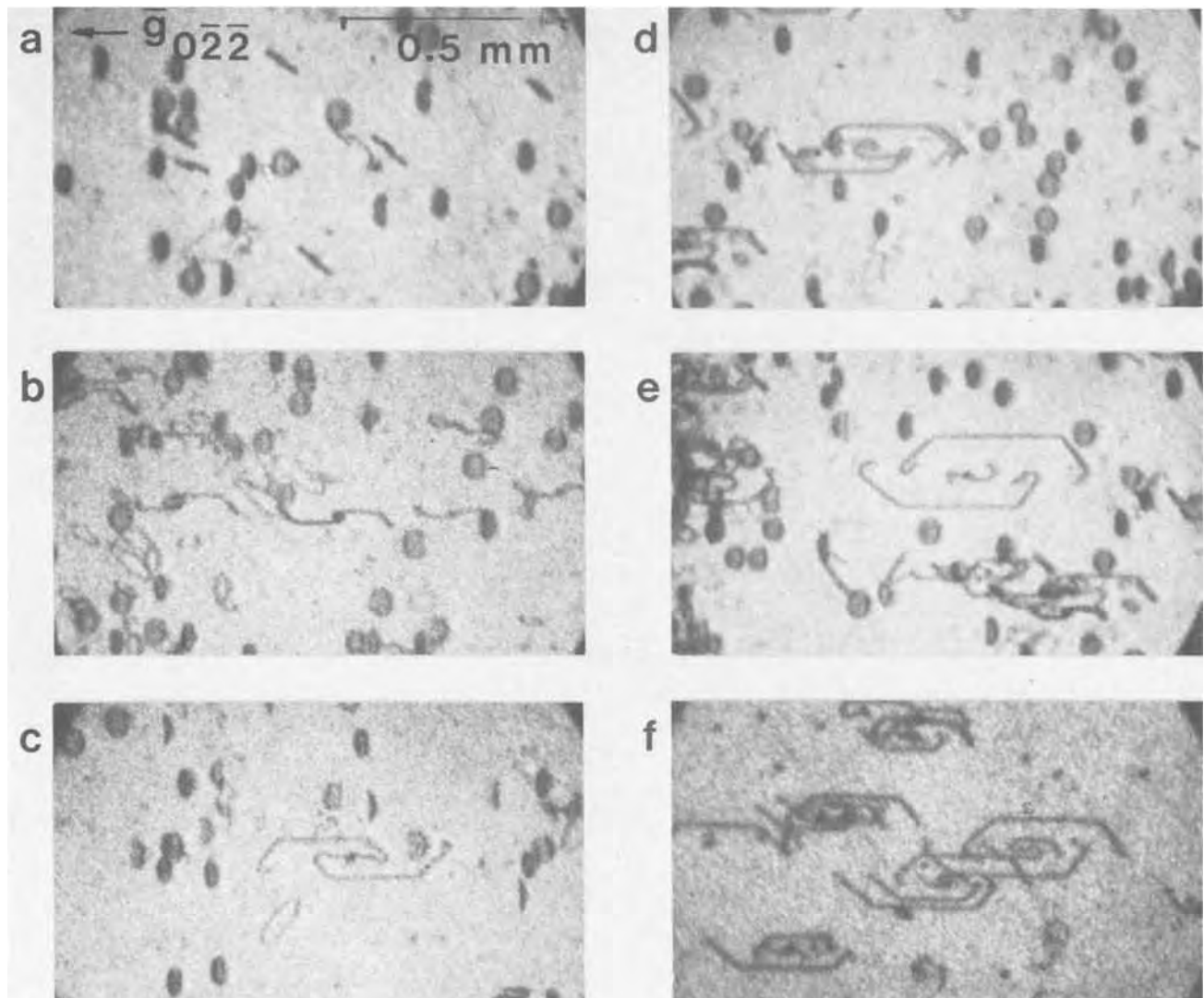


Fig. 4. Topographs showing various configurations of the dislocation half-loops. They seem to correspond to different stages of development.

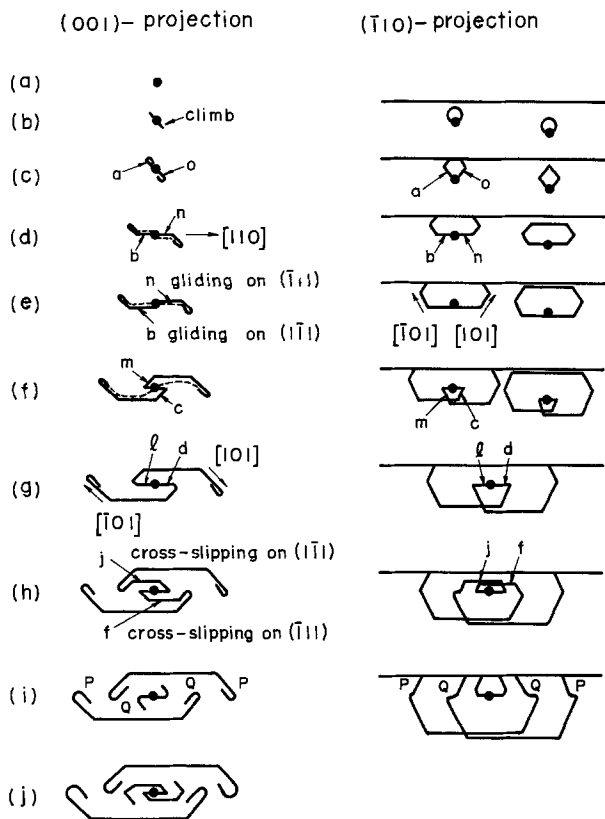


Fig. 5. Schematic illustrations showing successive views of development and multiplication processes as projections onto the (001) and (110) planes. Designations to the dislocation segments correspond respectively to those in Fig. 3.

location shapes projected onto the (001) and (110) planes. The dislocation half-loops shown in Fig. 4(a-f) would thus be expected to form by a combination of expansion of prismatic loops and their subjection to thermal stresses, as follows.

At the first stage, small prismatic loops of interstitial type attached to the precipitates may be emitted in

order to lower strain energy increased around the precipitates. Both ends of a single dislocation line would be connected to the surface of a single precipitate. Vacancy emission may be more accelerated at the side close to the surface than the side further from the surface, as shown in Fig. 5b. Incipient alignment of the dislocation line of the climbing dislocation may not be in a particular direction because of high density of jogs on the line. However, <110> alignments would be preserved after considerable expansion of the dislocation loops since hexagonal prismatic loops consisting of straight, <110>-oriented segments have been observed so far in heat-treated silicon crystals (11, 14-15, 18). Therefore, it can be expected that, as shown in the left side of the (110)-projections in Fig. 5(b and c), once a part of the dislocation loop line gets to a wafer surface, it is cut there and resolved into two dislocation lines which connect the precipitate surface and the wafer surface, and which will make a projection onto the (001) plane as is shown in Fig. 5(b and c) consistent with the actual feature of dislocations seen in Fig. 4a. Under the influence of thermal stresses which the specimen undergoes during a second thermal oxidation, each <110>-aligned segment of the prismatic dislocation loops lying in one of the inclined {111} planes would glide in the direction parallel to the Burgers vector. Since the Burgers vectors are $a/2$ <110> type parallel to the surface as already mentioned, the two <110> segments, e.g., segment a(M, [101]) in the (111) plane and segment o(M, [101]) in the (111) plane, as shown in Fig. 5d, glide inevitably in opposite directions from each other with respect to the precipitate, the phenomenon being related to the sense of resolved shear stress in each of the {111} planes. When the specimen is subjected to the thermal stress τ_1 in the [110] direction as shown in the upper part of Fig. 6, resolved shear stresses in the (111) and (111) planes are of such senses as seen in the right-hand part of Fig. 6, where \odot and \otimes mean directions in which the stresses drive the material normally above and below the sheet, respectively. It is apparent that another shear stress τ_2 does not play a role for the movement of the present dislocations because of a null Schmid factor for either the [110]/(111) or [110]/

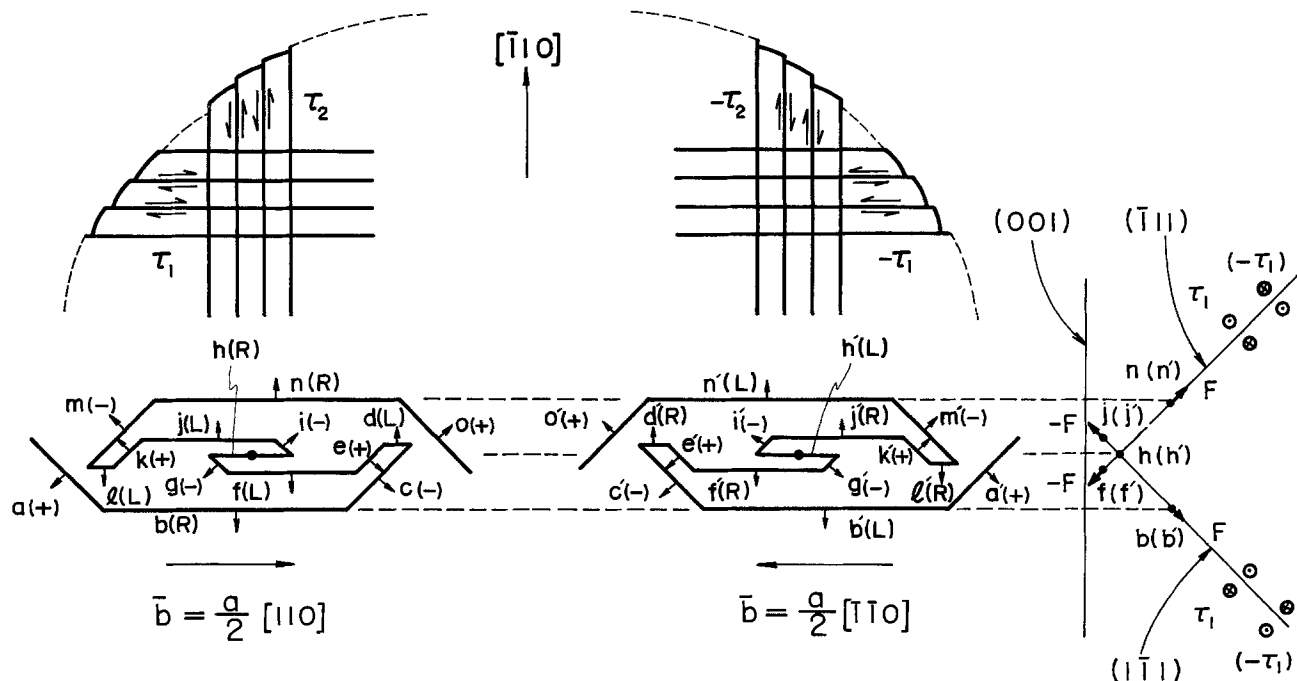


Fig. 6. Movement of each segment of half-loops under the influence of resolved shear stresses exerted parallel to the [110] directions. A 60° segment with the sign (+) has an extra half-plane above the glide plane whereas that with the sign (-) below the glide plane. A screw segment as noted by R in parentheses is of a right-hand screw character whereas that indicated by L is of a left-hand one.

($\bar{1}\bar{1}\bar{1}$) slip system. Supposing that extra half-planes which terminate at the lines of segments a and o exist above ($\bar{1}\bar{1}\bar{1}$) and ($\bar{1}\bar{1}\bar{1}$) planes, respectively [hereafter, segment r of 60° dislocation having an extra half-plane above the glide plane (on the side of the (001) surface) will be written as segment r(+, M, $\langle 110 \rangle$) while that below the glide plane (on the side of the (00 $\bar{1}$) surface as segment r(-, M, $\langle 110 \rangle$)], the a(+, M, $[\bar{1}0\bar{1}]$) segment on the ($\bar{1}\bar{1}\bar{1}$) plane should glide in the $[\bar{1}\bar{1}0]$ direction (to the left) and the o(+, M, $[10\bar{1}]$) segment on the ($\bar{1}\bar{1}\bar{1}$) plane should glide in the $[1\bar{1}0]$ direction (to the right), under the resolved shear stresses mentioned above. This process must leave a screw segment which connects segments a and o. This screw segment is regarded as made of two parts, i.e., segments b and n on both sides of the precipitate, as shown by the solid lines in Fig. 5d. From the above consideration, the screw segments should be right-hand screw dislocations [hereafter, segment r of this type will be written as segment r(R, S, $\langle 110 \rangle$), while that of left-hand screw type as segment r(L, S, $\langle 110 \rangle$)]. Apparently, both the b(R, S, $[110]$) segment in the ($\bar{1}\bar{1}\bar{1}$) plane and the n(R, S, $[110]$) segment in the ($\bar{1}\bar{1}\bar{1}$) plane exert motive forces, F , normal to the segment lines in each of the $\{111\}$ planes also due to the resolved shear stresses and, as a result, each of the screw segments glides independently deeper into the wafer thickness in one of these planes. Dislocation configuration as seen in Fig. 5e and actually as shown in Fig. 4b can be thus obtained, and furthermore, formation of the other two 60° dislocations as in segments c(-, M, $[01\bar{1}]$) and m(-, M, $[0\bar{1}\bar{1}]$) shown in Fig. 5f and of two screw dislocations as in segments d(L, S, $[110]$) and l(L, S, $[110]$) in Fig. 5g takes place. These segments move in such a way that each half-loop expands continuously in each glide plane, and the resulting feature is such a one as seen in Fig. 4c.

Another formation process of the dislocation shown in Fig. 5g may be possible in which the glide motions mentioned above precede arrival of a part of the dislocation line at the surface. The dislocations having not yet reached the surface are shown by the dashed lines in Fig. 5(c-f) in addition to the solid lines and are also shown in the right side of the ($\bar{1}\bar{1}0$)-projections. Dislocation features as seen in Fig. 7(a and b) appear to correspond to this case. By either development process, the dislocation configuration as shown in Fig. 5g can be explained. At this time, the most part of segments d and l in Fig. 5g exert motive forces, $-F$, whose sense is opposite to those on segments n and b as shown in Fig. 6. Therefore, they cross-slip on the ($\bar{1}\bar{1}\bar{1}$) and ($\bar{1}\bar{1}\bar{1}$) planes, respectively, turning themselves into f(L, S, $[110]$) and j(L, S, $[110]$) segments connected to a pair of the other 60° dislocations, i.e., e(+, M, $[0\bar{1}\bar{1}]$) and g(-, M, $[10\bar{1}]$) segments for segment f and k(+, M, $[01\bar{1}]$) and i(-, M, $[\bar{1}0\bar{1}]$) segments for segment j as shown in Fig. 5h and also actually seen in Fig. 1 and 4d. When segments f and j reach an oxidizing surface again, then these segments disappear and only 60° segments are left, being emergent at the surface as shown in Fig. 4e and 5i. Thus, the dislocation becomes the one that consists of two half-loops and also of one inside dislocation which is of mostly screw character and suspended at the surface. The latter is ready to give off another pair of half-loops by going through the same process all over again, since it is also a right-hand screw segment as are segments b and n. Accordingly, whenever left-hand screw segments cross-slip and emerge from the surface and hence annihilate there, dislocation multiplication takes place and in turn, formation of pairs of multi-fold half-loops occurs as shown in Fig. 4f and 5j.

It should be noted that part of the 60° segments on both of the ends of each half-loop seem to, at their

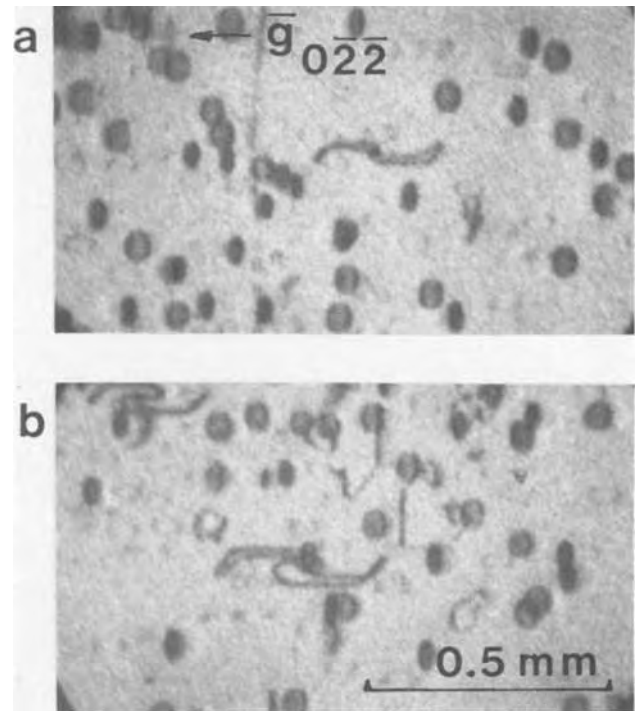


Fig. 7. Dislocations expanding by glide in the direction parallel to the surface before a part of each dislocation line arrives and annihilates at the surface. (a), Early and (b), later stages of development.

emerging points, depart from the initial glide planes since they are not in rectilinear alignments but are revealed in the shape of a hook on the projected topographs, as shown in Fig. 1 and 4e. In fact, stereotopographs give a nonplanar configuration of the dislocations at both the emerging points of each half-loop. George *et al.* (10) have reported that similar bends of the emergent segments observed in (111)-oriented wafers are caused by the cross-slip of screw segments. In the present case of the (001)-oriented wafers, however, this mechanism does not seem to hold since the emergent segments themselves are not screw but 60° dislocations. Apparently one of the bends in a single half-loop, connected to segment a or o as at P in Fig. 5i, is generated in an early stage of development, as already mentioned. The other bend, Q, is made of a 60° segment such as segment e or k, as a result of the disappearance of the cross-slipped screw segment such as f or j segment. After all, it is evident that formation of the two bends takes place due to interaction of the dislocations of screw character with the specimen surface.

The symmetry of the dislocation configuration illustrated in Fig. 2b seems quite reasonable since, as shown in Fig. 6, thermal shear stresses, felt by the dislocations in the opposite sides of the wafer with respect to the (110) plane normal to the stress direction, are in the opposite directions from each other and thus, screw segments of both the dislocations, e.g., segments b(R, S, $[110]$) and b'(L, S, $[110]$), are also of opposite senses, whereas the same development mechanism may preside over both the dislocations.

Another type of dislocation.—Another type of dislocation is observed to coexist with the dislocations described above, as marked by B in Fig. 1 and also as shown in Fig. 8, the former having the shape of a full hexagon, whether regular or partly perturbed, and the latter lacking some segments. Each hexagon on the topograph projected onto the (001) plane usually consists of four $\langle 110 \rangle$ segments and two $\langle 100 \rangle$ segments. Stereotopographs show that they are also lying in two sets of adjacent $\{111\}$ planes, as schematically shown

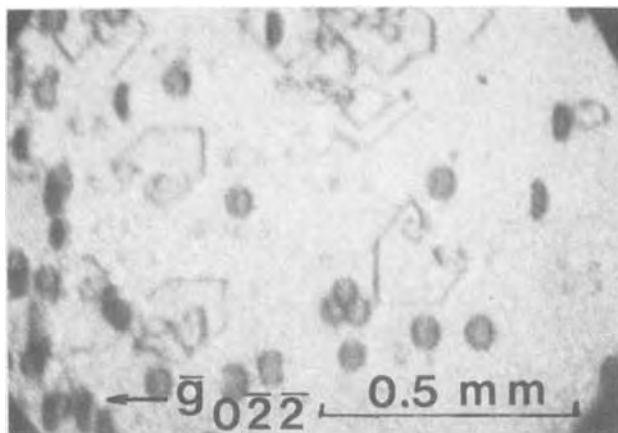


Fig. 8. Another type of dislocation of which Burgers vector is inclined to the wafer surface.

in Fig. 9. They are found to have a Burgers vector of $a/2\langle 110 \rangle$ inclined to the surface, and are also found to be prismatic dislocations which contain a pair of screw segments of opposite senses, e.g., as shown in Fig. 9, segments u (M, $[110]$) and v (S, $[011]$) are in the $(1\bar{1}1)$ plane, and segments x (M, $[\bar{1}\bar{1}0]$) and y (S, $[011]$) are in the $(\bar{1}\bar{1}1)$ plane, while segments w (M, $[\bar{1}\bar{1}0]$) and z (M, $[110]$) are in the $(\bar{1}\bar{1}1)$ and $(1\bar{1}1)$ planes, respectively, parallel to the x and u segments.

This type of dislocation is thought to develop through such processes as are schematically shown in Fig. 10. First, as well as the previous dislocations, sources of the dislocations are probably precipitates, although they are located at larger distances from the surface than those in the previous case. Then, round dislocation loops would be emitted from the precipitates by climb, since these loops seem to lie in planes

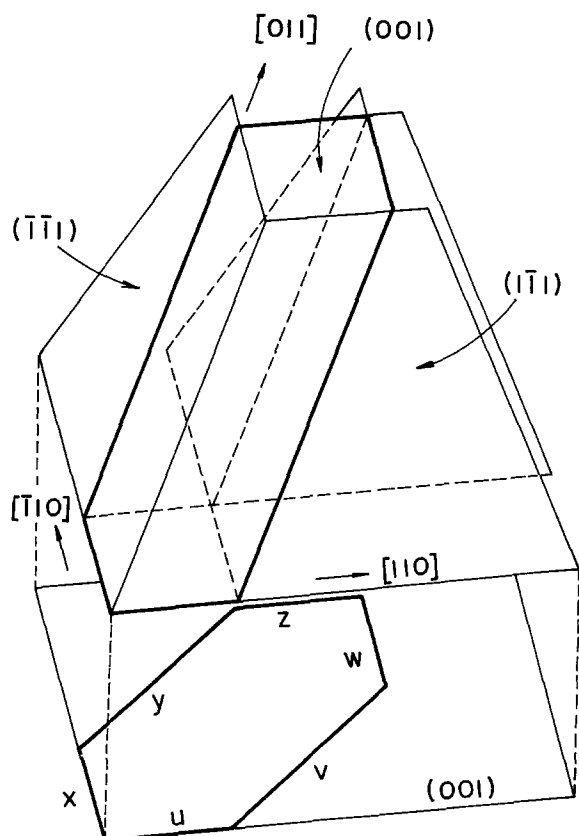


Fig. 9. Spatial illustration of a dislocation with an inclined Burgers vector as B in Fig. 1 and in Fig. 8, with its projection onto (001) plane.

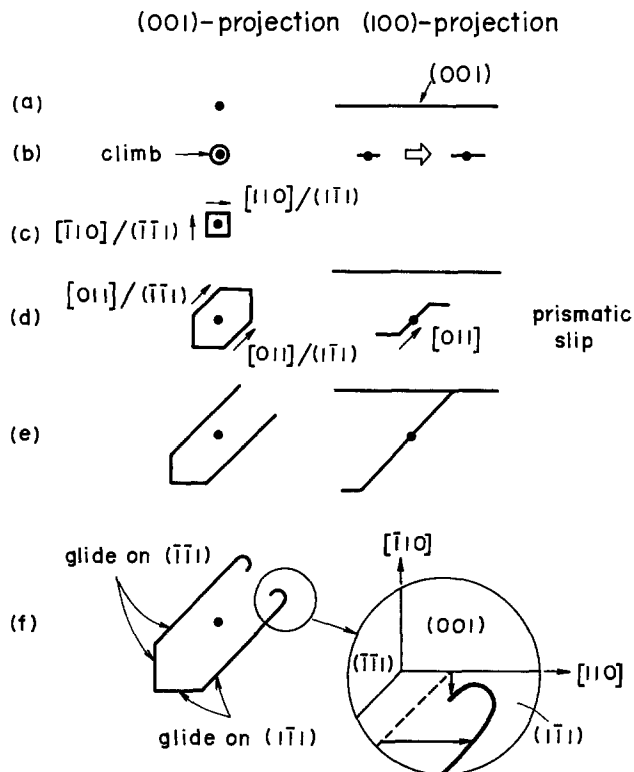


Fig. 10. Development processes of the dislocation with an inclined Burgers vector.

parallel to the (001) surface and no preference of the vacancy emission along the loop line is expected. The loops would turn to the ones with several $\langle 110 \rangle$ -aligned segments, as shown in Fig. 10c. When the crystal region containing the loops is affected by a resolved shear stress, two halves of each loop with the Burgers vector parallel to the stress might glide in opposite directions, and hence the dislocations would have shapes as shown in Fig. 9 and 10d. The dislocation feature is similar to the previous dislocation shown in the right side of the $(\bar{1}10)$ -projection in Fig. 5d except for orientation of the screw segments. Once one of the halves arrives and annihilates at a surface, only four segments are left. This four-segmented dislocation could also be obtained by a mechanism in which two segments with $\langle 110 \rangle$ orientation parallel to the surface originate at the surface due to surface irregularities and glide into the material leaving a pair of screw segments behind them. The fact that, by Sirtl-etching, the dislocations made of full hexagon or of four segments sometimes reveal an unidentified dot nearly at their center and sometimes not, seems to suggest the difference of nucleation sources, i.e., the precipitates or surface irregularities.

Additionally, two emergent screw segments of opposite senses often bend toward the inside on a topograph as seen in Fig. 8. The phenomenon is thought, in contrast with the previous dislocations, to be due to cross-slips of the emergent screw segments themselves, similar to the case observed by George *et al.* (10) in addition to the pinning effect of the surface; e.g., as shown in Fig. 10f, a part of the screw segment v would move in the $[110]$ direction on the $(\bar{1}\bar{1}1)$ plane, slower near the surface than at the inner part, and also could cross-slip in the $[1\bar{1}0]$ direction on the adjacent $(\bar{1}\bar{1}1)$ plane. As has been reported (10), this cross-slipping part can be a new source of another mobile dislocation. Thus, dislocation multiplication may occur also in the case of the present dislocations.

Conclusion

(001)-oriented silicon wafers subjected to two sequential thermal oxidations are found to reveal char-

acteristic dislocation configurations. These dislocations originate from the precipitates nucleated at some grown-in defects in dislocation-free silicon crystals on rapid cooling from a first thermal oxidation. Via small prismatic dislocation loops generated through climb, and under the influence of thermal stresses exerted during the course of a second thermal oxidation, the dislocations can develop and multiply giving off successively pairs of half-loops lying in two sets of symmetrically inclined $\{111\}$ planes. Another type of dislocation lying in the adjacent $\{111\}$ planes is also observed.

Acknowledgment

The author would like to thank Drs. S. Asanabe, Y. Nannichi, and T. Kawamura for their encouragements and discussions.

Manuscript submitted June 17, 1974; revised manuscript received March 30, 1975. This was Paper 106 presented at the Chicago, Illinois, Meeting of the Society, May 13-18, 1973.

Any discussion of this paper will appear in a Discussion Section to be published in the June 1976 JOURNAL. All discussions for the June 1976 Discussion Section should be submitted by Feb. 1, 1976.

Publication costs of this article were partially assisted by Nippon Electric Company, Limited.

REFERENCES

1. J. E. A. Miltat and D. K. Bowen, *Phys. Status Solidi (a)*, **3**, 431 (1970).
2. T. Abe, T. Ohtaki, and J. Chikawa, *Denki Kagaku*, **40**, 525 (1972).
3. J. R. Patel and B. W. Batterman, *J. Appl. Phys.*,

- 34, 2716 (1963); J. R. Patel, *Discussions Faraday Soc.*, **38**, 201 (1964).
4. T. Suzuki and H. Kojima, *Acta Met.*, **14**, 913 (1966).
5. M. C. Collet, *This Journal*, **117**, 259 (1970).
6. G. Granberg, *J. Appl. Phys.*, **43**, 4801 (1972).
7. A. R. Chaudhuri, J. R. Patel, and L. G. Rubin, *ibid.*, **33**, 2736 (1962).
8. J. R. Patel and P. E. Freeland, *Phys. Rev. Letters*, **18**, 833 (1967); *J. Appl. Phys.*, **41**, 2814 (1970).
9. E. Gerward, *Phys. Status Solidi (a)*, **2**, 797 (1970).
10. A. George, C. Escaravage, W. Schröter, and G. Champier, *Crystal Lattice Defects*, **4**, 29 (1973).
11. J. R. Patel, *J. Appl. Phys.*, **34**, 2788 (1963).
12. K. V. Ravi, *Met. Trans.*, **4**, 681 (1973); *J. Appl. Phys.*, **43**, 1785 (1972).
13. J. Matsui and T. Kawamura, *Japan. J. Appl. Phys.*, **11**, 197 (1972).
14. J. R. Patel and A. Authier, Paper S-171 presented at the Ninth International Congress of Crystallography, Kyoto, Japan, 1972; *J. Appl. Phys.*, **46**, 118 (1975).
15. S. Prussin, *ibid.*, **43**, 733 (1972); *ibid.*, **43**, 2850 (1972).
16. L. I. Bernewitz, B. O. Kolbesen, K. R. Mayer, and G. E. Schuh, *Appl. Phys. Letters*, **25**, 277 (1974).
17. J. Matsui and T. Kawamura, in "Semiconductor Silicon 1973," H. R. Huff and R. R. Burgess, Editors, p. 126, The Electrochemical Society Soft-bound Symposium Series, Princeton, N. J. (1973).
18. A. George, C. Escaravage, G. Champier, and W. Schröter, *Phys. Status Solidi (b)*, **53**, 483 (1972).
19. J. R. Patel, *J. Appl. Phys.*, **44**, 3903 (1973).
20. T. Abe, T. Samizo, and S. Maruyama, *Japan. J. Appl. Phys.*, **5**, 458 (1966).
21. A. J. R. DeKock, *Appl. Phys. Letters*, **16**, 100 (1972).
22. T. Iizuka, *Japan. J. Appl. Phys.*, **5**, 1018 (1966).
23. I. R. Sanders and P. S. Dobson, *Phil. Mag.*, **20**, 881 (1969).

Diffusion of Cobalt out of Cobalt-Hardened Gold Measured with Auger Electron Spectroscopy

Harland G. Tompkins

Bell Laboratories, Incorporated, Columbus, Ohio 43213

ABSTRACT

The diffusion of cobalt out of a gold layer is considered. The theory is discussed to relate measured quantities to diffusion coefficients. Measurements were taken and appropriate calculations made to obtain values for the coefficients at 100° and 150°C. Arrhenius plot extrapolations are then made to obtain approximate values at ambient temperatures.

Electroplated gold is a material often used in electrical contacts because of its excellent noncorrosive properties. Because pure gold is reasonably soft it is often modified by adding a small amount of cobalt as a hardening agent to reduce its sticking tendency. Cobalt does not have the noncorrosive properties of gold, however, and if a significant amount of the cobalt were to diffuse to the surface and become oxidized, the electrical contact properties would be significantly impaired. The purpose of this work is to study the diffusion of cobalt out of a gold matrix. The theory is developed for a simple model. Measurements of surface cobalt are described and diffusion coefficients (at slightly elevated temperatures) calculated. An Arrhenius plot is made which shows extrapolated diffusion coefficients down to ambient temperatures.

Key words: cobalt, gold, diffusion, Auger electron spectroscopy.

Theory

In setting up the appropriate boundary value problem, we make the following simplifying assumptions: (i) Except for the cobalt content, the gold layer is homogeneous throughout. (ii) The diffusion coefficient for cobalt in gold is independent of the concentration of cobalt within the ranges studied. (iii) The cobalt does not diffuse into the underlying material (i.e., into Cu or Ni). (iv) Cobalt which arrives at the outside surface of the gold is immediately oxidized. Formally, we say that a sink exists at the surface for the cobalt.

A few comments are in order about the appropriateness of the initial assumptions to real world conditions. This study concentrates on temperatures near ambient, gold thicknesses large enough to avoid porosity, and times of the order of 40 years or less. For these conditions we shall find that significant transfer of cobalt

occurs only near the surface of the gold and the system could have been treated as if the gold were a semi-infinite slab. We shall, however, consider a finite gold thickness, both for convenience and also to show when the diffusion process is affected by the finiteness of the gold. This information is particularly needed in the area of (possibly incorrect) accelerated aging of corrosion processes. With the semi-infinite idea in mind, the real world boundary condition at the back side of the gold is irrelevant and is chosen for mathematical convenience. The assumption of a sink at the outer surface involves assuming that the chemical and transport processes of oxidation in the film occur much faster than the transport phenomena in the gold. For an oxide with thickness of 60Å or less and gold with cobalt concentrations of tenths of a per cent, this seems reasonable.

We shall use the standard textbook approach (1, 2) in setting up and solving the boundary value problem. Let us make the following definitions. Time (in seconds) will be denoted as t . Distance (in centimeters) normal to the surface will be denoted as x (we will discuss later where the origin is to be chosen). The atomic concentration of cobalt will be denoted as c , and in fact $c = c(x)$, with the uniform concentration at time zero as c_i . The thickness of the gold layer will be taken as $h/2$ (the reason for the half will become obvious later).

The differential equation which is obeyed by the cobalt in the gold layer is

$$\frac{dc}{dt} = D \frac{d^2c}{dx^2} \quad [1]$$

where D is the diffusion coefficient (assumed to be independent of concentration).

The actual boundary conditions which seem reasonable are that the concentration is uniform at time zero, that the concentration of free cobalt at the outside surface of the gold is zero (i.e., the sink effect), and that the slope of the concentration at the inside gold surface is zero. The boundary value problem is simpler to solve, but equally applicable, if we consider the actual situation plus its mirror image. This is shown in Fig. 1 along with the appropriate mathematical boundary conditions necessary to represent the real world boundary conditions.

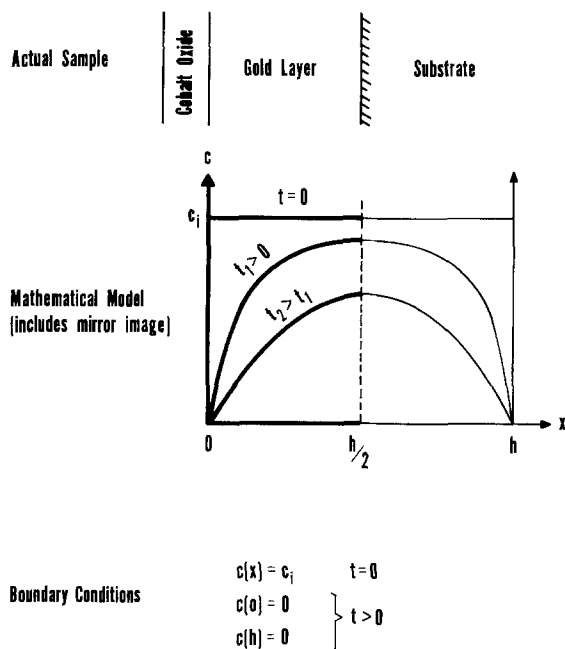


Fig. 1. Boundary value problem and boundary conditions, actual and mathematical.

The solution, expressed as an infinite sum is

$$c = \frac{4c_i}{\pi} \sum_{n=0}^{\infty} \frac{1}{2n+1} \sin \frac{(2n+1)\pi x}{h} \exp \left[-(2n+1)^2 \pi^2 \frac{Dt}{h^2} \right] \quad [2]$$

which has the form shown on Fig. 1.

The integral

$$\int_0^{h/2} c(x) dx = \frac{1}{2} \int_0^h c(x) dx \quad [3]$$

gives the total content of cobalt in the gold layer at any time, t . The quotient

$$\text{quotient} = \frac{\frac{1}{2} \int_0^h c(x) dx}{\frac{1}{2} \int_0^h c_i dx} = \frac{1}{c_i h} \int_0^h c(x) dx \quad [4]$$

gives the fraction of the original amount of cobalt remaining in the gold layer. It is clear that this fraction is the same whether we consider x from 0 to $h/2$ or from 0 to h . Let us denote the fraction of the cobalt which has been removed as F . Therefore

$$F = 1.0 - \frac{1}{c_i h} \int_0^h c(x) dx \quad [5]$$

performing this integration we get

$$F = 1.0 - \frac{8}{\pi^2} \sum_{n=0}^{\infty} \frac{1}{(2n+1)^2} \exp \left[-(2n+1)^2 \pi^2 \frac{Dt}{h^2} \right] \quad [6]$$

The reason for concerning ourselves with the cobalt which has been removed is that this is the cobalt which appears at the surface as an oxide and can be easily measured. The reason for considering the fraction, F , is that the fraction of material removed from one-half of the hypothetical system is the same as the fraction removed from the entire hypothetical system, hence the real world problem can be considered with the mathematical boundary value problem which we have set up (and shown in Fig. 1).

The infinite sum, in Eq. [6], is a function of the variables D , t , and h , and in fact these always appear as Dt/h^2 .

The infinite sum itself is not very illustrative of how these variables affect F . We can, however, with a simple Fortran program, solve for F , for various values of Dt/h^2 , and plot the result. This is shown in Fig. 2.

Crank (2) indicates that for small times an error function-type expression is applicable and if, in fact, the quantity Dt/h^2 is quite small the approximation

$$F = \frac{4}{\sqrt{\pi}} \sqrt{\frac{Dt}{h^2}} = 2.26 \sqrt{\frac{Dt}{h^2}} \quad [7]$$

is valid. This expression is also plotted in Fig. 2. Above $F = 0.6$ or $Dt/h^2 = 0.07$, the curve deviates significantly from the approximation.

The above expression provides some interesting insight in the following way. It is not clear at first thought, whether using a thicker gold layer (with the same cobalt concentration) will give a thicker cobalt oxide film or not. More total cobalt is available, but it has further to travel to arrive at the surface. Equation [7] shows that, in fact, the film growth will be the same, regardless of the thickness of the gold layer in the early stages. This can be seen by rearranging Eq. [7] as follows

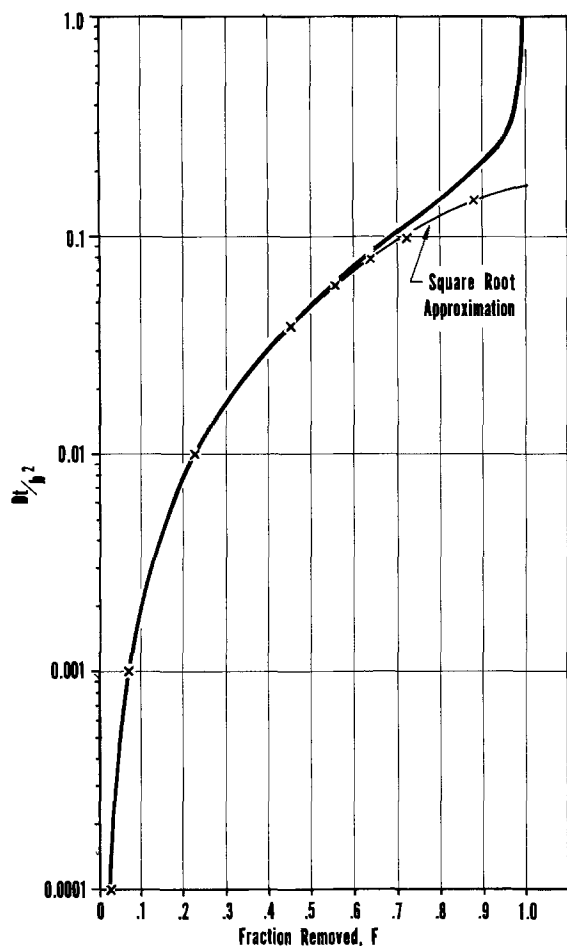


Fig. 2. Fraction of cobalt which has been removed from the gold film plotted vs. Dt/h^2 .

$$Fh = 2.26 \sqrt{Dt}$$

The amount of cobalt in the oxide film is simply the fraction removed times the original amount or
 amount = $F \cdot h \cdot (\text{area}) \cdot c_i$

$$= 2.26 \sqrt{Dt} \cdot (\text{area}) \cdot c_i$$

and hence is independent of thickness.

This is to say that until the fraction removed approaches 0.6, the thickness of the cobalt oxide film is independent of the gold layer thickness. It is very dependent, however, on the original concentration of cobalt in the gold. The dependence is one-to-one in that twice as much cobalt gives a film twice as thick.

Applying the theory, then, consists of measuring F , t , and h and calculating D , and then, by using values of D obtained, predicting values of F for other values of t and h (and as shown below, for different temperatures).

The diffusion coefficient is generally accepted to be a function of temperature and is usually represented with the Arrhenius equation

$$D = D_0 e^{-Q/RT}$$

where T is in degrees Kelvin, R is the gas constant, Q is the activation energy for diffusion, and D_0 is the preexponential factor. Data are then taken at elevated temperatures, and, using an Arrhenius plot, the values of D for lower temperatures are obtained by extrapolation using the obtained values. Calculations can then be made for F at the lower temperatures as a function of t and h . These extrapolations are based on one rather limiting assumption, i.e., that the mechanism of diffusion is the same for the measured values and the extrapolated values. Serious problems can arise when the diffusion mechanism changes (3). Accordingly, the extrapolation is more likely to be acceptable if the measured values are obtained at temperatures reasonably near the temperature for the extrapolated values.

Experimental Methods

The samples used were electroplated gold films which contained 0.26% (by weight) cobalt as a hardening agent. Some of the films were plated directly on the OFHC copper substrate, and some of the samples had a nickel underplate between the gold and the copper. Results were independent of which material was immediately under the gold. The gold thickness was determined by photomicrography. All except two of the samples had $3.3 \mu\text{m}$ of gold. Two samples had $50.8 \mu\text{m}$ of gold. The cobalt content was measured by atomic absorption. The samples were coupons approximately $4 \text{ cm}^2 \times 0.3 \text{ cm}$. These were heated in air at 150° and at 100°C for extended periods of time in ovens. Temperatures were controlled to within $\pm 1^\circ\text{C}$. At appropriate times, the coupons were removed from the ovens and small sections were cut out of the larger coupons. These smaller ($1 \times 0.5 \text{ cm}$) pieces were then analyzed for cobalt.

The cobalt analysis was made using Auger electron spectroscopy (4, 5) along with argon ion bombardment to obtain a depth profile of the cobalt along with other elements. A commercial instrument purchased from Physical Electronics Industries was used. Sputtering and Auger analysis are done simultaneously and a plot of peak-to-peak height vs. sputtering time can be obtained for up to six elements. Sputtering rate was obtained by prior calibration of the sputtering parameters for gold. Sputtering rate for cobalt oxide is assumed to be that of cobalt which in turn is taken to be one-half that of gold (6).

The thickness is measured as described above and combined with the calculated value of oxide thickness if all the cobalt were oxidized to give the fraction of the cobalt removed, or F . The stoichiometry of the oxide was not measured, but it was assumed to be CoO . When density and molecular weight are taken into account, the results are within 10% for either CoO

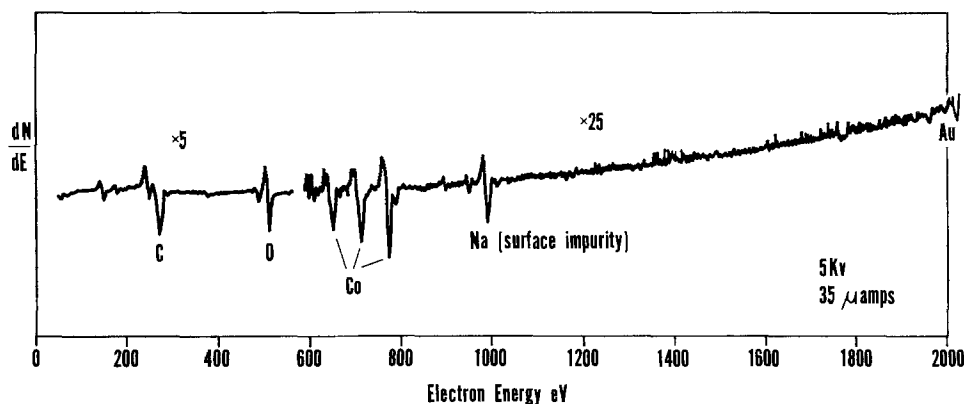


Fig. 3. Typical Auger spectrum taken before sputtering. Sample had been heated at 100°C for 6060 hr.

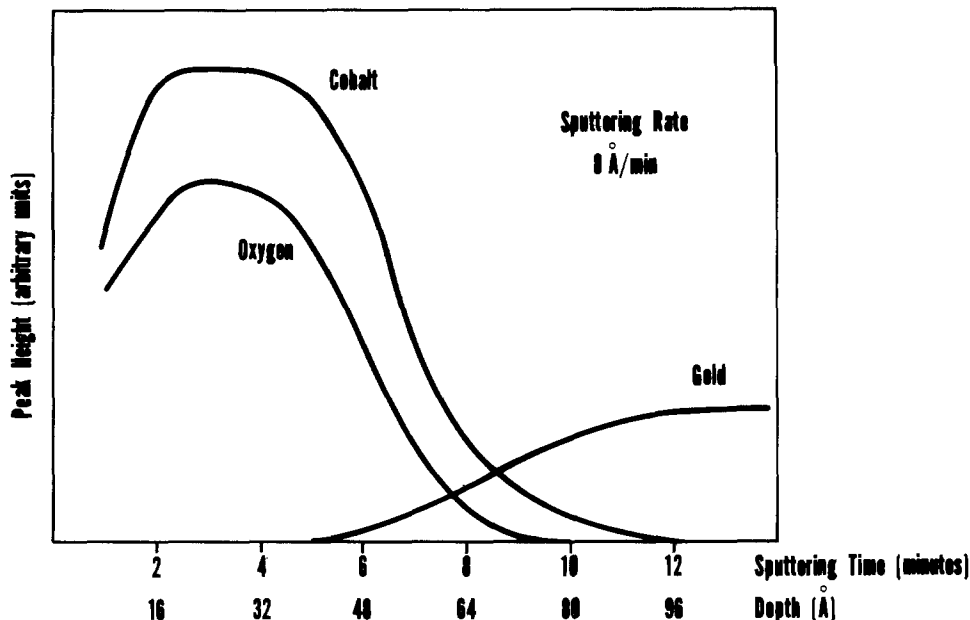


Fig. 4. Typical profile of the top few hundred angstroms. Sample had been heated at 150°C for 2927 hr.

or Co_3O_4 which are the two possibilities (7). For simplicity, then we assume CoO .

Results

Profiles were obtained for samples heated at 150°C for 2927 hr and samples heated at 100°C for 6060 hr. A typical Auger spectrum is shown in Fig. 3 and a typical profile is shown in Fig. 4.

The reason for the initial rise in the cobalt and oxygen signal is that a small layer of carbon (which typically exists on any sample which has been exposed to the atmosphere for any significant length of time) is being removed, thus, uncovering the underlying material.

The oxygen signal follows the cobalt rather closely which tends to indicate that this cobalt is in the oxide form. The gold signal goes from zero in the oxide to its bulk value after the oxide has been sputtered away. The model is, then, that the cobalt at the surface becomes oxidized leaving a lower free cobalt concentration, the cobalt in the bulk diffuses out and in turn is oxidized. The resulting structure is a cobalt oxide film on top of the gold.

Let us take the thickness where the peak height crosses the center point, half-way between maximum and zero, as the thickness of the cobalt oxide. Table I gives the values of time, temperature, thickness, and the corresponding value of diffusion coefficient obtained using methods discussed in the section on Theory.

One immediate observation is that the samples with 50.8 μm of gold give cobalt oxide films which are not significantly different in thickness from the films formed on the 3.3 μm samples. This tends to substantiate the theoretical conclusion that the amount of film formed should be independent of gold thickness.

Table I. Thickness of cobalt oxide and diffusion coefficients for various times and temperatures

Temperature, °C	Time, hr	Thickness, Å	D, cm^2/sec
150	2927	53	2.0×10^{-16}
150	2927	58	2.28×10^{-16}
150*	2927	64	2.95×10^{-16}
100	6060	7.0	1.85×10^{-19}
100	6060	11.0	4.2×10^{-19}
100	6060	9.6	3.2×10^{-18}
100*	7156	11.4	3.82×10^{-18}

* Gold thickness is 50.8 μm for these samples. Others are all 3.3 μm .

The main thrusts of this work are the description of how Auger spectroscopy can be used for diffusion measurements (along with the necessary diffusion theory) and the reporting of diffusion coefficients at reasonably low temperatures (100° and 150°C). A secondary benefit obtained is that these values of the diffusion coefficient can be plotted on an Arrhenius plot to obtain an activation energy for diffusion and to make rough estimates of diffusion coefficients at even lower temperatures.

Extrapolation beyond measured data is risky, at best, and the choice of the method used for the extrapolation is up to the extrapolator. The author has used a least squares fit along with the 95% confidence limits

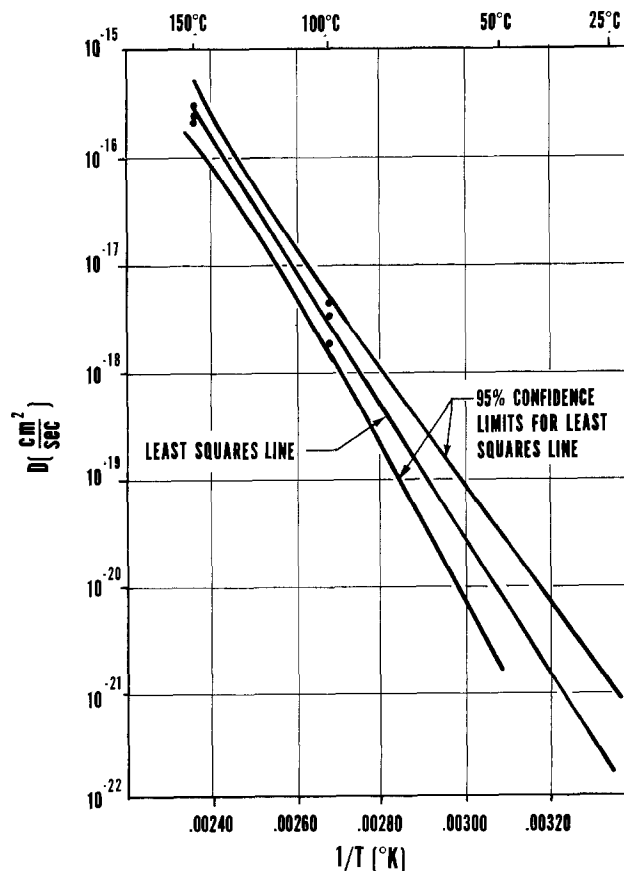


Fig. 5. Arrhenius plot of diffusion coefficient, D vs. $1/T$

of the least squares line. This is shown in Fig. 5. The activation energy for diffusion, Q , obtained from the least squares line is

$$Q = 28 \pm 6 \text{ kcal/mole}$$

Another point of interest is that the square root relation

$$F = 2.26 \sqrt{\frac{Dt}{h^2}}$$

holds for most systems of interest for this model. For gold thicknesses of $3.3 \mu\text{m}$ and temperature of 50°C (along with the corresponding diffusion coefficient $D = 10^{-19}$) the time corresponding to $F = 0.6$ is of the order of 10^4 years. If we use smaller thicknesses where the fraction might be appreciable, other transport mechanisms, e.g., porosity, would prevail and the model proposed here would not be applicable.

Summary

We have considered the diffusion of cobalt out of a gold layer. The theory is discussed first to relate measured quantities to diffusion coefficients. Measurements were taken and the appropriate calculations made to obtain values for the diffusion coefficients at different temperatures. Arrhenius plot extrapolations were then made to obtain rough values for the coefficients at lower temperatures.

Acknowledgments

The author would like to acknowledge Dr. Morton Antler for preparation and aging of the samples, Dr. M. R. Pinnel for useful discussion, and J. A. Smiley for assistance in taking the Auger spectra.

Manuscript submitted Oct. 9, 1974; revised manuscript received Feb. 4, 1975.

Any discussion of this paper will appear in a Discussion Section to be published in the June 1976 JOURNAL. All discussions for the June 1976 Discussion Section should be submitted by Feb. 1, 1976.

Publication costs of this article were partially assisted by Bell Laboratories.

REFERENCES

1. W. Jost, "Diffusion in Solids, Liquids, Gases," p. 35 ff, Academic Press, New York (1960).
2. J. Crank, "The Mathematics of Diffusion," p. 45 ff, Oxford University Press, London (1956).
3. M. R. Pinnel and J. E. Bennett, *Met. Trans.*, **3**, 1989 (1972).
4. C. C. Chang, *Surface Sci.*, **25**, 53 (1971).
5. P. W. Palmberg, *J. Vacuum Sci. Technol.*, **9**, 160 (1972).
6. G. Carter and J. S. Colligon, "Ion Bombardment of Solids," American Elsevier Publishing Co., New York (1968).
7. E. A. Gulbransen and K. F. Andrew, *This Journal*, **98**, 241 (1951).

Multilayer Metallization with Planar Interconnect Structure Utilizing CVD Al_2O_3 Film

H. Mutoh,* Y. Mizokami,* H. Matsui, S. Hagiwara, and M. Ino

OKI Electric Industry Company, Limited, Hachioji, Tokyo, Japan

ABSTRACT

A new, multilayer metallization system has been developed for the purpose of fabricating a planar interconnect structure. This system comprises two levels of metal interconnection, and the first-level metal layer is buried in a low temperature CVD Al_2O_3 film pyrolytically deposited by $\text{Al}(i\text{-C}_3\text{H}_7\text{O})_3$ at 420°C . The metal chosen for both layers is aluminum, and the insulator is phosphosilicate glass. In the metal processing, a self-aligned photolithographic technique is applied in which positive photoresist AZ-1350 plays an important role in forming the first-level Al layer and the Al_2O_3 film.

The recent development of large scale integration (LSI) of microcircuits has required the use of more than one level of metallization in order to achieve high packing density. In conventional multilevel structures, each metal layer is separated from the next by an insulating oxide, and there are many steps at metal edges which result in limiting the reliability and yield. In the fabrication of multilevel structures, it is highly desirable to provide a planar interconnect structure.

Recently, so-called "no step" metallizations appear to be possible by the use of anodically formed Al_2O_3 or polyimide (1, 2).

This paper describes a new multilayer metallization system in which a first-level metal layer is buried in chemically vapor deposited Al_2O_3 for the purpose of fabricating the planar interconnect structure.

Structure and Manufacturing Process

The schematic cross section of a two-level structure fabricated by this new method is shown in Fig. 1(a), in comparison with a conventional structure

* Electrochemical Society Active Member.

Key words: aluminum oxide film, planar interconnection, lift off, positive photoresist.

using a phosphosilicate glass (PSG) film as the insulating layer in Fig. 1(b). It was found that planarity of surface in the new structure is achieved with the first-level metal layer buried in Al_2O_3 .

The metal process steps used in the fabrication of this new planar interconnect structure are shown in Fig. 2. After the diffusion processes are finished, an Al_2O_3 film is deposited on the wafer by pyrolysis of aluminum triisopropoxide $\text{Al}(i\text{-C}_3\text{H}_7\text{O})_3$ (3-5) as shown in step (A). This CVD Al_2O_3 film can be deposited at a relatively low temperature of about 400°C so that the characteristics of the devices do not deteriorate. The required film patterns are prepared by photomasking with positive photoresist (AZ-1350) and etching in hot phosphoric acid as shown in steps (B) and (C). The Al_2O_3 film can be very quickly etched by phosphoric acid, which makes it possible to perform the etching process with negligible etching of the other oxide film underneath the etched Al_2O_3 film to form selectively desired patterns.

Next, without removing the photoresist, we evaporate aluminum onto the wafer up to the equivalent thickness of the Al_2O_3 film as shown in step (D).

Fig. 1. Schematic cross section of two-level structure. (a, left) Structure made by new method, (b, right) structure made by conventional method.

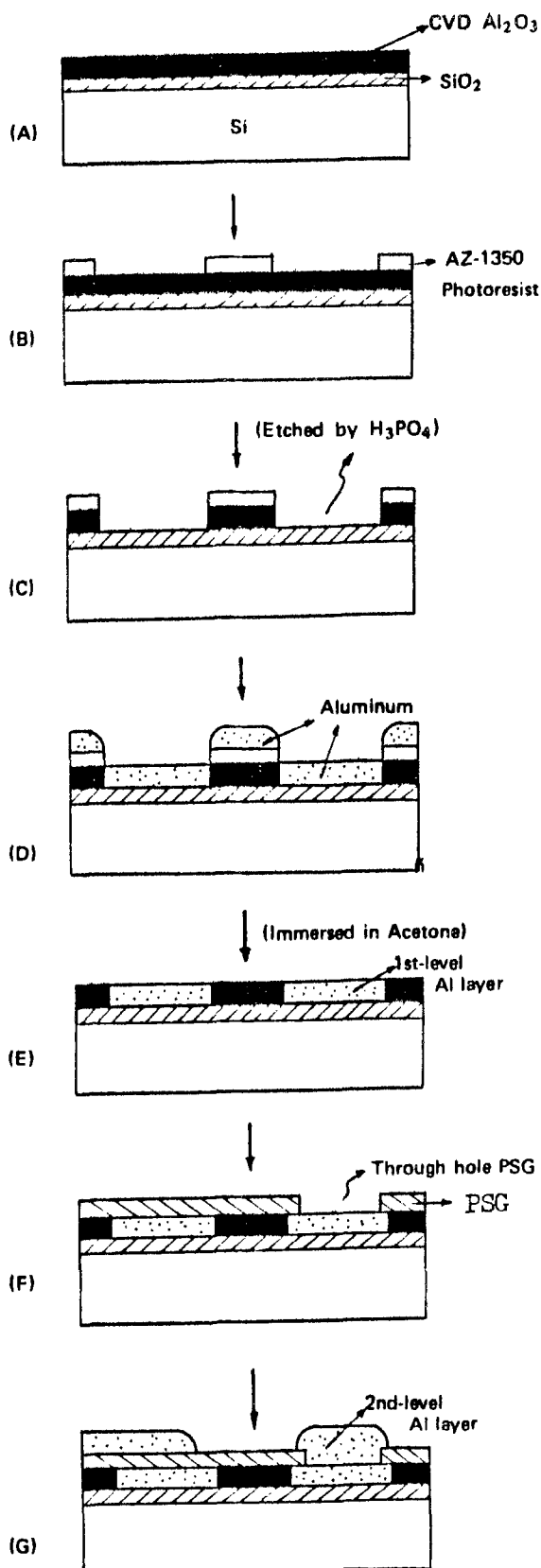
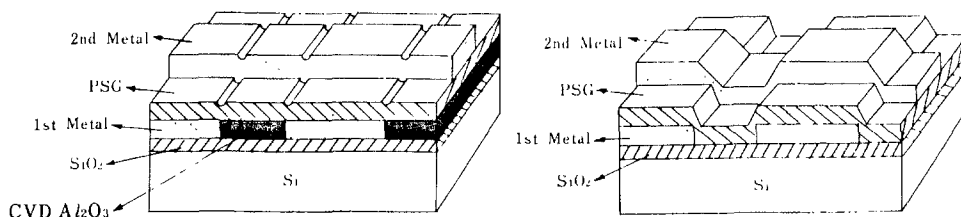


Fig. 2. Manufacturing process

When the wafer is immersed into a solution such as acetone or concentrated sulfuric acid, the AZ-1350 photoresist is dissolved in the solution and the aluminum on the resist is removed. As a result of this operation, the remaining aluminum in spaces between Al_2O_3 areas forms the first-level Al layer as shown in step (E). As mentioned, a self-aligned photolithographic technique is used in this new metallization process; i.e., AZ-1350 photoresist which has been used for formation of the Al_2O_3 areas is also utilized in forming the first-level Al layer.

Additional insulator and second-level Al layer processes are the same as for conventional metal interconnection as shown in steps (F) and (G).

The insulator used in this structure is phosphosilicate glass deposited by a chemical vapor deposition technique, the insulator "through-holes" are patterned by a photoengraving technique, and the second-level Al layer is finally formed. When etching through-holes, a "plasma etching technique" is employed in our process in order to protect the first-level Al layer from corrosion by electrochemical reaction in buffered HF liquid. The specific contact resistance between the first and second-level Al layers through the through-holes was observed to be $4\text{-}5 \times 10^{-8}$ ohm-cm².

Properties of CVD Al_2O_3 Film and Effects on Devices

Properties.—Formation of Al_2O_3 films.—The deposition apparatus consists essentially of a bell jar covering a rotating hot plate. A schematic of the apparatus for the deposition of Al_2O_3 film is shown in Fig. 3. Dry nitrogen gas passes through the aluminum triisopropoxide [$\text{Al}(i\text{-C}_3\text{H}_7\text{O})_3$] vaporizer at a constant temperature of 170°C (vapor pressure = 50 mm Hg), and the organic compound vapor is mixed with more nitrogen gas and transported to the hot plate in the bell jar, where the mixture pyrolyzes to form Al_2O_3 . We usually deposit at 420°C in our process, when the growth rate is typically 200 Å/min. If deposition is performed in the presence of additional oxygen, the growth rate will increase.

Dielectric breakdown strength measurements.—Some dielectric breakdown strength measurements of this CVD Al_2O_3 film were made using an Al- Al_2O_3 -Si structure. The results are shown in Fig. 4. The dielectric breakdown strength of films deposited at 420°C was approximately 4×10^6 V/cm, which is about half the breakdown strength of a thermal SiO_2 film.

Cracking.—In our experiments, we observed cracks developing if thick Al_2O_3 was deposited, or if the film was deposited in the presence of additional oxygen.

In our deposition process, however, we form the film under oxygen-free conditions, so no cracks occur for film thicknesses up to 15,000 Å.

Film etch rate.—This CVD Al_2O_3 film is highly soluble in phosphoric acid, especially at high temperature.

The etch rate of Al_2O_3 film in phosphoric acid is shown in Fig. 5, in comparison with that of a thermal SiO_2 film containing P_2O_5 . The etch rate for the Al_2O_3 film is approximately 4000 times that of the SiO_2 film.

As an example, the etch rate for the Al_2O_3 films prepared at 420°C was typically 4000 Å/min in 85% H_3PO_4 at 70°C, whereas that of the thermal SiO_2 film containing P_2O_5 was as low as 50 Å/hr. This considerable difference between the etch rates for Al_2O_3 and SiO_2 films makes it possible to delineate selectively buried Al_2O_3 films.

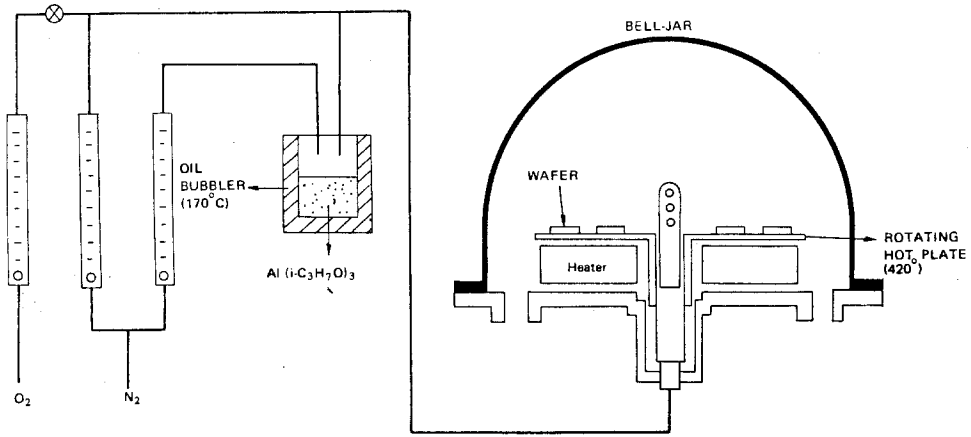


Fig. 3. Schematic of vapor deposition system for preparing Al_2O_3 film.

Effects of Al_2O_3 film on devices.—Since the CVD Al_2O_3 film is formed at a relatively low temperature of $400^\circ\text{--}500^\circ\text{C}$, it may show several electrical properties different from high temperature formed Al_2O_3 films, especially exhibiting bad interface properties with silicon. For example, it is known from the C-V behavior that Al- Al_2O_3 -Si (MAS) structures show unstable characteristics because of the presence of mobile electrons in the Al_2O_3 film and charge transfer at the gate electrodes (3, 4). In the new metallization system, however, the presence of the SiO_2 film between the Si and Al_2O_3 eliminates such effects associated with

charge transfer at the Si- SiO_2 interface. The flatband surface-state charge density (N_{FB}) characteristics of Al- Al_2O_3 - SiO_2 -Si structures are shown in Fig. 6, where N_{FB} is plotted as a function of the Al_2O_3 and SiO_2 film thicknesses. It is noted that the thicker the SiO_2 film becomes, the less pronounced the tendency of the Al_2O_3 film to make the surface of the Si more positive.

When this structure is applied to such devices as bipolar IC's, inversion of the collector conductivity may occur. The resistivity of the collector region, however, is usually as high as about 1 ohm-cm, and the thickness of the SiO_2 film is as high as about 7000\AA , so we consider it to be free from the influence of Al_2O_3 . In this metal process, the Al_2O_3 film is deposited after a contact photolithographic step. Therefore, an insulating layer may be formed on the exposed silicon in the bell jar, which would make it difficult to establish good ohmic contact or to form a Schottky barrier diode. This problem can be overcome by dipping the wafer in a buffered HF liquid just before the Al evaporation step.

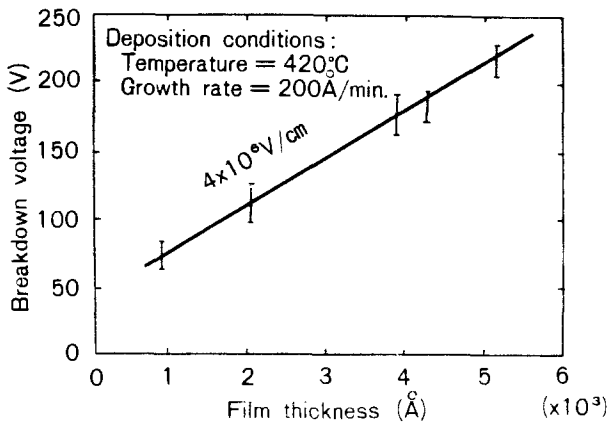


Fig. 4. Dielectric breakdown strength of CVD Al_2O_3 film

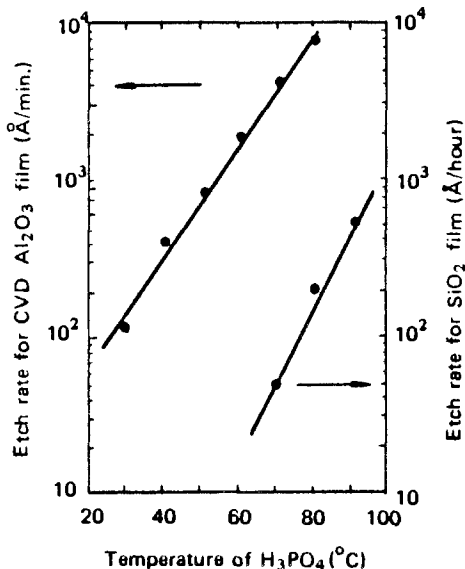


Fig. 5. Comparison of etch rates for CVD Al_2O_3 film and SiO_2 film.

Reliability

Continuity of second-level Al layer.—Observation by SEM and angle-lapping.—Scanning electron microscopy and angle-lapping were used to examine the features of crossovers of leads in new and conventional structures as shown in Fig. 7. Photograph (A) and (C) show the cross section of a chip made by the new method. The thickness of the first-level Al layer is 6500\AA , the same as that of the Al_2O_3 film, the inter-layer phosphosilicate glass 8000\AA , and the second-level Al layer $12,000\text{\AA}$. On the other hand, photograph (B) and (D) show the cross section of another chip made by a conventional method under the same conditions. These photographs indicate that the new structure is very beneficial in realizing surface planarity, whereas

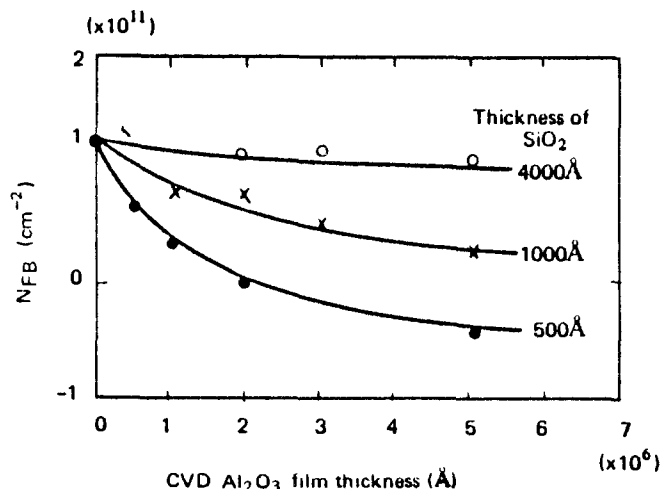
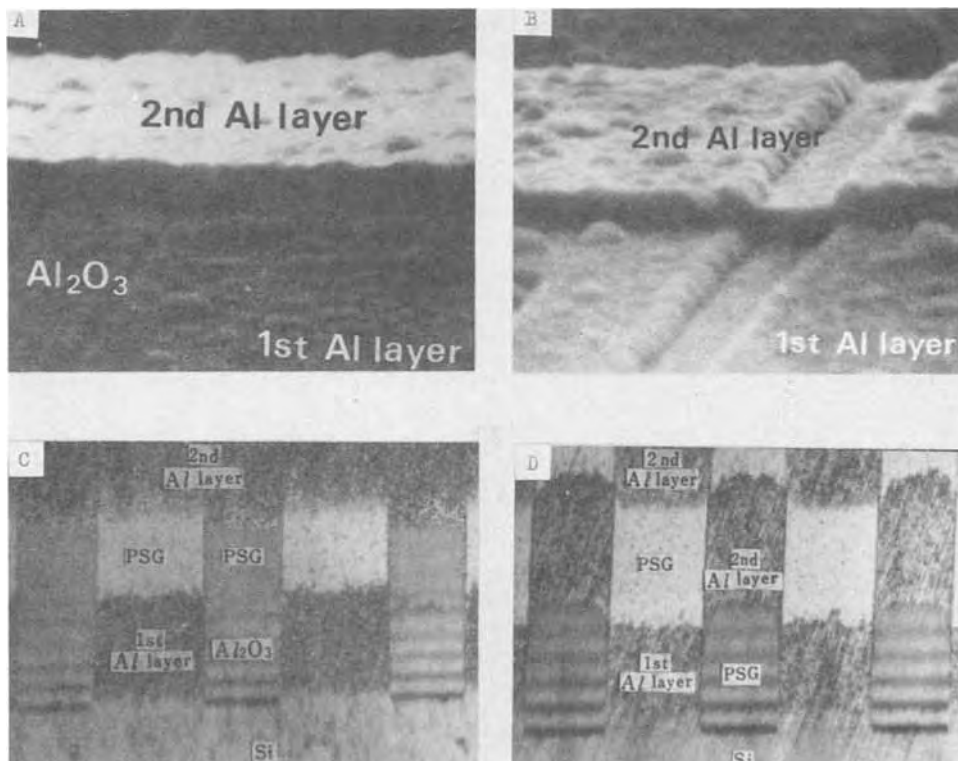


Fig. 6. Characteristics of N_{FB} in Al- Al_2O_3 - SiO_2 -Si structures

Fig. 7. Scanning electron micrographs (A and B) of crossover and optical photographs (C and D) of angle-lapped surface. A and C, structure made by new method; B and D, structure made by conventional method.



the second-level Al layer of the conventional structure is apt to be cut at the step.

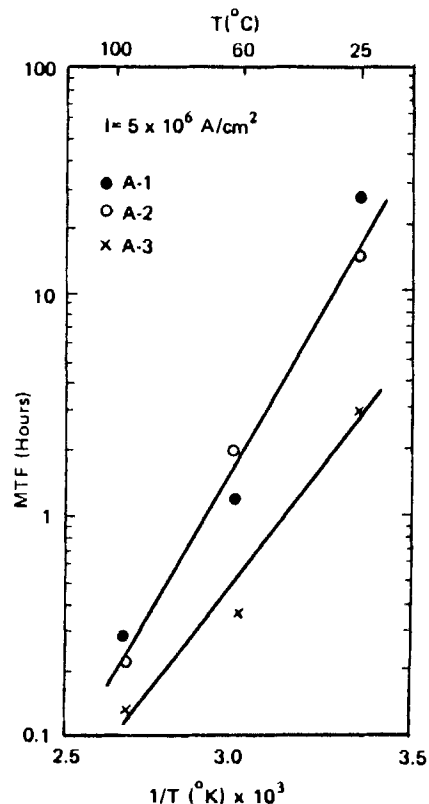
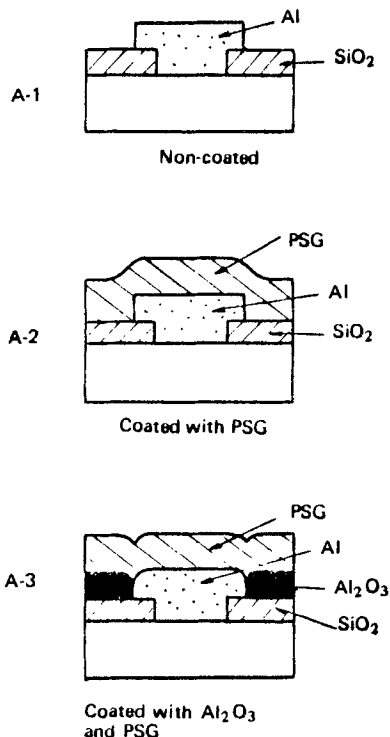
Opens in second Al layer.—The continuity of the second Al layer for several different thicknesses of the first Al layer was checked.

Test patterns were fabricated in which the first Al layers of 20 μm width were 3000, 4500, 7000, and 10,000 \AA thick, and the second Al layers of 20 μm width were maintained 12,000 \AA thick. There were the same number of chips for each structure and each chip had 800 crossover points.

The contrast between the number of opens in the second Al layers for the new and conventional structures is presented in Table I. These data show that as long as the thickness of the first Al layer is less than 4500 \AA , there are no opens for both the new and conventional structures. But when the first Al layer is up to 10,000 \AA in thickness, the new structure eliminates failures resulting from opens of the second Al layer.

Mean time to failure of the first and second Al layers.—*First Al layer.*—It has been observed that electromigration in aluminum is produced by high current

Fig. 8. Mean time to failure vs. temperature of first Al layer for three types of test structure. (a, left) Test structures, (b, right) MTF vs. temperature.



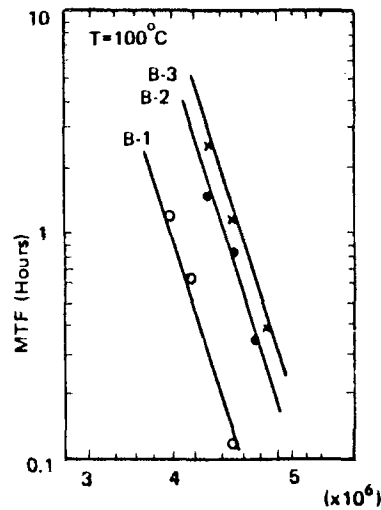
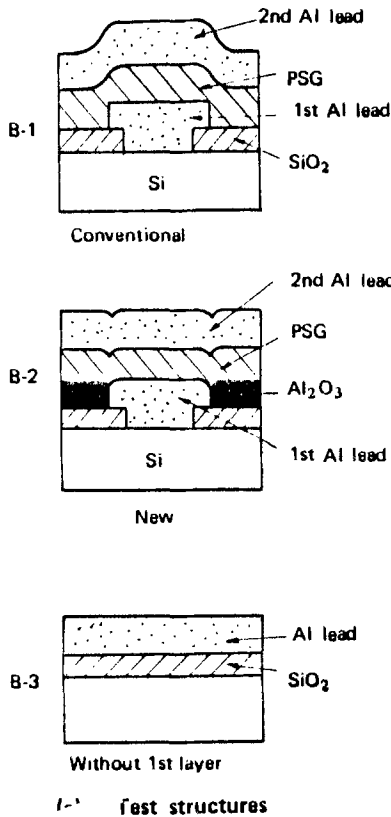


Fig. 9. Mean time to failure vs. current density of second Al layer for three types of test structures.

(b) MTF vs. current density

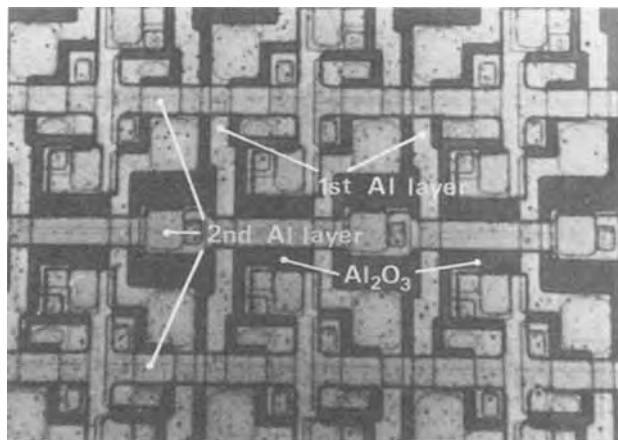


Fig. 10. Two-level LSI pattern using CVD Al₂O₃

densities, which decrease the mean time to failure (MTF) (6). The MTF can be increased by coating the aluminum layer. In the new metal structure, as the first Al layer is coated with Al₂O₃ and PSG films, the MTF is expected to be greater than that of a noncoated Al layer.

Experiments were carried out to evaluate the effects on the MTF of coated first Al layers. In order to compare the MTF of the new structure with others, three types of test structures A-1, A-2, and A-3 were fabricated as shown in Fig. 8(a) where the first Al layer of A-1 is noncoated, that of A-2 is completely coated with PSG, and that of A-3 is coated with Al₂O₃ and

Table I. Number of opens in second Al layer

Thickness of first Al layer, Å	New structure	Conventional structure
3,000	0/50	0/50
4,500	0/50	0/50
7,000	0/50	23/50
10,000	0/50	50/50

PSG. Test strips 20 μm in width and 3000Å in thickness were subjected to a current density of 5 × 10⁶ A/cm² at 25°, 60°, and 100°C. Aluminum was evaporated at a rate of 40 Å/sec using electron beam evaporation.

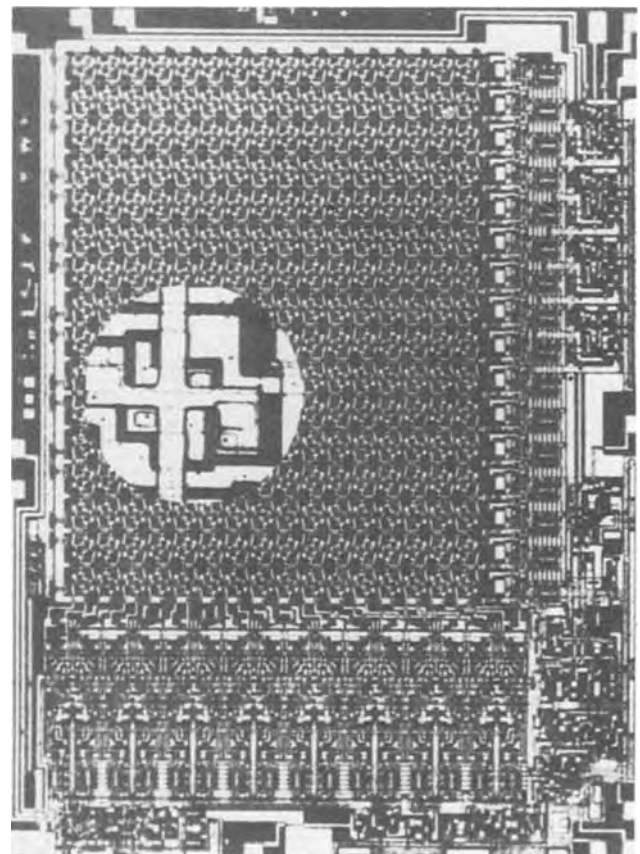


Fig. 11. 256 bit bipolar RAM chip with planar interconnect structure utilizing CVD Al₂O₃.

Data for each structure of MTF *vs.* temperature is presented in Fig. 8(b). We can see that both the new and conventional structures have almost equal MTF, which is greater than that of the noncoated structure.

Second Al layer.—Similarly, experiments were carried out to evaluate the MTF of the second Al layers. Test strips 15 μm in width and 12,000Å in thickness were subjected to a temperature of 100°C at various current densities. In order to compare the MTF of the new structure with others, three types of test structures B-1, B-2, and B-3 were fabricated as shown in Fig. 9(a), where B-1 is a conventional structure, B-2 is the new structure, and B-3 is a test structure without a first Al layer.

Data for each structure of the MTF *vs.* current density is presented in Fig. 9(b). The thickness of the first Al layer is 3000Å, and that of the PSG film is 8000Å. It is noticed that the MTF for the new structure is about five times greater than that of the conventional structure.

Applications

This new planar interconnection technique can be applied to fabricate various LSI chips.

Figure 10 shows an example of a two-level LSI pattern utilizing this technique, and a photograph of a 256 bit bipolar RAM chip fabricated using this new structure is shown in Fig. 11.

Conclusions

A new planar metallization technique has been described for fabricating a two-level structure utilizing CVD Al_2O_3 .

It has been shown that a planar interconnect structure can be fabricated using low temperature CVD Al_2O_3 as an insulator between areas of the first-level Al layer, a self-aligned photolithographic technique

can be applied in which positive photoresist AZ plays an important role in forming the first-level Al layer and the Al_2O_3 film, and the process for forming the CVD Al_2O_3 film is simple and economical.

This new structure should provide a useful method for establishing a new approach to LSI multilayer structures.

Acknowledgments

The authors would like to thank Dr. S. Nakaya and Dr. T. Imai for their support of this work, and Mr. T. Higashi and Mr. K. Suzuki for their advice and helpful discussions.

Manuscript submitted Aug. 27, 1974; revised manuscript received March 5, 1975. This was Paper 76 presented at the San Francisco, California, Meeting of the Society, May 12-17, 1974.

Any discussion of this paper will appear in a Discussion Section to be published in the June 1976 JOURNAL. All discussions for the June 1976 Discussion Section should be submitted by Feb. 1, 1976.

Publication costs of this article were partially assisted by OKI Electric Industry Company, Limited.

REFERENCES

1. H. Tsunemitsu and H. Shiba, "A Planar Multi-Layer Interconnection," IEDM Technical Program Abstract, Paper 18.4, October 1969.
2. K. Sato *et al.*, *IEEE Trans. Parts, Hybrids, Packag., PHP-9*, No. 3 (September 1973).
3. J. A. Aboaf, *This Journal*, **114**, 948 (1967).
4. M. T. Duffy and A. G. Revesz, *ibid.*, **117**, 372 (1970).
5. C. J. Santoro and D. L. Tolliver, *Proc. IEEE*, **59**, No. 10 (1971).
6. T. Satake, K. Sawaguchi, and S. Fujimoto, Paper 67, p. 165, Electrochemical Society Extended Abstracts, Spring Meeting, Washington, D. C., May 9-13, 1971.

Determination of Excess Zn in ZnO

The Phase Boundary $\text{Zn-Zn}_{1+x}\text{O}$

K. I. Hagemark and P. E. Toren

3M Central Research Laboratories, St. Paul, Minnesota 55101

ABSTRACT

The excess Zn of Zn-doped ZnO has been determined using two different methods. An electrochemical method was used as a direct method. Hall effect measurements at 77°-300°K were used as an indirect method. The agreement between the results from the two methods is good. The Zn- Zn_{1+x}O phase boundary is given in the range 700°-1100°C as $\log x_{\text{Zn}}$ (ppma) = $-4700/T + 5.6$.

Excess Zn accounts for the n-type character of ZnO. Small changes in the stoichiometric composition have a drastic effect on the physical and chemical properties. However, the Zn concentration level is less than 100 ppm and thus difficult to determine by conventional analytical techniques. Some chemical analytical methods have been reported previously (1-4).

In this paper we discuss the use of two methods, an electrochemical method as a direct chemical method and Hall effect measurements as an indirect method. ZnO single crystals have been equilibrated at 700°-1100°C in Zn vapors from Zn metal kept at the same temperature as ZnO and rapidly quenched to room temperature. As a result Zn-saturated ZnO crystals were obtained. After the Hall effect measurements at 77°-300°K, the crystals were analyzed by an electro-

Key words: zinc oxide, coulometry, Hall effect.

chemical technique similar to the one developed by Engell (3). The agreement between the methods is good.

Experimental

Crystals.—3M vapor phase grown ZnO crystals were used. Emission spectrometric and mass spectrographic analyses showed no major impurities above 1 ppma (atomic) (4.2×10^{16} atoms-cm⁻³) except for Si (10-20 ppma). The crystals were cut into bars of typical size 2 × 2 × 15 mm. Excess Zn was introduced into the ZnO crystals by heating the crystals in sealed silica ampuls in saturated vapor of Zn. Doping runs were performed at 700°, 800°, 900°, 1000°, and 1100°C for a length of 2 weeks at the lower temperatures to 2 days at the higher temperatures. After the heat-treatments the crystals were rapidly cooled to room

temperature. A hot concentrated H_3PO_4 etch was used to remove about 50μ from the surface.

Electrical measurements.—A conventional Hall method was used. Details of the method and apparatus are given elsewhere (5).

Electrochemical techniques.—Electrochemical measurements were carried out in a 3-compartment cell with fritted glass disks separating the compartments. The working electrode compartment contained a mercury pool which formed the electrical contact between the external circuit and the ZnO crystal which was floated on it. A platinum counterelectrode and a saturated calomel reference electrode (SCE) were placed in the other two cell compartments.

A Wenking potentiostat was used to maintain the ZnO crystal at a constant potential vs. the reference electrode.

Electrolysis current was integrated by a simple analog integrator, built in-house using "μA 741" integrated circuit operational amplifiers and a high quality $10\mu F$ integrating capacitor.

Experimental measurements were carried out by filling the cell compartments with 1.8M H_2SO_4 electrolyte solution, connecting the electrodes (with the mercury pool as the working electrode), and applying the desired working electrode potential while bubbling nitrogen through the stirred solution to remove dissolved oxygen. When the background current at the preset potential (usually $-0.2V$ vs. SCE) had decreased to its minimum level (less than 0.01 mA) a weighed crystal of ZnO was dropped into the cell and floated on the mercury pool. The current resulting from the oxidation of Zn^0 as the ZnO dissolved in the acid electrolyte was integrated and the result used to calculate the equivalents of oxidizable material present in the ZnO crystal. Most of the measurements were made at $40^\circ-50^\circ C$ to increase the dissolution rate of the ZnO and thus minimize the background current correction.

Results and Discussion

Electrical transport properties.—The electrical resistivity ρ , the carrier concentration n , and Hall mobility μ_H have been measured in the range $77^\circ-300^\circ K$. Only the results at 300° and $100^\circ K$ are given in Table I.

The concentration of excess Zn can be calculated from (i) the relationship of the carrier concentration vs. the temperature and (ii) the Hall mobility at lower temperatures where defect scattering is important.

Carrier concentration analysis.—From semiconduction statistics (6) the concentration of donors N_D and acceptors N_A can be calculated. A more detailed discussion of Zn-doped ZnO is given in Ref. (5) and (7). We have assumed that excess zinc is incorporated into ZnO lattice as hydrogen-type shallow donors. The results of the calculations are given in Table I. We are assuming the excess Zn, x_{Zn} , is simply given by

$$x_{Zn} = N_D - N_A \quad [1]$$

The ZnO crystal contains 4.21×10^{22} Zn atoms-cm $^{-3}$. Thus 1 ppma corresponds to 4.21×10^{16} atoms-cm $^{-3}$.

Hall mobility analysis.—The total mobility μ can be assumed to be expressed as

$$\frac{1}{\mu} = \frac{1}{\mu_L} + \frac{1}{\mu_I} + \frac{1}{\mu_N} \quad [2]$$

where the lattice mobility $\mu_L = 2.0 \times 10^3$ cm 2 -V $^{-1}$ -sec $^{-1}$ at $100^\circ K$ (9); μ_I is the ionized defect scattering mobility and μ_N is the neutral defect scattering mobility. The expressions for μ_I and μ_N are given in previous papers (5, 8).

The concentration of excess Zn can be estimated by calculating the concentration of ionized centers N_I and of neutral centers N_N . We will only consider the data at $100^\circ K$. Since we are dealing with strongly n-type ZnO we are assuming a low concentration of acceptors. Thus

$$N_I \approx n(100^\circ K)$$

where n is the carrier concentration at $100^\circ K$. By knowing N_I and n , μ_I can be calculated [from Ref. (5)]. The value for μ_N can then be found from Eq. [2]. The concentration of neutral centers is then (5)

$$N_N = \frac{5.39 \times 10^{20}}{\mu_N} \text{ (cm}^{-3}\text{)}$$

and the concentration of excess Zn is

$$x_{Zn} \approx n(100^\circ K) + N_N$$

The results of the calculations, given in Table I, compare favorably with the results from the carrier concentration analysis.

Electrochemical measurements.—The electrochemical method reported here is similar to Engell's in that both methods involve the measurement of electrochemical oxidation of zinc occurring simultaneously with the chemical dissolution of zinc oxide. Engell calculated the oxidation rate corresponding to a measured steady-state oxidation current, and compared it to the total dissolution rate of the oxide electrode. Our procedure, based on integration of the electrochemical current, is not limited to steady-state currents or electrodes of constant surface area.

Both procedures are based on two assumptions concerning the behavior of the ZnO crystal in the cell: (i) that the electrochemical oxidation of Zn^0 is much more rapid than the chemical solution of metallic zinc in dilute sulfuric acid, and (ii) that Zn^0 is the only oxidizable material present in the ZnO crystal. The first assumption was checked by adding small particles of metallic zinc to the cell in place of ZnO crystals. The integrated current corresponded to greater than 95% of that predicted by Faraday's law. The second assumption rested on the spectroscopic evidence that no metal other than zinc was present in the crystals.

The factors limiting measurement accuracy were the background current and possible integrator drift during the course of the measurement. The effect of both of these factors was minimized by carrying out the measurements at $40^\circ-50^\circ C$ instead of at room temperature. The higher temperature decreased the time required to dissolve a ZnO crystal from several hours to about 40 min.

Atomic ppm Zn was calculated from

$$\text{ppma} = \frac{(\text{coulombs}) (81.38) (10^6)}{(\text{mg ZnO}) (96.5) (2)}$$

Table I. Results

Doping temperature, °C	Electrical resistivity ρ and carrier concentration n				Analyses				
	300°K		100°K		Carrier conc		Mobility		El. Chem
	ρ (ohm-cm)	n (cm $^{-3}$)	n (cm $^{-3}$)	μ_H (cm 2 -V $^{-1}$ -sec $^{-1}$)	x_{Zn} (cm $^{-3}$)	x_{Zn} (ppma)	x_{Zn} (cm $^{-3}$)	x_{Zn} (ppma)	
700	0.36	1.1×10^{17}	2.0×10^{19}	930	1.6×10^{17}	4	2.2×10^{17}	5	—
800	0.14	3.1×10^{17}	6.6×10^{19}	580	5.6×10^{17}	13	4.8×10^{17}	11	23
900	0.060	7.3×10^{17}	2.0×10^{17}	350	1.0×10^{18}	24	9.5×10^{17}	23	30
1000	0.048	9.5×10^{17}	4.5×10^{17}	210	1.9×10^{18}	45	2.0×10^{18}	47	75
1100	0.017	3.6×10^{18}	3.4×10^{18}	100	$\sim 7 \times 10^{18}$	165	7.7×10^{18}	183	190

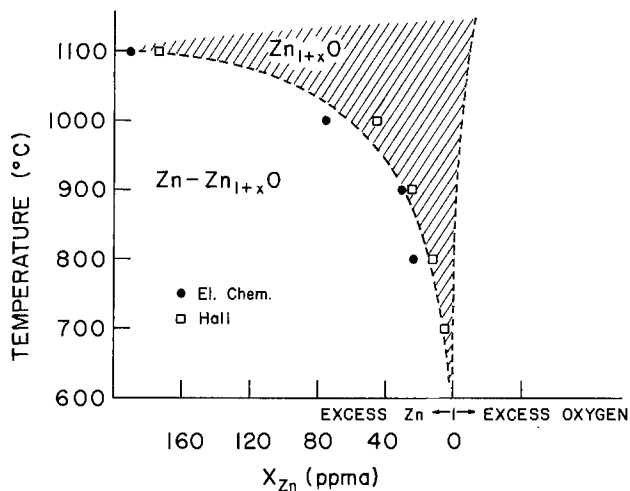


Fig. 1. A portion of the phase diagram $\text{Zn-Zn}_{1+x}\text{O}$ is shown. The excess Zn boundary has been determined. ● represents the electrochemical data and □ represents results from the Hall effect analysis. The excess oxygen boundary is suggested only.

Results of these measurements are summarized in the last column of Table I.

The phase boundary $\text{Zn-Zn}_{1+x}\text{O}$.—The values for x_{Zn} in Table I represent the phase boundary $\text{Zn-Zn}_{1+x}\text{O}$ (the maximum solubility of Zn in Zn_{1+x}O). A portion of the phase diagram $\text{Zn-Zn}_{1+x}\text{O}$ is shown in Fig. 1. The excess oxygen limit of Zn_{1+x}O is probably very close to stoichiometric ZnO (p-type ZnO has not yet been observed).

The phase boundary is also shown in Fig. 2 as $\log x_{\text{Zn}}$ vs. $1/T$ and may be represented as

$$\log x_{\text{Zn}} = -\frac{4700}{T} + 5.6$$

This corresponds to average values of the heat of solution $\Delta H = 22$ kcal/mole and entropy of solution $\Delta S = 26$ eu in the temperature range $700^\circ\text{--}1100^\circ\text{C}$ of Zn saturated ZnO.

Manuscript submitted Dec. 2, 1974; revised manuscript received Feb. 27, 1975.

Any discussion of this paper will appear in a Discussion Section to be published in the June 1976 JOURNAL.

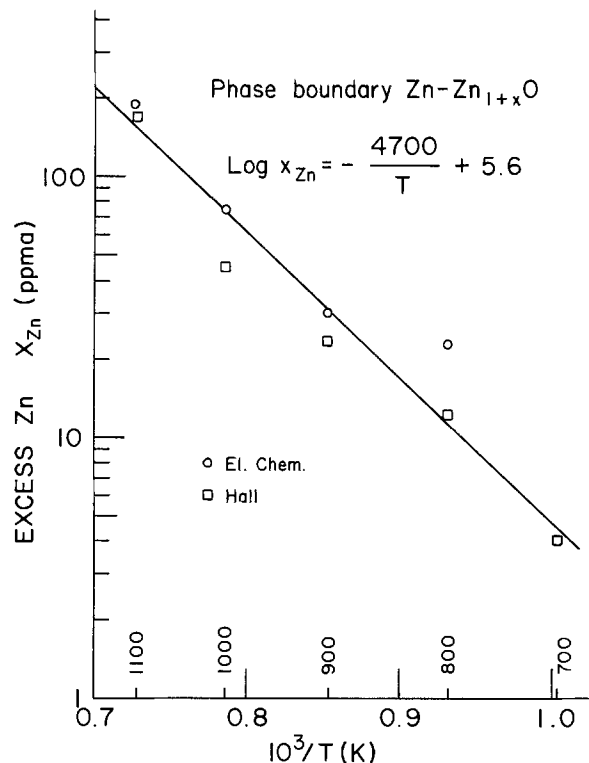


Fig. 2. The excess Zn boundary of Zn_{1+x}O as shown as $\log x_{\text{Zn}}$ (ppma) vs. $10^3/T$ ($^\circ\text{K}$).

All discussions for the June 1976 Discussion Section should be submitted by Feb. 1, 1976.

Publication costs of this article were partially assisted by the 3M Company.

REFERENCES

1. H. J. Allsopp, *Analyst*, **82**, 474 (1957).
2. V. J. Normann, *ibid.*, **89**, 261 (1964).
3. H. J. Engell, *Z. Elektrochem.*, **60**, 905 (1956).
4. J. M. Kruse, *Anal. Chem.*, **43**, 771 (1971).
5. K. I. Hagemark and L. C. Chacka, To be published in *J. Solid State Chem.*
6. J. S. Blakemore, "Semiconductor Statistics," p. 133, Pergamon Press, New York (1962).
7. D. G. Thomas, *J. Phys. Chem. Solids*, **3**, 229 (1957).
8. P. Wagner and R. Helbig, *ibid.*, **35**, 327 (1974).
9. A. R. Hutson, *Phys. Rev.*, **108**, 222 (1957).

The Preparation and Properties of Aluminum Nitride Films

T. L. Chu* and R. W. Kelm, Jr.*

Institute of Technology, Southern Methodist University, Dallas, Texas 75275

ABSTRACT

Aluminum nitride films have been deposited on silicon substrates at 800°-1200°C by the pyrolysis of an aluminum trichloride-ammonia complex, $\text{AlCl}_3 \cdot 3\text{NH}_3$, in a gas flow system. The deposit was transparent, tightly adherent to the substrate, and was confirmed to be aluminum nitride by x-ray and electron diffraction techniques. The deposited aluminum nitride films were found to be polycrystalline with the crystallite size increasing with increasing temperature of deposition. Other properties of aluminum nitride films relevant to device applications, including density, refractive index, dissolution rate, dielectric constant, and masking ability, have been determined. These properties indicate that aluminum nitride films have potential as a dielectric in electronic devices.

Aluminum nitride is a refractory, large energy gap material [sublimation temperature 2400°C (1), energy gap 5.9-6.2 eV (2, 3)] and has chemical, physical, and electrical properties suitable for several applications in electronic devices. For example, its large energy gap, good thermal stability [equilibrium vapor pressure of nitrogen at 1500°C: 0.05 Torr (4)], and chemical inertness [stable in air at temperatures up to 700°C (5)] suggest that aluminum nitride is a good dielectric for active and passive components in semiconductor devices. Aluminum nitride, being a piezoelectric material with a high acoustic velocity, is also well suited for the fabrication of surface wave acoustic devices.

Aluminum nitride has been prepared by several techniques, such as the direct combination of the elements and chemical reactions of gaseous aluminum and nitrogen-containing compounds on substrate surfaces. The direct combination technique requires temperatures in excess of 1500°C (2, 5, 6) and is not suitable for device applications. On the other hand, aluminum nitride films have been deposited on the surfaces of refractory metals, insulators, and semiconductors at considerably lower temperatures by the reaction of aluminum trichloride with ammonia (1, 3, 7-12) and the reaction of trimethylaluminum with ammonia (13). Aluminum nitride films up to 5 μm in thickness have also been deposited on metallic substrates by diode reactive sputtering, and the dielectric properties of sputtered aluminum nitride films were found to be superior to those of bulk polycrystalline material (14). The chemical deposition technique appears to be more compatible with the current device technology; however, the utilization of aluminum nitride in semiconductor devices has not been explored.

In this work, aluminum nitride films have been deposited on single crystal silicon substrates by the pyrolysis of an aluminum trichloride-ammonia complex in a gas flow system. The properties of the deposited films, such as structure, composition, density, refractive index, dissolution rate, dielectric constant, masking ability, etc., have been determined. The experimental methods and results are discussed in this paper.

Preparation of Aluminum Nitride Films

The ammonolysis of aluminum trichloride is commonly used for the deposition of aluminum nitride films. Because of the hygroscopic nature of aluminum trichloride, an aluminum trichloride-ammonia complex was used as the starting material. The complex

was prepared by saturating reagent grade anhydrous aluminum trichloride in a fused silica reaction tube with anhydrous ammonia at room temperature. The resulting mass was heated at 350°C in an ammonia flow, and the complex sublimed yielding a white crystalline powder. The composition of the complex, determined by dissolving a weighed amount of the specimen in a known volume of 0.1N hydrochloric acid and titrating the excess acid with 0.1N sodium hydroxide, was $\text{AlCl}_3 \cdot 3\text{NH}_3$. This complex is considerably more stable in the laboratory ambient than aluminum trichloride. Its vapor pressure was determined from the extent of vaporization in a sealed silica tube after heating at a predetermined temperature for 24 hr. The vapor pressure data in the temperature range 500°-800°K are shown in Fig. 1; the complex has sufficient vapor pressure at temperatures below 300°C for utilization in the deposition of aluminum nitride. The heat of vaporization of the complex calculated from the slope of this plot was 11.8 ± 0.2 kcal/mole.

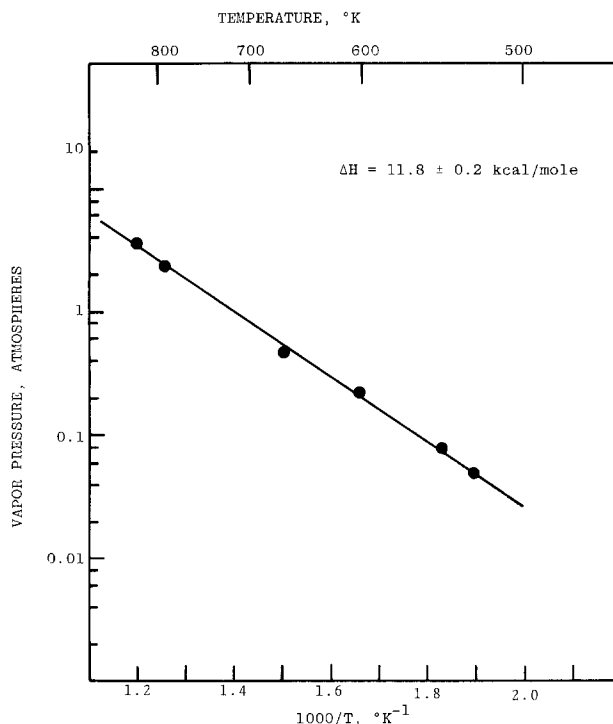


Fig. 1. Vapor pressure of aluminum trichloride-ammonia complex $\text{AlCl}_3 \cdot 3\text{NH}_3$.

* Electrochemical Society Active Member.

Key words: aluminum nitride, chemical deposition, electronic devices, silicon.

The deposition of aluminum nitride by the pyrolysis of the aluminum trichloride-ammonia complex in a gas flow system was carried out using an apparatus shown schematically in Fig. 2. The diluent gases used in the deposition process were commercial hydrogen purified by diffusion through a palladium-silver alloy and Matheson anhydrous ammonia of better than 99.99% purity. The reaction tube was made of clear fused silica, 55 mm ID and 3 ft long. A fused silica boat containing the aluminum trichloride-ammonia complex was maintained at 250°C by using an external resistance heater, and hydrogen or a 6:1 hydrogen-ammonia mixture at a flow rate of 30 liters/min was used to carry the complex to the substrate surface. The silicon substrates with main faces of {111} orientation were n-type, 5-20 ohm-cm resistivity, and were mechanically polished and chemically etched in the usual manner. They were supported on a silicon carbide-coated graphite susceptor, and the susceptor was heated externally by an rf generator. Prior to the deposition of aluminum nitride, the substrates were heated at 1150°C in hydrogen for ½ hr to remove the oxide on the surface. In some experiments, the substrate surfaces were etched *in situ* at 1170°C with a hydrogen-hydrogen chloride mixture containing 2% hydrogen chloride. The deposition of aluminum nitride was carried out at substrate temperatures in the range of 800°-1200°C, and the deposition time was usually 15-45 min. The thickness of aluminum nitride films on silicon substrates was determined by removing part of the film and measuring the height of the step generated with a Sloan Dektak and Graphic Chart Recorder.

Under the conditions described above, the deposited films are transparent and tightly adherent to the substrate. The average deposition rates in the temperature range 800°-1200°C are shown in Fig. 3. The deposi-

tion rate decreased with increasing temperature from 160 Å/min at 800°C to 120 Å/min at 900°C and 90 Å/min at 1000°C. This decrease of deposition rate is due presumably to the increased contribution of gas phase nucleation at high temperatures. The gas phase nucleation becomes more pronounced at higher concentrations of the aluminum trichloride-ammonia complex in the reactant mixture. For example, films deposited at a rate of 750 Å/min at 900°C had a cloudy appearance as a result of the enhanced gas phase nucleation.

The films deposited in the temperature range 800°-1100°C were analyzed by the x-ray diffraction technique. Silicon substrates were removed from the specimens by etching with a nitric acid-hydrofluoric acid mixture, and the resulting material was pulverized and examined by the Debye-Scherrer technique using nickel-filtered $\text{CuK}\alpha$ radiation. The diffraction patterns were identical with those reported for aluminum nitride (15), thus confirming that the deposited films were aluminum nitride.

Properties of Aluminum Nitride Films

Structure.—Aluminum nitride films deposited on silicon substrates under proper conditions were uniform, transparent, and highly adherent to the substrate. They showed no structural features when examined with an optical microscope. Several films were investigated by transmission electron microscopy using a Hitachi Model 11BU electron microscope after removing the substrates with a nitric acid-hydrofluoric acid mixture. Figure 4 shows the micrographs of aluminum nitride films deposited in the temperature range 800°-1100°C. All films were polycrystalline, and the average linear dimensions of the crystallites increased with increasing deposition temperature. Typical dimensions of crystallites were 100, 200, 600, 1100, and 2200 Å in films deposited at 800°, 900°, 1000°, 1100°, and 1200°C, respectively. This increase in crystallite size with temperature is to be expected. The diffraction patterns of aluminum nitride films deposited at various temperatures are shown in Fig. 5. The d-spacings measured from these patterns further confirm that all films are aluminum nitride. Figure 5

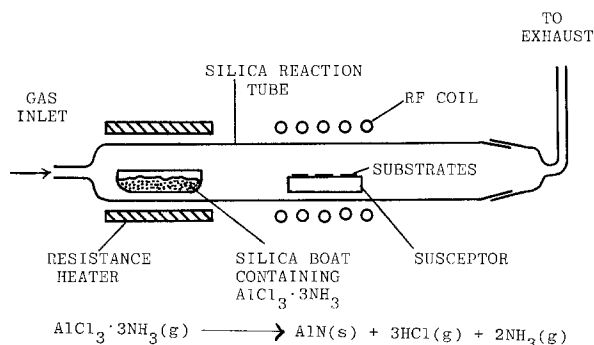


Fig. 2. Schematic of the apparatus used for the deposition of aluminum nitride films.

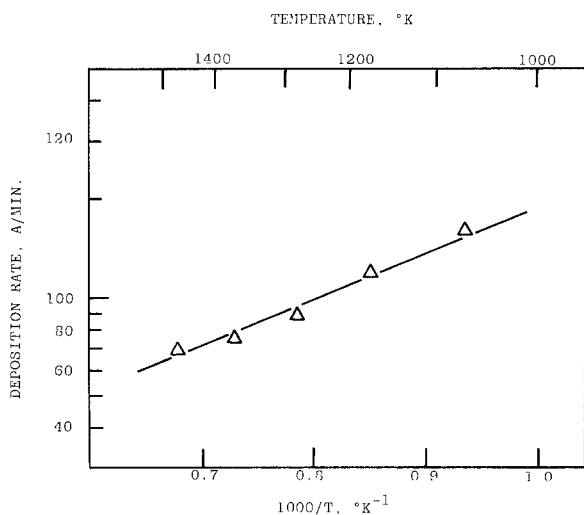


Fig. 3. Average deposition rate of aluminum nitride films as a function of temperature.

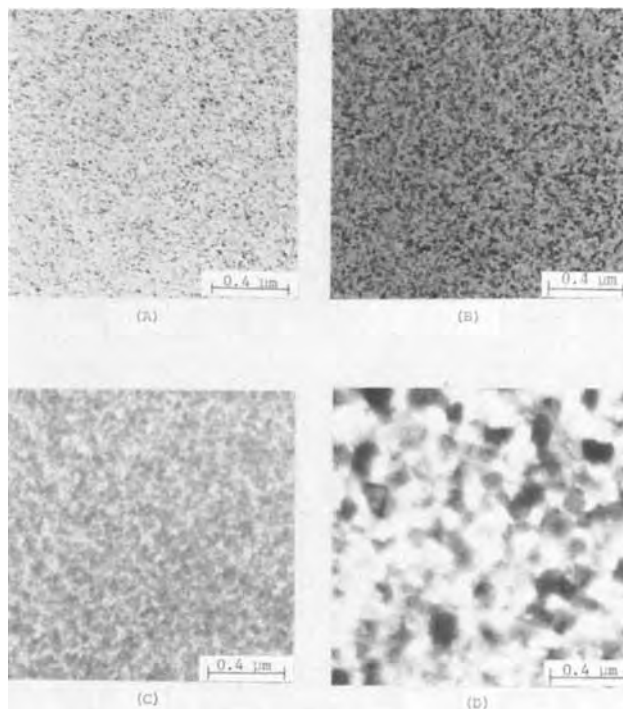


Fig. 4. Transmission electron micrographs of aluminum nitride films deposited at (A) 800°C, (B) 900°C, (C) 1000°C, and (D) 1100°C.

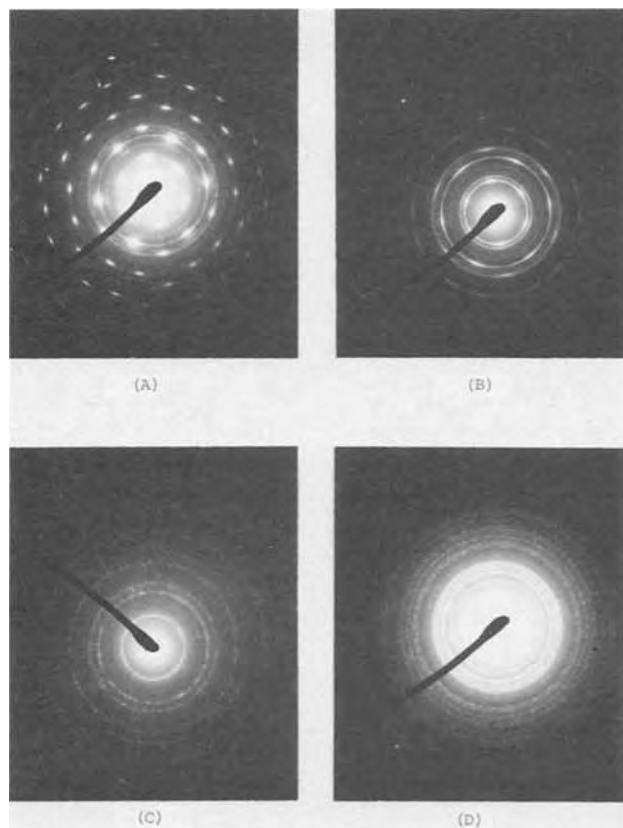


Fig. 5. Electron diffraction patterns of aluminum nitride films deposited at (A) 800°C, (B) 900°C, (C) 1100°C, and (D) 1200°C.

indicates that aluminum nitride films deposited at temperatures above 1000°K are polycrystalline and that preferred orientations are increasingly apparent with decreasing temperature of deposition. The single crystallinity of the substrates appears to have little or no effect on the structural properties of aluminum nitride since aluminum nitride films deposited on the surface of silicon dioxide were essentially the same as those on silicon substrates.

Density, refractive index, and optical absorption.—The density of aluminum nitride films deposited at various temperatures was determined by the floating equilibrium technique using a mixture of 1-bromo 2-iodo benzene and methylene iodide. The temperature of deposition was found to affect only slightly the

density of aluminum nitride. Aluminum nitride films deposited at 800°, 900°, 1000°, and 1100°C have densities of 3.15, 3.18, 3.18, and 3.20 ± 0.01 g/cm³, respectively, as compared with a reported value of 3.13 g/cm³ (12) and the theoretical density of 3.26 g/cm³.

The refractive index of aluminum nitride films deposited in the temperature range 800°–1200°C was determined by the Becke line method to be 1.991 ± 0.003 , irrespective of the deposition temperature. A few samples were also measured by the ellipsometric technique; the results, though not as reproducible, were usually in good agreement with those by the Becke line method. However, refractive indices as high as 2.17 ± 0.05 have been reported for single crystalline aluminum nitride prepared by the direct reaction of aluminum with nitrogen (16).

The optical absorption spectra of aluminum nitride films deposited under various conditions were taken on a Beckman Model DK-2 spectrophotometer at room temperature. Typical results are shown in Fig. 6, where the thickness of the aluminum nitride film was 18 μ m for curve A and 13 μ m for curve B. The fundamental absorption edge for all specimens measured was found to be 5.9 ± 0.2 eV, in agreement with that observed by others (2). However, the films deposited at very high rates, 700 Å/min or higher irrespective of deposition temperature, exhibited an additional absorption band in the 3.0 to 3.2 μ m region (curve A) while those deposited at low rates, 300 Å/min or lower, showed no absorption in this region (curve B). The absorption in the 3.0–3.2 μ m region is presumably due to the N-H or Al-Cl bonds in aluminum nitride films deposited at high rates. As stated previously, the gas phase nucleation becomes pronounced at high deposition rates. The decomposition of the aluminum trichloride-ammonia complex in the gas phase may not proceed to completion, and the deposited material contained N-H or Al-Cl bonds. Thus, the use of low deposition rates is essential for obtaining good quality aluminum nitride films.

Dissolution behavior.—The deposited aluminum nitride films are soluble in phosphoric acid and sodium hydroxide solutions. To determine the dissolution rate of aluminum nitride films, a portion of the specimen was covered with Apiezon Q wax or photoresist, and the specimen was immersed in the etchant with constant agitation for various lengths of time. The dissolution rate was then determined by removing the protective coating and measuring the difference in the step heights using the Dektak system.

The dissolution rate of aluminum nitride films, deposited in the temperature range 800°–1200°C, in a 10% sodium hydroxide solution was determined in the

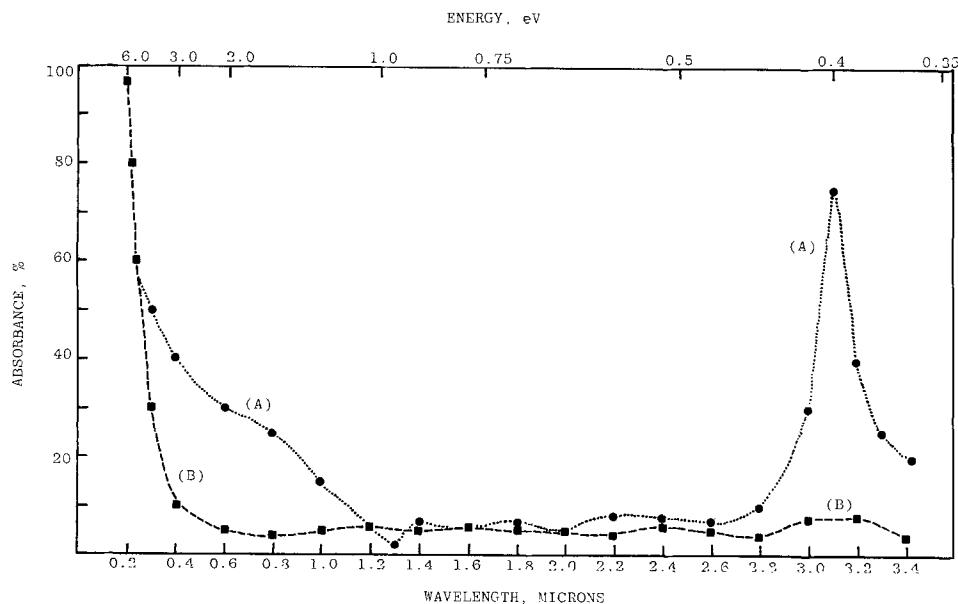


Fig. 6. Optical absorption spectra of aluminum nitride films deposited at a rate of about 700 Å/min (A) and at a rate of about 300 Å/min (B).

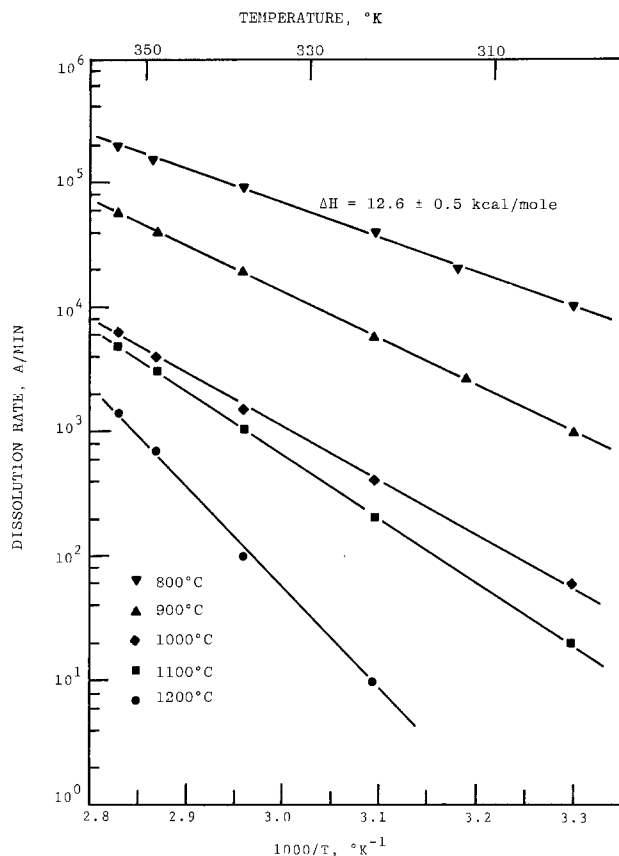


Fig. 7. Dissolution rate of aluminum nitride films, deposited in the temperature range 800°-1200°C, in 10% sodium hydroxide solution.

temperature range 30°-80°C. The results are shown in Fig. 7. At a given temperature, the dissolution rate of aluminum nitride films decreased with increasing deposition temperature, due presumably to the larger crystallites of aluminum nitride deposited at higher temperatures. Also, the dissolution rate of aluminum nitride films deposited at low temperatures was found to remain the same after annealing at higher temperatures, indicating negligible grain growth. The activation energy of dissolution for aluminum nitride films deposited at 800°C was found to be 12.6 ± 0.5 kcal/mole. The activation energy also increased with increasing deposition temperature. The relatively large activation energy indicates that the dissolution of aluminum nitride films is a surface-reaction controlled process.

The dissolution rate of aluminum nitride films deposited at 900°C was also determined using an 85% phosphoric acid solution. At temperatures up to 50°C, the dissolution rate of aluminum nitride was negligible. Figure 8 shows the dissolution rate in the temperature range 75°-150°C, and the activation energy of this dissolution was found to be 13.5 ± 0.5 kcal/mole, similar to the use of sodium hydroxide solution as an etchant.

Both sodium hydroxide and phosphoric acid solutions used in this work were found to produce clean and structureless surfaces, similar in appearance to the as-grown aluminum nitride films, when examined with an optical microscope.

Masking ability.—To explore the usefulness of aluminum nitride in silicon devices, its capabilities and limitations as masks against the diffusion of boron, phosphorus, aluminum, and gallium into silicon were investigated. Aluminum nitride films of 1000-1700Å thickness, deposited on silicon substrates at 900°C were used in the diffusion experiments. The substrates were n-type, 5-10 ohm-cm resistivity for the diffusion of boron, aluminum, and gallium, and were p-type, 10-20

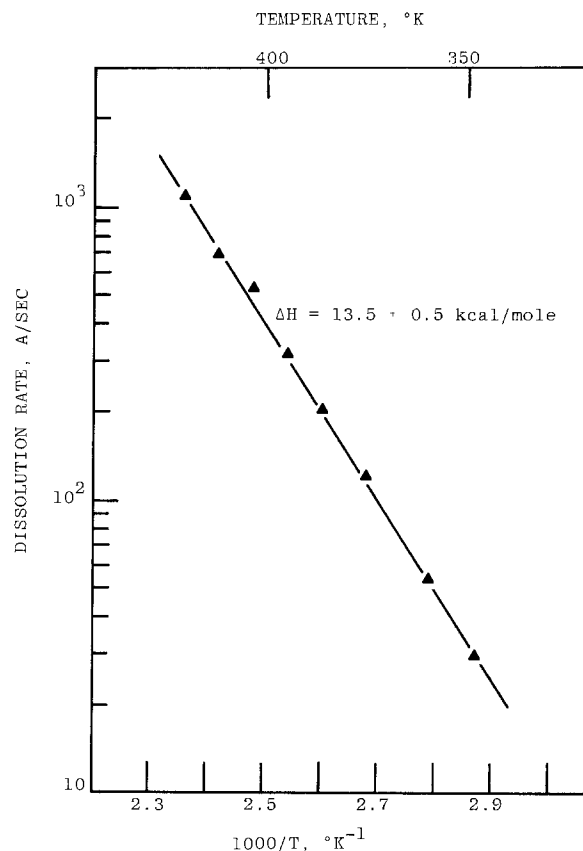


Fig. 8. Dissolution rate of aluminum nitride films deposited at 900°C in 85% phosphoric acid.

ohm-cm for the diffusion of phosphorus. The aluminum nitride film was removed completely from circular areas (usually 500 μm diameter) of the specimen by photolithographic techniques using sodium hydroxide or phosphoric acid as an etchant. Sharp, well-defined edges were obtained with virtually no undercutting.

The boron diffusion was carried out by depositing boron oxide glass on the specimen surface at 970°C for 40 min from a boron nitride source followed by redistribution at 1300°C for 1 hr. In the phosphorus diffusion process, phosphorus oxide glass was deposited on the specimen surface at 1000°C for 30 min using phosphorus oxytrichloride as the source, and the redistribution was carried out at 1150°C for 1.5 hr. After the diffusion process, an unmasked region of the specimen was angle-lapped, and the aluminum nitride mask was removed by etching. The resistivity profile on the masked and unmasked regions of the main face and on the beveled surface was measured by the spreading resistance technique (17). The results for the boron diffusion into n-type silicon and the phosphorus diffusion into p-type silicon are shown in Fig. 9. The silicon under the aluminum nitride film was found to have the same conductivity type with essentially no change in resistivity, while p-n junctions were formed in unmasked regions. Thus, aluminum nitride films are successful for masking the diffusion of boron and phosphorus under the conditions used here.

Subsequent to the boron and phosphorus diffusion process, the dissolution rate of the aluminum nitride masks in a 10% sodium hydroxide solution was measured. Aluminum nitride films with boron oxide or phosphorous oxide coatings showed no measurable change in dissolution rate or appearance after heating at 1150°C for 1.5 hr, indicating the inertness of aluminum nitride toward the dopant oxide. However, when the heat-treatment was carried out at 1250°-1300°C after the deposition of boron oxide, the dissolution rate of the nitride films decreased appreciably, indi-

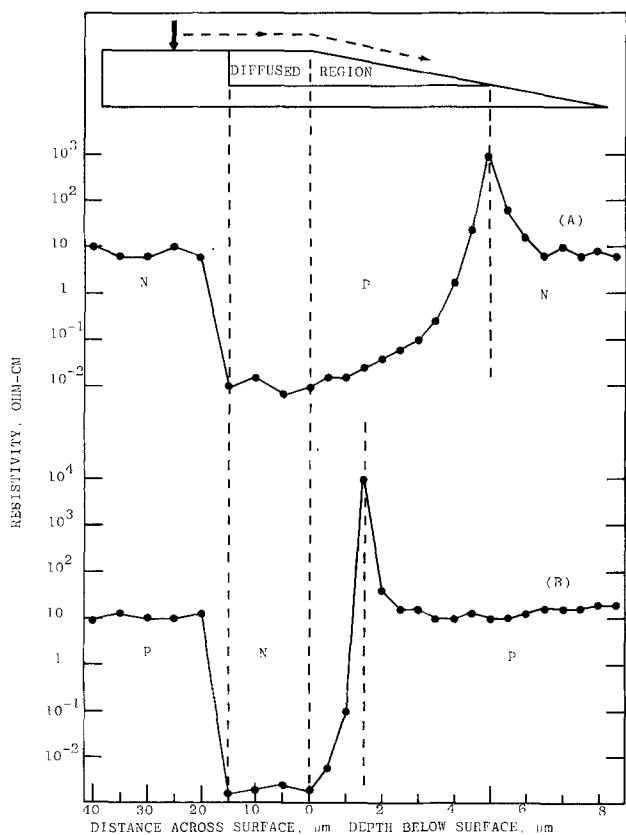


Fig. 9. Resistivity profiles in n-type (A) and p-type (B) silicon specimens after diffusion using aluminum nitride as a diffusion mask.

cating a reaction between aluminum nitride and boron oxide.

The aluminum and gallium diffusions were carried out at 1150°C for 1.5 hr in sealed fused silica tubes using the element as the source material. Aluminum nitride films failed to mask the diffusion of dopant in both cases. This is due presumably to the penetration of aluminum and gallium vapor through the grain boundaries in finely polycrystalline aluminum nitride films at high temperatures.

Dielectric properties.—The dielectric properties of aluminum nitride films were measured at room temperature using aluminum-aluminum nitride-silicon structures. Aluminum contacts of 2.5×10^{-2} cm diameter were deposited on aluminum nitride, and ohmic contacts were applied to the back surface of silicon substrates by electroless plating (18).

The dielectric strength of aluminum nitride films deposited in temperature range 800°–1000°C on low resistivity silicon substrates was measured at room temperature using d.c. and 400 kHz. The average dielectric strength of aluminum nitride was found to be 1.5×10^7 V/cm for films of 300–400 Å thickness, independent of deposition temperature; it decreased to the apparent bulk value of approximately 10^7 V/cm for film thicknesses greater than about 1000 Å. Aluminum nitride films deposited at 1100°C or above were found to have lower dielectric strength than those deposited at 800°–1000°C, due presumably to the inclusions in the films of the products of volume reaction where the decomposition of the aluminum trichloride-ammonia complex was not complete. The d-c dielectric strength of aluminum nitride films of 2000 Å thickness prepared at 800°–1000°C was also measured at higher temperatures and was found to be approximately 10^7 V/cm at 30°C, 5×10^6 V/cm at 100°C, 2.5×10^6 V/cm at 200°C, 1.5×10^6 V/cm at 250°C, and 10^6 V/cm at 300°C.

Capacitance measurements were made on aluminum-aluminum nitride-silicon structures using a Boonton

75C Direct Capacitance Bridge operated at frequencies up to 0.5 MHz. The insulator capacitance was used to obtain the dielectric constant value. The dielectric constant of aluminum nitride films prepared at 800°, 900°, and 1000°C was found to be 11.5 ± 0.2 , and that prepared at 1100°C was considerably lower, usually 8.1 ± 0.3 , as compared with 9.14 reported for the low-frequency dielectric constant of single crystalline aluminum nitride (19). Also, the dielectric constant of an aluminum nitride film prepared at 800°C was found to remain unchanged after heating at 1100°C in hydrogen for 1 hr, again indicating the structural stability of aluminum nitride. The dielectric constant of all aluminum nitride films prepared in the temperature range 800°–1100°C was found to be independent of frequency and temperature in the ranges 5–500 kHz and 100°–500°K, respectively.

It should be mentioned that the properties of aluminum nitride films discussed above are independent of the nature of the carrier gas, hydrogen or 6:1 hydrogen-ammonia mixture, used in the deposition process.

Summary and Conclusions

Aluminum nitride films have been deposited on silicon substrates at 800°–1200°C in a gas flow system by the thermal decomposition of an aluminum trichloride-ammonia complex, $\text{AlCl}_3 \cdot 3\text{NH}_3$. This complex was prepared by saturating aluminum trichloride with ammonia and purified by sublimation. The deposit was transparent, tightly adherent to the substrate and was verified by x-ray and electron diffraction techniques to be aluminum nitride. Transmission electron microscopy indicated that all aluminum nitride films were polycrystalline; the crystallite size increased with increasing temperature of deposition, and the preferred orientations became more apparent at lower deposition temperatures.

At deposition temperatures in the range of 800°–1000°C, the average density, refractive index, dielectric strength, and dielectric constant of aluminum nitride were found to be 3.18 g/cm³, 1.99, 10^7 V/cm, and 11.5, respectively. Aluminum nitride films are soluble in sodium hydroxide and phosphoric acid solutions, and the standard photolithographic technique can be readily applied. Aluminum nitride films were found to be capable of masking against the diffusion of boron and phosphorus into silicon from the oxide sources. These properties indicate that aluminum nitride films have great potential as a dielectric in solid-state devices.

Acknowledgment

This research was supported by the Langley Research Center of the National Aeronautics and Space Administration under Grant NGL 44-007-042.

Manuscript submitted Feb. 6, 1974; revised manuscript received March 12, 1975.

Any discussion of this paper will appear in a Discussion Section to be published in the June 1976 JOURNAL. All discussions for the June 1976 Discussion Section should be submitted by Feb. 1, 1976.

REFERENCES

1. Th. Renner, *Z. Anorg. Allg. Chem.*, **298**, 22 (1959).
2. G. A. Cox, D. O. Cummins, K. Kawabe, and R. H. Tredgold, *J. Phys. Chem. Solids*, **28**, 543 (1967).
3. W. M. Yim, E. J. Stofko, P. J. Zanzucchi, J. I. Panikove, M. Eitenberg, and S. L. Gilbert, *J. Appl. Phys.*, **44**, 292 (1973).
4. D. L. Hildenbrand and W. F. Hall, *J. Phys. Chem.*, **67**, 888 (1963).
5. K. M. Taylor and C. Lenie, *This Journal*, **107**, 308 (1960).
6. G. A. Wolf, I. Adams, and J. W. Mellichamp, *Phys. Rev.*, **114**, 1262 (1959).
7. T. L. Chu, D. W. Ing, and A. J. Noreika, *Solid-State Electron.*, **10**, 1023 (1967).
8. A. M. Lejus, J. Thery, J. C. Giller, and R. Colongues, *Compt. Rend.*, **257**, 157 (1963).

9. A. J. Noreika and D. W. Ing, *J. Appl. Phys.*, **39**, 5578 (1968).
10. A. A. Pletyushkin and N. G. Slavina, *Neorg. Mater.*, **4**, 893 (1968).
11. M. D. Lyutaya, I. G. Chernysh, and Z. A. Yaremenko, *ibid.*, **5**, 1929 (1969).
12. D. W. Lewis, *This Journal*, **117**, 978 (1970).
13. H. M. Manasevit, F. M. Erdmann, and W. I. Simpson, *ibid.*, **118**, 1864 (1971).
14. A. J. Noreika, M. H. Francomb, and S. A. Zeitman, *J. Vacuum Sci. Technol.*, **6**, 194 (1969).
15. M. Stackelberg and K. F. Spiess, *Z. Phys. Chem.*, **A175**, 140 (1935).
16. J. Pastrnak and L. Roskovcova, *Phys. Status Solidi*, **14**, K5 (1966).
17. R. G. Mazur and D. H. Dickey, *This Journal*, **113**, 255 (1966).
18. M. V. Sullivan and J. H. Eigler, *ibid.*, **104**, 226 (1957).
19. A. T. Collins, E. C. Lightowers, and P. J. Dean, *Phys. Rev.*, **158**, 833 (1967).

Technical Notes



Vapor Deposition of Sulfur-Doped GaAs Layers

K. H. Bachem*¹ and H. Bruch

*Institut for Semiconductor Electronics/Sonderforschungsbereich 56 "Festkörperelektronik,"
Technical University Aachen, Germany*

Sulfur is a commonly used dopant in the vapor growth of n-type GaAs epitaxial layers (1-7). The most straightforward approach is to use H₂S as a vapor dopant. This gas can be purchased diluted with hydrogen and bled into the deposition system using a variable leak. However, it appears to be difficult to obtain well-defined and reproducible dopant concentrations due to irreversible changes of the leak rates. Experiments have shown that the variable leaks (Varian, Leybold) commonly used in vacuum systems are calibratable only to within an order of magnitude. Another alternative, the stepwise dilution of the doping gas by using fine metering valves and ball flowmeters requires an extensive apparatus and time-consuming calibration also. These problems are most likely responsible for the large discrepancies in the literature data regarding the relationship between the H₂S concentration in the gas phase and the donor concentration in the epitaxial film (5, 6).

Other workers have used solid sulfur as a primary source (2, 7). The element can be vaporized into the reactor either directly or via an H₂S generator. A drawback of this method results from the difficulties in evaporating sulfur powder or grains with a well-defined vapor pressure. Both the evaporating surface area and the crystalline form and hence the vapor pressure of the sulfur may change during heat-treatment.

In the present investigation we have attempted to find improved sulfur doping methods and to clarify the discrepancies referred to above. This was accomplished by using a capillary for the controlled injection of H₂S or by adding a liquid sulfur compound to the AsCl₃ bubbler in the deposition system.

The H₂S doping experiments were carried out in a standard apparatus (8) for the Ga/AsCl₃/H₂ process (9). Well-defined concentrations of H₂S were added to the gas stream by controlling, via a reducing valve, the input pressure to a capillary tube of ≈150 μm diameter and 6 cm length used for injecting the doping gas into the hydrogen carrier. The system was calibrated by determining the time required to pass a defined amount of gas through the capillary at a given input pressure. The doping gas was a mixture of H₂S (985 ppm) in H₂, bottled in a steel cylinder.

For the second approach S₂Cl₂ was selected as a liquid sulfur dopant source. This compound appears to fulfill the main requirements for use in this application: (i) It can be obtained in a relatively pure form. (ii) It will decompose at the deposition temperature. (iii) In the working temperature range of the AsCl₃ source (15°-25°C) its vapor pressure is such that epitaxial layers in the 10¹⁶-10¹⁷ cm⁻³ doping range can be obtained.

The data in Fig. 1 show that the partial pressures of AsCl₃ (10) and S₂Cl₂ (11) are equal within approximately 10% around room temperature. Making the likely assumption that the two liquids form an ideal mixture, the ratio of their partial pressures in the vapor phase will be nearly the same as the ratio of their concentrations in the AsCl₃-bubbler.

For the S₂Cl₂ doping experiments a reactor was used with two Ga source tubes side by side, each connected to a bubbler, one for AsCl₃, the other for the AsCl₃-S₂Cl₂ mixture (Fig. 2). In the deposition zone the dopant concentration can be varied either by varying the proportion of the gas streams through the two bubblers or by changing the amount of S₂Cl₂ in the AsCl₃ bubbler. The results indicate that after saturation of the Ga source with As along with formation of a GaAs crust (12) a constant sulfur pressure is obtained in the system, and steady-state conditions can be expected during epitaxial growth.

The following starting materials were used: chromium-doped GaAs substrates ($\rho = 10^7$ - 10^8 ohm-cm, Monsanto) orientated 2° off {100} towards {110}, gallium (99.9999% Johnson Matthey), AsCl₃ (Suprapur, Merck), S₂Cl₂ (99%, Riedel-de Hean) redistilled, H₂S (985 ppm in H₂, Matheson). The hydrogen was purified in a Pd-diffuser.

The experimental results in Table I demonstrate the behavior of the deposition system using S₂Cl₂. The epitaxial layers were grown in the listed succession, at a deposition temperature of 740°C, a flow rate of 200 ml/min (tube diameters: source tube 25 mm, substrate tube 55 mm), and an AsCl₃-partial pressure of 9.9·10⁻³ atm. The deposition time was 1 hr. An amount of 5 μl of S₂Cl₂ was added to 100 ml of AsCl₃, giving a doping level of 3.4·10¹⁶ cm⁻³ determined by Hall effect measurements. By transferring the Ga source into the second source tube connected to the bubbler containing only AsCl₃ a doping level of 2.3·10¹⁵ cm⁻³ was reached under the same growth con-

* Electrochemical Society Active Member.

¹ Presently on leave of absence at the IBM Research Center, Yorktown Heights, New York 10598.

Key words: GaAs, epitaxy, sulfur doping, gas phase deposition.

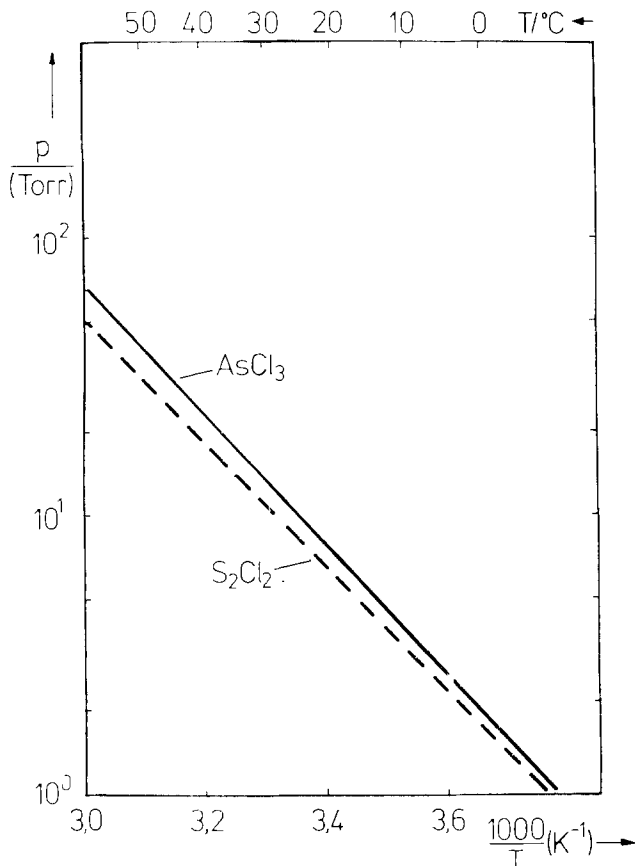


Fig. 1. Partial pressure of AsCl_3 and S_2Cl_2 vs. reciprocal temperature [after (9) and (10)].

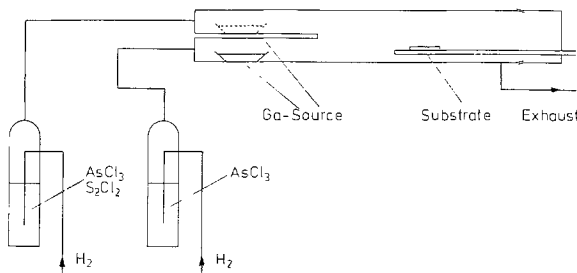


Fig. 2. Schematic diagram of the epitaxial deposition system

ditions. This value is in good agreement with the results obtained for undoped epitaxial layers grown earlier in the same reactor with identical starting material, where as an example a carrier concentration of $1.9 \cdot 10^{15}$ was obtained with an AsCl_3 pressure of $11.1 \cdot 10^{-3}$ atm. For the next runs the Ga source was returned to the source tube with the dopant gas stream. Carrier concentrations of $3.1 \cdot 10^{16} \text{ cm}^{-3}$ and $3.05 \cdot 10^{16}$ were obtained in successive runs. Knight *et al.* (4) found that the apparatus does not exhibit a memory effect when H_2S is injected into the reactor after the Ga source. Our results show that a memory effect is even absent when the entire system

Table I. Experimental results using S_2Cl_2

Sample	Mole fraction S_2Cl_2 in AsCl_3 bubbler	Bubbler used	Carrier conc (cm^{-3})
15	5×10^{-5}	with S_2Cl_2	3.4×10^{16}
16	0	without S_2Cl_2	2.3×10^{15}
17	5×10^{-5}	with S_2Cl_2	3.1×10^{16}
18	5×10^{-5}	with S_2Cl_2	3.05×10^{16}
19	1.5×10^{-4}	with S_2Cl_2	1.2×10^{17}
20	1.5×10^{-4}	both	7.8×10^{16}

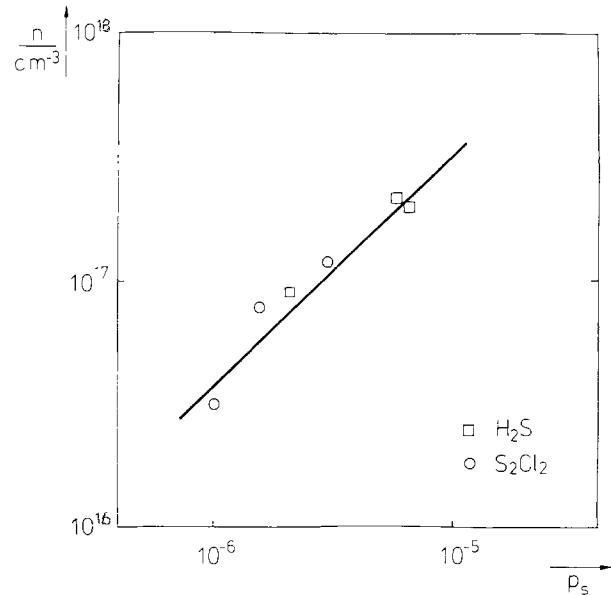


Fig. 3. Carrier concentration vs. partial pressure of sulfur in the gas phase for the H_2S and S_2Cl_2 systems.

including the Ga source has been exposed to sulfur vapor in a previous experiment. Tripling the amount of S_2Cl_2 in the bubbler leads to a roughly comparable increase in the carrier concentration. An intermediate value of $7.8 \cdot 10^{16} \text{ cm}^{-3}$ was reached by mixing both gas streams with each having a flow rate of 100 ml/min.

Figure 3 compares the carrier concentration obtained for various sulfur pressures in the gas phase both for the H_2S and the S_2Cl_2 systems. Notice first the good agreement between the data for both systems. Of course, such agreement should be expected since at the deposition temperature the composition of the gas phase will be identical in both cases. These results show the proportionality between sulfur pressure and electron density. In calculating the gas phase pressure it was assumed that the system $\text{AsCl}_3\text{-S}_2\text{Cl}_2$ behaves as an ideal solution. Under the assumption that all sulfur incorporated into the films is electrically active it also appears that a relationship analogous to Henry's law exists between sulfur pressure and sulfur concentration in the GaAs. Such behavior was also reported by Rai-Choudhury (13). Of course, it should be realized that the "Henry's law constant" (Table II) derived in this case is not obtained under equilibrium conditions with respect to the GaAs deposition.

Acknowledgment

The authors are indebted to Mr. Schiffers, Institute of Inorganic Chemistry of the Technical University Aachen, for redistilling our S_2Cl_2 dopant material. They would also like to thank Prof. P. Balk for his interest in this project.

Manuscript submitted Nov. 11, 1974; revised manuscript received April 2, 1975.

Any discussion of this paper will appear in a Discussion Section to be published in the June 1976 JOURNAL.

Table II. Relationship between sulfur concentration in epitaxial layer and sulfur concentration in vapor phase

Carrier conc (cm^{-3})	Atom fraction S in epitaxial layer	Atom fraction S in vapor phase	Henry's law constant	Dopant
3.4×10^{16}	7.7×10^{-7}	9.9×10^{-7}	1.28	S_2Cl_2
3.1×10^{16}	7.0×10^{-7}	9.9×10^{-7}	1.41	S_2Cl_2
7.8×10^{16}	1.8×10^{-6}	1.5×10^{-6}	0.83	S_2Cl_2
1.2×10^{17}	2.7×10^{-6}	3.0×10^{-6}	1.11	S_2Cl_2
2.2×10^{17}	5×10^{-6}	5.8×10^{-6}	1.16	H_2S
9.4×10^{16}	2.1×10^{-6}	2.3×10^{-6}	1.09	H_2S

All discussions for the June 1976 Discussion Section should be submitted by Feb. 1, 1976.

Publication costs of this article were partially assisted by the Technical University Aachen.

REFERENCES

1. E. W. Mehal and G. R. Cronin, *Electrochem. Technol.*, **4**, 540 (1966).
2. D. V. Eddolls, J. R. Knight, and B. L. H. Wilson, "GaAs, 1966 Symposium Proceedings," the Institute of Physics and the Physical Society, p. 3 (1967).
3. D. W. Shaw, R. W. Conrad, W. W. Mehal, and D. W. Wilson, *ibid.*, p. 10.
4. S. Knight, L. R. Dawson, J. V. DiLorenzo, and W. A. Johnson, "GaAs, 1970 Symposium Proceedings," the Institute of Physics and the Physical Society, p. 108 (1971).
5. J. V. DiLorenzo and G. E. Moore, Jr., *This Journal*, **118**, 1823 (1971).
6. F.-H. Dörbeck, Diss. Institute of Semiconductor Electronics, Technical University Aachen (1971).
7. S. Gisdakis, H. Kniekamp, and D. Schweizer, *Verhandl. DPG (VI)* **8**, 821 (1973).
8. K.-H. Bachem, G. Erlaki, and W. Markert, "Chemical Vapor Deposition, Fourth International Conference," G. F. Wakefield and J. M. Blocher, Jr., Editors, p. 296, The Electrochemical Society Softbound Symposium Series, Princeton, N. J. (1973).
9. J. R. Knight, D. Effer, and P. R. Evans, *Solid-State Electron.*, **8**, 178 (1965).
10. A. Boucher and L. Hollan, *This Journal*, **117**, 932 (1970).
11. A. Landolt-Börnstein, "Zahlenwerk und Funktionen aus Physik, Chemie, Astrophysik, Geophysik und Technik," 6. Aufl., Bd. II, T2a, p. 34, Springer Verlag, Berlin, Göttingen, Heidelberg (1960).
12. D. W. Shaw, *J. Crystal Growth*, **8**, 117 (1971).
13. P. Rai-Choudhury, *ibid.*, **11**, 113 (1971).

Postirradiation Alkali Migration

William Primak

Argonne National Laboratory, Argonne, Illinois 60439

During the course of his ion bombardment studies, Hines noted that the ion charge required to alter the refractive index of glass was greater than that required to alter the refractive index of quartz. He suspected the composition of the glass was altered by selective sputtering (1). Evidence for the migration of alkali ions during electron and ion bombardment appears in the temporal changes occurring during electron and ion probe microanalysis (2). The writer noted that areas of a lithium niobate surface which had been subjected to ion bombardment became decorated with droplets, and from these droplets (over a period of weeks) small crystals formed. They were identified as $\text{LiOH}\cdot\text{H}_2\text{O}$. The decoration could be washed off and would appear again over a period of weeks, repeatedly, evidence of a continuing migration of lithium to the surface (3). Now a number of commercial optical glasses have been subjected to ion bombardment, and the decoration phenomenon has been observed for some of them.

The glasses which were studied were a variety of commercial optical glasses, crown (C-1), borosilicate crown (BSC-2), telescope flint (TF), light barium crown (LBC-1), barium crown (BAK-5), light flint (LF-2), and dense flint (DF). Small areas of polished plates were subjected to ion bombardment with 140 keV D^+ ions for the following accumulated incident charge: 0.018, 0.036, 0.072, 0.108, 0.144, and 0.18 coulombs/cm², respectively. Decoration with droplets following ion bombardment during the summer (relative humidity in the laboratory varied between 40 and 60%, temperature controlled to within a degree of 24°C) was most severe on C-1, TF, LF-2, and DF. It was less severe on the barium crowns and was not seen on BSC-2. Decoration reappeared following washing, the time required to obtain droplets easily observed at 50-100X magnification being several days or weeks. Several months later, when the relative humidity had dropped to 20-40% with occasional days at 60%, the specimens were reexamined, and little mounds of solid were seen on the C-1 and TF glasses. Liquid droplets and some solid material were seen on the most highly bombarded areas of the LF-2 and DF glasses. The solid material can form exotic patterns. Probably these are caused by the crystallization rather than being related to structures formed by the ion bombardment. Examples of the decoration are shown in Fig. 1.

Key words: ion bombardment, glass, decoration, electrical leakage.

Water permitted to flow over the specimens will wet the bombarded areas more readily than the surrounding glass surface; and the water will cling to the bombarded areas, but not to the unbombarded areas. Such water adhesion has been interpreted as an indication of cleanliness of the glass surface. It is now seen to have quite a different cause: the bombarded areas have become hygroscopic because of the alkali migration.

The liquid droplets are probably alkali hydroxide solutions, and the deposits which develop are probably largely alkali carbonate. In the ion microprobe work (2), electric charge appeared to facilitate the migration of alkali ions in the solid, for the effects were reduced significantly by flooding the surface with electrons during bombardment or by using neutral atoms instead of ions. Although long-term storage of charge does occur in some materials, it probably did not (in the conventional sense) occur in these glasses which were covered with a solution film and which were washed with water. The freeing of the alkali ions is therefore attributed to a chemical change (such as the change in the valency of another ion or the substitution of some kind of center for the ion) or a structural change. It may be noted that the severity of the decoration effect for these glasses accords with their usually accepted chemical durability (3). Thus the factors which are involved in the chemical attack of glass by water and aqueous solutions (4) are involved in the transport of the alkali ions to the surface, which thus becomes a secondary process following the initial alteration of the glass by the ion bombardment.

When decoration of ion-bombarded lithium niobate was observed, it was the first example of the phenomenon seen in this laboratory. The appearance of liquid droplets could not be accounted for on the basis of the vapor pressure depression caused by lithium hydroxide, because the relative humidity in the laboratory was too low, and the possibility of an electrical effect associated with the charge of a strained piezoelectric material was considered. Now it has been found that irradiation can destroy the piezoelectric effect in lithium niobate. This may serve both to explain the reason why some highly bombarded surfaces showed a lesser decoration effect and to lend support to the hypothesis of an electrical effect. Such an effect is not necessary in the case of these glasses because they contain sodium, and sodium hydroxide is sufficiently more soluble than lithium hydroxide that liquid droplets could form at relative humidities occurring in

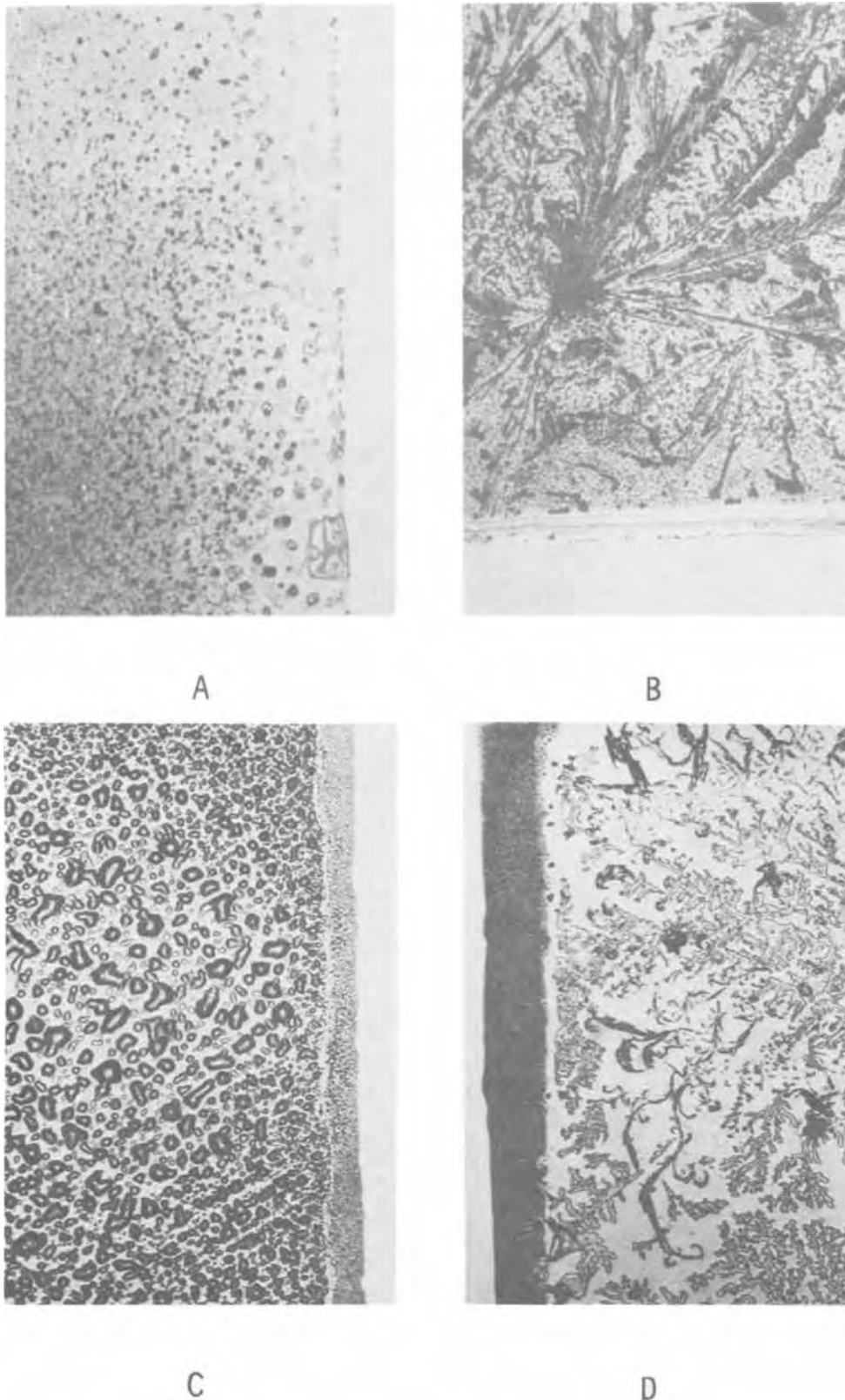


Fig. 1. Decoration of ion bombarded glass caused by water vapor condensation. The specimen areas shown are 0.75×1.08 mm. The "penumbral zones" are caused by lack of registry of masking arrangements. All of the decoration begins as liquid droplets. The crystallization depends on the relative humidity, length of storage, the particular glass, and the dose. All of these examples were seen following 140 keV deuteron bombardment (and may have been washed with water) for the following doses: A, C-1 glass, 0.018 coulombs/cm²; B, C-1 glass, 0.108 coulombs/cm²; C, TF glass, 0.036 coulombs/cm²; D, TF glass, 0.108 coulombs/cm².

our laboratory. However, the new observations raise the question whether surface impurities may be involved in some of the phenomena observed in the decoration of the lithium niobate. To this end it may be profitable to explore the system $\text{LiOH-NaCl-H}_2\text{O}$, and this is planned.

It had been customary to subject glass surfaces intended for coating to ion bombardment. The effect of alkali migration on the film should be considered.

Electrical leakage in ceramic electrical insulation used in radiation environments is a notorious problem. The problems arising from the formation of nitrates in

such environments was pointed out many years ago (6). Now effects caused by the alkali migration in these environments should be considered.

The alkali migration may contribute to the difficulties of evacuating glass vacuum systems and to the deterioration of glass structures subjected to bombardment or located in radiation fields.

Acknowledgment

This paper is based on work performed under the auspices of the U.S. Atomic Energy Commission.

Manuscript submitted Jan. 13, 1975; revised manuscript received March 17, 1975.

Any discussion of this paper will appear in a Discussion Section to be published in the June 1976 JOURNAL. All discussions for the June 1976 Discussion Section should be submitted by Feb. 1, 1976.

Publication costs of this article were partially assisted by Argonne National Laboratory.

REFERENCES

1. R. L. Hines, *J. Appl. Phys.*, **28**, 587 (1957); private communication.
2. D. V. McCaughan and R. A. Kushner, in "Characterization of Solid Surfaces," P. F. Kane and G. B. Larabee, Editors, chap. 22, pp. 627-640, Plenum Press, New York (1974).
3. G. W. Morey, "The Properties of Glass," Van Nostrand Reinhold Co., New York (1938).
4. R. H. Doremus, "Glass Science," pp. 242-250, Wiley-Interscience, New York (1973).
5. W. Primak, in "Electrets, Charge Storage and Transport in Dielectrics," M. M. Perlman, Editor, p. 546, The Electrochemical Society Softbound Symposium Series, Princeton, N. J. (1973).
6. W. Primak and L. F. Fuchs, *Nucleonics*, **13**, 3, 38 (1955); *Phys. Today*, **7**, 9, 15 (1954).



Cathodes for Seawater Activated Cells

Nehemiah Margalit*

ESB Incorporated, Technology Center, Yardley, Pennsylvania 19067

ABSTRACT

Temperature-humidity tests and discharge in an experimental cell were used to evaluate new cathode materials for magnesium seawater activated cells. Of the materials tested AgCl, Hg₂Cl₂, and CuI,S mixes were found promising. Mg/AgCl,Hg₂Cl₂ cells performed almost as well as Mg/AgCl cells due to an apparent intracathode reaction. The Mg/CuI,S system exhibited a lower operating voltage and will require further work for full evaluation.

The need to reduce silver content and loss associated with conventional Mg/AgCl seawater activated batteries has prompted searches for substitute cathodes. This search was directed towards the "silver group" of the classical qualitative analysis procedure (1) and copper(I) halide-sulfur mixes previously investigated by Reutschi *et al.* (2) for weather balloon applications.

Of the "silver group", aside from AgCl, PbCl₂ was found promising by other investigators (3); however, the use of Hg₂Cl₂ was hampered by the need to contain the discharge product, liquid mercury. Addition of silver powder for mercury amalgamation, as in the Ruben mercury(II) oxide electrode (4) has resulted in a low energy density cathode. Therefore a new method for making Hg₂Cl₂ electrodes was required.

Of the copper(I) halides, the bromide and the iodide exhibit low solubilities (5); thus their mixes with sulfur were evaluated as candidates for cathode material.

Preliminary Temperature Humidity Tests

In preliminary tests, copper(I) halide-sulfur mixes of the chloride (control), bromide and iodide were made and pelletized using the method described by Honer (6). The formulations for these mixes are shown in Table I.

Hg₂Cl₂ pellets were made using AgCl as an active binder. The AgCl active material-binder was precipitated, using reagent grade hydrochloric acid, from an aqueous solution of AgNO₃ (Fisher) in which Hg₂Cl₂ powder (Fisher) was suspended by stirring with a Teflon-coated magnetic stirring bar. The resultant white powder was collected by filtration, washed three times with deionized water and dried under vacuum. An analysis of the powder showed a 3-7 weight ratio of silver to mercury. X-ray data indicated only pure crystals of AgCl and Hg₂Cl₂ in the final product. This white product was pressed into pellets which turned yellow upon exposure to light.

Freshly made pellets were discharged in a weather balloon type cell using magnesium AZ31B as the anode and a 1% NaCl solution as the electrolyte. In this cell the electrodes were separated by a nonwoven cellulosic mat and contact to active materials was made

through carbonized steel sheets. At the same time, identical pellets were subjected to ten 24 hr cycles of a high temperature, high humidity test. During each cycle the pellets underwent a steady temperature rise from 38° to 50°C for 2 hr followed by a rest of 6 hr at 50°C and a gradual temperature drop to 38°C lasting 16 hr. The relative humidity was kept above 95% throughout this test.

Results

Only AgCl, Hg₂Cl₂, and CuI,S pellets passed the temperature, humidity test unchanged. CuBr,S pellets were covered with green droplets which dried to green crystalline spots, whereas CuCl,S pellets disintegrated.

When discharged after temperature, humidity testing, as shown in Table II, both AgCl,Hg₂Cl₂ and CuI,S cathodes exhibited behavior similar to fresh pellets, while CuBr,S cathodes gave unreliable results.

As seen in Table II, the AgCl,Hg₂Cl₂ cathodes exhibited 90% coulombic efficiency based on both chlo-

Table I. Composition of copper(I) halide mixes

Active material	% halide	% sulfur**	% graphite***
CuCl, industrial	63	31	7
CuBr, 99% pure*	69	24	7
CuI, 99% pure*	73	20	7

* Research Organic/Inorganic Chemical Corporation.

** Flowers, Fisher.

*** Texas Fines.

Table II. Discharge behavior of cells of weather balloon type construction

Mg/1.0% NaCl-water/temperature humidity cycled electrodes, cells (Room temperature) (16 Ohm load to a 1.0V cutoff)

Active material	Average voltage (V)	Maximum voltage (V)	Average current (mA)	Coulombic efficiency (%)
CuBr,S	1.37	1.43	21	69.1
CuBr,S	1.07	1.12	16	68.3
CuBr,S	1.20	1.34	18	75.1
CuI,S	1.32	1.35	20	88.3
CuI,S	1.35	1.37	20	89.9
CuI,S	1.31	1.33	20	95.2
AgCl,Hg ₂ Cl ₂	1.33	1.44	20	90.6
AgCl,Hg ₂ Cl ₂	1.30	1.47	20	89.5
AgCl,Hg ₂ Cl ₂	1.33	1.46	21	93.1

* Electrochemical Society Active Member.

Key words: seawater activated cell, magnesium anode, AgCl, Hg₂Cl₂-cathode, CuI,S-cathode.

EST

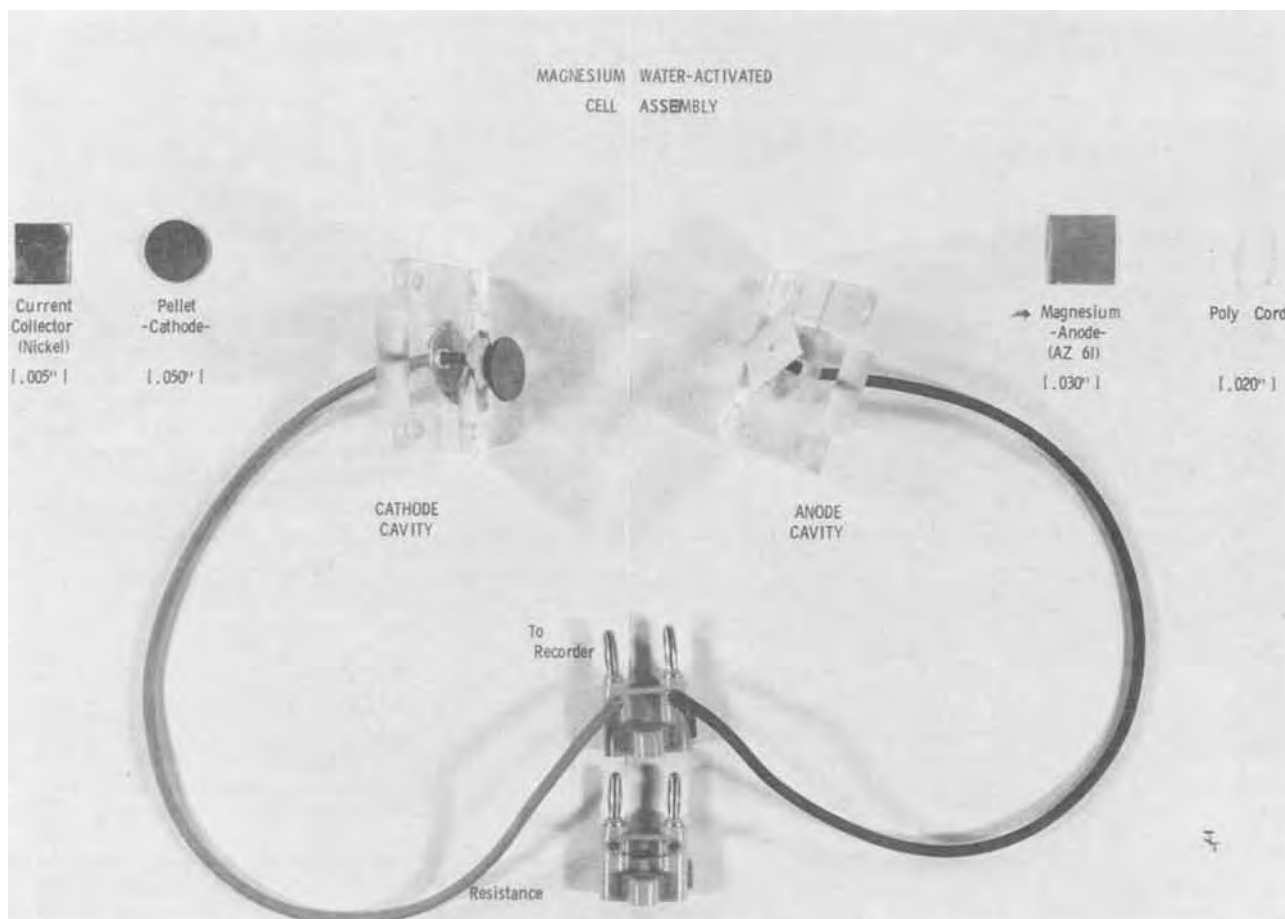


Fig. 1. Experimental cell assembly

rides. Furthermore, only one discharge plateau was observed with Mg/AgCl,Hg₂Cl₂ cells at a voltage close to that of Mg/AgCl control cells. Therefore the investigation of the discharge behavior of CuI,S and AgCl,Hg₂Cl₂ cathodes was extended by using simulated seawater as the electrolytic solution, and varying the ratio of the components in the AgCl,Hg₂Cl₂ cathode.

Experimental "Seawater Cell" Tests

Two series of AgCl,Hg₂Cl₂ cathode materials containing varying amounts of silver and mercury were prepared. One, the P (precipitated AgCl) series was prepared by the above-mentioned method, whereas the CP series was prepared by coprecipitation of both chlorides from an aqueous solution of their nitrates using hydrochloric acid. The amounts of starting materials are presented in Table III.

The composition of these materials was designed to produce discharge products of different silver mercury ratios starting with the γ phase (P-30) and ending with P-10 and CP-10 dilute amalgams (7).

Mixes of AgCl,Hg₂Cl₂ and CuI,S (Table I) were pressed at about 1000 kg into pellets 1.9 cm in diam-

eter and 0.11 cm thick and tested in a laboratory version of a seawater activated cell (Fig. 1), using simulated seawater (ASTM D1191-52, solution 2). Cells were placed in a perforated Plexiglas holder, inside a 400 ml beaker, to allow free circulation of the electrolytic solution. The solution temperature did not increase more than 1°C above room temperature throughout discharge.

Results

CuI,S.—Tests with CuI,S cathodes showed (Fig. 2) that at an average current density of 13 mA/cm² of cathode, in this test cell, the coulombic efficiency decreased to 66%. This apparent decrease of coulombic efficiency was traced to loss of active material due to shedding during discharge.

Table III. Starting materials for AgCl,Hg₂Cl₂ cathodes

Preparation*	AgNO ₃ (g)**	Hg ₂ Cl ₂ (g)**	Hg ₂ (NO ₃) ₂ ·H ₂ O (g)**
P-30	19.3	33.7	—
P-25	18.1	36.4	—
P-20	13.0	39.0	—
P-10	4.3	29.0	—
CP-15	8.4	—	41.7
CP-10	5.6	—	44.5

* The number indicates calculated percentage silver in the discharge product.

** Fisher Scientific.

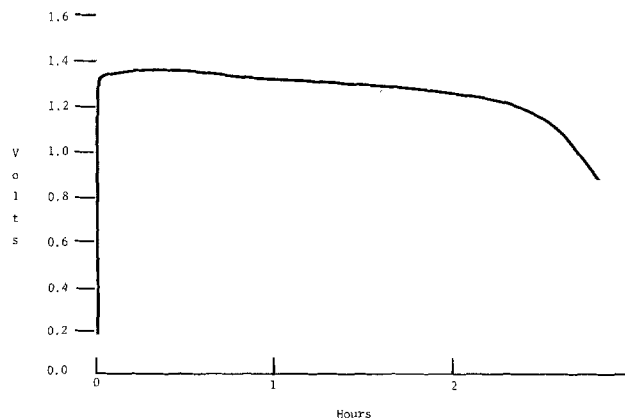


Fig. 2. Discharge behavior of the Mg(AZ61)/seawater/CuI,S experimental cell under a 32 ohm load at ambient temperature and pressure.

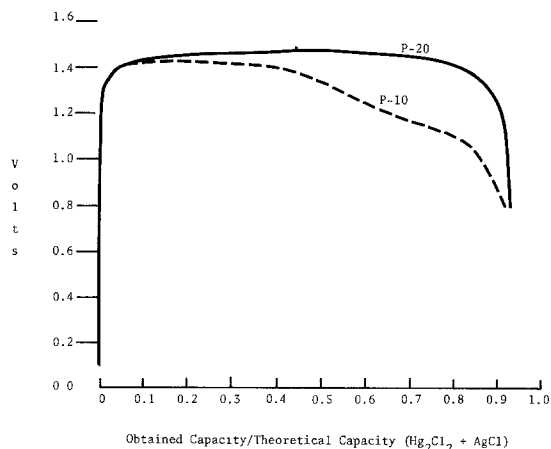


Fig. 3. Discharge behavior of Mg(AZ61)/"seawater"/ Hg_2Cl_2 , AgCl (precipitated binder) experimental cells under a 32 ohm load at ambient temperature and pressure. P-20 cathode composition, 78% Hg_2Cl_2 , 22% AgCl; P-10 cathode composition, 88.8% Hg_2Cl_2 , 11.2% AgCl.

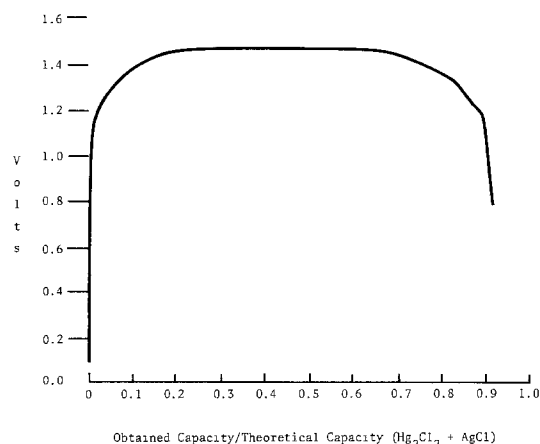


Fig. 4. Discharge behavior of the Mg(AZ61)/"seawater"/88.8% Hg_2Cl_2 , 11.2% AgCl (coprecipitated) experimental cell under a 32 ohm load at ambient temperature and pressure.

$\text{AgCl}, \text{Hg}_2\text{Cl}_2$.—Two typical discharge curves were obtained with $\text{AgCl}, \text{Hg}_2\text{Cl}_2$ active materials (Fig. 3). The first shows a fast rise followed by a single discharge plateau and a sharp knee, typical of CP-15 and silver-rich P cathodes. However, silver-poor cathodes of the P series such as P-10 gave a two-step discharge. A much shorter second plateau occurred with CP-10 electrodes (Fig. 4). A summary of discharge data for such cells is presented in Table IV.

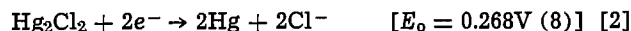
Discussion

In general, the discharge behavior of the Mg/ $\text{AgCl}, \text{Hg}_2\text{Cl}_2$ cells was almost identical to that of Mg/AgCl ones. The major exceptions were cells whose cathode consisted of a P-type silver-poor electrode, such as P-10. The virtual nonexistence of the second plateau when CP-10 electrodes were utilized and the

Table IV. Performance of experimental Mg/seawater/ $\text{AgCl}, \text{Hg}_2\text{Cl}_2$ cells

Active material	Average voltage	Current density mA/cm ² of cathode	Coulombic efficiency (%)
P-30	1.40	15.3	97
P-25	1.38	15.0	97
P-20	1.41	15.5	93
CP-15	1.39	15.3	94
P-10	1.29	14.1	84
CP-10	1.38	15.0	90
AgCl (control)	1.39	15.2	99

superior performance of CP-15 over P-20 cathodes indicate that intimate mixing of the electrode components improves cell performance. This behavior suggests that several processes take place simultaneously at the cathode. These postulated processes are



and amalgams [4]

The major electrochemical reaction, silver chloride reduction, is responsible for the high operating voltage of the cell. However, some contribution from Hg_2Cl_2 , especially with low silver content electrodes, is observed and both P-10 and CP-10 electrodes which show a second discharge plateau at 1.1V. Simultaneously, an intraelectrode reduction of mercury(I) chloride by silver, reaction [3], is replenishing the silver chloride, thus controlling the relative quantities of active materials within the electrode, hence determining the discharge voltage of the cell (9). Considering the operating current densities, such a rapid intracathode reaction must proceed either through a corrosion-like mechanism (10) or direct contact between the reacting species. Either way, the rate determining step will be mass transport dependent, hence the increase in cell performance with the increase in the physical proximity of the mix components in the active material.

The effect of the process described in Eq. 4 on the instantaneous silver activity, and thereby on the overall cathode behavior, is not clear. It was observed, especially with low silver content electrodes, that free mercury droplets required at least 24 hr to be absorbed into the discharged pellet. If this behavior is indicative of the rate of this process, then the change in silver activity, at least beyond the γ phase, is slow, thus allowing the intraelectrode reaction (reaction [3]) to proceed more efficiently.

The similarity between the $\text{AgCl}, \text{Hg}_2\text{Cl}_2$ and the AgCl cathodes extends beyond discharge voltage. The reduced mercury, like reduced silver, occupies slightly more than half the volume of the original chloride, and reaction [4] will further reduce the volume of the discharge product; hence solid, nonporous electrodes can be used in both cases. A final comparison between $\text{AgCl}, \text{Hg}_2\text{Cl}_2$ mixes and AgCl in terms of calculated volumetric capacity densities based on the known densities of AgCl and Hg_2Cl_2 (5), and assuming nonporous cathodes is presented in Table V.

Conclusions

$\text{AgCl}, \text{Hg}_2\text{Cl}_2$ cathode materials were found highly efficient and suitable for replacing AgCl cathodes with minimal changes in present cell design. Indeed, the $\text{AgCl}, \text{Hg}_2\text{Cl}_2$ cathode could be regarded as a highly efficient Ag/AgCl electrode in which the expensive active material, present in a small quantity, is regenerated by the reaction of the discharge product with Hg_2Cl_2 .

Table V. Calculated maxima of capacity-volume ratios* for AgCl, Hg_2Cl_2 cathodes

Per cent AgCl in active material	A-hr/DM ³ of active material	A-hr/DM ³ active material	
		A-hr/DM ³ AgCl	
100.0	1040	100.0	
32.6	900	86.5	
27.3	886	85.3	
22.0	873	83.9	
16.6	859	82.6	
11.1	849	81.2	

* Based on the known densities of AgCl and Hg_2Cl_2 (5) and assuming solid, nonporous electrodes.

The Mg/CuI,S system exhibited lower operating voltages and would require further improvement of cathode formulation and/or cell design in order to reduce the loss of coulombic efficiency due to shedding of active material during discharge. However, no silver is required for the operation of this system.

Both CuI,S and AgCl,Hg₂Cl₂ mixes could serve as cathode materials in magnesium water activated cells.

Acknowledgment

We thank Mr. L. C. Thompson, Jr., of our laboratory, for his assistance in the testing phase of this investigation.

Manuscript submitted Aug. 29, 1974; revised manuscript received April 16, 1975. This was Paper 43 presented at the Boston, Massachusetts, Meeting of the Society, Oct. 7-11, 1973.

Any discussion of this paper will appear in a Discussion Section to be published in the June 1976 JOURNAL. All discussions for the June 1976 Discussion Section should be submitted by Feb. 1, 1976.

Publication costs of this article were partially assisted by ESB Incorporated.

REFERENCES

1. C. H. Sorum, "Introduction to Semimicro Qualitative Analysis," 2nd ed., Prentice-Hall, Inc., Englewood Cliffs, N. J. (1953).
2. a. P. Ruetschi and R. F. Amlie, *This Journal*, **112**, 665 (1965),
b. R. F. Amlie, H. N. Honer, and P. Ruetschi, *ibid.*, **112**, 1073 (1965).
3. J. R. Coleman, *J. Applied Electrochem.*, **1**, 65 (1971).
4. S. U. Falk and A. J. Salkind, "Alkaline Storage Batteries," pp. 185-186, John Wiley & Sons, Inc., New York (1964).
5. R. C. Weast, "Handbook of Chemistry and Physics," The Chemical Rubber Co., Cleveland, Ohio (1971).
6. H. N. Honer, U.S. Pat. 3,205,696 (1965).
7. M. Hanson, "Constitution of Binary Alloys," 2nd ed., pp. 24-25, McGraw-Hill Book Company, New York (1958).
8. W. M. Latimer, "The Oxidation States of the Elements and Their Potentials in Aqueous Solutions," 2nd ed., Prentice-Hall, Englewood Cliffs, N. J. (1953).
9. J. O'M. Bockris and A. K. N. Reddy, "Modern Electrochemistry," Vol. 2, pp. 1269-1273, Plenum Press, New York (1970).
10. K. J. Vetter, "Electrochemical Kinetics," (English Translation), pp. 732-735, Academic Press, New York (1967).

Electrocatalytic Activity of Metals and Alloys Electrodeposited on Foreign Substrates

I. Some Aspects of Oxygen Reduction on Electrodeposited Silver Films on Pyrolytic Graphite

Ikram Morcos*

Hydro-Quebec Institute of Research, Varennes, Quebec, Canada

ABSTRACT

Oxygen reduction has been studied in alkaline medium on both bulk silver electrodes and electrodes prepared by the electrodeposition of a silver film on pyrolytic graphite, platinum, and silver substrates. The rotating disk technique was used throughout the work and the current potential data were obtained by slow scanning voltammetry. The effect of the starting potential and some surface pretreatments were also examined. The experimental results indicate that a silver surface electrodeposited on a foreign substrate is more catalytically active toward O₂ reduction than either bulk silver or silver electrodeposited on a silver substrate. A silver surface which has been electrochemically oxidized and subsequently reduced is more catalytically active than a surface which has been only subjected to the reducing potential. It appears that these variations in electrocatalytic activity are caused by variations in both surface area as well as the reversibility of adsorbed oxygen.

The electrocatalytic properties of electrodeposited metallic films on foreign substrates are important for both its fundamental and applied aspects. The cost of a catalyst in the form of an electrodeposited metal film on a substrate such as graphite could be less than one made of the corresponding bulk metal. The method of electrodeposition provides a better control on the reproducibility (e.g., on such properties as surface area, grain size, and impurities) of the metal surface and that may contribute to the obtainment of more reliable kinetic data. Moreover the topographical and metal-

lurgical analysis of thin metal films can be more easily carried out by a variety of optical and spectroscopic techniques.

In the present paper some aspects of O₂ reduction on electrodeposited silver films on pyrolytic graphite and platinum substrates will be compared to the corresponding phenomena observed on bulk silver and electrodeposited silver on bulk silver electrodes.

Experimental Procedure

The electrochemical reduction of oxygen was studied using a Teflon cell and electrode assembly as described in a previous work (1). The solution was 0.1N KOH prepared from A. R. quality potassium hydroxide and triply distilled water twice from a permanganate solution. The reference electrode was an Hg/HgO, 1.0N

* Electrochemical Society Active Member.

Key words: rotating disk electrode, electrocatalytic activity and nucleation of metals on pyrolytic graphite, oxygen reduction on silver, surface active area of electrodeposited silver on pyrolytic graphite, adsorption of oxygen on electrodeposited silver on pyrolytic graphite.

KOH. The rotating disk technique was applied throughout the work to control mass transfer of oxygen. Current-potential plots were obtained by slow scanning voltammetry, using a Tacusel function generator, a Wenking potentiostat, and a Honeywell X-Y recorder.

The bulk silver electrode consisted of a disk of 0.785 cm² area. Prior to the study the electrode was mechanically polished with 0.3 μ alumina powder on a felt wheel followed by cleaning in carbon tetrachloride, isopropyl alcohol, and triply distilled water. Other electrodes were prepared by electrodepositing silver from silver cyanide solution on pyrolytic graphite, platinum, and silver substrates. The areas of these electrodes were 0.338, 0.502, and 0.785 cm². Except where otherwise noted, the latter three electrodes were used after cleaning in triply distilled water without any further pretreatment.

Some surface area study was attempted using the capacity method. The potential dependence of the differential capacity was measured at 1000 Hz and using other experimental details as those described by Randin and Yeager (2). Topographical examination of silver deposits on pyrolytic graphite was carried out by the scanning electron microscope. For this, the deposited sample was bombarded with an electron beam of 20 kV.

Results and Discussion

The dependence of the cathodic current on potential in the range 0 to -1.0V and on rotation rate for O₂ reduction in oxygen-saturated 0.1N KOH on bulk silver electrode and on electrodeposited silver on silver substrate is given in Fig. 1 and 2. The corresponding plots obtained on silver electrodeposited on pyrolytic graphite and platinum substrates are given in Fig. 3 and 4. In Fig. 5 is shown the corresponding plots obtained on silver electrodeposited on pyrolytic graphite electrode which has been mechanically polished after the deposit was prepared. Figures 6 and 7 show similar plots obtained on mechanically polished bulk silver and silver electrodeposited on pyrolytic graphite electrodes which have been prior to the experiment (in both cases) immersed in dilute HNO₃ for about 5 sec.

Figures 8-10 show the dependence of the cathodic current on potential in the range 0.5 to -1.0V and on rotation rate in oxygen-saturated 0.1N KOH solution on bulk silver electrode, silver electrodeposited on pyrolytic graphite, and on platinum substrates, respectively.

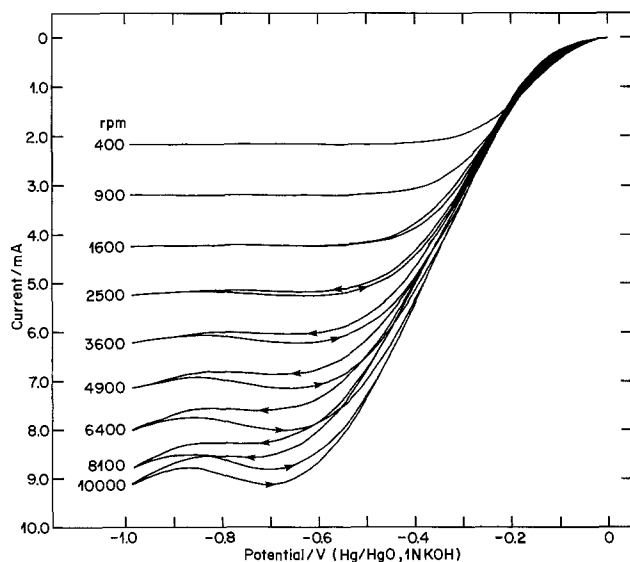


Fig. 1. Reduction of O₂ on bulk silver electrode at different rotation rates in O₂-saturated 0.1N KOH. Temperature 25°C, electrode area 0.786 cm², and potential scan from 0 to -1.0V at a rate of 1 V/min.

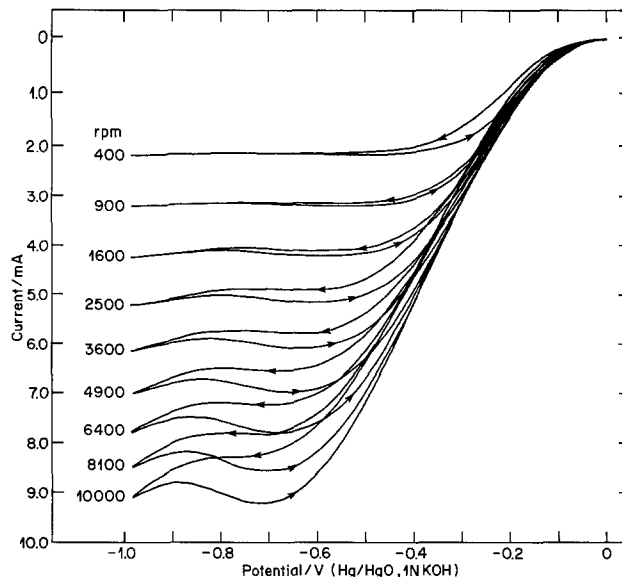


Fig. 2. Reduction of O₂ on electrodeposited silver on bulk silver at different rotation rates in O₂-saturated 0.1N KOH. Temperature 25°C, electrode area 0.786 cm², and potential scan from 0 to -1.0V at a rate of 1 V/min.

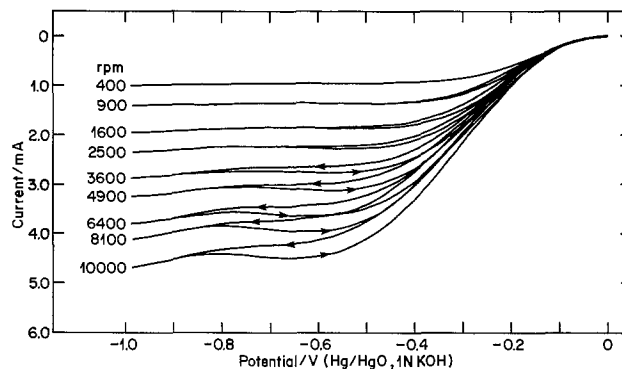


Fig. 3. Reduction of O₂ on electrodeposited silver on pyrolytic graphite substrate at different rotation rates in O₂-saturated 0.1N KOH. Temperature 25°C, electrode area 0.338 cm², and potential scan from 0 to -1.0V at a rate of 1 V/min.

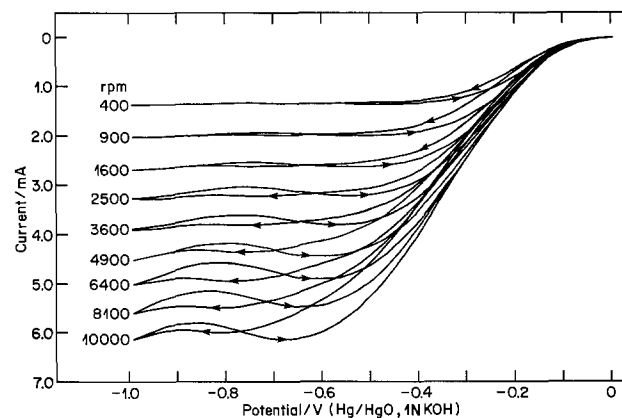


Fig. 4. Reduction of O₂ on electrodeposited silver on platinum substrate at different rotation rates in O₂-saturated 0.1N KOH. Temperature 25°C, electrode area 0.502 cm², and potential scan from 0 to -1.0V at a rate of 1 V/min.

In all the experiments reported in Fig. 1-10 a voltage scan rate of 1 V/min was used and the first potential scan was always started from the most anodic potential. The current-potential plots were independent of scan rate from 0.1-1 V/min. No faster scan rates than 1 V/min was attempted. The direction of the voltage sweeps are indicated by the arrows. Figure

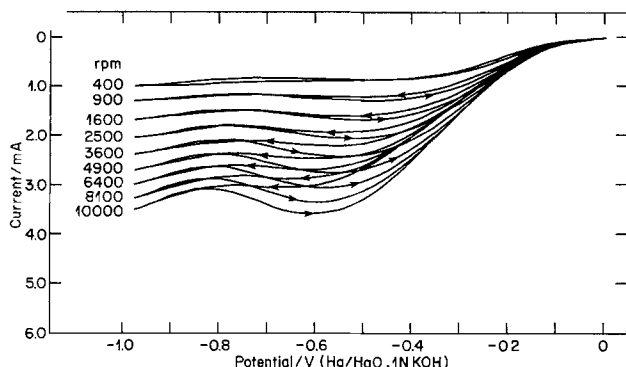


Fig. 5. Effect of mechanical polishing on reduction of O_2 on electrodeposited silver on pyrolytic graphite substrate at different rotation rates in O_2 -saturated 0.1N KOH. Temperature 25°C, electrode area 0.338 cm^2 , and potential scan from 0 to -1.0V at a rate of 1 V/min.

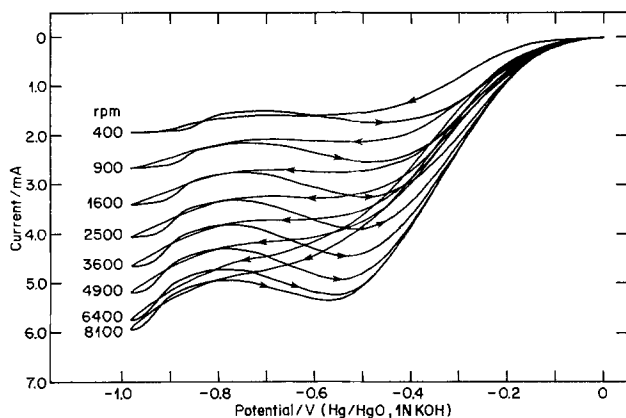


Fig. 6. Effect of pretreatment with dilute HNO_3 on reduction of O_2 on bulk silver electrode at different rotation rates in O_2 -saturated 0.1N KOH. Temperature 25°C, electrode area 0.786 cm^2 , and potential scan from 0 to -1.0V at a rate of 1 V/min.

11 shows the dependence of the current on potential in helium-saturated 0.1N KOH on bulk silver electrode for potential scans starting at both 0 and 0.5V, respectively. Figure 12 shows the corresponding curves obtained on silver electrodeposited on pyrolytic graphite. The current in both Fig. 11 and 12 exhibits no dependence on rotation rate.

The dependence of the cathodic limiting current/square centimeter on the square root of the rotation rate for the different experimental data of Fig. 1-10 is shown in Fig. 13-16. The latter figures were plotted after correction for the corresponding residual current

observed in Fig. 11 and 12. Whenever hysteresis exists between the cathodic and anodic potential scans, the value of the limiting current used is that corresponding to the anodic scan. Figure 13 also shows (the top curve) the theoretically calculated Levich plot for a 4-electron process oxygen reduction using the equation (3)

$$i_d = B\sqrt{\omega} \quad [1]$$

where i_d is the mass-transfer limiting current in mA, ω is the rotation rate in rev/min, and B is given by Newman (4) as

$$B = 10^3 (2\pi/60)^{1/2} \frac{nFAc\nu^{1/2} (0.621 Sc^{-2/3})}{1 + 0.298 Sc^{-1/3} + 0.145 Sc^{-2/3}} \quad [2]$$

where ν is the kinematic viscosity, D is the diffusion coefficient of oxygen (moles/ cm^3), n is the number of electrons transferred per mole of O_2 , F is the faraday, A is the disk electrode area (cm^2), c is the bulk concentration of O_2 (moles/ cm^3), $Sc = \nu/D$ is the Schmidt number. Using values of 1.22×10^{-6} mM and 1.9×10^{-5} cm^2/sec for the solubility and diffusion coefficient of oxygen in 0.1N KOH at 25°C reported in Ref. (5-6) a value of $B = 0.142$ was calculated for $n = 4$ and electrode surface area of 1 cm^2 .

The following are some important observations from Fig. 1-15.

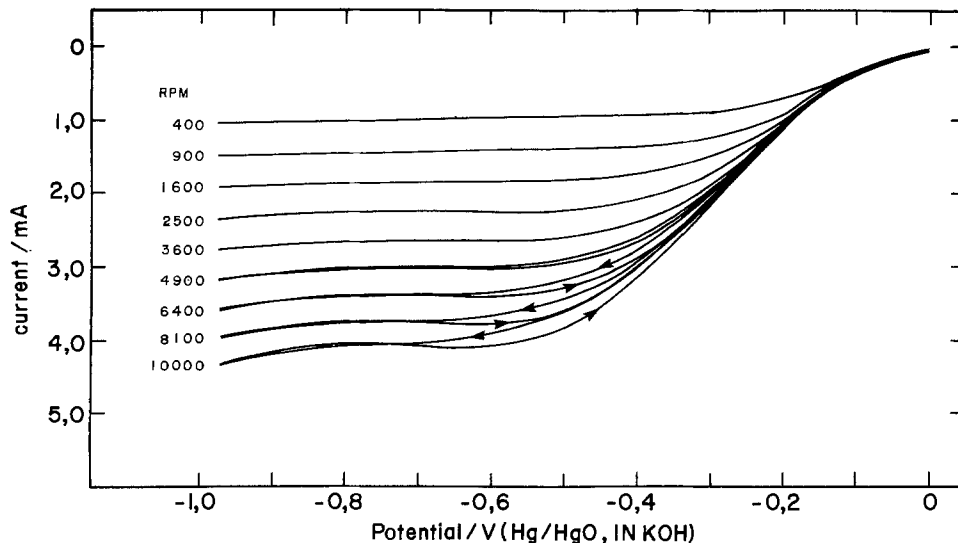
1. The dependence of the cathodic current density on rotation rate (Fig. 1-10) starts at a relatively small overpotential. Consequently the study of the kinetics of oxygen reduction on silver cathodes in the absence of a forced control of mass transfer will be restricted to a small potential region near the open-circuit value and therefore will be of limited use. In view of this, caution must be considered in analyzing kinetics data obtained over a relatively large potential region of few hundreds millivolts without the use of the rotating disk electrode.

2. The relative magnitude of the limiting current as compared to theoretically predicted values on the basis of the Levich equation (Fig. 13-16) depends on the rotation rate, the form of silver electrode used, the starting potential of the sweep, and electrode pretreatment.

With silver electrodeposited on pyrolytic graphite Levich plots are linear (throughout the range of rotation used) even in cases where the limiting current is slightly less (see Fig. 13) than that theoretically predicted. Deviation from linearity at higher rotation rates is very evident (Fig. 13) in the case of bulk silver and electrodeposited silver on silver substrate electrodes. Slight deviation from linearity is observed in the case of silver electrodeposited on platinum substrate electrodes.

When the starting potential is 0.5 instead of 0V, all the limiting currents (Fig. 14) shift to higher values

Fig. 7. Effect of pretreatment with dilute HNO_3 on reduction of O_2 on electrodeposited silver on pyrolytic graphite at different rotation rates in O_2 -saturated 0.1N KOH. Temperature 25°C, electrode area 0.338 cm^2 , and potential scan from 0 to -1.0V at a rate of 1 V/min.



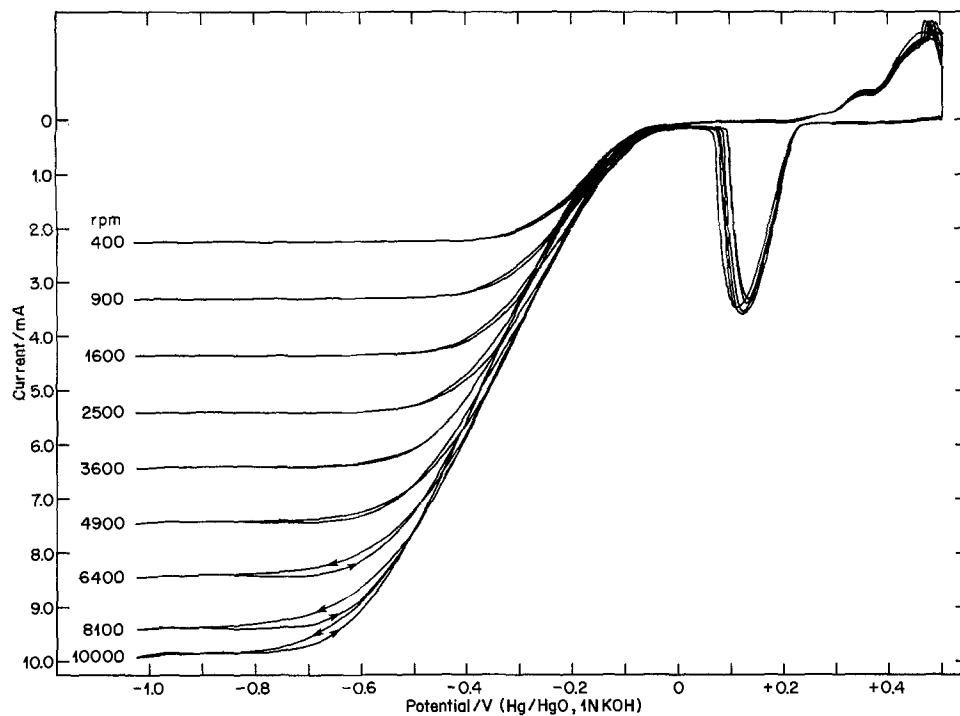


Fig. 8. Reduction of O_2 on bulk silver electrode at different rotation rates in O_2 -saturated 0.1N KOH. Temperature 25°C, electrode area 0.786 cm^2 , and potential scan from 0.5 to -1.0V at a rate of 1 V/min.

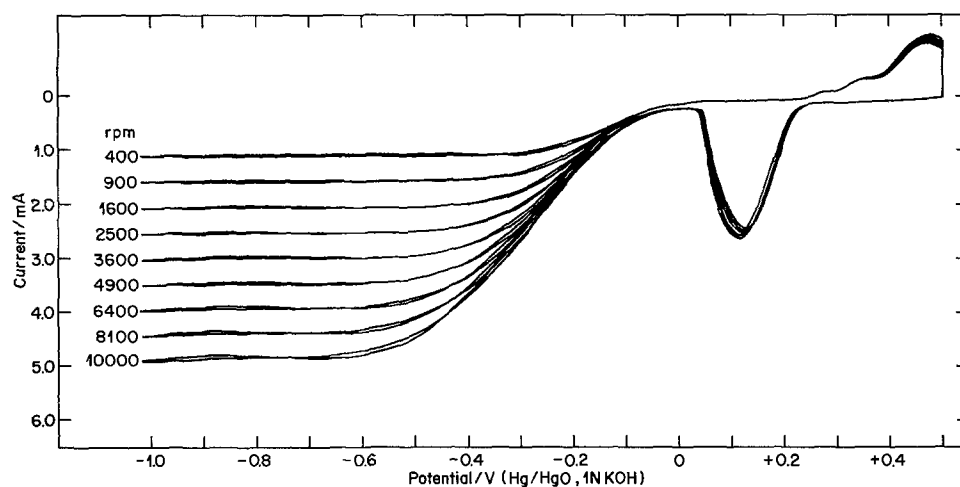


Fig. 9. Reduction of O_2 on electrodeposited silver on pyrolytic graphite at different rotation rates in O_2 -saturated 0.1N KOH. Temperature 25°C, electrode area 0.338 cm^2 , and potential scan from 0.5 to -1.0V at a rate of 1 V/min.

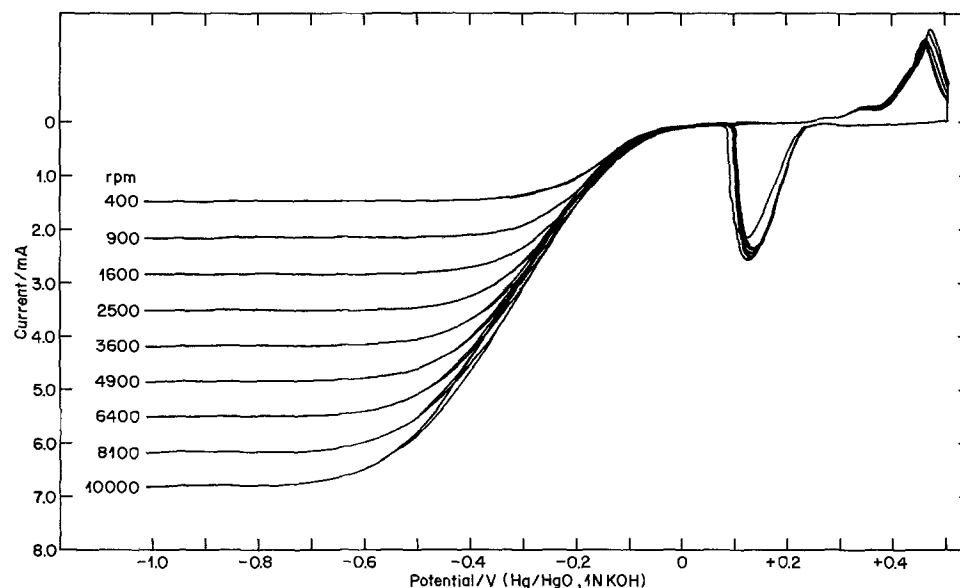


Fig. 10. Reduction of O_2 on electrodeposited silver on platinum substrate at different rotation rates in O_2 -saturated 0.1N KOH. Temperature 25°C, electrode area 0.502 cm^2 , and potential scan from 0.5 to -1.0V at a rate of 1 V/min.

(higher electrocatalytic activity) and generally approach the mass-transfer limiting currents. In the case of silver electrodeposited on pyrolytic graphite the limiting current coincides with the theoretical plot

(Fig. 14). With bulk silver electrodes however slight deviation from linearity is still observed (Fig. 14).

The electrocatalytic activity and limiting current are strongly influenced by electrode pretreatment pro-

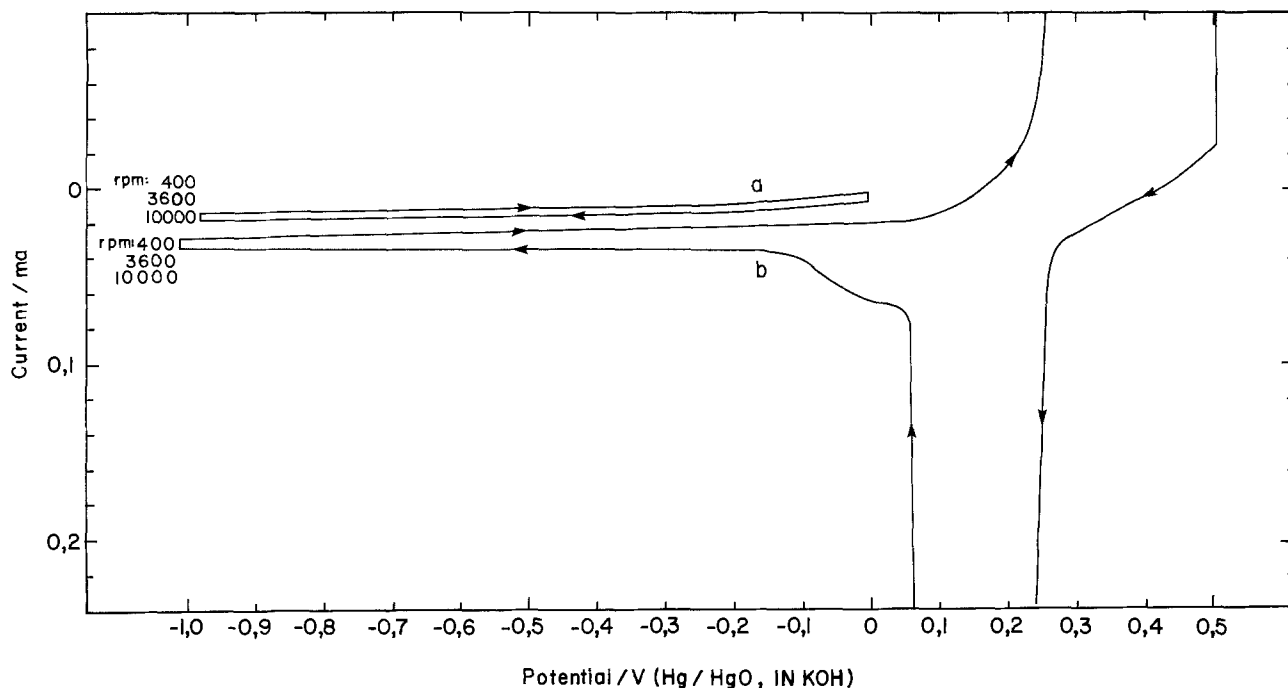


Fig. 11. Current-potential plots on bulk silver electrode at different rotation rates in He-saturated 0.1N KOH. Temperature 25°C, electrode area 0.786 cm², and potential scan: curve a, from 0 to -1.0V, and curve b, from 0.5 to -1.0V at a rate of 1 V/min.

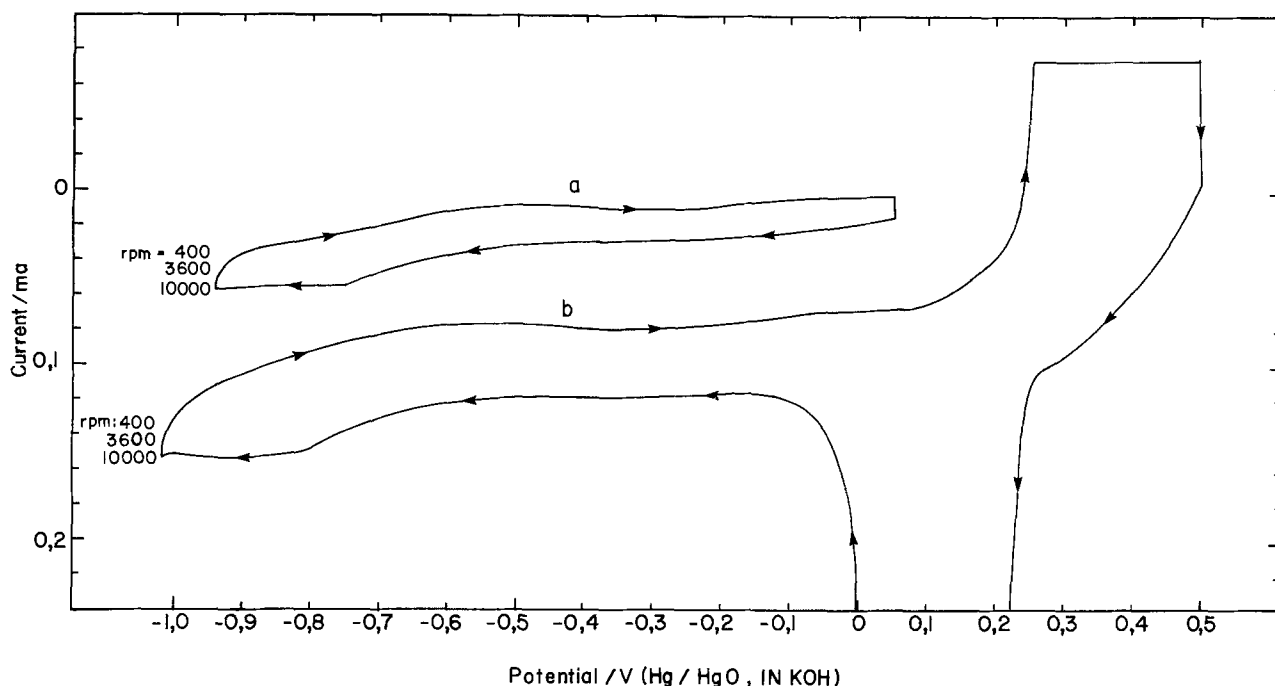


Fig. 12. Current-potential plots on silver electrodeposited on pyrolytic graphite at different rotation rates in He-saturated 0.1N KOH. Temperature 25°C, electrode area 0.338 cm², and potential scan: curve a, from 0 to -1.0V, and curve b, from 0.5 to -1.0V at a rate of 1 V/min.

vided that the starting potential used is 0 and not 0.5V. A drastic reduction in the cathodic current of a bulk silver electrode is observed (Fig. 15) when the electrode prior to the experiment is immersed for 5 sec in dilute HNO₃. The limiting currents after such treatment approach those corresponding to a 2-electron reduction process. H₂O₂ was detected in the cell after the experiment of Fig. 6 and its concentration was found to be $1 \times 10^{-5}N$. A far less reduction in the current is observed (Fig. 16) when the same treatment is applied to a silver surface electrodeposited on pyrolytic graphite. A stronger reduction in the limiting current of the latter surface is observed (Fig. 16), when the surface, prior to the experiment, is mechanically polished with alumina powder or even a filter paper.

3. The limiting currents in the case of silver electrodeposited on pyrolytic graphite or platinum substrates start at more positive potentials as compared to the limiting currents on bulk silver or electrodeposited silver on silver substrate (Fig. 1-10).

4. The increase in rotation rate, results, for the same silver surface, in a significant shift into more cathodic potentials of the limiting current. The only exception for this observation is the case in which the bulk silver electrode is immersed prior to the experiment in dilute HNO₃. In the latter case only slight shift is observed.

5. Hysteresis between the anodically and cathodically increasing potential scans is much more significant in curves where the starting potential is 0V than

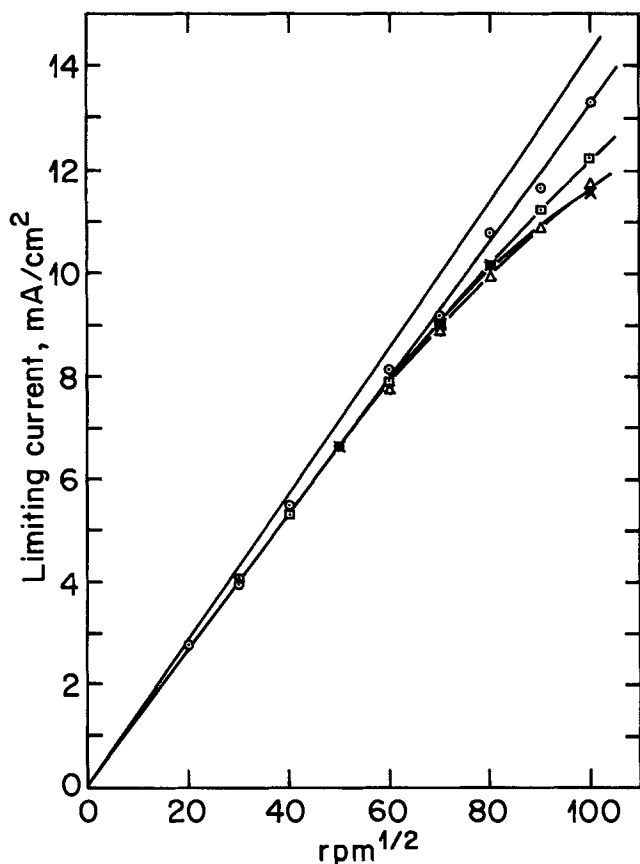
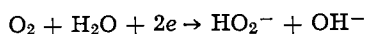


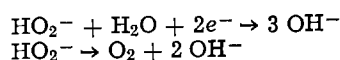
Fig. 13. Dependence of the limiting current/cm² on the square root of rotation rate at different silver surfaces. — Theoretical plot calculated by Eq. [1]; ○, data of Fig. 3 obtained on electro-deposited silver on pyrolytic graphite substrate potential scan from 0 to -1.0V; □, data of Fig. 4 obtained on electro-deposited silver on platinum substrate, potential scan from 0 to -1.0V; △, data of Fig. 1 on bulk silver, potential scan from 0 to -1.0V; x, data of Fig. 2 obtained on electro-deposited silver on bulk silver, potential scan from 0 to -1.0V.

when it is 0.5V (Fig. 1-10). Whenever hysteresis exists it increases with the increase in rotation rate. Hysteresis is generally higher with silver surfaces which have been prior to the experiment immersed in dilute HNO₃ or mechanically polished than with those surfaces which have not been subjected to such treatments.

The experimental results indicate that the total number of electrons transferred in the over-all reduction of O₂ on silver cathodes ranges between a value which is slightly above 2 electrons in the case of bulk silver electrodes (with a potential scan starting at 0V) pretreated in dilute nitric acid to 4 electrons in the case of silver electrodeposited on pyrolytic graphite with a potential scan starting at 0.5V. Such wide variation in the electrocatalytic activity of silver cathodes as a function of surface pretreatments is consistent with previously reported work (7-12). Also on the basis of previous work (13) it is known that oxygen reduction on silver may follow one or more of two routes. In one route oxygen is first reduced to peroxide



The resultant peroxide ion may be further reduced electrochemically or catalytically decomposed as shown by



If oxides are present, they may be reduced by the peroxide intermediate as shown by

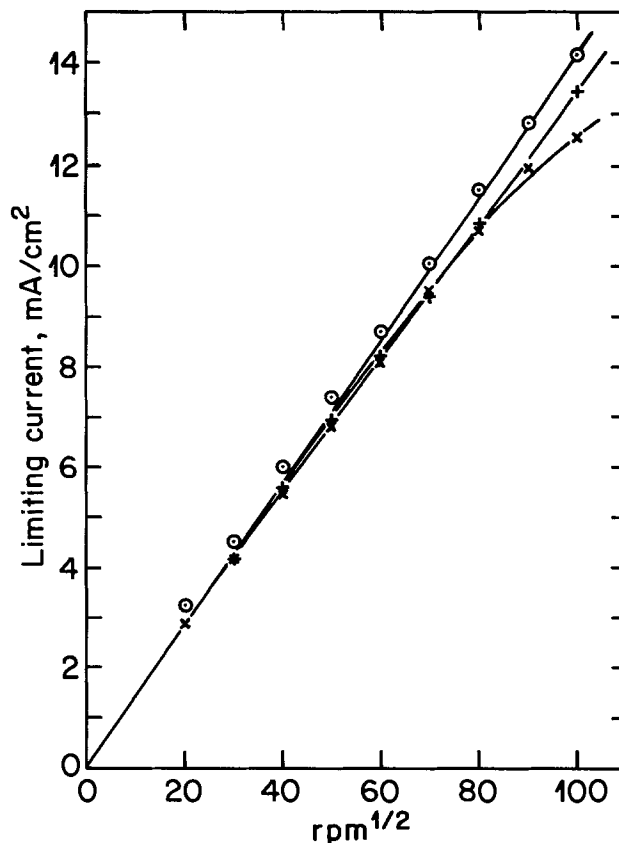
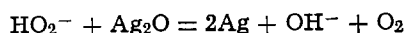
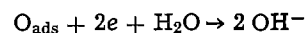


Fig. 14. Dependence of the limiting current/cm² on the square root of rotation at different silver surfaces. ○, Theoretical plot calculated by Eq. [1] and data of Fig. 9 obtained on electrodeposited silver on pyrolytic graphite substrate, potential scan from 0.5 to -1.0V; +, data of Fig. 10 obtained on silver electrodeposited on platinum substrate, potential scan from 0.5 to -1.0V; x, data of Fig. 8 obtained on bulk silver electrode, potential scan from 0.5 to -1.0V.

Also some of the peroxide may be removed into the bulk of the solution. In the second route oxygen is dissociatively adsorbed and the adsorbed oxygen atoms are directly reduced to hydroxide



A limiting current that corresponds to 2 electrons or slightly more than 2 electrons, as observed in the case of bulk silver electrodes pretreated in dilute HNO₃ and with a 0V starting potential, indicates that O₂ reduction occurs mostly via the peroxide route. It also indicates that the electrode surface is a poor catalyst for peroxide decomposition. The removal of formed peroxide into the bulk of the solution (as detected by chemical analysis) considerably reduces the amount of peroxide available for further electrochemical reduction. The pretreatment in dilute HNO₃ must result in the formation of an oxide or chemisorbed O₂ layer which is not easily reduced when the potential is scanned in the region of O₂ reduction. The formation of such a layer decreases the electrocatalytic activity of the electrode surface both by preventing the dissociative adsorption of O₂ as well as by reducing the catalytic activity for peroxide decomposition. This observation is consistent with the results of Palous and Buvet (8) and of Mazitov *et al.* (9) who observed two waves for O₂ reduction on silver electrodes preheated in oxygen. The fact that pretreatment in dilute HNO₃ causes by contrast very little reduction in the electrocatalytic activity of silver electrodeposited on pyrolytic graphite suggests that any formed oxide or chemisorbed O₂ layer is more easily removed when the potential is scanned in the region of O₂ reduction. That probably means that O₂ adsorbs more reversibly on a silver surface electrodeposited on pyrolytic graphite than on a bulk silver electrode.

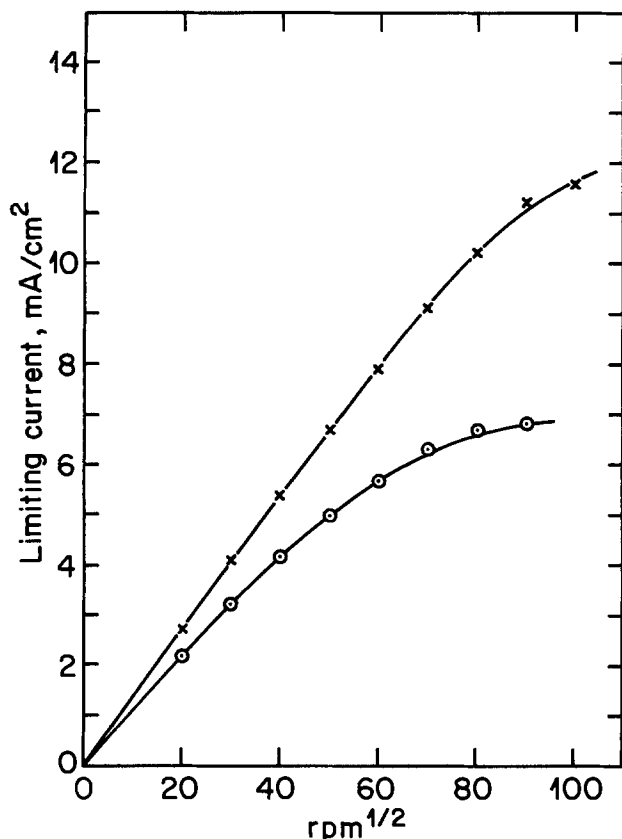


Fig. 15. Effect of pretreatment in dilute HNO_3 on the dependence of the limiting current/cm² on the square root of rotation for bulk silver electrode. x, Without pretreatment, data of Fig. 1, and o, with pretreatment, data of Fig. 6.

A limiting current that corresponds to 4 electrons as observed in the case of silver electrodeposited on pyrolytic graphite and with a 0.5V starting potential, may result from a reduction of oxygen via either route 1, route 2, or both routes. In case route 1 is followed either partially or completely, a 4-electron reduction limiting current can only mean that the reaction leading to peroxide formation is coupled with a second-order heterogeneous catalytic reaction with a rate constant for the catalytic reaction tending to infinity (14). If the latter condition is not satisfied, then a 4-electron limiting current may only result from the direct reduction of dissociatively adsorbed oxygen into hydroxide. This point cannot be settled however without the use of the rotating disk-ring electrode. Zhutaeva and co-workers (13) used the latter electrode and showed that in the case of a mechanically polished bulk silver electrode the relative fraction of the current going via the intermediate formation of H_2O_2 is at most 10% in the potential region between 0.7 and -0.2 (vs. H_2). At potentials more positive than 0.7 the proportion of H_2O_2 production increases and reaches 40% at 0.8V. On the basis of these results it may be concluded that the 4- and near 4-electron limiting currents observed in the present work must result mostly from the reduction of dissociatively adsorbed oxygen. The occurrence of the later reaction must be associated with the shift in potential as a function of rotation rate observed in Fig. 1-10. In Fig. 6 this shift is very slight because the 4-electron reduction of dissociatively adsorbed O_2 is largely absent.

The observed increase in the electrocatalytic activity when the silver surface is prepared by electrodepositing Ag on either graphite or platinum most probably results from the effect of electrochemical three-dimensional nucleation (associated with the electrodeposition of silver from silver cyanide on a foreign substrate such as graphite or platinum) in increasing the electrocatalytically active area of the silver surface.

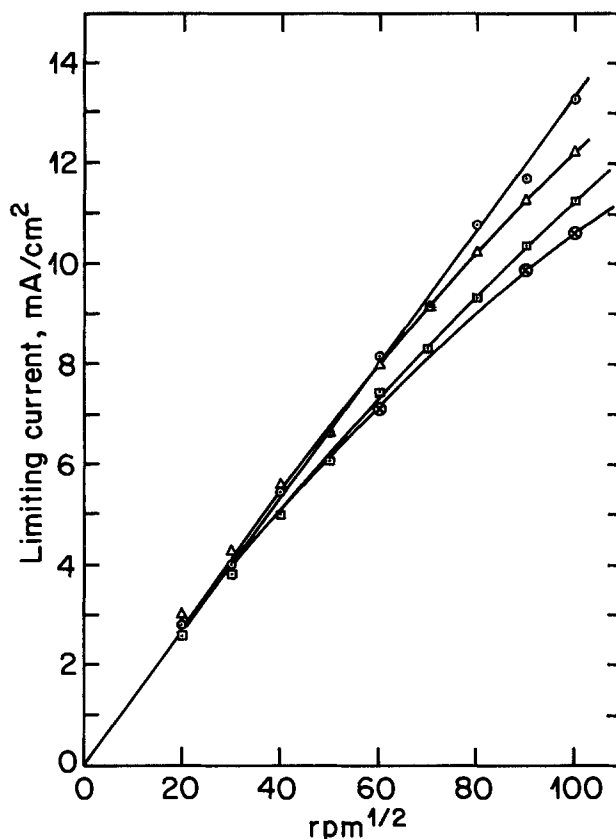


Fig. 16. Effect of different pretreatments on the dependence of the limiting current/cm² on the square root of rotation for silver electrodeposited on pyrolytic graphite. o, Without pretreatment, data of Fig. 3; Δ, pretreated in dilute HNO_3 , data of Fig. 7; □, polished with filter paper (data not shown previously); ⊗, polished with alumina powder, data of Fig. 5.

Other alternative explanations would be that impurities left on bulk silver surface from polishing with an alumina powder has a poisoning effect on such active area or that the difference between the residual current due to reduction of silver oxide species in both cases results in the observed difference in limiting current. In view of the fact that a silver surface prepared by electrodepositing silver on a bulk silver electrode exhibits the same electrocatalytic activity (Fig. 13) as that of bulk silver, the former objection is ruled out. Figures 11 and 12 also show that in helium-saturated solutions and with a 0V starting potential, the magnitude of the currents as well as the difference between the current-potential characteristics of both bulk silver and electrodeposited silver on graphite, are too insignificant to influence the currents in Fig. 1-4.

If three dimensional electrochemical nucleation of silver on a foreign substrate results in the observed higher electrocatalytic activity, one would anticipate that the nucleation mechanism of silver from silver cyanide on a foreign substrate (such as graphite or platinum) would be considerably different from the corresponding nucleation mechanism on the same silver substrate. Figure 17 shows that the electrodeposition of silver from silver cyanide on either pyrolytic graphite or platinum is accompanied with a very high nucleation overpotential.¹ In contrast the electrodeposition of silver on a silver substrate occurs without any such nucleation overpotential. The high nucleation overpotential in the case of graphite and platinum substrates results from the high energy barrier associated with nucleation. Silver cannot form mixed crystals with such foreign substrates and therefore can only condense on its surface and forms a granular

¹ For further information on the correlation between potential-time plots of Fig. 17 and nucleation overpotential, see Ref. (15).

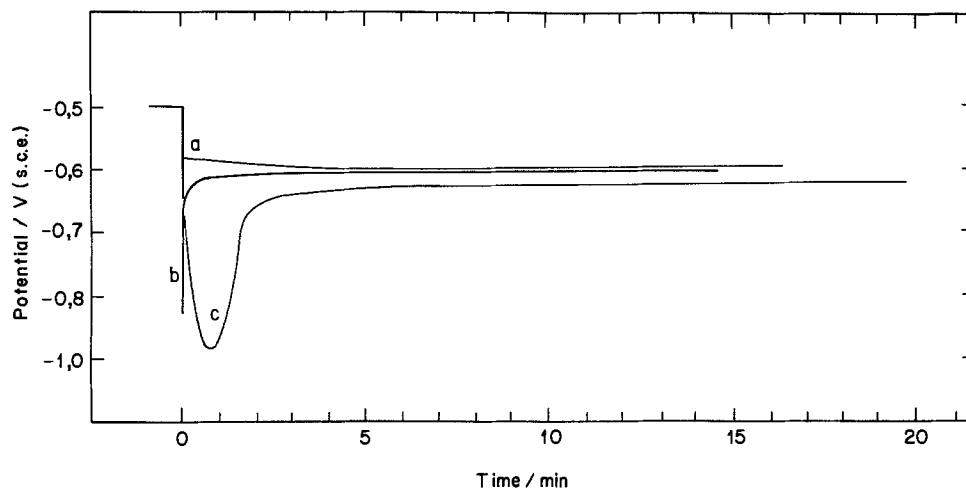


Fig. 17. Potential-time relationships at 0.3 mA/cm^2 for the electrodeposition of silver from silver cyanide on different substrates: (a) silver substrate; (b) platinum substrate; (c) pyrolytic graphite substrate.

deposit. The fact that such a granularly shaped deposit actually forms is seen in the scanning electron micrograph (Fig. 18) of a silver deposit obtained by electrodepositing silver on pyrolytic graphite from silver cyanide solution at a current density of 3 mA/cm^2 for 12 min.

The slightly higher electrocatalytic activity of silver electrodeposited on a pyrolytic graphite substrate as compared to that electrodeposited on a platinum substrate may be attributed to the formation of a higher number of nuclei/square centimeter in the former case. The higher number of nuclei is expected on the basis of the much higher nucleation time (see Fig. 17) observed with the graphite substrate.

In order to find out whether electrodeposited silver on pyrolytic graphite has a higher ratio of true/apparent surface area as compared to bulk silver electrodes, the potential dependence of the differential capacity for both surfaces was measured in $0.1N \text{ KOH}$. Figure 19 shows that the differential capacity in the

potential region of O_2 reduction is about $3\frac{1}{2}$ times larger with electrodeposited silver on graphite than with bulk silver electrodes.

The effect of the variation in true surface area (due to the change in the form of silver surface) on the experimental result can be quantitatively described as follows. The relationship between the observed limiting current, i_L , mass-transfer limiting current, i_d , and pure first-order kinetically controlled limiting current, i_K , is given (16) by

$$\frac{1}{i_L} = \frac{1}{i_K} + \frac{1}{i_D} = \frac{1}{i_K} + \frac{1}{B\sqrt{\omega}} \quad [3]$$

and a linear $1/i_L$ vs. $1/\sqrt{\omega}$ plot indicates that the reaction is first order. Now if the experimentally observed limiting current is equal to the mass transfer limiting current, the plot $1/i_L$ vs. $1/\sqrt{\omega}$ passes through the origin as shown in Fig. 20 for the case of O_2 reduction on an electrodeposited silver on pyrolytic graphite. But if $i_d \neq i_L$ as for the case of O_2 reduction on bulk silver or electrodeposited silver on silver substrate, the corresponding plot of Fig. 20 intercepts the Y axis at a value of $1/i_K$ or $i_K \approx 100 \text{ mA/cm}^2$. But from



Fig. 18. Scanning electron micrograph of silver deposit obtained at current density of 3.0 mA/cm^2 and 12 min. Magnification 1500X.

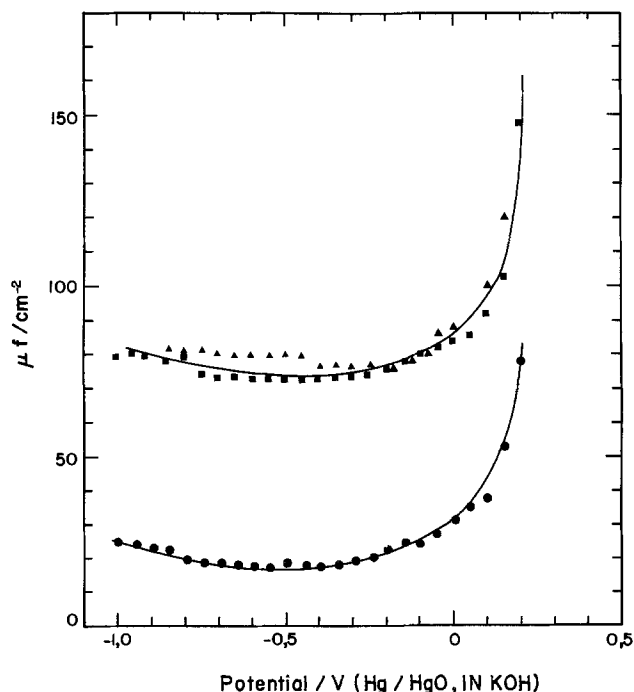


Fig. 19. Differential capacity vs. potential plots in helium-saturated $0.1N \text{ KOH}$ at 1000 Hz. ▲ and ■, Same experiment on silver electrodeposited on pyrolytic graphite; ●, on bulk silver electrode.

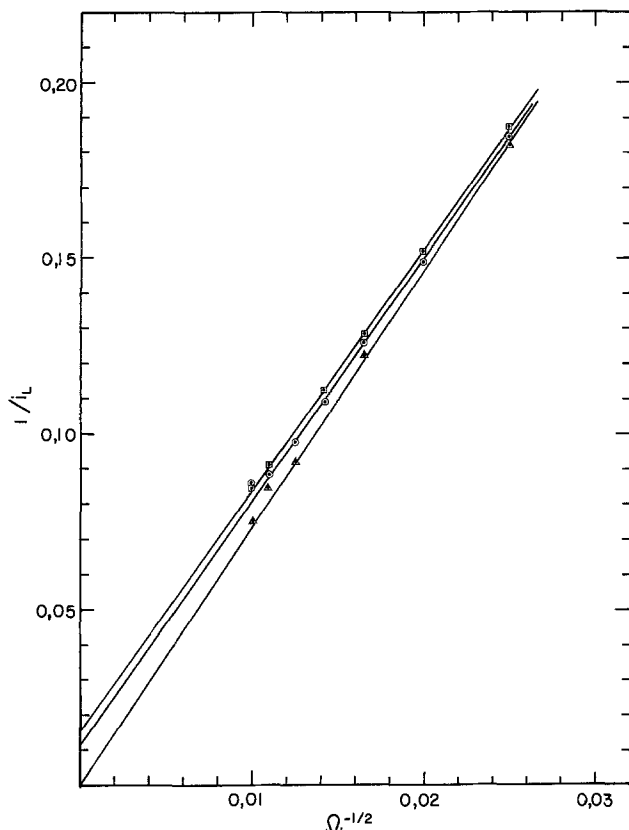


Fig. 20. Dependence of $1/i_L$ on $\Omega^{-1/2}$ for the data of Fig. 1, 2, and 3. □, Electrodeposited silver on silver substrate; ○, bulk silver; △, electrodeposited silver on pyrolytic graphite.

Eq. [3] one obtains

$$i_L = \frac{i_d i_K}{i_d + i_K} \quad [4]$$

Since the value of i_d (10–15 mA/cm²) at higher rotations is not negligible compared to 100 mA/cm², i_L will be under mixed mass-transfer and kinetic control and a plot of i_L vs. $\Omega^{1/2}$ will deviate from linearity as observed in Fig. 13. If it is assumed that the increase in electrocatalytic activity of the electrodeposited silver on pyrolytic graphite is proportional (17) to the increase in true surface area, i_K , for the latter surface is found to be ≈ 350 mA/cm². Since this value is much greater than the mass-transfer limiting current, Eq. [4] shows that the observed limiting current will be equal to i_d . The fact that a plot of i_L vs. $\Omega^{1/2}$ of Fig. 13, although linear, exhibits i_L values that are slightly less than those predicted on the basis of pure mass-transfer control probably results from the removal at higher rotation rates of some of the peroxide intermediate into the solution bulk.

Several objections could be raised against the preceding quantitative treatment; first there is no concrete proof that the increase in the electrocatalytic activity is directly proportional to the increase in true surface area. Second, it could be argued that Eq. [3] is only applicable for an electrode reaction that is determined both by electrode kinetics and by mass transfer (18) and not for the case of mixed control by a chemical reaction (which may be the case in the present work) and mass transfer. Third as shown by McIntyre (19) and Riddiford (16) it is possible for there to be intercepts in the plot of the reciprocal of the transfer limiting current vs. $\omega^{-1/2}$. But regardless of the validity or not of Eq. [3] for the present treatment, the conclusion would still be that silver electrodeposited on such foreign substrates as graphite and platinum exhibits higher electrocatalytic activity and therefore higher kinetically controlled limiting current as compared to bulk silver electrodes.

The strong decrease in the electrocatalytic activity observed when the electrodeposited silver on pyrolytic graphite electrode is mechanically polished must in view of the preceding discussion result from a decrease in active surface area. The dependence of hysteresis on the type of silver surface and rotation rate can be also easily interpreted in the light of the same discussion. A mass-transfer limiting current is a property of a certain species (O₂ in this case) in the electrolyte and therefore its magnitude should not depend on the variation of surface properties. In contrast a kinetically or chemically controlled limiting current may be influenced by the variation in surface properties and therefore would be expected to be less reproducible and to exhibit more hysteresis. Consequently, at lower rotation rates, where the limiting currents are mass-transfer controlled, no hysteresis is observed, and at higher rotation rates where the currents are under kinetic or chemical control hysteresis appears.

The higher electrocatalytic activity and far less hysteresis generally observed when the potential scan is started at 0.5V must be also related to the increase in the number of active surface sites as a result of surface oxidation and subsequent surface reduction. The oxidation and reduction processes are indicated by the two anodic and one cathodic peaks which are observed at about 0.45, 0.33, and 0.15V, respectively. These correspond to the formation of Ag₂O, AgOH, and silver surface, respectively (20).

On the basis of electron microscopic examination Stonehart (20) claims that the area of a smooth silver surface increases by more than 100× after one single potentiodynamic scan involving the previously mentioned oxidation and reduction processes. Differential capacity measurement by the present author has shown however that the increase in the surface area of a bulk silver electrode after one single potentiodynamic scan is only of the order of 3–4×. But even if the increase in surface area of the bulk silver electrode is only 3–4× one would have expected that with a starting potential scan of 0.5V the limiting current/square centimeter would reach as in the case of electrodeposited silver on graphite, the mass-transfer limiting value. The fact that the limiting current on bulk silver deviates from such value (Fig. 14) at 10,000 rpm suggests a lower frequency of active sites as compared to its frequency on the electrodeposited silver on graphite substrate. Figures 11 and 12 actually indicate that the amount of chemisorbed O₂ and/or Ag oxides reduced in He-saturated solutions and with a scan started at 0.5V, is about 8× larger² in the case of electrodeposited silver on graphite. This is consistent with the previously made conclusion that the adsorption of O₂ is probably more reversible on silver electrodeposited on graphite than on bulk silver electrodes. This higher reversibility is also consistent with the observation that the limiting currents in the case of electrodeposited silver on graphite start at more positive potentials as compared to the limiting currents on bulk silver or electrodeposited silver on silver substrates (Fig. 1–10). The fact that this shift in potential is related to the reversibility of O₂ adsorption rather than to a mere increase in surface area is supported by the observation that the magnitude of the shift in potential which is associated with the increase in rotation rate is not reduced when the surface area is presumably increased by the oxidation and subsequent reduction of the silver surface (compare Fig. 1–3 with Fig. 8–10).

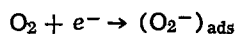
A detailed analysis of the mechanism of O₂ reduction on the different types of silver electrodes is too complex and will require further experimental work including the use of the rotating disk-ring electrode. On the basis of the present data some general conclusions are possible.

² After converting the currents of Fig. 11 and 12 into current densities.

It can be shown (1) that for a cathodic electrochemical reaction which is partially controlled by charge transfer and partially by mass transfer and in which the limiting current, i_L , is caused by either mass-transfer control or a potential insensitive chemical step, or both, with first-order kinetics with respect to the diffusing reactant, the following equation may be used

$$\eta = -\frac{RT}{\alpha F} \left[\ln \frac{i}{i_L - i} - \ln \frac{i_0}{-i_L} \right] \quad [5]$$

where η is the overpotential and i_0 the exchange current of the rate-determining step. The validity of Eq. [5] also requires that i_L is the product of the total diffusing reactant. Figure 21 shows that the plots of $\log [i/(i_L - i)]$ vs. the potential at different rotation rates for the data of Fig. 9 are linear with a Tafel slope that increases slightly with the increase in rotation rate. This suggests (i) that the same O_2 reduction mechanism takes place at the same O_2 concentration, and (ii) that a continuous change in the mechanism occurs as the concentration of O_2 reaching the surface is increased. At 400 rpm the Tafel slope is ≈ 0.12 V/decade. In accordance with previously attempted analysis (1, 12) of O_2 reduction mechanisms on silver as well as other electrodes a Tafel slope of 0.120 V/decade suggest that the rate-determining step is



assuming that α is equal to $1/2$ and that Langmuir conditions of adsorption prevail.

An increase in the value of the Tafel slope with the increase in rotation rate probably reflects the continuous increase in the contribution of the irreversible dissociative O_2 adsorption step which is known to become more dominant with the increase in current density. Figure 22 shows that similar $\log [i/(i_L - i)]$ vs. potential plots are obtained from the data of Fig. 8 on bulk

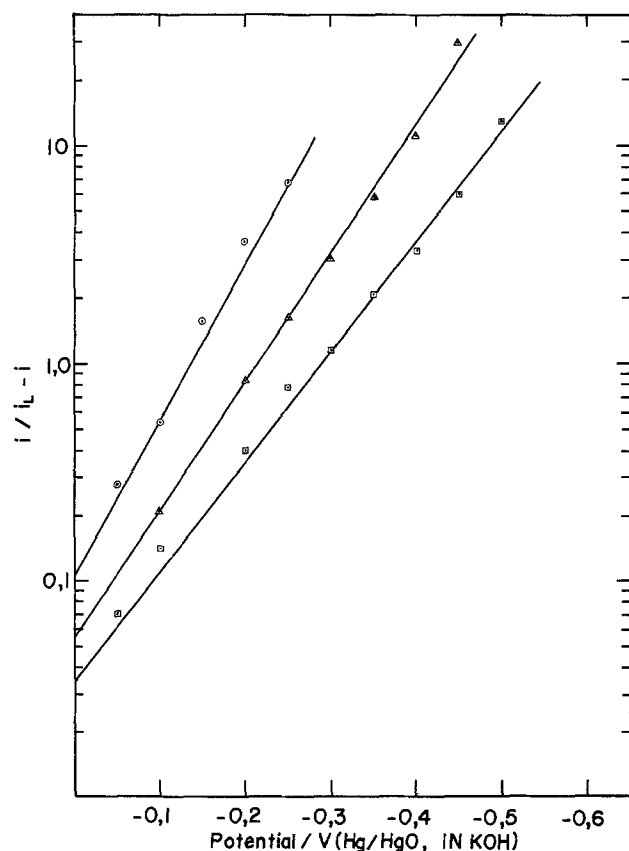


Fig. 21. Dependence of the potential on the function $\ln [i/(i_L - i)]$ at different rotation rates for silver electrodeposited on pyrolytic graphite, data of Fig. 9. \odot , 400 rpm; \triangle , 3600 rpm; \square , 10,000 rpm.

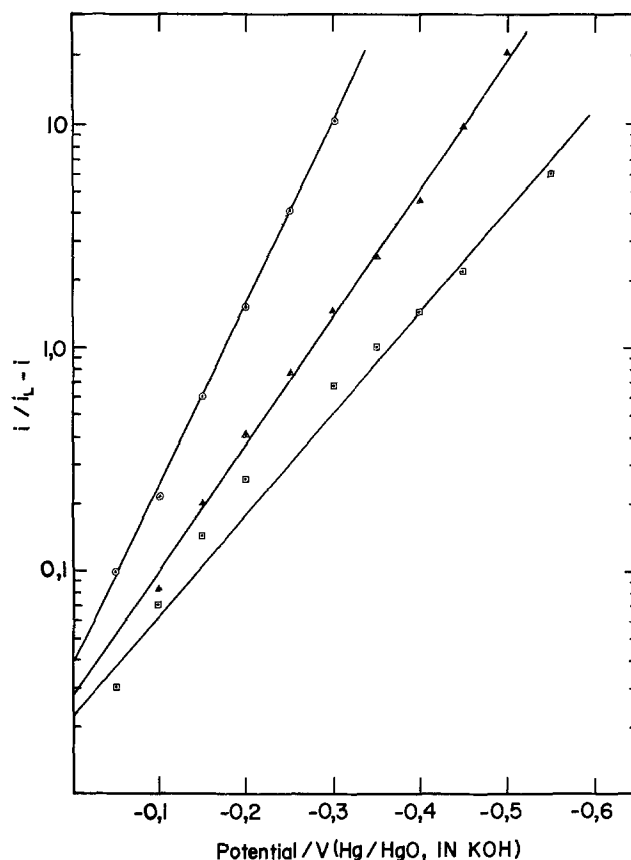


Fig. 22. Dependence of the potential on the function $\ln [i/(i_L - i)]$ at different rotation rates for bulk silver electrode, data of Fig. 8. \odot , 400 rpm; \triangle , 3600 rpm; \square , 10,000 rpm.

silver electrode. It is observed however that the increase in the value of the Tafel slope with the increase in rotation rate is larger, probably because of the higher irreversibility of O_2 adsorption.

Acknowledgments

The author acknowledges the help of Dr. J. P. Randin and Mr. A. Gendron in the capacity measurement. Gratitude is expressed for Mr. G. Larochelle for his assistance in the physical realization of the voltammetry curves. The author also thanks Dr. A. Vijh for helpful discussions.

Manuscript submitted Nov. 6, 1974; revised manuscript received March 21, 1975.

Any discussion of this paper will appear in a Discussion Section to be published in the June 1976 JOURNAL. All discussions for the June 1976 Discussion Section should be submitted by Feb. 1, 1976.

Publication costs of this article were partially assisted by Hydro-Quebec Institute of Research.

REFERENCES

- I. Morcos and E. Yeager, *Electrochim. Acta*, **15**, 953 (1970).
- J. P. Randin and E. Yeager, *J. Electroanal. Chem.*, **36**, 257 (1972).
- V. Levich, *Acta Phys. Chim. URSS*, **17**, 257 (1952); "Physico-chemical Hydrodynamics," Prentice Hall, Englewood Cliffs, N. J. (1952).
- J. Newman, *J. Phys. Chem.*, **70**, 1327 (1966).
- K. E. Gubbins and R. D. Walker, *This Journal*, **112**, 469 (1965).
- R. E. Davis, G. L. Horvath, and G. W. Tobias, *Electrochim. Acta*, **12**, 287 (1967).
- G. V. Zhutavaeva, N. A. Shumilova, and M. R. Tarasevich, *Dokl. Akad. Nauk SSSR*, **161**, 151 (1965).
- S. Palous and R. Buvet, *Bull. Soc. Chim. France*, 1602, 1606 (1962).
- Yu. A. Mazitov, K. I. Rozental, and V. I. Vevelovskii, *Elektrokhimiya*, **1**, 36 (1965).

10. V. S. Bagotskii, L. N. Nekrasov, and N. A. Shumilova, *Usp. Khim.*, **34**, 697 (1965).
11. S. Z. Beer and Y. L. Sandler, *This Journal*, **112**, 1133 (1965).
12. S. Sepa, M. Vojnovic, and A. Damjanovic, *Electrochim. Acta*, **15**, 1355 (1970).
13. G. V. Zhutaeva, N. D. Merkulova, N. A. Shumilova, and V. S. Bagotskii, *Elektrokhimiya*, **4**, 1253 (1968).
14. J. D. E. McIntyre, *J. Phys. Chem.*, **73**, 4102 (1969).
15. I. Morcos, *J. Electroanal. Chem.* **54**, 87 (1974).
16. A. C. Riddiford, "Advances in Electrochemistry and Electrochemical Engineering," Vol. 4, P. Delahay, Editor, Interscience Publishers, New York (1966).
17. P. H. Emmet, "Catalysis," p. 31, Reinhold Publishing Corp., New York (1961).
18. A. N. Frumkin and G. Tedoradse, *Z. Elektrochem.*, **62**, 251 (1958).
19. J. D. E. McIntyre, *J. Phys. Chem.*, **71**, 1196 (1967).
20. P. Stonehart, *Electrochim. Acta*, **13**, 1789 (1968).

On the Nature of Electrochemical Reactions at a Crack Tip during Hydrogen Charging of a Metal

B. G. Ateya*¹ and H. W. Pickering*

*Metallurgy Section, Department of Material Sciences,
The Pennsylvania State University, University Park, Pennsylvania 16802*

ABSTRACT

The electrochemical conditions within cracks in metals undergoing cathodic hydrogen charging in acid solutions are analyzed. The gradients of the electrical potential and concentrations of the various ionic species and the current distribution are calculated for a model crack. The actual potential profiles were measured in slots in Fe, Ni, and Cu samples during hydrogen charging using an electrical potential probe. The measured potential drop in the electrolyte in the slots of all three metals is often very large, e.g., 0.5V. This is about an order of magnitude larger than that calculated, and is in general at odds with the usually implicit assumption that the electrode potential is not an important variable within a growing crack. The reason for this discrepancy is shown to be the large potential variation caused by the presence of trapped hydrogen gas bubbles in the slot.

The measured electrode potentials in the slot during cathodic hydrogen charging are in the region of metal dissolution in the case of the two base metals, Fe and Ni. On the other hand, the outer surface of these metals is under perfect cathodic protection for the typical impressed cathodic currents of 5 or 10 mA cm⁻². Subsequent tests of electrolyte samples taken from within slots while the current was flowing, indeed, showed the presence of relatively large amounts of iron and nickel ions indicating that anodic dissolution of iron and nickel occurs within the slots, though not at the outer surface during cathodic hydrogen charging. Analysis of the solution at the outer surface of the slot under conditions of impressed current showed the absence of significant concentrations of metal ions.

It has long been recognized that the concentrations of the ionic species within probes and cracks in an electrode are always different from those at the outer surface, e.g., see the review paper by Szklarska-Smialowska (1). Some measure of these composition changes within pits have been obtained in a few cases (2-5). The electrode potential is another parameter that is known to vary as a function of position in a cavity (6-11), although the fact that the potential change can be quite large is not generally recognized.

There is also the possibility of additional or alternative electrochemical and/or chemical reactions in the cavity or crack. Pickering and Frankenthal (9) observed hydrogen evolution from inside pits in iron samples during strong anodic polarization; the electrode potential at the outer surface was >0.8V SHE. At this potential hydrogen evolution from the outer surface is not thermodynamically possible and was not observed. It was found that the electrode potential inside the pit, on the other hand, was so base as to allow hydrogen evolution. These measured large po-

tential drops were attributed to constrictions caused by trapped hydrogen gas bubbles.

More recently Beck (11) has obtained a similar result. He found hydrogen evolving from pits in titanium while the sample was anodically polarized at large noble potentials. The generation of hydrogen in this case would again seemingly require that at some location within the pit the electrode potential is in the region of hydrogen evolution.

A corresponding situation exists for cathodic polarization, although it has attracted little if any attention. For this case, in particular, one wishes to answer the question: Does metal dissolution occur at the bottom of cracks in samples being cathodically charged with hydrogen? This is important with regard to the question of crack propagation under corrosion conditions and during cathodic protection practices. Recent results show that metal dissolution does occur within pores and cracks for Fe-10Pt (12) and iron (13) samples during aggressive hydrogen charging.

The purpose of the present paper is to determine the electrochemical conditions and the ongoing electrode reactions within cracks in metals during cathodic charging. A model is proposed for the combined effect of ohmic, mass transfer, and concentration polarizations

* Electrochemical Society Active Member.

¹ Present address: Chemistry Department, Faculty of Science, Cairo University, Cairo, Egypt.

Key words: cathodic protection, current distribution, iron, nickel, copper.

on the current, concentration, and potential profiles inside the crack. The approach taken here is similar to that developed by Wagner (14) in electroplating. Related models and calculations for different conditions have appeared in the porous electrode literature (15-17). Experimental results are presented to test the validity of the proposed model.

Theoretical

Model, assumptions, and solution.—The model of a crack considered here is that of a narrow, deep slot whose outer surface is maintained at a large negative potential so that the only reaction taking place at the outer surface is hydrogen evolution. The cross section of the slot is a rectangle of dimensions a and b , and its depth is L such that $a \ll L$ and $a \ll b$, Fig. 1, in which case the reaction can be considered to occur only on the outer surface and on the side walls. A more precise condition for validity of the equations is $X \gg a$ where X is the characteristic distance defined later. It is assumed that mass transfer in the electrolyte takes place by molecular diffusion and ionic migration according to the Nernst-Einstein relation. The electrolyte is a simple acid, HY , which completely dissociates to give monovalent ions.

Performing a mass balance on an element dx , Fig. 1, under steady-state conditions, one has for the fluxes, j , of the H^+ and Y^- ions in the direction of the interior of the slot

$$j_{\text{H}^+} = -D_{\text{H}^+} \left(\frac{dc_{\text{H}^+}}{dx} + c_{\text{H}^+} \frac{\mathbf{F}}{RT} \frac{d\phi}{dx} \right) = \frac{i}{\mathbf{F}} \quad [1]$$

$$j_{\text{Y}^-} = -D_{\text{Y}^-} \left(\frac{dc_{\text{Y}^-}}{dx} - c_{\text{Y}^-} \frac{\mathbf{F}}{RT} \frac{d\phi}{dx} \right) = 0 \quad [2]$$

in which D is the diffusivity and c is the concentration of the indicated species, ϕ is the local electrical potential in the electrolyte in the crack with respect to the potential at the opening where $\phi = 0$ by definition, i is the local current density of cathodic hydrogen evolution, T is the absolute temperature, \mathbf{F} is the Faraday constant, and R is the gas constant. Since Y^- ions are neither produced nor consumed, the right-hand side of Eq. [2] equals zero.

The electroneutrality equation is

$$c_{\text{H}^+} = c_{\text{Y}^-} = c \quad [3]$$

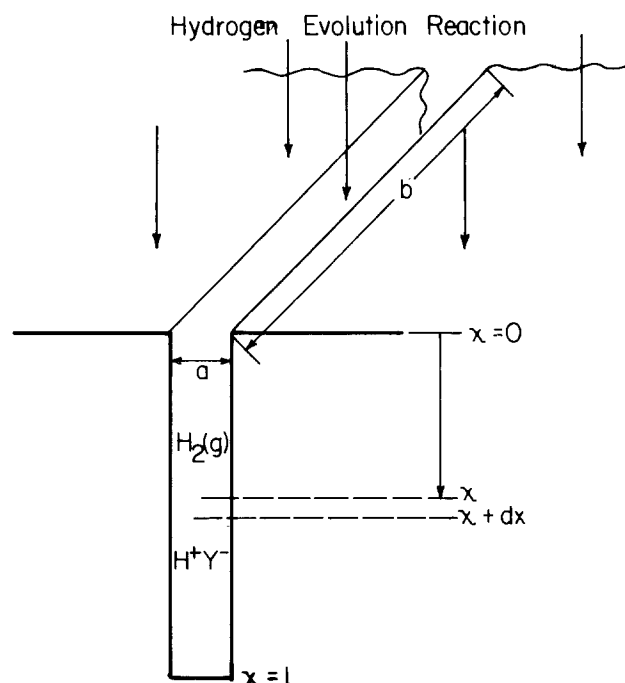


Fig. 1. Model of crack

The boundary condition at $x = 0$ for a bulk acid concentration of c_0 is

$$x = 0: c_{\text{H}^+} = c_{\text{Y}^-} = c_0 \text{ and } \phi = 0 \quad [4]$$

A boundary condition at $x = L$ is formulated below in Eq. [12]. Equations [1]-[4] are then used to find ϕ , c , and i as functions of x , c_0 , a and the local current density, i_s , at the outer surface, $x = 0$, far from the slot.

Rearranging, integrating Eq. [2], and using Eq. [3] and [4] yields

$$c = c_0 \exp \left(\frac{\mathbf{F}\phi}{RT} \right) \quad [5]$$

Note that $c(x > 0) < c_0$ since $\phi(x > 0)$ is negative in view of the current flow direction. Modifying Eq. [5] by Eq. [3] and substituting in Eq. [1] gives

$$j_{\text{H}^+} = -2D_{\text{H}^+} c_0 \exp \left(\frac{\mathbf{F}\phi}{RT} \right) \cdot \frac{\mathbf{F}}{RT} \frac{d\phi}{dx} \quad [6]$$

Let us consider a mass balance for the volume element $(ab)dx$. Equation [1] gives

$$(ab) dj_{\text{H}^+} = -(2bi/\mathbf{F}) dx \quad [7]$$

with $(2b)dx$ the lateral area of the element if $b \gg a$. Note that ab is the electrolyte cross-sectional area available for diffusion and migration of ions. If any gas bubbles accumulate in the slot this area effectively decreases. The local current density at distance x is (18)

$$i = i_s \left(\frac{c}{c_0} \right)^\beta \exp \left(\frac{\beta\mathbf{F}\phi}{RT} \right) \quad [8]$$

in which β is the transfer coefficient of the hydrogen evolution reaction. The value of i_s is given by the Tafel relation

$$i_s = i_0 \exp \left(\frac{\beta\mathbf{F}\eta}{RT} \right) \quad [9]$$

in which i_0 is the exchange current density at the bulk concentration of H^+ ions and η is the polarization at $x = 0$.

Introducing the auxiliary variable

$$\mu = \exp(\mathbf{F}\phi/RT) \quad [10]$$

and substituting Eq. [10] in Eq. [6] gives

$$j_{\text{H}^+} = -2D_{\text{H}^+} c_0 d\mu/dx \quad [6a]$$

and substituting Eq. [5] in Eq. [8], using Eq. [10] and taking $\beta = 1/2$ gives

$$i = i_s \mu \quad [8a]$$

Substituting with Eq. [6a] and [8a] in Eq. [7] gives

$$d^2\mu/dx^2 = (1/X^2)\mu \quad [11]$$

in which the characteristic length X is

$$X = (D_{\text{H}^+} c_0 \mathbf{F} a / i_s)^{1/2} \quad [11a]$$

X is an important parameter because it contains all the necessary parameters of the system, *i.e.*, the bulk concentration c_0 , the mass transfer constant D_{H^+} , the charging current i_s , and the important geometric property of the crack, a . Note that X is independent of the length L . For $X \gg a$ the use of one-dimensional transport equations in the x -direction is a valid approximation (14).

In terms of the new variable Eq. [4] becomes

$$x = 0 \quad \mu = 1 \quad [4a]$$

The boundary condition at $x = L$ in terms of μ can be obtained by equating Eq. [6a] and [8a] after dividing Eq. [8a] by \mathbf{F} , and then substituting Eq. [11a], since the current at the bottom of the slot is supported by the flux of H^+ ions at $x = L$. Thus

$$(d\mu/dx)_{x=L} = -(a/2X^2)\mu_L \quad [12]$$

The solution to the problem is obtained by solving Eq. [11] using Eq. [4a] and [12] as boundary conditions. Substituting by the equality

$$\frac{d^2\mu}{dx^2} = \frac{1}{2} \frac{d}{d\mu} \left(\frac{d\mu}{dx} \right)^2 \quad [13]$$

in Eq. [11], rearranging, and integrating with Eq. [12] as a boundary condition, one obtains

$$\left(\frac{d\mu}{dx} \right) = - \left(\frac{1}{X} \right) \left[\mu^2 - \mu_L^2 \left(1 - \frac{a^2}{4X^2} \right) \right]^{1/2} \quad [14]$$

The negative root is taken in Eq. [14] because μ decreases as x increases. Since the treatment is realistic only if $a \ll X$, it follows that $a^2/4X^2 \ll 1$ and the factor of μ_L in Eq. [14] can be set equal to unity as an approximation. Thus

$$\frac{d\mu}{dx} \simeq - \frac{1}{X} (\mu^2 - \mu_L^2)^{1/2} \quad [14a]$$

Integration of Eq. [14a] for $\mu = 1$ at $x = 0$ as a boundary condition yields

$$\mu = \frac{\cosh [(L-x)/X]}{\cosh [L/X]} \quad [15]$$

The validity of this solution can readily be checked upon substitution in Eq. [14a].

If the argument z of the cosh function is much greater than unity, one may use the approximation

$$\cosh z \simeq \frac{1}{2} \exp z \text{ if } z \gg 1$$

Then it follows from Eq. [15] that

$$\mu_L = \frac{1}{\cosh (L/X)} \simeq 2 \exp \left(- \frac{L}{X} \right) \text{ if } L \gg X \quad [16]$$

From Eq. [10] and [15] the potential in the electrolyte as a function of distance into the slot is given as

$$\phi = \frac{RT}{F} \ln \frac{\cosh [(L-x)/X]}{\cosh [L/X]} \quad [17]$$

The concentration and the current distribution are obtained by substituting Eq. [17] in Eq. [5] and Eq. [15] in Eq. [8a], to yield, respectively

$$c = c_0 \frac{\cosh [(L-x)/X]}{\cosh [L/X]} \quad [18]$$

$$i = i_s \frac{\cosh [(L-x)/X]}{\cosh [L/X]} \quad [19]$$

Equation [17] may be used to estimate the depth (using also Eq. [28]) at which the potential ϕ (in the electrolyte) assumes a sufficiently high negative value for anodic dissolution of the metal. Similarly, Eq. [18] and [19] may be used to estimate the depth at which depletion of H^+ and decrease in the hydrogen evolution rate became significant.

The potential, concentration, and current density at the bottom of the slot are obtained by substituting $x = L$ in Eq. [17]-[19]. Thus

$$\phi(x=L) = - \frac{RT}{F} \left(\frac{L}{X} - \ln 2 \right) \text{ if } L \gg X \quad [20]$$

$$c(x=L) = 2c_0 \exp \left(- \frac{L}{X} \right) \text{ if } L \gg X \quad [21]$$

and

$$i(x=L) = 2i_s \exp \left(- \frac{L}{X} \right) \text{ if } L \gg X \quad [22]$$

If $(L-x) \gg X$, Eq. [17] reduces to the linear relation

$$\phi \simeq - \frac{RT}{F} \cdot \frac{x}{X} \text{ if } (L-x) \gg X \quad [23]$$

and Eq. [18] and [19] reduce to

$$c \simeq c_0 \exp (-x/X) \text{ if } (L-x) \gg X \quad [24]$$

$$i \simeq i_s \exp (-x/X) \text{ if } (L-x) \gg X \quad [25]$$

From Eq. [6a], [10], and [14] one may calculate the relation between the current density i_n in the slot normal to the outer surface and the local potential ϕ

$$i_n = j_{H^+} + F = \frac{2D_{H^+} + c_0 F}{X} \left[\exp \left(\frac{2F\phi}{RT} \right) - \exp \left(\frac{2F\phi_L}{RT} \right) \left(1 - \frac{a^2}{4X^2} \right) \right]^{1/2} \quad [26]$$

where ϕ_L is the potential at the bottom of the slot. For the entrance of the slot ($x = 0$, $\phi = 0$), one obtains as an approximation

$$i_n(x=0) \simeq \frac{2D_{H^+} + c_0 F}{X} \text{ if } -\phi_L \gg \frac{RT}{F} \quad [26a]$$

Substituting Eq. [11a] and [9] with $\beta = 1/2$, one obtains

$$i_n(x=0) = 2 \left(\frac{D_{H^+} + c_0 F i_s}{a} \right)^{1/2} = 2 \left(\frac{D_{H^+} + c_0 F i_0}{a} \right)^{1/2} \exp \left(\frac{F\eta}{4RT} \right) \quad [27]$$

This is a Tafel equation with a slope of twice the normal value and an apparent exchange current density of $2(D_{H^+} + c_0 F i_0/a)^{1/2}$. The appearance of a double Tafel slope is common in porous electrode work (16, 17). This is attributed to both ohmic and mass transfer effects.

The results of the calculations are plotted in Fig. 2-5 for a slot of depth $L = 1$ cm and a diffusivity of H^+ ion at 25°C of $D_{H^+} = 10^{-4}$ cm² sec⁻¹ (19). Figure 2 shows the concentration of both H^+ and Y^- as a function of x and i_s for a slot width $a = 0.05$ cm. With increasing distance into the slot, the concentration of H^+ decreases as it is consumed by the electrode reaction at the walls. Under the existing potential gradient, c_{Y^-} decreases as x increases such that at any distance $c_{H^+} = c_{Y^-}$ as required by electroneutrality. Actually, c_{Y^-} may fall off less rapidly with increasing distance

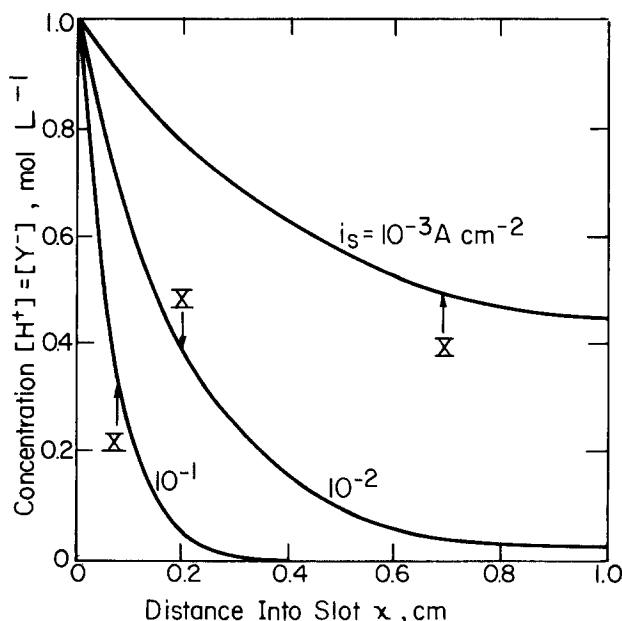


Fig. 2. Calculated concentration profiles of H^+ and Y^- ions in a slot of depth $L = 1$ cm and width $a = 0.05$ cm for three rates of cathodic hydrogen evolution at the surface, $x = 0$. See text for definition of the characteristic distance X .

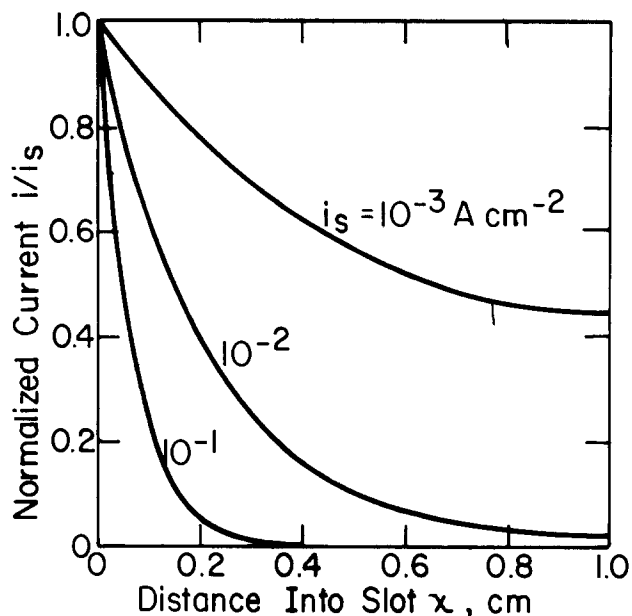


Fig. 3. Ratio of the calculated current density to the charging current density vs. distance into the slot for the same conditions as in Fig. 2.

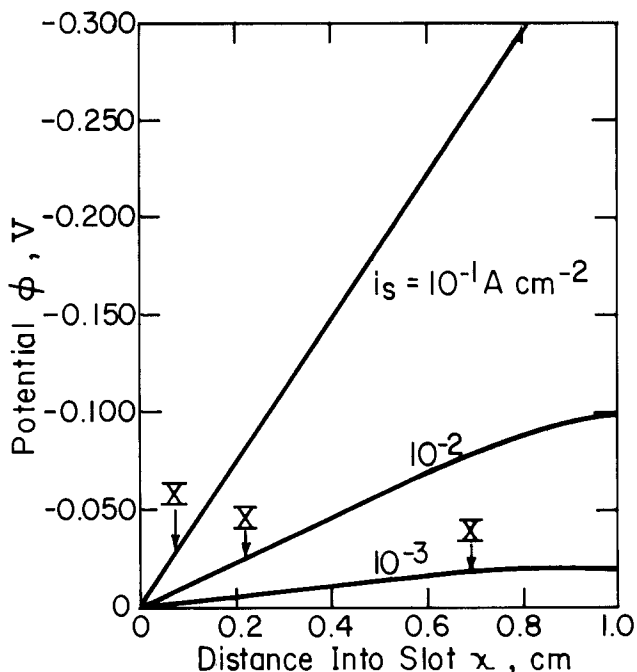


Fig. 4. Calculated profiles of the electrical potential in the electrolyte in a slot with respect to the potential at the opening where $\phi = 0$ for same conditions as in Fig. 2.

if anodic dissolution occurs near the crack tip to form metal ions, the presence of which was not considered in this model. It is shown later that metal dissolution does actually occur inside cracklike slots for the base metals, iron and nickel. It is also seen from Fig. 2 that as i_s increases, the H^+ (and Y^-) concentration profile becomes steeper.

The current distribution was found to behave similarly, Fig. 3. It decreases sharply with increasing distance into the slot, in agreement with an earlier analysis by Wagner (14). The distance into the slot at which the rate of hydrogen evolution becomes negligible decreases with increasing i_s , in agreement with established rules (20, 14) which state that the "throwing power" decreases with increasing current density.

Figure 4 shows that the electrical potential, ϕ , becomes more negative with increasing distance into the

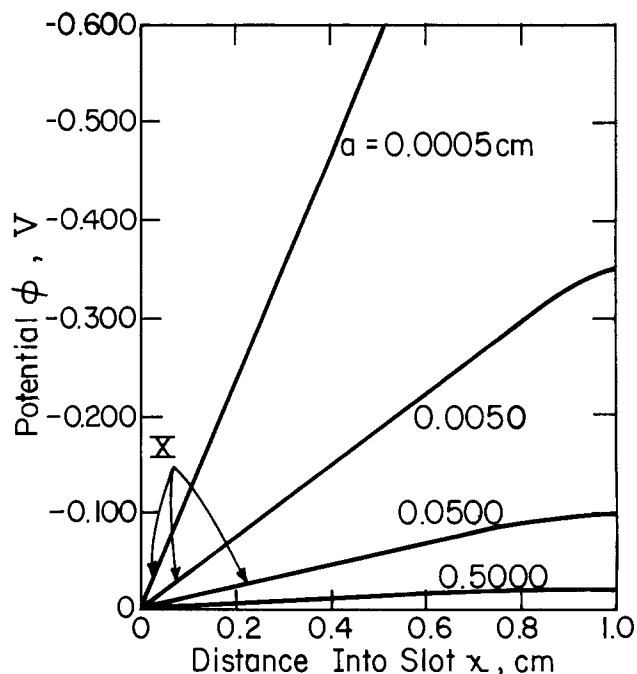


Fig. 5. Effect of crack width "a" on the electrical potential profile inside a crack of depth $L = 1$ cm at a constant hydrogen charging rate at the electrode surface of $i_s = 0.01$ $A\ cm^{-2}$.

slot ($a = 0.05$ cm). The magnitude of ϕ is seen to increase with increasing i_s and x . In the presence of metal ions (which may be produced by dissolution of the metal at the bottom of the slots) the electrolyte conductivity may be higher and accordingly the magnitude of ϕ lower.²

Figure 5 shows for $i_s = 10^{-2}$ $A\ cm^{-2}$ the important effect of slot width, a , on the potential profiles inside the slot. As the slot width decreases ϕ changes more sharply with distance into the slot. Correspondingly larger variations in current and concentration also occur as the slot width decreases. This is a particularly noteworthy feature of this model since cracks usually are very narrow, and since the effect of crack width on concentration and potential profiles is not generally recognized. The bulk electrolyte concentration has the same effect on the various profiles as the slot width since it is the product $c_0 a$ which influences the value of X , see Eq. [11a]. It follows that as the bulk concentration of the acid decreases (hence its conductivity decreases) the potential drop over a certain distance increases.

The potential ϕ involves an ohmic potential drop inside the slot and the contribution of a diffusion potential as well. The IR drop in the metal is negligible. Thus ϕ is equal to the difference of the electrode potentials E at $x = 0$ and $x > 0$, i.e.

$$\phi = E(x = 0) - E(x) \quad [28]$$

Thus, a more negative value of ϕ in the electrolyte corresponds to a more positive (noble) local electrode potential of the metal with respect to the solution, as pointed out previously by Wagner (14).

The results in Fig. 2 are reliable for $i_s = 10^{-3}$ and 10^{-2} $A\ cm^{-2}$, but of only marginal value for $i_s = 10^{-1}$ $A\ cm^{-2}$ for which $X = 0.07$ cm is not much larger than the slot width. The validity range of the equations increases as the slot width decreases, e.g., $X \gg a$ for all except the bottom curve in Fig. 5. Nevertheless, they apply quantitatively only at $x \gg X$ in view of appreciable three-dimensional transport at the slot opening. However, even precisely calculated current and concentration distributions have limited practical application since experimental data are often obtained

² It is shown later that the increase in resistance due to constrictions (gas) in the electrolyte path far outweighs the increase in conductivity due to anodically formed metal ions.

from laboratory experiments or industrial practice for which conditions in the crack differ from those in the idealized model, *e.g.*, the accumulation of gas to form a constriction, and the occurrences of additional chemical and electrochemical reactions. Gas accumulation is likely in cracks with a corresponding increase in the effective electrolyte resistance as shown previously by Pickering and Frankenthal (9). The consequence of such constrictions in the present study would be steeper gradients of H^+ , Y^- , i , and ϕ than in Fig. 2-4, and a more noble local electrode potential at the slot bottom, $E_{x=L}$, according to Eq. [28]. It is shown later that gas accumulation and larger-than-expected negative ϕ values occur in cracklike slots during hydrogen charging, and that anodic dissolution occurs in slots of base metals.

In summary, substantial changes in electrochemical conditions within pores or cracks during cathodic hydrogen charging are expected. This, in turn, means that the nature and the rates of the electrochemical reactions occurring inside the pores may be quite different from those at the outer surface. For example, at high hydrogen charging rates the electrode potential at the outer surface of iron in 1N H_2SO_4 may be sufficiently negative such that no significant iron dissolution occurs. Nevertheless, at some distance into a pore or crack iron dissolution may occur because the electrode potential is more positive. This shift of electrode potential is illustrated in Fig. 6 using the partial polarization curves according to Wagner and Traud (21).

Iron dissolution inside the pore or crack is also favored by the higher pH (Fig. 2). It is recognized now that the anodic current density of iron dissolution at a given potential increases with increasing pH (22-27). Thus, dissolution of iron inside a pore is favored, not only by the shift of the potential to more noble values with respect to the potential at the outer surface, but also by a decreasing hydrogen ion concentration inside the pore.

Experimental

General procedure.—An experimental system was set up to test the above hypothesis and conclusions. Cracklike slots, (see Fig. 1), were cut in the middle of cubes of Ferrovac E Fe, electrolytic Ni, and 99.999+ Cu ($a \approx 0.5$ -1.5 mm, $b \approx 1.2$ cm, $L \approx 1.2$ cm). The cutting procedure differed for the metals, with the result that the surfaces of the slot in the iron sample were smooth in comparison to those for the Ni and Cu

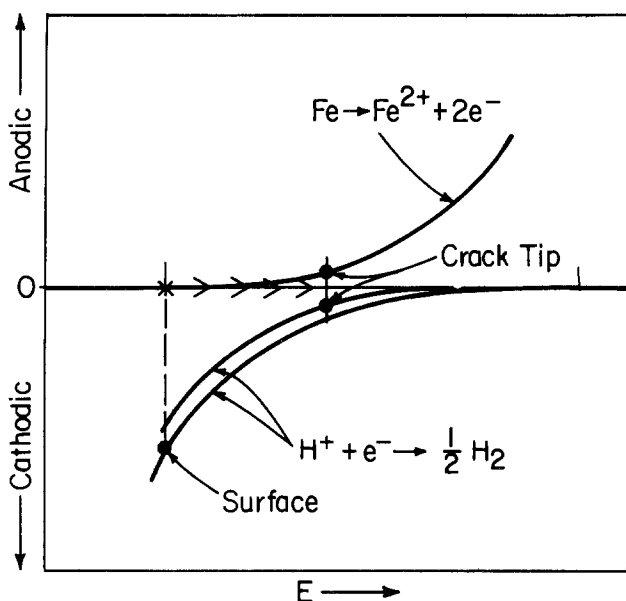


Fig. 6. Schematic partial polarization curves illustrating the shift of the local electrode potential E from the region of solely hydrogen evolution at the outer surface to the mixed potential region of iron dissolution and hydrogen evolution at the bottom of the crack.

samples. In order to shield the outer (except the top) surfaces from the electrolyte the sample was tight-fitted into a Teflon mount such that only the horizontal outer top and inner (slot) surfaces were accessible to the electrolyte. Electrical contact to the sample was made through a thin platinum wire attached to one side of the electrode before it was fitted inside the Teflon mount. The platinum wire was shielded from the electrolyte with an Alphex shrinkable tubing, the diameter of which decreases considerably on gentle heating.

This assembly was then put into a large volume of electrolyte (about 1.5 liter). The electrolytes used were 1M $HClO_4$ and a sodium acetate-acetic acid buffer, $pH \approx 5$ (0.5M each). All tests were made at room temperature. Electrode potentials are reported with respect to the standard hydrogen electrode (SHE).

A constant cathodic current was impressed on the sample. After a steady potential was obtained the potential of the metal with respect to the solution at the outer surface ($E_{x=0}$) and at various positions inside the slot (E_x) was measured using a Hg/Hg_2SO_4 (0.1N H_2SO_4) reference electrode and a fine Luggin capillary (diameter < 0.01 cm) (9). In order to avoid probe-induced ϕ values the probe diameter was 5-10 times smaller than the slot width, values at the slot bottom were obtained with the probe backed off the bottom, and a technique for detecting gas accumulation within the probe was developed. For these conditions the potential variation in the electrolyte ϕ between two positions of the Luggin capillary is the difference in the measured electrode potentials, Eq. [28].

A second procedure was also used which allowed direct measurement of the variation in potential ϕ inside the slot. In this arrangement two reference electrodes were used, one with Luggin capillary positioned at $x = 0$ and the other with a (adjustable) Luggin capillary at distance x into the slot. The two reference electrodes were connected to a high impedance voltmeter. The measured potential was the magnitude of ϕ over the distance x .

The position of the capillary inside the slot was adjusted and the distance measured using a micromanipulator. The counterelectrode was a spectrographically pure porous graphite rod positioned about 10 cm away from the iron sample to insure a uniform current distribution on the exposed outer (top) surface of the metal.

After reaching steady state and while the current was flowing, the solution inside the slot was extracted using a fine capillary glass tube and a simple suction mechanism. Qualitative tests for iron were done using the Standard Orthophenanthroline color procedure (28). Quantitative tests for Fe^{2+} , Cu^{2+} , and Ni^{2+} ions were made using atomic absorption spectrometry.

Electrode potential values and gas bubbles.—The measured potential variation ϕ inside a slot of $a = 0.05$ cm width in a Ferrovac E iron sample is shown in Fig. 7. The charging current density (comparable to i_s in the model) was 5.2 mA cm^{-2} cathodic and the electrolyte was acetate-acetic acid buffer, $pH \approx 5$. Although this pH is different than that used in the model, it is not an important consideration for reasons to be discussed; its choice was based on experimental considerations. Electrolytes which fit the model were used for the Ni and Cu samples.

It is seen from Fig. 7 that there is a significant difference between the measured potential at the outer surface and that at the bottom of the slot. The measured electrode potential at the outer surface was approximately $E_{x=0} \approx -0.9V$ SHE and that at the bottom was $E_{x=L} \approx -0.5V$. Since the ferrous ion concentration in the bulk electrolyte is extremely low, one may use the standard single electrode potential of iron minus $0.2V$ ($E = -0.64V$) as the limiting condition for virtually complete cathodic protection (29, 30). Hence, the outer iron surface was cathodically pro-

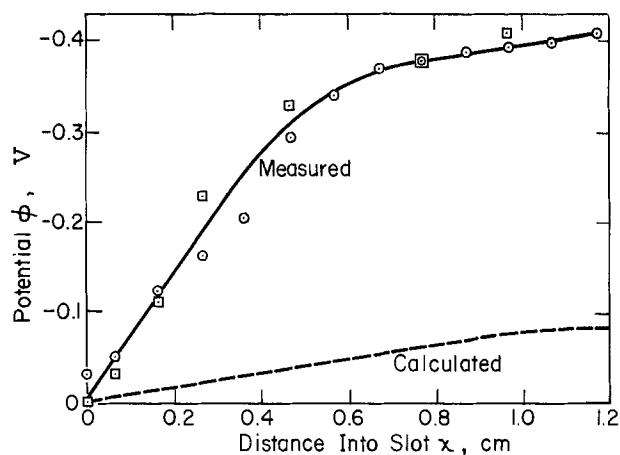


Fig. 7. The ϕ profile from the measured electrode potentials as a function of distance x into the slot in the iron sample exposed to the acetate-acetic acid solution for $i_s = 5.2 \text{ mA cm}^{-2}$ and $a = 0.05 \text{ cm}$. Points are for a traverse of the Luggin probe into (\circ) and out of (\square) the slot. Total time of traverse was 25 min. The calculated ϕ profile (Eq. [19]) is shown for comparison; $X = 0.3 \text{ cm}$.

tected well into the stable iron region. The electrode potential at the bottom corresponds to appreciable equilibrium concentrations of Fe^{2+} ions (see Appendix) and as such is a mixed potential value established by the iron and hydrogen reactions.

A second series of measurements made 3 hr later showed nearly the same potential variation within the slot as in Fig. 7, *viz.*, $\phi_{x=L} \approx -0.34 \text{ V}$. In a third series of measurements the potential variation in the electrolyte within the slot was measured directly using the alternative circuit and gave $\phi_{x=L} \approx -0.33 \text{ V}$, in good agreement with the above value.

Figure 8 shows the measured ϕ values inside a slot 0.15 cm wide and 1.4 cm deep in a Ni sample. The charging solution was 1M HClO_4 and the current density was 10 mA cm^{-2} cathodic. It is seen that part way inside the slot ϕ increases sharply. This behavior was very reproducible in all cases when a gas bubble was seen to occupy the bottom portion of the slot. The measured electrode potential at the opening of the slot

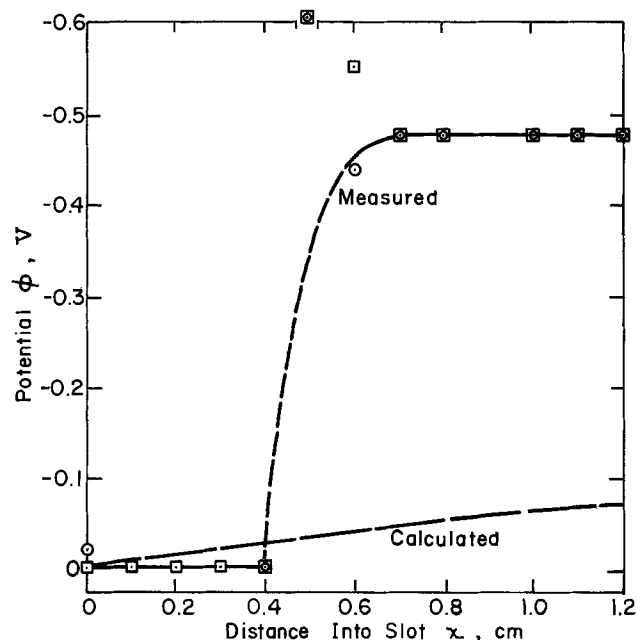


Fig. 8. The experimental and calculated ϕ profiles for a nickel sample in 1M HClO_4 for $i_s = 10 \text{ mA cm}^{-2}$ and $a = 0.15 \text{ cm}$; $X = 0.4 \text{ cm}$.

was $E_{x=0} \approx -0.6$ to -0.7 V , a value which is too negative for anodic dissolution of Ni ($E^\circ = 0.2 \text{ V} = -0.45 \text{ V}$). However, the electrode potential in the deeper portion of the slot, being 0.4-0.5V more noble at $E_{x>L/2} \approx -0.2 \text{ V}$ is in the region of Ni dissolution.

Some difficulty was encountered in the measurements, which may explain the scatter of values of ϕ about halfway into the slot (Fig. 8). The sharp increase in ϕ is attributable to the presence of a large gas bubble in the slot.

The large width of the slot in the nickel sample enabled information to be obtained on the nature of gas bubble formation and evolution within the slot. It was seen that accumulation of the gas occurred to give a large bubble which occupied most, if not all, of the cross section about halfway down the slot. Intermittently, a smaller bubble (though much larger in size than those evolving off the outer surface) evolved from the slot as if coming from the accumulated hydrogen gas "stuck" in the slot. Since only the small area at the edges of the slot were material other than iron (Teflon), the accumulation of gas occurs primarily, if not entirely, on the iron walls of the slot.

Data for the Cu sample were obtained for a charging current of 10 mA cm^{-2} in 1M HClO_4 . The slot was 0.5 mm wide and 1 cm deep. The measured electrode potential at the outer surface was $E_{x=0} \approx -0.7 \text{ V}$, a value which is well below that required for anodic dissolution of copper since $E^\circ = 0.2 \text{ V} = 0.14 \text{ V}$. The measured electrode potential inside the slot was erratic and oscillating very quickly. During the first traverse of the probe to the slot bottom a relatively small potential variation, $\phi_{x=L} = -0.10$ to -0.15 V , was measured. At a later time, a larger increase in potential, $\phi_{x=L} \approx 0.50 \text{ V}$, was noted. Gas accumulation was observed within the slot during the experiment.

Results with the Cu sample differed in an important way from those for iron and nickel. The potential variation, $\phi_{x=L} \approx -0.50 \text{ V}$, though large was not enough to shift the electrode potential into the region of copper dissolution. The most noble potential reached was $E_{x=L} \approx -0.2 \text{ V}$ which is well below the limiting value of $E = 0.14 \text{ V}$.

The measured potential data for the Fe, Ni, and Cu samples are summarized in Table I. Values listed for the slot bottom were the most noble ones measured for each sample, and in most cases could be associated with accumulated gas which was lodged in the slot.

Metal ion concentrations.—Tests for increased metal ion concentrations within slots of the samples were done on solution periodically extracted from the slots. The amount of solution extracted was several times larger than the volume of the slot, a relatively large volume of liquid being required for the analysis (about 0.5 cm^3). Thus, average values heavily weighed toward the bulk concentrations were obtained. Consequently, in those cases in which departures from the bulk concentrations were observed, the measured concentrations were only small fractions of the true concentrations at $x = L$. Contributing to this averaging effect is the fact that the greatest departure occurs in only a small fraction of the slot volume (slot bottom or the region of a trapped gas bubble) where the electrical potential in the solution differs most from that in solution at the outer surface. For these reasons the

Table I. The largest measured potential variations (ϕ) in slots of Fe, Ni, and Cu samples and the corresponding (approximate) electrode potential at the bottom and at the opening of the slots

Metal	$\phi_{x=L}, \text{ V}$	$E_{x=L}, \text{ V SHE}$	$E_{x=0}, \text{ V SHE}$
Fe	-0.4	-0.5	-0.9
Ni	-0.5	-0.2	-0.7 (approx)
Cu	-0.5	-0.2	-0.7

greatest concentration in the slot is estimated to be up to 100 times the difference in concentration of the measured bulk and slot values. The measured slot and bulk concentrations for Fe, Ni, and Cu specimens and the estimated limiting concentrations are shown in Table II.

Solution extracted from the slot of an iron sample ($a = 0.05$ cm) during cathodic charging at a rate of 5.2 mA cm^{-2} ($\phi_{x=L} = -0.36\text{V}$) showed an iron content of 50 ppm and gave a definite color in the orthophenanthroline test. Solution extracted at the same time from the bulk solution showed about 2 ppm Fe (as did the stock solution) and gave a barely detectable orthophenanthroline color. This was found to be reproducible on a daily basis for a period of 10 days of continuous hydrogen charging.

A similar result was obtained for a Ni sample. Quantitative analysis of electrolyte extracted from the slot during cathodic charging at 10 mA cm^{-2} showed 15 ppm of Ni^{2+} as compared to a negligible quantity in the bulk solution.

The results for the Cu specimens were quite different. The measured Cu^{2+} ion concentration in the slot was much lower than for iron and nickel.

One may calculate the lowest (most negative) electrode potential which will support the concentrations of metal ions shown in Table II. Using concentrations in place of activities in the Nernst equation one obtains $E = -0.53$ and -0.47V (SHE) for 50 and 5000 ppm iron, respectively; $E = -0.36$ and -0.30V for 15 and 1000 ppm nickel, respectively, and $E = 0.20\text{V}$ for 1 ppm copper. In the case of iron and nickel the measured electrode potentials at the slot bottom (Table I) are more noble than these values, indicating that the measured metal ion concentrations in the slot are stable. The 1 ppm copper level in the slot is not stable at the measured $E_{x=L} = -0.2\text{V}$, and indicates that either more positive electrode potentials exist in the slot³ or transport of Cu^{2+} in the electrolyte becomes a factor at these low concentrations. It may also be noted in this regard that the concentration of Cu^{2+} may be somewhat higher in the slot than in the bulk solution (where <1 ppm was measured) in view of the prevailing potential gradient within the solution.

Discussion

Comparison of the experimental results with the model.—The calculated ϕ potential from Eq. [17] is compared to the measured electrode potential for an iron sample in Fig. 7. It is clear that, although the direction of the potential change for calculated and measured values agree, the actual potential change is very much greater (order of magnitude) than that calculated. The disparity is much greater than that due to the use of a $\text{pH} = 5$ rather than a $\text{pH} = 0$ solution as called for in the model. Similar comparisons exist for Ni (Fig. 8) and Cu; in these cases the pH of the aqueous solutions fit the model. Large trapped gas bubbles were identified within the slot during the potential measurements, and are the most obvious reason for the deviation. Their presence would reduce the

³This is due to the possible occurrence of oxygen reduction, in addition to H^+ ion reduction, in which case the limiting electrode potential also is a more positive value.

Table II. The measured concentrations of Fe^{2+} , Ni^{2+} , and Cu^{2+} ions in samples of electrolyte extracted from within the "slot" and from the bulk solution are listed. From these data an estimated concentration at the slot bottom was obtained as described in the text.

Metal	Bulk [M^{2+}] (ppm)	"Slot" [M^{2+}] (ppm)	Estimated [M^{2+}] @ $x = L$ (ppm)
Fe	2	50	$\lesssim 5000$ ($\lesssim 0.1\text{M}$)
Ni	0.2	15	$\lesssim 1000$
Cu	—	1	—

available cross section for current flow in the electrolyte, i.e., comparable to a local reduction in the slot width a , Fig. 5. For a given current, the actual potential variation ϕ in the constricted (high resistance) region is necessarily larger than in the absence of the constriction. Hence, the measured ϕ is larger than that calculated, and in turn, so is the change in electrode potential per unit distance into the slot according to Eq. [28].

The present model and equations do correctly predict the signs of the gradients of the ionic species and of the electrical potential, and consequently are helpful in explaining and predicting the occurrence of electrochemical reactions inside a cavity when, as usual, only the electrochemical conditions at the outer surface are known. Furthermore, the solutions could apply in a quantitative sense to cracking situations in which constrictions are absent.

Role of gas bubbles and crack width.—Are constrictions likely in real cracks? Are they necessary for the attainment of large potential variations in real cracks? Since real cracks are usually much narrower than the slots used in this investigation, and since for all known conditions the vast majority of reduced H^+ ions becomes hydrogen gas, it seems likely that hydrogen gas will accumulate in real cracks. As to the second question, Fig. 5 shows that the gas may not be necessary for the attainment of large potential variations in the case of real cracks which are very narrow (small a). Recall that results in Fig. 5, which show the effect of slot width on the magnitude of the potential variation in the electrolyte, were obtained from a model which does not include constrictions. Hence, for a crack of $5 \mu\text{m}$ width ($a = 0.0005$ cm) and an impressed cathodic current of 0.01 A cm^{-2} , a potential variation of 0.5V exists over a distance of only 0.4 cm, i.e., $\phi_{x=0.4 \text{ cm}} \simeq -0.5\text{V}$. From these data it is clear that crack width also plays an important role in determining which reactions occur at the crack tip.

What is the upper limit of the electrode potential in a crack? The answer to this question for cathodic polarization (meaning a net cathodic current) is the reversible potential of the cathodic reaction. One has the basic condition that a net cathodic current (current flow into the slot) is required in the slot for ϕ to be negative. The more noble the electrode potential, the smaller is the rate of the cathodic reaction (hydrogen evolution) in accord with the general polarization behavior for a cathodic reaction. Since the rate goes to zero at the reversible potential of the hydrogen reaction, the local electrode potential in the slot can increase only to the point of approaching this value. Furthermore, if anodic reactions occur in the slot, a net zero current would occur at a more negative electrode potential than the local reversible hydrogen potential, and this "mixed" potential would then be the upper limit.

The experimental data are consistent with this concept of a limiting potential in the slot which is dictated by the cathodic (hydrogen) reaction. For the three metals investigated the most noble potentials measured were all negative of SHE. For two of the metals (Fe and Ni) whose anodic polarization behavior overlaps the cathodic polarization behavior of the hydrogen reaction, the measured electrode potential at the bottom of the slot may have been a mixed potential established by the metal and hydrogen reactions, in accord with the finding that Fe and Ni concentrations were significantly higher in the slots. In the case of Cu, anodic dissolution could not be expected (and was not observed) since the electrode potential at the bottom of the slot never attained a value near the dissolution potential. In this case, the measured electrode potential may have approached the reversible potential of the hydrogen evolution reaction at $x \simeq L$. A similar limiting potential criterion applies in the case of anodic polarization, and the available experimental data (6, 9) are consistent with such.

From a practical point of view it is an important finding that the local electrode potential in the slot may shift by much larger amounts than previously assumed. This means that the likelihood of additional electrochemical reactions occurring in a crack is substantially increased. In particular, the noble E_x values measured and the detection of substantial amounts of iron and nickel ions in the slot during cathodic polarization indicate that in the case of the base metals and base-metal alloys, metal dissolution within cracks, crevices, etc. has to be taken into account in applying protection methods, as well as in mechanistic analyses of crack propagation.

Conclusions

The most significant experimental results of this investigation of cathodic charging of metals are (i) that the electrode potential measured at the bottom of cracklike slots in iron, nickel, and copper are about 0.5V more noble than at the outer surface, and (ii) that relatively large concentrations of metal ions were detected at the bottom of slots in the iron and nickel samples.

It is concluded that metal dissolution occurs in the slots, though not at the outer surface, in iron and nickel samples during cathodic hydrogen charging. In the case of copper, no metal dissolves at the external surface or at the bottom of the slot, in accord with its positive standard potential. Since these results are a consequence of mass and charge transfer conditions in the electrolyte and depend on the metal only as to its nobility, metal dissolution in slots or cracks during cathodic hydrogen charging or during cathodic protection should be considered a possibility for all base metals and their alloys, including the vast majority of commercial alloys.

Based on a simple model, the electrode potential, ionic concentration, and current distributions within cracks undergoing cathodic hydrogen charging in acid solutions were analyzed. The calculated solutions of the model show that (i) the concentrations of both ionic species, H^+ and Y^- , decrease with increasing distance into the slot, and that both gradients become sharper as the charging current is increased or the slot width decreased (Eq. [18] and [11a], and Fig. 2); (ii) the current distribution on the walls of the crack is nonuniform and becomes even less uniform as the hydrogen charging rate increases or as the slot becomes narrower (Eq. [19] and [11a], and Fig. 3); (iii) the electrical potential ϕ in the solution decreases with increasing distance into the slot, and the ϕ gradient becomes sharper with increasing rate of hydrogen evolution and with decreasing width of the slot (Eq. [17] and [11a], and Fig. 4 and 5); and (iv) the local electrode potential E_x increases in the noble direction with increasing x (Eq. [28] and at some distance into the slot may cause metal dissolution (Fig. 6) as was indicated for iron and nickel.

The very large measured change in ϕ in the slots of Fe, Ni, and Cu samples showed that the model greatly underestimated the electrical potential change, and hence, the local electrode potential in the slot. This is not surprising since hydrogen gas was regularly observed to partially fill the slots, in which case the experimental conditions clearly departed from those stipulated in the model. The gas has the effect of restricting current flow and mass and charge transport. It follows that a new model should include accumulation of gas in the slot or a comparable reduced cross-section effect. The present model, therefore, is a limiting one. The presence of gas constrictions does not invalidate the above-mentioned conclusions of the model.

Acknowledgment

The authors gratefully thank Professor Carl Wagner of the Max-Planck-Institut für Biophysikalische Chemie for his help in formulating and solving the model described in the theoretical section. Financial

support by the Office of Naval Research under Contract No. 4330/N00014-67-A-0385-0022 is gratefully acknowledged.

Manuscript submitted Dec. 18, 1974; revised manuscript received April 4, 1975.

Any discussion of this paper will appear in a Discussion Section to be published in the June 1976 JOURNAL. All discussions for the June 1976 Discussion Section should be submitted by Feb. 1, 1976.

Publication costs of this article were partially assisted by The Pennsylvania State University.

APPENDIX

A check on the estimated Fe^{2+} concentrations shown in Table II can be made by assuming that the metal ion concentrations were in local equilibrium with the metal. For an electrode potential at the slot bottom of $E_{x=L} \simeq -0.5V$ (SHE), the Nernst equation gives a value of about 600 ppm Fe^{2+} ions (activity coefficient = 1) at $x = L$, which is midway between the measured and estimated values (Table II). A similar calculation is not realistic for the Ni sample since Ni is appreciably polarized at $E_{x=L} \simeq -0.2V$ in aqueous electrolytes.

REFERENCES

1. Z. Szklarska-Smialowska, *Corrosion*, **27**, 223 (1971).
2. M. Pourbaix, *ibid.*, **26**, 431 (1970).
3. B. F. Brown, C. T. Fujii, and E. P. Dahlberg, *This Journal*, **116**, 218 (1969).
4. J. H. Shively, F. R. Hehemann, and A. R. Troiano, *Corrosion*, **23**, 215 (1967); *ibid.*, **22**, 253 (1966).
5. H. Kaesche, *Korrosion*, **16**, 17 (1963); *Z. Phys. Chem. N.F.*, **34**, 114 (1962).
6. G. Herbsleb and H. J. Engell, *Z. Electrochem.*, **65**, 881 (1961); *Werkstoffe Korrosion*, **17**, 365 (1966).
7. N. D. Greene, W. D. France, Jr., and B. E. Wilde, *Corrosion*, **21**, 275 (1965).
8. C. M. Chen, F. H. Beck, and M. G. Fontana, *ibid.*, **27**, 234 (1971).
9. H. W. Pickering and R. P. Frankenthal, in Proceedings of the Conference on Localized Corrosion, Williamsburg, Va., December 6-10, 1971, R. W. Staehle, B. F. Brown, J. Kruger, and A. Agrawal, Editors, p. 261-269, N.A.C.E. (1974); *This Journal*, **119**, 1297 (1972).
10. M. H. Peterson and T. J. Lennox, Jr., *Corrosion*, **29**, 406 (1973).
11. T. R. Beck, *This Journal*, **120**, 1317 (1973).
12. H. W. Pickering and P. J. Byrne, *ibid.*, **120**, 607 (1973).
13. B. Ateya and H. W. Pickering, in "Hydrogen in Metals," I. M. Bernstein and A. W. Thompson, Editors, p. 207, American Society for Metals (1974).
14. C. Wagner, *Plating*, **48**, 997 (1961).
15. E. A. Grens, II, *Electrochim. Acta*, **15**, 1047 (1970), and references therein.
16. R. de Levie, in "Advances in Electrochemistry and Electrochemical Engineering," P. Delahay, Editor, Vol. 6, Interscience Publishers, New York (1967).
17. L. G. Austin, in "Handbook of Fuel Cell Technology," C. Berger, Editor, p. 184, Prentice Hall, Inc., Englewood Cliffs, New Jersey (1968).
18. A. N. Frumkin; see K. J. Vetter, "Elektrochemical Kinetics," p. 560, Academic Press, New York (1967).
19. M. Breiter and K. Hoffmann, *Z. Elektrochem.*, **64**, 462 (1960).
20. C. Wagner, *This Journal*, **98**, 116 (1951).
21. C. Wagner and W. Traud, *Z. Elektrochem.*, **44**, 391 (1938).
22. G. M. Florianovich, L. A. Sokolova, Ya. M. Kolytyrkin, *Electrochim. Acta*, **12**, 879 (1967).
23. T. Hurlen, *Acta Chem. Scand.*, **14**, 1533 (1960); **14**, 1555 (1960); **14**, 1564 (1960).
24. J. O'M. Bockris and H. Kita, *This Journal*, **108**, 676 (1961).
25. J. O'M. Bockris, D. Drazic, and A. R. Despic, *Electrochim. Acta*, **4**, 325 (1961).

26. K. Schwabe, *Electrochim. Acta*, **14**, 853 (1969).
 27. K. E. Heusler, *Z. Elektrochem.*, **62**, 582 (1958); **66**, 177 (1962).
 28. F. Feigl, "Spot Tests in Inorganic Chemistry," 6th Edition, American Elsevier Publishing Co., New York (1972).
 29. C. Wagner, *This Journal*, **99**, 1 (1952).
 30. M. Pourbaix, "Atlas of Electrochemical Equilibria in Aqueous Solutions," Pergamon Press, Inc., New York (1966).

Retentivities of Anodic Oxide Coatings on Aluminum Containing Electrodeposited Cobalt, Nickel, and Cobalt-Nickel

Satoshi Kawai

The Pilot Pen Company, Limited, Hiratsuka-Works, Kanagawa, Japan

ABSTRACT

Cobalt, nickel, and cobalt-nickel alloy were electrodeposited into the micropores of anodic oxide films on aluminum obtained in a sulfuric acid bath. The deposits in the micropores were separated from the oxide films and were observed as needlelike crystals about 100Å in diameter. The metallic deposits were quite dense at the bottom of the micropores and then gradually grew to the surface. Finally the deposits form layers distributed uniformly parallel to the surface. The density of residual magnetizations in cobalt and nickel deposits increase to about 1700 and 600G, respectively, when the outer layers are lapped down to a few microns in thickness. The films can be used as magnetic recording disks.

In the previous paper, it has been reported by the present author and his collaborator that the anodic oxide films of aluminum obtained from various electrolytic baths in which cobalt and Co-Ni alloy were electrodeposited showed characteristic magnetic anisotropies (1). These properties have been considered to be caused by the regular formation of micropores perpendicular to the substrate and the crystal orientation of metallic deposits in them. The coercivities of the films (about 500-1100 oe) showed rather higher values and the retentivities (about 1000G) indicated lower values compared to conventional magnetic thin films.

In the study of electrolytic coloring process of aluminum, Lichtenberger-Bajza *et al.* deposited copper crystals in the micropores by a-c electrolysis and observed with an electron microprobe analyzer that the metallic copper was deposited near the bottom of the pores (2). Sandera separated the deposits from the anodic oxide films which were pigmented in the baths contained metal salts and found under an electron microscope and by the diffraction method that the metal deposits such as gold and silver crystallized as very fine fibrous structures in the micropores (3).

Meanwhile, in the study of a magnetic recording system, Iwasaki presented an empirical equation concerning the relationship between the half-pulse width (W_{50}) of output and the magnetic property of thin films as follows

$$W_{50} \propto (\delta \cdot Br/Hc)^{0.5}$$

and he elucidated that the high bit density magnetic recording can be obtained by decreasing the value of W_{50} (4). Therefore, δ (film thickness) has to be thinner and Hc (coercivity) to be larger while Br (residual magnetization) should be maintained at the same strength.

In the present paper, for the purpose of maximizing the recording performance of the magnetic oxide films, the author has studied the structures and remanences of electrodeposited metals in the oxide films.

Key words: anodic oxide film, electron microprobe analyzer, saturation magnetization moment.

Experimental Procedures

Rolled aluminum sheets, 99.99% in purity, $0.5 \times 50 \times 100$ mm³ in size, were used as substrates. For the measurement with a magnetometer, the surfaces of the specimens were previously machined with a lathe to a surface roughness of about 1 μ m.

First, aluminum sheets were anodized in a sulfuric acid bath and then electrolyzed between a carbon electrode with a.c. in various metal sulfate solutions as shown in Table I. Cobalt, nickel, and cobalt-nickel alloy were deposited in the micropores of oxide films as reported in the first paper (1).

In order to observe the electrodeposited crystals under an electron microscope, the specimens were immersed in 3% mercuric chloride solutions for a few hours at room temperature to separate the oxide films from the substrates, and the stripped films containing magnetic metals were dissolved in 5% NaOH solutions at 50°C for several minutes. Then, the extracted crystals were washed thoroughly with clean water and transferred to collodion films to keep the deposits as they were.

By using an electron microprobe, an x-ray microanalysis was performed. The specimens were buried in polyester resins and the cross sections of films were polished to flat surfaces. The measuring conditions were as follows; diameter of emission electron beam, 2 μ m; scanning rate, 10 μ m/min; acceleration voltage,

Table I. Bath compositions

Procedures	Remarks
Degreasing	5%—NaOH, 60°C, 2 min
Desmut	5%—HNO ₃ , 23°C, 1 min
Anodizing	15%—H ₂ SO ₄ , 0.1%—Al, 1.3 A/dm ² , 20°C, 40-50 min
Electrodeposition	
Co	5%—CoSO ₄ ·7H ₂ O, 2%—H ₃ BO ₃ , 0.2%—glycerine, 15V (50 Hz), 20°C, pH 6.0, 40-150 min
Ni	5%—NiSO ₄ ·7H ₂ O, 2%—H ₃ BO ₃ , 0.2%—glycerine, 15V (50 Hz), 20°C, pH 6.0, 15-120 min
Co-Ni	3%—CoSO ₄ ·7H ₂ O, 7%—NiSO ₄ ·7H ₂ O, 2%—H ₃ BO ₃ , 0.2%—glycerine, 15V (50 Hz), 30°C, pH 6.0, 20-120 min
Sealing	1%—Ni(CH ₃ COO) ₂ ·4H ₂ O, 90°C, 20 min

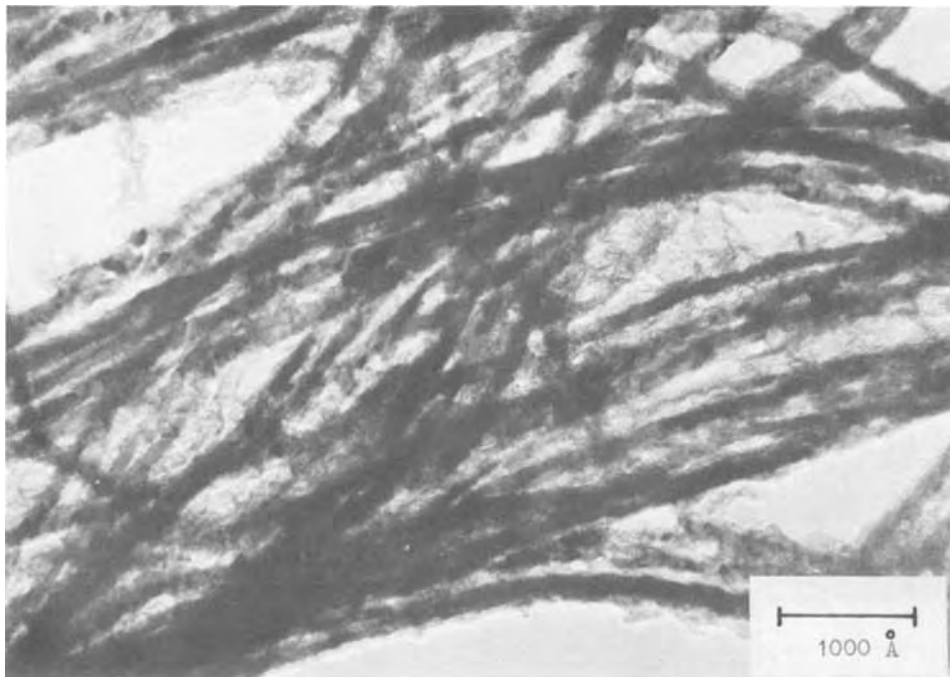


Fig. 1. Electron micrograph of nickel deposits extracted from anodic oxide film.

25 kV; absorbed electron current, 0.18 μ A. The electron beam scanned the cross-sectional area from the outer surface of the oxide to the aluminum substrate. X-ray intensities due to ferromagnetic and aluminum metals at each position of film were continuously described with an X-Y recorder. In addition, the same specimens were also observed with a scanning electron microprobe image.

The total amount of cobalt and nickel deposits in the oxide films were determined by an atomic absorption spectroscopy. The specimens, 20 \times 20 mm² in size, were immersed in 5% NaOH solutions at 50°C to dissolve the films from the substrates. Then the undissolved aluminum metals were washed and removed from the solutions. The caustic solutions which contained the metal deposits were dissolved in hydrochloric acid solutions and subjected to quantitative analyses.

With a lapping machine, the surfaces of the oxide films were abraded with aluminum oxide powder with a diameter of about 0.1 μ m. And with this procedure, the surface roughness of the films could be maintained at 0.05 μ m while the flatness was about 0.1 μ m in a 20 mm length. The thickness of the oxide films was reduced gradually by this polishing and finally reached a value of about 2 μ m. At each step in decreasing the thickness, the strength of magnetization was measured by the sample vibrating magnetometer as described in the previous paper (1).

Hysteresis loops were measured by the sample vibrating magnetometer in which 80 Hz vibration is applied to the specimen by a quartz oscillator. By using this method, the magnetic moment in the direction of vibration can be determined with high sensitivity. The specimens in the form of a disk, 6 mm in diameter, were inset on a quartz holder, and hysteresis curves were measured with an X-Y recorder under 5 kOe of magnetic field.

Experimental Results

The deposited crystal extracted from the oxide films showed needlelike structure, and the typical crystalline form of the nickel deposits is shown in Fig. 1.

Figure 2 (a) and (b) show the results of the cobalt deposits in the cross section of the oxide films as determined by the electron microprobe analysis. Samples (a) and (b) differ in the amount of cobalt deposits with different electrolysis time. Separate distributions for cobalt and aluminum were observed as a

function of thickness. The Al K α lines had two different intensities. The area showing the lower intensities indicated the anodic oxide film sections, because of the lower aluminum content in the oxide. In specimen (a), the x-ray intensity of Co K α was relatively high near the bottom of the micropores, but very low in the vicinity of the surface of the oxide film. On the other hand, the Co K α line of specimen (b) was nearly uniform from the bottom of the micropores to the outer surface of the oxide.

With the scanning electron microscope, the same sections of the oxide films were observed. Simultaneously the scanning x-ray images of aluminum and cobalt at the identical positions are indicated as shown in Fig. 3 of which the (a) and (b) portions are different in the amount of cobalt deposits, respectively. The thickness of the oxide layers observed under the electron microscope correlated well with the layers examined by the x-ray images of aluminum which were discerned clearly by the spot distributions. The spot density of cobalt deposits were found to be very homogeneous and the layer became thicker with increasing cobalt deposits. The same tendencies for cobalt were also recognized in the case of nickel and Co-Ni alloy.

Figure 4 indicates the amount of precipitated metals of cobalt and nickel which varied with the duration time of electrolysis. The deposition rate in each case decreased as the electrolysis time became longer.

The saturation magnetization moments calculated with the amount of deposited cobalt and nickel increased linearly and showed approximately equal

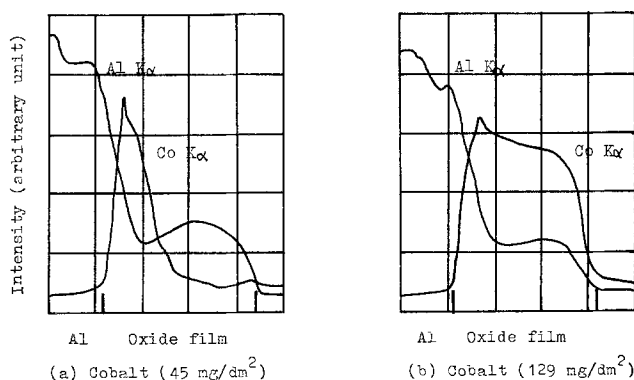


Fig. 2. Line profiles of Co and Al in cross section of oxide films

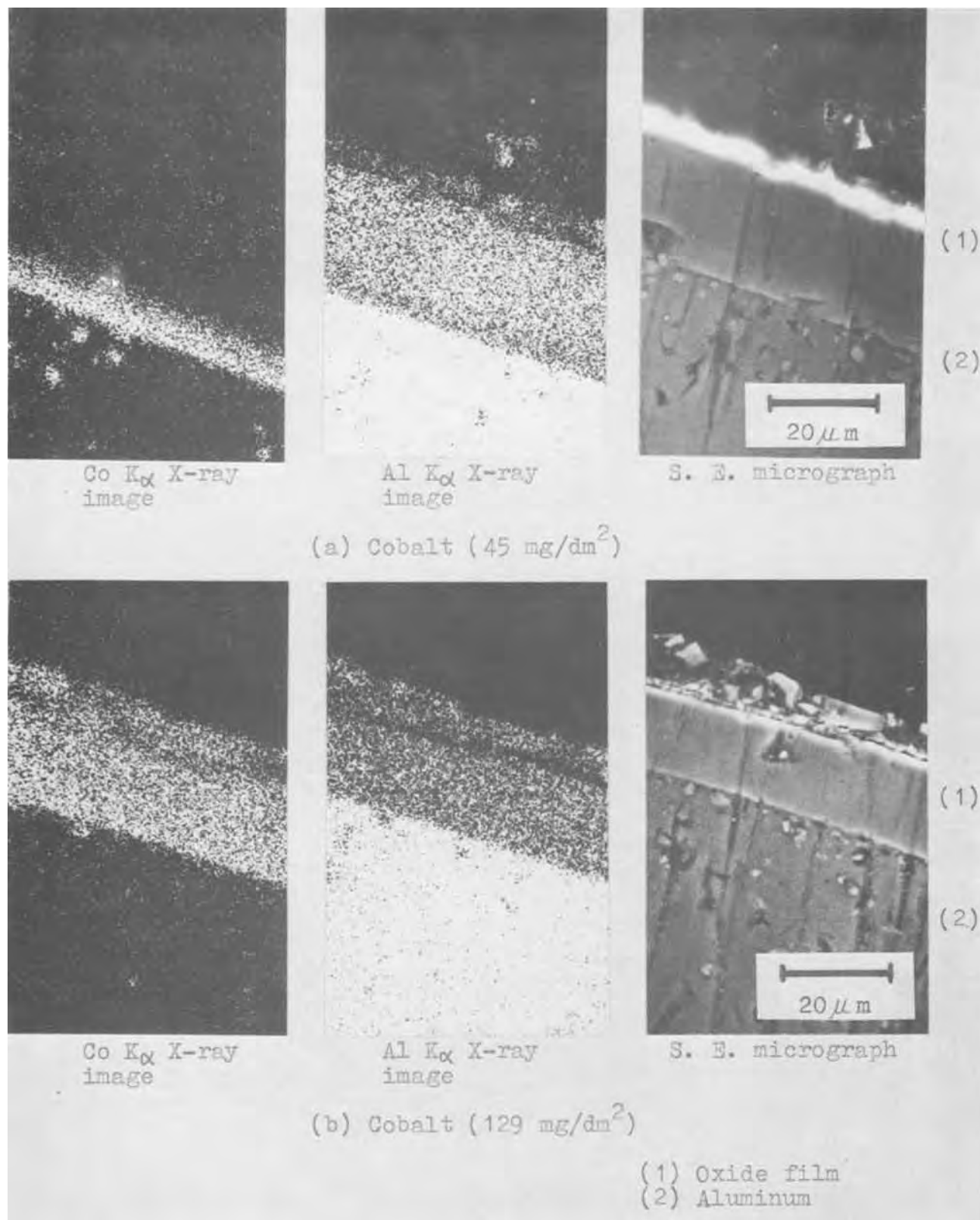


Fig. 3. Scanning electron and x-ray micrograph on the cross section of oxide films

strengths of pure bulk cobalt and nickel (σ_s) as shown in Fig. 5. From the hysteresis loops obtained by the magnetometer, it was found that the density of residual magnetization of films increased by degrees with decreasing film thickness and reached a definite value when the thickness was reduced to about $2 \mu\text{m}$ by polishing as shown in Fig. 6.

No particular changes in the other magnetic properties were observed on the oxide films thinned by mechanical treatments. The coercivities of cobalt and

nickel deposits remained at about 1100 and 750 Oe, and the squareness ratios measured about 70 and 95%, respectively.

Crystal Structures of Deposits

The deposits in the micropores formed fibrous structures about 100\AA in diameter which coincides well with the diameter of micropores anodized in a sulfuric acid bath. Each fibrous deposit consists of fine

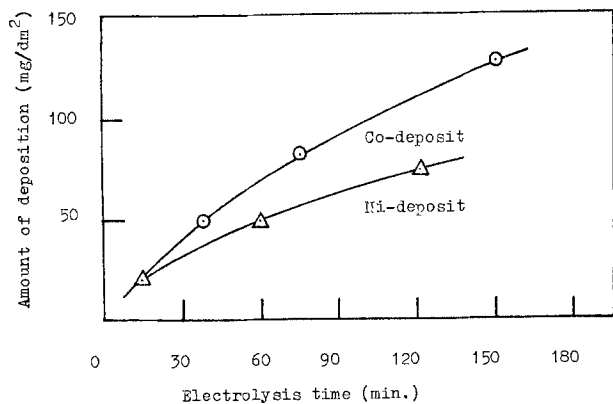


Fig. 4. Relationship between amount of deposits and electrolysis times.

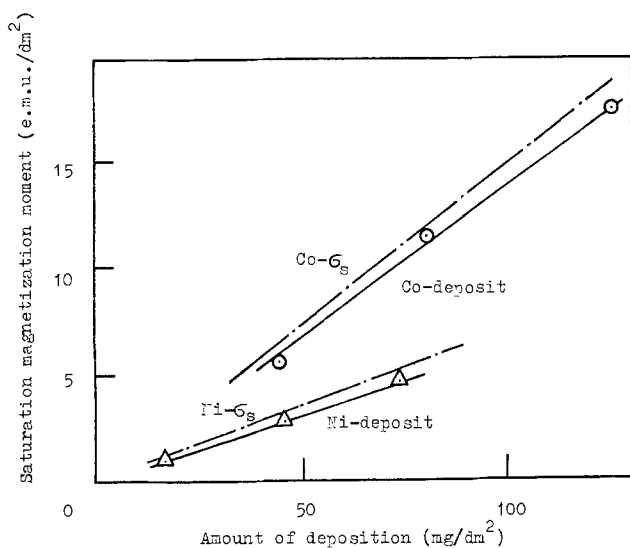


Fig. 5. Relationship between amount of deposits and saturation magnetization moments.

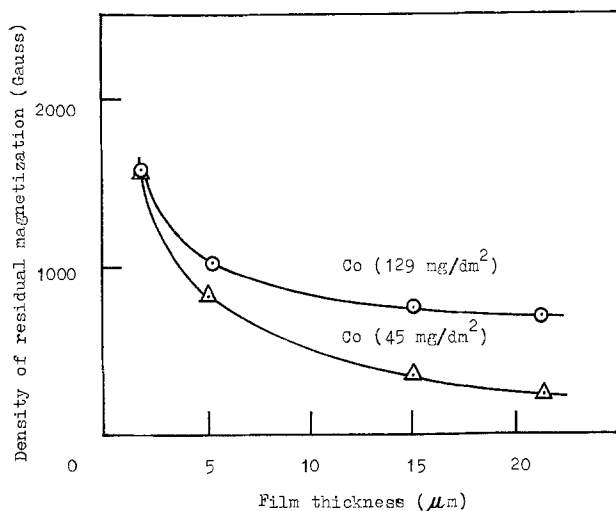


Fig. 6. Relationship between density of residual magnetizations and film thickness.

segmented crystals which are considered to show a spontaneous magnetization.

Although the length of deposits could not be measured exactly, the metals formed in cobalt and nickel

depositions were relatively long fibers, while the Co-Ni alloy deposits were somewhat shorter in length. These deposits may be caused by the crystal orientations in the micropores and form either a columnar or lamellar structure.

The deposits distributed uniformly in the micropores and were arranged regularly at intervals parallel to the surface. And the initial high current density of electrolysis has the effect of a heavy deposition of the metals at the bottom of the micropores, while the subsequent decreasing current density is attributed to decreasing metal deposition along the length of the micropores.

Retentivities of Deposits

When the thickness of oxide films containing cobalt and nickel were scraped from the surface within about 15-2 μm by using the lapping machine, the density of residual magnetizations increased and reached about 1700 and 600G, and the density of saturation remanences attained about 2400 and 630G, respectively.

Then, the saturation magnetization moments of the oxide films electrodeposited with cobalt and nickel are calculated to be about 136 and 54 emu/g. Whereas, in the case of pure bulk metals of cobalt and nickel, the same moments were reported at 161 and 54 emu/g (20°C), respectively (5). These values are almost equal to the former values.

According to Keller *et al.* (6) the pore volume of micropores to the whole film layer anodized in sulfuric acid bath under the same conditions of the present experiments has been revealed as about 10%. As the density of saturation magnetizations can be reckoned to be about 18,000 and 6,000G in each metal by referring to the specific gravity, the strength of remanences of these metals were found to be about 13 and 11% of those values in bulk metals. It may be noted that the micropores of anodic oxide films are fully packed with the metallic deposits by a-c electrolysis.

The thinned oxide films show not only the stronger remanences than the part of outer layers of the oxide films, but also can easily provide the very flat surface by mechanical polishings. It is considered that there are possible applications for magnetic recording disks.

Acknowledgments

The author expresses his sincere thanks to Professor R. Ueda, Waseda University in Tokyo, for his keen interests in the work, and also thanks to Messrs. I. Ishiguro and K. Kasahara of the Pilot Pen Company, Limited, for their help.

Manuscript submitted Dec. 16, 1974; revised manuscript received April 11, 1975.

Any discussion of this paper will appear in a Discussion Section to be published in the June 1976 JOURNAL. All discussions for the June 1976 Discussion Section should be submitted by Feb. 1, 1976.

Publication costs of this article were partially assisted by the Pilot Pen Company, Limited.

REFERENCES

1. S. Kawai and R. Ueda, *This Journal*, **122**, 32 (1975).
2. Edith Lichtenberger-Bajza, Ferenc Dömölki, and Iren Imre-Baán, *Metal Finishing*, **71**, 50 (1973).
3. L. Sandera, *Aluminum*, **49**, 535 (1973).
4. S. Iwasaki: *J. IECE Japan*, **52**, 1241 (1969).
5. R. Bozorth, "Ferro-Magnetism," p. 876, D. Van Nostrand Co., Inc., Princeton, N. J. (1968).
6. F. Keller, M. S. Hunter, and D. L. Robinson, *This Journal*, **100**, 411 (1953).

Kinetics of Decomposition of Silane (Diluted in Argon) in a Low Pressure Glow Discharge

G. Nolet

Laboratoire de Physique et Electronique de l'Etat Solide,
Université Catholique de Louvain, Institut d'Electricité, Bâtiment Maxwell, 1348 Louvain-la-Neuve, Belgium

ABSTRACT

The high temperature electrons in a plasma are able to excite as well as to ionize neutral atoms and molecules. At sufficiently low pressures, the inelastic collisions between electrons and molecules are generally considered to be the most effective mechanism for molecular dissociation in the positive column of a glow discharge. It is therefore expected to obtain, at constant current density, a first-order reaction with respect to the molar fraction of the reagent, if all other reactions are negligible. In the case of silane diluted in argon investigated in this work, the first-order rate equation $\ln X_{\text{SiH}_4} = -kt$ is not observed; in this equation k is the first-order rate constant, t the gas transit time in the discharge, and X_{SiH_4} the mole fraction of silane at time t . The k value increases with time during decomposition. This is attributed to an increase of the electronic temperature of the gaseous mixture during its transformation.

A bibliographical analysis of the achieved researches on electric discharge chemistry shows that very often one is mainly concerned with the aspects of empiricism and reactor stability (1, 2). Some attempts to explain the chemical reaction mechanisms and to establish a general theory were not successful because the investigated systems were too complex. On the other hand, the physical aspects of the electric discharges are not simple and have a large influence on the behavior of the chemical reactions.

Therefore, it is necessary (i) to study the influence of the physical parameters of the electric discharge on the total kinetics of an irreversible gaseous decomposition; (ii) to work at low pressure and low current density in order to dissociate the thermal and electric phenomena; (iii) to use low pressures in order to limit the number of parallel reactions; (iv) to work with the best known discharges, often studied in an inert medium (rare gases); (v) to study the total kinetics of gases with a simple chemical dissociation mechanism (irreversible decomposition, few synthesis products in low concentration, etc. If the kinetics may be overcome under the previous conditions, it will be possible to investigate more complicated systems (with side reactions, opposing reactions, etc.).

The purpose of this work is not to explain the decomposition mechanisms of a gas, but to examine the influences of the physical parameters of the discharge on the kinetics of gaseous decomposition. This paper only presents the experimental results on the silane kinetics.

Choice of the Experimental Conditions

Gases.—Silane, SiH_4 , has a simple structure and irreversibly decomposes to form an amorphous thin film on the walls of the reactor (3); the only gaseous reaction products found in our electric discharges are hydrogen with traces of disilane, Si_2H_6 . Furthermore, silane diluted in an inert gas is widely used in micro-electronic device technology and, more precisely, in its reactive plasma applications (3) for deposition of thin films on silicon substrates. These applications make use of an rf induced discharge, which is quite ideal since it limits the plasma extension to the neighborhood of the substrate and avoids the contamination of the thin films by internal electrodes. Diluted silane was chosen to obtain a small impact of the reaction on the reactant volume. The silane gas is prediluted in argon (10%

SiH_4 -90%Ar; Air Products) and it is always injected at the same concentration in a "plug-flow" tubular reactor which obviously the glow discharge tube is.

Electric discharge.—For microelectronics purposes diluted silane is injected in a rf discharge. However for our study this kind of discharge must be discarded for several reasons: (i) The power transmitted to the gas by the rf generator cannot be estimated with sufficient accuracy (4). (ii) Numerous problems, depending on the high frequency, are related to the measurement of parameters, such as electric field and electronic temperature. (iii) The theoretical value of the electronic temperature is a function of the tube radius, R , the gas nature and its pressure, P (as in the case of a d-c glow discharge), but also of the frequency and the electric field. The calculation of the electronic temperature becomes quite difficult when a gas mixture is present. (iv) It is difficult to obtain a large and homogeneous reaction zone. Furthermore, since rf and d-c discharges have similar properties (5), we decided to use the low pressure ($0.1 < P < 3$ Torr) d-c glow discharge because its physical properties are relatively well known and easily measurable (6).

Apparatus

Since silane and its derivatives decompose very rapidly in the presence of oxygen, a rapid and direct analysis of the gaseous mixture composition must be done (dynamic flow system). Mass spectrometry was chosen as the analytical technique. The measurement of the silane concentration is achieved on the pre-selected mass 30 of the SiH_2^+ ion which is the most characteristic for silane (7, 8). The apparatus is composed of four parts (Fig. 1).

Two low pressure rooms.—In the first one, 1, in Fig. 1, (glass tube of 3m length; internal diameter of the tube 13.4 mm; mean pressure 0.1 Torr) the decomposition of silane by the glow discharge occurs. In the second one, 8, (stainless steel tube; mean pressure 10^{-5} Torr) the gas analysis is achieved by the mass spectrometer, 9.

The differential pressure existing between the discharge tube, 1, and the analysis room, 8, is obtained by means of a diffusion pump, 3, coupled to a rotative pump, 2'. This allows a small fraction of the gas flowing along the discharge tube to be continuously extracted through a microleak, 15. The pressure gauges, 6, 6', and, 6'', are, respectively, of the Pirani, Penning, and McLeod type.

Key words: electric discharge, electronic temperature, plasma chemistry.

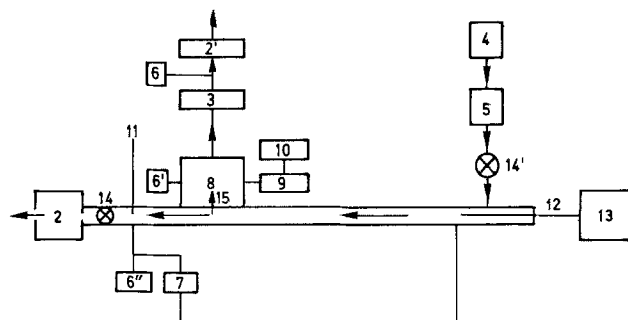


Fig. 1. Schematic diagram of the apparatus. The arrows show the directions of the gas flow. 1, Discharge tube; 2 and 2', primary pumps; 3, diffusion pump; 4, premixed gases; 5, flowmeter; 6, 6', and 6'', pressure gauges; 7, U-tube for $\Delta P/\Delta x$ measure; 8, analysis room; 9, mass spectrometer; 10, control console; 11, fixed cathode; 12, anode; 13, high voltage source; 14 and 14', taps; 15, microleak.

Gas flow system.—Before the injection of the premixed gases, 4, in the discharge tube, 1, the flow rate must be measured at atmospheric pressure, 5. Then the gases cross all the tube, 1, and are extracted by a rotative pump, 2. The taps, 14 and 14', allow the regulation, respectively, of the pressure and of the gas flow rate. The pressure gradient in the discharge tube is measured with a "U" gauge, 7.

Electric system.—A stabilized d-c high voltage source, 13, ($V_{\max} = 10,000\text{V}$; $I_{\max} = 150\text{ mA}$) creates an electric discharge between the grooving anode (high voltage, 12) and the fixed cathode (grounded, 11).

Gas analysis system.—At the exit side of the discharge tube, near the cathode, a VEECO GA 4R gas analyzer, 9 (with a regulation system, 10), is coupled to the gas analysis room, 8.

Experimental Results

The study of the decomposition of light hydrocarbons under electric discharge conditions has shown that the first-order rate law is well obeyed (9); a typical experimental result is shown in Fig. 2. We shall use the same presentation for our results in order to allow a better comparison. Hence, to plot the typical concentration *vs.* time graphs, we must first determine the transit time of the gas in the discharge.

Determination of the gas transit time, *t*.—The gas flow rate in the discharge tube involves the existence

of a pressure gradient all along the tube. Since the tube area is constant and since the transformation of the highly diluted gas only gives a small volume variation, the pressure gradient along the tube must be constant

$$P_x = P_0 + ax \quad a = \Delta P/\Delta x$$

where *a* is the pressure gradient (Torr/cm); P_0 , the pressure (Torr) at the reference point located at the microleak (15 in Fig. 1); P_x , the pressure (Torr) at the anode; and *x*, the tube length between the reference point and the anode (12 in Fig. 1).

The gas flow being laminar, the following gas flow rate relation holds

$$v = dx/dt = 760 D_0 T/S T_0 (P_0 + ax)$$

where D_0 is the NPT flow rate (cm^3/sec); *T*, the gaseous temperature in the plasma ($^{\circ}\text{K}$); T_0 , the reference temperature (298°K); and *S*, the tube area.

The transit time expression may then be written as

$$t = ST_0(P_0 + ax/2) x/760 D_0 T \quad [1]$$

By moving the anode, different *x* values may be obtained. Relation [1] is only valid for inert gases for reactions without volume variation. For highly diluted gases we may, as a first approximation, consider flow variation with *x* (or *t*) as negligible. For all other cases the constant flow rate D_0 must be replaced by a position dependent flow rate D_x .

In practice for the study investigated on 10% SiH_4 in Ar, the simple equation, Eq. [1], may be used. On the other hand, a kinetic study of the silane decomposition can only be done at low current levels ($I < 5\text{ mA}$); this implies a small variation of the gas temperature with respect to the reference temperature, T_0 . In general the correction term T_0/T is greater than 0.95.

Results on the kinetics.—To compare our results on diluted silane (typical examples are given in Fig. 3 and 4) with those of Loix (9) on hydrocarbons (Fig. 2), we have plotted graphs of $\ln X$ *vs.* *t*. Curves for different experimental conditions (the pressure was changed from 0.3 to 2.5 Torr and the current from 0.2 to 6 mA) all have the same shape.

The difference between the kinetics of the decomposition of a pure hydrocarbon and of a diluted silane gas is attributed to a difference in experimental conditions (initial concentration and current density).

For silane the rate constant always increases with time under constant pressure and current conditions.

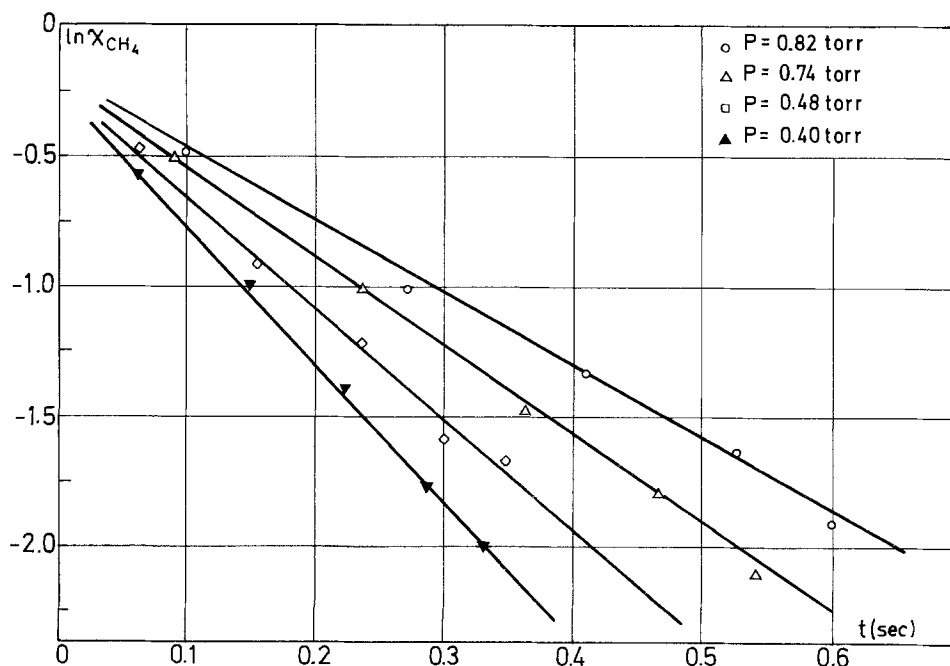


Fig. 2. Kinetics of methane decomposition. Experimental results ($I = 50\text{ mA}$).

Table I. Determination of the experimental rate constants k_0 and k_t in function of discharge current and pressure

P (Torr)	I (mA)								
	0.20	0.50	0.75	1.0	1.5	2.0	3.0	4.0	6.0
Rate constant k_0 (sec ⁻¹)									
0.30	0.77	2.3	4.5	5.4	8.2	14.1	19.6	33.1	
0.60		1.7	3.0	4.6					
0.75	0.70	1.5	2.1	3.4	5.1	7.6	10.6		
1.0	0.87	1.9	2.9	4.4	6.1	9.5	14.5		
1.5	0.80	1.9	2.7	3.8	5.5	7.9			
2.5	0.22	0.70	2.3	(4)	(6.4)				
Rate constant k_t (sec ⁻²)									
0.30			10.9	16.0	21.8	29.8	41.0	63.2	
0.60		7.0	9.2	13.0					
0.75			7.6	11.8	15.8	20.1	28.3		
1.0		4.8	7.1	10.3	15.0	21.0	26.6		
1.5		5.3	7.2	10.7	13.4	17.0			
2.5					12.7				

Table I presents, for each kinetic curve, the values of the following rate constants: k_0 (rate constant for $t = 0$, or $X^{\circ}_{\text{SiH}_4} = 0.1$) and k_t (rate constant for a large t , or $X_{\text{SiH}_4} < 0.01$). The values were obtained from the slope of the curves at the two points under consideration; the accuracy is relatively poor (10-20% error).

For all cases, the rate constant for a nearly complete silane transformation is greater than two times the initial rate constant at $t = 0$; such a variation may not be attributed to the experimental errors.

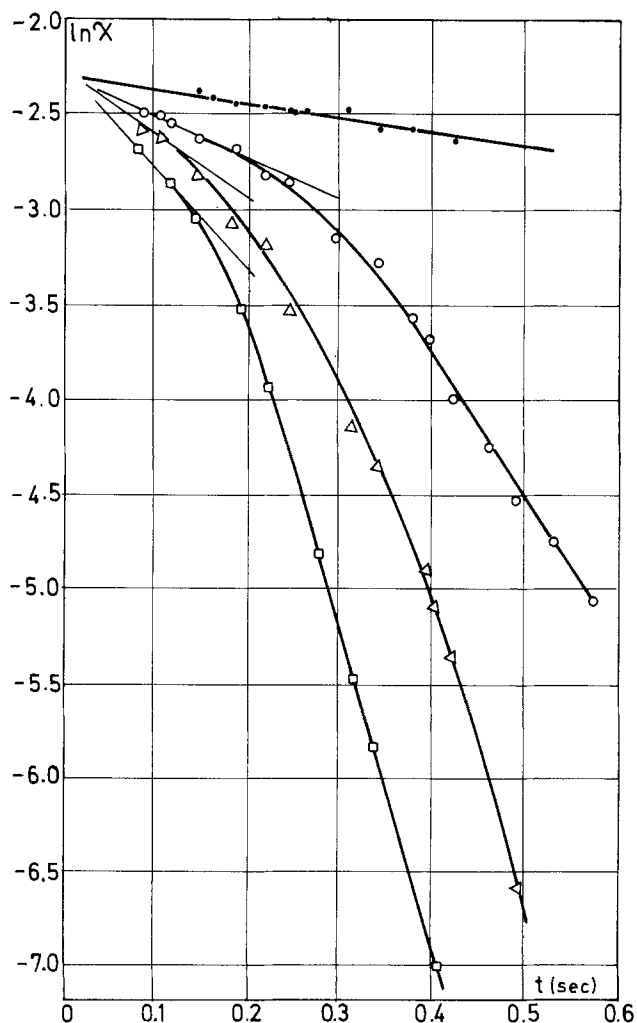


Fig. 3. Kinetics of silane decomposition. Experimental results ($p = 0.75$ Torr); ●, $I = 0.5$ mA; ○, $I = 1.0$ mA; △, $I = 1.5$ mA; □, $I = 2.0$ mA.

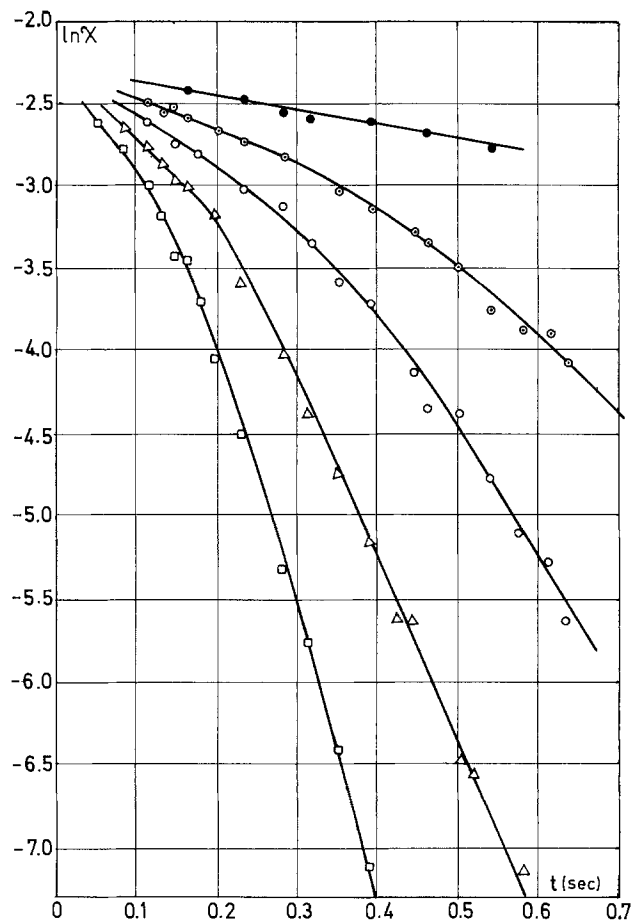


Fig. 4. Kinetics of silane decomposition. Experimental results ($P = 1.0$ Torr). ●, $I = 0.5$ mA; ○, $I = 0.75$ mA; ○, $I = 1.0$ mA; △, $I = 1.5$ mA; □, $I = 2.0$ mA.

Before examining these results, a theoretical approach of the phenomena must be pursued.

Theoretical Considerations

Hypothesis.—It is accepted that the electron molecule collisions form the initial step of the chemical transformation in the positive column of the low pressure glow discharge. A modification of the discharge parameters and particularly of the electron energy may then explain the particular shape of the experimental curves $\ln X_{\text{SiH}_4}$ as a function of t ; the electron energy (or electronic temperature) would increase during the silane transformation.

Indeed, at low pressure ($P \approx 0.1$ Torr), the electronic temperature T_e is much larger than the gas temperature T_g ($T_e > 15,000^\circ\text{K}$; $T_g < 350^\circ\text{K}$) whereas both temperatures are approximately equal ($T_e \approx T_g \approx 4000^\circ\text{K}$) at high pressure ($P > 10^2$ Torr). The gas temperature is quite insensitive to a variation of the gas mixture composition; furthermore, since low current densities are used, the gas temperature will remain near the reference temperature.

On the other hand it is known that the electronic temperature, T_e , is a function of the gas under consideration, of its ionization potential, V_i , and the pressure, P , in the tube of radius, R . The theoretical expression of the electronic temperature, in the case of a pure and inert gas, has been derived by Von Engel, following the extension of Schottky's diffusion theory (10)

$$(eV_i/kT_e)^{-1/2} \cdot \exp(+eV_i/kT_e) = 1.17 \times 10^7 c_i^2 P^2 R^2 \quad [2]$$

c_i being a constant for the gas i . One can find in the literature numerous examples of the sensitivity of the electronic temperature on the gas type used in the discharge (6, 11, 12). Figure 5 shows that pure inert gases

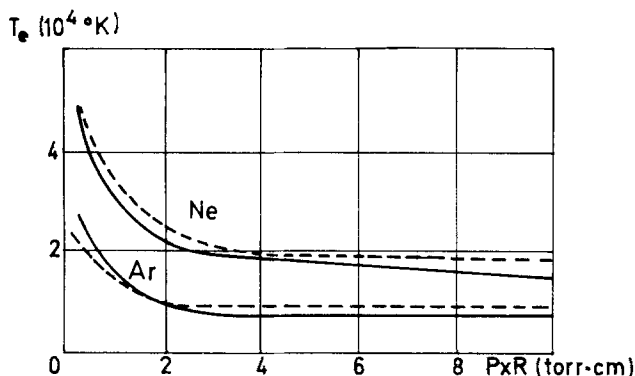


Fig. 5. Dependence of electronic temperature on PR . —, Measured; ---, calculated (13).

have a distinct electronic temperature for identical experimental conditions (13).

The total kinetics may however be affected by other possible reactions occurring in the plasma: electron-ion, radical-molecule, ion-molecule, radical-radical reactions; the wall effect on these reactions is not negligible (14).

For relatively high pressures ($P > 10$ Torr), the total kinetics of an irreversible gaseous decomposition necessarily implies the intervention of phenomena which may be neglected in the low pressure glow discharge: (i) trimolecular collisions; (ii) excitation of rare gas atoms on metastable levels; (iii) electron-molecule association [considered in the case of the CO_2 laser (15)]; and (iv) modification of the electron energy distribution function when the electron energy is used to excite levels of the vibration spectrum rather than of the electronic spectrum (16) (most frequent case when $P > 10$ Torr).

These miscellaneous effects are considered as negligible when a low pressure exists, because the electron energy is almost used for electronic excitation of the molecules which then dissociate into atoms and (or) radicals (16, 17). The electron-molecule collisions imply the intervention of the electron energy in the efficiency of the molecular dissociation; this fact can explain the evolution of the rate constants.

Kinetics of diluted silane.—Indeed, admitting that the reaction initiating step is due to the inelastic electron-molecule collision, one concludes that the electron must at last possess the necessary energy to excite the molecule on its first electronic level; one has to know the pattern of the electron energy distribution function. Among the two types of distribution generally used in the electric discharge field, the Maxwell-Boltzmann and the Druyvenstein-Penning functions, the Maxwell function must be used when the electrons transmit their energy essentially by inelastic collisions (16, 17).

The frequency of efficient collisions between silane molecules and electrons is given by

$$-dn_{\text{SiH}_4}/dt = \bar{\sigma}_e \bar{v}_e n_e^* n_{\text{SiH}_4} \quad [3]$$

where n_{SiH_4} and n_e^* are, respectively, the silane and efficient electron concentration; \bar{v}_e , the mean electron speed (cm/sec); and $\bar{\sigma}_e$, the mean collision cross section.

A more practical form is obtained when using the molar fraction of silane, X_{SiH_4}

$$-dX_{\text{SiH}_4}/dt = \bar{\sigma}_e \bar{v}_e n_e X_{\text{SiH}_4} \quad [4]$$

If the Maxwell-Boltzmann function is used, one obtains

$$dX_{\text{SiH}_4}/dt = \bar{\sigma}_e \bar{v}_e n_e X_{\text{SiH}_4} \exp(-eV_s/RT_e) \quad [5]$$

where V_s is the excitation potential of the silane molecule on its first electronic level. The current density

is $J = n_e e v_d$ and the electron drift velocity, v_d , is proportional to the electron thermal velocity, v_e (18)

$$-dX_{\text{SiH}_4}/dt = \alpha \bar{\sigma}_e J X_{\text{SiH}_4} \exp(-eV_s/RT_e) \quad [6]$$

where α is a constant; the rate constant k takes the form

$$k = \alpha \bar{\sigma}_e J \exp(-eV_s/RT_e) \quad [7]$$

The preexponential term $A = \alpha \bar{\sigma}_e J$ is independent of the pressure, P , and of the electronic temperature, T_e , for the usual conditions existing in the positive column. On the other hand, the exponential term only depends on the electronic temperature, which is function of the pressure, P , of the gas, the tube radius, R , the current density, J , and the composition of the gaseous mixture.

Some Qualitative Verifications of the Theory

Constant pressure and current.—The particular shape of the curves of Fig. 3 and 4 may be attributed to the change of the discharge parameters when the gas mixture composition is modified during the decomposition of silane. We consider the shape of the kinetic curves as essentially determined by a modification of the electronic temperature as a function of the gaseous composition. Indeed, at the start ($t = 0$) one has an argon-silane mixture, but when t becomes large the argon-silane-hydrogen mixture tends more and more to the pure argon-hydrogen mixture.

If T_{e0} and T_{et} are the electronic temperatures of the Ar-SiH₄ and Ar-H₂ mixtures, respectively, Eq. [7] may be written as

$$k_0 = A \exp(-eV_s/RT_{e0}) \quad [7']$$

$$k_t = A \exp(-eV_s/RT_{et}) \quad [7'']$$

where k_0 and k_t are the rate constants for the extreme compositions of the gaseous mixture (Table I).

Figures 3 and 4 are related to a first-order reaction, if $T_{et} > T_{e0}$. Further research is necessary to confirm this condition, both theoretically and experimentally.

Constant current.—Following Von Engel's law (Eq. [2]), any pressure increase reduces the electronic temperature (Fig. 6). If only the pressure is changed, the resulting change in electronic temperature will strongly affect the k_0 and k_t values, as seen in Eq. [7'] and [7'']. This is effectively observed in our experiments (Fig. 7).

Constant pressure.—For our experiments at constant pressure, the kinetics are almost entirely determined by the current effect. Figure 8 shows some results, in agreement with Eq. [7]. If the electronic temperature, T_e , remains constant, one should expect a linear relationship between k_t (or k_0) vs. J . Hence the observed deviation from linearity must be attributed to the variation of T_e with current. As the observed deviation is not too strong, a weak variation of T_e vs. J is suspected.

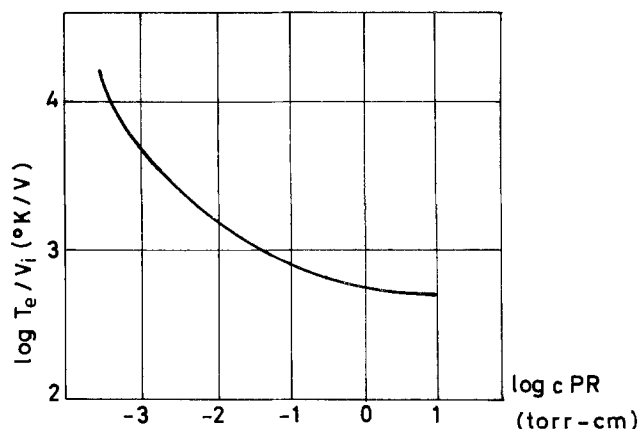


Fig. 6. T_e/V_i as function of cPR , plotted from Eq. [3]

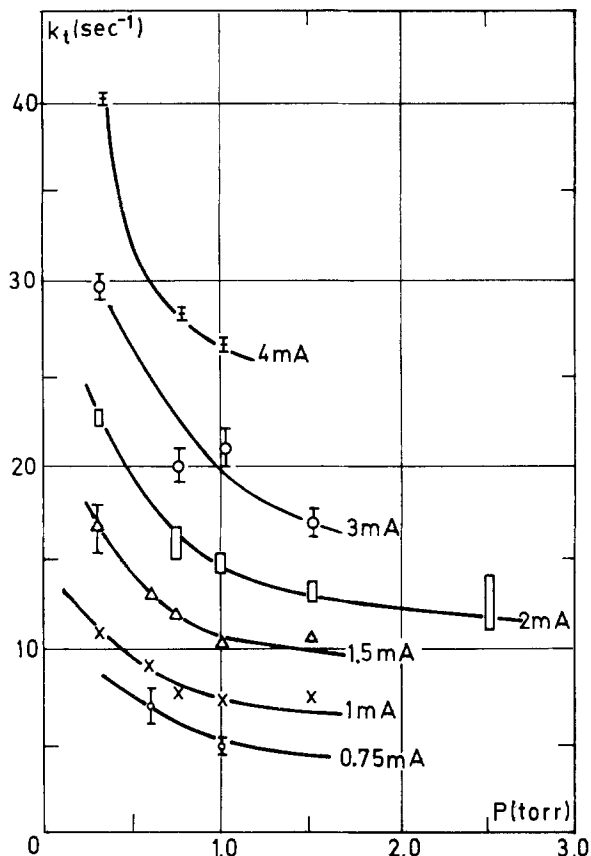


Fig. 7. Effect of the pressure of the k_t rate constants

The last fact remains to be confirmed by further experiments on the electronic temperature.

Conclusions

The shape of the kinetic curves for silane diluted in argon is related to a simple first-order rate equation, if a variation of the electronic temperature during the decomposition of silane is accepted. Experimental evidence of the validity of the rate equation is found by varying pressure and current parameters.

Manuscript submitted Sept. 9, 1974; revised manuscript received March 21, 1975.

Any discussion of this paper will appear in a Discussion Section to be published in the June 1976 JOURNAL. All discussions for the June 1976 Discussion Section should be submitted by Feb. 1, 1976.

Publication costs of this article were partially assisted by the Université Catholique de Louvain.

REFERENCES

1. M. Venugopalan, Editor, "Reactions Under Plasma Conditions," Vol II, John Wiley & Sons, Inc.,

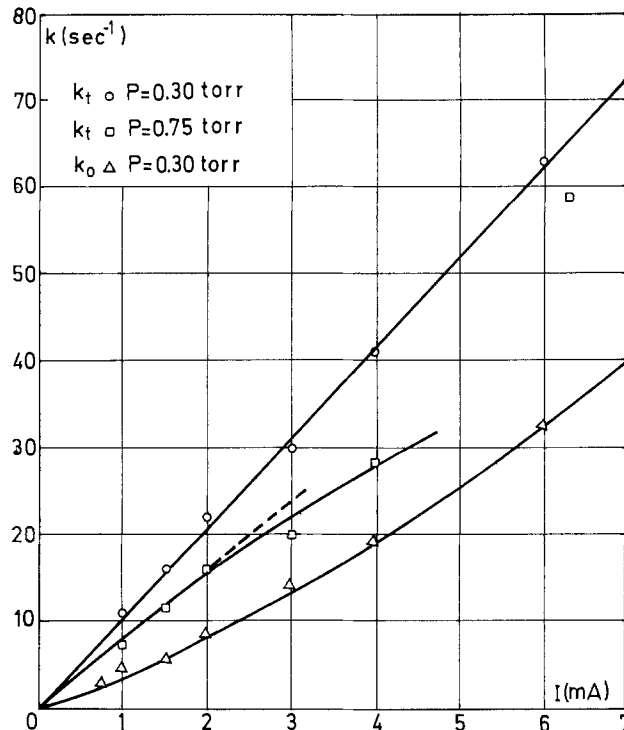


Fig. 8. Effect of current on rate constants. Experimental results

- New York (1971).
2. *Adv. Chem. Ser.*, **80**, (1969).
 3. H. F. Sterling and R. C. G. Swann, *Solid State Electron.*, **8**, 653 (1965).
 4. A. P. Bois d'Enghien, J. Vrebosch, and A. Van Tiggelen, *Bull. Soc. Chim. France*, 2315 (1968).
 5. R. G. Fowler, "Handbuch der Physik," Vol. XXII, p. 117, Springer Verlag, Berlin (1956).
 6. F. Francis, "Handbuch der Physik," Vol. XXII, p. 117, Springer Verlag, Berlin (1956).
 7. J. D. Pupezin and K. F. Zmbov, *Bull. Inst. Nucl. Sci.*, "Boris Kidrich" (Belgrade), **8**, 89 (1958).
 8. H. P. Agafonov, *Tr. Khim. Khim. Teknol.*, **4**, 227 (1961).
 9. R. Loix, Thesis K. U. Leuven (1969).
 10. A. Von Engel, "Elektrische Gasentladungen," Vol. II, p. 83, Springer Verlag, Berlin (1934).
 11. Badareu-Popescu, "Gaz ionisés," Dunod (1965).
 12. J. D. Cobine, "Gaseous Conductors," Dover Publications Inc., New York (1958).
 13. B. Klafeld, *J. Techn. Phys. USSR*, **5**, 725 (1938).
 14. F. Kaufmann, *Adv. Chem. Ser.*, **80**, 29 (1969).
 15. C. R. Claydon and G. A. Segal, *J. Chem. Phys.*, **52**, 3387 (1970).
 16. W. L. Nighan, *Phys. Rev.*, **2A**, 1989 (1970).
 17. M. J. Druyvenstein and F. M. Penning, *Rev. Mod. Phys.*, **12**, 87 (1940).
 18. R. Papoular, "Phénomènes Electriques dan les gaz," Dunod (1962).

A Novel Electrochemical Cell Employing a Rotating Bipolar Electrode

P. R. Nadebaum and T. Z. Fahidy

Department of Chemical Engineering, University of Waterloo, Waterloo, Ontario, Canada N2L 3G1

ABSTRACT

An overview of a recent study of a rotating bipolar cylindrical electrode (RBE) cell is presented. The central rotating electrode in this cell is surrounded by axially located wiper blades which form 2 (bipolar) or 3 (tripolar) compartments. An outer electrode governs in each compartment the central electrode potential, and conditions similar to potential and current pulsing can be obtained. The rotating electrode surface can be maintained in the state of continuous activation and the cell is well suited for refining, concentrating, and removal of impurities from electrolyte solutions.

It is well known (1-20) that the rate of oxidation of many fuels [e.g., H_2 , C_2H_4 , CH_3OH , $HCOOH$, and $(COOH)_2$] at a Pt electrode decreases with time and can be increased momentarily by a current or potential pulse. This increase in the rate of reaction can be caused by various factors, such as removal of adsorbed impurities and of partially oxidized substances from the electrode surface and removal of surface oxide layers. Many other electrode reactions can be significantly affected by voltage and current pulsing. It has been reported, for example, that pulsing can be used to control the product spectrum of electrolysis (21-29), to prevent passivation and improve the quality of deposits in the electrodeposition of metals and alloys (30-35), to avoid fouling of electrodes by alkaline earth salts during the electrochemical sterilization of sewage (36-39), and to prevent passivation during the electrochemical production of acrolein (40).

While the results of these studies have been interesting, there has been little or no commercial application of current and voltage pulsing because of the practical difficulty of controlling and varying the large amounts of current (>1000A) required by an industrial scale process.

An alternative approach to pulsing is to vary the electrode potential by mechanically moving the electrode through different potential regions, rather than by directly varying the applied potential (41). In this manner steady currents and potentials can be employed while still achieving the effects of potential or current pulsing.

One relatively simple way in which this can be done is to use a "rotating bipolar electrode" as shown in Fig. 1. The cell in its simplest form involves three main electrodes: a central rotating bipolar electrode and two counterelectrodes separated by an insulating barrier. As the center electrode rotates, its surface passes through a potential region determined first by V_{S1} and then by V_{S2} . Depending on the relative potentials of V_{S1} , V_{S2} , and V_M , the center electrode can first form either an anode or cathode in one compartment, and then either an anode or cathode in the other compartment. In this way an effect similar to "continuous" voltage or current pulsing is achieved. This method of performing the pulsing has an additional advantage, namely, that the products of the reaction can be separated from the products of the pulse treatment, thus avoiding some of the problems involved with the recombination of the products.

There have been many types of electrolytic reactors described in the literature which employ either stationary bipolar electrodes, rotating monopolar electrodes, or some sort of a "wiper" arrangement; however, a search of the literature (summarized in Table

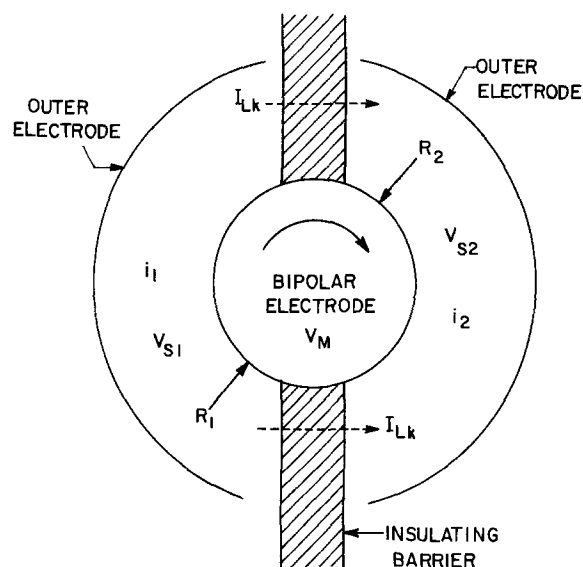


Fig. 1. Diagram of the rotating bipolar electrode cell. i represents the compartment current density; I_{LK} represents the leakage current between the compartments; R represents the reference electrodes, which sense the solution potential V_S near the center electrode; V_M represents the center electrode potential; E , the bipolar electrode, assumes a potential $E_1 = (V_M - V_{S1})$ and $E_2 = (V_M - V_{S2})$ in each compartment.

I) indicates only one cell employing the rotating bipolar electrode principle. This cell, recently designed

Table I. Survey of electrochemical cells incorporating either bipolar, rotating, or "wiped" electrodes*

Classification	Type	References
Bipolar (stationary)	Particulate	(43-44)
	Porous/powder	(45-47)
	Bipolar amalgam	(48-51)
	Cylindrical (fixed concentric)	(52-54)
	Fixed plate, alkali salts	(55-66)
	Fixed plate, miscellaneous	(67-78)
	Undetermined	(79-81)
Rotating (monopolar)	Fuel cell	(82-86)
	Hg cathode	(87-89)
	Alkali salts	(90-93)
	Disk	(94-96)
	Miscellaneous	(97-99)
	Strip steel plating	(100)
Wiped (monopolar)	Rotating, cylindrical	(101)
	Rotating wipers, cylindrical	(102)
	Rotating wipers, plate	(103-105)
	Abraded, rotating cylindrical	(106)
	Axially moving wipers, cylindrical	(107)
Rotating bipolar	Dual, cylindrical rotating bipolar electrode	(42)

* Key words: continuous activation, voltage pulsing, cost, mass transfer, refining.

* Also note recent reviews (108-111) of new types of electrochemical cells.

by Benner (42), consists of two side-by-side cylindrical rotating electrodes, and was created for the purpose of removing ions from solution. No further details are available to the authors at this time. There appears to be no mention in the literature of the use of a rotating bipolar electrode cell to achieve the conditions of voltage or current pulsing, other than a publication arising from some of the preliminary experimental results obtained in this work (41).

In this paper we summarize the operation and performance of two rotating bipolar electrode (denoted as RBE) cells, and provide an overview of recent work (112) carried out with these cells. For the purposes of discussion, we have selected only the most important experimental results; other results and a more detailed discussion can be found elsewhere (112) and will be available in further papers providing details on specific areas of the study.

Design and Construction of the Laboratory RBE Cells

Two RBE cells were constructed during the course of this work. The first cell to be constructed had two compartments (a "bipolar" cell), while the second cell, of considerably more sophisticated design, had three compartments (a "tripolar" cell).

In order to provide for rigorous cleaning of the cell and to avoid contamination of the electrolyte by traces of impurities, the cell bodies and fixtures were constructed entirely out of glass and Teflon. The electrodes were platinum (99.9%, Engelhard). While the use of Pt was desired by the reaction systems to be studied, it had the added advantage of being resistant to the corrosive effects of potential cycling. Because of the great cost of Pt, however, it was necessary to minimize the amount used and this considerably complicated the design of the rotating electrode. In its simplest form this electrode could merely be a solid, cylindrical rod.

The outer electrodes surrounding the center electrode were symmetric, forming compartments of equal size, and the interelectrode spacing was quite generous to permit insertion of reference electrodes and to allow inspection of the electrolyte flow patterns.

Bipolar and tripolar cells.—The principle and details of construction of the simple bipolar cells are shown in Fig. 1. The cell consisted of a glass outer body sandwiched between two Teflon plates. It was found that although the wiper blade design efficiently removed the electrolyte boundary layer at the electrode surface, considerable difficulty was experienced in obtaining a low level of current leakage between the compartments. For this reason the simple cell was not used extensively in actual bipolar operation. It was found to be suitable, however, to determine the mass transfer characteristics of such cells, a situation where current leakage is not important.

The principle of the more sophisticated tripolar cell is shown in Fig. 2 and 3. The cell body consisted of a Teflon cylinder supported by a steel sheath, properly sealed between the cylinder and the Teflon base plate and provided with inlet and outlet tubes. The central rotating electrode was a relatively large platinum cylinder fabricated from a 0.05 cm thick uniform Pt foil and was supported on a solid Teflon cylinder. The dimensions of the assembled electrode were: 12.50 cm in length, 3.176 ± 0.0075 cm in diameter, and 145.8 cm² in area. The estimated resistance of the electrode to the current flow was about 37 μ ohms. In order to avoid wear at the bottom Teflon-Teflon bearing surfaces, the electrode was located and supported by a top bearing so that a clearance of about 0.01 cm was maintained. Gas (O₂, N₂, or Ar as desired) was passed through the bottom bearing, thus obviating a continuous electrolyte film under the electrode and reducing current leakage. The design of the insulating barriers or wiper blades was critical, and their construction represents a compromise between flexibility (i.e., uniform wiping action) and a minimum current leakage.

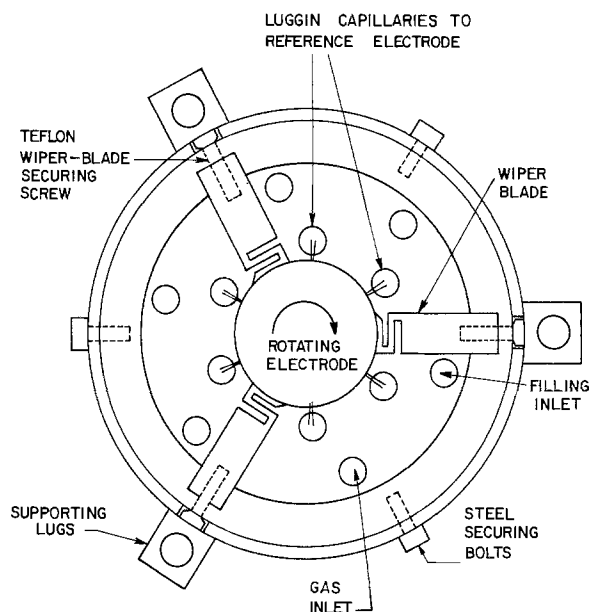


Fig. 2. Rotating tripolar electrode cell; top, inside view

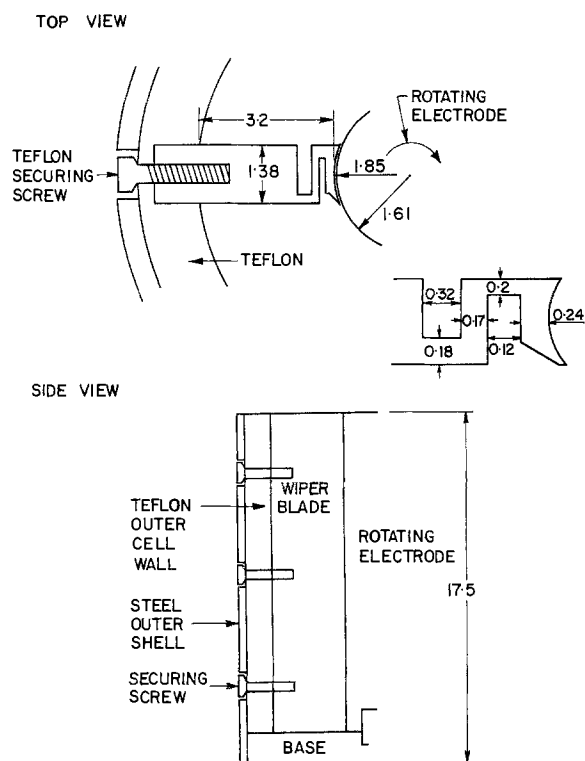


Fig. 3. Rotating tripolar electrode cell: wiper blade design (all dimensions in cm).

Amongst many configurations considered, the design shown in Fig. 3 was found the most satisfactory. Several points may be noted. The wiper blades are relatively thick in cross section, and the bearing surfaces are machined to a slightly smaller radius than the rotating cylinder, thus providing a good wiping action. The leading edge of each wiper blade is quite sharp and the electrolyte as it is removed from the electrode surface tends to further press the wiper blade onto the surface and improve the sealing action. The seal between the wiper blades and the outer cell body was simply achieved by machining a slot in the outer wall and pressing the wiper blades into it. The wiper blades were, in addition, secured by Teflon screws passing through the outer wall of the cell. The seal between the wiper blades and the cell bottom plate was achieved by pulling the blades hard down onto the bot-

tom plate by a Teflon screw inserted through the bottom plate into each wiper blade. The most significant feature is the slots machined into the wiper blade near the curved sealing surface. This arrangement is simple, easily constructed, and accurate machining is not necessary. Furthermore, considerable misalignment of the wiper blades could easily be accommodated without sacrificing the efficiency of the wiping action. The pressure exerted by the wiper blades on the central cylinder could easily be controlled by varying the dimensions of the slots. This design affords a relatively flexible sealing surface which can closely adapt itself to the contours of the electrode surface, even at quite high electrode rotation rates. Under these circumstances, an average gap size of less than 0.0015 cm was maintained; for an electrolyte of specific conductance of 0.01 Scm^{-1} , the minimum gap resistance was about 8000 ohms. For potential drops of 1V or less the magnitude of leakage current density was $1 \mu\text{A}/\text{cm}^2$ (based on the true surface area in the working compartment). The wear of the sealing surface was found to be negligible.

The temperature of the electrolyte was regulated by glass cooling coils which passed cold water through the top cell cover and dipped into the electrolyte in each compartment. Cooling was found to be adequate even at high power densities (50W/compartment), and the cell temperature was maintained without difficulty at $297^\circ \pm 1^\circ\text{K}$.

Gas was bubbled through the electrolyte via gas inlet tubes in each compartment. The inlet tubes consisted of a standard ground glass joint containing a fine porous frit fused into the end of the joint. This permitted a fine dispersion of the gas into the electrolyte. The three gas inlet tubes were fed via a single gas line, and the flow rate into each compartment was not individually adjusted. The gas flow rate was measured by the pressure drop across a small orifice plate.

Filling and emptying each compartment was accomplished via tubes let into the base of the cell, which were then connected via a stopcock to large funnels, or drain pipes.

Two Luggin capillaries were used in each compartment, and these were both connected to a single reference electrode chamber; in this manner an average solution potential was obtained. The location of the Luggin capillaries is shown in Fig. 2. The clearance between the capillaries and the rotating electrode was about 1 mm in order to eliminate the possibility of scratching the electrode surface should the electrode position vary slightly. The reference electrode chamber for each compartment was isolated from the cell electrolyte by a large diameter ground glass stopcock; the electrolyte film around the stopcock, while in the closed position, was of sufficiently low resistance for accurate potential measurement. This arrangement minimized the possible contamination of the electrolyte by the reference electrode solution.

In acid electrolyte reference electrodes of the type (Pt)Hg,HgSO₄/H₂SO₄ (1.0 mol/dm³) were used, and in alkaline solution a saturated calomel reference electrode was used. The reference potential was corrected for liquid junction potentials by measuring the potential of the reference electrode with respect to the potential of a reversible hydrogen electrode in the same solution. Potentials are reported with respect to RHE. At higher current densities correction for errors arising from the ohmic drop in the electrolyte was accomplished by the voltage interrupt methods (113-116). Current densities are reported with respect to the true surface area exposed in each compartment. The cell was cleaned by alternatively rinsing and allowing to stand with alcoholic KOH, dilute HNO₃, deionized water (approximately 10^{-6} - 10^{-7} S/cm specific conductance), and the desired electrolyte (prepared with reagent grade chemicals and 10^{-7} S/cm conductivity water).

While in some applications one power supply would be used (i.e., the central electrode would be floating with respect to the other electrodes), in this study a separate power supply was used for each compartment and conventional circuits employing operational amplifiers were used to control large power supplies [for a list of specific instruments employed for generating potential step and triangular waveforms, recording and stabilizing devices, etc., consult Ref. (112)]. The rise times of these potentiostats were in the range of 10^{-5} - 10^{-4} sec.

Rate of Mass Transfer at a Rotating Cylindrical Electrode with Wiper Blades

While the primary purpose of the wiper blades is to insulate one cell compartment from another, they also serve to significantly increase the rate of mass transfer to the electrode surface. Spencer *et al.* (101), for example, have used wiper blades to remove the diffusion layer on a rotating cylindrical electrode. They report large increases in the current efficiency of producing sodium dithionite from sodium bisulfite [c.f. (117)].

At the present time there seems to be no available theory which can predict the mass transfer rates expected at a rotating wiped electrode, although the case of concentric rotating cylinders without wiper blades has been treated in some detail (118-121). There is apparently no quantitative indication in the literature concerning the enhancement of mass transfer via wiper blades.

The mass transfer effects were studied in two cases: (a) the reduction of ferricyanide ions and (b) the reduction of oxygen, employing the rotating electrode as cathode. In the former reaction, the net change in composition is zero (the anode reaction is exactly the opposite of the cathode reaction) and at the low pH employed the chemical decomposition of the ferricyanide ions, whose concentration was determined by iodometric titration, is negligible. In the reduction of oxygen experiments, oxygen was bubbled rapidly through the cell before each measurement while the electrode potential was kept at 1.2V under no current load. Thus, the electrolyte was saturated with O₂ and the electrode was covered with oxide, thereby minimizing the side reaction producing H₂O₂. After these preliminaries, the electrode potential was quickly set to the value of interest and the measurements of current were begun. At each rotation rate typical polarization curves were obtained and the limiting current flows were determined. The results are summarized in Fig. 4 where the solid lines denote theoretical relationships between the limiting current density and electrode rotation rates, computed from the dimensionless relationship

$$\text{Nu}_R = \frac{2}{\pi} (1 - C) \sqrt{\frac{w}{1 - wd/2\pi R} \text{Re}_R \text{Sc}} \quad [1]$$

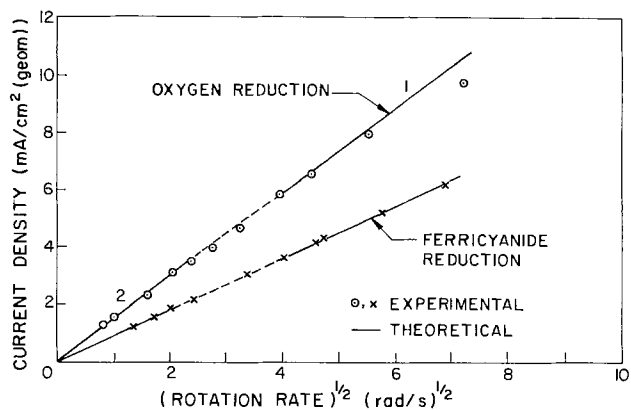


Fig. 4. Comparison of theory and experimental results in the mass transfer study.

Here, w and d represent the number and thickness of the wiper blades, respectively, R is the radius of the rotating electrode, and Re_R , Nu_R , and Sc are the Reynolds, Nusselt, and Schmidt numbers defined as follows

$$\begin{aligned} Re_R &= 2\Omega R^2/\nu \\ Nu_R &= 2\bar{i}_L R/(zFDc_b) \\ Sc &= \nu/D \end{aligned}$$

As usual, ν is the kinematic viscosity of the solution, D is the diffusion coefficient, c_b is the bulk activity of the reacting species, Ω is the angular rotation rate (rad/sec) of the electrode, z is the number of electrons transferred in the electrode reaction, and \bar{i}_L is the average limiting current density over the electrode surface. The term C represents a correction for the effects of convection arising from the rotation of the electrode. In general, this term is small for large Sc (less than 5% for Sc greater than 200) and acts to decrease the rate of mass transfer. This decrease occurs because convection arising through electrode rotation tends to transport fluid of lower concentration into regions of higher concentration near the electrode surface (112). The ranges of pertinent parameters are as follows: $392 \leq Sc \leq 1237$; $0.6 \leq \Omega$, rad/sec ≤ 52 ; $824 \leq Re_R \leq 71,300$; $0.181 \leq k_L \cdot 10^4$, cm/sec ≤ 145 ; $2.9 \leq Nu_R \leq 6850$ (k_L denotes the mass transfer coefficient). The results indicate that flow is essentially laminar at this set of experimental conditions, although the presence of relatively slow Taylor vortices was experimentally observed. This aspect and details of the rather involved mathematical analysis, including expressions for local mass transfer rates at the electrode surface, are presented elsewhere (122). As shown in Fig. 4, the rather good agreement between theory and experimental findings renders Eq. [1] a reliable design equation for a rotating cylindrical wiped electrode system, if the following conditions are met: the temperature, pressure, and density of the fluid are constant; there is no chemical reaction; there is a relatively high concentration of supporting electrolyte; the Sc number is high (> 200); there is no axial electrolyte flow; bubble formation (gas evolution) at the electrode surface is negligible; the rate of reaction is determined solely by the rate at which the reactants are transported to the electrode surface; and removal of the diffusion layer by the wiper blades is complete.

"Continuous" Activation via Impurity Stripping

It is well known that many reactions occurring at platinum electrodes are susceptible to poisoning by traces of impurities and that often this poisoning effect can be overcome (*i.e.*, the electrode surface can be "activated") by potential cycling or by an appropriate prepolarization treatment (11, 123-143). One such electrode reaction, occurring at Pt electrodes, which is particularly susceptible to poisoning is the reduction of oxygen (144-147). Impurities known to inhibit the rate of this reaction include, for example: various cations [*e.g.*, Ag^+ , Cd^{2+} , Tl^+ , Ba^{2+} , Sr^{2+} , Ca^{2+} (148-151)], anions [*e.g.*, halide and sulfate ions (11, 133, 146, 150, 152-156)], and organic impurities (146, 157, 158). Tindall, Cadle, and Bruckenstein (151) have shown that in the presence of Cu^{++} ions, inhibition occurs through the deposition of submonolayer Cu films. These films are deposited at very low Cu^{++} concentrations (< 1 ppm) and at "underpotentials," *i.e.*, at potentials more anodic than the reversible potential, in the potential range $E_{rev} < E < 0.8V$ (159, 160). This apparent violation of thermodynamics has been clarified by demonstrating (161) that if copper atoms absorbed on an inert surface are more stable than those in the copper lattice, such depositions are feasible from energy considerations.

The experiments were carried out in the tripolar cell, operated in a fashion similar to the general procedure described in the previous section, except for the flowing electrolyte (dilute aqueous solutions of $CuSO_4$)

and preparation of the active surface: prepolarization at 1.4V for 15 sec, and 0.0V for 0.5 sec. This treatment serves to strip off any Cu deposited on the electrode surface and also to reduce surface oxides during the anodic treatment. The rate of inhibition of the oxygen reduction current is determined by the diffusion-limited rate of copper deposition and is quite rapid.

The typical rate of poisoning of an "active" electrode surface observed in a relatively concentrated Cu^{++} solution is shown in Fig. 5, which also shows the steady-state uninhibited oxygen reduction current observed in the absence of Cu^{++} . The ability of a RBE to achieve "continuous" activation of the electrode surface in the same solution is shown by the following. The potential of the inner electrode was maintained at a sufficiently anodic potential in compartment 1 to strip off the Cu film (0.85-1.2V), and in compartments 2 and 3 it was maintained independently at the desired reduction potential (0.2V). As the electrode surface passes out of compartment 1 into compartment 2, there is an initial additional current flow arising from the reduction of surface oxides and double layer charging. In compartment 3, however, the measured current corresponds almost entirely to the oxygen reduction current, and the steady-state current thus obtained may be compared in Fig. 5 with the steady-state current in the absence of Cu^{++} . It can be seen from these results that the electrode can operate at high activity under conditions where ordinarily almost complete passivation would occur. Similar behavior is observed (112) at other reduction potentials (0.0-0.7V) and Cu^{++} concentrations (10^{-5} - 10^{-2} mol/dm³).

"Continuous" Activation by Decreasing the Thickness of the Surface Oxide Film

In some cases an apparent "activation" of the electrode surface is obtained in the absence of impurities.

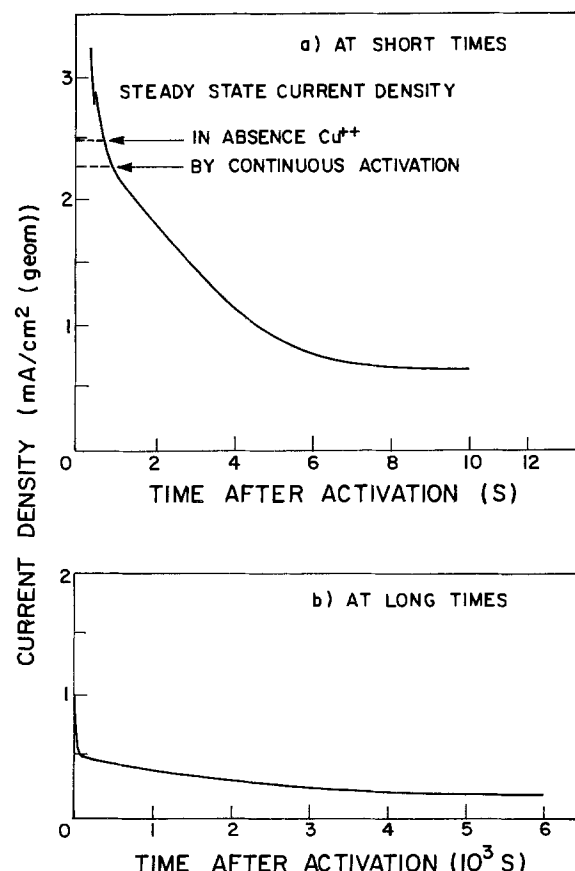


Fig. 5. Decay of oxygen reduction current density following activation in presence of Cu^{++} , compared with steady-state continuous activation. 10^{-3} mol/dm³ Cu^{++} + 0.05 mol/dm³ H_2SO_4 ; $\Omega = 0.78$ rad/sec, electrode roughness factor = 3.63. Electrode potential 0.2V RHE.

This can be seen, for example, in the large increases in the rate of oxygen evolution immediately following a cathode potential pulse at Pt (162-167) and other metals [e.g., Ni, Co, Fe, Au (168-175)], and for other reactions [e.g., the oxidation of CO, the reduction of Cl_2 (163), and the reduction of oxygen (176-186)]. Afonshin, Tyurin, Volodin, and co-workers (162, 186-188) and Schultze and Vetter (163-167) have studied the oxygen evolution reaction at Pt electrodes in detail, and have clearly established that the rate of oxygen evolution is directly dependent on the thickness and nature of the surface oxide film. Thus, the rate of oxygen evolution can be increased temporarily by an appropriate cathodic treatment which serves to reduce the oxide thickness. Although much of the oxide film is quickly reestablished at the anodic potentials necessary for oxygen evolution, the growth is logarithmic with time (166, 189, 190) and the rate of oxygen evolution is significantly higher than its steady-state rate even as long as 60 sec after activation. A steady-state oxide thickness is not reached until very long times have passed (> 1000 sec).

Utilizing these ideas, the ability of a RBE to effect large increases in the rate of oxygen evolution by controlling the thickness of the surface oxide layer was investigated. Oxygen was liberated at the platinum anode from a 3.5 mol/dm^3 aqueous H_2SO_4 solution; first, the cell was operated in a conventional monopolar manner, with the outer electrodes connected together and the inner electrode rotating at the speed of 1 revolution per 8 sec. A 0.3V cathodic potential was first applied to the rotating electrode for 15 sec to strip off the surface oxide film, and the potential was then raised to a working oxidation potential within the 1.4-2.1V range. The results obtained have been summarized in Fig. 6, where the current density (CD) arising from oxygen evolution and oxide formation 4, 60, and 1000 sec after a cathodic pretreatment of 15 sec at 0.3V is shown. It can be seen that the "activation" of the electrode is considerable and CD's are greater than the steady-state CD's (i.e., the CD's at times > 1000 sec) by more than one order of magnitude. These unsteady-state CD's can be compared with the steady-state CD's obtained at a RBE. The latter results were obtained with the potential of the rotating electrode in compartment 1 maintained at 0.3V, and independently at the desired potential E in compartments 2 and 3. As before, the CD's in compartment 3 are reported, since they can be expected to be relatively free from contributions from oxide formation and double layer charging (these processes will take place in compartment 2). The electrode rotation rate employed was 0.78 rad/sec (about 1 revolution every 8 sec) and was

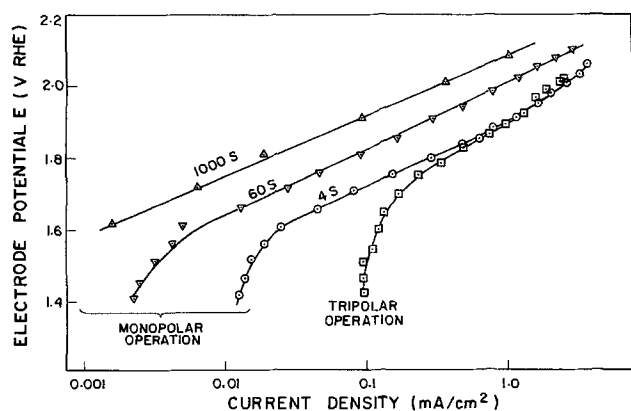


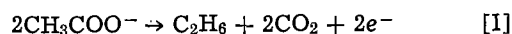
Fig. 6. Oxygen evolution current density vs. potential: tripolar operation compared with conventional (monopolar) operation. $3.5 \text{ mol/dm}^3 \text{ H}_2\text{SO}_4$; $\Omega = 0.78 \text{ rad/sec}$; roughness factor = 4.28; potentials corrected for ohmic drop. Tripolar operation: steady-state CD in compartment 3, $E_1 = 0.3\text{V}$, $E_2 = E_3 = E$. Monopolar operation: CD in compartment 3 at 4, 60, and 1000 sec after activation, $E_1 = E_2 = E_3 = E$.

selected so that the exposure of the electrode surface in compartment 3 occurs approximately 4 sec after exiting from the treatment compartment. It can be seen that the use of a RBE has effected large increases (more than 1 order of magnitude) in the steady-state CD, and corresponds quite well with the unsteady-state CD observed at 4 sec after cathodic activation. Further experiments showed that the steady-state CD's achieved with the RBE increase with electrode rotation rate and are higher in compartment 2 (which immediately follows the treatment compartment).

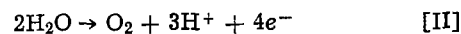
Two points can be noted regarding these results. Firstly, the enhanced CD's at lower potentials (1.4-1.7V) arise through current leakage from compartment 3 to compartment 1 and do not represent a useful increase in the oxygen evolution reaction. Leaving the results uncorrected in this form helps to portray the typical deviations which might be expected through this effect. Secondly, as further experiments have confirmed, the major portion of the observed current increase arises through an increase in the rate of oxygen evolution rather than simply through oxide film growth; at 1.8V, for example, the contribution of the oxide film growth to current was found to be less than 10%. This agrees generally with the work of Schultze (163), who has studied the relationships governing the relative portions of the total CD due to oxygen evolution and oxide film growth in some detail.

Control of the Relative Rate of Competing Electrode Reactions

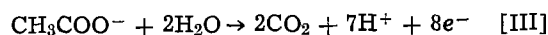
Under particular conditions of voltage and current pulsing the product spectrum of some electrode reactions can be altered, e.g., in the electrolysis of aqueous acetate solutions (21-29). Normal steady-state electrolysis at potentials greater than 2.1V yields largely ethane via the Kolbe dimerization reaction



Under current pulsing conditions (23), and to a lesser extent under voltage pulsing conditions (26), the yield of ethane decreases. At moderate frequencies (1-100 Hz) oxygen is evolved



and at higher frequencies (> 1000 Hz) acetate ions begin to be completely oxidized to CO_2



It is pertinent to note that during steady-state electrolysis of acetate solutions, the complete oxidation of acetate ions occurs at low potentials ($0.4 < E < 0.8\text{V}$), and at intermediate potentials ($1.5 < E < 2.1 \sim 1\text{V}$) oxygen is evolved (191).

A RBE can be used to obtain similar changes in the product spectrum if the electrode rotation rate is fast enough to correspond to the pulsing frequencies at which such changes occur. In order to study this application of the electrode, a $1 \text{ mol dm}^{-3} \text{ CH}_3\text{COOK} + 2 \text{ mol dm}^{-3} \text{ CH}_3\text{COOK}$ aqueous electrolyte mixture (pH buffered strongly at 5.5) was electrolyzed in the cell where the outer electrodes of compartments 1 and 2 were connected together. A constant current was applied to the compartments (the resulting CD was 2.82 mA/cm^2 , with a sign such that reduction occurred at the center electrode). Compartments 1 and 2 formed the "treatment" compartment. In compartment 3 a constant current corresponding to a CD of 27.4 mA/cm^2 was applied. The center electrode was rotated at 14.6 rad/sec (140 rpm), and Ar was bubbled through each cell compartment at $4 \text{ cm}^3/\text{sec}$. After 10 min of operation, the outlet gas from compartment 3 was sampled. The electrode rotation was then stopped, and the CD in compartment 3 was reduced by an amount equal to twice the treatment compartment CD (becoming 21.8 mA/cm^2). The CD in the treatment compartment 3 was again sampled.

The analysis of the anodic outlet gases is summarized in Table II. It can be seen that under conventional, steady-state electrolysis (with the electrode stationary), the Kolbe dimerization reaction proceeds with high efficiency, and the product gases consist mainly of C_2H_6 , CO_2 , with very little O_2 . Under simulated current pulsing conditions (while the electrode is rotating), however, the product spectrum changes considerably: evolution of ethane via Kolbe dimerization is almost completely nonexistent, instead of which the evolution of oxygen and other processes which yield CO_2 are observed. These results clearly illustrate that for some electrode reactions the relative yield of the various reaction products can be significantly altered using a RBE. This selectivity effect is manifest by the fact that at lower electrode potentials oxygen evolution proceeds in preference to the Kolbe dimerization, although only at low rates. Furthermore, the rate of oxygen evolution is greatly increased at short times, as demonstrated above, after a decrease in the thickness of the oxide layer on the electrode surface. Thus, under bipolar operation, the high CD's can be achieved by oxygen evolution taking place at relatively low electrode potentials, and at these lower potentials the Kolbe reaction does not proceed at a significant rate relative to the enhanced rate of oxygen evolution. The relative rate of the various electrode reactions is most likely determined by the thickness of the oxide film of the electrode. This is also very likely the cause of the increase in the complete oxidation reaction at shorter pulse times reported in the literature (21), since it is well known that complete oxidation takes place under conditions of very low oxide coverage and is inhibited by the formation of the oxide film (192). The additional observation that the changes in selectivity are greater during constant current operation (23) than constant potential operation (21) is also consistent with this view of the mechanism. In previous discussions of the unsteady-state nature of the Kolbe reaction [e.g., by Fleischmann *et al.* (21, 25, 27), Hickling and Wilkins (23), Vijn and Conway (193), and Nadebaum and Fahidy (28)], the particular importance of the oxide film thickness has not been adequately taken into account, and a new appraisal of the factors involved in the kinetics of the Kolbe dimerization reaction is required.

Concentration and Refining of Metals and Other Substances

In using a RBE to achieve activation via stripping of adsorbed impurities, it is apparent that when the impurity is, e.g., copper, the process involves deposition of Cu on the rotating electrode surface in one compartment and stripping in another. Thus, a net transfer of copper from one compartment to another takes place

Table II. Change in the product distribution of an electrochemical reaction with a rotating bipolar electrode cell

Operating conditions	Current efficiency* of production of anodic gases† (via chromatographic analysis)			
	O_2	C_2H_6	CO_2 (other than formed during C_2H_6 production)	CO_2 (total)
Simulated current pulsing (electrode rotating at 14.6 rad/sec)	25.0	4.0	19.9	27.9
Conventional constant current (electrode stationary)	0.7	94.7	2.9	192.4
Equivalent*	2	1	1	1

* Current efficiencies were calculated with respect to the percentage of hydrogen in the product gas

$$\text{current efficiency} = \frac{100 (\% \text{ product}) (\text{equivalent})}{(\% \text{ hydrogen})}, \%$$

† Qualitative determination of CH_4 and CO indicated the presence of very small amounts of these constituents.

and a "concentrating" effect is observed. This process was also studied in some detail and the findings (194) are summarized in Fig. 7, showing cupric ion concentration in each compartment. It can be seen that, commencing with about 0.85×10^{-3} mol/dm³ Cu(II) in all cell compartments, after several hours of operation almost all of the copper ions has been transferred to compartment 1. After about 20,000 sec, e.g., the concentration in compartments 1, 2, and 3 are 2.15×10^{-3} , 1.1×10^{-4} , and 8.5×10^{-6} mol/dm³, respectively. This process can be analyzed by carrying out a simple mass balance on the *i*th, cathodic compartment of a multi-compartment cell

$$\text{rate of removal} = \text{rate of deposition} + \text{rate of leakage via electrode gap}$$

At short times, the rate of decomposition is approximately linear, hence

$$-\frac{dc_i}{dt} = \frac{r_o}{c_o} c_i + \frac{L_e R \Omega g}{2V_{\text{compt}}} (c_i - c_{i-1}) \quad [2]$$

From this equation the maximum attainable ratio of the concentrations in adjacent compartments is given by

$$\frac{c_{i-1}}{c_i} = 1 + \frac{2(r_o/c_o) \cdot V_{\text{compt}}}{L_e \cdot R \cdot \Omega \cdot g} \quad [3]$$

$$\approx 1 + 4\pi \left(\frac{r_o/c_o}{w \cdot \Omega} \right) \left(\frac{G}{g} \right) \quad [4]$$

In these equations c_i = bulk copper concentration at time *t* in the *i*th compartment (mol/dm³), c_o = initial bulk copper concentration (mol/dm³), r_o = rate of deposition when $c_i = c_o$ (mol/dm³·sec), L_e = depth of the electrolyte in the compartment (m), V_{compt} = volume of electrolyte in the compartment (dm³), g = effective gap between the inner rotating electrode and the stationary wiper blade, G = annular gap between the inner and outer electrodes. These expressions indicate the following: (I) The rate of removal of Cu^{++} increases with deposition rate (r_o). Thus, if the deposition rate is mass transfer controlled, increasing the rotation rate (Eq. [1]) or agitating the electrolyte will increase the rate of transfer. (II) The maximum attainable concentration ratio can be increased by decreasing the leakage gap at the wiper blades, or by increasing the volume of the cell compartment (e.g., by increasing the gap between the inner and outer electrodes). (III) Multicompartment cells can sustain much greater concentration ratios than a simple two-compartment cell.

Similar concentration-time curves were obtained over a wide concentration range (10^{-5} - 10^{-2} mol/dm³ Cu^{++}). It was also found that the stripping process in compartment 1 can be effected chemically. Thus, in the

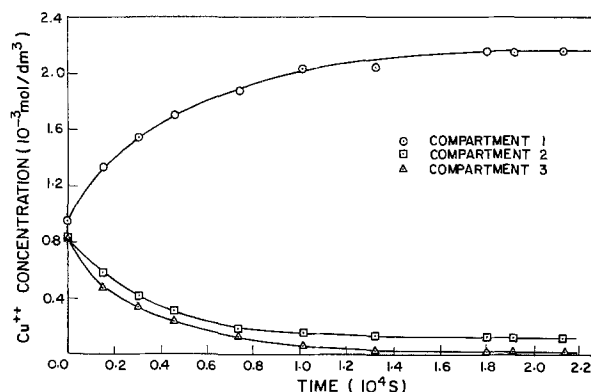


Fig. 7. Copper concentration vs. time in individual compartments under tripolar operation. $\sim 10^{-3}$ mol/dm³ Cu^{++} (initial) + 0.05 mol/dm³ H_2SO_4 ; $\Omega = 0.73$ rad/sec; oxygen flow rate 4.6 cm³/sec; $E_2 = E_3 = 0.2V$; compartment 3 short-circuited.

case of Cu, bubbling oxygen through the solution at open circuit rapidly strips deposited copper from the electrode surface. A more rapid stripping action can be achieved by short-circuiting the electrodes of the stripping compartment, the outer electrodes thus providing additional area for oxygen reduction. As explained in a previous section, the deposition process involves the formation of submonolayer films and can take place at potentials more anodic than the reversible potential.

Concluding Remarks

In this paper the concept, operation modes, and some applications of a rotating bipolar cell were described. Much more work remains to be done: at present reaction systems of importance in fuel-cell technology are being studied, and an investigation with respect to electrode materials other than platinum will soon begin.

While it is somewhat premature to draw definite conclusions on technological applicability, the RBE cell may become an attractive means of carrying out certain electrochemical reactions. The economics involved in the design and construction of an industrial cell will be the subject of a future publication by the authors.

Acknowledgment

Support of this work by the National Research Council of Canada via a research grant and a scholarship (to P.R.N.) is gratefully acknowledged.

Manuscript submitted Aug. 19, 1974; revised manuscript received March 24, 1975.

Any discussion of this paper will appear in a Discussion Section to be published in the June 1976 JOURNAL. All discussions for the June 1976 Discussion Section should be submitted by Feb. 1, 1976.

Publication costs of this article were partially assisted by the University of Waterloo.

REFERENCES

- H. Binder, A. Kohling, and G. Sanstede, in "From Electrocatalysis to Fuel Cells," G. Sanstede, Editor, pp. 15-31 and 43-79, Academic Press, New York (1972).
- J. O'M. Bockris, B. J. Piersma, E. Gileadi, and B. D. Cahan, *J. Electroanal. Chem.*, **7**, 487 (1965).
- J. O'M. Bockris and S. Srinivisan, "Fuel Cells—Their Electrochemistry," p. 315, McGraw Hill, New York (1969).
- S. B. Brummer, *Elektrokhimiya*, **4**, 243 (1968).
- R. P. Buck and L. R. Griffith, *This Journal*, **109**, 1005 (1962).
- J. Giner, *Electrochim. Acta*, **4**, 42 (1961).
- J. Giner, *ibid.*, **9**, 63 (1964).
- M. Green, J. Weber, and V. Drasic, *This Journal*, **111**, 721 (1964).
- G. Horanyi, D. Hegedus, and E. M. Rizmayer, *J. Electroanal. Chem.*, **40**, 393 (1972).
- A. G. Kornienko, L. A. Mirkind, and M. Ya. Fio-shin, *Elektrokhimiya*, **3**, 1370 (1967).
- M. L. Kronenberg, NASA Rept. CR54767 (1965).
- A. Kutshker and W. Vielstich, *Electrochim. Acta*, **8**, 985 (1963).
- F. B. Leitz, W. Glass, and D. K. Fleming, in "Hydrocarbon Fuel Cell Technology," B. S. Baker, Editor, p. 43, Academic Press, New York (1965).
- E. H. Lyons, U.S. Pat. 3,300,345 (1967).
- D. Pouli and J. R. Huff, in "Hydrocarbon Fuel Cell Technology," B. S. Baker, Editor, p. 103, Academic Press, New York (1965).
- R. A. Sanderson, C. L. Bushnell, and T. F. McKiernan, "Advances in Chemistry," Vol. 90, R. F. Gould, Editor, p. 60, American Chemical Society, Washington, D.C. (1969).
- S. Schuldiner, *This Journal*, **116**, 767 (1969).
- W. Vielstich and U. Vogel, *Ber. Bunsenges. Phys. Chem.*, **68**, 688 (1964).
- W. Vielstich, in "Hydrocarbon Fuel Cell Technology," B. S. Baker, Editor, p. 80, Academic Press, New York (1965).
- H. Wroblowa, B. J. Piersma, and J. O'M. Bockris, *J. Electroanal. Chem.*, **6**, 401 (1963).
- M. Fleischmann, J. R. Mansfield, and Lord Wynne-Jones, *ibid.*, **10**, 511, 522 (1965).
- Yu. M. Tyurin, G. N. Afonshin, and G. S. Shakimova, *Elektrokhimiya*, **4**, 491 (1968).
- A. Hickling and R. Wilkins, *Discussions Faraday Soc.*, **45**, 261 (1968).
- T. Dickinson and W. F. K. Wynne-Jones, *Trans. Faraday Soc.*, **58**, 382, 388, 400 (1962).
- G. Atherton, M. Fleischmann, and F. Goodridge, *ibid.*, **63**, 1468 (1967).
- M. Fleischmann, J. R. Mansfield, H. R. Thirsk, H. G. E. Wilson, and L. Wynne-Jones, *Electrochim. Acta*, **12**, 967 (1967).
- M. Fleischmann and F. Goodridge, *Discussions Faraday Soc.*, **45**, 254 (1968).
- P. R. Nadebaum and T. Z. Fahidy, *Electrochim. Acta*, **17**, 1659 (1972).
- P. R. Nadebaum and T. Z. Fahidy, "Symposium on Electrochemical Engineering," J. D. Thornton, Editor, Vol. 1, p. 1. 145, Institute Chemical Engineering, London (1973).
- S. Z. Batkin, *Chem. Abstr.*, **54**, 9548e (1960).
- H. Y. Cheh, *This Journal*, **118**, 551 (1971).
- A. Hickling and H. P. Rothbaum, *Trans. Inst. Metal Finishing*, **34**, 53, 199 (1957).
- N. Ibl and M. Braun, *Chem. Ing. Tech.*, **45**, 182 (1973).
- F. Grimm, Swiss Pat. 274,248 (1951).
- K. K. Popov, Lazarevic, and M. Kostic, *J. Appl. Electrochem.*, **3**, 161 (1973).
- J. O'M. Bockris, "Electrochemistry of Cleaner Environments," p. 126, Plenum Press, New York (1972).
- A. T. Kuhn, *Chem. Ind. (London)*, 946 (1971).
- A. T. Kuhn, in "Modern Aspects of Electrochemistry," J. O'M. Bockris and B. E. Conway, Editors, p. 273, Plenum Press, New York (1972).
- R. C. Rhees, Abstract 210, p. 531, The Electrochemical Society Extended Abstracts, Spring Meeting, Houston, Texas, May 7-11, 1972.
- D. G. M. Brooks, J. M. Coulson, and F. Goodridge, "Symposium on Electrochemical Engineering," J. D. Thornton, Editor, Vol. 1, p. 1.70, Institute Chemical Engineering, London (1973).
- P. R. Nadebaum and T. Z. Fahidy, *Nature (London)*, *Phys. Sci.*, **241**, (106), 45 (1973).
- P. E. Benner, U.S. Pat. 3,448,026 (1969).
- C. J. H. King, K. Lister, and R. E. Plimley, Abstract 239, p. 584, The Electrochemical Society Extended Abstracts, Spring Meeting, Chicago, Illinois, May 13-18, 1973.
- M. Fleischmann, J. W. Oldfield, and C. L. K. Tennakoon, "Symposium on Electrochemical Engineering," J. D. Thornton, Editor, Vol. 1, p. 1.53, Institute Chemical Engineering, London (1973).
- D. Kocot-Bonczakowa, *Prezem. Chem.*, **45**, 63 (1966).
- W. Tomassi, *ibid.*, **42**, 345 (1963).
- Union Carbide Corp., Ger. Pat. 1,225,256 (1966).
- N. I. Fulman, *Chem. Abstr.*, **60**, 15438d (1964).
- V. P. Gladyshev, G. A. Tembre, and K. Ya. Geinrikh, USSR Pat. 160,590 (1964).
- V. P. Gladyshev, L. M. Ruban, K. Ya. Geinrikhs, and V. A. Kulashov, *Chem. Abstr.*, **67**, 39547s (1967).
- L. F. Kozin, *ibid.*, **60**, 195e (1964).
- V. G. Formichev and V. P. Mashovets, *Zh. Fiz. Khim.*, **35**, 803 (1961); *Chem. Abstr.*, **55**, 2679 (1961).
- D. R. Kendall and H. Freund, *J. Electroanal. Chem.*, **34**, 253 (1972).
- Siemens and A. G. Halkse, Brit. Pat. 430,477 (1935).
- Central Elect. Gen. Board, Brit. Pat. 1,104,374 (1968).
- E. H. Cook and M. P. Morris, U.S. Pat. 3,475,301 (1969).
- Edison-Settore Chimico, Belg. Pat. 621,091 (1963); U.S. Pat. 3,278,403 (1963).
- D. G. Elliot, *Tappi*, **51**, A88 (1968).
- D. J. Evans, Brit. Pat. 1,080,756 (1967).
- Hooker Chemical Corp., Neth. Appl. 6,510,232 (1966).
- M. S. Kircher, U.S. Pat. 3,477,939 (1969).
- R. L. Lofffield, A. L. Bargato, H. W. Laub, and G. Messner, Ger. Pat. 1,467,236 (1970).

63. N. W. Meyers, U.S. Pat. 3,389,071 (1968).
64. I. Rousar, *This Journal*, **116**, 676 (1969).
65. J. W. S. Weed, U.S. Pat. 3,497,433 (1970).
66. G. O. Westerlund, Can. Pat. 854,706 (1970).
67. J. E. Colman, Can. Pat. 835,964 (1970).
68. Kh. Sh. Gabitov and S. T. Tadezhanov, USSR Pat. 254,101 (1969).
69. Farbwerke Hoechst Ag., Belg. Pat. 6 39,622 (1964).
70. F. H. Horne and R. Blevitzky, U.S. Pat. 3,287,251 (1966).
71. M. A. Knight, U.S. Pat. 3,484,290 (1969).
72. Oronzio de Nora, U.S. Pat. 2,846,384 (1968).
73. E. P. Pustovit, I. I. Kotov, V. G. Klets, and R. G. M. Savidge, Brit. Pat. 1,136,869 (1968); 1,056,889 (1967).
74. F. A. Scheider, Neth. Appl., 69 95,290 (1969); 68 02,763 (1968).
75. R. Schoeberle, Ger. Offen., 1,958,423 (1970).
76. A. Stranberg, U.S. Pat. 3,389,072 (1968).
77. J. Vosyka, Czech. Pat. 128,337 (1968).
78. L. M. Yakimanko, F. S. Sebryanskii, and L. I. Korneev, *Zh. Prikl. Khim.*, **44**, 1290 (1971).
79. A. J. MacDougall, U.S. Pat. 1,366,404 (1921).
80. Maschinenfabrik Oerlikon, Swiss Pat. 206,960 (1930); 242,830 (1946); 255,873 (1949).
81. I. G. Shcherbakov, Russ. Pat. 43,302 (1935).
82. M. Bonnemay, G. Bronoel, E. Levart, and A. A. Pilla, *Rev. Energ. Primaire*, **2**, (2), 67 (1966).
83. H. Huber and R. Le Bihan, U.S. Pat. 3,252,838 (1966).
84. R. J. Roethlein and H. J. R. Maget, *This Journal*, **114**, 1043 (1967).
85. V. A. Shepelin, *Elektrokhimiya*, **4**, 326 (1968).
86. Societe les Piles Wonder, Fr. Pat. 1,492,316 (1967).
87. Inventa Ag Fur Forschung and Patent Vertung, Swiss Pat. 281,429 (1952).
88. Kanegafuchi Spinning Co. Ltd., Japan. Pat. 7722; 7723 (1959).
89. S. Okada and S. Yoshizawa, *J. Electrochem. Soc. Japan*, **20**, 471 (1952).
90. K. C. Narasimham, S. Sundararajan, and H. V. K. Udupa, *Roczniki Chem.*, **36**, 685 (1962).
91. K. C. Narasimham and H. V. K. Udupa, *Bull. Acad. Pol. Sci., Ser. Sci. Chim.*, **16**, 123 (1968).
92. N. Subramanian, B. K. Sadananda Roa, H. V. K. Udupa, and B. B. Dey, *J. Sci. Ind. Res. (India)*, **15B**, 665 (1958).
93. Y. Tsuchi, Japan. Pat. 8059 (1955).
94. V. S. Bagotskii, Yu. B. Vassilev, and I. I. Pyshnograeva, *Electrochim. Acta*, **16**, 2141 (1971).
95. M. Kawakami, Japan. Pat. 4,563 (1952).
96. K. S. Udupa, G. S. Subramanian, and H. V. K. Udupa, *Bull. Chem. Soc. Japan*, **35**, 1168 (1962).
97. R. Berthold, Ger. Pat. 1,171,640 (1964).
98. T. B. Hoover, U.S. Pat. 3,119,759 (1964).
99. C. Wyche and F. X. McCawley, *Electrochem. Technol.*, **4**, 447 (1966).
100. D. A. Swalhein, *This Journal*, **86**, 395 (1944).
101. M. S. Spencer, P. J. H. Carnell, and W. J. Skinner, *Ind. Eng. Chem., Process Des. Develop.*, **8**, 191 (1969).
102. G. M. B. H. and Fischer Porter, Ger. Pat. 1,231,463 (1966).
103. Imperial Chemical Ind., Neth. Appl. 65 00,121 (1965).
104. Pei-Tai Pan, U.S. Pat. 3,432,420 (1969).
105. P. S. Roller, U.S. Pat. 3,182,010 (1965).
106. F. Strafelda and D. Kozak, *Collection Czech. Chem. Commun.*, **26**, 3168 (1961); **31**, 3042 (1966).
107. I. Jirovsky, Czech. Pat. 120,865 (1966).
108. T. Z. Fahidy, *Can. J. Chem. Eng.*, **51**, 521 (1973).
109. F. Goodridge, *Chem. Process Eng.*, **49**, 93 (1968).
110. C. L. Mantell, *Chem. Proc. Rev.*, No. 14, Noyes Dev. Corp. (1968).
111. A. P. Tomilov and Y. A. Fioshin, *Brit. Chem. Eng.*, **16**, 154 (1971).
112. P. R. Nadebaum, Thesis, University of Waterloo, Canada (1974).
113. W. Nernst, *Z. Phys. Chem.*, **2**, 613 (1888).
114. J. D. E. McIntyre and W. T. Peck, Jr., *This Journal*, **117**, 747 (1970).
115. J. Newman, *ibid.*, **117**, 507 (1970).
116. J. Postlethwaite, K. L. Ong, and D. J. Pickett, "Symposium on Electrochemical Engineering," J. D. Thornton, Editor, Vol. 1, p. 1.105, Institute Chemical Engineering, London (1973).
117. C. L. Wilson and H. V. Udupa, *This Journal*, **99**, 289 (1952).
118. J. R. Flower, N. McLeod, and A. P. Shahbenderian, *Chem. Eng. Sci.*, **24**, 637 (1969).
119. J. R. Flower, N. McLeod, and A. P. Shahbenderian, *ibid.*, **24**, 651 (1969).
120. D. R. Gabe and D. J. Robinson, *Electrochim. Acta*, **17**, 1129 (1972).
121. D. R. Gabe and D. J. Robinson, *ibid.*, **17**, 1121 (1972).
122. P. R. Nadebaum and T. Z. Fahidy, *Can. J. Chem. Engrg.*, In press.
123. M. Eisenberg, C. W. Tobias, and C. R. Wilke, *This Journal*, **101**, 306 (1954).
124. W. Bold and M. W. Breiter, *Electrochim. Acta*, **5**, 145 (1961).
125. M. W. Breiter, *J. Electroanal. Chem.*, **8**, 230 (1964).
126. H. Dietz and H. Gohr, *Electrochim. Acta*, **8**, 343 (1963).
127. S. W. Feldberg, C. G. Enke, and C. E. Bricker, *This Journal*, **110**, 826 (1963).
128. W. G. French and T. Kuwana, *J. Phys. Chem.*, **68**, 1279 (1964).
129. A. N. Frumkin, E. I. Krushteva, M. R. Tarasevich, and N. A. Shumilova, *Elektrokhimiya*, **1**, 17 (1965).
130. S. Gilman, "Electroanalytical Chemistry," A. J. Bard, Editor, Vol. 2, p. 117, Marcel Dekker, New York (1967).
131. J. Giner, *Z. Elektrochem.*, **64**, 491 (1960).
132. C. E. Icenhower, H. B. Urbach, and J. H. Harrison, *This Journal*, **117**, 1500 (1970).
133. S. D. James, *ibid.*, **114**, 1113 (1967).
134. S. D. James, *ibid.*, **116**, 1681 (1969).
135. D. C. Johnston, D. T. Napp, and S. Bruckenstein, *Electrochim. Acta.*, **15**, 1493 (1970).
136. H. A. Laitinen and C. G. Enke, *This Journal*, **107**, 773 (1960).
137. O. A. Petrii and I. G. Shchigorev, *Elektrokhimiya*, **4**, 370 (1968).
138. J. L. Sandler and E. A. Pantier, *This Journal*, **112**, 928 (1965).
139. S. Schuldiner, M. Rosen, D. R. Flinn, and C. H. Presbrey, Jr., *Electrochim. Acta*, **17**, 1637 (1972).
140. S. Shibata, *Bull. Chem. Soc. Japan*, **36**, 525 (1963).
141. S. Shibata, *ibid.*, **37**, 410 (1964).
142. F. G. Will and C. A. Knorr, *Z. Elektrochem.*, **64**, 258 (1960).
143. F. G. Will and C. A. Knorr, *ibid.*, **64**, 270 (1960).
144. U. R. Evans, *Nature*, **218**, 602 (1968).
145. U. R. Evans, *Electrochim. Acta*, **14**, 197 (1969).
146. A. Damjanovic, M. A. Genshaw, and J. O'M. Bockris, *This Journal*, **114**, 466 (1967).
147. M. A. Genshaw, A. Damjanovic, and J. O'M. Bockris, *J. Phys. Chem.*, **71**, 3722 (1967).
148. A. Kozawa, *J. Electroanal. Chem.*, **8**, 20 (1964).
149. L. Muller and V. V. Sobol, *Elektrokhimiya*, **1**, 111 (1965).
150. L. N. Nekrasov and T. K. Zolotava, *ibid.*, **4**, 362 (1968).
151. G. W. Tindall, S. H. Cadle, and S. Bruckenstein, *J. Am. Chem. Soc.*, **91**, 2119 (1969).
152. V. S. Bagotskii, N. A. Nekrasov, and N. A. Shumilova, *Usp. Khim.*, **34**, 1697 (1965).
153. G. Bianchi and T. Mussini, *Electrochim. Acta*, **10**, 445 (1965).
154. M. W. Breiter, *ibid.*, **9**, 441 (1964).
155. J. Koryta and K. Holub, *J. Electroanal. Chem.*, **9**, 167 (1965).
156. L. Muller and L. N. Nekrasov, *Electrochim. Acta*, **9**, 1015 (1964).
157. D. C. Johnston and S. Bruckenstein, *Anal. Chem.*, **43**, 1313 (1971).
158. J. P. Hoare, *This Journal*, **113**, 846 (1966).
159. M. W. Breiter, *Trans. Faraday Soc.*, **65**, 2197 (1969).
160. V. S. Bagotskii, M. R. Tarasevich, and V. Yu. Filinovskii, *Elektrokhimiya*, **5**, 1218 (1969).
161. J. T. Byrnes and L. B. Rogers, *This Journal*, **98**, 457 (1951).
162. G. N. Afonshin, G. F. Volodin, and Yu. M. Tyurin, *Elektrokhimiya*, **7**, 1338 (1971).
163. J. W. Schultze, *Z. Phys. Chem.*, **73**, 29 (1970).
164. J. W. Schultze and K. J. Vetter, *Electrochim. Acta*, **18**, 889 (1973).
165. K. J. Vetter, *ibid.*, **16**, 1923 (1971).
166. K. J. Vetter and J. W. Schultze, *J. Electroanal.*

- Chem.*, **34**, 131 (1972).
167. K. J. Vetter and J. W. Schultze, *ibid.*, **34**, 141 (1972).
 168. V. S. Bagotskii, N. A. Shumilova, G. P. Samoilov, and E. I. Krushcheva, *Electrochim. Acta*, **17**, 1625 (1972).
 169. B. E. Conway and E. Gileadi, *Trans. Faraday Soc.*, **58**, 593 (1962).
 170. T. S. De Gromoboy and L. L. Shreir, *Electrochim. Acta*, **11**, 895 (1966).
 171. L. M. Elina, T. I. Borisova, and T. I. Zalkind, *Zh. Fiz. Khim.*, **28**, 785 (1954).
 172. A. C. Makrides, *This Journal*, **113**, 1158 (1967).
 173. N. A. Shumilova and V. S. Bagotzky, *Electrochim. Acta*, **13**, 285 (1968).
 174. A. I. Tsinman, *Elektrokhimiya*, **1**, 326 (1965).
 175. Y. I. Turyan and A. I. Tsinman, *Zh. Fiz. Khim.*, **36**, 659 (1962).
 176. A. Damjanovic, A. Dey, and J. O'M. Bockris, *Electrochim. Acta*, **11**, 791 (1966).
 177. A. Damjanovic and J. O'M. Bockris, *ibid.*, **11**, 376 (1966).
 178. A. Damjanovic and V. Brusic, *ibid.*, **12**, 615 (1967).
 179. E. I. Krushcheva, N. A. Shumilova, and M. R. Tarasevich, *Elektrokhimiya*, **1**, 730 (1965).
 180. L. Muller and L. N. Nekrasov, *J. Electroanal. Chem.*, **9**, 282 (1965).
 181. L. Muller, *Electrochim. Acta*, **12**, 557 (1967).
 182. M. R. Tarasevich and V. A. Bogdanovskaya, *Elektrokhimiya*, **7**, 1072 (1971).
 183. A. V. Yuzhanina, V. I. Lukyanycheva, N. A. Shumilova, and V. S. Bagotskii, *ibid.*, **6**, 1054 (1970).
 184. Ku. Ling-Ying, N. A. Shumilova, and V. S. Bagotskii, *ibid.*, **3**, 460 (1967).
 185. D. T. Sawyer, and L. V. Interrante, *J. Electroanal. Chem.*, **2**, 310 (1961).
 186. Yu. M. Tyurin and G. F. Volodin, *Elektrokhimiya*, **5**, 1203 (1969).
 187. Yu. M. Tyurin and G. F. Volodin, *ibid.*, **6**, 1188 (1970).
 188. Yu. M. Tyurin, G. F. Volodin, L. A. Smirnova, and Yu. V. Battalova, *ibid.*, **9**, 532 (1973).
 189. D. Gilroy and B. E. Conway, *Can. J. Chem.*, **46**, 875 (1968).
 190. J. L. Ord and F. C. Ho, *This Journal*, **118**, 46 (1971).
 191. M. Ya. Fioshin and Yu. B. Vasilev, *Izv. Akad. Nauk SSSR, Otd. Khim. Nauk*, 437 (1963).
 192. D. F. A. Koch and R. Woods, *Electrochim. Acta*, **13**, 2101 (1968).
 193. A. K. Vijh and B. E. Conway, *Chem. Rev.*, **67**, 623 (1967).
 194. P. R. Nadebaum and T. Z. Fahidy, *J. Appl. Electrochem.*, In press.

Electrochemical Oxidation of Ferrous Iron in Very Dilute Solutions

George B. Adams* and Roger P. Hollandsworth

*Chemistry Department, Lockheed Missiles and Space Company, Incorporated,
Palo Alto Research Laboratories, Palo Alto, California 94304*

and Douglas N. Bennion*

*Energy and Kinetics Department, School of Engineering and Applied Science,
University of California, Los Angeles, California 90024*

ABSTRACT

Experimental results are presented for the anodic oxidation of ferrous iron in dilute ferrous sulfate-sulfuric acid solutions. A conductive fixed-bed, flow-through, electrochemical reactor in which electric current flow is parallel to the direction of electrolytic solution flow was used. Steady-state anodic polarization curves were obtained at seven different flow rates, ranging from 1.5 to 10 ml/min in a cell of 81.1 cm² cross section. Input ferrous iron concentrations were 725 μg/ml in an acid mine water simulant containing 1430 μg/ml of sulfuric acid. Conversion efficiency for ferrous to ferric iron exceeded 99.9% at the lower flow rates. Design equations have been developed which predict performance of the system. Measured limiting currents exceed theoretical values by 6-14%. A preliminary cost analysis for a million gallons per day acid mine water treatment plant for oxidizing ferrous to ferric iron using parallel current-electrolytic solution flows predicts 7.5¢ per thousand gallons of which 4.6¢ per thousand gallons is assigned to capital costs. An additional 22.3¢ per thousand gallons must be added for following limestone treatment and precipitation of the ferric iron.

A serious industrial water pollution problem associated with coal mining operations results from the oxidation of iron pyrite in coal by exposure to air and water. This results in the formation of a dilute solution of ferrous sulfate and sulfuric acid, each product concentration varying typically from several hundred to several thousand micrograms/milliliter (acid mine water). To avoid pollution, this effluent must be neutralized and freed of iron before discharge into receiving waters.

A number of processes have been investigated for acid mine water treatment, including ion exchange,

reverse osmosis, freezing, foaming, microbiological oxidation-limestone neutralization, ozone oxidation-limestone neutralization, and combination limestone-lime neutralization with aeration. Except for special circumstances, poor efficiencies, adverse economics, or both appear to rule out present use of most of these approaches. The principal treatment now in use commercially is the lime neutralization with aeration process.

An alternate approach is to preoxidize the ferrous ion electrolytically with subsequent iron precipitation and acid neutralization effected by addition of ground limestone. Certain economic advantages are claimed for this approach over the lime neutralization with

* Electrochemical Society Active Member.

Key words: ferrous oxidation, flow-through electrodes, water treatment.

eration process (1-3). These previous studies report on processes in which electrolytic preoxidation was carried out in a conductive packed bed, flow-through reactor with current flow perpendicular to the direction of electrolytic solution flow. Maximum conversion efficiency for ferrous to ferric iron electro-oxidation of about 73% was achieved in the bench-scale reactor used. A rather complete mathematical analysis for that cell geometry has been presented by Alkire and Ng (4).

In the present work, a packed bed, flow-through reactor with powdered graphite filler was used with current flow parallel to the direction of electrolytic solution flow. Design and operation of this reactor, shown schematically in Fig. 1, is similar to that described by Bennion and Newman (5) and further tested by Wenger (6) and by Yip (7). The iron oxidation cell consists essentially of the anode half of the Bennion-Newman cell with a stainless steel cathode. Electrolytic solution was gravity-flowed through the cell, downward through the cathode screen, through a thick, porous anode, and then discharged through a micrometer control valve.

Design Principles

In order to achieve maximum utilization of the reactor volume, all or most of the volume must be involved in converting ferrous to ferric ions. The object is to maximize the average conversion rate per unit volume for the whole reactor and maintain product quality while minimizing the cost of the reactor and associated operating costs. The principal operating costs are electrical energy, pumping to overcome pressure drop across the cell, and associated labor and maintenance costs. Various geometries can be considered. However, this discussion is limited to the geometric cell configuration shown in Fig. 1 in which solution flow is parallel to electrical current flow and the counterelectrode is upstream of the working electrode. For this configuration, it has been shown (5, 6) that the pumping costs are very small. The details of labor costs are beyond the scope of this study. In the following calculations it is assumed that the system is capital intensive and that the primary objective is to achieve maximum conversion rates per unit volume. The effects

of electrical energy costs on the design can be considered later. The basic principles used here are very similar to those presented earlier for a copper system (5).

As fluid flows through the porous electrode, ferrous ions are transported from the bulk solution to the electrode surface and react to form ferric ions. The larger the electrode surface area per unit volume, a , the greater will be the reaction rate. It is assumed there is an excess of supporting electrolyte and that ferrous ions are transferred from bulk solution within the pores to the electrode surface by diffusion only. Thus the rate of reaction of the ferrous ions per unit area is proportional to the concentration difference between the bulk, c_b , and the surface, c_s . It is convenient to express the surface reaction rate in terms of the local transfer current density, j . Based on Faraday's law, the volumetric reaction rate, R , can be written as follows

$$R = \frac{aj}{F} = ak_m(c_b - c_s) \quad [1]$$

k_m is the effective mass transfer coefficient. In order to maximize R , c_s must go to zero. This condition is achieved by applying a sufficiently large electrical potential driving force. The driving force must not be so large as to create excessive oxygen evolution.

Oxygen bubbles trapped in the packed bed will cause channeling and reduce the effective value of ak_m . The parameter combination ak_m is determined experimentally from the limiting current for ferrous to ferric conversion prior to O_2 evolution. Electrolytically evolved oxygen or other oxidant diffusing into the bulk of a pore and oxidizing ferrous iron in the pore leads to values of j larger than predicted by Eq. [1] based on ferrous diffusion only. This latter effect will be dominant in early stages of oxygen evolution, but, as oxygen bubbles continue to plug the bed more and more, the effects of oxygen evolution can decrease over-all performance.

A material balance on the ferric ion yields the concentration distributed within the flow-through porous electrode

$$v \frac{dc_b}{dy} = -R = -ak_m c_b \quad [2]$$

The symbols are defined at the end of the paper. The variation of the potential driving force is described by Ohm's law and the conservation of charge

$$i = \kappa \frac{d\phi}{dy} \quad [3]$$

$$aj = \frac{di}{dy} \quad [4]$$

i is the superficial or observed current density and κ is an effective, electrolytic conductance in the porous bed.

The boundary conditions are

$$c_b = c_o \text{ at } y = 0 \quad [5]$$

$$i = 0 \text{ at } y = L \quad [6]$$

$$\phi = 0 \text{ at } y = L \quad [7]$$

$$c_b = c_L \text{ at } y = L \quad [8]$$

The final condition is not really a boundary condition, but more of a design criterion. Given c_L , the optimum electrode thickness, L , and flow rate, v , can be determined. The solution to these equations is

$$c_b = c_o \exp(-\alpha y) \quad [9]$$

$$i = Fvc_o [\exp(-\alpha y) - c_L/c_o] \quad [10]$$

$$\Delta\phi = \beta [\exp(-\alpha y) - 1 + \alpha y c_L/c_o] \quad [11]$$

where

$$\alpha = ak_m/v \quad [12]$$

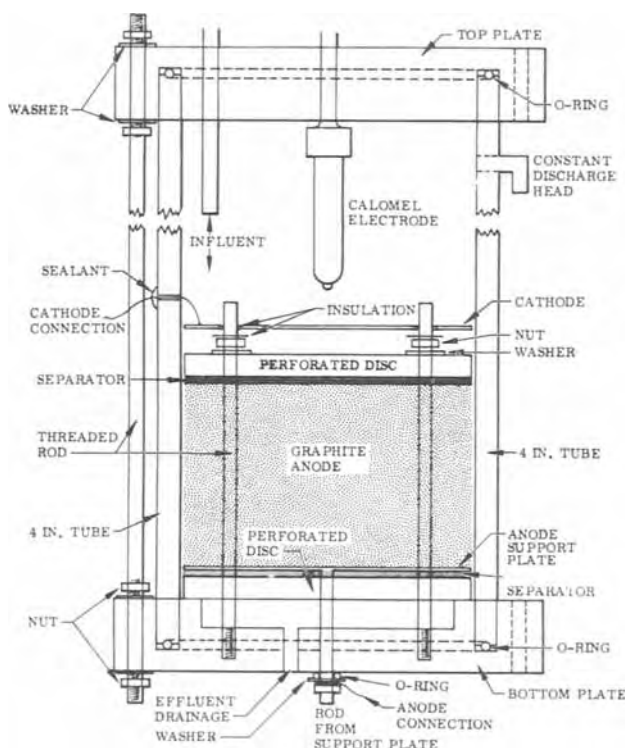


Fig. 1. Four-inch, flow-through electrolytic reactor

$$\beta = Fv^2c_0/ak_m\kappa \quad [13]$$

As a first approximation, the cost of a processing plant will depend on the volume or weight of cells required to process a given feed flow rate of acid mine waters to be treated. The volume of cells is just the area, A , times the thickness, L . The area, A , is the feed flow rate, F , in cm^3/sec divided by the maximum allowable feed velocity through the cell, v

$$A = F/v \quad [14]$$

The larger the velocity v , the smaller A , and the lower the capital cost. Typically k_m depends on the velocity through the bed and the bed geometry expressed through the area per unit volume, a , and the particle shape factor, ψ . A correlation suggested by Bird *et al.* (8) has been used

$$\frac{k_m}{aD} = 0.91 \frac{\rho v^{0.49}}{a\mu\psi} \psi^2 \text{Sc}^{1/3} \quad [15]$$

Given c_0 , c_b^L , a , $\Delta\phi$, and κ , Eq. [9], [11], and [15] can be solved for v , L , and κ_m . Equation [15] assumes no channeling. If there is channeling, one must use an effective a which may be much smaller than the geometric a based on particle size alone. The larger the magnitude of $\Delta\phi$, the larger will be v . L also increases with $\Delta\phi$, but the gain in v more than offsets any increased size associated with the larger L . The larger the magnitude of $\Delta\phi$, the greater the rate of oxygen evolution. A value of about $-1.7V$ appeared optimum for the experiments reported on here. For higher magnitude $\Delta\phi$, the oxygen which formed caused channeling which reduced the effective value of a and thus v_{max} decreased with further increase in magnitude of $\Delta\phi$. The optimum value of $\Delta\phi$ could vary considerably with local operating conditions.

The effective electrolytic conductivity in the porous electrode, κ , was estimated using the Bruggemann equation (9, 10)

$$\kappa = \kappa_0 \epsilon^{1.5} \quad [16]$$

where κ_0 is the bulk electrolytic solution conductivity and ϵ is the porosity of the electrode.

Given c_0 , c_b^L , L , v , and κ from experimental observations, it is possible to calculate effective values of $\Delta\phi$, a , and k_m . If the effective a is much smaller than a calculated from the geometric area of the packing material, it implies there is channeling of the flow through the bed. It was not possible to measure $\Delta\phi$ directly. However, by placing a reference electrode in the effluent stream and measuring its potential relative to the anode, one measures a potential V_p . This V_p is essentially $\Delta\phi$ plus any electronic resistance losses in the matrix, surface overpotential at the front of the electrode, local concentration overpotential at the front of the electrode, and possibly a constant term which depends on the particular reference electrode selected. These local effects in comparing V_p and $\Delta\phi$ have been discussed by Wenger (6). It seems sufficient to state here that V_p is related to $\Delta\phi$. The larger V_p , the larger the magnitude of $\Delta\phi$ and the greater the tendency for oxygen evolution.

In experimental runs, current is increased by increasing the cell voltage, V_f , and measuring V_p . When limiting current is reached throughout the cell, c_s everywhere very much less than c_b , further increases in the cell voltage increase V_p , but the current no longer changes. The length of the I vs. V_p plateau is a measure of the excess capacity of the cell. As v is increased, the length of the limiting current plateau decreases. When the plateau just disappears with increasing v , the maximum velocity is assumed to have been established experimentally, see Fig. 2 and 3. For a given set of input and output conditions, the larger the value of the effective a , the larger will be the maximum v . Thus the importance should be clear of minimizing channeling and realizing an effective a as close to the geometric or true a as possible.

Experimental

Cell construction.—The experimental reactor is shown in Fig. 1. It is constructed of Plexiglas tubing, 4 in. ID, with two end plates consisting of Plexiglas disks fitted with O-rings to close off both ends of the tube. Sealing is effected by compression of six external, threaded, steel rods located peripherally on the end plates at 60 degree intervals. The graphite bed is contained between two Plexiglas support plates containing 72 $\frac{1}{4}$ -in. and 18 $\frac{3}{8}$ -in. perforations spaced in a geometrical pattern to give a uniform flow rate and still maintain structural strength. These support plates are compressed by means of six internal stainless steel threaded rods. Cloth separators, placed below the top perforated support plate and below the perforated anode support plate, prevent graphite particles from washing out of the bed by the electrolytic solution flow. The graphite used in the bed was Stackpole Carbon Company, Grade 6026 graphite, sized to $-100 + 150$ mesh.

Electrical circuit.—Circuitry was similar to that used by Bennion and Newman (5). Influent and effluent were monitored continuously for pH and conductance. Anode potential was measured vs. saturated calomel reference electrodes located above the cathode (V_f) and below the anode (V_p) in the effluent stream. Conductance was measured with Beckman flow-through conductivity cells (cell constant 0.5 cm^{-1}). Anode potential, cell voltage, and pH were measured with an Orion Model 601, digital pH meter; cell resistance was measured with a General Radio tube 1650-A impedance bridge. Power was supplied to the cell from a Gerhard Bark, Wenking potentiostat in which the impressed current is regulated at a constant potential between anode and a calomel reference electrode placed above the cathode (V_f).

Flow control.—Flow of effluent being discharged was controlled with a Nulcear Products Company micrometer valve. Influent flow rate was adjusted always to exceed that of the effluent, the overflow being discharged through an outlet located near the top of the reactor in order to maintain a constant head of electrolytic solution on the micrometer valve exit port. This was necessary in order to minimize fluctuations in flow rate over 24 hr periods. Flow rates were determined using graduated cylinders to collect known volume of effluent over measured time intervals.

Electrolyte concentrations.—The electrolytic solution was an acid mine water simulant, 725 $\mu\text{g}/\text{ml}$ in ferrous iron (as ferrous sulfate heptahydrate) and 1430 $\mu\text{g}/\text{ml}$ in H_2SO_4 . Solutions were made up from deionized water and reagent grade (J. T. Baker) chemicals. The pH of the influent electrolyte ranged from 1.9 to 2.1 with a mean conductivity of 0.065 mho/cm. Influent temperature varied between 22° and 26°C.

After reaching a steady state for V_p at each V_f setting for a given flow rate, the effluent was analyzed for the ferrous and total iron concentration. Analysis was made spectrophotometrically, using a Beckman Model D2 spectrophotometer. Either 1-10 phenanthroline or α - α' bipyridyl procedures were followed (11), depending on the ferrous iron concentration.

For solutions containing less than 10 $\mu\text{g}/\text{ml}$ of ferrous iron, two parts (by volume) of the sample were diluted by addition of one part of saturated potassium fluoride solution to complex ferric ions, thereby inhibiting formation of the colored ferric complex. An additional one part of α - α' bipyridyl solution (2% in 6N HCl) was then added to form the yellow ferrous complex which was determined spectrophotometrically at 415 $m\mu$. For solution containing more than 10 $\mu\text{g}/\text{ml}$ ferrous iron, the sample was suitably diluted to give 0-3 $\mu\text{g}/\text{ml}$, and the red 1-10 phenanthroline ferrous complex was determined at 515 $m\mu$. Total iron was determined by using a 500 \times dilution treated with solid hydroxylamine hydrochloride to reduce ferric to fer-

rous iron, followed by spectrophotometric determination of the red O-phenanthroline complex.

Above 20 $\mu\text{g/ml}$, accuracy of the analytical determinations was about 7%; at the lower limit of the measurements near 1 $\mu\text{g/ml}$, the accuracy was 10%.

Materials compatibility.—It was found necessary to thicken gold plate 316 stainless steel anode support plate and the six internal tie rods, washers, and nuts. All other metal exposed to the electrolyte was unplated 316 stainless steel. The cell body was Plexiglas. Separators were cut from Webril material, a non-woven Dacron cloth.

Results

Figures 2 and 3 show the family of anodic polarization curves (I vs. V_p) at seven flow rates ranging from 1.5 to 10 ml/min, or 3.1×10^{-4} to 2.1×10^{-3} cm/sec. These results were obtained under steady-state conditions with an electrolytic solution of acid mine water simulant containing from 705 to 725 $\mu\text{g/ml}$ ferrous iron. Runs were made at constant flow rate. Variations in flow rate of up to 10%, in some cases, occurred due mainly to temperature variations occurring overnight with consequent viscosity changes in the solution. Flow rates for each point have been normalized to the value shown for each curve and the corresponding current values corrected accordingly. From 4 to 24 hr are required to reach a true steady state for each point on the curve after each change in the control potential V_f . Superficial residence time is of the order of 8 hr. It normally takes about three superficial residence times to achieve a steady state. This point is discussed in greater detail by Bennion and Newman (5) in their work on copper deposition. Shapes of the curves are typical (at flow rates up to 6.85 ml/min) for an electrode process approaching and then establishing a limit current. A reasonably identifiable plateau is established before the rapid rise due to oxygen evolution occurs.

Analysis of the effluent stream for ferrous and total iron concentrations was carried out for each run. Coulombic conversion efficiencies of over 99.9% were obtained at the lower flow rates. Effluent ferrous iron concentration is given in micrograms/milliliter beside each datum point. Effluent total iron concentration was lowered from that of the influent by electrodeposition of some metallic iron at the cathode.

Discussion

Current increment.—Table I is a summary of steady-state, limiting current operation at various flow rates. Comparing the calculated current based on Eq. [10] and the observed current shows the observed current to be consistently 10–12 mA higher. This effect is also shown by comparing the dashed lines and plateau positions in Fig. 2 and 3. One possible explanation of this difference is that hydrogen produced at the cathode and dissolved in the electrolyte is oxidized in the bed to give the observed increment of current. It is difficult to account for more than half this difference, however, assuming the solution is saturated (not supersaturated) with hydrogen at a solubility concentration of 1.34 ppm. An experiment was conducted at 1.50 cm³/min to test this concept using a Nafion XR-475 ion

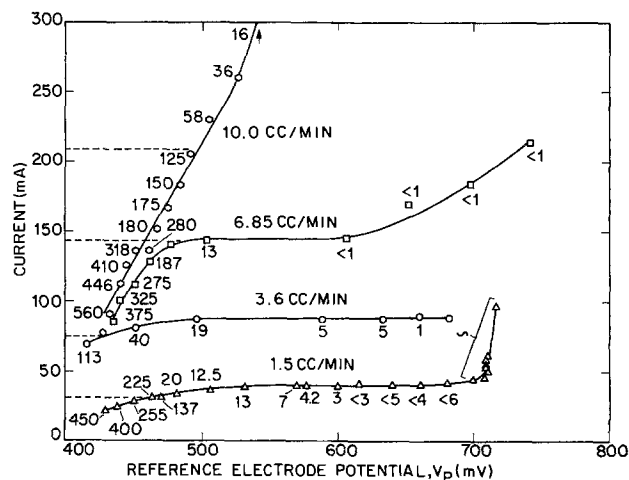


Fig. 2. Polarization curves for porous, flow-through anode. 81.1 cm² cross section, 7.4 cm length, $\kappa_{in} = 6.5 \times 10^{-3}$ mho/cm, $\kappa_{out} = 5.3 \times 10^{-3}$ mho/cm, $\text{Fe}^{++}_{in} = 725$ ppm, Fe^{++}_{out} noted by numbers next to experimental points. Average total iron out = 705 ppm. Flow rate noted beside each curve. --- shows calculated limiting currents.

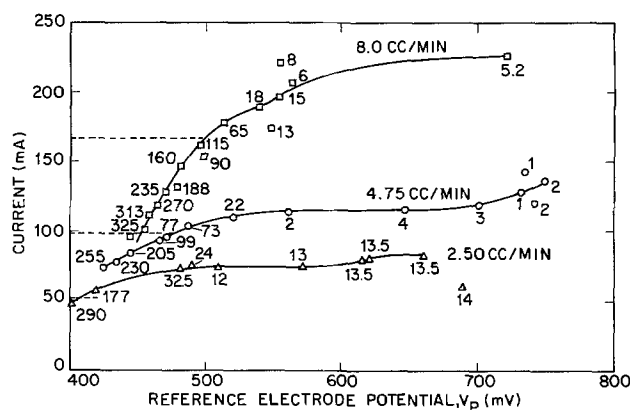


Fig. 3. Polarization curves for porous, flow-through anode. Conditions same as for Fig. 2, only for different flow rates.

exchange membrane to separate the dissolved hydrogen formed at the cathode from the anode bed. No decrease in limiting current was observed. This experiment supports the view that the anomalous current increment is not due to electro-oxidation of hydrogen.

Another point mitigating against the concept of oxidation of dissolved hydrogen is that the incremental current observed should increase with increasing flow rate for any dissolved species being oxidized. This does not occur; the incremental current remains essentially constant at about 10–12 mA.

Another explanation of the anomalously high observed limiting current and the relatively constant value of the current increment at increasing flow rates is that the incremental current is due to the anodic oxidation of the graphite surface. Since the oxidation product may be a solid and remain on the surface of

Table I. Analysis of operating conditions

Electro-oxidation of Fe^{++} to Fe^{+++} , $\epsilon = 0.5$, $A = 81.073$ cm², $S_c = 1366$, $\kappa^{\circ} = 5 \times 10^{-8}$ mho/cm.

Input data				Calculated values			Other observed data		
L , cm	Flow, cm ³ /min	c_L , $\mu\text{g/ml}$	c_o , $\mu\text{g/ml}$	a , cm ⁻¹	$-\Delta\phi$, V	I , mA	I , mA	V_p , mV	V_x , mV
7.4	1.46	0.6	695	8.89	0.212	29.2	41.2	-681	-996
7.4	2.23	1.35	705	9.47	0.368	45.2	62.0	-616	-1025
7.4	3.64	0.5	725	12.36	0.536	75.9	87.8	-633	-1175
7.4	4.75	0.4	775	13.87	0.720	105.9	115.8	-647	-1398
7.4	6.90	0.1	755	17.56	0.866	150.0	146.0	-606	-1496
7.4	8.14	6.0	725	12.30	1.742	168.5	211.0	-564	-1801
7.4	9.25	58.0	760	12.99	2.048	200.9	213.0	-506	-1799

the graphite, no dissolved species would be involved, and hence no increase in incremental current with flow rate would occur. A recent study (12) has shown that hydroquinone-like groups on a graphite surface are anodically oxidized to quinone-like groups. These quinone-like surface species could eventually react with the ferrous ions to establish a steady-state condition. Other observations favoring this point are that the bed appeared to improve with age, and that a yellow colloidal layer appeared above the packed graphite bed when the reactor was back flushed after running above oxygen evolution potentials for a prolonged period. Quinoidal compounds are usually colored.

If carbon is reacting, eventually the carbon bed will be destroyed. Over a three month period of operation, the graphite bed used in these experiments showed no noticeable deterioration. If impurities in the graphite are involved, eventually they would be used up and the excess current would no longer be observed. If the impurity level is estimated at 5% of the graphite by weight and to have an effective equivalent weight of 50, a graphite bed of 700g would contain 0.7g equivalents of impurities. Assuming operation for 20 days at 10 mA excess current implies consumption of only 0.18g equivalents in some Faradaic reaction other than ferrous iron oxidation. (This calculation is only good to about an order of magnitude.) Hence, it is concluded that for the length of time involved, impurities could have been reacting or possibly graphite breakdown would not have been extensive enough to be noticed.

Another more obvious explanation for the excess current is oxygen evolution. If bubbles of oxygen form, they are expected to plug the porous electrode flow channels and cause electrolyte channeling, which should result in poor iron oxidation rates. Since observed oxidation rates were high, it could be that oxygen did not nucleate, but reacted with ferrous iron as fast as it formed at the graphite surface. It is known that the uncatalyzed reaction of molecular oxygen with ferrous iron is a slow reaction (13). However, this reaction is catalyzed by activated carbon (14). Hence, the rapid oxidation of ferrous iron by the active oxygen forming in the bulk of the electrode pores cannot be ruled out.

A difficulty with both the quinone and oxygen evolution explanations for the anomalous limiting current increment is that the anomaly is observed at potentials below those required for either oxygen evolution or surface quinone formation.

It seems improbable that peroxide, formed by partial oxidation from water, could be the active intermediary, since at pH 2 the oxidation of ferrous iron by hydrogen peroxide is incomplete unless a large excess of peroxide is present.

The experimental results presented here are not sufficient to determine the precise secondary reaction or reactions taking place. However, the results do indicate that electrochemical oxidation of ferrous ions is feasible and that the proposed design equations and procedures work and yield conservative design conditions. The unaccounted for side reactions apparently do not hinder operation so far as has been determined to date. Their possible beneficial effects should not be counted upon until more is known about them and under what conditions they occur.

Conversion efficiency.—As shown in Fig. 2, conversion efficiency of ferrous to ferric iron is over 97% at the highest flow rate (10 cm³/min), the last point indicated on the curve. This high conversion efficiency is achieved even though no limiting current is established at this high flow rate. Normally one would expect a relatively low conversion efficiency under these conditions, since ferrous iron flows through the bed faster than it can diffuse to the anodic surfaces and be oxidized. Surface quinone formation at the anode, as discussed above, could serve as a solid redox couple and catalyze the oxidation of ferrous ion, especially if it

were partially soluble in the electrolyte. In effect, it would increase the effective mass transport coefficient of ferrous ion by rapidly oxidizing it within the pores of the graphite anode surface.

Cost analysis.—Using actual data at a cell flow rate of 8.14 cm³/min, feed of 725 μg Fe⁺⁺/ml, feed conductivity of 0.005 mho/cm, effluent concentration of 6 μg Fe⁺⁺/ml, bed length of 7.4 cm, and a bed shape factor of 0.86 yields an effective surface area per unit volume for the bed of 12.3 cm⁻¹ and an allowable resistance loss through the bed of 1.768V. The effective surface area is quite low compared to an estimated geometric specific surface area of over 100 cm⁻¹. By optimizing the packing material to get more uniform size distribution, the specific surface can probably be increased substantially, possibly to between 26 and 50 cm⁻¹. For design estimates here, specific area of 14 cm⁻¹ and 1.7V resistance potential drop across the packed bed will be used. In order to compare costs with previous estimates (3), feed of 500 μg Fe⁺⁺/ml and effluent with 95% conversion¹ (25 μg Fe⁺⁺/ml) will be used as the design basis. These conditions imply an optimum bed length of 4.8 cm and a flow velocity of 2.7 × 10⁻³ cm/sec or 57 gal/day·ft². To take advantage of any soluble oxidant or dissolved oxygen production in the cell, the cell should be made a little longer than 4.8 cm, possibly up to 7 cm.

To handle one million gallons per day, the above cell design implies that 17,544 ft² of cell area will be needed. If the cells are coated concrete slabs and walls with a packed bed on top, a separator, a cathode, the concrete container filled with electrolytic solution, and a hood to collect the hydrogen, the construction cost is assumed to be similar to that of a concrete slab warehouse for which the construction cost is estimated (15) as \$9.50/ft². Detailed cost estimating procedures for copper removing flow-through electrodes yield \$4 to \$15/ft², depending on design details and cost bases. It seems reasonable to assume a cost of \$10/ft² for a large-scale reactor of this type.

At \$10/ft², the cost of a one million gallon per day reactor will be \$175,440. For purposes of comparison, straight line depreciation over ten years with no interest charges is assumed. This gives a fixed cost of \$17,544 per annum or 4.8¢ per thousand gallons of acid mine water treated. For cell voltage of 3V, it requires 2.73 kW-hr to treat one thousand gallons of feed assuming 100% current efficiency for the Fe⁺⁺ → Fe⁺⁺⁺ + e⁻ reaction. If power costs 1¢/kW-hr, energy costs will be 2.7¢ per thousand gallons of feed. Other costs for limestone precipitation have been estimated (3) to be 22.3¢ per thousand gallons based on 500 μg Fe⁺⁺/ml and 1000 μg/ml total acidity. This implies a total treatment cost of 29.8¢ per thousand gallons. This cost figure compares to 36¢ per thousand gallons for the Tyco Laboratories estimate (3). A credit of 6¢ per thousand gallons for salable hydrogen gas produced is deductible from each of these figures for comparison with non-electrolytic processes. Sludge handling costs are not included in these estimates.

Cost estimates of this type are of necessity approximate. They should be useful for preliminary comparisons and to illustrate how the costs are capital intensive at today's energy costs. By achieving higher flow rates per unit geometric area and/or lower cost per unit geometric area of the electrode, more favorable economic situations should be possible. In particular, larger values of the effective specific surface area, *a*, should allow for higher flow rates. This might be achieved by minimizing channeling of electrolytic solution flow through the bed and increasing the actual specific surface area within the bed.

Other applications.—This use of flow-through, porous electrode reactors should be applicable to the anodic oxidation of cyanide ions from dilute solutions

¹This is reported to be (3) the lowest conversion efficiency for Fe⁺⁺ that will allow complete precipitation of iron by addition of limestone.

such as plating rinse waters for cyanide concentrations up to several hundred parts/million. It should also be applicable to the reduction of chromate to chromic ions in plating bath rinse waters from acid chromium plating baths. In addition it should be possible to cathodically strip gold, silver, copper, and nickel from plating bath rinse waters. The details for metal recovery are discussed elsewhere (5, 6, 16). By using a combination of cyanide destruction and ion recovery, it may be possible to clean rinse waters for reuse.

Acknowledgment

This research was supported as part of the 1973 Lockheed Independent Research Program.

Manuscript submitted Nov. 8, 1974; revised manuscript received April 1, 1975.

Any discussion of this paper will appear in a Discussion Section to be published in the June 1976 JOURNAL. All discussions for the June 1976 Discussion Section should be submitted by Feb. 1, 1976.

Publication costs of this article were partially assisted by Lockheed Missiles and Space Company, Incorporated.

SYMBOLS

a	specific surface area, cm^{-1}
A	geometric cross sectional flow channel area, cm^2
c_b	bulk ferrous ion concentration in pores, mol/cm^3
c_L	effluent ferrous ion concentration, mol/cm^3
c_o	influent ferrous ion concentration, mol/cm^3
c_s	ferrous ion concentration at surface of pore walls, mol/cm^3
D	diffusion coefficient of ferrous ions, cm^2/sec
F	Faraday constant, 96,487 coulombs/equiv.
i	superficial or geometric current density, A/cm^2
I	total current, A
j	transfer current density across pore walls, A/cm^2
k_m	mass transfer coefficient, cm/sec
L	length of porous anode, cm
R	effective reaction rate per unit volume within anode, $\text{mol}/\text{cm}^3 \cdot \text{sec}$
Sc	Schmidt number, $\mu/\rho D$
v	superficial fluid velocity, cm/sec
V_f	potential of a saturated calomel reference electrode in feed solution relative to anode, V
V_p	potential of a saturated calomel reference electrode in effluent solution relative to anode, V
y	distance along porous anode in direction of flow, cm
α	ak_m/v , cm^{-1}
β	$Fv^2 c_o/ak_m \kappa$, V

ϵ	void fraction, dimensionless
κ	effective or superficial electrical conductivity of catholyte, mho/cm
μ	viscosity of feed solution, $\text{g}/\text{cm} \cdot \text{sec}$
ρ	density of feed solution, g/cm^3
ϕ	potential in solution, V
$\Delta\phi$	potential drop in solution across porous electrode, V
ψ	particle shape factor, 0.86 for flakes, dimensionless

REFERENCES

1. Bituminous Coal Research, Inc., E.P.A. Report, Water Pollution Control Research Series DAST-33, 14010 E1Z61/70 (Jan. 1970).
2. Bituminous Coal Research, Inc., E.P.A. Report, Environmental Protection Technology Series, 14010 EZ12/71 (Dec. 1971).
3. Tyco Laboratories, Inc., E.P.A. Report, Water Pollution Control Research Series, 14010 FNQ 02/72 (Feb. 1972).
4. Richard Alkire and P. K. Ng, *This Journal*, **121**, 95 (1974).
5. D. N. Bennion and John Newman, *J. Appl. Electrochem.*, **2**, 113 (1972).
6. R. S. Wenger, M.S. Thesis, School of Engineering, Univ. of California, Los Angeles (Feb. 1974).
7. H. K. Yip, M.S. Thesis, Chemical Engineering Dept., Univ. of California, Berkeley (June 1973).
8. R. B. Bird, W. E. Stewart, and E. N. Lightfoot, "Transport Phenomena," John Wiley & Sons, Inc., New York (1960).
9. R. E. de la Rue and C. W. Tobias, *This Journal*, **106**, 827 (1959).
10. D. A. G. Bruggemann, *Ann. Physik.*, **24**, 636 (1935).
11. W. M. Banick, Jr. and G. F. Smith, *Talanta*, **1**, 153 (1958). Also "Standard Methods for Examination of Water and Wastewater," 12th Ed., p. 156, (1965), prepared and published by A.P.H.A., A.W.W.A., and W.P.C.F.
12. K. F. Blurton, *Electrochimica Acta*, **18**, 869 (1973).
13. Harvard University, Water Pollution Control Research Series 14010-06/69, Water Quality Office, U.S. Environmental Protection Agency, Washington, D. C.
14. C. T. Ford and J. F. Royer, Environmental Protection Technology Series, EPA-R2-73-150 (Jan. 1973), Office of Research and Monitoring, U.S. Environmental Protection Agency, Washington, D. C.
15. "The National Construction Estimator," 18th ed. p. 174, Craftsman Book Co., Solana Beach, Calif. (1970).
16. D. N. Bennion and John Newman, U.S. Pat. 3,804,733 (April 16, 1974).

Investigation of the Reaction Between Liquid Lithium and Lithium Chloride-Potassium Chloride Melts

Randall N. Seefurth* and Ram A. Sharma*

Electrochemistry Department, Research Laboratories, General Motors Corporation, Warren, Michigan 48090

ABSTRACT

The fumes over lithium chloride-potassium chloride melts containing lithium were determined to be potassium vapors resulting from the exchange reaction between the lithium and the potassium chloride in the melt. The rate of this reaction was measured by using a simple electrochemical half-cell containing two lithium electrodes. The amount of unreacted lithium was determined at any desired time by transporting it electrochemically between the electrodes. The reaction rate was determined at various current densities up to 3000 A/m² over a temperature range of 648°-773°K; it was found to be independent of current density, potassium chloride concentration in the melt, and electrode-melt interfacial area. The activation energy was found to be 111 kJ/mol of lithium, which is nearly equal to the heat of potassium vaporization (115 kJ/mol) from the melt. Since the activation energy is about equal to the heat of potassium vaporization, the rate of the reaction of lithium with potassium chloride is considered to be controlled by the rate of potassium vaporization from the melt.

In the course of Li-S cell studies in a helium atmosphere, fumes of varying intensity were observed when lithium metal, held in a stainless steel matrix, was dipped into the molten LiCl-KCl electrolyte at 673°K. The fumes, which became more pronounced as the temperature was increased, were reddish-brown and gave a grayish-purple to violet deposit on condensation. When the condensate was smeared, it appeared to be very soft and had a metallic luster.

The metallic lithium which dissolves in LiCl-KCl melts should not be the source of the fumes, as no fumes have been observed over Li-LiCl solutions at about 923°K. The partial vapor pressure of lithium is expected to be lowered by dissolution in these melts if the solution is similar in behavior to that of alkaline earth metals in their respective chlorides. The partial vapor pressures of the alkaline earth metal in their respective chlorides have been observed to be lowered (1).

Hammer *et al.* (2) calculated the standard decomposition potentials of the alkali halides and indicated that the LiCl-KCl melt can be used as an electrolyte in galvanic cells with lithium anodes. The LiCl-KCl melt is used as an electrolyte in the electrolytic production of lithium metal (3). But both of these sources did not give any information as to what extent the lithium reacts with the potassium chloride under the existing conditions. The reaction of lithium with potassium chloride at cell operating temperatures (~673°K) may proceed to the extent where the activity of the potassium may be high enough to give appreciable vapors, and consequently may be the source of the fumes seen in the lithium-sulfur studies. Some indication of potassium vaporization at higher temperatures (above 773°K) from a LiCl-KCl melt in contact with lithium may be obtained from the emf work of Foster *et al.* (4) where they observed potassium condensate on the cooler sections of the electrode leads of cells with Li anodes, Li-Bi cathodes, and LiCl-KCl electrolyte. Therefore, a systematic investigation was undertaken to identify the volatile product and the sources of its formation and to determine its rate of formation and the rate-controlling step.

Experimental

Materials.—Lithium metal of 99.97% purity and a compressed nickel-fiber sheet of 80% porosity with an

* Electrochemical Society Active Member.

Key words: lithium electrode, molten salt electrolyte, lithium chloride-potassium chloride, exchange reaction, potassium vaporization.

average pore size of 40 μm (pore range $\approx 20\text{--}60 \mu\text{m}$) were used to make the test electrodes.

Lithium chloride of 99.6% purity and potassium chloride of 99.9% purity were used in preparing the eutectic mixture. The eutectic mixture was purified by bubbling chlorine through the melt at about 723°K for 2 hr and subsequently scavenging the chlorine by bubbling helium for about 1 hr. The exact purity level of the prepared electrolyte was not determined. However, lithium cycling tests yielded a mean current efficiency of $97 \pm 5\%$ which was taken to indicate no gross amount of impurities. In addition, the low electronic conductivity, $8 \times 10^{-3} \text{ ohm}^{-1}\text{cm}^{-1}$ at 723°K (5) is not expected to have any influence on the measurements. This may also be observed from the current efficiency.

Electrode preparation.—The lithium electrodes were prepared by cutting rectangular pieces, 13 \times 25 mm each, from the 1.6 mm thick nickel-fiber sheet. A 1.5 mm hole was drilled through each of the matrices near the narrow edge (Fig. 1). A 1.5 mm diameter by 450 mm long rod of 304 stainless steel was then inserted through the hole, bent to form a hook, and then arc welded to provide an intimate contact with the nickel-fiber matrix. This rod served as the electrical lead during testing. The matrices were hydrogen-fired at 1100°C for 2 hr to remove oxides from their surfaces before use.

The electrode matrices were loaded by immersing them in a molten pool of lithium at approximately 973°K. After loading, the counterelectrode was electrolytically stripped of its lithium in a separate cell.

Apparatus.—The furnace was a clamshell heater, 150 mm long and 75 mm ID, insulated with firebricks. This simple furnace was convenient to use in the dry box. The furnace temperature was controlled with a proportional-band temperature controller. A millivolt potentiometer and a Chromel-Alumel thermocouple were used for temperature measurements. The electrical instruments included a d-c power supply, together with the necessary logic and switching circuitry to cycle the cell automatically according to a preset charge-discharge program, and a dual channel recorder for measuring cell potential and current.

A bell-shaped condenser made from 304 stainless steel, large enough to cover the clamshell heater, was used for the condensation of the fumes. The condenser had a central tube to allow the hot gases to escape. A tray inside the condenser, which was attached at the

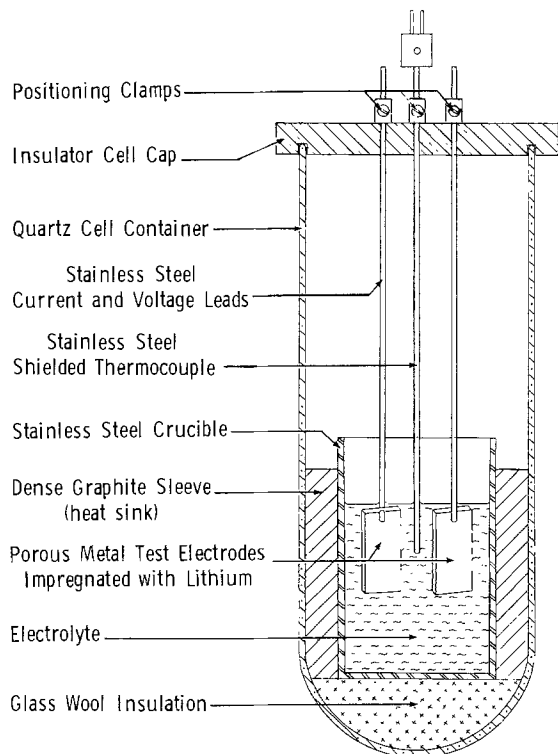


Fig. 1. Lithium electrode test cell

bottom end of the central tube for collecting the condensate, also served as a baffle.

The cell used for cycling the lithium between the two electrodes is shown in Fig. 1. It consisted of a quartz enclosure (70 mm diam, 300 mm deep) fitted with a cap which served to position the two electrodes and a thermocouple. A 304 stainless steel cup (50 mm diam, 100 mm deep) was used to hold the electrolyte.

Procedure.—About 50g of purified LiCl-KCl eutectic was placed into a hydrogen-fired stainless steel container, 100 mm long and 50 mm ID inside a helium-atmosphere dry box. The container with the eutectic was placed inside the furnace and heated to 673°K. While the melt was maintained at this temperature, lithium metal was slowly added. After about 15 min, reddish-brown fumes were observed to be coming from the melt. (These fumes were similar in appearance to cigarette smoke.) The condenser was positioned above the melt container to condense the fumes. After a week, the condensate was scraped from the condenser and sent for chemical analysis.

To determine the rate of product volatilization, the test cell (Fig. 1) was assembled inside the dry box holding the electrodes above the solid electrolyte (usually 200g). The cell was placed inside the furnace,

heated to the desired temperature, and the electrodes were lowered into the molten electrolyte. The immersion depth was kept at a minimum so that the electrode leads would not contribute appreciably to the electrode areas. After thermal equilibrium was reached, the testing was accomplished by continuously cycling the cells at varying current densities with the aid of the automatic cycling device. The usual test consisted of discharging the working electrode at constant current until an increase in voltage (5-10 mV at 0.1A) indicated that the lithium was depleted from the electrode. After a short recovery time (300 sec), the current was reversed and the lithium was recharged onto the working electrode until a similar voltage increase again indicated the complete transfer of lithium. The cycling was continued in this manner for several hours to determine the loss in lithium capacity as a function of time under the test conditions. In addition, visual inspection of the electrodes was made periodically to determine the wetting characteristics and the general appearance of the deposited lithium. These determinations were made at various temperatures and current densities.

Results and Discussion

Identification of the volatile product and the source of its formation.—The condensate that was obtained from over the Li-LiCl-KCl melt was gray. It appeared to be very soft when rubbed with a stainless steel spatula. The chemical analysis of this condensate gave >99.0% potassium and 0.1% lithium. This indicates that potassium vapors may have been the source of the fumes seen during lithium-sulfur cell studies. As stated earlier, potassium vapor formation has also been reported by Foster *et al.* (4) during their emf measurements of cells with Li anodes, Li-Bi cathodes, and LiCl-KCl electrolyte above 773°K. Another recent work has also reported vaporization of potassium from Li-LiCl-KCl solutions at 400°C (6). Together, these findings indicate the possibility of the following reaction



The standard free energy changes, ΔG° , calculated at various temperatures, from the data given in the JANAF compilation (7), are given in Table I. The value of ΔG° varies from 18.8-16.1 kJ/mol of lithium (4490-3855 cal/mol of lithium) in the temperature range 627°-823°K. The activity of potassium may be calculated from the equilibrium constant

$$K = \frac{a_{\text{LiCl}} a_{\text{K}}}{a_{\text{KCl}} a_{\text{Li}}} \quad [2]$$

where a is the activity of the designated component.

The values of K at various temperatures were calculated from the relation

$$K = e^{-\Delta G^\circ/RT} \quad [3]$$

Table I. Standard free energy change, ΔG° , equilibrium constant, K , and activities a , of the components for the reaction $\text{KCl(s)} + \text{Li(l)} = \text{LiCl(s)} + \text{K(l)}$, and partial vapor pressures of K, P_K

Temperature, °K	ΔG° , kJ/mol or (cal/mol)	Equilibrium constant, K	Activities*			Partial pressure, P_K , Pa or (mm Hg)
			a_{LiCl}	a_{KCl}	a_K	
627	18.8 (4490)	0.02728	1	1	0.0273	4.853 (0.0364)
648	18.5 (4420)	0.03229	0.933	0.959	0.0332	10.306 (0.0773)
673	18.2 (4340)	0.03894	0.865	0.916	0.0412	22.811 (0.1911)
698	17.8 (4260)	0.04634	0.805	0.878	0.0505	47.703 (0.3578)
723	17.5 (4175)	0.05468	0.753	0.843	0.0612	94.846 (0.7114)
773	16.8 (4015)	0.07323	0.668	0.785	0.086	325.307 (2.44)
823	16.1 (3855)	0.09466	0.601	0.736	0.116	952.722 (7.146)

* With respect to solid.

and are given in Table I. The activity of LiCl in LiCl-KCl melts with respect to pure solid LiCl were calculated in the usual way using the open-circuit potentials for LiCl-KCl melts reported by Anthony *et al.* (8). The relation reported by Bradley and Sharma (9)

$$E^{\circ} = 4.184 - 7.96 \times 10^{-4}T \pm 0.010V \quad (600^{\circ} - 881^{\circ}K) \quad [4]$$

was used for those of pure LiCl. The activities of KCl with respect to pure solid KCl were calculated using the Gibbs-Duhem relation. These activities are given in Table I. The activities of K at various temperatures were calculated by Eq. [2] at unit activity of Li using the values of K , a_{LiCl} , and a_{KCl} given in Table I. Pure lithium at unit activity will be present under the conditions of the calculations as potassium is not appreciably soluble in lithium (10). The calculated potassium activities also given in Table I are less than unity in each case, indicating that under these conditions potassium will be present only in solution in the eutectic melt. The vapor pressures of potassium (mm Hg) can be calculated using the equation (11)

$$\log P_K = -4770/T - 1.37 \log T + 11.58 \quad [5]$$

The partial vapor pressures of potassium, P_K , over the melt of Li and LiCl-KCl eutectic electrolyte, were calculated from the activity of potassium and its vapor pressure at various temperatures, and are given in Table I. The partial vapor pressure of potassium is quite appreciable at these temperatures. Therefore, reaction [1] appears to occur forming K which vaporizes giving fumes over the LiCl-KCl melt. The enthalpy change of the reaction is 27.2 kJ/mol of lithium (6.5 kcal/mol of lithium) and the entropy change is 64.4 J/K per mol of lithium (15.4 cal/deg per mol of lithium) at these temperatures. So the reaction appears to occur due to the change in entropy.

Rate of the reaction at various current densities and temperatures.—Twelve cells were assembled to generate the data. The matrices made from nickel fiber retained lithium metal better than other metal-fiber matrices tested. A fully loaded matrix had a capacity of 2.5 kC of lithium. Results of typical tests in terms of lithium electrode capacity vs. elapsed time are presented in Fig. 2 and 3.¹ The results at various current densities are given in Fig. 4, whereas the results at various temperatures are shown in Fig. 5. Figure 6 presents the rates of lithium loss obtained from Fig. 5 plotted against temperature reciprocals.

The data were obtained after the electrolyte had been in contact with lithium for more than 300 ksec in order to ensure saturation. Similar melts, such as molten magnesium chloride, have been observed to be saturated with magnesium within 5.5 ksec (12) and molten calcium chloride with calcium within 10 ksec (13).

The data in Fig. 2 also indicate electrolyte saturation with lithium before the measurements were made. In this case, the electrolyte had been in contact with lithium for 30 ksec, then the lithium loss rate was measured at 500°C before and after an interval of 340 ksec at 400°C. The lithium loss rates before and after the interval were the same. This observation indicates that the electrolyte had been saturated with lithium within 30 ksec and remained so during the measurements.

Lithium loss by droplet formation can also be discounted from the data in Fig. 2. As may be observed from the plots in this figure, the lithium loss rate with time remains constant at 500°C, then decreases with change in temperature to 400°C, and regains its original value when the temperature was raised to 500°C. This regularity in loss rate with temperature is most unlikely if droplet formation is occurring. However, under certain conditions, especially at lower tempera-

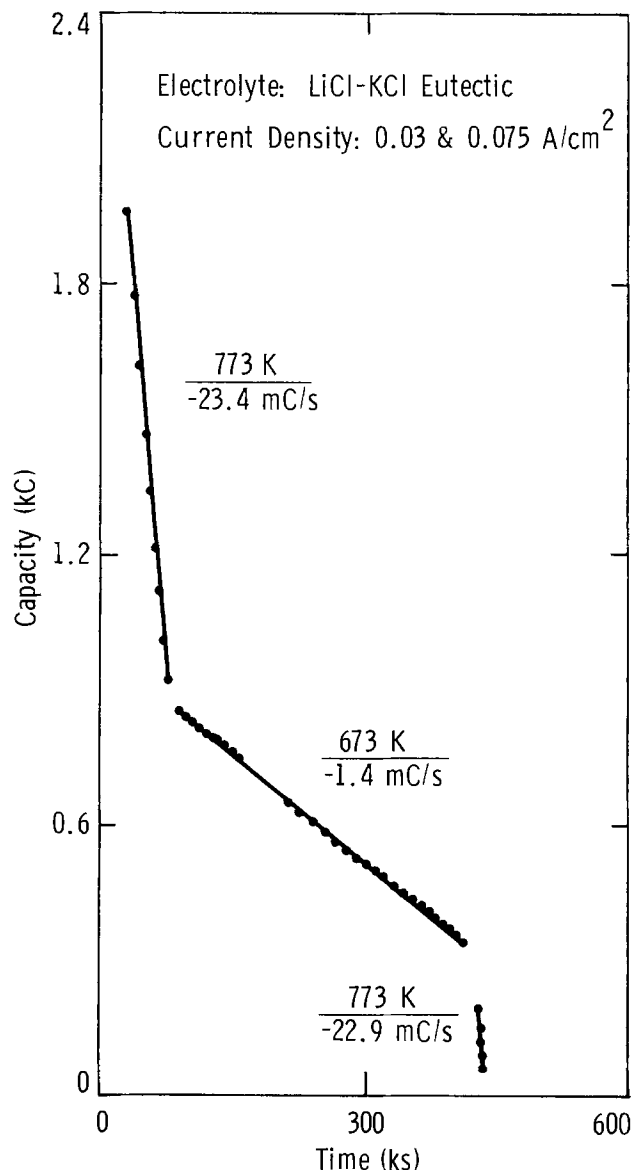


Fig. 2. Lithium content of electrode vs. elapsed time

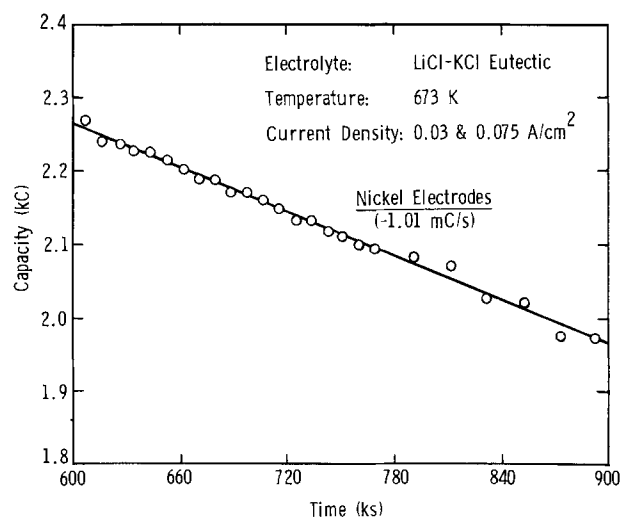


Fig. 3. Lithium content of electrode vs. elapsed time

tures ($\sim 400^{\circ}C$), lithium loss has been observed by droplet formation. In these experiments, the lithium loss with time was observed to be erratic. The loss increased in an erratic manner with increase in current density, *i.e.*, droplet formation appeared to increase with increase in current density. The droplets in the electrolyte could also be seen visually. The present

¹ The curves shown in these and subsequent figures in the text are a least squares fit to the data. For clarity, the individual data points were not included in Fig. 4.

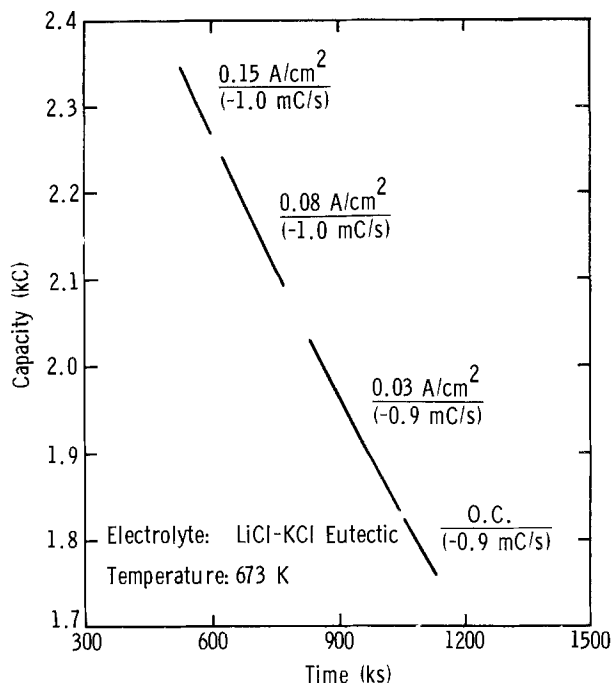


Fig. 4. Lithium content vs. elapsed time at various current densities.

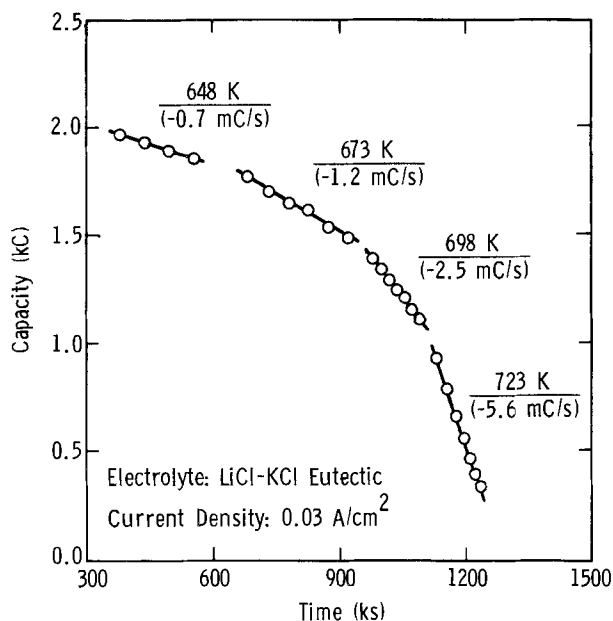


Fig. 5. Lithium content vs. elapsed time at different temperatures.

data are from experiments where the lithium loss with time was linear (Fig. 2 and 3). It remained constant with change in current density from 0 to 1500 mA (Fig. 4) and no lithium droplets were observed in the electrolyte.

Figures 2-5 show the lithium loss rate to be independent of the change in concentration of lithium chloride [+1.0 weight per cent (w/o) maximum] and potassium chloride (-1.0 w/o maximum) which occurred during the period of the experiments. It also is not affected by the possible lithium chloride and potassium chloride concentration gradients which could occur with current density variations (Fig. 4).

The rate of lithium loss increases exponentially with decreasing reciprocal temperature and follows an Arrhenius relationship as may be seen in Fig. 6. The activation energy calculated from this plot is 111 kJ/mol of lithium. This is nearly equal to the heat of

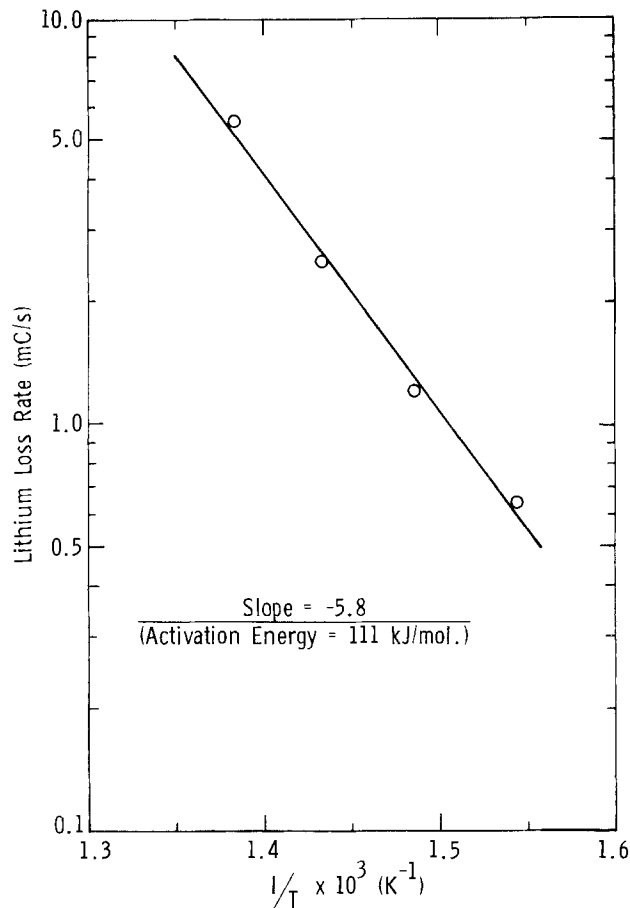


Fig. 6. Effect of temperature on lithium loss rates

vaporization of potassium (115 kJ/mol of potassium) which was calculated from the equilibrium potassium vapor pressures over the lithium chloride-potassium chloride melts at various temperatures given in Table I.

Determination of the rate-controlling step.—In the homogeneous Li-K-LiCl-KCl melt, the number of K molecules reaching a unit surface in unit time may be taken to be

$$n_K/2 V_x \quad [6]$$

where n_K is the number of potassium molecules per cubic centimeter and V_x is the velocity component perpendicular to the surface.

The term $1/2$ implies that only one-half of the potassium molecules are moving toward the surface and the other half are moving in the opposite direction.

The number of molecules in a velocity interval between V_x and $V_x + dV_x$ can be obtained from the Maxwell distribution (14-17) as

$$dn_{V_x} = n_K/2 \sqrt{\frac{M}{2\pi RT}} e^{-MV_x^2/2RT} dV_x \quad [7]$$

where M is the molecular weight, R is the gas constant, and T is the temperature in degrees K.

The number of molecules reaching the surface in unit time within this velocity interval is given by

$$dn_{K'} = V_x n_K/2 \sqrt{\frac{M}{2\pi RT}} e^{-MV_x^2/2RT} dV_x \quad [8]$$

Now all of the molecules having a velocity less than a certain limiting value, V_L , will be pulled back by the attractive forces of the other molecules in the interior. Only those molecules which have velocities greater than V_L can pass through this zone of attraction and escape as vapors. The number of these molecules can be determined by integrating the above equation be-

tween $V_x = V_L$ and $V_x = \infty$ and so

$$n_K' = n_K/2 \int_{V_L}^{\infty} \sqrt{\frac{M}{2\pi RT}} e^{-MV_x/2RT} V_x dV_x \quad [9]$$

Upon integration

$$n_K' = n_K/2 C e^{-MV_L/2RT} \quad [10]$$

where C is a constant equal to $\sqrt{Rt/2\pi M}$.

The expression $MV_L^2/2$ represents the kinetic energy of one mole of potassium atoms moving with the limiting velocity, V_L , and which are just capable of escaping into the gas sphere. According to the law of conservation of energy, this amount of energy must be equal to the work performed against the attractive forces of the atoms in the interior, i.e., it is equal to the work of vaporization of potassium from the melt. The work of vaporization can be taken equal to the heat of vaporization, ΔH_v , which gives $MV_L^2/2 = \Delta H_v$. Therefore

$$n_K' = n_K/2 C e^{-\Delta H_v/RT} \quad [11]$$

a relation which shows the activation energy equal to the heat of vaporization of potassium.

In a general way, the Li losses in Li-LiCl-KCl melts may be considered to occur in the following steps: (i) contact of lithium with potassium chloride either through solution or by transport of potassium chloride to the lithium-electrolyte interface, (ii) $\text{Li(l)} + \text{KCl(melt)} = \text{LiCl(melt)} + \text{K(melt)}$ reaction, (iii) transport of lithium chloride and potassium away from the reaction zone, and (iv) evaporation of potassium by the reaction: $\text{K(solution)} \rightleftharpoons \text{K(vapors)}$.

As was observed earlier, the activation energy calculated from the rate of lithium loss vs. temperature has been found equal to the heat of vaporization of K from Li-K-LiCl-KCl melts. The heat of vaporization of potassium was calculated from the equilibrium partial vapor pressures of potassium over these melts at different temperatures. Since the activation energy is equal to the heat of vaporization under these conditions, the rate-controlling step appears to be the potassium vaporization reaction. This also implies that the electrolyte has equilibrium concentrations of potassium and lithium.

Acknowledgment

The authors are thankful to Dr. Elton J. Cairns for helpful discussions.

Manuscript submitted Jan. 10, 1975; revised manuscript received March 28, 1975.

Any discussion of this paper will appear in a Discussion Section to be published in the June 1976 JOURNAL. All discussions for the June 1976 Discussion Section should be submitted by Feb. 1, 1976.

Publication costs of this article were partially assisted by General Motors Corporation.

REFERENCES

1. J. A. Van Westenburg, PhD Thesis, Iowa State University of Science and Technology, Ames, Iowa (1964).
2. W. J. Hamer, M. S. Malmberg, and B. Rubin, *This Journal*, **103**, 8 (1956).
3. G. T. Motock, *Electrochem. Technology*, **1**, 122 (1963).
4. M. S. Foster, S. E. Wood, and C. E. Crouthamel, *Inorg. Chem.*, **3**, 1428 (1964).
5. R. J. Heus and J. J. Egan, *J. Phys. Chem.*, **77**, 1989 (1973).
6. P. A. Nelson *et al.*, USAEC Report ANL-8058, Argonne National Laboratory, Argonne, Ill. (1974).
7. JANAF Thermochemical Data, Vol. I, The Dow Chemical Co., Midland, Mich. (Dec. 1960).
8. R. G. Anthony, B. J. Welsh, and R. J. Steele, *Australian J. Chem.*, **21**, 789 (1968).
9. T. G. Bradley and R. A. Sharma, in the 26th Power Sources Conference, Atlantic City, N. J. (April 30, 1974).
10. Max Hansen, "Constitution of Binary Alloys," p. 875, McGraw-Hill Book Co., New York (1958).
11. O. Kubaschewski, E. LL. Evans, and C. B. Alcock, "Metallurgical Thermochemistry," Pergamon Press, New York (1967).
12. M. Krumpelt, J. Fischer, and I. Johnson, *J. Phys. Chem.*, **72**, 506 (1968).
13. R. A. Sharma, *ibid.*, **74**, 3896 (1970).
14. W. J. Moore, "Physical Chemistry," pp. 215, 235, Prentice-Hall International Inc., Englewood Cliffs, N. J. (1964).
15. J. R. Partington, "An Advanced Treatise on Physical Chemistry," Vol. I, p. 251, Longman, Green and Co., London (1951).
16. J. R. Partington, "An Advanced Treatise on Physical Chemistry," Vol. II, p. 245, Longman, Green and Co., London (1951).
17. S. Glasstone, "Textbook of Physical Chemistry," pp. 264, 449, D. Van Nostrand Co. Inc., New York (1946).

Silver/Silver Chloride Electrode: Charging of a Porous Structure

S. Szpak and A. Nedoluha

Electronic Materials Sciences Division, Naval Electronics Laboratory Center, San Diego, California 92152

and T. Katan*

Materials and Structures, Lockheed Palo Alto Research Laboratory, Palo Alto, California 94304

ABSTRACT

Reaction profiles for the charging of porous silver electrodes in 1N KCl are investigated. The effects of changes in the rate-determining step on the reaction profile are calculated and compared with experiment for galvanostatically held superficial current densities of 2-25 mA/cm² for 2-8 hr. Interpretations are given for the experimentally determined distributions of anodically formed silver chloride and for the morphology of the silver chloride deposits as observed with the scanning electron microscope as a function of distance into the porous structure.

In recent years several approaches to battery electrode modeling have been proposed. Perhaps the best known and most comprehensive one is that of Bennion and co-workers (1, 2) which is based on the solution of a set of coupled partial differential equations representing the various applicable laws of transport and conservation. An effective computer program is available so that, in principle, the reaction profile can be constructed once the details of the reaction mechanism and transport processes within the porous structure have been established (3). In practice, the difficulty in electrode modeling arises from a lack of sufficiently detailed information concerning the nature of the controlling elementary processes and their dependence on the degree of electrode discharge. Nevertheless, some success has been reported in a comparison of the experimental data of Bro and Kang (4), with the computer simulated behavior using the solution-diffusion model (3).

Experimental efforts in studying the time-dependent evolution of reaction profiles, which are of interest in battery technology, involve the determination of pertinent factors from the analysis of the degree of conversion as a function of distance at externally controlled discharge conditions, *e.g.*, potentiostatic, galvanostatic, or an otherwise programmed discharge mode. In general, it is not possible to assign a reaction path on the basis of a chemical analysis of the reaction products as a function of distance alone. Thus, in addition to the usual analytical procedures, Katan (5) and Katan *et al.* (6, 7) studied surface morphology after charge and discharge in an attempt to obtain data necessary for modeling the sparingly soluble reactant-conductive matrix system. In an extension of this approach, Bennion *et al.* (8) selected a different geometry to simulate the electrode behavior and employed x-ray element scanning analyses combined with scanning electron microscopy to arrive at the nature of the controlling elementary process.

While electrode modeling can be used to predict electrode behavior and to show very clearly the effects of various elementary processes, modeling *per se* cannot be used to predict the elementary processes. It is the purpose of this communication to illustrate how a gain into describing the working of battery electrodes can be achieved using a more restrictive model for which analytical solutions can be given. In particular, we shall consider the situation where the rate determining step changes during the course of electrode discharge.

This model is less restrictive than that of Winsel (9) where the reaction path is invariant with time, but certainly is more restrictive than that of Bennion and co-workers (1, 2). The silver/silver chloride electrode will be used here to demonstrate essential features of this model.

Equivalent Circuit Concept

Elementary model of porous electrode.—An extensive review of the equivalent electric circuit concept was given by de Levie (10). The reaction density profile for a one-dimensional porous electrode of length l , and subject to a galvanostatic mode of operation, *i.e.*, for boundary conditions given by

$$i(0, t) = i_0, i(l, t) = 0 \quad [1]$$

is as follows

$$j(x) = \kappa_1 i_0 \frac{\cosh[\kappa_1(l-x)]}{\sinh(\kappa_1 l)} \quad [2]$$

The transfer (faradaic) current density is given by Eq. [3]

$$j = - \frac{\partial i}{\partial x} \quad [3]$$

The dimensionless parameter $\kappa_1 = (R_1/Z_1)^{1/2}$, is the square root of the ratio of solution resistance to electrode reaction impedance, both per unit length and unit cross section of the porous electrode.

Equation [2] exhibits an exponential behavior; for $j(x) > 0$, the slope $j'(x)$ is negative and its magnitude decreases with an increase in distance. The rate at which $j(x)$ bends away from the x axis depends on the numerical value of κ_1 . Thus, Winsel (9) refers to κ_1 as the reduced pore length, Bro and Kang (4) prefer the name of electrochemical Thiele parameter. Other terms, such as electrode effectiveness factor and depth of penetration, are also associated with it. A formulation by Nanis (11) is especially useful because it reflects the importance of electrode structure as well as the electrochemical process. Regardless of the manner in which this number has been introduced, its use is limited to electrodes under a steady-state regime.

Unfortunately, a true steady-state operation cannot be realized in the course of battery discharge, because the supply of reactant is continually diminishing. Corresponding structural changes occur, and when all active material is used up, the electrode ceases to function. The time-dependent reaction profile is thus related to the material used up, or, alternatively, to the material still present. It is not surprising, therefore, that the experimentally determined Thiele parameter

* Electrochemical Society Active Member.

Key words: silver chloride, porous electrode, charge distribution, current distribution, reaction profile.

has been found to vary with the electrode discharge (4, 12).

Porous electrode with change of reaction path.—An electrochemical process, as a rule, consists of a series of consecutive elementary processes. Consequently, there exists a relation

$$Z(x, t) = \sum_k Z_k(x, t) \quad [4]$$

as can be inferred from Van Rysselberghe's analysis of the complex reaction path (13), as indicated by de Levie (10), and as explicitly derived by Dunning (3) for the "solution-diffusion" model.

Usually one elementary process dominates the overall reaction path, so that the right side of Eq. [4] contains essentially one term. If, in the course of electrode reaction a change in the rate determining step (rds) takes place, only the numerical value of Z is affected, that is to say, again only one term dominates expression [4]. A typical example is the reduction of thin films of silver chloride partially covering the silver substrate. It was recently shown that, as the individual patches of silver chloride become smaller, a change in the rds from chloride diffusion to silver chloride dissolution occurs (6). If this process is allowed to occur within the confinements of a porous structure, a change in the rds is likely because of the wide variety of local conditions caused by the distribution in transfer current density and the decreased accessibility of electrolyte which effectuates a change in local concentrations.

Consider an electroactive substance uniformly dispersed within the conductive matrix. Assume that the reaction path is initially governed by one elementary process throughout the electrode thickness. The reaction density profile is described by Eq. [2], with R_1 and Z_1 associated with the assumed reaction path. Due to the nonlinear reaction profile, the amount of the active material used up varies with distance. Assume further that, when the amount of active material initially present is reduced to an *a priori* specified level, another reaction path begins to operate. The reaction density profile given by Eq. [2] then no longer applies.

The graphical representation of a change in the rds within the porous electrode is shown in Fig. 1. The change from one mechanism to another has occurred at $x = x_c$. To the right, i.e., for $x_c < x \leq l$, the initial reaction path operates, while for $0 \leq x < x_c$, another process dominates the electrode discharge.

Obviously, the location at which the change in controlling reaction takes place is determined by the extent of the electrode discharge or charge. It follows that the rational description of electrode operation requires specification of three time intervals, namely, the time before the second mode of electrode operation is initiated, the time during which the first and second modes operate simultaneously, each with its own rds,

and the time after the first mode of operation has completely disappeared. The determination of these time intervals, the corresponding reaction profiles, and the velocity at which the plane of change in the rds propagates through the porous structure can be used to constitute the basis for electrode evaluation. The plane at which the change in the rds occurs will henceforth be referred to as the mode interface.

Analytical Formulation

Basic concepts.—Consider a small section of an equivalent electric circuit analogue, shown in Fig. 1(b). The current density, $i(x, t)$, and the electrostatic potential in the solution phase relative to the metal matrix, $u(x, t)$, are related by Eq. [5] and [6]

$$\frac{\partial u}{\partial x} = -Ri \quad [5]$$

$$\frac{\partial i}{\partial x} = -\frac{u}{Z} \quad [6]$$

The degree of electrode discharge or charge at point, x , and time, t , is given by Eq. [7]

$$M(x, t) = M_0 - \alpha Q(x, t) \quad [7]$$

Here, M_0 is the initial amount of electroactive material uniformly distributed within the porous structure, α is a proportionality constant, and $Q(x, t)$ is the transferred charge. If the discharge process is initiated at $t = 0$, the charge transferred at time t is given by Eq. [8]

$$Q(x, t) = \int_0^t j(x, t') dt' \quad [8]$$

We consider $Q(x, t)$ to be always positive and express it in Asec/cm³. When the amount of charge transferred exceeds an *a priori* given amount, that is, when $Q(x, t) > Q_c$, a new reaction path becomes operative, characterized by R_2 and Z_2 , as illustrated in Fig. 1(a). Thus, the introduction of R_1 , Z_1 , R_2 and Z_2 , identifies two regions within the electrode structure. The region to the left, i.e., for $0 \leq x < x_c$, will be designated as region 2, while the region to the right of the dividing plane at $x = x_c$, will be referred to as region 1.

With the adapted nomenclature, we identify $x_c(t)$ as the position where a change in the rds takes place, for example, from diffusion to dissolution controlled, as illustrated in Fig. 1. All relevant quantities pertaining to position $x_c(t)$ will be denoted by subscript *c*. The quantities of interest in the present communication are: Q_c , the amount of charge transferred, or extent of electrochemical reaction necessary to initiate the change in the rds; $t_c(x)$, the time at which the mode interface arrives at an *a priori* selected position x ; $v_c(x)$, the velocity at which the mode interface penetrates the porous structure.

The extent of the electrochemical conversion is defined by Eq. [8]; the critical time $t_c(x)$ is the inverse of $x_c(t)$. For j bounded, it follows from Eq. [8] that a critical time, $t_c(0)$, exists such that all of the electrode belongs to region 1 for $t \leq t_c(0)$. Within this time period the electrode operates under one mode, that is to say, the same reaction path operates throughout the electrode structure. As discharge of the electrode is carried beyond time $t_c(0)$, the mode interface begins to penetrate into the porous structure, reaching the electrode's backside at time $t_c(l)$. Thus, at a time greater than $t_c(0)$ but less than $t_c(l)$, the electrode operates under two modes, with the change of the rds occurring at position $x_c(t)$.

At times greater than $t_c(l)$, the reaction profile is once again controlled by a single mode, i.e., by the new reaction path which supplanted the original one.

The physical significance of $x_c(t)$, and of the charge transferred, Q_c , is clear; practical utilization, however, requires a knowledge of the dependence of these quantities on the nature of electrochemical reaction and the

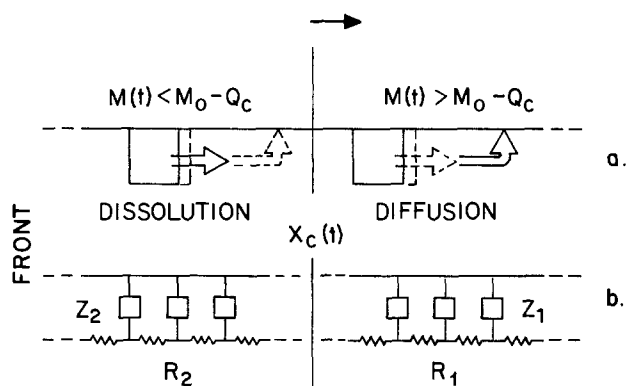


Fig. 1. Schematic representation of a segment of porous electrode. Upper: change in reaction path at $x = x_c(t)$; initial reaction path at $x > x_c(t)$, newly created path at $x < x_c(t)$. Lower: electric circuit analogue, subscript 1 initial path, 2 reaction path after $Q > Q_c$.

electrode's structure, and information is needed on changes in these dependences which occur during the course of reaction. Specifically, we need the reaction profile at any time, t , the rate of penetration of the mode interface, and the amount of charge transferred. The depth of penetration of the mode interface and the rate of penetration are experimentally accessible (12) without electrode destruction. The reaction profile, on the other hand, is usually not accessible to direct measurement; it is inferred from the changes in chemical composition as a function of time and position. If the reaction profile is known and the model is given, one can compute the corresponding charge transferred; conversely, from experimental information on the extent of the electrode reaction as a function of position and time, the reaction profile can be reconstructed.

Determination of critical time, $t_c(0)$.—From the initiation of electrode discharge at $t = 0$ to the time $t_c(0)$, the reaction profile is given by Eq. [2]. The local rate of electrode reaction, $j(x)$, during this period is taken to be independent of time until charge Q_c is accumulated, which is an approximation. Hence, it follows from Eq. [8] that

$$Q(x, t) = j(x) \cdot t \quad [9]$$

which, together with Eq. [2], results in

$$t_c(0) = \frac{Q_c}{\kappa_1 i_0} \tanh(\kappa_1 l) \quad [10]$$

Evidently, the time necessary for the initiation of a new reaction path is determined by the electrode thickness as well as the initial reaction path. The critical time can be experimentally controlled by the total discharge current density, i_0 in Eq. [10].

Transfer current density profile, $j(x, t)$.—The transfer current density distribution representing the reaction rate profile prior to initiation of the new reaction path is given by Eq. [2]. A similar expression applies also at times greater than $t_c(l)$, except that R_1 and Z_1 are replaced by R_2 and Z_2 , denoting the new reaction mechanism.

In this section we will calculate the discharge profiles when the electrode operates with a change of reaction mechanism, that is, discharge profiles for $t_c(0) < t < t_c(l)$. The general form for the solution of Eq. [5] and [6] is given by Eq. [11] and [12]

$$i = Ae^{\kappa_2 x} + Be^{-\kappa_2 x} \text{ for } 0 \leq x < x_c \quad [11]$$

$$i = Ce^{\kappa_1 x} + De^{-\kappa_1 x} \text{ for } x_c < x \leq l \quad [12]$$

Coefficients A , B , C , and D are evaluated using the

boundary conditions in Eq. [1] for the galvanostatic discharge together with the condition of continuity for current, i , and potential, u , at $x = x_c(t)$. After some manipulations, we obtain the coefficients as follows

$$A = -i_0 e^{-\kappa_2 x_c} M^{(-)}/2N \quad [13a]$$

$$B = i_0 e^{\kappa_2 x_c} M^{(+)} / 2N \quad [13b]$$

$$C = -i_0 \xi_2 e^{-\kappa_1 l} / 2N \quad [13c]$$

$$D = i_0 \xi_2 e^{\kappa_1 l} / 2N \quad [13d]$$

where

$$M^{(\pm)} = \xi_1 \cosh[\kappa_1(l - x_c)] \pm \xi_2 \sinh[\kappa_1(l - x_c)] \quad [14]$$

$$N = \xi_1 \sinh(\kappa_2 x_c) \cosh[\kappa_1(l - x_c)]$$

$$+ \xi_2 \cosh(\kappa_2 x_c) \sinh[\kappa_1(l - x_c)] \quad [15]$$

and

$$\xi_k = (R_k Z_k)^{1/2} \text{ with } k = 1, 2$$

Appropriate substitutions of Eq. [13]-[15] into Eq. [11] and [12], followed by differentiation with respect to distance, yield corresponding local current transfer densities

$$j(x) = \frac{\kappa_2 i_0}{N} \{ \xi_1 \cosh[\kappa_1(l - x_c)] \cosh[\kappa_2(x_c - x)] + \xi_2 \sinh[\kappa_1(l - x_c)] \sinh[\kappa_2(x_c - x)] \} \quad \text{for } 0 \leq x < x_c \quad [16]$$

$$j(x) = \frac{\kappa_1 \xi_2 i_0}{N} \cosh[\kappa_1(l - x)] \quad \text{for } x_c < x \leq l \quad [17]$$

Typical current density profiles associated with the change in the reaction path are shown in Fig. 2(a), 2(b), and 2(c). They were computed for a selected set of parameters R_1 , R_2 , Z_1 , and Z_2 to demonstrate the various types of transfer current density profiles that may arise in the course of electrode discharge or charge. For example, by changing values of R_1 , R_2 , Z_1 , and Z_2 two kinds of interferences affecting the evolution of reaction profile can be surmised with the derived equations, and they are designated as choking or blockage of the first and second kind. Specifically, Fig. 2(a), curve c, demonstrates the effect of choking of the first kind where the principal reaction zone, i.e., that portion of the electrode that carries the bulk of the transfer current, is shifted towards the front of the porous structure. This behavior is associated with an increase in electrolyte resistance, R_2 , either due to depletion by reactive consumption or because of formation of a voluminous precipitate suspended in the

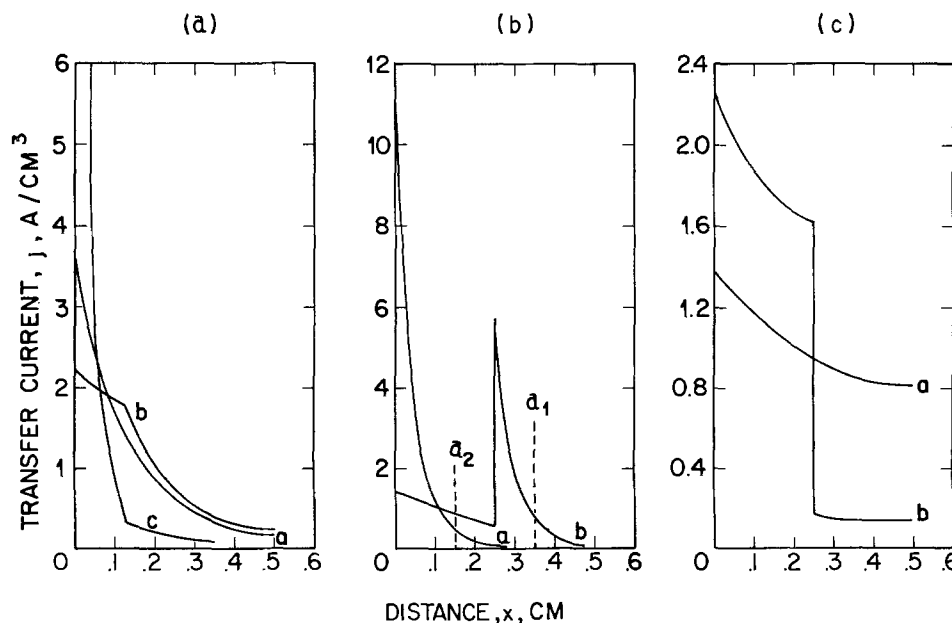


Fig. 2. Transfer current density profiles (from Eq. [16] and [17]) for selected set of parameters: R , Z , and x_c . All curves for $i_0 = 5 \text{ mA cm}^{-2}$ and $l = 0.5 \text{ cm}$. Note that at $x_c = 0$ only R_1 and Z_1 operate and R_2 and Z_2 are nonexistent while for $x_c > 0$ both R_1, Z_1 and R_2, Z_2 are operative. (a) $R_1 = 5, Z_1 = Z_2 = 10^{-1}$. Curve a, $x_c = 0$; curve b, $R_2 = 1, x_c = 0.125$; curve c: $R_2 = 50, x_c = 0.125$. (b) $R_1 = 5, R_2 = 1, Z_1 = 10^{-2}$, and $Z_2 = 10^{-1}$. Curve a, $x_c = 0$; curve b, $x_c = 0.25 \text{ cm}$. (c) $R_1 = R_2 = 5, Z_1 = 1, Z_2 = 0.1, x_c = 0.25 \text{ cm}$. Curve a, $x_c = 0$; curve b, $x_c = 0.25 \text{ cm}$.

electrolyte. Another type of choking, called that of the second kind, results in an opposite behavior when Z_2 is large, Fig. 2(b), curve b; the principal reaction zone is then shifted into the electrode interior.

Figure 2(c), curve b, illustrates another set of circumstances that may arise when Z_2 is small, *i.e.*, when the electrode reaction becomes faster as more electroactive substance has been converted. In practice, this may occur with complexing of the reaction product.

In our model the transfer current density profile consists of two regions, with a discontinuity at $x = x_c(t)$. By definition

$$\Delta j_c = \lim_{\epsilon \rightarrow 0} \{j[x_c(t) + \epsilon, t] - j[x_c(t) - \epsilon, t]\}, \epsilon > 0$$

hence, it follows from Eq. [16] and [17] that

$$\Delta j_c = (Z_2 - Z_1) \frac{i_0 \kappa_2 \kappa_1}{N[x_c(t)]} \cosh[\kappa_1(l - x_c(t))] \quad [18]$$

Sharp discontinuities as shown in Fig. 2 would be smoothed in real electrodes where the change in rate determining step occurs over a finite length. The magnitude of the discontinuity depends on both reaction paths and becomes smaller as the mode interface penetrates deeper into the electrode structure.

Rate of penetration of mode interface, $v_c(x)$.—The determination of the velocity at which the $x_c(t)$ plane penetrates the electrode structure can be used as a tool in the examination of simple models (12) of electrode discharge.

The charge transferred at any point within region 1 is specified by substitution of Eq. [17] into Eq. [8]

$$Q(x, t) = \kappa_1 i_0 z_1 \cosh[\kappa_1(l - x)] \int_0^t \frac{dt'}{N[x_c(t')]} \quad [19]$$

but, at $x = x_c(t)$, $Q(x, t) = Q_c$, which is a constant, thus Eq. [19] is an integral equation for $x_c(t)$

$$\int_0^t \frac{dt'}{N[x_c(t')]} = \frac{Q_c}{\kappa_1 i_0 z_1} \operatorname{sech}[\kappa_1(l - x_c(t))] \quad [20]$$

Upon differentiation of Eq. [20] with respect to t , an expression for the rate of penetration of the mode interface into the porous structure, $v_c(x_c(t)) = dx_c/dt$, can be written as follows

$$v_c(x) = \frac{i_0}{Q_c} \coth[\kappa_1(l - x)] \left\{ \frac{\xi_1}{\xi_2} \sinh[\kappa_2 x] + \cosh[\kappa_2 x] \tanh[\kappa_1(l - x)] \right\}^{-1} \quad [21]$$

The functional dependence of v_c on the depth of penetration x_c for a selected group of parameters characteristics of the new reaction path, R_2 and Z_2 , is shown in Fig. 3. It is seen that, immediately after the initiation of a new reaction path, the velocity of propagation of the mode interface is calculated by taking the limit of Eq. [21]

$$v_c(0) = \frac{i_0}{Q_c} \coth^2[\kappa_1 l] \quad [22]$$

The velocity, v_c , is thus independent of the kinetics of the newly formed reaction.

For penetration of the mode interface to some distance, x_c , which is small enough ($\kappa_2 x_c \ll 1$) so that $\sinh \kappa_2 x_c \approx \kappa_2 x_c$, another simplified relationship can be derived

$$v_c(x) = \frac{i_0}{Q_c} \coth[\kappa_1(l - x)] \left\{ \frac{\xi_1}{Z_2} x + \tanh[\kappa_1(l - x)] \right\}^{-1} \quad [23]$$

The rate of penetration is dependent on the reaction

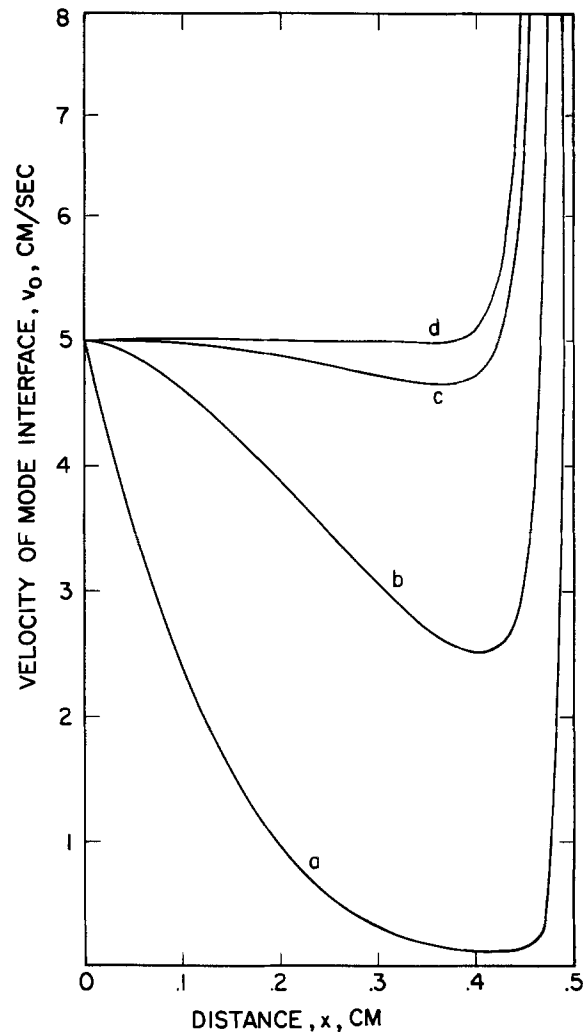


Fig. 3. Rate of penetration of the mode interface, $x = x_c$, into the electrode structure as function of reaction impedance. Curve a, $Z_1 = 10^{-2}$, $Z_2 = 5 \times 10^{-2}$; curve b, $Z_1 = 10^{-2}$, $Z_2 = 5 \times 10^{-1}$; curve c, $Z_1 = 10^{-2}$, $Z_2 = 5$; curve d, $Z_1 = 10^{-2}$, $Z_2 = \infty$; $R_1 = R_2 = 5$.

impedance of the new reaction path. Hence, the larger the value of Z_2 , the faster the rate of penetration. As Z_2 becomes infinite, as in the case treated by Winsel (9), Eq. [23] becomes the following

$$v_c = \frac{i_0}{Q_c} \coth^2[\kappa_1(l - x_c)] \quad [24]$$

Equation [24] no longer exhibits a minimum in the rate of penetration, as indicated in Fig. 3, *e.g.*, curve d.

Charge transfer.—Direct determination of the transfer current density profile in the course of battery electrode operation has not been demonstrated experimentally thus far, although earlier work by Euler (14) has dealt with simulated behavior. Verification of any proposed or assumed mechanism is usually sought via chemical analysis of the electrode interior. Such an approach essentially involves a comparison of the time integral $\int_0^t j(x, t') dt'$, calculated for an assumed model with the results of chemical analysis. In what follows, we will derive analytical expressions for the charge transferred, *i.e.*, for the extent of reaction, valid for the considered mechanism of two reaction paths operating within the electrode structure at various degrees of electrode discharge.

Consider again Fig. 2(b) and select positions within the porous structure as indicated, *e.g.*, $x = a_1$ and $x = a_2$. Transfer current densities at these locations are given by Eq. [2], [16], and [17] with the extent of reaction obtained from appropriate substitutions into

Eq. [8]. The integration indicated by Eq. [8] extends over distinct time intervals reflecting the occurrence of significant events within the electrode structure, that is, based on the position where the change in the rds takes place.

The first time interval, characteristic of the assumed model, is the time before the onset of the new reaction path. This time has been denoted by $t_c(0)$. The integration indicated by Eq. [8] is particularly simple because the reaction profile is time independent. Hence, by Eq. [9]

$$Q(a_1, t) = i_0 \kappa_1 \frac{\cosh[\kappa_1(l - a_1)]}{\sinh(\kappa_1 l)} t \quad [25]$$

which, at $t = t_c(0)$, by Eq. [10] becomes

$$Q[a_1, t_c(0)] = Q_c \frac{\cosh[\kappa_1(l - a_1)]}{\cosh(\kappa_1 l)} \quad [26]$$

As the reaction is carried on beyond the critical time, $t_c(0)$, i.e., after the new reaction path is well established, two regions are distinguished. The first region covers depths greater than the position where the change in the rds has taken place, i.e., where $x_c(t) < a_1 \leq l$. The second region is concerned with the locations to the left of $x_c(t)$, i.e., for depths less than determined by the location of the mode interface, that is to say, when $0 \leq a_2 < x_c(t)$.

The charge transferred at any point within region 1 is less than Q_c and is given by Eq. [19]. At $x = a_1$ together with Eq. [20], this yields

$$Q(a_1, t) = Q_c \frac{\cosh[\kappa_1(l - a_1)]}{\cosh[\kappa_1(l - x_c(t))]} \quad [27]$$

It is seen that the charge transferred depends on the position $x_c(t)$ and only indirectly on the newly generated reaction path.

The calculation of charge transfer in region 2 is performed somewhat differently. The charge accumulated must exceed Q_c (by definition), thus the time integral, Eq. [8], may be split as follows

$$Q(a_2, t) = Q_c + \int_{t_c(a_2)}^t j(a_2, t') dt' \quad [28]$$

Here, it is convenient to change the integration variable through the use of the expression $v_c(x) = dx_c/dt$, and obtain

$$Q(a_2, t) = Q_c + \int_{a_2}^{x_c(t)} \frac{j[a_2, t_c(x')]}{v_c(x')} dx' \quad [29]$$

The $j(a_2, t_c(x'))$ and $v_c(x')$, needed in Eq. [29], are given by Eq. [16] and [21], respectively. Upon substitution we obtain

$$Q(a_2, t) = Q_c \left\{ 1 + \kappa_2 \int_{a_2}^{x_c(t)} \tanh[\kappa_1(l - x')] \left\{ \frac{\xi_1}{\xi_2} \cosh[\kappa_2(x' - a_2)] + \tanh[\kappa_1(l - x')] \sinh[\kappa_2(x' - a_2)] \right\} dx' \right\} \quad [30]$$

At times greater than $t_c(l)$, the electrode once again operates in a single mode of discharge or charge. The expression for the charge transferred is

$$Q(a_2, t) = Q[a_2, t_c(l)] + i_0 \kappa_2 \frac{\cosh[\kappa_2(l - a_2)]}{\sinh[\kappa_2 l]} \cdot [t - t_c(l)] \quad [31]$$

Figure 4 summarizes the behavior of the porous electrode operating with the change in the reaction path when the charge transferred exceeded a given

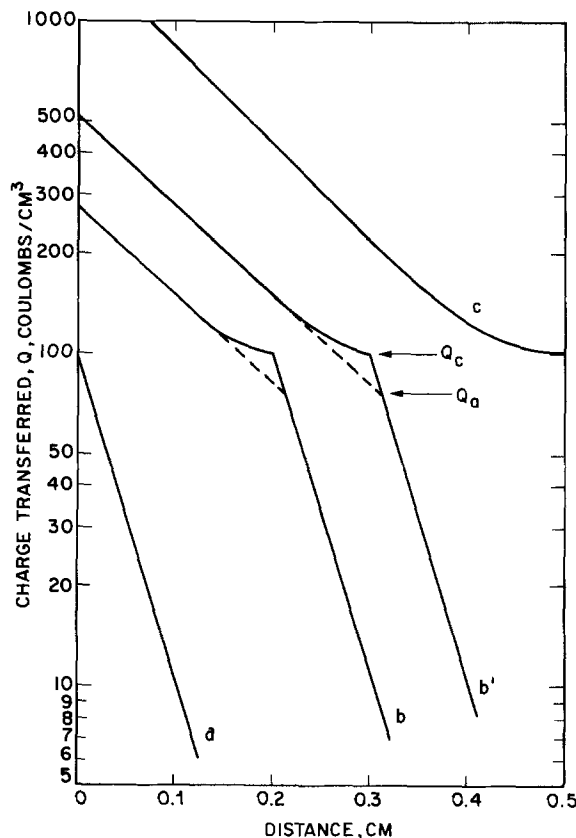


Fig. 4. Reaction product distribution at various time or electrode operation. Curve a, for $t = t_c(0)$; curve b and b', for $t_c(0) < t < t_c(l)$; curve c, for $t = t_c(l)$. Arbitrarily selected parameters: $i_0 = 0.25 \text{ mAcm}^{-2}$, $Q_c = 100.0$; $R_1 = 5.0$, $R_2 = 5.0$; $Z_1 = 10^{-1}$, $Z_2 = 10^{-2}$.

value, Q_c . In particular, curve a is a plot of Eq. [26] at $t = t_c(0)$, i.e., for $x_c = 0$. Curve b illustrates the Q - x relationship at times $t_c(0) < t < t_c(l)$, when the electrode experiences a change in the rds at $0 < x_c(t) < l$. The curve denoted by b', represents the Q - x relationship for the same electrode mechanism, but at some later time. It is seen that the curves are displaced to the right, but are otherwise very similar. The relevant equations are: Eq. [27] for the lower part and Eq. [30] for the upper part. The rate at which the displacement penetrates the electrode structure is, of course, the velocity given by Eq. [21]. Finally, curve c illustrates the behavior at time $t \geq t_c(l)$, i.e., when the electrode once again operates in a single mode.

Comparison with Experiment

Before we proceed with the interpretation of experimental results, it is necessary to review briefly the applied experimental procedures and relate them to the basic assumptions underlying the theoretical development.

The details of the experimental arrangement, including the construction and geometry of the porous electrode employed, were given elsewhere (5, 6). Here, we restrict remarks on experimental procedure to the fact that the porous electrode was constructed by confining loosely packed silver spheres in a glass cylinder and resting the spheres on a silver backing-plate. Such packing assured good electrical conductivity in the electrode matrix, satisfying the assumption of negligibly small ohmic resistance of the matrix in the formulation of the fundamental differential equations, Eq. [5] and [6]. Direct measurements showed that the specific resistance is about 1 ohm-cm at the beginning of the charging process, which is indeed negligible when compared with the ohmic resistance of the electrolyte occupying the voids of the porous structure.

For convenience, quantities useful in the interpretation of experimental results pertaining to the porous

Table I. Summary of relevant parameters of porous electrode

Sphere diameter	$(37.2 \pm 4) \times 10^{-4}$ cm
Weight of Ag per unit	0.49g
Volume of experimental unit	0.078 cm ³
Volume of Ag per unit	0.0484 cm ³
Volume of electrolyte	0.030 cm ³
Surface area per unit	78.3 cm ²
Equivalents of Cl ⁻ ions per unit	2.90 coulombs
Electrolyte	1N KCl
Cross-section area	1.56 cm ²
Unit thickness	0.05 cm

electrode used in this investigation, are given in Table I.

The Q - x curves.—Data first obtained by Katan (5) were plotted in Fig. 5 as the logarithm of the charge transferred, $\log Q$, vs. the position within the porous structure, x . The charging current, i_0 , and the charging time, t , were used as parameters. The charge transferred, Q , was determined from the amount of silver chloride found within the experimental unit volume. Atomic absorption spectrometry was the analytical technique employed.

Qualitatively, the predicted behavior is evidenced by displacement of the Q - x curves with change in the charging current, a corollary of Eq. [21] which relates the velocity of penetration of the change in the rds to the charging current. Similar displacement was recorded when the electrode was charged at constant current for various periods of time. Disregarding the first 0.3 cm, further qualitative agreement is found in the invariance of slopes with the degree of conversion.

Quantitatively, the dotted lines shown in Fig. 5 are the constructed Q - x curves, Eq. [27] and [30], obtained by using R 's and Z 's determined from the experimental data shown by the solid line and under the assumption that $Q_c = 1$ coulomb/experimental unit. The bases for

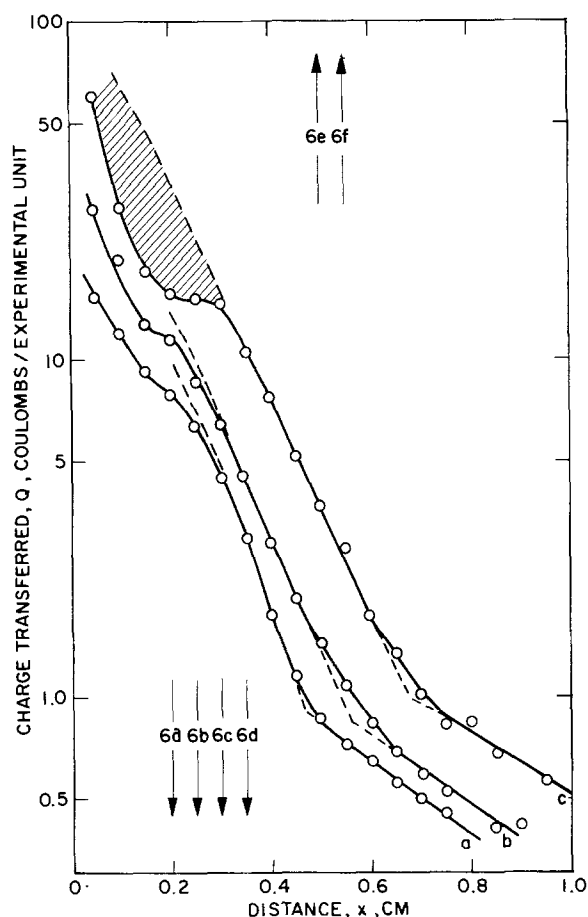


Fig. 5. A plot of experimental data of Q vs. x as a function of charging current i_0 . Curves a, b, and c for $i_0 = 5, 8,$ and 25 mA cm^{-2} , respectively. Arrows indicate positions of segments examined by SEM (see Fig. 6).

this selection of Q_c and details of the calculations are given in subsequent sections.

Microscopic examination.—In order to determine causes for the aforementioned presence of an additional break in the Q - x curves, located at approximately $x = 0.3$ cm and independent of the applied charging current, i_0 , microscopic examinations of the electrode's interior were undertaken. Representative photographs, showing elements of electrode surface at depths indicated (alongside curve b), Fig. 5, are assembled in Fig. 6(a)-6(f).

As one would expect, the electrode surface close to the bulk electrolyte is heavily converted to silver chloride. Nevertheless, the points of contact between the spheres are seen to be preserved, remaining uncoated, so that good electrical conductivity is maintained. The characteristic feature of the front portion of the electrode is the appearance of a sludge-like, enveloping deposit, resembling in fact, a dried clay. It is noteworthy that the sludge-like deposit is evident until we approach the critical distance, $x = 0.30$ cm, and then it abruptly disappears to be replaced by crystallites. The density of the crystallized conversion product decreases with the electrode depth.

This examination suggests that the porous structure in the proximity of the bulk electrolyte is engaged in processes which are different than those predominant at greater depths.

Origin of the first break in the Q - x curves, a qualitative analysis.—A qualitative analysis based on microscopic examinations (Fig. 6) and experimental Q - x curves (Fig. 5) is given in this section to indicate our interpretation for the origin of the first break. It is seen in Fig. 5, curve b, that the number of coulombs passed through the first experimental unit is approximately 28.0, a number which exceeds by a factor of 10 the initially available chloride ion content. A similar estimate for $x = 0.3$ cm shows that twice as much chloride was used in that segment as was initially present in the pores during the 4 hr of electrode charging at $i_0 = 8.0$ mA cm^{-2} . Consequently, chloride must be supplied from the bulk electrolyte. An order of magnitude calculation shows that the necessary chloride could have been supplied by diffusional transport alone and that local chloride concentrations in the pores would be quite low. Significant changes would occur in electrolytic conductivity during the course of electrode charging and some pore blockage takes place (see Fig. 6). Increase in electrolytic resistivity would shift the reaction toward the electrode-bulk electrolyte interface, promoting localized surface coverage. Increase in surface coverage by a nonconductive film, however, would tend to force the transfer current deeper into the electrode structure, thus shifting the region of low chloride content to greater depths. Further shifts are essentially determined by respective interactions of transport and reaction impedances.

This situation is shown in Fig. 7. For $x < a$, the reactive surface within the experimental volume is approaching a condition of full coverage and surface blockage with silver chloride. This forces the transfer current deeper into the electrode structure. Eventually the highest rate of conversion and, consequently, the lowest concentration of available chloride occurs at $x = b$. Although chloride transport will originate at both sides of $x = b$, chloride influx will be principally from the bulk electrolyte. Diffusing potassium chloride then comes into contact with deposited silver chloride to form a complex, $\text{AgCl}_n^{-(n-1)}$. The complex ions will diffuse along the path indicated in Fig. 7. The complex ions diffusing toward the bulk electrolyte are irretrievably lost and are most likely deposited on the counterelectrode. Those ions that diffuse inward will encounter a region deficient in chloride, thus favoring nucleation and crystal growth of AgCl from the liquid phase. This disappearance of the diffusing complex ions sharpens the diffusion front of diffusing $\text{AgCl}_n^{-(n-1)}$,

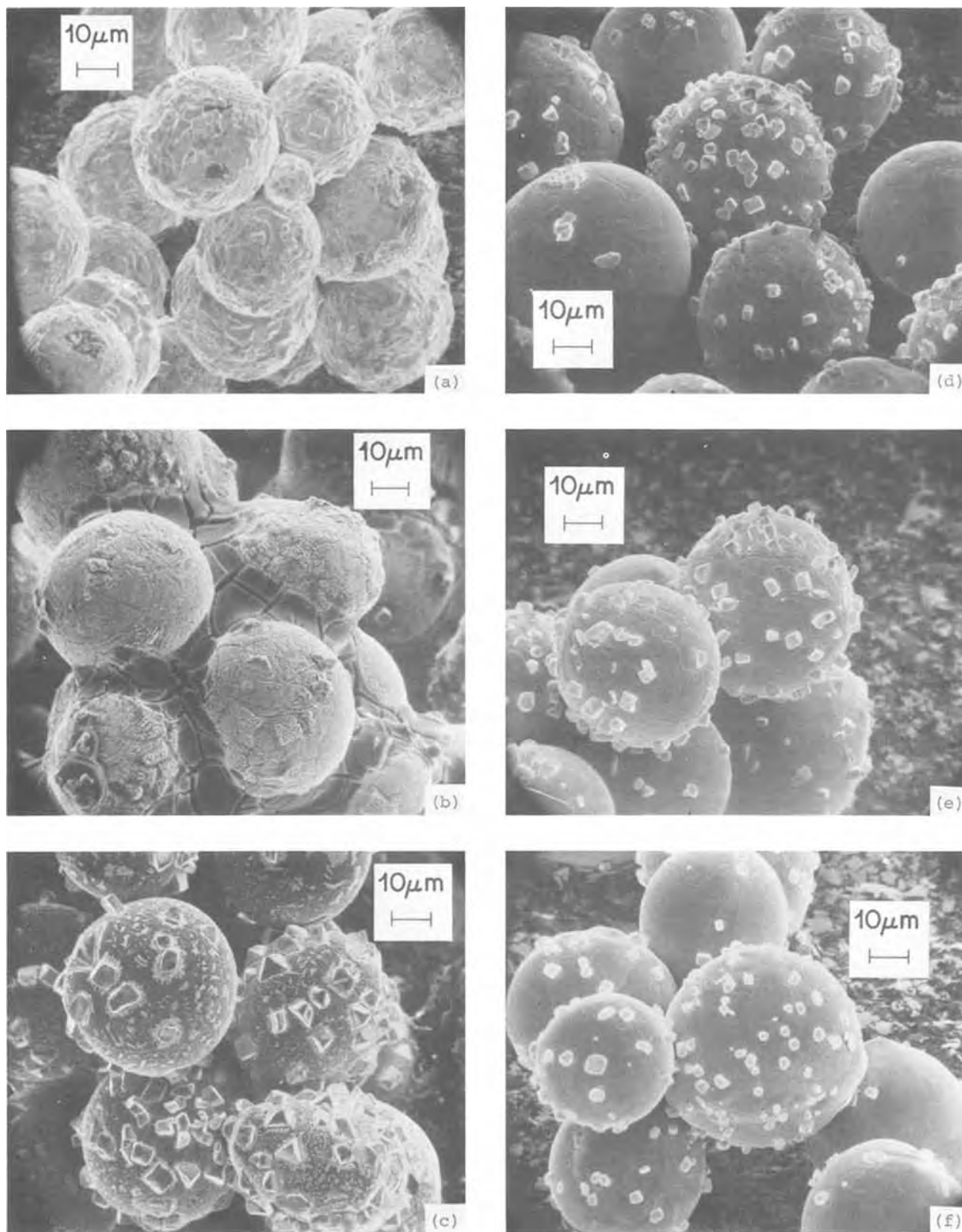


Fig. 6. Surface morphology at various depths indicated in Fig. 5

i.e., increases the concentration gradient, so that there is a rapid termination in diffusing $\text{AgCl}_n^{-(n-1)}$ species, and can account for the observed abrupt change in surface morphology at $x = 0.3$ cm [Fig. 6(c)]. Precipitation of AgCl from complex ions releases chloride ions, which further modifies diffusional transport.

Results tabulated in Table II are in qualitative agreement with the processes shown in Fig. 7. The last column of Table II lists the differences in the number

of coulombs supplied by the external circuit and that calculated on the basis of chemical analysis. This difference depends on the charging time for a constant charging current and on charging current for a constant charging time in a manner consistent with the loss of silver ions by the mechanism illustrated in Fig. 7. It is known that the electrochemical conversion of silver to silver chloride is 100% efficient, and the differences therefore are attributed to subsequent dis-

Table II. Faradaic losses upon charging*

i_0 mAcm ⁻²	t , hr	Q_a /exp unit	x_a	% loss
2.0	4.0	1.03	0.262	22.59
5.0	4.0	1.22	0.478	21.72
8.0	4.0	1.1	0.593	23.8
5.0	8.0	1.5	0.62	36.0

Q_a charge determined from an intercept, coulombs/experimental unit

x_a distance determined from intercept, in cm.

* Based on differences obtained between experimentally impressed charges and charges determined by chemical analyses of the sections.

solution and transport out of the porous structure. For current densities less than 10 mA cm⁻² and times less than 20 min, faradaic efficiencies of 100% were always maintained in the 1N KCl. In fact, from Table II it is seen that the longer the charging time, the greater the loss. It is noteworthy that the number of coulombs calculated from the extension of the slope shown in Fig. 5, from the shaded area, corresponds to within 10% to the differences tabulated in Table II. This may be considered as evidence for the correctness of the general assumptions.

Quantitative aspects of electrode charging.—This section is devoted to the quantitative analysis of the experimental curves (solid lines) and calculated values (dotted lines) shown in Fig. 5. For this analysis we require, as was shown in previous sections, the specification of transport and reaction impedances, R_1 , R_2 , Z_1 , and Z_2 , and the value of charge transferred, Q_c , associated with the change in reaction path. Of these quantities only one, R_1 , can be estimated because the initial concentration of electrolyte is known. In the present work, $R_1 = 14.0$ ohm-cm is used. The other impedances are determined from a selection of four points taken from the Q - x curve and from the estimated value of Q_c .

The estimate of the critical charge, Q_c , is not a straightforward procedure. In a semilogarithmic plot of Q vs. x , the transferred charge at a sufficient distance above and below x_c is in good approximation represented by straight lines. One might attempt to obtain Q_c as the intersection of the extensions of these straight lines, but this is justified under special conditions only. In region 2, i.e., for $0 \leq x < x_c(t)$, the transferred charge $Q(x, t)$ is given by Eq. [30]; in region 1, i.e., for $x_c(t) < x \leq l$, the transferred charge obeys Eq. [27]. For convenience and without committing a serious error, we assume $l \rightarrow \infty$ which reduces Eq. [30] to

$$Q_2(x, t) = Q_c + \kappa_2 Q_c \int_x^{x_c(t)} \left\{ \frac{\xi_1}{\xi_2} \cosh[\kappa_2(x' - x)] + \sinh[\kappa_2(x' - x)] \right\} dx' \quad [32]$$

and Eq. [27] to

$$Q_1(x, t) = Q_c e^{\kappa_1[x_c(t) - x]} \quad [33]$$

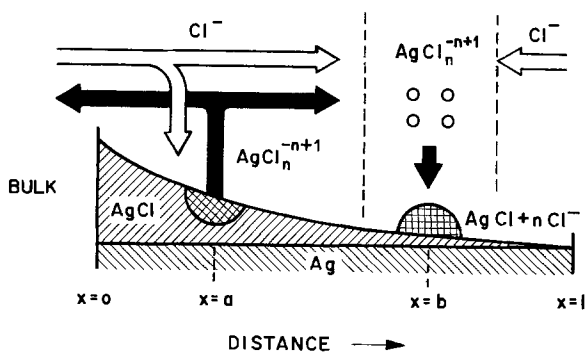


Fig. 7. Schematic representation of nonelectrochemical processes within the porous structure.

Upon integration, Eq. [32] yields

$$Q_2(x, t) = Q_c + Q_c \left\{ \frac{\xi_1}{\xi_2} \sinh[\kappa_2(x' - x)] + \cosh[\kappa_2(x' - x)] \right\} \Big|_x^{x_c(t)} \quad [34]$$

For $\kappa_2[x_c(t) - x] \gg 1$, Eq. [34] takes the form

$$Q_2(x, t) = \frac{1}{2} Q_c \left(\frac{\xi_1}{\xi_2} + 1 \right) e^{\kappa_2[x_c(t) - x]} \quad [35]$$

The asymptotic expressions [33] and [35] intersect at a point x_a with a corresponding charge $Q_1(x_a, t) = Q_2(x_a, t) = Q_a$. We shall designate Q_a as the asymptotic charge. By equating Eq. [33] and [35], we obtain

$$x_c(t) - x_a = \frac{1}{\kappa_1 - \kappa_2} \ln \left[\frac{1}{2} \left(\frac{\xi_1}{\xi_2} + 1 \right) \right] \quad [36]$$

Upon substitution of Eq. [36] into Eq. [33], an expression for the relationship between the asymptotic charge Q_a and the critical charge, Q_c , is obtained, namely

$$Q_a = Q_c \left[\frac{1}{2} \left(\frac{\xi_1}{\xi_2} + 1 \right) \right]^{\frac{\kappa_1}{\kappa_1 - \kappa_2}} \quad [37]$$

Hence, for finite κ_1 and κ_2 , the asymptotic charge Q_a will agree with Q_c only if $R_1 Z_1 = R_2 Z_2$.

Evidently, the information contained in the asymptotics of the Q - x curves is insufficient for an unambiguous determination of the critical charge. For this reason, a trial and error procedure was devised, consisting of a selection of "nearly" correct value for Q_c , taken in the vicinity of Q_a (see Fig. 5).

In this investigation the following procedure was adapted: Select an arbitrary value for Q_c in the vicinity of Q_a (charge transfer density from the intercept) and compute the associated electrode parameters, R_2 , Z_1 and Z_2 ; the R_1 is known from the concentration of the dissolved salt. The calculated values are assembled in Table III.

On purely physical grounds we reject those Q_c 's which yield R_2 less than R_1 since otherwise we would accept an increase in salt concentration (here potassium chloride) while none can be produced as a result of electrochemical reaction. Also, we reject those Q_c 's that yield values higher than 50 ohm-cm. This is equivalent to the statement that the concentration of potassium chloride in region 2 cannot be less than 0.3N. This appears to be a reasonable value in view of the diffusional processes summarized in Fig. 7. On this basis alone, a value $0.88 < Q_c < 1.0$ coulomb/exp unit was selected. Further decision is made by inspecting the last column of Table III where the Z_2 values are tabulated. Since the reaction impedance is assumed to be independent of the charging current, we seek such Q_c that the Z_2 values for both charging currents agree. $Q_c = 0.94$ coulomb/exp unit was selected.

The experimental evaluation of constants: R_1 , R_2 , Z_1 , Z_2 , and Q_c are sufficient to describe the electrode be-

Table III. Experimentally determined summary of relevant parameters

i_0	Q_c	x_c	κ_1	κ_2	ξ_1/ξ_2	R_1	Z_1	R_2	Z_2
5.0×10^{-3}	0.75	0.54	3.11	10.72	0.071	13.99	1.44	676	5.98
	0.80	0.518	3.10	10.76	0.24	13.99	1.45	199	1.72
	0.88	0.48	3.10	10.65	0.61	13.99	1.45	78	0.69
	0.92	0.46	3.10	10.41	0.88	13.99	1.45	53.3	0.49
	0.98	0.45	3.10	9.50	1.51	13.99	1.45	28.2	0.31
8.0×10^{-3}	0.80	0.59	3.31	8.48	0.532	13.99	1.27	67.3	0.93
	0.84	0.57	3.31	8.45	0.66	13.99	1.27	53.4	0.75
	0.88	0.56	3.31	8.42	0.80	13.99	1.27	44.13	0.62
	0.94	0.54	3.31	8.33	1.06	13.99	1.27	33.14	0.47
	1.00	0.52	3.31	8.17	1.35	13.99	1.27	25.58	0.38
	1.20	0.46	3.31	5.72	4.05	13.99	1.27	5.93	0.181

havior. An additional check on correctness of the reported constants can be obtained by comparing the experimentally located $x_c(t)$ with that calculated for a given current density of the charging process.

Upon integration of Eq. [21], we obtain the information sought, *i.e.*, the time necessary for the change in the reaction mechanism to occur at the position $x_c(t)$, namely

$$t_c(x) = t_c(0) + \frac{Q_c}{i_0} \int_0^x \tanh[\kappa_1(l - x')] \left\{ \frac{\xi_1}{\xi_2} \sinh[\kappa_2 x'] + \cosh[\kappa_2 x'] \tanh[\kappa_1(l - x')] \right\} dx' \quad [38]$$

Note that the Q_c needed in Eq. [38] must be given in coulombs/cm³ whereas the values tabulated in Table III used for the determination of electrode process parameters were given per volume of experimental unit, *i.e.*, 0.078 cm³. When the value $Q_c = 0.94/0.078 = 12.05$ coulombs/cm³, was employed and the integral in Eq. [38] evaluated, $t_c(0.54) = 15,700$ sec was obtained. This value compares rather well with the experimental charging time of 14,400 sec. The agreement between the experimental value and the calculated value is within 10%.

Reconstructed $j(x)$ curves.—The theoretical transfer current density profile for $R_1 = 14.0$ ohm-cm, $R_2 = 33.14$ ohm-cm, $Z_1 = 1.27$ ohm-cm³, $Z_2 = 0.47$ ohm-cm³, and $i_0 = 8 \times 10^{-3}$ as a function of position $x_c(t)$ is plotted in Fig. 8. These parameters are based on the data of Fig. 5.

It is seen that for the first 8.0 min [$t_c(0) = 452$ sec] the electrode operated with a single reaction path. The

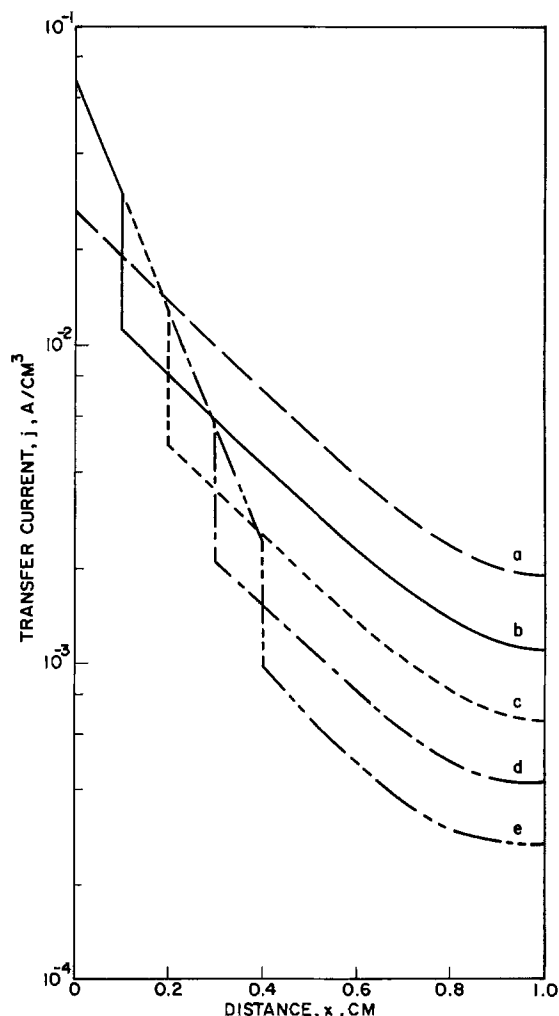


Fig. 8. Reconstructed $j(x)$ curves for the charging of silver/silver chloride system. $R_1 = 13$ ohm-cm, $R_2 = 33.1$ ohm-cm, $Z_1 = 1.27$ ohm-cm³, $Z_2 = 0.47$ ohm-cm³, $i_0 = 8.0$ mA/cm²

current density was exponential within $0 < x < 0.6$ cm and starts to flatten out for $x > 0.6$ cm. As the new reaction path was established and the electrode operated with a change in the reaction mechanism, most of the current was shifted toward the bulk electrolyte side of the porous structure. Upon initiation of the change in the rds, the contribution in region 1 became insignificant, being less as region 2 was expanding. The velocity of penetration also became less. These two observations are consistent with the surface morphology shown in Fig. 6.

One would expect on the basis of reconstructed curves very little difference in surface coverage at depths greater than 0.45 cm. Inspection of Fig. 6(d)-6(f) confirms this and indicates that the observed surface coverage in this region was completed within the first 8 min, *i.e.*, before the new reaction path became operative. Within this time the difference between the current densities is relatively small, $j(0.45) = 6 \times 10^{-2}$ Acm⁻², $j(0.9) = 2 \times 10^{-2}$ Acm⁻². It is also seen that irrespective of the location of x_c , most of the current is concentrated near the bulk electrolyte. The small changes in Z_2 are not associated with the surface coverage, but rather they are due to the difference in concentration of Cl⁻ ions.

The reconstructed $j(x)$ curves shown in Fig. 8 do not prove but are consistent with the surface morphology exhibited in Fig. 6. It is seen that at depths $x > 0.45$ cm the extent of surface coverage is almost uniform and is developed in the first 8 min, *i.e.*, before the new reaction path was established. When the new mechanism became operative, the reaction profile was shifted toward the bulk electrolyte, which for the galvanostatic case, reduced the transfer current density from $j(0.9) = 2 \times 10^{-2}$ to 0.7 mA/cm² when the rds reaction front advanced to $x_c = 0.4$ cm. Before the change in the rds, the transfer current density was more uniformly distributed throughout the porous structure. For example, when $x_c = 0$, $j(0.4) = 60$ mAcm⁻² and $j(0.9) = 20$ mA/cm².

Summary

An analytical method has been formulated to describe the transfer current density in a porous electrode as function of position and time. The mathematical model assumes the electrode mechanism to depend on the amount of the locally transferred charge and accounts for a change in the rate determining step. Application to the silver-silver chloride system and comparison with experiment shows that the depletion of chloride ions initially present in the porous structure is primarily responsible for the location and depth of the principal reaction zone. The performance characteristics of the electrode is further affected by the dissolution of silver chloride and subsequent transport of complex ions. These conclusions were corroborated by examination of the surface morphology.

Acknowledgment

This work was supported by the Office of Naval Research.

Manuscript submitted April 29, 1974; revised manuscript received Dec. 24, 1974.

Any discussion of this paper will appear in a Discussion Section to be published in the June 1976 JOURNAL. All discussions for the June 1976 Discussion Section should be submitted by Feb. 1, 1976.

Publication costs of this article were partially assisted by Lockheed Palo Alto Research Laboratory.

LIST OF SYMBOLS

- | | |
|-----|--|
| a | a constant, defined in text |
| i | current density (also current in external circuit) in electrolyte, Acm ⁻² |
| j | $-di/\partial x$, transfer current (faradaic) density, Acm ⁻³ |
| k | running index ($k = 1, 2, \dots$) |
| l | electrode thickness, cm |

M	amount of electroactive material, gcm^{-3}
$M^{(\pm)}$	a function of x_c , defined by Eq. [14]
N	a function of x_c , defined by Eq. [15]
Q	charge transferred, Asec/cm^2
R	ohmic resistance, ohm-cm
t	time, sec
u	potential, V
v	velocity of penetration of rds change, cm/sec
Z	reaction impedance, ohm-cm^2
x	distance, cm

Greek Symbols

α	a proportionality constant, g/Asec
ϵ	a small number
κ_k	$(R/Z_k)^{1/2}$, dimensionless parameter
ξ_k	$(R_k Z_k)^{1/2}$, resistance, ohm-cm^2

Subscripts

c, a, o defined in text

REFERENCES

1. J. S. Dunning, D. N. Bennion, and J. Newman, *This Journal*, **118**, 1251 (1971).
2. J. S. Dunning and D. N. Bennion, Proc. Advances in Battery Technology Symposium, The Electrochemical Society, Inc., Southern California-Nevada Section, Vol. 5, 1972.
3. J. S. Dunning, Ph.D. Thesis, UCLA (1972).
4. P. Bro and H. Y. Kang, *This Journal*, **118**, 519 (1971).
5. T. Katan, "Electrochemical Characteristics of Porous Silver/Silver Chloride Electrode," Final Report, LMSC—D 309658 (1972).
6. T. Katan, S. Szpak, and D. N. Bennion, *This Journal*, **120**, 883 (1973).
7. T. Katan, S. Szpak, and D. N. Bennion, *ibid.*, **121**, 757 (1974).
8. D. N. Bennion, H. Gu, and R. K. Hebbbar, "Failure Analysis of Porous Electrodes," UCLA-ENG 7347 (May 1973).
9. A. Winsel, *Z. Elektrochem.*, **66**, 287 (1962).
10. R. de Levie, in "Advances in Electrochemistry and Electrochemical Engineering," Vol. 6, Interscience Publishers, New York (1966).
11. L. Nanis, *Plating*, **58**, 805 (1971).
12. S. Szpak and G. E. McWilliams, *This Journal*, **120**, 635 (1973).
13. P. Van Rysselberghe, in "Modern Aspects of Electrochemistry," Vol. 4, Plenum Press, New York (1966).
14. K. J. Euler, *Electrochim. Acta*, **13**, 1533 (1968).

An Experimental Study of Reaction Profiles in Porous Electrodes

S. Szpak

Electronic Materials Sciences Division, Naval Electronics Laboratory Center, San Diego, California 92152

and T. Katan*

Materials and Structures, Lockheed Palo Alto Research Laboratory, Palo Alto, California 94304

ABSTRACT

An electrode for monitoring the time-dependent distribution of transfer current density in porous electrodes is developed. When applied to the Ag/AgCl system, predicted behavior is obtained, showing interaction of resistances manifested within the pores and on the pore walls. Good correlation is found of the developed experimental electrode to a porous structure similar to those of practical interest.

The aim of porous electrode modeling has been to provide design criteria for electrochemical devices which can operate according to prescribed modes. For realistic representation, this modeling must be based on analyses of actual elementary processes occurring within confines of the porous structure. Principal elements of the analyses are then local and bulk transport, and charge transfer kinetics. Variation in driving force naturally occurs as a function of distance and morphological change for any given mode of operation.

Theoretical aspects of electrode modeling have advanced to a high degree of sophistication. From the simple picture presented by Daniel'-Bek (1) in 1948, that of fixed geometry and invariant reaction kinetics, complex models have evolved. Models now contain such considerations as the effect of surface morphology and the change in pore geometry upon passage of charge as well as the change in transport behavior. Detailed reviews of progress, both historical and conceptual, can be found in numerous publications (2-4). Little progress can be claimed, however, for experimental verification of these models, at least as they apply to battery technology.

It is the purpose of this communication to describe an experimental technique, based on a concept of the segmented electrode, for the study of time-dependent behavior of battery electrodes. In particular, it is shown that a simple geometrical arrangement, such as a slotted pore, can represent the behavior of a geometrically more complex porous structure.

Elements of Experimental Modeling

Before presenting details of the segmented electrode, some of the relevant techniques used in the experimental study of battery electrodes are summarized.

Distribution functions.—One of the most important distribution functions relevant to battery electrode modeling is the time-dependent, spatial distribution of transfer current density $j(x,t)$. Unfortunately, under normal conditions, this distribution is not accessible to direct measurement without some modification of the electrode structure. This modification may involve prior electrode slicing into segments and reassembly with interspaced separators (5, 6). The introduction of separators, however, can seriously distort the distribution, especially in cases where transport processes are participating.

* Electrochemical Society Active Member.

Key words: silver chloride, charge distribution, current distribution, segmented electrode.

The second, equally important distribution function, is the time-dependent overpotential-distance relationship, $\eta(x,t)$. Again, this is not accessible to direct measurement. Insertion of Luggin capillaries into the porous structure (7) not only changes local geometry but it interferes with local flow of current.

Because of these considerations, experimental reconstructions of reaction profiles have typically involved determinations of the amount of charge transferred across the metal-electrolyte interface at selected times and locations. In practice, this requires slicing of the electrode after a given charge or discharge and analyses for the reactant or product in each slice (6, 7). Recently, x-ray element scanning was introduced to provide point-by-point analysis of the extent of reaction in a single pore arrangement (8). Useful but less detailed information was also obtained by slow cycling of the electrode combined with cell power output measurements (9); the thickness of the reaction layer and its position within the electrode structure as a function of electrode discharge was determined.

Experimental reconstruction of reaction profile.—The reconstruction of reaction profile, based on analyses of amounts of charge transferred as a function of position and time, requires a considerable effort: The function $j(x,t)$ is reconstructed from the relationship

$$i(t)t' = \int_0^l \int_0^{t'} j(x,t) dx dt \quad [1]$$

where $i(t)$ is the impressed current in the external circuit, t' is the duration of the experiment, and l is the electrode thickness. For the frequently used galvanostatic mode of discharge the current in the external circuit is kept constant, $i(t) = i_0$.

Upon completion of the experiment, at $t = t'$, the electrode is divided into a number of segments, usually 0.05 cm in thickness (10, 11) and they are analyzed for the amount of charge transferred. In terms of Eq. [1], it is assumed that $j(x,t)$ is a continuous function within the rectangle bounded by the lines $x = 0$, $x = l$, $t = 0$, and $t = t'$, so that the order of integration is immaterial. By sectioning the electrode into k equal parts, so that $l = k\lambda$, Eq. [1] can be written as follows

$$i_0 t' = \int_0^{t'} \left\{ \int_0^\lambda j(x,t) dx + \int_\lambda^{2\lambda} j(x,t) dx + \dots + \int_{(k-1)\lambda}^{k\lambda} j(x,t) dx \right\} dt \quad [2]$$

Application of the mean value theorem to the integrals in the brackets yields Eq. [3]

$$i_0 t' = \int_0^{t'} \left\{ \lambda \sum_0^k j(\bar{x}_k, t) \right\} dt \quad [3]$$

The time evolution of reaction profile requires a similar expansion of the time integral in Eq. [3], thus

$$i_0 t' = \lambda \tau \sum_0^k \sum_0^m j(\bar{x}_k, \bar{t}_m) \quad [4]$$

where $t' = m\tau$, and \bar{x}_k and \bar{t}_m denote points at which j is evaluated.

Equations [3] and [4] form the basis for the experimental determination of the time evolution of reaction profile utilizing chemical analyses of the electrode interior. The frequently cited Bro and Kang (12) data, for example, were obtained for time intervals of hours rather than minutes, and consequently some of the details of the time evolution of the reaction profile could be lost.

Experimental models of porous electrodes.—A necessary condition for substitute arrangements of electrodes used to simulate behavior of practical porous

electrodes is that they must reflect essential features of the real structure.

An approach that gained popularity in recent years has evolved from the concept of the "inverted pore" used to simulate behavior of the gas-diffusion electrode (13). The geometrical analog of this concept for flooded electrodes would be a thin film of electrolyte immobilized between a metal electrode and an inert surface. In practice, a drop of electrolyte can be placed on a smooth metal surface and a flat glass plate may be placed over this drop at a distance of several tens of microns, forcing excess electrolyte away (8, 14). The physical dimensions of concern to electrode modeling, such as electrode film thickness and electrode length, are experimentally controlled variables.

Such an arrangement can be useful in providing information necessary for electrode modeling. Whether or not it directly simulates the behavior of practical porous electrodes should be assessed by comparisons with geometrically realistic structures, such as a packing of metallic spheres of uniform diameter (11). Further, direct measurements of $j(x,t)$ are possible, if the electrode is sectioned and measurements made in a manner free from objections attributed to placement of separators, *i.e.*, if the electrode-separator geometry is clearly defined.

Experimental

The concept of a segmented electrode as an experimental tool for the study of $j(x,t)$ dependence is not new (5, 15). The rather infrequent use of this technique is attributed to difficulties in assembly and questionable validity in interpretation of results. Some of the difficulties can be eliminated by taking advantage of technology developed for the microelectronics industry. Reference is made to techniques of photographic transfer of a pattern and vapor phase deposition of metal films, which greatly enhance reproducibility and accuracy of fabricated microstructures (16, 17). Very small, detailed analogs of electrode structure can be repeatedly prepared on a variety of substrates by using these techniques.

Cell design and principles of measurements.—The prerequisite for direct measurements of space-time distributions of transfer current, $j(x,t)$, is to isolate thin segments of the electrode structure and to provide each segment with a separate current take-off lead. This should be done so that the sectioning will not appreciably change the structure and elementary processes that comprise the over-all reaction path. Also, provisions must be made to assure the monitoring of current in each segment without altering the original $j(x,t)$ distribution. The arrangement shown in Fig. 1 was adopted.

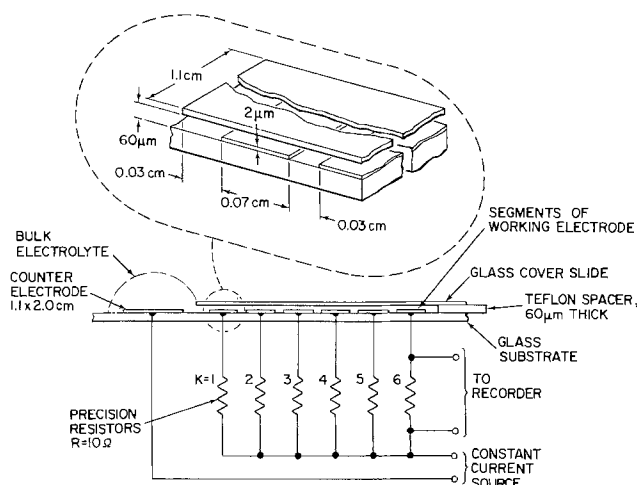


Fig. 1. Schematic representation of the segmented electrode concept. Upper part shows a small section of the segmented electrode showing dimensions.

The silver working electrode consisted of six segments which were vapor deposited onto a glass microscope slide and which had connecting electrical leads insulated by Teflon tape as shown in Fig. 1 and 2. The counterelectrode was similarly formed. As illustrated, the pore structure was simulated by placing and aligning a microscope cover slide onto a drop of electrolyte so that the slide rested on the Teflon tape and was parallel with the segments and slide. The cover slide extended beyond the first segment by approximately 0.03 cm, the distance of separation between the individual segments. Bulk electrolyte protruded around the counterelectrode as shown. The counterelectrode was made large, 1.1×2 cm, compared with the working electrode, 0.07×1.1 cm per segment, and was separated by a distance of 1.0 cm from the counterelectrode.

To measure the $j(x,t)$ distribution, the current in each segment, $j_k(t)$, was obtained by measuring the potential drops across $R_k = 10$ ohm resistors in series with the segments. The resistors deviated by less than 0.005 ohm from their rated values. The measured currents never exceeded 0.6×10^{-3} A, so that the effect on current density by the presence of resistors was quite small, at worst less than 6 mV in reaction overpotential.

Electrode fabrication and assembly.—Silver, deposited from vapor on a glass substrate, constituted the main element of the experimental arrangement. Fabrication of the silver pattern was accomplished in two steps: First, a thin platinum film was deposited onto the masked glass microscope slide, and then, silver was deposited with the mask in place in multiple layers to assure thicknesses sufficient to withstand charge and discharge modes. Vapor deposition was carried out at pressures of $ca. 5 \times 10^{-5}$ Torr on slides which were preheated by maintaining filament temperature just below the melting point of the deposited metal for $ca. 15$ min. The mask was prepared from magnetic stainless steel foil and fastened magnetically to the slide.

Prior to the vapor deposition, the Corning No. 2947 microscope slides were roughened with No. 4/0 emery polishing paper and then thoroughly washed in acetone, water, boiling potassium permanganate solution, hydrochloric acid solution, and deionized water, respectively. They were then ultrasonically cleaned in conductivity water, oven dried, and stored in a desiccator.

After vapor deposition, the areas of the working electrode, counterelectrode, and pore thickness were defined by affixing a U-shaped piece of Teflon tape, $60 \mu\text{m}$ thick, as shown in Fig. 2. The slide could then be placed in a holder for electrical connections, and the

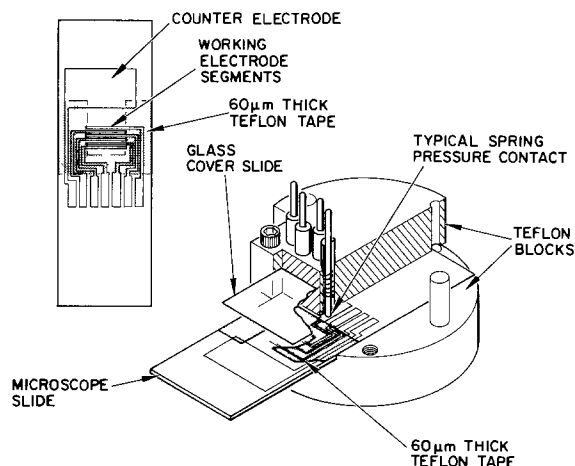


Fig. 2. Experimental cell assembly. Lower right: details of holder construction, electrical connections, and positioning of segmented electrode. Upper left: construction of segmented electrode showing vapor deposited silver on a glass substrate. The shaded area is a U-shaped Teflon tape, $60 \mu\text{m}$ thick.

electrolyte and cover glass could be attached as required.

The electrode holder was constructed of Teflon and consisted of two parts: The lower part was provided with a groove and a locating pin to position the microscope slide. In addition, there were two more pins to guide the location of the upper part which contained seven pressure loaded contacts to connect the individual segments and counterelectrode to the galvanostat and to the instrumentation for recording currents $j_k(t)$.

Electrode preparation for the $j(x,t)$ measurements.—Two sets of measurements of transfer current distributions are discussed: those associated with electrode discharge and those associated with electrode charging. Each set requires different preconditioning of the electrode surface.

Preconditioning for the discharge curves was as follows: Each segment of the electrode assembly was individually charged in 1N KCl solution and received 0.25 A-sec/cm², which corresponds to about 22% surface coverage by a film of AgCl (18). Unless otherwise noted, each segment was charged for 4 min at 80×10^{-6} A in 1N KCl solution. The resulting error in Q_k ($k = 1, 2, \dots, 6$) was determined by discharging each segment galvanostatically while observing the polarization, and it never exceeded 1.5%. Q_k increased in accordance with charging sequence, indicating charge loss by dissolution. To attain better uniformity, the charging sequence was specified, namely, segments 1, 3, 5, 6, 4, and 2, respectively.

After preconditioning, the cover glass was placed as shown in Fig. 1 to construct the single pore assembly. The pore discharge was carried out at preselected currents, in the range of 80 – $600 \mu\text{A}$.

A somewhat different procedure was followed in order to prepare the single pore electrode for studying the charging process. It was found that conversion of freshly deposited silver to silver chloride by an anodic current at 80×10^{-6} A for 2 min, followed by a cathodic current also at 80×10^{-6} A, for 3 min, yielded reproducible results. Following the surface conditioning, the segmented electrode was thoroughly washed in triply distilled water and with electrolyte used in the experimental run.

Failure modes.—The most common cause of failure was severance of the deposited silver film due to "overcharging," *i.e.*, after complete conversion to silver chloride occurred at some location. This type of failure was eliminated by using thicker films of platinum to assure electrical conduction or, alternatively, by limiting the level of charging.

A second type of failure was associated with the current take-off arrangement. Electrolyte would occasionally seep to the location where the pressure loaded contacts pressed against the deposited silver leads, and the dissimilar metal contact would then modify the measured currents. This was prevented by placing a thin film of Apiezon grease only at the pressure loaded contacts to act as a barrier.

Results and Discussion

Experimental results and their interpretation are presented here separately for the discharge process, $\text{AgCl} \rightarrow \text{Ag}$, and for the charging process, $\text{Ag} \rightarrow \text{AgCl}$. In both processes, the effects of varying impressed current, i_0 , and concentration of KCl are given. Finally, comparisons are made of the time evolution of reaction profile for a simulated segmented pore with that of a porous electrode comprised of packed spheres, all of the same diameter.

The Discharge Process: $\text{AgCl} \rightarrow \text{Ag}$

A summary of the time evolution of reaction profiles is given in Fig. 3, 4, and 5, for 0.1, 1, and 2N KCl solutions, respectively, and for a range of discharge currents, 80 – $300 \mu\text{A}$.

Effect of discharge current, i_0 .—For the applied discharge currents, i_0 , j_k vs. t curves were observed to be

quite similar. In fact, when reduced currents, j^* , where $j^* = j_k/i_0$, and reduced time, t^* , where $t^* = t/t_0$, were employed, all data could be presented by a single plot, as shown in Fig. 3-5. Here, t_0 refers to the time necessary for complete discharge of the initial charge, Q_0 , by the discharge current, i_0 .

Such behavior implies that the over-all discharge path is independent of discharge current, at least

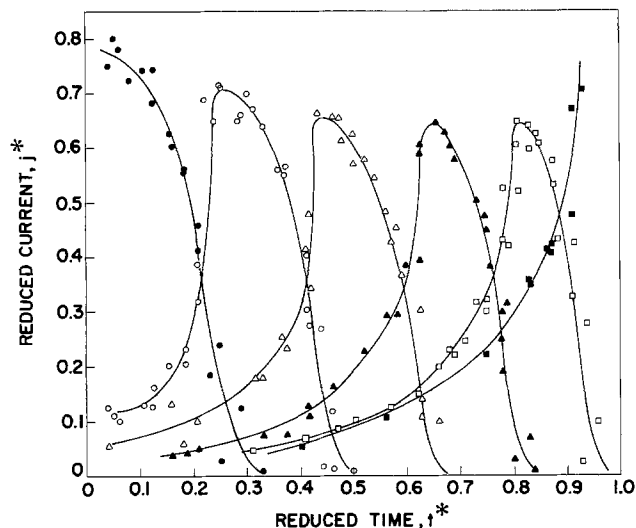


Fig. 3. Time evolution of discharge profiles in 0.1N KCl. Range of discharge currents: 80 to 300 μ A.

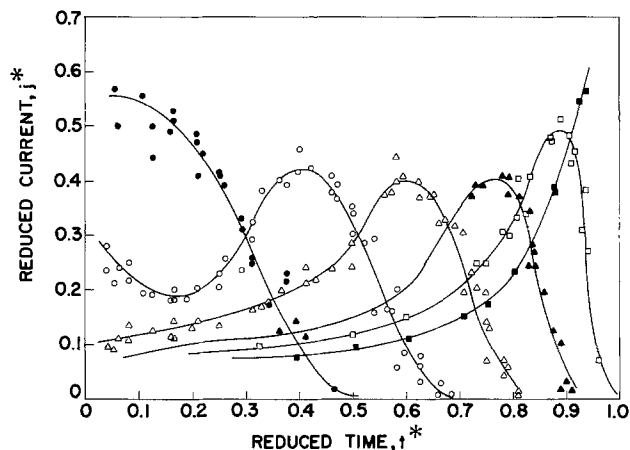


Fig. 4. Time evolution of discharge profiles in 1N KCl. Range of discharge currents: 80 to 300 μ A.

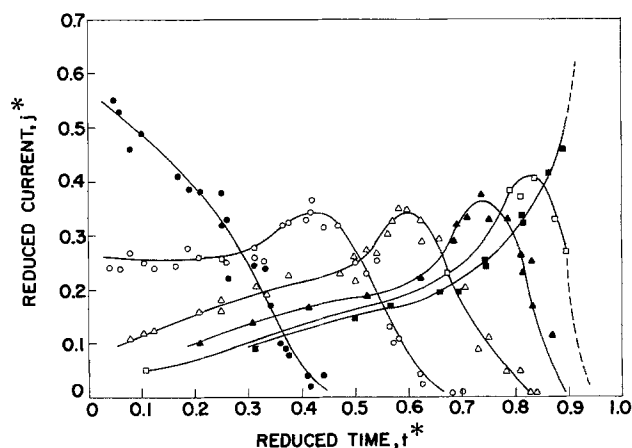


Fig. 5. Time evolution of discharge profiles in 2N KCl. Range of discharge currents: 80 to 300 μ A.

within the range of 80-300 μ A which is equivalent to superficial current densities of 12.1-45.4 mA/cm².¹

With the exception of the first and last segment, partial transfer currents, $j_k(t)$, always increased with time, reached a maximum, and then decreased monotonically to zero, Fig. 3-5. Evidently, the nature of local change in discharge for each segment is similar, and this behavior does not clearly indicate that a change in the mechanism of electrochemical reaction has occurred, as could be concluded from j/t relationships established for various degrees of surface coverage (18). It can be assumed that measurements with the present design of the segmented electrode are insensitive to the relatively small changes in current-potential dependence which have been found to occur with varying state of charge. Better resolution may be anticipated for finer division by the segments.

Effect of concentration, c_0 .—Examination of Fig. 3-5 reveals also the effects of electrolyte concentration. It is seen that, as the concentration of KCl is increased, the transfer current is distributed more uniformly while the similarity of the currents is retained in each segment. For the more concentrated solutions, the decrease in ohmic resistance of electrolyte within the pore enables a more uniform participation of each segment in the over-all discharge current.

For the more dilute solution, e.g., 0.1N KCl, as the reaction proceeds deeper into the electrode structure, the maximum transfer current remains essentially the same with increase in segment number, k . However, in 1 and 2N electrolytes, we notice that the maximum transfer current decreases and then increases again, as the electrode discharge is nearing its completion. It is noteworthy that the increase in current maximum begins earlier for higher concentrations of KCl. This effect of the electrolyte concentration on the time evolution of transfer current during electrode discharge can be interpreted in terms of a moving reaction layer.

Concept of reaction layer.—The concept of a reaction layer is well established in many branches of chemistry and chemical engineering (19-21). It is also one of the first concepts that guided the early discussions of porous electrode behavior (22, 23). The reaction layer thickness thus has been defined in many ways. Here, we define the reaction layer thickness as the distance along the x -coordinate which yields the area of the triangle OAB equal to the area under the $j(x,t)$ curve, placed in a manner as to retain the initial slope, as shown in Fig. 6a. The initial portion of the $j(x)$ vs. x curves for concentrations and currents investigated ex-

¹ Superficial current density is defined here as i_0/A , where $A = 6.8 \times 10^{-3}$ cm², the cross-sectional area of the pore, cf. Fig. 1.

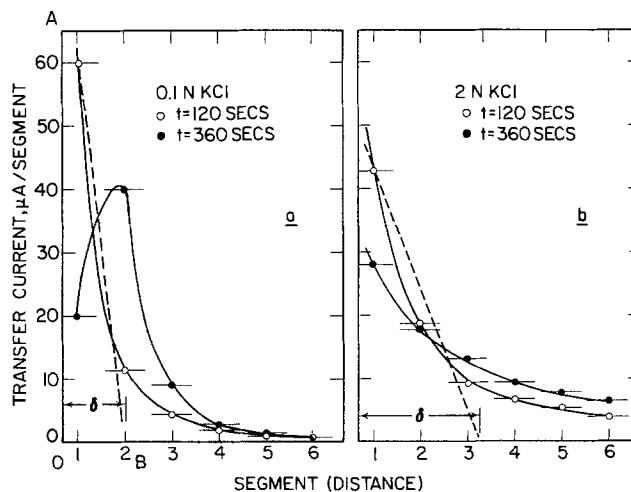


Fig. 6. Initial evolution of reaction profile on discharge and a graphical determination of reaction layer thickness: a, in 0.1N KCl; b, in 2N KCl. Discharge current, $i_0 = 80 \mu$ A; δ is defined as the reaction layer thickness.

hibit exponential behavior as shown in Fig. 6. The transfer current falls off rapidly with the distance, in accordance with an expression of the form

$$j(x) = A \cosh [\kappa(l - x)] \quad [5]$$

where $A = ki_0/\sinh(\kappa l)$ is a constant for a given set of experimental conditions and electrode dimensions.

The thickness of the reaction layer, $\delta(c_0)$, can be determined directly from Fig. 6a and b. We note that the thickness depends strongly on electrolyte concentration, since in both cases the discharge current was the same, namely, $i_0 = 80 \times 10^{-6}$ A. Accordingly, we find $0.07 < \delta(0.1) < 0.14$ cm and $0.14 < \delta(2) < 0.21$ cm in 0.1 and 2N KCl solutions, respectively.

Application of the reaction layer concept.—Before applying the reaction layer concept to the interpretation of results summarized in Fig. 3-5, and introducing additional supporting experimental evidence, the following is noted: The transfer currents, j_k , are expressed here as currents rather than current densities and represent the integrated values of local currents over the segment's area. Time is accurately known; partial currents were recorded every 20 sec. Also, the initial charge deposited on the individual segments, $Q_k = 19.2$ mA-sec/segment, was maintained constant, independent of the running index, k .

In our previous communication (11) we discussed the behavior of a porous electrode operating with a change in reaction path when a predetermined conversion has taken place. We derived the $j(x,t)$ dependence when the reaction path characterized by electrolyte resistance, R_1 , and the reaction impedance, Z_1 , changed to other values designated by R_2 and Z_2 . It was shown that an electrode operating under this restriction is adequately described by the position of the mode interface, x_c , and the velocity, v_c , at which the mode interface penetrates the electrode structure ($v_c = dx_c/dt$).

To simplify the discussion, we consider the electrode discharge as a special case, namely, no reaction occurs in region 2. That is, we assume $Z_2 = \infty$, within region $0 \leq x < x_c$. For finite R_2 and $Z_2 = \infty$, it follows that $\kappa_2 = 0$ and $\zeta_2 = \infty$, where $\kappa_2 = (R_2/Z_2)^{1/2}$ and $\zeta_2 = (R_2 Z_2)^{1/2}$. Under these conditions the developed equations of Ref. (11) are reduced as follows

$$j(x) = 0 \quad \text{for } 0 \leq x < x_c \quad [6]$$

and

$$j(x) = ki_0 \cosh[\kappa(l - x)]/\sinh[\kappa(l - x)] \quad \text{for } x_c < x \leq l \quad [7]$$

Equations [6] and [7] are identical with those derived by Winsel (22) and represent the exponential distribution within the region where discharge is taking place. Similarly, the velocity of penetration can be obtained

$$v_c = (i_0/Q_0)/\coth^2[\kappa(l - x_c)] \quad [8]$$

It is advantageous to examine the time evolution of discharge profiles in terms of the moving reaction layer concept. Consider Fig. 6a: Two minutes after initiation of the discharge reaction, most of the current is located in the first segment, with only a small fraction in the second and third segments. Four minutes later, most of the current is found in the second segment with only minor increase in the third segment and almost none at greater electrode depths. Bearing in mind that the recorded current in any segment is the integrated current over the segment area, we conclude that for the one-dimensional case, the original current (local current) distribution, given by Eq. [7], is retained, but its zero point, x_c , is shifted into the electrode interior. It indicates that

$$\int_{x_c}^{0.07} j(x)_t dx < \int_{0.07}^{0.14} j(x)_t dx \quad [9]$$

that is, an increase in the current recorded in the sec-

ond segment is due to the decrease in the active area of the first segment rather than in the value of local transfer current density, $j(x)$, in the first segment.

The time necessary for a similar development in 2N solution of potassium chloride is longer than 6 min after the initiation of the electrode discharge. It is seen that the exponential character is retained. This is a consequence of thicker reaction layer, since both electrodes contained initially the same amount of charge, $Q_0 = 19.2$ mA-sec, and were discharged with the same current, $i_0 = 80 \times 10^{-6}$ A. Using the same concept, we can interpret the (j/i_0) vs. (t/t_0) curves shown in Fig. 3-5.

Consider Fig. 3: It depicts the time evolution of the discharge profile in 0.1N KCl. The existence of the j_k max, in all segments except the first and the last one, has just been discussed, Eq. [9]. The sharpness and lack of overlap of the curves of the reduced current implies the presence of a reaction layer on the order of the segment thickness with a layer thickness unaffected by the degree of electrode discharge, i.e., by the position of mode interface, x_c . The independence of the j_k max of the running index, k , i.e., of the position of x_c , suggests further the validity of Eq. [8], and, therefore also, of Eq. [10]

$$\Delta j_c = j(x_c) = ki_0 \coth[\kappa(l - x_c)] \quad [10]$$

These equations are independent of x_c , as long as $\coth[\kappa(l - x_c)] \approx 1$, i.e., as long as $[\kappa(l - x_c)] \geq 3$. The sharp increase in the transfer current as the discharge process is nearly completed may also be noted. This implies that δ becomes greater than the remaining electrode depth of the active portion.

The form of the (j/i_0) vs. (t/t_0) plot is preserved as the chloride concentration is increased. Disregarding the initial contraction of the reaction layer (decrease in j_2), the situation is similar. Since the reaction layer is thicker due to decrease in ohmic resistance of the electrolyte, the j_k max are less, the penetration of the reaction layer is somewhat slower, as indicated by the position of j_k max on the reduced time scale, except when the reaction layer just entered the last segment.

The effect of the reaction layer thickness on details of the discharge profile is also demonstrated in Fig. 5. Here, the j_k max are less than those observed in 1N KCl; this is consistent with the increase in the layer's thickness. Also, the penetration rate is less at the beginning of the discharge process, and increases toward the end of the discharge. The increase in the rate of penetration occurred at an earlier time than in 1N KCl, and this is also consistent with the increase in the reaction layer thickness.

The degree of a segment's discharge at the time of j_k max is given in Table I. It is seen that the amount of material used up before the event of j_k max is hardly dependent on the discharge current, i_0 , but is affected by the position; more material is used up for greater depth. This observation is again consistent with the concept of moving reaction layer.

It has been indicated that the reaction layer thickness is a strong function of electrolyte concentration. However, it did not change with the progress of elec-

Table I. Surface coverage and reactant charge content at j_k max in 1N KCl

i_0	$Q(2)$	$\theta(2)$	$Q(3)$	$\theta(3)$	$Q(4)$	$\theta(4)$	$Q(5)$	$\theta(5)$
80×10^{-3}	5.6	0.291	5.0	0.260	4.4	0.229	4.0	0.208
100×10^{-3}	7.8	0.406	5.4	0.285	4.21	0.219	3.6	0.187
120×10^{-3}	6.8	0.354	5.9	0.307	4.83	0.251	3.4	0.177
160×10^{-3}	7.2	0.375	6.01	0.313	5.2	0.270	4.1	0.213

Values computed from formula:

$$\theta = \frac{19.2 \times 10^{-3} - Q(k,t)}{19.2 \times 10^{-3}}$$

where $Q(k,0) = 19.2 \times 10^{-3}$ A-sec/segment, $Q(k,t) = 19.2 \times 10^{-3} - Q$ (transferred), Q (transferred) by integration under the $j(x,t)$ curves.

trode discharge, which should be particularly evident in 0.1N solution. A complete discharge of a segment, initially containing 19.2 mA-sec/segment will add, upon discharge, 15.25 mg Cl^-/cm^3 . To assure electro-neutrality, a corresponding amount of potassium ions must be brought from the bulk. Transport processes must obviously participate. However, their effect on the local current density distribution, on the thickness of the reaction layer, will be relatively unimportant, because the changes in concentration due to the transport phenomena will be restricted to regions toward the pore mouth. Therefore, although the concentration of potassium chloride has increased to about 0.4N solution, no effects of change in δ (c_0) were noted. The same observations can be made for 1 and 2N solutions.

Similar evolution of a discharge profile was reported for another sparingly soluble reactant-conductive matrix system (24).

The Charging Process: $\text{Ag} \rightarrow \text{AgCl}$

The charging process considered here took place within the geometrical constraints of a porous structure and differs from the discharge process in that chloride ions are used up. Thus, diffusional processes and, in general, transport processes of Cl^- are directed into the porous structure rather than into the bulk electrolyte. This fact alone would imply the possibility of an effect of concentration changes in the porous structure on the time evolution of reaction profile which was not noted in the course of electrode discharge.

We present the experimental data in somewhat different manner, namely, we start the discussion with the presentation of the evolution of reaction profile in 2N KCl.

Evolution of reaction profile on charging.—Significant events which occurred during the evolution of the transfer current during charging in 2N solution are inferred from the experimental distribution shown in Fig. 7. Shortly after the initiation of charging, at $t = 2$ min, a typical distribution was recorded. At some later time, the exponential distribution degenerated into one exhibiting a minimum and a maximum. Taking into consideration that the recorded currents are in fact integrated values, we may visualize the "degenerated" curves as composed of two exponential branches with the discontinuity, as shown in Fig. 7 by a broken line. As the charging process is being carried out, the discontinuity penetrates into the electrode structure. After

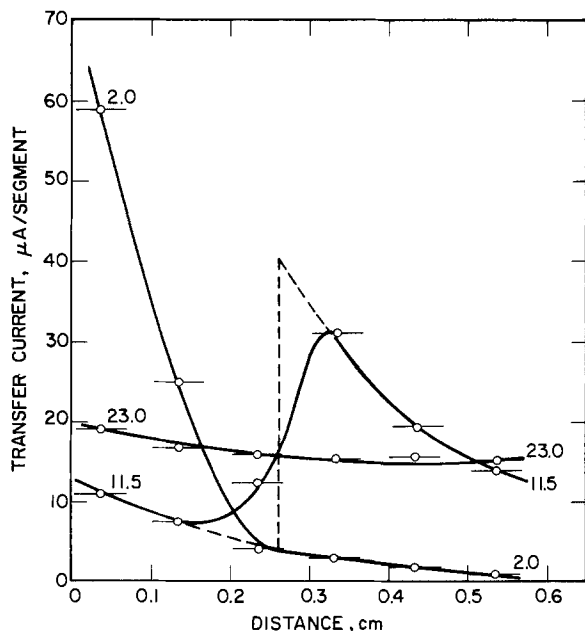


Fig. 7. Evolution of reaction profile on charging in 2N KCl. Time in minutes indicated along corresponding curves.

11 min of electrode charging, the discontinuity has reached the fourth segment of the experimental analog. As the charging process was carried out further, a leveling in the distribution was observed. This was interpreted as a disappearance of the upper branch of the distribution curve, at $t = 23$ min. Such profile evolution is in agreement with the predicted behavior for the case of a change in the rds in the course of electrode operation (11).

To seek further confirmation, a plot of $\log Q$ vs. the distance has been prepared, Fig. 8. The charge transferred, or extent of reaction, in each segment was determined by mechanical integration of the experimentally recorded $j-t$ curves. The similarity of this plot and one based on theoretical calculations and reported previously (11), is evident.

The critical charge accumulation, *i.e.*, the critical extent of reaction, associated with the change in the reaction path, corresponds to about 14% of surface coverage, cf. Fig. 8. It follows from the evidence presented in Fig. 7 and 8 that the change in reaction mechanism is due to inhibition of charge transfer, rather than to an increase in the ohmic resistance of the electrolyte in the electrode pore.

The change in the reaction path appears to be independent of the charging current within the range of

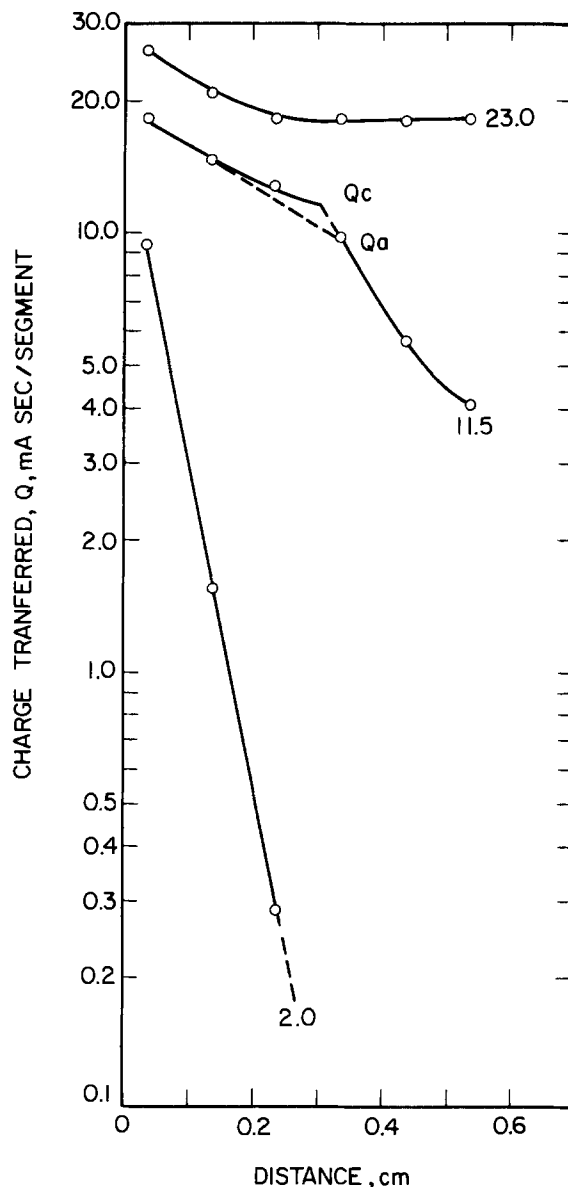


Fig. 8. Charge transferred as a function of distance at $t = 2.0$, 11.5, and 23 min; critical and asymptotic charges, Q_c and Q_a , are indicated [cf. Ref. (11)].

$80\text{--}200 \times 10^{-6}\text{A}$. This range was essentially imposed by the limited speed of sampling and recording of the j - t curves. No significant changes in the curves were noted at currents as high as $600 \times 10^{-6}\text{A}$.

The experimental evidence is wholly consistent with the concept of a change in reaction path due to a change in electrochemical mechanism, rather than to an increase in solution resistance. Disregarding the transport from bulk electrolyte, the change in chloride ion concentration did not exceed 12%.

Theoretical analysis (11) has shown that the time evolution of the reaction profile, associated with the increase in interfacial impedance is characterized by the position dependent rate of penetration of the mode interface which, in turn, is associated with the numerical value of the discontinuity at x_c [cf. Eq. [18], Ref. (11)]. Examination of Fig. 8 indicates an increase of about one order of magnitude of the interfacial impedance, after approximately 14% of the available surface has been covered by silver chloride (18).

A plot of (j/i_0) vs. t^* , where t^* is the reduced time and is calculated according to the formula $t^* = t/t(l)$, is shown in Fig. 9. Here, $t(l)$ is the time of charge to obtain complete surface coverage (18). Because of the finite dimensions of the segment employed, an error in the dimensionless time $t(l)$ is introduced when complete coverage is judged by the motion of the reaction profile. However, this error appears to be insignificant in view of the correlation obtained for the various charging currents, Fig. 9.

Effect of changing ohmic resistance on the evolution of transfer current distribution.—The effect of a change in solution resistance on the evolution of the reaction profile is of special interest to electrode design. In most systems, especially those containing no supporting electrolyte and having a small ratio of volume to surface engaged in charge transfer, large changes in composition may develop because of an electrochemical process. Chemical changes, in turn, give rise to transport processes and promote the development of interactions between the charge transfer and other processes. The development of this progressive interaction is illustrated in Fig. 10a, b, and c, where the j - t curves for the segmented electrode operation in 1N KCl are shown. Charging currents of 200, 300, and 400 μA were used.

Consider Fig. 10a, where for the purpose of clarity in illustration, currents in the first three segments only are shown. The j - t curves are essentially similar to those obtained in 2N KCl solutions. It is seen that, if a j - x plot were constructed at $t = 2.5$ min, or greater, it would be analogous to the one shown in Fig. 7. Thus, we can reasonably conclude that choking (blockage) of the second kind dominates the transfer current evo-

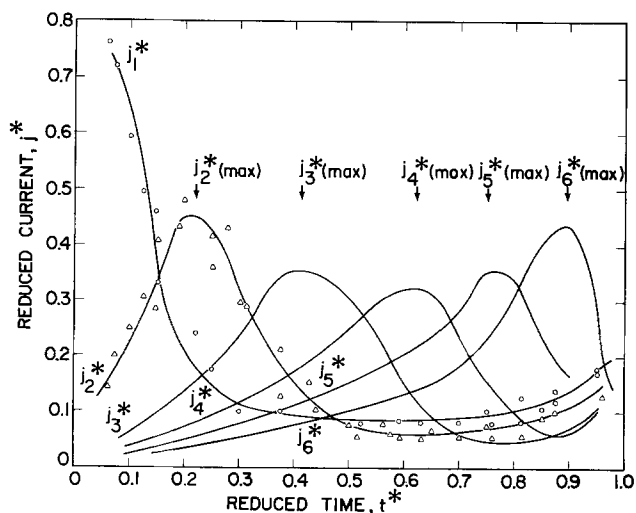


Fig. 9. Time evolution of reaction profile on charging in 2N KCl; charging currents: $i_0 = 80\text{--}600 \mu\text{A}$.

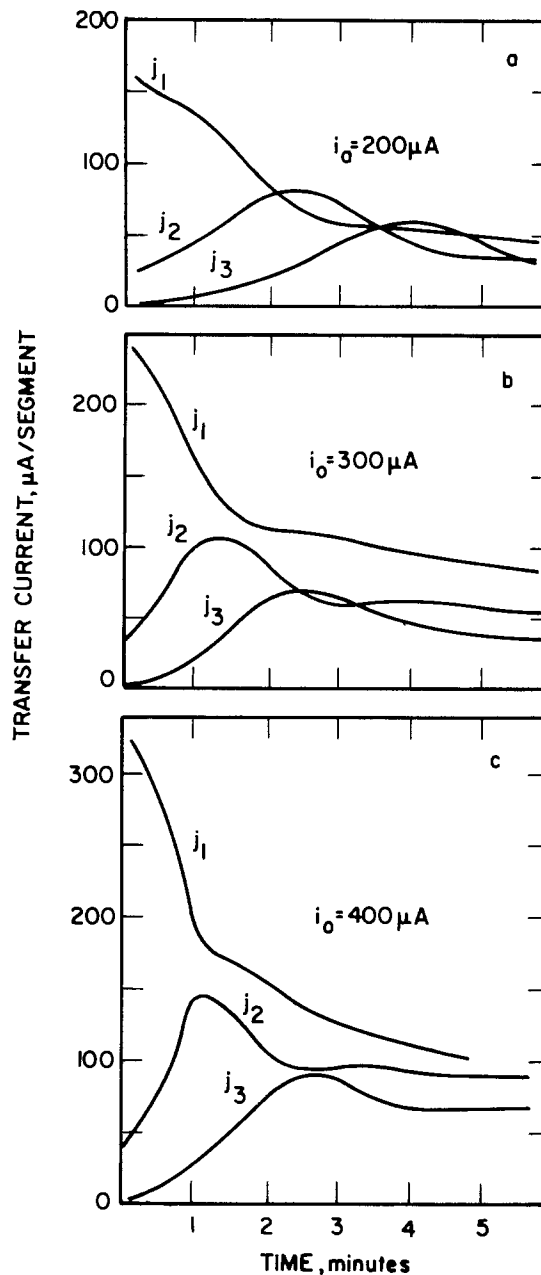


Fig. 10. Time evolution of reaction profile on charging in 1N KCl; charging currents: a, $i_0 = 200 \mu\text{A}$; b, $i_0 = 300 \mu\text{A}$; c, $i_0 = 400 \mu\text{A}$.

lution under those circumstances, i.e., the reaction resistance increases; choking of the first kind has been defined as the shift of current profile toward the electrolyte side caused by an increase in solution resistivity (11).

As the charging current was increased to 300 μA , Fig. 10b, we noted a shift in the transfer current toward the front of the electrode. The current recorded in the first segment was never less than in the second, third, etc. That is, the transfer current distribution "opened up." It is also seen that, at times greater than 2.5 min, the transfer current in the third segment exceeded that in the second. This can be interpreted as an evidence that choking of the second kind still operates, but at greater depths only. As the charging current was increased further, i.e., to 400 μA , the transfer current distribution was further modified in a sense of further "opening up"; at no time were we able to find $j_{k+1} > j_k$. The j - x curve was no longer exponential, except at the beginning of the charging process. Maxima and minima in the distribution curves are expected instead.

The effect of solution resistance on the development of reaction profile is even more dramatically demon-

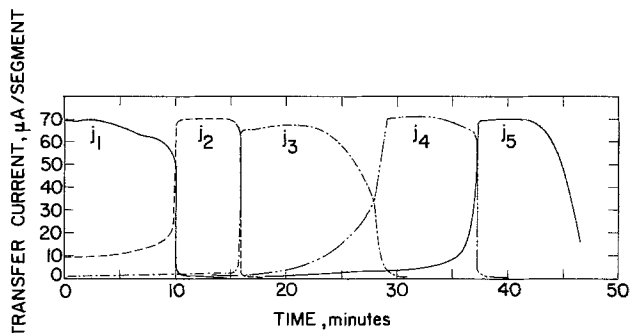


Fig. 11. Time evolution of reaction profile in charging in 0.1N KCl; charging current, $i_0 = 80 \mu\text{A}$.

strated in Fig. 11. It is seen that in 0.1N KCl, the transfer current was almost entirely located in the first segment, with only a small fraction found in the second, and practically none passed through the third. Thus, the reaction was limited to the first two segments: in the concept of reaction layer, $\delta(0.1) < 0.14 \text{ cm}$. When approximately 40 mA-sec has passed through the first segment, there was a rapid termination of reaction in the first segment and a rapid increase in the second. However, no increase in the transfer current in the third segment was noted. Reaction entered the third segment after approximately 36 mA-sec has been accumulated in the second, again after an abrupt termination. In terms of the reaction layer concept, the reaction layer became less thick, $\delta(c) < 0.07 \text{ cm}$.

At later times, i.e., after the reaction entered the third segment, the reaction layer increased in size to the same thickness as at the beginning; the participation of the fourth segment was observed. Again, when approximately 40 mA-sec were accumulated in the third segment, the reaction layer penetrated further. The reaction layer thickness again became less than before.

This behavior appears to be consistent with the motion of a layer, provided that its thickness varies with position. On the basis of the progressive evolution of the transfer current distribution illustrated in Fig. 10a, b, and c, the changing thickness of the reaction layer demonstrated in Fig. 11, should be associated with the interaction between the charge transfer reaction and the transport of reactant.

Effect of Electrode Structure on Evolution of Reaction Profile

The segmented electrode concept provided direct experimental support to the fact that an electrode process operating with a change in electrode mechanism in the interior of porous electrode can be found and shows an excellent qualitative agreement with predicted behavior (11). From a point of view of electrode design, it is more relevant if the segmented electrode concept could be used as a tool in an experimental approach to electrode modeling. In what follows, we shall compare the evolution of reaction profile in a structure generated by loosely compacted spheres of uniform diameter, with those derived from Fig. 10b.

The reaction profiles given in Fig. 12 are based on atomic absorption spectrometric analyses of silver chloride produced on galvanostatic charging of sphere bed electrodes and reconstructed using Eq. [3] and [4]. The sphere bed electrodes were charged at constant current density of 50 mA/cm^2 for periods of $\frac{1}{2}$, $1 + \frac{1}{2}$, $2 + \frac{1}{2}$, etc., min. The experimental technique was outlined previously (18). The time evolution profile in the segmented electrode constructed from data given in Fig. 10b is also shown in Fig. 12.

The similarity in the transfer current evolution is quite evident. In both cases, the initial distribution was exponential with well-defined depth of penetration. As the charging was continued, the usual advancement in the penetration was observed: the distribution was less steep and the exponential character was retained.

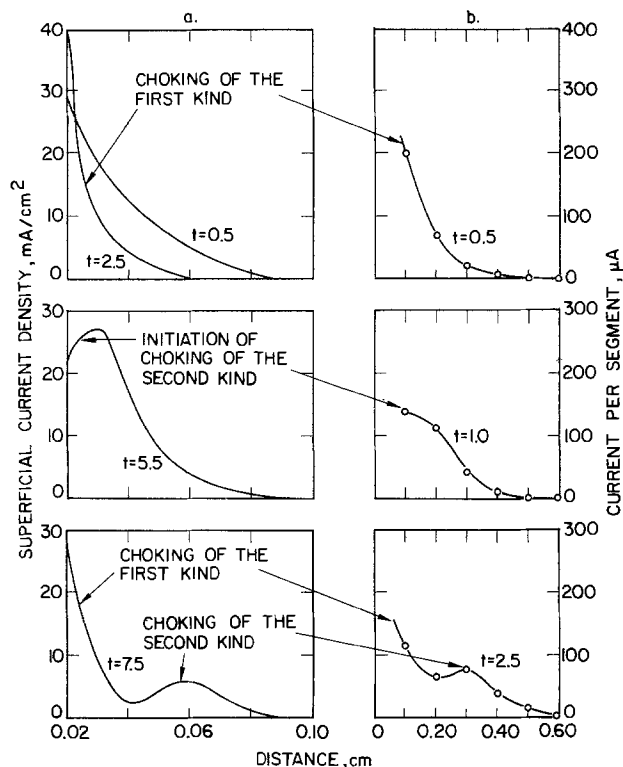


Fig. 12. Comparison of experimentally obtained reaction profile evolutions in 1N KCl. a, Sphere bed electrode, with $i_0 = 50 \text{ mA/cm}^2$; b, segmented electrode, with $i_0 = 300 \mu\text{A}$.

Shortly thereafter, at about 2.5 min of charging, the shift toward the pore mouth in the distribution was noted; that is, choking of the first kind was observed. The origin of this choking, i.e., whether due to the increase in solution resistance due to reactant exhaustion or the onset of voluminous precipitation, cannot be ascertained without independent examination such as electron scan microscopy. Somewhat later, at 5.5 min of charging, choking of the second kind was observed. A noticeable decrease in the current density in the proximity of electrode-electrolyte interface developed. Again, at a later time, at 7.5 min, we observe the formation of a maximum and a minimum in the distribution curve, i.e., the development of reaction profile characteristic of one associated with penetration of choking of the second kind.

The lack of coincidence in time, for the evolution of reaction profiles in the two electrodes can be attributed to differences in detailed structure of the electrodes. The over-all agreement, however, corroborates the usefulness of segmented electrodes as used here in interpreting behavior of more complex geometrical structures.

Conclusions

A segmented, single pore electrode may be prepared to show experimentally the manifestations of reaction regions during the course of charge or discharge for the Ag/AgCl system in aqueous KCl electrolyte. Evolution of the reaction profile and change in the rate determining process could be detected and followed. Further, changes in the distribution of transfer current with varying electrolyte concentration, 0.1, 1.0, and 2.0N KCl, could be distinguished, and a distinction was made from the reaction profiles between choking of the first and second kinds.

In comparison with another, multipore electrode, correspondence between the response of the segmented, single-pore analog and a geometrically three-dimensional porous electrode with interconnected pores were found. In view of insight gained from these studies and practical applications for battery electrodes, important future use of the described technique is anticipated.

Acknowledgment

This work was supported by the Office of Naval Research.

Manuscript submitted June 24, 1974; revised manuscript received Dec. 26, 1974.

Any discussion of this paper will appear in a Discussion Section to be published in the June 1976 JOURNAL. All discussions for the June 1976 Discussion Section should be submitted by Feb. 1, 1976.

Publication costs of this article were partially assisted by Lockheed Palo Alto Research Laboratory.

LIST OF SYMBOLS

c	concentration, mol/liter
i_0	charging current (in external circuit), A
j	transfer current, A and A/cm ²
j^*	dimensionless (reduced) current, defined in text
k	running index referring to distance
l	electrode thickness, cm
m	running index, referring to time
Q	charge transferred, A-sec/cm ²
R	ohmic resistance, ohm; also solution resistance as ohm-cm
t	time, sec
t^*	dimensionless (reduced) form, defined in text
$t(l)$	time of charge for complete coverage (18), sec
t_0	time for complete discharge of electrode, sec
t'	time of duration of experiment, sec
v	velocity of penetration, cm/sec
Z	reaction impedance, ohm-cm ³
x	distance, cm
δ	thickness of reaction layer, cm
κ	$(R/Z)^{1/2}$ -parameter, cm ⁻¹
ζ	$(RZ)^{1/2}$ -resistance, ohm-cm ²
λ	section thickness, cm
τ	time interval, sec

REFERENCES

1. V. S. Daniel'-Bek, *Zh. Fiz. Khim.*, **22**, 697 (1948).
2. E. A. Grens II, *Electrochim. Acta*, **15**, 1047 (1970).
3. J. O'M. Bockris and S. Srinivasan, "Fuel Cells: Their Electrochemistry," Chap. V, McGraw Hill Book Co., New York (1969).
4. R. de Levie, in "Advances in Electrochemistry and Electrochemical Engineering," Vol. 6, P. Delahay, Editor, Interscience Publishers, New York (1966).
5. J. J. Coleman, *This Journal*, **98**, 26 (1951).
6. L. S. Sergeeva and I. A. Selitzkii, *Zh. Fiz. Khim.*, **39**, 204 (1965).
7. R. J. Brodd, *Electrochim. Acta*, **11**, 1107 (1966).
8. D. N. Bennion, H. Gu, and R. K. Hebbbar, *UCLA-ENG 7347* (1972).
9. S. Szpak and G. E. McWilliams, *This Journal*, **120**, 635 (1973).
10. Z. Nagy and J. O'M. Bockris, *ibid.*, **119**, 1129 (1972).
11. S. Szpak, A. Nedoluha, and T. Katan, *ibid.*, **122**, 1054 (1975).
12. P. Bro and H. Y. Kang, *ibid.*, **118**, 519 (1971).
13. F. G. Will, *ibid.*, **110**, 145 (1963); *ibid.*, **110**, 152 (1963).
14. F. G. Will and J. H. Hess, *ibid.*, **120**, 635 (1973).
15. S. Szpak, J. D. Elwin, and T. Katan, *Electrochim. Acta*, **11**, 934 (1966).
16. M. Fogiel, "Modern Microelectronics," Research and Education Association, New York (1972).
17. L. Holland, "Vacuum Deposition of Thin Films," John Wiley & Sons, Inc., New York (1956).
18. T. Katan, S. Szpak, and D. N. Bennion, *This Journal*, **120**, 883 (1973).
19. E. W. Thiele, *Ind. Eng. Chem.*, **31**, 916 (1939).
20. A. Wheeler, "Advances in Catalysis," Vol. III, Academic Press, Inc., New York (1951).
21. L. Nanis, *Plating*, **58**, 805 (1971).
22. A. Winsel, *Z. Elektrochem.*, **66**, 287 (1962).
23. O. S. Ksenzhek, *Russ. J. Phys. Chem.*, **36**, 121 (1962).
24. J. S. Dunning, D. N. Bennion, and J. Newman, *This Journal*, **120**, 906 (1973).

Electrochemical Studies on Single Crystalline CuCl Solid Electrolyte

A. V. Joshi*¹ and J. Bruce Wagner, Jr.*

Department of Materials Science and Materials Research Center, Northwestern University, Evanston, Illinois 60201

ABSTRACT

The d-c polarization technique, relaxation technique, and the charge transfer technique have been applied to cuprous chloride single crystals for the determinations of electronic conductivity, mobility of electronic carriers, and the double layer capacitance at CuCl/graphite interface. A method to separate the electronic charge transfer is presented. It has been shown that the redistribution of electronic carriers within the solid electrolyte in which the concentrations of electronic carriers exponentially increase with the applied potential may make a significant contribution to transient measurements involving a polarization cell. Further, ideal polarization kinetics were observed for the CuCl/graphite interface in the temperature range of 200°-300°C, because the electronic charge transfer was made negligible by selecting the proper parameters such as thickness of the electrolyte and the magnitude of the applied potential step $\Delta E (E_1 - E_2)$ as well as the values of the applied potentials, E_1 and E_2 , on the polarization cell.

In two previous papers (1, 2) electrochemical measurements on CuCl single crystals were described. However, the experimental details and some of the data could not be presented due to the limitations of space. The purpose of the present paper is to supple-

ment and to review the available information on the electrochemical properties of cuprous chloride.

Very little is known about the transport properties of cuprous halides compared to silver halides. In contrast to AgCl or AgBr, cuprous chloride is a p-type conductor (3) when equilibrated with its parent metal, copper. The present study mainly uses a d-c polarization cell of the type, M|MX| inert electrode, to determine the following properties of single crystalline

* Electrochemical Society Active Member.

¹ Present address: P. R. Mallory & Company, Inc., Burlington, Massachusetts 01803.

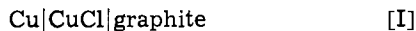
Key words: electrical conductivity, transport numbers, double layer capacitance.

cuprous chloride: (i) electronic conductivity, (ii) drift mobility and concentrations of electronic carriers, and (iii) double layer capacitance at CuCl|graphite interface.

Essentially, three electrochemical techniques are used in the present study. These are: (a) the polarization technique (4), (b) the relaxation technique (5), and (c) the charge transfer technique (6, 7). In what follows, the theory of each type of experiment and the experimental results are discussed.

Theory

D-C polarization study.—These measurements are essentially steady-state measurements. A conductivity cell of the type



where a sample of cuprous chloride is sandwiched between a reversible electrode, copper, and a blocking electrode, graphite, is used as a d-c polarization cell; a positive d-c potential (much below the decomposition potential of cell) is applied to the right-hand electrode. Wagner (4) showed that the total electronic current, I_T , passing through a cell under steady-state conditions is given by

$$I_T = RTA/LF \{ \sigma_{\ominus}^{\circ} [1 - \exp(-EF/RT)] + \sigma_{\oplus}^{\circ} [\exp(+EF/RT) - 1] \} \quad [1]$$

where I_T = total current due to excess electrons and electron holes at steady state, A = cross-sectional area of the interface between graphite and the CuX, L = thickness of the sample, F = Faraday's constant, σ_{\ominus}° = electronic conductivity due to excess electrons in CuX coexisting with copper, σ_{\oplus}° = electronic conductivity due to excess electron holes in CuX coexisting with copper. The other symbols have their usual meaning. If $\sigma_{\oplus}^{\circ} \gg \sigma_{\ominus}^{\circ}$, then the current due to electron holes, I_{\oplus} , becomes

$$I_{\oplus} = RTA/LF \{ \sigma_{\oplus}^{\circ} [\exp(EF/RT) - 1] \} \quad [2]$$

and when $E \gg RT/F$, Eq. [2] can be written as

$$I_{\oplus} = RTA/LF \{ \sigma_{\oplus}^{\circ} \exp(EF/RT) \} \quad [3]$$

Equation [3] is very useful in determining the electronic hole conductivity of CuCl equilibrated with copper from a plot of the log of current *vs.* the applied potential, E .

Relaxation study.—Weiss (5) suggested the relaxation technique to measure the drift mobility of electronic carriers in crystals of AgBr. AgBr is an n-type conductor when equilibrated with its parent metal Ag. The theory can be extended for p-type conductor (*e.g.*, the cuprous halides) as follows.

Consider a typical cell of type [I]. On applying a voltage below decomposition potential of CuCl to cell [I] with the positive pole on the graphite side, the activity of copper at the blocking electrode (*e.g.*, graphite) interface is given by

$$a_{\text{Cu}} = \exp(-EF/RT) \quad [4]$$

Since cuprous halides of ideal composition exhibit mostly cationic conduction and there are substantial concentrations of interstitial cations and cation vacancies, small changes in stoichiometry do not affect the chemical potential of cations but do affect that of electrons or electron holes which are present in concentrations several orders of magnitude less than that of the lattice defects. The concentrations of excess electrons and electron holes at the blocking electrode interface are given by

$$\begin{aligned} C_{\ominus} &= C_{\ominus}^{\circ} [\exp(-EF/RT)] \\ C_{\oplus} &= C_{\oplus}^{\circ} [\exp(EF/RT)] \end{aligned} \quad [5]$$

where E is applied potential and C_{\ominus}° and C_{\oplus}° are the concentrations of electrons and electron holes, respectively, at the Cu-CuX interface.

When the applied potential is removed from cell [I], the concentration of electron holes at the CuX/graphite interface will decrease with time. The open-circuit potential as a function of time $\Delta V(t)$ is given by

$$\Delta V(t) = [RT/F] \ln [C_{\oplus}(t)/C_{\oplus}^{\circ}] \quad [6]$$

where $\Delta V(t)$ = measured open-circuit potential difference across cell [I] as a function of time, and $C_{\oplus}(t)$ = time dependent electron hole concentration at the CuX/graphite interface.

In ionic compounds where the electronic species are minority defects, it can be shown that the effective diffusion coefficient represents the diffusion coefficient of majority electronic carriers (8). This effective diffusion coefficient in cuprous halides represents the diffusion coefficient of electron holes under the conditions where ionic conduction prevails. Fick's second law may be applied to this case where there is a concentration gradient across the sample. The concentration gradient in the sample of length L is constant, *i.e.*, a linear change in concentration is assumed. Thus

$$C_{\oplus}(x) = C_{\oplus}^{\circ} + \frac{x}{L} [C_{\oplus}(x=L) - C_{\oplus}^{\circ}] \quad \text{for } t = 0 \quad 0 \leq x \leq L \quad [7]$$

where $C_{\oplus}(x)$ = concentration of electron holes at a distance x from the Cu/CuX interface. Also

$$\left(\frac{\partial C}{\partial x} \right)_{x=L} = 0 \quad \text{for } t = 0 \quad [8]$$

With these boundary conditions, the solution to Fick's second law is given by (9)

$$\frac{C_{\oplus}(x,t) - C_{\oplus}^{\circ}}{C_{\oplus}(t=0) - C_{\oplus}^{\circ}} = \frac{4}{\pi^2} \sum_{\nu=0}^{\infty} \frac{(-1)^{\nu}}{(2\nu+1)^2} \sin \left[\frac{\pi x(2\nu+1)}{2L} \right] \cdot \exp \left[-\frac{\pi^2(2\nu+1)^2 D_{\oplus} t}{4L^2} \right] \quad [9]$$

$$\approx \frac{4}{\pi^2} \exp \left[-\frac{\pi^2 D_{\oplus} t}{4L^2} \right] \quad [10]$$

where D_{\oplus} denotes the effective diffusion coefficient of electron holes.

Substituting Eq. [5] and [6] in Eq. [10] yields

$$D_{\oplus} t = -\frac{4L^2}{\pi^2} \ln \left[\frac{\pi^2 \exp \left(\frac{\Delta V(t) F}{RT} \right) - 1}{4 \exp(EF/RT) - 1} \right] \quad [11]$$

For $\Delta V(t) F \gg RT$, Eq. [11] becomes

$$D_{\oplus} t = -\frac{4L^2}{\pi^2} \left[\frac{\Delta V(t)}{RT} F - \left(\frac{EF}{RT} \right) + \ln \left(\frac{\pi^2}{4} \right) \right] \quad [12]$$

Thus the slope of a plot of $\Delta V(t)$ *vs.* time will yield the value of D_{\oplus} .

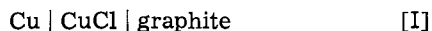
In the case of an n-type conductor such as AgBr, electrons are the majority carriers when the crystal is equilibrated with silver. In that case the concentrations of electrons are substituted in Eq. [10] instead of electron holes. The expression for \tilde{D}_{\ominus} will be

$$D_{\ominus} t = -\frac{4L^2}{\pi^2} \ln \left[\frac{\pi^2}{8} \cdot \frac{1 - \exp[-F\Delta V(t)/RT]}{1 - \exp[-EF/RT]} \right] \quad [13]$$

Charge transfer study.—Raleigh (6) suggested the charge transfer method in order to separate the double layer charge transfer from the bulk electronic charge transfer for the case of AgBr. The theory can be extended to p-type conductors (*e.g.*, cuprous halides) as follows.

When a steady-state bias voltage, E_1 , on the polarized cell [I] is changed from E_1 to E_2 ($E_2 > E_1$), charge transfer occurs by three processes. These are: (i) the charging or discharging, as the case may be, of a double layer capacitor at the inert electrode-solid electrolyte interface, (ii) the redistribution of electronic carriers within solid electrolyte, and (iii) diffusion of copper or other impurities into the graphite electrode until the graphite electrode becomes equilibrated with the new activity of copper at the CuCl | graphite interface.

The third process can be neglected for the present case. This is accomplished experimentally by choosing an inert electrode (graphite) which exhibits virtually no solid solubility for copper or chlorine at temperatures of the investigations. We now derive the expression for the charge transfer due to the second process, namely, the distribution of electronic carriers. Consider the typical cell



in which CuCl exhibits electron hole conduction. The total number of electron holes, N_{\oplus} , when the cell is polarized with potential E_1 is given by (6)

$$N_{\oplus} = \frac{1}{2} AL [C_{\oplus}^{\circ} + C_{\oplus}(o)] \quad [14]$$

where A = area of the interface CuCl/graphite, L = length of the CuCl sample, C_{\oplus}° = concentration of electron holes at the Cu/CuCl interface, and $C_{\oplus}(o)$ = concentration of electron holes at the CuCl/graphite interface.

$$N_{\oplus} = \frac{1}{2} AL C_{\oplus}^{\circ} [\exp(E_1 F/RT) + 1] \quad [15]$$

Now if the potential is changed to some other value, E_2 , then the total number of electron holes, N_{\oplus}' , at this new potential is given by

$$N_{\oplus}' = \frac{1}{2} AL C_{\oplus}^{\circ} [\exp(E_2 F/RT) + 1] \quad [16]$$

Thus, the total amount of electronic charge transfer involved in the polarizing potential step ($E_2 - E_1$) is given by

$$Q_e = \frac{1}{2} e AL C_{\oplus}^{\circ} [\exp(E_2 F/RT) - \exp(E_1 F/RT)] \quad [17]$$

where e is the electronic charge.

The total charge transfer, Q_T , in response to the potential step, ($E_2 - E_1$), involves double layer recharging, Q_{dl} , as well as electronic charge transfer, Q_e (neglecting diffusion charge transfer into the inert electrode). Therefore, we can write

$$\begin{aligned} Q_T &= Q_e + Q_{dl} \\ &= \frac{1}{2} e AL C_{\oplus}^{\circ} \{ \exp(E_2 F/RT) - \exp(E_1 F/RT) \} \\ &\quad + A C_{dl} [E_2 - E_1] \end{aligned} \quad [18]$$

where C_{dl} = double layer capacitance at the CuCl/graphite interface. For the case of AgBr, which ex-

hibits electron conduction when equilibrated with silver as in the cell Ag|AgBr|graphite, the electronic charge transfer is given by

$$Q_e = \frac{1}{2} e AL C_{\ominus}^{\circ} [\exp(-E_1 F/RT) - \exp(-E_2 F/RT)] \quad [19]$$

where C_{\ominus}° is the electron concentration at the Ag|AgBr interface.

In order to separate the contribution of Q_e and Q_{dl} , Eq. [18] is very useful. Consider a double cell, as shown in Fig. 1, involving two identical specimens of cuprous chloride solid electrolyte differing only in specimen length. One sample is of length L_1 and the other of L_2 , ($L_1 > L_2$). If a potential step, E_1 to E_2 , is applied to such a cell, the contribution Q_{dl} may be separated from Q_e because if Q_{dl} is the same for each of the two samples, then for a sample of length, ($L_1 - L_2$), one has

$$Q_e = \frac{1}{2} e A (L_1 - L_2) C_{\oplus}^{\circ} [\exp(E_2 F/RT) - \exp(E_1 F/RT)] \quad [20]$$

for a p-type conductor and a similar expression for an n-type conductor. Moreover, by subtracting the value of Q_e for a sample of length L_1 (or L_2) from the total charge transfer, Q_T for a single cell, then the value of Q_{dl} and hence the double layer capacitance may be obtained. Experimentally it is convenient to use $E_2 \gg E_1$, whereupon the first exponential term in Eq. [20] is much larger than the second so that

$$\ln Q_e = \ln \left\{ \frac{1}{2} e A (L_1 - L_2) C_{\oplus}^{\circ} \right\} + E_2 F/RT \quad [21]$$

and the resulting slope yields a value of F/RT if the experiment is in accord with theory. The intercept yields the value of C_{\oplus}° .

If the value of the specific electronic hole conductivity, σ_{\oplus}° , has been obtained from the steady-state, d-c polarization measurements, then the mobility, μ_{\oplus} , may be obtained using

$$\mu_{\oplus} = \frac{\sigma_{\oplus}^{\circ}}{C_{\oplus}^{\circ} \cdot e} \quad [22]$$

Determination of electron hole mobility by current-time analysis.—The charge transfer technique described previously, basically involves measurement of current as a function of time for a fixed potential step. In a cell of type [I], if the electronic charge transfer is predominant over the capacitive charge transfer for a fixed potential step, then a current-time relationship can be derived in order to determine the electronic carrier mobility in a solid electrolyte as follows.

Consider cell [I] of length L subjected to some potential E_1 . If the electron hole concentration at Cu|CuCl interface is denoted by C_{\oplus}° then the concentration of electron holes at CuCl|graphite interface under the potential E_1 is given by

$$C_{\oplus} = C_{\oplus}^{\circ} \exp(E_1 F/RT) \quad [23]$$

Under this steady-state condition, the electron hole concentration at any distance x from the blocking elec-

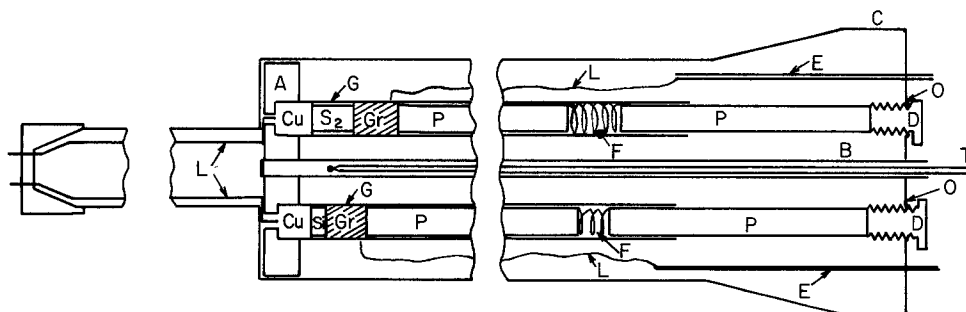


Fig. 1. Schematic diagram of setup for two polarization cells called double cell. A, Lavite block; B, stainless steel tube; C, Teflon plug; D, stainless steel bolt; E, copper leads; F, springs; G, glass tube cell holder; L, platinum leads; O, O-rings; P, plungers; T, thermocouple; S₁, small sample of CuCl; S₂, long sample of CuCl; Cu, copper pellet; Gr, graphite pellet.

trode interface where $x = 0$ can be expressed as

$$C_{\oplus}(x,0) = C_{\oplus}^{\circ} \exp(E_1 F/RT) - \frac{x}{L} [C_{\oplus}^{\circ} \exp(E_1 F/RT) - C_{\oplus}^{\circ}] \quad [24]$$

This is the initial condition.

When the applied potential on the cell is changed from E_1 to E_2 , the concentration of electron holes at blocking electrode interface changes to a value of $C_{\oplus}^{\circ} \exp(E_2 F/RT)$. For the present experimental conditions this process occurs in 1 or 2 sec. Therefore, the following boundary condition holds

$$C_{\oplus}(0,t) = C_{\oplus}^{\circ} \exp(E_2 F/RT) \quad \text{at } x = 0 \quad t > 0 \quad [25]$$

When the new potential fixes the concentration of electron holes at the blocking electrode interface ($x = 0$), diffusion of electron holes will occur in the solid electrolyte until the steady-state electron hole current passes through the sample. The solution of Fick's second law with the above mentioned initial and boundary conditions is given by

$$C_{\oplus}(x,t) = \left\{ C_{\oplus}^{\circ} \exp(E_2 F/RT) \operatorname{erfc} \frac{x}{2\sqrt{D_{\oplus} t}} + C_{\oplus}^{\circ} \exp(E_1 F/RT) \operatorname{erf} \frac{x}{2\sqrt{D_{\oplus} t}} - [C_{\oplus}^{\circ} \exp(E_1 F/RT) - C_{\oplus}^{\circ}] x/L \right\} \quad [26]$$

The above solution is for the semi-infinite rod and is valid for early times (≈ 100 to 200 sec in the present case).

Differentiation of Eq. [26] with respect to x can be written as

$$\frac{\partial C_{\oplus}}{\partial x} \Big|_{x=0} = \left\{ -\frac{C_{\oplus}^{\circ} \exp(E_2 F/RT)}{\sqrt{\pi D_{\oplus} t}} + \frac{C_{\oplus}^{\circ} \exp(E_1 F/RT)}{\sqrt{\pi D_{\oplus} t}} - \frac{1}{L} [C_{\oplus}^{\circ} \exp(E_1 F/RT) - C_{\oplus}^{\circ}] \right\} \quad [27]$$

The flux is given by

$$J = -D \frac{\partial C_{\oplus}}{\partial x} \Big|_{x=0} \quad [28]$$

Therefore, the current due to electron holes is given by

$$I_{\oplus}(t) = -(eAD_{\oplus}) \left(\frac{\partial C_{\oplus}}{\partial x} \Big|_{x=0} \right) \quad [29]$$

$$= \left(\frac{eAD_{\oplus}}{\sqrt{\pi D_{\oplus} t}} \right) C_{\oplus}^{\circ} [\exp(E_2 F/RT) - \exp(E_1 F/RT)] + [eAD_{\oplus} C_{\oplus}^{\circ}/L] [\exp(E_1 F/RT) - 1] \quad [30]$$

Substituting $D_{\oplus} = \mu_{\oplus} RT/F$ and $\sigma_{\oplus}^{\circ} = C_{\oplus}^{\circ} e \mu_{\oplus}$ in the above expression, we get

$$I_{\oplus}(t) = \frac{L}{\sqrt{\pi D_{\oplus} t}} [I_{\oplus}(E_2) - I_{\oplus}(E_1)] + I_{\oplus}(E_1) \quad [31]$$

where

$$I_{\oplus}(E_2) = (RTA/LF) \sigma_{\oplus}^{\circ} [\exp(E_2 F/RT) - 1]$$

and

$$I_{\oplus}(E_1) = (RTA/LF) \sigma_{\oplus}^{\circ} [\exp(E_1 F/RT) - 1]$$

Experimental

Cuprous chloride crystallizes in the zinc blende lattice up to 407°C and in a wurtzite (hexagonal) lattice from 407°C to its melting point at 422°C. Crystals grown at temperatures below 407°C can crystallize directly in the zinc blende phase and exhibit no strains

(10). The single crystals provided to us were grown by the same technique using fluxes to suppress the melting point below 407°C.

Preparation of pellets.—For the measurements of electronic conductivity, electronic mobility, and double layer capacitance, the double cell arrangement as shown in Fig. 1 was used. For this type of arrangement two specimens of single crystalline CuCl with different lengths were used. The pellets were cut from one long cylinder of CuCl (9 mm diam) by using a diamond wire saw. The pellets were then polished mechanically on polishing wheels saturated with abrasives in an acetone solution. After polishing these cylinders were washed successively in acetone, dilute HCl, and acetone. The pellets were then ready for the experimental use. The mass spectrographic analysis for the cuprous chloride is given in Table I. For the reversible copper electrode 99.999% pure copper rod (obtained from American Smelting and Refining Company) was used. For the nonreversible graphite electrode, pyrolytic graphite (obtained from the Union Carbide Company) was used. The pellets of copper and pyrolytic graphite electrodes were also given the same surface treatment as the cuprous chloride pellets. All measurements were carried out in the double cell as shown in Fig. 1.

Apparatus.—The prepared samples of cuprous chloride, copper, and pyrolytic graphite were mounted in a polarization double cell as shown in Fig. 1. The contact was insured by applying slight pressure with springs attached to the plunger P. At temperatures near their melting points, most solid electrolytes tend to soften. Because of this, annealing to a bulk metal electrode under light spring pressure resulted in an excellent interface contact. The electronic conductivity measurements, the drift mobility of electronic carriers by the relaxation technique, the charge transfer technique, and the total conductivity measurements were carried out on the same double cell under a purified Linde argon atmosphere. Purification of the argon was carried out by passing the gas over heated copper turnings (99.999% pure) at approximately 500°C. The gas was then passed through the tubes of Linde molecular sieves and silica gel. A Marshall resistance furnace was used in a horizontal position. The temperatures were controlled to $\pm 1^{\circ}\text{C}$ by a Leeds and Northrup Electromax controller using Chromel-Alumel thermocouples. A copper tube heat sink was fitted around the cells with a controlled thermocouple within the core of the tube. Shielded wires were used to connect with the digital voltmeters. Various stable d-c potentials were

Table I. Impurity concentrations in northwestern cuprous chloride (in parts per million by weight)

Element ^(a)	Detection limit ^(b)	CuCl
Li	0.05	0.15
C	0.3	1400 ^(c)
N	0.3	11
O	0.3	23
F	0.3	23
Na	0.1	13
Al	0.3	0.97
Si	0.3	27
S	0.7	2.7
K	0.1	4.7
Ca	0.3	6.5
Mn	0.6	180
Fe	1	26
Ni	1	1.4
Zn	3	25
Br	3	120
Rb	0.3	11

^(a) No analysis was made for hydrogen. Analyses for tantalum and gold are not given since tantalum slits are used in the mass spectrometer and the sample was sparked against a high purity gold counterelectrode. Residuals in the mass spectrometer interfere with the analyses for gallium and arsenic. Other impurities not listed were not detected and have concentrations less than 3 ppm atomic.

^(b) Determined for 3×10^{-8} coulomb exposure.

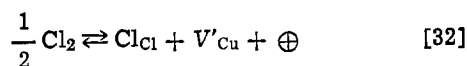
^(c) The high concentration of carbon was due to the graphite inert electrode which was pressed against the surface of the CuCl crystal analyzed.

applied via a Keithley 260 nanovolt source. For the measurement of charge transfer the voltage steps were applied on the two samples. The circuitry for applying voltage steps was similar to that used by Raleigh (15) and is shown in Fig. 2. The cell current in response to such a step is monitored across a resistor using a Tektronix Model 564A storage oscilloscope for initial short times and Doric Digital microvoltmeter for longer times. The Doric digital micrometer is a six range instrument with a digital read out and microvolt sensitivity. The maximum reading rate of this instrument is about 2 readings per second. The readings were recorded by the Datatotal digital printout. The applied voltage on the cell was measured by the other similar Doric digital voltmeter. The total charge transfer was determined by measuring the area under the plot of the transient current vs. time. For the relaxation measurements the open-circuit potentials were recorded every 1 sec by the Datatotal printer. The total conductivity measurements were done on the same cells as used for the previous measurements of electronic conductivity, mobility, etc. These measurements were carried out after all the other measurements were completed. A General Radio Bridge (1650A) was used to measure the total electrical conductivity. Before making these measurements some copper was deposited on the graphite electrode by applying positive potential on the copper electrode.

Results and Discussion

Measurement of ionic and electronic conductivity of CuCl.—Current voltage characteristics were measured on the cuprous chloride single crystal mounted between copper and graphite electrode. Equation [3] predicts that logarithm of hole current ($\log I_{\oplus}$) vs. applied voltage (E) should yield a straight line plot, the intercept of which would yield the value of the specific hole conductivity of cuprous chloride equilibrated with copper. Vander Meulen and Kröger (11) reported that for heavily doped samples of silver chloride, there is an additional current flow which is due to surface leakage. In the present experiments, the data were analyzed by plotting I vs. $\exp(EF/RT)$ or by $\log I$ vs. E . The slopes of $\log I$ vs. E plots were found to be close to the theoretically predicted slope of F/RT . The average ratio of theoretical to experimental slope of $\log I$ vs. E plot was found to be 1.01. This suggests that there was no appreciable surface leakage in the cell [see Ref. (11)].

The hole conductivity in cuprous chloride can be due to the excess chlorine as follows



where Cl_{Cl} represents a chlorine ion on chlorine site and V'_{Cu} represents the singly ionized cation vacancy. Since the degree of cationic disorder in cuprous chloride is large compared to its range of stoichiometry, the cationic vacancy concentration is independent of chlorine pressure. Thus, the mass action law applied to Eq. [32] yields

$$[V'_{\text{Cu}}] [\oplus] / p_{\text{Cl}_2}^{1/2} = K \quad [33]$$

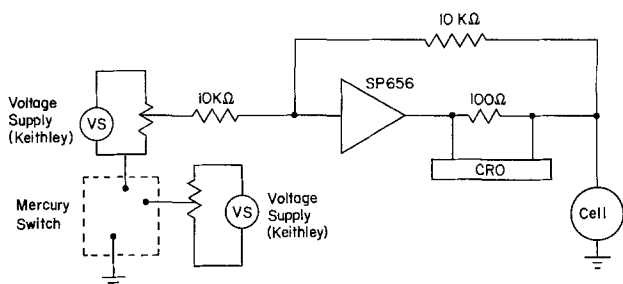


Fig. 2. Circuit diagram for application of stable d-c potential steps to the cell.

From the previous argument

$$[V'_{\text{Cu}}] = K_1 = \text{constant} \quad [34]$$

$$[\oplus] \propto p_{\text{Cl}_2}^{1/2} \quad [35]$$

Thus one can see that hole conductivity varies as the square root of chlorine pressure. The observation that slopes of $\log I$ vs. E plots are close to the value of (F/RT) at all temperatures of the present investigation is in agreement with the prediction that the electronic conductivity of cuprous chloride is proportional to the square root of the partial pressure of chlorine.

A typical plot of I vs. $\exp(EF/RT)$ at a particular temperature (383°C) for the case of single crystalline cuprous chloride is shown in Fig. 3. The electronic conductivity was calculated from the value of the slope of the I vs. $\exp(EF/RT)$ plot. The geometric factor, $L/A \equiv G$, was determined by making a series of a-c measurements and is discussed later. The electronic conductivity values were then plotted against temperature as $\log \sigma_{\text{e}}^{\circ}$ vs. $1/T$. The plot of $\log \sigma_{\text{e}}^{\circ}$ vs. $1/T$ for two different samples is shown in Fig. 4. The electronic conductivity values were determined in the temperature range of $100^\circ\text{--}400^\circ\text{C}$. The dependence of electronic conductivity on $1/T$ for single crystalline cuprous chloride can be expressed as

$$\sigma_{\text{e}}^{\circ} = 78 \exp \left\{ \frac{-24,900 \pm 300}{RT} \right\} \quad [36]$$

Following the polarization measurements, the same cells were used to measure the total conductivity of cuprous chloride single crystals by an a-c technique. Previous a-c measurements on cuprous chloride were made by Wagner and Wagner (3) on pressed pellets and by Hsueh and Christy (12) on single crystals. The present measurements were intended to check our

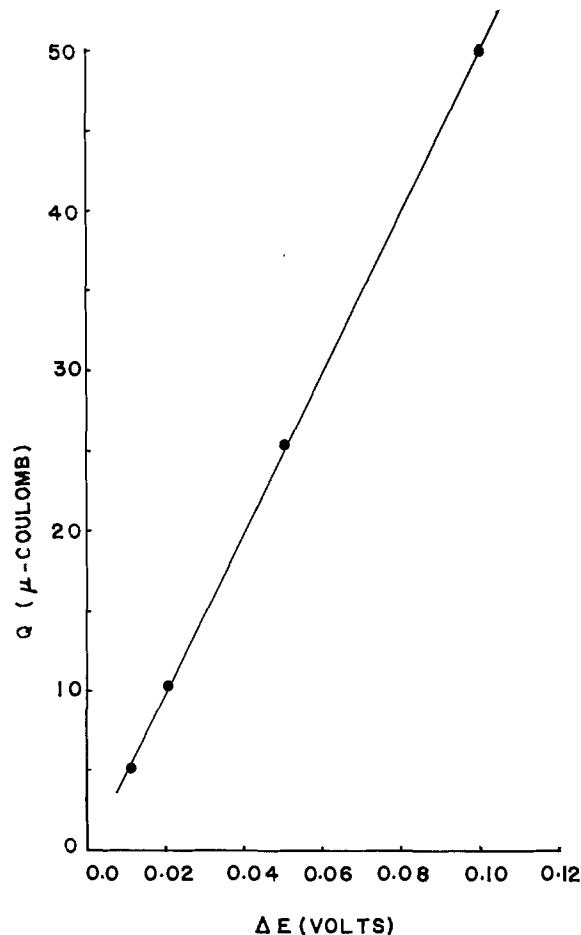


Fig. 3. Typical plot of current vs. $\exp(EF/RT)$ for the case of CuCl at temperature of 383°C .

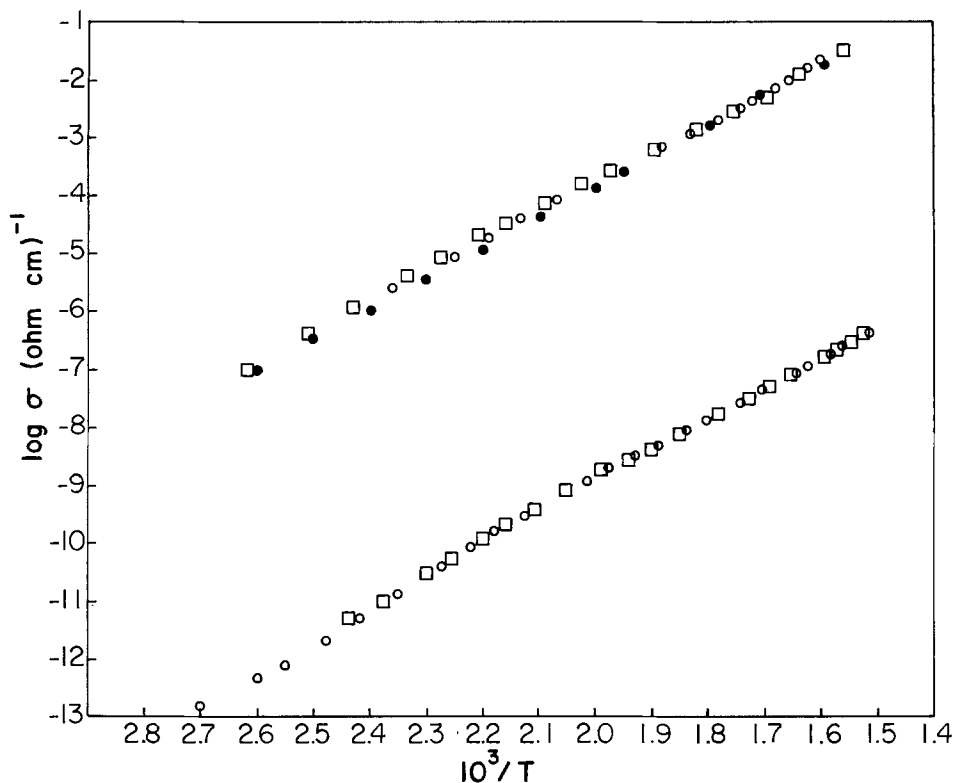


Fig. 4. Logarithm of electron hole conductivity equilibrated with copper $\log(\sigma_{\oplus}^{\circ})$ vs. $1/T$ for single crystal of CuCl. \square , Run 300 series; \circ , run 200 series; \bullet , as obtained by Hsueh and Christy (12) and by Wagner and Wagner (3).

measurements and also to determine the geometric factor $G = L/A$.

In the present study prior to carrying out a-c measurements, a positive current was passed through the copper electrode in order to plate some copper onto the graphite electrode. This arrangement would then be equivalent to sandwiching the cuprous chloride sample between two reversible copper electrodes as was used by Wagner and Wagner (3) and by Hsueh and Christy (12). The resistance of the sample was measured with a-c method using a General Radio Type 1650 A impedance bridge at 1000 Hz. The measurements were carried out on two different samples and the data were compared to previous measurements. The present measurements were in good agreement with the data reported previously (3, 12). These measurements also determined the geometric factor G . If R is the measured resistance of the crystal used and σ is the specific conductivity then $G = R\sigma$.

The conductivity results are summarized in Fig. 4. It can be seen that cuprous chloride is predominantly an ionic conductor throughout the temperature range investigated. Tubandt and Bandowin (13) in the 1930s reported that cuprous chloride becomes predominantly an electronic conductor below 200°C. Recently Maidanovskaya *et al.* (14) reported that cuprous chloride does not exhibit predominantly ionic conduction until the melting point temperature is obtained. The transference numbers of the electronic species in CuCl reported by Tubandt and Bandowin and by Maidanovskaya *et al.* are shown in Fig. 5. Their results are in disagreement with each other and also are in disagreement with present results. The present authors suggest that the probable cause for the discrepancies was due to oxygen, either dissolved or as a second phase, in their samples and that pure CuCl is predominantly an ionic conductor.

Measurement of drift mobility and the concentration of electronic carriers in cuprous chloride equilibrated with copper by the charge transfer technique.—As mentioned above, the electronic charge transfer and double layer capacitive charge transfer in a polarized cell [I] can be separated by the so called charge transfer technique. The charge transfer values were measured on two identical polarized cells of type [I] differing only in sample length. These values are measured

by applying a fixed potential step on both cells at a given temperature. The concentration of electron holes at the Cu/CuCl interface, C_{\oplus}° , is determined using Eq. [23]. The total charge transfer values for each sample and the calculated values of concentration of electron holes at the reversible electrode (C_{\oplus}°) for CuCl are shown in Table II. The values shown are the average values obtained at each temperature. A deviation of $\pm 3\%$ was observed between successive runs. It can be seen from these measurements that double layer charge transfer at CuCl/graphite interface is negligible compared to the electronic charge transfer for samples longer than 1 cm in the temperature range of 300°–400°C. Therefore, Eq. [21] can be used to test the theory. For this case, charge transfer values on the

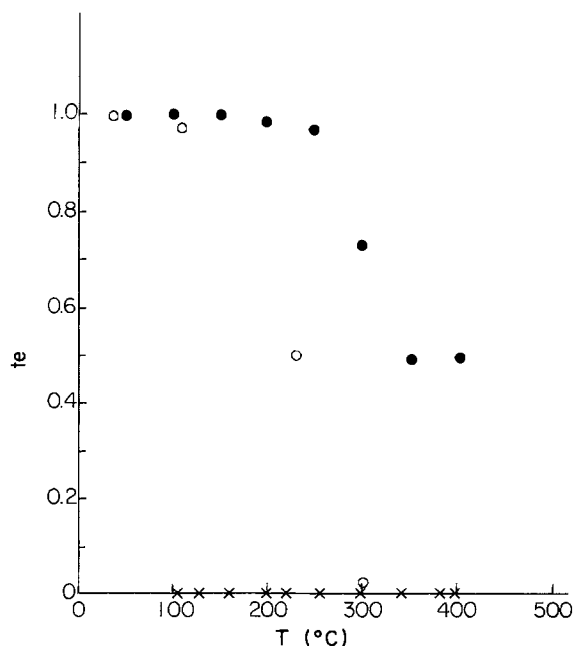


Fig. 5. Transference numbers for electron (t_e) vs. temperature (T) plot for the case of CuCl. \bullet , Maidanovskaya *et al.* (14); \circ , Tubandt and Bandowin (13); \times , present measurements.

Table II. Values of charge transfer concentration of electron holes at various temperatures and voltage steps for the case of cuprous chloride

Run	Charge transfer [$\mu\text{coulombs}$]		C_{\oplus}° , No./cm ³	Temper- ature, °K	Step, V
	Long sample $L_1 = 1.672$ cm	Short sample $L_2 = 0.21$ cm			
303	27,200 \pm 300	3,389 \pm 110	5.6×10^{13}	655	0.2871-0.4878
304	22,815 \pm 150	2,805 \pm 90	4.03×10^{13}	646	0.2880-0.4898
305	17,991 \pm 200	2,100 \pm 60	2.7×10^{13}	634.5	0.2881 \rightarrow 0.4895
306	14,416 \pm 180	1,822 \pm 40	1.93×10^{13}	626	0.2885-0.4893
307	11,059 \pm 170	1,407 \pm 50	1.30×10^{13}	615	0.2883 \rightarrow 0.4898
308	19,489 \pm 150	2,387 \pm 80	8.8×10^{12}	605	0.2883-0.5348
309	13,229 \pm 100	1,800 \pm 50	4.1×10^{12}	590.5	0.2442-0.5393
310	11,400 \pm 110	1,479 \pm 30	2.5×10^{12}	578	0.2434-0.5453
311	6,539 \pm 50	852 \pm 40	1.05×10^{12}	561	0.2432-0.5499

longer sample (1.672 cm) were measured as a function of E_2 . The lower value of applied potential (E_1) was always maintained at a value such that $\exp(E_2F/RT) \gg \exp(E_1F/RT)$. Figure 6 shows the plot of logarithm of total charge transfer vs. E_2 for the longer sample (1.672 cm) of CuCl at 353°C. The plot of $\log Q_T (\cong \log Q_E)$ vs. E_2 yielded a slope which was essentially equal to the theoretical slope of F/RT between 300° and 400°C. This is a very good proof for the argument that the electronic charge transfer in polarized cells of type [I] is predominant over other processes under the conditions as described earlier. The values of concentrations of electrons (C_{\oplus}°) as calculated from Table II or from Fig. 6 were in good agreement with each other. Figure 7 shows the plot of $\log C_{\oplus}^{\circ}$ vs. $1/T$ for cuprous chloride equilibrated with copper. The plot shows a very good linear dependence of $\log C_{\oplus}^{\circ}$ on $1/T$. This dependence can be expressed as

$$C_{\oplus}^{\circ} = 1.04 \cdot 10^{24} \exp(-31,000 \pm 500/RT) \text{ (No./cm}^3\text{)} \quad [37]$$

where 31 kcal/mole is the value for the heat of solution of chlorine in CuCl.

The electron hole mobility was determined by using the values of concentrations of electron holes determined by charge transfer technique. The electron hole mobility is given by Eq. [22].

The values of electron hole conductivity, mobility and the concentrations at various temperature for CuCl equilibrated with copper are tabulated in Table III. Figure 8 shows the plot of $\log \mu_{\oplus}$ vs. $\log T$ for CuCl

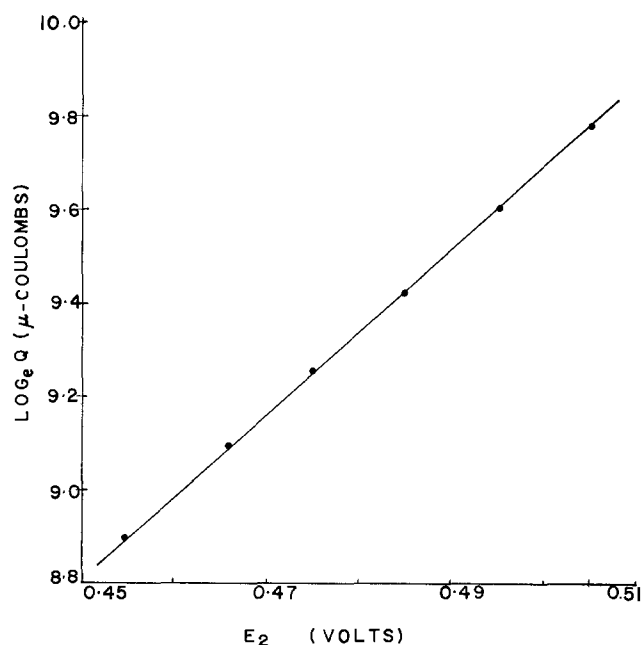


Fig. 6. Plot of logarithm of total charge transfer vs. final potential E_2 for CuCl where $\exp E_2F/RT \gg \exp E_1F/RT$ and double layer charge transfer is negligible compared to the total charge transfer.

Table III. Values of electronic conductivity, concentration, and mobility at various temperatures for cuprous chloride

σ_{\oplus}° , ohm-cm	C_{\oplus}° , No./cm ³	μ_{\oplus}° , cm ² /sec-V	Temper- ature, °K
4×10^{-7}	5.60×10^{13}	4.46×10^{-2}	655
3.09×10^{-7}	4.03×10^{13}	4.79×10^{-2}	646
2.17×10^{-7}	2.7×10^{13}	5.0×10^{-2}	634.5
1.64×10^{-7}	1.93×10^{13}	5.32×10^{-2}	626
1.16×10^{-7}	1.30×10^{13}	5.62×10^{-2}	615
8.6×10^{-8}	8.8×10^{12}	6.1×10^{-2}	605
5.1×10^{-8}	4.1×10^{12}	7.77×10^{-2}	590.5
3.31×10^{-8}	2.5×10^{12}	8.27×10^{-2}	578
1.69×10^{-8}	1.05×10^{12}	1.05×10^{-1}	561

in the temperature range of 300°-400°C. The dependence of mobility on temperature can be expressed as

$$\mu_{\oplus} \propto T^{-5.6 \pm 0.2} \quad [38]$$

Raleigh (15, 19) reports a similar dependence of electron hole mobility on the temperature in the case of AgBr.

Measurement of drift mobility of electronic carriers by the relaxation technique.—The relaxation technique as suggested by Weiss (5) for the case of AgBr could be applied for the case of CuCl since it was found that the electronic charge transfer predominates over other processes for samples longer than 1 cm and in the temperature range of 300°-400°C. A typical plot of $\Delta V(t)$ vs. time for CuCl is shown in Fig. 9. Equation [12] was

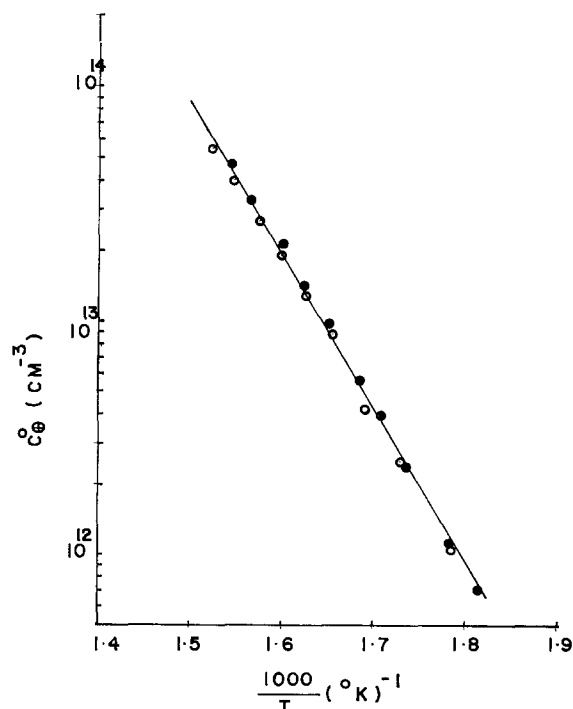


Fig. 7. Log of concentration of electron holes in cuprous chloride equilibrated with copper vs. $1/T$ plot. ●, Run 200 series; ○, run 300 series.

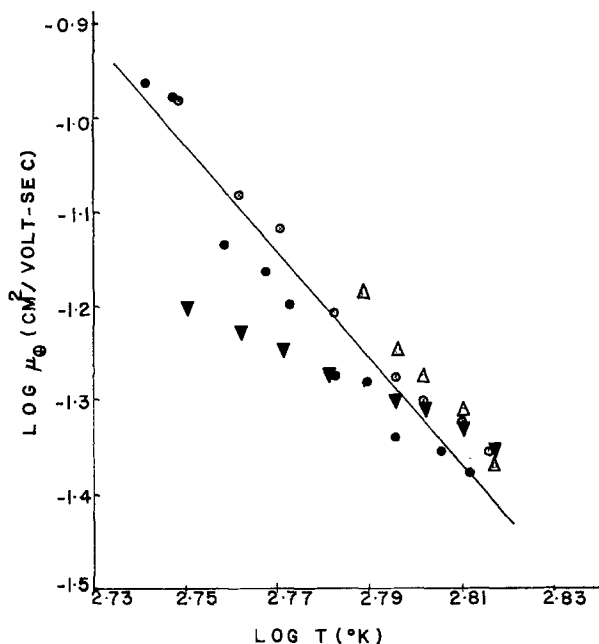


Fig. 8. Plot of logarithm of mobility for electron holes vs. logarithm of temperature for the case of CuCl. ●, Run 200 series, charge transfer techniques; ○, run 300 series, charge transfer techniques; △, I vs. $1/\sqrt{t}$ analysis; ▼, relaxation technique.

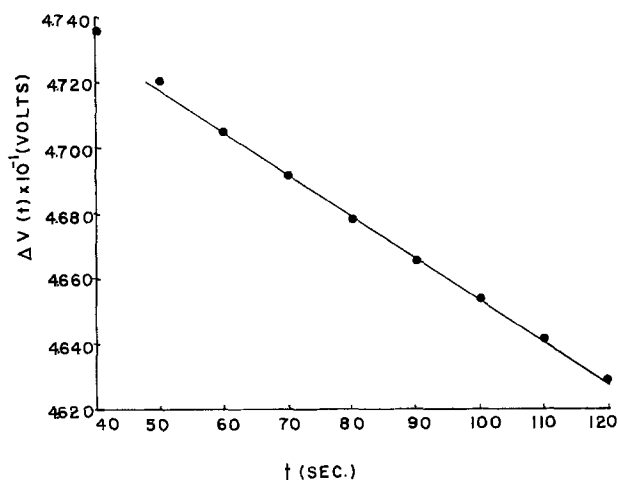


Fig. 9. Typical plot of $\Delta V(t)$ vs. time for the case of cuprous chloride at temperature of 646°K.

used to determine the diffusion coefficient of electron holes from the knowledge of the slopes of $\Delta V(t)$ vs. time plots. The mobility was then calculated by using Nernst-Einstein relation

$$D_{\oplus} = \mu_{\oplus} \frac{RT}{F} \quad [39]$$

These values are shown in Fig. 8.

Determination of electron hole mobility by current-time analysis.—The charge transfer measurements described earlier involve the measurement of transient currents as a function of time for a fixed potential step. The present authors derived the relationship between the transient current and time under the condition that the charge transfer due to electronic carriers is predominant over the other process. This relationship is given by Eq. [31].

Plots of the transient current, $I(t)$, vs. $1/\sqrt{t}$ for the case of CuCl (1.672 cm) at various temperatures are shown in Fig. 10. The magnitudes of the potential steps are shown in Table I. The diffusion coefficients of electron holes were calculated using the slopes of $I(t)$ vs. $1/\sqrt{t}$ plots at various temperatures using Eq.

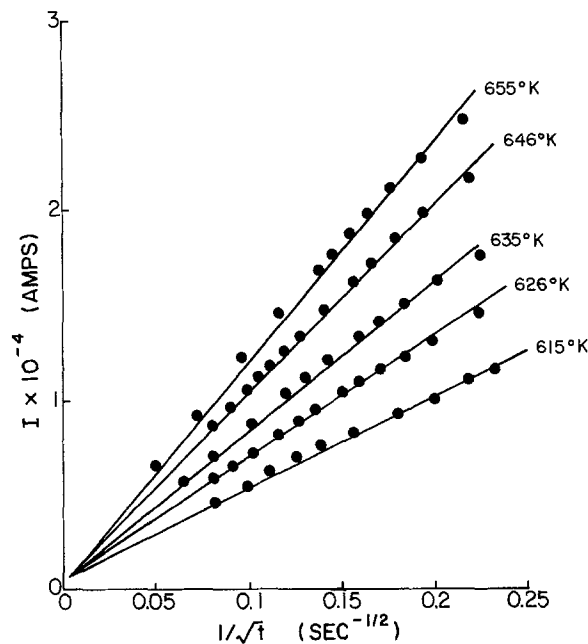


Fig. 10. Plot of current I vs. $1/\sqrt{t}$ for the case of CuCl when the potential on the polarized cell changed from E_1 to E_2 . The slope of plot changes according to the temperature as can be seen from the figure.

[31]. The mobility is then calculated by using Nernst-Einstein relation (Eq. [39]). Equation [31] suggests that the intercept of $I(t)$ vs. $1/\sqrt{t}$ plot should yield a value of $I_{\oplus}(E_1)$, if the measurements are in accord with the theory. The values of the intercept for $I(t)$ vs. $1/\sqrt{t}$ plot for CuCl were indeed close to the values of $I_{\oplus}(E_1)$ for temperatures between 340° and 400°C. The mobility values obtained by this analysis are plotted in Fig. 8. It can be seen that these values agree with the values obtained by charge transfer method.

Measurement of double layer capacitance at CuCl | graphite interface at lower temperatures.—Raleigh (15, 19) made various measurements on AgBr to determine the double layer capacitance of the AgBr | inert electrode interface. For the measurement of double layer capacitance at the AgBr | graphite interface, the voltage steps were applied to the polarization cell Ag | AgBr | graphite and transient currents in response to such voltage steps were recorded as a function of time. All the charge transfer involved in the above process was due to the double layer capacitive charging. The electronic charge transfer was negligible as has been shown by Raleigh (6). In Raleigh's experiment the plots of $\log I$ vs. time were linear at longer times. For initial times they were not linear. The reason for this was attributed by Raleigh to the nonlinear effect in chemical double layer capacitance. The present authors (20) attributed such nonlinearity to the electronic charge transfer at early times. Hull and Pilla (21) also studied the AgI | graphite and the AgI | platinum interfaces at room temperature. They reported pure double layer behavior of such interfaces.

For the case of cuprous chloride at temperatures greater than 350°C the plots of $\log I$ vs. time were not linear. The reason for this was that the electronic charge transfer contributed significantly, although a small voltage step was applied to the cell. The electronic charge transfer is dependent upon the length of the specimen, the magnitude of the voltage step, and the concentration of electron holes at the reversible electrode. It was therefore decided to work at lower temperatures with very thin samples. A sample of length 0.085 cm was used for the measurements. Various small voltage steps of about 20 mV were applied in the voltage range of 200–450 mV. On the lower side of this voltage range, the plots of $\log I$ vs. time were

linear for times greater than 30 msec. On the other hand, at the higher side of this voltage range, *i.e.*, between 400 and 450 mV, the plots of $\log I$ vs. time were not linear. Figure 11 shows this difference. The dotted curve in Fig. 11 represents the characteristics for the voltage step of 0.4287 \rightarrow 0.4489. This is due to the contribution from the electronic charge transfer. The calculation of electronic charge transfer can be carried out by using Eq. [17]. The concentration of electron holes equilibrated with copper at 264°C can be obtained by extrapolating our high temperature data (see Fig. 7). The calculation shows that the electronic charge transfer due to potential steps of 0.2476 \rightarrow 0.2677V, 0.2678 \rightarrow 0.2879V, and 0.2878 \rightarrow 0.3089V at 242°C amounts to less than 5% of the total charge transfer. However, the electronic charge transfer due to a potential step of 0.4287 \rightarrow 0.4489 constitutes about 50% of the total charge transfer. This is the reason for the nonlinearity of dotted curve in Fig. 11. Figure 12 shows plots of $\log I$ vs. time for two temperatures. It was found that for the three temperatures investigated, the double layer capacitance of the CuCl | graphite interface remained constant as has been observed by Raleigh for the case of the AgBr | graphite interface. The double layer capacitance was determined by the slope of $\log I$ vs. time plot. The current and time relation is given by

$$I = I_0 \exp(-t/R C_{dl}) \quad [41]$$

where R = resistance of electrolyte and C_{dl} = double layer capacitance at the CuCl | inert electrode interface. The average value of the double layer capacitance was found to be $729 \pm 60 \mu\text{F}/\text{cm}^2$. Figure 13 shows the plot of the total charge transfer vs. the magnitude of voltage steps. Care has been taken not to exceed the electronic transfer more than 5% of the total charge transfer.

The linear relation between total charge transfer and the magnitude of voltage steps suggests that the double layer charge transfer is predominant over electronic charge transfer for this thin sample.

General comments on the above measurements.—We have discussed, in general, three methods of obtaining mobility of electronic carriers in cuprous chloride. These methods are applicable to any mixed conductor

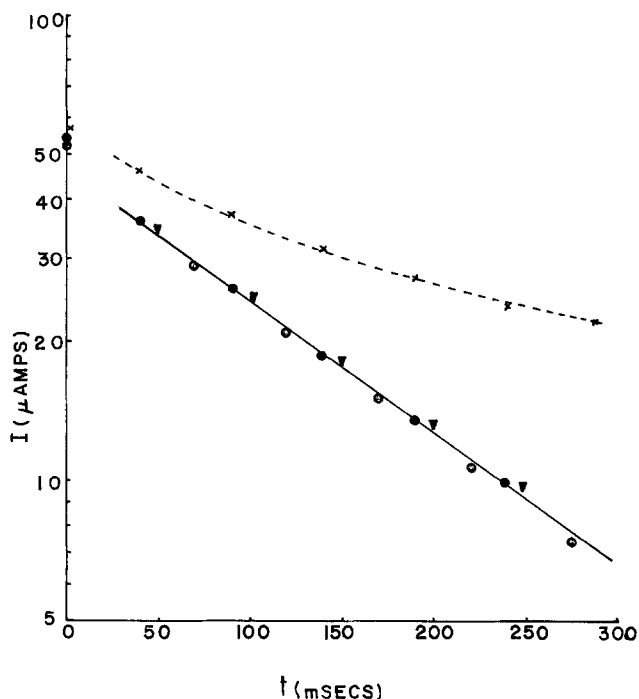


Fig. 11. Plot of $\log I$ vs. time for the case of thin sample of cuprous chloride for various applied voltage steps at a temperature of 242°C. ●, 0.2476-0.2677V; ○, 0.2678-0.2879V; ▼, 0.2878-0.3089V; ×, 0.4287-0.4489V.

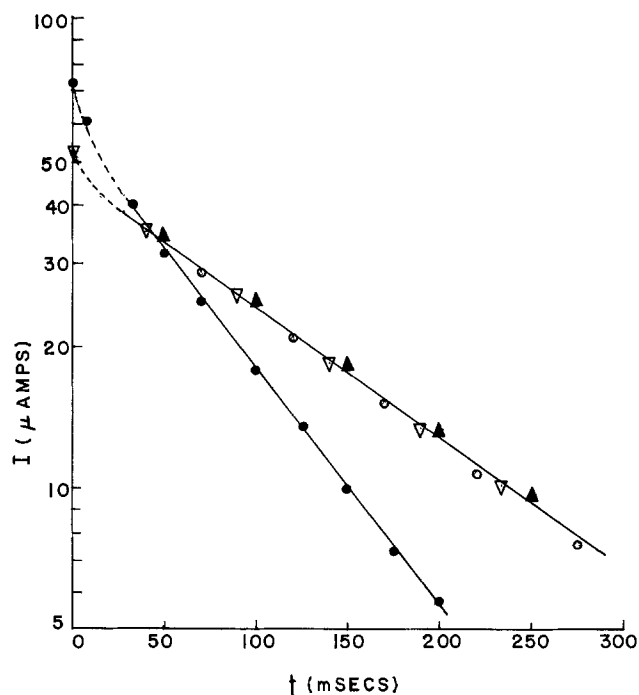


Fig. 12. Plot of $\log I$ vs. time for the case of thin sample of cuprous chloride. The line through triangles and open circles represents the behavior at 242°C while the line through the dark circles represents the behavior at 264°C.

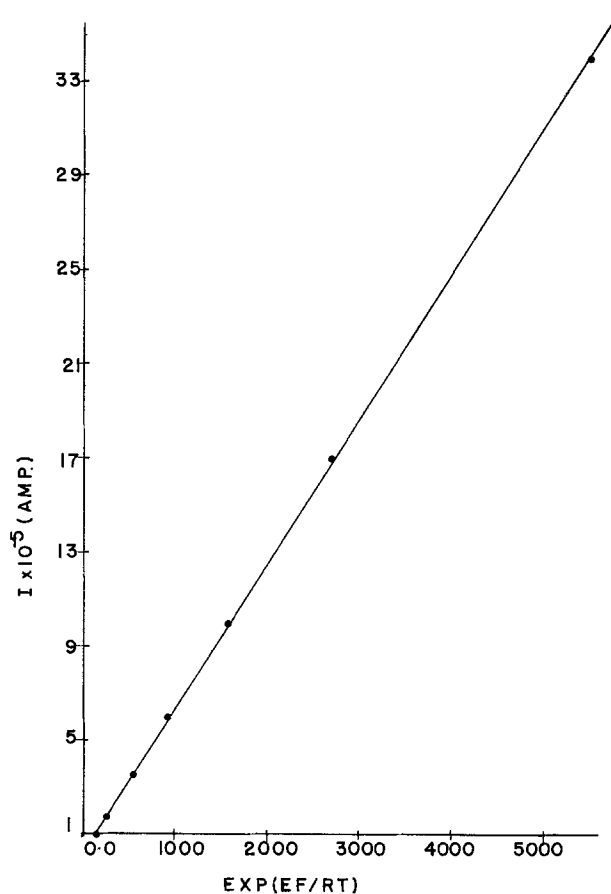


Fig. 13. The plot of total charge transfer Q vs. the value of voltage step for the case of thin sample of cuprous chloride at a temperature of 264°C.

MX in which the electronic charge transfer can be made predominant with respect to other processes. This can be easily achieved in a polarized cell, if the concentration of electronic carriers exponentially increases with the applied potential. In such a case, the

electronic charge transfer can be made predominant over the other processes by using a longer sample and also by using a large potential step.

Among the three techniques used in this study, we found the charge transfer technique was the most reliable. In the other two methods the effect of other interface processes (e.g., diffusion of copper in an inert electrode and double layer capacitance) if present, could interfere with the determination of electron hole diffusivity. This problem is entirely eliminated in our use of the charge transfer technique since the technique eliminates the effects due to interfaces by carrying out the measurements on two samples of different lengths. These measurements also indicate that the requirement that the transference number by virtual unity is not a sufficient condition for an electrolyte to be used for a galvanic cell for the various thermodynamic measurements as has been described by Wagner (2) and Joshi (7).

The exponential increase of concentrations of electron holes with the applied voltage at the blocking electrode interface can be the limiting factor in the use of the electrolyte for electrochemical diffusion measurements of the elemental component of an electrolyte into an inert electrode. Recently Goldman and Wagner (22) have successfully used a cell $\text{Cu} | \text{CuCl} | \text{Au}$ to measure the diffusion of Cu in Au. These workers insured that the electron hole current contribution to the total transient current was negligible. This was achieved by using a very thin sample of CuCl and by using temperatures higher than 350°C. Thus, in the measurements involving transient currents, one should be aware of the transient electronic current resulting from the redistribution of electronic carriers in response to the new potential. The electronic current is especially important in ionic conductors where the concentration of electronic carriers exponentially increases with the applied potential.

Summary and Conclusions

The measurements of conductivity, mobility, and concentrations of electron holes were carried out on single crystals of cuprous chloride. The half-power dependence of electron hole conductivity on chlorine pressure was indirectly verified in the temperature range of 100°-400°C. Further it was found that cuprous chloride is predominantly an ionic conductor throughout the above temperature range. The concentrations and mobility of electron holes in cuprous chloride was determined by three methods; namely, charge transfer, relaxation, and I vs. $1/\sqrt{t}$ analysis. The mobility values obtained by the above three methods are in excellent agreement with each other in the temperature range of 300°-400°C. The double layer capacitance of $\text{CuCl} | \text{graphite}$ interface was also measured at lower temperatures (200°-300°C). Ideal polarization behavior was observed for this interface.

Acknowledgments

The authors wish to thank Professor C. Wagner, Professor John Patterson, and Dr. D. O. Raleigh for helpful discussions during this work. The authors are also grateful to Dr. Okabe of Shizuoka University (Japan) for a gift of cuprous chloride single crystals. This work was supported by contract DAHC 15 67 C 0213 from the Advanced Research Projects Agency through the Materials Research Center of Northwestern University.

Manuscript submitted Sept. 26, 1974; revised manuscript received Feb. 27, 1975.

Any discussion of this paper will appear in a Discussion Section to be published in the June 1976 JOURNAL. All discussions for the June 1976 Discussion Section should be submitted by Feb. 1, 1976.

REFERENCES

1. A. V. Joshi, in "Proceedings of NATO Conference, Belgirate, Italy, Sept. 5-15, 1972," W. van Gool, Editor, p. 173.
2. J. B. Wagner, *ibid.*, p. 489.
3. J. B. Wagner and C. Wagner, *J. Chem. Phys.*, **26**, 1597 (1957).
4. C. Wagner, "Proc. 7th International Committee for Electrochemical Thermodynamics and Kinetics, London, 1955," Butterworths Scientific Publications, London (1956).
5. K. Weiss, *Z. Physik Chem. (N.F.)*, **59**, 242 (1968).
6. D. O. Raleigh, *ibid.*, **60**, 319 (1969).
7. A. V. Joshi, Ph.D. Thesis, Northwestern University (1972).
8. C. Wagner, *J. Phys. Chem. Solids*, **29**, 1925 (1968).
9. H. S. Carslaw and J. S. Jeager, "Conduction of Heat in Solids," Clarendon Press, Oxford (1968).
10. M. Soga, R. Imaizumi, Y. Kondo, and F. Okabe, *This Journal*, **114**, 388 (1967).
11. Y. J. Vander Meulen and F. A. Kröger, *This Journal*, **117**, 69 (1970).
12. V. W. Hseuh and R. W. Christy, *J. Chem. Phys.*, **39**, 3519 (1963).
13. C. Tubandt and M. Bandowin, Landolt-Börnstein "Physikalisch-chemische Tabellen," 5th ed., Springer-Verlag, Berlin, Haupt Werk II, 1923 Ergänzungsband I (1927), II (1931), and III (1935-1936).
14. L. G. Maidanovskaya, I. A. Kirovskaya, and G. L. Lomanova, *Izv. Akad. Nauk SSSR, Inorganic Materials*, **3**, 936 (1967).
15. D. O. Raleigh, *J. Phys. Chem.*, **70**, 689 (1966).
16. D. O. Raleigh, *ibid.*, **71**, 1785 (1967).
17. D. O. Raleigh, *J. Phys. Chem. Solids*, **29**, 261 (1968).
18. D. O. Raleigh, *Phys. Status Solidi*, **4**, 215 (1971).
19. D. O. Raleigh, *This Journal*, **118**, 79 (1971).
20. A. V. Joshi and J. B. Wagner, *J. Phys. Chem. Solids*, **33**, 205 (1972).
21. M. N. Hull and A. A. Pilla, *This Journal*, **118**, 72 (1971).
22. J. Goldman and J. B. Wagner, *ibid.*, **121**, 1318 (1974).

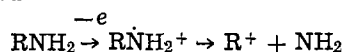


Electrochemical Oxidation of *tert*-Butylamine to 2,2'-Azoisobutane

A. U. Blackham,* Solim Kwak, and J. L. Palmer

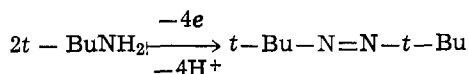
Departments of Chemistry and Chemical Engineering, Brigham Young University, Provo, Utah 84602

The electrochemical oxidation of primary aliphatic amines in aqueous solution is complicated by the closeness of the oxidation potentials of the amine and the solvent water. Barnes and Mann (1) have studied the electrochemical oxidation of several primary amines at a platinum anode in acetonitrile to avoid this interference by the solvent. Two reaction paths were postulated to account for the products observed. Most of the amines studied followed both reaction paths simultaneously. However, *tert*-butylamine followed only one path. In one of the steps of this path a carbonium ion was generated



Accordingly, the reaction products observed were *tert*-butyl alcohol and isobutylene.

We report in this note an electrochemical oxidation of *tert*-butylamine in sharp contrast to the above reaction as the concentration of the *tert*-butylamine is drastically changed. The major anodic product from a concentrated solution in which *tert*-butylamine is essentially the solvent as well as the reactant is azo-*tert*-butane (2,2'-azoisobutane)



Our initial concern in this study was the development of a satisfactory synthesis of azo-*tert*-butane. A few preliminary electrolyses were run in a small H-cell. The progress of the reaction was determined by gas chromatographic detection of the products soluble in 2,2,4-trimethylpentane. In dilute aqueous solutions of *tert*-butylamine with both platinum and graphite anodes only traces of azo-*tert*-butane were detected. As the concentration of *tert*-butylamine in the electrolyte was increased, more azo-*tert*-butane was observed. Also, azoxy-*tert*-butane and nitroso-*tert*-butane were detected. These trends suggested a high concentration of *tert*-butylamine would favor the synthesis of azo-*tert*-butane. Accordingly, a large scale preparative cell was constructed. The following experimental details are for a run made in this cell.

Experimental

Preparative cell.—The anodes were cut from a block of graphite. Each had the dimensions 0.60 × 7.0 × 25.0 cm with a small tab at the top for contact with a copper rod. The cathodes were cut from a sheet of stainless steel. Each had the same length and width as the anodes and with a similar tab. An alternating array of 22 anodes and 23 cathodes were placed in a box 10 × 36 × 36 cm constructed from acrylic plastic. Spacers between the electrodes permitted a distance of 0.5–0.7 cm between the anodic and

cathodic surfaces. The evolution of hydrogen provided a stirring action to the electrolyte. This cell design was based on the assumption that the hydrogen gas liberated at the cathode and the azo-*tert*-butane formed at the anode would not react further at opposite electrodes.

Synthesis.—The electrolytic solution was prepared by mixing 2500g *tert*-butylamine, 366g water, and 34g NaClO₄·6H₂O. Therefore this was an 86% *tert*-butylamine solution. This solution which measured about 4 liters was placed in the cell and electrolyzed at 3.0V. A current of about 2.0A flowed through the cell until 23.0f of charge had passed. The calculated current density for an 80% immersion of the electrodes was 0.33 mA/cm². The reaction mixture was diluted with water resulting in two phases. The upper organic phase was distilled yielding 423g of azo-*tert*-butane and 50g of azoxy-*tert*-butane. Of the charge that passed through the cell 41% accounted for the azo compound and 5% for the azoxy compound. About 20g of a white crystalline solid was recovered from the diluted reaction mixture. This was later characterized as di-*tert*-butylurea. The progress of the reaction was periodically determined by gas chromatography. A 2 ml sample of the reaction mixture was mixed with 2 ml of 2,2,5-trimethylhexane and 10 ml water. The gas chromatograms of the hydrocarbon phase had large peaks for the azo and azoxy compounds. Other compounds shown to be present in smaller amounts were isobutylene, isobutane, and nitroso-*tert*-butane. The gaseous product from the reaction contained hydrogen, isobutylene, isobutane, nitrogen, and oxygen. However, the gaseous products were not analyzed accurately and periodically to establish complete material and charge balances. The aqueous phase from the reaction product contained unreacted *tert*-butylamine.

Characterization of products.—Azo-*tert*-butane¹ was distilled at 105°C at 650 Torr (lit. value 109–110 at 760) (2, 3). The NMR spectrum gave a singlet at 1.13 δ. Azoxy-*tert*-butane¹ was distilled at 141°C at 650 Torr. The NMR spectrum gave two singlets at 1.27 and 1.47 δ (lit. values 1.28 and 1.48) (4). The nitroso-*tert*-butane was characterized by its NMR spectrum from gas chromatographic collection in carbon tetrachloride. The solution was blue. The NMR spectrum gave a singlet at 1.24 δ (lit. value 1.25 δ) (4).

The di-*tert*-butylurea was easily sublimed and a mass spectrum was taken of a pure sample. The mass spectrum gave a parent peak at 172 amu with major fragments at 100 (t-BuNHCO)⁺, 72 (t-BuNH)⁺, 56 (C₄H₈)⁺, and 15 (CH₃)⁺. Some infrared spectral assignments were a NH peak at 3352 cm⁻¹, a CH absorption for *tert*-butyl group at 1388–1319, and a carbonyl absorption at 1630 cm⁻¹. The NMR spectrum (run with

* Electrochemical Society Active Member.
Key words: amine oxidation, electrochemical synthesis, azoalkane, nitrene.

¹ Azo-*tert*-butane and azoxy-*tert*-butane are available from Fairfield Chemical Company, Blythewood, South Carolina 29016.

chloroform as the solvent) gave two peaks at 1.29 and 1.44 δ in a ratio of 9:1. The melting point in a sealed tube was 258°-260°C (lit. value 245°C) (5). In an open capillary tube vigorous sublimation was observed at 242°-250°C.

Discussion

We are considering two possible reaction pathways for this electrolytic oxidation of *tert*-butylamine. The first step may involve a one-electron loss leading to the formation of a free radical, *t*-BuNH \cdot , or a two-electron loss leading to the formation of a nitrene, *t*-BuN. The reaction products isolated can be explained by both intermediates. However, di-*tert*-butylhydrazine which would be expected from the dimerization of *t*-BuNH was not found as a reaction product.

This electrochemical synthesis offers some advantages over chemical oxidations of *tert*-butylamine. Farenhorst and Kooyman (3) prepared the N-chloro-*tert*-butylamine and reacted it with silver oxide to obtain a 5% yield of azo-*tert*-butane. Stevens (6) oxidized *tert*-butylamine with IF₅ to obtain a 48% yield. Stowell (7) reacted N,N'-di-*tert*-butylsulfamide with NaOCl to obtain an 84% yield.

Compared with these chemical methods, the electrochemical synthesis of azo-*tert*-butane can be conducted with cheaper reactants and reagents and with a higher or comparable percentage conversion.

Further work is in progress to establish complete material and charge balances; to determine yields as a function of current density and concentration; and to determine the number of electrons in the first electrochemical step.

Acknowledgment

This research was supported in part by a grant from the estate of Patricia B. Fish.

Manuscript submitted Aug. 26, 1974; revised manuscript received March 28, 1975.

Any discussion of this paper will appear in a Discussion Section to be published in the June 1976 JOURNAL. All discussions for the June 1976 Discussion Section should be submitted by Feb. 1, 1976.

Publication costs of this article were partially assisted by Brigham Young University.

REFERENCES

1. K. K. Barnes and C. K. Mann, *J. Org. Chem.*, **32**, 1474 (1967).
2. A. U. Blackham and N. L. Eatough, *J. Am. Chem. Soc.*, **84**, 2922 (1962).
3. E. Farenhorst and E. C. Kooyman, *Rec. Trav. Chem.*, **72**, 993 (1953).
4. J. P. Freeman, *J. Org. Chem.*, **28**, 2508 (1963).
5. R. A. Franz, F. Applegath, F. V. Morriss, and F. Baiocchi, *ibid.*, **26**, 3306 (1961).
6. T. E. Stevens, *ibid.*, **26**, 2531 (1961).
7. J. C. Stowell, *ibid.*, **32**, 2360 (1967).

Comparison of Some Solutions for the Warburg Impedance of a Rotating Disk Electrode

E. Levart and D. Schuhmann

Laboratoire d'Électrolyse du Centre National de la Recherche Scientifique, 92190 Bellevue, France

Homsy and Newman (1) have recently given the following solution for the Warburg impedance of a rotating disk electrode, valid only for high frequencies and large Schmidt numbers

$$\theta'(0) = -\sqrt{jK} + 3j/4K + 0(K^{-5/2}) \quad [1]$$

In this equation (Eq. [12] in their paper), K represents a dimensionless frequency and $\theta'(0)$ is the derivative of a complex dimensionless time-varying concentration on the disk surface.

Using the corresponding expressions obtained for $\text{Re}[1/\theta'(0)]$ and $\text{Im}[1/\theta'(0)]$, these authors have evaluated the real and imaginary parts of the Warburg impedance. The error between their results and the exact solution does not exceed 2% for $K = 10$, which evidently offers an improvement over the Nernst stagnant diffusion-layer approximation in the region of intermediate to large K .

Meanwhile, we have published a general method for evaluation of the concentration impedance for a rotating disk electrode (2) which includes the problem above as a particular case. Our asymptotic solution, valid for high frequencies and any finite value of the Schmidt number involved in electrochemistry, was given in the following form

$$M^\circ(\tau, \sigma) = a^{-1/3} \tau [u^{-1/2} - \frac{1}{4}u^{-2} + 0.3\tau u^{-5/2} + 0(u^{-3})] \quad [2]$$

where $\tau = \text{Sc}^{-1/3}$ and $u = \chi + j\sigma$. The dimensionless complex variable, u , is related to the frequency by

Key words: Warburg impedance, rotating disk electrode, asymptotic approximation, dimensionless quantity, complex plane graphical representation.

$\sigma = \omega/\Omega\tau a^{2/3}$ and to the rate constant k of the chemical reaction following or preceding charge transfer by $\chi = k/\Omega\tau a^{2/3}$ (for a first-order reaction, $k = \bar{k} + \bar{k}^-$). $M^\circ(\tau, \sigma)$, a dimensionless concentration impedance, is the value of a very general transfer function $M(z, \tau, \sigma)$ at the surface of the disk. M , which may be considered as the inverse of the Nusselt (Sherwood) function (3), is proportional to the local variations in the concentration.

For the case of the pure Warburg impedance without chemical complications, Eq. [2] may be written for very large Schmidt numbers as follows

$$M^\circ(\tau, \sigma) = a^{-1/3} \tau [(j\sigma)^{-1/2} - \frac{1}{4}(j\sigma)^{-2} + 0(\sigma^{-7/2})] \quad [3]$$

Since Eq. [3] is not usable for $\tau = 0$, we divide by $M^\circ(\tau, 0) = (3/a)^{1/3} \Gamma(4/3)\tau$, obtaining

$$\Phi^\circ = M^\circ(\tau, \sigma)/M^\circ(\tau, 0) = [(j\sigma)^{-1/2} - \frac{1}{4}(j\sigma)^{-2} + 0(\sigma^{-7/2})]/3^{1/3}\Gamma(4/3) \quad [4]$$

If we replace σ and Φ° in Eq. [4] by their respective equivalents $K/3^{2/3}$ and $1/\theta'(0)\Gamma(4/3)$, we get the following equation

$$1/\theta'(0) = (jK)^{-1/2} + 3/4K^2 + 0(K^{-7/2}) \quad [5]$$

which is more advantageous than Eq. [1].

First of all, the expressions for the real and imaginary parts of the Warburg impedance derived from Eq. [5]

$$\text{Re}[1/\theta'(0)] = 1/\sqrt{2K} + 3/4K^2 \quad [6]$$

and

$$\text{Im}[1/\theta'(0)] = -1/\sqrt{2K} \quad [7]$$

are simpler than the corresponding formulas of Homzy and Newman, (Ref. (1), Eq. [13] and [14]). Of course, the contrary may be said about the corresponding expressions for the Warburg admittance.

The important point is that the results obtained using Eq. [6] and [7] agree much better with the numerical exact solution than do the results from Homzy and Newman's equations. As a matter of fact, our error does not exceed 0.2% for $K = 10$, which is one order of magnitude better than the 2% stated by these authors. The same error of 2% which they have for $K \approx 10$, we get for $K \approx 5$. Table I summarizes these results.

We have found that by continuing the (nonconvergent) series expansion of Homzy and Newman we obtain the same result as on inverting our continued expansion. Thus the lower error of our expression (limited, as is that of Homzy and Newman, to the two first terms) results from the smaller contribution of the truncated terms.

We wish to take this opportunity to add a word of caution concerning the graphical representation of such results in the complex plane. Such a representation, frequently used, can be misleading if the corresponding frequencies are not indicated on the graph. For example, looking only at Fig. 1 of Ref. (1), we may think that the proposed asymptotic solution agrees with the exact solution over the entire region where both curves are superimposed, that is, up to $K \approx 4$. In view of their accompanying numerical data, this is evidently not the case. We believe that for this purpose it is more convenient to represent separately the real and imaginary parts of the reduced impedance vs. the reduced frequency, as we show here on Fig. 1. The data calculated by Homzy and Newman and those from our asymptotic solution are compared with the exact solution (continuous curves). The black dots represent the results obtained by another approximation, valid only for low and intermediate frequencies, which we had proposed in the paper quoted above (2). These last data were calculated by dividing the values of $\text{Re}(\lambda^{\circ}_1)$ and $\text{Im}(\lambda^{\circ}_1)$, published in Table 3 of that paper, by $(3/a)^{1/3} = 1.8049$. They agree perfectly with the exact solution over the entire region of frequencies from $K = 0$ to $K = 30$ at least.

Manuscript submitted Dec. 30, 1974; revised manuscript received March 25, 1975.

Table I. Solutions for the real and imaginary parts of $1/\theta'(0)$

K	Homzy and Newman		Levart and Schuhmann		Exact solution	
	Re	-Im	Re	-Im	Re	-Im
3.5	0.4055	0.3398	0.4392	0.3780	0.4561	0.3474
5	0.3304	0.2991	0.3462	0.3162	0.3556	0.3115
7.5	0.2647	0.2510	0.2715	0.2510	0.2735	0.2588
10	0.2273	0.2197	0.2311	0.2236	0.2314	0.2240
20	0.1591	0.1572	0.1600	0.1581	0.1600	0.1581

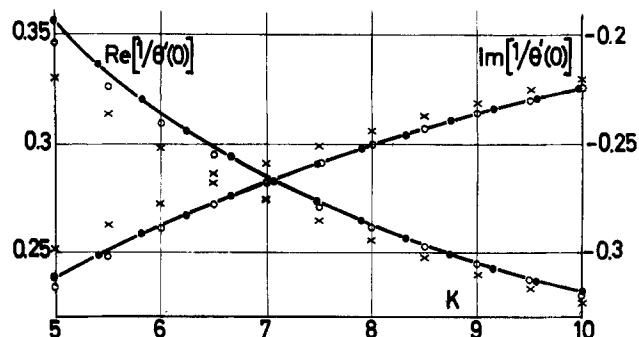


Fig. 1. The dependence of the real and imaginary parts of the Warburg impedance $1/\theta'(0)$ on the reduced frequency K . (X), Homsy and Newman's asymptotic solution; (O), our asymptotic solution; (●), our low-frequency solution; continuous curves, exact numerical solution.

Any discussion of this paper will appear in a Discussion Section to be published in the June 1976 JOURNAL. All discussions for the June 1976 Discussion Section should be submitted by Feb. 1, 1976.

Publication costs of this article were partially assisted by Centre National de la Recherche Scientifique.

SYMBOLS

Generally used:

a	0.510233
j	$\sqrt{-1}$
Re, Im	real and imaginary parts of a complex quantity
k	chemical-reaction rate constant, sec^{-1}
ω	angular frequency (pulsatance) of alternating current, rad/sec
Ω	rotation speed of disk, rad/sec
Sc	Schmidt number

Used by Homzy and Newman (all are dimensionless):

θ	complex time-varying concentration
$1/\theta'(0)$	Warburg impedance
K	frequency

Used by Levart and Schuhmann (all are dimensionless):

M°	concentration impedance
u	complex variable related to χ and σ
Φ°	Warburg impedance
λ°_1	first coefficient in the series expansion of M° in powers of τ
σ	frequency
τ	$\text{Sc}^{-1/3}$
χ	reaction rate constant

REFERENCES

1. R. V. Homzy and J. Newman, *This Journal*, **121**, 521 (1974).
2. E. Levart and D. Schuhmann, *J. Electroanal. Chem.*, **53**, 77 (1974).
3. D. Schuhmann, 25th I.S.E. Meeting, September 1974, Brighton, Extended Abstracts, p. 104.



Note on the Stability of Impregnated Paper Separators

Barbara A. Campbell and J. R. Dafler*

ESB Incorporated, Yardley, Pennsylvania 19067

Impregnated paper separators, made by typical paper-forming techniques, then impregnated with thermosetting resins, are widely used in automotive battery technology. They possess distinct cost advantages compared with microporous rubber or sintered polymer separators. They are adequate for shallow cycling use typical of automotive storage batteries. They tend to fail after a few hundred cycles when discharged at 5 and 10 hr rates. The mechanism of failure is not clearly defined but related to physical and chemical stability.

Our investigation of stability is based on x-ray diffraction measurements of the crystalline cellulose present in the separator matrix. Hermans and Weidinger have explored the question of crystallinity and recrystallization in a series of papers (1-3). The question on order or crystallinity of cellulose has been discussed at some length (4-6). For the purposes of this study the term crystallinity serves well.

We have not used the same technique but have concentrated on direct x-ray comparisons of the crystalline material in unimpregnated paper, finished, and used separators. Using typical diffractometer techniques and postsample monochromated Cu-radiation ($\lambda = 1.543\text{\AA}$), we obtained patterns very similar to those Hermans and Weidinger (1) obtained with a microcamera and a carefully compressed plug of sample. As in the case of Hermans and Weidinger, all samples tested gave diffuse peaks in the region $8\text{--}15^\circ 2\theta$, and a much taller, less diffuse peak in the neighborhood of $22^\circ 2\theta$. All samples tested were derived from the same source of α -cellulose.

Experimental

A large bundle of impregnated paper separators was selected and cut in quarters, the samples then shuffled and divided into groups for storage in sulfuric acid. About 50 such chips were stored at 125°F in sulfuric acid of three concentrations. In addition, one acid medium was saturated with PbSO_4 . The acid concentrations were defined by the following specific gravities; 1.260, 1.280, and 1.325. Samples were taken from acid storage at intervals and examined by x-ray diffraction.

A number of automotive batteries were fabricated and put on cycle testing. The testing (SAE Schedule K) consisted of discharging for 1 hr at 20A followed by charging at 5A for 5 hr. Separators were taken at 5 and 9 week intervals and washed thoroughly in cold water to free the surfaces of Pb-salt accumulations. After drying the samples, representative chips were taken for x-ray analysis. All sets of x-ray diffraction scans were made with a "blank" chip of the basic α -cellulose used in the paper matrix. This was done to allow normalization of diffractometer intensities to a standard value. A Philips Electronics Mark II x-ray diffractometer was used to obtain x-ray intensity data. The analyses were done at Cu-target parameters of 35 kVA and 15 mA x-ray current. Figure 1 indicates typical diffractometer traces for unimpregnated paper, virgin separators, and separators stored 3690 hr in 1.280

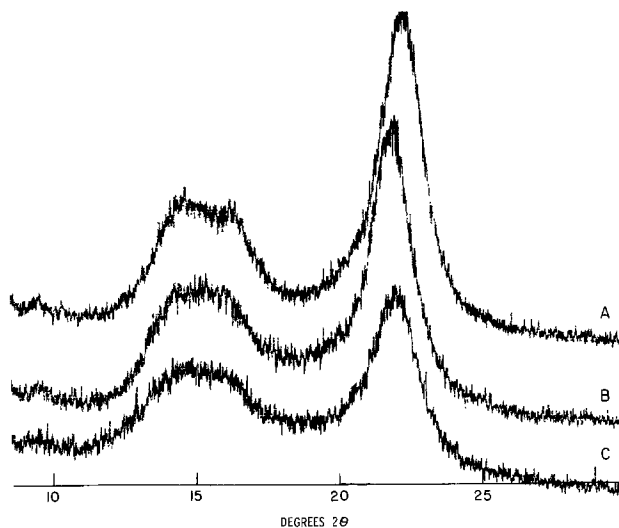


Fig. 1. X-ray diffraction traces. A, Scan of α -cellulose raw material; B, unused separator; C, separator after storage in 1.280 specific gravity H_2SO_4 at 125°F for 3690 hr. All scans were done at the same x-ray field strength and tube current.

specific gravity H_2SO_4 . Counts and relative intensities were also normalized with respect to density of the cellulose compacts.

Discussion

Hermans and Weidinger and others compared integrated intensity measurements to arrive at a measure of cellulose crystallinity. In this work, the integrated value of the major crystalline peaks are compared with those obtained with samples of unimpregnated paper. The measurement was made by establishing an arbitrary baseline on the line between intensities at 8 and 30° . The integrated areas, A_x , are then compared to those of the untreated source of α -cellulose, A_{std} , then corrected for density. Table I shows data from separators stored in 1.280 H_2SO_4 , 1.325 H_2SO_4 , and separators taken from batteries cycled for 5 and 9 weeks.

Table I. Crystallinity index: paper separators A_x/A_{std}

Specific gravity	Acid storage Hours at 125°F			Cycled battery samples Weeks cycled at 125°F	
	0	1360	3690	5 (140 cycles)	9 (252 cycles)
1.280	0.59	0.55	0.42	0.063	0.080
1.325	0.59	0.48	0.42		

Work in this study shows that impregnated paper separators possess excellent long-term resistance to attack by H_2SO_4 at specific gravities much higher than those encountered in automotive batteries. The basic α -cellulose structure, measured by an index of crystallinity, is not severely attacked during static storage. During cycling, however, the index of crystallinity decreases very rapidly. Work started here suggests this

* Electrochemical Society Active Member.

Key words: cellulose, crystallinity, x-ray diffraction, lead-acid separators.

Table II. Crystallinity index: separators stored in 1.260 H₂SO₄ saturated with PbSO₄

Hours at 125°F	A_x/A_{std}
0	0.55
1360	0.39
2400	0.29

may be due to physical damage. Uncycled separator pieces, stored at 125°F in 1.260 H₂SO₄ saturated in PbSO₄, suffer a similar decrease in crystallinity over similar storage periods. The data are summarized in Table II. It is indicated that the dynamic processes of solution/dissolution of the PbSO₄ imbibed in the fiber matrix may stress the fiber matrix to a sufficient extent to damage the basic material, lowering the crystallinity index.

The greater resistance to degradation in 1.325 H₂SO₄ compared to the losses of crystallinity in 1.260 acid plus PbSO₄ support this argument. In cycling, the dynamic processes of solution/dissolution degrade the cellulose matrix to a greater degree over shorter periods of time.

Independent microscopic examination of cycled separators found frequent examples of brittle fracture of

the fibers. In cycled separators, in which considerable amounts of Pb-salts are imbibed and trapped in the fiber matrix, considerable physical damage to the cellulose is expected. Shedding and shape change of electrodes deposit salts and stress the cellulose in a significant way.

Manuscript submitted March 10, 1975; revised manuscript received April 1, 1975.

Any discussion of this paper will appear in a Discussion Section to be published in the June 1976 JOURNAL. All discussions for the June 1976 Discussion Section should be submitted by Feb. 1, 1976.

Publication costs of this article were partially assisted by ESB Incorporated.

REFERENCES

1. P. H. Hermans and A. Weidinger, *J. Am. Chem. Soc.*, **68**, 2547 (1946).
2. P. H. Hermans and A. Weidinger, *J. Appl. Phys.*, **19**, 491 (1948).
3. P. H. Hermans and A. Weidinger, *J. Polymer Sci.*, **4**, 135, 709 (1949); **5**, 565 (1950).
4. J. L. Matthews, H. S. Peiser, and R. B. Richards, *Acta Cryst.*, **2**, 85 (1949).
5. L. Segal, J. J. Creely, A. E. Martin, Jr., and C. M. Conrad, *Textile Res. J.*, **29**, 786 (1959).
6. W. O. Statton, *J. Polymer Sci.*, **C18**, 33 (1967).



Absolute X-Ray Efficiencies of Some Phosphors

J. A. de Poorter and A. Brill

Philips Research Laboratories, Eindhoven, Netherlands

ABSTRACT

Efficiencies of various powder phosphors under x-ray excitation are determined. Thin layers are used to minimize the loss in light output due to scattering and absorption of the emitted luminescence. The luminescence of the layer is measured with the aid of a calibrated photomultiplier. The absorbed x-ray radiation is measured with a scintillation crystal. The efficiencies found are of the order of the cathode-ray efficiencies; calcium tungstate has the largest deviation.

A review of published data (1-5) on the efficiencies of phosphors with x-ray excitation is given in the paper of Ludwig (6). The author reports efficiencies of powder phosphor layers irradiated with x-rays generated by radioisotopes with energies between 27 and 122 keV. The light output was measured as a function of the weight per square centimeter of the layer while the x-ray absorption was calculated with the aid of tables published by Storm and Israel (7).

As is well known, the light output of a phosphor screen used as a front screen is often different from the light output when used as a back screen. (Front screen output means the output at the nonirradiated side; back screen that at the irradiated side). This difference in light output is due to absorption of the luminescent radiation in the layer. The path length of this radiation is much longer than the real thickness of the layer (the latter is generally more than $100 \mu\text{m}$) because of scattering of the luminescent radiation by the phosphor grains. With the aid of the formulas of Hamaker (8) and Klasens (2) the measured light output can be corrected for the loss. This was done by Ludwig, who found a reasonable agreement between cathode-ray efficiencies and the corrected x-ray efficiencies of the phosphors considered. However, the disadvantage of this method is that very large corrections are generally necessary, the real efficiency being 3 to 6 times higher than the values measured. Sometimes the difference is even greater. The marked influence of the scattering is demonstrated in Fig. 1, where the output curves are given for the small grain size fraction ($< 8 \mu\text{m}$) and the large grain size fraction ($> 26 \mu\text{m}$) of CsI-Na powder layers as a function of powder weight. We determined these curves experimentally; the spectral power distribution of the exciting x-ray source is given in Fig. 2. The optimum front screen output of the small grain size fraction is very small compared with that of the large grain size fraction due to the stronger scattering (i.e., more absorption) as a consequence of the smaller grain size.

This is contrary to the case of cathode-ray excitation of, e.g., 20 keV, where the correction required for front screen output is only small [generally 10% or less, see Brill and Klasens (9)], due to the fact that the penetration depth of fast electrons is only a few micrometers. Therefore thin layers can be used in that case for max-

imum absorption of the cathode rays. In order to obtain a negligible correction for the light output with x-ray excitation we used thin layers in the latter case too.

The absorption of the x-rays in the layer was also measured, because the values given in the tables are

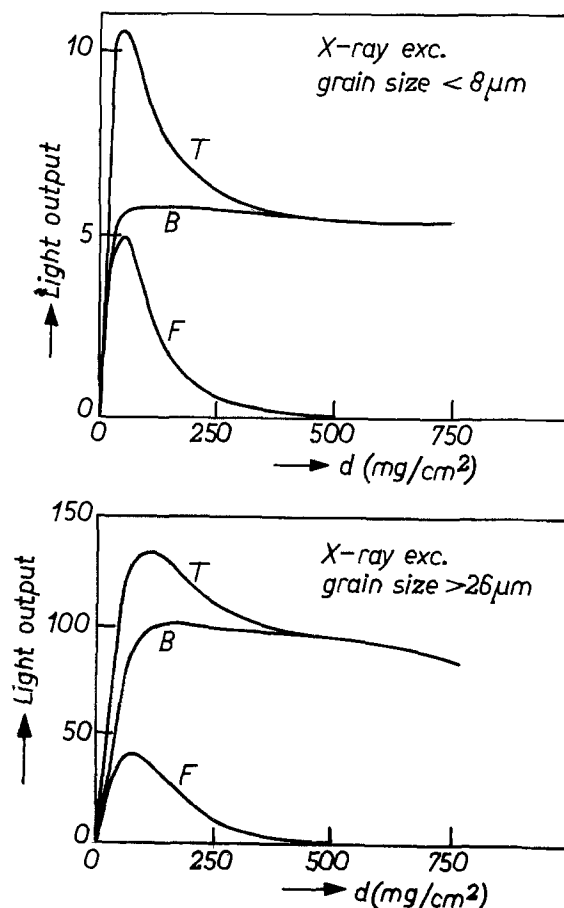


Fig. 1. Front screen (F), back screen (B), and total light output (T) as a function of layer thickness for a sample of CsI-Na. (a) Grain size $< 8 \mu\text{m}$, (b) grain size $> 26 \mu\text{m}$.

Key words: luminescence, fluorescence, x-ray excitation, radiant efficiencies.

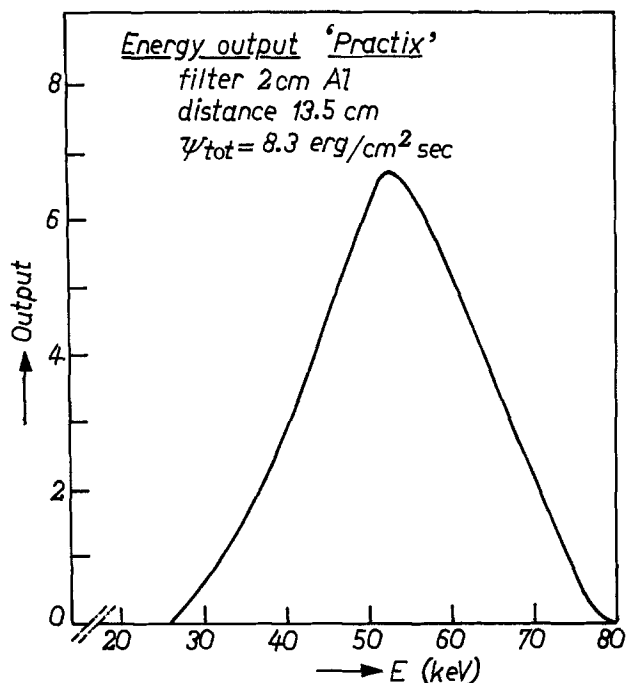


Fig. 2. The spectral power distribution of the x-rays emitted by the "Practix" x-ray tube, filtered by 2 cm Al.

not quite valid for use in the case of x-ray luminescence for reasons explained in the last section.

Experimental

The x-ray source used was a Philips "Practix" tube, operated at a voltage of 75 kV and a tube current of 1 mA. An aluminum filter with a thickness of 2 cm was placed in front of the tube to make the spectral bandwidth narrower. The spectral power distribution and absolute output of the combination was measured in our laboratory by Van der Linden and De Wijk (10) with the aid of a scintillation spectrometer in which a NaI crystal with photomultiplier was employed as a detector. The spectral power distribution is shown in Fig. 2. We chose the thickness of the phosphor layer as equivalent to a screen weight of 25 mg/cm². The layer was applied between two quartz plates. From Hamaker's formulas it was calculated that the loss in light output due to scattering in such thin layers is only a few per cent for a wide range of x-ray absorption coefficients.

A schematic drawing of the setup used for measuring the luminescence output of the phosphors is shown in

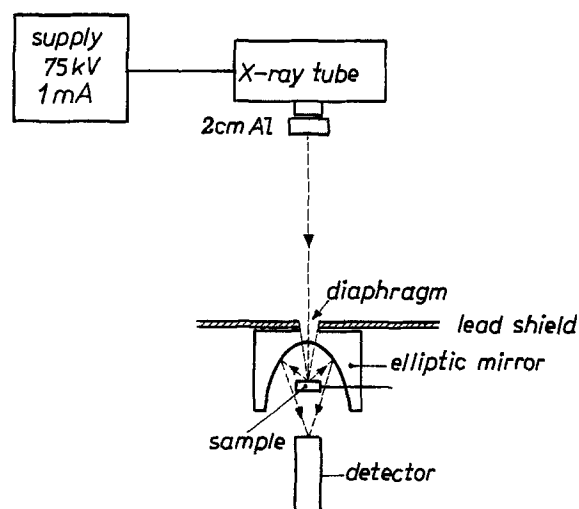


Fig. 3. Schematic diagram of the light output measurement

Fig. 3. The x-ray beam falls on the phosphor layer through a lead diaphragm producing an irradiated area of 1 cm diameter on the sample. Just below the sample a blackened lead shield is placed to prevent x-rays from reaching the photomultiplier and to absorb the luminescence emitted from the front side of the layer. The total back screen emission is collected by a 2 π -geometry elliptic mirror (11) and focused onto the detector. The light transmission of the system is calibrated by first directing a light beam via a magnesium oxide screen toward the photomultiplier. Then the MgO screen is taken away, so that the light beam falls directly onto the detector. The transmission of the elliptic mirror system was found in this way to be 63%. The spectral and absolute response of the photomultiplier we used was measured with the aid of a Philips 150 uv photocell calibrated by the National Physical Laboratory in Teddington (Great Britain).

The x-ray absorption coefficients were both calculated and measured. The measurement was carried out in the following way (see Fig. 4). The x-rays transmitted by the phosphor layer are converted into visible radiation by a plaque of CsI-Tl which covers the window of a photomultiplier. The latter collects the generated visible radiation. In order to obtain a more accurate value of the absorption, thicker layers are used in this case than for the luminescence measurements. To obtain the x-ray absorption coefficient two measurements are carried out: (i) The transmission of the x-rays is measured with the sample placed at a large distance from the detector (Fig. 4a). (ii) The transmission of the x-rays is measured when the sample is placed on the detector (Fig. 4b). In the latter case nearly half of the escaping x-ray fluorescence also reaches the detector. From these two measurements the mass absorption coefficients can be calculated: $(\mu/\rho)_F$ when the escaping parts of the x-ray fluorescence is taken into account and $(\mu/\rho)_{NF}$ when the x-ray fluorescence is not considered (see next section). The x-ray absorption coefficient is denoted by μ , the density by ρ .

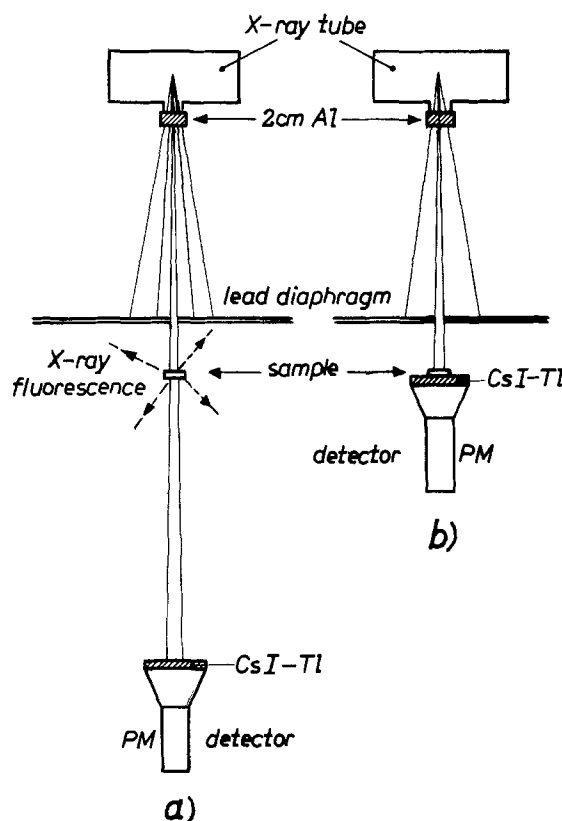


Fig. 4. Schematic diagram of the x-ray absorption measurement. (a) Detector and sample far apart, (b) detector and sample as close as possible to each other. PM = photomultiplier tube.

Table I. Calculated and measured x-ray absorption coefficients

Phosphor	$(\mu/\rho)_{\text{tot,a}}$ (calculated), cm ² /g	$(\mu/\rho)_{\text{NF}}$ (measured), cm ² /g	$(\mu/\rho)_{\text{tot,en}}$ (calculated), cm ² /g	$(\mu/\rho)_{\text{F}}$ (measured), cm ² /g	K-absorption edge, keV
CaWO ₄ , NBS No. 1026	3.83	3.48	3.50	3.53	69.5
Zn ₂ SiO ₄ , NBS No. 1021	1.64	1.90	1.54	1.43	—
ZnS-Ag, NBS No. 1020	1.97	2.05	1.83	1.85	—
BaSi ₂ O ₅ -Pb, NBS No. 1032	6.19	5.2	3.15	4.75	37.4
(0.58 Zn, 0.42 Cd) S-Ag (TV-sample)	4.86	5.02	3.43	4.00	26.7
(0.64 Zn, 0.36 Cd) S-Ag (large grain size)	4.48	3.86	3.19	3.75	26.7
CsI-Tl	11.7	10.1	6.27	8.15	33.2-36.0
La ₂ O ₂ S-Tb	9.20	9.3	4.82	7.5	38.9
Gd ₂ O ₂ S-Tb	8.08	7.7	4.14	5.7	50.2

Results and Discussion

We compare the measured absorption coefficients with those calculated from the extensive tables published by Storm and Israel (7). From the coefficients given in these tables $(\mu/\rho)_{\text{tot,a}}$ refers to the absorption determined by the difference of the incident monochromatic x-radiation and the transmitted x-radiation of the same wavelength. The coefficient $(\mu/\rho)_{\text{tot,en}}$ also accounts for the escape of the emitted x-ray fluorescence of longer wavelengths than that of the incident x-rays. In practice however, only part of the x-ray fluorescence is absorbed and gives rise to luminescence. Therefore $(\mu/\rho)_{\text{tot,en}}$ does not give the correct absorption for our efficiency measurements; moreover in the table all data refer to the element in consideration while the phosphors are composed of a number of elements. Consequently the absorption of the x-ray fluorescent radiation will be different from that assumed in the table, especially in cases where the K-absorption edges of one or more of the constituent elements of the phosphor lie within the region of the spectral power distribution of the x-rays. Therefore, it is better to use the absorption coefficient $(\mu/\rho)_{\text{F}}$ as defined in the experimental section. From the foregoing it is evident that the measured absorption coefficients $(\mu/\rho)_{\text{F}}$ will have a value between $(\mu/\rho)_{\text{tot,a}}$ and $(\mu/\rho)_{\text{tot,en}}$. The results of the absorption measurements are given in Table I, together with $(\mu/\rho)_{\text{tot,a}}$ and $(\mu/\rho)_{\text{tot,en}}$ from Storm and Israel's tables. We see that the measured $(\mu/\rho)_{\text{F}}$ does indeed lie between the calculated $(\mu/\rho)_{\text{tot,a}}$ and $(\mu/\rho)_{\text{tot,en}}$ within the error of measurement, and that the deviation between $(\mu/\rho)_{\text{F}}$ and $(\mu/\rho)_{\text{tot,en}}$ is large in the cases where the K-absorption edges of the phosphor elements play a role, as is expected (e.g., CsI-Tl and La₂O₂S-Tb).

We also see from the table that the calculated absorption coefficient $(\mu/\rho)_{\text{tot,a}}$ is in reasonable agreement with the absorption coefficient $(\mu/\rho)_{\text{NF}}$ measured with the detector at a large distance, as should be the case. However, these figures $(\mu/\rho)_{\text{NF}}$ cannot be used in our

experiment because of the reason mentioned above. Table II gives the radiant efficiencies of the phosphors as determined from the measured absorption coefficient $(\mu/\rho)_{\text{F}}$ and the measured light output. Also given in the table are the radiant efficiencies we obtained with cathode-ray excitation [excitation voltage 20 kV; thick layer in a demountable tube, see Ref (9)].

A reasonable agreement is found for most phosphors when the efficiencies for x-ray and cathode-ray excitation are compared. An exception is CaWO₄, which is often used for x-ray screens. We found for x-ray excitation about twice the value for cathode-ray excitation, for which we have no explanation up to now.

Acknowledgments

We are indebted to Prof. Dr. W. J. Oosterkamp for valuable discussions and for the measurement of the spectral power distribution of the x-ray tube carried out in his research group. Acknowledgments are also due to Dr. Ludwig for drawing our attention to the various tables of Storm and Israel, and to the departments of Ir. Schuil, Dr. Wanmaker, and Mr. Snethorst for the preparation of a part of the phosphor samples.

Manuscript submitted Feb. 4, 1975; revised manuscript received April 14, 1975. This was Paper 114 presented at the San Francisco, California, Meeting of the Society, May 12-17, 1974.

Any discussion of this paper will appear in a Discussion Section to be published in the June 1976 JOURNAL. All discussions for the June 1976 Discussion Section should be submitted by Feb. 1, 1976.

Publication costs of this article were partially assisted by Philips Research Laboratories.

REFERENCES

1. J. W. Coltman, E. G. Ebbinghausen, and W. Altar, *J. Appl. Phys.*, **18**, 530 (1947); J. W. Coltman, in "Preparation and Characteristics of Solid Luminescent Materials," p. 416, John Wiley & Sons, Inc., New York (1948).
2. H. A. Klasens, *Philips Res. Rept.*, **2**, 55 (1947).
3. H. A. Klasens and W. de Groot, *Philips Tech. Rev.*, **9**, 321 (1947).
4. J. Broser, H. Kallmann, and U. M. Markus, *Z. Naturforsch.*, **4a**, 2041 (1949).
5. F. Grum, L. F. Costa, and J. L. Donovan, *J. Opt. Soc. Am.*, **59**, 848 (1969).
6. G. W. Ludwig, *This Journal*, **118**, 1152 (1971).
7. E. Storm and H. I. Israel, Report LA-3753, Los Alamos Scientific Laboratory of the University of California (1967).
8. H. C. Hamaker, *Philips Res. Rept.*, **2**, 55 (1947).
9. A. Brill and H. A. Klasens, *ibid.*, **7**, 401 (1952).
10. P. W. J. van der Linden and J. J. F. de Wijk, Private communication.
11. J. W. van der Does de Bijle, *Rev. Sci. Instr.*, **40**, 320 (1969).

Table II. Radiant efficiencies

Phosphor	X-ray excitation, %	Cathode-ray excitation (20 keV), %
CaWO ₄ , NBS No. 1026	6.5	3
CaWO ₄ , larger grain size	8	3.5
Zn ₂ SiO ₄ , NBS No. 1021	11.5	8
ZnS-Ag, NBS No. 1020	17	21
BaSi ₂ O ₅ -Pb, NBS No. 1032	3.5	4
BaSi ₂ O ₅ -Pb, own sample	3.5	4
(0.58 Zn, 0.42 Cd) S-Ag (TV-sample)	14.5	21
(0.64 Zn, 0.36 Cd) S-Ag (large grain size)	19	19.5
CsI-Tl	10	9
La ₂ O ₂ S-Tb	12.5	11
Gd ₂ O ₂ S-Tb	13	11

Resolution of X-Ray Intensifying Screens

A. F. Sklensky,* R. A. Buchanan, T. G. Maple,* and H. N. Bailey

Lockheed Palo Alto Research Laboratory, Palo Alto, California 94304

ABSTRACT

The purpose of this study is to experimentally explore the dependence of the speed and resolution of radiographs on the thickness and phosphor packing density of rare earth oxysulfide intensifying screens. The quantitative dependence of resolution on the following parameters is also discussed: the wavelength of the emitted light, the presence of a reflective backing, the concentration of dye in the binder, and the use of double screens and film *vs.* single screens and film. It is found that a trade-off exists between speed and resolution for variation of screen thickness, the placement of a reflective backing on the screen, and dye in the binder, and the use of double screens and film. The green-emitted light gives a slight, but usually negligible decrease in resolution over blue-emitted light. Increased packing density increases the speed with little or no sacrifice of resolution.

The resolution that an x-ray intensifying screen permits on a radiograph is a key factor in determining radiographic quality. Nevertheless, we have been unable to find any literature treating screen construction technique.

X-ray intensifying screen properties are only one factor in determining quality. Image quality is determined by many factors. First, we have the properties of the subject itself such as x-ray absorption contrast, scattering, and the spatial frequency of the image. Next are the properties of the x-ray source and the geometry involved, such as focal spot size and shape, the film to focal spot distance, and the energies of the x-ray photons. Finally, we have the film characteristics and screen characteristics. Screen characteristics may be broken down into categories, such as technique (single screen and film *vs.* double screen and film), phosphor properties (speed, optical properties, response to x-ray photons of different energies, and the energy of emitted photons), and manufacturing parameters (uniformity, phosphor particle size, the presence or absence of a reflective backing, the optical properties of the binder, the thickness of the screen, and particle packing density).

Of these many factors, our interest is in the effect that an increase in phosphor speed can have on the speed and resolution of a radiographic system. It is self-evident that greater speed in the phosphor permits greater speed in the screen for a given resolution. The purpose of this paper is to show some ways in which greater speed in the phosphor also permits greater resolution for a given speed.

The reason for our interest in the changes in radiographic quality that result from an increase in phosphor speed, is that the oxysulfide phosphors were developed in our laboratory (1-3). We have been exploring the implications of their use in intensifying screens.

Other work in the area of image quality in radiographs has been done by Rao (4-6) and Morgan (7-8). Rao has integrated considerations of film gamma, subject contrast, scattering, quantum mottle and spatial frequency of the subject, and frequency response of the screen-film system, into a single expression for a quantity he calls the image contrast function.

It is shown in this paper that variations in screen manufacturing parameters result in variations in the speed and resolution obtainable with screens. Generally, but not always, a trade-off exists between speed and resolution. The amount of speed that must be traded for increased resolution is greater for some variations in manufacturing techniques than for others. We present here the effect of varying (i) the screen

thickness, (ii) dye concentration in the binder, (iii) the use of a diffusely reflecting layer between the phosphor coating and the Mylar substrate, (iv) the packing density of the phosphor particles, (v) the wavelength of the light emitted by the phosphor, and (vi) the use of two screens and double-coated film in place of a single screen and single-coated film.

Experimental Technique

Screens and films used.—Commercially available phosphors from various sources were used in the manufacture of the screens. The rare earth oxysulfide (REOS) materials yttrium oxysulfide (YOS), lanthanum oxysulfide (LOS), and gadolinium oxysulfide (GOS) were the primary materials studied. The particle size within each batch varied from 10 to 20 μm down to a fraction of a micron. In addition, the average particle size in each batch of phosphor varied from about 10 to about 3 μm . Since extensive milling of the powders damages their fluorescent properties and separation is difficult, we did not control particle size and particle size was not studied as a parameter.

Screens were prepared in our laboratory by dispersing the phosphor material in a binder (B48N from Rohm and Haas) and drawing the mixture with a doctor blade. A 10-mil Mylar substrate was used. When a reflective backing was applied, the material used was TiO_2 . It was also drawn with a doctor blade. For the dye experiments, Oil Red O was added to the binder. To determine the effects of a greater packing density, a portion of our phosphor was sent to Hyman laboratories where screens were pressed under a force of 725 psi. A density of 4.13 g/cm^3 was achieved, compared to 3.25 g/cm^3 that results from our standard laboratory procedure of simply drawing the screen. The bulk density for GOS is 7.4 g/cm^3 .

Four different film types were used. For applications where single-coated film was needed, Kodak SB-54 was used as the blue-sensitive film, and Kodak Type O was used as the green-sensitive film. Du Pont Cronex 4 was the double-coated blue-sensitive film, and an early prototype green-sensitive film from 3M was used for the double-coated green-sensitive film. Where two screens have been used, the back screen is the same thickness as the front screen.

Speed and resolution measurements.—To determine the properties of the screens, a standard tungsten target medical x-ray source was used. Characteristic curves were determined by placing an optical step wedge between the screen and the film. The speed measurements at 90 kV_p were made by placing a 1 in. thick aluminum plate in the beam. A coarse stationary grid (60 lines per inch, 6:1 ratio) was used in these experiments to reduce the scattered radiation level.

* Electrochemical Society Active Member.

Key words: intensifying screen construction, radiography, rare earth oxysulfides.

The speed measurements at 30 kV_p were made without the aluminum plate or the stationary grid.

Most resolution measurements were made with a single screen and single-coated film with the emulsion touching the screen. The screen was placed between the x-ray source and film. All resolution measurements were made at 30 kV_p. A lead bar pattern from Emil Funk (Type 53G) was placed immediately in front of the cassette. The lead grid is 50 μm thick and the bar pattern spatial frequency varies from 0.25 to 10 lp/mm. The film densities behind the grid for each spatial frequency were converted from maximum and minimum exposures through the characteristic curves previously determined at the same kV_p. We then plotted $(E_{\max} - E_{\min}) / (E_{\max} + E_{\min})$ vs. spatial frequency. In other cases, cross plots are shown of the frequency at which $(E_{\max} - E_{\min}) / (E_{\max} + E_{\min})$ drops to 0.2.

The effects of noise on resolution are not considered here. Noise in a radiograph has many sources; for example nonuniformities in the screen construction or in the film, film grain, and quantum mottle. The slit height on our densitometer is 2 mm, so all but the lowest spatial frequency noise components are averaged out of our measurements.

The decision to measure the speed at 90 kV_p and resolution at 30 kV_p was somewhat arbitrary. The 90 kV_p, heavily filtered, speed measurement corresponds to typical diagnostic medical procedures. However, the 30 kV_p single-screen technique for measuring the resolution does not. These latter conditions were chosen so that the x-rays would be absorbed far from the film and the light would have a significant distance to scatter through the screen. This maximizes the effect on the resolution of the various parameters being varied. In addition, the contrast from our lead foil resolution grid is greatest at the low kV_p, so we can measure the resolution differences more accurately.

Experimental Results and Discussion

Screen thickness.—Figure 1 shows the changes in speed at 90 kV_p and resolution at 30 kV_p that result from changes in the screen thickness. Measurements were made on both GOS and LOS screens. All the exposures were made with green sensitive film except the frequency response of GOS which was measured with SB-54 film. Speed measurements were made with double screens, the 1 in. aluminum block, and the stationary grid.

The scales that were chosen for presentation of these data were linear in both the spatial frequency and exposure. That is, a factor of 2 increase in exposure time will appear the same on these plots as a factor of 2 increase in resolution. This should be kept in mind while interpreting our results.

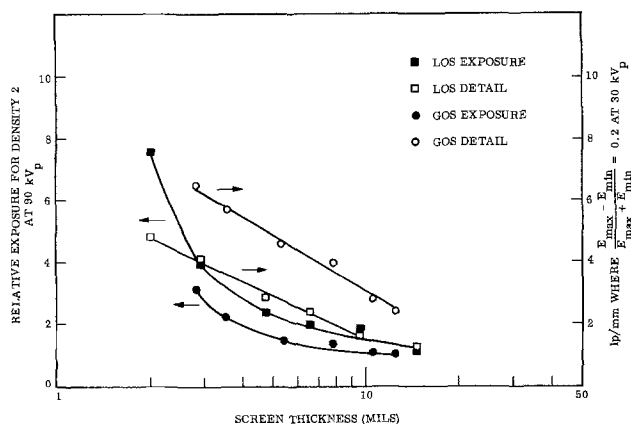


Fig. 1. Speed and resolution as a function of screen thickness. Screens are drawn, have no dye, and no reflective backing. Exposure values measured with double screens, and with green-sensitive, double-coated film. Resolution of LOS was measured with Type 0 film; of GOS with SB-54 film.

For both phosphors, at large thickness values (> 6 mils) the 90 kV_p exposure decreases little with increasing screen thickness, while the 30 kV_p resolution continues to decrease. At small thickness values (below 5 mils) exposure increases rapidly, even on the log scale used, toward the no-screen exposure value. Resolution increases with the same slope as at higher screen thickness values. The difference in resolution between LOS and GOS screens is tentatively ascribed to the difference in particle size between the phosphors. It is not believed to be due to a difference in phosphor properties, such as the x-ray absorption or energy conversion efficiencies.

Resolution changed by about a factor of 3 over the range of thickness values studied, while exposure varied over a factor of 3-6.

Dye concentration.—Figure 2 shows the improvement in resolution that is obtained through the use of dye in the binder. The increased exposure necessary is also shown. Both measurements were made at 30 kV_p.

Most of the light emitted by the LOS is green. GOS emits light in both the green and the blue. The red dye placed in the binder absorbs the light emitted by both phosphors. Since light that is scattered a greater distance from the energy conversion event travels a longer path length than light that is scattered less, the former undergoes greater attenuation and resolution is increased by the inclusion of dye in the binder. However, all the emitted light undergoes attenuation, so the exposure increases with dye concentration also.

For the thick GOS screens, there is a larger increase in resolution at low dye concentrations than at higher dye concentrations. For the thinner LOS screens, the initial improvement in resolution appears to require no increase in exposure. Over the entire range of the measurements for both phosphors, a 25% increase in resolution requires about a 100% increase in exposure. That is, only a relatively small increase in resolution was observed for a large increase in exposure time.

Packing density.—The high packing density screen displayed an increase in the speed at 90 kV_p (Fig. 3) with a negligible decrease in resolution at 30 kV_p (Fig. 4). The 7.2 mil high packing density screen required less exposure than the 12.5 mil drawn screen. The 7.2 mil high packing density screen has the same amount of phosphor per square centimeter as a 9.2 mil drawn screen.

Since we only had one screen available and were unwilling to cut it to obtain two screens for a double-screen, double-film experiment, all the data shown in

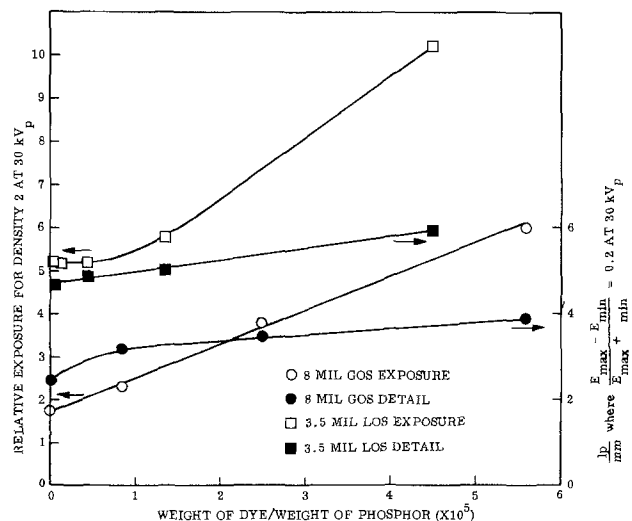


Fig. 2. Speed and resolution as a function of dye concentration. Screens are drawn and have no reflective backing. Exposure and resolution of GOS screens measured with SB-54 film, and of LOS screens with Type 0 film.

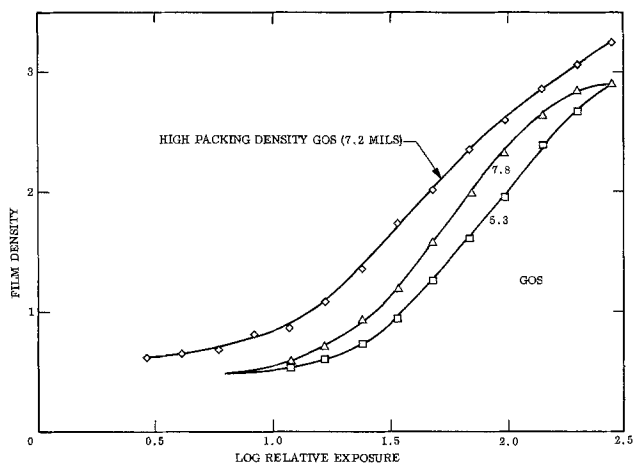


Fig. 3. Comparison of screen speed at 90 kV_p between a high packing density screen and drawn screens. One inch of aluminum and a stationary grid were placed in the x-ray beam. All measurements use single screens and SB-54 film.

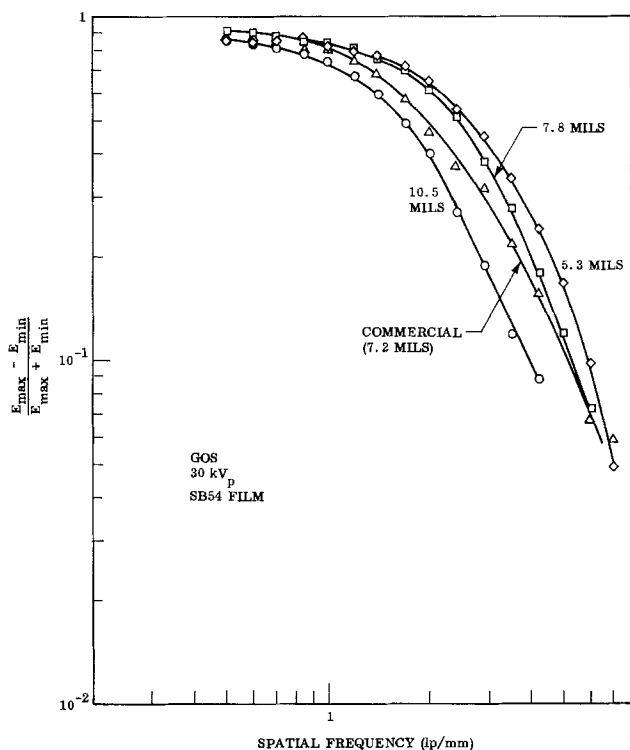


Fig. 4. Comparison of GOS screen resolution at 30 kV_p between a high packing density screen and drawn screens. SB-54 film was used.

the figures were taken with single screens and single-coated film.

Reflective backing.—Figure 5 shows the decrease in resolution at 30 kV_p that occurs when a reflective backing is placed on the screen. Evidently the increased scattering the reflected light undergoes decreases the resolution.

At low spatial frequencies, the two curves are nearly coincident, as would be expected if the SWRF for both is to go to 1 as $f \rightarrow 0$. At high frequency, the two curves join again. About a 30% decrease in exposure time results in about 13% decrease in resolution at the 20% $(E_{\max} - E_{\min}) / (E_{\max} + E_{\min})$ point.

Wavelength of emitted photons.—Figure 6 shows the resolution of thin YOS screens at 30 kV_p as measured by green-sensitive film and by blue-sensitive film. Green-emitted light is seen to give poorer resolution than blue-emitted light. Since the film sensitivity is broadband the effect is small. However, it does appear

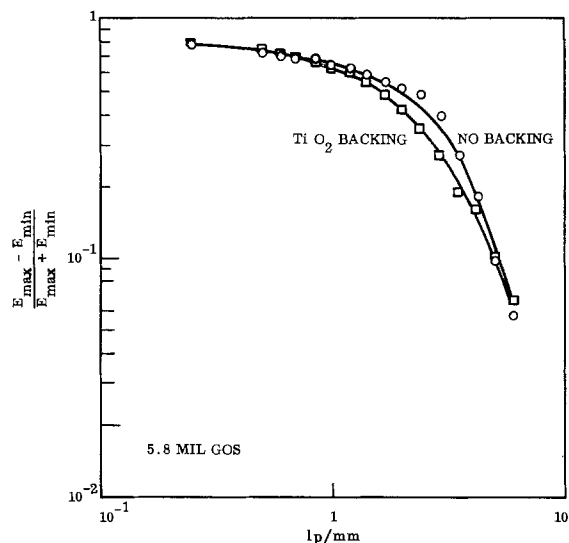


Fig. 5. Resolution of screens with and without a reflective backing. The exposure at 30 kV_p using the screen with the backing was about 70% that used for the screen without the backing. SB-54 film was used.

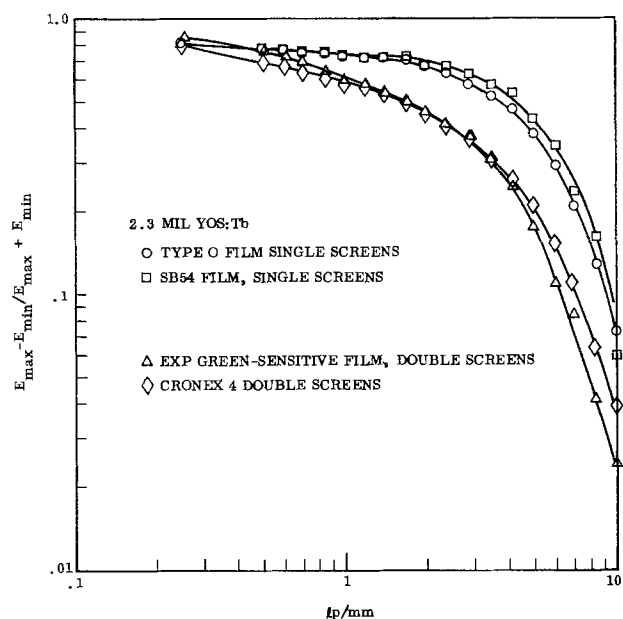


Fig. 6. Resolution of single and double screens, with no reflective backing, using blue-sensitive and green-sensitive film. The double-screen measurements were made with 25 sec exposures and ffd = 98 cm. The SB-54 film was exposed 4.8 sec and the Type 0 for 27 sec at ffd = 47 cm.

to be real. It was observed for both single and double screens, as may be seen in the figure. The experiments were repeated for GOS screens, and similar results were obtained. In addition, $(E_{\max} - E_{\min}) / (E_{\max} + E_{\min})$ was measured as a function of frequency for the films without screens and their frequency response was found to be the same, within the accuracy of the measurements.

Double screens.—The decrease in resolution at 30 kV_p that results from using double screens and double-coated film is also evident in Fig. 6. The decreased resolution is presumed to be due to spreading of light as it traverses the greater distance through the film base to the emulsion that is not in contact with the screen that emitted the light. At MTF = 0.2 the resolution is decreased by about 30% for double screens and double-sided film relative to single screens and single-sided film. The decrease in exposure necessary is not known, but would not be expected to be greater than 50%.

Conclusions

An empirical study has been presented of six of the many screen parameters that affect resolution, which may be varied at the screen designer's discretion. Most involve a trade-off between speed and resolution. High phosphor packing density, however, appears to increase speed with little or no sacrifice of resolution. The trade-off for green-sensitive film vs. blue-sensitive film depends on the phosphor. For CaWO_4 and YOS there is no speed advantage for the green-sensitive film (4), and thus, no reason to use it. For GOS and LOS the speed advantage is sufficiently great that the small decrease in resolution is of little consequence. That is, the GOS and LOS phosphor speed with green-sensitive film is sufficiently great that screens made from them can be made faster and with better resolution than screens made from slower phosphors using blue-sensitive film.

The remaining screen parameters require a significant trade-off between exposure and resolution. Qualitatively we can say that a fast, low resolution screen-film system may be given greater resolution by decreasing the screen thickness, or by removing the reflective backing with about the same incremental increase in resolution for a given incremental increase in exposure. Adding dye to the binder requires a significantly larger incremental increase in exposure for an incremental increase in resolution.

Considerable benefit could result from a study that is more analytical than the one presented here. For example, an analytical description of speed and resolu-

tion as functions of wavelength of emitted light and particle size could indicate optimal values where experiments are difficult.

Manuscript submitted Dec. 2, 1974; revised manuscript received April 14, 1975. This was Paper 115 presented at the San Francisco, California, Meeting of the Society, May 12-17, 1974.

Any discussion of this paper will appear in a Discussion Section to be published in the June 1976 JOURNAL. All discussions for the June 1976 Discussion Section should be submitted by Feb. 1, 1976.

Publication costs of this article were partially assisted by Lockheed Palo Alto Research Laboratory.

REFERENCES

1. A. F. Sklensky, R. A. Buchanan, T. G. Maple, and H. N. Bailey, *IEEE Trans. Nucl. Sci.*, **NS-21**, 685 (1974).
2. R. V. Alves and R. A. Buchanan, *ibid.*, **NS-20**, 415 (1973).
3. R. A. Buchanan, *ibid.*, **NS-19**, 81 (1972).
4. G. U. V. Rao, *Am. J. Roentgenol., Radium Therapy Nucl. Med.*, **118**, 293 (1973).
5. G. U. V. Rao, "The Modulation Transfer Function in Radiology and Nuclear Medicine," 14th Meeting of Am. Ass. Phys. Med. (1972).
6. G. U. V. Rao, *Intern. J. Appl. Radiation Isotopes*, **21**, 571 (1970).
7. R. H. Morgan *Am. J. Roentgenol., Radium Therapy Nucl. Med.*, **93**, 982 (1965).
8. R. E. Sturm and R. H. Morgan, *ibid.*, **62**, 617 (1949).
9. J. W. Coltman, *J. Opt. Soc. Am.*, **44**, 468 (1954).

Passivation Coatings on Silicon Devices

G. L. Schnable,* W. Kern,* and R. B. Comizzoli*

RCA Laboratories, Princeton, New Jersey 08540

ABSTRACT

Passivation coatings are widely used to improve the performance and reliability of silicon devices of various types, ranging from discrete mesa-type diodes and transistors to complex planar silicon integrated circuits, and including both hermetic and plastic-encapsulated devices. This paper reviews the materials and techniques used to apply passivation coatings to completed silicon devices. Principal production techniques used in passivation of silicon devices include thermal oxidation, high-temperature diffusion, high-temperature chemical vapor deposition of Si_3N_4 or Al_2O_3 , low-temperature chemical vapor deposition of glasslike SiO_2 or phosphosilicate layers (deposited at approximately 400°C), rf sputtering of SiO_2 , mechanical deposition of glass frit layers which are subsequently fused, and application of organic polymer films.

The effects of passivation layers on silicon device reliability are discussed, and the interrelationships among the silicon device, the passivation layer or layers used and the final encapsulation are indicated. Pertinent references on passivation and on related topics are cited in the text.

Passivation coatings are widely used to improve the performance and reliability of silicon devices of various types, ranging from discrete mesa-type diodes and transistors to complex planar integrated circuits, and including both hermetic and plastic-encapsulated devices. This paper outlines the materials and techniques used in the semiconductor device industry to achieve silicon device passivation.

Passivation coatings may be classified as primary if they are directly in contact with the single-crystal silicon from which the device is fabricated, and as secondary if they are separated from the silicon by an underlying dielectric layer. The function of the primary passivation layer is to provide good dielectric properties, low surface recombination velocity, con-

trolled immobile charge density, and device stability at elevated temperatures under bias or operating conditions. The functions which are served by the secondary passivation layer are to provide additional stability in various ambients, in both production and use, and to serve as getter, impurity barrier, or mechanical shield.

This paper reviews primary and secondary passivation materials and the techniques used to obtain them, including thermal oxidation, high-temperature diffusion, low-temperature deposition of SiO_2 and binary silicates, deposition of alkali barrier-type layers, and deposition of glass frit or application of preforms followed by fusion. The effect of passivation layers on silicon device reliability is discussed, and the interrelationship among the techniques used for final encapsulation, the passivation layers used, and device reliability is indicated. Emphasis is given to those proc-

* Electrochemical Society Active Member.

Key words: silicon device passivation, silicon dioxide, glass passivation, phosphosilicate glass, silicon device reliability.

esses and materials which have been widely used to fabricate semiconductor devices in production, rather than to processes used only to fabricate exploratory developmental devices. A total of 363 references (listed alphabetically) have been cited to indicate the type of information which has been published on passivation layers and on related topics (1-363).

Thermally Grown Silicon Dioxides

The most commonly used primary passivation material is thermally grown SiO_2 , with thickness ranging typically from 0.5 to 1.5 μm . In addition to passivation, two other very important functions of thermal oxides on silicon wafers are to serve as diffusion masks, and to serve as the insulator between the expanded metallization pattern and the underlying silicon in planar devices. Thermally grown oxides are prepared by high-temperature oxidation, at atmospheric pressure, of silicon wafers in atmospheres of dry oxygen, wet oxygen, or steam (11, 70, 114, 259, 72, 226, 348). For surface-sensitive devices, oxidation is frequently followed by one or more annealing steps (heat-treatments) in appropriate nonoxidizing atmospheres to improve the electrical properties of the Si- SiO_2 interface (259, 47, 220, 361, 307).

The cleanliness of the silicon surface is of great practical importance in device processing. Organic and inorganic surface contaminants (159, 149, 150, 137, 199, 152) are frequently introduced during many of the wafer processing steps and must be removed effectively to achieve high-quality oxide layers and interfaces. Decontamination is especially important just prior to heat-treatments and can be carried out by wet chemical methods (159, 124, 213).

The presence of alkali ions in thermally grown SiO_2 can result in device instability (296, 130, 114, 236, 173). Also alkali ions are undesirable because they can lead to devitrification of SiO_2 (202, 224, 212) and are a factor in SiO_2 dielectric breakdown (346, 83, 233). Accordingly, precautions are taken to minimize the level of alkali ion contamination during oxidation, and in some cases subsequent treatments are used to remove alkali ions (206). Whatever the process used, the results achieved are readily monitored by measuring stability of capacitance-voltage curves of metal-oxide-silicon capacitors subjected to bias at an elevated temperature (114, 362, 72, 226) such as 300°C.

In recent years, the technique of oxidation in atmospheres containing a small percentage of HCl (or Cl_2) has been widely used to getter alkali ions, thereby producing thermally grown oxides with very low levels of alkali ion contamination (260, 171, 172, 184, 231, 335, 173). The HCl gettering process, in addition to gettering alkali ions from SiO_2 , also removes fast-diffusing interstitial contaminants from silicon, thus increasing bulk lifetime (260, 261, 53) and improving device properties (50, 192).

The thermally grown layer, which is amorphous, may be pure SiO_2 , may contain boron if formed by oxidation of a boron-doped region (115), may contain hydroxyl if prepared by wet oxidation (25), or may contain chlorine if prepared using a chlorine-containing oxidizing ambient (211, 52, 334).

A very large body of literature exists concerning thermal oxides on silicon (11, 259, 226, 74, 334) and on the effects of oxidation conditions on the electrical properties and stability of the Si- SiO_2 interface (259, 71, 163, 72-74, 227). This information, to a large extent generated in connection with studies of MOS devices (270-272, 3), is applicable to a wide variety of oxide-passivated silicon devices. Considerable information has also been published on the radiation hardness of various types of SiO_2 (353, 132, 112). Accordingly, SiO_2 primary passivation phenomena will not be treated in detail in this paper. The ambient and temperature during application, or during subsequent fusion or heat-treatment of the secondary passivating layer may, however, modify the electrical properties of the Si-

SiO_2 interface, including the mobile and immobile charge density and the fast surface-state density (75, 294, 309, 274, 76, 193, 361, 16). While this is particularly true of high-temperature depositions or heat-treatments (temperatures greater than approximately 800°C), it also occurs to some extent during low-temperature deposition processes [performed at 450°C or lower (274)].

Sequence of Application of Dielectric Layers

Figure 1 shows the sequence of application of passivation layers to various types of silicon devices. Passivation coatings may be applied before or after metallization, depending on the type of device. Some devices contain several different types of passivation layers, each having specific functions.

Table I, II, and III show some of the physical properties of commonly used passivation materials. Single-crystal silicon, thermally grown silicon dioxide, aluminum, and gold are included for comparison purposes.

Considerable information exists on the properties and stability of double dielectric structures such as MNOS memory devices (55, 272, 3, 16, 349). In such structures, the second dielectric layer serves primarily as part of the active device rather than as a secondary passivation layer, and thus is not considered in this paper.

Thermal oxides which have served as high-temperature diffusion masks will have an overlying layer of borosilicate glass and/or phosphosilicate glass. In NPN bipolar transistors and bipolar IC's, the thin layer of phosphosilicate glass (EPSG), formed on the surface of the thermally grown SiO_2 during emitter diffusion, remains on the device and serves as a getter for alkali ions present at that point (164) or introduced during later processing steps. In some processes, a phosphosilicate glass (206) or emitter diffusion layer (phosphorus-doped) (42) is used to getter alkali, and is subsequently removed by etching.

A very thin phosphosilicate layer has also been applied over gate oxides of some MOS transistors and IC's for gettering purposes (17, 266, 91, 141). Typically, this is accomplished at approximately 800°C using a diffusion source such as POCl_3 . (Gettering of alkali

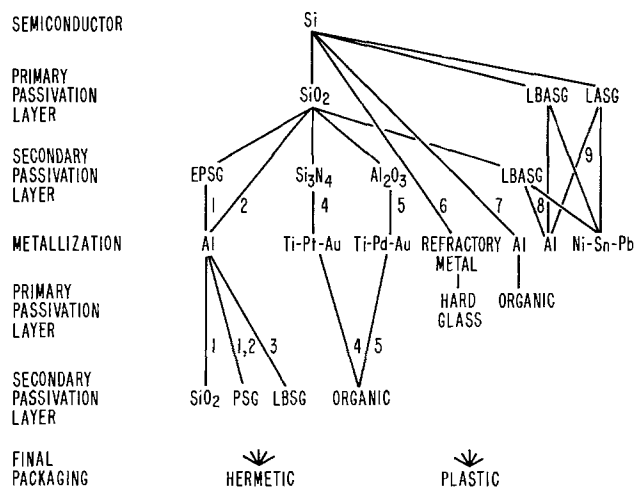


Fig. 1. Sequence of application of passivation layers to various types of silicon devices. Typical devices made by the sequences indicated by numbers are as follows: 1, NPN transistors, digital and linear bipolar IC's; 2, MOS transistors, p-channel MOS IC's, CMOS; 3, face-bonded chips; 4, beam-lead sealed-junction bipolar devices, plastic encapsulated Au-metallized devices; 5, beam-lead sealed-junction MOS IC's; 6, axial-lead diodes; 7, high-power diodes, high-power transistors, thyristors, devices with beveled junction; 8, high-voltage devices, high-voltage power devices; 9, high-voltage devices. Designations for glasses are as follows: EPSG, phosphosilicate glass formed by NPN bipolar transistor emitter diffusion; LASG, lead aluminosilicate glass; LBASG, lead borosilicate glass; PSG, phosphosilicate glass.

Table I. Growth and properties of typical low-temperature passivation materials. Some of the properties of thermally grown SiO₂ are given for comparison purposes.

Film type	Source material	Growth temperature, °C	Growth rate, Å-min ⁻¹	Film composition	Melting range, °C	IR band maxima, μm	Etch rate,* Å-sec ⁻¹
Sputtered SiO ₂	SiO ₂	100-450	50-200	SiO ₂	1600-1700	9.3-9.5	4-12
CVD SiO ₂	SiH ₄ + O ₂	325-475	500-5000	SiO ₂	1600-1700	9.3	16-20
CVD PSG	PH ₃ + SiH ₄ + O ₂	350-450	1000-4000	3 m/o P ₂ O ₅ (3 w/o P) in P ₂ O ₅ -SiO ₂	900-1000	7.6, 9.3	40-50
CVD BSG	B ₂ H ₆ + SiH ₄ + O ₂	400-450	1000-4000	17 m/o B ₂ O ₃ in B ₂ O ₃ -SiO ₂	850-950	7.4, 9.3	50-70
Thermal SiO ₂	Si + H ₂ O	900-1250	17-170	SiO ₂	1600-1700	9.2	1.8-2.0

* P-etch, 25.0°C: 2HNO₃:3HF:60 H₂O.

ions from thermally grown SiO₂ by an overlying phosphosilicate layer involves a different mechanism than the high-temperature process of gettering of interstitial impurities such as Au, Cu, Fe, and Ni from Si by phosphosilicate glasses in direct contact with silicon.) Where PSG is used over the gate oxide of MOS devices (under the gate metal), close control of the P-concentration and layer thickness is required to avoid undesirable polarization effects (293, 294, 92, 82).

For MOS and PNP bipolar transistor applications in which an underlying high-temperature phosphosilicate glass is not present, special precautions are taken to insure that deposited films do not contain alkali. For example, deposited Al metal must be alkali-free.

Thermally grown SiO₂ is not used for passivation of some discrete devices, particularly high-voltage devices, because of drift effects and high, immobile charge density. Primary passivation in these devices is achieved by use of a silicate glass or an organic polymer coating. When an organic polymer is applied directly to a silicon surface, it must be recognized that real silicon surfaces contain a native SiO₂ layer (9, 135) on the order of 20Å thick. The exact nature of the processing prior to application of the polymer material and of the polymer itself (135, 190) are significant factors in determining initial device properties, and also device stability.

With both Al- and Au-based metallization systems, the maximum temperature which can be used in processing after metallization is limited by the melting point of the eutectic formed between silicon and the metallization (the Al-Si eutectic temperature is 577°C; the Au-Si eutectic is 370°C) rather than the melting point of the metal itself.

Deposited Thin-Film SiO₂ and Silicates

With IC's and small-signal planar transistors, a secondary passivation coating is applied to completed devices after Al metallization (147, 197, 34, 275, 278, 142). Originally, functions of the deposited layer were to provide resistance to scratching of the metallization pattern during chip handling (142), and to provide immunity to effects of loose conductive particles in her-

metic packages. It was subsequently realized that additional benefits could accrue from these coatings. These benefits include reduced effects of ion motion on the surface (273, 275, 280), lower susceptibility to metal corrosion (215, 275), decreased susceptibility of metal stripes to electromigration failure (31, 297, 32, 81), improved stability and reliability of thin-film resistors (144, 342, 234), and alkali-gettering capability in the case of phosphosilicate glasses (PSG). Anodic Al₂O₃ has also been reported to reduce susceptibility of Al metallization to electromigration (180, 77, 178, 263, 81).

Silicon devices in hermetically sealed packages are susceptible to the effects of loose conducting particles in the package (209, 207, 101) unless the devices are coated with a dielectric. In Al-metallized devices, deposited SiO₂ or PSG is quite effective. In Au-metallized devices, organic coatings are generally used (345, 239) since deposited oxides have low adhesion to gold (63).

Most commonly, chemical vapor deposition (CVD) of SiO₂ on Al-metallized circuits is accomplished at atmospheric pressure at a temperature of approximately 400°C using SiH₄ plus excess O₂ in N₂ as carrier (106, 145, 301, 147, 6, 19, 155, 191, 15, 27, 360, 154); PSG and BSG (borosilicate glass) are deposited using, respectively, PH₃- and B₂H₆-containing mixtures under similar conditions (321, 147, 157, 6, 155, 269, 275, 191, 15, 27, 360, 286, 287, 154). Typically, CVD layers are on the order of 1 μm thick. Tetraethyl orthosilicate (TEOS) has also been used as a source for CVD of SiO₂ (6). CVD SiO₂ layers are in tensile intrinsic stress as deposited (303, 104). Because silicon has a higher coefficient of thermal expansion (CTE) than silicon dioxide, the residual stress in CVD SiO₂ films on Si at room temperature is somewhat lower than the intrinsic stress of films as deposited, but the films are still in considerable tension (175, 19, 302, 303) (see Table II).

Deposited SiO₂ or PSG films, when heated above the deposition temperature, are put in additional tension, particularly in regions over the edges of delineated Al metal films. Accordingly, there is some correlation between the intrinsic tensile stress in deposited films and the temperature increment above deposition temperature which can be attained before cracks begin to form (269, 303).

SiO₂ secondary passivation layers on Si wafers have also been obtained by rf sputtering (251, 61, 188, 99). The sputtering conditions can be adjusted to produce good coverage of topography (188, 339, 161) and to result in low stress (compressive) at room temperature (251, 325). Sputtering processes produce radiation damage in the thermally grown SiO₂ which can adversely affect sensitive devices such as MOS transistors and integrated circuits (251, 188, 58, 187, 205, 318, 204). Most, but not all of the radiation-induced charge can be annealed out by suitable heat-treatments. Techniques which reduce the amount of radiation damage during sputtering have recently been described (58, 187, 205, 318).

Layers of PSG have been widely used because they are in less stress (tensile) than layers of SiO₂ as deposited by CVD (269, 302, 235) and have the ability to getter alkali ions (269). PSG is thus particularly ad-

Table II. Stress in low-temperature deposited passivation layers. Some of the properties of thermally grown SiO₂ and of Si, Al, and Au are given for comparison purposes.

Material	CTE, × 10 ⁻⁶ /°C	Internal stress, dynes/cm ² (350°-400°C)	Total stress on Si (at 25°C)	Total stress over Al edges (450°C)
CVD SiO ₂	0.5	High T* (1-4 × 10 ⁹)	High T* (0.5-2 × 10 ⁹)	Very high T*
Sputtered SiO ₂	0.5	Low	C**	T
CVD PSG	0.5	Moderate T	T	High T
Thermal SiO ₂	0.5	—	C	—
Si	3.5	—	—	—
Al	26.0	Low	T	—
Au	15.0	—	—	—

* T = tensile.
** C = compressive.

vantageous for MOS devices, which are more surface sensitive than digital bipolar IC's.

CVD has been more widely used than rf sputtering for depositing layers of SiO₂, PSG, or BSG, because it is faster (see Table I), requires simpler equipment, and, in contrast to rf sputtering, produces no radiation damage in the thermally grown SiO₂.

Deposited SiO₂ or silicate films are sometimes densified by a heat-treatment in a suitable ambient to improve their properties (148, 305, 158). Higher phosphorus contents in the CVD PSG glass reduce intrinsic tensile stress (which tends to cause cracking) (269, 303, 235) and increase the alkali-ion gettering capability of the passivation layer. On the other hand, PSG layers with excessively high phosphorus concentration tend to be hygroscopic and may have poor stability in humid atmospheres (225). These effects can be reduced by depositing a thin SiO₂ layer over the PSG layer (158).

Excessively thin passivation layers tend to contain more pinholes than thicker layers (85) and are less effective in covering topography such as delineated metal lines. Also, any charges which move along the surface of the passivation layer are closer to the Si-SiO₂ interface and thus exert more influence on device characteristics (273). Thicker layers, however, are more likely to contain nodules and are more likely to crack.

The effectiveness of a passivation layer in providing protection against metallization scratches increases with increasing passivation layer thickness (277). It is possible to deposit and delineate crack-free BSG or PSG layers 3 μm thick (157, 158) which afford very good scratch protection. With thicker layers, it is necessary to deposit the layers under conditions in which stress is not excessive. Consideration must also be given to the effects of mismatches in thermal coefficients of expansion. Borosilicate containing 17 mole per cent (m/o) B₂O₃ approximates the linear coefficient of thermal expansion (CTE) of silicon (158). Crack-free layers of BSG over 10 μm in thickness can readily be obtained by CVD at 450°C (157, 158).

Regardless of deposited passivation layer thickness, layers of deposited dielectrics must be applied to properly cleaned wafers under suitable conditions to avoid metal penetration (20) and lateral charge spreading or lateral ion migration effects at the interface between thermally grown SiO₂ and deposited dielectric (273, 118, 280, 39).

There is some reaction of Al metal with SiO₂, BSG, or PSG at relatively low temperatures (289), such as 400°C (277, 232, 253). Thus, an intermediate aluminosilicate film forms during SiO₂ deposition. Subsequent high-temperature processing steps such as chip-to-header eutectic bonding and package sealing, particularly in frit-sealed ceramic packages, which are sealed at temperatures on the order of 500°C (200, 343), can cause additional Al-glass interaction. The Al-SiO₂ reaction tends to be accelerated at localized oxide defects and thus is dependent on oxide quality (51, 232).

Low-temperature deposited films of SiO₂, PSG, and BSG are amorphous. Delineation of deposited SiO₂ and PSG films (to expose bonding pads and open scribe lines) is accomplished using buffered hydrofluoric acid. Delineation of BSG films is preferably performed using unbuffered hydrofluoric acid mixtures because of the higher etch rate (158).

In Si-gate MOS IC's, CVD phosphosilicate is frequently used as the dielectric between polycrystalline silicon and overlying metal; in these devices it also serves as a passivation layer. In some cases the PSG layer is subjected to a heat-treatment at a temperature such as 1000°C to obtain some flow of the PSG (222, 161, 153, 340, 10).

Characterization of Dielectric Films

The characterization of dielectric films used in silicon device passivation is based both on standard chemical, physical, and electrical methods established for surface and thin-film analysis (198, 199, 138, 139) and on methods developed specifically for the analysis of thin dielectric films (341, 137). Special electrical methods include metal-insulator-semiconductor (MIS) measurements of the capacitance-voltage (C-V) relationship before and after bias heat-treatment (116, 296, 259, 362, 72). From these measurements one can calculate the density of electronic states, interface charges, and bulk charges, all of which play important roles in the electrical properties and stability of deposited dielectrics (296, 114, 294, 309, 226). Measurements of the sheet resistivity of a silicon wafer after heat-treatment at temperatures over 1000°C is often used to estimate the composition of a deposited binary oxide film from the resulting doping concentration in the silicon (18, 38, 10). X-ray fluorescence analysis (246, 306, 82), backscattering (186), and Auger electron spectroscopy (292) have been used to determine the composition of deposited dielectric films. Infrared spectroscopy has been used extensively for compositional and structural analysis of deposited SiO₂ (251, 305, 158, 264, 265, 151, 37, 223, 247), PSG (60, 158, 265, 37, 64, 317, 247, 286, 287), and BSG (251, 148, 158, 264, 151, 315, 37, 247, 8, 312) films. Chemical etch rate measurements have also been used to determine film composition and relative density for films as deposited (251, 146, 54, 321, 305, 158, 282, 120, 136, 110, 316) or after densification heat-treatment (321, 305, 158, 156). Moisture absorption and adsorption, and resistance of deposited dielectric films to moisture are important aspects of passivating films and have been examined by various authors (265, 151, 64, 8). Measurements of surface conductivity (46), stress (129, 268, 267, 175, 302, 303, 104, 331), and index of refraction (251, 106, 305, 158) of various deposited dielectrics have been reported. Methods for characterizing localized structural defects in dielectric films have been reviewed recently (153). Coverage of topography by deposited films is important for device reliability (107, 140, 161, 10, 179).

Alkali Barrier Layers

In some high-reliability devices, silicon nitride (Si₃N₄), which serves as both a getter and an effective alkali barrier (322, 65, 100, 41), is applied over the thermally grown SiO₂ prior to metallization. Aluminum oxide (Al₂O₃), which is also an alkali ion barrier (329, 330), has been used in some MOS devices (49, 174, 105). Examples of devices with ion barriers include nitride-passivated bipolar devices (195, 279), beam-lead sealed-junction devices (279, 239), and MNOS devices (262). Silicon nitride can also be deposited over refractory metals (160) such as W and Mo, or over the polycrystalline silicon used in silicon-gate MOS devices. A considerable amount of information has been published on deposition (54, 109, 87, 208, 191, 216, 347, 258) and properties (75, 54, 109, 344, 168, 87, 265, 216, 194, 347, 193) of Si₃N₄, and on device applications (322, 279, 262, 109, 78, 310, 337, 351, 196, 160, 355, 195, 125, 12).

Typically, Si₃N₄ layers are formed by reaction of SiH₄ or of SiCl₄ with excess NH₃ at temperatures of 800°-900°C at atmospheric pressure. Layer thicknesses of 0.1-0.2 μm are generally used as alkali barrier layers in bipolar devices. Al₂O₃ is prepared by CVD from Al₂Cl₆ + H₂ + CO₂ (328, 329, 86, 326) at approximately 900°C.

Delineation of Si₃N₄ or Al₂O₃ films is performed using hot (180°C) phosphoric acid (336). In MOS devices in which the Si₃N₄ is used under the gate metal, the thickness of the Si₃N₄ is on the order of 0.03-0.05 μm (262, 12). Both thickness and dielectric constant must be closely controlled in this type of MOS application.

Although defect-free silicon nitride layers are effective diffusion barriers, it must be recognized that many

nitride-passivated devices have exposed underlying thermal oxide at each contact cut and at the periphery of the chip. Although procedures exist for sealing the edges with nitride, this is frequently not done because of the additional process complexity and the chip area penalty involved. With unsealed oxide edges, lateral migration of alkali is possible, and has been shown to adversely affect silicon device reliability (208). While the effects of alkali ions on stability of threshold voltage of MOS devices have been the subject of many studies, it has also been clearly established that alkali ions can adversely affect bipolar devices (279, 310, 208, 195, 77).

Fused Glass Layers

Fused glass films are used on various device types. Table III shows the composition and properties of typical fused glasses used in silicon device passivation. Planar, aluminum-metallized IC's have made use of a thin ($\sim 1 \mu\text{m}$) fused glass layer applied over metal (68, 69, 323). The high CTE permits only very thin layers, which can be applied by careful sedimentation of fine powder as is described later. Pinholes in the glass film on such devices can lead to metal corrosion (7). Power devices of planar or mesa structure often use fused glass as a direct passivant on the high-voltage junction (169, 126). Various techniques for high-voltage axial-lead diode passivation make use of beads of fused glass powder (79, 80), glass sleeves with metal studs (56, 44), or glass sleeves with glass beads as end seals (67).

The composition of glass used to form fused layers for device passivation depends on the device processing restrictions and designed operating characteristics. Important properties of the starting glass are particle size (in the case of powders), fusion temperature, and melt viscosity. For the fused layer, the important properties are chemical durability, CTE, and dielectric properties, in particular, ionic mobility at intended device operating temperature. Since the CTE increases and chemical durability decreases with decreasing fusion temperature, tradeoffs based on device processing requirements and intended use must be made (214, 354). As an example, low melting glasses used over aluminum can be applied in thicknesses of only a few microns (242).

Because of their good chemical stability, lead oxide-containing glasses are widely used, but the high ionic mobility of the lead ion above about 125°C in some glasses of this type limits device operating temperature (162, 295, 40, 290). For example, lead aluminosilicate glasses (LASG) are used in mesa grooves for thyristor and other high power device passivation (351, 352, 62) where device operating temperature of 125°C is sufficient. The low CTE of such glasses permits the application of thick layers directly on silicon in the grooves (355, 356), and the chemical stability permits contact etching and nickel plating of the device after high-temperature fusion ($\sim 900^\circ\text{C}$) of the glass powder. The addition of boron oxide (LBASG) (40, 221, 357) permits further decrease of ionic mobility and also of fusion temperature (to about 700°C), rendering the glass suitable for use on higher operating temperature devices (88), such as power transistors. However, CTE is increased (see Table I). ZnO is usually added to such glasses (LAZBSG) to moderate the CTE increase.

With boron-containing glass of high fusion temperature ($\cong 900^\circ\text{C}$), it is not possible to fuse the glass directly on the silicon because of doping effects. An intermediate SiO_2 barrier layer is then necessary. Glasses with ZnO and B_2O_3 as major constituents have higher device operating temperature capability because of reduced ionic mobility (162, 45, 221). In some cases, however, reduced chemical resistance of such glasses limits subsequent processing options.

For scratch and ambient protection over metallization on planar IC's and small-signal transistors, where the glass is applied over the entire wafer, the glass must fuse at a temperature compatible with the metallization. This is an important restriction in the case of Al metallization since, as previously indicated, the Al-Si system forms a eutectic melting at 577°C . Also the low-melting glasses used have a high CTE, and therefore, to avoid cracking, only very thin layers can be used (240, 242, 133, 325, 88, 125).

Depending on thickness desired, the powdered glass may be deposited by several methods. For thin, pinhole-free films on the order of 1 or $2 \mu\text{m}$ thickness, sedimentation in a centrifuge is suitable. Procedures for dispersing the glass powder in the suspending liquid and choice of liquid(s) are important for obtaining thin, uniform, pinhole-free, and adherent glass films (248, 240, 250, 249) by this technique.

For thicker layers of about 5-25 μm , doctor-blading of a slurry, electrophoretic deposition, spinning on of photoresist-glass mixtures, application of beads of glass powder in a slurry, and silk screening (245) can be used. Doctor-blading requires a step- or groove-type geometry for the selective placement of the glass, and is suited to mesa-type devices. Electrophoretic deposition (123, 313, 217) is used for various power devices, and can be made selective by using insulator films to mask areas where no glass is desired (283-285). Photoresist-glass powder compositions permit removal of unwanted glass before fusion, thus eliminating an etching step (13).

For axial-lead diodes passivated with fused glass powder, a drop of slurry can be formed about the diode and stud lead assembly. In the case of preforms, the glass tubes for axial diodes are fitted over the device and fused into contact. High ambient pressure applied during fusion permits a lowering of fusion temperature (56). Combinations of glass powder as a bonding agent, and preforms as the passivating layer, have also been described (218).

Other glass application techniques include the use of various oxide thin films as a bonding layer between fused glass powder and the silicon surface (241, 244, 251, 243) and the formation of a glass *in situ* by firing of a silicon device with deposited glass-forming oxide powders (134).

The various analytical techniques already noted for grown or deposited layers are also useful for characterizing fused glass materials (247, 153). In addition, differential thermal analysis (102), microhardness testing (331), and particle size analysis (143) of the powder are valuable test methods to assure the attainment of high-quality layers.

Table III. Typical fused glasses. Some of the properties of silicon are given for comparison purposes.

Glass	Composition (% by wt)						Fusion temperature ($^\circ\text{C}$)	CTE ($^\circ\text{C}^{-1}$)	Devices	Deposited
	PbO	B_2O_3	Al_2O_3	ZnO	SiO_2	Other				
LABSG	51	9	3	—	29	$\text{Na}_2\text{O}:1.6$; other oxides:5.4	570	6.2×10^{-6}	Planar IC's	Over metal on completed chip
LBASG	30	13	7	—	50	—	950	3.5×10^{-6}	Power devices	Over SiO_2 in mesa grooves
LASG	50	—	10	—	40	—	900	4.0×10^{-6}	High-voltage power devices	On Si in mesa grooves
LZABSG	46	10	3	2	39	—	700	4.6×10^{-6}	Power trans. and diodes	On Si; glass bead
ZBSG	2	25	—	60	10	$\text{CeO}_2:3$	700	4.5×10^{-6}	Power trans. and diodes	On Si; glass bead
Si	—	—	—	—	—	—	1410	3.5×10^{-6}	—	—

Passivation Layers and Silicon Device Reliability

Most of the presently available small-signal planar transistors and integrated circuits are Al-metallized and are passivated with a thin layer of SiO₂ or PSG. The primary purposes of this layer are to provide scratch protection during handling (142), to achieve immunity to shorts caused by loose particles in packages with a cavity, to reduce susceptibility of the Al metallization to corrosion (275), and to meet customer specification requirements. With complex IC's, increased electrical and visual inspection yields frequently more than compensate for the costs of applying and delineating a passivation layer. Glass passivation layers, deposited over the metallization pattern, have also been shown to significantly increase device reliability (197, 97, 276, 125, 185, 324, 127).

Glass passivation is frequently performed on all wafers by the same process, without regard to whether the final product will be commercial or high-reliability, in plastic or in hermetic packages, or will be rated for limited temperature or full temperature operation. Obviously, the thickness and composition of the passivation layer which meet all of these diverse requirements involve some tradeoffs and compromises. Our experimental studies (156) have shown that in a substantial portion of the integrated circuits manufactured in the last several years, the passivation layer contains pinholes, cracks, or a combination of these. A number of publications also confirm this finding (157, 278, 140, 144, 210, 89, 153, 338, 21).

Cracks in passivation layers, when present, frequently occur at and run along topographic steps or along the edges of delineated metal conductors or thin-film resistors (140, 144), and thus cannot be seen by optical microscopy. Pinholes in the dielectric over alloyed metal are generally very difficult to see by optical microscopy because of the rough topography of the recrystallized aluminum. Both cracks and pinholes can be revealed by scanning electron microscopy (SEM), or by subjecting the chip to immersion in an etchant which does not dissolve the dielectric but is capable of dissolving the underlying material (85, 254, 144, 89, 153). After chemical etching to undercut the Al, the actual pinhole in the dielectric is generally visible, by optical microscopy, in the center of the undercut area (153).

Pinholes in the passivating glass can occur for a variety of reasons. They may be present in the passivation layer as deposited (85, 27), may arise during etching to open the bonding pads (because of holes in the photoresist layer), or may be created by the contact printing operation or by impact during chip handling (142).

In a recent study (156), two classes of pinholes were evident in samples of IC's from six manufacturers. The more common class was pinholes in the central regions of aluminum lines. Another type observed was pinholes along the edge of the delineated metal lines (153). The edge pinholes are attributed to inadequate coverage of metal edges by the photoresist and can generally be avoided by the use of thicker photoresist layers or improved photoresist application techniques. Those pinholes which occurred in the central areas of delineated lines are to a large extent believed to be attributable to the presence of hillocks in the aluminum which occur because of recrystallization of the aluminum during the contact alloying step (188, 179, 156). Even if a hillock is completely covered with dielectric during the subsequent step of deposition of the passivation layer, the hillock may not be adequately covered by photoresist, the photoresist may be pushed away from the peak of the hillock during contact printing, or the contact printing step may fracture the dielectric over the hillock. Any of these three conditions, or a combination, will result in a pinhole through the passivation layer, exposing a region of underlying metal. Handling of wafers can result in impact cracks and scratches (142).

Al-metallized IC's are considerably more susceptible to failure due to opens as a result of Al corrosion during operation if the passivation layer contains cracks (235, 358) or pinholes (156) over the metal lines. Defects in passivation layers also increase susceptibility to ionic contaminant effects (156, 111). The requirements for attaining crack-free, pinhole-free passivation layers are very similar to the requirements for a first-layer deposited dielectric in multilevel-metallized integrated circuits. These include minimizing hillocks, low-stress dielectric deposition conditions, good coverage of the edges of delineated metal, and proper photolithographic procedures (303, 278, 104, 161, 103, 153, 340).

Phosphosilicate layers with an excessively high concentration of phosphorus are hygroscopic and have led to aluminum corrosion problems (235, 358, 93, 359). On the other hand, the use of low-phosphorus glass compositions which result in cracks over or along the edges of aluminum metal lines can lead to localized metal corrosion problems (235). The density and structure of phosphosilicate films are factors which influence the optimum phosphorus content (225).

The effectiveness of a passivation layer can be assessed by accelerated techniques in which the devices are exposed to high relative humidities. One commonly used condition is reverse bias or operating life at 85% relative humidity at 85°C. A considerably more severe test is to apply bias to devices which are in a pressure cooker, for example, at 15 psig (121°C).

Moisture plus bias can result in electrochemical corrosion of metal. Electrochemical corrosion normally would be expected to result in open metal lines which have positive (anodic) bias relative to adjacent lines (298, 166); with Al-metallized integrated circuits, corrosion of circuit lines which are cathodic has also been reported (166, 235). Stress-corrosion cracking (30) may be a factor in accelerating cathodic corrosion of Al metallization lines at grain boundaries. Corrosion mechanisms of Al can be chemical as well as electrochemical, and in either case temperature (5), pH (252, 170), and presence of chlorides (252, 170) are important factors in determining corrosion rate and corrosion products.

The more costly metallization system Ti-Pt-Au, with Au wire bonds, has been shown to be superior to Al for corrosion resistance (350, 119, 165). With Au metallization systems, electrolytic corrosion can, however, result in formation of dendrites which form shorts between conductors (170, 203, 288, 117).

Device Encapsulation

Final encapsulation of silicon devices may be in hermetically sealed packages (181, 94, 35, 22, 200, 343, 255), in molded plastic packages (181, 22, 4, 165, 113, 189, 23), in cast plastic, or by conformal plastic coating of chips mounted on hybrid substrates (345, 122). The encapsulation process provides the final means for passivation of the device. The device reliability, in terms of both stability of electrical characteristics and susceptibility to catastrophic failure, is a complex function of the device design and processing techniques and materials used, including the metallization, the passivation layer or layers, and the final encapsulation.

Early silicon devices were primarily sealed in hermetic packages. The plastic-encapsulated silicon devices initially offered had reliability limitations (183, 215, 310, 36, 276, 98, 108, 304) which, to a large extent, have now been overcome (24, 95, 98, 165, 113). Plastic encapsulation does permit lower costs, provides mechanically rugged packages, provides freedom from loose particle problems, and permits smaller package size.

Hermetically sealed devices are not totally immune to ionic contamination and moisture effects (20, 209, 140, 319, 332, 239). Ionic contaminants may be inadvertently sealed in the package (319, 320). Also, a percentage of the devices in completed electronic equip-

ment are not actually hermetically sealed (300, 209, 1), either because they escaped hermeticity screening tests, or because the hermetic seal became damaged during device handling or equipment assembly (1). In such cases, a suitable passivation layer can provide some protection against Al corrosion or electrolytic Au migration reactions.

The plastic formulations initially used for molding silicon devices were based on phenolics, epoxies, and silicones (128, 36, 28, 200, 97, 121, 201, 165, 113). In many cases a junction coat (layer of plastic such as an epoxy, silicone varnish, or room-temperature vulcanizing silicone elastomer) was applied prior to molding (84, 97, 121, 311, 165, 2). Plastics can be a source of ions (182, 128, 230, 228, 29, 166, 177, 308) or impurities (183, 230, 135, 298, 176) which adversely affect silicon devices, particularly in moist atmospheres and under bias conditions. In the last several years, a considerable number of process and materials changes has been made to improve the reliability of plastic-encapsulated silicon integrated circuits (96, 24, 95, 98, 165, 113). Most notable of the improvements is the use of novolac epoxy formulations with high glass transition temperatures (165).

Silicones are extensively used for encapsulation of power devices (201, 26) and for beam-lead devices (345, 237). In general, silicones permit high in-process temperatures and higher maximum storage temperatures (201, 257) than epoxy- or phenolic-based encapsulating compounds.

Various test devices and accelerated testing techniques have been developed for evaluating the stability of passivated devices under severe environmental conditions (314, 256, 238, 257). For plastic-encapsulated devices, a moisture-containing ambient constitutes an effective means for accelerating ion migration effects or chemical or galvanic corrosion of the metallization pattern on the chip (182, 28, 237, 33, 7, 90, 256, 121, 29, 238, 229, 291, 236, 257, 189, 23, 166, 176, 177). Moisture is an important factor since surface conductivity of SiO₂ and of other passivation materials increases by several orders of magnitude with increase in relative humidity (131, 46).

In general, passivation techniques provide only partial protection against ambient effects. For example, silicon nitride-passivated devices may be protected against alkali penetration into the underlying SiO₂, but may be influenced by potential buildup at insulator-insulator interfaces or at the ambient-upper dielectric interface. Increased device stability is frequently obtained by specific device construction features which make the device less surface sensitive. Examples include resistive overlays (57), use of diffused channel stoppers (273, 49), field plates (48, 43, 363, 59), ion implanted surfaces (299, 219), and use of beveled junctions (66, 167, 327, 14, 62) in high-voltage devices.

The most reliable silicon devices are those in which device design, wafer processing, metallization, passivation, assembly, encapsulation, and electrical testing are all specified to minimize the incidence of conditions which result in known failure mechanisms, and adequate in-process controls (39) are applied during the entire device fabrication sequence; thus reliability (278, 333, 281, 324, 236, 239) is designed into the product.

Acknowledgments

The authors gratefully acknowledge the contributions of A. W. Fisher and R. D. Vibronek to the experimental results presented in this paper, and the assistance of R. E. Allen and P. L. Pado in preparation of the manuscript. We also thank A. W. Fisher, K. W. Hang, and J. L. Vossen for the helpful discussions and for reviewing the manuscript. We also thank F. P. Jones, S. Merrin, and G. S. Sheldon for bringing several references on fused glass to our attention, and M. H. Woods for supplying several references on double dielectric structures.

This work was in part supported by the Air Force Materials Laboratory, Wright-Patterson Air Force Base, Ohio, under Contract No. F33615-74-C-5146.

Manuscript submitted Nov. 22, 1974; revised manuscript received Feb. 26, 1975. This was Paper 215 presented at the New York, New York, Meeting of the Society, Oct. 13-17, 1974.

Any discussion of this paper will appear in a Discussion Section to be published in the June 1976 JOURNAL. All discussions for the June 1976 Discussion Section should be submitted by Feb. 1, 1976.

Publication costs of this article were partially assisted by RCA Corporation.

REFERENCES

- G. E. Adams, 11th Ann. Proc. Reliab. Phys., pp. 95-97 (1973).
- J. D. Adams, 1/4-1 to 1/4-7 in IEEE 1974 INTERCON—Improving Producibility II, IEEE Cat. No. 74CHO904-3 (1974).
- A. H. Agajanian, *IEEE Trans. Electron. Devices*, **ED-20**, 757 (1973); IBM Technical Report No. TR 22.1559 (November 1972).
- L. Altman, *Electronics*, **46**, No. 9, 85 (April 26, 1973).
- R. S. Alwitt, *This Journal*, **121**, 1322 (1974).
- J. A. Amick and W. Kern, in "Chemical Vapor Deposition," J. M. Blocher, Jr. and J. C. Withers, Editors, pp. 551-570, The Electrochemical Society Softbound Symposium Series, New York (1970).
- E. S. Anolick, A. Amendola, and P. J. Levitz, 9th Ann. Proc. Reliab. Phys., pp. 228-232 (1971).
- E. Arai and Y. Terunuma, *This Journal*, **121**, 676 (1974).
- J. R. Archer, *ibid.*, **104**, 619 (1957).
- W. E. Armstrong and D. L. Tolliver, *ibid.*, **121**, 307 (1974).
- M. M. Atalla, E. Tannenbaum, and E. J. Scheibner, *Bell System Tech. J.*, **38**, 749 (1959).
- T. G. Athanas, *Solid State Technol.*, **17**, No. 6, 54 (1974).
- S. S. Baird and J. A. Cunningham, U.S. Pat. 3,355,291 (1967).
- M. Bakowski and K. I. Lundstrom, *IEEE Trans. Electron. Devices*, **ED-20**, 550 (1973).
- B. J. Baliga and S. K. Ghandhi, *J. Appl. Phys.*, **44**, 990 (1973).
- P. Balk, Review paper prepared for inclusion in Proc. ESSDERC 1973 (European Solid State Device Research Conference), Munich (September 18-21, 1973) (Preprint).
- P. Balk and J. M. Eldridge, *Proc. IEEE*, **57**, 1558 (1969).
- M. L. Barry, *This Journal*, **117**, 1405 (1970).
- M. L. Barry, in "Chemical Vapor Deposition," J. M. Blocher, Jr. and J. C. Withers, Editors, pp. 595-617, The Electrochemical Society Softbound Symposium Series, New York (1970).
- J. J. Bart, *IEEE Trans. Electron. Devices*, **ED-16**, 351 (1969).
- J. J. Bart, Paper No. 3.6 presented at the International Reliability Physics Symposium, Las Vegas, Nevada, April 2, 1975.
- A. T. Batch, *Electronic Pkg. Prod.*, **11**, No. 3, 45, (1971).
- D. M. Baugher and L. J. Gallace, 1/2-1 to 1/2-8 in IEEE 1974 INTERCON—Improving Producibility II, IEEE Cat. No. 74CHO904-3 (1974).
- R. Beard, 10th Ann. Proc. Reliab. Phys., pp. 72-77 (1972).
- K. H. Beckmann and N. J. Harrick, *This Journal*, **118**, 614 (1971).
- W. P. Bennett and L. J. Gallace, *IEEE Trans. Broadcast Television Receivers*, **BTR-20**, 322 (1974).
- W. C. Benzing, R. S. Rosler, and R. W. East, *Solid State Technol.*, **16**, No. 11, 37 (1973).
- J. R. Bevington, J. P. Cook, and D. R. Little, 8th Ann. Proc. Reliab. Phys., pp. 73-80 (1970).
- A. Bimson, in "Mikroelektronik 5," L. Steipe, Editor, pp. 395-421, R. Oldenbourg Verlag, München (1973).
- W. W. Binger, E. H. Hollingsworth, and D. O. Sprowls, in "Aluminum, Vol. 1, Properties, Physical Metallurgy and Phase Diagrams," K. R.

- Van Horn, Editor, pp. 209-276, American Society for Metals, Metals Park, Ohio, 1967.
31. J. R. Black, *IEEE Trans. Electron. Devices*, **ED-16**, 338 (1969).
 32. J. R. Black, *Proc. IEEE*, **57**, 1587 (1969).
 33. B. L. Blair and E. A. Herr, 8th Ann. Proc. Reliab. Phys., pp. 110-113 (1970).
 34. I. Blech, H. Sello, and L. V. Gregor, in "Handbook of Thin Film Technology," L. I. Maissel and R. Glang, Editors, pp. 23-1 to 23-23, McGraw-Hill Book Co., New York (1970).
 35. F. H. Bower, *Solid State Technol.*, **13**, No. 8, 56 (1970).
 36. J. B. Brauer, V. C. Kapfer, and A. L. Tamburrino, 8th Ann. Proc. Reliab. Phys., pp. 61-72 (1970).
 37. D. M. Brown, M. Garfinkel, M. Ghezzi, E. A. Taft, A. Tenney, and J. Wong, *J. Crystal Growth*, **17**, 276 (1972).
 38. D. M. Brown and P. R. Kennicott, *This Journal*, **118**, 293 (1971).
 39. G. A. Brown, K. Lovelace, and C. Hutchins, 11th Ann. Proc. Reliab. Phys., pp. 203-207 (1973).
 40. R. C. Buchanan and M. A. Zuegel, *J. Am. Ceram. Soc.*, **51**, 28 (1968).
 41. T. E. Burgess, J. C. Baum, F. M. Fowkes, R. Holmstrom, and G. A. Shirn, *This Journal*, **116**, 1005 (1969).
 42. R. S. Buritz, A. Fafarman, R. F. McGowan, and S. L. Webster, Proc. 1969 Electron. Comp. Conf., pp. 304-321 (1969).
 43. H. R. Camenzind, B. Polata, and J. Kocsis, *Electronics*, **42**, No. 7, 90 (March 31, 1969).
 44. J. N. Carman, U.S. Pat. 3,200,310 (1965).
 45. J. N. Carman, U.S. Pat. 3,392,312 (1968).
 46. R. Castagne, P. Hesto, and A. Vapaille, *Thin Solid Films*, **17**, 253 (1973).
 47. P. L. Castro and B. E. Deal, *This Journal*, **118**, 280 (1971).
 48. P. P. Castrucci and J. S. Logan, *IBM J. Res. Develop.*, **8**, 396 (1964).
 49. G. T. Cheney, R. L. Freyman, and A. A. Mamele, 9th Ann. Proc. Reliab. Phys., pp. 62-66 (1971).
 50. Y. C. Cheng, J. W. Haslett, E. J. M. Kendall, R. J. Krieger, and F. J. Scholz, *Proc. IEEE*, **62**, 859 (1974).
 51. N. J. Chou and J. M. Eldridge, *This Journal*, **117**, 1287 (1970).
 52. N. J. Chou, C. M. Osburn, Y. J. van der Meulen, and R. Hammer, *Appl. Phys. Letters*, **22**, 380 (1973).
 53. C. K. Chu, J. E. Johnson, and A. J. Riding, Abstract 30, p. 86, The Electrochemical Society Extended Abstracts, Spring Meeting, San Francisco, California, May 12-17, 1974.
 54. T. L. Chu, *J. Vacuum Sci. Technol.*, **6**, 25 (1969).
 55. T. L. Chu, J. R. Szedon, and C. H. Lee, *Solid-State Electron.*, **10**, 897 (1967).
 56. J. E. Clark, U.S. Pat. 3,193,366 (1965).
 57. L. E. Clark and D. S. Zoroglu, *Solid-State Electron.*, **15**, 653 (1972).
 58. R. H. Collins and J. S. Logan, U.S. Pat. 3,616,403 (1971).
 59. F. Conti and M. Conti, *Solid-State Electron.*, **15**, 93 (1972).
 60. E. A. Corl and W. E. Reese, *Metallurg. Trans.*, **1**, 747 (1970).
 61. R. L. Cormia, *Solid State Technol.*, **12**, No. 12, 56 (December 1969).
 62. J. Cornu, S. Schweitzer, and O. Kuhn, *IEEE Trans. Electron. Devices*, **ED-21**, 181 (1974).
 63. H. E. Culver, H. Schilling, and R. E. Thun, *J. Vacuum Sci. Technol.*, **10**, 170 (1973).
 64. K. S. Dagher, Abstract 268, p. 666, The Electrochemical Society Extended Abstracts, Fall Meeting, Miami Beach, Florida, Oct. 8-13, 1972.
 65. J. V. Dalton and J. Drobek, *This Journal*, **115**, 865 (1968).
 66. R. L. Davies and F. E. Gentry, *IEEE Trans. Electron. Devices*, **ED-11**, 313 (1964).
 67. E. K. Davis and K. W. Hansen, U.S. Pat. 3,723,835 (1973).
 68. E. M. Davis, W. E. Harding, and R. S. Schwartz, Wescon 1963, San Francisco, August 1963, Part 2, Paper 13.1.
 69. E. M. Davis, W. E. Harding, R. S. Schwartz, and J. J. Corning, *IBM J. Res. Develop.*, **8**, 102 (1964).
 70. B. E. Deal, *This Journal*, **110**, 527 (1963).
 71. B. E. Deal, Abstract 93, p. 259, The Electrochemical Society Extended Abstracts, Fall Meeting, Detroit, Michigan, Oct. 5-9, 1969.
 72. B. E. Deal, in *Silicon Device Processing*, NBS Spec. Pub. 337, pp. 36-50, November 1970.
 73. B. E. Deal, Abstract 39, p. 108, The Electrochemical Society Extended Abstracts, Spring Meeting, San Francisco, California, May 12-17, 1974.
 74. B. E. Deal, *This Journal*, **121**, 198C (1974).
 75. B. E. Deal, R. J. Fleming, and P. L. Castro, *ibid.*, **115**, 300 (1968).
 76. B. E. Deal, E. L. MacKenna, and P. L. Castro, *ibid.*, **116**, 997 (1969).
 77. C. J. Dell'Oca and M. L. Barry, *Solid-State Electron.*, **15**, 659 (1972).
 78. R. Denning and C. L. Tollin, U.S. Pat. 3,465,209 (1969).
 79. N. E. DeVolder, U.S. Pat. 3,505,571 (1970).
 80. N. E. DeVolder, U.S. Pat. 3,533,832 (1970).
 81. F. M. d'Heurle and R. Rosenberg, in "Physics of Thin Films," Vol. 7, G. Hass, M. H. Francombe, and R. W. Hoffman, Editors, pp. 257-310, Academic Press, New York (1973).
 82. G. DiGiacomo, *This Journal*, **121**, 419 (1974).
 83. T. H. DiStefano, *J. Appl. Phys.*, **44**, 527 (1973).
 84. O. Dobson, *Electron. Eng. (London)*, **43**, No. 3, 47 (March 1971).
 85. V. Y. Doo and V. M. L. Sun, *Metallurg. Trans.*, **1**, 741 (1970).
 86. V. Y. Doo and P. J. Tsang, *This Journal*, **116**, 116C, (1969).
 87. M. T. Duffy and W. Kern, *RCA Rev.*, **31**, 742 (1970).
 88. M. Dumesnil and R. Hewitt, *This Journal*, **117**, 100 (1970).
 89. G. H. Ebel and H. A. Engelke, 11th Ann. Proc. Reliab. Phys., pp. 108-116 (1973).
 90. H. C. Edfors, Proc. 1972 Ann. Rel. & Maint. Symp., pp. 479-491 (January 1972).
 91. J. M. Eldridge and D. R. Kerr, *This Journal*, **118**, 986 (1971).
 92. J. M. Eldridge, R. B. Laibowitz, and P. Balk, *J. Appl. Phys.*, **40**, 1922 (1969).
 93. C. J. Elia, *Wall Street Journal*, p. 31, May 2, 1974.
 94. G. K. Fehr, *Solid State Technol.*, **13**, No. 8, 41 (1970).
 95. J. E. Feldt and E. R. Hnatek, 10th Ann. Proc. Reliab. Phys., pp. 78-81 (1972).
 96. F. Fischer, 8th Ann. Proc. Reliab. Phys., pp. 94-100 (1970).
 97. P. Flaskerud, Proc. 1971 Semicond./IC Proc. and Prod. Conf., pp. 40-47, Ind. and Sci. Conf. Mtg., Chicago, Ill. (1971).
 98. J. L. Flood, 10th Ann. Proc. Reliab. Phys., pp. 95-99 (1972).
 99. P. Z. Fox and W. J. Nestork, *IBM J. Res. Develop.*, **15**, 384 (1971).
 100. I. Franz and W. Langheinrich, *Solid-State Electron.*, **12**, 145 (1969).
 101. B. T. French, J. E. Mann, and G. E. Ereckson, 10th Ann. Proc. Reliab. Phys., pp. 26-31 (1972).
 102. R. G. Frieser, R. R. Tummala, and W. Fedrowitz, Abstract 5, p. 18, The Electrochemical Society Extended Abstracts, Spring Meeting, San Francisco, California, May 12-17, 1974.
 103. P. B. Ghate, W. R. Gardner, and D. L. Crosthwait, *IEEE Trans. Reliability*, **R-22**, 186 (1973).
 104. P. B. Ghate and L. H. Hall, *This Journal*, **119**, 491 (1972).
 105. A. P. Gnadinger and W. Rosenzweig, *ibid.*, **121**, 700 (1974).
 106. N. Goldsmith and W. Kern, *RCA Rev.*, **28**, 153 (1967).
 107. A. J. Gonzales, 9th Ann. Proc. Reliab. Phys., pp. 142-148 (1971).
 108. C. R. Gray, 10th Ann. Proc. Reliab. Phys., pp. 100-101 (1972).
 109. L. V. Gregor, in "Thin Film Dielectrics," F. Vratny, Editor, pp. 447-488, The Electrochemical Society Softbound Symposium Series, New York (1969).
 110. L. V. Gregor, *Proc. IEEE*, **59**, 1390 (1971).
 111. A. J. Gregoritsch and R. G. Berger, Paper No. 3.5 presented at the International Reliability Phys-

- ics Symposium, Las Vegas, Nevada, April 2, 1975.
112. B. L. Gregory and C. W. Gwyn, *Proc. IEEE*, **62**, 1264 (1974).
 113. S. E. Grossman, *Electronics*, **46**, No. 21, 80 (Oct. 11, 1973).
 114. A. S. Grove, "Physics and Technology of Semiconductor Devices," John Wiley and Sons, New York (1967).
 115. A. S. Grove, O. Leistiko, Jr., and C. T. Sah, *J. Appl. Phys.*, **35**, 2695 (1964).
 116. A. S. Grove, E. H. Snow, B. E. Deal, and C. T. Sah, *ibid.*, **35**, 2458 (1964).
 117. F. J. Grunthamer, T. Griswold, and H. Bright, Paper No. 3.2 presented at the International Reliability Physics Symposium, Las Vegas, Nevada, April 2, 1975.
 118. J. R. Haberer and J. J. Bart, 10th Ann. Proc. Reliab. Phys., pp. 106-111 (1972).
 119. E. B. Hakim, G. Malinowski, and R. Holevinski, 11th Ann. Proc. Reliab. Phys., pp. 230-235 (1973).
 120. L. Hall, *This Journal*, **118**, 1506 (1971).
 121. M. C. Halleck, 10th Ann. Proc. Reliab. Phys., pp. 88-94 (1972).
 122. D. W. Hamer and J. V. Biggers, in "Thick Film Hybrid Microcircuit Technology," pp. 277-302, Wiley-Interscience, New York (1972).
 123. W. E. Harding and R. S. Schwartz, U.S. Pat. 3,280,019 (1966).
 124. R. C. Henderson, *This Journal*, **119**, 772 (1972).
 125. E. A. Herr, 10th Ann. Proc. Reliab. Phys., pp. 69-71 (1972).
 126. E. A. Herr, A. Fox, and J. S. Read, G.E. Report No. R73 EGP8, November 19, 1973; Annual IEEE Chicago Fall Conference, December 1973.
 127. E. A. Herr, A. Fox, and J. S. Read, *IEEE Trans. Broadcast Television Receivers*, **BTR-20**, 117 (1974).
 128. H. Hirsch, *Solid State Technol.*, **13**, No. 8, 48 (1970).
 129. R. W. Hoffman, in "Measurement Techniques for Thin Films," B. Schwartz and N. Schwartz, Editors, pp. 312-333, The Electrochemical Society Softbound Symposium Series, New York (1967).
 130. S. R. Hofstein, *IEEE Trans. Electron Devices*, **ED-14**, 749 (1967).
 131. L. Holland, in "The Properties of Glass Surfaces," pp. 448-528, Chapman and Hall, London (1964).
 132. A. G. Holmes-Siedle, *Proc. IEEE*, **62**, 1196 (1974).
 133. H. M. Hoogendorn and S. Merrin, U.S. Pat. 3,303,399 (1967).
 134. G. C. Huth, U.S. Pat. 3,669,731 (1972).
 135. J. A. Jackson, J. R. Szedon, and T. A. Temofonte, *This Journal*, **119**, 1424 (1972).
 136. J. S. Judge, *ibid.*, **118**, 1772 (1971).
 137. P. F. Kane and G. B. Larrabee, Editors, "Characterization of Semiconductor Materials," pp. 33-65, McGraw-Hill Book Co., New York (1970).
 138. P. F. Kane and G. B. Larrabee, in *Annual Review of Materials Science*, **2**, 33 (1972).
 139. P. F. Kane and G. B. Larrabee, "Characterization of Solid Surfaces," Plenum Press, New York (1974).
 140. V. C. Kapfer and J. J. Bart, 10th Ann. Proc. Reliab. Phys., pp. 175-182 (1972).
 141. L. H. Kaplan and M. E. Lowe, *This Journal*, **118**, 1649 (1971).
 142. L. K. Karstadt, W. G. Burger, C. M. Hsieh, and W. A. Cosgrove, *Solid State Technol.*, **16**, No. 8, 41 (August 1973).
 143. B. Kaye, *Int. Sci. and Technol.*, No. 27, 40-48 (March 1964).
 144. W. F. Keenan and W. R. Runyan, *Microelectron. Reliab.*, **12**, 125 (1973).
 145. W. Kern, *RCA Rev.*, **29**, 525 (1968).
 146. W. Kern, *ibid.*, **29**, 557 (1968).
 147. W. Kern, U.S. Pat. 3,481,781 (1969).
 148. W. Kern, *This Journal*, **116**, 251C, (1969).
 149. W. Kern, *RCA Rev.*, **31**, 207 (1970).
 150. W. Kern, *ibid.*, **31**, 234 (1970).
 151. W. Kern, *ibid.*, **32**, 429 (1971).
 152. W. Kern, *Solid State Technol.*, **15**, No. 1, 34 (1972), and **15**, No. 2, 39 (1972).
 153. W. Kern, *RCA Rev.*, **34**, 655 (1973); *Solid State Technol.*, **17**, No. 3, 35, and No. 4, 78, 89 (1974).
 154. W. Kern, Proc. Natl. Aerosp. Electr. Conf., pp. 93-100 (IEEE Cat. No. 75CHO956-3 NAECON), June 1975.
 155. W. Kern and A. W. Fisher, *RCA Rev.*, **31**, 715 (1970).
 156. W. Kern, A. W. Fisher, and R. D. Vibronek, Unpublished work (1974).
 157. W. Kern and R. C. Heim, *This Journal*, **117**, 562 (1970).
 158. W. Kern and R. C. Heim, *ibid.*, **117**, 568 (1970).
 159. W. Kern and D. Puotinen, *RCA Rev.*, **31**, 187 (1970).
 160. W. Kern and J. M. Shaw, *This Journal*, **118**, 1699 (1971).
 161. W. Kern, J. L. Vossen, and G. L. Schnable, 11th Ann. Proc. Reliab. Phys., pp. 214-223 (1973).
 162. D. R. Kerr, *IBM J. Res. Develop.*, **8**, 385 (1964).
 163. D. R. Kerr, 8th Ann. Proc. Reliab. Phys., pp. 1-8 (1970).
 164. D. R. Kerr, J. S. Logan, P. J. Burkhardt, and W. A. Pliskin, *IBM J. Res. Develop.*, **8**, 376 (1964).
 165. H. Khajezadeh, 11th Ann. Proc. Reliab. Phys., pp. 236-244 (1973); *Microelectronics (London)*, **5**, No. 2, 28 (1973).
 166. H. Koelmans, 12th Ann. Proc. Reliab. Phys., pp. 168-171 (1974).
 167. G. Kohl, *Solid-State Electron.*, **11**, 501 (1968).
 168. W. A. Kohler, *Metallurg. Trans.*, **1**, 735 (1970).
 169. R. A. Kokosa, B. R. Tuft, and E. D. Wolley, IEEE Industry Applications Meeting Proceedings, Milwaukee, Wisc., p. 87 (October 1973).
 170. S. C. Kolesar, 12th Ann. Proc. Reliab. Phys., pp. 155-167 (1974).
 171. R. J. Kriegler, *Thin Solid Films*, **13**, 11 (1972).
 172. R. J. Kriegler, in "Semiconductor Silicon 1973," H. R. Huff and R. R. Burgess, Editors, pp. 363-375, The Electrochemical Society Softbound Symposium Series, Princeton, N.J. (1973).
 173. R. J. Kriegler, 12th Ann. Proc. Reliab. Phys., pp. 250-258 (1974).
 174. E. E. Lampi and E. F. Labuda, 10th Ann. Proc. Reliab. Phys., pp. 112-119 (1972).
 175. R. Lathlaen and D. A. Diehl, *This Journal*, **116**, 620 (1969).
 176. R. W. Lawson, 12th Ann. Proc. Reliab. Phys., pp. 243-249 (1974).
 177. R. W. Lawson and J. C. Harrison, Paper No. 6, presented at the First International Conference on Plastics in Telecommunications (IEE), London, November 26-27, 1974 (preprint).
 178. A. J. Learn, *J. Appl. Phys.*, **44**, 1251 (1973).
 179. A. J. Learn, *Thin Solid Films*, **20**, 261 (1974).
 180. A. J. Learn and W. H. Shepherd, 9th Ann. Proc. Reliab. Phys., pp. 129-134 (1971).
 181. I. A. Lesk and E. D. Metz, in "Handbook of Semiconductor Electronics," 3rd ed., L. P. Hunter, Editor, pp. 9-1 to 9-25, McGraw-Hill Book Co., New York (1970).
 182. J. J. Licari, in "Plastic Coatings for Electronics," pp. 278-313, McGraw-Hill Book Co., New York (1970).
 183. J. J. Licari and G. V. Browning, *Electronics*, **40**, No. 4, 101 (April 17, 1967).
 184. J. R. Ligenza, Paper presented at Solid State Device Physics and Technology Seminar, Dept. of Elec. Eng., Princeton Univ., Princeton, N.J., November 20, 1973.
 185. J. H. Lindwedel, Final Report to RADC by Autonetics Div., North American Rockwell Corp., RADC-TR-73-127, May 1973.
 186. G. Linker, O. Meyer, and W. Scherber, *Phys. Status Solidi (a)*, **16**, 377 (1973).
 187. P. Lloyd, *Thin Solid Films*, **10**, 159 (1972).
 188. J. S. Logan, F. S. Maddocks, and P. D. Davidse, *IBM J. Res. Develop.*, **14**, 182 (1970).
 189. R. L. Lohn, 1/1-1 to 1/1-18 in IEEE 1974 INTERCON Improving Producibility II, IEEE Cat. No. 74CHO904-3 (1974).
 190. C. P. Lue, J. A. Jackson, and Y. P. Han, Abstract 199, p. 490, The Electrochemical Society Extended Abstracts, Fall Meeting, New York, New York, Oct. 13-17, 1974.
 191. E. L. MacKenna, Proc. 1971 Semicond./IC Proc. and Prod. Conf., 71-83, Ind. and Sci. Conf. Mtg., Chicago, Ill. (1971).
 192. E. L. MacKenna, Abstract 216, p. 531, The Electrochemical Society Extended Abstracts, Fall

- Meeting, New York, New York, Oct. 13-17, 1974.
193. E. M. MacKenna and P. Kodama, *This Journal*, **119**, 1094 (1972).
194. H. G. Maguire and P. D. Augustus, *ibid.*, **119**, 791 (1972).
195. C. F. Maguire, Q. T. Jarrett, and C. Y. Bartholomew, *Solid State Technol.*, **15**, No. 4, 46 (1972).
196. C. F. Maguire, F. J. Koons, and Q. T. Jarrett, *ibid.*, **14**, No. 8, 37 (1971).
197. C. C. Mai and T. S. Whitehouse, *IEEE Trans. Reliability*, **R-19**, 71 (1970).
198. "Handbook of Thin Film Technology," L. I. Maissel and R. Glang, Editors, McGraw-Hill Book Co., New York (1970).
199. Proc. of the Symp. on Modern Methods of Surface Analysis 1970, in "Modern Methods of Surface Analysis," P. Mark and J. D. Levine, Editors, North-Holland Publishing Co., Amsterdam (1971).
200. H. W. Markstein, *Electronic Pkg. Prod.*, **10**, No. 10, 20 (October 1970).
201. H. W. Markstein, *Electronic Pkg. Prod.*, **13**, No. 3, 25 (March 1973).
202. J. R. Mathews, W. A. Griffin, and K. H. Olson, *This Journal*, **112**, 899 (1965).
203. J. J. Mazenko, ISHM Symp. Proc. 1974, pp. 450-459 (1974).
204. D. V. McCaughan and R. A. Kushner, *Proc. IEEE*, **62**, 1236 (1974).
205. D. V. McCaughan, R. A. Kushner, and V. T. Murphy, in "Semiconductor Silicon 1973," H. R. Huff and R. R. Burgess, Editors, pp. 376-384, The Electrochemical Society Softbound Symposium Series, Princeton, N. J. (1973).
206. D. V. McCaughan, R. A. Kushner, and S. Wagner, *This Journal*, **121**, 724 (1974).
207. R. E. McCullough, 10th Ann Proc. Reliab. Phys., pp. 19-22 (1972).
208. B. A. McDonald, *Solid-State Electron.*, **14**, 17 (1971).
209. W. McQuitty and C. R. Lively, *Electronic Pkg. Prod.*, **11**, No. 11, 112 (November 1971).
210. P. B. Mee, *Honeywell Computer Journal*, **5**, 115 (1971).
211. R. L. Meek, *This Journal*, **120**, 308 (1973).
212. R. L. Meek and R. H. Braun, *ibid.*, **119**, 1538 (1972).
213. R. L. Meek, T. M. Buck, and C. F. Gibbon, *ibid.*, **120**, 1241 (1973).
214. S. Merrin, *EDN*, **15**, No. 23, 35 (December 1, 1970).
215. E. D. Metz, *Proc. IEEE*, **57**, 1606 (1969).
216. J. T. Milek, "Silicon Nitride for Microelectronic Applications, Part 1, Preparation and Properties," p. 1-118, IFI/Plenum, New York (1971).
217. K. Miwa, M. Kanno, S. Kawashima, S. Kawamura, and T. Shibuya, *Denki Kagaku*, **40**, 478 (1972).
218. J. P. Mize, U. S. Pat. 3,689,243 (1972).
219. R. A. Moline and G. W. Reutlinger, *IEEE Trans. Electron Devices*, **ED-20**, 1129 (1973).
220. F. Montillo and P. Balk, *This Journal*, **118**, 1463 (1971).
221. W. J. Morrissey, U.S. Pat. 3,752,701 (1973).
222. C. T. Naber, *This Journal*, **119**, 301C, (1972).
223. N. Nagasima, *J. Appl. Phys.*, **43**, 3378 (1972).
224. N. Nagasima and H. Enari, *Jap. J. Appl. Phys.*, **10**, 441 (1971).
225. N. Nagasima, H. Suzuki, K. Tanaka, and S. Nishida, *This Journal*, **121**, 434 (1974).
226. E. H. Nicollian, *J. Vacuum Sci. Technol.*, **8**, S39 (1971).
227. E. H. Nicollian, 12th Ann. Proc. Reliab. Phys., pp. 267-272 (1974).
228. R. W. Nufer and L. C. Anderson, *Solid State Technol.*, **14**, No. 8, 33 (1971).
229. T. Ohtsuki, O. Shintaku, and H. Fukuwatari, Abstract 156, p. 400, The Electrochemical Society Extended Abstracts, Fall Meeting, Boston, Massachusetts, Oct 7-11, 1973.
230. R. C. Olberg, *This Journal*, **118**, 129 (1971).
231. C. M. Osburn, *ibid.*, **121**, 809 (1974).
232. C. M. Osburn and N. J. Chou, *ibid.*, **120**, 1377 (1973).
233. C. M. Osburn and S. I. Raider, *ibid.*, **120**, 1369 (1973).
234. W. M. Paulson, 11th Ann. Proc. Reliab. Phys., pp. 61-68 (1973).
235. W. M. Paulson and R. W. Kirk, 12th Ann. Proc. Reliab. Phys., pp. 172-179 (1974).
236. C. G. Peattie, J. D. Adams, S. L. Carrell, T. D. George, and M. H. Valek, *Proc. IEEE*, **62**, 149 (1974).
237. D. S. Peck, 8th Ann. Proc. Reliab. Phys., pp. 81-93 (1970).
238. D. S. Peck and C. H. Zierdt, Jr., 11th Ann. Proc. Reliab. Phys., pp. 146-152 (1973).
239. D. S. Peck and C. H. Zierdt, Jr., *Proc. IEEE*, **62**, 185 (1974).
240. J. A. Perri, *Solid State Technol.*, **8**, No. 5, 19 (1965).
241. J. A. Perri and J. Riseman, U.S. Pat. 3,247,428 (1966).
242. J. A. Perri and J. Riseman, *Electronics*, **39**, No. 20, 108 (October 3, 1966).
243. J. A. Perri and J. Riseman, U.S. Pat. 3,546,013 (1970).
244. J. A. Perri, J. Riseman, and R. L. Ruggles, Jr., U.S. Pat. 3,300,339 (1967).
245. A. J. Pikor, Abstract 34, p. 96, The Electrochemical Society Extended Abstracts, Spring Meeting, San Francisco, California, May 12-17, 1974.
246. F. X. Pink and V. Lyn, *Electrochem. Technology*, **6**, 258 (1968).
247. W. A. Pliskin, in "Semiconductor Silicon 1973," H. R. Huff and R. R. Burgess, Editors, pp. 506-509, The Electrochemical Society Softbound Symposium Series, Princeton, N. J. (1973).
248. W. A. Pliskin and E. E. Conrad, *Electrochem. Technol.*, **2**, 196 (1964).
249. W. A. Pliskin and E. E. Conrad, U.S. Pat. 3,212,921 (1965).
250. W. A. Pliskin and E. E. Conrad, U.S. Pat. 3,212,929 (1965).
251. W. A. Pliskin, P. H. Davidse, H. S. Lehman, and L. I. Maissel, *IBM J. Res. Develop.*, **11**, 461 (1967).
252. M. Pourbaix, "Lectures on Electrochemical Corrosion," translated by J. A. S. Green, pp. 145-146, 165-171, Plenum Press, New York (1973).
253. K. Prabripataloong and M. R. Piggott, *This Journal*, **121**, 430 (1974).
254. I. J. Pugacz-Muraszkiewicz, *IBM J. Res. Develop.*, **16**, 523 (1972).
255. T. H. Ramsey, Jr., *Solid State Technol.*, **17**, No. 9, 51 (September 1974).
256. B. Reich and E. B. Hakim, 10th Ann. Proc. Reliab. Phys., pp. 82-87 (1972).
257. B. Reich and E. B. Hakim, Proc. 1974 Ann. Reliab. and Maint. Symp., pp. 396-402 (January 1974).
258. A. R. Reinberg, Abstract 6, p. 19, The Electrochemical Society Extended Abstracts, Spring Meeting, San Francisco, California, May 12-17, 1974.
259. A. G. Revesz and K. H. Zaininger, *RCA Rev.*, **29**, 22 (1968).
260. P. H. Robinson and F. P. Heiman, *This Journal*, **118**, 141 (1971).
261. R. S. Ronen and P. H. Robinson, *ibid.*, **119**, 747 (1972).
262. J. C. Sarace, R. E. Kerwin, D. L. Klein, and R. Edwards, *Solid-State Electron.*, **11**, 653 (1968).
263. T. Satake, K. Yokoyama, S. Shirakawa, and K. Sawaguchi, *Jap. J. Appl. Phys.*, **12**, 518 (1973).
264. K. Sato, *This Journal*, **117**, 1065 (1970).
265. J. Sato, Y. Ban, and K. Maeda, 9th Ann. Proc. Rel. Phys., pp. 96-106 (1971).
266. K. Sato, Y. Nishi, and T. Abe, in "Thin Film Dielectrics," F. Vratny, Editor, pp. 378-406, The Electrochemical Society Softbound Symposium Series, New York (1969).
267. P. M. Schaible and R. Glang, in "Thin Film Dielectrics," F. Vratny, Editor, pp. 577-594, The Electrochemical Society Softbound Symposium Series, New York (1969).
268. R. J. Scheuerman, in "Thin Film Dielectrics," F. Vratny, Editor, pp. 561-576, The Electrochemical Society Softbound Symposium Series, New York (1969).
269. M. M. Schlacter, E. S. Schlegel, R. S. Keen, R. A. Lathlaen, and G. L. Schnable, *IEEE Trans. Electron Devices*, **ED-17**, 1077 (1970).
270. E. S. Schlegel, *ibid.*, **ED-14**, 728 (1967).

271. E. S. Schlegel, *ibid.*, **ED-15**, 951 (1968).
272. E. S. Schlegel, "A Categorized MIS Bibliography," Philco-Ford Corp., Blue Bell, Pa. (1971).
273. E. S. Schlegel, R. S. Keen, and G. L. Schnable, 8th Ann. Proc. Reliab. Phys., pp. 9-16 (1971).
274. E. S. Schlegel and G. L. Schnable, *IEEE Trans. Electron Devices*, **ED-16**, 386 (1969).
275. G. L. Schnable, IEEE '71 Intern. Conv. Digest, pp. 586-587 (1971).
276. G. L. Schnable, H. J. Ewald, and E. S. Schlegel, *IEEE Trans. Reliability*, **R-21**, 12 (1972).
277. G. L. Schnable and R. S. Keen, *Proc. IEEE*, **57**, 1570 (1969).
278. G. L. Schnable and R. S. Keen, in "Advances in Electronics and Electron Physics," Vol. 30, L. Marton, Editor, pp. 79-138 Academic Press, New York (1971).
279. G. H. Schneer, W. van Gelder, V. E. Hauser, and P. F. Schmidt, *IEEE Trans. Electron Devices*, **ED-15**, 290 (1968).
280. W. Schroen, 11th Ann. Proc. Reliab. Phys., pp. 117-123 (1973).
281. W. H. Schroen, J. G. Aiken, and G. A. Brown, 10th Ann. Proc. Reliab. Phys., pp. 42-48 (1972).
282. R. O. Schwenker, *This Journal*, **118**, 313 (1971).
283. G. S. Sheldon, U. S. Pat. 3,642,597 (1972).
284. G. S. Sheldon, U. S. Pat. 3,644,801 (1972).
285. G. S. Sheldon, U.S. Pat. 3,735,483 (1973).
286. M. Shibata and K. Sugawara, *This Journal*, **122**, 155 (1975).
287. M. Shibata, T. Yoshimi, and K. Sugawara, *ibid.*, **122**, 157 (1975).
288. A. Shumka and R. R. Piety, Paper No. 3.1 presented at the Intl. Reliab. Phys. Symp., Las Vegas, Nevada, April 2, 1975.
289. R. Silverman, *This Journal*, **115**, 674 (1968).
290. B. R. Singh, *J. Phys. D: Appl. Phys.*, **7**, 443 (1974).
291. F. N. Sinnadurai, *Microelectron. Reliab.*, **13**, 23 (1974).
292. J. N. Smith, S. Thomas, and K. Ritchie, *This Journal*, **121**, 827 (1974).
293. E. H. Snow and B. E. Deal, *ibid.*, **113**, 263 (1966).
294. E. H. Snow and B. E. Deal, *Trans. Met. Soc. AIME*, **242**, 521 (1968).
295. E. H. Snow and M. E. Dumesnil, *J. Appl. Phys.*, **37**, 2123 (1966).
296. E. H. Snow, A. S. Grove, B. E. Deal, and C. T. Sah, *ibid.*, **36**, 1664 (1965).
297. S. M. Spitzer and S. Schwartz, *IEEE Trans. Electron Devices*, **ED-16**, 348 (1969).
298. R. S. Spriggs and A. H. Cronshagen, 10th Ann. Proc. Reliab. Phys., pp. 201-203 (1972).
299. J. D. Stansbury, *IEEE Trans. Electron Devices*, **ED-20**, 473 (1973).
300. R. L. Stewart and G. R. Neff, Proc. 1971 Semicond. IC Proc. and Prod. Conf., pp. 48-56, Ind. and Sci. Conf. Mtg., Chicago, Ill. (1971); *Evaluation Engineering*, **10**, No. 2, 32, (March/April 1971).
301. K. Strater, *RCA Rev.*, **29**, 618 (1968).
302. H. Sunami, Y. Itoh, and K. Sato, *J. Appl. Phys.*, **41**, 5115 (1970).
303. H. Sunami, Y. Itoh, and K. Sato, Proc. 2nd Conf. Sol. St. Dev., Tokyo, 1970, Suppl. to *J. Jap. Soc. Appl. Phys.*, **40**, 67 (1971).
304. R. E. Sundius, 10th Ann. Proc. Reliab. Phys., pp. 102-104 (1972).
305. B. Swaroop, in "Thin Film Dielectrics," F. Vratny, Editor, pp. 407-431, The Electrochemical Society Softbound Symposium Series, New York (1969).
306. B. Swaroop, *This Journal*, **118**, 913 (1971).
307. B. Swaroop, *IEEE Trans. Pts., Hybrids Pkg., PHP-9*, 234 (1973).
308. J. R. Szedon, *ibid.*, **PHP-10**, 251 (1974).
309. J. R. Szedon and R. M. Handy, *J. Vacuum Sci. Technol.*, **6**, 1 (1969).
310. J. R. Szedon and J. P. Stelmak, *IEEE Trans. Elec. Insulation*, **EI-5**, 3 (1970).
311. J. R. Szedon, T. A. Temofonte, J. A. Jackson, and D. C. Philips, *J. Vacuum Sci. Technol.* **10**, 284 (1973).
312. E. A. Taft, *This Journal*, **118**, 1985 (1974).
313. E. G. Tefft, U.S. Pat. 3,639,975 (1972).
314. T. A. Temofonte and J. R. Szedon, 9th Ann. Proc. Reliab. Phys., pp. 107-113 (1971).
315. A. S. Tenney, *This Journal*, **118**, 1658 (1971).
316. A. S. Tenney and M. Ghezze, *ibid.*, **120**, 1091 (1973).
317. A. S. Tenney and M. Ghezze, *ibid.*, **120**, 1276 (1973).
318. L. Terry, Abstract 228, p. 533, The Electrochemical Society Extended Abstracts, Spring Meeting, San Francisco, California, May 12-17, 1974.
319. R. W. Thomas, Proc. Govt. Microcirc. Appl. Conf. (GOMAC), pp. 31-36, October 1972.
320. R. W. Thomas and D. E. Meyer, *Solid State Technol.* **17**, No. 9, 56 (September 1974).
321. T. Tokuyama, T. Miyazaki, and M. Horiuchi, in "Thin Film Dielectrics," F. Vratny, Editor, pp. 297-326, The Electrochemical Society Softbound Symposium Series, New York (1969).
322. N. C. Tombs, H. A. R. Wegener, R. Newman, B. T. Kenney, and A. J. Coppola, *Proc. IEEE*, **54**, 87 (1966).
323. P. A. Totta, Proc. 1971 Electronic Components Conf., pp. 275-284 (IEEE 71C7-PMP) (May 1971).
324. P. A. Totta, 11th Ann. Proc. Reliab. Phys., p. 92 (1973).
325. P. A. Totta and R. P. Sopher, *IBM J. Res. Develop.*, **13**, 226 (1969).
326. T. Tsujide, S. Nakanuma, and Y. Ikushima, *This Journal*, **117**, 703 (1970).
327. B. R. Tuft, U.S. Pat. 3,643,136 (1972).
328. S. K. Tung and R. E. Caffrey, *Trans. Met. Soc. AIME*, **233**, 572 (1965).
329. S. K. Tung and R. E. Caffrey, *This Journal*, **114**, 275C (1967).
330. S. K. Tung and R. E. Caffrey, in "Thin Film Dielectrics," F. Vratny, Editor, pp. 286-296, The Electrochemical Society Softbound Symposium Series, New York (1969).
331. M. N. Turetzky, J. B. Jenkins, and H. R. Fraser, Jr., *This Journal*, **121**, 1098 (1974).
332. J. Vaccaro, *Proc. IEEE*, **62**, 169 (1974).
333. H. W. van Beek, 10th Ann. Proc. Reliab. Phys., pp. 36-41 (1972).
334. Y. J. van der Meulen, *J. Vacuum Sci. Technol.*, **11**, 985 (1974).
335. Y. J. van der Meulen and J. G. Cahill, *J. Electronic Materials*, **3**, 371 (1974).
336. W. van Gelder and V. E. Hauser, *This Journal*, **114**, 869 (1967).
337. R. R. Verderber, G. A. Gruber, J. W. Ostroski, J. E. Johnson, K. S. Tarneja, D. M. Gillott, and B. J. Coverston, *IEEE Trans. Electron Devices*, **ED-17**, 797 (1970).
338. A. A. Viele, 12th Ann. Proc. Reliab. Phys., pp. 16-21 (1974).
339. J. L. Vossen, *J. Vacuum Sci. Technol.*, **8**, S12 (1971).
340. J. L. Vossen, G. L. Schnable, and W. Kern, *ibid.*, **11**, 60 (1974).
341. "Thin Film Dielectrics," F. Vratny, Editor, The Electrochemical Society Softbound Symposium Series, New York (1969).
342. R. K. Waits, *J. Vacuum Sci. Technol.*, **10**, 285 (1973).
343. C. H. Wang and W. T. Wakely, 18/1-1 to 18/1-3 in 1974 IEEE INTERCON Technical Program Papers, IEEE Cat. No. 74CHO898-7 (1974).
344. W. A. Westdorp and G. H. Schwuttke, in "Thin Film Dielectrics," F. Vratny, Editor, pp. 546-560, The Electrochemical Society Softbound Symposium Series, New York (1969).
345. M. L. White, *Proc. IEEE*, **57**, 1610 (1969).
346. R. Williams and M. H. Woods, *J. Appl. Phys.*, **43**, 4142 (1972).
347. V. D. Wohlheiter and R. A. Whitner, *This Journal* **119**, 945 (1972).
348. H. F. Wolf, in "Semiconductors," pp. 342-362, Wiley-Interscience, New York (1971).
349. M. H. Woods, 12th Ann. Proc. Reliab. Phys., pp. 259-266 (1974).
350. J. C. Wright, 11th Ann. Proc. Reliab. Phys., pp. 224-229 (1973).
351. Staff Article, "Fabrication Changes Soup Up Power Devices," *Electronics*, **44**, No. 10, 43 (May 10, 1971).
352. Staff Article, "Double Mesa is Key to Triac Chip Process," *ibid.*, **44**, No. 15, 28 (July 19, 1971).
353. See, for example, *IEEE Trans. Nuclear Science*, **NS-18**, No. 6 (December 1971); **NS-19**, No. 6 (December 1972), **NS-20**, No. 6 (December 1973); and **NS-21**, No. 6 (December 1974).

354. Staff Article, "Tailor-Made Glasses Can be Made Strong, Flexible, and Inert," *Product Engineering*, **43**, No. 2 (February 1972).
355. Staff Article, "Westinghouse Speeds High-Power Device," *Electronics*, **45**, No. 4, 41 (February 14, 1972).
356. Staff Article, "Diode Chips are Glass Passivated," *ibid.*, **46**, No. 2, 207 (January 18, 1973).
357. Staff Article, "GI Pushes High-Voltage Technology," *ibid.*, **46**, No. 21, p. 36 (October 11, 1973).
358. Staff Article, "How Phosphorus Abets IC Destruction," *ibid.*, **47**, No. 8, 34 (April 18, 1974).
359. Staff Article, "Defective ICs Halted Philco TV Output," *Electronic News*, p. 34 (May 20, 1974).
360. Staff Article, "Vapor Deposition Unit is Modular," *Electronics*, **47**, No. 18, p. 138 (September 5, 1974).
361. Y. T. Yeow, J. W. Clancy, and D. R. Lamb. *Int. J. Electronics*, **34**, 115 (1973).
362. K. H. Zaininger and F. P. Heiman, *Solid State Technol.*, **13**, No. 5, p. 49, and No. 6, 46 (1970).
363. D. S. Zoroglu and L. E. Clark, *IEEE Trans. Electron Devices*, **ED-19**, 4 (1972).

The Nucleation Reaction on Photosensitive TiO₂ Films

J. J. Kelly and J. K. Vondeling

Philips Research Laboratories, Eindhoven, The Netherlands

ABSTRACT

The nucleation reaction, which occurs when transparent TiO₂ films in contact with palladium ions are exposed to u.v. light, has been investigated. The nuclei, thus formed, may serve as catalytic centers for electroless deposition of various metals. The photographic procedure, which has a high light sensitivity, may be used for the photoselective plating of nonconducting substrates. It has been shown, by electron diffraction and ellipsometry, that metallic palladium is formed on the TiO₂ during exposure. The minimum number of palladium atoms required to initiate electroless metal deposition has been estimated.

Considerable interest exists for systems with which nonconducting substrates can be nucleated and then plated by means of electroless metal deposition. One such system involves a sensitization and activation procedure using stannous chloride and palladium chloride solutions, respectively. It was generally believed that metallic palladium is formed during the nucleation. Recent evidence (1, 2) has shown, however, that this is not always the case. The presence of metallic palladium is therefore not a necessary prerequisite for successful nucleation.

Titanium dioxide, coated from a dispersion as a thin film on various substrates, has been used as a light-sensitive compound for selective nucleation in the fields of printed circuitry (3) and photographic reproduction (4). For the former application the TiO₂ film is dipped in a silver or palladium salt solution, dried, and then exposed image-wise to u.v. light. The nuclei formed in the exposed areas of the film can be developed by electroless deposition to yield a visible metallic image. For photographic reproduction (4) the oxide film is activated in silver nitrate solution after exposure, and the nuclei are developed by silver deposition.

The use of a palladium salt instead of a silver salt as the sensitizing agent presents a more attractive system for electronic applications, since nuclei formed by exposure can be developed, not only with silver, but also with other metals, e.g., copper, nickel, cobalt, and gold (3).

The photocatalytic reaction on TiO₂ has been explained by a number of workers (5-9) in terms of a semiconductor model involving photoexcited electrons and holes. Electrons trapped at surface sites act as reducing centers for metal ions.

Photosensitive TiO₂ films have also been made by pyrolysis of various titanium compounds (10, 11). In this paper we describe an investigation of the photoselective nucleation reaction, occurring on transparent TiO₂ films formed on glass by pyrolysis of titanium acetylacetonate. We considered various techniques for studying the nucleation reaction. The nuclei produced during exposure could not be directly

observed by electron microscopy. The amount of product formed by u.v. exposure of dried PdCl₂-sensitized films was very small. Radioactive tracer analysis is sufficiently sensitive to study the total amount of palladium on the surface but it does not distinguish between the different forms of palladium, metallic or otherwise, which may be present. In order to increase the amount of reaction product we exposed TiO₂ films in palladium salt solutions and used electron diffraction, optical absorption, spectrophotometric analysis, and ellipsometry to study the product formed.

It has been shown (1, 12) that ellipsometric measurements can be used to detect the presence of very thin films on substrates. A clean substrate is characterized by the ellipsometric parameters Δ and ψ , which are determined by the optical constants (i.e., extinction coefficient and refractive index) of the material. Formation of an adsorbed film on the substrate generally leads to changes, $\delta\Delta$ and $\delta\psi$, in these parameters. The magnitude of these changes depends on the optical constants of the film and on its thickness. For very thin films ($\leq 10\text{\AA}$) $\delta\psi$ is directly proportional to the extinction coefficient (1). This means that a film with low extinction coefficient at the measuring wavelength has an effect in $\delta\Delta$ only, whereas a film with a high extinction coefficient involves changes in both Δ and ψ . Since metallic palladium films have a stronger optical absorption at 632 nm than palladium salts (1) we hoped to be able to use the ellipsometric technique to distinguish between metallic and nonmetallic product and to get a semiquantitative estimate of the film thickness.

In the first part of the paper we describe the photographic properties of the TiO₂/PdCl₂ system with special reference to the use of transparent TiO₂ films for photoselective metal deposition. Various techniques were then used to study the nature and the extent of the photonucleation reaction. From the results of these studies an estimate was made of the minimum number of palladium atoms required to initiate electroless deposition.

The mechanism of the primary photocatalytic reaction on these layers has been discussed elsewhere by Möllers *et al.* (9).

Table I. Solutions used for image formation on TiO₂ films

		Sensitization	
A.	PdCl ₂ 5.6 × 10 ⁻³ mol/liter HCl 1.2 × 10 ⁻¹ mol/liter Tensagex DP-24 0.4% (weight) aqueous solution	B.	PdCl ₂ 5.6 × 10 ⁻³ mol/liter HCl 1.2 × 10 ⁻¹ mol/liter CH ₃ OH 80% (Vol) H ₂ O
		Development	
Silver	49 ml solution (i) +	{ 0.1 mol/liter metol ^a 0.1 mol/liter citric acid 2.5 mol/liter AgNO ₃ 0.28 mol/liter CuSO ₄ ·5H ₂ O 0.30 mol/liter Na ₄ EDTA 0.65 mol/liter NaOH 35% formaldehyde	
	1 ml solution (ii)		
Copper	42 ml solution (iii) +		
	8 ml solution (iv)		
Nickel		D.	NiSO ₄ ·6H ₂ O 2.7 × 10 ⁻² mol/liter Na ₂ P ₂ O ₇ ·10H ₂ O 7.8 × 10 ⁻² mol/liter NaH ₂ PO ₂ ·H ₂ O 1.1 × 10 ⁻¹ mol/liter pH = 9.15, temp. 50°C
C.	NiCl ₂ ·6H ₂ O 1.3 × 10 ⁻¹ mol/liter NaH ₂ PO ₂ ·H ₂ O 9.4 × 10 ⁻² mol/liter NH ₂ CH ₂ COOH 4.0 × 10 ⁻¹ mol/liter pH = 3.8, temp. 95°C		

^a Metol is methyl-p-aminophenol sulfate.

Experimental

Titanium dioxide films.—Light-sensitive TiO₂ films were prepared on glass by pyrolysis of titanium acetylacetonate (TAA), supplied by Dynamit Nobel (Muhlheim, West Germany) as a 50% solution in isopropanol. For the photographic experiments a mixture containing 20g TAA solution and 80g diacetonealcohol was applied to Pyrex plates by whirl-coating at 1500-3000 rpm. Thin quartz plates lifted from a 12.5% TAA solution in isopropanol were used for the rate experiments. In both cases the layer was pyrolyzed in air at 500°C. The thickness of the resulting TiO₂ film was approximately 50 nm for the whirl-coated and 38 nm for the lifted samples. Electron and x-ray diffraction data for the TiO₂ films on Pyrex indicated the presence of polycrystalline anatase. The films were optically transparent in the visible spectral region but absorbed appreciably at wavelengths below 350 nm.

Rate of the photoreaction.—Kinetic runs were performed at 25°C and virtually constant palladium salt concentrations. The TiO₂ film in contact with the solution in a quartz cuvette was exposed through the quartz substrate to light from a filtered mercury lamp (Philips HPK lamp; λ > 280 nm). The increase in absorption of the film at wavelengths greater than 500 nm due to product formation could be measured continuously during exposure by means of a Philips 90 AV photocell and filter system. The extent of the photoreaction was measured by dissolving the product film in nitric acid and determining the palladium spectrophotometrically using p-nitrosodimethylaniline (13). For the quantum efficiency measurements monochromatic light from a Bausch and Lomb grating monochromator was used instead of the HPK lamp. The output of the monochromator was calibrated using ferrioxalate actinometry (14).

Ellipsometric measurements.—The ellipsometer and the measuring cell have been described elsewhere (1). The TiO₂ film was mounted rigidly at the center of the cell. The cell was provided with quartz windows and a water-jacket through which water from a thermostat could be circulated to maintain a constant cell temperature (25° ± 0.1°C). A helium-neon laser (λ = 632.8 nm) was used for making the ellipsometric measurements. The angle of incidence was 47°.

A HPK lamp together with a shutter arrangement was used to irradiate both the TiO₂ films in palladium salt solutions and the dried PdCl₂-sensitized films.

Results

Photographic image formation on TiO₂ films.—The procedure used for photoselective metal deposition on TiO₂ films consisted of four steps: sensitization, nucleation, fog inhibition, and development.

The TiO₂ film was sensitized by introducing a palladium salt onto its surface. For this purpose the film

was lifted from a solution of the metal salt (cf. Table I) at a controlled rate and dried superficially during lifting by warm air or IR radiation. Tensagex DP-24, a sodium alkylphenolpolyglycolether sulfate supplied by Labaz Holland N. V. (the Hague, the Netherlands) was used as a wetting agent in the aqueous solution A. The PdCl₂-sensitized TiO₂ film was then exposed through a mask to a high pressure mercury lamp (Philips HPR 125W) or to monochromatic light. In the exposed areas the film became activated due to the formation of nuclei.

In the nonexposed areas, metal ions remained on the surface of the oxide, even after thorough rinsing with water. A radiotracer study using Pd¹⁰⁹Cl₂ showed that a TiO₂ film sensitized with solution A, contained 0.03 μg Pd/cm² (approximately 1.7 × 10¹⁴ palladium ions/cm²) after rinsing with water. The presence of palladium salt, in certain cases, caused fogging during development since bivalent palladium could be reduced by the reducing agent of the electroless solution, giving rise to nucleation centers. Solutions containing strong complexing agents for bivalent palladium were effective in drastically reducing the amount of adsorbed metal salt. Satisfactory results were obtained with aminoacetic acid (0.4 mol/liter) and triethanolamine (1.0 mol/liter). Tensagex solution (1-2%) also considerably reduced the amount of palladium salt present on TiO₂ and therefore could be used as an efficient antifogging agent.

The nuclei produced by exposure were developed by electroless deposition of silver, copper, and nickel, with the solutions listed in Table I. Nickel patterns containing 5-10 μm details were made using solutions A and C of Table I.

The photographic sensitivity of the system was measured by exposing the PdCl₂-sensitized films to monochromatic light (λ = 300 nm). Values for E_m, the minimum exposure required to initiate electroless deposition, and for D, (= log I₀/I) the density of the developed image after various development times, are given in Table II for Ni and Ag deposition. The sen-

Table II. Photographic sensitivity of TiO₂ films

Nuclei	Development	D ^c	E _m (μJ/cm ²)
Pd (λ = 300 nm)	Ni ^a	1 min	2.1
	Ni ^a	2 min	4.7
	Ag ^b	½ min	2.0
	Ag ^b	1 min	4.3
High resolution silver halide λ = 436 nm			240

^a Using sensitizing solution A and nickel solution C.

^b Using sensitizing solution A.

^c D is the optical density = log I₀/I measured after a given development time.



Fig. 1. A 60 kV RHEED pattern of the product film formed on TiO_2 during exposure in sensitizing solution A.

sitivity of this $\text{PdCl}_2/\text{TiO}_2$ system at 300 nm is comparable to that of high resolution silver halide emulsions at 436 nm (15).

Light of wavelengths less than 350 nm was effective in producing developable nuclei on these TiO_2 films. In agreement with the optical absorption spectrum of the films, photographic sensitivity was found to increase as the wavelength decreased from 350 to 290 nm.

Exposure of TiO_2 films in PdCl_2 solution.—As a result of u.v. exposure of TiO_2 films in palladium salt solutions a product layer was formed on the surface of the oxide. For all the cases studied, reflection high energy electron diffraction (RHEED) measurements gave the same diffraction pattern, as shown in Fig. 1. This pattern is characteristic of a polycrystalline fcc lattice. The lattice parameters derived from Fig. 1 are given in Table III and are in agreement with the published values for metallic palladium. The oxide film acted as a light-sensitive catalyst for the formation of polycrystalline palladium (9).

The light reaction was followed discontinuously by determining the palladium product spectrophotometrically as a function of exposure time. The same TiO_2 film could be used many times for the photocatalytic reduction without loss of sensitivity. The reaction could also be followed continuously by measuring the increase in absorption of the quartz/ TiO_2 film at $\lambda > 500$ nm as a function of exposure time. The optical density of the palladium product film was directly proportional to the amount of metal present on the TiO_2 .

The rate of reduction of palladium ions from a solution containing 5.6×10^{-3} mol/liter PdCl_2 and 0.12 mol/liter HCl was relatively low (Fig. 2, curve a). Compounds which are known to undergo photocatalytic oxidation on illuminated n-type oxide semiconductors (16-18) gave a considerable increase in the rate of palladium deposition, indicating the importance of the oxidation process. Results are shown in Fig. 2 for additions of methanol, ethanol, and 1-propanol (all 80% by volume). Optimum concentrations of the additives were not determined. We found that Tensagex

Table III. Lattice parameters in Å corresponding to Fig. 1

hkl	Values for Pd metal ^a	Experimental values
111	2.246	2.24
200	1.945	1.95
220	1.376	1.38
311	1.173	1.17
222	1.123	1.13
400	0.972	0.97
331	0.892	0.89
420	0.870	0.87

^a Values from Swanson and Tatge NBS Circular 539, Vol. 1, 21 (1953).

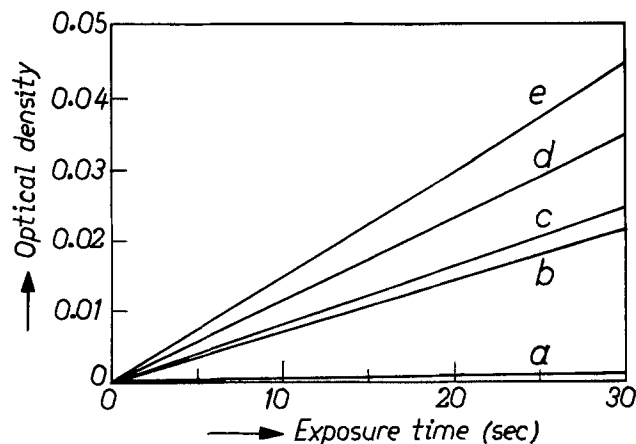


Fig. 2. The effect of certain additives, to a solution containing 5.6×10^{-3} mol/liter PdCl_2 , 1.2×10^{-1} mol/liter HCl, on the relative rate of palladium deposition. The increase in optical density of the product film is plotted as a function of exposure time for the solution containing (a) no additive, (b) 1-propanol (80% vol), (c) ethanol (80% vol), (d) Tensagex DP-24 (0.4% weight), (e) methanol (80% vol).

also markedly increased the rate of formation of palladium on exposed TiO_2 (Fig. 2, curve d).

The quantum efficiency Q , defined as the number of palladium atoms produced per photon, was measured by exposing TiO_2 films to monochromatic light ($\lambda = 300$ nm) in the two sensitizing solutions given in Table I. At the light intensities studied ($\leq 3 \times 10^{16}$ photons/cm² min), Q was independent of intensity. For the methanolic solution B, Q varied between 0.1 and 0.3, and for solution A values between 0.05 and 0.15 were found. The quantum efficiency for the corresponding PdCl_2 -HCl solution without additives was at least a factor of 30 lower.

In Fig. 3 the changes in the ellipsometric parameters, Δ and ψ , as a function of exposure time are plotted for a TiO_2 film exposed in a solution containing 1.4×10^{-4} mol/liter PdCl_2 and 3.3×10^{-3} mol/liter HCl. For these experiments a diluted PdCl_2 solution without additive had to be used because light absorption by the usual sensitizing solutions at the exposure wavelength (~ 300 nm) was too great. Exposure led to a decrease in Δ and an increase in ψ . For palladium film thickness $\geq 10\text{Å}$ the metal could be determined spectrophotometrically. In this region a linear relationship between film thickness and $\delta\Delta$ was observed. A palladium film with an average thickness of 10Å gave changes in Δ and ψ of approximately 20° and 4.5° , respectively. The magnitude of these changes is consistent with the formation of a metallic film on the oxide (1).

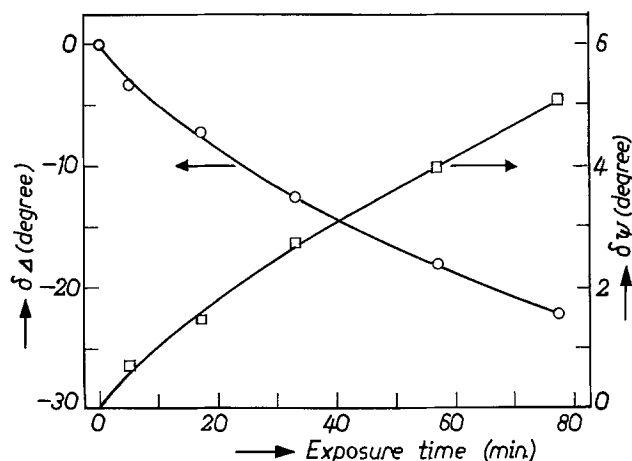


Fig. 3. Changes in the ellipsometric parameters of a TiO_2 film, due to exposure in a solution containing 1.4×10^{-4} mol/liter PdCl_2 , 3.3×10^{-3} mol/liter HCl, as a function of exposure time.

Exposure of PdCl₂-sensitized TiO₂ films.—For the ellipsometric measurements using dried PdCl₂-sensitized films, the two sensitizing solutions shown in Table I were used. The TiO₂/glass film was mounted in the cell containing deionized water and the ellipsometric measurements were made. The water was then replaced by a PdCl₂-sensitizing solution. After 5 min this solution was removed and the oxide film was rinsed by filling and emptying the cell 5 times with water. The changes in Δ and ψ caused by irreversible adsorption in the dark of palladium species from the sensitizing solution were measured in water.

The cell was then refilled with the same PdCl₂ solution for 5 min and, when this solution had been removed, the film was dried using compressed air and exposed in the dried sensitized state to u.v. light. The exposed film was then rinsed 5 times with deionized water and the ellipsometric measurements were again performed with water in the cell.

In both cases adsorption of PdCl₂ species in the dark gave only very slight negative changes in ψ as shown in Table IV. Exposure of the dried sensitized films caused substantial changes in both Δ and ψ with Δ decreasing and ψ increasing as a function of exposure time. The direction of the changes in these parameters was the same as found for experiments involving exposure in solution (Fig. 3). These results, especially the considerable increases in ψ , indicated that metallic films are also formed on dried sensitized films.

Activity of nuclei for Ni deposition.—We observed certain anomalies concerning electroless Ni deposition on nuclei formed by exposure of PdCl₂-sensitized TiO₂ films. Nuclei obtained using sensitizing solution A could be developed with Ni, Ag, and Cu. However, when sensitizing solution B was used, the nuclei formed during exposure could be developed with Ag or Cu but not with Ni. Aqueous PdCl₂/HCl and Pd(NO₃)₂/HNO₃ solutions without Tensagex also gave "Ni-inactive" palladium nuclei.

When the TiO₂ film sensitized using solution A was overexposed to u.v. light, the activity of the nuclei for electroless Ni deposition was destroyed. Thus when a sensitized TiO₂ film was exposed at 300 nm at a light intensity of 6×10^{16} photons/cm² min, a threshold exposure as reported in Table II was found. However, on increasing the exposure by a factor of 100 at the same intensity the nuclei became inactive for Ni deposition, while remaining active for Ag and Cu deposition.

Discussion

Exposure of TiO₂ films in palladium salt solutions led to the formation of polycrystalline metallic films on the oxide. The presence of metallic nuclei after exposure of dried PdCl₂-sensitized films was shown by ellipsometry. It seems likely therefore that the catalytic nuclei for electroless deposition consist of metallic palladium particles. By assuming that the quantum efficiency for the initial stages of exposure of the PdCl₂-sensitized TiO₂ film does not differ seriously from the value found experimentally for exposure of TiO₂ in PdCl₂ solution, an estimate can be made of the minimum palladium coverage required for electroless

deposition. The product of the minimum exposure (Table II) and the quantum efficiency, measured using the same exposure system, gives an indication of the minimum number of atoms required. Results are shown in Table V. If we assume that the palladium is distributed as atoms which each occupy 10Å² of the surface, then these values range from 8×10^{-3} of a monolayer for Ag deposition to 3.2×10^{-2} of a monolayer for Ni deposition. This suggests that very low palladium coverages are sufficient to catalyze electroless deposition.

The ellipsometric measurements indicate that this order of magnitude is correct. Thirty seconds exposure of the film sensitized using solution A gave a change in Δ of -0.8° (Table IV). This corresponds to approximately 0.1 of a monolayer. The exposure time required for Ag development with this system was 1 sec. Assuming a linear increase in palladium coverage with exposure time in this range, this is equivalent to a surface coverage of approximately 3×10^{-3} of a monolayer.

Behrntdt (19) was able to achieve reproducible surface coverages of from 10^{-3} monolayers upwards of gold and silver on glass and TiO₂ substrates by controlled deposition using a rate-controlled evaporation source, a shutter arrangement, and a quartz crystal oscillator detector system. These films could be developed by Ag deposition. In this way it was possible to specify the number of silver or gold atoms necessary to give Ag development. There is a good similarity between their minimum Au and Ag coverages on TiO₂, given in Table V, and our estimated Pd coverages also shown in the same table. Hamilton and Logel (20) report that for electroless deposition of nickel, from a dimethylamineborane bath, on palladium nuclei evaporated onto amorphous carbon substrates, a coverage of 5×10^{14} atoms/cm² is required. Their work suggests that nuclei containing at least 4 palladium atoms are required for Ni deposition.

The results found in the present work do not explain why certain palladium nuclei were not catalytic for deposition of Ni from the solutions used here. The deactivation of "Ni-active" nuclei due to overexposure of the films with u.v. light is also not explained. Chow and co-workers (21) found an analogous effect with nuclei prepared by SnCl₂ sensitization, PdCl₂ activation of Formvar substrates. Freshly activated substrates were catalytic for Ni and Co deposition. For the activated films they found a diffuse electron diffraction pattern, difficult to attribute to any one symmetry. Recent investigations (1) have shown the absence of metallic palladium on activated glass substrates. Chow *et al.* found that 50 min irradiation of activated films caused the nuclei to become inactive for Ni and Co deposition while remaining active for Cu deposition. They observed an increase in the degree of crystallization of the activated film due to irradiation. They speculate that the increased crystallinity of the palladium may inhibit deposition of Ni and Co, which unlike Cu, give an initial glassy, noncrystalline structure.

Table IV. Changes in the ellipsometric parameters, Δ and ψ , of TiO₂ films as a result of PdCl₂ treatments

Solution	Treatment	$\delta\Delta$	$\delta\psi$
PdCl ₂ -sensitizing solution A	Not exposed	-0.22	-0.06
	Exposed ½ min ^a	-0.80	+0.16
	Exposed 1½ min ^a	-1.30	+0.30
PdCl ₂ -sensitizing solution B	Not exposed	-0.10	-0.02
	Exposed 1 min ^a	-0.74	+0.13

^a Exposed in the dry state.

Table V. Number of metal atoms on TiO₂ films required for electroless deposition

Nuclei	Development	Atoms/cm ^{2a}
Pd ^b	Ag	8×10^{14}
Pd ^c	Ag	1.6×10^{15}
Pd ^d	Ni	3.2×10^{15}
Au ^e	Ag	2×10^{15}
Ag ^e	Ag	1.2×10^{15}

^a These values have not been corrected for the surface roughness factor of the TiO₂ film, which in our case was shown by a BET measurement to be 3.7.

^b Using sensitizing solution A.

^c Using sensitizing solution B.

^d Using sensitizing solution A and nickel solution C.

^e From Ref. (19).

Conclusions

As a result of u.v. exposure of transparent TiO₂ films in the presence of various palladium salts, catalytic nuclei are formed. Such nuclei can be developed by electroless deposition of different metals. Electron diffraction and ellipsometric measurements have shown the light reaction product to be polycrystalline metallic palladium. Using the results of quantum efficiency and ellipsometric measurements, the minimum palladium coverages required for electroless Ag and Ni deposition were estimated. The values found ranged from 8×10^{-3} of a monolayer for Ag to 3×10^{-2} of a monolayer for Ni. Two factors contribute to the high photographic sensitivity (100-500 $\mu\text{J}/\text{cm}^2$) of the PdCl₂/TiO₂ film system: the quantum efficiency for the production of metallic palladium is relatively high, while the minimum palladium coverage required for electroless deposition is very low.

Acknowledgments

The authors wish to thank Dr. A. J. van Bommel, Dr. F. Meyer, and Mr. G. Loyen of this laboratory for their assistance with the RHEED and ellipsometric measurements. The authors are also grateful to Dr. C. J. G. F. Janssen of Philips Product Division Elcoma, Eindhoven and to Dr. R. Memming, Dr. F. Möllers, and Ing. H. J. Tolle of Philips Forschungslaboratorium, Hamburg for very useful discussions.

Manuscript submitted Jan. 17, 1975; revised manuscript received April 11, 1975.

Any discussion of this paper will appear in a Discussion Section to be published in the June 1976 JOURNAL. All discussions for the June 1976 Discussion Section should be submitted by Feb. 1, 1976.

Publication costs of this article were partially assisted by Philips Research Laboratories.

REFERENCES

1. C. H. de Minjer and P. F. J. v.d. Boom, *This Journal*, **120**, 1644 (1973).
2. N. Feldstein, M. Schlesinger, N. E. Hedgecock, and S. L. Chow, *ibid.*, **121**, 738 (1974).
3. a. H. Jonker, C.J.G.F. Janssen, C. J. Dippel, Th.P.G.W. Thijssens, and L. Postma, *Phot. Sci. Eng.*, **13**, 45 (1969).
b. C.J.G.F. Janssen, H. Jonker, and A. Molenaar, *Plating*, **58**, 42 (1971).
4. E. Berman, *Phot. Sci. Eng.*, **13**, 50 (1969).
5. W. C. Clark and A. G. Vondjidis, *Can. J. Phys.*, **46**, 1775 (1968).
6. P. Vohl, *Phot. Sci. Eng.*, **13**, 120 (1969).
7. R. R. Addiss and F. G. Wakim, *ibid.*, **13**, 111 (1969).
8. P. D. Fleischauer, H. K. Alan Kan, and J. R. Shepherd, *J. Am. Chem. Soc.*, **94**, 283 (1972).
9. F. Möllers, H. J. Tolle, and R. Memming, *This Journal*, **121**, 1160 (1974).
10. Itek Corporation, Brit. Pat. 1,138,858 (1969).
11. Philips, Brit. Pat. 1,370,584 (1974).
12. G. A. Bootsma and F. Meijer, *Surface Sci.*, **14**, 52 (1969).
13. E. B. Sandell, "Colorimetric Determination of Traces of Metals," p. 714, Interscience, New York (1959).
14. J. G. Calvert and J. N. Pitts Jr., "Photochemistry," pp. 783-786, John Wiley and Sons, Inc., New York (1966).
15. H. Jonker, L. K. H. van Beek, H. J. Houtman, F. T. Klostermann, and E. J. Spiertz, *J. Phot. Sci.*, **20**, 53 (1972).
16. W. P. Gomes, T. Freund, and S. R. Morrison, *This Journal*, **115**, 818 (1968).
17. H. Yoneyama, Y. Toyoguchi, and H. Tamura, *J. Phys. Chem.*, **76**, 3460 (1972).
18. J. Cunningham and H. Zainal, *ibid.*, **76**, 2362 (1972).
19. M. E. Behrndt, *J. Vacuum Sci. Technol.*, **8**, 724 (1972).
20. J. F. Hamilton and P. C. Logel, *J. Cat.*, **29**, 253 (1973).
21. S. L. Chow, N. E. Hedgecock, M. Schlesinger, and J. Rezek, *This Journal*, **119**, 1013 (1972).

Properties of Epitaxial GaAs Layers from a Triethyl Gallium and Arsine System

Yasuo Seki and Koetsu Tanno

Central Research Laboratories, Nippon Electric Company, Limited,
1753, Shimonumabe, Nakahara-ku, Kawasaki, Japan

and Kazuo Iida and Eiichi Ichiki

Light Metal Division, Kikumoto Works, Sumitomo Chemical Company, Limited,
Kikumoto-cho, Niihama, Ehime, Japan

ABSTRACT

GaAs epitaxial layers with low electron concentrations were obtained from an alkylgallium and arsine system by use of triethylgallium. The highest Hall mobility of the layer, with an electron concentration of $7.0 \times 10^{13}/\text{cm}^3$ at 77°K was 120,000 $\text{cm}^2/\text{V sec}$. Carrier concentration and carrier type of the layer could be changed in the range of from 10^{12} to $\sim 10^{16}/\text{cm}^3$ by changing the arsine to triethyl gallium mole ratio introduced into a deposition zone. This fact was expected to be due to the amphoteric impurity sharing between the arsenic and the gallium sites of GaAs crystal.

Although the extension of carrier concentration to the lower range resulted from impurity compensation, mobility data of the layers of electron concentrations higher than about $10^{14}/\text{cm}^3$ were almost the same as those from the usual $\text{AsCl}_3\text{-Ga-H}_2$ system. Dominant acceptor impurities observed in the photoluminescence measurements were discussed and were correlated with amphoteric silicon and carbon impurities. This was consistent with the result obtained on the impurities of the layer by mass spectroscopic analysis.

One of the most commonly used techniques for growing high purity GaAs epitaxial layers from vapor phase is one using the $\text{AsCl}_3\text{-Ga-H}_2$ system (1). Because of extensive efforts for growing high purity GaAs over the past several years (2-8), it is now possible to obtain GaAs with total ionized impurity concentration ($N_D + N_A$) in the $10^{13}/\text{cm}^3$ range (4). Although recent reports throw light on the preparation of high purity GaAs (5-8), the $\text{AsCl}_3\text{-Ga-H}_2$ system is rather complicated and somewhat unstable (9).

A system using alkylgallium and arsine, first reported by Manasevit (10), seems to have some advantage compared with the $\text{AsCl}_3\text{-Ga-H}_2$ system. This system required only one temperature zone, whose temperature is easily controlled inductively by r.f. power. Crystal growth takes place on the substrate on a heated pedestal in a quartz tube with a cool wall. The system does not contain reactive halogen. This seems to be an important factor to suppress impurity incorporation into the layer from the reactor system.

In spite of extensive experiments on the deposition of the layer by this method (11-15), total impurity ($N_D + N_A$) seems to be higher than $10^{16}/\text{cm}^3$ so far. Rai-Chaudhury (12) and Ito *et al.* (15) detected a large quantity of impurities in the layer, such as silicon, carbon, and others by the mass spectroscopic analysis. Shallow active impurities of the layer were examined by the photoluminescence measurement and were expected to be carbon and/or silicon which mainly come from the trimethylgallium source (15). These reports seemed to show that a high purity gallium source, whose silicon and carbon impurities are reduced, should be used to obtain a high purity GaAs layer. Lindeke *et al.* (16) used distilled gallium diethyl chloride as gallium source, but the electron Hall mobility data at 77°K showed that impurity concentration was nearly the same as that from the trimethylgallium source.

In this experiment, high purity triethylgallium (TEG) was used as gallium source in place of trimethylgallium (TMG), in order to reduce carbon con-

tamination. It has been pointed out that decomposition reaction of trimethyl compounds of metallic elements was accompanied with formation of carbide (17), whereas triethyl compound decomposed to pure metal through some alkyl-metal-hydrides and metal-hydride formation steps, in the case of aluminum alkyl compounds (18).

Although no experiment has been reported on gallium-carbide formation by trimethylgallium decomposition, the above experiments on aluminum compounds suggested that less carbide formation (less carbon incorporation) would be expected when TEG was used in place of TMG. Manasevit and Simpson (11) used TEG in their earlier experiment and determined the feasibility of obtaining a signal crystal on a germanium substrate. However few experiments on the electronic properties of a layer from a TEG source have been reported.

In this experiment, an epitaxial layer was deposited on a GaAs substrate by use of TEG and AsH_3 . Conduction type conversion, the Hall mobility, compensation ratio, and photoluminescence spectra of the layer are discussed.

Experimental

Epitaxial growth apparatus used in the experiments was a vertical one and almost the same as reported before (15). Gas mixing apparatus was made of a stainless steel tube, joints, and mass flow sensors. Air leak through joint fittings was eliminated as much as possible. Si- and Cr-doped GaAs wafers with (100) face were used as substrates. These were mechanically polished and then etched in a $3\text{H}_2\text{SO}_4\text{-H}_2\text{O}_2\text{-H}_2\text{O}$ solution. A quartz bubbler containing TEG was kept at 21°C during the growth. Vapor saturation rate of TEG through the bubbler was found to be over 95% in the experimental condition. Two TEG sources used,¹ TEG-2 and TEG-6, were chemical analysis grade and electronic grade, respectively. AsH_3 diluted to about 1% with a high purity argon,² 99.9999%, was used.

¹TEG sources are commercial products and were supplied by Sumitomo Chemical Company, Limited, Japan.

² AsH_3 was made by Phoenix Research Corporation, U.S.A., and was diluted to -1% with argon by Nihon Sanso Company, Limited, Japan.

Key words: crystal growth, chemical vapor deposition, silicon in GaAs, carbon in GaAs, high purity GaAs, GaAs Hall effect, GaAs mobility, GaAs photoluminescence.

Nominal purity of the original AsH_3 was 99.999% and this contained <1 ppm of O_2 , N_2 , CH_4 , and CO_2 as dominant impurities, respectively.

Flow rates of AsH_3 were varied in the ranges from 2×10^{-4} to 3.6×10^{-3} mole/min to a fixed TEG flow rate of 3×10^{-4} mole/min. An additional H_2 flow was added to keep the total gas flow rate constant (3000 cm^3/min).

Deposition temperature was 650°C . AsH_3 flow started when the substrate temperature reached about 500°C , prior to the introduction of TEG into the reactor, in order to prevent substrate decomposition. After the deposition was completed, the AsH_3 flow was continued until the substrate temperature had dropped to 500°C . Growth rate of the layer was about $0.2 \mu\text{m}/\text{min}$.

For electronic and optical measurements, layers $\geq 10 \mu\text{m}$ thick were used. Hall measurement of a layer deposited on Cr-doped semi-insulating substrate was carried out in a magnetic field of 6000G. The shell measurements and the C-V measurements using a palladium Schottky barrier gave the same carrier concentrations. Deviation of thickness homogeneity was about 10% throughout the layer with $\sim 5 \text{ cm}^2$ area. Carrier profile measurement using an impurity profile plotter (J.A.C. Electronic Limited, England, Model 366) showed flat profiles, independent of the layer thickness, and no anomaly at the epitaxial-substrate interface was observed.

Photoluminescence measurement of the layer was carried out at near liquid He temperatures by He-Ne laser beam excitation, using nearly the same method reported before (19). Monochromator resolution was 0.2 meV.

Results and Discussion

Effect of the arsine to triethylgallium mole ratio on carrier concentration.—Figure 1 shows the effect of the AsH_3 to TEG mole ratio ($[\text{As}]/[\text{Ga}]$ ratio) fed into the reactor during the growth on the carrier concentration for two TEG sources. All data were obtained by changing the AsH_3 flow rate to a fixed TEG flow rate of 3×10^{-4} mole/min. At low $[\text{As}]/[\text{Ga}]$ ratios, the layers show p-type conduction. Conduction type of the layer was changed from p- to n-type by increasing the $[\text{As}]/[\text{Ga}]$ ratio. Electron concentration of the layer was increased by further increasing of the $[\text{As}]/[\text{Ga}]$ ratio. The figure shows some changes in the maximum carrier level and in transition points, where n- to p-type conversion occurred, depending on the TEG source lots, TEG-2 and -6. These were not changed so much, though AsH_3 cylinders were changed. These changes, accompanied with TEG source change, are expected to be due to the difference in residual impurities of the sources. Shift of p- to n-type conversion point is assumed to be due to the fact that there is more column II acceptor in TEG-2 source or more column VI donor impurity in TEG-6 source.

Although there are some few difference in the result between two sources, as seen in Fig. 1, the main features, where carrier concentration change and p- to n-type conversion occurred by changing the $[\text{As}]/[\text{Ga}]$ ratio, are the same for the layers from two sources. The same $[\text{As}]/[\text{Ga}]$ ratio effect, even in the TMG- AsH_3 system, has been observed by Thorsen and Manasevit (14) for a heteroepitaxy case and by Ito *et al.* (5) for a homoepitaxy case. These results seem to show that the $[\text{As}]/[\text{Ga}]$ ratio is an essential factor in defining the properties of the GaAs layers from the alkylgallium and arsine system.

It has been said that compositional deviation from stoichiometry induces some defects in GaAs, which affect the electronic properties. The direct effects of defects were considered by Blanch *et al.* (20) and others (21-23) in which the conversion of n-type to p-type GaAs by heat-treatment was ascribed to such defects. Also, the effects in the vapor epitaxial growth were considered by Nakagawa and Ikoma (24), Okamoto and Sakata (25), and Ihara *et al.* (26), in which the carrier concentration change was ascribed to the

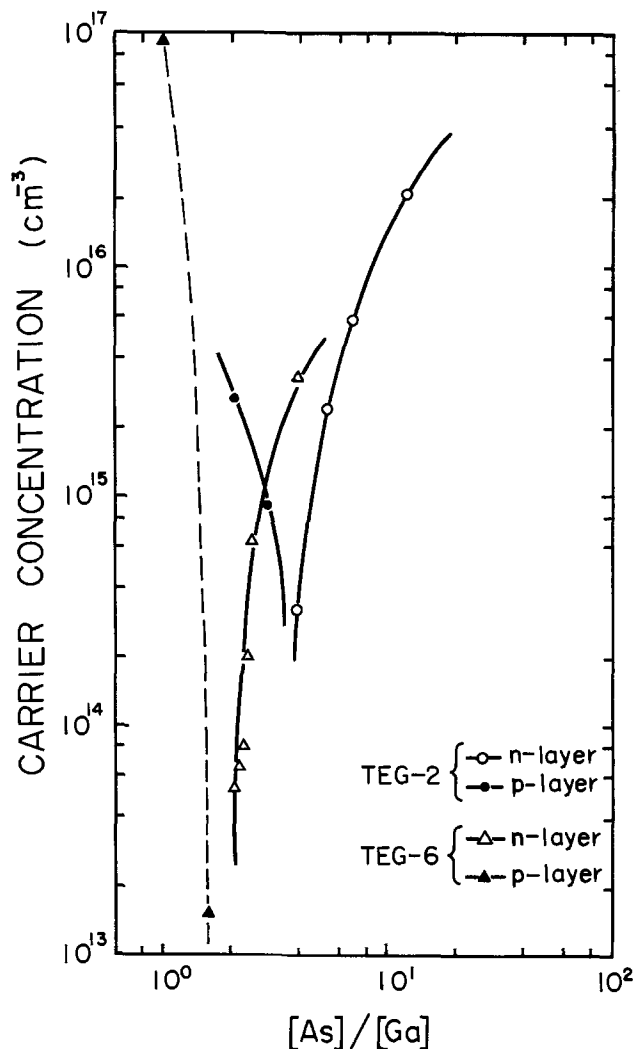


Fig. 1. Effect of the $[\text{As}]/[\text{Ga}]$ ratio on carrier concentration of the layer. TEG-2 source contained higher silicon impurity than TEG-6.

reaction between the amphoteric impurity and defects. Also, thermodynamic considerations were made by Logan and Hurle (27) for the case without impurity and by Kroger (28) and others (24, 26) for the case with impurity. It is assumed, also, for the alkylgallium and arsine system that the $[\text{As}]/[\text{Ga}]$ ratio change during the growth affects the stoichiometry which changes properties of the growing GaAs layer.

Thorsen and Manasevit (14) reported that occurrence of p-type layer at a low $[\text{As}]/[\text{Ga}]$ ratio is ascribed to the arsenic vacancy. But, there have been few experiments reported which show that the arsenic vacancy forms a shallow acceptor. It seems to be difficult to explain the feature, as seen in Fig. 1, from the viewpoint of arsenic vacancy. Ito *et al.* (15) reported that the $[\text{As}]/[\text{Ga}]$ ratio effect is ascribed to carbon and/or silicon. However they did not identify carbon and silicon, respectively. Detailed experiments are needed in order to explain the $[\text{As}]/[\text{Ga}]$ ratio effect, as seen in Fig. 1.

Column II element forms a shallow acceptor in GaAs. But, as will be reported in the following section, the layer does not contain column II element and main impurities are assumed to be carbon, silicon, and sulfur. The following model, based on the reaction between these column IV impurities and vacancies, seems to explain the $[\text{As}]/[\text{Ga}]$ ratio effects, as well as the mobility data and the photoluminescence results which will be discussed in the following sections. Since TEG was checked containing 0.5 ppm silicon, column IV elements, such as carbon and silicon in the layer, were thought to come from the TEG sources. Column

IV elements have been thought to be amphoteric impurities, e.g., silicon on gallium site is acceptor and that on arsenic site is donor in GaAs. From a simple thermodynamic consideration, vacant site concentrations of gallium and arsenic are expected to be proportional to $[As]/[Ga]^{-m}$, respectively.³

Amphoteric impurities shared from vapor phase to gallium and arsenic sites of the crystal are thought to be proportional to the respective vacant site concentrations. So, it is assumed that, at a low $[As]/[Ga]$ ratio, amphoteric impurities shared to arsenic sites rather than to gallium sites are dominant and the layer becomes p-type. On the contrary, at a high $[As]/[Ga]$ ratio, amphoteric impurities shared to gallium sites are dominant and the layer becomes n-type. This model can explain the reason why, at lower $[As]/[Ga]$ ratios, the layers are p-type and become n-type by increasing the $[As]/[Ga]$ ratio, as seen in Fig. 1.

However in Fig. 1, the p-type layer with the highest carrier concentration of $\sim 10^{17}/\text{cm}^3$ from TEG-6 source may come from another origin. At such a low $[As]/[Ga]$ ratio, ~ 1 , it was difficult to deposit an epitaxial layer with good quality. In this case, the layer showed poor crystallinity, and some kind of defects should be the origin for the high hole density.

Effects of the $[As]/[Ga]$ ratio on Hall mobility and compensation ratio.—The Hall mobility was measured at room temperature and 77°K. The layers with electron concentration in the range from 5×10^{13} to $8 \times 10^{15}/\text{cm}^3$ were obtained by changing the $[As]/[Ga]$ ratio, where AsH_3 flow rate was changed to a fixed TEG flow rate of 3×10^{-4} mole/min. Room temperature Hall mobilities varied in the range from 7400 to 8500 $\text{cm}^2/\text{V sec}$ for the layers from TEG-6 source and from 6500 to 7800 $\text{cm}^2/\text{V sec}$ for the layers from TEG-2 source, corresponding to the carrier concentration. These room temperature data are nearly the same as the reported values (8, 29).

Figure 2 shows the correlation between the Hall mobility and the electron concentration at 77°K. Also plotted are curves showing the theoretical 77°K mobility as a function of electron concentration for several fixed compensation ratios (29). Some data plotted in the figure are mobility of the layer with (100) orientation obtained from the Ga/AsCl₃/H₂ system (8). Figure 2 shows that mobilities of layers with an elec-

³ $m = \frac{1}{2}$. Detailed thermodynamical consideration will be reported in the future.

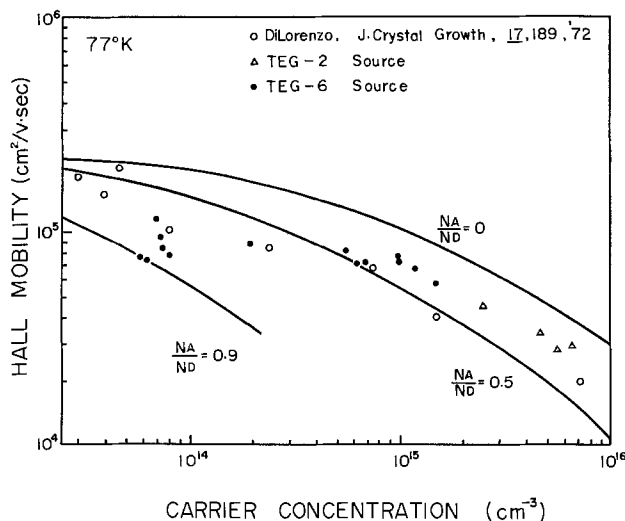


Fig. 2. Variation of 77°K mobility with the carrier concentration ($N_D - N_A$) showing the effects of variable compensation. Carrier concentration of undoped layer was changed by changing the $[As]/[Ga]$ ratio during the growth. Thickness of the layer was in the range from 15 to 30 μm . Symbols Δ and \circ represent present work; \bullet represents DiLorenzo's using the Ga/AsCl₃/H₂ system (8); K , compensation ratio calculated by Wolfe et al. (30).

tron concentration higher than $\sim 10^{14}/\text{cm}^3$ are almost the same as those from the usual Ga/AsCl₃/H₂ system.

Also, this figure shows that layers with a lower electron concentration have a higher compensation ratio and the decrease of electron concentration of the layer is accompanied with an increase in the compensation ratio. This fact is consistent with the result of thermodynamic consideration, in which amphoteric impurities are shared between gallium sites and arsenic sites, according to the $[As]/[Ga]$ ratio. According to the amphoteric impurity share model, the compensation ratio for the n-type region is expected to be proportional to $([As]/[Ga])^{-m}$.³ This seems to explain the experimental result as shown in Fig. 2, wherein the donor concentration is nearly the same as that of acceptor ($K \approx 1$) in the layer deposited at low $[As]/[Ga]$ ratios and the compensation ratio becomes smaller in the layers deposited at higher $[As]/[Ga]$ ratios.

Photoluminescence experiment.—Shallow acceptor levels of the layer were examined by use of the photoluminescence measurement at low temperatures. Figure 3 shows the photoluminescence spectra of an n-type sample at 10°K. There are five emission peaks near the bandgap in the range from 8180 to 8220Å. Bogardus and Bebb (31) and Rossi et al. (32) reported that there are five emission peaks near the bandgap energy in high purity epitaxial GaAs. According to Bogardus and Bebb (31), these are expected to be due to the free exciton (X), the exciton-neutral donor (D^0 , X), neutral donor-band (D^0 , h), exciton-ionized donor (D^+ , X), and exciton-neutral acceptor (A^0 , X) recombinations.

It is noted that there are three emission peaks in the range from 8250 to 8450Å.

Figure 4 shows the photoluminescence spectra at 11°K of p- and n-type layers, with different carrier concentrations in the range from 8250 to 8450Å. The spectra of n-type layers consist of three emission lines, indicated as A, B, and C in the figure. Intensities of the emissions are increased in the layers which have lower electron concentrations and are the most intense in the p-type layer. This seems to show that the layer deposited at lower $[As]/[Ga]$ ratios contains many more acceptors. Emission spectra of a p-layer in this range consist of B and C emission. Many workers have pointed out that the photoluminescence spectra of high purity GaAs in this wavelength range have several luminescence peaks involving acceptors (31, 33-35). Recently, Rossi et al. (35) identified the origin for the emission line multiplicity in this wavelength region by a photoluminescence experiment under a magnetic field. They identified three emission peaks in the photoluminescence spectra of their high purity n-type GaAs, associated with two shallow acceptors having different binding energies, respectively. Thus, the data indicated that two acceptor levels were present in the sample and that two free-electron neutral-acceptor emissions and two donor-acceptor pair emissions were expected, but two of these emissions were overlapped.

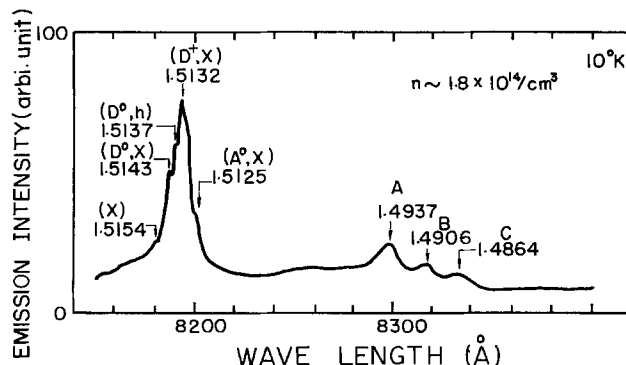


Fig. 3. Photoluminescence spectra from n-type layer at 10°K. Identification of near bandgap emissions, (X), (D^0 , X), (D^0 , h), (D^+ , X), and (A^0 , X) follow after Bogardus and Bebb (31).

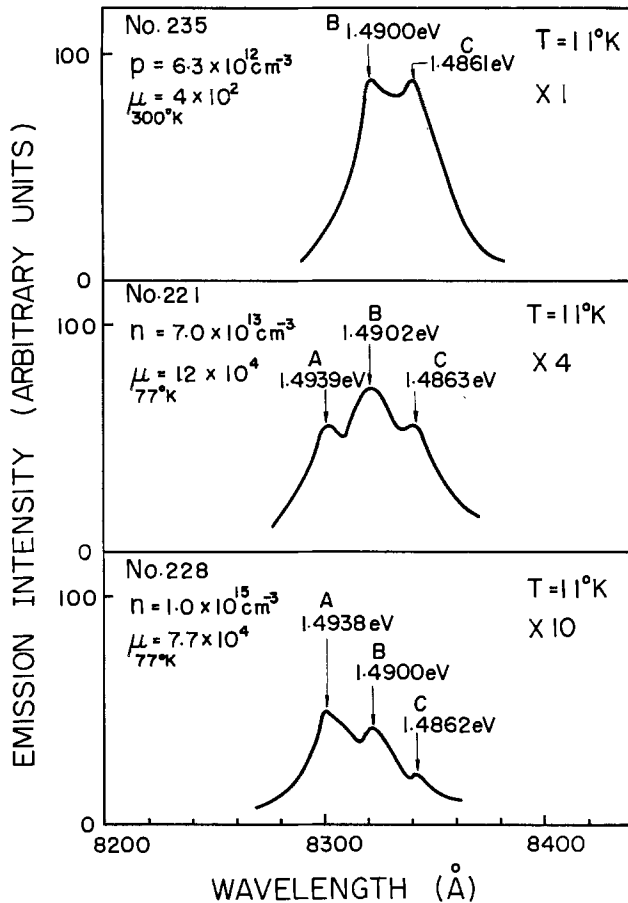


Fig. 4. Photoluminescence spectra of p- and n-layers with different carrier concentration, corresponding to emission peaks A, B, and C in Fig. 3.

If the present photoluminescence results were the same as in the above experiments, binding energies of two acceptors are 25.6 and 29.4 meV, respectively, using a bandgap energy of 1.5194 eV (47). This assumption is consistent with the following experiment on temperature dependence of the photoluminescence spectra. Emission peak C of 1.4869 eV at 11°K was annihilated by increasing temperature, whereas emission peaks A and B shifted toward the higher energy side, but the emission intensities did not change so much, as shown in Fig. 5.

These facts show that emission peaks A and B are due to free electron and to two different acceptor recombinations, respectively, and emission peak C is due to a donor-acceptor pair recombination, being of the same origin of acceptor as emission peak B. It is assumed that an emission due to donor to acceptor pair recombination, being the same acceptor origin as emission A, has not been identified with emission peak B, because of the overlap of this pair emission and the emission peak B.

There have been many reports on the shallow acceptor levels in GaAs. Data are shown in Table I. The acceptor with a binding energy of 25.6 meV in this experiment is assumed to be carbon. However, there are two different results for the acceptor with a binding energy of 29.4 meV. This acceptor is assumed to be either silicon or zinc. Therefore, it cannot be decided, from these reports, whether silicon or zinc is respon-

Table I. Binding energies of shallow acceptors (meV)

	C	Si	Zn	Ge	Cd
Williams and Bebb (36)		30			34.5
Nakanishi (37)		31		41	
White et al. (38)	26.7	35.2	31.4	41.2	35.4
Ozeki et al. (39)	26.5	35.1	30.2	41.3	34.5

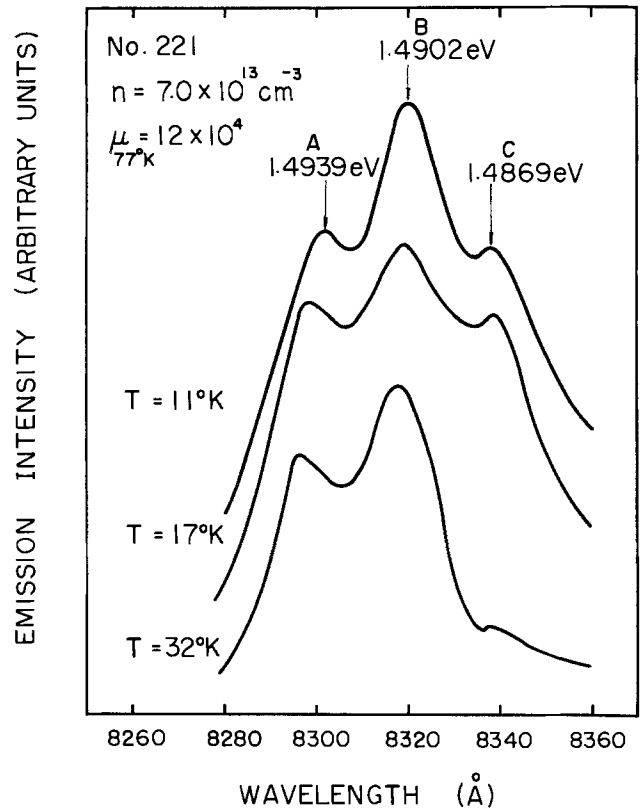


Fig. 5. Variation of photoluminescence showing the increase in intensity of free electron to acceptor recombinations, 1.4939 and 1.4902 eV, with a simultaneous decrease in donor to acceptor pair emission of 1.4869 eV due to increasing temperature.

sible for emission peaks B and C. However, it should be noted that the emission peaks B and C become more intense in n-type layers with lower electron concentrations and become dominant in a p-type layer, as shown in Fig. 4. This fact means that emission peaks B and C are more intense in a layer which is deposited under the low [As]/[Ga] ratios. The layer deposited under the low [As]/[Ga] ratios could be expected to contain higher density of impurity substituting arsenic sites than gallium sites of the crystal.

It is reasonable to think that the impurities substituted on the arsenic sites to form acceptors are the origin for the emissions. Thus, silicon substituted on the arsenic sites is expected to be the acceptor responsible for emission peaks B and C in this sample, rather than zinc. Emission spectra of the p-type layer consist of B and C emissions, in Fig. 1. The C emission was observed to be annihilated at higher temperatures. This seems to show that B emission is due to free electron to silicon acceptor recombination and silicon is a dominant acceptor in the p-type layers.

This expectation was supported by the result of a mass spectroscopic analysis of the layer, as shown in Table II. Carbon, silicon, and sulfur were detected as major impurities, but zinc was not detected within the zinc detection limit of ~ 0.03 ppm. Mass spectroscopic analysis was carried out on the GaAs sample deposited on the lightly sulfur-doped germanium as an electronic

Table II. Impurities in GaAs layer determined by mass spectroscopic analysis (ppm)

	C	Si	S	Fe	P	Al	Ca	Zn
TEG-6	8	0.4	0.7	0.5	0.1	0.6	0.2	N.D.

Spark source mass spectroscopic analyzer was used. Samples were made by depositing the GaAs layer on sulfur-doped Ge crystal containing C (8 ppm), Si (0.4 ppm), S (0.7 ppm), and Fe (0.5 ppm).

conductive support. The germanium support was found to be containing C(8 ppm), Si(0.4 ppm), S(0.7 ppm), and Fe(0.5 ppm). Analytical data show that the GaAs layer does not contain these impurities exceeding the above values, at least. The carbon contamination (<8 ppm) for the layer from TEG source of less than the 25 ppm for the layer from the TMG source (15) seems to show that TEG is an appropriate source for reducing carbon contamination.

From the amphoteric impurity share model, dominant donor impurities are assumed to be carbon and silicon on gallium sites. Silicon has been thought to form a donor, but no experiment has been reported to show that carbon forms a donor. In order to confirm the existence of a carbon donor, additional experiments, such as carbon doping, are needed. This is a future problem.

Conclusion

High purity epitaxial GaAs has been deposited on GaAs substrate using high purity triethylgallium and arsine as source materials.

The layer carrier type was changed by changing the [As]/[Ga] ratio introduced into the reactor. A higher [As]/[Ga] ratio made the layer more n-type.

Carrier type conversion and carrier concentration change accompanying the [As]/[Ga] ratio change were explained by the sharing of amphoteric impurities between gallium sites and arsenic sites. The Hall mobility data, carrier compensation effect, and photoluminescence results were consistent with the amphoteric impurity sharing model. Dominant impurity active impurities were expected to be carbon and silicon. This agreed with the impurities determined by the mass spectroscopic analysis.

Triethylgallium is a useful source material for growing a high purity epitaxial layer. A higher purity layer would be deposited by eliminating silicon impurity from the source materials.

Electron Hall mobility at room temperature and at 77°K of the layers with an electron concentration higher than $\sim 10^{14}/\text{cm}^3$ was nearly the same as those obtained by the usual Ga-AsCl₃-H₂ system. The highest electron Hall mobility at 77°K was 120,000 cm²/V sec for the layer with an electron concentration of $7 \times 10^{13}/\text{cm}^3$.

Three emission peaks were observed in the wavelength range from 8250 to 8450Å in photoluminescence and were due to two shallow acceptors with binding energies of 25.6 and 29.4 meV, which corresponded to carbon and silicon in the arsenic sites, respectively.

Acknowledgment

The authors are grateful to Dr. S. Asanabe for his encouragement and support.

Grateful acknowledgement is made for helpful discussions on the photoluminescence experiment with Dr. K. Sugibuchi and Mr. H. Iwasaki.

Manuscript submitted Oct. 18, 1974; revised manuscript received April 16, 1975.

Any discussion of this paper will appear in a Discussion Section to be published in the June 1976 JOURNAL. All discussions for the June 1976 Discussion Section should be submitted by Feb. 1, 1976.

Publication costs of this article were partially assisted by Nippon Electric Company, Limited.

REFERENCES

1. J. R. Knight, D. Effer, and P. R. Evans, *Solid State Electron.*, **8**, 178 (1965).
3. M. Maruyama, S. Kikuchi, and O. Mizuno, *This Journal*, **116**, 413 (1969).
3. C. M. Wolfe, G. E. Stillman, and E. B. Owens, *ibid.*, **117**, 129 (1970).
4. C. M. Wolfe, G. E. Stillman, and J. O. Dimmock, *J. Appl. Phys.*, **41**, 504 (1970).
5. C. M. Wolfe and G. E. Stillman, Proc. 3rd Int. Symp. on Gallium Arsenide, Paper 1 (1970).
6. S. Knight, L. R. Dawson, J. V. DiLorenzo, and W. A. Johnson, *ibid.*, Paper 12.
7. J. V. DiLorenzo and G. E. Moore, Jr., *This Journal*, **118**, 1823 (1971).
8. J. V. DiLorenzo, *J. Crystal Growth*, **17**, 189 (1972).
9. H. Watanabe and Y. Seki, ICCG-4, *Collected Abstracts*, 143 (1974).
10. H. M. Manasevit, *Appl. Phys. Letters*, **12**, 156 (1968).
11. H. M. Manasevit and W. I. Simpson, *This Journal*, **116**, 1725 (1969).
12. P. Rai-Chaudhury, *ibid.*, **116**, 1745 (1969).
13. H. M. Manasevit and A. C. Thorsen, *Metal. Trans.*, **1**, 623 (1970).
14. A. C. Thorsen and H. M. Manasevit, *J. Appl. Phys.*, **42**, 2519 (1971).
15. S. Ito, T. Shinohara, and Y. Seki, *This Journal*, **120**, 1419 (1973).
16. K. Lindeke, W. Sack, and J. J. Nickl, *ibid.*, **117**, 1316 (1970).
17. K. Ziegler, K. Nagel, and W. Pfohl, *Annal. der Chem.*, 629 (1960).
18. W. L. Smith and T. Wartik, *J. Inorg. Nucl. Chem.*, **29**, 629 (1967).
19. H. Iwasaki and K. Sugibuchi, *Appl. Phys. Letters*, **18**, 420 (1971).
20. J. Blanc, R. H. Bube, and L. R. Weisberg, *J. Phys. Chem. Solids*, **25**, 225 (1964).
21. H. Otsuka, K. Ishida, and J. Nishizawa, *Japan. J. Appl. Phys.*, **8**, 632 (1969).
22. E. Muñoz, W. L. Snyder, and J. L. Moll, *Appl. Phys. Letters*, **16**, 262 (1970).
23. J. Nishizawa, H. Otsuka, S. Yamakoshi, and K. Ishida, *Japan. J. Appl. Phys.*, **13**, 46 (1974).
24. M. Nakagawa and H. Ikoma, *ibid.*, **10**, 1345 (1971).
25. H. Okamoto and S. Sakata, *J. Appl. Phys.*, **44**, 1316 (1973).
26. M. Ihara, K. Dazai, and O. Ryuzan, *ibid.*, **45**, 528 (1974).
27. R. M. Logan and D. T. J. Hurle, *J. Phys. Chem. Solids*, **32**, 1739 (1971).
28. F. A. Kröger, "The Chemistry of Imperfect Crystals," North Holland Publishing Co., Amsterdam (1964).
29. C. Hilsum, *Electron. Letters*, **10**, 259 (1974).
30. C. M. Wolfe, G. E. Stillman, and W. T. Lindley, *J. Appl. Phys.*, **41**, 3088 (1970).
31. E. H. Bogardus and H. B. Bebb, *Phys. Rev.*, **176**, 993 (1968).
32. J. A. Rossi, C. M. Wolfe, G. E. Stillman, and J. O. Dimmock, *Solid State Commun.*, **8**, 2021 (1970).
33. M. A. Gilileo, P. T. Bailey, and D. E. Hill, *Phys. Rev.*, **174**, 898 (1968).
34. J. Shah, R. C. C. Leite, and R. E. Nahory, *ibid.*, **184**, 811 (1969).
35. J. A. Rossi, C. M. Wolfe, and J. O. Dimmock, *Phys. Rev. Letters*, **25**, 1614 (1970).
36. E. W. Williams and H. B. Bebb, *J. Phys. Chem. Solids*, **30**, 1289 (1969).
37. T. Nakanishi, *Japan. J. Appl. Phys.*, **12**, 1263 (1973).
38. A. M. White, P. J. Dean, D. J. Ashen, J. B. Mullin, M. Webb, B. Day, and P. D. Green, *J. Phys. C: Solid State Phys.*, **6**, 1243 (1973).
39. M. Ozeki, K. Nakai, K. Dazai, and O. Ryuzan, *Japan. J. Appl. Phys.*, **13**, 1121 (1974).

Investigation of Breakdown and Resistivity Striations in High-Voltage Silicon Diodes

A. Mühlbauer, F. Sedlak, and P. Voss

Siemens AG, Bereich Bauelemente, 8 München, F. R. Germany

ABSTRACT

The breakdown behavior of high-voltage diodes prepared from silicon wafers that were cut parallel to the rod axis was observed by means of the infrared breakdown radiation. The breakdown patterns were striated and could be correlated to spreading resistance measurements on a microscopic scale. It could be confirmed experimentally that the breakdown in material with resistivity variations not only depends on the absolute resistivity value at each location, but also to a large extent on the wave form and the period of the variations. Only in diodes in which the microscopic resistivity variations had high amplitudes and a distinct periodicity with wavelengths longer than the extent of the space charge region did individual minima lead to individual clearly separated breakdown lines.

The incorporation of dopants during the growth of silicon crystals from the melt is usually layerlike (1). Microscopic dopant variations are generated in this way along the axis of the rod. They are normally determined by means of a resistivity measurement with high local resolution (1,2).

The effect of these fluctuations on device properties depends to a large degree on their geometrical extent as compared to the dimensions of a single active element of the device. The critical dimension can be given by a lateral dimension or by the extent of a space charge region.

For small-area discrete devices the influence is easily estimated, since in these the resistivity remains virtually constant within one single element. The resistivity variations manifest themselves in variations of the properties from one device to the other. An example is the multidiode vidicon in which the resistivity variations become visible in the dark current display (3).

In the large-area discrete devices used for power applications, e.g., in thyristors and in rectifiers, the period of the variations may be small compared with the lateral dimensions and of the same order or smaller than the extent of the space charge region. Therefore, it is significantly more difficult to estimate the influence of the resistivity variations on the device properties. For example, it is no longer possible to assume a one-to-one relationship between a measured resistivity profile and the breakdown behavior of a p-n junction.

The breakdown of a p-n junction is determined by the field strength at the junction. In homogeneously doped silicon the applied voltage needed to reach the breakdown field strength is proportional to the resistivity, according to Poisson's equation. The breakdown field strength itself varies slightly with resistivity due to the sensitivity of the breakdown to the gradient of the field strength (4).

Cornu and Sittig (5) have investigated theoretically the influence of resistivity variations on the distribution of the electrical field strength for a constant applied voltage. They considered resistivity minima in the shape of a sinusoidal half-wave or of rectangular shape that were arranged perpendicular to the p-n junction. They concluded that as compared with an equivalent one-dimensional resistivity reduction a 10% dip of the resistivity causes hardly any increase in the maximum field strength, if its width is less than the extent of the space charge region.

On the other hand, for a width twice the extent of the space charge region, the increase in field strength reaches 70% of that of the one-dimensional increase.

Key words: spreading resistance measurements, infrared breakdown radiation, breakdown lines, space charge region.

Therefore, in this case breakdown will occur predominantly at the location of the resistivity minimum.

For low-voltage devices and for low current densities there may exist influences on the breakdown behavior other than that of the resistivity, e.g., influences of lattice defects like dislocations, stacking faults, and "swirls." So far we have found no experimental indication that there are any such influences on the high current density breakdown of high-voltage diodes made from dislocation-free silicon of the type investigated in this paper. This was particularly evident when the diodes were manufactured from silicon homogeneously doped by neutron irradiation (6).

The purpose of this paper is to clarify experimentally the correlation between microscopic resistivity variations and the breakdown behavior of high-voltage diodes for devices made from wafers that were cut parallel to the rod axis (lengthwise cuts). In lengthwise cuts the arrangement of the resistivity variations is easier to survey than in normal cuts, i.e., cuts that are perpendicular to the rod axis. While in the first case the dopant layers are arranged perpendicular to the p-n junction across the entire area, the intersection angle varies in the second case (see Fig. 1).

The distribution of the infrared breakdown radiation was observed (7) and the resistivity profile in the same diodes determined by means of spreading resistance (SR) measurements (2).

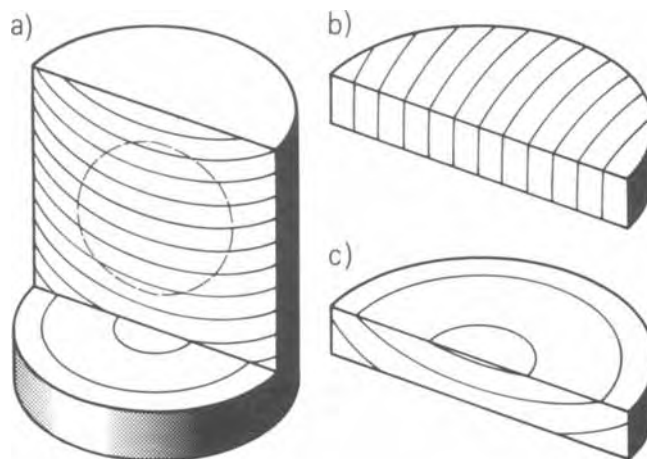


Fig. 1. Schematic representation of the way striations are located in a silicon rod and in wafers sliced from it. (a) Silicon rod. (b) Lengthwise cut wafer. (c) Normal cut wafer.

Experimental

The results that are reported were obtained with diodes made from two, dislocation-free, float-zoned silicon rods that were phosphorus-doped. The average resistivity of the first rod (No. 340) was 70 ohm-cm. The macroscopic resistivity variations in this silicon were less than $\pm 10\%$ which is considered quite homogeneous by common standards. Such material is used for the fabrication of power devices. The breakdown voltage of the diodes was higher than 2000V. The second rod (No. 4214B) had a resistivity dip in the center (dopant core). The minimum resistivity was 52 ohm-cm.

The investigated samples were cut from the $\langle 111 \rangle$ -oriented silicon rod parallel to the rod axis in a $\{112\}$ plane. Figure 1 indicates schematically how resistivity striations are distributed inside slices that are cut perpendicular to the rod axis as compared with slices cut parallel to the axis.

Starting from slices approximately 470 μm thick, diodes were fabricated by diffusion as described in Ref. (7). The p-n junction was located 90 μm below the surface. The slices were alloyed onto molybdenum on the p-doped side. The other side was provided with an evaporated grid electrode of aluminum, to make possible the observation of the breakdown radiation. The grid spacing was 3 mm. In one case an arrangement of observation holes, 0.5 mm apart, was used for a p-n-p structure [as in Ref. (7)].

As the first step in the investigation, the distribution of the breakdown radiation emitted from the entire area of each diode was recorded. Then, the aluminum electrode and a layer of the silicon approximately 100 μm wide¹ were removed. The silicon surface was mechanically-chemically polished in preparation for the spreading resistance measurement.

An ASR-100 (Solid-State Measurements) with two probes at a distance of 0.6 mm was used to determine the distribution of the microscopic resistivity variations. The probes were aligned perpendicular to the growth axis. All measurement tracks were parallel to the axis. The distance between steps was 25 μm .

Results

The breakdown radiation emitted from diodes that were cut in the normal fashion perpendicular to the axis from rod No.340 showed a quite regular spiraling pattern (Fig. 2). It thus clearly indicated the presence of periodic resistivity variations.

¹ In lengthwise cut slices, the width of the removed layer is not critical for the result of the measurement, as long as one stays inside the original material. This fact will become evident in the next section.

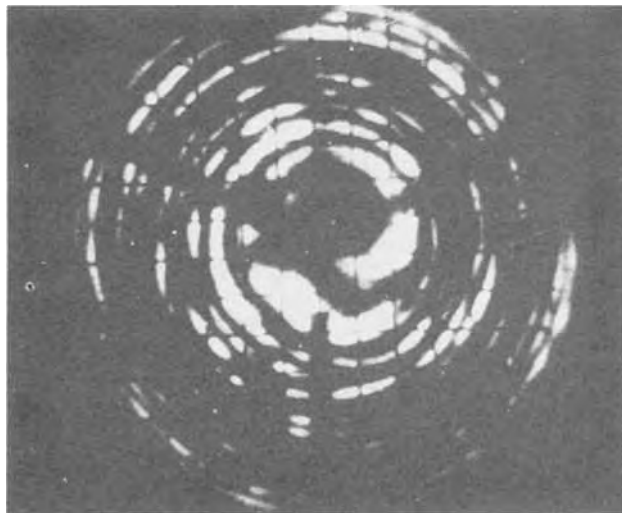


Fig. 2. Breakdown pattern of a normal cut diode from rod No. 340; breakdown current 50A. Grid electrode spacing is 3 mm. The three dark bars separated by 120° are current terminals.

In order to demonstrate that in lengthwise cuts the resistivity distribution virtually does not change perpendicular to the p-n junction over a distance of several hundred microns, we prepared p-n-p structures with the two junctions 300 μm apart. An example of the two breakdown radiation patterns obtained from a p-n-p structure is given in Fig. 3. Only a very close inspection of the patterns reveals that there are actually small differences. Thus, it is justified to compare the breakdown patterns with SR measurements that are taken at some distance from the p-n junction.

Figure 4 shows two examples of diode breakdown patterns. The diameter of the diodes is 33 mm. The slices used for these diodes were cut at position 3.6 and 17.8 mm from the rod axis. The breakdown patterns became more homogeneous at higher current levels. The radiation patterns are clearly striated. The minimum distance between striations is the same (290 μm) as the distance obtained from a striation etch. With larger distance from the rod axis the distribution of the breakdown radiation becomes more homogeneous across the area.

The comparison between breakdown pattern and SR measurement was performed with the diode cut 3.6 mm away from the rod axis (Fig. 4a). The measuring track is indicated in Fig. 5, which is the magnified center section of Fig. 4a, turned 90 degrees. As mentioned above, two SR probes at a distance of 0.6 mm were

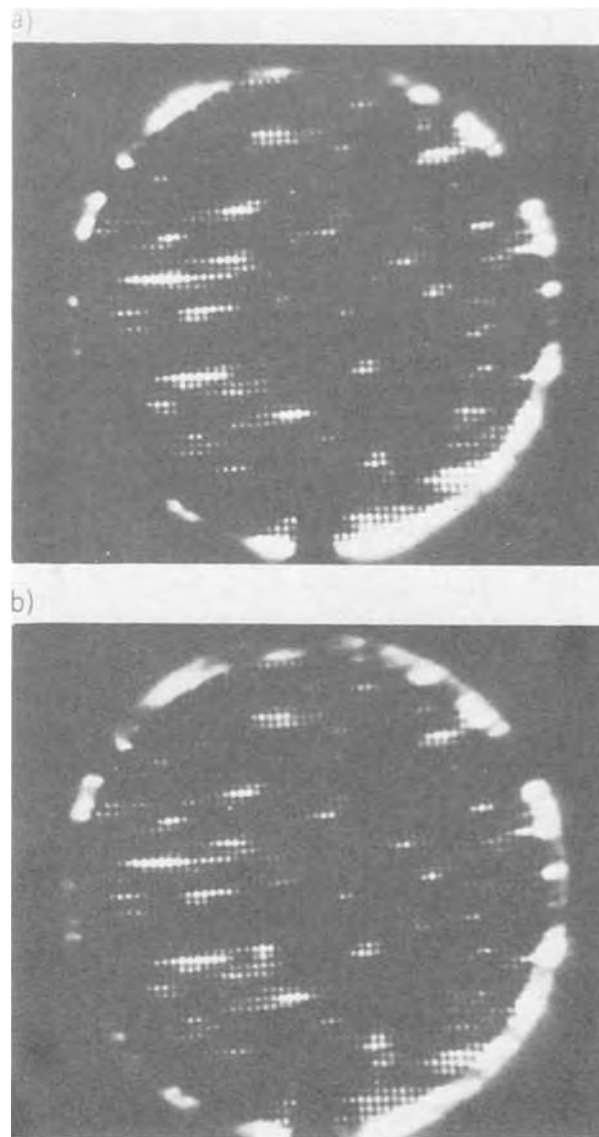


Fig. 3. Breakdown patterns of the two junctions in a p-n-p structure (lengthwise cut); 28 mm diameter of the electrode.

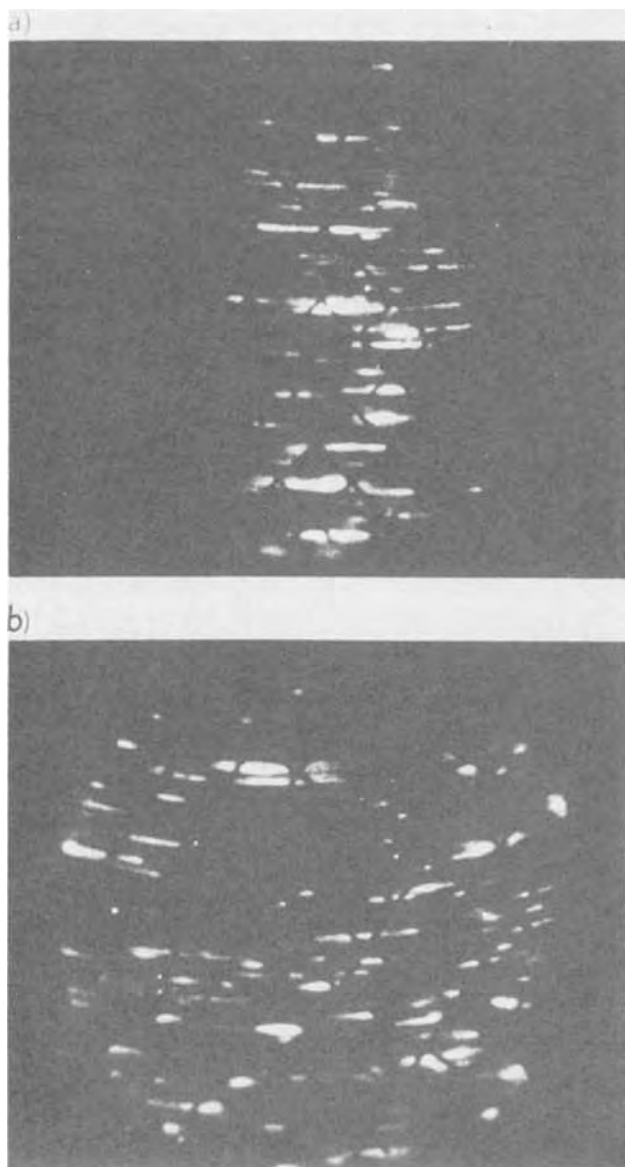


Fig. 4. Breakdown patterns of lengthwise cut diodes at a breakdown current of 7A. The grid electrode spacing is 3 mm. (a) Cut 3.6 mm off the rod axis. (b) Cut 17.8 mm off the rod axis.

used, *i.e.*, the probes were applied to the silicon surface 0.3 mm to both sides of the indicated track. In Fig. 6 the results of the SR measurement and the breakdown pattern magnified to the same scale are arranged adjacently. The spatial resolution of the breakdown pattern in Fig. 5 and 6 is approximately 200 μm .

The SR profile shows a quite regular fluctuation pattern. The amplitudes average to approximately $\pm 20\%$, the period to 290 μm .

The breakdown patterns in Fig. 4-6 are representative for the breakdown in diodes in which the period of the resistivity variations is longer (290 μm) than the extent of the space region (180 μm), while the width of the individual minima is slightly smaller. The results given in Fig. 7 and 8 are examples for a silicon crystal that shows less regular microscopic resistivity variations with a distance between pronounced minima (125 μm) that is slightly shorter than the extent of the space charge region (140 μm). The etched silicon surface revealed straight striations (facets), also at a distance of approximately 125 μm . The detail of Fig. 8c was taken independently with an optical arrangement with higher resolution. The spatial resolution in Fig. 7 and 8b is approximately 200 μm and better than 100 μm in Fig. 8c.

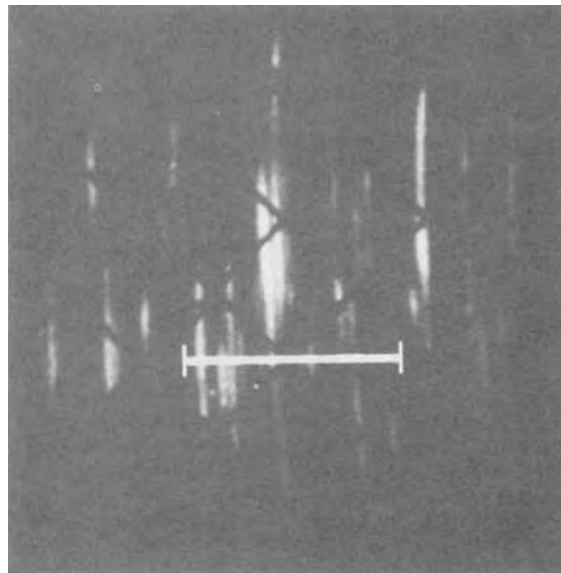


Fig. 5. Breakdown pattern of diode cut 3.6 mm off the axis. Detail from Fig. 4. Indicated is the location of the spreading resistance measurement track.

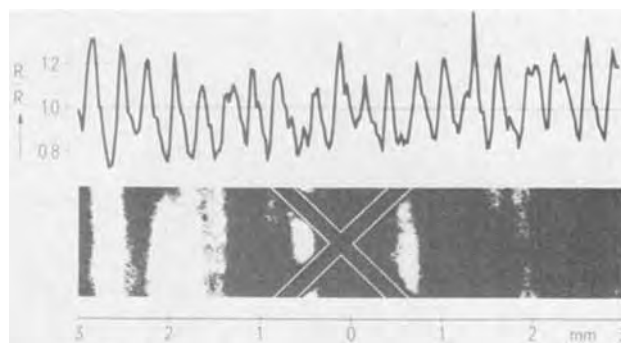


Fig. 6. Correlation between breakdown pattern of diode cut 3.6 mm off the axis with spreading resistance measurement along the track indicated in Fig. 5. Grid electrode outlined.

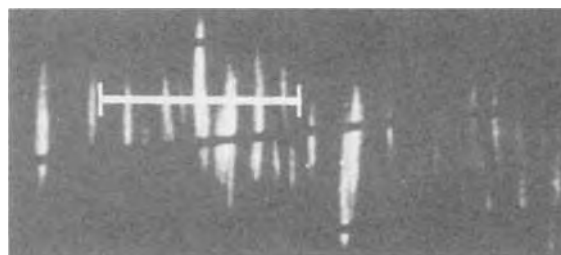


Fig. 7. Breakdown pattern of diode cut 1 mm off the axis from a rod with a central dopant core; breakdown current 2A. Indicated is the location of the spreading resistance measurement track. The grid electrode spacing is 3 mm.

The general appearance of the breakdown pattern in Fig. 7 is similar to that in Fig. 5 (which is of the same scale), only that the breakdown lines are somewhat shorter due to the dopant core. In Fig. 7 the minimum distance between lines is approximately 250 μm . Figure 8a shows the result of the SR measurement along the track indicated in Fig. 7. Figure 8b is a magnified section of Fig. 7.

Discussion

Especially Fig. 4b could be interpreted as indicating that the dopant is very inhomogeneously incorporated in the direction of the rod axis as well as along the slightly curved striations which correspond to the solid-liquid interface during growth. However, since

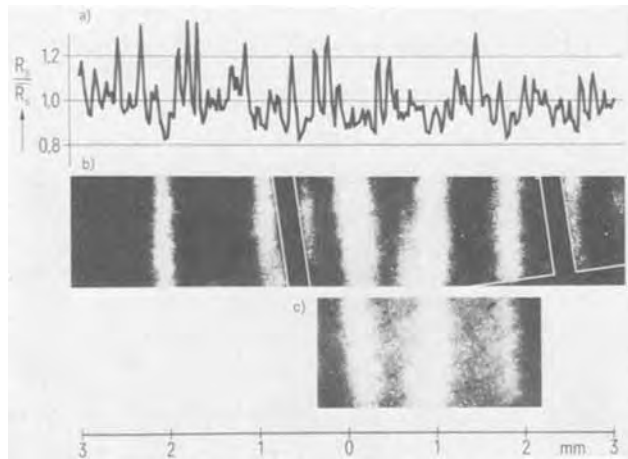


Fig. 8. Correlation between breakdown pattern of Fig. 7 and spreading resistance measurement. (a) SR measurement. (b) Enlarged detail of Fig. 7; optical resolution approximately $200\ \mu\text{m}$. (c) Detail. Optical resolution better than $100\ \mu\text{m}$. This photograph is slightly cushion-distorted and has an intensity fall-off toward the edges. The slanted square pattern visible in the photograph originates from the fiber optics in the infrared system.

the breakdown current density rises very sharply once the local breakdown voltage is surpassed, such intensity variations can basically be caused by resistivity fluctuations of only a few per cent.

When one compares the details of the breakdown patterns and the resistivity wave forms in Fig. 6, it becomes evident that all breakdown striations coincide with minima of the resistivity profile, though some of the adjacent lines are only barely separated. For these current and observation conditions there is no breakdown visible for local resistivity minima that lie more than 12% above the absolute minimum.

The intensities of different breakdown lines do not always correspond exactly to the resistivity values of the related minima. This is easily understood in the framework of the calculations of Cornu and Sittig (5): The field distribution is not only determined by the resistivity of the minimum but also by its width and by the resistivity of the surrounding material. Still, for this particular material there is a clear correlation between the resistivity values and the breakdown behavior.

The breakdown patterns in Fig. 7 and 8 are examples for the breakdown in a diode in which the width of some of the individual resistivity minima is markedly smaller than the extent of the space charge region (approximately half).

One could suspect that in Fig. 7 and 8b several of the broad lines are optically not resolved into individual lines due to the lack of optical resolution. However, even the higher resolution of Fig. 8c does not reveal such lines. The juxtaposition of the breakdown pattern and the SR measurement in Fig. 8 indicates that a resolution into narrow lines is not to be expected for the broad line to the left of Fig. 8c, since even the SR measurement shows essentially only a wide macroscopic minimum with little structuring in its bottom. For the broad center line in Fig. 8c the SR measurement shows two distinct narrow minima, i.e., in this broad line a separation into narrower lines is basically possible, but is not observed.

Thus, the experiment shows that for this material the individual variations level out to macroscopic resistivity distributions whose minima lead to breakdown. Wide minima cause a stronger breakdown than narrow ones. When one keeps this in mind it becomes evident that here also the agreement between the breakdown pattern and the SR measurement is quite good.

From these results we can in turn conclude that the SR measurement gives reliable information as far

as the form and the relative position of the minima are concerned. However, we cannot determine how accurate the measurement of the absolute resistivity variations might be.²

Summary and Conclusion

We were able to observe the breakdown behavior of high-voltage, large area diodes fabricated from silicon slices that were cut parallel to the rod axis. The breakdown patterns were striated similarly to the well-known etched striation patterns. We further attempted to obtain a correlation between the observed breakdown patterns and resistivity fluctuations measured with the spreading resistance technique. It was found that:

1. In silicon of 70 ohm-cm resistivity which contained distinct, regular resistivity fluctuations with periods larger than the extent of the space charge region, the minimum distance between breakdown striations was equal to that between resistivity fluctuations. The breakdown took place at the positions of the microscopic resistivity minima.

2. For faceted silicon of 52 ohm-cm resistivity that showed less pronounced and less regular microscopic resistivity variations with a period slightly smaller than the extent of the space charge region, we also observed a striated breakdown pattern. However, the distance between breakdown striations was at least twice that of the minimum distance between resistivity minima.

The results verified that the individual microscopic resistivity striations in high-voltage diodes do not necessarily lead to equivalent individual breakdown lines. The influence of resistivity variations is leveled as the extent of the space region becomes large as compared with the width of a resistivity minimum. Particularly when the period of the resistivity variations and the extent of the space charge region are of the same order, it may be difficult to deduce the breakdown pattern from a given resistivity profile. For the same reason, a breakdown pattern alone does not give any unequivocal indication as to the microscopic resistivity variations in the bulk material. The observation of the breakdown still has the advantage that it supplies direct information on the device performance over a large area.

Acknowledgment

The authors would like to thank J. M. Andreu, A. Steidel, and M. Süss for their technical assistance and Dr. H. Benda and Dr. J. Krausse for helpful discussions. This work has been partially supported by the technological program of the Federal Department of Research and Technology of the FRG. The authors alone are responsible for the content.

Manuscript submitted Sept. 4, 1974; revised manuscript received April 7, 1975.

Any discussion of this paper will appear in a Discussion Section to be published in the June 1976 JOURNAL. All discussions for the June 1976 Discussion Section should be submitted by Feb. 1, 1976.

Publication costs of this article were partially assisted by Siemens AG.

² Krausse (8) has compared the results of spreading resistance measurements taken with an arrangement of diffused contact areas of defined geometry [nonblocking aluminum-silicon contacts (9)] with standard metal probe measurements taken in different experimental setups. He found that the absolute resistivity variations measured with the standard arrangement may depend on the particular measurement conditions. Aluminum-silicon contacts could not be used in our experiments because they are not suited for the close spacing needed with lengthwise cut material.

REFERENCES

1. A. Mühlbauer, R. Kappelmeyer, and F. Keiner, *Z. Naturforsch.*, **20a**, 1089 (1965).
2. R. G. Mazur, *This Journal*, **114**, 255 (1967).
3. S. Yoshikawa and J. Chikawa, *Appl. Phys. Letters*, **23**, 636 (1973).
4. S. M. Sze, "Physics of Semiconductor Devices,"

- pp. 111 ff., John Wiley & Sons, Inc., New York (1969).
5. J. Cornu and R. Sittig, *IEEE Trans. Electron. Devices*, **ED-22**, 108 (1975).
6. M. Schnöller, *ibid.*, **ED-21**, 313 (1974).

7. P. Voss, *ibid.*, **ED-20**, 299 (1973).
8. J. Krausse, In preparation.
9. J. Krausse, Spreading Resistance Symposium, National Bureau of Standards, Gaithersburg, Md., June 1974, J. R. Ehrstein, Editor, p. 109.

Liquid-Phase Epitaxial Growth of ZnTe and $Zn_{1-x}Cd_xTe$

Akihiro Kanamori,¹ Tadahisa Ota,² and Kiyoshi Takahashi

Department of Electronics, Tokyo Institute of Technology, O-okayama, Meguro-ku, Tokyo, Japan

ABSTRACT

ZnTe and $Zn_{1-x}Cd_xTe$ crystals were grown on ZnTe substrates by using the liquid-phase epitaxial method in an open system. In, Ga, Sn, and Bi were used as solvents for growing ZnTe, while $Zn_{1-x}Cd_xTe$ with any alloy composition could be grown from both In and Bi solutions. $Zn_{1-x}Cd_xTe$ layers showing n-type conduction could be grown in the composition range $0.6 \leq x \leq 1.0$ from both In and donor-doped Bi solutions. n- $Zn_{1-x}Cd_xTe$ /p-ZnTe heterodiodes emitted green light at 77°K in the forward-bias region.

Since ZnTe has a bandgap of 2.26 eV at room temperature, it is potentially a good material for visible light-emitting diodes. However, to prepare n-type ZnTe is very difficult because of self-compensation (1). We have therefore investigated the possibility of using the heteroepitaxy technique for making p-n junction devices with ZnTe.

Liquid-phase epitaxial growth (LPE) is one of the principal methods used to obtain high-quality epitaxial layers of the III-V compounds. The application of this method to the II-VI compounds is difficult because of the high vapor pressure of their constituent elements. However, several authors have used the LPE method to prepare layers of ZnTe on ZnSe (2, 3) and on ZnTe (4), and of CdTe on CdTe (5),

In this study, ZnTe and $Zn_{1-x}Cd_xTe$ epitaxial layers were grown on ZnTe substrates from In, Ga, Bi, or Sn solutions by the LPE method, and their growth properties were examined. Since $Zn_{1-x}Cd_xTe$ crystals containing sufficient CdTe are expected to be amphoteric, their electrical properties have been examined to determine the dependence of amphoteric behavior on the alloy composition and growth conditions. $Zn_{1-x}Cd_xTe$ -ZnTe heterodiodes were fabricated, and their electrical and optical properties are briefly described.

Experimental Procedure

The LPE apparatus used here is an open-tube slide system in which a growth solution is brought into contact with a substrate and separated from the substrate after the completion of growth, by moving a graphite solution holder in a hydrogen atmosphere. A diagram of the experimental arrangement is shown in Fig. 1a. The substrates were (111) slices cut from As-doped ZnTe single crystals prepared by the Bridgman method, and they were chemically etched in bromine-methanol solution after mechanical polishing for the epitaxial growth. The solutes for ZnTe and $Zn_{1-x}Cd_xTe$ layers were ZnTe and CdTe + ZnTe, respectively. The ZnTe and CdTe were prepared by the Bridgman method and crushed into small pieces to facilitate dissolution. In,

Ga, Bi, and Sn were used as solvents for growing ZnTe layers, and In and Bi for $Zn_{1-x}Cd_xTe$ layers. The ratio of ZnTe to the solvent was determined by the solubility of ZnTe in that solvent (6, 7) at the desired growth temperature. For $Zn_{1-x}Cd_xTe$ crystals, the ratio of CdTe to ZnTe in the growth solution was determined by the desired alloy composition.

The substrate is placed in the depression in the thin graphite plate and is initially covered with the solution holder in order to minimize contamination and thermal etching before it is brought into contact with the solution.

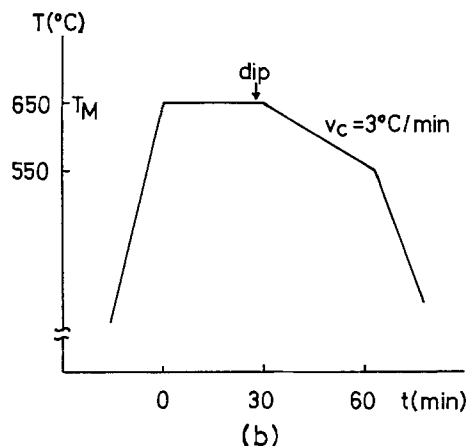
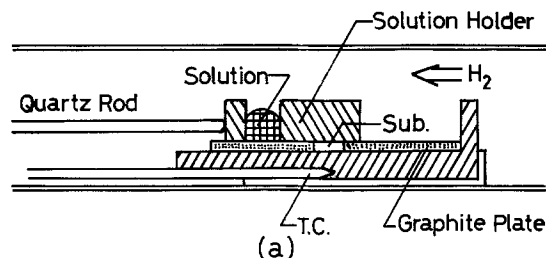


Fig. 1 (a). Apparatus for liquid-phase epitaxial growth of ZnTe and $Zn_{1-x}Cd_xTe$. (b) Typical temperature program employed for LPE.

¹ Present address: IC Division, Nippon Electric Company, Ltd., Kawasaki-shi, Kanagawa, Japan.

² Present address: Electrical Communication Laboratory, Nippon Telegraph and Telephone Public Corporation, Musashino-shi, Tokyo, Japan.

Key words: II-VI compounds, solution growth, light emitting diodes, heteroepitaxy.

Table I. Conditions for LPE growth of ZnTe and $Zn_{1-x}Cd_xTe$

Grown layer	Solvent	$T_M(^{\circ}C)$	$v_c(^{\circ}C/min)$
ZnTe	Bi	700-850	1-3
	Sn	650-700	1-3
	Ga	650-750	1-3
	In	600-650	3
$Zn_{1-x}Cd_xTe$	Bi	550-750	1-6
	In	550-650	1-3

A typical temperature program employed for LPE is shown in Fig. 1b. The holding temperatures (T_M) and the cooling rates (v_c) used for each solvent are summarized in Table I. The holding period (t_1) for dissolving the solute was 20-30 min. The solution and the substrate were kept in contact at T_M for 1-3 min, and the solution was separated from the substrate at about $100^{\circ}C$ below T_M to terminate growth. The thickness of the grown layers obtained by this program is typically a few micrometers.

Results and Discussion

Epitaxial growth of ZnTe.—High-quality epitaxial layers of ZnTe could be obtained by using any of the four solvents studied. The layers grown from Ga solutions are more reddish in color than those grown from other solvents, possibly because of high Ga doping.

The surfaces of ZnTe epitaxial layers grown from In, Ga, or Sn solutions were flat and mirror-smooth, as

shown in Fig. 2a, and the values of T_M and v_c had no significant influence on the properties of the layers. However, the surface condition of the layers grown from Bi solutions was influenced by the cooling rate as illustrated by Fig. 2b and c, where two typical examples are shown for $v_c = 3$ and $1^{\circ}C/min$, respectively.

Though the quality of ZnTe layers did not depend on whether (111)Zn or (111)Te substrates were used, the orientation of the substrate seems to be important in obtaining flat layers like the one shown in Fig. 2a. For example, layers on (110) substrates were granular and rough. Electron diffraction measurements showed that the epitaxy of ZnTe layers on (111) faces is very good. For this orientation, the interface between the ZnTe layer and the substrate was found to be very flat by examining a 5° angle-lapped cross section which was stained with an etchant containing dichromate and $AgNO_3$.

The solvents used here can be dopants in ZnTe, so that ZnTe layers showed various photoluminescence (PL) spectra, especially in the near infrared region, depending on the solvent. The differences are illustrated by Fig. 3, which shows PL spectra obtained from nondoped, Ga-doped, In-doped, and Al-doped ZnTe layers, all grown from Bi solutions. For comparison, the PL spectrum for nondoped bulk ZnTe annealed in an H_2 atmosphere is also shown.

Epitaxial growth of $Zn_{1-x}Cd_xTe$.— $Zn_{1-x}Cd_xTe$ crystals over the entire alloy composition range could be

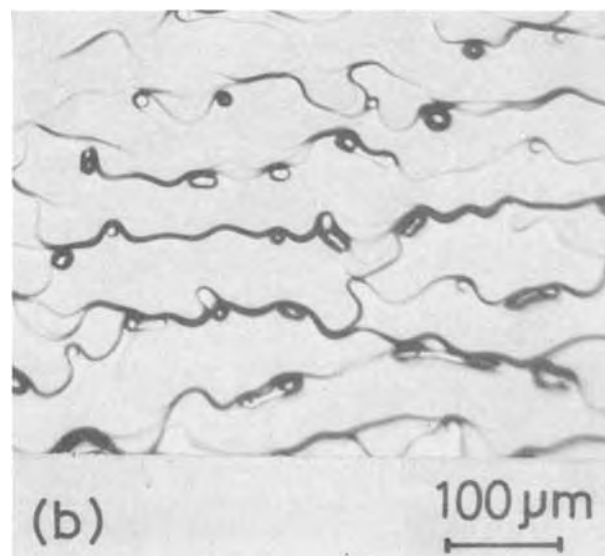
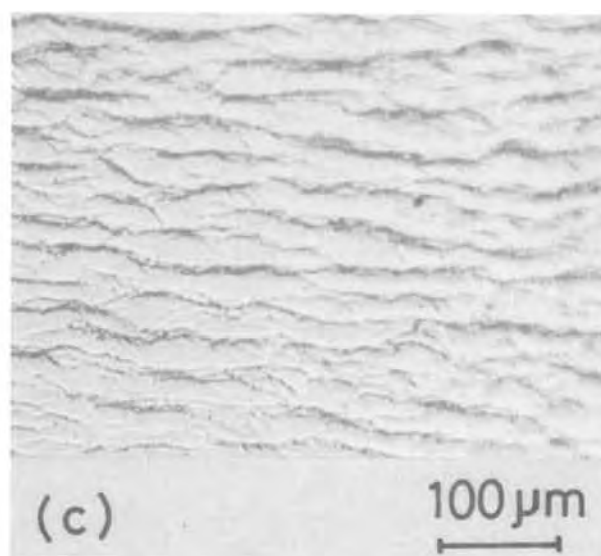
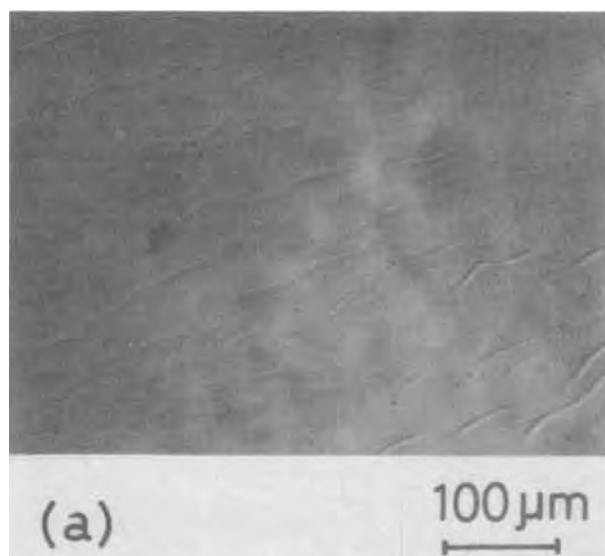


Fig. 2. Photomicrographs of the surfaces of ZnTe layers: (a) In solvent, $T_M = 600^{\circ}C$, $v_c = 3^{\circ}C/min$; (b) Bi solvent, $T_M = 700^{\circ}C$, $v_c = 3^{\circ}C/min$; (c) Bi solvent, $T_M = 700^{\circ}C$, $v_c = 1^{\circ}C/min$.

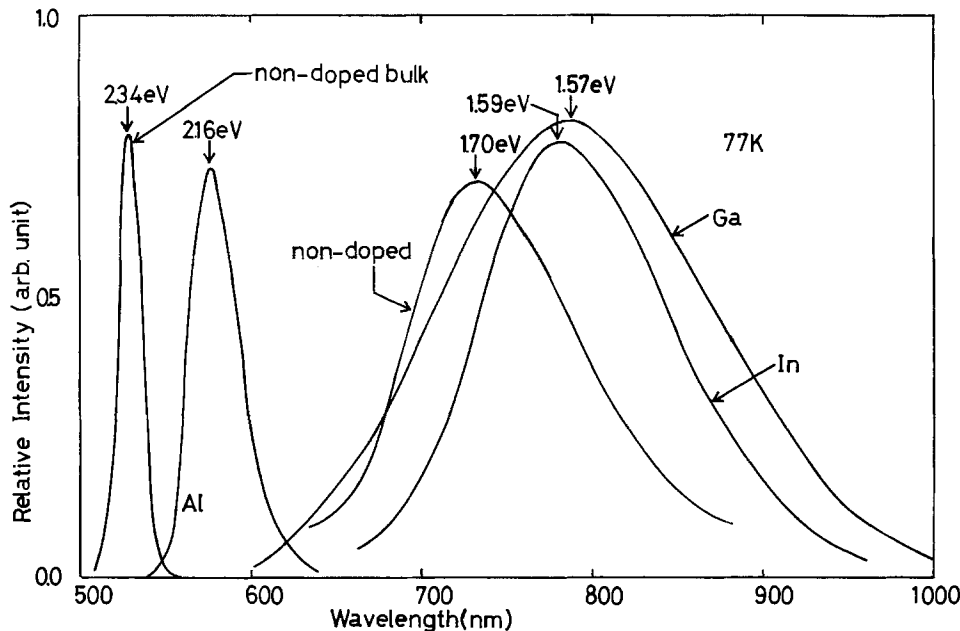


Fig. 3. Photoluminescence spectra at 77°K of ZnTe layers grown from nondoped, Ga-doped, In-doped, and Al-doped Bi solutions.

grown from both Bi and In solvents. CdTe and ZnTe were used as solutes. If the constituent elements are used as solutes, because of their high vapor pressures it is very difficult to obtain good epitaxial layers or to control the composition of the mixed crystals. For example, when Cd was used instead of CdTe, the grown layers had a rough surface and a composition close to ZnTe. Moreover, these layers could be grown only on the (111)Te face, but not on (111)Zn face of ZnTe substrates; when CdTe was used, layers could be grown successfully on both faces.

The composition x of the mixed crystals was determined from the results of x-ray diffraction measurements, assuming that Vegard's law is valid (8). Optical transmittance measurements were also used to determine the x -values, where the relationship between bandgap and composition of $Zn_{1-x}Cd_xTe$ crystals obtained by Saito *et al.* (9) was used. No attempt was made to investigate homogeneity with respect to alloy composition in the direction of growth. For compositions close to CdTe, flat layers as shown in Fig. 4a could be obtained from both In and Bi solutions. However, for composition close to ZnTe, flat surfaces could be obtained only from In solution. Mixed crystals with

intermediate compositions had rough surfaces as shown in Fig. 4b.

Electron diffraction measurements made on the surface of the $Zn_{1-x}Cd_xTe$ layers yielded patterns like the one shown in Fig. 5, where strong spots and dim Debye-Scherrer rings were observed. The interfaces between the mixed layers and the ZnTe substrates were irregular, as shown in Fig. 6a, and thus inferior to those obtained for ZnTe epitaxial layers. The cleaved and stain-etched cross section of a mixed layer grown from In solution is shown in Fig. 6b. This figure shows that a region of In-doped ZnTe about 30 μm thick adjacent to the interface was formed by diffusion of In into the substrate. Similar diffused regions were observed when growth took place from Al- or In-doped Bi solutions, but not when undoped Bi solutions were used.

In this work the composition of the $Zn_{1-x}Cd_xTe$ layers was controlled by adjusting the concentration of CdTe in the growth solution and by varying the holding temperature T_M . Figure 7 shows the relationship between the layer composition and the CdTe concentration in Bi solutions for values of T_M between 650° and 750°C. The CdTe/Bi ratio is the ratio of moles

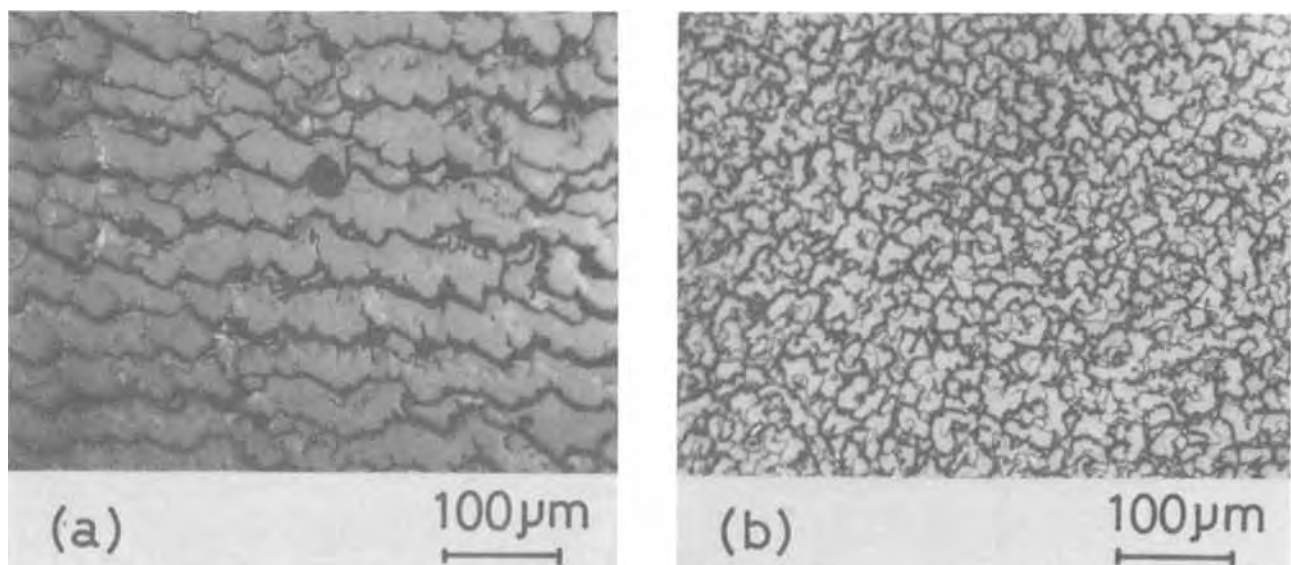


Fig. 4. Photomicrographs of the surfaces of $Zn_{1-x}Cd_xTe$ layers grown on ZnTe (111)Te faces. (a) Composition close to CdTe ($x = 0.89$, $T_M = 650^\circ C$, $v_c = 3^\circ C/min$, Bi solvent); (b) composition close to ZnTe ($x = 0.05$, $T_M = 750^\circ C$, $v_c = 3^\circ C/min$, Bi solvent).

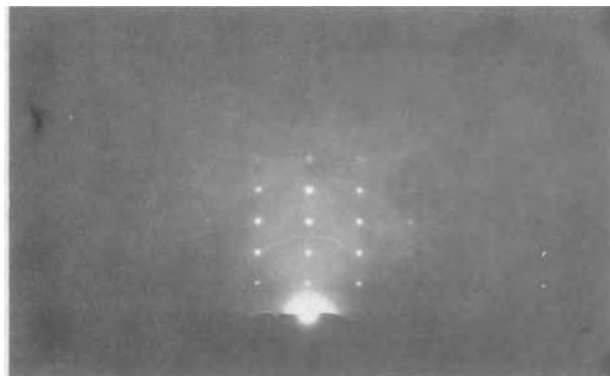


Fig. 5. Electron diffraction pattern of $Zn_{1-x}Cd_xTe$ layer with $x = 0.89$, grown from Bi solution.

CdTe to atoms of Bi. This range of temperatures was chosen in order to give sufficient solubility of ZnTe and CdTe in Bi (5, 6). In this range, mixed layers with any desired composition could be obtained by selecting suitable values of T_M and CdTe concentration. The solubilities of ZnTe in Bi are 0.0060, 0.0084, and 0.0120 at 650°, 700°, and 750°C, respectively. These solubilities were obtained by extrapolating Rubenstein's data (6) to the lower temperatures. The ZnTe/Bi ratios used for $T_M = 650^\circ$, 700°, and 750°C were 0.022, 0.032, and 0.043, respectively. The excess ZnTe was used in order to saturate the solutions. The undissolved ZnTe floated to the top of the solution, so that it did not interfere with epitaxial growth. As an example, the weights of ZnTe, CdTe, and Bi used to form the growth solution for CdTe/Bi = 0.065 and $T_M = 700^\circ C$ were 0.030, 0.070, and 1g, respectively. X-ray diffraction analysis showed that CdTe and Bi do not form any compounds.

The cooling rate v_c also has a strong influence on the composition of the $Zn_{1-x}Cd_xTe$ layers, as shown in Fig. 8. This dependence is presumably due to deviations from equilibrium during the growth process. It appears that only ZnTe is grown on ZnTe substrates under equilibrium conditions (*i.e.*, slow cooling rate).

When In was used as the solvent, mixed crystals with any desired composition could be obtained for $T_M = 600^\circ C$. At higher growth temperatures, however, it was difficult to obtain mixed crystals with compositions close to CdTe: *e.g.*, only ZnTe could be grown for $T_M = 650^\circ C$, regardless of the concentration of CdTe in the solution. When a large amount of CdTe was added to a solution at $T_M = 650^\circ C$, the grown layers became rough due to precipitation of some compound formed between CdTe and In.

In an earlier study (10), it was found that n-type conductivity could be obtained in Al-doped $Zn_{1-x}Cd_xTe$ crystals with $x > 0.3$ which were grown by the Bridgman method in sealed quartz ampuls. In the present work, the conductivity type of the epitaxial layers was determined by Schottky barrier formation or by using

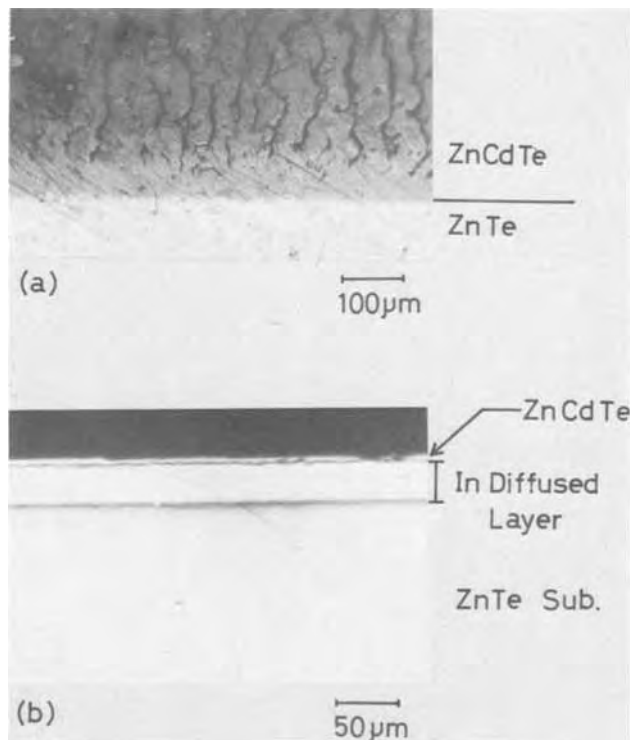


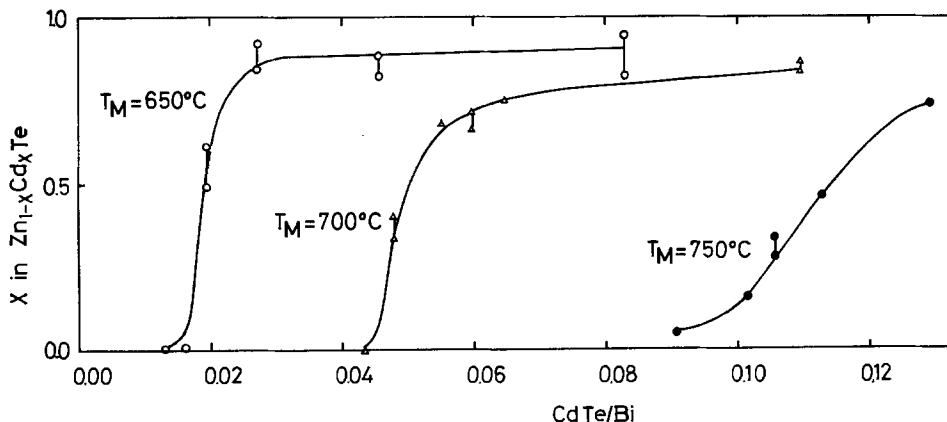
Fig. 6. Typical interfaces between ZnTe substrates and $Zn_{1-x}Cd_xTe$ layers: (a) 5° angle-lapped cross section of a layer with $x = 0.89$ grown from Bi solution, (b) stain-etched cleaved cross section of a layer with $x = 0.80$ grown from In solution.

the hot probe method. It was very difficult to determine the type without illumination because the layers had high resistivities (10^2 - 10^5 ohm-cm). Measurements made under illumination showed that n-type conductivity could be obtained in Al- and In-doped layers with $x > 0.6$.

Figure 9 shows the relationship between the composition and dark resistivity of Al- and In-doped layers grown from Bi solutions. It is seen that the resistivity becomes lower with increasing Cd content. The same result was obtained for the layers grown from In solutions. For layers grown from Al- or In-doped Bi solutions, the alloy composition was not influenced by doping when the concentration of dopant was small, though addition of the dopants did influence the flatness of the layers.

$Zn_{1-x}Cd_xTe$ -ZnTe heterodiodes.—n- $Zn_{1-x}Cd_xTe$ /p-ZnTe heterodiodes were fabricated by making ohmic contacts to the ZnTe substrates and the $Zn_{1-x}Cd_xTe$ layers by electroless plating of Ag and vacuum deposition of In, respectively. The diodes were annealed at 300°C for 5 min to obtain better ohmic contacts to ZnTe.

Fig. 7. Relationship between the ratio of moles of CdTe to atoms of Bi in growth solution and composition of epitaxial layers of $Zn_{1-x}Cd_xTe$ for $T_M = 650^\circ$, 700°, and 750°C with $v_c = 3^\circ C/min$.



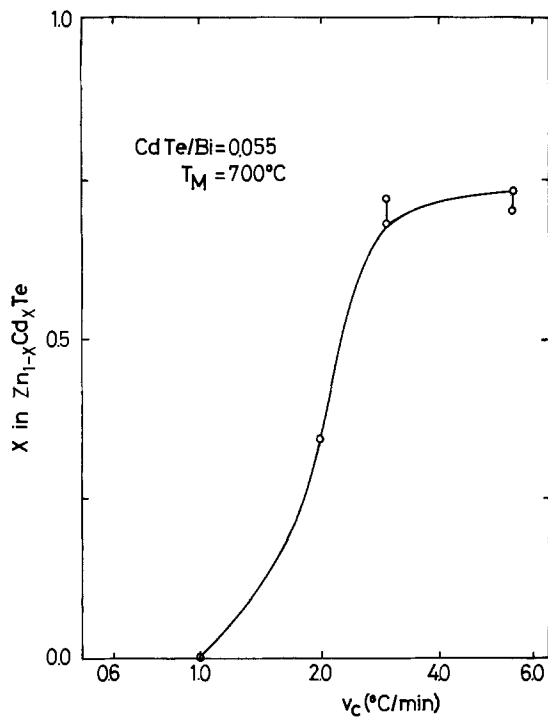


Fig. 8. Relationship between cooling rate v_c (logarithmic scale) and composition of $Zn_{1-x}Cd_xTe$ layers ($CdTe/Bi = 0.055$, $T_M = 700^\circ C$).

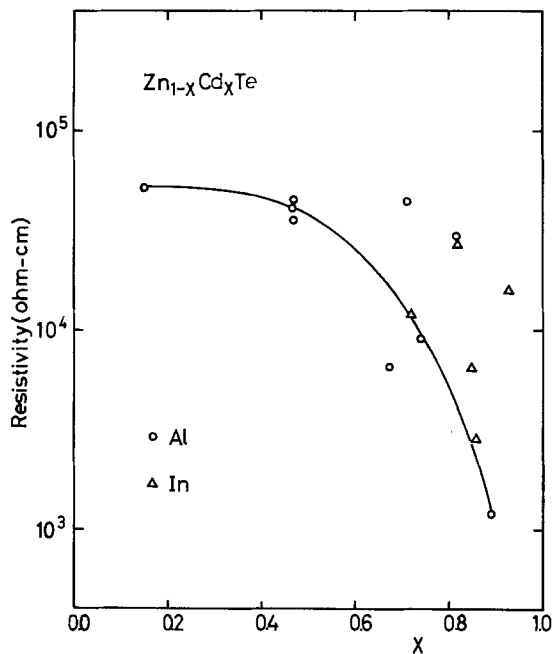


Fig. 9. Relationship between composition x and resistivity of Al- and In-doped $Zn_{1-x}Cd_xTe$ layers grown from Bi solutions.

Figure 10 shows the room-temperature photovoltaic spectra of $Zn_{1-x}Cd_xTe$ -ZnTe heterodiodes grown from In solutions for various x -values determined by x-ray diffraction measurements of the lattice constants. The cutoff wavelengths in the long wavelength region agree well with the bandgaps corresponding to the x -values. In the case of $x = 0.13$, the resistivity of the $Zn_{1-x}Cd_xTe$ layer is very high, so that the photovoltage results from the i-p junction.

The current-voltage (I - V) characteristics of the heterodiodes grown from In solutions were dominated by a semi-insulating region which was formed by diffusion of In into the ZnTe substrates. From C-V measurements this semi-insulating region is estimated to be about $30 \mu m$ thick, in agreement with the observa-

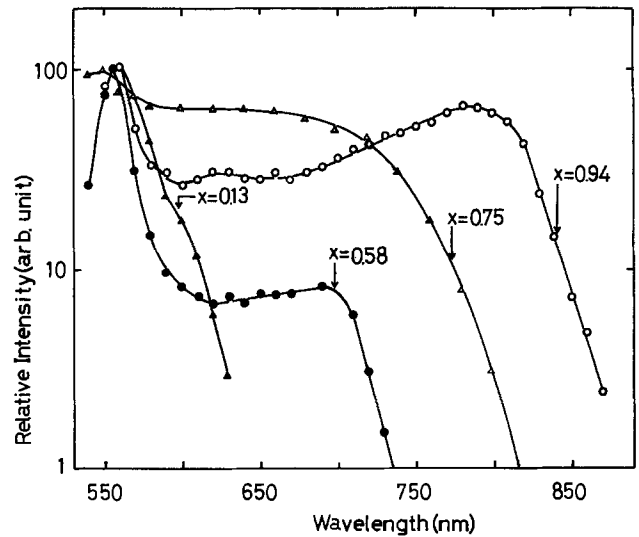


Fig. 10. Photovoltaic spectra at room temperature of $Zn_{1-x}Cd_xTe$ -ZnTe heterodiodes with various x -values.

tions on the etched cross section shown in Fig. 6b. The I - V characteristics of the heterodiodes ($x = 0.87$) grown from Al-doped Bi solution could be expressed by $I \propto \exp(eV/nkT)$ where $n = 2.7$ at $300^\circ K$ and $n = 7.5$ at $77^\circ K$, as shown in Fig. 11, though a very thin Al-diffused layer ($< 0.25 \mu m$ thick) was formed.

At $77^\circ K$, the heterodiodes ($x = 0.87$) prepared from Al-doped layers grown from Bi solutions appeared green under forward bias and red under reverse bias. The emission spectra are shown in Fig. 12. Emission peaks are located at 530, 620, and 720 nm in the forward-bias region and at 620 nm in the reverse-bias region. In the forward-bias region, a shoulder at 550 nm corresponding to yellow emission was also observed, though sometimes it did not appear clearly.

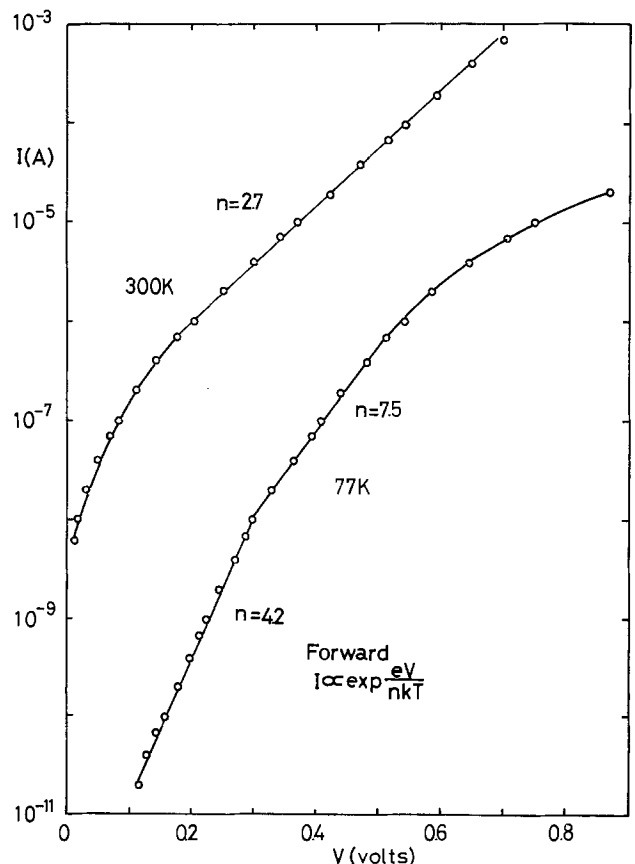


Fig. 11. I - V characteristics in the forward-bias region of $Zn_{0.13}Cd_{0.87}Te$ -ZnTe heterodiodes at 300° and $77^\circ K$.

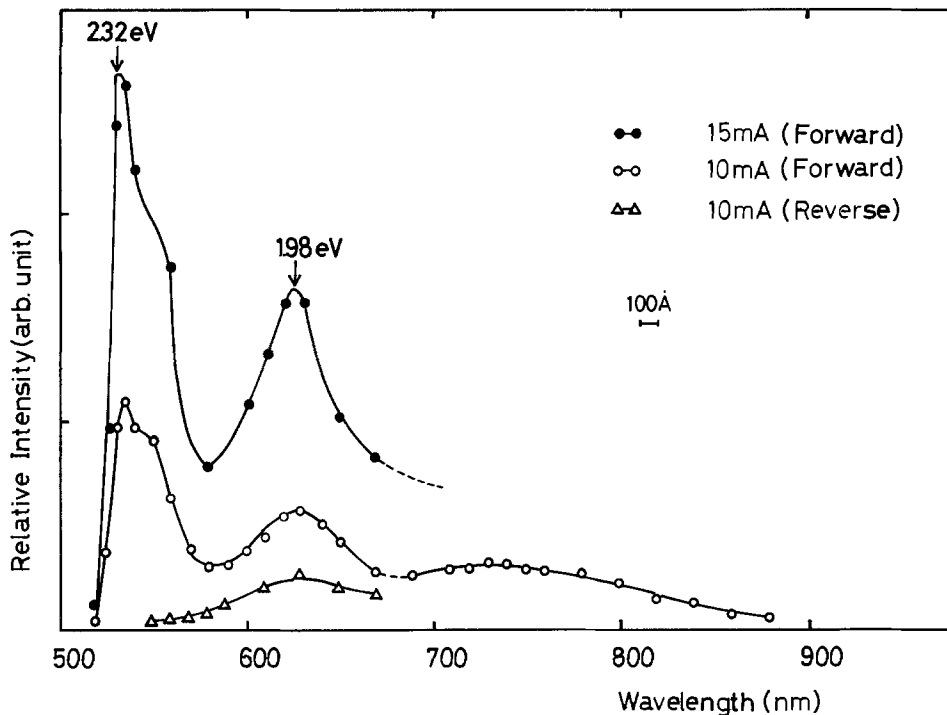


Fig. 12. Electroluminescence spectra at 77°K of Al-doped $Zn_{0.13}Cd_{0.87}Te-ZnTe$ heterodiodes (photomultipliers used are R-453 for 500-670 nm and 7102 for 700-900 nm).

This emission is believed to be due to Al-diffusion into ZnTe, because the shoulder was not observed for the heterodiodes prepared from In-doped samples. The green emission at 530 nm is believed to be due to radiative recombination via As acceptor centers. Since this emission was not observed for the heterodiodes prepared from In-doped samples, In centers may act as killer centers for the green emission. The peak at 720 nm may have the same origin as the peak at that wavelength observed in PL spectra of ZnTe layers grown from nondoped Bi solutions (Fig. 3). Though no attempt was made to measure the electroluminescence efficiency, the green emission could be perceived by the naked eye under room light at a forward current of 20 mA.

Summary

ZnTe and $Zn_{1-x}Cd_xTe$ crystals have been grown on ZnTe substrates by the LPE method using various metals as solvents in an open-tube system. High-quality epitaxial layers with flat interfaces were obtained under suitable growth conditions. $Zn_{1-x}Cd_xTe$ layers showing n-type conductivity, but with high resistivities, were obtained in the composition range $0.6 \leq x \leq 1.0$ from both In solutions and donor-doped Bi solutions. Heterodiodes prepared from Al-doped $Zn_{1-x}Cd_xTe$ layers showed green light emission at 77°K under forward bias.

Acknowledgments

The authors would like to thank Professor Y. Sakai for his encouragement and Associate Professor T. Moriizumi for invaluable discussions.

Manuscript submitted May 24, 1974; revised manuscript received Dec. 12, 1974.

Any discussion of this paper will appear in a Discussion Section to be published in the June 1976 JOURNAL. All discussions for the June 1976 Discussion Section should be submitted by Feb. 1, 1976.

Publication costs of this article were partially assisted by Tokyo Institute of Technology.

REFERENCES

1. G. Mandel, *Phys. Rev.*, **134**, A1073 (1964).
2. S. Fujita, F. Moriai, S. Arai, and T. Sakaguchi, *Japan. J. Appl. Phys.*, **12**, 1841 (1973).
3. S. Fujita, S. Arai, K. Ito, F. Moriai, and T. Sakaguchi, *Appl. Phys. Letters*, **20**, 317 (1972).
4. R. Widmer, D. P. Bortfeld, and H. P. Kleinknecht, *J. Crystal Growth*, **6**, 237 (1970).
5. H. Ischida and K. Tanaka, Proc. 3rd Conf. Solid State Devices, Japan (1971).
6. M. Rubenstein, *This Journal*, **113**, 623 (1966); *J. Crystal Growth*, **3-4**, 309 (1968).
7. P. Wagner and M. R. Lorenz, *J. Phys. Chem. Solids*, **27**, 1749 (1966).
8. J. C. Woolley and B. Ray, *ibid.*, **13**, 151 (1951).
9. K. Saito, A. Ebina, and T. Takahashi, *Solid State Commun.*, **11**, 841 (1972).
10. F. F. Morehead and G. Mandel, *Phys. Rev.*, **137**, A924 (1965).

Effect of Nitrogen and Oxygen/Nitrogen Mixtures on Oxide Charges in MOS Structures

D. W. Hess* and B. E. Deal*

Research and Development Laboratory, Fairchild Camera and Instrument Corporation, Palo Alto, California 94304

ABSTRACT

The positive fixed charge, Q_{ss} , associated with thermally oxidized silicon, has been investigated as a function of annealing time in nitrogen and oxygen/nitrogen mixtures at 1200°C. The effective density of Q_{ss} was found to increase during long time high temperature treatments in nitrogen, but this increase can be controlled by using O_2/N_2 mixtures in place of nitrogen. The trends in Q_{ss} observed during nitrogen annealing are dependent on the furnace used to do the annealing. A correlation was found to exist between Q_{ss} and interface state generation in the various furnaces, and the dependence of interface state generation on annealing ambient has been investigated. In most cases, an equilibrium Q_{ss} is obtained after a certain annealing time in both nitrogen and oxygen/nitrogen atmospheres. Results obtained from reoxidation of oxides equilibrated in nitrogen suggest that these oxides are more oxygen deficient than those equilibrated in oxygen/nitrogen mixtures.

It is well established that the thermal oxidation of silicon results in a positive fixed charge (designated Q_{ss}) located in the oxide-silicon interface region (1-4). This charge is a function of the SiO_2 -Si interface structure and its magnitude depends on the silicon crystal orientation, the oxidation conditions, and subsequent annealing treatments. Q_{ss} , along with other oxide charges, can affect many semiconductor device characteristics, such as MOS threshold voltages, junction breakdown voltages, leakage between devices, and others. Due to the importance of these effects, numerous studies have been carried out to characterize Q_{ss} and to determine its dependence on processing conditions. Such studies have resulted in reasonable control of this oxide charge.

In general, the lowest possible density of Q_{ss} is desirable from a device fabrication standpoint, and this has been attained by using inert gas anneals at temperatures between 900° and 1200°C. Recently, it was recognized that an increase in effective Q_{ss} could result from long time (> 30 min), high temperature (1200°C), inert gas anneals (5, 6). This effect is similar to that observed by Hess and Fowkes (7), where an increase in Q_{ss} resulted from exposure of thermal oxides to a reducing atmosphere at 910°C. Such increases could be due to the breaking of additional Si-O bonds in the somewhat strained oxide interfacial region, and thus a dependence on the silicon surface orientation is expected.

Since no information was available concerning 1200°C nitrogen annealing of thermal SiO_2 films for times greater than 2 hr, and also since the orientation dependence of such anneals had not been determined, this study was initiated to investigate these effects. Also, if the oxygen deficiency or ionized silicon model for this Q_{ss} increase during long time, high temperature, inert gas treatments is correct, subsequent oxidation should eliminate the observed increase. In addition, since Q_{ss} is affected by the amount of oxygen present in the annealing atmosphere, the dependence of Q_{ss} on the oxygen partial pressure was investigated.

Experimental Procedure

The silicon wafers used in this investigation were 4-6 ohm-cm, phosphorus doped, with (100) and (111) orientation. They were cleaned using sulfuric-peroxide, aqua regia, a hydrofluoric acid dip, and several de-ionized water rinses. Oxidations were carried out at 1200°C in a resistance-heated furnace containing an

ultra-high purity Mullite liner and a fused quartz oxidation tube. The samples were oxidized for 39 min and then slow pulled (~2 min) in dry oxygen. This procedure resulted in ~1600Å oxides. The (100) and (111) oxides were then annealed simultaneously in nitrogen or oxygen/nitrogen mixtures at 1200°C in various furnaces. The standard push and pull times were approximately 1 and 2 min, respectively, both in the annealing ambient.

After the anneal, the oxide thicknesses were measured with an Applied Materials (AME-500) ellipsometer. The reproducibility of the oxide thickness over the range investigated was ±4%. The oxides were then stripped from the backs of the wafers. Aluminum dots were evaporated on the front of the wafers through metal masks, and the backs of the slices were coated with aluminum using a cold substrate EB evaporation. The wafers were then annealed for 10 min in dry nitrogen at 500°C, and the MOS capacitors evaluated using the capacitance-voltage technique. In order to separate out any effects due to ionic contamination (Q_o), bias-temperature (B-T) stress measurements were made on the MOS capacitors at 300°C, ±5V, for 3 min. Q_o ranged from less than $3 \times 10^{10} \text{ cm}^{-2}$ for short (under 4 hr) annealing times to $7 \times 10^{10} \text{ cm}^{-2}$ for 16 hr annealing in the various O_2/N_2 mixtures. The fixed charge (Q_{ss}) was calculated from the negatively B-T stressed C-V curve using the following equation

$$\frac{Q_{ss}}{q} = \frac{(2.13 \times 10^{10})(-V_{FB})}{x_o(\mu)} \text{ charges/cm}^2$$

where the work function difference, ϕ_{MS} , is essentially zero for the n-type silicon. The Q_{ss} values were found to be reproducible to $\pm 3 \times 10^{10} \text{ cm}^{-2}$.

The flow meters utilized in this study were calibrated using a Matheson Electronic Mass Flowmeter and a Porter-Vol-U-Meter. The total flow rate was 1 liter/min, which corresponded to a gas velocity of ~1 cm/sec. The oxygen and nitrogen used were from a liquid source and were further dried and filtered by passage through a Matheson Model 451 gas purifier.

Results and Discussion

Effect of N_2 anneal on fixed charge (Q_{ss}).—The variation of the fixed surface state charge (Q_{ss}) with nitrogen annealing time at 1200°C is shown in Fig. 1 and 2 for (100) and (111) silicon surface orientations, respectively. The observed increase in effective Q_{ss} during long time anneals in nitrogen at 1200°C has been reported previously (6) for anneal times up to 2 hr

* Electrochemical Society Active Member.
Key words: silicon dioxide, MOS, oxide charge.

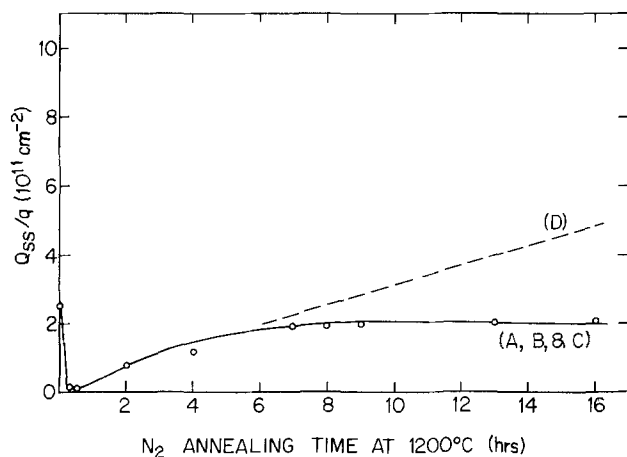


Fig. 1. Dependence of effective Q_{ss} on the time of nitrogen annealing at 1200°C for 1600\AA oxides in four different furnaces. The silicon surface orientation is (100).

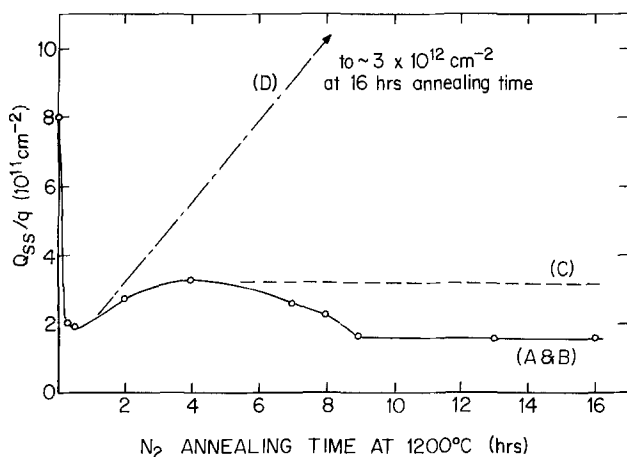


Fig. 2. Dependence of effective Q_{ss} on the time of nitrogen annealing at 1200°C for 1600\AA oxides in four different furnaces. The silicon surface orientation is (111).

and (111) silicon surface orientation. It has been proposed (6) that this effect may be related to the breaking of additional Si-Si or Si-O bonds near the Si-SiO₂ interface, which creates additional positive charge in the oxide. The solid line in Fig. 1 represents data obtained from three different furnaces (denoted A, B, and C), while the dotted line represents data obtained from a fourth furnace, D. Similarly, the data presented in Fig. 2 were obtained from the same four furnaces as those in Fig. 1.

The data from furnaces A and B were taken at the various anneal times indicated by the circles in Fig. 1 and 2, while data points for furnaces C and D were taken up to 2 hr of annealing time, and then results obtained for 16 hr of N₂ annealing in both furnaces. The curves were then extrapolated to these 16 hr points (dotted lines). It can be seen from Fig. 1 and 2 that three of the furnaces gave identical (within experimental error) results for (100) samples, while the results of (111) oriented silicon showed three different results for the four furnaces. Particularly interesting is the result obtained in furnaces A and B for (111) samples, where, as for the (100), the effective Q_{ss} increases after one-half hour of nitrogen annealing, but subsequently decreases and reaches a steady state near the original Q_{ss} minimum.

At present, we cannot explain the observed dependence of Q_{ss} on the furnace used to do the annealing, although it should be mentioned that furnace A was the only furnace that utilized a liner. However, the fact that furnace B did not have a liner, yet the results from this furnace agreed within experimental error to those obtained from furnace A, seems to preclude any

effect of a liner on the observed Q_{ss} . Also, no differences in mobile ion concentration could be detected among the various furnaces.

In order to determine whether the addition of chlorine to the oxide would affect the value of Q_{ss} obtained during nitrogen annealing, a series of (100) and (111) samples in which chlorine was incorporated during oxidation by passing a small amount of oxygen through a bubbler of trichloroethylene, was prepared at 1100°C . Nitrogen anneals were then performed for times ranging from 15 min to 16 hr in furnace A at 1200°C , and the Q_{ss} values agreed within experimental error to those obtained with nonchlorine oxides in this furnace.

Effect of N₂ anneal on interface states.—In the case of the (111) samples, an interesting correlation existed between the shapes of the C-V curves and the value of Q_{ss} obtained in the different furnaces (see Fig. 2). At an annealing time of 7 hr in nitrogen (furnaces A and B), the shape of the C-V curve was nearly ideal (Fig. 3), but a relatively large flatband shift was observed. However, as the anneal time was gradually increased from this point, a distortion of the C-V curve became apparent as the flatband voltage decreased. This distortion increased rather noticeably as longer anneal times were used (Fig. 3). Even when the flatband (and thus Q_{ss}) reached a constant value (approximately 9 hr), the distortion continued to increase. The distortion is physically similar to that produced by interface states occurring between the intrinsic level and conduction band of silicon as reported by Deal, MacKenna, and Castro (8). However, the present state could not be eliminated by a nitrogen anneal at 500°C with aluminum dots present on the wafer (anneal), suggesting that this is not a normal interface state since it cannot be eliminated by hydrogen produced during the anneal process (9). The (100) samples annealed simultaneously with the (111) showed no evidence of such distortion. (It should be noted that all curves shown in Fig. 3 represent samples which have received an anneal at 500°C .)

Furnace C, which gave an intermediate value of Q_{ss} for the (111) sample ($\sim 3.2 \times 10^{11} \text{ cm}^{-2}$) generated the same distortion of the C-V curve as furnaces A and B, but the distortion was much less pronounced (Fig. 4). Finally, furnace D, which gave the highest value of Q_{ss} for the (111) and (100) samples, generated no detectable distortion of either the (111) or (100) C-V curves. To more specifically indicate the differences in the C-V curves of the various samples obtained after nitrogen annealing, a quantity V_{IS} , which represents the "width" of the break in the C-V curve in volts and is apparently due to some kind of interface

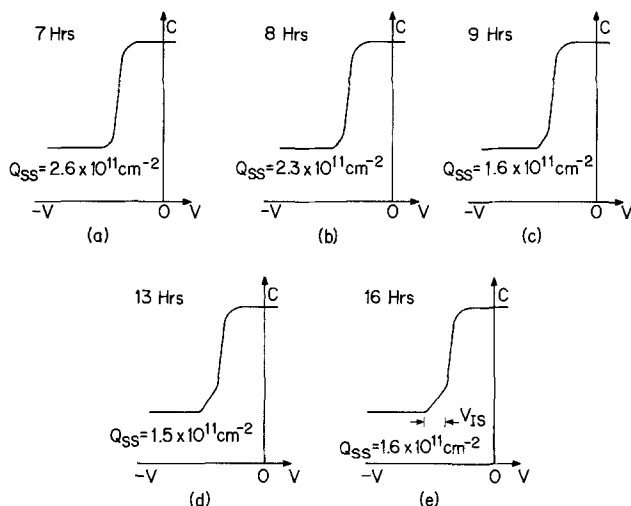


Fig. 3. Effect of nitrogen annealing at 1200°C in furnaces A and B on the shape of the C-V curve for various annealing times. V_{IS} is the magnitude of the "break" observed in the C-V curve in volts. All oxide thicknesses were 1600\AA . See Table II.

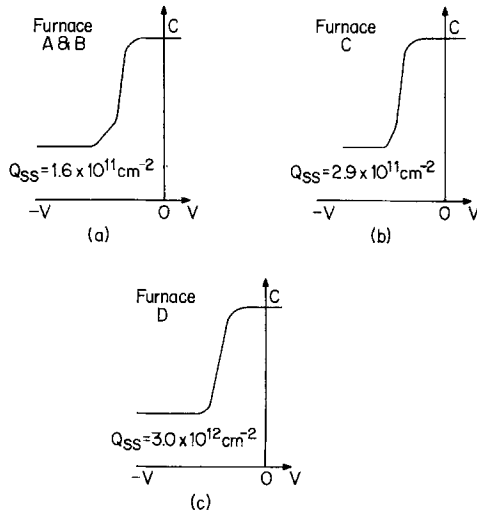


Fig. 4. Effect of nitrogen annealing at 1200°C for 16 hr in furnaces A, B, C, and D on the shape of the C-V curves. All oxide thicknesses were 1600Å. See Table II.

state, was defined as shown in Fig. 3e. Also, the slopes of the C-V curves obtained after N₂ treatments were measured and compared on the basis of the voltage (V_{slope}) required to go from 0.8 to 0.5 C_{max}. These slopes, along with the V_{IS} values, are given in Table I. The values of V_{slope} indicate that interface states, as measured by distortion of C-V curves, are generated in furnace D, and these states, like those observed in furnaces A, B, and C, are not eliminated by an anneal. These data suggest that the distribution of states in furnace D may be different from the distribution in furnaces A, B, and C. Indeed, preliminary conductance-voltage experiments (10) have shown little difference in interface state densities between samples annealed in furnaces A, B, C, or D. However, while the samples annealed in furnaces A, B, and C showed a rather narrow distribution of states, samples annealed in furnace D showed a relatively broadened distribution.

As with Q_{ss}, we can at present offer no explanation or possible description of the interface states causing the effect reported here. Considering the fact that hydrogen is ineffective in eliminating these states, and also that the results are furnace dependent, an effect such as a heavy metal impurity is suspected. However, reoxidation results that are presented later show that a structural defect in the SiO₂ is also a possibility.

Effect of O₂/N₂ anneals on oxide charges.—Before describing the results of O₂/N₂ mixtures on oxide charges, it should be noted that several selected experiments, utilizing both N₂ and O₂/N₂, were carried out in furnaces A, B, C, and D, and of these, the nitrogen annealing studies described above were the only ones that indicated any dependence on the furnace used.

As stated above, if the ionized silicon or oxygen deficiency model for the Q_{ss} increase during long time,

Table I. Comparison of the shapes of C-V curves obtained from different furnaces used for the nitrogen annealing of Si-SiO₂ samples at 1200°C

All oxide thicknesses are 1800-1650Å.
The silicon surface orientation is (111)

Furnace	N ₂ anneal time (hr)	V _{IS} (V)*	V _{slope} (V)*
A and B	8	0.9	0.7
A and B	9	1.0	0.7
A and B	13	1.4	0.7
A and B	16	1.8	0.7
C	16	1.1	0.7
D	16	Not detectable	1.1

* See explanation in text.

high temperature, inert gas treatments is correct, it should be possible to control this Q_{ss} increase during such anneals if a small amount of oxygen is present during the heat-treatment. The effect on the fixed charge due to treating thermal oxides in various O₂/N₂ mixtures at 1200°C and pulling the samples from the furnaces in the annealing ambient is shown in Fig. 5-8. In these figures, any increase of the oxide thickness during O₂/N₂ treatment was taken into account for the purpose of Q_{ss} calculation.

Figures 5 and 6 show that the initial effect of 2 and 5% O₂/N₂ mixtures is to significantly lower Q_{ss} as in nitrogen up to a time of approximately 2 hr, after which a slight decrease and "leveling off" occurs. As might be expected, an increase in the Q_{ss} minimum is experienced as the oxygen percentage is increased from 2 to 5%. Apparently, at longer anneal times, an equilibrium situation is attained where the increase in Q_{ss} caused by the pure nitrogen treatment is compensated by the oxygen present in the annealing atmosphere. As the oxygen diffuses through the oxide, and a "new interface" begins to form, the Q_{ss} approaches an equilibrium value. This agrees with the data obtained for 10 and 50% mixtures (Fig. 7 and 8) where, after the initial Q_{ss} decrease, an almost immediate equilibrium situation with regard to Q_{ss} is established.

It should be noticed that the times necessary for equilibration decrease with increasing oxygen partial pressure, substantiating the necessity of forming a "new interface" before Q_{ss} can reach a constant value. Figures 5-8 show that for each oxygen partial pressure, the Q_{ss} for (111) oriented silicon is approximately

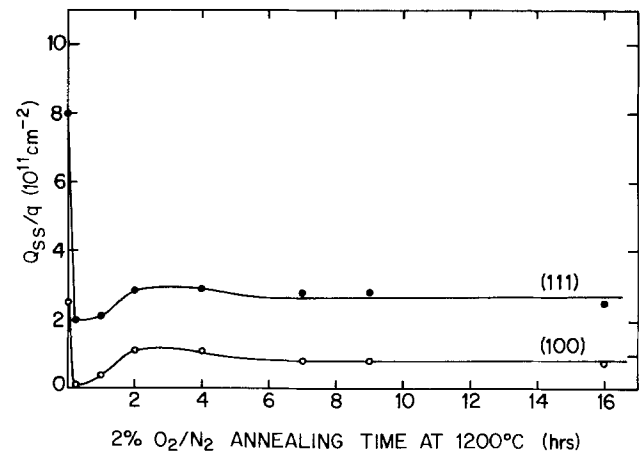


Fig. 5. Dependence of effective Q_{ss} on the time of annealing in 2% O₂/N₂ fixtures at 1200°C. All initial oxide thicknesses were 1700Å.

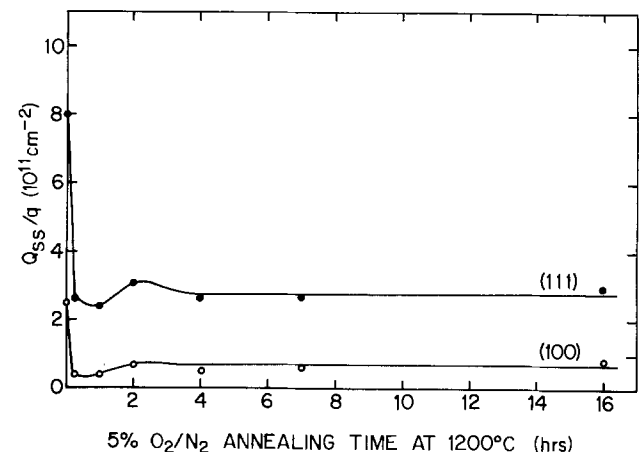


Fig. 6. Dependence of effective Q_{ss} on the time of annealing in 5% O₂/N₂ mixtures at 1200°C. All initial oxide thicknesses were 1600Å.

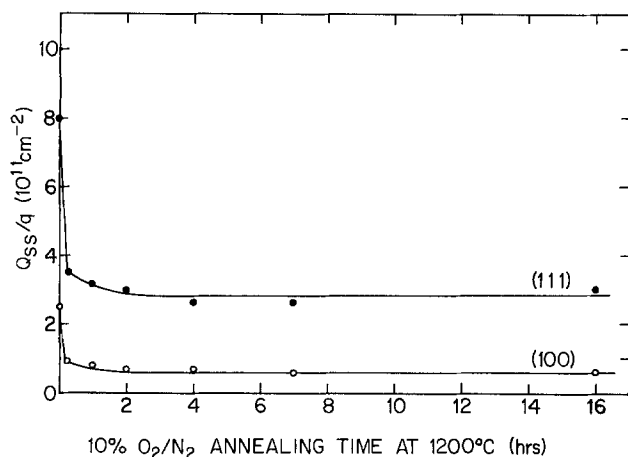


Fig. 7. Dependence of effective Q_{ss} on the time of annealing in 10% O_2/N_2 mixtures at 1200°C. All initial oxide thicknesses were 1600Å.

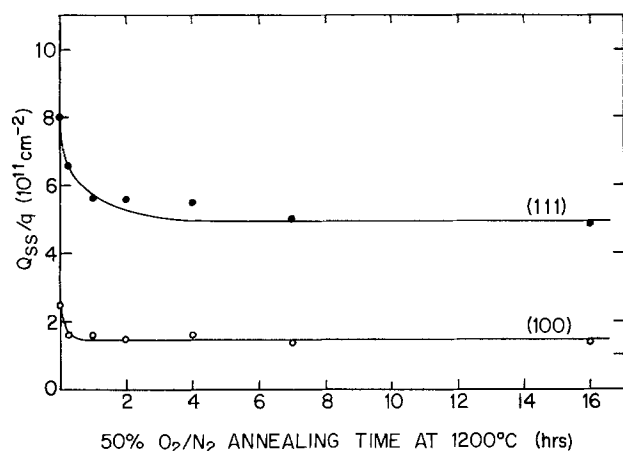


Fig. 8. Dependence of effective Q_{ss} on the time of annealing in 50% O_2/N_2 mixtures at 1200°C. All initial oxide thicknesses were 1600Å.

three to four times that of (100). This is the normally observed orientation dependence (1).

Mention should be made of the pull rate dependence of Q_{ss} experienced during this study. Although slight variations were observed, the pull rate was not found to be critical for the 2, 5, and 10% mixtures, but was quite critical for the 50% mixture. This is in agreement with previous results (1) which showed the difference in Q_{ss} between fast and slow pulling in oxygen. As the percentage of oxygen in the annealing atmosphere increases, the pull rate will determine the final Q_{ss} value for the same O_2/N_2 mixture, where Q_{ss} will increase with increasing pull time. Consideration of the equilibrium Q_{ss} values indicates that up to an oxygen partial pressure of 0.1, the exact amount of oxygen present in the annealing atmosphere is not critical, since the equilibrium values of Q_{ss} are approximately $0.7 \times 10^{11} \text{ cm}^{-2}$ and $2.7 \times 10^{11} \text{ cm}^{-2}$ for the (100) and (111) wafers, respectively, for 2, 5, and 10% mixtures. Also, it is important to recognize that no distortion of the C-V curves such as those shown in Fig. 3 and 4 and tabulated in Table I were observed for any of the O_2/N_2 mixtures investigated.

Effect of O_2 anneals on oxide charges.—It has been postulated that Q_{ss} results from a silicon excess or oxygen deficiency at the Si-SiO₂ interface (1, 7). If this is true, it should be possible to "reoxidize" the present oxides, which have been equilibrated in a deficiency of oxygen and thereby return Q_{ss} to more normal values. Therefore, using (100) and (111) oriented silicon wafers, two sets of oxides were prepared, one of which was equilibrated in 2% O_2/N_2 and the other

equilibrated in N_2 only (furnace C) at 1200°C. The oxides were fabricated such that the final oxide thicknesses were the same for all samples ($1600 \pm 20\text{Å}$). They were then pushed into the furnace in nitrogen and oxidized in 100% O_2 at 1200°C for times of 1, 2, and 3 min. At the end of these times, some of the samples were slow pulled (2 min) from the furnace in oxygen and some received a 15 min nitrogen anneal prior to being slow pulled from the furnace in nitrogen.

The results of Q_{ss} measurements for the wafers slow pulled in oxygen indicate no difference between samples equilibrated in 2% O_2/N_2 or N_2 alone, and the Q_{ss} values agreed with initially oxidized samples which had been slow pulled in oxygen [$Q_{ss} \approx 2.5 \times 10^{11} \text{ cm}^{-2}$ for (100) and $8 \times 10^{11} \text{ cm}^{-2}$ for (111)]. The final Q_{ss} values for samples which received a 15 min nitrogen cycle at the end of the reoxidation are given in Table II. It can be seen that after equilibration of the oxides in 2% O_2/N_2 , little oxygen is required to compensate for the oxygen deficiency established during equilibration. However, the samples equilibrated in N_2 required substantially more oxygen prior to nitrogen annealing to lower the Q_{ss} significantly.

Similarity of thermal and electrical charge generation.—The increase in Q_{ss} and the simultaneous generation of interface states during 1200°C nitrogen treatments for times greater than 7 hr is quite similar to the effect produced by a negative field applied to MOS capacitor structures at elevated temperatures (1, 11-14). In the latter case, an oxygen vacancy or silicon excess model has been proposed to account for the increase in fixed charge and interface state density (6, 12). Such a model is in agreement with the observed dependence of the generated fixed charge on the initial Q_{ss} density (1). Likewise, the results of the present investigation might be explained by the breaking of additional Si-O bonds, resulting in a higher positive charge, accompanied by an increase in surface-state density. Whereas the negative field at elevated temperatures may break bonds primarily by electrical means, in the present work, as in Ref. (7), the breaking of bonds might be due to thermal energy.

Summary

Using the C-V technique, the fixed oxide charge, Q_{ss} , was studied as a function of annealing time in nitrogen and oxygen/nitrogen mixtures at 1200°C. These investigations have shown that after the initial decrease of Q_{ss} due to nitrogen annealing, an increase is observed up to approximately 4-7 hr, possibly resulting from the breaking of additional Si-Si or Si-O bonds at the Si-SiO₂ interface. Longer nitrogen annealing times give scattered results for Q_{ss} , which apparently depend on the oxidation system (furnace) used for the annealing. In most furnaces, these long time nitrogen anneals generate interface states which are observed as

Table II. Reoxidation of oxides equilibrated in 2% O_2/N_2 and N_2 only* at 1200°C

All samples were pushed into the furnace in N_2 , oxidized at 1200°C in 100% O_2 for the indicated time, annealed in N_2 for 15 min, and slow pulled (2 min) from the furnace in N_2

Equilibrating atmosphere	Orientation	Equilibrium Q_{ss} (10^{11} cm^{-2})	Oxidation time (min)	Final Q_{ss} (10^{11} cm^{-2})
2% O_2/N_2	(100)	0.9	1	0.3
2% O_2/N_2	(100)	0.9	2	0.4
2% O_2/N_2	(100)	0.9	3	0.4
2% O_2/N_2	(111)	3.4	1	2.7
2% O_2/N_2	(111)	3.4	2	2.7
2% O_2/N_2	(111)	3.4	3	2.7
N_2^*	(100)	2.1	1	2.2
N_2^*	(100)	2.1	2	1.0
N_2^*	(100)	2.1	3	1.2
N_2^*	(111)	3.6	1	3.6
N_2^*	(111)	3.6	2	2.3
N_2^*	(111)	3.6	3	2.1

* The initial N_2 annealing was done for 16 hr in furnace C.

distortions of the C-V curve and cannot be eliminated by a 500°C anneal. A reoxidation of the samples in 100% oxygen, however, does eliminate the distortions. This suggests that the interface states or levels responsible for these distortions may be related to a structural defect in the SiO₂ lattice. No differences in the values of Q_{ss} or interface states were observed between oxides which did or did not contain chlorine (for a given annealing treatment).

After a particular annealing time in oxygen/nitrogen mixtures at 1200°C, Q_{ss} reached an equilibrium value. The fact that the oxidation time necessary to reach equilibrium depended on the oxygen partial pressure, indicated that a "new interface" had to form before Q_{ss} could reach a constant value. Up to a partial pressure of 0.1 this equilibrium value was a rather insensitive function of the oxygen partial pressure. No distortions of the C-V curves such as those generated during nitrogen annealing were observed for any O₂/N₂ mixtures. Also, unlike the nitrogen anneals, all O₂/N₂ mixtures resulted in the normal orientation dependence of Q_{ss} over all times investigated. Reoxidation of samples equilibrated in 2% O₂/N₂ and samples equilibrated in nitrogen suggested, as expected, that there is a difference in oxygen deficiency depending on the oxygen partial pressure of the atmosphere used for equilibration.

Acknowledgments

The authors wish to thank Maija Sklar for helpful discussions during the course of this work, and Ying Shum for conductance-voltage experiments. Also, most of the experimental procedures were conducted by Julia Bien.

Manuscript received March 5, 1975.

Any discussion of this paper will appear in a Discussion Section to be published in the June 1976 JOURNAL. All discussions for the June 1976 Discussion Section should be submitted by Feb. 1, 1976.

Publication costs of this article were partially assisted by Fairchild Camera and Instrument Corporation.

REFERENCES

1. B. E. Deal, M. Sklar, A. S. Grove, and E. H. Snow, *This Journal*, **114**, 266 (1967).
2. E. Kooi, "The Surface Properties of Oxidized Silicon," N. V. Philips Gloeilampenfabrieken, Eindhoven, The Netherlands (1967).
3. P. V. Gray, *Proc. IEEE*, **57**, 1543 (1969).
4. A. Goetzberger and S. M. Sze, "Applied Solid State Science," Vol. 1, pp. 154-238, Academic Press, New York (1969).
5. S. D. Brotherton, D. R. Lamb, and J. W. Clancy, *Intern. J. Electron.*, **31**, 629 (1971).
6. B. E. Deal, *This Journal*, **121**, 198C (1974).
7. D. W. Hess and F. M. Fowkes, Paper 303 RNP presented at The Electrochemical Society Meeting, Chicago, Ill., May 13-18, 1973; *Appl. Phys. Letters*, **22**, 377 (1973).
8. B. E. Deal, E. L. MacKenna, and P. L. Castro, *This Journal*, **116**, 997 (1969).
9. P. Balk, Paper 109 presented at The Electrochemical Society Meeting, San Francisco, California, May 9-13, 1965.
10. E. H. Nicollian and A. Goetzberger, *Appl. Phys. Letters*, **7**, 216 (1965).
11. A. Goetzberger and H. E. Nigh, *Proc. IEEE*, **54**, 1454 (1966).
12. Y. Miura and Y. Matukura, *Japan. J. Appl. Phys.*, **5**, 180 (1966).
13. F. H. Reynolds, Proc. 11th Annual Reliability Physics Symposium, Las Vegas, Nevada, April 3-5, 1973.
14. M. Nakagiri, *Japan. J. Appl. Phys.*, **13**, 1610 (1974).

Effects of MOS Metallization Geometry and Processing on Mobile Impurities

Arthur J. Learn

Research and Development Laboratory, Fairchild Camera and Instrument Corporation, Palo Alto, California 94304

ABSTRACT

The possible effects on MOS structures of metallization material, method of vacuum deposition, method of electrode delineation, electrode size and geometry, post-metallization heat-treatments, and hydrogen incorporation were investigated. It was found that a minimum in the level of mobile ionic contamination (Q_0) was achieved in a time the order of 15 min for annealing at 500°C in dry nitrogen. The minimum Q_0 values were proportional to either the diameter of circular electrodes or the width of rectangular electrodes in the range of 5-30 mil. Results were similar for both aluminum and aluminum-copper-silicon metallization as well as for either shadow masked or photo-masked electrodes. The assumed presence of hydrogen, either arising from that produced in the deposition chamber during filament and electron beam evaporation as monitored by residual gas analysis or from hydrogen anneals prior to metallization, resulted in increased Q_0 for short anneal times. In interpreting the results, consideration was given mechanisms which would decrease Q_0 , such as diffusion of contaminant (probably sodium) to and evaporation from the electrode periphery, and increase Q_0 , such as introduction of contaminant and/or aluminum from the electrodes or substitution of protons for contaminant ions at traps.

The importance of minimizing mobile alkali ion contamination (Q_0) in silicon device processing is well recognized (1). Such contamination in silicon dioxide can affect the threshold voltage and stability of MOS devices. Adverse effects on bipolar devices, primarily

Key words: mobile impurity monitoring, MOS electrode size effects, hydrogen effects, annealing effects.

related to silicon surface inversion and channeling, can also be observed as a consequence of ionic contamination. Many of the processing steps may introduce contamination with one of the more suspect (2) being metallization.

Extensive investigations of the behavior of charges, including Q_0 , in oxides have been made (1). Tech-

niques for minimizing Q_0 levels have been developed including gettering by phosphorus (3) or chlorine (4) incorporated in the oxide. In such studies the metallization for the MOS structure is considered to play a passive role, other than serving as an electrode, with the following two exceptions. The annealing of fast surface states in the presence of aluminum is presumed (5) to be a consequence of hydrogen evolution through an aluminum-water vapor reaction. In addition, sintering conditions for the aluminum metallization have been found (6) to affect radiation hardness of MOS structures.

The possibility of the metallization and metallization processing influencing Q_0 is more directly examined here. The effects on Q_0 of the method of metallization deposition and fabrication into electrodes, electrode size and geometry, temperature treatments, and hydrogen were considered. It was found to be necessary, in interpreting the results, to postulate ionic contamination diffusion to and vaporization from the electrode periphery combined with either activation of contamination in the oxide or introduction of mobile contamination from the electrode. Enhanced mobilization of ionic alkali contamination in the oxide with hydrogen present was also proposed.

Experimental Procedure

The thermal oxidation of silicon wafers of $\langle 111 \rangle$ orientation in dry oxygen was performed under clean conditions. The oxide thickness was either 0.1 or 0.2 μ . The metal providing contact to the backside of the wafers was deposited after scratching through the oxide. Frequently this metal was deposited and then sintered in dry nitrogen or hydrogen before deposition on the front side of the wafers. Heat-treatment of wafers after front-side metallization was performed in dry nitrogen at 500°C.

Both aluminum and aluminum-alloy metallization of about 1 μ thickness were deposited in oil-diffusion-pumped vacuum chambers. Aluminum was deposited by electron beam, tungsten filament, or flash evaporation (7) while only the latter technique was used for aluminum-4% copper-2% silicon deposition. The source material used was always of at least 99.999% purity. The gas composition within the deposition chamber was investigated for each technique. A quadrupole residual gas analyzer attached to the chamber was used for this purpose. Deposition was normally onto wafers heated to temperatures of 300°-350°C. With other conditions held constant, it was found that the increased heating time necessary in order to attain progressively higher wafer temperatures during deposition resulted in increased Q_0 . Accordingly, substantially higher temperatures were sometimes used in flash evaporation in order to increase Q_0 to readily measurable levels. By the same reasoning, wafers were not heated during flash evaporation when the objective was to gain a measure of Q_0 in the prepared oxides. The metal electrodes were formed either by shadow masking during deposition or by subsequent photomasking. The shadow masks were thoroughly cleaned chemically before use. Circular electrodes having nominal diameters of 5, 10, 15, and 30 mil were formed by both techniques. Rectangular electrodes having widths of 6 and 14 mil were prepared by photomasking.

Capacitance measurements at a frequency of 1 MHz were performed on completed capacitors. Room temperature capacitance-voltage traces were obtained for as-formed capacitors and following application of positive or negative bias for 3 min at 300°C. A field of 25 V/ μ was used with the electrode negatively biased and 50 V/ μ for the positive bias. The samples were rapidly quenched to room temperature following removal of the bias. The values of Q_0/q in charges cm^{-2} were calculated from the usual equation (8)

$$\frac{Q_0}{q} = \frac{2.1 \times 10^{10}}{x_0} \Delta V$$

where x_0 is the oxide thickness in μ and ΔV is the voltage shift between the capacitance-voltage characteristics following negative and positive bias-temperature stress. It was determined by this procedure, when clean metallization processes such as cold-substrate flash evaporation were used, that the Q_0 levels in the oxide were typically in the low 10^{10} cm^{-2} range for 30 mil diameter electrodes. Such measurements also served to establish the cleanliness of the annealing furnace used for all nitrogen anneals.

Results

Effect of anneal time and masking procedure.—Values of Q_0 as a function of anneal time at 500°C in nitrogen are shown in Fig. 1 for circular (dot) electrodes of two diameters. The sample was prepared by heated substrate deposition of aluminum-copper-silicon through a shadow mask. A minimum in Q_0 is noted for both dot sizes. A longer anneal time was required in order to achieve the minimum for the larger dot.

Results are presented in Fig 2 for a sample similar to that of Fig. 1 except that the dots were formed by photomasking. Two values of Q_0 are indicated for the smaller dot at zero anneal time. The larger value was obtained from the initial capacitance-voltage measurement. The second and subsequent measurements on the same dot or other dots of the same size yielded the lower Q_0 value. Apparently the bias stress temperature (300°C) was sufficient to alter the contamination for the smaller dots. No such effect was observed with the larger dots but it should be noted that the measurements on such dots were performed last. As was true for the shadow-masked dots, anneals at 500°C resulted in a minimum Q_0 . The data are not sufficiently detailed to determine whether or not a longer anneal time was required to minimize Q_0 for the larger dots. However, results presented below suggest that this was the case.

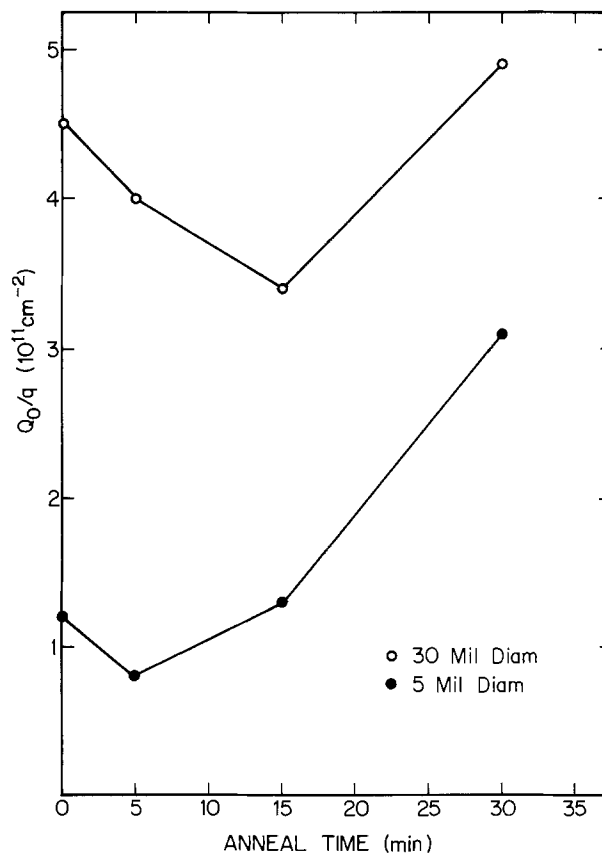


Fig. 1. Dependence of Q_0 on the time of annealing in nitrogen at 500°C for a sample with hot-substrate aluminum alloy metallization. Circular electrodes of the nominal dimensions indicated were formed by shadow masking.

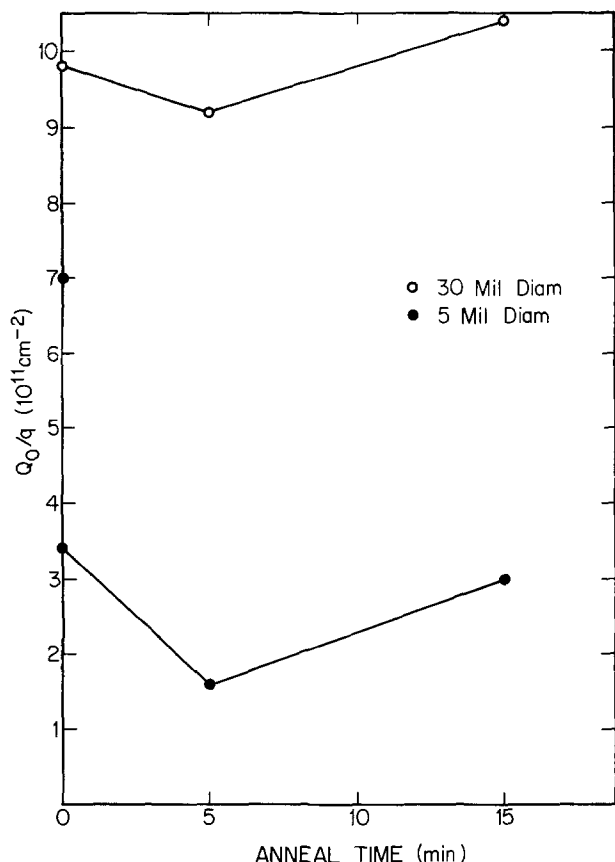


Fig. 2. Dependence of Q_0 on the time of annealing in nitrogen at 500°C for a sample with hot-substrate aluminum alloy metallization. Circular electrodes of the nominal dimensions indicated were formed by photomasking.

Effect of dot dimensions.—The indication from Fig. 1 and 2 is that the minimum Q_0 for smaller dots were reached after approximately 5 min anneals. The attainment of minimum Q_0 for larger dots apparently requires somewhat longer anneals but probably the levels reached are not substantially different from Q_0 values after 5 min anneals. Accordingly, a 5 min anneal at 500°C was considered to be a useful condition for more complete investigation of the dependence of Q_0 on dot size. Values of Q_0 after this treatment are plotted as a function of the dot diameter in Fig. 3. Results are shown for aluminum dots formed through a shadow mask and aluminum-copper-silicon dots formed either by shadow masking or photomasking. All of the films were deposited by flash evaporation onto heated wafers. Also included for reference are some of the data of Fig. 1 and 2. The actual dot diameters, as determined from photomicrographs of the dots, were used. In the case of the shadow masked dots the diameters differed substantially from nominal values as a consequence of penumbral effects occurring during deposition.

In all cases, Q_0 was found to increase approximately linearly with increasing dot diameter. This was true for both aluminum and the aluminum alloy as well as for both shadow masked and photomasked samples. The two data points shown for the larger dots from the sample of Fig. 1 are the minimum Q_0 and the Q_0 following a 5 min anneal. While somewhat better fit to a straight line through the origin might be obtained with strict use of minimum Q_0 , the basic nature of the curves would remain unchanged.

Effect of hydrogen.—It has been reported (9) that substantial amounts of hydrogen are present in the vacuum chamber during aluminum evaporation from pyrolytic boron nitride which is radiatively heated. The data presented in Fig. 4 show this to be true for tungsten filament and electron beam evaporations as

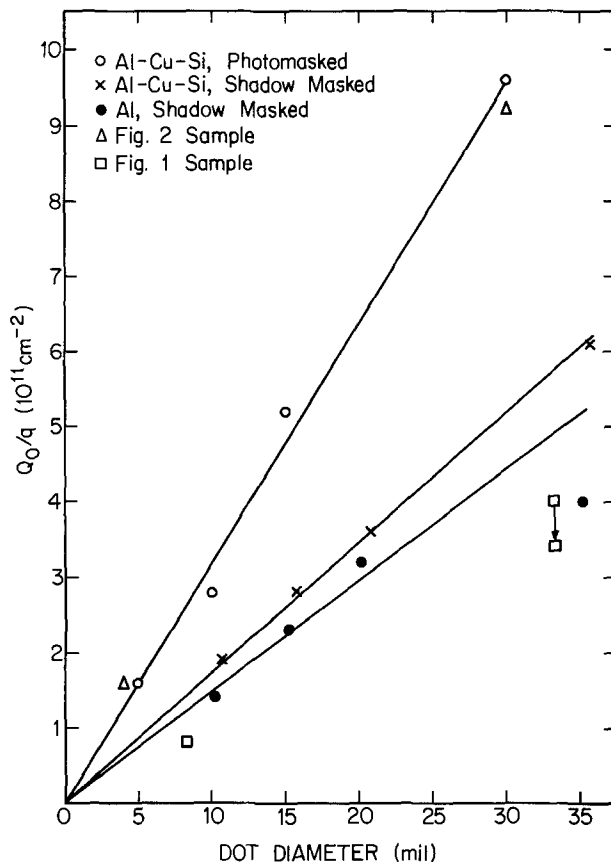


Fig. 3. Dependence of Q_0 , obtained after a 5 min anneal at 500°C , on electrode diameter for hot-substrate samples as indicated.

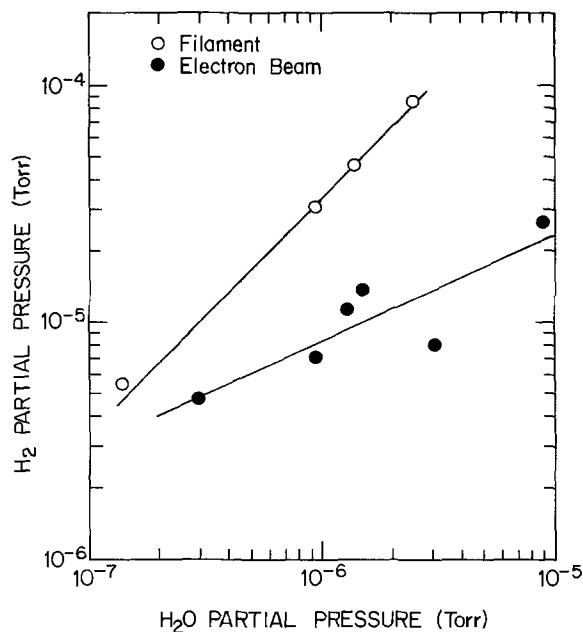


Fig. 4. Partial pressures of H_2 and H_2O in the deposition chamber during filament and electron beam evaporation of aluminum.

well. The partial pressures are averages over the few minute periods of deposition. Prior to melting of the aluminum source material the major gas present was water vapor. Some hydrocarbons were detected both before and during deposition but the concentrations were relatively small. The predominant species of hydrogen observed was H_2 although atomic hydrogen was present in significant concentrations, particularly for filament evaporations. The higher total pressures were obtained by restricting the area of the pumping

line between the vacuum chamber and the diffusion pump. For filament evaporation the data are fitted by a line of unit slope consistent with a constant ratio of H_2 to H_2O partial pressures of approximately 30. The data for electron beam evaporation exhibited considerable scatter. The line shown is a least squares fit. For a typical deposition pressure ($\sim 10^{-5}$ Torr) the ratio of H_2 to H_2O partial pressures is about 10.

The hydrogen presumably is generated through reaction of the aluminum and water vapor. The reaction could occur both on the molten aluminum and on freshly deposited film surfaces. The surface area of the filament was an order of magnitude larger than that of the molten aluminum in the electron gun hearth. The more pronounced H_2 evolution with the filament deposition is an indication then that reaction on molten aluminum is more significant. Some reaction does occur at this surface as evidenced by the buildup of an oxide dross on the electron beam aluminum source material. Further support for such a mechanism is provided by results obtained with flash evaporation. In this case little H_2 was present during deposition. It would be expected that the reaction would be limited with flash evaporation since the molten aluminum is confined in area and remains on the flash bar only for a short period of time. Undoubtedly, reaction also occurs at film surfaces as evidenced by the effect (9) of water vapor on several film properties. It is presumed, however, that the partial pressure of water vapor of importance in this respect is that remaining after reaction with the molten aluminum. It was found, for example, that the properties of filament deposits were much more tolerant of total pressure than electron beam deposits consistent with the lower partial pressure of water vapor in the former case (Fig. 4). A source of hydrogen alternative to that present during deposition may appear when oxides are subjected to heat-treatment in hydrogen prior to metallization.

Values of Q_0 for two dot sizes are presented as a function of anneal time at 500°C in Fig. 5 for three samples. The samples were formed by deposition onto unheated wafers using filament evaporation of aluminum (shadow masked), by electron beam deposition of aluminum onto heated wafers (photomasked), or by flash evaporation of aluminum alloy onto heated wafers preannealed in hydrogen (shadow masked). The filament and flash evaporated samples clearly exhibited a maximum in Q_0 for short anneal times. For longer anneal times, behavior was similar to that of samples discussed above. For all samples, a longer time is required to achieve minimum Q_0 for the larger dots. Meaningful measurements on the electron beam evaporated samples could not be made without an anneal to remove radiation damage (1). It does not appear that the electron beam evaporated sample exhibited maxima for Q_0 , although the crossover in Q_0 values for small and large dots at an anneal time of 15 min may be attributable to the presence of hydrogen. In general, the results were more widely scattered for such samples possibly because of the variability of the hydrogen level generated during deposition.

If the minimum (or near-minimum) values of Q_0 are considered, they are in rough proportion to the dot diameter as before. It should be noted that for the filament-evaporated sample the dots were elliptical and the major axis dimension ratio was only about 2.5 for the dots of nominal diameter equal to 30 and 5 mil.

Room temperature drift measurements were performed on samples for which hydrogen was assumed to be present. Some drift was observed but was an order of magnitude smaller than the increases noted in Fig. 5 for short anneal times. Therefore it is probable that the additional Q_0 introduced is traceable to alkali ions rather than hydrogen ions.

Effect of electrode geometry.—In addition to circular electrodes, rectangles having widths of 6 or 14 mil and containing at least 5 squares were tested. The electrode material was the aluminum alloy deposited on heated

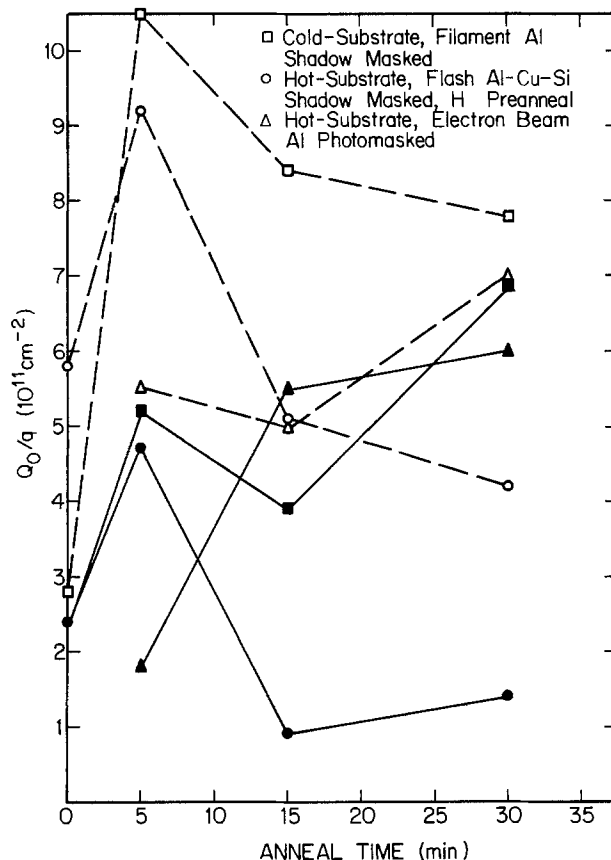


Fig. 5. Dependence of Q_0 on the time of annealing in nitrogen at 500°C for samples as indicated. Open symbols denote results for electrodes of nominal 30 mil diameter and solid symbols for nominal 5 mil diameter.

wafers simultaneously with the sample of Fig. 2. The electrodes were delineated by photomasking. Figure 6 illustrates that the general nature of Q_0 variation with anneal time was similar to that for dots similarly prepared (Fig. 2). As discussed in connection with Fig. 2, probably the initial values of Q_0/q shown have been reduced from a value of about $9 \times 10^{11} \text{ cm}^{-2}$ by the bias stress at 300°C. The minimum values of Q_0 are in approximate proportion to the widths and would appear to be about the same as for dots of the same diameter. The anneal time required to reach the minimum Q_0 was longer for the wider rectangle, analogous to the case for dots, but was greater than for dots of corresponding diameter.

No systematic dependence of Q_0 on rectangle length was observed even though the number of squares examined on a given wafer was 5, 15, and 43 for the wider rectangle and 12, 30, and 100 for the narrower rectangle. A range of Q_0 , sometimes noted for the different lengths is indicated by the bars in Fig. 6.

Other effects.—For shadow masked samples it was invariably found that the contamination was originally at or very near the metal-silicon dioxide interface. The original capacitance-voltage trace would therefore overlap the trace following negative bias stress (curve A of Fig. 7). The original trace for photomasked samples, such as curve B of Fig. 7, was typically displaced from curve A toward more negative voltages indicating that the ionic contamination was originally located away from the metal-oxide interface. This is presumably a consequence of shorting of the metal to the silicon at the edge of the wafer or at pinholes in the oxide which allows movement of contamination away from the interface. An effect of this type has been categorized (10) as drift XVIII and adds to a previously compiled list of drifts of silicon oxide technology (11).

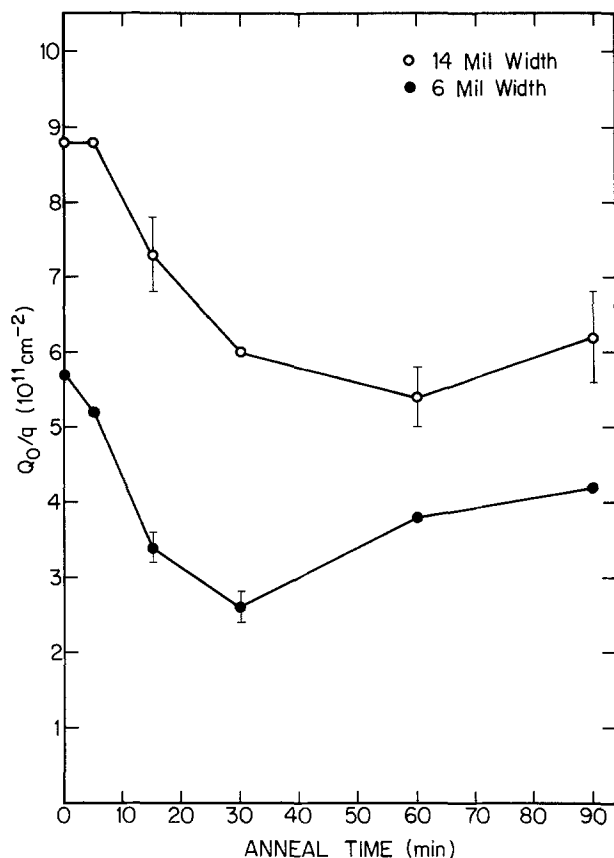


Fig. 6. Dependence of Q_0 on the time of annealing in nitrogen at 500°C for samples with hot-substrate aluminum alloy metallization. Rectangular electrodes of the widths indicated were formed by photomasking.

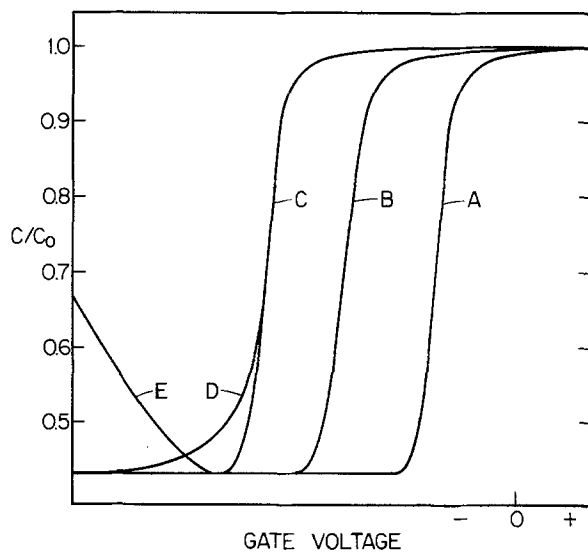


Fig. 7. Capacitance-voltage plots observed under various conditions as discussed in the text.

Annealing at 500°C was found to move the ionic contamination closer to the metal-oxide interface for photomasked samples. For times yielding near-minimum Q_0 , the contamination had moved essentially to the interface. Such an effect was more noticeable for the largest dots and the wider rectangles.

The shape of the capacitance-voltage trace was frequently altered in two respects by long anneals. A tail on the trace following positive bias stress, as typified by curve D in Fig. 7, was observed. Again, this was more prevalent for the capacitors with the largest electrode dimensions. Secondly, the trace sometimes returned to higher capacitance values in the inversion

region as indicated by curve E in Fig. 7. Such behavior was more common with p-type than with n-type wafers. Apparently defects in the silicon were generated by the anneals which acted as sources of minority carriers.

Discussion

The majority of the effects observed can be explained in terms of the following three postulates:

(i) A reduction in ionic contamination level in the oxide under the electrodes as a consequence of heating. A possible mechanism might be diffusion of contaminants to the edge of the electrodes and subsequent vaporization.

(ii) Activation of immobilized contamination under short-term heating with hydrogen as a catalyst. This may occur through substitution of protons for sodium ions at trapping sites. An opposite effect in which protons were released from adsorbed water, in the presence of sodium, has been observed (12).

(iii) An increase in mobile ionic contamination under prolonged annealing. A release of ionic contamination from the metal or effects associated with diffusion of aluminum into the oxide may produce such a result. As regards the latter, it is noted (6) that the immobilized sodium content near the aluminum-oxide interface increased for more extensive annealing. It is not clear, however, that this would lead to increased Q_0 .

The combination of (i) and (iii) or (i), (ii), and (iii) will obviously reproduce the general features of the curves in Fig. 1 and 2 or Fig. 5, respectively. Also on this basis no fundamental difference would be expected between shadow masked and photomasked electrodes. However, the original (nominally zero anneal time) results for heated wafer, shadow masked samples may actually be appropriate to short anneals. That some annealing effect can occur at temperatures of 300°C is apparent from the behavior of Q_0 under electrical stress for photomasked samples (Fig. 2).

Consideration of the mechanism mentioned in (i) suggests that the effect of heating in reducing Q_0 would be more pronounced for smaller dots and narrower rectangles where the circumference to area ratio is larger. This is, of course, the empirical finding. By the same token, in the absence of heating, no dependence of Q_0 on electrode size would be anticipated. The initial results for the filament evaporation on unheated wafers in Fig. 5 demonstrate that this is the case. Efforts were made to minimize stress effects at 300°C on Q_0 for these measurements by utilizing separate chips from one wafer for the two dot sizes and by performing the positive bias stress first.

A further consequence of (i) would be that the time to reduce Q_0 to a given level would be larger for larger dots because of the longer diffusion distance required. Again this was observed experimentally. The occurrence of a minimum in Q_0 for 30 mil diameter dots after an anneal time t of approximately 15 min implies a diffusion coefficient D of $1.7 \times 10^{-7} \text{ cm}^2/\text{sec}$ if a diffusion length $2\sqrt{Dt}$ of about 10 mil is assumed. Such a value for D would not be considered incompatible with sodium diffusion. For comparison, an extrapolation of data (13) for bulk diffusion of sodium in fused silica to a temperature of 500°C yields a value of approximately $3 \times 10^{-8} \text{ cm}^2/\text{sec}$. In addition, ready evaporation of sodium would be anticipated since the vapor pressure of sodium at this temperature is about 4 Torr (14). The possibility was also considered that the hydrogen arising from the aluminum-water vapor reaction (5) plays a role when present in the oxide. Diffusion of this species to electrode edges and evaporation therefrom would be expected to reduce Q_0 since sodium ions could then be retrapped in the oxide. An increase in Q_0 for short term anneals of flash-evaporated metallization, as for the samples of Fig. 5, would be anticipated in such a case. However, an increase of this type was not observed. Apparently the ratio of

circumference to area is also of some significance as regards diffusion since times to reduce Q_0 are longer for a rectangular than a circular electrode with width equal to diameter. In such a case the circumference to area ratio for the circle is twice that of the rectangle, assuming a rectangle of length much greater than width. Also, somewhat less uniform contamination under the larger dots or wider rectangles might be expected if diffusion to the dot edge is involved. It was previously noted that a tail on the capacitance-voltage trace, indicative of nonuniform contamination (15), was most prevalent for the capacitors with the larger electrodes.

The logical extension of (i) would be that for sufficiently long anneal times Q_0 would approach a low value which would be independent of electrode size. This does not occur because of factor (iii). The approximately proportionate dependence of minimum Q_0 on dot diameter and rectangle width was observed for a wide variety of sample types. This would appear to be more than fortuitous and suggests a possible relationship between (i) and (iii). It is difficult to see, however, that a mechanism involving introduction of aluminum or sodium from the electrode could lead to a size dependence. A convergence of Q_0 values for different sizes and shapes, as typically observed for long anneal times, is more consistent with such a mechanism. It should also be noted that no consideration has been given possible effects arising from the aluminum-silicon dioxide reaction. On the basis of one set of reported data (16) about 300Å of silicon dioxide would be reduced to aluminum oxide in 60 min and some consequence might be anticipated. On the other hand no significant reduction of this type is apparent in a later study (6).

Finally, it is probable that for sufficiently large electrodes little or no reduction in Q_0 could be effected through heating. The proportionality to size would then saturate. The data in Fig. 2 for the 30 mil diameter dots indicate that this condition may be approached with only slightly larger dimensions than this.

Summary and Conclusions

It was found that the value of Q_0 measured on MOS capacitors is dependent on the annealing of the structure and on the electrode size and geometry. A minimum in Q_0 is achieved with annealing time, and this minimum value is proportional to either the diameter of circular electrodes or the width of rectangular electrodes. These observations were interpreted to be a consequence of ionic contamination diffusion to and vaporization from the periphery of the electrodes together with eventual introduction of ionic contamination from the electrodes and/or activation of immobilized contamination. The long-term increase in Q_0 has evidently been observed previously (10) and was attributed to contamination from the electrodes. The decrease in Q_0 with anneal time or electrode dimension has not been noted heretofore. The dependence on size is, of course, the opposite of the normal edge effect where ionic contamination is introduced at the electrode periphery. In addition, substantial evidence was gathered to indicate that active contamination levels

can be increased appreciably by annealing when hydrogen is incorporated in the capacitor structure.

The consequences of these findings in connection with semiconductor device fabrication are obvious since several factors may lead to variations in Q_0 and therefore induce similar variations in device properties. The results are also of relevance as regards the common use of auxiliary MOS wafers to monitor Q_0 at various processing steps (17), in particular metalization. The ideal approach would utilize electrode sizes and shapes closely approximating those on device wafers. In addition, the monitor wafers would experience heat-treatments identical to those of device wafers. Electrode delineation by photomasking rather than shadow masking would also be more in keeping with the processing of device wafers.

Acknowledgments

Bruce Deal and Maija Sklar were the source of many useful conversations and comments. Many of the metallization depositions and Q_0 measurements were performed by Ed Dovichi. Pat Kodama was helpful in obtaining materials for evaluation.

Manuscript submitted Feb. 24, 1975; revised manuscript received April 25, 1975.

Any discussion of this paper will appear in a Discussion Section to be published in the June 1976 JOURNAL. All discussions for the June 1976 Discussion Section should be submitted by Feb. 1, 1976.

Publication costs of this article were partially assisted by Fairchild Camera and Instrument Corporation.

REFERENCES

1. B. E. Deal, *This Journal*, **121**, 198C (1974).
2. K. G. Aubuchon, *IEEE Trans. Nucl. Sci.*, **NS-18**, 117 (1971).
3. D. R. Kerr, J. S. Logan, P. J. Burkhardt, and W. A. Pliskin, *IBM J. Res. Develop.*, **8**, 376 (1964).
4. R. J. Kriegler, Y. C. Cheng, and D. R. Colton, *This Journal*, **119**, 388 (1972).
5. P. Balk, Paper 111 presented at The Electrochemical Society Meeting, Buffalo, N. Y., October 10-14, 1965.
6. H. L. Hughes, R. D. Baxter, and B. Phillips, *IEEE Trans. Nucl. Sci.*, **NS-19**, 256 (1972).
7. A. J. Learn, *Thin Solid Films*, **20**, 261 (1974).
8. E. H. Snow, A. S. Grove, B. E. Deal, and C. T. Sah, *J. Appl. Phys.*, **36**, 1664 (1965).
9. R. K. Dheer, Proc. Twentieth Electronic Components Conf., p. 76, IEEE, New York (1970).
10. B. E. Deal, Unpublished.
11. B. E. Deal, Abstract 39, p. 108, The Electrochemical Society Extended Abstracts, Spring Meeting, San Francisco, Calif., May 12-17, 1974.
12. S. R. Hofstein, *IEEE Trans. Electron Devices*, **ED-14**, 749 (1967).
13. A. S. Grove, "Physics and Technology of Semiconductor Devices," p. 41, John Wiley and Sons, Inc., New York (1967).
14. R. C. Honig, *RCA Rev.*, **23**, 567 (1962).
15. M. J. McNutt and C. T. Sah, *J. Appl. Phys.*, **45**, 3916 (1974).
16. J. R. Black, in *Silicon Device Processing*, NBS Special Publication 337, p. 398, (November 1970).
17. R. J. Kriegler, Proc. Twelfth Reliability Physics Symp., p. 250, IEEE, New York (1974).

The Standard Thermodynamic Functions for the Formation of Electrons and Holes in Ge, Si, GaAs, and GaP

C. D. Thurmond*

Bell Laboratories, Murray Hill, New Jersey 07974

ABSTRACT

The forbidden energy gaps of Ge, Si, GaAs, and GaP have been used to obtain the standard Gibbs energy, enthalpy and entropy of formation of electrons and holes for each semiconductor up to the melting points. The forbidden energy gap is the standard Gibbs energy of formation of electrons and holes and the enthalpy and entropy have been obtained from the energy gap as a function of temperature and familiar thermodynamic relationships. Energy gaps as a function of temperature, available in the literature, have been fit to the semiempirical equation of Varshni and used to extrapolate the energy gaps and thereby the three thermodynamic functions to the melting points. It is well known that the energy gaps, i.e., the Gibbs energies, decrease with increasing temperature but it is not well known that the enthalpy of formation increases with temperature and that it is proportional to the slope of the familiar logarithmic plot of the intrinsic carrier concentration over $T^{3/2}$ vs. $1/T$. Examples of the utility of the enthalpy function are given. It is the entropy that leads to the decrease in energy gap with increasing temperature and its magnitude is large near the respective melting points (10-13 cal/deg, i.e., 4 to 5.6×10^{-4} eV/deg) arising from the interactions of electrons and holes with the lattice. The intrinsic carrier concentrations were calculated from the forbidden energy gaps and the average effective masses which were estimated for the higher temperatures.

The forbidden energy gap of a semiconductor is known to be a Gibbs energy, $G = H - TS$ (1-3). It is the Gibbs energy of formation of electrons and holes. More specifically the forbidden energy gap is the standard Gibbs energy of formation of electrons and holes as described by the equilibrium reaction (4)



There is now sufficient information in the literature to permit the forbidden energy gaps of the four principal semiconductors, Ge (5-8), Si (7-9), GaAs (10-12), and GaP (11, 14, 15), to be reasonably estimated at all temperatures from 0°K to the respective melting points. In fact, the forbidden energy gap is known with sufficient accuracy to make possible the estimation of the standard enthalpies and entropies of formation of electrons and holes as functions of temperature. In addition, estimates can be made of the standard heat capacity changes for reaction [1] for these four semiconductors but with a greater degree of uncertainty. After an opening discussion of the forbidden energy gap as a standard Gibbs energy and the thermodynamic relationships giving the standard enthalpy, entropy, and heat capacity from the forbidden energy gap, the measurements of the energy gap are reviewed. These measurements are analyzed with the help of a semiempirical equation due to Varshni (16), which gives the forbidden energy gap as a function of temperature. The standard thermodynamic functions ΔG° , ΔH° , ΔS° , and ΔC_p° are obtained at all temperatures up to the respective melting points by extrapolation of the Varshni equation. An estimate of the uncertainties of these functions is made. The intrinsic carrier concentrations have been calculated from the forbidden energy gap and the average effective mass of electrons and holes, available from reported experiments at lower temperatures but estimated at higher temperatures. In addition, the utility of the standard enthalpy of formation of electrons and holes is illustrated in a discussion of the widely used linear approximation to the forbidden energy gap as a function of temperature and in an alternative explanation of a once anomalous property of the Au energy level in Si.

* Electrochemical Society Active Member.

Key words: semiconductors, energy gap, Gibbs energy, enthalpy, entropy.

Thermodynamics

It has been long recognized (1-3, 17) that for a semiconductor the product of the electron concentration, n , and the hole concentration, p , is not a function of concentration when the concentrations are low. This product has been shown by statistical mechanical methods to be proportional to an exponential containing the energy gap (1, 2, 17)

$$np = n_c n_v \exp(-\Delta E_{cv}/kT) \quad [2]$$

The symbol ΔE_{cv} will be used for the forbidden energy gap as recommended by Phillips (18), who suggests that the symbol E_g be reserved for the average bond energy gap. In the following, the terms forbidden energy gap, minimum energy gap, and energy gap will be equivalent. The two terms, n_c and n_v , are the effective density of states for electrons in the conduction band and holes in the valence band.

Equation [2] has a form similar to that of a chemical equilibrium constant. The equilibrium constant would be the fraction $np/n_c n_v$ and the energy gap, ΔE_{cv} , would be the standard Gibbs energy of formation of electrons and holes. That this is, in fact, true can be shown from the following argument.

The condition to be met for electrons and holes to be at equilibrium at some temperature T and some constant external pressure is that the Gibbs energy (19, 20) of the system be a minimum with respect to a change in the number of electrons or holes. This condition for equilibrium can also be expressed in terms of the chemical potentials of electrons and holes the sum of which must be zero

$$0 = \mu_n + \mu_p \quad [3]$$

(Equation [3] is the equilibrium condition implied by Eq. [1] for the formation of electrons and holes.)

The chemical potentials of electrons and holes at low concentrations as a function of composition and temperature may be written as follows

$$\begin{aligned} \mu_n &= \mu_n^\circ + kT \ln x_n \\ \mu_p &= \mu_p^\circ + kT \ln x_p \end{aligned} \quad [4]$$

The standard chemical potentials μ_n° and μ_p° are the values of the respective chemical potentials when the

composition fractions, x_n and x_p , are unity. If the compositions are expressed in terms of concentration ratios, x_n would be n/n° and x_p would be p/p° where n° and p° are the concentrations of electrons and holes, respectively, in the standard states. From Eq. [3] and [4] it follows that

$$np = n^\circ p^\circ \exp(-(\mu_n^\circ + \mu_p^\circ)/kT) \quad [5]$$

an equation identical in form to Eq. [2].

The choice of the standard states is based on a statistical and quantum mechanical model of free electrons and free holes in the conduction and valence bands, respectively, of a semiconductor (1). The Fermi level, the electron chemical potential, is referred to the minimum energy of conduction band states, E_c , and therefore $\mu_n^\circ = E_c$. The hole chemical potential (the negative of the Fermi level) is referred to the maximum energy of the valence band states, E_v , and therefore $\mu_p^\circ = -E_v$. Since the energy gap, ΔE_{cv} , is $E_c - E_v$ it follows that

$$\mu_n^\circ + \mu_p^\circ = E_c - E_v = \Delta E_{cv} \quad [6]$$

The standard chemical potentials of Eq. [6] are also Gibbs energies since the equilibrium conditions of interest are constant temperature and pressure. Consequently the standard chemical potential sum is the standard Gibbs energy, ΔG_{cv}° , for formation of electrons and holes and is also the forbidden energy gap

$$\mu_n^\circ + \mu_p^\circ = \Delta E_{cv} = \Delta G_{cv}^\circ \quad [7]$$

The standard state concentration, n° , is the electron concentration, n_c , which places the Fermi level at the conduction band edge, while the standard state concentration, p° , is the hole concentration, n_v , which places the Fermi level at the valence band edge. The concentration n_c is also the effective density of states in the conduction band and the concentration n_v is also the effective density of states in the valence band (21). They can be obtained from the two equations

$$\begin{aligned} n_c &= 2(2\pi m_n kT/h^2)^{3/2} \\ n_v &= 2(2\pi m_p kT/h^2)^{3/2} \end{aligned} \quad [8]$$

where m_n and m_p are the effective masses of electrons and holes, respectively, and the other symbols have their usual meanings.

Since the forbidden energy gap as a function of temperature is the standard Gibbs energy for formation of electrons and holes as a function of temperature, the standard enthalpy, entropy, and heat capacity of formation of electrons and holes can be calculated from familiar thermodynamic relationships

$$\Delta E_{cv} = \Delta H_{cv} - T\Delta S_{cv} \quad [9]$$

$$d(\Delta E_{cv})/dT = -\Delta S_{cv} \quad [10]$$

$$d(\Delta E_{cv}/T)d(1/T) = \Delta H_{cv} = \Delta E_{cv} - Td(\Delta E_{cv})/dT \quad [11]$$

$$\Delta C_{cv} = d(\Delta H_{cv})/dT = Td(\Delta S_{cv})/dT \quad [12]$$

The superscript $^\circ$ which has been used to designate standard functions has been dropped for the subscript cv. Thus ΔH_{cv} , ΔS_{cv} , and ΔC_{cv} are the standard enthalpy, entropy, and heat capacity of formation of electrons and holes.

Experimental

Ge and Si.—Macfarlane, McLean, Quarrington, and Roberts have measured the forbidden energy gaps of Ge (5-8) and Si (7-9). The absorption coefficient was measured as a function of wavelength and temperature at high optical resolution in the wavelength region of the band edge. Fine structure in the absorption edge permitted identification of four phonon transitions characteristic of these indirect gap semiconductors. Each phonon transition was found to have a component related to an optical transition. The phonon and optical transition energies were obtained by curve fitting. The

optical process measured in this way differs from the energy of the forbidden gap by a small amount, the dissociation energy of the exciton. The optical transition measured is the formation energy of an exciton, ΔE_{ex}^f , and this energy plus the dissociation energy of the exciton ΔE_{ex}^d , is the forbidden energy gap

$$\Delta E_{cv} = \Delta E_{ex}^f + \Delta E_{ex}^d \quad [13]$$

The exciton dissociation energy in Ge is 2.7 ± 0.2 meV according to McLean (8). A value of 10.0 meV was estimated for the exciton in Si (8) but a more recent measurement by Shaklee and Nahory (22) gives 14.7 ± 0.4 meV.

High resolution measurements of the Si forbidden energy gap as a function of temperature have been reported recently by Bludau, Onton, and Heinke (23). The derivative of the absorption coefficient with respect to wavelength was measured. The energy of formation of the exciton was sharply defined and 140 experimental points between 2° and 300°K were taken on high purity silicon. Thirty points at 10 degree intervals were obtained by quadratic averaging of the measurements. In order to obtain the energy gap, the exciton dissociation energy of 14.7 meV must be added, but in addition, a momentum conserving phonon energy must be subtracted (22) both of which are assumed to be independent of temperature.

The Ge and Si measurements are shown in Fig. 1. The difference between the value of the energy gap at T and its value at 0°K is plotted against T . A characteristic shape is exhibited. The curves drawn in Fig. 1 are obtained from a fit of the measurements to a semiempirical equation suggested by Varshni (16) and will be discussed below. The curves approach 0°K quadratically and at high temperatures approach linearity.

GaAs.—The measurements of Sell and co-workers (12, 13) and of Panish and Casey (11) have been used. Sell, Casey, and Wecht (12) obtained the energy gap at 297°K from reflectivity measurements. Panish and Casey measured the shift in absorption edge at constant absorption coefficient from 297°K to four temperatures up to 973°K. The measured shift added to the value of the energy gap at 297°K is assumed to give the energy gap at the higher temperatures. [Panish and Casey used the 294°K measurement of Sturge (10) to get high temperature values of the energy gap but the more recent reflectivity measurements of Sell, Casey, and Wecht (12) on unstrained GaAs and at higher resolution than used by Sturge are to be preferred.]

The differences between the energy gap at T and 0°K are plotted in Fig. 2 for GaAs.

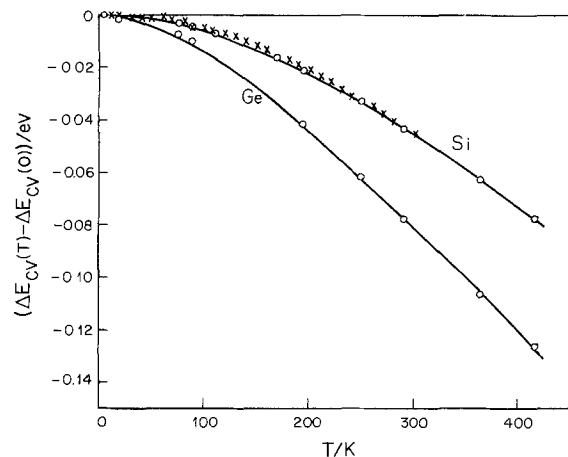


Fig. 1. The difference between the forbidden energy gap at T and 0°K, $\Delta E_{cv}(T) - \Delta E_{cv}(0)$, as a function of temperature for Ge and Si. \circ (Ge), Macfarlane et al. (5-8); \times (Si), same authors (7-9); \times , Bludau, Onton, and Heinke (23); — Eq. [14], with the appropriate constants of Table I.

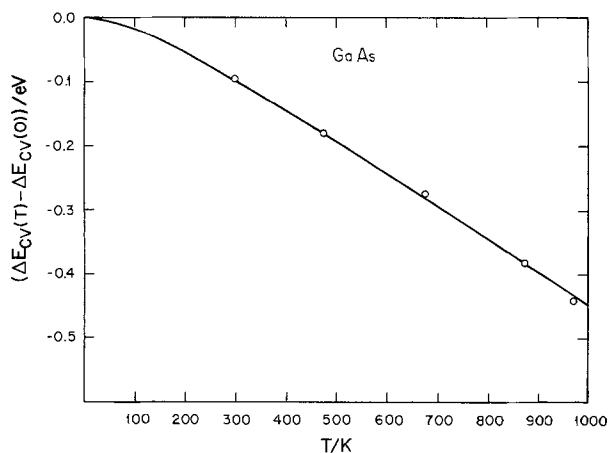


Fig. 2. The difference between the forbidden energy gap at T and at 0°K , $\Delta E_{cv}(T) - \Delta E_{cv}(0)$, for GaAs as a function of temperature. \circ , Panish and Casey (11); point at 297°K from Sell, Casey, and Wecht (12); $\Delta E_{cv}(0)$ from Sell, Stokowski, Dingle, and DiLorenzo (13) (see Table III); — Eq. [14] with the appropriate constants of Tables I and III.

GaP.—Lorenz, Pettit, and Taylor (14) have made absorption measurements up to 868°K . The measurements below 400°K give the energy gap from an analysis of spectral features equivalent to those used for Ge and Si. Between 400° and 868°K , the energy gap shift was estimated from the absorption edge shift at constant absorption coefficient. Panish and Casey (11) have measured the absorption edge shift at constant absorption coefficient from 300° to 1273°K . Figure 3 gives the experimental data as a plot of the energy gap difference between T and 0°K as a function of temperature.

The Evaluation of the Experimental Data

Varshni (16) has proposed a simple equation for the temperature dependence of the energy gap

$$\Delta E_{cv}(T) - \Delta E_{cv}(0) = -\alpha T^2 / (T + \beta) \quad [14]$$

Equation [14] is based upon two assumptions; that the energy gap should be proportional to T at high temperatures and proportional to T^2 at low temperatures. The constant β was to be a reasonable approximation to the Debye temperature. The support for the use of the equation comes from the fact that it is a good representation of experiment (11, 16).

The method previously used to evaluate the three constants of Eq. [14] was to plot the energy gap,

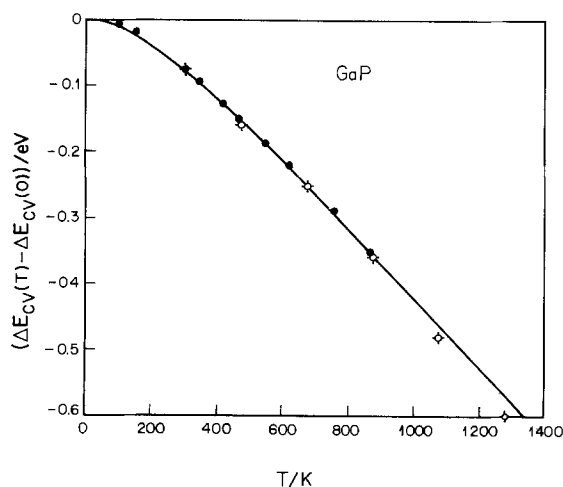


Fig. 3. The difference between the forbidden energy gap at T and at 0°K , $\Delta E_{cv}(T) - \Delta E_{cv}(0)$, for GaP as a function of temperature. \circ , Panish and Casey (11) and \bullet , Lorenz, Pettit, and Taylor (14); — Varshni Eq. [16], with the appropriate constants of Tables I and III.

$\Delta E_{cv}(T)$ vs. $T^2/(T + \beta)$ and find the value of β for which a straight line was obtained. The intercept was $\Delta E_{cv}(0)$ and the slope was α . It is found that there is a rather wide range of values of α and β which gives a satisfactory fit to the data. An alternate method of evaluating these two constants will be used here which leads to a direct graphical solution for α and β and an estimate of uncertainties.

The question of the value of the energy gap at 0°K can be dealt with separately since the same value of the exciton dissociation energy applies to all values of the energy gap (Eq. [13]). The constants α and β can be obtained from the difference function, $\Delta E_{cv}(T) - \Delta E_{cv}(0)$, plotted in Fig. 1, 2, and 3. Equation [14] can be rearranged to give

$$T^2 / (\Delta E_{cv}(0) - \Delta E_{cv}(T)) = \beta / \alpha + T / \alpha \quad [15]$$

If the experimental data are to fit Varshni's equation, the term on the left of Eq. [15] will depend linearly on temperature.

The measured energy gap differences are plotted according to Eq. [15] in Fig. 4, 5, 6, and 7. The values of α and β obtained and their estimated uncertainties are given in Table I. The values previously used are given for comparison. An uncertainty of 0.5 meV has been estimated for Ge and Si energy gap differences; an uncertainty of 4 meV has been estimated for GaAs and GaP. The uncertainty in α and β was obtained by passing one line of maximum slope through the selected data points and another of minimum slope. The values of α and β obtained from these two lines give

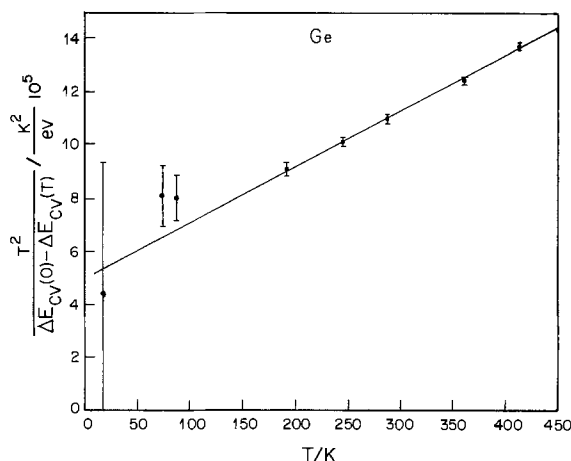


Fig. 4. The function $T^2 / (\Delta E_{cv}(0) - \Delta E_{cv}(T))$ vs. T for Ge. \bullet , Macfarlane et al. (5-8); — Eq. [14], Table I.

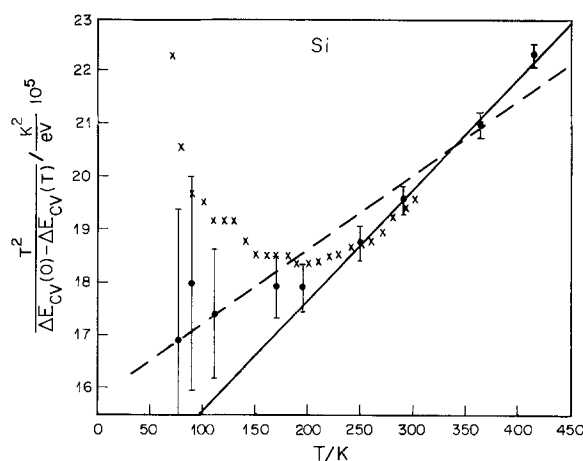


Fig. 5. The function $T^2 / (\Delta E_{cv}(0) - \Delta E_{cv}(T))$ vs. T for Si. \bullet , Macfarlane et al. (7-9); \times , Bludau, Onton, and Heinke (23); — Eq. [14], Table I; - - - Varshni Eq. [14] with constants from Varshni (16), see Table I.

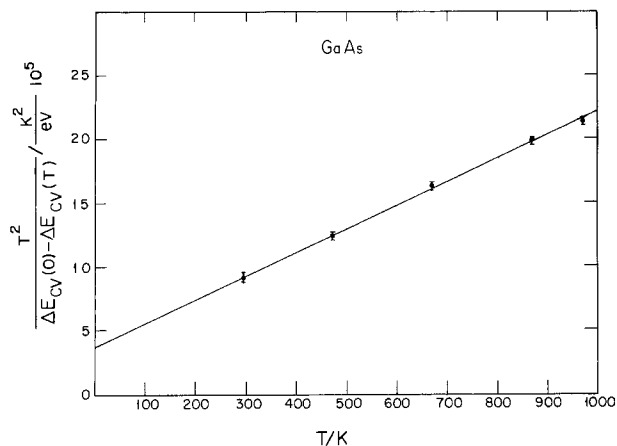


Fig. 6. The function $T^2/(\Delta E_{cv}(T) - \Delta E_{cv}(0))$ vs. T for GaAs. Data from Panish and Casey (11); point at 297 from Sell, Casey, and Wecht (12), — Eq. [14], Table I.

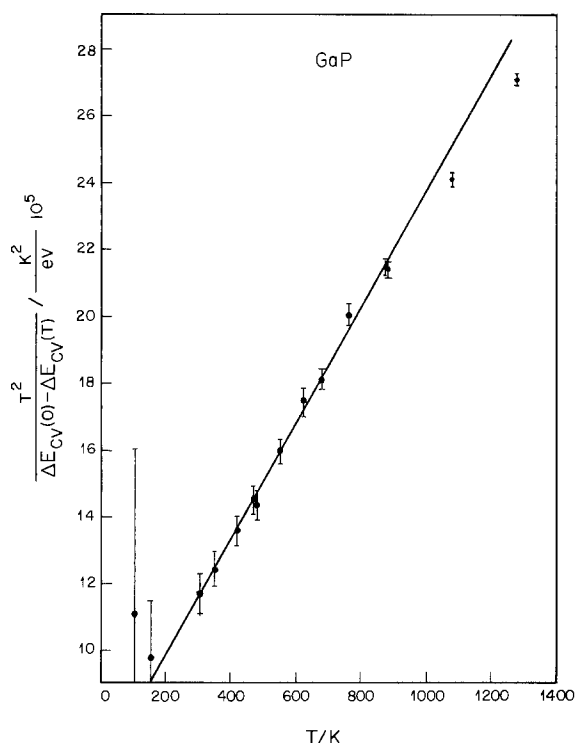


Fig. 7. The function $T^2/(\Delta E_{cv}(T) - \Delta E_{cv}(0))$ vs. T for GaP. Data from Panish and Casey (11), and from Lorenz, Pettit, and Taylor (14); — Eq. [14], Table I.

the spread in values which are twice the uncertainties given in Table I.

The curves shown in Fig. 1, 2, and 3 were calculated from Eq. [14] and the constants of Table I. The standard deviations of the experimental points from the calculated curves are given in Table II where they are compared with previous fits to the Varshni equation.

Table I. The coefficients α and β of the Varshni equation [14], $\Delta E_{cv}(T) - \Delta E_{cv}(0) = -\alpha T^2/(T + \beta)$. Comparisons are made with earlier work. The 0°K Debye temperature, $\theta_D(0)$, is also given

	$\alpha/10^{-4}$ eV K $^{-1}$	β/K	$\theta_D(0)/K$
Ge	4.774 ± 0.30	235 ± 40	374 (24)
	4.561 (16)	210 (16)	
	4.730 ± 0.25	636 ± 50	645 (24)
Si	7.021 (16)	1108 (16)	
	5.405 ± 0.25	204 ± 45	344 (25)
	5.8 (11)	300 (11)	
GaAs	5.771 ± 0.55	372 ± 95	446 (25)
	6.2 (11)	460 (11)	

Table II. The standard deviation of the experimental energy gap difference, $\Delta E_{cv}(T) - \Delta E_{cv}(0)$, from the Varshni equation [14], using the coefficients of Table I. These are compared in the last column with standard deviations calculated using coefficients obtained by others

	Standard deviation/meV	
Ge	1.1	1.3 (16)
Si	0.6 (0.9) ^a	1.2 (16)
GaAs	2.6 ^b	2.1 (11)
GaP	2.7 ^c	4.0 ^c (11)

^a Measurements of Bludau, Onton and Heinke (23) included.

^b Sturge (10) measurements not used.

^c The two points at highest temperatures not included.

It is clear from Fig. 5 that below 250°K, the measurements of Bludau, Onton, and Heinke (23) deviate significantly from the Varshni equation. The low temperature points of Macfarlane *et al.*, (5-9), for Si and for Ge indicate similar deviations. The measurements of Bludau join those of Macfarlane at 250°K and above as can be seen in Fig. 5. The dashed line is equivalent to the fit to the Macfarlane *et al.* data made by Varshni (16).

The GaAs measurements at 297°K and above are satisfactorily represented by Varshni's equation (Fig. 6). No measurements have been used below 297° to fit the Varshni equation but absorption measurements by Sturge (10), photoluminescence measurements by Nathan and Burns (26), and injection luminescence by Sarace *et al.* (27) all below 297°K, give values of the energy gap that can be compared to values calculated from the Varshni equation fit to the temperature measurements above 297°. The energy gap values obtained by Sturge (10) at 90°, 55°, and 21°K agree within +3 meV with the Varshni equation. When Sturge's strain correction is not used and a value of 4.2 meV is used for the exciton dissociation energy, the 185° and 294°K values differ by about +5 meV from the Varshni equation. The energy gap values reported by Nathan and Burns are all higher than the Varshni equation calculations varying from 6.7 meV at 197°K to 3.7 meV at 65°K. The only other point lies at 4.2°K and is in good agreement with the calculated value (-0.5 meV). The experimental emission peaks have been assumed to be from free exciton annihilation, and a value of 4.2 meV has been added for the exciton dissociation energy to obtain the energy gap. Sarace *et al.* (27), have measured the recombination radiation from injected holes into n-type GaAs at 77° and 298°K. Their measures agree within 1 meV of the values of the energy gap calculated from the Varshni equation.

The GaP measurements are fit satisfactorily by the Varshni equation except for the two highest points, one at 1073°, the other at 1273°K. These two points have not been used in obtaining the constants of Eq. [15].

It was suggested by Varshni (16) that the constant α should have a value near that of the Debye temperature, but he found poor agreement among the examples he had. Panish and Casey (11) found better agreement for GaAs than did Varshni and their measurements, with those of Lorenz *et al.* (14), led to reasonable agreement for GaP. Table I includes a value for the Debye temperature evaluated at 0°K, $\theta_D(0)$. The value of β for Si, 636°K, is now in much better agreement with the Debye temperature, 645°K, than the 1108°K found by Varshni. The values of β now fall close to a straight line ($\beta = 1.51 \theta_D - 324$) revealing the relationship suggested by Varshni.

In order to obtain the value of the energy gap as a function of temperature, the value of the energy gap at 0°K is needed. These are given in Table III along with the exciton dissociation energies used.

The Thermodynamic Functions

It is now proposed to use the Varshni equation to obtain the various thermodynamic functions of inter-

Table III. The forbidden energy gap at 0°K, $\Delta E_{cv}(0)$, and the exciton dissociation energy ΔE_{ex}^d

	$\Delta E_{cv}(0)/\text{eV}$	$\Delta E_{ex}^d/\text{meV}$
Ge	0.7437 ± 0.001 (9)	2.7 ± 0.4 (9)
Si	1.1700 ± 0.001 (9, 23)	14.7 ± 0.4 (22)
GaAs	1.519 ± 0.001 (13)	4.2 ± 0.2 (28)
GaP	2.338 ± 0.002 (14)	10.0 ± 1.0 (15)

est and to use it at all temperatures up to the melting point. An estimate will be made in a following section of the uncertainties that may be expected in the various functions.

From Eq. [10] and [14] it follows that the entropy of formation of electrons and holes, i.e., the gap entropy, is given by the equation

$$\Delta S_{cv}(T) = \alpha T(T + 2\beta)/(T + \beta)^2 \quad [16]$$

From Eq. [11] it follows that the enthalpy of formation of electrons and holes, i.e., the gap enthalpy, is

$$\Delta H_{cv}(T) = \Delta H_{cv}(0) + \alpha\beta(T/(T + \beta))^2 \quad [17]$$

The thermodynamic functions, Gibbs energy, ΔE_{cv} , the enthalpy, ΔH_{cv} , and the entropy, ΔS_{cv} , are plotted as functions of temperature in Fig. 8, 9, 10, and 11 for each of the four semiconductors of interest.

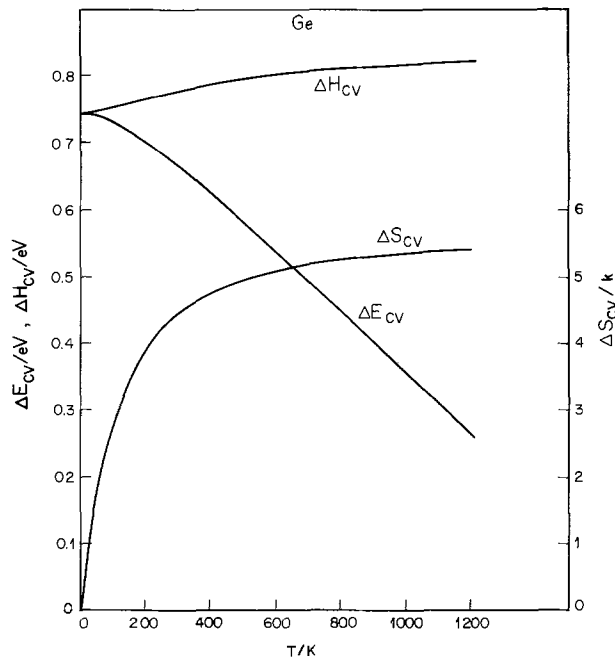


Fig. 8. The Gibbs energy, ΔE_{cv} in eV, the enthalpy, ΔH_{cv} in eV and the entropy, ΔS_{cv} in units of k, as functions of T for Ge.

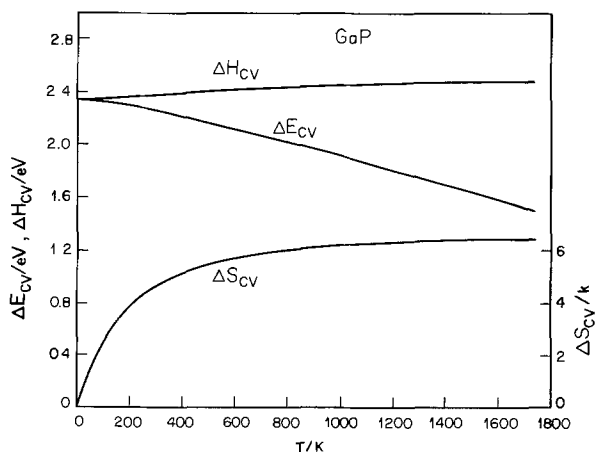


Fig. 9. The Gibbs energy, ΔE_{cv} in eV, the enthalpy, ΔH_{cv} in eV and the entropy, ΔS_{cv} in units of k, as functions of T for Si.

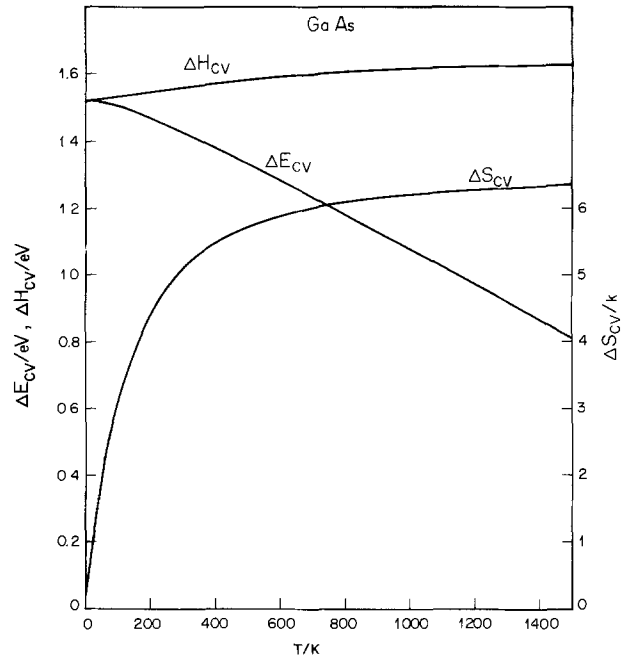


Fig. 10. The Gibbs energy, ΔE_{cv} in eV, the enthalpy, ΔH_{cv} in eV and the entropy, ΔS_{cv} in units of k, as functions of T for GaAs.

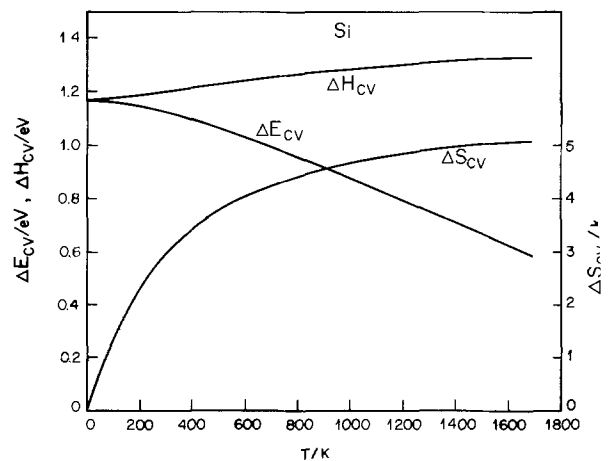


Fig. 11. The Gibbs energy ΔE_{cv} in eV, the enthalpy, ΔH_{cv} in eV and the entropy, ΔS_{cv} in units of k, as functions of T for GaP.

The heat capacity, ΔC_{cv} , can be obtained from Eq. [12] and Eq. [17]

$$\Delta C_{cv} = 2\alpha\beta^2 T/(T + \beta)^3 \quad [18]$$

and is plotted in Fig. 12.

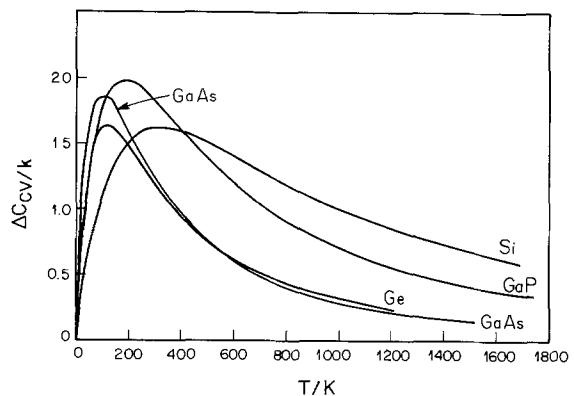


Fig. 12. The heat capacity change, ΔC_{cv} in units of k, for the formation of electrons and holes as a function of T for Ge, Si, GaAs, and GaP.

Discussion

Uncertainties.—An estimate of the uncertainties in the forbidden energy gap and the derived thermodynamic functions can be made based upon the uncertainties in the coefficients α and β of the Varshni equation. Of particular interest are the uncertainties at high temperatures. Table I lists the uncertainties in α and β estimated from Fig. 4-7. The uncertainties in ΔE_{cv} , ΔH_{cv} , ΔS_{cv} , and ΔC_{cv} can be obtained using the α and β uncertainties and Eq. [14], [16], [17], and [18]. Table IV gives the estimated uncertainties for each material at 300°K and at its melting point. At room temperature ΔE_{cv} and ΔH_{cv} are known to within a few tenths per cent; at the melting points, to within 2-7%. The uncertainties in ΔH_{cv} are smaller because it is the larger quantity at the melting point. The entropies are known to a per cent or so at 300°K and 5-8% at the melting points. The heat capacities have the largest uncertainties ranging from 5 to 50%.

The energy gaps of Ge and Si have been measured near the melting points by Glassbrenner and Slack (29). They measured the thermal conductivity of Ge and Si and found that at high temperatures nearly half was determined by the electrons and holes present. From their measurements, they obtained a value of the energy gap of Ge, at its melting point, of 0.26 ± 0.08 eV. The value given in Fig. 8, obtained from the Varshni equation (Eq. [14]) and the constants in Tables I and III, is 0.260 eV with an estimated uncertainty of ± 0.018 eV from Table IV. The value given for Si at its melting point by Glassbrenner and Slack (29) was 0.6 ± 0.1 eV. The value given by the extrapolated Varshni equation is 0.591 eV with an estimated uncertainty of 0.018 eV from Table IV. The agreement is well within the estimated uncertainties.

Si below 300°K.—Recent measurements of the energy gap by Bludau, Onton, and Heinke (23), between 0° and 300°K, are in agreement with the measurements of Macfarlane *et al.* (9), between 250° and 300°K. Below 250°K, however, definite departures occur from the values obtained from the Varshni equation (see Fig. 1 and Fig. 5). These departures are relatively small; less than 0.1% for ΔE_{cv} and less than 0.4% for ΔH_{cv} at all temperatures, less than 7% at 300°K for ΔS_{cv} (at 50°K the maximum departure of 25% occurs for ΔS_{cv}) and less than about 30% for ΔC_{cv} at all temperatures below 300°K.

The function used by Bludau *et al.* (23), to represent their measurements in the 0°-190°K temperature range, has a linear term, and as a consequence the calculated value of ΔS_{cv} is not zero at 0°K. The averaged data points given by the authors are consistent, however, with T^2 dependence near 0°K and no linear term is needed.

The intrinsic carrier concentration, n_i .—The concentrations of electrons and holes are equal in a pure semiconductor. From Eq. [2] and [8] the intrinsic concentration is given by

$$n_i = 2(2\pi k/h^2)^{3/2} \langle m \rangle^{3/2} T^{3/2} \exp(-\Delta E_{cv}/2kT) \quad [19]$$

The average density of states effective mass, $\langle m \rangle$, is the geometric mean of the electron and hole density of

states effective masses

$$\langle m \rangle = (m_n m_p)^{1/2} \quad [20]$$

Since values of the energy gap have now been either measured or estimated at all temperatures for Ge, Si, GaAs, and GaP, values of n_i can be calculated from Eq. [19] if $\langle m \rangle$ is known as a function of temperature. Casey (30) has used this method to obtain an estimate of n_i to the melting points for GaAs, GaP, and a number of other 3-5 compounds.

Si.—Barber (31) has concluded that the effective masses of electrons and holes in silicon are functions of temperature and from available literature information and his own calculations has obtained values up to 600°K. Values of n_i calculated from Eq. [19] using these effective masses were compared to the Hall measurements of n_i by Morin and Maita (32) and by Putley and Mitchell (33). Best agreement was obtained with the Putley and Mitchell measurements when it was assumed that the exciton dissociation energy was zero.

An alternative approach is to use Eq. [19] to calculate the average effective mass, $\langle m \rangle$, from the measured values of n_i and from ΔE_{cv} obtained from Eq. [14] and the constants given in Tables I and II

$$\Delta E_{cv}(T) = 1.1700 - 4.73 \times 10^{-4}(T^2/(T + 636)) \quad [21]$$

The calculated values of $\langle m \rangle$ for Si, given in units of the electron rest mass, are shown in Fig. 13 as a function of temperature. They are to be compared to the $\langle m \rangle$ curve calculated from Eq. [20] using the electron and hole effective masses recommended by Barber (31). The experimental values of n_i were calculated from the equations used by Morin and Maita (32) to fit their data over the temperature range 300°-1200°K

$$n_i = 3.87 \times 10^{16} T^{3/2} \exp(-(0.605 + \Delta\epsilon)/kT) \quad [22]$$

$$\Delta\epsilon = -7.1 \times 10^{-10}(n_i/T)^{1/2}$$

Putley and Mitchell (33) made measurements over the temperature range 370°-500°K, and the data were well represented by the equation

$$n_i = 3.10 \times 10^{16} T^{3/2} \exp(-0.603/kT) \quad [23]$$

It is estimated that the average deviation of the experimental points from the fitting curves in both cases is about 5%.

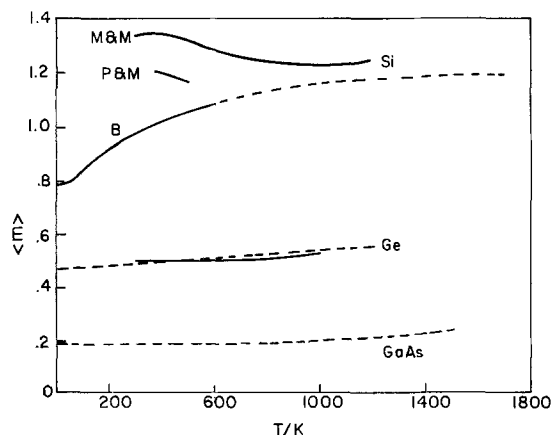


Fig. 13. The density of states average effective mass, $\langle m \rangle$, in units of the electron rest mass, as a function of T . The Si-M&M curve is based upon the n_i measurements of Morin and Maita (32), the Si-P&M curve is based upon the n_i measurement of Putley and Mitchell (33); the Si-B curve is from Barber (31); the dashed extension of the Barber curve is the present estimate of $\langle m \rangle$ to the melting point of Si. The Ge-M&M curve is based upon the n_i measurements of Morin and Maita (34); the straight line is the present estimate of $\langle m \rangle$ from 0°K to the melting point of Ge. The GaAs curve was obtained from Casey (30).

Table IV. The per cent uncertainty in the calculated thermodynamic functions arising from the uncertainty in α and β (Table I) and $\Delta E_{cv}(0)$ (Table III)

	T/K	Uncertainty, per cent			
		ΔE_{cv}	ΔH_{cv}	ΔS_{cv}	ΔC_{cv}
Ge	300	0.3	0.5	2	15
	1210	7	2	5	35
Si	300	0.1	0.1	0.1	5
	1685	3	1	4	15
GaAs	300	0.3	0.3	0.6	20
	1511	2	1	4	45
GaP	300	0.2	0.2	1	15
	1738	3	2	8	50

Barber pointed out a discrepancy between the early measurements by Morin and Maita and the later measurements by Putley and Mitchell on higher purity silicon. This discrepancy in the measured values of n_i is evident in the two upper curves of Fig. 13 of $\langle m \rangle$ as a function of temperature. Barber found that the measurements of Putley and Mitchell were in satisfactory agreement with the temperature dependent effective masses he found to represent the best available effective mass measurements. This agreement, however, rested upon the assumption that the exciton dissociation energy was zero. It is now known that for low temperatures the exciton dissociation energy is 14.7 meV (22) and is not expected to be a significant function of temperature. The difference between the Putley and Mitchell curve of Fig. 13 and the Barber curve is due to the exciton dissociation energy of 14.7 meV ignored by Barber.

The high temperature Morin and Maita measurements which should be less sensitive to impurities than the lower temperature data suggest that the average effective mass does not vary much with temperature. We have arbitrarily extrapolated Barber's curve to the melting point of silicon guided to some extent by the high temperature measurements of Morin and Maita.

Ge.—The average effective mass, $\langle m \rangle$, of electrons and holes in Ge has been calculated from the measurements of n_i by Morin and Maita (34)

$$n_i = 1.76 \times 10^{18} T^{3/2} \exp(-0.785/2kT) \quad [24]$$

and the forbidden energy gap

$$\Delta E_{cv} = 0.7437 - 4.774 \times 10^{-4} (T^2/(T + 235)) \quad [25]$$

The measurements of n_i were made over the temperature range of 300°–1000°K. The calculated values of $\langle m \rangle$ are plotted in Fig. 13. They show a slow increase with temperature and good agreement with the value of 0.47 near 0°K obtained from an effective mass for the electron of 0.55 and for the hole of 0.40 (35). We have estimated the value of the average effective mass up to the melting point by the straight line shown in Fig. 13. This approximation is expected to be satisfactory at all temperatures not too near 0°K where the average effective mass is expected to approach 0°K with zero slope as shown for Si in the curve given by Barber (31).

GaAs.—No measurements of n_i as a function of temperature have been made. Casey (30) has calculated n_i from the forbidden energy gap and an average effective mass consistent with low temperature measurements and an estimated temperature dependence based upon the GaAs band structure

$$\langle m \rangle = 0.186 (1 + 16.67 \exp(-0.36/kT)) \quad [26]$$

$\langle m \rangle$ is again measured in units of the electron rest mass. Equation [26] is shown in Fig. 13 from 0°K to the melting point of GaAs.

GaP.—The intrinsic carrier concentration, n_i , has not been measured as a function of temperature. Low temperatures effective masses of electrons and holes give a value for $\langle m \rangle$ of 1.15 which Casey (30) has used to calculate n_i as a function of temperature. The same assumption has been made here.

Values of n_i are shown in Fig. 14 up to the respective melting points. The calculations for GaAs and GaP are nearly identical to those made by Casey (30). We have used the same values of the effective masses and nearly the same values of the forbidden energy gap. At 300°K, n_i calculated by Casey for GaAs and GaP are approximately a factor of 2 larger than given in Fig. 14. At the melting points, Casey calculated a value for GaAs 40% higher than given here and for GaP, about 15% smaller than given in Fig. 14.

Recently, Jain *et al.* (36) have estimated n_i for Si to the melting point. Their value of n_i at 300°K is about

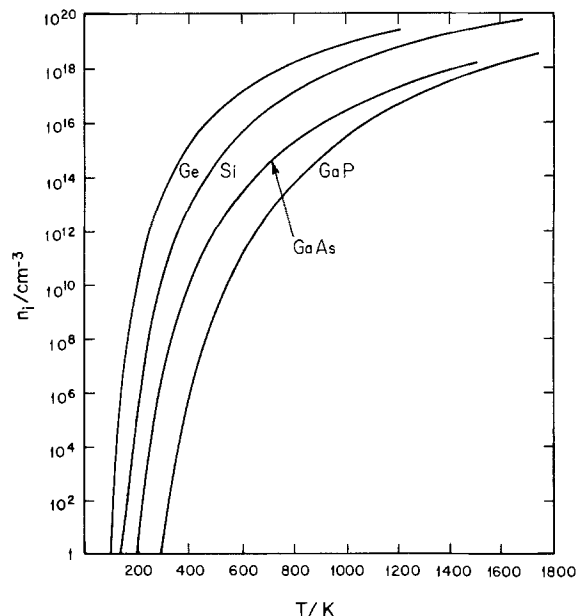


Fig. 14. The intrinsic carrier concentration, n_i in cm^{-3} , as a function of T for Ge, Si, GaAs, and GaP.

25% larger than given here, while at the melting point, n_i is a factor of 1/3 lower than given in Fig. 14.

The assumption that classical statistics can be used to give the electron and hole chemical potentials as a function of composition and temperature (Eq. [4]) receives its severest test at the highest temperatures attainable. The values of n_i calculated using classical statistics rather than Fermi-Dirac statistics are too large at the respective melting points by 10% for Ge, 4% for Si, 2% for GaAs, and 0.2% for GaP. It has been assumed in these calculations that the effective masses of the electron and the hole are the same in each material at its melting point. When room temperature effective mass ratios are used instead, the only significant change is for GaAs, changed from 2% to 4%. It is clear that classical statistics satisfactorily represent n_i for these four semiconductors.

The enthalpy of formation of electrons and holes, ΔH_{cv} .—The temperature dependence of the intrinsic carrier concentrations, n_i , frequently written in the form

$$n_i/T^{3/2} = A \exp(-\Delta E_{cv}/2kT) \quad [27]$$

$$A = 2(2\pi\langle m \rangle kT/h^2)^{3/2}$$

which follows from Eq. [19]. The assumption is generally made that the average effective mass is independent of T . It was found by Pearson and Bardeen (2) and later confirmed by Morin and Maita (32) that a plot of $\log(n_i/T^{3/2})$ vs. $1/T$ was a straight line for Si, but the magnitude of the constant A did not agree with theory. Pearson and Bardeen suggested that the inconsistency arose because ΔE_{cv} was temperature dependent. They then assumed a linear dependence and found a reasonable value for the modified preexponential coefficient. The slope of the line was the extrapolated value of the energy gap at 0°K.

In fact, a plot of $\log(n_i/T^{3/2})$ vs. $1/T$ will, in general, not be a straight line but will be a slowly varying function of T and at any temperature the slope at that temperature gives the enthalpy, ΔH_{cv} . Changes in effective mass with temperature are expected to be sufficiently small to have a negligible effect on the slope. That the slope is the enthalpy, ΔH_{cv} , follows directly from Eq. [27] and the derivative of the exponent with respect to T

$$\begin{aligned} d(\Delta E_{cv}/T)/d(1/T) &= \Delta E_{cv} - T(d\Delta E_{cv}/dT) \\ \Delta E_{cv} + T\Delta S_{cv} &= \Delta H_{cv} \end{aligned} \quad [28]$$

Since ΔH_{cv} is an increasing function of temperature, the slope of the $\log n_i$ vs. $1/T$ plot should increase with temperature. This effect is clearly shown in the measurements of Morin and Maita (32) on silicon at higher temperatures. At lower temperatures, over the usual temperature ranges studied, the slope will be constant within experimental uncertainties.

It is frequently assumed that the temperature dependence of the energy gap is a linear function of temperature. The line will usually be a good approximation to the tangent of the curve that gives the correct temperature dependence of the energy gap. The intercept of this tangent line at $T = 0^\circ\text{K}$, the extrapolated energy gap at 0°K , is the enthalpy, ΔH_{cv} , at the temperature T where the line is tangent to the curve. These relationships are shown in Fig. 15 and follow from the thermodynamic relationships of Eq. [9], [10], and [11].

An example of how the gap enthalpy, ΔH_{cv} , can be used to clarify a problem is found from the work of Parillo and Johnson (37). They measured the temperature dependence of the electron emission rates from the Au energy level in Si, and after correcting the experimental slope for the temperature dependence of thermal velocities, capture cross sections, and the effective density of states in the conduction band, concluded that they had fixed the position of the level below the conduction band edge. Similar measurements of the hole emission rates fixed the position of the level above the valence band edge. They found, however, that the two energies did not add to give the value of the energy gap at their average temperature, 328°K . Their measurements gave the sum, 1.21 ± 0.03 eV; the value of ΔE_{cv} was 1.12 eV (1.117 ± 0.001 eV present value). The anomaly was explained by assuming that the energy gap and the energy level were functions of temperature, specifically, linear functions of temperature. This led to the conclusion that the energy levels obtained from the temperature dependences of the emission rates were, in fact, energy levels at 0°K . Their sum, 1.21 eV, should compare to the extrapolated energy gap at 0°K , 1.20 eV, giving satisfactory agreement.

This explanation of the anomaly is basically correct. There is no necessity, however, to assume a linear dependence on temperature for the energy gap and the energy level when it is recognized that the energy level measured is an enthalpy level and the sum should be compared to the gap enthalpy, ΔH_{cv} . The comparison is, then, between the sum, 1.21 ± 0.03 meV and ΔH_{cv} at 328°K , 1.204 ± 0.001 eV, with agreement well within estimated uncertainties.

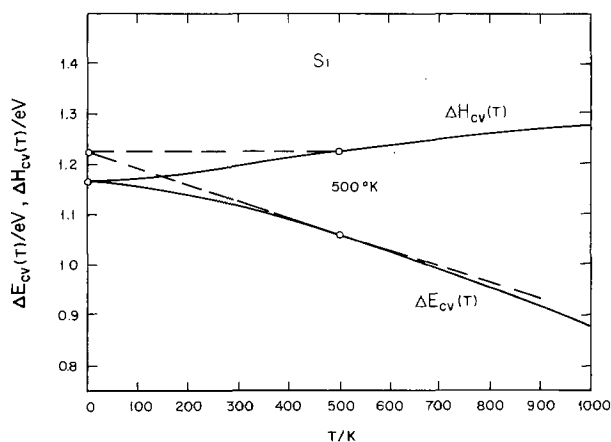


Fig. 15. The forbidden energy gap, ΔE_{cv} in eV, and the enthalpy, ΔH_{cv} in eV, vs. T for Si. It is shown that the tangent to the ΔE_{cv} curve at 500°K intersects the $T = 0^\circ\text{K}$ axis at a value equal to the enthalpy, ΔH_{cv} , at 500°K . The same relationship holds at any temperature.

A comment about the apparent anomaly of the optically measured energy gap being a Gibbs energy.

—In the section on thermodynamics a chemical thermodynamic argument is given for the forbidden energy gap as a Gibbs energy and optical absorption measurements were later used to obtain the energy gap. This implies that the absorption of light by the crystal should occur at constant temperature and pressure since it involves a Gibbs energy, but this certainly is not so. The absorption of a photon by the lattice is a very rapid process. The crystal does not have time to come to thermal equilibrium and therefore absorption of light occurs at constant entropy, and also constant volume. Under these conditions it is the internal energy, U , that changes in the formation of the electron and hole, not the Gibbs energy, G . But a fundamental thermodynamic relationship can be used to show that these two functions are of equal magnitude. The fundamental thermodynamic relationship defines the chemical potential (38)

$$\mu_i = \left(\frac{\partial G}{\partial N_i} \right)_{P,T,N_j} = \left(\frac{\partial U}{\partial N_i} \right)_{S,V,N_j} \quad [29]$$

The change in total Gibbs energy, G , with the number of atoms of i , N_i , at constant pressure, temperature and all other components, N_j , and the change in the total internal energy, U , with atoms of i at constant entropy, volume and N_j , are both the chemical potential of i , μ_i . It has been shown (section on thermodynamics) that the energy gap is a chemical potential. It follows that the energy gap measured optically at conditions of constant entropy and volume is identical to the energy gap measured at constant pressure and temperature. With recognition that these are, in fact, standard functions and using the symbol N for the number of electron-hole pairs, the equalities can be expressed in a modified form of Eq. [29]

$$\mu_n^\circ + \mu_p^\circ = \Delta E_{cv}(\text{thermal}) \\ = \left(\frac{\partial \Delta G^\circ}{\partial N} \right)_{P,T} = \left(\frac{\partial \Delta U^\circ}{\partial N} \right)_{V,S} = \Delta E_{cv}(\text{optical}) \quad [30]$$

Table columns and figure axes.—The headings of table columns and the labeling of figure axes follows the recommendation of McGlashan (41).

Summary

The Gibbs energy, the enthalpy and the entropy of formation of electrons and holes in Ge, Si, GaAs, and GaP have been obtained over the temperature ranges 0°K to the respective melting points. The Gibbs energy for the electron-hole formation reaction is the forbidden energy gap of the semiconductor. The enthalpy and entropy of the reaction are obtained from the forbidden energy gap as a function of temperature by familiar thermodynamic relationships.

The forbidden energy gaps of Ge, Si, GaAs, and GaP are available in the literature but over limited temperature ranges. A semiempirical equation by Varshni (16) has been used to fit the available forbidden energy gap measurements as a function of temperature and provides the basis for extrapolation to the melting points. A different fitting method from that used by Varshni has led to the resolution of an anomaly found by Varshni for Si. One of the constants of the Varshni equation was expected to have a value near that of the Debye temperature. The value found by Varshni for Si was surprisingly large (1108° vs. 645°K). The new fit leads to an acceptable value (636°K).

While the forbidden energy gaps decrease with temperature, the enthalpies slowly increase with temperature implying a positive heat capacity change in the formation of electrons and holes. The entropy changes

are large, approximately 12 cal/deg or 5×10^{-4} eV/deg at high temperatures. It follows that the decrease with temperature of the forbidden energy gaps is predominately due to the relatively large entropies of formation of electrons and holes. These entropies arise from the interaction of electrons and holes with the lattice. The thermodynamic functions ΔE_{cv} , ΔH_{cv} , and ΔS_{cv} , are independent of the concentrations of electrons and holes are the so-called "standard" functions of chemical thermodynamics.

The intrinsic carrier concentrations have been calculated from the forbidden energy gaps and the average density of states effective masses. Estimates of the average effective masses have been made.

The forbidden energy gap as a function of temperature is frequently approximated by a straight line. In general, ΔE_{cv} is not linear in T and the extrapolated value of the energy gap at 0°K is larger than the true value $\Delta E_{cv}(0)$. When the line is a good approximation to the tangent, at T , of the curve giving $\Delta E_{cv}(T)$, the extrapolation to 0°K gives ΔH_{cv} , the enthalpy of formation of electrons and holes at the temperature T .

Acknowledgments

Discussions with H. C. Casey, Jr. and J. A. Van Vechten have been particularly helpful. Help on specific problems was received from R. Dingle, C. H. Henry, J. J. Hopfield, M. B. Panish, M. Sturge, and from H. Reiss.

Manuscript received April 2, 1975. This was Paper 152 presented at the San Francisco, California, Meeting of the Society, May 12-17, 1974.

Any discussion of this paper will appear in a Discussion Section to be published in the June 1976 JOURNAL. All discussions for the June 1976 Discussion Section should be submitted by Feb. 1, 1976.

Publication costs of this article were partially assisted by Bell Laboratories.

LIST OF SYMBOLS

ΔC_{cv}	standard constant pressure heat capacity change for the formation of electrons and holes, Eq. [1]
ΔE_{cv}	forbidden energy gap; the standard Gibbs energy of formation of electrons and holes, Eq. [1]
ΔE_{ex}^f	molar Gibbs energy of formation of an exciton
ΔE_{ex}^d	molar Gibbs energy of dissociation of an exciton
ΔG_{cv}°	standard Gibbs energy of formation of electrons and holes, Eq. [1, 7]; the forbidden energy gap
ΔG°	total standard Gibbs energy of formation of electrons and holes, Eq. [1, 30]
ΔH_{cv}	standard enthalpy of formation of electrons and holes Eq. [1]; the enthalpy gap
h	Planck's constant
k	Boltzmann's constant
m_n, m_p	the effective masses of electrons and holes, respectively
$\langle m \rangle$	the average effective mass, $(m_n m_p)^{1/2}$
n, n°	electron concentration and reference state electron concentration, respectively, in number/cm ³
n_c, n_v	effective density of states in the conduction band and valence band, respectively
n_i	intrinsic electron concentration, $n_i = n = p$
p, p°	hole concentration and reference state electron concentration in number/cm ³
ΔS_{cv}	the standard entropy of formation of electrons and holes, Eq. [1]; the entropy gap
ΔU°	total standard internal energy of formation of electrons and holes, Eq. [1, 30]
x_n	electron composition fraction, n/n°
x_p	hole composition fraction p/p°
μ_n, μ_p	chemical potentials of electrons and holes, respectively

REFERENCES

- H. Brooks, *Advan. Electron. Electron Phys.*, **7**, 85 (1955).
- G. L. Pearson and J. Bardeen, *Phys. Rev.*, **75**, 865 (1949).
- F. A. Kröger, "The Chemistry of Imperfect Crystals," p. 252, John Wiley and Sons, Inc., New York (1964).
- F. A. Kröger, "The Chemistry of Imperfect Crystals," p. 253, John Wiley and Sons, Inc., New York (1964).
- G. G. Macfarlane, T. P. McLean, J. E. Quarrington, and V. Roberts, *Phys. Rev.*, **108**, 1377 (1957).
- G. G. Macfarlane, T. P. McLean, J. E. Quarrington, and V. Roberts, *Proc. Phys. Soc. (London)*, **71**, 863 (1958).
- G. G. Macfarlane, T. P. McLean, J. E. Quarrington, and V. Roberts, *J. Phys. Chem. Solids*, **8**, 388 (1959).
- T. P. McLean, "Progress in Semiconductors," Vol. 5, p. 53, Heywood and Co., Ltd., London (1960).
- G. G. Macfarlane, T. P. McLean, J. E. Quarrington, and V. Roberts, *Phys. Rev.*, **111**, 1245 (1958).
- M. D. Sturge, *ibid.*, **127**, 768 (1962).
- M. B. Panish and H. C. Casey, Jr., *J. Appl. Phys.*, **40**, 163 (1969).
- D. D. Sell, H. C. Casey, Jr., and K. W. Wecht, *ibid.*, **45**, 2650 (1974).
- D. D. Sell, S. E. Stokowski, R. Dingle, and J. V. DiLorenzo, *Phys. Rev.*, **B7**, 4568 (1973).
- M. R. Lorenz, G. D. Pettit, and R. C. Taylor, *ibid.*, **171**, 876 (1968).
- P. J. Dean and D. G. Thomas, *ibid.*, **150**, 690 (1966).
- Y. P. Varshni, *Physica*, **39**, 149 (1967).
- R. H. Fowler, "Statistical Mechanics," 2nd ed., Chap. 11, Cambridge University Press, London (1936).
- J. C. Phillips, "Bonds and Bands in Semiconductors," p. 11, Academic Press, New York (1973).
- K. Denbigh, "The Principles of Chemical Equilibrium," 3rd ed., Chap. 4, p. 133, Cambridge University Press, London (1971).
- G. N. Lewis and M. Randall, "Thermodynamics," 2nd ed., revised by K. S. Pitzer and L. Brewer, Chap. 13, p. 138, McGraw-Hill Book Co., New York (1961).
- J. S. Blakemore, "Semiconductor Statistics," pp. 64, 68, Pergamon Press, New York (1962).
- K. L. Shaklee and R. E. Nahory, *Phys. Rev. Letters*, **24**, 942 (1970).
- W. Bludau, A. Onton, and W. Heinke, *J. Appl. Phys.*, **45**, 1846 (1974).
- P. Flubacher, A. J. Leadbetter, and J. A. Morrison, *Phil. Mag.*, **4**, 273 (1959).
- E. F. Steigmeir, *Appl. Phys. Letters*, **3**, 6 (1963).
- M. I. Nathan and G. Burns, *Phys. Rev.*, **129**, 125 (1963).
- J. C. Sarace, R. H. Kaiser, J. M. Whelan, and R. C. C. Leite, *ibid.*, **137**, 623 (1965).
- D. D. Sell, *ibid.*, **B6**, 3750 (1972).
- C. J. Glassbrenner and G. A. Slack, *ibid.*, **134**, 1058 (1961).
- H. C. Casey, Jr., "Atomic Diffusion in Semiconductors," D. Shaw, Editor, Appendix 6A, p. 422, Plenum Press, New York (1973).
- H. D. Barber, *Solid-State Electron.*, **10**, 1039 (1967).
- F. J. Morin and J. P. Maita, *Phys. Rev.*, **96**, 28 (1954).
- E. H. Putley and W. H. Mitchell, *Proc. Phys. Soc. (London)*, **A72**, 193 (1958).
- F. J. Morin and J. P. Maita, *Phys. Rev.*, **94**, 1525 (1954).
- M. Neuberger, "Handbook of Electronic Materials, Group IV Semiconducting Materials," Vol. 5, pp. 18-19, IFI/Plenum, New York (1971).
- R. K. Jain and R. J. Van Overstraeten, *IEEE Trans. Electron Devices*, **ED-21**, 155 (1974).
- L. C. Parrillo and W. C. Johnson, *Appl. Phys. Letters*, **20**, 104 (1972).
- Following a suggestion by J. A. Van Vechten.
- G. N. Lewis and M. Randall, "Thermodynamics," 2nd ed., revised by K. S. Pitzer and L. Brewer, p. 80, McGraw-Hill Book Co., New York (1961).
- B. N. Taylor, W. H. Parker, and D. N. Langenberg, *Rev. Mod. Phys.*, **41**, 375 (1969), Tables 32 and 33, pp. 477-479.
- M. L. McGlashan, "Annual Review of Physical Chemistry," pp. 51-76, see p. 59, Quantity Calculus, Annual Reviews Inc., Palo Alto, Calif. (1973).

Growth of Single Crystals of CdO by Molten Hydrrous KOH Solutions

Krishna Kumar

Department of Physics, Indian Institute of Technology, New Delhi 110029, India

ABSTRACT

Octahedral crystals of CdO have been grown at 450°C using KOH melt as flux. Three dimensional dendrites are also reported. Supersaturation and crystal growth were promoted by the high temperature dissociation of a complex with the solvent.

CdO is a high bandgap, n-type degenerate semiconductor having NaCl structure. The electrical, optical, thermal, and other properties of CdO have not been investigated in detail due to the difficulty in growing single crystals of the material. The high melting point and the absence of suitable crucible material limit its growth by the conventional melt growth technique. The floating zone technique has been unsuccessful in melting the sintered mass of CdO. The low vapor pressure (1) of CdO at the softening temperature of quartz ($\approx 1200^\circ\text{C}$) imposes severe restrictions for growth of single crystals by the vapor phase technique. Fahrig (2) used a horizontal tube made of CdO powder supported by a quartz tube at 1200°C and obtained small single crystals. Konak *et al.* (3, 4) and Fischer and Spear (5) succeeded in obtaining bigger size crystals from the vapor phase. In all these cases crystals grew on the charge itself. Thermal decomposition of cadmium oxalate (6, 7) at 600°C resulted in needle-type crystals. The hydrothermal method has been suggested by Moody (8) for the growth of CdO single crystals. The author has attempted to grow CdO single crystals using NaOH and KOH melts as flux; the former was found to be unsuitable whereas the latter proved to be a good solvent for CdO. The present paper deals with the flux growth of single crystals of CdO using KOH melt as the solvent.

Experimental

The experimental setup and the temperature profile of the furnace were similar to those used by Kashyap (9) and Krishna (10), to grow ZnO crystals. To find the optimum amount of CdO to be mixed with KOH, 60g of KOH (AR) was melted in a silver crucible and different amounts of CdO (AR, supplied by Reanal, Hungary) were dissolved in different runs in it by constant stirring with a silver rod, as it was not possible to find the exact solubility of CdO in the KOH melt. The crucible was then covered with a silver lid and kept in the constant temperature zone of the furnace, which was heated at a rate of $50^\circ\text{--}60^\circ\text{C/hr}$ to the desired temperatures ($400^\circ\text{--}600^\circ\text{C}$) in different runs; the charge was left at this temperature for different durations of time varying from 20–80 hr. After the completion of a run, the furnace was cooled at a rate of $10^\circ\text{--}15^\circ\text{C/hr}$ to room temperature. CdO crystals were separated by dissolving the KOH in water; the crystals were investigated by optical microscopy, x-ray (Laue method), and spectroscopic methods.

Results and Discussion

Unlike in other flux growth experiments where supersaturation is achieved either by lowering the temperature of the solution or by evaporating the solvent or by a combination of both, in the present case it is caused by an altogether different mechanism. This was indicated by the fact that when program cooling of the solution was employed no crystal was observed to grow. Again the nonvolatile nature of the KOH sug-

gests that supersaturation cannot be promoted by the evaporation of solvent in the present case. It is suggested that KOH which absorbs water molecules from its surroundings, forms a complex in a fashion similar to the ZnO-KOH system (9). This complex dissociated at higher temperature and gives rise to CdO which leads to the growth of CdO crystals. The rate of dissociation increases with the increase in growth temperature. This was indicated by our observation that at low temperature (400°C) of charge no crystals grew, whereas the use of high temperature ($\approx 600^\circ\text{C}$) yielded a large number of small crystals. Best crystals were grown at 450°C when 5g of CdO was dissolved in 60g of KOH melt, which was actually found to contain 40g of KOH and 20g of water, and the duration of growth was 40 hr. Emission spectroscopic analysis confirmed that crystals were of CdO and that the metallic impurities were the same as in the initial charge except that a small amount of Ag ($\approx 0.001\%$) was observed.

The crystals were black in color. This has been attributed to the deficiency of oxygen in the crystals (3, 6). The crystals were octahedral in morphology (Fig. 1) with one corner in contact with the crucible wall indicating heterogeneous nucleation. X-ray investigations (Laue photograph) confirmed their single-crystal nature. In many of these crystals hopper growth was observed on (111) faces (Fig. 2), while in many others these faces were smooth. The four (111) faces which were near the wall were invariably rough because of a high initial growth rate; later on the surface area for growth increased resulting in the decrease in local supersaturation and smoother faces. Hopper growth arises near the center of the face of the crystal, probably due to absorption of impurities on the growing face (10) and due to the high viscosity of



Fig. 1. Single crystal of CdO showing (111) faces. Octahedral morphology ($\times 40$).

Key words: crystal growth, CdO, flux method, solubility.



Fig. 2. Hopper growth on (111) face of a crystal ($\times 30$)



Fig. 3. Figure shows the initiation of dendritic growth at one corner of the octahedron ($\times 40$).

the solvent which in turn reduces the supply. Basic morphology of the crystals was found to be independent of growth temperature, only the crystal size changes.

When the solution was rapidly cooled at the end of the run, three dimensional dendritic crystals grew from the corner of the octahedron which is farthest from the wall (Fig. 3 and 4) and also from the wall of crucible near the melt surface (Fig. 5). The arms of the dendrites protruded in four directions, each perpendicular to the main arm. X-ray study (Laue photograph) of these dendrites revealed the branching was along $\langle 100 \rangle$ directions.

Acknowledgments

Sincere thanks are to Dr. S. D. Sharma for valuable discussions. Thanks are also due to CSIR, India for the award of a research fellowship.

Manuscript submitted Oct. 10, 1974; revised manuscript received Feb. 20, 1975.

Any discussion of this paper will appear in a Discussion Section to be published in the June 1976 JOURNAL. All discussions for the June 1976 Discussion Section should be submitted by Feb. 1, 1976.

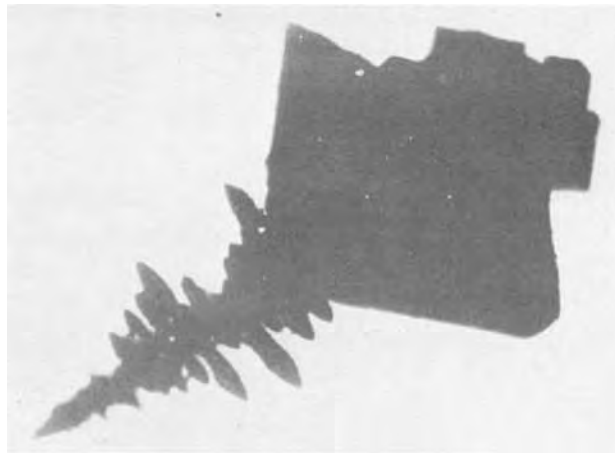


Fig. 4. A crystal of octahedron morphology which has transformed into three dimensional symmetrical dendrite ($\times 40$).

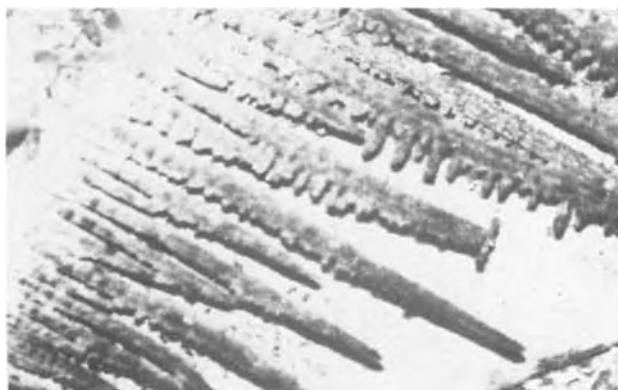


Fig. 5. Dendrites which grow at the surface of a melt from the wall of the crucible ($\times 30$).

REFERENCES

1. "American Institute of Physics Handbook," D. E. Gray, Editor, pp. 4-129, 9-25, McGraw-Hill Book Co., New York (1963).
2. R. H. Fahrig, *J. Appl. Phys.*, **34**, 234 (1963).
3. P. Höschl, C. Konak, and V. Prosser, *Mater. Res. Bull.*, **4**, 87 (1969).
4. C. Konak, P. Höschl, J. Dillinger, and V. Prosser, in "Crystal Growth," H. S. Peiser, Editor, p. 341, Pergamon, Oxford (1967).
5. K. J. Fischer and K. F. Spear, *J. Crystal Growth*, **16**, 142 (1972).
6. S. Van Houten, *Nature*, **195**(4840), 484 (1962).
7. Krishna Kumar, To be published.
8. J. W. Moody and R. C. Himps, *Battelle Tech. Rev.*, **14**, 3 (1965).
9. S. C. Kashyap, *J. Appl. Phys.*, **44**, 428 (1973).
10. Krishna Kumar, *J. Crystal Growth*, In press.

Chemical Vapor Deposition of Transparent, Electrically Conductive Tin Oxide Films Formed from Dibutyl Tin Diacetate

James Kane and H. P. Schweizer

Laboratories RCA Limited, Zurich, Switzerland

and Werner Kern*

RCA Laboratories, Princeton, New Jersey 08540

ABSTRACT

The reactions of volatile tin organometallic compounds with oxygen have been investigated as a method for preparing transparent, electrically conducting layers of tin oxide. Several organometallic tin compounds were examined before the process was systematically optimized using dibutyl tin diacetate with excess O_2 and H_2O as reactants and N_2 as carrier gas at a substrate temperature of $420^\circ C$ in 10-20 min of deposition. The presence of water vapor during oxidation is beneficial.

Important optical, electrical, structural, and chemical properties of the films have been examined. Typical SnO_2 coatings are 800-5000Å thick, transmit 90-95% of visible light, have sheet resistances of 500-1700 ohms/square, resistivities of 0.005-0.09 ohm-cm, a carrier concentration of $9 \times 10^{18} \text{ cm}^{-3}$, and a Hall mobility of $10 \text{ cm}^2/V \text{ sec}$. Films of 0.4-0.5 μm consist of a mixture of polycrystalline tetragonal stannic oxide as evidenced by x-ray diffraction, and of amorphous tin oxide phases as concluded from infrared spectroscopy. Electron diffraction analysis has indicated that the surface layers to a depth of 50Å are amorphous.

Semitransparent, electrically conducting thin films are required in many modern opto-electronic devices. Numerous materials have been prepared for this purpose by a variety of physical and chemical deposition processes (1-5). For many applications not requiring very low sheet resistance, nonstoichiometric (oxygen-deficient) tin oxide without dopant addition is a satisfactory conductor which is reasonably transparent to light in the visible wavelength region.

Tin oxide films are most commonly deposited by vapor or spray hydrolysis of stannic chloride onto hot glass surfaces in the temperature range of 500° - $800^\circ C$ (1-4, 6-12). However, the properties of these films are hard to reproduce, the optical quality is often poor, and the SnO_2 lattice is frequently contaminated with chlorine (12). The object of the present investigation was to develop a convenient, economical, and reproducible process for the preparation, on a production scale, of transparent, electrically conducting layers of tin oxide of high optical quality that are essentially free of chemical and particulate contaminants. A chemical vapor deposition process that is based on the use of a volatile organometallic tin compound has been developed to meet these requirements.

A number of volatile organometallic tin compounds was considered as potential source materials for vapor phase oxidation to tin oxide films at relatively low temperatures (350° - $500^\circ C$). Initial screening experiments indicated that a deposition process could be developed using any one of a number of compounds, including bis-(tri-n-propyl tin) oxide, bis(tributyl tin) oxide, tetraphenyl tin, tetra isopropyl tin, and dibutyl tin diacetate. Polymeric dibutyl tin oxide, $[C_4H_9SnO]_x^-$, and stannous oxalate did not work, and tetraphenyl tin could be considered to be a failure since most of the compound was not decomposed in the reactor.

The process we now describe was optimized using dibutyl tin diacetate, for a number of reasons. Dibutyl

tin diacetate, also known as dibutyl-diacetoxystannate, $(C_4H_9)_2Sn(OOCCH_3)_2$, is an oily, air-stable, colorless liquid compound having a vapor pressure of 1 Torr at $120^\circ C$, which makes it convenient for transporting its vapor in CVD work. The compound does not pose severe safety hazards and is much cheaper and more readily available than any of the other compounds we considered.

Most of the experimental work was carried out with 1 in. square plates of polished borosilicate glass. The deposition method is equally applicable to any substrate material that is unaffected by the deposition conditions, namely $420^\circ C$ in an atmosphere containing oxygen. Transparent, conducting layers of tin oxide were also obtained on a variety of silicate glasses, vitreous quartz, and a number of single crystal materials including silicon, sapphire, spinel, strontium titanate, and gallium phosphide. For analytical purposes representative deposits of tin oxide were prepared on polished, high-resistivity silicon wafers.

Film Deposition

Apparatus.—The deposition apparatus was a single rotation hotplate reactor similar in construction to that devised for oxide and glass coating of semiconductor device wafers (13). The radial temperature profile across the 8 in. diameter rotating plate was checked using a Barnes "TEMPTRON" infrared pyrometer. At a nominal temperature of $420^\circ C$ the actual temperature range measured across the plate was $420^\circ \pm 5^\circ C$.

A schematic drawing of the assembled apparatus is shown in Fig. 1. The entire system was constructed in a chemical exhaust hood to avoid exposure to toxic organometallic vapors. The reaction chamber was rigidly mounted to allow the use of stainless steel connections to the gas inlet system. The rotating hotplate unit was mounted on a laboratory jack for easy loading and unloading of the substrates.

The organometallic tin compound was contained in a fritted glass bubbler which was maintained at a controlled temperature in the range 70° - $150^\circ C$. A

* Electrochemical Society Active Member.

Key words: tin oxide, CVD, transparent conductors, thin films, semiconductors.

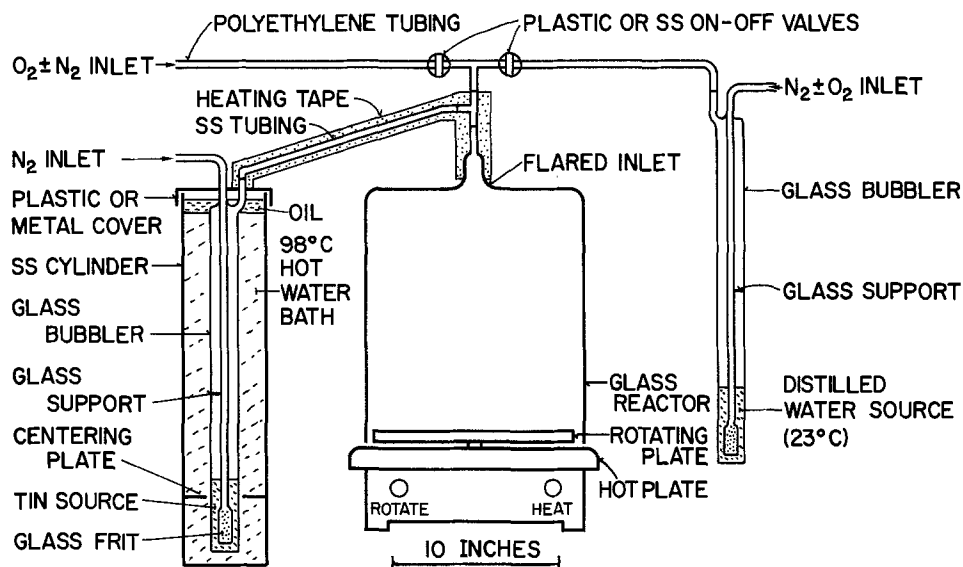


Fig. 1. Schematic of CVD reactor and gas flow systems.

boiling water bath is a simple and convenient method of temperature control.

Study of deposition parameters.—The effects of deposition variables on film properties were systematically explored to define optimum process conditions. The variables included source and substrate temperatures, rate of film growth, reactant and carrier gas flow rates, concentration of water vapor, and nature of substrate. In general, one variable was tested at a time by keeping all other variables constant. It was found that a minimum tin source temperature of 70°C was required to start film deposition, but that 90°C was needed to produce sufficient vapor for acceptable film deposition rates. Temperatures up to 150°C have been used with satisfactory results. A temperature of 98°C was adopted so that a boiling water bath could be employed for automatic temperature control.

Substrate temperatures in excess of 375°C were found necessary to oxidize the dibutyl tin diacetate vapor for depositing tin oxide films. All work was conducted at a fixed temperature of 420°C, which was found to yield good deposition rates. A heat-up time of 5 min was required to thermally equilibrate the substrates before starting the deposition. A postdeposition flush nitrogen of ½ min was sufficient to exhaust the reactant vapors from the bell jar before opening.

A relatively large nitrogen flow rate was used to suppress homogeneous gas phase nucleation and to avoid the formation of powdery wall deposits. Similar results have already been obtained in silicate glass synthesis by CVD (14, 15). The optimum flow rate was selected in conjunction with uniformity and other properties of the films, including absence of particulate defects.

The oxygen flow rate, in relation to the organotin input, affects the stoichiometry of the resulting tin oxide to some extent but is not very critical as long as some oxygen is present. The presence of water vapor has beneficial effects on the optical and electrical properties of the films.

The rate of film deposition was controlled primarily by the flow rate of nitrogen carrier gas through the tin source bubbler. A deposition time of 5 min was considered a minimum period to allow good control of film thickness, whereas periods greater than 20 min were undesirable due to the deterioration of the electrical properties of the films.

Once conditions for good film deposition had been established a series of runs was conducted to test the reproducibility of the films in terms of electrical resistance. The effect of variations in the flow of oxygen and water vapor was also studied. The results of these experiments are summarized in Table I. The beneficial effects of water vapor are evident from the marked improvement in film conductivity.

Film Properties

Surface morphology.—The films were deposited under the conditions listed in Table I. The general features of the tin oxide film surfaces were established by visual examination and by low-power optical microscopy, including Nomarski differential interference contrast. Typical samples exhibited very smooth, structureless surfaces on which could be found an occasional impurity particle that may have originated from the vapor phase during CVD.

Details of surface morphology on borosilicate glass were studied at magnifications up to 20,000X by scanning electron microscopy in the secondary electron emissive mode with a Cambridge "Steroscan." No pretreatment of the specimens was required, since the SEM image is generated by secondary electrons emitted from the surface being scanned. Typical scanning electron micrographs of three CVD samples (Fig. 2A-C) were compared with one sample that had been produced by the standard tin halide spray-deposition process (Fig. 2D). The photographs for the CVD films exhibit a very fine-grained surface with few defects; in contrast, the spray-deposited film is grainy, non-uniform, and covered with deep scratches and particulate impurities.

Electrical properties.—The electrical resistance of the films was measured using a conventional four-point probe. Resistance and resistivity data for samples obtained under various gas flow rate conditions are presented in Table I. The conditions stated are particularly desirable and have been selected from a large number of experiments. Sheet resistance values for

Table I. Preferred wet and dry CVD conditions and electrical resistance of tin oxide films grown at 420°C

Sample No.	Deposition time, min	N ₂ , cm ³ /min	O ₂ , cm ³ /min	Film thickness, Å	Sheet resistance, ohms/square	Film resistivity, ohm-cm
Wet						
With H ₂ O						
1	10	12,600	1,020	900	544	0.005
2	15	12,600	1,020	2,900	634	0.018
3	10	12,600	1,380	700	725	0.005
4	15	12,600	6,300	2500	815	0.020
Dry						
Without H ₂ O						
5	20	6,700	650	3,400	1,404	0.045
6	15	6,700	650	3,400	1,404	0.048
7	15	6,700	480	3,600	1,586	0.057
8	25	6,700	650	5,300	1,721	0.091

Additional constant deposition conditions as follows: carrier gas through tin source (N₂-Sn), 4400 cm³/min; Sn-source temperature, 98°C; H₂O source temperature, 23°C; substrate temperature, 420°C; substrate thermal equilibration time, 5 min; postdeposition purge time, ½ min N₂.

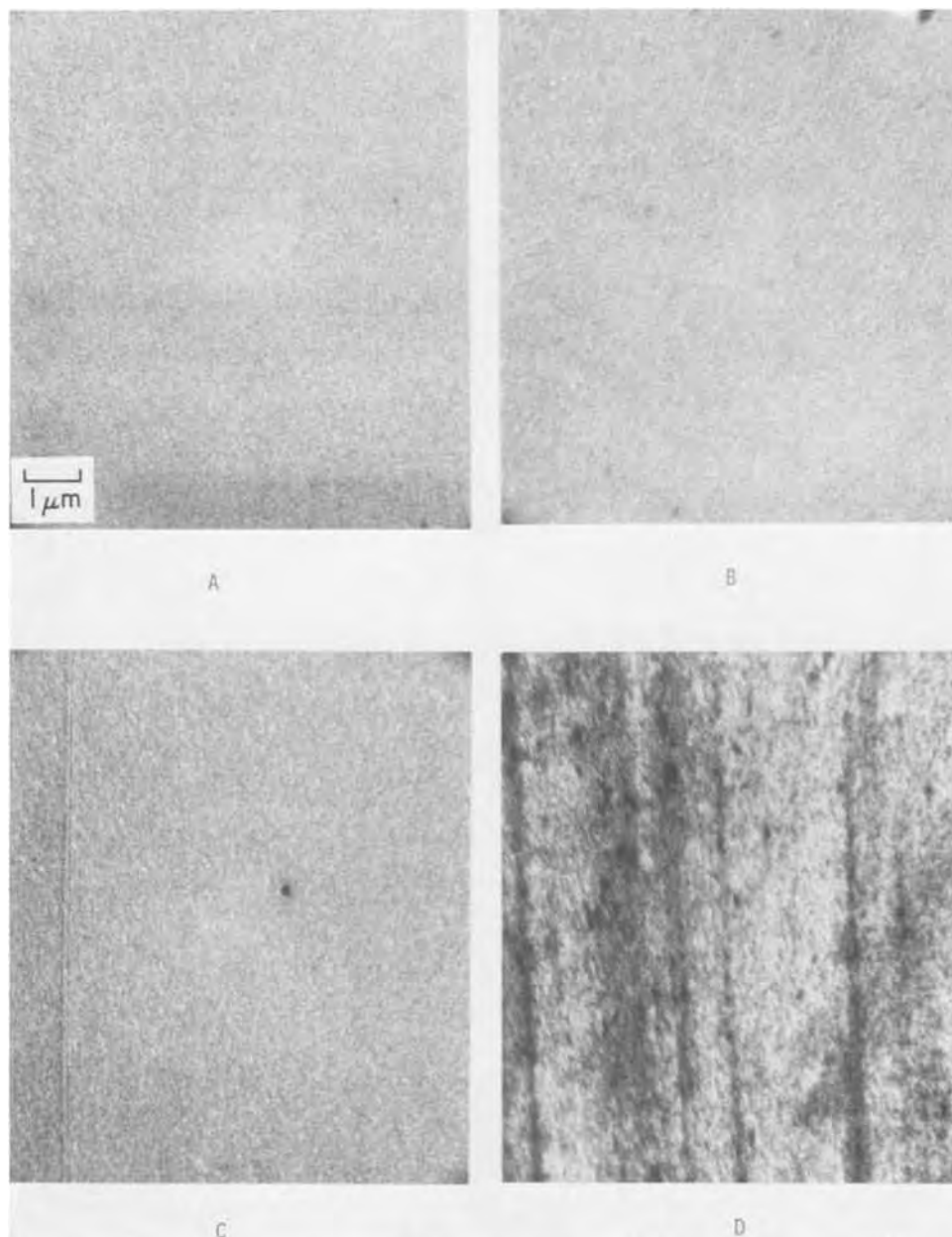


Fig. 2. Scanning electron micrographs of tin oxide films on glass plates (at a tilt of 45°). Three typical CVD samples (A, B, C) compared with a typical tin halide spray-deposited sample (D).

typical wet and dry CVD conditions are also shown graphically as a function of deposition time in Fig. 3. These curves show decreasing resistivity as the film thickness increases up to about a 20 min deposition period. With longer periods of deposition, especially in the case of dry CVD conditions, there is an increase in sheet resistance, perhaps due to the diffusion of ionic impurities from the substrate and the effect of annealing on the stoichiometry of the tin oxide.

Hall measurements were performed at room temperature using the standard Van der Pauw technique. The magnetic field was 16 kG. The tin oxide was found to be n-type with an average carrier concentration of $9 \times 10^{18} \text{ cm}^{-3}$ and a mobility of $10 \text{ cm}^2/\text{V sec}$.

No controlled tests were conducted on the long term film stability although the electrical resistance remained constant for periods of at least several months. The films showed no signs of devitrification.

Optical properties.—For device fabrication the tin oxide films are required to have good optical transmission throughout the visible spectrum in addition to low electrical resistance. The transmission spectrum of a 6500\AA thick film of tin oxide together with the corresponding reflection spectrum are shown in Fig. 4. As can be seen from a comparison of these two curves, the actual absorption losses are quite small. Since tin

oxide is a high refractive index material, a considerable proportion of the incident radiation is reflected.

The transmission spectrum was measured with an uncoated glass plate in the reference beam of the spectrometer. Per cent transmission values measured for the wavelengths 4000, 4400, 4800, 5200, 5600, and 6000\AA are presented in Table II for the same samples listed in Table I. An optical transmission of 85% net with a sheet resistance of 2000 ohms/square is readily attainable.

Since the most important film characteristics are sheet resistance and optical transparency, a figure of merit for the films has been derived from these characteristics to facilitate comparison. This figure has been calculated by dividing per cent average light transmission (arithmetic mean of per cent transmission at 4000, 4400, 4800, 5200, 5600, and 6000\AA) by the sheet resistance. Figures of merit for preferred deposition conditions are included in Table II. Figure 5 exemplifies graphically the effect of film growth time on the figure of merit for a wet and a dry CVD condition.

The refractive index of tin oxide films deposited under various reaction conditions was measured using a Rudolph ellipsometer (Model 436-200 E) at a wavelength of 5461\AA . For these measurements representative films were deposited on polished silicon wafers.

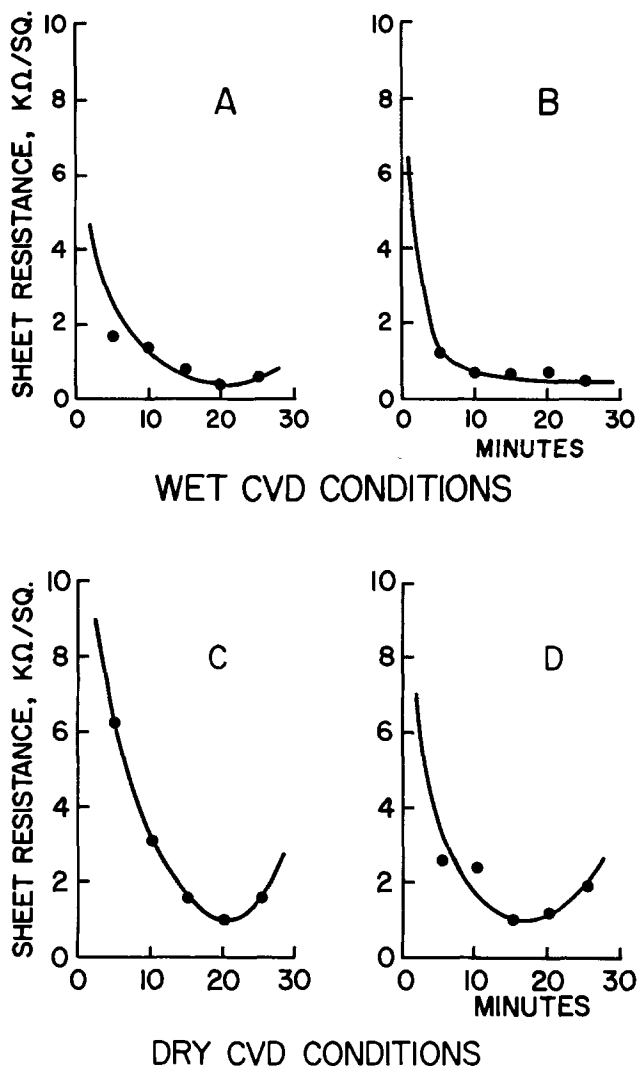


Fig. 3. Sheet resistance of tin oxide films as a function of growth time for typical wet (A, B) and dry (C, D) CVD deposition conditions.

The films were assumed to be nonabsorbing and the optical constants of the silicon substrate were taken to be 4.05 for the real part of the refractive index and 0.28 for the imaginary part. The angle of radiation incidence used was 70°. Samples prepared with various tin-to-oxygen vapor ratios, both with and without water vapor, were examined. The addition of water vapor reduced the refractive index but there was no ob-

Table II. Light transmission and figure of merit for tin oxide films deposited by preferred wet and dry CVD conditions*

Sample No.	Transmission in per cent at wavelength stated, Å						Calculated average transmission, (per cent net per T)	Figure of merit,** (per cent square/ohm)
	4000	4400	4800	5200	5600	6000		
Wet								
1	94.8	96.1	93.0	89.6	87.0	85.1	90.7	0.167
2	87.0	96.8	99.1	98.7	96.0	88.0	94.3	0.149
3	98.3	95.0	92.0	88.9	87.9	85.8	90.6	0.125
4	91.4	98.5	99.0	96.2	91.2	89.0	94.3	0.116
Dry								
5	85.8	86.3	97.0	94.0	86.8	88.0	89.7	0.0791
6	91.6	86.7	88.6	96.8	99.0	96.0	93.1	0.0663
7	85.0	85.4	96.6	99.4	97.1	92.2	92.6	0.0584
8	82.0	85.3	97.0	86.1	88.7	98.0	89.5	0.0520

* Same conditions and samples listed in Table I. Average net per cent T

** $\frac{\text{ohms/square}}{\text{ohms/square}}$

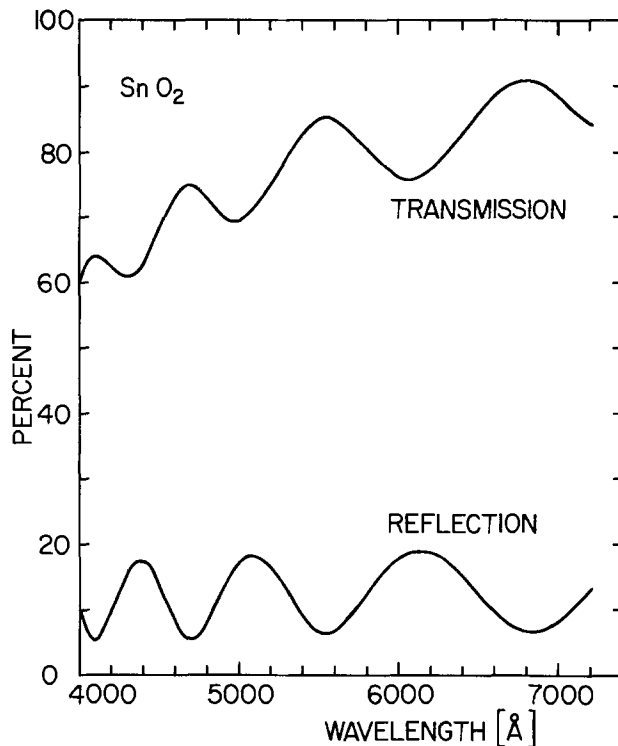


Fig. 4. Transmission and reflection spectra of a 6500Å thick film of tin oxide as a function of wavelength in the visible region of the spectrum.

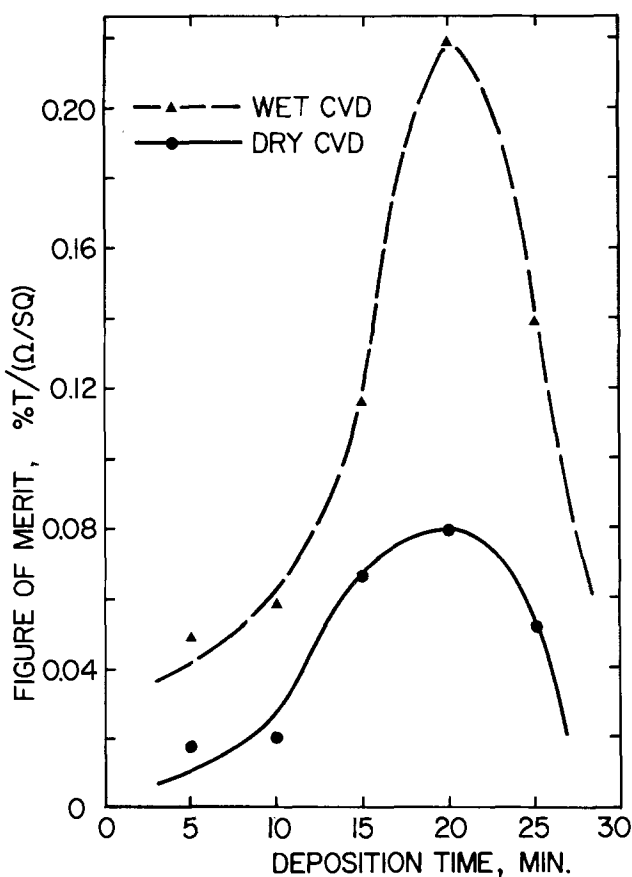


Fig. 5. Figure of merit as a function of growth time for typical wet (A) and dry (B) CVD conditions.

vious correlation of the refractive index with the oxygen-to-tin vapor ratio. The results are summarized in Table III.

Infrared absorption.—Films of about 6000-7500Å thickness were deposited on special infrared-transparent silicon for spectroscopic studies by the tech-

Table III. Index of refraction and layer thicknesses of CVD tin oxide films on silicon by ellipsometry

Film deposition conditions		Refractive index		Film thickness, Å
H ₂ O	O ₂ /Sn gas ratio*	<i>n</i>	Confidence limits for <i>n</i>	
no	0.295	2.3084	2.3023-2.3145	6047
no	0.109	2.1089	2.1061-2.1116	6236
no	0**	2.2681	2.2666-2.2695	3300
yes	1.43	1.7539	1.6922-1.8141	7529
yes	0.232	1.9098	1.9060-1.9136	3845
yes	0.109	2.1906	2.1785-2.2023	2960

(O₂ ± H₂O) cm³/min⁻¹

(N₂ through Sn source) cm³/min⁻¹

** No O₂ used for comparison. These films are brownish colored due to the presence of carbonized material.

niques described previously for silicate glasses (16). Double-beam infrared recording spectrophotometers (Perkin Elmer Model 137-B and Model 457 for detailed studies) were used, scanning the wavelength range from 2.5 to 40 μm. Infrared absorption spectra from samples prepared by dry or wet oxidation were weak, showing broad band absorption centered about 500 cm⁻¹ and, possibly, some weak discrete band structure near 600, 450, and 230 cm⁻¹. For comparison, the oscillator frequencies for stannic oxide single crystals are E_{lc} 243, 284, and 605 cm⁻¹ and E_{jc} 465 cm⁻¹ (17). The presence of combined broad and discrete structure in our samples suggests that the coatings contain both amorphous and crystalline phases.

Lattice structure.—Examination of the surfaces of several tin oxide coatings by electron diffraction showed an amorphous structure to a depth of 50Å. This is in contrast to the spray-deposited material which is polycrystalline with ordering. Both dry and wet grown films were analyzed with the same results.

Since the tin oxide coatings were too thin to be examined directly by x-ray diffraction, samples were removed for x-ray powder diffraction studies. The coating was composed of very fine tetragonal tin dioxide crystallites of less than 1000Å maximum dimension.

Chemical impurities.—Gaseous impurities given off by the tin oxide coating at elevated temperatures would be detrimental in certain applications. To ascertain the nature and quantity of these impurities, several samples were analyzed using a AEI MS-10 gas mass spectrometer.

Samples were contained in an evacuated quartz ampul at controlled temperatures up to 300°C. Outgassing of the samples was compared with samples of the uncoated substrate glass. The analysis showed that the gaseous impurities which could be attributed to the tin oxide were insignificant. The major outgassing impurities, carbon dioxide and water vapor, were evolved in similar quantities from both coated and uncoated samples.

Routine chemical analysis of the films using an AEI MS-7 solids mass spectrograph revealed only minor quantities of metallic impurities. Calcium and chlorine in quantities up to 25 ppm together with smaller quantities of other metals were found in all samples analyzed. Since only reagent grade chemicals were employed, the presence of small quantities of metallic impurity was not unexpected. Chlorine is also a likely contaminant of the organometallic compound.

Discussion of Results

A set of optimized deposition parameters is shown in Table I. The basis for selection was sheet resistance (arbitrary maximum of 3000 ohms/square) and optical transmission (minimum 85%) in the wavelength

range of 4000-6000Å. Additional criteria were acceptable film uniformity, freedom from particulate contaminants, and film stability. Due to optical interference effects it is possible to maximize the transmission of thin films at a particular wavelength. This is a useful technique to extend the transmission at the blue end of the visible spectrum if the sheet resistance is low enough to meet the specifications. The optical transmission of a relatively thick layer of tin oxide (2500Å) is shown in Fig. 4 to demonstrate these interference effects.

The distinct minimum in the sheet resistance which occurs after a deposition time of 20 min can be attributed to a number of factors: migration of alkali cations from the substrate into the oxide layer, changes in the oxygen stoichiometry, or crystallization of the tin oxide. All of these processes are known to occur and all lead to higher resistivity material.

By comparison of data from quartz and soda lime substrates it was clear that in the case of soft soda lime glass substrates the diffusion of alkali metal cations is the dominant process. The mobile alkali cations act as a p-type doping agent in the n-type tin oxide film, thus neutralizing some of the charge carriers. All attempts to prepare a 1000Å tin oxide with a sheet resistivity of 2000 ohms/square on such glass were unsuccessful. The sheet resistivities were at least a factor of 10 higher than comparable layers on borosilicate glass or vitreous quartz. The effect of the alkali metal contamination is so strong that the mere presence of soda lime glass in the reaction chamber during a tin oxide deposition significantly affects the film resistance on other substrates being coated. Subsequent deposition runs are also affected and a thorough cleaning of the apparatus is required before high-quality films can again be produced.

To examine the effect of heat-treatment on the oxygen stoichiometry a number of samples on glass, quartz, and silicon substrates were annealed for 15 min at 420°C in air or in nitrogen. All samples increased in sheet resistance, regardless of substrate material. The increase was by a factor of 15-25 in the case of the air annealed samples and of 1.5-3.0 for the nitrogen annealed material. These data indicate that the resistance increases are predominantly due to oxidation effects of nonstoichiometric (oxygen deficient) tin oxide (SnO, stannous oxide) shifting toward stannic tin dioxide (SnO₂, stannic oxide) structure. This is in accordance with the thermodynamic stability of the two oxides, the stannic oxide being the more stable compound (18).

Conclusions

Dibutyl tin diacetate at a deposition temperature of 420°C was found particularly suitable for preparing tin oxide films by vapor phase oxidation. Nitrogen is a suitable diluent and carrier gas to transport the organotin vapor from the liquid source maintained at 98°C. Oxygen is necessary as an oxidizing agent, but the ratio of organotin vapor to oxygen is not critical. In addition, water vapor is beneficial in producing high-quality tin oxide films.

Important optical, electrical, structural, and chemical properties of the films have been examined. Typical SnO₂ coatings on borosilicate glass are hard, clear, uniform, and 800-5000Å thick. They transmit 90-95% (net) of visible light. The ellipsometrically determined index of refraction varies with the conditions of film deposition, particularly the presence of water vapor. The films are n-type semiconductors, having sheet resistances of 500-1700 ohms/square and resistivities of 0.005-0.09 ohm-cm.

The infrared absorption spectra of 0.6-0.75 μm thick layers deposited on silicon indicate the presence of both amorphous and crystalline phases. Surface layers to a depth of about 50Å are amorphous, as shown by electron diffraction analysis. On the basis of x-ray diffraction, thicker layers (0.4-0.5 μm) are polycrystalline and were identified as tetragonal SnO₂. Scanning

electron microscopy at 10,000X magnification exhibited rather smooth surfaces with very much less particulate contamination and film damage than observed on tin halide spray-deposited samples.

On the basis of results obtained from mass spectrographic analysis we conclude that the films are essentially free of volatile impurities. Gas mass spectrometry showed that CO₂, CO, and H₂O were given off on heating but in quantities similar to those observed for the uncoated substrate glass.

The electrical resistance of tin oxide films deposited by this process on substrates high in alkali, such as soda lime glasses, is very high due to p-type doping by alkali ions. The resistance of films of comparable thickness on vitreous quartz or silicon is about half of that on a borosilicate glass containing 1 weight per cent (w/o) Na₂O and 8 w/o K₂O.

The growth period for the films should be the minimum period compatible with control of the film thickness. Periods beyond 20 min lead to rapid increases in resistivity due to chemical changes in the film stoichiometry and the diffusion of alkali metals from the glass substrate.

It must be realized that these conductive tin oxide films are nonstoichiometric and are therefore metastable compounds with fluctuating properties that cannot be controlled with high precision. For many applications these undoped tin oxide coatings are quite satisfactory; but if higher conducting or thermal stability is required then a suitable dopant must be introduced. We have found that antimony in the form of the pentachloride is compatible with the present process and can be used to produce more highly conductive films of SnO₂:Sb (19).

Acknowledgments

The authors would like to thank the following persons for their contributions in the instrumental analysis part of the project: E. Meier, H. Meier, and D. P. Bortfeld at Zurich; E. M. Botnick, D. C. McCarthy, J. J. McGinn, H. McCandless, R. J. Paff, B. J. Seabury, J. M. Shaw, R. D. Vibronnek, and P. J. Zanzucchi at Princeton. We are indebted also to H. W. Lehmann (Zurich) for reviewing the manuscript.

Manuscript submitted Sept. 25, 1974; revised manuscript received March 3, 1975. This was Paper 15RNP presented at the San Francisco, California, Meeting of the Society, May 12-17, 1974.

Any discussion of this paper will appear in a Discussion Section to be published in the June 1976 JOURNAL. All discussions for the June 1976 Discussion Section should be submitted by Feb. 1, 1976.

Publication costs of this article were partially assisted by RCA Laboratories.

REFERENCES

1. L. Holland, "Vacuum Deposition of Thin Films," Chap. 16, p. 493, Chapman and Hall Ltd., London (1963).
2. F. v.d. Maesen and C. H. M. Witmer, Proc. 17th Intern. Conf. on the Phys. of Semiconductors, p. 1211. Paris (1964).
3. W. M. Feist, S. R. Steele, and D. W. Ready, in "Physics of Thin Films," Vol. 5, G. Hass and R. E. Thun, Editors, p. 310, Academic Press, New York (1969).
4. L. Maissel, in "Handbook of Thin Film Technology," L. I. Maissel and R. Glang, Editors, Chap. 18, McGraw-Hill Book Company, New York (1970).
5. E. Giani and R. Kelly, *This Journal*, **121**, 394 (1974).
6. A. Fischer, *Z. Naturforsch.*, **9a**, 508 (1954).
7. K. Ishiguro, T. Sasaki, T. Arai, and I. Imai, *J. Phys. Soc. Japan*, **13**, 296 (1958).
8. R. G. Livesay, E. Lyford, and H. Moore, *J. Phys. E-Sci. Instr.*, **1**, 947 (1968).
9. E. W. Wartenburg and P. W. Ackerman, *Glastech. Ber.*, **41**, 55 (1968).
10. V. M. Novikov, *Steklo i Keram.*, **25**, 13 (1968).
11. R. F. Bartholomew and H. M. Garfinkel, *This Journal*, **116**, 1205 (1969).
12. J. A. Aboaf and V. C. Marcotte, *ibid.*, **120**, 701 (1973).
13. W. Kern, *RCA Rev.*, **29**, 525 (1968).
14. K. Kern and A. W. Fisher, *ibid.*, **31**, 715 (1970).
15. W. Kern and R. C. Heim, *This Journal*, **117**, 562 (1970).
16. W. Kern, *RCA Rev.*, **32**, 1429 (1971).
17. R. Summit, *J. Appl. Phys.*, **39**, 3762 (1968).
18. L. D. Loch, *This Journal*, **110**, 1081 (1973).
19. J. Kane, W. Kern, and H. P. Schweizer, *ibid.*, **121**, 375C (1974).

Technical Notes



A Note on the Chemistry of Lead Sulfide Sensitization for Infrared Detection

G. M. Wolten

The Aerospace Corporation, El Segundo, California 90245

The chemical deposition of mirrorlike films of PbS has been known for at least 65 years (1). It is the basis for the production of modern lead sulfide detectors for near infrared radiation. In order to render the films highly photoconductive, an "oxidant," usually hydrogen peroxide, is added to the deposition bath. Published speculations concerning the role of H₂O₂ ignore a body of basic chemical information that has been readily available for many decades.

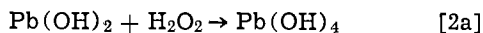
Key words: lead sulfide detectors, chemical deposition.

For example, a 1937 textbook (2) describes the following quantitative reaction

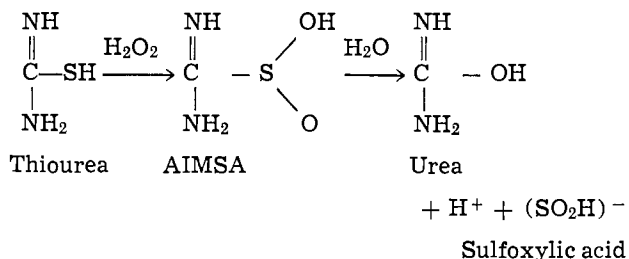


In the manufacture of PbS photodetectors, H₂O₂ is present in the solution of thiourea and a lead salt before it is rendered highly alkaline (pH⁺ > 10) to commence the reaction. In order to test the validity of reaction [1] under these conditions, a typical "deposition" was carried out with the H₂O₂ content in-

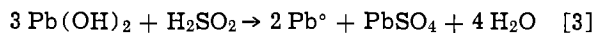
creased to the stoichiometric equivalent (100%) of the lead content instead of the typical 30%. Under these conditions, the sole product, identified by x-ray diffraction, was PbSO_4 . The reaction proceeded in two recognizable steps, as follows



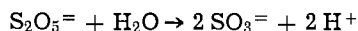
Kunze *et al.* (3) have pointed out that it is theoretically possible for H_2O_2 to oxidize thiourea to aminomethanesulfonic acid (AIMSA), which then hydrolyzes to sulfoxylic acid, as indicated in the following sequence



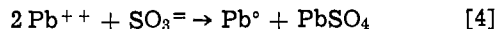
The sulfoxylic ion is a strong reducing agent that would reduce lead ions to metallic lead. Kunze *et al.* therefore proposed that the sensitization was due to metallic lead. They obtained highly sensitive films by substituting AIMSA or other sulfur-bearing organic compounds for H_2O_2 . What they overlooked was that reduction of lead ions by sulfoxylic necessarily leads to oxidation of the sulfoxylic ion. In order to investigate this reaction, AIMSA was added to a solution of a lead salt. The gray precipitate obtained contained colloidal lead and, after drying, gave a diffraction pattern of PbSO_4 and nothing else. The reaction is



Two patents, assigned to the Eastman-Kodak Company (4, 5), describe the use of sodium sulfite, Na_2SO_3 , or metabisulfite, $\text{Na}_2\text{S}_2\text{O}_5$, respectively, in place of H_2O_2 . These do not differ substantially since the metabisulfite ion hydrolyses to sulfite in solution



Since the sulfite ion will react with lead ions according to reaction [4]



it is clear that lead sulfate is formed in all the sensitization procedures discussed here.

Vinchakov (6) proposed, on the basis of electrical measurements, that PbSO_4 or $\text{PbO}\cdot\text{PbSO}_4$ are likely identities for the sensitizing centers.

Normally, not enough PbSO_4 is incorporated into the films to be detectable. Roth *et al.* (7) have reported finding Lanarkite, $\text{PbO}\cdot\text{PbSO}_4$.

One would suppose that if the sulfate ion is responsible for sensitization, it would have to be present as part of the PbS structure rather than as a separate phase and that its concentration would be likely to be the same as the carrier concentration, which is of the order of $5 \times 10^{16}/\text{cm}^3$.

The ionic radius of $\text{S}^=$ is 1.84Å, and its tetrahedral covalent radius is 1.04Å. According to Dalven (8), PbS is about 50% ionic, and this suggests an effective radius of 1.44Å. The ionic radius of $\text{SO}_4^=$ is quite close to this, namely 1.49Å.

We therefore expect that during deposition, a solid solution, containing a low concentration of PbSO_4 in PbS, is formed. This does not necessarily mean that the $\text{SO}_4^=$ ion itself is responsible for the sensitization. It is conceivable that the sulfate, once it is formed, may undergo further processes of an as yet unknown nature.

Manuscript submitted Dec. 2, 1974; revised manuscript received April 9, 1975.

Any discussion of this paper will appear in a Discussion Section to be published in the June 1976 JOURNAL. All discussions for the June 1976 Discussion Section should be submitted by Feb. 1, 1976.

Publication costs of this article were partially assisted by The Aerospace Corporation.

REFERENCES

1. National Bureau of Standards Circular 389, page 13, Washington, D.C. (1931).
2. A. I. Vogel, "A Textbook of Qualitative Chemical Analysis," p. 116, Longmans, London, England (1937).
3. O. A. Kunze *et al.*, *Z. Naturforsch.*, **26B**, 8 (1971).
4. G. W. Hammar, U.S. Pat. 2,917,413 (Dec. 15, 1959).
5. J. S. Dunn and F. C. Bennett, Jr., U.S. Pat. 3,017,296 (Jan. 16, 1962).
6. V. N. Vinchakov, *Sov. Phys.—Semiconductors*, **4**, 813 (1970).
7. L. M. Roth *et al.*, *Phys. Rev.*, **85**, 724 (1952).
8. R. Dalven, *Infrared Phys.*, **9**, 141 (1969).

Growth and Characterization of $\text{Al}_x\text{Ga}_{1-x}\text{Sb}$

S. M. Bedair¹

Electrical Engineering Department, Carnegie-Mellon University, Pittsburgh, Pennsylvania 15213

The preparation of a number of ternary III-V semiconductor compounds is now of interest, due to the need for materials with a wide range of energy gaps. It has been suggested that the Al-Ga-Sb heterojunction (1) may be of interest for optoelectron devices.

In this work liquid-phase epitaxial layers of $\text{Al}_x\text{Ga}_{1-x}\text{Sb}$ are grown on GaSb substrates. The liquidus and the corresponding solidus isotherms in the Ga rich corner of the Al-Ga-Sb phase diagram have been determined at 600°C. Variation of the optical energy gap with the AlSb concentration in the grown layer has also been examined.

¹ Permanent address: Nuclear Engineering Department, Alexandria University, Alexandria, Egypt.

Key words: liquid phase epitaxy, phase diagram, energy gap.

A horizontal growth system with a palladium purified hydrogen environment and a graphite boat similar to the one for multiple layer epitaxy (2) was used. A saturation technique was applied to determine the liquidus composition along the 600°C isotherm. Such a technique has been previously used to determine liquidus isotherms and gave results in agreement with those obtained by differential thermal analysis (3, 4). Known weights of Ga (about 2g), and Al were contained in a separate compartment of the boat and by sliding were moved onto or off the GaSb single crystal seed used for liquid saturation. The boat was tightly covered to decrease any losses of Sb by vaporization. In each saturation experiment the Al + Ga solution was initially maintained at 600°C, then contact with

the seed crystal was achieved. Heating times of the order of days were found to be necessary for high Al concentrations in the melt after which the solution was removed from the seed and the boat was cooled to room temperature. The antimony solubilities in this ternary system are calculated from the weight loss of GaSb seed. No correction has been applied to allow for any vaporization of Sb, since no vapor deposits were observed on the growth tube. The liquidus isotherm at 600°C is shown in Fig. 1.

Saturation was considered to be attained when further heating for periods equal to those which have been previously applied resulted in an increase in the Sb dissolved by less than 1%. Thus, this stop in the seed dissolution with time indicates that a true equilibrium had been established. This probably occurs by the formation, on the surface of the seed that was initially in contact with the liquid, of a very thin epitaxial layer of the equilibrium ternary alloy, which protects the seed from further dissolution. A similar phenomenon is observed in the Al-Ga-As and the Al-Ga-P systems (3, 4).

Epitaxial layers of $\text{Al}_x\text{Ga}_{1-x}\text{Sb}$ were then grown from saturated Ga solutions on (110) and (111)B oriented GaSb substrates. The growth cycle starting with a saturated melt at 600°C involved cooling at a rate of 0.2°C/min over a temperature interval of 10°C. Grown layer thicknesses were between 15 and 50 μm , with the higher growth rate for low Al concentration in the melt. Surfaces of the grown layers on the (111) substrates were smooth and shiny, whereas those grown on the (110) substrates showed some roughness. X-ray back Laue patterns showed that the grown layers were single crystals with the same orientation as the corresponding substrate.

The compositions of the grown layers were determined by electron microprobe analysis with the Colby correction program applied (5). The solidus isotherm for the Al-Ga-Sb system derived is shown in Fig. 2. Since the growth range was from 600° to 590°C, the resulting changes in the concentrations of the grown layers are within the standard deviation error expected for the electron microprobe technique, and the observations showed no depletion in the Al concentration in the grown layers. There are no published data, of which we are aware, to compare with the present results.

In order to determine the variation of the optical absorption with AlSb concentration in the grown film, samples were mounted on separate glass (or quartz) sides with transparent wax. The GaSb substrate was ground off, followed by lapping until the grown layer became shiny. In the lapping process water was

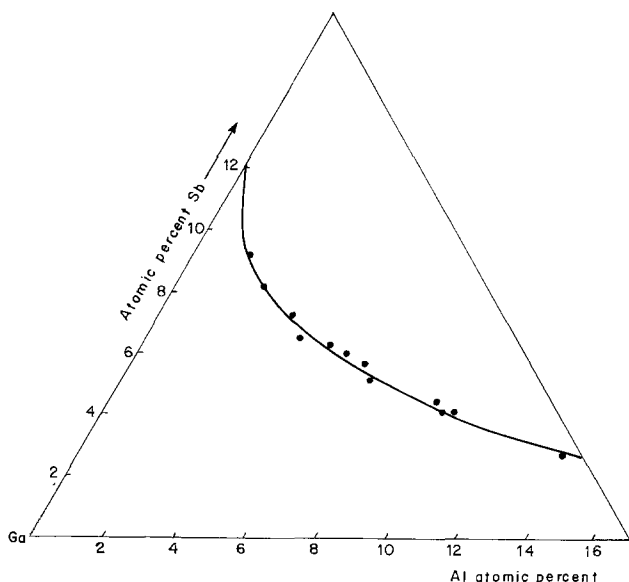


Fig. 1. Liquidus isotherm for the Al-Ga-Sb system at 600°C

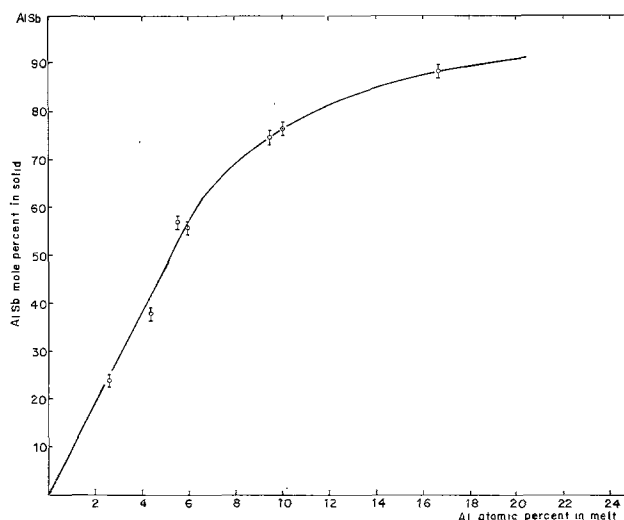


Fig. 2. Solidus isotherm for the Al-Ga-Sb system at 600°C

avoided (replaced by alcohol) to minimize any oxide growth on the grown layer especially for those having high AlSb concentration. The absorption measurement was done at room temperature on a Cary 14 double beam spectrometer with a reference aperture on a glass plate having the same area as the film under test. Measurements were performed on grown layers with AlSb concentrations varying from zero (GaSb) to 90% and typical transmission spectra are shown in Fig. 3. The optical energy gap was calculated at the intercept of the absorption edge (6) with the zero-transmission abscissa and the results are shown in Fig. 4. Extrapolation of these results gives 1.6 eV for the energy gap for AlSb in agreement with previous measure-

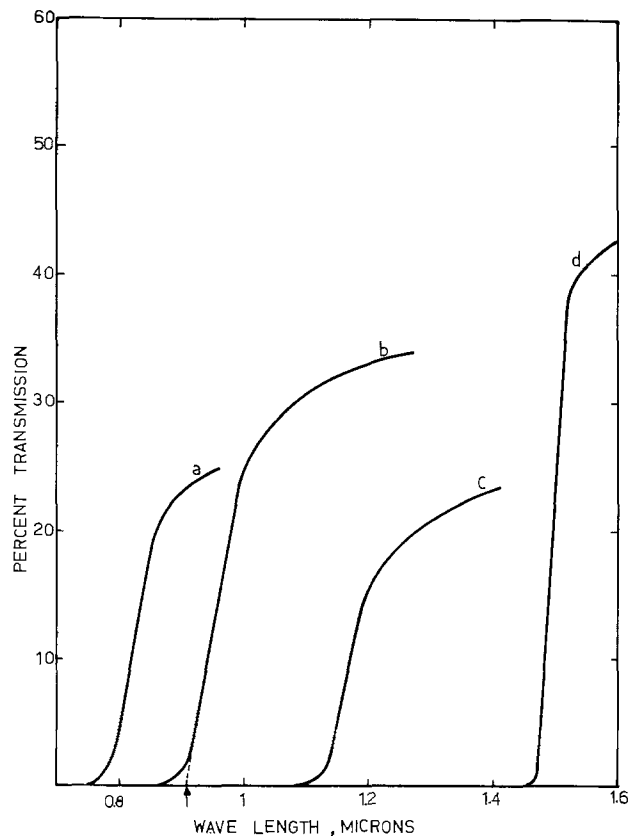


Fig. 3. Transmission spectra for different AlSb mole per cent. a, 81%; b, 56%; c, 34%; d, 13%. Sample thickness after the lapping process was about 1 mil, and the optical energy gap is determined at the intercept of the absorption edge with the zero transmission abscissa as shown for case (b).

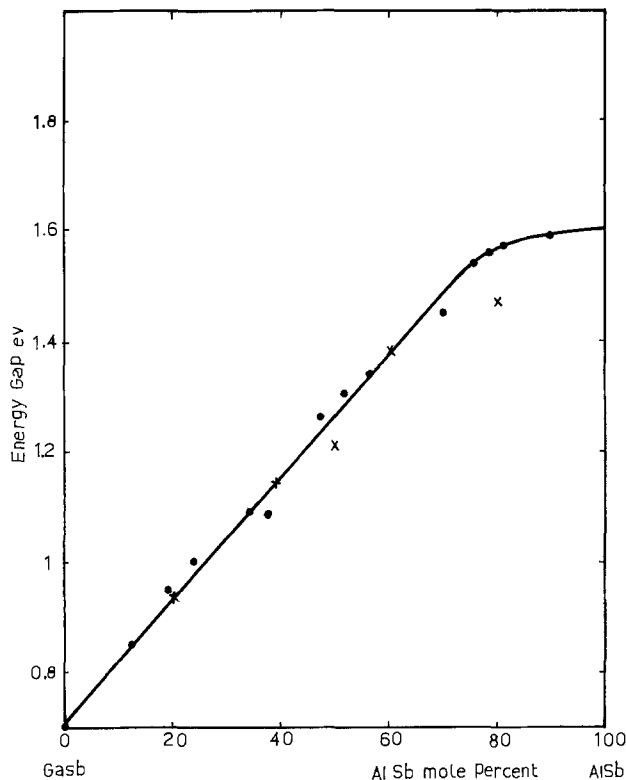


Fig. 4. Dependence of the optical energy gap on the AlSb concentration in $\text{Al}_2\text{Ga}_{1-x}\text{Sb}$ mixed crystal. (●) Present work, film grown by liquid phase epitaxy; (×) from Ref. (9) alloyed polycrystalline film.

ments (7) and 0.1 eV higher than that obtained from photoresponse measurements (8). In Fig. 4, we have also included some results (9) obtained for AlSb-GaSb polycrystalline alloys prepared by a zone casting method. For high AlSb concentration these data for energy gap fall below the corresponding ones in the present work. This may be because alloys prepared by this method (10) show a decrease in the AlSb concentration as the solidification process proceeds, possibly since the Al has a higher distribution coefficient than

Ga in the Al-Ga-Sb system. Inhomogeneous polycrystalline mixed crystals result in a lower value for the optical energy gap than a homogeneous one with the same average composition. Similar observations of the effect of inhomogeneity on the effective energy gap had been reported for the Al-Ga-As system (11).

Acknowledgments

The author is indebted to Professors A. G. Milnes and D. L. Feucht for helpful discussions and for financial assistance. The author wishes also to thank UNESCO for financial support. The work was supported in part by the U.S. Army Research Office, Durham.

Manuscript submitted June 27, 1974; revised manuscript received Feb. 27, 1975.

Any discussion of this paper will appear in a Discussion Section to be published in the June 1976 JOURNAL. All discussions for the June 1976 Discussion Section should be submitted by Feb. 1, 1976.

Publication costs of this article were partially assisted by Carnegie-Mellon University.

REFERENCES

1. A. G. Milnes and D. L. Feucht, "Heterojunctions and Metal Semiconductor Junctions," Academic Press, New York (1972).
2. B. I. Miller, E. Pinkas, I. Hayashi, and R. J. Capik, *J. Appl. Phys.*, **43**, 2817 (1972).
3. M. Ilegems and G. E. Pearson, in Proc. 1968 Symposium on GaAs, p. 3, The Institute of Physics and the Physical Society, London (1969).
4. M. Ilegems and M. B. Panish, *J. Crystal Growth*, **20**, 77 (1973).
5. I. W. Colby, in "Advances in X-Ray Analysis," Vol. 77, J. B. Newkirk, G. R. Mallet, and H. G. Pfeifer, Editors, Plenum Press, New York (1968).
6. J. I. Pankove, "Optical Processes in Semiconductors," Prentice Hall, Englewood Cliffs, N.J. (1971).
7. W. J. Turner and W. E. Reese, *Phys. Rev.*, **117**, 1003 (1960).
8. C. A. Mead and W. G. Spitzer, *Phys. Rev. Letters*, **11**, 358 (1963).
9. I. I. Burdigan, *Sov. Phys.-Solid State*, **1**, 1246 (1960).
10. J. F. Miller, H. L. Goering, and R. C. Himes, *This Journal*, **107**, 527 (1960).
11. J. F. Black and S. M. Ku, *ibid.*, **113**, 250 (1966).

Brief Communication



Modified Contact Metallizations for GaP to Provide Barrier Action Against Gallium Migration

W. A. Brantley,¹ B. Schwartz,* V. G. Keramidas, A. K. Sinha, and G. W. Kammlott

Bell Laboratories, Murray Hill, New Jersey 07974

In the chemical oxidation of GaP in aqueous H_2O_2 , native oxide thickness quickly reaches a limiting value, in the range of 200–400 Å, and does not change with continued exposure to the oxidant (1). In the galvanic

oxidation of GaP with ohmic contacts, the cathodic component of the reaction proceeds unhindered at the noble metal ohmic contact. The resulting oxide layers are thick and the ultimate thickness is limited only by the diffusion of the oxidant through the oxide. However, in a number of cases, relatively thin oxides were formed on contacted GaP. It was determined that both Ga and P were present in appreciable

* Electrochemical Society Active Member.

¹ Present address: Department of Dental Materials, School of Dentistry, Marquette University, Milwaukee, Wisconsin 53233.

Key words: ohmic contacts, compound semiconductors, barrier metallization, secondary ion mass spectrometry.

quantities on the Au-based ohmic contacts before as well as after oxidation (2).

In a recent investigation (3), we reported the extent of Ga and P migration through the ohmic contact metallizations. The migration principally occurs when the contacts are formed with GaP.² During subsequent galvanic oxidation, gallium and phosphorus oxides form on the ohmic contacts, and the presence of these oxides is believed to cause the inhibition of thick oxide growth. In this communication, we report the successful utilization of intermediate layers in the contact metallizations which serve as barriers to gallium migration.

The conventional (4,5) contact metallizations for GaP LED's were evaporated on <111>-oriented GaP wafers. The p-contact consisted of a Be-Au alloy, and these films were deposited on GaP having

$N_A - N_D \sim 5 \times 10^{17} \text{ cm}^{-3}$. The n-contact consisted of a Si-Au alloy, and these films were deposited on

GaP having $N_D - N_A \sim 3 \times 10^{17} \text{ cm}^{-3}$. Specimens were alloyed at 600°C for 5 min to obtain ohmic contacts.

A thin titanium or tungsten film was considered to have promise as a barrier to gallium migration because no gallium interdiffusion at 500°C into thin titanium (6) or tungsten (7) films on GaAs could be detected by 2 meV ⁴He⁺ backscattering. In addition, experiments had indicated (8) some effectiveness for Ti/Pt films in reducing gallium migration through gold-based contacts to GaAs.

Accordingly, three modified metallization schemes for GaP were investigated, in which the following layers were deposited successively over the initial Be-Au or Si-Au layer: (i) Ti/Au, (ii) Ti/Pt/Au, and (iii) W/Ti/Au. (The outermost layer in each case is gold.) The tungsten (9) and gold depositions for (iii) were performed in different stations, so that a titanium layer had to be included to provide adhesion which would otherwise be marginal between gold and tungsten films exposed to air. Specimens for groups (i), (ii), and (iii) were alloyed in two different manners. For half of the specimens, the Be-Au or Si-Au film only was alloyed with GaP at 600°C for 5 min, followed by deposition of the remaining layers. For the other half, the entire composite metallization was alloyed with GaP at 600°C for 5 min, after deposition of all the layers.

The effectiveness of the modified metallizations for reducing the gallium migration was evaluated by secondary ion mass spectrometry³ (SIMS) (10-12), using O₂⁺ ions as the primary sputtering species. With this technique, relative comparisons of the extent of the gallium migration through the metallizations can be obtained. The ⁶⁹Ga⁺ secondary ion signals from the outermost gold films were compared at some arbitrary depth such as 1000Å where the near-surface signal enhancement (12, 13) resulting from the presence of a surface gallium oxide is no longer significant (3). Absolute gallium concentrations were not established, due to the lack of appropriate chemical standards and possibly different sputtering rates for the various gold matrices. Because the SIMS apparatus has a much lower sensitivity for phosphorus (as ³¹P⁺) than gallium, the effectiveness of the modified metallizations for reducing the phosphorus migration was not investigated.

The ⁶⁹Ga⁺ signals at an estimated 1000Å depth for the various specimens are summarized in Table I. These signals are normalized to a value of unity for a reference specimen consisting of a pure gold film on a quartz substrate. The data are presented in a decade format, where each entry is the logarithm of the upper limit of the decade(s) within which the relative Ga⁺ signal values lie.

² The term "formed" is employed to denote any heat-treatment process for achieving ohmic contacts.

³ SMI-300, Cameca Instruments, Incorporated, Elmsford, New York.

Table I. Gallium migration through contact metallizations on GaP

Metallization group	Relative ⁶⁹ Ga ⁺ signal at 1000Å depth*
I. Reference specimen: pure gold on quartz substrate	0
II. Conventional (4,5) alloyed p- or n-contact	5-6
III. Ti/Au over Si-Au or Be-Au	
A. Only Si-Au or Be-Au alloyed	1-2
B. Entire metallization alloyed	6
IV. Ti/Pt/Au over Si-Au or Be-Au	
A. Only Si-Au or Be-Au alloyed	2-3
B. Entire metallization alloyed	
1. Be-Au initial layer	1
2. Si-Au initial layer	3
V. W/Ti/Au over Si-Au or Be-Au	
A. Only Si-Au or Be-Au alloyed	2
B. Entire metallization alloyed	5-6

* These values are logarithms of the upper limit of the decade(s) within which the relative Ga⁺ signal values lie. For example, an entry of 3 corresponds to a relative signal between 101 and 1000. All the relative Ga⁺ signals are normalized to that for the reference specimen which has been assigned a value of unity (and thus a logarithm of 0).

It is evident that the near-surface gallium concentration is considerably decreased for some of the modified metallizations in Groups III through V, compared to that for the conventional alloyed contacts to GaP in Group II. In general, the most efficient barrier to gallium migration was obtained if the Ti/Au, Ti/Pt/Au, or W/Ti/Au layers were deposited after the underlying Si-Au or Be-Au layer was alloyed with GaP. No significant effect on gallium migration was found for variation of deposition rates for the Si-Au and Be-Au layers by an order of magnitude. For these specimens, there appear to be no noteworthy differences in barrier action for the three different structures. However, microstructural imperfections in the alloyed Si-Au or Be-Au layers, observed with the scanning electron microscope, may diminish the effectiveness of the barrier layers. A note of caution is also necessary for the simple Ti/Au metallization; when Ti/Au couples are aged in air, titanium migrates along the gold grain boundaries and subsequently forms an oxide layer on the surface of the gold (14).

On the other hand, if the entire composite structure was instead alloyed with GaP, no barrier to gallium migration was provided by the metallizations containing the W/Ti or titanium layers. However, with this alloying procedure, the near-surface Ga⁺ signals for the Ti/Pt/Au modified metallizations were comparable to those for the efficient barrier structures where only the initial Si-Au or Be-Au films were alloyed with GaP. Inferior behavior for the alloyed Ti/Pt/Au films deposited over a Si-Au initial layer, compared to that when deposited over a Be-Au layer (cf. Group IVB), may be associated with microstructural imperfections, which were more prevalent for the Si-Au films. (The near-surface gallium signal was not measured in these regions.)

The effective barrier action of the alloyed Ti/Pt/Au metallizations in Group IVB is unexpected in view of the extensive gallium migration through the alloyed Ti/Au metallizations (Group IIIB) and since it is known (15) that gallium migration occurs freely through platinum films on GaP. It may be that interaction between platinum and gallium or, instead, among titanium, platinum, and gallium [with the possible formation of intermetallic compounds (16) in either case] impedes the gallium. The reason for the gallium barrier effectiveness of the alloyed Ti/Pt/Au films remains to be established.

Two different multilayer metallization approaches thus may be possible to reduce the near-surface gallium concentration in ohmic contacts to GaP. One approach is the deposition of appropriate metal layers, after alloying the initial Si-Au or Be-Au layer with GaP, to provide a barrier to gallium migration. An alternative approach involves alloying the entire composite metallization, whereby the migrating gallium is

trapped by interacting, and possibly forming intermetallic compounds, with an intermediate layer. The former approach is considered more attractive in view of possible adverse effects of intermetallic compounds on mechanical properties of the contact films and on potential device reliability in general.

Acknowledgments

The authors are grateful to R. K. Lewis and B. Aulier of Cameca Instruments for performing the SIMS analyses, to P. A. Barnes and R. T. Hepplewhite for use of their thin-film deposition facilities, to T. E. Smith and L. J. Smith for assistance in performing the depositions, and to E. F. Labuda for helpful discussions.

Manuscript received April 4, 1975.

Any discussion of this paper will appear in a Discussion Section to be published in the June 1976 JOURNAL. All discussions for the June 1976 Discussion Section should be submitted by Feb. 1, 1976.

Publication costs of this article were partially assisted by Bell Laboratories.

REFERENCES

1. B. Schwartz and W. J. Sundburg, *This Journal*, **120**, 576 (1973).
2. K. Yoshida and D. R. Wonsidler, Unpublished research.
3. W. A. Brantley, B. Schwartz, V. G. Keramidas, G. W. Kammlott, and A. K. Sinha, *This Journal*, **122**, 434 (1975).
4. N. E. Schumaker and G. A. Rozgonyi, *ibid.*, **119**, 1233 (1972).
5. J. M. Ralston, *J. Appl. Phys.*, **44**, 2635 (1973).
6. A. K. Sinha, T. E. Smith, M. H. Read, and J. M. Poate, Unpublished research.
7. A. K. Sinha and J. M. Poate, *Appl. Phys. Letters*, **23**, 666 (1973).
8. W. A. Brantley, B. Schwartz, V. G. Keramidas, G. W. Kammlott, and A. K. Sinha, Unpublished research.
9. A. K. Sinha, T. E. Smith, T. T. Sheng, and N. N. Axelrod, *J. Vacuum Sci. Technol.*, **10**, 436 (1973).
10. J. V. DiLorenzo, R. B. Marcus, and R. Lewis, *J. Appl. Phys.*, **42**, 729 (1971).
11. J. V. DiLorenzo, *This Journal*, **118**, 1645 (1971).
12. J. M. Morabito and R. K. Lewis, *Anal. Chem.*, **45**, 869 (1973).
13. R. K. Lewis, J. M. Morabito, and J. C. C. Tsai, *Appl. Phys. Letters*, **23**, 260 (1973).
14. A. K. Sinha, J. D. Speight, and Y. Okinaka, Unpublished research.
15. V. Kumar, Unpublished research.
16. M. Hansen and K. Anderko, "Constitution of Binary Alloys," McGraw-Hill Book Co., New York (1958).



C. V. King—Acheson Medalist

David A. Vermilyea¹



Dr. David A. Vermilyea delivers introductory remarks about the Acheson Award Medalist.

The Acheson Medal and Prize is awarded not more than every two years for "distinguished contributions to the advancement of any of the objects, purposes, or activities of The Electrochemical Society." This is the twenty-third Acheson Medal to be awarded.

In the short time available it is not a simple matter to provide an adequate picture of the long and distinguished career of Dr. King, and it is even more difficult to convey an impression of the man himself to those who do not know him. I shall mainly attempt a very brief outline of his scientific, educational, and industrial careers and of his contributions to The Electrochemical Society.

First, with respect to his work in science, education, and industry, he was off to a good start with a formal education which started at Indiana University, moved through Columbia University, and finished with a post doctoral stay at Copenhagen with Professor Brønsted. He next spent three years as an instructor at Columbia, and then moved to New York University where he spent the next 35 years of his academic career. While there he taught inorganic and physical chemistry and, with his co-workers, he published more than 70 papers in solution electrochemistry, ionic transport, acid-base catalysis, homogeneous kinetics, corrosion, inhibition and ion exchange at surfaces. He co-authored the book "Experiments in Physical Chemistry." He trained more than 100 graduate students. He became a fellow of the New York Academy of Sciences, a fellow of the American Association for the Advancement of Science, was admitted to the Fellowship of the American-Scandinavian Foundation, and became a member of Sigma Xi and Phi Lambda Upsilon. In addition to The Electrochemical Society, he is a member of the American Chemical Society, the National Association of Corrosion Engineers, the Instrument Society, the Vacuum Society, and the Cryogenic Society.

Following his acquisition of the title "Emeritus"—he did not retire—he became president of the American Gas and Chemical Company, a post he still holds.

¹ Introductory remarks by David A. Vermilyea, General Electric Company, Schenectady, New York, on the occasion of the presentation of the Acheson Medal Award to Cecil V. King on October 15, 1974 at the New York, New York, Meeting of the Society.

The company specializes in leak detection and industrial pollutants; Dr. King has two patents on leak detection. I asked Dr. King how the company was named, and was told that the name was deliberately selected to permit the Company to do nearly anything.

Let us turn to Dr. King's contributions to The Electrochemical Society. He has been Chairman of the Corrosion Division and Chairman of the New York Chapter, and has been very active in both that Division and that chapter. He was editor of the *Journal of The Electrochemical Society* from 1954 to 1968, and was President of The Electrochemical Society from 1971 to 1972. Among his many contributions to the Society one stands out in my mind as being unique, namely, his many editorials in the *Journal of The Electrochemical Society* during his years as editor. I can remember reading these witty, cogent, informative, thoughtful editorials with great relish. Many were on Society matters, often pertaining to publications, but many were on a great variety of other subjects. They all contributed greatly to my own understanding of these subjects and stimulated my thoughts significantly. As an example of the breadth of his interests, consider the following titles, a few selected from the more than 100 he wrote: The St. Lawrence Seaway, Our National Highways, Dielectric Materialism, Future of Mankind, Inflation, Russian Literature, Of Satellites and of Men, Wisdom, Bell for St. Michaels, Growing Up Absurd, What Are We Teaching Our Students?, How Long to Boil an Egg?, Las Cucarachas y las chinchas, Salty Waters, Science Fiction, Search For Life on Earth. Truly, our lives have been enriched by these editorials; I recommend their rereading.

Dr. King did not spend all his time on his scientific, educational, and industrial careers and working for the Society. He has become an expert in golf, chess, ping pong, and croquet, and even now, I'm told, he still plays an occasional game of football. At least once he fell through the ice while skating at Chatham, and was soaked to the skin. He spent much time with his family in a variety of activities and trips which involved many experiences they will all long remember. For instance, an early trip to Indiana was made in a car which boiled over regularly every 100 miles on the Pennsylvania Turnpike, necessitating frequent trips with a mason jar down embankments to streams for water. Dr. King was a parent who believed that the rod should not be spared. I'm told that he once sprained his thumb chastising his son Peter. He likes homemade beer. He is a violin player and a trumpet player, and plays trumpet duets. He is a PUNdit. He likes the story of the moron who sat up all night trying to figure where the sun went when it went down. Finally it dawned on him!

Although these comments do not do him full justice, I hope that you have some picture before you of the twenty-third Acheson medalist, the man and his career. And now, "For distinguished contributions to Solution Chemistry and to The Electrochemical Society" it is my very great pleasure to present this Acheson gold medal, a bronze replica thereof, and a check for \$2000 to one of the great men of electrochemistry, Dr. Cecil V. King.

Research in Review²

Cecil V. King



Dr. Cecil V. King presents the Acheson Medal Award Address.

I was introduced to electrochemistry in the laboratory of Professor Oliver W. Brown at Indiana University, in 1917. We learned to electrodeposit copper quantitatively from solution, and found that stirring made the deposition go much faster. One method of stirring was to place the beaker in a solenoid coil. We made our own potentiometers by stringing a resistance wire along the laboratory bench, making contact with alligator clips, and measuring distances with a meter stick. One of my assignments was to make a fused quartz tube by burying a carbon rod in quartz sand and heating it electrically. This was done in the university powerhouse beside a large switchboard, and it was tempting to close one more switch to be sure the carbon rod was hot enough. The quartz tube was perfect, but part of the campus was without light or power for a while.

Professor Brown had a set of lead-acid storage cells which he maintained would last at least 30 years if he could care for them personally.

During that year I learned the names AQUA-DAG and OIL-DAG, even then registered trade names of the Acheson Company; DAG standing for Deflocculated Acheson Graphite.

One of my nominators for the Acheson Award mentioned that my first research was done with ova, and that I started in a modest way with pigeon eggs. The facts are, that when I got out of college I was much interested in the ova that are served with bacon for breakfast, and was willing to do whatever I was told to earn them. And the eggs to be studied were not pigeon eggs, but hybrid African ring dove eggs. Is there an analogy with crow's eggs compared to pheasant eggs under glass?

This work was done in the laboratory of Dr. Oscar Riddle at the Carnegie Experimental Station on Long Island, and there was much to be learned. For example, the birds could be fed calcite crystals, but they put aragonite crystals in their egg shells. I first learned of the superiority of the female over the male with respect to adverse conditions. One of my duties was to prepare oxygen-rich or -deficient atmospheres in which to incubate the eggs; fewer eggs hatched under these abnormal conditions, and the proportion of surviving females was greater than normal. Higher or lower than normal incubation temperatures had a similar effect.

I also learned how easy it is to operate on a bird, or a hen, and insert a capsule containing a message in the upper oviduct; the capsule serves as a yolk, receiving an albumin coating and a shell. The birds recover immediately from such an operation. This is evidently the procedure used to obtain a large egg with a small

egg inside, both complete with yolks and shells, as has been demonstrated on television.

Let me review some background material for my doctoral research. In the early 1900's several investigators studied binary compound formation between acids and such oxygen-containing compounds as esters, aldehydes, ketones, and ethers. The criterion of compound formation was the familiar maximum in the binary freezing point curve, at the composition of the compound. Earlier investigators had often postulated that changes in slope of physical property-composition curves could indicate compound formation. The eminent Russian chemist Dmitri Mendeleev examined the specific gravity of ethyl alcohol-water mixtures and decided that three compounds must be formed [*Trans. Chem. Soc. (London)*, **51**, 778 (1887)]. The compound $C_2H_5OH \cdot 12 H_2O$ could be isolated at -17° , he said, and $C_2H_5OH \cdot 3 H_2O$ at the temperature of "solid carbonic acid anhydride;" the compound $C_2H_5OH \cdot H_2O$ required a still lower temperature. Of course no one since has been able to isolate any alcohol-water compounds, and the freezing point curves show no maxima. At about -17° the appearance of the ice crystals formed on freezing changes noticeably, and this is probably what Mendeleev observed.

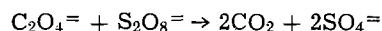
Professor James Kendall, my research sponsor, had students isolate acid-ester compounds as a means of studying the mechanism of ester hydrolysis. James Booge studied three compounds which had sharp melting points, i.e., they were stable at least at and below their melting points. He measured the freezing points of benzene solutions of the separate components and of equimolar mixtures. The results indicated that in the aprotic solvent the compounds were somewhat, but not fully, dissociated.

My research was essentially to repeat this work with water as the solvent. There was no evidence of any acid-ester compound remaining; the freezing points of equimolar mixtures of ethyl acetate and trichloroacetic acid, for example, were strictly the sum of those of the components; and the effect of the ester on the conductance of the acid was due to the increased viscosity.

Such negative results do not exclude the view that trace amounts of fleeting compounds are involved in the kinetic mechanism of ester hydrolysis. But the negative results are to be expected on the basis of the Brønsted acid-base theory; water is a far stronger base than ethyl acetate, or the trichloroacetate ion, and neither can compete for protons in the presence of water. In aqueous acetic acid the acetate ion can retain most of the protons, but an ester cannot compete in base strength even with the acetate ion.

Considerations similar to these led Brønsted to formulate his acid-base theory. The evidence was equally available to many other chemists who failed to review and correlate it.

To explain my eventual interest in metal dissolution and inhibition, it is necessary to introduce some background. After a year in Brønsted's laboratory my interest centered in the study of reaction kinetics and catalysis in dilute solution, and the interpretation of salt effects on the rates. One system, for example, was the peroxydisulfate oxidation of various compounds with silver ion as catalyst. The reaction with oxalate looks as if it should be especially simple

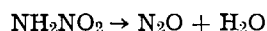


Without a catalyst the reaction is extremely slow. Small amounts of silver ion speeded it up, but the rates were not reproducible; two experiments run side by side perhaps differing by 200%. With excess peroxydisulfate the reaction was autocatalytic, not

² Acheson Award Address delivered on October 15, 1974 at the New York, New York, Meeting of the Society.

just at the start but until the oxalate was used up; the CO₂ pressure in the apparatus increased faster and faster up to the end. This behavior indicates that an intermediate accumulated in the solution; trivalent silver ion has often been suggested. It was later shown elsewhere that purity of the water is important in these experiments; traces of copper from a copper still probably enhance the silver ion catalysis.

Eventually we became aware of experiments on general acid and base catalysis. For example, it was shown in Brønsted's laboratory that the nitramide decomposition

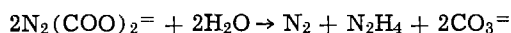
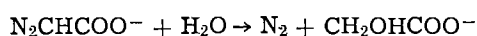


is catalyzed not only by hydroxyl ion, but by other basic ions and molecules as acetate ion and aniline molecules. The mutarotation of glucose and the enolization of acetone were found subject to both general acid and general base catalysis. It was found that a plot of log rate constant *vs.* log base (or acid) strength constant was linear, indicating a rate law

$$k_m = G(K_A)^x$$

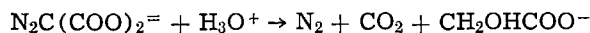
where *x* is the slope of the log-log plot and the constant *G* is characteristic of the reaction. Brønsted and Kai Pedersen were able to formulate a derivation of this equation, based on reasonable intermediate formation in the Brønsted-Bjerrum sense. Actually the equation needs a simple statistical correction depending on the charge type of the catalyzing species.

We studied in detail two cases of general acid catalysis: the decomposition of diazoacetate ion and of azodicarbonate ion



In both cases the Brønsted relation was obeyed over the range of acid strength from H₂O to H₃O⁺, a range of 10¹⁸ in strength constants. The azodicarbonate reaction is so sensitive that it was necessary to use extremely weak acids like sucrose, maltose, acetoxime, in alkaline solutions. In both cases the slope of the log-log lines, the exponent *x*, was approximately 0.8; a similar value of *x* had been found in the nitramide decomposition, but in the acid catalyzed glucose mutarotation the value of *x* was about 0.3.

A similar study of the decomposition of diazomalonnate was rather disappointing. The reaction uses up hydrogen ion



In strong acids the rate is approximately proportional to the acid concentration and it was expected that the rate would be low in weak acid buffers. Actually, in 0.1M acetic acid, 0.1M sodium acetate the decomposition was as fast as in 0.1M perchloric acid. The reaction showed general base catalysis, and several anionic and neutral bases were studied. Since hydrogen ions are used up the analysis of the measured rates was difficult and the range of base strengths was limited. A Brønsted slope of 0.27 was indicated for some of the bases, but H₂O did not fall on the line.

With this background we proceed to the study of metal dissolution. Around 1930 Martin Kilpatrick published experiments on the rate of dissolution of rotating magnesium cylinders in weak and strong acids. As he described a preliminary experiment: in 0.1M HCl, hydrogen was evolved at the rate of 0.5 cm³/min. In 1.7M formic acid, 0.1M sodium formate the hydrogen ion concentration is half as great but the hydrogen evolution was about 100 cm³/min. This might indicate that weak acid molecules react directly with the metal and the Brønsted relation for general catalysis might apply. The log-log points for several acids, including hydrogen ion, fell near a straight line with a slope of about 0.08, much lower than for any case of homogeneous catalysis.

Brønsted and Kane at about the same time measured the rate of dissolution of sodium from its amalgams in acids. Their conclusion was that diffusive transport of strong acids to the amalgam was rate-controlling, but that with extremely weak acids the slow chemical reaction controlled the rates.

Since metal dissolution offered the possibility for further studies of acid reactivity, we decided to study zinc dissolution. Since the reaction in pure acids was known to be erratic, depending on the amount and nature of impurities in the metal and their effect on hydrogen evolution, the effect of oxidizing depolarizers was investigated. It was found that nitrates or hydrogen peroxide were equally suitable, giving the same rates when added (in excess) to hydrochloric acid; in such solutions zinc dissolved at about the same rate as magnesium did with or without the additives. A log-log plot of rate *vs.* acid strength constants was similar to the plot for magnesium, with a slope of 0.05. Very weak acids such as ammonium ion, fell far below the line.

Our conclusion, of course, was that the observed rates were those of convective and diffusive transport of acid to the metal surface, as had been postulated many years earlier by a number of investigators. The diffusion layer theory was developed by Nernst and by Brunner in 1904. Van Name and his co-workers at Yale University (1910-1916) had perhaps carried out the most extensive and convincing experiments with several metals dissolving in ferric and other solutions where no special depolarizers were needed.

In our first experiments we used rotating zinc disks but soon abandoned them in favor of cylinders so that the entire surface would have equal velocity with respect to the solution. We operated in the turbulent region and had no idea that V. Levich at about the same time was solving the hydrodynamic problem of flow for disks rotating in the nonturbulent region. The rotating disk and later the ring disk have of course been extremely useful in many problems. The hydrodynamic relations for the rotating cylinder have not been solved, but the dimensionless group analysis has had useful applications in turbulent flow experiments.

If diffusion of acid or other reagent to the metal surface is rate controlling, then theoretically one cannot learn anything about the reaction mechanism. For example, one does not know whether a weak acid molecule reacts directly, or gives up its proton to a water molecule, allowing the H₃O⁺ ion to react. One would suspect the latter, since the H₃O⁺ diffuses faster and new ionic equilibria are established almost instantly. When I was asked if I considered the metal dissolution an electrochemical process, I replied that it was an oxidation-reduction with electron transfer, but we did not know if that transfer took place at every collision with the metal surface. I should have realized at once that since the metal usually becomes rough, evidently some spots do dissolve faster than others; there are anodic and cathodic sites on the surface and a considerable flow of electrons within the metal.

In some cases, notably nickel dissolving in acidified ferric and ceric solutions, while the rates are transport controlled, the metal becomes extremely rough and there may even be undercutting and spallation of nickel particles. The roughness also increases the turbulence in the solution at a given rotational speed. This was observed and treated by Makrides and Hackerman.

Some of the metal cylinders acquire a gray or black coating during dissolution. This was observed with zinc and cadmium, and even with magnesium in certain alcohol-water mixtures. In some experiments with cadmium we removed the coating by wiping gently with filter paper. Microanalysis showed nothing but cadmium. Since such fine particles could hardly have been formed by undercutting and there was no visible spallation, we must conclude that cadmium, already dissolved, can replate on the surface.

In the course of the metal dissolution experiments it became necessary to measure many diffusion coefficients of the acids and other reagents since values were not available in the literature. These measurements were carried out in cells with two compartments separated by fritted glass disks, as pioneered by McBain. As an offshoot of these experiments one student made diffusion measurements with acid in one compartment, base in the other, neutralization occurring within the porous disk. Another student was able to make cylinders of benzoic acid and measure the rate of solution in sodium and potassium hydroxides, neutralization taking place within the diffusion layer. Addition of phenolphthalein gave a self-indicating endpoint.

It was expected that with a fixed degree of stirring, the dissolution rates would be proportional to the diffusion coefficients of the reagents. The plots were linear within experimental error, but did not extrapolate to the origin, as if a reagent which could not diffuse could still dissolve the metal. A log-log plot was linear and showed that the diffusion coefficients should be raised to about the 0.7 power. This indicates that the "effective diffusion layer" thickness is not the same for all reagents but is related to the diffusion coefficients.

We were able to measure the dissolution rates of thin wires of zinc, cadmium, and copper in suitable reagents and compare them with heat dissipation from a thin platinum wire which was heated electrically and show that the heat transfer coefficients and thermal diffusivity could be included in the same relation.

Having studied the dissolution of several metals under convective-diffusive control, it was natural to try to inhibit such dissolution. Only a few of these attempts will be mentioned here. It was found that as little as 0.005% of certain surfactants, such as sodium dioctyl sulfosuccinate, could reduce the dissolution

rate of iron, zinc, or cadmium in acid nitrate solution from 100 mg in a few minutes to 3 or 4 mg in the same time. However, more surfactant did not block the surface much more, and addition of other inhibitors did not help.

Cupferron and neocupferron form very insoluble complexes with ferrous and ferric ions, and it was thought that they might be strongly adsorbed on an iron surface and form an impervious film. It soon became obvious that iron first dissolved, then the chelate precipitated on the metal surface to form a barrier layer which inhibited dissolution only as long as excess cupferron was present. Since these compounds are not very stable in acid solution, inhibition could be maintained for only a few hours and eventually the iron began to pit.

Experiments on the rate of dissolution of silver in ferric salt solutions showed that silver ion, formed in the reaction or added separately, had an inhibiting effect. The presence of silver and ferrous ions reduces the driving potential for the reaction, and the inhibition could be explained quantitatively as due to adsorption of silver ion on the metal. These results led to a serious study of metal ion adsorption on metals: if dilute silver nitrate is allowed to trickle down through a column of finely divided silver, pure water comes out at first. The advent of radioactive isotopes naturally led to studies of exchange as well as adsorption.

Our research program was made possible and in fact was made mandatory by the large number of master's and doctoral candidates at New York University starting in the 1920's. It was promoted by the helpful attitude and support of the university, and by the availability of government financial assistance after 1946. I am grateful for the cooperation of scores of students, most of whose work has not been mentioned here.



Alkaline Primary Cells¹

S. Ruben*

Ruben Laboratories, New Rochelle, New York 10801

I would like to relate some history and development of sealed zinc/mercuric oxide alkaline cells. Thirty-two years have passed since the work on sealed zinc/mercuric oxide alkaline cells was initiated, and its history may be of interest.

At the start of World War II there was a need for transceiver batteries having the ability to withstand tropical conditions with high capacity per unit volume, and maintain a low voltage drop during their effective discharge life.

In 1942 the work initiated at my laboratory utilized the experience obtained in the mid thirties in developing the hermetically sealed C-bias cell and the dry electrolytic capacitor. The bias cell had as its anode

a cadmium container separated by a grommet and crimped to the cathode composed of a sintered disk of vanadium pentoxide, sealing in an enclosed gel electrolyte of ammonium glyco-borate. The first sealed alkaline cell structure utilized the type of capacitor structure shown in Fig. 1, with a wide area rolled anode and close spacing to its cathode for low internal resistance (Fig. 2). The cathode in the rolled structure was a 2 mil sandblasted steel strip coated with a layer of cupric oxide and graphite, bonded with a 5% polystyrene solution. This coated strip was rolled at high pressure, producing a low resistance flexible cathode layer. The spacers were a combination of an ionically conductive cellophane layer as a barrier in contact with the oxide to prevent migration of cathode particles, and an absorbent nylon gauze element in contact with the zinc. A dusting of mercuric oxide was applied to the anode before winding, so as to cause amalgamation of its surface when in contact with the alkaline electrolyte. In order to reduce solubility of the cupric oxide in the potassium hydroxide electrolyte, a solidified high concentration electrolyte was used and impregnated into the rolled unit at the electrolyte melting point. After impregnation and electrolyte solidification, the unit was fastened to a composite insulating top. The cupric oxide coulombic capacity and its voltage of 1.06 was not adequate, and other oxide coatings such as mercuric oxide, manganese dioxide, cadmium oxide, and silver oxide were comparatively tested. The mercuric oxide (1.34V) produced the best over-all results. Since the main object was to provide a sealed alkaline cell with maximum capacity per unit volume, the design was changed to one using a steel can cathode in the bottom of which a densely pressed mixture of mercuric oxide and micronized graphite was consolidated. The anode was composed of a spirally wound corrugated zinc strip with an intervening absorbent cotton paper spacer. The winding was in an offset manner, so that the corrugated zinc extended at one end, and paper at the other. Corrugation of the anode was found essential, since it provided space for the zinc oxide produced at the anode when the cell was discharged. After impregnation of the wound unit and its porous spacers, the anode was amalgamated by applying a measured quantity of mercury to the exposed turns of the corrugated zinc, providing an amalgamated junction with zinc top contact without local galvanic action. The barrier was a microporous dialysis paper disk, and other barriers such as sintered magnesium oxide were also used. The potassium hydroxide electrolyte was zincated by dissolving zinc oxide at a temperature of about 100°C.

In order to obtain maximum anode area, another type of rolled anode was used in which zinc was sprayed onto one side of cellophane strip with a "Schori" gun, producing a powdered porous layer of zinc. This was corrugated, wound, and amalgamated in the same manner as the solid zinc strip, but did not make suitable cells because of impurities derived from the spraying equipment. In later cells, the use of pressed

* Electrochemical Society Emeritus Member.
¹ Introductory address at the Alkaline Primary Cells Symposium at the New York, New York, Meeting of the Society, Oct. 13-17, 1974.

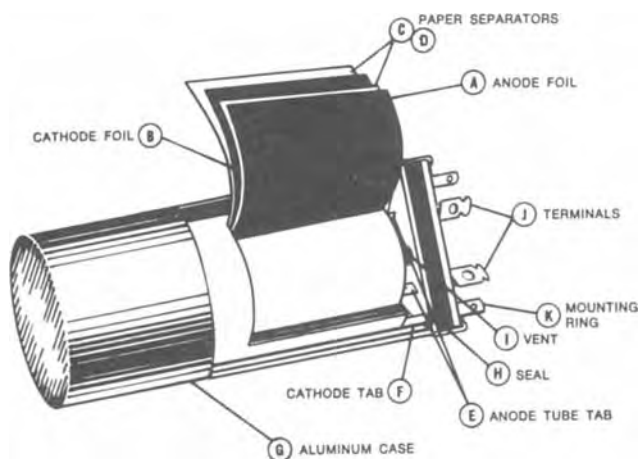


Fig. 1. Dry electrolytic capacitor structure

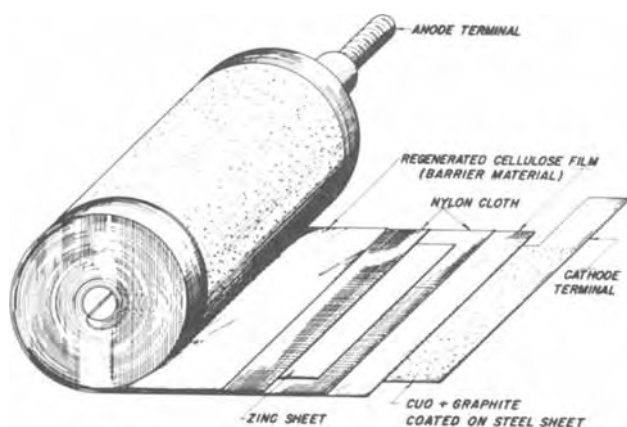
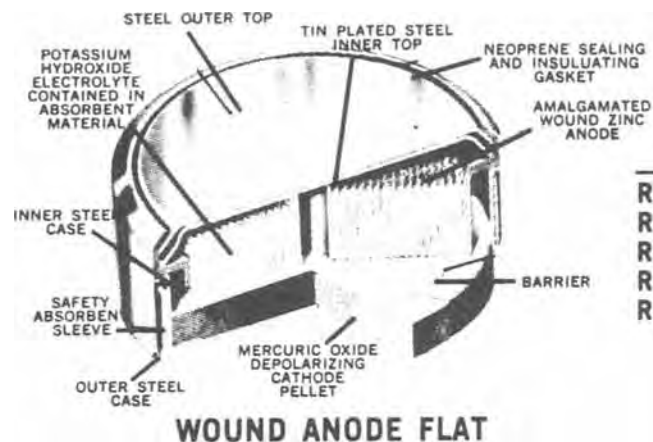


Fig. 2. Wound anode/cathode assembly on first alkaline sealed cells tested.



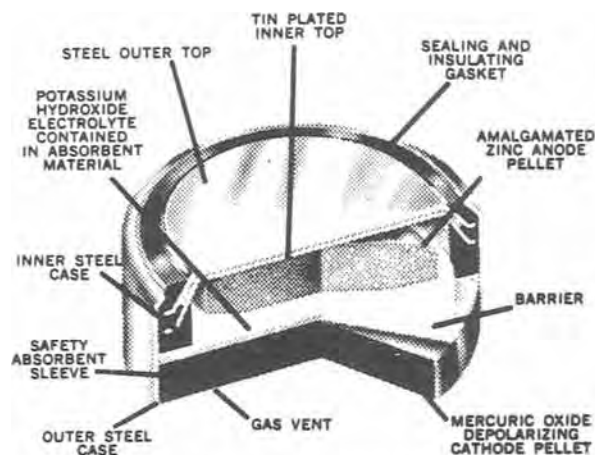
WOUND ANODE FLAT

Wound Anode Cells

Type #	Max. Diam. (cm)	Height (cm)	Weight (g)	Rated Capacity (mah)
RM 640	1.587	0.965	9.68	360
RM 3	2.498	1.37	22.56	1500
RM 1438	3.71	1.003	36.22	2700
RM 1450	3.71	1.36	51.80	4500
RM 2550	6.58	1.394	165.20	13,000

Table 1

Fig. 3. Relation of geometry to capacity of wound anode RM cells



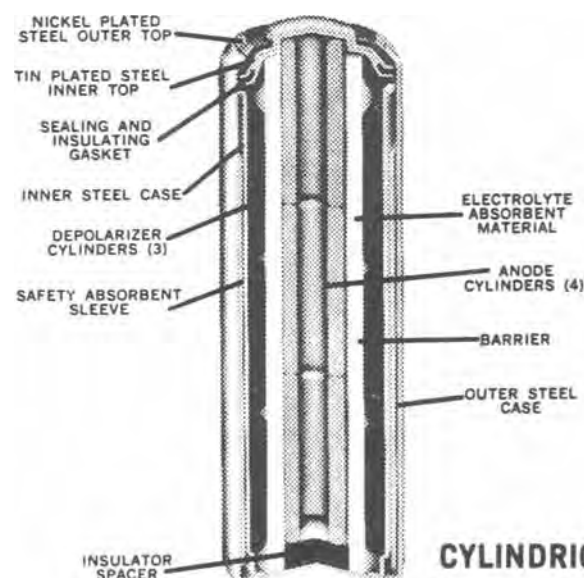
FLAT PELLET STRUCTURE

Flat Pressed Powder Cells

Type #	Max. Diam. (cm)	Height (cm)	Weight (g)	Rated Capacity (mah)
RM 312	0.87	0.34	0.56	36
RM 575	1.143	0.33	1.4	100
RM 675	1.143	0.54	2.24	160
RM 630	1.549	0.58	4.76	350
RM 640	1.574	1.104	7.84	500
RM 4R	3.02	1.66	40.88	3,400

Table 2

Fig. 4. Pressed powder flat and button RM cells



CYLINDRICAL STRUCTURE

Cylindrical Pressed Powder Cells

Type #	Max. Diam. (cm)	Height (cm)	Weight (g)	Rated Capacity (mah)
RM 24	1.0	4.396	14.0	900
RM 601	1.59	2.857	34.16	1800
RM 3R	2.489	1.651	28.56	2200
RM 502	1.358	4.90	30.44	2400
RM 401	1.133	2.844	11.20	800
RM 1R	1.579	1.638	12.04	1000
RM 12R	1.519	4.959	30.88	3600
RM 42R	2.922	6.032	148.33	14,000

Table 3

Fig. 5. Pressed powder cylindrical cathode/anode RM cells

powdered zinc amalgam served the same purpose without the impurity factor.

The most important development for producing sealed alkaline cells was the development of the coulombmetrically balanced cell having equivalent anode and cathode capacities. Since the hydrogen deposition potential is 0.989V and the container overvoltage is

0.15V, the sum of both is less than the zinc half-cell potential of 1.332V in the electrolyte, so that any residual unoxidized zinc would cause hydrogen generation at cathode on continued application of load after the oxygen content of the depolarizer was exhausted. It also basically required that the anode top contact be composed of a nonconsumable but amal-

gamatable material such as copper or tinned steel. In order to compensate for errors in the required measured weights of the anode and cathode materials, an excess amount of cathode was used, in most cases the addition of a small per cent of electrolytic manganese dioxide sufficing. On larger cells an added safety factor against possible gas producing impurities in the cathode materials is applied by using a pressure-vented structure with an outer steel container separated by a cardboard tube which absorbs any electrolyte that may be vented.

Natural manganese ore, on account of its ferrous content, was found to produce dendritic growth on the

zinc that caused internal discharge. The available large scale supply of pure manganese dioxide has made possible sealed manganese alkaline cells which, while not having the small voltage change of mercuric oxide during discharge and being of lower capacity per unit volume, have lower cost and are produced on a high volume scale.

Figures 3, 4, and 5 show the relation of capacity to the geometry of the present three types of sealed zinc mercury cells; corrugated wound anode, pressed powder anodes in flat or button form, and pressed powder cylindrical anode cells.



Technique for the Measurement of the Viscosity of a High Vapor Pressure Organic Electrolyte

H. Y. Kang and P. Bro

*P. R. Mallory & Company, Incorporated, Laboratory for Physical Science,
Northwest Industrial Park, Burlington, Massachusetts 01803*

ABSTRACT

A capillary flow viscometer was developed to measure the viscosity of high vapor pressure organic solvent electrolytes over a wide temperature range. Inert electrodes and associated circuits were used to observe the passage of the meniscus through the viscometer. The viscometer was kept inside a sealed aluminum container to minimize the pressure differential between the test solution and the ambient and to contain the high vapor pressure solutions if the viscometer should rupture. Measurements were made on sulfur dioxide/organic solvent electrolytes containing lithium bromide at temperatures between -60° and 70°C and at vapor pressures to 15 atm. The viscosity varied between 0.6 and 22 cp, being higher the lower the temperature and the lower the SO_2 concentration. The activation energy calculated from the temperature effect was about 4 kcal/mole for electrolyte compositions close to those used in Li/ SO_2 batteries. The data indicated the occurrence of strong ion/solvent interactions in this system.

The rate capability of high energy density lithium batteries depends more strongly on the transport properties of the electrolyte than does that of an alkaline battery because of the generally low electrolytic conductivity of organic solvent electrolytes. The search for high-rate lithium batteries is, therefore, in part a search for suitable high-conductivity organic electrolytes. An important property that affects the conductivity of a solution is the viscosity of the medium in which ionic transfer takes place, and the analysis of the conductivity of organic solvent electrolytes requires the availability of viscosity data.

The sulfur dioxide/organic solvent electrolytes have a high conductivity and a low activation energy for ionic transfer over a wide temperature range, and they provide an interesting model system on which to study the structural and other factors that affect the solution conductivity. The measurement of the transport properties of the sulfur dioxide electrolytes poses a problem because of the high vapor pressure of the electrolyte. Concentrated SO_2 solutions have vapor pressures approaching that of pure SO_2 , i.e., close to 15 atm at the highest temperature of interest for battery applications. When we were confronted with the need for viscosity data on the sulfur dioxide/organic solvent electrolytes, we found no available viscometer suitable for such high vapor pressure solutions and had to adapt a conventional capillary viscometer to our needs. The modified viscometer is described in this report, together with some experimental data on a sulfur dioxide/organic solvent electrolyte containing dissolved lithium bromide. The chosen electrolyte com-

positions are representative of the solutions used in lithium/sulfur dioxide batteries.

Experimental Techniques

Viscometry.—The viscometer is shown schematically in Fig. 1. It was made of Pyrex and consisted of two compartments, A and B, connected with a capillary tube, C, and a side tube, D. Three metallic probes, P_1 , P_2 , and P_3 , are located in A. The glass-to-metal seals were made with a tungsten wire and uranium glass, and the wire tips were gold plated to prevent corrosion by the electrolyte. At the bottom of the B compartment, the glass tube was sealed to Kovar K which was, in turn, soft soldered to a threaded brass ring, F. The viscometer was tightly screwed into the bottom of the aluminum pressure cell, E_2 , with O-rings placed as shown to prevent any leakage of electrolyte from the viscometer. The probes P_1 and P_2 were connected to a triggering circuit by the feed-throughs, G_1 and G_2 , on the container E_2 , and probe P_3 was grounded to the aluminum container. The aluminum pressure cell, E_1 and E_2 , was sealed as indicated to prevent leakage of SO_2 gas to the atmosphere should the viscometer be broken by the high vapor pressure. The viscometer was filled at low temperatures via port H and then sealed. The container was kept with the A compartment down until the desired temperature had been reached, then the viscometer was inverted to allow the electrolyte to flow through capillary C. When the meniscus of the electrolyte passed probe P_1 , the electrical connection between P_1 and P_3 through the conductive electrolyte was broken which triggered the timer. When the meniscus passed P_2 , the stopping trigger circuit stopped the timer. The trigger circuit is shown in Fig. 2. It was used in conjunction with a Beckman Berkeley Di-

* Electrochemical Society Active Member.
Key words: capillary viscometer, density, lithium batteries, Li/ SO_2 battery electrolyte.



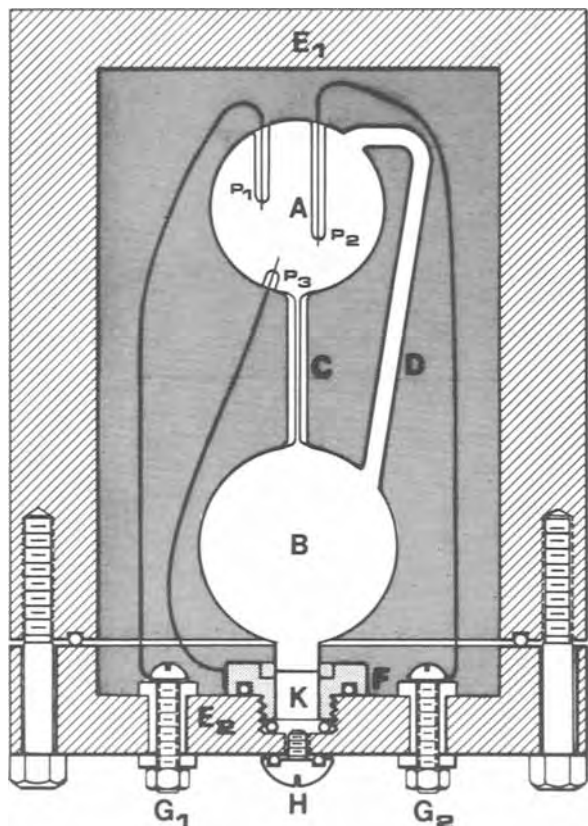


Fig. 1. Schematic diagram of viscometer (refer text)

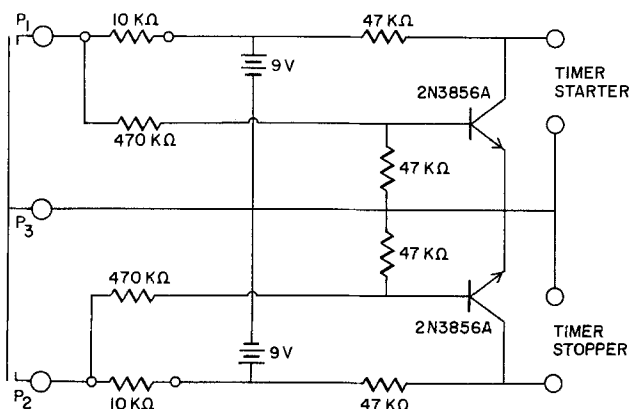


Fig. 2. Trigger circuit

vision Model 7360 Universal Timer Unit. The viscometer was kept in a vertical position by aligning the capillary section with the center line of the aluminum vessel, and the latter, in turn, was supported on a horizontal surface. Vibrations were reduced to a minimum by turning off the compressor on the refrigerator dur-

ing the actual measurements and by removing any other sources of vibration from the proximity of the viscometer work area. No significant thermal drifts occurred during the refrigerator off-periods.

A Statham Model SP-60-1 Temperature Test Chamber was used for the temperature control of the viscometer. A check on the rate of change of the temperature of the electrolyte inside the viscometer while controlling with the Statham Chamber was carried out using a calibrated iron-constantan thermocouple. The electrolyte reached a temperature within 5°C of the set temperature in 30 to 45 min, then gradually approached the set point temperature in 60 min, and stabilized at that temperature within $\pm 1.5^{\circ}\text{C}$. At least 90 min was allowed for thermal equilibration prior to each measurement.

The viscosity of the mixed acetonitrile-propylene carbonate-sulfur dioxide solvents with no LiBr was measured by determining the efflux time visually. Due to the low conductivity of these solvents, the triggering mechanism could not be used. A thick glass bell was pressed tightly onto the bottom part of aluminum cell E_2 (see Fig. 1) in place of E_1 . Then the viscometer was connected to a handle installed in a Blue M Versa-Range Test Chamber (window provided) that could be used to turn the viscometer from the outside. At each temperature the flow of the liquid was observed visually and the flow time was measured by operating the Berkeley Timer manually. The calibration of the viscometer is discussed in a following section.

The efflux time was measured three to five times for each determination. The standard deviation of the measurements ranged from about 1% at room temperature to about 5% at 70°C and -60°C . Typical data are listed in Table I. In addition to the error in efflux time, the error in the viscometer constant introduced during the calibration (estimated to be about 3%) and the error in the density (about 1%, see the following section) contribute to the error of the viscosity values. The error of the viscosity measurements was estimated from the linear contributions of these factors to be $\pm 5\%$ at room temperature and $\pm 10\%$ at -60° and 70°C .

Density measurements.—The density measurements were made with 10 ml Pyrex pipettes with 0.1 ml subdivisions. A small bulb was blown at one end of the pipette, and the volume of the attached bulb up to the first subdivision mark was calibrated with distilled water. The coefficient of thermal expansion of the glass was used to calculate the pycnometer volume at other temperatures, but the change was less than 1% and no thermal corrections were used. The sample electrolyte was injected into the tube through a septum attached at the other end of the pipette while the tube was chilled in a dry ice bath. The tube was then flame sealed at the top. The weight of the sample electrolyte was determined by weighing the original tube, the sealed tube with the sample, and the piece of glass removed during the sealing operation. To prevent the hazards that might be caused by a possible rupture of

Table I. Efflux time of the Li/SO₂ electrolytes measured by the new viscometer

Temperature, $^{\circ}\text{C}$	Solution 13, viscometer No. 1			Solution 23, viscometer No. 2		
	Seconds	Average	Standard deviation, %	Seconds	Average	Standard deviation, %
-60	6.035, 5.879, 6.201	6.038 ± 0.161	2.67	12.241, 10.966, 11.447, 10.706	11.340 ± 0.675	5.95
-50	5.775, 5.302, 5.456	5.511 ± 0.242	4.39	11.045, 10.427, 9.987, 10.321	10.445 ± 0.442	4.23
-40	5.485, 4.916, 5.023	5.141 ± 0.302	5.87	10.069, 9.089, 9.987, 9.221	9.591 ± 0.508	5.30
-30	4.688, 4.645, 4.848, 4.925, 4.835	4.788 ± 0.117	2.44	9.005, 8.465, 8.802, 8.800	8.768 ± 0.224	2.55
-20	4.535, 4.664, 4.543, 4.498	4.560 ± 0.072	1.58	8.328, 8.281, 8.018, 7.845	8.118 ± 0.227	2.80
-10	4.324, 4.369, 4.301	4.331 ± 0.035	0.81	7.625, 7.364, 7.502, 7.609	7.525 ± 0.120	1.60
0	4.141, 4.068, 4.400, 4.065	4.168 ± 0.158	3.80	6.639, 6.978, 7.135, 6.879	6.651 ± 0.211	2.98
10	4.058, 4.200, 4.199, 4.108, 4.049	4.123 ± 0.074	1.79	6.639, 6.757, 6.538, 6.670	6.551 ± 0.091	1.37
20	4.002, 4.036, 4.028	4.022 ± 0.018	0.45	6.239, 6.112, 6.288, 6.103	6.198 ± 0.105	1.69
30	4.005, 3.980, 3.976, 3.997	3.990 ± 0.016	0.38	5.916, 5.639, 5.977, 5.882	5.866 ± 0.124	2.11
40	3.942, 3.927, 3.924	3.931 ± 0.010	0.25	5.685, 5.478, 5.519, 5.498	5.545 ± 0.095	1.71
50	3.624, 3.807, 3.740, 3.733	3.726 ± 0.076	2.04	5.444, 5.195, 4.989, 5.348	5.244 ± 0.199	3.79
60	3.523, 3.650, 3.359	3.511 ± 0.146	4.16	5.089, 4.865, 4.991, 5.007	4.988 ± 0.093	1.86
70	3.374, 3.572, 3.416, 3.166	3.382 ± 0.167	4.94	5.069, 4.597, 4.689, 4.533	4.722 ± 0.240	5.08

the tube due to the pressure buildup at elevated temperatures, the density tube was placed in a thick-walled Pyrex tube plugged with a stopper. The volume of the electrolyte was read at various temperatures in a Blue M temperature chamber provided with a window. The temperature of the Blue M chamber was determined with a Fisher certified thermometer inside the chamber. Each measurement was made 30 min after the temperature reading had stabilized within $\pm 1^\circ\text{C}$ of the control temperature. The composition of the sample electrolytes other than the stock solutions was calculated from the density of the solutions at the acetone/dry ice temperature and the amount of the stock solution used to prepare the given volume of the electrolyte at the dry ice temperature. The error of the density measurements was estimated to be $\pm 1\%$ based on the errors of the weighing and the volume readings.

Materials.—Eastman Kodak practical grade propylene carbonate was fractionally distilled at reduced pressure, and the distillate at $120^\circ\text{--}122^\circ\text{C}/1.0\text{ mm}$ was collected.

Eastman Kodak practical grade acetonitrile was dried over molecular sieve 4A and then fractionally distilled in an atmosphere of argon. The water content of the purified solvents was less than 20 ppm as determined by infrared spectroscopy. The Foote Mineral lithium bromide, anhydrous (99.6% pure), was dried in a vacuum oven at 150°C for approximately 48 hr before use. The purified solvents and the lithium bromide were stored in an argon atmosphere dry box.

The desired amounts of LiBr, acetonitrile, and propylene carbonate were weighed and mixed in a volumetric flask in the argon atmosphere dry box. The sealed flask with the mixture was taken out of the dry box and SO_2 gas was slowly admitted to the mixture. A cold water bath (10°C) was used to minimize evaporation of the solvents and to enhance SO_2 dissolution. When the volume of the solution reached the calibration mark on the volumetric flask the amount of SO_2 that had been introduced was determined by weighing. The solution thus prepared was used as a stock electrolyte solution from which other electrolytes were made by diluting the stock electrolyte solution with liquid SO_2 in a dry ice cold bath as illustrated in Fig. 3. A given amount of the stock solution was poured into volumetric flask A which was connected to the line at joint J_1 , and cooled in a cold bath C. SO_2 gas was added to the stock solution through the three-way stopcock S_1 and tube T_2 until the meniscus of the electrolyte reached mark M. Pressure buildup in flask A was avoided by opening S_2 . The sample electrolyte was transferred to the vacuum jacketed burette B through tube T_1 by closing S_2 and pressurizing A with argon admitted through S_1 . The sample electrolyte was injected into the viscometer or the pycnometer through the hypodermic needle N. The ingress of moisture from the outside air to the cold solution inside A was limited by attaching drying tubes to stopcocks S_1 , S_2 , and S_3 . The portion of tube T_1 that joined A and B was wrapped with glass wool to minimize heat transfer to the cold electrolyte during its transfer from A to B. The water content of final electrolyte varied between 150 and 200 ppm as determined by Karl Fisher titrations (no cell was available for infrared absorption measurements on the high vapor pressure electrolyte).

Experimental Results

The densities of the various solutions are shown in Fig. 4 and 5 and their compositions are given in Table II. At each temperature between -60° and 70°C the density increased linearly with the LiBr concentration, except below 1.0 weight per cent (w/o) LiBr where it increased as a higher degree function of the LiBr concentration. The density of the solutions decreased linearly as the temperature increased, the temperature coefficient of expansion being slightly greater for the more concentrated LiBr solutions. It may be noted

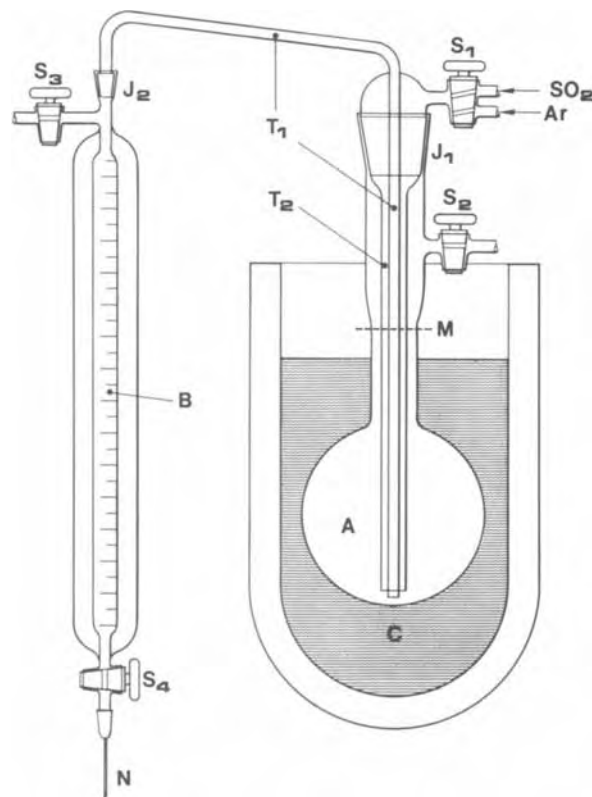


Fig. 3. Schematic diagram of electrolyte injection apparatus (refer text).

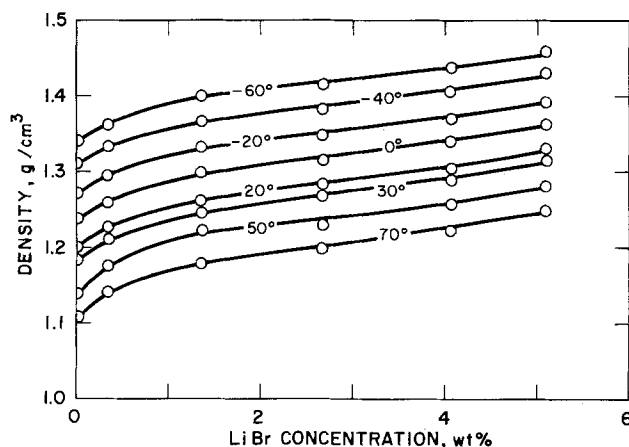


Fig. 4. The effect of the LiBr concentration on the density of the electrolyte. Solutions: 13, 23, 33, 43, 53, and 63.

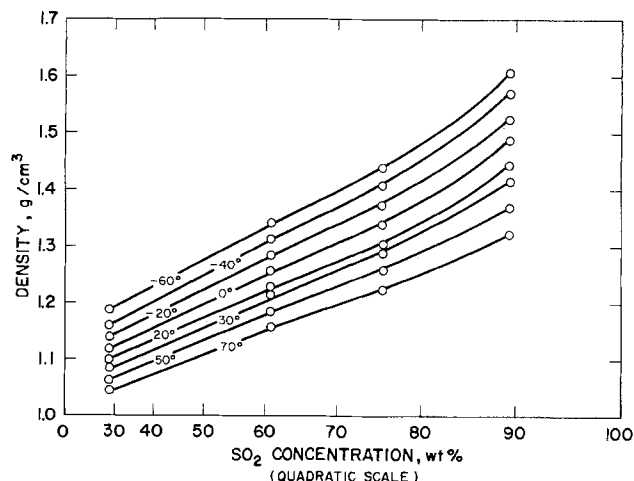


Fig. 5. The effect of the SO_2 concentration on the density of the electrolyte. Solutions: 20, 22, 23, and 25.

Table II. Solution compositions
(Weight per cent)

Solution No.	13	23	33	43	53	63	03	20	22	25
Component:										
LiBr	5.1	4.1	2.7	1.4	0.4	0.09	0	11.9	6.5	1.8
AN*	13.4	13.6	13.8	14.1	14.3	14.4	14.4	39.7	21.6	6.0
PC**	6.9	7.0	7.1	7.2	7.4	7.4	7.4	20.4	11.1	3.1
SO ₂	74.6	75.3	76.4	77.3	77.9	78.1	78.2	28.0	60.8	89.1

* AN = acetonitrile.
** PC = propylene carbonate.

that the mass ratios of the non-LiBr constituents remained the same for all the data points shown in Fig. 4.

As the SO₂ concentration increased for a constant mass ratio of the other constituents the density increased approximately as a second degree function of

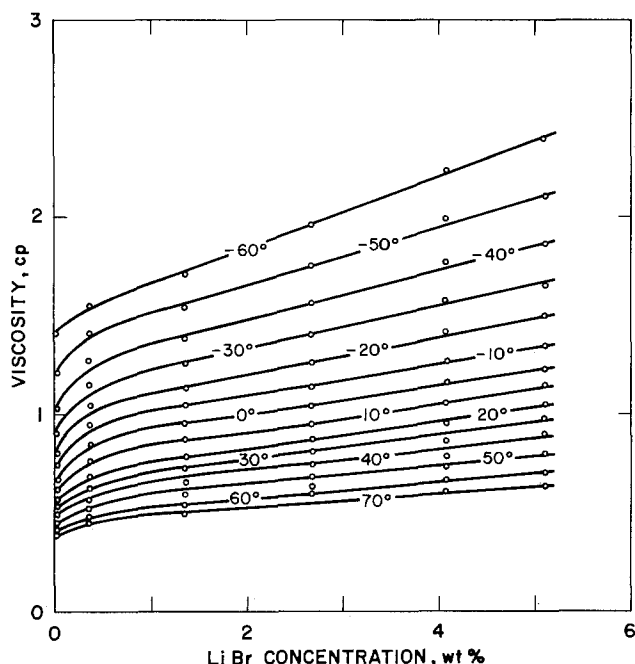


Fig. 6. The viscosity of the electrolyte as a function of the LiBr concentration. Solutions: 13, 23, 33, 43, 53, and 63.

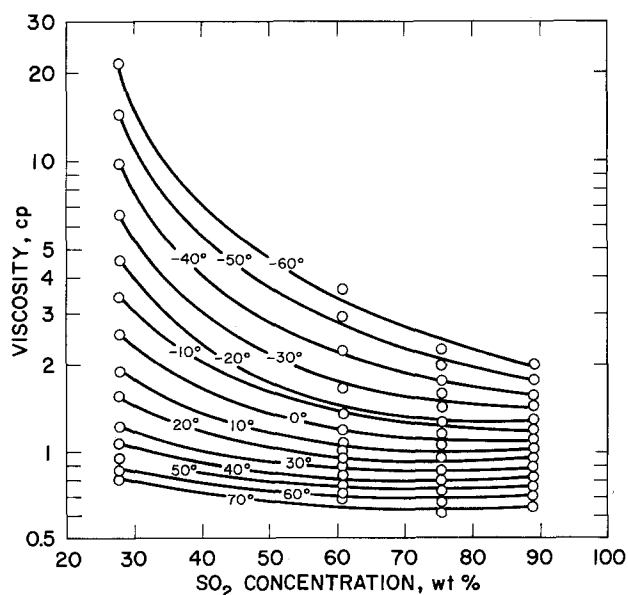


Fig. 7. The viscosity of the electrolyte as a function of the SO₂ concentration. Solutions: 20, 22, 23, and 25.

the SO₂ concentration between 30 and 90 w/o of SO₂. As expected, the density decreased as the temperature increased for a given composition, and it was approximately linear in the temperature between -60° and 70°C.

The viscosity data for the same solutions are presented in Fig. 6 and 7. The viscosity increased linearly with the LiBr concentration at each temperature except in the range below 0.1 w/o LiBr where nonlinearity was observed. At 20°C the viscosity changed from 0.58 cp for the pure solvent mixture to 1.05 cp for the 5.1 w/o LiBr solution, and at -60°C it changed from 1.41 to 2.40 cp, respectively, over the same concentration range. The viscosity decreased as the temperature increased, the change being more pronounced at the lower temperatures.

The SO₂ was quite effective in reducing the viscosity of the electrolyte, especially in the low temperature range; the rate of change being greater than that of a simple exponential function of the SO₂ concentration. At -60°C the viscosity decreased from 21.6 to 2.0 cp as the SO₂ concentration increased from 28 to 89 w/o. At 0°C it changed from 2.5 to 1.1 cp over the same concentration range. The viscosity remained a non-linear function of temperature over the SO₂ concentration range studied, decreasing as the temperature increased.

Discussion

The viscosity technique.—The basic theory of viscosity measurements by kinematic instruments can be derived from the Poiseuille-Hagenbach equation (1)

$$\eta = \frac{\pi R^4 (P_0 - P_1) t}{8Vl} \quad [1]$$

where η is the viscosity, V is the volume of the liquid flowing through the capillary tube of length l and inside radius R in time t , and P_0 and P_1 are the pressures at the two ends of the liquid column. Equation [1] assumes a steady, laminar flow with no slip of an incompressible, Newtonian fluid. Departures from these conditions in actual viscometers necessitate the introduction of correction factors, and Eq. [1] becomes

$$\eta = \frac{\pi R^4 h_m g d t}{8V(1+b)} - \frac{Mvd}{8\pi(1+b)t} \quad [2]$$

where h_m is the mean height of the liquid column during the flow, g the acceleration due to gravity, d the density of the liquid, and M and b the coefficients for the Hagenbach and the Couette corrections, respectively. The pressure difference between the two ends of liquid, $P_0 - P_1$ in Eq. [1], is replaced by $h_m g d$ in Eq. [2].

The most important correction in designing a viscometer is the correction for the nonsteady flow which is expressed as the second term in Eq. [2] (kinetic energy or Hagenbach correction). The numerical coefficient M is introduced to account for the particular shape of the capillary ends, and it is close to unity. It is seen from the kinetic energy correction term that it can be reduced most easily by decreasing the rate of flow and by using a small efflux volume. In the present viscometer the efflux volume was kept small by making the distance between probes P_1 and P_2 small ($V \approx 1.5$ ml).

A low rate of flow is important not only to prevent departures from steady-state flow but also to assure laminar flow conditions. In the flow of liquids through uniform tubes, turbulence may be expected for Reynolds numbers above about 2000. The size of the capillary was chosen to give a Reynolds number below 300. However, there is a practical limit to the extent to which the radius of the capillary may be decreased because of the sensitive dependence of the reproducibility of the data on the presence of dust particles in the fine capillary and because of the difficulty involved in transferring liquid from compartment B to A prior to

each measurement. A compromise was adopted by employing a capillary radius of about 0.04 cm (Reynolds number about 100).

The Couette correction coefficient b relates to the viscous energy dissipated at the entrance and at the exit of the capillary. This correction is of minor importance experimentally if the kinetic energy correction term is negligible, since the viscometer can be calibrated with a standard fluid of known viscosity without considering the complications due to the second term in Eq. [2]. The present viscometer design minimizes the loading error common with the Cannon-Fenske viscometers. Any differences in the volume of liquid discharging through the Cannon-Fenske viscometer will be reflected in the mean driving fluid head h_m . However, in our viscometer (an Ubbelohde type) the loading error is practically eliminated since the mean head is not dependent on the liquid level in the lower reservoir B, but terminates at the junction of the capillary with bulb B. This is made possible by gas pressure equalization between the lower and upper bulbs through the side tube D.

Another error may arise from the surface tension difference between the calibrating liquid and the sample electrolytes. In the present viscometer surface tension will affect not only the adhesion of the liquid to the walls of the bulbs but also the adhesion of the liquid to the probes P_1 and P_2 , and thus the error due to surface tension is more significant than with other viscometers. This error was reduced by calibrating the viscometer with a low vapor pressure stock solution whose viscosity was determined separately with a certified Cannon-Fenske viscometer. The efflux times of the standard electrolyte through both the new viscometer and the certified viscometer were measured at several temperatures to obtain the required calibration data.

The construction of the confining vessel and the contact structures appeared to be satisfactory and gave trouble-free operation of the unit. Although the actual pressures did not exceed about 15 atm, it is reasonable to think that the viscometer can be used at higher pressures. However, it may be necessary to provide a means of pressure equalization either by the use of a pressurized inert gas or a volatile inert solution inside the confining vessel external to the viscometer tube if pressures much above 15 atm are involved.

The solution properties.—It is our intention to discuss the solution properties in some detail at a later time in conjunction with the conductivity of the SO_2 electrolyte, and we limit this section to a few brief remarks on the viscosity data.

The electrolyte chosen for the viscosity measurement was selected because of its usefulness in Li/ SO_2 batteries. Each solution component serves a useful function in these batteries. The SO_2 is the active depolarizer, the acetonitrile forms a complex with the lithium bromide and causes it to dissolve in the sulfur dioxide to give a highly conductive solution, and the propylene carbonate inhibits the reactivity of lithium toward acetonitrile and sulfur dioxide. Since the SO_2 concentration decreases during discharge, it was of interest to determine the viscosity over an appreciable SO_2 concentration range.

The data correlated well as a function of the specific volume of the solutions, Fig. 8, according to the Batschinski equation as written by Hildebrand (2)

$$\frac{1}{\eta} = K \frac{\bar{v} - V_0}{V_0} \quad \bar{v} = \frac{1}{d} \quad [3]$$

where η is the viscosity, d the solution density, V_0 the empirical constant (specific volume of "hole-free" liquid), and K the empirical constant. The fluidity ($1/\eta$) was an almost linear function of the free volume ($\bar{v} - V_0$) of the solution over the entire temperature range for all the solutions. Slight deviations from

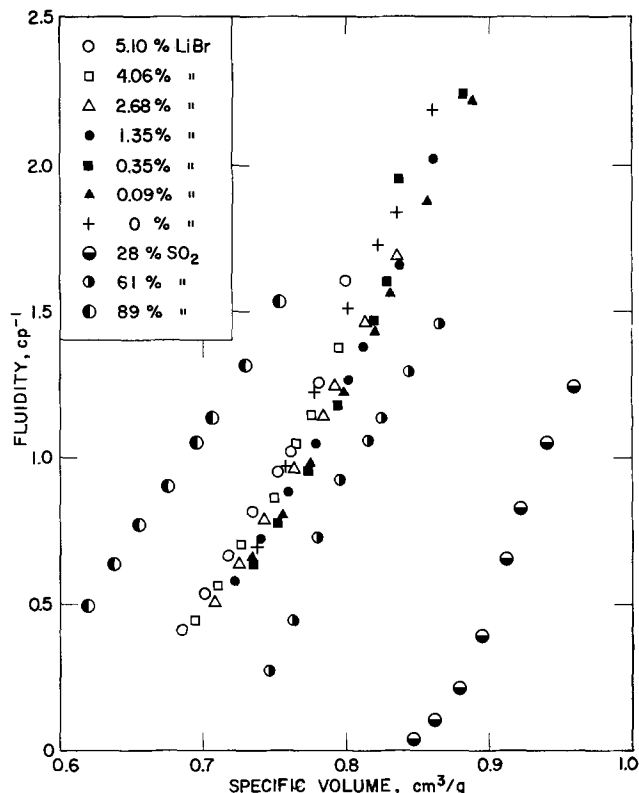


Fig. 8. The free volume theory correlation of the electrolyte viscosity.

linearity occurred in the region of the smaller specific volumes, i.e., at the lower temperatures. Interestingly, solutions with different LiBr concentrations defined the same fluidity/specific volume curve to a first approximation. The SO_2 concentration, however, displaced the curves noticeably. The greater the SO_2 concentration, the more the fluidity curves shifted toward the smaller specific volume range. The effect of the SO_2 concentration on the constants in the free-volume viscosity equation is given in Table III.

The specific volume constant V_0 approached the specific volume of liquid SO_2 (0.61 cm^3/g) at the melting point of SO_2 as the concentration of the SO_2 increased. This is in reasonable agreement with the model considerations on which the free volume viscosity equation is based (3).

The viscosity data reflected the strong solvent/solute interactions thought to occur in the $\text{SO}_2/\text{AN}/\text{PC}/\text{LiBr}$ solutions. Apart from the low LiBr concentration range, the viscosity was linear in the LiBr concentration, Fig. 6

$$\eta/\eta_0 = 1 + BC \quad [4]$$

where η_0 is the viscosity of solvent, C the LiBr molar concentration, B the empirical constant; and the value of B was found to be $B = 0.79 \pm 0.02$, independent of the temperature. This value is characteristic of non-aqueous electrolyte solutions containing small ions (4). The dominance of the linear concentration term in the Jones-Dole equation above is taken to signify strong solvent/solute interactions (5), presumably the solvation of Br^- by acetonitrile and sulfur dioxide in this case.

Table III. The effect of the SO_2 concentration on the free volume equation constants (Eq. [3])

SO_2 concentration (w/o)	K (1/cp)	V_0 (cm^3/g)
28	10.1	0.85
61	6.4	0.70
75	6.2	0.66
89	5.0	0.57

The same general conclusion may be derived from Einstein's equation for the viscosity of dilute solutions of uncharged spherical molecules (6)

$$\eta/\eta_0 = 1 + 2.5 C\bar{V} \quad [5]$$

where \bar{V} is the molar volume of solute species, from which $\bar{V} = 316 \text{ cm}^3/\text{mole}$ for LiBr in the $\text{SO}_2/\text{AN}/\text{PC}$ solvent. Since the sum of the ionic volumes of Li^+ and Br^- is about $19 \text{ cm}^3/\text{mole}$, it is apparent that the ions must be strongly solvated in this solution.

The data may also be analyzed in terms of an Arrhenius type of activated process (3, 7, 8) despite some doubts about the validity of such a model for momentum transfer (9).

As the concentration of LiBr increased from 0 to 5% (weight) the activation energy increased from about 2 to 4 kcal/mole, Table IVA.

SO_2 exerted a more pronounced effect on the activation energy; Table IVB. At low SO_2 concentrations, the activation energy was close to 44 kcal/mole, and at high SO_2 concentrations it approached 3 kcal/mole or less. This pattern reflects the highly beneficial effect of the SO_2 on the transport properties of the SO_2 electrolyte used in the Li/ SO_2 batteries. The changes in the

Table IV. The activation energy for momentum transfer in the SO_2 electrolyte

A. The effect of the LiBr concentration*	
LiBr concentration, w/o	Activation energy, cal/mole
0	2347
0.09	2777
1.35	2745
2.68	3328
5.10	4058
B. The effect of the SO_2 concentration**	
SO_2 concentration, w/o	Activation energy, kcal/mole
28	44.2
61	7.0
89	3.4

* AN/PC/ SO_2 mass ratio: 1.95/1/10.6.

** LiBr/AN/PC mass ratio: 1/3.3/1.7.

activation energy also reflect the complicated interactions that occur between the dissolved species and the solvents in these solutions.

Conclusions

The capillary flow viscometer was found to function satisfactorily for the high vapor pressure SO_2 organic solvent electrolyte over the temperature and pressure range explored in these experiments: -60° to 70°C and pressures below 15 atm.

A high concentration of SO_2 in the electrolyte decreased the solution viscosity markedly, and the viscosity increased linearly with the LiBr concentration at temperatures between -60° and 70°C . This functional dependence indicated the occurrence of strong solvent/solute interactions in the SO_2 electrolyte.

The effect of the temperature on the viscosity agreed reasonably well with that expected from the free volume theory of momentum transfer.

Manuscript submitted Sept. 3, 1974; revised manuscript received April 21, 1975. This was Paper 52 presented at the Boston, Massachusetts, Meeting of the Society, Oct. 7-11, 1973.

Any discussion of this paper will appear in a Discussion Section to be published in the June 1976 JOURNAL. All discussions for the June 1976 Discussion Section should be submitted by Feb. 1, 1976.

Publication costs of this article were partially assisted by P. R. Mallory & Company, Incorporated.

REFERENCES

1. R. H. Stokes and R. Mills, "Viscosity of Electrolytes and Related Properties," chap. 2, Pergamon Press, London (1965).
2. J. H. Hildebrand, *Science*, **174**, 490 (1971).
3. S. Glasstone, K. J. Laidler, and H. Eyring, "The Theory of Rate Processes," chap. IX, McGraw-Hill Book Co., New York (1941).
4. J. I. Padova, in "Modern Aspects of Electrochemistry," B. E. Conway and J. O'M. Bockris, Editors, Vol. 7, p. 55, Plenum Publishing Corp., New York (1972).
5. R. H. Stokes and R. Mills, *ibid.*, chap. 4.
6. R. H. Stokes and R. Mills, *ibid.*, chap. 5.
7. F. C. Collins, *J. Chem. Phys.*, **26**, 398 (1957).
8. D. Feakins, D. J. Freemantle, and K. G. Lawrence, *J. Chem. Soc., Faraday Trans. I*, **70**, 795 (1974).
9. J. Adler and T. Einwohner, *J. Chem. Phys.*, **43**, 3399 (1965).

Lead-Acid Batteries: Use of Carbon Fiber-Lead Wire Grids at the Positive Electrode

J. L. Weininger* and C. R. Morelock

General Electric Company, Research and Development Center, Schenectady, New York 12301

ABSTRACT

Conducting carbon fibers were introduced into the positive grid of the lead-acid battery in a structure which resembled a grid of pipecleaners. The carbon fibers are compatible with the environment of the positive electrode of the cell. In conjunction with Pb-Ca-Sn alloy wires or pure lead wires, the fibers prolong the cycle life of the battery, increase the high discharge rate capability, and can decrease the weight of the battery. Scanning electron microscopy showed the function of the carbon fibers to be an extension of the lead wire grid, thereby participating in the solution-precipitation mechanism of the electrode reaction. For comparison, a grid with glass fibers was also studied.

In most applications of the lead-acid battery, the factors limiting performance and lifetime of the battery are utilization of the active material, adhesion of this material to the grid of the positive plate, and corrosion of the grid structure. Furthermore, an improvement in the energy density of the battery requires an increase in the utilization of the active material and a decrease in the weight of structural materials, especially of the grid.

The work described here deals with an attempt to achieve these ends with a radically different positive grid, as compared with the conventional cast or expanded lead grids. In the new structure, carbon fibers are combined with lead wires. The fibers interlock with each other and with the lead grid. This combined grid could still be pasted with active material and treated in the conventional manner to produce positive plates by curing, forming, and cycling. The purpose of the addition of carbon fibers was to (a) strengthen the lead grid, (b) improve the adhesion of the active material to the grid, and (c) reduce the resistive path from the metallic substrate to the site of electrochemical activity owing to the conductivity of the carbon fibers, thereby improving utilization.

In this report an experiment to prove the compatibility of carbon fibers with the lead-acid battery environment is described, as are the design and preparation of the grid and the performance of cells in which the carbon fiber-lead wire combination serves as the positive grid.

Use of Carbon Fiber at Positive Plate

It is common practice to improve conductivity of electrodes in galvanic cells by addition of carbon blacks or various grades of graphite. However, carbon fibers have not yet been used in the lead-acid cell. The pyrolyzed polyacrylonitrile (PAN) fibers used in this work have a conductivity in the range 0.86×10^{-3} to 2.5×10^{-3} mho/cm which compares to the values of 2.2×10^{-5} mho/cm for metallic lead and 1×10^{-3} and 4×10^{-3} mho/cm for α -PbO₂ and β -PbO₂, respectively. For this application, it was necessary to prove that the fibers can stand up to the strongly oxidizing conditions of the positive electrode. To test the stability of carbon fibers in this environment, an expanded grid of Pb-0.065% Ca-1.0% Sn alloy (St. Joe Minerals Corporation, RDP-16) was wound with carbon fibers (Hercules, Type A). This electrode was placed in 1.28 sp gr H₂SO₄ and was maintained poten-

tially at 1.40V vs. a Hg/Hg₂SO₄ reference electrode. The test lasted the equivalent of more than 700 cycles, if it is assumed that the plate must stand this high voltage for 20 min in each cycle. After 234 hr, the carbon fibers had lost their metallic grayish surface sheen and some colloidal carbon was suspended in the solution. There was no measurable weight loss which may have been compensated by oxidation of the surface with nascent oxygen. The texture of the surface observed in the scanning electron microscope (SEM) was not changed during the experiment. Instead, almost all fibers were at least partly split parallel to their long axis (Fig. 1). This would not interfere with their functioning as an extension of the positive lead grid. Furthermore, as will be seen later, during the actual operation of the lead-acid cell, the fibers became thoroughly covered with the active electrode material so that their exposure to acid, adsorbed oxygen, and to oxidizing potentials was less severe in the battery than during this compatibility test.

Grid Preparation

Figure 2 shows three substrates (grids) for electrodes of lead-acid cells. On the right is a lead-plated

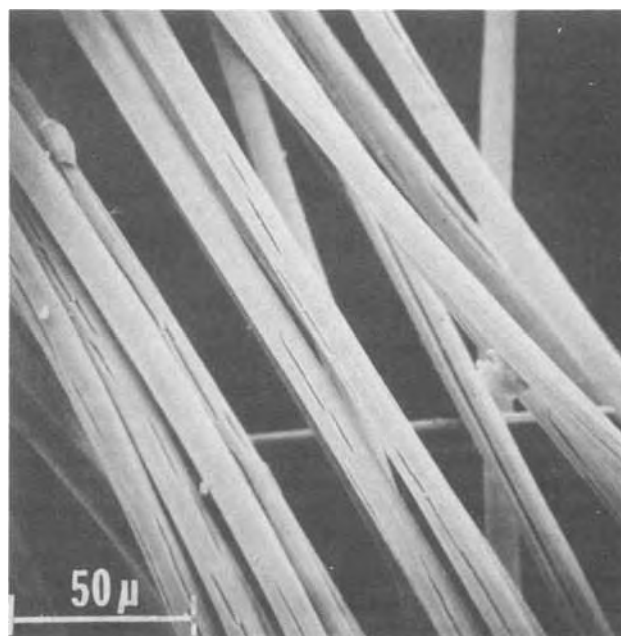


Fig. 1. SEM of carbon fiber after compatibility test

* Electrochemical Society Active Member.

Key words: lead-acid battery, positive grid, lead-calcium alloy, carbon fibers.

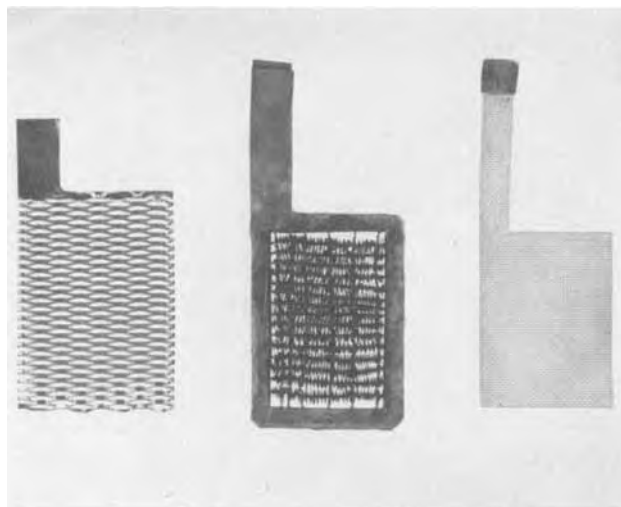


Fig. 2. Grids. For positive electrodes: left, expanded RDP-16 alloy; center, carbon fiber/Pb alloy wire combination. For negative electrode: right, lead-coated copper screen.

copper screen and on the left an expanded RDP-16 alloy grid which were used, respectively, for negative and positive electrodes. In the center of the figure is a combination of lead wires and carbon fibers, framed in RDP-16 alloy. The horizontal strands of the grid are structures resembling pipecleaners. They consist of two twisted RDP-16 alloy wires which hold the carbon fibers in place. During the twisting operation, while the wires are twisted, the carbon fibers are caught and aligned radially to the pipecleaner. Each 360 degree turn of the wire strand, about two complete twists, contains approximately 1000 carbon fibers. Their radial orientation is ideal for gripping the active battery material during and after pasting and curing. Figure 2 shows one of the first pipecleaner grids. The ends of wire strands were pressed between frames of 0.018 in. RDP-16 sheets which were welded on the outside of the frame.

Experimental Results

Four cells were assembled with identical components except for the positive plates to be examined. In each cell the positive electrode was placed in a Daramic (W. R. Grace Company) separator bag and was sandwiched between two negative electrodes of larger combined capacity than that of the positive. The grid of the control cell consisted of RDP-16 alloy with a 500/1 expanded grid pattern. The cells Pb/C-2 and Pb/C-3 had carbon fiber/lead wire grids; that of Pb/C-3 is shown in Fig. 2. Finally, as a further check on the utility of carbon fibers, the fourth cell, Pb/G-1, had a positive grid in which the carbon fibers were replaced by glass fibers.

The plates were pasted and cured in the conventional manner. Their weights, dimensions, and additions of H_2SO_4 and water during pasting are given in Table I. The larger weight of fiber structures was due to the excess weight of the lead frame in which the fiber grid was anchored.

Formation of the plates was also performed in the customary manner at charge rates of C/20 for 24 hr in 1.05 sp gr acid, followed by C/24 for 20 hr in 1.28 sp gr acid. Before each charging step the plates were soaked in the acid electrolyte for 1-2 hr.

The cells were cycled at constant current to cut-off voltages of 2.70V on charge and 1.75V on discharge. With these conditions the charge rate varied with cycle life, but except for the first few cycles, during which the capacity decreased rapidly, the rates were approximately C/2 for the control and Pb/C-2 cells and C/4 for Pb/C-3 and Pb/G-1. For the latter pair of cells the rate was changed to C/6 after 40 cycles.

Table I. Dimensions and weights of grids and other cell components

Substrate	Control alloy RDP-16 grid pattern 500/1	Pb/C-2 C fiber/RDP-16 wire	Pb/C-3 C fiber/RDP-16 wire	Pb/G-1 glass fiber/RDP-16 wire
Electrode area (cm ²)*	37.0	25.2	35.4	35.4
Fiber area (cm ²)*	—	18.2	21.8	21.8
Fiber diam (μ)	—	3-10	3-10	12-14
Pb wire diam (cm)	—	0.043	0.043	0.043
Substrate { positive	9.7	17.5	25.5	24.2
wt (g) { negative**			9.0	
Active mix { positive			12.25	
(g) { negative**			14.00	
H ₂ O (g) { positive			1.76	
{ negative			1.51	
H ₂ SO ₄ (sp. gr. { positive			1.64	
1.40) (g) { negative			1.39	
Weight of both electrodes (g)***	47.1	53.7	61.7	60.4
Separator (g)			1.2	
Housing and leads (g)			16.0	
Electrolyte (g)			26.0	
Total cell weight (g)	90.3	96.9	104.9	103.6

- * One side of electrode only.
- ** Two electrodes.
- *** Approximately 8% weight loss during pasting and curing.

The experimental results are plotted in Fig. 3-5. Figure 3 gives the cell voltage as a function of time for the first two cycles for all four cells. Figure 4 shows the variation of discharge capacity up to cycle 25 and Fig. 5 extends this to the end of cycle life.

There is a large decrease in discharge capacity between the first and second cycle (Table II, Fig. 3). Although this has also been observed to a lesser extent with negative electrodes (1), it is much more pronounced with the positive electrodes. After the first discharge there was little difference between the plates containing carbon fibers or glass fibers until after cycle 25 (Fig. 3a and 4), but there was a large difference between these plates and the control electrode even in the second cycle, particularly at high discharge rates (Fig. 3b and 4).

A broad band of slowly decreasing values in Fig. 4 indicates small differences between individual fiber electrodes which can be attributed to the automatic

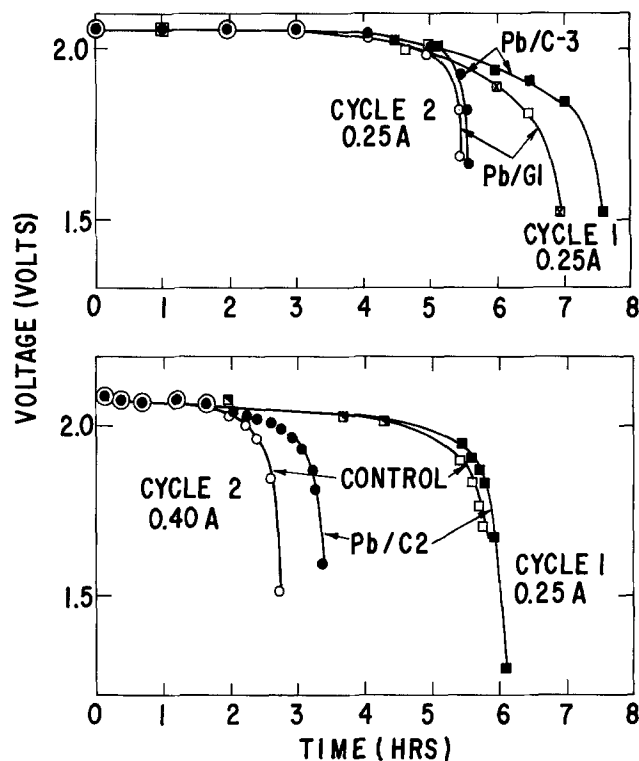


Fig. 3. Voltage-time plots during discharge of cycles 1 and 2. a, Top; b, bottom.

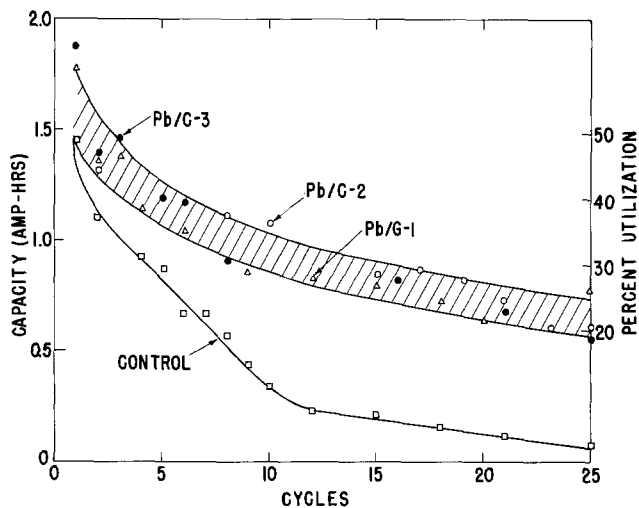


Fig. 4. Capacity and per cent utilization for first 25 cycles

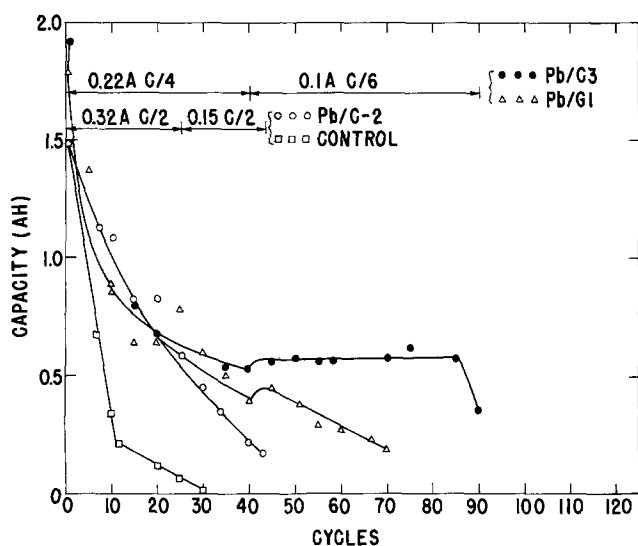


Fig. 5. Capacity during total cycle life

cycling equipment. However, the control cell, based on the expanded RDP-16 alloy grid, deteriorated rapidly and failed after about 10 cycles. This control cell and cell Pb/C-2 were cycled at the high rate of C/2. The other cells were cycled at C/4, and then at C/6, the change having been made to explore the possibility of prolonging cell life of Pb/C-3 and Pb/G-1 by decreasing the rate of charge and discharge (Fig. 5). This was the case for the electrode containing the carbon fibers, which showed superior charge acceptance over that with glass fibers after about cycle 30-35. This became more pronounced with increased cycle life. Pb/C-3 lasted 90 cycles and Pb/G-1 about 50 cycles

Table II. Performance of positive grids

	Control	Pb/C-2	Pb/C-3	Pb/G-1
Active positive material (g)	—	—	12.25	—
Equivalent capacity (A-hr)	—	—	3.0	—
Discharge 1				
Current (A)	—	—	0.25	—
Capacity (A-hr)	1.48	1.48	1.89	1.76
Duration (hr)	5.92	5.92	7.57	6.97
Rate	C/6	C/6	C/8	C/7
Utilization (%)	49.0	49.0	63.0	58.0
Energy density (W-hr/lb)	15.3	13.6	15.9	15.1
Discharge 2				
Current (A)	0.40	0.40	0.25	0.25
Capacity (A-hr)	1.10	1.32	1.39	1.38
Duration (hr)	2.75	3.30	5.51	5.55
Rate	C/3	C/3	C/6	C/6
Utilization (%)	37.0	44.0	47.0	46.0
Energy density (W-hr/lb)	11.4	12.1	11.8	12.3

before falling below the arbitrary limit of 0.50 A-hr capacity.

The serviceable life of the carbon-fiber cell Pb/C-3 is illustrated in Fig. 6 by the potential measurements of the individual electrodes against a Hg/Hg₂SO₄ reference electrode during the charge portion of cycle 81. Gas evolution occurred at approximately the same stages for both electrodes. It started at about 4 hr, became pronounced after 5 hr and predominant for the last 20-30 min of the 6-hr charge. The corresponding potential-time curves for discharge were more linear, with smaller time dependence, almost to the end of discharge, at which time the potential decayed rapidly.

An inset in Fig. 6 shows the typical coup de fouet or Spannungsberg which has been observed at the beginning of charging a previously completely discharged positive electrode (2). This phenomenon has been attributed to resistance polarization. In cell Pb/C-3 the potential maximum of the coup de fouet varied with charge current as follows: 1368, 1310, and 1264 mV, respectively, for currents of 150, 100, and 75 mA. The approximately linear relation of these values would be characteristic of an insulating PbSO₄ film on the positive electrode with resistance of the order of 1 ohm.

Examination of cell components at the end of cycle life showed few changes in the negative electrodes which were still functioning normally. The carbon-fiber electrodes had retained much of the active positive material, but in the case of the expanded grid, adhesion was so poor that the cell could not be taken apart without losing from the grid whatever material still adhered to it. This is shown in Fig. 7.

Scanning Electron Microscopy (SEM)

The appearance of the positive plates after use (Fig. 7) indicated that adhesion of the active material was improved by the use of carbon fiber-lead wire grids. SEM further helped to elucidate the role of the carbon fibers in the positive plate. It showed that the active material was distributed uniformly between individual

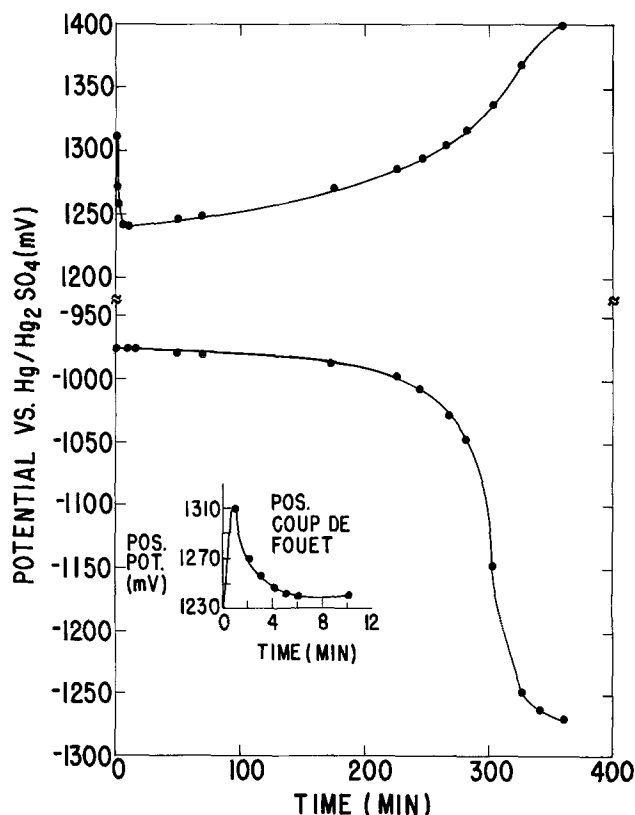


Fig. 6. Electrode potentials vs. Hg/Hg₂SO₄ reference electrode, cell Pb/C-3, cycle 81.

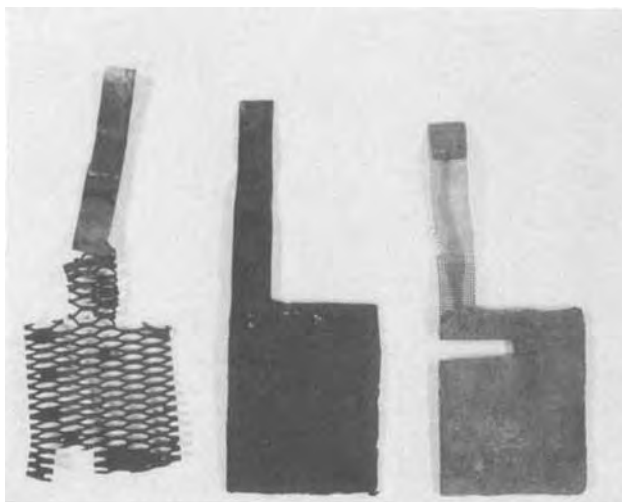


Fig. 7. Grids of Fig. 2 after use in the control cell (left), in cell Pb/C-2 (center), and as negative counterelectrode (right).

carbon fibers and that the fibers acted as nucleation sites for growth of the active material. For example, Fig. 8 shows a single carbon fiber which is heavily encrusted with PbSO_4 crystals. This barnacled appearance was typical of the deposits on the fibers. A similar deposit and growth were found at a bundle of fibers taken from the positive plate of cell Pb/C-3 (Fig. 9). Individual PbSO_4 crystals, their aggregates, and nucleation sites at the carbon fibers can be seen.

The materials in Fig. 8 and 9 were taken at the end of the useful life of cell Pb/C-3 so that they may have been very nearly inactive. However, a completely passivated PbSO_4 deposit is shown in Fig. 10 where the large crystal size rules out any effective electrode reactions. Conversely, where the deposit is still active, different smaller crystal structures, typical of PbO_2 were found (see Fig. 15 below).

The insulating glass fibers in cell Pb/G-1 were useful to the extent that they added structural support to the active material. But unlike the carbon fibers, they did not provide a substrate for crystal growth. This is shown in Fig. 11, which is a view of many isolated, but closely spaced, glass fibers. That they are not covered with active material is clearly shown in

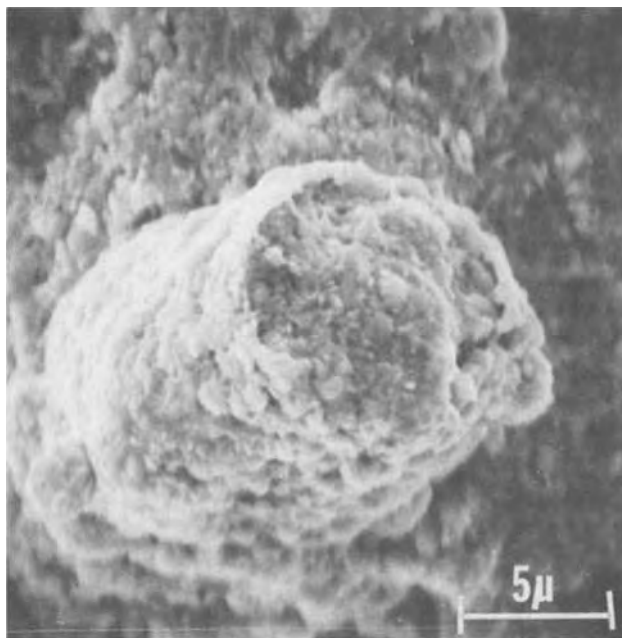


Fig. 8. Carbon fiber with deposit of positive active material

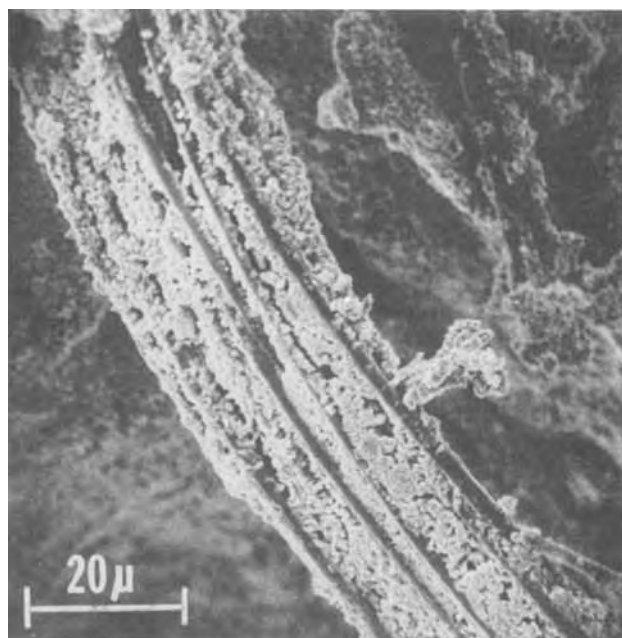


Fig. 9. Bundle of carbon fibers, each 3μ thick, with positive active material, at end of cycle life of cell Pb/C-3. Note growth characteristics of solution-precipitation mechanism.

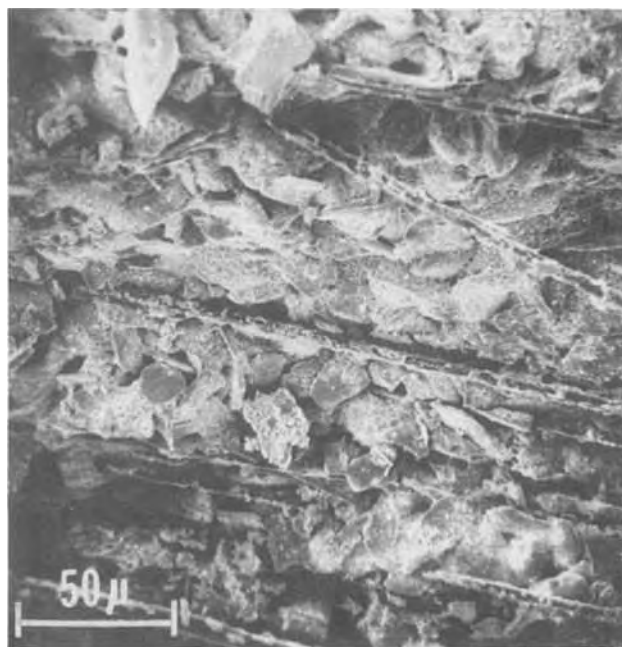


Fig. 10. Passivating PbSO_4 crystals between carbon fibers of electrode Pb/C-2 at end of cycle life.

the enlargement of one of the central glass fibers of Fig. 11 in Fig. 12.

Another interesting SEM observation, not directly related to the use of carbon fibers, is that of the passivated layer on the Pb/Ca/Sn alloy wire of the fiber-wire grid. Figure 13 is the cross section of the wire, originally 0.043 cm in diameter, at the end of experiment Pb/C-3. Two layers of active material adjacent to the wire are noted. They have different color and texture. The inner, lighter layer is made up of large PbSO_4 crystals. It is believed to be the corrosion layer which has the passivating effect on cell operation. Figure 14 is the enlargement of the central portion of the SEM of Fig. 13. The PbSO_4 crystals are densely packed, but considerable porosity is maintained, even in the corrosion layer. The darker, finer

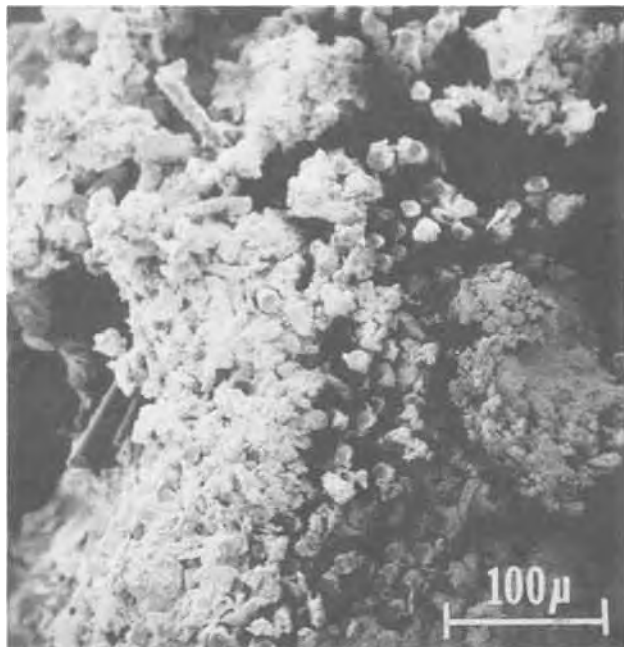


Fig. 11. Isolated but closely spaced glass fibers in electrode Pb/G-1 at end of cycle life.

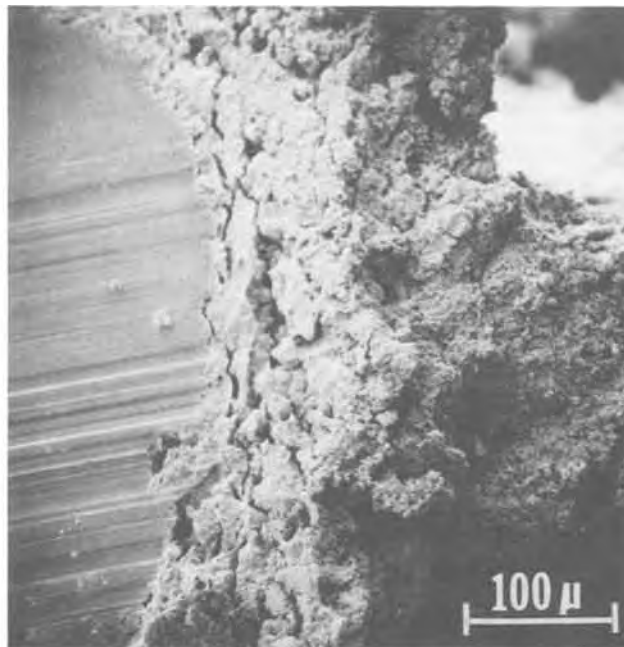


Fig. 13. Cross section of Pb-Ca-Sn alloy wire from C fiber/Pb wire grid at end of Pb/C-3 cycle life. There are two layers of deposits on the wire.

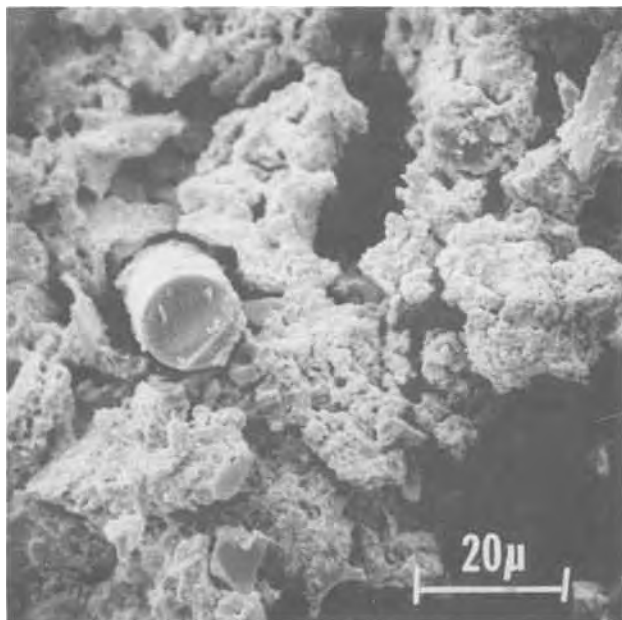


Fig. 12. Same electrode area as in Fig. 11, at larger magnification. There is little contact with glass fibers and no deposit of the active material on the glass fiber.

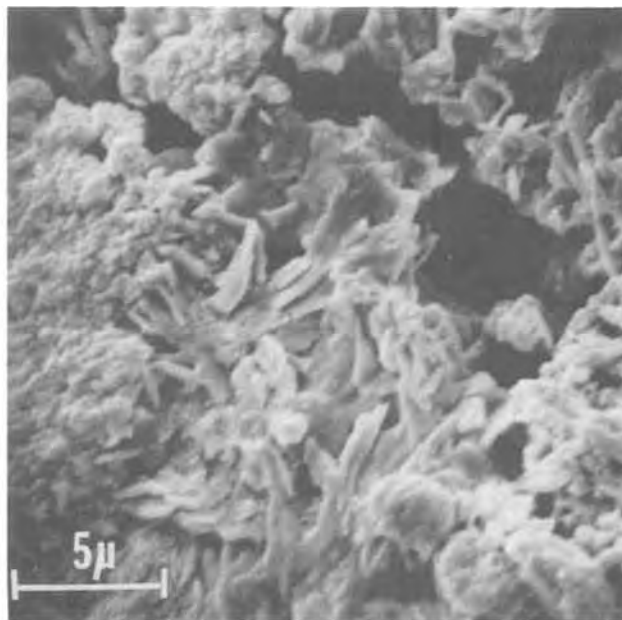


Fig. 14. Enlargement of the central portion of Fig. 13, showing PbSO_4 crystals which constitute the dense lighter layer adjacent to the Pb alloy wire.

textured active material of the positive plate, located to the right of the central portion of Fig. 13, is shown in the enlargement of Fig. 15. The porosity and crystallite sizes in Fig. 15 are typical of active PbO_2 material.

Discussion

Use of alloyed lead and carbon fibers.—In the present work the main objectives of improving the cycle life of positive plates and of the utilization of the positive active material were combined with the search for a suitable Sb-free grid structure. The new grid structure makes use of conducting carbon fibers as an extension of a Pb-Ca-Sn alloy wire grid. This combination, resembling a grid of pipecleaners, results in greater strength, better adhesion of the active material, and longer cycle life of the positive electrode.

Two important aspects of the contribution of the carbon fibers are: (a) their relatively ordered, radial arrangement, with respect to the Pb or Pb alloy wire grid, and (b) their electrical conductivity. The former leads to an intimate combination of carbon fibers and active material on a microscopic scale providing nucleation sites for growth of the active material. This is made possible by the conductivity of the carbon fibers which allows the fibers to act as extension of the grid (see below).

Performance of test cells.—Figures 4 and 5 show the longer lifetime of the carbon-fiber cells Pb/C-2 and Pb/C-3 than those of the control cell and the glass-fiber cell Pb/G-1. The control cell had a positive substrate of expanded Pb-Ca-Sn alloy with an expansion

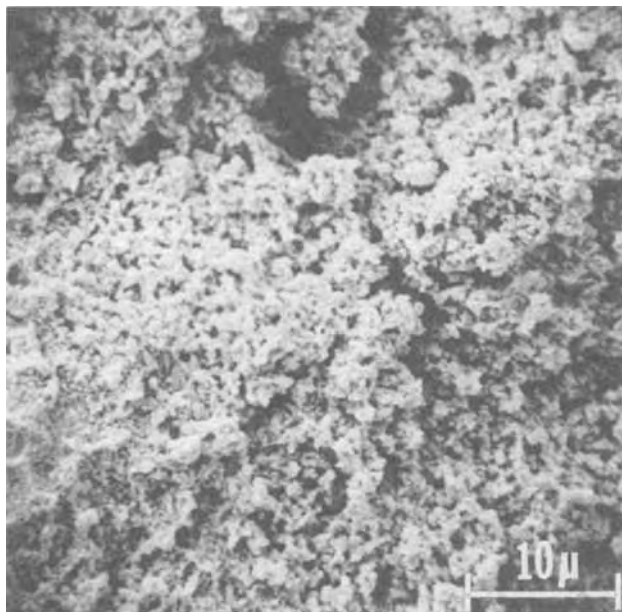


Fig. 15. Enlargement of a portion of Fig. 13 which contained the more porous, darker layer. The active material of the positive electrode.

pattern that resembled slightly that of the conventional cast grid (Fig. 1). But the lack of adhesion of the active material (see Fig. 7) was the decisive factor in the poor performance of the control cell, particularly with the rigorous cycle regime of 100% depth of discharge. The glass-fiber cell kept pace with the carbon-fiber cell for approximately the first 25 cycles (Fig. 3 and 4), showing a similar structural improvement of the positive electrode, due to the incorporation of fibers. In the later stages of cycle life, when previously active sites were passivated, the advantages of the carbon-fiber grid became more pronounced (Fig. 5). They can be related to the mechanism of the electrode reactions, discussed below.

The better cycle life of cells, containing positive electrodes with carbon fibers, is evident from the data represented in Fig. 5. This preliminary finding holds out hope that the life of a specialty "maintenance-free" battery with Pb-Ca-Sn grid wires can be brought up to the level of heavy-duty batteries, employing antimonial lead grids.

Electrode design.—The grid design incorporating fiber electrodes was intended to prove the feasibility of the carbon-fiber grid structure. It did not constitute a design for best performance, utilization, or energy density. There was excessive weight in construction of the lead alloy frame and of the cell as a whole. Furthermore, another observation indicated that the life of cells containing carbon fibers was not limited by the usual factors contributing to deterioration of the positive plate, such as lack of utilization, passivation, or shedding of active material. Instead, an extraneous introduction of a resistive contact, produced by corrosion of the alloy at points of contact between the ends of the carbon-lead pipecleaners and the lead alloy frame, may have been responsible for lower capacity in the later cycles of Pb/C-3. The contacts were made by pressing and cold-welding the ends of the pipe-cleaner strand between two frames of Pb alloy and melting the outside edges of the frames. Optical microscopy showed that this connection was not leak-proof. The acid electrolyte seeped into the cracks between the two frames and corroded the contact points. It is, therefore, quite plausible that with a better design of the grid frame, for example, by anchoring the ends of the carbon fiber/lead wire strands in a suitable material, better results will be obtained with an advanced electrode design.

Utilization of positive material.—The decrease in the utilization of the positive material from 50-60%, encountered in the first cycle, to approximately 40-47% in the second cycle (see Table II) is disappointing. It may be tentatively ascribed to the passivation of the Pb-Ca-Sn alloy which over the life of the cell is pronounced. It is illustrated in the SEM's of Fig. 13 to 15.

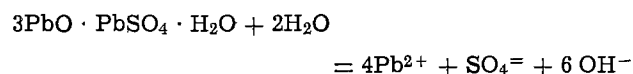
Some methods of carbon-fiber grid construction do not depend on the mechanical strength of the lead alloy. It is then possible to use pure lead wire for the carbon-fiber grid. This may be an advantage electrochemically and economically, but the same sulfation problem and, hopefully, the same remedies that apply to the Pb-Ca-Sn alloy will also apply to pure lead.

High rate discharge.—Electrodes containing carbon fibers will have a better capability to deliver power at high rates. This conclusion is again based on the concept of extending the grid by means of the carbon fibers into the active material. The effect of sulfation will be alleviated insofar as the carbon fibers act as an active electrode surface. Also, more utilization and capacity at higher current drain may be obtained than with conventional grids. This is shown to some extent by the discrepancy of the performance of cells Pb/C-2 and of the control cell, between the first cycle at C/6 discharge rate (small difference) and the second cycle at C/3 (considerable advantage to the cell containing the carbon fiber).

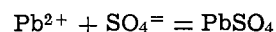
Scanning electron microscopy.—SEM studies of active constituents of the lead-acid cell were first described by Hughel and Hammar (3) who showed many interesting SEM's of positive and negative materials in various stages of charge. Since that publication, SEM has become a powerful and popular tool in battery research. It has recently been described for the negative electrode of the lead-acid cell (1). In the present work, the function of the carbon fibers as conducting substrates in positive plates was also elucidated by SEM. This is discussed in connection with the solution-precipitation mechanism of the electrode reactions.

Solution-precipitation mechanism.—Evidence for this mechanism is derived from SEM's. Figure 9 shows the crystal growth and nucleation sites on carbon fibers, whereas in the comparable construction with glass fibers (Fig. 11) no such crystal growth occurred. The reaction in question may take place even before cycling, during the formation of the positive active material which is discussed in detail by Pavlov and co-workers (4).

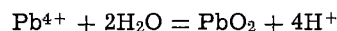
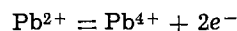
During formation, Pb(II) ions have a limited solubility in equilibrium with tribasic lead sulfate



This may be followed by (a) direct precipitation of the sulfate



or (b) by oxidation and subsequent precipitation of α or β PbO_2 , depending on the acidity at the site of PbO_2 precipitation



The existence of this solution-precipitation mechanism is particularly important for the proper distribution of active material in the carbon-fiber grid. There are approximately 1000 strands to a single tow of the carbon fibers, each of which has a very small diameter. Consequently, during pasting, the carbon fibers cannot be expected to be individually coated. Only later during formation and cycling can it be expected that the carbon fibers will be uniformly covered with the active material.

Conclusions

A new positive grid structure has been developed which, by means of carbon fibers, extends the active lead wire grid into microscopic contact areas with the active material. The resulting performance of lead-acid cells with these grids shows longer cycle life and better capability at higher discharge rates than control cells made with expanded Pb-Ca-Sn alloy or cells in which the carbon fiber is replaced by glass fibers.

Acknowledgment

The authors wish to express their appreciation to P. C. Lord with whom the basic invention of the carbon fiber-lead grid was a joint effort; to F. W. Secor who designed and prepared the test cells; and to M. D. McConnell for the scanning electron microscopy.

Manuscript submitted Dec. 18, 1974; revised manuscript received April 28, 1975. This was Paper 12 pre-

sented at the Toronto, Canada, Meeting of the Society, May 11-16, 1975.

Any discussion of this paper will appear in a Discussion Section to be published in the June 1976 JOURNAL. All discussions for the June 1976 Discussion Section should be submitted by Feb. 1, 1976.

Publication costs of this article were partially assisted by General Electric Company.

REFERENCES

1. J. L. Weininger, *This Journal*, **121**, 1541 (1974).
2. D. Berndt and E. Voss, "Batteries 2," Proc. Internatl. Symp., Brighton, 1964, p. 17.
3. T. J. Hughel and R. H. Hammar, "Power Sources 3," Proc. 7th Internatl. Symp., Brighton, 1970, p. 35.
4. D. Pavlov, G. Papazov, and V. Iliev, *This Journal*, **119**, 8 (1972).

Anodic Behavior of Silver in Alkaline Solutions

D. B. Gibbs, B. Rao, R. A. Griffin, and M. J. Dignam*

Department of Chemistry, University of Toronto, Toronto, Ontario, Canada M5S 1A1

ABSTRACT

The anodic behavior of silver was investigated under controlled diffusion conditions in alkaline solutions. Experiments were carried out under linear flow control and also using a rotating disk electrode. The electrical and optical properties of the silver oxide films were measured. On the basis of these results, we point out the difficulties involved with surface roughness in interpreting diffusion layer kinetics. Finally, we suggest a mechanism for Ag_2O film formation under stirred conditions, involving dissolution of silver followed by precipitation, the rate-controlling step for which is nucleation of steps on the oxide surface.

Interest in the anodic behavior of silver in alkaline solutions (1-3) has been stimulated in recent years by the widening use of silver/silver oxide electrodes in storage batteries. The plateaus on the potential-time charging curves obtained at constant current have been associated (4) with the formation of Ag_2O , AgO , and other higher oxides. The first anodic product is Ag_2O which may be grown to several thousand angstroms in thickness (5). Its growth is terminated rather abruptly with the rapid increase of electrode potential to be followed by the formation of AgO and possibly higher oxides, before oxygen is eventually evolved. The physical and chemical properties of these silver oxides have been reviewed in detail by Allen (6) and MacMillan (7).

This paper is concerned primarily with the investigation of the initial electrode process, namely the formation of Ag_2O . A mechanism for the formation of this oxide would in general consist of a series of elementary steps involving solid-state point defects as well as species in solution and on the electrode surface, and would include reactions both within the film and at the interfaces. It was found that the kinetic behavior of silver electrodes was profoundly influenced by surface conditions (5) and it would thus seem that further studies should be carried out on smooth well-defined surfaces. The earlier work of the galvanostatic investigation (5) of both etched and electropolished silver electrodes in aqueous Ag_2O saturated NaOH solutions, included an examination of the effect of stirring of the electrolyte. The results were explained by postulating that at least two dif-

ferent mechanisms were involved in the Ag_2O film formation: one a dissolution-precipitation process and the other a direct interfacial reaction. Evidence for this hypothesis came from observations such as: (a) the apparent existence of two different overpotentials about 40 mV apart for oxidation, (b) the marked dependency of current efficiency on stirring, particularly at low current densities, and (c) the very different appearance of films formed under stirred and unstirred conditions, the former having a transparent glassy appearance, the latter a dull opaque one. In this work an attempt is made to examine further this hypothesis through the use of both a flow system and a rotating disk electrode. In addition, the electrical and optical properties of the films formed are determined, both to provide additional information on which to base kinetic arguments and also for reasons of intrinsic interest.

Experimental Details

The experimental procedure used involved a flow system, with adjustable flow rates, designed to circulate the electrolyte solution past the electrode surface at very high speeds. A schematic of the system is shown in Fig. 1. The system was constructed entirely of plastic materials (Teflon, polypropylene, and high density polyethylene) since the experiments involved the use of concentrated alkaline solutions. A Teflon lined pump P circulated the solution from a storage reservoir S through the cell C and a flow meter F. The flow meter was calibrated by measuring the time needed to pump a given volume of the solution through the system for a given manometer deflection. The flow rate was variable over a range of 25 to 100 ml sec⁻¹.

The storage reservoir S was placed in an outer tank containing water thermostated at 27°C. Through the

* Electrochemical Society Active Member.

Key words: silver oxide, rotating disk electrode, nucleation mechanism, electrical properties.

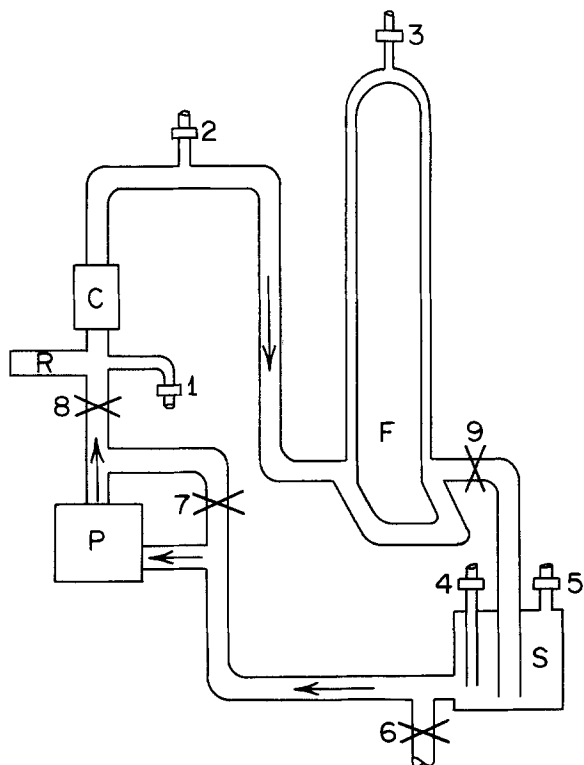


Fig. 1. Schematic of the flow system: C, polypropylene cell; R, reference electrode chamber; P, pump; F, flow meter; and S, storage tank.

top of the tank were sealed two tubes, for nitrogen inlet (a porous polyethylene gas dispenser) and an outlet such as to provide isolation from the atmosphere. Two auxiliary electrodes were also installed in the tank, one of platinum gauze and the other of silver foil, used for the preelectrolysis of the solution. A Hg/HgO microelectrode prepared on a piece of platinum foil (3) was used as the reference electrode. The nitrogen used in the system was purified by passage through vanadous chloride solution and amalgamated zinc (8) followed by a bubbler containing 0.7N NaOH solution.

The electrochemical cell was designed to place the test electrode in the center of a rectangular flow channel with counterelectrodes at each side as shown in Fig. 2(a). The pieces are from top to bottom: polypropylene tubing (main flow line) joined by a sleeve to a tapered end piece, electrode locater, center piece locater, and finally a tapered end piece joined by sleeve to the tubing. The center piece plan is shown in Fig. 2(b). The counterelectrodes N consisted of silver plates covered with anodically formed Ag_2O . Electrical contacts were made by sharpened silver wires which were forced against the back of the electrodes and sealed into the cell walls using first molten polypropylene and then reinforcing with epoxy cement. The electrical contact to the test electrode was made by a sharpened silver wire, this time sealed into the tight fitting polypropylene plug H. The electrode locaters [Fig. 2(c)] were small annular disks with three grooves to accommodate the ends of the electrodes and served to keep the test electrode at the center of the channel and parallel to the counterelectrodes. The center hole of each locater had a diameter just small enough to support the test electrode and prevent it from being swept downstream during the operation of the system. With the present cell, flow velocities ranging from 100 to 400 cm sec^{-1} could be produced.

The electrolyte was prepared from analytical grade NaOH and was found to contain 0.8% by weight of carbonate. The electrolyte was saturated with Ag_2O either by adding the powdered oxide into the electrolyte solution or by the anodic oxidation of the silver

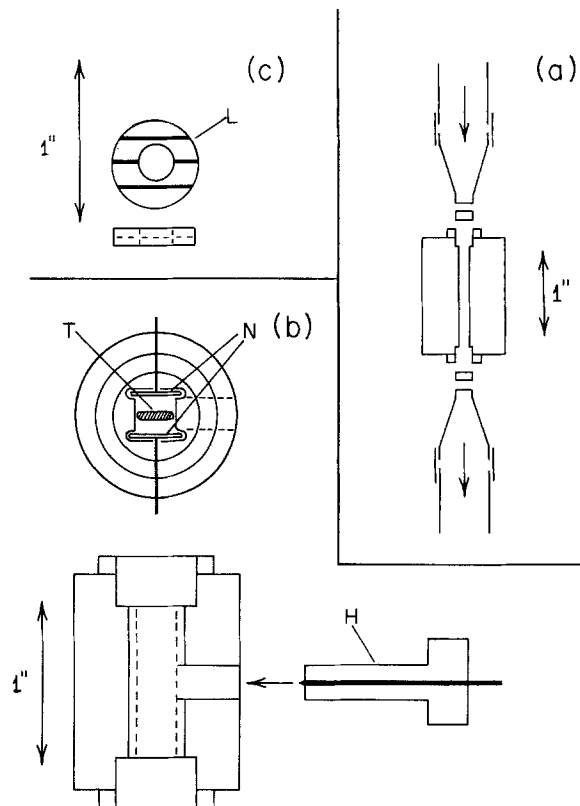


Fig. 2. Details of polypropylene cell. (a) Cross sectional view of the cell. (b) Central part of the cell: T, test electrode; N, counter electrode; and H, plug with lead for test electrode. (c) Electrode locater, L.

auxiliary electrode and subsequent agitation of the solution with the use of a mechanical shaker. Oxygen was removed from the solution by bubbling prepurified nitrogen for several hours. The test electrode was punched from 0.13 cm bright rolled silver sheet (99.95% pure) in the form of paddles with a blade approximately 2.54×0.63 cm and with a handle of 0.18 cm. Following a preliminary annealing in flowing hydrogen at 500°C for 1 hr, the electrodes were electropolished in a cyanide bath (10). They were rinsed in running distilled water and subjected to a further annealing in hydrogen at 500°C for 1 hr. The geometrical area of the electrode was 4.4 cm^2 .

The rotating disk electrode (Pine Instrument Company) experiment was carried out employing a demountable electrode assembly (9) as shown in Fig. 3. Silver electrodes (99.95% pure) 1 cm in diameter and 0.6 cm thick were imbedded in a thermoplastic. These were metallographically polished to 0.25μ and then subsequently electropolished (10) to remove the worked layer. The rotational speed was varied from 0-10,000 rpm. Electrolyte preparation and other procedures were similar to that used in the flow system.

For studying the effect of roughness on the diffusion layer kinetics, silver electrodes for use in the rotating disk assembly were prepared in two different ways. In the first, electrodes mounted in the rotating head were metallographically polished and subsequently electropolished, then a silver film was deposited on the top of the polished surface by vacuum evaporation. In the second method, circular optical flats made of Pyrex were seated into the face of the rotating disk electrode assembly and silver film was deposited on the exposed face of the optical flat by vacuum evaporation. Electrical contact with the film was made by means of a fine silver wire protruding through a small hole (10μ diameter) in the center of the optical flat. The electronic equipment consisted of a standard galvanostat/potentiostat combination built with a set of operational amplifiers.

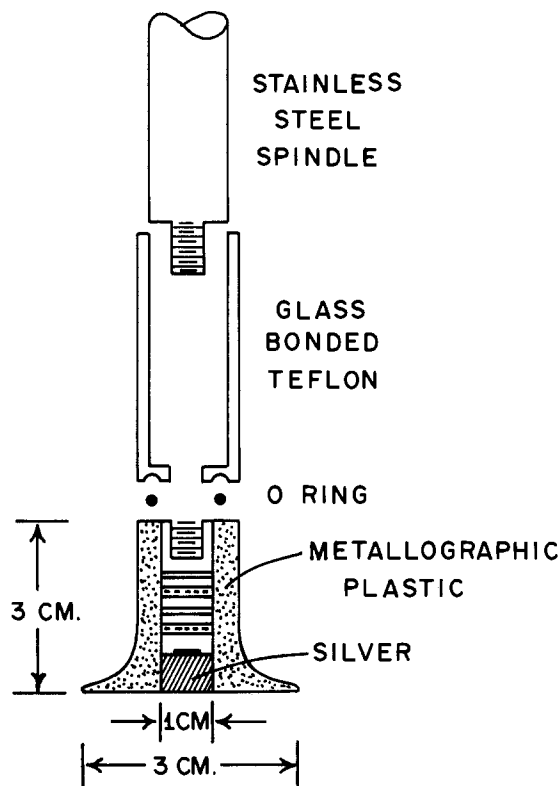


Fig. 3. Rotating disk electrode with demountable head suitable for electrical and optical measurements.

The optical studies consisted of direct reflection spectroscopy in the infrared region to observe lattice vibrational modes and ellipsometry in the visible spectral region to determine the thickness and optical constants of the silver oxide films. A Perkin-Elmer 350 spectrophotometer ($0.35\text{--}217\mu$) and a Beckman IR-11 spectrophotometer ($12\text{--}150\mu$) were used to obtain the specular reflectance spectrum of the silver oxide films. Also, for the sake of comparison, transmission spectra of Ag_2O powder were recorded. The ellipsometric measurements were carried out, using a method involving light intensity measurements (11), over the wavelength region $4000\text{--}7000\text{\AA}$.

In addition, electrical measurements were carried out on the oxide films. These were done by subjecting the system Ag/anodic oxide/Al to measurements of direct current *vs.* voltage, and capacitance (10^6 Hz) *vs.* d-c polarizing voltage. For this purpose a uniform square grid of superpurity aluminum spots of 0.04 cm was evaporated on to the silver oxide surface to provide electrical contacts. The type of charge carrier was identified at room temperature by means of thermoelectric measurements. The sign of the thermoelectric power for the oxide film was determined by observing the sign of the potential developed between a heated probe against that of a room temperature probe on adjacent aluminum spots.

Results

Electrochemical studies.—In the absence of stirring, a freshly installed silver electrode was found to assume an initial open-circuit potential of about 0.20V *vs.* Hg/HgO reference electrode and then slowly increased toward the reversible Ag/ Ag_2O potential of 0.244V . This was however speeded up under stirring conditions and remained stable at that value. Figure 4 shows a typical oxidation-reduction curve of potential *vs.* time at 27°C for silver in Ag_2O saturated alkaline solution. The general shape of the anodic curve was found to be unaffected by stirring. The cathodic curves were always recorded in the absence of stirring, since otherwise reducible species such as silver in solution and residual oxygen would be transported to the electrode,

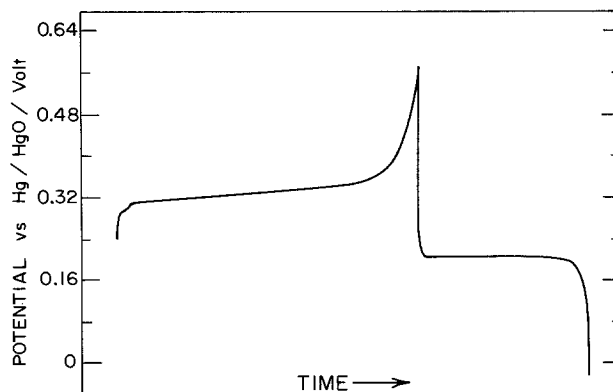


Fig. 4. Oxidation and reduction curves for Ag_2O film formation under a flow rate of 350 cm sec^{-1} at 27°C oxidation: $i = 0.33\text{ mA cm}^{-2}$, time = 7.6 min reduction: $i = 0.39\text{ mA cm}^{-2}$, time = 4.3 min.

making meaningful reduction measurements impossible. The cathodic curve normally consisted of only one plateau and always exhibited a distinct abrupt drop toward hydrogen evolution, which was taken to signify the end of Ag_2O film reduction. It was, however, found that it is essential to saturate the electrolyte with Ag_2O , otherwise the electrochemically formed oxide film tended to dissolve in the electrolyte. Examination of the Ag_2O film formed under rapid stirring conditions showed it to have a smooth shiny finish, compared to those formed under unstirred conditions, which were dull brown in color.

The plot of current efficiency (defined as the ratio of the reduction charge to the oxidation charge) *vs.* total current density is shown in Fig. 5. At median current densities, the measured current efficiencies were less than 100%, and independent of whether the electrode was reduced immediately following oxidation or whether a period of open-circuit stirring was allowed before reduction. The experimental points in Fig. 5 are represented fairly well by two intersecting straight lines. A more or less similar behavior was observed with the rotating electrode system. The intersection of the two lines falls near 0.25 mA cm^{-2} , the current density noted by Dignam *et al.* (5) to be unique. Below this current density, the current efficiency falls off precipitously and would appear to reach a value of zero at about 0.06 mA cm^{-2} .

Mean film thicknesses were calculated from the number of coulombs needed to reduce the films, assuming unit roughness factor and using bulk density (6) values for the Ag_2O . The limiting film thickness as calculated was found to be a decreasing function of current density, as shown in Fig. 6. The reduction charge (proportional to the film thickness) and current efficiency for silver oxide films at varying current densities and different flow rates are shown in Table I.

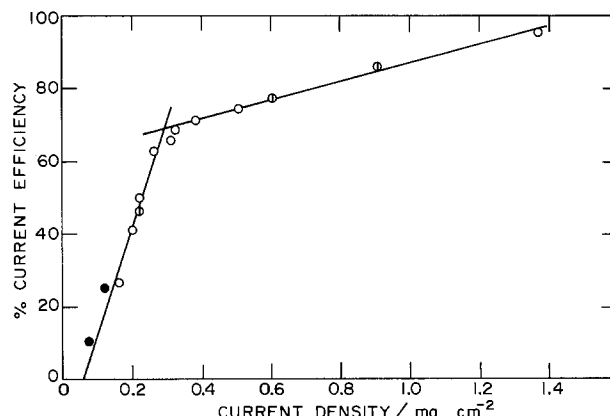


Fig. 5. Current efficiency for Ag_2O formation as a function of current density under a flow rate of 350 cm sec^{-1} and at 27°C .

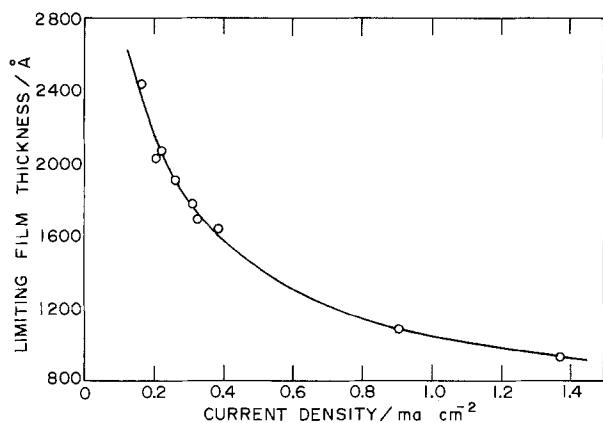


Fig. 6. Limiting film thickness as a function of current density under a flow rate of 350 cm sec⁻¹ and at 27°C.

Examination of the amount of charge required for reduction shows clearly that the limiting film thickness is independent of flow rate over the entire range investigated in our experiments. Thus Ag₂O film formation ceases when a certain thickness has been reached, independent of the contribution of the dissolution process. As regards current efficiency data for unstirred conditions, the efficiency is very high at all current densities, but has dropped significantly by the time a flow of 150 cm sec⁻¹ is reached. Thus it would appear that at least for the range of flow rates accessible here, the current efficiency is independent of flow rate except at very low flow rates.

The dependence of current efficiency on the per cent complete formation of Ag₂O film is given in Table II. These results indicate that the efficiency is independent of film thickness. The linear segments of the anodic potential vs. time curves were extrapolated to zero time. The resulting potential intercept, η_0 , is seen to be approximately constant at about 60 mV (Table III) except at very low current densities where it drops rapidly with decreasing current.

Table I. Current efficiency and reduction charge for completed films as functions of flow rate at various current densities

	Flow rate, cm/sec	Oxidation charge, mcoulomb/cm ²	Reduction charge, mcoulomb/cm ²	Current efficiency, %
$i = 0.905$ mA/cm ²	0	67.3	65.1	96.7
	150	78.7	69.7	88.6
	275	80.9	72.0	89.1
	350	75.4	65.1	86.2
$i = 0.387$ mA/cm ²	150	135.0	92.9	69.1
	350		97.6	71.1
$i = 0.328$ mA/cm ²	0	111.0	105.0	94.4
	275	140.0	100.0	71.8
	350	147.0	100.0	68.5
$i = 0.225$ mA/cm ²	0	133.0	124.0	93.0
	150	227.0	119.0	52.2
	275	266.0	132.0	49.8
	350	246.0	123.0	50.0

Table II. Current efficiency as a function of extent of completion of film

	Oxidation charge, mcoulomb/cm ²	Reduction charge, mcoulomb/cm ²	Current efficiency, %	% Completion of film
$i = 0.387$ mA/cm ²	137.0	97.6	71.1	100
	81.3	59.3	72.9	61
	35.1	25.6	72.8	26
	13.9	9.8	70.0	10
$i = 0.225$ mA/cm ²	246.0	123.0	50.0	100
	129.0	59.0	45.9	48
	67.6	31.4	46.4	25
		11.9	46.1	10
	25.7			

Table III. Overpotential intercept η_0 and partial current densities i_f , i_s as functions of applied current density i

i , mA/cm ²	η_0 , mV	i_f , mA/cm ²	i_s , mA/cm ²
0.905	53.5	0.780	0.125
0.905	64.3	0.802	0.103
0.905	62.3	0.806	0.099
0.509	52.1	0.380	0.129
0.387	60.9	0.275	0.112
0.387	69.1	0.267	0.120
0.328	67.0	0.236	0.092
0.328	73.1	0.225	0.103
0.313	73.8	0.206	0.107
0.264	65.7	0.166	0.098
0.225	57.6	0.113	0.112
0.225	61.6	0.117	0.108
0.225	63.6	0.112	0.113
0.225	74.5	0.105	0.120
0.209	49.4	0.086	0.123
0.168	74.5	0.044	0.122
0.123	21.0	0.031	0.092
0.077	17.0	0.008	0.069

The current efficiency for film formation may be written as

$$\text{C.E.} = i_f / (i_f + i_s) = i_f / i \quad [1]$$

where i_f is the current density associated with film formation and i_s that for metal dissolution. Their sum i is the total current density. The film current density i_f can be calculated as the product of total current density and current efficiency, the values of i_s being subsequently found by subtraction. The results are shown in Table III. While i_f increases regularly with current density, being nearly zero at the lowest current density, i_s is virtually constant (~ 0.1 mA cm⁻²) except at the lowest current densities. Indeed, the variation of i_s with i is very similar to that of η_0 with i described earlier. It was further found that oxidation reduction cycling does not appreciably affect the current efficiency. However, limiting film thicknesses calculated were somewhat greater ($\sim 30\%$) which suggests some surface roughening has occurred. This observation is consistent with earlier studies (5).

Diffusion layer studies.—The results of diffusion layer studies using rotating silver disk electrodes prepared by vacuum evaporation on both smooth and rough surfaces suggest that roughness effects might be a problem in obtaining reproducibility in the system Ag/Ag₂O/(Ag₂O saturated aqueous NaOH) under anodic conditions. This conclusion was verified by the results of the study of redox reactions as a function of rotational speed for both smooth and rough electrodes. The behavior of the rotating disk electrodes under both potentiostatic and galvanostatic conditions as a function of angular velocity were determined in three different electrolytes. Figure 7 shows the result for I₃⁻-I⁻, for a rough Ag rotating disk electrode under cathodic conditions. Thus under potentiostatic control the limiting current density is found to vary in direct proportion to $\omega^{1/2}$, where ω is the angular velocity, a result expected on the basis of the hydrodynamic theory (12), since diffusion layer thickness is predicted to vary in inverse proportion to $\omega^{1/2}$. A similar behavior was observed for the case of Fe(NO₃)₃-Fe(NO₃)₂ under anodic conditions.

In contrast, the electrodes were found to behave very differently under conditions in which the minor constituent is generated at the electrode surface, such as Fe(NO₃)₃-Fe(NO₃)₂ under cathodic conditions and Ag₂O saturated NaOH under anodic conditions where Ag(OH)₂⁻ is presumed to be generated at the electrode surface. Thus the rough electrode surfaces (i.e., those surfaces formed by silver evaporation onto metallographically polished surfaces) show very little change in overpotential with rotational speed under galvanostatic conditions (Fig. 8), while relatively smooth electrode surfaces (i.e., those formed by silver

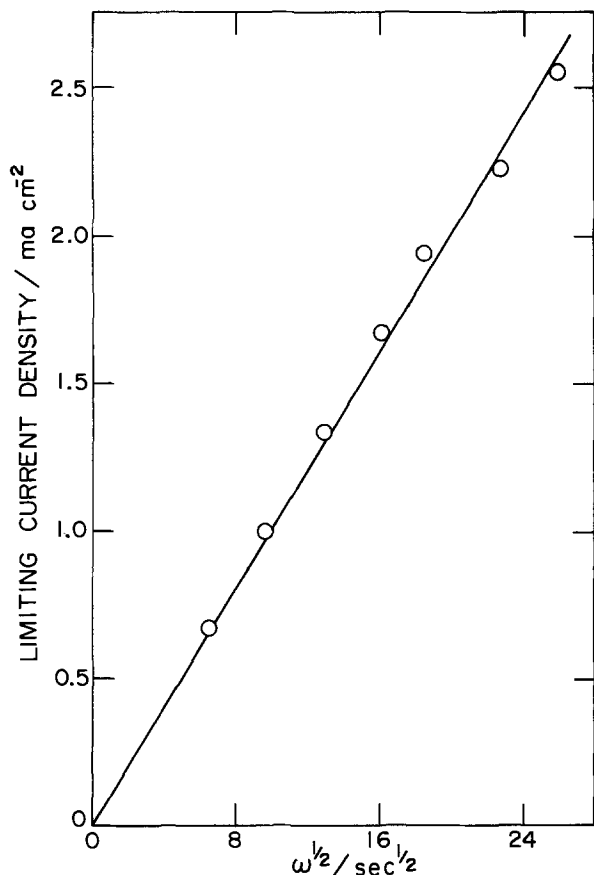


Fig. 7. Limiting current density as a function of the rotational speed using a rough silver rotating disk electrode under cathodic conditions for the redox system $\text{I}_3^- - \text{I}^-$.

evaporation onto optically polished Pyrex flats) display a substantial change, though much less than that predicted theoretically.

A plausible, though not entirely convincing, explanation of these results follows: If the surface is rough on a scale of the order of the hydrodynamic boundary layer thickness, then under rotation, the electrolyte lying in the valleys on the surface will be more or less stagnant compared with that in the vicinity of the peaks. Thus a hydrodynamic layer will be formed extending from the bulk of the solution up to a plane defined approximately by the positions of the peaks on the surface. Species diffusing up to the electrode to undergo electrochemical reaction will have to diffuse through this boundary layer before reacting at the mountain peaks. If this description is correct, then the roughness should not affect the diffusion kinetics significantly under these conditions, *i.e.*, the species diffusing up to the surface, *e.g.*, $\text{I}_3^- - \text{I}^-$ under cathodic conditions and $\text{Fe}^{+2} - \text{Fe}^{+3}$ under anodic conditions. If, on the other hand, the diffusing species are generated at the electrode surface and diffuse into the bulk of the solution, they must not only diffuse through the hydrodynamic boundary layer but also through a portion of the stagnant layer lying in the valleys. As the rotational speed will not alter the thickness of the stagnant layer, the rougher the surface, the less the effect of rotational speed on overpotential or current density as the case may be, in agreement with the data presented for the case of Ag electrodes (with varying roughness characteristics) in Fig. 8 and for the case of $\text{Fe}^{+3} - \text{Fe}^{+2}$ under anodic conditions.

Optical measurements.—The optical results for the silver oxide films consisted primarily of ellipsometric data. From these measurements the ellipsometric parameters Δ and ψ for the film free surface, and Δ and ψ for the oxide film covered surface were calculated at each wavelength (13). In order to determine the thick-

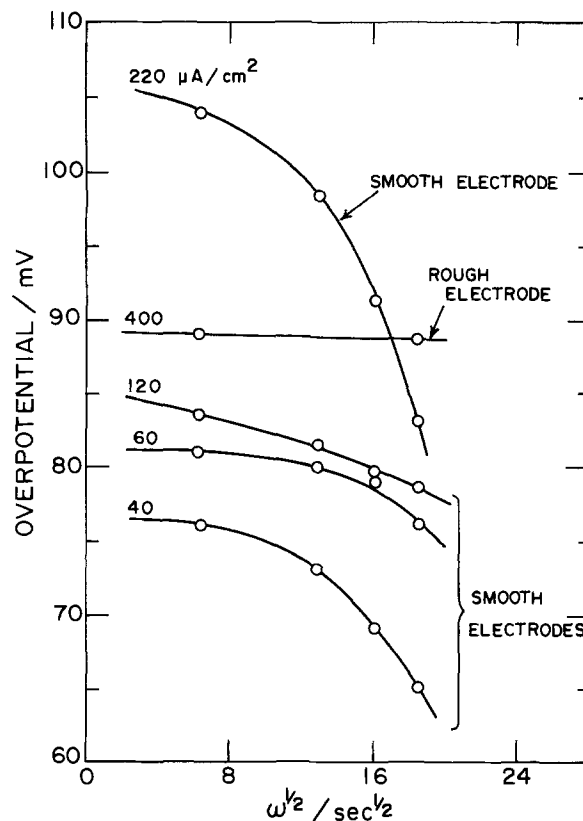


Fig. 8. Overpotential vs. rotational speed for both rough and smooth silver rotating disk electrodes under anodic conditions in Ag_2O saturated NaOH electrolyte solution.

ness and the spectrum of optical constants of the oxide film, we have used a procedure described elsewhere (14). The method involves the expansion of the complex dielectric constant of the film as a series of Lorentzian functions (15), the Lorentzian function parameters and the film thickness being chosen to minimize the variance (sum of the square differences between the measured and calculated values) of the optical measurements. Three Lorentzian functions were used in the expansion of the dielectric constant, so that a total of ten parameters was used to fit the experimental data for a range of trial film thickness values. For a typical case, the film thickness corresponding to the minimum variance 960Å, is to be compared with 1015Å, the thickness of the film determined by coulometric reduction (16) assuming bulk density and unit roughness factor. Figures 9 and 10 show the

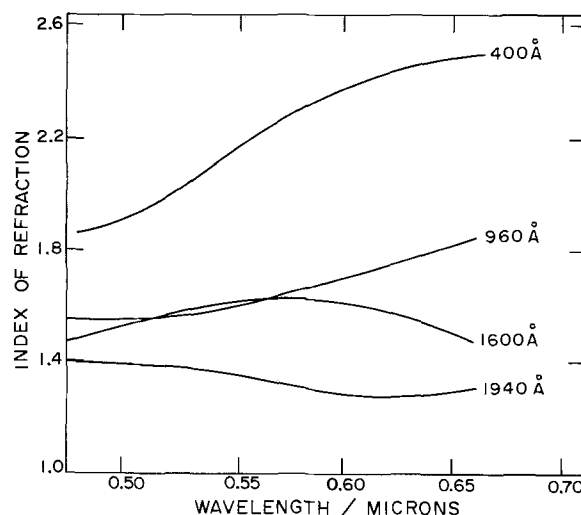


Fig. 9. Spectrum of refractive index for selected silver oxide films.

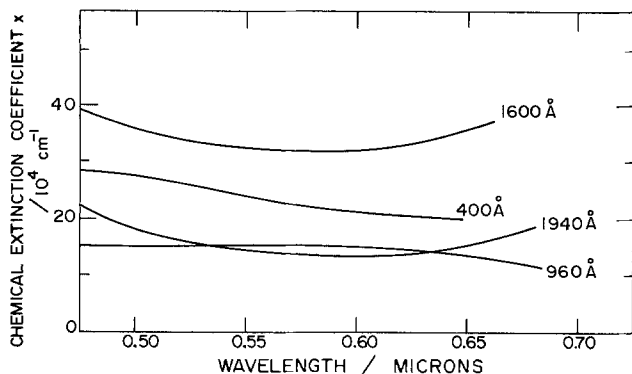


Fig. 10. Absorption spectrum for selected silver oxide films

resulting spectra of the refractive index and chemical extinction coefficient. The Ag_2O film exhibits broad absorption features, an indication of its semiconducting properties. In addition, the infrared and far infrared reflectance spectra of the Ag_2O film were found to agree with the transmission spectrum of chemically prepared Ag_2O , in its main features.

Electrical measurements.—The d-c current-voltage characteristics for a Ag_2O film formed at 0.2 mA cm^{-2} to a thickness of 450 Å is shown in Fig. 11. The results indicate ohmic behavior for silver biased with a positive voltage with specific resistivity ($\sim 3 \times 10^7 \text{ ohm-cm}$) being close to that for bulk Ag_2O (6). For silver biased with a negative voltage, however, the film appears to be blocking up to electrical breakdown. In contrast, the results for the oxide film formed at 0.017 mA cm^{-2} show almost perfect ohmic behavior for both positive and negative electrode bias and a much lower specific resistivity ($\sim 10^4 \text{ ohm-cm}$) (Fig. 12). An explanation for the very different electrical behavior of the films formed under high (0.2 mA cm^{-2}) and low

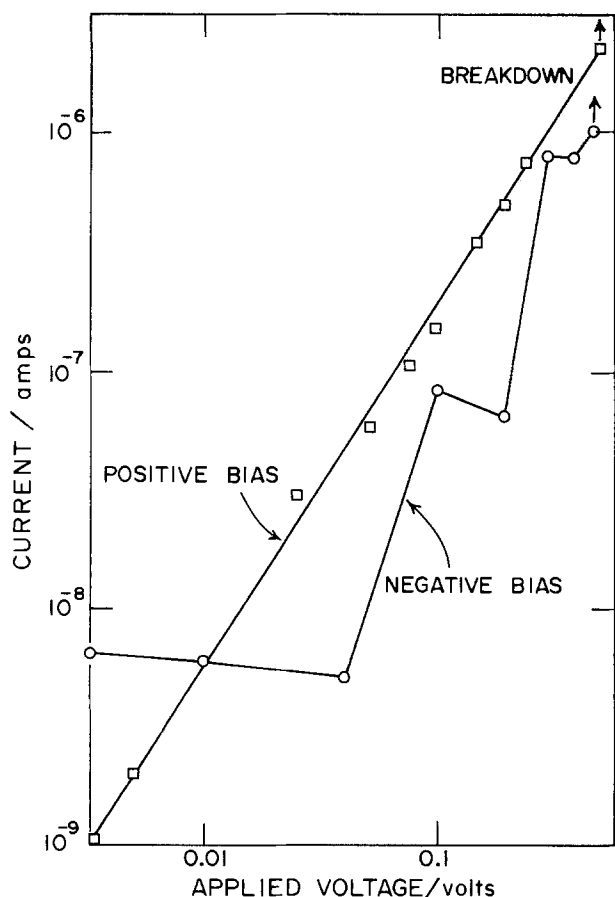


Fig. 11. Direct current-voltage curves for a 450 Å thick Ag_2O film formed at 0.2 mA cm^{-2} in $0.3N \text{ NaOH}$ solution.

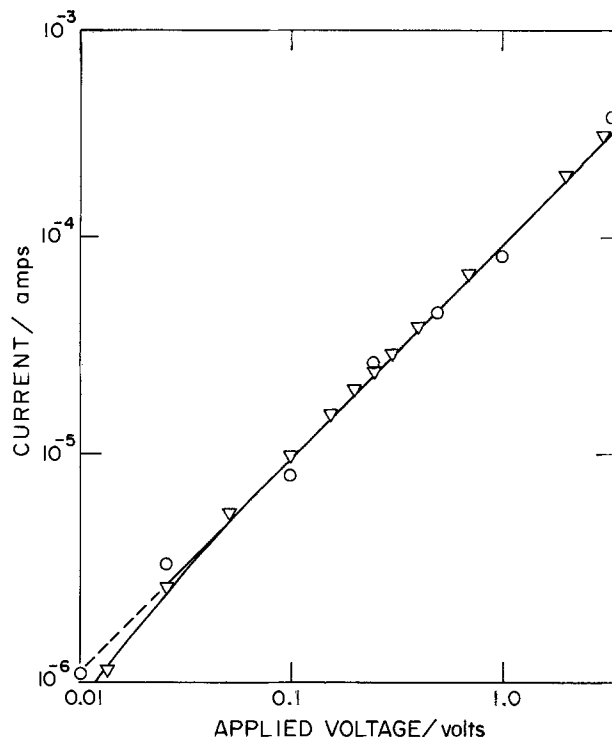


Fig. 12. Direct current-voltage characteristics for a Ag_2O 1260 Å film formed at a current density of 0.017 mA cm^{-2} in a $0.3N \text{ NaOH}$ solution.

(0.017 mA cm^{-2}) current densities follows: The two current densities used differ by a factor of ten, and thus in the case of the film grown under high current densities, a larger concentration gradient of the diffusing species exists in the film, remitting in its non-symmetrical electrical behavior, in contrast with the film grown under appreciably lower current densities. Further, the specific resistivity ($\sim 10^4 \text{ ohm-cm}$) is substantially below that accepted for Ag_2O powders. The capacitance-voltage characteristics for films formed at 0.2 mA cm^{-2} are displayed in Fig. 13. The lack of symmetry for positive and negative bias is indicative of asymmetry in the film itself. The thermoelectric power for films formed as above was found to be negative, a result expected for n-type semiconductors. To confirm the results the method was checked against both n- and p-type sections of silicon, in both cases the expected result being obtained. This is a surprising result as Ag_2O has generally been regarded as metal-deficient and hence p-type analogous to Cu_2O .

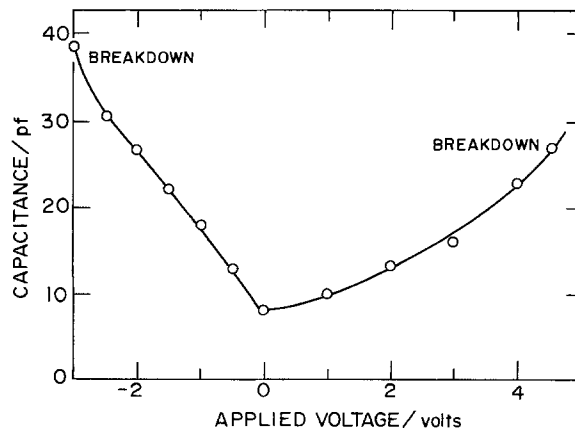


Fig. 13. Capacitance (1 MHz) vs. d-c polarizing voltage for the system $\text{Ag}/\text{anodic oxide}/\text{Al}$, the anodic oxide Ag_2O being 450 Å thick, formed at a current density of 0.2 mA cm^{-2} in $0.3N \text{ NaOH}$ solution.

We suggest that perhaps the n-type properties are conferred upon the film by the presence of colloidal silver.

Discussion

In this section we attempt to correlate some of the experimental observations in order to obtain an insight into the nature of the Ag/Ag₂O electrode.

A plot of current density i vs. $1/X_L$ (where X_L is the limiting film thickness) was clearly nonlinear, but a plot of the form i vs. $1/(X_L - A)$ (where A is a constant) produced an excellent straight line (Fig. 14). In this plot, the intercept has been set equal to zero and the optimum value of A was found by a least squares procedure to be 695Å. This suggests that diffusion within the film determines the limiting film thickness, though the presence of the constant A does pose a problem. It is possible that it arises due again to surface roughness.

Since current efficiency was found to be independent of film thickness, one is led to the conclusion that the pathways for Ag₂O film formation and metal dissolution share a common step in transport through the film, and differ only in the reaction path at the film solution interface. The most obvious mechanism which satisfies this condition is one in which film formation occurs entirely by a dissolution precipitation mechanism. The relevant equations for such a mechanism, when it is further assumed that the rate-controlling step for film growth is the nucleation of step sites on the oxide film, take the following form (17)

$$i_s = i_s^0 [e^{\eta_0/V_s} - 1] \quad [2]$$

and

$$i_f = i_f^0 e^{\eta_0/V_s} e^{-V_f/\eta_0} \quad [3]$$

where i_f is the current density associated with film formation, i_s is the current density for metal dissolution, η_0 is the overpotential, $V_s = kT/e$ (k being the Boltzmann constant, T the absolute temperature, and e the electronic charge), $V_f = \pi\rho^2 a/kTe$ (ρ being the step free energy per unit length and a is the area per molecule in the oxide surface), i_s^0 is a constant (equal to $DFCo/\delta$, where D is the diffusion coefficient for the dissolved ionic silver species, Co is the bulk concentration, and δ is the diffusion layer thickness), and i_f^0 is a constant which contains the preexponential factor for step site nucleation. The total current density, made up of i_s and i_f defined in terms of Eq. [2] and [3], was fitted to the measured current efficiency and overpotential, using an optimization procedure (18) involving

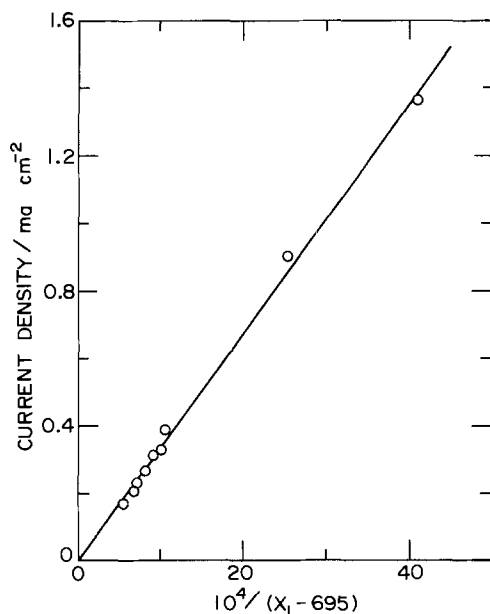


Fig. 14. Plot of current density vs. $1/(X_L - A)$, where X_L is the limiting film thickness and A is a constant (695Å).

a three parameter fit (i_s^0 , i_f^0 , and V_f). Figures 15 and 16 show the fit of the current efficiency and the overpotential, respectively. The fit for the current efficiency vs. current density is extremely good, that for the overpotential within experimental scatter. The scatter in the overpotential arises in part from the fact that the experimental points represent different electrodes, leading to at least a 10 mV uncertainty in the overpotentials. From the value of i_s^0 , and assuming a value for the diffusion constant of 10^{-5} cm² sec⁻¹, the diffusion layer thickness was calculated to be 0.008 cm in good agreement with that predicted under stirred conditions (19). From the value for the film crystallization parameter, V_f , the step free energy per unit length was calculated to be 4.4×10^{-6} ergs·cm⁻¹ in good agreement with the value quoted for a standard situation involving nucleation of steps on the surface (17). Further, the surface free energy per square centimeter, σ , is related to ρ through the approximate equation

$$\sigma \approx \rho/r \quad [4]$$

where r is the step height in centimeters and ρ is the step free energy per unit length. Taking r to be the unit cell length, σ is calculated to be 120 ergs·cm⁻², a value which closely matches that for ionic crystals (20).

In conclusion we suggest a mechanism for the Ag₂O film formation under stirred conditions, involving dis-

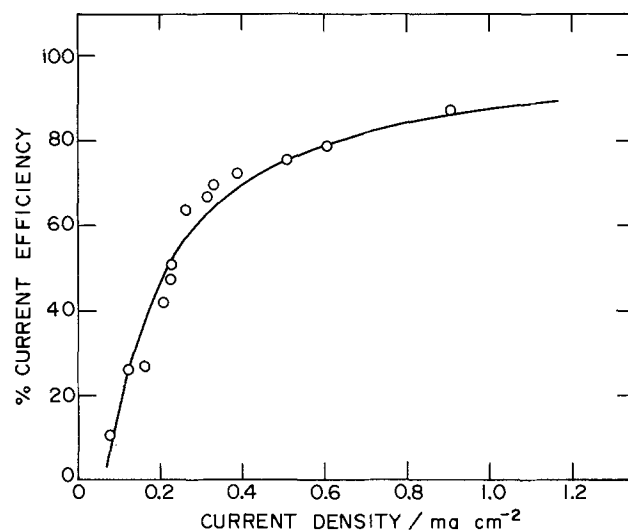


Fig. 15. Theoretical fit of the current efficiency vs. current density for Ag₂O film formation (solid line, theoretically generated; circles, experimental points).

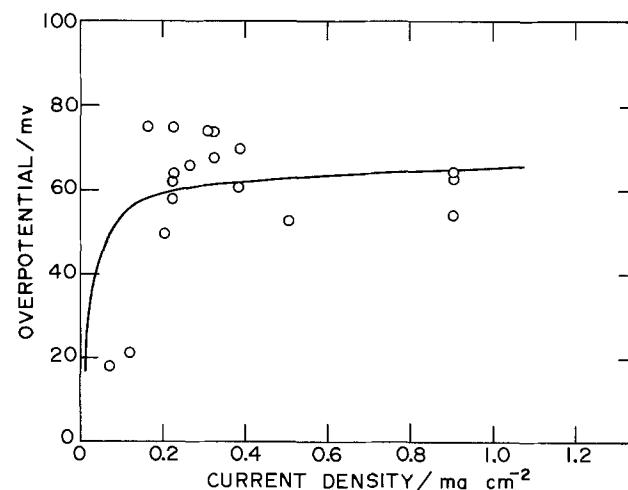


Fig. 16. Theoretical fit for the overpotential vs. current density for Ag₂O film formation (solid line, theoretically generated; circles, experimental points).

solution of silver followed by precipitation, the rate of which is controlled by the formation of steps on the oxide surface. We point out the difficulties involved with surface roughness in interpreting diffusion layer kinetics, difficulties which led to the previous erroneous interpretation of the kinetics as arising from two mechanisms for film formation. The electrical properties point to the interesting semiconducting nature of these oxide films, grown under the stated conditions, with the optical properties being consistent with those of an electronic conducting material.

Acknowledgment

The authors are grateful to the Defence Research Board of Canada for supporting this research.

Manuscript submitted Oct. 28, 1974; revised manuscript received Jan. 22, 1975.

Any discussion of this paper will appear in a Discussion Section to be published in the June 1976 JOURNAL. All discussions for the June 1976 Discussion Section should be submitted by Feb. 1, 1976.

Publication costs of this article were partially assisted by the Defence Research Board of Canada.

REFERENCES

1. T. P. Dirske, *This Journal*, **106**, 453 (1959).
2. G. H. Fraser, Ph.D. Thesis, University of Toronto (1964).
3. B. D. Cahn, J. B. Ockerman, R. F. Amlie, and P. Rüetschi, *This Journal*, **107**, 725 (1960).
4. J. P. Hoare, "The Electrochemistry of Oxygen," p. 219, Interscience Publishers, New York (1968).
5. M. J. Dignam, H. M. Barrett, and G. D. Nagy, *Can. J. Chem.*, **47**, 4253 (1969).
6. J. A. Allen, in "Proc. First Australian Conference on Electrochemistry," p. 72, Pergamon Press, London (1965).
7. J. A. McMillan, *Chem. Rev.*, **62**, 65 (1962).
8. L. Meites, "Polarographic Techniques," p. 89, Interscience Publishers, New York (1965).
9. A. C. Riddiford, in "Advances in Electrochemistry and Electrochemical Engineering," P. Delahay, Editor, Vol. 3, Interscience Publishers, New York (1966).
10. F. Sullivan and E. H. Newton, *This Journal*, **107**, 886 (1960).
11. J. R. Beattie, *Phil. Mag.*, **46**, 236 (1955).
12. V. G. Levich, "Physicochemical Hydrodynamics," 2nd Ed., Physics Math Publication, Moscow (1959).
13. M. J. Dignam and M. Moskovits, *Appl. Opt.*, **9**, 1868 (1970).
14. J. Roth, B. Rao, and M. J. Dignam, *J. Chem. Soc., Faraday II*, **71**, 86 (1975).
15. H. Verleur, *J. Opt. Soc. Am.*, **48**, 1356 (1958).
16. J. O'M. Bockris and A. K. N. Reddy, "Modern Electrochemistry," Plenum Press, New York (1970).
17. K. J. Vetter, "Electrochemical Kinetics," pp. 317-325, Academic Press, New York (1967).
18. M. J. D. Powell, *Comp. J.*, **7**, 155 (1964).
19. L. L. Bircumshaw and A. C. Riddiford, *Quart. Rev. (London)*, **6**, 157 (1952).
20. W. E. Garner, "Chemistry of the Solid State," p. 175, Butterworths, London (1955).

The Anodic Oxidation of Hydrogen on Platinized Tungsten Oxides

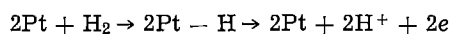
III. Mechanism of H₂ Oxidation on Platinized Lower Tungsten Oxide Electrodes

B. S. Hobbs and A. C. C. Tseung

Department of Chemistry, The City University, London EC1V 4PB, England

ABSTRACT

The anodic oxidation of hydrogen at platinized electrodes of the lower tungsten oxides (WO_y, where 2 < y < 3) occurs via a route involving hydrogen tungsten bronze formation on the surface of WO₃ film



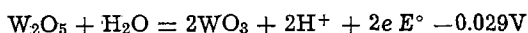
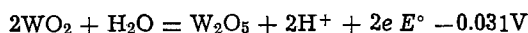
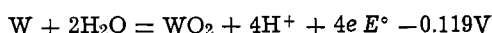
Initial performance of the platinized lower tungsten oxide electrodes is lower than the corresponding WO₃ electrodes. However, their performance improves with time as the surface is converted to WO₃ rich layers until a limiting thickness is reached. The bulk of the lower tungsten oxide is then protected from further oxidation and does not participate in the over-all electrode reaction. It does, however, provide a conducting pathway to the current collector, even under flooded hydrogen-starved conditions, thus ensuring long-term stability in performance as compared with platinized WO₃ electrodes.

The anodic oxidation of hydrogen at platinized WO₃ electrodes occurs by a synergistic mechanism involving predissociation of molecular hydrogen on the platinum, followed by migration of H atoms into the WO₃ lattice to form hydrogen tungsten bronzes (H_xWO₃). These "bronzes" subsequently undergo electrochemical oxidation (1, 2). This paper is concerned with hydrogen electrode reactions on platinized mixtures of the lower

tungsten oxides, WO_y, where 2 < y < 3. There is a prolific number of these oxides quoted in the literature, but from a crystallographic standpoint only three stable compounds exist: β-oxide (W₂₀O₅₃), γ-oxide (W₁₈O₄₉), and δ-oxide (WO₂) (3-5). All other compounds are either metastable or consist of mixtures and solid solutions of these three phases and α-oxide (WO₃). The lower tungsten oxides are nonstoichiometric n-type semiconductors with electrical resistivities decreasing from about 1 ohm-cm for WO₂ to a minimum of 0.1

Key words: electrocatalysis, H₂ oxidation, lower tungsten oxides, stability.

ohm-cm for $WO_{2.75}$, then rising sharply to 2×10^5 ohm-cm as the composition tends to WO_3 . Colors depend on stoichiometry and particle size, but normally vary from brown WO_2 through red-violet $W_{18}O_{49}$ to blue $W_{20}O_{58}$. These oxides are insoluble in acid solutions due to the formation of a protective WO_3 film, their standard potentials being below hydrogen (6). The electrochemical literature (6) quotes standard potential values for W_2O_5 and does not apparently consider the true phases, $W_{18}O_{49}$ and $W_{20}O_{58}$. Three distinct equilibria are identified



It is very likely that true equilibrium is not obtained in electrochemical systems and that the W_2O_5 phase represents a metastable oxidation state. Whatever the nature of the oxides, it is recognized that tungsten electrodes in contact with water progressively oxidize at the surface in a stepwise manner, eventually forming a WO_3 outer layer (7-9). The thickness of this layer increases with anodic polarization, but the crystalline bulk remains essentially unchanged.

In view of the close crystallographic relationship between WO_3 and the lower tungsten oxides and the possible existence of a WO_3 surface film, it is likely that a similar synergic mechanism for hydrogen oxidation exists with Pt/WO_y as for Pt/WO_3 . Two reaction pathways are possible with the lower oxides: (i) Migrating H atoms from the Pt form bronzes of the type H_xWO_y which then undergo anodic oxidation as for H_xWO_3 . (ii) Bronze formation is restricted to the surface layers of WO_3 to give H_xWO_3 , with the WO_y crystallite bulk merely acting as a conducting support.

The following investigations were carried out to establish the mechanism of H_2 oxidation at platinized lower tungsten oxide electrodes, using the techniques developed for Pt/WO_3 (1, 2).

Experimental

Preparation and analysis of lower tungsten oxides.— WO_3 impregnated with 0.8% by weight Pt (1) was heated in a stream of hydrogen at 300°C for 2 hr and cooled to room temperature before admitting air. The product, a blue powder, was identified by x-ray diffraction and thermogravimetric oxidation in air. No further reduction of the oxide occurred on prolonged heating under the conditions of temperature, hydrogen pressure, and flow rate. The reduced powder was used for composition studies in hydrogenated slurries with 5N H_2SO_4 as described for WO_3 , using x-ray diffraction and chemical analysis (1).

Electrode preparation and testing.—A series of platinized WO_3 hydrophobic electrodes were prepared with varying platinum loadings between 0.100 and 0.007 mg cm^{-2} . Preparation of electrodes having similar physical structures and platinum crystallite morphology, but varying widely in their Pt loadings, has been described (2). Tungsten oxide loadings were 10 mg/ cm^2 . Electrodes were tested in a "floating electrode cell" after converting the WO_3 to lower tungsten oxides by heating the electrodes at 300°C in H_2 as above. The electrolyte was 5N H_2SO_4 at 25°C. The purification of materials for these tests is described in Ref. (1) and (2).

Polarization curves were measured under 1 atm of flowing H_2 . Background corrosion currents were also measured by replacing the H_2 with white spot N_2 . The reduced oxides gave higher initial corrosion currents than Pt/WO_3 electrodes, ca. 1 mA/ cm^2 maximum between 0-600 mV vs. RHE, compared to 0.1 mA/ cm^2 for Pt/WO_3 . These currents, however, decreased to the Pt/WO_3 level after an hour or so and must have included contributions from the conversion of immediate surface layers to WO_3 .

Results and Discussion

Composition of tungsten oxide electrocatalyst.—The reduced WO_3 was a blue powder, stable in air at room temperature, and unaffected by boiling acidic dichromate solution. On heating in air at 400°C, it reverted to a pale yellow solid identified by x-ray diffraction as WO_3 . From weighings before and after thermal oxidation, an empirical formula of $WO_{2.87(\pm 0.02)}$ was calculated which approximates to the phase $W_{20}O_{58}$. The x-ray pattern exhibited marked line broadening, rendering identification difficult. Subsequent BET measurements confirmed a decrease in average particle size from 0.11 to 0.10 μm during the reduction.

A slurry of the reduced platinized oxide in 5N H_2SO_4 absorbed 0.22 moles hydrogen per mole oxide. This product was easily reoxidized to $WO_{2.87}$ by warm air and acidified dichromate solution. X-ray diffraction patterns of the hydrogenated product were identical to the original $WO_{2.87}$, although line broadening made accurate measurements impossible.

A coarser sample of WO_3 used as the starting material had better x-ray line definition. The H_2 -reduced product had an empirical formula of $WO_{2.84}$, in fair agreement with the finer material. The x-ray pattern was complex and not characteristic of any one tungsten oxide phase. It probably consisted of solid solutions of lower tungsten oxides, and none of the strong WO_3 lines were present. The hydrogen uptake of this powder in 5N H_2SO_4 slurries was only 0.09 moles per mole oxide, i.e., half the finer material, and no change was detected in the x-ray pattern.

From BET surface area measurements, it was estimated that the amount of H_2 absorbed by both fine and coarse powders was considerably more than that required for monolayer coverage, indicating migration into the bulk of the crystallites. But the absence of a measurable change in diffraction pattern after hydrogenation supports the hypothesis that bronze formation is confined to immediate, oxidized surface layers of WO_3 which are not detectable and that the existence of lower oxide bronzes is doubtful.

Anodic oxidation of hydrogen.—The electrochemical behavior of the lower tungsten oxide electrodes differed from WO_3 electrodes with regard to the long term stability of electrode performance. Table I compares typical long-term characteristics of WO_3 and lower oxide electrodes. The reduced oxide electrodes underwent improvement with time and eventually achieved a steady performance after a few days. The performance of WO_3 electrodes, however, progressively decayed with time.

The stabilized performances of lower tungsten oxide hydrogen electrodes were very high and comparable with initial performances of WO_3 electrodes (Fig. 1). Thus a synergic mechanism is indicated.

The participation of the tungsten oxide in the electrode reaction may be confirmed as for WO_3 (2) by measuring the performances of a series of electrodes having similar catalyst morphologies and electrode structures, but varying in their Pt loadings. A plot of performance against Pt loading, for these electrodes is characteristic of an "active" support (Fig. 2). This plot is also characteristic of Pt/WO_3 electrodes in hav-

Table I. Typical life characteristics of platinized WO_3 and lower tungsten oxide electrodes

5N H_2SO_4 , 1 atm H_2 , iR free overvoltage
100 mV Pt loadings 0.1 mg/ cm^2 , 25°C

	Tungsten trioxide WO_3 current density (mA/ cm^2)	Lower tungsten oxide WO_y current density (mA/ cm^2)
Initial	480	125
2nd day	200	300
3rd day	110	350
4th day	—	360
5th day	—	360
6th day	—	380

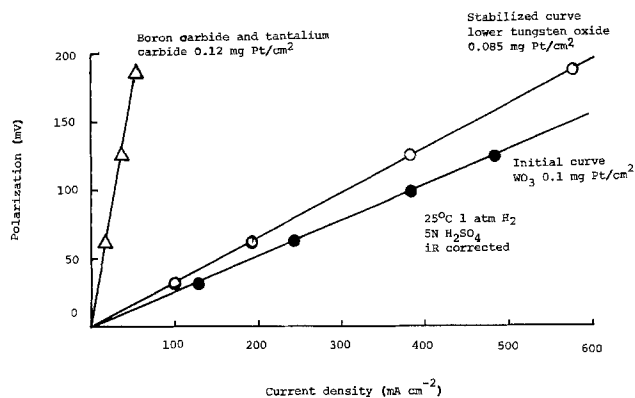


Fig. 1. Polarization for various platinumized substrates

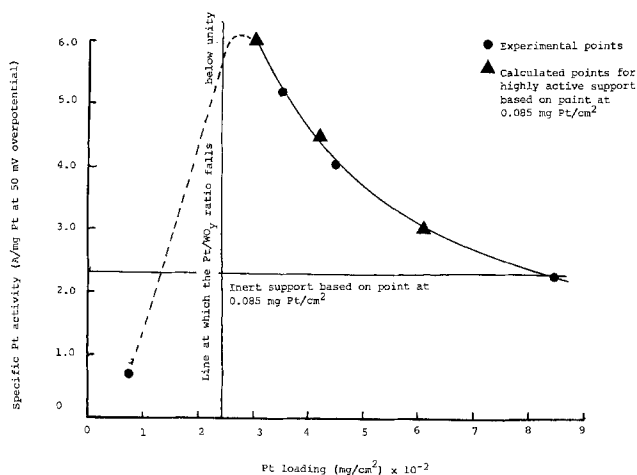


Fig. 2. Variation of specific Pt activity with Pt loading on lower tungsten oxide support.

ing a cutoff point at which the ratio of WO_3 to Pt particles falls below unity (2).

These results do not differentiate between the two possible reaction pathways for the lower tungsten oxide supports. A deeper insight into the exact mechanism is provided by considering further the performance/time variations exhibited by tungsten oxide electrodes.

The attainment of a stable performance with lower tungsten oxide electrodes was achieved within several hours by subjecting them to anodic pretreatments. The most convenient method of anodic treatment was to leave the electrodes at open circuit with oxygen fed to the gas compartment. Optimum performances were achieved in about 3 hr with this treatment (Fig. 3). Oxygen evolution also speeds the attainment of a stable performance, but the gassing had deleterious

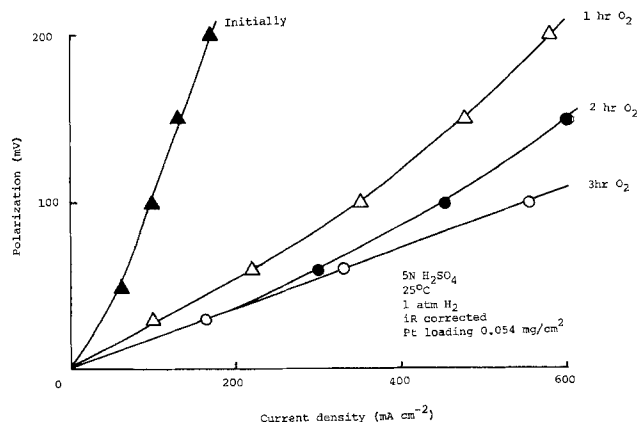


Fig. 3. Effect of O_2 treatment at 0°C V on a lower tungsten oxide electrode performance.

effects on the electrode structures and final performances were lower.

This behavior supports the findings of the compositional studies that WO_3 and its bronzes are the "active" agents in platinumized tungsten oxide hydrogen electrodes. The anodic treatment would result in faster growth of the WO_3 film with corresponding improvements in performance. Optimum performance would then correspond to the stage at which the WO_3 film reached the limiting thickness controlled by the oxidation conditions. The possibility of the increased performance being due to anodic oxidation of impurities can be dismissed since no improvement in performance was observed when similar pretreatments were carried out on platinumized electrodes of WO_3 , boron carbide, or tantalum carbide.

The progressive decay in Pt/WO_3 electrode performance requires an explanation. Several possibilities exist:

(i) Poisoning by impurity adsorption on the Pt can be discounted since it should apply equally to lower oxide electrodes and other substrates studied, i.e., B_4C and TaC.

(ii) WO_3 has a slight solubility in sulfuric acid solution (6), forming tungstate ions which may discharge onto and poison the Pt surfaces. A similar effect has been reported by Radovici and Totir with MoO_3 substrates in acid media (10). However, the effect should equally apply to the lower oxide electrodes which form WO_3 layers on anodic treatment. Performance of hydrogen cured electrodes was also unaffected when left in contact for several days with an electrolyte presaturated with WO_3 .

(iii) The aqueous PTFE dispersion used to wet-proof the electrodes (2) contains a surfactant to stabilize the suspension. It is possible that a higher proportion of this material remained in the WO_3 electrodes, which were cured in static air at 300°C (2), than in the lower oxide electrodes cured in flowing H_2 at the same temperature. The hydrophobicity of the WO_3 electrodes would therefore be lower and render them more susceptible to "flooding" with electrolyte, producing a higher degree of gas mass transfer polarization. However, a WO_3 electrode cured in flowing nitrogen had exactly the same decay pattern as those cured in static air.

A "spent" WO_3 electrode was regenerated, almost to its original performance, by washing in distilled water and drying in static air at 300°C (Fig. 4). Continued operation of the electrode resulted in more rapid loss of performance, and successive "resuscitations" became less effective; after the third cycle, performance after resuscitation was actually worse. The reasons for this behavior could be many, thus steam may be forming in the catalyst pores causing disruption of the elec-

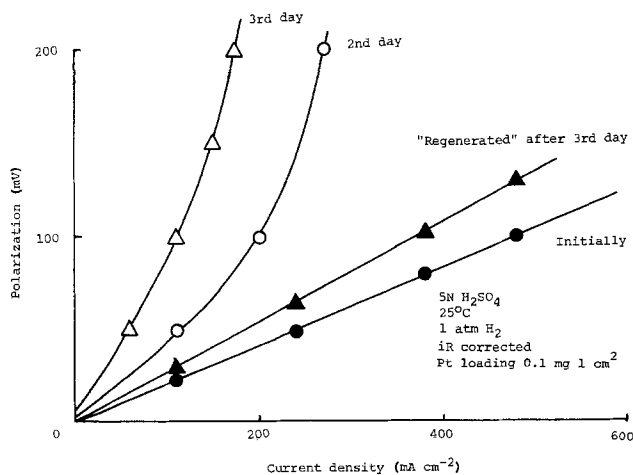


Fig. 4. Pt/WO_3 electrode performance decay and effect of first regeneration after third day.

trode structure, sintering may be reducing the activity of the components, etc. Nevertheless, it is clear that flooding is a major cause of performance decay in WO_3 electrodes. There is no reason to suspect that the lower tungsten oxide electrodes were any more resistant to flooding. The explanation of their improved long-term performance characteristics must therefore lie with their ability to cope under flooded conditions.

The lower tungsten oxides are more resistant to oxidation of their crystalline bulk than tungsten bronzes of the type H_xWO_3 . Thus the blue oxides prepared in this work were unaffected by air or boiling dichromate solution, whereas the hydrogen bronzes revert rapidly and completely to WO_3 in either of these conditions (1). Similar effects were noted during anodic polarization under nitrogen. In a flooded catalyst aggregate, the bronze oxidation rate may exceed the hydrogen supply and the value of x in the H_xWO_3 will diminish with a corresponding reduction in conductivity. With WO_3 electrodes, oxidation can penetrate deeply in the crystallite bulk causing severe ohmic polarization of the electrode. The lower oxides, however, are more resistant to bulk oxidation which does not proceed beyond the layer formed during anodic pretreatment. Although the flooded portion of the catalyst aggregate is subject to a degree of gas concentration polarization, the electrical conductivity of the electrodes is not so markedly reduced.

Acknowledgments

This work has been carried out with the support of Procurement Executive, Ministry of Defense.

Manuscript submitted Jan 6, 1975; revised manuscript received May 16, 1975.

Any discussion of this paper will appear in a Discussion Section to be published in the June 1976 JOURNAL. All discussions for the June 1976 Discussion Section should be submitted by Feb. 1, 1976.

REFERENCES

1. B. S. Hobbs and A. C. C. Tseung, *This Journal*, **119**, 580 (1972).
2. B. S. Hobbs and A. C. C. Tseung, *ibid.*, **120**, 766 (1973).
3. K. C. Li and C. Y. Wang, "Tungsten," Reinhold Press (1955).
4. A. E. Vol, in "Handbook of Binary Metallic Systems," N. V. Ageer, Editor, p. 727, Israel Program Sci. Trans. (1966).
5. A. D. Wadsley, in "Nonstoichiometric Compounds," L. Mandelcorn, Editor, Academic Press, Inc., New York (1964).
6. M. Pourbaix, "Atlas of Electrochemical Equilibria in Aqueous Solutions," p. 280, Pergamon Press, Inc., Elmsford, New York (1966).
7. S. E. S. Wakkad, H. A. Rizk, and I. G. Ebaid, *J. Phys. Chem.*, **59**, 1004 (1955).
8. V. S. Bagotsky and S. A. Jofa, *Compt. Rend. Acad. Bulgare Sci.*, **53**, 5, 439 (1946).
9. N. R. Stalica, Ph.D. Thesis, University of Pennsylvania, Philadelphia, Pa. (1964).
10. O. Radovici and N. Totir, *Rev. Roumaine Chimie*, **12**, 10, 119 (1967).

A Rutherford Scattering Study of Catalyst Systems for Electroless Cu Plating

I. Surface Chemistry of Mixed Pd, Sn Colloids

Ronald L. Meek*

Bell Laboratories, Murray Hill, New Jersey 07974

ABSTRACT

Rutherford ion backscattering has been used to obtain quantitative data on the surface concentration of Pd and Sn on substrates catalyzed with Pd-Sn colloid solutions. The alteration of these catalyzed substrates due to subsequent processing solutions, *i.e.*, the accelerator and electroless Cu bath, was also examined. The early stage of catalyst deposition saturates at a few monolayers of particles. The Pd/Sn ratio at this stage is $\lesssim 1$. The accelerator solution partially removes extraneous Sn and leaves a final average Pd surface coverage of $2-4(10)^{15}$ atom cm^{-2} independent of initial value. The Pd/Sn ratio at this stage is ~ 3 . The Pd/Sn ratio in the catalyst core particle on which Cu deposition takes place is ~ 6 . Sn lost into the electroless Cu bath is codeposited on subsequent samples.

Electroless copper plating of insulating substrates is widely used in printed circuit and decorative plating technology. Sensitization of the substrate, usually with Pd-Sn catalyst solutions, is required to provide catalytic sites for initiation of the autocatalytic electroless plating reaction (1). At present, very little useful quantitative data is available characterizing the behavior of these catalyst systems.

In the past, catalysis has been accomplished by sensitization in SnCl_2 solutions followed by activation in PdCl_2 solutions but, in recent years this process has been somewhat supplanted by the use of mixed Pd-Sn colloids. This paper will be concerned only with the

Pd-Sn colloidal solutions and the process utilizing separate sensitization and activation will be examined separately (2).

Recent publications (3, 4) have questioned the colloidal nature of the solutions of interest. However, the experiments of Cohen and West (5, 6) indicate their colloidal nature, and, insofar as possible, the present results will be interpreted in terms of their model which is based on Mössbauer spectroscopy results. In a separate paper (7), we will combine results obtained by Rutherford backscattering, transmission electron microscopy, and Mössbauer spectroscopy, as well as discuss apparent disagreements with other published results. Suffice it to say here that when experimental methods, which have the inherent capability of re-

* Electrochemical Society Active Member.

Key words: catalysis, electroless plating, Pd-Sn colloids, printed circuit processing.

vealing colloidal particles in the $\sim 20\text{\AA}$ size range, are applied, the colloidal nature of the catalyst is revealed.

The purpose of the present study is to obtain quantitative information on the amount of Pd and Sn present on catalyzed surfaces and to examine the interaction of these catalyzed surfaces with the solutions used in subsequent process steps.

Experimental Details

Solution preparation.—In order to insure relevance to real life production situations, the catalysts used were prepared from commercial concentrates. The S catalyst solution was prepared by mixing 33 ml H_2O , 33 ml conc (37%) HCl, and 33 ml Shipley 9F conc.¹ The M solution was made up by mixing 55 ml H_2O , 20 ml conc HCl, and 25 ml MacDermid 9070 concentrate.² As prepared, the S solution contains 0.38 g/liter Pd and the equivalent of 33 g/liter Sn^{++} as $\text{SnCl}_2 \cdot 2\text{H}_2\text{O}$, while the M solution contains 0.29 g/liter Pd and 13 g/liter Sn^{++} . Pd was determined spectrophotometrically and Sn^{++} via titration.

Substrate catalysis is followed by immersion in an accelerator solution such as dilute fluoroboric acid. The accelerator used in the present work was prepared by mixing 5 H_2O to 1 Shipley 19 accelerator concentrate.

The early stage of electroless Cu plating on the various catalyzed substrates was studied using the MacDermid 9072 D bath with mechanical agitation at room temperature. In all cases, fresh solutions were prepared immediately before use and kept in clean polyethylene containers. Each step, catalysis, acceleration, and plating, is normally followed by a rinse. In this work a standard rinse of 30 sec in DI water was selected and the results were established to be independent of rinse time for times greater than 15 sec.

Substrates were prepared for analysis by immersing 1 cm^2 samples in 100 cm^3 of the appropriate solution, or series of solutions, with gentle stirring. They were then carefully dried by placing the sample edge on filter paper and immediately (within 15 min) examined. Substrate selection and the surface analytical technique are discussed in the following subsection.

Rutherford ion scattering.—Backscattering of high energy (2 MeV) He^+ ions has been fruitfully applied to a number of problems in surface, interface, and thin-film analysis (8, 9). Details of the technique as

used by the author may be found elsewhere (10). Through conservation of energy and momentum, the energy of a backscattered ion yields the mass of the atom from which it scattered. Through the well-established Rutherford scattering cross section, the number of backscattered ions yields the number of scattering atoms. Thus, the technique qualitatively and quantitatively identifies the nature of the surface and near-surface layers.

It should be emphasized that the Rutherford scattering event takes place between nuclei well inside the innermost electron shell so that the information obtained is independent of the chemical state of the atoms. That is, essentially one identifies and counts the number of atomic nuclei. Depth information may be obtained due to the fact that an ion scattered from an atom of given mass at some depth into the substrate will possess a lower energy than will an ion scattered from an identical atom at the surface of the substrate due to the inelastic (electronic stopping) energy loss as the ion enters into and exits from the material.

Cleaved graphite substrates ($\sim 1 \text{ cm}^2$) were chosen for the present study.³ A scattered ion spectrum from a control (untreated) substrate is shown in Fig. 1. The low mass of C eliminates substrate interference and, furthermore, graphite may be obtained in a very pure form. By using a freshly cleaved surface, unwanted surface impurities can be minimized. The surface peaks in Fig. 1 correspond to O [$5(10)^{14}$ atoms cm^{-2}] and P and Si ($\sim 10^{14}$ cm^{-2}).

A typical spectrum from a surface layer produced by immersion in a catalyst solution and rinsing is shown in Fig. 2. Here O [$3(10)^{15}$ cm^{-2}], Cl (10^{15} cm^{-2}), Pd [$3(10)^{15}$ cm^{-2}], and Sn [$3.5(10)^{15}$ cm^{-2}] can be clearly seen. Results with other substrates, e.g., epoxy-glass composites, were found to be roughly equivalent when the real to apparent surface area ratio is taken into account.

The substrate area examined by the ion beam is 0.78 mm^2 . The statistical counting error in a given measurement is typically 3% for heavy mass impurities (Cu, Pd, Sn) and 10% for light masses (O, Cl). During the experiments it became apparent that significant differences (a factor of two) can exist from point to point on a given substrate. Thus 3-5 separate measurements were made at randomly selected points on a given sample. Throughout this paper, bars on data points indicate the point to point variation found, not

¹ Shipley Company, Newton, Massachusetts.

² MacDermid, Incorporated, Waterbury, Connecticut.

³ UCAR graphite, Union Carbide Corporation, New York.

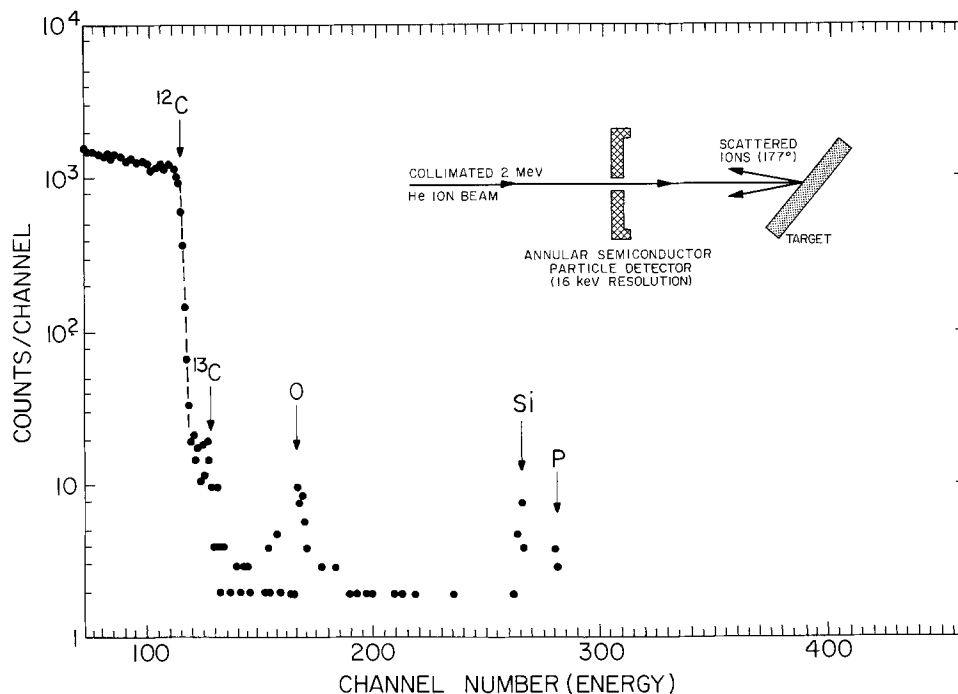


Fig. 1. Scattered ion spectrum (scattered ion yield as counts per channel vs. scattered ion energy as channel number) from graphite control substrate. The inset shows schematically the typical experimental arrangement.

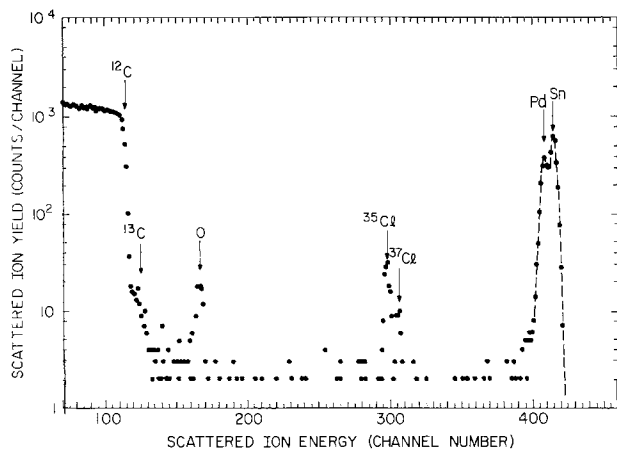


Fig. 2. Scattered ion spectrum from sample treated for 60 sec with S catalyst and rinsed.

an error bar. Of course, surface concentration variations on a smaller scale, smaller than the beam spot size, may be even greater. Two or more samples treated in the same way gave equivalent results within the point to point variations just mentioned.

Results and Discussion

Catalyst.—Figure 3 shows Pd and Sn surface concentration vs. time in the S catalyst solution. In the early stages ($t \lesssim 100$ sec) the Pd or Sn increases roughly as the square root of time, but begins to saturate at about $5(10)^{15}$ Pd cm^{-2} and $8(10)^{15}$ Sn cm^{-2} . Note that not only is there a significant point to point variation in the Pd and Sn concentration, but also there is a considerable variation in the observed Pd/Sn ratio. Figure 4 shows similar data for the M solution. In this case the Pd and Sn values at a given time are

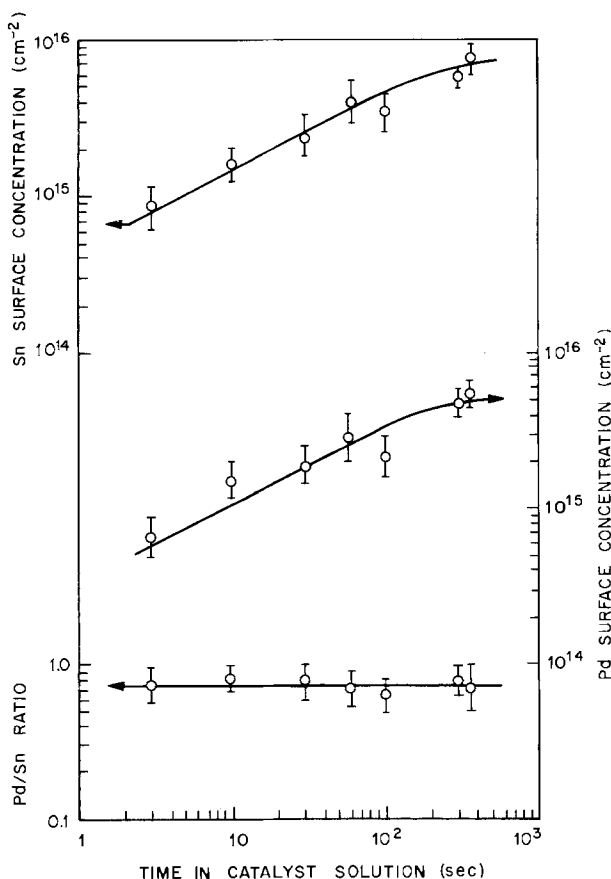


Fig. 3. Pd and Sn surface concentration vs. immersion time in S catalyst solution.

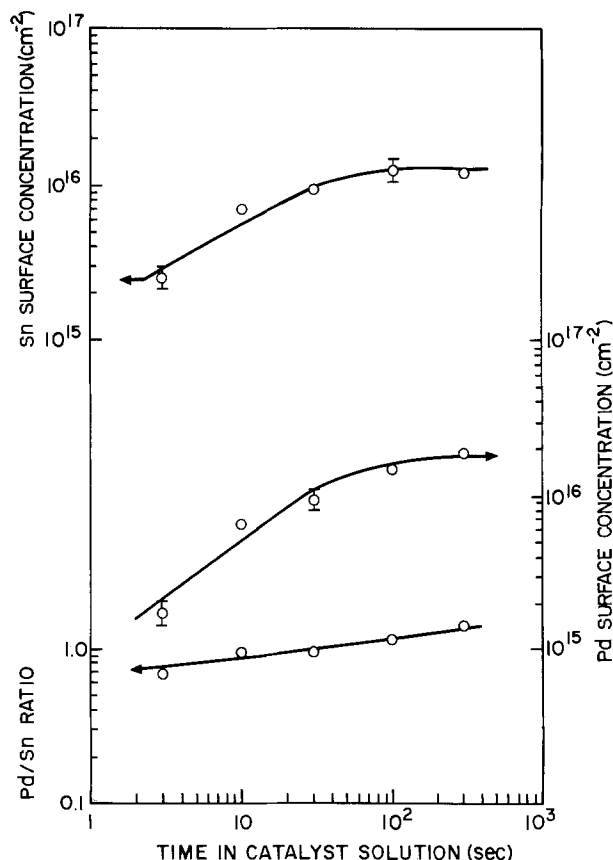


Fig. 4. Pd and Sn surface concentration vs. immersion time in M catalyst solution.

larger than for the S solution and there is considerably less point to point spread.

The Cl and O surface concentrations were also determined. The O/Sn ratio is essentially unity while the Cl/Sn ratio is about 0.3.

It will be convenient to discuss the results of this study in terms of adsorption of colloidal, Pd-containing catalyst particles. Because of the large excess of Sn present in the solutions, adsorption of other species may also be important and, furthermore, we must expect Sn to be deposited due to hydrolysis during the rinse step. The extent to which this is an influence is examined in Fig. 5. Twenty g/liter $\text{SnCl}_2 \cdot 2\text{H}_2\text{O}$ was added to the M solution so that the excess Sn concentration was the same as for the S solution. Little change is apparent in the surface coverage values except for a slightly reduced Pd concentration and Pd/Sn ratio at the longest times. Thus we have some confidence in interpreting the data in terms of adsorption of the Pd-Sn catalyst.

Cohen and West (5, 6) have stated that the Pd catalyst particles consist of a Pd-Sn alloy core in which the Pd/Sn ratio is about 6 surrounded by a divalent Sn stabilizing sheath which is probably SnCl_3^- ions. The over-all diameter of these colloidal particles was judged to be about 20\AA and the over-all Pd/Sn ratio to be in the range 0.5-1, depending on particle size (5, 6).

The square root of time dependence for early times suggests that the adsorption is diffusion controlled. The solutions were gently stirred, but it should be noted that even if the external flow is fully turbulent, for times such that the mass transfer boundary layer thickness is less than the distance from the surface to which the turbulent fluctuations penetrate, the mass flux to the surface will be essentially independent of fluid motion effects. Using periodic viscous sublayer theory (11, 12) and the usual turbulent boundary layer theory (13), it can be estimated that this is the case as long as the free stream velocity is less than about 10 cm/sec, which is appropriate for these ex-

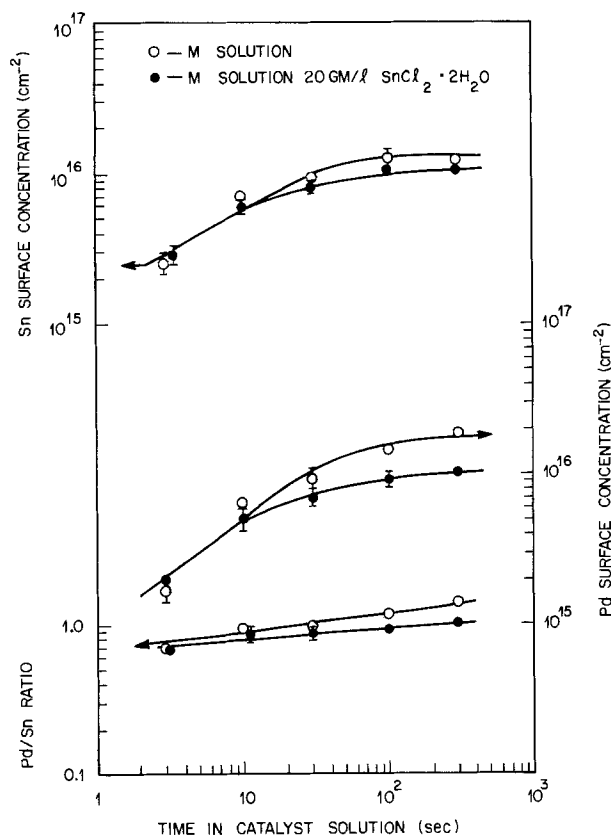


Fig. 5. Comparison of Pd and Sn surface concentration vs. catalysis time for M solution with and without added $\text{SnCl}_2 \cdot 2\text{H}_2\text{O}$ (20 g/liter).

periments. For short times, such that adsorption dominates desorption, the Pd surface concentration, n_{Pd} , is related to the bulk solution concentration, C_{Pd} , the effective diffusivity, D , and time, t , by

$$n_{\text{Pd}} = C_{\text{Pd}}(Dt)^{1/2} \quad [1]$$

Using the Stokes-Einstein equation (14), the diffusivity for a colloidal particle of the expected size (20Å) may be estimated as $10^{-6} \text{ cm}^2 \text{ sec}^{-1}$. Then from the above equation

$$n_{\text{Pd(S)}} = 1.3(10)^{15}t^{1/2}$$

and

$$n_{\text{Pd(M)}} = 0.9(10)^{15}t^{1/2}$$

for the S and M solutions, respectively, where n has units of atom cm^{-2} and t is in seconds. The experimentally observed coefficients are $4(10)^{14}$ and $(10)^{15}$, respectively; the differences are probably within the approximations involved.

If the adsorbed material is regarded as being entirely the catalyst particles, the observed Pd/Sn ratio may be used to deduce an apparent particle size based on the model developed by Cohen and West (5, 6). We will assume that the particle is spherical, in agreement with TEM observations (7), and that the Pd/Sn ratio in the core is 6 (5, 6). Then the number of Pd atoms in the core is

$$\frac{6}{7} \frac{4\pi r_c^3}{3V}$$

where r_c is the core radius and V is the volume occupied by an atom in the core (14.7Å^3) (5). Similarly the number of Sn atoms in the core is

$$\frac{1}{7} \frac{4}{3} \frac{\pi r_c^3}{V}$$

and the number of Sn atoms in the stabilizing sheath is

$$\frac{4\pi r_c^2}{\Delta^2}$$

where Δ is the characteristic dimension of the divalent Sn group in the sheath (4Å) (5). That is, the total diameter of the particle, d , in terms of the particle's over-all Pd/Sn ratio is

$$d = \frac{\left(\frac{7V}{\Delta^2}\right)\left(\frac{\text{Pd}}{\text{Sn}}\right)}{1 - \frac{1}{6}\left(\frac{\text{Pd}}{\text{Sn}}\right)} + 2\Delta \quad [2]$$

Apparent particle sizes deduced in this way are presented in Table I for comparison to ultracentrifuge (6) and TEM (7) observations. Furthermore, it would appear from Fig. 3 and 4 that the S solution has a somewhat smaller and more variable particle size, that is, a smaller and more variable Pd/Sn ratio, than does the M solution; again in agreement with the observations and arguments of Cohen and West (6). Also, Fig. 5 indicates that the apparent particle size estimated in this way is not much affected by changing the excess Sn concentration in solution. It can be noted that the presence of Sn as species other than the Pd-Sn colloid serves to decrease the apparent particle size estimated from Eq. [2] so that the values in Table I must be thought of as lower limits.

For particles approximately 20Å in diameter, coverage of the surface with one layer of particles would correspond to about $5(10)^{15}$ Pd atoms cm^{-2} . Thus the saturation surface coverage is equivalent to a few layers of particles. The fact that considerably more O than Cl is found implies that most of the Sn in the stabilizing layer, or Sn adsorbed as species extraneous to the catalyst particle itself, has been converted to oxides or hydroxides in the washing and drying steps. Recent Mössbauer results (7) show that, in fact, essentially all Sn, except that in the Pd-Sn core, is in the form of hydroxous stannic oxide at this stage.

Accelerator.—Figures 6 and 7 show the change in Pd and Sn surface concentration observed when catalyzed substrates are treated with the accelerator solution. In all cases, the Sn concentration decreases by a factor of from 3 to 10. For substrates catalyzed in the S solution, there is only a slight decrease in the Pd concentration. For the M solution, however, the Pd concentration also decreases significantly, by a factor of about 3 in Fig. 7 for example. Note that in all cases, the final Pd concentration is about $2-4(10)^{15} \text{ cm}^{-2}$; that is about one monolayer of particles according to the arguments in the preceding subsection. Five to ten minutes in the accelerator are in general sufficient to reduce the Sn concentration to its asymptotic value. After treatment in the accelerator solution, the O/Sn ratio is about 3 and the O/Cl ratio increases to about 6 for both catalysts. In all cases the Pd/Sn ratio rises to roughly 3. It thus appears that the accelerator both removes Sn in the stabilizing sheath and perhaps changes the chemical state of the remaining Sn. If all Sn in the sheath were removed we would expect a Pd/Sn ratio of 6, based on the model (5). As will be seen, one does achieve this ratio during electroless deposition. The purpose of an accelerator solution is thought to be to remove the Sn sheath, or any other Sn species extraneous to the core particle itself, thus exposing the catalytically active core particle. The present accelerator, HBF_4 , seems to be only partially successful in achieving this objective on these substrates.

Table I. Colloidal particle size (Å)

Solution	From surface Pd/Sn ratio*	Ultracentrifuge (6)	TEM (7, 15)
S	10-16	10-20	~20
M	13-18	10-20	~20
M + SnCl_2	12-16	—	—

* See text, Eq. [2].

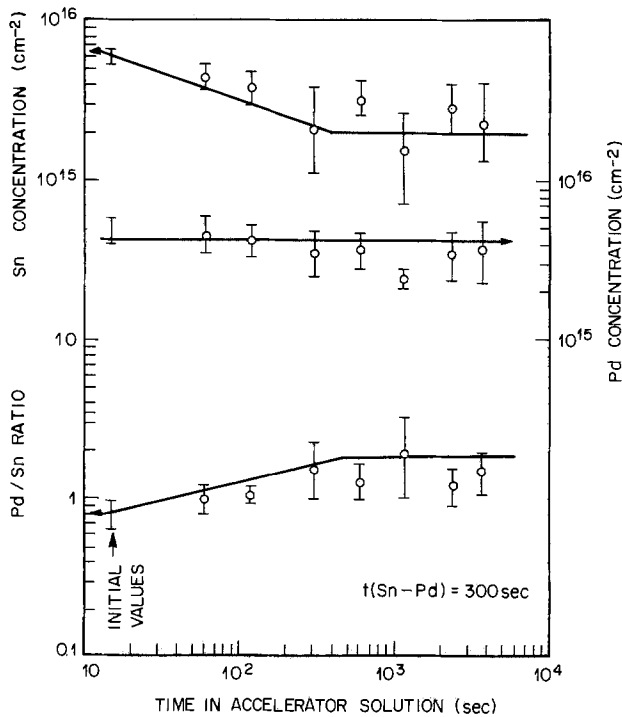


Fig. 6. Pd and Sn surface concentration vs. accelerator time for a S solution catalysis time of 300 sec.

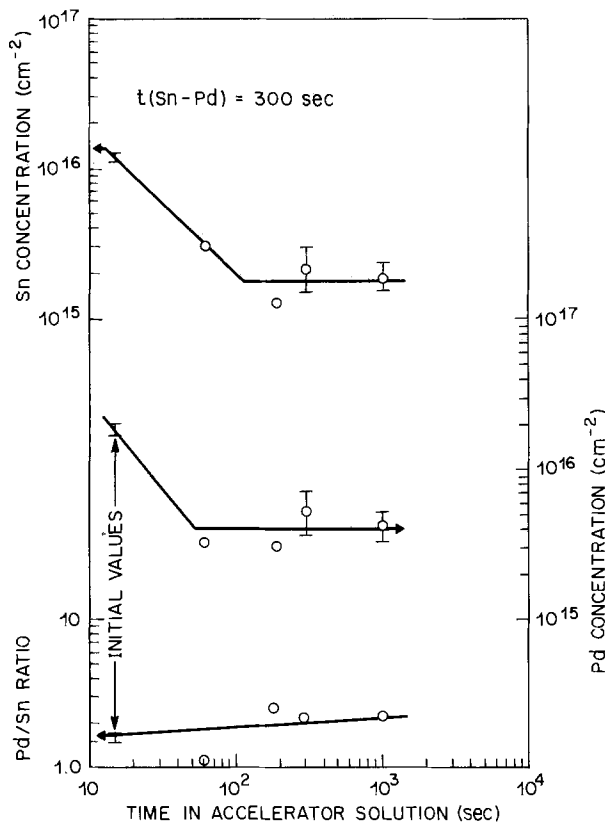


Fig. 7. Pd and Sn surface concentration vs. accelerator time for a M solution catalysis time of 300 sec.

Electroless copper.—Figure 8 shows the high energy portion of the Rutherford scattered ion spectrum from a substrate which had been briefly immersed (30 sec) in the electroless Cu bath after catalysis. This material system (Cu, Pd, Sn) is well suited to study by ion scattering because of the convenient mass (energy) separations between Cu, Pd, and Sn. Not only can the three peaks be easily resolved, but also the peak for scattering from Cu occurs at a lower energy than from

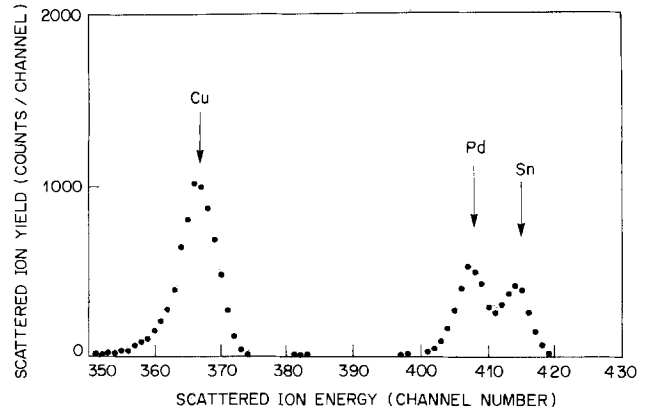


Fig. 8. Scattered ion spectrum from sample for which $t_{catalyst(S)} = 300$ sec, $t_{accelerator} = 60$ sec, and $t_{Cu} = 30$ sec.

Pd or Sn so that the processing can be allowed to proceed to significant Cu thickness ($\sim 1000\text{\AA}$) while still allowing observation of the Pd and Sn peaks.

Figures 9 and 10 show copper coverage data (as atoms cm^{-2} or equivalent average thickness) vs. time in the electroless Cu bath. The line labeled $2.2 \text{\AA}/\text{sec}$ is the rate at which this bath plates Cu on Cu as determined by a method which will be described later. It can be seen that the accelerator solution may or may not accelerate the initial metal plating rate. Reducing the catalysis time to 10 sec results in a rather long ($\sim 10^3$ sec) initiation time for significant plating to begin; i.e., $>10^{15}$ Cu atom cm^{-2} . For surfaces in the S solution for 300 sec (Fig. 9) the Cu coverage for times of 30 sec or less is greatest for intermediate accelerator times. For greater plating times, equivalent thickness $>100\text{\AA}$, the data converge to the Cu on Cu line. Microscopic observation indicates complete coverage also occurs at about this stage. For the M catalyst solution, Fig. 10, the largest Cu coverage values for short times

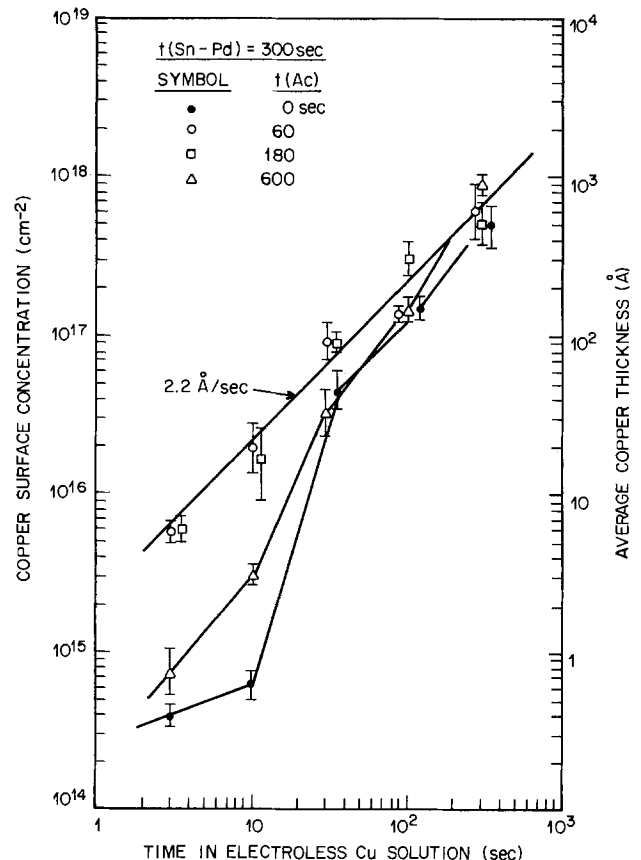


Fig. 9. Copper surface concentration vs. time in electroless Cu solution for a S solution catalysis time of 300 sec and various accelerator solution times.

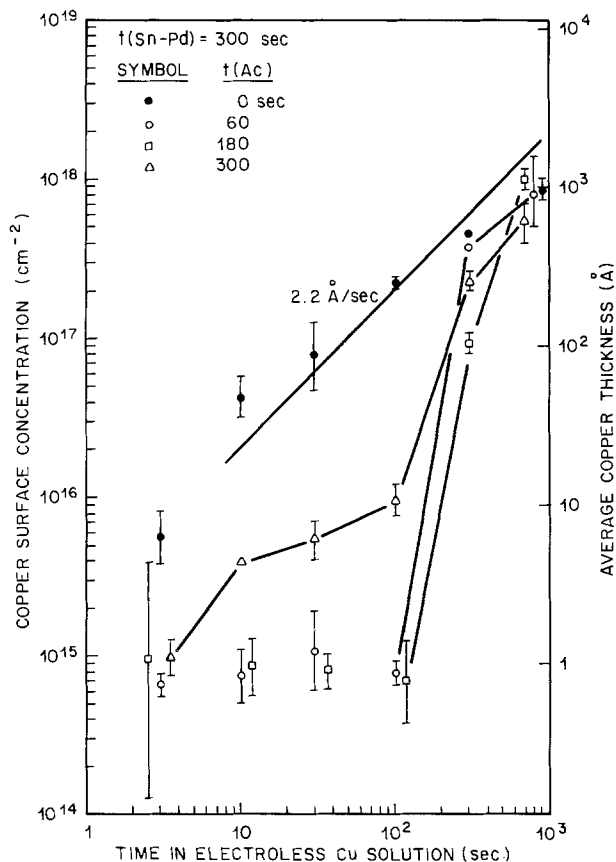


Fig. 10. Copper surface concentration vs. time in electroless Cu solution for a M solution catalysis time of 300 sec and various accelerator solution times.

correspond to no accelerator at all. It will be recalled from the previous discussion that the surfaces catalyzed in the M solution lose Pd in the accelerator step so that the zero accelerator time sample has a considerably greater Pd concentration (~3X) than do the other samples. It can also be noted that there is a considerably greater (100 sec as opposed to 10 sec) initiation time apparent in Fig. 10 than in Fig. 9. This may relate to particle size and distribution differences. In any case, the effects of the accelerator treatment appear rather complex and probably include removal of catalyst particles, partial removal of the stabilizing sheath and other excess deposited Sn, and perhaps chemical changes.

Figures 11 and 12 give the Pd and Sn surface concentrations corresponding to the samples represented in Fig. 9 and 10 for the S and M catalyst solutions, respectively. There is no evidence of significant decrease in Pd concentration, but the Sn concentration does further decrease so that by the time the catalyst particles are covered the Pd/Sn ratio has risen to 6/1; that is, only the core particle remains. The reduction of Sn surface concentration implies that Sn has been lost into the electroless Cu bath; the implication of this result is discussed further below. It was also found that the Cl peak completely disappears after the first stage of Cu plating (3 sec); the O peak cannot be meaningfully interpreted because of surface oxidation of copper.

It can also be noted that the present results are not in accord with the supposition that a well-defined Pd₃Sn compound is the catalytically active species (15). This and other apparent discrepancies with some of the published literature will be discussed in more detail elsewhere (7).

Figure 13 is the scattered ion spectrum for a sample which had been plated to a mean equivalent Cu thickness of ~500Å. The arrows labeled Cu, Pd, and Sn denote the channel numbers (energies) for scattering from Cu, Pd, and Sn at the surface. The Pd peak has

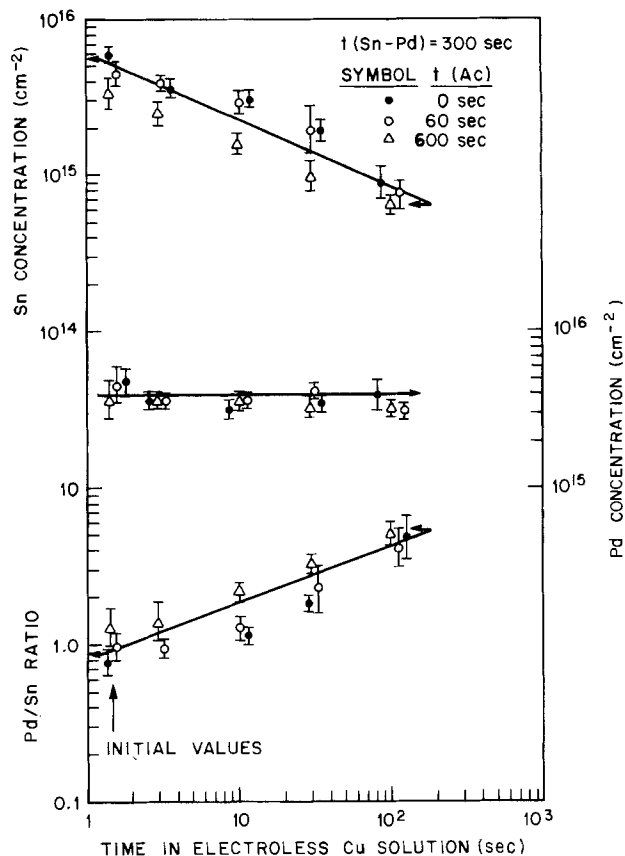


Fig. 11. Pd and Sn surface concentration vs. time in electroless Cu for a S solution catalysis time of 300 sec and various accelerator times.

been shifted to lower energy, i.e., the Pd lies at the Cu-substrate interface. As discussed above, this shift

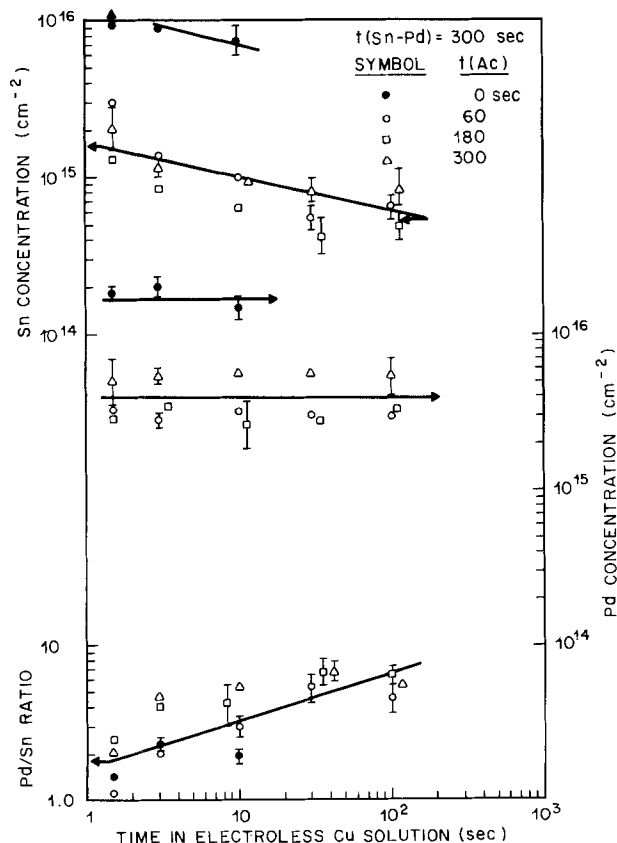


Fig. 12. Pd and Sn surface concentration vs. time in electroless Cu for a M solution catalysis time of 300 sec and various accelerator times.

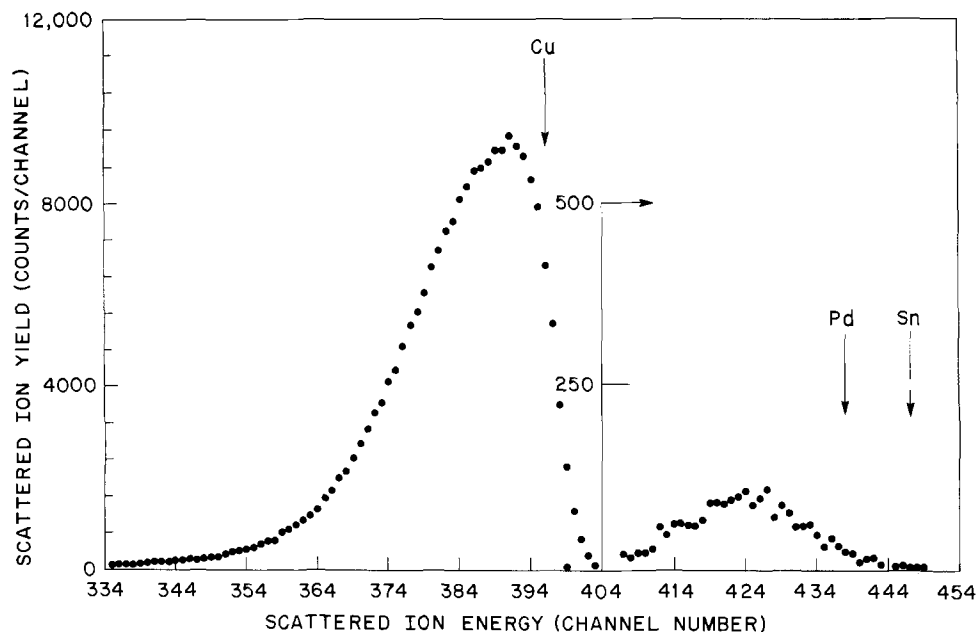


Fig. 13. Scattered ion spectrum for a sample for which $t_{\text{catalyst}(S)} = 300$ sec, $t_{\text{accelerator}} = 60$ sec, $t_{\text{Cu}} = 300$ sec.

is due to the loss in energy as the ion penetrates into and exits from the overlying Cu layer. The broadening of the Pd peak and the low energy edge of the Cu peak is due to nonuniformity of the Cu film over the area examined by the beam. This nonuniformity is estimated to be 25-50% of the mean Cu thickness in the range from a few hundred to a few thousand angstroms. (Slit-scattering and straggling also contribute to this broadening but are not of significance here.) In this particular spectrum, definition of the Sn peak has been lost in the broadened Pd peak. The shift in the Pd peak with increasing Cu thickness may be used to monitor the plating rate for Cu on Cu. That is, the Pd is used as an interface marker. It is in this way that the line labeled 2.2 Å/sec on the previous figures was determined. For longer times, the plating rate can be determined by weight-gain methods, with the same result.

In the experiments discussed thus far, care was taken to use fresh solutions. Figure 14 shows the result observed when a sample was plated for 100 sec in a bath which had been used to process about ~10 previous samples. Although the Pd peak is shifted down a few channels, that is, it is at the interface, a sharply defined Sn peak is apparent at the surface; i.e., on top of the Cu. Figure 15 shows the result when the Cu bath is allowed to become even further contaminated with Sn. Here the mean Cu thickness is about 1000 Å and approximately 5% Sn has been codeposited with the Cu. The Sn contamination at this stage is estimated to be ~10 ppm. Further study of the effects of metallic impurities is now underway. It may be of interest to note that it has been found that Pb was also codeposited when an electroless copper bath was inadvertently contaminated with Pb.

Other substrates.—The experimental observations obtained when the S solution was used to catalyze a variety of substrates appropriate to printed circuit board fabrication are similar to those obtained using graphite substrates. Surface roughness measurements on the substrates indicated that the data are in reasonable quantitative agreement with the graphite substrate data when this factor is taken into consideration. However, important effects on surface coverage *vs.* time, for example, cannot be ruled out if the substrate is charged or perhaps otherwise chemically active.

Catalyst aging and contamination.—Cohen and West have shown that the presence of enough divalent Sn to form a stabilizing sheath around the core particle is necessary and sufficient for the solution to be stable with respect to oxidative coagulation (5, 6). Oxidation

due to atmospheric aging and the presence of transition metal ions has been examined.

For the aging experiments, the S and M solutions were prepared and kept in sealed polyethylene containers. This serves to cut down evaporation losses, but the containers are rather permeable to oxygen. Periodically, samples of the solutions were withdrawn and their catalytic behavior was examined. The life, defined as the time when the colloid coagulates and precipitates out of solution, was determined to be 12 ± 1 week for the S solution and 8 ± 1 week for the M

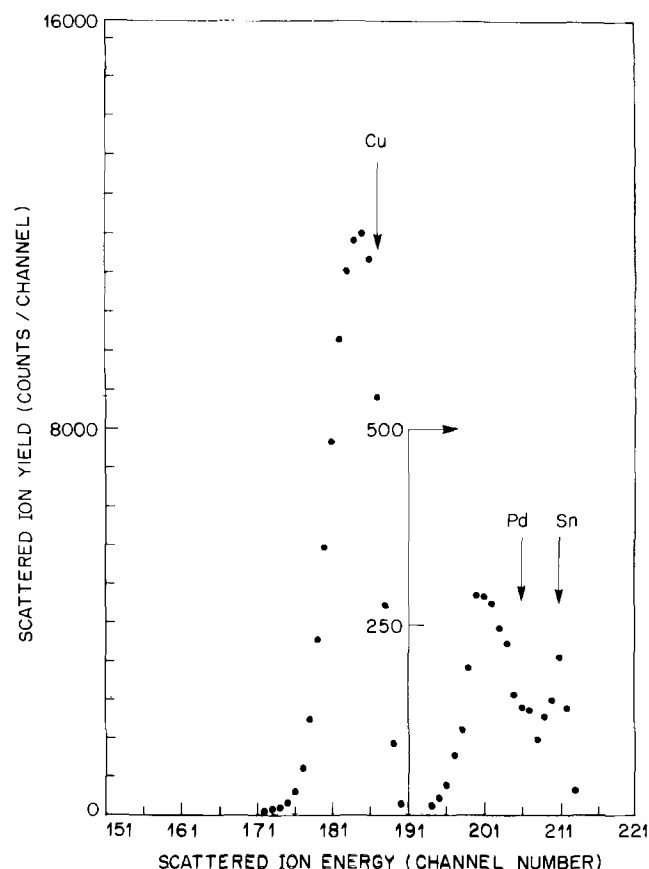


Fig. 14. Scattered ion spectrum from a sample for which $t_{\text{catalyst}(S)} = 300$ sec, $t_{\text{accelerator}} = 180$ sec, $t_{\text{Cu}} = 100$ sec. Electroless copper solution had been used to process ~10 previous samples.

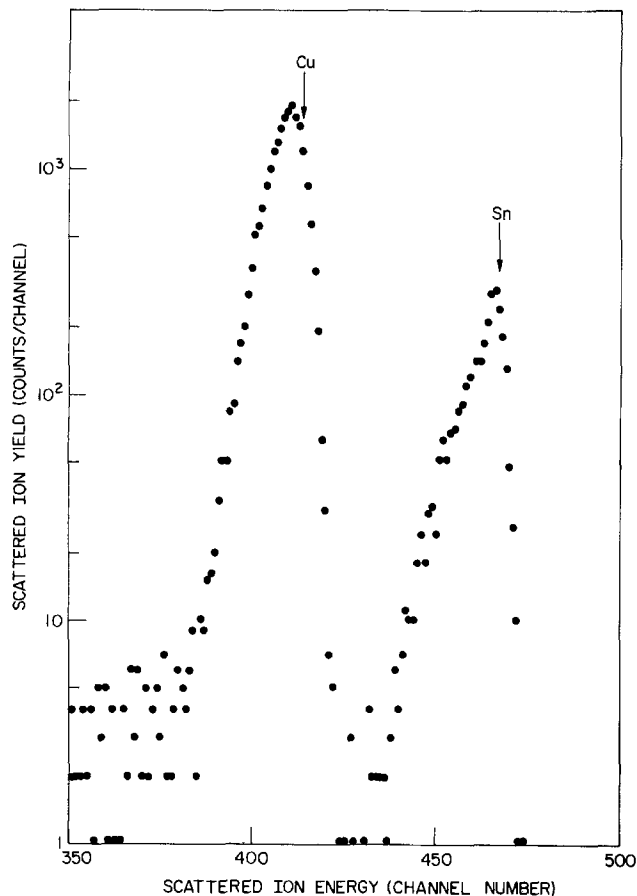
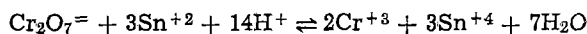


Fig. 15. Scattered ion spectrum from a sample for which $t_{\text{catalyst(S)}} = 300$ sec, $t_{\text{accelerator}} = 180$ sec, $t_{\text{Cu}} = 300$ sec. Electroless Cu solution had been used to process ~50 previous samples. Shows ~5% Sn codeposited with Cu.

solution. This result is in accord with the larger divalent Sn content of the S solution. The catalytic activity, in terms of amount of Pd and Sn adsorbed and in terms of the plating behavior, was unchanged at least up to 90% of the life of the solutions. Thus it is concluded that degradation of the solution does not occur progressively, but rather suddenly when nearly all the Sn^{+2} is oxidized to Sn^{+4} . It should also be noted that in production environments these solutions can remain stable for many months when suitable replenishment schemes are used to maintain concentrations near nominal values.

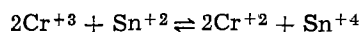
The effect of addition of Cr ions in the +3 and +6 valence states has also been studied. When Cr is added as the dichromate ion, the S and M solutions will tolerate 800 and 300 ppma Cr, respectively.

The reaction



has a large negative free energy change (16), and 3Sn^{+2} ions are oxidized for every $\text{Cr}_2\text{O}_7^{=2}$ ion added. The S solution, e.g., contains 0.14 mole $\text{Sn}^{+2}/\text{l}^{-1}$ so that one would expect to need 0.05 mole $\text{Cr}_2\text{O}_7^{=2}/\text{l}^{-1}$ to coagulate the solution. The experimental value is 0.07 mole $\text{Cr}_2\text{O}_7^{=2}/\text{l}^{-1}$.

In the case of trivalent Cr ions, the reaction



has a positive free energy change (16) so the reaction does not proceed as written to any great extent. Experimentally it is found that at least 10^4 ppma Cr^{+3} can be added without adverse effect.

Also, it is found that when the $\text{Cr}_2\text{O}_7^{=2}$ added is less than that necessary to cause oxidative coagulation, no significant changes in catalytic activity are noted. Any adsorbed Cr on the sample surfaces is less than the

detection limit ($< 10^{14}$ Cr cm^{-2}) for 400 ppma Cr^{+6} added or 2000 ppma Cr^{+3} added.

Conclusions

Rutherford scattering has been used to quantitatively measure adsorption from Pd, Sn colloid catalyst systems, and the behavior of the adsorbed material during subsequent steps in the electroless deposition sequence. The present findings are in general agreement with the colloidal model of Cohen and West (5, 6) insofar as it is possible to interpret the results on that basis. The early stages of catalyst adsorption appear to be diffusion controlled and obey at $t^{1/2}$ dependency. The particle sizes deduced (10-20Å) are in agreement with other work and it appears that a few monolayers of particles lead to saturation.

The effect of the accelerator solution appears to be rather complex. Although it does partially remove the excess Sn, its use may or may not accelerate the initial plating rate. The Pd surface concentration found after the accelerator treatment is in the range 2-4(10)¹⁵ Pd atoms cm^{-2} regardless of the solution used for catalysis times greater than 30 sec, so that there is little point in using solution concentrations or treatment times which give significantly greater Pd surface coverage after the catalysis step. Accelerator times of 10 min are sufficient to remove all Sn which can be removed in HBF_4 . The primary virtue of the accelerator treatment appears to be to reduce subsequent contamination of the electroless copper bath with Sn.

The early stages of electroless copper plating have also been studied. In this process, the remaining excess Sn is removed and the copper plates over the core particle in which the Pd/Sn ratio is approximately 6. Tin lost into the bath may be subsequently codeposited into the Cu layer on succeeding samples.

Catalyst aging and contamination (with Cr^{+3} and Cr^{+6}) indicate that oxidative coagulation is precipitous rather than progressive in nature.

Acknowledgments

The author would like to thank R. L. Cohen, R. Sard, and L. N. Schoenberg for several illuminating discussions and P. Skurkiss for performing the spectrophotometric Pd determinations.

Manuscript submitted Jan. 17, 1975; revised manuscript received April 30, 1975.

Any discussion of this paper will appear in a Discussion Section to be published in the June 1976 JOURNAL. All discussions for the June 1976 Discussion Section should be submitted by Feb. 1, 1976.

Publication costs of this article were partially assisted by Bell Laboratories.

REFERENCES

1. N. Feldstein, *Plating*, **60**, 611 (1973).
2. R. L. Meek, To be published.
3. A. Rantell and A. Holtzman, *Trans. Inst. Metal Finishing*, **51**, 62 (1973).
4. A. Rantell and A. Holtzman, *Plating*, **61**, 326 (1974). For comment see E. Matijevic, *ibid.*, **61**, 1051 (1974) and R. L. Cohen and K. W. West, *ibid.*, **61**, 1053 (1974).
5. R. L. Cohen and K. W. West, *Chem. Phys. Letters*, **16**, 128 (1972).
6. R. L. Cohen and K. W. West, *This Journal*, **120**, 502 (1973).
7. R. L. Meek, R. L. Cohen, and A. G. Cullis, in *Proceedings of the V Symposium on Plating in the Electronics Industry*, New York (March 1975).
8. M. A. Nicolet, J. W. Mayer, and I. V. Mitchell, *Science*, **177**, 841 (1972).
9. W. K. Chu, J. W. Mayer, M. A. Nicolet, T. M. Buck, G. Amsel, and F. Eisen, *Thin Solid Films*, **17**, 1 (1973).
10. R. L. Meek, T. M. Buck, and C. F. Gibbon, *This Journal*, **120**, 1241 (1973).
11. R. L. Meek and A. D. Baer, *A.I.Ch.E. J.*, **16**, 841 (1970).

12. R. L. Meek and A. D. Baer, *Intern. J. Heat Mass Transfer*, **16**, 1385 (1973).
13. H. Schlichting, "Boundary Layer Theory," p. 537, McGraw-Hill Book Co., New York (1960).
14. R. B. Bird, W. E. Stewart, and E. N. Lightfoot, "Transport Phenomena," p. 514, John Wiley & Sons, Inc., New York (1960).
15. N. Feldstein, M. Schlesinger, N. E. Hedgecock, and S. L. Chow, *This Journal*, **121**, 738 (1974).
16. W. M. Latimer, "The Oxidation States of the Elements and Their Potentials in Aqueous Solution," Prentice-Hall, Inc., Englewood Cliffs, New Jersey (1952).

Hydrodynamic Studies of Bubble Effects on the *IR*-Drops in a Vertical Rectangular Cell

F. Hine,* M. Yasuda, R. Nakamura, and T. Noda

Nagoya Institute of Technology, Gokiso-cho, Showa-ku, Nagoya 466, Japan

ABSTRACT

The bubble effects on the resistivity of solution under various conditions of electrolysis was examined with a rectangular cell, in which hydrogen evolution took place from a stainless steel cathode in dilute caustic soda solution. The resistivity of electrolyte containing hydrogen bubbles was a function of the current density, the operating temperature, the flow rate of solution, and the geometry of channel. An experimental equation was obtained.

Bubble effects on the terminal voltage of electrolyzer are important, especially at high current densities. Increase in the resistivity of electrolyte due to suspensions of nonconducting particles has been studied by La Rue and Tobias (1), and Tobias has also described a theoretical treatment of the effect of gas on the current distribution in a vertical cell (2). Hine *et al.* studied the *IR*-drops in the chlor-alkali cells, and discussed preferable geometry and arrangement of the graphite anode for the horizontal cell (3-7).

Gardiner stated that the apparent resistivity of the brine between the graphite anode and the amalgam cathode of the Olin E-11 cell was practically free of chlorine bubbles when the anode-to-cathode gap was more than 0.13 in., whereas the resistivity of brine was affected by bubbles if the gap was narrow (8). MacMullin pointed out that the vertical-type diaphragm cell such as the Hooker cell is a "good pump," because gas lift near the anode enhances circulation of the brine and it causes significant reduction of the *IR*-drop between two electrodes (9, 10). The cell voltage of the amalgam-type chlorine cells operated at high flow rate of mercury cathode is relatively low even at high current densities, because chlorine bubbles under the graphite anodes are removed quickly (11, 12).

Electrolytic cells with gas evolution are important not only with respect to chlor-alkali cells but some others such as the water electrolyzer. The *IR*-drop due to involvement of bubbles in the brine is a major factor of high voltage in chlor-alkali cells. The water electrolyzer stores a certain amount of electrolytic solution, but, in some cases, the cell is operated with forced flow of solution along the electrode. The *IR*-drop depends on the flow rate in the latter case (13-16). Agitation of solution with bubbles enhances the mass- and heat-transfer in the cell (17-24).

Experimental Procedure

Electrolysis of dilute NaOH solution with a rectangular cell under flow conditions has been carried out, and the effects of hydrogen bubbles on the *IR*-drop have been investigated.

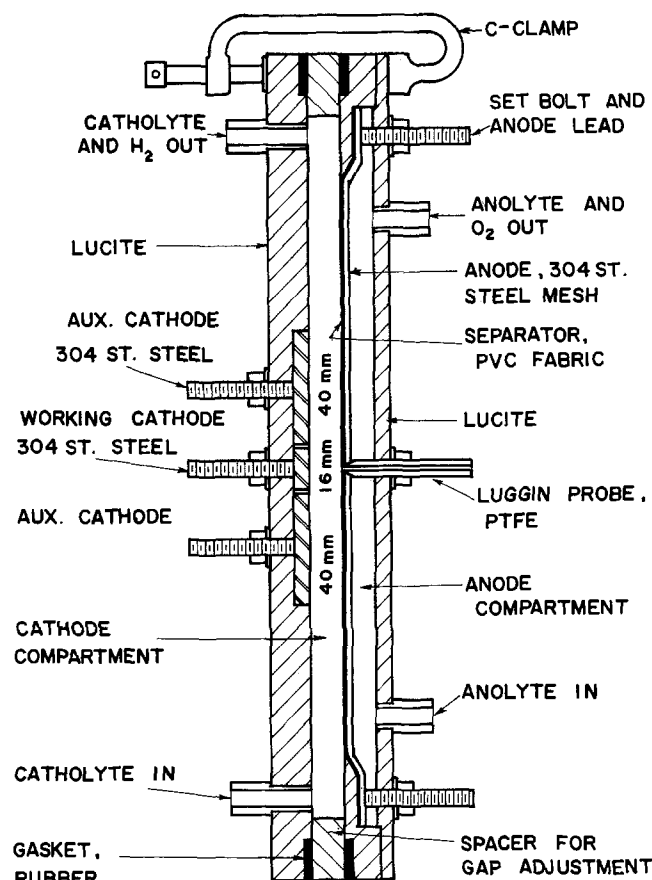
A rectangular cell, made of Lucite resin, 240 mm long and 10 mm wide is shown in Fig. 1. The anode-to-cathode gap can be changed with spacers 2, 3, 5, and 7 mm thick.

* Electrochemical Society Active Member.

Key words: hydrodynamic studies, bubble effects, *IR* drops, brine flow, rectangular cell, void fraction.

The working cathode of AISI 304 stainless steel is 10 mm wide and 16 mm long and is placed at the center of the cathode compartment. At both sides 2 mm from the working cathode, the auxiliary cathodes (10 mm wide and 40 mm long) are arranged so as to yield uniform current distribution on the test electrode.

The anode screen, also Type 304 SS, is covered by a PVC fabric diaphragm and is parallel to the cathode.



NOTE: ELECTRODES ARE
10 mm WIDE.

Fig. 1. Experimental cell in vertical position

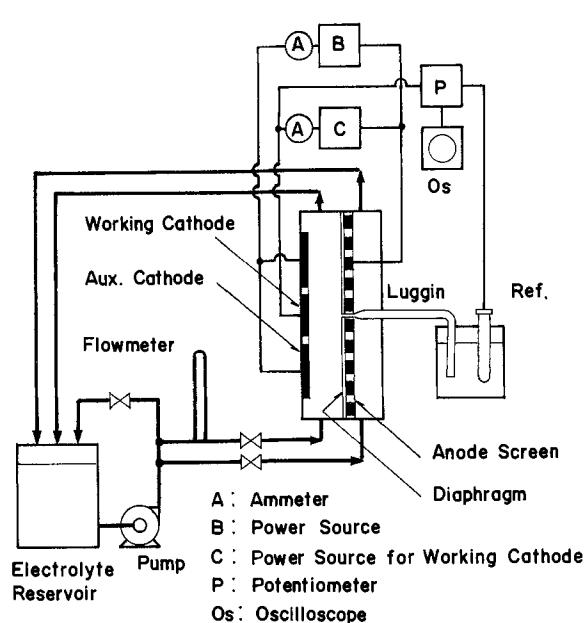


Fig. 2. Flowsheet of system

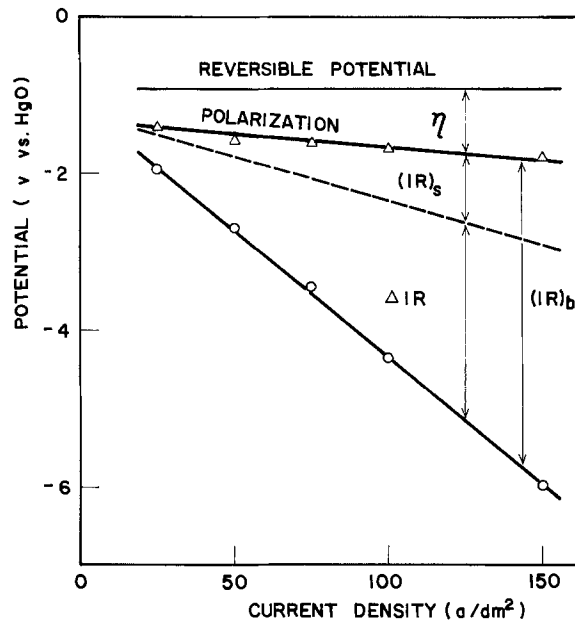
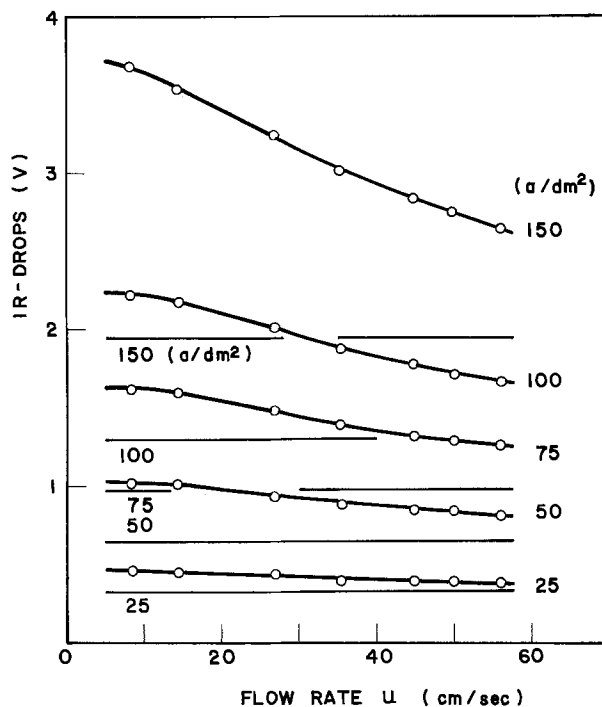
A Luggin probe made of PTFE resin is screwed and pressed to the back side of a diaphragm from the anode compartment, and is connected to a reference electrode consisting of Hg/HgO/1.75N NaOH. The IR -drop between the Luggin and the working cathode is determined by means of the current interruption technique. The auxiliary electrodes are polarized at an equal current density with the working cathode by a separate d-c power source.

The flowsheet of the system is shown in Fig. 2. The electrolytic cell is placed vertically. Caustic soda solution (1.75N NaOH) is pumped up from the thermostated reservoir to the cell bottom and flows through the channel under controlled rate. The solution returns to the reservoir of about 50 liters in volume, where hydrogen and oxygen are purged. Properties of a 1.75N NaOH solution employed are shown in Table I.

Results and Discussion

An example of the voltage balance between the working cathode and the Luggin probe is shown in Fig. 3. The hydrogen overvoltage is relatively small compared to the IR -drops in the solution containing bubbles, $(IR)_b$. The broken line shows the estimated IR -drop in the solution free of bubble, $(IR)_s$, which is also small in comparison to $(IR)_b$. The ratio of $(IR)_b$ to $(IR)_s$ is proportional to the normalized resistivity, ρ/ρ_0 , where ρ and ρ_0 are the conductivity of solutions with and without bubbles, respectively.

Figure 4 shows the IR -drop vs. flow rate at given current densities. The thin lines show the estimated $(IR)_s$. The voltage reduces with the increase of flow rate, especially at high current densities, and tends to the corresponding $(IR)_s$. At low flow rate, less than 10 cm/sec, the IR -drop fluctuated and bubbles were swept out intermittently from the electrode due to natural convection. The IR -drop was not linear to the current density in the solution containing bubbles. It was also a function of the temperature. The IR -drop was low due to increase in the conductivity and to decrease of the viscosity at high temperature ranges.

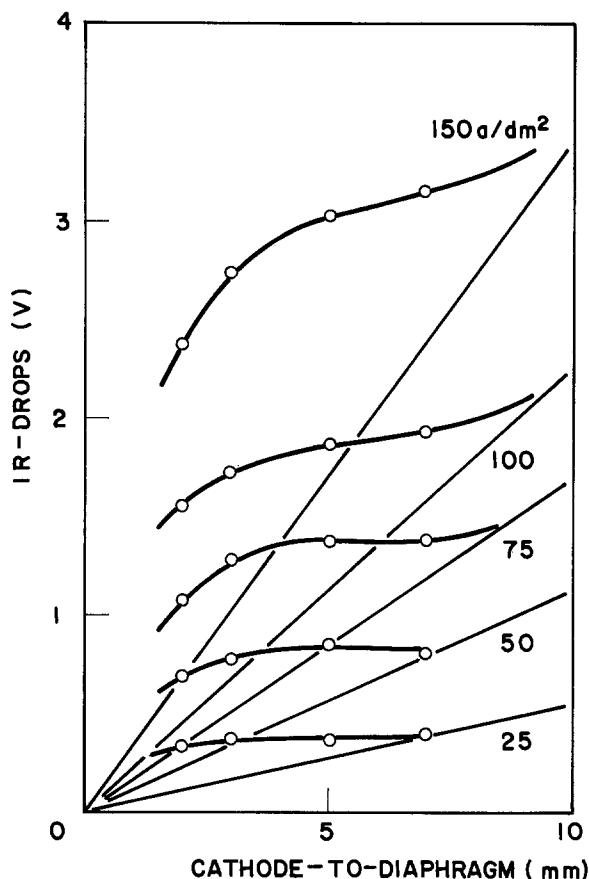
Fig. 3. Potential vs. current density curves. $l = 2$ mm, $t = 30^\circ\text{C}$, $u = 10$ cm/sec.Fig. 4. IR -drop vs. flow rate curves. $l = 5$ mm, $t = 50^\circ\text{C}$

The IR -drop vs. cathode-to-diaphragm gap showed the S-shaped curve (Fig. 5). The thin lines show $(IR)_s$ as reference. In the wide channel, such as a 10 mm gap, the IR -drop is close to $(IR)_s$, whereas it becomes large in the narrow channel. There is a maximum of ρ/ρ_0 at about 2-3 mm in gap.

The normalized resistivity is a function of the ratio of gas flow to liquid flow, V_g/V_l , the ratio of gap width

Table I. Properties of a 1.75N NaOH solution

	Temperature, $^\circ\text{C}$						Reference
	30	40	45	50	60	70	
Resistivity, ρ_0 , ohm · cm	3.33	2.86	2.68	2.51	2.25	2.05	Observed
Vapor pressure, P_{H_2O} , atm	0.039	0.068	0.088	0.114	0.185	0.289	26
Viscosity, μ , cp	1.17	0.97	0.89	0.81	0.69	0.59	27
Density, d , g/cm ³	1.0667	1.0623	1.0598	1.0575	1.0521	1.0464	Observed

Fig. 5. IR-drop vs. distance curves. $t = 60^\circ\text{C}$, $u = 20\text{ cm/sec}$

to electrode width, l/L , and the Reynolds number, Re , as follows (25)

$$\frac{\rho}{\rho_0} = K \left(\frac{V_g}{V_1} \right)^\alpha \left(\frac{l}{L} \right)^\beta (Re)^\gamma \quad [1]$$

where Re is assumed to be

$$Re = \frac{D_{eq} u d}{\mu} \quad [2]$$

Equivalent diameter, D_{eq}

$$\begin{aligned} &= \frac{4 \times (\text{Sectional area of channel})}{\text{Total length of wall of section}} \\ &= \frac{4Ll}{2(L+l)} = \frac{2l}{1+l} \quad (\because L = 1\text{ cm}) \end{aligned} \quad [3]$$

where K , α , β , and γ are the coefficients. The area of gap is $lL\text{ cm}^2$, and the approach velocity of liquid is $u\text{ cm/sec}$. The flow of liquid is, therefore, $V_1 = lLu$. On the other hand, the volume rate of gas, V_g in cm^3/sec , is represented as follows

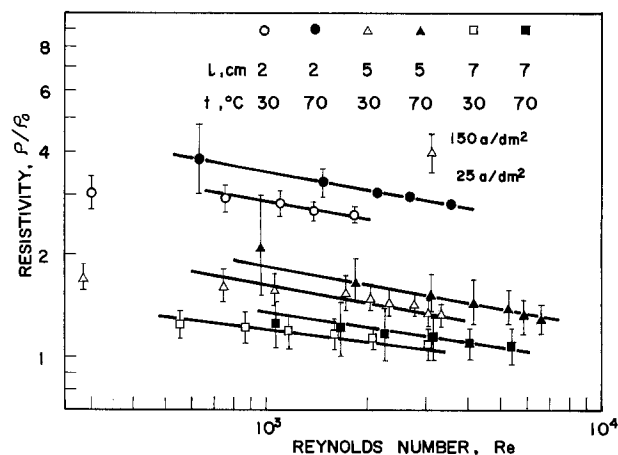
$$V_g = \left(\frac{i}{2F} \right) \left(\frac{RT}{p_{H_2}} \right) LH \quad [4]$$

where LH is the total cathode area in cm^2 . The hydrogen partial pressure, p_{H_2} in atm, is as follows

$$p_{H_2} = 1 - p_{H_2O} \quad [5]$$

where p_{H_2O} is the water vapor pressure on NaOH solution (see Table I).

Figure 6 shows the logarithmic plots of ρ/ρ_0 vs. Re under given conditions of l/L and the temperature. It is somewhat complicated that V_g/V_1 varies with the solution flow, also the kinematic viscosity, μ/d , would change with the void fraction, ϵ . It is impossible to change those two factors separately. The higher the temperature in a narrow channel the larger is the ρ/ρ_0 .

Fig. 6. Resistivity vs. Reynolds number. Average slope, $\gamma = -0.18$.

At high current densities, the ρ/ρ_0 becomes large. The plots in this figure are the average values of the data shown by the bar under given conditions. The slope of the curve is small: $\gamma = -0.18$, and is almost independent of the gap width and the temperature.

The (ρ/ρ_0) vs. (l/L) is shown in Fig. 7, where the slope, β , is -0.65 . The (ρ/ρ_0) vs. (V_g/V_1) is shown in Fig. 8. The Re is not specified in this figure, because the V_g/V_1 contains some influences of Re as stated above. The slope α is 0.12 and is almost independent of l .

With use of those coefficients, Eq. [1] has been applied for all the data, but we have found some deviations. On the other hand, Fig. 9 is a trial of the plots of Eq. [6], where (V_g/V_1) involves the influence of Re . This equation fits the data quite well rather than Eq. [1]

$$\frac{\rho}{\rho_0} = K_1 \left(\frac{V_g}{V_1} \right)^\alpha \left(\frac{l}{L} \right)^\beta \quad [6]$$

where K_1 is a coefficient.

The void fraction due to holdup of bubbles is as follows

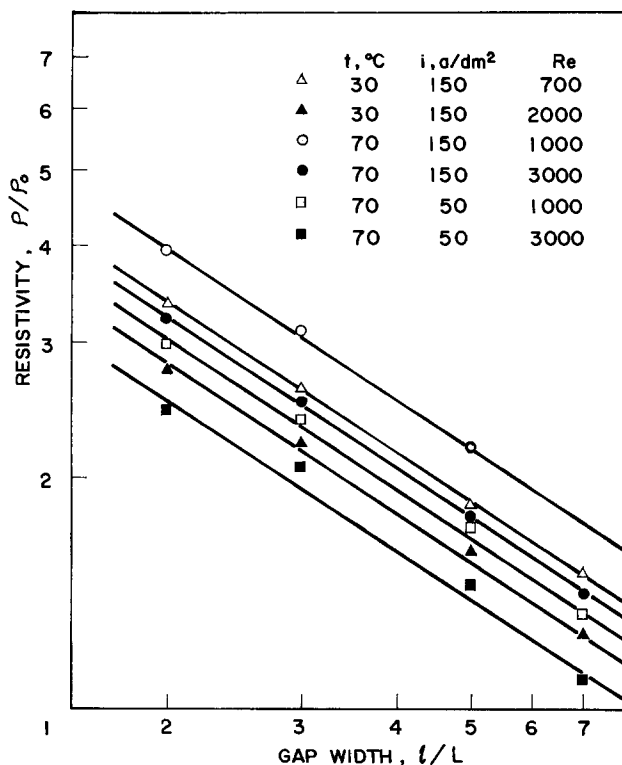
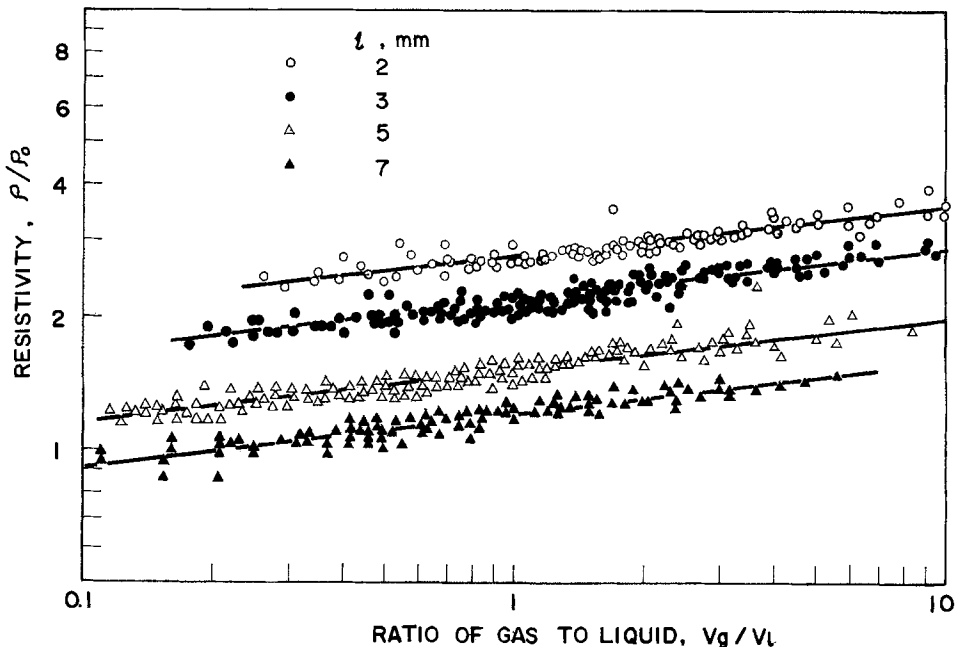
Fig. 7. Resistivity vs. gap width. Average slope, $\beta = -0.65$

Fig. 8. Resistivity vs. ratio of gas flow to liquid flow. Average slope, $\alpha = 0.12$.



$$\text{Void fraction} = \frac{\text{Bubble volume}}{\text{Solution} + \text{bubbles}} \quad [7]$$

The bubbles generated at the upper stream of the channel may disturb the working cathode, and the flow of gas halfway up is $V_g/2$. Therefore

$$\epsilon = \frac{V_g/2}{V_g/2 + V_l} = \frac{V_g/V_l}{V_g/V_l + 2} \quad [8]$$

Substituting this into Eq. [6], we have

$$\frac{\rho}{\rho_0} = K_1 \left(\frac{2\epsilon}{1-\epsilon} \right)^\alpha \left(\frac{l}{L} \right)^\beta \quad [9]$$

La Rue and Tobias have shown an equation (1)

$$\frac{\rho}{\rho_0} = (1 - \epsilon)^{-3/2} \quad [10]$$

This equation differs from Eq. [9], probably due to

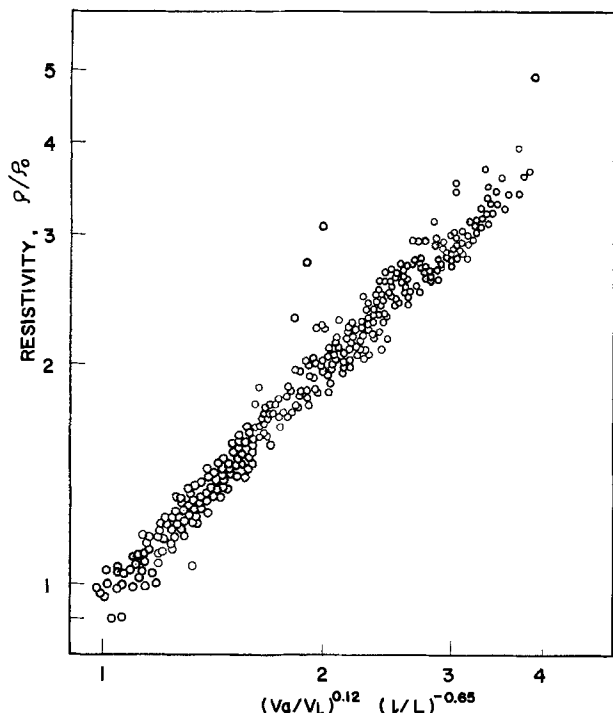


Fig. 9. Resistivity represented by Eq. [6]. $K_1 = 1.03$

conditions of the brine flow. Equation [10] was obtained with the assumption of uniform distribution of bubbles in the anode-to-cathode gap. Under flow conditions, on the other hand, a major part of bubbles is crowded in the vicinity of the electrode surface, and the solution flows away in the center of channel. Figure 10 shows simple models of the distribution of bubbles across the gap. With Eq. [10], the (ρ/ρ_0) is represented as follows (25)

$$\frac{\rho}{\rho_0} = \left(1 - \frac{\epsilon}{\lambda} \right)^{-3/2} \lambda + (1 - \lambda) \quad [11]$$

and

$$\frac{\rho}{\rho_0} = \frac{(1 - 2\epsilon)^{-1/2} - 1}{\epsilon} \quad [12]$$

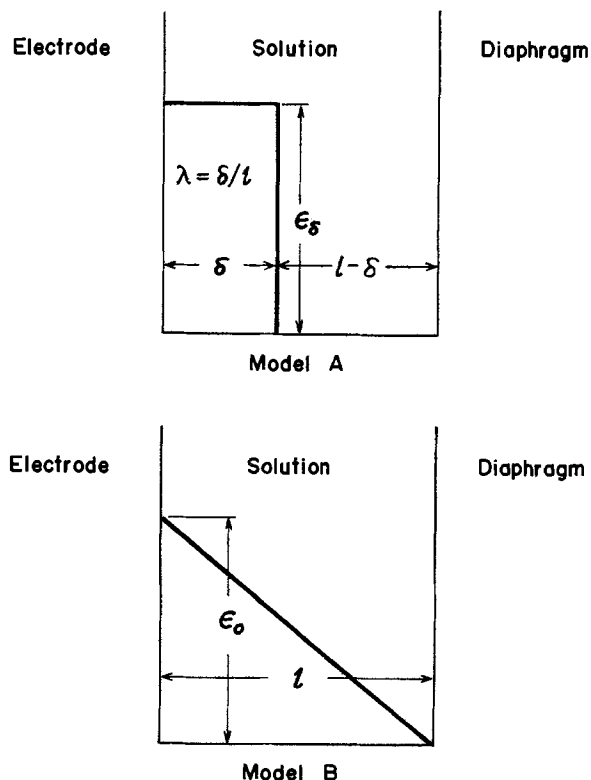


Fig. 10. Two models of the distribution of bubbles across the gap. ϵ_δ , void fraction of crowded zone, δ , ϵ_0 , void fraction at electrode surface.

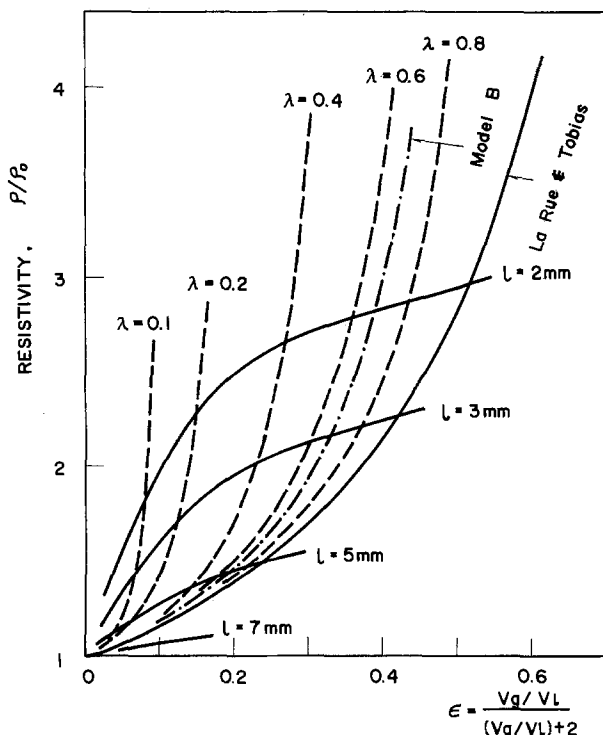


Fig. 11. Resistivity vs. void fraction. MacMullin equation,

$$\rho/\rho_0 = \left(1 - \frac{\epsilon}{\lambda}\right)^{-3/2} \lambda + (1 - \lambda)$$

for models A and B, respectively, where $\lambda = \delta/l$, and δ is a crowded zone in model A. Those curves are still concave as shown in Fig. 11, and differ from the experimental data labeled *l*.

It is assured that a part of the electrode surface is covered with the "fixed layer" of gas bubbles, which depends on the operating conditions such as current density and temperature. The actual current density at the working surface of electrode thus increases, and the *IR*-drop near the electrode surface and the overvoltage become large compared to the predicted values in the case of uniform distribution across the gap. Those phenomena would be significant in the narrow channel.

The "fixed gas layer" would differ somewhat from the models shown in Fig. 10. Suppose the gas is fixed into a layer, δ_1 cm, at the electrode surface, and the solution in the remaining layer, $(1 - \delta_1)$, contains gas dispersion. The ρ/ρ_0 is shown by the equation

$$\rho = \rho_f \left(\frac{\delta_1}{l}\right) + \rho_1 \left(1 - \frac{\delta_1}{l}\right)$$

or

$$\frac{\rho}{\rho_0} = \frac{\rho_1}{\rho_0} + \left(\frac{\rho_f + \rho_1}{\rho_0}\right) \left(\frac{\delta_1}{l}\right) \quad [13]$$

where ρ_f and ρ_1 are the resistivity of the fixed layer and of the remaining layer, respectively. The second term of the right-hand side is large enough compared to the first term in the narrow channel, and hence, the ρ/ρ_0 is dependent largely on the gap width. In a wide channel, on the other hand, the second term diminishes. The ρ becomes small and uniform. The *IR*-drop across the wide gap can be represented by $i\rho_1 l \cong i\rho_0 l$. It would be a major reason of why the plots in Fig. 11 appear below the curve by La Rue and Tobias at large *l* and ϵ .

Experiments described above were carried out with the rectangular channel under controlled flow conditions. The electrode surface is covered by fine bubbles, and hence, the overvoltage increases significantly. The resistivity of the solution near the electrode is very large due to dispersion of fine bubbles. The resistivity

of the solution containing bubbles depends largely on the geometry of the channel and the bubble size as well as the void fraction. It is evident from Eq. [13] that the tighter the spacing of the channel the larger is the resistivity, especially in the narrow channel, which is important from the viewpoint of practical electrolysis.

In conclusion, the bubble effects on the terminal voltage depend on a variety of operating conditions and the cell geometry. The apparent resistivity of the solution containing bubbles is a function of those factors as well as the void fraction. Differences between our experimental data and the theory by La Rue and Tobias have not been clarified.

Acknowledgment

The authors wish to thank Dr. P. A. Danna for his suggestions and Olin Research Center, New Haven, Connecticut, for support in setting up the research program. We appreciate very much the important suggestions and discussion of Mr. R. B. MacMullin, R. B. MacMullin Associates, Niagara Falls, New York. Some of his comments have been quoted in this paper. A part of this work was covered by the financial support of Japanese Ministry of Education, No. 875416.

Manuscript submitted Jan. 14, 1975; revised manuscript received April 7, 1975. This was Paper 346 presented at the Toronto, Canada, Meeting of the Society, May 11-16, 1975.

Any discussion of this paper will appear in a Discussion Section to be published in the June 1976 JOURNAL. All discussions for the June 1976 Discussion Section should be submitted by Feb. 1, 1976.

Publication costs of this article were partially assisted by F. Hine.

SYMBOLS

<i>d</i>	density, g/cm ³
<i>D</i> _{eq}	equivalent diameter for Re, cm
<i>F</i>	Faraday constant, 96,500 coulombs/g-equiv.
(<i>IR</i>) _b	<i>IR</i> -drop with bubbles (= <i>i</i> <i>l</i>), V
(<i>IR</i>) _s	<i>IR</i> -drop without bubble (= <i>i</i> ρ_0 <i>l</i>), V
ΔIR	increment of <i>IR</i> -drop (= (<i>IR</i>) _b - (<i>IR</i>) _s), V
<i>H</i>	electrode length, cm
<i>i</i>	current density, A/cm ²
<i>l</i>	cathode-to-diaphragm spacing, cm
<i>L</i>	electrode width (= 1 cm), cm
<i>p</i> _{H₂}	hydrogen partial pressure, atm
<i>p</i> _{H₂O}	water vapor pressure, atm
<i>R</i>	gas constant, 82.1 atm·cm ³ /g-mol·°K
Re	Reynolds number
<i>T</i>	temperature, °K
<i>t</i>	temperature, °C
<i>u</i>	flow velocity, cm/sec
<i>V</i> _g	volume rate of evolved hydrogen, cm ³ /sec
<i>V</i> _l	volume flow of liquid, cm ³ /sec
ϵ	void fraction due to bubbles
ρ and ρ_1	apparent resistivity with bubbles, ohm·cm
ρ_0	resistivity of solution, ohm·cm
$\rho\delta$	resistivity in crowded layer, ohm·cm
ρ_f	resistivity in fixed layer, ohm·cm
η	hydrogen overvoltage, V
μ	viscosity, poise
δ	thickness of crowded layer, cm
δ_1	thickness of fixed layer, cm
λ	dimensionless thickness of gassy layer (= δ/l)

REFERENCES

- R. E. De La Rue and C. W. Tobias, *This Journal*, **106**, 827 (1959).
- C. W. Tobias, *ibid.*, **106**, 833 (1959).
- F. Hine, S. Yoshizawa, and S. Okada, *Denki Kagaku (J. Electrochem. Soc. Japan)*, **24**, 370 (1956).
- S. Okada, S. Yoshizawa, F. Hine, and Z. Takehara, *ibid.*, **26**, 165, 211 (1958).
- S. Yoshizawa, F. Hine, Z. Takehara, and M. Yamashita, *ibid.*, **28**, 205 (1960).
- F. Hine, S. Yoshizawa, S. Okada, and T. Uesugi, *Kogyo Kagaku Zasshi (J. Chem. Soc. Japan, Ind. Chem. Section)*, **57**, 554 (1954).
- R. B. MacMullin, in "Chlorine," ACS Monograph 154, J. S. Sconce, Editor, p. 127, Reinhold Publishing Corp., New York (1962).

8. W. C. Gardiner, *Electrochem. Technol.*, **1**, 71 (1963).
9. R. B. MacMullin, *ibid.*, **1**, 5 (1963).
10. R. B. MacMullin, *Denki Kagaku*, **38**, 570 (1970).
11. M. Murozumi, *Electrochem. Technol.*, **5**, 236 (1967).
12. H. Shibata and Y. Yamasaki, *ibid.*, **5**, 239 (1967).
13. D. Landolt, R. Acosta, R. H. Müller, and C. W. Tobias, *This Journal*, **117**, 839 (1970).
14. A. Cohen, *Z. Elektrochem.*, **29**, 1 (1923).
15. B. Kabanow and A. Frumkin, *Z. Physik. Chem.*, **A165**, 433 (1933).
16. K. Takada and H. Morishita, *Denki Kagaku*, **32**, 378, 586 (1964).
17. T. Murakawa, *J. Electrochem. Soc. Japan*, **25**(5), E-61 (1957).
18. D. E. Westerheide and J. W. Westwater, *Am. Inst. Chem. Engrs. J.*, **7**, 357 (1961).
19. J. P. Glas and J. W. Westwater, *Intern. J. Heat Mass Transfer*, **7**, 1427 (1964).
20. A. E. Debarr and D. A. Oliver, "Electrochemical Machining," p. 61, MacDonald, New York (1968).
21. J. Venczel, *Electrochim. Acta*, **15**, 1909 (1970).
22. L. J. J. Janssen and J. G. Hoogland, *ibid.*, **15**, 1013 (1970).
23. N. Ibl and J. Venczel, *Metalloberfläche*, **24**, 365 (1970).
24. N. Ibl, *Chem.-Ing. Tech.*, **43**, 202 (1971).
25. R. B. MacMullin, Private communication.
26. G. Alerlöf and G. Kegeles, *J. Am. Chem. Soc.*, **62**, 620 (1940).
27. Lando t-Börnstein, "Zahlenwerte und Funktions," 6 Auflage, Band II, 5 Teil, Bendteil A, p. 316, Julius Springer, Berlin (1969).

A New Approach to the Analysis of Chemiluminescence Transients from Step Experiments

Larry R. Faulkner*

Department of Chemistry, University of Illinois, Urbana, Illinois 61801

ABSTRACT

A study has been made of problems associated with extracting fundamental parameters from chemiluminescence decay curves generated by electrochemical step experiments. Emphasis is placed on the use of data obtained early in the transient, and a new approach based on curve fitting is advanced. A general ST mechanism provides the fitting function, and the Marquardt algorithm plays the key role in implementing the fit. However, a perimeter search routine has been developed to remove the unreliability that the Marquardt algorithm displays with noisy decay curves. The effectiveness of the entire procedure has been tested on sets of noisy transients, and fitting precision is reported as a function of the size and time domain of the data base, the noise level, and the percentage of S emission in the over-all luminescence. The effects of error in the calibration of absolute luminescence measurements are also discussed.

Studying light emission in single pulses from electrochemical step experiments has been an important aid in understanding chemiluminescent electron transfer processes. These experiments involve a planar working electrode which is held initially at rest in a solution of the electrochemical precursors to the reactants that will ultimately yield luminescence. To begin, the potential is stepped to the mass-transfer-limited region for creation of the first reactant. For example, the cation radical of rubrene might be generated from the parent hydrocarbon in a benzonitrile solution. The width, t_f , of this forward step might range from 10 sec to 10 μ sec. It is terminated by switching the potential to a value in the mass-transfer-limited region for creation of the second reactant (e.g., the rubrene anion radical). Thus, the two reactants diffuse together near the electrode and yield luminescence, which appears as a pulse that decays by a nonexponential form. Often this reverse step has a width equal to t_f , and it is nearly always ended by a return to the original rest potential.

Feldberg was early in pointing out the diagnostic utility of the luminescence transient (1, 2). He presented treatments of S- and T-route cases (see below), and showed that one should usually obtain a linear plot of the form

$$\log \omega_1 = a_1 + b_1(t_r/t_f)^{1/2} \quad (t_r/t_f \geq 0.2) \quad [1]$$

where ω_1 is proportional to intensity and t_r is time measured into the second step from its start. The slope,

* Electrochemical Society Active Member.
Key words: chemiluminescence, electrogenerated chemiluminescence, curve fitting, Feldberg treatment.

b_1 , of this "Feldberg plot" was shown to be sensitive to the type of light producing mechanism (2). A number of experimental studies have pursued these ideas (3-7).

Later Cruser and Bard adopted the Feldberg format for their study of the effects of reactant instability on the shapes of light decay curves. Their publications include both theoretical analysis and experimental results (8, 9).

More recently, Bezman and Faulkner added some refinements to Feldberg's reaction schemes, and they showed that certain aggregates of rate and efficiency parameters could be evaluated from a_1 and b_1 , if absolute luminescence measurements were available (10, 11). They later constructed a suitable apparatus and reported data for several systems (11-13).

Analyzing experimental results by linearizing the light transient has been very convenient, especially for the limited amounts of information one can obtain by oscilloscopic recording. Even so, the procedure carries several important drawbacks:

(i) Only data for $t_r/t_f \geq 0.2$ are examined. For still earlier times, the decay is rapid, hence the intensities that are actually studied are low compared to those that can be recorded, and they have relatively poor signal-to-noise ratios.

(ii) Obviously a linearized curve can yield only two parameters; hence, studies that are restricted to the later time domain cannot deal with ST systems, which require at least three parameters for description (see below).

(iii) Eliminating the short-time intensities, which decay in a more complex fashion than the later ones,

reduces the opportunity for critical comparisons with theory, even with S- and T-route systems, for which the linear approach is, in principle, valid.

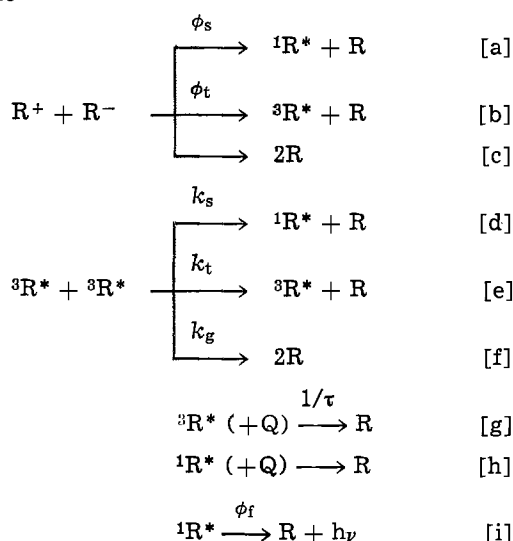
(iv) The parameters a_i and b_i are synthetic intermediates with no fundamental meaning of their own. They must be related to mechanistic variables in an imperfect manner via working curves.

(v) The need for linearity in the transformed decay curve limits the generality of the interpretive procedure. Complications introduced into the mechanisms for light generation often yield intensities that cannot be linearized in the usual format, hence quantitative comparisons with theory become difficult.

All of these problems are remedied by the new approach to transient analysis that is described below. Virtually the entire decay curve is used, without logarithmic transformation, in a curve fitting algorithm that can accept a general fitting function. The function used for this work describes light emitted from an ST system in a manner much like the one advanced by Feldberg (2). Sets of noisy synthetic decay curves have been used to assess the performance of the algorithm, and it is shown below that this procedure is a realistic approach to the evaluation problem.

A Generalized ST Mechanism

Prior knowledge of the functional form of any kinetic transient is a prerequisite for evaluating fundamental parameters from it, hence a presumed fitting function must be derived from a postulated mechanism. The analysis below is based on the following scheme



The notation here duplicates that used previously (10). In general, ϕ 's, τ 's, and k 's represent branching efficiencies, lifetimes, and rate constants according to usual practice. Note, however, that τ is the triplet lifetime in the absence of triplet-triplet annihilation and that $k_a = k_s + k_t + k_g$. This mechanism represents the generation of light via two parallel paths: The emitting singlets ${}^1R^*$ may be produced directly in electron transfer (the S route, reactions [a] and [i]) or indirectly through triplet intermediates (T route, reactions [b], [d], [e], [f], and [i]).

Feldberg's treatment of this scheme involves the presumption that events [a]-[i] take place in a reaction zone to which the ion radicals are fed by diffusion (2, 10). The over-all redox reaction rate, N (moles/sec), is then fixed by the diffusion process. The linkage between light emission and the redox rate is expressed (10) by

$$\omega_i = \beta - (\beta^2 + \alpha\beta\omega_n)^{1/2} + 0.5\alpha\omega_n + \gamma\omega_n \quad [2]$$

where ω_i and ω_n are dimensionless variables proportional to light intensity and redox reaction rate, re-

spectively. They are defined explicitly in the symbols list. The first three terms describe light emission from the T route via two aggregate parameters $\alpha = \phi_f\phi_{tt}\phi_t/(1-g)$ and $\beta = \phi_f\phi_{tt}f t_f/8k_a(1-g)^2\tau^2C$. Here $\phi_{tt} = k_s/k_a$, $g = k_t/2k_a$, f is a dimensionless reaction zone thickness [in units of $(Dt_f)^{1/2}$], and C is the bulk concentration of the substrate from which R^+ and R^- are generated. S route emission is registered in the fourth term, where $\gamma = \phi_s\phi_f$. The efficiency parameters α and γ are potentially useful because they contain the excitation yields, but β is of little value (10).

In general the redox rate function ω_n is obtained from a digital simulation of the experiment (1, 10), and it can be used directly as the numerical array. For this study, however, it was obtained in an analytical form by linearizing it to determine the longest-lived exponential, subtracting that term from each numeric ω_n , then repeating the process twice more with the residues from the preceding subtraction steps. Figure 1 displays about 10% of the information used in the third (and most uncertain) stage of this process for ω_n data based on an infinite redox rate constant. The result

$$\begin{aligned}
 \omega_n = & 4.70 \exp[-3.272(t_r/t_f)^{1/2}] \\
 & + 11.4 \exp[-11.35(t_r/t_f)^{1/2}] \\
 & + 34.9 \exp[-34.6(t_r/t_f)^{1/2}] \quad [3]
 \end{aligned}$$

closely approximates the numeric form for $t_r/t_f \geq 0.005$. The three terms were obtained from simulations involving 2,500, 10,000, and 100,000 iterations/step, respectively.¹ At shorter times, additional exponential terms contribute, but they are of no consequence to this work. The first term is better recognized in Feldberg's linear format (1)

$$\log \omega_n = (0.672 \pm 0.002) - (1.421 \pm 0.003)(t_r/t_f)^{1/2} \quad [4]$$

which is valid for $(t_r/t_f) > 0.5$.

The functions [2] and [3] describe the intensity-time relationship for a light pulse generated in the step format, provided the assumptions involved in deriving [2] are valid. They have been considered in the literature (10), and only the presumed steady state in ${}^3R^*$ needs reexamination here. The use of data taken early in the curve, where intensity changes are rapid, makes it necessary to support this approach. Thus, a comparison was made of the light intensities predicted by that approximation and by the integrated rate equation (10) for ${}^3R^*$. For these calculations, f was taken as $(\tau'/t_f)^{1/2}$, where $1/\tau' = 1/\tau + k_a[{}^3R^*]$. [See Ref. (10).] For a realistic case, $t_f = 1$ sec, $\phi_t = 0.1$, and $\tau = 10^{-4}$ sec, and the two predicted intensities become equal within 2% by the time $t_r = 30$ μ sec. Longer time constants characterize systems with lower ϕ_t or longer τ . A worst case can be taken as $t_f = 1$ sec, $\phi_t = 0.001$, and $\tau = 10^{-2}$ sec, and it features an 8% discrepancy after 10 msec. In the algorithm proposed below, data are considered only for $t_r/t_f > 0.01$, hence it is likely that the steady-state treatment is always valid for the data analysis as long as $t_f > 0.1$ sec. For experiments

¹ During the review of this manuscript, Professor J. T. Maloy pointed out that the oscillations in ω_n could be eliminated by equalizing the dimensionless redox rate constant, $k t_f C$, with the number of iterations/step in a given simulation. One can further argue that such a procedure is the most appropriate method to obtain ω_n for diffusion controlled conditions. It gives rise to the analytical rate-time function

$$\begin{aligned}
 \omega_n = & 4.74 \exp[-3.275(t_r/t_f)^{1/2}] \\
 & + 11.99 \exp[-11.604(t_r/t_f)^{1/2}] \\
 & + 37.34 \exp[-36.33(t_r/t_f)^{1/2}].
 \end{aligned}$$

This function deviates from the numeric data set by 0.4% at the most and 0.2% on the average. It deviates from [3] by 0.5% at the most and 0.3% on the average. The two analytical representations give virtually identical precision in fitting operations.

The smoothness of ω_n from Maloy's approach is noteworthy, however. For example, one obtains an analog to Fig. 1 that is absolutely straight and noise free from $0.07 \leq (t_r/t_f)^{1/2} \leq 0.13$. When fitting operations involve numeric (rather than analytical) ω_n , the smoothness is a great advantage.

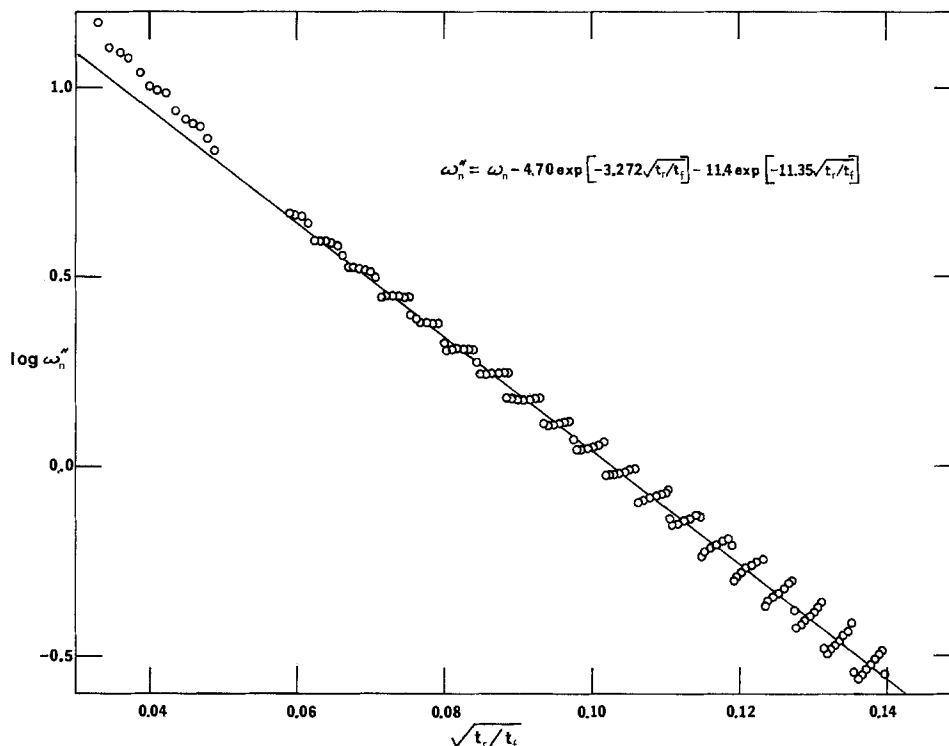


Fig. 1. The residue of ω_n following subtraction of the two longer-lived exponentials in Eq. [3]. The circles represent approximately every tenth value of ω_n produced by a simulation involving 100,000 iterations/step. The oscillatory behavior of ω_n is an artifact arising from the discrete nature of the concentration arrays in the simulation. The line is a plot of the shortest lived exponential in Eq. [3].

of shorter duration or for very inefficient systems, one might have to consider the more exact approach.

Strategy for Evaluating Parameters

The heart of the proposed method for extracting information from decay curves is the Marquardt curve fitting algorithm (14, 15). Like other least squares methods, it seeks the minimum point on the surface $\chi^2(\alpha, \beta, \gamma)$, which is defined as

$$\chi^2(\alpha, \beta, \gamma) = \sum_{\text{all points}} [\omega_i(\alpha, \beta, \gamma) - (\omega_i)_{\text{meas}}]^2 / \sigma_n^2 \quad [5]$$

The sum in [5] covers the whole array of measured intensity-time pairs $[(\omega_i)_{\text{meas}}, t_r/t_f]_n$, and the weighting factor σ_n is proportional to the standard deviation in the intensity of the n^{th} point.

The Marquardt algorithm requires as input a working point, i.e., some set (α, β, γ) . The shape of the χ^2 surface at that point is examined, and the routine adjusts the three parameters in a manner that yields a smaller $\chi^2(\alpha, \beta, \gamma)$. The new working point is then used as input for another cycle, and the whole procedure continues until the working point arrives at a minimum on the χ^2 surface.

This procedure is accurate and efficient. If one supplies a data set which is calculated from given α , β , and γ values via [2], it will report exactly those values regardless of what initial point is chosen. Unfortunately, the reliability is much worse when noisy data are used because the noise introduces into the χ^2 surface shallow secondary minima that can serve as traps. They usually are located fairly near the true result, but our observations include cases in which the fitting results are erroneous by an order of magnitude in one or more parameters. In the presence of noise, then, fitting operations using only the Marquardt algorithm are imprecise, sometimes grossly incorrect, and may yield results that depend strongly on one's choice of the initial working point. It is a key aspect of this work that the Marquardt procedure has been supplemented to improve its reliability.

The improvements are derived from a second routine which is executed after a first pass through Marquardt's algorithm. Since the working point that exists on entry to this routine defines a minimum in χ^2 , one cannot easily use surface contour there to obtain a

better working point. Instead, the approach is to search a perimeter of 26 selected points surrounding it. These points are the set $(\alpha + u_1\delta\alpha, \beta + u_2\delta\beta, \gamma + u_3\delta\gamma)$ where $u_i = 0, \pm 1$. The increments $\delta\alpha/\alpha$, $\delta\beta/\beta$, and $\delta\gamma/\gamma$ do not exceed 0.5, but they are usually large enough that χ^2 for some peripheral point is larger than that at the working point by factors from 2 to 10. Selecting them so helps to ensure that the perimeter will extend over the ridges defining the secondary traps in the χ^2 surface. If one or more of the peripheral points has χ^2 smaller than the working point, then the best of these is taken as the new working point, and a new perimeter search is made. When the improvement is within the fitting tolerance, the iteration is stopped, and a final pass through the Marquardt algorithm is made. Its output is taken as the best fit to the data.

The perimeter search is inefficient and accounts for about 70% of the typical fitting time; but it virtually eliminates gross errors, it improves fitting precision markedly, and dependences in the final fit on the initial guess became quite rare. For a 150 point array of data, a program written in Fortran IV for a Data General Nova 820 minicomputer requires about 3 min for execution.

This fitting procedure is prefaced by several other operations. In our implementation, data from experiments or from calculations of trial synthetic curves exist on tape cassettes in an array which contains 501 intensities corresponding to times 0.002 unit apart in the range $0 \leq t_r/t_f \leq 1$. These data are first subjected to a 7-point quartic smooth for $0 \leq t_r/t_f \leq 0.06$ and a 19-point quartic smooth for $t_r/t_f > 0.06$ (16, 17). Since a 501 point array is unmanageably large for the fitting operation, some selection of points must be made. In much of the work reported below, the data sent to the fitting algorithm were taken at even time intervals over the range $0 \leq t_r/t_f \leq 1$. Better precision is attained when they are selected at intervals as even as possible in a $(t_r/t_f)^{1/2}$ format, hence this procedure was adopted for the version now being used for experimental work. Data for $t_r/t_f \leq 0.01$ are discarded. The weight σ_n for any given point is taken as the average of the smoothing corrections made for it and for the two selected points immediately adjacent to it.

Following smoothing and point selection, the Feldberg parameters are determined, and the ratio of ω_1 at $t_r/t_f = 0.05$ to that at 0.2 is calculated. A comparison

of these three indices of curve shape with those in a large catalog of data from theoretical curves permits one to enter an initial working point that is not too far from the final value.

Performance.

To characterize the precision that could be expected from this procedure, a study of fitting performance has been made for synthetic curves which first were calculated from [2] and then had noise superimposed upon them. The sets of deviations making up the noise were Gaussian, and the deviations in any set ranged from $3\sqrt{2}\sigma$ to $-3\sqrt{2}\sigma$, where σ was the standard deviation of the distribution. One could change the absolute noise level by altering σ . Two kinds of noisy curves were studied: (i) For most work, ω_1 was perturbed in a manner such that σ/ω_1 was constant. Thus the noise falls with the intensity decay, and the signal-to-noise ratio is constant. (ii) A few studies involved the application of a constant noise level, expressed as $(\sigma/\omega_1)_{t_r/t_f=1}$, to the entire curve. In this case, the signal-to-noise ratio worsens as the decay proceeds.

Performance has been defined for variations in several operating parameters, including the number of data points used in the fit, the range of times over which the points are taken, the noise level, and the fraction of S route emission. In addition, the effect of an error in calibrating absolute emission measurements has been examined. The results are as follows:

Number of data points.—Figure 2 portrays the precision of determining α , β , and γ from a set of five noisy transients all of which had the same noise level and the same true values of those parameters. Precision is expressed for each parameter as $\bar{\Delta}$, the relative average deviation from the mean fitting result. In every case the mean was within Δ of the true value.

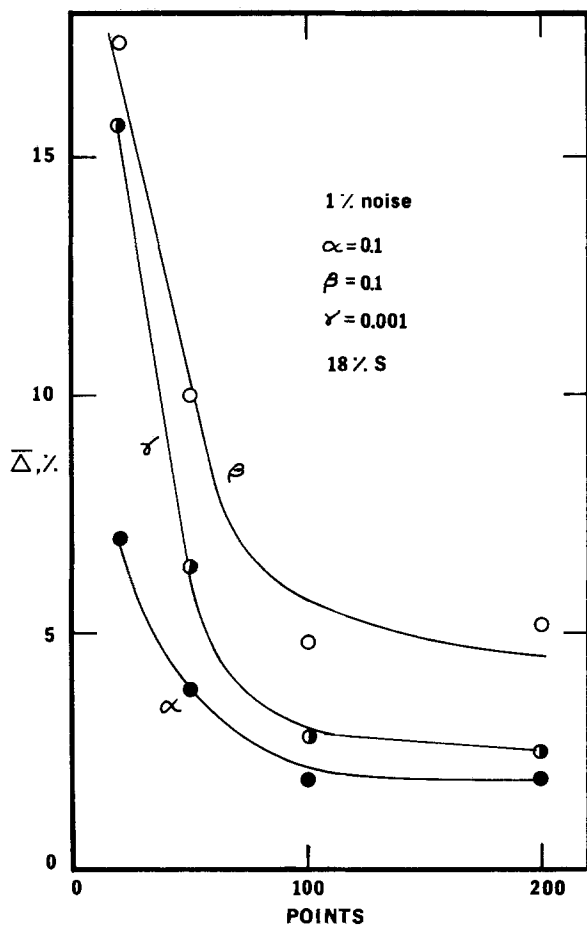


Fig. 2. Relative average deviations in fitting α , β , and γ vs. size of the data array. Noise is of type (i).

Table I. Effect of data base time domain on fitting precision^a

Time domain	$\bar{\Delta}\alpha$ (%)	$\bar{\Delta}\beta$ (%)	$\bar{\Delta}\gamma$ (%)
$0.01 \leq t_r/t_f \leq 1$	1.9	4.8	2.8
$0.1 \leq t_r/t_f \leq 1$	3.0	7.8	3.2

^(a) 100 points; type (i) noise at 1% level; true curve: $\alpha = 0.1$, $\beta = 0.1$; $\gamma = 0.001$; 18% S.

The noise was of type (i) described above, and its standard deviation was 1% of the intensity ω_1 . In peak-to-peak terms, this level is 3-5% of ω_1 throughout the time domain. For the particular combination of α , β , and γ taken here, the S route supplies 18% of the total emission. Performance improves markedly with increases in the data set when the number of points is below 100. However, the slight improvement obtained with still larger sets has led us to settle on 100 or 150 points for the analysis of real data.

Time domain.—Table I shows the effect on Δ values of taking data later in the transient. Deleting the early information has disadvantages enumerated above, but it may be necessary whenever the step rise time or the validity of the steady-state approximation becomes a problem. The fitting procedure remains useful if one retains some information for $t_r/t_f \leq 0.2$, but raising the lower bound on t_r/t_f causes increases in Δ values. Note that the increases are much larger for α and β than for γ . This situation derives from the T route's sensitivity to $[^3R^*]^2$, and it emphasizes the importance of the early information for evaluating T route parameters and the later data for determining the role of the S pathway.

Errors in the absolute measurement of ω_1 .—It is not a trivial task to calibrate a detector to yield absolute measurements, and disagreement continues over the validity of calibration procedures. It is therefore important to determine the effect on the fitting outcome of a constant multiplicative error in all values of ω_1 . The general rule can be found from Eq. [2]. Note that if a given set ω_1 is associated with the given parameters α , β , and γ , then the set of intensities $k\omega_1$, which has the same shape as ω_1 if k is constant, must be associated with $(k\alpha, k\beta, k\gamma)$. The important conclusion is that the curve shape depends only on the ratios of α , β , and γ . The ratios of the parameters, hence the percentage of S emission, can be determined even from relative measurements of intensity. Absolute data are needed if the magnitudes of the parameters are wanted, and any error factor in evaluating ω_1 will show up identically in all three parameters. Tests with the fitting procedure have borne out this expectation.

Contributions from the S route.—Figure 3 depicts fitting precision as a function of S route contribution to the total emission arising from an ST system. For a constant relative noise level, Δ values hardly depend at all on the absolute magnitudes of α , β , and γ . As one expects, the ability to define α and β deteriorates as one moves to larger S participation, and γ shows the opposite trend. When the S contribution is between 10 and 90%, both important parameters, α and γ , seem adequately defined.

Noise level.—The deterioration in precision with increasing noise is shown in Fig. 4, where the abscissa expresses the standard deviation of superimposed noise of type (i) as a percentage of ω_1 . The efficiency parameters α and γ are sufficiently well defined to make the fitting procedure worthwhile even at a 5% level (15-25% peak-to-peak), and Fig. 3 suggests that they generally will be so for pure S or pure T cases and for ST systems with S contributions ranging from 10-90%.

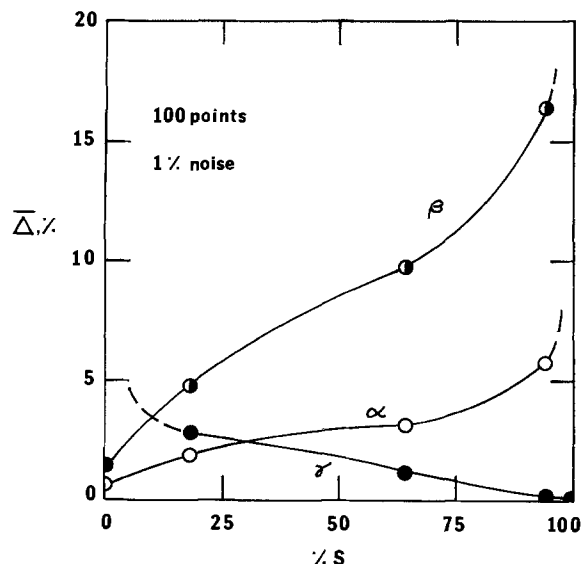


Fig. 3. Relative average deviations in fitting α , β , and γ vs. percentage contribution of S-route luminescence to total emission. Noise is of type (i).

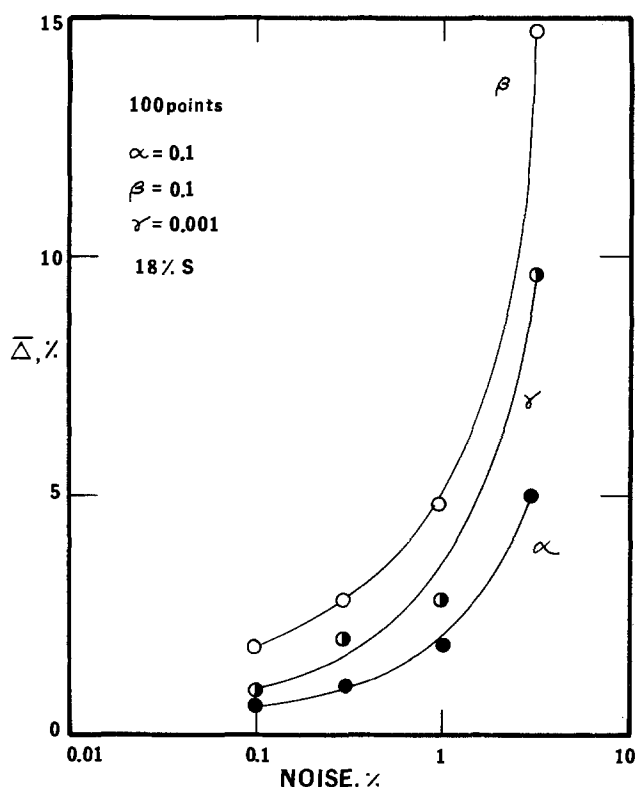


Fig. 4. Effect of noise level on fitting precision. Noise is of type (i).

A brief study dealt also with noise of type (ii) For $\alpha = 0.1$, $\beta = 0.1$, and $\gamma = 0.001$ (18% S) and for σ being 50% of ω_1 at $t_r/t_f = 1$, $\bar{\Delta}$ values for the three parameters were 0.3, 1.8, and 6.4%, respectively. When σ was 200% of ω_1 at $t_r/t_f = 1$, these figures rose to 0.9, 5.7, and 23%. The importance of the early emission for determining T route parameters is again demonstrated: For 50% noise of type (ii), the precision in α and β is comparable to that obtained with noise of type (i) at a level of 0.1%; yet γ is only as precise as with a 2-3% level of type (i).

Conclusion

The foregoing paragraphs demonstrate the viability of this procedure for transients having noise levels no larger than those considered here. Such signals are ex-

perimentally realistic. In work with the rubrene homomolecular ion annihilation in benzonitrile, we record transients with noise patterns resembling type (ii) with a 50% level. Thus, it seems reasonable to use this approach with real data, and efforts along that line are in progress. Being able to examine an entire transient with precision will make a rigorous test of the theory behind [2] possible for the first time. If it or a successor is found to be valid, the fitting approach should prove worthwhile for routinely extracting information about excitation efficiencies.

LIST OF SYMBOLS

A	electrode area, cm^2
a_i, b_i	intercept and slope of Feldberg plot
C	concentration of reactant precursor, moles/ cm^3
D	diffusion coefficient of reactant precursor, cm^2/sec
f	width of reaction zone along diffusion axis (dimensionless) (2, 10)
g	$k_t/2k_a$
I	absolute light intensity, einstein/sec
k_a	$k_s + k_t + k_g$
k_s, k_t, k_g	rate constants for triplet-triplet annihilation
N	redox reaction rate, mole/sec
t_f	duration of the forward step, sec
t_r	time measured into the reverse step from its start, sec
α	$\phi_f \phi_{tt} \phi_t / (1 - g)$
β	$\phi_f \phi_{tt} f t_f / 8 k_a \tau^2 (1 - g)^2 C$
γ	$\phi_f \phi_s$
σ_n	standard deviation in the measurement of the η^{th} ω_i value
σ	standard deviation of the distribution of absolute noise deviations
τ	lifetime of $^3R^*$ in the absence of triplet-triplet annihilation
ϕ_f	fluorescence efficiency of $^1R^*$
ϕ_s	singlet yield of electron transfer
ϕ_t	triplet yield of electron transfer
ϕ_{tt}	k_s/k_a
χ^2	index function for fitting, see [5]
ω_i	$I t_f^{-1/2} / A D^{1/2} C$
ω_n	$N t_r^{-1/2} / A D^{1/2} C$

Acknowledgments

The author is grateful for the support of the National Science Foundation through Grant GP37335X and for a fruitful suggestion by Professor N. Winograd.

Manuscript submitted Jan. 15, 1975; revised manuscript received May 1, 1975. This was Paper 292 presented at the San Francisco, California, Meeting of the Society, May 12-17, 1974.

Any discussion of this paper will appear in a Discussion Section to be published in the June 1976 JOURNAL. All discussions for the June 1976 Discussion Section should be submitted by Feb. 1, 1976.

Publication costs of this article were partially assisted by the University of Illinois.

REFERENCES

1. S. W. Feldberg, *J. Am. Chem. Soc.*, **88**, 390 (1966).
2. S. W. Feldberg, *J. Phys. Chem.*, **70**, 3928 (1966).
3. R. E. Visco and E. A. Chandross, *Electrochim. Acta*, **13**, 1187 (1968).
4. J. Chang, D. M. Hercules, and D. K. Roe, *ibid.*, **13**, 1197 (1968).
5. E. W. Grabner and E. Brauer, *Ber. Bunsenges. Phys. Chem.*, **76**, 106 (1972).
6. E. W. Grabner and E. Brauer, *ibid.*, **76**, 111 (1972).
7. R. P. Van Duyne and S. F. Fischer, *Chem. Phys.*, **5**, 183 (1974).
8. S. A. Cruser and A. J. Bard, **91**, 267 (1969).
9. S. A. Cruser, Ph.D. Dissertation, University of Texas at Austin (1968).
10. R. Bezman and L. R. Faulkner, *J. Am. Chem. Soc.*, **94**, 3699 (1972).
11. R. Bezman and L. R. Faulkner, *ibid.*, **94**, 6331 (1972); **95**, 3083 (1973).
12. R. Bezman and L. R. Faulkner, *ibid.*, **94**, 6317 (1972); **95**, 3083 (1973).

13. R. Bezman and L. R. Faulkner, *ibid.*, **94**, 6324 (1972); **95**, 3083 (1973).
 14. D. W. Marquardt, *J. Soc. Ind. Appl. Math*, **11**, 431 (1963).
 15. P. R. Bevington, "Data Reduction and Error Analysis for the Physical Sciences," pp. 235-242, McGraw-Hill Book Co., New York (1969).
 16. A. Savitzky and M. J. E. Golay, *Anal. Chem.*, **36**, 1627 (1964).
 17. J. Steinier, Y. Termonia, and J. Deltour, *ibid.*, **44**, 1906 (1972).

Studies in Derivative Chronopotentiometry

I. Instrumentation and Diffusion-Controlled Systems

P. E. Sturrock,* J. L. Hughey, B. Vaudreuil, and G. E. O'Brien

School of Chemistry, Georgia Institute of Technology, Atlanta, Georgia 30332

and R. H. Gibson*

Department of Chemistry, University of North Carolina at Charlotte, Charlotte, North Carolina 28223

ABSTRACT

Theoretical correction and instrumental compensation of charging current are discussed for both conventional and derivative chronopotentiometry. Experimental results indicate that either correction or compensation is effective in reducing the error due to charging the electrical double layer, but that best results are obtained by application of both techniques. In diffusion-controlled systems, derivative chronopotentiometry shows significant advantages over conventional chronopotentiometry.

Relationships governing chronopotentiometry in its simplest form have been derived, and the technique has been discussed in some detail (1-5). The relationships given in the references do not include the unavoidable complication of double-layer charging, probably the most serious problem encountered in chronopotentiometry. Because of this, it is often difficult to obtain a highly precise correspondence of experimental results and theoretical predictions. Despite these problems, the chronopotentiometric technique offered sufficient promise of utility to encourage our examination. Most of our efforts have been in the evaluation of derivative chronopotentiometry (6) and its comparison with the conventional technique. In this paper, we report the instrumentation required for derivative chronopotentiometry, its application to simple systems, and a comparison of derivative and conventional results. Included are suggestions for obtaining chronopotentiometric data corrected for the effects of double-layer charging.

Conventional Chronopotentiometry

Application of the Sand equation (3) requires that all current supplied to the cell be used in the faradaic process. In reality this requirement is never met. A part of the current supplied is used in charging the electrical double layer. This has the effect of decreasing the amount of charge available for the faradaic process. In addition, the double-layer capacity is potential-dependent and the rate of potential change is highly nonlinear so that the fraction of current devoted to the charging process is not constant. These two effects produce not only a lengthening of the apparent transition time beyond its predicted value based upon the value of the applied current, but also a distortion of the potential-time curve. These effects become most important at short times (high current densities) and low concentrations.

Considerable effort has been expended in recent years in attempts to obtain chronopotentiometric data unperturbed by double-layer charging (7-9). One approach to the distortion problem has been the sug-

gestion that instrumental compensation, usually requiring positive feedback, be used (10). A promising instrumental method, evaluated in this work, is based upon the fact that the rate of double-layer charging is a function of the rate of potential change. Electronic differentiation of the potential-time curve produces a voltage signal proportional to dE/dt , and a portion of this signal is converted to a current which is then added to the applied current by positive feedback (6). The fixed proportion of the differentiator output which is used for feedback is based on the double-layer capacitance in the potential range of interest. Further details are given in the instrumentation section.

The various graphical and potential-interval techniques and correction approaches have been compared by others (11). After considerable investigation, we have chosen to base our estimate of the conventional transition time upon the measuring technique suggested by Noonan (12) (Fig. 1) and the correction model suggested by Bard (13). Noonan defines the initial time ($t = 0$) as the intersection of tangents to

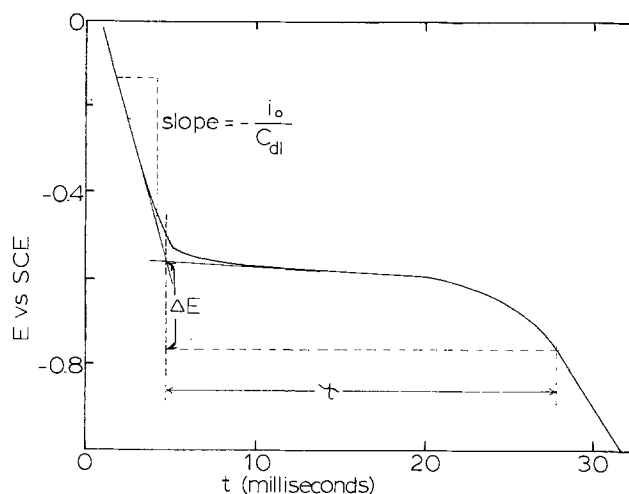


Fig. 1. Noonan technique for measurement of transition time and double-layer capacitance.

* Electrochemical Society Active Member.

Key words: dropping mercury electrode (dme), current compensation, positive feedback.

the initial, rapid potential change and the initial portion of the plateau region of the potential-time curve. The uncorrected transition time, τ , is then defined as the time interval from this point to the time at which the potential has changed by 200 mV. The choice of potential interval magnitude is somewhat arbitrary, but the interval must be large enough to ensure that the surface concentration of electroactive species approaches zero. Of course, the larger the interval the more nonfaradaic charge is included in the measurement, and the greater the probability that more highly potential-dependent regions of double-layer charging will be encountered. No charging correction is obtained in the measuring technique itself. This is accomplished by treating the data in the manner suggested by Bard, who utilized a split current model

$$i_o = i_F + i_{dl} + i_{ads} \quad [1]$$

where i_o = total applied current density; i_F = faradaic current density; i_{dl} = double-layer current density; and i_{ads} = adsorption current density. The model assumes that the component currents comprising i_o are all constant throughout the experiment. In the absence of adsorption, the equation becomes after substitution

$$i_o = nF(\pi D)^{1/2} C / 2\tau^{1/2} + C_{dl}\Delta E / \tau \quad [2]$$

where C_{dl} = average double-layer capacitance per cm^2 over interval ΔE volts and τ = measured transition time. A useful form of this equation is

$$i_{o\tau} = nF(\pi D)^{1/2} C \tau^{1/2} / 2 + C_{dl}\Delta E \quad [3]$$

$$i_{o\tau} = A C \tau^{1/2} + B$$

where A = true chronopotentiometric constant = $nF(\pi D)^{1/2} / 2$ and $B = C_{dl}\Delta E$. Thus, if the model is applicable, a plot of $i_{o\tau}$ vs. $C\tau^{1/2}$ should yield a straight line with a slope of A and an intercept of B for a series of data obtained at varying current densities. Once B is known, it may be applied in various ways to correct chronopotentiometric data. Corrected individual chronopotentiometric constants can be calculated from Eq. [4]

$$A = (i_{o\tau} - B) / C\tau^{1/2} = (i_o\tau^{1/2} - B/\tau^{1/2}) / C \quad [4]$$

Corrected individual values of τ (as $\tau^{1/2}_{corr}$) can be calculated from Eq. [5]

$$\tau^{1/2}_{corr} = AC / i_o = \tau^{1/2} - B / i_o\tau^{1/2} \quad [5]$$

An alternative method of determining B was suggested by Noonan (12); in this method, one measures the slope of the initial, sharply changing segment of the chronopotentiometric potential-time curve just prior to its breaking over to the plateau region (Fig. 1). The slope is related to the double-layer capacity by

$$\text{Slope} = i_o / C_{dl} \quad [6]$$

The value of C_{dl} thus calculated is used with the known ΔE over which τ is measured to yield a value of B . This value can be used in the same ways as outlined above. This procedure is most useful in kinetically complicated systems.

The Noonan-Bard approaches were used with the results given below. Details as to the specific mode of correction used are given in the Results and Discussion section.

The assumptions, explicit and implicit, in the Bard model have been discussed in some detail in the work of de Vries (14), Nicholson (11), and Rodgers and Meites (15). Their more complex treatments of the double-layer effect indicate that the Bard model is open to some criticism on both theoretical and physical grounds. While these criticisms may be valid, in our hands the model does yield data substantially free of double-layer error and in close agreement with theoretical predictions. It is possible that this occurs because of fortuitous cancellations of errors contained

in the model; nonetheless, the model appears to provide a simple, empirical method for obtaining chronopotentiometric data substantially free of charging error.

Derivative Chronopotentiometry

In derivative chronopotentiometry, the chronopotentiometric potential-time curve is electronically differentiated as a function of time. The differentiator output, dE/dt , can be displayed vs. time or potential. During the chronopotentiometric trace, dE/dt reaches a minimum which is quantitatively related to the transition time. For a cathodic process dE/dt is a negative quantity while for an anodic process it is a positive quantity. The term minimum here refers to the minimum of the absolute values of the derivative. Previous published work in derivative chronopotentiometry is rare. The derivative concept has been applied to cyclic chronopotentiometry (16), and Peters and Burden (6) have derived the theoretical relationship between the transition time and the minimum in the dE/dt curve. Noonan (12) deals with the technique to a limited extent; others have reported initial attempts to apply the technique to submicroformal concentrations (17) and to multicomponent systems (18).

For reversible systems, Peters and Burden derived the following expression

$$(dE/dt)_{\min} = -27RT/8nF\tau = -0.08664/n\tau \quad \text{at } 25^\circ\text{C} \quad [7]$$

The authors claim that this equation provides the first theoretically justifiable method for the evaluation of transition times and point out that the minimum in the dE/dt function is relatively insensitive to double-layer charging. Although this is true and, as a result, derivative chronopotentiometric data are less distorted by double-layer effects than conventional data, it is evident that the experimentally determined dE/dt function retains a double-layer charging term. We have chosen to treat the derivative data in a similar fashion (Bard model) to that chosen for conventional data. As mentioned above, the Bard model assumes a constant ratio of i_F/i_{dl} over the chronopotentiometric curve. Although this can only be approximately true over the entire chronopotentiogram in the conventional technique, the ΔE over which the derivative is taken is much smaller. Thus, the derivative technique is performed using conditions which more nearly approach those postulated in the model. As a consequence, insofar as the model is applicable at all, it should be more applicable to the derivative than to the conventional technique. Results are given below.

Use of the derivative approach is not without its price. The original instrumentation used by Peters and Burden is severely limited in its ability to yield data over a broad time range. Expanding the time range of the instrumentation required some added complexity compared to conventional chronopotentiometry. Most of the additional complexity is directly traceable to the well-known difficulties of electronic differentiation.

More serious disadvantages are those associated with the nature of the charge-transfer process. Theoretical chronopotentiometric transition times depend only upon mass-transfer properties; in principle, the detailed nature of the potential-time curve does not affect τ . Derivative chronopotentiometry, however, requires differentiation of the potential-time curve; thus, relating $(dE/dt)_{\min}$ to τ requires a detailed knowledge of the degree of reversibility of the electrochemical process. In addition, IR drop (uncompensated resistance) may be more important in the derivative method than in the conventional technique. Despite some problems, the work we report here and in succeeding papers will, we believe, demonstrate the continued utility of the chronopotentiometric technique and the potential of the derivative approach.

Instrumentation

Several different chronopotentiometers have been built in this laboratory which represent various stages of development from the instrument described previously (16). The major differences in these instruments are in the characteristics of the amplifiers used, the devices used for switching, and in the number of differentiators employed.

In all the instruments the same basic galvanostat circuit has been used with the test electrode connected to the summing point (at virtual ground) and the counterelectrode connected to the output of the galvanostat amplifier (Fig. 2). The reference electrode is connected to the input of a second amplifier which is used as a voltage follower. The output of the follower serves as the potential output of the instrument and is also connected to one or two differentiators and the voltage sensors of the control circuit. In the earlier instruments, the current source for the galvanostat was an operational amplifier with output voltage limited by a pair of Zener diodes connected back to back. In the latest instrument, regulated power supplies are used for the current sources.

To control the potential of the working electrode prior to the application of the current step, the cell connections are not changed but the summing point of the galvanostat is disconnected from the current sources and connected to the movable tap of the voltage divider (R_3) between the \pm or $-$ supply and the output of the follower. The galvanostat amplifier then controls the voltage of the cell so that the tap of the voltage divider is at ground potential. The potential control is quite effective if no cell current flows at this setting. If cell current does flow at this setting, the nominal electrode potential will be in error since current will be drawn from the voltage divider; however, the potential control is adequate for most purposes and, in any event, the output of the follower will indicate the electrode potential plus a small fraction of the total IR drop in the cell. This circuit has the advantage that the cell is connected to the galvanostat and follower amplifiers at all times and thus switching transients are minimized.

In order to perform chronopotentiometry with a dropping mercury electrode, some device must be employed to synchronize the drop action so that the current step is applied at a reproducible time in the drop life and, hence, on a reproducible electrode area. For this purpose a drop-detaching solenoid is actuated by the cycle timer. The detacher must be designed so that the drop will be dislodged without causing significant continued oscillation of the capillary. The solenoid is mounted in a jig which also holds the capillary. The capillary is held in a semicircular groove by an elastic band or metal spring. The spring tension is just sufficient to return the capillary to its original position. The back side of the groove is covered with a section of rubber tubing to damp the recoil motion when the

capillary is resealed. The solenoid may be positioned in the jig so as to obtain the minimum necessary amount of capillary movement when the solenoid is actuated.

A master timing and control circuit is used to actuate the drop detaching solenoid and to control the input switches to the galvanostat amplifier. When the timer pulses the solenoid, the current control switches, S_1 and S_2 , are set nonconducting and the potential-control switch, S_3 , is set conducting. At the end of the predetermined delay time, the potential control is switched off and either S_1 or S_2 is made conducting so that a cathodic or anodic current is switched into the input of the galvanostat amplifier to start the chronopotentiometric process. The magnitudes of the anodic and cathodic currents are set independently with R_1 and R_2 . When the electrode potential, as represented by the follower output, reaches a preset limiting value, a voltage-sensing circuit reverses the states of S_1 and S_2 , thus reversing the direction of cell current. When the electrode potential reaches a second preset limiting value, both S_1 and S_2 are again set nonconducting and S_3 is set conducting to restore potential control. Alternatively, when the second limiting potential value is reached, the states of S_1 and S_2 are again reversed so that another chronopotentiometric cycle is started. In this way, cyclic chronopotentiometry can be performed. At the end of the cycle time, the drop-detaching solenoid is pulsed again and a new cycle is started. A push-button switch is also provided to serve as a manual start for experiments on stationary electrodes. In this series of instruments, the switching elements have ranged from toggle switches through mercury-wetted relays and diode gates to MOS field-effect transistors.

Operational amplifier differentiators are used to obtain the dE/dt readout and as a signal source for the positive feedback loop used for compensation for the cell capacitance current. A series of differentiator time constants is selectable by switching the input capacitor and feedback resistor. Careful attention to the frequency response of the circuit is necessary to obtain a stable, fast, low noise differentiator. Both a series resistor in the input of the circuit and a parallel capacitor in the feedback loop of the differentiator are necessary. These are switched together with the input capacitor and feedback resistor. In addition, it is necessary to use Zener diodes in a low impedance feedback loop which comes into use when the differentiator output voltage nears its limit. If this is not done, the summing point of the differentiator circuit will leave virtual ground when the limiting output voltage is reached. The circuit recovers very slowly from this condition, especially if a chopper-stabilized amplifier is used.

For derivative readout it is desirable to have a differentiator circuit with a rise time at least two orders of magnitude faster than the transition time being measured. This requires a fast amplifier for transition times of less than a msec. On the other hand, for charging-current compensation, the rise time of the differentiator must be slower than that of the galvanostat-cell circuit; otherwise, the entire circuit will break into oscillation. Thus, it is clear that optimum results can be obtained only if different differentiators are used for readout and feedback. Only one of the instruments used in these studies had two differentiators and the quality of some of the results obtained with the other instruments was curtailed by this omission.

Due to the evolutionary nature of our instruments, still in process, we prefer not to supply specific values of circuit elements in this paper. Interested readers may contact us for further details of specific circuit elements.

Results and Discussion

The first results discussed are conventional. By "conventional" is meant the usual experiment in which the chronopotentiometric potential-time curve, as opposed to its derivative, is the waveform of interest. In all

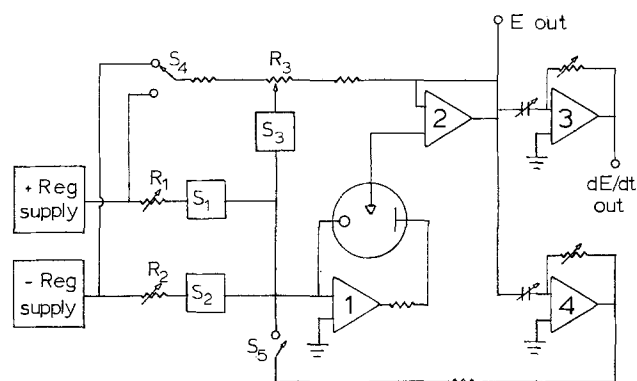


Fig. 2. Schematic diagram of chronopotentiometer. Amplifiers: 1, galvanostat; 2, voltage follower; 3, readout differentiator; 4, feedback differentiator; see text for other details.

cases the measurement of τ was made using the 200 mV interval technique discussed above. Both cadmium and lead systems, of varying concentrations, were examined; the supporting electrolyte was 1.0M KNO_3 in all cases. The conventional results obtained are presented in Tables I and II. In these tables, the column heading "microfarads compensation" refers to the amount of positive feedback utilized, a larger number meaning higher current feedback. The range of τ gives the longest and shortest transition time observed for a given set. The quantity $i\tau^{1/2}/C$ is given as a range in the table, but note that the ranges are somewhat larger than would be obtained using a graphical method for τ measurement; our reasons for adopting the potential-interval measuring technique are given above. The intercept and slopes given are the values obtained by applying the Bard model to the chronopotentiometric data. In all cases this is a plot of $i\tau$ vs. $C\tau^{1/2}$ where τ is the measured transition time, C is concentration of electroactive species, and i is the applied current chosen instrumentally. Such a plot corresponds to

Eq. [3] with all terms multiplied by the electrode area, a , and yields a slope of $i\tau^{1/2}/C$ and an intercept on the $i\tau$ axis which equals $aC_{d1}\Delta E$. Thus, the slope, insofar as the model applies, should be equal to the average value of $i\tau^{1/2}/C$ obtained by correcting individual values of experimental $i\tau/C$, using the procedure outlined previously, and should be equal to the true chronopotentiometric constant multiplied by the electrode area. The intercept value provides a value of C_{d1} . In all cases the slopes and intercepts were obtained by least squares computer analysis, rather than by hand plotting. The column headed $i\tau^{1/2}/C$ (corrected) presents the average of Bard-corrected values thus obtained. Note that slopes and corrected values are in good agreement, implying not only linearity of the data but also close adherence to the Bard model. The number of values given is the actual number of individual values to determine the range and average reported for each set. The number of points used for the over-all average does not always agree with the total due to the statistical procedure of eliminating points whose standard

Table I. Conventional chronopotentiometry of $\text{Pb}(\text{NO}_3)_2$; dme electrode area = 0.0280 cm^2

	Microfarads compensation	τ range (in msec)	$\frac{i\tau^{1/2}}{C}$ range	Intercept	Slope*	$\frac{i\tau^{1/2}}{C}$ corrected	Number of values	Summaries
A. $10^{-3}\text{M Pb}(\text{NO}_3)_2$	0	92-1.5	14.1-19.4	0.250	13.3	13.3	6	$\frac{i_0\tau^{1/2}}{C} = 471 \pm 6^*$
1M KNO_3	0.2 0.4	89-1.3 85-1.1	13.8-18.1 14.1-16.9	0.179 0.127	13.3 13.1	13.3 13.1	6 6	$C_{d1} = 29 \mu\text{f}/\text{cm}^2$
				over-all avg.		13.2	17	
B. $5 \times 10^{-4}\text{M Pb}(\text{NO}_3)_2$	0	90-1.4	15.0-24.3	0.202	13.3	13.3	6	$\frac{i_0\tau^{1/2}}{C} = 467 \pm 7^*$
1M KNO_3	0.3 0.5 0.7	81-1.0 75-0.71 68-0.38	14.2-20.9 13.7-17.2 12.6-13.1	0.123 0.0646 0.0067	13.1 13.0 12.7	13.1 13.0 12.8	6 5 5	$C_{d1} = 26 \mu\text{f}/\text{cm}^2$
				over-all avg.		13.1	21	
C. $2 \times 10^{-4}\text{M Pb}(\text{NO}_3)_2$	0	80-1.3	18.0-40.2	0.162	13.2	13.1	5	$\frac{i_0\tau^{1/2}}{C} = 464 \pm 12^*$
1M KNO_3	0.3 0.5 0.7	68-0.89 59-0.48 47-0.22	16.7-32.8 15.5-24.1 13.8-16.5	0.098 0.046 0.004	13.0 13.0 12.3	13.0 13.1 12.5	5 5 5	$C_{d1} = 28 \mu\text{f}/\text{cm}^2$
				over-all avg.		13.0	19	
D. $1 \times 10^{-4}\text{M Pb}(\text{NO}_3)_2$	0	77-1.2	21.8-67.5	0.149	13.4	13.3	5	$\frac{i_0\tau^{1/2}}{C} = 471 \pm 11^*$
1M KNO_3	0.3 0.5 0.7	61-0.72 50-0.39 35-0.21	19.5-52.9 17.6-38.7 14.6-28.3	0.089 0.046 -0.005	13.3 13.2 13.0	13.3 13.3 12.9	5 4 4	$C_{d1} = 29 \mu\text{f}/\text{cm}^2$
				over-all avg.		13.2	20	

* Units of $\frac{i\tau^{1/2}}{C}$ and slopes are $\frac{\text{amp}\cdot\text{sec}^{1/2}\cdot\text{ml}}{\text{mole}}$; units of $\frac{i_0\tau^{1/2}}{C}$ are $\frac{\text{amp}\cdot\text{sec}^{1/2}\cdot\text{ml}}{\text{mole}\cdot\text{cm}^2}$. Precision analysis is standard deviation. Values of $\frac{i_0\tau^{1/2}}{C}$ are obtained from corrected $\frac{i\tau^{1/2}}{C}$.

Table II. Conventional chronopotentiometry of $\text{Cd}(\text{NO}_3)_2$; electrode (dme) area = 0.0280 cm^2

	Microfarads compensations	τ range (in msec)	$\frac{i\tau^{1/2}}{C}$ range	Intercept	Slope*	$\frac{i\tau^{1/2}}{C}$ corrected	Number of values	Summaries
A. $10^{-3}\text{M Cd}(\text{NO}_3)_2$	0	90-1.2	13.0-17.5	0.176	12.4	12.4	6	$\frac{i_0\tau^{1/2}}{C} = 436 \pm 6^*$
1M KNO_3	0.2 0.4 0.6	85-1.0 81-0.85 77-0.60	12.7-16.2 12.3-14.6 12.0-12.3	0.129 0.075 0.020	12.2 12.1 12.0	12.2 12.1 11.9	6 6 6	$C_{d1} = 24 \mu\text{f}/\text{cm}^2$
				over-all avg.		12.2	23	
B. $5 \times 10^{-4}\text{M Cd}(\text{NO}_3)_2$	0	87-1.1	13.8-20.8	0.147	12.7	12.8	6	$\frac{i_0\tau^{1/2}}{C} = 436 \pm 15^*$
1M KNO_3	0.3 0.5 0.7	77-0.78 70-0.50 64-0.27	13.0-18.1 12.4-14.5 10.6-11.8	0.083 0.046 0.012	12.4 11.8 11.9	12.4 11.9 11.9	6 5 6	$C_{d1} = 24 \mu\text{f}/\text{cm}^2$
				over-all avg.		12.2	23	

* For units, see Table I.

deviation is greater than 2σ . In the summary column are presented chronopotentiometric constants in conventional units; also presented are values of C_{dl} calculated from intercepts. Observe the close agreement of corrected chronopotentiometric constants and C_{dl} over a wide range of concentrations and τ 's and with different values of compensation.

The conventional chronopotentiometric results obtained for the lead system are presented in Table I. Detailed examination of the results in Table I reveals a number of salient features. For no compensation, the values of $i\tau^{1/2}/C$ obtained increase drastically, not only with decreasing τ in a single concentration but also with decreasing concentration; in the absence of double-layer charging, this value should be constant. For example, the values obtained for $10^{-3}M$ range from 14.1 to 19.4, whereas for $10^{-4}M$ the range is 21.8-67.5. These results are expected and are in agreement with the observations of other workers. On the other hand, even with zero compensation, the corrected values are virtually constant within experimental error. A second feature is that exhibited by the results obtained using positive feedback. Generally, as compensation increases (increasing feedback current), the range of uncorrected $i\tau^{1/2}/C$ values decreases within each concentration studied, but does not decrease sufficiently to indicate that electronic compensation alone can provide completely corrected data; a Bard correction is still necessary. An interesting result is revealed by the data for the $10^{-4}M$ solution at compensation 0.7; the negative intercept obtained indicates "overcompensation" and is a further suggestion that electronic compensation alone is inadequate in conventional chronopotentiometry.

The third salient feature of the data in Table I is revealed by examination of corrected values of $i\tau^{1/2}/C$; virtual constancy in the quantity is obtained over the concentration range studied. Although the trend is not statistically meaningful, corrected values obtained with zero compensation are slightly larger than those obtained with positive feedback; yet, too high a level of compensation can be used, as evidenced by the negative intercept discussed above. Therefore, it would appear that, if conventional chronopotentiometry is used, the optimum approach is to use some compensation and to invoke the correction system by Bard. A somewhat less optimum approach is to use no compensation, but to use only the correction technique; this approach would provide data usable for most applications. Data obtained at the concentration levels and transition times of Table I are virtually useless without correction, and electronic compensation (positive feedback) further improves the data. At higher concentrations (2-10 mM), it may be possible to obtain corrected data using only electronic compensation, but at these higher concentrations and at longer transition times correction is often unnecessary. The success of the correction approach and of the application of electronic compensation has particular significance in kinetics studies where theoretically predicted behavior must be obtained; the significance of these results in analytical application is dealt with in a later paper of this series. The fourth important feature of Table I is revealed in examination of the values of $i_0\tau^{1/2}/C$, the chronopotentiometric constant. Values of the quantity, calculated using the corrected value of $i\tau^{1/2}/C$ and the electrode area, are in good agreement with values previously obtained in our laboratories under more favorable concentration and transition time conditions and, thus, much less subject to double-layer charging error.

The conventional chronopotentiometric results obtained for the cadmium system are presented in Table II. The results in set A of the table are illustrated in Fig. 3. These results confirm and strengthen the conclusions and observations obtained using the lead results. They are also useful in the comparison of derivative and conventional approaches given below. In addition, a few important features require comment. Ob-

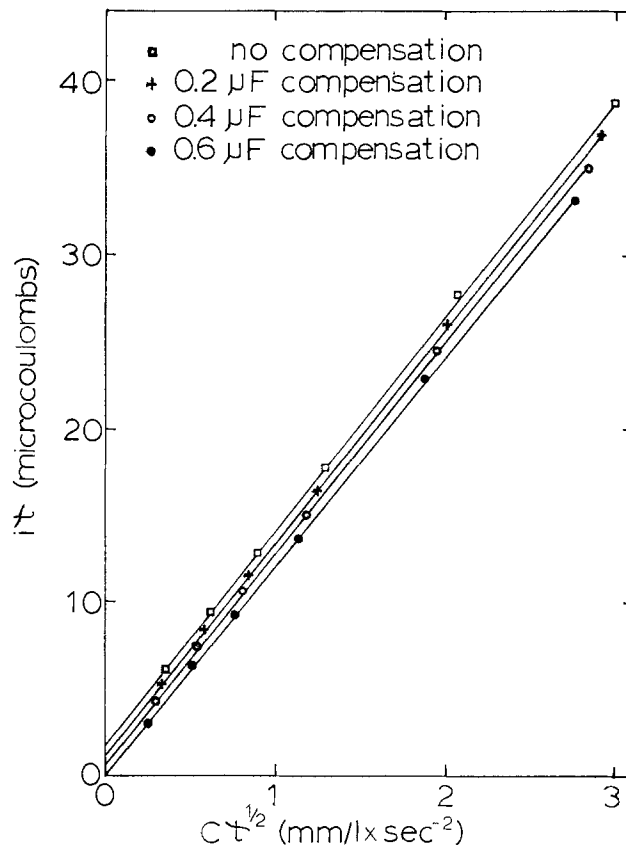


Fig. 3. Bard plots for Cd^{2+} , Set A of Table II

serve that the cadmium system is somewhat more well behaved than the lead in that the ranges of experimental $i\tau^{1/2}/C$ are somewhat smaller. This is probably due to the smaller average double-layer capacitance encountered in the cadmium system, where reduction occurs at $-0.6V$ vs. SCE, than that encountered in the lead system where reduction occurs at $-0.4V$ vs. SCE. In fact the electronically compensated ($0.6 \mu F$) but uncorrected values of $i\tau^{1/2}/C$ obtained in $10^{-3}M$ $Cd(NO_3)_2$ compare rather favorably with corrected values. The data in Table II also provide some indication, as do the data of Table I, that zero-compensated data yield larger values of corrected $i\tau^{1/2}/C$ than do compensated data; again, the trend may not be statistically meaningful. Finally, note that constancy in $i\tau^{1/2}/C$ is achieved over a wide range of transition times.

Derivative chronopotentiometric results are presented in Table III. Note that the concentration of cadmium is low and thus provides a good test of the derivative technique compared to the conventional approach. Calculated transition times in the table were obtained from Eq. [7] presented earlier. Actual differentiator readout is a potential waveform, the minimum of which permits calculation of $(dE/dt)_{min}$ by the relationship

$$(dE/dt)_{min} = -E_{min}/R_f C_i \quad [8]$$

where R_f and C_i are the respective values of the feedback resistance and input capacitance of the differentiator circuit. The quantity $i\tau$ is the product of the calculated experimental transition time and the controlled current chosen instrumentally. Other quantities in the table were determined as in Tables I and II. Observe that each entry in Table III is a single data point, whereas the entries in Tables I and II are averages of several measurements. Set A of Table III are uncompensated (no positive feedback) results. Note that the uncorrected values of $i\tau^{1/2}/C$ show a definite trend towards higher values as τ decreases; although the

Table III. Derivative chronopotentiometry of Cd(NO₃)₂; electrode (dme) area = 0.0290 cm²

	Calculated τ (msec)	$i\tau$	$i\tau^{1/2}$ *		Summaries
			uncorrected	corrected	
A. $4 \times 10^{-4}M$ Cd(NO ₃) ₂	39.4	0.984	12.4	12.2	$\frac{i_0\tau^{1/2}}{C} = 420 \pm 0^*$
1M KNO ₃ no positive feedback (uncompensated)	28.0	0.838	12.5	12.2	(corrected)
	16.0	0.642	12.7	12.2	$\frac{i_0\tau^{1/2}}{C} = 440 \pm (\text{drift})$
	10.3	0.516	12.7	12.2	(uncorrected)
	7.22	0.433	12.8	12.1	
	5.41	0.379	12.9	12.2	
	4.20	0.336	13.3	12.2	
	avg.			12.8	12.2
$\text{Slope } \frac{i\tau^{1/2}}{C} = 12.2$ $\text{Intercept} = 0.050$					
B. $4 \times 10^{-4}M$ Cd(NO ₃) ₂	27.1	0.812	12.3	12.3	$\frac{i_0\tau^{1/2}}{C} = 423 \pm 4^*$
1M KNO ₃ optimum positive feedback (compensated)	15.5	0.619	12.4	12.3	(corrected)
	9.84	0.492	12.4	12.3	
	7.10	0.426	12.6	12.5	$\frac{i_0\tau^{1/2}}{C} = 427 \pm 4$
	4.97	0.348	12.4	12.2	(uncorrected)
avg.			12.4	12.3	
$\text{Slope } \frac{i\tau^{1/2}}{C} = 12.3$ $\text{Intercept} = 0.012$					

trend is present, the values are more nearly constant than equivalent conventional results presented in Table II. Corrected values of $i\tau^{1/2}/C$ are constant, and the value of the chronopotentiometric constant obtained (420) is in fair, though not excellent, agreement with the value of 436 (Table II) obtained conventionally with a different instrument and cell more than a year earlier. Set B of Table III are results for the same concentration of cadmium as in Set A, but were obtained using optimum compensation (*i.e.*, use of as much positive feedback as possible without introducing observable distortion of the conventional chronopotentiometric waveform). Note that, in the case of Set B, corrected and uncorrected data are virtually identical; this result suggests that the derivative technique does indeed provide data significantly less affected by double-layer charging than does conventional chronopotentiometry. These results were obtained with an instrument having only one differentiator for both readout and feedback.

Conclusions

These results are encouraging in that they confirm the utility of electronic compensation (positive feedback) and the Bard correction approach in removing double-layer charging error from chronopotentiometric data and, thus, extend application of the technique downwards to lower concentrations and shorter transition times using either the conventional or derivative technique. Although optimum results can be achieved using derivative chronopotentiometry, positive feedback, and the correction system, those electroactive species exhibiting irreversible charge transfers can still be studied using the conventional technique with feedback and correction. Further, should the use of positive feedback be undesirable or inconvenient, good results can still be achieved using conventional or derivative results with correction.

Manuscript submitted Jan. 2, 1975; revised manuscript received May 7, 1975.

Any discussion of this paper will appear in a Discussion Section to be published in the June 1976 JOURNAL. All discussions for the June 1976 Discussion Section should be submitted by Feb. 1, 1976.

Publication costs of this article were partially assisted by Georgia Institute of Technology.

REFERENCES

- H. J. S. Sand, *Phil. Mag.*, **1**, 45 (1901).
- L. Gierst and A. Juliard, Proc. Intern. Comm. Electrochem. Thermodynam. and Kinet., 2nd Meeting, pp. 117, 279, Milan (1950).
- P. Delahay, "New Instrumental Methods of Electrochemistry," Chap. 8, Interscience Publishers, New York (1954).
- Z. Karaoglanoff, *Z. Elektrochem.*, **12**, 5 (1906).
- R. W. Murray and C. N. Reilley, *J. Electroanal. Chem.*, **3**, 64, 182 (1962).
- D. G. Peters and S. L. Burden, *Anal. Chem.*, **38**, 530 (1966); S. L. Burden, Jr., Ph.D. Dissertation, Indiana University, (1966).
- P. Delahay and T. Berzins, *J. Am. Chem. Soc.*, **75**, 2486 (1953); W. H. Reinmuth, *Anal. Chem.*, **33**, 485 (1961).
- C. N. Reilley, G. W. Everett, and R. H. Johns, *ibid.*, **27**, 483 (1955); J. D. Voorhies and N. H. Furman, *ibid.*, **30**, 1656 (1958).
- J. J. Lingane, *J. Electroanal. Chem.*, **1**, 379 (1960); F. C. Anson, *Anal. Chem.*, **33**, 1123 (1961); R. W. Laity and J. D. E. McIntyre, *J. Am. Chem. Soc.*, **87**, 3806 (1965).
- W. D. Shults, F. E. Haga, T. R. Mueller, and H. C. Jones, *Anal. Chem.*, **37**, 1415 (1965).
- M. L. Olmstead and R. S. Nicholson, *J. Phys. Chem.*, **72**, 1630 (1968).
- D. C. Noonan, Ph.D. Dissertation, Columbia University (1967).
- A. J. Bard, *Anal. Chem.*, **35**, 340 (1963).
- W. T. de Vries, *J. Electroanal. Chem.*, **17**, 31 (1968).
- R. S. Rodgers and L. Meites, *ibid.*, **16**, 1 (1968).
- P. E. Sturrock, *ibid.*, **8**, 425 (1964).
- P. E. Sturrock, G. Privett, and A. R. Tarpley, *ibid.*, **14**, 303 (1967).
- P. E. Sturrock, W. D. Anstine, and R. H. Gibson, *Anal. Chem.*, **40**, 505 (1968).

Electrode Kinetics of Antimony in Acidic Chloride Solutions

L. L. Wikstrom,* N. T. Thomas,* and Ken Nobe*

School of Engineering and Applied Science, University of California, Los Angeles, California 90024

ABSTRACT

The kinetics of the electrode processes of antimony in KCl-HCl solutions have been investigated. The rest potential of antimony in acidic chloride solutions can be expressed empirically by the equation

$$E^e = 0.182 - 0.060 \text{ pH} + 0.020 \log [\text{Sb(III)}]$$

and is attributed to the redox reaction



The empirical rate equations for the electrodisolution and electroreduction reactions near the rest potential are

$$I_a = \bar{k}_a [\text{OH}^-] [\text{Sb(III)}]^{-1} e^{2FE/RT}$$

and

$$I_c = \bar{k}_c [\text{H}^+]^2 e^{-FE/RT}$$

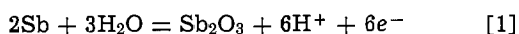
The rate of electrodeposition of Sb(III) can be expressed as

$$I_{c, \text{dep}} = \bar{k}_{c, \text{dep}} [\text{H}^+] [\text{Sb(III)}] e^{-FE/2RT}$$

A mechanism which is consistent with the experimental results is proposed.

Although there has been interest in antimony as a reference electrode, electrocatalyst for electrochemical energy conversion and inhibitor in the corrosion control of iron and steel (1), there has been little work on the kinetics of electrodisolution and electroreduction of antimony. The use of antimony as a reference electrode has focused studies on the thermodynamic properties and open-circuit electrochemical behavior of antimony and antimony oxides. Stock, Purdy, and Garcia (2) and Ives and Janz (3) have reviewed this work.

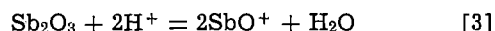
Park and Beard (4, 5) surmised that the rest potential of antimony was determined by the redox reaction



with the equilibrium potential following the relation

$$E^e = 0.152 - 0.059 \text{ pH, volts} \quad [2]$$

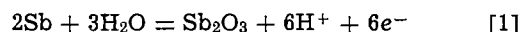
The Sb_2O_3 was assumed to be a surface film on the antimony electrode and formed antimony ions (SbO^+) in strong acid solutions by the reaction



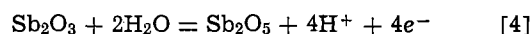
Although Bishop and Short (6) and Stock, Purdy, and Garcia (2) obtained the same redox potential, they attributed it to different reaction steps. Bishop and Short (6) suggested Sb(OH)_3 as an intermediate, while Stock, Purdy, and Garcia (2) suggested Sb^{+3} as an intermediate. These investigators report that the experimental rest potential was more noble than the theoretical value but approached it as oxygen was removed from the system. Schuhmann (7), and Robert and Fenwick (8) report $E^e = 0.15\text{V}$ for the $\text{Sb/Sb}_2\text{O}_3$ reaction in deaerated perchloric acid and acidic chloride solutions, respectively. On the other hand, Tourkey and Musa (9) report about a 0.1V higher value for E^e and conclude that the value, $E^e = 0.15\text{V}$, can only be obtained with finely divided antimony. Schuhmann's actual measured rest potential of antimony in deaerated perchloric acid was 0.212V (7). He attributed this rest potential value to the Sb/SbO^+ redox reaction. According to Schuhmann, the SbO^+ forms as

given in Eq. [3]. It should be noted that Cotton and Wilkinson (10) question the existence of SbO^+ .

Bishop and Short (11) investigated the electrochemistry of antimony in oxygenated 0.03M KCl ($\text{pH} = 7$). They attributed the potential controlling process at low cathodic currents and high oxygen concentrations to



and at high anodic current densities to



Similarly, from galvanostatic charging transients, El Wakkad and Hickling (12) suggested that antimony oxidized to Sb_2O_3 at low currents and to Sb_2O_5 at high currents. However, they surmised that although the antimony electrode was covered by a porous Sb_2O_3 film, Sb_2O_5 was formed by direct oxidation of antimony.

Huq, Rosenberg, and Makrides (13) investigated the anodic dissolution of single crystal antimony in 1M HClO_4 ($\text{pH} = 0.04$). In acid solution an anodic Tafel slope of 120 mV was obtained. An active-passive transition was observed at 0.40V vs. SHE with a critical current density of $4.5 \times 10^{-3} \text{ A/cm}^2$. Passivation was attributed to the formation of Sb_2O_5 . In a further study (14) these investigators obtained a Tafel slope of 180 mV and an exchange current density of $2 \times 10^{-6} \text{ A/cm}^2$ for the hydrogen evolution reaction on antimony in 1M HClO_4 .

This paper reports on kinetic studies of the electrooxidation and electroreduction processes at the antimony electrode and the electrodeposition of Sb(III) on Sb in acidic chloride solution.

Experimental

A common 3-electrode electrochemical cell was used for this investigation. The electrolyte was deaerated with prepurified nitrogen which was passed through scrubbers before entering the cell. All experiments were performed with the cell and scrubbers in a glove box filled with prepurified nitrogen gas. Temperatures were maintained at $23^\circ \pm 1^\circ\text{C}$.

Electrical connections were made with shielded leads and BNC connectors. A Kepco power supply was used for long galvanostatic pulses. Differential capacitances

* Electrochemical Society Active Member.

Key words: electrodisolution, electrodeposition, polarization.

were determined by the d-c pulse method with the Rutherford pulse generator and a specially constructed cathode follower. The potential transients were measured and recorded with a Type 564 Tektronix oscilloscope. Potentiostatic polarization was performed with a Wenking potentiostat.

Saturated calomel electrodes were used as reference electrodes which were in contact with the electrolyte close to the electrode surface through a Haber-Luggin capillary. Potentials were measured with either a Keithley 621 or 603 electrometer.

The antimony electrodes were prepared from a bar stock of 99.9996% antimony. All electrodes were cut with a carborundum wheel with water used as the lubricant. The cylindrical electrodes were drilled and tapped dry. The exterior surfaces were ground with the carborundum wheel and then with carborundum paper 4/0 to a cylindrical shape. The planar electrodes were 1 cm × 1.5 cm and the cylindrical electrodes were 0.63 cm diam. × 0.75 cm length. The planar electrodes were cut flat with a carborundum wheel and soldered to a platinum wire passed through a 6 mm Pyrex tube. The electrode was masked with purified paraffin wax except for one surface of the antimony. The cylindrical electrode assembly was rotated at 500 rpm ($V_t = 35$ cm/sec) while the planar electrode was stationary.

Just prior to immersion into the electrolyte, the electrode was etched in CP-4A (HNO₃, 5 parts; 48% HF, 3 parts; acetic acid, 3 parts) for 4-8 sec, washed, and immersed in distilled water and then placed immediately in the cell.

All solutions were prepared from C.P. grade chemicals: B & A HCl, KCl, and Sb₂O₃. Solutions of constant ionic strength of unity were used throughout the investigation. All solutions were prepared from 1N HCl with the desired pH obtained by the addition of KOH. The pH values of 0, 1, and 2 were investigated.

After immersion of the electrode in the electrolyte, the system was held at open circuit for at least 2 hr before polarization. During the 2 hr period, the rest potential was monitored and recorded. If, at the end of the 2 hr period, the potential drift was in excess of 2 mV/hr, the system was kept at open circuit until the drift was 2 mV/hr or less. After a steady-state rest potential was observed, the electrode was polarized.

Two-minute current steps were used to polarize the antimony electrode. The 2 min steps were chosen since it was observed that an apparent steady-state was achieved for both anodic and cathodic currents after about 90 sec. At each absolute value of current density, anodic polarization was first obtained and then switched to cathodic polarization. This same procedure was followed with each increasing increment of current density.

Results

Sb/Sb(III) reaction.—The dependence of the rest potential on the pH, as shown in Fig. 1, is

$$\frac{\partial E^e}{\partial \text{pH}} = -0.06\text{V} \quad [5]$$

An E^e vs. log Sb(III) plot shows that

$$\frac{\partial E^e}{\partial \log \text{Sb(III)}} = 0.02\text{V} \quad [6]$$

Except for the extreme negative potential region where mass transfer effects become important, the polarization data obtained with stationary and rotating electrodes were identical. Figures 2 and 3 show the polarization behavior of antimony in 1M Cl⁻ of pH = 0, 1, and 2 solutions in the absence and presence of Sb(III), respectively. The anodic dissolution increased with increase in pH. On the other hand, both the rates of the cathodic reaction near the rest potentials and at large negative potentials decreased with increase in pH. Near the rest potential the anodic and cathodic Tafel slopes in both the absence and presence of Sb(III)

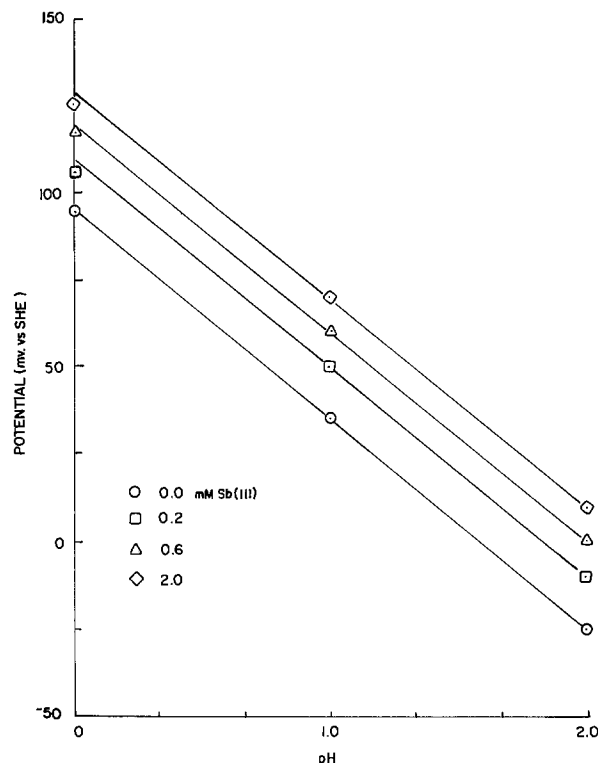


Fig. 1. Rest potential of antimony in acidic chloride solutions vs. pH.

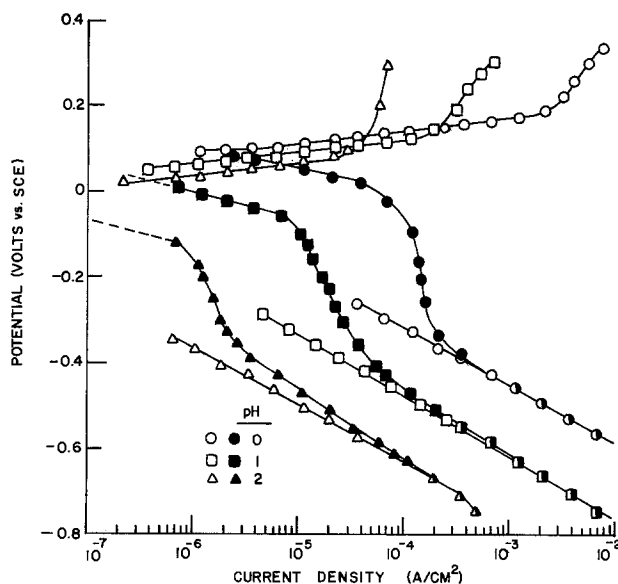


Fig. 2. Effect of pH on the polarization of antimony in acidic chloride solutions.

are 30 and 60 mV/decade, respectively. Figure 4 shows some typical results of the effect of Sb(III) on the polarization behavior of antimony. It is shown that anodic dissolution decreased with increase in the concentration of Sb(III) while the rate of the cathodic reaction near the rest potential was independent of the Sb(III) concentration, i.e.

$$\frac{\partial \log |I_c|}{\partial \log [\text{Sb(III)}]} = 0 \quad [7]$$

This latter result suggests that the electroreduction process near the rest potential is not electrodeposition of Sb(III) from the bulk solution. Figure 5 shows the variation of the cathodic reaction in this same region with pH

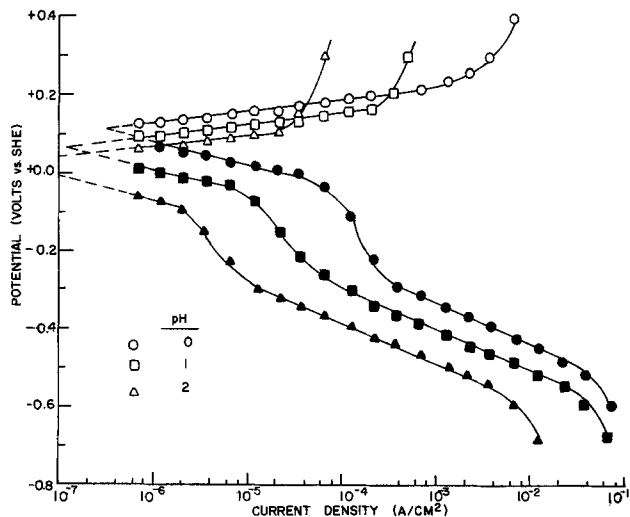


Fig. 3. Effect of pH on polarization of antimony in acidic chloride solutions 0.6 mM Sb(III).

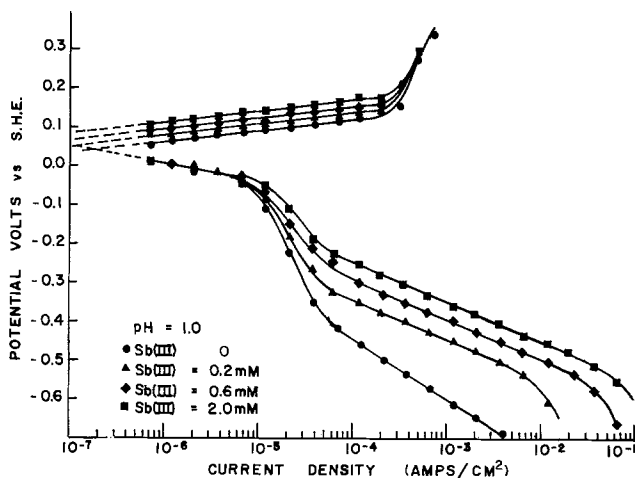


Fig. 4. Effect of Sb(III) on polarization of antimony in pH = 1 solutions.

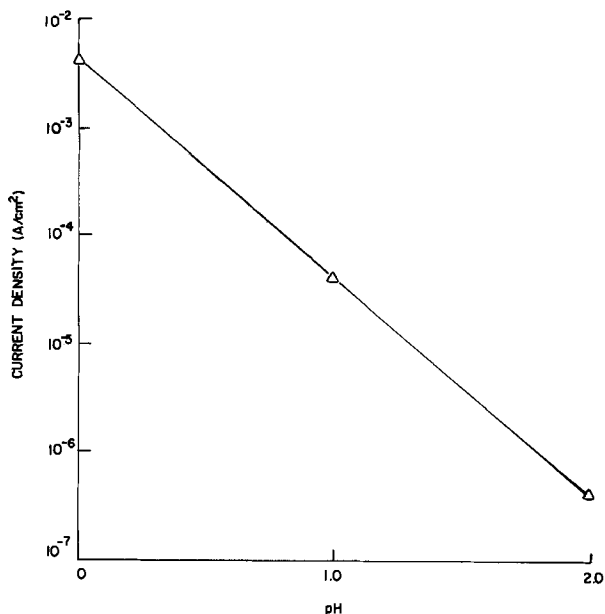


Fig. 5. Reaction order of electroreduction of antimony near the rest potential with respect to pH. -0.1V.

$$\frac{\partial \log |I_c|}{\partial \text{pH}} = -2 \quad [8]$$

The dependence of anodic dissolution on pH and

Sb(III) concentration is

$$\frac{\partial \log I_a}{\partial \text{pH}} = 1 \quad [9]$$

and

$$\frac{\partial \log I_a}{\partial \log [\text{Sb(III)}]} = -1 \quad [10]$$

as shown in Fig. 6 and 7, respectively.

The variation of the exchange current density of the electrode reaction near the rest potential with pH, as shown in Fig. 8, is

$$\frac{\partial \log I_0}{\partial \text{pH}} = -1 \quad [11]$$

A log I₀ vs. log [Sb(III)] plot shows that

$$\frac{\partial \log I_0}{\partial \log [\text{Sb(III)}]} = -\frac{1}{3} \quad [12]$$

From the experimental results given above, the rate of the anodic and cathodic reactions near the rest potential can be written in the following empirical form

$$I_a = \bar{k}_a [\text{OH}^-] [\text{Sb(III)}]^{-1} e^{2FE/RT} \quad [13]$$

and

$$|I_c| = \bar{k}_c [\text{H}^+]^2 e^{-FE/RT} \quad [14]$$

Electrodeposition of Sb(III).—The cathodic Tafel region at the higher negative potentials in Fig. 2 shows hydrogen evolution on antimony by discharge of hydrogen ions with a Tafel slope of 130 mV/decade and a reaction order of one. The closed points represent the descending polarization curves, and the open points represent the ascending ones.

Figure 4 shows the codeposition of hydrogen ions and Sb(III) at the higher negative potentials. The rate of electrodeposition of Sb(III) can be readily obtained by subtracting the rate of hydrogen evolution from the rate of codeposition. The cathodic polarization curves thus obtained representing electrodeposition of Sb(III) have Tafel slopes of 110 mV/decade. The dependence of electrodeposition of Sb(III) on pH and the concentration of Sb(III) is shown in Fig. 9 and 10, respectively. These results indicate that

$$\frac{\partial \log |I_{c,\text{dep}}|}{\partial \text{pH}} \approx -1 \quad [15]$$

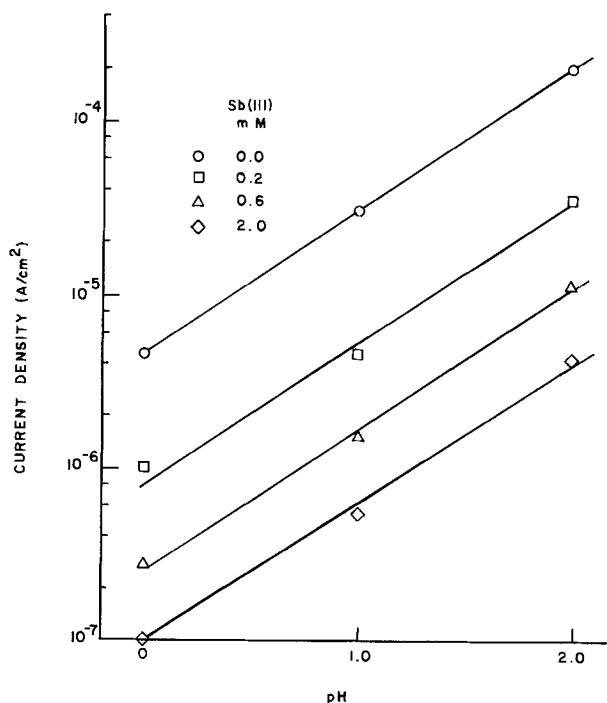


Fig. 6. Reaction order of electrodisolution with respect to pH. 0.1V.

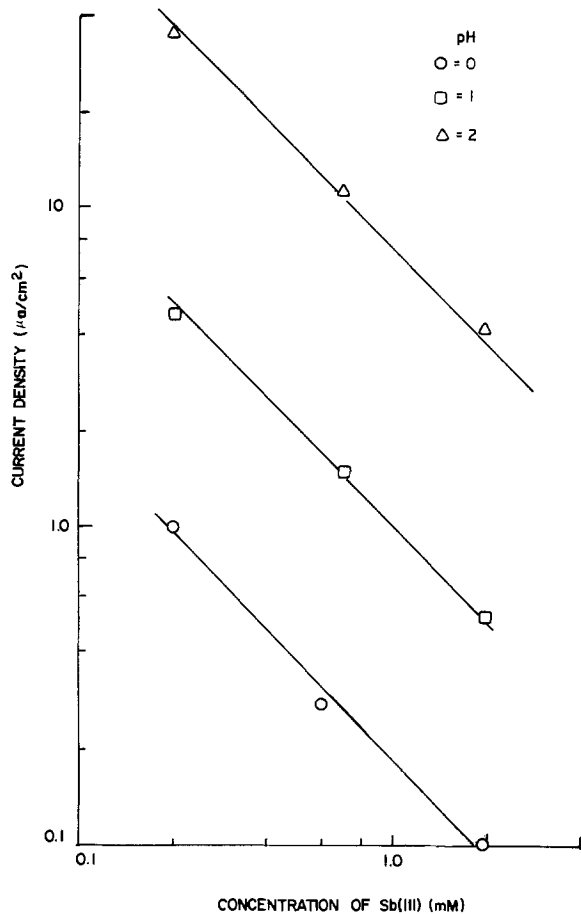


Fig. 7. Reaction order of electrodisolution with respect to Sb(III) concentration. 0.1V.

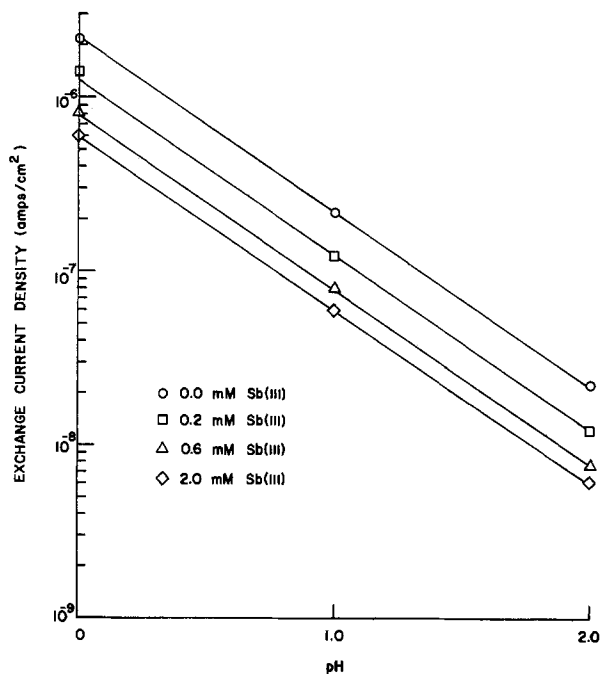


Fig. 8. Exchange current density of Sb/Sb(III) reaction vs. pH

and

$$\frac{\partial \log |I_{c,dep}|}{\partial \log [Sb(III)]} = 1 \quad [16]$$

Thus, the rate of electrodeposition of Sb(III) in acidic chloride solutions can be expressed empirically as

$$I_{c,dep} = \bar{k}_{c,dep} [Sb(III)][H^+] \exp - (FE/2RT) \quad [17]$$

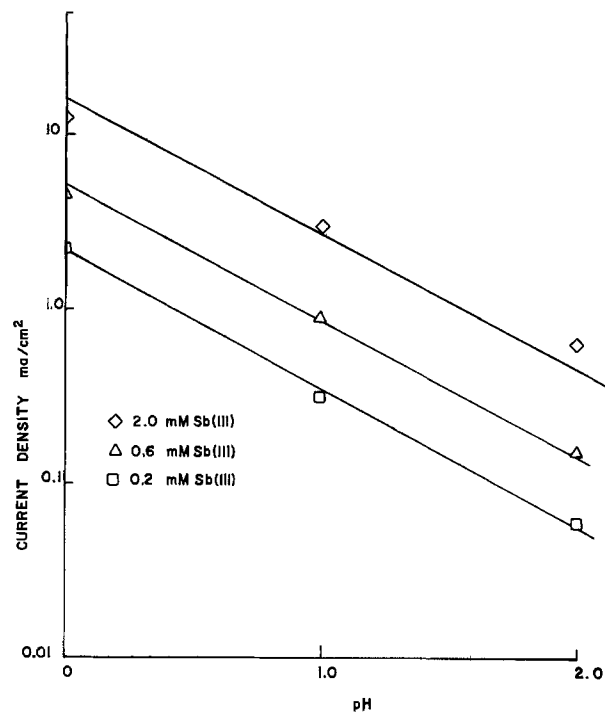


Fig. 9. Reaction order of electrodeposition of Sb(III) with respect to pH. -0.4V.

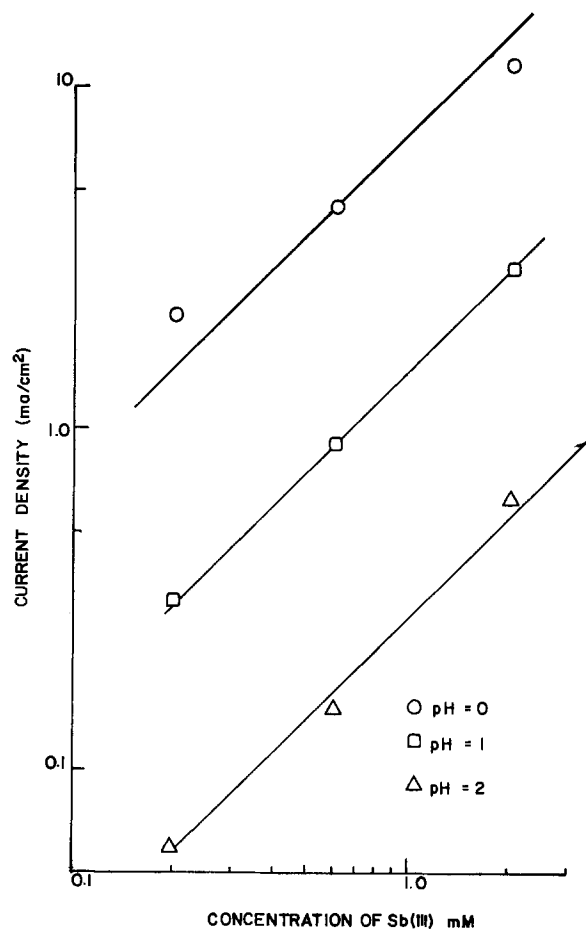
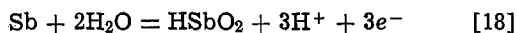


Fig. 10. Reaction order of electrodeposition of Sb(III) with respect to Sb(III) concentration. -0.4V.

Discussion

Thermodynamic considerations.—Pourbaix (1) reports that $HSbO_2$ is the predominant Sb species in aqueous solution between pH = 1-11. The Sb/ $HSbO_2$ redox reaction



has an equilibrium potential

$$E^e = E^o + (RT/3F) \ln [\text{HSbO}_2] + (RT/F) \ln [\text{H}^+], \text{V} \quad [19]$$

where E^o is 0.23V. Equation [14] shows that

$$\frac{\partial E^e}{\partial \text{pH}} = -0.060\text{V}$$

and

$$\frac{\partial E^e}{\partial \log [\text{Sb(III)}]} = 0.020\text{V}$$

in accord with the experimental results (Eq. [5] and [6]). The values of E^e calculated for Eq. [19] are compared in Table I with the measured rest potentials, E^e_{obs} , and the rest potentials determined by the intersection of the experimental anodic and cathodic Tafel lines, E^e_x . It is seen that the rest potentials were about 50 mV less than the equilibrium potentials calculated from Eq. [19].

If it is assumed that the observed rest potential of antimony in acidic chloride solutions, which can be expressed empirically as

$$E^e = 0.182 - 0.060\text{pH} + 0.020 \log [\text{HSbO}_2], \text{V} \quad [20]$$

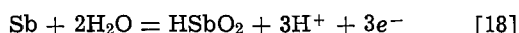
is the equilibrium potential of the redox reaction, Eq. [18], the standard electrode potential, E^o , can be determined. These values are presented in Table I. The mean value of E^o is 0.182V. Therefore, ΔG^o (Eq. [18]) = 12.6 kcal/mole and $\Delta G^o_f(\text{HSbO}_2) = -100.8$ kcal/mole. Latimer (15) determined the free energy of formation of HSbO_2 , $\Delta G^o_f(\text{HSbO}_2) = -97.5$ kcal/mole, from the solubility and the free energy of formation of Sb_2O_3 .

The rest potential of antimony in the absence of Sb(III) in the supporting electrolyte can also be attributed to the above redox reaction. The incipient oxide, Sb_2O_3 , on the electrode surface forms HSbO_2 by the following reaction

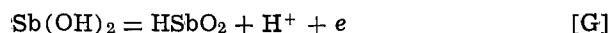
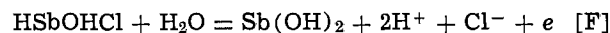
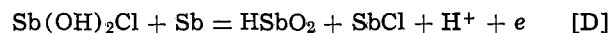
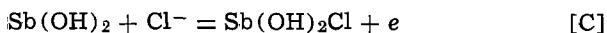
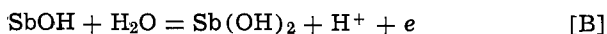
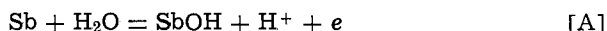


The concentration of HSbO_2 at the electrode-electrolyte interface can be determined from Eq. [20]. These interface concentrations of HSbO_2 , $[\text{HSbO}_2]_i$, for solutions of pH 0, 1, and 2 not containing Sb(III) in the bulk solution, are given in Table I.

Mechanism of the Sb/Sb(III) reaction near the rest potential.—The experimental data indicate that the over-all electrochemical reaction is



To interpret the experimental kinetic data in light of the above over-all reaction, the following mechanism is proposed for the anodic reaction



If step [E] is the rate determining step, the rate of electrodisolution of antimony is

$$r_a = k_{a,(E)}\theta_{\text{SbCl}} \quad [22]$$

By assuming reaction steps [A], [B], [C], and [D] are at quasi-equilibrium, the surface coverage of Sb(OH)_2 , $\theta_{\text{Sb(OH)}_2} \rightarrow 1$, and the surface coverages of the other surface intermediates SbOH , $\text{Sb(OH)}_2\text{Cl}$, SbCl , and Sb(OH)Cl , are very small, the kinetic equation for electrodisolution can be obtained from Eq. [22]

$$I_a = \bar{k}_a [\text{OH}^-] [\text{HSbO}_2]^{-1} e^{2FE/RT} \quad [23]$$

Similarly, if step [E] is the rate determining step for electroreduction, the corresponding rate can be expressed as

$$r_c = k_{c,(E)}\theta_{\text{HSbOHCl}} \quad [24]$$

By assuming reaction steps [G] and [F] are at quasi-equilibrium and that surface coverages of the surface intermediates are the same as above, the kinetic equation for electroreduction near the rest potential can be derived from Eq. [24]

$$I_c = \bar{k}_c [\text{H}^+]^2 e^{-FE/RT} \quad [25]$$

Thus, Eq. [23] and [25] show that the proposed mechanism for electrodisolution and electroreduction of antimony in acidic chloride solutions near the rest potential is consistent with the experimental results which can be expressed by the empirical relations, Eq. [13] and [14], respectively.

Mechanism of the electrodeposition of Sb(III).—Reaction steps [G] to [A] also comprise the mechanism for the electrodeposition of Sb(III). However, in this case, reaction step [G] is assumed to be the rate determining step. Thus, the rate of electrodeposition can be expressed as

$$r_{c,\text{dep}} = k_{c,\text{dep}} [\text{HSbO}_2] [\text{H}^+] e^{-\beta FE/RT} \quad [26]$$

If $\beta = 1/2$, the kinetic equation for electrodeposition of Sb(III) can be obtained from Eq. [26]

$$I_{c,\text{dep}} = \bar{k}_{c,\text{dep}} [\text{HSbO}_2] [\text{H}^+] e^{-FE/2RT} \quad [27]$$

Equation [27] shows that the proposed mechanism for the electrodeposition of Sb(III) is consistent with the experimental data correlated by the empirical expression, Eq. [17].

Acknowledgment

L. L. W. gratefully acknowledges a Standard Oil of California fellowship, NSF Traineeship and a Ford Foundation loan during this investigation. This work is part of the University of California research program in seawater desalination.

Manuscript submitted Oct. 23, 1974; revised manuscript received April 29, 1975.

Any discussion of this paper will appear in a Discussion Section to be published in the June 1976 JOURNAL. All discussions for the June 1976 Discussion Section should be submitted by Feb. 1, 1976.

REFERENCES

1. M. Pourbaix, "Atlas of Electrochemical Equilibrium in Aqueous Electrolyte at 25°C," p. 524, Pergamon Press, Cebelcor, Brussels, Belgium (1966).
2. J. T. Stock, W. C. Purdy, and L. M. Garcia, *Chem. Rev.*, **58**, 611 (1958).
3. D. J. G. Ives and G. J. Janz, "Reference Electrodes," p. 351, Academic Press, New York (1961).
4. L. R. Park and H. C. Beard, *J. Phys. Chem.*, **37**, 822 (1933).

Table I. Electrochemical parameters

pH	[Sb(III)] mM	E^e	E^e_x mV vs. SHE	E^e_{obs}	E^e_{calc}	[HSbO ₂] _i μM
	0		95	80		44
	0.2	156	105	100	179	
0	0.6	166	118	105	183	
	2.0	176	125	115	179	
	0		35	30		40
	0.2	97	50	50	183	
1	0.6	107	60	60	184	
	2.0	117	70	70	183	
	0		-25	-35		35
	0.2	38	-10	-10	182	
2	0.6	48	0	0	183	
	2.0	58	10	15	182	
avg = 182						

5. L. R. Park and H. C. Beard, *ibid.*, **37**, 821 (1933).
6. E. Bishop and G. D. Short, *Talanta*, **11**, 393 (1964).
7. R. Schuhmann, *J. Am. Chem. Soc.*, **46**, 52 (1923).
8. E. J. Roberts and F. Fenwick, *ibid.*, **50**, 2125 (1928).
9. A. R. Tourkey and A. A. Mousa, *J. Chem. Soc.*, 752 (1948).
10. F. A. Cotton and G. Wilkinson, "Advances in Inorganic Chemistry," 2nd ed., p. 509, Interscience Publishers (1966).
11. E. Bishop and G. D. Short, *Anal. Chem.*, **37**, 962 (1965).
12. S. E. S. El Wakkad and A. Hickling, *J. Phys. Chem.*, **57**, 203 (1953).
13. A. K. M. Huq, A. J. Rosenberg, and A. C. Makrides, *This Journal*, **111**, 278 (1964).
14. A. K. M. Huq and A. J. Rosenberg, *ibid.*, **111**, 270 (1964).
15. W. M. Latimer, "Oxidation Potentials," 2nd ed., Prentice-Hall, Englewood Cliffs, N. J. (1952).

On a Model for the Electrocrystallization of Zinc Involving an Autocatalytic Step

I. Epelboin,* M. Ksouri, and R. Wiart

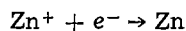
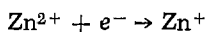
*Groupe de Recherche n°4 du C.N.R.S. "Physique des Liquides et Electrochimie,"
associé à l'Université Pierre et Marie Curie, 75230 Paris Cedex 05, France*

ABSTRACT

The model presented involves the autocatalytic step $Zn^{2+} + Zn^{+}_{ads} + e^{-} \rightleftharpoons 2Zn^{+}_{ads}$ and the adsorption at the interface of three species, hydrogen, an anion, and the Zn^{2+} cation which can be complexed. The model is compared with results obtained, after eliminating the influence of convective diffusion, during the electrocrystallization of zinc in: (i) an acid sulfate solution, (ii) a Leclanché cell electrolyte, and (iii) an alkaline zincate solution commonly used in accumulators. The experimental results are in good agreement with the model, although the three electrolytes are markedly different. The model accounts indeed for the variation of the electrocrystallization efficiency with the current, for the appearance of multiple steady states revealed by S-shaped current-potential curves, and for the existence of an inductive faradaic impedance characterized by at least three time-constants.

The study of the electrocrystallization of zinc is now of high interest, mainly because this metal is more and more employed in electrochemical generators. In this paper, basing ourselves on a kinetic study of the electrocrystallization of zinc in several acidic and basic electrolytes (commonly used for industrial purposes), we shall propose a reaction model for the electrocrystallization of this metal in such electrolytic media.

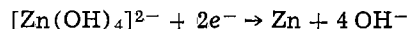
Several mechanisms have been proposed for the electrocrystallization of zinc at acidic pH's. According to certain authors (1), the adatoms resulting from the simultaneous transfer of two electrons diffuse on the surface before being incorporated into the crystal lattice. Other authors (2-5) believe on the contrary that charge transfer occurs from the bivalent metal ion Zn^{2+} , which can either be solvated or form a complex in the electrolyte, in two successive monoelectronic steps involving a monovalent intermediate Zn^{+} which can also form complexes with certain anions (4, 5)



Although the reaction mechanism of the electrocrystallization of zinc is still a matter for discussion, it now seems accepted that the adsorption of hydrogen plays an important role in acidic medium. As a matter of fact, hydrogen evolution takes place within the same potential range as for zinc deposition (6) and it is known that hydrogen is always present in zinc electrodeposited from acid solutions (7). In addition, the polarization curve which characterizes the electrocrystallization of this metal considerably depends on the electrolyte pH (5, 8, 9).

In very alkaline medium, the electrolytic deposition of zinc is known to occur mainly from zincate ions

$[Zn(OH)_4]^{2-}$ (10-12). In addition, it is generally accepted that charge transfer occurs in several steps, but the mechanism of the over-all reaction



is still under discussion. As a matter of fact, the reaction schemes differ in the number and the nature of the hydroxyl species involved as reaction intermediates (13-16).

In the case of the electrocrystallization of zinc from a Leclanché cell electrolyte, it is known that, when the influence of mass transfer is cancelled out, three different current density values correspond to a given potential value (17). Consequently, these multiple steady states cannot be attributed, as in the case of iron passivation in sulfuric acid medium, to a coupling between mass transfer and heterogeneous reactions (18-20).

The above-mentioned reaction mechanisms of the electrocrystallization of zinc are based only on the idea of elementary interfacial steps associated with simple activation processes; therefore, it is highly probable that they are not sufficient to predict the existence of multiple steady states. Now, in homogeneous kinetics, it is known that the presence of an autocatalytic reaction in the reaction scheme can give rise to instabilities and to continuous oscillations of the system (21) and can be the origin of multiple steady states (22, 23). This is the idea we based ourselves on, and therefore the model of heterogeneous reactions relative to the electrocrystallization of zinc, which is put forward in this paper, involves by analogy an autocatalytic reaction.

In zincate solutions as well as in certain acidic media such as the Leclanché cell electrolyte, it is known that several complexed ions are in chemical equilibria. In the model we shall describe, the heterogeneous reactions which occur at the interface will be only considered, whereas the chemical reactions taking place in

* Electrochemical Society Active Member.

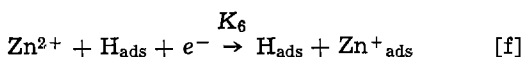
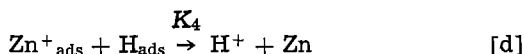
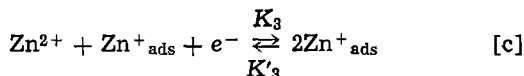
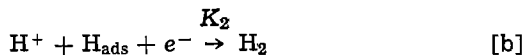
Key words: multiple steady states, faradaic impedance, efficiency, rotating disk electrode, heterogeneous reactions.

the homogeneous solution will be neglected. The good agreement between this model and the experimental results justifies such an approximation.

Theoretical

The model we shall describe is based on a coupling between heterogeneous reactions one of them being autocatalytic, i.e., of the form $A + X \rightleftharpoons 2X$, where A and X are reacting species.

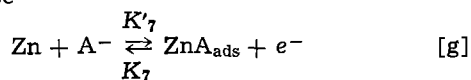
Let us consider that the following reactions take place at the interface



Reaction [a] corresponds to the hydrogen adsorption and reaction [b] to the hydrogen evolution. This evolution the mechanism of which is not well known on zinc may also occur through the recombination $\text{H}_{\text{ads}} + \text{H}_{\text{ads}} \rightarrow \text{H}_2$, so that reaction [b] must be considered only as a possible path.

The Zn^{2+} ion, which may be either complexed or solvated in the electrolyte, is adsorbed through the autocatalytic reaction [c] and also through reaction [f] which is catalyzed by H_{ads} and this adsorption gives the intermediate Zn_{ads}^+ , which may also be complexed. From this intermediate, reduction to the metal finally occurs through the chemical reaction [d] and through the electrochemical reduction [e].

In order to simplify the calculations, the reverse reactions of [a], [b], [d], [e], and [f], which may occur at low cathodic polarizations, have been neglected. As a matter of fact, the coupling of reaction [a] to [f] is sufficient to cause multiple steady states of the interface (24). Reactions [a]-[f] imply that both the intermediate adsorbed Zn_{ads}^+ species and the adsorbed hydrogen H_{ads} exist at the interface. Now, it is known that the reactions which lead to the corrosion and to the anodic dissolution of zinc can involve the adsorption of anions such as OH^- (25, 26). That is the reason why we shall also take into account the following reaction which corresponds to the reversible adsorption of an anion A^- the nature of which may depend on the electrolyte



Equations of the system.—Using a method already described in detail in the case of electrocrystallization of nickel and cobalt in acidic medium (27), we first establish the balance of mass and electrons at the interface. To this end, we shall accept the following hypotheses:

1. The three species H_{ads} , Zn_{ads}^+ , and ZnA_{ads} adsorb according to the Langmuir isotherm. Their surface concentrations are $\beta_1\theta_1$, $\beta_2\theta_2$, and $\beta_3\theta_3$, respectively; θ_1 , θ_2 , and θ_3 are the coverage fractions; and β_1 , β_2 , and β_3 represent the maximal surface concentrations related to a total coverage of the electrode by the corresponding species.

2. The electrochemical rate constants K_i and K'_i vary with the cathodic potential V according to Tafel's law: $K_i = k_i \exp(b_i V)$ for the cathodic reactions and $K'_i = k'_i \exp(-b'_i V)$ for the anodic reactions where $b_i =$

$\alpha_i F/RT$ and $b'_i = (1 - \alpha_i) F/RT$; α_i , F , R , and T represent the transfer coefficient of the cathodic reaction, the Faraday constant, the ideal gas constant, and the absolute temperature, respectively.

With these hypotheses, the equations accounting for the variation of the system with time, can be written as

$$\beta_1 \frac{d\theta_1}{dt} = A_1(1 - \theta_1 - \theta_2 - \theta_3) - A_2\theta_1 - A_4\theta_1\theta_2 \quad [1]$$

$$\beta_2 \frac{d\theta_2}{dt} = A_6\theta_1 - A_4\theta_1\theta_2 + (A_3 - A_5)\theta_2 - A'_3\theta_2^2 \quad [2]$$

$$\beta_3 \frac{d\theta_3}{dt} = A'_7(1 - \theta_1 - \theta_2 - \theta_3) - A_7\theta_3 \quad [3]$$

$$\frac{J}{F} = (A_1 - A'_7)(1 - \theta_1 - \theta_2 - \theta_3) + (A_2 + A_6)\theta_1 + (A_3 + A_5)\theta_2 - A'_3\theta_2^2 + A_7\theta_3 \quad [4]$$

where J is the current density and where

$$\left. \begin{aligned} A_1 &= K_1[\text{H}^+] & A_2 &= K_2\beta_1[\text{H}^+] \\ A_3 &= K_3\beta_2[\text{Zn}^{2+}] & A_4 &= K_4\beta_1\beta_2 \\ A'_3 &= K'_3\beta_2^2 & A_5 &= K_5\beta_2 \\ A_6 &= K_6\beta_1[\text{Zn}^{2+}] & A_7 &= K_7\beta_3 \\ & & A'_7 &= K'_7[A^-] \end{aligned} \right\} \quad [5]$$

Steady-state current potential curve.—Under steady-state conditions the coverage fractions can be expressed by the following equations

$$\theta_1 = \frac{A_1(1 - \gamma)(1 - \theta_2)}{A_1(1 - \gamma) + A_2 + A_4\theta_2} \quad [6]$$

$$\theta_2^3 + B\theta_2^2 + C\theta_2 + D = 0 \quad [7]$$

$$\theta_3 = \gamma(1 - \theta_1 - \theta_2) \quad [8]$$

where

$$\gamma = \left(1 + \frac{A_7}{A'_7}\right)^{-1} \quad [9]$$

The coefficients in Eq. [7] are

$$B = \frac{A_1(1 - \gamma) + A_2}{A_4} - \frac{A_1(1 - \gamma) + A_3 - A_5}{A'_3} \quad [10]$$

$$C = \frac{A_1}{A'_3}(1 - \gamma) \left(1 + \frac{A_6}{A_4}\right) - (A_3 - A_5) \frac{A_1(1 - \gamma) + A_2}{A'_3 A_4} \quad [11]$$

$$D = -\frac{A_1 A_6}{A'_3 A_4}(1 - \gamma) \quad [12]$$

Under these conditions, the steady-state current density is

$$J_s = 2F[\theta_2(A_5 + A_4\theta_1) + A_2\theta_1] \quad [13]$$

and the efficiency η of the electrocrystallization is

$$\eta = \frac{\theta_2(A_5 + A_4\theta_1)}{\theta_2(A_5 + A_4\theta_1) + A_2\theta_1} \quad [14]$$

When adequate values are employed for the parameters A_i and b_i , it can be found that there exists a potential range within which Eq. [7] has three real roots between 0 and 1, to which correspond three values of θ_1 and θ_3 , also between 0 and 1, and three values of J_s . We then obtain an S-shaped curve for the dependence of current density on the steady-state potential, similar to curve 1 in Fig. 1(a). Curve 1 has been computed using the values for parameters A_i and b_i indicated in the caption to Fig. 1(a). On the other hand, curve 2 in Fig. 1(a), which corresponds to a different set of parameters, is no longer S-shaped. Curve 2 has been

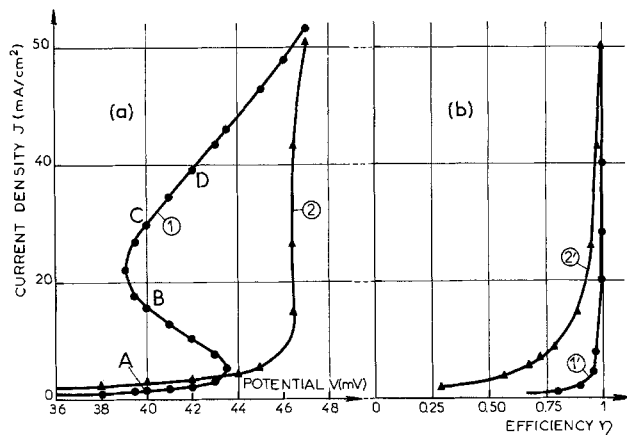


Fig. 1. Simulation of the influence of pH (a), on current density-potential curves with respect to an arbitrary origin, and (b), on current density-deposition efficiency curves. Curves (1) and (1') have been calculated taking the following values for parameters b_i (in V^{-1}): $b_1 = 19.3$, $b_2 = 29.3$, $b_3 = 33.8$, $b'_3 = 4.8$, $b_5 = 38.6$, $b_6 = 19.3$, $b_7 = 19.3$, $b'_7 = 19.3$ and, at $V = 0$, for parameters A_i (in $cm^{-2} sec^{-1}$): $A_1 = 0.16591 \cdot 10^{-6}$, $A_2 = 0.3 \cdot 10^{-9}$, $A_3 = 0.8763 \cdot 10^{-7}$, $A'_3 = 0.1229 \cdot 10^{-6}$, $A_4 = 10^{-7}$, $A_5 = 0.54 \cdot 10^{-7}$, $A_6 = 10^{-10}$, $\gamma = 0.1$. Curves (2) and (2') have been calculated from the same set of parameters by multiplying A_1 and A_2 by 10.

obtained from curve 1 by multiplying by 10 the parameters A_1 and A_2 , which simulates a decrease of a unity in the pH. Consequently, a decrease of the electrolyte pH tends to eliminate the multiple steady states of the interface. Correlatively, we can see from Fig. 1(a) that a decrease in the pH shifts the current-potential curve towards higher cathodic polarizations, which corresponds to an inhibiting effect of adsorbed hydrogen.

Calculation of the coverage fractions shows that when the current increases, θ_1 decreases whereas θ_2 increases, which means that the adsorbed H_{ads} species are progressively replaced by Zn^{+}_{ads} species. In addition, it was found that the anion coverage θ_3 first increases, and then decreases, with increasing current.

Figure 1(b) shows the variation of the efficiency η of the metal deposition with current. In order to simulate a variation of pH, curves 1' and 2' have been computed using the values of the parameters corresponding to curves 1 and 2, respectively. Figure 1(b) reveals that η , which is lower than 1 due to hydrogen evolution, increases with increasing current and tends to 1. In addition, a decrease of a unity in the pH leads to a decrease in η at a given current density.

Electrode impedance.—The faradaic impedance Z_f of the electrode is calculated using a method described elsewhere (27) which consists in linearizing Eq. [1]–[4] for small sinusoidal variations $\Delta V = |\Delta V| e^{j\omega t}$ from conditions for steady state. We thus obtain Eq. [15]–[18]

$$\frac{1}{Z_f} = \frac{\Delta J}{\Delta V} = \left(\frac{\partial J}{\partial V} \right)_{\theta_i} + \sum_i \left(\frac{\partial J}{\partial \theta_i} \right)_V \cdot \frac{\Delta \theta_i}{\Delta V} \quad [15]$$

$$(j\omega\beta_1 + A_1 + A_2 + A_4\theta_2) \frac{\Delta \theta_1}{\Delta V} + (A_1 + A_4\theta_1) \frac{\Delta \theta_2}{\Delta V} + A_1 \frac{\Delta \theta_3}{\Delta V} = A_1 b_1 (1 - \Sigma \theta_i) - A_2 b_2 \theta_1 \quad [16]$$

$$(A_4\theta_2 - A_6) \frac{\Delta \theta_1}{\Delta V} + (j\omega\beta_2 + A_4\theta_1 + 2A'_3\theta_2 + A_5 - A_3) \frac{\Delta \theta_2}{\Delta V} = A_6 b_6 \theta_1 + (A_3 b_3 - A_5 b_5) \theta_2 + A'_3 b'_3 \theta_2^2 \quad [17]$$

$$A'_7 \frac{\Delta \theta_1}{\Delta V} + A'_7 \frac{\Delta \theta_2}{\Delta V} + (A_7 + A'_7 + j\omega\beta_3) \frac{\Delta \theta_3}{\Delta V} = - [A_7 b_7 \theta_3 + A'_7 b'_7 (1 - \Sigma \theta_i)] \quad [18]$$

The first term in Eq. [15] corresponds to the transfer resistance R_t and can be calculated from Eq. [4]

$$\frac{1}{R_t} = \left(\frac{\partial J}{\partial V} \right)_{\theta_i} = F[(A_1 b_1 + A'_7 b'_7) (1 - \Sigma \theta_i) + (A_2 b_2 + A_6 b_6) \theta_1 + (A_3 b_3 + A_5 b_5) \theta_2 + A'_3 b'_3 \theta_2^2 + A_7 b_7 \theta_3] \quad [19]$$

Terms $\left(\frac{\partial J}{\partial \theta_i} \right)_V$ are also deduced from Eq. [4]

$$\left(\frac{\partial J}{\partial \theta_1} \right)_V = F(A_2 + A_6 - A_1 + A'_7) \quad [20]$$

$$\left(\frac{\partial J}{\partial \theta_2} \right)_V = F(A'_7 + A_3 + A_5 - A_1 - 2A'_3 \theta_2) \quad [21]$$

$$\left(\frac{\partial J}{\partial \theta_3} \right)_V = F(A_7 + A'_7 - A_1) \quad [22]$$

Terms $\Delta \theta_i / \Delta V$ are obtained by solving, using the Cramer method, the linear system formed by Eq. [16], [17], and [18].

By taking account of the electrochemical double-layer capacity C_d considered in parallel with Z_f , we finally obtain the electrode impedance Z

$$\frac{1}{Z} = \frac{1}{Z_f} + jC_d \omega \quad [23]$$

With certain values of the parameters, Z is inductive at low frequencies. As an example, we represented in Fig. 2 the impedance $R-jG$ diagrams calculated at points A, B, and C of curve 1 in Fig. 1(a). These diagrams were obtained using the values of parameters A_i and b_i already employed to establish the current-potential curve, and the values of the parameters A_7 , β_1 , β_2 , β_3 , and C_d which are indicated in the caption to Fig. 2. On each diagram, where the parameter is frequency in Hertz, the capacitive semicircle corresponds to the circuit formed by the capacity C_d in parallel with the transfer resistance R_t . At low frequencies, the faradaic impedance Z_f , which is then inductive, prevails and three time-constants corresponding to the relaxation of the coverage fractions θ_1 , θ_2 , and θ_3 , are observed. The limit of Z_f at zero frequency coincides with the polarization resistance R_p , given by the slope of the steady-state current-potential curve. As shown in Fig. 2, this resistance is either positive (points A and C) or negative (point B).

Figure 2 reveals that with the values chosen for the parameters, the three time-constants remain clearly different when current varies. This is not always the case. Thus, by attributing for example to parameters β_1 , β_2 , and β_3 another set of values (indicated in the caption to Fig. 3), we can see that the shape of the impedance diagram changes when the current varies, and the three time-constants become more or less clearly separated. The diagrams depicted in Fig. 3 have been calculated at points A, B, and D in Fig. 1. We can see that the three inductive loops clearly appear at point B, where the polarization resistance is negative, whereas at points A and D only two inductive loops can be observed.

Experimental

Electrolytic solutions and electrolysis cell.—In order to compare the theoretical model with our experimental results, we chose three types of electrolytes which are commonly used in zinc industry. One of them, (1M Na_2SO_4 + 1.5M $ZnSO_4$) is used in the metallurgy of zinc; the pH of this medium is varied by addition of small amounts of H_2SO_4 . To vary the pH of the second acidic medium (2.67M NH_4Cl + 0.72M $ZnCl_2$, which is a Leclanché cell electrolyte), we added small amounts of NH_4OH or of HCl . The third electrolyte, we chose, was an alkaline medium (7M KOH

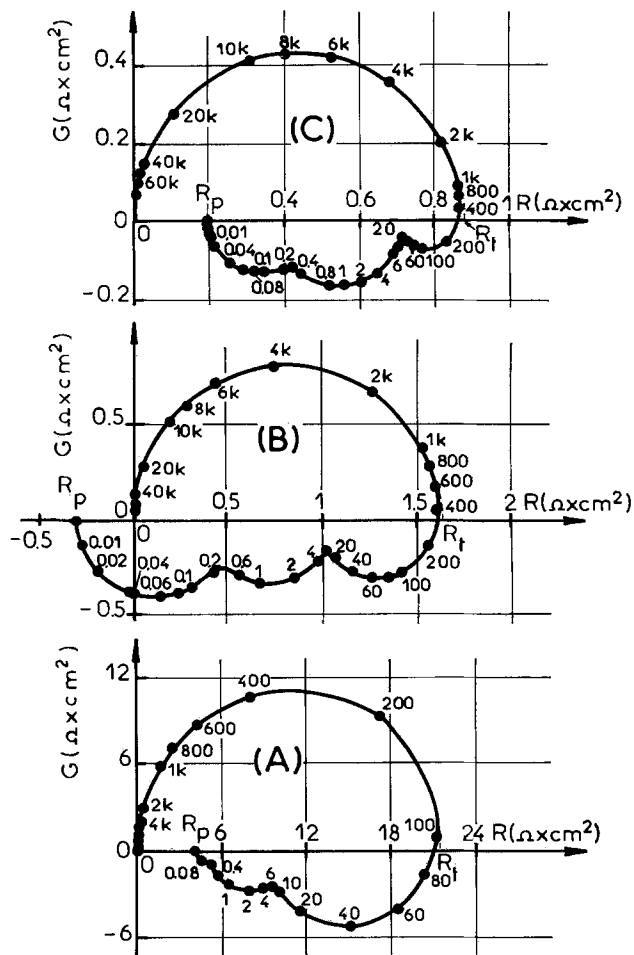


Fig. 2. Impedance diagrams simulated at the same potential ($=40$ mV) as for points A (3 mA/cm 2), B (15.5 mA/cm 2), and C (30 mA/cm 2) of Fig. 1(a) by introducing the following parameters: $C_d = 25 \mu\text{F/cm}^2$, $\beta_1 = 1.36 \cdot 10^{-7}$ at·g·cm $^{-2}$, $\beta_2 = 9.067 \cdot 10^{-11}$ at·g·cm $^{-2}$, $\beta_3 = 8.10 \cdot 10^{-9}$ at·g·cm $^{-2}$ and at $V = 0$: $A_7 = 4.62 \cdot 10^{-9}$ cm $^{-2}$ sec $^{-1}$.

+ 0.5 to 1.24M ZnO) employed in accumulators. The most concentrated ZnO solutions were prepared by dilution and cooling of ZnO solutions in 21M KOH previously obtained by heating (14). All the solutions were prepared with twice ion-exchanged water and "Merck" compounds of analytical purity.

During the electrolysis, the electrolyte was maintained at $26^\circ \pm 0.5^\circ\text{C}$. The atmosphere in the cell remained inert by argon bubbling. The anode was generally a cylinder of zinc of high purity (99.999%). In the most acidic solutions ($\text{pH} \leq 2$), it was replaced by a platinum gauze in order to avoid chemical attack, and the anodic and cathodic compartments were separated by a sinter wall. Besides, at $\text{pH} = 5.2$, we have verified that the plotting of the current-potential curve and the measurement of the impedance do not depend on the nature of the anode (zinc or platinum) in our experimental conditions. In all cases, the reference electrode was immersed in the electrolyte, and consisted of two compartments separated by fritted-glass. The compartment containing the calomel electrode was filled with a KCl saturated solution, the other one contained the electrolyte of the cell.

Metal deposition was performed on the cross section of a zinc cylinder having an area of 0.28 cm 2 . The wall of the cylinder was isolated from the electrolyte with a coat of a "Specifix" type resin. The electrode was rotated uniformly round a vertical axis and constituted a rotating disk whose speed could range from 0 to 5000 rpm. This speed was always sufficiently high so that the current-potential curve was independent of the rotation speed, i.e., of the transfer by convec-

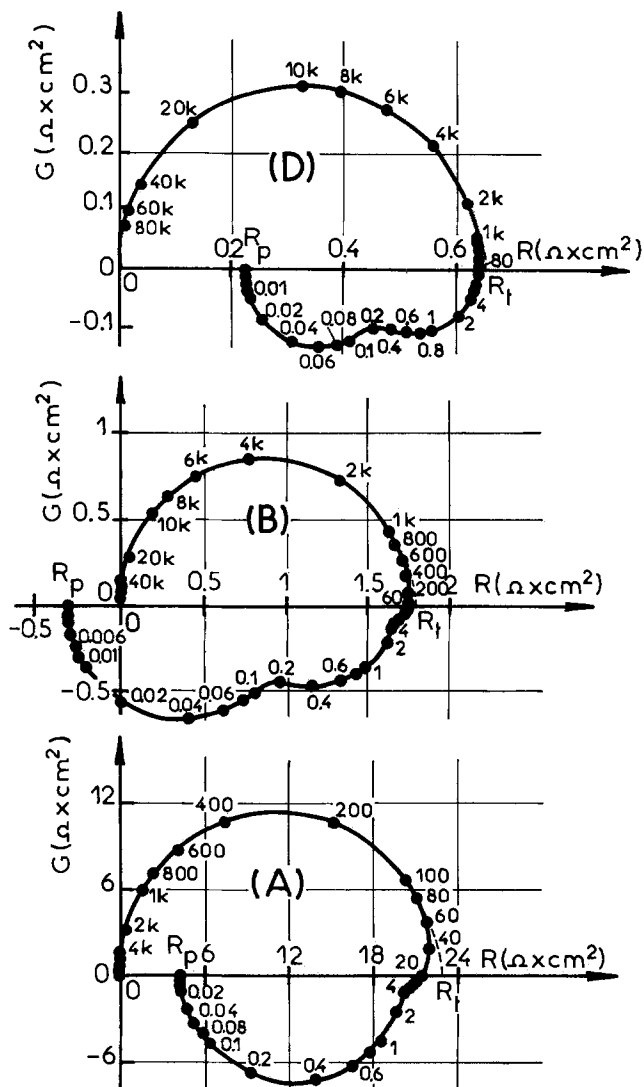


Fig. 3. Impedance diagrams simulated at points A (40 mV, 3 mA/cm 2), B (40 mV, 15.5 mA/cm 2), and D (42 mV, 39 mA/cm 2) of curve 1 in Fig. 1(a) by introducing the following parameters: $C_d = 25 \mu\text{F/cm}^2$, $\beta_1 = 2.72 \cdot 10^{-7}$ at·g·cm $^{-2}$, $\beta_2 = 1.904 \cdot 10^{-8}$ at·g·cm $^{-2}$, $\beta_3 = 2.72 \cdot 10^{-10}$ at·g·cm $^{-2}$, and at $V = 0$: $A_7 = 4.62 \cdot 10^{-9}$ cm $^{-2}$ sec $^{-1}$.

tive diffusion of the chemical species towards the electrode.

In order to obtain a reproducible plotting of the current-potential curve, the electrode surface was polished by emery paper (600 grade) before each deposition, then immersed into a nearly 50% HCl solution for some seconds. It is finally rinsed with twice ion-exchanged water and used immediately after.

Plotting of the current-potential curve and measurement of the impedance.—Considering that during the electrocrystallization of zinc the current varies very rapidly with the cathodic polarization (28, 29), the plotting of the $I(V)$ current-potential curve and the measurement of the impedance have been performed under galvanostatic conditions. Provided that the applied electrolysis current remain sufficiently low, dendritic growth of zinc is avoided (30, 31) and steady-state conditions for the electrocrystallization of the metal are maintained. As a matter of fact, the recording of the electrode-potential as a function of time reveals, after a short-time variation of potential (about 1 min), a plateau which defines the steady-state potential. The lower the current, the more extended the plateau is; particularly, at current lower than 10 mA, this plateau is longer than 15 min. In order to obtain the potential V , the steady-state potential was measured and corrected for ohmic drop (term in $R_e I$,

where R_e is the resistance of the electrolyte between the cathode and the reference electrode). This ohmic drop term has been determined using an interruptor method (32) and, also, from the high-frequency limit of the impedance. The accuracy was better than 4% and was sufficient to reveal an S-shaped current-potential curve. Each curve, which has been recorded both with increasing and decreasing values of current intensity, shows no hysteresis effects.

The electrode impedance was obtained by superimposing on the direct current a sinusoidal alternating current of small amplitude. Measurements were performed with a correlation transfer function analyzer (Solarton JM 1600 + JX 1639) connected to a wide-band galvanostat built in our laboratory (33). Such a device allows an easy measurement of the electrochemical impedance between 10^{-3} Hz and 50 kHz. As a matter of fact, it is necessary to measure the interface impedance up to its zero-frequency limit in order to reach the elementary steps of any electrochemical reaction (27, 34, 35). Now, most of the impedance measurements relative to a zinc electrode have hitherto been performed at frequencies higher than a few hundred Hertz (1, 36) or at a few ten Hertz (37-40), and therefore they only lead to the double-layer capacity and the transfer resistance.

Efficiency of the electrocrystallization.—To perform a reproducible electrocrystallization of the metal, it is indispensable not to dry the electrode before the electrolysis, and this prohibits any weighing of the electrode before the experiment. The efficiency measurements have therefore been carried out using an electrode constituted by a Johnson-Matthey (99.999%) copper disk kept in electric contact with the zinc rotating cylinder by means of a thermoplastic coat.

After electrolysis, the disk was separated from the zinc cylinder. The amount of the zinc deposit is equal to the difference between the weight of the copper disk covered by the deposit and that of the disk after dissolution of the deposit by 50% HCl. Before each weighing, the disk was rinsed with ethyl acetate, then dried under vacuum. Weighings were performed with a "Cahn Division" electrobalance and allowed us to determine the electrocrystallization efficiency η to better than 0.5%.

Results

The acid sulfate solution.—In Fig. 4(a) we represented the current-potential curves obtained when the influence of mass transfer is eliminated in the case of the acid sulfate solution ($1M Na_2SO_4 + 1.5M ZnSO_4$) at two different pH values. The curves were recorded with currents lower than 10 mA, which is the limit beyond which conditions are no longer those for steady state. At a pH of 4.3, curve 1 is S-shaped, and multiple steady states are observed at potentials between -1.045 and -1.049 V/SCE. At a pH of 2, however, the

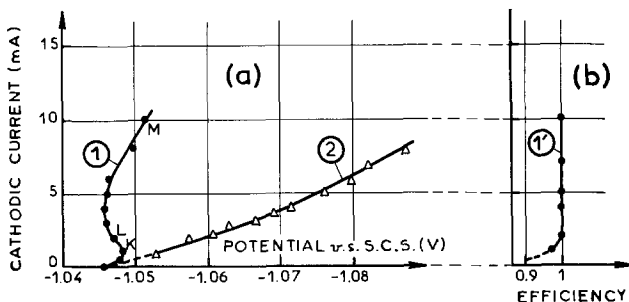


Fig. 4. Influence of the pH on the steady-state current-potential curves (a) and influence of the current on the deposition efficiency (b) for the electrocrystallization of zinc obtained with the following electrolyte: ($1M Na_2SO_4 + 1.5M ZnSO_4$) and a rotating disk electrode (area $0.28 cm^2$; rotation speed Ω , 3000 rpm) at $26 \pm 0.5^\circ C$: Curve 1 and 1', pH = 4.3 ± 0.1 ; curve 2, pH = 2.0 ± 0.1 ; K, $I = 2 mA$, $V = -1.0485 V/SCE$; L, $I = 3 mA$, $V = -1.047 V/SCE$; M, $I = 10 mA$, $V = -1.0515 V/SCE$.

current-potential curve is single valued and is shifted towards higher cathodic polarizations.

At low cathodic currents, the electrocrystallization efficiency η is an increasing function of current. For example, at pH = 4.3, it can be seen in Fig. 4(b) (curve 1') that the efficiency is equal to 0.97 at 1 mA and that it remains nearly equal to unity as soon as the current becomes higher than 2 mA.

With such an electrolytic medium, the shape of the impedance diagrams is similar to that we already obtained with the Leclanché cell electrolyte (29). At high frequencies, the faradaic impedance is shunted with the double-layer capacity, and the impedance becomes reduced to the electrolyte resistance R_e . At frequencies higher than about 100 Hz, there appears a capacitive loop whose shape is nearly a semicircle and which corresponds to the circuit formed by the double-layer capacity in parallel with the transfer resistance R_t .

At low frequencies, the impedance is inductive and is characterized by three time-constants; Fig. 5 gives an example of the variation of the impedance diagrams ($Z = R - jG$) with current at pH = 4.3. Diagrams (K), (L), and (M) correspond to points K, L, and M on curve 1 in Fig. 4. The electrolyte resistance R_e is taken as origin of the R-axis in the complex plane and is equal here to 9.0 ± 0.1 ohms. Extrapolating the capacitive loop leads to the transfer resistance R_t . This loop also allows us to calculate the double-layer capacity which has an average value of $40 \mu F/cm^2$ for diagrams (K) and (L), and of $50 \mu F/cm^2$ for diagram (M). At low frequencies, all three diagrams lead to three well-defined time-constants, since they show clearly three inductive loops. For example, dia-

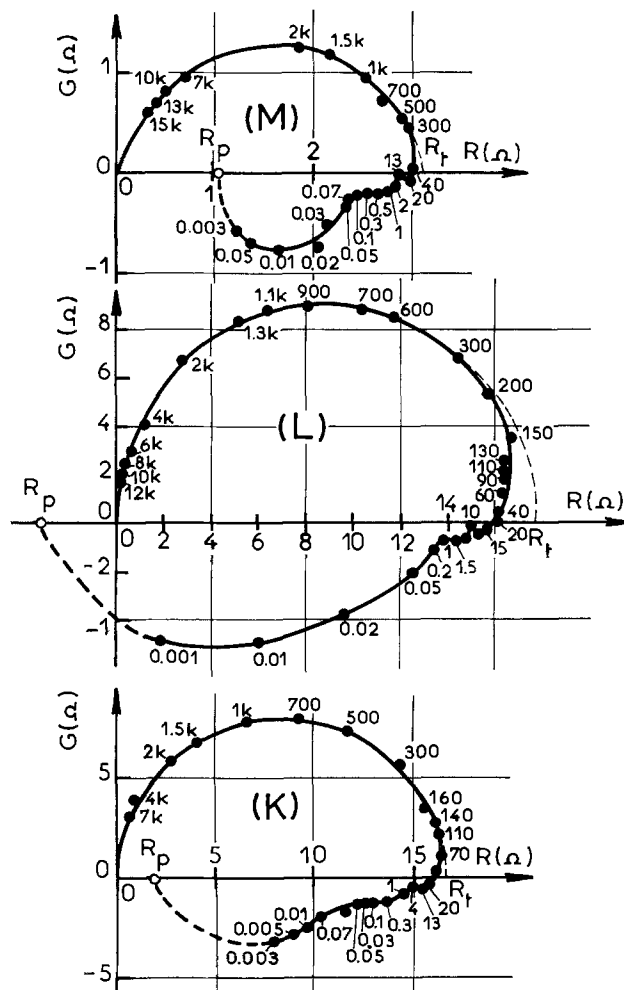


Fig. 5. Complex impedance $Z = R - jG$ corresponding to the electrocrystallization of zinc under the same conditions as for points K, L, and M of curve 1 in Fig. 4 (frequency in Hz).

gram (L) shows three loops located within the 0-1, the 1-10, and the 10-40 Hz frequency ranges approximately. Finally, by extrapolating each diagram at zero frequency, we find the polarization resistance; in particular extrapolation in diagram (L) actually leads to a negative resistance.

The Leclanché cell electrolyte.—With this electrolyte we can determine the current-potential curve under conditions for steady state as long as the current remains lower than about 20 mA. In addition, electrode rotation speeds higher than 1000 rpm no longer have an influence on the current-potential plots. Figure 6(a) shows the current-potential curves obtained at two different values of pH. Curve 1, recorded at pH = 5.2, is S-shaped and is characteristic of multiple steady states between -1.057 and -1.059 V/SCE. As in the case of the acid sulfate solution, the multiple steady states disappear when the pH decreases; this is why the curve becomes single valued at pH = 2 (curve 2). In addition, contrarily to the case of the acid sulfate solution, a decrease of the pH gives rise to a shift of the current-potential curve towards lower cathodic polarizations.

As in the case of the acid sulfate solution, an increase of the efficiency η is found when the current increases. This variation is illustrated in Fig. 6(b) where the three current-efficiency curves correspond to 5.2, 2, and 0.5 pH values, respectively. It can be seen that for a given current value, the more acid the solution the lower the efficiency. For example, at pH = 5.2, η becomes equal to unity as soon as the current exceeds 2 mA (curve 1'), whereas at pH = 0.5 it is still equal to 0.97 for a current of 20 mA (curve 3').

Figure 7 shows the variation of the impedance diagrams with the current at pH = 5.2. Diagrams (N), (P), and (Q) correspond to points N, P, and Q on curve 1 in Fig. 6a. In this medium, which is more conducting than the acid sulfate electrolyte, the electrolyte resistance is equal to 2.8 ± 0.2 ohms. The average value of the capacity shunted by the transfer resistance is equal to 50, 40, and 200 $\mu\text{F}/\text{cm}^2$ at points N, P, and Q, respectively. At low frequencies, impedance becomes inductive, and three relaxation processes are observed. As a matter of fact, three time constants are clearly shown on diagram (P), whereas they are not as well

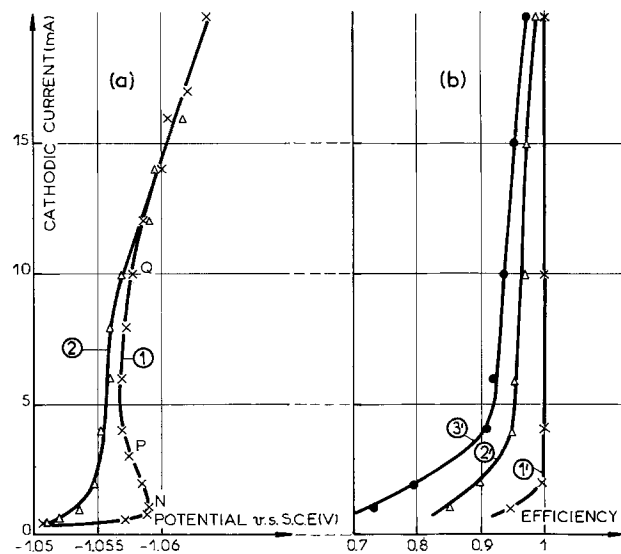


Fig. 6. Influence of the pH (a) on the steady-state current-potential curves, and (b) on the current deposition efficiency curves recorded during the electrocrystallization of zinc from a Leclanché cell electrolyte ($0.72\text{M ZnCl}_2 + 2.67\text{M NH}_4\text{Cl}$) with a rotating disk electrode (area, 0.28 cm^2 ; rotation speed Ω , 3000 rpm) at $26^\circ \pm 0.5^\circ\text{C}$. Curves 1 and 1', pH = 5.2; curves 2 and 2', pH = 2; curve 3', pH = 0.5. N, $I = 1\text{ mA}$, $V = -1.059\text{ V/SCE}$; P, $I = 3\text{ mA}$, $V = -1.0575\text{ V/SCE}$; Q, $I = 10\text{ mA}$, $V = -1.0575\text{ V/SCE}$.

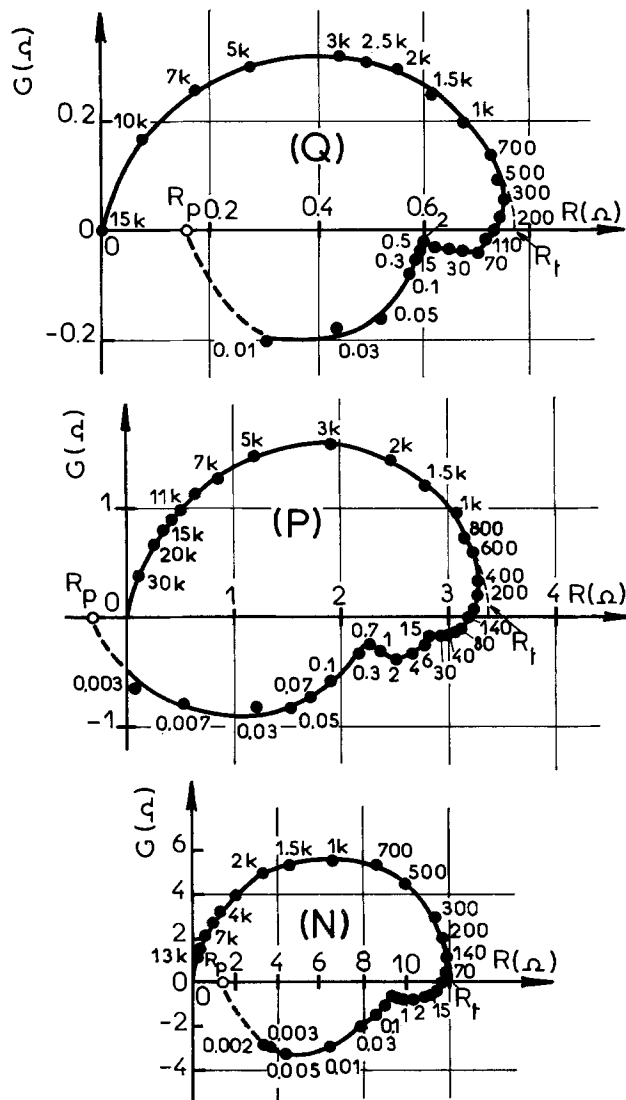


Fig. 7. Complex impedance $Z = R - jG$ corresponding to the electrocrystallization of zinc under the same conditions as for points N, P, and Q on curve 1 in Fig. 6(a) (frequency in Hz).

separated on diagrams (N) and (Q) where only two inductive loops can be seen.

The alkaline zincate solution.—Curves 1 and 2 in Fig. 8 represent the steady-state current-potential curves obtained after eliminating the influence of mass transfer with the alkaline zincate solution at two different zinc oxide concentrations (1.24 and 0.5M, respectively). These curves reveal that, in alkaline medium like in acidic medium, the electrocrystallization of zinc is markedly activated when the cathodic polarization increases. This activation is more and more important as the concentration of zinc becomes higher in the electrolyte. The dependence of the current-potential curve on concentration is similar to that we observed with the Leclanché cell electrolyte (29).

The impedance diagrams obtained in alkaline medium are also similar to those obtained in acidic medium. As a matter of fact, the mean values of the double-layer capacity as calculated from diagrams (I), (J), and (H) in Fig. 8, which correspond to points I, J, and H, are close to those determined in acidic medium, since they are equal to 40, 60, and 30 $\mu\text{F}/\text{cm}^2$, respectively. Moreover at low frequencies, three relaxation processes presenting an inductive character are most frequently found here as shown by the three inductive loops which clearly appear on the three diagrams as in the case of acidic solutions. However, the three diagrams reveal a further faradaic time-constant as shown by a fourth loop which is either inductive [diagram (I)], or capacitive [diagram (J) and (H)].

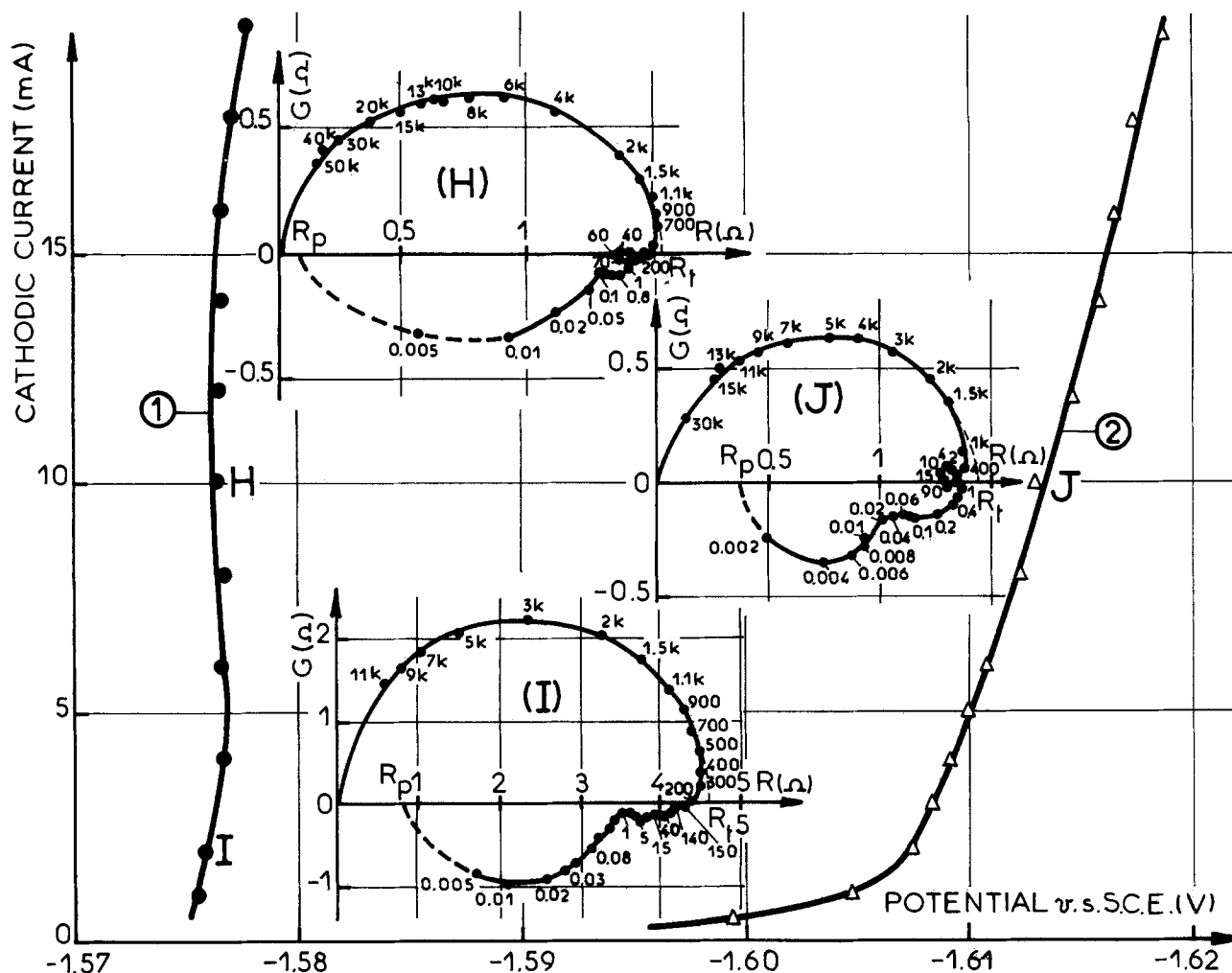


Fig. 8. Influence of the concentration x of ZnO in 7M KOH on the steady-state current-potential curves relative to the electrocrystallization of zinc obtained with a rotating disk electrode (area, 0.28 cm^2) at $26^\circ \pm 0.5^\circ\text{C}$. Curve 1, $x = 1.24\text{M}$, rotation speed $\Omega = 3000 \text{ rpm}$; curve 2, $x = 0.25\text{M}$; Ω , 5000 rpm. H (10 mA, -1.576 V/SCE); I (2 mA, -1.5755 V/SCE); J (10 mA, -1.613 V/SCE). Impedance diagrams (H), (I), and (J) obtained under the same conditions as for points I, J, and H (frequency in Hz).

Let us finally note that, with such alkaline electrolytes, the efficiency η increases with increasing current in a manner analogous to that in acidic medium. For example, at a zinc oxide concentration of 0.5M , the influence of the current on η is similar to that represented in Fig. 4b: η is equal to 0.98 with a current of 1 mA and becomes equal to unity as soon as the current is higher than 2 mA.

Discussion

Our experimental results have been obtained by: (i) eliminating the influence of mass transfer, (ii) correcting the current-potential curve for the ohmic drop term related to the electrolyte resistance, and (iii) measuring the faradaic impedance of the interface up to very low frequencies. Our experimental results agree, on the whole, with the model proposed and confirm that the mechanism of electrocrystallization is more complicated in alkaline medium than in acidic medium. As a matter of fact, in alkaline medium, the impedance diagrams reveal not only the three inductive loops predicted by the model but also a fourth faradaic time-constant (Fig. 8). This leads us to believe that, in fact, the electrocrystallization of zinc from zincate ions involves at least four adsorbed species at the interface, unless chemical reactions between different complex species are the origin of a further time-constant, as in the case of the cupri-prochloride reduction on a platinum electrode (41).

It is evident that the hypotheses upon which our model is based and which concern the behavior of the interface and the mechanism of adsorption, are over

simplified. In particular, assimilating the active surface of the electrode with an ideal plane by neglecting all roughness at a macroscopic level as well as at that of atomic steps, constitutes a rough approximation. Now, it is known that the roughness of zinc deposits depends on the current value (42); a change of the roughness with the electrode polarization might therefore influence the values of the time-constants. However, the time-constants measured here, even the highest one, do not seem to be caused by a slow relaxation of the electrode area, as shown by a recent attempt to establish such a relationship in the case of the Cu/CuSO₄ interface (43). Therefore, the most probable cause for this time-constant remains a coverage process, at least in the present study.

In addition, the hypotheses accepted here do not take account of the extreme mobility of adsorbed hydrogen and of its penetration into the metal. These approximations might explain why, in order to calculate the magnitude of the highest time-constant measured and compare it to the experimental results, it is necessary to choose a relatively high value of the coefficient β_1 , since this value is 100 times as great as the surface concentration $\beta_0 = 2.72 \cdot 10^{-9} \text{ at}\cdot\text{g}\cdot\text{cm}^{-2}$ of the zinc atoms in the compact plane (0001), where the interatomic distance is 2.659\AA . On the other hand, the values of β_2 and β_3 , relative to Zn_{ads} and ZnA_{ads} , chosen for a good agreement between our model and experiment are close to or lower than β_0 .

It is known that the Leclanché cell electrolyte may contain several complex ions (6) but the structure of the charged species that adsorb remains unknown. It

is possible that a change of the pH entails a change of another parameter such as the concentration of Zn^{2+} and A^- ions. Therefore, it is not surprising that a decrease of the pH for such an electrolyte can alter the electrolysis conditions in a way different than the condition which is simulated simply by increasing parameters A_1 and A_2 (Fig. 1a). Thus, with an electrolyte of this type, a decrease of the pH gives rise to a decrease of the cathodic polarizations at low current values (Fig. 6a) which is contrary to the inhibiting effect of hydrogen adsorption predicted by our model. On the other hand, with the acid sulfate solution, which is known to form complexes with zinc much less readily than the Leclanché cell electrolyte, a decrease of the pH actually entails an increase of the inhibiting effect of hydrogen adsorption (Fig. 4a), which is in good agreement with our model.

Experimentally, it is observed that a decrease in the concentration of zinc in the electrolyte leads to a shift of the steady-state current-potential curve towards more cathodic polarizations, and simultaneously cancels out the multiple steady states. Such an influence was shown up in basic medium (Fig. 8) as well as in acidic medium (29). It is not obvious that this influence can be interpreted in terms of the model described in this paper. As a matter of fact, with the set of parameters used to simulate curve 1 in Fig. 1(a), a decrease of the concentration of Zn^{2+} (corresponding to a decrease of parameters A_3 and A_6) does not tend to make the curve single valued. This might be due to the choice of the relative values of parameters A_1 and b_1 employed to perform the simulation. Considering the complexity of this type of model, due to the number of parameters and the nonlinearity of the equations of the system, it is very difficult to make sure that a given set of parameters is optimal, even if these parameters can account for the magnitude of the electrolysis current and the components of the faradaic impedance. As a matter of fact, because it is not possible to fit the theoretical parameters to the experimental results and because the nature and the concentration of the Zn^{2+} and A^- ions are not well-known, the values of the quantities K_1 and β_1 specific of each electrolyte cannot be determined.

Besides, it might be possible that the concentration effect be interpreted more satisfactorily in terms of a different coupling between the heterogeneous reactions. For example, when the reaction [f] is replaced by another one such as $Zn^{2+} + e \rightarrow Zn^{+}_{ads}$, it becomes possible to simulate the effect of the concentration of zinc in the electrolyte on the steady-state current-potential curves. Unfortunately, with such a new coupling of heterogeneous reactions, an increasing of parameters A_1 and A_2 simulates no more the inhibiting effect of hydrogen adsorption.

The reaction model presented here agrees with certain basic facts relative to the electrocrystallization of zinc experimentally performed with very different electrolytic media, although it presents some imperfections probably due to the relatively simple hypotheses on which it is based.

This model takes account of the influence of hydrogen evolution on the efficiency η of the electrocrystallization of zinc. The variation of η with current, which is observed experimentally, agrees entirely with the theoretical variation depicted in Fig. 1(b). As a matter of fact, both in acidic and in alkaline medium, η is actually an increasing function of current [Fig. 6(b)]. In addition, the experimental variation of η with the electrolyte pH is also in good agreement with our theory, since the experimental values confirm that a decrease of the pH leads to a decrease of the efficiency at constant current [Fig. 6(b)].

The model, which involves an autocatalytic interfacial step, also predicts the appearance of multiple steady states of the interface which are revealed by an S-shaped current-potential curve. In agreement with the model, after eliminating the influence of con-

vective diffusion, we showed up such curves with the two acidic electrolytes [Fig. 4(a) and 6(a)] and also with the alkaline medium we investigated (Fig. 8). Moreover, a decrease of the pH, in the case of the Leclanché cell electrolyte as well as the acid sulfate solution, cancels out the multiple steady states, and the current-potential curve becomes single valued [Fig. 4(a) and 6(a)]. This effect is also in good agreement with the behavior predicted by our model.

The shape of the impedance diagrams we obtained experimentally is also in conformity with the theoretical model. In fact, with the two acidic media, and even with the alkaline medium where a further time-constant appears, an inductive impedance can be measured at low frequencies and three time-constants are revealed. These time-constants correspond to the relaxation of the partial coverages of the electrode by the three adsorbed species predicted by the model. Finally, the variation of the impedance diagrams with current in acidic medium also agrees with the model. As a matter of fact, according to the values of the parameters used to simulate the interface impedance, we may predict a more or less clear separation of the three time-constants when the current varies. For example, the variation of the diagrams verified with the Leclanché cell electrolyte supports the simulated variation (Fig. 3). Similarly, the diagrams recorded with the acid sulfate solution (Fig. 5) agree with those calculated (Fig. 2).

Obviously, relaxation experiments are indirect methods for detecting intermediates in electrode reactions and cannot give an unambiguous picture of what intermediates are involved (44). Nevertheless, other experimental results confirm the outstanding role played by the autocatalytic step in the reaction mechanism of the electrocrystallization of zinc. So, it has been shown that the interactions between the interfacial reactions [a] to [f] and the surface diffusion of the Zn^{+}_{ads} adions can give rise to a distribution of the current-density on the electrode (45). This spatial structuration of the electrode accounts for the appearance of spongy, compact or dendritic deposits which are observed successively when the current intensity increases, both in acidic and alkaline electrolytes. Consequently, the model is able to make a correlation between the morphology of the electrodeposits and the heterogeneous reactions.

Conclusion

The model for the electrocrystallization of zinc presented in this paper reveals that several species such as hydrogen, certain anions, and Zn^{+} are involved. It also allows one to show the outstanding role played in the mechanism of the electrocrystallization of zinc by an autocatalytic step during which a monovalent intermediate is formed. Comparison of the model with the experimental results obtained with three markedly different electrolytes shows up the importance of this autocatalytic step both in acidic and in alkaline medium, despite the probably different nature of the chemical species implied in the three media investigated. As a matter of fact, not only does our model account for the influence of hydrogen adsorption on the efficiency of electrocrystallization, but it also explains the appearance of multiple steady states and the existence of an inductive faradaic impedance characterized by at least three time-constants. This type of model allows one to calculate, from the elementary steps occurring at the interface, parameters such as the electrocrystallization efficiency, the electrolysis current, and the various components of the faradaic impedance. This opens promising outlooks for the study of the electrocrystallization of zinc because it is perhaps possible to relate one or several of the parameters defined here to certain properties specific to the interface.

Any discussion of this paper will appear in a Discussion Section to be published in the June 1976 JOURNAL. All discussions for the June 1976 Discussion Section should be submitted by Feb. 1, 1976.

Publication costs of this article were partially assisted by Centre National de la Recherche Scientifique.

LIST OF SYMBOLS

A_i and A'_i	defined by Eq. [5], $\text{cm}^{-2}\text{sec}^{-1}$
b_i	$\alpha_i F/RT, \text{V}^{-1}$
b'_i	$(1 - \alpha_i) F/RT, \text{V}^{-1}$
B	defined by Eq. [10], dimensionless
C	defined by Eq. [11], dimensionless
C_d	electrochemical double layer capacity, F
D	defined by Eq. [12], dimensionless
F	Faraday's constant, 96,500 coulombs/g-equivalent
G	imaginary part of the electrode impedance
Z	
I	current intensity, A
J	current density, $A \text{ cm}^{-2}$
J_s	steady-state current density, $A \text{ cm}^{-2}$
j	$\sqrt{-1}$
$(K_i)_{i=1,3,5,7}$	electrochemical rate constants of cathodic reactions
$(K'_i)_{i=3,7}$	electrochemical rate constants of anodic reactions
K_4	chemical rate constant, $\text{cm}^2 \text{ sec}^{-1}$
R	real part of the electrode impedance Z
R_e	electrolyte resistance
R_p	polarization resistance
R_t	transfer resistance
Q	ideal gas constant
T	temperature, $^{\circ}\text{K}$
t	time, sec
V	cathodic potential, V
Z	electrode impedance
Z_f	faradaic impedance
α_i	transfer coefficient of the cathodic reactions
β_i	maximal surface concentrations, $\text{at} \cdot \text{g cm}^{-2}$
γ	defined by Eq. [9], dimensionless
η	efficiency of the electrocrystallization, dimensionless
ω	angular frequency, rad. sec^{-1}
θ_i	coverage fractions

REFERENCES

- W. Lorenz, *Z. Physik. Chem. N.F.*, **19**, 377 (1959).
- L. Gaiser and K. E. Heusler, *Electrochim. Acta*, **15**, 161 (1970).
- T. Hurlen and E. Eriksrud, *J. Electroanal. Chem.*, **45**, 405 (1973).
- K. E. Heusler and R. Knodler, *Electrochim. Acta*, **18**, 855 (1973).
- D. M. Dražić, S. Hadži-Jordanov, and Z. Nagy, *Croat. Chem. Acta*, **45**, 199 (1973).
- Ph. Brouillet and F. Jolas, *Electrochim. Acta*, **6**, 245 (1962).
- E. Raub and A. Knödler, *Trans. Inst. Metal Finishing*, **38**, 131 (1961).
- V. N. Titova and A. T. Vagramyan, *Elektrokhimiya*, **2**, 1149 (1966); *Zasch. Metall.*, **3**, 102 (1967).
- A. T. Vagramyan and M. Jamagortcjan, "Electrocrystallization of Metals and Inhibiting Adsorption," Chap. 2, Moscow (1969).
- T. P. Dirkse, *This Journal*, **101**, 328 (1954).
- J. S. Fordyce and R. L. Baum, *J. Chem. Phys.*, **43**, 843 (1965).
- G. H. Newman and G. E. Blomgreen, *ibid.*, **43**, 2744 (1965).
- J. O'M. Bockris, Z. Nagy, and A. Damjanovic, *This Journal*, **119**, 285 (1972).
- N. A. Hampson, G. A. Herdman, and R. Taylor, *J. Electroanal. Chem.*, **25**, 9 (1970).
- D. A. Payne and A. J. Bard, *This Journal*, **119**, 1665 (1972).
- T. P. Dirkse and N. A. Hampson, *Electrochim. Acta*, **17**, 1113 (1972).
- I. Epelboin, E. Lejay, and R. Wiart, *Compt. Rend. Acad. Sci. Paris*, **274C**, 178 (1972).
- I. Epelboin, M. Keddam, and J. C. Lestrade, *Faraday Discussions of Chem. Soc.*, **264** (1973).
- I. Epelboin, C. Gabrielli, M. Keddam, J. C. Lestrade, and H. Takenouti, *This Journal*, **119**, 1632 (1972).
- C. Gabrielli and M. Keddam, *J. Electroanal. Chem.*, **45**, 267 (1973).
- P. Glansdorff and I. Prigogine, "Structure, Stabilité et Fluctuations," Masson, Paris (1971).
- C. Vidal, *Compt. Rend. Acad. Sci. Paris*, **274C**, 1713 (1972).
- B. B. Edelstein, *J. Theoret. Biol.*, **29**, 57 (1970).
- E. Lejay and R. Wiart, *Compt. Rend. Acad. Sci. Paris*, **277C**, 833 (1973).
- V. V. Batrakov and A. I. Sidnin, *Elektrokhimiya*, **8**, 122 (1972).
- L. M. Baugh and J. A. Lee, *J. Electroanal. Chem.*, **48**, 55 (1973).
- I. Epelboin and R. Wiart, *This Journal*, **118**, 1577 (1971).
- R. Wiart, E. Lejay, and F. Lenoir, 8th Interfinish Symposium, Bâle, September 1972, p. 84.
- I. Epelboin, M. Ksouri, E. Lejay, and R. Wiart, 25th Meeting of I.S.E., Brighton (1974), Extended Abstracts p. 143; *Electrochim. Acta*, In press.
- F. Mansfield and S. Gilman, *This Journal*, **117**, 1521 (1970).
- J. W. Diggie and A. Damjanovic, *ibid.*, **119**, 1649 (1972).
- Ph. Morel, *Traitement de Surface*, n°. 89, 9 (1969) et n°. 91, 37 (1970).
- C. Gabrielli and M. Keddam, *Electrochim. Acta*, **19**, 355 (1974).
- I. Epelboin and M. Keddam, *This Journal*, **117**, 1052 (1970).
- I. Epelboin, F. Lenoir, and R. Wiart, *J. Crystal Growth*, **13/14**, 417 (1972).
- J. T. Clark and N. A. Hampson, *J. Electroanal. Chem.*, **26**, 307 (1970).
- J. P. G. Farr and N. A. Hampson, *Trans. Faraday Soc.*, **62**, 3493 (1966).
- K. J. Euler, *Metalloberfläche*, **25**, 13 (1971).
- K. J. Euler, *Electrochim. Acta*, **17**, 619 (1972).
- N. Petric and B. Lovreček, *Werkstoffe Korrosion*, **270** (1972).
- I. Epelboin and R. Wiart, *J. Chim. Phys.*, **589** (1973).
- M. Froment and G. Maurin, *Electrodeposition and Surface Treatment*, In press.
- F. Wenger and R. Wiart, *J. Chim. Phys.*, **1307** (1974).
- H. Gerischer, *Faraday Discussions of Chem. Soc.*, **7** (1973).
- I. Epelboin, M. Ksouri, and R. Wiart, *J. Electroanal. Chem.*, **58**, 433 (1975).



Calculation of Diffusion Coefficients from Rotating Disk Electrode Data

Stanley Bruckenstein*

Department of Chemistry, State University of New York, Buffalo, New York 14214

Levich's equation (1)

$$i_o = 0.62048 n F Sc^{-2/3} (\nu\omega)^{1/2} C^b \quad [1]$$

relates the convective-diffusion limiting current density, i_o , to the number of electrons exchanged per molecule of electroactive species, n ; to the Faraday constant, F ; to the kinematic viscosity, ν ; to the rotation speed, ω ; to the bulk concentration, C^b ; and to the Schmidt number, Sc . In turn, the Schmidt number is a function of ν and the diffusion coefficient, D

$$Sc = \nu/D \quad [2]$$

Newman (2) derived an improved version of Eq. [1] and obtained

$$i_o = \frac{0.62048 n F Sc^{-2/3} (\nu\omega)^{1/2} C^b}{1 + a Sc^{-1/3} + b Sc^{-2/3}} \quad [3]$$

where $a = 0.2980$ and $b = 0.14514$. Equation [3] is accurate to 0.1% for $Sc > 100$ as compared to a numerical treatment of this problem. If we denote D_L as the diffusion coefficient that would be calculated from a set of experimental data using Eq. [1], and D as the diffusion coefficient given by Eq. [3], it follows that

$$D = D_L [1 + a Sc^{-1/3} + b Sc^{-2/3}]^{3/2} \quad [4]$$

From Eq. [4] we see that D_L is always smaller than D . Table I presents the dependence of D/D_L upon Sc .

Table I. D/D_L vs. Schmidt number

D/D_L	1.108	1.100	1.090	1.080	1.070	1.060	1.050	1.040	1.030
Sc	100	124	165	228	330	509	851	1608	3685

Their ratio varies significantly from one over the entire range of Schmidt numbers likely to be encountered. Current practice involves a number of successive approximation techniques and graphical methods (3, 4) for evaluating D using Eq. [3].

The purpose of this note is to demonstrate that no graphical or successive approximation procedure is

* Electrochemical Society Active Member.

Key words: diffusion coefficients, rotating disk electrode.

required when using Newman's rotating disk relationship. A simple algebraic manipulation leads to an analytical solution for Sc , from which D is calculated.

Equation [3] may be written in the form

$$J = \frac{Sc^{-2/3}}{1 + a Sc^{-1/3} + b Sc^{-2/3}} \quad [5]$$

where

$$J = \frac{i_o}{0.62048 n F (\omega\nu)^{1/2} C^b} \quad [6]$$

hence

$$J^{-1} = Sc^{2/3} + a Sc^{1/3} + b \quad [7]$$

which is a quadratic function of $Sc^{1/3}$. Its solution is

$$Sc^{1/3} = \left(J^{-1} - b + \frac{a^2}{4} \right)^{1/2} - \frac{a}{2} \quad [8]$$

and the explicit expression for D is

$$D = \nu [(J^{-1} - 0.122939)^{1/2} - 0.1490]^{-3} \quad [9]$$

The evaluation of D using Eq. [9] poses no particular computational problem and will yield a result whose accuracy is limited only by that of Eq. [3].

Acknowledgment

This work was supported by the Air Force Office of Scientific Research under Grant No. 74-2572.

Manuscript submitted April 25, 1975; revised manuscript received May 13, 1975.

Any discussion of this paper will appear in a Discussion Section to be published in the June 1976 JOURNAL. All discussions for the June 1976 Discussion Section should be submitted by Feb. 1, 1976.

REFERENCES

- V. G. Levich, *Acta Physicochimica*, USSR, **17**, 257 (1942).
- J. S. Newman, *J. Phys. Chem.*, **70**, 1327 (1966).
- J. S. Newman, "Electrochemical Systems," p. 309, Prentice-Hall, Inc., Englewood Cliffs, New Jersey (1973).
- B. Miller, Private communication.



Thermal Oxidation of Silicon

In Situ Measurement of the Growth Rate Using Ellipsometry

M. A. Hopper,^{*1} R. A. Clarke,² and L. Young*

Department of Electrical Engineering, University of British Columbia, Vancouver 8, British Columbia, Canada

ABSTRACT

The formation of oxide films on resistively heated silicon in dry oxygen was followed *in situ* using a computer controlled ellipsometer. For (111) silicon surfaces two distinct growth regions were observed. Our results on the growth above 300Å were found to agree with previous investigations. For films 200Å or less (for which little previous data exist) the kinetics did not obey any existing model of the growth process. The rate of growth of the oxide on (111) surfaces in the 20-200Å region was investigated from 700° to 950°C and at oxygen pressures between 50 and 1200 Torr. A possible explanation of the thin film kinetics is given and its relation to the thick film data is discussed.

Because the production of oxide films on silicon by thermal oxidation is of importance to the semiconductor industry, many studies have been made on various aspects of the process. Despite this, the mechanism is not fully understood, partly because of lack of experimental data. In particular, kinetic data for films less than 300Å in thickness are limited. The purpose of the present work was to help fill this gap by using an automated ellipsometer to observe the growth of the films *in situ* on the hot substrate. Some form of *in situ* film measurement process is desirable for this range of thickness and it turns out that the thermal radiation from the specimen does not interfere with the ellipsometric technique.³

Investigation of the thermal oxidation process of silicon in oxygen gas is complicated by its sensitivity to impurities and additions, some of which (H₂O, Cl₂) are important in the production of films for electronic devices. Papers on the oxidation process in pure dry oxygen mostly fall into two categories: those on the formation of the first few layers of oxide, say up to 50Å, mostly at temperatures below 600°C, and those dealing with relatively thick films at relatively high temperatures. Continued growth at any reasonable rate above 300Å requires temperatures above 800°C.

In the thick film region Deal and Grove (1) made a comprehensive study of the thermal oxidation of silicon in dry oxygen and reported that the dependence of the oxide thickness L , on the oxidation time, t , for oxides greater than 230Å, could be described by the equation

$$\frac{L_2}{k_p} + \frac{L}{k_1} = t + \tau \quad [1]$$

where k_p and k_1 are the parabolic and linear rate con-

stants. A relation of the form of Eq. [1] may be interpreted as resulting from a growth mechanism where the oxidizing species diffuses through the oxide film (giving rise to the parabolic term) and reacts with the silicon at the silicon-oxide interface (giving the linear term). Equation [1] could not be applied to the data below 230Å as the growth rate in that region was greater than that predicted by fitting the equation to the thicker film data. In the region below 50Å the growth law is uncertain. Fehlner (2) has shown that his data, and that obtained by earlier investigations [e.g. Goodman and Breece (3)] in the very thin film region, can equally well be described by several alternative growth laws. He has, in addition, pointed out the effect of certain impurities on the kinetics in the thin film region.

Only van der Meulen (4) and Smith and Carlan (5) have given thickness-time data over the thickness range 30-300Å. The results given by these authors show significant differences.

Experimental

All oxidations were carried out in a stainless steel vacuum chamber fitted with windows to allow optical probing of the sample surface. Attached to the chamber through the appropriate valves was a sorption pump, a titanium sublimation pump, and two sputter-ion pumps. The system pressure could be reduced routinely to less than 10⁻⁸ Torr and into the 10⁻¹⁰ Torr range if the integral baking heaters were employed. A residual gas analyzer pumped by a separate ion pump was attached to the chamber through a variable leak valve to allow the composition of the oxidizing atmosphere to be monitored during an oxidation. Oxidations were carried out at pressures between 50 and 1200 Torr, these pressures being measured with a calibrated integrated circuit piezoresistive strain gauge (National Semiconductor LX 1603) mounted in a small chamber connected to the oxidation cell by large diameter, high vacuum valve. This gauge has an accuracy of ±10 Torr but changes in pressure of the order of 2 Torr can be detected.

* Electrochemical Society Active Member.

¹ Present address: Xerox Research Canada, Mississauga, Ontario, Canada.

² Present address: Garrett Manufacturing, Rexdale, Ontario, Canada.

Key words: silicon thermal oxidation, silicon oxide films, kinetics, oxidation of silicon, silicon dioxide film.

³ Dr. van der Meulen has informed us of a concurrent project using the same technique in his laboratory.

The silicon substrates used in this investigation were cut from standard 2 in. diameter Monsanto wafers of the appropriate orientation and doping. The samples, in the form of strips 3 cm long and 3 mm wide, were chemically cleaned using the acid-peroxide process (6) and given a HF dip before having platinum contacts sputtered on to each end. The samples were then clamped to the sample holder (made of Inconel sputtered with platinum where the sample made contact with the holder), which was designed to allow the samples to be heated directly. The sample holder was fixed to a high vacuum, high current feedthrough which was fitted onto the oxidation chamber using a bellows connector. This arrangement allowed the position of the sample to be adjusted so that the optical beam probed the center of the sample.

The computer controlled nulling ellipsometer is similar in general construction to that described by Ord and Wills (7). A Rudolph ellipsometer (Type 43603-200E) was modified by the addition of stepping motor drives on the analyzer and polarizer. Anti-backlash gears were used with one motor step giving the optical element a rotation of 0.01° . A difference in design from that of Ord and Wills is that absolute, brush-type shaft encoders were used to read the analyzer and polarizer angles. The light source used with the instrument was a He-Ne laser, wavelength 632.8 nm, and the quarter-wave plate, a Babinet-Soleil compensator, was placed between the polarizer and the input window of the oxidation chamber. The ellipsometer was aligned using the procedure given by Aspnes and Studna (8). The retardation of the compensator was determined by the method of McCrackin (9). An angle of incidence of 70.0° was used for all measurements, this angle being fixed by the cell and the requirement that the light beam pass normally through the oxidation cell windows. Comparison between the two zone average measurements of the ellipsometric parameters of the sample, when measured in and out of the cell (both before and after the oxidation), gave the correction required to adjust measurements made in the cell for any window birefringence. A method for determining the correction has been described by Azzam and Bashara (10).

To ensure a reproducible starting surface before carrying out an oxidation the sample was heated to 1200°C for 30 sec in a vacuum better than 10^{-7} Torr and allowed to cool to room temperature. This procedure removes the thin oxide film that forms on the etched silicon surface on exposure to air. This "flashing" technique was found to be the only reliable way of removing this oxide while maintaining an optically flat surface. The surface prepared in this way did not remain oxide free if left for any extended period at 10^{-8} Torr. From changes in the optical parameters no more than a monolayer of oxygen appeared to react with the surface if left under these conditions for a few hours. Details of an extensive investigation of the optical properties of silicon surfaces and various techniques of oxide removal will be described elsewhere.

Starting with the "clean" flashed surface, ultra high purity Matheson oxygen was admitted to the system until the desired pressure was reached. The sample was then heated by the passage of d-c current from a constant current power supply. During the oxidation the ellipsometer completed a null every 3 sec allowing an almost continuous monitoring of the oxide thickness-time relation to be determined. The temperature of the sample during the oxidation was measured with an optical pyrometer having an effective wavelength of 650 nm. The true sample temperature could be determined from the observed sample temperature by applying the appropriate emissivity correction. As this correction is intimately connected with the optical constants of the silicon it is discussed in the appropriate section below.

Results

Temperature dependence of the optical constants.—During an oxidation, changes in the ellipsometric parameters, Δ and Ψ , for the hot silicon surface were recorded. Analysis of this optical data to obtain the thickness-time relation for oxide growth is possible only if the refractive indices of the silicon ($\bar{n}_s = n_s - ik_s$) and the oxide ($\bar{n}_f = n_f - ik_f$) are known at the oxidation temperature. The temperature dependence of these indices may be estimated for 632.8 nm from certain ellipsometric data.

A silicon surface covered by a film of oxide of thickness such that the value of Δ for the system is close to 180° has certain unique features. For this surface the Ψ value depends mainly on n_s and to a lesser extent on k_f , whereas changes in Δ arise from changes in k_s , n_f and the thickness of the oxide film. By making ellipsometric measurements on at least two samples (each with a different oxide coverage) in this region, changes in n_s with temperature can be distinguished from changes in the other parameters.

Figure 1 shows the ellipsometric results obtained when silicon samples covered with approximately 18Å (a) and 2810Å (b) are heated. This experiment was performed in vacuo to prevent growth of oxide during the course of the measurements. The figure also shows three curves of the Δ - Ψ locus that would be traced out on the growth of a film of index $\bar{n}_f = 1.46 - i0.0$, on a substrate for n_s equal to 3.9, 4.1, and 4.3, respectively. k_s was assumed to be less than 0.2. The experimental points X_1 and X_2 correspond to the same apparent temperature (900°C) as measured by the optical pyrometer. Determination of the actual temperature of the sample at these points requires estimation of the emissivity correction.

The spectral emissivity, e_λ , and the reflectance, R_λ , at a wavelength λ for a medium which absorbs the radiation are related (11) by the expression

$$e_\lambda = 1 - R_\lambda$$

The value of R_λ for an oxide-covered surface depends on the optical constants of the substrate and the thickness and refractive index of the oxide layer (12). R_λ is also related to the ellipsometric parameters Δ and Ψ . Vedam *et al.* (13) have shown that R_λ is not sensitive to oxide coverage, for a film within 100Å of that required to make $\Delta = 180.00^\circ$. This observation, which can be checked by computation of R_λ for the films used to obtain the data shown in Fig. 1, implies that X_1 and X_2 correspond to the same surface temperature. As the effective wavelength of the optical pyrometer is close to the wavelength used with the ellipsometer, the refractive index of the surface, actually n_s , is taken to

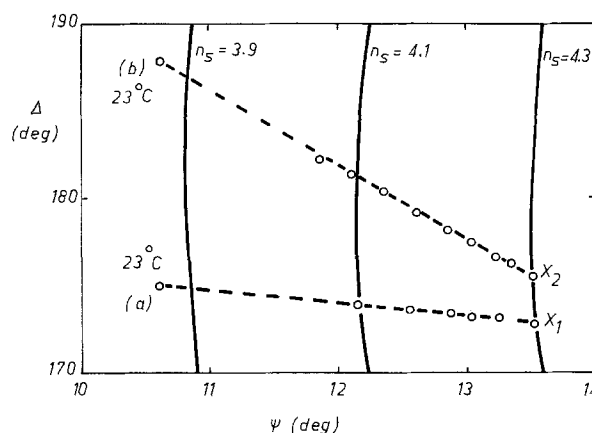


Fig. 1. Changes in Δ and Ψ with temperature for silicon samples covered with (a) 18Å and (b) 2810Å of oxide. Points X_1 and X_2 correspond to a temperature of 930°C . The solid curves show the computed Δ , Ψ locus for the growth of a nonabsorbing film, of index 1.46, on a substrate having the indicated index.

be 4.30 for points X_1 and X_2 . Using the relations given by Sato (14) the emissivity at this temperature was estimated to be 0.61. For an observed temperature of 900°C this emissivity implies a true surface temperature of 930°C. The resistivity of the sample was also used to estimate changes in the temperature of the silicon. The data of Fulkerson *et al.* (15) being used to relate temperature and resistance. For temperatures below 700°C where the optical pyrometer cannot be used to probe the surface temperature, resistivity measurements alone were used.

The temperature dependence of n_s , determined from our results given in Fig. 1, is plotted in Fig. 2. The temperature dependence we obtain is the same as that reported by van der Meulen and Hien (16) and is consistent with the infrared results of Lukes (17) and the emissivity measurements of Sato (14). The ellipsometric results of Ibrahim and Bashara (18) are quite different from our results as seen when their data are plotted on Fig. 2 (dashed curve). The differences are probably due to an overestimation of the surface temperature by Ibrahim and Bashara because of their method of measuring temperature (a thermocouple in contact with the substrate heater).

The results given in Fig. 1 show that the value of n_s for silicon for any particular temperature is independent of the thickness of the oxide film on the surface. This result also implies that the absorption coefficient of the oxide, k_s , is negligible at all temperatures used in this work.

The refractive index of the oxide and its temperature dependence can be estimated by performing ellipsometric measurements similar to those described above with the silicon covered by between 1000 and 1800 Å of oxide. The value of n_f was found to increase from 1.458 at 23°C to 1.467 at 930°C. These results are in good agreement with published values of the refractive index of fused silica (19).

Other quantities which might change on heating an oxide-covered silicon sample are the film thickness, L , and the absorption coefficient of the substrate, k_s . Changes in these two quantities result in essentially similar changes in Δ and Ψ for a film of any thickness and are thus difficult to determine separately using ellipsometric measurements alone. Assuming that the thermal expansion coefficient of the oxide is identical to that of fused silica (19), and knowing the variation of n_s and n_f with temperature, we can estimate how k_s varies with temperature. In addition the room temperature value of $k_s = 0.023$, as determined by the bulk transmission measurements of Philipp (20), has to be assumed. With these assumptions the value of k_s at 930°C was determined at many oxide thicknesses. A consistent value of 0.172 ± 0.003 was measured for all oxides greater than 100 Å. For thinner oxide films

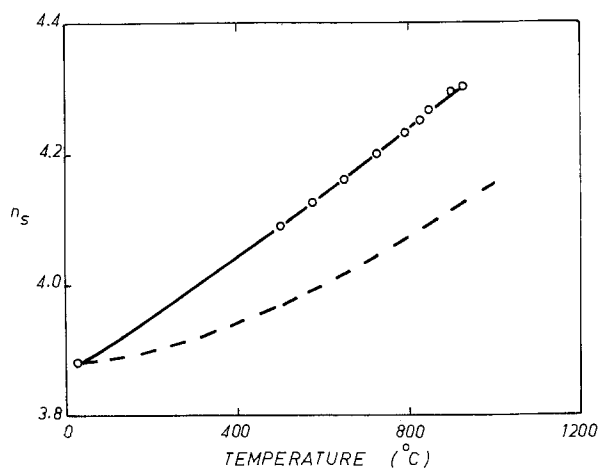


Fig. 2. Temperature dependence of the refractive index of silicon at 632.8 nm. The dashed line shows the relation between n_s and T given by Ibrahim and Bashara (17).

the apparent value of k_s decreased with decreasing thickness. At 18 Å of oxide k_s has the value of 0.140. The reason for this low value in the thin film region is uncertain but may be associated with the composition of the thin oxide film. Backscattering results of Sigmon *et al.* (21) and ESCA measurements made in this laboratory (to be published) indicate that the oxide close to the silicon-oxide interface is silicon-rich having a composition closer to SiO than SiO_2 .

From the thick film measurements the variation of k_s with temperature was determined using the above assumptions. These results are summarized in Fig. 3.

Oxidation kinetics for (111) silicon.—Oxidation of (111) silicon surfaces was investigated at temperatures between 650° and 950°C in oxygen atmospheres between 50 and 1200 Torr. To illustrate the general characteristics that we observe in all our experiments the data for both 870° and 930°C at 760 Torr oxygen are discussed in detail. Under these conditions the oxide grows to 1000 Å in a reasonable period of time, and sufficient data can be obtained for films less than 100 Å to allow an accurate comparison of the growth rate in the thick and thin film regions to be made.

The thickness for both the 870° and 930°C runs in 760 Torr oxygen increased smoothly with time. The thickness-time data obtained from fitting the ellipsometric measurements for these runs are given in Fig. 4. Only every fifth point obtained is plotted in this figure. Examination of the results summarized by Fig. 4 shows that there is no region of oxide thickness where the oxide grows linearly with time. The data are curved

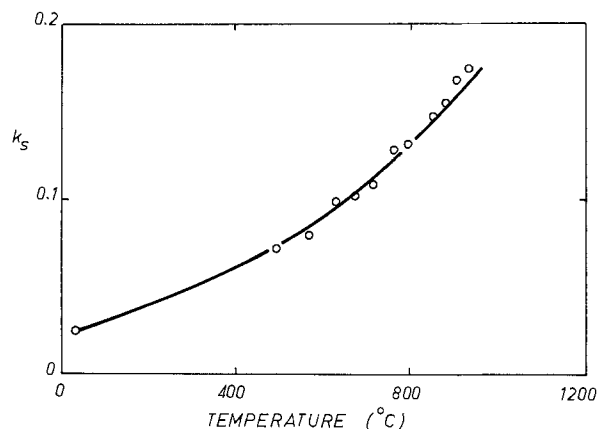


Fig. 3. Temperature dependence of the absorption coefficient of silicon at 632.8 nm. Experimentally estimated values of k_s are plotted as circles.

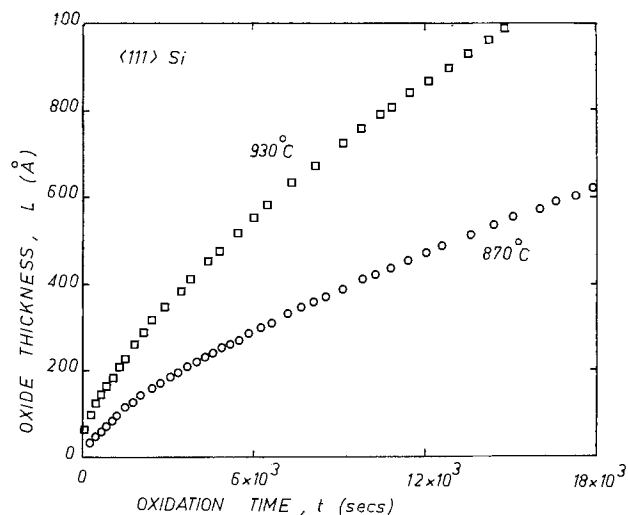


Fig. 4. Thickness-time dependence observed for oxidation of (111) silicon at 870° and 930°C in 760 Torr dry oxygen.

over the whole region investigated. Guided by approaches used by previous workers we attempted to fit the thickness-time data for each run in such a way that meaningful kinetic parameters could be estimated. This procedure proved unsuccessful as no single expression, that can be given a useful kinetic interpretation, was found that adequately describes our data over the whole range of thickness covered. As we have many data points in every thickness range it was decided that the growth rate could be determined directly by appropriate differentiation of the thickness-time data.

To facilitate comparison with theory (see the Discussion section) it is more useful to determine the thickness dependence of the inverse of the growth rate rather than the growth rate itself. For an oxide of thickness, L , at time, t , dt/dL is determined using the following procedure. All data lying within $\pm 50\text{\AA}$ of the point are least squares fitted with an expression of the

form $t = \sum_{i=0}^{\lambda} c_i L^i$. Once the values of c_i have been

estimated, it is an easy manipulation to determine dt/dL at the point. This procedure is applied over the whole thickness range available.

The thickness dependence of dt/dL obtained using the above procedure, for the oxidation runs summarized by Fig. 4 is given in Fig. 5. The error bars shown on the 870°C data indicate the spread in dt/dL expected, at 100 and 500 \AA , if the only error involved in obtaining this data was an uncertainty of $\pm 2^\circ\text{C}$ in the temperature of the substrate. Figure 5 shows dt/dL increasing with increasing oxide coverage for any particular oxidation. The 930°C data show that above 300 \AA , dt/dL increases linearly with L .

In Fig. 6 the variation of dt/dL with L for films less than 200 \AA in thickness is plotted. Both the 870° and 930°C data appear linear in this region, the slope in the thin film region being greater than that found for the thicker films. This characteristic behavior was found for all oxidations of (111) silicon carried out in this investigation.

As we have found two distinctly different regions of oxidation behavior, our results for the dependence of the oxide thickness on time for (111) silicon are best summarized in the following manner. Below 200 \AA the time t is related to the oxide thickness L by the relation

$$t = a_0 + a_1 L + a_2 L^2 \quad [2]$$

and above 300 \AA by

$$t = b_0 + b_1 L + b_2 L^2 \quad [3]$$

For (111) silicon surfaces oxidized in pure dry oxygen at 760 Torr the temperature dependence of the parameters a_0 , a_1 , and a_2 are given in Table I. In the

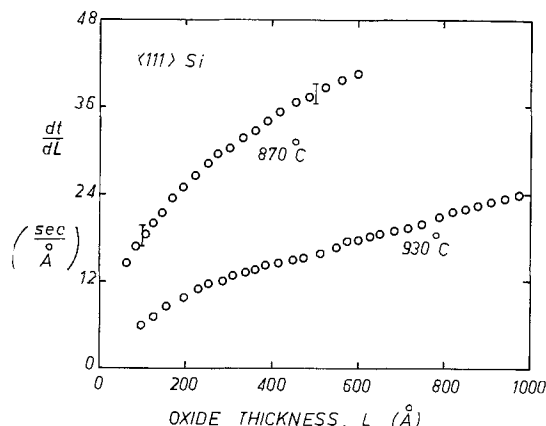


Fig. 5. Dependence of the inverse of the growth rate on oxide thickness for (111) silicon at 870° and 930°C in 760 Torr dry oxygen.

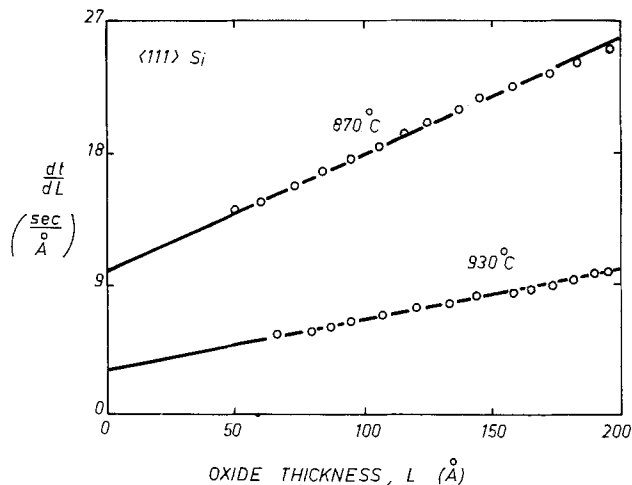


Fig. 6. Increase in the inverse of the growth rate with oxide thickness for films less than 200 \AA for the data shown in Fig. 5.

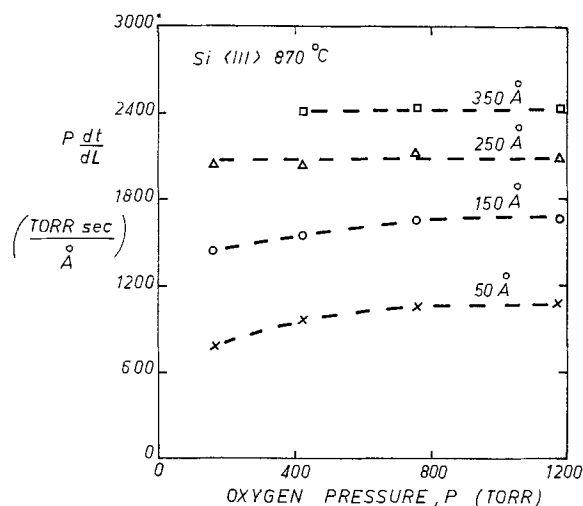


Fig. 7. Dependence of the inverse of the growth rate on oxygen pressure for (111) silicon at 870°C as a function of oxide thickness.

thick film region b_0 , b_1 , and b_2 have the values -1222.5 sec, 19.41 sec- \AA^{-1} , and 1.86×10^{-2} sec- \AA^{-2} , respectively, at 870°C and -634.8 sec, 7.38 sec- \AA^{-1} , and 8.4×10^{-3} sec- \AA^{-2} , respectively, at 930°C . Our measurements indicate that all these values are independent of the doping of the silicon substrate (0.1 and 10 ohm-cm n-type and 10 ohm-cm p-type samples were tested).

The dependence of the oxidation rate on the pressure of the reactive gas often is of considerable use in elucidating the mechanism of the oxidation reaction. In the present case the pressure dependence is far from simple. To illustrate this pressure dependence it is convenient to plot $p \cdot dt/dL$ (at a particular oxide thickness) against p , where p is the oxygen pressure.

The results obtained for a (111) silicon surface at 870° are presented in this way in Fig. 7. The value of $p \cdot dt/dL$ is independent of pressure above approximately 300 \AA . Below this thickness $p \cdot dt/dL$ decreases

Table I. Temperature dependence of growth parameters of (111) Si at 760 Torr oxygen for films less than 200 \AA

Temperature ($^\circ\text{C}$)	a_0 (sec)	a_1 (sec- \AA^{-1})	a_2 (sec- \AA^{-2})
720	-4386.0	251.7	0.621
780	-576.0	58.5	0.268
832	-216.0	24.0	0.0654
870	-162.6	10.0	0.0396
930	-92.4	3.0	0.0174

with decreasing pressure. The curve fitting parameters in Eq. [2] and [3] were determined where possible at all the pressures investigated. The pressure dependence of a_1 and a_2 was found to be rather complex, these parameters both vary approximately as $p^{0.8}$ at 870°C.

Oxidation of (100) silicon.—Oxide growth on (100) silicon surfaces is far slower than that on the (111) surface. The change of dt/dL with thickness found for an oxidation of a (100) surface at 870°C at a pressure of 760 Torr oxygen is shown in Fig. 8. For comparison the data obtained under similar conditions for the (111) surface is also given in the figure. An almost linear increase in dt/dL , below 200Å, with thickness was found and the parameters a_0 , a_1 , and a_2 have the values 246.0 sec, 17.1 sec-Å⁻¹, and 0.0806 sec-Å⁻², respectively. The second linear section of the dt/dL vs. L plot was not observed until the oxide is more than 600Å thick. The temperature dependence of oxidation of (100) surfaces has not been extensively investigated.

Discussion

The rate of growth of an oxide film on silicon during thermal oxidation in dry oxygen was found to show a complicated dependence on oxide thickness. In general agreement with the results of Deal and Grove (1) we find that growth in the thin film region differs markedly from that of thicker films. Deal and Grove applied the linear-parabolic law (Eq. [1]) to (111) silicon oxidation only for oxides thicker than 230Å, growth of thinner films being faster than that predicted by their general formula. They gave no explanation of the thin film kinetics, but the present results on (111) surfaces indicate that the thickness above which the kinetics show the characteristics of the Deal and Grove model varies with temperature and oxygen pressure.

The model of oxidation in the thick film region involves the diffusion of the oxidizing species through the oxide layer and reaction at the silicon oxide interface. These two processes are essentially in series, the over-all rate being controlled by the slowest process at any temperature. Under interface control the growth rate, dL/dt , is constant. If diffusion limits the growth rate $dL/dt \propto L^{-1}$. When the two growth rates are comparable

$$\frac{dt}{dL} = b_1 + 2b_2L \quad [4]$$

where b_1 and b_2 are related to the rate constants. Equation [4] is the differential form of Eq. [3]. Comparison with Eq. [1] gives $b_1 = 1/k_1$ and $b_2 = 1/k_p$.

For thick oxide films (>300Å) we find dt/dL increases linearly with L . From the slope of dt/dL vs. L plots we can estimate a value of k_p . Our results for k_p at 870° and 930°C for 760 Torr oxygen are in good agreement with the data given by Deal and Grove. The pressure dependence of k_p provides information

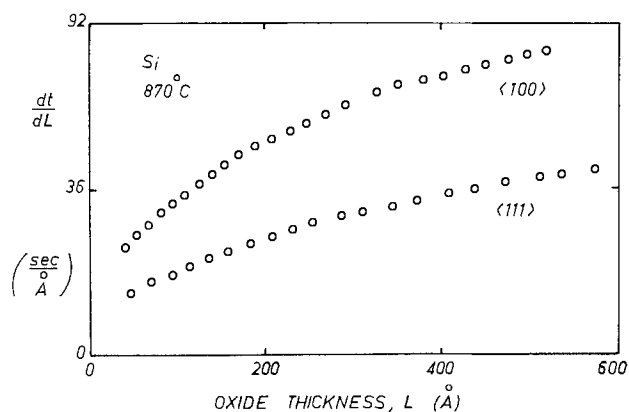


Fig. 8. Comparison of the oxide thickness dependence of the inverse of the growth rate obtained with (111) and (100) silicon at 870°C in 760 Torr oxygen.

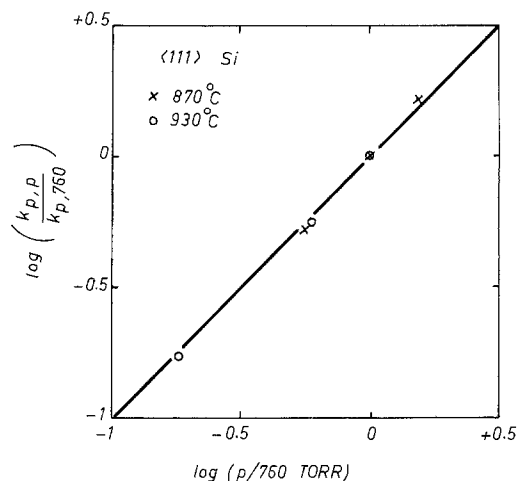


Fig. 9. Pressure dependence of the parabolic rate constant, k_p , estimated from the growth rate for films thicker than 300Å on (111) silicon at 870° and 930°C. For each temperature the value of k_p measured at 760 Torr oxygen ($k_{p,760}$).

on the nature of the diffusing species. Figure 9 shows our results for the pressure dependence of k_p at both 870° and 930°C. In this plot the values of k_p are normalized to the 760 Torr value of this constant for the temperature of interest. This procedure eliminates the effects of temperature allowing the pressure dependence to be compared directly. The data clearly indicate that k_p depends linearly on oxygen pressure. Deal and Grove observed that k_p showed a linear pressure dependence for temperatures above 1000°C. According to Wagner (22) a linear dependence of this parameter, which is related to the diffusion coefficient, implies that the diffusing species is either O_2 or O_2^{n-} .

The linear rate constant, k_1 , is apparently known with far less certainty than is k_p . Deal and Grove give values of k_1 from 700° to 1200°C. Revesz and Evans (23) in their study of oxidation in dry oxygen above 900°C obtain values of k_1 that are quite different from those of Deal and Grove. The activation energy for the k_1 data of Revesz and Evans is only half that measured by Deal and Grove. We can estimate the corresponding k_1 value from our thick film fits. This gives values of k_1 that are smaller than those given by both Deal and Grove and by Revesz and Evans but they show the temperature dependence observed by Deal and Grove. k_1 was found not to vary linearly in oxygen pressure, but appears to vary as $p^{0.6}$.

We would question whether the method used to obtain k_1 , by simply fitting the thick film data, actually provides a measure of the rate constant of the process occurring at the interface. Admittedly this value is sensitive to surface orientation, as seen by the results given in Fig. 8, which is an indication that it is related to the nature of the surface, but the value obtained may also reflect some influence of the processes that occur in the thin film region.

In his study of thin film oxide growth van der Meulen (4) measured the thickness-time dependence of both (111) and (100) silicon surfaces from 700° to 100°C for thicknesses up to 300Å. Our thickness-time data generally agree with those given by van der Meulen, but the kinetic parameters cannot be compared as he assumed that the thick film value of k_p (given by Deal and Grove) could be applied to the thin film region. Our results do not agree with the measurements of Smith and Carlan (5) and the complex growth they observed is unexplained.

Two explanations of the "fast" growth found for films less than 200Å have been advanced. One, due to Revesz and Evans (23) invokes the existence of a process in which the normal diffusion is effectively

short circuited by "fast" diffusion through "micro-channels" that are presumably about 200Å in length. This model should tend to enhance the effect of the linear rate constant in the thin film region which makes dt/dL independent of thickness until the film is sufficiently thick to obey the bulk diffusion model. dt/dL , however, changes more rapidly with thickness for thin films than it does above 300Å. To obtain an adequate description of the thin film process, the Revesz and Evans model needs further development.

To explain some of the results of van der Meulen, Ghez and van der Meulen (24) have proposed a reaction process for the interface oxidation which modifies the form of the linear-parabolic equation. Using the expressions given by Ghez and van der Meulen we have computed the thickness dependence of dt/dL predicted by their assumptions. The effect of this modification to the model of the interface process is to decrease the dependence of dt/dL on L for thinner films, thus contradicting the present experimental results.

The observation that dt/dL increases linearly with L over the range 20-200Å has not been observed previously in silicon. It is interesting to note that the slope of the dt/dL vs. L plot for thin films is approximately twice what it is above 300Å at the same temperature, while the intercept for $L = 0$ is half the thick film value.

From Eq. [2] we can write

$$dt/dL = a_1 + 2a_2L$$

Assuming a_1 and a_2 correspond to some physical process, their temperature dependence should be governed by an Arrhenius-type law. Figure 10 shows how a_1 and a_2 vary with $1/T$ for oxidation of (111) silicon at 760 Torr oxygen. These results show that a_1 and a_2 do vary as expected with temperature, but have almost identical activation energy, about 1.95 eV.

The existence of two linear segments in the dt/dL vs. L plots, and the behavior of the thin film slope, suggests that oxidation of silicon might be proceeding by two parallel paths. Each process involved would have to have both an interface reaction and a diffusion-limited step. The diffusion coefficients for the two processes, and thus the "parabolic" rate constants, must differ sufficiently that one dominates in the thick film region.

The growth rate for two such parallel independent processes is

$$\frac{dL}{dt} = \frac{dL}{dt} \Big|_1 + \frac{dL}{dt} \Big|_2$$

where

$$\frac{dL}{dt} \Big|_i = \frac{1}{A_i + B_i L}$$

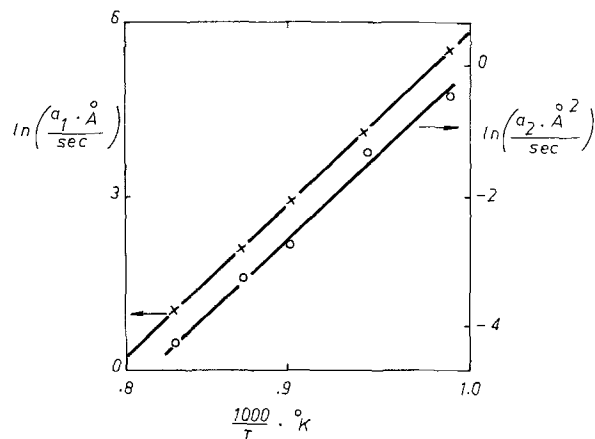


Fig. 10. Temperature dependence of the rate parameters a_1 and a_2 (see text) obtained from oxidation data for film growth below 200Å on (111) silicon in 760 Torr dry oxygen.

The over-all value of dt/dL is thus

$$\frac{dt}{dL} = \frac{A_1 A_2 + (B_1 A_2 + B_2 A_1) L + B_1 B_2 L^2}{(A_1 + A_2) + (B_1 + B_2) L} \quad [5]$$

where A_1 and B_1 refer to one process and A_2 and B_2 to the other. For certain values of these parameters Eq. [5] has interesting limiting behavior. For $A_1 \sim A_2$ and $B_1 \ll B_2$, at thin films where $B_1 B_2 L^2 \ll B_2 A_1 L$ and $B_2 L \ll A_1 + A_2$

$$\frac{dt}{dL} = \frac{A_1 A_2}{A_1 + A_2} + \frac{A_1}{A_1 + A_2} \cdot B_2 L \quad [6]$$

and for thick films ($L \rightarrow \infty$)

$$dt/dL \propto B_1 L$$

Under these assumptions this type of model predicts that dt/dL increases with L and the slope of the dt/dL vs. L plot decreases as thickness increases. Under the given assumptions this model might explain the experimental dt/dL vs. L plots.

A possible explanation of the two parallel processes arises from the studies of Jorgensen (25). At high temperatures with a porous metal electrode attached to the oxide he has shown the growth rate of the oxide could be increased or decreased by applying a current of appropriate polarity. This experiment, as analyzed by Raleigh (26), indicates that both ionic and molecular motion might be possible in these oxide films. The existence of both ionic and molecular motion diffusion could be the reason for our observed rate data. As the diffusion coefficient and activation energy for these two processes are not necessarily equal, these processes might contribute to the over-all growth rate in a manner similar to that summarized by Eq. [5].

The parallel reaction model described above does explain, at least qualitatively, the over-all shape of the experimental dt/dL vs. L plots. No attempt was made to fit the data using a relation having the form of Eq. [5] because some of our results indicate that even this fairly complex model might not be a complete description of the oxidation process.

In the model leading to the growth rate given by Eq. [5] we would expect that the two diffusion processes would be independent of silicon surface orientation. For any oxidation temperature B_1 and B_2 (in Eq. [5]) should thus not differ for (111) and (100) surfaces. The interface parameters, A_1 and A_2 , can differ for different orientations but the ratio $A_1(111)/A_1(100)$ and $A_2(111)/A_2(100)$ should be similar. From these observations, and assuming the validity of Eq. [6], the slope of the dt/dL vs. L plot (d^2t/dL^2) in the thin film region should be the same for both (111) and (100) surfaces at any fixed temperature. Experimentally we find, at 870°C, that d^2t/dL^2 for a (100) surface is more than twice as large as the corresponding (111) value.

Two other experimental results are difficult to reconcile with the present theory. The first of these is the observation that the kinetic parameters a_1 and a_2 (in the thin film region) both vary approximately as $P^{0.8}$ with oxygen pressure for a (111) surface at 870°C. This result is surprising and it is not obvious how the theory would account for this behavior. Secondly, the results for the temperature dependence of a_1 and a_2 at fixed oxygen pressure are unusual. Both these parameters were found to have the same activation energy.

Despite these unexplained results the mechanism of two parallel competing processes appears to be the only model of the oxidation that can describe the general characteristics of the rate behavior we observe experimentally. Further studies on this model are required to determine whether it can be modified to account for all the experimental results.

Conclusions

The use of an *in situ* technique to follow the rate of growth of an oxide film on silicon in dry oxygen shows

the existence of two distinctly different regions of oxidation behavior. Oxidation appears to proceed in one manner from 20 to approximately 200Å of oxide coverage and in a different manner at greater oxide thicknesses. The thickness above which characteristic thick film behavior is observed was found to vary with temperature, oxygen pressure, and silicon substrate orientation. No earlier kinetic description of the process adequately describes the observed results. A mechanism is proposed that qualitatively accounts for the general behavior of the oxidation kinetics.

This work was supported by the Department of Communications Contract DSS OSU4-0180.

Manuscript submitted Nov. 26, 1974; revised manuscript received April 9, 1975.

Any discussion of this paper will appear in a Discussion Section to be published in the June 1976 JOURNAL. All discussions for the June 1976 Discussion Section should be submitted by Feb. 1, 1976.

Publication costs of this article were partially assisted by The University of British Columbia.

REFERENCES

1. B. E. Deal and A. S. Grove, *J. Appl. Phys.*, **36**, 3770 (1965).
2. F. P. Fehlner, *This Journal*, **119**, 1723 (1972).
3. A. M. Goodman and J. M. Brece, *ibid.*, **117**, 982 (1970).
4. Y. J. van der Meulen, *ibid.*, **119**, 530 (1972).
5. T. Smith and A. J. Carlan, *J. Appl. Phys.*, **43**, 2455 (1972).
6. W. Kern and D. A. Puotinen, *RCA Rev.*, **31**, 187 (1970).
7. J. L. Ord and B. Wills, *Appl. Opt.*, **6**, 1673 (1967).
8. D. E. Aspnes and A. A. Studna, *ibid.*, **10**, 1024 (1971).
9. F. L. McCracken, *J. Opt. Soc. Am.*, **60**, 57 (1970).
10. R. M. A. Azzam and N. M. Bashara, *ibid.*, **61**, 773 (1971).
11. H. O. McMahon, *ibid.*, **40**, 376 (1950).
12. M. Born and E. Wolf, "Principles of Optics," Pergamon Press, Inc., Oxford (1964).
13. K. Vedam, W. Knausenberger, and F. Lukes, *J. Opt. Soc. Am.*, **59**, 64 (1969).
14. T. Sato, *Japan. J. Appl. Phys.*, **6**, 339 (1967).
15. W. Fulkerson, J. P. Moore, R. K. Williams, R. S. Groves, and D. L. McElvoy, *Phys. Rev.*, **167**, 765 (1968).
16. Y. J. van der Meulen and N. C. Hien, *J. Opt. Soc. Am.*, **64**, 804 (1974).
17. F. Lukes, *J. Phys. Chem. Solids*, **11**, 342 (1959).
18. M. M. Ibrahim and N. M. Bashara, *J. Vacuum Sci. Technol.*, **9**, 1259 (1972).
19. D. E. Gray, Editor, "American Institute of Physics Handbook," 3rd ed., pp. 6-29; pp. 4-138.
20. H. R. Philipp, *J. Appl. Phys.*, **43**, 2335 (1972).
21. T. W. Sigmon, W. K. Chu, E. Lugujo, and J. W. Mayer, *Appl. Phys. Letters*, **24**, 105 (1974).
22. C. Wagner, in "Chemistry of Solid State," W. E. Garner, Editor, Academic Press, New York (1955).
23. A. G. Revesz and R. J. Evans, *J. Phys. Chem. Solids*, **30**, 551 (1969).
24. R. Ghez and Y. J. van der Meulen, *This Journal*, **119**, 1101 (1972).
25. P. J. Jorgensen, *J. Chem. Phys.*, **49**, 1594 (1968).
26. D. O. Raleigh, *This Journal*, **113**, 782 (1966).

Concentration Dependence Curves of Y₂O₂S:Eu

Lyuji Ozawa* and Herbert N. Hersh*

Zenith Radio Corporation, Chicago, Illinois 60639

ABSTRACT

Concentration dependence curves for Y₂O₂S:Eu over a range of excitation conditions have been determined for transitions from the ⁵D₀ to various ⁷F levels. It is shown that the optimum Eu concentration for the ⁵D₀ → ⁷F₂ transition is lower for cathode-ray excitation than for photoexcitation. The absorption spectrum of Y₂O₂S:Eu has also been determined; it suggests the possibility that the change in optimum concentration might be qualitatively explained in terms of a preferential increase in reabsorption of the ⁵D₀ → ⁷F₂ emission, however the calculated average population increase does not seem to be large enough to provide quantitative validation.

The optimum activator concentration of cathodoluminescent phosphors is an important practical and theoretical parameter in discussing the efficiency of a phosphor. In rare earth activated phosphors the optimum activator concentration occurs at different values for different types of excitation, e.g., cathode-ray excitation, host photoexcitation, and direct activator photoexcitation (1). For direct photoexcitation of the activator, one can obtain the true concentration dependence curves only where the radiation is weakly absorbed. For phosphors with high optical absorption coefficients, the optimum activator concentration shifts to lower concentrations due to a decrease in penetration depth of the exciting radiation with activator concentration (1). For a wide range of activator concentrations (10⁻⁶-10⁻²), the concentration dependence curves of phosphors excited by cathode-rays are almost identical to the curves obtained for host photoexcitation (because apparently the same mechanisms are involved in the excitation process), except for the

fact that the optimum concentration under cathode-ray excitation is always slightly lower (2).

Since host photoexcitation is usually very superficial (penetration depth <1 μm) whereas cathode-ray excitation is deeper (penetration depth >1 μm) and increases with cathode voltage, the smaller value of the optimum concentration for cathodoluminescence has been hypothesized as being due to de-excitation at the surface of the phosphor particles (3-5) or to radiationless sinks which interfere with the energy transfer process between the excited host and activators. In those experiments the total phosphor luminescence has usually been measured rather than the spectral intensities of the individual lines.

The transition probabilities between the states of Eu⁺³ ion in crystal are determined by the selection rules and crystal parameters; they are independent of the energy transfer process involved in the phosphor (such as surface de-excitation and radiationless sink), of excitation conditions, and of phosphor temperature. Thus, for each of the ⁵D₀ luminescences, the same normalized concentration dependence curve is expected.

* Electrochemical Society Active Member.

Key words: absorption, saturation, cathodoluminescence.

However in the present work it has been found that all of the 5D_0 concentration dependence curves are not the same. By analyzing the normalized curves and the absorption spectrum one can obtain qualitative intimations of the presence of nonthermal populations of some of the terminal states of the activators.

Experimental

The study was made using $Y_2O_3S:Eu$ phosphor in which conditions are simpler and better defined than in other Eu^{+3} activator phosphors. This arises because of more easily identified luminescence lines which make spectroscopic studies and interpretation relatively simple and unambiguous.

The preparation of the $Y_2O_3S:Eu$ phosphors has been described elsewhere (6). To obtain the concentration dependence curves, the spectral luminescence intensities were measured on powder samples which were packed in planchettes to a depth of 2 mm. For cathodoluminescence measurements, the samples were excited in a demountable cathode-ray apparatus under steady-state excitation conditions at $1 \mu A$ beam current per 5 mm spot diameter ($= 5 \mu A/cm$). Photoluminescence and excitation spectra were obtained with Perkin-Elmer Fluorescence Spectrometer MPF-3. The host photoexcitation intensity was estimated to be $10 \mu W/cm^2$ on the phosphor surface. The luminescence intensities of selected lines of Eu^{+3} luminescences were determined from the amplitudes of the recorded luminescence spectra.

Measurements were also made using a 19-in. tricolor television picture tube under pulsed, high excitation conditions. The picture tube was mounted in a production television chassis, which was driven by a signal generator. The anode voltage was a nominal 30 kV. The current densities were calculated from the anode current and beam size (7). To ensure that the phosphor dot on the screen was excited in a regular television scanning mode, *i.e.*, 50 nsec pulses every 1/30 sec, a single scanning line was used. This was accomplished by blanking the entire raster except for one scanning line at the center of the screen. To increase the pumping rate, multiple excitation (8) was used: by shrinking the vertical raster, the raster line separation becomes smaller than the electron beam diameter, and hence each phosphor dot was multiply excited by the scanning beam, with a 60 μsec interval between excitations. The degree of multiple excitation depends on the ratio of the beam diameter to the shrunken raster height.

Results

It was found that there are some differences in the concentration dependence curves of the luminescences from one emitting level to the various lower levels, 7F , on which the transitions terminate. Concentration dependence curves for the 5D_0 emitting level to the 7F levels are reported here but similar results also occur for the 5D_1 and 5D_2 levels.

Figure 1A shows the normalized concentration dependence curves for host photoexcited luminescence. Note the difference between the 7F_2 curve and the 7F_1 and 7F_0 curves; the optimum activator concentration, C_{opt} , is 2 mole per cent (m/o) for the 7F_0 and 7F_1 , and 4 m/o for the 7F_2 . Under cathode-ray excitation, C_{opt} for the 7F_2 luminescence shifts to a lower value, 2.5 m/o (Fig. 1B) and the curve closely approaches the 7F_0 curve. The 7F_1 and 7F_0 curves are hardly affected in going from host photoexcitation to cathode-ray excitation.

The 7F_4 curves for host photoexcitation (not shown) are close to the 7F_1 curves and are only slightly shifted by cathode-ray excitation. The 7F_3 curves were not studied because of their weak intensities; the 7F_5 and 7F_6 luminescences were not in the range of our interest.

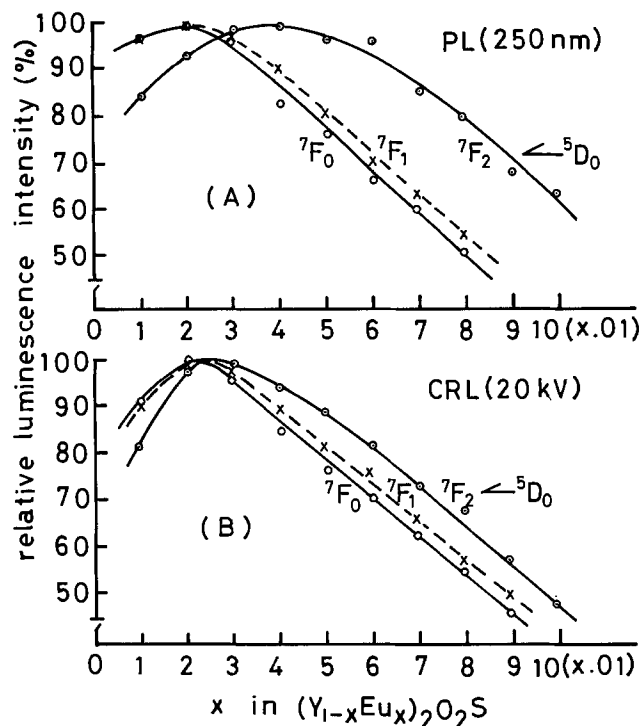


Fig. 1. Concentration dependence curves of $^5D_0 \rightarrow ^7F_0$, 7F_1 , and 7F_2 luminescences for host photoexcitation (A) and for 20 kV cathode-ray excitation (B).

Discussion

A difference in the maxima of the concentration dependence curves for the $^5D_0 \rightarrow ^7F_2$ luminescence using cathode-ray and photon excitation has been observed. This shift of C_{opt} with the type of excitation cannot be explained by the bulk-to-surface effect (9) (surface de-excitation of the 5D emitting state), because this would not differentially affect the individual 7F terminal levels. Thus, the relative $^5D \rightarrow ^7F$ luminescence intensities would not be expected to change by this mechanism, and the normalized concentration dependence curves should be the same for each terminal level. Thus another explanation must be sought.

Since the relative luminescence intensities from the 5D_0 emitting level should be independent of excitation conditions, the difference may possibly be explained by a quenching mechanism involving the ground 7F states.

A phenomenon commonly overlooked in cathodoluminescence studies is the possible reabsorption of the luminescence. Reabsorption by the activator is a general phenomenon operating in all phosphors to limit the photon yield (10, 11) but it has not been considered in cathodoluminescence, possibly because no absorption band in the spectral region of the luminescence has been reported in practical phosphors.

Boltzmann population of 7F states.—The excitation spectrum for the $^5D_0 \rightarrow ^7F_4$ luminescence at 707 nm is given in Fig. 2. This spectrum is equivalent to the absorption spectrum because the absorptions are weak. Optical absorption only occurs from states populated by electrons. At $T = 0^\circ K$, the 7F_0 state is fully populated. At higher temperatures the population is also distributed in the 7F_1 to 7F_6 states in accordance with the Boltzmann distribution law. The Boltzmann population at room temperature is computed as 0.1 for each 7F_1 state and 0.0016 for each 7F_2 state. It is clear that at room temperature no absorption will occur from the 7F_3 and 7F_4 in unexcited phosphors because the Boltzmann populations of these levels are negligible.

At room temperature, strong absorption from the 7F_0 and 7F_1 state and two weak absorptions from the 7F_2 state are seen in Fig. 2. These results indicate

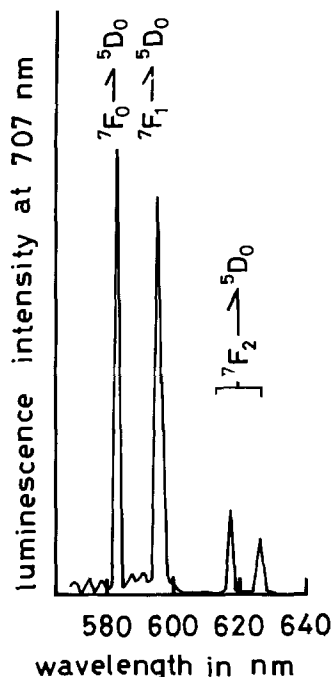


Fig. 2. Excitation spectrum for 707 nm (${}^5D_0 \rightarrow {}^7F_4$) luminescence of $Y_2O_2S:Eu$ phosphor.

that reabsorption of the ${}^5D_0 \rightarrow {}^7F_{0,1,2}$ luminescences exists at room temperature.

The absorption intensity of the 7F_2 is about 20% of the intensities for the 7F_0 and 7F_1 , although the Boltzmann population is about 10^{-3} of the 7F_0 state. This fact indicates that the absorption coefficient for the ${}^7F_2 \rightarrow {}^5D_0$ transition is about two orders greater than the coefficient for the ${}^7F_{0,1} \rightarrow {}^5D_0$ transitions. Because of the low Boltzmann population (0.0016) and high absorption coefficient for the 7F_2 state, the absorption from the 7F_2 should be more sensitive to the change in the population than the 7F_1 and 7F_0 . This conclusion seems to be supported by the facts that the 7F_0 and 7F_1 dependence curves (Fig. 1) are not affected in going from photon to cathode-ray excitation and that only the 7F_2 curves shift to lower values with cathode-ray excitation.

Cathode-ray pumped population.—One may compute the average cathode-ray (CR) pumped population as follows: Assuming that the penetration depth of 20 kV electrons is $6 \mu m$ ($6 \times 10^{-4} cm$) (12), the excitation effective volume, Δ , of the phosphor particles is calculated to be $6 \times 10^{-4} cm^3$ for a circular homogeneous beam of 0.5 cm diameter. The Eu^{+3} ions/ Δ are calculated as

$$\frac{\Delta x (\text{density of phosphor}) \times N \times (\text{Eu ions in molecule})}{\text{molecular weight}} \quad [1]$$

where N is Avogadro's number. For 5 m/o europium this corresponds to 7.4×10^{17} ions/ Δ . Taking the center-of-gravity of five 7F_2 states as $1000 cm^{-1}$ above the ground state, the fractional thermal excitation at room temperature ($T = 300^\circ K$, $kT = 206 cm^{-1}$) is 0.0078. Because the population quickly thermalizes among the five 7F_2 states, the fraction for each 7F_2 state is $0.0078/5 = 0.0016$. Thus, the thermal population of each 7F_2 state is

$$7.4 \times 10^{17} \times 0.0016 = 1.2 \times 10^{15} Eu^{+3} \text{ ions}/\Delta \quad [2]$$

Under steady-state CR excitation, the rate equation of the population for each 7F_2 state is

$$\frac{dn}{dt} = \dot{N} - n/\tau = 0 \quad [3]$$

Therefore, the average population, n , for the average lifetime τ of the 7F_2 state is given by

$$n = \dot{N} \tau \quad [4]$$

where \dot{N} is the average number of ${}^5D_0 \rightarrow {}^7F_2$ luminescence transitions per second as calculated by Eq. [5]

$$\dot{N} = \frac{(\text{input power}) \times (\text{power efficiency of luminescence})}{\text{photon energy of luminescence}} \quad [5]$$

The input power for steady-state CR excitation of 20 kV, $5 \mu A/cm^2$ is $0.1 W/\Delta$. Assuming that the luminescence photon energy is 2 eV and the efficiency of the ${}^5D_0 \rightarrow {}^7F_2$ transitions for the CR excitation is 0.06 W/W, one can get 1.8×10^{16} transitions/ Δ -sec. Each downward transition populates one of the 7F_2 states. This excess population would thermalize very quickly among the five 7F_2 states, so that \dot{N} for each 7F_2 state would be

$$\dot{N} = \frac{1.8 \times 10^{16}}{5} = 3.6 \times 10^{15} Eu^{+3} \text{ ions}/\Delta\text{-sec} \quad [6]$$

Unfortunately we could not measure the lifetime of the 7F states. The reported decay times for the 5D luminescence under CR excitation are shorter in going to order of the 5D_0 , 5D_1 , and 5D_2 (13) and the decay time of the 5D_0 luminescence is about $500 \mu sec$ (13, 14). If τ for the 7F_2 is about $100 \mu sec$ ($10^{-4} sec$), the CR pumped population is computed as

$$\dot{N} \tau = 3.6 \times 10^{15} \times 10^{-4} = 3.6 \times 10^{11} Eu^{+3} \text{ ions}/\Delta \quad [7]$$

Thus, the computed CR population (10^{11} ions) is too small to perturb the thermal population (10^{15} ions), even if the calculation is made for one-tenth the electron penetration depth (5).

The CR pumped population can be increased by increasing the beam current density. An increase in the steady-state beam current density results in a significant increase in phosphor temperature. We have measured the luminescence intensities from the phosphor screen of a 19-in. color television picture tube (30 kV) as a function of beam current density (to avoid a temperature increase). The results obtained with two extremes of the pulsed excitation (30 Hz and 15 kHz) on the picture tube screen are shown in Fig. 3.

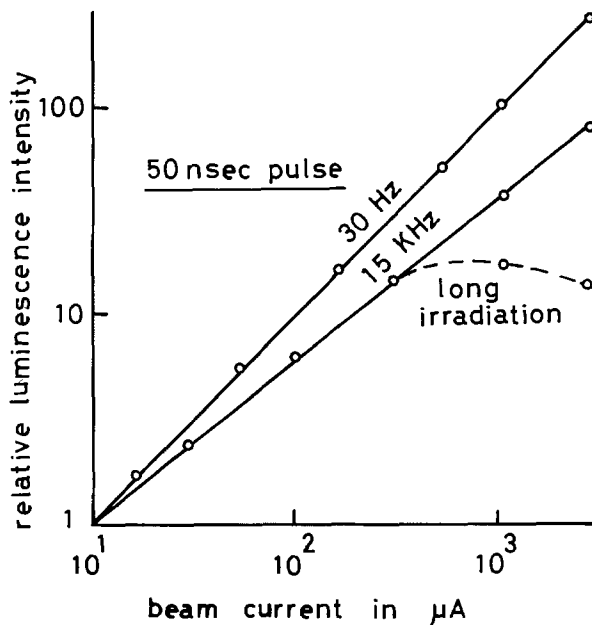


Fig. 3. Relative 5D_0 - 7F_2 luminescence intensities of $Y_2O_2S:Eu$ phosphor on 19-in. tricolor television picture tube screen as a function of beam current. The phosphor dots on the screen are excited by 50 nsec pulses at 1/30 Hz and 15 kHz, respectively. Quenching (dashed lines) only occurs for long CR irradiation under multiple excitation conditions at high beam current.

The phosphor dot (0.3 mm diameter) in the 19-in. television picture tube is instantaneously excited for 50 nsec by a single horizontal scan. The instantaneous excitation intensity for 50 mA/cm² corresponds to 1500 W/Δ or 6×10^{15} Eu⁺³ ions pumped in each 7F_2 state/Δ under steady-state excitation. When the phosphor screen was excited by 50 nsec pulses every 1/30 sec using a single scanning line, all of the luminescence intensities increased linearly with beam current up to 3 mA [estimated as 70 mA/cm² current density on the phosphor screen (7)]. No change in the relative 5D_0 luminescence intensities was observed. Under multiple excitation, sublinear response (0.9 slope for the 5D_0 luminescence) and quenching at high beam current (dashed lines) for long CR irradiation were observed. No change in the relative 5D_0 luminescence intensities was observed in the straight line region. The quenching was enhanced on increasing the degree of multiple excitation and the CR irradiation time. Therefore, the quenching is related to reabsorption of the luminescence because the relative intensities of the 5D_0 luminescence were markedly changed in this region; the 7F_2 was quenched more than the 7F_1 . Longer CR irradiation with a short pulse interval heats up the phosphor temperature, resulting in an increase in the thermal population of the 7F_1 and 7F_2 states.

The temperature rise for continuous CR excitation in this study (20 kV, 5 μA/cm²) is too small to change the thermal population of the 7F_2 state. The phosphor temperature rise during the steady CR excitation can be determined accurately by measuring the ${}^5D_1/{}^5D_0$ luminescence intensity ratio of $Y_2O_3S:Eu$ phosphor (15). Because this ratio measurement uses an internal reference method, the accuracy is high enough to determine the temperature difference within a few degrees centigrade. For the measurement it is convenient to select two luminescence lines located at 583 and 587 nm which are ${}^5D_0 \rightarrow {}^7F_0$ and ${}^5D_1 \rightarrow {}^7F_3$ transitions, respectively (15). No change in the ratio was detected for steady CR excitation in this study. Thus, the change in the 7F_2 curves is also hard to attribute to a thermal effect.

Concluding Remarks

We have shown that the concentration dependence curves of $Y_2O_3S:Eu$ depend on the mode of excitation. The absorption spectrum (Fig. 2) shows the existence of reabsorption of luminescence. However, our calculations allow one to conclude that the decrease of the optimum activator concentration of the ${}^5D_0 \rightarrow {}^7F_2$ luminescence in going from host photoexcitation to steady-state cathode-ray excitation (Fig. 1) cannot be

attributed to the increase in absorption due to the change in the average population in the 7F_2 state caused by CR pumping or temperature rise. It may be necessary to consider the instantaneous population, or otherwise to clarify the energy transfer mechanism from host to activators, before one can calculate theoretical concentration dependence curves for host excitation.

Acknowledgment

The authors wish to thank Dr. M. Stevens for his cathodoluminescence measurements on the picture tube screen and Ms. H. Stanczyk for her assistance in preparation of samples.

Manuscript submitted July 19, 1974; revised manuscript received May 21, 1975.

Any discussion of this paper will appear in a Discussion Section to be published in the June 1976 JOURNAL. All discussions for the June 1976 Discussion Section should be submitted by Feb. 1, 1976.

Publication costs of this article were partially assisted by Zenith Radio Corporation.

REFERENCES

1. L. Ozawa, H. Forest, P. M. Jaffe, and G. Ban, *This Journal*, **118**, 482 (1971).
2. H. Forest and L. Ozawa, Paper 211RNP presented at the Electrochemical Society Meeting, Washington, D.C., May 9-13, 1971.
3. G. Gergely, *J. Phys. Chem. Solids*, **17**, 112 (1960).
4. J. D. Kingsley and G. W. Ludwig, *This Journal*, **117**, 354 (1970).
5. J. D. Kingsley and J. S. Prener, *J. Appl. Phys.*, **43**, 3073 (1972).
6. L. Ozawa and P. M. Jaffe, *This Journal*, **117**, 1297 (1970).
7. M. Stevens, L. Ozawa, G. Ban, and H. N. Hersh, *IEEE Trans. Consumer Electron.*, **CE-21**, 1 (1975).
8. M. Stevens, G. Ban, L. Ozawa, and H. N. Hersh, Preprint No. 155, Japanese Luminescence Soc., November 1974.
9. U. Fano, *Phys. Rev.*, **58**, 544 (1940).
10. D. Curie, "Luminescence in Crystals," p. 224, John Wiley & Sons, Inc., New York (1960).
11. A. Bril, *Physica*, **15**, 361 (1949).
12. C. Feldman, *Phys. Rev.*, **117**, 455 (1960).
13. Y. Kobayashi and T. Takamura, *Japan. J. Appl. Phys.*, **6**, 114 (1967).
14. G. E. Peterson, in "Transition Metal Chemistry," Vol. 3, p. 202, R. L. Carlin, Editor, Marcel Dekker, Inc., New York (1966).
15. W. H. Fonger and C. W. Struck, *J. Chem. Phys.*, **52**, 6364 (1970).

Low Carbon Contamination of Epitaxial Germanium Films Produced by Pyrolysis of Alkyl Germanium Compounds

Y. Avigal,¹ D. Itzhak, and M. Schieber²

Department of Materials Science, School of Applied Science and Technology,
Hebrew University of Jerusalem, Jerusalem, Israel

ABSTRACT

Thin films of Ge produced by the pyrolysis of alkyl germanium tetramethyl germanium and tetraethyl germanium compounds have been studied for their rates of deposition, crystallinity, and carbon contamination. The pyrolysis reaction has been found to be of first order, and the activation energies have been found to vary with concentration of the alkyl germanium compound between the limits of 25-30 kcal/mole for both tetramethyl and tetraethyl germanium. The morphology and crystallinity of the films vary with the chemical and crystalline structure of the substrate. Good quality and uniform films are produced on monocrystalline germanium substrates preetched *in situ* with HCl gas. The carbon contamination is found to be strongly dependent on the substrate material, and it varies between 25 ppm for germanium and 200-50,000 ppm for tungsten substrates.

Pyrolysis and oxidation of alkyl silicon compounds for the chemical vapor deposition of SiC or SiO₂ have been studied recently in our laboratories (1, 2). The experiments have shown that the pyrolytically dissociated silicon tends to combine with the carbon from the alkyl radical to form SiC, and it is also contaminated with large amounts [up to about 7 weight per cent (w/o)] of free carbon (1, 3). The tendency to form SiC is attributed to the larger chemical affinity of Si for C. Since GeC is known to be unstable, it is expected that the pyrolysis of alkyl germanium compounds would lead to the formation of pure germanium. It was therefore considered interesting to study the epitaxy of germanium by pyrolysis of alkyl germanium compounds and to compare the carbon content of the resulting deposits with the carbon found in films grown by pyrolysis of alkyl silicon compounds (1, 3). The rates of deposition and the morphology of the grown films were also studied and are reported here.

Homoepitaxial thin films of germanium are usually deposited by hydrogen reduction of GeCl₄ (4-7) or by the pyrolysis of GeH₄ (8-12). Chemical transport with iodine is limited to close systems only, and direct vacuum sublimation (13-15) is limited by the high cost of the equipment and the difficulty of controlling the deposition process. Heteroepitaxial films of germanium on various substrates are usually deposited by the pyrolysis of GeH₄ (16-20). The main disadvantages of GeCl₄ and GeH₄ as sources for deposition are their high chemical reactivity at room temperature, which makes them highly corrosive (GeCl₄) or flammable (GeH₄) and also causes difficulties with the purification process (21). Alkyl germanium compounds have the advantages of being noncorrosive, nonhazardous, and easy to purify.

Experimental Procedure and Rates of Deposition

The alkyl germanium compounds used in the present investigation have been tetramethyl germanium (CH₃)₄Ge (TMG) and tetraethyl germanium (C₂H₅)₄Ge (TEG) purchased from Alpha Chemicals. The vapor pressure of these compounds is not available from the literature and, therefore, has been determined dynamically for TEG and statically for TMG (1). The results are shown in Fig. 1. The substrates used for crystallinity studies of epitaxy were single crystals of (111) Ge whereas substrates of polycrystalline tungsten were used for studies of deposition rates and carbon con-

tamination. The diluent gases were high purity H₂ and He (Matheson) which was further purified *in situ* in one laboratory (1).

The experimental procedure of deposition is similar to the one used for SiC and is described elsewhere (1, 3). The relations of deposition rates and deposition parameters have been studied by measuring the rate of increase in weight, *R*, as a function of the tungsten substrate temperature (Fig. 2 and 3) and the molar fraction of the alkyl germanium which was regulated either by the flow rate through the saturator or by its temperature (Fig. 4 and 5). It can be seen from Fig. 2 and 3 that for both TMG and TEG, a measurable deposition rate starts at about 700°C, increases with the temperature of the substrate, and tends to stay constant at around 1000°C. While in the case of TMG hydrogen was used exclusively as the gas diluent, in the case of TEG depositions, either hydrogen or helium were used as the gas diluent. Figure 3 shows that *R* is unchanged by the gas diluent, a behavior which is different from the case of the alkyl silanes (1) where *R* is strongly dependent on whether the diluter is H₂ or He.

The different behavior between the pyrolysis of alkyl silane and alkyl germanium compounds in the presence of H₂ is an indication that H₂ does not participate chemically in the deposition of the films of Ge. In comparing the units of Fig. 2 and 3 it is interesting to note that *R* for TMG is much larger than *R* for TEG

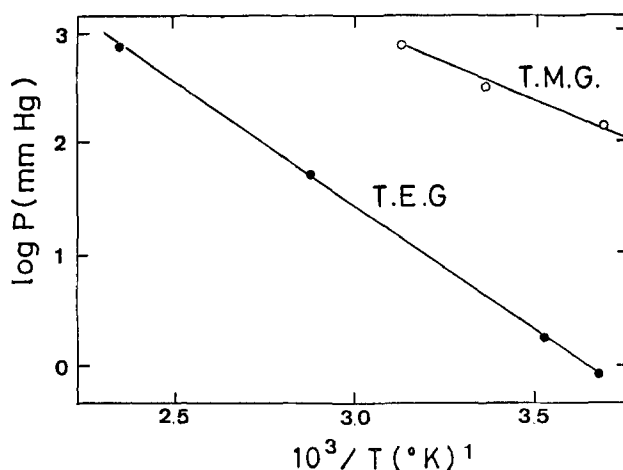


Fig. 1. Vapor pressure vs. the inverse temperature for TMG and TEG.

¹ Present address: Battery Division, Tadiran, Israel Electronics Industries, Rehovoth, Israel.

² Also at EG&G, Inc., Santa Barbara, Goleta, California 93017.

Key words: low carbon contamination, epitaxial germanium films, pyrolysis, alkyl germanium compounds.

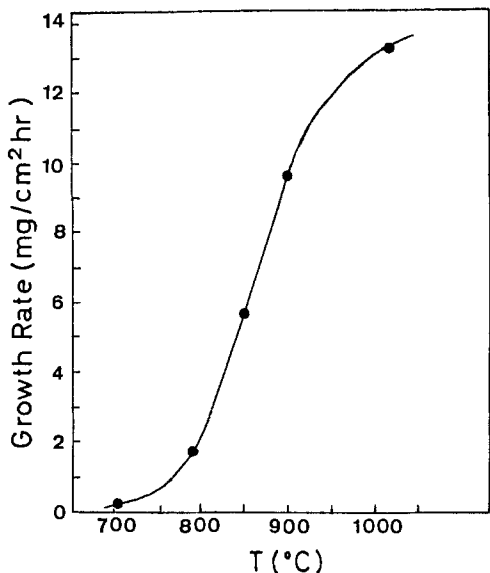


Fig. 2. Growth rate vs. temperature of Ge films on tungsten substrates prepared by the pyrolysis of TMG in H₂. Molar fraction is 2.0×10^{-2} and total flow is 1.5 liters/min.

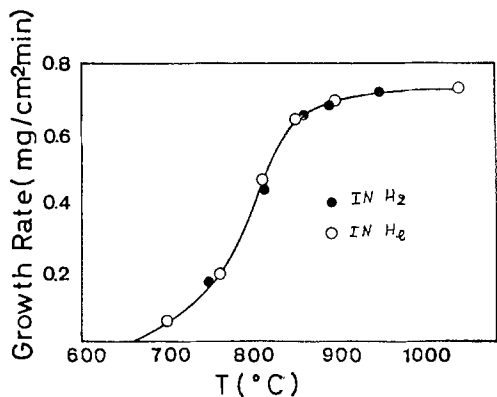


Fig. 3. Growth rate vs. temperature of Ge films on tungsten substrates prepared by the pyrolysis of TEG in H₂ or He. The molar fraction is 3.7×10^{-3} and total flow is 1.5 liters/min.

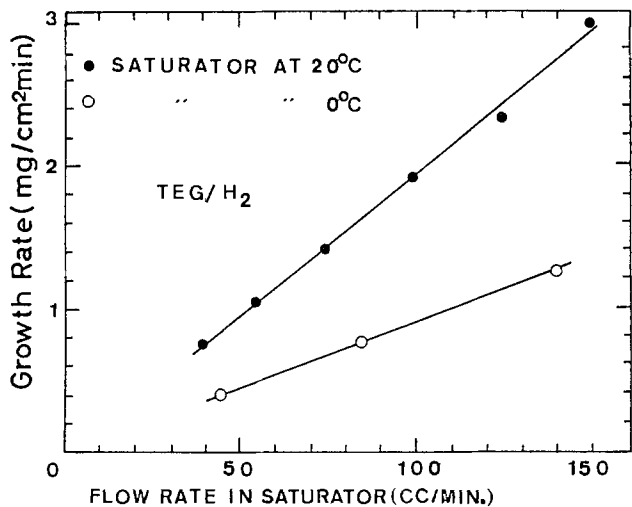


Fig. 4. Growth rate vs. H₂ flow rate in the saturator of TEG. All experiments were performed at a constant temperature of 800°C of the tungsten substrates.

at about the same conditions of deposition. The linear relations of Fig. 4 and 5 indicate a first order for the over-all reaction of deposition. An Arrhenius plot of $\log R$ vs. T^{-1} is shown in Fig. 6 for both TMG and

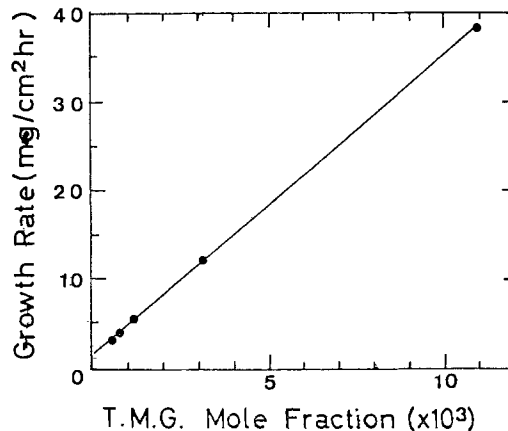


Fig. 5. Growth rate vs. mole fraction of TMG in H₂. All experiments were performed at a constant temperature of 850°C of the tungsten substrates. The total gas flow is 1.5 liters/min.

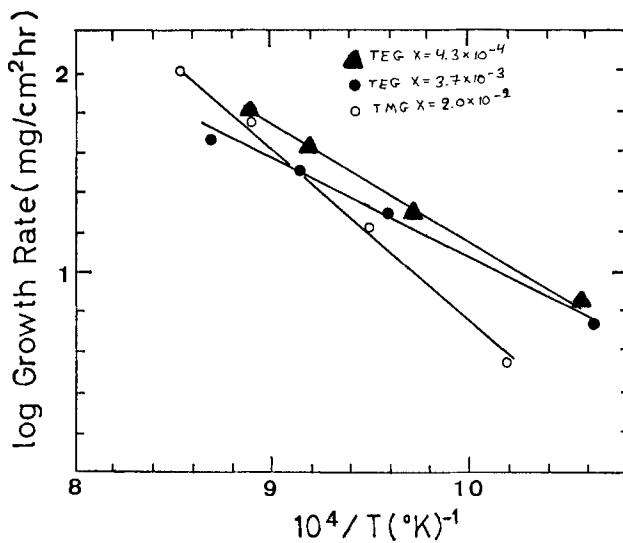


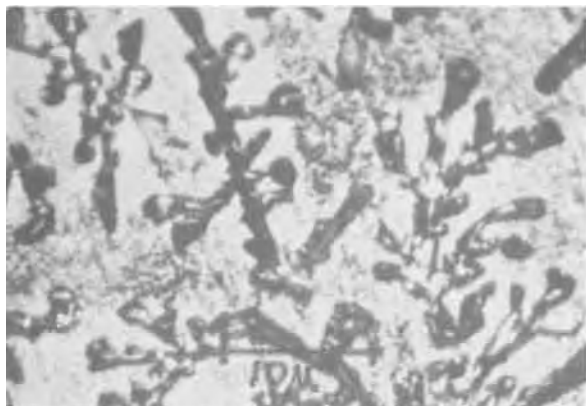
Fig. 6. Arrhenius plot of the log of growth rate vs. inverse temperature of the tungsten substrates for TEG at a molar fraction of 4.3×10^{-4} and 3.7×10^{-3} and for TMG at a molar fraction of 2.0×10^{-2} on H₂. The total gas flow is 1.5 liters/min.

TEG, and for two different values of the molar fraction X for TEG. The activation energies calculated from these plots are 31.6 kcal/mole for TMG for $X = 2.0 \times 10^{-2}$, and 31.3 and 25.0 kcal/mole for $X = 4.3 \times 10^{-4}$ and 3.7×10^{-3} , respectively, for TEG.

Characterization of the Films

The Ge thin films grown on (111) Ge and polycrystalline tungsten have been characterized using scanning electron microscopy (SEM), electron diffractions, and microchemical analysis of the carbon content. An optical examination shows that all films of Ge grown in H₂ were metallic in appearance and shiny, whereas the films grown in He showed various degrees of gray coloring.

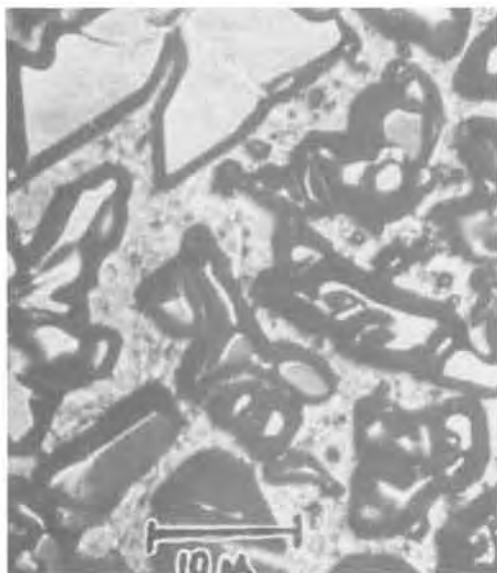
The morphology determined by the SEM examination varies according to the deposition temperature and also the nature and the pretreatment procedure of the substrate. Lower temperatures of deposition, e.g., 750°C, show relatively poor quality films. The dendritic appearance of the Ge on polycrystalline tungsten at 750°C (Fig. 7a) is changed at 850°C to a polygonal type of growth (Fig. 7b) whose lateral sites still increase further if the substrate has been preetched in HCl (Fig. 7c). The homoepitaxial film on (111) Ge (Fig. 7d) shows irregular shaped steps of growth. Raising the substrate temperature to about 850°C and etching with HCl *in situ* improved the morphology of the grown films, as can be seen in Fig. 7e and f, respectively. HCl



a. On polycrystalline tungsten at 750°C



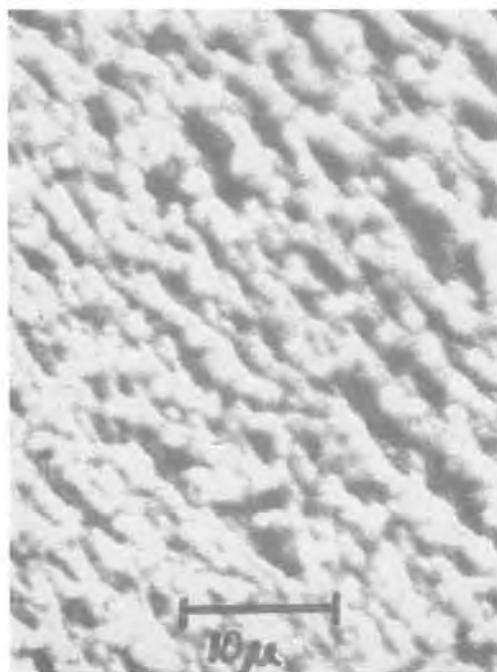
b. On polycrystalline tungsten at 850°C



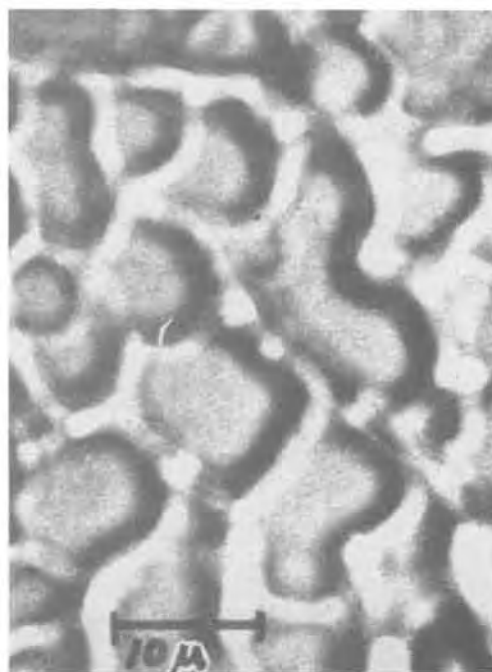
c. On polycrystalline tungsten at 850°C with HCl preetching



d. On (111) Ge at 750°C



e. On (111) Ge at 850°C



f. On (111) Ge at 850°C with HCl preetching

Fig. 7. SEM micrographs of Ge films about 10 μm thick deposited by the pyrolysis of TEG on H_2

in situ etch did not give any substantial improvement for films grown at 750°C.

The crystallinity of the grown films has been studied both by x-ray Laue low angle diffractions, transmission electron microscopy (TEM) diffractions, and reflection electron diffractions (RED). Films of about 10 μm thick were deposited on (111) Ge for these measurements which showed the single crystallinity of the homoepitaxial layer of Ge grown both on H_2 or He atmosphere.

The films grown on polycrystalline tungsten substrates also show an appearance of twinned (111) single crystalline deposits. However, this is due to the natural tendency of Ge to grow as twins in the (111) plane.

The carbon contamination of the films grown on cleaned tungsten and (111) Ge substrates has been analyzed microchemically, as reported previously for SiC films (1). The carbon content of blank substrates treated in a similar way as the ones covered with Ge films was subtracted from the total carbon content of the samples. Etching with HCl *in situ* was not used for carbon concentration studies. The epitaxial films of Ge on (111) Ge contained no more than about 25 ppm of carbon. It was seen, however, that the tungsten substrate influenced the results and that the carbon contamination was much higher, varying between 800 to 4700 ppm. This is probably due to the tendency of W to form WC, as in the case of SiC, which causes the production of free carbon during the pyrolysis of the alkyl radicals. The results of the carbon contamination are summarized in Table I. Table I shows that no clear cut correlation can be found between the carbon concentration and the deposition temperature, the mole fraction of the alkyl germane and the chemical identity of the alkyl germane. This is in contrast to the case of alkyl silanes where such correlations were found. The only factor which we found to affect the carbon concentration is the nature of the diluent gas, where the carbon concentration is higher for depositions performed in He rather than in H_2 .

Discussion

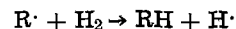
Comparing the results obtained in the present investigation with those reported for the heteroepitaxy of SiC (1) we can conclude that the alkyl compounds have a tendency to deposit free carbon whenever they

Table I. Weight percentage of carbon, C (w/o), at various deposition temperatures, $T(^{\circ}\text{C})$, and molar fractions, ($\times 10^3$), diluting gases, and transporting alkyl germanium, found in Ge on polycrystalline tungsten films

Number	Transporting agent	Diluting gas	Molar fraction $\times 10^3$	T ($^{\circ}\text{C}$)	C (w/o) ^(a)
G50	TMG	He	1.30	880	4.71
G52	TMG	He	1.30	980	4.42
G23	TEG	He	0.44	1060	2.65
G32	TMG	H_2	2.00	790	0.10
G47	TMG	H_2	11.00	890	0.21
G40	TMG	H_2	2.00	900	0.11
G26	TEG	H_2	0.43	760	0.33
G24	TEG	H_2	0.43	890	0.08
G30	TEG	H_2	3.7	900	0.46

^(a) The analysis of carbon has been performed on both the substrates covered or not covered with films of Ge. The uncovered substrates were analyzed as blanks and their carbon content was subtracted from the total amount of carbon determined on the film. Expressing in weight percentages it can be seen that the total carbon content varies between 0.1 to 5% and is larger in films of Ge produced in a He rather than an H_2 atmosphere.

can form with a given element a stable carbide. Since Ge does not form a stable carbide the homoepitaxial layers of Ge have a low carbon content. Alkyl germanium deposits less carbon in the presence of H_2 than in He. Hydrogen promotes the reaction similar to the behavior of alkyl silicon (1), preventing the decomposition of the alkyl radical R into free carbon



It can be concluded that the optimum conditions of growth of thin films of Ge, starting from alkyl germanium, are as follows: (i) use a substrate composed of elements which do not tend to form a stable carbide; (ii) preetch the substrate *in situ* with HCl; (iii) deposit in the presence of H_2 ; (iv) use higher temperatures of deposition in excess of 850°C, in order to promote lateral growth and thus increase the over-all growth rates; and (v) use higher molar fractions of the alkyl germanium which increase the rates of growth without giving any clear indication that it would also cause an unwanted increased contamination of carbon in the grown films.

Acknowledgments

The authors are indebted to Mr. R. Levin for performing the microchemical carbon analyses. This paper is part of the Ph.D thesis of Y. Avigal submitted to the Hebrew University.

Manuscript submitted Oct. 21, 1974; revised manuscript received March 20, 1975.

Any discussion of this paper will appear in a Discussion Section to be published in the June 1976 JOURNAL. All discussions for the June 1976 Discussion Section should be submitted by Feb. 1, 1976.

REFERENCES

- Y. Avigal, M. Schieber, and R. Levin, *J. Crystal Growth*, **24/25**, 188 (1974).
- Y. Avigal, I. Beinglass, and M. Schieber, *This Journal*, **121**, 1103 (1974).
- Y. Avigal and M. Schieber, *J. Crystal Growth*, **9**, 127 (1971).
- E. F. Cave and B. R. Czorny, *RCA Rev.*, **24**, 523 (1963).
- N. N. Sheftal, N. P. Kokorisk, and A. V. Krasilov, *Izvest. Akad. Nauk. SSR., Ser. Fiz.*, **21**, 140 (1957).
- R. P. Ruth, J. C. Marinace, and W. C. Dunlap, *J. Appl. Phys.*, **31**, 995 (1960).
- C. H. Thenere *et al.*, *Proc. I.R.E.*, **48**, 1642 (1960).
- M. Tamaru, M. Bondart, and H. Taylor, *J. Phys. Chem.*, **59**, 801 (1955).
- P. J. Fersham, K. Tamatu, M. Bondart, and H. Taylor, *ibid.*, **59**, 806 (1955).
- M. Davis and R. F. Lever, *J. Appl. Phys.*, **27**, 835 (1956).
- E. Roth, H. Gossenberger, and J. A. Amick, *RCA Rev.*, **24**, 499 (1963).
- J. C. Marinace, *IBM J. Res. Develop.*, **4**, 248 (1960).
- E. T. Handelman and E. I. Povrilonis, *This Journal*, **111**, 201 (1964).
- R. C. Newman, *Microelectron. Rev.*, **3**, 121 (1964).
- O. S. Heavens, *Proc. Phys. Soc. London*, **65B**, 788 (1952).
- Becker and L. Horovitz, *Proc. Nat. Electronics Conf.*, **8**, 506.
- J. L. Porter and R. G. Woltson, *J. Appl. Phys.*, **36**, 3690 (1965).
- D. J. Dumin, *This Journal*, **114**, 752 (1967).
- R. F. Trampusch, *Appl. Phys. Letters*, **2**, 83 (1966).
- J. A. Amick, E. A. Roth, and H. Gossenberger, *RCA Rev.*, **24**, 473 (1963).
- M. S. Brooks and J. K. Kennedy, Editors, "Ultra-purification of Semiconductor Materials," McMillan Co., New York (1962).

Observations on Si Contamination in GaP LPE

O. G. Lorimor, S. E. Haszko, and P. D. Dapkus

Bell Laboratories, Murray Hill, New Jersey 07974

ABSTRACT

Silicon has long been known to be an unintentional impurity often present in GaP; however, the concentration of the Si and its effects have not been known. It has been observed that the net donor concentration in undoped LPE layers fluctuates from $\sim 1 \times 10^{16} \text{ cm}^{-3} \lesssim N_d - N_a \lesssim 2-4 \times 10^{17} \text{ cm}^{-3}$ for different growth runs when growth is in ~ 1 atm of H_2 . This background $N_d - N_a$ is attributed to unintentionally present Si donors. The Si concentrations in these as well as S- and Zn-doped layers as determined by ion micro-analyzer measurements range from $\sim 6 \times 10^{16} \text{ cm}^{-3} \lesssim X_{\text{Si}}^{\text{s}} \lesssim 2 \times 10^{18} \text{ cm}^{-3}$ with the typical value being $\sim 5 \times 10^{17} \text{ cm}^{-3}$. In the undoped layers X_{Si}^{s} often exceeds $N_d - N_a$. The variations in both background $N_d - N_a$ and X_{Si}^{s} are attributed to variations in the oxygen level of the gas ambient which is inversely related to the X_{Si}^{s} . An important reaction resulting in Si contamination is H_2 reduction of the quartz used in the construction of the LPE growth system. With a growth sequence designed to grow both a Zn- and oxygen-doped p-layer onto an undoped n-layer in the same growth run, SiO_2 precipitates have been observed in the p-layer near the p-n junction. The identification of these precipitates as SiO_2 is further proof of the high levels of Si contamination that can occur during LPE growth. Minority carrier lifetimes for Si-doped LPE layers with $N_d - N_a \gtrsim 5 \times 10^{17} \text{ cm}^{-3}$ are considerably longer than have been obtained by doping with S or Te. The increased lifetime is attributed to either a reaction involving Si which results in the reduction in the concentration of an important nonradiative center or the fact that the usual dopants S and Te themselves are involved in a nonradiative center.

For several years it has been known that Si is often found as an unintentional impurity in GaP (1); however, this Si contamination has received little attention, especially in the LPE layers used in LED's. In this paper we review both previous work and present additional data which together provide a better understanding of Si contamination resulting from LPE growth.

Early work by Trumbore *et al.* (2) studied Si incorporation into intentionally Si-doped samples. One observation was that emission spectroscopic measurements always yielded a higher value for the Si concentration than did a spectrophotometric (a chemical separation followed by a spectroscopic measurement) determination. They felt that the spectrophotometric analysis was more accurate and so weighed those data points more heavily in their analysis. However, the same data were later reinterpreted (3) by suggesting that the spectrophotometric method yields the isolated Si (or Si-Si pairs) in solid solution while the emission spectroscopic (as well as electron microprobe) method yields the total Si content including Si in the form of some second phase (*e.g.*, SiO_2) or complex which is insoluble in the reagents used to dissolve the GaP for the spectrophotometric analysis. Thus, there is early evidence that the incorporation of Si into GaP may be complicated in that the total Si concentration in GaP may exceed that truly in solid solution.

More recently, it has been observed that the background net donor concentration, $N_d - N_a$, measured in LPE layers grown in a quartz dipping system from both 1000° and 900°C have varied nonsystematically (4) from $\sim 1 \times 10^{16} \text{ cm}^{-3}$ to $2-4 \times 10^{17} \text{ cm}^{-3}$. C, Si, S, and N have been identified in these layers from photoluminescence or optical absorption measurements (5). The S and N concentrations are typically $\lesssim 5 \times 10^{15} \text{ cm}^{-3}$ as determined by optical absorption. This implies that Si, for which no concentration could be determined by optical absorption, is the donor providing the measured background $N_d - N_a$.

To investigate Si incorporation further two crystal growth runs were made where radioactive Si was used as a dopant. In one experiment an LPE layer was grown from 925°C from a melt containing 0.01 atom per cent (a/o) radioactive Si (5). The net donor concentration, $N_d - N_a$, was $1.6 \times 10^{18} \text{ cm}^{-3}$ while the total Si concentration, X_{Si}^{s} , was $1.7 \times 10^{19} \text{ cm}^{-3}$. The total Si concentration exceeds $N_d - N_a$ by a decade.

In the second experiment, the melt was undoped except that a small piece of irradiated quartz with an area of $\sim 1 \text{ cm}^2$ was floated on the surface of the melt. The 15g melt was held at 800°C in a H_2 atmosphere for $2\frac{1}{2}$ hr. After this treatment, the melt contained $2.3 \mu\text{g}$ of Si from the irradiated piece of quartz. This amount of Si in the melt would Si dope an LPE layer so that $N_d - N_a \approx 3 \times 10^{16} \text{ cm}^{-3}$. However, considering that the temperature is low compared to that normally used for GaP LPE, and the small size of the piece of the "hot" quartz compared to the total area of quartz in the system, $2.3 \mu\text{g}$ of Si is judged to be quite a high level of contamination. Thus, Si from the quartz used in the growth systems can contaminate the melt.

There is direct evidence for the presence of Si in many undoped LPE layers. Trumbore (3) has studied Si in GaP using the ion microanalyzer. By using a few highly Si-doped samples whose Si concentration could accurately be measured by other analytical techniques, an absolute calibration for Si was obtained. The Si concentrations in a number of undoped crystals grown under varying conditions were measured. These results are shown in Table I along with two additional samples (the last two) recently studied. In obtaining these values for the Si concentration in the solid GaP, X_{Si}^{s} , it is assumed that the entire positive ion signal at mass 28 is due to Si^+ ions. The minimum Si concentration that could be detected was $\sim 2 \times 10^{17} \text{ cm}^{-3}$.

The primary observation that can be made from Table I is that Si concentrations vary from sample to sample from $6 \times 10^{16} \text{ cm}^{-3}$ to over 10^{18} cm^{-3} . As with the background $N_d - N_a$ found in undoped layers, the variation of X_{Si}^{s} from sample to sample is in general

Key words: LED, light-emitting diodes, liquid phase epitaxy.

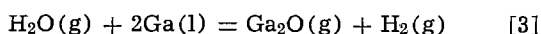
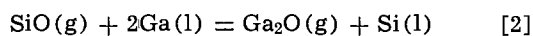
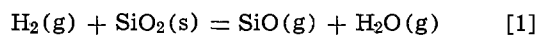
Table I. Si concentrations in GaP LPE layers as measured by the ion microanalyzer

Crystal	Growth conditions: (temp, boat material, gas ambient)	Dop- ants	$N_d - N_a$ (cm^{-3})	X_{Si}^{s} (cm^{-3})
1-474	900°C, pyrolytic C, H ₂	N	6.5×10^{18}	1×10^{18}
1-471	900°C, quartz, H ₂	S,N	2×10^{18}	2×10^{18}
2-388	1000°C, BN, H ₂	—	—	8×10^{17}
2-432	1000°C, quartz, H ₂ (melt prebaked in vacuum)	N	1.1×10^{18} (p)	4×10^{17}
2-430	1000°C, quartz, H ₂	S,N	4.7×10^{17}	2×10^{17}
1-468	900°C, quartz, H ₂	—	2.5×10^{18}	6×10^{16}
2-364	900°C, BN, H ₂	N	—	2×10^{18}
X-112873	1000°C, quartz, H ₂	—	3.5×10^{17}	4×10^{17}
X-120473	1000°C, quartz, He	—	2×10^{18} (p)	$< 2 \times 10^{17}$

nonsystematic. Although one might expect less Si to enter the melt when the boat material is BN or C rather than quartz, Table I shows no such correlation. Instead X_{Si}^{s} appears to fluctuate randomly. The last two samples in Table I were grown under as nearly leak-free conditions as possible. Less Si was found in the sample grown under an ambient of high purity He compared to the sample grown under H₂. However, one cannot quantitatively compare the relative Si concentrations in these two samples because of the relatively high detectability limit of the ion microanalyzer compared to their Si concentrations. A general conclusion from the data in Table I is that values of X_{Si}^{s} in the mid- 10^{17} cm^{-3} range appear to be quite common when the ambient is ~ 1 atm H₂.

We propose that the Si enters the melt from the quartz used in the construction of the LPE system when the ambient is ~ 1 atm H₂. The large variations observed in X_{Si}^{s} and background $N_d - N_a$ are attributed to the effects of varying water vapor pressure resulting from inadvertent and fluctuating air leaks in the gas system. (The oxygen that is admitted by an air leak is assumed to be essentially entirely converted to H₂O by the ~ 1 atm of hot H₂.)

For a system consisting of the liquid Ga melt, the quartz reactor tube, and the H₂ and H₂O gases, we consider the following reactions which result in Si contamination of the melt



Making the usual assumptions such as ideal dilute solutions, we obtain from reactions [1]-[3]

$$K_1 = \frac{p_{\text{SiO}} p_{\text{H}_2\text{O}}}{p_{\text{H}_2}} \quad [1a]$$

$$K_2 = \frac{p_{\text{Ga}_2\text{O}} \gamma_{\text{Si}} X_{\text{Si}}^{\text{l}}}{p_{\text{SiO}}} \quad [2a]$$

$$K_3 = \frac{p_{\text{Ga}_2\text{O}} p_{\text{H}_2}}{p_{\text{H}_2\text{O}}} \quad [3a]$$

The general effect of increasing the water vapor is to decrease the Si contamination of the melt. Figure 1 illustrates this effect by the solution of Eq. [1a]-[3a]. X_{Si}^{l} is shown as a function of the inlet partial pressure of water in the gas stream, $p_{\text{H}_2\text{O}}^{\text{l}}$. $p_{\text{H}_2\text{O}}^{\text{l}}$ is determined by the oxygen entering the gas stream through leaks as well as any other source of water or oxygen present in the inlet gases. Table II gives the values of the reaction constants used in these calculations. At the higher values of $p_{\text{H}_2\text{O}}^{\text{l}}$, the reduction of the quartz is negligible and thus $p_{\text{H}_2\text{O}} = p_{\text{H}_2\text{O}}^{\text{l}}$ with the consequence $X_{\text{Si}}^{\text{l}} \propto (p_{\text{H}_2\text{O}}^{\text{l}})^{-2}$. X_{Si}^{l} saturates at the lower values of $p_{\text{H}_2\text{O}}^{\text{l}}$ at a value determined by the reduction of the quartz. One should note that, in equilibrium, X_{Si}^{l} can be quite large, $> 10^{-3}$ atom fraction, at both 900° and 1000°C. Values of $X_{\text{Si}}^{\text{l}} \approx 1 \times 10^{-4}$ are sufficient to

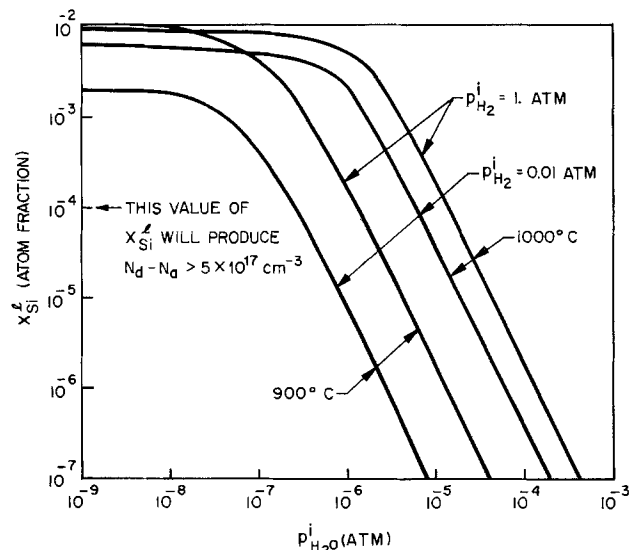


Fig. 1. Concentration of Si in the melt, X_{Si}^{l} , as a function of inlet water vapor partial pressure, $p_{\text{H}_2\text{O}}^{\text{l}}$.

dope an LPE layer so that $N_d - N_a > 5 \times 10^{17} \text{ cm}^{-3}$ (2).

However, the rate at which Si enters the melt is highly dependent upon the growth conditions, $p_{\text{H}_2\text{O}}^{\text{l}}$, and the boat material. Calculations have shown that the rate of Si contamination for a nonquartz boat where the Si must be transported to the melt via the vapor is much slower than for a quartz boat where the Si may dissolve directly into the melt (6, 7). These calculations also showed that for a quartz boat, 1 atm H₂, and $p_{\text{H}_2\text{O}}^{\text{l}} \lesssim 10^{-5}$ atm equilibrium is not reached for typical LPE growth times. However, the actual rate at which these reactions approach equilibrium may differ from that calculated as the idealized assumptions used in the calculations are most likely not entirely met experimentally. However, the generalized conclusions that Si contamination occurs faster in quartz boats than inert boats and that equilibrium is not reached for low values of $p_{\text{H}_2\text{O}}^{\text{l}}$ for typical LPE growth times are most likely true experimentally. Thus, the very high levels of X_{Si}^{l} shown in Fig. 1 for low values of $p_{\text{H}_2\text{O}}^{\text{l}}$ are probably not attained experimentally.

There is one final piece of evidence for high levels of Si contamination in GaP LPE layers. When unintentionally doped n-layers were grown followed by an oxygen-doped p-layer in the same growth run, precipitates were often observed in the p-layer at the p-n junction. The n-layer was first grown from 1020°C under ~ 1 atm of H₂. After n-growth the furnace was held at constant temperature and the H₂ ambient replaced by ~ 0.9 atm He, ~ 0.1 atm H₂, $\sim 2 \times 10^{-3}$ atm Zn, and $\sim 1 \times 10^{-2}$ atm O₂ at the inlet to the reactor tube. After allowing 1 hr for equilibration of the melt, the furnace is heated $\sim 2^\circ$ to melt back a small amount of the n-layer and then cooled for p-growth.

Figure 2 shows an SEM photograph using secondary electron emission of one of these precipitates. The p-region is lighter than the n-region due to voltage enhancement of the secondary emission. Using the

Table II. Equilibrium constants for reactions [1], [2], and [3] and the activity coefficient for Si in liquid gallium used to compute the curves shown in Fig. 1

Equilibrium constant or activity coefficient	900°C	1000°C	Reference
K_1	1.0×10^{-14}	5×10^{-18}	12, 13
K_2	6.7×10^{-8}	2.3×10^{-2}	13, 14, 15
K_3	0.27	0.8	12, 14, 15
γ_{Si}	3	2.5	8

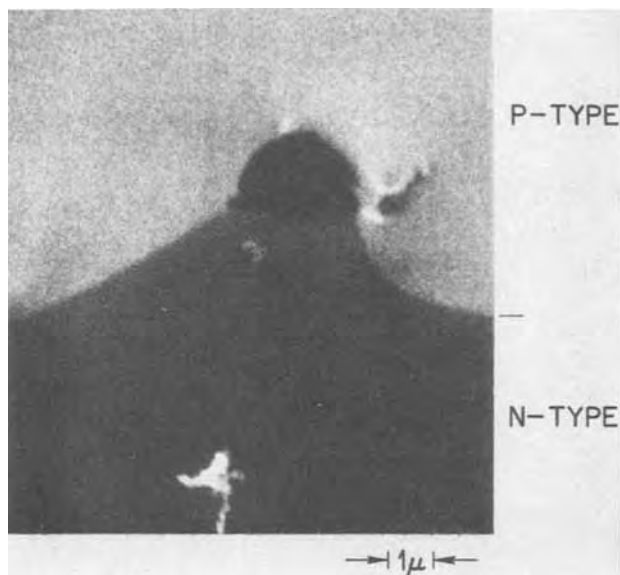


Fig. 2. Scanning electron microscope photograph using secondary electron emission showing precipitate in the p-layer at the p-n junction.

energy dispersive x-ray unit, a strong Si signal as well as background Ga and P signals were identified with the electron beam on the precipitate. We judge these precipitates to be largely SiO_2 . (Oxygen and all the lighter elements are not detected with the x-ray unit.) This conclusion is reached because these precipitates are not produced if O_2 is deleted from the same growth procedure, and elemental Si will not precipitate from a Ga+P melt at 975°C for Si concentrations in the melt $\leq 15\%$ (8).

During n-growth the melt becomes heavily contaminated with Si via reactions [1]-[3]. During the equilibration period, the introduction of oxygen causes the Si to be precipitated from the melt as SiO_2 . These SiO_2 precipitates evidently grow on the surface of the n-layer which results in their hemispherical shape. Eventually, the melt is almost entirely depleted of Si and precipitate growth stops. The precipitate acts as a mask during the meltback and thus is sitting on the mesa of n-layer. If n-growth is under 1 atm He, no precipitates are observed, indicating that the Si contamination of the melt is greatly reduced compared to growth in an H_2 ambient.

It is felt that these precipitates have not been present in earlier LPE studies because a unique growth cycle is required to produce them. First the melt must be heavily contaminated with Si and then the oxygen must be added. If the oxygen were added initially, the melt would not become Si contaminated as the large concentration of oxygen dissolved in the melt causes X_{Si}^1 to be very small.

The presence of these precipitates is strong evidence that the melt was highly Si contaminated during n-growth. Typically the density of these precipitates is $\sim 10^5 \text{ cm}^{-2}$ and $\sim 5\mu$ diameter over a growth area of $\sim 2 \text{ cm}^2$. If they were solid SiO_2 , the total weight of Si in the precipitates is $\sim 20 \mu\text{g}$. This amount of Si is a lower limit on the total Si contamination of the melt as it is highly unlikely that all, or perhaps even most, of the SiO_2 precipitates out onto the n-layer which is at the bottom of the melt. For example, the density of SiO_2 is $\sim 2.5 \text{ g/cm}^3$ compared to 5.6 g/cm^3 for Ga, with the consequence that the SiO_2 particles should float to the surface. This $\sim 20 \mu\text{g}$ of Si represents a minimum $X_{\text{Si}}^1 = 1 \times 10^{-5}$ atom fraction in the 5g melt used in these experiments. A deliberate addition $X_{\text{Si}}^1 = 1.0 \times 10^{-5}$ atom fraction to the melt is sufficient to dope to $N_d - N_a = 3 \times 10^{17} \text{ cm}^{-3}$ when growth is from 900°C . Consequently, it is observed again that the unintentional Si-contamination level is sufficient to produce

$N_d - N_a = \text{several} \times 10^{17} \text{ cm}^{-3}$. The total Si concentration in these LPE layers is undoubtedly much higher.

Intentionally Si-doped crystals with $N_d - N_a \gtrsim 5 \times 10^{17} \text{ cm}^{-3}$ grown in the dipping system from both 900° and 1000°C were found to have long minority carrier lifetimes compared to those which could be obtained with other dopants. Figure 3 shows the minority carrier lifetimes (τ) as determined from the green-PL time decay (9), as a function of $N_d - N_a$ for Si, S, Te, and undoped LPE layers. The values of τ for the S, Te, and undoped LPE layers are the highest which were measured during several years of LPE growth. It should be noted that these lifetimes are substantially longer than those reported for similar crystals doped with nitrogen.

For $N_d - N_a \gtrsim 5 \times 10^{17} \text{ cm}^{-3}$ the value of τ for Si-doped material is larger than the correspondingly S- or Te-doped layers by at least a factor of 2. At lower doping densities the dopant dependence of τ decreases. At $N_d - N_a \lesssim 1.2 \times 10^{17} \text{ cm}^{-3}$ it appears that the addition of Si has little, if any, effect upon the lifetime. However, $N_d - N_a \approx 1.2 \times 10^{17} \text{ cm}^{-3}$ is just the background value often measured and that has been attributed to unintentional Si doping in a nearly oxygen-free system. An undoped layer should probably be more properly called a lightly Si-doped layer.

From Fig. 3, we can conclude that the defect limiting the minority carrier lifetime in the S- and Te-doped samples where $N_d - N_a \gtrsim 5 \times 10^{17} \text{ cm}^{-3}$ does not consist of Si alone or Si-intrinsic GaP defect complexes. If it did, the corresponding Si-doped samples would not be expected to have a longer lifetime. Instead it appears that the Si, through a reaction in the Ga melt or during impurity incorporation, is reducing the concentration of the defect limiting τ . One of the simplest but most likely possibility is that the Si in the melt is reducing the oxygen in the melt via $\text{Si}(l) + 2 \text{O}(l) = \text{SiO}_2(s)$. An important nonradiative recombination center in the LPE layer involving oxygen is then being reduced in concentration. Deliberate doping with 10 to 30 ppm oxygen has been observed to reduce both τ and the electroluminescent efficiency of green-emitting LED's (11). In other work, a complex involving Si and oxygen has been observed to be an important nonradiative center when large concentrations of O_2 were added to Si-doped melts (5). Consequently, if the reduction in O_2 concentration of the melt results in the longer minority carrier lifetimes, one should be able to add to the melt an impurity which has a strong affinity for oxygen but is not incorporated into the

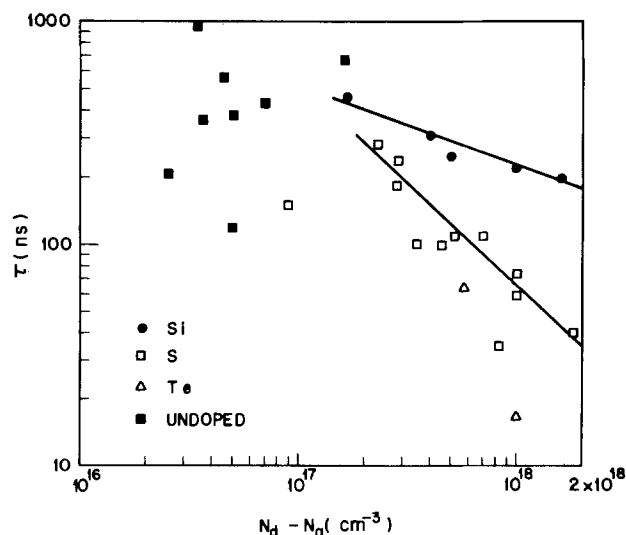
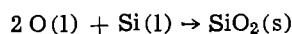


Fig. 3. Minority carrier lifetime as a function of net donor concentration for S-, Te-, and Si-doped LPE layers.

GaP in an appreciable concentration as a means of increasing the minority carrier lifetime. A second possibility is that the shorter lifetimes for $N_d - N_a \gtrsim 5 \times 10^{17} \text{ cm}^{-3}$ in the S- and Te-doped crystals is that the Te and S themselves are involved in the defect limiting the lifetime. In this case, when Si is used as the n-dopant this defect is eliminated.

Discussion and Summary

The background net donor concentration in LPE layers, which is attributed primarily to Si donors, has been observed to fluctuate from $\sim 1 \times 10^{16} \text{ cm}^{-3} \lesssim N_d - N_a \lesssim 2-4 \times 10^{17} \text{ cm}^{-3}$. This behavior is attributed to variations in the oxygen partial pressure (actually H_2O) in the gas ambient which in turn varies the oxygen content of the melt and thus the Si content of the melt via the reaction



The lower the oxygen content of the gas stream, the lower the oxygen in the liquid Ga and the higher the concentration of Si in the melt, and a higher resultant $N_d - N_a$. Thus, a high ($> 1 \times 10^{17} \text{ cm}^{-3}$) value of $N_d - N_a$ is to be expected in undoped LPE layers grown in an oxygen-free system for growths under $\sim 1 \text{ atm}$ of H_2 .

Measurements of the Si concentration in unintentionally Si-doped layers with the ion microanalyzer give absolute numbers for the Si concentration. Fluctuations have been noted in X_{Si}^s from layer to layer which do not correlate with the boat material. Thus, it appears that Si contamination through H_2 reduction of the quartz in the LPE growth system is an important mechanism for Si contamination. The fact that less Si contamination was observed when growth is under 1 atm He compared to 1 atm H_2 is consistent with this conclusion. The observed fluctuations in X_{Si}^s often result in values higher than $N_d - N_a$. In a crystal lightly doped with radioactive Si, X_{Si}^s exceeded $N_d - N_a$ by a decade.

Precipitates of SiO_2 have been observed which are further evidence of Si contamination during LPE growth. A rough estimate shows that the Si contained in these precipitates is consistent with that required in the melt to dope the LPE layers to the 10^{17} cm^{-3} levels.

Measurements of the minority carrier lifetimes of intentionally Si-doped layers have been made. For $N_d - N_a \gtrsim 5 \times 10^{17} \text{ cm}^{-3}$, these values of τ , ~ 200 - 350 ns , are the longest that have been achieved by any means at these doping densities. At lower doping densities it appears that the lifetimes of the Si-doped layers should be comparable to those of the undoped layers. We attribute these long lifetimes in the Si-doped layers to the effects of Si reactions in either the melt or the LPE layer which reduce the concentration of defects which are responsible for limiting τ to the usually observed values. The most probable reaction is the reduction of oxygen in the melt through the formation of SiO_2 .

One should note that the large concentrations of Si (10^{17} cm^{-3} range) that often occur in LPE layers not intentionally Si doped are apparently not limiting τ to values less than several hundred nanoseconds. This amount of Si may even be beneficial by causing the

reduction in concentration of another defect which is more important in limiting τ . However, in green-emitting LED's, the simultaneous doping of the n-layer with N precludes the use of Si as a dopant (16). The Si and N react in the melt forming Si_3N_4 until the melt is depleted in one of the dopants, which, in practice, is Si. In red-emitting LED's Si should be a superior n-dopant to Te, which is now commonly used (17, 18).

Acknowledgments

The authors are indebted to many persons for assistance with this work. L. R. Dawson and K. B. Wolfstirn for the use of unpublished data obtained from radioactive Si doping experiments, J. A. Armstrong and D. D. Roccasecca for LPE crystal growth, S. F. Nygren and D. Dahms for ion microanalyzer measurements. Thanks are also due to L. B. Hooker for time decay measurements, F. A. Trumbore for many helpful discussions, and to R. H. Saul for critical readings of the manuscript.

Manuscript submitted July 8, 1974; revised manuscript received May 20, 1975.

Any discussion of this paper will appear in a Discussion Section to be published in the June 1976 JOURNAL. All discussions for the June 1976 Discussion Section should be submitted by Feb. 1, 1976.

Publication costs of this article were partially assisted by Bell Laboratories.

REFERENCES

1. P. J. Dean, C. J. Frosch, and C. H. Henry, *J. Appl. Phys.*, **39**, 5631 (1968).
2. F. A. Trumbore, H. G. White, M. Kowalchik, C. L. Luke, and D. L. Nash, *This Journal*, **112**, 1208 (1965).
3. F. A. Trumbore, Unpublished.
4. O. G. Lorimor and L. R. Dawson, Paper 212 RNP presented at the Electrochemical Society Meeting, Cleveland, Ohio, Oct. 3-7, 1971.
5. R. Z. Bachrach, O. G. Lorimor, L. R. Dawson, and K. B. Wolfstirn, *J. Appl. Phys.*, **43**, 5098 (1972).
6. P. D. Greene, *J. Phys. D; Appl. Phys.*, **6**, 1552 (1973).
7. M. E. Weiner, *This Journal*, **119**, 496 (1972).
8. A. S. Jordan and M. E. Weiner, *ibid.*, **121**, 1634 (1974).
9. R. Z. Bachrach and O. G. Lorimor, *J. Appl. Phys.*, **43**, 500 (1972).
10. P. D. Dapkus, W. H. Hackett, Jr., O. G. Lorimor, G. W. Kammlott, and S. E. Haszko, *Appl. Phys. Letters*, **22**, 227 (1973).
11. O. G. Lorimor, P. D. Dapkus, and W. H. Hackett, Jr., *This Journal*, **122**, 407 (1975).
12. G. V. Raynor, Editor, "Metallurgical Thermochemistry", Pergamon Press, Oxford (1967).
13. JANAF Thermochemical Tables, Published by U.S. Dept. of Commerce (1965).
14. C. D. Thurmond and C. J. Frosch, *This Journal*, **109**, 144 (1962).
15. D. R. Stull and G. C. Sinke, "Thermodynamic Properties of the Elements," Am. Chem. Soc. Advances in Chem. Series (1956).
16. O. G. Lorimor and M. E. Weiner, *This Journal*, **119**, 1576 (1972).
17. R. C. Vehse and D. D. Manchon, Paper 230 presented at Electrochemical Society Meeting, Miami Beach, Florida, Oct. 8-13, 1972.
18. O. G. Lorimor, R. H. Saul, L. R. Dawson, and C. R. Paola, *Solid State Electron.*, **16**, 1289 (1973).

Influence of an Oxidizing Annealing Ambient on the Distribution of As, Sb, and Ga Implanted into Silicon

H. Müller,¹ J. Gyulai,² W. K. Chu,* and J. W. Mayer*

California Institute of Technology, Pasadena, California 91125

and T. W. Sigmon

Hewlett-Packard Laboratories, Palo Alto, California 94304

ABSTRACT

The redistribution of As, Sb, and Ga implants into silicon during wet oxidation was investigated by MeV He backscattering and channeling techniques. Oxidation produces an accumulation of nonsubstitutional As and Sb at the interface of the advancing oxide front. In contrast, the implanted Ga accumulates at the front surface of the oxide layer. In subsequent diffusion all three species are highly substitutional at concentrations at or below the solubility. Loss of As and Sb is minimal during oxidation or subsequent diffusion; however, for Ga diffusion encapsulation with Si₃N₄ was required.

A number of papers has been published describing the redistribution of diffused impurities (1-4) in Si in an oxidizing ambient. The results of these investigations have shown that n-type impurities accumulate at the oxide silicon interface while p-type impurities are depleted from the substrate.

The purpose of the present investigation was to study the influence of the oxidation process on the distribution and lattice location of a number of implanted dopant species in Si. Since the use of heavily implanted layers is increasing in silicon technology we were interested in determining whether or not the segregation of impurities at a SiO₂/Si interface was different in implanted samples as compared to published work on diffused samples. Based on studies of gettering of heavy metal ions in damaged layers (5) it might be anticipated that Group V dopants, for example, would show enhanced segregation at the interface between damaged Si and SiO₂. Also because oxidation is used to consume the disorder caused by high-dose heavy-ion implants, it is essential to gain information about incorporation of impurities in these oxide layers. It has been reported, for example, in As implants that the As is driven into the Si by use of a high-temperature oxidizing ambient (6).

In the present work, As and Sb were chosen for the n-type species because of their difference in solid solubility. Ga was chosen as a p-type dopant having a similar solid solubility to that of Sb. The thickness of the thermally grown SiO₂ layers was chosen to consume an amount of Si greater than the projected range of the implanted species. Low temperature wet oxidation was used to minimize diffusion of the impurities during the oxidation cycle. Backscattering techniques were used to determine the depth distribution of implanted impurities and channeling was used to determine lattice locations.

Experimental Techniques

The silicon wafers used for this investigation were n-type, 2-4 ohm-cm resistivity of <111> orientation with a low damage surface preparation. Arsenic implantations were performed at 200 keV with doses of $1-2 \times 10^{16}$ cm⁻². The crystals were oriented in a random direction to the beam and the substrate was initially at room temperature. The gallium and antimony implantations were done at 80 keV with doses between

10^{15} and 1.6×10^{16} cm⁻². The annealing in a non-oxidizing ambient was carried out in dry N₂. Thermal oxidation was performed in steam between temperatures of 850° and 1000°C. The carrier gas was pure O₂.

The oxide growth rate has been found previously to depend on the concentration of the impurity species (7, 8). For implanted Si samples, it has been found that the oxide growth rate depends on both impurity concentration and residual damage (9, 10). In both implanted and diffused cases, the change can be characterized by a change in the linear rate constant, the parabolic rate constant remaining roughly the same.

In our case, the oxide thicknesses were determined by backscattering and ellipsometry measurements. For a steam oxidation at 850°C, oxides of about 2400Å were grown in 30 min for a well annealed 2×10^{16} cm⁻² As implant. This thickness is about twice that grown on low concentration n-type Si. For the case of Sb a similar behavior is found. These results are in agreement with those found by Nomura *et al.* on Sb and P implanted Si. The thickness of our oxide layers grown on the Ga implanted samples were found to be about 10-20% less than that of a nonimplanted 2 ohm-cm n-type sample.

Channeling and backscattering measurements were made with 2 MeV ⁴He⁺ ions. The backscattered particles were detected by a surface barrier detector mounted at an angle of 168° to the incident beam direction. For the conversion of energy depth, the stopping cross sections of Ziegler and Chu (11) were used.

Experimental Results

Arsenic implantations.—The implanted distribution was first measured by backscattering, then the samples were oxidized and the distribution remeasured both with the oxide layer and with the layer etched away. Channeling measurements were also performed on annealed samples without the oxide layer. Typical results obtained are shown in Fig. 1. Here, the upper portion of the figure is the random spectrum for a sample implanted with 10^{16} As/cm². The lower portions are spectra taken after oxidation and subsequent oxide removal, respectively.

It can be seen in Fig. 1a, that the broad plateau with a front edge at 1.13 MeV is due to particles backscattered from the Si and the peak at 1.55 MeV corresponds to As. The peak of this As distribution is located approximately 50 keV below the surface position (1.61 MeV) and corresponds to a projected range value of approximately 1100Å (12).

After oxidation of the sample the As distribution (solid curve) is found to shift to lower energies (1.38

* Electrochemical Society Active Member.

¹ Permanent address: Lehrstuhl für Integrierte, Schaltungen, Technical University, Munich, West Germany.

² Permanent address: Central Research Institute for Physics, Budapest, Hungary.

Key words: ion implantation, redistribution of dopants, oxidizing anneal ambient.

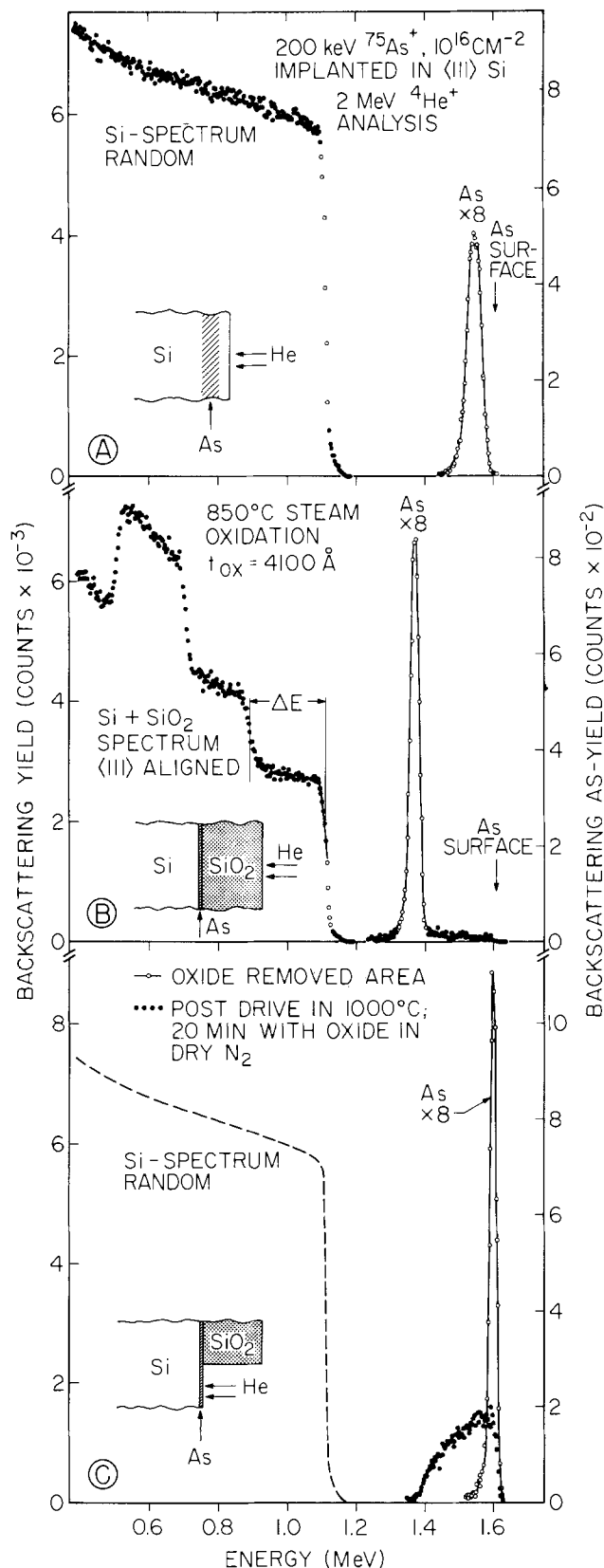


Fig. 1. Random spectra for 2 MeV He^+ backscattered from As-implanted silicon: (a) as implanted, (b) after wet oxidation at 850°C , and (c) after oxide removal. Solid points represent As diffusion profile following 1000°C , 20 min anneal with oxide in place.

MeV in Fig. 1b) and to narrow in width. The step observed in the Si spectrum represents scattering from Si in the SiO_2 layer. The width (ΔE) of the Si step is directly related to the thickness of the SiO_2 layer. The shift of the As signal is also directly related to the depth of the As below the surface. Comparison of the

width of the oxide layer and the position of the As indicates that the As is located at the Si/ SiO_2 interface. Less than 5% of the As atoms are located within the outer regions of the SiO_2 layer as indicated by the sum of the counts in the energy interval 1.4–1.6 MeV.

More details on the width of the As distribution can be obtained by removing the SiO_2 layer. The As signal in Fig. 1c for the oxidized and stripped sample appears at an energy corresponding to the As surface position. The integrated number of counts of the As signal is reduced by about 20% which indicates that there is little loss of the As during the oxide removal in HF. Channeling measurements show the absence of any residual oxide layer within our experimental sensitivity (i.e., less than 5×10^{15} oxygen/ cm^2). The FWHM of this measured As signal corresponds to that of the system resolution. From this result we can determine that the As is confined in a layer which is less than 200Å wide. Tilting the sample by 60° to double the depth to energy conversion did not produce a significant shift in the major portion of the As spectrum confirming that the location of the As is at the silicon surface.

The solid points in Fig. 1c represent the As profile obtained after annealing the sample at 1000°C for 20 min in dry N_2 with the oxide layer in place. Diffusion of the As profile is observed to extend more than 4000Å below the surface. The integrated signal from the As after the diffusion was found to be 5% less than that of the original implant. From this we conclude that little As was lost during the oxidation and diffusion.

During the thermal oxidation of As-implanted Si, the As distribution is determined by the pileup of As at the advancing oxidation front coupled with some diffusion which leads to a spreading away from this front (1). The distribution and lattice location of As are illustrated in Fig. 2 for three samples that had oxide layers grown at 850° , 920° , and 1000°C .

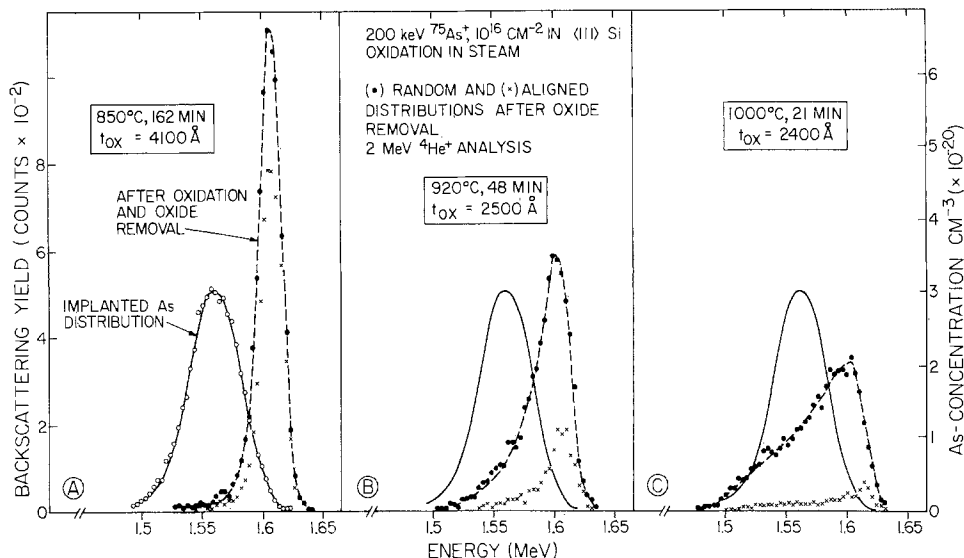
The spectra in Fig. 2 were taken after the oxide layer was removed and are compared with the original distribution (solid line). The 850°C sample (Fig. 2a) exhibits a narrower As distribution after oxidation than the original implant caused by the pileup effect. The aligned $\langle 111 \rangle$ yield is $\sim 75\%$ of the random yield which indicates that the majority of the As is nonsubstitutional after the oxidation.

The As distribution for the sample oxidized at 920°C (Fig. 2b) has a deeper profile and an aligned yield which exhibits peak at the surface. About two-thirds of the As located near the surface is substitutional with an increasing component extending deeper into the crystal. The 1000°C sample has an even deeper distribution which extends 3000Å below the surface and an even higher substitutional component.

Antimony implantations.—Similar to the results obtained with As implantations, Sb is pushed deeper into the sample by the advancing oxide front. The backscattering spectra for $1.2 \times 10^{16} \text{ cm}^{-2}$ Sb implanted at 80 keV and then oxidized at 850°C is shown in Fig. 3. The distribution of the implanted Sb before oxidation is located with the peak at about 370Å below the surface corresponding to R_p (13). After oxidation the major portion of the Sb is located near the Si/ SiO_2 interface. Less than 5% of the Sb is found within the oxide layer, the majority of which is found near the oxide surface. There is a loss of greater than 90% of the Sb during oxide removal. This indicates that either the Sb atoms are incorporated within the SiO_2 layer at the interface, or that the Sb atoms reside at the interface and are removed by HF.

After oxidation, the Sb can be diffused deeper into the Si. The depth distribution of the Sb following oxidation at 850°C and subsequent diffusion in dry N_2 at 1050°C is shown in Fig. 4. With the oxide cap in place, the spectra in Fig. 4 indicate that the majority of the Sb remains near the interface. The deeply penetrating distributions within the Si represent diffusion

Fig. 2. Random spectra for 2 MeV He showing competition between As pileup and diffusional broadening of As-implanted silicon during wet oxidation at different temperatures. Arsenic distributions are shown after oxide removal for the as-implanted condition (solid line) and following oxidation.



of the Sb by standard mechanisms. Removal of the oxide cap reduced the Sb peak at the surface indicating that Sb is located at the interface but did not change the depth distribution for the deeper component. The origin of the depth scale in Fig. 4 was placed at the break of the two profile parts.

The solid curves are calculated for an erfc distribution using an Sb surface concentration C_0 of $3.4 \times 10^{19}/\text{cm}^3$ and a diffusion coefficient $D = 8.0 \times 10^{-15} \text{ cm}^2\text{-sec}^{-1}$ (14). These values are representative of the bulk solubility and diffusion coefficient of Sb in Si. The concentration at this point corresponds to the equilibrium solubility of Sb in Si (15). The data points and the calculated curves are in reasonable agreement suggesting that the Sb distribution is determined by bulk diffusion processes. Channeling effect measurements performed on these samples indicated that greater than 85% of the Sb atoms below the surface are on sub-

stitutional sites while the Sb atoms located near the surface are predominantly nonsubstitutional.

Gallium implantations.—Figure 5 represents 2 MeV ^4He backscattering spectra for a sample implanted at 80 keV with $1.2 \times 10^{16} \text{ Ga}/\text{cm}^2$ before (solid curve) and after (dashed curve) oxidation. In this figure the vertical and horizontal axes of the Ga component were expanded. In the implanted sample, Ga is distributed with a peak about 500 Å below the surface. After oxidation, the gallium distribution is shifted toward the surface and the total amount of Ga decreases by about 20%. The high energy edge of the Ga distribution appears at the sample surface as shown in Fig. 5 and nearly all the remaining Ga is incorporated within the oxide layer. The left-hand portion of Fig. 5 shows the change in the Si spectrum observed after oxidation. The same features are found

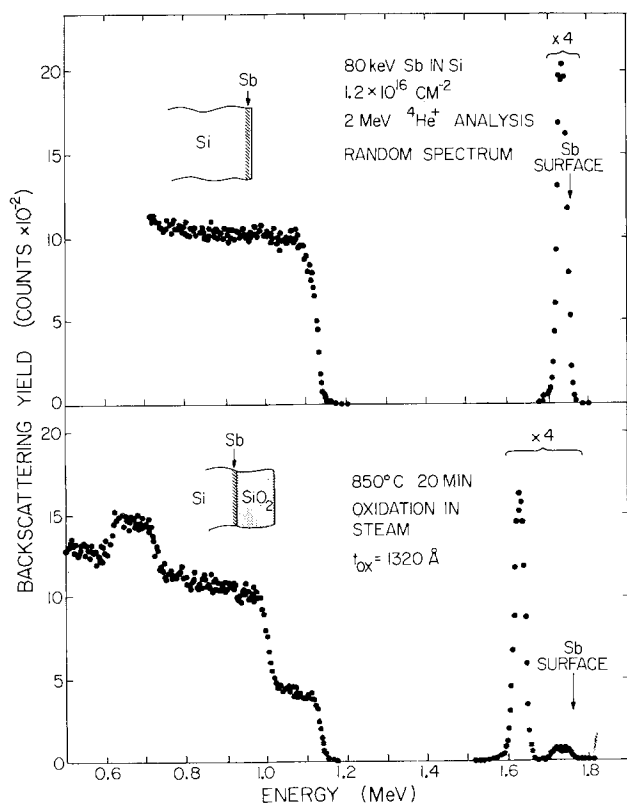


Fig. 3. Backscattering spectra for 2 MeV He^+ on Sb-implanted silicon before and after wet oxidation at 850°C, 20 min.

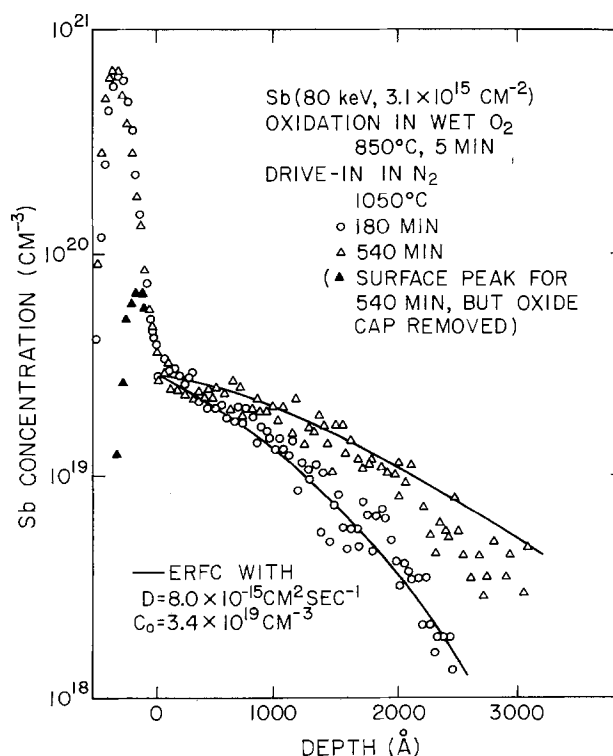


Fig. 4. Sb-drive-in diffusion profiles following wet oxidation at 850°C, obtained by 2 MeV He backscattering on samples with oxide layer in place. Solid triangles show reduction of Sb surface concentration after oxide removal.

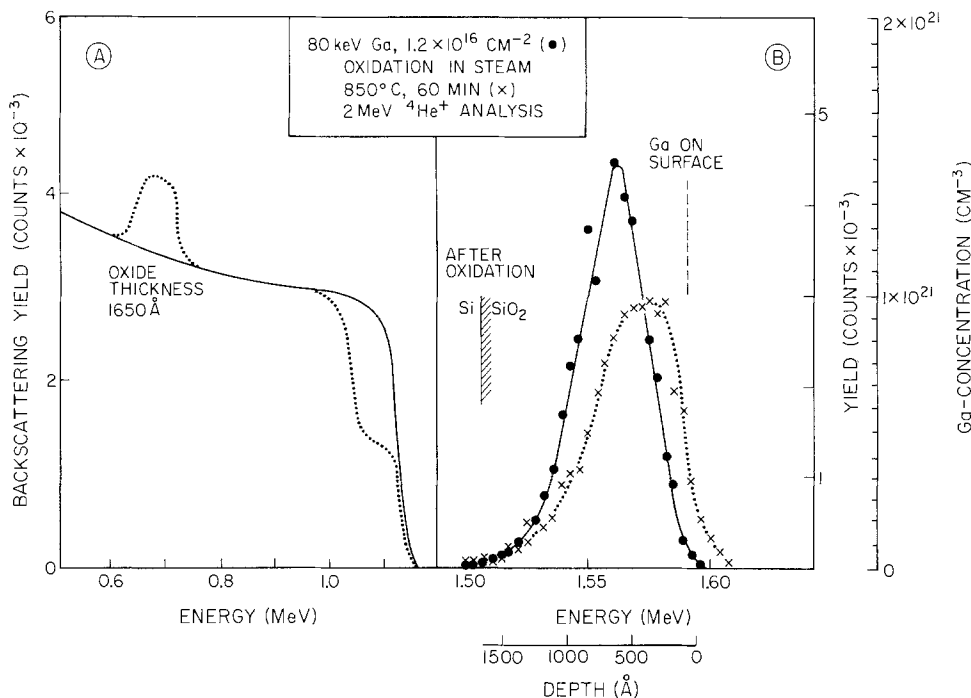


Fig. 5. Random spectra for 2 MeV He on Ga-implanted silicon before and after wet oxidation at 850°C, 60 min. Both the energy and yield scales are expanded for the Ga component. The depth scale is determined for Ga in SiO₂.

as in the case of an As-implanted sample (Fig. 1b) except that the oxide layer is thinner.

Wet oxidation at 850°C was carried out on samples implanted at 80 keV with doses of $0.6\text{--}1.2 \times 10^{16}$ Ga/cm². For all samples there was a shift in the Ga concentration to the oxide front surface and a loss of 20–35% of the total amount of Ga. The maximum concentration of Ga in the Si following these diffusions was less than 8×10^{18} cm⁻³, well below the thermal equilibrium solubility. These results indicate that the Ga is incorporated in the oxide layer. This oxidation cycle is not suitable to act as an encapsulating layer for Ga drive-in diffusions.

As an alternative encapsulating layer, Si₃N₄ was deposited by reactive sputtering. Figure 6 shows random and aligned backscattering spectra for a sample annealed at 1050°C for 45 min after the Si₃N₄ was removed. An almost constant depth distribution for the Ga is observed over the accessible depth (7000 Å). The concentration of the Ga is between 3 and 3.5×10^{19} cm⁻³ which is comparable to the equilibrium solubility at this temperature (15). The dashed curve represents the calculated erfc diffusion distribution using bulk values (14). The disagreement between the experimental data and the calculated curve indicates the enhancement of the Ga penetration during the anneal. The aligned spectrum for this sample indicates that more than 80% of the Ga is on lattice sites.

Discussion and Speculation

Since the diffusion coefficients (extrapolated) of As and Sb in SiO₂ are $\sim 1/10\text{--}1/100$ of that in Si at the temperatures of 805°–1000°C, the pileup of these two impurities at the oxidation interface will be a function mainly of the oxidation temperature. At higher temperatures ($> 1000^\circ\text{C}$) the diffusion velocity of As and Sb is higher than the oxidation front velocity and they diffuse away from the advancing oxidation front. In the case of As the diffusion coefficient is known to be concentration dependent (16) so the transition between pileup and diffusion may be also expected to depend on total implanted dose.

For the As there appears, even at 850°C, a substitutional component (Fig. 2) indicating that substitutional incorporation in the lattice is starting to take place. However, for Sb there is no evidence for substitutional incorporation at 850°C. We believe that for both Sb and As the dopant accumulates at the

interface. Although the evidence is indirect for Sb it is rather clear for As. This speculation disagrees with the recent findings of Chou *et al.* for phosphorus in Si.

The situation is much less clear for Ga. Competition between the oxidation of the Ga and Si can lead to the formation of (Ga₂O₃)_xSiO₂. Presently, we have no direct evidence that the Ga accumulation at the outer surface of the SiO₂ layer is caused by the oxidation of the Ga.

It is evident (Fig. 6) that encapsulation of the implanted sample with Si₃N₄ can prevent the interaction of oxygen with Ga. The anomalous feature of our data is the enhanced penetration of the Ga under the Si₃N₄ layer. We speculate that this is due to lattice strain caused by the mismatch of the expansion coefficients between Si₃N₄ and Si.

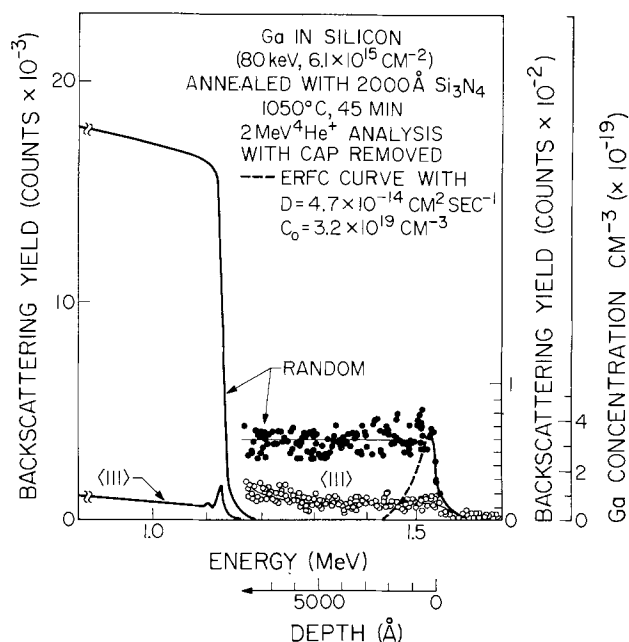


Fig. 6. Backscattering spectra for 2 MeV He⁺ on Ga-implanted silicon after drive-in diffusion at 1000°C, 45 min using sputtered Si₃N₄ as a protective encapsulating layer.

Summary

The most pronounced feature of the low temperature oxidation of As and Sb implanted samples is the pileup effect where the implanted dopant accumulates at the advancing oxide interface.

For As, the low temperature oxidation results in a nonsubstitutional accumulation at the advancing oxide front. At higher oxidation temperatures (920°, 1000°C) the As profile exhibits diffusional broadening and an increased substitutional component. The backscattering data show that the maximum concentration of As in Si to that in SiO₂ is greater than a factor of 50. It is found that less than 5% of the As is lost during the oxidation.

For the Sb case a somewhat greater amount (up to 10-20%) is found in the SiO₂ layer. There is also a pileup of Sb at the front surface of the oxide layer. With the oxide layer in place, the Sb at the interface acts as a diffusion source. The resultant diffusion profiles follow an erfc distribution, described by bulk values of the Sb concentration and diffusion coefficient. Channeling effect measurements showed that the diffused Sb profile was highly substitutional.

For the case of As, we find that the As is incorporated in the Si at the interface. This result differs from that of Chou *et al.* (4) for thermal oxidation of phosphorus-doped Si. They found that a phosphorus-rich layer was located in the SiO₂ film near the interface but not in the silicon substrate. Our results for Sb show that the Sb either resides in the oxide layer near the interface or is at the interface and dissolved by HF.

In contrast to the results with implanted Sb and As the implanted Ga accumulates at the front surface of the oxide layer and therefore does not act as a diffusion source. The maximum Ga concentration in Si was less than $8 \times 10^{18} \text{ cm}^{-3}$, well below the value for the equilibrium solubility. As an alternative procedure we found that sputter-deposited Si₃N₄ acted as a protective cap layer during drive-in diffusion. The Ga concentration at the surface was at the thermal equilibrium solubility and channeling effect measurements showed that the Ga was highly substitutional. However, the penetration is anomalously deep.

Acknowledgments

The authors wish to acknowledge the assistance of Jim Hansen of Hewlett-Packard, who provided As-implanted samples and of E. Pasztor from the implantation group at the Central Research Institute

for Physics, Budapest, who provided Ga and Sb implants. We wish to thank Fred Eisen for helping us by providing cap layers. This work is part of the Caltech-Central Research Institute for Physics joint program, sponsored by the National Science Foundation and the Institute of Cultural Relations, Budapest.

Manuscript submitted Dec. 9, 1974; revised manuscript received May 12, 1975. This was Paper 125 presented at the Toronto, Canada, Meeting of the Society, May 11-16, 1975.

Any discussion of this paper will appear in a Discussion Section to be published in the June 1976 JOURNAL. All discussions for the June 1976 Discussion Section should be submitted by Feb. 1, 1976.

Publication costs of this article were partially assisted by California Institute of Technology.

REFERENCES

1. A. S. Grove, O. Leistiko, Jr., and C. T. Sah, *J. Appl. Phys.*, **35**, 2695 (1964).
2. R. N. Ghostagore, *Phys. Rev. Letters*, **25**, 856 (1970).
3. B. E. Deal, A. S. Grove, E. H. Snow, and C. T. Sah, *This Journal*, **112**, 308 (1965).
4. N. J. Chou, Y. J. van der Meulen, R. Hammer, and J. Cahill, *Appl. Phys. Letters*, **24**, 200 (1974).
5. T. E. Seidel, R. L. Meek, and A. G. Cullis, *J. Appl. Phys.*, **46**, 600 (1975).
6. A. U. MacRae, Proc. 2nd Intern. Conf. on Ion Implantation in Semiconductors, I. Ruge and J. Graul, Editors, p. 329, Springer-Verlag, Berlin (1970).
7. B. E. Deal and M. Sclar, *This Journal*, **112**, 430 (1965).
8. W. A. Pliskin, *IBM J. Res. Develop.*, **10**, 198 (1966).
9. G. Fuller, Hewlett-Packard, Private communication.
10. K. Nomura, Y. Hirose, Y. Akasaka, K. Horie, and S. Kawazu, Proc. IV Intern. Conf. Ion Implantation in Semiconductors and Other Materials, Osaka, Japan, p. 681, Plenum Press, New York (1975).
11. J. F. Ziegler and W. K. Chu, *Atomic Data and Nucl. Data Tables*, **13**, 463 (1974).
12. T. W. Sigmon, W. K. Chu, H. Muller, and J. W. Mayer, *Appl. Phys.*, **5**, 347 (1975).
13. W. S. Johnson and J. F. Gibbons, "Projected Range Statistics," Distributed by Stanford University Bookstore (1970).
14. B. I. Boltaks, "Diffusion in Semiconductors," Academic Press, New York (1963).
15. F. A. Trumbore, *Bell System Tech. J.*, **39**, 205 (1960).
16. R. B. Fair and G. R. Weber, *J. Appl. Phys.*, **44**, 273 (1973).

Investigations of the Fabrication of Thin Silicon Films for Microwave Semiconductor Transit Time Devices

Jürgen Freyer

Institut für Allgemeine Elektrotechnik der Technischen Universität München, 8 München 2, Germany

ABSTRACT

The fabrication of thin silicon films for microwave semiconductor devices is investigated using polishing and etching methods. With the described bubble etching method the thickness of the Si film can be monitored during etching. Si-films with a thickness down to 3 μm could be fabricated with this process. The etched films are free of strain and etch pits and are sufficiently plane parallel as required by microwave transit devices. The fabrication of an MnM Baritt diode and a double diffused Impatt diode without substrate is given as example.

For application in microwave semiconductor devices very thin semiconductor layers or films are useful, for example for Impatt, Baritt, or pin diodes. The

Key words: etching, polishing, Impatt diodes, Baritt diodes.

thickness of these films varies between 2 and 10 μm depending on the application. For Impatt diodes without any substrate [MnM-Impatt diodes (1)] silicon films with a thickness of 4 μm are required for X-band

frequencies. For Baritt diodes in the same frequency range the film thickness must be about 8-10 μm (2, 3). The semiconductor layers in any case have to be plane parallel, free of strain and of dislocations, and without any damage at the surface. To meet these requirements the fabrication of thin silicon films was investigated by polishing and etching methods.

Polishing

In order to achieve the required thin silicon films the reduction of the thickness first was performed by polishing. The base, the polish, and the pressure on the silicon slice during polishing could be varied. Plane glass plates and Pellon cloths on plane glass plates were used for the base. The Pellon cloths had different degrees of hardness. The polish was Al_2O_3 powder (0.25 μm ϕ), diamond paste (1 μm ϕ), and Lustrox.¹ The apparatus used for thinning slices was the same as for conventional mechanical lapping and polishing and was similar to that used by Mash *et al.* (4) who fabricated silicon slices down to 10 μm . Thinning was also performed using a vibration polishing machine. Above 10 μm the thickness of the films can be measured with an accurate dial gauge, below 10 μm the thickness must be measured by the aid of the transparency colors of the silicon because the pressure of the dial gauge would damage the thin film.

In Table I the results from polishing are summarized for two thickness ranges of the films: 10-15 and 4-6 μm . In the last two rows in Table I the results using a vibration polishing machine are also listed. The surface of these polished slices often is not plane but convex and has an orange skinlike structure. The dislocation density caused by polishing was high on all polished films and became higher if the pressure on the silicon slices during polishing was exceeded.

Etching

The polished silicon slices show many disadvantages for many applications for solid-state devices; *i.e.*, the dislocation density caused by polishing is high at the polished surface and the slices are often crumbly especially for very thin films. Therefore, in the following work the silicon slices are thinned only by etching. Unvala *et al.* (5) describe a large-scale process for the fabrication of thin semiconductor layers but the thickness of the layers is limited to about 20 μm . Theunissen *et al.* (6) developed a preferential electrochemical etching process with which very thin

silicon films can be fabricated. One disadvantage, however, is that a special doping structure of the initial material is needed and that an additional layer has to be etched away.

Generally bubbles of gaseous reaction products at the surface of the slices to be thinned lead to non-uniform etching. One method to remove these bubbles is the use of a rotating beaker. The results of this method are also listed in Table I. In the following an etching method is described which is especially sensitive for the fabrication of thin films (<10 μm). The etching process is similar to that published by Stoller *et al.* (7) who fabricated slices with a thickness less than 25 μm . With this described bubble etching method thin films down to 3 μm could be attained. The determination of the thickness is performed during etching and the thickness is monitored by means of the transparency colors.

Figure 1 shows a schematic cross section of the etching apparatus. The apparatus consists of a Teflon or polyethylene vessel which at the bottom has a thin polyethylene plate perforated with many holes 0.1 mm in diameter. Carbon dioxide is blown through these holes under low pressure. In this way bubbles rise into the upper volume which is filled with the etching solution. The silicon slice which is fixed on a quartz plate with beeswax is slowly rotated in this etching solution to ensure uniform etching.

To investigate the etching process more in detail several parameters were varied: the ingredients of the etching solution, the pressure and the rate of flow of carbon dioxide, respectively, and the rotation velocity of the sample. If the sample is not rotated a concave surface results; on the other hand a convex surface is obtained if the silicon sample is only rotated and if the rotation velocity is too high. It has been found that the etched films are plane if the sample is alternately rotated and not rotated during etching and if the ratio of the rotation time to the time without rotation is 2:1. In this case the rotation velocity has a value of 8 rpm. Similar to the rotation of the sample the pressure respectively the rate of flow of the gas influences the plane parallelism of the film. A high rate of flow brings a lot of whirls into the etching solution and a too low flow is not sufficient to remove the gaseous reaction products from the surface: in both cases a nonuniform etching results. A rate of flow of 4 liters/min gave the best results with the described etching apparatus.

The ingredients of the etching solution normally have no influence on the plane parallelism of the

¹ Lustrox: trademark.

Table I. Quality of thinned silicon films for several polishing and etching methods. Two thickness ranges 10-15 and 4-6 μm have been investigated

Polishing method	Thickness of the Si-film, μm	Quality of the Si-films ^(b)			
		Plane parallelism of the whole slice	Solidity of the slice	Properties of the surface	Dislocation density caused by polishing
Diamond paste on glass plate	10-15	+	- crumbly	○ crashes	-
	4-6	+	- crumbly	○ crashes	- high
Al_2O_3 -powder on glass plate	10-15	+	-	+	-
	4-6	+	- crumbly	+	- high
Diamond paste on Pellon cloth (hard)	10-15	○	○	+	- high
	4-6	○	- fragile	○ sometimes crashes	- high
Al_2O_3 -powder on Pellon cloth (soft)	10-15	- convex	+	+	○ fairly high
	4-6	- convex	○ sometimes crumbly	+	○ fairly high
Lustrox on Pellon cloth (hard)	10-15	+	+	+	- high
	4-6	+	○ sometimes crumbly	+	- high
Lustrox on Pellon cloth (soft)	10-15	- convex	+	+	○ fairly high
	4-6	- convex	○	+	○ fairly high
Vibration polishing machine (Al_2O_3 -powder, hard Pellon cloth)	10-15	○ orange skin	+	+	○
	4-6	○ orange skin	○ sometimes crumbly	+	○
Vibration polishing machine (Al_2O_3 -powder, soft Pellon cloth)	10-15	- orange skin, convex	+	+	○
	4-6	- orange skin, convex	○	+	○
Stirring etching method ^(a)	10-15	+ sometimes convex	+	+	+ { no additional dislocations
	4-6	○ sometimes convex	+	+	+ { no additional dislocations

^(a) The determination of the thickness during etching is difficult.

^(b) + = good, ○ = medium, - = bad.

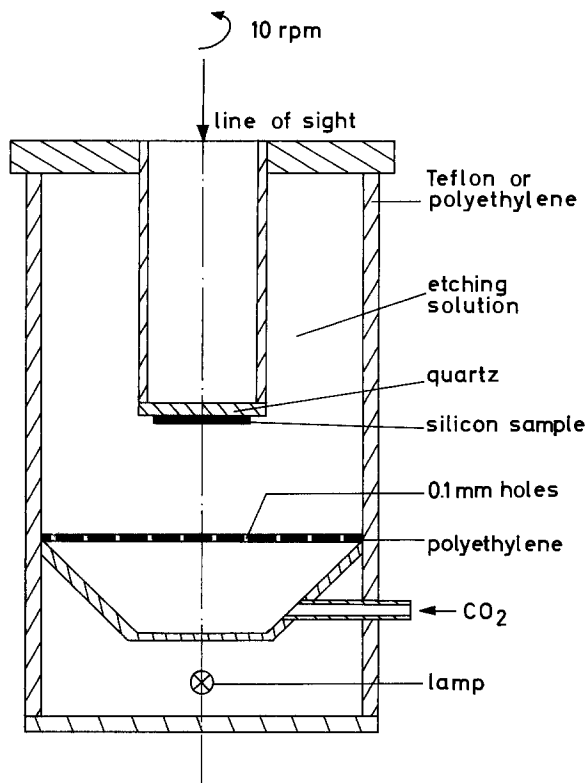


Fig. 1. Schematic cross section of the etching apparatus for the fabrication of thin silicon films.

sample but on the surface behavior. As etching solution only a mixture of nitric acid and hydrofluoric acid was used. Other additional ingredients such as glacial acetic acid often lead to bad surface characteristics such as high etch pit density and passivation layers. The etching solution used with the described bubble etching method consists of a mixture of 10 parts HNO_3 (65%) and one part HF (50%) resulting in an etching rate of 12-15 $\mu\text{m}/\text{min}$ depending on the material, i.e., on the dislocation density of the material.

The thickness of the silicon films is monitored during etching by means of the transparency colors. For calibration, thin silicon films were fabricated and their thicknesses were measured by the aid of a microscope. In this way each thickness can be coordinated to a transparency color. Using the apparatus shown in Fig. 1, the color changes from brown to light yellow in a thickness range of 15-1 μm can be observed. The etching process can be stopped immediately when the color corresponding to the desired thickness appears.

With the aid of this bubble etching process silicon films with a thickness down to 3 μm could be fabricated reproducibly. The deviation of the plane parallelism is less than 0.3 μm over the whole area of the silicon film (the used silicon slices had an area of approximately 1 cm^2), even if the initial material has a thickness of approximately 200-300 μm .

Device Fabrication

Normally silicon epitaxial wafers with a total thickness of approximately 200 μm are used as initial material for the fabrication of microwave semiconductor transit time devices. The entire substrate and part of the epitaxial layer are etched away until the desired

thickness of the silicon film is reached. It is advantageous to use epitaxial wafers because the exact doping concentration of the epi-layer can be obtained easily, the epitaxial layer is plane and free of damages, and no additional dislocations at the surface are generated by polishing.

Baritt diodes and Impatt diodes have been produced using the thin films fabricated with the described bubble etching method. For MnM Baritt diodes (for X-band frequencies) silicon layers in the thickness range of 7-10 μm are needed. On both sides of the n-layer a Schottky contact is performed and after plating a heat sink on one side, standard photoresist technology is applied on the other side for separating the diodes by mesa etching. By the aid of the thin silicon films it was possible to investigate the behavior of MnM-Baritt diodes (2) which can find application as local oscillators for communication systems.

In a similar fabrication process double-diffused X-band Impatt diodes without any substrate have been fabricated. The initial silicon films had a thickness of 6-7 μm and were simultaneously diffused on one side with p^+ and on the other side with n^+ . By this means it was possible to fabricate Impatt diodes with two very abrupt junctions. The advantage of such a structure in comparison to a diode with epitaxial transitions is a smaller series resistance and a resulting higher efficiency and power output (8). The efficiency of these diodes could be increased from 6.5 to 11.5% at a power output of 0.8W.

Conclusion

The fabrication of thin films for microwave semiconductor devices has been investigated. Thin silicon films which satisfy the requirements for microwave transit time devices such as plane parallelism, good surface characteristics, and a minimum of dislocations can be obtained by the bubble etching method. The minimum thickness of the slice was 3 μm even if the initial material has a thickness of more than 200 μm . The measurement of the thickness is performed by the aid of the transparency colors of the silicon during etching. With these thin silicon films MnM-Baritt diodes and double diffused Impatt diodes without any substrate have been fabricated.

Acknowledgment

The author thanks W. Harth for many helpful discussions and the Deutsche Forschungsgemeinschaft for financial support.

Manuscript submitted Feb. 3, 1975; revised manuscript received May 19, 1975.

Any discussion of this paper will appear in a Discussion Section to be published in the June 1976 JOURNAL. All discussions for the June 1976 Discussion Section should be submitted by Feb. 1, 1976.

REFERENCES

1. M. Claassen, Patent pending.
2. J. Freyer, M. Claassen, and W. Harth, *AEÜ*, **26**, 150 (1972).
3. D. J. Coleman and S. M. Sze, *Bell System Tech. J.*, **50**, 1695 (1971).
4. D. H. Mash, G. D. Henshall, and B. A. Eales, *J. Phys. D: Appl. Phys.*, **3**, 1199 (1970).
5. B. A. Unvala, D. B. Holt, and Aung San, *This Journal*, **119**, 318 (1972).
6. M. J. J. Theunissen, J. A. Appels, and W. H. C. G. Verkuylen, *ibid.*, **117**, 959 (1970).
7. A. I. Stoller, R. F. Speers, and S. Opresko, *RCA Rev.*, **31**, 265 (1970).
8. J. Freyer, To be published.

Diffusion of Ion-Implanted B in High Concentration P- and As-Doped Silicon

Richard B. Fair* and Paul N. Pappas

Bell Laboratories, Reading, Pennsylvania 19604

ABSTRACT

The diffusion of ion-implanted B in Si in the presence of a uniform background of high concentration P or As has been studied by correlating numerical profile calculations with profiles determined by secondary-ion mass spectrometry (SIMS). Retarded B diffusion is observed in both As- and P-doped Si, consistent with the effect of the local Fermi-level position in the Si bandgap on B diffusivity, D_B . It is shown that D_B is linearly dependent on the free hole concentration, p , over the range $0.1 < p/n_{ie} < 30$, where n_{ie} is the effective intrinsic electron concentration. This result does not depend on the way in which the background dopant has been introduced (implantation predeposition or doped-oxide source), nor the type of dopant used (P or As).

In earlier papers (1, 2) the theory was discussed that the diffusion of B in Si is controlled by donor-type monovacancies. This model predicts that the diffusivity of B increases linearly with B concentration for $C_B > n_i$ when the concentration of n-type dopants, C_N , is $\ll n_i$. The combined observations of many workers verify this fact. It has also been demonstrated (2) that the diffusivity of B in uniform As-doped Si ($C_N \approx 1.5 \times 10^{20} \text{ cm}^{-3}$) is retarded approximately linearly with the decrease in the normalized hole concentration, p/n_i , also predicted by the donor-type monovacancy model. Some ambiguity may exist in interpreting these results, since the retarded diffusion of B in Si in the presence of a diffusing As layer has been attributed to other effects (3, 4). Therefore, additional data have been obtained by implanting and diffusing B into uniform P- and As-doped Si layers. Retarded B diffusion in both P- and As-doped Si has been observed, consistent with the theory of a Fermi-level-controlled concentration of donor-type vacancies which directly affect B diffusivity. The significance of this result is that transistor modeling programs must take this first-order effect into account, since the diffusion of B in the presence of n-type dopants is invariably encountered. Examples of numerically calculated B diffusion profiles in n-type Si are presented in which the local diffusivity is determined from the local hole concentration, p . Heavy-doping effects (5) on the Fermi-level calculation are included. These calculations are compared with experimental profiles obtained by secondary-ion mass spectrometry (SIMS) analysis.

Experimental

Ion-implantation and doped-oxide source diffusions were both used to introduce P and As into Si slices. Silicon slices [(100) orientation, 1 ohm-cm, p-type] were implanted with $5 \times 10^{15} \text{ cm}^{-2}$, 50 keV P, and then were diffused at 1050°C for 45 min in a N_2/O_2 ambient. In other slices, arsenic implantations were performed ($5 \times 10^{15} \text{ cm}^{-2}$, 50 keV), and these samples were diffused at 1050°C for 2 hr, also in N_2/O_2 . In both cases, $\sim 600\text{\AA}$ of SiO_2 grew on the Si surface, which was retained through the subsequent B implantation. P- and As-doped oxide depositions were performed on another group of Si slices, and diffusions were performed in O_2 at 1050°C for 2 hr. The oxide sources were etched off in HF prior to the subsequent B implantations.

B was implanted into all of the slices at $1 \times 10^{15} \text{ cm}^{-2}$, 50 keV. Diffusion was performed at 1050°C for 23 min in N_2 . The B and n-type dopant diffusion profiles were determined by mass analysis of secondary ions ejected from the samples by 15 keV oxygen ion

bombardment (predominantly O_2^+) using a Cameca IMS-300 Ion Analyzer. Secondary ions were selected and counted using an AS-200 multichannel analyzer. The analyzer data were converted to impurity concentrations by measuring the depths of the sputtered holes in the samples, and from calibration achieved by knowing the total implanted dose in the Si. For the diffused P and As profiles, spreading resistance measurements were used to establish the surface concentrations and, thus, the calibration for the SIMS data.

Analysis

The coupled diffusion equations for C_B and C_N have been described previously (3, 4). These equations were solved numerically by transforming them into explicit differential-difference equations and by integrating with respect to time by the Runge-Kutta technique. Since the B was implanted to a known dose in all cases, the accuracy of the numerical results was checked by the equation

$$\int_0^\infty C_B(x, t) dx = \int_0^\infty C_B(x, 0) dx \quad [1]$$

which stipulates the conservation of the total B concentration.

The local B diffusivity was calculated according to the equation

$$D_B = D_i(p/n_{ie}) \quad [2]$$

where $pn = n_{ie}^2$ [effective intrinsic electron concentration at the diffusion temperature (5)], D_i is the intrinsic diffusion coefficient

$$p/n_{ie} = \exp(-(E_F - E_{Fi})/kT) \quad [3]$$

is the normalized free hole concentration, and E_F is the local Fermi level. Calculations of E_F have been made by Jain and Van Overstraeten, taking into account band-tailing and impurity-band formation (heavy-doping effects). Their results have been approximated over limited concentration ranges and for three diffusion temperatures are

$$1000^\circ\text{C} \quad E_F = -0.4 + 0.074 \ln\left(\frac{C_N}{10^{19}}\right) + 0.041\left(1 - \frac{C_B}{10^{20}}\right) \quad [4]$$

$$1100^\circ\text{C} \quad E_F = -0.35 + 0.083 \ln\left(\frac{C_N}{3 \times 10^{19}}\right) + 0.036\left(1 - \frac{C_B}{10^{20}}\right) \quad [5]$$

* Electrochemical Society Active Member.
Key words: boron diffusion, cooperative diffusion, profile calculations, secondary ion mass spectrometry.

1200°C

$$E_F = -0.36 + 0.077 \ln \left(\frac{C_N}{3 \times 10^{19}} \right) + 0.03 \left(1 - \frac{C_B}{10^{20}} \right) \quad [6]$$

for $10^{19} < C_N < 5 \times 10^{20} \text{ cm}^{-3}$ and $0 < C_B < 2 \times 10^{20} \text{ cm}^{-3}$. The intrinsic Fermi level is calculated from the equation

$$E_{F1} = -\frac{E_g(T)}{2} - 0.0133 \left(\frac{T}{300} \right) \quad [7]$$

where $E_g(T)$ is the silicon bandgap given by

$$E_g(T) = 1.156 - \frac{7.02 \times 10^{-4} T^2}{(T + 1108)} \quad [8]$$

Results

An example of B diffusion in Si with a pre-diffused P layer ($R_S = 46 \text{ ohms}/\square$, $x_J = 1.5 \mu\text{m}$, doped-oxide source) is shown in Fig. 1. The agreement between the SIMS data and the calculated final P and B profiles is quite good. The B diffusivity calculated during the final time increment of the Runge-Kutta integration is also shown plotted as a function of depth. The resulting B profile when diffusion was performed in a P implanted-diffused sample is shown in Fig. 2. The average P doping over the B-doped region was $\sim 1.5 \times 10^{20} \text{ cm}^{-3}$. As a result, even less relaxation of the implanted B has occurred than is shown for the case in Fig. 1. The average diffusivity of the B in Fig. 2 was $\sim 1.5 \times 10^{-14} \text{ cm}^2/\text{sec}$ which is 0.2 times D_i . These results show unambiguously that the B diffusivity is reduced by the presence of the P.

The sensitivity of the redistribution of the implanted B layer to background n-type doping is illustrated in Fig. 3. The calculated curves show the final B profiles following a 1050°C, 23 min diffusion for several uniform background concentrations of n-type dopant. The SIMS data were taken from a slice with a pre-diffused

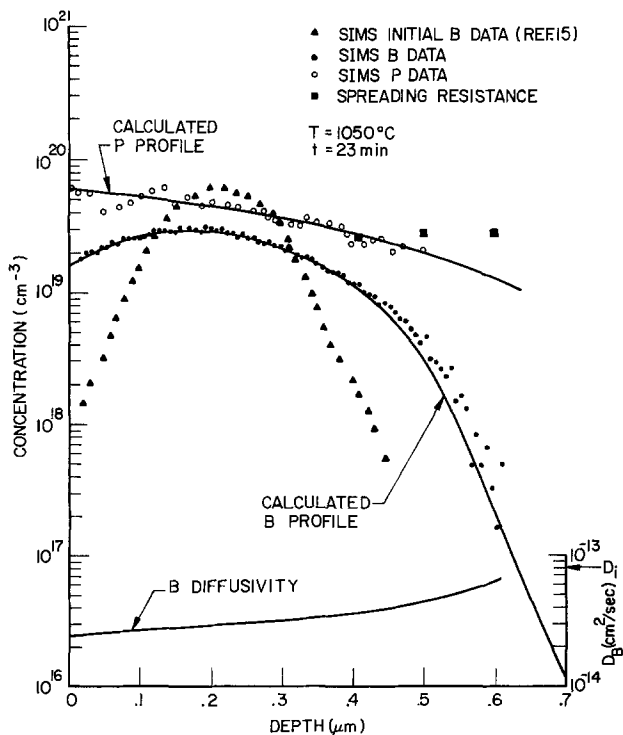


Fig. 1. Experimental SIMS data of as-implanted B ($1 \times 10^{15} \text{ cm}^{-2}$, 50 keV: ▲ data), the subsequently diffused B (1050°C, 23 min in N_2 : ● data), and the background P doping (○ data) introduced from a doped-oxide source (1050°C, 2 hr in O_2) before the B implant. The calculated B and P profiles are shown as well as the calculated B diffusivity as a function of depth.

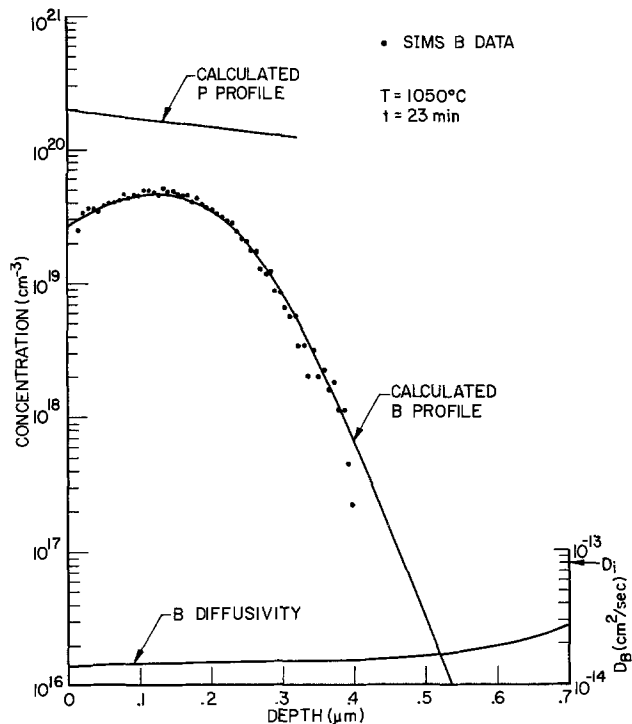


Fig. 2. Experimental SIMS data of B implanted through 600Å of SiO_2 ($1 \times 10^{15} \text{ cm}^{-2}$, 50 keV) and diffused at 1050°C for 23 min in N_2 . The background doping is implanted P ($5 \times 10^{15} \text{ cm}^{-2}$, 50 keV), diffused at 1050°C for 45 min prior to the B implantation. Calculated profiles and the B diffusivity are also shown.

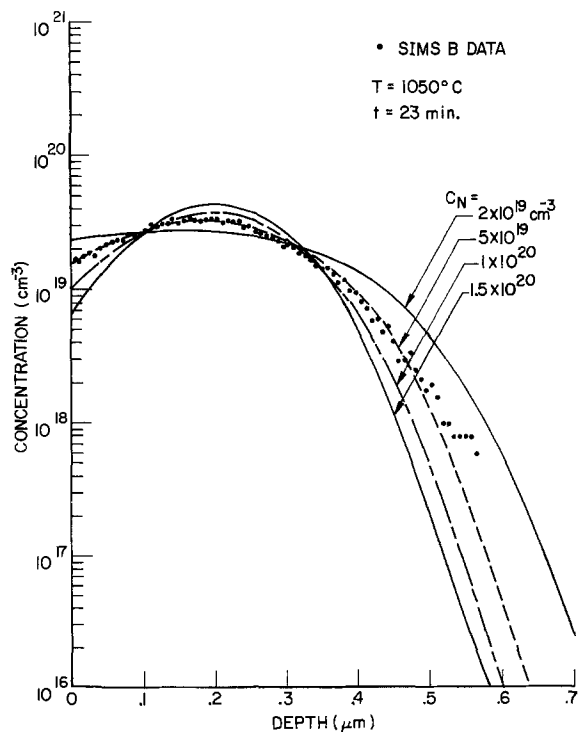


Fig. 3. Calculated B profiles as a function of n-type background doping, C_N . Experimental SIMS data of B ($1 \times 10^{15} \text{ cm}^{-2}$, 50 keV) diffused at 1050°C for 23 min in N_2 in a P-diffused (doped-oxide source) background ($R_S = 16 \text{ ohms}/\square$, $x_J = 2.1 \mu\text{m}$, $C_N \approx 5 \times 10^{19} \text{ cm}^{-3}$).

P layer ($R_S = 16 \text{ ohms}/\square$, $x_J = 2.1 \mu\text{m}$, doped-oxide source).

For the case of B diffusion in the presence of As, experimental and calculated profiles are shown in Fig. 4. The As was implanted and then diffused in this sam-

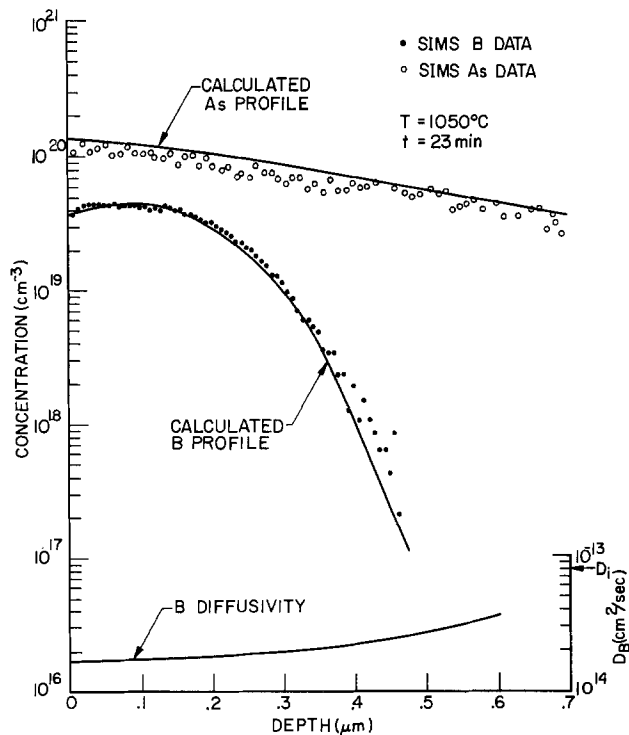


Fig. 4. Experimental SIMS data of B implanted through 600Å of SiO₂ ($1 \times 10^{15} \text{ cm}^{-2}$, 50 keV) and diffused at 1050°C for 23 min in N₂. The background doping is implanted As ($5 \times 10^{15} \text{ cm}^{-2}$, 50 keV), diffused at 1050°C for 2 hr prior to B implantation. Calculated profiles and the B diffusivity are also shown.

ple. A similar reduction in the B diffusivity is observed.

To summarize the published results on B diffusion (and Ga diffusion), normalized diffusivity is plotted vs. p/n_{ie} in Fig. 5. The data representing B diffusion in n-type Si (this study) were obtained by averaging D_B and p/n_{ie} over the diffused B regions. Also included is the data of Crowder *et al.* (2) (Δ and \circ) which has been corrected in terms of the p/n_{ie} ratio which takes into account the effects of heavy doping on band structure. The type of n-type dopant background is indicated next to each data point. By considering the previously published data (1) from B diffusions into lightly doped substrates, it can be seen

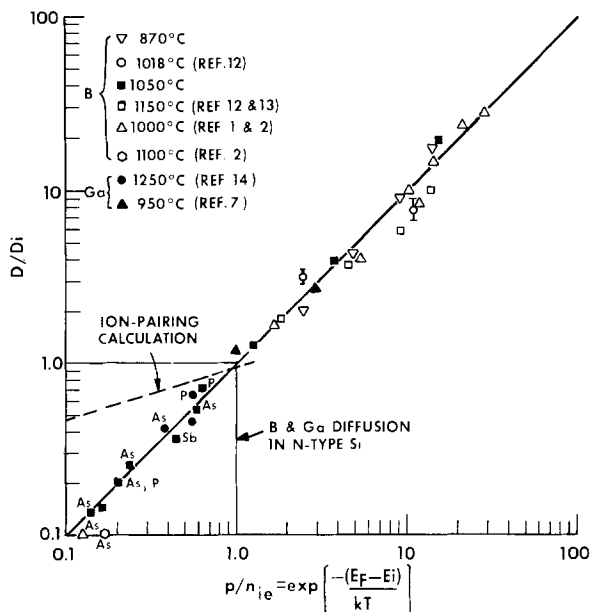


Fig. 5. Diffusivity of boron and gallium in silicon as a function of the normalized hole concentration.

that D_B/D_i is linear with p/n_{ie} over 2½ orders of magnitude. These latter data are plotted by assuming that $n_{ie} \approx n_i$, since it has been shown that heavy-doping effects on band structure are less pronounced in degenerate p-type Si as compared with degenerate n-type Si (6). All of the data shown (for $p/n_{ie} > 1$) were obtained from B diffusions with surface concentrations less than $2 \times 10^{20} \text{ cm}^{-3}$. Above this concentration, heavy-doping effects certainly should not be neglected.

Also shown in Fig. 5 is previously published Ga diffusivity data. These results indicate that Ga diffusion in Si is also controlled by the position of the Fermi level in the bandgap, which was pointed out by Makris and Masters (7). These authors concluded that a donor-type vacancy is probably responsible for Ga diffusion in Si.

Discussion

Arguments supporting the donor-type monovacancy diffusion model have been previously discussed (1, 2, 7). The data reported in this paper provide additional support for the concept of a simple, positively charged defect being responsible for B diffusion in Si when the diffusion ambient is a nonoxidizing ambient. The additional influence of Si self-interstitials extrinsically generated at an oxidizing Si surface have been discussed previously (1, 8). The conclusion that the donor-type monovacancy is the primary defect which controls B diffusion is based on the following observations:

1. Both quenching and diffusion experiments indicate that the dominant native defect in high temperature silicon has an entropy of $\sim 5k$ (k = Boltzmann constant). This value is much too large for simple neutral monovacancies or interstitials, nor can the existence of divacancies, semivacancy pairs, or similar complexes be used to explain this result (9). However, the entropy of ionization of the vacancy is quite large at high temperatures. Thus, the large entropy associated with the dominant defect can be accounted for by the entropy of formation of the neutral vacancy ($1.1k$) plus the ionization entropy of the vacancy ($5.1k$), which is within the experimental uncertainty of the measured value (10).

2. The defect involved in atomic diffusion could not be a self-interstitial because the energy of formation of interstitials is too large and their migration is too rapid and athermal (10).

3. The existence of a vacancy in the Si lattice will cause a perturbation such that states will be split from the valence and conduction bands of the surrounding atoms a few tenths of an electron volt into the bandgap (10). Thus, the energy levels associated with simple donor- and acceptor-type vacancies are such that at high temperatures both V^+ and V^- would be more numerous than neutral vacancies.

4. The quenching experiments of Elstner and Kamp-rath (11) indicate that an energy level exists at $E_v + 0.37 \text{ eV}$ associated with donor-type complexes in p-type Si samples. The effect of vacancy association should shift the ionization energy of the donor level by only a small amount. Assigning the $E_v + 0.37 \text{ eV}$ level to a V^+ vacancy means that above 800°K, V^+ is the dominant charge state of the monovacancy in p-Si.

It was pointed out earlier (1) that one other mechanism could possibly account for retarded B diffusion in highly doped n-type Si-ion pairing. For this situation the B diffusion coefficient can be expressed as (3)

$$\frac{D_B}{D_i} = \frac{1}{2} \left[\frac{C_B - C_N + \frac{1}{\Omega} + 1}{2 \left[\frac{1}{4} \left(C_B - C_N - \frac{1}{\Omega} \right)^2 + \frac{C_B}{\Omega} \right]^{1/2}} \right] \quad [9]$$

where $\Omega(T)$ is the ion-pairing equilibrium constant. Using the charge neutrality condition, Eq. [9] can be rewritten as

$$\frac{D_B}{D_i} = \frac{1}{2} \left[\frac{A + \frac{1}{\Omega}}{2 \left\{ \frac{1}{4} \left(A - \frac{1}{\Omega} \right)^2 + \frac{C_B}{\Omega} \right\}^{1/2}} + 1 \right] \quad [10]$$

where

$$A = \frac{n_{ie} [(p/n_{ie})^2 - 1]}{(p/n_{ie})} \quad [11]$$

The experimental data in Fig. 5 show that D_B/D_i is independent of temperature and n-type dopant. However, $\Omega(T)$ is dependent on both of these variables ($\Omega(1050) = 1.1 \times 10^{-20}$ for the $[As^+B^-]$ pair, while $\Omega(1050) = 1.25 \times 10^{-20}$ for the $[P^+B^-]$ pair). Also, the parameter A depends on temperature. Equation [10] is plotted in Fig. 5 for the $[As^+B^-]$ pairing condition at $1050^\circ C$. It can be seen that this phenomenon cannot be used to explain the data.

The B diffusivity expressed explicitly in terms of C_B and C_N can be obtained by substituting Eq. [4] or [5] or [6] into Eq. [3], depending on the temperature (valid only over the concentration ranges indicated). For example, plots of D_B/D_i (or p/n_{ie}) vs. C_B for values of C_N are shown in Fig. 6 for diffusions performed at $1000^\circ C$.

Conclusions

The diffusion of ion-implanted B in the presence of a uniform background of n-type dopant (P and As) has been studied. In the absence of any previously observed cooperative-diffusion effects (3, 4) (electric-

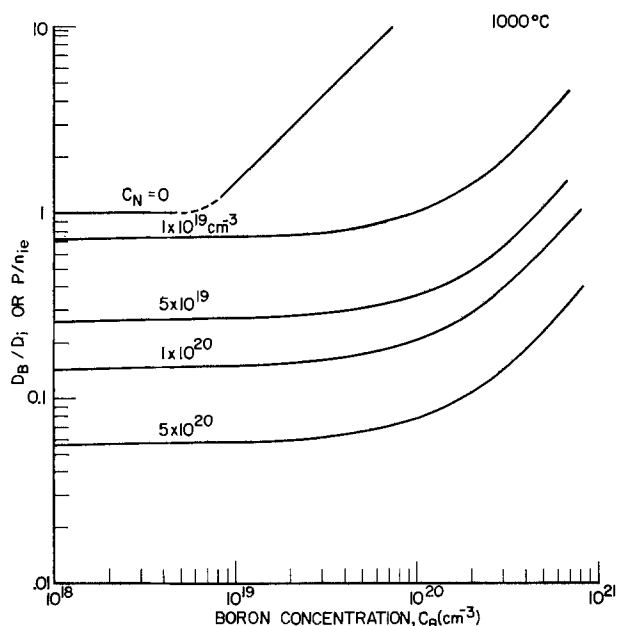


Fig. 6. Boron diffusivity vs. concentration at $T = 1000^\circ C$ for several values of n-type background doping density.

field interaction, ion-pairing, vacancy transients, etc.), a retarded B diffusion has been observed to be consistent with the local Fermi-level position in the Si bandgap, as determined by the net free hole concentration. The native defect most likely responsible for the diffusion of B is the donor-type monovacancy with a level at $\sim E_v + 0.37$ eV.

Numerical calculations of B diffusion profiles in which the B diffusivity is locally determined from the equation

$$D_B = D_i p/n_{ie} \quad [2]$$

with p/n_{ie} given by Eq. [3] have yielded good agreement with profiles experimentally determined by the SIMS analysis. The results did not depend on the way in which the background dopant had been introduced (implantation, predeposition or doped-oxide source), nor the type of background dopant used (P or As).

Acknowledgments

The authors would like to thank Mr. J. D. Abbott of the Western Electric Company for performing the SIMS measurements.

Manuscript submitted Dec. 2, 1974; revised manuscript received May 5, 1975.

Any discussion of this paper will appear in a Discussion Section to be published in the June 1976 JOURNAL. All discussions for the June 1976 Discussion Section should be submitted by Feb. 1, 1976.

Publication costs of this article were partially assisted by Bell Laboratories.

REFERENCES

1. R. B. Fair, *This Journal*, **122**, 800 (1975).
2. B. L. Crowder, J. F. Ziegler, and F. F. Morehead, in "Ion-Implantation in Semiconductors and Other Materials," B. L. Crowder, Editor, p. 267, Plenum Publishing Corp., New York (1973).
3. R. B. Fair, *J. Appl. Phys.*, **44**, 283 (1973).
4. S. M. Hu and S. Schmidt, *ibid.*, **39**, 4272 (1968).
5. R. K. Jain and R. J. Van Overstraeten, *IEEE Trans. Electron Dev.*, **ED-21**, 155 (1974).
6. A. A. Vol'fson and V. K. Subashiev, *Sov. Phys. Semicond.*, **1**, 327 (1967).
7. J. S. Makris and B. J. Masters, *J. Appl. Phys.*, **42**, 3750 (1971).
8. S. M. Hu, *ibid.*, **45**, 1567 (1974).
9. A. Seeger, in "Radiation Effects in Semiconductors," by J. W. Corbett and Watkins Corbett, p. 29, Gordon and Breach Science Publishers, Inc., New York (1971).
10. J. A. Van Vechten, Inter. Lattice Defects Conf., Freiburg, Germany, July 1974.
11. Elstner and Kamprath, *Phys. Stat. Sol.*, **22**, 541 (1967).
12. G. L. Vick and K. M. Whittle, *This Journal*, **116**, 1142 (1969).
13. R. K. Jain and R. Van Overstraeten, *J. Appl. Phys.*, **44**, 2437 (1973).
14. M. Okamura, *Japan. J. Appl. Phys.*, **10**, 434 (1971).
15. J. C. C. Tsai, Unpublished results.

Phase Diagram of Al-Ga-In-As Quaternary System

Kazuo Nakajima, Koza Osamura, and Yotaro Murakami

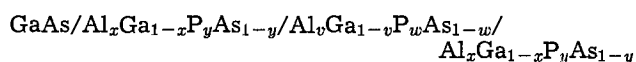
Department of Metallurgy, Faculty of Engineering, Kyoto University, Kyoto, Japan

ABSTRACT

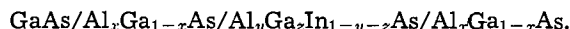
The phase diagram of the Al-Ga-In-As quaternary system has been determined experimentally for several Al isoconcentration sections. The liquidus data were obtained by DTA, and the solidus data were determined from liquid epitaxial layers grown on GaAs substrates by using EPMA. The phase diagram was calculated by using a simple solution model. Most of the nine interaction parameters necessary for the present calculation are the same as those used in the corresponding binary and ternary phase diagrams, and the remaining three parameters, Ω^{GaAs} , $\Omega^{\text{AlAs-InAs}}$, and $\Omega^{\text{GaAs-InAs}}$, were determined by fitting each calculated phase diagram to the experimental data.

It has been reported that various, closely lattice-matched heterojunction devices based on quaternary III-V solid solutions are possible which permit the independent variation between lattice constant and bandgap (1). Several devices based on such systems have been reported, for example, $\text{Ga}_x\text{In}_{1-x}\text{P}_y\text{As}_{1-y}/\text{InP}$ photocathode emitter (1, 2), $\text{Al}_x\text{Ga}_{1-x}\text{P}_y\text{As}_{1-y}/\text{GaP}_y\text{As}_{1-y}$ heterojunction lasers (3), and $\text{Al}_x\text{Ga}_{1-x}\text{As}_y\text{Sb}_{1-y}/\text{GaAs}_y\text{Sb}_{1-y}$ heterojunction lasers (4, 5). For producing these devices, the accurate knowledge of their quaternary phase diagrams is desired.

The GaAs- $\text{Al}_x\text{Ga}_{1-x}\text{As}$ double heterostructure device is presently one of the most important of the III-V mixed crystal systems, because very low threshold semiconductor lasers can be made from it which can operate continuously at room temperature. At the region of the heteroboundary, however, stresses remain at room temperature due to the different lattice constants of the two layers involved (6). These interface stresses are the primary factors that shorten the lifetime of the lasers. It is possible to get a good match between the lattice constant of the different constituent layers of the diodes by the addition of a fourth component P or In, that is, by making such structures as



or



It is difficult, however, to grow the alloys with exactly controlled compositions with the first system, because the addition of a small amount of P substantially raises the melting temperatures of the alloys, the vapor pressure of phosphorus in the alloys is very high, and the atomic ratio of P to As in the quaternary solid solutions varies rapidly with a small change of As concentration in the liquid (7). Consequently, because of their low melting temperatures and the fact that there is only one volatile component, As, it is better to use the second system for growing crystals with closely controlled compositions

In the present paper, the experimental and calculated phase diagrams of Al-Ga-In-As system were determined to facilitate the preparation of closely lattice-matched heterojunction devices.

Experiments and Results

Liquidus.—Differential thermal analysis was used for the determination of the liquidus isotherms of the Al-Ga-In-As system. In this work, the materials used were semiconductor grade Ga, In, Al, and GaAs. The required amounts of these materials were sealed under vacuum into a fused silica capsule as reported earlier (8). The capsule was held above the melting point of GaAs, then cooled at a constant rate of 3.0°C/min.

Key words: LPE, III-V semiconductors, quaternary, lattice matching, heterojunctions.

After it had been cooled below an inflection point, T_c , that was observed in the cooling curve, it was again heated with a constant heating rate of 3.0°C/min to above an inflection point, T_h , that was observed in the heating curve. The temperature, T_h , was read from the foot point on the higher temperature side of the peak due to the latent heat of fusion of the solid in the heating curve. It is considered that the last solid completely dissolves and the evolution of the heat finishes off slightly below this point. The temperature, T_c , at which a primary crystal appears in the melt, tends to be lower than the equilibrium liquidus temperature due to the supercooling effect. Therefore, in the present analysis, an average of T_c and T_h was taken to be the transformation temperature. These temperatures are listed in Table I.

In solutions containing $X^{\text{Al}} = 0.001, 0.002, \text{ and } 0.005$, the liquidus at the cross sections of $X^{\text{As}}/(X^{\text{Ga}} + X^{\text{In}} + X^{\text{As}}) = 0.05, 0.10, \text{ and } 0.20$ are shown in Fig. 1, 2, and 3, where X^i represents the atomic fraction of the element i in the liquid. These Al compositions were taken from the previously calculated phase diagram to permit growth of $\text{Al}_x\text{Ga}_{1-x}\text{As}$ ($x = 0-0.3$) epitaxial layers within a reasonable temperature range. These figures show that addition of Al to the melt raises the liquidus and decreases the solubility of As in the liquid.

Table I. Liquidus temperatures determined by DTA in the Al-Ga-In-As quaternary system

X^{Al}	Atomic fraction			(°C)		
	X^{Ga}	X^{In}	X^{As}	T_h	T_c	T
0.001	0.89910	0.0	0.09990	997	963	980
0.001	0.84915	0.04995	0.09990	984	946	965
0.001	0.79920	0.09990	0.09990	977	947	962
0.001	0.74925	0.14985	0.09990	972	944	958
0.001	0.69930	0.19980	0.09990	945	922	934
0.001	0.94905	0.0	0.04995	920	899	910
0.001	0.89910	0.04995	0.04995	919	882	900
0.001	0.84915	0.09990	0.04995	922	838	880
0.001	0.79920	0.14985	0.04995	892	852	872
0.001	0.74925	0.19980	0.04995	908	842	875
0.002	0.74850	0.04990	0.19960	1102	1081	1092
0.002	0.64870	0.14970	0.19960	1092	1053	1073
0.002	0.54890	0.24950	0.19960	1064	1026	1045
0.002	0.39920	0.39920	0.19960	1029	987	1008
0.002	0.24950	0.54890	0.19960	995	953	974
0.002	0.84830	0.04990	0.09980	1001	968	985
0.002	0.74850	0.14970	0.09980	991	947	969
0.002	0.64870	0.24950	0.09980	953	937	945
0.002	0.49900	0.39920	0.09980	944	892	918
0.002	0.34930	0.54890	0.09980	948	873	911
0.002	0.89820	0.04990	0.04990	957	890	924
0.002	0.79840	0.14970	0.04990	930	872	901
0.002	0.69860	0.24950	0.04990	910	860	885
0.002	0.54890	0.39920	0.04990	902	839	871
0.002	0.39920	0.54890	0.04990	860	820	840
0.005	0.74625	0.04975	0.19900	1126	1085	1106
0.005	0.69650	0.09950	0.19900	1083	1078	1081
0.005	0.59700	0.19900	0.19900	1068	1048	1058
0.005	0.49750	0.29850	0.19900	1068	1022	1045
0.005	0.84575	0.04975	0.09950	1014	977	996
0.005	0.79600	0.09950	0.09950	995	966	981
0.005	0.59700	0.29850	0.09950	972	952	962
0.005	0.89550	0.04975	0.04975	952	915	934
0.005	0.84575	0.09950	0.04975	923	908	916
0.005	0.74625	0.19900	0.04975	941	884	913

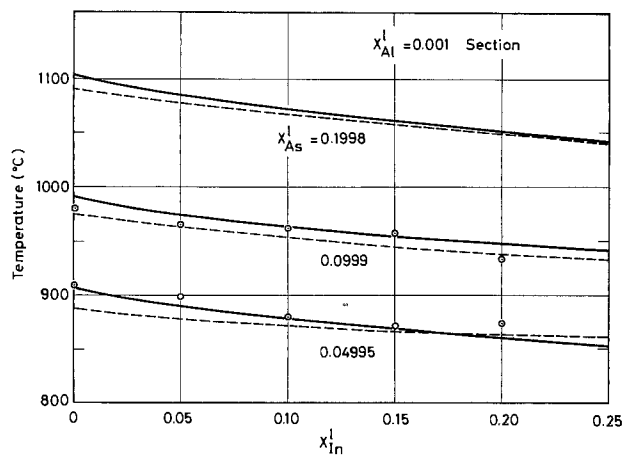


Fig. 1. Liquidus curves at isoconcentration section of $X_{Al}^I = 0.001$ in the Al-Ga-In-As system. \odot , DTA data. - - - - and — represent the calculated liquidus for the first (I) and second (II) sets of interaction parameters given in Table III, respectively.

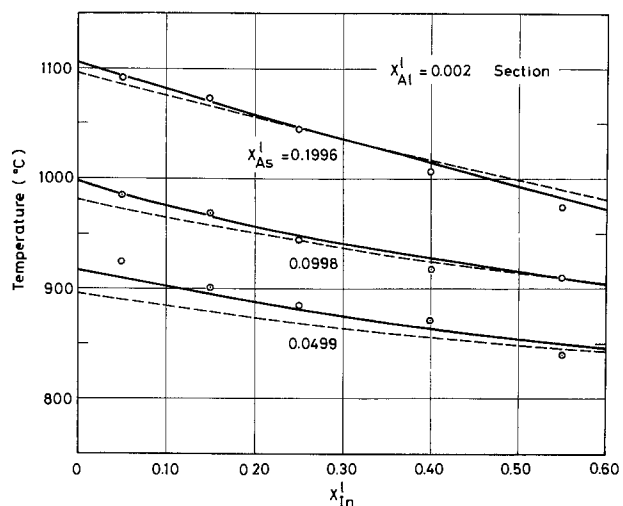


Fig. 2. Liquidus curves at isoconcentration section of $X_{Al}^I = 0.002$ in the Al-Ga-In-As quaternary system. \odot , DTA data. - - - - and — represent the calculated liquidus for the first (I) and second (II) sets of parameters given in Table III, respectively.

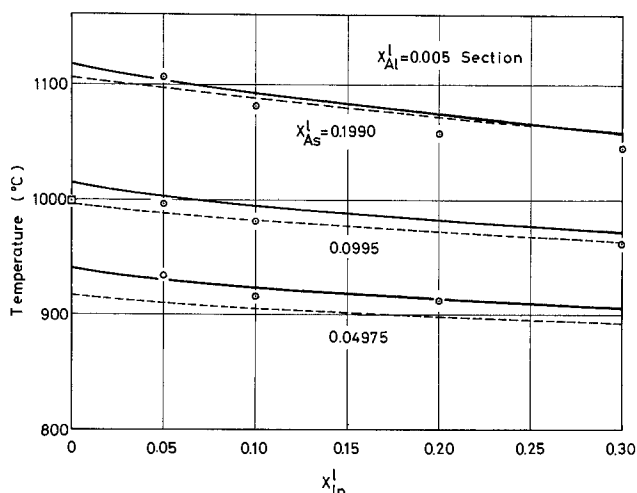


Fig. 3. Liquidus curves at isoconcentration section of $X_{Al}^I = 0.005$ in the Al-Ga-In-As quaternary system. \odot , DTA data. - - - - and — represent the calculated liquidus for the first (I) and second (II) sets of parameters given in Table III, respectively.

Solidus.— $Al_xGa_yIn_{1-x-y}As$ epitaxial layers were grown onto Cr-doped or Te-doped GaAs (100) or (111)A substrates from quaternary solutions to deter-

mine the solidus isotherms. The apparatus consisted of a horizontal furnace, a fused silica tube, and a sliding graphite boat. At the start of a run, the apparatus was heated rapidly to 50°C above the starting temperature of the growth and maintained there for about 1 hr. It was then cooled with a constant cooling rate of 1.0°C/min. At the desired growth temperature, the substrate was brought into contact with the solution by moving the slider. The growth ranges were 805°–775°C and 905°–875°C. After the growth, the solution was separated from the seed by sliding the boat, then the apparatus was rapidly cooled to room temperature. Layer thicknesses were in the range of 20 to 30 μ m.

Ga and In concentrations were determined on cleaved sections of epitaxial layers with EPMA. A scanning electron microscope equipped with an energy-dispersive x-ray analyzer was used. An electron beam energy of 25 keV was used and the peak energy of the Ga-L α emission bands was measured. GaAs and InSb were used as the EPMA standard for Ga and In, respectively. The measured relative x-ray intensities were normalized by performing the atomic number, absorption, and fluorescence corrections.

The quaternary layers on GaAs substrates were single crystal. The surfaces of the layers grown from 800°C were generally smoother than those from 900°C. The layers grown from the liquidus containing $X_{In}^I > 0.3$ showed uneven surfaces and generally were polycrystalline. The condition of the surfaces was not influenced by Al concentration in the liquid within the range of the present experiments. The variation of the crystal composition was due to the depletion of Al in the melt near the growing interface during cooling. The composition of the layer near the interface between the GaAs substrate and the epitaxial layer was adopted as the solidus composition of the primary precipitated crystal.

The solidus isotherms in equilibrium with the quaternary liquids containing $X_{In}^I < 0.4$ and $X_{Al}^I = 0.001, 0.002,$ and 0.005 were determined. The solidus data values are listed in Table II. Figures 4 and 5 show the solid solubility isotherms for Al in the quaternary liquids at 800° and 900°C, respectively. These solidus isotherms show that the lower the growth temperature, the larger the distribution coefficient for Al becomes. Figures 6 and 7 show the solid solubility isotherms for In in the quaternary liquidus at 800° and 900°C, respectively. These isotherms indicate that the higher the growth temperature and the lower X_{Al}^I , the larger the distribution coefficient for In becomes.

Discussion

This experimental phase diagram showed that the solubility of In in the solid was very small and almost linearly dependent on X_{In}^I , and that the distribution

Table II. Solidus compositions in equilibrium with the Al-Ga-In-As quaternary liquidus determined by EPMA

Liquidus temperature (°C)	Atomic fraction				Mole fraction (mean value)	
	X_{Al}^I	X_{Ga}^I	X_{In}^I	X_{As}^I	X_{AlAs}^s	X_{InAs}^s
800	0.001	0.92308	0.04995	0.02597	0.17886	0.00114
800	0.001	0.87113	0.09990	0.02797	0.18415	0.00193
800	0.001	0.81918	0.14985	0.02997	0.22455	0.00291
800	0.001	0.76723	0.19980	0.03197	0.24370	0.00395
800	0.002	0.93413	0.04990	0.01397	0.38304	0.00090
800	0.002	0.88024	0.09980	0.01796	0.41125	0.00153
800	0.002	0.82834	0.14970	0.01996	0.40335	0.00246
800	0.002	0.77744	0.19960	0.02096	0.45555	0.00289
800	0.002	0.67764	0.29940	0.02096	0.51145	—
800	0.002	0.57285	0.39920	0.02595	0.55108	—
800	0.005	0.93132	0.04975	0.01393	0.58900	—
900	0.001	0.88611	0.04995	0.06294	0.10152	0.00191
900	0.001	0.82917	0.09990	0.06993	0.12520	0.00336
900	0.001	0.77323	0.14985	0.07592	0.13045	0.00499
900	0.001	0.71528	0.19980	0.08392	0.15415	0.00663
900	0.002	0.89022	0.04990	0.05788	0.25224	0.00157
900	0.002	0.83832	0.09980	0.05988	0.25300	0.00260
900	0.002	0.78044	0.14970	0.06786	0.24800	0.00393
900	0.002	0.72754	0.19960	0.07086	0.26258	0.00565
900	0.005	0.89649	0.04975	0.04876	0.45000	—

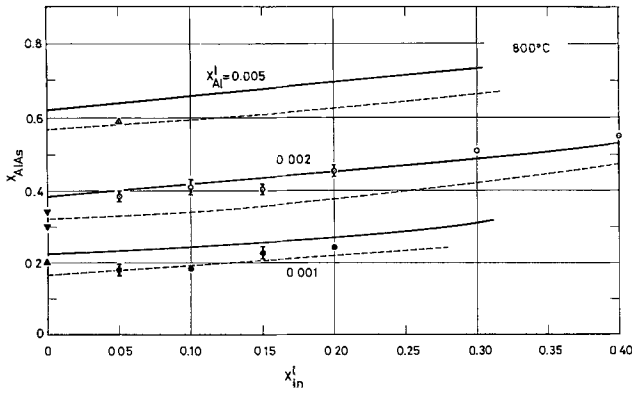


Fig. 4. 800°C AlAs solidus isotherms in the Al-Ga-In-As system at $X_{Al}^I = 0.001, 0.002, \text{ and } 0.005$. ●, $X_{Al}^I = 0.001$; ○, $X_{Al}^I = 0.002$; △, $X_{Al}^I = 0.005$. - - - - and — represent the calculated solidus for the first (I) and second (II) sets of parameters given in Table III, respectively.

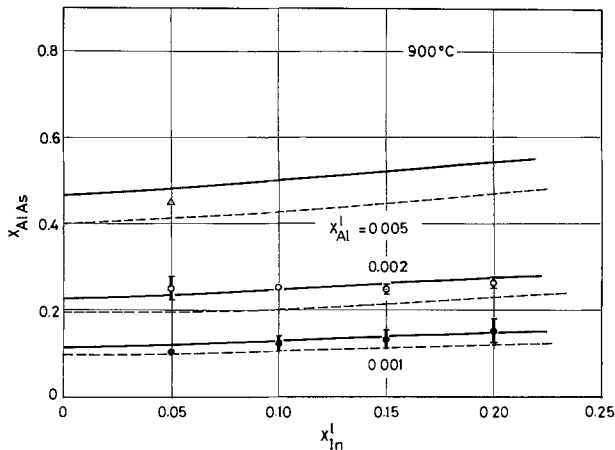


Fig. 5. 900°C AlAs solidus isotherms in the Al-Ga-In-As system at $X_{Al}^I = 0.001, 0.002, \text{ and } 0.005$. ●, $X_{Al}^I = 0.001$; ○, $X_{Al}^I = 0.002$; △, $X_{Al}^I = 0.005$. - - - - and — represent the calculated solidus for the first (I) and second (II) sets of parameters given in Table III, respectively.

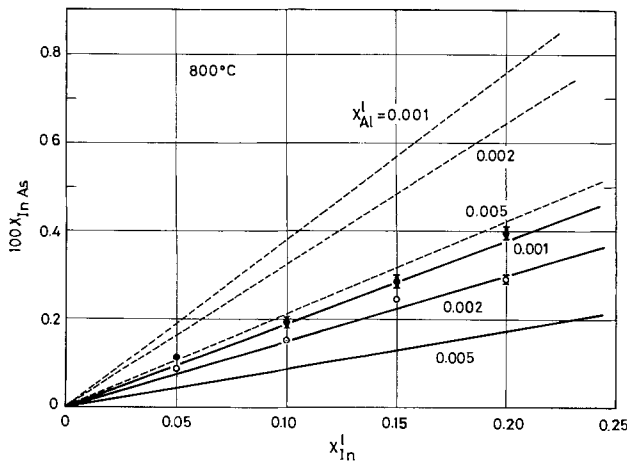
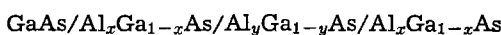


Fig. 6. 800°C InAs solidus isotherms in the Al-Ga-In-As system at $X_{Al}^I = 0.001 \text{ and } 0.002$. ●, $X_{Al}^I = 0.001$; ○, $X_{Al}^I = 0.002$. - - - - and — represent the calculated solidus for the first (I) and second (II) sets of parameters given in Table III, respectively

coefficient for Al was nearly independent of X_{In}^I ($X_{In}^I \leq 0.2$). A quaternary layer which has the same bandgap as the active layer, $Al_yGa_{1-y}As$ of the



structure and whose lattice is matched with that of

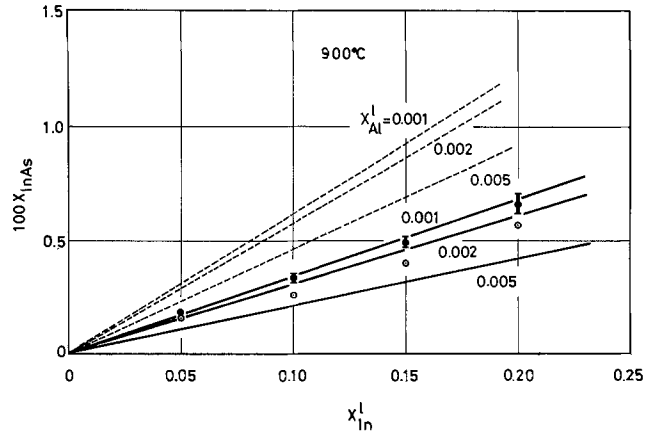


Fig. 7. 900°C InAs solidus isotherms in the Al-Ga-In-As system at $X_{Al}^I = 0.001 \text{ and } 0.002$. ●, $X_{Al}^I = 0.001$; ○, $X_{Al}^I = 0.002$. - - - - and — represent the calculated solidus for the first (I) and second (II) sets of parameters given in Table III, respectively.

$Al_xGa_{1-x}As$ can be easily prepared by using the information contained in the phase diagram. That is, the desired amount of In can be easily dissolved in the solid at the appropriate Al composition.

The Al-Ga-In-As phase diagram was calculated by treating the quaternary liquid and solid as a simple solution (11, 12) in which the interaction parameters are approximated by a linear temperature dependent function. The basic equations given by Huber (13) expressing the chemical equilibrium between the pseudoternary solid of the type $A_xB_yC_{1-x-y}D$ and the quaternary liquid were used. These equations are useful for the calculation of the $III_A-III_B-III_C-V_D$ type phase diagram because the solid of the type $A_xB_yC_{1-x-y}D$ is completely analogous to the pseudobinary solid. The reasonable values found in the literature were used as the interaction parameters necessary for the calculation. These values are listed in Table III. The calculated results represented by dashed lines in Fig. 1-7, however, did not agree well with every experimental one. For obtaining the reasonable agreement, the values of three parameters, Ω_{GaAs}^I , $\Omega_{AlAs-InAs}^S$, and $\Omega_{GaAs-InAs}^S$, had needed to be changed as $\Omega_{GaAs}^I = 6100 - 9T$, $\Omega_{AlAs-InAs}^S = 4800$, and $\Omega_{GaAs-InAs}^S = 4800$ cal/mole, but the implication of the magnitude of these parameters presented here is not clear. The calculated results are represented by solid lines in Fig. 1-7. Figure 8 shows the liquidus isotherms and the AlAs and InAs solidus isotherms on the entire cross section of 0.2 atom per cent Al in the liquid which are calculated by using such changed parameters. Figure 8 summarizes the results of Fig. 4-7.

Table III. Thermodynamic input data for phase diagram calculation

The diagram was calculated for two sets of interaction parameters. Each set is consisted of nine parameters. Six are common parameters in two sets and the remaining three parameters, $\Omega_{GaAs}^I, \Omega_{AlAs-InAs}^S$, and $\Omega_{GaAs-InAs}^S$, are not. The first and the second sets are marked with I and II, respectively.

Input data	
T_{AlAs}^F	$= 2043.0^\circ K$ (14, 15)
T_{GaAs}^F	$= 1511.0^\circ K$ (16, 17)
T_{InAs}^F	$= 1215.0^\circ K$ (18, 19)
ΔS_{AlAs}^F	$= 15.60 \text{ cal/mole}^\circ K$ (12)
ΔS_{GaAs}^F	$= 16.64 \text{ cal/mole}^\circ K$ (20)
ΔS_{InAs}^F	$= 14.52 \text{ cal/mole}^\circ K$ (20)
Ω_{AlGa}^I	$= 104 \text{ cal/mole}$ (12)
Ω_{AlIn}^I	$= 2000 \text{ cal/mole}$ (21)
Ω_{GaIn}^I	$= 1060 \text{ cal/mole}$ (12)
Ω_{AlAs}^I	$= -6390 - 5.5T \text{ cal/mole}$ (10)
Ω_{GaAs}^I	$= \begin{cases} 5160 - 9.16T \text{ cal/mole} & \text{(22) (I)} \\ 6100 - 9T \text{ cal/mole} & \text{(II)} \end{cases}$
Ω_{InAs}^I	$= 4300 - 9.16T \text{ cal/mole}$ (23)
$\Omega_{AlAs-GaAs}^S$	$= -3892 + 4.0T \text{ cal/mole}$ (10)
$\Omega_{AlAs-InAs}^S$	$= \begin{cases} 2500 \text{ cal/mole} & \text{(12) (I)} \\ 4800 \text{ cal/mole} & \text{(II)} \end{cases}$
$\Omega_{GaAs-InAs}^S$	$= \begin{cases} 3000 \text{ cal/mole} & \text{(12) (I)} \\ 4800 \text{ cal/mole} & \text{(II)} \end{cases}$

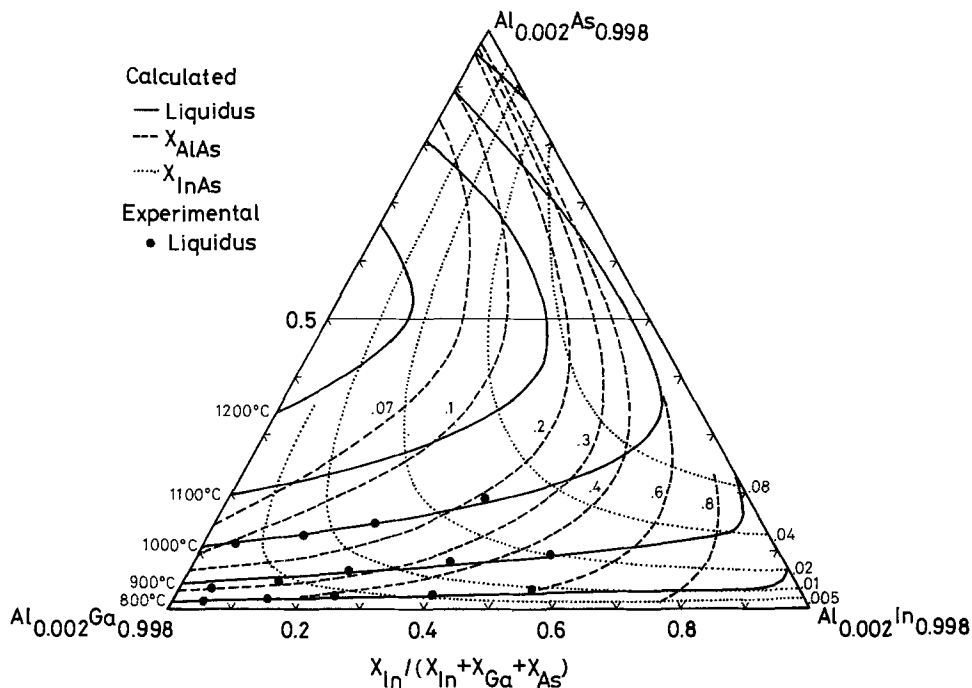


Fig. 8. The calculated Al-Ga-In-As quaternary phase diagram on the entire cross section of $X_{Al}^{Al} = 0.002$ for the second (II) set of parameters given in Table III. — Calculated liquidus isotherms; - - - - calculated AlAs solidus isotherms; calculated InAs solidus isotherms; ●, DTA data.

Acknowledgments

The authors wish to express their hearty thanks to the Research Laboratory of Fujitsu Ltd. and Sumitomo Electric Industries Ltd. for a supply of the experimental materials. They also wish to acknowledge helpful discussions with Mr. S. Isozumi.

Manuscript submitted Dec. 26, 1974; revised manuscript received April 1, 1975.

Any discussion of this paper will appear in a Discussion Section to be published in the June 1976 JOURNAL. All discussions for the June 1976 Discussion Section should be submitted by Feb. 1, 1976.

Publication costs of this article were partially assisted by Kyoto University.

REFERENCES

- G. A. Antypas, R. L. Moon, L. W. James, J. Edgecumbe, and R. L. Bell, "Proceeding of the 1972 Symposium on GaAs," p. 48, The Institute of Physics, London (1973).
- G. A. Antypas and R. L. Moon, *This Journal*, **120**, 1574 (1973).
- R. D. Burnham, N. Holonyak, H. W. Korb, H. M. Macksey, D. R. Scifres, J. B. Woodhouse, and Zh. I. Alferov, *Appl. Phys. Letters*, **19**, 25 (1971); *Soviet Phys.-Semicond.*, **6**, 77 (1972).
- K. Sugiyama and H. Saito, *Japan. J. Appl. Phys.*, **11**, 1057 (1972).
- G. A. Antypas and R. L. Moon, *This Journal*, **12**, 416 (1974).
- F. K. Reinhart and R. A. Logan, *J. Appl. Phys.*, **44**, 3171 (1973).
- M. Ilegems and M. B. Panish, *J. Phys. Chem. Solids*, **35**, 409 (1974).
- K. Osamura, J. Inoue, and Y. Murakami, *This Journal*, **119**, 103 (1972).
- Zh. I. Alferov, V. M. Andreyev, S. G. Konnikov, V. G. Nikitin, and D. N. Trilyakov, "Proceedings of International Conference on Heterojunctions I," p. 93, Academy of Sciences, Budapest (1971).
- M. B. Panish, *J. Appl. Phys.*, **44**, 2667 (1973).
- E. A. Guggenheim, "Thermodynamics," 5th ed., p. 197, North Holland, Amsterdam (1967).
- M. B. Panish and M. Ilegems, "Progress in Solid State Chemistry," Vol. 7, p. 39, H. Reiss and J. O. McCaldin, Editors, Pergamon Press, Inc. New York (1969).
- D. Huber, *J. Phys. Chem. Solids*, **34**, 1859 (1973).
- W. Kischio, *Z. Anorg. Allgem. Chem.*, **328**, 187 (1964).
- L. M. Foster, J. E. Scardefeld, and J. F. Woods, *This Journal*, **119**, 765 (1972).
- W. Köster and B. Thoma, *Z. Metallk.*, **46**, 291 (1955).
- C. D. Thurmond, *J. Phys. Chem. Solids*, **26**, 785 (1965).
- T. S. Lin and E. A. Peretti, *Trans ASM*, **45**, 677 (1953).
- G. A. Antypas, *This Journal*, **117**, 1393 (1970).
- B. D. Lichten and P. Sommelet, *Trans. AIME*, **245**, 1021 (1969).
- K. Osamura, K. Nakajima, and Y. Murakami, *J. Japan. Inst. Metals*, **36**, 744 (1972).
- J. R. Arthur, *J. Phys. Chem. Solids*, **28**, 2257 (1967).
- G. A. Antypas, *This Journal*, **117**, 1393 (1970).

The High-Temperature Oxidation Behavior of a $\text{HfB}_2 + 20$ v/o SiC Composite

J. W. Hinze* and W. C. Tripp

Systems Research Laboratories, Incorporated, Dayton, Ohio 45432

and H. C. Graham

Metallurgy and Ceramics Research Laboratory, Aerospace Research Laboratories,
Wright-Patterson Air Force Base, Ohio 45433

ABSTRACT

The high-temperature oxidation behavior of a $\text{HfB}_2 + 20$ v/o SiC composite was investigated in the temperature range 1200°-1550°C and in oxygen partial pressures at 1400°C ranging from 2.6×10^{-9} to 3.3×10^{-1} atm. Oxidation kinetics in pure oxygen were parabolic, with the rate constants exhibiting linear Arrhenius behavior. The rate of oxygen consumption is described by $k_p = 1.62 \times 10^7 \exp(-106,000/RT)$ $\text{g}^2\text{-cm}^{-4}\text{-hr}^{-1}$ in the range 1350°-1550°C. The oxide scale formed in this range consisted of an inner HfO_2 layer in series with an outer SiO_2 layer. The oxidation rate was found to be controlled by initial short-circuit oxygen diffusion through the HfO_2 , followed by volume diffusion through the SiO_2 scaling layer. Below 1350°C, rapid oxidation kinetics were observed, HfO_2 being the primary scale constituent.

Interest in diboride composites stems from their potential use in high-temperature oxidizing environments. These materials hold promise due to their chemical inertness, thermal-shock resistance, retained strength at high temperature, and oxidation resistance. Early studies by Kaufman *et al.* (1) on the oxidation of undoped diborides showed the oxidation resistance of HfB_2 to be superior to that of its Zr, Ti, Ta, and Nb counterparts based on a comparison of the total diboride recession after a 1 hr exposure to oxygen at temperatures ranging from 1300°-2000°K. Later, Kaufman *et al.* (2) and Berkowitz-Mattuck (3) studied the oxidation rate of HfB_2 and ZrB_2 as a function of temperature and oxygen partial pressure in order to determine the mechanism of oxidation. The oxidation kinetics were observed to obey a parabolic rate law, and oxygen diffusion through the scaling layer was found to be rate determining. More recently, Clougherty *et al.* (4) investigated the oxidation behavior of HfB_2 and ZrB_2 containing additions of SiC as a function of temperature only, and total diboride recession was measured after 1 hr of oxidation. The SiC addition was found to increase the oxidation resistance; however, kinetic data were not obtained.

The oxidation of ZrB_2 and $\text{ZrB}_2 + 20$ v/o SiC has been investigated by Tripp *et al.* (5-7) as a function of temperature and oxygen partial pressure using thermogravimetric techniques. The oxidation reaction was found to be controlled by diffusion through a SiO_2 scaling layer. In the present investigation, the oxidation behavior of $\text{HfB}_2 + 20$ v/o SiC was studied as a function of temperature and oxygen partial pressure. The oxidation resistance of the $\text{HfB}_2 + \text{SiC}$ composite was compared to that of its constituent components as well as its zirconium counterpart in order to define the rate-determining oxidation mechanism.

Experimental

The diboride composite used in this study was prepared by Man Labs, Inc. under contract with the Air Force Materials Laboratory. The $\text{HfB}_2 + 20$ v/o SiC powders had been hot pressed at 2200°C under a pressure of 3000 psi for 90 min, and the resulting billet was 88% dense. Coupons ($\sim 1 \times 0.5 \times 0.1$ cm) were

cut from the billet, ground with 600-grit SiC paper, and ultrasonically cleaned in acetone and methanol.

Oxidation kinetics were determined using an oxygen-consumption technique (5-7) which is very useful for studying oxidation where one or more of the reaction products is volatile at sample temperature but condensable at lower temperatures. With this technique the volatile species are collected on the walls of a cold alumina crucible which is suspended over the sample, and the weight of the sample plus crucible is monitored continuously with time. In this way the weight gain due to the oxygen used to form both the solid and volatile products can be measured. The measurement of sample weight change alone does not give a true indication of the reaction kinetics because sample weight gains and losses occur simultaneously. In the present work nonvolatile HfO_2 and SiO_2 are formed as well as volatile B_2O_3 and SiO . The CO and CO_2 which are formed as oxidation products cannot be condensed on the cold crucible; however, their weight is only 10-15% of the total weight change.

The kinetics of total oxygen consumption were studied using a Cahn RH electrobalance having a capacity of 100g and a sensitivity of $\pm 2 \mu\text{g}$. The balance assembly has been described previously (5, 8). The diboride specimen and crucible were preheated for ~ 15 hr in Ar at 500°C in the balance assembly. The furnace was then quickly heated to the desired temperature and the oxidant (O_2 , O_2/Ar , or CO/CO_2) admitted into the furnace chamber until the desired total pressure was reached. In all cases the oxidation experiments were conducted in flowing gas at $\sim 60 \text{ cm}^3$ (STP)/min.

Postoxidation analysis of the specimens consisted of x-ray analysis for determining scale constituents, microprobe analysis for elemental distribution, and optical and scanning electron microscopy for scale morphologies.

Results

Oxidation in pure oxygen.—The oxidation behavior in pure oxygen was studied in the temperature range 1200°-1550°C; the results of a typical experiment are shown in Fig. 1. In all experiments parabolic behavior was observed after an initial transient period, the initial rapid kinetics being due to short-circuit diffusion (see Discussion section). Scaling rate constants com-

* Electrochemical Society Active Member.

Key words: boride, oxygen consumption, electrobalance, silicon carbide, hafnium diboride, diboride ceramic composite.

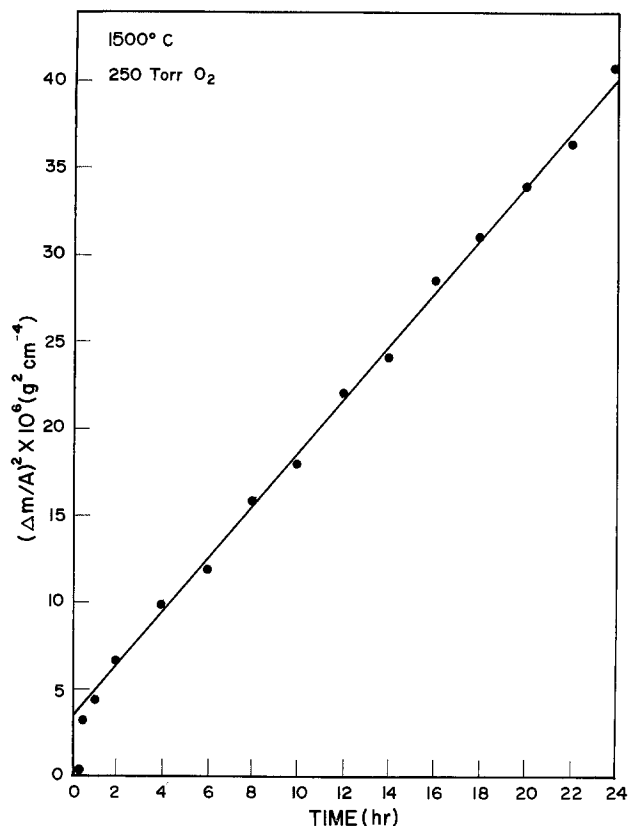


Fig. 1. Typical parabolic plot of kinetic data for $\text{HfB}_2 + \text{SiC}$ oxidation in 250 Torr O_2 .

puted from the slopes of the parabolic plots are given in Arrhenius form in Fig. 2. The activation energy for oxidation in the range 1350°-1550°C is 106 kcal/mole with

$$k_p = 1.62 \times 10^7 \exp(-106,000/RT) \text{ g}^2\text{-cm}^{-4}\text{-hr}^{-1}$$

The scaling rate increases abruptly below 1350°C due

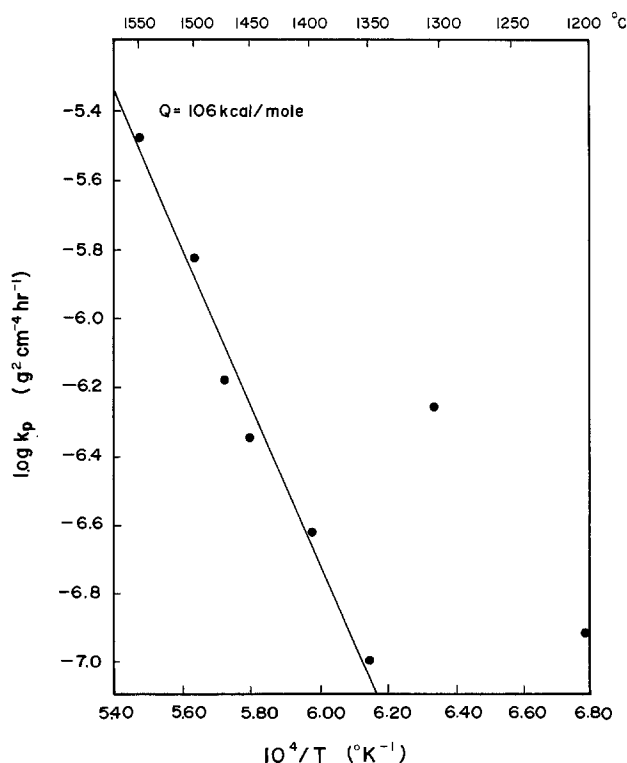


Fig. 2. Arrhenius plot of parabolic rate constants for total oxygen consumption of $\text{HfB}_2 + \text{SiC}$ in 250 Torr O_2 .

to selective oxidation of the HfB_2 with very slow attack of the SiC . Only small amounts of SiO_2 were found on the samples oxidized at these low temperatures. Therefore, the beneficial effect of the addition of SiC appears to be lost in this temperature range.

Figure 3 is an optical micrograph of the polished cross section of a sample oxidized for 24 hr at 1400°C in 250 Torr oxygen. The scale formed consists of an amorphous SiO_2 layer on top of a HfO_2 layer and is typical of those formed in the high-temperature region. The HfO_2 is porous and of uniform thickness, the dark regions being a combination of voids and SiC particles. The matrix beneath the scale contains a uniform distribution of SiC particles and no SiC depletion is observed.

X-ray diffractometer analysis of the oxidized specimens indicated that monoclinic HfO_2 and tetragonal HfSiO_4 are the primary scale constituents. The expected amorphous silica hump and cristobalite peak could not be found with this technique. The location of the scale constituents was obtained using the electron-beam microprobe. Figure 4 is a microprobe scan of the sample oxidized at 1400°C. The zone between 19 and

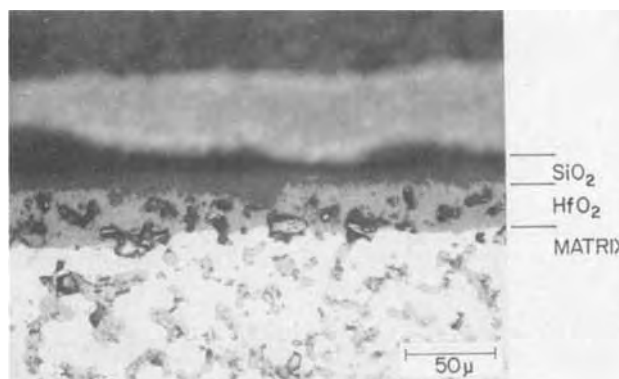


Fig. 3. Optical micrograph of a $\text{HfB}_2 + \text{SiC}$ specimen oxidized at 1400°C in 250 Torr O_2 for 24 hr.

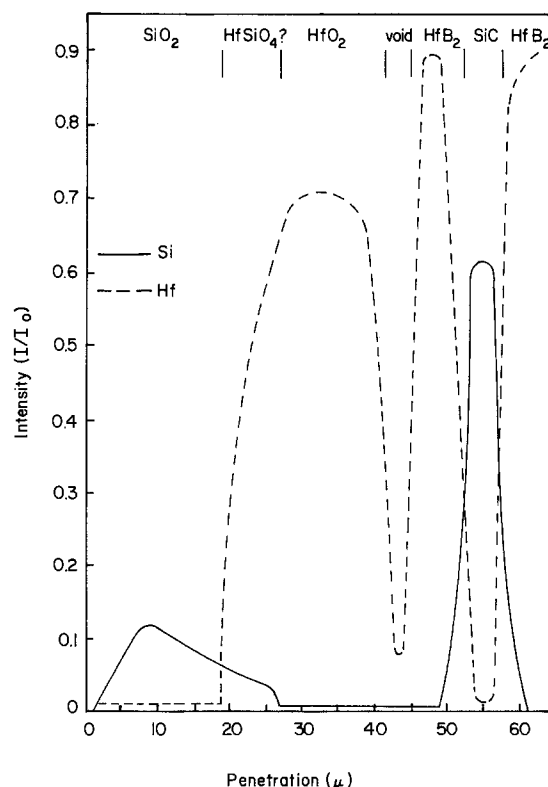


Fig. 4. Electron-beam microprobe scan of a $\text{HfB}_2 + \text{SiC}$ specimen oxidized at 1400°C in 250 Torr O_2 for 24 hr.

27μ may be HfSiO_4 ; however, since the intensity of the Hf peak varies throughout this range, the thickness of the HfSiO_4 cannot be determined. The HfSiO_4 probably exists as a very thin reaction layer between the SiO_2 and HfO_2 scaling layers. No B was found in the microprobe scans of the scales, suggesting that B diffuses through the scale and vaporizes as B_2O_3 at the scale-ambient interface.

Oxidation at reduced oxygen partial pressures.—The oxygen partial pressure dependence of the rate of oxygen consumption was investigated at 1400°C . Reduced oxygen partial pressures in the range 3.6×10^{-9} to 3.3×10^{-1} atm were established with premixed O_2/Ar and CO/CO_2 gas mixtures obtained from Air Products and Chemicals, Inc., the total system pressure being maintained at 250 Torr. A parabolic plot of the data is presented in Fig. 5. Oxidation kinetics are slower than parabolic in the O_2/Ar mixtures except at a P_{O_2} of 3.2×10^{-4} atm where rapid linear oxidation kinetics are exhibited. At this P_{O_2} active oxidation of the SiC occurs, with gaseous SiO being formed as the reaction product. A weight gain, rather than a weight loss, is observed because the volatile species is collected as SiO_2 on the cold crucible surrounding the $\text{HfB}_2 + \text{SiC}$ sample. The rate of oxygen consumption is found to increase with decreasing P_{O_2} in O_2/Ar gas mixtures down to 3.2×10^{-4} atm. Below this pressure CO/CO_2 gas mixtures were used, and the trend is reversed. The oxidation kinetics are parabolic in CO/CO_2 mixtures as in pure oxygen, suggesting that the reaction is diffusion controlled; however, the oxidation rates at the low oxygen partial pressures established by these mixtures are much higher.

Figure 6 is a light micrograph of the sample oxidized at a P_{O_2} of 3.2×10^{-4} atm. As expected, the SiO_2 scale is absent, and a thick HfO_2 layer has formed. The SiC particles have been depleted in the matrix due to rapid active oxidation. This micrograph is in contrast to that of the sample oxidized in pure oxygen (Fig. 3)

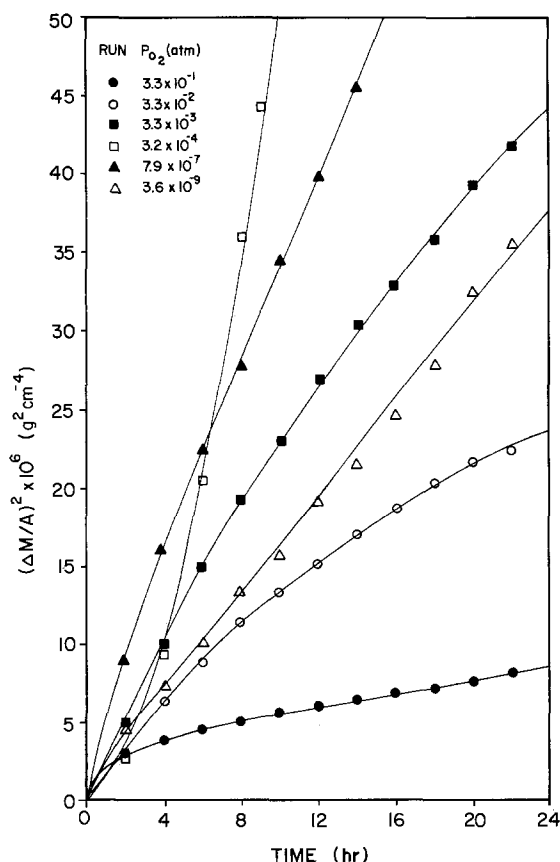


Fig. 5. Total oxygen consumption of $\text{HfB}_2 + \text{SiC}$ as a function of oxygen partial pressure at 1400°C : ● O_2 ; ○, ■, □ O_2/Ar ; ▲, △ CO/CO_2 .

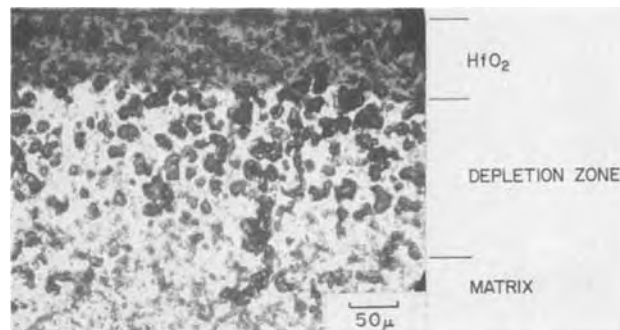


Fig. 6. Light micrograph of a $\text{HfB}_2 + \text{SiC}$ specimen oxidized at 1400°C in 975 ppm O_2/Ar ($P_{\text{O}_2} = 3.2 \times 10^{-4}$ atm) for 24 hr.

where no such depletion zone is present. Figure 7 is a comparison of scanning electron micrographs of these two specimens oxidized at 1400° in a P_{O_2} of 3.3×10^{-1} and 3.2×10^{-4} atm. The HfO_2 scale formed at the higher P_{O_2} appears to be more coherent than that formed at the lower P_{O_2} which contains pores and pinholes through which SiO escaped during oxidation.

Light micrographs of samples oxidized in CO/CO_2 mixtures are shown in Fig. 8. The HfO_2 scale formed on these samples has a greater thickness than that formed in pure oxygen, and globules of SiO_2 rather than a coherent layer are formed on the HfO_2 layer. No active oxidation of the SiC particles was found, as evidenced by the absence of a SiC depletion zone near the matrix-oxide interface.

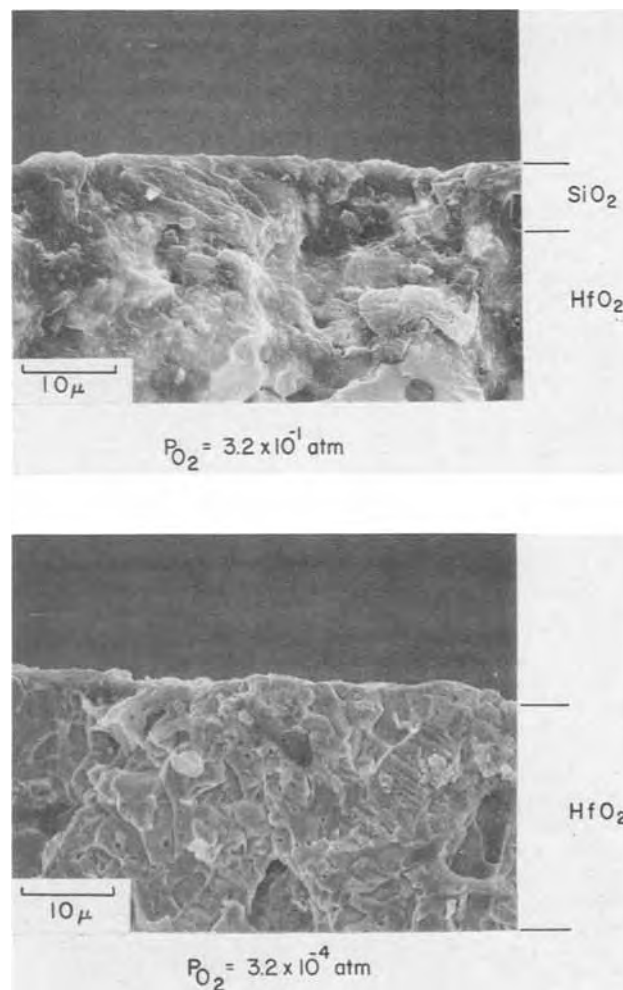


Fig. 7. SEM micrographs showing the effect of oxygen partial pressure on oxide scale morphologies. Specimens were oxidized at 1400°C for 24 hr.

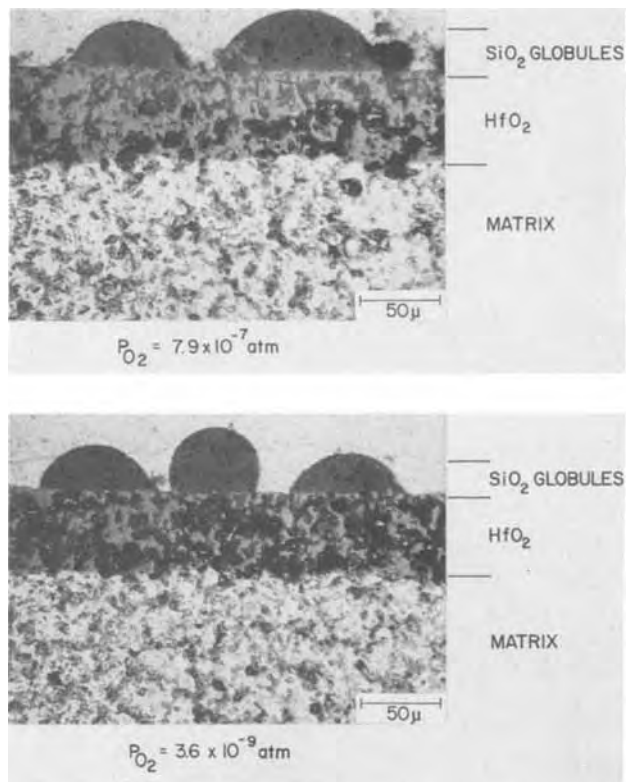


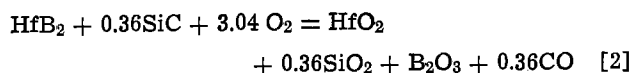
Fig. 8. Light micrographs of two $\text{HfB}_2 + \text{SiC}$ samples oxidized at 1400°C in CO/CO_2 gas mixtures for 24 hr.

Discussion

The parabolic oxidation kinetics observed in pure oxygen indicate that the oxidation reaction is diffusion controlled. Oxidation may be controlled by one of several mechanisms, including inward diffusion of oxygen through either the HfO_2 or SiO_2 layer or outward diffusion of Si, C, or B through the HfO_2 or SiO_2 . If the oxidation mechanism is via oxygen transport through the HfO_2 scale, the oxidation rate and activation energy for Hf and HfB_2 oxidation. The rates of oxidation for $\text{HfB}_2 + \text{SiC}$, HfB_2 , and Hf in 250 Torr O_2 are compared in Fig. 9. In order to compare the oxidation kinetics for the three materials, the rates of HfO_2 formation were computed from the experimental parabolic rate constants, assuming that the diboride materials oxidize stoichiometrically according to the reactions



and



The low-temperature (600°C - 1200°C) data by Smeltzer and Simnad (9) for Hf oxidation were extended into the range of interest. For the oxidation of Hf and HfB_2 , the agreement in rates of HfO_2 formation and activation energies is quite good, which suggests that the oxidation mechanism is the same for the two materials. However, the SiC addition to the HfB_2 significantly alters the kinetics and activation energy for oxidation. Although volume diffusion of oxygen through the HfO_2 layer has been found to control the oxidation of Hf (9) and HfB_2 (3), this mechanism is not rate determining during the oxidation of $\text{HfB}_2 + \text{SiC}$.

If the oxidation of $\text{HfB}_2 + \text{SiC}$ is controlled by diffusion of oxygen through the SiO_2 scaling layer, the activation energy and kinetics of oxidation should agree with those of other silicon-based materials. Generally activation energies of 28-30 kcal/mole are re-

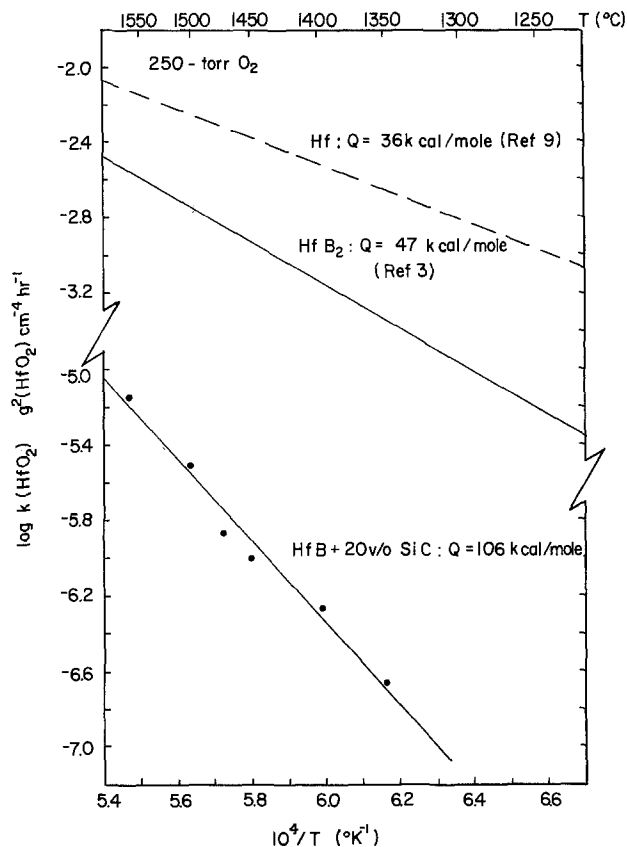


Fig. 9. Comparison of the rates of HfO_2 formation during oxidation of $\text{HfB}_2 + 20 \text{ v/o SiC}$, Hf, and HfB_2 in 250 Torr O_2 .

ported for silicon oxidation in the range 800°C - 1200°C (10-12). However, in recent investigations on the oxidation of silicon (13) and hot-pressed silicon carbide (14-16), activation energies of ~ 70 -115 kcal/mole were reported. In Fig. 10 the oxidation kinetics of $\text{HfB}_2 + \text{SiC}$ are compared with those for SiC oxidation obtained by the present authors (15, 16). The rates of SiO_2 formation were compared for the two materials using the stoichiometric oxidation reaction (2) and

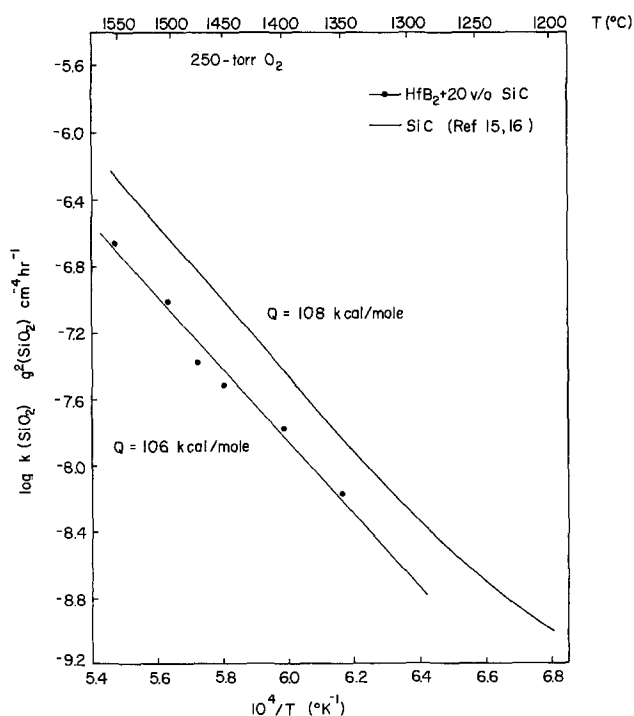
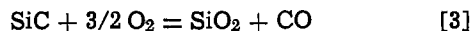


Fig. 10. Comparison of the rates of SiO_2 formation during oxidation of $\text{HfB}_2 + 20 \text{ v/o SiC}$ and hot-pressed SiC in 250 Torr O_2 .

the reaction

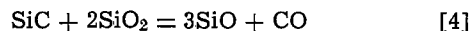


The agreement in rates and activation energies is excellent, confirming that the oxidation mechanism is the same for the two materials. Therefore, outward diffusion of B through the scale is eliminated as a possible rate-controlling mechanism. For SiC oxidation a mechanism involving outward diffusion of C was shown to be unlikely. Instead, volume diffusion of oxygen through the scale was found to be rate controlling, the valence of the oxygen species being indeterminate (15-16). Thus, in pure oxygen, the oxidation mechanism of both $\text{HfB}_2 + \text{SiC}$ and SiC is inward diffusion of oxygen through the silica scale.

Some question arises as to the manner in which the external SiO_2 scale forms atop the internal HfO_2 layer. The optical micrographs and microprobe scans of the oxidized specimens reveal the presence of SiC particles in the HfO_2 layer. It is believed that a number of these particles are present at or near the ambient HfO_2 interface following the initial transient oxidation period and that the SiO_2 which subsequently forms on the SiC particles spreads laterally across the HfO_2 surface forming a protective layer. In view of the similarity between the oxidation behavior of SiC and that of $\text{HfB}_2 + \text{SiC}$, it appears that any rate-controlling mechanism involving outward Si diffusion through the HfO_2 layer is improbable.

The oxygen partial pressure dependence of the oxidation rate is quite different for SiC and $\text{HfB}_2 + \text{SiC}$. At reduced oxygen partial pressures in O_2/Ar gas mixtures, the oxidation rate of SiC was parabolic and increased with P_{O_2} . In the present investigation the rate decreased with increasing P_{O_2} in the same mixtures. The rapid rate of oxidation at a P_{O_2} of 3.2×10^{-4} atm has already been interpreted in terms of active oxidation of the SiC particles in the HfB_2 matrix. However, at larger oxygen partial pressures, no evidence for active oxidation through depletion of the SiC particles was found. The downward curvature of the parabolic plots at these pressures suggests that the oxidation rate is controlled by oxygen diffusion along short-circuit paths through the HfO_2 layer, the number of paths decreasing with time. Such short-circuit diffusion has been observed and interpreted by Smeltzer *et al.* (17) for the initial oxidation of Zr and Hf. If the rate of SiO_2 formation decreases with decreasing P_{O_2} , as observed for SiC oxidation, it will take longer to form a coherent SiO_2 layer at reduced P_{O_2} , and the short-circuit diffusion found initially in pure oxygen will occur for a longer period of time. Therefore, in O_2/Ar mixtures the oxidation mechanism is essentially the same as it is in pure oxygen except that the period of short-circuit diffusion is extended.

In CO/CO_2 gas mixtures the oxidation rates were parabolic after a brief transient period, decreased with decreasing P_{O_2} , and were larger than in pure oxygen. The SiO_2 formed in these mixtures appeared as globules and was not protective. Although the cause of the globule formation is not clear, volume oxygen diffusion through the HfO_2 layer is believed to be rate determining in these mixtures. Active oxidation of the SiC particles was not observed in CO/CO_2 mixtures. In these mixtures the partial pressure of CO in the gas surrounding the sample is large causing the active oxidation reactions



and



to be retarded or driven to the left.

The rates of total oxygen consumption of $\text{HfB}_2 + \text{SiC}$ and $\text{ZrB}_2 + \text{SiC}$ composites in 250 Torr O_2 are compared in Fig. 11. The 1400°C data for the ZrB_2 -based composite are those of Tripp *et al.* (7) converted to a parabolic plot. The initial rapid oxidation kinetics of the two composites are controlled by short-circuit

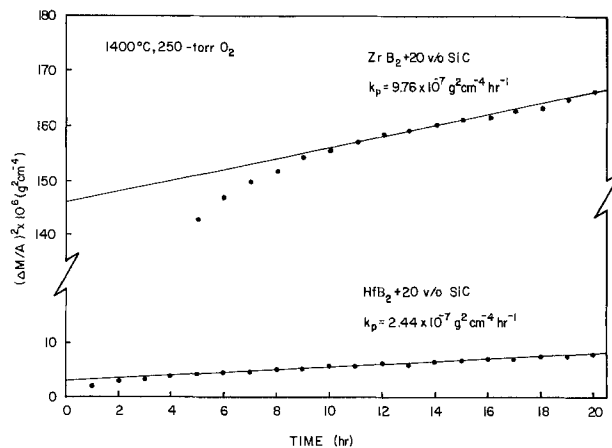


Fig. 11. Comparison of the rates of total oxygen consumption for $\text{HfB}_2 + 20 \text{ v/o SiC}$ and $\text{ZrB}_2 + 20 \text{ v/o SiC}$ at 1400°C in 250 Torr O_2 .

diffusion through the inner HfO_2 or ZrO_2 scales; however, the reason for the large difference in initial oxidation rates is unknown. After ~ 10 hr the oxidation rate of the $\text{ZrB}_2 + \text{SiC}$ composite is only a factor of four larger than that of the $\text{HfB}_2 + \text{SiC}$. Since each composite contains ~ 26 -27 m/o SiC, the stoichiometric oxidation reactions are essentially the same for the two materials. Hence, the rates of silica formation during oxidation can be compared directly and agree well within one order of magnitude. The oxygen partial pressure dependences of the oxidation rates are also similar. Therefore, the same mechanism, initial short-circuit oxygen diffusion through the HfO_2 or ZrO_2 followed by oxygen diffusion through the SiO_2 scaling layer, controls the oxidation of the two materials.

Acknowledgment

The authors wish to thank J. E. Henry for his assistance with the balance measurements and R. H. Duff for conducting the microprobe analyses of the scales. This work was supported in part by U. S. Air Force Contract F33615-71-C-1841. This paper was presented in part at the 75th Annual Meeting of the American Ceramic Society, Cincinnati, Ohio, May 1, 1973 (Basic Science Division, No. 83-B-73).

Manuscript submitted Aug. 7, 1974; revised manuscript received ca. April 7, 1975.

Any discussion of this paper will appear in a Discussion Section to be published in the June 1976 JOURNAL. All discussions for the June 1976 Discussion Section should be submitted by Feb. 1, 1976.

Publication costs of this article were partially assisted by the U.S. Government.

REFERENCES

1. L. Kaufman and E. V. Clougherty, Air Force Materials Laboratory Report RTD-TDR-63-4096, Part 1, Air Force Materials Laboratory, Wright-Patterson Air Force Base, Ohio (December 1963).
2. L. Kaufman, E. V. Clougherty, and J. B. Berkowitz-Mattuck, *Trans. Met. Soc. AIME*, **239**, 458 (1967).
3. J. B. Berkowitz-Mattuck, *This Journal*, **113**, 908 (1966).
4. E. V. Clougherty, D. Kalish, and E. T. Peters, Air Force Materials Laboratory Report AFML-TR-68-190, Air Force Materials Laboratory, Wright-Patterson Air Force Base, Ohio (July 1968).
5. W. C. Tripp and H. C. Graham, *This Journal*, **118**, 1195 (1971).
6. H. C. Graham, H. H. Davis, I. A. Kvernes, and W. C. Tripp, in "Ceramics in Severe Environments," W. W. Kriegel and H. Palmour III, Editors, p. 35, Plenum Publishing Co., New York (1971).
7. W. C. Tripp, H. C. Graham, and H. H. Davis, *Am. Ceramic Soc. Bull.*, **52**, 612 (1973).

8. W. C. Tripp and H. C. Graham, *Air Force Res. Rev.*, **1**, 26 (July-August 1970).
9. W. W. Smeltzer and M. T. Simnad, *Acta. Met.*, **5**, 328 (1957).
10. B. E. Deal and A. S. Grove, *J. Appl. Phys.*, **36**, 3770 (1965).
11. A. G. Revesz and R. J. Evans, *J. Phys. Chem. Solids*, **30**, 551 (1969).
12. K. Motzfeldt, *Acta. Chem. Scand.*, **18**, 1596 (1964).
13. W. C. Tripp, J. W. Hinze, and H. C. Graham, Paper No. 27-B-74 presented at the 76th Annual Meeting of the American Ceramic Society, Chicago, Ill., April 28-May 2, 1974.
14. S. C. Singhal and F. F. Lange, Paper No. 38-BC-73F presented at the Fall 1973 Meeting of the American Ceramic Society, Pittsburgh, Pa., Sept. 23-26, 1973.
15. J. W. Hinze, W. C. Tripp, and H. C. Graham, Paper No. 28-52-74 presented at the 76th Annual Meeting of the American Ceramic Society, Chicago, Ill., April 28-May 2, 1974.
16. J. W. Hinze, W. C. Tripp, and H. C. Graham, in "Mass Transport in Ceramics," A. H. Heuer and A. R. Cooper, Editors, Plenum Publishing Co., New York (In press).
17. W. W. Smeltzer, R. R. Haering, and J. S. Kirkaldy, *Acta Met.*, **9**, 880 (1961).

Kinetics of Phosphorus Predeposition in Silicon Using POCl_3

P. Negrini, D. Nobili, and S. Solmi

C.N.R.—LAMEL, Via Castagnoli, 1, 40126 Bologna, Italy

ABSTRACT

Phosphorus predeposition in silicon using a POCl_3 source and oxidizing conditions has been studied over a wide range of temperature (850°-1200°C) and doping gas compositions, by determining the total and electrically active dopant and the thickness of the surface oxide. The dependence of the fraction of electrically inactive phosphorus on temperature, time, and doping gas composition was studied; and it is reported that phosphide precipitation takes place in the course of the predeposition. These observations lead to the conclusion that the flux of phosphorus is not limited by the solubility of this element in silicon, and this is confirmed by the results of the study of the kinetics, which are reported. They show that the rate-determining process of phosphorus predeposition and the associated oxide growth is the diffusion across the oxide layer. The amount Q of dopant predeposited in an isothermal process increases with a parabolic time law

$$Q = \sqrt{K_0 \exp(-E_K/kT) \cdot t}$$

and a similar behavior is observed for the oxide thickness

$$X_0 = \sqrt{B_0 \exp(-E_B/kT) \cdot t}$$

It is shown that E_K and E_B are constants in a wide range of experimental conditions, and the dependence of K_0 and B_0 on gas composition is reported. A method, based on surface resistivity measurements after drive-in, which provides quantitative determinations of the predeposited phosphorus in satisfactory agreement with activation analysis, is reported in the Appendix.

A considerable amount of information exists in the literature on the electrical properties of phosphorus-doped layers in silicon as a function of the main parameters of the predeposition process (1-4).

It has been noticed by several authors that only a fraction of the predeposited phosphorus is electrically active and that it changes with subsequent heat-treatments (5, 6). Several hypotheses, among which is that of precipitation, have been put forward to explain the phenomenon (7, 8).

In silicon device technology, predeposition is generally followed by heat-treatments (drive-in, oxidation, annealing) which can therefore result in an unpredictable change of the amount of electrically active dopant.

In industrial practice this uncertainty is by-passed by using standard procedures for device production.

Determination of the total phosphorus content as a function of the main parameters of the predeposition thus has practical interest and is a necessary procedure for an analysis of the kinetics of this process.

Further, determination of the functional relations between the physical and chemical variables and the

electrically active and total dopant can contribute to clarifying the nature of the electrically inactive phosphorus.

Experimental

Low dislocation density ($< 500 \text{ cm}^{-2}$), (111) oriented, boron-doped, Czochralski-pulled silicon of nominally $1 \text{ ohm}\cdot\text{cm}$, about $300 \mu\text{m}$ thick, has been used in our experiments. Slices, produced by Wacker, were mirror finished on one side.

Predeposition experiments were carried out under oxidizing conditions in an open tube furnace¹ having an internal diameter of 55 mm. Temperature uniformity in the flat zone of the quartz tube ($\sim 30 \text{ cm}$) was kept within $\pm 0.5^\circ\text{C}$.

Experiments were run at 850°, 920°, 1000°, 1100°, and 1200°C using a POCl_3 source kept at 24°C (corresponding to a vapor pressure of 34 Torr).

The predeposition atmosphere consisted of high purity nitrogen bubbled through the phosphorus oxychloride source and mixed, before entering the furnace, with the main carrier gas (nitrogen plus high purity oxygen).

Key words: silicon, phosphorus oxychloride, kinetics of predeposition, phosphorus precipitation.

¹ B.T.U. Engineering Corporation, Model DC. LH1.

A set of experiments has been carried out at various partial pressures of dopant, always keeping the ratio between POCl_3 and O_2 constant; another set by changing only oxygen partial pressure and a third set by changing only that of POCl_3 . In any case the total gas flow was kept constant (1580 ml/min) by adjusting the main nitrogen flow. Calibrated flow meters² were used to control the predeposition atmosphere.

Prior to each deposition a 5 min warm-up period was given without the flow of dopant and, afterwards, a further 3 min flushing as a health precaution.

Extraction from the furnace was, unless specified, rapid (about 1 sec). Specimens were left to cool in an air stream, and a quartz boat of low thermal capacity was used.

The thickness of the phosphorus glass formed during the predeposition was accurately measured by a Taly-step (maximum sensitivity 20Å) by making at least 10 determinations for each specimen.

We have determined both the electrically active and the total content of phosphorus. As discussed in the Appendix the latter quantity has been measured by neutron activation analysis and electrical resistivity after suitable drive-in. These were carried out at 1100° or 1200°C in a $\text{N}_2 + 10\% \text{O}_2$ atmosphere, after removal of the phosphorus glass in dilute hydrofluoric acid.

Both after predeposition and drive-in processes sheet resistivity was measured by the four-point probe technique; five distinct determinations were executed on each specimen after removing oxide with dilute HF. At least three specimens were processed for each experimental point.

The presence of precipitates in predeposited specimens has been checked both by transmission electron microscopy (TEM) using an Elmiskope 101 electron microscope, and by x-ray topography using a Lange camera and $\text{CuK}_{\alpha 1}$ radiation.

TEM observations have been carried out on the polished side after thinning the slice by etching the opposite surface with a jet technique. Also the specimens for x-ray topography were chemically thinned to eliminate the damaged lapped side.

Results and Discussion

Total and electrically active predeposited phosphorus.

—We report first the values of Q and Q_{el} (total and electrically active phosphorus) for a predeposition time of 27 min at 920°C. In Fig. 1 these quantities are plotted vs. the concentration of POCl_3 at a constant O_2 concentration of 5.7%.

In Fig. 2 the values of Q and Q_{el} are reported vs. the concentration of O_2 at a constant POCl_3 concentration of 0.27%.

In Fig. 3 we report the values for a simultaneous change of O_2 and POCl_3 keeping constant the ratio of their concentrations (~ 21.5).

In the composition range considered our data of Q_{el} are in qualitative agreement with those reported earlier (1) and show that this quantity is relatively insensitive to the variables under control. On the contrary, Q is a sensitive property which decreases as the concentration of oxygen rises, increases with that of POCl_3 , and increases also, but less steeply, with their simultaneous increase. In any case the ratios Q/Q_{el} turn out to be larger than 1.

For a more comprehensive analysis of this effect in the range of experimental conditions typical of device technology we report in Fig. 4 the ratios Q/Q_{el} as a function of time for predeposition processes at 850°, 920°, 1000°, 1100°, 1200°C at constant gas composition (5.7% O_2 and 0.27% POCl_3). In Fig. 5 the ratios Q/Q_{el} are reported for processes at the above-mentioned temperatures and at a constant predeposition time (27 min) as a function of O_2 and POCl_3 concentrations, simultaneously increased.

² Fischer and Porter.

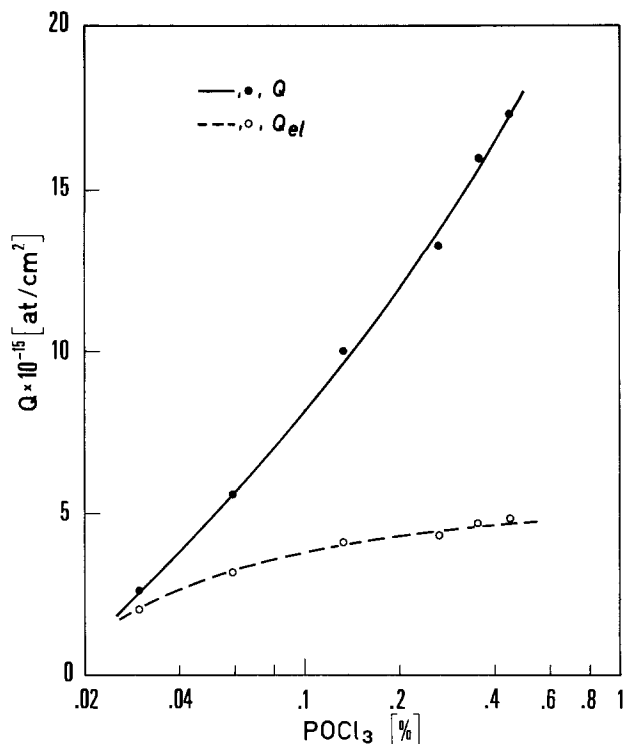


Fig. 1. Total, Q , and electrically active phosphorus, Q_{el} , vs. POCl_3 concentration, in constant time (27 min) predepositions at 920°C. Oxygen concentration is constant (5.7%).

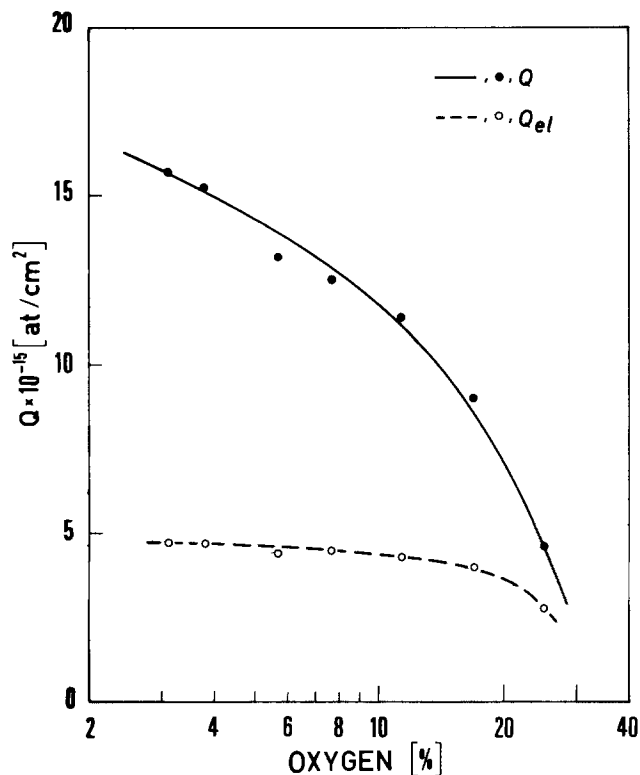


Fig. 2. Total, Q , and electrically active phosphorus, Q_{el} , vs. oxygen concentration, in constant time (27 min) predepositions at 920°C. POCl_3 concentration is constant (0.27%).

These results confirm that the situation evidenced by comparing electrical profiles and chemical data is verified in a wide range of experimental conditions: i.e., the amount of phosphorus determined by resistivity measurements after predeposition is systematically lower than the total, and the discrepancy can be very large. They show that the ratio increases with increasing concentration of POCl_3 and decreasing tempera-

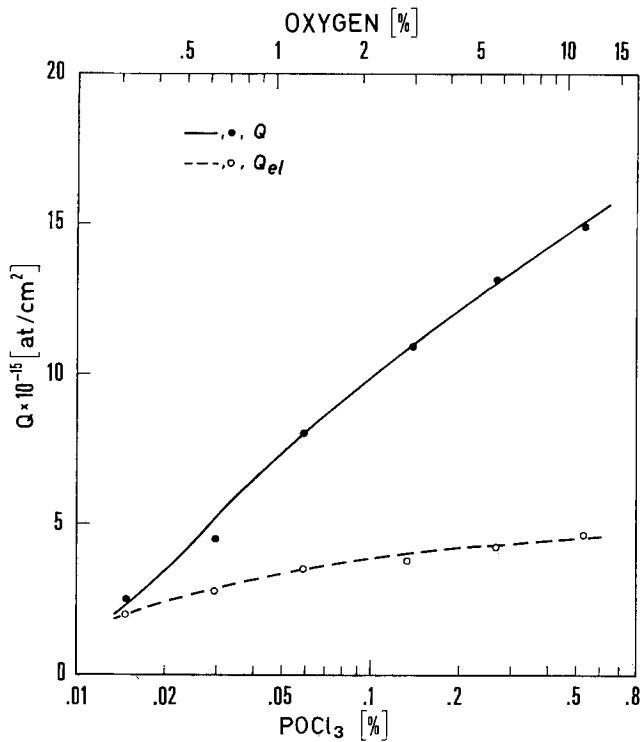


Fig. 3. Total, Q , and electrically active phosphorus, Q_{el} , vs. $POCl_3$ and oxygen concentrations increased keeping constant their ratio (~ 21.5). Conditions of predepositions are the same as for Fig. 1 and 2.

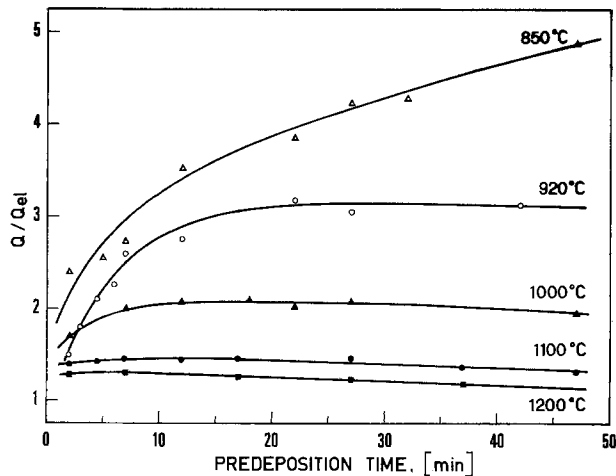


Fig. 4. Time dependence of the ratio Q/Q_{el} between total and electrically active phosphorus. Doping gas composition is 5.7% O_2 and 0.27% $POCl_3$.

tures. Further, these ratios keep nearly constant after an initial time which increases with decreasing temperature.

We have determined, by changing the time of extraction from the furnace from 1 to 60 sec, that these ratios are unaffected by the extraction rate.

TEM and x-ray topography examinations carried out using the techniques described have shown evidence of precipitation taking place in the course of the predeposition process.

This phenomenon can account for the electrical inactivity of at least part of the phosphorus. Qualitatively, the amount of the precipitated phase increases as the ratio Q/Q_{el} rises.

A detailed study on the morphology and structure of the precipitates will be presented in a separate paper (10).

We report in Fig. 6 and 7 typical examples of the precipitates observed: the particles in the former look like those observed by Jaccodine (7); the precipitates

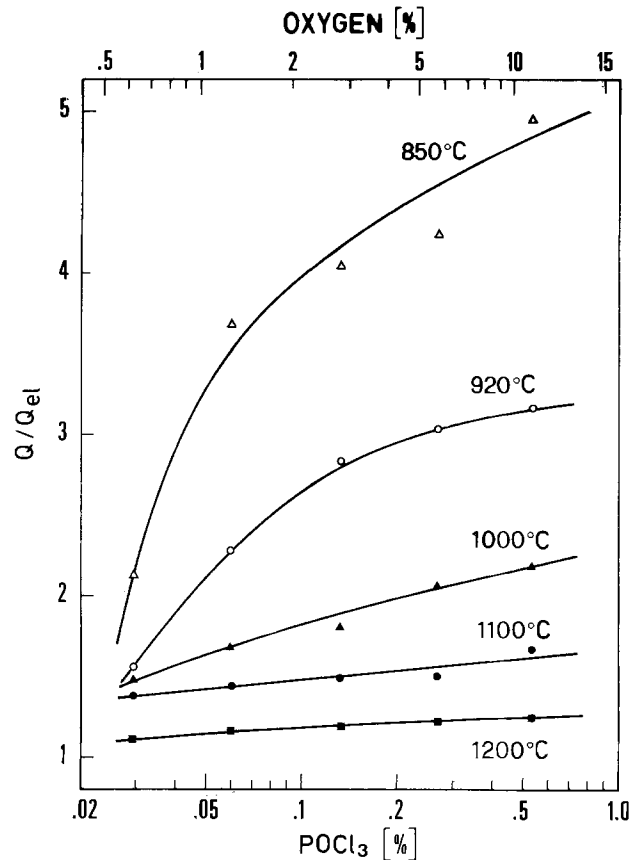


Fig. 5. Ratio Q/Q_{el} between total and electrically active phosphorus vs. $POCl_3$ and oxygen concentration increased keeping constant their ratio (~ 21.5). Predeposition time is constant (27 min).

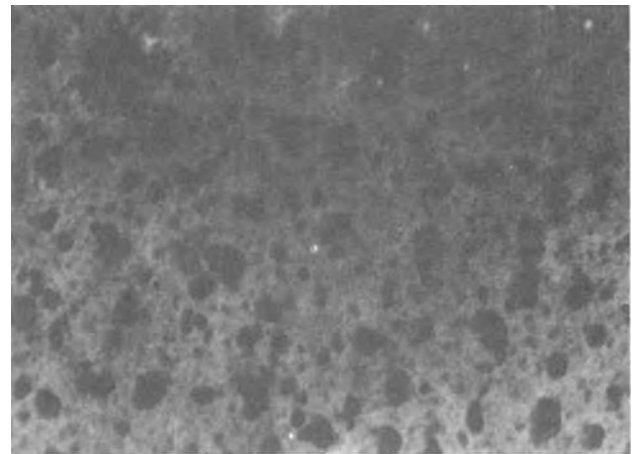


Fig. 6. Electron micrograph showing dotlike particles of silicon phosphide in a 1000°C, 22 min predeposited silicon wafer. 130,000X.

in Fig. 7 are plateletlike, similar to those observed by Levine *et al.* (11).

It has been verified by systematic observations carried out after anodic oxide stripping that the precipitates are not confined to the surface but lie within the diffused region.

Further, it has been shown, by changing the time of extraction from the furnace from about 1 to 60 sec, that both the structure and density of the precipitates are unaffected by the extraction rate. This is in agreement with the above-mentioned result that Q/Q_{el} is unaffected by the extraction and is a further evidence that precipitation takes place in the furnace.

The presence of these precipitates shows that in a wide range of conditions, typical of device technology, the chemical potential of phosphorus at the glass-silicon interface and in the adjacent Si matrix can

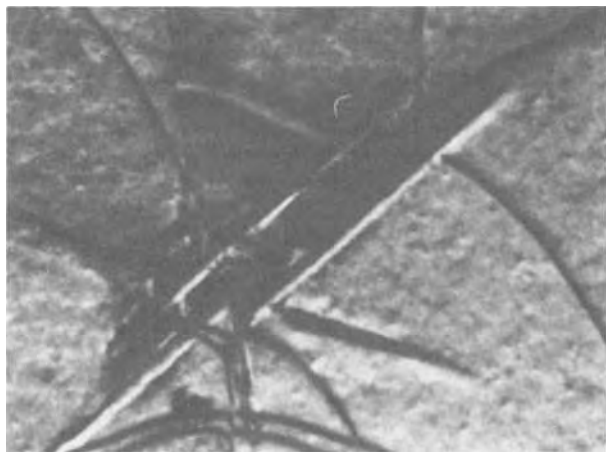


Fig. 7. Electron micrograph showing platelets of silicon phosphide in a 920°C, 42 min predeposited silicon wafer. The precipitates are parallel to $\langle 220 \rangle$ direction. 50,000X.

overcome the value corresponding to the solubility limit. A supersaturated solid solution of phosphorus in silicon is formed and precipitates can nucleate inside the silicon matrix.

It is important to point out that these precipitates act as sinks for the dopant, therefore, the flow of phosphorus across the glass-silicon interface is not limited by the primary solid solubility of this element in silicon.

Kinetics of oxide growth and of phosphorus doping.

—To obtain information about the kinetics, the values of the total phosphorus content Q and of the oxide thickness X_o resulting from predeposition experiments at given doping gas compositions have been determined as a function of time t at different temperatures, 850°, 920°, 1000°, 1100°, and 1200°C. In Fig. 8 we report the Q data obtained with POCl_3 and O_2 concentrations of 0.27 and 5.7%, respectively. The corresponding thicknesses X_o of oxide are reported in Fig. 9. In spite of the indeterminateness in the predeposition time due to the experimental procedure, the plots extrapolate well to the origin. These results show, at all temperatures, a parabolic oxide growth $X_o = \sqrt{Bt}$; a similar kinetics $Q = \sqrt{KT}$ is observed for phosphorus. B and K are coefficients which depend, as discussed below, only on temperature and gas composition.

The process of doping, as well as the oxide growth go through several consecutive steps. A detailed treatment of the thermal oxidation of silicon is reported by Grove: the reacting species must be transported

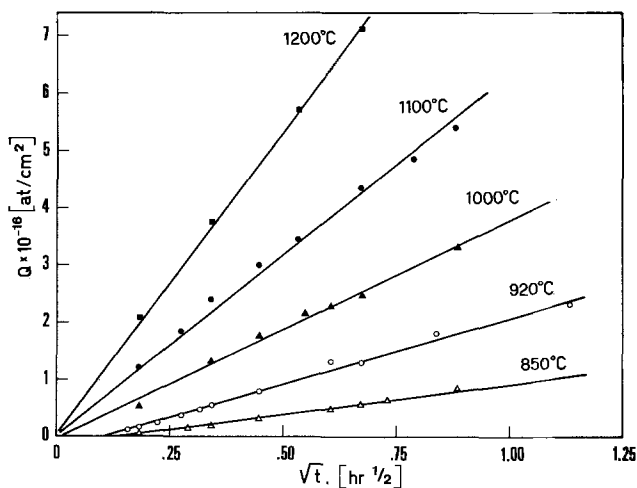


Fig. 8. Parabolic increase of the amount of phosphorus with predeposition time. POCl_3 and O_2 concentrations are 0.27 and 5.7%, respectively.

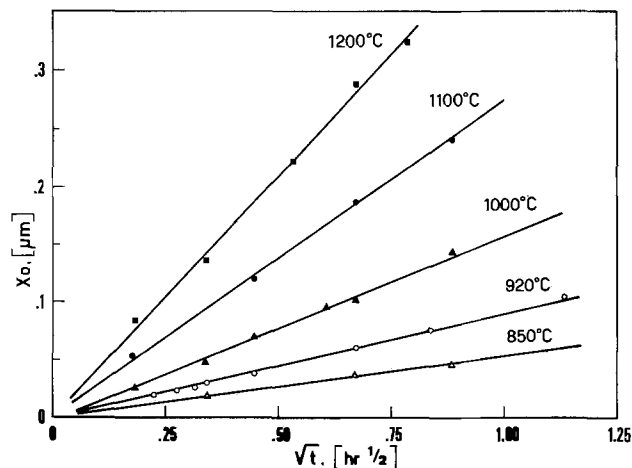


Fig. 9. Parabolic increase of the oxide thickness with predeposition time. POCl_3 and O_2 concentrations are 0.27 and 5.7%, respectively.

from the bulk of the gas to the oxide surface, diffuse across the oxide layer, and then react at the Si surface. In the steady state the fluxes corresponding to each step are equal and the kinetics is controlled by the slowest one. This treatment leads to the conclusion that a parabolic growth results from a diffusion limited process (9). Our data fit with the following rate equation

$$\frac{dQ}{dt} = \frac{D(C_o - C_i)}{x(t)} \quad [1]$$

where D is the diffusion coefficient, C_o and C_i the steady-state concentration of phosphorus at the gas oxide and at the oxide silicon interface, respectively, and x the oxide thickness, which increases parabolically with time. This indicates that also in case of phosphorus diffusion the passage across the oxide is the controlling step.

These conclusions can be verified by observing the effect of thin, preformed oxide films on the velocity of these processes.

In diffusion-limited conditions, with an initial oxide thickness x_i , the law of oxide growth becomes (9)

$$x = \sqrt{Bt + x_i^2} \quad [2]$$

and the integral of Eq. [1] results

$$Q = Q_o \left[\sqrt{1 + \left(\frac{x_i}{x_o}\right)^2} - \frac{x_i}{x_o} \right] \quad [3]$$

where Q_o and x_o are, respectively, the amount of predeposited phosphorus and the oxide thickness resulting from the process with $x_i = 0$.

For Eq. [3] to be valid C_o and C_i must attain their steady values in a negligible time; this is a further reason for keeping $x_i \ll x_o$.

We have carried out constant time (27 min) predepositions at 920° and 1000°C on slices with x_i up to about 300 and 500Å, respectively. Doping gas conditions were kept the same as in Fig. 8 and 9. The oxide films had been obtained by thermal oxidation at 920°C in a dry oxygen atmosphere.

We report in Fig. 10 the experimental values of $Q(x_i)$ together with those of the thickness $(x - x_i)$ of the newly formed oxide as a function of the thickness x_i of the preformed oxide. A very good agreement is observed between these and the theoretical curves obtained by Eq. [2] and [3], respectively; they are verified in a wide range up to $x_i = \frac{1}{2} x_o$. This confirms the validity of the simplified model in Eq. [1] and that both phosphorus predeposition and oxide growth are limited by diffusion across the oxide layer. Both processes show an exponential temperature dependence

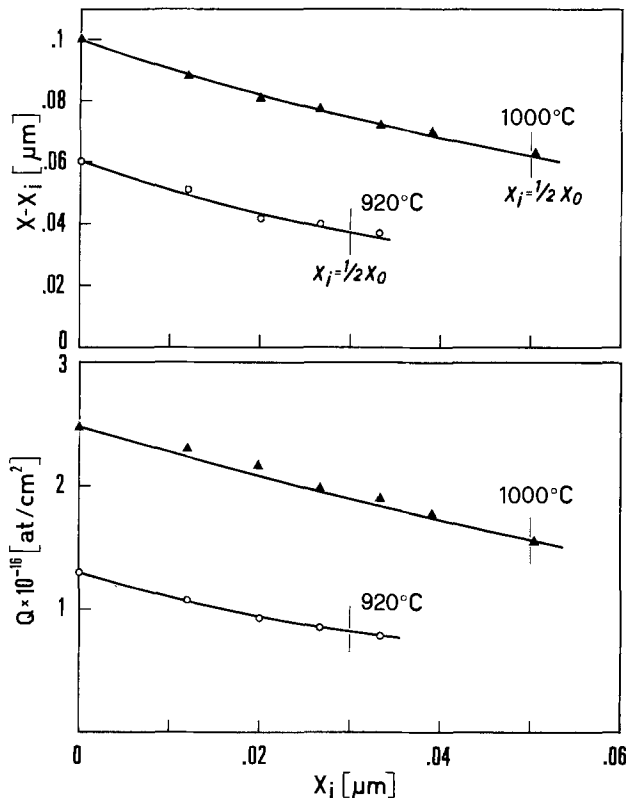


Fig. 10. Experimental values and calculated curves of pre-deposited phosphorus and of the associated oxide growth, reported vs. the thickness x_i of preformed oxide layers. Constant time (27 min) predepositions at the same doping gas compositions as in Fig. 8 and 9.

which can be analyzed by considering the values of the coefficients B and K .

We have verified by further experiments that the exponential factors keep constant in a wide range of gas compositions. In Fig. 11 and 12 are reported Arrhenius plots of B and K values, respectively, obtained by constant time (27 min) predepositions carried out at 850°, 920°, 1000°, 1100°, and 1200°C. The concentration of POCl_3 was varied in the range between 0.06 and 0.53%, by keeping constant the O_2/POCl_3 ratio (21.5). In the whole temperature range, B turns out to have the general form $B = B_0 \exp(-E_B/kT)$ with $E_B = 1.7$ eV.

A similar relation $K = K_0 \exp(-E_K/kT)$, valid up to 1100°C, is observed in Fig. 12 with $E_K = 2.2$ eV.

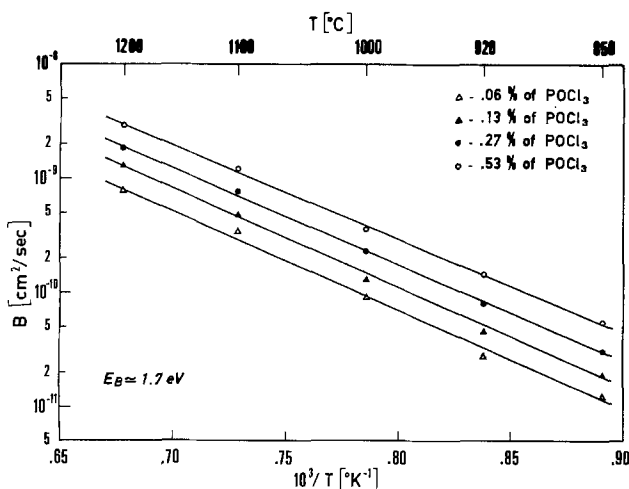


Fig. 11. Dependence on temperature and on doping gas composition of the coefficient B . The ratio O_2/POCl_3 is kept constant (21.5).

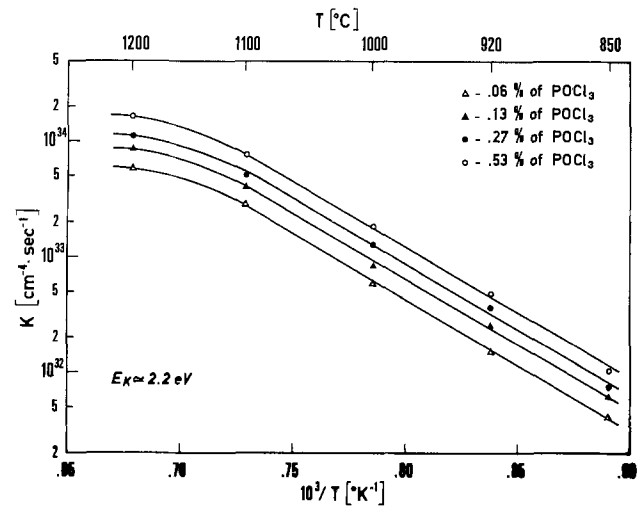


Fig. 12. Dependence on temperature and on flux composition of the coefficient K , compositions are the same as in Fig. 11.

Only the pre-exponential factors B_0 and K_0 depend on gas composition and decrease with decreasing oxygen and POCl_3 concentrations.

The energy term in the temperature dependence of Q results $\frac{1}{2} E_K = 1.1$ eV; lower than the corresponding term of Q_{el} (about 1.6 eV) resulting from our experimental data. The latter value is in agreement with those calculated by the data in literature (6, 9, 12, 13).

This accounts for the increase of the ratio Q/Q_{el} with decreasing temperature observed in Fig. 4, and confirms that Q and Q_{el} depend on distinct phenomena.

We have shown that the total phosphorus content Q is limited by diffusion across the oxide layer; on the other hand Q_{el} , as reported in literature, is limited by the solubility and diffusivity of the dopant in silicon (9).

Finally, we notice that in our experimental conditions both Q_{el} and Q turned out to be fairly reproducible.

From statistics we have determined that the fractional standard deviation, $\sigma = \frac{1}{\bar{X}} \sqrt{\frac{\sum_1^n (\bar{X} - X_j)^2}{n-1}}$,

were 1.5 and 3% for Q_{el} and Q , respectively, in slices processed together. For different predepositions carried out in the same conditions we have obtained for Q_{el} and Q values of σ of 4 and 9%, respectively.

A more extensive study on the correlation between gas composition and the properties of the oxide phase is under way and the results will be reported.

Conclusions

A simple method which provides a satisfying precision for the quantitative determination of phosphorus predeposited in silicon, is the measurement of surface resistivity after suitable drive-in. The results of this technique, described in the Appendix, are in good agreement with those obtained by activation analysis.

In a wide range of experimental conditions typical of device technology using a POCl_3 source, the amount of electrically active predeposited phosphorus Q_{el} , is lower than the total dopant content Q . The fraction of electrically inactive phosphorus increases with the rising concentration of POCl_3 and decreasing temperature.

The electrically inactive phosphorus is due, at least in part, to phosphide precipitates within the diffused region. Precipitation takes place in the course of the predeposition process, therefore these precipitates act as sinks for the dopant. As a consequence the flux of phosphorus is not limited by the primary solid solubility of this element in silicon.

Study of the kinetics has shown that the rate-determining process of both phosphorus doping and the as-

sociated oxide growth is diffusion across the oxide layer.

Phosphorus predeposition follows a parabolic law $Q = \sqrt{Kt}$; a similar behavior $X_o = \sqrt{Bt}$ is observed for oxide thickness.

The relations $K = K_o \exp(-E_K/kT)$, with $E_K \approx 2.2$ eV, and $B = B_o \exp(-E_B/kT)$, with $E_B \approx 1.7$ eV, are satisfied over a wide range of temperature and flux compositions. The pre-exponential factors K_o and B_o increase with the concentrations of oxygen and $POCl_3$.

Acknowledgments

The authors wish to thank A. Armigliato and M. Servidori for their results of structural observations, F. Mousty for activation analysis, and G. Masetti for useful discussion. Acknowledgments are due to E. Gabilli and S. Guerri for cooperation in setting up the experimental facilities.

Manuscript submitted June 27, 1974; revised manuscript received April 1, 1975. This was Paper 221 presented at the New York, New York, Meeting of the Society, Oct. 13-18, 1974.

Any discussion of this paper will appear in a Discussion Section to be published in the June 1976 JOURNAL. All discussions for the June 1976 Discussion Section should be submitted by Feb. 1, 1976.

Publication costs of this article were partially assisted by C.N.R.—LAMEL.

APPENDIX

The amount of phosphorus predeposited in silicon can be accurately determined by activation analysis.

We have verified, according to the observations formerly reported by Tannenbaum (5), that it is possible to derive the same information by electrical measurements carried out after suitable drive-in.

As a prior step we have established the agreement between chemical and electrical profiles.

Our determinations were carried out on silicon slices processed in parallel at different predeposition and drive-in temperatures and times. Chemical profiles have been obtained by neutron activation analysis and an automated technique (14). The electrical profiles were obtained by conventional anodic oxide stripping and resistivity measurements (5). The dependence of mobility on concentration was considered based on accurate measurements carried out in our laboratory (15).

To avoid out-diffusion of phosphorus we have tried two procedures with good results. The first consisted of depositing a film of SiO_2 about 1 μm thick by sputtering; subsequent drive-in was performed in nitrogen.

The same results have been obtained, more simply, by performing the drive-in process in an oxidizing atmosphere ranging from pure O_2 to $N_2 + 10\% O_2$. This last composition has been adopted.

The amount of phosphorus lost turned out to be negligible; this is because the phosphorus segregation coefficient between SiO_2 and Si is very small (9) and the diffusivity of phosphorus is much smaller in SiO_2 than in Si (16).

Our determinations have shown that after suitable drive-in, as detailed below, the chemical and electrical profiles coincide fairly well.

Further, if the out-diffusion of phosphorus is inhibited by using the above techniques, the integral of the chemical profile after predeposition agrees with those of the profiles, chemical as well as electrical, after drive-in.

A typical example of our results is reported in Fig. 13.

The determination of the amount of predeposited phosphorus by analysis of the electrical profile is very tedious and time consuming. As a further step we have verified that a rapid technique which provides satisfying precision is the measurement of the surface resistivity after suitable drive-in.

The surface resistivity is given by the well-known relation

$$\rho_s = \frac{1}{e \cdot \int_0^{X_j} [C(x) - C_B] \cdot \mu(x) dx} \quad [A-1]$$

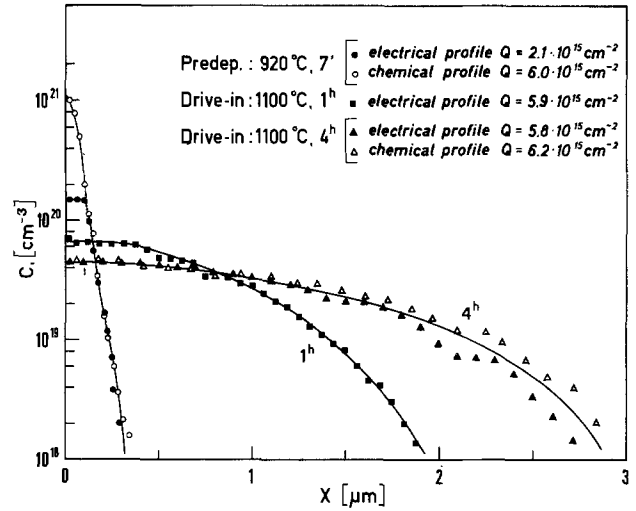


Fig. 13. Chemical and electrical phosphorus profiles after predeposition and drive-in. The latter has been carried out in $N_2 + 10\% O_2$ atmosphere.

where $C(x)$ is the concentration of the diffused dopant, C_B the concentration in the bulk (which was negligible in our experiments), X_j the junction depth, μ the electron mobility, which depends on the total impurity concentration, and e the charge of the electron.

Defining an "effective mobility" by the ratio

$$\mu_{eff} \equiv \frac{\int_0^{X_j} C(x) \cdot \mu(x) dx}{\int_0^{X_j} C(x) dx} \quad [A-2]$$

where

$$\int_0^{X_j} C(x) dx = Q$$

one obtains

$$\rho_s = \frac{1}{e \cdot \mu_{eff} \cdot Q} \quad [A-3]$$

which allows determination of the content of dopant Q by a simple measurement of the surface resistivity, provided that the values of μ_{eff} are known. Actually for concentrations above 10^{19} at./ cm^3 phosphorus mobility depends only slightly on the concentration (15, 17).

This results in values of μ_{eff} which are nearly independent of the process of predeposition and drive-in,

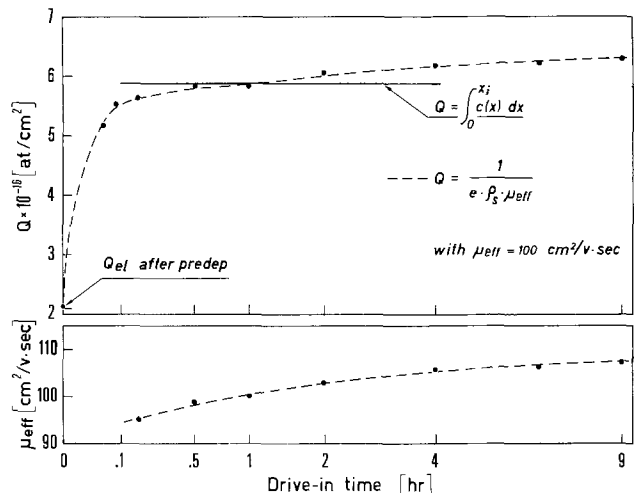


Fig. 14. Experimental determination of the apparent total phosphorus content vs. the drive-in time, assuming a constant value of μ_{eff} . In the lower part of the figure the real effective mobility, as deduced from the knowledge of the total diffused charge Q (solid line), are reported vs. the drive-in time.

Table I

Predeposition temp (°C)	Drive-in temp (°C)	Drive-in time (min)
850	1100	30
920	1100	30
1000	1100	60
1100	1200	30
1200	1200	30

provided that most of the dopant is in regions of the profile with concentration exceeding 10^{19} at./cm³.

By Eq. [A-2] we have calculated the value of μ_{eff} for all the specimens whose profile has been determined.

The value after predeposition was 95 cm²/V-sec, fairly independent of the conditions of the process.

Further, we have verified that, provided the surface concentration of the dopant keeps high, the "effective mobility" depends only slightly on the conditions of drive-in, our mean value being about 100 cm²/V-sec.

As a typical example we report in Fig. 14 our results for specimens having received a predeposition treatment of 7 min at 920°C followed by drive-in at 1100°C. The plot reports μ_{eff} vs. time of drive-in, calculated by Eq. [A-3] using the known value of Q . The values of Q calculated by using a constant value of $\mu_{\text{eff}} = 100$ are also shown.

Initially Q increases rapidly with time, corresponding to the formation of new active dopant; subsequent changes in the calculated values of Q are slight corresponding to increases in μ_{eff} with modifications in the distribution of the dopant.

It is noticed in Fig. 14 that a more than 50 times increase of the heating time results in a change of Q

of about 10%. These results show that, above a given time, the conditions of drive-in suitable for the determination of Q , are not critical.

Experiments like those in Fig. 1 have been carried out to determine the temperature and time of drive-in for the different predeposition processes. The conditions chosen for the present work are reported in Table I.

REFERENCES

1. M. S. R. Heynes and J. T. Wilkerson, *Electrochem. Technol.*, **5**, 464 (1967).
2. P. C. Parekh, *This Journal*, **119**, 173 (1972).
3. M. S. R. Heynes and P. G. G. van Loon, *ibid.*, **116**, 890 (1969).
4. J. S. Kesperis, *ibid.*, **117**, 554 (1970).
5. E. Tannenbaum, *Solid-State Electron.*, **2**, 123 (1961).
6. F. N. Schwettmann and D. L. Kendall, *Appl. Phys. Letters*, **19**, 218 (1971).
7. R. J. Jaccodine, *J. Appl. Phys.*, **39**, 3105 (1968).
8. M. L. Joshi and S. Dash, *IBM J.*, **11**, 271 (1967).
9. A. S. Grove, "Physics and Technology of Semiconductor Devices," John Wiley & Sons, Inc., New York (1967).
10. A. Armigliato and M. Servidori, *J. Mater. Sci.*, **10**, 306 (1975).
11. E. Levine, J. Washburn, and G. Thomas, *J. Appl. Phys.*, **38**, 87 (1967).
12. I. M. Mackintosh, *This Journal*, **109**, 392 (1962).
13. S. Maekawa, *J. Phys. Soc. Japan*, **17**, 1592 (1962).
14. G. Restelli, F. Girardi, F. Mousty, and A. Ostidich, *Nucl. Instr. Methods*, **112**, 581 (1973).
15. F. Mousty, P. Ostojica, and L. Passari, *J. Appl. Phys.*, **45**, 4576 (1974).
16. M. L. Barry, *This Journal*, **117**, 1405 (1970).
17. G. Baccarani and P. Ostojica, *Solid-State Electron.*, **18**, 579 (1975).

Anisotropy of Spontaneous Macro stresses in Ferromagnetic Films Induced by Magnetization

I. Anisotropic Macro stresses in Films of Nickel and Iron-Nickel Alloy Deposited in a Magnetic Field

M. Perakh (M. Ya. Popereka)*

Graduate School of Applied Science, The Hebrew University of Jerusalem, Jerusalem, Israel

ABSTRACT

When depositing nickel and iron-nickel alloy films in a magnetic field parallel to the substrate, the spontaneous macro stresses in the films are anisotropic. The absolute magnitude of the stresses can, depending on the composition of the alloy and the deposition conditions, be either substantially smaller or larger than in films deposited without the application of such a field. In layers of nickel electrodeposited from a solution free of organic inhibitors, the tensile macro stresses acting along the lines of a magnetic field are larger than those acting across the lines of a field. The introduction of saccharin into the solution effects an inversion of the influence of the magnetic field on the macro stresses: the tensile macro stresses acting across the lines of the field are now larger than those acting along these lines. In alloy films having a negative magnetostriction, the tensile stresses along the lines of the field are smaller than those across the lines. A change in the sign of the magnetostriction leads to an inversion of the field effect on the stresses: in alloys with a positive magnetostriction, the tensile macro stresses acting along the field are larger than those acting across it.

In ferromagnetic films obtained in vacuum by oblique incidence of the atom beam, the planar macro stresses possess a definite degree of anisotropy (1-3). However, the above means of precipitation is not the only source of the anisotropy of macro stresses. Thus,

* Electrochemical Society Active Member.

Key words: internal stress, measurement of anisotropic stress, anisotropy of magnetic films, electrodeposition of nickel and nickel-iron alloys, influence of magnetic field on electrodeposition.

McDonald (4) has already pointed out that films deposited in a magnetic field possess an anisotropic component of macro stresses in the direction of the field.

The creation of anisotropy of the macro stresses by a magnetic field (or, more accurately, by magnetization) is interesting, first, because of the possible contribution of macro stresses to magnetic anisotropy, and second, because its study may develop an understanding

of the origin of spontaneous macrostresses. The contribution made by spontaneous macrostresses to the uniaxial magnetic anisotropy of films, the composition of which is about 83% nickel and 17% iron, and the magnetostriction coefficient which is in the order of -10^{-5} , has been previously reported (5).

The purpose of this work was to measure spontaneous anisotropic macrostresses in iron-nickel films of a wide range of compositions and to investigate the basic behavior of the phenomenon (to which Part I of this work is dedicated), and to attempt to form a quantitative interpretation of the phenomenon (see Part II) (6).

Experimental

Two methods were used to measure spontaneous macrostresses in electrolytic films of an iron-nickel alloy. The first used an alternate bending of two mutually perpendicular flat substrates (3, 7), one directed along and the other across the line of the field. The deflections of the substrates were registered automatically by a highly sensitive device, roughly identical to the one previously described (8). The substrates were polished copper plates of 1.5 mm thickness, on the lower side of which the film was deposited, while the upper side was kept outside the electrolyte. The computation of the absolute magnitude of real [not the average over the film thicknesses (1, 4)] macrostresses was made according to the following formulas (7)

$$\sigma_x = \frac{1}{3} \frac{E_0 d^2}{l^2 (1 - \mu_0^2)} \left(\frac{df_x}{dt} + \mu_0 \frac{df_y}{dt} \right);$$

$$\sigma_y = \frac{1}{3} \frac{E_0 d^2}{l^2 (1 - \mu_0^2)} \left(\frac{df_y}{dt} + \mu_0 \frac{df_x}{dt} \right) \quad [1]$$

where E_0 is Young's modulus of elasticity, μ_0 is Poisson's ratio of the substrate material, l is the length of that part of the substrate covered by the film, d is the thickness of the substrate, f_x and f_y are the deflections of the free ends of the substrates directed along (x axis) and across (y axis) the lines of the field. Magnitudes df_x/dt and df_y/dt are determined by graphical differentiation of the "deformation curves," i.e., the relationship of deflections f_x and f_y , recorded on the diagram tape, to the film thickness.

In addition, a second method was specially developed which, although more laborious, measures σ_x and σ_y simultaneously using only one sample, as compared to two required by the first method; the second method enables a stricter control over the similarity of conditions for measuring σ_x and σ_y . Because of its tediousness, the second method was chiefly used to check the results. It is based on the spontaneous tension-compression (in two mutually perpendicular directions) of the flat substrate covered on both sides by the film being studied. A device schematically pictured in Fig. 1 was used. Fixture 1 fixes one corner of the flat substrate 2 to the Teflon frame 3, which is being inserted into the guides 5 of the carriage 6. The device is placed on the table of a microhardness meter. A diamond indenter is used to make imprints A and B_x on the substrate opposite the reference marks C_1 and C_2 on part 7 which is fixed to carriage 8. Frame 3 with the substrate 2 is then turned through 90° and carriage 6 is used to fix imprint A opposite mark C_2 ; carriage 8 is used to introduce mark C_1 in the field of vision of the microscope, and imprint B_y is made opposite it on the substrate. Then, frame 3 (without the flat table 4) is placed in the cell, where the film being studied is grown on both sides of the substrate until it reaches the required thickness. After that, frame 3 with the substrate and film (and with table 4) is again inserted into guides 5. Screw 9 is used to move carriage 6 in the grooves of carriage 8 until imprint A coincides with reference mark C_1 (or C_2). Carriage 8 is moved in the grooves 10 by turning screw 11 until mark C_2 and imprint B_x (or, correspondingly, C_1 and B_y) appear in

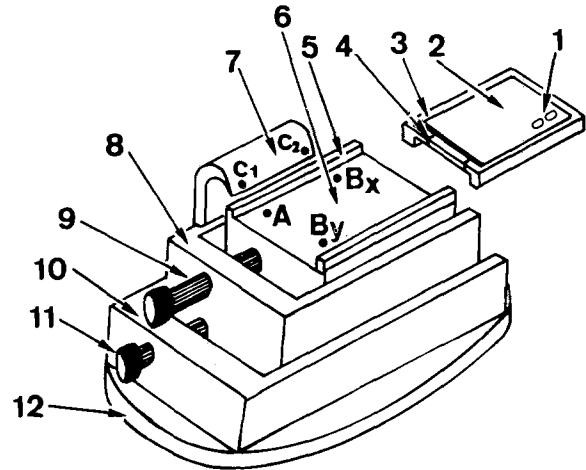


Fig. 1. Diagram of device for the measurement of anisotropic spontaneous macrostresses in films according to the method of biaxial tension-compression of the substrate plate. See text for explanation of numbers; 4, supporting table used to press the indenter into the sample.

the field of vision of the microscope. Stresses in the film produce a deformation of the substrate: the distance between imprint A and imprints B_x and B_y change by magnitudes Δ_x and Δ_y . The above deformations (i.e., the distance between C_2 and B_x or between C_1 and B_y after the deposition of the film) are measured using a measuring eyepiece (graduation $0.2 \mu\text{m}$).

In order to obtain the dependencies Δ_x vs. t and Δ_y vs. t (t is the thickness of deposit) it is needed to repeat the procedure described, specifying in every run the definite thicknesses t_1, t_2, \dots, t_n . Thus, although the σ_x and σ_y are determined by this method simultaneously and error due to the difference in experimental conditions while measuring these magnitudes separately is eliminated, error due to the use of a series of consecutive runs of measurement needed to obtain one "deformation curve" is greater than it is by using the first method (margins of error indicated in Fig. 2 and 3 correspond in all cases to maximum error obtained in series of specimens by using both methods).

The measurement base l (i.e., the distance between C_1 and C_2) was 3 cm. The substrates were plates of copper (thickness $25 \mu\text{m}$). The substrate deformed freely as the film was deposited. For such conditions, the computation of the absolute magnitude of actual macrostresses is made according to the formula (7)

$$\sigma_x(t) = \left[\frac{E_0 d}{1 - \mu_0^2} + \frac{E_1 t}{1 - \mu_1^2} \right] \frac{1}{l} \frac{d\Delta_x}{dt}$$

$$+ \left[\frac{E_0 \mu_0 d}{1 - \mu_0^2} + \frac{E_1 \mu_1 t}{1 - \mu_1^2} \right] \frac{1}{l} \frac{d\Delta_y}{dt} \quad [2]$$

and a similar equation for σ_y , which is obtained by replacing indexes x by y and vice versa. In Eq. [2], E_1 is the modulus of elasticity, μ_1 Poisson's ratio for the material of the film, t the sum total thickness of deposit on both sides of the substrate. Magnitudes $d\Delta_x/dt$ and $d\Delta_y/dt$ are determined by graphical differentiation of the experimental deformation curves Δ_x-t and Δ_y-t . The Young's modulus and Poisson ratios for substrates and deposits were determined using the method previously described (9).

While using the two-cantilever technique, stress is determined simultaneously with the film's growth in a magnetic field, thus the magnetostrictive deformation does not affect the results. When use is made of the second method described, the specimen is taken out of the magnetic field before strain measurement, thus a magnetostrictive deformation is added algebraically to that caused by stress. However, the difference of stresses determined using both methods described, did not exceed the margins presented in Fig. 2 and 3. Hence, the

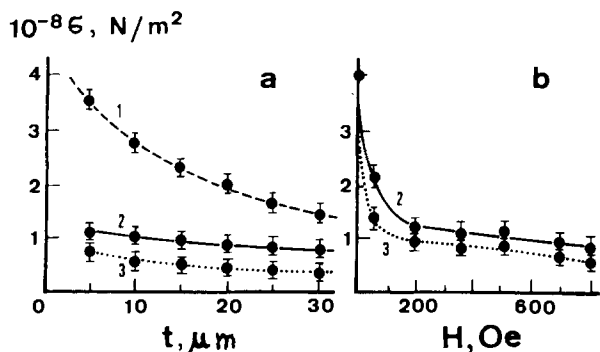


Fig. 2. Dependence of spontaneous macrostresses in electrolytic nickel films on the film thickness (a) and on the intensity of the technological magnetic field, used while the film is growing, parallel to the substrate (b). Curve 1, Stresses in the film deposited without a field; curve 2, macrostress along, and curve 3, across the field lines. For (a), curves 2, 3, $H_T = 520$ oe. For (b), curves 2 and 3, $t = 10 \mu\text{m}$.

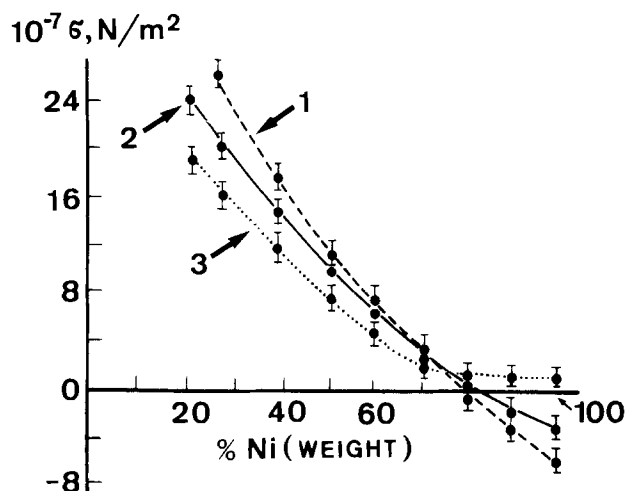


Fig. 3. Dependence of spontaneous macrostress in iron-nickel alloy films on composition. Curve 1, Stresses in films deposited without a field; curve 2, stresses along, and curve 3, across the field lines (300 oe). Film thickness $10 \pm 0.2 \mu\text{m}$.

regularities stated in this paper cannot be ascribed to the ordinary magnetostriction itself. Indeed, the coefficient of magnetostriction, for instance, for nickel is about $\lambda_s = -3.4 \times 10^{-5}$, while the initial strains discovered in nickel films were about $(0.5 \div 2) \times 10^{-3}$; the difference of strains appearing in two mutually perpendicular directions was up to 3×10^{-4} , which is almost ten times more than a maximum possible magnetostrictive strain in one direction. Moreover, the difference of strains, longitudinal and transverse, respectively, which are due to the magnetostriction, must be of the same sign regardless of operating conditions; actually, the difference of stresses longitudinal and transverse, respectively, changes its sign when, for instance, saccharin is introduced into the solution. Therefore, it is not the ordinary magnetostrictive strain which is responsible for the phenomenon described below.

The compositions of the solutions and the deposition conditions used to prepare the films under investigation are given in Table I.

The temperature of the specimen while measuring the stress using the second method was kept quite identical to that while depositing.

The thickness of the films was measured on an "Ultraoptimeter" (graduation scale $0.2 \mu\text{m}$). The rectangular cell was placed between the poles of the electromagnet (homogeneous field up to 10^3 oe). Uniformity of thickness of the deposited film over the sub-

Table I. Conditions of the deposition of nickel and iron-nickel films

Figure	Composition of solution, g/liter	Current density, A/dm ²	pH	Temperature, °C
2	NiSO ₄ · 7H ₂ O NiCl ₂ · 6H ₂ O H ₃ BO ₃	300 80 40	2.3	20 ± 0.25
3	(NiSO ₄ · 7H ₂ O + (FeSO ₄ · 7H ₂ O) H ₃ BO ₃ Rochelle salt Saccharin	294* 30 25 1	2.3	20 ± 0.25

* The ratio of the nickel and iron salts in the solution was changed (10) in order to obtain an alloy of the required composition (including 100% nickel).

strate was ensured by special limiters (11) of the electric field in the electrolyte.

Results and Discussion

Many properties of films studied were reported elsewhere (17, 18). Particularly, in these films, neither crystallographic texture nor the "columnar" structure were observed.

The characteristic experimental data are shown in Fig. 2 and 3. Let us note some of the basic features of the regularities thus discovered:

1. When depositing nickel and iron-nickel alloy films in a magnetic field, the spontaneous macrostresses are anisotropic.

2. In films of nickel deposited from a solution not containing organic inhibitors, the tensile stresses along the line of field (σ_x) are larger than the tensile stresses across the field (σ_y), Fig. 2. In nickel films deposited from a solution containing saccharin (as also in films deposited from the same solution without the superposition of a magnetic field), compressive macrostresses are registered in the direction of the lines of the technological magnetic field, while in the direction perpendicular to the field, tensile macrostresses are observed (Fig. 3).

The macrostresses observed in the experiment may be considered (12-14) as the algebraic sum of stresses of both signs, created independently. Hence, the above observation can be interpreted by assuming that the tensile macrostresses across the magnetic field are larger than those acting along the field. (The latter are in this case so small that they are exceeded by independently emerging compressive stresses and, as a result, excess compressive stresses are registered.) Thus, the introduction of saccharin into the solution leads to an inversion of the field's effect on macrostresses.

3. In films of iron-nickel alloy deposited from a solution containing saccharin and possessing a negative magnetostriction, the macrostresses along the lines of the field are smaller than those acting across it. Conversely, the macrostresses along the lines of the field are larger than the stresses across it in films of alloys possessing a positive magnetostriction (those containing less than $\sim 81\%$ nickel). Thus, a change of the sign of the magnetostriction leads to an inversion of the field effect on macrostress.

4. When depositing nickel and iron-nickel films in a magnetic field, the mean arithmetic magnitude of the stresses acting in both directions changes greatly as compared with those in films obtained without the superposition of a field. Such a change can greatly exceed the difference between the stresses acting along and across the field. Depending on the composition of the alloy and the deposition conditions, the mean magnitude of the stresses obtained by deposition in a magnetic field can be considerably smaller or larger than that obtained by the deposition without the superposition of a field.

An interpretation of items 1-3 will be proposed in Part II of this work (6). A full explanation regarding item 4 will not be attempted here. However, several

hypotheses could be proposed to explain the possible causes of this phenomenon. It has been found (15) that by depositing iron films in a magnetic field, a change occurred in the density of the crystal defects of the film. Indeed, this density of defects is one of the main factors determining the macrostress level (12-14). Changes in density of the defects may depend on changes in the amount of hydrogen (16) reduced together with the metal and adsorbed on the crystals of the growing film. Adsorption of hydrogen has a major effect on the surface tension of the crystal, thereby changing the condition of the outflow of defects and with it, the macrostress level (12). Causes of the changes in amount of hydrogen reduced together with the metal during deposition in a magnetic field are as yet unclear. (It may be that the magnetic field changes the height of the potential barrier being negotiated by the discharging hydrogen ion.)

Acknowledgments

The experiments, the results of which are given in this report, were carried out with the valuable assistance of B. S. Zolotkovskii, to whom the author wishes to express his sincere gratitude.

Manuscript submitted Dec. 2, 1974; revised manuscript received May 7, 1975.

Any discussion of this paper will appear in a Discussion Section to be published in the June 1976 JOURNAL. All discussions for the June 1976 Discussion Section should be submitted by Feb. 1, 1976.

REFERENCES

1. J. Finnegan and R. Hoffman, *J. Appl. Phys.*, **30**, 597 (1959).
2. J. Finnegan and R. Hoffman, Coll. "Eighth Natl. Symp. on Vac. Techn. Trans.," p. 935, Pergamon Press, New York (1961).
3. J. Priest, H. Caswell, and Y. Budo, *J. Appl. Phys.*, **34**, 347 (1963).

4. J. McDonald, *Proc. Phys. Soc., London*, **A64**, 968 (1951).
5. V. G. Balagurov, B. S. Zolotkovskii, M. Ya. Popereka, and V. M. Romanov, "Fizika plionok," Vol. 1, p. 3, Publ. Kalinin University, Kalinin (1972).
6. M. Perakh (M. Ya. Popereka), *This Journal*, **122**, 1263 (1975).
7. M. Ya. Popereka, "Elektroosazhdionie plionki," p. 5, Publ. Kalinin Pedagogical Institute, Kalinin (1970).
8. V. M. Bystrov, I. V. Nikityshev, and M. Ya. Popereka, *ibid.*, p. 89.
9. M. Ya. Popereka and V. G. Balagurov, *Fiz. Tverd. Tela*, **11**, 3507 (1969) (English transl., *Soviet Phys.-Solid State*).
10. A. Brenner, "Electrodeposition of Alloys," Academic Press, New York (1960).
11. L. I. Kadaner, *Ravnomernost galvanischeskikh pokrytiy* (Russ.), Publ. Kharkov Univ. (1962).
12. M. Ya. Popereka, *Fiz. Metal. metalloved.*, **23**, 753 (1965) [English transl., *Phys. Metals Metallog. (USSR)*].
13. M. Ya. Popereka, "Vnutrenie napryazheniya elektroliticheskoy osazhdayemykh metallov," West Siberian Book Press, Novosibirsk (1966) [English transl., "Internal Stresses of Electrolytically Deposited Metals," India Nat. Sci. Doc. Center, New Delhi, India (1970), translated for NBS and NSF, Washington, D.C., USA].
14. M. Ya. Popereka, *Proc. of the Third Intern. Congress on Metallic Corrosion*, Vol. 3, Publ. "Myr," Moscow (1968).
15. A. I. Vyrlan and A. S. Parsadanyan, Coll. "Navodorozhivanie metallov i borba s vodorodnoy khrupkostyu," p. 203, Publ. Moscow House of Scientific and Technical Propaganda, Moscow (1968).
16. A. S. Parsadanyan and N. P. Torodiy, *ibid.*, p. 200.
17. B. S. Zolotkovskiy and M. Ya. Popereka, *Fiz. Metal. Metalloved.*, **33**, 64, 268 (1972); **34**, 217, 1101 (1972) [English transl., *Phys. Metals Metallog. (USSR)*].
18. M. Ya. Popereka and B. S. Zolotkovskiy, *Izv. Akad. Nauk SSSR, Ser. Fiz.*, **36**, 1189 (1972) (English transl., *Bull. Acad. Sci. USSR, Phys. Series*).

Anisotropy of Spontaneous Macro stresses in Ferromagnetic Films Induced by Magnetization

II. Dislocation Model of the Anisotropy of Spontaneous Macro stresses in Films Grown in a Magnetic Field

M. Perakh (M. Ya. Popereka)*

Graduate School of Applied Science, The Hebrew University of Jerusalem, Jerusalem, Israel

ABSTRACT

A model of the appearance of anisotropy of the spontaneous tensile macro stresses in films grown in a magnetic field is considered. The model is based on the idea that the microscopic areas along the lines of the edge dislocations interact (as a result of magnetostriction) with the magnetization. This interaction effects the partial orientation of the dislocation lines and that of the normals to them, lying in the slip planes. This orientation appears during the growth of the film crystals in the magnetic field. In the system of partly orientated dislocations, the withdrawal of a fraction of them to the surface of the crystals creates a tendency for anisotropic reduction of the volume. This tendency is hampered by the adhesion of the film to the substrate, creating an anisotropic state of stress. The calculated values of anisotropy are close to the experimental observations; the equation derived offers an explanation for the principal experimental regularities.

In Part I of this work (1), the results of the measurement of anisotropic macro stresses in films of nickel

and iron-nickel alloy electrodeposited in a magnetic field were described, and the regularities observed in the experiments were stated. In this report, attempts are made to interpret the phenomena described in Part I. The consideration is based on a model (2-4), ac-

* Electrochemical Society Active Member.

Key words: dislocations in electrodeposits, anisotropy of internal stress, theory of stress, influence of magnetic field on electrodeposition.

ording to which a definite fraction of the tensile macrostresses results from the tendency of crystals in the film to decrease their volume. This tendency is due to the egress of a fraction of the growth dislocations from the volume of the crystals to the surface. Since adhesion of the film to the substrate prevents the decrease of volume, a plane state of stress sets in.

The assumption that the withdrawal of dislocations may contribute to the creation of spontaneous macrostresses in growing films (2-4) was confirmed by later experiments, the principal results of which can be summarized as follows:

1. Direct determinations of the density of dislocations, p_0 , in films [see for example (5)], gave results coinciding with the values of p_0 postulated to correlate the formulas with experimental data (2-4).

2. It was found that measures applied to the films to facilitate the escape of dislocations (for example, cathode polarization of the film in an electrolyte (6), which decreases its surface tension) increase spontaneous tensile macrostresses. This falls in with the predictions of the theory (2-4).

3. Direct observation by means of electron microscopy of high resolving power made it possible to observe the withdrawal of individual dislocations from a newly formed crystal of the film during the latter's growth (7). Observation confirmed the existence of the postulated mechanism (2-4).

4. A spontaneous decrease of the density of the stacking faults was reported (8, 9), i.e., a removal from the crystal of partial dislocations. This process, which occurs in electrodeposited copper films, is characterized by an activation energy of ~ 0.37 eV, which is lower than that for the motion of vacancies (~ 0.7 eV). The latter was thus not observed. The enumerated data give grounds to believe that the concept (2-4) can be used to interpret experimental data.

At the same time, it should be noted that the withdrawal of dislocations cannot be the only (and in many cases, not even the main) factor responsible for the appearance of spontaneous tensile macrostresses. Indeed, the presence of dislocations with a density of p_0 (the Burgers vector being b) brings about an increase in the specific volume of the crystal by magnitude (10)

$$\theta \cong 2 p_0 b^2$$

If the density of dislocations decreases as a result of the withdrawal of a fraction, κp_0 , of them (where $\theta < \kappa < 1$), a linear strain (along an arbitrary axis) of the order of $1/3 \kappa \cdot 2 p_0 b^2$ will result. To this linear strain (which is due to the adhesion of the film to the substrate) corresponds a linear macrostress of the order

$$\sigma \cong E \frac{1}{3} \kappa \cdot 2 p_0 b^2$$

where E is the modulus of elasticity of the film material. The computation of σ , using the above relation and based on experimental values (5) of p_0 at $\kappa \sim 0.1$, shows that for some films (e.g., for copper, antimony, manganese, tin, etc.) the withdrawal of dislocations may be responsible for the magnitudes of tensile macrostresses, observed experimentally. At the same time, for some other films (e.g., for chromium, iron, nickel, cobalt), the escape of dislocations, judging from the above relation, can account only for a part (ca. 0.1-0.3 of the total) of the observed values of the stresses. This indicates that there must also be other mechanisms responsible for the creation of tensile macrostresses [for example, the outflow of vacancies (11), phase and structural changes, interdiffusion on the interface, etc.].

This paper attempts to show that the mechanism of the withdrawal of dislocations should be regarded as the main reason for the creation of the anisotropic component of tensile macrostresses, as applies to films grown in a magnetic field.

In close-packed structures (which include, in particular, nickel and iron) vacancies are practically isotropic defects. The annihilation of vacancies or their removal from the crystal, assumed, for example, to be one of the main causes of the appearance of macrostresses (11), can therefore hardly explain the creation of the anisotropic component of them. The assumption that the withdrawal of a fraction of the dislocations is the cause of the appearance of macrostresses, however, makes it possible, owing to the anisotropic nature of the dislocations themselves, to propose a model for the creation of anisotropic macrostresses for films grown in a magnetic field.

In this model neither the origin of edge dislocations nor their types, nor any other particular properties of dislocation are essential. Only three facts are to be employed for the consideration, namely, (a) that presence of dislocation causes an increase in the volume; (b) that a partial egress of dislocations occurs; and, consequently, (c) that this egress causes an anisotropic change in volume, which is due to the anisotropic structure of dislocations.

Computation of the Orientation of the Dislocation Lines by Magnetization

Figure 1 shows a model of a segment AB of an edge dislocation line (DL), which segment is of unit length and has a definite orientation. The escape of such a segment from the crystal causes linear dilatation in the direction of the normal (NSP) to the dislocation line, which normal lies in the slip plane. In the direction of DL, the dislocation withdrawal will cause no dilatation. In an arbitrary direction, coinciding neither with DL nor with NSP, the escape of the segment under consideration will cause a dilatation, the magnitude of which is equal to the projection on the given direction of the dilatation observed along NSP. Thus, the level of the macrostresses acting in the given direction is determined by the statistically averaged orientation of the normal NSP to the dislocation line.

Crystalline anisotropy leads to the formation, within a single grain, of some predominant orientations of DL and NSP. However, in a polycrystalline body the orientation of the dislocations, as averaged for the body, is random. The superposition of a magnetic field, while the crystal is growing, creates the additional factor of anisotropy. The area of the lattice adjacent to the line of dislocation interacts in the ferromagnetic body with magnetization, owing first to the existence, along the line of dislocation, of demagnetizing fields and second, to magnetostriction. [According to calculations, for example (12), the intensity of the magnetostrictive interaction is by two orders of magnitude greater than that of the magnetostatic.] Energy of the interaction of the dislocation with magnetization must depend on the angle θ , which is formed between DL and the magnetization vector M , and angle ϕ , formed

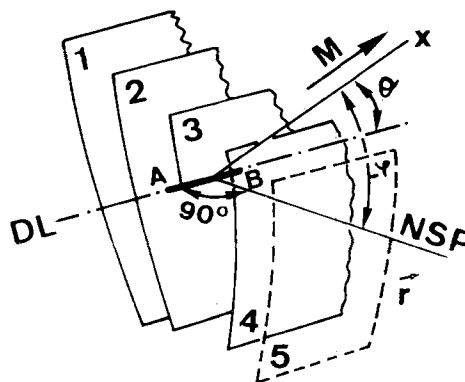


Fig. 1. Schematic presentation of edge dislocation. 1-5, Atomic planes; DL, line of dislocation; NSP, normal to dislocation line in the slip plane. The x-axis is directed along the vector of magnetization, M .

between NSP and M (Fig. 1). Considering the magnetostrictive interaction as the main factor, let us write the energy of the interaction between the dislocation and magnetization in a form similar to that introduced by Néel (13, 14) and Taniguchi (15), for anisotropic groups of point defects, the only difference being that in our case, the role not of one, but of two angles ϕ and θ must be taken into account

$$E(\theta, \phi) = K_1 \left(\cos^2\phi - \frac{1}{3} \right) + K_2 \left(\cos^2\theta - \frac{1}{3} \right) \quad [1]$$

where K_1 and K_2 are the constants of the postulated interaction. The sign of these constants is determined by the sign of the magnetostriction. Their magnitude depends on the magnetization and on the coefficient of magnetostriction of the given material. The value of $2(K_1 + K_2)/3$ is equal to the energy of the interaction between the dislocation and the magnetization when DL as well as NSP are perpendicular to the magnetization (Fig. 1). (The constants K_1 and K_2 are introduced here phenomenologically; the evaluation of their physical nature is beyond the scope of our task.)

In order to select the distribution law of dislocations, according to energies of their interaction with magnetization, let us take into account the following considerations.

1. The "solution" of the dislocations in the film may be considered as a rather "dilute" one: even at a dislocation density of $\sim 10^{12} \text{ cm}^{-2}$, a line of dislocation is encountered on an average of once in every $\sim 10^3$ "regular" atom planes.

2. It is known (10) that the dislocations are non-equilibrium defects. Indeed, the presence of dislocations in crystal increases simultaneously the free energy and the entropy of the latter. The increase of free energy, however, due to distortions in the crystallographic order, is considerably larger than the decrease due to the increase of entropy; the appearance of dislocations always increases the free energy. Thus the dislocation density does not depend on temperature: because of a large elastic energy connected with dislocation existence (which is much greater than the heat energy: $W \gg kT$), thermal fluctuations are not able to create a new dislocation.

The presence of an additional factor, magnetization, causes the distribution of dislocation lines according to angles θ and ϕ . This distribution could depend on temperature, as the energy of interaction between dislocation and magnetization, as well as the rotation energy of dislocation segments, are lower than the heat energy, and naturally, than W . Hence, as far as the distribution of dislocation line segments upon θ and ϕ is concerned, a behavior of a quasi-equilibrium system might be inherent in the "solution" of dislocations. This makes it possible to postulate the applicability of the Boltzmann formula to the distribution of dislocations according to angles θ and ϕ .

At the same time, it might be expected that the entropy of dislocation segment rotation is considerably small. The ratio of magnetoelastic energy to the entropic term TS can scarcely be estimated at present for the case of dislocation rotation. If this ratio is large enough, this factor could annihilate the dependence of dislocation line directions on temperature. On the other hand, however, the consideration of possible distribution functions have shown that the distribution differing from that of Boltzmann could give a much smaller stress anisotropy as compared with an observed one.

Hence, in order to estimate whether the mechanism assumed can ensure the level of stress anisotropy observed, let us postulate the Boltzmann law for distribution of dislocation line directions upon θ and ϕ . Introducing such a postulate, the distribution function is

$$\rho(\theta, \phi) = A \exp(-\alpha_1 \cos^2\phi - \alpha_2 \cos^2\theta) \quad [2]$$

where A is a constant to be determined from the nor-

malization conditions, while

$$\alpha_1 = \frac{K_1}{kT}; \quad \alpha_2 = \frac{K_2}{kT} \quad [3]$$

where k is the Boltzmann constant, T the absolute temperature.

Let us now imagine that all segments DL, every one of unit length, are transferred to the beginning of the coordinates, while the orientation of every one of them is preserved. The ends of all these segments will now lie on a sphere of a unit radius, as shown in Fig. 2. Since the density of the dislocations in films is considerable (10^{10} - 10^{12} cm^{-2}) (3, 7), let us replace the actual discrete distribution of the unit segments DL with a quasi-continuous one. Let us now consider a film built up in an intense field, sufficiently intense for magnetic saturation. In this case, the magnetization will coincide during growth of the crystals throughout the volume of the film, with the direction of the technological magnetic field, so that the x-axis is directed along that field.

On an element of the sphere under consideration (Fig. 2), having an area of $dS = 1 \times 2\pi \sin\theta d\theta$, terminate $\rho_1(\theta)2\pi \sin\theta d\theta$ of segments DL, where $\rho_1(\theta)$ is the quasi-continuous function of the distribution of dislocation line unit segments according to angle θ . The magnitude $\rho_1(\theta)$ can be computed if each such segment is matched with a unit vector of the normal to DL in the slip plane. Imagining a transfer of all these unit vectors to the beginning of the coordinates, we shall obtain a picture identical to that in Fig. 2, the sole difference being that instead of angle θ we shall have angle ϕ .

Figure 3 shows that if θ remains constant, ϕ can be changed within the limits of $\pi/2 - \theta$ to $\pi/2 + \theta$. Then, if $\rho(\theta, \phi)$ is the function of the distribution of the NSP unit vectors, according to angle ϕ at a fixed θ , we shall obtain for $\rho_1(\theta)$ the following

$$\rho_1(\theta) = 2 \int_{\pi/2-\theta}^{\pi/2} 2\pi \sin\phi \rho(\theta, \phi) d\phi \quad [4]$$

Taking into account Eq. [2] and [4], we shall find the total number of NSP unit vectors (or, equally, of the unit DL segments) equal to the dislocation density in the film crystal

$$p_0 = 8\pi A \int_0^{\pi/2} \sin\theta \int_{\pi/2-\theta}^{\pi/2} \exp(-\alpha_1 \cos^2\phi - \alpha_2 \cos^2\theta) \sin\phi d\phi d\theta \quad [5]$$

The dilatation along the x-axis is determined by the sum of the projections on the x-axis of all the random orientated NSP unit vectors. Projection of each unit vector on the x-axis depends on the magnitude of $\cos\phi$ (Fig. 3). Then, considering Eq. [5] as a condi-

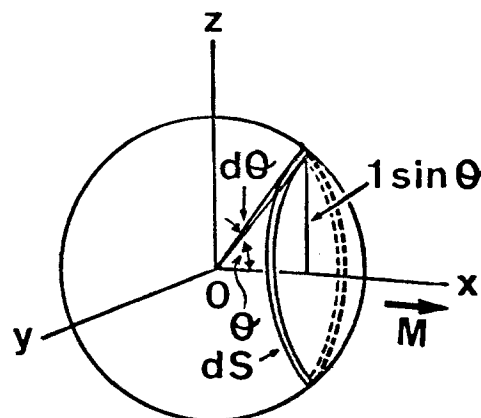


Fig. 2. Diagram illustrating the computation of distribution functions. The x-axis is directed along the magnetization, the z-axis along the normal to the film.

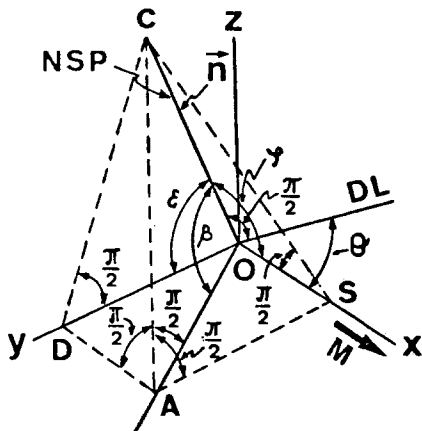


Fig. 3. Diagram for the computation of p_o^x and p_o^y parts of the density of the dislocations, the outflow of which results in the emergence of anisotropic macrostresses along the x and y axes.

tion for normalization for A, we shall find the sum of the projections of all NSP unit vectors on the x-axis

$$p_o^x = \frac{p_o \int_0^{\pi/2} \sin \theta \int_{\pi/2-\theta}^{\pi/2} \sin \phi \cos \phi \exp(-\alpha_1 \cos^2 \phi - \alpha_2 \cos^2 \theta) d\theta d\phi}{\int_0^{\pi/2} \sin \theta \int_{\pi/2-\theta}^{\pi/2} \sin \phi \exp(-\alpha_1 \cos^2 \phi - \alpha_2 \cos^2 \theta) d\theta d\phi} \quad [6]$$

The dilatation along the y-axis is determined by an identical expression, where however, instead of $\cos \phi$, we write $\cos \epsilon$ (the angle ϵ is shown in Fig. 3). Figure 3 shows that

$$\cos \epsilon = \sqrt{\cos^2 \beta - \cos^2 \phi} \quad [7]$$

For fixed ϕ and θ , β can change within the range 0 to ϕ . The value of β does not affect the energy of the interaction between the dislocations and magnetization, so that all values of β within the above limits are equally probable. The average magnitude of $\cos \epsilon$ in that case is

$$\overline{\cos \epsilon} = \frac{1}{\phi} \int_0^{\phi} \sqrt{\cos^2 \beta - \cos^2 \phi} d\beta \quad [8]$$

Thus, for the sum of the projections of all NSP unit vectors on the y-axis we shall obtain

$$p_o^y = \frac{p_o \int_0^{\pi/2} \sin \theta \int_{\pi/2-\theta}^{\pi/2} \sin \phi \left[\frac{1}{\phi} \int_0^{\phi} \sqrt{\cos^2 \beta - \cos^2 \phi} \cdot \exp(-\alpha_1 \cos^2 \phi - \alpha_2 \cos^2 \theta) \right] d\theta d\phi d\beta}{\int_0^{\pi/2} \sin \theta \int_{\pi/2-\theta}^{\pi/2} \sin \phi \exp(-\alpha_1 \cos^2 \phi - \alpha_2 \cos^2 \theta) d\theta d\phi} \quad [9]$$

We shall assume (13-15) that the energy of the interaction between the defect and magnetization is considerably lower than the heat energy

$$\alpha_1 = \frac{K_1}{kT} \ll 1; \quad \alpha_2 = \frac{K_2}{kT} \ll 1 \quad [10]$$

Then, replacing the exponents in Eq. [6] and [9] by the first members of the corresponding series, we shall reduce the denominators of both expressions [6] and [9] and the numerator in [6] to table integrals; the numerator of [9] can be found by numerical integration. As a result of the computation of the integrals in [6] and [9], we obtain

$$p_o^x \cong 0.425 p_o \frac{1 - 0.4\alpha_1 - 0.125\alpha_2 + 0.057\alpha_1\alpha_2}{1 - 0.563\alpha_1 - 0.25\alpha_2 + 0.042\alpha_1\alpha_2}$$

$$p_o^y \cong 0.425 p_o \frac{1 - 0.244\alpha_1 - 0.211\alpha_2 + 0.039\alpha_1\alpha_2}{1 - 0.563\alpha_1 - 0.25\alpha_2 + 0.042\alpha_1\alpha_2} \quad [11]$$

From expression [11] it will be seen that for $\alpha_1 \neq 0$ and $\alpha_2 \neq 0$, the sums of the NSP vector unit projec-

tions on the x-axis coinciding with the direction of the field, and the y-axis, normal to the technological field, differ from one another. This makes for different dilatations in the directions of the indicated axes and, hence, also for different macrostresses.

Computation of Macro stresses in the Films Growing in a Magnetic Field

Let us compute the macro stresses σ_x in the direction of the x-axis and σ_y in the direction of the y-axis.

Let p_R be the density of dislocations which are preserved in the crystal after the process of their outflow has stopped. Let p_R^x be the sum of the projection of all the NSP unit vectors, normal to the lines of the "remaining" dislocations, on the x-axis, and let p_R^y be the same for the y-axis. Then, the decrease of the sum of projections of the NSP unit vectors on the x-axis (as a result of the outflow of a part of the dislocations) will amount to $\Delta p_x = p_o^x - p_R^x$, and on the y-axis, $\Delta p_y = p_o^y - p_R^y$. If W_o is the linear energy of the dislocation, the withdrawal of a part of the dislocations will bring about a decrease of the total dislocation energy in the crystal by $W_o \cdot \Delta p$, where $\Delta p = p_o - p_R$.

Let us now introduce a coefficient q

$$q(\Delta p_x + \Delta p_y) = \Delta p \quad [12]$$

Thus, for example, if $p_R^x/p_o^x = p_R^y/p_o^y = p_R/p_o$, we obtain from [11] the following

$$q^{-1} = 0.425 \frac{2 - 0.644\alpha_1 - 0.336\alpha_2 + 0.096\alpha_1\alpha_2}{1 - 0.563\alpha_1 - 0.25\alpha_2 + 0.042\alpha_1\alpha_2} \quad [13]$$

In this case, the decrease of the total energy of the dislocations (as a result of their partial withdrawal) can be presented as $\Delta W = W_o q(\Delta p_x + \Delta p_y)$, where part of the decrease of energy to the amount of $W_o q \Delta p_x$ is connected with a change in the sum of the projections

of all NSP unit vectors on the x-axis and part $W_o q \Delta p_y$ on the y-axis.

On the other hand, in the event of a plane state of stresses with stresses σ_x and σ_y , the potential energy corresponding to the elastic deformation along the x-axis is (16)

$$\frac{1}{2} \sigma_x \epsilon_x = \frac{1}{2} \sigma_x \left[\frac{1}{E} (\sigma_x - \mu \sigma_y) \right] = \frac{1}{2E} (\sigma_x^2 - \mu \sigma_x \sigma_y) \quad [14]$$

(ϵ_x and ϵ_y are the strains along the x and y axes); for the y-axis it will be

$$\frac{1}{2} \sigma_y \epsilon_y = \frac{1}{2E} (\sigma_y^2 - \mu \sigma_y \sigma_x) \quad [15]$$

where E is Young's modulus of the elasticity and μ Poisson's ratio of the film material.

While the dislocations, which outflow from the crystals, carry away the energy in amount ΔW , only a fraction χ of ΔW is converted to macrostress energy; the

rest of ΔW , expressed as $(1 - \chi)\Delta W$, is scattered as heat. The estimation of a value χ will be proposed in the discussion. As to the nature of this quantity, it scarcely can be explained at this stage of theory's development. Hence, we must be limited by the introduction of, instead of ΔW , a magnitude $\chi\Delta W$ in following relations. Then, the energy balance is

$$\begin{aligned}\chi W_0 q \Delta p_x &= \frac{1}{2E} (\sigma_x^2 - \mu \sigma_x \sigma_y) \\ \chi W_0 q \Delta p_y &= \frac{1}{2E} (\sigma_y^2 - \mu \sigma_y \sigma_x)\end{aligned}\quad [16]$$

The solution of the system of equations in [16] provides formulas

$$\left. \begin{aligned}\sigma_x &= \sqrt{\frac{\chi q W_0 E}{1 - \mu^2}} \cdot \sqrt{\mu^2 \delta p_{xy} + 2\kappa_x p_o^x + \sqrt{(\mu^2 \delta p_{xy} + 2\kappa_x p_o^x)^2 - 4(1 - \mu^2)\kappa_x^2 p_o^{x2}}} \\ \sigma_y &= \sqrt{\frac{\chi q W_0 E}{1 - \mu^2}} \cdot \sqrt{\mu^2 \delta p_{yx} + 2\kappa_y p_o^y + \sqrt{(\mu^2 \delta p_{yx} + 2\kappa_y p_o^y)^2 - 4(1 - \mu^2)\kappa_y^2 p_o^{y2}}}\end{aligned}\right\} [17]$$

into which the following notations are introduced

$$\delta p_{xy} = -\delta p_{yx} = p_o^x - p_o^y; \quad \kappa_x = \frac{\Delta p_x}{p_o^x}; \quad \kappa_y = \frac{\Delta p_y}{p_o^y} [18]$$

[The sign in front of the inner square root in both equations [17] is determined by letting α_1 and α_2 approach zero and comparing formulas [17] to the corresponding ones for the isotropic case (2-4).]

Discussion

Relations [17], taking into account formulas [11], make it possible to explain the experimental regularities stated in Part I (1) (section on Results and Discussion, items 1-3).

1. If $\alpha_1 \neq 0$ and $\alpha_2 \neq 0$, i.e., according to Eq. [11], $p_o^x \neq p_o^y$, from relations [17] it is evident that σ_y must differ from σ_x . The obtained result shows how the small energies of magnetic interaction control the large energies of elastic deformation: even if K_1 and K_2 are small and, hence, the orientation of the dislocation lines and the normals to them are not substantial, the high density of the dislocations makes this small degree of orientation sufficient for the creation of a measurable anisotropy of the macrostresses.

For a quantitative evaluation of the anisotropy of the macrostresses being induced by the above mechanism, let us assume that in Eq. [11], $\alpha_1 \cong \alpha_2 \cong 0.1$ which is within the admissible limits given in Eq. [10]. We then obtain from [11]: $p_o^x = 0.437p_o$, $p_o^y = 0.444p_o$. In nickel films electrodeposited in a magnetic field, the tensile macrostresses are of an order of (1): $\sigma \sim 2 \times 10^7 \text{ N}\cdot\text{m}^{-2}$. Let us assume, for example, that ~ 0.02 of the initial density of dislocations is removed from the crystal, i.e., $p_R \cong 0.98p_o$. Then, by taking the limit of Eq. [11] for $\alpha_1 \rightarrow 0$, we obtain: $p_R^x = p_R^y \cong 0.425p_R \cong 0.425 \cdot 0.98p_o$; and from relations [17] and [19]: $\sigma_x = \sqrt{\chi q} \cdot 1.25 \times 10^9 \text{ N}\cdot\text{m}^{-2}$, $\sigma_y = \sqrt{\chi q} \cdot 1.4 \times 10^9 \text{ N}\cdot\text{m}^{-2}$. In order to correlate the calculated σ_x and σ_y with the experimental ones, we have to assume that $\chi q \cong 1.5 \times 10^{-3}$. From [13] it can be seen that the factor q , introduced by relation [12], is of the order of ~ 1 . Hence, there must be: $\chi \cong 1.5 \times 10^{-3}$. Thus, if less than 1% of the energy of the dislocations, which was removed from the crystal, converts to the energy of the macrostresses, the postulated mechanism will ensure the level of macrostresses observed in experiments. Here, the anisotropy of the macrostresses caused by the partial orientation of the dislocations in the magnetic field is also of the same magnitude as the experimental one (in the above example $\sigma_y/\sigma_x \cong 1.12$).

2. When the sign of the magnetostriction changes, the constants K_1 and K_2 and, hence, also α_1 and α_2 , change their sign. As can be seen from Eq. [11] and [17], when $\alpha_1 > 0$ and $\alpha_2 > 0$ we obtain $\sigma_y > \sigma_x$. When

$\alpha_1 < 0$ and $\alpha_2 < 0$ there is an inversion, $\sigma_y < \sigma_x$, which corresponds to the inversion observed experimentally when the sign of the magnetostriction was changed (1).

3. Equations [11] and [17] also provide an explanation for the effect of saccharin on the anisotropy of macrostresses of the films studied here. It has been observed (1) that saccharin inverts the influence of the magnetic field on the macrostresses. Since, as was postulated, K_1 and K_2 and with them also α_1 and α_2 (see Eq. [10]) characterize the magnetostrictive interaction, the magnitude of the coefficient of magnetostriction λ_s determines the absolute values α_1 and α_2 . It is known (17) that the stresses affect the magnetostriction λ_s substantially. But introduction of saccharin into

the solution leads to a considerable increase in the defect concentration and raises the microstress level. [For example, in a nickel film the introduction of saccharin into the solution raises the microstresses by more than 5-fold (18).] This must greatly alter the absolute values of α_1 and α_2 . On the other hand, from Eq. [11] and [17], it will be seen that a change in the absolute value of α_1 and α_2 can bring about an inversion of the relation between σ_x and σ_y . For example, at $\alpha_1 \cong 10^{-3}$, $\alpha_2 \cong 2 \times 10^{-3}$, we obtain from [11]: $p_o^x > p_o^y$ and hence, according to [17] also $\sigma_x > \sigma_y$. If, however, $\alpha_1 \cong 3 \times 10^{-3}$, $\alpha_2 \cong 2.5 \times 10^{-3}$ then $p_o^x < p_o^y$ and correspondingly $\sigma_x < \sigma_y$.

Thus, the regularities of the anisotropy of macrostresses, observed in films of nickel and iron-nickel alloy deposited in a magnetic field and described in Part I of this work (1), can be explained on the basis of the above concept.

Adoption of the dislocation model of the creation of the macrostresses, as well as of their anisotropy, does not exclude the possible role of other mechanisms. However, from the above discussion, it is seen that a considerable part of the anisotropy of macrostresses could very likely be ascribed to the effect of the partial withdrawal of dislocations from the film crystals and to the partial orientation of dislocations under the influence of technological factors (as in the case under consideration, the magnetic field).

Manuscript submitted Dec. 2, 1974; revised manuscript received May 7, 1975.

Any discussion of this paper will appear in a Discussion Section to be published in the June 1976 JOURNAL. All discussions for the June 1976 Discussion Section should be submitted by Feb. 1, 1976.

REFERENCES

1. M. Perakh (M. Ya. Popereka), *This Journal*, **122**, 1260 (1975).
2. M. Ya. Popereka, *Fiz. Metal. Metalloved.*, **20**, 753 (1965) [English transl., *Phys. Metals Metallog. (USSR)*].
3. M. Ya. Popereka, "Vnutrenniye napriazheniya elektroliticheski osazhdayemykh metallov," West Siberian Book Press, Novosibirsk (1966). [English transl., "Internal Stresses of Electrolytically Deposited Metals," India Nat. Sci. Doc. Center, New Delhi, India (1970), translated for NBS and NSF, Washington, D.C., USA].
4. M. Ya. Popereka, Proc. of the 3rd Intern. Congress on Metallic Corrosion, Vol. 3, Publ. "Myr," Moscow (1968).
5. M. P. Arbutov, E. S. Bushuyev, and A. L. Leontovich, *Izv. Vysshikh Uchebn. Zavedeniy SSSR, Ser. Fiz.*, No. 2 (1969) (English transl., *Sov. Phys. J.*).
6. Yu. M. Polukarov, *Elektrokhimiya*, **2**, 937 (1966).

7. M. Jacobs, D. Pashley, and M. Stowell, *Phil. Mag.*, **13**, 121 (1966).
8. Yu. M. Polukarov and Y. D. Gamburg, Coll. "Vsesoyuznaya konferentsia po elektrokhemii," p. 529, Tbilissi (1969).
9. Yu. M. Polukarov and Yu. D. Gamburg, *Elektrokhemiya*, **7**, 717 (1971).
10. R. W. Cahn, Editor, "Physical Metallurgy," North Holland Publishing Co., Elsevier (1963).
11. M. Ya. Fuks, V. V. Bieleziorov, and Yu. F. Boyko, *Fiz. Metal. Metalloved.*, **33**, 571 (1972) [English transl., *Phys. Metals Metallog.* (USSR)].
12. F. Vicena, *Czech. Phys. J.*, **5**, 11 (1955).
13. L. Néel, *Compt. Rend.*, **237**, 1468, 1613 (1953).
14. L. Néel, *J. Phys. Rad.*, **15**, 525 (1954).
15. S. Taniguchi, *Sci. Rep. Res. Inst., Tohoku Univ.*, **A1**, 269 (1955).
16. L. D. Landau and E. M. Lifshitz, "Teoriya uprugosti" ("Theory of Elasticity") (Russ.), Publ. "Nauka," Moscow (1965).
17. S. V. Vonsovski, "Magnetizm," (Russ.), Publ. "Nauka," Moscow (1971).
18. B. S. Zolotkovskiy and M. Ya. Popereka, *Fiz. Metal. Metalloved.*, **33**, 268 (1972) [English transl., *Phys. Metals Metallog.* (USSR)].

Technical Notes



Vapor Deposition of High P₂O₅ Content Binary Phosphosilicate Films on Silicon

J. Wong* and M. Ghezso*

General Electric Company, Research and Development Center, Schenectady, New York 12301

The stability enhancement of Si devices by binary phosphosilicate glass (PSG) films as gettering sources for metallic impurities (1-7) and passivation layers (8-12), and the utilization of these materials as n-diffusion sources for the fabrication of p-n junctions in Si (13-15) have been demonstrated by a number of authors. Much of the preparation, material characterization studies, and device application of PSG so far has been confined to films with less than 20 mole per cent (m/o) P₂O₅ (16-24). High P₂O₅ content phosphosilicate glasses are of considerable interest, especially in studies such as structural aspects of this type of material (25) which require systematic property investigations across the whole composition of the binary system.

In this paper, we report the vapor deposition of binary PSG films with composition ranging from one end component to the other using a PH₃-SiH₄-O₂-Ar (or N₂) reaction system at substrate temperatures in the range 300°-400°C. The rate of deposition and film composition has been investigated systematically as a function of temperature and concentration of reactive and carrier gases.

Experimental Procedure

Ten ohm-cm p-type (111) oriented silicon wafers, 2.5 cm in diameter and 0.05 cm thick, were used as substrates for film deposition. These were heavily etched in a conc HNO₃-conc HF solution (3:1 by volume), rinsed thoroughly in distilled water, and spindried prior to deposition. The phosphine and silane sources used were semiconductor grade obtained from the Matheson Company as a calibrated 1% mixture in Ar. Union Carbide ultrapure grades of O₂, Ar, and N₂ were used as the oxidizing medium and carrier gases, respectively, in the CVD process. The gas-flow system and vertical reactor used in the present study are similar to those used for the study of arsenosilicate film reported earlier (26).

Depositions were made at substrate temperatures of 300°, 350°, and 400°C controlled to within ±2°C. All

flow meters were calibrated with the corresponding gases or mixtures using two Brook flow calibrators having capacities of 0-70 and 0-1000 cc. In all depositions, the molar ratio of O₂ to total hydride in the reactive mixture was maintained at about 10 to assure complete oxidation of both PH₃ and SiH₄, which theoretically requires an O₂/hydride ratio varying from 1 to 1.25 depending on composition across the PSG system.

Deposition rate was conveniently determined by continuously recording the color of the film *in situ* during deposition and using the color thickness chart devised by Tenney and Ghezso (22b) from the data of Pliskin and Conrad for thermal SiO₂ (27) to plot film thickness *vs.* time of deposition. The actual thickness of PSG films may be 5-10% (see error bars in Fig. 1-3) lower than that obtained by color because of the higher refractive indices of PSG films (1.50-1.60 depending on composition) (28) compared to a value of 1.46 for thermal SiO₂. Interestingly enough, it was found experimentally that by reducing the substrate temperature to 300°C and using a high flow rate of PH₃ with Ar, but not N₂, as carrier gas, a pure P₂O₅ film can be reproducibly vapor deposited at a fairly high rate. The uniformity of the P₂O₅ film can be greatly improved by first coating the bare Si substrate with a 200Å layer of SiO₂ prior to the P₂O₅ deposition.

Film compositions were determined by electron microprobe analysis for silicon and phosphorus using high purity, undoped samples of silicon and gallium phosphide, respectively, as standards. Films containing 20 m/o P₂O₅ and higher are hygroscopic; to protect these high P₂O₅ content films from moisture attack during handling, a thin covering layer (~300Å thick) of SiO₂ was deposited *in situ* immediately after the PSG deposition by simply turning off the PH₃ supply. For films containing 50-100 m/o P₂O₅, a double covering layer was necessary in order to avoid cracking (due to thermal stress) of the covering layer when cooled from the deposition temperature to room temperature. The double covering layer consisted of a 20 m/o PSG film (~300Å thick) followed by a pure SiO₂ layer (also ~300Å thick). When stored in a desiccator,

* Electrochemical Society Active Member.

Key words: thin dielectric glass films, preparation.

moisture attack on the underlying binary film can be obviated for as long as a week which is indicated by the reproducibility of the infrared spectrum of the as-deposited film and absence of the OH absorption in the 3μ region. The accuracy of the microprobe technique was estimated to be within $\pm 3\%$ or better for all films.

Results and Discussion

Deposition rate.—The deposition rate of PSG films has been studied as a function of the mole fraction of PH_3 (x_{PH_3}) in the hydride mixture, substrate temperature, and gas flow conditions. Figure 1 shows the results obtained at $400^\circ C$ by varying the flow rate of PH_3 (1% in Ar) in the range $0-900\text{ cc min}^{-1}$, while holding constant flow rates of O_2 , SiH_4 (1% in Ar), and carrier gas Ar at 40, 100, and 2800 cc min^{-1} , respectively. The deposition rate increases monotonically with x_{PH_3} and exhibits a maximum at $x_{PH_3} \sim 0.8$.

At lower substrate temperatures, higher flow rates of reactant gases are necessary in order to facilitate deposition rate measurements within a reasonable time scale. The results at 350° and $300^\circ C$ in the N_2 system are shown in Fig. 2 and 3. In the range $0 \leq x_{PH_3} \leq 0.45$, the flow rate of PH_3 (1% in Ar) was allowed to increase, while those of O_2 , SiH_4 (1% in Ar), and N_2 were held constant at 40, 400, and 2800 cc min^{-1} , respectively. Again, the deposition rate increases with x_{PH_3} . In the range $0.5 \leq x_{PH_3} \leq 1.0$, the flow rate of PH_3 (1% in Ar), O_2 , and N_2 were held constant at 473, 40, and 2800 cc min^{-1} , respectively, while that of SiH_4 (1% in Ar) was progressively lowered to obtain high x_{PH_3} values. In this range the deposition rate decreases monotonically to zero with increase in x_{PH_3} (Fig. 3).

However, when Ar was used instead of N_2 as the carrier gas at $300^\circ C$, a maximum similar to that shown in Fig. 1 was again observed at $x_{PH_3} \sim 0.85$. At $x_{PH_3} = 1$, the deposit rate in the Ar system shown in Fig. 3 could be maintained at $\sim 1300\text{ \AA min}^{-1}$ under the gas flow conditions of 473, 40, and 2800 cc min^{-1} for PH_3 (1% in Ar), O_2 , and Ar, respectively. The deposition corresponds to that of a pure P_2O_5 film. The above data for the N_2 system shown in Fig. 2 and 3 clearly indicate an inhibitive effect of N_2 on the deposition of PSG

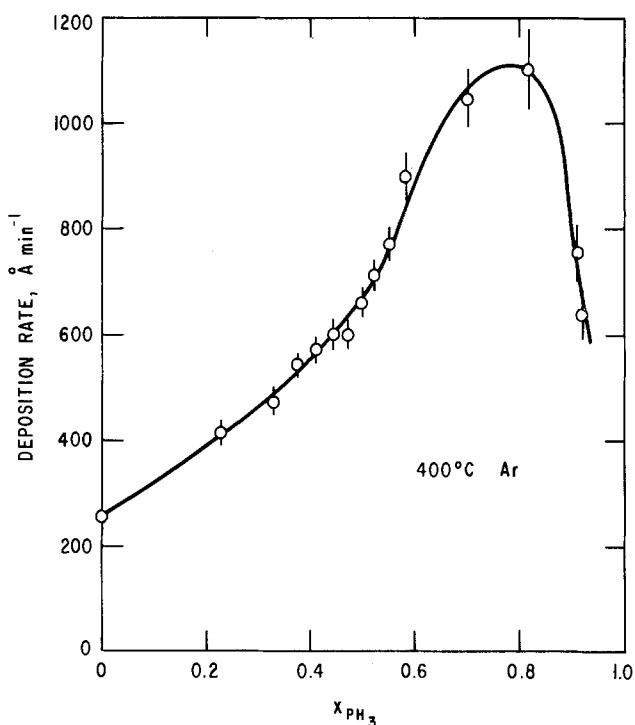


Fig. 1. Deposition rate of PSG films at $400^\circ C$ vs. x_{PH_3} . The flow rates of O_2 , SiH_4 (1% in Ar), and Ar were held constant at 40, 100, and 2800 cc min^{-1} , while that of PH_3 (1% in Ar) was made to vary so as to obtain the corresponding x_{PH_3} in the hydride mixture.

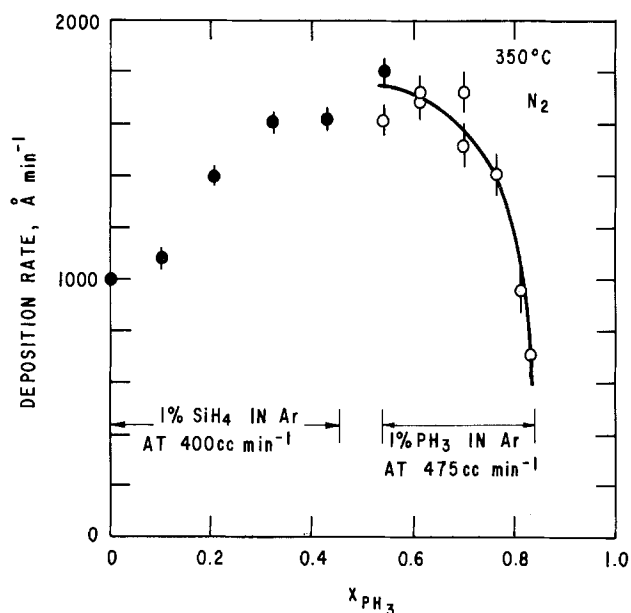


Fig. 2. Deposition rate of PSG films at $350^\circ C$ vs. x_{PH_3} in N_2 . Flow rates in cc min^{-1} for $0 \leq x_{PH_3} \leq 0.42$: $O_2 = 40$, $SiH_4 = 400$, $N_2 = 2800$, and PH_3 variable; for $0.5 \leq x_{PH_3} \leq 0.83$, $O_2 = 40$, $PH_3 = 473$, $N_2 = 2800$, and SiH_4 variable. Flow rates of both SiH_4 and PH_3 are those of the 1% mixtures in Ar.

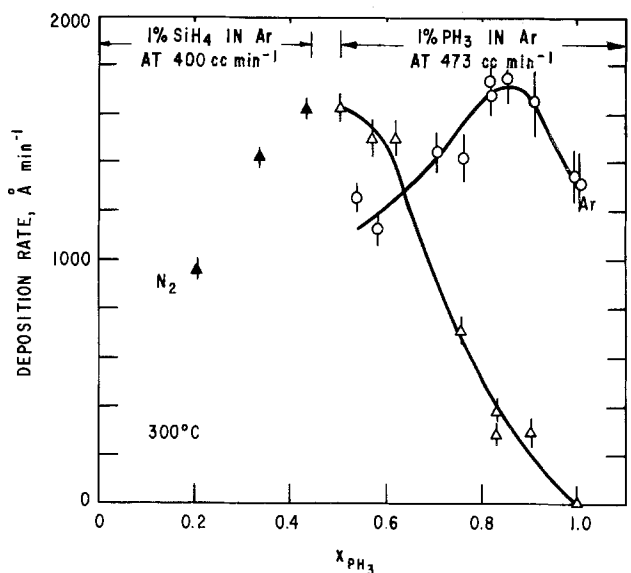


Fig. 3. Deposition rate of PSG film at $300^\circ C$ vs. x_{PH_3} . Flow rates in cc min^{-1} for $0.2 \leq x_{PH_3} \leq 0.43$: $O_2 = 40$, $SiH_4 = 400$, $N_2 = 2800$, and PH_3 variable; for $0.5 \leq x \leq 1.0$: $O_2 = 40$, $PH_3 = 473$, N_2 or Ar = 2800 , and SiH_4 variable. Flow rates of both SiH_4 and PH_3 are those of the 1% mixtures in Ar.

film in the region of high x_{PH_3} values. In the absence of further detailed kinetic data, it could only be speculated that N_2 may retard the generation of oxygen free radicals that are necessary to initiate the oxidation of PH_3 ; complex with intermediate species, thus preventing further oxidation to higher oxides; or terminate chain propagation in the polymerization process.

Deposition of pure P_2O_5 films.—The above systematic study of the rate of deposition of PSG films from the PH_3 - SiH_4 - O_2 system leads to a formulation for depositing a pure P_2O_5 film at low substrate temperature and high PH_3 flow rate. Pure P_2O_5 films deposited on bare Si substrates are rather nonuniform in thickness as shown by the color distribution of the deposit. It was found experimentally that by depositing a thin layer of CVD SiO_2 ($\sim 200\text{ \AA}$ thick) on the bare Si sub-

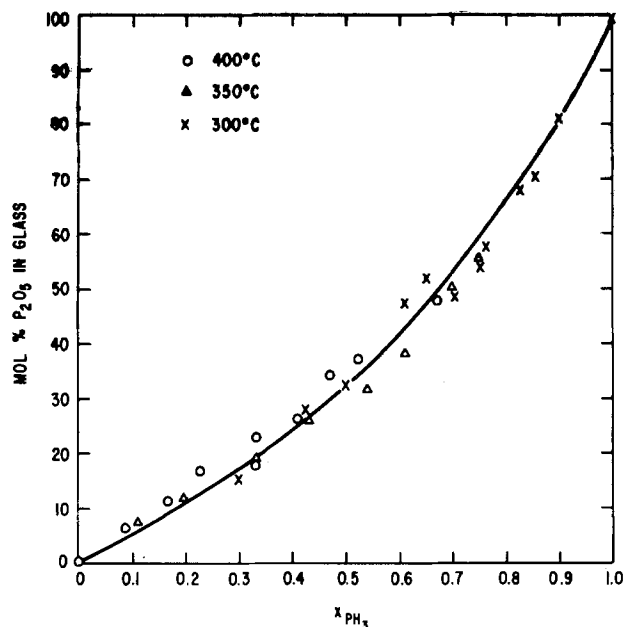


Fig. 4. Film composition determined by electron microprobe analysis vs. x_{PH_3} at various deposition temperatures. The line is calculated by using the formula $m/o \text{ P}_2\text{O}_5 = \frac{x_{\text{PH}_3}}{2 - x_{\text{PH}_3}}$.

strate prior to the P_2O_5 film, uniformity of the latter was greatly enhanced. This "priming" procedure enables reproducible deposition of very uniform P_2O_5 films.

Film composition.—Compositions of PSG film prepared under the above-mentioned substrate temperatures and gas flow conditions have also been determined. It was found that the amount of P_2O_5 that can be incorporated in the film depends strongly on x_{PH_3} and substrate temperature. The results are given in Fig. 4 in which the film composition in m/o P_2O_5 is plotted vs. x_{PH_3} at various deposition temperatures. The points represent the data obtained by electron microprobe analysis after having been corrected for the respective covering layers, while the curve corresponds to those calculated from the molar concentration of PH_3 and SiH_4 in the reaction mixture using the formula: $m/o \text{ P}_2\text{O}_5 = x_{\text{PH}_3} / (2 - x_{\text{PH}_3})$ which assumes stoichiometric oxidation of each hydride component. Within ± 5 m/o or better, composition of CVD PSG films can be expected to follow that determined by the relative concentrations of the hydride components in the presence of excess O_2 . Furthermore, in the

range 0–20 m/o P_2O_5 , the microprobe data agree well with those obtained from the infrared data of Tenney and Ghezzi (22) using the intensity ratio of the $\text{P} = \text{O}$ band and Si-O band at 1320 and 1100 cm^{-1} as a composition calibration of PSG films deposited from the same reaction system in the range 300°–700°C.

The amount of P_2O_5 that can be incorporated in the PSG films increases with decreasing substrate temperature in agreement with the findings of Tenney and Ghezzi (22), as well as the more recent data of Shibata *et al.* (29). At 400°C, the maximum concentration is about 50 m/o P_2O_5 (see Fig. 4 for the data point at 400°C). Increasing the amount of PH_3 gas (hence x_{PH_3}) will lead only to heavy fuming at the gas-substrate interface, indicative of vaporization loss of reaction products, especially P_2O_5 . This probably gives rise to the drop in deposition rate beyond $x_{\text{PH}_3} = 0.8$. When the substrate temperature was lowered to 350° and 300°C, the concentration of P_2O_5 in the film can be extended to ~60 and even to 100 m/o P_2O_5 as shown in Fig. 4. The decrease in P_2O_5 concentration in the film with increasing substrate temperature appears to be due to a decrease in the sticking coefficient of the P_2O_5 component with temperature. That this is the case is substantiated by direct observation of a progressive decrease in thickness (Fig. 5 inset) of a pure P_2O_5 film deposited initially at 300°C as it was being heat-treated *in situ* in the reactor from 325° to 550°C holding the temperature constant for 3 min at 25°C intervals. Accordingly, the infrared spectrum of the heat-treated film shows a decrease in intensity in all the corresponding absorption bands (Fig. 5). The vibrational spectra and structural analysis of these CVD PSG films will be given in a subsequent paper (30). In fact, the occurrence of the band at 1300 cm^{-1} which is characteristic of the $\text{P} = \text{O}$ vibration and its persistence in the spectra of all as-deposited binary PSG films suggest that the oxidation product of PH_3 under the present CVD conditions is indeed phosphorus pentoxide.

Summary

Binary phosphosilicate glass films of varying composition across the binary system have been prepared by a CVD technique using a $\text{PH}_3\text{-SiH}_4\text{-O}_2$ reaction system at low substrate temperatures (300°–400°C). The deposition characteristics of these films may be summarized as follows: (i) The P_2O_5 content in the film increases monotonically with the mole fraction of PH_3 (x_{PH_3}) in the hydrides mixture in the presence of excess O_2 . (ii) At 400°C film composition is restricted to no higher than 50 m/o P_2O_5 . Higher P_2O_5 content PSG films can be deposited by lowering the substrate temperature to 300°C, at which a pure P_2O_5 film may be deposited using only $\text{PH}_3\text{-O}_2$ and Ar, but

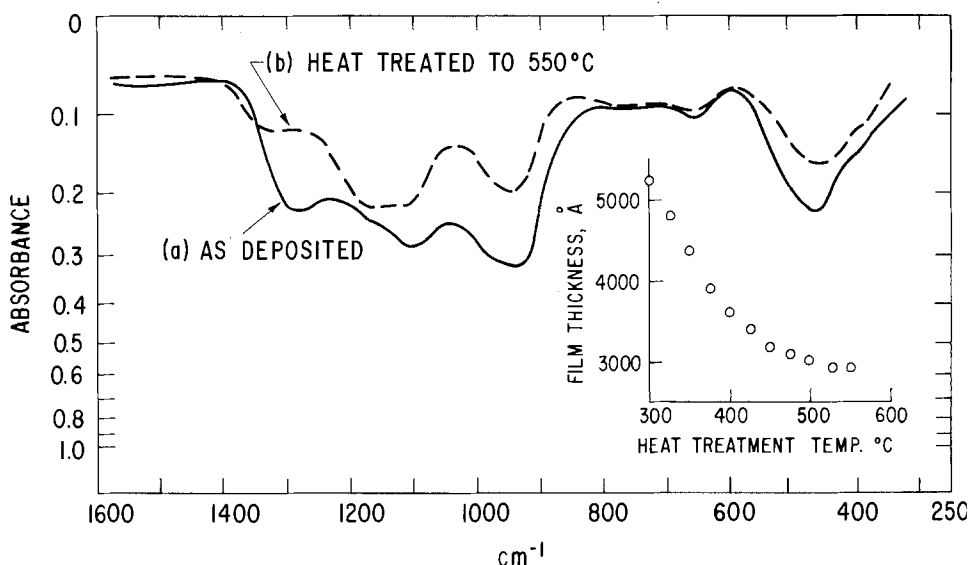


Fig. 5. Room temperature infrared transmission spectra of pure P_2O_5 films deposited on silicon (a) as-deposited and (b) heat-treated to 550°C. The priming layer of SiO_2 and double covering layer have been compensated accordingly on a reference Si substrate. Inset is a plot of film thickness vs. *in situ* heat-treatment temperature.

not N₂, as the carrier gas. (iii) The deposition rate increases initially with x_{PH_3} at all temperatures studied. A maximum rate at $x_{\text{PH}_3} \sim 0.8$ is observed in the Ar system, but not the N₂ system. (iv) Deposition of high P₂O₅ content films, i.e., at $x_{\text{PH}_3} > 0.5$, appears to be inhibited by the presence of N₂.

Acknowledgment

The authors would like to thank P. Sargent for technical assistance and M. McConnell for performing the microprobe analysis.

Manuscript submitted March 4, 1975; revised manuscript received May 6, 1975.

Any discussion of this paper will appear in a Discussion Section to be published in the June 1976 JOURNAL. All discussions for the June 1976 Discussion Section should be submitted by Feb. 1, 1976.

Publication costs of this article were partially assisted by the General Electric Company.

REFERENCES

1. A. Goetzberger and W. Shockley, *J. Appl. Phys.*, **31**, 1821 (1960).
2. S. W. Ing, R. E. Morrison, R. E. Alt, and R. W. Aldrich, *This Journal*, **110**, 533 (1963).
3. J. L. Lambert, K. Roy, and M. Reese, *Solid-State Electron.*, **10**, 877 (1967).
4. J. L. Lambert and M. Reese, *ibid.*, **11**, 1055 (1968).
5. M. Nakamura, T. Kato, and N. Oi, *Japan. J. Appl. Phys.*, **7**, 512 (1968).
6. S. Dash, in "Semiconductor Silicon 1973," H. R. Huff and R. R. Burgess, Editors, p. 626, The Electrochemical Society Softbound Symposium Series, Princeton, N. J. (1973).
7. R. L. Meek and C. F. Gibbon, *This Journal*, **121**, 444 (1974).
8. D. R. Kerr, J. S. Logan, P. J. Burkhardt, and W. A. Pliskin, *IBM J. Res. Develop.*, **8**, 376 (1964).
9. E. H. Snow and B. E. Deal, *This Journal*, **113**, 263 (1966).
10. J. M. Eldridge and P. Balk, *Trans. Met. Soc. AIME*, **242**, 539 (1968).
11. P. Balk and J. M. Eldridge, *Proc. IEEE*, **57**, 1558 (1969).
12. M. M. Schlacter, E. S. Schlegel, R. S. Keen Jr., R. A. Lathlaen, and G. L. Schnable, *IEEE Trans. Electron Devices*, **ED-17**, 1077 (1970).
13. E. Kooi, *This Journal*, **111**, 1383 (1964).
14. M. L. Barry, *ibid.*, **117**, 1405 (1970).
15. J. Middlehoek and J. Holleman, *ibid.*, **121**, 132 (1974).
16. W. A. Pliskin, *J. Appl. Phys.*, **7**, 158 (1965).
17. E. A. Corl, S. L. Silverman, and Y. S. Kim, *Solid-State Electron.*, **9**, 1009 (1966).
18. Y. Miura, R. S. Tanaka, Y. Matukura, and H. Osafune, *This Journal*, **113**, 399 (1966).
19. W. Kern and R. C. Heim, *ibid.*, **117**, 562 (1970); *ibid.*, **117**, 568 (1970).
20. B. J. Baliga and S. K. Ghandhi, *J. Appl. Phys.*, **44**, 990 (1972).
21. M. Ghezzi, *This Journal*, **119**, 1428 (1972).
22. (a) A. S. Tenney and M. Ghezzi, *ibid.*, **120**, 1276 (1973); (b) *ibid.*, **120**, 1091 (1973).
23. G. Linker, O. Meyer, and W. Scherber, *Phys. Status Solidi*, **16**, 377 (1973).
24. N. Nagasima, H. Suzuki, Keizo Tanaka, and S. Nishida, *This Journal*, **121**, 434 (1974).
25. A. S. Tenney and J. Wong, *J. Chem. Phys.*, **56**, 5516 (1972).
26. J. Wong and M. Ghezzi, *This Journal*, **118**, 1540 (1971).
27. W. A. Pliskin and E. E. Conrad, *IBM J. Res. Develop.*, **8**, 43 (1964).
28. A. N. Winchell and H. Winchell, "The Microscopical Characters of Artificial Inorganic Solid Substances: Optical Properties of Artificial Minerals," p. 66, Academic Press, New York (1964).
29. M. Shibata and K. Sugawara, *This Journal*, **122**, 155 (1975).
30. J. Wong, *J. Non-Crystalline Solids*, **17** (1975).

Silicon Nitride Films by Direct RF Sputter Deposition

G. J. Kominak

Sandia Laboratories, Albuquerque, New Mexico 87115

Silicon nitride, because of its chemical stability (1), is of considerable importance in the electronics industry for use in passivating semiconductor surfaces (2, 3), as a barrier to diffusion in silicon device technology (2, 4-10), and in MNOS device technology (11-16). Nonelectronic applications of silicon nitride layers include: the formation of glass to metal seals (17), a proposed antireflection coating for a solar-thermal collector (18), and as an electrode insulator in high temperature electrochemistry (19).

Among the several methods which have seen general use for the deposition of amorphous layers of silicon nitride are: the pyrolysis of silane in the presence of gaseous nitrogen compounds (4, 20-30), rf and microwave discharge induced CVD (31-34), ion beam techniques (35), and reactive sputter deposition from a high-purity silicon target (36-39). The most common method of film formation appears to be the CVD techniques.

A disadvantage to the pyrolysis schemes is the high substrate temperatures needed (500°-1000°C) (28-30). Glow discharge induced CVD methods alleviate this disadvantage since deposition occurs at temperatures below 100°C (34). These low temperature films appear to have residual hydrogen content (40), which may

limit their usefulness. Direct rf sputter deposition of silicon nitride films from a pressed powder target of silicon nitride has been avoided because of the difficulty in obtaining high purity targets (40), the danger of silicon oxide incorporation into the films because of gases trapped in the target (41), and variations in stoichiometry in the resulting films due to dissociation reactions at the target (42). Gregor (43) has reported that reproducible films of silicon nitride may be sputtered from a nitride target, but only at high rf power levels.

Here we report the formation of transparent thick films (up to 10 μ) of silicon nitride by direct rf sputter deposition. These films are prepared at low rf power levels from an Si₃N₄ target using a mixture of argon and nitrogen.

Experimental

The silicon nitride films were directly sputter deposited on water-cooled substrates of silicon, fused SiO₂, gold, platinum, and T-12[®] infrared windows using an MRC IC² grade Si₃N₄ target. The depositions were carried out in a conventional planar rf sputtering system. The substrates were biased by inserting a tuning network between the substrate holder and

¹ Registered Trademark, Harshaw Chemical Company.

² Materials Research Corporation, Advanced Materials Division, Orangeburg, New York.

Table I.

Target voltage (kV)	Input power (watts)	Lattice absorption (cm^{-1})	Refractive index	Etch rate ($\text{\AA}/\text{sec}$)
1.0	300	870	2.08	~ 8
1.2	450	850	2.00	~ 15
1.5	700	830	1.90	~ 20
Bulk	—	935	2.1	—
CVD	—	830	2.0-2.06	1.5^{20}
Glow discharge CVD (low temp)	—	870	1.75-2.18	100^{40}

ground (44). Gas mixtures were admitted and adjusted to the operating pressure with the high vacuum valve open in an effort to maintain a high gas throughput. Low throughput resulted in films with considerable oxygen (26) content as evidenced by a distinct infrared absorption band at 1100 cm^{-1} . A nitrogen concentration in the discharge gas of $<20\%$ produced films which were silicon rich, while a percentage greater than $\sim 25\%$ gave clear adherent films but severely reduced the deposition rate. The principal variable in this investigation was the target voltage (input power) (45). The substrate circuit was tuned for +20V bias and held constant from run to run.

The width and position of the lattice absorption band (46, 47), the index of refraction (46, 48), the ultraviolet absorption (40), film density, and the etch rate (48) were used to evaluate the quality of the film.

Results

Figure 1 shows the infrared absorption spectrum (curve A) of a 2000\AA film of silicon nitride deposited in argon-20% nitrogen at a target voltage of 1 kV ($P_{\text{in}} \sim 300\text{W}$). The lattice absorption is fairly broad with the maximum occurring at 870 cm^{-1} as compared to $\sim 830 \text{ cm}^{-1}$ for CVD material (4, 25) (curve B) and $\sim 935 \text{ cm}^{-1}$ for bulk silicon nitride (curve C) (4, 6). As these films were shown to be amorphous by x-ray diffraction, the shift in lattice absorption to lower frequencies may be attributed to bond stretching in the amorphous film (4, 36). Increasing the target voltage to 1.5 kV ($P_{\text{in}} \sim 700\text{W}$) resulted in a general increase in the infrared absorption in the range $1000\text{--}1200 \text{ cm}^{-1}$ and a shift in the maximum to $\sim 830 \text{ cm}^{-1}$. The shift in the band maximum may be attributed to porosity (49) or an increased bond strain in the resulting films (50). These infrared properties were obtained only if the target was presputtered for approximately 1 hr prior to film deposition. Proceeding without presputtering gave rise to films with additional absorption bands at $\sim 3300 \text{ cm}^{-1}$ (N-H) (40) and $\sim 2100 \text{ cm}^{-1}$ (Si-H) (33, 40). This is comparable to low temperature glow discharge CVD coatings (40). In this

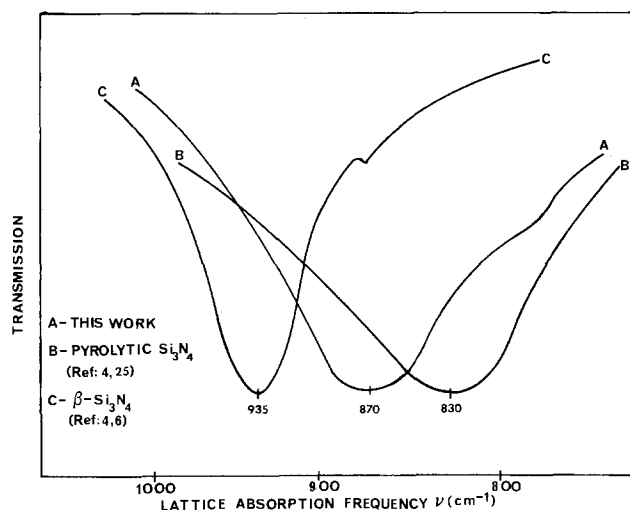


Fig. 1. Position of lattice absorption band. A, Direct sputter Si_3N_4 ; B, CVD Si_3N_4 ; C, bulk Si_3N_4 .

case, the hydrogen probably originated as an adsorbed impurity in the target surface (41).

For measurements of refractive index and optical absorption, Si_3N_4 layers were deposited on chromium-coated soft glass and fused silica, respectively. The chromium layer was opaque and was partially masked during nitride deposition to facilitate measurement of the optical constants of both the chromium substrate and the nitride layer. The refractive index was measured at $\lambda = 5461 \text{\AA}$ using an ellipsometer and the energy gap was calculated from the position of the ultraviolet absorption edge.

Silicon nitride films deposited at 1 kV ($P_{\text{in}} \sim 300\text{W}$) exhibited an index of refraction of 2.08 (bulk — 2.1) (36); the optical gap was $\sim 5 \text{ eV}$. Increasing the target voltage to 1.5 kV ($P_{\text{in}} \sim 700\text{W}$) reduced the refractive index to 1.90 and increased the energy gap to $\sim 5.5 \text{ eV}$. These results along with an increase in infrared absorption in the vicinity of $\sim 1100 \text{ cm}^{-1}$ are suggestive of oxygen incorporation in the 1.5 kV deposit. Examination of these films by sputter-Auger spectroscopy indicated the presence of ~ 9 atomic per cent (a/o) oxygen. In addition, the films produced at high target voltages were uniformly absorbing in the visible. This absorption is probably a result of damage caused by particle bombardment of the film during growth (51-55).

The density, as determined by weight gain, of 10μ thick nitride films deposited at 1 kV, was $\sim 3 \text{ g/cm}^3$. This is comparable to that found for films produced by other techniques (56).

The room temperature etch rate in 48% hydrofluoric acid was found to range from 8 $\text{\AA}/\text{sec}$ for films deposited at 1 kV (300W) to $\sim 20 \text{ \AA}/\text{sec}$ for films deposited at 1.5 kV (700W). As preliminary investigation of the composition of these films did not indicate large changes, the variation in etch rate may be related (at least in part) to changes in internal stress with deposition conditions (57, 58).

Summary

Thick ($\sim 10 \mu$), transparent films of amorphous silicon nitride were deposited at low temperatures ($< 100^\circ\text{C}$), at rates of 30-60 $\text{\AA}/\text{min}$ by direct rf sputtering of a Si_3N_4 target. The films were prepared using a mixture of Ar/20% nitrogen as the sputtering gas. Nitrogen levels $< 20\%$ result in films which are silicon rich, while concentrations $> 25\%$ drastically reduce the deposition rate. The density and optical properties of the films were comparable to those of pyrolytic and glow discharge CVD deposits. Contrary to the results of Gregor (43), these properties tend toward those of crystalline material when deposited at low rf power levels. Increasing the input power by a factor of ~ 2 broadens the lattice absorption band and further shifts its position to longer wavelengths. Simultaneously, the films become absorbing in the visible, and the index of refraction decreases from 2.08 to 1.90. Along with changes in optical properties, the power increase during deposition results in an increase in the 48% HF etch rate of approximately a factor of 3.

Acknowledgment

I wish to thank G. T. Gay for x-ray analysis and P. Thatcher for measurements of the index of refraction.

This work was supported by the U. S. Energy Research and Development Administration.

Manuscript submitted March 7, 1975; revised manuscript received April 21, 1975.

Any discussion of this paper will appear in a Discussion Section to be published in the June 1976 JOURNAL. All discussions for the June 1976 Discussion Section should be submitted by Feb. 1, 1976.

Publication costs of this article were partially assisted by Sandia Laboratories.

REFERENCES

1. J. F. Collins and R. W. Gerley, *J. Metals*, **7**, 612 (1955).
2. M. T. Grieco, F. L. Worthing, and B. Schwartz, *This Journal*, **113**, 212C (1966).
3. H. Seki, S. Ohosaka, M. Kanda, Y. Kawasaki, H. Yamazaki, and M. Fujimoto, *Rev. Elec. Commun. Lab.*, **20**, 810 (1972).
4. S. M. Hu, *This Journal*, **113**, 693 (1966).
5. V. Y. Doo, *IEEE Trans. Electron Devices*, **ED-13**, 561 (1966).
6. S. M. Hu and L. V. Gregor, *This Journal*, **114**, 826 (1967).
7. W. Meer and D. Dommerrenig, *Z. Angew. Phys.*, **23**, 369 (1967).
8. T. L. Chu, J. R. Szedon, and C. H. Lee, *Solid-State Electron.*, **10**, 897 (1967).
9. J. V. Dalton and J. Drobeck, *This Journal*, **115**, 865 (1968).
10. B. Swaroop, "Proceedings of the Annual Conference on Electrical Insulation and Dielectric Phenomena," Buck Hill Falls, Pa., p. 75, IEEE, Washington, D.C. (1972).
11. Y. Hsia, "Proceedings," Wescon, Los Angeles, Vol. 16, IEEE (1972).
12. H. A. R. Wegener, M. B. Doig, P. Marraffino, and B. Robinson, *IEEE Trans. Nucl. Sci.*, **19**, 291 (1972).
13. J. R. Cricchi, F. C. Blaha, and M. D. Fitzpatrick, in "Technical Digest," International Electron Devices Meeting, Washington, D.C., p. 126, IEEE, New York (1973).
14. L. S. Wei and J. G. Simmons, *Solid-State Electron.*, **17**, 591 (1974).
15. P. K. Chaudari and D. C. Beyar, *This Journal*, **121**, 89C (1974).
16. C. A. Barile, R. C. Dockerty, and A. Nagarajan, *ibid.*, **121**, 907 (1974).
17. A. I. Stoller, W. Schilp, and J. Benbenek, *RCA Rev.*, **31**, 443 (1970).
18. B. O. Seraphin and V. A. Wells, NSF Report GI-36731X.
19. W. C. Waggener, Personal communication.
20. V. Y. Doo, D. R. Nichols, and G. A. Silvey, *This Journal*, **113**, 1279 (1966).
21. K. E. Bean, P. S. Gleim, R. L. Yeakley, and W. R. Runyan, *ibid.*, **114**, 733 (1967).
22. S. Yoshioka and S. Takayanagi, *ibid.*, **114**, 962 (1967).
23. V. Y. Doo, D. R. Kerr, and D. R. Nichols, *ibid.*, **115**, 61 (1968).
24. M. J. Grieco, F. L. Worthing, and B. Schwartz, *ibid.*, **115**, 525 (1968).
25. J. A. Aboaf, *ibid.*, **116**, 1736 (1969).
26. S. Yamazaki, K. Wada, and I. Taniguchi, *Japan. J. Appl. Phys.*, **9**, 1467 (1970).
27. H. Goral and T. Zalesica, *Electronika*, **26** (1970).
28. M. T. Duffy and W. Kern, *RCA Rev.*, **31**, 742 (1970).
29. P. C. Parekh, *Solid-State Electron.*, **16**, 954 (1973).
30. J. J. Tietjen, in "Annual Review of Materials Science," Vol. 3, R. A. Higgins, Editor, p. 317, Palo Alto (1973).
31. H. F. Sterling and R. C. G. Swann, *Solid-State Electron.*, **8**, 653 (1965).
32. R. C. G. Swann, R. R. Mehta, and T. P. Cauge, *This Journal*, **114**, 713 (1967).
33. T. Sugano, H. Sakai, and Y. Mori, *Ann. Rep. Eng. Res. Inst.*, **30**, 205 (1971).
34. A. Reinberg, *This Journal*, **121**, 85C (1974).
35. G. A. Vorob'ev, K. I. Smirkova, and Z. A. Shandra, *Sov. Phys. J. (USA)*, **13**, 839 (1970).
36. A. R. Janus and G. A. Shirn, *J. Vacuum Sci. Technol.*, **4**, 37 (1967).
37. S. C. Audisio and H. Leidheiser, Jr., *This Journal*, **119**, 408 (1972).
38. W. Rothemund and C. R. Fritsch, *Thin Solid Films*, **15**, 199 (1973).
39. E. Erdesz, *Finommech and Mikroteck*, **12**, 263 (1973).
40. E. A. Taft, *This Journal*, **118**, 1341 (1971).
41. J. L. Vossen, *J. Vacuum Sci. Technol.*, **8**, 751 (1971).
42. J. L. Vossen and J. J. O'Neill, *RCA Rev.*, **29**, 566 (1968).
43. L. V. Gregor, Tech. Report: AFAL-TR-67-248, September 1967.
44. J. S. Logan, *IBM J. Res. Develop.*, **14**, 172 (1970).
45. L. T. Lamont and T. Turner, *J. Vacuum Sci. Technol.*, **11**, 47 (1974).
46. W. A. Pliskin, in "Physical Measurements and Analysis of Thin Films," E. M. Murt and W. G. Guldner, Editors, Chap. 8, Plenum Press, New York (1969).
47. H. R. Philip, *This Journal*, **120**, 295 (1973).
48. W. A. Pliskin and S. J. Zanin, in "Handbook of Thin Film Technology," L. I. Maissel and R. Glang, Editors, pp. 11-49, McGraw-Hill Book Co., New York (1969).
49. W. A. Pliskin and H. S. Lehman, *This Journal*, **112**, 1013 (1965).
50. D. M. Mattox and G. J. Kominiak, *ibid.*, **120**, 1535 (1973).
51. I. Brodie, L. T. Lamont, Jr., and D. O. Myers, *J. Vacuum Sci. Technol.*, **6**, 124 (1969).
52. T. W. Hickmott, *J. Appl. Phys.*, **43**, 2339 (1972).
53. J. W. Coburn and E. Kay, *ibid.*, **43**, 4965 (1972).
54. P. K. Chaudhari, J. M. Franz, and C. P. Acker, *This Journal*, **120**, 991 (1973).
55. D. V. McCaughan and R. A. Kushner, *Proc. IEEE*, **62**, 1238 (1974).
56. T. L. Chu, *J. Vacuum Sci. Technol.*, **6**, 25 (1969).
57. D. M. Mattox and G. J. Kominiak, *ibid.*, **9**, 528 (1972).
58. R. D. Bland, G. J. Kominiak, and D. M. Mattox, *ibid.*, **11**, 671 (1974).

Growth of GaN Thin-Films from Triethylgallium Monamine

J. E. Andrews

Research Triangle Institute, Research Triangle Park, North Carolina 27709

and M. A. Littlejohn

North Carolina State University, Raleigh, North Carolina 27607

Vapor phase deposition of gallium nitride from organometallic compounds and NH_3 offers the possibility of lower growth temperatures compared to Ga-halide compounds due to the weaker Ga-organic radical bonds compared to the Ga-halide bonds (1). Lower

Key words: organometallic compounds, epitaxial growth, diethylgallium amide.

growth temperatures could be desirable since the dissociation temperature of GaN has been reported to be as low as 600°C (2), depending on the growth conditions (3).

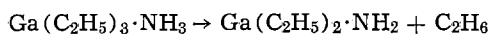
Although GaN growth was obtained from trimethylgallium $[\text{Ga}(\text{CH}_3)_3]$, (4) triethylgallium monamine $[\text{Ga}(\text{C}_2\text{H}_5)_3 \cdot \text{NH}_3]$ was selected over $\text{Ga}(\text{CH}_3)_3$ for

several reasons. First, a nitrogen atom is already bonded to the Ga atom, and although this is a weak bond, some Ga-N pairs may survive long enough to be incorporated into the film growth without an external source of N. Second, it is not pyrophoric as are both triethylgallium and trimethylgallium. Finally, this compound is a liquid at room temperature, providing slightly more convenient handling than $\text{Ga}(\text{CH}_3)_3 \cdot \text{NH}_3$ which is solid (mp $31^\circ\text{-}32^\circ\text{C}$) (5).

Published information on the physical and thermodynamic properties of $\text{Ga}(\text{C}_2\text{H}_5)_3 \cdot \text{NH}_3$ was not available. Only one commercial source is known to date.

Preparation of $\text{Ga}(\text{C}_2\text{H}_5)_3 \cdot \text{NH}_3$

The $\text{Ga}(\text{C}_2\text{H}_5)_3 \cdot \text{NH}_3$ used in this research¹ was prepared by saturating $\text{Ga}(\text{C}_2\text{H}_5)_3$ with NH_3 at -10°C . The material so formed was reported to be pale yellow and apparently underwent a slow decomposition, possibly by the reaction



Distillation resulted in further decomposition with C_2H_6 positively identified as a by-product. Upon completion of the decomposition, the product was easily distilled in a vacuum of 0.25-0.4 mm Hg. The material's reported boiling range was $64^\circ\text{C}/0.25 \text{ mm Hg}$ - $83^\circ\text{C}/0.4 \text{ mm Hg}$, and an analysis indicated the material to be predominantly diethylgallium amide.

The as-received material was colorless and "air-sensitive." Several droplets of the liquid turned into a white waxy-type substance when exposed to air over a period of approximately two days at room temperature. H_2O was nearly immiscible with the liquid and converted, at least ten times its own volume of the liquid into a beige-colored solid substance over a period of several days at room temperature.

Growth System Description

The growth system constructed for this research used a horizontal steady-state flow, 5 cm ID, cylindrical quartz reactor heated with a 700w Type FM305 Hoskins furnace. The reactor was operated at atmospheric pressure with a N_2 carrier gas stream for reactant vapor transport.

The triethylgallium monamine source material was shipped in a pressurized (N_2 gas, 12 psig), stainless steel sample cylinder and connected to the growth system shown in Fig. 1 directly over the bubbler. The bubbler is Pyrex and is connected to the stainless steel tubing through a Kovar glass-to-metal seal. The entire system was evacuated and the lines baked out from the gas supplies toward the vacuum system (reactor was removed and vacuum system was connected in its place) to aid the desorption of O_2 and H_2O from the interior tube walls. The system was evacuated, sealed

¹ Prepared and characterized by Dr. T. F. Jula and Dr. Bernd Schneider, Ventron Corporation, Alfa Inorganics, following essentially the technique described on p. 172 of Ref. (4).

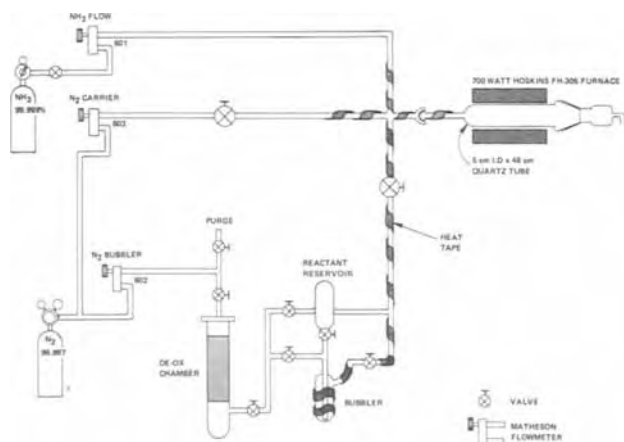


Fig. 1. GaN growth system

off, and leak-back rate measurements made to verify system integrity.

The N_2 tanks were rated at 20-30 ppm O_2 and required the addition of a de-oxygenation catalyst² and chamber (Fig. 1) to reduce this impurity to the sub-ppm levels. It should be noted that the system shown in Fig. 1 was designed to afford the maximum protection to the source material from O_2 and H_2O contamination. This precaution was essential in prolonging the useful life of the source material.

After several runs were made, the source material became noticeably darker and more viscous. The vapor pressure apparently decreased (based on a decrease in the deposition rate), and the films grown did not appear to be as transparent as those grown during the first run with fresh source material. Preliminary tests were carried out to characterize the vapor evolved from the material remaining in the bubbler.

Source Material Characterization

The purpose of this characterization was twofold: first, to establish a temperature range over which the vapor pressure was reproducible and stable; second, to identify the vapor being introduced into the furnace and to obtain some indications as to the nature of the decomposition or reaction path.

A cold trap was designed and constructed which allowed the chemical vapors that normally enter the reactor (Fig. 1) to be collected for analysis. The trap was fitted with aseptum so that the material could be withdrawn with a syringe for transfer to the liquid inlet of an AEI MS-12 mass spectrometer. A thermoelectric cooler was used to lower the trap temperature to -20°C .

The material was collected by vacuum transfer from the bubbler to the cold trap. The bubbler was maintained at 130°C during sample collection, and in 20 min approximately 1 cm of material was collected. Continued heating eventually left a dry, tan-colored residue in the bubbler.

The material collected consisted initially of a white precipitate and a clear, colorless liquid. It took approximately 2 hr after the trap was brought to room temperature before the precipitate apparently dissolved, again leaving a clear, colorless liquid in the trap. This material had the same appearance as the fresh source material.

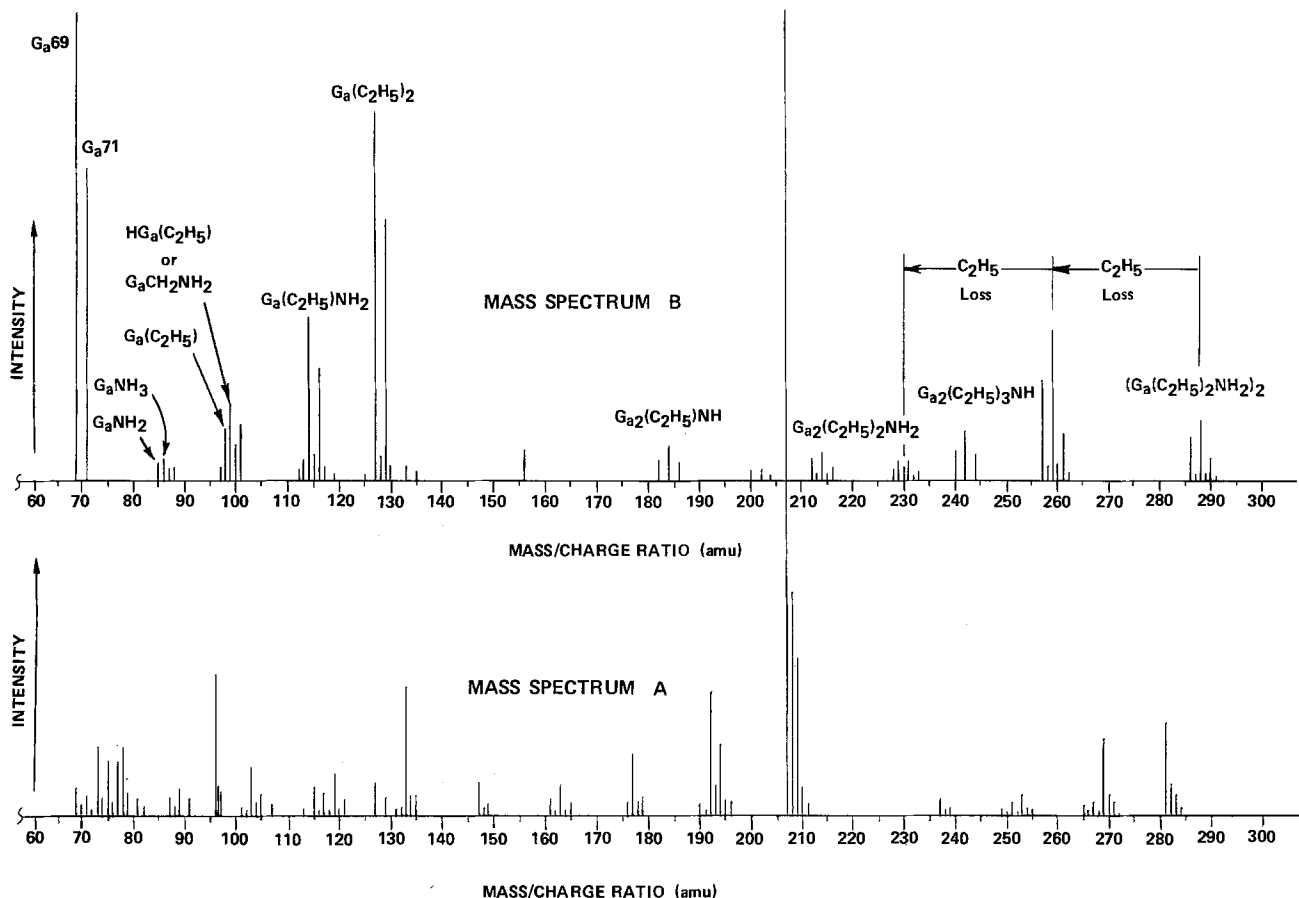
Mass spectra were obtained on the clear liquids both before and after the precipitate dissolved. These spectra are shown in Fig. 2. The two mass spectra were completely different, indicating that a reaction had taken place. The molecular fragments from the clear liquid collected initially did not contain Ga. The mass spectrum taken after the precipitate dissolved does show Ga-containing fragments, with the heaviest fragment (286-288-290 amu) tending to support the existence of a diethylgallium amide dimer. The diethylgallium amide dimer, if a constituent of the original source material, would be consistent with the supplier's analysis that indicated the existence of diethylgallium amide initially. The relative abundance ratios of the Ga^{69} and Ga^{71} isotopes were used to identify Ga-containing fragments.

Subsequently, vapor pressure stability of the collected material vs. temperature was studied by evacuating the cold trap and monitoring the pressure at the trap inlet. Above 71°C the pressure was erratic due apparently to the occurrence of a reaction. At 71°C or below, the pressure was well behaved; this was used as a basis for defining a maximum working temperature for the source.

Film Properties

Nearly transparent, yellow deposits were obtained on (0001) and ($\bar{1}\bar{1}02$) single crystal $\alpha\text{-Al}_2\text{O}_3$ substrates with deposition rates up to $2 \mu/\text{hr}$, with $0.5 \mu/\text{hr}$ being typical. These films were analyzed with x-ray and re-

² Alfa De-OX supplied by Ventron Corporation, Alfa Inorganics.



NOTES:

1. Spectrum A was from the clear liquid that was observed with the white precipitate when the sample was first collected.
2. Spectrum B was from the same sample but taken after the white precipitate dissolved leaving again a clear liquid.

Fig. 2. Mass spectra of source material collected from bubbler

reflection electron diffraction techniques and found to have a wurtzite structure with a c/a ratio of 1.63 and interplanar spacings corresponding to those published for GaN in the ASTM powder diffraction data analysis.

The GaN films were n-type with electron concentrations ranging from $5 \times 10^{14}/\text{cm}^3$ to $7 \times 10^{19}/\text{cm}^3$. Hall mobilities from 20 to 30 $\text{cm}^2/\text{V}\cdot\text{sec}$ can and have been routinely obtained, with the highest Hall mobility observed to date being 34 $\text{cm}^2/\text{V}\cdot\text{sec}$, $n = 1.5 \times 10^{19}/\text{cm}^3$, (room temperature data) for films grown at 800°C. Growth at 600°C yielded high resistivity films ($\sim 10^3$ ohm-cm) with carrier concentrations in the $10^{15}/\text{cm}^3$ range, but the Hall mobilities were low due in part to poorer quality substrate surface finishes used in that sequence of runs.

A more comprehensive report on the evaluation of the films grown to date will be published.

Summary

In summary, the triethylgallium monamine used in this research did lead to the growth of thin epitaxial layers of GaN. The preliminary analyses of the source material indicate that it is diethylgallium amide $[\text{Ga}(\text{C}_2\text{H}_5)_2\cdot\text{NH}_2]$ and probably exists as a dimer. $\text{Ga}(\text{C}_2\text{H}_5)_3\cdot\text{NH}_3$ decomposition to $\text{Ga}(\text{C}_2\text{H}_5)_2\cdot\text{NH}_2$ during preparation or in the bubbler does not preclude GaN growth since this is expected to be an intermediate step in the decomposition process that leads to the formation of GaN. However, this change and further decomposition in the bubbler makes vapor pressure control difficult. Heating the material to not more than

71°C does permit reasonably stable reactant vapor pressures suitable for thin film growth.

Acknowledgments

The authors want to thank Dr. J. R. Hauser and Dr. J. W. Harrison for their helpful comments and suggestions which contributed to the writing of this paper. Also, we are indebted to Dr. T. F. Jula and Dr. Bernd Schneider for their preparation of and discussions on the properties of this compound. Finally, we gratefully acknowledge the financial support of the Office of Naval Research.

Manuscript submitted Feb. 20, 1975; revised manuscript received May 21, 1975.

Any discussion of this paper will appear in a Discussion Section to be published in the June 1976 JOURNAL. All discussions for the June 1976 Discussion Section should be submitted by Feb. 1, 1976.

Publication costs of this article were partially assisted by North Carolina State University.

REFERENCES

1. K. I. Chopra, "Thin Film Phenomena," p. 47, McGraw-Hill Book Co., New York (1969).
2. T. L. Chu, *This Journal*, **118**, 1200 (1971).
3. F. P. Kesmanly, *Sov. Phys. Sem.*, **8**, 147 (1974).
4. H. M. Manasevit, F. M. Erdmann, and W. I. Simpson, *This Journal*, **118**, 1864 (1971).
5. I. A. Sheka, I. S. Chaus, and T. T. Mityureva, "The Chemistry of Gallium," p. 172, Elsevier Publishing Co., Amsterdam (1966).



Elimination of Random Compositional Inhomogeneities in Czochralski Grown Silicon

A. Murgai, A. F. Witt,* and H. C. Gatos*

Department of Materials Science and Engineering,
Massachusetts Institute of Technology, Cambridge, Massachusetts 02139

Thermal conditions were achieved, in a standard Czochralski system, under which the random compositional inhomogeneities in silicon crystals are consistently eliminated. This growth configuration was obtained for the generally employed rate of seed rotation (ranging from 3 to 30 rpm) by establishing pronounced thermal asymmetry through the introduction of an off-centered heat sink above the melt.

In earlier studies on the microsegregation in Czochralski grown semiconductor crystals, random compositional fluctuations were attributed to turbulent thermal convection (1); they were also found to become more pronounced with increasing melting point of the material grown (2). Thus, it was shown that the formation of these microsegregation inhomogeneities is readily suppressed by seed rotation of moderate rates in InSb and germanium crystals. In silicon, however, grown at the commonly used pulling rates and rates of seed rotation, random compositional inhomogeneities are invariably present (3).

The thermal configuration achieved is of fundamental importance as it permits the quantitative study of the effects of seed rotation and of crucible rotation on growth and segregation without interference from turbulent convection; moreover, it now becomes possible to determine quantitatively the effect of turbulent convection on segregation and growth behavior.

The reported results were obtained in a standard Czochralski system, with design features, including

* Electrochemical Society Active Member.

Key words: silicon, crystal growth, dopant inhomogeneities.

interface demarcation (4), for an extensive study of growth and segregation behavior of silicon. In this system a graphite resistance heater was used (7 cm in diameter and 16 cm long) in conjunction with a concentric cylindrical tantalum heat shield (14 cm in diameter and 11 cm long). Silicon melts up to 75g were employed. Numerous crystals grown invariably exhibited the familiar random compositional inhomogeneities. The thermal configuration leading to microsegregation free of random convection effects was first obtained after introducing a stainless steel pipe 5 mm in diameter (wall thickness, 0.5 mm) running horizontally through the water-cooled furnace wall to a distance of 3 cm from the rotational axis and bent downwards with its end located 2 cm above the upper rim of the crucible. Growth experiments under various thermal conditions indicated that the presently reported critical thermal configuration may be achieved not only by establishing asymmetric heat loss from the melt (as described above), but also through pronounced asymmetric heat input, *i.e.*, by displacing the crucible containing the melt from the rotational axis of the growth system. A quantitative characterization of the thermal conditions leading to segregation without interference from thermal convection is in progress.

The microsegregation in silicon before and after the modification of the thermal configuration is shown in Fig. 1(a) and 1(b). It is seen that the random compositional fluctuations present in Fig. 1(a) are eliminated in Fig. 1(b). The widely spaced lines of Fig. 1(b)

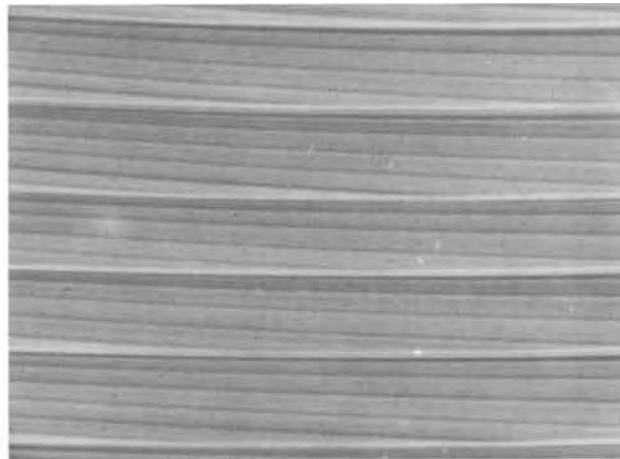
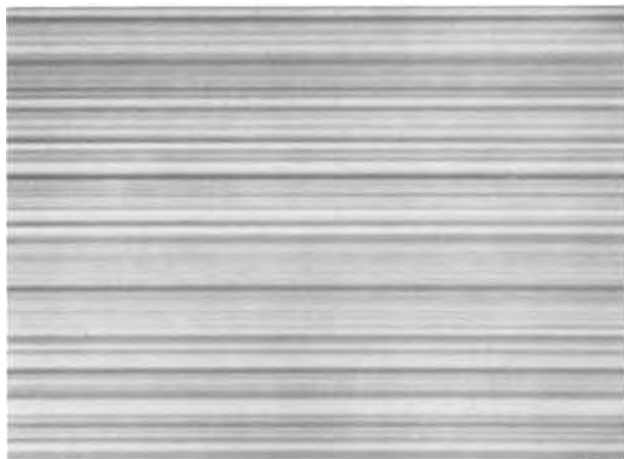


Fig. 1. Microsegregation in Czochralski type silicon (Sb doped to $5 \times 10^{18}/\text{cm}^3$) pulled at a rate of 3.4 cm/hr with seed rotation (5 rpm). Figure 1(a, left) shows the normal segregation behavior, characterized by the appearance of random nonrotational striations caused by thermal convection. Figure 1(b, right) shows the segregation behavior in silicon grown under the presently reported thermal conditions; periodic rotational striations now become well defined and random striations are eliminated. The number of rate striations (fine lines between successive rotational striations) introduced at 1 sec intervals reveal that the crystal segment remaining after backmelting for each rotational cycle (12 sec) corresponds to about 4 sec of growth. The samples were etched in 1 part [25g CrO_3 in 50 cm^3 H_2O] + 1 part HF (conc) by successive immersions for periods of 5 sec (total etching time 1 min).

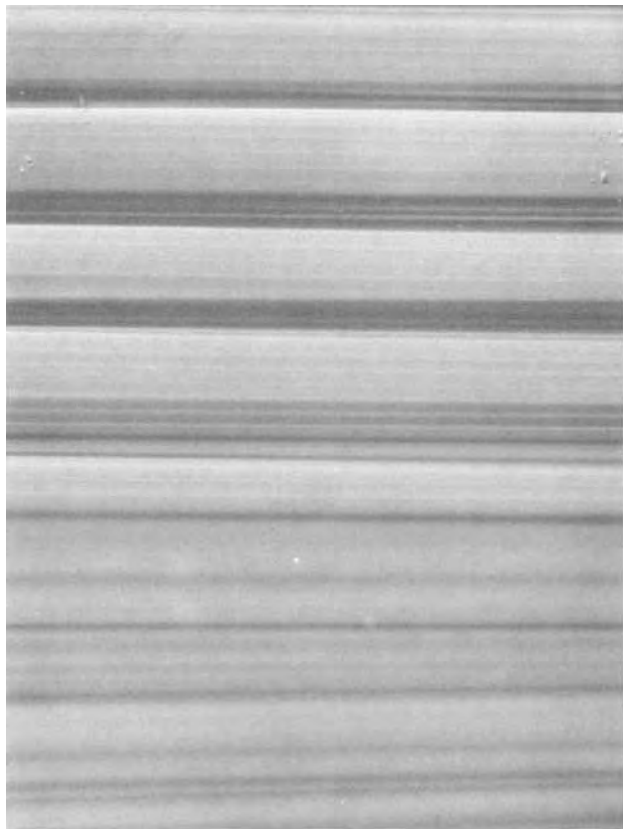


Fig. 2. Microsegregation behavior in silicon pulled under the presently reported thermal configuration. Note the abrupt transition from forced convection controlled segregation (top portion) to thermal convection controlled segregation (bottom portion) which occurred as the melt level was decreased and the aspect ratio exceeded the value of 2.5.

were introduced by interface demarcation, employing current pulses of 10 A/cm² at 1 sec intervals. These rate striations show clearly the existence of pronounced thermal asymmetry and the occurrence of periodic rotational backmelting during growth. With the given thermal configuration, growth without convective interference was reproducibly achieved for aspect ratios (d/h) of the melt less than 2.5. For the crucible employed (5 cm in diameter), these aspect ratios corre-

spond to melt heights greater than 2.1 cm. As the melt height decreased below 2.1 cm, it was found that the growth system changes abruptly to the normally encountered conditions associated with turbulent convection controlled growth and segregation. The critical aspect ratio (2.5) was found to be independent of the pulling rate and of the diameter of the crystal grown. The segregation behavior above and below the critical aspect ratio is shown in Fig. 2.

It is of interest to note that temperature measurements in the melt, with a thermocouple located 0.5 cm below the initial growth interface, indicated the presence of pronounced irregular temperature fluctuations (up to $\pm 8^\circ\text{C}$) of frequencies up to 5 Hz during growth both above and below the critical aspect ratio. In the light of the observed growth and segregation, the detailed study of the thermal configuration and the prevailing thermohydrodynamics of the melt should be of fundamental significance.

The reported thermal asymmetry effect on microsegregation in silicon now makes it possible to isolate forced convection from thermal convection effects and to investigate quantitatively their respective influence on growth and segregation.

Acknowledgment

The authors are indebted to the National Science Foundation for financial support.

Manuscript submitted April 4, 1975; revised manuscript received May 6, 1975.

Any discussion of this paper will appear in a Discussion Section to be published in the June 1976 JOURNAL. All discussions for the June 1976 Discussion Section should be submitted by Feb. 1, 1976.

Publication costs of this article were partially assisted by Massachusetts Institute of Technology.

REFERENCES

1. A. Müller and M. Wilhelm, *Z. Naturforschung*, **19A**, 254 (1965); W. R. Wilcox and L. D. Fullmer, *J. Appl. Phys.*, **36**, 2201 (1965); K. M. Kim, A. F. Witt, and H. C. Gatos, *This Journal*, **119**, 1218 (1972).
2. A. F. Witt, M. Lichtensteiger, and H. C. Gatos, *ibid.*, **120**, 1119 (1973).
3. T. F. Ciszek, in "Semiconductor Silicon," R. R. Haberecht and E. L. Kern, Editors, p. 116, The Electrochemical Society Softbound Symposium Series, New York (1969).
4. M. Lichtensteiger, A. F. Witt, and H. C. Gatos, *This Journal*, **118**, 1013 (1971).

Erratum

In the paper "The Free Energy of Formation of Iridium Oxide by Solid Electrolyte Galvanic Cell" by E. S. Ramakrishnan, O. M. Sreedharan, and M. S. Chandrasekharaiah which appeared on pp. 328-331 in the March 1975 JOURNAL, Vol. 122, No. 3, Eq. [5] should read as follows

$$E_2(\text{mV}) \pm 1.0 = 14.5 + 6.20 \times 10^{-2}T; \\ 1175^\circ \leq T \leq 1375^\circ\text{K}$$

Also in Table I, the third line from the bottom of the table should read

$$E_{\text{III}}(\text{mV}) \pm 1.0 \quad 291.6 \quad 284.4 \quad 277.2 \quad 270.1 \quad \text{This work}$$



The Catalytic Activity of Platinum Supported on Carbon for Electrochemical Oxygen Reduction in Phosphoric Acid

H. R. Kunz and G. A. Gruver

Power Systems, Division of United Technologies Corporation, South Windsor, Connecticut 06074

ABSTRACT

An experimental program was conducted to determine the catalytic activity of high surface area platinum supported on carbon for the electrochemical reduction of oxygen in phosphoric acid. The Tafel slope at 160°C in 96 weight per cent phosphoric acid was found to be approximately 90 mV/decade. The exchange current per unit of real surface area of the supported platinum was found to be approximately the same as that of platinum black or a flat platinum sheet if the effect of electrode prepolarization is considered. Additional tests at other temperatures indicated that the Tafel slope varies as RT/F and is similar in sulfuric and phosphoric acid at the same temperature. The prediction that a double Tafel slope exists when oxygen diffusional resistance becomes significant in a Teflon-bonded porous electrode was confirmed.

Although a considerable amount of experimental work had been done to determine the Tafel slope and exchange current for the electrochemical reduction of oxygen in acidic electrolytes, uncertainty still existed concerning the true value of these quantities for high surface area platinum when supported on carbon. These uncertainties were present for a number of reasons.

First, the experimental data on Tafel slope were not in good agreement. For example, the data of Vogel and Lundquist (1) at 120°C in 85% phosphoric acid indicated a Tafel slope of 60 mV/decade for platinum black, whereas the data of Appleby (2) indicated a Tafel slope of 80 mV/decade at 116°C in 85% phosphoric acid in what he considered to be an oxide-free platinum sheet. Vogel and Lundquist indicated that this difference could be due to a true difference between the catalytic properties of the two surfaces or due to impurities on the platinum when tested as a smooth surface.

Secondly, the measured temperature effect on Tafel slope was not consistent. Appleby found the Tafel slope in 85% phosphoric acid to be equal to RT/F on a flat sheet. However, Vogel and Lundquist found the Tafel slope in 85% phosphoric acid at 120°C to be approximately 60 mV/decade and about equal to that in 50% phosphoric acid at 70°C and 20% sulfuric acid at 70°C.

Thirdly, the data of Vogel and Lundquist for platinum black in phosphoric acid was obtained at potentials above 0.9V with respect to a hydrogen reference electrode in the same electrolyte. This was necessary because diffusional resistance to oxygen migration through the electrolyte within the platinum black was found to occur at lower potentials. The Tafel slope was not measured in phosphoric acid at potential levels significantly lower than 0.9V. Since a change in the

oxidation state of the platinum surface occurring in the vicinity of 0.9V might cause a change in the mechanism for oxygen reduction (3), extrapolating a linear Tafel line to lower potentials is not justifiable. An extensive study of the surface oxidation state of platinum has been made by Conway *et al.* (4-6).

Fourth, a measurement of the Tafel slope for platinum supported on carbon is difficult at potentials above 0.9V because of the mixed potential caused by oxidation of platinum and carbon.

Finally, if a high surface area platinum supported on carbon is considered, the catalytic properties can be affected by the size of platinum crystallites and the support. Small crystallite sizes of the supported platinum as compared to those of platinum black might affect the Tafel slope and exchange current. Also, a catalytic interaction between the platinum and carbon might be present for small platinum crystallites.

Because of the uncertainties that existed concerning the true activity of high surface area supported platinum for the reduction of oxygen in acidic electrolyte, a theoretical and experimental program was undertaken to clarify this situation.

Theory

A number of theoretical studies have been performed on Teflon-bonded platinum black electrodes. Brown and Horve (7) derived a model based on cylindrical platinum agglomerates and applied this to cathodes operating in potassium hydroxide electrolyte. This model was also used by Giner (8). Kosinski (9) applied this model to phosphoric acid electrolyte and found the model capable of rationalizing the platinum black data of Vogel and Lundquist using a Tafel slope of 65 mV/decade at 120°C in 85% phosphoric acid. This value was essentially the same as that extracted by Vogel and Lundquist.

The use of such a theoretical model is definitely limited because of the number of fitting parameters

Key words: platinum, oxygen reduction, phosphoric acid, cathode theory, Tafel slope.

that are needed to rationalize the experimental data and the assumptions that are made in the model. Tafel slope, exchange current, agglomerate diameter, agglomerate porosity, agglomerate tortuosity, and electrolyte film thickness surrounding the agglomerate are all fitting parameters. Nevertheless, a great deal of information can be obtained about the operating characteristics of electrodes through the use of a theoretical model.

At low levels of current and high potentials, the polarization of an electrode is controlled by a mixed potential between the reduction of oxygen and oxidation of carbon, platinum, and possible impurities (10). As the current is increased, the polarization should follow the Tafel line of the electrochemical reaction if the currents are high enough to make mixed potential effects negligible and other losses are adequately small. These include the losses associated with oxygen, ion, and electron migration to the reaction site. This region of the data can be used to obtain the Tafel slope and exchange current.

Once the centers of the majority of agglomerates start to experience a significantly reduced oxygen activity, the polarization curve starts to follow a slope which is twice the Tafel slope, in the absence of significant ohmic polarization and electrolyte concentration gradients. If a wide distribution of agglomerate sizes is present, a wide transitional region will exist with slopes between the Tafel slope and double Tafel slope. The current at which the polarization curve changes from a single to a double Tafel slope can be used to obtain a measure of an average agglomerate size.

This model was extended to Teflon-bonded electrodes containing supported platinum in order to get a better understanding of their operation. The resulting equations are similar to those derived previously for unsupported catalyst. When all of the electrode polarization is that associated with the finite rate of the electrochemical reaction, the Tafel equation results in the form

$$i = W_{Pt} S_g i_0 e^{\alpha N F \eta / RT} \quad [1]$$

where i = electrode current density, A/cm² frontal area; W_{Pt} = platinum loading, g/cm² frontal area; S_g = platinum surface area, cm²/g; i_0 = exchange current, A/cm² Pt real area; α = transfer coefficient; N = number of electrons in the rate-determining step, equiv./mole; F = Faraday constant, coulomb/equiv.; η = polarization, V; R = gas constant, joule/mole^oK; T = temperature, ^oK.

When the ability of oxygen to diffuse through the electrolyte in a porous cylinder of supported catalyst is also controlling, the following equation results for suitably large values of

$$i = \frac{2W_{Pt}}{R_{agg}} \left[\frac{NFD_{O_2} \alpha_{O_2} S_g i_0}{\rho_s W_{Pt} / W_s} \cdot \frac{\theta}{(1-\theta)\tau} \right]^{1/2} e^{\alpha N F \eta / 2RT} \quad [2]$$

where R_{agg} = agglomerate radius, cm; L = electrode thickness, cm; W_s = support loading, g/cm² frontal area; $D_{O_2} \alpha_{O_2}$ = oxygen diffusivity-solubility product, mole/cm sec; ρ_s = support density, g/cm³; θ = agglomerate porosity; τ = agglomerate tortuosity.

As demonstrated by Eq. [1], the theory of supported platinum electrodes indicates that in the Tafel region the current at a given potential varies linearly with the catalyst loading if the catalyst specific activity is constant. In the double Tafel region described by Eq. [2], however, if the carbon loading is fixed and the platinum specific activity is fixed, the current at a given potential should vary with the square root of the platinum loading. Therefore, it was concluded that, if experimental data could be obtained over a wide range of platinum loading, the variation of current with loading could be used to determine whether the

single or double Tafel slope is occurring. The Tafel slope could therefore be obtained. Since as the catalyst loading is reduced the relative importance of the diffusional resistance to oxygen in the catalyst layer is diminished, it was thought that experimental data on Tafel slope would become available at lower levels of potential, in the range of 0.7V. This potential is significantly below that at which a change in the oxidation state of the platinum occurs.

Such a test series was therefore performed in this study together with investigations of the effect of temperature in phosphoric acid and the effect of changing the electrolyte to sulfuric acid. The latter tests were run to determine whether or not the Tafel slope varies with RT/F as found by Appleby and to compare results with those of other investigators. Experiments were also performed on cathodes with reduced Teflon content to increase the effective agglomerate size. A well-defined double Tafel slope was hoped to result in these experiments and therefore confirm the findings obtained in the study in which platinum loading was varied. Finally, some experiments were performed on a flat platinum sheet to obtain data at temperatures higher than those investigated by Appleby.

Experiments

The electrodes used in this study contained platinum supported on Vulcan XC-72 (Cabot Corporation). The nitrogen BET surface area of this support was measured and found to be about 220 m²/g. Platinum was deposited upon this carbon and it was fabricated into Teflon-bonded electrodes.

Electron micrographs of this carbon-containing platinum are shown in Fig. 1 and 2 for untested specimens. Figure 1 is a "bright field" micrograph in which the platinum appears as dark particles overlaid on the semitransparent carbon. In Fig. 2 the white spots are "reflections" arising from (111) platinum (same sample field as in Fig. 1). This micrograph confirms that the dark spots in Fig. 1 are in fact platinum. Platinum

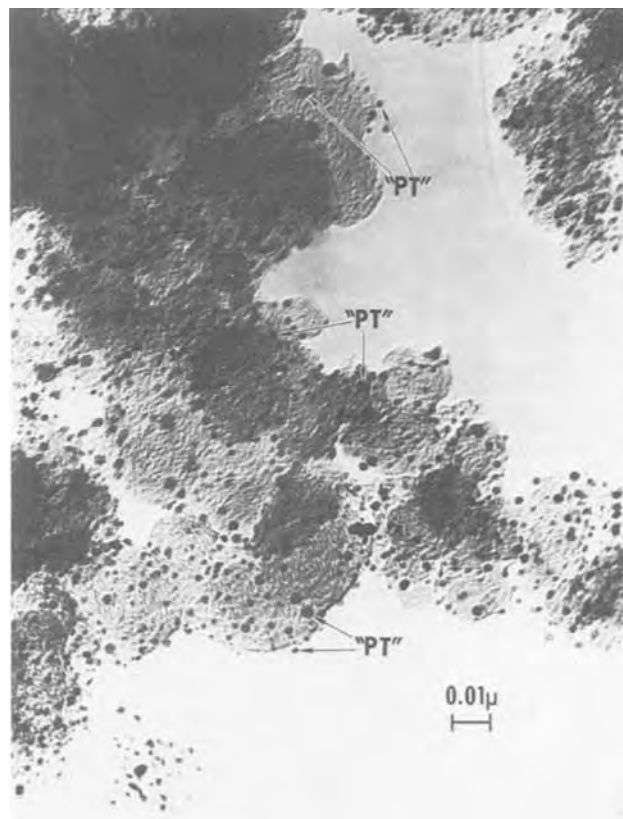


Fig. 1. Electron photomicrograph of platinum supported on Vulcan XC-72 (bright field).

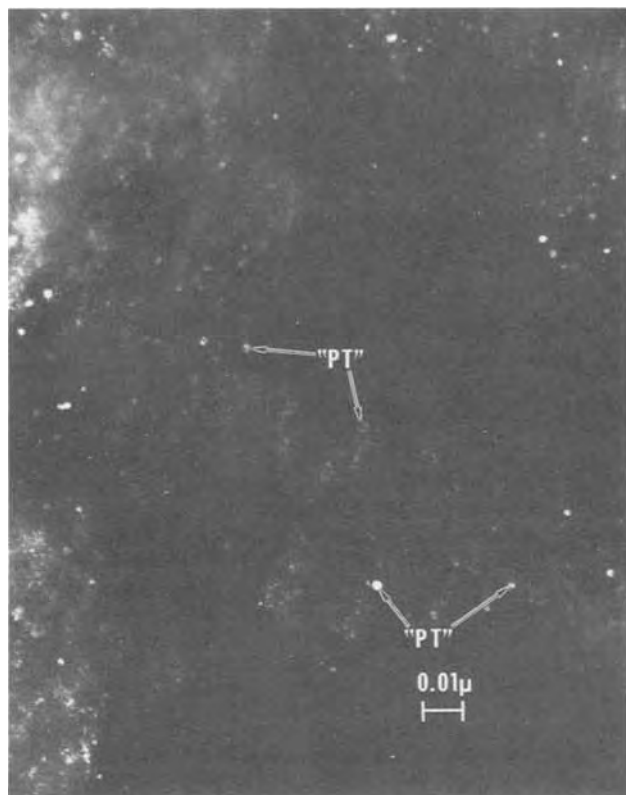


Fig. 2. Electron photomicrograph of platinum supported on Vulcan XC-72 (dark field).

crystallite sizes were measured from these micrographs and found to result in a platinum surface area of approximately $130 \text{ m}^2/\text{g}$, assuming the particles to be spherical and all of the platinum surface exposed. The range of surface areas from micrographs of other samples of this catalyst was $109\text{--}175 \text{ m}^2/\text{g}$.

Platinum surface areas were also measured electrochemically using hydrogen adsorption in sulfuric acid for samples of electrodes containing about $0.25 \text{ mg Pt}/\text{cm}^2$. These areas were found to be about $60\text{--}70 \text{ m}^2/\text{g}$ after the electrodes had been tested. These areas are considerably lower than the areas calculated from platinum crystallite sizes measured using the electron microscope micrographs.

The difference in surface areas obtained from the micrographs and from hydrogen adsorption might be due to a number of reasons. For example, some of the platinum crystallite surface is in contact with the carbon and might be blocked with respect to hydrogen adsorption. In addition, part of the platinum area is lost due to recrystallization, part might not be adequately wet by electrolyte to act as effective catalyst, and some might be in poor electronic contact. Since the important platinum area with respect to the determination of catalytic activity is that which is used in an electrode, a typical area of $70 \text{ m}^2/\text{g}$ was used in the rest of this study.

The supported platinum was fabricated into electrodes using Teflon 30 (E. I. du Pont de Nemours & Company). A photograph of the cross section of an electrode is shown in Fig. 3. Figure 4 shows an electron micrograph of a microtomed section of a catalyst layer. The Teflon and the carbon can be seen to be present in distinct segregated regions.

Electrodes were tested in a glass half-cell apparatus as 1 cm^2 floating electrodes as shown in Fig. 5. The catalyst layer was located facing the electrolyte with the carbon paper facing upward toward the reactant supply. A platinum black hydrogen reference electrode operating in the same electrolyte was used in conjunction with a Luggin capillary. The counterelectrode was a platinum screen enclosed in a separate electrolyte

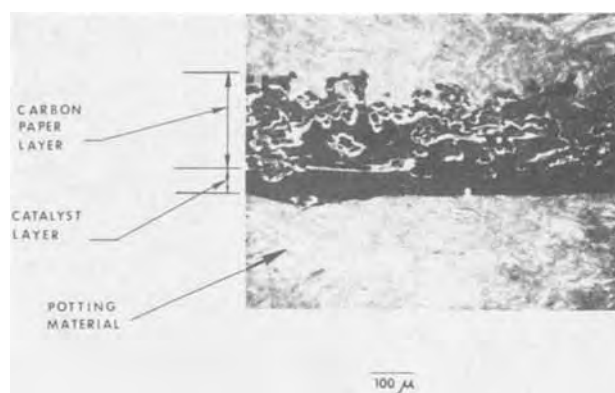


Fig. 3. Optical photomicrograph of an electrode cross section

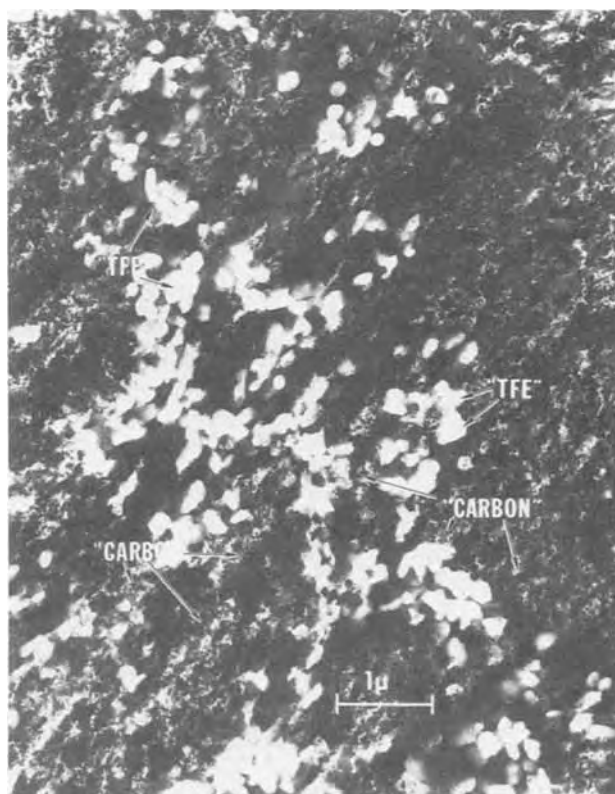


Fig. 4. Electron photomicrograph of an ultramicrotomed section of an electrode catalyst layer.

region. Current was collected from the top of the working electrode using a platinum spring. The volume of electrolyte in the apparatus was approximately $30\text{--}40 \text{ ml}$. Both Baker and Adamson reagent grade H_3PO_4 and acid which had been electrochemically cleaned by absorption of impurities on platinum black at hydrogen potential were used. Temperature was controlled using an electrically heated mantle surrounding the electrolyte vessel with the sensing thermocouple in the electrolyte. Electrode potentials, E^* , were measured relative to a hydrogen reference electrode in the same electrolyte and were corrected for external resistance by using a current interrupter. Load currents were supplied by a constant current source and were measured using a precision 1% resistor located in the counterelectrode line. Electrode voltage and current were monitored using either an electronic digital voltmeter accurate to 0.2% of full scale (1.999V) or an electromechanical voltmeter accurate to 0.5%. Reactant gases were saturated to provide a water vapor pressure in equilibrium with the electrolyte.

No prepolarization of electrodes was performed in general since this might introduce errors in the steady-

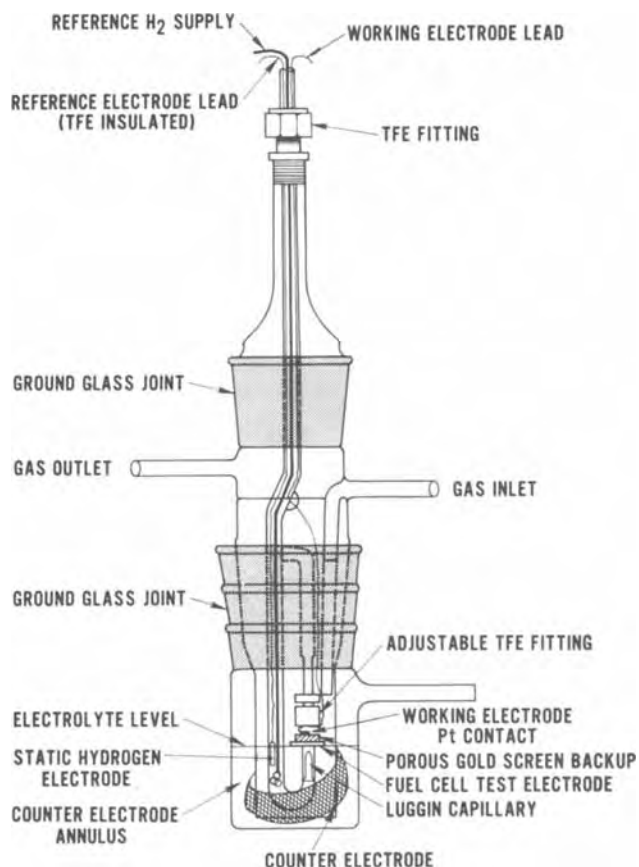


Fig. 5. Half-cell apparatus

state activity due to possible effects of phosphate anion adsorption and the extent of adsorbed oxygen coverage (11). Data were obtained by both increasing current in steps and decreasing current in steps through the potential range of interest, about 0.9-0.7V. Little difference in results was found. Potentials in this range were stable for at least 5 min. Data at higher potentials changed somewhat with time due possibly to anion desorption, platinum oxidation, or mixed potential effects due to oxidation of the carbon, platinum, and possible impurities. Data at high current densities changed with time due to possible electrode heating. Some experiments were performed on a flat platinum sheet to investigate the effect of prepolarization since both Appleby and Vogel and Lundquist incorporated prepolarization treatments.

Results

As discussed in the Theory section, a number of separate experimental studies were conducted to evaluate the activity of platinum. The first of these involved an investigation of the effects of a variation of the platinum loading with a constant carbon loading with phosphoric acid electrolyte. Others involved investigations of the effect of temperature and of operation with sulfuric acid rather than phosphoric acid. In addition, electrodes were evaluated in which definite diffusional losses had been introduced. A final investigation involved tests on flat sheets in order to obtain an extension of the data of Appleby to higher temperatures. The results obtained in these various investigations are presented in the following sections.

Variation of platinum loading.—A series of electrodes were prepared containing 15, 1.5, and 0.15 weight per cent (w/o) platinum applied to Vulcan XC-72. The weight per cent of Teflon in the supported catalyst and Teflon mixture was held constant at 50%. These weight per cents of platinum resulted in platinum loadings of about 0.25, 0.025, and 0.0025 mg/cm²,

respectively. These platinum loadings were verified by chemical analysis.

Each one of these electrodes was tested as a floating electrode in the half-cell apparatus on both oxygen and air at atmospheric pressure at 160°C in unpurified 96% H₃PO₄. Graphs of the experimental data for these various electrodes are presented in Fig. 6 through 8.

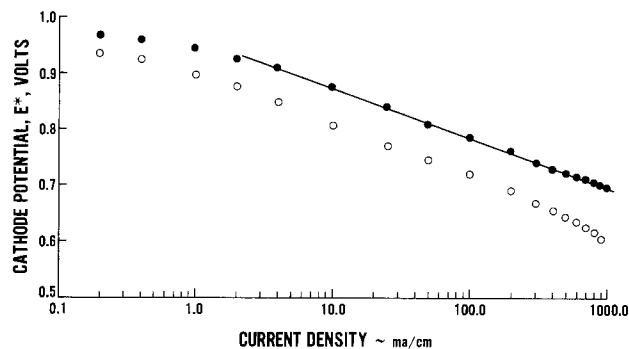


Fig. 6. Cathode performance for 0.25 mg Pt/cm² supported on Vulcan XC-72 at 160°C in 96% H₃PO₄. ●, Oxygen; ○, air. A straight line with a slope of 90 mV/decade has been drawn through the oxygen data.

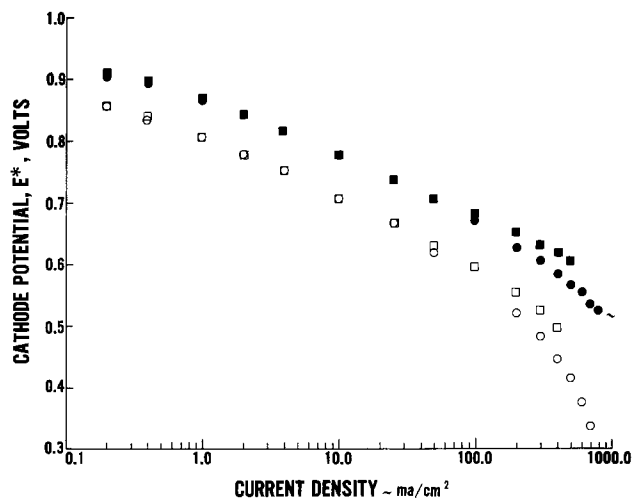


Fig. 7. Cathode performance for 0.025 mg Pt/cm² supported on Vulcan XC-72 at 160°C in 96% H₃PO₄. ●, Oxygen; ○, air; with high concentration platinum solution. ■, Oxygen; □, air; with low concentration platinum solution (two sets of data).

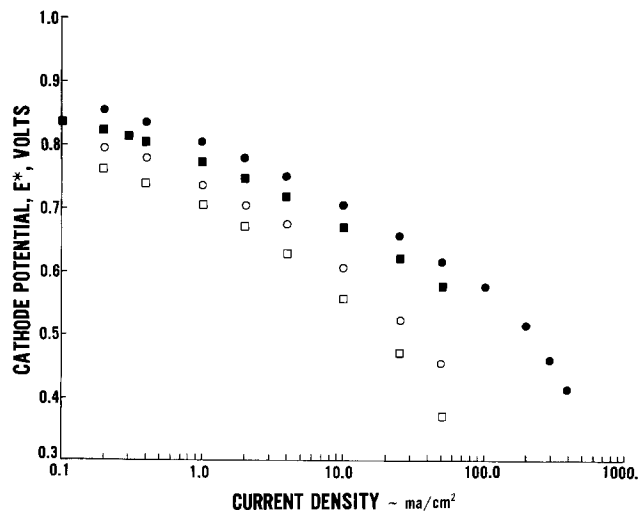


Fig. 8. Cathode performance for 0.0025 mg Pt/cm² supported on Vulcan XC-72 at 160°C in 96% H₃PO₄. ●, Oxygen; ○, air; with high concentration platinum solution. ■, Oxygen; □, air; with low concentration platinum solution.

During the fabrication of the electrodes with the loadings of 0.025 and 0.0025 mg Pt/cm², two different concentrations of the platinum catalyzation solution were used. This was done in order to investigate whether or not the small quantity of platinum was being uniformly distributed throughout the Vulcan. The data presented in Fig. 7 and 8 show that adequately uniform catalyzation of the Vulcan had been achieved.

By investigating Fig. 6-8 some of these electrodes can be seen to demonstrate a straight line variation of cathode potential with the logarithm of current density over a range of potential below 0.9V. As discussed in the Theory section, if the variation of current at a given potential varies linearly with platinum loading in a straight line region, the straight line region represents a region in which the Tafel slope is occurring. If the variation of current at a given potential varies with the square root of the loading, this straight line region is a double Tafel region rather than a single Tafel region. For this reason a graph was made of current density at 0.7V cathode potential vs. loading. This graph is shown in Fig. 9. As can be seen in this figure, all the experimental points fall along an approximate straight line with a slope of 45°, thereby showing a linear dependence between the current at a given potential and the loading. The straight line segments on the performance curves of these various cathodes in the range of 0.7-0.9V therefore represent the true single Tafel slope for the reduction of oxygen. The value of this slope is approximately 90 mV/decade.

The possibility existed in this investigation that a systematic change in the electrode structure might be occurring as the platinum loading is being changed, thereby leading to an erroneous conclusion. To eliminate this possibility, an electrode was fabricated containing no platinum with the same quantity of Vulcan as was used in the study in which the platinum content was varied between 0.25 and 0.0025 mg/cm². This electrode was subsequently catalyzed with 0.25 mg Pt/cm² and resulted in essentially the same experimental results as the electrode which was precatalyzed with 0.25 mg Pt/cm². Therefore, no systematic effect of electrode structure was present in the data.

The theory of fuel cell electrodes indicated that the limiting current should not depend on the platinum loading for a given carbon loading. However, the experimental data obtained here indicated limiting currents on air of approximately 2000 mA/cm² for the 0.25 mg/cm² loading, 1300 mA/cm² for the 0.025 mg/cm² loading, and 110 mA/cm² for the 0.0025 mg/cm² loading. This result at first indicated that perhaps the results for the lowest loading were not being interpreted correctly. However, a theoretical investigation of oxy-

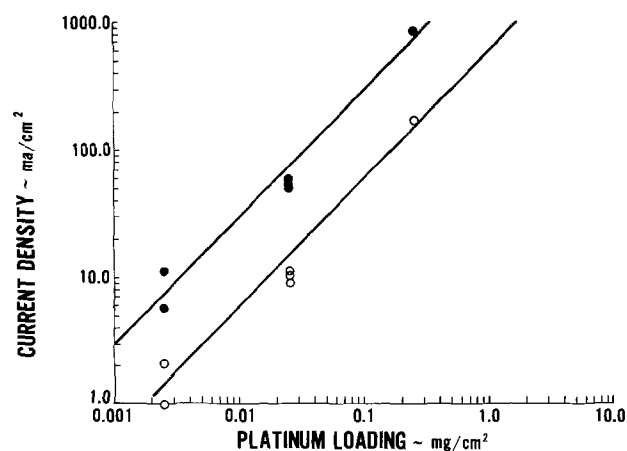


Fig. 9. Variation of current density with Pt loading for Pt supported on Vulcan XC-72 at 160°C in 96% H₃PO₄. ●, Oxygen; ○, air. $E^* = 0.7$ V. Lines represent a linear relationship between variables for oxygen and air.

gen diffusion through the electrolyte film surrounding the agglomerate to single platinum crystallites on the surface of the agglomerate indicated that, with this loading, an additional diffusional resistance of oxygen in the electrolyte was present due to the scarcity of the platinum crystallites on the surface of the agglomerate. This additional diffusional resistance was calculated to be absent at the low currents and high potentials occurring in the range of data that was being used to evaluate the variation of current at a given potential with platinum loading. Therefore, the fact that the limiting current declined with loading is probably of no consequence.

A variation of the platinum specific area with loading would also affect the variation of electrode performance with loading. The platinum specific area might be expected to increase as the loading is reduced. This would tend to make the variation of current at a given potential vary in less than a linear manner with loading in the Tafel region, just as the presence of a diffusional resistance would. Therefore, the variation of platinum specific area with loading is probably not causing this linear dependence. The specific area could not be measured electrochemically for the loadings of 0.025 and 0.0025 mg/cm² because of the greater relative capacitive effect of the Vulcan.

Variation of temperature.—A series of tests was performed on the 0.25 mg Pt/cm² cathode to determine the variation of the Tafel slope and the current at a given potential with temperature. These tests were run using both unpurified 96% H₃PO₄ and purified and unpurified 85% H₃PO₄ in the half-cell apparatus. The cathode performance data are presented in Fig. 10 and 11. Figures 12 and 13 present a comparison with the experimental data of Appleby. The data on Tafel slope obtained with unpurified 85% H₃PO₄ in this study are in good agree-

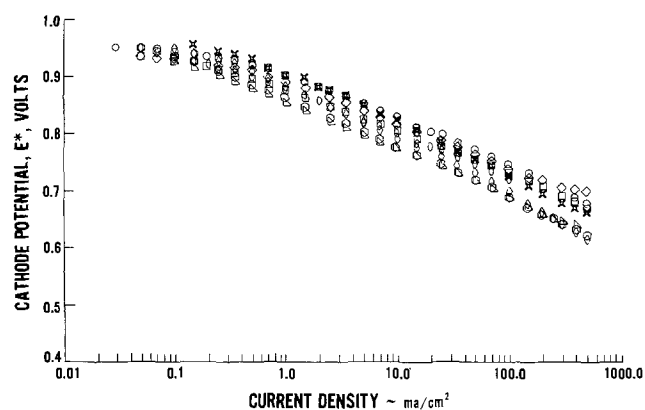


Fig. 10. Cathode performance on oxygen for 0.25 mg Pt/cm² supported on Vulcan XC-72 at various temperatures. ○, 121°C; □, 113°C; ◇, 95°C; X, 77°C; ◇, 66°C; ◇, 54°C; △, 49°C with unpurified 85% H₃PO₄. ○, 46°C with purified 85% H₃PO₄.

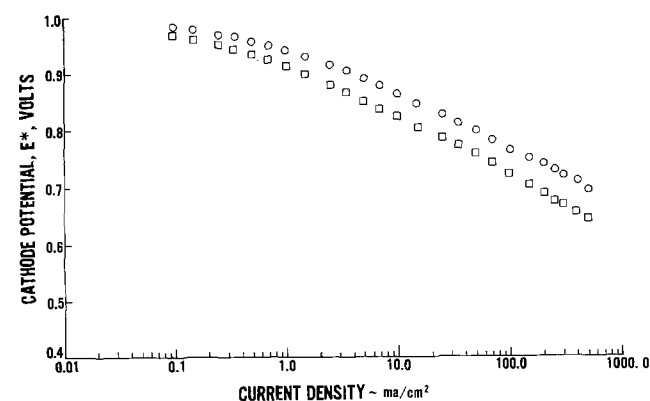


Fig. 11. Cathode performance on oxygen for 0.25 mg Pt/cm² supported on Vulcan XC-72 at various temperatures with unpurified 96% H₃PO₄. ○, 129°C; □, 91°C.

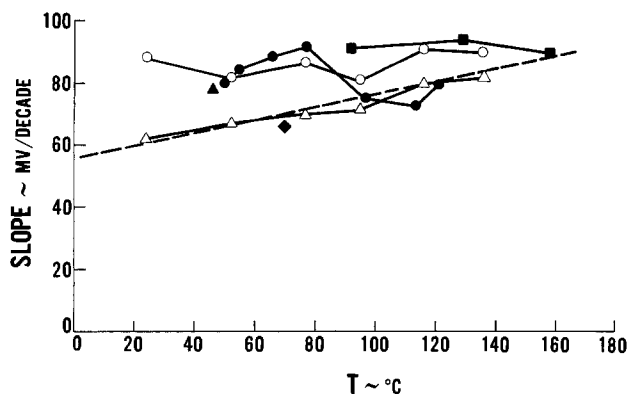


Fig. 12. Variation of oxygen Tafel slope with temperature for various acid compositions. Data of Appleby: Δ , purified 85% H_3PO_4 ; \circ , analytical grade H_3PO_4 . Data of this study: \blacktriangle , purified 85% H_3PO_4 ; \bullet , unpurified 85% H_3PO_4 ; \blacksquare , unpurified 96% H_3PO_4 ; \blacklozenge , 20% H_2SO_4 . The dotted line represents a Tafel slope which is proportional to absolute temperature.

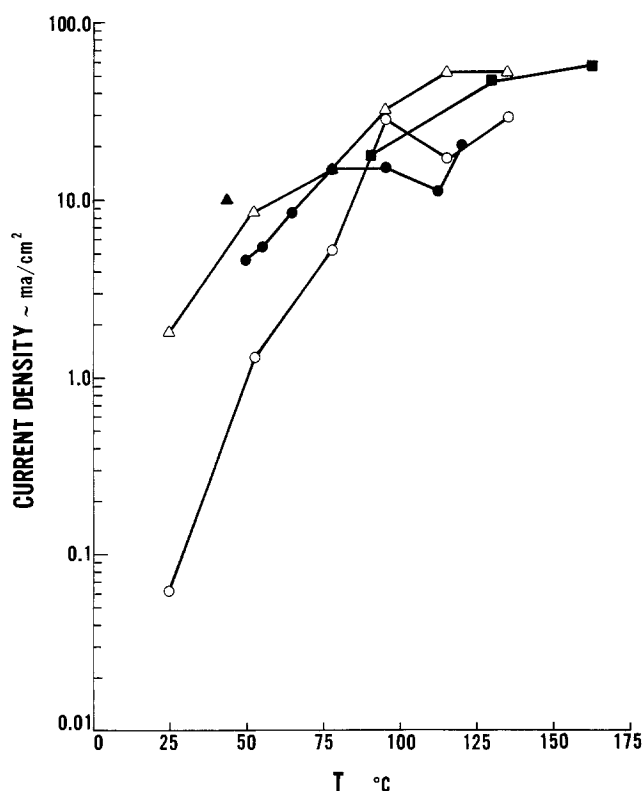


Fig. 13. Variation of oxygen reduction current at 0.8V with temperature for various acid compositions. Data of Appleby: Δ , purified 85% H_3PO_4 ; \circ , analytical grade H_3PO_4 . Data of this study: \blacktriangle , purified 85% H_3PO_4 ; \bullet , unpurified 85% H_3PO_4 ; \blacksquare , unpurified 96% H_3PO_4 .

ment with the data of Appleby for purified acid at temperatures above 95°C. This agreement could be due to the smaller effect of electrolyte impurities on the larger platinum surface area in the fuel cell electrode used here compared to that of the flat sheet used by Appleby. Below 95°C, the Tafel slope obtained with the fuel cell electrode in unpurified and purified 85% H_3PO_4 is in agreement with the data of Appleby for unpurified electrolyte. This increase in Tafel slope at lower temperatures for the fuel cell electrode is probably due to an increase in the relative importance of electrolyte impurities at lower temperature. With unpurified 96% H_3PO_4 , the Tafel slope was 90 mV/decade at 160°C, was relatively insensitive to temperature, and showed a trend similar to that of Appleby for unpurified 85% H_3PO_4 . This result might be caused by an increase in the effect of impurities in the more highly concentrated electrolyte.

In the comparison of the variation of current at a given potential with temperature with the variation found by Appleby, the area of the platinum on the fuel cell electrode was considered to be 70 m^2/g . Using this value of surface area, the value of current at a given potential can be seen to be in fair agreement with the data obtained by Appleby for 85% H_3PO_4 . The data obtained in this study at 96% H_3PO_4 were somewhat higher than that obtained with 85% H_3PO_4 .

Tests using sulfuric acid.—Tests were run in 20% H_2SO_4 at 70°C on a sample of a 0.25 $\text{mg Pt}/\text{cm}^2$ electrode that demonstrated 90 mV/decade Tafel slope using 96% H_3PO_4 at 160°C. These data are presented in Fig. 14. The data with H_2SO_4 can be seen to indicate a slope of about 65 mV/decade at the currents at which 90 mV/decade occurs with H_3PO_4 . The limiting current for air in H_2SO_4 was about 2500 mA/cm^2 , a value near that using H_3PO_4 . Since the diffusivity-solubility products of oxygen in these two electrolytes are probably of the same order, the same mechanisms are probably controlling performance in the two electrolytes in the 65 and the 90 mV/decade slope ranges. Therefore, the type electrode tested here is probably activation limited with a slope of 65 mV/decade for H_2SO_4 and 90 mV/decade for H_3PO_4 . This 65 mV/decade is about what would be expected in H_3PO_4 at 70°C if the Tafel slope varied as RT/F , that is, linearly with temperature as predicted by theory with constant transfer coefficient. This data with H_2SO_4 are shown in Fig. 12 and compares well with Appleby's data with phosphoric acid at the same temperature. It should be noted, however, that the absolute performance level with sulfuric acid was less reproducible than that with H_3PO_4 .

Flooded electrode tests.—An electrode was fabricated with 5 w/o Teflon using 15 w/o platinum supported on Vulcan. A small percentage of Teflon was used to cause the electrode to flood with electrolyte and thereby introduce diffusional losses. This electrode was tested in the half-cell apparatus at 160°C in unpurified 96% phosphoric acid and the data are shown in Fig. 15. A slope of 180 mV/decade resulted for almost 2 decades on oxygen. This value is twice the 90 mV/decade slope and indicates that the single Tafel slope is probably 90 mV/decade.

Flat plate tests.—A platinum sheet electrode was submerged in unpurified 96% H_3PO_4 in the half-cell apparatus at 160°C with oxygen over the electrolyte. The data for this electrode are shown in Fig. 16 both with and without oxygen bubbling over the surface of the sheet. Data are also presented both with and without polarization of the electrode to 500 mV prior to the obtaining of each data point. The higher performance obtained with prepolarization is probably due to the desorption of anions or impurities occurring during the prepolarization. Appleby found a similar effect by prepolarizing to 50 mV. This electrode can be seen

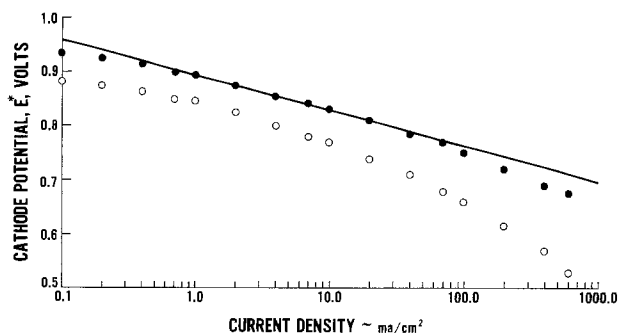


Fig. 14. Cathode performance for 0.25 $\text{mg Pt}/\text{cm}^2$ supported on Vulcan XC-72 with 20% H_2SO_4 at 70°C. \bullet , Oxygen; \circ , air. A straight line with a slope of 65 mV/decade has been drawn through the oxygen data.

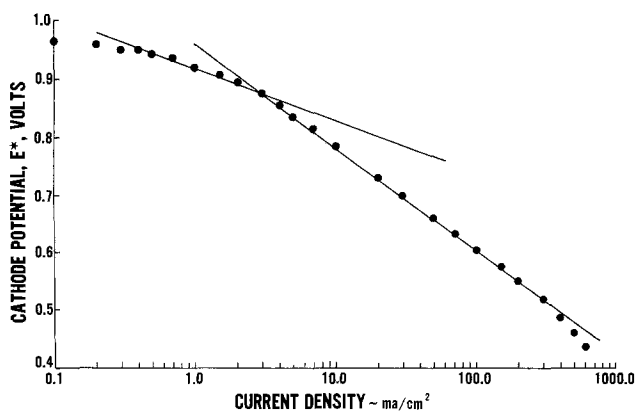


Fig. 15. Cathode performance on oxygen for flooded electrode tested in half-cell apparatus at 160°C in 96% H_3PO_4 . Straight lines with slopes of 90 and 180 mV/decade have been drawn through the data.

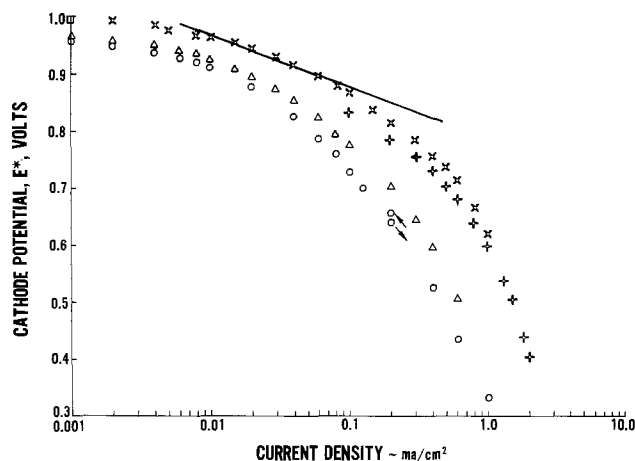


Fig. 16. Cathode performance for oxygen on a flat sheet submerged in unpurified 96% H_3PO_4 in the half-cell apparatus at 160°C. \circ , No bubbling, no prepolarization; Δ , no bubbling, with prepolarization to 500 mV; $+$, with bubbling, no prepolarization; \times , with bubbling, with prepolarization to 500 mV. A line with a slope of 90 mV/decade has been drawn through the highest data.

to have resulted in only a short Tafel slope region. A straight line was drawn through the data obtained using prepolarization to 500 mV and bubbling oxygen and an exchange current calculated. The exchange current, corrected to 1 atm oxygen pressure, is plotted in Fig. 17 where good agreement with an Arrhenius-type extrapolation of Appleby's data can be seen.

Discussion

All the experimental data obtained in this study indicate that the true Tafel slope for the reduction of oxygen in 96% H_3PO_4 at 160°C in the range of potentials below 0.9V is approximately 90 mV/decade.

The series of electrodes that were fabricated with various platinum loadings with a constant carbon loading indicated a linear dependence between current at a given potential and the platinum loading. This result indicated that the performance of these electrodes was controlled only by the activity of platinum. Since these electrodes had a slope on semilogarithmic coordinates of 90 mV/decade this slope is the Tafel slope.

The test sequence that was conducted to investigate the effect of temperature variation with 85% phosphoric acid resulted in data in good agreement with the results obtained by Appleby on a flat platinum sheet above 95°C. The Tafel slope varied as RT/F and is equal to 90 mV/decade at 160°C.

The tests using H_2SO_4 indicated a Tafel slope of 65 mV/decade with 20% H_2SO_4 at 70°C. This Tafel slope is in agreement with that found by Appleby at the

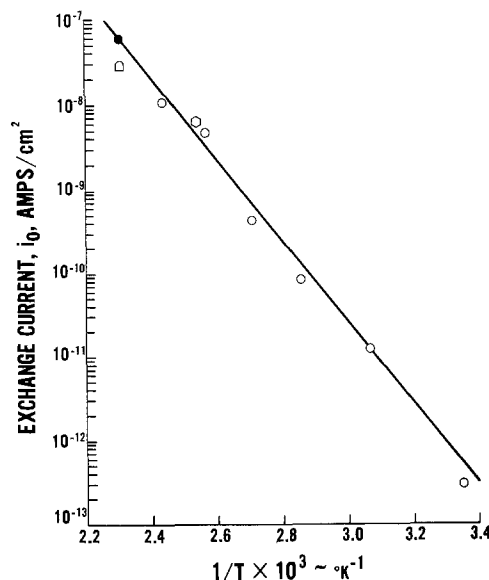


Fig. 17. Exchange current for oxygen reduction as a function of reciprocal temperature. \circ , Flat sheet, Appleby, purified 85% H_3PO_4 ; \bullet , flat sheet, this study, 96% H_3PO_4 ; \diamond , platinum black, Vogel and Lundquist, 85% H_3PO_4 , 82 mV/decade Tafel slope; Δ , platinum on Vulcan, this study, 96% H_3PO_4 . The straight line represents a fit to the experimental data.

same temperature in 85% H_3PO_4 . Therefore, the rate-limiting reactions for the reduction of oxygen in H_2SO_4 and H_3PO_4 are most likely the same. The flooded electrode tests indicated a double Tafel slope of 180 mV/decade, again confirming that the Tafel slope is 90 mV/decade for H_3PO_4 at 160°C.

The experiment conducted on a flat platinum sheet was in good agreement with an extrapolation of Appleby's data. The platinum specific activity obtained from a flat platinum sheet was found to be in fair agreement with the experimental results obtained with platinum supported on carbon as shown in Fig. 17. This means that, down to the range of platinum crystallite sizes obtained with the supported platinum in this study, no large change in the properties of the platinum are occurring with respect to activity. Also, there is apparently no large interaction between the platinum and the carbon with respect to platinum activity.

However, one set of experimental data must still be rationalized, that of Vogel and Lundquist. They found that at 120°C with 85% H_3PO_4 the Tafel slope was apparently 60 mV/decade on platinum black. These experimental data were fit by Kosinski (9) using the cylindrical agglomerate model to obtain a Tafel slope of 65 mV/decade. In order to rationalize the platinum black data of Vogel and Lundquist, additional calculations were performed to determine whether the newly determined Tafel slope in this experimental study could be used to fit their experimental cathode performance curves.

The Tafel slope determined by Appleby for a platinum sheet was used so that the number of fitting parameters was reduced to essentially four: the exchange current, the agglomerate diameter, the agglomerate porosity, and the electrolyte film thickness. Since Vogel and Lundquist's data were obtained at 120°C, a Tafel slope of 82 mV/decade was used in the fitting of their experimental data. A comparison of their experimental data with the results obtained by fitting the cylindrical agglomerate model is shown in Fig. 18 and 19. Figure 18 shows a comparison between the calculated and experimental results of cathode potential vs. current density for one catalyst loading. Figure 19 shows the comparison of current densities vs. catalyst loading for various cathode potentials. As can be seen from these figures, an excellent fit was obtained. A comparison between the results of the cylindrical ag-

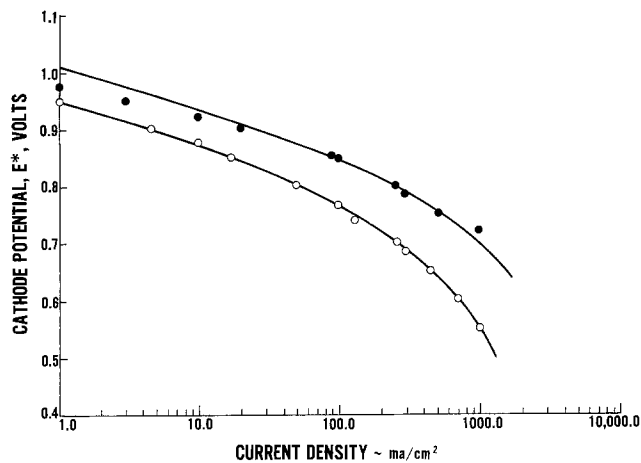


Fig. 18. Comparison between the experimental data of Vogel and Lundquist and calculated results of cathode potential vs. current density for one catalyst loading at 120°C in 85% H_3PO_4 at 1 atm gas pressure. ●, Oxygen; ○, air. Values of parameters used in the calculations: exchange current = 6.5×10^{-9} A/cm²; Tafel slope = 82 mV/decade; Pt loading = 6.0 mg/cm²; Pt surface area = 24 m²/g; agglomerate porosity = 0.80; agglomerate length = 0.0762 mm; agglomerate diameter = 4.0 μ ; tortuosity = 1.0; electrolyte film thickness = 0.05 μ ; electrolyte conductivity = 0.42 (ohm-cm)⁻¹; oxygen diffusivity-solubility product = 1.0×10^{-11} mole/cm-sec; density of Pt = 21.4 g/cm³.

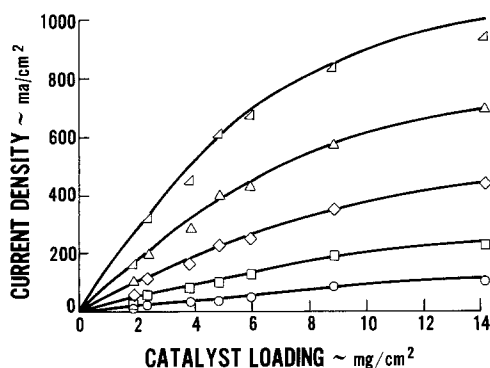


Fig. 19. Comparison between the experimental data of Vogel and Lundquist and calculated results showing the effect of loading upon cathode performance at 120°C in 85% H_3PO_4 with 1 atm air reactant pressure. Cathode potential (mV): \triangle , 600; \triangle , 650; \diamond , 700; \square , 750; \circ , 800. Calculated results used same values of parameters as used in Fig. 18.

glomerate model and the experimental data using a 65 mV/decade slope obtained previously by Kosinski are shown in Fig. 20 and 21. As can be seen from these figures, an excellent agreement was obtained in this case also.

The comparison between the results of the cylindrical agglomerate model and the experimental data was somewhat better for the 65 mV/decade case at potentials greater than 0.9V. However, since the surface oxidation state of platinum changes above approximately 0.9V, no conclusion can be reached as to which fit of Vogel and Lundquist's data is the better. The value of the exchange current obtained using the 82 mV/decade value of Tafel slope was added to Fig. 17. As can be seen, this value of exchange current for the platinum black electrode is in good agreement with Appleby's results for a flat sheet. A measured surface area of 24 m²/g was used for the platinum black. Both fits of the experimental data lead to reasonable values of agglomerate diameter, agglomerate porosity, and electrolyte film thickness.

Experimental data obtained on an electrode fabricated using platinum supported on Vulcan XC-72 were

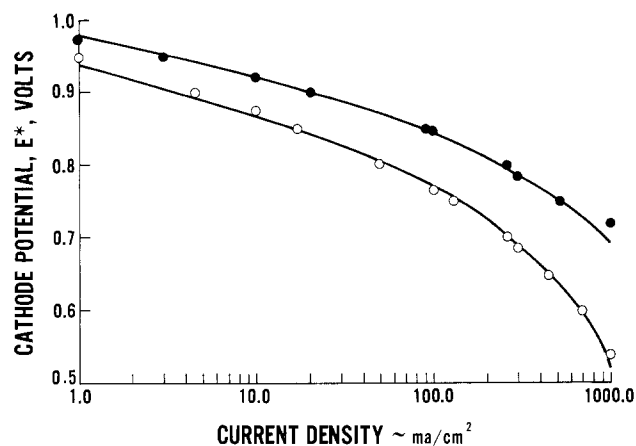


Fig. 20. Comparison between the experimental data of Vogel and Lundquist and calculated results of cathode potential vs. current density for one catalyst loading at 120°C in 85% H_3PO_4 at 1 atm gas pressure. ●, Oxygen; ○, air. Values of parameters used in the calculations: exchange current = 5.3×10^{-10} A/cm²; Tafel slope = 65 mV/decade; Pt loading = 6.0 mg/cm²; Pt surface area = 24 m²/g; agglomerate porosity = 0.60; agglomerate length = 0.0762 mm; agglomerate diameter = 6.0 μ ; tortuosity = 1.0; electrolyte film thickness = 0.05 μ ; electrolyte conductivity = 0.42 (ohm-cm)⁻¹; oxygen diffusivity-solubility product = 1.0×10^{-11} mole/cm-sec; density of Pt = 21.4 g/cm³.

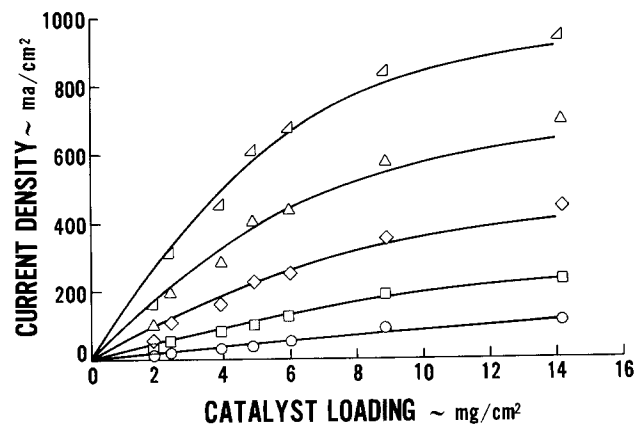


Fig. 21. Comparison between the experimental data of Vogel and Lundquist and the calculated results showing the effect of catalyst loading upon cathode performance at 120°C in 85% H_3PO_4 with 1 atm air reactant pressure. Cathode potential (mV): \triangle , 600; \triangle , 650; \diamond , 700; \square , 750; \circ , 800. Calculated results used same values of parameters as used in Fig. 20.

also fit using the cylindrical agglomerate model to determine if reasonable values of fitting parameters would be obtained. Data were obtained at 160°C so a Tafel slope of 90 mV/decade was used. A comparison of the results of the cylindrical agglomerate model with the data using only the exchange current, the agglomerate diameter, porosity, and electrolyte film thickness as fitting parameters are shown in Fig. 22. Good agreement resulted in this case.

The value of exchange current, corrected to 1 atm oxygen pressure, was added to Fig. 17. This value is lower than the value expected based on the results for 96% H_3PO_4 on a flat sheet. This difference can be partially attributed to the absence of prepolarization in the supported platinum electrode test as shown in Fig. 16. Other reasons for the results of the supported platinum electrode exchange current being low might be that regions of the Teflon-bonded catalyst were excessively flooded by electrolyte, that some regions of the Teflon-bonded electrode were in poor ionic or electronic contact, that slight surface roughness existed on the flat sheet (assumed to be 1.0), and that a slight effect of platinum crystallite size is present. A lower value of current in the supported platinum electrode in 85% H_3PO_4 can also be seen in Fig. 13.

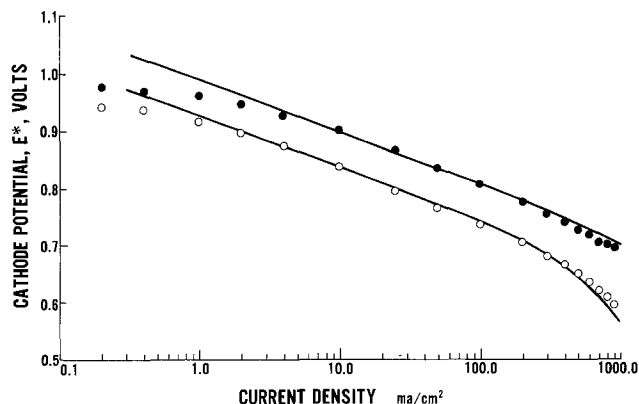


Fig. 22. Comparison of data of the present study with the calculated results of the cylindrical agglomerate model at 160°C in 96% H_3PO_4 ; 0.31 mg Pt/cm². ●, Oxygen; ○, air. Values of parameters used in the calculations: exchange current = 2.4×10^{-8} for oxygen; exchange current = 0.73×10^{-8} for air; Pt surface area = 70 m²/g; agglomerate porosity = 0.60; agglomerate length = 0.0382 mm; agglomerate diameter = 1.6 μ ; tortuosity = 1.0; electrolyte film thickness = 0.20 μ ; electrolyte conductivity = 0.57 (ohm-cm)⁻¹; oxygen diffusivity-solubility product = 0.63×10^{-11} mole/cm-sec; density of carbon = 2.0 g/cm³.

The values of the agglomerate diameter, porosity, and electrolyte film thickness for the supported platinum electrode were also reasonable considering the electron micrographs obtained for this type of electrode shown in Fig. 4. The agglomerate diameter appears to be somewhat small. This might be due to an effect of the carbon and/or Teflon on the diffusivity-solubility product of the oxygen in the electrolyte.

Again, a slight deviation between the predicted results using the model and the experimental data occurred above 0.9V. However, this might be expected in this case due to mixed potential effects caused by carbon, platinum, or impurity oxidation or perhaps a change in the catalytic properties of the platinum.

The fact that the cylindrical agglomerate model can be used to fit the experimental data for both the platinum black electrodes of Vogel and Lundquist and the supported platinum electrodes in this study does not confirm results obtained in this study but merely indicates that experimental data on both these types of electrodes can be rationalized using the results of this study. In all probability, the Tafel slope and exchange current for platinum black, platinum supported on carbon, and a flat platinum sheet are all the same, since the results obtained for platinum black and platinum supported on carbon are in such good agreement with the flat sheet results.

Conclusions

The following conclusions can be made from the results obtained in this study.

1. Platinum with an area as high as about 70 m²/g when supported on carbon has approximately the same specific activity as a flat platinum sheet if the effect of electrode prepolarization is considered.
2. The specific activity of platinum black is most likely the same as that of a flat platinum sheet.
3. Crystallite size is relatively unimportant with respect to specific activity for oxygen reduction in the range of crystallite sizes studied and carbon does not interact significantly with the platinum.

4. The experimental data of Appleby are valid with respect to platinum activity in the potential range below 0.9V.

5. The mechanism for oxygen reduction is the same over a temperature range from 70° to 160°C for purified 85% phosphoric acid and is probably the same in both sulfuric and phosphoric acid. The Tafel slope varies as RT/F .

6. Data above approximately 0.9V for platinum on carbon catalyzing pure oxygen reduction are confused by at least mixed potential effects and therefore cannot be used to obtain Tafel slope information for application to lower potential levels.

7. Data obtained for platinum black above approximately 0.9V indicate that possibly a change in mechanism for oxygen reduction may be occurring, perhaps through a change in the oxidation state of the surface.

8. Because the catalyst surface area for supported platinum determined using the electron microscope is larger than the electrochemical area and because the activity of the supported catalyst is somewhat lower than that anticipated using the data of Appleby, some of the catalyst in the supported platinum electrodes may be ineffective due to poor electronic or ionic paths.

Acknowledgments

The authors wish to thank Dr. A. Kaufman, M. Katz, and S. Organ for their assistance in the experimental phases of this work. The assistance of J. Kosinski in the theoretical studies and D. Pilney in the investigations with the electron microscope are also acknowledged.

Manuscript submitted Feb. 13, 1975; revised manuscript received May 16, 1975. This was Paper 40 presented at the New York, New York, Meeting of the Society, Oct. 13-17, 1974.

Any discussion of this paper will appear in a Discussion Section to be published in the June 1976 JOURNAL. All discussions for the June 1976 Discussion Section should be submitted by Feb. 1, 1976.

REFERENCES

1. W. M. Vogel and J. T. Lundquist, *This Journal*, **117**, 1512 (1970).
2. A. J. Appleby, *ibid.*, **117**, 328 (1970).
3. J. O'M. Bockris and A. Damjanovic, "The Mechanism and Electrocatalysis of Oxygen Reduction," *Troisiemes Journees Internationales D'Etude Des Piles A Combustible*, Brussels, 1969.
4. H. Angerstein-Kozlowska, B. E. Conway, and W. B. A. Sharp, *J. Electroanal. Chem.*, **43**, 9 (1973).
5. B. E. Conway and S. Gottesfeld, *J. Chem. Soc., Faraday Trans. I.*, **69**, 1090 (1973).
6. B. V. Tilak, B. E. Conway, and H. Angerstein-Kozlowska, *J. Electroanal. Chem.*, **48**, 1 (1973).
7. R. Brown and L. Horve, Paper 203, p. 109, *The Electrochemical Society Extended Abstracts*, Vol. I-5, Spring Meeting, Dallas, Texas, May 7-12, 1967.
8. J. Giner and C. Hunter, *This Journal*, **117**, 1124 (1969).
9. J. Kosinski, Paper 32, p. 90, *The Electrochemical Society Extended Abstract Fall Meeting*, Detroit, Michigan, Oct. 5-9, 1969.
10. D. A. J. Rand and R. Woods, *J. Electroanal. Chem.*, **47**, 353 (1973).
11. M. Paucirova, D. M. Drazic, and A. Damjanovic, *Electrochim. Acta*, **18**, 945 (1973).

Rate Capability and Electrochemical Stability of Carbon Fluorine Compounds in Organic Electrolytes

Herbert F. Hunger* and Joseph E. Ellison

Power Sources Technical Area, U.S. Army Electronics Technology and Devices Laboratory (ECOM),
Fort Monmouth, New Jersey 07703

ABSTRACT

Polarization measurements of cathodes containing various carbon fluorine compounds, CF_n ($n = 0.24-1.5$), as the active depolarizer material were made in 1M $LiClO_4$ -propylene carbonate at 298°K. The polarization (free of ohmic iR drop) was measured, using the periodically interrupted sine wave pulse current technique. The open-circuit potentials and polarization data were analyzed, considering their mixed potential character. The two major factors that influenced the data were the C/F ratio and the electrode compression pressure. With graphite fluorides, activation polarization was prevalent and Tafel behavior was observed ($b = 0.12$). The exchange currents were low, peaking at $n = 0.93$ with $10^{-22}A$. From the exchange currents, the cathodic currents at the mixed potentials were computed. For $n = 0.93$, a value of about $7 \cdot 10^{-10}A$ was obtained, indicating a depolarizer shelf life of about 10^6 years. Compounds with higher rate capabilities, such as polymeric, perfluorinated, and polycyclic hydrocarbons, show a very short shelf life by oxidizing rapidly the organic solvent. The experimental behavior of such compounds can be explained by the mixed potential theory. Shifts in open circuit, mixed potentials to more positive values are predicted for compounds with higher rate capability and can be observed experimentally.

The energy densities of lithium organic electrolyte batteries with graphite fluorides as depolarizers can reach 150 W-hr/lb; their rate capability, however, is limited to about 5-10 mA/cm² at room temperature. This limitation is mainly due to a relatively high polarization at the cathode at these current densities. The shape of the cathodic polarization curve indicates strong activation polarization (1). It would be desirable to decrease this overvoltage in order to obtain higher energy densities and rate capabilities in lithium batteries using carbon fluorine compounds as the cathodic material. Therefore, in our study, the polarization behavior of carbon fluorine compounds with various compositions and structures was investigated, but limited to a one solvent-electrolyte system.

Experimental

The electrochemical measurements and associated handling of cell materials were carried out in a dry lab in pure, dried argon or helium atmosphere. The water vapor level was between one and five parts per million.

Solvents and electrolytes.—The solvent employed in this investigation was propylene carbonate, purified by vacuum distillation. The electrolyte used in this study was one molar solution of anhydrous lithium perchlorate in propylene carbonate.

Depolarizer materials.—Graphite fluorides, covering the composition range from tetracarbon monofluoride to polycarbon monofluoride, were investigated as cathode materials. These materials were obtained from Rice University. Their preparations and purities have been described previously (2). Further, polymeric carbon fluorine compounds were investigated, such as the oxygen crosslinked polymers of perfluoro anthracene, perfluoro decacyclene, perfluoro phthalocyanine, and fluorinated paracyanogene. These compounds were prepared and characterized for the U.S. Army Electronics Command by Professor Lagow of MIT (3).

Preparation of electrodes.—The cathodes were prepared by a dry press technique. This involves preparing a dry cathodic depolarizer mixture of 80 weight per cent (w/o) depolarizer, 15 w/o graphite (spectro-

scopic grade), and 5 w/o Teflon powder. About 0.3g of the mixture were pressed into a highly porous nickel matrix of 10 cm² cross section. Both anode and reference electrode consisted of lithium foil pressed onto a nickel screen.

Electrochemical cell.—The electrochemical cell was assembled by placing the cathode, surrounded by a separator, between two lithium electrodes identical in size to the cathode. One of the lithium electrodes served as the anode and the other as the reference electrode. The cell design has been described in detail previously (1).

Electrochemical measurements.—Since the cathode polarization measurements included a substantial resistance polarization, it was essential to separate the resistance polarization component from the others. For that purpose, the periodically interrupted sine wave pulse current technique, invented by Kordes and Marko, was chosen for polarization measurements free of the ohmic iR drop (4).

The circuit used in the measurements is shown in Fig. 1. The electrochemical cell C is connected with a load circuit (D_1) and two voltage measurement circuits (S_3 positions a and b). A gating switch circuit (D_2 and D_3) permits the cathode potential to be measured, free of the ohmic iR drop, during the brief

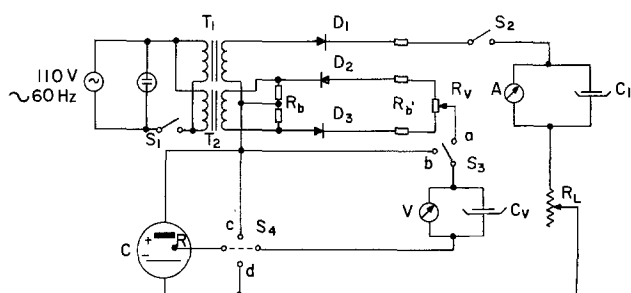


Fig. 1. Periodically interrupted sine wave pulse current circuit. Components: $T_1 = T_2 = 110V/24V, 1A$. $D_1 = 50V, 1A$. $D_2 = D_3 = 250V, 200 mA, i_{rev} = 0.05 \mu A$. $R_b = 20$ ohms, 35W each. $R'b = 250$ ohms, 38W each. $R_v = 50$ ohms. $C_v = 10 \mu F, 150V$. $C_1 = 100 \mu F, 500V$.

* Electrochemical Society Active Member.

Key words: graphite fluorides, mixed potential, perfluoro anthracene, perfluoro decacyclene, perfluoro phthalocyanine.

period of current interruption (1/120 sec). The selection of the circuit components had to consider the higher cell voltages and the ohmic resistance characteristics of the lithium batteries which influence mainly the choice of the transformers (T_1 and T_2), the components in the gating switch circuit, and the condenser, C_V , parallel to the voltmeter. The latter had to be adjusted to the time constant of the voltage measurement circuit (S_3 position a).

Thus quasi steady-state current-cell voltage and current-cathode potential curves of lithium/graphite fluoride cells, including or excluding the ohmic iR drop, could be measured. In the case of polymeric carbon fluorine compounds as depolarizers, galvanostatic discharge curves were measured.

Results and Discussion

Standardization of cathode preparation.—Before a study of the kinetics of various graphite fluorides was started, the cathode preparation technique had to be optimized and standardized. It was found that the major two factors influencing the performance of the cathode were the carbon to fluorine ratio and the compression pressure applied in preparing the cathodes. The compression pressure was varied within the range of 400 to 30,000 lb/electrode. Using the dry press technique a pressure of about 2000 lb/in.² yielded graphite fluoride cathodes with the lowest polarization up to 5 mA/cm².

Mixed potential theory of CF_n reduction.—The key to the analysis of the polarization data was the mixed potential theory of CF_n reduction. The open-circuit potential of graphite fluoride cathodes is a mixed potential, the reduction of graphite fluoride being the cathodic reaction and solvent oxidation being the anodic reaction (1). The electrochemical behavior of carbon fluorine compounds is shown schematically in terms of the mixed potential theory in Fig. 2. E_{CF} is the potential of a carbon fluoride cathode vs. a lithium reference electrode, computed from thermodynamic data. It is numerically identical to the electromotive force of a corresponding lithium-carbon fluoride cell. The emf of such cells, covering the composition range from $CF_{0.24}$ to $CF_{1.13}$, have been determined recently by Professor Margrave and co-workers at Rice University (2). The values range from 5.23 to 4.56V at 298°K. Note that the potentials decrease with increasing fluorine content in the compounds. There are three current-potential curves shown in Fig. 2, covering three cases of CF kinetics, slow, medium, and fast. E_s is the oxidation potential of the organic solvent. The average potential of graphite electrodes in 1M $LiClO_4$ -PC is 2.56V vs. lithium. Tiedemann has found that the potential of a completely discharged $(CF)_n$ electrode is approximately 2.5V vs. lithium (5). A_s is the solvent oxidation and C_s the solvent reduction curve.

The open-circuit potential of a CF electrode, e.g., E_m , is a mixed potential and a function of its state of

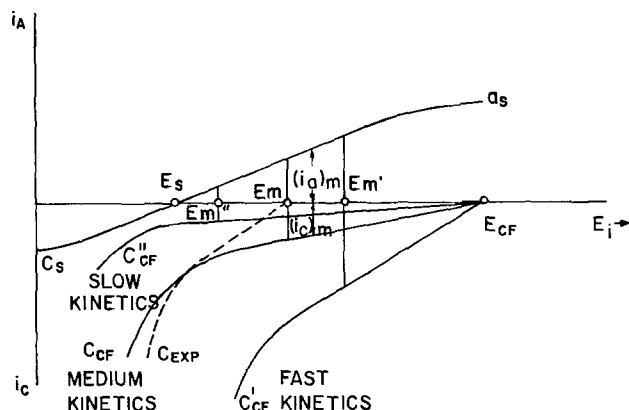


Fig. 2. Current-potential curves of carbon fluorine compounds and organic solvents.

discharge (1). Experimental E_m values, ranging from 2.56 to 3.36V, have been observed with poly carbon monofluoride at 298°K. The variations are caused by the type of CF used and by the electrode compression pressure.

A mixed potential, E_m , is established when the cathodic current of CF reduction and the anodic current of solvent oxidation are equal. The open-circuit potential, E_m , is thus a function of the kinetics of the partial electrode processes (6, 7). According to the principle of the additive composition of all partial electrode processes, we should observe experimentally the interrupted curve, C_{exp} . The theoretical curve for CF reduction and the experimental curve are, however, practically identical between E_m and E_s due to the smallness of the solvent oxidation current.

CF_n cathode polarization data.—In Fig. 3, polarization data, free of ohmic iR drop, of graphite fluoride cathodes are shown. The polarization here is defined as the difference between the cathode potential, calculated from thermodynamic data, and the cathode potential at a given current measured vs. the lithium reference electrode. Each data point was taken after quasi steady state, defined by a change of less than ± 5 mV/5 min, was reached. The average error in the polarization data, e.g., for $CF_{0.93}$, for the 0.15 to 50 mA range was 38 mV or less than 1.8% at polarizations between 2.5 and 2.74V. At higher current densities, above 2 mA/cm² (20 mA), a slow, continuous increase in polarization with time was observed. In these cases, the initial data points taken are shown in the graph. The upper two curves (Fig. 3) are for white CF [dry press technique and wet preparation technique (1)] and the lower two curves for gray CF (dry press technique, two different metal current collectors).

A range of linear behavior with a slope of about 0.12V/decade of current can be observed. The deviations at higher currents from linearity could be due to blocking of parts of the inner surface area of the electrodes with reaction products, mainly lithium fluoride; the deposition will be proportional to current and time. Since no limiting currents have been observed up to 100 mA, any concentration polarization can be neglected due to its smallness.

Exchange currents of CF_n reduction.—From the linear part of the polarization curves, the exchange currents, i_0 , for cathodic CF reduction could be computed, using the following equation

$$E_{CF} - E_i = 0.116 \log i_c - 0.116 \log i_0 \quad [1]$$

Values of exchange currents for various graphite fluorides are shown in Table I. The highest exchange

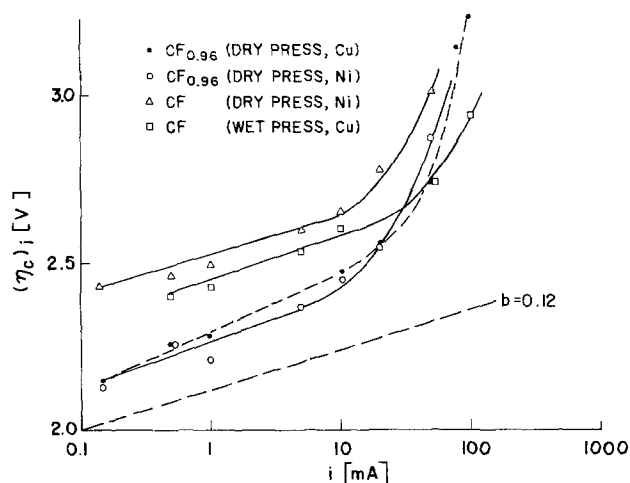


Fig. 3. Polarization data of CF_n cathodes free of ohmic iR drop. ● $CF_{0.93}$ (dry press technique, Cu collector), ○ $CF_{0.93}$ (d.p.t., Ni collector), △ CF (d.p.t., Ni collector), □ CF [wet preparation technique (1)] 1M $LiClO_4$ -PC, 25°C.

Table I. Exchange currents of graphite fluorides CF_n in 1M $LiClO_4$ -PC at 298°K for about 2% discharge of the cathodes

n	i_0 (A)	$(i_m)_c$ (A)	E_m (V)	τ (Y)
0.237	$3 \cdot 10^{-26}$			
0.55	$8.9 \cdot 10^{-28}$			
0.93	$1 \cdot 10^{-28}$	$6.9 \cdot 10^{-10}$	3.09	$3.05 \cdot 10^{+4}$
0.96	$2.2 \cdot 10^{-28}$			
1.0	$6.4 \cdot 10^{-24}$			
1.09	$3.6 \cdot 10^{-24}$	$3.39 \cdot 10^{-11}$	3.05	$9 \cdot 10^{+5}$

current was observed with $CF_{0.93}$. Considering the inner surface areas of the graphite fluorides (2), which range from 230 to 270 m^2/g , the exchange current density for gray CF should be in the order of $1.7 \cdot 10^{-28}$ A/cm² and that of white CF about $5.4 \cdot 10^{-30}$ A/cm²; however, blocking of active, inner surface area by compression during electrode preparation has to lead to higher exchange current densities.

Electrochemical stability of CF cathodes.—From the exchange currents, the cathodic currents of CF_n reduction at the mixed potentials, $(i_m)_c$ (third column, Table I), could be computed via Eq. [2]

$$E_{CF} - E_m = 0.116 \log (i_m)_c - 0.116 \log i_0 \quad [2]$$

For gray CF we obtain $(i_m)_c = 6.9 \cdot 10^{-10}$ A. This value is significant in that it relates to the electrochemical stability of the CF cathode on open circuit. A cathodic current at the mixed potential of about 10^{-11} A corresponds to a depolarizer shelf life, τ , (last column, Table I) in the electrolyte of about 10^6 years.

It can be estimated that hypothetical compounds with a higher rate capability than gray CF, e.g., with exchange currents of $(i_0)_{CF_n} = 10^{-12}$ or 10^{-7} A, would have, based on the computed $(i_m)_c$, a far shorter depolarizer shelf life in the electrolyte of about 3 years or 1 day, respectively.

In computing the depolarizer shelf life of such compounds from i_m , we have to consider the shift in E_m due to the faster kinetics of the CF_n reduction. E_m , i_m , and consequently τ , can be computed from the two equations [3] and [4] with two unknowns E_m and i_m

$$E_m - E_s = 0.12 \log i_m - 0.12 \log (i_0)_s \quad [3]$$

$$E_{CF_n} - E_m = 0.12 \log i_m - 0.12 \log (i_0)_{CF_n} \quad [4]$$

As mentioned earlier, E_s was found experimentally to average 2.56V. The exchange current of the solvent $(i_0)_s$ could be determined indirectly from i_m , e.g., for $CF_{1.09}$, under assumption of activation control, using Eq. [3], E_m being the mixed potential of $CF_{1.09}$; $(i_0)_s$ was also determined directly by measuring the anodic oxidation of propylene carbonate at $CF_{1.09}$. With 1M $LiClO_4$ -PC at 25°C, a Tafel slope of 0.12 was found and an $(i_0)_s$ of 10^{-16} A; $(i_0)_s$ determined indirectly was about 10^{-15} A.

E_{CF_n} can be estimated using Eq. [5] (2) and [6]

$$G^{298} = -(104.2n + 1.158) \text{ (kcal mole}^{-1}\text{)} \quad [5]$$

$$E^{298}_{CF_n} = G^{298}/n + 23.053 \quad (V) \quad [6]$$

The polymeric carbon fluorine compounds, mentioned earlier, fall apparently into the category of high rate depolarizers by showing initially a far better kinetics than white CF, but also a strong reactivity with the organic solvent. Figure 4 shows the cathodic reduction of polymeric carbon fluorine compounds and of white CF. The discharge was performed galvanostatically at 1 mA/cm². In the figure the cathode potential measured vs. a lithium reference electrode is plotted vs. the discharge time in minutes. Oxygen crosslinked perfluoro anthracene, perfluoro decacyclene, perfluoro phthalocyanine, and fluorinated paracyanogene showed initially about 1V higher discharge potentials than poly carbon monofluoride. After a certain time, however, reactions between depolarizer and solvent consume the cathodes. Highly soluble depo-

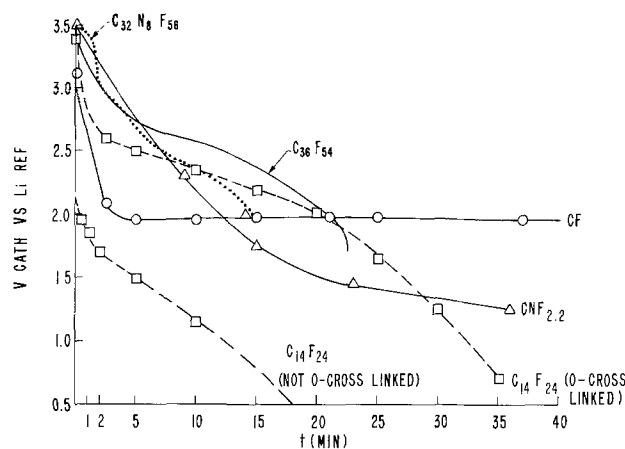


Fig. 4. Cathodic reduction of polymeric carbon fluorine compounds compared with CF (1 mA/cm²). 1M $LiClO_4$ -PC, 30°C. $C_{14}F_{24}$ perfluoro anthracene (oxygen crosslinked), $C_{36}F_{54}$ perfluoro decacyclene (oxygen crosslinked), $C_{32}N_8F_{56}$ perfluoro phthalocyanine (oxygen crosslinked), $CNF_{2.2}$ fluoro paracyanogene, CF poly carbon monofluoride.

larizers, such as oxygen crosslinked perfluoro anthracene, show inferior discharge behavior.

A more detailed explanation of the experimental behavior of these compounds is submitted: When the cathode is submerged for the first time in the electrolyte, reduction takes place initially at a high rate, corresponding perhaps to an $i_0 = 10^{-7}$ A, at a mixed potential of about 3.95V. For 100% bulk utilization of the depolarizer, a time of about 1 day would be required; for depletion of active species at the surface, however, far less time would be required. This depletion will change the kinetics to a slower one, e.g., to an $i_0 = 10^{-12}$ A. A mixed potential of about 3.62V would be the consequence. This would approximately correspond to the starting points of our discharge experiments in Fig. 4. Drawing a cathodic current of 10^{-2} A at about 3.32V would result in a fast consumption of the remaining active depolarizer material which is indicated in Fig. 4 by a strong drop in discharge potential.

The mixed potential theory predicts a shift in E_m to more positive potentials for compounds with faster reduction kinetics (see Fig. 2). This could be observed experimentally in the case of oxygen crosslinked perfluoro anthracene, perfluoro decacyclene, perfluoro phthalocyanine, and fluoro paracyanogene. The mixed potentials of these compounds measured vs. a lithium reference electrode are given in Table II.

Such compounds could make excellent depolarizers with higher rate capabilities if solvents and electrolytes could be found that would be stable to oxidation by the compounds. The theoretical energy capacities of these compounds exceed those of graphite fluorides, 2050 W-hr/lb of cell reactants vs. 1785 W-hr/lb.

Manuscript submitted Nov. 13, 1974; revised manuscript received May 20, 1975. This was Paper 25 presented at the New York, New York, Meeting of the Society, Oct. 13-17, 1974.

Any discussion of this paper will appear in a Discussion Section to be published in the June 1976 JOURNAL. All discussions for the June 1976 Discussion Section should be submitted by Feb. 1, 1976.

Table II. Mixed potentials of polymeric carbon fluorine compounds in 1M $LiClO_4$ -PC at 298°K vs. the lithium reference electrode

Compound	E_m (V)
$CF_{0.93}$	3.09
Oxygen crosslinked perfluoro Anthracene $C_{14}F_{24}$	3.46
Decacyclene $C_{36}F_{54}$	3.47
Phthalocyanine $C_{32}N_8F_{56}$	3.47
Fluoro paracyanogene $CNF_{2.2}$	3.58

Publication costs of this article were partially assisted by the U.S. Army.

REFERENCES

1. H. F. Hunger and G. J. Heymach, *This Journal*, **120**, 1161 (1973).
2. A. J. Valerga, R. B. Badachhape, G. D. Parks, P. Kamarchik, J. L. Wood, and J. L. Margrave, Final Report, Contract DAAB07-73-C-0056 (ECOM), Rice University, March 1974.
3. R. J. Lagow and J. L. Adcock, Final Report, Contract DAAB07-72-C-0166 (ECOM), MIT, May 1974.
4. K. Kordesch and A. Marko, *This Journal*, **107**, 480 (1960).
5. W. Tiedemann, *ibid.*, **121**, 1308 (1974).
6. K. J. Vetter, "Electrochemische Kinetik," p. 588, Springer-Verlag (1961).
7. C. Wagner and W. Traud, *Z. Elektrochem.*, **44**, 391 (1938).

High Conductivity Solid Electrolytes

Double Salts of Substituted Organic Ammonium Halides and Cuprous Halides

Anthony F. Sammells,* Jack Z. Gougoutas,¹ and Boone B. Owens*²

Gould Incorporated, Gould Laboratories, St. Paul, Minnesota 55165

ABSTRACT

Copper solid electrolytes have been synthesized by the solid-state reaction between substituted organic ammonium halides and cuprous halides. High conductivity electrolytes were found with both high and low symmetry organic ammonium halides, indicating that high symmetry in the latter need not be necessary in this class of electrolytes. Initial experiments with these materials in galvanic cells and coulometers indicated some instability.

Many of the highly conducting solid electrolytes investigated over the past decade have been silver ion conductors. The most conductive of these, RbAg_4I_5 , has a conductivity of $0.27 \text{ ohm}^{-1}\cdot\text{cm}^{-1}$ at ambient temperatures (1) and has found application in galvanic cells (2). Silver electrolytes have also been synthesized through compound formation between AgI and various substituted ammonium halides (4, 5) and also between AgI and sulfonium iodides (6). The single-crystal structures of certain of these unique phases have been investigated (7-11) to determine the structural features that permit fast ion diffusion in solids. It was observed that the iodide ions form face-sharing polyhedra (generally tetrahedra), with the silver ions situated within these polyhedra. On the average there are two or three vacant sites per silver ion, thus permitting ready diffusion through the faces of the polyhedra.

Because of the similar properties of Ag^+ and Cu^+ together with the much lower cost of copper compared to silver, it has been of considerable interest to synthesize copper electrolytes with ionic transport properties analogous to those of the above referenced silver electrolytes. Such materials were recently reported to exhibit ionic conductivities as high as $0.045 \text{ ohm}^{-1}\cdot\text{cm}^{-1}$ (12-13).

In the present investigation, following procedures similar to those of Takahashi, Cu^+ ion conducting solid electrolytes were synthesized by the combination of NN' -dimethyltriethylenediamine dibromide + cuprous bromide, NN -dihydrotriethylenediamine dibromide + cuprous bromide, and N -hydrohexamethylenetetramine chloride + cuprous chloride, in good agreement with the results of Takahashi *et al.* (12, 13).

The organic cations that are presumably stabilizing the high conductivity phase in the above three electrolytes have both high symmetry and a saturated cage-type structure. In order to determine whether ionic conduction is limited to the hydrohalides of triethyl-

enediamine and hexamethylenetetramine and their derivatives, and investigate the relative importance of high symmetry, the cage-type structure, and the onium nitrogen atoms, we have investigated several other systems. Our choice of substituents for the most part has been empirical since no crystallographic structural information is available to suggest those molecular features which the organic moiety should possess in order to form an ionically conducting phase. The possibility of ionically conductive cuprous halide phases being stabilized by quinuclidine, quinuclidone, pyridinium, dimethylpiperazine, NN' , NN' -diethylenedipyrilidinium, and 1-adamantanamine halides was investigated.

Conductivity measurements have been reported both at 1000 Hz and ∞ Hz. Extrapolation to ∞ Hz was made to eliminate the faradaic impedance ΔR , which may be proportional to the square root of frequency (14, 15).

$$\Delta R = kf^{-1/2}$$

where f is frequency and k a proportionality constant. The measured resistance R_m will contain both the bulk electrolyte resistance R and any faradaic impedance effects that may exist at the interface

$$R_m = R + \Delta R = R + kf^{-1/2}$$

The error caused by ΔR was minimized by extrapolating the measured resistance to infinite frequency.

The conductivity-temperature function was determined for some of these electrolytes and activation energies reported. The stability of these electrolytes under a potential was evaluated by fabricating galvanic cells with copper anodes and various cathodes, including CuBr_2 , MoO_3 , V_2O_3 , tetrapropylammonium tribromide, tetrabutylammonium tribromide, and triethylenediamine dibromide.

Experimental

Electrolyte syntheses.—3-quinuclidone hydrochloride, quinuclidine hydrochloride, and 1-adamantanamine were obtained from Aldrich Chemical Company. Triethylenediamine was purchased from Eastman Kodak Chemical Company. Cuprous chloride and bromide were very carefully purified by recrystallization from the appropriate halogen acid, followed by wash-

* Electrochemical Society Active Member.

¹ Present address: Chemistry Department, University of Minnesota, Minneapolis, Minnesota 55455.

² Present address: Medtronic Incorporated, Minneapolis, Minnesota 55418.

Key words: copper ion diffusion, frequency measurements, symmetry, organic ammonium halides, activation energy, galvanic cells.

ing with glacial acetic acid, and ethanol. While still moist with ethanol, the cuprous halide was stirred with tetrahydrofuran and rapidly transferred to a round bottom flask, where the remaining solvent was removed under vacuum. After solvent removal the cuprous halides were not exposed to the atmosphere in any subsequent operation.

The electrolyte materials were synthesized under a nitrogen atmosphere by intimately mixing the appropriate mole quantities of cuprous halide and organic material in a round bottom flask, using sufficient ethanol to make a slurry. The ethanol was then vacuum distilled. After thorough washing and drying the materials were transferred to a dry box where they were pressed into pellets at 57,000 psi. These pellets were then heated under the conditions illustrated in Table I. After the solid-state reaction, the pellets were transferred to a dry box, ground up, and repressed at 57,000 psi into conductivity cells of the configuration Cu,E/E/Cu,E (E is the electrolyte). The electrodes consisted of powdered copper intimately mixed with electrolyte in the weight ratio 2:1. Some of the conductivity cells were annealed under high purity nitrogen to remove any excess halogen that may be present. However, attempts to anneal the electrolytes containing quinuclidine and 3-quinuclidone resulted in deterioration of these materials.

Synthesis of electrolyte components.—NN'-dimethyltriethylenediamine dibromide.—Methyl bromide (2 moles) was reacted with triethylenediamine (1 mole) in benzene. The product was recrystallized from tetrahydrofuran. [Br: found 51.70%, calculated 52.98% (13).] This material was also prepared from NN'-dimethylpiperidine and 1-2-dibromoethane.

NN'-dihydrotriethylenediamine dibromide.—Triethylenediamine was reacted with an excess of a 47% aqueous HBr solution. The solution was allowed to stir overnight; the product was recrystallized from EtOH/water. [Br: found 57.4%, calculated 58.39% (13).]

N-hydrohexamethylenetetramine chloride.—Hexamethylenetetramine was reacted with 1 mole equiv. of 47% aqueous HBr in ethanol and was recrystallized from ethanol. [Cl: found 19.37%, calculated 20.11% (12).]

Quinuclidine hydrobromide.—Quinuclidine hydrochloride was treated with 1M NaOH, stirred with MgSO₄, and then reacted with a slight excess of HBr. The product was recrystallized from ethanol. (Br: found 40.94%, calculated 41.66%.)

Quinuclidine methylbromide.—As above except treated with 3 moles methylbromide. The product was recrystallized from ethanol. (Br: found 37.70%, calculated 38.83%.)

3-Quinuclidone hydrobromide.—This material was synthesized by passing quinuclidone hydrochloride through an anion exchange resin (amberlite IR-45) and the product was recrystallized from ethanol. (Br: found 40.18%, calculated 38.46%.)

Pyridinium bromide.—This extremely hygroscopic salt was prepared by titrating an aqueous solution of pyridine with 47% aqueous HBr. After evaporation of the solvent, the solid was recrystallized from acetone/ethanol. (Br: found 45.17%, calculated 41.66%.)

NN'-dimethylpiperazine dihydrochloride.—NN'-dimethylpiperazine was treated with 2 moles of aqueous hydrochloric acid. Crystals were obtained by concentration of the solution and were recrystallized from ethanol. (Cl: found 34.74%, calculated 37.96%.)

NN',NN'-diethylenedipyrrolidinium dibromide.—Pyrrolidine was reacted with ethylenedibromide, the solution was clarified using NORITE (activated charcoal) and the product was recrystallized from iPrOH. [Br: found 45.28%, calculated 44.94% (16).]

Synthesis of cathode materials.—Tetramethylammonium tribromide.—Tetramethylammonium bromide was reacted with bromine in carbon tetrachloride. The excess bromine was pumped off.

Tetrabutylammonium tribromide.—Tetrabutylammonium was reacted in carbon tetrachloride with a 0.05 mole Br₂/CCl₄ solution (14).

Triethylenediamine dibromine complex of.—Triethylenediamine was dissolved in benzene and was stirred with excess bromine in benzene. The yellow product was filtered, washed with benzene, and air dried. The product was recrystallized from glacial acetic acid.

Experimental measurements.—Cell resistances were measured at frequencies between 500 and 20,000 Hz using a General Radio 1608A impedance bridge with an external Hewlett-Packard 209A oscillator. The measurements were made on cells maintained in an inert atmosphere. The cell voltages were measured with an HP3430A digital voltmeter. X-ray powder diffraction patterns were run on a GE XRD-6 x-ray spectrometer using CuK_{α1} lines.

Table I. Conductivity results

Electrolyte	Conductivity ohm ⁻¹ · cm ⁻¹ at 25°C				Electrolyte synthesis	Conductivity cell anneal
	1000 Hz		∞ Hz			
	Before anneal	After anneal	Before anneal	After anneal		
Quinuclidine-HBr-CuBr (87.5 m/o)	4.2 × 10 ⁻³	1.3 × 10 ⁻³	8.7 × 10 ⁻³	3.0 × 10 ⁻³	190°C 16 hr under vac	110°C 8 hr N ₂ flow
Quinuclidine-MeBr-CuBr (87.5 m/o)	6.0 × 10 ⁻³		1.6 × 10 ⁻²		150°C 16 hr under vac	
Quinuclidine-HCl-CuCl (85 m/o)	1.8 × 10 ⁻⁴		4.0 × 10 ⁻⁴		160°C 16 hr under vac	
3-Quinuclidone-HBr-CuBr (80 m/o)	2.4 × 10 ⁻⁴		3.0 × 10 ⁻⁴		175°C 16 hr under vac	
3-Quinuclidone-HCl-CuCl (80 m/o)	2.6 × 10 ⁻³		2.5 × 10 ⁻²		120°C 16 hr under vac	
Pyridinium bromide-CuBr (87.5 m/o)	7.4 × 10 ⁻⁴		3.3 × 10 ⁻³		100°C under H ₂	
NN'-dihydrotriethylenediamine dibromide-CuBr (87.5 m/o)		2.0 × 10 ⁻³		6.5 × 10 ⁻²	190°C 16 hr under vac	170°C 8 hr N ₂ flow
NN'-dimethyltriethylenediamine dibromide-CuBr (94 m/o)	2.7 × 10 ⁻³	6.5 × 10 ⁻³		1.4 × 10 ⁻²	190°C 16 hr under vac	170°C 8 hr N ₂ flow
N-hydrohexamethylenetetramine chloride-CuCl (87.5 m/o)	5.4 × 10 ⁻⁴	2.4 × 10 ⁻³	2.5 × 10 ⁻³	2.7 × 10 ⁻³	120°C 16 hr under vac	120°C 8 hr N ₂ flow
Dimethylpiperazine-2HCl-CuCl (87.5 m/o)	9.6 × 10 ⁻⁷	3.3 × 10 ⁻⁷			110°C 16 hr under vac	
NN',NN'-diethylenedipyrrolidinium dibromide-CuBr (87.5 m/o)		4.0 × 10 ⁻³				110°C 8 hr N ₂ flow
1-Adamantylamine-HCl-CuCl (80 m/o)	3.1 × 10 ⁻⁷	1.2 × 10 ⁻⁷			180°C 16 hr under vac	140°C 8 hr N ₂ flow
Triethylenediamine-CuBr (90 m/o)		No conductivity			100°C 16 hr N ₂ flow	
Triethylenediamine-CuCl (90 m/o)	1.3 × 10 ⁻⁷				100°C 16 hr N ₂ flow	

Results

The systems reported on are shown in Fig. 1. These are (I) quinuclidine hydrobromide-CuBr, (II) quinuclidine methylbromide-CuBr, (III) quinuclidine hydrochloride-CuCl, (IV) 3-quinuclidone hydrobromide-CuBr, (V) 3-quinuclidone hydrochloride, (VI) pyridinium bromide-CuBr, (VII) NN'-dihydrotriethylenediamine dibromide-CuBr, (VIII) NN'-dimethyltriethylenediamine dibromide-CuBr, (IX) N-hydrohexamethylenetetramine chloride-CuCl, (X) dimethylpiperazine dihydrochloride-CuCl, (XI) NN',NN'-diethylenedipyrrolidinium dibromide-CuBr, (XII) 1-adamantanamine hydrochloride-CuCl, (XIII) triethylenediamine-CuBr, (XIV) triethylenediamine-CuCl.

A typical frequency dependence for a conductivity cell resistance is shown in Fig. 2 for the electrolyte NN'-dimethyltriethylenediamine dibromide-CuBr [94 mole per cent (m/o)]. If we plot cell resistance values at 1 kHz against cell length, the resultant faradaic impedance, as represented by the intercept, is generally several ohms. However, by plotting the extrapolated conductivity values at ∞ Hz against cell length, the intercept is at the origin, demonstrating that the impedance effect has been minimized, as shown in Fig. 3. All of our results for both 1 kHz and ∞ Hz are summarized in Table I. The highest conductivity found was for NN'-dihydrotriethylenediamine chloride-CuBr (87.5 m/o) at $6.5 \times 10^{-2} \text{ ohm}^{-1} \cdot \text{cm}^{-1}$ at ∞ Hz, which is in reasonable agreement with the value of $4 \times 10^{-2} \text{ ohm}^{-1} \cdot \text{cm}^{-1}$ at 1000 Hz reported by Takahashi.

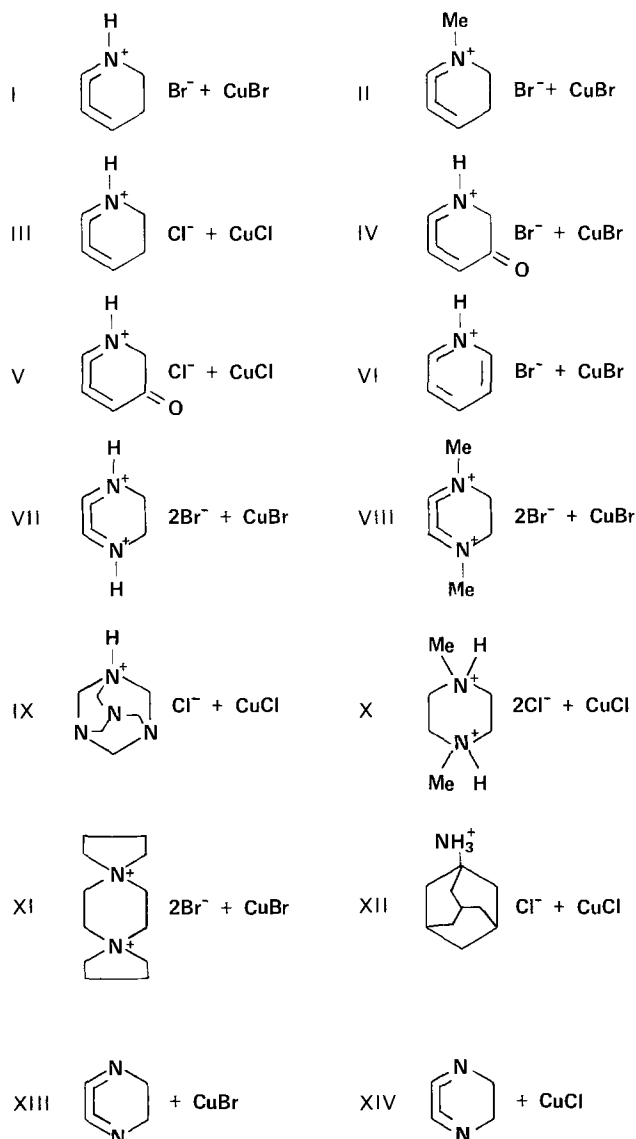


Fig. 1. Copper electrolyte systems investigated

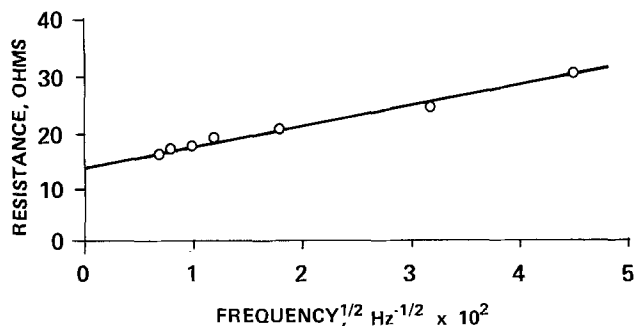
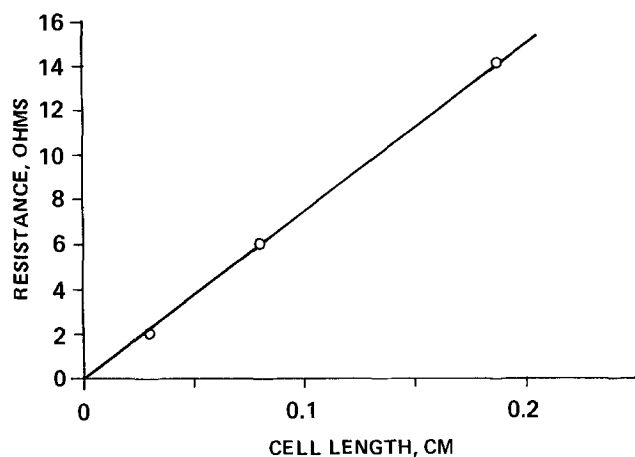


Fig. 2. Frequency dependence for dimethylenediamine dibromide + CuBr(94 m/o).

Fig. 3. Cell resistance vs. cell length at ∞ Hz for dimethyltriethylenediamine dibromide + CuBr(94 m/o).

The composition dependence of the conductivity was determined for the more conductive systems investigated. The compositions at which maxima occurred are summarized in Table I. The synthesis temperatures chosen were those where new phase materials could be detected from x-ray patterns. The presence of the new phases was then correlated with directly measured conductivity values to find the synthesis temperature at which the most conductive samples were produced.

The optimized stoichiometries for maximum conductivity were quite distinct, but were generally not sharp.

The observed temperature dependence of the conductivity for quinuclidine hydrobromide-CuBr (87.5% m/o) over the temperature range 50° to -20°C is shown in Fig. 4. The slope corresponds to an activation energy of 2.7 kcal/mole. The activation energies observed in the present study varied from 2.7 up to 6.7 kcal/mole as shown in Table II.

X-ray powder diffraction patterns were routinely run on samples of optimized stoichiometry. All samples showed lines characteristic of the starting materials together with, in some cases, new phases, indicating that the phases were not optimized to equilibrium.

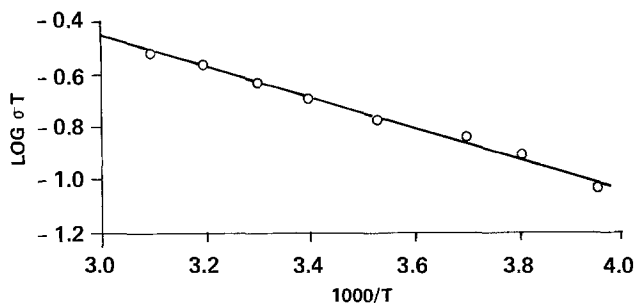


Fig. 4. Conductivity temperature dependence for quinuclidine hydrobromide + 87.5 m/o CuBr.

Table II. Activation energies for copper solid electrolytes

Electrolyte	ΔE , kcal/mole
Quinuclidine-HBr-CuBr (87.5 m/o)	2.68
Quinuclidine-MeBr-CuBr (87.5 m/o)	3.6
3-Quinuclidone-HBr-CuBr (80 m/o)	6.72
Pyridinium-HBr-CuBr (87.5 m/o)	4.19
NN'-dihydrotriethylenediamine dibromide-CuBr (87.5 m/o)	4.55
NN'-dimethyltriethylenediamine dibromide-CuBr (94 m/o)	5.7
N-hydrohexamethylenetetramine chloride-CuCl (87.5 m/o)	5.46

Table III. Galvanic cells investigated

System	Initial voltage, mV
Cu Hexamethylenetetramine-HCl-CuCl Triethylenediamine dibromide	674
Cu Hexamethylenetetramine-HCl-CuCl Propyl ₄ NBr, Br ₂	618
Cu Hexamethylenetetramine-HCl-CuCl Butyl ₄ NBr, Br ₂	618
Cu Hexamethylenetetramine-HCl-CuCl MoO ₃	378
Cu Hexamethylenetetramine-HCl-CuCl V ₂ O ₅	423
Cu Dihydrotriethylenediamine dibromide-CuBr Triethylenediamine dibromide	710
Cu Hexamethylenetetramine-HCl-CuCl CuBr ₂	672
Cu 3-Quinuclidone-HCl-CuCl Triethylenediamine dibromide	581
Cu 3-Quinuclidone-HCl-CuCl Propyl ₄ NBr, Br ₂	527
Cu 3-Quinuclidone-HCl-CuCl Butyl ₄ NBr, Br ₂	592

To evaluate the utility of these copper electrolytes in solid-state galvanic cells, various cells were made. Initial voltages are reported in Table III. A load curve for the cell Cu/hexamethylenetetramine-HCl-CuCl (87.5 m/o) CuBr₂ is shown in Fig. 5. During discharge or upon standing on open circuit, the electrolyte phase in our cells deteriorated and became black in appearance. There was a concurrent loss of cell voltage, possibly due to electronic conductivity in the electrolyte decomposition product.

The plating characteristics of copper in these materials was investigated for a simple coulometer cell. The plate, deplate cycle for the cell Cu/pyridinium bromide-CuBr (87.5 m/o) graphite is shown in Fig. 6.

Some preliminary work was performed on identification of the ionically conductive phase or phases present in these copper electrolytes by the use of single-crystal techniques. Single crystals of a conductive phase of pyridinium bromide-CuBr were prepared from an aqueous solution. A preliminary crystallographic survey of the single crystals suggested an orthorhombic unit cell ($a = 11.8\text{\AA}$, $b = 14.1\text{\AA}$, $c = 13.1\text{\AA}$). The observed density of 3.178 g/cm^3 and unit

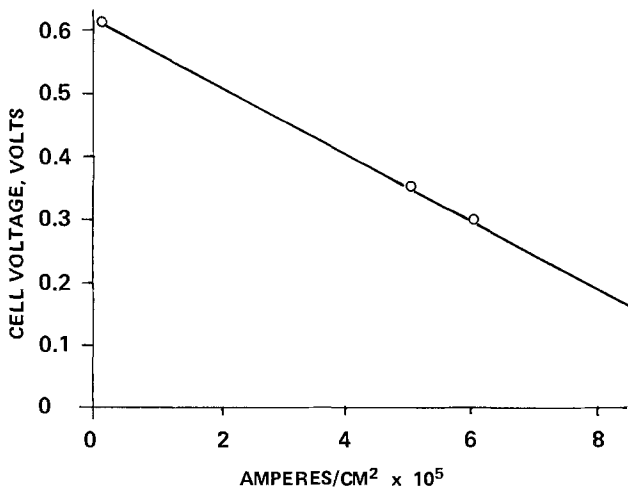


Fig. 5. Load curve for Cu/hexamethylenetetramine-HCl/CuBr₂ + CuCl(87.5 m/o).

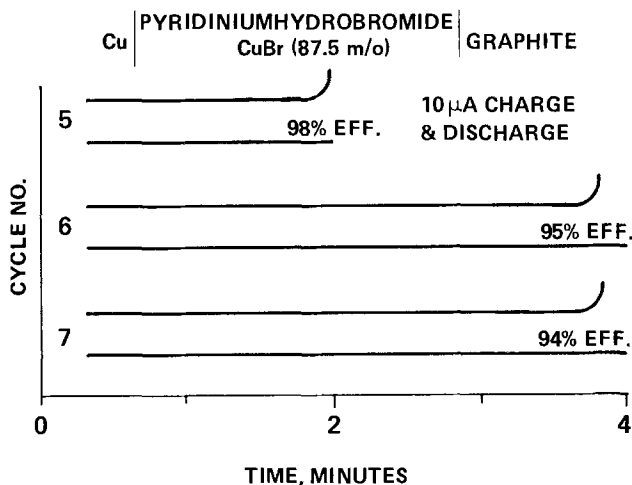


Fig. 6. Application in coulometers

cell volume agree with a unit cell containing 20 CuBr and 8 C₅H₆NBr.

Discussion

The present results indicate that copper ion conducting phases can be stabilized not only by substituted organic ammonium compounds of high symmetry (D_{3h}) as reported by Takahashi (12, 13) but also by species in which some lowering of the over-all symmetry occurs. High conductivity has been observed for double salts of copper halides with quinuclidine hydrobromide, quinuclidine methylbromide, and quinuclidine hydrochloride, where there is still a high symmetry organic ammonium halide, but one of the "onium" nitrogens of the NN'-dialkyltriethylenediamine halide has been removed. In fact, the conductivity at infinite frequency found for quinuclidine methylbromide-CuBr (87.5 m/o) was close to that observed in this laboratory for NN'-dimethyltriethylenediamine dibromide-CuBr (94 m/o), Table I. The molecular symmetry of quinuclidine may be C_{3v} or C₃, but it was clear that the cation need not contain rotational axes or mirror planes of symmetry perpendicular to the three-fold axis. It also followed that a doubly charged cation was not essential for the formation of a conducting phase.

Asymmetry was introduced into the quinuclidine structure by introduction of an oxygen atom at the three-position, giving the quinuclidone-type structure. High conductivity was found for 3-quinuclidone hydrochloride-CuCl (80 m/o) and 3-quinuclidone hydrobromide-CuBr (80 m/o), showing that highly symmetric organic nitrogen compounds are not necessary for the formation of highly conductive phases.

However, it is possible that the carbonyl group represents only a relatively small perturbation on the cage structure which, accordingly, may be axially disordered at 120° rotational intervals in the crystal structure of the double salt and thereby simulate three-fold symmetry. A crystallographic study of such possible positional disorder in the double salt would be required to clarify this possibility.

The formation of conductive phases with cations not having a cage structure was evaluated in the systems: dimethylpiperazine dihydrochloride-CuCl and NN', NN'-diethylenedipyrrolidinium dibromide-CuBr, the structures of which are shown in Fig. 1, No. X and XI, respectively. No significant conductivity was observed with either of these materials. One might infer from the low conductivity of these two materials that removal of the cage structure from a saturated species such as NN'-dimethyltriethylenediamine dibromide appears to prevent the stabilization of conductive phases. However, by analogy with previous work on silver conductors (8, 10) high conductivity was found with pyridinium bromide-CuBr (87.5 m/o) where the

organic cation has a planer aromatic ring and in particular, three-fold symmetry is absent.

The possible conductivity of the 1-adamantanamine hydrochloride-CuCl system (Fig. 1, No. XII) was investigated by analogy to the electrolyte N-hydrohexamethylenetetramine chloride-CuCl (87.5 m/o) (Fig. 1, No. IX). Conductivities only a little greater than 10^{-7} ohm $^{-1}$ ·cm $^{-1}$ were achieved with the samples investigated.

From conductivity measurements the optimum Cu/substituted organic ammonium halide mole ratios were found to be 7:1 for CuBr-quinuclidine hydrobromide, CuBr-quinuclidine methylbromide, and CuBr-pyridinium bromide, close to 6:1 for CuCl-quinuclidine hydrochloride, and 4:1 for CuBr-3-quinuclidone hydrobromide and CuCl-3-quinuclidone hydrochloride. The conductive materials used in these investigations were not single phase, as determined by x-ray diffraction, and optimized stoichiometries may be somewhat contingent upon experimental details used for electrolyte synthesis. Further comment on the stoichiometry of the conductive phase or phases in these electrolytes must await single-crystal structural determinations.

The conductivity of an ionic conductor can be represented by $\sigma = n\mu q$ (17), where n is the concentration of migrating species, μ is the ionic mobility, and q is the charge on the migrating species. Assuming that a univalent copper ion is the migrating species in these electrolytes, q will be essentially constant. The concentration of ions n in these copper electrolytes will vary between one material and another, being dependent on how much ionically conducting phase is present. Therefore, to compare conductivity values between the more highly conductive copper electrolytes might be somewhat erroneous.

The mobility μ of such ionic conductors can be represented by (17)

$$\mu = \mu_0 e^{-\Delta E/kT}$$

where ΔE is the activation energy for ionic migration and the other symbols have their usual significance. The concentration of migrating species n will be difficult to predict in the absence of single-phase material; it may therefore be more meaningful to compare ΔE values obtained from the conductivity-temperature dependence than absolute conductivity values.

The lowest activation energies were found for electrolytes (Table II) stabilized by the quinuclidine structure. The conductivities of these electrolytes are comparable to those found for electrolytes stabilized by NN'-dihydro and dimethyltriethylenediamine dibromide. The activation energies of the latter materials were found to be higher than those of the quinuclidine-CuX electrolytes, which suggests that there may be more mobile copper ions in the latter materials.

The introduction of an oxygen double bond into the three-position of quinuclidine causing the possible loss of symmetry in the 3-quinuclidone increased the activation energy for copper migration from 2.7 kcal/mole for quinuclidine hydrobromide-CuBr (87.5 m/o) to 6.7 kcal/mole for 3-quinuclidone hydrobromide-CuBr (80 m/o). The optimum stoichiometric ratios are also changed from 7:1 to 4:1 indicating a different structure and possibly a different conduction mechanism. The electrolyte 3-quinuclidone hydrochloride-CuCl (80 m/o) was not stable at the temperatures used for temperature dependence measurements, however assuming an activation energy comparable to that found in 3-quinuclidone hydrobromide-CuBr (80 m/o) there must be a high concentration of mobile species available since a conductivity of 2.5×10^{-2} ohm $^{-1}$ ·cm $^{-1}$ was recorded at ∞ Hz.

These results indicate that high molecular symmetry in the substituted organic ammonium cations is not essential in achieving high conductivity, but does appear to give a lower ΔE value for copper ion migration in the solid phase. For example, the activation energy for NN'-dimethyltriethylenediamine dibromide-CuBr

(87.5 m/o) is greater (5.7 kcal/mole) than for NN'-dihydrotriethylenediamine dibromide-CuBr (87.5 m/o) 4.55 kcal/mole), and quinuclidine methylbromide-CuBr (87.5 m/o) is greater (3.6 kcal/mole) than quinuclidine hydrobromide (2.68 kcal/mole). We tentatively conclude that introduction of a larger group on the onium nitrogen atom leads to larger ΔE values. However, the over-all conductivity will be contingent also on the number of migrating species available in the phase that is stabilized as indicated earlier.

All of the copper electrolytes were evaluated in galvanic cells and were observed to lose voltage upon standing on open circuit, with electrolyte deterioration, even when stored in a dry box under an argon atmosphere. With halide cathode materials the initially white electrolyte became black both upon standing and during discharge. This color change appears to be a direct chemical reaction. By pressing pellets of the configuration CuBr $_2$ /electrolyte/CuBr $_2$ the initially white electrolyte was observed to become black upon standing, indicating that even in the absence of any voltage breakdown of the electrolyte, a direct chemical path was also available for reaction with the copper electrolyte. This chemical instability was only observed in the stabilized conductive electrolyte phases and not in the organic nitrogen halide compounds used for the electrolyte synthesis. No color change was observed in pellets CuBr $_2$ /organic nitrogen halide/CuBr $_2$ upon extended standing. The electrolytes were also stable to copper since conducting cells Cu/electrolyte/Cu were stable over several months without evidence of chemical breakdown.

The chemical change taking place in galvanic cells containing halide cathode materials, probably involves a halide migration which could cause the formation of electron holes, and/or the formation of Cu $^{2+}$ species in the electrolyte, thus explaining the loss of cell voltage. The presence of electron holes in cuprous halides containing an excess of halogen is well known (18, 19). Four cells of the configuration Cu/electrolyte/graphite + electrolyte were charged up initially to around 600 mV; these cells slowly began to lose their charge with the simultaneous decomposition of the electrolyte (detected by the color change), and finally held a voltage of around 350 mV for several months.

In cells using V $_2$ O $_5$ or MoO $_3$ as cathode materials, the cell voltage similarly deteriorated with time; however, no electrolyte color change was observed. This indicates that voltage breakdown of the electrolytes is probably occurring leading to some electronic conduction path. Preliminary attempts using x-ray diffraction techniques to identify the electrolyte decomposition products were not conclusive.

The performance of these electrolytes in solid-state coulometers is illustrated by the cell Cu/pyridinium bromide-CuBr (87.5 m/o)/graphite (Fig. 6). The first few cycles charging and discharging at 10 μ A showed high coulombic efficiencies, indicating that initially the materials were predominantly Cu $^+$ ion conducting; however, upon extended cycling the efficiency began to decrease, probably due to electrolyte breakdown caused by the voltage drop across the cell.

The fact that high ionic conduction has been found in copper electrolytes stabilized by substituted organic ammonium compounds of lower symmetry than previously reported, indicates that such electrolyte phase stabilization is more general than might have previously been thought. From the evidence presently available it would appear that these materials are somewhat unstable when applied in galvanic cells. Whether these copper electrolyte materials can find any useful applications in solid-state devices must await the syntheses or isolation of the phase or phases that are responsible for the ionic conduction, together with the necessary structural determination and stabilization of the electrolytes in cells.

Acknowledgment

The partial support of this investigation by the National Science Foundation (NSF Faculty Research Participation Project, Grant No. GZ-2939) and the assistance of Patricia M. Schultz who performed many of the technical measurements are gratefully acknowledged.

Manuscript submitted March 31, 1975; revised manuscript received June 4 1975. This was Paper 19 presented at the New York, New York, Meeting of the Society, Oct. 13-17, 1974.

Any discussion of this paper will appear in a Discussion Section to be published in the June 1976 JOURNAL. All discussions for the June 1976 Discussion Section should be submitted by Feb. 1, 1976.

Publication costs of this article were partially assisted by Gould Incorporated.

REFERENCES

1. D. O. Raleigh, *J. Appl. Phys.*, **41**, 1536 (1970).
2. a. B. B. Owens, J. S. Sprouse, and D. L. Warburton, 25th Power Sources Conference, 1972, p. 8.
b. J. E. Oxley and B. B. Owens, Power Sources 3, D. H. Collins, Editor, Oriel Press, Boston (1970).
3. B. B. Owens, *This Journal*, **117**, 1536 (1970).
4. B. B. Owens, J. H. Christie, and G. T. Tiedemann, *ibid.* **118**, 1144 (1971).
5. B. B. Owens, in "Advances in Electrochemistry and Electrochemical Engineering," P. Delahay and C. W. Tobias, Editors, Vol. 8, p. 1-61, Wiley-Interscience, New York (1971).
6. J. H. Christie, B. B. Owens, and G. T. Tiedemann, Abstract 20, p. 53, The Electrochemical Society Extended Abstracts, Fall Meeting, New York, New York, Oct. 13-17, 1974.
7. S. Geller, *Science*, **157**, 310 (1967).
8. S. Geller and M. D. Lind, *J. Chem. Phys.*, **52**, 5854 (1970).
9. S. Geller, *Science*, **176**, 1016 (1972).
10. S. Geller and B. B. Owens, *J. Phys. Chem. Solids*, **33**, 1241 (1972).
11. S. Geller, P. M. Skarstad, and S. A. Wilber, *This Journal*, **122**, 332 (1975).
12. T. Takahashi, O. Yamamoto, and S. Ikeda, *ibid.*, **120**, 1431 (1975).
13. T. Takahashi and O. Yamamoto, *ibid.*, **122**, 83 (1975).
14. E. Warburg, *Ann.*, **6**, 125 (1901).
15. G. Jones and S. M. Christian, *J. Am. Chem. Soc.*, **57**, 272 (1935).
16. F. F. Blicke and E. B. Hatelling, *ibid.*, **76**, 2427 (1954).
17. W. Jost, "Diffusion in Solids, Liquids, and Gases," E. M. Laebl, Editor, Academic Press Inc., New York (1960).
18. C. Wagner, *J. Chem. Phys.*, **18**, 62 (1950).
19. J. B. Wagner and C. Wagner, *ibid.*, **26**, 1597 (1957).

On the Kinetics of the Breakdown of Passivity of Preanodized Aluminum by Chloride Ions

Z. A. Foroulis*¹ and M. J. Thubrikar

Department of Metallurgy and Materials Science, New York University, New York, New York 10019

ABSTRACT

The kinetics of passivity breakdown and nucleation of pitting of preanodized aluminum by chloride ions has been investigated using aluminum supporting oxide films of reasonably well-known thickness and structure. The kinetics of passivity breakdown at the steady-state, critical pitting potential is influenced by chloride ion concentration, temperature, and oxide film thickness; it was found to be independent of solution pH in the range 5-10. It is postulated that passivity breakdown and nucleation of pitting at the critical pitting potential occurs by a process of Cl⁻ adsorption (assisted by the field at the oxide-solution interface) on the hydrated oxide surface and formation of a soluble, basic chloride salt with the lattice cation which readily goes in solution. This process of localized dissolution of the hydrated oxide film via formation of a soluble, basic, aluminum chloride salt once initiated is likely to continue in an "autocatalytic" fashion until the oxide is locally "penetrated" and dissolution of the substrate metal begins.

The breakdown of passivating oxide films on aluminum, by "aggressive" anions such as chlorides at sufficiently positive anodic potentials is frequently responsible for the failure of aluminum and its alloys in aqueous chloride solutions because it usually leads to severe pitting of the underlying metal. Several mechanisms for the breakdown process have been suggested (1-7). However, there is little experimental information on the kinetics of the oxide film breakdown process which could be used to establish the mechanism of pit nucleation of aluminum by chloride ions. Considerably more research is required to better understand the physical and chemical processes occurring during pit nucleation. In particular, there is considerable need to understand the role of surface films, Cl⁻ concentration, solution pH, and temperature on the

kinetics of passivity breakdown and nucleation of pitting.

The work described in this report was undertaken to study the kinetics of pit nucleation of preanodized aluminum by chloride ions, as a function of Cl⁻ concentration, solution pH, and temperature. The purpose of prefilming of aluminum by anodization was to obtain oxide films of reasonably well-known thickness and structure.

Experimental

The electrodes, about 4-7 cm² total exposed area were cut from 99.99% pure aluminum. The electrode assembly was similar to the one described previously (8). Surfaces were abraded through 4-0 emery paper and then metallographically polished using 1 and 0.5 μ alumina. This surface preparation produced a mirror like surface.² Following rinsing in distilled water,

² This type of surface preparation was essential for the microscopic observation of pits.

* Electrochemical Society Active Member.

¹ An Adjunct Professor and also associated with Exxon Research and Engineering Company, Florham Park, New Jersey 07932.

Key words: aluminum, pitting, corrosion, passivity breakdown, kinetics.

specimens were anodized using two different methods. One method involved constant current anodization in sulfuric acid using 15% w/v sulfuric acid (sp gr 1.84) for various times at 25 mA/cm² (20-21V) with a standard rate of stirring. Following anodization, the specimens were sealed in boiling distilled water. In general, the ratio of anodizing time to sealing time in boiling distilled water was 1:30. In some instances, however, longer times of sealing were also used. The unsealed films produced consisted of a thin barrier layer adjacent to the metal and a thick outer porous layer. The oxide film prior to sealing in water is essentially γ -Al₂O₃. During exposure in boiling water, sealing of pores due to hydration of γ -Al₂O₃ and formation of the less dense boehmite, AlO(OH), or Al(OH)₃ is well known (9-12). The sealing procedure gives an essentially pore free film (9). The over-all thickness of the oxide films produced by anodization was estimated from values reported by Hoar and Wood (9).

Another method of prefilming of aluminum specimens was constant voltage anodization in 3% ammonium tartrate. In this case different anodizing voltages were used in order to get different film thicknesses. Films formed in ammonium tartrate solution are much thinner, nonporous, and did not require sealing. The oxide films produced by anodization in ammonium tartrate are similar to the air formed oxides and consist essentially of γ -Al₂O₃. The thickness of oxides produced by anodizing in ammonium tartrate solutions were estimated from values reported by Hass (13).

Solutions for the kinetic studies of film breakdown and pit initiation were prepared from distilled water and reagent grade KCl, KOH, and H₂SO₄. The cell design was essentially identical to the one described previously (14). Solutions were deaerated by bubbling prepurified nitrogen prior and throughout each run. Additional purification was done by passing it through copper turnings heated at 500°C. Potential control was obtained by means of an electronic potentiostat. Potentials were measured against SCE using a vacuum tube millivoltmeter (high impedance). Current was measured by recording the potential drop across a standard resistor using a millivolt recorder. Temperature control was achieved either by means of a heat mantle fitted to the lower part of the cell or by using suitable cooling baths.

Since the aim of this investigation was to gain an understanding of the mechanism of nucleation of pitting, it was felt of particular significance to study the kinetics of film breakdown at the steady-state, critical pitting potential. The procedure was to anodically polarize the electrode, in steps of 10 to 20 mV,³ after a rest period of a few minutes at the open-circuit potential. At each step the potential was kept constant at a given value, while the current was recorded continuously for as long as 24 hr and the electrode was then observed under a low power microscope for pitting. The potential at and above which pitting was observed was taken as the potentiostatic, critical pitting potential, E_c . It was also observed that at and above E_c , the current, after an initial induction period (τ) during which the current remained essentially constant, began and continued to increase with time, eventually reaching current values higher by two or more orders of magnitude. At potentials smaller than the critical, the current generally <1 μ A/cm², remained essentially constant and pits were not observed. Reproducibility of the critical pitting potential was within about 10-15 mV. All potentials are reported with reference to the SCE.

To gain information regarding the kinetics of film breakdown and pit nucleation at the critical pitting potential, the induction time τ was determined experimentally as a function of Cl⁻ ion concentration, tem-

perature, oxide film thickness, and solution pH. The induction time τ is defined as the initial period of time (generally a few minutes) at the critical pitting potential during which the anodic current (induction current) is very low and essentially constant, prior to a beginning of a continuous increase of current with time which eventually reaches current values higher than the induction current by two or more orders of magnitude as shown in Fig. 1.

The continuous increase of the over-all anodic current at the critical potential at times higher than τ is attributed to growth of minute pits initiated on a microscale during the induction time. As the minute pits grow the over-all, anodic current density, due to active metal dissolution at the very small pit or pits and the passive current passing through most of the electrode surface which remains passive, continues to increase with time as the size of pits grow and perhaps additional pits nucleate. The localized, anodic current density due to active metal dissolution at the small pit or pits is expected to be higher by several orders of magnitude as compared with the current density passing through the passive surface. It should be mentioned that pits could actually be observed under a low power microscope only after the electrode was maintained at the critical potential for an extended period of time beyond the induction time τ during which pits grew to sufficient size to be visible under the microscope.

In a typical experiment for the induction time determination, the preanodized aluminum electrode was introduced in the cell and its potential was set and maintained at the steady-state critical potential for pitting while the current was recorded continuously. The time required for the current to begin its sharp and continuous increase was measured as τ , the induction time for the oxide film breakdown and nucleation of pitting.

The measurement of the induction time τ for pit nucleation was not very reproducible. The poor reproducibility of the induction time for pit nucleation as seen by the spread of the experimental data points is probably due to several reasons, such as nonuniform thickness of the oxide film produced by anodization due to nonuniform current distribution on the specimen surface (edge effects), small variations in surface finish, and perhaps other oxide surface discontinuities. Since the induction time τ relates to the very precise process of current increase at the critical pitting potential, the relative accuracy of measuring τ is also affected by the uncertainty of 10-15 mV in reproducing the critical pitting potential (15). The reported, induction time data represent clearly defined values using specimens with carefully prepared surface finish, as described previously.

Results and Discussion

A typical experiment showing the variation of current with time at and below the critical pitting potential is shown in Fig. 1. The data were obtained with preanodized aluminum exposed to 3.0M KCl at 25°C.

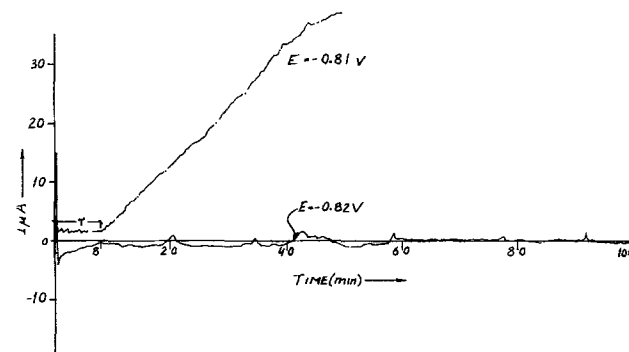


Fig. 1. Typical current-time curve for preanodized pure aluminum electrode potentiostated at -0.81 and -0.82 V (SCE) in 3M KCl at 25°C.

³ Prior to each potential setting, the electrode was subjected to new surface preparation (polishing, anodization, and sealing for specimens anodized in sulfuric acid).

The critical pitting potential in this case was $-0.81V$ (SCE) and the induction time, τ , for pit nucleation was about 8 min. At the lower potential of $-0.82V$ (SCE) the current remained relatively constant and very low and no pits were observed for up to 24 hr.

The dependence of the induction time on chloride ion concentration was measured at $25^\circ C$ in the concentration range $0.01-3M$ KCl; the pH of these solutions was in the range 5.9-6.1. The data for a series of experiments with preanodized⁴ aluminum are plotted in Fig. 2. The data show that the induction time for pit nucleation decreases from about 23 min in $0.01M$ KCl to about 4 min in $3M$ KCl. The slope, n , of the $\log 1/\tau$ vs. $\log C_{Cl^-}$ line is approximately $n \approx -0.1$ in the concentration range $0.01-1M$ KCl. At higher chloride ion concentrations the induction time appears to decrease rapidly as indicated by the approximate slope of $n \approx -0.9$ which was drawn through the available experimental points. One may question the relative accuracy of the slopes drawn through the data points; the significant thing is not the precise value of the slopes but rather the general conclusion drawn from the data that in low Cl^- concentrations there is a very weak dependence of τ on KCl concentration but in higher KCl concentrations there is a tendency for higher dependence of τ on Cl^- concentration.

Temperature as might be expected has also considerable influence on the rate of pit nucleation as indicated by data on the temperature dependence of τ plotted in Fig. 3. This figure shows an Arrhenius-type plot for the temperature variation of τ of preanodized aluminum in $0.1M$ KCl solution. The plot shows an apparent activation energy of about 6.7 kcal/mole for the pit nucleation process.

The solution pH in the range 5-10, at constant chloride ion concentration, was found to have no effect

⁴Unless otherwise indicated, specimens were anodized for 1 min in 15% H_2SO_4 and sealed for 30 min in boiling distilled water.

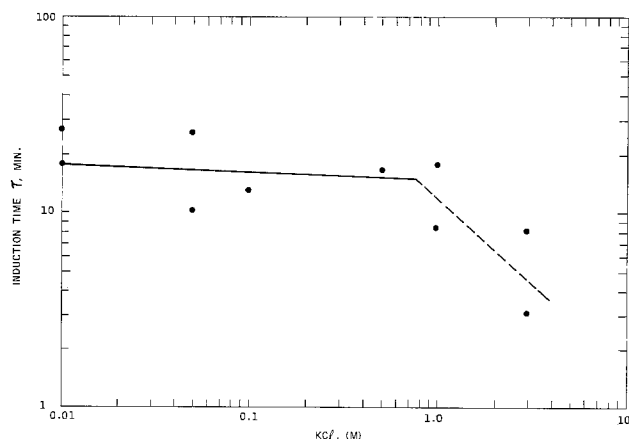


Fig. 2. Dependence of the induction time for pit nucleation on chloride ion concentration in the pH range 5.9-6.0 at $25^\circ C$. Preanodized pure aluminum.

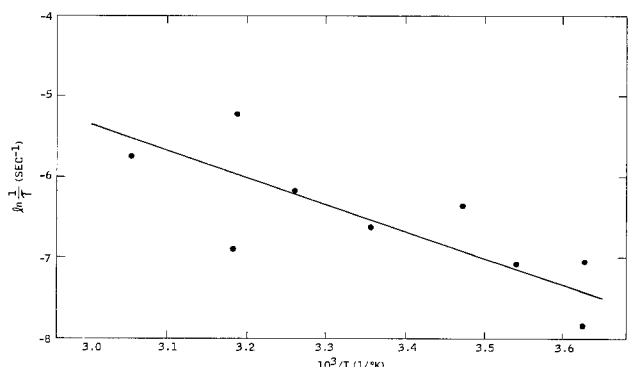


Fig. 3. Arrhenius-type plot for temperature dependence of induction time for pit nucleation. Preanodized aluminum, $0.1M$ KCl.

on the rate of pit nucleation, as measured by the induction time. This is shown with the data plotted in Fig. 4. These data were obtained with preanodized aluminum in $0.1M$ KCl in the pH range 5-10. Solution pH was adjusted as required with either H_2SO_4 or KOH.

In order to study the influence of oxide film thickness on the rate of film breakdown and pit nucleation, a series of experiments was carried out with oxide films of a broad thickness range. Most oxide films on aluminum were prepared by anodization in 15% H_2SO_4 followed by sealing in distilled water as described in the experimental section. This procedure produced oxide films in the thickness range 0.8 to about 40μ . Several oxide films of considerably smaller thicknesses, in the range of $260-1300\text{\AA}$, were also produced by anodization in 3% ammonium tartrate solution.

The dependence of the incubation time τ for pit nucleation on the oxide film thickness is shown in Fig. 5. The data show essentially a linear dependence of τ on oxide film thickness. The data plotted in Fig. 5 were obtained in 0.1 and $3M$ KCl solutions with aluminum preanodized in H_2SO_4 and sealed in distilled water and in $0.1M$ KCl solutions with aluminum preanodized in 3% ammonium tartrate solution.

Table I shows the dependence of the steady-state, critical pitting potential on the thickness and structure of the oxide film. The data show that the critical pitting potential of specimens covered with oxide films in the thickness range of $0.026-0.130\mu$ is essentially the same within the $\pm 10-15$ mV (experimental error) of the average value. However, in the case of much

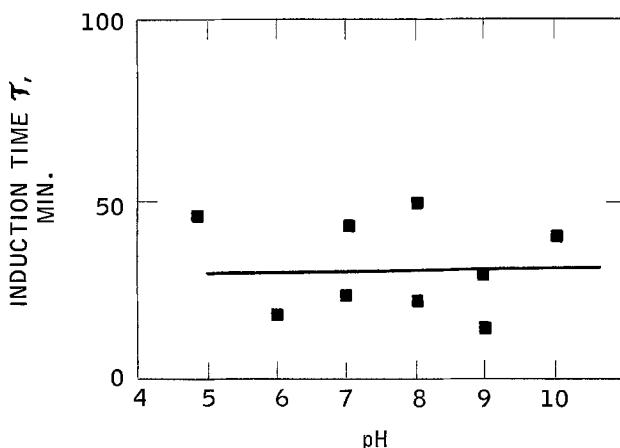


Fig. 4. Dependence of induction time for pit nucleation of preanodized aluminum in $0.1M$ KCl on solution pH.

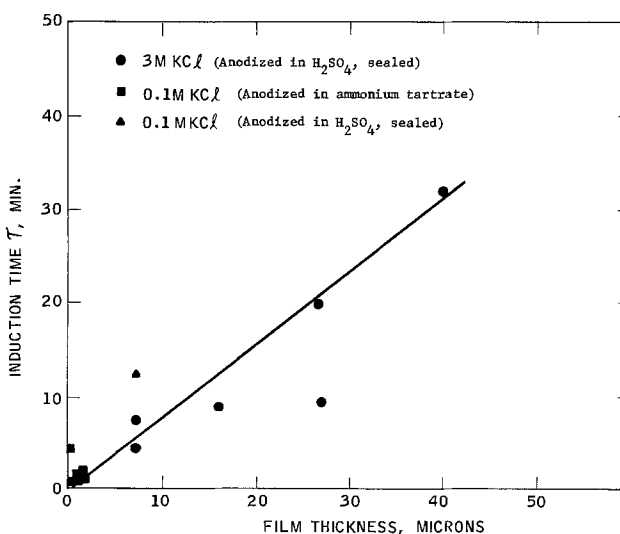


Fig. 5. Dependence of induction time for pit nucleation on oxide film thickness in 0.1 and $3M$ KCl, $25^\circ C$.

Table I. Steady-state critical pitting potentials, E_c vs. SCE

Electrolyte	Surface preparation	Oxide film thickness, μ	E_c , V (SCE)
0.1M KCl 25°C	Anodization in 3% ammonium tartrate	0.026	-0.73
0.1M KCl 25°C	Anodization in 3% ammonium tartrate	0.097	-0.72
0.1M KCl 25°C	Anodization in 3% ammonium tartrate	0.130	-0.71
0.1M KCl 25°C	As polished		-0.73
0.1M KCl 25°C	Anodization in 15% H ₂ SO ₄ and sealed in boiling dist. H ₂ O	0.79	-0.68

higher oxide film thickness (about 0.79 μ) there is clear evidence that E_c increases with oxide film thickness. The apparent increase in E_c with oxide film thickness suggests that with increasing oxide film thickness, due to potential drop (pd) within the oxide film, a higher applied anodic potential is required to attain the minimum pd across the oxide-solution interface which is required to achieve the penetration of Cl⁻ through the electric double layer at the oxide-solution interface and its adsorption on the hydrated oxide surface.

Following the arguments of Engell and Stolica (16), Hoar and Jacob (17), and Bogar and Foley (18), it is assumed that $1/\tau$ is an approximate estimate of the rate of the limiting process leading to pit nucleation of aluminum. Then the slope of the straight lines in Fig. 2 is interpreted as the order n of the rate-determining step during pit initiation with respect to the concentration of chloride ion in solution.

The very weak dependence of τ on chloride ion concentration in dilute chloride solution, as shown in Fig. 2, and the low apparent activation energy of about 6.7 kcal/mol (Fig. 3) suggest that in dilute chloride solutions the rate-determining step in the process of pit initiation is likely to be a diffusion or adsorption step. Lattice diffusion of chloride ions through the aluminum oxide film via lattice defects or by place exchange of oxide ions and chloride ions would be energetically consistent with the measured activation energy and the weak dependence of τ on C_{Cl^-} , but the diffusion rate itself would be much too slow to account for the induction time observed (19).

If we suppose that the relationship between the concentration of Cl⁻ adsorbed on the hydrated oxide surface and the bulk solution is that of a Freundlich adsorption isotherm, and assuming that pitting is initiated at the critical pitting potential when a critical concentration of Cl⁻ is established at one or more sites on the hydrated oxide surface, then $1/\tau$ should be related to the bulk chloride ion concentration C according to the Freundlich adsorption isotherm. The data plotted in Fig. 2 in dilute solutions follow such a functional relationship

$$\frac{1}{\tau} \simeq k_1 C^{1/n'} \simeq k_1 C^n$$

where k_1 and $1/n'$ are constants of a Freundlich-type isotherm and n is the stoichiometric factor described previously.

In higher chloride ion concentrations, the induction time apparently decreases much faster with chloride ion concentration as indicated by the approximate dotted line slope of about $n \simeq -0.9$. The stronger dependence of τ on the bulk chloride ion concentration in concentrated KCl solutions suggests that the rate-determining step in the over-all process of passivity breakdown changes from a step involving adsorption from solution on the hydrated oxide surface to that of a chemical reaction on the hydrated oxide surface which involves approximately one Cl⁻ per aluminum cation.

The stoichiometric factor n obtained in this study for the pit initiation process of aluminum is considerably smaller than the values of 2.5-4.5 reported by

Hoar and Jacob (17) for the breakdown of passivity in 18-8 stainless steel by chloride ion in sulfuric acid solution of pH 2.05, in the potential range of 0.4-0.8V (SHE). These authors also found an apparent activation energy of about 60 kcal/mole for the breakdown of passivity in acidic solutions. Values of n in the range 3.0-11.1 were also reported by Foley and Bogar (18) for pit initiation of aluminum alloys in sulfuric acid solutions containing chloride ions in the pH range 0.0-3.5. Their data on the temperature dependence of the breakdown process give apparent activation energies in the range of 22.9 kcal in pH 0.0 and 12.0 kcal/mole in pH 6.08. Reasons for the considerable difference in stoichiometric numbers n and activation energies between the present study and those of Foley and Bogar (18), Hoar and Jacob (17), and Engell and Stolica (16) are not known. It is assumed, however, that this difference is probably caused by the considerable difference in pH of the solutions used in the various breakdown experiments, and the difference in alloy and passive film compositions. This explanation is consistent with the decreasing stoichiometric number and apparent activation energy reported by Foley and Bogar (18) with increasing solution pH for the passivity breakdown process of an aluminum alloy potentiostated at 0.18V (SCE) in sulfuric acid solution.

General Discussion

Several mechanisms for the action of chloride ions to initiate pitting corrosion have been suggested in the literature. These include: (a) Cl⁻ penetration of the protective oxide film which covers the metal surface through pores or other weak places (1, 20, 21), (b) competitive adsorption of Cl⁻ and oxygen or OH⁻ for sites on the metal surface (22, 23), (c) migration of chloride ions inward through the oxide lattice (4), (d) peptization of the oxide film by a strong negative charge caused by adsorbed anions (5) and by dynamic breakdown-repair mechanism (7). Aluminum provides a good opportunity to evaluate the influence of an oxide on the process of pit initiation since well-known methods are available for preparing oxide films of different thicknesses and structure by anodization.

The results of the present study provide considerable experimental evidence to test the various mechanisms for passivity breakdown and initiation of pitting in nearly neutral solutions by chloride ions.

Chloride ion migration through pores or other weak places in the oxide film (1, 20, 21) followed by competitive adsorption between chloride ions and adsorbed oxygen or hydroxyl ions at the metal/solution interface as a mechanism of pit initiation (22, 23) is an unlikely mechanism for several reasons. Migration of Cl⁻ through pores or other weak spots in the oxide film as the rate-determining step can be ruled out, since by treating the aluminum specimens as a porous electrode it can be shown (24) that the mass transport limiting current for a porous and a corresponding flat electrode are the same both being determined by mass transport in the hydrodynamic layer outside the electrode. Furthermore, it is considered unlikely that continuous pores through the oxide film to the bare aluminum surface are present in oxide films prepared by anodization in ammonium tartrate or in H₂SO₄ with subsequent sealing.

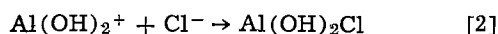
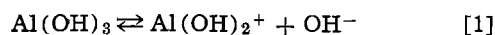
Competitive adsorption (22, 23) between chloride ions and adsorbed oxygen or OH⁻ on a bare metal surface is also considered an unlikely mechanism. There is abundant evidence that aluminum metal (even without a thick barrier-type film) in neutral solutions is covered with a thin persistent and fairly protective film of aluminum oxide (25). A dynamic passivity breakdown-repair mechanism (7) which attributes to the Cl⁻ the role of inhibiting repassivation rather than promoting passivity breakdown, cannot account for the observed increase in induction time τ with the thickness of the oxide film. The passivity breakdown-repair mechanism (7) conceptually is similar to the com-

petitive adsorption mechanism (22, 23) and assumes in essence competitive adsorption between Cl^- and OH^- (or H_2O) on the metal surface as the rate-limiting process of pit nucleation. If this were the rate-limiting process in pit nucleation, the induction time should be independent of the thickness of the oxide film (which must in some way be "penetrated" before Cl^- can adsorb on the bare metal surface). This, of course, is contrary to the data shown in Fig. 5, which indicate that the induction time increases with oxide film thickness.

Migration of chloride ions inward through lattice diffusion, as discussed previously, is much too slow to account for the induction time observed (19).

The kinetic data presented in this paper are consistent with a pit nucleation model (26) which involves field-assisted adsorption of chloride ions from solution on the hydrated oxide surface followed by oxide dissolution as the rate-determining steps in the process of passivity breakdown and pit nucleation of aluminum in nearly neutral solutions. The over-all passivity breakdown and nucleation of pits according to this model involves the following sequence of reaction steps: (a) adsorption of Cl^- on the oxide-solution interface under the influence of the electric field (at the oxide-solution interface) in competition with OH^- or H_2O molecules for surface sites on the hydrated oxide surface; (b) formation of a basic hydroxychloride aluminum salt with aluminum oxide cations on the hydrated oxide surface, which immediately separates from the oxide lattice and readily goes in solution.

It is suggested that a probable reaction describing formation of such a readily soluble basic chloride aluminum salt is reaction [2]



Reaction [1] describes the ionization of the hydrated aluminum oxide surface in nearly neutral solution. This reaction accounts for the positive charge on the hydrated oxide surface as indicated by ζ potential measurements (27-29).

This process of field assisted Cl^- adsorption on the hydrated oxide surface and formation of a soluble aluminum chloride salt leading to localized oxide dissolution will have a high probability of repeating itself at the same site, since at constant anode potential the applied field at the oxide-solution interface will tend to be stronger at the "thinned" point of the oxide film. Thus, the process of localized dissolution of the oxide film via the formation of a basic chloride aluminum salt ($\text{Al}(\text{OH})_2\text{Cl}$) is likely to continue until the oxide film is locally dissolved; once the oxide film is locally "dissolved," dissolution of the substrate metal begins and the anodic current density at the very small pit or pits increases by several orders of magnitude compared with the current density of the passivated surface.

Localized dissolution of the oxide (leading to pitting of the underlying metal), rather than general dissolution of the oxide film occurs at the critical pitting potential because of the "autocatalytic" character of the localized oxide film dissolution at the critical pitting potential. Once a critical concentration of chloride ions is adsorbed on a particular site on the hydrated oxide surface via this mechanism (26), and one or more, adjacent, aluminum oxide lattice cations are transformed to chloride-containing soluble salts, they are likely to immediately separate from the oxide cations in the lattice and go in solution.⁵ The probability of this localized oxide dissolution to continue on the same sites is considerable because of the higher potential drop (pd) at the oxide-solution interface (under con-

stant, applied anodic potential) expected on these sites.

This argument implies that preferential sites for pit initiation are likely to be areas of oxide surface defects such as scratch lines, voids or other surface flaws where the oxide thickness is smaller than in adjacent areas and therefore the pd across the oxide-solution interface is higher (30).

The question may be raised as to why the high field across the oxide film would not rapidly repair the film in areas where it is locally thinned by dissolution and thereby prevent film breakdown. The answer to this lies in the supposition that on the oxide-solution interface a competition exists between Cl^- and OH^- (or H_2O molecules) for oxide surface sites. Once oxide dissolution is initiated via the proposed mechanism, a high probability exists that as aluminum cations advance through the oxide film at the thinned points of the film (under the influence of the field across the oxide film) instead of oxide forming OH^- or H_2O molecules, they are likely to meet Cl^- and OH^- so that a high probability exists for formation of a readily soluble aluminum hydroxychloride salt rather than an insoluble aqueoaluminum complex required for oxide film repair.

In low chloride ion concentrations adsorption of chloride ions, from solution, on the hydrated aluminum oxide surface under the influence of the field at the oxide-solution interface is assumed to be the rate-determining step in the process of passivity breakdown. In higher chloride ion concentrations, the reaction step leading to formation and dissolution of the hydroxychloride aluminum salt on the hydrated oxide surface is likely to become the rate-determining step in the process of pit initiation.

The induction time for passivity breakdown and pit initiation according to the proposed mechanism is a direct measure of the rate of the localized dissolution of the passive aluminum oxide film via the sequence of Cl^- adsorption and formation of a readily soluble chloride containing aluminum salt (Eq. [2]).

On this basis, it is expected that the induction time τ for pit initiation should increase with the thickness of the oxide film. Data plotted in Fig. 5 on the dependence of the induction time for preanodized aluminum on oxide film thickness show that τ increases with oxide thickness following essentially a linear dependence.

The hypothesis in the proposed mechanism that a readily soluble, chloride-containing aluminum salt is locally formed on the solution side of the aluminum oxide surface, once the chloride ions under the influence of the applied anodic potential have penetrated the electric double layer at the oxide-solution interface and adsorbed on the hydrated oxide surface, is consistent with literature data (31, 32) indicating that hydrated aluminum oxides form soluble aluminum salts in acidic or nearly neutral aqueous solutions containing chloride ions.

Acknowledgment

The authors are pleased to acknowledge support of this research by the Ocean Engineering Research Program in the Department of Metallurgy and Materials Science of New York University, and the encouragement and support provided by Dr. H. Margolin.

Manuscript submitted Feb. 10, 1975; revised manuscript received June 2, 1975.

Any discussion of this paper will appear in a Discussion Section to be published in the June 1976 JOURNAL. All discussions for the June 1976 Discussion Section should be submitted by Feb. 1, 1976.

REFERENCES

1. U. R. Evans, L. C. Bannister, and S. C. Britton, *Proc. Roy. Soc.*, **A131**, 366 (1931).
2. H. Bohni and H. H. Uhlig, *This Journal*, **116**, 906 (1969).

⁵ It is worth noting that the solubility of hydrated aluminum oxide cations present in the film without the participation of the activating chloride ions is considerably lower; the very low rate of dissolution in this case is uniform throughout the oxide surface.

3. Ya. M. Kolotyarkin, *Corrosion*, **19**, 263t (1963).
4. T. P. Hoar, D. C. Mears, and G. P. Rothwell, *Corrosion Sci.*, **5**, 279 (1965).
5. T. P. Hoar, *ibid.*, **7**, 341 (1967).
6. M. A. Heine, D. S. Keir, and M. J. Pryor, *This Journal*, **112**, 24 (1965).
7. J. Zahavi and M. Metzger, in "Localized Corrosion," B. F. Brown, J. Kruger, and R. W. Staehle, Editors, p. 132, NACE, Houston (1975).
8. M. Stern and A. C. Makrides, *This Journal*, **107**, 782 (1960).
9. T. P. Hoar and G. Wood, *Electrochim. Acta*, **7**, 333 (1962).
10. J. E. Draley, S. Mori, and R. E. Loess, *This Journal*, **110**, 622 (1963).
11. J. E. Draley and W. E. Ruther, *ibid.*, **103**, 441 (1956).
12. S. Mori, R. E. Loess, and J. E. Draley, *Corrosion*, **19**, 165 (1963).
13. G. Hass, *J. Opt. Soc. Am.*, **39**, 532 (1949).
14. Z. A. Foroulis, *This Journal*, **113**, 532 (1966).
15. Z. A. Foroulis and M. J. Thubrikar, *Werkstoffe Korrosion*, **26**, 350 (1975).
16. H. Engell and N. Stolika, *Z. Physik. Chem. N.F.*, **20**, 113 (1959).
17. T. P. Hoar and W. R. Jacob, *Nature*, **216**, 1299 (1967).
18. F. D. Bogar and R. T. Foley, *This Journal*, **119**, 462 (1973).
19. A. E. Paladino and W. D. Kingery, *J. Chem. Phys.*, **37**, 457 (1962).
20. T. P. Hoar and U. R. Evans, *This Journal*, **99**, 212 (1952).
21. M. Streicher, *ibid.*, **103**, 375 (1956).
22. H. Leckie and H. Uhlig, *ibid.*, **113**, 1262 (1966).
23. Y. Kotolyrkin, *Corrosion*, **19**, 261t (1963).
24. R. deLevie, in "Advances in Electrochemistry and Electrochemical Engineering," Vol. 6, p. 329, P. Delahay and C. Tobias, Editors, John Wiley & Sons, Inc., New York.
25. M. J. Pryor, *Z. Elektrochem.*, **62**, 782 (1958).
26. Z. A. Foroulis, Presented at the 5th International Congress on Metallic Corrosion, Tokyo, Japan. Proceedings to be published by NACE; Z. A. Foroulis, *Werkstoffe Korrosion*, Submitted.
27. J. A. Yopps and D. W. Fuerstenau, *J. Coll. Sci.*, **19**, 61 (1964).
28. H. J. Modi and D. W. Fuerstenau, *J. Phys. Chem.*, **61**, 640 (1957).
29. V. C. P. Morphopoulos and H. C. Pareira, *Corrosion Sci.*, **7**, 241 (1967).
30. J. A. Richardson and G. C. Wood, *ibid.*, **10**, 313 (1970).
31. K. F. Lorking and J. E. O. Mayne, *J. Appl. Chem.*, **11**, 170 (1961).
32. E. A. Devuyst and I. H. Warren, in "Oxide-Electrolyte Interfaces," R. S. Alwitt, Editor, p. 112, The Electrochemical Society Softbound Symposium Series, Princeton, N. J. (1973).

Rate of Propagation of Growth Layers on Cubic Crystal Faces in Electrocrystallization of Silver

V. Bostanov, G. Staikov, and D. K. Roe*¹

Central Laboratory of Electrochemical Power Sources, Bulgarian Academy of Sciences, Sofia, Bulgaria

ABSTRACT

The advancement rate of mono- and polyatomic growth steps was measured on perfect, screw dislocation-free cubic faces of silver single crystals during electrocrystallization of silver. For low overvoltages, a linear dependence of the rate on overvoltage was found. It was established that the advancement rate of the steps depends on the surface conditions of the crystal face and is about two times larger on a "fresh" surface than on an "aged" one. It was also found that mono- and polyatomic steps advance with the same rate on a fresh surface. A polyatomic step is considered as a ledge composed of monoatomic steps. The ledge spacing of this composite step was estimated. On the basis of these experimental results as well as on the experimentally determined value of the exchange current of adatoms with metal ions of the electrolyte, it is concluded that the electrolytic deposition of silver in 6M solution of silver nitrate is carried out according to the direct transfer mechanism. The value of the exchange current of the edge atoms at the steps with ions of the electrolyte was determined to be $i_{o,st} = 200 \text{ A}\cdot\text{cm}^{-2}$ for an aged surface and $i_{o,st} = 370 \text{ A}\cdot\text{cm}^{-2}$ for a fresh surface.

The kinetics of growth of an equilibrium-form, close packed crystal face depends on the rate of advancement of the growth steps on its surface. The theory of electrocrystallization assumes two basic mechanisms of step growth offered by Volmer (1) and Brandes (2): the direct transfer mechanism and the surface diffusion mechanism. According to the first, the ionic transfer onto the crystal surface through the double layer occurs directly at the kink sites of the steps. The ions are discharged and incorporated simultaneously into the crystal lattice. According to the second mechanism the transfer is carried out on completely built areas of the surface. Here the ions discharge and remain adsorbed (adatoms) for a certain period of time.

By surface diffusion the adatoms can reach the kink sites and be incorporated into the crystal lattice.

The dependence of the current density, i ($\text{A}\cdot\text{cm}^{-2}$), on the overvoltage, η , in the case of surface diffusion was derived for the first time by Lorenz (3) and has the form

$$i = i_{o,ad} [e^{zF\eta/RT} - e^{-(1-\alpha)zF\eta/RT}] \frac{\lambda_o}{x_o} \tanh \frac{x_o}{\lambda_o} \quad [1]$$

In this equation, $i_{o,ad}$ ($\text{A}\cdot\text{cm}^{-2}$) is the exchange current density of the adatoms with the metal ions of the electrolyte; $2x_o$ (cm) is the average distance between the monoatomic steps which can also be given by the total step length L_s ($\text{cm}\cdot\text{cm}^{-2}$) per unit area; λ_o (cm), the surface diffusion penetration, is defined by

$$\lambda_o = (zFD_s c_{o,ad} / i_{o,ad})^{1/2} e^{-zF\eta/2RT}$$

where D_s ($\text{cm}^2\cdot\text{sec}^{-1}$) is the surface diffusion coefficient.

* Electrochemical Society Active Member.

¹ Present address: Chemistry Department, Portland State University, Portland, Oregon 97207.

Key words: crystal growth, electrocrystallization, silver single crystal, growth layer propagation.

cient and c_{ad}^0 ($\text{mol}\cdot\text{cm}^{-2}$) the equilibrium adatom concentration.

In the case of direct transfer the dependence of the current density on overvoltage is described by a Volmer-type equation

$$i = i_{\text{o, st}} \delta L_s [e^{\alpha z F \eta / RT} - e^{-(1-\alpha) z F \eta / RT}] \quad [2]$$

here $i_{\text{o, st}}$ ($\text{A}\cdot\text{cm}^{-2}$) is the exchange current density of the edge atoms of the monoatomic step with the metal ions of the electrolyte and δ (cm) is the width of an atomic row in the crystal lattice parallel to the step.

The normal velocity of step growth or the advancement rate of the step v ($\text{cm}\cdot\text{sec}^{-1}$) and the current density are connected in the relation

$$v = i v_M / z F h L_s \quad [3]$$

where v_M ($\text{cm}^3\cdot\text{mol}^{-1}$) is the molar volume and h (cm) is the height of a monoatomic step. For low overvoltages, under the assumption that the surface diffusion penetration is small as compared to the average step half-distance, $\lambda_0/x_0 \ll 1$, from Eq. [1] and [2] one obtains a linear dependence of the current density on step length and overvoltage

$$i = \kappa L_s \eta \quad [4]$$

where the constant κ ($\text{ohm}^{-1}\cdot\text{cm}^{-1}$) is given by

$$\kappa = i_{\text{o, ad}} 2 \lambda_0 z F / RT \quad [5]$$

for surface diffusion, and

$$\kappa = i_{\text{o, st}} \delta z F / RT \quad [6]$$

for direct transfer. Under these conditions the advancement rate of the steps is linearly dependent on overvoltage

$$v = k_v \eta \quad [7]$$

where the advancement rate constant k_v ($\text{cm}\cdot\text{sec}^{-1}\cdot\text{V}^{-1}$) is given by

$$k_v = \kappa v_M / z F h \quad [8]$$

Experimental

The advancement rate of growth steps in electrocrystallization of silver was studied on perfect, dislocation-free, (100) crystal faces. These were obtained by the capillary method described in detail earlier (4, 5). The essence of the method is the electrolytic growth of a silver single crystal in a capillary along a definite crystallographic axis. If this axis is $\langle 100 \rangle$, a (100) face would appear as a frontal face of the single-crystal filament. Under specified conditions of electrolysis, the face may fill up the whole cross section of the capillary. These conditions require high purity of the electrolyte, high concentration of silver ions, and, above all, modulation of the direct current of growth with an alternating 50 Hz current. At slow growth conditions of the single-crystal filament ($20 \text{ mA}\cdot\text{cm}^{-2}$) and a suitably chosen amplitude of the alternating current, the number of screw dislocations intersecting the front face gradually decreases and a perfect face can be obtained.

It was experimentally shown that dislocation-free (100) faces grow by two-dimensional nuclei (5), in agreement with the theory of crystal growth. The critical overvoltage for the nucleation process is about 6 mV, and if an overpotential lower than this value is applied, charge flow through the electrolytic cell is not observed. A potentiostatic pulse with suitable amplitude and duration (e.g., 12 mV, 100 μsec) leads to the creation of only one nucleus. If after the pulse the face remains at a potential lower than the critical overvoltage, current flows through the cell, passing through a maximum and subsequently decreasing to zero. This current is connected with the growth of the newly formed monolayer and is proportional to the length of growing monoatomic step, in accordance with Eq. [4]. The value of the constant κ in this equation may be determined from the current-time curves following nu-

cleation overvoltage pulses which produce different supersaturations. The round shape of the face complicates this task. The experiment is considerably simplified if the crystal face has the shape of an elongated rectangle.

Rate of Propagation and Form of Monoatomic Layers

The capillary method was developed using capillaries with round cross section. Crystal faces filling up the entire cross section and free of screw dislocations can also be obtained in capillaries with a rectangular cross section (e.g., $400 \times 100 \mu\text{m}$) (6). At constant rate of growth of a monoatomic layer on a perfect face with rectangular form, a plateau should be expected in the current-time curve, since after a definite time interval a step would be advancing along the face with a constant length. This was experimentally confirmed and Fig. 1 represents three characteristic experimental current-time curves at constant overvoltage.

As shown in Fig. 2, the value of the growth current of a monoatomic step with constant length is linearly dependent on overvoltage, according to Eq. [4]. However, to determine exactly the constant κ in Eq. [4], one should know the step length. Besides on the capillary width, the step length depends also on the form of the monoatomic layer, or whether the layer is round or polygonized. If polygonized, it would also depend on the orientation of the layer, i.e., on the orientation of the seed crystal with respect to the capillary cross section. In Fig. 2 the straight line a refers to the case when the long axis of the rectangular section of the capillary is parallel to the crystallographic direction $\langle 100 \rangle$, and the straight line b, when this axis is parallel to the direction $\langle 110 \rangle$. The slopes of both straight lines differ by $\sqrt{2}$. Therefore it can be concluded that

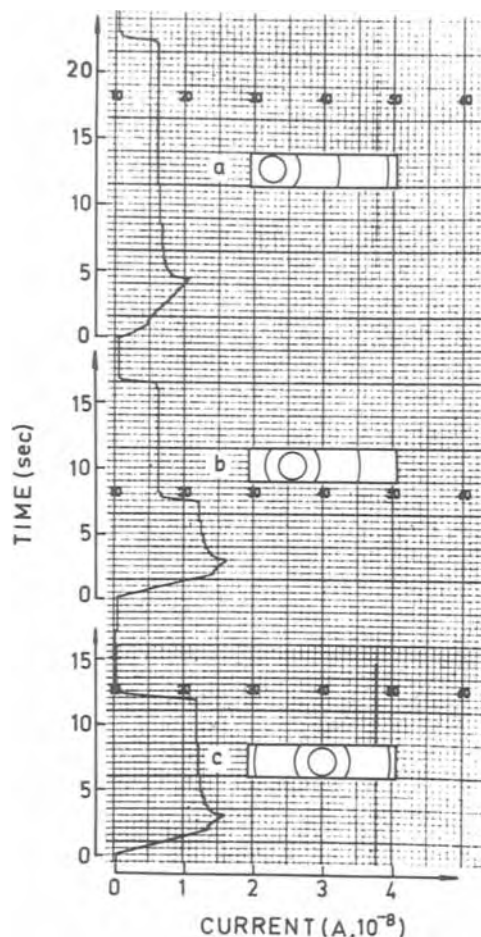


Fig. 1. Current-time curves at 3 mV overvoltage following a nucleation overvoltage pulse on a perfect (100) face with rectangular form ($0.1 \times 0.4 \text{ mm}$). The probable site of nucleation is schematically indicated in each case.

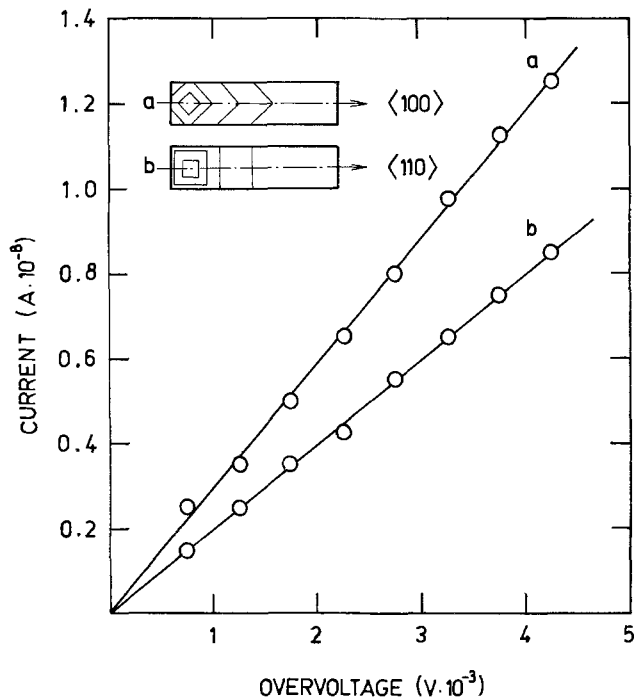


Fig. 2. The stationary value of the current (Fig. 1) as dependent on overvoltage, for two orientations of the seed crystal in respect to the rectangular cross section of the capillary: straight line a, the longitudinal axis of the cross section coincides with the direction 100; straight line b, with the direction 110.

the monoatomic layers are polygonized and have a square form and that the growth steps are parallel to the crystallographic direction $\langle 110 \rangle$. So the step length is known and the constant κ in Eq. [4] can be exactly calculated. At 45°C and in 6M solution of AgNO_3 the value obtained is $\kappa = 2 \cdot 10^{-4} \text{ ohm}^{-1} \cdot \text{cm}^{-1}$. The advancement rate constant k_v can be obtained from this constant, according to Eq. [8] and is $k_v = 1.0 \text{ cm} \cdot \text{sec}^{-1} \cdot \text{V}^{-1}$.

Rate of Propagation of Polyatomic Layers

On a dislocation-free (100) face the rate of propagation of polyatomic layers was now studied. Polyatomic layers sometimes originate after an overvoltage pulse having higher amplitude and longer duration (e.g., 50-60 mV, several milliseconds).

At higher overvoltages a dislocation-free face grows according to the multinuclear, multilayer growth mechanism (7, 8). During the pulse action several tens of monoatomic layers are deposited on its surface. After the pulse the face surface has a complex relief, comprising several lattice planes. Under the action of a low overvoltage applied after the pulse, the face begins to flatten and the current drops slowly to zero.

The crystal face is generally expected to be homogeneous in respect to the process of two-dimensional nucleation. The surface becomes then randomly rough during and immediately after the pulse. In some cases, however, on a specific, more "active" center the nucleation proceeds with a higher rate resulting in a more pronounced hillock at this site. During the subsequent flattening this hillock gives the origin of a polyatomic front of growth. By means of the interference contrast device after Nomarski, this front, if sufficiently thick, is already visible under the microscope as a strip advancing on the face. The current accompanying the process during the flattening stabilizes to a stationary value proportional to the front length and thickness, Fig. 3. This growth front can be considered either as a single polyatomic ledge or as a composite step consisting of several monoatomic layers.

The advancement rate of such steps was measured as described below. After the stabilization of the current at the stationary value two flash light pictures

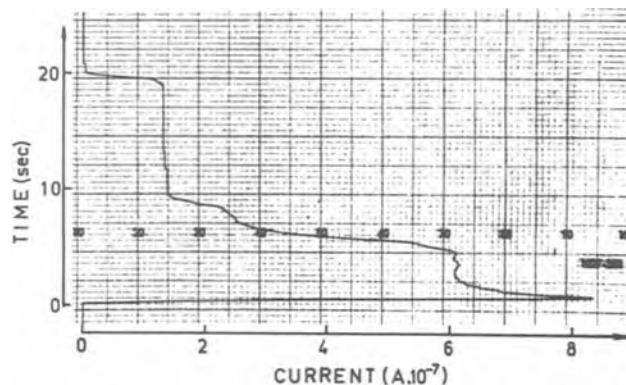


Fig. 3. Current-time curve following an overvoltage pulse with amplitude 60 mV and duration 5 msec on a perfect (100) face with rectangular form. The stationary value of the current results from the growth of a visible in the microscope polyatomic step retaining a constant length.

are taken in sequence on the same frame. With the first flash an electronic chronometer is triggered which is stopped by the second one. A picture made in this way is shown in Fig. 4. Two positions of the growth step are clearly fixed by the two consecutive flash exposures. The distance traveled by the step for the time interval between the flash exposures can be measured quite accurately. The time interval is indicated by the chronometer so that the rate of advancement of the step is directly determined. From the rate of advancement and the stationary value of the current (Fig. 3), the height of the polyatomic step is evaluated.

Using the interference contrast after Nomarski, steps higher than 10Å (equivalent to 5 monoatomic layers) can be visually detected, while steps above 30Å can be photographed, as shown in Fig. 4. It was also found that independently of their thickness, steps up to 80Å advance with the same velocity. A measurable decrease in the velocity is observed only for steps higher than 100Å. Figure 5 shows the dependence of the advancement rate of steps 30-80Å high on overvoltage. From the slope of the straight line the value of the constant k_v in Eq. [7], $k_v = 1.9 \text{ cm} \cdot \text{sec}^{-1} \cdot \text{V}^{-1}$ is obtained. The value of k_v is roughly two times higher than the value obtained for monoatomic steps. This unexpected difference can be explained by the assumption that the polyatomic steps under the conditions of their creation advance on a "refreshed" surface. Immediately before their origination during the high amplitude pulse, several tens of monoatomic layers have been deposited on the face obviously refreshing the surface. This assumption is confirmed by the fact that if the surface prior to the creation of a mono-

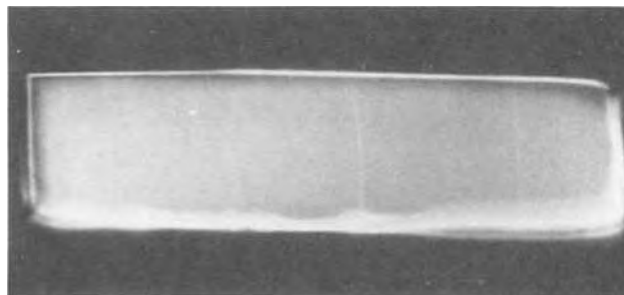


Fig. 4. Two overlapping flashlight photographs of a perfect (100) crystal face in a glass capillary with rectangular form of the cross section (0.1 × 0.4 mm). The two bright strips represent the polyatomic step with height 30Å advancing along the face in the moment of the first and the second photographs.

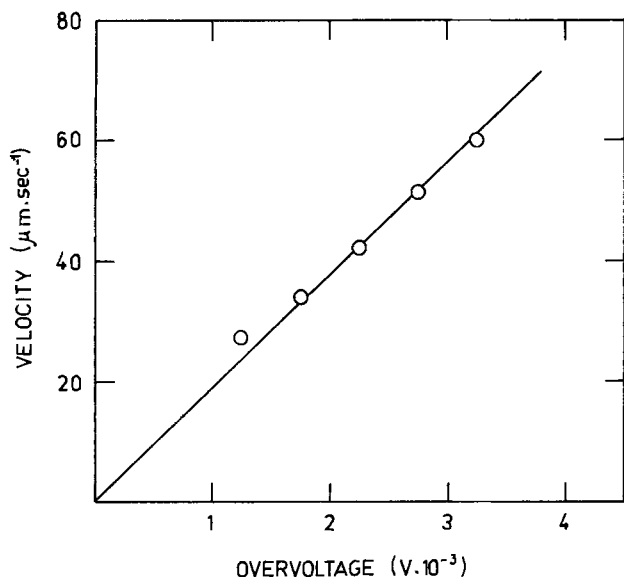


Fig. 5. The dependence of the rate of advancement of polyatomic steps up to 80Å high on overvoltage.

atomic layer is refreshed by a high amplitude pulse as described above, one obtains the curve a in Fig. 6, instead of the curve b observed on an aged surface. It is readily seen that the slope of curve a is nearly two times higher than that of curve b. From the slope of curve a one obtains $\kappa = 3.7 \cdot 10^{-4} \text{ ohm}^{-1} \cdot \text{cm}^{-1}$, and for $k_v 1.9 \text{ cm} \cdot \text{sec}^{-1} \cdot \text{V}^{-1}$ which is equal to the value found for a polyatomic step.

It is interesting to note that by the propagation of monoatomic layers the surface is not refreshed. Such a refreshing occurs only when more than several tens of layers are deposited simultaneously.

Ledge Spacing in a Composite Polyatomic Step

As already mentioned, a growing polyatomic step can be considered as a "train" of parallel monoatomic steps. By means of the interference contrast device the polyatomic step is seen under the microscope as a darker or brighter thin strip. The width of the strip on this

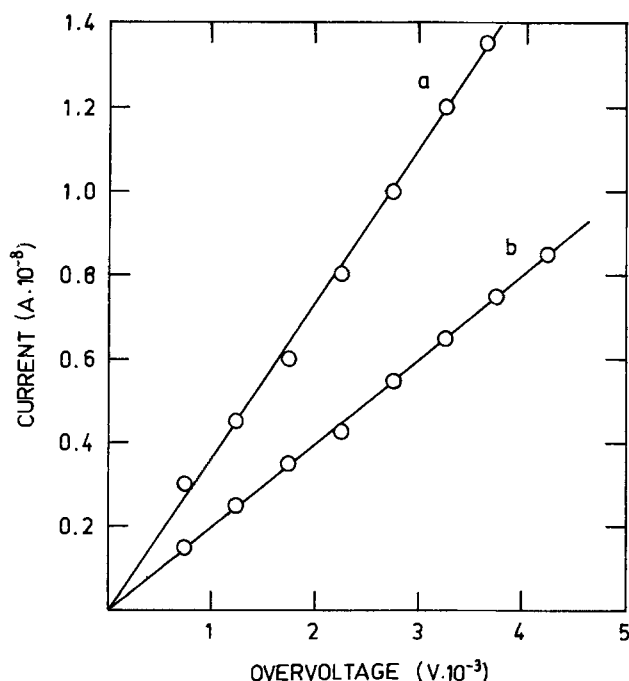


Fig. 6. Current (stationary value)-overvoltage curve at the growth of a monoatomic layer. The straight line a refers to a fresh surface; and b, to an aged surface.

interferential picture is not related in a simple manner to the width of the step train.

The advancement rate of the polyatomic step at constant overvoltage is known. The step height is determined by the rate and the growth current. Then the average ledge spacing can be determined from the time required for disappearance of the ledge into the capillary wall which is strictly parallel to it. This time can be measured from the current drop to zero accompanying the ledge disappearance. As has been demonstrated, the ledges are parallel to the crystallographic direction $\langle 110 \rangle$ and advance toward the narrow capillary wall. To orientate the seed crystal so that the direction $\langle 110 \rangle$ is strictly parallel to these walls is a very difficult task. This difficulty can be overcome if, instead of in the capillary wall, the ledge is made to disappear in a crystal edge parallel to it. This can be easily achieved if the crystal face filling up the capillary cross section is grown for a specified time by a suitably modulated direct current at which its dimensions begin to decrease. Between the crystal face and the narrow capillary walls crystal edges and dislocation-free (111) faces of small dimensions appear. Figure 7 shows an experimental curve of the current drop recorded at the disappearing of a polyatomic step in a crystal edge. From the curve the average ledge spacing $2x_0$, at the step train is determined to 160Å.

It should be noted that the above estimation indicates the maximum possible value of the average ledge spacing. This distance can in fact be smaller because any deviation of the ledge from a straight line parallel to the edge increases the time of disappearance of the polyatomic steps. For example the curve in Fig. 7 can be obtained from a very steep polyatomic step curved in an arc with a radius of 2.5 mm, *i.e.*, with side wings advancing only 0.5 μm after the central part of the step. It is obvious that it is impossible to determine a curvature of this magnitude and hence it is excluded in the observation conditions of our case. In fact in many cases longer periods of ledge disappearance have been observed which are obviously connected with an already visible curvature or any other irregularity of the ledge.

Mechanism of Electrolytic Deposition of Silver

As shown above, on a "fresh" surface the monoatomic and all polyatomic steps with a height up to 80Å advance with one and the same rate. The average ledge spacing in some of the polyatomic steps does not exceed 160Å. From these two relevant experimental findings a conclusion elucidating the mechanism of electrolytic deposition of silver can be drawn.

The rate of advancement of the growth steps does not depend at all on the step distance if the metal ions are directly incorporated in kink sites along the steps. If the crystal lattice is built up by surface diffu-

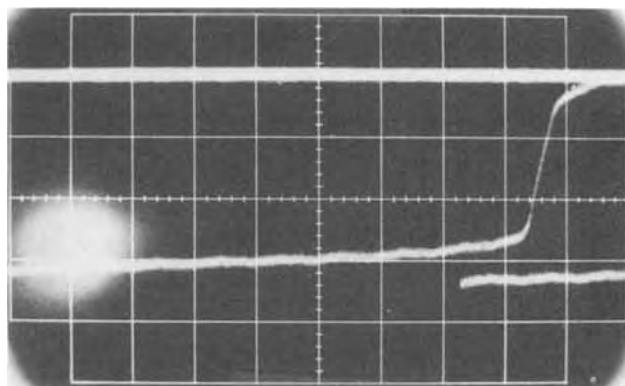


Fig. 7. Curve of current drop to zero, accompanying the disappearance of the polyatomic step in a crystal edge parallel to it. Height of the step, 61Å (30 monoatomic layers); rate of advancement, $48 \cdot 10^{-4} \text{ cm} \cdot \text{sec}^{-1}$ (overvoltage 2.5 mV). Vertical sensitivity, $1 \cdot 10^{-7} \text{ A} \cdot \text{cm}^{-1}$, time base, $20 \text{ msec} \cdot \text{cm}^{-1}$.

sion of adatoms, the advancement rate of the steps does not depend on the distance between them only if the depth of the surface diffusion penetration is small compared to the average half-distance between the steps, $\lambda_0/x_0 \ll 1$. Obviously, if one assumes the surface diffusion mechanism of deposition of silver, λ_0 must be $\leq 80\text{\AA}$.

The constant κ of Eq. [4] in the case of surface diffusion mechanism is given by Eq. [5] and contains $i_{0,ad}$ and λ_0 . Under experimental conditions similar to ours, the exchange current $i_{0,ad}$ for crystal (100) face has been determined by high frequency impedance measurements on a perfect completely built up aged face and was found to be $i_{0,ad} = 0.06 \text{ A}\cdot\text{cm}^{-2}$ (9). Preliminary impedance measurements carried out now on a fresh crystal face lead to the conclusion that the value of the exchange current of the adatoms is smaller than the one for aged surface. The value of λ_0 is unknown but it is not larger than 80\AA . If the constant κ is now evaluated with these values of $i_{0,ad}$ and λ_0 , one obtains $\kappa = 3.5 \cdot 10^{-6} \text{ ohm}^{-1}\cdot\text{cm}^{-1}$ which is two orders of magnitude smaller than the one experimentally observed here. It follows therefore that the electrolytic deposition of silver occurs almost exclusively by direct incorporation. The contribution of the surface diffusion would not exceed 1%. From the experimentally found values of κ , according to Eq. [6], for the exchange current of the step edge atoms with metal ions in the electrolyte two values were found: $i_{0,st} = 200 \text{ A}\cdot\text{cm}^{-2}$ for an aged surface and $i_{0,st} = 370 \text{ A}\cdot\text{cm}^{-2}$ for a fresh one.

This conclusion pertaining to the mechanism of electrolytic deposition of silver was made by Vitanov, Popov, and Budevski (10) on the basis of: (i) the results of impedance measurements at high frequency on a (100) face, atomically smooth (9) and with a surface relief defined by spiral growth (10); (ii) the results of the experimental check of the theory of spiral growth by the electrocrystallization of silver of a (100) face (11). The value of the exchange current determined by these authors is $i_{0,st} = 170 \text{ A}\cdot\text{cm}^{-2}$ and refers

to an aged surface. This value is very close to the one $i_{0,st} = 200 \text{ A}\cdot\text{cm}^{-2}$, given here for the same surface.

Acknowledgment

The authors wish to thank Prof. Dr. E. Budevski for the helpful discussions throughout the course of this work. The participation of D. K. Roe was through the scientific exchange program between the Bulgarian Academy of Sciences and the National Academy of Sciences; this cooperative support is gratefully acknowledged.

Manuscript submitted April 14, 1975; revised manuscript received June 6, 1975.

Any discussion of this paper will appear in a Discussion Section to be published in the June 1976 JOURNAL. All discussions for the June 1976 Discussion Section should be submitted by Feb. 1, 1976.

REFERENCES

1. M. Volmer, "Das elektrolytische Kristallwachstum," Verlag Herman, Paris (1934).
2. H. Brandes, *E. Physik. Chem.*, **142**, 97 (1929).
3. W. Lorenz, *Z. Naturforsch.*, **9A**, 716 (1954).
4. V. Bostanov, A. Kotzeva, and E. Budevski, *Bull. Inst. Chim. Phys., Acad. Bulgare Sci.*, **6**, 33 (1967).
5. E. Budevski, V. Bostanov, T. Vitanov, Z. Stoynov, A. Kotzeva, and R. Kaishev, *Phys. Status Solidi*, **13**, 577 (1966); *Electrochim. Acta*, **11**, 1697 (1966).
6. V. Bostanov, R. Roussinova, and E. Budevski, *Chem.-Ing.-Techn.*, **45**, 179 (1973).
7. R. Armstrong and J. Harrison, *This Journal*, **116**, 328 (1969).
8. V. Bostanov, R. Roussinova, and E. Budevski, *ibid.*, **119**, 1347 (1972).
9. T. Vitanov, E. Sevastianov, V. Bostanov, and E. Budevski, *Elektrokhimiya*, **5**, 451 (1969); T. Vitanov, E. Sevastianov, Zdr. Stoinov, and E. Budevski, *ibid.*, **5**, 238 (1969).
10. T. Vitanov, A. Popov, and E. Budevski, *This Journal*, **121**, 207 (1974).
11. V. Bostanov, R. Roussinova, and E. Budevski, *Comm. Dept. Chem., Bulgare. Acad. Sci.*, **2**, 885 (1969).

Compensation of Ohmic Potential Interactions Occurring at Ring-Disk Electrodes

Mani Shabrang* and Stanley Bruckenstein**

Chemistry Department, State University of New York at Buffalo, Buffalo, New York 14214

ABSTRACT

Pseudocollection and inverse pseudocollection effects caused by potential drops at ring-disk electrodes can be eliminated by positive feedback. A potential proportional to a fraction of the disk electrode current is fed back to the ring electrode potentiostat, eliminating changes in ring potential and current that arise due to the variations of the disk electrode potential and current. Analogously, feedback of a potential proportional to a fraction of the ring current to the disk electrode potentiostat prevents variations of disk electrode potential and current that are due to the variations in ring electrode potential and current. The two positive feedback networks function independently and no *a priori* knowledge of the uncompensated resistance is required.

Many investigators have considered the problems of positive feedback compensation of the ohmic potential drop that exists in an electrochemical cell between the working and the reference electrode (1-10). Roe (11) and Nicholson (12) have summarized recent work on this subject while Smith (13) has reviewed work prior

* Electrochemical Society Student Member.

** Electrochemical Society Active Member.

Key words: inverse pseudocollection effect, pseudocollection effect, uncompensated resistance, positive feedback.

to 1972. In all these studies the ohmic potential drop occurred between the reference electrode and a single working electrode. Two working electrodes exist when a rotating ring-disk electrode (RRDE) is used, and some unique ohmic potential compensation problems can arise in an electrochemical cell having a RRDE.

Recently an equivalent circuit for the uncompensated primary resistances existing at a RRDE was proposed by us (14). The validity of this circuit was veri-

fied, and the circuit is shown within the circled region of Fig. 1. Point T represents the tip of the Luggin capillary leading to the reference electrode. The tip's location in the electrochemical cell determines its effective position on three of the resistors making up the equivalent circuit. In this paper we are concerned with treating the case in which the tip lies on the R_C , the resistance that is common to the current path between the Luggin capillary tip and the two working electrodes, the ring and the disk. In Fig. 1, R_{aux} represents the resistor between the Luggin capillary tip and the auxiliary electrode. The total uncompensated resistance between the capillary tip and the disk electrode is $R_C + R_D$, and is $R_C + R_R$ between the capillary tip and the ring electrode. E_D , E_R , and E_{Ref} represent the half-cell potentials of the disk, ring electrode, and reference electrode, respectively, and include all the impedances characteristic of the electrode processes that are occurring. I_D and I_R are the corresponding disk and ring electrode currents, and no current flows through the reference electrode.

Full compensation for the total uncompensated ohmic potential drops between the Luggin capillary and the ring and disk electrodes is not considered in this paper. Full compensation is an elusive concept when dealing with working electrodes that have nonuniform current distributions such as those that can exist at disk, ring, and other electrode geometries. Under such circumstances positive feedback circuitry cannot compensate for the nonuniform potential distribution that is inherent to the electrolysis cell.

The ohmic potential drop dealt with in this paper is associated with the flow of current through resistor R_C , the resistor common to the ring and disk electrodes. The pseudocollection effect (14) is the term we have

used to represent the current phenomena occurring at the ring electrode produced as a result of varying uncompensated potential drops associated with a changing disk electrode current. Conversely, the inverse pseudocollection effect corresponds to the current phenomena produced at the disk electrode as a result of varying uncompensated ohmic potential drops produced by varying ring electrode currents.

Appropriate positive feedback compensation has the effect of repositioning the Luggin capillary at point O of Fig. 1 and thus eliminates the pseudocollection effect and the inverse pseudocollection effect. This kind of feedback compensation involves only partial compensation of the total ohmic potential drop and does not give rise to any of the conceptual difficulties associated with full compensation in the presence of a nonuniform current density, nor are there experimental problems of potentiostat stability which arise when full compensation of an ohmic potential drop at an electrode is attempted.

Experimental

Reagents.—Solutions of 0.01M sulfuric acid were prepared from triply distilled water and a Baker reagent grade sulfuric acid.

Cell.—The glass cell and the auxiliary equipment are described elsewhere (15, 16).

Electrodes.—The four electrodes used in the experiments were: electrode I, a platinum-ring platinum-disk with a diameter, d_1 , of 7.6 mm and ring-inner diameter, d_2 , of 8.0 mm and ring-outer diameter, d_3 , of 8.4 mm; electrode II, a platinum-ring gold-disk with $d_1 = 7.6$ mm, $d_2 = 8.0$ mm, and $d_3 = 11.0$ mm; electrode III, a gold-ring platinum-disk with $d_1 = 7.6$ mm,

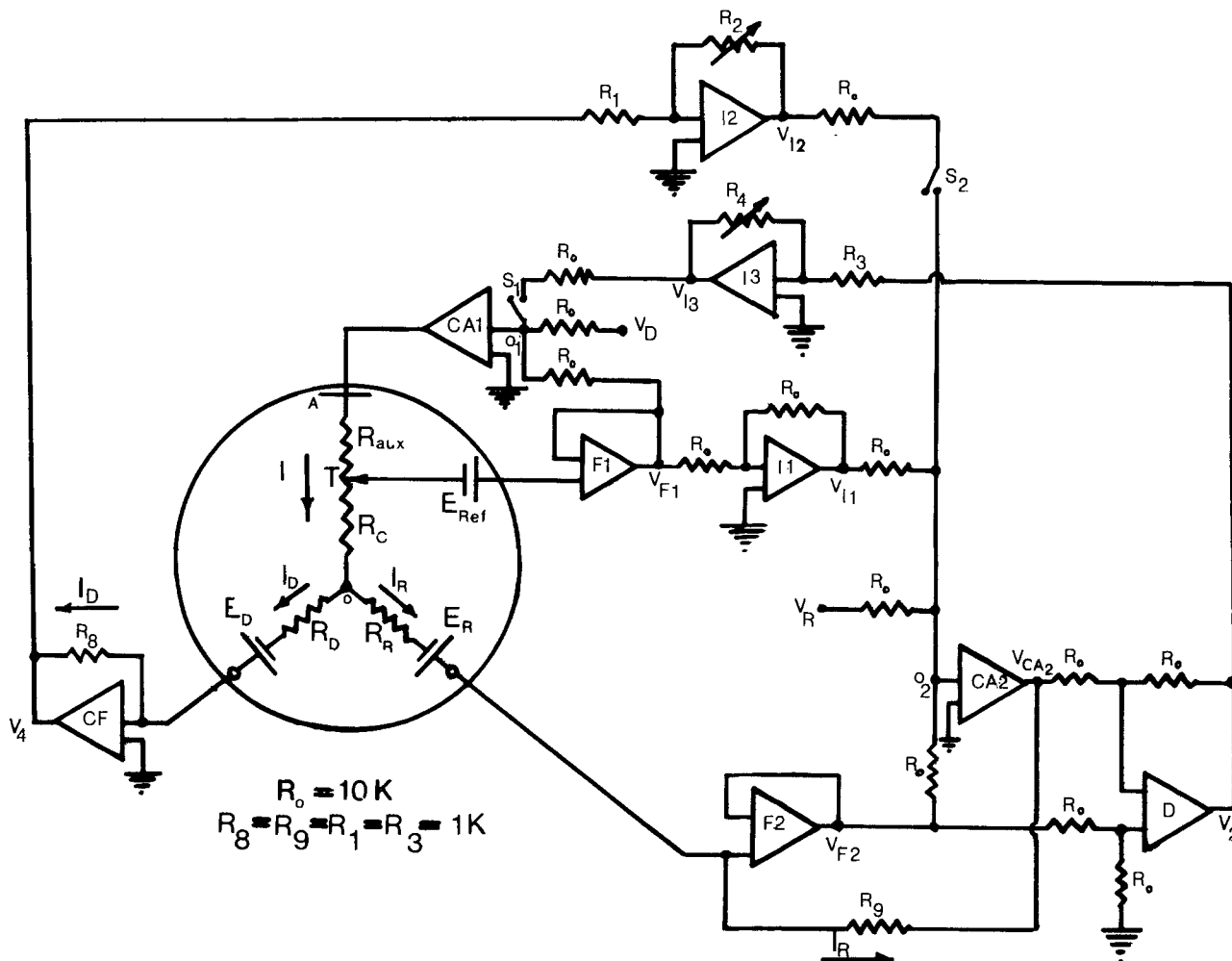


Fig. 1. Conventional four-electrode potentiostat with the additional positive feedback network. The equivalent circuit for the uncompensated ohmic resistance at ring-disk electrodes is enclosed by the circle.

$d_2 = 8.0$ mm, and $d_3 = 11.0$ mm; and electrode IV, a gold-ring gold-disk with $d_1 = 7.6$ mm, $d_2 = 8.0$ mm, and $d_3 = 8.4$ mm. Teflon was used as the insulating material for all electrodes.

These electrodes were electrochemically pretreated before each experiment, as discussed in Ref. (17), and were all polished to a final mirror finish using 0.05 μ alumina on Buehler microcloth.

Instrumentation.—A conventional four-electrode analog instrument for independent potentiostatic control of the ring and the disk was used (18-20), and the I - E curves obtained were recorded on an EA1, X-Y-Y' 1131 Variplotter, Model 141 A. Analog Devices operational amplifiers were used in the positive feedback networks.

The operational amplifier instrument for independent galvanostatic control of the ring and the disk used for the common resistance measurement is described elsewhere (14).

A Heathkit Model IG-18 function generator was used to supply the a-c signal.

All potentials were measured and reported *vs.* the saturated calomel electrode. Experiments were run at 25°C. The Luggin capillary was positioned, by eye, to lie on the axis of rotation, unless otherwise stated.

Theoretical

Four electrode potentiostat with finite cell resistance.—Consider Fig. 1, which includes the electronic schematic and the ring-disk electrode equivalent circuit. We intend to obtain the expression for the disk electrode potential *vs.* the reference electrode, $E_D - E_{Ref}$, and the ring electrode potential *vs.* the reference electrode $E_R - E_{Ref}$, in terms of various currents and cell resistances, and the voltages applied to control amplifiers CA1 and CA2. It is instructive to consider the original four electrode potentiostatic circuit first, *i.e.*, S-1 and S-2 open, before undertaking the analysis of circuit with positive feedback, since this analysis was not given earlier (18).

No-ohmic drop compensation.—Disk electrode.—If switches S-1 and S-2 are open, the circuit corresponds to a slightly modified version of the original by Johnson, Napp, and Bruckenstein (18). The various relations of interest in obtaining the disk potential control function are:

summing point restraint at CA1

$$V_{F1} + V_D = 0 \quad [1]$$

and the output of the voltage follower, F1

$$V_{F1} = E_D - E_{Ref} + I_D R_C + I_R R_C + I_D R_D \quad [2]$$

Defining

$$E_D^* \equiv E_{Ref} - E_D \quad [3]$$

we obtain

$$E_D^* = V_D + I_D (R_C + R_D) + I_R R_C \quad [4]$$

and we see that the disk potential contains an uncompensated ohmic resistance, R_C , through which the ring electrode current passes. Changes in the ring current will therefore produce changes in the disk potential even though V_D is held constant. The partial derivative

$$\left(\frac{\partial E_D^*}{\partial I_R} \right)_{I_D} = R_C \quad [6]$$

is a convenient measure of this resistance, which we term the inverse pseudocollection resistance.

Ring electrode.—The various relations of interest in obtaining the ring electrode potential control functions are the summing point restraint at CA2

$$V_{F2} + V_R + V_{I1} = 0 \quad [7]$$

the output of voltage follower 2

$$V_{F2} = E_D - E_R - I_R R_R + I_D R_D \quad [8]$$

the output of I1

$$V_{I1} = -V_{F1} \quad [9]$$

and the output of F1 given by Eq. [2] above. Defining

$$E_R^* \equiv E_{Ref} - E_R \quad [10]$$

and solving for E_R^* using Eq. [2] and [7]-[9], yields

$$E_R^* = -V_R + I_R (R_C + R_R) + I_D R_C \quad [11]$$

Thus, we see that there is an uncompensated resistance through which the disk electrode current can affect the ring potential. This resistance R_C is given by

$$\left(\frac{\partial E_R^*}{\partial I_D} \right)_{I_R} = R_C \quad [12]$$

and is termed the pseudocollection resistance.

The pseudo and inverse pseudocollection resistances are identical, hence, the magnitude of the pseudo and inverse pseudocollection effects for a given value of R_C depend on slope of the current-potential curves at the ring and disk electrodes and the remaining uncompensated potential drops at these two indicator electrodes. For example, if the ring electrode is set on the rising portion of a current-potential curve, variations of the disk current produce changes in the ring electrode potential that can be accompanied by large relative changes in the faradaic current.

In addition, the double layer capacity at the ring and disk electrodes can play a significant, even major, role in the case where there are time-varying currents, *e.g.*, the sinusoidal variation of current through a rotating disk electrode (Albery papers) will produce a sinusoidal variation in the ring electrode potential and thus a double layer charging current. The treatment presented above was a d-c analysis, and for simplicity was not presented in a-c terms, although this extension is quite straightforward. The d-c analysis is also used below to discuss the positive feedback circuitry.

Compensation for R_C .—Disk electrode.—Assume switch S-1 is closed. Then Eq. [1] must be replaced by

$$V_{F1} + V_D + V_{I3} = 0 \quad [13]$$

where

$$V_{I3} = -V_2 \frac{R_4}{R_3} \quad [14]$$

and

$$V_2 = I_R R_9 \quad [15]$$

Using Eq. [13]-[15] and Eq. [8] and [13] yields

$$E_D^* = V_D + I_D (R_C + R_D) + I_R (R_C - R_4 R_9 / R_3) \quad [16]$$

for the relationship describing the disk potentiostat behavior. Hence, when

$$\frac{R_4 R_9}{R_3} = R_C \quad [17]$$

the inverse pseudocollection effect vanishes. In practice, R_4 is increased from zero, and the magnitude of the effect is seen to decrease to zero and to change sign as $R_4 R_9 / R_3$ becomes greater than R_C .

Ring electrode.—Assume switch S-2 is closed at CA2, the summing point condition leads to

$$V_{F2} + V_R + V_{I1} + V_{I2} = 0 \quad [18]$$

instead of Eq. [7]. Also

$$V_{I2} = -\frac{R_2}{R_1} V_4 \quad [19]$$

and

$$V_4 = -I_D R_8 \quad [20]$$

Thus, using Eq. [18]-[20] along with Eq. [8]-[10] yields

$$E_R^* = -V_R + I_R (R_C + R_R) + I_D \left(R_C - \frac{R_2 R_8}{R_1} \right) \quad [21]$$

Hence, compensation from the pseudocollection effects occurs when

$$\frac{R_2}{R_1} R_3 = R_C \quad [22]$$

Again, experimentally, partial or overcorrection (with change in sign) for the pseudocollection phenomena is observed by continuously varying R_2 from zero to larger values.

In both of the derivations for compensation of R_C , note that the position of S-2, when S-1 was closed, or S-1, when S-2 was closed, is irrelevant. The position of the other switch does not affect the statement of Eq. [2], which is common to both derivations even though the values of E_D , I_D , and I_R may be affected. Any change in these quantities is accounted for by the other relationships involved in the derivations. Therefore, one may elect to compensate for either the pseudo or inverse pseudocollection effect, or both, as the experimental needs dictate.

Discussion

Pseudocollection-faradaic processes.—As was shown earlier (14, 21-24) the current of a ring electrode which is potentiostated at "constant" potential can be affected by the currents that pass through the disk electrode. Figure 2 illustrates the pseudocollection phenomena strikingly. The platinum ring electrode has been potentiostated on the rising portion of the hydrogen evolution current (at -0.400V in $0.01\text{M H}_2\text{SO}_4$). As the potential of the gold disk electrode is scanned at $\pm 130\text{ mV/sec}$, the changing disk electrode currents produce a change in the ring electrode potential. Cathodic disk electrode currents produce more anodic ring electrode currents, and vice versa; as a result of decreasing or increasing the hydrogen evolution current. This result is consistent with the idea of a common uncompensated ohmic resistance, represented by R_C in Fig. 1. This result also indicates the difficulty in detecting an intermediate produced during nonsteady-state disk current conditions if the required ring electrode potential lies on the rising portion of a voltammetric wave, e.g., either the solvent or supporting electrolyte decomposition.

One approach to eliminating the pseudocollection effect was suggested earlier by us (14). The position of the Luggin capillary in the cell determined the value

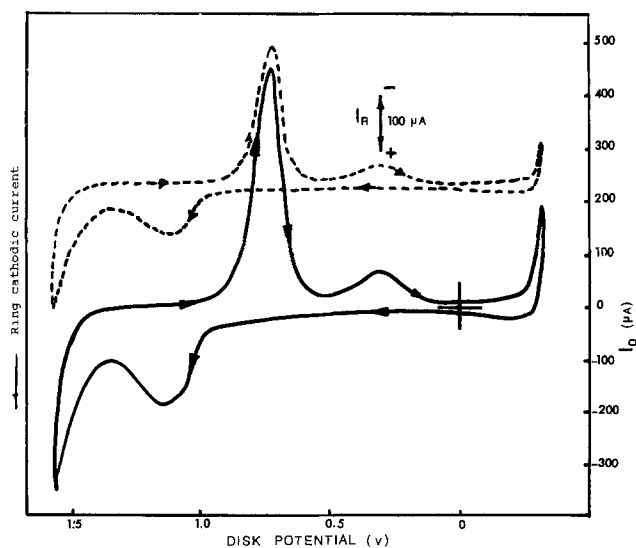


Fig. 2. Pseudocollection effect. $0.01\text{M H}_2\text{SO}_4$ using electrode No. 2. Solid curve and dashed curve represent disk and ring voltammograms, respectively. The gold ring electrode is potentiostated at -0.400V , where $2\text{H}^+ + 2\text{e}$ occurs. Ring current offset arbitrarily from zero. Scan rate = 130 mV/sec ; rotation speed = 2500 rpm . There is a trace of platinum left on the gold disk after polishing, and it is visible in the I - E curve at $\sim 0.4\text{V}$.

of R_C , and thus by proper positioning (trial and error) the Luggin tip can be placed at point O of Fig. 1 (i.e., $R_C = 0$). In fact if the capillary is brought extremely close to the electrode, the pseudocollection response reverses since the capillary is in effect located on R_D . The results of such an experiment in $0.01\text{M H}_2\text{SO}_4$ is shown in Fig. 3. As the Luggin capillary is moved down the axis of rotation toward the disk electrode, the pseudocollection effect becomes smaller (curves b-d), vanishes (at curve e), and reappears with a reversed sign (curves f, g). This result is in accordance with the physical representation of the capillary tip, T in Fig. 1, moving toward point O, through point T and then down R_D toward E_D . Curve e, corresponding to complete compensation ($R_C = 0$), is produced when the capillary is very close to the electrode ($\leq 1\text{ mm}$) and it requires some patience to locate this point exactly. There are a number of positions of the Luggin which give very little evidence of the pseudocollection effect, but there appears to be only one position that compensates for both the pseudo and inverse pseudocollection effect, which in our equivalent circuit corresponds to locating the capillary precisely at point O.

Figures 4 and 5 demonstrate the behavior of the compensation circuitry in Fig. 1. The faradaic ring electrode reaction in both cases is the evolution of hydrogen at the platinum ring electrode in a supporting electrolyte of $0.01\text{M H}_2\text{SO}_4$. Figure 4 illustrates the case of no compensation (curve b) and over compensation (curve c) in which case there is a reversal in the appearance of the ring electrode current shape, as predicted by Eq. [22] when $R_2R_3/R_1 > R_3$. Note that severe overcompensation (by a factor of more than two) does not produce any instability in the circuit.

The circuit response in the vicinity of ideal compensation, i.e., $R_2R_7/R_1 = R_C$, is shown in Fig. 5. Curve d shows no pseudocollection effect, while a $\pm 3\%$ change in the value of R_2 produces a visible pseudocollection response.

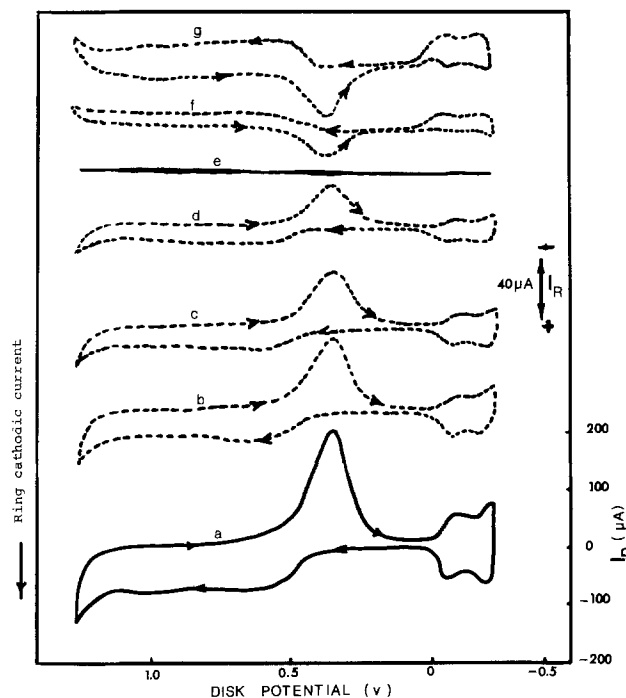


Fig. 3. Pseudocollection compensation by positioning of Luggin capillary. $0.01\text{M H}_2\text{SO}_4$ using electrode No. 1. Solid curve and dashed curves represent disk and ring electrode voltammograms, respectively. Ring is potentiostated at -0.370V . All ring current curves are zero offset to allow for current due to $2\text{H}^+ + 2\text{e} = \text{H}_2$. Scan rate = 120 mV/sec ; rotation speed = 2500 rpm . The approximate distance of the Luggin capillary tip from the plane of the rotating ring-disk electrode is 1 in., 6, 3, 2, and 1 mm, and a fraction of mm for curves b, c, d, e, f, and g, respectively. The tip has been positioned by eye, on the axis of rotation.

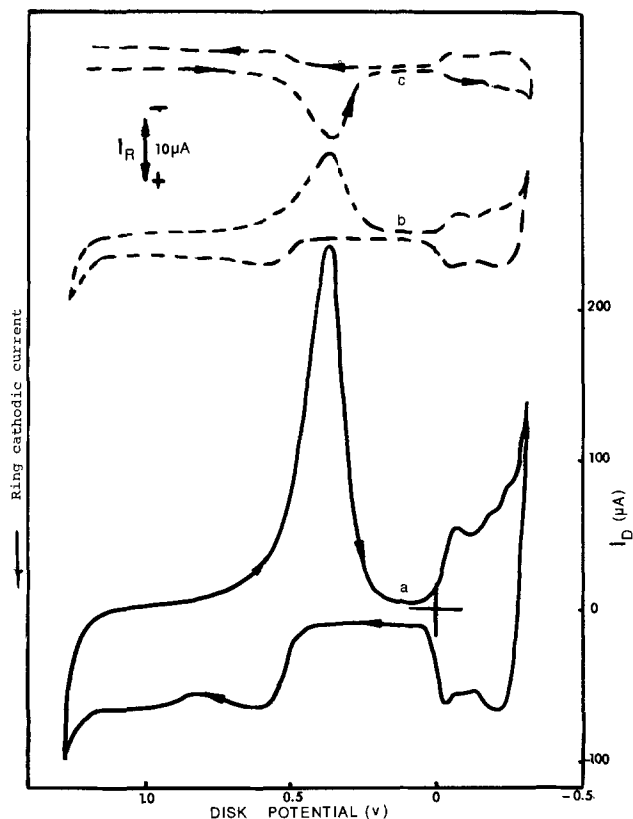


Fig. 4. Pseudocollection compensation by positive feedback. 0.01M H₂SO₄ using electrode No. 1. Solid curve and dashed curves represent disk and ring voltammograms, respectively. Ring is potentiostated at -0.325V. Ring current arbitrarily offset from zero. Scan rate = 130 mV/sec; rotation speed = 2500 rpm. The value of the resistor R₂ is 0 and 90 ohms for curves b and c, respectively.

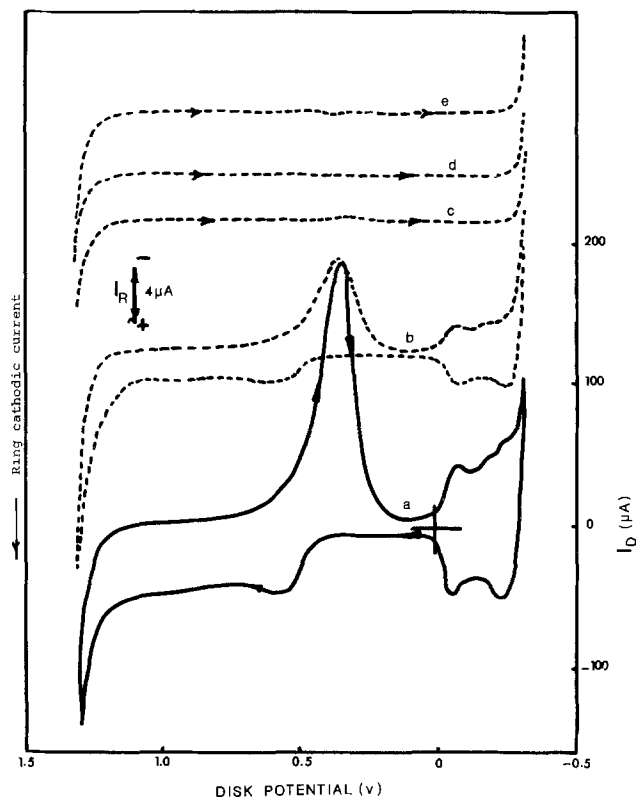


Fig. 5. Pseudocollection compensation by positive feedback. 0.01M H₂SO₄ using electrode No. 1. Solid curve and dashed curves represent disk and ring voltammograms, respectively. Ring is potentiostated at -0.300V. Ring current is arbitrarily offset from zero. Scan rate = 110 mV/sec. Rotation speed = 2500 rpm. R₂ = 0, 32, 33, and 34 for curves b, c, d, and e, respectively. The curves c, d, and e are recorded only when the disk potential is scanned in the cathodic direction.

The pseudocollection resistance ($R_2R_8/R_1 = R_C$) is readily found by varying R_2 and observing the ring electrode current trace in the potential region where the oxidized disk electrode is reduced. Table I presents the results of pseudocollection resistance measurements obtained by this procedure at five different locations of the Luggin capillary. Also listed in Table I are the corresponding values of R_C found using our earlier procedure (14). The agreement between these two methods is excellent.

Inverse pseudocollection.—Another test of the equivalent circuit was performed by interchanging the leads to the ring and disk electrodes, i.e., the ring electrode to the input of F2. The effect of this change to position R_R at the input of CF and R_D at the input of F2. Thus varying the ratio R_2R_8/R_1 compensates the disk electrode potential for effects caused by ring electrode currents passing through R_C , i.e., compensates for the inverse pseudocollection effect.

Table II lists the values of the inverse pseudocollection resistance found by the above procedure at three

different locations of the Luggin capillary. Also listed are the values of the pseudocollection resistance found when the disk electrode lead was connected to CF and the ring electrode lead was connected to F2, i.e., the original configuration. The agreement between the pseudo and inverse pseudocollection resistances found in this way is good.

Pseudo and Inverse Pseudocollection Effects: Double Layer Charging Currents

Albery (23) in his a-c studies at the ring-disk electrode noticed that an a-c ring electrode current flows in the ring electrode circuit even when only an a-c double layer charging current flows through the disk electrode and correctly ascribed this phenomenon to an uncompensated ohmic potential drop caused by the disk current flowing through a solution resistance that is coupled to the ring electrode. The equivalent circuit for this situation is shown in the circled region in Fig. 1 in which E_D and E_R should be considered to contain the double layer capacitances of the disk and ring electrodes. Our model contains the Albery *et al.* features and in addition predicts the reciprocal effects of current at one electrode on the other electrode's poten-

Table I. Determination of pseudocollection resistance. 0.01M H₂SO₄. Rotation speed = 2500 rpm

Electrode No.	R _C (ohm)	
	Method of Ref. (14) ^(a)	Using Eq. [22]
1	53	52
1	61	60
1	26	25
2	45	43
3	50	50
4	50	51

^(a) Using Eq. [31].

Table II. Comparison of pseudo and inverse pseudocollection resistances. Electrode No. 1, 0.01M H₂SO₄. Rotation speed = 2500 rpm

R _C (ohm)	
Pseudocollection resistance	Inverse pseudocollection resistance
42	45
53	55
55	56

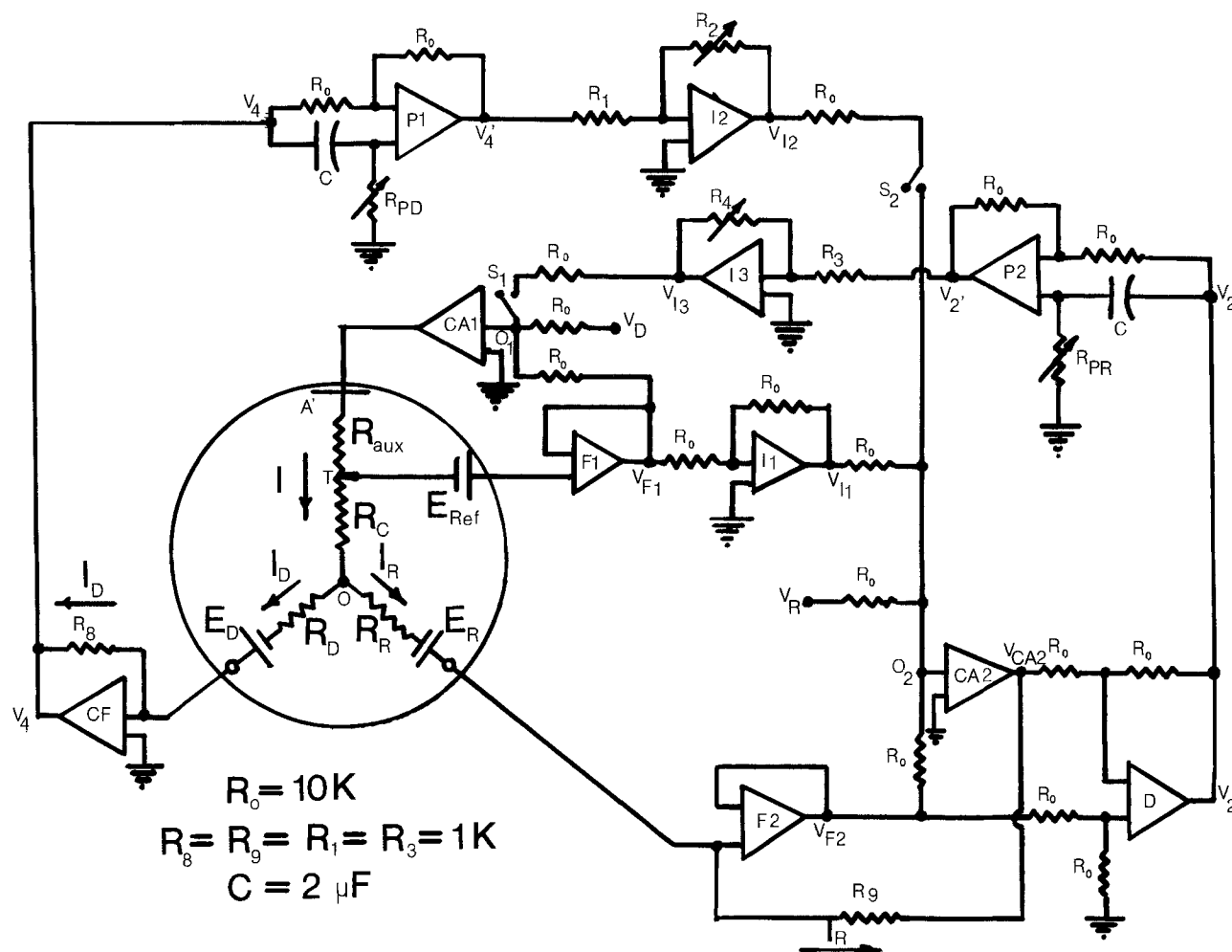


Fig. 6. The four-electrode potentiostat and the positive feedback circuitry with modification for a-c compensation. The equivalent circuit for the uncompensated ohmic resistances at ring-disk electrodes is enclosed by the circle.

tial. The a-c voltage fluctuation across the common resistance, R_C , of Fig. 1, produces potential fluctuations across the ring electrode double layer capacitance, and thus double layer charging currents at the ring electrode. Analogously, as is shown below, an inverse pseudocollection effect can be produced by an a-c current flowing at the ring electrode.

The ring and disk electrode currents involved in these capacitive pseudo and inverse pseudocollection effects are out of phase with each other as a result of the differing value of R_R , R_D , the ring electrode double layer capacitance and the disk electrode to double layer capacitance. Hence, the derivation leading to Eq. [17] and [22] would have to be suitably modified to account for this phase shift. This was not done, since it is seen that if the proper phase shifted fraction of I_D is fed back to the ring control amplifier CA2, the inverse pseudocollection effect can be eliminated. Similarly, by feeding back the appropriate phase shifted fraction of I_R to the disk control amplifier, the inverse pseudocollection effect can be eliminated. The circuit used to accomplish these results is given in Fig. 6, in which a phase shifting circuit P1 and P2 was introduced into the ring and disk current positive feedback loops. P1 and P2 are identical circuits, and have the property of unity gain at all frequencies, shifting the phase of an a-c signal from 180° to 360° , depending on values of the R_P 's and C 's and the frequency.

In an actual a-c pseudocollection compensation experiment, both R_2 and R_{PD} are adjusted until there is no a-c ring current in the absence of a faradaic process at the disk electrode. The analogous adjustment of R_4 and R_{PR} compensates for the a-c inverse pseudocollection effect.

The results of such a-c compensation experiments at 10, 100, and 200 Hz are given in Table III. The currents listed in parenthesis are the a-c pseudo or inverse pseudocollection currents. The values of R_2R_8/R_1 and R_4R_9/R_3 produce the resistance values necessary after adjusting the phase shift resistors, R_{PR} or R_C , as measured by the d-c method in which the faradaic currents flow through the ring and disk electrodes. R_C values measured in this way are given in the last column of Table III, and agree well in all pseudo and inverse pseudocompensation studies.

The positive feedback networks function completely independently of each other when the inverse pseudocollection effect is compensated according to Eq. [17], the pseudocollection phenomenon is unaffected, and visa versa when the condition of Eq. [22] is met. When the conditions of Eq. [17] and [22] are both met, both effects vanish.

Conclusion

The uncompensated common resistance R_C , between the reference electrode and the ring and disk electrodes can be a significant fraction of the uncompensated resistance found at ring-disk electrodes. Pseudo and inverse pseudocollection effects arise due to this common resistance. These effects can be completely eliminated, in both d-c and a-c experiments, by appropriate positive feedback networks, without any noticeable loss of dual potentiostat stability. The positive feedback networks used are our earlier equivalent circuit for the uncompensated resistances occurring at ring-disk electrodes (14) and the success of the positive feedback networks in eliminating pseudo and inverse

Table III. A-C pseudo and inverse pseudocollection compensation. 0.01M H₂SO₄.
Rotation speed = 2500 rpm, electrode No. 1, C = 2 μF

Experiment type	Frequency (Hz)	E (mV)	E' (mV)	I _D (μA)	I _R (μA)	R _{PD} (k-ohm)	R _P (k-ohm)	R ₂ R ₈ /R ₁ (ohm)	R ₄ R ₈ /R ₈ (ohm)	R _C ^(a) (ohm)
Pseudo	10	400	0	1200	(15)	100		44		44
Pseudo	100	30	-300 ^(a)	250	(100)	14		44		44
Pseudo	100	30	0	250	(100)	14		44		44
Pseudo	200	200	0	2000	(200)	33		44		44
Inverse ^(b)	200	80	0	(350)	600	35		46		44
Inverse	200	0	20	(20)	450		12		45	44
Pseudo	200	0	20	18	(170)	6		44		44
Pseudo	200	0	200	2000	(160)	55		45		44
Pseudo	100	10	-300 ^(a)	70	(20)	10		36		37
Pseudo	100	200	-300 ^(a)	1500	(360)	18		36		37
Pseudo	100	130	0	40	(120)	20		38		37
Inverse	100	0	130	(800)	36		20		38	37

^(a) D-C values.

^(b) Method of Table II.

^(c) Procedure of Ref. (14), Eq. [3].

pseudocollection effects is considered to be a further test for the validity of the model.

Acknowledgment

This research was supported in part by Henry Woodburn Fellowship from S.U.N.Y.A.B. (M.S.) and by AFSOR Grant No. 505034A.

Manuscript submitted March 8, 1975; revised manuscript received May 28, 1975.

Any discussion of this paper will appear in a Discussion Section to be published in the June 1976 JOURNAL. All discussions for the June 1976 Discussion Section should be submitted by Feb. 1, 1976.

REFERENCES

- G. Lauer and R. A. Osteryoung, *Anal. Chem.*, **38**, 1106 (1966).
- E. R. Brown, T. G. McCord, D. E. Smith, and D. D. DeFord, *ibid.*, **38**, 1119 (1966).
- A. A. Pilla, *This Journal*, **118**, 702 (1971).
- C. Lamy and P. Malaterre, *J. Electroanal. Chem.*, **32**, 137 (1971).
- D. Garreau and J. M. Saveant, *ibid.*, **35**, 309 (1972).
- N. S. Sarma, L. Sankar, A. Krishnan, and S. R. Rajagoplan, *ibid.*, **41**, 503 (1973).
- E. R. Brown, H. L. Hung, T. G. McCord, D. E. Smith, and G. L. Booman, *Anal. Chem.*, **40**, 1424 (1968).
- E. R. Brown, D. E. Smith, and G. L. Booman, *ibid.*, **40**, 1411 (1968).
- A. Bewick, *Electrochim. Acta.*, **13**, 825 (1968).
- A. A. Pilla, *This Journal*, **116**, 1105 (1969).
- D. K. Roe, *Anal. Chem. Rev.*, **46**, 8R (1974).
- R. S. Nicholson, *ibid.*, **44**, 478R (1972).
- D. E. Smith, *CRC Crit. Rev. Anal. Chem.*, **2**, 247 (1971).
- M. Shabrang and S. Bruckenstein, *This Journal*, **121**, 1439 (1974).
- D. C. Johnson and S. Bruckenstein, *ibid.*, **117**, 460 (1970).
- D. T. Napp, Ph.D. Thesis, University of Minnesota (1967).
- D. F. Untereker and S. Bruckenstein, *Anal. Chem.*, **44**, 1009 (1972).
- D. T. Napp, D. C. Johnson, and S. Bruckenstein, *ibid.*, **39**, 481 (1967).
- D. F. Untereker, Ph.D. Thesis, S.U.N.Y.A.B. (1973).
- S. H. Cadle, Ph.D. Thesis, S.U.N.Y.A.B. (1972).
- C. Gabrielli, M. Keddani, and H. Takenouti, *J. Chem. Phys.*, **4**, 737 (1972).
- M. Shabrang, *This Journal*, **121**, 50C (1974).
- W. J. Albery, A. H. Davis, and A. J. Mason, *Discussions Faraday Soc.*, **56**, 317 (1973).
- B. Miller, Private communications.

Studies in Derivative Chronopotentiometry

II. Analysis of Multicomponent Systems

P. E. Sturrock* and B. Vaudreuil

School of Chemistry, Georgia Institute of Technology, Atlanta, Georgia 30332

and R. H. Gibson*

Department of Chemistry, University of North Carolina at Charlotte, Charlotte, North Carolina 28213

ABSTRACT

Instrumental compensation for diffusion current of prior steps is investigated for the derivative chronopotentiometry of multicomponent systems. This technique, in combination with the instrumental compensation and mathematical correction for charging current described in a previous paper (1) is applied to the analysis of multicomponent systems by standard addition and titration. As examples, an amount of 0.2 μmoles of cadmium was determined by standard addition in the presence of 100 μmoles of lead and an amount of 2 μmoles of cadmium was titrated with EGTA in the presence of 50 μmoles of copper.

Chronopotentiometry of solutions containing two or more electroactive substances which undergo con-

secutive electrode reactions suffers the inherent disadvantage that the faradaic current for the second and subsequent components is reduced by the amount of the residual diffusion current from the more easily

* Electrochemical Society Active Member.

Key words: current correction, standard addition, titration, DME.

electrolyzed components. This has the effect of increasing the transition times for the subsequent components. In addition, the shape of the chronopotentiogram for the second component is altered, thus complicating the relationship between transition time and the minimum of the dE/dt curve.

Previous attempts to correct the transition time of the latter component were based on theoretical concentration-transition time relationships derived by Delahay and Mamantov (2) for two consecutive processes and which were extended to multicomponent systems by Reilly *et al.* (3). Sturrock, Anstine, and Gibson (4) derived the theoretical potential-time relationships for multicomponent derivative chronopotentiometry. They found it is possible to evaluate τ for second and third components by using a computer prepared tabulation of a parameter which is dependent on $(dE/dt)_{\min}$ for the component in question, and the sum of the transition times for the preceding waves.

The same authors proposed a standard addition type analysis to determine the concentration of the component in question. However, this type of analysis cannot be applied to very dilute solutions or to transition times much shorter than 3 msec because it is impossible to apply a Bard-type separation of faradaic and capacitive currents to correct for double-layer charging.

Bowman and Bard (5), working with stationary electrodes, were able to decrease the effect of a preceding wave by imposing a constant potential between the two waves for a measured time before applying the constant current for the chronopotentiometry of the second component. Extension of the potential step technique was undertaken in the present work in which all experiments were performed on a DME. If the prebias potential is applied for a long enough time, the diffusion current of the first component decays to a small and nearly constant value. If the chronopotentiometric current is applied at any time within the flat portion of the i vs. τ curve, the diffusion current can be considered to be constant over the short (1-50 msec) time span of the chronopotentiometric wave. The constant diffusion current, i_d , can be subtracted from the applied current to give the current going toward the faradaic process for the second component, i_f . The value of i_f is used with the observed transition time to calculate the $i\tau^{1/2}/C$ ratio for the second component. The chronopotentiometric constant is stated in terms of a corrected current, rather than a corrected transition time. If the value of i_f is known, or can be held constant, analytical applications are possible.

There are various methods, based on the Cottrell and Ilkovic equations of obtaining a value for i_d . The disadvantage of calculating instantaneous currents by the Ilkovic equation lies in the inaccuracies introduced by the use of so many measured parameters. To reduce the number of experimentally measured parameters involved, a new expression was derived in the course of this work combining the Cottrell and Sand equations. The concentration of electroactive substance in the bulk solution was expressed in terms of the Sand equation, then this expression was substituted for C in the Cottrell equation along with a factor, $\sqrt{7/3}$, to account for the expansion of the drop. The resulting equation is

$$i_d = (2/\pi) (7/3t)^{1/2} i_f \tau^{1/2} \quad [1]$$

where t is the delay time (the length of time that the growing drop is subject to the prebias before the chronopotentiometric current is applied) and i and τ are obtained from a chronopotentiogram of the first component, without prebias, at time t in the drop life. Essentially, i_d for a single component is calculated from a single chronopotentiogram of that component.

In the course of this investigation, a simpler method was discovered to determine diffusion currents. A prebias potential beyond the first wave is maintained for time t , as the electrode drop grows, then upon switch-

ing to galvanostat mode, sufficient current is applied from a continuously variable calibrated source so that the prebias potential is maintained. Under such conditions, the applied current is equal to the diffusion current of the first species. If the applied current is less than the diffusion current, the concentration of electroactive species will increase at the electrode surface and the potential will change in accord with the Nernst equation. Likewise, if too large a current is applied the potential will move in the opposite direction. The diffusion current measured in this way is subtracted from the total current to the next drop of the DME to obtain i_f . A simpler method is to use an uncalibrated, variable current source adjusted to supply just the current necessary to equal the diffusion current and maintain the prebias potential. Then this current can be electronically added to the current, applied to the next drop of the DME so that nominally all the applied current is available for the second faradaic process. In a multicomponent situation where one is trying to measure a transition for a wave on top of several others, this method is superior to the use of the Sand-Cottrell calculation which can be applied only with difficulty to multicomponent systems. It is also superior to the application of the Ilkovic equation which involves summing the diffusion currents for each of the preceding waves. In the new instrumental method, the total residual diffusion controlled current is measured without regard to the number or magnitude of its components.

Experimental Verification of Applied Corrections

The validity of the various corrections proposed was tested on lead-cadmium solutions using potassium nitrate as the supporting electrolyte. The transition for the reduction of lead occurs at approximately $-0.4V$ vs. SCE. The reduction wave for cadmium occurs at a potential about 0.2V more negative. Both metals are reduced reversibly, and neither species is known to be adsorbed on a mercury electrode.

Calculation and measurement of diffusion currents.— Diffusion controlled currents for lead were determined by four methods; direct measurement at $-0.52V$, Sand-Cottrell calculation, Ilkovic calculation based on $D^{1/2}$ obtained from derivative chronopotentiometry, and Ilkovic calculation based on polarographic literature value of $D^{1/2}$.

To 50 ml of 1M KNO_3 supporting electrolyte were added 2 ml portions of $2 \times 10^{-2}M$ $Pb(NO_3)_2$. The solution was deaerated after each addition and allowed to become quiet. The delay time for switching from prebias to controlled current modes was 2.625 sec into the drop life. The diffusion current was measured by adjusting the calibrated main cathodic current control to exactly maintain the prebias voltage for a period of 50 msec, thus giving a horizontal trace on the oscilloscope. The magnitude of the applied current was read directly from the dial of the current control potentiometer.

To obtain data required for the Sand-Cottrell calculation derivative chronopotentiograms were run on the above solutions with the prebias at $-0.2V$. Values of $(dE/dt)_{\min}$ for the lead wave were converted to transition times. Using delay time, t , equal to 2.625 sec, and combining numerical terms, the modified Sand-Cottrell equation (Eq. [1]) reduces to

$$i_{d(\text{in } \mu A)} = 0.600 (i_f \tau^{1/2}) \quad [2]$$

Experimental values of i and τ were used to calculate i_d for solutions with different lead concentrations.

The Ilkovic calculation was based on the following experimentally measured parameters

$$D^{1/2} = 0.00290 \text{ cm/sec}^{1/2}, \quad t = 2.625 \text{ sec}, \\ m = 2.393 \text{ mg/sec}, \quad C = (\text{variable}) \\ \text{mmoles/liter}$$

Combining numerical terms, the Ilkovic equation reduces to

$$i_{d(\text{in } \mu\text{A})} = 8.63C \quad [3]$$

When using a literature value of $D^{1/2}$ from polarographic data (6), Eq. [3] becomes

$$i_{d(\text{in } \mu\text{A})} = 9.00C \quad [4]$$

The values of i_d obtained for lead solutions over a concentration range from $7.69 \times 10^{-4}\text{M}$ to $4.38 \times 10^{-3}\text{M}$ are summarized in Table I. Diffusion current is a linear function of concentration of the diffusing species. Values for diffusion currents calculated by the Sand-Cottrell and the Ilkovic equations based on chronopotentiometric $D^{1/2}$ values agree well. However, the diffusion currents obtained by direct measurement were consistently higher by about 6% and in close agreement with the Ilkovic calculation based on literature value of polarographic $D^{1/2}$ (6).

The discrepancy noted in Table I was thought to be due to the depletion of electroactive substance in the vicinity of successive drops. A semiquantitative evaluation of the magnitude of the depletion effect was obtained by examining the changes in successive chronopotentiograms of an electroactive substance as the depleted layer, resulting from a prebias, is replenished by continued diffusion after the prebias is switched off.

A cadmium solution ($1.1 \times 10^{-3}\text{M}$ in 1.0M KNO_3) was subjected to a prebias of -0.76V until a steady-state diffusion current ($10 \mu\text{A}$) was observed at the usual delay time. Then the prebias was switched off manually to coincide as closely as possible to drop detachment. Derivative and conventional chronopotentiograms were run on the next four drops of the DME. With an applied current of $100 \mu\text{A}$ and an electrode area of 0.0290 cm^2 , $\tau^{1/2}$ values were 0.128, 0.145, 0.152, and $0.153 \text{ sec}^{1/2}$. The increase in $\tau^{1/2}$ from the first to the fourth drop indicates a corresponding increase in the apparent concentration of cadmium at the electrode surface. Stated in another way, application of a prebias to a DME electrode results in a residual concentration polarization such that the concentration of electroactive species seen by the newly formed drop may be much less than the true bulk concentration. The directly measured diffusion currents presented in Table I were obtained after a steady state of depletion was reached. The same steady-state conditions were used in subsequent work. During the application of the prebias, the situation at the electrode is exactly the same as in polarography and one would expect the Ilkovic equation to be applicable provided polarographic values of $D^{1/2}$ are used.

No depletion effect was observed on any chronopotentiograms run normally, that is, without a prebias beyond the reduction potential for that substance. Chronopotentiograms on the first and subsequent drops were identical for single component systems. For multicomponent systems, with a prebias set between the reduction potentials of the different components, chronopotentiograms of the first few drops were not identical. Discrepancies between first and subsequent drops can be explained by considering the variation of current required to set up the diffusion layer for the more active component. As the current required to set up the diffusion layer decreases, the fraction of the total current which is used for the chronopotentiometric process increases. Once a steady state is reached in the diffusion of the more active component, the chronopotentiograms of the less active component will superimpose so that successive traces on a storage oscilloscope appear as one trace.

Contributions to the apparent diffusion current from charging the double layer of the growing drop at the prebias potential are insignificant. For a drop area change of 1% ($\Delta a = 0.0003 \text{ cm}^2$) and a typical double-layer capacitance of $20 \mu\text{f/cm}^2$, charging the double layer required approximately $0.006 \mu\text{coul/V}$. At a prebias of -0.52V over a time of 50 msec, the required current would be

$$i = \frac{0.006 \mu\text{coul} \times 0.1\text{V}}{0.05 \text{ sec}} = 0.012 \mu\text{A}$$

This is insignificant compared to the magnitude of the diffusion currents reported in Table I.

Consistency of the chronopotentiometric constant for cadmium in the presence of lead.—A series of solutions which were $3.8 \times 10^{-6}\text{M}$ to $4.3 \times 10^{-3}\text{M}$ in cadmium and 2.0×10^{-3} in lead was prepared by adding portions of solutions which were $1.0 \times 10^{-3}\text{M}$ or $1.0 \times 10^{-4}\text{M}$ in cadmium and also $2.0 \times 10^{-3}\text{M}$ in lead and 1.0M in KNO_3 to a solution which was $2.0 \times 10^{-3}\text{M}$ in lead and 1.0M in KNO_3 . A series of chronopotentiograms was run on these solutions using a prebias of -0.52V and instrumental compensation for the lead diffusion current. The diffusion current was checked after each addition and was found to be invariant. The chronopotentiograms were run with and without instrumental double-layer compensation and the transition times measured with the derivative technique (1).

Three sets of chronopotentiometric constants were calculated: from the uncompensated (double-layer) and uncorrected data; from uncompensated (double-layer) data corrected according to Bard (7); and from data compensated (double-layer) instrumentally. The results are shown in Table II. Consistency was achieved for cadmium concentrations as low as $1.66 \times 10^{-5}\text{M}$ both by Bard corrections and by instrumental compensation. For Cd solutions on the order of 10^{-6}M , Bard-corrected results were more consistent than were the instrumentally compensated results. The results from the latter were improved by applying Bard corrections; $i\tau$ vs. $C\tau^{1/2}$ plots of the instrumentally compensated data showed a residual double-layer effect of about $0.0036 \mu\text{coul}$. This is one-tenth the double-layer effect in the uncompensated data and becomes insignificant at concentrations of 10^{-5}M and higher, but it consumes significant portions of the very low currents used for lower concentrations.

The lowest current setting available on the instrument used was $1 \mu\text{A}$. For a $3.8 \times 10^{-6}\text{M}$ cadmium solution using double-layer compensation, this lowest current yielded a τ of 7.73 msec, too near the lower limit imposed by the speed of the differentiator for an attempt to analyze more dilute solutions. There is reason to believe that with a lower applied current and a more sophisticated double-layer compensator, this concentration limit can be extended to the lower 10^{-6} range and perhaps beyond.

It should be emphasized that in these experiments the amount of lead present was 0.5-500 times the amount of cadmium. Consistency of $i\tau^{1/2}/aC$ was attained despite the large amounts of lead.

Table I. Lead diffusion currents

Conc. Pb (mmoles/ liter)	Diffusion current (μA)			
	Direct measure- ment	Sand- Cottrell calcu- lation	Ilkovic calculation	
			Chronopotentiometric polarographic $D^{1/2}$	$D^{1/2}$
0.77	7.3	6.72	6.63	6.91
1.48	13.6	12.8	12.8	13.3
2.14	19.6	18.6	18.5	19.3
2.76	25.2	23.8	23.8	24.8
3.33	30.3	28.6	28.7	30.0
3.87	35.4	33.4	33.4	34.8
4.38	40.1	37.5	37.8	39.4

Application to Analysis

The concentration of an electroactive substance can be determined by chronopotentiometry by substituting experimental values for the other parameters into the Sand equation and solving for C . The value obtained, however, is subject to considerable error owing to the large number of variables used. Standard addition and titration methods offer a better approach. A series of chronopotentiograms is used to obtain data for the analytical curves.

Table II. Chronopotentiometric constants for cadmium in the presence of $2 \times 10^{-3}M$ lead

Conc. Cd (moles/ liter)	Uncompensated data					Instrumentally compensated data				
	Uncorrected			Bard-corrected		Uncorrected			Bard-corrected	
	i (μA)	τ (msec)	$i\tau^{1/2}$ aC	i_t (μA)	$i_t\tau^{1/2}$ aC	i (μA)	τ (msec)	$i\tau^{1/2}$ aC	i_t (μA)	$i_t\tau^{1/2}$ aC
4.29×10^{-3}	400	19.7	451.2	398.5	449.5	400	19.7	451.2		
3.15×10^{-3}	300	19.7	460.9	298.5	458.4	300	19.7	460.9		
1.37×10^{-3}	150	15.5	469.8	148.1	463.6	150	14.9	461.5		
7.4×10^{-4}	100	10.2	470.8	97.1	457.0	100	9.62	457.4		
5.83×10^{-4}	50	25.5	472.3	48.7	460.3	50	24.1	458.9		
3.62×10^{-4}	50	10.31	483.9	46.9	454.0	50	9.02	452.6		
1.89×10^{-4}	20	18.1	490.4	18.2	447.1	25	9.84	452.7		
1.42×10^{-4}	30	5.70	550.2	24.4	447.3	25	5.55	452.6		
9.09×10^{-5}	30	3.38	662.3	20.5	453.5	15	6.37	454.3		
6.25×10^{-5}	20	4.25	719.4	12.5	448.7	10	6.99	461.3		
3.22×10^{-5}	10	6.66	874.5	5.19	454.7	10	1.86	462.4		
1.66×10^{-5}	20	2.28	1982.4	4.43	439.1	2.0	12.74	469.1		
1.07×10^{-6}	30	1.35	3549.4	3.70	438.2	2.0	8.02	577.5	1.55	448.0
7.4×10^{-8}	20	1.99	4158.0	2.16	449.2	1.0	15.47	579.8	0.11	446.1
3.8×10^{-8}	20	1.92	7970.1	1.56	621.0	1.0	7.73	798.4	0.54	426.3

Note i = applied current; $a = 0.0290$ cm²; $i_t = i - B/\tau$; B for uncompensated data = 0.035 μ coul; B for compensated data = 0.0036 μ coul. Units for $\frac{i\tau^{1/2}}{aC}$ in $\frac{\mu A \cdot sec^{1/2} \cdot liter}{cm^2 \cdot mmole}$.

Constancy of the $i\tau^{1/2}/C$ ratio is a necessity if chronopotentiometry is to be used for standard addition or titrimetric determinations. Either instrumental compensation of double-layer charging or arithmetic corrections as described previously (1) can be used to assure the constancy of $i\tau^{1/2}/C$ over the range of concentration to be spanned during the titration or standard addition. Generally, instrumental compensation will yield values for τ that can be used directly in plotting an analytical curve.

Standard addition determinations.—For a standard addition determination it is essential that a plot of $i\tau^{1/2}$ vs. C (which is equivalent to a Bard-type plot of $i\tau$ vs. $C\tau^{1/2}$) intercept the C -axis at the point $C = 0$. If double-layer effects are not eliminated by compensation or corrections, the $i\tau^{1/2}$ vs. C line may be displaced upward, indicating a higher concentration of the substance than is actually present. As derived in an earlier paper on derivative chronopotentiometry of single component systems (8), double-layer charging can be corrected for by maintaining a constant value for current density and plotting $\tau^{1/2} - \tau_{res}/\tau^{1/2}$ on the ordinate. In order to create a perfectly linear plot, it is necessary to correct for dilution.

If the solution which is being determined contains two or more electroactive species, these species can be determined independently in the same solution. In this study, cadmium was determined in the presence of lead by using the prebias and diffusion current compensation techniques discussed above. As aliquots of a standard cadmium solution are added to the test solution, the concentration of lead present is decreased. Thus the lead diffusion current changes after each Cd addition, and the diffusion current must be checked and the compensation readjusted.

When a sufficient number of additions (3-5) has been made and data obtained for the cadmium standard addition curve, the prebias can be lowered to a potential below the lead wave and aliquots of a standard lead solution added, yielding data for the lead determination. A solution of several electroactive substances can be analyzed by this means as long as the reduction potentials for the substances are separated sufficiently for a prebias to be imposed between the waves.

It is important that the substance which is reduced at a more negative potential be determined first. The additional amount of that substance which remains in the solution as a result of the standard addition acts as supporting electrolyte and does not interfere when the more easily reduced species is determined. If, on the other hand, the more easily reduced species is determined first, the additional amount present in the test solution interferes in the determination of the less

easily reduced species. The more of the former present, the more difficult it becomes to compensate for it.

Another precaution is worthy of note. To achieve the best precision, the amount of electroactive substance added in each increment should be of the same order of magnitude as the total amount of that substance initially present. Addition of considerably larger amounts greatly compresses the concentration axis and reduces the precision by which small amounts may be determined. If, on the other hand, the increments are much smaller than the amount to be determined, extrapolation over a long distance adds to the uncertainty of the result.

An example of a two component standard addition determination is presented in Fig. 1. Cadmium in the amount of 0.2 μ moles was determined, in the presence of 100 μ moles of lead, by derivative chronopotentiometry.

Titration using chronopotentiometric end point detection.—Cadmium can be titrated with EGTA ([ethylene bis(oxyethylenenitrate)] tetraacetic acid) in the presence of copper if an ammonia-ammonium buffer of pH 10 is used. The ammonia strongly complexes the copper and masks it for reaction with EGTA. The $Cd(NH_3)_4^{2+}$ complex is weaker and does react with the EGTA. End point detection is difficult, however, because copper interferes with metallo-chromic indicators such as Eriochrome Black-T which is routinely used for the EGTA titration of cadmium.

As EGTA complexes cadmium during the course of the titration, chronopotentiometry can be used to measure the decreasing concentration of uncomplexed cadmium.

As the concentration of cadmium decreases, double-layer effects become prominent. Bard corrections work well to deal with these effects. The τ measured by derivative means which occurs beyond the equivalence point is τ_{res} , the apparent transition time due to double-layer charging (8). It is constant at points well beyond the equivalence point where the concentration of cadmium not complexed by EGTA is essentially zero. If $\tau^{1/2} - (\tau_{res}/\tau^{1/2})$ is plotted vs. ml EGTA added, the portion of the titration curve beyond the equivalence point coincides with the x-axis. Thus the point where the extrapolated initial portion of the titration curve intersects the x-axis is taken as the end point.

If volume changes during the titration are significant, volume corrections must be applied, just as they are in the case of standard addition determinations. Chronopotentiometric end point determination lends itself to the use of concentrated titrant which can be added in small volume, eliminating the need for volume corrections. In the vicinity of the end point, titrant can be added in larger increments, so long as several

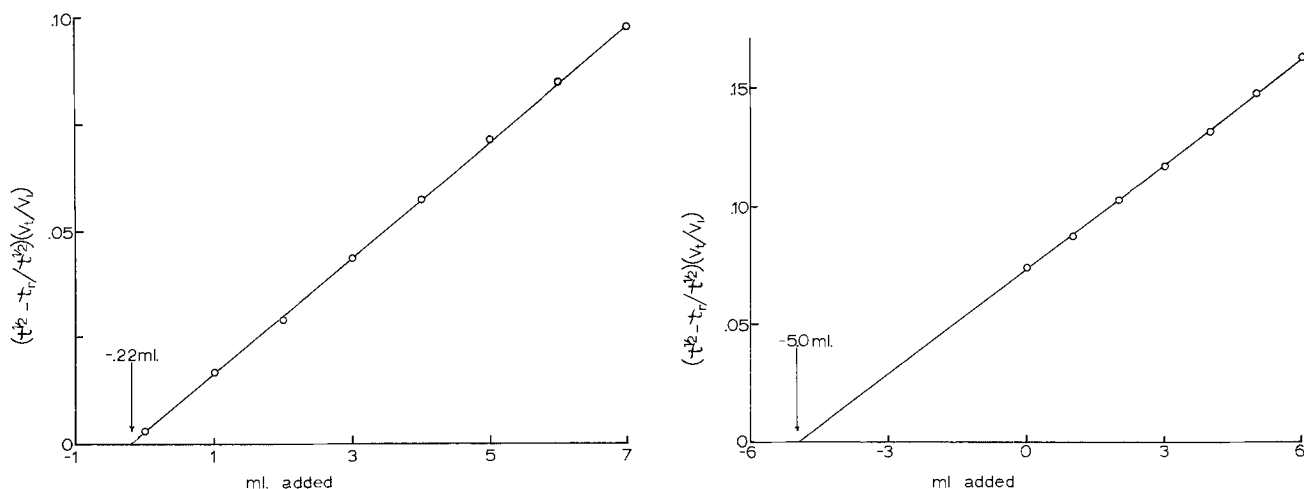


Fig. 1. Standard addition curves: (a, left). 0.2μ moles of cadmium in presence of 100μ moles of lead. Addition of $1.0 \times 10^{-3} F$ $Cd(NO_3)_2$. 0.22μ moles Cd found. (b, right). 100μ moles lead. Additions of $1.0 \times 10^{-2} F$ $Pb(NO_3)_2$. 100μ moles lead found.

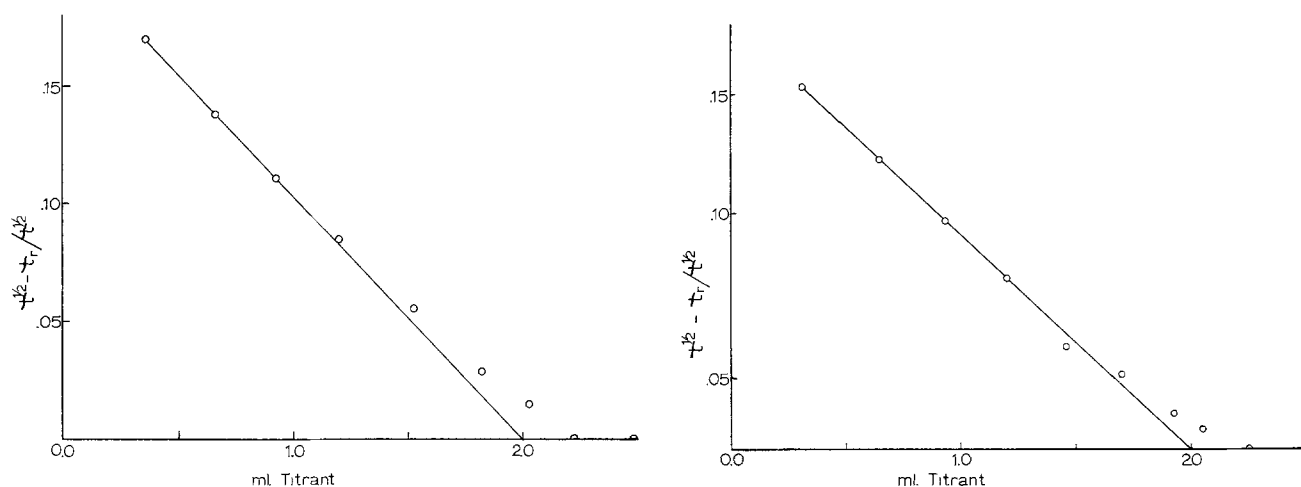


Fig. 2. Titration curves. (a, left). 2μ moles of cadmium and no copper. (b right) 2μ moles of cadmium and 50μ moles of copper

points are obtained in the linear regions before and beyond the end point.

An EGTA solution was standardized against a standard cadmium solution using Eriochrome Black-T and an ammonia-ammonium nitrate buffer of pH 10. A series of identical solutions was made as follows: 1.00 ml standard Cd solution (2μ moles Cd) was added to 5 ml buffer, 10 ml 1.0M KNO_3 , and sufficient water to make 50 ml total. The concentration of Cd in these test solutions was $4.00 \times 10^{-5} M$. The EGTA titrant was determined to be exactly $1.00 \times 10^{-3} M$.

The same titration was performed using chronopotentiometry. The chronopotentiometric titration curve is presented in Fig. 2a. For this determination, electrode area = 0.02899 cm^2 , current = $30 \mu A$, and pre-bias = $-0.66V$. The cadmium-ammonia complex is reduced at $-0.8V$.

The same procedure was repeated on a new test solution, identical to the preceding one except for the presence of 50μ moles copper. Diffusion current compensation was used to eliminate interference from the Cu. The titration curve is presented in Fig. 2b.

The results of the two cadmium titrations using chronopotentiometric end point detection are identical to the result of the series of titrations using Eriochrome

Black-T, and demonstrate the feasibility of titrating multicomponent mixtures using chronopotentiometry.

Manuscript submitted March 24, 1975; revised manuscript received June 4, 1975.

Any discussion of this paper will appear in a Discussion Section to be published in the June 1976 JOURNAL. All discussions for the June 1976 Discussion Section should be submitted by Feb. 1, 1976.

Publication costs of this article were partially assisted by Georgia Institute of Technology.

REFERENCES

1. P. E. Sturrock, J. Hughey, B. Vaudreil, G. O'Brien, and R. Gibson, *This Journal*, **122**, 1195 (1975).
2. P. Delahay and G. Mamantov, *Anal. Chem.*, **27**, 478 (1955).
3. C. N. Reilley, G. W. Everett, and R. H. Johns, *ibid.*, **27**, 483 (1955).
4. P. Sturrock, W. Anstine, and R. Gibson, *ibid.*, **40**, 505 (1968).
5. J. Bowman and A. Bard, *Anal. Letters*, **1**, 533 (1968).
6. L. Meites, "Polarographic Techniques," p. 270, Interscience, New York (1955).
7. A. Bard, *Anal. Chem.*, **35**, 340 (1963).
8. P. Sturrock, G. Privett, and A. Tarpley, *J. Electroanal. Chem.*, **14**, 303 (1967).

The Frequency Response of Limiting Currents to Sinusoidal Speed Modulation at a Rotating Disk Electrode

Koichi Tokuda* and Stanley Bruckenstein*

State University of New York, Buffalo, New York 14214

and Barry Miller*

Bell Laboratories, Murray Hill, New Jersey 07974

ABSTRACT

When a sinusoidal modulation is superimposed on the rotation speed of a rotating disk electrode, the corresponding modulated current follows the Levich equation closely for sufficiently low ratios of the modulation frequency to the constant center rotational frequency. In this work, the frequency response of the modulated current (amplitude and phase) is derived for the general case and the results experimentally confirmed over a wide range of Schmidt numbers (230-2100 Sc) and modulation to rotational frequency ratios for the reduction of Fe^{+3} to Fe^{+2} in 1.0M H_2SO_4 over the temperature range 25°-85°C. Tables are given of the phase and amplitude factors which would be encountered for the normal range of both modulation and solution parameters.

In recent papers (1-6), we have considered various theoretical and experimental aspects of hydrodynamic voltammetry at the rotating disk (RDE) and ring-disk electrodes (RRDE). In these studies, the angular velocity of the RDE, ω , was programmed as a function of time, t , or current, i . With the exception of one study (4) involving step speed change, this work dealt with conditions for which the Levich equation always applied, *i.e.*, a quasi-steady state existed in which the concentration gradients adjacent to the RDE could be described adequately using the instantaneous angular velocity, ω , of the electrode and the von Kármán (7)-Cochran (8) approach. Recently, using the results of Benton (9), we considered the current transient produced by a step change in angular velocity, $\Delta\omega$, of a RDE held at a limiting current. After such a step change in ω , the fluid velocities in the region adjacent to the RDE adjust very rapidly from values characteristic of the initial velocity, ω_0 , to those characteristic of the final velocity, $\omega_0 + \Delta\omega$, while the concentration profiles adjust somewhat more slowly.

We consider here the problem of describing the limiting, convective-diffusion controlled current at a disk subjected to a rotational velocity program of the form

$$\omega^{1/2} = \omega_0^{1/2}(1 + \epsilon \cos \sigma t) \quad [1]$$

In Eq. [1]

$$\epsilon = \Delta\omega^{1/2}/\omega_0^{1/2} \quad [2]$$

and σ is the modulation frequency in radians/sec. In this paper, we refer to this class of techniques as sinusoidal hydrodynamic voltammetry (SHM) to distinguish it from other uses now being made of the term "hydrodynamic voltammetry (10)."

Equation [1] will describe the experimental situation for all values of ω_0 , ϵ , and σ , including those for which the angular acceleration, $d\omega/dt$, is too high for the quasi-steady state assumptions used in our previous studies of a sinusoidal modulation of ω to apply. These broader experimental conditions will produce current responses deviating from those (5, 6) found for Levich-type conditions ($\epsilon\sigma$ small), *i.e.*, the current is not given by

$$i = i_{\omega_0} + \Delta i \cos \sigma t \quad [3]$$

where

* Electrochemical Society Active Member.
Key words: hydrodynamic modulation, frequency dependence, convective-diffusion.

$$\Delta i = i_{\omega_0} \Delta\omega^{1/2}/\omega_0^{1/2} = i_{\omega_0}\epsilon \quad [4]$$

and i_{ω_0} is the convective-diffusion limiting current at a constant angular velocity of ω_0 .

Instead, as will be shown later, i is given by

$$i = i_{\omega_0} + \Delta i_1 \cos(\sigma t - \varphi_1) + \Delta i_2 \cos(2\sigma t - \varphi_2) + \dots \quad [5]$$

In our experiments we have determined Δi_1 and φ_1 by appropriate techniques and have therefore restricted the detailed theoretical analysis to the first harmonic term, *i.e.*, to the calculation of Δi_1 and φ_1 as a function of the Sc number. The results for the amplitude response are reported in terms of the dimensionless parameter A

$$A = \Delta i_1/\Delta i \quad [6]$$

where $A \rightarrow 1$ as $\sigma \rightarrow 0$.

The need to predict values of Δi_1 and φ_1 had been prompted by unpublished studies of certain applications of SHM. These results indicated the desirability of performing experiments at larger values of σ/ω_0 than those to which we restricted the earlier work. For example, where potential scanning programs are used, higher modulation frequencies permit using higher scanning rates before undue distortion of Δi_1 - E curves is found, shortening experiments, reducing sensitivity to impurity poisoning, and thus leading to a better response to convective-diffusion controlled reactions.

Excellent agreement between the theory for A and φ_1 and experiment has been found for the reduction of Fe^{+3} to Fe^{+2} in 1.0M H_2SO_4 over the temperature range 25°-85°C (230-2100 Sc).

Theoretical

The normal component of the fluid velocity, w_0 , for an infinite disk rotating at constant angular velocity was first studied by von Kármán (7) and later by Cochran (8). After quasi-steady state is reached, w_0 is given by

$$w_0 = (\omega\nu)^{1/2}H_0(\eta) \quad [7]$$

where ν is the kinematic viscosity and

$$\eta = (\omega/\nu)^{1/2}z \quad [8]$$

For small η

$$H_0(\eta) = -0.51023\eta^2 + 0.33333\eta^3 - 0.10267\eta^4 + \dots \quad [9]$$

where the value of the second derivative of $H(\eta)$ with respect to η at $\eta = 0$ is the one given by Cochran (8).

Sparrow and Gregg (11) analyzed the analogous rotating disk problem for the case in which the angular velocity was a time dependent quantity. Their expression for the instantaneous normal component of the fluid velocity w , was obtained by a series expansion about the value found at quasi-steady state, i.e.

$$w = (\omega\nu)^{1/2}\{H_0(\eta) + \beta_1 H_1(\eta) + \beta_2 H_2(\eta) + \dots\} \quad [10]$$

where

$$\beta_1 = (d\omega/dt)/\omega^2 \quad [11]$$

$$\beta_2 = (d^2\omega/dt^2)/\omega^3 \quad [12]$$

and the $H_i(\eta)$ are axial velocity functions that satisfy the equations

$$H_i(\eta) = \frac{1}{2} H_i''(0)\eta^2 = c_i\eta^2 \quad [13]$$

for all i values at small values of η .

The values of the $H_i(\eta)$ functions were given graphically (11) for $0 \leq \eta \leq 20$, and the values of $H_2''(0)$ were given in their Table I. However, the values of higher derivatives at $\eta = 0$ were not given. Using their Table I data, we obtain

$$\begin{aligned} c_0 &= -0.51023 \\ c_1 &= 0.204835 \\ c_2 &= -0.023112 \end{aligned} \quad [14]$$

and

$$w = -0.51023(\omega^3/\nu)^{1/2}z^2\{(1 - 0.65327\eta + 0.20121\eta^2) - 0.40144\beta_1 + 0.04530\beta_2\} \quad [15]$$

as a good approximation to w when $\beta_{i+1} \leq \beta_i$. Note that when $\beta_1 = \beta_2 = 0$, Cochran's result, as used by Newman (12), is obtained. It is therefore possible to solve the Levich problem for small oscillations in ω , given its time dependence.

As stated previously, the superposition of a sinusoidal $\omega^{1/2}$ modulation, $\Delta\omega^{1/2}$, about a constant value, $\omega_0^{1/2}$, is advantageous from the experimental viewpoint, and the problem we deal with assumes that

$$\omega = \omega_0(1 + \epsilon \cos \sigma t)^2 \quad [16]$$

It is also convenient to define

$$p = \sigma/\omega_0 \quad [17]$$

Thus, the values of β_1 and β_2 are

$$\beta_1 = -2\epsilon p \sin \sigma t (1 + \epsilon \cos \sigma t)^{-3} \quad [18]$$

and

$$\beta_2 = -2\epsilon p^2\{\cos \sigma t + \epsilon(\cos^2 \sigma t - \sin^2 \sigma t)\} (1 + \epsilon \cos \sigma t)^{-6} \quad [19]$$

Substituting Eq. [18] and [19] into Eq. [15] and assuming $\epsilon \ll 1$ yields the expression for the instantaneous normal component of the fluid velocity

$$w = w_0\{1 + \epsilon(a_{01} \cos \sigma t + a_{10} \sin \sigma t) + \epsilon^2(a_{02} \cos 2\sigma t + a_{11}) + \dots\} \quad [20]$$

where

$$\begin{aligned} w_0 &= -0.51023(\omega_0^3/\nu)^{1/2}z^2(1 - 0.65327\eta_0 + 0.20121\eta_0^2) \\ a_{01} &= (3 - 2.6131\eta_0 + 1.0060\eta_0^2 - 0.090591p^2)/(1 - 0.65327\eta_0 + 0.20121\eta_0^2) \\ a_{10} &= 0.80288p/(1 - 0.65327\eta_0 + 0.20121\eta_0^2) \end{aligned} \quad [21]$$

$$\begin{aligned} a_{02} &= (1.5 - 1.9598\eta_0 + 1.0060\eta_0^2 - 0.04530p^2)/(1 - 0.65327\eta_0 + 0.20121\eta_0^2) \\ a_{11} &= (1.5 - 1.9598\eta_0 + 1.0060\eta_0^2 - 0.13589p^2)/(1 - 0.65327\eta_0 + 0.20121\eta_0^2) \end{aligned}$$

and

$$\eta_0 = (\omega_0/\nu)^{1/2}z$$

However, if $\epsilon < 1$ rather than $\epsilon \ll 1$, only the amplitude of the second harmonic expression in Eq. [20] will be in error, while the amplitude of the first harmonic with which we are experimentally concerned remains unchanged.

In order to obtain the time dependent convective-diffusion limiting current, the convective-diffusion equation

$$\frac{\partial C}{\partial t} = D \frac{\partial^2 C}{\partial z^2} - w \frac{\partial C}{\partial z} \quad [22]$$

must be solved for the boundary conditions

$$\begin{aligned} z = 0 : C &= 0 \\ z \rightarrow \infty : C &\rightarrow C^\circ \text{ (bulk concentration)} \end{aligned} \quad [23]$$

$u(z, t)$ given by Eq. [20] and [21] and for steady sinusoidal variations.

Taking into account the form of Eq. [20], a solution of the convective-diffusion equation is

$$C = C^\circ u(z, t) \quad [24]$$

where

$$\begin{aligned} u(z, t) &= u_0(z) + \epsilon\{u_{01}(z) \cos \sigma t + u_{10}(z) \sin \sigma t\} \\ &+ \epsilon^2\{u_{02}(z) \cos 2\sigma t + u_{20}(z) \sin 2\sigma t + u_{11}(z)\} + \dots \end{aligned} \quad [25]$$

Thus, we substitute Eq. [24] and Eq. [20] into Eq. [22], equate the coefficients of all terms having the same time dependence in the resulting expression, and obtain a set of ordinary differential equations involving functions of z . These equations are not written out here but may be simplified by using the dimensionless variable

$$\xi = \{0.51023(\omega_0^3/\nu)^{1/2}/3D\}^{1/3}z = 0.55405 \text{ Sc}^{1/3}\eta_0 \quad [26]$$

where $\text{Sc} (\equiv \nu/D)$ is the Schmidt number, and they lead to the set of equations below where the various u 's are functions of ξ and the primes represent differentiation with respect to ξ

$$u''_0 - f(\xi)u'_0 = 0 \quad [27]$$

$$u''_{01} - f(\xi)(u'_{01} + a_{01}u'_0) = bu_{10} \quad [28]$$

$$u''_{10} - f(\xi)(u'_{10} + a_{10}u'_0) = -bu_{01} \quad [29]$$

$$u''_{02} - f(\xi)(u'_{02} + a_{02}u'_0) = 2bu_{20} \quad [30]$$

$$u''_{20} - f(\xi)u'_{20} = -2bu_{02} \quad [31]$$

$$u''_{11} - f(\xi)(u'_{11} + a_{11}u'_0) = 0 \quad [32]$$

where

$$f(\xi) = -3\xi^2 + 3.5372 \text{ Sc}^{-1/3} \xi^3 - 1.9663 \text{ Sc}^{-2/3} \xi^4 \quad [33]$$

The quantity b is defined by

$$b = \{9\nu/(0.51023)^2D\}^{1/3}p = 3.2576 \text{ Sc}^{1/3}p \quad [34]$$

The boundary conditions become

$$\begin{aligned} \xi = 0 : u_0 &= u_{01} = u_{10} = u_{02} = u_{20} = u_{11} = 0 \\ \xi \rightarrow \infty : u_0 &\rightarrow 1, u_{01}, u_{10}, u_{02}, u_{20}, \text{ and } u_{11} \rightarrow 0 \end{aligned}$$

It is readily shown that the form of Eq. [25] leads to a current of the form given by Eq. [5].

The limiting convective-diffusion current, i , is defined by

$$i = nF\pi r^2D(\partial C/\partial z)_{z=0} \quad [35]$$

or in terms of ξ

$$i = nF\pi r^2DC^\circ(d\xi/dz)(\partial u(\xi, t)/\partial \xi)_{\xi=0} \quad [36]$$

where r is the radius of the disk electrode. Combining Eq. [25] and [36] with Eq. [26] yields

$$\begin{aligned} i &= i_{\omega_0} + i_{\omega_0}I(\infty)\epsilon a_1 \cos(\sigma t - \varphi_1) \\ &+ i_{\omega_0}I(\infty)\epsilon^2\{a_2 \cos(2\sigma t - \varphi_2) + a_3\} + \dots \end{aligned} \quad [37]$$

where

$$a_1 = [\{u'_{01}(0)\}^2 + \{u'_{10}(0)\}^2]^{1/2} \quad [38]$$

$$\varphi_1 = \cos^{-1}\{u'_{01}(0)/a_1\} = \sin^{-1}\{u'_{10}(0)/a_1\} \quad [39]$$

$$a_2 = [\{u'_{02}(0)\}^2 + \{u'_{20}(0)\}^2]^{1/2} \quad [40]$$

$$\varphi_2 = \cos^{-1}\{u'_{02}(0)/a_2\} = \sin^{-1}\{u'_{20}(0)/a_2\} \quad [41]$$

$$a_3 = u'_{11}(0) \quad [42]$$

and

$$i_{\omega_0} = 0.6205nF\pi r^2 D^{2/3} \nu^{-1/6} \omega_0^{1/2} C \Gamma(4/3) / I(\infty) \quad [43]$$

The above value for i_{ω_0} is obtained by solving Eq. [27] to obtain

$$u_0(\xi) = I(\xi) / I(\infty) \quad [44]$$

where

$$I(\xi) = \int_0^\xi \exp \left[\int_0^\xi f(x) dx \right] d\xi$$

$$= \int_0^\xi \exp \left(-\xi^3 + 0.8843Sc^{-1/3}\xi^4 - 0.3932Sc^{-2/3}\xi^5 \right) d\xi \quad [45]$$

and $I(\infty)$ is given by

$$I(\infty) = 0.89294 + 0.26610Sc^{-1/3} + 0.12960Sc^{-2/3} \quad [46]$$

which was obtained by Newman (12) for the correction of the Levich equation and holds for $Sc \geq 100$.

The experiments we have performed involve detecting the magnitude and phase of the current at the frequency used to modulate $\omega^{1/2}$; hence we need only solve Eq. [28] and [29] and we have postponed consideration of the behavior of the terms associated with the second harmonic.

Equations [28] and [29] were solved numerically (13) for various values of p in the range 0-1.0 and for selected values of Sc in the range 100-2100. In addition, A and φ_1 corresponding to specific experimental Sc values were calculated where required.

The effect of p on amplitude response for selected values of Sc is given in Table I, using the parameter A defined by Eq. [6].

By comparing the coefficients of the $\cos(\sigma t - \varphi_1)$ of Eq. [5] and [37] it is seen that

$$\Delta i_1 = i_{\omega_0} I(\infty) \epsilon a_1 \quad [47]$$

Substituting Eq. [47] and [46] into Eq. [6] yields

$$A = (0.89294 + 0.26610Sc^{-1/3} + 0.12960Sc^{-2/3}) a_1 \quad [48]$$

The theoretical values of a_1 at constant p and Sc are calculated using the numerical values of $u'_{01}(0)$ and $u'_{10}(0)$ obtained through Eq. [28] and [29] and applying Eq. [38]. The phase shift φ_1 is calculated from Eq. [39] and is given in Table II.

In using Tables I and II, linear interpolation at low Sc values is not accurate. A more sophisticated interpolation technique or graphing of the tabulated values of A and φ_1 is necessary if an error less than that found experimentally is to be achieved.

In the above discussion, both the deviation of hydrodynamics from quasi-steady state and the simultaneous relaxation of the diffusion layer were taken into account. It is of interest to estimate the conditions under which the current response is controlled almost completely by convective-diffusion, i.e., the conditions under which the hydrodynamic situation deviates by only a small percentage from quasi-steady state. Since we propose to obtain only an estimate for this condition, only the large Schmidt number limit for the normal velocity component, obtained from Eq. [15], will be used, i.e.

$$w = -0.51023 \{ \omega(1 - 0.40144\beta_1 + 0.04530\beta_2)^{2/3} \nu \}^{1/2} z^2 \quad [49]$$

From Eq. [49] it is seen that small deviations of ω from quasi-steady state are approximately given by $2/3 \times 0.401\beta_1\omega$. Since the deviation in the percentage current error, ϵ , is twice that in angular velocity, it follows that relationship between the error in ω and i is given by

$$\beta_1 = \frac{\dot{\omega}}{\omega^2} = -2p \frac{\sin \sigma t}{(1 + \epsilon \cos \sigma t)^3} \leq 0.0187\epsilon \quad [50]$$

Table I. Values of A for values of p and Sc

p	0.05	0.10	0.15	0.20	0.25	0.30	0.40	0.50	0.60	0.70	0.80	0.90	1.00
Sc													
100.0	0.9903	0.9626	0.9205	0.8687	0.8118	0.7535	0.6420	0.5447	0.4635	0.3970	0.3426	0.2982	0.2616
140.0	0.9872	0.9545	0.9057	0.8468	0.7836	0.7202	0.6028	0.5037	0.4233	0.3588	0.3070	0.2653	0.2314
200.0	0.9848	0.9458	0.8886	0.8215	0.7514	0.6829	0.5601	0.4604	0.3817	0.3200	0.2714	0.2329	0.2020
315.0	0.9809	0.9318	0.8623	0.7837	0.7047	0.6303	0.5030	0.4045	0.3296	0.2726	0.2288	0.1946	0.1677
400.0	0.9783	0.9230	0.8461	0.7612	0.6777	0.6008	0.4722	0.3753	0.3031	0.2490	0.2078	0.1768	0.1512
446.0	0.9784	0.9200	0.8395	0.7517	0.6664	0.5883	0.4593	0.3633	0.2923	0.2394	0.1994	0.1687	0.1448
600.0	0.9745	0.9066	0.8160	0.7203	0.6300	0.5496	0.4209	0.3261	0.2611	0.2122	0.1757	0.1480	0.1266
615.0	0.9741	0.9054	0.8139	0.7175	0.6269	0.5463	0.4177	0.3232	0.2586	0.2100	0.1739	0.1464	0.1252
800.0	0.9672	0.8888	0.7875	0.6843	0.5901	0.5111	0.3840	0.2952	0.2327	0.1877	0.1547	0.1298	0.1107
890.0	0.9639	0.8812	0.7758	0.6700	0.5745	0.4953	0.3694	0.2825	0.2217	0.1784	0.1467	0.1235	0.1053
1000.0	0.9630	0.8756	0.7658	0.6571	0.5603	0.4808	0.3560	0.2708	0.2119	0.1700	0.1396	0.1169	0.0996
1200.0	0.9606	0.8652	0.7483	0.6354	0.5369	0.4548	0.3325	0.2508	0.1950	0.1559	0.1276	0.1067	0.0912
1400.0	0.9557	0.8529	0.7299	0.6138	0.5170	0.4351	0.3151	0.2361	0.1828	0.1458	0.1192	0.0995	0.0846
1600.0	0.9537	0.8444	0.7162	0.5974	0.4972	0.4159	0.2984	0.2222	0.1714	0.1369	0.1112	0.0928	0.0792
1800.0	0.9506	0.8352	0.7024	0.5814	0.4809	0.4002	0.2850	0.2112	0.1630	0.1289	0.1050	0.0880	0.0748
2100.0	0.9475	0.8239	0.6851	0.5616	0.4608	0.3810	0.2688	0.1980	0.1517	0.1202	0.0979	0.0815	0.0692

Table II. Values of phase shift for values of p and Sc

p	0.05	0.10	0.15	0.20	0.25	0.30	0.40	0.50	0.60	0.70	0.80	0.90	1.00
Sc													
100.0	10.6	21.0	30.8	40.1	48.7	56.5	70.3	81.8	91.5	99.8	107.0	113.2	118.8
140.0	11.5	22.7	33.3	43.1	52.1	60.2	74.3	85.9	95.5	103.7	110.7	116.7	122.1
200.0	12.6	24.7	36.1	46.5	55.9	64.3	78.6	90.2	99.7	107.7	114.4	120.3	125.4
315.0	14.2	27.7	40.2	51.3	61.2	70.0	84.4	95.9	105.1	112.8	119.1	124.6	129.3
400.0	15.1	29.4	42.5	54.1	64.2	73.0	87.6	98.9	109.0	115.4	121.5	126.6	131.3
446.0	15.5	30.2	43.5	55.2	65.5	74.4	88.9	100.1	109.1	116.3	122.4	127.5	132.0
600.0	16.8	32.6	46.7	58.9	69.3	78.3	92.8	103.8	112.5	119.4	125.2	130.0	134.2
615.0	16.9	32.8	46.9	59.2	69.7	78.7	93.1	104.1	112.8	119.7	125.4	130.2	134.4
800.0	18.3	35.3	50.1	62.8	73.5	82.3	96.6	107.4	115.7	122.3	127.7	132.3	136.2
890.0	18.9	36.3	51.5	64.3	75.1	83.9	98.2	108.8	117.1	123.6	128.9	133.1	136.9
1000.0	19.5	37.4	52.8	65.8	76.6	85.4	99.5	110.0	118.1	124.4	129.6	133.9	137.6
1200.0	20.5	39.1	54.9	68.1	79.0	88.0	102.1	112.4	120.2	126.3	131.3	135.4	138.7
1400.0	21.4	40.7	57.0	70.4	81.0	90.0	103.9	113.9	121.5	127.4	132.2	136.2	139.6
1600.0	22.2	42.1	58.6	72.1	83.1	92.1	105.8	115.6	123.0	128.5	133.4	137.3	140.3
1800.0	23.0	43.4	60.2	73.8	84.7	93.7	107.3	116.9	123.9	129.7	134.2	137.6	140.9
2100.0	24.0	45.0	62.2	75.9	86.8	95.7	109.0	118.3	125.3	130.6	134.9	138.5	141.6

The maximum value of β_1 , β_{\max} , is

$$\beta_{\max} = 2\epsilon p \frac{\sqrt{1 - \left(\frac{1 - \sqrt{1 + 24\epsilon^2}}{4\epsilon}\right)^2}}{\left(\frac{5 - \sqrt{1 + 24\epsilon^2}}{4\epsilon}\right)^3} = 2\epsilon p f(\epsilon) \quad [51]$$

so that the relationship between p , and ϵ and α is

$$2\epsilon p f(\epsilon) \leq 0.0187\alpha \quad [52]$$

Sparrow and Gregg (11) considered the problem of determining under what condition the shear stress would deviate by less than 5% from its quasi-steady state value and found that

$$\beta_1 \leq 0.0834$$

which, by comparison with Eq. [50], corresponds to an α of 4.5%.

Table III gives the values of p vs. selected ϵ 's which cannot be exceeded if the deviation from hydrodynamic quasi-steady state is not to produce a current error exceeding 4.5%

The significance of Table III is merely that, within specified restrictions on p and ϵ , the total current is determined by convective-diffusion processes rather than by the coupling of convective-diffusion and a deviation from a hydrodynamic quasi-steady state.

Experimental

The motor drive and operational amplifier control systems have been described previously (3, 5). The entire system (mechanical plus electronic) bandwidth for modulation was examined by recording the motor tachometer's voltage amplitude and phase shift with respect to the driving waveform. The latter signal was the sum of a linear voltage ramp and a sinusoidal voltage of constant frequency and amplitude. The ramp voltage was selected to scan the center motor speed, ω_0 from 6.67 Hz (400 rpm) to above 125 Hz (7500 rpm).

Typical tracings of a-c motor response to this kind of program are shown in Fig. 1; e.g., at a constant modulation (signal) amplitude of $3 \text{ rpm}^{1/2}$ and a frequency of 6 Hz, the tachometer amplitude agrees with the a-c driving signal to $\pm 1\%$ and the phase shift is constant within $\pm 1^\circ$ at least up to a center speed of 84 Hz (>5000 rpm). The amplitude circuitry in the Dranetz Phasemeter automatically switches ranges during experiments since a constant $\Delta\omega^{1/2}$ at all speeds produces a-c voltages (related to $\Delta\omega$) which typically vary by a factor of more than four. The observed constant phase shift level in each trace is determined solely by modulation frequency, up to the rotational frequencies indicated by the roll-offs in Fig. 1.

All experiments were carried out with combinations of modulation frequency, amplitude, and center rotational speed frequency for which any amplitude and phase errors due to the above sources were well within $\pm 1\%$ and $\pm 1^\circ$, respectively. Thus, correction of the modulated disk electrode current response for $\Delta\omega^{1/2}$ variations was eliminated, and a full-wave rectifier circuit was used to obtain the amplitude in Δi -experiments. In these experiments, the amplitude response Δi_1 was determined as a function of p . Extrapolations of the Δi_1 data to $p = 0$ yield the maximum amplitude response, and A values were calculated by dividing

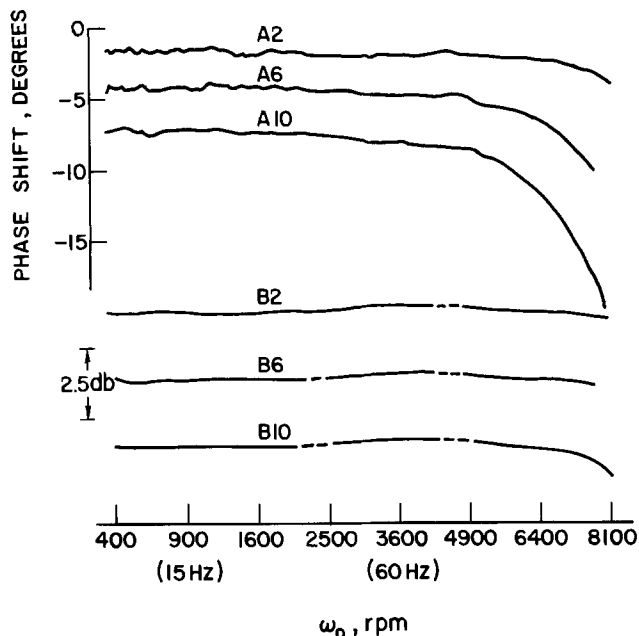


Fig. 1. A-C motor response to sinusoidal modulation. Curves A are phase shift, tachometer vs. signal; curves B are log of amplitude ratio, tachometer to signal. Signal amplitude set to constant $\Delta\omega^{1/2}$ of $3 \text{ rpm}^{1/2}$; center was scanned from low to high. Fixed frequency of modulation (Hz) indicated by number following A or B. Constant phase shift levels were, for A2, A6, and A10, respectively, -1.6° , -4.3° , and -7.2° , expressed as deviation from the theoretical 180° (no lag) shift. Amplitude plots arbitrarily displaced from common value; dashed regions indicate interruption of measurement due to ranging of phasemeter.

this value into the observed amplitude response at the various p values.

The phase shift of the sinusoidal Δi response relative to the $\Delta\omega$ tachometer output was continuously recorded with a Dranetz Model 305 Phasemeter equipped with a Model 3009A plug-in, after prefiltering each signal with matched 0.64-32 Hz two-pole bandpass amplifiers that introduced $<0.5^\circ$ of phase shift uncertainty. In a typical experiment, ω_0 was scanned from 400 to ca. 8000 rpm and back, and the φ data averaged to correct for a small hysteresis related to time constant effects. The experimental abscissas were converted to $p = \sigma/\omega_0$ values and the φ data were used without further reduction.

The electrochemical experiments were all carried out with a 0.313 cm^2 platinum disk electrode and a $2.17 \text{ mM Fe}^{+3} - 1.0 \text{ M H}_2\text{SO}_4$ solution, prepared from reagent chemicals and triply distilled (the last two from quartz) water. The Sc was varied by performing experiments at $10^\circ\text{C} \pm 0.5^\circ\text{C}$ increments between 25° and 85°C . The supporting electrolyte kinematic viscosities, ν were determined with a Cannon-Fenske viscometer that was calibrated with water over the $25^\circ-75^\circ\text{C}$ range. The diffusion coefficients for Fe^{+3} were calculated at the various temperatures from the slopes of Levich plots (i_L vs. $\omega^{1/2}$) for the limiting current of Fe^{+3} reduction, utilizing the ν values determined independently above and Eq. [46]. Log plots of Sc , D , and ν vs. $1/T^\circ\text{K}$ are shown in Fig. 2.

All data in this paper were obtained at 0.00V vs. an unthermostated SCE. This potential was in the limiting current region over the $25^\circ-85^\circ\text{C}$ cell temperature range.

Results and Discussion

The phase shift, φ_1 , of the modulated limiting disk current output, Δi_1 , produced by $\omega^{1/2}$ modulation at the frequency $f = \sigma/2\pi$ Hz, was directly measured for the reduction of Fe^{+3} to Fe^{+2} in $1.0 \text{ M H}_2\text{SO}_4$, using the constant modulation frequency- ω_0 variation technique described in the Experimental Section. The value of A , however, was, as noted, not calculated directly from the defined value of $\Delta i_1/\Delta i$ but rather from $\Delta i_1/$

Table III.

ϵ	p
0.01	≤ 4.17
0.05	≤ 0.825
0.1	≤ 0.399
0.2	≤ 0.176
0.3	≤ 0.095

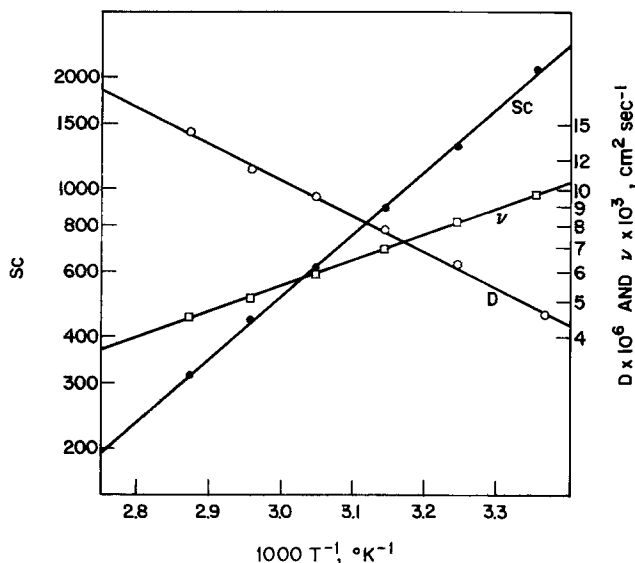


Fig. 2. Log plots of Sc , D , and ν vs. $1000/T^\circ K$.

$(\Delta i_1)_{p \rightarrow 0}$ where $(\Delta i_1)_{p \rightarrow 0}$ is the extrapolated value of Δi_1 at $p = 0$. Satisfactory agreement between $(\Delta i_1)_{p \rightarrow 0}$ and Δi_1 has been established previously by us (5), and the present procedure cancels a number of possible sources of small determinate errors associated with the electronic instrumentation including bandpass, gain, and rectification efficiency.

Theoretical plots and experimental values of A and ϕ_1 as a function of p for three values of Sc (315, 890, and 2100) are given in Fig. 3 and 4. Other sets of data obtained for different Sc (not plotted) agree equally well with theory. The Sc range illustrated in Fig. 3 and 4 covers the great majority of aqueous solution cases that will be encountered.

Satisfactory experimental tests of the theory for A and ϕ_1 dependence on Sc for five constant p values from 0.2 to 0.6 are given in Fig. 5 and 6. The theoretical values of A and ϕ_1 for these particular Sc values may also be accurately obtained by graphical interpolation in the tables of A and ϕ_1 given earlier, assuring the general experimental usefulness of the tabulations.

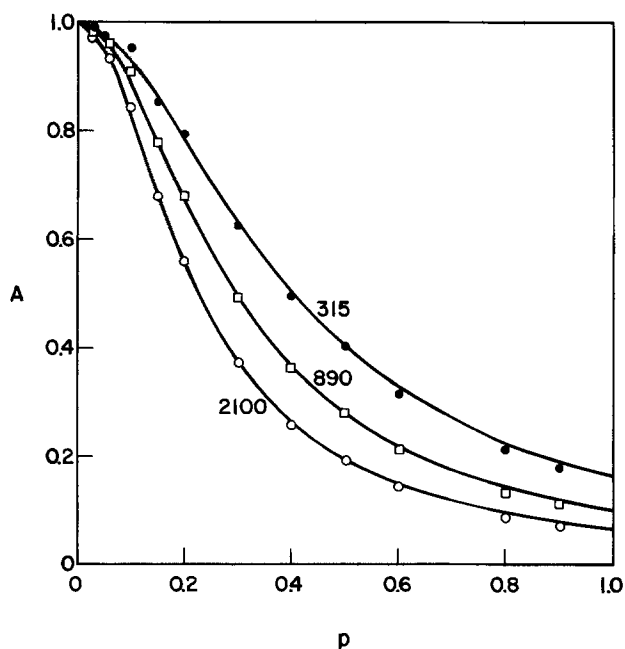


Fig. 3. Amplitude factor A as a function of p for Sc values of 315, 890, and 2100, as marked. Solid lines are theoretical, points are experimental.

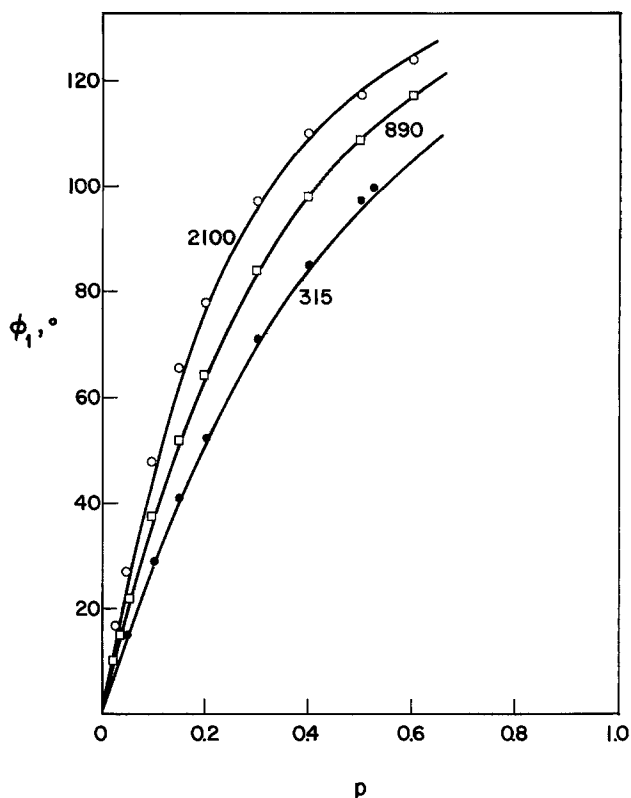


Fig. 4. Phase shift ϕ_1 as a function of p for Sc values of 315, 890, and 2100. Sc values marked. Solid lines are theoretical, points are experimental.

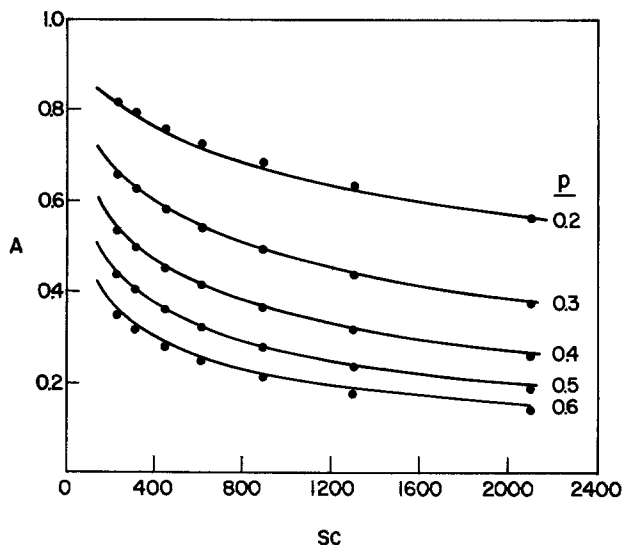


Fig. 5. Amplitude factor as a function of Sc at constant p . Values of p indicated at right of curves. Solid curves are theoretical, points are experimental.

The criteria of Table III, expressing maximum limits of p and ϵ for which the total current is essentially determined by convective-diffusion processes, have been exceeded in certain of our measurements by a factor of as much as three. Our theory explicitly takes into account the region in which convective-diffusion and hydrodynamics couple. Nevertheless, it was of significance to examine experimentally whether the $p\epsilon$ product at these levels, rather than just p alone, influenced the value of A in a given solution. Therefore, Δi_1 was measured as a function of $\Delta\omega^{1/2}$ under conditions of constant p , while $\Delta\omega^{1/2}$ was varied so that $p\epsilon$ was either always ≤ 0.04 , exceeded 0.04 at an intermediate value of $\Delta\omega^{1/2}$, or was ≥ 0.04 for all $\Delta\omega^{1/2}$. We

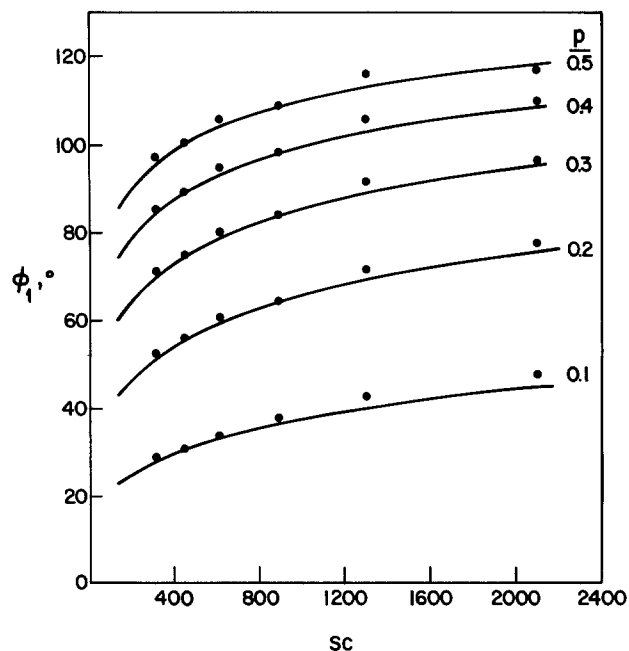


Fig. 6. Phase shift ϕ_1 as a function of Sc for constant p . Values of p indicated at right of curves. Solid curves are theoretical, points are experimental.

chose 0.04 simply as the approximate level of the pe products collected in Table III.

These results for Fe^{+3} reduction in 1.0M H_2SO_4 are shown in Fig. 7. The points taken for $p = 0.2$ cover pe from 0.004 to 0.03, those for $p = 0.4$ cover 0.012-0.093, and those for $p = 0.8$ cover 0.04-0.26. All three plots are linear and both the slope ratios (A ratios) and absolute A values are in satisfactory correspondence to the theory given above. Absolute A values were estimated in this case by determining Levich plots of i_{ω_0} vs. $\omega_0^{1/2}$ for various $\omega_0^{1/2}$ and comparing the slopes with those of the Fig. 7 plots. By combining Eq. [43] with Eq. [6], a definition of A related to this experimental approach is obtained, i.e.

$$A = \frac{\Delta i_1}{\Delta \omega^{1/2}} \bigg/ \frac{i_{\omega_0}}{\omega_0^{1/2}} \quad [53]$$

Hence, the slopes of the SHM data in Fig. 7, when divided by the slopes of the Levich plots, give the A values for the particular p values.

As far as the SHM technique is concerned, exceeding the pe criterion for deviation from a hydrodynamic quasi-steady state by even a factor of six appears to have little detectable effect on $\Delta i_1 - \Delta \omega^{1/2}$ plots. This result, predicted by theory, has the significance for practical use of the SHM technique at higher modulation frequencies (larger p) that, to a large extent, much of the loss of current sensitivity associated with a decreasing A factor at higher p values may be compensated by a $\Delta \omega^{1/2}$ increase. At present, the practical limitations of this sort of approach appear to reside mostly in the amplitude and frequency response of the motor system.

The A and ϕ_1 functions are independent of the concentration of the electroactive species and its n value in the electrode process. This property suggests a method for determining the diffusion coefficient of an electroactive species without *a priori* knowledge of the n value (or concentration), as is required by RDE and other voltammetric steady-state diffusion layer techniques. From the A (or ϕ_1) vs. p data for an unknown system, Sc for the electroactive species can be determined by interpolation in Table II (or I). D can then be calculated from the readily determined kinematic viscosity of the solution. This value of D may be in error by $\pm 10-15\%$, because of the combination of experimental error and relative insensitivity of the A or ϕ_1 vs. p function to some values of Sc . However, if i_{ω_0} and the electroactive solute's concentration are known, substituting these data and the estimate of D into Eq. [43] will permit determination of the integral value of n , and thence a precise value of D .

Application of the SHM technique to solutions containing two or more electroactive components leads to certain difficulties if phase sensitive detection is used to determine Δi_1 . In such mixtures, each electroactive species has its unique value of Sc , and thus a corresponding phase shift. The detection of Δi_1 response for regions on the current-voltage curve involving simultaneous reduction (or oxidation) of more than one species is thus complicated by the varying phase shifts for each component. There are obvious experimental stratagems to correct for this difficulty, e.g., manual tuning of the phase shift for each of the components is feasible. However, the variation of phase angles as a function of Sc at constant p , as can be seen from Table I or Fig. 3, is not large. The phase angle effect is modest when compared to the phase angle setting accuracy requirements of lock-in amplifiers. Phase errors of $\pm 10^\circ$ are necessary for $1\frac{1}{2}\%$ signal loss and, if the spread of Sc values is not extreme, errors due to this source will probably be small in most practical situations.

It should be noted that, if a tuned filter used to isolate the a-c response to SHM is followed by either full-wave rectification or RMS detection, the phase problem is completely avoided.

The theory presented here does not apply to the case of mixed electron and mass transfer control, which we have already considered for the $p \rightarrow 0$ limit (6). There are effects in those situations (further diminishing A and increasing ϕ_1) which require a more involved treatment.

Acknowledgments

Work done at the State University of New York at Buffalo was supported by the Air Force Office of Scientific Research through AFOSR Grant No. 74-2572 to the Research Foundation of the State of New York.

Manuscript submitted February 6, 1975; revised manuscript received June 13, 1975. This was Paper 397 presented at the Toronto, Canada, Meeting of the Society, May 11-16, 1975.

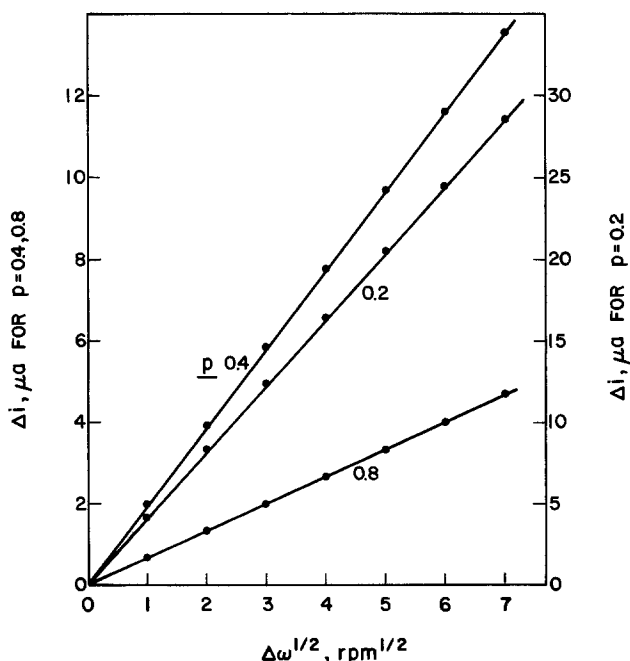


Fig. 7. Δi_1 as a function of $\Delta \omega^{1/2}$ at constant p values of 0.2, 0.4, and 0.8, as marked. Modulation frequency 6 Hz (all curves), center speed held at 30, 15, and 7.5 Hz. Abscissa is convertible to pe values by multiplication by 0.00472, 0.0133, and 0.0377 for $p = 0.2, 0.4, \text{ and } 0.8$, respectively.

Any discussion of this paper will appear in a Discussion Section to be published in the June 1976 JOURNAL. All discussions for the June 1976 Discussion Section should be submitted by Feb. 1. 1976.

Publication costs of this article were partially assisted by Bell Laboratories.

REFERENCES

1. B. Miller and S. Bruckenstein, *This Journal*, **117**, 1032 (1970).
2. B. Miller, M. I. Bellavance, and S. Bruckenstein, *ibid.*, **118**, 1082 (1971).
3. B. Miller, M. I. Bellavance, and S. Bruckenstein, *Anal. Chem.*, **44**, 1983 (1972).
4. S. Bruckenstein, M. I. Bellavance, and B. Miller, *This Journal*, **120**, 1351 (1973).
5. B. Miller and S. Bruckenstein, *Anal. Chem.*, **46**, 2026 (1974).
6. B. Miller and S. Bruckenstein, *This Journal*, **121**, 1557 (1974).
7. Th. von Kármán, *Z. Angew. Math. Mech.*, **1**, 233 (1921).
8. W. G. Cochran, *Proc. Cambridge Phil. Soc.*, **30**, 365 (1934).
9. E. R. Benton, *J. Fluid Mech.*, **24**, 781 (1966).
10. K. Tokuda and H. Matsuda, *J. Electroanal. and Interfac. Electrochem.*, **52**, 41 (1974).
11. E. M. Sparrow and J. L. Gregg, *J. Aerospace Sci.*, **27**, 252 (1960).
12. J. Newman, *J. Phys. Chem.*, **70**, 1327 (1966).
13. IBM Application Program, System/360 Scientific Subroutine Package, Version III, Programmer's Manual Program Number 360A-CM-03X, 5th ed, 1970.

Technical Note



The Cathodic Reaction of Iron Disulfide Electrode in KCl-LiCl Eutectic Electrolyte

Katsushi Abe and Takewo Chiku*

Toyota Central Research and Development Laboratories, Incorporated,
2-12, Hisakata, Tempaku-ku, Nagoya 468, Japan

The molten salt battery will be given more attention in the near future because of its high specific power and high specific energy. However, in the present state, there are various difficulties involving the battery construction, particularly the risk at high temperature operation from the use of liquid (1) or gaseous (2) active material as the positive electrode.

Vissers *et al.* (3) studied the molten salt secondary cells with iron sulfide as the positive material. This study was useful because it showed that there was no significant deterioration of electrical performance with cell operation.

Tomczuk, Martin, and Steunenberg (4,5) found that metal sulfides, such as nickel or cobalt sulfide, were solid-state materials that could serve as a positive electrode for a molten salt battery, and they proposed that the charge reaction of iron disulfide proceeds by three steps. The present authors have also examined various metal sulfides as solid-state active material for a battery with KCl-LiCl eutectic electrolyte.

It is the purpose of the present note to elucidate the discharge reaction of iron disulfide in KCl-LiCl eutectic electrolyte by a combination of the polarization character and x-ray diffraction analyses.

Experimental

The test electrodes were prepared, as shown in Fig. 1, by putting a definite quantity of iron disulfide powder in a hole (3.2 mm diameter, about 3 mm depth) drilled in spectroscopic graphite rod (6 mm diameter, 150 mm length), then filling it with electrolyte salt powder; the lower part of the rod was fixed by baking Aremco alumina adhesive and glazed Pyrex to separate it from the electrolyte except the hole. To prevent iron disulfide from escaping, the hole was sealed by wind-

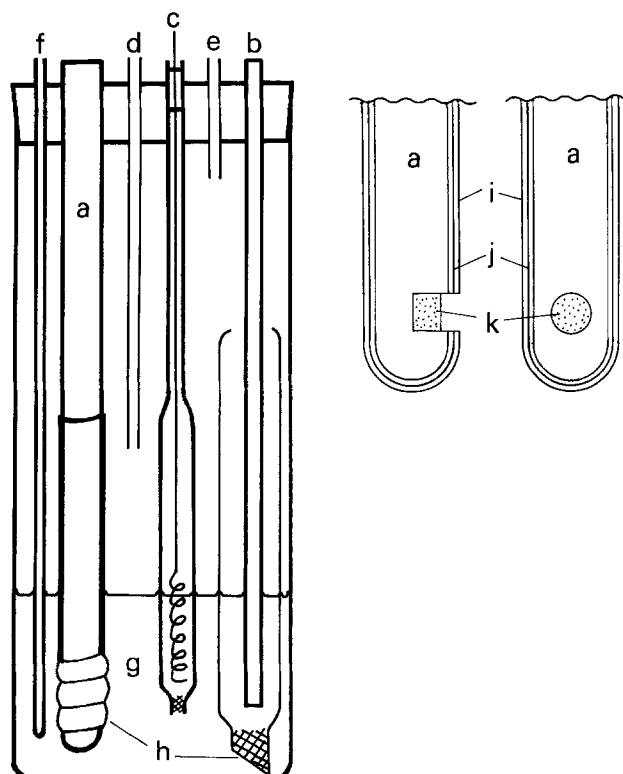


Fig. 1. Electrolysis cell and electrode construction. a, Graphite (test electrode); b, glassy carbon counterelectrode; c, reference electrode; d, Ar gas inlet; e, Ar gas outlet; f, thermocouple; g, KCl-LiCl eutectic; h, quartz wool; i, Pyrex glass seal; j, alumina adhesive; k, FeS₂ powder.

* Electrochemical Society Active Member.

Key words: iron pyrite, discharge reaction, molten salt electrolyte, high temperature cell.

ing the rod with quartz wool. The iron disulfide powder sample used in this study was a commercial pyrite (99.9% purity) containing only a trace of marcasite as shown by x-ray diffraction analysis.

The 58 mole per cent (m/o) LiCl-42 m/o KCl eutectic electrolyte was prepared by combining reagent grade lithium chloride and potassium chloride in a Pyrex vessel at 400°C, bubbling hydrogen chloride gas for about 1 hr and then high purity argon gas (O_2 : ~1 ppm, dew point: -65°C) for several hours. A Pyrex tube 28 mm inner diameter and 150 mm height was used as the electrolysis cell; the anode and the cathode compartments were separated by quartz wool. Figure 1 shows a schematic representation of its construction. The iron disulfide electrodes were discharged and charged at 400°C in the electrolyte with glassy carbon as the counterelectrode. High purity argon gas was made to flow continuously over the electrolyte during the experiments. The electrode potential was measured against a Pt/0.01 mole $PtCl_2$ reference electrode with the supporting electrolyte.

The reaction products used for x-ray measurements were taken from the electrode at various stages of charge and discharge in the following way: The respective electrodes were removed from the circuit and cooled in argon atmosphere, the products extracted from the graphite rods were crushed and pulverized in the atmosphere, then were covered with a thin film of Mylar. No washing or drying procedures were performed so as to prevent any change in the chemical composition.

Results and Discussion

Discharge and charge characteristics.—Figure 2 shows potential/time curves for the iron disulfide electrode with the repetition of discharge and charge cycles at a constant current of 200 mA/cm². The potential curve obtained during the first discharge to -2.0V shows several steps, and similar steps also were obtained in the curve with the subsequent charge to -0.7V, in which open-circuit potential before the discharge was about -0.7V. When repeating the cycle, the corresponding curves have little change in the shapes and the discharge capacities, at least up to 40 cycles. There is an additional step at about -0.8V in the discharge curve. However, judging from the fact that the upper limit of the charging potential was equal to the open-circuit potential at the initial state, the open-circuit potential could not be that of iron disulfide itself.

Figure 3 shows the discharge and charge curves at a constant current density of 100 mA/cm² and open-circuit potentials in various discharge and charge states; a stationary value obtained about 30 min after the circuit was opened at each state served for the open-circuit potential. It is seen that both the open-circuit potential curves in the discharge and charge were composed of four steps, and they are in close agreement with each other. These results suggest that the discharge-charge reaction proceeds through four reversible processes. At this current density, the polarization curve in discharge also shows four distinct steps corresponding to those in the open-circuit potential curve, but the four steps grow less distinct as the discharge current increases.

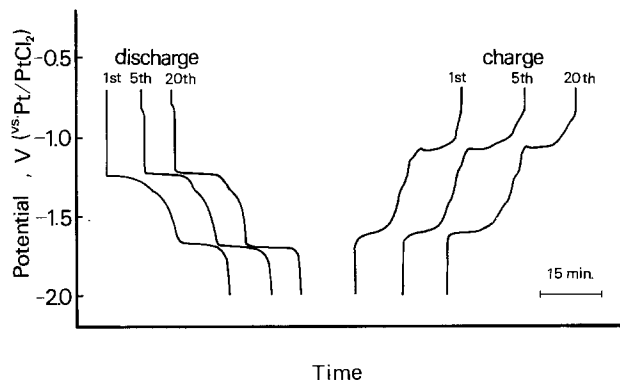


Fig. 2. Typical potential/time curves for FeS_2 electrode in discharge-charge cycling at a constant current density of 200 mA/cm².

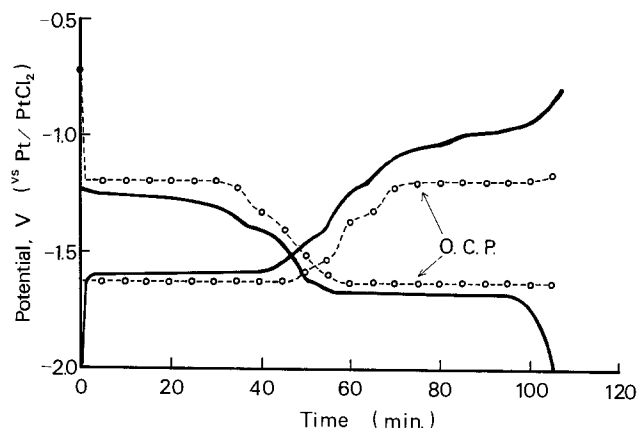


Fig. 3. Discharge-charge curves at a constant current density of 100 mA/cm² and open-circuit potentials in various discharge and charge states, for 20 mg FeS_2 at 400°C.

X-ray diffraction analyses.—Five electrodes, each containing 70 mg of iron disulfide, were placed in the discharge and charge states in the KCl-LiCl electrolyte. Three of them were partially discharged to -1.3, -1.6, or -2.0V at a current density of 50 mA/cm². The fourth electrode was completely discharged to -2.0V intermittently at 25 mA/cm². The last electrode was discharged to -2.0V at 100 mA/cm², then immediately recharged to -0.7V, the level of initial potential, at the same current density. X-ray diffraction analyses were carried out as a function of the depth of discharge. The results are summarized in Table I. As seen from the table, the starting material is pyrite containing a trace of marcasite. Phases gradually decrease with progressive discharge and are eventually exhausted at about -1.6V. At -2.0V, lithium sulfide and iron were observable as the final products. It is noted here that by recharging the electrode, the diffraction peaks of lithium sulfide and iron disappear accompanied by the reformation of pyrite together with a trace of pyrrhotite. However, many unknown peaks were present in the diffraction pattern at the partial discharge states. As shown in the last column

Table I. Results of x-ray diffraction analyses; Co-K α , 2θ ; 30° ~ 80°

No. of sample	Sampling potential (V)		Discharge state (%)	Identified material	Unknown peaks
	Discharge	Charge			
—	—	—	0	Pyrite, Marcasite (trace)	
1	-1.3	—	35	(Decrease) Marcasite	(A) ↓
2	-1.6	—	40	(Not detected)	(B) ↓
3	-2.0	—	85	Li_2S , Fe	Decrease (C) ↓
4	-2.0	—	100	Li_2S , Fe	Increase ↓
5	(-2.0)	-0.7	3	Pyrite, $Fe_{1-x}S$ (trace)	Not detected

of Table I, the unknown peaks were divided into three groups denoted by A, B, and C, respectively. These classifications show a partial increase or decrease as the discharge takes place. To ascertain if said peaks may have been caused by atmospheric oxidation or hygroscopicity during the sample preparation, the same examination was carried out with the sample specially prepared in a high purity argon atmosphere. No change, however, was observed in the diffraction pattern.

The results suggest at least that the corresponding substances were formed with the discharge process and that they transform to a stable substance at the final stage. In fact, the unknown peaks disappeared at the complete discharge state, and lithium sulfide and iron, which are considered to be the final products, could only be detected. These results corroborate previous findings that suggested four reversible processes make up the discharge-charge reaction.

Acknowledgments

The authors wish to thank Dr. K. Nakajima of Toyota Central Research and Development Laboratories for his helpful suggestions during this study.

Manuscript submitted Jan. 27, 1975; revised manuscript received June 9, 1975.

Any discussion of this paper will appear in a Discussion Section to be published in the June 1976 JOURNAL. All discussions for the June 1976 Discussion Section should be submitted by Feb. 1, 1976.

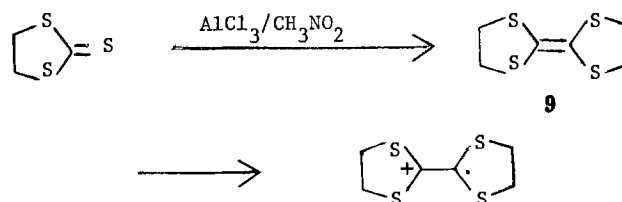
Publication costs of this article were partially assisted by Toyota Central Research and Development Laboratories, Incorporated.

REFERENCES

1. L. A. Heredy, N. P. Yao, and R. C. Saunders, International Electric Vehicle Symp., Nov. 5-7, 1969, p. 325.
2. D. A. J. Swinkels, *This Journal*, **113**, 6 (1966).
3. D. R. Vissers, Z. Tomczuk, and R. K. Steunenberg, *ibid.*, **121**, 665 (1974).
4. Z. Tomczuk, A. E. Martin, and R. K. Steunenberg, Paper 53 presented at the Electrochemical Society Meeting, New York, N.Y., Oct. 13-17, 1974.
5. A. E. Martin, R. K. Steunenberg, and Z. Tomczuk, Paper 54 presented at The Electrochemical Society Meeting, New York, N.Y., Oct. 13-17, 1974.

Erratum

In the paper "Electrochemistry of Multisulfur Heterocycles: Trithiocarbonates and Trithiocarbenium Ions" by P. R. Moses, J. Q. Chambers, J. O. Sutherland, and D. R. Williams which appeared on pp. 608-615 in the May 1975 JOURNAL, Vol. 122, No. 5, several bonds were omitted from the structure in Eq. [5]. The equation should read as follows:



of Table I, the unknown peaks were divided into three groups denoted by A, B, and C, respectively. These classifications show a partial increase or decrease as the discharge takes place. To ascertain if said peaks may have been caused by atmospheric oxidation or hygroscopicity during the sample preparation, the same examination was carried out with the sample specially prepared in a high purity argon atmosphere. No change, however, was observed in the diffraction pattern.

The results suggest at least that the corresponding substances were formed with the discharge process and that they transform to a stable substance at the final stage. In fact, the unknown peaks disappeared at the complete discharge state, and lithium sulfide and iron, which are considered to be the final products, could only be detected. These results corroborate previous findings that suggested four reversible processes make up the discharge-charge reaction.

Acknowledgments

The authors wish to thank Dr. K. Nakajima of Toyota Central Research and Development Laboratories for his helpful suggestions during this study.

Manuscript submitted Jan. 27, 1975; revised manuscript received June 9, 1975.

Any discussion of this paper will appear in a Discussion Section to be published in the June 1976 JOURNAL. All discussions for the June 1976 Discussion Section should be submitted by Feb. 1, 1976.

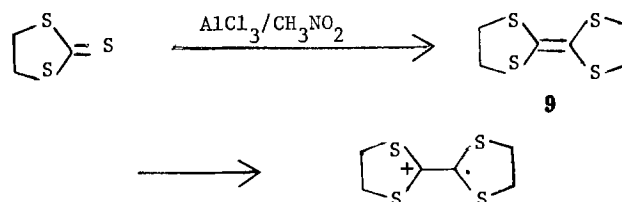
Publication costs of this article were partially assisted by Toyota Central Research and Development Laboratories, Incorporated.

REFERENCES

1. L. A. Heredy, N. P. Yao, and R. C. Saunders, International Electric Vehicle Symp., Nov. 5-7, 1969, p. 325.
2. D. A. J. Swinkels, *This Journal*, **113**, 6 (1966).
3. D. R. Vissers, Z. Tomczuk, and R. K. Steunenberg, *ibid.*, **121**, 665 (1974).
4. Z. Tomczuk, A. E. Martin, and R. K. Steunenberg, Paper 53 presented at the Electrochemical Society Meeting, New York, N.Y., Oct. 13-17, 1974.
5. A. E. Martin, R. K. Steunenberg, and Z. Tomczuk, Paper 54 presented at The Electrochemical Society Meeting, New York, N.Y., Oct. 13-17, 1974.

Erratum

In the paper "Electrochemistry of Multisulfur Heterocycles: Trithiocarbonates and Trithiocarbenium Ions" by P. R. Moses, J. Q. Chambers, J. O. Sutherland, and D. R. Williams which appeared on pp. 608-615 in the May 1975 JOURNAL, Vol. 122, No. 5, several bonds were omitted from the structure in Eq. [5]. The equation should read as follows:





Role of Anodic Processes in the Electrolytic Coloration of Alkali Halides

M. T. Montojo¹ and F. Jaque

Departamento de Física, Universidad Autónoma, Cantoblanco, Madrid, Spain

and C. Sánchez

FEMSA, D.E.P. Investigación, Hnos. García Noblejas No. 19, Madrid 17, Spain

ABSTRACT

An investigation has been made into the origin of Zone IV (1) of the current *vs.* time curves obtained during electrolytic coloration of alkali halides with a pointed cathode and a flat metallic anode mechanically pressed against the crystal. Zone IV is not intrinsic and is not due to the crystal volume itself, but is related to processes occurring in the crystal-metallic anode interface. Whenever these processes are inhibited, *e.g.*, by using a vacuum evaporated metallic anode, Zone IV is suppressed and intrinsic current *vs.* time curves are obtained. These curves resemble those corresponding to space charge limited currents in insulators and semiconductors. The following anodic processes are mentioned: An electrical arc was produced in the thin and irregular gap between the crystal and the anodic plate. The intensity of the light emitted from this arc correlates with electrical current during Zone IV and the spectral distribution shows a complicated multippeak structure. The number and position of the peaks are quite independent of the alkali halide crystal, anodic material, and gas filling the furnace. Most of the spectrum peaks correspond fairly well in position to those of the air component discharge. The main characteristics of the arc are due to air (water vapor) adsorbed on the anodic crystal surface. A tentative explanation of how this electrical arc can determine the properties of Zone IV is proposed.

Electrolytic coloration has been extensively used as a procedure to create F-centers in alkali halides (2); the number of F-centers produced depending upon the experimental conditions. Experiments are usually carried out at constant temperatures ($\sim 350^{\circ}$ – 700° C) and applied voltages (50 – 10^3 V). Currently, a pointed cathode and a flat metallic anode mechanically pressed against the crystal are used. Atmospheres surrounding the crystals are air, vacuum, or an inert gas.

The evolution of the electrical current through the crystal during the electrolytic coloration has been recorded in KCl and KBr (1, 3, 4). Figure 1 shows an example of this behavior in KBr single crystals. F-center density changes in a parallel fashion, as shown by the dashed curve, although a time lag exists. Four zones appear in the *i-t* curve. Zone I has been accounted for as being due to purely ionic transport (1, 4, 5). This process leads to the formation of an injecting contact at the cathode-crystal interface (6). Once this contact is formed electrons are injected from the pointed cathode into the crystal. Electronic current marks the start of Zone II. The kinetics of this zone in KCl has been explained by Heiland (3) and Karabascheff (7) as due to F-center diffusion. Equations describing the slope of this zone have also been proposed.

In spite of the wide use of electrolytic coloration, several questions relating to its physical mechanisms

still remain open. Briefly, these questions relate to: (i) The appearance of Zone IV in KBr and KCl which corresponds to an enhancement of the electrical current and F-center density in the crystal. According to Heiland (3) Zone II should be followed by an equilib-

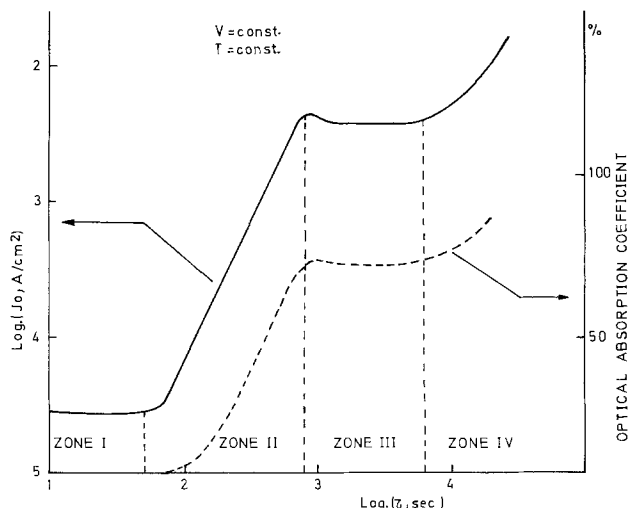


Fig. 1. Electrical current (continuous line) and F-center density (dashed line) *vs.* time during electrolytic coloration of KBr single crystals. [After Andreev *et al.* (1)].

¹ Also: C.I.D.A., Arturo Soria No. 289, Madrid, Spain.
 Key words: solid electrolytes, injected carriers, color centers, dielectric breakdown.

rium stage (Zone III) in all cases, and Zone IV should never appear. (ii) The F-color cloud starts at the cathode and propagates through the crystal. Pisarenko (8) has observed a coloration starting at the region surrounding the anode after the conductivity increased in Zone IV in KCl crystals at temperatures between 250°-350°C.

Herein are reported some new experimental results in relation to these points. It is shown that Zone IV is exclusively due to processes occurring at the anode-crystal frontier. These processes can be inhibited, therefore suppressing Zone IV. They are responsible for the high current and high F-center concentrations that characterize Zone IV.

Experimental

A vacuum-sealed furnace was used to electrolytically color the crystals. Temperature was controlled with $\pm 1^\circ\text{C}$ and measured with a Chromel-Alumel thermocouple. Experiments were performed in either air, vacuum, nitrogen, or argon atmospheres. A pointed cathode (stainless steel, Pt) and a flat anode (tungsten, aluminum foils, and graphite) were used. In some experiments the anode was a vacuum-evaporated film.

A couple of quartz windows in the furnace allowed for luminescence measurements and photographing the crystals. A high intensity Bausch and Lomb monochromator and an EMI 9558 QB photomultiplier were used in the range 2500-4500Å. Single crystals of KBr, NaCl, KCl, KI, and CsI of $\sim 10 \times 5 \times 5$ mm were colored. Other experimental details are described in (4).

Results

In the process of electrolytically coloring KBr single crystals with a stainless steel pointed cathode and a tungsten foil anode mechanically pressed against the crystal, a light emission was detected. The samples were placed between the electrodes in the open air and the sample holder was then introduced into the furnace. Air was evacuated and nitrogen was let into the furnace at a pressure slightly higher than the atmospheric one. The sample was heated and once the working temperature ($\sim 350^\circ\text{C}$ - 550°C) was stabilized, the electric field was turned on in order to color the crystal. Light emission was also measured with other crystals (KCl, KI, NaCl, and CsI), electrodes (platinum point, aluminum foils, and graphite), and atmospheres (air and argon).

Photographs taken during the coloration process proved that in all cases the light is generated at the anode-crystal frontier. The crystal is shown in Fig. 2 with a black line and the pointed cathode is at the top of the picture. The light emitted has a multipeak spectrum as shown in Fig. 3. The width of the lines

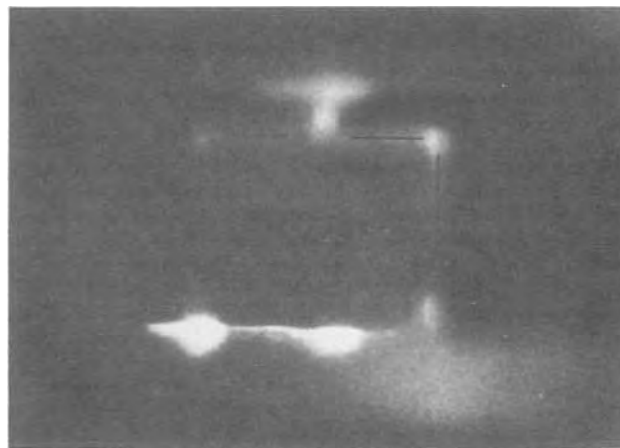


Fig. 2. Photograph of a KBr crystal during coloration in Zone IV shows light emission in the anodic region. The crystal is marked with a black line.

cannot be considered as a reliable datum due to the monochromator we used. The intensities of the lines were highly dependent on the experimental conditions and no systematic study of this point has been made.

In order to elucidate the possible origin of the electrical arc and the light emission, experiments were performed with different alkali halides, electrodes, and atmospheres. In all cases, the experimental procedure was that described above. The most relevant parameters from the obtained spectra were the peak positions. Table I shows some of the experimental results: the crystal, cathode and anode material, and the atmosphere used in each experiment are indicated. The main air component discharge is also quoted for comparison purposes. It is clear from the table that most of the peak positions are quite independent of the various crystals, electrodes, and atmospheres. In our experiments with KBr and KCl single crystals, we were able to obtain measurements only for wavelengths shorter than $\sim 4700\text{Å}$ due to the emission of the furnace walls: A much lower temperature is required to color CsI than to color KBr and KCl. All the wavelengths in the table are affected by an error of $\pm 50\text{Å}$. At this point it is interesting to note that whenever a graphite anode was used, the peak intensities were much weaker than with an Al or W anode. Furthermore, with air filling the furnace the intensities of all the lines were considerably improved.

The intensity of the emitted light is a function of time during the coloration process: we never detected

Table I. Peak position wavelengths (Å) of the anodic emission spectra obtained by electrolytically coloring different alkali halides with several electrodes and atmospheres. The major lines of the air component discharge are also included. All the values are affected by an error of $\pm 50\text{Å}$.

Crystal Electrodes Atmosphere	CsI SS*-W Nitrogen	CsI Pt-Al Nitrogen	CsI Pt-W Nitrogen	KBr SS* graphite Nitrogen	KBr SS*-W Nitrogen	KBr Pt-Al Nitrogen	KBr SS*-W Argon	KCl SS*-W Nitrogen	Principal air Lines**	
	5865	5800	5880	5830					5888	
	5680		5740	5656					5750	
			5400	5304					5330	
	4980	~5100	5020	5018					4969	
		4750	4700						4705	
	4650		4600	4660					4649	
	4300	4300	4330	4292	4270	4300	4370		4349	
	4040		4000	4028		4050	4090	4040	4070	
Peak posi- tions (Å)		3900	3940	3900					3995	
		3700	3770	3750	3800	3810	3760	3790	3749	
		3600	3600	3610	3570	3570	3580	3590		
		This range has not been covered					3345	3380	3330	3350
						3120	3140	3120	3100	3390
						2950				3332
						2810		2850		3329
						2680	2600	2750		2733
								2650		2678

* SS = stainless steel.

** Wavelength tables for spectrum analysis, Adam Hilger Ltd., London (1931).

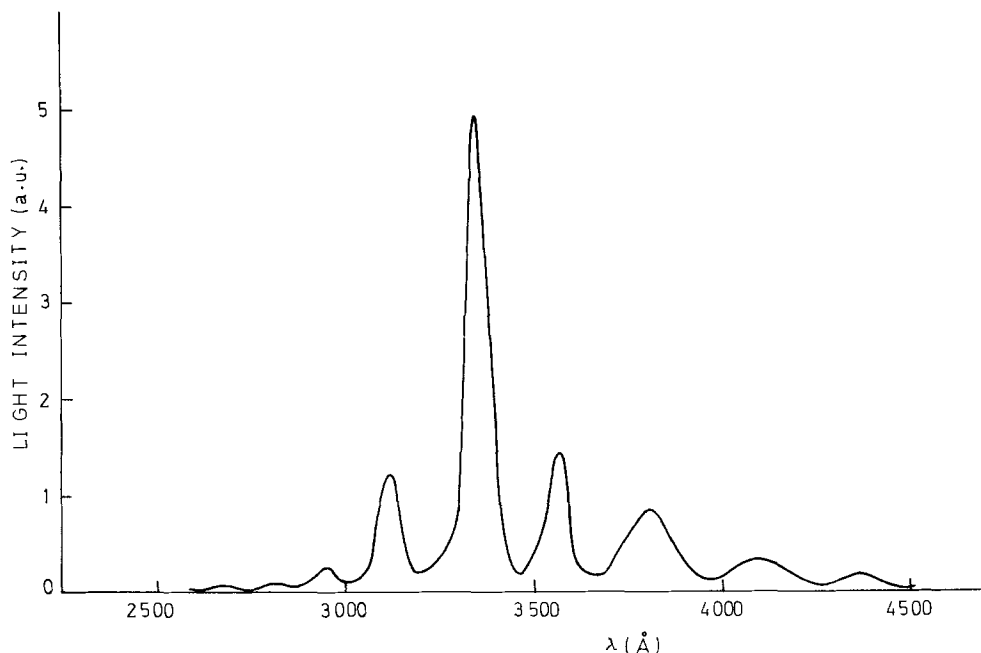


Fig. 3. Spectral distribution of light emitted during electrolytic coloration of KBr with a W foil as anode and nitrogen atmosphere.

light during Zone I of the coloration curve; a very weak emission was measured sometimes during Zone II and at other times during Zone III; but the emission of light was highly efficient during Zone IV. This behavior is depicted in Fig. 4(a) where the evolution of the electrical current (curve A) and the light intensity measured at $\lambda = 3570\text{\AA}$ (curve B) during the electrolytic coloration of KBr are shown. A time lag between the current and light is observed initially; but in Zone IV both curves rise up proportionally as represented in Fig. 4(b). This behavior appears in all the materials we have studied. The slope of the straight line and the value of the electrical current when there is no light intensity are a function of the experimental conditions, but are more affected by the applied electric field and the sample temperature. It was also noted that at temperatures below 500°C the F-coloration originating at the cathode during Zone II is very weak, but on reaching Zone IV a dense line of coloration from the anode propagates through the crystal and begins its dielectric breakdown when it joins the cathode.

Discussion

It is clear from Fig. 2 that the emission of light during Zone IV of the current-time curve is due to processes occurring in the crystal-anode interface. All the experimental results already described were obtained by using a metallic anodic plate mechanically pressed against the sample; the conventional method used to electrolytically color alkali halides. The experimental procedure followed in all cases was that described above.

It is also evident that a close parallelism exists between the electrical behavior in Zone IV and the anodic processes responsible for the light emission. In order to examine this parallelism more closely, the anodic contact was changed. Crystals with vacuum (10^{-6} Torr)-evaporated metallic (Au, Al) anodes were prepared. The rest of the experimental procedure was as previously described: The same stainless steel or platinum pointed cathode was used. While coloring the crystal with these new anodes, the electrical current passing through the sample was recorded. Curve A in Fig. 5(a)

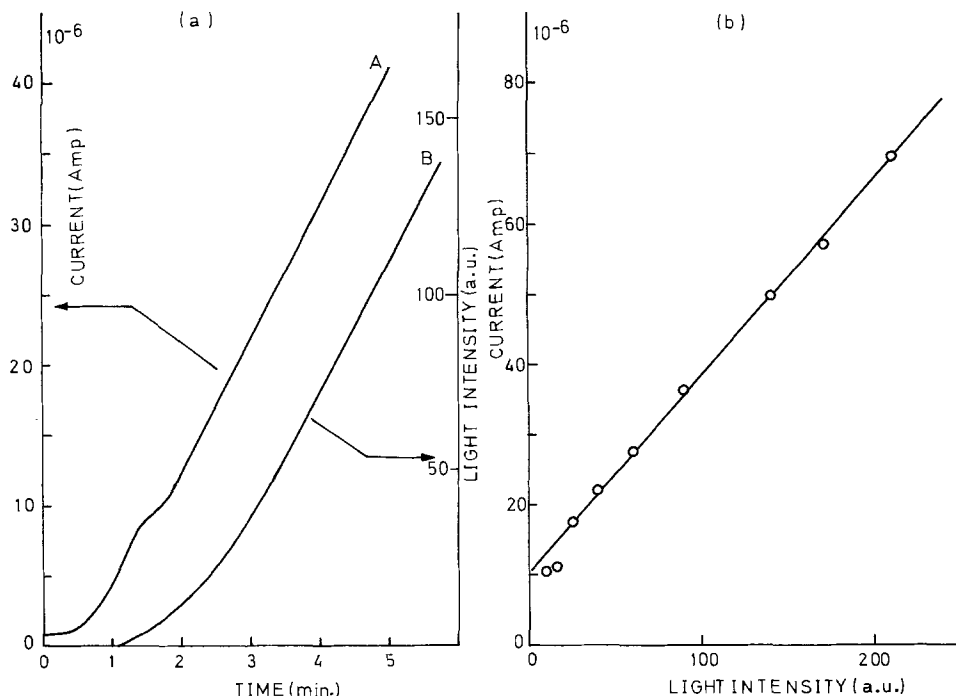


Fig. 4. (a). Electrical current (curve A) and light intensity at $\lambda = 3570\text{\AA}$ (curve B) during electrolytic coloration of KBr at $T = 422^\circ\text{C}$, $V = 600\text{V}$. (b) Relationship between current and light intensity.

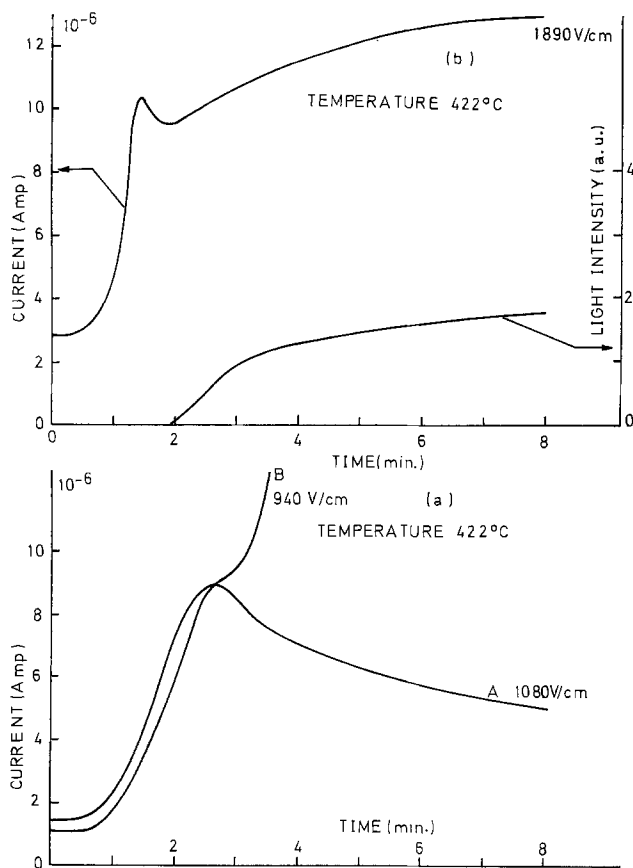


Fig. 5. (a). Electrical current during electrolytic coloration of KBr with a vacuum-evaporated Al film as anode (curve A). Curve B is shown for comparison purposes and has been obtained with a tungsten plate. (b). Shows the effect of increasing the voltage to higher values than those commonly used in our experiments. The anode was a vacuum-evaporated film.

represents the results obtained. At the same time it must be emphasized that no light emission was detected along the whole coloration process. It is clear from Fig. 5(a) that Zone IV does not appear. The electrical current follows Zones I and II, reaches a maximum, and finally decreases; the difference between the maximum and the final steady value of the current being a function of the applied voltage and the crystal temperature. From these experiments it was concluded that Zone IV of the curves is not intrinsic and is due to the processes occurring in the crystal-anode interface while electrolytically coloring alkali halides by conventional means. If these phenomena are inhibited, at least partially, Zone IV disappears. The anodic processes are not totally avoided by using vacuum evaporated anodes as can be seen from Fig. 5(b) where the applied voltage has been increased to much higher values than those commonly used in these experiments. Current again increases, leading to a very reduced Zone IV. At the same time, a very slight light emission is detected [Fig. 5(b)] proving that both light emission and electrical current in Zone IV have the same origin. For comparison purposes a typical curve obtained with a tungsten foil anode mechanically pressed against the crystal at the same temperature is shown as curve B in Fig. 5(a).

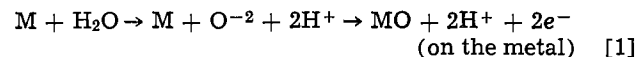
It is worthwhile to note that curve A in Fig. 5(a) closely resembles those obtained in insulators and semiconductors (9) whenever space charge controlled mechanisms are operating. Results regarding the role played by these mechanisms in the electrolytic coloration of alkali halides will be published elsewhere.

As to the physical nature of the processes occurring in the crystal-anode interface, it is clear from Table I that the peak positions of the emission spectra are widely independent of the crystals, electrodes, and gas filling the furnace. On the other hand, a very narrow

correspondence (within the experimental error) exists between these values and those shown by the principal lines of the air component discharge (last column of Table I). These two experimental facts, and the evidence that on using vacuum-evaporated anodes there is no light emission, lead to the suggestion that the air (essentially water vapor) adsorbed in the anodic crystal face during the cleaving and the storing of the samples plays a major role in all the described phenomena. This water vapor is probably desorbed during the heating of the sample and retained in the thin and irregular gaps between the crystal and the anodic plate due to the overpressure of the nitrogen (or argon) introduced in the furnace. As a consequence, the main characteristics of the emission spectra correspond to those of the air component discharge. A confirmation of this hypothesis was obtained by the following experiments: with the same primitive flat anode (tungsten or aluminum foils), the crystal holder was introduced into the furnace and the crystal heated in a dynamic vacuum (without introducing inert gas) up to the working temperature, then the vacuum was maintained for some time (~ 1 hr) before letting nitrogen or argon in. With this procedure we tried to partly eliminate the water vapor adsorbed in the crystal surface. On applying the electric field to color the crystal, curves similar to curve A in Fig. 5(a) are obtained and no light emission exists. Whenever the water vapor retained in the gaps between the crystal and the metallic anode is removed, Zone IV disappears and there is no luminous phenomena. Not all the observed phenomena are due exclusively to this water vapor, no doubt there is some influence from the gas filling the furnace and the electrode materials, but these should be rather small in comparison with the contribution of the adsorbed water vapor.

Regarding the origin of the electrical arc in the crystal anode interface, no clear conclusion can be obtained from these results. According to the shape of the curve in Fig. 1 it can be suggested that during Zone II a high negative space charge accumulates at the crystal anodic face and a very high electric field is produced through the narrow gaps between the crystal and the anode. This suggestion has some experimental support in that the arc appears either during or at the end of Zone II.

Finally, the means by which the electrical arc in the anodic face can give place to Zone IV of the curves should be discussed. The whole process appears to be very complicated, and some speculation seems unavoidable. Our results suggest that water vapor molecules desorbed from the anodic face of the crystal are decomposed by the arcing, and oxygen ions react with the metal plate to produce oxides. In fact, the area of the anodic foil in contact with the crystal shows a very dark stain, clear evidence of a chemical reaction. On the other hand, the principal emission lines that were measured correspond to those of the second ionization of oxygen. One possible mechanism for this decomposition could be



although the whole process must be much more complicated and other quantitative combinations are possible. M signifies the anodic metal (W, Al, Mo). Reactions like Eq. [1] have been observed in different metallic surfaces under the action of an electric arc (10).

In order to account for the high value of electrical current in Zone IV, it is plausible to think that protons liberated in the arc region are injected into the crystal under the electric field existing in the gap. Their high mobility should produce a considerable contribution to the electrical current. Phenomena parallel to those we are discussing now have been shown to take place in some glasses when atmospheric moisture is present (11). Further experimental work is needed before all these possible mechanisms can be confirmed.

The final conclusion in relation to the electrolytic coloration process is that only Zones I, II, and III are intrinsic; Zone IV is not due to the crystal itself. From our results it appears that water vapor adsorbed in the anodic face of the crystal plays an important role in relation to Zone IV of the curve. But it is not yet possible to determine the exact processes taking place in the electrical arc at the anode region.

Acknowledgments

The authors gratefully recognize "Ayudas Manuel Aguilar" which partly supported this work. Fruitful discussions with the members of C-IV (U.A.M.) have been a continuous encouragement.

Manuscript submitted July 1, 1974; revised manuscript received May 23, 1975.

Any discussion of this paper will appear in a Discussion Section to be published in the June 1976 JOURNAL. All discussions for the June 1976 Discussion Section should be submitted by Feb. 1, 1976.

Publication costs of this article were partially assisted by FEMSA.

REFERENCES

1. G. A. Andreev, G. B. Semushkin, and A. N. Tsikin, *Soviet Phys. Solid State*, **9**, 2564 (1968).
2. J. J. Markham, "F-centers in Alkali Halides," Academic Press, Inc., New York (1966).
3. G. Heiland, *Z. Physik*, **127**, 144 (1950).
4. M. T. Montojo and C. Sánchez, *J. Phys. Chem. Solids*, **35**, 1437 (1974).
5. N. Paramo and C. Sánchez, *J. Phys. Soc. Japan*, **30**, 1106 (1971).
6. M. T. Montojo and C. Sánchez, *Solid State Commun.*, **14**, 485 (1974).
7. N. Karabasheff, *Z. Physik*, **118**, 718 (1942).
8. V. F. Pisarenko, *Soviet Phys. Solid State*, **3**, 2184 (1962).
9. M. A. Lampert and P. Mark, "Current Injection in Solids," Academic Press Inc., New York (1970).
10. G. Amsel, in "Physics of Solid Electrolytes," J. Hladik, Editor, p. 133, Academic Press Inc., London (1972).
11. K. Hughes and J. O. Isard, *ibid*, p. 368.

The Transport of Chromium in Cr₂O₃ Scales in Sulfidizing Environments

G. Romeo,^{*1} H. S. Spacil,* and W. J. Pasko

Research and Development Center, General Electric Company, Schenectady, New York 12301

ABSTRACT

The diffusivity of chromium in Cr₂O₃ scales formed during the oxidation of chromium at 900°-1000°C appears to increase by several orders of magnitude when an initially present oxide scale is exposed to sulfur-bearing atmospheres at low oxygen partial pressure. As a result chromium sulfide scales grow on both sides of the preexisting oxide layer. The transition from oxidation to sulfidation corresponds to a change from parabolic to linear weight gain, indicating that the sulfide growth is controlled by a constant rate of supply of chromium through the oxide to the outer oxide-sulfide interface, under fixed experimental conditions. The sulfidation rate increases with sulfur partial pressure, indicating that chromium transport in the oxide is affected by changes in the defect structure of Cr₂O₃ induced by the presence of sulfur. A model is proposed in which sulfur enters the oxide as an electron donor, thereby increasing the concentration of chromium vacancies and interstitials.

Hot corrosion phenomena of gas turbine superalloys frequently result in the formation of mixed oxide/sulfide scales. Sulfidation has been reported as due to the reaction of the alloy surface with sodium sulfate deposits, considering the sulfate, with a very low sulfur activity, as the only source of sulfur (1). However, the presence of sulfur at an activity above the equilibrium value for sulfide formation would provide an additional mechanism for accelerated corrosion. Such high sulfur activities could arise from local reducing conditions in an otherwise oxidizing environment (2). Internally precipitated sulfides are frequently observed under Cr₂O₃ scales formed on Ni-base alloys. It is then possible that a mechanism involving the transport of sulfur across these scales from a high activity source is responsible for the presence of sulfide particles. The diffusion of sulfur in polycrystalline Cr₂O₃ has been studied by Seybolt (3), who reported a tracer diffusion coefficient of about 1.5×10^{-10} cm²/sec at 1000°C. No mechanism was proposed for the migration of sulfur species through the oxide. A recent paper by Chang *et al.* (4) on the diffusion of S³⁵ in hot-pressed α -Cr₂O₃ reported a diffusion coefficient for S³⁵ varying from 5.1×10^{-11} to 5.2×10^{-10} cm²/sec in the temperature range 700°-1050°C.

In a previous publication (5) we have reported preliminary results on the sulfidation kinetics and scale morphologies of chromium specimens preoxidized and subsequently exposed at 900°C to 10% H₂S-H₂ gas mixtures. This paper summarizes the results of further experiments in which the sulfidation of preoxidized chromium was studied at different partial pressures of sulfur.

Experimental

Rectangular specimens of high purity "iochrome" (99.997%) approximately $1.5 \times 0.7 \times 0.15$ cm were cut from a cast ingot. After a suspension hole was drilled in each, these were wet ground through 600 grit silicon carbide paper and cleaned with acetone and methanol. Finally, their dimensions were measured with a micrometer.

Reaction kinetics were determined by following the weight gain of a specimen with a spring balance, the basic design of which has been described in a previous publication (6). Some modifications were made to this equipment in order to run experiments at low sulfur pressures. These could be attained by bubbling argon or a carbon monoxide/argon mixture through a flask containing molten sulfur. The flask was immersed in a silicone oil bath which was held at temperatures controlled within 1°C. Argon was used as an inert carrier

* Electrochemical Society Active Member.

¹ Present address: General Electric Company, Vallecitos Nuclear Center, Pleasanton, California 94566.

Key words: sulfidation, chromium diffusion, chromium oxide.

for sulfur, while carbon monoxide could provide a reducing environment. Gas mixtures of composition ranging from 0.001-10 volume per cent (v/o) hydrogen sulfide in hydrogen were also used as a source of sulfur. Linde commercial mixtures of "ultra high purity" gases were employed directly or appropriately diluted with hydrogen for this purpose. When the sulfur bath was used, the vapor pressure of S_2 was known from the temperature of the bath; by assuming saturation of the argon carrier, the S/CO ratio in the final gas mixture could be specified. With either H_2S-H_2 or $CO-S_2$ mixtures, the equilibrium sulfur partial pressure can be found by employing thermodynamic data for the relevant species. For the latter mixtures, formation of COS, CO_2 , and SO_2 must be considered. Data from the JANAF Tables were used for this purpose (7).

Prior to each sulfidation run the chromium specimen was oxidized isothermally with oxygen at atmospheric pressure at temperatures of 900° or 1000°C, the latter value being chosen to allow the formation of thicker oxide layers. The oxygen flow was then stopped, the reaction cell was purged with argon, and the furnace temperature was adjusted to a value of 900°C prior to sulfidation, with the exception of a few runs carried out at 800° and 1000°C. The temperature of 900°C was chosen for its relevance to gas turbine operations.

After completion of each run the specimens were mounted in epoxy resin and cross-sectioned for metallographic examination and microprobe analysis of the scale. Also, after some runs the scale composition was identified by the Debye-Scherrer method.

Results

As reported elsewhere (5), a dramatic change in reaction rate and mechanism took place when a previously oxidized chromium specimen was exposed to a sulfur-containing atmosphere. Figure 1 shows that the weight gain curve of a specimen exposed directly to a 10% H_2S-H_2 gas mixture at 900°C followed a parabolic rate law, with a rate constant of $52 \text{ mg}^2\text{-cm}^{-4}\text{-min}^{-1}$, in quite good agreement with the value $92 \text{ mg}^2\text{-cm}^{-4}\text{-min}^{-1}$ reported by Strafford and Hampton for the sulfidation of chromium at 925°C with a 30% H_2S-H_2 gas mixture (8). Figure 2 shows the weight gain curve of a specimen preoxidized and subsequently exposed at 900°C to the 10% H_2S-H_2 gas mixture. In the latter instance, switching from an oxidizing to a sulfidizing atmosphere brought about a change from a parabolic to a linear rate law after an incubation period.

Figure 3 shows an example of scale structure formed after a complete preoxidization and sulfidation run (No. 4 in Table II). Chromium sulfide can be formed on both sides of the oxide layer initially present, with

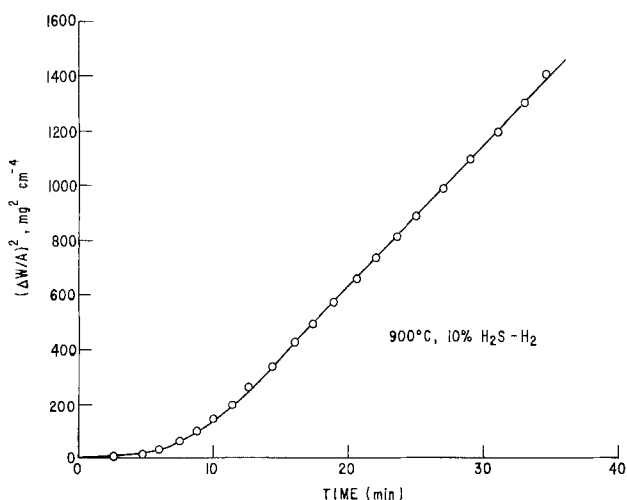


Fig. 1. Parabolic plot of weight gain vs. time for the sulfidation of chromium at 900°C with a 10% H_2S-H_2 gas mixture.

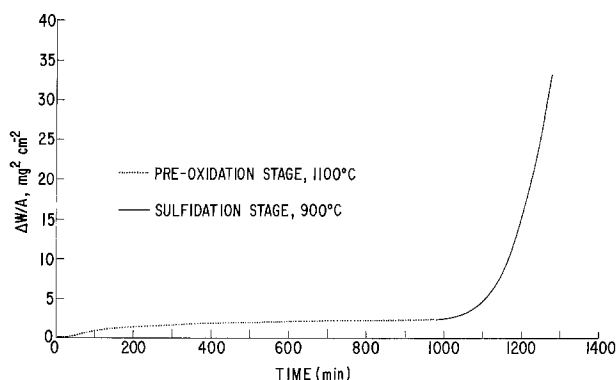


Fig. 2. Weight gain of a chromium specimen first exposed to oxygen at 1 atm and 1100°C, then to a 10% H_2S-H_2 gas mixture at 900°C.

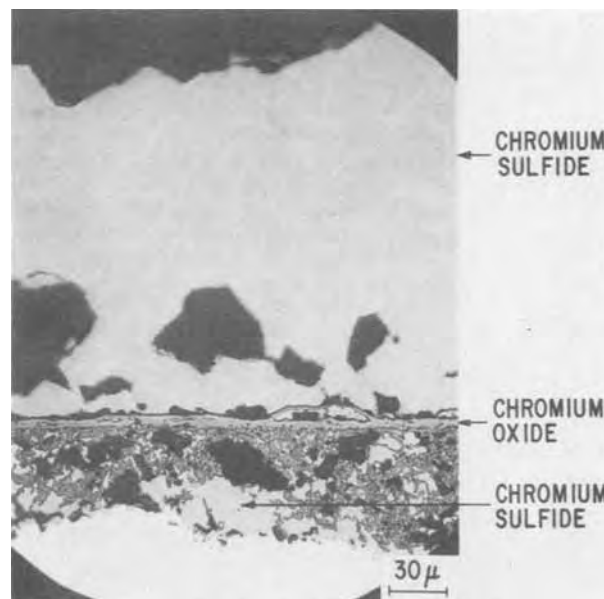


Fig. 3. Scale structure of a chromium specimen preoxidized and subsequently exposed for 20 hr to a 0.1% H_2S-H_2 gas mixture at 900°C.

the outer portion of the sulfide scale much thicker than the inner portion. Although the initial compactness of the oxide layer has been altered by the growth of the inner chromium sulfide layer, a fairly uniform layer of chromium oxide exists between the chromium sulfide scales.

Table I summarizes the values of the linear rate constant k_1 obtained during sulfidation for three different thicknesses of pregrown oxide. The sulfidation was carried out in each case at 900°C in a 10% H_2S-H_2 gas mixture. The corresponding weight gain curves have been reported previously (5).

To verify the lower limits of sulfur pressure at which sulfidation does not take place on a preoxidized chromium specimen, similar experiments were also carried out in a much lower range of sulfur pressures. The experimental conditions and linear rate constants are

Table I. Linear rate constants in sulfidizing atmosphere of 10% H_2S-H_2

No.	Oxidation temperature (°C)	Weight of oxide at end of oxidation ($\text{mg} \times \text{cm}^{-2}$)	k_1 (sulfidation) ($\text{mg} \times \text{cm}^{-2} \times \text{min}^{-1}$)
1	900	0.6	0.50
2	1100	2.3	0.23
3	1200	3.2	0.11

Table II. Linear rate constants in low sulfidizing atmospheres

No.	Oxidation temperature ($^{\circ}\text{C}$)	Weight of oxide at end of oxidation ($\text{mg} \times \text{cm}^{-2}$)	Atmosphere compositions (v/o)	k_1 (sulfidation) ($\text{mg} \times \text{cm}^{-2} \times \text{min}^{-1}$)
1	1000	2.7	$\text{H}_2\text{S}-\text{H}_2$ 0.001	—
2	1000	1.6	0.05	0.01
3	1000	1.6	0.1	0.06
4	900	1.1	0.1	0.09
5	900	0.5	0.2	0.09

summarized in Table II. Figure 4 shows the corresponding weight gain curves, in which time zero is the time at which the sulfidizing mixture was introduced into the reaction cell. Again, after an incubation period which varied with the thickness of the pregrown oxide, sulfidation took place in all cases according to an approximately linear rate law, except for run No. 1 of Table II.

A similar weight gain curve was obtained when the sulfidation stage was carried out using a reacting gas mixture of carbon monoxide bubbled through a sulfur melt held at 175°C . The purpose of this experiment was to observe whether a decrease in oxygen activity in the reacting gas mixture due to a reducing agent other than hydrogen would result in a comparable sulfidation mechanism. Indeed the corresponding weight gain curve, labeled with an asterisk in Fig. 4, followed the same trend as the curves obtained with $\text{H}_2\text{S}-\text{H}_2$ atmospheres. However, the morphology of the corrosion product was different in this case, as shown in Fig. 5. X-ray and microprobe analysis identified the outer layer of the scale as Cr_3S_4 , the dark layer underneath it as a mixture of sulfides and carbides of chromium, and the innermost layer as primarily chromium together with chromium oxide and carbide particles. Saturation of the carrier gas with sulfur was more difficult to accomplish, and the vapor pressure of sulfur in the gas may have been below the nominal value of 10^{-3} atm corresponding to the temperature of the sulfur bath.

Discussion

The equilibrium phases that would be expected at 900°C in the Cr-O-S system are shown in Fig. 6, which is the stability diagram for this system in terms of the chemical potentials of oxygen and sulfur. These chemical potentials are given by $\mu_X = RT \ln p_{X_2}^{1/2}$, where X represents either oxygen or sulfur and p_{X_2} is the equilibrium partial pressure of O_2 or S_2 . Data on sulfide stability were obtained from Young *et al.* (9), except for CrS, where an average of data from Young *et al.* with that of Hager and Elliott (10) was used. Data on

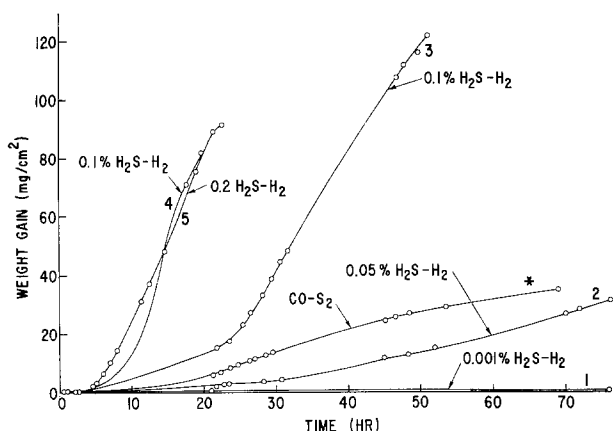


Fig. 4. Weight gain curves of chromium specimens preoxidized and subsequently sulfidized at 900°C with $\text{H}_2\text{S}-\text{H}_2$ gas mixtures of different composition. The experimental conditions corresponding to the curves labeled with numerals are listed in Table II. The curve labeled with an asterisk corresponds to a sulfidation stage carried out with a $\text{CO}-\text{S}_2$ gas mixture.

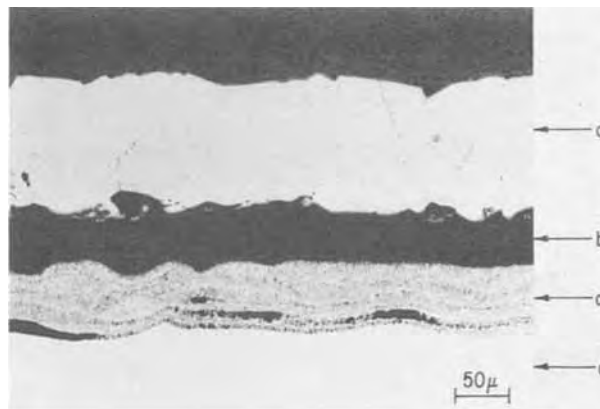


Fig. 5. Scale structure of a chromium specimen preoxidized and exposed at 900°C for about 70 hr to a $\text{CO}-\text{S}_2$ gas mixture: a, chromium sulfide (Cr_3S_4); b, mixture of sulfides and carbides of chromium; c, mixture of chromium with some oxides and carbides; d, chromium.

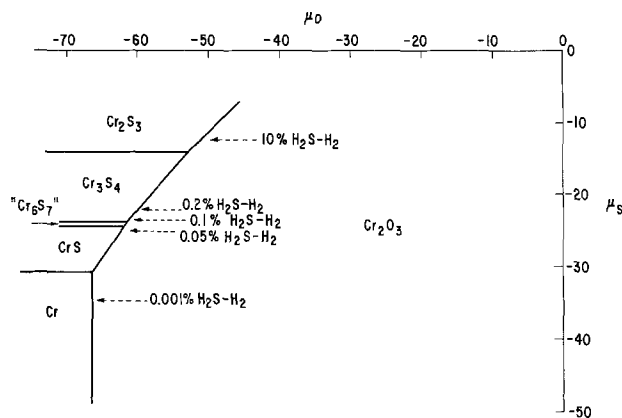


Fig. 6. Stability diagram of the Cr-O-S system at 900°C (μ_{O} , μ_{S} in kcal/mole).

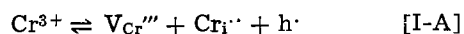
oxide stability were taken from Elliott and Gleiser (11). The phase " Cr_6S_7 " represents an average of data for the phases Cr_5S_6 and Cr_7S_8 reported by Young *et al.*; the equilibrium S_2 pressures for these two phases in equilibrium with Cr and Cr_3S_4 , respectively, are sufficiently close to allow treating them as one phase for the present purpose.

Figure 6 also shows the sulfur potentials corresponding to the various $\text{H}_2\text{S}-\text{H}_2$ compositions of Tables I and II. It is immediately apparent from this figure that the lowest composition of 0.001% H_2S is thermodynamically incapable of forming any sulfide. Thus run No. 1 of Table II would be expected to show no sulfide formation. All other compositions, however, can lead to sulfide formation at oxygen potentials below that of oxide/sulfide equilibrium. Since sulfide was formed, it can be presumed that the oxygen contents of the sulfidizing atmospheres were sufficiently low to satisfy this condition. Direct measurements of the oxygen potential in the sulfidizing atmospheres employed for the experiments summarized in Table I showed that this requirement was met (5).

Figure 3 shows that the oxide scale remains relatively intact during sulfidation even though Fig. 4 would predict conversion of the oxide to sulfide under any combination of sulfur and oxygen potentials that lead to sulfide formation. Since this conversion does not occur appreciably during the sulfidation time periods employed, it can be concluded that transport of oxygen through the external sulfide layer formed during sulfidation is very slow. Further, the linear growth of the sulfide at a rate which is low compared to direct sulfidation (see Fig. 2) suggests that Cr trans-

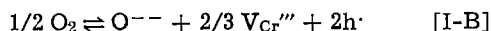
port through the oxide layer is the limiting step during sulfidation. Thus a probable "reaction path" for the sulfur and oxygen potentials across the reaction products of a specimen during sulfidation is shown in Fig. 7, which is a simplified version of Fig. 6 that does not distinguish between the various chromium sulfides. Point A represents the gas/external sulfide layer interface, point B the external sulfide layer/oxide layer interface, point C the oxide layer/internal sulfide layer interface, and point D the internal sulfide layer/metal interface. Since the sulfidation rate in the presence of an oxide layer is much less than that of direct sulfidation, the sulfur potential gradient in both sulfide layers has been assumed to be nearly zero. Most of the sulfur potential drop then occurs across the oxide layer as shown in Fig. 7.

The mechanism of Cr transport in Cr_2O_3 has not been determined unambiguously. This oxide is a p-type semiconductor, but its electrical conductivity at relatively high oxygen pressures is nearly independent of oxygen pressure, indicating a lack of any strong reaction between O_2 and electron holes (12). The oxidation rate of Cr metal to Cr_2O_3 is likewise essentially independent of oxygen pressure in a similar pressure range, indicating that while Cr diffusion under such conditions may involve a defect mechanism, the defect concentration is not determined by a defect- O_2 reaction (13). Thus Hauffe and Block have proposed that the principal defects in Cr_2O_3 are Cr vacancies, Cr interstitials, and electron holes, formed in accordance with the equilibrium (12)



where Cr^{3+} is a normal Cr ion on a cation site, V_{Cr}''' is a triply charged (negative) Cr vacancy, Cr_i' is a doubly charged (positive) Cr interstitial, and $h \cdot$ is a positively charged electron hole.

Kassner *et al.* studied the oxidation of Cr metal and the tracer diffusion of Cr^{51} in Cr_2O_3 at the low equilibrium oxygen pressures generated by H_2 - H_2O mixtures (14). They observed an oxygen partial pressure dependence of the oxidation rate and of the tracer diffusion coefficient which led them to propose that the principal defects in Cr_2O_3 are Cr vacancies and electron holes formed in accordance with the equilibrium



where O^{--} is a normal O ion on an anion site.

The presence of other cations in Cr_2O_3 would be expected to affect the oxidation rate of Cr metal if these cations were either electron donors or electron acceptors. Reactions [I-A] and [I-B] both indicate that such cations would modify the intrinsic hole concentration and thus Cr diffusivity through changing Cr defect concentration. This effect has been demonstrated

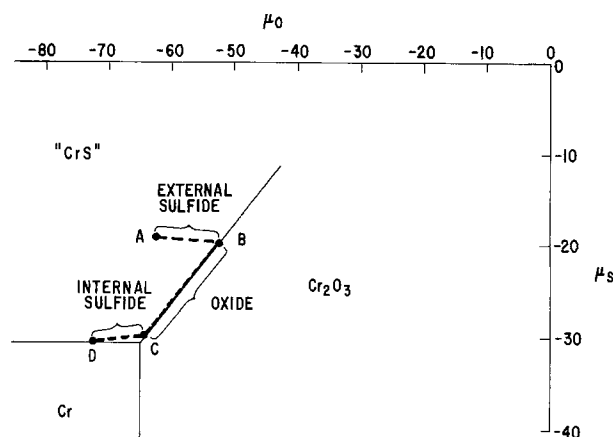
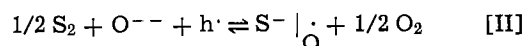


Fig. 7. Schematic reaction path in the Cr-O-S system during sulfidation at 900°C.

as a change in oxidation rate (15). If sulfur were an electron donor in Cr_2O_3 , it would likewise be expected to increase the Cr diffusivity in the oxide through decreasing the hole concentration and consequently increasing the Cr defect concentration as either reaction [I-A] or [I-B] are shifted to the right. Konev *et al.* have proposed that sulfur enters NiO as S^- ions rather than S^{--} ions (16). Wagner and his co-workers have also suggested that S^- ions may be the form in which sulfur generally enters into solution in most oxides (4). The sulfur could act as an electron donor according to the equilibrium



where $\text{S}^- |_{\text{O}}$ is a singly ionized sulfur ion on an anion site, and is thus a singly charged (positive) defect with respect to the anion lattice.

The equilibrium constants for reactions [I-A], [I-B], and [II] can be expressed in terms of x_v , x_i , x_h , and x_s which are, respectively, the mole fractions of Cr vacancies, Cr interstitials, electron holes, and singly ionized sulfur ions on anion sites. These equilibrium constants will also involve the oxygen and sulfur activities, which are defined as $a_o = p_{\text{O}_2}^{1/2}$ and $a_s = p_{\text{S}_2}^{1/2}$. It can be noted that the chemical potentials are then given by $\mu_X = RT \ln a_X$, where X represents either oxygen or sulfur, allowing the activities corresponding to specific phase equilibria to be obtained from Fig. 6.

From reaction [II], the value of x_s is obtained as $x_s = K_{\text{II}}(a_s/a_o)x_h$, where K_{II} is the equilibrium constant for reaction [II]. We will assume that in the H_2 - H_2S gas mixtures considered in the following analysis that the oxygen activity is sufficiently low to cause $K_{\text{II}}(a_s/a_o)$ to be much greater than unity. The vacancy concentrations corresponding to reactions [I-A] and [I-B] can then be obtained as

$$x_v = K(a_s^{1/3}/a_o^{1/3}) \quad [\text{I-a}]$$

and

$$x_v = K(a_s^{3/4}/a_o^{3/8}) \quad [\text{I-b}]$$

where K in each instance represents some combination of the equilibrium constants $K_{\text{I-A}}$ and K_{II} or $K_{\text{I-B}}$ and K_{II} . If reaction [I-A] is assumed to take place, then $x_i = x_v$ and Cr transport could occur either through interstitial or vacancy defects. Whether reaction [I-A] or [I-B] is assumed to prevail, however, a Cr defect concentration gradient could exist across the sulfur-containing Cr_2O_3 layer during sulfidation to act as a driving force for Cr transport through this layer.

The sulfur and oxygen activities on each side of the Cr_2O_3 layer during sulfidation of any specimen used in the present work can be obtained from Fig. 6, assuming that a reaction path such as that shown schematically in Fig. 7 applies to the sulfidation process. A general form of Eq. [I-a] or [I-b] is

$$x_D = K(a_s^f/a_o^g) \quad [2]$$

where x_D is the Cr defect concentration, whether vacancies or interstitials. The outward molar flux of Cr through the Cr_2O_3 layer is then given by the proportionality relationship

$$\Gamma_{\text{Cr}} \propto (x_{D,B} - x_{D,C})/m \quad [3]$$

where Γ_{Cr} is the Cr flux, m is the mass per unit area of the oxide layer, and the subscripts B and C refer to the external sulfide/oxide interface and the oxide/internal sulfide interface, respectively (cf. Fig. 7). Assuming that the linear sulfidation is due primarily to the formation of the external sulfide layer of composition Cr_2S_y , the linear rate constant for sulfidation is given by the proportionality relationship

$$k_1 \propto ((y/x)/m)\phi \quad [4]$$

where the factor ϕ is defined as

$$\phi = (a_{S,B}/a_{S,C})^f (a_{O,C}/a_{O,B})^g - 1 \quad [5]$$

Since k_1 , the ratio y/x , and m are experimentally accessible, they can be consolidated into a single parameter, using Eq. [4], defined by

$$k = (x/y)mk_1 \quad [6]$$

Thus the value of k should be proportional to ϕ for any run, or the value of k/ϕ should be constant for all runs in which sulfide was formed at a single temperature of 900°C. The ratio k/ϕ was calculated for each of the runs of Tables I and II. Values for $a_{S,C}$ and $a_{O,C}$ were taken as those corresponding to the Cr/CrS/Cr₂O₃ equilibrium of Fig. 6, and remain the same for all runs. Values for $a_{S,B}$ and $a_{O,B}$ as well as for x and y were those corresponding to the appropriate Cr_xS_y/Cr₂O₃ equilibrium of Fig. 6 at the sulfur potential level indicated by the dashed line for each H₂-H₂S composition. Since the absolute magnitude of the ratio k/ϕ has no significance, the value of the ratio was normalized using the average values obtained in arbitrary units of each set of runs treated. Three pairs of values of the exponents f and g were used: $f = 0$ and $g = 0$; $f = 1/3$ and $g = 1/3$; $f = 3/4$ and $g = 3/8$. These represent, respectively, an absence of any influence of sulfur or oxygen on Cr defect concentration, a Cr defect concentration established according to Eq. [1-a], and a Cr defect concentration governed by Eq. [1-b].

Table III summarizes the normalized k/ϕ ratios obtained for each pair of exponents. Averages and variances are also presented. Since the average must be unity for the normalized k/ϕ ratio, the variances are direct indications of how well the three assumed models for the influence of sulfur on Cr diffusivity fit the experimental observations. Either of the models involving the presence of sulfur as an electron donor gives a better fit than the assumption of no interaction between sulfur and Cr defects. It is thus proposed that sulfur enters Cr₂O₃ as an electron donor, thereby reducing the electron hole concentration. This reduction leads to an increase in Cr defect concentration through reactions similar to [I-A] or [I-B]. Such a general model can be qualitative only at present, but it is suggested that a parameter containing an equilibrium constant and both sulfur and oxygen activities, in the form given by Eq. [2], describes the effect of sulfur on the Cr defect composition.

An enhanced Cr diffusivity in Cr₂O₃ due to the presence of sulfur could be either a grain boundary or volume effect. It is not possible to distinguish between these two types of mechanism at this time. Factors which may contribute variations in linear sulfidation rate are deviations from the nominal gas compositions, differences in Cr₂O₃ layer grain size as a result of different oxidation temperatures, and partial disruption of the Cr₂O₃ layer during sulfidation. Thus no more detailed analysis of the data appears warranted.

The single test undertaken with a CO-S₂ mixture (Fig. 4) was performed to show that the observed enhancement of Cr transport through Cr₂O₃ during sulfidation was not uniquely dependent on the use of H₂

to achieve the low oxygen potentials that thermodynamically allow sulfide formation. Figure 5 indicates that the Cr₂O₃ layer was at least partially converted to one or more Cr carbides during this run. While not conclusively demonstrating that neither hydrogen nor carbon is affecting defect equilibria, the result shows that hydrogen is not unique and that the sulfur itself is most probably responsible for the enhanced diffusivity of Cr in Cr₂O₃ exposed to sulfur at low oxygen potentials. Since the reaction products of the specimen were not the same as those of other tests, no attempt was made to treat this test quantitatively.

Conclusions

Exposure of preoxidized Cr to an ambient atmosphere of sufficiently high sulfur potential and low oxygen potential results in the linear growth of Cr sulfide on both sides of the Cr₂O₃ layer formed during oxidation. Most of the sulfide growth takes place in the external sulfide layer by transport of Cr through the relatively intact Cr₂O₃ layer which is metastable as a result of limited oxygen transport through Cr sulfides. The sulfidation rate in this situation reflects a much higher Cr diffusivity in the Cr₂O₃ than would be expected in the absence of sulfur. A model for the defect equilibria in Cr₂O₃ exposed to sulfur can be formulated, in which sulfur enters the oxide as an electron donor, thereby increasing the concentration of Cr defects.

Acknowledgment

The technical support of the Materials Characterization Operation staff of the General Electric Research and Development Center is gratefully acknowledged.

Manuscript submitted July 22, 1974; revised manuscript received April 22, 1975. This was Paper 184 presented at the San Francisco, California, Meeting of the Society, May 12-17, 1974.

Any discussion of this paper will appear in a Discussion Section to be published in the June 1976 JOURNAL. All discussions for the June 1976 Discussion Section should be submitted by Feb. 1, 1976.

Publication costs of this article were partially assisted by General Electric Company.

REFERENCES

1. J. A. Goebel, F. S. Pettit, and G. W. Goward, *Met. Trans.*, **4**, 261 (1973).
2. D. W. McKee and G. Romeo, *ibid.*, **4**, 1877 (1973).
3. A. U. Seybolt, *Trans. Met. Soc. AIME*, **242**, 752 (1968).
4. D. R. Chang, R. Nemoto, and J. B. Wagner, Jr., *Met. Trans.*, In press.
5. G. Romeo and H. S. Spacil, in "High Temperature Gas-Metal Reactions in Mixed Environments," S. A. Jansson and Z. A. Foroulis, Editors, p. 299, TMS-AIME (1973).
6. G. Romeo, W. W. Smeltzer, and J. S. Kirkaldy, *This Journal*, **118**, 740 (1971).
7. JANAF Thermochemical Tables, Second Edition, D. R. Stull and H. Prophet, Editors, Nat. Bur. of Standards, Washington, D.C. (1971).
8. K. N. Strafford and A. F. Hampton, *J. Less Common Metals*, **21**, 305 (1970).
9. D. J. Young, W. W. Smeltzer, and J. S. Kirkaldy, *This Journal*, **120**, 1121 (1973).
10. J. P. Hager and J. F. Elliott, *Trans. AIME*, **239**, 513 (1967).
11. "Thermochemistry for Steelmaking," Vol. 1, J. F. Elliott and M. Gleiser, Editors, Addison-Wesley Publishing Co., Reading, Mass. (1960).
12. K. Hauffe and J. Block, *Z. Phys. Chem.*, **198**, 232 (1951).
13. W. C. Hagel, *Trans. ASM*, **56**, 583 (1963).
14. T. F. Kassner, L. C. Walters, and R. E. Grace, in "Thermodynamics," Proc. Symposium on Thermodynamics, Vol. II, organized by IAEC/IUPAC, p. 357, IAEC (1966).
15. C. S. Tedmon, Jr. and W. C. Hagel, *This Journal*, **115**, 147 (1968).
16. V. N. Konev, V. N. Cherbotin, N. V. Suntsov, and L. I. Startseva, *Zashchita Metal.*, **6**, 448 (1970), available as Consultants Bureau Translation UDC 620.193.5 (1970).

Table III. Values of ratio of sulfidation parameter defined by Eq. [6] to sulfur and oxygen activity function defined by Eq. [5]. The designation of each run corresponds to numbering in Tables I and II.

Run	$(k/\phi) / (\overline{k/\phi})$		
	$f = 0$ $g = 0$	$f = 1/3$ $g = 1/3$	$f = 3/4$ $g = 3/8$
I-1	1.44	1.32	0.59
I-2	2.52	2.30	1.03
I-3	1.66	1.50	0.68
II-2	0.12	0.20	0.61
II-3	0.52	0.70	1.75
II-4	0.53	0.70	1.80
II-5	0.25	0.29	0.57
Average	1.00	1.00	1.00
Variance	± 0.89	± 0.75	± 0.55

The Deposition of Tin Oxide Films from a D-C Glow Discharge

D. E. Carlson

RCA Laboratories, Princeton, New Jersey 08540

ABSTRACT

Tin oxide films have been deposited on soda-lime-silicate glass using a d-c glow discharge in atmospheres of $\text{Sn}(\text{CH}_3)_4$ and O_2 , and SnCl_4 and O_2 . The sodium ions were removed from the surface of the glass during the film deposition by forcing the current to pass through the heated glass substrates. Film properties were studied as a function of atmospheric composition, current density, and deposition time.

Many investigators (1-12) have reported the deposition of thin films on various substrates using a-c and d-c glow discharges in appropriate gases or vapors (typically at a pressure of 0.1-10 Torr). The glow discharge breaks chemical bonds and promotes complex reactions in the gas or gas mixture, and the films result from the deposition of certain reactive components on substrates in the vicinity of the discharge.

Most of the published work involves films deposited on substrates placed in rf or microwave glow discharges. This technique has been used to produce films of organic polymers (2,3), silicon oxides (4,5), silicon nitride (5,6), aluminum oxide (7), amorphous silicon (8,9), etc. (9,10). The substrate may or may not be heated depending on the type of film desired.

Much less work (11,12) has been reported on the deposition of films from a d-c glow discharge. The scarcity of work in this area has been attributed to poor reproducibility of film composition and contamination of the film due to sputtering effects (1,4). However, the present study shows that good quality tin oxide films can be produced on the cathode in a d-c discharge and that the sputtering action of the discharge can be controlled. Moreover, the d-c technique is simple in practice and readily allows the uniform deposition of thin films over large areas. An additional benefit is gained in the deposition of films on glass substrates since the glass surface will be either ion-depleted (13,14) or proton-exchanged (15) during the deposition. In either case, the removal of alkali ions from the glass surface allows high quality films to be deposited (14).

Experimental Procedure

The apparatus used in the present study is depicted schematically in Fig. 1. The major components of the system were a vacuum bell jar, a mechanical vacuum pump, and a high voltage d-c power supply (5 kV, 5A). A heating plate was located in the center of the bell jar on a thin-walled, fused silica pedestal. Power for the heater was provided by coupling through an isolation transformer to a variable auto-transformer.

For glass substrates, the bottom was first painted with a conductive coating such as Ag or graphite so that at elevated temperatures the current passed through the glass. The substrate to be coated was then placed on the heating plate with the negative lead (0.005 in. Pt wire) from the power supply in electrical contact with the bottom of the substrate. That part of the negative lead not under the substrate was electrically shielded with a fused silica tube.

The anode was a metal sheet (usually Pt) placed ~2 cm above the substrate. The ceramic spacers that held the anode were several cm to either side of the substrate so that they were outside of most of the glow discharge region. A limiting resistor (10^5 ohm, 100W) was used to stabilize the discharge. The current

was monitored by measuring the voltage drop across a 10^3 ohm resistor.

The system was evacuated to a pressure of ~5 mTorr with the substrate hot (200° - 550°C) before any gases or vapors were admitted. The procedure for admitting vapors such as tetramethyltin ($\text{Sn}(\text{CH}_3)_4$) was to freeze a vial of $\text{Sn}(\text{CH}_3)_4$ in liquid nitrogen while pumping on it. Once a pressure of ~5 mTorr was attained, the sample was warmed until the desired vapor pressure was achieved. The appropriate gases or vapors were sequentially bled into the system, and the pressure during each admission was monitored with a thermocouple vacuum gauge. Since the thermocouple gauge was calibrated for air, a McLeod vacuum gauge was used to measure the pressure after each admission. The total pressure was in the range of 0.5-2.0 Torr for most of the film depositions.

The minimum voltage for deposition of uniform films was determined by adjusting the applied voltage so that the negative glow of the discharge covered the entire cathode substrate. This is the beginning of the regime for the abnormal fall of potential near the cathode (16). Operating at this voltage assures a uniform deposition while minimizing sputtering effects. Increasing the voltage beyond this value will increase the deposition rate, but eventually sputtering effects will decrease the rate and may even prevent film deposition. Normally, a constant current density was maintained during the film deposition. The applied voltage had to be increased during the deposition when a glass substrate was used. (As the depleted region in the glass increased in thickness, the resistance increased.)

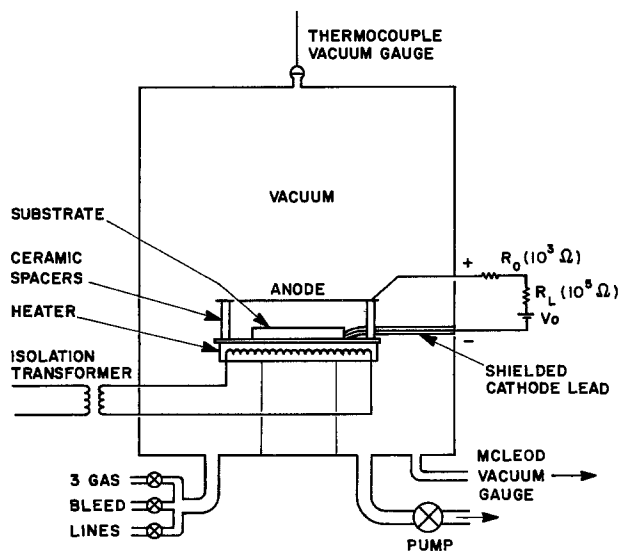


Fig. 1. Schematic diagram of the apparatus used for film deposition from a d-c glow discharge.

Key words: glass, semiconductor, ion-depletion.

The films could be deposited in patterns by using either insulating or conducting masks. Insulating masks perturbed the field distribution in the discharge and generated borders that were not sharp, *i.e.*, the film thickness increased gradually up to a distance of a few mm from the edge of the mask. Conducting masks did not affect the field distribution, and the film edges were sharp to within a few microns. When glass substrates were used, Na was removed from the glass surface beneath both the depositing film and the conducting mask.

Since the edges of the cathode substrates were high field regions, the film thickness varied near the edges. Uniform deposition over the entire substrate was achieved by placing another cathode material around the edges of the substrate. This effectively moved the high field regions of the cathode out beyond the edges of the substrate. For uniform deposition, the total pressure was maintained at $\lesssim 1$ Torr since the discharge tended to localize at higher pressures.

The thickness of various films was measured with a stylus profilometer (Bendix Linear Piloter, Type RLC). The surface resistivity was measured with an RCA VoltOhmyst or a Keithley Electrometer (Model 610C) after painting parallel stripes on the surface of the film with air-drying Ag paint. The transmission of visible light was measured with a Cary spectrophotometer (Model 14R).

Results and Discussion

Tin oxide films were deposited on soda-lime-silicate glass¹ substrates using d-c glow discharges in vapors of $\text{Sn}(\text{CH}_3)_4$ and oxygen, and in vapors of SnCl_4 and O_2 . The inclusion of the glass substrate in the electrical circuit caused the glass surface to be either ion-depleted (13,14) (for a discharge in SnCl_4 and O_2) or proton-exchanged (15) (for a discharge in $\text{Sn}(\text{CH}_3)_4$ and O_2) during the film deposition. The Na ions were typically removed from the glass surface to a depth of $\sim 2000\text{\AA}$. The removal of Na ions from the glass surface during the deposition gave rise to sodium-free films with excellent optical and electrical properties. Moreover, the Na-depleted region is little affected by thermal treatment below the transformation temperature of the glass ($\sim 510^\circ\text{C}$), so the films should remain Na free during any subsequent thermal processing below this temperature. (The thermal stability of the ion-depleted region is due to the removal of the nonbridging oxygen ions (13) during the film deposition.)

Figure 2 shows how the volume resistivity of films deposited in a discharge of $\text{Sn}(\text{CH}_3)_4$ and O_2 depended on the composition of the atmosphere. The current density and treatment time were held constant, and the thickness of the films increased as the ratio of $\text{Sn}(\text{CH}_3)_4$ to O_2 was increased (from 350\AA at a ratio of 0.10 to 1250\AA at a ratio of 0.23). When the ratio of $\text{Sn}(\text{CH}_3)_4$ to O_2 was small ($\lesssim 0.10$), the films were fairly resistive ($\rho > 10^{-2}$ ohm-cm). When the ratio of $\text{Sn}(\text{CH}_3)_4$ to O_2 was large (~ 0.23), the films were also resistive and acquired a yellowish coloration and became less scratch-resistant. The coloration is probably due to an oxygen deficiency in the films; only ~ 0.2 atomic per cent (a/o) of C was found in these colored films. When the optimum ratio was selected, films with resistivities of $\sim 3 \times 10^{-3}$ ohm-cm were obtained; these films had a surface resistivity of ~ 400 ohm/ \square ($\sim 750\text{\AA}$ thick) and an average light transmission as compared to uncoated glass of $\sim 87\%$ (over the wavelength range of $3500\text{--}6500\text{\AA}$). Approximately 0.5 a/o of C was present in the most conductive films.

These films were relatively insensitive to thermal cycling and exhibited only 10-20% reduction in conductivity after baking for 24 hr at 400°C in air. (Baking for 1 hr at 550°C caused a decrease of 50%.) If the conduction were due only to donor states arising from

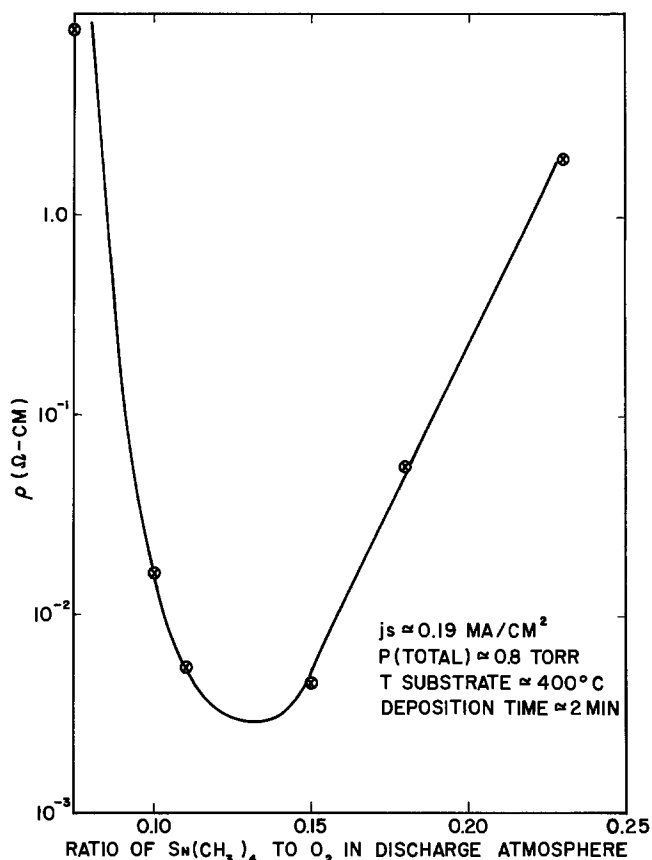


Fig. 2. Volume resistivity of tin oxide films as a function of the ratio of $\text{Sn}(\text{CH}_3)_4$ to O_2 in the discharge atmosphere.

oxygen vacancies, the resistivity should have increased by more than an order of magnitude (17,18). One possibility is that donor levels are created by the presence of OH groups in the tin oxide structure. The glow discharge is expected to produce OH groups because of the large number of hydrogen atoms per $\text{Sn}(\text{CH}_3)_4$ molecule and the large per cent of O_2 in the initial discharge atmosphere ($\sim 88\% \text{O}_2$).

Figure 3 shows how the film thickness and the surface resistivity varied with time for a discharge in $\text{Sn}(\text{CH}_3)_4$ and O_2 . The deposition rate was ~ 1200 $\text{\AA}/\text{min}$ for the first 15 sec and slowed to ~ 225 $\text{\AA}/\text{min}$ after 1 min. The average volume resistivity decreased from $\sim 4 \times 10^{-2}$ ohm-cm at 15 sec to $\sim 10^{-2}$ ohm-cm at 4 min. The composition or stoichiometry of the film varied with thickness since the percentage of Sn in the discharge atmosphere decreased with time.

Figure 4 shows how the surface resistivity of films formed from a discharge in $\text{Sn}(\text{CH}_3)_4$ and O_2 varied with current density. For low current densities, the deposition rate increased as the current density increased. As the current density (or cathode fall potential) became larger, the deposition rate decreased due to the influence of sputtering. At large current densities ($\gtrsim 1.0$ mA/cm^2), film deposition did not occur and the glass surface was slowly sputter etched.

Tin oxide films were deposited on glass substrates at temperatures as low as 200°C using a d-c glow discharge in $\text{Sn}(\text{CH}_3)_4$ and O_2 . These films can be deposited at temperatures much lower than with chemical vapor deposition (CVD) ($\gtrsim 375^\circ\text{C}$) (17) because the discharge dissociates the molecules and drives the positive ions to the substrate with appreciable kinetic energies ($\sim 10\text{--}100$ eV depending on the deposition parameters). Thus, the positive ions arriving at the substrate are on the order of 10^3 times "hotter" than the substrate.

The average light transmission and volume resistivity of the best films deposited at 250°C were com-

¹ Approximate composition by weight per cent (w/o): 73 w/o SiO_2 ; 13.5 w/o Na_2O ; 9 w/o CaO ; 4 w/o MgO ; 0.2 w/o Al_2O_3 .

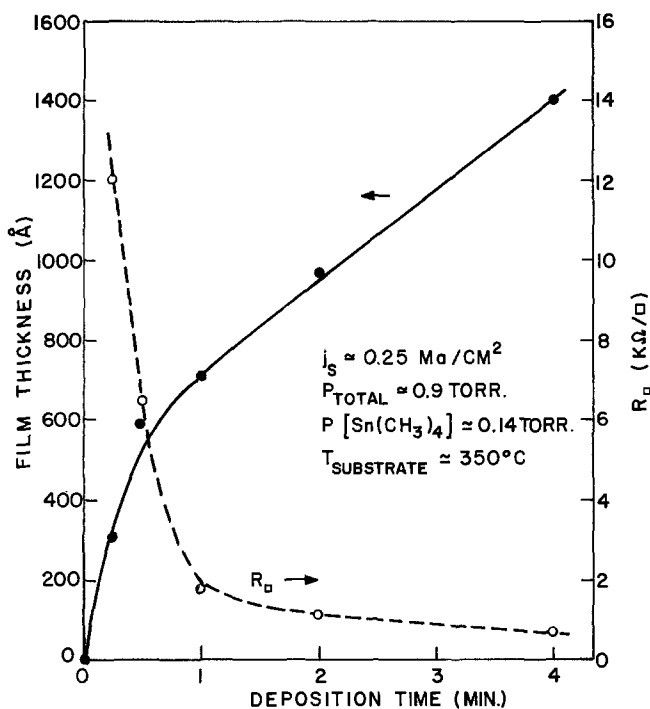


Fig. 3. Thickness and surface resistivity of tin oxide films as a function of deposition time.

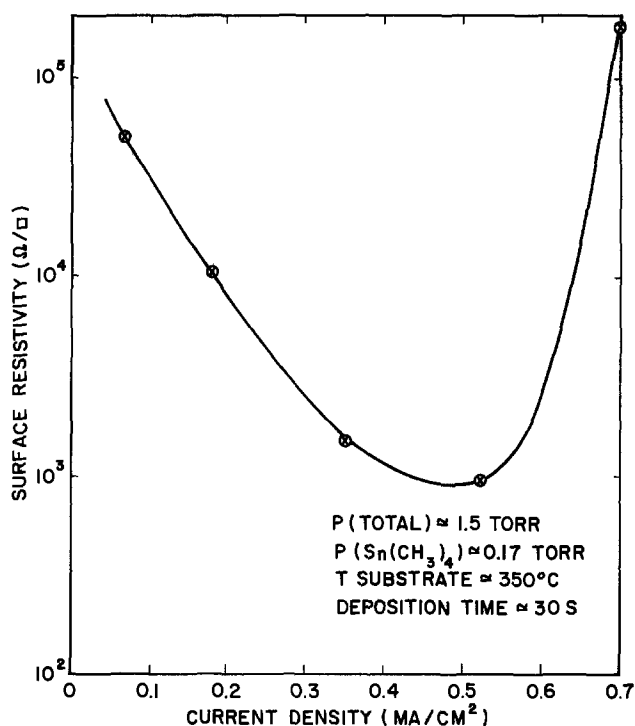


Fig. 4. Surface resistivity of tin oxide films as a function of current density.

parable to those deposited at 400°C. However, the films deposited at lower temperatures appeared to be slightly less scratch-resistant.

As the deposition temperature was reduced, the highest conductivity films were produced at decreasing ratios of $\text{Sn}(\text{CH}_3)_4$ to O_2 . For example, at a deposition temperature of 400°C, the ratio was ~ 0.13 (Fig. 2), while at 250°C the ratio was ~ 0.04 . A larger ratio was probably necessary at higher temperatures to compensate for the thermal decomposition of some of the $\text{Sn}(\text{CH}_3)_4$ in the vicinity of the heater coils.

By admitting SbCl_5 to an atmosphere of $\text{Sn}(\text{CH}_3)_4$ and O_2 , films with volume resistivities as low as 1.7

$\times 10^{-3}$ ohm-cm were produced. The variation of volume resistivity with varying amounts of SbCl_5 in the atmosphere is shown in Fig. 5. Mass spectrometry (solids) showed that the most conductive film contained ~ 0.33 a/o of Cl and less than 0.06 a/o of Sb. The average light transmission for this film was $\sim 90\%$.

SnO_2 films were also made from glow discharges in SnCl_4 and O_2 . For depositions at 400°C, a current density of ~ 0.2 – 0.5 mA/cm² was applied for 2 min. The ratio of SnCl_4 to O_2 was typically 0.3–0.5 ($P_{\text{total}} \approx 0.8$ Torr) and was not as critical as in the case of $\text{Sn}(\text{CH}_3)_4$ and O_2 (Fig. 2).

The most conductive films made from a discharge in SnCl_4 and O_2 had a resistivity of $\sim 1.5 \times 10^{-3}$ ohm-cm. These films only showed a 20–40% increase in resistivity after baking for 24 hr at 400°C in air. (Baking for 1 hr at 550°C caused a 70% increase.) The doping must be caused mainly by substitutional incorporation of chlorine (18, 19) since mass spectrometry (solids) showed that the films contained ~ 1 a/o of Cl. However films that are halogen-doped during spray deposition do not usually show the stability to thermal cycling in air that the discharge-produced films do. For example, films formed by spraying solutions of stannic bromide on hot fused silica showed an order of magnitude increase in resistivity after baking in air for 24 hr at 400°C (20). Films made by spraying stannic chloride solutions on hot glass show similar thermal degradation in air. The films produced by a d-c glow discharge may be more dense than those produced by spraying, and thus halogen diffusion may be reduced in the discharge-produced films.

Electron diffraction by reflection has shown that discharge-produced films have a crystallite grain size less than 100Å for deposition temperatures below $\sim 400^\circ\text{C}$. The grain size was slightly larger in films produced from discharges in SnCl_4 and O_2 than those from $\text{Sn}(\text{CH}_3)_4$ and O_2 for the same deposition temperature.

In conclusion, the present study shows that a d-c glow discharge in the appropriate atmosphere can be

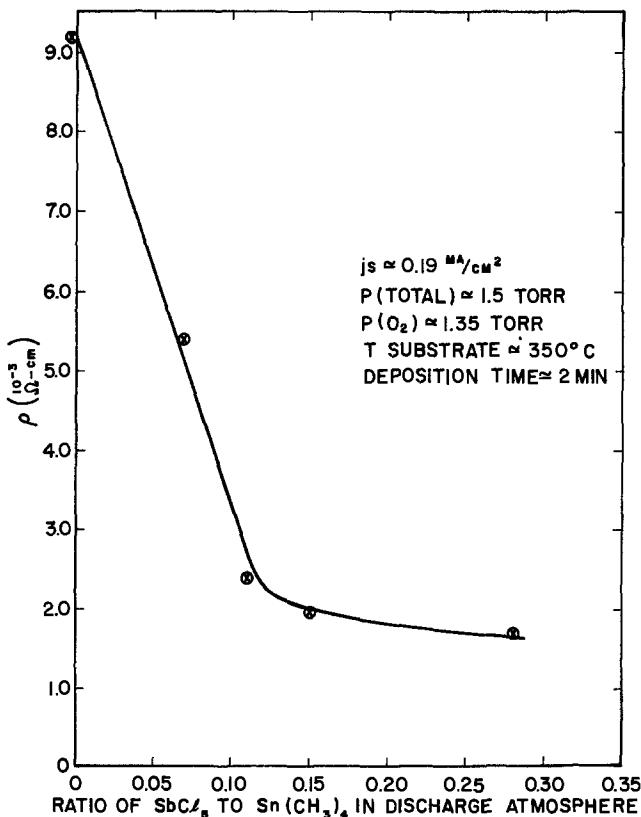


Fig. 5. Volume resistivity of doped tin oxide films as a function of the ratio of SbCl_5 to $\text{Sn}(\text{CH}_3)_4$ in the discharge atmosphere.

used to deposit good quality, tin oxide films on the surface of a soda-lime-silicate glass.

Acknowledgments

The author thanks P. J. Zanzucchi for making the optical transmission measurements and E. M. Botnick for providing the mass spectrometry (solids) data.

Manuscript received Feb. 6, 1975; revised manuscript received June 12, 1975.

Any discussion of this paper will appear in a Discussion Section to be published in the June 1976 JOURNAL. All discussions for the June 1976 Discussion Section should be submitted by Feb. 1, 1976.

Publication costs of this article were partially assisted by RCA Laboratories.

REFERENCES

1. A. M. Mearns, *Thin Solid Films*, **3**, 201 (1969).
2. J. Goodman, *J. Polymer Sci.*, **44**, 551 (1960).
3. F. J. Vastola and J. P. Wightman, *J. Appl. Chem.*, **14**, 69 (1964).
4. L. L. Alt, S. W. Ing, Jr., and J. H. Alexander, *This Journal*, **110**, 465 (1963).
5. R. J. Joyce, H. F. Sterling, and J. H. Alexander, *Thin Solid Films*, **1**, 481 (1967/1968).
6. R. C. G. Swann, R. R. Mehta, and T. P. Cange, *This Journal*, **114**, 713 (1967).
7. H. Katto and Y. Koga, *ibid.*, **118**, 1619 (1971).
8. H. F. Sterling, J. H. Alexander, and R. J. Joyce, *Le Vide*, p. 80 (1966).
9. H. F. Sterling and R. C. G. Swann, U. S. Pat. 3,655,438 (1972).
10. J. Goodman, U. S. Pat. 3,239,368 (1966).
11. H. Pagnia, *Phys. Status Solidi*, **1**, 90 (1961).
12. B. G. Carbajal III, *Trans. Met. Soc. AIME*, **236**, 364 (1966).
13. D. E. Carlson, *J. Am. Ceram. Soc.*, **57**, 291 (1974).
14. D. E. Carlson, K. W. Hang, and G. F. Stockdale, *ibid.*, **57**, 295 (1974).
15. D. E. Carlson, *ibid.*, **57**, 461 (1974).
16. F. M. Penning, "Electrical Discharges in Gases," The Macmillan Co., New York (1957).
17. J. Kane, H. P. Schweizer, and W. Kern, Paper 15 RNP presented at Electrochemical Society Meeting, San Francisco, California, May 12-17, 1974.
18. C. A. Vincent, *This Journal*, **119**, 515 (1972).
19. J. A. Aboaf and V. C. Marcotte, *ibid.*, **120**, 701 (1973).
20. H. Kim and H. Laitinen, presented at 76th Annual Meeting of the American Ceramic Society, 1974; *Am. Ceram. Soc. Bulletin*, **53**, 342 (1974).

Microstructural and Electrical Properties of Thin PtSi Films and Their Relationships to Deposition Parameters

R. M. Anderson and T. M. Reith

IBM System Products Division, East Fishkill Facility, Hopewell Junction, New York 12533

ABSTRACT

The intimate relationships among the microstructure, electrical characteristics, and deposition parameters of thin PtSi films deposited on {001}, {011}, and {111} Si wafers are discussed. PtSi morphology and crystallinity fall into several distinct categories, according to substrate surface preparation, deposition conditions, heat-treatment, and electrical performance. *In situ* sputter cleaning before PtSi deposition and formation gives better films. Also, the microstructure and sheet resistance of PtSi are strongly affected when deposition and formation are followed by heat-treatment at temperatures from 400° to 950°C.

PtSi films have recently been the subject of much investigation because of their usefulness in forming near-ideal ohmic and Schottky contacts to both n- and p-type Si (1, 2). The crystallography and morphology of PtSi films have received considerable attention (3-8), as have the kinetics of their formation (9-12). This paper discusses the intimate interrelations of the microstructure of thin PtSi films, their electrical properties, and their dependence on deposition conditions.

Experimental

Preparation of samples.—In the present study we have examined both sputter- and e-beam-deposited PtSi films, although we have concentrated on the former. For the sputter-deposited films, an oil diffusion-pumped vacuum system with a Pt target 30 cm in diameter was used. It had provisions for *in situ* rf sputter cleaning and d-c sputtering of Pt. A Pt-coated stainless steel substrate holder resting on a Cu block with an embedded heating element enabled us to heat the wafers to 450°C before, during, or after Pt deposition (Fig. 1). The *in situ* sputter cleaning, when performed and unless otherwise indicated, was for 2

min at an rf power of 100W and an Ar pressure of 10 mTorr. Figure 2 shows the amounts of Si and SiO₂ removed as a function of time and rf power. The curves were obtained by sputter etching bare and thermally oxidized 3.2 cm Si wafers, which were partially masked with chromium to create a step in the surface. The step height was subsequently measured by use of a Talystep apparatus.

Extrapolation of the appropriate curves indicates that, for 2 min at 100W of rf power, about 75Å of SiO₂ and 175Å of Si are removed. The Pt was d-c sputter deposited with a 2 kV potential applied to the target and at 40-50 mTorr of Ar pressure unless otherwise noted. Various heat-treatments were used to form the PtSi, either *in situ* or externally in dry, flowing N₂. After PtSi formation, any unreacted Pt was removed in aqua regia at 60°-65°C. An oil diffusion-pumped vacuum system with a 180° four-pocket Cu-hearth e-beam source was used for the evaporated PtSi films. The pressure in the deposition system was 1-5 × 10⁻⁶ Torr during all evaporations. A spiral-wound tungsten wire heater was used to heat the substrates to ~300°C during deposition. The PtSi was formed externally in dry N₂, and unreacted Pt was stripped in aqua regia.

Key words: electron microscopy, platinum-silicon, electrical measurements.

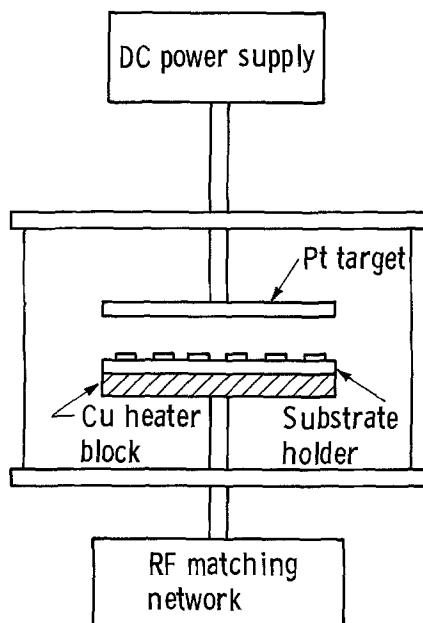


Fig. 1. Pt sputtering system

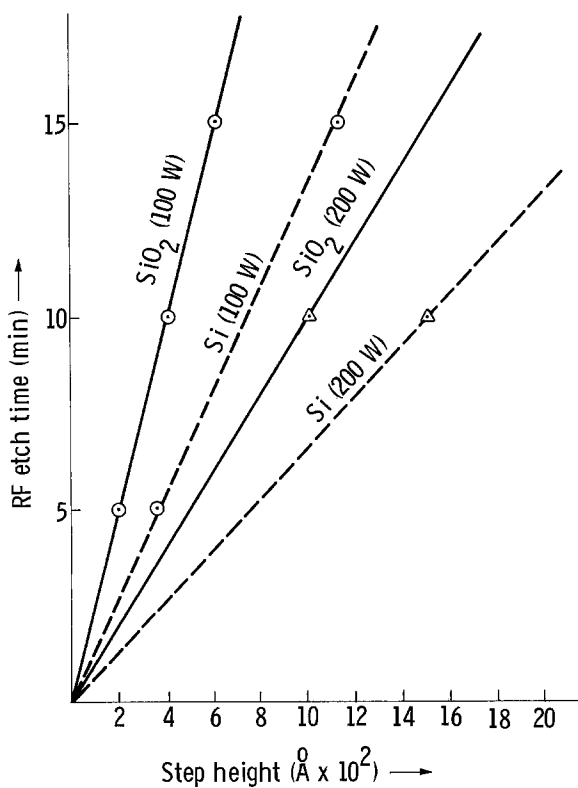


Fig. 2. RF etch time

To examine the dependence of PtSi microstructure on the dopant level and species of the Si on which it is formed, and the stability of the compound as a function of high heat-treatment temperature, 500Å of Pt was sputter deposited on the entire surface of several 3.2-cm Si wafers that had been diffused with either boron or arsenic to various dopant concentrations. After the wafers were cleaned by rf sputtering, the Pt was d-c sputter deposited as described previously. The substrates were heated to 450°C during the Pt deposition to form PtSi *in situ*. Any unreacted Pt that may have been present was removed in hot aqua regia. The sheet resistance of films was measured as a function of dopant and anneal by use of an in-line four-point probe apparatus. No attempt was made to convert the measurements into resistivity units, because there was

some uncertainty about the total thickness of the PtSi. As before, all heat-treatments subsequent to the *in situ* PtSi formation at 450°C were done in dry, flowing N_2 . The resulting microstructures were then examined by transmission electron microscopy (TEM).

To examine the effects of *in situ* rf sputter cleaning, bare 10-20 ohm-cm As-doped Si wafers, 3.2 cm in diameter, were sputter etched for 5 min at 100 and 500W of rf power. These specimens were analyzed by transmission electron microscopy, reflection electron diffraction (RED), low-angle-Laue, Berg-Barrett surface topography, and electron microprobe methods to determine whether any microstructural changes could be induced on the Si surfaces as a result of the *in situ* sputter cleaning. Also, some of the device structures described earlier were sputter cleaned for 15 min at rf power levels of 100 and 200W and examined by scanning electron microscopy (SEM) and electron microprobe analysis to determine whether SiO_2 can be back sputtered from the areas surrounding the opened contacts onto the exposed Si in these contacts by the sputter-cleaning operation. All sputter cleaning performed was either of longer duration or at higher power than would normally be used and hence represented an extreme condition.

Electrical testing procedure.—By use of the test structure shown in Fig. 3, the specific contact resistance of the various PtSi-Si contacts formed was measured. Since the only point in common between the current and voltage loops is the PtSi-Si contact, the measured voltage drop is that which occurs across the PtSi-Si interface, if spreading resistances are neglected. The test structures were defined by standard photolithographic methods. To simulate a typical "base" contact, boron was diffused into 10-20 ohm-cm phosphorus-doped <001> Si wafers. After reoxidation, the measured junction depth was about 0.5 μm , and the surface concentration was 2.4×10^{19} atoms/cm³. To simulate a typical "emitter" contact, slightly smaller cuts were opened photolithographically on half the devices through the reoxidized SiO_2 above the "bases" and an arsenic diffusion was done. After reoxidation, the junction depth was approximately 0.25 μm , and the surface concentration was 1.1×10^{21} atoms/cm³. To complete the structures, contact holes 0.05 mm in diameter were etched to expose the doped Si surfaces. After PtSi deposition and formation, 1000Å of Cr and 10,000Å of

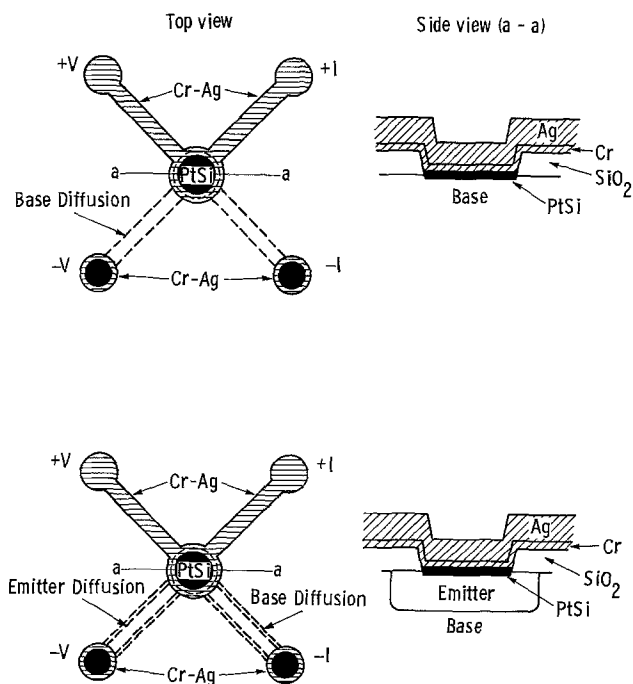


Fig. 3. Electrical test structure

Ag were evaporated through a molybdenum mask 0.1 mm thick to facilitate electrical probing. Unlike Al, Cr (13, 14) will not react with PtSi until temperatures well above those typically encountered in semiconductor device processing are reached. This fact was confirmed by four-point probe resistivity measurements and particle backscattering analysis. All measurements of contact resistance were made with a constant-current source and a digital voltmeter. Finally, HCl was used to stripe the Cr-Ag metallization to expose the electrically characterized PtSi contacts for subsequent TEM analysis.

Transmission electron microscopy specimen preparation.—The electrically characterized wafers were scribed and broken up into specimens, each containing one device, of a size that would fit the specimen holder of the JEM 200A electron microscope. After appropriate masking, the Si was thinned from the backside of the specimen down to the intermetallic film in a mixture of HF-HNO₃-CH₃COOH (1:2:3). Specimens were thinned further, as required, in a Commonwealth ion milling machine.

Results

Microstructure vs. electrical properties.—At this point it would be well to stop and look at what “good” and “bad” PtSi microstructures are like. As we have learned, the key to “good” and “bad” microstructures lies in the cleanliness of the Si surface before Pt deposition. Pt deposited on a clean Si surface will begin to form a satisfactory PtSi film during deposition or subsequent heat-treatments, even without substrate heating. Unreacted Pt on Si films are due primarily to the presence of a contamination layer between the Pt and the Si which prevents the formation of PtSi, even after extensive heat-treatments. Quite often, especially with thin (<150Å) initial Pt depositions, the as-deposited Pt films are not fully coalesced and do not become so after subsequent heat-treatment. Selected area electron diffraction (SAD) of thin, poor Pt on Si films shows randomly oriented Pt diffraction rings superimposed on Si reflections. Subsequent heat-treatment brings no change; the Pt has not reacted with the Si, and the SAD patterns still show Pt rings and Si substrate spots.

For thicker initial Pt depositions on randomly and unintentionally contaminated Si, the as-deposited Pt films still do not fully coalesce. After heat-treatment these films undergo simultaneous grain growth and void enlargement, producing lacelike Pt films on Si. Whenever the initial Pt deposition fails to show a preferred orientation to the Si wafer, the microstructure observed after heat-treatment is poor, and no PtSi phase forms. Where the contamination film is itself incomplete, allowing islands of more or less continuous PtSi to form, the stress evolved as the PtSi phase shrinks during formation dissipates itself through void enlargement. One obvious observed consequence of the failure to form PtSi over contaminated Si is that when the aqua regia etch for unreacted Pt is applied, the film disappears. Where PtSi forms in islands, the unreacted Pt over contaminated Si is etched away. Any subsequent metallurgy forms a “capacitor,” with the contaminant film as a very leaky “dielectric.” Moreover, the metallurgy contacts the Si because of the circular channel of bare Si exposed around the islands of PtSi (opened up by shrinkage of the PtSi phase). No electrical data were taken on the very poor Pt on Si films discussed above, because no PtSi phase formed.

The contamination film on the Si was analyzed by x-ray microprobe and ESCA methods. It consists primarily of oxygen (as SiO₂) and carbon films, 50-100Å thick. It builds up in the perimeters of contacts. ESCA has also shown the presence of a thin SiO₂ film (<100Å thick) on top of freshly prepared PtSi films. Heat-treating the PtSi films in air instead of nitrogen results in a surface containing less platinum and more oxygen. The etching in aqua regia may promote the

formation and growth of the thin SiO₂ film on the PtSi. This phenomenon has been observed by other investigators (15).

When Pt is deposited on clean Si, but not heat-treated *in situ* or later, the electron microscope shows a continuous Pt film with a very strong <111> preferred orientation to the Si substrate. As was mentioned earlier, this strong orientation is a good indication that a satisfactory PtSi film will form upon heat-treatment. When these films are heated *in situ* in the electron microscope while being recorded in the SAD mode on 16-mm motion picture film, it is possible to edit frames from the sequence and index the SAD patterns. By this method we find that the phases formed are Pt + Si → Pt₃Si → Pt₂Si → PtSi. The complete reaction occurs in approximately 20 sec at 450°C. Often one or more rings from the Pt₂Si phase remains in the PtSi phase diffraction pattern despite prolonged heat-treatment.

PtSi films <500Å thick, deposited or heat-treated in the range of 400°-850°C, can have several different morphologies, each with its own associated crystallography and, as will be shown later, concentration of dopant in the substrate. For Si substrates that are less than atomically clean, or high concentrations of Si dopant, we see a continuous, polycrystalline PtSi film, randomly oriented to the Si and having high-angle grain boundaries separating grains that are randomly oriented toward each other. Figure 4a is typical of such a PtSi film. For very clean Si substrates and intrinsic-to-moderate Si dopant levels, the PtSi film is hetero-epitaxial to the Si substrate and consists of very small nodules of PtSi, having a high degree of orientation toward each other and separated by discontinuities, or voids, 20-150Å wide. This important result indicates that PtSi, by itself, could not be used as an effective diffusion barrier to prevent interaction between the subsequently deposited device interconnective metal and the substrate. Figure 4b is an example of such a film on a <001> Si substrate; the SAD pattern in the insert exhibits anomalous symmetry, greater than two-fold. These two morphologies are extremes; many morphologies may be observed between these limits.

The results for microstructure vs. electrical performance are summarized in Table I. Here the specimens observed are divided into groups as functions of deposition conditions. The specific contact resistance data in the table are the statistical means of the data for the specimens in any particular group. Any difference between the forward and reverse values gives a measure of the contact's departure from ohmic behavior. When an occasional sample in one of the superior

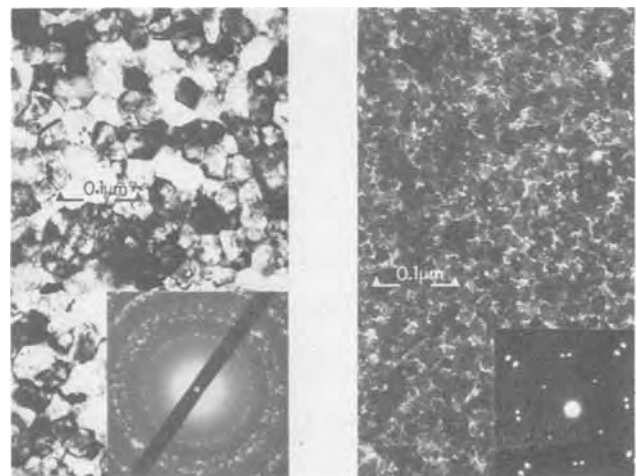


Fig. 4. PtSi morphology: extremes. Corresponding diffraction patterns are shown in the insets. (a, above left) High-angle grain-boundaries; sample is described in Table I, I (base). (b, above right) PtSi nodules; sample is described in Table I, III (base).

Table I. PtSi properties related to deposition parameters

Group	Substrate preparation	Heat-treatment	Diffusion	Specific contact resistance: forward, reverse (ohm-cm ² × 10 ⁻⁴)	Morphology	Crystallinity
I	Chemical cleaning plus sputter cleaning, performed <i>in situ</i>	450°C <i>in situ</i> during Pt deposition; substrates cooled <i>in vacuo</i>	Base	5.48, 6.29	Nodules (300Å), taken as definitive, 10-50Å. Buildup of larger, thicker nodules in contact hole perimeter (Fig. 5a)	Type A pattern, taken as definitive
Ia	Same as I	Same as I	Emitter	0.406, 0.507	Nodules (210Å). Internodule voids, 10-50Å. Nodules have textured surface or internal structure, build up in perimeter	Type A pattern
Ib	Same as I	Same as I	Emitter Base	13.6, 13.4 0.528, 2.64 19.1, 19.1	As above except discontinuity in perimeter 2000-3000Å wide, exposing bare Si	Type A pattern in PtSi
II	Same as I	450°C for 20 min <i>in situ</i> after deposition	Emitter Base	0.812, 1.22 15.2, 15.0	Same as base PtSi as in groups I, Ia, and Ib on different samples with no change in contact resistance	Type A pattern in PtSi As in group Ia
III	Chemical cleaning	550°C for 30 min externally in clean furnace	Emitter Base	0.771, 0.771 17.5, 17.7	Same as base plus an occasional large void, 500-1000Å High-angle g.b.* Some large voids. Perimeter effects as in group II	Type A pattern mixed with regions of type B pattern
IIIa	Same as I	Same as III	Emitter Base	1.68, 1.68 13.4, 13.2	Same as base Mixed nodules and high-angle g.b., porous	Same as base Type B patterns mixed with type C; some unreacted Pt
IV	Chemical cleaning	Same as III, but in a contaminated furnace**	Emitter Base	0.446, 1.91 102, 81.2	Same as base but more porous High-angle g.b. Large grains, some voids, etching damage, perimeter effects	Type C pattern plus some unreacted Pt
Effect-of-thickness samples	Same as I	550°C for 30 min in clean furnace	Emitter Base	40.6, 40.6 16.1, 16.1	Same as base; contamination evident Two-layer film; nodules next to substrate, and very porous, very small grain layer above (Fig. 5c)	Same as base Type A pattern next to substrate; broad, diffuse Pt rings above
Evaporated Pt-I	Chemical cleaning; deposition at 300°C	Same as effect-of-thickness samples	Emitter Base	1.81, 1.02 12.4, 12.2	Same as base except that nodule layer was thinner Same as groups Ia and Ib	Same as base Same as group Ia
Evaporated Pt-II	Same as evaporated Pt-I	Same as effect-of-thickness samples	Emitter Base	0.790, 0.821 24.8, 24.6	Same as group Ia High-angle g.b.;* two-layer structure; etch damage (Fig. 5d)	Same as group Ia Poly PtSi below; broad, diffuse Pt rings above
			Emitter	12.03, 11.42 (when PtSi film is present)	Same as base; or, for some samples, Pt did not react with Si and was etched off during the aqua regia step	Same as base or no film at all

* g.b. = grain boundary.

** The furnace was intentionally contaminated with oxygen.

specimen groups had electrical data more typical of one of the contaminated groups, and electron microscopy confirmed the presence of a contaminated or anomalous microstructure, the data for such specimens are presented in a separate statistical subgroup in the table.

For brevity, codes were adopted. In the morphology section, "high-angle g.b." refers to the first limiting case, described above, of a continuous, random, polycrystalline PtSi film with high-angle grain boundaries. "Nodules" refers to the second limiting case of highly oriented, heteroepitaxial, small, discontinuous nodules (lacking grain boundaries) of PtSi; the width of the void between modules is specified in the table. "Poly PtSi" refers to a diffraction pattern of randomly oriented PtSi phase with no preferred orientation. A "type A pattern" is a single-crystal PtSi diffraction pattern consisting of one diffraction zone.¹ A "type B pattern" is a mixture of two or more PtSi diffraction zones, and a "type C pattern" is a mixture of one or more diffraction zones with polycrystalline PtSi rings. The morphology types are illustrated in Fig. 4a and b. For comparison, Table I includes data from thicker sputtered specimens and from films e-beam evaporated and subsequently heat-treated.

Some of the points brought forth in the table merit detailed discussion. The contact perimeter effects that distinguish groups I, Ia, Ib, and II from one another and are illustrated in Fig. 5a and b are due to different degrees of cleanliness in the contact holes combined with the volume contraction, about 500Å, associated

¹ The diffraction zone of the pattern is a function of the Si substrate orientation and will be identified along with the n-fold anomalies of the diffraction patterns in the Discussion section.

with the formation of the PtSi phase. Even when the contacts are sputter cleaned *in situ* before Pt deposition, microanalysis methods often disclose an increased level of chemical etchant residues within 5000Å of the SiO₂ step-down to the Si around the perimeter of the contact hole. When this contamination is present, the Pt immediately adjacent to the SiO₂ step fails to react with the Si, with the result that the aqua regia strip leaves a ring of exposed Si around the contact, as in Ia, or a ring plus scallops, as in Ib. The group I samples occur when the sputter cleaning effectively eliminates the contaminating residue. *In situ* heat-treatment of group II samples in the electron microscope reveals that the Pt on the walls and the top of the SiO₂, having no Si to react with, rapidly diffuses down to feed the reaction in the contact hole perimeter, yielding thicker PtSi nodules in the perimeter. This phenomenon is observed only for sputtered Pt samples in which edge coverage of the oxide step-down is very good. The group II PtSi films had a somewhat poorer heteroepitaxy than the group I films, with an apparently concomitant insensitivity of the specific contact resistance to perimeter effects.

The formal Discussion section will deal with the nodular plus void morphology we attribute to pure PtSi. We believe that the high-angle g.b. morphology is a manifestation of PtSi formed in the presence of low levels of surface contamination that prevents the PtSi from becoming heteroepitaxial to the Si. For PtSi films more than 300-400Å thick, we often see remnants of the Pt₂Si diffraction pattern mixed with diffraction patterns of types A, B, and C. *In situ* heat-treatment in the electron microscope has shown that when the substrate conditions are appropriate for the

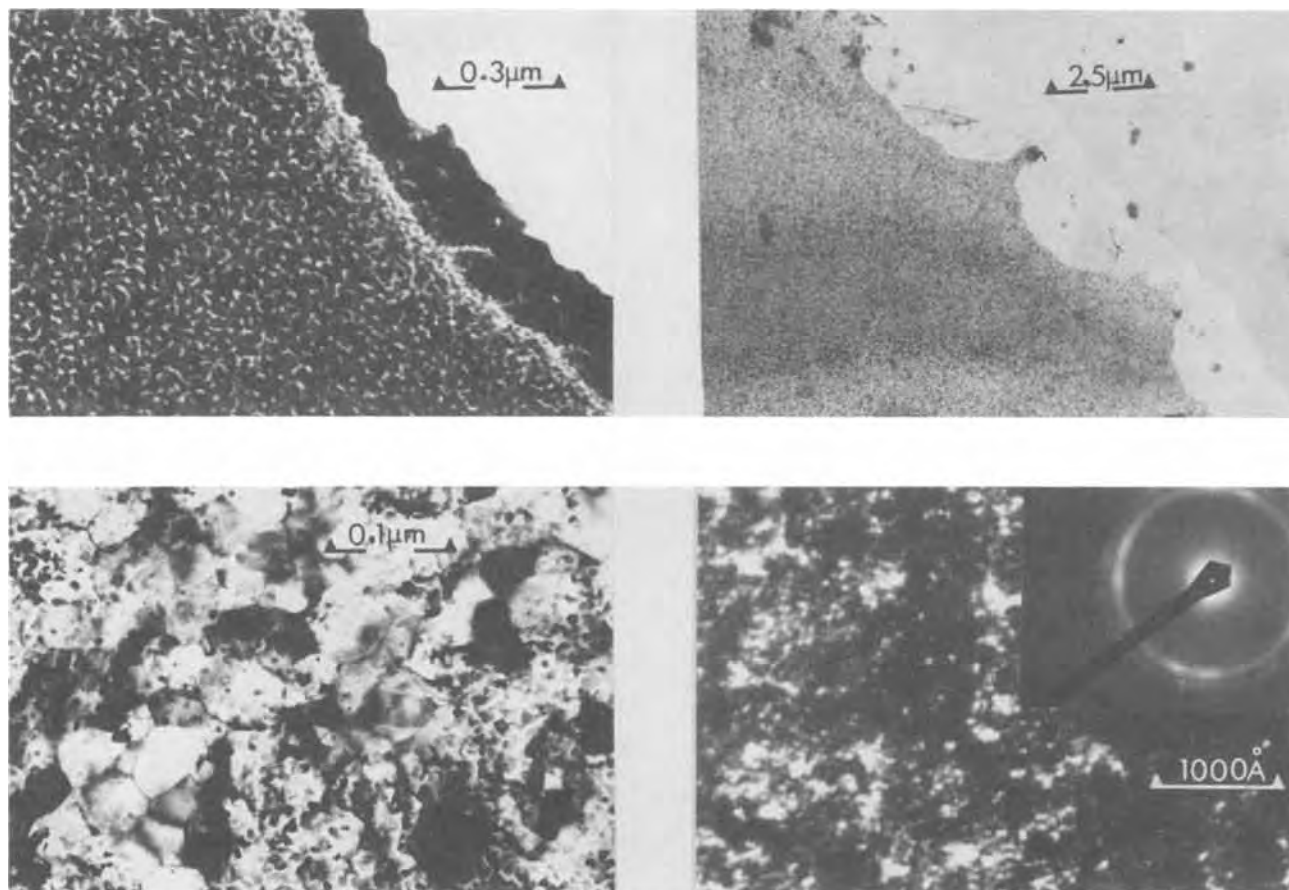


Fig. 5. Anomalies in morphology of PtSi. (a, top left) Buildup of thicker grains of PtSi in perimeter of contact. (b, top right) Opened-up contact perimeter with scallops. (c, bottom left) Remnants of nodule layer beneath recrystallized Pt₂Si₇. (d, bottom right) Porous Pt with diffraction pattern showing diffuse Pt rings.

formation of high-angle g.b. PtSi, heat-treatment at a temperature of over 500°C for more than 1 or 2 min may induce void growth.

The "effect-of-thickness" samples introduce a new morphological type: the two-layer film. The two discrete layers are detected visually in the transmission and scanning electron microscopes and by their different chemical etching behavior. Both layers yield Pt and Si spectra in energy and wavelength dispersion studies in the x-ray microprobe. As is mentioned in Table I, the layer adjacent to the Si substrate has a nodular morphology that often compares well with the group II samples. The top layer has a very slow etch rate and has a spongelike morphology consisting of grains 50-75Å in size in a matrix that is about 50% small grains and 50% voids. Electron diffraction patterns from the top layer are indexed as fcc Pt, but the Pt rings are very broad and diffuse. On this evidence, we identify the top layer as porous Pt, an etching residue.²

For these samples, the heteroepitaxial PtSi nodules are diffusion limited to a maximum thickness of 200-500Å before, presumably, stoichiometric deficiencies cause the PtSi to renucleate in a randomly oriented polycrystalline morphology, as has been observed on unetched specimens. Figure 5c depicts a thick sample that has been thinned from below; the remnants of the nodules can be seen under the large renucleated Pt_xSi_y ($x > y$) grains. This Pt_xSi_y is attacked by the aqua regia etch to produce porous Pt (Fig. 5d). The thickness of Pt_xSi_y/porous Pt is maximized, for a given Pt thickness, by poor contact hole cleaning and/or higher concentrations of B or As dopants in the Si, as is discussed later.

PtSi formed from evaporated Pt presents a study in contrasts. The evaporated Pt group I samples, which are typical of most of the evaporated Pt-PtSi examined, compare very favorably with sputtered samples of groups Ia and Ib. In all cases, evaporated Pt contacts exhibited deleterious contact perimeter effects. When evaporated Pt-PtSi contacts are made in large lots, with no intentional changes in deposition parameters, electrical tests occasionally reveal wafers with high specific contact resistances. TEM analysis of these wafers reveals the microstructure identified as evaporated Pt group II in Table I. The morphology and crystallinity of evaporated Pt samples in group II combine the worst features of sputtered group IV and the effect-of-thickness samples. Often the perimeter discontinuity expands to the center of the contact, leaving only a small region of PtSi.

The authors believe that the poor quality of the microstructures in the evaporated Pt samples in group II is directly attributable to contamination of the Si contacts. Support for this belief comes from ESCA and SEM/Auger analysis, which reveals higher levels of carbon that presumably are due to residues of chemical cleaning and photoresist left before deposition. Often the high contact resistance of evaporated Pt group II samples can be lowered somewhat by additional heat-treatment before the aqua regia etch. Heat-treatments of up to 2 hr at 550°C were used. This is additional, indirect evidence of contact contamination; one can assume that hydrocarbons in the contacts are breaking down and allowing the Pt to react with the Si.

Dopant C₀ dependence.—During our analysis of PtSi thin films, we noted that the microstructure of the PtSi films is sensitive to the dopant species and surface concentration in the underlying Si substrate. As was noted in the section on preparing specimens, the dopant-C₀-dependence PtSi was formed on the seven wafers listed in Table II. The Si dopant species and the range of dopant concentrations were chosen with the aim of encompassing all of the Si-dopant possi-

bilities germane to the production of viable contacts. The 2.0×10^{15} boron wafer is taken as the intrinsic Si case. Sheet resistances were measured on the as-deposited films and after the external heat-treatments as listed in Table II. The heat-treatments were performed after the unreacted Pt strip, to prevent any unreacted Pt present from adding to the volume of PtSi phase formed during the deposition *in situ* heat-treatment. The drop in sheet resistance observed after the heat-treatment at 750° or 850°C is due to the expansion of the heteroepitaxial film via the partial consumption of the thin polycrystalline PtSi (or porous Pt) film overlying the heteroepitaxial nodules. We postulate not that the sheet resistance is lower because of the more perfect microstructure of the PtSi films, but rather that the electrical properties of the films are degraded as the increased heat-treatment temperature drives the finite amount of Pt deeper into the Si at the expense of the stoichiometry of the PtSi films. The films heat-treated at 950°C have been completely recrystallized. The PtSi is now completely randomly oriented polycrystalline, with high-angle grain boundaries and no voids. Paralleling Sinha's findings (8), the polycrystalline PtSi film is covered with discontinuous clusters of agglomerated large grains of PtSi protruding from the smooth film. Note in Table II that the complete absence of stoichiometric heteroepitaxial PtSi in the 950°C samples is invariably accompanied by an increase in sheet resistance.

Space does not permit us to include representative micrographs and diffraction patterns for all of the combinations of Si dopants and heat-treatments reported in Table II. Let us start with the intrinsic (2.0×10^{15} B) Si sample. The as-deposited, two-layer PtSi film has a complete nodule layer over the Si and an incomplete poly PtSi/porous Pt film over the nodules. After heat-treatment at 750°C, there is much less poly PtSi/porous Pt in evidence; after heat-treatment at 850°C, there is none at all in discrete areas on the intrinsic Si. The morphology of the film after the heat-treatment at 950°C consists of protruding large PtSi grains on randomly oriented continuous PtSi film.

The most obvious effect of increasing the Si dopant in the substrate is to improve the coverage of the as-deposited samples by poly PtSi/porous Pt. The As 1.0×10^{19} sample was covered about as well as the intrinsic Si sample, about 50%. On the other hand, the As 1.0×10^{20} and the B 4.0×10^{18} as-deposited samples were 70-90% covered over the heteroepitaxial nodules. At higher dopant levels of either species in Si, the nodules were completely covered with poly PtSi/porous Pt. The microstructural effects of heat-treatment of all the as-deposited films parallel the sequence described for intrinsic Si: at 750° or 850°C the poly PtSi/porous Pt loses its identity as a discrete film, and at 950°C it recrystallizes. The only exception to the general trend was that the As 1.0×10^{21} sample heat-treated at 850°C was partly recrystallized.

Effect of in situ sputter cleaning on the silicon surface.—We have stressed the importance of contact hole

Table II. Sheet resistance (ohm/sq) of PtSi as a function of dopant concentration and heat-treatment. All heat-treatments lasted 1 hr

Dopant	Heat-treatment, °C	Dopant concentration (cm ⁻³)		
		2×10^{15} *	5×10^{18}	4×10^{19}
Boron	As deposited	13.50	0.721	0.697
	750	9.36	0.493	0.694
	850	6.50	0.546	0.659
	950	6.86	0.497	0.689
			1×10^{19}	1×10^{20}
Arsenic	As deposited	12.74	5.14	4.51
	750	7.67	4.41	4.20
	850	6.90	4.37	4.36
	950	7.74	5.54	5.47

* Taken as the intrinsic case.

² A porous reaction occurs when an intermetallic alloy, consisting of a noble metal and a nonnoble metal, is etched: the noble metal is leached from the alloy lattice, leaving the noble metal in a highly disordered state. The remnant lattice will produce a diffraction pattern consisting of broad, diffuse lines. The porous metal product has a spongelike morphology and is not amenable to further etching.

cleanliness on the microstructure of the subsequently deposited PtSi film. We have shown that *in situ* sputter cleaning before Pt deposition produces improved PtSi films and minimizes or eliminates contact perimeter effects. In this section we deal with the side effects of *in situ* sputter cleaning. Specifically, are the SiO₂ surrounding the contacts, and Pt from the nearby Pt fixtures, being backsputtered into the contacts during the cleaning?

TEM analysis of the 100W and 500W sputtered wafers showed contrast effects on the Si that were found to be associated with a rough surface morphology, very small dislocation loops, or the nucleation of a foreign material on the Si surface. Electron diffraction patterns showed single-crystal Si reflections, polycrystalline Si rings, and a ring pattern indexed as Pt.

A part of each sample was analyzed by reflection electron diffraction analysis (RED), comparing the center of the wafer with observations out to the edge. RED showed polycrystalline Si rings, Pt rings, and one ring identified as PtSi on the sample that had not been heat-treated. The only Si single-crystal reflections seen were very weak; this indicates that the thickness of the polycrystalline Si is nearly as great as the depth to which the electron beam from the RED apparatus penetrates into the substrate, about 300Å. The Pt reflections were broadened; this, in turn, indicates that the Pt is very thin. Both the polycrystalline Si and the Pt were more intense near the edges of the wafers than at the centers. Neither the thin polycrystalline Si nor the Pt showed in a low-angle Laue x-ray photograph. A Berg-Barrett surface topograph revealed no surface damage, within the limit of resolution of this method.

In view of the diffraction results, the samples were given a heat-treatment designed to clear up the ambiguity in the TEM observations of the surface. A heat-treatment would cause nucleated Pt to form PtSi with a resolvable size and/or any Si defects, such as dislocation loops, to grow to analyzable dimensions. After a heating cycle that peaked at 750°C after 30 min, TEM revealed isolated islands of PtSi with a strong PtSi $\langle 110 \rangle$ orientation relationship normal to the Si. No polycrystalline Si was detected.

For corroboration, the 500W sample was analyzed in the x-ray microprobe for Pt as a step function of distance from the center of the wafer to its edge. Pt was detected from the center out to the edge; its concentration was lowest at the center and peaked approximately 5 mm from the edge. The total counts at each step were low, indicating a very thin layer.

By use of the ESCA and Auger/SEM methods and the x-ray microprobe, we searched for backsputtered SiO₂ in the contact windows that had been sputter cleaned *in situ*. All three analyses confirmed that oxygen and/or SiO₂ were present, along with carbon, in the contact holes. However, the amount of contamination was very close to the above method's detectability limits and to the amount of SiO₂/carbon present on control samples that had not been sputter etched; hence the few monolayers of contamination that we see may well be native oxide films grown on the Si after sputter etching and artifactual carbon contamination induced in the analyzing instrumentation.

Apparently, then, the effect of rf sputter cleaning the Si wafer, if we neglect SiO₂ and carbon contamination, is to introduce a thin layer of polycrystalline Si on the surface (which is probably caused by backsattering or reflection of sputter-etched Si falling back on the surface) and to backscatter some Pt from the Pt-coated sputter-etching cathode and the nearby Pt d-c sputter-deposition cathode. When the samples were heat-treated, the Pt reacted preferentially, with the polycrystalline Si consuming it in the formation of PtSi. No dislocation loops or other line defects were observed in the Si. Although twins and other remnants of the existence of the polycrystalline Si layer could

be expected in the heat-treated samples, none was observed.

The presence of backscattered Pt on the Si is desirable (16). The amount and distribution of it can be controlled by manipulation of the sputtering conditions.

The formation of a polycrystalline Si layer is probably not harmful. In fact, it may speed the formation of the PtSi phase.

Excessive sputter etching may produce an amorphous Si layer on top of the polycrystalline Si; however, we found no evidence of such a layer.

Discussion

PtSi diffraction anomalies.—The anomalous greater than twofold symmetry observed in diffraction patterns taken of orthorhombic PtSi was explained in earlier works (11-13). There we identified the epitaxial relationship of PtSi on {100} Si to be PtSi ($\bar{1}10$) parallel to Si (001) and PtSi [001] parallel to Si [110]. The fourfold symmetry arises from double positioning of PtSi [001]'s on the two cubic $\langle 110 \rangle$ of the surface in neighboring PtSi nuclei.

In an illustration, we see that the PtSi on the {100} Si diffraction pattern in Fig. 6a exactly matches the computer plot in Fig. 6b. The computer plot was made by first drawing a PtSi [$\bar{1}10$] zone (asterisks) and then

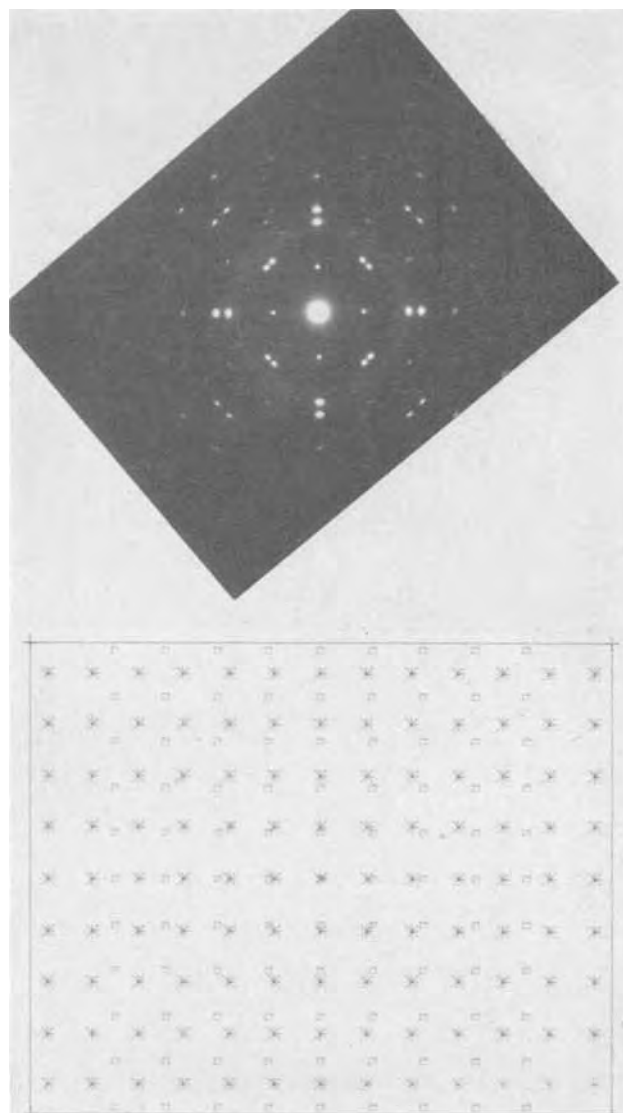


Fig. 6. Comparison of {100} diffraction pattern and computer plot for PtSi on {001} Si. (a) Diffraction pattern. (b) Computer plot, containing two PtSi [110] zones plotted with a 90° mutual rotation.

redrawing the same $\{1\bar{1}0\}$ zone (squares) after a 90° rotation about the common zone normals. The same explanation applies to the anomalous threefold diffraction patterns observed for PtSi on $\{111\}$ Si wafers. In this case the PtSi (010) is parallel to the Si (111), and the PtSi [010] is triply positioned on three equivalent $\langle 224 \rangle$ of the Si. In Fig. 7 a diffraction pattern and a computer plot are compared as before except that the computer plots the PtSi [010] zone twice after two 60° rotations. The nonmatching reflections plotted by the computer are structure-factor-forbidden PtSi reflections that are present in the [010] zone. Figure 7a also contains oriented Pt_2Si reflections.

For completeness, we have also investigated the epitaxial relationships of PtSi formed on $\{011\}$ Si substrates. The 150Å of PtSi was formed *in situ* during sputtering with conditions the same as those which produce type A PtSi. The blanket samples exhibited a type A nodule morphology. The diffraction patterns exhibited greater than twofold symmetry, but it was obvious that more than one crystallographic zone was present in the patterns. Figure 8a depicts the morphology of PtSi on $\{011\}$ Si, and Fig. 8b shows the corresponding diffraction pattern. The heteroepitaxial relationships, obtained from Fig. 8b, are as follows:

PtSi on $\{011\}$ Si

Major orientation—double positioning of

PtSi (133) || Si (011)

PtSi [301] || Si [022]

Coexisting minor orientations

(a) PtSi (120) || Si (011)

PtSi [002] || Si [022]

(b) PtSi (011) || Si (011)

PtSi [$\bar{1}1\bar{1}$] || Si [400]

The samples with PtSi on $\{011\}$ Si were also used to find a solution for another electron diffraction puzzle observed on $\{001\}$ and $\{111\}$ Si. When a thin type A film is observed in SAD mode over a thin wedge of Si tilted into perfect zonal orientation, clusters of satellite reflections are formed around the Si matrix diffraction spots (Fig. 9a). Multiple diffraction effects, superlattice formation, and film formation on twinned Si surface regions were suggested as mechanisms for the satellite spot formation (17). Silicon twins primarily across (111) planes; the $\{011\}$ samples, which have two (111) planes perpendicular to the surface, are ideal vehicles to test the twinning argument.

The assumption of twinning across the two (111) traces in Fig. 9a accounts for all of the anomalous reflections in what appears to be an $n/3$ relationship to the Si reflections. The close-by satellite reflections are not accounted for in this manner; they are presumed to arise from a combined multiple-diffraction-twinning mechanism, not yet determined, involving the substrate and the heteroepitaxial film. Analogous satellite arrangements for $\{001\}$ and $\{111\}$ substrates are seen in Fig. 9b and c.

The one significant conclusion drawn from the identification of the twin reflections in Fig. 9a is that local regions of the Si surface bear twin relationships to one another. Therefore, PtSi films formed heteroepitaxially on one region of Si will bear a twin relationship to PtSi formed on a neighboring, twinned region of Si. This in turn leads to an alternative argument to account for the greater than twofold symmetries observed in PtSi diffraction patterns. For example, the major asymmetry of Fig. 8b, ascribed to double positioning of $\{133\}$ PtSi zones, could be equivalently produced by forming $\{133\}$ PtSi over twinned regions of Si. Unfortunately, the Si planes over which the PtSi $\{133\}$ must be mirrored are the Si (011) and (001), which have not been observed to be Si twinning axes. An attempt to extend the twinning argument to account for the high symmetry of PtSi on $\{001\}$ and $\{111\}$ Si wafers is also unsuccessful because the assumption of twinning over the previously reported $[111]$, $[123]$, and $[511]$ Si twinning axes cannot account for the anomalous symmetry.

With the epitaxial relationships established, we can explain the observed morphology of thin, clean, epitaxial PtSi in thicknesses from 100 to 500Å. For PtSi on Si $\{100\}$ wafers, we would expect an epitaxial PtSi film consisting of grains of PtSi abutting with 90° grain boundaries. Contrary to expectation, the morphology of such a film (Fig. 10a) consists of small disconnected nodules of PtSi with random shapes. This morphology probably arises because large misfit energies make neighboring PtSi nuclei with 90° rotations between PtSi $\langle 001 \rangle$ directions unable to coalesce during film deposition or recrystallization.

By carefully tilting a PtSi film on a $\{100\}$ Si specimen in the goniometer stage of the electron microscope, it was possible to extinguish the PtSi reflections and leave one Si (400) reflection in a selected-area electron diffraction pattern. The Si (400) reflection was used to produce a high-magnification dark-field micrograph (Fig. 10b) of the area seen in Fig. 10a. Here the internodule regions are illuminated. This establishes that the epitaxial PtSi nodules are surrounded by un-

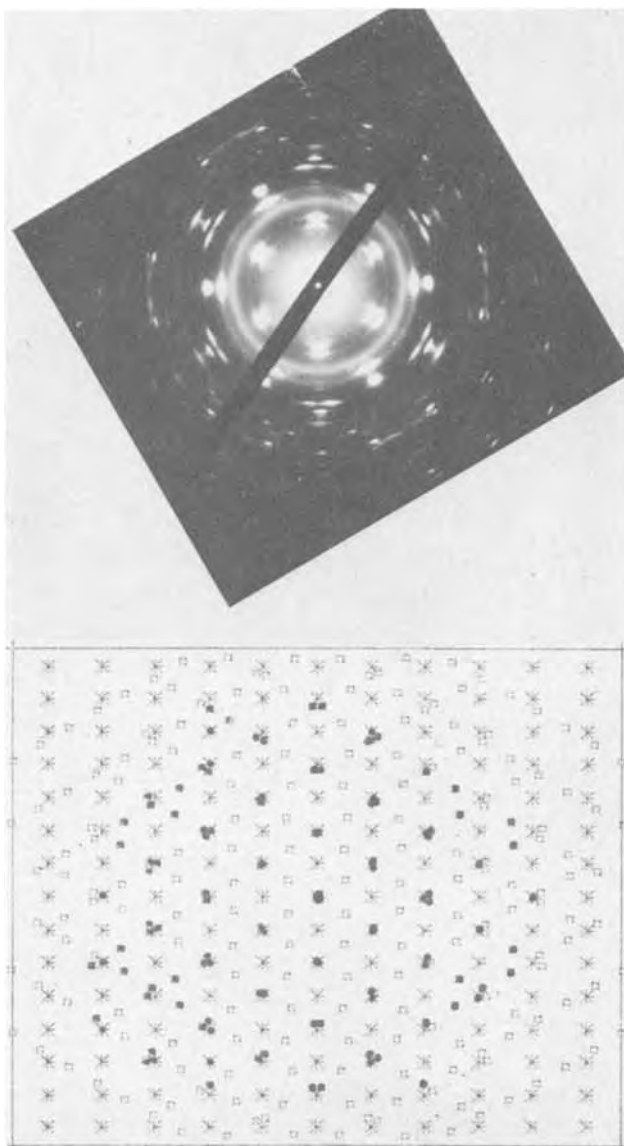


Fig. 7. Comparison of $\{111\}$ diffraction pattern and computer plot for PtSi on $\{001\}$ Si. (a) Diffraction pattern, which contains a Pt_2Si reflection that also shows anomalous symmetry. (b) Computer plot, containing three PtSi [010] zones plotted with 60° mutual rotations.

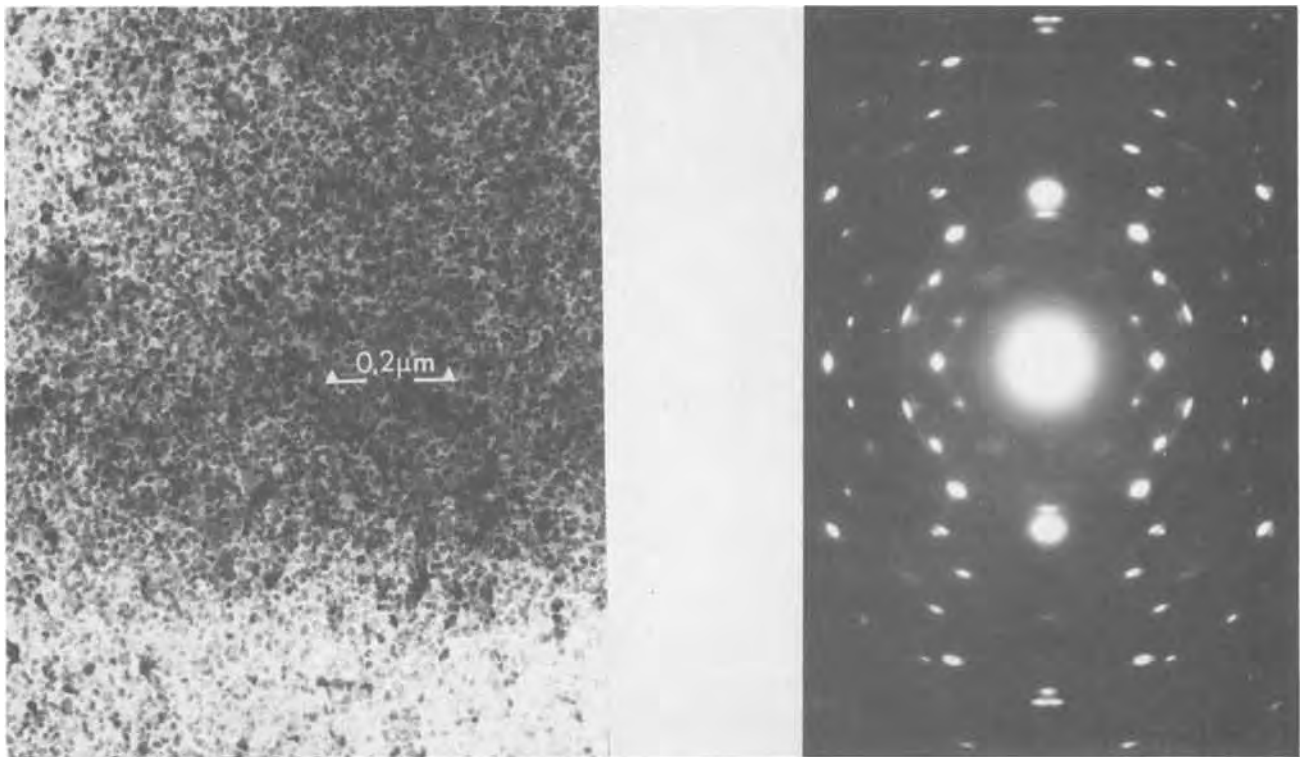


Fig. 8. PtSi on {011}. (a, above left) Nodule morphology. (b, above right) Corresponding diffraction pattern, containing two PtSi [133] zones rotated 180° plus minor orientations.

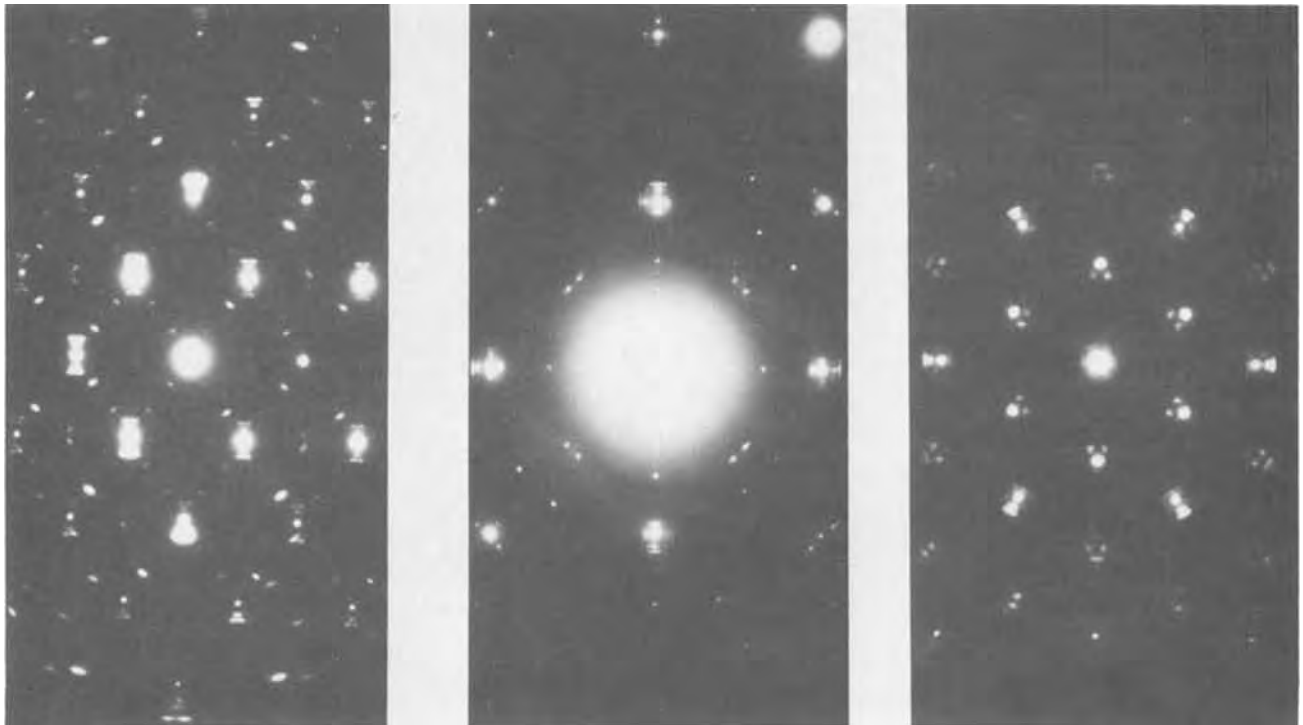


Fig. 9. Extra reflections observed when thin PtSi over Si is brought to perfect Si zonal orientation. (a, above left) {011} Si. (b, above middle) {001} Si. (c, above right) {111} Si.

reacted Si channels approximately 20-30Å wide. Apparently the misfit energy associated with the coalescence of two PtSi nodules oriented 90° with respect to each other overcomes the driving force of the intermetallic phase formation, leaving, presumably, very highly stressed, unreacted Si between nodules.

The same explanation applies to the identical epitaxial PtSi morphology observed on {111} and {110} Si wafers.

Relationship of electrical properties of morphology and crystallinity.—Clearly, the best electrical contacts, *i.e.*, the lowest in specific contact resistance and the closest to ohmic behavior, produce single-crystal PtSi diffraction patterns consisting of one diffraction zone (type A). Morphologically, such structures consist of heteroepitaxial PtSi nodules 200-500Å in diameter separated by voids of 10-50Å, as shown in Fig. 10a. Not surprisingly, the PtSi microstructure that yields the

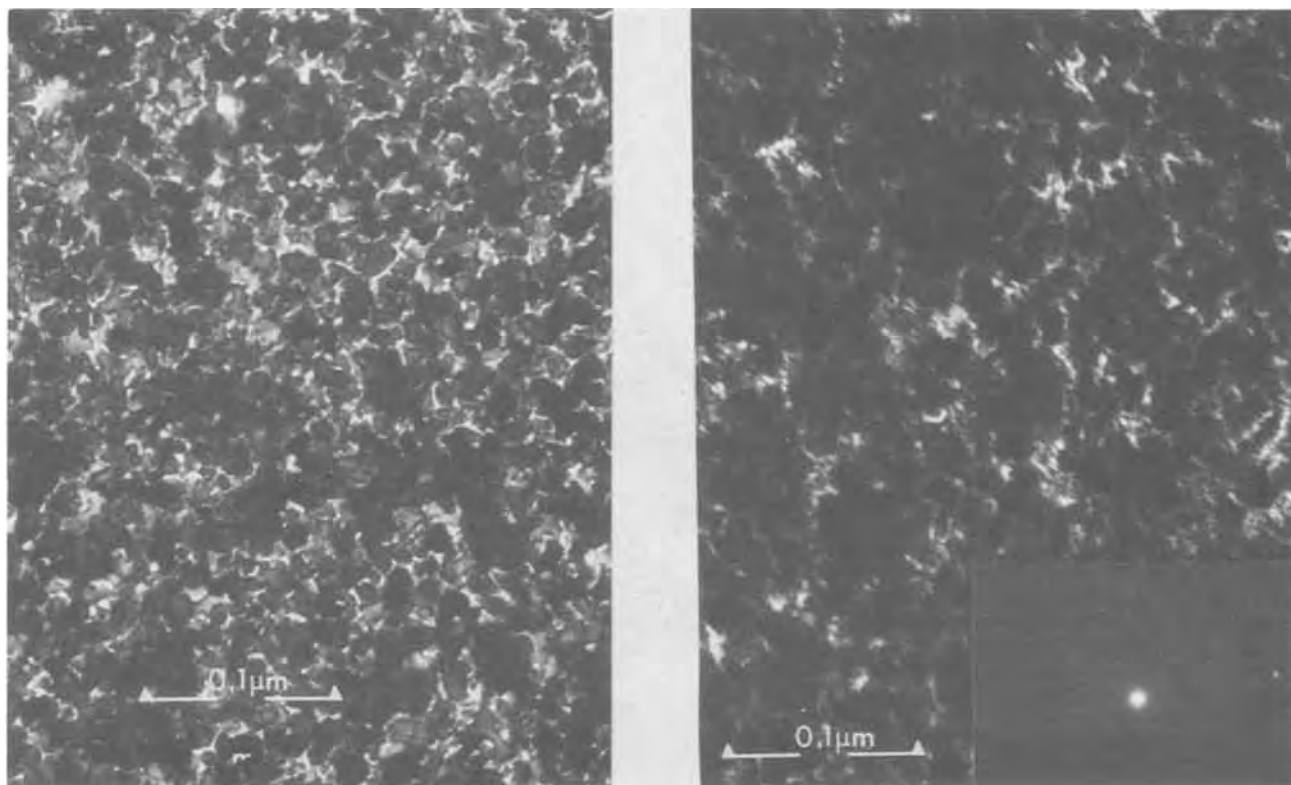


Fig. 10. Unreacted Si between PtSi nodules. (a, above left) Bright-field micrograph. (b, above right) Companion dark-field micrograph taken by use of a Si (400) reflection.

best electrical base contacts also gives the best emitters. Type A PtSi, therefore, appears to be the best from a pragmatic as well as an esthetic point of view.

Relationship of microstructure to deposition conditions.—We have found that the best PtSi films could be formed most consistently by sputter depositing at elevated substrate temperature ($\sim 450^\circ\text{C}$) after *in situ* sputter cleaning. Heat-treating *in situ*, but after rather than during the deposition, produced microstructurally and electrically better contacts than heat-treating externally in a flowing dry N_2 furnace, even with the furnace 100°C higher in temperature. Both methods, however, are inferior to *in situ* heating during deposition.

Chemical cleaning plus *in situ* sputter cleaning also gave consistently better results than chemical cleaning alone. No direct comparison of *in situ* sputter-etched sputter-deposited PtSi and *in situ* sputter-etched, e-beam-evaporated films was made, but sputter depositing should be better, if only because it covers the perimeters of the contact holes better. Perimeter coverage is an extremely important factor when the PtSi is used on lightly doped n-type Si to form a rectifying (Schottky) contact, in which edge effects play a dominant role in reverse-bias operation.

Conclusions

A number of conclusions can be drawn from this study:

1. A direct relationship has been established between the microstructural and the electrical properties of PtSi thin films. We are now able to predict with certainty, by only a microstructural examination, when a PtSi contact will be electrically acceptable. Conversely, we have related unsatisfactory electrical performance to specific microstructures, which are in turn related to certain deposition conditions; this finding makes it possible to adjust microstructures on the production line on the basis of electrical data.

2. A direct relationship has been established between PtSi deposition parameters and microstructural properties (and hence electrical properties). The best PtSi

films, microstructurally and electrically, are formed by sputter depositing Pt while continuously forming PtSi *in situ* at approximately 450°C on Si that has been rf sputter cleaned *in situ*.

3. Sputter cleaning forms a thin layer of polycrystalline Si and deposits a small amount of unreacted Pt on the surfaces of the Si contacts. Neither effect is detrimental; in fact, the formation of polycrystalline Si may aid in the efficient, uniform formation of PtSi.

4. A PtSi film more than $200\text{--}500\text{\AA}$ thick has two layers. The layer next to the Si substrate often compares well to the best single-layer PtSi. The top layer, after etching, has been identified as "porous Pt" and is poorer microstructurally than the layer beneath. A porous reaction occurs in intermetallic alloys of a noble metal and a nonnoble metal when the latter is leached from the lattice, leaving the noble metal in a highly disordered state.

5. The microstructure and the electrical sheet resistance of a PtSi thin film are sensitive to the dopant species and surface concentration of the Si on which the film is formed, and to subsequent heat-treatment in the range from 750° to 950°C . For a given heat-treatment, the best microstructures are observed on the lowest doped Si, and the lowest sheet resistances on the highest doped Si. For films formed on Si with any dopant species and surface concentration, sheet resistance decreases in the $750^\circ\text{--}850^\circ\text{C}$ range, but increases at 950°C because discontinuous clusters of large PtSi grains form and any stoichiometric heteroepitaxial PtSi is completely destroyed.

Manuscript submitted April 24, 1975; revised manuscript received June 12, 1975.

Any discussion of this paper will appear in a Discussion Section to be published in the June 1976 JOURNAL. All discussions for the June 1976 Discussion Section should be submitted by Feb. 1, 1976.

Publication costs of this article were partially assisted by IBM Corporation.

REFERENCES

1. D. Kahng and M. P. Lepselter, *Bell System Tech. J.*, **44**, 1525 (1965).

2. M. P. Lepselter, *ibid.*, **45**, 233 (1966).
3. R. M. Anderson and S. Dash, *EMSA Proc.*, p. 120 (1969).
4. R. M. Anderson, *EMSA Proc.*, p. 518 (1972).
5. G. A. Walker, R. C. Wnuk, and J. E. Woods, *J. Vacuum Sci. Technol.*, **7**, 543 (1970).
6. F. B. Koch and P. B. Byrnes, Paper 191 presented at Electrochemical Society Meeting, Atlantic City, N.J., Oct. 4-8, 1970; *This Journal*, **117**, 262c (1970).
7. H. N. S. Lee, F. B. Koch, and W. R. Costello, Paper 70 presented at Electrochemical Society Meeting, Washington, D.C., May 9-13, 1971; *This Journal*, **118**, 72c (1971).
8. A. K. Sinha, R. B. Marcus, T. T. Sheng, and S. E. Haszko, *J. Appl. Phys.*, **43**, 3637 (1972).
9. H. Muta and D. Shenoda, *ibid.*, **43**, 2913 (1972).
10. A. Hiraki, M.-A. Nicolet, and J. W. Mayer, *Appl. Phys. Letters*, **18**, 178 (1971).
11. T. Kawamura, D. Shenoda, and H. Muta, *ibid.*, **11**, 101 (1967).
12. J. M. Poate and T. C. Tisone, *ibid.*, **24**, 8 (1974).
13. H. H. Hosack, *ibid.*, **21**, 256 (1972).
14. H. H. Hosack, *J. Appl. Phys.*, **44**, 8 (1973).
15. M. J. Rand, *This Journal*, **120**, 685 (1973).
16. J. L. Vossen, J. J. O'Neill, Jr., K. M. Finlayson, and L. J. Royer, *RCA Rev.*, **31**, 2, 293 (1970).
17. G. Das, Private communication.

An ESCA Study of the Oxide at the Si-SiO₂ Interface

R. A. Clarke,¹ R. L. Tapping², M. A. Hopper,^{*3} and L. Young^{*}

*Department of Electrical Engineering and Department of Chemistry,
The University of British Columbia, Vancouver, British Columbia, Canada*

ABSTRACT

Thermally grown oxide films on silicon were investigated using ESCA (electron spectroscopy for chemical analysis). Evidence was obtained which confirmed previous indications from other techniques that there is a transition layer of about 15 or 20 Å thickness next to the silicon. In this layer the oxide changes from SiO close to the silicon to SiO₂ in the rest of the film.

The silicon/silicon oxide interface has a part in controlling the rate of thermal oxidation of silicon (1). Conversely, the atomic arrangement at this interface (which is important in determining several electrical properties of MOS systems) is itself affected by the variables of the oxidation process (2). The aim of the present work was to see what information could be obtained about the composition of the oxide near the interface with ESCA. Using this method, the shift of the 2p electron levels in silicon atoms, due to changes in the chemical environment of silicon atoms in oxide of different oxygen content, was observed. Confirmation of previous evidence from various techniques [including helium ion backscattering (3), secondary ion spectroscopy (4, 5), and optical reflectance (6, 7)] was obtained showing that there is a silicon-rich layer near the interface.

Experimental Procedures

The x-ray source of the Varian IEE-16 photoelectron spectrometer produces $h\nu = 1254$ eV photons. Absorption of a photon raises an electron from the 2p level of the silicon. Neglecting any loss of energy in escaping from the material, the kinetic energy E_k of the freed electron would be $E_k = h\nu - E_b$ where E_b is the difference in energy between the vacuum level and the 2p level. Electrons thus released will not be collected by the detector if the potential difference across the intervening vacuum is of appropriate sign and slightly greater than E_k/e (where $e =$ magnitude of charge on electron). For this condition to exist, the observable difference in Fermi levels between the two electrodes and their work functions is related by $(E_F^d + \phi^d) - (E_F^s + \phi^s) = E_k$, where d refers to the detector and s to the specimen. Consequently

$$E_b = h\nu - (\phi^d - \phi^s) - eV$$

where V is the applied voltage (sample positive). Rather than estimate the work function difference, the energy calibration of the electron spectra was accomplished by taking the binding energy of some other known observable level. Either a film of gold was deposited on the sample and the higher energy Au 4f level was taken as 87.5 eV or the 2p line of the bulk silicon was used as a reference. The latter can, of course, be used only if the oxide is not too thick to prevent the escape of electrons from the substrate. Located with respect to the above gold standard, this level was found to be 99.5 ± 0.3 eV for the n-type 10 ohm-cm material which we used. Different values of the energy of the silicon peak were observed for different doping densities (e.g., 98.9 ± 0.2 eV for degenerate p-type silicon and 99.9 ± 0.2 eV for degenerate n-type silicon). This is expected since the work function of the silicon is, of course, changed by doping. In this work we are interested in shifts of the level due to silicon atoms in the oxide. To circumvent complications due to doping as well as to band-bending, all bulk silicon peaks used as a reference were arbitrarily taken as having an absolute energy of 98.9 eV.

The silicon samples were commercially polished n-type (111)-oriented 10 ohm-cm material. They were cleaned by immersion in 1:1 H₂O₂-H₂SO₄, 4:1:1 H₂O-H₂O₂-HCl, and dilute HF and were oxidized in steam or pure oxygen in a quartz furnace tube.

The thickness of the oxide films was estimated using ellipsometry. For very thin films on silicon, thickness and refractive index differences cannot readily be distinguished using ellipsometry. The thicknesses were calculated using 1.458 for the refractive index of the oxide at 6328 Å, which was the value found for thicker "dry" oxides. For very thin films of low oxygen content, and also for "wet" oxides, this index will, of course, be slightly in error.

For the ESCA measurements the oxide was removed from the back surface with HF and silver paste was

* Electrochemical Society Active Member.

¹ Present address: Garrett Manufacturing Company, 40 Voyager Court North, Rexdale, Ontario, Canada.

² Present address: Chalk River Nuclear Laboratories, Atomic Energy of Canada Limited, Chalk River, Ontario, Canada.

³ Present address: Xerox Research Centre of Canada, Mississauga, Ontario, Canada.

Key words: silicon, ESCA, oxidation, thin films.

used to mount pieces of wafer on the gold-plated brass specimen holders.

Since fluorine is a likely contaminant and would cause a shift in the peaks, a search was made but no detectable signals were found from any of the fluorine orbitals. The pressure in the ESCA system was typically 2×10^{-7} Torr.

Results and Discussion

Spectra from silicon with not too thick an oxide contained two peaks, as illustrated in Fig. 1. The lower energy peak is due to silicon atoms in the substrate. The higher energy peak is due to silicon atoms in the oxide and, as shown in Fig. 1, the energy of this "oxide" peak depends on how the oxide was prepared and on its thickness.

The solid curve in Fig. 1 was obtained with a specimen from which oxide had been removed with HF immediately before insertion in the ESCA system. It is believed to have had about 5Å of oxide giving an unresolved peak at 102 eV. Three features of the ESCA spectra will be discussed. These are (i) the ratio P defined as the "oxide" peak height divided by the sum of the "oxide" and "silicon" peak heights, (ii) the line width of the "oxide" signal, and (iii) the energy shift between the "oxide" and the "substrate" peaks.

By defining the quantity P in terms of peak height rather than peak area it is possible to avoid the problem of deconvolving the rather closely spaced oxide and bulk silicon peaks. While not the ideal approach, this definition allows the general trends to be observed as shown in Fig. 2 where P is plotted as a function of oxide thickness for dry and wet oxides. The so-called escape depth from any material was taken to be that depth at which probability of escape of an excited electron is $1/e$ of its value at the surface (8). In silicon (8) this depth was calculated to be 20 ± 5 Å. An analysis of Fig. 2 indicates that the escape depth from the oxide is somewhat greater than this. The figure also shows a significant difference between "wet" and "dry" oxides, presumably due to inclusion of H_2O or OH in the former. This difference merely implies less silicon in a thin film containing water than in one not containing water but of equal thickness as determined by ellipsometry assuming the same refractive index.

Figure 3 shows spectra of three films: (i) 16Å dry oxide, (ii) 16Å grown in O_2 bubbled through water at 95°C, and (iii) 29Å grown in steam. All gave the same P . Clearly the line width is larger when there is more water in the oxidation ambient. The increased

width, however, is insufficient to account for the extra silicon required to provide an oxide of 29Å.

Figure 4 shows the energy of the oxide peak as a function of film thickness for films grown in dry oxygen at different temperatures. Also shown are data for films etched back in buffered HF to the thickness show from an initial 150Å (produced at 900°C). The figure shows data referred to the substrate silicon peak and also data referred to the gold level. In both cases, the oxide peak shifts with increasing thickness in the direction which, as shown below, corresponds to a change from SiO to SiO₂. Because of the limited escape depth of electrons, the ESCA technique samples only the outer part of the thicker films. However, the etch-back data show that these thicker films have an SiO-like layer near the silicon, similar in composition to the initial thin layers.

To calibrate the shift of position of the ESCA "oxide" peak as a function of composition, measurements were made on powdered fused silicon dioxide and on pow-

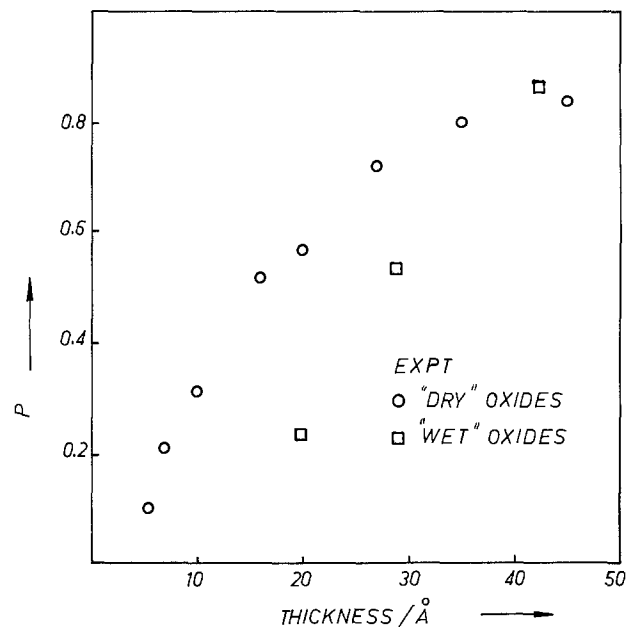


Fig. 2. Ratio P of the "oxide" signal to the total signal as functions of thickness for "wet" and "dry" oxides.

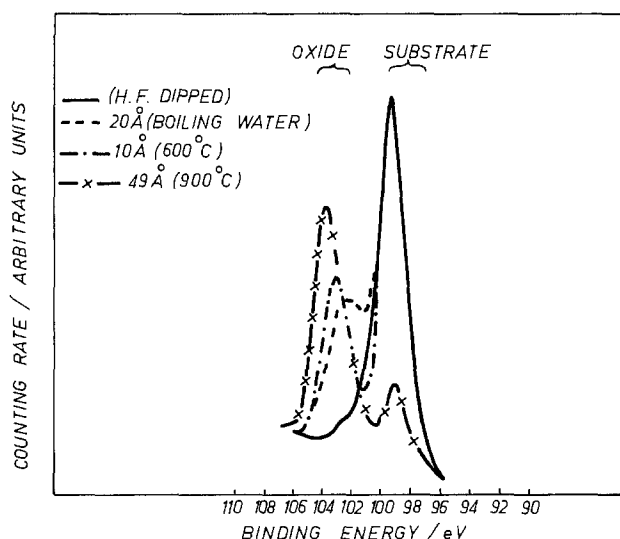


Fig. 1. ESCA spectra for silicon 2p electrons, indexed to gold, obtained with silicon wafers with thin film of oxide prepared in the ways shown inset.

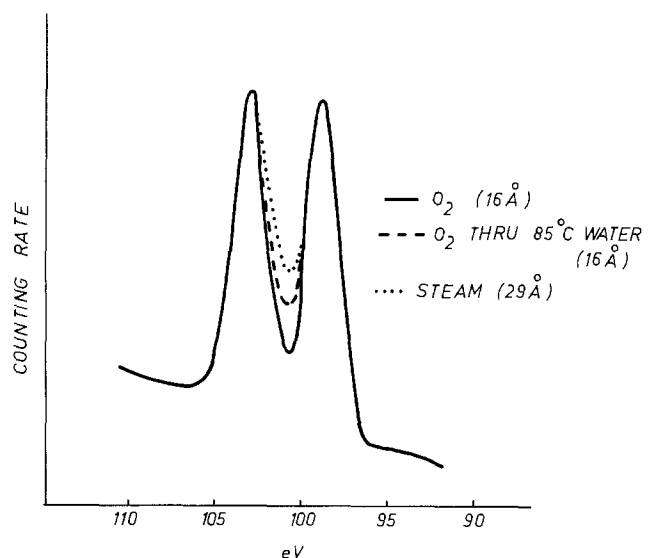


Fig. 3. Oxide and substrate peaks showing increasing linewidth of oxide peak in going from ——— 16Å dry oxide to - - - - - 16Å of oxide grown in O bubbled through H_2O at 95°C to 29Å of oxide grown in steam.

dered Linde Corporation "silicon monoxide." It is, of course, well known that SiO is not a stoichiometrically well-defined compound. As a further complication, our ESCA studies showed that our samples of the Linde product contained a small amount of elemental silicon. The spectra of SiO₂ and "SiO" powders are shown in Fig. 5. The order of line positions is reversed from that reported by previous authors (9). However, the theory developed later shows that the order observed by us is to be expected.

One source of error in ESCA measurements is the build-up of charge on insulating samples. Some tests were made to see if charging was occurring. A technique (10) was used in which a gold layer evaporated onto both the powder and the supporting metal block. Charging, if it occurs, is indicated by an asymmetry of the gold line. No charging was observed with the "SiO" or with the oxide-coated silicon wafers. About 0.8V of charging was observed with the SiO₂ powder. The difference between the gold-referenced data and the silicon-referenced data in Fig. 4 are believed due to band-bending effects rather than to charging.

A theoretical treatment is now given which allows the observed differences in energy and line width between the ESCA peaks for "SiO" and SiO₂ to be accounted for, and which, in fact, allows predictions to be made of these quantities for oxide of arbitrary composition, SiO_x. The theory is based on an analysis of the structure of the amorphous forms of SiO_x due to Philipp (6). He noted that the tetrahedral configuration of oxygen around the silicon atoms in SiO₂ is

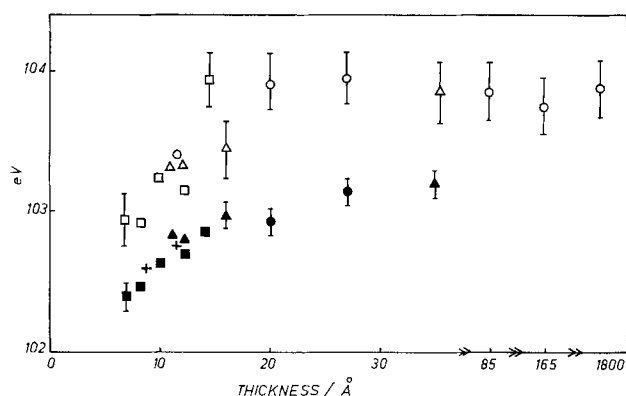


Fig. 4. "Oxide" peak energy as function of oxide film thickness. Open symbols, referred to gold peak; solid symbols, referred to substrate peak. \square and \blacksquare grown at 600°C; \triangle and \blacktriangle grown at 750°C; \circ and \bullet grown at 900°C; + etched back from films greater than 150Å thickness.

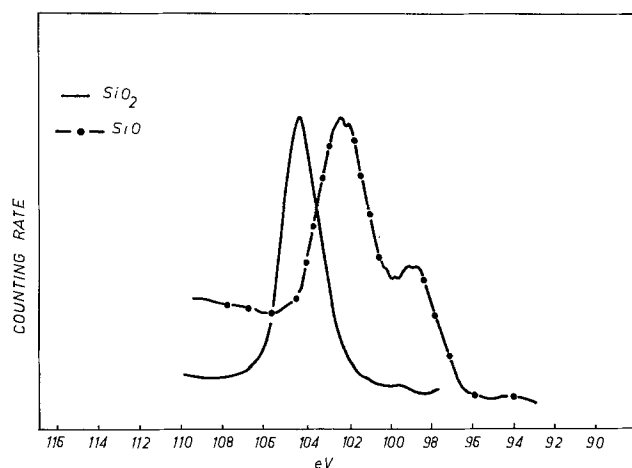


Fig. 5. ESCA spectra for bulk powders — SiO₂ and —○— SiO. Energies referred to gold peak.

maintained in SiO_x except that some silicons replace oxygen, the average tetrahedron containing not four oxygens but $(4 - y)$ oxygens and y silicons (with a relation implied between x and y). Any given individual tetrahedron must be one of five kinds (i.e., with $y = 0, 1, 2, 3,$ or 4). The proportions of each of the five kinds are shown in Table I for different values of x in SiO_x. Considering only nearest-neighbor interaction, the chemical shift in the 2p level of a given silicon atom will depend on which of the five types of tetrahedron it has around it. It should be understood that the observed peaks represent a superposition of contributions from individual atoms, but that these contributions produce a single peak; the spectrometer does not resolve separate peaks from atoms in each type of tetrahedral coordination. The greater line width found in Fig. 5 with SiO as compared to SiO₂ is, for example, explained in that, in the former, all 5 tetrahedra are present, whereas only one type is present in SiO₂. Also, the shift for SiO will be expected to be less than of SiO₂, as we observed.

From the above theory it should be clear that homogeneous materials of formula SiO_x can be simulated, for the purposes of ESCA, by making heterogeneous mixtures of SiO₂ and "SiO" and hence varying the relative concentrations of each type of tetrahedron so as to produce an averaged peak corresponding to that given by any required homogeneous oxide with $1 < x < 2$.

Figure 6(a) and 6(b) shows the energy and width of the composite line observed with mixtures of various mole fraction χ of Linde "SiO." These confirm the direction of shift in peak energy and line width seen with the separate powders. The lines labeled "theory" in Fig. 6 were calculated for hypothetical SiO_x with x corresponding to a homogeneous oxide of the same over-all composition as our mixtures of "SiO" and SiO₂. The separation between "SiO" and SiO₂ was taken as 1.5 eV and the observed line widths for the separate powders were used together with the proportions of the types of tetrahedra from Table I.

Agreement between theory and experiment in Fig. 6 is substantially improved if the presence of elemental silicon in the Linde "SiO" is taken into account. Based on the height ratio of the two peaks in the "SiO" spectra of Fig. 5, it can be shown that the true values of χ_{SiO} for the mixture are $\sim 20\%$ lower than the values shown. With this correction, for instance, the mole fraction at which equal oxide signal magnitude are obtained from each component of the mixture is seen to be $\chi \sim 0.67$ both experimentally and theoretically. It should be noted that this is greater than the value of 0.5 that might have been expected for such a condition if one assumed the "SiO" structure contained only a single tetrahedral form as is the case with SiO₂.

Oxide-coated wafers with graded oxide composition would give a line corresponding to some average composition of SiO_x where the averaging process would involve the escape depth. It can be inferred, therefore, from Fig. 4 that the outer 50Å of silicon oxide layers on silicon approaches SiO₂ in composition only for oxide thickness $> 50\text{Å}$. The continuing presence at all thicknesses of a thin (15-20Å) transition layer at the oxide-silicon interface of "average" composition SiO

Table I. Proportion of 5 possible tetrahedron types in oxides of various Si to O atom ratios*

	SiO ₂	SiO _{1.5}	SiO	SiO _{0.5}	Si
Si—(O ₄)	1.0000	0.3164	0.0625	0.0039	0.0000
Si—(SiO ₃)	0.0000	0.4219	0.2500	0.0469	0.0000
Si—(Si ₂ O ₂)	0.0000	0.2109	0.3750	0.2109	0.0000
Si—(Si ₃ O)	0.0000	0.0469	0.2500	0.4219	0.0000
Si—(Si ₄)	0.0000	0.0039	0.0625	0.3164	1.0000

* H. R. Philipp, *J. Phys. Chem. Solids*, 32, 1935 (1971).

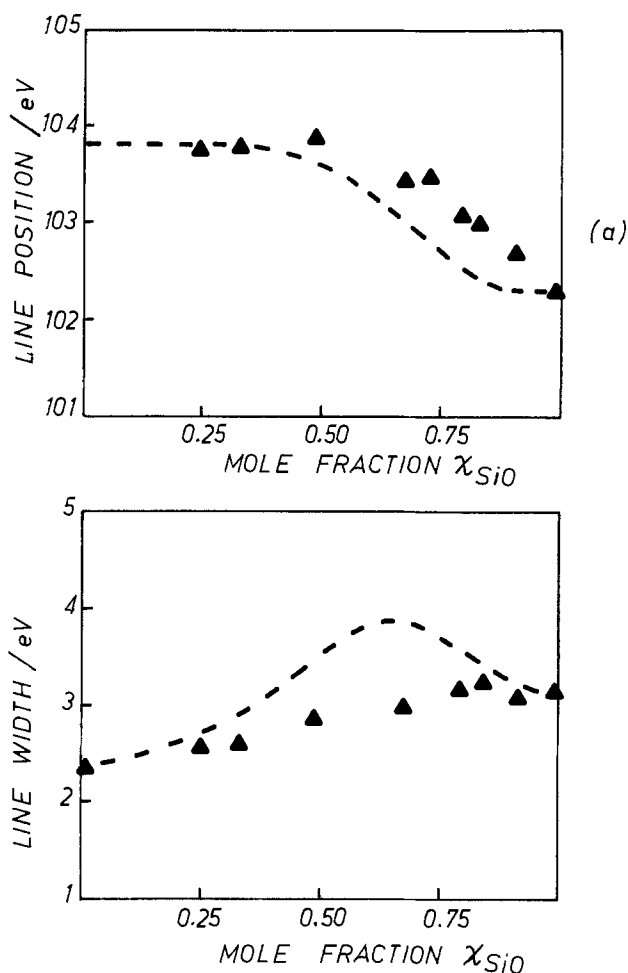


Fig. 6. Points are observed (a) peak energies and (b) line widths for mixtures of SiO and SiO₂ powders. Lines are calculated as discussed in text.

would account for energy shifts in the oxide peaks observed for oxides <50Å.

Conclusions

ESCA studies of the 2p electron spectral line of silicon atoms in thermally grown silicon oxides showed that the width and energy of this line varies with oxide thickness and oxidation ambient. For oxides less

than 40Å in thickness, the width of the line increased and the binding energy decreased with decreasing film thickness and with increasing water vapor content in the oxidizing ambient. No effect was found of oxidation temperature and oxide thickness before etchback. Comparison between thermal oxide data and data obtained with mixtures of "SiO" and SiO₂ shows that the oxide at the interface of the Si-SiO₂ structure has the form SiO_x with x increasing from 1 to 2 with increasing distance from the silicon surface up to about 20Å. The transition region is thicker for the steam grown oxides but is of more uncertain Si:O ratio because of the probable presence in the oxide of OH or H₂O. The shifts in the peaks for oxides of different compositions were discussed using Phillip's model for the structure of oxides of the form SiO_x.

Acknowledgments

We thank Professors C. A. McDowell and D. Frost for the use of the ESCA system and for their interest and helpful comments. The work was supported by the CRC (DSS Contract Serial No. OSU4-0180) and the NRC of Canada. R. A. Clarke, R. L. Tapping, and M. A. Hopper thank the University of British Columbia for teaching Post Doctoral Fellowships.

Manuscript submitted Dec. 12, 1974; revised manuscript received April 21, 1975.

Any discussion of this paper will appear in a Discussion Section to be published in the June 1976 JOURNAL. All discussions for the June 1976 Discussion Section should be submitted by Feb. 1, 1976.

Publication costs of this article were partially assisted by the University of British Columbia.

REFERENCES

1. B. E. Deal and A. S. Grove, *J. Appl. Phys.*, **36**, 3770 (1965).
2. A. G. Revesz and K. H. Zaininger, *R C A Rev.*, **29**, 22 (1968).
3. T. W. Sigmon, W. K. Chu, E. Lugujo, and J. W. Mayer, *Appl. Phys. Letters*, **24**, 105 (1974).
4. A. Benninghoven, *Surface Sci.*, **35**, 427 (1973).
5. A. Benninghoven and S. Storp, *Appl. Phys. Letters*, **22**, 170 (1973).
6. H. R. Philipp, *J. Phys. Chem. Solids*, **32**, 1935 (1971).
7. H. R. Philipp, *J. Appl. Phys.*, **43**, 2835 (1972).
8. C. J. Powell, *Surface Sci.*, **44**, 29 (1974).
9. R. Norberg, H. Brecht, R. G. Albridge, A. Fahlman, and J. R. Van Wazer, *Inorg. Chem.*, **9**, 2469 (1970).
10. D. J. Hnatowich, J. Hudis, M. L. Perlman, and R. C. Ragani, *J. Appl. Phys.*, **42**, 4883 (1971).

Formation and Properties of Porous Silicon and Its Application

Y. Watanabe, Y. Arita, T. Yokoyama, and Y. Igarashi

Musashino Electrical Communication Laboratory, Nippon Telegraph and Telephone Public Corporation,
Musashino-shi, Tokyo, Japan

ABSTRACT

Preparation, properties, and applications of porous silicon film were investigated. Silicon single crystal is converted into porous silicon film by anodization in concentrated hydrofluoric acid at currents below the critical current density. When an n-type silicon was anodized, the silicon surface was illuminated to generate holes which were necessary for this anodic reaction. The growth rate of the film, from n-type silicon, was larger than that from p-type silicon in this experimental condition. The crystalline structure was the same as that of silicon single crystal. A new isolation technique for bipolar integrated circuits was proposed by making use of the properties of the film such that it can be formed several microns thick and oxidized easily to form an insulator. The main feature of the technique is that it provides a means to form thick insulating film inlaid through the n-type epitaxial layer without prolonged heat-treatment. A preliminary experiment was carried out to test the practical usage of the technique.

With the increasing usage of silicon integrated circuits, their fabrication techniques have developed remarkably. However, many problems are left for each fabrication process. Improvement of the isolation process for bipolar integrated circuits is one of the most important and difficult problems. The conventional diffusion method for isolation has various parasitic effects. In addition, the spreading of the isolation region due to sideways diffusion limits the integration density.

Recently, many new structures for isolation have been proposed. Some of them have been considerably successful in avoiding the above mentioned effects. One typical example is the isoplanar technique, in which passive oxide layers are substituted for the usual diffused layers. In this partial oxidation method, however, prolonged heat-treatment is necessary to form thick silicon dioxide films. In the bipolar integrated circuits, the intense heat-treatment has serious problems. For example, when a buried collector exists, the additional diffusion of the buried impurities toward the surface may affect the breakdown characteristics of the fabricated devices.

The authors have also been investigating the isolation technique in silicon integrated circuits and have found a new technique (1) called the IPOS technique. IPOS is an abbreviation of insulation by oxidized porous silicon. The IPOS technique is roughly divided into two processes. The first one is a selective anodization of a silicon epitaxial wafer in hydrofluoric acid. The parts of silicon, where isolation layers are to be formed, are converted into porous silicon, which seems to be the same as the thick anode film reported by Turner and others (2, 3). The other process is a subsequent heat-treatment in oxidizing atmosphere. The porous silicon film can easily be oxidized to a thick insulating film because of its porosity and active nature. Through these processes, isolated islands of silicon single crystal, similar to those of the isoplanar technique, can be formed without long heat-treatment.

There are also two approaches in applying IPOS to the isolation of bipolar integrated circuits, namely n-type method and p-type method. They are shown in Fig. 1. In the former method, the n-type epitaxial layer is directly converted into porous silicon film under illumination. In the latter method, the film is anodized after acceptor diffusion is carried out, as in the usual diffusion isolation. Since the p-type silicon is anodized at lower forming voltage than n-type silicon, only the diffused p-type regions are converted without mask and illumination.

This paper describes preparation, properties of the porous silicon film, and isolation process of the n-type method.

Experimental

Preparations and properties of porous silicon films.—Porous silicon films were prepared by anodization of the silicon single crystals in 48% concentrated hydrofluoric acid under constant current densities. The cathode was the platinum.

Since positive holes are necessary for the reaction to occur (2), hole generation was induced by xenon lamp illumination to anodize n-type silicon. The light intensities were 10 ~ 60 mW/cm². P-type silicon was anodized without illumination.

At first the growth rates of the porous silicon films were measured with respect to both p-type and n-type silicon. Next, measurements of apparent specific gravities by volumes and weights, observations of film structure by scanning electron microscope, and weight change measurements in an oxidizing atmosphere were performed.

Preparation of samples for testing isolation characteristics.—The structures of the sample is shown in Fig. 2. N on P silicon epitaxial wafers were used. The thicknesses of the n-type epitaxial layers and p-type substrates were, respectively, 2 ~ 4 μ and 200 μ , and the

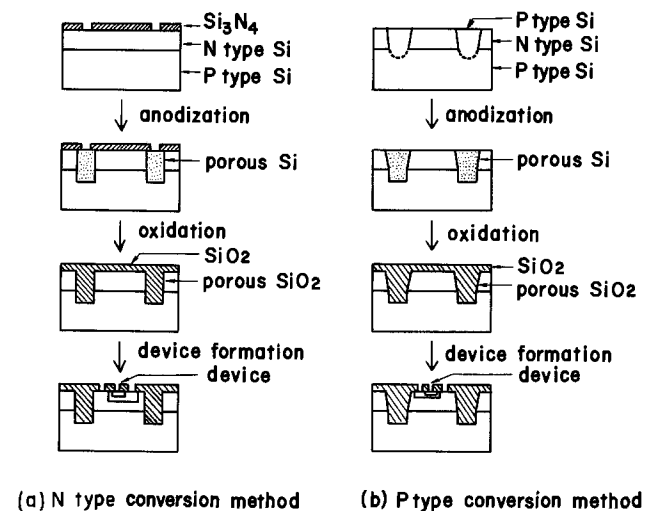


Fig. 1. Two IPOS processes

Key words: silicon, IC, porous, anodize, isolation.

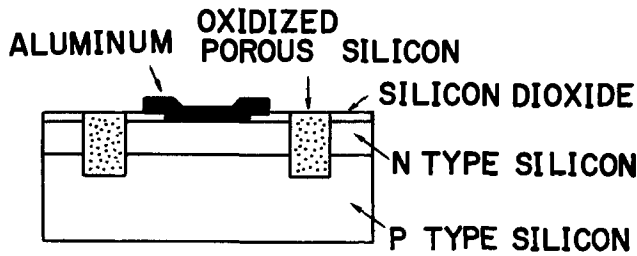


Fig. 2. Structure of the sample for measuring isolation characteristics.

resistivities of the former and the latter were 0.3 ohm-cm and 0.3 ~ 30 ohm-cm, respectively.

For selective formations of porous silicon films to make isolated islands, silicon nitride films were used as hydrofluoric acid-proof mask patterns. The 1500Å thick nitride films were deposited on the wafers by the vapor phase reaction of silane and ammonium, and then were partially removed by the usual photolithographic etch process. On anodization, the silicon portions, where the nitride films had been removed, were converted into porous silicon films.

In order to obtain films of uniform thickness, aluminum films were formed on the back of the wafers by vacuum evaporation to act as equipotential low resistivity contact layers. Moreover, acid-proof wax was coated over the aluminum films to prevent current flow from the films to hydrofluoric acid.

After anodization, wax, aluminum films, and nitride films were removed. The wafers were washed in hot phosphoric acid and boiled in water to improve the film properties. Subsequently, they were heated in a wet oxygen atmosphere to convert the porous silicon films into insulators. Heating was done for 30 min at 1100°C.

The above processes form islands of n-type epitaxial silicon, isolated from each other by the oxidized porous silicon and p-n junctions. Conventional silicon planar technology may then be applied to fabricate the integrated circuits. In this experiment, a metallization process was followed to make ohmic contact directly to the island for testing the isolation properties by the n-type method.

Electrical characteristics measurements.—To investigate the isolation characteristics of the samples, leakage currents and capacitances were measured. As the isolation characteristics in this case are reduced to those of the reverse biased mesa diodes, their d-c leakage currents and capacitances were measured. The frequency used for measuring the capacitances was 1 MHz. All measurements were made at room temperature.

Results and Discussion

Porous silicon film preparation and properties.—Figure 3 shows the relation between the growth rates and the anodizing current densities. The growth rates for n-type silicon were larger than those for p-type silicon for equal current densities.

Though the growth rates were not proportional to the current densities, the total amount of dissolved silicon was proportional to the total electric charge. On the other hand, the film thickness increased in proportion to the square root of the anodizing time. One of these relations is shown in Fig. 4.

The specific gravity of the porous film depends on the anodizing condition. Figure 5 shows the relation of the specific gravities and the current densities. In the case of p-type silicon, specific gravities decreased with current densities. For n-type silicon, however, maxima appeared at about 40 mA/cm² and they decreased with increasing light intensities.

Pore diameters at the sample surface were smaller than 10Å for both p-type and n-type silicon. Those of the inner part of the film were 10 ~ 10,000Å. A cross-sectional view of porous silicon prepared from n-type

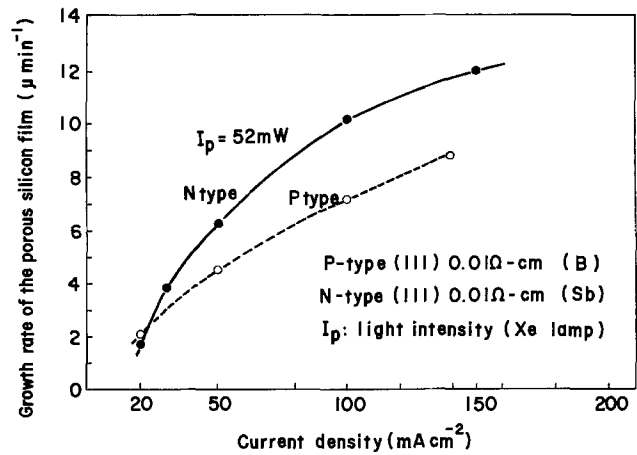


Fig. 3. Relation between growth rate and current density

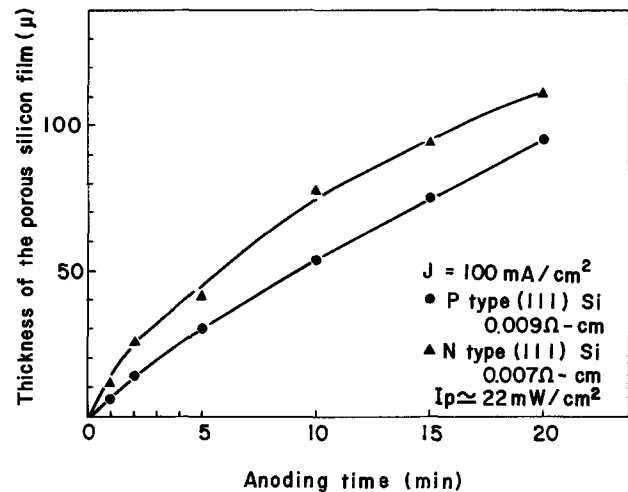


Fig. 4. Relation between the porous silicon thickness and anodizing time.

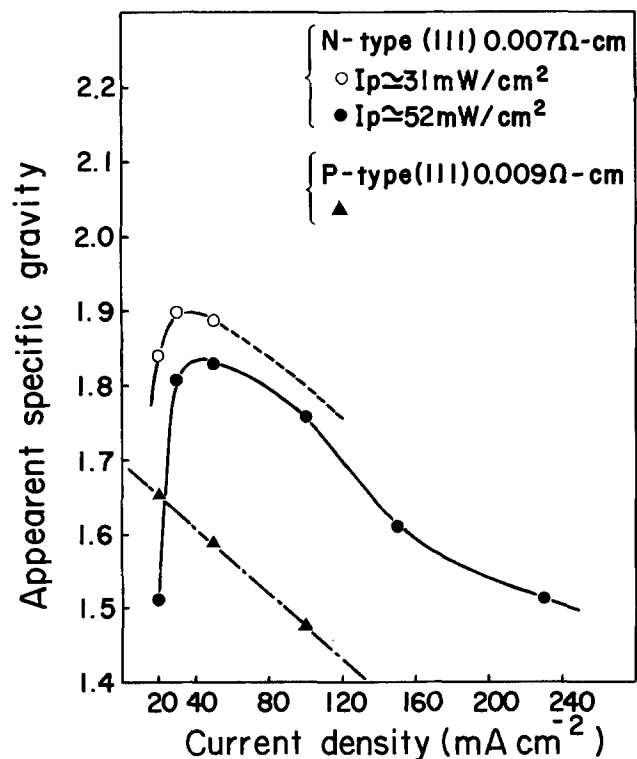


Fig. 5. Relation between apparent specific gravity and anodizing current density of porous silicon film.

silicon with low donor density at small current density is shown in Fig. 6. In this case, the pore diameter was about 1μ . At the surface of the film, however, the pores were very fine.

It is interesting that the crystal structure of the porous silicon was the same as that of the silicon single crystal. This fact was confirmed by x-ray diffraction and electron diffraction. The films are probably a mixture of the unreacted original silicon crystal and the silicon that was the product of the disproportionation reaction of silicon difluoride proposed by Turner (2).

The porous silicon is oxidized very rapidly in oxygen or steam at elevated temperatures. This was confirmed by infrared absorption spectrum and the weight change measurement. Figure 7 shows the relation between weight change of a wafer in which the porous silicon film was formed during oxidation in oxygen at 1000°C

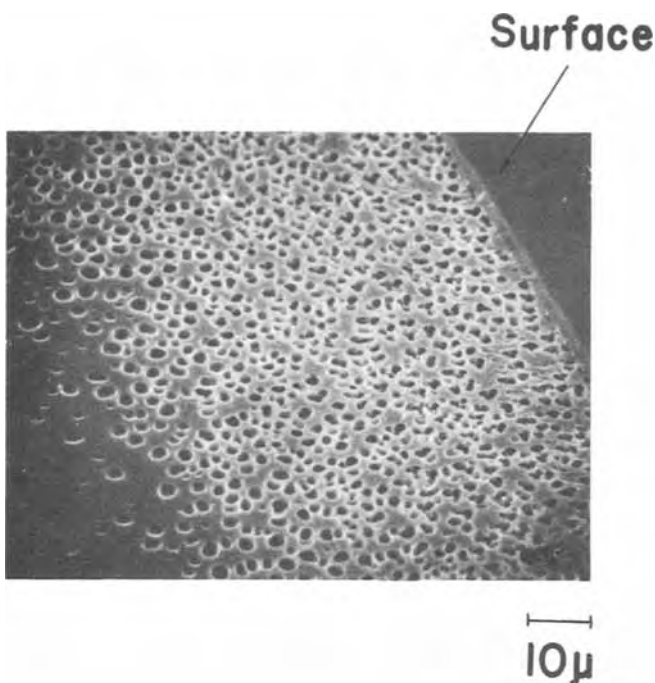


Fig. 6. Cross-sectional view of porous silicon film observed by SEM ($\times 5000$). Sample was bevelled at an angle of 5° .

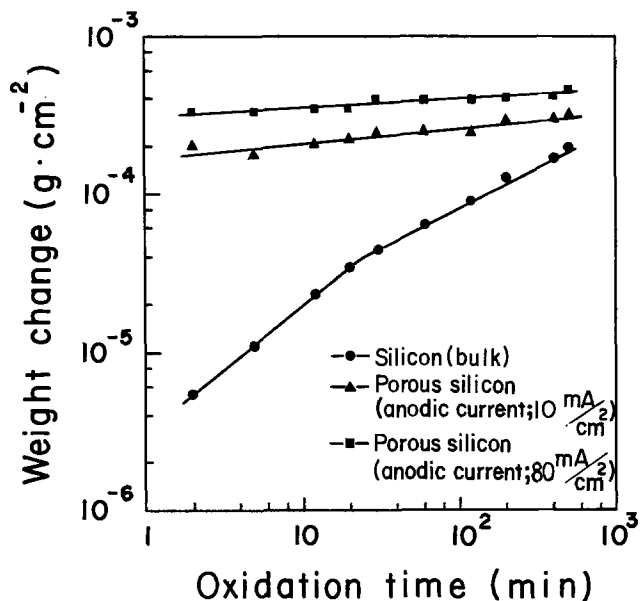


Fig. 7. Relation between weight change and oxidation time at 1000°C in wet oxygen.

and the oxidation time. Most of the weight change occurred in a very short time and, thereafter, no remarkable change was found. This implies that the greater part of silicon in the film was oxidized within a few minutes. There are two reasons why the oxidation velocity is very large. One is the existence of many pores in the film; oxygen and steam can penetrate through the pores. The other is the nature of the film constituents.

Isolation processes.—Figure 8 shows a comparison of the original isolation pattern with the porous silicon pattern. Figure 8(a) is one of the original mask patterns. The width of the isolation zone is 6μ . Figure 8(b) is the porous silicon pattern formed using the above mentioned mask pattern. In this case, the thickness of the film was 6μ . It was observed that sideways spreading of the anodized zone occurred beyond the original zone. The ratio of the spreading width to the thickness of the porous film was about 7:10. This ratio was the same in other anodizing conditions and it is slightly smaller than that of the diffusion isolation.

A cross-sectional view of the isolation region is shown in Fig. 9. In this picture the nail-like line across the n-type layer is the isolation region. When the width of the isolation zone is large, the anodic reaction seems to proceed more rapidly at the edge of the region than at the inner part, due to the current concentration effect.

Current densities suitable for forming proper quality porous films were $200 \sim 400 \text{ mA/cm}^2$. Proper quality means that the films could be easily oxidized sufficiently deep compared with the thickness of the epi-

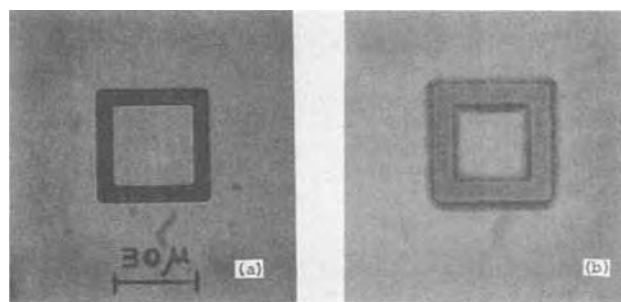


Fig. 8. Isolation pattern. (a) Original mask pattern. Isolation width, 6μ . Inside area, $900\mu^2$. (b) Porous silicon pattern formed by using a pattern (a). Thickness was 6μ .

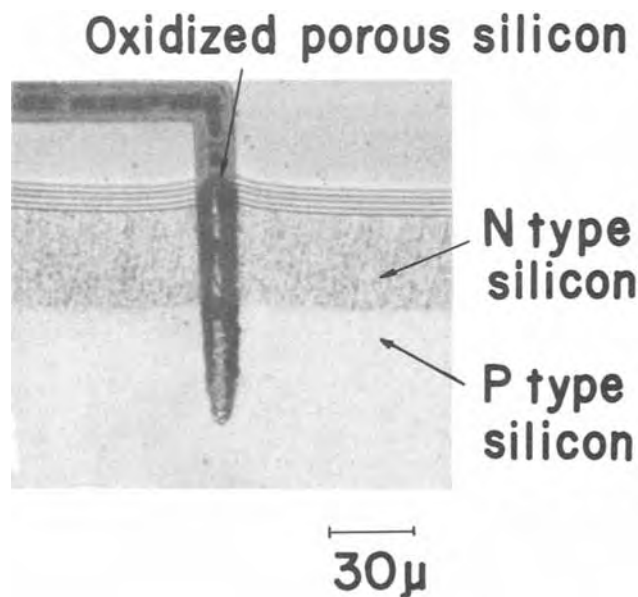


Fig. 9. Cross-sectional view of the isolation region bevelled at an angle of 5° .

taxial layers and have flat surfaces after the oxidation process.

Below 100 mA/cm² it was difficult to obtain films that were converted into a high resistivity insulator. This fact is probably in connection with the specific gravities and the pore diameters. On the other hand, at current densities over 500 mA/cm² peeling off of the oxidized film occurred and a large surface roughness was observed. In particular, it was marked at the edges of the isolation regions.

Heat-treatment in a wet oxygen atmosphere at 1100°C for 30 min was sufficient to make the porous film prepared at the above mentioned current densities insulating. Under this condition, silicon dioxide film of 0.5 μ thick was grown on silicon single crystal. On the other hand, porous silicon films greater than 5 μ thick were wholly oxidized as was verified by measurements of leakage currents. There was still slight unevenness at the surface of the oxidized porous silicon. Figure 10 shows a typical example of the surface observed by scanning electron microscopy. The unevenness was also measured by Talystep. It has been confirmed that the interconnecting metallization and photolithographic processes were not affected by this unevenness because their heights were less than 0.5 μ and the slopes were gradual. When single crystal silicon is oxidized, the volume of the oxide is about two times that of the original crystal. In the case of the porous film, the ratio of the volume increase is very small because of the porous nature.

Electrical characteristics.—A typical current voltage relation between two islands is shown in Fig. 11. The apparent breakdown voltage was about 210V. This value was larger than that of the diffusion isolation whose breakdown voltage was about 60V, limited by the epitaxial layer resistivity. However, if the isolation process by the IPOS technique were successfully carried out, higher breakdown voltage determined by the resistivity of the substrate of the wafer should be realized. Accordingly, it is considered that the breakdown in this case occurred at the damaged p-n junction parts that were adjacent to the oxidized porous sili-

con. More detailed leakage current behavior of the same sample is shown in Fig. 12. The current was smaller than 1×10^{-8} A at applied voltages below 100V and increased gradually with increasing voltage. This value is slightly larger than that of diffusion isolation. Most of the leakage current was considered to flow at the same place where breakdown occurred. Leakage of this order does not prevent practical use of IPOS for bipolar integrated circuits. However, in the isolation of the MOS integrated circuits, smaller leakage currents are desired. It is probable that further reduction can be achieved by improving the fabricating processes.

Leakage currents were reduced with the reduction of substrate resistivities. For example, a sample with the substrate resistivity of 0.3 ohm-cm showed an order of 10^{-11} A at 10V.

The relation between capacitances and bias voltages of the sample was measured and the result is shown in Fig. 13. The capacitance was inversely proportional to the cube root of the voltage. This is the same relationship as that of the graded p-n junction. Figure 14 shows the capacitances of two different areas. These

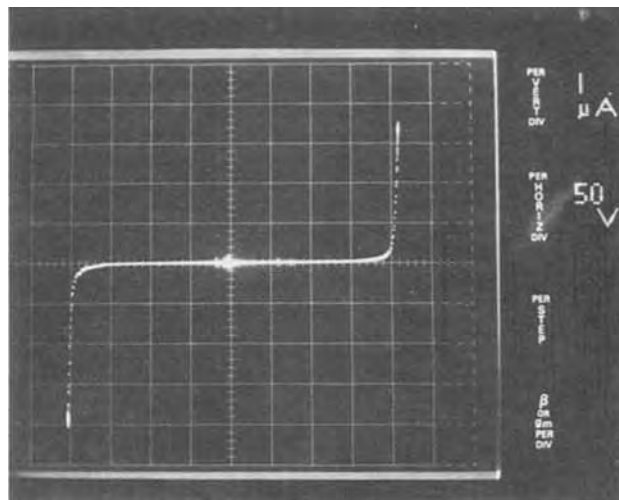


Fig. 11. Current/voltage relation between two islands. Epitaxial layer: 2 μ , 0.3 ohm-cm, n-type. Substrate: 200 μ , 30 ohm-cm, p-type.

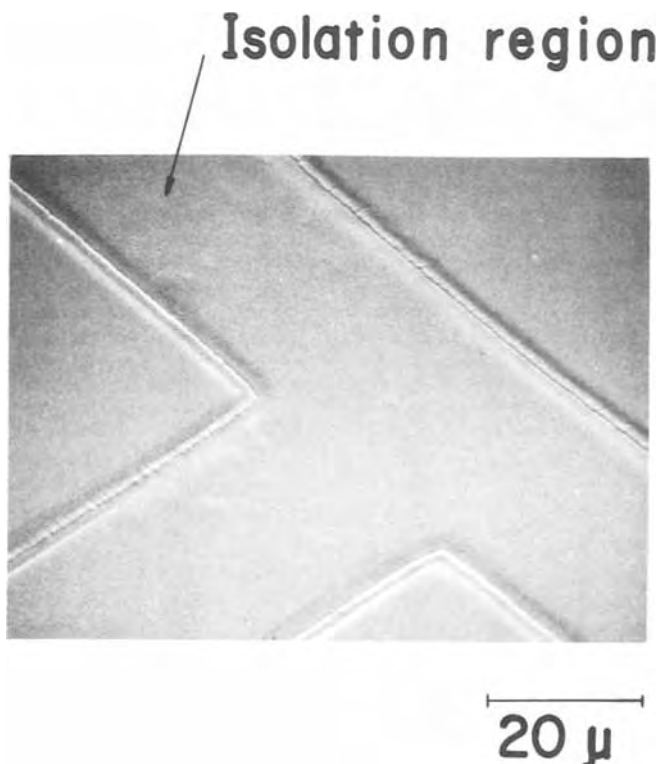


Fig. 10. Surface of isolation region, observed by SEM

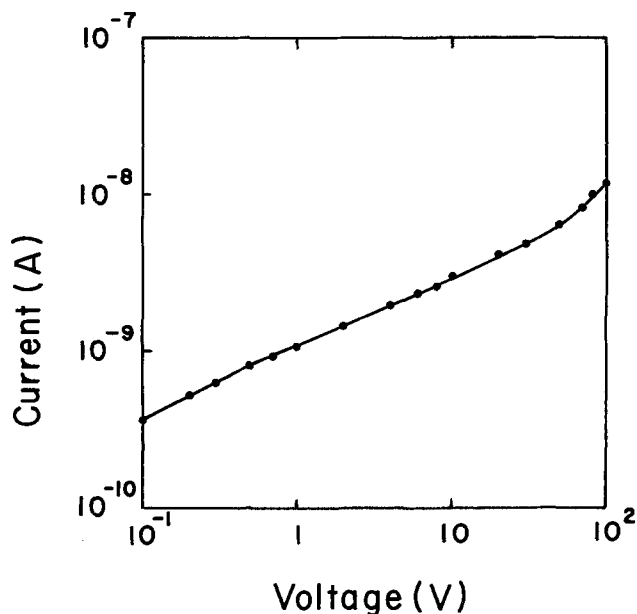


Fig. 12. Current/voltage relation between an island and substrate. Epitaxial layer: 2 μ , 0.3 ohm-cm, n-type. Substrate: 200 μ , 30 ohm-cm, p-type. Area of island: 10,000 μ^2 .

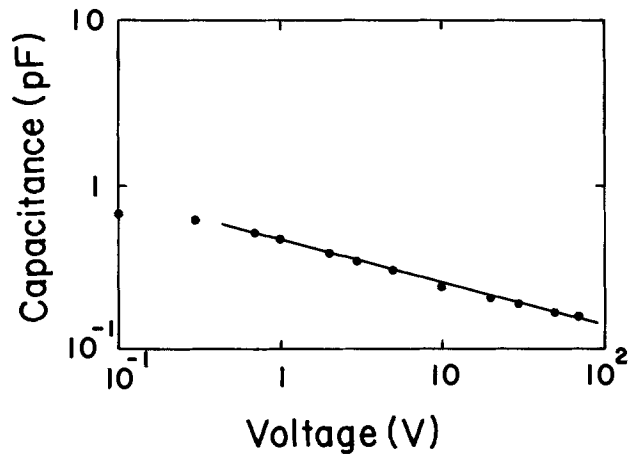


Fig. 13. Capacitance/voltage relation between an island and substrate. Epitaxial layer: 2μ , 0.3 ohm-cm , n-type. Substrate: 200μ , 30 ohm-cm , p-type. Area of island: $10,000\mu^2$.

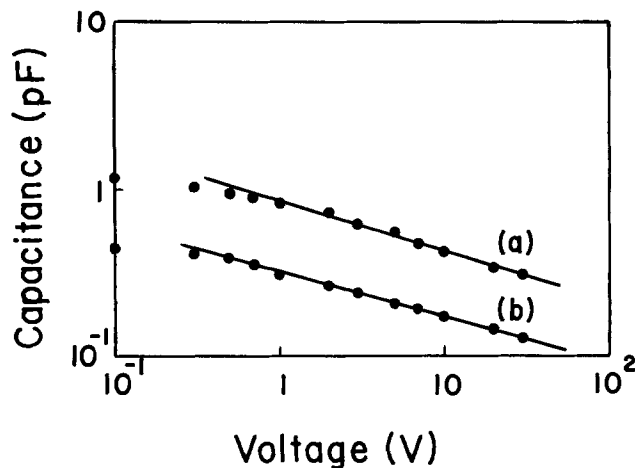


Fig. 14. Capacitance/voltage relations between an island and substrate. Epitaxial layer: 2μ , 0.3 ohm-cm , n-type. Substrate: 200μ , 5 ohm-cm , p-type. Area of islands: (a) $10,000\mu^2$, (b) $3600\mu^2$.

values agree exactly with the estimated values from the areas of the islands and the substrate resistivities.

From these data, the capacitances of the oxidized porous silicon layers can be considered negligible. It implies that the isolations of small capacitances can be realized using the IPOS technique because the isolation

capacitances are only due to the p-n junctions between n-type epitaxial layers and p-type substrates.

As described above, the n-type method IPOS technique can be advantageously applied to bipolar integrated circuits isolation. Though the experimental result concerned only samples whose epitaxial layers were 2μ thick, the same results have also been obtained for those above 4μ thick.

Conclusion

A thick porous silicon film retaining a flat surface was prepared by anodization of silicon single crystal in hydrofluoric acid. The silicon surface was illuminated when the n-type silicon was anodized. The growth rate of the film from n-type silicon was larger than that from p-type silicon. Apparent specific gravity and pore diameter of the film on n-type silicon were affected by the current density and donor density. The crystalline structure of the film was the same as that of silicon single crystal.

The film was oxidized very rapidly in oxidizing atmospheres. A preliminary attempt was made to apply the porous silicon film to bipolar integrated circuits isolation. An oxidation step at 1100°C for 30 min was sufficient to make an insulating film 4μ thick. Small excess leakage current was observed in the sample. Capacitance/voltage relation was similar to that of a graded p-n junction, $C \propto V^{-1/3}$.

The IPOS technique may be applicable to fabricating not only bipolar integrated circuits, but also MOS integrated circuits. Some problems still remain to be resolved. For example, a lower leakage current is desired for application to MOS devices.

Acknowledgments

The authors would like to thank Dr. T. Suzuki and Dr. K. Ono for their helpful guidance.

Manuscript submitted Oct. 31, 1974; revised manuscript received April 30, 1975. This was Paper 117 presented at the Boston, Massachusetts, Meeting of the Society, October 7-11, 1973.

Any discussion of this paper will appear in a Discussion Section to be published in the June 1976 JOURNAL. All discussions for the June 1976 Discussion Section should be submitted by Feb. 1, 1976.

Publication costs of this article were partially assisted by the Nippon Telegram and Telephone Public Corporation.

REFERENCES

1. Y. Watanabe and T. Sakai, *Rev. Elec. Commun. Lab.*, **19**, 899 (1971).
2. D. R. Turner, *This Journal*, **105**, 402 (1958).
3. A. Uhlir, *Bell System Tech. J.*, **35**, 333 (1956).

Temperature Dependence of Characteristics of Plastic Film Thermoelectrets

K. Ikezaki, K. Wada, and I. Fujita

Department of Instrumentation, Faculty of Engineering, Keio University, Yokohama, Japan

ABSTRACT

The initial charge and its decay characteristics of Teflon FEP thermoelectrets have been investigated at different polarizing and storage temperatures. The decay of the electrets strongly depends on the polarizing temperature T_p , even when they are stored under the same conditions. For low polarizing temperatures, the initial charge is fairly large but it decreases as the polarizing temperature increases. After it reaches a minimum value at $T_p \approx 100^\circ\text{C}$, it increases again with T_p . On the other hand, for low T_p , the residual charge which is measured 60 min after polarization, is small in spite of the fairly large initial charge and it increases with T_p . From these experimental results, it is concluded that the polarizing temperature plays an essential role for charge stability in electrets. Observed temperature dependence of the initial charge and its decay characteristics are discussed briefly.

Recently plastic film thermoelectrets have been investigated owing to the practical interest in the electret microphone (1). For several plastic film electrets, the time variation of the surface charge was studied as a function of the storage temperature for estimating the lifetime of electrets (2).

Usually, most of the values of surface charge densities reported in the literature are order of $10^{-9} \sim 10^{-10}$ coulomb/cm². In these electrets with relatively low charge densities, effects of molding and stripping charges also become important (3,4). In these electrets charge reversal often takes place. The effect of storage temperature on the charge reversal was investigated for various electret materials (5,6). Pillai *et al.* (3,7) investigated the effect of polarizing temperature on initial charge and its decay characteristics for polyvinylchloride and polyvinylacetate electrets. The importance of polarizing temperature and electric field is also pointed out in the thermoelectrets of polyvinylchloride and polymethylmethacrylate (8). Recently, Perlman and Unger (9) studied the polarizing temperature effect on charge trapping in Teflon film electrets with the use of the thermally stimulated current technique (10). They reported that both molecular motion and thermal excitation are important for charge release. With the use of the thermally stimulated current technique, Takamatu and Fukada also studied the polarizing temperature effect (11,12).

For practical purpose, however, it is desirable to produce electrets having large charge density, and to study forming conditions for good electrets is useful not only for deeper understanding of basic mechanisms of electret phenomena but also for practical application of electrets. To get a practical film electret with large homocharge, several techniques have been developed (2,13,14). In the present paper, initial charge and its decay characteristics are studied in thermoelectrets of Teflon FEP film which are polarized at various polarizing temperatures with use of the technique of dielectric insert (14).

Experimental

The electret material used in this investigation is a film of Teflon FEP (copolymer of tetrafluoroethylene and hexafluoropropylene) of 12μ in thickness. A film sample and a disk of soda glass (0.75 mm thick) metallized on one face were placed between brass electrodes of a polarizing holder. As shown in Fig. 1, this glass disk was inserted between the sample and the negative electrode in order to obtain an electret with a

large homocharge without arcing during the polarization process (14).

Electrets were obtained as follows: a sample was heated to a polarizing temperature T_p and then a polarizing voltage V_p (800V) was applied across the electrodes. After 10 min under the electric stress at the temperature of T_p , the sample was cooled down to room temperature under the same electric stress. The cooling process took about 40 min. In order to exclude a confusing contribution of unstable charges which stay on the surface of electrets, after polarization all electrets were kept for 5 min between brass electrodes short-circuited, and then the net surface charges were measured by the vibrating electrode method developed by Reedyk and Perlman (15). The decay characteristics of the surface charges for various storage temperatures were observed as a function of storage time t_s by measuring the surface charges of electrets which were stored in free (unshort-circuited) at a temperature of T_s .

Results

The time variations of the surface charge were investigated for the samples which were polarized at various temperatures. Since the decay of the charge on the anode surface of the sample was almost the same as that of the cathode except for some irregular behavior, the charge on the cathode surface was chiefly investigated.

The net surface charge observed in this study was a homocharge and the charge reversal did not take place.

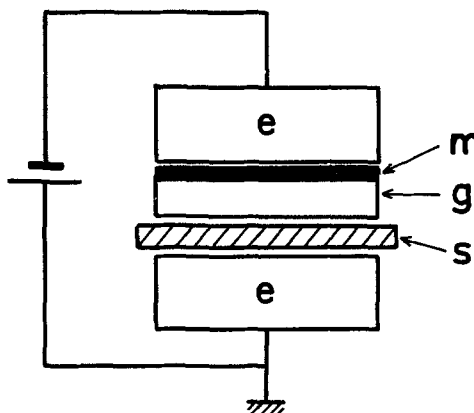


Fig. 1. Electrode assembly. e, Brass electrode; g, glass disk; m, metal layer.

Key words: Teflon FEP, polarizing temperature, initial charge, residual charge.

Observed values of the initial surface charge scattered from sample to sample even when the electrets were produced under the same conditions, and the electrets slightly differed in their decay characteristics. Therefore, normalized decay curves were determined from the several measurements as shown in Fig. 2. For various polarizing temperatures, the normalized decay curves are shown in Fig. 3 and 4. As is seen from

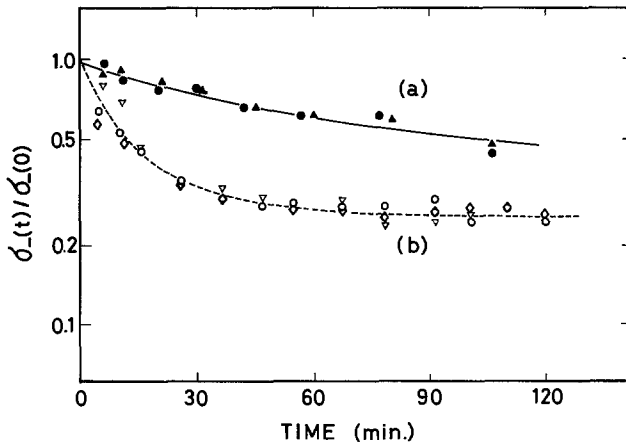


Fig. 2. Normalized decay curve of surface charge on the cathode side of Teflon FEP thermoelectrets. Curve (a), $T_p = 180^\circ\text{C}$, $T_s = 100^\circ\text{C}$, $V_p = 800\text{V}$. Curve (b), $T_p = 60^\circ\text{C}$, $T_s = 80^\circ\text{C}$, $V_p = 800\text{V}$.

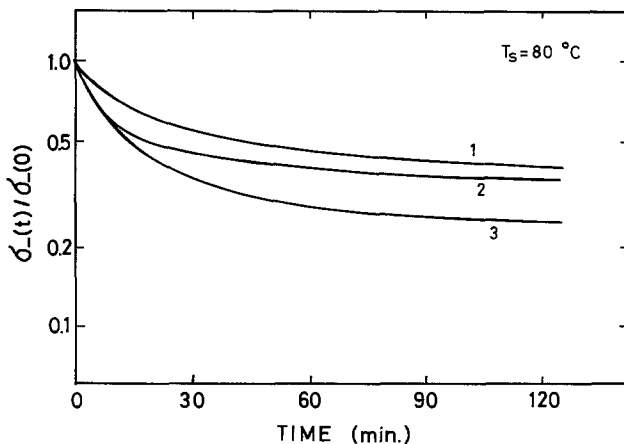


Fig. 3. Normalized decay curves of surface charge on the cathode side of Teflon FEP thermoelectrets stored at 80°C . Curve 1, $T_p = 140^\circ\text{C}$; curve 2, $T_p = 80^\circ\text{C}$; curve 3, $T_p = 60^\circ\text{C}$.

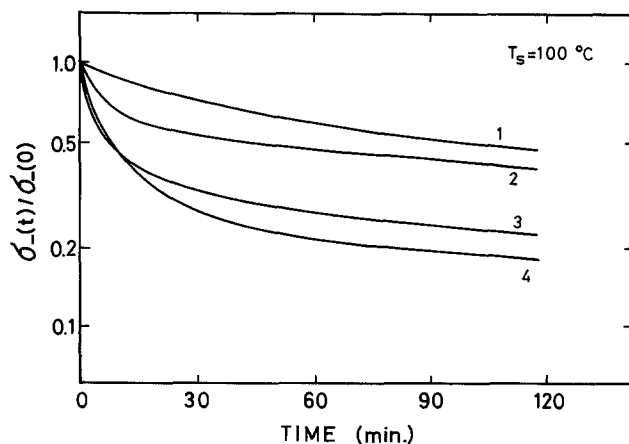


Fig. 4. Normalized decay curves of surface charge on the cathode side of Teflon FEP thermoelectrets stored at 100°C . Curve 1, $T_p = 180^\circ\text{C}$; curve 2, $T_p = 110^\circ\text{C}$; curve 3, $T_p = 80^\circ\text{C}$; curve 4, $T_p = 60^\circ\text{C}$.

these figures, the decay characteristics of Teflon FEP electrets are nonexponential and they strongly depend on T_s and T_p . Mean values of the initial charge densities on the anode and cathode surfaces, $\sigma_+(0)$ and $\sigma_-(0)$, and their mean errors are presented in Fig. 5. Their values were determined by taking averages of 12-34 samples which were polarized under the same conditions (12 samples for $T_p = 60^\circ\text{C}$, 34 for $T_p = 80^\circ\text{C}$, 26 for $T_p = 110^\circ\text{C}$, 25 for $T_p = 140^\circ\text{C}$, and 14 for $T_p = 180^\circ\text{C}$). In Fig. 5, the values of $\sigma_-(60)$ defined as residual charge on the cathode surface after storage of 60 min at T_s , are also plotted against T_p for various storage temperatures. These values of the residual charge were determined from the mean values of $\sigma_-(0)$ and the normalized decay curves.

Discussion

In electrets there are two kinds of surface charge (16), a homocharge and a heterocharge. The heterocharge is due to the volume polarization and it decays more rapidly as compared with the homocharge in many electrets (17). The electrets which are produced with a suitable dielectric insert as in this study, have a large homocharge (2, 13, 14). This homocharge is thought to be due to the discharge in the air gap between the sample and the polarizing electrodes (18-22). The charge produced by this discharge is then trapped by the various trapping sites in the sample. In real electrets there are many kinds of traps. The kinds of traps and the trap densities depend on several factors such as the physical and chemical properties of the material used and the polarizing conditions of electrets. In addition to these facts, in real electrets the heterocharge may be present. Therefore, the decay characteristics of the surface charge become complicated and cannot be expected to obey strictly a simple exponential function. In many electrets, however, the decay form is found to be quasiexponential: After decay has taken place for some time, the subsequent decay can be expressed by a simple exponential curve (17).

For our Teflon FEP electrets, it is found from Fig. 2-4, that the decay curves of the surface charge consist of two components: an initial fast decay component and the subsequent, slow and somewhat exponential component. Similar decay curves have been reported in the electrets with high homocharge (2, 13). As is

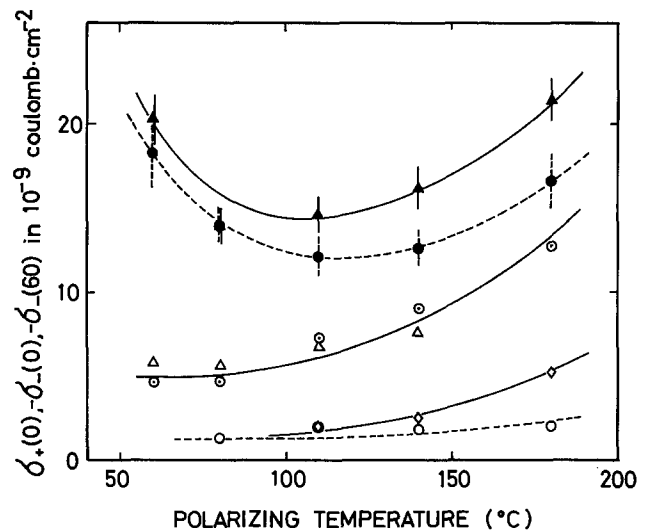


Fig. 5. Effect of polarizing temperature on the initial and residual surface charge densities of Teflon FEP thermoelectrets. \bullet , $\sigma_+(0)$; \blacktriangle , $\sigma_-(0)$; \triangle , $\sigma_-(60)$ at $T_s = 80^\circ\text{C}$; \odot , $\sigma_-(60)$ at $T_s = 100^\circ\text{C}$; \diamond , $\sigma_-(60)$ at $T_s = 120^\circ\text{C}$; \circ , $\sigma_-(60)$ at $T_s = 150^\circ\text{C}$; where $\sigma_+(0)$ and $\sigma_-(0)$ are initial charge densities on the anode and the cathode surfaces, respectively, and $\sigma_-(60)$ is residual charge density on the cathode surface which is measured after storage of 60 min at various storage temperatures.

seen from Fig. 2-4, relative values of these components vary depending on T_s and T_p . In general, the fast component is more remarkable in electrets polarized at low T_p and stored at high T_s than in electrets polarized at high T_p and stored at low T_s . This T_p -dependence of the charge trapping was recently investigated by Perlman and Unger (9). They observed that the curves of thermally stimulated currents in electro-electrets of Teflon vary depending on the polarizing temperature and the current spectra shift toward higher temperature with increasing sample temperature during polarization. This peak shift in thermally stimulated current spectra was also observed by Takamatu and Fukada (11, 12). They found that there are two kinds of peaks in thermally stimulated current spectra in polyvinylidene fluoride, polyethylene, and polytetrafluoroethylene thermoelectrets. For one kind of peaks, the peak position does not depend on polarizing temperature and it locates at low temperatures (most of these peaks appear below 0°C). For the other kind of peaks, the peak position is T_p -dependent and peaks appear at the temperature several degrees higher than that of polarizing temperature. From these facts it is suggested that polarizing temperature plays an essential role for charge trapping in electrets.

Figure 5 shows T_p -dependence of the initial charges. It is almost the same on both anode and cathode sides but the surface charge on the cathode side is slightly larger. In Teflon FEP electrets, negative charges seem to be more stable than the positive. The initial charges on both sides have large values for low T_p and they decrease as T_p increases. After the charges have minimum values at $T_p \approx 100^\circ\text{C}$, they increase again with T_p and have large values for high T_p . On the other hand, the residual charge becomes large with increasing T_p .

In our electrets, the homocharge is thought to be produced by the following process (18, 19): Applying a voltage between electrodes increases the field in the air gap. Eventually, this field will exceed the breakdown strength of the air gap and the spray discharge will occur. The homocharge deposition by this spray discharge continues until the surface density of the deposited charge attains a certain threshold value which reduces the field in the gap below breakdown and quenches the discharge. In order to discuss qualitatively the observed T_p -dependent initial charges and their decay characteristics, we make an assumption for simplicity that there are two kinds of charge traps in our electrets, low energy traps and relatively deep traps. Then, a part of the homocharges produced by the spray discharge is held in the two kinds of traps, σ_1 in shallow traps and σ_2 in deep traps. The remainder of the spray charges contributes to a forming current or to an unstable charge σ_0 which stays on the surface of the sample and easily escapes while the electret is kept for 5 min between the electrodes short-circuited or handled prior to measurements. Since the quenching of the discharge in the air gap is determined only by the threshold value of the deposited charge and it does not depend on the kind of traps in which the charge falls, just after polarization the total value of $\sigma_0 + \sigma_1 + \sigma_2$ is thought to be constant and independent of T_p as long as the polarizing voltage remains constant.

Observed T_p -dependent behavior of the electrets is explained as follows on the basis of an idea that the relative values of σ_0 , σ_1 , and σ_2 vary depending on T_p .

For electrets polarized at low temperatures, the charge trapped in the shallow traps predominantly contributes to the initial charge. Therefore, at high storage temperature the detrapping rate from the shallow traps is large and the surface charge rapidly decreases in the initial part of the decay. In this case the residual charges are small in spite of the large initial charge.

For electrets polarized at high temperatures, emission probability from the shallow traps increases and the equilibrium net trapping rate by the shallow traps

decreases. For this reason the unstable charge σ_0 may be large and the initial charge becomes small.

When the polarizing temperature T_p is much higher, the contribution from the charge held in the shallow traps becomes smaller and smaller due to increase of detrapping probability, but the charges released from the shallow traps migrate much more easily at high T_p and are retrapped more easily by the deeper traps. As a result, the charge held in the deep traps contributes much more to the threshold charge density which quenches the spray discharge. Therefore, the initial charge becomes large again and the residual charge also increases with T_p . In this case the initial rapid decay is not observed.

The charge retrapping was reported by Sessler and West (13). From analysis of thermally stimulated currents, they found that charges in polyethyleneterephthalate and Teflon FEP electrets are subjected to considerable retrapping. This charge retrapping is also supported from the following experiment. Two kinds of electrets were polarized under the same V_p and T_p but different polarizing time t_p , 3 hr and 10 min, respectively. Figure 6 shows charge decay curves of these electrets. As is seen from Fig. 6, the initial charge of the electrets polarized with applying V_p for 3 hr is larger than the electrets polarized with applying V_p for 10 min, and these two kinds of electrets show quite different decay characteristics. In the electrets with t_p of 3 hr, no initial rapid decay is observed and the residual charge is larger. As the polarizing time increases, emitted charges from the shallow traps have much more chance to be retrapped by the deeper traps, so that the unstable component σ_0 decreases and the ratio of σ_2 to σ_1 becomes large even when the values of V_p and T_p are kept constant. This results in a larger initial charge and no initial rapid decay, as is found for the electrets with a long t_p in Fig. 6.

Although the detailed natures of the two kinds of traps are not clear at this stage, the charge σ_1 may be loosely bound on the surface of an electret and decay chiefly by surface recombination. On the other hand, it is found from Fig. 5 that, when T_s is 120° or 150°C , the values of the residual charges decrease abruptly in comparison with the cases of $T_s = 80^\circ$ and 100°C . This suggests that the deep traps may be associated with the motion of the main chain of Teflon FEP because the glass transition temperature of the film is about 130°C (23).

Summary

The observed results are summarized as follows.

1. The initial charge density and its decay charac-

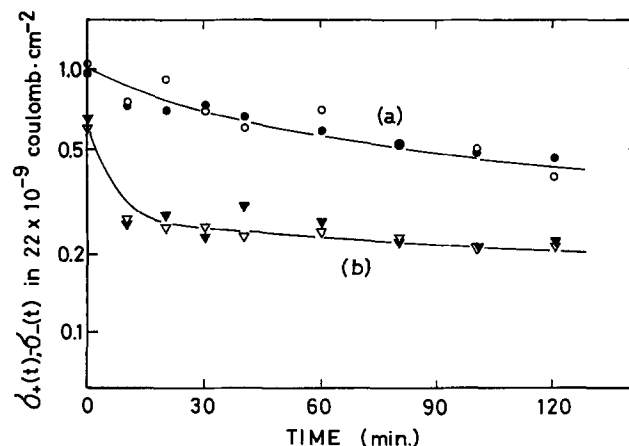


Fig. 6. Effect of polarizing time on charge decay of Teflon FEP thermoelectrets (average over 3 electrets). The storage temperature T_s is 100°C . Curve (a), $t_p = 3$ hr, $T_p = 75^\circ\text{C}$, $V_p = 800\text{V}$. Curve (b), $t_p = 10$ min, $T_p = 75^\circ\text{C}$, $V_p = 800\text{V}$. \circ , ∇ , Surface charge densities on the anode surface. \bullet , \blacktriangledown , Surface charge densities on the cathode surface.

teristics of Teflon FEP thermoelectrets strongly depend not only on the storage temperature but also on the polarizing temperature.

2. The decay curves of the electrets are nonexponential and they consist of two components, a fast decay component and a slow component.

3. For electrets polarized at relatively low T_p , the fast decay component becomes remarkable. In this case the surface charge is predominantly held in shallow traps and the residual charge density is small in spite of its large initial charge density.

4. As the polarizing temperature increases, the initial charge density decreases and it has a minimum value when the polarizing temperature is around 100°C.

5. For electrets polarized at T_p higher than about 100°C, the relative amount of the charge trapped by deep traps becomes large, and both initial and final charges increase with T_p .

6. To get a stable electret, the polarizing temperature should be high enough to produce many deep trapping sites and the polarizing time should be long enough for charge retrapping by deeper traps.

Acknowledgment

The authors wish to thank Messrs. J. Nakamura, K. Okazaki, and Y. Suzuki of the Research and Development Department, Aiwa Company, Limited for their technical help.

Manuscript submitted Oct. 15, 1974; revised manuscript received April 30, 1975.

Any discussion of this paper will appear in a Discussion Section to be published in the June 1976 JOURNAL. All discussions for the June 1976 Discussion Section should be submitted by Feb. 1, 1976.

Publication costs of this article were partially assisted by Keio University.

REFERENCES

1. G. M. Sessler and J. E. West, *J. Acoust. Soc. Am.*, **40**, 1433 (1963).
2. M. M. Perlman and C. W. Reedyk, *This Journal*, **115**, 45 (1968).
3. P. K. C. Pillai, V. K. Jain, and G. K. Vig, *ibid.*, **116**, 836 (1969).
4. G. G. Wiseman and G. R. Feaster, *J. Chem. Phys.*, **26**, 521 (1957).
5. B. Hilczner, B. Blaszyk, and S. Goderska, *Phys. Status Solidi*, **23**, 419 (1967).
6. J. Handerek and R. Wilk, *Acta Phys. Polon.*, **29**, 623 (1966).
7. P. K. C. Pillai and V. K. Jain, *J. Phys. D., Appl. Phys.*, **3**, 829 (1970).
8. M. Latour, *Compt. Rend.*, **272**, serie B, 469 (1971).
9. M. M. Perlman and S. Unger, *Appl. Phys. Letters*, **24**, 579 (1974).
10. C. Bucci, R. Jieschi, and G. Guidi, *Phys. Rev.*, **148**, 816 (1966).
11. T. Takamatu and E. Fukada, *Rept. Inst. Phys. Chem. Res. (Tokyo)*, **45**, 1 (1969).
12. T. Takamatu and E. Fukada, *ibid.*, **45**, 73 (1969).
13. G. M. Sessler and J. E. West, *J. Appl. Phys.* **43**, 922 (1972).
14. K. Ikezaki, I. Fujita, K. Wada, and J. Nakamura, *This Journal*, **121**, 591 (1974).
15. C. W. Reedyk and M. M. Perlman, *ibid.*, **115**, 49 (1968).
16. B. Gross, *Phys. Rev.*, **54**, 57 (1940).
17. H. J. Wintle, *J. Acoust. Soc. Am.*, **53**, 1578 (1973).
18. B. Gross, *J. Chem. Phys.*, **17**, 886 (1949).
19. B. Gross, *Brit. J. Appl. Phys.*, **1**, 259 (1950).
20. J. W. Wild and J. D. Stranathan, *J. Chem. Phys.*, **27**, 1055 (1957).
21. R. A. Draughn and A. Catlin, *This Journal*, **115**, 391 (1968).
22. J. Roos, *J. Appl. Phys.*, **40**, 3135 (1969).
23. Plastic Handbook, S. Maruhashi, R. Oda, and M. Imoto, Editors, p. 461, Asakura shoten, Tokyo (1969).

The Formation and Structure of Anodic Films on Beryllium

M. T. Shehata* and Roger Kelly*

Institute for Materials Research, McMaster University, Hamilton, Ontario, Canada, L8S 4M1

ABSTRACT

The present, as well as previous, work on the anodizing of Be confirms that most electrolytes yield films characterized by one or more of being porous, being subject to extensive dissolution, or being crystalline. This includes electrolytes based on the following: aqueous KOH, a $\text{CrO}_3\text{-HNO}_3$ mixture, aqueous Na_2CO_3 , $(\text{C}_2\text{H}_5)_2\text{HPO}_4$, a $(\text{C}_2\text{H}_5)_2\text{SO}_4\text{-H}_2\text{SO}_4$ mixture, acetic acid. Significantly different results are obtained with ethylene glycol which is saturated with Na_2HPO_4 or KH_2PO_4 or both Na_2HPO_4 and Na_2SO_4 . The films are then nonporous, as shown by scanning electron microscopy. They are formed with negligible dissolution, as follows by implanting the Be with 30-keV Kr^{85} before anodizing and noting the loss of activity during anodizing. They are nominally amorphous, as inferred by reflection electron diffraction, though crystallize to hexagonal BeO at a temperature lying somewhere below 300°C. It will be shown in a subsequent paper that the films formed in an ethylene-glycol-based electrolyte can be quantitatively removed and that Be can therefore be microsectioned.

Anodic films on metals are often classified as porous or nonporous. Nonporous films, which are the more usual, are normally found to form in electrolytes in which the oxide has a low solubility, and to grow until they reach an almost limiting thickness which, for a given time scale, is proportional to the applied potential. They are characterized by a high resistivity and by conduction which is mainly ionic in character. Nonporous films are often amorphous though there are many exceptions, including Sn (1) and Zr (2, 3) in

general and Mo (4), Ta (4, 5), Ti (3, 5), U (6), V (4), and W (4) under particular conditions.

On the other hand, electrolytes in which the oxide is somewhat soluble are occasionally found to support the growth of porous films which increase more or less indefinitely in thickness while the applied potential varies slightly or not at all. They are characterized by a low resistivity. Though normally described as "crystalline," they are variously amorphous [Al anodized at room temperature (5)] or crystalline [Be (7, 8), probably Sn (9, 1)].

* Electrochemical Society Active Member.

Key words: beryllium, anodization, thin films, anodic sectioning.

Films formed on Be have invariably been found to show one or more of the characteristics of a porous film. Thus no films at all were obtained with some dilute aqueous electrolytes (7, 8). Those formed with HNO_3 , CrO_3 , or mixed $\text{CrO}_3\text{-HNO}_3$ were crystalline (7, 8) and had thicknesses up to ~ 400 nm (7) or more (10). Those formed with ammonia in ethylene glycol appeared to have had a low resistivity and to have been subject to dissolution (7, 8), while use of $0.5\text{M Na}_2\text{CO}_3$ resulted in crystalline films (11).

The object of the present work was to attempt to form anodic films on Be which, unlike those of previous work, were simultaneously nonporous, formed with minimal or no dissolution, and nominally amorphous. This goal was achieved, such that films could be formed under conditions when the potential drop across the film was about 19×10^8 V/m and the efficiency at 30V for fixed current was 0.95 ± 0.02 . Beryllium can thus be made to anodize in a similar manner as with most other metals (Table I). The formation of such films is in principle of importance in the understanding of anodic oxidation from an electrochemical point of view, but we regard it of greater interest to work on diffusion or on ion-solid collisions. It leads first of all to a microsectioning technique, thence to the possibility of studying diffusion and ion depth distributions in Be (12). It leads secondly to the possibility of studying secondary particle emission from BeO in a manner similar to what was done with Al_2O_3 (13).

Experimental

The specimens used throughout this work were polycrystalline Be foils with dimensions of approximately $25 \times 12.5 \times 0.25$ mm and with purities claimed to be 99.5%. They were obtained from Ventron Corporation (Alpha Products). After an initial polishing with a series of increasingly fine SiC papers, the specimens were given further treatment consisting either of chemical polishing [in 5 weight per cent (w/o) sulfuric acid, 75 w/o phosphoric acid, 7 w/o chromic acid, and 13 w/o water] or else of mechanical polishing using $6 \mu\text{m}$ and $1 \mu\text{m}$ diamond paste with kerosene as a lubricant. For experiments where reproducible flat surfaces were required, the specimens were finally anodized and sectioned 5 times. The anodizings were carried out at 50V in ethylene glycol which is saturated in both Na_2HPO_4 and Na_2SO_4 and will be subsequently called "electrolyte A." The sectionings were accomplished by exposing the films to 10% KOH for 1 min (12). Such treatment may be assumed to remove submicroscopic irregularities, though this matter will be investigated explicitly in work now underway.

All anodizings were performed at room temperature ($\sim 22^\circ\text{C}$) using a power supply such that limits to both the current and potential could be preset (Hewlett-Packard Model 6186B). The cathode was made of platinum gauze in the form of a cylinder with an inside diameter of 25 mm. Potentials refer to the total value from anode to cathode rather than to the value across the oxide film. For electrolyte A and a current of 3 mA/cm^2 these values differ by $\sim 5\text{V}$ (as determined

using a Ni wire near the Be as a probe), though with none of the results to follow is this of importance. The anodizings were carried out in unstirred electrolytes and without protection from air, and the electrolytes were therefore discarded after 5 or 6 anodizings or 1 hr, whichever came first.

The extent of metal dissolution during anodizing was determined using a depth-distribution technique due to Giani (1). Kr^{85} , which is beta-active, was implanted in Be at 30 keV to a dose of 2×10^{15} ions/ cm^2 , and the activity was noted before and after anodizing. The experimental depth distribution of such an implant is shown in Fig. 1 (12) and enables the retained activity fraction to be expressed as a depth. Such a depth is a lower limit to the metal loss during anodizing the lower-limit aspect entering due to the possibility of film formation by outward migration of Be, thence to a burying of the marker in the manner shown by Pringle (14) for Ta.

Results

Dilute aqueous electrolytes.—It was concluded by Levin (8) that no film at all is formed on Be in 1% H_2SO_4 or 1% KOH, though 1% HNO_3 led to crystalline BeO if the current density was high enough. Survey experiments undertaken in the course of the present work have largely confirmed these results, except for an indication of film formation with 1% KOH. This follows from the V-t and I-t behavior (Table II).

To provide new information on the use of dilute aqueous electrolytes the depth-distribution technique was applied. Unacceptable extents of metal dissolution during anodizing were revealed (Table II).

$\text{CrO}_3\text{-HNO}_3$.—A $\text{CrO}_3\text{-HNO}_3$ mixture consisting of 200 g/liter of CrO_3 in 10% HNO_3 is known to yield crystalline films with Be, which grow in thickness linearly with time while the current remains constant (7,8). Anodic films have also been obtained using as electrolyte 20% aqueous CrO_3 (10,15). The results were interpreted in terms of the initial formation of a nonporous layer of small but constant thickness fol-

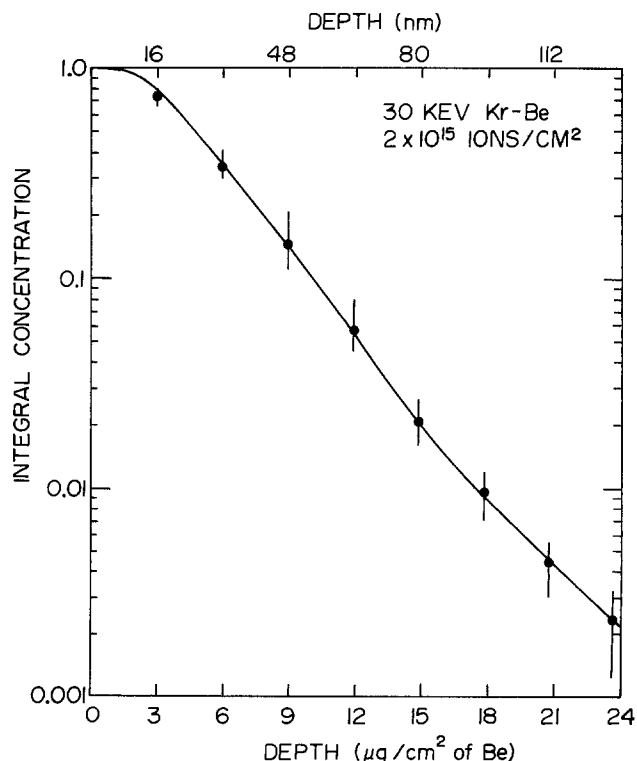


Fig. 1. Integral depth-distribution curve for 30-keV Kr in polycrystalline Be as determined by anodic sectioning (12). Such a curve enables retained activity fractions, i.e., integral concentrations, to be expressed as depths.

Table I. Comparison of fields and efficiencies for anodizing various metals

Metal	Electrolyte	Field to form a 50-V film (10^8 V/m)	Efficiency at constant current of 2 or 3 mA/ cm^2	Ref.
V	Mainly acetic acid	2.8	0.95	19, 23
Mo	Mainly acetic acid	2.9	0.95	17, 23
Nb	Aqueous	3.4	$\sim 1.0^a$	16, 24
Zr	Aqueous	4-6	0.50	25
W	Mainly acetic acid	4.6	0.96	16, 23
Ta	Aqueous	6.2-6.6	0.99	20
Al	Aqueous	8.7-9.1	0.90	20
Be	Electrolyte A	19.0	0.95 ± 0.02 here, Eq. [1]	

^a Not for constant current.

Table II. *V-t* behavior, *I-t* behavior, and dissolution for the anodization of Be (Present potential 30V with 1% KOH, 50V otherwise)

Electrolyte	Final potential (V)	Time to reach preset potential (min)	Initial current (mA/cm ²)	Final current (mA/cm ²)	Total anodizing time (min)	Fraction of Kr implant which is retained	Inferred loss of Be ^b (nm)
1% H ₂ SO ₄	~0	Never	20	20	5	<0.003	≧120
1% HNO ₃	~3	Never	20	20	5	0.15 ± 0.01	≧50
1% KOH	30	4	20	3	10	0.07 ± 0.02	≧60
CrO ₃ -HNO ₃ mixture	~3	Never	30	30	2	0.19 ± 0.05	≧40
0.5M Na ₂ CO ₃	50	6	10	0.4	15	0.13 ± 0.03	≧50
(C ₂ H ₅) ₂ HPO ₄	50	14.5	5	4.5	20	<0.01	≧90
(C ₂ H ₅) ₂ SO ₄ -H ₂ SO ₄ mixture	50 ^a	0.3 ^a	20	~20	10	<0.01	≧90
Mainly acetic acid	50	0.5	10	1	15	0.06 ± 0.01	≧60
Electrolyte A	50	0.3	3	10.35	1.5	0.986 ± 0.006	≧1

^a The voltage rose to 50V in 0.3 min and then fell slowly to 30V by 10 min.

^b Deduced from the preceding column with the help of Fig. 1.

lowed by a thick film which could be shown to be porous.

We have undertaken a limited number of additional experiments using the CrO₃-HNO₃ electrolyte of Ref. (7, 8). The *V-t* behavior, as shown in curve A of Fig. 2 and also in Table II, suggests (though does not prove) that thick, porous films are formed. The extent of porosity was investigated explicitly by means of scanning electron microscopy. The results, given in Fig. 3 show clearly the porous nature of the films, the

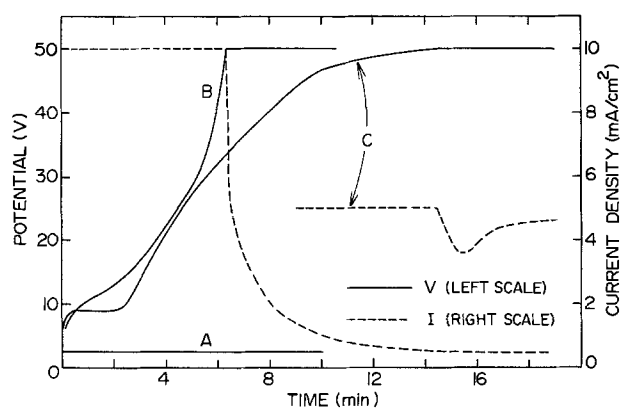


Fig. 2. Typical *V-t* and *I-t* curves for the anodization of Be in CrO₃-HNO₃ (curve A, always 30 mA/cm²), 0.5M Na₂CO₃ (curve B), and (C₂H₅)₂HPO₄ (curve C). Solid lines: *V-t*, with potential as in scale at left. Dashed lines: *I-t*, with current as in scale at right.

scale of the porosity being 100-1000 nm. The extent of metal dissolution during anodizing was determined by the depth-distribution technique and found to be significant (Table II).

In conclusion, the anodic films formed on Be with the CrO₃-HNO₃ electrolyte of Ref. (7, 8) have none of the properties which were desired regarding porosity, dissolution, and structure.

Na₂CO₃.—Heusler (11) was able to form films on Be with an electrolyte consisting of 0.5M Na₂CO₃. The films were crystalline, could be formed up to a thickness of ~250 nm (at 200V), and were accompanied by oxygen evolution.

We have sought to obtain additional information on the use of 0.5M Na₂CO₃. The *V-t* and *I-t* behavior, as shown in curve B of Fig. 2 and also in Table II, suggests (though does not prove) that nonporous films result. The extent of porosity was again investigated by scanning electron microscopy. The results, given in Fig. 4, show that the films are mainly nonporous, but with evidence for both local and general dissolution. Metal dissolution during anodizing occurred to a significant extent (Table II).

The use of 0.5M Na₂CO₃ as the electrolyte for anodizing Be is thus unsatisfactory in the present context for two reasons: the dissolution and the crystallinity. Porosity, on the other hand, is not a problem.

Nonaqueous electrolytes.—An indication that nonaqueous electrolytes may be of interest with Be is found in work by Kerr and Wilman (7). They established, using a 25 g/liter solution of ammonia in ethylene glycol, that 30 nm thick amorphous films could be

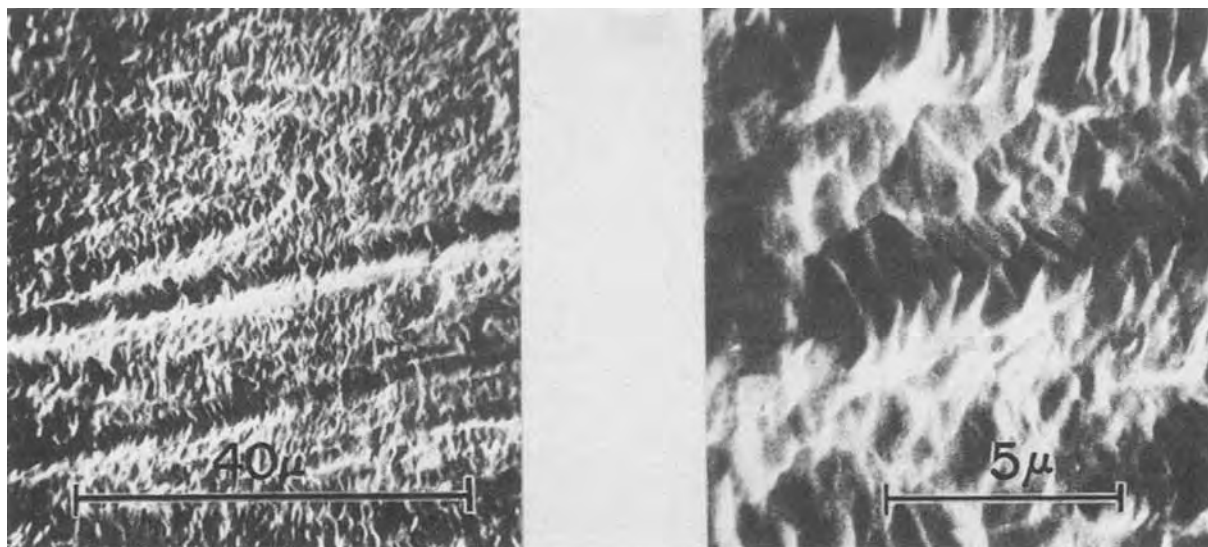


Fig. 3. Scanning electron micrographs with different magnifications of film formed by anodizing Be in CrO₃-HNO₃ for 2 min at 30 mA/cm². The films are markedly porous, the scale of the porosity being 100-1000 nm.

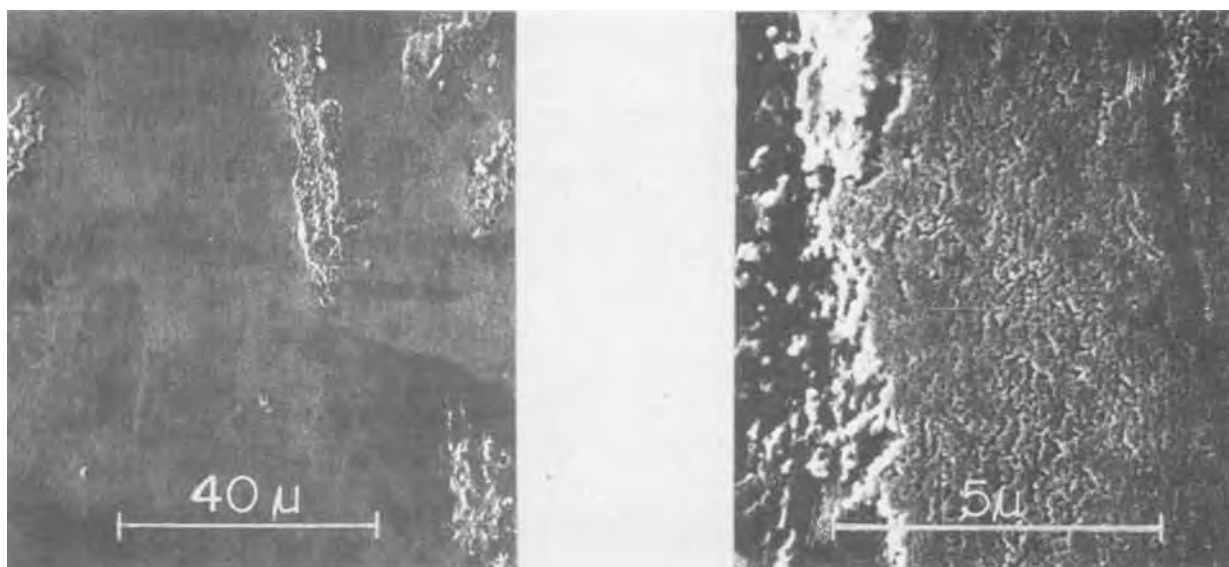


Fig. 4. Scanning electron micrographs with different magnifications of film formed by anodizing Be in 0.5M Na_2CO_3 for 15 min with a preset current of 10 mA/cm^2 and a preset potential of 50V. The films are mainly nonporous, though show features suggestive of both local and general dissolution.

formed. Unfortunately, the current remained roughly constant, as if the films were not insulating or alternatively were dissolving.

In the present work we have investigated nonaqueous electrolytes of four types.

(i) $(\text{C}_2\text{H}_5)_2\text{HPO}_4$. Anodizing Be in diethyl phosphate results in a $V-t$ curve suggestive of a nonporous film but an $I-t$ curve leading to the converse conclusion (curve C of Fig. 2 and also Table II). To gain further information, the extent of metal dissolution during anodizing was determined and found to be unacceptably high (Table II).

(ii) $(\text{C}_2\text{H}_5)_2\text{SO}_4\text{-H}_2\text{SO}_4$. A mixture of 75% $(\text{C}_2\text{H}_5)_2\text{SO}_4$ and 25% H_2SO_4 has been successfully used in the anodic sectioning of Nb and Ta (16). Anodizing Be in this electrolyte results in $V-t$ and $I-t$ curves of nonideal type (Table II). The electrolyte is implied by this to be unsatisfactory, and this conclusion was confirmed by finding similar metal dissolution to occur during anodizing as with diethyl phosphate (Table II).

(iii) *Acetic acid*. An acetic-acid based electrolyte, consisting of acetic acid, $\text{Na}_2\text{B}_4\text{O}_7 \cdot 10\text{H}_2\text{O}$, and water, is one of the few which permits Mo (17) and V (18,19) to be anodized. Its use with Be appeared at first sight encouraging in view of the $V-t$ and $I-t$ behavior (Table II); however, unacceptable metal dissolution occurs (Table II).

(iv) *Ethylene glycol*. More satisfactory results were obtained with ethylene glycol which has been saturated with certain salts. As seen in Fig. 5, the choice of Na_2CO_3 (curve A) or Na_2SO_4 (curve B) as the salt is unsatisfactory owing to the low value of dV/dt , whence an implied low efficiency. The choice of Na_2HPO_4 (curve C) or KH_2PO_4 or both Na_2HPO_4 and Na_2SO_4 (curve D and also Table II), however, results in $V-t$ and $I-t$ curves similar to those found when nonporous films are formed on Nb, Ta, V, or W (16, 19). We will subsequently refer to the electrolyte consisting of ethylene glycol saturated with both Na_2HPO_4 and Na_2SO_4 as "electrolyte A".

Anodizing efficiency with electrolyte A.—Experiments of two kinds were done to determine the anodizing efficiency with electrolyte A. First of all, Be thicknesses inferred by integrating $I-t$ curves with expanded time scales, such as those shown in curves A and B of Fig. 6, were compared with true Be thicknesses obtained gravimetrically by stripping the films in 10%

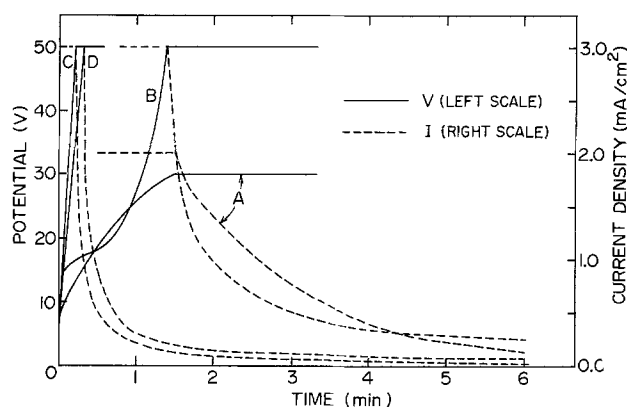


Fig. 5. Typical $V-t$ and $I-t$ curves for the anodizing of Be in ethylene-glycol-based electrolytes. Curve A: ethylene glycol saturated with Na_2CO_3 (abnormally low dV/dt). Curve B: ethylene glycol saturated with Na_2SO_4 (abnormally low dV/dt). Curve C: ethylene glycol saturated with Na_2HPO_4 (no anomalies). Curve D: ethylene glycol saturated with both Na_2HPO_4 and Na_2SO_4 (electrolyte A, no anomalies). Solid lines: $V-t$, with potential as in scale at left. Dashed lines: $I-t$, with current as in scale at right.

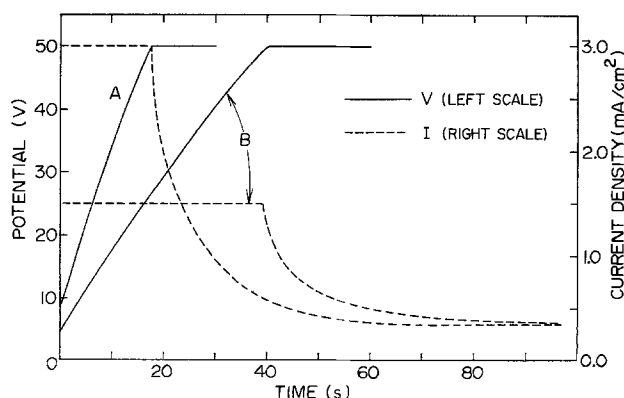


Fig. 6. Like curve D of Fig. 5 but plotted with an expanded time scale. An appropriate analysis of such curves is shown to yield the anodizing efficiency for conditions both of constant current and of constant current followed by constant potential.

Table III. Anodizing efficiency for Be using electrolyte A

Preset potential (V)	Anodizing time (sec)	Charge passed ^a (C/cm ²)	Be thickness from Faraday's law ^b ($\mu\text{g}/\text{cm}^2$ of Be)	True Be thickness from Eq. [1] ($\mu\text{g}/\text{cm}^2$ of Be)	Anodizing efficiency
25	55	454 \pm 10	2.12 \pm 0.05	1.50 \pm 0.08	0.71 \pm 0.04
50	65	920 \pm 30	4.29 \pm 0.14	2.90 \pm 0.15	0.68 \pm 0.04

^a Given by the total area under $I-t$ curves as in Fig. 6 for an initial current density of 3.0 mA/cm². Repeated 3 times for each present potential.

^b Calculated assuming an efficiency of 1.00.

KOH for 1 min. The true thicknesses are shown elsewhere (12) to be given by the relation

thickness $\approx 0.1 + (0.056 \pm 0.003) \times V \mu\text{g}/\text{cm}^2$ of Be [1]

which is valid provided the preset current is 3 mA/cm² and the current is allowed to drop, following the attainment of the preset potential, for 45 sec. The re-

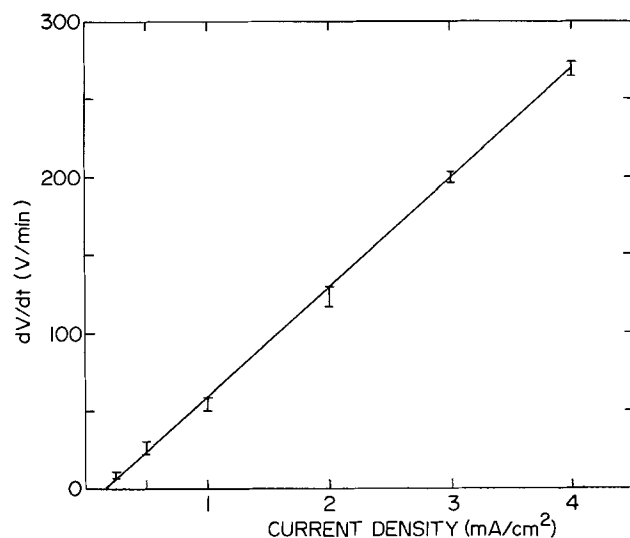


Fig. 7. dV/dt at 30V vs. I for the anodization of Be in electrolyte A. Given that dV/dt is proportional to the ionic current as in Eq. [2], these curves serve to separate the total current of 3 mA/cm² into an ionic part of 2.85 ± 0.05 mA/cm² and a non-ionic part of 0.15 ± 0.05 mA/cm².

sults, summarized in Table III, indicate an efficiency of ~ 0.7 , valid for conditions of fixed current followed by fixed potential.

The dependence of dV/dt on the total current I can be used to estimate the efficiency under conditions of fixed current. The basic relation, which remains valid even if (as in the present work) the IR drop in the electrolyte is not corrected for, is

$$\frac{dV}{dt} \propto i_1 = k(I - i_2 - i_3) \quad [2]$$

where i_1 is the ionic current, i_2 is the electronic current (which usually causes oxygen evolution), and i_3 is the current leading to film dissolution (20). Accordingly, a second group of experiments was carried out. The primary data were as in Fig. 6, and from these plots of dV/dt at 30V vs. I as in Fig. 7 were constructed. The intercept with the current axis represents the non-ionic current density, namely

$$i_2 + i_3 = 0.15 \pm 0.05 \text{ mA/cm}^2 \quad (\text{at } 30\text{V})$$

when I is 3 mA/cm². The efficiency follows as 0.95 ± 0.02 and is thus markedly greater for fixed current than for fixed current plus potential. This result is understandable if it is remembered that the contribution of $i_2 + i_3$ will depend on the total anodizing time (19) and the times were ~ 15 sec at fixed current but 65 sec at fixed current plus potential.

A slight curvature in the rising portions of the curves in Fig. 6 will be noted. We have not studied this effect in detail and therefore cannot say whether it is due to a change (with V or t) of the field in the anodic film or of the efficiency. The discrepancy between $i_2 + i_3 = 0.15$ mA/cm² and the leakage current in Fig. 6, 0.35 mA/cm², becomes less for longer times.

Porosity, dissolution, and crystallinity with electrolyte A.—Figure 8 shows scanning electron micrographs obtained for a film formed on Be and electrolyte A. Comparison with Fig. 3 and 4 suggests a significant freedom from porosity.

The depth-distribution technique showed that the metal dissolution during anodizing was essentially zero (Table II). Electrolyte A differs in this respect from all others that were examined. Stated in other terms, the dissolution current, i_3 , is evidently less important than the electronic current, i_2 , in lowering the anodizing efficiency to ~ 0.7 for conditions of fixed current plus potential.

Figure 9a shows a reflection electron diffraction pattern typical of a film as formed with electrolyte A.

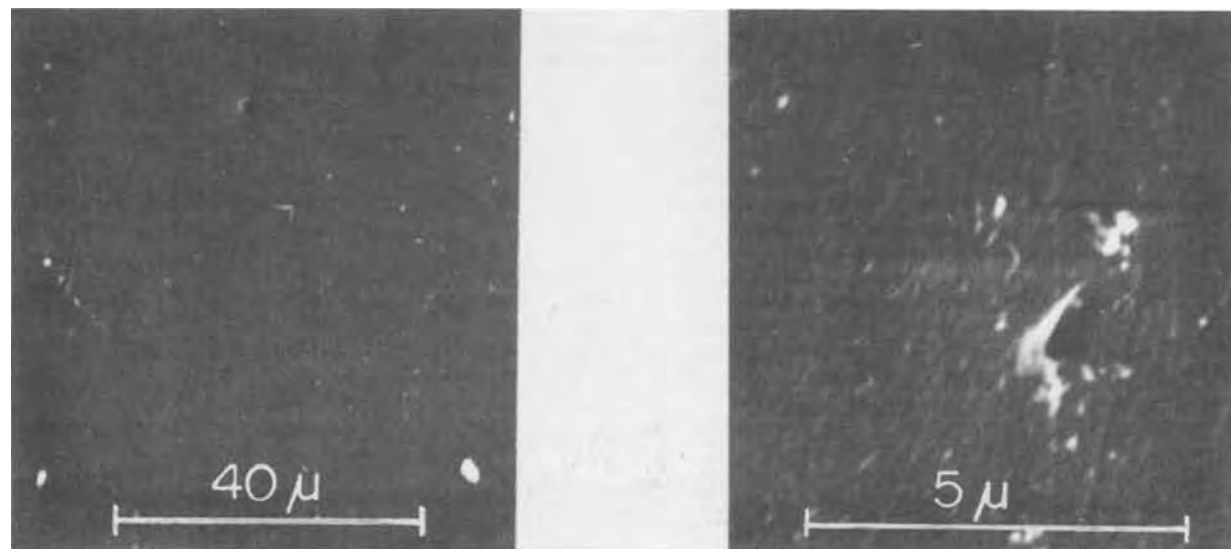


Fig. 8. Scanning electron micrographs with different magnifications of film formed by anodizing Be in electrolyte A for 1.5 min with a preset current of 3 mA/cm² and a preset potential of 50V. The films are significantly free from porosity.

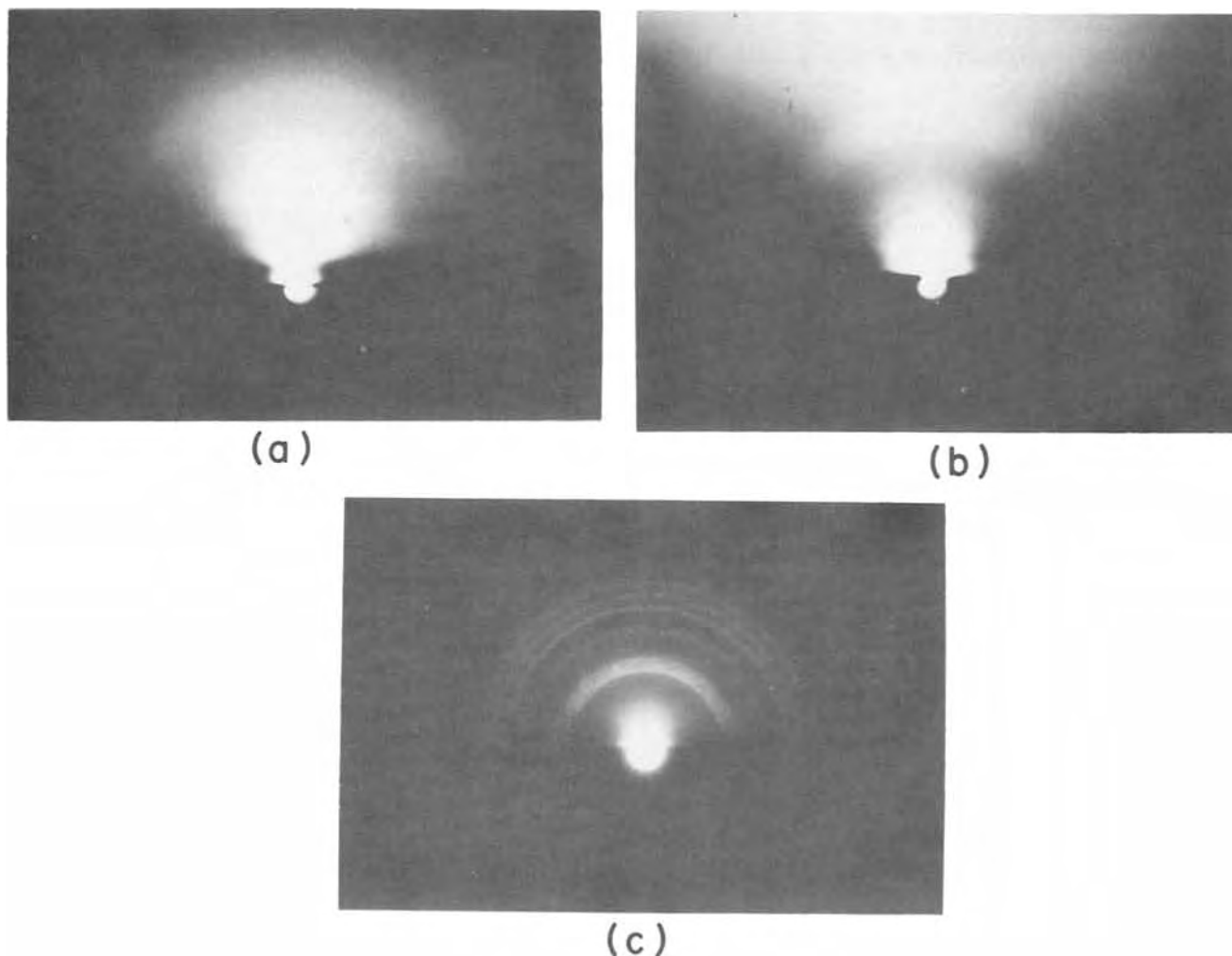


Fig. 9. Reflection electron diffraction patterns taken at 60 or 80 kV of film formed by anodizing Be in electrolyte A for 1.5 min with a preset current of 3 mA/cm^2 and a preset potential of 50V. Image (a): as-formed film, showing halos such as are conventionally ascribed to an amorphous structure though can also arise from microcrystallites having sizes of 1-2 nm. Image (b): film heated for 30 min in a vacuum of $1 \times 10^{-4} \text{ Pa}$ at 300°C , showing the halos to have split into diffuse rings. Image (c): film heated for 30 min in vacuum at 600°C , showing sharp rings identifiable as hexagonal BeO.

The film is nominally amorphous. After heating the films for 30 min in a vacuum of about $1 \times 10^{-4} \text{ Pa}$ at 300°C (Fig. 9b) or 600°C (Fig. 9c), the diffraction patterns revealed increasing degrees of crystallinity, such that the heating at 600°C led to overt polycrystallinity. The rings were identifiable as those of hexagonal BeO.

Discussion and Conclusions

Type of film.—The results presented here have shown that the behavior of Be with regard to anodizing is much like that of Al (5) and Sn (1, 9). Porosity, dissolution, and crystallinity can be varied almost at will depending on the electrolyte, with over-all results as in Table IV. The most interesting electrolytes would appear to be those consisting of ethylene glycol saturated with Na_2HPO_4 or KH_2PO_4 or both Na_2HPO_4 and Na_2SO_4 (electrolyte A). The $V-t$ and $I-t$ behavior suggested that a voltage-dependent limiting film thick-

ness was obtained (Fig. 5 and 6). The films were found to be nonporous (Fig. 8) and dissolution to be undetectable (Table II). The films were nominally amorphous, with a crystallization temperature lying somewhere below 300°C and with the crystallization product consisting of hexagonal BeO (Fig. 9). Their structure thus more nearly resembled the chemically precipitated BeO studied by Kerr (21) than the anodic films obtained in previous work (7, 8, 11). Anion incorporation in the anodic film from the electrolyte, such as that demonstrated with Ta (16, 22) may or may not have played a role and will be investigated in subsequent work.

Anodizing efficiency.—The anodizing efficiency using electrolyte A was determined in two ways: from Faraday's law and from dV/dt . Use of the former gave a value of ~ 0.7 , valid for conditions of fixed current

Table IV. Summary of Be anodizing

Electrolyte	Film?	Current at fixed potential	Porous?	Dissolution?	Crystallinity
1% H_2SO_4 or 1% HNO_3	No	Constant		Yes	
1% KOH	Yes	Falls slowly		Yes	
CrO_3 - HNO_3 mixture	Yes	Constant	Yes	Yes	Crystalline (7)
0.5M Na_2CO_3	Yes	Falls rapidly	No	Yes	Crystalline (11)
$(\text{C}_2\text{H}_5)_2\text{HPO}_4$	Yes	Nearly constant		Yes	
$(\text{C}_2\text{H}_5)_2\text{SO}_4$ - H_2SO_4 mixture	Yes	Constant or nearly constant		Yes	
Mainly acetic acid	Yes	Falls rapidly		Yes	
Electrolyte A	Yes	Falls rapidly	No	No	Nominally amorphous

followed by fixed potential. Use of dV/dt gave a value of 0.95 ± 0.02 , valid at 30V for fixed current. Efficiencies of less than unity will arise whenever electronic current, i_2 , or dissolution current, i_3 , play a role. The lack of dissolution (Table II) shows that i_2 is the more important in the present case. We attribute this role of electronic current to the relatively low thicknesses of the anodic films formed on Be (Eq. [1]) such that the resulting fields across the films are higher than with most other metals (Table I).

Anodic sectioning of Be.—The present work constitutes the first instance in which Be has been anodized under controlled conditions, the important feature being the choice of electrolyte. We will in a subsequent paper (12) treat the converse of film formation, namely the quantitative removal of films. This leads first of all to a microsectioning technique, thence to the possibility of studying diffusion and ion depth distributions in Be. We note in this connection that Be is a particularly interesting material for depth-distribution work in view of its low mass. Film removal also has a purely electrochemical interest, in that it leads to explicit information on efficiencies such as that in Table III.

Acknowledgment

This research was supported by a grant from the National Research Council, Ottawa, Canada.

Manuscript submitted March 7, 1975; revised manuscript received June 16, 1975.

Any discussion of this paper will appear in a Discussion Section to be published in the June 1976 JOURNAL. All discussions for the June 1976 Discussion Section should be submitted by Feb. 1, 1976.

Publication costs of this article were partially assisted by McMaster University.

REFERENCES

1. E. Giani and R. Kelly, *This Journal*, **121**, 394 (1974).
2. P. H. G. Draper and J. Harvey, *Acta Met.*, **11**, 873 (1963).
3. D. G. Brandon, J. Zahavi, A. Aladjem, and J. Yahalom, *J. Vacuum Sci. Technol.*, **6**, 783 (1969).
4. M. R. Arora and R. Kelly, Submitted to *J. Mater. Sci.*
5. R. A. Harrington and H. R. Nelson, *AIMME, Inst. Metals Div.*, **137**, 62 (1940).
6. O. Flint, J. J. Polling, and A. Charlesby, *Acta Met.*, **2**, 696 (1954).
7. I. S. Kerr and H. Wilman, *J. Inst. Metals*, **84**, 379 (1955-1956).
8. M. L. Levin, *Trans. Faraday Soc.*, **54**, 935 (1958).
9. R. Kerr, *J. Soc. Chem. Ind.*, **57**, 405 (1938).
10. R. M. Al'tovskii, A. G. Fedotova, M. I. Urazbaev, and S. I. Korolev, *Prot. Metals*, **5**, 172 (1969).
11. K. E. Heusler, *Ber. Bunsengesellschaft*, **67**, 943 (1963).
12. M. T. Shehata and R. Kelly, Submitted to *Rad. Effects*.
13. R. Kelly and K. Kerkdijk, *Surface Sci.*, **46**, 537 (1974).
14. J. P. S. Pringle, *This Journal*, **120**, 398 (1973).
15. A. I. Vol'fson, N. E. Markova, V. V. Chernyshev, V. N. Lebedev, and V. V. Vavakin, *Prot. Metals*, **9**, 321 (1973).
16. M. R. Arora and R. Kelly, *Electrochim. Acta*, **19**, 413 (1974).
17. M. R. Arora and R. Kelly, *This Journal*, **119**, 270 (1972).
18. R. G. Keil and R. E. Salomon, *ibid.*, **15**, 628 (1968).
19. M. R. Arora and R. Kelly, *ibid.*, **120**, 128 (1973).
20. J. Siejka, J. P. Nadai, and G. Amsel, *ibid.*, **118**, 727 (1971).
21. I. S. Kerr, *Acta Cryst.*, **9**, 879 (1956).
22. G. Amsel, C. Cherki, G. Feuillade, and J. P. Nadai, *J. Phys. Chem. Solids*, **30**, 2117 (1969).
23. M. R. Arora, Ph.D. Thesis, McMaster University (1974).
24. N. Q. Lam and R. Kelly, *Can. J. Phys.*, **48**, 137 (1970).
25. A. Charlesby, *Acta Met.*, **1**, 340 (1953).

Photoluminescence of Epitaxial ZnSe Layers Grown on Ge

F. Chernow, G. F. Ruse, and G. W. Eldridge

Department of Electrical Engineering, University of Colorado, Boulder, Colorado 80302

ABSTRACT

The epitaxial growth of ZnSe on (100) Ge using the close-spaced transport process is described. Substrate temperature of 575°C and source temperatures of 675°C yield 10μ single-crystal layers in 10 hr. The Ge substrate provides a nonreplenishable, chemical transport agent and the epitaxial layer thickness is limited to approximately 10μ . As-grown epitaxial layers show excellent photoluminescence structure at 77°K. As-grown layers exhibit high resistivity, annealing in Zn vapor at 575°C reduces the resistivity to 10-100 ohm-cm. Zinc vapor annealing quenches the visible photoluminescence.

The literature on the epitaxy of ZnSe on Ge is relatively large. Growth techniques include vacuum deposition (1-3), chemical vapor transport (4), close-space vapor transport (5), and close-space, chemical vapor transport (5). The pair of semiconductors is particularly attractive for electronic applications such as transistors with wide bandgap emitters (6,7) due to the small lattice mismatch and low concentration of interface states achievable (8). Vacuum-deposited layers exhibit strain and adhesion problems that may make

Key words: close-spaced transport.

them unacceptable for devices (1,2). Chemical transport techniques lead to incorporation of substantial halogen concentrations which create donors and comparable densities of deep acceptors (4,5,9). The close-spaced growth process using pure H₂ gas and undoped ZnSe sources minimizes doping and compensation in a configuration that is inherently clean and efficient (10).

The present work was motivated by a need to prepare ZnSe substrates suitable for ion-implanted electroluminescent devices. Required characteristics include morphology adequate for ion implantation,

low doping to minimize the dose required for compensation, and high luminescence efficiency. Layers grown using the close-space technique were examined for morphology and macroscopic uniformity, behavior under Zn vapor annealing, and photoluminescence structure. Photoluminescence measurements provide information on both the defect structure of the ZnSe layer and a suggestion of its electroluminescence potential. Little has been reported on the photoluminescence of ZnSe epitaxial layers and the reported results are somewhat disappointing (4).

Experimental Procedure

Growth system.—The close-space transport system employed in this work is shown in Fig. 1. This configuration is similar to that described by Hovel and Milnes (5). The insert in Fig. 1 shows the actual growth region. The high purity quartz crown establishes the source to substrate separation and aids in controlling the vapor pressure over the substrate. Slots cut in this crown provide access for the flow gas. Several variations in the access area were used, but no dependence of the growth behavior on this area could be determined. The source and substrate are clamped by high purity, low porosity carbon blocks which act as absorbers heated by external 600W tungsten-iodide lamps. These susceptors are supported by high purity quartz tubes. Thermocouples inserted in these tubes are used to monitor the temperatures of the susceptors and control the power to the lamps. Dual, digital, set point indicators, current modulators, and SCR power circuits control the substrate temperature (T_{sub}) and the source-substrate temperature difference (ΔT). Rapid response with little or no overshoot and temperature control of better than 1°C was easily achieved.

A gas flow and mixing system was designed to accommodate HCl chemical transport growth as well as the work described here. It was constructed of Monel, Type 316 stainless steel, and inert plastics. This system

was made leak tight to within the 10^{-10} atm-cm³/sec sensitivity of a helium leak detector. The hydrogen flow gas used during the growths was palladium-diffusion purified. Electronic grade HCl and prepurified argon were employed. Argon was used as a continuous flushing gas when the systems were not in use. (Several glass envelope-susceptor systems were constructed; each system was used exclusively for particular substrate and flow gas combination except where it is noted otherwise.) Systems were open to the atmosphere for source or substrate replacement for a few minutes at most. Prior to growth, the growth region was baked at 350°C in flowing H_2 for a minimum of 1 hr.

Substrate and source preparation.—Substrates were prepared from 2/3 mm thick, (100) oriented germanium wafers. The Ge was nominally undoped (40-100 ohm-cm, p-type). The dependence of epitaxial layer morphology on substrate surface structure was complicated by selective Se etching of the Ge during growth. The best results in terms of ZnSe uniformity and surface morphology were obtained when the substrates were mechanically polished using 1μ Al_2O_3 and then etch polished using concentrated NaOCl on a low nap pad (11). This produces optically flat, scratch-free Ge surfaces. A final etch in dilute I_2 -HF to remove 3-5 mils was used to reduce surface damage resulting from the polishing procedure.

Since the close-space transport is very efficient, approximately twenty 10μ thick growths can be made before the source-substrate gap changes appreciably. The work described here is the result of two separate source charges of which each were used twenty times. Sources were prepared from two, separate, high purity, melt grown, ZnSe single crystals purchased from Eagle-Picher Industries. Both crystals had high dark resistivity and both contained numerous grain boundaries. Emission spectroscopy analysis of the as-received crystals revealed an impurity concentration of 540 ppm (500 ppm Si, 20 ppm Fe) in the first crystal and an impurity concentration of 70 ppm (50 ppm Si, 20 ppm Fe) in the second crystal. These emission spectroscopy estimates exclude copper which was measured by atomic absorption at 87 and 0.4 ppm, respectively. The first crystal was ground down to $\sim 50\mu$ grains to form a "crushed-crystal" source. The second crystal was cut and polished to fit the quartz crown to form a "single-crystal" source. Surface damage and contamination were removed by etching in H_2SO_4 - $\text{K}_2\text{Cr}_2\text{O}_7$ in the latter case (12). No chemical analysis was performed on the completed sources.

Analysis techniques.—Surface morphology was observed using a 27-1250 \times microscope with a Nomarski phase-contrast attachment. The front surface of the ZnSe layer was always examined; in some cases the ZnSe layer was removed by etching in 5% bromine in methanol to permit examination of the Ge substrate for etching by Se vapor during growth (5). Samples were cleaved for microscopic examination to determine the thickness of the ZnSe layers. Uniformity of both the growth and substrate etching were also noted. Crystallinity of the ZnSe layers was examined using Laue x-ray reflection and glancing, high energy, electron diffraction techniques. As a consequence of the thin layers ($\leq 10\mu$) and good lattice match, the x-ray data is dominated by reflections from the substrate.

Several samples were annealed in a Zn vapor atmosphere at 575°C . No attempt was made to protect the Ge substrate from attack by the Zn vapor, and this precluded annealing in liquid Zn (5). The samples were placed in high purity quartz ampuls with a weighed quantity of metallic Zn (99.9995% pure) sufficient to achieve the Zn_1 - Zn_g equilibrium at the annealing temperatures while minimizing the quantity of excess, liquid Zn (13, 14). The ampuls were evacuated to 10^{-6} Torr and sealed. Annealing was performed for times between 1 and 36 hr. The ampuls were inserted into a

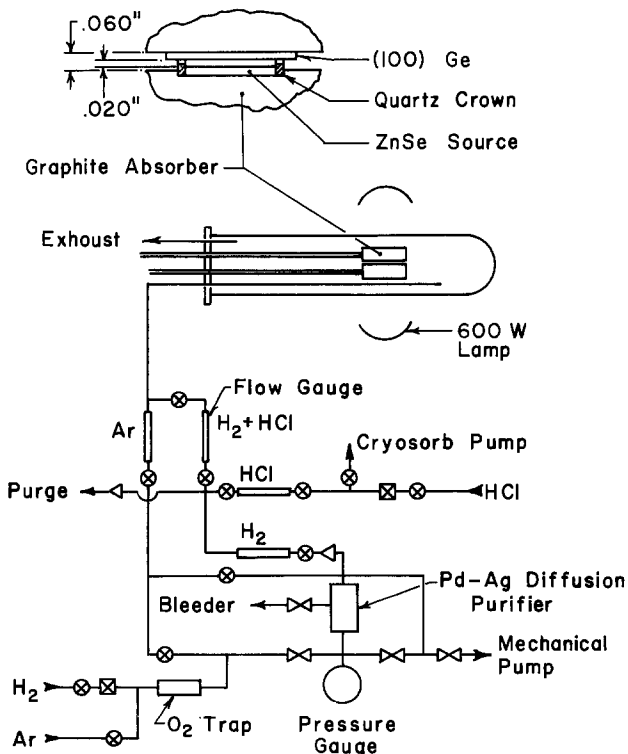


Fig. 1. ZnSe growth system. Graphite absorbers are $1\frac{1}{2}$ in. diam \times $7/16$ in. thick; Ge substrates are $1/2$ in. square, and the ZnSe growth region is 0.34 in. in diameter. Gases are vented through bubblers to prevent back diffusion. For $\text{H}_2 + \text{HCl}$ growths pure H_2 flows through the Ar flow gauge and a large fraction of the initial $\text{H}_2 + \text{HCl}$ mixture is dumped at the purge port in order to obtain low HCl concentrations.

preheated furnace and quench-cooled upon removal. Annealed samples were examined for cracks and peeling which would indicate stress and adhesion problems. Four terminal resistivity measurements were performed, and the ZnSe layer was etched back in steps and the resistivity measurement repeated to determine the uniformity of the induced conductivity.

Ultraviolet-stimulated luminescence measurements were performed to assess the quality of the ZnSe epitaxial layers. Samples were clamped to a cold finger in an evacuated Dewar and held at liquid nitrogen temperature. Light from a high pressure, 100W mercury lamp was filtered (Corning No. 7-51) to remove visible components and focused on the sample. The spectrum was resolved using a double pass monochromator and detected using a photomultiplier with an S-10 photocathode. None of the spectra were corrected for system response.

Experimental Results

Growth.— T_{sub} and ΔT were varied from 550° to 800°C and 5° to 125°C, respectively, to determine optimum growth conditions. Optimum conditions for this case are defined as best surface morphology, best crystal structure, with acceptable growth rate. The optimum conditions were $T_{\text{sub}} = 575^\circ\text{C}$, $\Delta T = 100^\circ\text{C}$ at a hydrogen flow of 300 cm³/min.

Ten micron thick films were grown in 10 hr under optimum conditions. Increasing T_{sub} leads to severe pitting of the Ge substrate while almost no pitting was observed under optimum conditions. There is always evidence of Ge etching in the area where the quartz crown makes contact with substrate. At the inside diameter of the crown, erosion reaches depths of a few microns. This erosion decreases continuously toward the outside diameter where isolated, square etch pits are found. No etching is observed outside the crown except in the immediate neighborhood of the slots. Decreasing ΔT increases substrate pitting as well as reducing the growth rate. For $T_{\text{sub}} = 575^\circ\text{C}$, ΔT must be greater than 50°C for the ZnSe thickness to exceed the erosion depth of the substrate. As T_{sub} is increased, ΔT must also be increased for this condition to be met. Increasing ΔT above 125°C leads to faceting and macroscopic nonuniformity of the layer but HEED and x-ray analysis indicated that all the epitaxially grown films were single crystal.¹ T_{sub} must exceed 500°C to achieve usable growth rates.

It has not been possible to define a ZnSe growth rate for this configuration. Increasing the growth time from 10 to 20 hr does not increase the layer thickness by more than 20%. Similar evidence for saturation of the layer thickness is found when the growth time is reduced. Any conclusions, however, must be qualified due to a $\pm 20\%$ uncertainty in the layer thickness under supposedly identical conditions.

The first series of growths were performed using the crushed crystal source. A Nomarski photograph of the ZnSe layer produced in run No. 12 is shown in Fig. 2a. The source had been used for 54 hr growing time prior to this run without replenishment. Earlier runs show projecting yellow needles as well as the uniform epitaxial layer. The density of dendritic needles decreases continuously to zero over the first 75 hr of source use. There also appears to be some improvement in the uniformity of the continuous layer with each succeeding growth.

Figure 2b is a Nomarski photograph of a ZnSe layer produced using the single-crystal source after 144 hr of prior use. In contrast to the powder source results, dendritic growth appears in only the first epitaxial layer and no further systematic changes occur in the morphology of the epitaxial layers.

¹ Experiments were performed to determine the growth rate for the single crystal to polycrystal transition at the optimum substrate temperature. Addition of 0.6% HCl leads to a growth rate of 30 μ /hr and induces this transition. This agrees with a linear extrapolation of the transition data for ZnSe epitaxy on (100) Ge presented by Calow et al. (2).



Fig. 2a. Surface of ZnSe epitaxial layer grown from the crushed-crystal source: Nomarski phase contrast; calibration marks correspond to 5 μ .

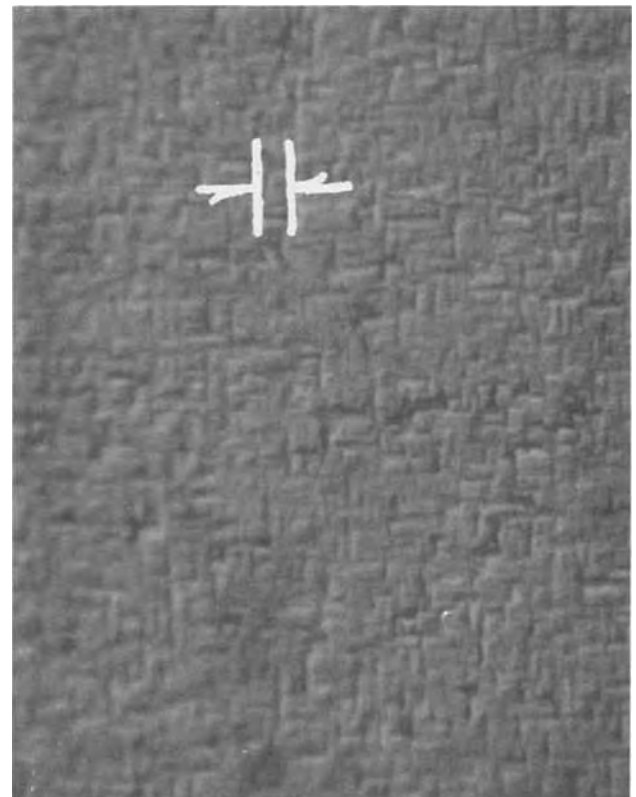


Fig. 2b. Surface of ZnSe epitaxial layers grown from the single-crystal source: Nomarski phase contrast; calibration marks correspond to 5 μ .

Photoluminescence.—Figure 3 shows the visible photoluminescence spectra of a series of ZnSe layers

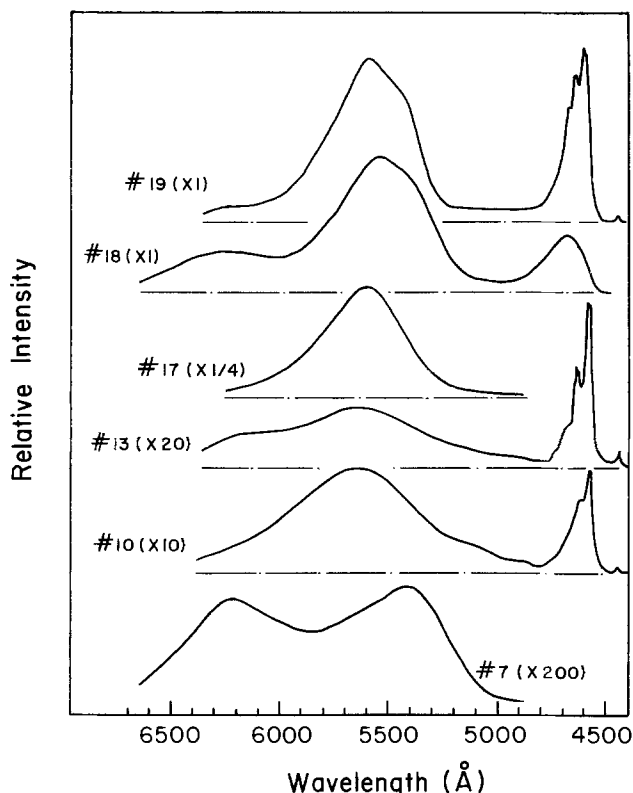


Fig. 3. Luminescence of ZnSe layers grown from a crushed-crystal source. The numbers in parentheses are the scaling factors used to multiply the intensity of the original data in preparing this figure. The relationship between run number and the accumulated hours of source use is No. 7, 20 hr; No. 10, 39 hr; No. 13, 65 1/2 hr; No. 17, 107 hr; No. 18, 119 hr; and No. 19, 131 hr. Run No. 17 employed a GaAs substrate.

grown using the crushed-crystal source. The chronological sequence of the growths is indicated by the run number; all of these growths were performed with approximately optimal parameter values. There is also a reduction in dendritic growth in this progression. The dendritic growth was brushed off the sample prior to taking the spectra shown in Fig. 3. Etching to remove any residue of the dendrites did not alter the spectra.

The evolution of the luminescence from layer to layer using the same source is too complex to be described completely by Fig. 3. The epitaxial layers grown when the source is new are of relatively poor quality and the luminescence is characterized by a broad, weak line peaking between 5900 and 6100 Å. As the source is used, epitaxial layers exhibit a 5400 Å line of increasing intensity followed by the gradual appearance of a line at 6240 Å and simultaneous decrease in the intensity of the 6000 Å line (No. 7). In turn, the 6240 Å line decays and what appears to be an unresolved pair of lines at ~6000 and ~5625 Å grows in intensity. Still later growths from the same source result in epitaxial layers that exhibit a reduction in intensity of the 6000 Å line with no change in the 5625 Å line. Appearance of the blue emission band at 4560-4720 Å and the line at 4450 Å occurs with extinction of the 6000 Å band (No. 10). Continued use of the source leads to epitaxial layers that show increased intensity and better resolution in the blue emission band (No. 13).

Run No. 17 was performed on a GaAs substrate. A 5 μ epitaxial ZnSe layer was grown on the (100) GaAs substrate in 10 hr. T_{sub} and ΔT were maintained at 575° and 100°C, respectively. In contrast to normal procedure, neither the growth tube nor the ZnSe source were changed. Figure 3, No. 17 shows substantial intensity enhancement and line width reduction of the 5625 Å line. No other lines were observed in the spectrum. Run No. 17 was followed by additional growths on germanium substrates using the same source and

growth tube. The 6240 Å red band and a structureless blue band reappears in No. 18. Figure 3, No. 19 indicates a return to the spectrum shown in Fig. 3, No. 13. Later runs show that the return to the original spectra is erratic and slower than might appear from the data appearing in Fig. 3, No. 18 and 19.

Figure 4 details the behavior of the blue emission. The phonon-assisted emission series seen in the run No. 13 sample has been identified as resulting from a free to bound transition by Dean and Merz (15). The LO phonon energy implied is 30.5 ± 1 meV in agreement with published results (15, 16). The blue emission band for the run No. 18 sample is typical of ZnSe with high Al and Na concentrations (16). The line at 4450 Å is a combination of unresolved I_1 , I_2 , and I_x lines (17).

ZnSe layers grown from single-crystal sources show similar luminescence spectra with notable exceptions. The structure of the blue emission changes in an erratic manner from growth to growth and never develops the detail observed in the spectra of the epitaxial layers grown from the powdered source. The 4450 Å line is observed in all epitaxial layers from the onset of use of the source. Layers grown during the initial runs show the ~5600 Å band and blue emission in the 4560-4720 Å range is absent. The broad 6000 Å emission band may appear alone or with a line at approximately 5400 Å. Other epitaxial layers exhibit a 6240 Å emission band appearing with a line peaking anywhere between 5600 and 5400 Å. The 4560-4720 Å blue emission is present only when the 6000 Å band is absent. Luminescence intensity in epitaxial layers grown from both sources is comparable.

Although growth of ZnSe epitaxial layers using HCl as a chemical transport agent is not the subject of this paper, some reference to the luminescent spectra obtained is useful. Layers grown using single-crystal sources and less than 0.1% HCl in H_2 show a green emission band centered at 5300 Å. At higher HCl concentrations the layers show a broad 6000 Å band and the blue emission is either structureless and very weak or absent. The photoluminescence spectra indicate no persistent contamination of the ZnSe source as a result of using HCl. Cutting off the HCl flow yields epi-

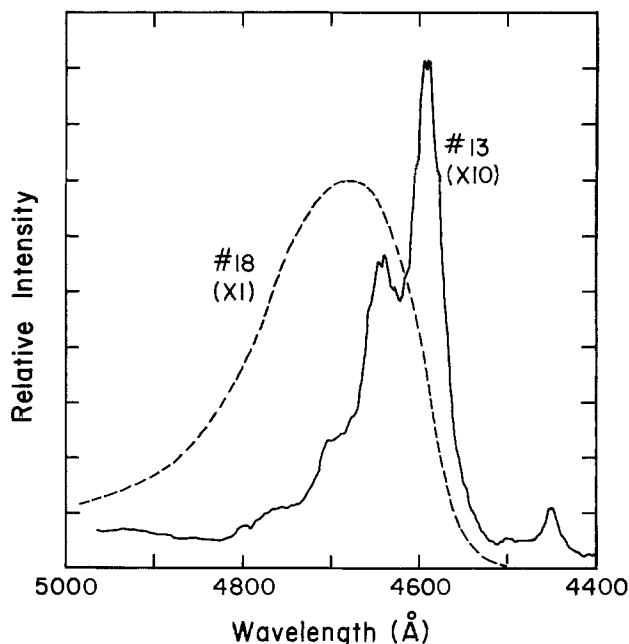


Fig. 4. Detail of blue luminescence of ZnSe layers. The spectra of the layer obtained from run No. 13 is typical of those obtained from runs No. 12 through No. 16. Run No. 18 was preceded by one run on a GaAs substrate. The numbers in parentheses are scaling factors for the data as defined in Fig. 3.

taxial layers showing 6240 and 5400Å emission bands and good blue emission in the following growth.

Sources used in HCl also show ~6200 and ~5400Å emission bands but do not show either intense or highly structured blue emission. Examination in regions with and without exposed grain boundaries shows that most of the emission originates at the grain boundaries. Small shifts in the peak wavelengths and changes of the line width of both the 6200 and 5400Å band demonstrate that the higher intensity observed at grain boundaries is not due to scattering. Unused source wafers do not exhibit uniform luminescence intensity or structure except that blue emission is usually not present. Sources used in H₂ only show a single, weak luminescence band peaking at 5400Å.

Zinc annealing.—All as-grown epitaxial layers exhibit resistivities greater than 10⁸ ohm-cm as measured with a four-point probe. Uncertain junction isolation between the n-type epitaxial layer and the p-type substrate sets this value as a lower limit. Annealing in saturated Zn vapor at 575°C for 18 hr reduces the resistivity to 10-100 ohm-cm. Etching studies indicate that the conductivity modification is uniform throughout the epitaxial layer thickness. Similar changes are observed upon annealing ZnSe source crystals under the same conditions. These results are typical of bulk ZnSe (15). In contrast to bulk ZnSe crystals annealed under these conditions, ZnSe epitaxial layers grown on Ge by H₂ transport show no visible photoluminescence at 77°K. Etching experiments demonstrate that this absence persists throughout the layer. Annealing in saturated Zn vapor at 575°C for times such that the resistivity is reduced to the 10⁴ ohm-cm range results in a fourfold reduction in luminescence intensity and broadening of the blue emission lines.

It might be hypothesized that photoluminescence is killed by a deep trapping and recombination center. Hovel has reported a Ge-ZnSe heterojunction switching device that depends on the presence of deep traps (18). Measurements on these annealed samples do not show switching behavior strongly suggesting that deep traps are not present.

Annealed samples did not exhibit lifting or cracking. In contrast to other ZnSe-Ge epitaxy studies employing different deposition techniques and/or thickness, this work did not show an adhesion or stress problem that can be revealed by annealing.

Discussion

Approximately 10μ thick ZnSe layers can be grown on (100) Ge using the close-space technique without using a chemical transport agent. Nonlinearity in the growth rate confirms Hovel and Milnes' observation that Ge itself acts as a chemical transport agent (15). Hovel and Milnes also obtained no growth on GaAs (B surface) under conditions similar to those used here; i.e., $T_{\text{sub}} = 590^\circ\text{C}$, $\Delta T = 110^\circ\text{C}$, and 0.02% HCl in H₂. (HCl should increase the growth rate but we have not observed measurable increases at this low concentration.) In contrast, a 5μ thick ZnSe layer was obtained ($T_{\text{sub}} = 575^\circ\text{C}$, $\Delta T = 100^\circ\text{C}$, and pure H₂) on (100) GaAs using a source that had been used for repeated growths on Ge. Although conditions are not identical, the most probable explanation for the discrepancy is persistent Ge contamination of the source powder. Parker *et al.* obtain Ge concentrations of 50-100 ppm in ZnSe epitaxial layers grown by HBr transport on ~500°C Ge substrates (4), and Hovel and Milnes demonstrate that this Ge is provided by Se rather than halogen etching of the substrate (5). It must be concluded that under optimum growth conditions, when there is no visible etching under the ZnSe layer, the GeSe_x concentration is replenished via etching at the quartz crown-substrate interface. Etching in only this region implies very low Zn and ZnSe mobility on the substrate surface and very fast reaction of H₂Se with the exposed Ge. Slightly higher substrate tem-

perature at this interface may also enhance the selectivity of the etching.

Gradual changes in the morphology of layers grown from the crushed-crystal source and absence of similar changes in layers grown from the single-crystal source can be explained by several models. The large surface area of the crushed-crystal source, uncertain thermal contact, and latent heat of vaporization may cooperate to yield supersaturation and dendritic and atypical growth. Morphology improves as smaller grains are consumed or "fused" together to reduce the surface area and improve thermal contact. It is also possible that the ZnSe source surface must equilibrate at nonstoichiometric Zn and Se concentrations in order to achieve stoichiometric deposition. The higher impurity concentration of the crushed-crystal source may have an adverse effect on morphology. Crushing ZnSe also exposes grain boundary surfaces and the impurity concentration on these surfaces is expected to be higher than the bulk. Repeated sublimation from these surfaces may lead to successively purer epitaxial layers.

The photoluminescent spectra of the best epitaxial layers is superior to both that previously reported for epitaxial layers (9, 19) and the source crystals employed in this work. "Superior" in this case refers to the dominance and structural detail achieved in the blue emission region. Blue emission has been identified with Na acceptors (16), but the origin of Na has not been established in this case. Emission spectroscopy reveals no Na in the ZnSe sources and 2 ppm Na in the graphite absorbers. The Ge substrates were not analyzed.

The consistent reduction of the long wavelength emission of layers grown from the crushed-crystal source and the erratic behavior of this emission in layers grown from the single-crystal source suggests that with the exception of the 5625Å line these lines are associated with chemical impurities originating preferentially from grain boundaries in the source. An abnormally high concentration of chemical impurities at grain boundaries is expected and examination of the source luminescence confirms a higher concentration of optically active defects at grain boundaries. Crushing the source exposes these high impurity concentration regions so they are sublimed and incorporated in the early grown epitaxial layers. Single-crystal sources release these impurities for incorporation as sublimation and preferential sublimation at grain boundaries exposes impurity pockets. This model requires that these impurities do not both diffuse freely along the grain boundaries and sublime preferentially at the source surface.

Only speculative identifications can be made as to the specific origin of the long wavelength lines. The luminescence band at 6000Å is thought to be equivalent to the self-activated blue luminescence center in ZnS (20). The S-10 photocathode response distorts the luminescence data in this wavelength range. Correction for the S-10 response brings the center wavelength and the linewidth of the 6000Å band into agreement with the self-activated emission band reported by Jones and Woods (21). This center has been suggested to consist of a Zn vacancy associated with a halogen or a Group III donor (22). Appearance of this line in layers grown in high HCl concentrations suggests the halogen donor is responsible.

Cu has been associated with emission bands at approximately 5300 and 6300Å (19, 22-24). Aven and Halstead observed green emission in compensated ZnSe:Cu:Cl and red emission in ZnSe:Cu:Al containing excess Cu (22). Cl does not appear to be optically active in the former case while an optically active Cu-Al complex appears to form in the latter case (22, 25). Similar processes may lead to the 5300Å band in layers grown using low HCl concentration and reappearance of the 6240Å band after contamination of the growth apparatus with Ga (19). Correction for the

S-10 photocathode response bring the center wavelength and the linewidth of the 6240Å band into agreement with the copper-red emission band reported by Jones and Woods (21). The relative behavior of layers grown from the two sources is not consistent with the initial Cu concentrations, however.

Both the 5625Å line in layers grown from the crushed crystal and the 5600-5440Å line in layers grown from the single crystal appear to be the so-called yellow self-activated luminescence (26, 27). Variability in the peak in the latter case is thought to be due to a varying defect concentration.

The ZnSe source material used for this study is similar to that employed by Dean and Merz and by Chatterjee *et al.* in regard to both electrical and photoluminescent behavior (15, 16). Prior to Zn vapor annealing the epitaxial layers also exhibited similar photoluminescent behavior. The initial conductivity of the epitaxial layers and their response to Zn vapor annealing is also similar. Dean and Merz annealed their ZnSe samples in Zn vapor to create or enhance the Q and Q^{F→B} emission lines (15). This procedure should reduce the Zn vacancy concentration. Chatterjee *et al.* indicate that Na substituting for Zn is responsible for the Q emission series (16). The presence of substitutional Na must be accompanied with a reduction in Zn vacancies if the blue emission is to be enhanced. If not, the deeper Zn vacancies would tend to dominate the photoluminescence and lead to longer wavelength emission. The epitaxial layers show no visible photoluminescence when Zn is vapor annealed to achieve similar electrical properties. This implies either that a killer center involving Ge impurities is formed or that the optically active centers are gettered by the substrate.

Approximately 75 hr of firing the source powder at the growth temperature is an impractical method for stabilizing and purifying the source material. Even this preparation does not achieve surface morphology comparable to that obtained using a single-crystal source. It is possible that prefring single-crystal sources in liquid zinc would make these sources more uniform and achieve some purification by a solvent extraction process (28).

Some form of chemical analysis of the epitaxial layers would have been helpful in explaining the luminescence data. The luminescence is a complex function of the concentrations of more than one chemical species in general, and these concentrations may lie in the range of 1 ppm or less in ZnSe (27).

Manuscript submitted Feb. 14, 1975; revised manuscript received May 27, 1975.

Any discussion of this paper will appear in a Discussion Section to be published in the June 1976 JOURNAL. All discussions for the June 1976 Discussion Section should be submitted by Feb. 1, 1976.

Publication costs of this article were partially assisted by The University of Colorado.

REFERENCES

1. J. T. Calow, S. J. T. Owen, and P. W. Webb, *Phys. Status Solidi*, **28**, 295 (1968).
2. J. T. Calow, D. L. Kirk, and S. J. T. Owen, *Thin Solid Films*, **9**, 409 (1972).
3. A. San, *J. Appl. Phys.*, **44**, 523 (1973).
4. S. G. Parker, J. E. Pinnell, and L. N. Swink, *J. Phys. Chem. Solids*, **32**, 139 (1971).
5. H. J. Hovel and A. G. Milnes, *This Journal*, **116**, 843 (1969).
6. H. Kroemer, *Proc. IRE*, **45**, 1535 (1957).
7. H. J. Hovel and A. G. Milnes, *IEEE Trans. Electron Devices*, **ED-16**, 766 (1969).
8. A. G. Milnes and D. L. Feucht, "Heterojunctions and Metal-Semiconductor Junctions," Academic Press, New York (1972).
9. S. G. Parker, *J. Cryst. Growth*, **9**, 177 (1971).
10. F. H. Nicoll, *This Journal*, **110**, 1165 (1963).
11. A. Reisman and R. Rohr, *ibid.*, **111**, 1425 (1964).
12. V. S. Park, C. R. Geesner, and B. K. Shin, *Appl. Phys. Letters*, **21**, 567 (1972).
13. R. E. Honig, *RCA Rev.*, **23**, 567 (1962).
14. P. Goldfinger and M. Jeunchemme, *Trans. Faraday Soc.*, **59**, 2851 (1963).
15. P. J. Dean and J. L. Merz, *Phys. Rev.*, **178**, 1310 (1969).
16. P. K. Chatterjee, A. J. Rosa, and B. G. Streetman, *J. Luminescence*, **8**, 176 (1973).
17. A. Rosa, Private communication.
18. H. J. Hovel, *Appl. Phys. Letters*, **17**, 141 (1970).
19. C. Auzary Roindessault and F. Lebourg, *Compt. Rend. Acad. Sci. Paris*, **272**, 691 (1971).
20. J. S. Prener, and D. J. Weil, *This Journal*, **106**, 409 (1959).
21. G. Jones and J. Woods, *J. Luminescence*, **9**, 389 (1974).
22. M. Aven and R. Halstead, *Phys. Rev.*, **137A**, 228 (1965).
23. G. B. Stringfellow and R. H. Bube, *Phys. Rev.*, **171**, 903 (1968).
24. L. Yz. Markovskii, I. A. Mironov, and Yu. S. Ryzhkin, *Bull. Acad. Sci. USSR*, **33**, 887 (1969).
25. S. G. Parker and J. E. Pinnell, *Trans. Met. Soc. AIME*, **245**, 541 (1969).
26. S. Iida, *J. Phys. Soc. Japan*, **26**, 1140 (1969).
27. S. Iida, *ibid.*, **25**, 177 (1968).
28. M. Aven and H. H. Woodbury, *Appl. Phys. Letters*, **1**, 53 (1962).

Poly(Vinyl Arene Sulfones) as Novel Positive Photoresists

M. J. Bowden and E. A. Chandross

Bell Laboratories, Murray Hill, New Jersey 07974

ABSTRACT

The synthesis and photosensitivities of a number of copolymers of sulfur dioxide and various arylenes are described. Irradiation with ultraviolet light causes chain scission and increases the solubility of these polymers; thus they function as positive photoresists.

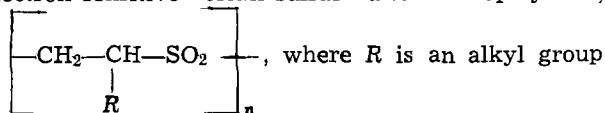
All commercial positive photoresists appear to depend on the same photochemical process, *viz.*, the rearrangement and hydration of a quinone diazide to form a carboxylic acid which solubilizes the resist in

Key words: polysulfones, positive resist, photoresist.

mild alkali (1). Process operations using these materials have not been entirely satisfactory. The resist solutions are complex mixtures and batch to batch variation in properties can make developing procedures unsatisfactory. Positive resists have limited chem-

ical resistance to etching solutions and are readily soluble in alkaline etchants. Certain difficulties also arise when positive resists are used in conjunction with gallium arsenide substrates since the substrate is attacked by the developing solution, leading to marked undercutting of the resist and attendant loss of resolution.

We have investigated a new type of positive photoresist, analogous to the recently described electron-sensitive olefin-sulfur dioxide copolymers,



(2). This group of polymers does not absorb ultraviolet light in a useful region of the spectrum ($\lambda > 250$ nm) and it is not possible to sensitize photodegradation. We thought that polysulfones containing R = aromatic hydrocarbon should show photochemical cleavage of the benzylic carbon-SO₂ bond. Related photochemical reactions are known for cyclic sulfones (3). We have found that the copolymers of arylated olefins, such as styrene, and sulfur dioxide are sensitive to ultraviolet light that is absorbed by the hydrocarbon moiety and that these copolymers function as positive photoresists with useful differential solubility.

Styrene is known to form a 2:1 copolymer with sulfur dioxide under certain conditions (4). We chose this material for our initial studies and found it to be sensitive to ultraviolet light absorbed by the pendant benzene rings (ca. 265 nm). The solubility of this polymer is increased by irradiation, indicating that chain scission is the principle mode of degradation as in the electron beam resists; thus it functions as a positive photoresist. The sensitivity is rather low because the absorbance is weak and lies in a region where there is relatively little output from the high pressure mercury arc lamp.

In order to increase the photosensitivity of this type of polymer we replaced some or all of the benzene groups with larger aromatic hydrocarbon systems having greater ultraviolet absorbance at somewhat longer wavelength. The systems studied are summarized in Table I. The sensitivity presumably depends not only on the aforementioned factors but also on the inherent instability of the polymer and the mechanism of photodecomposition.

The most promising member of this class of compounds was a terpolymer based on styrene, acenaphthylene and SO₂, whose sensitivity was about 500 mJ cm⁻² for ultraviolet light in the wavelength region 200-400 nm. This paper reports a more detailed investigation of the properties of this resist.

The photochemical reaction appears to proceed most readily from the excited singlet state as triplet sensitization, e.g., benzophenone was extremely inefficient. This may reflect the energy required to break the carbon-SO₂ bond which is comparable to the triplet energy of the naphthalene group (60 kcal mole⁻¹). These polymers decompose at elevated temperatures

and the photochemical reaction may be a hot ground state thermal reaction.

The acenaphthylene section of the polymer contains the grouping $-\text{CH}-\text{CH}-\text{SO}_2$ which has the aryl group



attached to two atoms of the main chain. We believe that the increased sensitivity of this polymer over the related vinylnaphthalene polymer is due to the strain introduced by the five-membered ring of the acenaphthylene group.

Experimental

Poly(styrene-acenaphthylene sulfone) (PASS).—A solution of acenaphthylene (8.75g, 0.057 mole) in freshly distilled styrene (30g, 0.29 mole) containing azobisisobutyronitrile (0.1g) and dimethylformamide (5 ml) was degassed by several freeze-thaw cycles. Sulfur dioxide (ca. 50g, 0.8 mole) was added and the flask was sealed. It was immersed in a water bath at 50°C for 72 hr. The polymer was precipitated by pouring the viscous mixture into a large excess of methanol. It was redissolved in dioxane and reprecipitated into methanol and then dried under vacuum at room temperature.

The elemental analyses of various batches of the polymer are given in Table II. The u.v. absorption spectrum is shown in Fig. 1. Acenaphthylene groups in the polymer are responsible for the absorption in the 290 nm region and their concentration can be determined from the u.v. spectrum.

Sensitivity.—The polymers were dissolved in Kodak Photoresist Thinner (methoxyethyl acetate) and films were spun on Si/SiO₂ substrates using a Headway photoresist spinner. Films were baked for 30 min at 200°C. The films were irradiated through a mask with collimated light from a 200W high pressure mercury arc source. The light was filtered through a Corning 7-54 filter which transmits the 220-400 nm region of the spectrum. The intensity, measured with a thermopile, was 20 mW cm⁻² at the resist surface.

Following exposure, the irradiated areas of the film were spray-developed with a 60 (dioxane)/40 (isopropyl alcohol) mixture. This developer did not attack the remaining film.

Resolution was checked by exposing the resist through a contact mask and developing the image as described. The resist was then postbaked (30 min at 200°C) and the substrate was etched in buffered HF.

Results and Discussion

Polymerization.—Styrene and sulfur dioxide form a 2:1 copolymer under the conditions used in our experiments. The addition of acenaphthylene (AcN) markedly reduces the over-all polymerization rate. Elemental analyses of the terpolymer indicated that acenaphthylene is incorporated into the chain in either $-\text{Sty}-\text{AcN}-\text{SO}_2-$ or $-\text{Sty}-\text{Sty}-\text{AcN}-\text{SO}_2-$ sequences interspersed between the $-(\text{Sty})_2-\text{SO}_2$ sequences of the normal copolymer. The marked retarda-

Table I. Properties and exposure parameters of poly(vinyl arene sulfones)

Name	Monomer formula	(Vinyl arene / SO ₂) copolymer	ϵ	λ max (nm)	Sensitivity (Jcm ⁻²)
Poly(styrene sulfone)		2	200	265	18.4
Poly(4-vinylbiphenyl sulfone)		2	16,000	250	6.0
Poly(1-vinylnaphthalene sulfone)		This material was not further investigated since yields were very low			
Poly(styrene-co-acenaphthalene sulfone)*		2 (25 mole % AcN)	7,000 200	290 320	<0.50

* Acenaphthalene did not form a homopolysulfone. Attempts were also made to synthesize the polysulfone from N-vinylcarbazole but were unsuccessful.

Table II. Analysis of PASS samples*

Sample No.	Initial mole feed composition sty/AcN/SO ₂	Initiation	C (%)	H (%)	S (%)	%AcN (u.v. spectrum)	Comments
2	3/1/15	tBuOOH at 0°C	70.12 (71.6)	6.18 5.65	11.48 (11.3)	14 (13.4)	2/1 copolymer with approximately every 8th styrene unit replaced by an AcN unit
3	3/1/15	AIBN at 50°C	75.87 (75.86)	5.77 5.74	9.10 9.19	23 (22)	5/2 copolymer with approximately every 5th styrene unit replaced by an AcN unit
4	5/1/15	AIBN at 50°C	72.92 (73.6)	6.05 5.65	10.27 10.26	20.8 (19.5)	11/5 copolymer with 2 AcN units per 11 vinyl arene units

* Values shown in parentheses are theoretical values based on assumed composition.

tion of the over-all rate indicates a kinetically unfavorable addition reaction to acenaphylene and of the acenaphthylene radical to SO₂. Thus the reaction must be carried out at moderate temperatures in order to obtain reasonable yields of product. The upper limit will, however, be determined by reversibility of the addition of SO₂ (ceiling temperature considerations) which tends to reduce its incorporation into the polymer. The rate retardation by acenaphthylene also results in a substantial reduction in molecular weight. This, alone, reduces the photosensitivity which is dependent on the rate of separation of molecular weight distributions; this rate is dependent on the initial molecular weight (5).

We found that cationic homopolymerization could sometimes occur readily in these systems but that it could be suppressed by the addition of small amounts of dimethylformamide. The amide was added routinely to avoid this undesired side reaction.

Film properties.—It was observed that, upon spray developing the exposed areas of the substrate, the unexposed areas developed a "frosted" appearance after extended spraying. This was not observed in the exposed areas which developed normally. Microscopic examination of the frosted regions showed that a myriad of semimicro cracks had developed in the film. In several cases, the film had markedly pulled away, exposing large areas of substrate. Some photomicrographs of these regions are shown in Fig. 2. This effect was only observed in films with thickness > 300 nm. At thicknesses ≤ 300 nm, the resists developed normally, leaving the unexposed film completely intact.

Several reasons may be advanced for this phenomenon. It was thought that the effect could be due to residual stress in the film which was not annealed during prebaking (the resists were initially prebaked at 100°C). It is generally considered advisable to prebake above the glass transition temperature in order to remove residual stress from the film. The T_g , as measured by differential thermal analysis, was found to

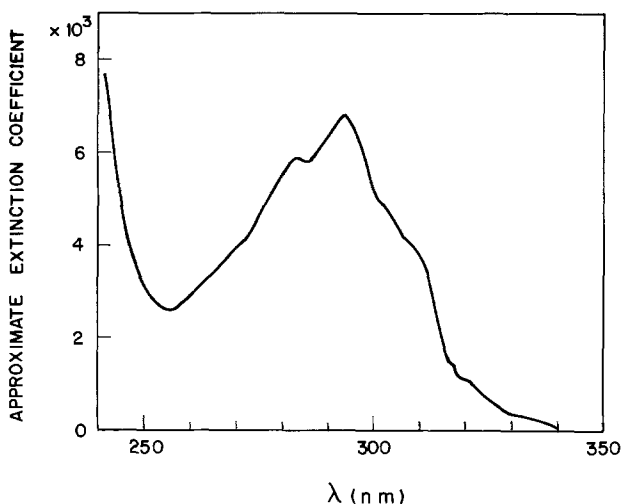


Fig. 1. U.V. absorption spectrum of poly(acenaphthalene styrene) sulfone.

be 186°C. Thermal degradation of the resist did not occur until 275°C. TGA and DTA analysis results are shown in Fig. 3. Some decrease in the tendency of the resist to crack was observed on increasing the prebaking temperature to 200°C but it was never entirely eliminated.

It appears that the reason for cracking of the film lies in the extreme brittleness of the film. It was not even possible to cast a film on mercury for infrared



Fig. 2. Micrograph of "frosted" unirradiated regions of developed film showing development of microcracks.

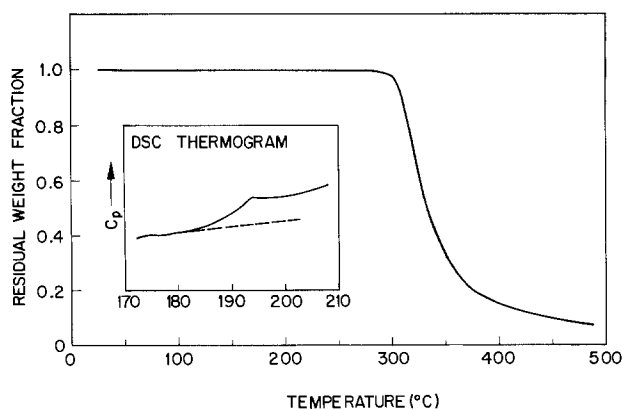
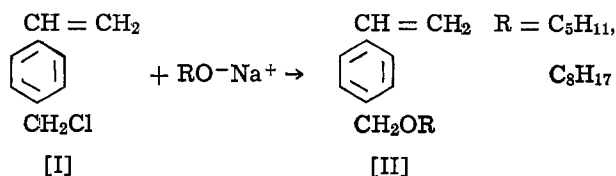


Fig. 3. TGA and DTA curves for PASS

measurement without the film breaking up during the final states of solvent evaporation.

Accordingly, attempts were made to "plasticize" the film by incorporating other groups into the polymer chain. The most practical approach was to attach groups to the *para* position of the polystyrene units in the chain. A typical approach is outlined below



These films did not crack under prolonged spraying by developing solutions. Unfortunately, the polymer derived underwent cross-linking during u.v. irradiation, presumably through cleavage of the ether bond and cross-linking to another chain.

It may be possible to obviate the cracking problem by increasing the molecular weight of the initial polymer. The addition of acenaphthylene to the mixture of styrene and SO_2 markedly reduces the over-all rate of polymerization and degree of polymerization of the resultant mixture. Reasonable yields of PASS were obtained where the initial mole ratio of styrene to acenaphthylene was 5/1. Acenaphthylene did not form a polysulfone by itself.

Resist evaluation.—The following results were obtained using sample PASS No. 4 which is a 11/5 copolymer of vinyl aryl groups/ SO_2 with two acenaphthalene units per eleven aryl groups. Evaluation was made on films of 300 nm thickness.

As can be seen in Fig. 1 acenaphthene absorbs strongly at 294 nm with a tail extending out to 330 nm. Exposures were accordingly made through the Corning 7-54 filter which transmits the 220–400 nm region of the spectrum. The sensitivity under these conditions was 500 mJ cm^{-2} . It was found that the sensitivity of the polymer film was unaltered by a 1 mm Pyrex filter (cutoff $\lambda \sim 285 \text{ nm}$). When the absorption peak of acenaphthene is matched against the output of the Hg lamp, it appears that the photochemical reaction is primarily due to the Hg line at 313 nm. Since more than half of the light passed by the 7-54 filter lies outside the polymer absorption band, the sensitivity at this wavelength is $<200 \text{ mJ cm}^{-2}$. This may be compared with a value of $\sim 60 \text{ mJ cm}^{-2}$ for the AZ positive photoresists (6).

PASS is an excellent etching mask against buffered HF. Some patterns etched in SiO_2 are shown in Fig. 4.

Conclusions

The major drawback to these resists is the region of the spectrum over which they absorb. Admittedly, they are sensitive enough, but they only use a small fraction of the output of the Hg lamp. In addition, one would need to use quartz optical systems for collimat-

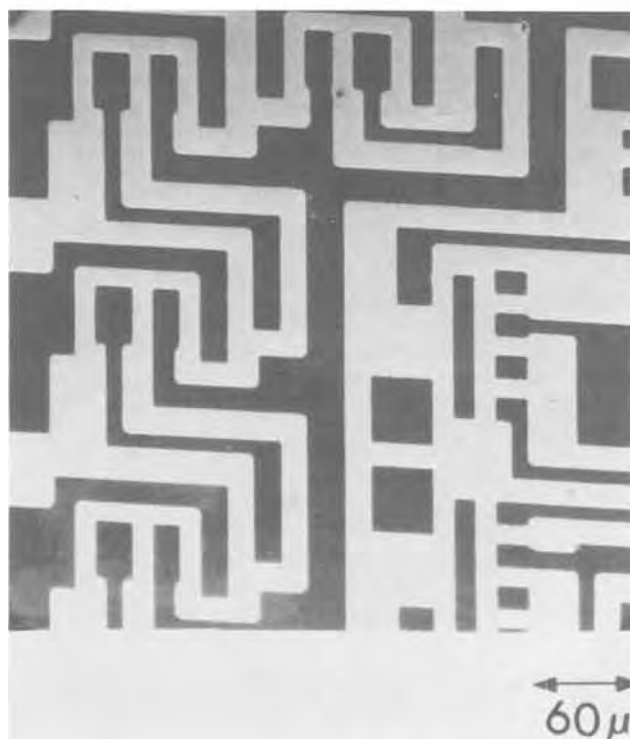
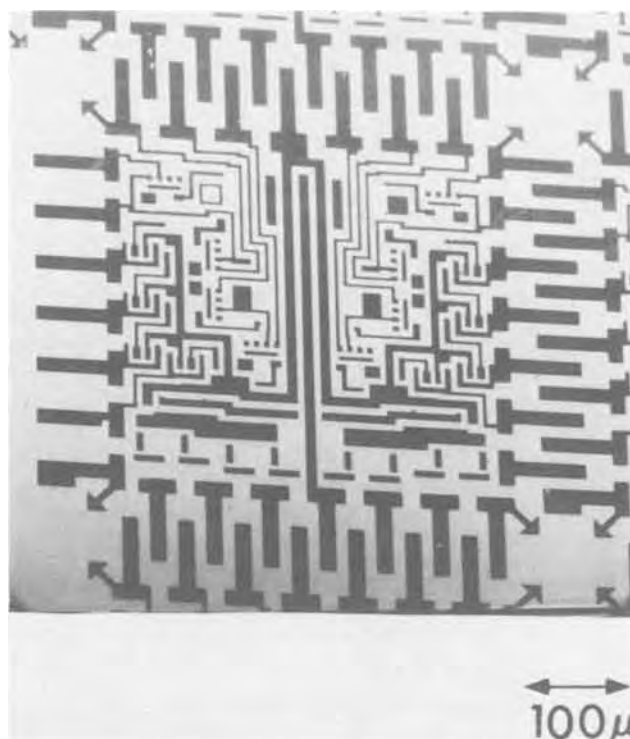


Fig. 4. Micrographs of test patterns etched in SiO_2

ing the light, etc. However, for those special situations where current available materials are unsatisfactory, as in the patterning of gallium arsenide, it is felt these resists offer a viable alternative.

It would obviously be desirable to extend the sensitivity into the 365 nm region of the ultraviolet where the lamp output is high and glass optics are usable. Studies directed toward this goal are underway.

Acknowledgments

We thank Mrs. A. H. Schiebel for synthesizing the alkoxy styrene monomers, H. Bair for the DTA measurement, and E. D. Feit for the use of his irradiation apparatus.

Manuscript submitted May 22, 1974; revised manuscript received Oct. 10, 1974.

Any discussion of this paper will appear in a Discussion Section to be published in the June 1976 JOURNAL. All discussions for the June 1976 Discussion Section should be submitted by Feb. 1, 1976.

Publication costs of this article were partially assisted by Bell Laboratories.

REFERENCES

1. A. A. Lamola and N. J. Turro, "Energy Transfer and Organic Photochemistry," p. 371, John Wiley and Sons, New York (1969).
2. M. J. Bowden and L. F. Thompson, *J. Appl. Polymer Sci.*, **17**, 3211 (1973).
3. M. P. Cava, R. H. Schlessinger, and J. P. Van Meter, *J. Am. Chem. Soc.*, **86**, 3173 (1964).
4. K. J. Ivin and J. B. Rose, *Adv. Macromol. Chem.*, **1**, 335 (1968).
5. M. J. Bowden, *J. Polymer Sci.*, **49**, 221 (1975).
6. M. S. Htoo, *Photo Sci. Eng.*, **12**, 169 (1968).

Comparison of Group IV and VI Doping by Implantation in GaAs

D. Eirug Davies, J. K. Kennedy, and C. E. Ludington

Air Force Cambridge Research Laboratories, Air Force Systems Command, Bedford, Massachusetts 01730

ABSTRACT

Factor important in attaining higher n-type conductivity on implanting GaAs have been investigated. These are reflected in a comparison of Group IV and VI dopants where the difference in behavior can be ascribed to the different sublattice occupation. The importance of Ga outdiffusion with SiO₂ encapsulated layers is seen on incorporating Ga within the oxide prior to initiating any heat-treatment. For sulfur, the electrical activity is doubled by the presence of the oxide gallium. Such an oxide is detrimental for implanted Si⁺ layers and indicates that some Ga outdiffusion is desirable. Presumably the same applies and inadvertently occurs with the traditionally simpler p-type implants. The annealing of S⁺ and Se⁺ implants with a dose-dependent, optimum annealing temperature differs significantly from Si⁺ which requires higher annealing for comparable doping. The advantage gained by implanting Group VI dopants at elevated temperatures is not as pronounced with Si and in this respect Si resembles the p-type dopant Zn which does not exhibit any strong dependence on implantation temperature.

One of the limiting factors in GaAs technology is the difficulty of forming thin, heavily doped n-type regions. In diffusion, problems can arise in working with arsenic overpressures and through many of the dopants reacting chemically with the GaAs wafer surface. When the dopants are introduced by implantation, it is difficult to get a substantial fraction electrically active and uncompensated. Details of early implantation work have been given by Allen (1) while more recent results are summarized by Eisen (2).

Both Group IV and VI elements can be used for n-type doping in GaAs. While Group VI elements are n-type dopants on the As sites, Group IV elements are amphoteric and in contrast exhibit n-type conductivity on the Ga sites. Thus, implanted Group IV and VI ions might be expected to behave somewhat differently and particularly during postimplantation annealing.

An area that has received considerable attention in investigating n-type implants is surface encapsulation. Such a layer is required to prevent thermal erosion that otherwise occurs during annealing. The simplest dielectric to apply is SiO₂ and though it fulfills its initial intent of containing the arsenic, Ga will outdiffuse into the oxide (3). While this Ga loss may be detrimental for Group VI dopants, a certain concentration of Ga vacancies so formed could conceivably benefit Si and other Group IV dopants.

All Group VI dopants exhibit better conductivity when implanted at elevated temperatures, in addition to the usual postimplantation annealing. Foyt *et al.* (4) reported the most efficient Se doping as occurring at the upper end of the room temperature to 500°C range

investigated. Better Te doping was obtained by Harris *et al.* (5) when implanting at 150°C rather than at room temperature. For S, an increase in utilization as dopants occurs ~150°C (6), coinciding with the temperature required to avoid lattice disorder (7), and no further improvement occurs at higher temperatures (up to 500°C). As no significant reduction in compensation occurs on implanting hot (6), the inferior room temperature results are attributed to the failure of these ions when so implanted to act as substitutional dopants on the arsenic sublattice. Thus, Group IV elements would not necessarily exhibit the same behavior with regard to implantation temperature in becoming n-type dopants on Ga sites. In this respect, Si or Sn might be expected to follow p-type dopants such as Zn which does not show any great dependence on implantation temperature (8, 9).

Here, S, Se, and Si have been implanted with the intent of comparing and contrasting their annealing behavior. Earlier work on compensation has indicated that even though annealing occurs at 225° and 525°C, this compensation arising from irradiation defects is still only partially recovered at least up to 600°C (10). As a consequence, any n-type doping regardless of the dopant implanted will require annealing to well over 600°C. Annealing temperatures used on this study range from 700° to 900°C. The influence of Ga loss into SiO₂ has been investigated by the use of oxides containing an initial quantity of Ga prior to any outdiffusion. Some implants have also been annealed using Si₃N₄ and AlN instead of SiO₂. Finally, the implantation temperature dependence of Si, taken as representative of the Group IV dopants, is compared to the Group VI dopant behavior.

Key words: GaAs doping, implantation, surface encapsulation.

Experimental

Epitaxial GaAs grown by the hydride vapor phase method has been used in the present work. It is grown 2° off the <100> direction and to a thickness of

1-1½ μm. The doping is held $\approx 10^{15}$ cm⁻³ and will have negligible effect compared to the implanted conductivity to be investigated. Any dependence of the implanted electrical activity on the initial material is minimized by confining the work to this epitaxial material which is grown as required under near identical conditions. In contrast, some earlier Si implants into chrome-doped bulk GaAs exhibited carrier concentrations and mobilities that were only around 75% of what is generally attainable with the epitaxial layers.

The SiO₂ used as a surface encapsulant is spun on from an alcohol solution.¹ Following an HF cleaning treatment the oxide is applied and spun at 3000 rpm. The oxide is baked at 180°C and film thicknesses are generally ~1700Å. The gallium-SiO₂ layers are similarly applied using oxides meant primarily to be Ga sources for diffusion into silicon and containing Ga to concentrations of 10²¹ cm⁻³. The Si₃N₄ and AlN are sputtered on (using targets of the same composition and not reactively). The AlN contains considerable oxide while the Si₃N₄ is relatively pure. Wafer deterioration becomes physically apparent with the oxide encapsulation after heat-treatment to 875°-900°C. Si₃N₄, on the other hand, can withstand temperatures up to at least 925°-950°C.

The encapsulating layers are generally applied prior to implantation and so protect the GaAs during both implantation and postannealing. Most of the S⁺ implants to be reported were carried out at 500°C while temperatures within the 200°-300°C range were used for both Se and Si. It should be noted that as there is no advantage in implanting S⁺ at 500°C rather than at 200°-300°C (6), the lower temperatures should also be preferred for S⁺ (and particularly if implanting prior to applying the surface encapsulant were required).

All the implants have been performed at 1 MeV. Other than one series of S⁺ implants at 3 × 10¹⁴ cm⁻² a dose of 10¹⁴ cm⁻² has been used throughout. SiH⁺ has been implanted instead of Si⁺ to avoid contamination from other mass 28 species. Annealing is carried out in a nitrogen ambient for 10 min. For performing Hall measurements tin contacts are alloyed into the implanted layer and no contracting problems are encountered at the dose levels mentioned.

Results

Table I compares the electrical activity resulting from sulfur implants when SiO₂ containing Ga, "pure" SiO₂, and Si₃N₄ are used as the encapsulants. The variation in implantation temperature (170°-360°C) should have minimal effect on the resulting activity. All the samples were implanted to a dose of 10¹⁴ cm⁻² and then similarly annealed at 825°C for 10 min. It will be observed that the highest active concentration is given by the Ga-SiO₂ encapsulated layer, indicating that the presence of Ga has a direct bearing on the resulting activity. Si₃N₄, though better than straight SiO₂, does not at present measure up to Ga-SiO₂. Some implants were also undertaken with AlN as the protective layer but the corresponding activity was much

¹ Commercially available from Emulsitone, Whippany, New Jersey.

Table I. Doping efficiency of 10¹⁴ S⁺ cm⁻² implants annealed at 825°C with different encapsulants

Encapsulant	T _{impl.} (°C)	R _s (ohm/□)	μ (cm ² /V-sec)	N _s (cm ⁻²)
Ga-SiO ₂	360	51	3100	4.0 × 10 ¹⁸
	170	57	2750	4.0 × 10 ¹⁸
Si ₃ N ₄	240	81	3100	2.5 × 10 ¹⁸
SiO ₂	299	99	3150	2.0 × 10 ¹⁸
	240	127	2050	2.4 × 10 ¹⁸

lower with only 1-2 × 10¹³ cm⁻² becoming electrically active. It should be borne in mind that as no information has been obtained on the relative effectiveness of the encapsulants in retaining the as-implanted distributions, the increase in integrated (sheet) concentrations may also reflect some profile widening.

The annealing temperature of 825°C used in Table I is near the optimum annealing temperature for 10¹⁴ cm⁻² S⁺ implants. This can be seen in Fig. 1 where both the sheet carrier concentration and the mobility are shown as a function of annealing temperature. The maximum concentration of 3.6 × 10¹³ cm⁻² is lower than the 4 × 10¹³ cm⁻² value given in Table I for similarly capped (Ga-SiO₂) implants. The reduction presumably arises from the 500°C implantation temperature used in Fig. 1 and which is marginally close to the onset of a deterioration in activity that occurs on implanting at temperatures \lesssim 500°C (6).

The improvement in mobility at 750°-800°C despite the accompanying rise in free carrier concentration suggests that considerable defect annealing is occurring. Relocation of S onto substitutional sites alone would lead to increased impurity scattering and a reduction in mobility. The maximum mobility of 3000 indicates a high degree of damage recovery. These mobilities correspond to 10¹⁸ cm⁻³ doping in bulk GaAs.

It is presumed that the fall off in conductivity that occurs above 825°C is surface related. The activity still attainable at higher temperatures for Si₃N₄ encapsulated Te implants (7) suggests that certain dielectrics may not be as restrictive as SiO₂ in this respect. More clarification is required, however. The same optimum annealing feature is followed at higher doses as can be seen in Fig. 2 for a 3 × 10¹⁴ cm⁻² dose level. At 800°C both the carrier concentration and mobility are close to what was obtained from the 10¹⁴ cm⁻² implant with similar annealing. The mobility then falls to reflect the higher active carrier concentration and, despite using similarly applied Ga-SiO₂, the optimum annealing condition of 800°-825°C in Fig. 1 shifts to 850°-875°C.

Similar annealing features are exhibited by Se⁺. This is shown in Fig. 3 where Se⁺ has been implanted to doses of 10¹⁴ cm⁻² at 250°C and annealed with SiO₂ containing Ga. The highest activity occurs at the same annealing temperature seen in Fig. 1 with sulfur. The mobilities are generally lower than those already observed for sulfur and what can be obtained from Si⁺ implants.

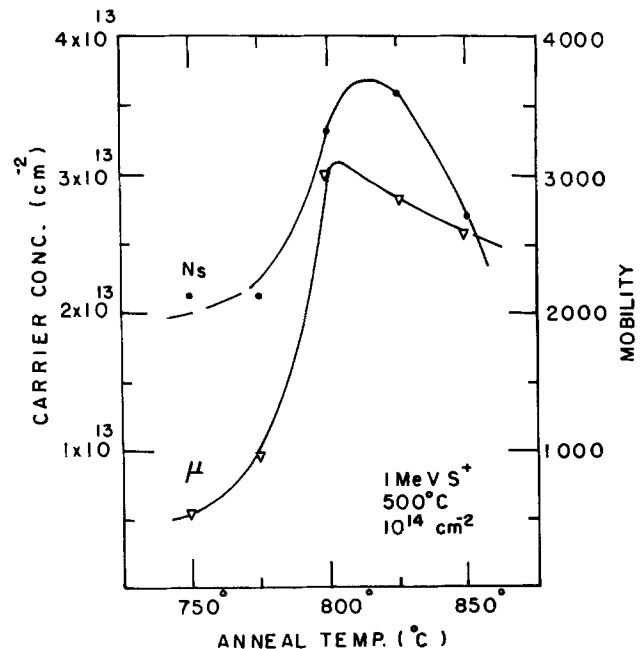


Fig. 1. Dependence of the sheet carrier concentration and mobility on annealing temperature for sulfur encapsulated with Ga-SiO₂.

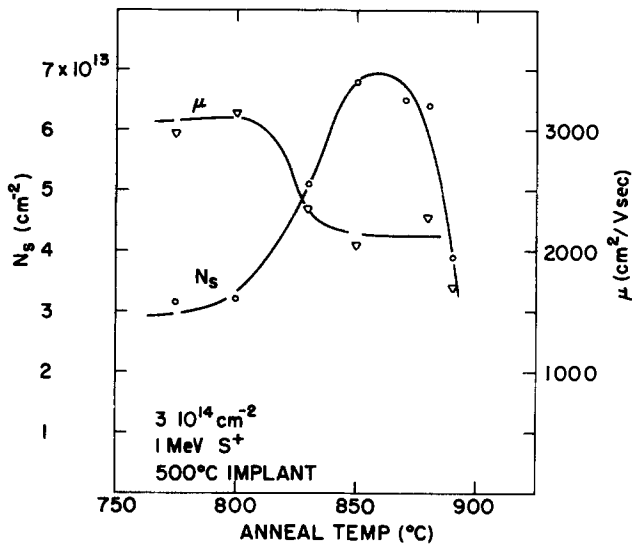


Fig. 2. Annealing of sulfur showing the higher temperatures required for the heavier 3 × 10¹⁴ cm⁻² dose level.

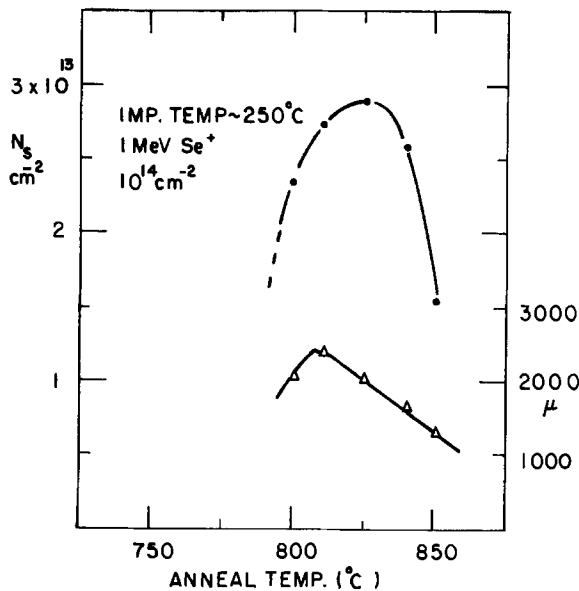


Fig. 3. Annealing of selenium-implanted layers passivated with Ga-SiO₂.

Turning to Group IV dopants, the influence of various dielectric coatings on the annealing of Si⁺-implanted layers is shown in Table II. Doses of 10¹⁴ cm⁻² were implanted at 250°-300°C and then annealed to 800°C. Contrary to the behavior with S⁺, the presence of Ga within the oxide now becomes detrimental to achieving high electrical activity. It thus appears again that Ga-SiO₂ reduces the out-diffusion of Ga but here, unlike with S⁺, such an out-diffusion seems desirable. The Si₃N₄ and AlN annealed layers are intermediate between the two oxide extremes.

Table II. Doping efficiency of 10¹⁴ Si⁺ cm⁻² implants annealed at 800°C with different encapsulants

Encapsulant	T _{impl.} (°C)	R _s (ohm/□)	μ(cm ² /V-sec)	N _s (cm ⁻²)
Ga-SiO ₂	260	496	2100	0.6 × 10 ¹³
AlN	300	340	2300	0.8 × 10 ¹³
	290	149	3000	1.4 × 10 ¹³
	250	142	2600	1.7 × 10 ¹³
Si ₃ N ₄	270	139	2500	1.8 × 10 ¹³
SiO ₂	290	99	3000	2.1 × 10 ¹³
	240	87	3000	2.4 × 10 ¹³

The 800°C annealing for the implants of Table II is not the most ideal for Si. This is illustrated in Fig. 4 where it can be seen that Si does not exhibit the 800°-825°C optimum temperature observed earlier with both S⁺ and Se⁺ at the same 10¹⁴ cm⁻² dose. These Si⁺ implants, at 220°-240°C, were annealed using Ga-free SiO₂. The sheet carrier concentrations up to 3.6 × 10¹³ cm⁻² (R_s = 52 ohm/□) are limited by the temperature which the oxide can withstand and which presently is ~900°C. Possibilities for improvement include overcoating the oxide with a nitride layer which would withstand higher temperatures or going to an oxynitride layer which may allow some Ga out-diffusion.

The corresponding mobilities together with those of other Si⁺ layers annealed with various oxides including As-SiO₂ are shown in Fig. 5. An improvement occurs at ~825°C but this stage is not as pronounced as that seen ~775°C with S⁺ (Fig. 1).

The effect of implantation temperature on S, Se, and Si layers can be seen in Table III. All ions have been implanted above 150°C as well as at room temperature. The sulfur results are taken from earlier work (6) while those for Se are in agreement with Foyt *et al.*

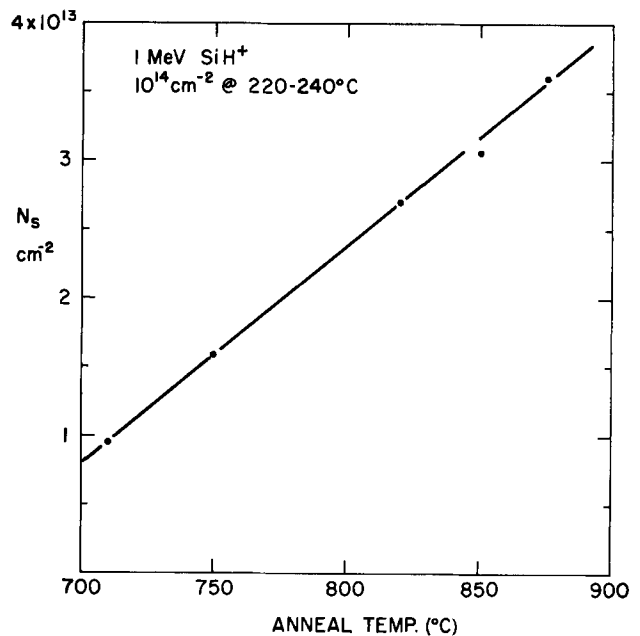


Fig. 4. Annealing of silicon with SiO₂ as the encapsulant

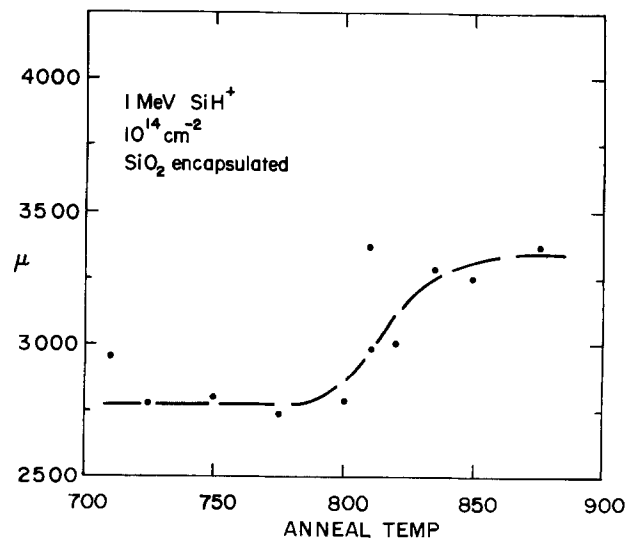


Fig. 5. Dependence of mobility on annealing for silicon implanted layers.

Table III. Effect of implantation temperature on S⁺, Se⁺, and Si⁺ electrical activity

Ion	T _{Impl.} (°C)	T _{Anneal} (°C)	Encapsulant	μ(cm ² / V-sec)	N _s (cm ⁻²)	Heated N _s
						R.T. N _s
S	360	825°	Ga-SiO ₂	3100	4.0 × 10 ¹³	2.5
	20	825°	Ga-SiO ₂	3000	1.6 × 10 ¹³	
Se	280	825°	Ga-SiO ₂	2050	2.9 × 10 ¹³	3.2
	20	825°	Ga-SiO ₂	1650	0.9 × 10 ¹³	
Si	235	825°	As-SiO ₂	2750	2.2 × 10 ¹³	1.2
	20	825°	As-SiO ₂	2700	1.9 × 10 ¹³	
Si	295	810°	SiO ₂	3000	2.3 × 10 ¹³	1.3
	20	810°	SiO ₂	3350	1.8 × 10 ¹³	

(4). The most significant factor is the relative insensitivity of Si to implantation temperature. It is clear that Si becomes substitutional more readily than the Group VI dopants when implanted at room temperature.

The comparatively lower activity in Table III that is shown for Si⁺ arises through annealing at similar temperatures to the S⁺ and Se⁺ layers rather than at the more ideal higher temperatures indicated by Fig. 4. Both SiO₂ and As-SiO₂ have been used in annealing these Si⁺ implants. It may be noted that incorporation of As within the oxide does not produce any improvement comparable to that obtained for S with Ga-SiO₂. It appears that As loss is not a problem, in agreement with Gyulai *et al.* (3) who established from back-scattering measurements that Ga alone out-diffuses through SiO₂.

In summary, significant differences arise in the behavior of implanted S⁺ or Se⁺ and Si⁺. These differences are attributed to Group VI and Group IV dopants occupying different sublattice sites. Incorporation of Ga into SiO₂ resulted in a marked improvement with S⁺ implants but was detrimental to achieving high conductivity with Si. It is concluded from such behavior that the gallium within the oxide at least partially inhibits the gallium loss from the wafer surface. Further, some Ga loss seems desirable in the case of Si⁺ and presumably the same applies and inadvertently occurs on implanting Group II p-type dopants which can in general be more readily rendered electrically active (2). The annealing characteristics of S and Se with an optimum annealing temperature contrast sharply with Si which requires higher annealing temperatures to achieve similar doping levels. Finally, the substantial difference in the electrical activity resulting from implanting Group VI elements at room temperature and $\lesssim 150^\circ\text{C}$ does not apply to Si. In this respect Si resembles Zn which does not exhibit any strong dependence on implantation temperature.

Acknowledgment

We would like to thank Dr. Genser of Emulstone for valuable advice on the use of spin on oxides. The technical assistance of M. Deane and J. Hawley with sample preparation is gratefully acknowledged.

Manuscript submitted March 5, 1975; revised manuscript received June 9, 1975.

Any discussion of this paper will appear in a Discussion Section to be published in the June 1976 JOURNAL. All discussions for the June 1976 Discussion Section should be submitted by Feb. 1, 1976.

Publication costs of this article were partially assisted by Air Force Cambridge Research Laboratories.

REFERENCES

1. R. M. Allen, "European Conference on Ion Implantation," p. 126, Peter Peregrinus Ltd. (1970).
2. F. H. Eisen, Presented at Fourth Int. Conf. on Ion Implantation, Osaka, Japan, 1974.
3. J. Gyulai, J. W. Mayer, and I. V. Mitchell, *Appl. Phys. Letters*, **17**, 332 (1970).
4. A. G. Foyt, J. P. Donnelly, and W. T. Lindley, *ibid.*, **14**, 372 (1969).
5. J. S. Harris, F. H. Eisen, B. Welch, J. D. Haskell, R. D. Pashley, and J. W. Mayer, *ibid.*, **21**, 601 (1972).
6. D. E. Davies, S. Roosild, and L. Lowe, *Solid State Electron.*, **18**, 733 (1975).
7. F. H. Eisen, J. S. Harris, B. Welch, R. D. Pashley, D. Sigurd, and J. W. Mayer, in "Ion Implantation in Semiconductors and Other Materials," B. L. Crowder, Editor, p. 631, Plenum Press, New York (1973).
8. V. M. Zelevenskaya, G. A. Kachurin, N. B. Pridachin, and L. S. Smirnov, *Soviet Phys.-Semiconductors*, **4**, 1529 (1971).
9. Y. Yuba, K. Gamo, K. Masuda, and S. Namba, *Japan J. Appl. Phys.*, **13**, 641 (1974).
10. D. E. Davies, J. K. Kennedy, and A. C. Yang, *Appl. Phys. Letters*, **23**, 615 (1973).

Vapor-Phase Etching and Polishing of Gallium Arsenide Using Hydrogen Chloride Gas

Rajaram Bhat,* B. Jayant Baliga,**,1 and Sorab K. Ghandhi†

Electrical and Systems Engineering Department, Rensselaer Polytechnic Institute, Troy, New York 12181

ABSTRACT

Vapor-phase etching of (100) and $\bar{1}\bar{1}\bar{1}$ GaAs substrates has been conducted in HCl-H₂-AsH₃ gas mixtures. Specular surfaces, suitable for epitaxy, were obtained for substrates doped with Cr, Te, Si, and Zn when the substrates were etched at temperatures above 870°C. It is shown that the etching reaction is mass-transport limited at these temperatures for both (100) and $\bar{1}\bar{1}\bar{1}$ surfaces. At lower temperatures, faceting results from the unequal etch rates for the different orientations. Etch rates of 0.02-14 $\mu\text{m}/\text{min}$ were obtained in this study.

The capability for *in situ* etching of substrates has often been incorporated in systems for vapor-phase epitaxy to insure a clean and damage-free surface prior to growth. It is an inherent feature of gallium arsenide epitaxial systems utilizing arsenic trichloride but details of the etching step are not available. Lin, Chou, and Miller (1) have studied the vapor-phase etching of $\bar{1}\bar{1}\bar{1}$ and (100) gallium arsenide using hydrogen-water vapor mixtures. Shaikh, Chou, and Donaghey (2) have studied hydrogen chloride etching of (100) gallium arsenide in a hydrogen-arsine ambient. The emphasis in their study was on the modeling of the mass transfer process to account for the etch rates observed experimentally. HCl etching of Si-, Te- and Sn-doped (100) GaAs surfaces has been studied by Moon and James (3) using Auger electron spectroscopy but no details of the surface morphology were published.

In this paper we wish to report studies conducted on the vapor-phase etching of a variety of gallium arsenide substrates using anhydrous hydrogen chloride gas in a hydrogen and arsenic ambient. High quality surfaces, with etch rates ranging from 0.02-14 $\mu\text{m}/\text{min}$, were obtained for (100) and $\bar{1}\bar{1}\bar{1}$ substrates, at temperatures exceeding 870°C. The etching reaction for all orientations was mass-transport limited at these temperatures. Under these conditions the partial pressure of arsenic did not significantly influence the etch rate or surface morphology, provided sufficient arsenic was present to prevent decomposition.

Experimental Conditions

Apparatus.—Etching was carried out in a 50 mm ID, 37 cm long, rf heated, horizontal quartz tube. A 50 by 25 by 13 mm graphite susceptor, coated with pyrolytic graphite, was placed approximately 16 cm from the input end of the reaction chamber, at an angle of 7° to the direction of gas flow. Temperature was monitored using a Pt/Pt-13% Rh thermocouple enclosed in a quartz sheath and inserted into the susceptor. The temperature was verified using infrared pyrometric measurements. Gases were delivered to the reaction chamber through stainless steel tubing, except in the case of HCl where Monel tubing was used to minimize contamination. The apparatus was similar to the one used for the growth of III-V compounds (4).

Gases.—The purity of the hydrogen chloride gas was found to have considerable effect on the quality of the etched surface. Electronic grade hydrogen chloride gas obtained from Matheson Gas Products² resulted in

poor surfaces under all experimental conditions. Similar difficulties have been reported by Amick, Roth, and Gossenberger (5) in the etching of germanium. Etching with electronic grade HCl, diluted to 1% in six-nines purity hydrogen,³ gave excellent results. The arsine gas used in this investigation was either a 2% mixture in five-nines purity hydrogen² or a 10% mixture in six-nines purity hydrogen.³ Ultrahigh purity hydrogen,² passed through a deoxidizer and molecular sieve,⁴ was used as the carrier gas.

Substrates.—Most experiments were performed with boat-grown, (100) oriented, Te-doped GaAs as the substrates.⁵ Some investigations were also conducted using boat-grown (100) Cr- and Zn-doped⁵ GaAs, $\bar{1}\bar{1}\bar{1}$ Te-doped,⁶ Zn-doped,⁶ Cr-doped,⁶ and Si-doped⁷ GaAs substrates. All wafers were obtained chemi-mechanically polished on one side. The wafers were degreased in methanol, etched in Caro's etch [10H₂SO₄ (97%):1H₂O₂ (30%):1H₂O] for 2 min at room temperature, rinsed in deionized water, and blown dry in filtered air after a final rinse in methanol. This procedure ensured a featureless, damage-free surface prior to *in situ* etching. More elaborate cleaning procedures, such as successive boiling in trichloroethylene, acetone, and methanol were attempted with no significant improvement in the quality of the etched wafer.

Procedure.—Substrates measuring 5 by 6 mm were placed centrally on the susceptor. The system was first purged with prepurified argon (2 liters/min) for 15 min, followed by a 5 min purge with ultrahigh purity hydrogen (3 liters/min). The susceptor was then heated to the etching temperature after introducing the required amount of arsine to prevent decomposition of the GaAs substrate. Substrates were maintained in hydrogen for 15 min at the etching temperature. This step served to remove traces of oxide on the gallium arsenide substrates and resulted in improving the quality of the etched surfaces. HCl gas was then introduced at the desired rate of flow and the substrates were usually etched for 2 min. The system was maintained at the etching temperature for 3 min, after the HCl gas was shut off. Typical flow rates were 3-18 ml/min for arsine gas,⁸ 250-8100 ml/min for hydrogen, and 0.1-5 ml/min for HCl gas.⁸ Typical etch rates ranged from 0.02-23 $\mu\text{m}/\text{min}$ at 900°C.

³ Precision Gas Products, Inc., Rahway, New Jersey 07065.

⁴ The use of a Pd-diffuser did not result in any improvement in the quality of the etched wafers.

⁵ Electronic Materials Corporation Pasadena, California 91107.

⁶ Texas Materials Laboratory, Inc., Garland, Texas 75041.

⁷ Supplied by Dr. W. Tantraporn, General Electric Company, Schenectady, New York 12301.

⁸ In this paper, flow rates for AsH₃ and HCl are all quoted in terms of the actual arsine and hydrogen chloride content of the diluted gas.

* Electrochemical Society Student Member.

** Electrochemical Society Active Member.

† Electrochemical Society Life Member.

¹ Present address: General Electric Company, Research and Development Center, Schenectady, New York 12301.

² Matheson Gas Products, East Rutherford, New Jersey 07073.

Key words: vapor etching, vapor polishing, gallium arsenide, hydrogen chloride gas, epitaxy.

Etch rate definition and determination.—Figure 1 shows the decrease in substrate thickness with increasing etch time for a typical etching experiment. The decrease in GaAs substrate thickness is seen to be a linear function of time, for times less than approximately 5 min. The deviation from linearity for etch times greater than 5 min is due to the loss of planarity of the substrates. Based on these considerations, it was decided that all measurements of etch rate would be made for an etch period of 2 min. Since the etch rate was constant for this period, it was defined in terms of the substrate thickness removed per unit time. The change in substrate thickness was obtained gravimetrically.

Experimental Results

Temperature.—The effect of temperature on etch rate was determined for (100) and (111) oriented, Te-doped GaAs substrates using a flow of 900 ml/min of hydrogen, 3 ml/min of arsine, and 2 ml/min of HCl gas. Under these conditions, the etching reaction of (100) GaAs substrates was mass-transport limited at temperatures above 850°C and kinetically controlled below this temperature with an activation energy of 1.25 eV/molecule. The etching reaction of the (111) GaAs substrates was mass-transport limited at temperatures above 870°C and kinetically controlled below this temperature with an activation energy of 1.85 eV/molecule. As expected, equal etch rates were observed at temperatures above 870°C, as shown in Fig. 2. [The data in Fig. 2 have not been corrected for the change in linear velocity with temperature (6)].

Surfaces of both (100) and (111) GaAs substrates etched below 870°C became increasingly faceted, with the simultaneous formation of either etch pits or hillocks,⁹ due to the unequal etch rates for different substrate orientations. Above 870°C, where the etch rates for the different orientations were equal, etched (100) and (111) substrate surfaces were featureless, as seen in the photomicrographs of Fig. 3 and 4.¹⁰

Chemical polishing of semiconductor substrates occurs when the etch rate for all crystallographic orientations is equal. This is achieved when the etching reaction is mass-transport limited, provided that the adsorption of the etchant on the substrate surface is independent of perturbations present on the surface (7).

⁹ Distinguished by scanning electron microscopy.

¹⁰ In this paper, all photomicrographs were taken using the Nomarski interference contrast technique.

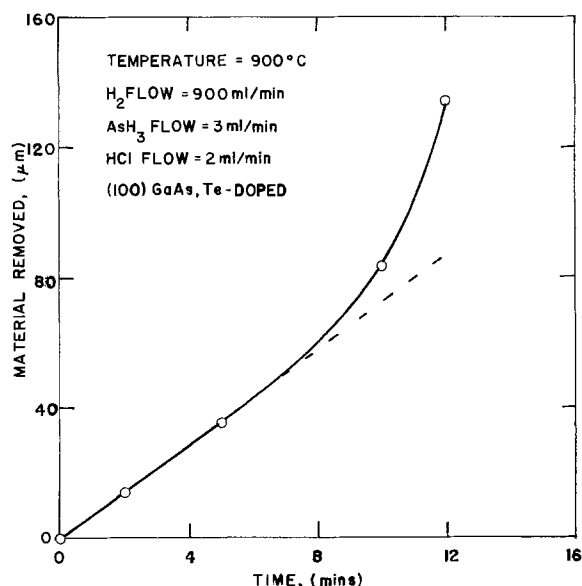


Fig. 1. Change in thickness of the wafers as a function of time

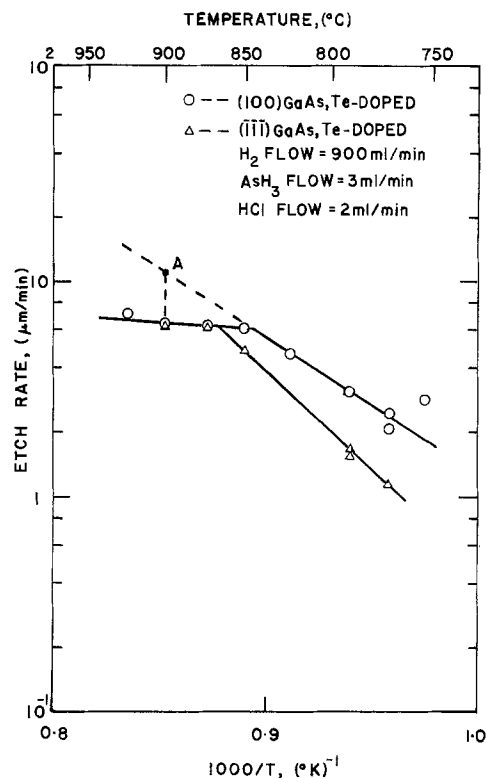


Fig. 2. Effect of substrate temperature on etch rate

The latter condition is apparently met during the vapor-phase etching of GaAs by HCl gas.

Hydrogen flow.—Figure 5 shows the variation of etch rate with hydrogen flow at 900°C for (100), Te-doped GaAs. In these experiments, the arsine and HCl gas flow was varied in proportion to the hydrogen flow to keep their partial pressures constant at 3.3×10^{-3} atm and 2.22×10^{-3} atm, respectively. It is seen that the etch rate varies linearly as the square root of the hydrogen flow for flows below 2.5 liters/min. This is because the etch rate varies directly with the rate of transport of HCl atoms to the substrate under mass-transport limited kinetics. This rate of transport varies directly with the boundary layer thickness at the substrate, and hence as the square root of the hydrogen flow under laminar flow conditions. At higher flows the etch rate saturates at 10.7 μ/min. This independence of etch rate at high hydrogen flow indicates the etching mechanism has become kinetically limited. If the data representing kinetically controlled etching shown in Fig. 2 is extrapolated to 900°C (point A), the value of the etch rate obtained is indeed the same as the observed saturated value.

The rate of transport of As to the GaAs surface decreases with decreasing hydrogen flow due to the increase in the boundary layer thickness. Consequently, substrate decomposition can be expected to occur at low hydrogen flows. This was indeed found to be the case for hydrogen flow rates below 0.45 liter/min. Verification of this fact was carried out by heating substrates under the above conditions without performing HCl etching. Surfaces of the HCl etched and the heated substrates were found to have similar features for identical hydrogen flow rates.

Arsine flow.—The effect of arsine flow on etch rate and surface quality under mass-transport limited conditions was investigated at 900°C using a hydrogen flow of 900 ml/min. It was found that at least 3 ml/min of arsine was required to prevent the decomposition of the substrate. For arsine flows between 3 and 18 ml/min, there was no appreciable change in surface quality, and the etch rate did not change within experimental error. Under similar flow conditions at 790°C,

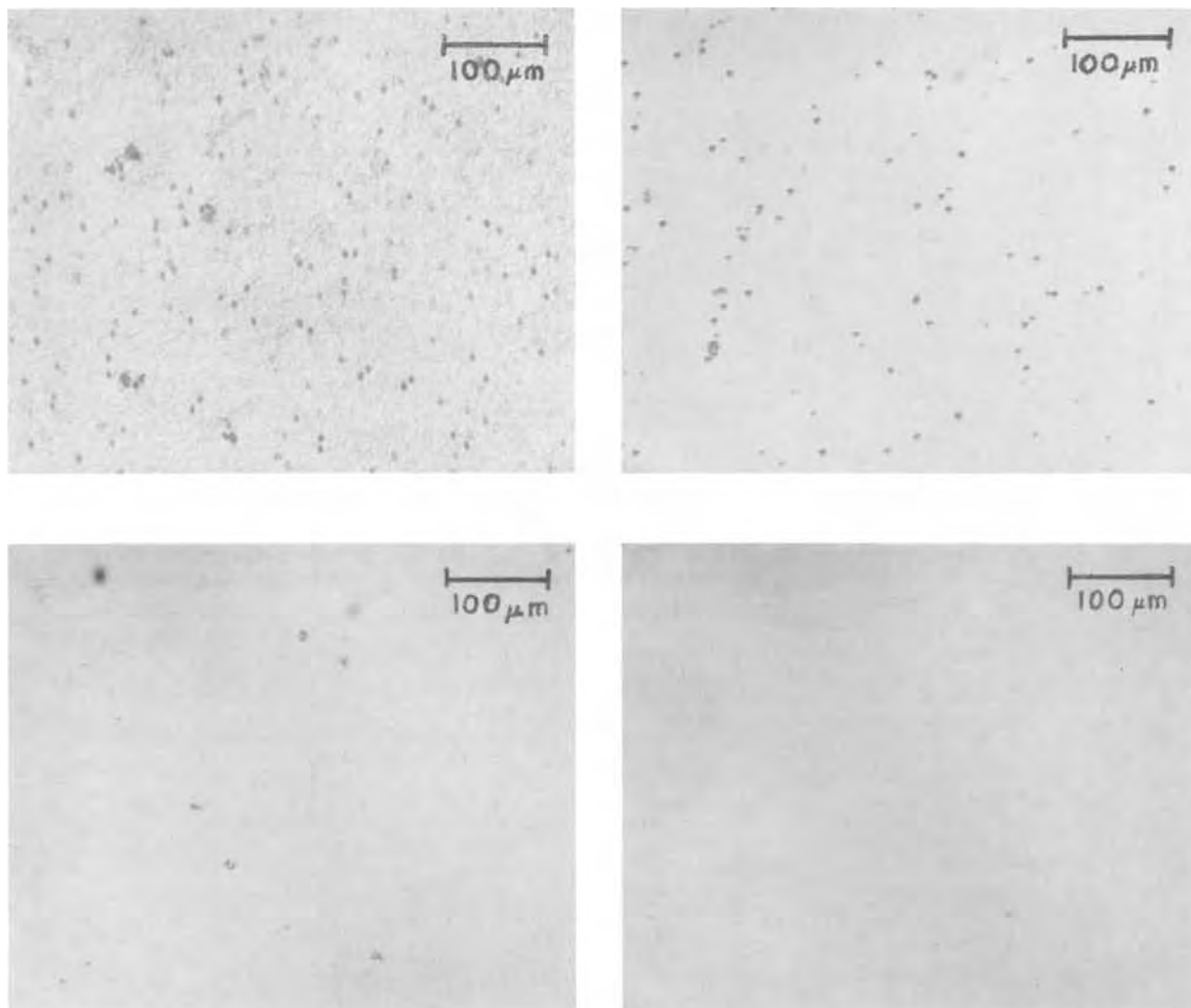


Fig. 3. Effect of temperature on the surface morphology of (100) Te-doped GaAs etched at (a, top left) 750°C, (b, top right) 825°C, (c, bottom left) 850°C, and (d, bottom right) 900°C.

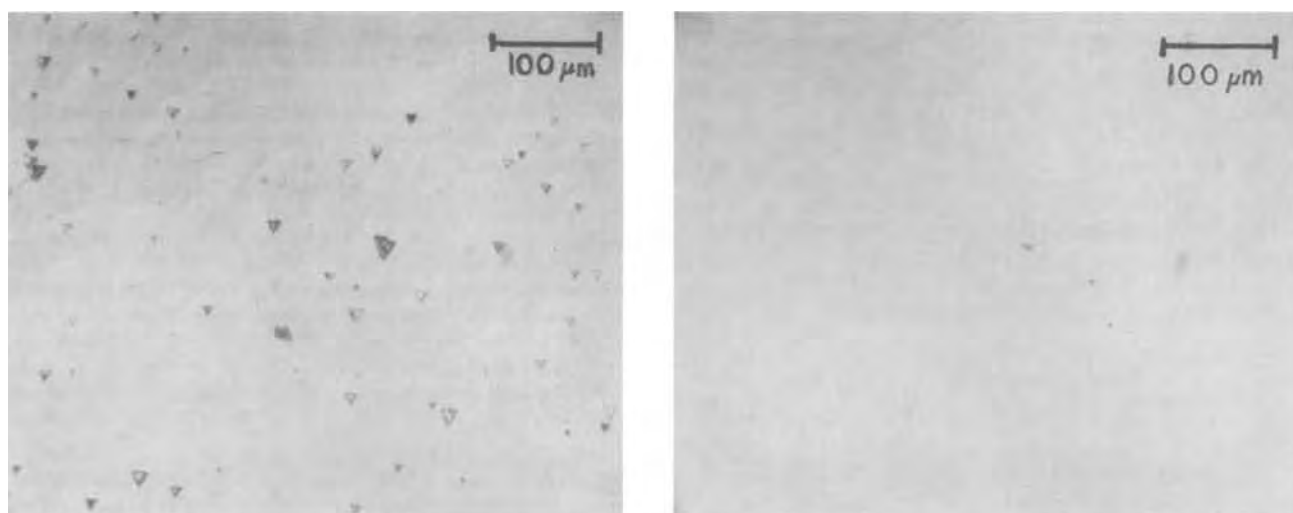


Fig. 4. Effect of temperature on the surface morphology of $(\bar{1}\bar{1}\bar{1})$ Te-doped GaAs etched at (a, left) 790°C and (b, right) 900°C

where the etching was kinetically controlled, the etch rate was found to decrease with increasing arsine flow.

HCl flow.—Figure 6 shows the etch rate of (100), Te-doped GaAs substrates as a function of the HCl gas flow. These experiments were conducted at a temperature of 900°C using a total hydrogen flow of 900

ml/min and an arsine flow of 3 ml/min. The etch rate was found to vary superlinearly with HCl concentration. Similar nonlinear dependence of the etch rate on etchant gas flow, under mass-transport limited conditions, has been observed in the vapor-phase etching of Si (8, 9) and Ge (6). Ideally, under mass-transport

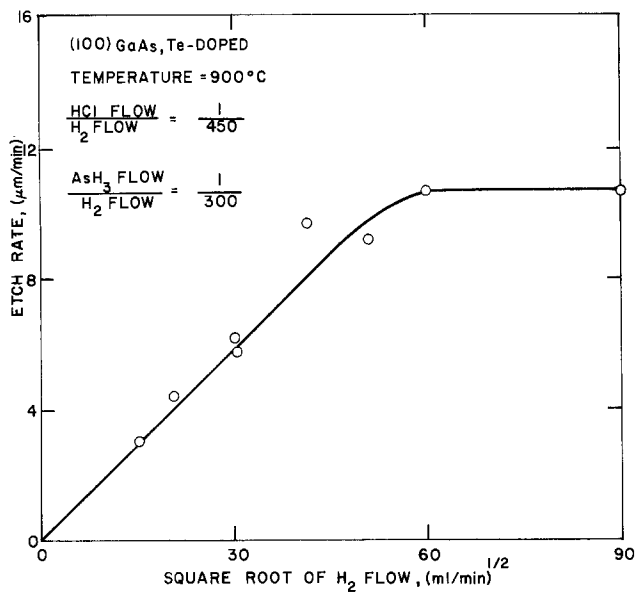


Fig. 5. Effect of hydrogen flow on etch rate

limited conditions, the etch rate should vary parabolically with the etchant concentration at low etchant partial pressures (9).

Orientation and dopant type.—The etch rate and the surface quality of (100) and $\bar{1}\bar{1}\bar{1}$ GaAs substrates with different dopants were also evaluated. The etch rate observed for Zn- and Cr-doped (100) and Si,¹¹ Zn-, and Cr-doped $\bar{1}\bar{1}\bar{1}$ GaAs substrates, under both mass-transport limited and kinetically controlled conditions, was the same as for their Te-doped counterparts. Therefore, the etch rate is insensitive to the type of dopant incorporated in the GaAs.

¹¹ Si-doped (100) GaAs was not available to us at the time this investigation was carried out.

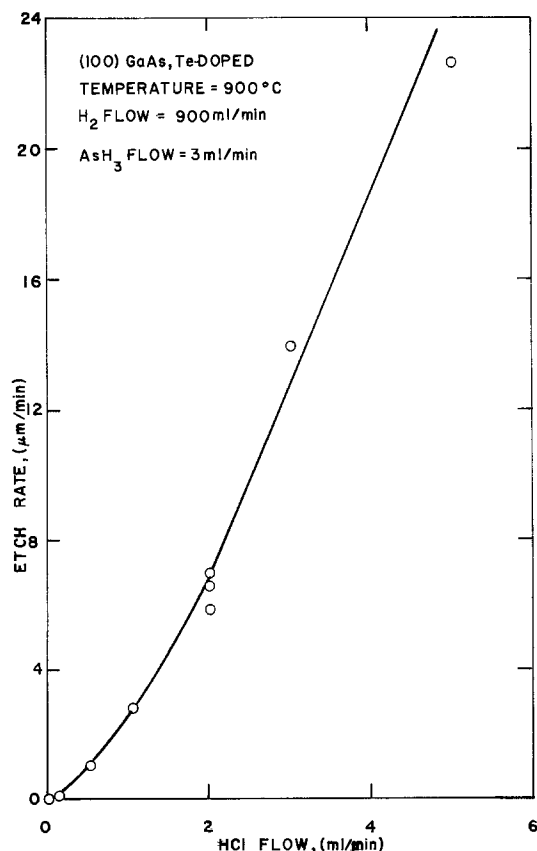


Fig. 6. Effect of HCl gas flow on etch rate

All substrates etched at 900°C using a hydrogen flow of 900 ml/min, arsine flow of 3 ml/min, and a HCl gas flow of 2 ml/min were specular to the unaided eye. However, the quality of etched (100) Cr-doped and $\bar{1}\bar{1}\bar{1}$ Si- and Cr-doped GaAs substrate surfaces was inferior to those obtained with Te- and Zn-doped GaAs substrates under microscopic examination (Fig. 7). This

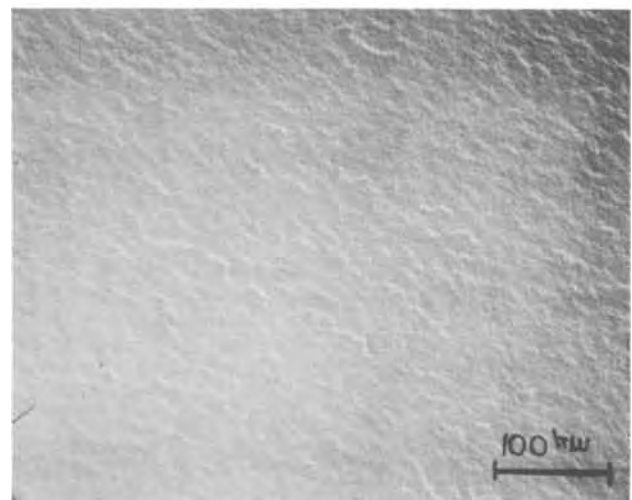
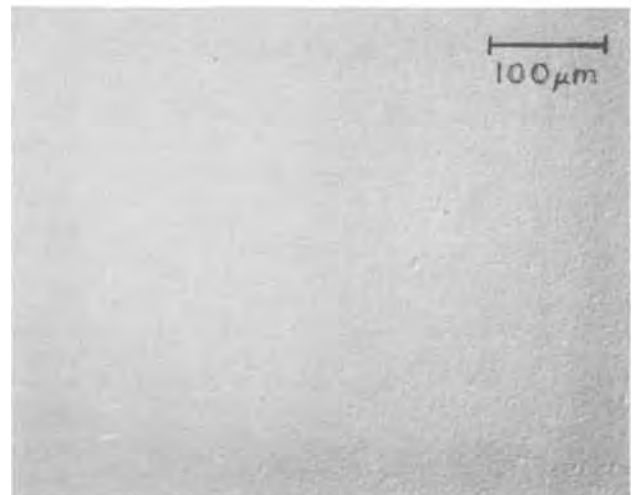


Fig. 7. Surface morphology of etched (a, top) Si-doped, $\bar{1}\bar{1}\bar{1}$ GaAs, (b, center) Cr-doped, (100) GaAs, and (c, bottom) Cr-doped, $\bar{1}\bar{1}\bar{1}$ GaAs substrates. Temperature 900°C, H₂ flow 900 ml/min, AsH₃ flow 3 ml/min, HCl gas flow 2 ml/min.

difference in etching behavior is believed to be due to greater inhomogeneities in the doping and dislocation densities in Cr- and Si-doped substrates.

Conclusions

Vapor-phase HCl etching of GaAs substrates can be performed to yield specular surfaces, suitable for epitaxy, with etch rates ranging from 0.02 to 14 $\mu\text{m}/\text{min}$, for (100) and ($\bar{1}\bar{1}\bar{1}$) Cr-, Te-, Zn-, and Si-doped GaAs substrates. A necessary condition for obtaining specular surfaces is that all orientations have the same etch rate. This condition is achieved at sufficiently high temperatures where the etch rate is mass-transport limited for all orientations. The quality of etched (100) and ($\bar{1}\bar{1}\bar{1}$) Si- and Cr-doped substrate surfaces was inferior to those obtained for Te- and Zn-doped GaAs substrates.

Acknowledgment

This work was partly supported by Grant No. GK-31332 from the National Science Foundation. The authors are indebted to Dr. W. Tantraporn for providing the Si-doped gallium arsenide and to Ms. R. Rafun for assistance in manuscript preparation.

Manuscript submitted March 24, 1975; revised manuscript received May 9, 1975.

Any discussion of this paper will appear in a Discussion Section to be published in the June 1976 JOURNAL. All discussions for the June 1976 Discussion Section should be submitted by Feb. 1, 1976.

Publication costs of this article were partially assisted by Rensselaer Polytechnic Institute.

REFERENCES

1. C. Lin, L. Chow, and K. L. Miller, *This Journal*, **117**, 407 (1970).
2. S. A. Shaikh, H. K. Chou, and L. F. Donaghey, Abstract 151, p. 364, Electrochemical Society Extended Abstracts, Spring Meeting, San Francisco, Calif., May 12-17, 1974.
3. R. L. Moon and L. W. James, *This Journal*, **120**, 581 (1973).
4. B. J. Baliga and S. K. Ghandhi, *ibid.*, **121**, 1642 (1974).
5. J. A. Amick, E. A. Roth, and H. Gossenberger, *RCA Rev.*, **24**, 473 (1963).
6. A. Reisman and M. Berkenblit, *This Journal*, **118**, 812 (1965).
7. H. C. Gatos and M. C. Lavine, *ibid.*, **107**, 427 (1960).
8. G. A. Lang and T. Stavish, *RCA Rev.*, **24**, 488 (1963).
9. W. H. Shepherd, *This Journal*, **112**, 988 (1965).

Chemical Processes in Vapor Deposition of Silicon

I. Deposition from SiCl_2H_2 and Etching by HCl

Vladimir S. Ban* and Stephen L. Gilbert

RCA Laboratories, Princeton, New Jersey 08540

ABSTRACT

Chemical processes occurring in the vapor deposition of silicon from SiCl_2H_2 and in the etching of silicon by HCl were studied by means of a mass spectrometer coupled to the CVD reactor. This setup was successfully used for the qualitative and quantitative analysis of the composition of the vapor phase in the Si-Cl-H system. Species found in the vapor phase were H_2 , HCl, SiCl_2 , SiCl_2H_2 , SiCl_3H , and SiCl_4 , and their partial pressures were measured as a function of temperature, value of the Cl/H ratio, and of the chemical nature of the initial gaseous mixture entering the reactor. The experimentally determined partial pressures were compared with the equilibrium partial pressures of vapor species, calculated from the newest thermochemical data for the Si-Cl-H system. On the basis of these results we discuss the nature and the extent of chemical processes in systems studied.

The chemical vapor deposition (CVD) of thin layers of silicon is among the most important processes in the electronic industry. For this purpose, various Si-containing gases are used, e.g., SiH_4 or various chlorosilanes such as SiH_3Cl , SiH_2Cl_2 , SiHCl_3 , and SiCl_4 . Typically, a mixture consisting of approximately 1% of Si-containing gas and 99% of carrier gas, usually H_2 or He, is introduced into the CVD reactor, where it comes into contact with substrates placed on a hot susceptor. The deposition of a layer of Si then takes place on these substrates through chemical reactions, the nature of which depends on experimental conditions, such as temperature, partial pressures and nature of the gaseous mixture, reactor geometry, etc. The purpose of this article is to discuss our studies of chemical processes leading to the deposition of Si. In particular, we studied the deposition of Si from SiCl_2H_2 as well as the reverse of this process, i.e., the HCl etching of Si. Dichlorosilane, SiCl_2H_2 , is becoming an increasingly important starting material for the deposition of Si-layers (1).

In general, CVD processes in any system can be understood through the chemical thermodynamics of that system. Thermodynamical calculations should in principle yield information on the feasibility of CVD processes, possible efficiencies of these processes, and on the expected structure and composition of the product. However, in order to apply thermodynamics correctly, one has to know the following about the systems: (a) the composition of the condensed and gaseous phases under all experimental conditions; (b) the magnitude and the nature of possible kinetic effects, the existence of which may determine the applicability of thermodynamics to the system in question; and (c) a set of reliable and consistent thermochemical data should be available.

In growth of Si from SiCl_2H_2 and in etching of Si by HCl, the pertinent system is Si-Cl-H. Thermodynamical calculations were applied to this system previously (2, 3). These calculations predicted the composition of the vapor phase, as well as the efficiency of the deposition of Si under various experimental conditions. However, neither the applicability of thermodynamics to the system nor the results of cal-

* Electrochemical Society Active Member.

Key words: mass spectrometry, CVD, thermodynamics, kinetics.

culations were experimentally verified. One could therefore suspect that the actual situation in the CVD reactor is perhaps different from the situation predicted by calculations. In this paper, we present results of the experimental qualitative and quantitative determination of the composition of the vapor phase and, in view of these results, discuss the applicability of thermodynamics to the system. The experimental and the calculated values of partial pressures are compared, and the nature and the extent of deviations from thermochemical equilibrium, *i.e.*, the role of kinetics, are assessed.

The determination of the composition of the vapor phase was done by means of a time-of-flight mass spectrometer connected directly to the CVD reactor. This method was successfully employed in studies of CVD of various III-V compounds (4-6).

Instrumental

Although the essential part of the mass spectrometer-CVD reactor setup has been described previously (4), we shall briefly review the main points as well as describe modifications made for the study of the Si-Cl-H system.

The reactor used in our studies is a tubular reactor with hot walls, similar to the reactor used in synthesis of III-V materials. This reactor is quite different from reactors normally used in deposition of Si-films, but it nevertheless enabled us to study the pertinent chemical processes. The deposition of Si took place either on the quartz wall of the reactor or on the layer of Si deposited there in previous experiments. Similarly, the HCl also reacted with this deposit in the etching experiments. The residence time of the gas phase as well as the Si area exposed to the gas phase was larger than in the normally used horizontal reactor used for CVD of Si. This should actually facilitate the attainment of chemical equilibrium in the system without altering the nature of reactions. The reactor was heated by a 4-segment tubular furnace. Measurements described here were done in the temperature range of 800°-1300°K. The length of the hot zone could be varied by switching one or two of the segments off. Gases were fed into the reactor through a combination of calibrated Fischer and Porter flow meters and Matheson electronic mass flow transducers. In this way, it was possible to introduce known amounts of SiCl₂H₂, HCl, H₂, or He into the reactor, and create a starting mixture of desired composition. There are also provisions for usage of SiCl₃H and SiCl₄ in the reactor, but this will be described in another publication.

The reactor is connected to the mass spectrometer via a small quartz capillary. In this way, it is possible to sample hot vapor from the reactor under normal CVD conditions, *i.e.*, 1 atm and temperatures of over 1000°C. The capillary is maintained at the temperature of the sampled gas and since it is made from the same material, *i.e.*, quartz, as the reactor, no interactions different from those in the reactor would occur in the capillary. The capillary reduces pressure from 1 atm in the reactor to 10⁻⁵ Torr in the mass spectrometer. From it emanates a stream of hot gas directly into the ion source of the mass spectrometer. Since a mean free path at the pressure of 10⁻⁵ Torr is much longer than the distance between the capillary and the ion source (*ca.* 12 cm), most molecules enter the source without undergoing any interactions in the area between the capillary and the source. We therefore believe that the sample entering the mass spectrometer is representative of the gaseous phase in the CVD reactor. The mass spectrometer can be calibrated for quantitative studies. One can introduce into the reactor gaseous mixtures where partial pressures of constituents are known, *e.g.*, mixtures of SiCl₂H₂ and H₂, or HCl, SiCl₂H₂ and H₂, and then relate peak intensities in the mass spectra to corresponding partial pressures.

Schematic representation of the mass spectrometer-reactor combination is given in Fig. 1.

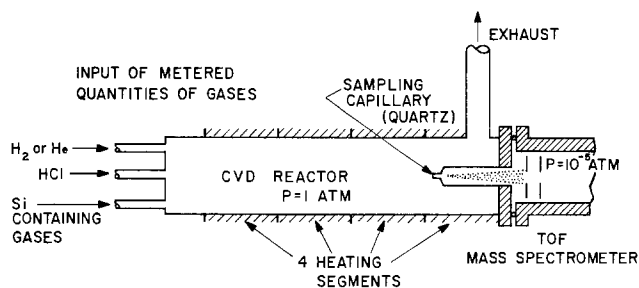


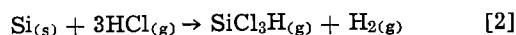
Fig. 1. Schematic representation of the system mass spectrometer-CVD reactor.

Thermodynamical Calculations

Calculations of equilibrium partial pressures of vapor species in the Si-Cl-H system have been done by several authors (2, 3, 7) and we shall describe the method only briefly. Basically, one deals with a 3-component system, where the gaseous phase is in equilibrium with the solid phase, *i.e.*, silicon. Therefore, according to the Gibbs rule, the system has three degrees of freedom. These are pressure, temperature, and a compositional variable Cl/H. This Cl/H ratio remains constant throughout the deposition process because neither Cl nor H atoms are added or removed from the system during the deposition (or etching) of Si. Its value is determined by partial pressures of gases in the initially introduced mixture. From the previously referenced works, we learned that the following eight species are most abundant in the Si-Cl-H system: H₂, HCl, SiH₄, SiH₃Cl, SiH₂Cl₂, SiHCl₃, SiCl₄, and SiCl₂. Other possibly existing species, such as Cl, Cl₂, Si₂Cl₆, etc., would be present in negligible amounts only. In order to calculate equilibrium partial pressures of the eight species mentioned above, one must have a set of eight independent, generally nonlinear equations, which specify relationships between these species. Six of these equations represent chemical equilibria between species



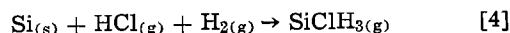
$$K_{p(1)} = \frac{P_{\text{SiCl}_4} \cdot P_{\text{H}_2}^2}{a_{\text{Si}} \cdot P_{\text{HCl}}^4}$$



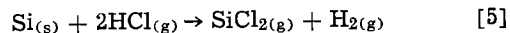
$$K_{p(2)} = \frac{P_{\text{SiCl}_3\text{H}} \cdot P_{\text{H}_2}}{a_{\text{Si}} \cdot P_{\text{HCl}}^3}$$



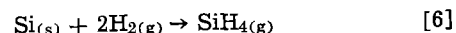
$$K_{p(3)} = \frac{P_{\text{SiCl}_2\text{H}_2}}{a_{\text{Si}} \cdot P_{\text{HCl}}^2}$$



$$K_{p(4)} = \frac{P_{\text{SiClH}_3}}{a_{\text{Si}} \cdot P_{\text{HCl}} \cdot P_{\text{H}_2}}$$



$$K_{p(5)} = \frac{P_{\text{SiCl}_2} \cdot P_{\text{H}_2}}{a_{\text{Si}} \cdot P_{\text{HCl}}^2}$$



$$K_{p(6)} = \frac{P_{\text{SiH}_4}}{a_{\text{Si}} \cdot P_{\text{H}_2}^2}$$

The activity of Si is represented by *a*; *a* = 1.

The remaining two equations specify the Cl/H ratio and state that the total pressure in the system is 1 atm

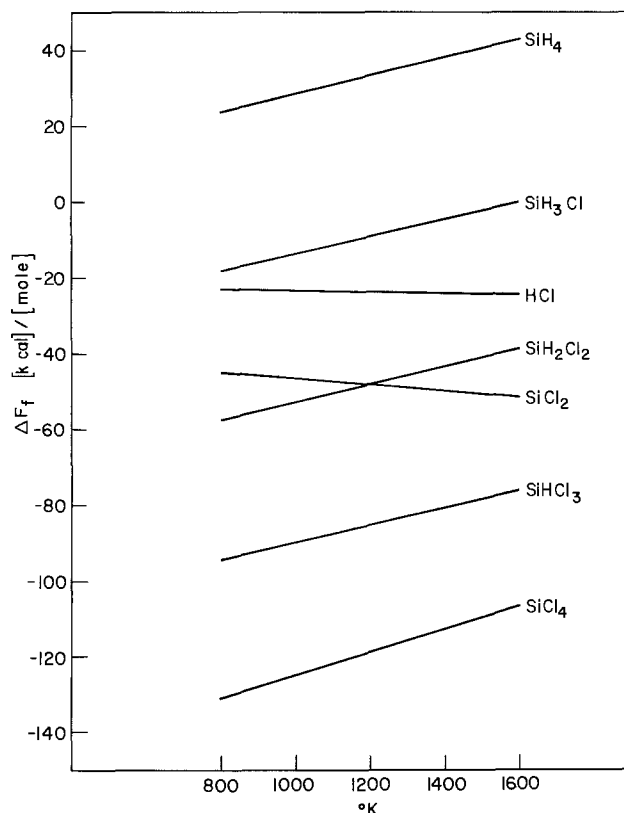


Fig. 2. Free energies of formation of important gaseous species in the Si-Cl-H system in the temperature interval of 800°-1600°K.

10^{-3} , 10^{-2} , 10^{-1} , and 10^0 ; the temperature was varied from 800° to 1600°K, in increments of 200°K. Results of calculations are given in Table I.

Thermodynamical calculations can also be used to determine the theoretical efficiency of the deposition process. The efficiency can be defined as

$$\eta = \frac{[\text{Si/Cl}]_{\text{in}} - [\text{Si/Cl}]_{\text{eq}}}{[\text{Si/Cl}]_{\text{in}}}$$

where $[\text{Si/Cl}]_{\text{in}}$ is the ratio of Si to Cl atoms in the starting mixture, and $[\text{Si/Cl}]_{\text{eq}}$ is this ratio in the equilibrium mixture. A negative value of η means that etching of Si is taking place in the system.

Experimental Results

Mass spectra of chlorosilanes.—Since the determination of the mass spectra of Si-containing gases in our setup is being reported elsewhere (9), we only briefly discuss this topic here. Vapor species in the reactor were identified by means of the attached mass spectrometer. The analysis is complicated by the fact that mass spectra of various chlorosilanes should be quite similar, due to the fragmentation of parent molecules by the ionizing electrons. We determined mass spectra of SiCl_4 , SiCl_3H , SiCl_2 , and SiCl_2H_2 in our experimental setup. A mixture containing 1% of these gases in He or H_2 (this change produces no difference in spectra) was introduced into the reactor and mass spectra were taken at room temperature, where no chemical reactions which would change the mixture occurred. The observed intensities of major peaks in these mixtures did not differ by more than 15%, thus indicating that our experimental setup is about equally sensitive for all chlorosilanes. Mass spectra of SiCl_2 were deduced from the high temperature mass spectrometry of SiCl_4 -He mixtures where the only present vapor

$$\text{Cl/H} = \frac{4P_{\text{SiCl}_4} + 3P_{\text{SiCl}_3\text{H}} + 2P_{\text{SiCl}_2\text{H}_2} + 2P_{\text{SiCl}_2} + P_{\text{SiCl}_3\text{H}} + P_{\text{HCl}}}{2P_{\text{H}_2} + P_{\text{SiCl}_3\text{H}} + 2P_{\text{SiCl}_2\text{H}_2} + 3P_{\text{SiCl}_3\text{H}} + P_{\text{HCl}} + 4P_{\text{SiH}_4}} \quad [7]$$

and

$$P_{\text{SiCl}_4} + P_{\text{SiCl}_3\text{H}} + P_{\text{SiCl}_2\text{H}_2} + P_{\text{SiCl}_3\text{H}} + P_{\text{SiCl}_2} + P_{\text{SiH}_4} + P_{\text{HCl}} + P_{\text{H}_2} = 1 \quad [8]$$

Of course, when growing Si from a mixture of SiCl_2H_2 and H_2 partial pressures of all other species are initially equal to zero.

In order to find values of $K_{p(1-8)}$, the most convenient data to have are free energies of formation, ΔF_f , of all species in the temperature interval of interest. Values of ΔF_f of all species were calculated from thermochemical data for the Si-Cl-H system recently collected by Hunt and Sirtl (3). Figure 2 shows values of ΔF_f vs. temperature in the form of the so-called Ellingham diagrams (8).

Once values of K_p 's were known, we calculated the equilibrium partial pressures of all eight species, using a simple iterative method on a time sharing computer. In these calculations, the Cl/H ratio was set to be

species were SiCl_4 , SiCl_2 , and He. Mass spectra of SiCl_3H were not determined, but as the calculations have shown, this should be a scarce species, and besides, using the analogy with other chlorosilanes, one could deduce its mass spectra with a fair degree of accuracy.

In determination of these spectra, 70 eV ionizing electrons were used. No corrections due to differences in ionization cross section of various species, possible mass discrimination of the instrument, etc., were applied, since we were primarily interested in the relative intensities of various peaks under our experimental conditions. Mass spectrum of SiCl_4 agrees reasonably well with the published data (10). Mass spectra of SiH_4 , HCl , and H_2 are known. Results of the determination of mass spectra of SiCl_4 , SiCl_3H , SiCl_2H_2 , and SiCl_2 are graphically represented in Fig. 3. From the relative intensities of various peaks, one can calculate relative abundances of various species in the

Table I. Calculated values of equilibrium partial pressures (in atmospheres) of vapor species in the Si-Cl-H system

T, °K	Cl/H	H ₂	HCl	SiCl ₄	SiHCl ₃	SiH ₂ Cl ₂	SiH ₂ Cl	SiH ₄	SiCl ₂
1000	10 ⁰	6.28 × 10 ⁻¹	1.52 × 10 ⁻²	2.74 × 10 ⁻¹	8.01 × 10 ⁻²	2.70 × 10 ⁻²	5.05 × 10 ⁻⁵	2.55 × 10 ⁻⁷	1.99 × 10 ⁻⁴
1000	10 ⁻¹	9.39 × 10 ⁻¹	1.07 × 10 ⁻²	3.03 × 10 ⁻²	1.88 × 10 ⁻²	1.34 × 10 ⁻²	5.33 × 10 ⁻⁵	5.70 × 10 ⁻⁷	6.62 × 10 ⁻⁵
1000	10 ⁻²	9.90 × 10 ⁻¹	5.40 × 10 ⁻³	1.74 × 10 ⁻³	2.26 × 10 ⁻³	3.39 × 10 ⁻⁴	2.83 × 10 ⁻⁵	6.34 × 10 ⁻⁷	1.59 × 10 ⁻⁵
1000	10 ⁻³	9.98 × 10 ⁻¹	1.67 × 10 ⁻³	1.55 × 10 ⁻⁵	6.58 × 10 ⁻⁵	3.22 × 10 ⁻⁵	8.78 × 10 ⁻⁶	6.45 × 10 ⁻⁷	1.50 × 10 ⁻⁶
1200	10 ⁰	6.0 × 10 ⁻¹	5.80 × 10 ⁻²	2.61 × 10 ⁻¹	7.36 × 10 ⁻²	2.92 × 10 ⁻²	5.95 × 10 ⁻⁵	3.43 × 10 ⁻⁷	5.01 × 10 ⁻³
1200	10 ⁻¹	9.18 × 10 ⁻¹	3.97 × 10 ⁻²	2.44 × 10 ⁻²	1.54 × 10 ⁻²	1.37 × 10 ⁻²	6.23 × 10 ⁻⁵	8.02 × 10 ⁻⁷	1.53 × 10 ⁻³
1200	10 ⁻²	9.83 × 10 ⁻¹	1.50 × 10 ⁻²	4.30 × 10 ⁻⁴	7.72 × 10 ⁻⁴	1.94 × 10 ⁻⁴	2.52 × 10 ⁻⁵	9.22 × 10 ⁻⁷	2.03 × 10 ⁻⁴
1200	10 ⁻³	9.98 × 10 ⁻¹	1.98 × 10 ⁻³	1.26 × 10 ⁻⁷	1.74 × 10 ⁻⁶	3.38 × 10 ⁻⁶	3.37 × 10 ⁻⁶	9.49 × 10 ⁻⁷	3.49 × 10 ⁻⁵
1400	10 ⁰	5.37 × 10 ⁻¹	1.38 × 10 ⁻¹	2.16 × 10 ⁻¹	5.99 × 10 ⁻²	2.63 × 10 ⁻²	5.75 × 10 ⁻⁵	3.64 × 10 ⁻⁷	4.62 × 10 ⁻²
1400	10 ⁻¹	8.81 × 10 ⁻¹	8.63 × 10 ⁻²	1.22 × 10 ⁻²	8.89 × 10 ⁻³	1.03 × 10 ⁻²	5.88 × 10 ⁻⁵	9.77 × 10 ⁻⁷	1.10 × 10 ⁻²
1400	10 ⁻²	9.81 × 10 ⁻¹	1.85 × 10 ⁻²	2.07 × 10 ⁻⁵	7.84 × 10 ⁻⁵	4.71 × 10 ⁻⁵	1.40 × 10 ⁻⁵	1.21 × 10 ⁻⁶	4.52 × 10 ⁻⁴
1400	10 ⁻³	9.98 × 10 ⁻¹	1.98 × 10 ⁻³	2.66 × 10 ⁻⁹	9.56 × 10 ⁻⁸	5.44 × 10 ⁻⁷	1.53 × 10 ⁻⁶	1.25 × 10 ⁻⁶	5.13 × 10 ⁻⁶

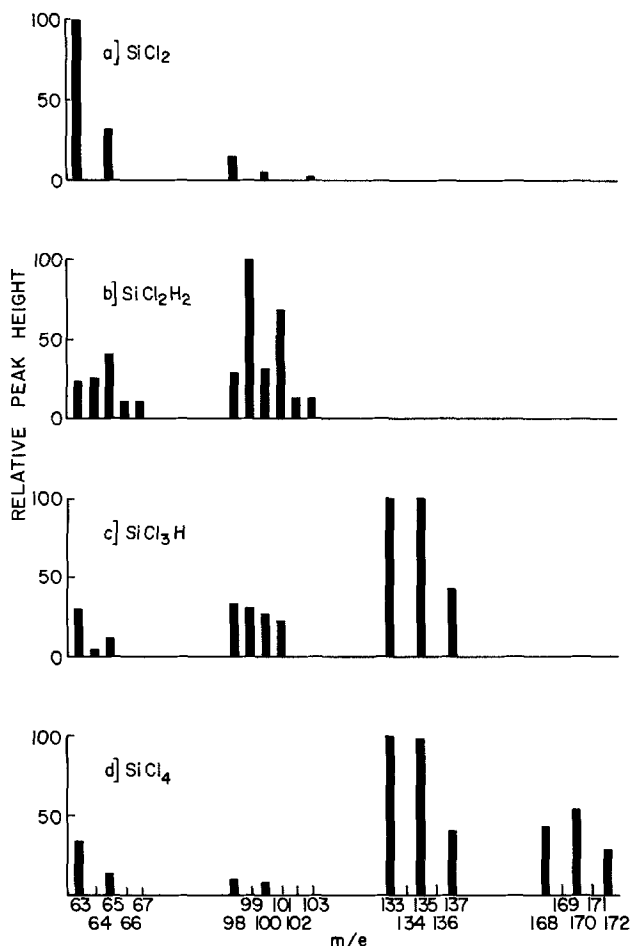


Fig. 3. Relative abundances of peaks in mass spectra of (a) SiCl_2 ; (b) SiCl_2H_2 ; (c) SiCl_3H ; and (d) SiCl_4 . The most abundant peak in each spectra is assigned a value of 100.

vapor phase; i.e., one can perform the qualitative and the quantitative analysis of the vapor phase in the reactor.

Determination of partial pressures.—The qualitative and quantitative analysis results in determination of partial pressures of all detected species. Effects of temperature and of the Cl/H ratio, as well as possible effects of the nature of starting mixture on values of partial pressures of various species were studied. Measurements were done at 1000° , 1200° , and 1300°K ; Cl/H ratios of 10^{-2} , 10^{-1} , and 10^0 were used. Mixtures with identical values of Cl/H ratio were prepared in two ways: by mixing pure SiCl_2H_2 with H_2 , or by mixing the appropriate amounts of SiCl_2H_2 and HCl with H_2 . The exact amounts mixed are given in Table II. In this way the effect of the nature (i.e., of the presence or the absence of HCl) of starting mixture on the composition of the vapor phase could be studied. In cases of $\text{Cl}/\text{H} = 10^0$, either pure SiCl_2H_2 or pure HCl were introduced into the reactor. Of course, the deposition of Si will occur in the former, and the etching of Si will occur in the latter case, but the composition of the vapor phase in contact with solid Si should nevertheless be the same, providing that chemical equilibrium has been established.

Table II. Amounts of gases used to prepare starting mixtures

Cl/H	Symbol in Fig. 4	SiCl_2H_2 , cm^3/min	HCl , cm^3/min	H_2 , cm^3/min
0.01	○	20	0	2000
0.01	●	20	20	2970
0.1	△	200	0	1800
0.1	▲	100	100	1350
1.0	□	200	0	0
1.0	■	0	200	0

Mass spectra of initial mixtures at room temperature contained only peaks characteristic for the gases comprising the mixture in question. At elevated temperatures new peaks appeared indicating the appearance of new species in the vapor phase. Under our experimental conditions, the following species were found to exist in appreciable amounts: H_2 , HCl , SiCl_2 , SiCl_2H_2 , SiCl_3H , and SiCl_4 . Species such as SiClH_3 and SiH_4 were not detected; Si_2Cl_6 was detected but only in very small amounts. The last three species were therefore ignored in the quantitative determination of partial pressures. When different Si-containing species coexist in the vapor phase, some of the peaks in the mass spectra comprise contributions from more than one species. For example, if the relative intensity of the peak with $m/e = 133$ is 100 and the relative intensity of the peak with $m/e = 170$ is only 25, one concludes that this gas mixture contains SiCl_4 (as evidenced by the existence of the peak at $m/e = 170$) and also SiCl_3H , because ratio of intensities of peaks with $m/e = 133$ and $m/e = 170$ is larger than in the mass spectrum of pure SiCl_4 (see Fig. 3) This means that some other species must contribute to the peak with $m/e = 133$. From Fig. 3 it is obvious that this can be only SiCl_3H . The relative amounts of SiCl_4 and SiCl_3H can be obtained in this way. Once the relative amounts of SiCl_4 and SiCl_3H are known, one proceeds to determine the relative amount of SiCl_2H_2 by subtracting the contribution of SiCl_3H to the peak with $m/e = 99$. The relative amount of SiCl_2 is determined from the intensity of peak at $m/e = 63$, after subtracting contributions from SiCl_4 , SiCl_3H , and SiCl_2H_2 to this peak. After the above procedure is completed, one obtains ratios of partial pressures of SiCl_3H , SiCl_2H_2 , and SiCl_2 respective to the partial pressure of SiCl_4 . We shall illustrate this on the previously given example, where relative intensity of $m/e = 133$ was 100, and of $m/e = 170$ was 25, respectively. The contribution of the SiCl_4 spectrum to the peak at $m/e = 133$ can be obtained by multiplying the ratio of relative intensities of $m/e = 133$ and $m/e = 170$ in the pure SiCl_4 spectrum with the relative intensity in the spectrum of the mixture

$$\frac{I_{133}(\text{SiCl}_4)}{I_{170}(\text{SiCl}_4)} \times I_{170(\text{mix})} = \frac{100}{53} \times 25 = 47.2$$

The contribution of SiCl_3H to the peak at $m/e = 133$ can be obtained by subtracting 47.2 from 100, i.e., its contribution is 52.8. Since partial pressures of species are proportional to mass spectrometric intensities, one has

$$\frac{47.2}{52.8} = \frac{P_{\text{SiCl}_4}}{P_{\text{SiCl}_3\text{H}}} = 0.89$$

and one can express $P_{\text{SiCl}_3\text{H}}$ in terms of P_{SiCl_4}

$$P_{\text{SiCl}_3\text{H}} = 1.12 P_{\text{SiCl}_4}$$

This procedure can be repeated for SiCl_2H_2 and SiCl_2 , so that partial pressures of these species are also expressed in terms of P_{SiCl_4} .

The partial pressure of HCl was determined through direct calibration. Intensities of HCl peaks in the mass spectra were measured at temperatures of interest in mixtures containing only HCl and H_2 in known proportions. Since Si was not present in these experiments, no reaction could occur in the reactor and measured HCl intensities can be directly correlated with the partial pressure of HCl .

Now one can proceed with calculations of actual values of partial pressures of SiCl_4 , SiCl_3H , SiCl_2H_2 , SiCl_2 , and H_2 from mass spectrometric data. Partial pressures must satisfy Eq. [7] and [8]. Expressing partial pressures of all present chlorosilanes in terms of P_{SiCl_4} and neglecting mass spectrometrically nondetectable species, Eq. [7] and [8] can be written as

$$\frac{\text{Cl}}{\text{H}} = \frac{4P_{\text{SiCl}_4} + 3aP_{\text{SiCl}_3\text{H}} + 2bP_{\text{SiCl}_2\text{H}_2} + 2cP_{\text{SiCl}_3\text{H}} + P_{\text{HCl}}}{2P_{\text{H}_2} + aP_{\text{SiCl}_4} + 2b\text{SiCl}_4 + P_{\text{HCl}}} \quad [9]$$

and

$$P_{\text{SiCl}_4} + aP_{\text{SiCl}_3\text{H}} + bP_{\text{SiCl}_2\text{H}_2} + cP_{\text{SiCl}_3\text{H}} + P_{\text{HCl}} + P_{\text{H}_2} = 1 \quad [10]$$

where a , b , and c are mass spectrometrically obtained ratios connecting partial pressure of SiCl_4 with partial pressures of SiCl_3H , SiCl_2H_2 , and SiCl_2 , respectively.

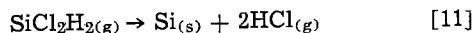
Since P_{HCl} is known from calibration experiments, we deal with the system of two linear equations containing two unknowns, *i.e.*, P_{H_2} and P_{SiCl_4} . After solving for P_{H_2} and P_{SiCl_4} one obtains $P_{\text{SiCl}_3\text{H}}$, $P_{\text{SiCl}_2\text{H}_2}$, and P_{SiCl_2} from known values of a , b , and c , respectively.

In Fig. 4(a)-(e), the experimentally determined partial pressures of vapor species are compared with calculated partial pressures at corresponding temperatures and Cl/H values. Lines represent the temperature variation of calculated partial pressures of pertinent species; Cl/H = 10^0 for the top line, Cl/H = 10^{-1} for the middle, and Cl/H = 10^{-2} for the bottom line. Square symbols are to be compared with the top line, triangular symbols with the middle, and circular symbols with the bottom line. Open symbols represent values of partial pressures in mixtures where HCl was not initially present; the full symbols represent partial pressures in mixtures where HCl was initially present. The reproducibility of these data from experiment to experiment is about $\pm 20\%$.

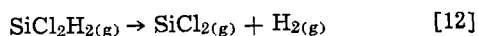
Discussion

In this section we discuss the nature and the extent of chemical reactions occurring in the system. From the presence of H_2 , HCl , SiCl_2 , SiCl_2H_2 , SiCl_3H , and SiCl_4 , one can conclude which reactions occur.

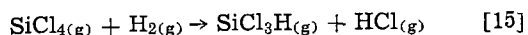
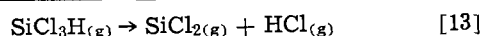
The drop of partial pressure of entering SiCl_2H_2 and the appearance of HCl in the system infers the following reaction (reverse of reaction [3]) by which the deposition of Si occurs



The HCl created in this way reacts with the Si deposit to form other thermodynamically stable species; SiCl_4 , SiCl_3H , and SiCl_2 are formed via reactions [1], [2], and [5], respectively. Reactions of equilibration between various vapor species can be also considered, *e.g.*



$$\frac{\text{Si}}{\text{Cl}} = \frac{P_{\text{SiCl}_4} + P_{\text{SiCl}_3\text{H}} + P_{\text{SiCl}_2\text{H}_2} + P_{\text{SiCl}_3\text{H}} + P_{\text{SiH}_4} + P_{\text{SiCl}_2}}{4P_{\text{SiCl}_4} + 3P_{\text{SiCl}_3\text{H}} + 2P_{\text{SiCl}_2\text{H}_2} + P_{\text{SiCl}_3\text{H}} + 2P_{\text{SiCl}_2} + P_{\text{HCl}}} \quad [16]$$



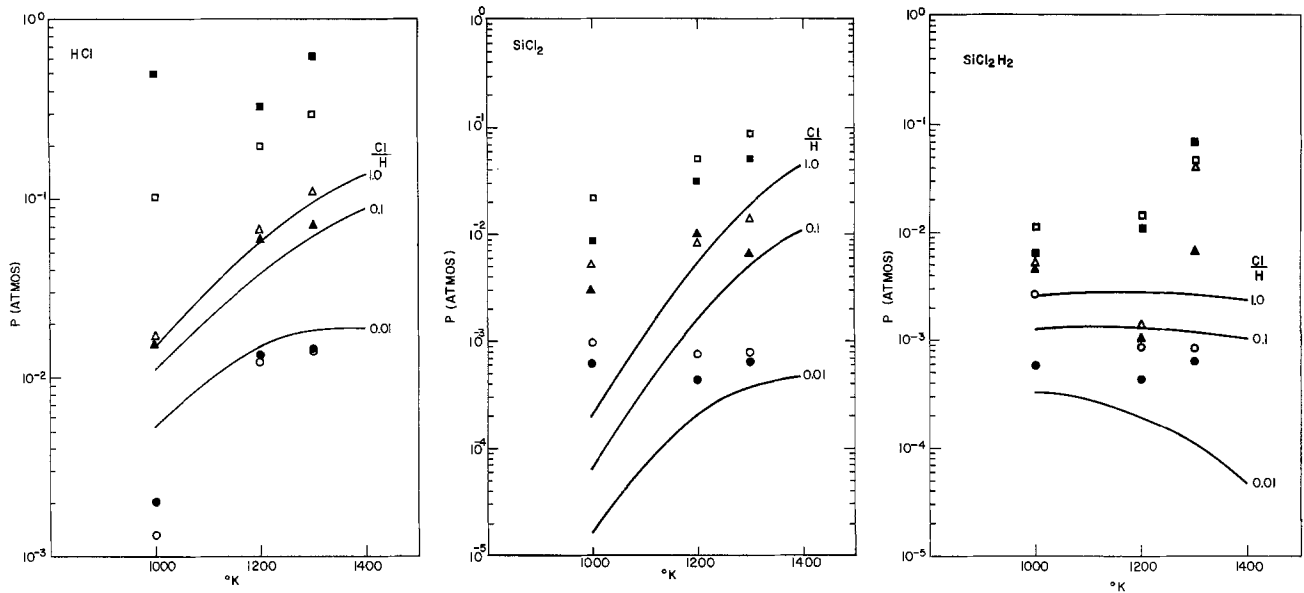
It is possible to draw some conclusions about the mechanism and the kinetics of the above reactions by referring to Fig. 4(a)-(e). The comparison of calculated with equilibrium partial pressures shows that deviations from equilibrium exist, but their nature varies from species to species. In almost all instances P_{SiCl_2} and $P_{\text{SiCl}_2\text{H}_2}$ are higher than their equilibrium values; P_{HCl} is also higher except for Cl/H < 10^{-1} . On the other hand, P_{SiCl_4} is almost always lower than the equilibrium value, and $P_{\text{SiCl}_3\text{H}}$ is also lower for $T > 1000^\circ\text{K}$. From these observations, one can conclude that the creation of species which require more HCl molecules to form (*i.e.*, reactions [1] and [2]) proceeds slower than the creation of species which require less HCl (*i.e.*, reactions [3] and [5]). This suggests a dearth of HCl molecules at the Si surface, which could be caused either by the poor transport of HCl to the surface or by the poor adsorption of HCl at the surface.

The increase of P_{HCl} by the addition of pure HCl to the gas phase increases the transport of HCl to the surface, but nevertheless, the relative abundance of vapor species does not change significantly. At higher Cl/H ratios one observes that the abundance of HCl in the vapor is higher than equilibrium data predict. This points toward the poor adsorption of HCl on silicon surface. The consequence is that species requiring more HCl for their formation (*i.e.*, SiCl_3H and SiCl_4) will form less readily than species such as SiCl_2 , which need only two HCl molecules for their formation. Recently, Robinson and Goldsmith obtained Si growth from mixtures of SiCl_2H_2 and HCl, where HCl content was so high that thermodynamic calculations predicted etching of Si rather than its growth (11). This indicates that in their system the reaction of HCl with Si also did not reach equilibrium.

The incomplete dissociation of SiCl_2H_2 (reaction [3]) could also contribute to the relatively high $P_{\text{SiCl}_2\text{H}_2}$. It is also possible that reaction [12] occurs in the system. This reaction is thermodynamically more feasible at our experimental temperatures than other homogeneous gas reactions, *i.e.*, reactions [13], [14], and [15]). Most likely, neither reactions [13], [14], and [15], nor their reverse reactions occur to a significant extent in our system. If they did occur, one would observe a strong dependence of P_{SiCl_4} and $P_{\text{SiCl}_3\text{H}}$ on the presence of free HCl in the reactor. This has not been observed. We thus conclude that events on the Si surface were the principal factor in determining the composition of the vapor phase. A similar conclusion was reached by crystal growers, who consider Si deposition up to about 1250°K as surface kinetics controlled (12, 13). Our mass spectrometric data indicate that these deviations from thermochemical equilibrium also reflect themselves in the composition of the vapor phase. Nevertheless, all major species predicted by thermodynamic calculations have been detected, and in most cases, their measured partial pressures are of the same order of magnitude as the equilibrium values.

It was already mentioned that one can calculate the efficiency of the Si deposition process by comparing values of Si/Cl ratio in the initial mixture with the Si/Cl in the equilibrium mixture at some given temperature. The efficiency obtained in this way is the theoretical efficiency of the Si-deposition process. The comparison of the initial Si/Cl ratio with the Si/Cl ratio determined from mass-spectrometric values of partial pressures yields the experimental efficiencies. The Si/Cl ratio is defined by the following equation

Of course, in the initial mixtures, only $P_{\text{SiCl}_2\text{H}_2}$ and P_{HCl} (when present) should be considered; in the determination of the value of Si/Cl from the experimental data, the partial pressures of undetected species such as SiCl_3H and SiH_4 are considered to be equal to zero. In Table III, the experimental and the theoretical efficiencies are listed. Efficiencies are expressed in terms of percentage of the introduced Si converted into the solid Si. From data in Table III, it can be seen that, in general, the experimental efficiencies are significantly lower than theoretical ones in cases of lower temperatures and Cl/H values. The experimental efficiencies approach theoretical values with increasing temperatures and Cl/H values. In some cases, they are even higher than the theoretical efficiencies. This can be explained by the already discussed low rates of the HCl-Si interaction. If the deposition of Si from SiCl_2H_2 proceeds at higher rates than the back-etching of the deposit by HCl, a net accumulation of Si larger than the equilibrium amount will occur, leading to the observed higher than theoretical efficiencies. This is consistent with data in Ref. (11).



(a) Comparison between the calculated and experimental pressure of HCl.

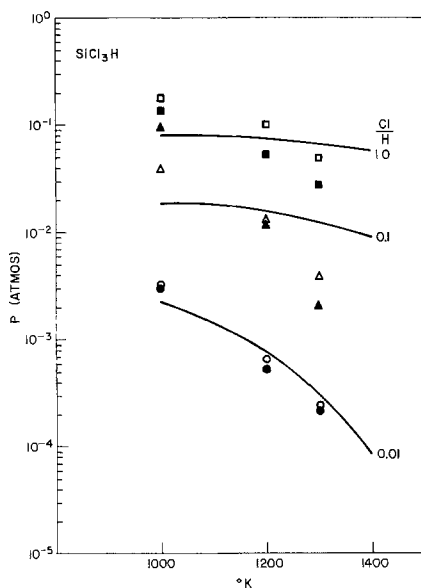
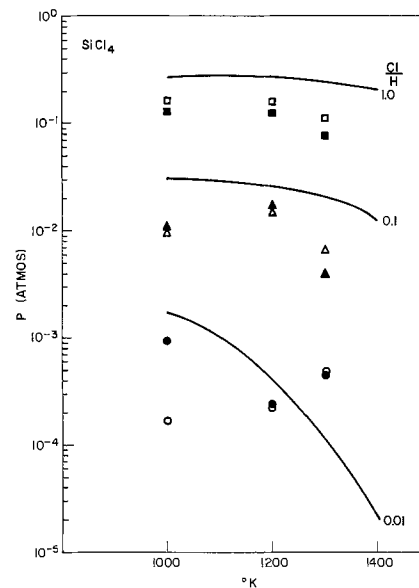
(b) Comparison between the calculated and experimental pressure of SiCl_2 .(c) Comparison between the calculated and experimental pressure of SiCl_2H_2 .(d) Comparison between the calculated and experimental pressure of SiCl_3H .(e) Comparison between the calculated and experimental pressure of SiCl_4 .

Fig. 4. Comparison between the calculated and the experimental partial pressures of detected species. Lines represent calculated temperature variations of partial pressures with Cl/H value as a parameter. Square symbols are to be compared with the top line (Cl/H = 10⁰), triangular symbols with the middle (Cl/H = 10⁻¹), and circular symbols with the bottom line (Cl/H = 10⁻²). Full symbols represent partial pressures in mixtures where HCl was initially present; the open symbols represent partial pressures in mixtures where HCl was not initially present.

In experiments where pure HCl was introduced into the reactor (i.e., Cl/H = 10⁰), the etching of the previously deposited Si occurred. The efficiency of etching can be obtained by comparing the experimentally determined amount of Si in the gas phase with the corresponding calculated amounts. Such comparison yields that the HCl-etching is 80, 64, and 71% efficient at 1000°, 1200°, and 1300°K, respectively. This again confirms the observation that the extent of HCl-Si interaction is lower than calculated.

Summary and Conclusions

The presented study of the chemical processes in deposition of Si from SiCl_2H_2 and of etching of Si by HCl is summarized in this section.

1. The mass spectrometer-CVD reactor setup has been successfully used for the qualitative and quanti-

Table III. Comparison of theoretically and experimentally determined efficiencies of Si deposition from SiCl_2H_2

Cl/H	Presence of HCl in initial mix	1000°K		1200°K		1300°K	
		Theor. η	Exp. η	Theor. η	Exp. η	Theor. η	Exp. η
0.01	No	55.9	25.0	83.6	73.6	91.1	76.0
0.01	Yes	33.8	9.8	75.4	73.2	86.6	70.9
0.1	No	47.1	39.2	54.8	58.9	60.3	67.1
0.1	Yes	20.6	5.3	32.2	35.4	40.4	54.9
1.0	No	47.4	44.8	48.8	48.8	49.4	49.1

tative analysis of the vapor phase in the Si-Cl-H system.

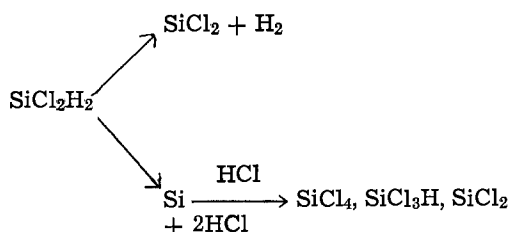
2. Mass spectra of SiCl_4 , SiCl_3H , SiCl_2H_2 , and SiCl_2 have been determined.

3. Species found in the vapor phase were H_2 , HCl , SiCl_2 , SiCl_2H_2 , SiCl_3H , and SiCl_4 , and their partial pressures were measured as a function of temperature, value of the Cl/H ratio, and of the chemical nature of the initial gaseous mixture entering the reactor.

4. The equilibrium partial pressures of all vapor species present in the Si-Cl-H system were calculated from the newest and most consistent set of thermochemical data available.

5. The comparison between the calculated and the experimentally determined partial pressures indicates that there are certain deviations from the thermochemical equilibrium which reflect themselves in the composition of the vapor phase. Notably, partial pressures of HCl , SiCl_2 , and SiCl_2H_2 tend to be higher, and partial pressures of SiCl_3H and SiCl_4 lower than the corresponding equilibrium partial pressures. Nevertheless, under most of our experimental conditions (particularly when $T > 1200^\circ\text{K}$), the measured and the calculated partial pressures were of the same order of magnitude. The equilibrium calculations thus provide useful information on the composition of the vapor phase and on the deposition and etching of Si, although the complete equilibrium situation has not been established.

6. The main chemical reactions occurring in the reactor are summarized by the following scheme



The incoming SiCl_2H_2 decomposes either to SiCl_2 through a loss of two H atoms or to Si through a loss of two HCl molecules; other species are then formed by the HCl-Si interaction.

7. From the nature and the extent of the deviations from the equilibrium, one concludes that their pos-

sible causes are the retarded HCl adsorption on Si and the incomplete dissociation of SiCl_2H_2 .

8. The calculated and the experimentally determined efficiencies of the deposition and etching processes were compared and found to be similar when $T > 1000^\circ\text{K}$ and $\text{Cl}/\text{H} > 10^{-2}$.

Acknowledgments

The authors gladly acknowledge helpful and informative discussions with D. Richman, N. Goldsmith, and G. Cullen.

Manuscript submitted Oct. 29, 1974; revised manuscript received June 2, 1975.

Any discussion of this paper will appear in a Discussion Section to be published in the June 1976 JOURNAL. All discussions for the June 1976 Discussion Section should be submitted by Feb. 1, 1976.

Publication costs of this article were partially assisted by RCA Corporation.

REFERENCES

1. N. Goldsmith and P. H. Robinson, *RCA Rev.*, **34**, 358 (1973); W. C. Benzing, A. E. Ozias, and H. B. Bradley, Paper 75 presented at Electrochemical Society Meeting, Washington, D. C., May 9-13, 1971.
2. R. F. Lever, *IBM J. Res. Develop.*, **8**, 460 (1964).
3. L. P. Hunt and E. Sirtl, *This Journal*, **119**, 1741 (1972).
4. V. S. Ban, *ibid.*, **118**, 1473 (1971).
5. V. S. Ban, *J. Crystal Growth*, **17**, 19 (1972).
6. V. S. Ban and M. Ettenberg, *J. Phys. Chem. Solids*, **34**, 1119 (1973).
7. L. P. Hunt and E. Sirtl, in "Chemical Vapor Deposition, Second International Conference," J. M. Blocher, Jr. and J. C. Withers, Editors, The Electrochemical Society Softbound Symposium Series, New York (1970).
8. H. J. T. Ellingham, *J. Soc. Chem. Ind.*, **63**, 125 (1944).
9. V. S. Ban, *Mat. Res. Bull.*, **10**, 81 (1975).
10. "Index of Mass Spectral Data," ASTM Committee E-14 on Mass Spectrometry, Philadelphia, Pa. (1969).
11. P. H. Robinson and N. Goldsmith, *J. Electron. Mat.*, **12**, 313 (1975).
12. J. Bloem, in "Semiconductor Silicon 1973," p. 180, H. R. Huff and R. R. Burgess, Editors, The Electrochemical Society Softbound Symposium Series, Princeton, N.J. (1973).
13. E. Sirtl, L. P. Hunt, and D. H. Sawyer, *This Journal*, **121**, 919 (1974).

Chemical Processes in Vapor Deposition of Silicon

II. Deposition from SiCl_3H and SiCl_4

Vladimir S. Ban*

RCA Laboratories, Princeton, New Jersey 08540

ABSTRACT

Chemical processes occurring in the vapor deposition of silicon from SiCl_3H and SiCl_4 were studied by means of a mass spectrometer coupled to the CVD reactor. Species identified in the vapor phase were H_2 , HCl , SiCl_2 , SiCl_2H_2 , SiCl_3H , and SiCl_4 . Their partial pressures were measured at temperatures of 1000°, 1200°, and 1300°K; the Cl/H value was 10^{-1} . Values of these partial pressures were compared with the calculated equilibrium partial pressures for the Si-Cl-H system, as well as with partial pressures determined in the deposition of Si from SiCl_2H_2 . On the basis of the obtained results, we discuss the nature and the extent of chemical processes occurring during the deposition of Si from SiCl_4 and SiCl_3H .

In the preceding paper of this series (1), the chemical processes occurring in the deposition of Si from SiCl_2H_2 and in the HCl-etching of Si were discussed. The topic of the present paper is chemical processes occurring in the deposition of Si from SiCl_3H and from SiCl_4 . Both of these gases are important sources for the deposition of Si on the industrial scale.

In principle, the deposition of Si from all chlorosilanes should proceed in identical manner, because in all cases one deals with the Si-Cl-H system. The rate and the efficiency of the deposition, as well as the composition of the vapor phase should be uniquely determined by specifying the temperature, the total pressure, and the Cl/H ratio in the system, providing that the thermochemical equilibrium has been established. In reality, however, significant differences in the rate and the efficiency of Si deposition from various chlorosilanes have been observed (2). This implies that certain deviations from the thermochemical equilibrium occur, and that the nature of the input gas affects the deposition.

We studied possible causes and the extent of these effects by experimentally determining the composition of the gas phase by means of a mass spectrometer in a manner described previously (1). The deposition from SiCl_3H and from SiCl_4 are compared with the deposition from SiCl_2H_2 discussed in Ref. (1). Values of the experimentally determined partial pressures will also be compared with the previously calculated equilibrium partial pressures of vapor species in the Si-Cl-H system (1). On the basis of these comparisons, we shall discuss chemical processes occurring during the Si deposition and the effect of the nature of the input chlorosilanes on these processes.

Experimental

The mass spectrometer-CVD reactor combination has been described in Ref. (1). Controlled amounts of SiCl_3H or of SiCl_4 were introduced into the reactor by means of the Tylan Source I Vaporizer Controller. The SiCl_3H and SiCl_4 were drawn from 50-lb tanks. Gases were of semiconductor grade purity and supplied by the M&T Chemicals Inc. The Matheson electronic mass flow transducers were used to introduce known amounts of carrier gases, such as H_2 or He, into the reactor. Therefore, partial pressures of Si-containing gases in the input mixtures were known.

The composition of initial mixtures was adjusted so that Cl/H = 10^{-1} . For the case of $\text{SiCl}_3\text{H-H}_2$ mixture, the Cl/H ratio is given by the following expression

$$\text{Cl/H} = \frac{3P_{\text{SiCl}_3\text{H}}}{P_{\text{SiCl}_3\text{H}} + 2P_{\text{H}_2}} \quad [1]$$

The corresponding expression for the $\text{SiCl}_4\text{-H}_2$ mixture is given by

$$\text{Cl/H} = \frac{4P_{\text{SiCl}_4}}{2P_{\text{H}_2}} \quad [2]$$

In the above expressions, $P_{\text{SiCl}_3\text{H}}$, P_{SiCl_4} , and P_{H_2} are the partial pressures of these gases at their entrance into the reactor. The $\text{SiCl}_3\text{H-H}_2$ mixture was prepared by combining flows of 100 cm^3/min of SiCl_3H with 1450 cm^3/min of H_2 . In the case of $\text{SiCl}_4\text{-H}_2$ mixture, 132 cm^3/min of SiCl_4 was mixed with 2640 cm^3/min of H_2 .

The effect of replacing H_2 by He as a carrier gas was also studied. For this purpose, 132 cm^3/min of SiCl_4 was mixed with 2640 cm^3/min of He. Partial pressures of gases in this mixture will be compared with partial pressures in the mixtures containing H_2 .

Results

Following the method described in Ref. (1), one can determine the qualitative and the quantitative composition of the vapor phase by means of a mass spectrometer. Briefly, various vapor species can be identified by their characteristic mass spectra. Values of partial pressures can then be determined from the mass spectrometrically measured relative amounts of various species and the specified Cl/H ratio and the total pressure in the system, which is 1 atm. Vapor species detected in the Si-Cl-H system, when either SiCl_3H or SiCl_4 was used in the initial mixture, were: HCl , SiCl_2 , SiCl_2H_2 , SiCl_3H , SiCl_4 , and H_2 . In the Si-Cl-He system, only SiCl_2 , SiCl_4 , and He were detected. In Table I, the experimentally determined par-

Table I. Experimental partial pressures of vapor species in $\text{SiCl}_2\text{H}_2\text{-H}_2$, $\text{SiCl}_3\text{H-H}_2$, and $\text{SiCl}_4\text{-H}_2$ mixtures (Cl/H = 10^{-1} in all cases) and their comparison with the calculated equilibrium partial pressures for the Si-Cl-H system

Temperature, °K	Species	P_p (atm) (Eq.)	P_p (atm) (SiCl_2H_2)	P_p (atm) (SiCl_3H)	P_p (atm) (SiCl_4)
1000	HCl	1.1×10^{-2}	1.7×10^{-2}	1.4×10^{-2}	1.9×10^{-2}
	SiCl_2	6.6×10^{-5}	5.2×10^{-3}	4.0×10^{-3}	$<10^{-5}$
	SiCl_2H_2	1.3×10^{-3}	5.2×10^{-3}	3.6×10^{-4}	$<10^{-5}$
	SiCl_3H	1.9×10^{-2}	3.6×10^{-2}	1.6×10^{-2}	1.2×10^{-2}
	SiCl_4	3.0×10^{-2}	9.8×10^{-3}	1.2×10^{-2}	3.8×10^{-2}
	H_2	0.939	0.9268	0.954	0.9478
1200	HCl	4.0×10^{-2}	6.5×10^{-2}	4.2×10^{-2}	2.8×10^{-2}
	SiCl_2	1.5×10^{-3}	8.5×10^{-3}	1.1×10^{-2}	2.8×10^{-3}
	SiCl_2H_2	1.4×10^{-3}	1.4×10^{-3}	1.1×10^{-3}	$<10^{-5}$
	SiCl_3H	1.5×10^{-2}	1.3×10^{-2}	1.0×10^{-2}	1.8×10^{-2}
	SiCl_4	2.4×10^{-2}	1.4×10^{-2}	2.2×10^{-2}	2.5×10^{-2}
	H_2	0.918	0.900	0.914	0.9256
1300	HCl	6.4×10^{-2}	1.1×10^{-1}	8.4×10^{-2}	6.4×10^{-2}
	SiCl_2	5.0×10^{-3}	1.4×10^{-2}	1.8×10^{-2}	1.7×10^{-2}
	SiCl_2H_2	1.3×10^{-3}	6.6×10^{-3}	5.3×10^{-3}	5.3×10^{-3}
	SiCl_3H	1.2×10^{-2}	4.0×10^{-3}	5.7×10^{-3}	3.9×10^{-3}
	SiCl_4	2.0×10^{-3}	6.5×10^{-3}	1.1×10^{-2}	1.7×10^{-2}
	H_2	0.8977	0.8589	0.876	0.8721

* Electrochemical Society Active Member.

Key words: mass spectrometry, CVD, thermodynamics, kinetics.

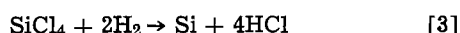
Table II. Comparison of the experimentally measured with the calculated equilibrium partial pressures of vapor species detected in the SiCl₄-He mixtures; Cl/He = 0.2, T = 1000°, 1200°, and 1300°K

Species	1000°K		1200°K		1300°K	
	P _{eq} (atm)	P _{exp} (atm)	P _{eq} (atm)	P _{exp} (atm)	P _{eq} (atm)	P _{exp} (atm)
SiCl ₂	1.15 × 10 ⁻⁴	>10 ⁻⁵	2.6 × 10 ⁻³	7.3 × 10 ⁻³	9.34 × 10 ⁻³	1.2 × 10 ⁻²
SiCl ₄	4.74 × 10 ⁻²	4.8 × 10 ⁻³	4.61 × 10 ⁻²	4.4 × 10 ⁻²	4.27 × 10 ⁻²	4.1 × 10 ⁻²
He	0.95268	~0.95240	0.95127	0.94890	0.94796	0.95873

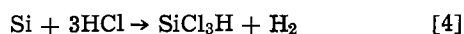
tial pressures of vapor species present in the SiCl₂H₂-H₂, SiCl₃H-H₂, and SiCl₄-H₂ mixtures as well as the calculated equilibrium partial pressures in the Si-Cl-H system are listed. For all cases, Cl/H ratio is 10⁻¹; pressure values for temperatures of 1000°, 1200°, and 1300°K are listed. In Table II we compare the equilibrium and the experimentally determined partial pressures in the Si-Cl-He system at the above temperatures.

Discussion and Conclusions

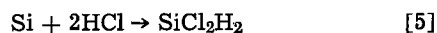
Results listed in Table I permit one to compare the deposition of Si from various chlorosilanes. There are some noticeable differences. At T = 1000°K, most of the SiCl₄ remains undecomposed, and practically no deposition of Si occurs. This is consistent with the relatively high stability of SiCl₄ in comparison with other chlorosilanes (1) and with the observed lower growth rate of Si from SiCl₄ (2). Differences between the deposition from SiCl₂H₂ and from SiCl₃H are smaller. With increasing temperatures, the values of pressures of vapor species become more similar for all three chlorosilanes and also closer to the calculated equilibrium partial pressures. In other words, the system approaches thermochemical equilibrium. However, at T = 1300°K, one still notices differences between the equilibrium and the experimental partial pressures. In particular, partial pressures of species containing two or less chlorine atoms (i.e., HCl, SiCl₂, and SiCl₂H₂) tend to be higher than their equilibrium values, while partial pressures of SiCl₃H and SiCl₄ tend to be lower than their equilibrium values. It is not clear whether the partial pressure of the incoming SiCl₄ indeed drops below its equilibrium value, or if this small deviation (~15%) is caused by the uncertainties of temperature measurement and/or of the thermochemical data used. Similar results have been reported in Ref. (1), and results described here provide some additional information which basically supports our previous discussion, where we concluded that the adsorption of HCl on the Si surface is retarded. In the case of growth of Si from SiCl₄ which occurs via the following reaction



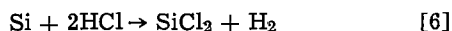
four molecules of HCl are supplied. It seems that their residence time at the Si surface is short and that they desorb easily. This would lead to the relatively smaller probability of forming, say, SiCl₃H where three molecules of HCl are needed



than of forming SiCl₂ or SiCl₂H₂ where only two molecules of HCl are needed



or



Nevertheless, all of the above reactions occur and the resultant partial pressures of all vapor species at T > 1200°K are never more than a factor of 3 or 4 apart from the equilibrium partial pressures.

The equilibrium partial pressures in the Si-Cl-He were calculated by employing the following system of three equations

$$P_{\text{SiCl}_4} + P_{\text{SiCl}_2} + P_{\text{He}} = 1.0 \quad [7]$$

$$\frac{\text{Cl}}{\text{He}} = \frac{4P_{\text{SiCl}_4} + 2P_{\text{SiCl}_2}}{P_{\text{He}}} = 0.2 \quad [8]$$

and

$$\text{SiCl}_{4(g)} + \text{Si}_{(s)} \rightarrow 2\text{SiCl}_{2(g)}; k_p = \frac{P_{\text{SiCl}_2}^2}{a_{\text{Si}} \cdot P_{\text{SiCl}_4}} \quad [9]$$

The first of these equations specifies the total pressure in the system, the second one the Cl/He ratio, and the third one the chemical reaction involving the Si-containing gaseous species. In Eq. [9], a_{Si} represents the activity of solid silicon; a_{Si} = 1.0. Values of k_p at 1000°, 1200°, and 1300°K were calculated from thermochemical data given in Ref. (1).

The results of these calculations are given in Table II, along with the experimentally determined partial pressures of SiCl₂, SiCl₄, and He. An inspection of Table II shows that SiCl₄ does not react at T ≤ 1000°K. At higher temperatures, significant amounts of SiCl₂ are detected, indicating that reaction [9] takes place. At 1200° and 1300°K the observed partial pressures are relatively close to the equilibrium pressures. Again, the P_{SiCl₄} appears to be slightly below the equilibrium value, but the extent of these deviations is smaller than the uncertainty in experimental temperatures and thermochemical data. Both P_{SiCl₂} and P_{SiCl₄} are considerably higher than the corresponding pressures in the Si-Cl-H system. This is so because, due to the absence of hydrogen, species such as SiCl₂H₂, SiCl₃H, and HCl cannot form. It is quite probable that in the Si-Cl-H system, where reactions such as [4], [5], and [6] are possible, reaction [9] occurs to a smaller extent.

Finally, we shall discuss the efficiencies of the Si deposition from SiCl₃H and from SiCl₄. These efficiencies can be obtained by comparing the Si/Cl ratios of the initial mixture with ratios at elevated temperatures. The same method was used in Ref. (1). In Fig. 1, the experimentally obtained efficiencies (full lines) are compared with the deposition efficiencies available under the equilibrium conditions (dotted lines). These efficiencies give the amount of Si deposited as percentages of Si introduced into the system. One notices that in the case of SiCl₃H, the experimental efficiencies run close to the theoretical efficiencies. In the case of SiCl₄, the theoretical and experimental efficiencies are significantly lower. At T < 1100°K, actual etching of the previously deposited Si takes place when SiCl₄-H₂ mixture with Cl/H = 10⁻¹ is introduced into the system. Of course, in the Si-Cl-He system, etching occurs at all temperatures via the reaction [9]. The upper curves in Fig. 1 represent the theoretical and the experimental efficiencies of the deposition of Si from SiCl₂H₂. These results are taken from the previous paper and indicate that for the given temperature and Cl/H ratio of the initial mixture, SiCl₂H₂ is the most efficient source of Si among the chlorosilanes examined.

The presented work could be summarized as follows:

1. Chemical processes in the deposition of Si from SiCl₃H-H₂ and SiCl₄-H₂ mixtures with Cl/H = 10⁻¹ were examined by the mass spectrometer at temperatures of 1000°, 1200°, and 1300°K.

2. Vapor species detected at elevated temperatures were H₂, HCl, SiCl₂, SiCl₂H₂, SiCl₃H, and SiCl₄; their partial pressures were measured and compared with partial pressures detected in SiCl₂H₂-H₂ mixtures and

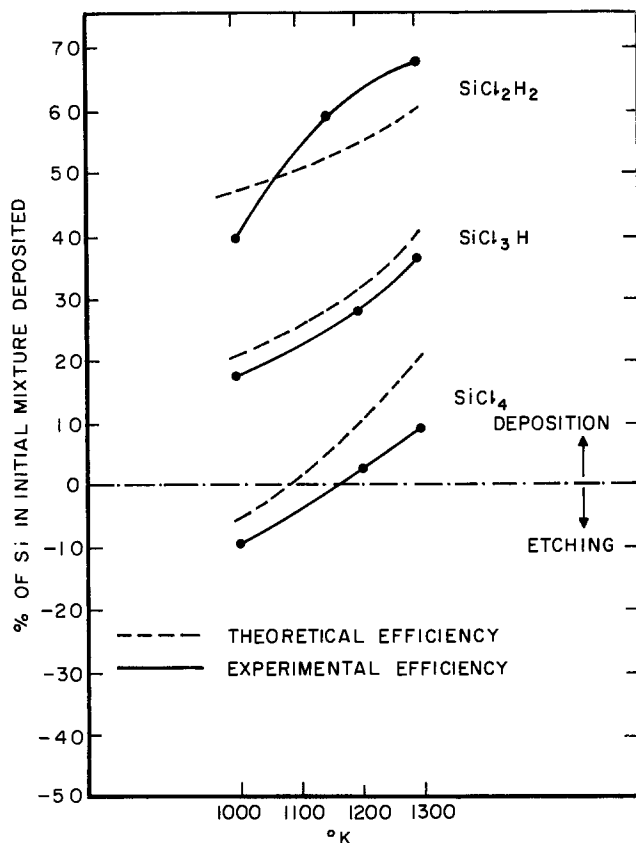


Fig. 1. Theoretical and experimental efficiencies of deposition of silicon from SiCl_2H_2 , SiCl_3H , and SiCl_4 in temperature interval of 1000°K - 1300°K ; $\text{Cl}/\text{H} = 10^{-1}$ in all cases.

with the calculated equilibrium partial pressures.

3. In the Si-Cl-He system, SiCl_4 , SiCl_2 , and He were present in the vapor and their partial pressures were measured and compared with the calculated equilibrium partial pressures for this system.

4. Measured values of partial pressures indicate that there are some significant deviations from the thermochemical equilibrium in the system, especially at lower temperatures where SiCl_4 remains largely undecomposed; at $T > 1200^\circ\text{K}$, partial pressures resemble more closely the equilibrium partial pressures, particularly in the Si-Cl-He system.

5. The calculated and experimentally determined efficiencies of the deposition of Si from SiCl_2H_2 , SiCl_3H , and SiCl_4 were compared and found to decrease in order $\eta\text{-SiCl}_2\text{H}_2 > \eta\text{-SiCl}_3\text{H} > \eta\text{-SiCl}_4$.

Acknowledgments

The author acknowledges helpful discussions with D. Richman, N. Goldsmith, G. W. Cullen, and M. Ettenberg.

Manuscript submitted Oct. 29, 1974; revised manuscript received June 2, 1975.

Any discussion of this paper will appear in a Discussion Section to be published in the June 1976 JOURNAL. All discussions for the June 1976 Discussion Section should be submitted by Feb. 1, 1976.

Publication costs of this article were partially assisted by RCA Corporation.

REFERENCES

1. V. S. Ban and S. L. Gilbert, *This Journal*, **122**, 1382 (1975).
2. F. C. Eversteyn, *Philips Res. Rept.*, **29**, 45 (1974).

A Solid-State Galvanic Cell Study of the Ti_2O_3 , Ti_3O_5 Equilibrium

Ronald G. Sommer*¹ and E. David Cater

Department of Chemistry, University of Iowa, Iowa City, Iowa 52242

ABSTRACT

The chemical potential of oxygen of the coexisting phases Ti_2O_3 , Ti_3O_5 was found to be given by $\Delta\bar{G}_{1/2\text{O}_2}(\text{Ti}_2\text{O}_3, \text{Ti}_3\text{O}_5) = -86,030 + 15.30T(\text{K}) \pm 180$ cal (1 std dev.) from a study of the cell $\text{Nb, NbO/YDT [7.5 weight per cent (w/o) yttria]/Ti}_2\text{O}_3, \text{Ti}_3\text{O}_5$ between 1022° and 1495°K . In the evaluation of the data obtained for the above cell the relationship $\Delta G^\circ_f(\text{NbO}) = -99,870 + 21.51T(\text{K}) \pm 150$ cal (1 std dev.) which was determined from a study of the cell $\text{Nb, NbO/YDT (15 w/o yttria)/Fe, Fe}_2\text{O}$ between 1089° and 1426°K was used. The data for $\text{Ti}_2\text{O}_3, \text{Ti}_3\text{O}_5$ correlate well with calorimetric measurements at lower temperatures and vaporization studies at higher temperatures.

This paper presents a study of the equilibrium chemical potential of oxygen in the coexisting solid phases $\text{Ti}_2\text{O}_3, \text{Ti}_3\text{O}_5$ from 1022° to 1495°K by a galvanic cell technique. For convenience idealized formulas are utilized in this paper for the various solid phases except where their actual nonstoichiometric compositions are of interest. The solid phases in the Ti-O system are of considerable interest because of the wide range of nonstoichiometry and unusual defect ordering near $\text{O}/\text{Ti} = 1$ (1, 2) and the multitudinous array of phases

$\text{Ti}_n\text{O}_{2n-1}$ based on crystallographic shear in the composition range O/Ti from 1.667 to 2.00 (1, 3, 4). At the time this work was begun thermodynamic data from calorimetric measurements were available for presumably stoichiometric TiO , Ti_2O_3 , Ti_3O_5 , and TiO_2 [references summarized in JANAF (5)]. Knudsen cell and mass spectrometric studies at temperatures above about 1700°K had explored the nature and thermodynamics of the vaporization processes (6-8) of the phases from $\text{O}/\text{Ti} = 1.0$ -2.0. Several thermodynamic discrepancies and uncertainties existed in the literature, arising from uncertainties regarding effects of nonstoichiometry and heats of transition. Equilibrium gravimetric studies involving gas-solid equilibria have

* Electrochemical Society Active Member.

¹ Present address: Corning Glass Works, Sullivan Park, Corning, New York 14830.

Key words: thermodynamics, titanium oxides, niobium monoxide, yttria-doped thoria.

been reported for systems with O/Ti ratios greater than 1.67 (Ti_3O_5), but this technique has not been successfully applied to systems with the low oxygen potentials found in $\text{O/Ti} < 1.67$ (9, 10).

The present work was undertaken to provide thermochemical information on the intermediate oxide phases Ti_2O_3 and Ti_3O_5 by an equilibrium technique, in the range of temperatures between the calorimetric and vaporization studies and at lower oxygen potentials than could be explored with gravimetric techniques. Of particular interest was the question of whether the calorimetric data on stoichiometric materials were valid when extrapolated to higher temperatures where the coexisting phases might exhibit significant nonstoichiometry.

The use of solid oxide electrolyte galvanic cells for the direct determination at elevated temperatures of the chemical potential ($\Delta\bar{G}_{1/2\text{O}_2}$) or partial pressure (P_{O_2}) of oxygen of two phases which coexist in some metal-oxygen system is by now well known (11, 12). Prior to the recently published, extensive study of the Ti-O system with yttria-doped thoria (YDT) electrolyte cells by Suzuki and Sambongi (9), the two-phase region $\text{Ti}_2\text{O}_3, \text{Ti}_3\text{O}_5$ had not been investigated via this technique, although a galvanic cell study of the adjoining two-phase region $\text{Ti}_3\text{O}_5, \text{Ti}_4\text{O}_7$ had been performed by Vasil'eva and Shaulova, along with studies on higher oxide phases (13). A measurement of the difference in oxygen potential of the electrodes "Ti,TiO" and "TiO, Ti_2O_3 " with a calcia-stabilized zirconia (CSZ) electrolyte cell attempted by Hoch *et al.* (14) was of questionable value because of incorrect assumptions about the Ti-O phase diagram and the useful region of CSZ. In the region $\text{O/Ti} > 1.6$, emf and gas-solid equilibrium studies have been surveyed by Suzuki and Sambongi (9) and critically reviewed by Merritt *et al.* (10).

The determination of $\Delta\bar{G}_{1/2\text{O}_2}$ for the region $\text{Ti}_2\text{O}_3, \text{Ti}_3\text{O}_5$ has been carried out in this laboratory via a study of the cell $\text{Nb}_2\text{NbO}/\text{YDT}$ (7.5 w/o yttria)/ $\text{Ti}_2\text{O}_3, \text{Ti}_3\text{O}_5$. Although the equilibrium partial pressures of oxygen exhibited by these electrodes, on the order of 10^{-25} and 10^{-22} atm at 1000°C , respectively, are very low, Etsell (15) indicates that the average ionic transport number (\bar{t}_i) of the YDT electrolyte for such a cell is greater than 0.99 at 1000°C .

A preliminary investigation of the cell $\text{Nb}_2\text{NbO}/\text{YDT}$ (15 w/o yttria)/ $\text{Fe,Fe}_x\text{O}$ (x indicates the boundary composition of iron-saturated wüstite) was performed in order to evaluate the emf apparatus and redetermine $\Delta G^\circ_f(\text{NbO})$. The majority of the emf data that have been reported for this cell are in excellent agreement (16, 17).

Experimental

Materials used in preparing electrodes were niobium and niobium pentoxide powders, both of 99.8% purity, and titanium powder of 99.5% purity from A. D. MacKay, Inc., hydrogen-reduced iron powder of Fisher Certified Reagent grade (labeled "95.8%" via an analysis which did not include oxygen), Matheson, Coleman, and Bell reagent grade iron oxide (Fe_2O_3) of 99% purity, and Baker Analyzed Reagent titanium dioxide powder, whose analyzed-for impurities totaled 0.0581%. X-ray powder diffraction was used to identify phases present in electrode and electrolyte materials.

Dense, $\frac{1}{8}$ in. thick, $\frac{1}{2}$ in. diameter disks of metal-to-oxide mole ratio 5:1, pressed at 3 kbar, functioned as the electrodes in the $\text{Nb}_2\text{NbO}/\text{Fe,Fe}_x\text{O}$ cell. The NbO phase was prepared by sintering the appropriate mixture of Nb_2O_5 at 1300°C for 12 hr in an inductively heated tungsten crucible within an evacuated quartz-walled chamber. The $\text{Fe,Fe}_x\text{O}$ electrode was generated *in situ* from an $\text{Fe,Fe}_2\text{O}_3$ disk by holding the cell at 750°C overnight prior to any emf measurements.

The coexisting phases $\text{Ti}_2\text{O}_3, \text{Ti}_3\text{O}_5$ were prepared by vacuum sintering the appropriate mixture of Ti + TiO_2 at 900 – 1500°C for 12 hr. The O/Ti ratio was found to

be 1.63 both before and after use, by combustion in air at 1000°C to a product taken to be stoichiometric TiO_2 . A mechanically sound $\text{Ti}_2\text{O}_3, \text{Ti}_3\text{O}_5$ disk could not be made, so the $\text{Ti}_2\text{O}_3, \text{Ti}_3\text{O}_5$ powder was packed into a flat-bottomed, 7.5 w/o YDT tube to function as the upper electrode in the $\text{Nb}_2\text{NbO}/\text{Ti}_2\text{O}_3, \text{Ti}_3\text{O}_5$ cell. The tube had a nominal wall thickness of $1/16$ in. and outside diameter of $\frac{1}{2}$ in. A new electrolyte disk and the previously used Nb,NbO electrode completed the cell.

Powders obtained by crushing Zircoa (Zirconium Corporation of America, Solon, Ohio) slipcast YDT electrolyte tubes were used in preparing electrolyte disks of nominal composition 7.5 and 15 w/o yttria. Isaacs (18) has discussed the impurity level of such YDT. The disks were pressed at 3 kbar and densified by sintering in vacuum at 2000°C for 4 hr followed by firing in air at 1200°C . Disks of $\frac{1}{2}$ in. diameter and $\frac{3}{8}$ in. thickness, of densities 9.2 and 7.2 g/cm^3 [103 and 92% of theoretical density (19)] were obtained.

The 7.5 w/o YDT tubes received from Zircoa were found by x-ray diffraction to contain detectable amounts of a second phase identified as thoria. However, the second phase was not detected in the electrolyte disks prepared by us.

The emf apparatus is shown in Fig. 1. A cell was supported in the inductively heated tantalum furnace tube and electrical contact to each electrode was made by a disk of platinum foil to which the bead of a platinum, platinum-10% rhodium thermocouple was attached. All insulators and cell supports were of recrystallized alumina. Springs at the top and bottom pushed the assembly together. A second concentric tantalum tube within the furnace tube shielded cells from the high frequency field. The environment of the cell and furnace was a clean dynamic vacuum, routinely 10^{-6} Torr.

A Rubicon precision potentiometer alone, or in combination with a Cary Model 31-CV vibrating reed electrometer, with appropriate filtering (14, 20) to remove high frequency signals, was used to measure emf's. No interference by the high frequency field was observed in cell emf measurements reported here. Cells containing the $\text{Ta, Ta}_2\text{O}_5$ electrode had been found to display high emf's within this apparatus when the induction coil was energized (20), presumably because of rectification by tantalum oxide films on tanta-

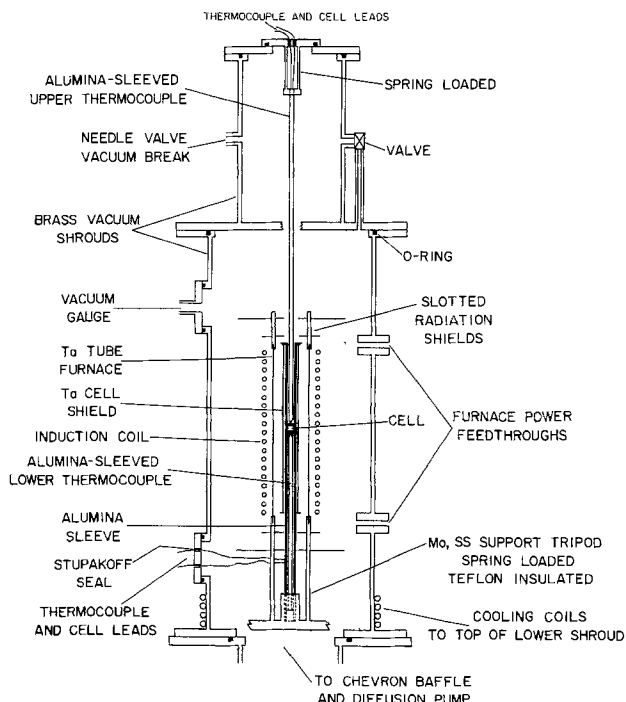


Fig. 1. High temperature inductively heated emf apparatus

lum. Temperatures have an estimated precision of $\pm 1^\circ$ and uncertainty of $\pm 4^\circ$. The latter estimate includes an observed temperature gradient of from zero degree at 1100°K to 4° at 1400°K. Two runs were made with each cell. The emf data were taken after equilibration at temperatures both sequentially increased and decreased. Equilibration times were from 1.3 to 25.6 hr with the majority less than 3 hr. Both cells were still operating excellently after a total time at 900°K or above of approximately one week.

Apparently reversible, and clearly reproducible, emf's were displayed by the cells. Somewhat less scatter in the cell emf's, and also distinctly shorter equilibration times, were evident above about 1250°K. The Fe,Fe_xO electrode of the cell Nb,NbO/YDT/Fe,Fe_xO literally welded itself to the electrolyte disk, with staining of the YDT occurring to a depth of 80 μ m. Others (21, 22) have previously reported similar phenomena. An electron microprobe study was made of a section sliced perpendicularly through the Fe,Fe_xO-YDT interface. Although the study was somewhat inconclusive due to excitation of the elements by secondary x-rays produced within the sample, no convincing evidence was obtained for diffusion of Fe into the electrolyte or Y into the Fe,Fe_xO disk. No gradient of Y, Fe, or O was detected near the interface and no evidence was found for formation of other phases such as the YFeO₃ reported by Worrell (21).

In the study of Ti₂O₃,Ti₃O₅, considerable coloration was developed by the YDT. However, no evidence was obtained for formation of any new phase such as, for example, YTiO₃ (23).

Results and Discussion

The data obtained in this laboratory for the cells Nb,NbO/YDT (15 w/o yttria)/Fe,Fe_xO and Nb,NbO/YDT (7.5 w/o yttria)/Ti₂O₃,Ti₃O₅ are plotted, respectively, in Fig. 2 and 3.

The raw data for the cell Nb,NbO//Fe,Fe_xO from 1089° to 1426°K when fit by an unweighted least squares analysis yield

$$E(\text{obs, mV}) = (797.9 \pm 5.6) - (0.1312 \pm 0.0044)T(\text{K}) \quad [1]$$

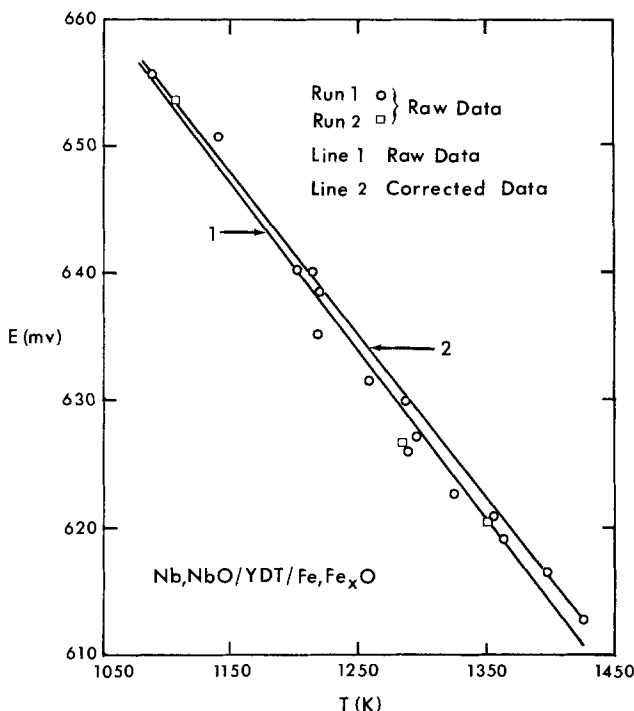


Fig. 2. Emf of cell Nb,NbO/YDT(15 w/o yttria)/Fe,Fe_xO vs. temperature. Line 1, least squares fit to data as measured (Eq. [1]); line 2, least squares fit to data adjusted for solubility of O in Nb (Eq. [2]).

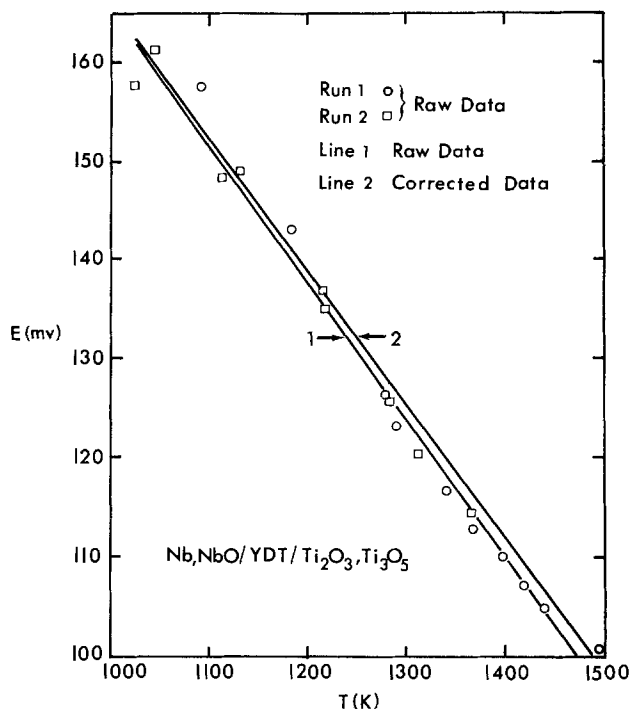


Fig. 3. Emf of cell Nb,NbO/YDT (7.5 w/o yttria)/Ti₂O₃,Ti₃O₅ vs. temperature. Line 1, least squares fit to data as observed (Eq. [7]); line 2, least squares fit to data adjusted for solubility of O in Nb (Eq. [8]).

To obtain the standard free energy of formation of NbO, the emf data were corrected point by point for the solubility of oxygen in niobium, giving

$$E(\text{corr, mV}) = (794.3 \pm 5.7) - (0.1275 \pm 0.0044)T(\text{K}) \quad [2]$$

Uncertainties in slopes and intercepts in these and subsequent equations are standard deviations. The emf's have standard deviations about the line of ± 1.7 and ± 1.8 mV in [1] and [2], respectively. The correction for oxygen solubility was made by using Bryant's solubility data (24) and assuming that Henry's law is valid for oxygen dissolved in niobium, while Nb obeys Raoult's law. Thus

$$E(\text{corr}) = E(\text{obs}) - (RT/nF) \ln X_{\text{Nb}} \quad [3]$$

This correction amounts to at most 1.8 mV at 1426°K.

Correspondingly, from the Nernst relation $\Delta G = -nFE$

$$\Delta G^{\circ}_{1/2 \text{ O}_2}(\text{cell}) = (-36,640 \pm 260) + (5.88 \pm 0.20)T(\text{K}) \pm 80 \text{ cal} \quad [4]$$

The value of Faraday's constant F was taken to be 23,061 cal/mV-equiv. Using the relationship for the free energy of formation of the iron-rich wüstite phase from 873°-1600°K derived by Steele and Alcock (25) from the work of Darken and Gurry (26)

$$\Delta G^{\circ}_f(\text{Fe}_x\text{O}) = -63,235 + 15.63T(\text{K}) \pm 125 \text{ cal mole}^{-1} \quad [5]$$

it was found that

$$\Delta G^{\circ}_f(\text{NbO}) = -99,870 + 21.51T(\text{K}) \pm 150 \text{ cal mole}^{-1} \quad [6]$$

for 1089°-1426°K.

Tabulated in Table I are values of $\Delta G^{\circ}_f(\text{NbO})$ which were calculated from the above relationship, from a study representative of the literature on the same cell, that of Ignatowicz and Davies (27), values from Worrell's results (21) based on cells different from the one studied here, along with those published by JANAF Thermochemical Tables (17). Also tabulated for comparison are values of $\Delta G^{\circ}_{1/2 \text{ O}_2}$ for the coexisting

Table I. Comparison of $\Delta G^\circ_f(\text{NbO})$ from this work with literature values

	$\Delta G^\circ_f(\text{NbO}, \text{kcal})$			
	1100°K	1200°K	1300°K	1400°K
This work (1089°-1426°K)	-76.21	-74.06	-71.91	-69.76
Worrell (21) (1050°-1300°K)				
1. NbO,NbO ₂ //NbO ₂ ,Nb ₂ O _{4.8}	-76.79	-74.65	-72.50	(-70.36)*
2. Nb,NbO//NbO,NbO ₂	-76.18	-74.02	-71.87	(-69.71)*
Ignatowicz and Davies (27)** (1073°-1373°K)	-76.18	-74.11	-72.03	(-69.95)*
JANAF (17)	-76.46	-74.39	-72.33	-70.28
$\Delta \bar{G}_{1/2\text{O}_2}(\text{Nb,NbO})$, this work	-76.19	-74.02	-71.85	-69.98

* Parentheses indicate ΔG°_f at temperature outside of experimental range.

** Corrected as herein for the solubility of oxygen in niobium.

phases Nb,NbO calculated from Eq. [1] and [5]. Worrell's first relationship was derived from $\Delta G^\circ_f(\text{NbO}_2)$ (28) and $\Delta G^\circ_f(\text{Fe}_x\text{O})$ (29) obtained from reviews in the literature along with data from the cells NbO₂,Nb₂O_{4.8}//Fe,Fe_xO and NbO,NbO₂//NbO₂,Nb₂O_{4.8}. His second relationship was derived from the same $\Delta G^\circ_f(\text{NbO}_2)$ (28) and data from the cell Nb,NbO//NbO,NbO₂. JANAF (17) has adopted $\Delta H^\circ_{f,298}$ based on the average of those from seven equilibrium (emf) studies. Five of these, including that of Ignatowicz and Davies (27), were of the cell Nb,NbO//Fe,Fe_xO. Worrell's data (21) for the cell Nb,NbO//Ta,Ta₂O₅ were also used. It is evident that the values tabulated for $\Delta G^\circ_f(\text{NbO})$ in Table I agree within better than 1% for 1100°-1400°K. Note that $\Delta G^\circ_f(\text{Fe}_x\text{O})$ of Steele and Alcock (25) and that adopted by Blumenthal and Whitmore (29), which was used by Worrell (21) and by Ignatowicz and Davies (27), agree within 33 cal in this range. JANAF (17) has tabulated $\Delta G^\circ_f(\text{Fe}_{0.947}\text{O})$, incorrectly implying a constant lower phase boundary composition for wüstite (26, 30), which are approximately 100 cal more negative than the other data. Giddings and Gordon (30, 31) in presenting the latest analysis on oxygen activities and phase boundaries of wüstite and of the use of Fe,Fe_xO electrode, prefer the equation for $\Delta G^\circ_f(\text{Fe}_x\text{O})$ of Rizzo *et al.* (32), which gives values at 1100° and 1400°K, respectively, 220 and 80 cal more positive than those chosen here.

The excellent agreement of our results for $\Delta G^\circ_f(\text{NbO})$ with those in the literature is taken as evidence that our apparatus and technique are giving valid results, and that the Nb,NbO electrode is a suitable reference for measurements on Ti₂O₃,Ti₃O₅.

The raw data for the cell Nb,NbO//Ti₂O₃,Ti₃O₅ from 1022° to 1495° plotted in Fig. 3 were fit by unweighted least squares to obtain

$$E(\text{obs, mV}) = (303.6 \pm 5.0) - (0.1382 \pm 0.0040)T(\text{K}) \quad [7]$$

while the data corrected for the solubility of oxygen in niobium via Eq. [3] fit the relationship

$$E(\text{corr, mV}) = (300.1 \pm 5.0) - (0.1346 \pm 0.0040)T(\text{K}) \quad [8]$$

The standard deviation of E about the lines in [7] and [8] is ± 2.3 mV. Correspondingly

$$\Delta G^\circ_{1/2\text{O}_2}(\text{cell}) = (-13,840 \pm 230) + (6.21 \pm 0.18)T(\text{K}) \pm 110 \text{ cal} \quad [9]$$

and

$$\Delta \bar{G}_{1/2\text{O}_2}(\text{Ti}_2\text{O}_3, \text{Ti}_3\text{O}_5) = -86,030 + 15.30T(\text{K}) \pm 180 \text{ cal} \quad [10]$$

for 1089°-1426°K. For internal consistency our Eq. [6] for $\Delta G^\circ_f(\text{NbO})$ was used in deriving this equation.

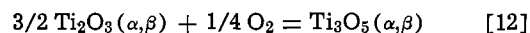
Tabulated in Table II are values of $\Delta \bar{G}_{1/2\text{O}_2}(\text{Ti}_2\text{O}_3, \text{Ti}_3\text{O}_5)$ which were calculated from the above relationship, from the graphically presented emf data of Suzuki and Sambongi (9) for the cell TiO_{1.6}//

Cr,Cr₂O₃, and from the recently revised JANAF Thermochemical Tables (17) for Ti₂O₃(c) and Ti₃O₅(β). Suzuki and Sambongi have published the only previous study of Ti₂O₃,Ti₃O₅ by emf techniques. They used the cells TiO_{1.6}/YDT/Cr,Cr₂O₃ and Ta,Ta₂O₅/YDT/TiO_{1.6} in a flowing argon atmosphere from 940° to 1740°K. Here, TiO_{1.6} represents several compositions in the range 1.560 < O/Ti < 1.648 in the Ti₂O₃,Ti₃O₅ two-phase region. They intercompared their Ta,Ta₂O₅ and Cr,Cr₂O₃ reference electrodes directly by means of the cell Ta,Ta₂O₅/YDT/Cr,Cr₂O₃, and both were measured against Fe,Fe_xO from 990° to 1520°K. Unfortunately their emf data and thermodynamic results for the Ti-O system are presented only graphically and they give no indication of how the lines in their figures were drawn among the data points. Their Eq. [20] for $\Delta G^\circ_f(\text{Fe}_x\text{O})$ taken from Ref. (20) contains two typographical errors. Numerous inconsistencies exist among their figures and equations. By carefully measuring their published figures and deriving equations from these measurements, we obtained the following equation which we believe to be the best representation of their data for the Ti₂O₃,Ti₃O₅ equilibrium

$$\Delta \bar{G}_{1/2\text{O}_2}(\text{Ti}_2\text{O}_3, \text{Ti}_3\text{O}_5) = -86,418 + 15.82T(\text{K}) \text{ cal} \quad [11]$$

As shown in Table II, our free energies and those of Suzuki and Sambongi (9) for oxygen in Ti₂O₃,Ti₃O₅ are in excellent agreement. This supports the validity of both sets of measurements, because different reference electrodes, physical arrangements, and equilibration procedures were employed. Above 1773°K their emf's rapidly dropped because of reaction of the TiO_{1.6} electrode and YDT electrolyte pellets.

The data in Table II calculated from the JANAF Tables (17) for Ti₂O₃(c) and Ti₃O₅(β) are derived principally from calorimetric measurements on stoichiometric material. Our emf results agree well (within about 1% in $\Delta \bar{G}_{1/2\text{O}_2}$) with these. JANAF (α-Ti₃O₅ table) (17) notes that the graphical emf data of Suzuki and Sambongi and "the authors' self-consistent data for the reference couples" yield ΔH and ΔS for the reaction



consistent with JANAF's adopted values. In addition, third law values of ΔH°_{298} for reaction [12], calculated from Suzuki and Sambongi's data, were in agreement with combustion calorimetric data.

Two further comments should be made in comparing the emf results to the JANAF data. First, use of the JANAF table for Fe_{0.947}O with the emf data would reduce the small differences of Table II by approximately 0.1 kcal per 1/2 mole O₂. Secondly, $\Delta \bar{G}_{1/2\text{O}_2}$ for the reference electrode Cr,Cr₂O₃ obtained in Suzuki and Sambongi's work (9) is systematically more positive than the data adopted for that system obtained by JANAF (17) by about 800 cal from 1000° to 1500°K. JANAF apparently did not use the emf work of Suzuki and Sambongi in drawing up their Cr₂O₃ tables, although Suzuki and Sambongi's data on Ti₂O₃,Ti₃O₅ were used by JANAF. However, both we and Suzuki and Sambongi have referenced our cells ultimately to the same free energies for Fe,Fe_xO (25) so that their Cr,Cr₂O₃ and our Nb,NbO couples are in a sense only intermediate standards. JANAF (17) utilized other data of Suzuki and Sambongi's taken with the Cr,Cr₂O₃ reference electrode in drawing up tables for Ti₄O₇. Suzuki's oxygen potentials for oxide pairs in 1.67 < O/Ti < 2.0 are in agreement with those determined by Merritt *et al.* (10) near 1300°K.

It appears from our results that the upper phase boundary (upb) composition of the Ti₂O₃ phase in equilibrium with the Ti₃O₅ phase from 1089° to 1426°K is not appreciably different from the stoichiometric composition. This is inferred because oxygen potentials we obtained from the equilibrium mixtures agree with those calculated from JANAF (17) for the stoichio-

Table II. Comparison of chemical potential of oxygen in Ti₂O₃,Ti₃O₅ from this work with literature values

	$\Delta\bar{G}_{1/2}O_2(Ti_2O_3, Ti_3O_5, \text{kcal})$					
	1000°K	1100°K	1200°K	1300°K	1400°K	1500°K
This work (1022°-1495°K)	(-70.73)*	-69.20	-67.67	-66.14	-64.61	(-63.08)*
Suzuki and Sambongi (9) (940°-1740°K)	-70.60	-69.02	-67.43	-65.85	-64.27	-62.69
JANAF (17)	-71.13	-69.66	-68.11	-66.51	-64.88	-63.24

* Parentheses indicate $\Delta\bar{G}_{1/2}O_2(Ti_2O_3, Ti_3O_5)$ at temperature outside of experimental range.

metric compounds. Ti₃O₅ was shown to be a line phase by Merritt *et al.* (10) near 1300°K from their gas-solid equilibration studies. Vaporization studies above 1800°K by Gilles and Wahlbeck and their co-workers (6-8) showed that Ti₃O₅ vaporizes congruently at the stoichiometric composition, and the reported partial pressures of oxygen for Ti₃O₅ and Ti₂O₃,Ti₃O₅ are compatible with the JANAF extrapolation of lower temperature data for the two stoichiometric compounds. Hence it appears that the upb of Ti₂O₃ deviates little from the ideal composition up to the melting point, and that the phase width $1.49 \leq O/Ti \leq 1.51$ suggested by Andersson *et al.* (33) is not unreasonable and may be too generous.

This conclusion is in marked contrast to the range $1.425 < O/Ti < 1.585$ around Ti₂O₃, shown by Suzuki and Sambongi in their Fig. 14 from 1273° to 1873°K. Their suggested composition range was deduced from a statistical thermodynamic argument patterned after Anderson (34), but the defect model they used is physically unrealistic, the calculated upb is richer in oxygen than TiO_{1.56}, one of their two-phase mixtures, the P_{O₂} values at the TiO_{1+x}-Ti₂O₃ phase boundary used in their calculations are probably (15) too low for valid measurement using YDT, and the resulting P_{O₂} at the proposed upb is inconsistent with either our or their emf data. Their suggested composition range for Ti₂O₃ is thus unrealistic.

In conclusion it seems reasonable to accept the thermodynamic data for Ti₂O₃ and Ti₃O₅ as tabulated by JANAF (17), because this recent compilation successfully correlates calorimetric, emf, and vaporization data over a very large range of T and P_{O₂}.

More precisely stated, the JANAF tabulation presents smoothed enthalpy, entropy, and free energy functions from somewhat discordant calorimetric measurements (35, 36), extrapolated to higher temperatures. These may be combined with free energy data from high temperature equilibrium (emf and vaporization) studies to obtain ΔH°_{298} for the solids which agree satisfactorily with the calorimetric values. However, if P_{O₂} is to be calculated, we recommend direct use of the high temperature equilibrium data, for example, our Eq. [10]. This is because a discrepancy of $\pm 1\%$ in $\Delta\bar{G}_{1/2}O_2(Ti_2O_3, Ti_3O_5)$ at, say, 1300°K corresponds to ± 14 mV in cell potential, or $\pm 50\%$ in P_{O₂}.

One remaining source of discrepancy between the emf and tabulated data is the transition from α to β Ti₃O₅ at $450^\circ \pm 20^\circ\text{K}$, for which JANAF (17) estimates $\Delta H^\circ_t = 3.17 \pm \text{kcal mole}^{-1}$, because of some uncertainty in the drop calorimetric measurements (35, 36) and a DTA study (37).

Acknowledgments

This paper is based on a thesis submitted to the University of Iowa by Ronald G. Sommer in partial fulfillment of the requirements for the Ph.D. degree, December 1974, and was reported in part at the 10th Midwest Regional Meeting of the American Chemical Society, Iowa City, November 1974. The work was supported in part by the USAEC through contract AT(11-1)-1182 with the University of Iowa and in part by the National Science Foundation under grant No. GP-33457. We are greatly indebted to Mr. Yasuyuki Ishikawa for translating the article by Suzuki and

Sambongi. Dr. F. D. Ingram and Mary Jo Ingram of the Department of Physiology and Biophysics kindly performed the microprobe analysis of our samples.

Manuscript submitted Feb. 24, 1975; revised manuscript received May 19, 1975.

Any discussion of this paper will appear in a Discussion Section to be published in the June 1976 JOURNAL. All discussions for the June 1976 Discussion Section should be submitted by Feb. 1, 1976.

Publication costs of this article were partially assisted by Corning Glass Works.

REFERENCES

- P. G. Wahlbeck and P. W. Gilles, *J. Am. Ceram. Soc.*, **49**, 180 (1966).
- D. Watanabe, O. Terasaki, A. Jostens, and J. R. Castles, *J. Phys. Soc., Japan*, **25**, 292 (1968); "The Chemistry of Extended Defects in Non-Metallic Solids," L. Eyring and M. O'Keeffe, Editors, p. 238, North-Holland, Amsterdam, (1970).
- S. Andersson and co-workers, *Acta Chem. Scand.*, **11**, 1641, 11653 (1957), and numerous later papers.
- L. A. Bursill and B. G. Hyde, *Prog. Solid State Chem.*, **7**, 177 (1972).
- JANAF Thermochemical Tables, Dow Chemical Co., NSRDS-NBS-37, U.S. Govt. Printing Office (1971).
- P. W. Gilles, K. D. Carlson, H. F. Franzen, and P. G. Wahlbeck, *J. Chem. Phys.*, **46**, 2461 (1967), review older data and establish the general picture. Subsequent data are discussed in Ref. (7,8).
- P. J. Hampson and P. W. Gilles, *ibid.*, **55**, 3712 (1971).
- H. Y. Wu and P. G. Wahlbeck, *ibid.*, **56**, 4534 (1972).
- K. Suzuki and K. Sambongi, *Tetsu To Hagane*, **58**, 1579 (1972), *Chem. Abstr.*, **77**, 169559q (1972). English translation by R. G. Sommer and Y. Ishikawa (1973).
- R. R. Merritt, B. G. Hyde, L. A. Bursell, and D. K. Philp, *Phil. Trans. Roy. Soc. London*, **A274**, 627 (1973).
- K. Kiukkola and C. Wagner, *This Journal*, **104**, 308 (1957).
- K. Kiukkola and C. Wagner, *ibid.*, **104**, 379 (1957).
- I. A. Vasil'eva and E. Yu. Shaulova, *Russ. J. Phys. Chem.*, **43**, 1713 (1969); **45**, 1141 (1971).
- M. Hoch, A. S. Iyer, and J. Nelken, *J. Phys. Chem. Solids*, **23**, 1463 (1962).
- T. H. Etsell, *Z. Naturforsch.*, **27a**, 1138 (1972).
- T. H. Etsell and S. N. Flengas, *Chem. Rev.*, **70**, 339 (1970).
- JANAF Thermochemical Tables, Dow Chemical Co. Midland, Mich.: Ti₂O₃(c) 6-30-73, Ti₃O₅(α, β) 12-31-73, Ti₄O₇(c) 12-31-73, Cr₂O₃(c) 12-31-73, and NbO(c) 12-31-73 to appear in 1975 in *J. Chem. Phys. Ref. Data*.
- H. S. Isaacs, *This Journal*, **119**, 455 (1972).
- E. C. Subbarao, P. H. Sutter, and J. Krizo, *J. Am. Ceram. Soc.*, **48**, 443 (1965).
- R. G. Sommer, Ph.D. Thesis, University of Iowa (1974).
- W. L. Worrell, "Thermodynamics," Vol. 1, p. 131, International Atomic Energy Agency, Vienna (1966).
- M. F. Lasker and R. A. Rapp, *Z. Phys. Chem. N.F.*, **49**, 198 (1966).
- G. P. Shreikin and G. V. Bazuev, *Russ. J. Inorg. Chem.*, **18**, 155 (1973).

24. R. T. Bryant, *J. Less-Common Metals*, **4**, 62 (1962).
25. B. C. H. Steele and C. B. Alcock, *Trans. Met. Soc. AIME*, **233**, 1359 (1965).
26. L. S. Darken and R. W. Gurry, *J. Am. Chem. Soc.*, **67**, 1398 (1945).
27. S. Ignatowicz and M. W. Davies, *J. Less-Common Metals*, **15**, 100 (1968).
28. H. L. Schick, Fifth Progress Report (Sept. 15, 1963), Arco-Everrett Report, RAD-SR-63-183.
29. R. N. Blumenthal and D. H. Whitmore, *J. Am. Ceram. Soc.*, **44**, 508 (1961).
30. R. A. Giddings and R. S. Gordon, *ibid.*, **56**, 111 (1973), and references given therein.
31. R. A. Giddings and R. S. Gordon, *This Journal*, **121**, 793 (1974).
32. H. F. Rizzo, R. S. Gordon, and I. B. Cutler, *Proc. Nat. Bur. Standards Symp. on Mass Transport in Oxides*, Oct. 1967, NBS Special Publication 296, pp. 129-142 (1968).
33. S. Andersson, B. Collen, U. Kuylenstierna, and A. Magneli, *Acta Chem. Scand.*, **11**, 1641 (1957).
34. J. S. Anderson, *Proc. Roy. Soc. London*, **A185**, 69 (1946).
35. F. Naylor, *J. Am. Chem. Soc.*, **68**, 1077 (1946).
36. N. P. Slyusar, A. D. Krivorotenko, E. N. Fomichev, A. A. Kalashnik, and V. P. Bondarenko, *Teplofiz. Vysokikh Temperatur, Akad. Nauk SSSR*, **11**, 213 (1973).
37. C. N. R. Rao, S. Ramdas, R. E. Loehman, and J. M. Honig, *J. Solid State Chem.*, **3**, 83 (1971).

Mechanisms of Decomposition of Organochromium Compounds in the CVD Process. Cycloheptatriene Chromium Tricarbonyl

T. J. Truex, R. B. Saillant, and F. M. Monroe

Ford Motor Company, Dearborn, Michigan 48121

ABSTRACT

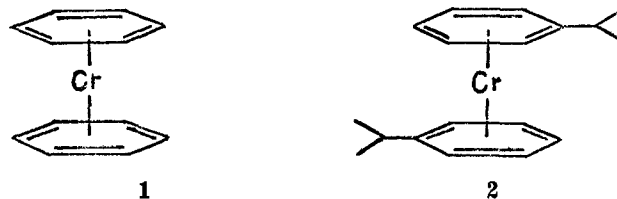
A general method for studying the decomposition of organometallic compounds in the low temperature chemical vapor deposition (CVD) process is described. Gas chromatographic and mass spectral analyses have been used to identify volatile by-products from CVD reactions and determine their relationship to deposit composition. The technique, in conjunction with ^{13}C labeling experiments, has been used to determine the mechanism of decomposition of cycloheptatriene chromium tricarbonyl $[(\text{C}_7\text{H}_5)\text{Cr}(\text{CO})_3]$. $(\text{C}_7\text{H}_5)\text{Cr}(\text{CO})_3$ pyrolyzes at temperatures $> 300^\circ\text{C}$ to give deposits containing mainly chromium and carbon with small amounts of oxygen present. Reactions involving the CO ligands, including CO disproportionation, make only minor contributions to deposit composition with the majority of deposited carbon ($>85\%$) resulting from reactions involving the cycloheptatriene ring. The use of thermogravimetric analysis and differential scanning calorimetry to screen potential CVD compounds is described.

We have undertaken a program to evaluate the use of organometallic compounds in the low temperature chemical vapor deposition (CVD) process for two reasons: to develop general methods for studying the mode of decomposition of these compounds, and to determine the detailed mechanism(s) of decomposition of selected organochromium compounds.

The use of new organometallic compounds (1) for low temperature ($< 550^\circ\text{C}$) CVD provides the potential of depositing metals, oxides, carbides, or nitrides on light metals, glass, and other materials not resistant to glow temperatures. The development of this process depends upon an understanding of the relationship between process variables (chemical and physicochemical) and deposit compositions and properties (2). In particular, an understanding of the mechanisms of decomposition of organometallic compounds could explain the origins of deposit compositions and conceivably indicate ways to control these compositions.

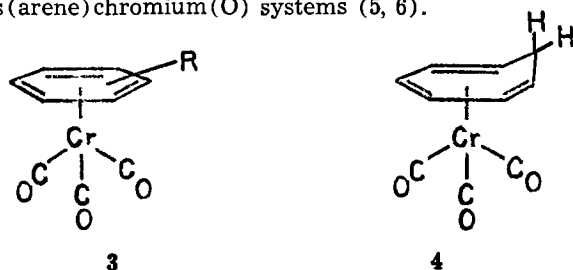
Several organochromium compounds have been used in the past to deposit chromium, chromium carbide, and/or chromium oxide by the CVD process. Lander and Germer (3) and also Owen and Webber (4) studied the decomposition of chromium hexacarbonyl, $\text{Cr}(\text{CO})_6$. Deposits containing varying amounts of Cr, Cr_3C_2 , and Cr_2O_3 were obtained depending upon reaction conditions. Decompositions using the bis(arene)-chromium(O) compounds, bis(benzene)chromium(O) **1** (5), and bis(cumene)chromium(O) **2** (6) also produced carbide deposits of varying compositions. Of the

latter two systems, the bis(cumene)chromium(O) compound has been the most extensively studied. It decomposes at substrate temperatures between 325° and 550°C producing chromium carbide deposits containing 8-12 weight per cent (w/o) carbon. Mechanistic studies on this compound have been precluded due to the unavailability of pure starting material. Chemical decomposition of commercially available bis(cumene)chromium(O) in this and other laboratories (7) reveals that it is a mixture of bis(arene)chromium(O) compounds containing benzene, cumene, diisopropylbenzenes, and triisopropylbenzene. Recently there has been a report of the preparation of pure bis(cumene)-chromium(O) (8) which we hope to utilize for the preparation of pure samples for mechanistic studies.



A third class of organochromium complexes which has received little attention as a potential source of CVD compounds is the arene chromium tricarbonyls **3** (9). These compounds are of particular interest for mechanistic studies because they incorporate structural features of both the $\text{Cr}(\text{CO})_6$ and bis(arene)-chromium(O) systems. Thus, decomposition studies of these systems could reveal reactions involving the CO

ligands leading to oxide and/or carbide formation as suggested for the metal hexacarbonyls of Cr, Mo, and W (3) and/or carbide formation from decomposition of the arene ligands as implied from results on the bis(arene)chromium(O) systems (5, 6).



Differential thermal analysis (DTA), differential scanning calorimetry (DSC), and preliminary plating studies on a series of arene chromium tricarbonyl compounds (*vide infra*) had also indicated that cycloheptatriene chromium tricarbonyl **4** (10) was a promising candidate for study. It is only slightly air-sensitive under ambient conditions, but thermally decomposes at temperatures $> 300^{\circ}\text{C}$. It is easily sublimed at 70°C and 1.0 mm pressure.

Results are reported on the mechanism of decomposition of cycloheptatriene chromium tricarbonyl. In addition, general procedures for studying the decomposition of organometallic compounds are presented.

Experimental Procedure

Chemicals.—All organometallic compounds were obtained from Strem Chemicals Incorporated, Beverly, Massachusetts. Comparison of observed melting points, solution infrared, nmr, and mass spectra with literature data indicated all compounds were pure as received.

Apparatus and procedure.—A diagram of the experimental apparatus is shown in Fig. 1. The glass (Pyrex) or aluminum substrate was attached to a graphite block which was heated inductively. The substrate temperature was recorded by a thermocouple imbedded in the block. The pressure was measured with a thermocouple gauge. Condensable gaseous by-products were collected in cold traps at liquid N_2 (-196°C), Dry Ice/acetone (-76°C), or ice-methanol ($\sim -20^{\circ}\text{C}$) temperatures. Noncondensable gaseous by-products were collected in a 1 liter evacuated glass bulb and then pumped via a Toeppler pump into a 50 cm^3 volume.

DTA and DSC were performed under an N_2 atmosphere using a du Pont Model 900 analyzer.

The condensable by-products in the CVD reactions were analyzed by separating the components using a gas chromatograph interfaced with a mass spectrometer. These analyses were done at Shrader Analytical and Consulting Laboratories, Incorporated, Detroit, Michigan.

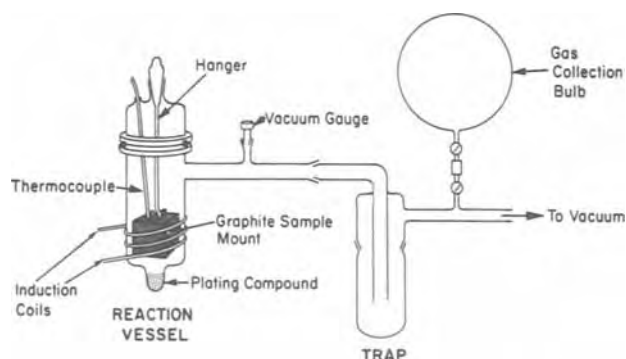


Fig. 1. Schematic diagram of apparatus for studying the mechanisms of decomposition of organometallic compounds.

Mass spectral analyses of the noncondensable gaseous by-products were performed using an Aero Vac Model AVA/61 residual gas analyzer. This instrument was calibrated for intensity vs. partial pressure for samples of air, CO , CO_2 , H_2 , CH_4 , and C_2H_4 .

Deposit compositions were determined by electron microprobe analyses.

In a typical plating run the following procedure was used. The reaction vessel was charged with the plating compound, the substrate/graphite holder was attached and the apparatus evacuated to the desired pressure. The induction furnace was then turned on and the substrate heated to the plating temperature. After the substrate temperature was stabilized, a preheated oil bath was placed around the bottom of the reaction vessel causing the complex to sublime. The condensable by-products were collected in the cold trap as described above. Noncondensable gases were collected in a 1 liter evacuated flask as described previously. All of the experiments with cycloheptatriene chromium tricarbonyl were done with a sublimation temperature of 70°C and a pressure of ~ 0.3 mm Hg on glass (Pyrex) or aluminum substrates.

^{13}C labeling experiment.—The ^{13}C exchange reaction described below is similar to that used to prepare the substituted compounds $(\text{C}_7\text{H}_5)\text{Cr}(\text{CO})_2\text{X}$, where X is triphenylphosphine or triphenylphosphite (11). 6.84g (30 mmole) of cycloheptatriene chromium tricarbonyl was dissolved in 150 ml of degassed cyclohexane (distilled under N_2 from CaH_2). This was placed in a Vycor reaction vessel, with care taken to exclude air, and attached to a vacuum line. After several freeze-thaw cycles under vacuum, 100 cm^3 at 0.7 atm of 90% enriched ^{13}C (Stohler Isotopes Incorporated) was introduced. The exchange reaction was allowed to proceed at room temperature under 3500Å irradiation for 36 hr. The reaction was then stopped, the solution frozen, and the gases above it replaced with a fresh supply of 90% enriched ^{13}C (100 cm^3 at 0.5 atm). The reaction was then allowed to proceed an additional 36 hr under the same conditions as above. At the end of this period the gases above the solution were again replaced with a fresh supply (350 cm^3 at 0.36 atm) and irradiation continued for a final 36 hr. The solution was filtered under N_2 and the product isolated by evaporation *in vacuo*. The extent of enrichment was determined by mass spectroscopic analysis. The parent ion region was analyzed for increases due to ^{13}C -containing species and the ratio of ^{13}C and ^{12}C was determined by analysis of the $m = 29$ and $m = 28$ peaks. The reaction can be followed qualitatively by monitoring the appearance and growth of a ^{13}C stretching band at 1855 cm^{-1} (cyclohexane solvent) in the infrared spectrum. Two samples of labeled compound were prepared; one contained 7.5% ^{13}C and the other 8.7% ^{13}C .

Results and Discussion

Selection of potential CVD compounds.—The quick and systematic evaluation of potential CVD compounds is a continuing problem for new materials. DTA and DSC show promise as reliable screening techniques which provide sublimation and decomposition data. A linear correlation was observed, Fig. 2, when the initial decomposition temperatures were plotted against the minimum plating temperatures¹ under CVD conditions. The less-than-unity slope results from the difference between the DTA/DSC measurements and our criterion for "initial plating." These data led to the study of cycloheptatriene chromium tricarbonyl. In the future, these DTA/DSC studies will be extended to a number of other classes of compounds to determine if the observed correlation persists.

Experimental procedure and rationale.—Figure 3 represents the interaction between product and process

¹ For CVD this is necessarily qualitative and arbitrary. For our purposes it is the minimum substrate temperature at which a uniform opaque deposit forms during 30 min of reaction time.

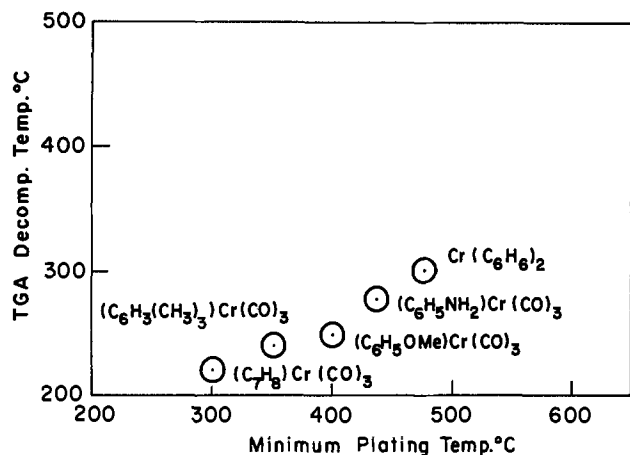


Fig. 2. Plot of DTA/DSC decomposition temperature vs. minimum CVD decomposition temperature.

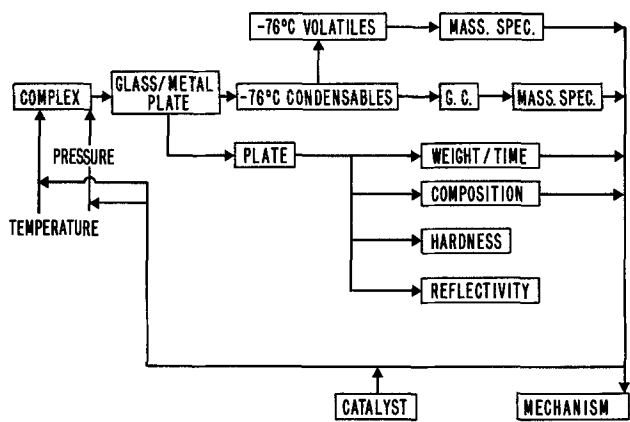


Fig. 3. Schematic representation of relationship between products and process variables in the CVD process.

variables. In this study we have controlled the pressure, and the substrate and sublimation temperatures. For a given set of these variables a deposit is formed which can be analyzed for different properties, some of which are shown. The property of interest for this study was coat composition. The reaction by-products can be experimentally separated into condensables and noncondensables by varying trap temperatures and analyzed as described in the experimental section. This procedure allows the correlation of deposit properties (composition) and reaction by-products with plating compound and variables from which a mechanism can be deduced.

The principle behind this approach is mass balance. Thus, a change in deposit composition must be accompanied by corresponding variations (molecular and/or concentration) in reaction by-products. Isotopic labeling has also been used in the present study to complement mass balance information and unambiguously identify specific carbon sources.

Results of decomposition studies on cycloheptatriene chromium tricarbonyl $(C_7H_8)Cr(CO)_3$.— $(C_7H_8)Cr(CO)_3$ is a slightly air-sensitive red crystalline solid which must be stored in an inert atmosphere but can be handled in air for short periods of time without noticeable decomposition. Its volatility is high enough that adequate sublimation rates are obtained at temperatures $\geq 70^\circ C$. Rapid pyrolysis of $(C_7H_8)Cr(CO)_3$ occurs at temperatures $\geq 300^\circ C$. The temperature range which produces uniform, smooth, continuous, adherent, mirror-bright films is 350° – $450^\circ C$. Below $350^\circ C$ some spontaneous peeling of the film from Pyrex glass substrates is observed (this problem has not been encountered with aluminum substrates) and above $500^\circ C$

formation of a black sooty material in the reaction chamber indicates that some of the vapor decomposes before it reaches the hot substrate. Although all deposition studies were conducted at a sublimation temperature of $70^\circ C$ and a pressure of 0.3 mm Hg, it is probable that the optimum substrate temperatures will change as a function of other variables. We have not explored this possibility in detail but have instead chosen to vary substrate temperature while holding all other variables constant in an attempt to simplify the mechanistic analysis. The substrate temperature range studied was 300° – $600^\circ C$.

The deposited films were analyzed for Cr, C, and O by electron beam microprobe analyses. The results show that deposits formed from $(C_7H_8)Cr(CO)_3$ decomposition in the 300° – $600^\circ C$ range contain mainly chromium and carbon with smaller amounts of oxygen. Average chromium and carbon contents [atomic per cent (a/o)] as a function of temperature were as follows:

300°C	63.6 a/o Cr	28.4 a/o C
400°C	62.4 a/o Cr	32.5 a/o C
500°C	58.8 a/o Cr	36.0 a/o C
600°C	59.1 a/o Cr	32.1 a/o C

Although quantitative oxygen analyses were not performed on all samples, in the analyzed samples oxygen accounted for the remainder of the film. In addition, no foreign elements other than chromium, carbon, or oxygen were detected in any of the films. These results show a fairly uniform composition throughout the temperature range with somewhat higher oxygen contents at both extremes of temperature. A poorly defined x-ray pattern was obtained for one deposit laid down at $600^\circ C$. The pattern could be associated with Cr_7C_3 although some known lines were absent. All other film deposits were amorphous. This type of behavior has been noted previously in chromium carbide films deposited at low temperatures (6b) where it was observed that annealing leads to crystallization. This has not been tried with films produced by $(C_7H_8)Cr(CO)_3$ decomposition since the major interest has been in as-deposited films. Of primary interest is the source of the deposited carbon and oxygen found in these films.

The variation in condensable by-products for $(C_7H_8)Cr(CO)_3$ decomposition in the temperature range 300° – $600^\circ C$ is shown in Fig. 4. The relative proportion of the major component, cycloheptatriene, steadily decreases as the deposition temperature is increased. However, the relative proportions of benzene, toluene, cycloheptadiene, and styrene increased with temperature. The benzene and cycloheptadiene concentrations pass through maxima at $\sim 500^\circ C$. This may indicate secondary reactions involving decomposition of these compounds above $550^\circ C$. Benzene decomposition has been noted in other CVD studies at temperatures $> 500^\circ C$ (5b).

The major component of the noncondensable by-products was CO , with the second largest component being H_2 [~ 10 – 15 molecular per cent (m/o) of the noncondensable gas fraction]. Minor components of methane and ethylene were observed together with trace amounts of CO_2 (0–2 m/o) and C_2 and C_3 hydrocarbons. It was noted that the relative compositions of the noncondensable by-products do not vary in a significant manner throughout the 300° – $600^\circ C$ temperature range.

The appearance of the different chemical species found in the condensable by-products implies that the net chemical reactions presented in Fig. 5 are taking place during decomposition. Only benzene formation involves a loss of carbon and is therefore a possible source of deposited carbide. The other reactions involve no net change in carbon or, as in the case of styrene, the addition of one carbon atom. The carbon loss through benzene formation is ~ 7 – 10 a/o between 300° – $400^\circ C$ and ~ 20 – 30 a/o at decomposition temperature $> 450^\circ C$. Since styrene formation, and the associated carbon addition in this reaction is ~ 0 – 2 m/o throughout the decomposition temperature range, the

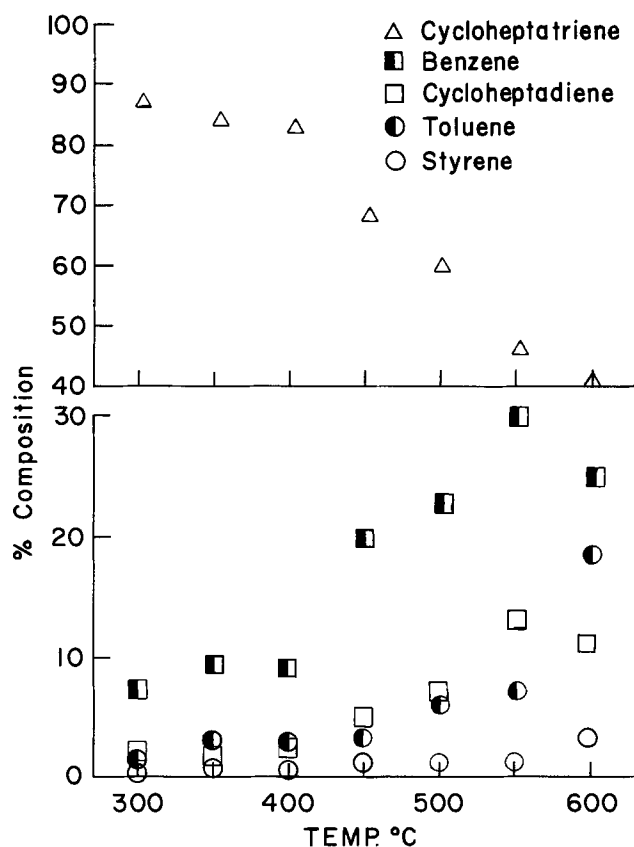


Fig. 4. Variation of condensable by-products for $(C_7H_8)Cr(CO)_3$ decomposition in the temperature range 300°-600°C.

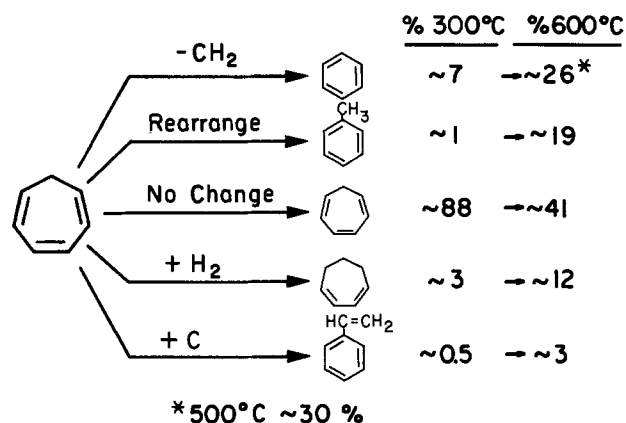


Fig. 5. Chemical reactions implied by the formation of condensable by-products in $(C_7H_8)Cr(CO)_3$ decomposition

majority of the carbon freed in the benzene reaction is available for carbide formation. Thus, below 400°C the benzene reaction can account for ~25-30% of the deposited carbon and above 400°C it can account for ~55-95% of deposited carbon.

The noncondensable gas results provide a complement to the condensable by-product conclusions. First, the absence of considerable amounts of CO_2 indicates that the CO disproportionation reaction proposed as a source of carbon formation in the decomposition of other carbonyl containing organometallics (3) is not significantly operative. This does not completely rule out participation of CO in deposit formation by some reaction pathway other than disproportionation. This point will be raised again during discussion of results from ^{13}C labeling experiments. The second point involves the large H_2 component seen in the noncondensable gas fraction. This implies that considerable reaction involving cycloheptatriene is taking place. Part of this is explained by the benzene formation re-

action mentioned previously, but this will not account for all of the H_2 observed, especially below 400°C. This, together with the absence of lower hydrocarbons ($<C_6$), suggests that some total degradation of cycloheptatriene is taking place.

Definitive information on the relative participation of CO and cycloheptatriene in deposit formation has been provided by ^{13}C labeling experiments. ^{13}CO labeled cycloheptatriene chromium tricarbonyl was used for deposition studies at 300°, 400°, and 500°C (runs at 600°C were precluded due to interference from gas phase decomposition). The deposits from these runs were then combusted and the CO_2 given off collected and analyzed mass spectrometrically to determine the $^{13}CO_2/^{12}CO_2$ ratio. The results of these experiments are shown in Table I together with the calculated per cent of observed carbide formation coming from reactions involving CO. These data show that the fraction of carbide formation due to CO was a maximum of ~13% at 400°C with average values of 7.3% at 300°C, 10.0% at 400°C, and 2.0% at 500°C. These results confirm the conclusions drawn from the noncondensable gas analyses. Specifically, CO participation in carbide formation is small compared to that of cycloheptatriene. The presence of 5-9 a/o oxide in the deposits could arise from reaction of the oxygen atom in CO with deposited chromium, or from the presence of residual O_2 in the system which has a background pressure of $\sim 1\mu$.

Conclusions

As part of an over-all program to determine mechanisms of decomposition of organometallic compounds, a study of the decomposition of cycloheptatriene chromium tricarbonyl has been made. $(C_7H_8)Cr(CO)_3$ decomposes at substrate temperatures of $\geq 300^\circ C$ to form deposits on glass and aluminum substrates containing mainly chromium and carbon, with lesser amounts of oxygen present. Mechanistic studies utilizing comparisons of deposit compositions and condensable and noncondensable by-products analyses and ^{13}CO labeling studies allow the following conclusions concerning $(C_7H_8)Cr(CO)_3$ decomposition:

(i) Reactions involving CO account for less than 13% of deposited carbon in the deposition pressure and temperature ranges studied.

(ii) The majority of deposited carbide comes from the cycloheptatriene ring. Two specific reactions appear to account for this. First, transformation of cycloheptatriene into benzene with loss of a carbon atom and one molecule of hydrogen. This reaction is operative to only a minor extent at low temperatures, but at $>450^\circ C$ it can account for ~55-95% of the deposited carbide. Second, total degradation of cycloheptatriene into carbon and hydrogen. This reaction must be operative throughout the temperature range 300°-600°C, but below 450°C it produces the majority of the carbide formed (~70-75%). It should be noted that in separate experiments pure cycloheptatriene was found not to decompose under the deposition conditions used here. This implies that complexation to chromium activates decomposition, or an initially formed chromium deposit catalyzes the decomposition.

(iii) Several other reactions of cycloheptatriene which do not contribute to deposit formation were observed. These included formation of toluene, cycloheptadiene, and styrene.

Table I. ^{13}C labeling experiment results

Deposition temperature, °C	Per cent ^{13}CO in $(C_7H_8)Cr(CO)_3$	Per cent ^{13}C in deposit (range)	Per cent of deposited carbon from CO (range)
300	7.5	1.57(1.49-1.67)	7.3(6.1-8.9)
400	7.5	1.74(1.56-1.92)	10.0(7.2-13.0)
500	8.7	1.25(1.10-1.35)	2.0(0.0-3.3)

(iv) The presence of small amounts of oxygen in the films suggests some reaction of deposited chromium with oxygen from CO and/or background O₂ in the reaction system.

This study demonstrates the utility of the experimental approach used in determining mechanisms of decomposition of organometallic compounds in the CVD process. In the future these studies will be extended to other arene chromium tricarbonyl compounds and also other classes of organometallic compounds with the goal of developing thermodynamic models for the prediction of decomposition mechanisms of these systems.

Acknowledgments

The authors would like to thank Barbara Bergman and Jack Tabock of the Technical Services Department of the Ford Scientific Research Staff for performing the DTA and electron microprobe analyses, respectively.

Manuscript submitted Dec. 26, 1974; revised manuscript received May 27, 1975. This was Paper 307RNP presented at the Boston, Massachusetts, Meeting of the Society, Oct. 7-11, 1973.

Any discussion of this paper will appear in a Discussion Section to be published in the June 1976 JOURNAL. All discussions for the June 1976 Discussion Section should be submitted by Feb. 1, 1976.

Publication costs of this article were partially assisted by the Ford Motor Company.

REFERENCES

1. F. G. A. Stone and R. West, *Advances in Organometallic Chemistry*, Vol. 1 (1964); Vol. 11 (1973), Academic Press, New York.
2. K. H. Bloss and H. Lukas, *Electrodeposition and Surface Treat.*, **2**, 47 (1974).
3. J. J. Lander and L. H. Germer, *Metals Technol.*, **14**, TP 2259 (1947); *Metal Ind.*, (London), **71**, 459, 487 (1947).
4. B. B. Owen and R. T. Webber, *Metals Technol.*, **15**, TP 2306 (1948).
5. (a) M. Tsutsui and C. J. Marsel, Air Force Cambridge Research Laboratories, ARCRL-64-934, Bedford, Massachusetts (1964).
(b) B. D. Nash, T. T. Campbell, and F. E. Block, *U.S. Bur. Mines, Rept. Invest. 7112*, Washington, D.C. (1968).
6. (a) R. Tomono, E. Yagi, and Y. Togashi, *Kinzoku Hyomen Gijyutsu (J. Metal Finishing Soc. Japan)* **16**, 210 (1965).
(b) J. E. Knap, B. Pesetsky, and F. N. Hill, *Plating*, **53**, 772 (1966).
7. Y. A. Sorokin and G. G. Petukhov, *J. Gen. Chem. USSR*, **35**, 2123 (1966).
8. R. Middleton, J. R. Hull, S. R. Simpson, C. H. Tomlinson, and P. L. Timms, *J. Chem. Soc., Dalton Trans.*, 120 (1973).
9. R. L. Pruett, *Prep. Inorg. Reactions*, **2**, 187 (1965).
10. E. W. Able, M. A. Bennett, R. Burton, and G. Wilkinson, *J. Chem. Soc.*, 4559 (1958).
11. W. P. Anderson, W. G. Blenderman, and K. A. Drews, *J. Organomet. Chem.*, **42**, 139 (1972).

Theoretical Aspects of the Peltier Effect on the Temperature Distribution in Crystal Grown by the Czochralski Technique

S. Vojdani, A. E. Dabiri, and M. Tavakoli

Materials and Energy Research Center, Arya-Mehr University of Technology, Tehran, Iran

ABSTRACT

A theoretical treatment is given for the temperature distribution in a Czochralski system with and without the presence of the Peltier effect. The effect of Peltier heating on the crystal diameter during growth is also considered. The results indicate that the Peltier current necessary to control a given diameter of a crystal during intermediate stages of growth is dependent on T_c , the crucible temperature, and h_c , the height of crucible above the melt.

Recently the use of the Peltier effect has been reported for the control of the diameter of pulled Ge crystals (1). The effect has also been used in connection with modulation of dopant segregation in Czochralski-grown InSb (2). The Peltier effect is produced at the solid-liquid interface without time lag and can be reversed by reversing the current through the crystal.

Some theoretical attempts have been made to determine the solid-liquid interface shape (3) and the temperature distribution in the axial direction of a crystal and the melt in a Czochralski crystal growth system (4, 5) by solving computationally the steady-state heat transfer equation. In such computations the convective processes in the melt are generally ignored. In practice crystal rotation in Czochralski technique is introduced to provide a forced convection flow in the liquid, which tends to isolate the interface from thermal convection in the bulk liquid.

The objective of this paper is to investigate theo-

retically the effect of Peltier heating at a solid-liquid interface on such parameters as temperature distribution in the solid and the melt, temperature gradients in the solid and the melt, and in particular the control of crystal diameter.

Theoretical Method

The crystal growth arrangement used for the present analysis is shown schematically in Fig. 1.

Assumptions made in solving the heat transfer equation are as follows: (i) The heat loss from the crystal and the melt is only through radiation. (ii) Convection in the melt is neglected. (iii) Joule heating due to the Peltier current in the crystal and the melt for normally used current densities (~ 20 A-cm⁻²) is neglected (6).¹ (iv) Thickness of the crucible wall is neglected. (v) The interface is assumed to be planar.

¹ The resistivity of the solid Ge, ρ_s , at the melting point is $\sim 10^{-3}$ ohm-cm; that of the liquid, ρ_L is about 1/5 this value. Assuming a normally used current density (~ 20 A-cm⁻²), the Peltier heat at the interface is 1.7 W-cm⁻² while the Joule heat in the solid and the liquid within 5 mm of the interface is 0.2 and 0.04 W-cm⁻², respectively.

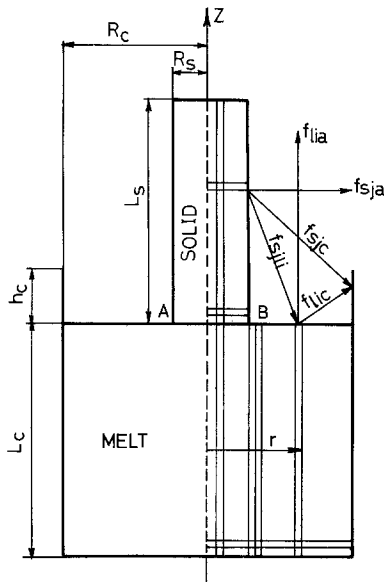


Fig. 1. Schematic diagram of crystal growth arrangement ($L_c = 5$ cm, $L_s = 5$ cm, $R_c = 2.5$ cm, $R_s = 1$ cm).

Assuming that the steady-state condition for the temperature distribution in the crystal and the melt is governed by the Laplace equation, and using the notation in the Appendix 1, we have

$$\frac{\partial^2 T}{\partial r^2} + \frac{1}{r} \frac{\partial T}{\partial r} + \frac{\partial^2 T}{\partial z^2} = 0 \quad [1]$$

Subject to the following boundary conditions: On the crystal axis by symmetry we have

$$\frac{\partial T}{\partial r} = 0 \quad [2]$$

On the crystal side surfaces

$$-K_s \left(\frac{\partial T}{\partial r} \right)_{sj} = q_{sj} \quad [3]$$

where q_{sj} is the net heat flux radiated from a point j on the side surface of the crystal and is given by

$$q_{sj} = \epsilon_s \sigma \left[\sum_{i=1}^n \epsilon_i f_{sji} (T_{sj}^4 - T_{ii}^4) + \epsilon_c f_{sjc} (T_{sj}^4 - T_c^4) + f_{sja} (T_{sj}^4 - T_a^4) \right] \quad [4]$$

In the above expression f 's are the geometry factors between any two points in the growth arrangement as shown in Fig. 1. The exact calculation of the geometry factors are given in Appendix 2.

Furthermore

$$-K_s \left(\frac{\partial T}{\partial z} \right)_{z=L_s} = q_{ti} \quad [5]$$

where q_{ti} is the net heat flux radiated from a point i on the top surface of the crystal and is given by

$$q_{ti} = \epsilon_s \sigma (T_{si}^4 - T_a^4) \quad [6]$$

on the melt free surface

$$-K_l \left(\frac{\partial T}{\partial z} \right)_{z=0} = q_{li} \quad [7]$$

where q_{li} is the net heat flux radiated from a point i on the free surface of the liquid and is given by

$$q_{li} = \epsilon_l \sigma \left[\sum_{j=1}^m \epsilon_s f_{lisj} (T_{li}^4 - T_{sj}^4) \right]$$

$$+ \epsilon_l f_{lic} (T_{li}^4 - T_c^4) + f_{lia} (T_{li}^4 - T_a^4) \quad] \quad [8]$$

and on the solid-liquid interface we have

$$-K_s \left(\frac{\partial T}{\partial z} \right)_{z=0} = -K_l \left(\frac{\partial T}{\partial z} \right)_{z=0} + LG + Q_P \quad [9]$$

where Q_P is the heat flux given to the interface by the Peltier heating current and is given by

$$Q_P = \alpha I_P T_m \quad [10]$$

Finally on the point A and B of Fig. 1

$$T = T_m$$

Solving Eq. [1] computationally with the above-mentioned boundary conditions, the following results can be obtained: (i) temperature distribution inside liquid and solid with and without Peltier effect, (ii) temperature gradients inside solid and liquid with and without Peltier effect, (iii) crucible temperature for a desired diameter with a given h_c (it should be noted that T_c is not taken as a boundary condition), (iv) the amount of Peltier current required to keep the diameter constant (with a given initial h_c), and (v) the crucible temperature changes required to keep the diameter constant with a given initial h_c .

Results

As an example Ge has been chosen. The following representative values were used: $T_a = 300^\circ\text{K}$, $T_m = 1210^\circ\text{K}$, $\epsilon_l = \epsilon_s = 0.2$, $K_s = 0.24 \text{ W-cm}^{-1} \text{ deg}^{-1}$, $K_l = 0.71 \text{ W-cm}^{-1} \text{ deg}^{-1}$, $L = 2.16 \times 10^3 \text{ joule cm}^{-3}$, $R_c = 2.5$ cm, $L_c = 5$ cm, $R_s = 1$ cm, $L_s = 5$ cm, $\epsilon_c = 1$, $\alpha = 7 \times 10^{-5} \text{ V deg}^{-1}$, and $G = 1 \text{ mm min}^{-1}$.

Figures 2 and 3 show the temperature distribution and the temperature gradient along the axis of a 5 cm long crystal with and without application of Peltier heating current. With Peltier current employed (24 A-cm^{-2}) no detectable change is observed in temperature distribution or temperature gradient along the axis of the crystal. However when the Peltier current is applied, the T_c must be lowered in order to have the same diameter. Lowering T_c especially for $h_c \geq 2$ cm has the effect of reducing the temperature difference between the bottom of the crucible and the melt surface along the axis of the crucible. This should tend to reduce convection in the melt. Since even in the presence of Peltier effect and crystal rotation, convection in the melt cannot be completely removed, the result in Fig. 4 can only be approximate. Another effect noticed was the movement of the interface toward the crystal upon the application of Peltier heating.

Control of diameter by Peltier heating.—Figure 5 shows the variation of Peltier current with crystal length for different values of h_c . The curves show that to keep the diameter constant during growth, for a fixed h_c (and therefore T_c), the Peltier current must be increased continuously. The saturation effect seen over longer crystal lengths is related to small variations on total radiation losses from the crystal as the length of the crystal increases. This is shown as a plot of Q_s vs. length of the crystal in Fig. 6. It is important to note that the Peltier effect does not change the radiation losses. However since the total area of a crystal increases, therefore the net radiation losses increase and the Peltier effect must compensate this increase of loss. The effect of increasing h_c for a fixed crystal diameter is shown to lower the Peltier current. This is due to decrease of net radiation from the crystal with increasing h_c .

Control of diameter by changing T_c .—Another way to control the diameter of the crystal during growth is to program T_c instead of Peltier current. Figure 7 shows the variation of T_c to keep the diameter of Ge constant with different h_c 's.

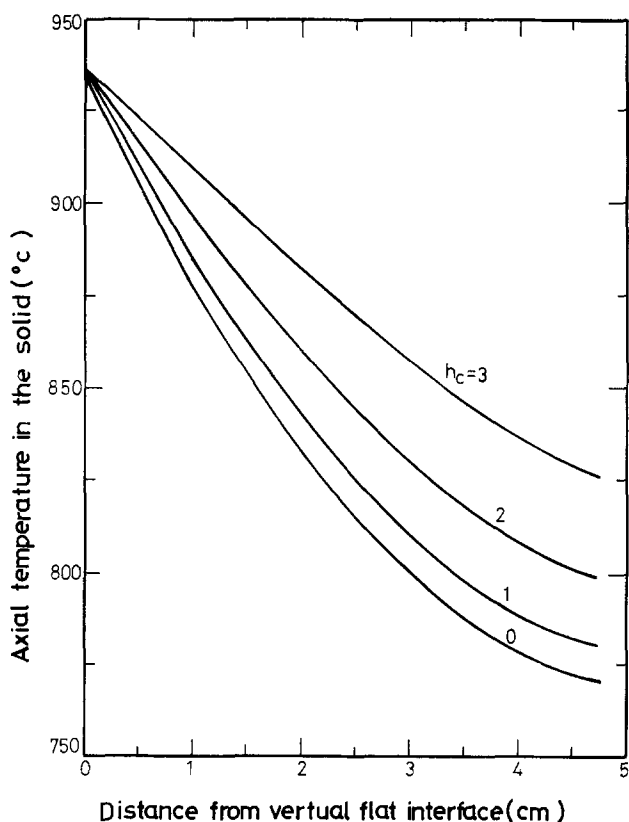


Fig. 2. Axial temperature distribution in the solid vs. distance from virtual flat interface.

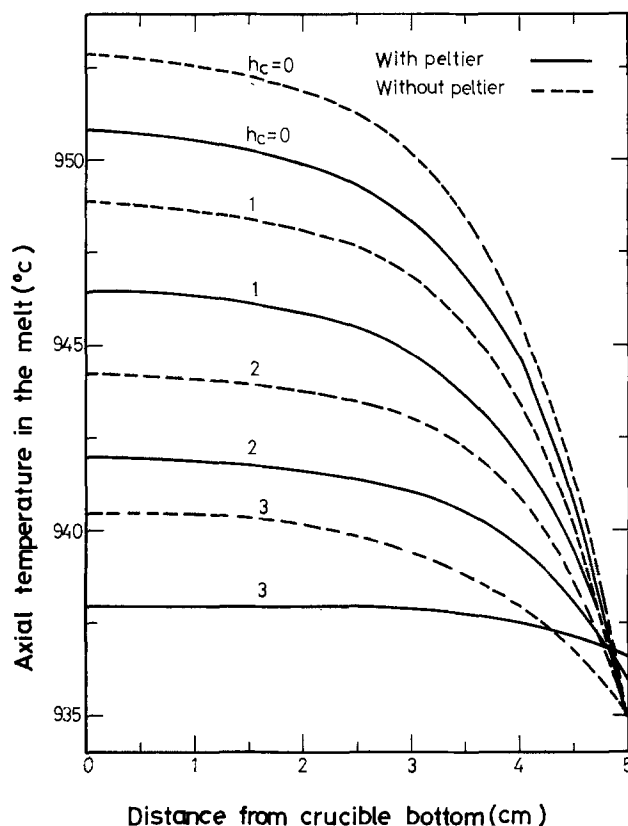


Fig. 4. Axial temperature distribution in the melt vs. distance from crucible bottom.

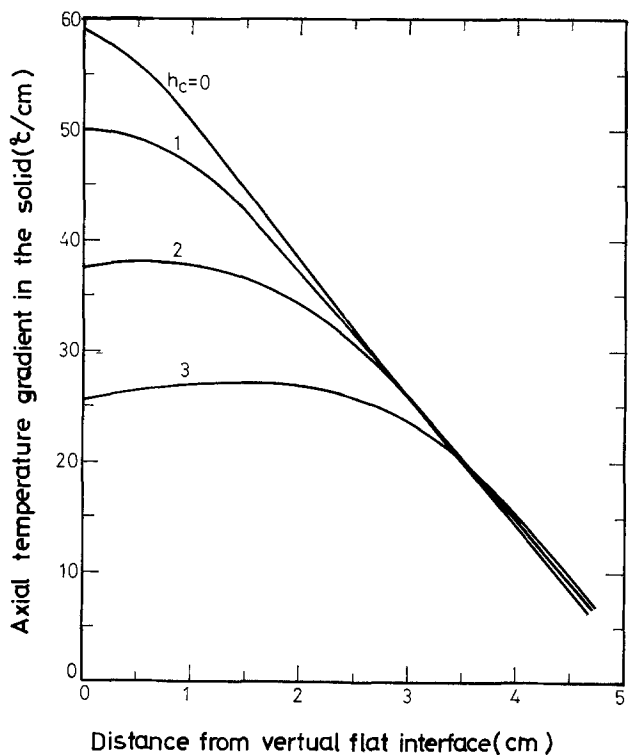


Fig. 3. Axial temperature gradient in the solid vs. distance from virtual flat interface.

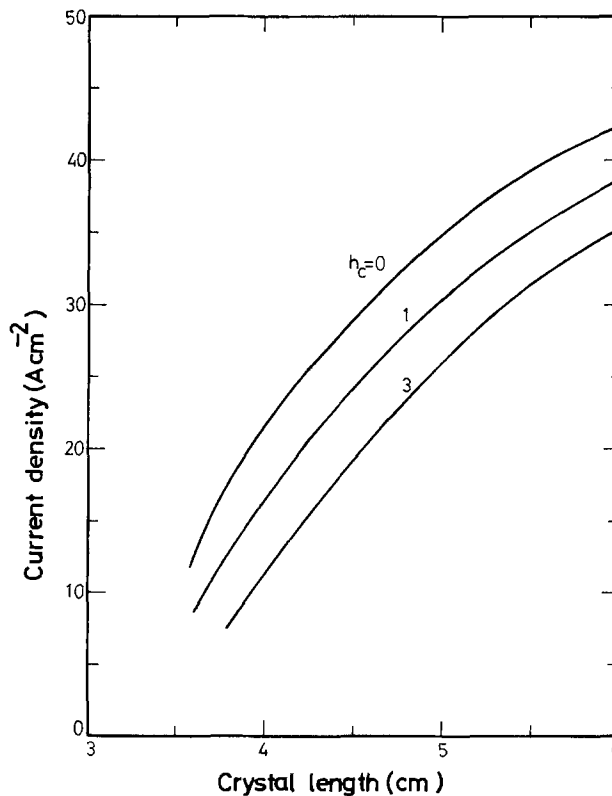


Fig. 5. Variation of current density vs. crystal length to control the diameter of the crystal at 2 cm for different h_c .

Conclusion

From the curves shown in Fig. 2-7 it has been demonstrated clearly that:

(a) The Peltier heating effect caused at the interface has no appreciable effect on the temperature distribution or gradients in the crystal.

(b) For a given diameter and T_c for every h_c the path of increasing the Peltier current to keep the diameter constant can be predicted. It must be noted that for large crystal diameters to keep the Peltier current

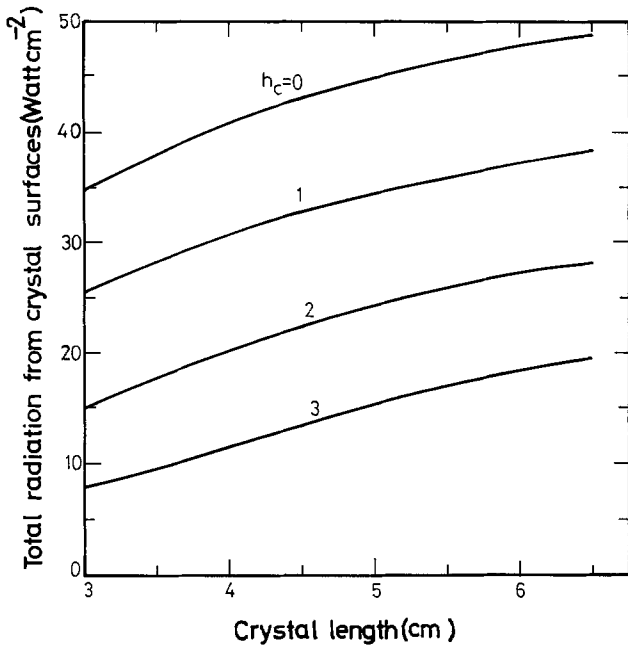


Fig. 6. Variation of total radiation from crystal surfaces with crystal length.

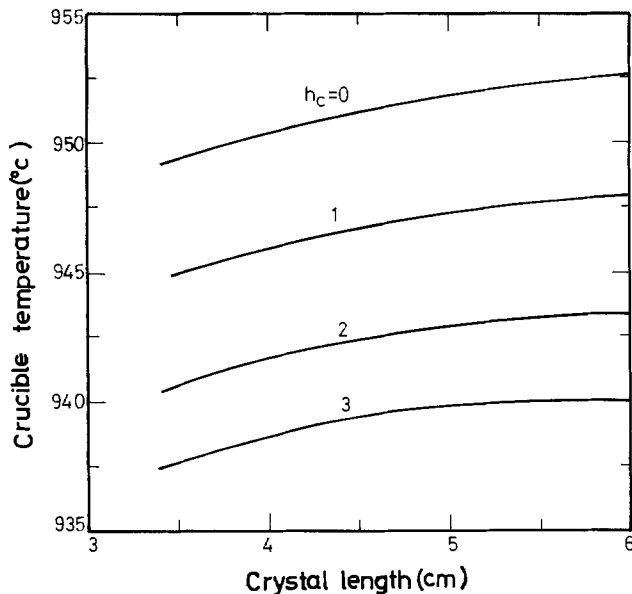


Fig. 7. Variation of crucible temperature with crystal length to control the diameter of the crystal at 2 cm for different h_c .

relatively low for diameter control, higher h_c (essentially an after heater) should be used. The Peltier current necessary for controlling the diameter saturates after, a certain length, a result which is known experimentally.

(c) The same control of crystal diameter can be obtained by changing T_c during growth. This is the process generally used in practice.

Manuscript submitted Dec. 11, 1974; revised manuscript received April 25, 1975.

Any discussion of this paper will appear in a Discussion Section to be published in the June 1976 JOURNAL. All discussions for the June 1976 Discussion Section should be submitted by Feb. 1, 1976.

Publication costs of this article were partially assisted by Arya-Mehr University of Technology.

Appendix 1

- 1. Geometry factor f
- 2. Rate of crystallization G

- 3. Height above melt surface h_c
- 4. Peltier current I_p
- 5. Liquid thermal conductivity K_l
- 6. Solid thermal conductivity K_s
- 7. Latent heat of fusion L
- 8. Crucible height L_c
- 9. Crystal length L_s
- 10. Heat flux q
- 11. Peltier heat Q_p
- 12. Radial coordinate r
- 13. Crucible radius R_c
- 14. Crystal radius R_s
- 15. Temperature T
- 16. Atmosphere temperature T_a
- 17. Crucible temperature T_c
- 18. Melting point T_m
- 19. Axial coordinate Z
- 20. Difference between absolute Seebeck coefficients of solid and liquid α
- 21. Liquid resistivity ρ_L
- 22. Solid resistivity ρ_s
- 23. Emissivity e
- 24. Stefan-Boltzmann constant σ

Appendix 2

Calculation of Geometry Factors

1. $f_{li \rightarrow b}$.—The problem is to find the geometry factor of a point li on the melt-free surface and an annulus b . This can be obtained by differentiating $f_{li \rightarrow ss}$ (ss denotes solid surface) with respect to Z . $f_{li \rightarrow ss}$ is the same as $f_{d \rightarrow ss}$. Considering the relations between geometry factors we have

$$2\pi\rho d\rho f_{d \rightarrow ss} = 2\pi R_s L_s f_{ss \rightarrow d} \quad [A-1]$$

or

$$f_{d \rightarrow ss} = \frac{R_s L_s}{\rho d \rho} f_{ss \rightarrow d}$$

but

$$f_{ss \rightarrow d} = \frac{\partial f_{ss \rightarrow ls}}{\partial \rho}$$

where ls is the subscript for liquid-free surface. From definition of geometry factor, we may write

$$f_{ss \rightarrow ls} + f_{ss \rightarrow 5} + f_{ss \rightarrow (3+4)} = 1$$

but $f_{ss \rightarrow ls} = f_{ss \rightarrow 5}$ and therefore

$$f_{ss \rightarrow ls} = \frac{1}{2} (1 - f_{ss \rightarrow (3+4)}) \quad [A-2]$$

but

$$f_{ss \rightarrow (3+4)} = \frac{R_c}{R_s} f_{(3+4) \rightarrow ss}$$

and $f_{(3+4) \rightarrow ss}$ is given by (7)

$$f_{(3+4) \rightarrow ss} = \frac{R_s}{R_c} \left\{ 1 - \frac{1}{\pi} \left\{ \cos^{-1} \frac{L_s^2 - R_c^2 + R_s^2}{L_s^2 + R_c^2 - R_s^2} - \frac{1}{2R_s L_s} \left[\sqrt{(L_s^2 + R_c^2 + R_s^2) - 4R_s^2 R_c^2} \right] \right\} \right\} + \cos^{-1} \frac{R_s(L_s^2 - R_c^2 + R_s^2)}{R_c(L_s^2 + R_c^2 - R_s^2)} + (L_s^2 - R_c^2 + R_s^2) \sin^{-1} \left[\frac{R_s}{R_c} - \frac{\pi}{2} (L_s^2 + R_c^2 - R_s^2) \right] \quad [A-3]$$

Substituting Eq. [A-3] into Eq. [A-2], and using Eq. [A-1], we get

$$f_{d \rightarrow ss} = f_{li \rightarrow ss} = \frac{1}{2\pi} \left[\cos^{-1} \left(-\frac{R_s}{\rho} \right) - \frac{L_s^2 + \rho^2 - R_s^2}{\sqrt{(L_s^2 + \rho^2 + R_s^2) - 4R_s^2 \rho^2}} \cos^{-1} \frac{R_s^2(L_s^2 - \rho^2 + R_s^2)}{(L_s^2 + \rho^2 - R_s^2)} \right] \quad [A-4]$$

2. $f_{li \rightarrow 3}$.—According to Fig. 8, $f_{li \rightarrow 3}$ could be approximated by the following equation

$$f_{li \rightarrow 3} = f_{d \rightarrow 3} = 1 - f_{d \rightarrow 6} - f_{d \rightarrow x} \quad [\text{A-5}]$$

but

$$f_{d \rightarrow 6} = \frac{\partial f_{7 \rightarrow 6}}{\partial \rho} d\rho$$

and $f_{7 \rightarrow 6}$ is given by (7)

$$f_{7 \rightarrow 6} = \frac{h_c^2 + \rho^2 + R_c^2 - \sqrt{(h_c^2 + \rho^2 + R_c^2)^2 - 4\rho^2 R_c^2}}{2R_c^2}$$

$f_{d \rightarrow x}$ could be evaluated from Eq. [A-4] where L_s is replaced by x . ($x = \frac{h_c}{R_c + \rho} (\rho - R_s)$ if $x < L_s$ and $x = L_s$ when $x \geq L_s$).

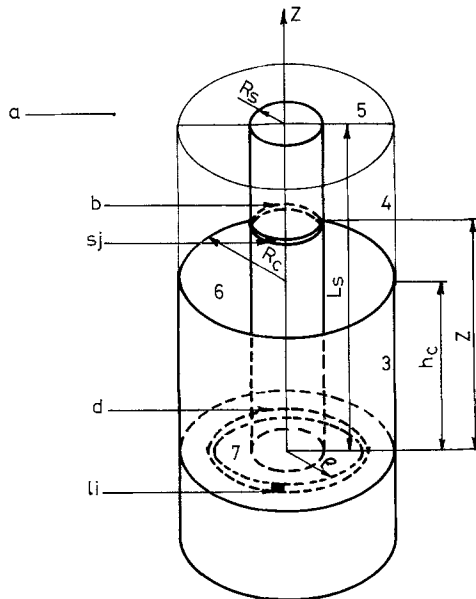


Fig. 8. Schematic diagram of crystal growth arrangement used for calculation of geometry factors.

3. $f_{li \rightarrow a}$.—The geometry factor of a point li on the melt-free surface and the atmosphere is given by

$$f_{li \rightarrow a} = 1 - f_{li \rightarrow 3} - f_{li \rightarrow ss} \quad [\text{A-6}]$$

4. $f_{sj \rightarrow d}$.—The problem is to find the geometry factor of a point sj on the crystal side and an annulus d on the melt-free surface. This can be obtained by differentiating $f_{sj \rightarrow ls}$ which is given by (7)

$$f_{sj \rightarrow ls} = \frac{1}{2\pi} \left\{ \cos^{-1} \frac{Z^2 - R_c^2 + R_s^2}{Z^2 + R_c^2 - R_s^2} - \frac{Z}{R_c} \left[\frac{Z^2 + R_c^2 - R_s^2}{\sqrt{(Z^2 + R_c^2 + R_s^2)^2 - 4R_c^2 R_s^2}} \right. \right. \\ \left. \left. \cos^{-1} \frac{R_s(Z^2 - R_c^2 + R_s^2)}{R_c(Z^2 + R_c^2 - R_s^2)} - \cos^{-1} \frac{R_s}{R_c} \right] \right\} \quad [\text{A-7}]$$

5. $f_{si \rightarrow 3}$.—This could be obtained by the following equations

$$f_{sj \rightarrow 3} = f_{sj \rightarrow 6} - f_{sj \rightarrow ls} \quad (\text{if } L_s > h_c)$$

The value of $f_{sj \rightarrow 6}$ is obtained from Eq. [A-7] if Z is replaced by $Z - h_c$. And if $L_s < h_c$, then

$$f_{sj \rightarrow 3} = 1 - (f_{sj \rightarrow 6} + f_{sj \rightarrow ls})$$

6. $f_{sj \rightarrow a}$.—

$$f_{sj \rightarrow a} = 1 - (f_{sj \rightarrow ls} + f_{sj \rightarrow 3})$$

REFERENCES

1. S. Vojdani, A. E. Dabiri, and H. Ashoori, *J. Crystal Growth*, **24/25**, 374 (1974).
2. M. Lichtensteiger, A. F. Witt, and H. C. Gatos, *This Journal*, **118**, 1013 (1971).
3. W. R. Wilcox and R. L. Duty, *J. Heat Transfer*, *ASME*, **88C**, 45 (1966).
4. K. Akiyama and J. Yamaguchi, *J. Appl. Phys.*, **33**, 1899 (1962).
5. T. Arizumi and N. Kobayashi, *J. Crystal Growth*, **13/14**, 615 (1972).
6. W. G. Pfann, K. E. Benon, and J. H. Wernick, *J. Electronics*, No. 2, 597 (1957).
7. H. Leuenberger and R. A. Person, *Am. Soc. Mech. Engrs.*, No. 56-A-144, 1 (1956).

Mass Spectrometric Analyses of Vapor in Chemical Vapor Deposition of Alumina

Sin-Shong Lin

Army Materials and Mechanics Research Center, Watertown, Massachusetts 02172

Current interest in improving techniques to fabricate a thick layer of translucent to transparent polycrystalline alumina with superior optical properties prompted the present investigation of the vapor phase composition in the preparation of alumina. Previous studies (1-3) relied mostly on analyses of deposits after the completion of a run. The present study extracts gaseous species directly from the deposition reaction, which may furnish basic information concerning vapor molecules existing in the reaction. The sampling of vapors from the process is accomplished by direct injection of these species from the hot furnace into vacuum followed by mass spectrometric detection. Thus the knowledge gained from vapor constituents of the reaction together with examination of the deposits provides valuable information in understanding the chemical deposition process.

Figure 1 shows a block diagram of the sampling device for the chemical vapor deposition of aluminum oxide by hydrolysis-oxidation of aluminum chloride. The experimental arrangement consists of gas inlet lines, a miniature chemical vapor deposition furnace, and a three-stage differential pumping system including a quadrupole mass filter and a modulated beam mechanism. Aluminum chloride is prepared by passing chlorine-hydrogen mixture in a 1:3 ratio over molten aluminum, and water vapor-oxygen mixture in a 1:4 ratio is obtained by bubbling oxygen through water at room temperature. Hydrogen as a carrier gas in the first mixture, reacts with oxygen at temperatures of the deposition to produce more water. Excess oxygen is used to avoid incomplete oxidation of the aluminum chlorides, and water is added not only to serve as a reactant but also to improve transparency of deposited materials. For the deposition reaction, these two gas mixtures are separately introduced into the hot furnace at the same flow rate. The initial flow rates of these gases are in the range of 2-5 cm³/min.

The miniature furnace is built on the flange of the first chamber of the vacuum system as indicated on Fig. 2. The core of the furnace consists of two high-purity

closed-end alumina tubes of 1/2 and 1/4 in. OD in a concentric configuration. On the tip of each tube an orifice is drilled on the axial line. The orifice diameter of the 1/4 in. tube is fixed at 0.006 in. and that of the outer 1/2 in. tube is either 0.04 or 0.06 in. A spacer or collar, cut from a 3/8 in. OD alumina tubing in lengths from 3/8 to 1/4 in. is inserted between these two tips to define a hot reaction zone and to serve as a substrate. The spacing between the tips can be reduced to the position of an intimate contact to examine varying extents of the interaction. The heating element is molybdenum wire of a 0.03 in. diameter wound directly around the outer combustion tube. For uniform heating, the winding begins from the orifice edge and extends about 4 in. along the length of the tube. At least two layers of zirconia felt are wrapped around the heating element as insulation. The cylindrical water jacket and the water channel flange are located outside the felt to circulate cooling water. A Pt-10% Rh/Pt thermocouple is placed inside the inner tube near the tip to record temperature and to regulate the heating alternating current supplied to the furnace. The vacuum system, as shown on the right side of Fig. 1, consists of three chambers individually evacuated by three pumping assemblies. The vacuum in the first chamber was maintained at 2×10^{-4} Torr or lower so that a molecular beam could be formed for sampling. The quadrupole mass spectrometer manufactured by Extranuclear Laboratories, Inc., has a high efficiency detection and is designed to operate in a mass range 0-4000 amu. The theory and practice of this sampling technique has been summarized by Milne and Greene (4), and the operation of the present system is given elsewhere (5, 6).

Provision was made to establish and to monitor pressures and flow rates of the reactant gases. The wet oxygen was introduced axially into the furnace through the core of the inner combustion tube and the chlorine-hydrogen mixture was fed into the furnace through the annulus between the inner and the outer combustion tubes. Aluminum metal was placed about 1 in. from the tip of the combustion tube in the annular space so that it melted and reacted with chlorine at temperatures above 600°C to provide aluminum

Key words: aluminum chloride hydrolysis, aluminum chloride oxidation, aluminum-chlorine reaction.

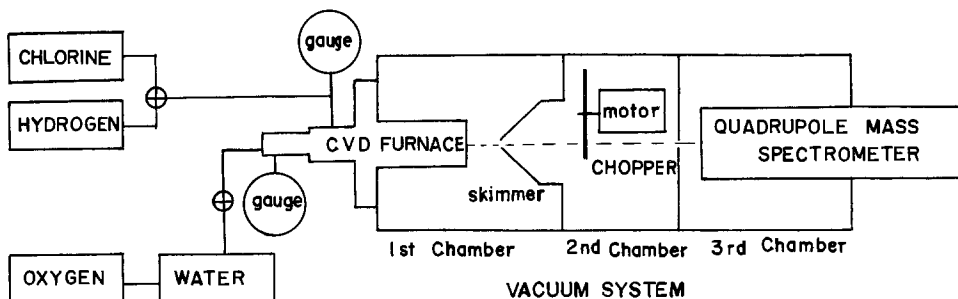
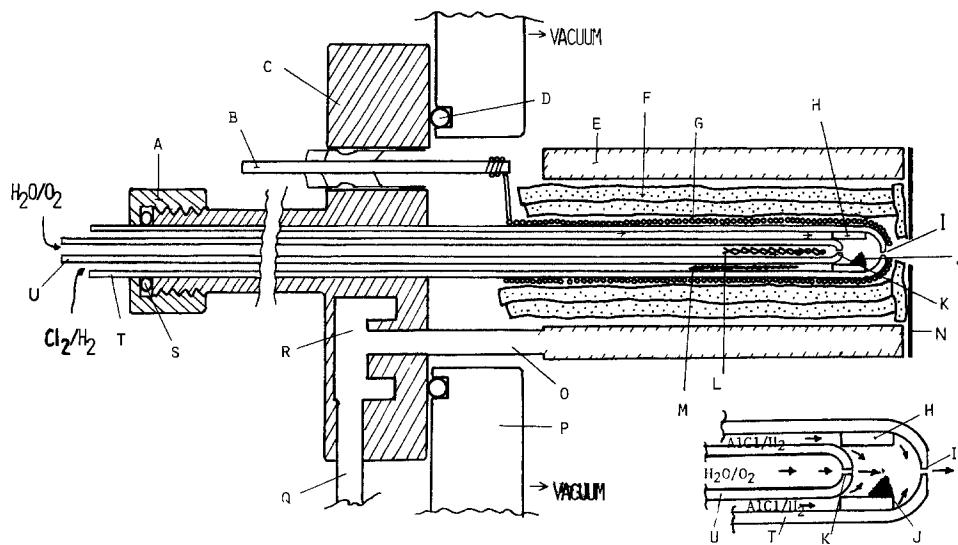


Fig. 1. Block diagram of CVD sampling device.

Fig. 2. Chemical vapor deposition furnace assembly, cross sectional view. Legend: A, quick coupling; B, electric feedthrough; C, vacuum flange; D, O-ring; E, cylindrical water jacket; F, zirconia felt; G, molybdenum heating wire; H, spacer or substrate; I, outer orifice; J, alumina deposit; K, inner orifice; L, Pt-10%Rh/Pt thermocouple; M, aluminum metal; N, tantalum heat shield; O, stainless steel tube; P, vacuum wall of the first chamber; Q, inlet and outlet water tubes; R, water channels; S, O-ring seal; T, 1/2 in. OD alumina combustion tube; U, 1/4 in. OD alumina combustion tube. The enlarged sketch of the reaction zone and the two orifices is shown on the right lower corner, and the direction of gas flows is indicated by arrows.



chloride vapors. Since the metal was not placed in a boat, the surface area of molten aluminum tended to decrease after a period of reaction. The experiments were carried out at temperatures from 800°-1400°C, and the pressures of both gaseous mixtures in the furnace were 50-100 mm Hg initially. The pressure of the reaction zone is estimated to be in the range of a few mm Hg. During the run, the Cl₂/H₂ passage tended to clog gradually due to the formation of Al₂O₃ and the displacement of molten aluminum. Consequently the flow rate decreased and the source pressure increased. Alumina deposits resulting from the interaction of the two mixtures were found mostly on the inner cylindrical surface near the exit end of the spacer. All vapors including reactants and products were exhausted into vacuum through the outer orifice for detection. The run was terminated after either the source pressure had reached 1 atm from clogging or a period of 6 hr had elapsed. At the end of a run, gases were shut off and furnace was allowed to cool. The entire furnace was then disassembled and the substrate was separated from the combustion tube.

The extent of the interaction between aluminum and chlorine was examined first. The study was carried out by passing a chlorine-argon mixture over aluminum at temperatures up to 1400°C. Mass spectra were

recorded continuously with rising temperatures. The gas-solid reaction begins somewhere around 300°C, and the products from the reaction depend on the surface area of aluminum and the partial pressure of the reactant. Ion species of Cl⁺, unreacted Cl₂⁺, AlCl⁺, AlCl₂⁺, AlCl₃⁺, Al₂Cl₅⁺, and a trace of Al₂Cl₆⁺ were observed at low temperatures. The ions resulting from the dimer, Al₂Cl₆ diminish in abundance as the temperature rises to 900°C. At this temperature all ions containing two Al atoms disappear and no chlorine ions are detected. As the temperature is increased further, AlCl⁺ becomes more abundant. Finally at temperatures above 1000°C, the monochloride ion becomes the predominant species and in most cases is the only major reaction product observed. The substitution of hydrogen for argon in the gas mixture did not change the reaction products except to produce HCl. Typical abundances of ions observed in the mass spectra are listed in the first half of Table I. The variation of the ion intensities of observed species with the partial pressure of chlorine-argon at 1365°C is illustrated in Fig. 3. At the high end of the chlorine pressure, the chlorine-rich ions are abundant, and at the low end AlCl⁺ is a dominant ion species.

Prior to the deposition experiments, vapor species existing in argon carrier gas over AlCl₃ powders were

Table I. Relative abundances of ion species present in aluminum-chlorine reaction and chemical vapor deposition process of alumina. The magnitudes of signals are obtained directly from strip charts and computer printouts without corrections for the sensitivity and efficiency of the detector. Due to variations in the experimental conditions, the data represent only relative ion intensities in a run

Reaction	Run No.	Gas mixture	Temperature Pressure	Relative ion intensity											
				H ⁺ H ₂ ⁺	OH ⁺ H ₂ O ⁺	Al ⁺	N ₂ ^{+(a)}	O ₂ ⁺	Cl ⁺	HCl ⁺	AlCl ⁺	Cl ₂ ⁺	AlCl ₃ ⁺	AlCl ₅ ⁺	Al ₂ Cl ₆ ⁺
Al + Cl ₂	111772	Ar/Cl ₂	475°C	—	—	20	—	—	15	—	14	1.2	60	25	16
Al + Cl ₂	020773	Ar/Cl ₂	155 mm Hg	—	—	18	—	—	11	15	21	1	58	29	1.5
Al + Cl ₂	020873	Ar/Cl ₂	600°C	—	—	10	—	—	10	—	9	0.3	30	15	2.5
Al + Cl ₂	112873	Ar/Cl ₂	870°C	—	—	43	—	—	14	—	69	—	23	7	—
Al + Cl ₂		Ar/Cl ₂	200 mm Hg	—	—	—	—	—	—	—	—	—	—	—	—
Al + Cl ₂		Ar/Cl ₂	1300°C	—	—	—	—	—	—	—	—	—	—	—	—
Al + Cl ₂		Ar/Cl ₂	200 mm Hg	—	—	—	—	—	—	—	—	—	—	—	—
CVD of alumina	030774	(d)	1200°C	(b)	153	—	79	870	642 ^(c)	—	—	—	—	—	—
CVD of alumina	030574	(d)	1000°C	(b)	116	—	147	1230	92 ^(c)	—	—	—	—	—	—
CVD of alumina	041974	(d)	1200°C	47	135	—	75	995	867 ^(c)	—	—	—	—	—	—

(a) N₂ is present due to leaks in the H₂O/O₂ inlet line.

(b) Ion intensities of H⁺ and H₂⁺ are not recorded.

(c) Sum of HCl⁺ and Cl⁺ ion intensities.

(d) Ratios of gas mixtures; H₂O/O₂ = 1/4 and Cl₂/H₂ = 1/3, see text for details.

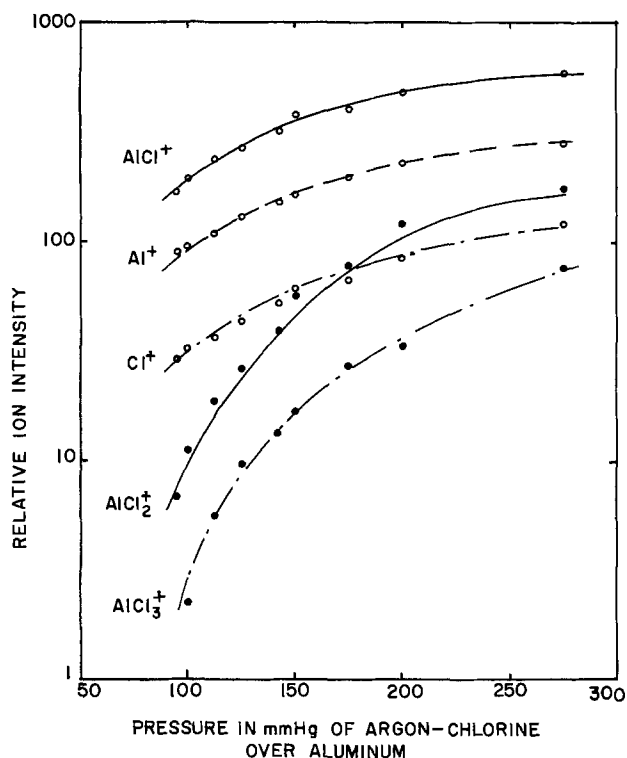


Fig. 3. Relative abundances of vapor ion species in aluminum-chlorine reaction at 1365°C. The data are taken from run 112872, Ar/Cl₂ ratio = 2/1, electron ionization energy = 40 eV, no correction is made for the detection efficiency. The fragmented ions are Al⁺ and Cl⁺ from AlCl, and AlCl₂⁺ from AlCl₃.

also examined. At low temperatures up to 400°C, Al₂Cl₅⁺ is the most abundant species, but at 1200°C, only AlCl⁺ and AlCl₂⁺ ion molecules exist and are equally abundant.

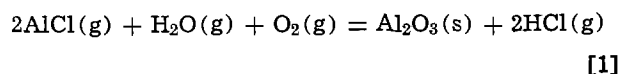
The mass spectra obtained during the deposition reaction at temperatures of 900°-1400°C reveal only the presence of H⁺, H₂⁺, O⁺, OH⁺, H₂O⁺, O₂⁺, Cl⁺, and HCl⁺ ions. The typical distribution of ion species is tabulated in the second half of Table II. The relative abundances may vary from run to run due to variation and fluctuation in the experimental conditions. In general there were no ions containing aluminum present, which indicated that the deposition reaction was nearly complete. During the experiments, the mass spectrometer was used repeatedly to scan up to mass 1000 amu to ascertain that no large mass ion or cluster ion was present in the deposition system. If there was a high mass ion present, the abundance must be less than 10⁻⁵ of the most abundant species in the spectra.

Under the condition of the present experiments, the chemical vapor deposition of alumina from aluminum-chloride/hydrogen and water/oxygen is predominantly a heterogeneous process in contrast to the earlier report (3) that vapor phase homogeneous nucleation

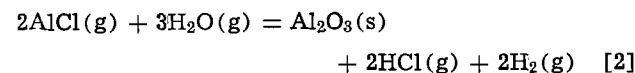
might take place. If vapor phase homogeneous nucleation had occurred, it would proceed via the random growth of small condensed aggregates and clusters of vapor molecules. The present result reveals the absence of aluminum-oxygen molecular species which are presumably the precursors of the aggregates and clusters, and Al₂O₃ nuclei in vapor phase. One might question the ability of the spectrometer to detect large microparticles from electron impact ionization processes. Since the existence of AlO⁺ and Al₂O⁺ ion species detected by the spectrometer has been reported (7, 8), there is no reason to suspect that the clusters of Al-O species would not have been detected if they had been present in the system in excess of 10⁻⁵ of the most abundant species. Perhaps large microcrystals dissociate into Al⁺ and large neutral fragments upon electron impact ionization, but this is highly improbable.

Examples of polycrystalline alumina deposits obtained from this study are shown in Fig. 4. These deposits were obtained from the CVD process under similar experimental conditions except for temperature, which was found to have a dominant influence over the textures of the deposits. The presence of whiskers grown on surfaces of the deposit at T = 1100°C (Fig. 4c) suggests that the surface nucleation is an important reaction mechanism.

The major vapor molecule from the aluminum-chlorine reaction at the present deposition temperature and pressure is AlCl. The exhaust gases from the CVD process of Al₂O₃ are HCl, Cl₂, O₂, H₂O, and H₂. The over-all deposition reaction should be written according to existing vapors as



and



¹The Cl⁺ ion intensity was greater than could be accounted for by HCl fragmentation; the monatomic chlorine probably resulted from dissociation of unreacted Cl₂.

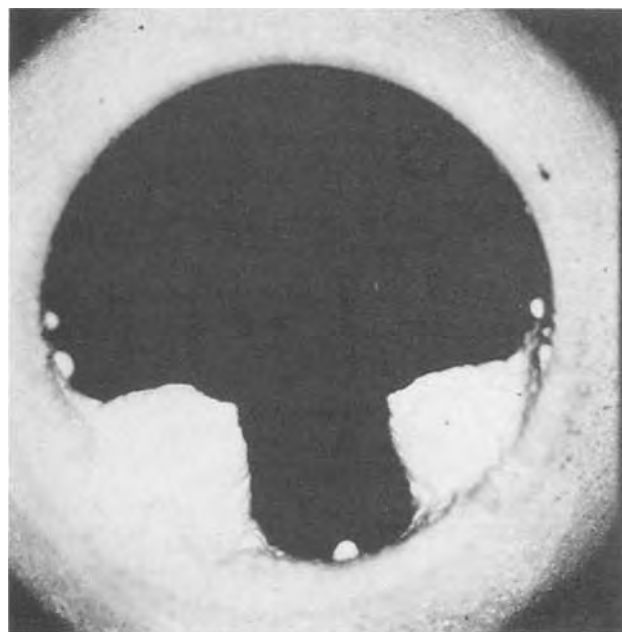
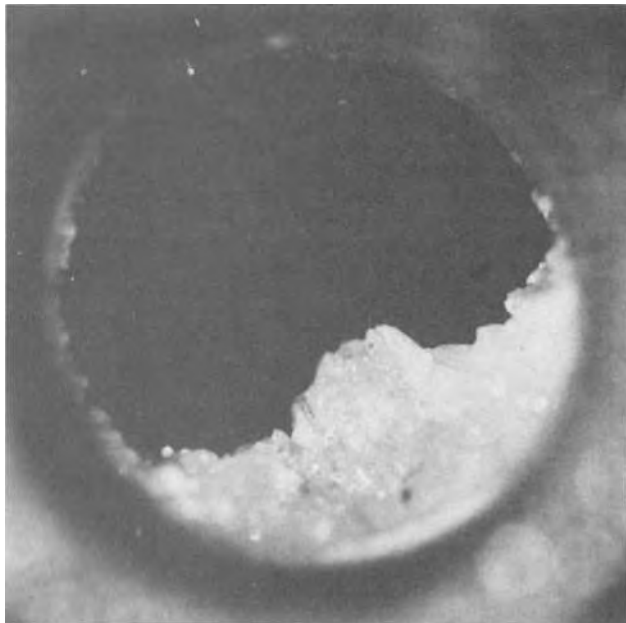


Fig. 4. Microphotographs (×7) of Al₂O₃ polycrystalline deposits obtained from chemical vapor deposition process. The deposits are grown on the cylindrical inner surface of the substrates cut from a 3/8 in. OD alumina tube under same gaseous reactants. a. White polycrystalline deposits obtained at 900°C. The similar white deposits were also obtained at temperatures above 1300°C and below 900°C.

Table II. Free energy changes of reactions between aluminum chlorides and water/oxygen in deposition of Al₂O₃ at various temperatures

Reaction	Free energy change in kcal-mole ⁻¹		
	1300°K	1500°K	1700°K
[1] 2AlCl(g) + H ₂ O(g) + O ₂ (g) = Al ₂ O ₃ (s) + 2HCl(g)	-235.4	-217.3	-199.5
[2] 2AlCl(g) + 3H ₂ O(g) = Al ₂ O ₃ (s) + 2HCl(g) + 2H ₂ (g)	-151.4	-138.7	-126.4
[3] 2AlCl(g) + 3/2 O ₂ (g) = Al ₂ O ₃ (s) + Cl ₂ (g)	-228.4	-206.9	-185.9
[4] 2AlCl ₃ (g) + 3H ₂ O(g) = Al ₂ O ₃ (s) + 6HCl(g)	-77.1	-77.8	-78.6



b. Opaque to transparent alumina obtained at 1000°C.

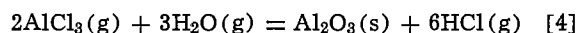


c. Whiskers on surfaces of opaque deposits obtained at 1200°C.

These reactions occur at the surfaces of substrates and/or Al_2O_3 crystals. The reaction

$2\text{AlCl}(g) + 3/2 \text{O}_2(g) = \text{Al}_2\text{O}_3(s) + \text{Cl}_2(g)$ [3]
is thermodynamically feasible, but the formation of Al_2O_3 from this reaction is neither observed by the

previous work (3) nor in this investigation. Table II tabulates the free energy changes of reactions leading to the formation of alumina. For the CVD of Al_2O_3 the first two reactions are both possible. The free energy change of reaction [1] is more negative than that of reaction [2], and reaction [1] seems to be kinetically more favorable because it requires fewer molecules to yield Al_2O_3 on the substrate surfaces. In reaction [1], oxygen is essential in the formation of Al_2O_3 . The earlier report (3) proposed the over-all reaction in which AlCl_3 is the only major Al-containing reactant



It would have been of interest to duplicate the conditions of the earlier work at higher pressures (3) to confirm the importance of AlCl_3 in the reaction; however the very small orifice [e.g., 0.01 cm (5)] necessary to isolate the high pressure region would have plugged with Al_2O_3 almost immediately, making measurements impossible.

At least, judging from analyses of vapor species in the present deposition data and associated experiments, the existence of AlCl molecule at the high temperature of the CVD process is highly probable. Furthermore, nonequilibrium kinetics in the chlorine-aluminum reactions could lead to AlCl vapor formation.

Competitive heterogeneous and gas-phase nucleation reactions leading to the formation of Al_2O_3 are believed to take place in the CVD process. The surface reaction is more favorable in the present experiments. Vapor phase nucleation is almost impossible because of fairly low pressures used in the present investigation. Perhaps vapor phase nucleation would have prevailed in the CVD system at much higher pressures.

Manuscript submitted Aug. 23, 1974; revised manuscript received June 2, 1975.

Any discussion of this paper will appear in a Discussion Section to be published in the June 1976 JOURNAL. All discussions for the June 1976 Discussion Section should be submitted by Feb. 1, 1976.

Publication costs of this article were partially assisted by The Department of the Army.

REFERENCES

1. P. S. Schaffer, *J. Am. Ceram. Soc.*, **4B**, 508 (1965).
2. R. Ellis, Raytheon Research Division, Contract DA-19-066-AMC-318(X), Final Report, AMMRC CR67-08(F), September 1968.
3. P. Wong and McD. Robinson, *J. Am. Ceram. Soc.*, **53**, 617 (1970).
4. T. A. Milne and F. T. Greene, in "Advances in High Temperature Chemistry," LeRoy Eyring, Editor, Vol. 2, p. 107, Academic Press, New York, London (1969).
5. S.-S. Lin, *Rev. Sci. Instr.*, **44**, 516 (1973).
6. S.-S. Lin, Army Material & Mechanics Research Center, AMMRC TR 73-9, March 1973.
7. K. J. D. MacKenzie, *J. Brit. Ceram. Soc.*, **58**, 83 (1968).
8. K. R. Thompson, *High Temp. Sci.*, **5**, 62 (1973).



Low Temperature Thermal Oxidation of Silicon by Dry Oxygen Pressure above 1 Atm

R. J. Zeto,* C. G. Thornton,* E. Hryckowian, and C. D. Bosco

U.S. Army Electronics Technology and Devices Laboratory (ECOM), Fort Monmouth, New Jersey 07703

It is widely recognized that the cost, reliability, and performance of integrated circuit devices are adversely affected by the large number of process-induced chemical and physical defects that result from high processing temperatures in the range 950°-1250°C. High thermal oxidation temperatures may also destroy specific desired impurity distributions achieved in previous processing steps. Consequently, there is strong motivation for developing an oxidation process that can produce gate, field, and other masking and passivating oxides at lower processing temperatures for silicon integrated circuit devices. It is also desirable that reduced oxidation temperatures be achieved by a dry oxidation method since problems due to oxide defects and contamination may be more serious for oxides prepared by wet oxidation. Although the use of high pressure steam (1) has long been known as a method for achieving low temperature thermal oxidation, attractive electrical characteristics have not been reported and the method is not generally used. On the other hand, it is known (2) that the oxidation of silicon is accelerated by dry oxygen partial pressures to 1 atm, but to our knowledge there are no oxidation data reported for dry oxygen pressures above 1 atm. On the basis of these considerations, dry pressure-oxidation of silicon is a logical possibility for achieving improved electrical properties *via* accelerated oxide growth and reduced oxidation temperatures.

The purpose of this communication is to report the initial results of experiments which demonstrate that dry pressure-oxidation, P-OX, significantly reduces the required oxidation temperatures of semiconductor silicon used for integrated circuit devices. The rate of oxidation of arsenic-doped (111) silicon at 800°C, 140 atm dry oxygen pressure was measured and compared with conventional (2, 3) thermal oxidation methods. The results are shown in Fig. 1. It is evident that oxide growth by 140 atm dry P-OX at 800°C is faster than either 1 atm dry or wet oxidation at 800°C, and is comparable to 1200°C dry oxidation at 1 atm. The 400°C reduction in dry oxidation temperature by the application of only 140 atm oxygen pressure is remarkable. Since 140 atm pressure (2060 psi) is less than the pressure supplied in conventional pressurized gas cylinders that are widely used and ordinarily handled, the technique is expected to be amenable to practical utilization.

The experimental oxidation system is readily assembled from commercially available components. It consists of a pressurized cylinder of oxygen gas, an oxygen gas pump, a vacuum pump, a cold-seal pressure vessel of the type used for hydrothermal crystal growth, an external resistance furnace, and stainless steel pressure lines. Rectangular samples, 8 × 10 mm,

were cut from a 1 in. silicon wafer and positioned in a quartz sample holder at the bottom of a 9 in. quartz tube (Amersil T08) that lined the inside of a 0.5 in. ID pressure vessel (Rene 41 alloy). The pressure-oxidations were conducted in a closed system with separate substrates for each experiment. Temperature and pressure were maintained within ±2°C and ±10 atm, respectively, during the course of the oxidations. Oxide thickness was measured with a Rudolph RR100 ellipsometer. The over-all uncertainty in thickness ranged from ±20Å for thin oxides to a maximum of ±200Å for some of the thicker oxides.

Special attention was given to the potential role of water vapor in the P-OX kinetics shown in Fig. 1. Scientific Gas Company electronic grade oxygen gas, 99.998% minimum purity, less than 3 ppm water vapor, and less than 1 ppm hydrocarbons as methane, was used. The stated moisture level was verified by measurements with a Panametrics Model 2000 hygrometer with a cell probe rated for operation to 5000 psi. Less than 14 ppm H₂O was measured in the exit gas from several overnight experiments. Using an identical hygrometer sensor element, Irene (4) recently compared the thermal oxidation kinetics of silicon at 1 atm oxygen pressure for conditions of less than 1 ppm water vapor *vs.* 20-30 ppm water vapor. This data for (111) silicon at 800°C is shown in Fig. 2 for comparison with the 800°C/140 atm P-OX data. With the ordinate scale used, both of Irene's cases are encompassed by the indicated points in Fig. 2. It was, therefore, concluded that the accelerated oxidation observed in the P-OX experiments was due to the effect

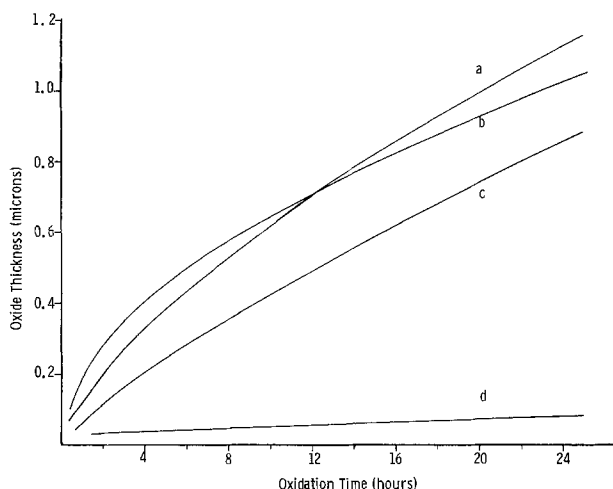


Fig. 1. Comparison of thermal oxidation conditions for (111) silicon: (a) 140 atm dry pressure-oxidation at 800°C, (b) 1 atm dry pressure-oxidation at 1200°C, (c) 1 atm steam oxidation at 800°C, (d) 1 atm dry oxidation at 800°C.

* Electrochemical Society Active Member.

Key words: silicon oxidation, dry oxygen pressure, oxide growth, MOS properties, passivation.

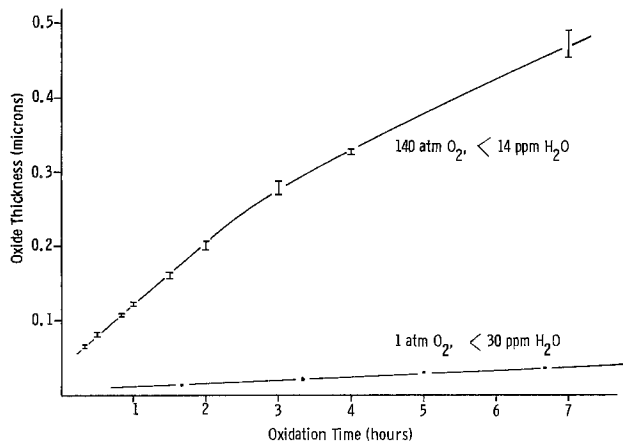


Fig. 2. Comparison of oxidation rate and moisture conditions for 800°C/140 atm P-OX and 800°C/1 atm (4) thermal oxidation of (111) silicon.

of dry oxygen pressure rather than moisture. For the P-OX conditions stated in Fig. 2, the oxide growth rate was linear between 650-2500Å with a value of about 14 Å/min.

Oxides for a wide range of applications in integrated circuit devices can be obtained at reduced temperatures by dry pressure-oxidation. A 1200Å gate oxide can be grown in 1 hr at 800°C/140 atm. Exploratory 3 hr oxidations at other temperature/pressure conditions yielded 4700Å at 800°C/500 atm and 16,000Å at 900°C/500 atm. Additional data on dry pressure-oxidation kinetics and detailed information on the P-OX experimental system will be reported.

According to the model of Deal and Grove (2), the thermal oxidation of silicon is initially reaction-rate limited at the oxide-silicon interface followed by diffusion control of the oxidant through the oxide. The corresponding coefficients in the oxidation equation $x_o^2 + Ax_o = B(t + \tau)$ are given in Table I for oxidation by 1 atm and 140 atm oxygen pressure at 800°C. Both the parabolic, B , and linear, B/A , rate constants are one to two orders of magnitude larger for 140 atm dry oxidation, indicating that both of these stages of the oxidation process are accelerated by pressures above 1 atm. The pressure variation of the coefficients, however, indicates that the pressure-oxidation mechanism is not completely described by

Table I. Coefficients for the dry thermal oxidation of (111) silicon according to $x_o^2 + Ax_o = B(t + \tau)$ for 1 atm (2) and 140 atm oxygen pressure at 800°C.

Oxidation pressure (atm)	A (μ)	B (μ^2/hr)	B/A (μ/hr)	τ (hr)
1	0.37	0.0011	0.0030	9.0
140	1.03	0.100	0.097	0.45

the model. The coefficient A is not independent of pressure, and neither the parabolic nor the linear rate

constants are proportional to pressure. The pressure-oxidation mechanism will be examined as additional P-OX data are determined.

A pressure vessel was recently put into operation to evaluate the MOS properties of samples prepared by the dry P-OX of 1 in. silicon wafers using clean-room conditions and state-of-the-art procedures. Evaporated aluminum dots were used for electrical contact, and conventional capacitance-voltage measurements were made. MOS structures from initial experiments showed negligible ($<0.1V$) shift in flatband voltage under bias temperature stress and Q_{ss} values in the range $3-8 \times 10^{10} \text{ cm}^{-2}$. These samples were (111) phosphorus-doped 1-5 ohm-cm silicon with 1000Å oxides prepared by 800°C/150 atm dry P-OX. Previous program effort was directed at an assessment of the dry pressure-oxidation kinetics, and for MOS properties exploratory experiments without clean-room conditions were made at 140 atm, 700°-800°C, with 8×10 mm samples of arsenic-doped silicon. Q_{ss} values in the range $2-7 \times 10^{11} \text{ cm}^{-2}$ were obtained, and under bias temperature conditions gross shifts in flatband voltage typical of alkali ion contamination were not present. These results indicate that significant benefits may be transferred to electrical properties by reduced temperature dry oxidation. Experimental conditions and procedures are currently being investigated to optimize electrical properties.

The characteristics of P-OX are advantageous for the preparation of oxide-isolated silicon devices with reduced impurity redistribution during dielectric isolation. This application of P-OX for bulk silicon and silicon-on-sapphire is currently under study. Initial results are promising and are reported separately (5).

Acknowledgments

The authors are indebted to G. J. Iafrate and S. Marshall for helpful discussions and advice, and E. Kostyk and J. Harthman for sample preparation.

Manuscript received Feb. 27, 1975.

Any discussion of this paper will appear in a Discussion Section to be published in the June 1976 JOURNAL. All discussions for the June 1976 Discussion Section should be submitted by Feb. 1, 1976.

Publication costs of this article were partially assisted by the U.S. Army Electronics Technology and Devices Laboratory.

REFERENCES

1. M. M. Atalla, in "Proceedings of the Conference on Elemental and Compound Semiconductors," H. Gatos, Editor, Interscience Publishers, New York (1960).
2. B. E. Deal and A. S. Grove, *J. Appl. Phys.*, **36**, 3770 (1965).
3. "Integrated Silicon Device Technology, Volume VII: Oxidation," p. 49, Research Triangle Institute, Durham, North Carolina (1965).
4. E. A. Irene, *This Journal*, **121**, 1613 (1974).
5. S. Marshall, R. J. Zeto, and C. G. Thornton, *This Journal*, **122**, 1411 (1975).

Dry Pressure Local Oxidation of Silicon for IC Isolation

S. Marshall, R. J. Zeto,* and C. G. Thornton*

U.S. Army Electronics Technology and Devices Laboratory (ECOM), Fort Monmouth, New Jersey 07703

This communication reports the use of dry pressure-oxidation (P-OX) for obtaining oxide-isolated device structures in both bulk silicon and epitaxial silicon on sapphire (SOS). Dry P-OX is a new low temperature oxidation technique which, compared with conventional dry thermal oxidation, reduces required oxidation temperatures as much as 400°C for equivalent oxide film growth. It has been shown, for example, that oxidation of silicon by 140 atm dry oxygen at 800°C is comparable to 1 atm dry oxidation at 1200°C (1).

Localized oxide isolation of silicon devices in integrated circuits utilizes silicon nitride as an oxidation mask (2). In the present work two structures were examined, one in which the Si_3N_4 was deposited directly on the silicon surface and one in which a 500-1000Å conventional thermal oxide was grown prior to the nitride deposition. The nitride was grown by the $\text{SiH}_4\text{-NH}_3$ process and was defined by supplemental CVD masking and etching in phosphoric acid. When the intermediate oxide layer was used, silicon areas were exposed by HF etching. The local oxidation process with dry P-OX was explored under a variety of experimental conditions, i.e., 700°-880°C, 140-500 atm oxygen pressure, and oxidation times of 3-24 hr. Optimum pressure-temperature-time conditions have not yet been determined, but at 850°C and 250 atm, the average oxidation rate was about 17 Å/min for <100> silicon. For <111> silicon the rate was 47 Å/min at 850°C and 500 atm. Scanning electron microscopy (SEM) was utilized to reveal the morphology of the P-OX structures.

The application of P-OX to dielectric isolation in bulk silicon and SOS devices is illustrated in Fig. 1, where the nitride mask has been applied directly to the surface of the silicon. Figure 1(a) shows the required oxidized structure as achieved in bulk material by the dry P-OX process at oxidation temperatures where undesired impurity redistribution effects are

very small. The oxide thickness is 1μ and was grown in 3½ hr at 850°C and 500 atm. In Fig. 1(b) the oxide extends completely through the $1\mu\text{m}$ epitaxial silicon layer of an SOS structure, thus effecting dielectric isolation of adjacent silicon elements. In this case, the oxide happened to be grown in 23 hr at 850°C, 250 atm. A more optimum set of conditions can obviously be chosen from available data (1).

Following the P-OX treatment the structures were well defined, lateral oxidation under the nitride mask was negligible, and cracks in the nitride film were absent. The use of a chromate dislocation etch (3) failed to reveal significant nitride induced defects in the cleaved low temperature pressure oxidized structures examined. This observation is contrasted with results reported in Ref. (2) where application of the nitride directly to the silicon surface resulted in severe dislocation damage under higher temperature oxidation. Thus, an intermediate oxide "buffer" layer may not be needed to avoid undesirable defects at the silicon-nitride interface.

Local pressure oxidation of silicon using a more conventional nitride/oxide/silicon structure is illustrated in Fig. 2(a) and 2(b) for bulk silicon and SOS, respectively. It is evident from a comparison of Fig. 1 and 2 that lateral oxidation underneath the nitride mask is much more pronounced in the presence of an intermediate oxide layer, an observation originally reported by Appels and Paffen (4) for silicon oxidized at 1 atm. The shape of the oxide edge is similar to that reported by Powell *et al.* (5) for silicon oxidized in steam. The experimental conditions for bulk silicon and SOS are the same as reported above for Fig. 1.

The degree of lateral oxidation has an important bearing on device design since lateral oxidation establishes a minimum size for adjacent isolated structures. This point is illustrated in Fig. 3 in which the lateral oxide growth undermines the original 8.5μ width of the nitride mask. The ratio of lateral oxidation L to isolation oxide thickness t for the specific P-OX sample shown in Fig. 2(a) (<111> Si, 500 atm,

* Electrochemical Society Active Member.

Key words: pressure oxidation, selective oxidation, dielectric isolation, SOS.

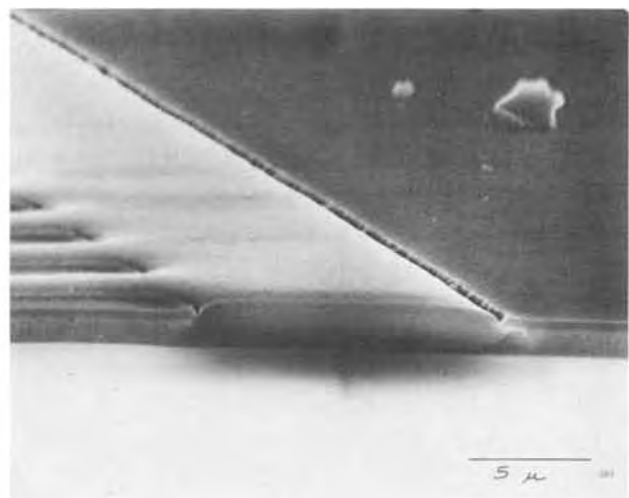
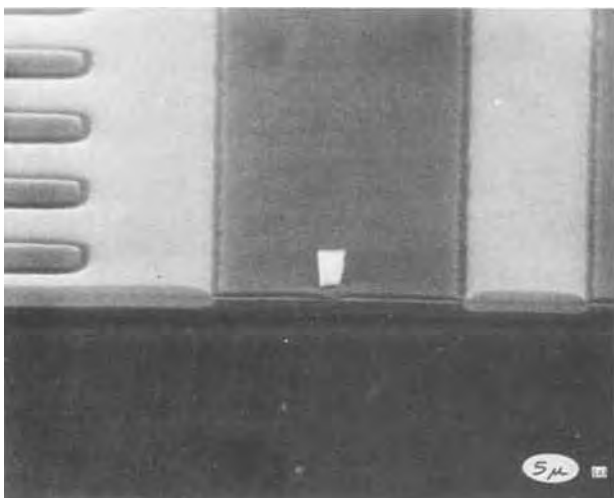


Fig. 1. Dry pressure-oxidation of nitride on silicon structures: (a) Bulk <111> silicon showing 1μ oxide (light) and masking nitride (dark); (b) $1\mu\text{m}$ <100> SOS showing complete dielectric isolation.

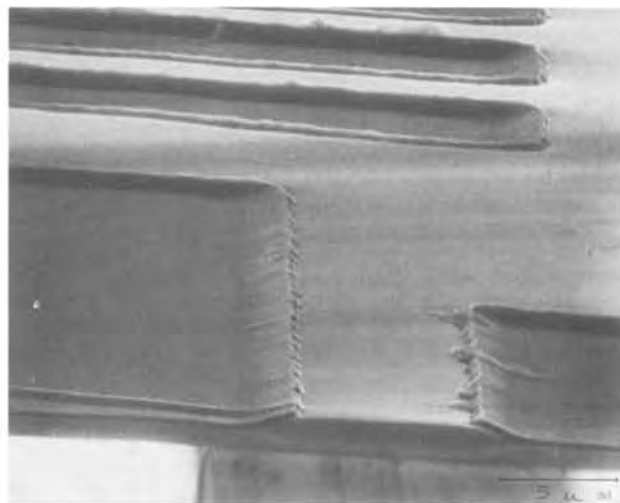
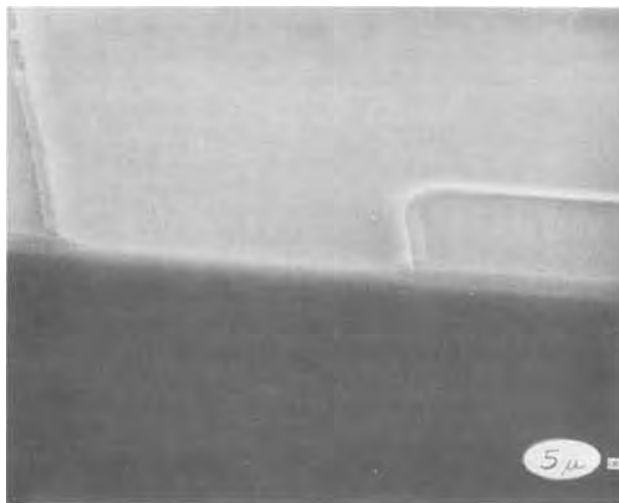


Fig. 2. Dry pressure-oxidation of nitride on thermal oxide on silicon structures: (a) bulk $\langle 111 \rangle$ silicon showing $1 \mu\text{m}$ pressure oxide; (b) $1 \mu\text{m}$ $\langle 100 \rangle$ SOS with 2700 \AA of silicon remaining. The extent of lateral oxidation is much greater than for the nitride-oxide structures of Fig. 1.

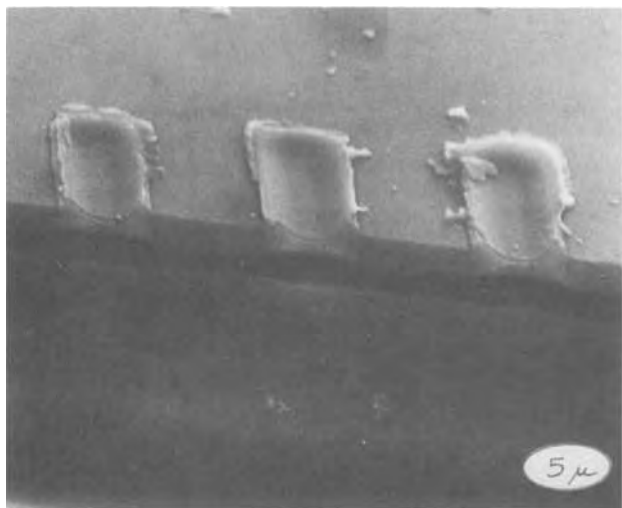


Fig. 3. LOCOS structure showing the limit imposed on device geometry by lateral oxidation beneath the nitride mask. Center to center pad spacing is $12 \mu\text{m}$. The initial mask consisted of $8.5 \mu\text{m}$ wide nitride bars separated by $3.5 \mu\text{m}$ spaces. The nitride was deposited on 1000 \AA thermal oxide on bulk $\langle 111 \rangle$ silicon.

850°C) is 2.8. For comparison, a ratio of 3.3 is calculated from the data of Powell *et al.* (5) (steam oxidation at 60 atm, 675°C). The P-OX L/t ratio is 2.2 for the $\langle 100 \rangle$ SOS sample of Fig. 2(b) (250 atm, 850°C). For equivalent conditions with nitride/oxide/silicon structures it would be expected that the L/t ratio would be higher for high pressure steam due to the high solubility and diffusivity of water in the initially present oxide layer. For either process, selective etching of the silicon prior to the pressure oxidation, as described in Ref. (4) will decrease the oxidation time needed to achieve oxide isolation, reduce the lateral

oxidation, and result in a desirable planar surface topography.

Subsequent work in this area will investigate in greater detail the effect of P-OX conditions on the generation of surface defects in nitride masked structures. Consideration will also be given to the oxidation kinetics of the nitride masking film and to the evaluation of "P-OX device" characteristics.

Acknowledgments

The authors are indebted to Mr. C. Cook for the SEM analysis and for many helpful discussions. They also wish to thank Ms. J. Harthman, Mr. A. Rogel, and Mr. E. Hryckowian for the preparation of the experimental samples.

Manuscript received Feb. 24, 1975.

Any discussion of this paper will appear in a Discussion Section to be published in the June 1976 JOURNAL. All discussions for the June 1976 Discussion Section should be submitted by Feb. 1, 1976.

Publication costs of this article were partially assisted by the U.S. Army Electronics Technology and Devices Laboratory.

REFERENCES

1. R. J. Zeto, E. Hryckowian, C. D. Bosco, G. J. Iafrate, R. W. Brower, and C. G. Thornton, Paper 206 presented at Electrochemical Society Meeting, New York, New York, Oct. 13-17, 1974.
2. J. A. Appels *et al.*, *Philips Res. Rep.*, **25**, 118 (1970).
3. B. M. Berry, "Integrated Silicon Device Technology," Vol. XII, p. 52, Air Force Avionics Laboratory (1966).
4. J. A. Appels and M. M. Paffen, *Philips Res. Rep.*, **26**, 157 (1971).
5. R. J. Powell, J. R. Ligenza, and M. S. Schneider, *IEEE Trans. on Electron Devices*, **ED-21**, 636 (1974).

New Method of Manufacturing Sintered-Type Aluminum Solid Electrolytic Capacitor

Sadao Okuma

Department of Applied Science, Tokyo Electrical Engineering College, Tokyo, Japan

The sintered-type aluminum solid electrolytic capacitor has been prepared by a new method, where first either nitrogen or hydrogen gas at 1 atm is used during the sintering of the aluminum powder to form the porous anode, and second either ammonium dihydrogen phosphate or ammonium borate solution is used during the anodization to form the dielectric.

The capacitors prepared by this method gave better characteristic properties than other electrolytic capacitors.

The preparation of the aluminum-sintered anode has been said to be difficult, because aluminum unlike tantalum easily forms a hard oxide at sintering temperature.

The author could prepare the aluminum-sintered anode in this experiment based upon the assumption that adequate sintering would take place in the gaseous atmosphere mentioned above.

This makes us suppose that the aluminum-sintered body has a large surface area with a suitable porous property and the interior surface can be converted to a good dielectric film by the usual anodization techniques.

Consequently, for the manufacture of the sintered-type aluminum solid electrolytic capacitor on this study, it has been understood that both ammonium dihydrogen phosphate as the forming solution and hydrogen gas as the sintering atmosphere gave better dielectric properties, respectively.

If the manufacturing steps are considered, the new method used in this study would be much simpler than the normal vacuum sintering method.

This communication reports a comparison of the characteristic properties with the ones obtained in this study.

Experimental

Materials.—99.98-99.99% pure aluminum powder was obtained from commercial sources. Particle sizes of the aluminum powder were 20, 35-150, 150-200, and 200 mesh, respectively. The binder used for sintering was less than 1 weight per cent (w/o). Gaseous atmosphere during sintering was at about 1 atm pressure. The forming solution was either 3% ammonium borate solution or 0.3% ammonium dihydrogen solution.

Apparatus.—The characteristic properties of the dielectric substance were measured by a Universal Bridge which was manufactured by Yokogawa Electrical Manufacturing Company.

Procedure.—The compacting pressure was either 0.1 ton/5 mm diameter or 0.2 ton/5 mm diameter. The size of the compact was 5 mm diameter by about 5 mm high. The sintering was at 600°C for about 120-180 min in each gas as mentioned above.

The anodization was performed at a constant current of 50 mA until 150V was reached, and the voltage was maintained at 150V until the current dropped to 2 mA.

The total formation time was 120 min. After formation the anodized pellet was washed for 60 min with water, and then dried at 500°C for 60 min.

Manganese dioxide, produced from thermal decomposition of a highly concentrated manganous nitrate solution at 300°C for 60 min, was used to form the interior semiconductor contact.

Finally, colloidal carbon was spread on the coated

anode, dried, coated with silver paint, and dried at 500°C for 60 min.

Results and Discussion

Table I shows the characteristic properties for the sintered-type aluminum solid electrolytic capacitor manufactured in this study.

In spite of fact that the dielectric constant of aluminum oxide is lower than other dielectric of metal oxide, the sintered-type aluminum solid electrolytic capacitor obtained in this study gave a capacitance of 0.5-7.4 μF .

The capacitance per unit weight of the aluminum solid electrolytic capacitor is 2-40 $\mu\text{F/g}$. Then anodization voltage to form the aluminum capacitors is much higher than the tantalum, niobium, or zirconium capacitors, and consequently the anodic oxide film is much thicker. Consequently, it can be said that this method was effective enough for the preparation of the dielectric substance.

The dissipation factor of the aluminum capacitor was somewhat inferior to other capacitors; however, it was considered that it might be lowered to some extent by eliminating the naturally formed aluminum oxide. This proposal has not yet been tried. Instead further comparisons were made using either hydrogen or nitrogen gas as the sintering atmosphere and either ammonium dihydrogen phosphate or ammonium borate solution as the forming solution.

First, the dielectric film was formed using each forming solution and then transformed into the sintered-type aluminum solid electrolytic capacitor ac-

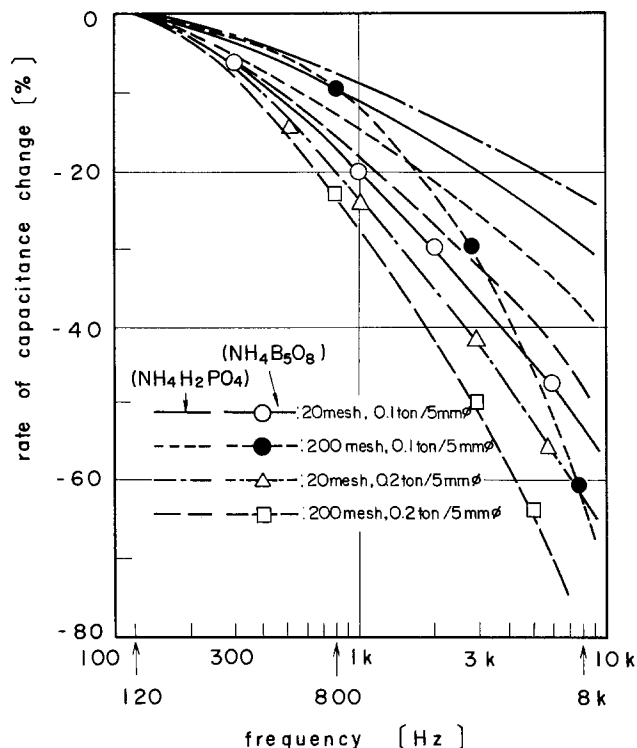


Fig. 1. Rate of capacitance change vs. frequency at 20°C (N_2 atmosphere).

Key words: aluminum, capacitor, sintered-type, solid, dielectric.

Table I. Comparison of various solid electrolytic capacitors at 20°C

Anode	Form	Etching done+none	Gaseous atmosphere to sintering	Forming solution	Density (g/cm ³)	Forming voltage (V)	Capacitance			Leakage* current (μA)		
							(μF)	Area (μF/cm ²)	Volume (μF/cm ³)		Weight (μF/g)	Dissipation factor (%)
Al	Foil	Done	—	Ammonium borate NH ₄ B ₂ O ₈	2.7	150	1.6 ~ 7.4	5.0 2.7 0.6	16 ~ 75	11 ~ 40	10 8 6	0.07 0.05 0.03
Al in this study	Sintered	None	Nitrogen	Ammonium borate NH ₄ B ₂ O ₈	1.4 ~ 1.8	150	1.6 ~ 7.4	1.6 ~ 7.4	16 ~ 75	11 ~ 40	13 ~ 40	0.16 ~ 0.21
	Sintered	None	Nitrogen	Ammonium dihydrogen phosphate NH ₄ H ₂ PO ₄	1.4 ~ 1.8	150	0.5 ~ 2.5	0.5 ~ 2.5	4.6 ~ 25	2 ~ 20	11 ~ 25	0.16 ~ 0.21
	Sintered	None	Hydrogen	Ammonium dihydrogen phosphate NH ₄ H ₂ PO ₄	1.5 ~ 1.8	150	0.5 ~ 1.6	0.5 ~ 1.6	5.6 ~ 1.7	4 ~ 11	7.5 ~ 13	0.16 ~ 0.21

* Measured at 4-6V.

ording to above procedure. The characteristic properties of these capacitors were measured.

Figure 1 gives the rate of capacitance change vs. frequency (at 20°C) of capacitors prepared in the sintering atmosphere of nitrogen gas as a function of the compacting pressure. Consequently, the element formed from ammonium dihydrogen phosphate solution is better than the one produced from ammonium borate solution.

Figure 2 shows the rate of capacitance and the dissipation factor of the capacitors made in a sintering atmosphere of hydrogen gas.

From these results, hydrogen gas was considered a better sintering atmosphere for it gave more stable dielectric characteristic properties than those prepared in nitrogen (1-3).

Conclusion

This study was carried out with the purpose of increasing the capacitance and the improvement of other characteristic properties of the dielectric substance.

The sintered-type aluminum solid electrolytic capacitors were prepared using either nitrogen or hydrogen gas as the sintering atmosphere and either ammonium borate or ammonium dihydrogen phosphate solution of the forming solution. Measurements were made of the characteristic properties of these capacitors.

The following conclusions can be made:

1. The anode in the capacitor has a large surface area with sufficient porosity to impregnate with manganese nitrate solution.
2. The dissipation factor is somewhat less satisfactory. However, it may be possible to improve it by a surface pretreatment before anodization.
3. Hydrogen gas as the sintering atmosphere and ammonium dihydrogen phosphate solution as the forming solution, each gave better dielectric properties than nitrogen gas and ammonium borate solution.
4. The new method used in this study would be more useful in the industrialization of the sintered-type aluminum solid capacitor than the vacuum mechanism method used hitherto.

Acknowledgment

The author wishes to thank Dr. Gisaku Ohara of Tokyo Electrical Engineering College for his actual

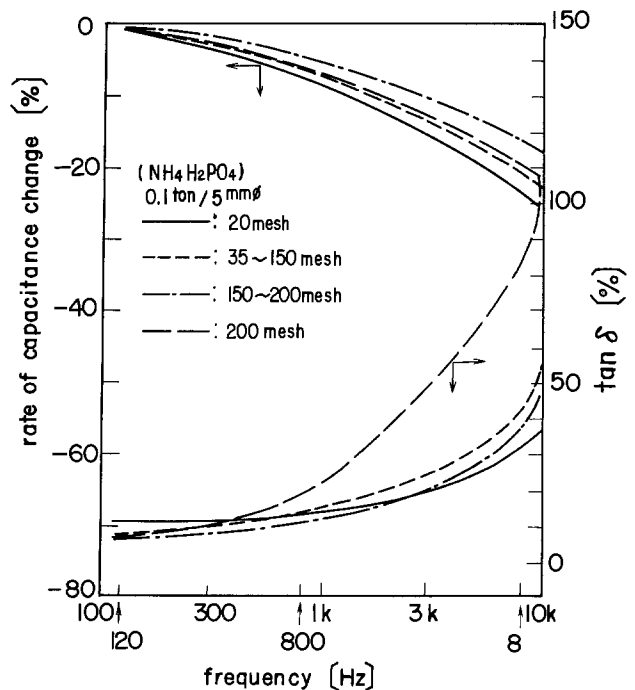


Fig. 2. Rate of capacitance change and dissipation factor vs. frequency at 20°C (H₂ atmosphere).

instruction in this study, and Mr. Hozui Okubo and Mr. Tomihiro Nemoto of the same college for their cooperation in submission of this paper.

Manuscript submitted Oct. 31, 1974; revised manuscript received June 13, 1975.

Any discussion of this paper will appear in a Discussion Section to be published in the June 1976 JOURNAL. All discussions for the June 1976 Discussion Section should be submitted by Feb. 1, 1976.

Publication costs of this article were partially assisted by Tokyo Electrical Engineering College.

REFERENCES

1. S. Okuma and T. Nemoto, *J. Metal Finishing Soc. Japan*, **23**, 204 (1972).
2. S. Okuma and T. Nemoto, *ibid.*, **24**, 376 (1973).
3. S. Okuma, *ibid.*, **24**, 626 (1973).



Optimal Working Parameters for Some Silver Gas Electrodes

I. Solacolu, Maria Mavrodin-Tărăbîc, and Ioana Onaca

Centre of Physical Chemistry, Bucharest, Romania

ABSTRACT

The effect of oxygen overpressure (200-600 mm Hg), temperature (15°-65°C) and electrolyte concentration (2-9N) were studied on silver gas electrode polarization by dispersional analysis. The values of apparent activation energies were calculated. The optimal working parameters were established for different apparent current densities.

Recent studies (1-5) showed the low polarization of silver gas electrodes during oxygen reduction in KOH medium. This study has tried to maximize a set of operating parameters for the silver gas electrodes not previously obtained (6).

Experimental

Electrode preparation and characterization.—The silver gas electrodes, having a DSK type structure, were fabricated by pressing ($2.8 \cdot 10^8$ N/m²) a homogenous mixture containing 81.25% silver carbonate (less than 5 μ m powder) and 18.75% ammonium dicarbonate (40-60 μ m powder). The resultant pellets (10 mm diameter, 3 mm thick) were sintered under a hydrogen atmosphere (15 min at 375°C). In a horizontal electric furnace (hydrogen flow rate 2 liters/min, heating 2°C/min, temperature steps, 1 hr at 100°C and 1 hr at 140°C, cooling 3°C/min with 30 min steps at every 100°C).

The microscopic examination showed a uniform distribution of pores in the whole electrode mass. The over-all porosity (as determined by weighing before and after soaking with toluene) was 50.5%.

Polarization measurements.—The study of oxygen reduction in KOH medium on silver gas electrodes was carried out by the potentiostatic technique, previously reported (7, 8). The following equipment was used: a Tacussel potentiostat Type PRT 500 LC (± 1 mV precision), an electronic Radiometer Type 22 millivoltmeter (± 1 mV precision), a DU 20 milliammeter ($\pm 1\%$ precision). The auxiliary electrode was a 99.9% nickel tape, the reference electrode was a saturated calomel electrode. The working cell (120 \times 72 \times 56 mm) was made from polystyrene. The polarization curves were obtained by applying potential steps of 10 mV at 1 min intervals.

The electrodes were supplied with oxygen at constant overpressure (± 2 mm Hg) (6). The working cell was kept at constant temperature ($\pm 0.1^\circ$ C). The electrolyte was prepared from pA KOH (Merck).

The values of the working parameters were varied as follows: oxygen overpressure from 200 to 600 mm Hg (100 mm Hg steps), electrolyte temperature from 15° to 65°C (5°C steps), and KOH concentration from 2 to 9N (1 mequiv./cm³ steps).

Effect of Changes in Working Parameters

The optimization study established the effect of change of working parameters upon the silver gas

Key words: silver, oxygen electrode, dispersional analysis, activation energy.

electrode polarization at different values of apparent current density between 10 and 70 mA/cm². Overvoltage values were obtained by interpolation from polarization curves. $\eta = f_P(P)$, $\eta = f_c(c)$, and $\eta = f_t(t)$ curves were plotted (Fig. 1, 2, and 3).

Effect of oxygen overpressure.—The family of curves in Fig. 1 shows the increase of oxygen overpressure from 200 to approx. 400-500 mm Hg has a favorable effect upon the performance of the studied electrodes whenever the apparent current densities are larger than 10 mA/cm². This is explained by an alteration of conditions under which oxygen electroreduction takes place (active surface increase and meniscus thickness reduction) and by the increase of oxygen solubility. The effect is more evident the larger the apparent current density (curves 2, 3, and 4) and the lower the electrolyte concentration (curves 4 and 5) and working temperature (curves 4 and 6). The increasing of oxygen overpressure above 500 mm Hg helps to increase the electrode polarization (more evident in curves 5 and 6).

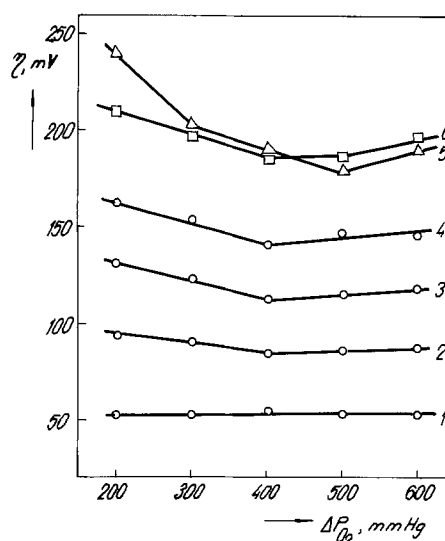


Fig. 1. The effect of oxygen overpressure on electrode polarization. Curve 1, 6N, 55°C, 10 mA/cm²; curve 2, 6N, 55°C, 30 mA/cm²; curve 3, 6N, 55°C, 50 mA/cm²; curve 4, 6N, 55°C, 70 mA/cm²; curve 5, 4N, 55°C, 70 mA/cm²; curve 6, 6N, 40°C, 70 mA/cm².

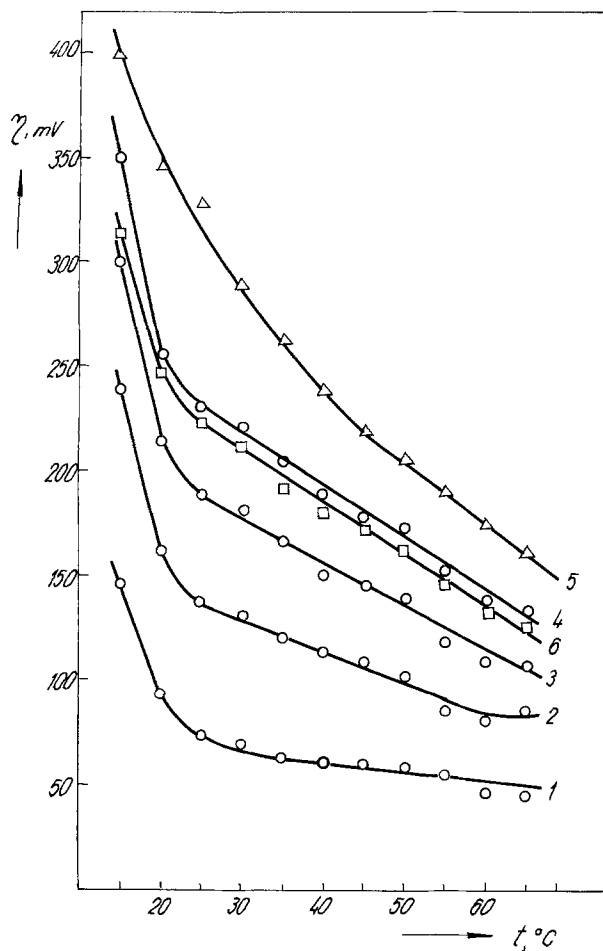


Fig. 2. The effect of electrolyte temperature on electrode polarization. Curve 1, 6N, 400 mm Hg, 10 mA/cm²; curve 2, 6N, 400 mm Hg, 30 mA/cm²; curve 3, 6N, 400 mm Hg, 50 mA/cm²; curve 4, 6N, 400 mm Hg, 70 mA/cm²; curve 5, 4N, 400 mm Hg, 70 mA/cm²; curve 6, 6N, 500 mm Hg, 70 mA/cm².

Effect of electrolyte temperature.—Examination of $\eta = f_t(t)$ curves in Fig. 2 shows the oxygen reduction in KOH is enhanced by increasing temperature over the range of 15°–65°C. This effect becomes more obvious as the temperature and electrolyte concentration are lowered (curves 4 and 5), and the apparent current density is increased (curves 1, 2, 3, and 4). The behavior of these gas electrodes is accounted for by unlike effects of temperature variation upon electrolyte conductivity (9), solubility of oxygen in KOH solution (10), and diffusion of reacting species and products to/from reaction zone, i.e., oxygen solubility decreases while conductivity and diffusion increase. At apparent current density higher than 10 mA/cm², the effect is more obvious over the entire range because, under these conditions, the contribution of concentration and ohmic polarization to the over-all electrode polarization is larger. A plateau is reached as a result of the two effects compensating each other, at 10 mA/cm² and temperatures higher than 40°C.

Effect of electrolyte concentration.—The electrode polarization decreases continuously as electrolyte concentration increases over the range of 2–6N KOH ($\eta = f_c(c)$ curves shown in Fig. 3). This effect becomes more obvious as the concentration and temperature are lowered (curves 4 and 5) and the apparent current density is increased (curves 1–4). The variation of the oxygen overpressure within the range 400–500 mm Hg has no notable effect upon the $\eta = f_t(t)$ and $\eta = f_c(c)$ functions (curves 4 and 6 in Fig. 2 and 3).

The increase of electrolyte concentration up to approximately 6N has a very favorable effect upon the electrolyte conductivity (9), which prevails over the

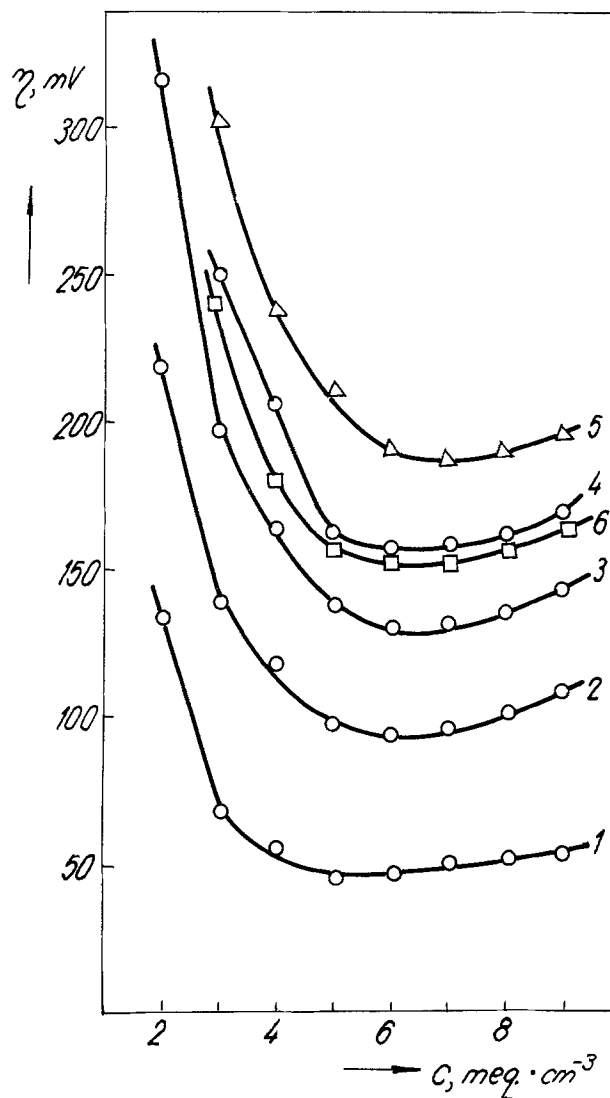


Fig. 3. The effect of electrolyte concentration on electrode polarization. Curve 1, 50°C, 400 mm Hg, 10 mA/cm²; curve 2, 50°C, 400 mm Hg, 30 mA/cm²; curve 3, 50°C, 400 mm Hg, 50 mA/cm²; curve 4, 50°C, 400 mm Hg, 70 mA/cm²; curve 5, 40°C, 400 mm Hg, 70 mA/cm²; curve 6, 50°C, 500 mm Hg, 70 mA/cm².

unfavorable effect upon the oxygen solubility (10) (Fig. 3). These two effects are compensated over the range of 6–7N. Above this concentration range the electrode polarization increases.

The data presented outline the complexity of the effect of working parameters upon silver gas electrode polarization. The same data show that the optimal parameters depend on the apparent current density (11) for low current densities (approx. 10 mA/cm²) at KOH concentration 4–5N, temperature 45°–55°C, and for apparent current densities higher than 30 mA/cm² at KOH concentration 5–6N, temperature 55°–65°C.

Apparent Activation Energies

The apparent activation energies (E_{ap}) were calculated from the plots $\log i_0$ vs. $1/T$. The results are given in Table I.

Examination of data in Table I shows the exchange current increases with increasing electrolyte temperature and concentration. The apparent activation energies decrease as the concentration increases, their lowest values corresponding to 6–7N KOH. Values of 4–5 kcal/mol, corresponding to 6–7N, prove the electrode process is diffusion-controlled which is in agreement with the literature data (12) obtained for oxygen reduction on coal gas electrodes.

Table I. Apparent exchange current densities (i_0) and activation energies (E^*_{ap})

Working temperature	3N			4N			5N			6N			7N			8N		
	300 mm Hg	400 mm Hg	500 mm Hg	300 mm Hg	400 mm Hg	500 mm Hg	300 mm Hg	400 mm Hg	500 mm Hg	300 mm Hg	400 mm Hg	500 mm Hg	300 mm Hg	400 mm Hg	500 mm Hg	300 mm Hg	400 mm Hg	500 mm Hg
293	-0.35	-0.18	-0.32	-0.05		-0.12	0.14	0.11	0.02	0.24	0.04	0.18	0.02	0.13	0.14	0.20	0.20	0.33
298	-0.30	-0.15	-0.25	0	-0.08	-0.06	0.37	0.18	0.09	0.34	0.21	0.26	0.20	0.30	0.45	0.30	0.32	0.48
303	-0.16	-0.03	-0.18	0.05	-0.10	-0.04	0.41	0.21	0.04	0.41	0.24	0.33	0.31	0.30	0.48	0.35	0.40	0.70
308	-0.08	0.05	-0.02	0.50	0.05	0.19	0.55	0.39	0.08	0.51	0.31	0.38	0.48	0.33	0.52	0.41	0.52	0.88
log i_0	313	0	0.10	0.20	0.26	0.15	0.31	0.58	0.47	0.38	0.59	0.33	0.52	0.38	0.55	0.52	0.65	0.91
mA/cm ²	318	0.21	0.23	0.46	0.41	0.36	0.58	0.68	0.57	0.60	0.63	0.35	0.40	0.65	0.48	0.63	0.64	0.74
	323	0.32	0.29	0.56	0.54	0.56	0.71	0.73	0.70	0.65	0.66	0.39	0.46	0.68	0.55	0.71	0.70	1.00
	328	0.43	0.43	0.61	0.56	0.63	0.70	0.76	0.73	0.71	0.74	0.45	0.51	0.73	0.62	0.71	0.80	0.92
	333	0.55	0.44	0.69	0.65	0.66	0.75	0.77	0.76	0.72	0.84	0.47	0.62	0.74	0.60	0.70	0.84	1.00
	338	0.67	0.71	0.75	0.78	0.70	0.84	0.75	0.74	0.69	0.80	0.45	0.63	0.72	0.66	0.78		
E^*_{ap} kcal/mol	10.5	10.8	10.2	9.3	9.6	9.2	6.9	7.4	7.1	4.4	4.0	4.5	5.0	4.5	4.4	5.9	5.6	6.2

Optimal Working Parameters

To establish the optimal values of working parameters for the different apparent current densities considered (10, 30, 50, and 70 mA/cm²), the polarization data were tested by dispersal analysis in order to eliminate those parameters whose variation had non-significant effects. Then, by using a factorial experiment program, the values of the parameters with significant effect were computed in order to minimize the electrode polarization.

Dispersal analysis.—The overvoltages yielded by the gas electrodes under consideration, at various apparent current densities, within optimal working domain are given in Table II.

A 3 factor (A = oxygen overpressure, B = KOH concentration, and C = working temperature) and two, three, and four levels (Table II) model (13) was chosen in order to carry out the dispersal analysis of polarization data. The results are given in Table III.

Examination of Table III shows that for all apparent current densities the effect of variation of factor A and of second order interactions AB and AC is not significant. At 10 mA/cm² the effect of the variation of factor C is significant while, at the other current densities, the effects of factors B , C , and of second order interaction BC are significant. The relatively low dispersion induced by random factors (residual dispersion, s_r) indicates satisfactory accuracy of experimental data and points out the fact that the third order interaction ABC is not significant.

These results were used in building up the interaction table (Table IV) and so figuring out the effect of variation of significant parameters upon the polarization of the silver gas electrodes. The interpretation of these data was done by computing the values of the reliability interval (13) for a significance limit $\alpha = 0.1$.

The data listed in Table IV lead to the following optimal operation zones which are to be further explored in optimization: for 10 mA/cm², concentration

Table II. Silver gas electrode overvoltages (mV) in different working conditions

	Working temperature	400 mm Hg				500 mm Hg			
		4N		5N		4N		5N	
		4N	5N	6N	7N	4N	5N	6N	7N
10 mA/cm ²	45°C	55	53	59	65	52	65		
	50°C	55	45	57	51	45	58		
	55°C	55	47	54	56	44	52		
	60°C	47	43	46	43	43	44		
30 mA/cm ²	50°C		90	97	90	89	94	90	
	55°C		87	85	96	85	86	92	
	60°C		80	81	97	85	80	98	
	65°C		87	87	96	86	78	98	
50 mA/cm ²	50°C		130	133	125	127	129	123	
	55°C		123	113	126	120	116	120	
	60°C		118	109	119	113	108	125	
	65°C		117	107	123	116	108	122	
70 mA/cm ²	50°C		162	171	157	161	167	154	
	55°C		155	144	153	153	141	149	
	60°C		150	137	149	143	136	145	
	65°C		146	132	145	144	132	143	

KOH 5N, temperature 50°C; for 30 mA/cm², 5N, 60°C; for 50 mA/cm², 6N, 60°-65°C; for 70 mA/cm², 6N, 60°-65°C.

Optimizing.—One considers the regression functions which describe the relation between the significant independent variables, concentration (x_1) and temperature (x_2), and the dependent variable, electrode overvoltage (y)

$$y = b_0 + b_1x_1 + b_2x_2 + b_{12}x_1x_2 + b_{11}x_1^2 + b_{22}x_2^2$$

The calculation of coefficients of regression functions (b_0 - b_{22}) for each apparent current density was carried out by starting up with data obtained from a factorial experiment program (13). The steps of 1 mequiv./cm³ and 5°C were considered characteristic to variations working parameters in the optimal zone. The coded values of independent variables correspond to

for 10 mA/cm²:

$$-1 = 4N; \quad 0 = 5N; \quad 1 = 6N \text{ (for } x_1)$$

$$-1 = 45^\circ\text{C}; \quad 0 = 50^\circ\text{C}; \quad 1 = 55^\circ\text{C (for } x_2)$$

for other C.D.

$$-1 = 5N; \quad 0 = 6N; \quad 1 = 7N \text{ (for } x_1)$$

$$-1 = 55^\circ\text{C}; \quad 0 = 60^\circ\text{C}; \quad 1 = 65^\circ\text{C (for } x_2)$$

To check up the validity of regression function, the overvoltage values (y_{calc}) for each apparent current

Table III. Dispersal analysis of the effect of parameter change

Current density, mA/cm ²	Dispersion source	Square sum	Degrees of freedom	Dispersion	F	F_α	Obs
10	S_A	54	1	54	4.61	5.99	
	S_B	62	2	31	2.65	5.14	
	S_C	592	3	197.3	16.86	4.76	*
	S_{AB}	90	2	45	3.85	5.14	
	S_{AC}	56	3	18.7	1.59	4.76	
	S_{BC}	146	6	24.3	2.08	4.28	
	S_r	70	6	11.7			
30	S_A	4	1	4	2.18	5.99	
	S_B	451	2	225.5	133.22	5.14	*
	S_C	78	3	29.3	16.01	4.76	*
	S_{AB}	0	2	0			
	S_{AC}	3	3	1	0.55	5.99	
	S_{BC}	433	6	72.1	39.40	4.28	*
	S_r	11	6	1.83			
50	S_A	19	1	19	5.43	5.99	
	S_B	211	2	105.5	30.14	5.14	*
	S_C	575	3	191.6	54.74	4.76	*
	S_{AB}	6	2	3	0.86	5.14	
	S_{AC}	8	3	2.7	0.74	4.76	
	S_{BC}	363	6	61	17.43	4.28	*
	S_r	21	6	3.5			
70	S_A	60	1	60	4.88	5.99	
	S_B	170	2	85	6.91	5.14	*
	S_C	1344	3	448	36.42	4.76	*
	S_{AB}	0	2	0			
	S_{AC}	18	3	6	0.49	4.76	
	S_{BC}	378	6	63	5.12	4.28	*
	S_r	74	6	12.3			

* Significant effect.

Table IV. Concentration-temperature interaction effect

Current density, mA/cm ²	Reliability interval, mV		45°C	50°C	55°C	60°C	65°C
10	±6.5	4N	55 } 60	55 } 53	55 } 55.5	47 } 45	
			65 } 52.5	51 } 45	56 } 45.5	43 } 43	
		5N	52 } 62	45 } 56.5	44 } 53	43 } 45	
			59 } 62	57 } 56	54 } 52	46 } 44	
		6N	65 } 62	56 } 56	52 } 52	44 } 44	
30	±2.6	5N	90 } 89.5	87 } 86	80 } 82.5	87 } 86.5	
			89 } 89.5	85 } 85	85 } 82.5	86 } 82.5	
		6N	97 } 95.5	85 } 85.5	81 } 80.5	87 } 82.5	
			94 } 90	86 } 94	80 } 97.5	78 } 97	
		7N	90 } 90	92 } 94	98 } 97.5	96 } 97	
50	±3.6	5N	130 } 128.5	123 } 121.5	118 } 115.5	117 } 116.5	
			127 } 131	120 } 114.5	113 } 108.5	116 } 107.5	
		6N	133 } 131	113 } 114.5	109 } 108.5	107 } 107.5	
			129 } 124	116 } 123	108 } 122	108 } 122.5	
		7N	125 } 124	126 } 120	119 } 125	123 } 122	
			123 } 124	120 } 120	125 } 125	122 } 122	
70	±6.8	5N	162 } 161.5	155 } 154	150 } 146.5	146 } 145	
			161 } 169	153 } 144	143 } 136.5	144 } 132	
		6N	171 } 169	141 } 144	137 } 136.5	132 } 132	
			167 } 155.5	147 } 151	136 } 147	132 } 144	
		7N	157 } 155.5	153 } 149	149 } 145	145 } 143	
			154 } 155.5	149 } 149	145 } 145	143 } 143	

Table V. Regression functions for silver gas electrodes polarization ($\Delta P_{O_2} = 400-500$ mm Hg)

Current density, mA/cm ²	No.	x_1	x_2	y_1	y_2	\bar{y}	y_{calc}	
10	1	-1	-1	55	65	60.0	60.0	
	2	0	-1	53	52	52.5	50.9	$s_1^2 = 11.24$
	3	1	-1	59	65	62.0	61.7	$s_r^2 = 4.67$
	4	-1	0	55	51	53.0	53.8	$F = 2.36$
	5	0	0	45	45	45.0	45.3	$F_a = 6.99$
	6	1	0	57	56	56.5	55.5	
	7	-1	1	55	56	55.5	55.9	51.5°C
	8	0	1	47	44	45.5	46.7	4.97N
	9	1	1	54	52	53.0	56.3	44.7 mV
30	1	-1	-1	87	85	86.0	87.9	$s_1^2 = 11.46$
	2	0	-1	85	86	85.5	84.3	$s_r^2 = 2.92$
	3	1	-1	98	98	97.0	97.5	$F = 3.97$
	4	-1	0	80	85	82.5	84.1	$F_a = 6.99$
	5	0	0	81	80	80.5	81.6	
	6	1	0	97	98	97.5	96.0	
	7	-1	1	87	86	86.5	84.2	61.5°C
	8	0	1	87	78	82.5	82.8	5.63N
	9	1	1	99	99	99.0	98.3	77.9 mV
50	1	-1	-1	123	120	121.5	122.3	$s_1^2 = 12.82$
	2	0	-1	113	116	114.5	114.9	$s_r^2 = 3.31$
	3	1	-1	126	120	123.0	125.7	$F = 3.87$
	4	-1	0	118	113	115.5	116.5	$F_a = 6.99$
	5	0	0	109	108	108.5	110.2	
	6	1	0	119	125	122.0	122.2	
	7	-1	1	117	116	116.5	114.6	64.1°C
	8	0	1	107	108	107.5	109.4	5.8N
	9	1	1	123	122	122.5	122.5	106.7 mV
70	1	-1	-1	155	153	154.0	154.9	$s_1^2 = 13.68$
	2	0	-1	141	147	144.0	144.4	$s_r^2 = 3.61$
	3	1	-1	153	149	151.0	151.6	$F = 3.78$
	4	-1	0	150	143	146.5	148.0	$F_a = 6.99$
	5	0	0	137	136	136.5	138.7	
	6	1	0	149	145	147.0	147.2	
	7	-1	1	146	144	145.0	142.5	78.9°C
	8	0	1	132	132	132.0	134.4	5.75N
	9	1	1	145	143	144.0	144.2	128.8 mV

density were calculated and the deviation of observed values from these calculated (that is the linearity of the regression function) was verified. By equating to zero the partial derivatives of regression functions with respect to the two independent variables, a system of two linear equations was obtained for each apparent current density. Solving the system has allowed the establishing of optimal values of independent variables which yield minimum polarization. The results are given in Table V.

Data in Table V show that the electrodes present minimal overvoltage at 400-500 mm Hg oxygen overpressure, 5-6N KOH concentration, and different temperatures depending upon current density: 51°C (10 mA/cm²), 61.5°C (30 mA/cm²), 64.1°C (50 mA/cm²), 78.9°C (70 mA/cm²).

Manuscript submitted Jan. 6, 1975; revised manuscript received July 15, 1975.

Any discussion of this paper will appear in a Discussion Section to be published in the June 1976

JOURNAL. All discussions for the June 1976 Discussion Section should be submitted by Feb. 1, 1976.

REFERENCES

1. J. P. G. Farr and N. A. Hampson, *J. Electroanal. Chem.*, **13**, 433 (1967).
2. J. Jausta, *Collection Czech. Chem. Commun.*, **33**, 160 (1968).
3. I. Lindholm, *This Journal*, **116**, 1150 (1969).
4. J. Mrha and J. Jindra, *Collection Czech. Chem. Commun.*, **34**, 2465 (1969).
5. O. Radovici, M. Mavrodin-Tărăbîc, I. Onaca, and I. Solacolu, *Rev. Roum. Chim.*, **18**, 767 (1973).
6. O. Radovici, M. Mavrodin-Tărăbîc, I. Onaca, and I. Solacolu, *Rev. Roum. Chim.*, **17**, 1153 (1972).
7. I. Solacolu, M. Mavrodin-Tărăbîc, and I. Onaca, *ibid.*, In press.
8. M. Mavrodin-Tărăbîc, I. Onaca, and I. Solacolu, *ibid.*, **18**, 1121 (1973).
9. E. L. Simons, D. W. McKee, and E. J. Cairns, "Comptes Rendus des Troisièmes Journées d'étude des piles à combustible," p. 132, Presses Académiques Européennes, Bruxelles (1969).
10. A. Seidell, "Solubilities of Inorganic and Metal Organic Compounds," Vol. I, p. 1352, Van Nostrand Co., New York (1953).
11. J. J. Gilvarry and J. Slaughter, *Electrochim. Acta*, **8**, 711 (1963).
12. D. B. Lucesoli, Thesis, Univ. Paris, (1971).
13. G. E. P. Box and N. R. Draper, "Evolutionary Operation," p. 63, J. Wiley & Sons Inc., New York (1965).

Electrochemical Studies at Silver/Alpha-Silver Sulfide Interfaces

I. The Sulfidation of Silver

C. J. Warde,*¹ J. Corish, and C. D. O'Briain²

Department of Chemistry, University College, Belfield, Dublin 4, Ireland

ABSTRACT

Kinetic measurements have been made in the temperature range 220°-340°C of the growth of α -silver sulfide from three different samples of high purity silver rods. These measurements confirm the parabolic nature of the reaction in the terminal stages although thermodynamic equilibrium is not established at the silver/ α -silver sulfide interface. Values for the parabolic rate constant have been derived from the experimental data and are found to be in excellent agreement with values calculated using the modified Wagner theory. New measurements of the partial ionic conductivity of silver ions in α -silver sulfide, accurate values of which are required for these calculations, are also reported. The sulfidation rates were found to be strongly dependent on the particular batch of silver used. Preannealing of the silver samples, which, as revealed by metallurgical examination increased grain size, was shown to produce corresponding changes in their rates of sulfidation.

Because it serves as an excellent model system the reaction between bulk silver and liquid sulfur has attracted much attention in the literature (1-5). The high temperature form of the sulfidation product α -Ag₂S provides fast-ion transport for silver ions and it has been known for some time that the latter stages of the reaction, when the product layer is thick, exhibit parabolic kinetics for which the rate-determining step is the diffusion of the silver ions through the sulfide (1, 6). The differential form of the rate equation may be written simply as

$$dx/dt = k_0/x \quad [1]$$

where x is the thickness of the sulfide layer and k_0 is the parabolic rate constant. It is feasible to obtain reliable kinetic data for this system since the problem of the formation of porous product layers may be overcome by introducing, and maintaining a load on, a compacted tablet of α -Ag₂S between the reactants (2). Assuming that the movement of silver through the product layer is an electrochemical process involving the transport of silver ions and electrons and that equilibrium exists at the interfaces, an equation of the Wagner theory of the oxidation of metals (7, 8) may be used to deduce an expression for the parabolic rate constant as follows

$$k_0 = \frac{\sigma_{Ag^+}}{c_{Ag}F^2} \{ \mu^0_{Ag}(Ag_2S) - \mu^*_{Ag}(Ag_2S) \} \quad [2]$$

where σ_{Ag^+} is the silver partial ionic conductivity in silver sulfide, c_{Ag} is the number of equivalents of silver/cm³ of sulfide, $\mu^0_{Ag}(Ag_2S)$ the chemical potential of silver in silver sulfide in equilibrium with pure silver, and $\mu^*_{Ag}(Ag_2S)$ the chemical potential of silver in silver sulfide in equilibrium with liquid sulfur. Although experimental values of k_0 and the k_0 values calculated using Eq. [2] were of the same order of magnitude acceptably close agreement was found only at 400°C or above (2, 5). The discrepancies between experimental and theoretical values of k_0 at lower temperatures have been shown by Rickert (2) to be due to the fact that thermodynamic equilibrium is not attained at the Ag/Ag₂S interface at temperatures below 400°C. He used the cell



the emf, E , of which may be related to the chemical potentials of silver in pure silver $\mu_{Ag}(Ag)$ and in silver sulfide $\mu_{Ag}(Ag_2S)$ by the relationship

$$-FE = \{ \mu_{Ag}(Ag_2S) - \mu_{Ag}(Ag) \} \quad [4]$$

to measure any departure from equilibrium occurring at the Ag/Ag₂S interface and found that when the sulfide layer exceeded ~0.5 cm in thickness the potential attained a steady value E^θ . The experimental kinetics of the reaction then agreed with values of the rate constant given by the modified theoretical equation

$$k_0 = \frac{\sigma_{Ag^+}}{c_{Ag}F^2} \{ E^* - E^\theta \} \quad [5]$$

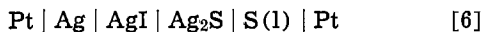
where E^* is the emf of the cell

* Electrochemical Society Active Member.

¹ Present address: Westinghouse Research Laboratories, Pittsburgh, Pennsylvania, 15235.

² Deceased.

Key words: silver iodide, parabolic rate, partial ionic conductivity, grain size, annealing.



Thus the parabolic rate law was still obeyed in spite of a large, but constant, departure from equilibrium at one of the interfaces (5, 9).

All previous work with this system has been reported by workers using, in any one study, a single type of silver sometimes rather loosely described as simply high purity silver. Involvement with processes of this kind over a lengthy period in this laboratory (9-11) has indicated that differences in the type of high purity silver used might be responsible for observed anomalies in experimental results. This paper reports a systematic and detailed investigation of the kinetics of sulfidation of three different samples of high purity silver in the temperature interval 220°-340°C. The kinetic data have been analyzed by computer and the parabolic rate constants obtained are compared with those calculated using Eq. [5]. The results of new measurements of the silver ion partial ionic conductivity in α -Ag₂S are also reported. These were deemed necessary because of systematic differences between observed and calculated values of k_0 , using earlier measurements of σ_{Ag^+} made in this laboratory (11). The effects on the rates of sulfidation when the silver samples were preannealed have been investigated in an attempt to elucidate the factors which govern the behavior of the system.

In the following paper (Part II) measurements of the overpotentials observed during the electrochemical passage of silver from three types of high purity silver across the Ag/ α -Ag₂S interface are reported and these again reveal differences in behavior between the samples. Such results are of interest both from a phenomenological point of view and because measurements of this type have been used to explain the kinetics of the sulfidation of silver by liquid sulfur (3, 9).

Experimental

Materials.—The three types of silver used in the basic kinetic measurements were supplied as rods of 6 mm diameter as follows: (i) Johnson-Matthey Chemicals Limited, major impurity, copper <5 ppm over-all purity 99.999%; (ii) Degussa Feinsilber, major impurity, copper <300 ppm, over-all purity 99.97%; (iii) Johnson-Matthey Chemicals Limited, major impurity, copper <50 ppm, over-all purity 99.99%. These samples will be referred to as JM1, D1, and JM2, respectively, and the impurity levels quoted are the result of an analysis carried out by Johnson-Matthey Limited. The behavior of a number of samples of the Degussa Feinsilber used previously by Duffy (11) (to be referred to later as D2) was also examined. The samples were prepared to fit into the apparatus to be described later using a high speed lathe and were then thoroughly degreased (12) using A.R. grade benzene and A.R. grade acetone. The purity of the silver iodide, which was supplied by Sherman Chemicals Limited was checked by testing for electronic leakage through cell [3] at 300°C in an atmosphere of pure nitrogen. After establishment of a cell potential of 100 mV by withdrawal of silver from the Ag₂S tablet, the cell was left on open circuit. A negligible rate of potential drop indicated the absence of electronic leakage. The sulfur was a spectrographically standardized substance of purity 99.999% supplied by Johnson-Matthey Chemicals Limited. The Ag₂S tablets used at the interface were fabricated from silver sulfide rods which had been grown in the laboratory in earlier experiments. These rods were ground to a uniform fine powder using a specially constructed filing machine. Disks of 0.8 mm thickness were then produced by pressing the powder to $6.1 \times 10^3 \text{ kg cm}^{-2}$ in a die designed for the preparation of KBr disks for IR measurements. Finally tablets of 9 mm diameter and with a 2 mm tag to carry the Ag/AgI probe electrode (see Fig. 1) were punched from these Ag₂S disks. The nitrogen atmosphere used for all experiments was produced from

the British Oxygen Company "white spot" product by removal of the residual oxygen with Fieser's Solution (13). The gas line employed also provided for the removal of any traces of hydrogen sulfide using saturated lead acetate solution and for the careful drying of the nitrogen before admission to the reaction assembly.

Apparatus for the kinetic measurements.—The essential components of the system constructed to measure the rate of unidimensional growth of α -Ag₂S and to measure simultaneously the difference in chemical potential of the silver atoms across the Ag/Ag₂S interface are shown schematically in Fig. 1. In contrast to the arrangement used by Rickert (2) it was the sulfide tablet which was rigidly supported. This was done using a platinum disk with a hole in the center which allowed the silver rod being sulfidized to move upwards under continuous spring pressure. The Ag₂S formed by the reaction grew upwards in the glass tube, shown full of liquid sulfur, and thus the level of the Ag₂S/S(l) interface rose. The Ag/AgI probe electrode shown pressed against the tag portion of the Ag₂S tablet was fabricated from a 5 cm piece of 3 mm OD glass tubing drawn to a tip at one end and filled with AgI. A glass spring (not shown) was used to press a piece of silver rod into the AgI and to maintain good contact between the probe and the Ag₂S tablet. The probe together with the platinum support disk formed a cell as shown in Eq. [3] and was used to measure the chemical potential drop for silver atoms across the Ag/Ag₂S interface. The emf of this solid-state cell was measured with a Honeywell 19 Elektronik recorder, checked frequently with a vibrating-reed electrometer accurate to 1 mV (Vibron 33C, E.I.L. Ltd.) and a Tinsley potentiometer (accuracy $\pm 10 \mu\text{V}$).

The complete apparatus is shown in Fig. 2. The upper end of the long glass tube which contained the liquid sulfur and the main body of the dial gauge were held at opposite ends of a rigid steel frame. The top of the dial gauge plunger supported a precision glass rod which moved freely through a precision tube and held the silver specimen, which was wedged into a Kovar

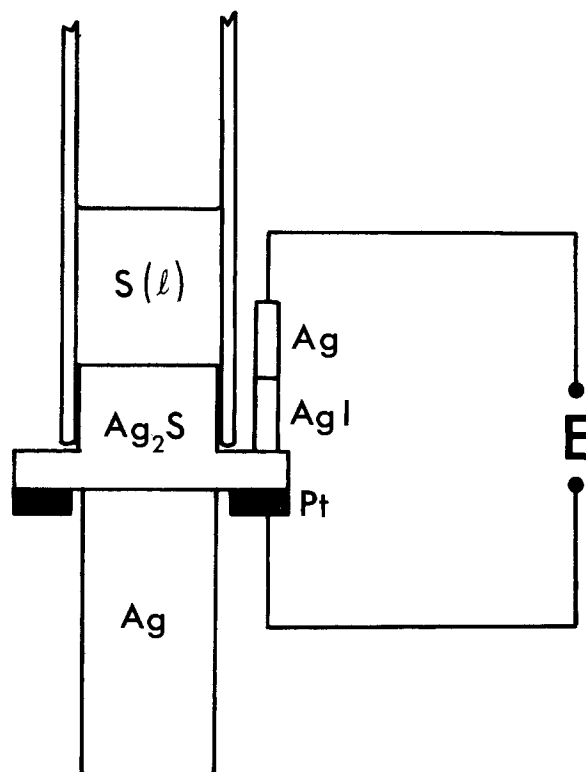


Fig. 1. Schematic diagram of the cell arrangement used to measure the overpotential, E , at the Ag/ α -Ag₂S interface during the formation of compact α -Ag₂S.

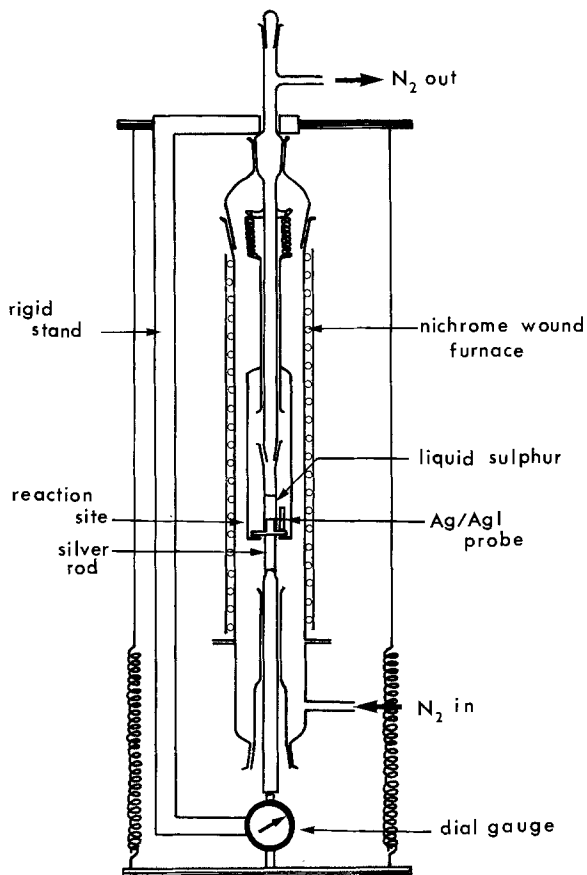


Fig. 2. Over-all apparatus to measure one-dimensional sulfidation of a silver rod by liquid sulfur.

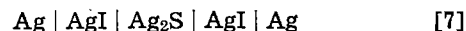
metal to glass seal, against the lower surface of the Ag_2S tablet. The other end of the dial gauge plunger was spring-loaded so that the pressure on the Ag/Ag $_2\text{S}$ contact was 6 kg/cm^2 . The rate of consumption of silver could be followed by means of the micrometer dial gauge which registered the decrease in length of the silver rod correct to $2.5 \times 10^{-4} \text{ cm}$. The rate of growth of Ag_2S was calculated from this measurement and the accuracy of this procedure was checked periodically by measuring the thickness of the sulfide layer with a cathetometer and finally by measuring the over-all length of the sulfide with a micrometer screw gauge after each experiment. The entire assembly was contained in a wide-bore air-jacketed glass tube which was heated by nichrome strip windings fed from a stabilized voltage source. The temperature at the reaction site was measured by a calibrated Chromel-Alumel thermocouple and was constant to $\pm 1^\circ\text{C}$ over the period of an experiment.

Polishing and etching of silver rods.—Silver samples, as received, after the kinetic runs at 220°C , and after annealing, were mounted in cold-setting resin cylinders. The cylinders were ground, parallel to the axis of the silver rods, on silicon carbide papers (Grades 220, 320, 400, and 600 sequentially). After exposure of an adequate section, polishing and etching were carried out by a procedure recommended by Darling (14). This involved polishing of the samples for 1-2 min on a velvet-covered turntable, rotating at 250 rpm, with "Brasso"³ employed as a lubricant. After washing, the samples were further lightly polished for 3 min on a velvet-covered stationary smooth glass plate with "Silvo"³ as lubricant. The surfaces were now etched by applying a solution, comprising one part of 1 weight per cent (w/o) H_2SO_4 and one part of a one-tenth saturated solution of $\text{K}_2\text{Cr}_2\text{O}_7$, to the samples by means of a cotton wool swab. Photomicrographs of the etched surfaces were

³ Supplied as proprietary products by Reckett's (Ireland) Limited.

prepared using a Union Optical metallurgical microscope Model UMG-Bi.

Experimental determination of σ_{Ag^+} .—Measurements of the partial ionic conductivity of $\alpha\text{-Ag}_2\text{S}$ were made using a modified form of the procedure originally suggested by Hebb (15) and improved by Wagner (16) and later followed by Duffy (11). Cylindrical specimens of Ag_2S 2-3 cm long obtained in the kinetic studies were turned down slightly to a uniform diameter and their cross-sectional area, a , determined using a micrometer. They were then made part of the electrochemical cell



and two small Ag/AgI probes, made in a manner similar to that described previously were pressed against its side. The distance between these probes, d , was measured using a cathetometer. Two platinum probes also touched the specimen, at points on the other side, opposite the Ag/AgI probes. A circuit diagram is shown in Fig. 3. Two AgI tablets were necessary between the Ag_2S specimen and each silver electrode to avoid formation of silver dendrites through individual AgI tablets. The materials used were as described previously for the kinetic measurements. The assembly of tablets and electrodes was contained in an air-jacketed nichrome wound furnace under an atmosphere of purified nitrogen and with temperature at the specimen constant to $\pm 1^\circ\text{C}$ during an experiment. The temperature was measured by a calibrated Chromel-Alumel thermocouple in close proximity to one end of the sulfide rod and a Pt/Pt-13% Rh thermocouple pressed against the other end and agreement between these two thermocouples was within the error quoted at all times. A constant 120V d-c source was used with variable high resistances in series with the specimen to achieve currents in the range 5-10 mA. This arrangement minimized the effects of any slight changes occurring in the resistance of the tablet assembly. If E is the potential difference between the two Ag/AgI probes the silver partial ionic conductivity is given by

$$\sigma_{\text{Ag}^+} = \frac{i_{\text{Ag}^+} d}{Ea} \quad [8]$$

where i_{Ag^+} , the current under steady-state conditions, was measured using a Cambridge precision microammeter. This experimental arrangement also allowed investigation of the effect on σ_{Ag^+} of changes in the stoichiometry of the silver sulfide. By applying a voltage between one of the platinum probes and one of the silver electrodes, silver could be added to or removed from the sulfide. The associated change in μ_{Ag} (Ag_2S) was determined by measuring the potential difference between the other platinum probe and an Ag/AgI probe.

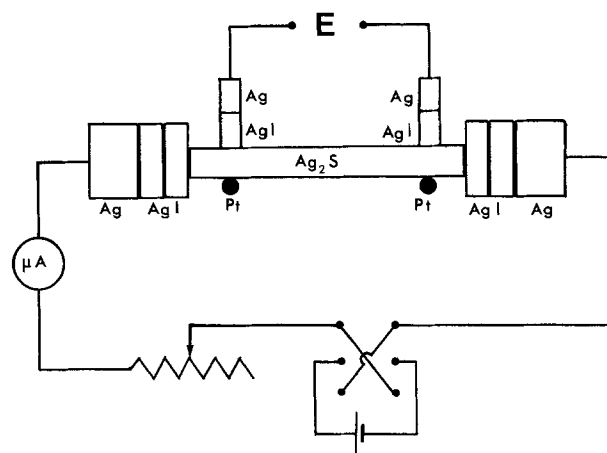


Fig. 3. Circuit to measure the silver partial ionic conductivity of $\alpha\text{-Ag}_2\text{S}$.

Results and Discussion

Kinetics of the sulfidation of silver.—In general, if equilibrium at either, or both of the interfaces, Ag/Ag₂S and Ag₂S/S(1), is established only gradually, and the kinetics of the reaction conform to the parabolic law in the later stages, the most satisfactory method (2) with which to represent the experimental data is to plot $(x + x_0)$ vs. $(t - t_0)/(x - x_0)$, where t and x represent the time and the thickness of the sulfide layer, respectively. x_0 corresponds to t_0 and is the least value of x which makes the greatest number of experimental points fit a straight line. The slope of such a plot is $2k_0$, where k_0 is the parabolic rate constant and is given by the equation

$$k_0 (\text{expt.}) = d(x + x_0)/2d(t - t_0)/(x - x_0) \quad [9]$$

The basic experimental data of time and length of silver rod consumed were processed together with the necessary conversion factors by a linear regression computer program, thus yielding values for k_0 . Three kinetic plots for D1 specimens are shown in Fig. 4, and it is evident from the similarity of the slopes that at the same temperature the sulfidation rate of identical samples is reproducible. Plots of the overpotential at the Ag/Ag₂S interface as a function of time for the three different kinds of silver at 260°C are shown in Fig. 5. The difference which is evident here between JM1 on the one hand and JM2 and D1 on the other was found to be pronounced at all the temperatures at which measurements were made. The very low overpotentials at the Ag/Ag₂S interface for the former are reflected in high values for the experimental parabolic rate constant as now a greater fraction of the affinity of the reaction is available for the diffusion process. A summary of the experimental values of k_0 as given by the computer fit and values calculated using Eq. [5] for the three types of silver used and at all the temperatures at which measurements were made is given in Table I. As is evident there is good agreement between experimental and calculated values in all cases but the rates of sulfidation measured under otherwise identical conditions are strongly dependent on the particular sample of high purity silver under investigation.

Properties of the bulk silver samples which it was felt might be responsible for the present observations were considered to include (i) impurity concentration, (ii) grain size, and (iii) grain orientation. Since all the samples were of a comparatively high purity (i) might not appear to be an important factor but it should be noted that the order of ascending steady-state overpotential (and thus of decreasing k_0) was the same as

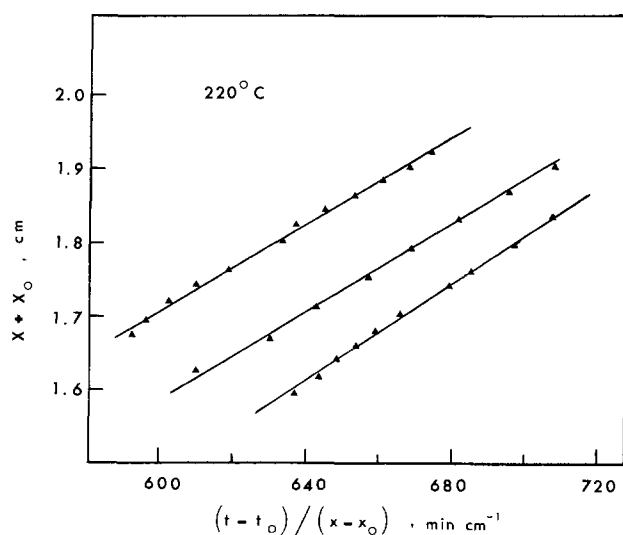


Fig. 4. Parabolic plots for the growth of α -Ag₂S from three separate experiments using samples of Degussa Feinsilber at 220°C.

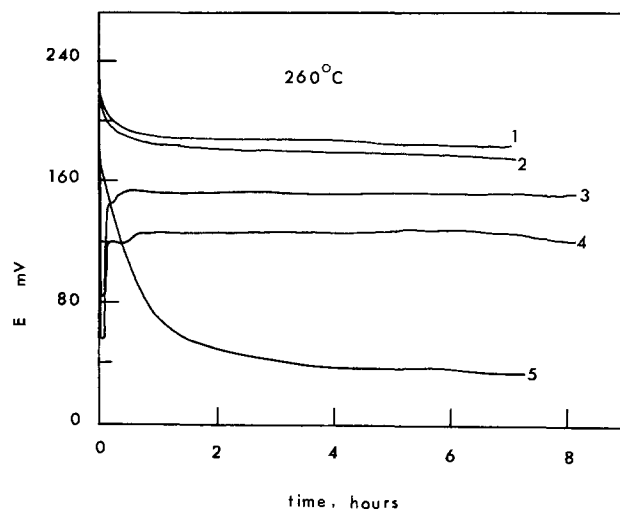


Fig. 5. Overpotential vs. time traces for annealed and unannealed silver samples at 260°C. The samples shown are: curve 1, D1 unannealed; curve 2, JM2 unannealed; curve 3, D1 annealed; curve 4, JM2 annealed; curve 5, JM1 unannealed.

the order of increasing impurity content. To investigate any possible correlation between the grain size and orientation in the bulk silver [(ii) and (iii) above] and its behavior during sulfidation, a specimen of each type of silver was polished and etched as described earlier. Figure 6(a) shows typical etch patterns observed for as-received samples of JM2 6 mm silver rod. Similar patterns were observed for D1 samples. It was deduced from the elongation of the grains parallel to the rod axis, and the extent of cold working, that the JM2 and D1 rods were drawn at temperatures well below 200°C, the recrystallization temperature for cold-worked silver. In marked contrast the JM1 sample had been drawn at temperatures much higher than 200°C and probably in the 750°-900°C range. As a result the grains were very large, by comparison with the other specimens, and were elongated along the axis of the rod, while the matrix accommodating the grains appeared to be a single crystal. A typical photomicrograph for JM1 silver is shown in Fig. 6(b). Examination of similarly etched samples which had been used in a kinetic experiment showed that recrystallization and grain growth were taking place in JM2 and D1 during the course of a sulfidation reaction even at 220°C [see Fig. 6(c)].

At this stage of the investigation all of the supply of JM1 6 mm rods had been used. It was realized that it would be impossible to reproduce the grain shape, size, and orientation of this silver sample but since it appeared that the extraordinary behavior might well be due mainly to the large grain size an attempt was made to increase the grain size in the JM2 and D1 silver. Annealing of samples of each type of silver was carried out in vacuo at 660°C for 100 hr followed by cooling at 6°C/hr. Some other samples of Degussa Feinsilber

Table I. Experimental and calculated parabolic rate constants for three kinds of silver

Temp (°C)	Sample	E^* (mV)	E^0 (mV)	k_0 (expt.) (10^{-6} cm ² sec ⁻¹)	k_0 (calc.) (10^{-6} cm ² sec ⁻¹)
220	D1	224	192	2.37	2.42
	JM1	224	37	12.4	13.6
	JM2	224	193	2.91	2.26
260	D1	230	184	3.72	3.69
	JM1	230	25	17.2	16.5
	JM2	229	176	4.59	4.33
300	D1	233	163	6.87	6.23
	JM1	233	30	18.5	17.7
	JM2	230	169	5.52	5.61
340	D1	235	146	8.11	8.46
	JM1	233	42	18.3	18.0
	JM2	237	117	12.5	11.2

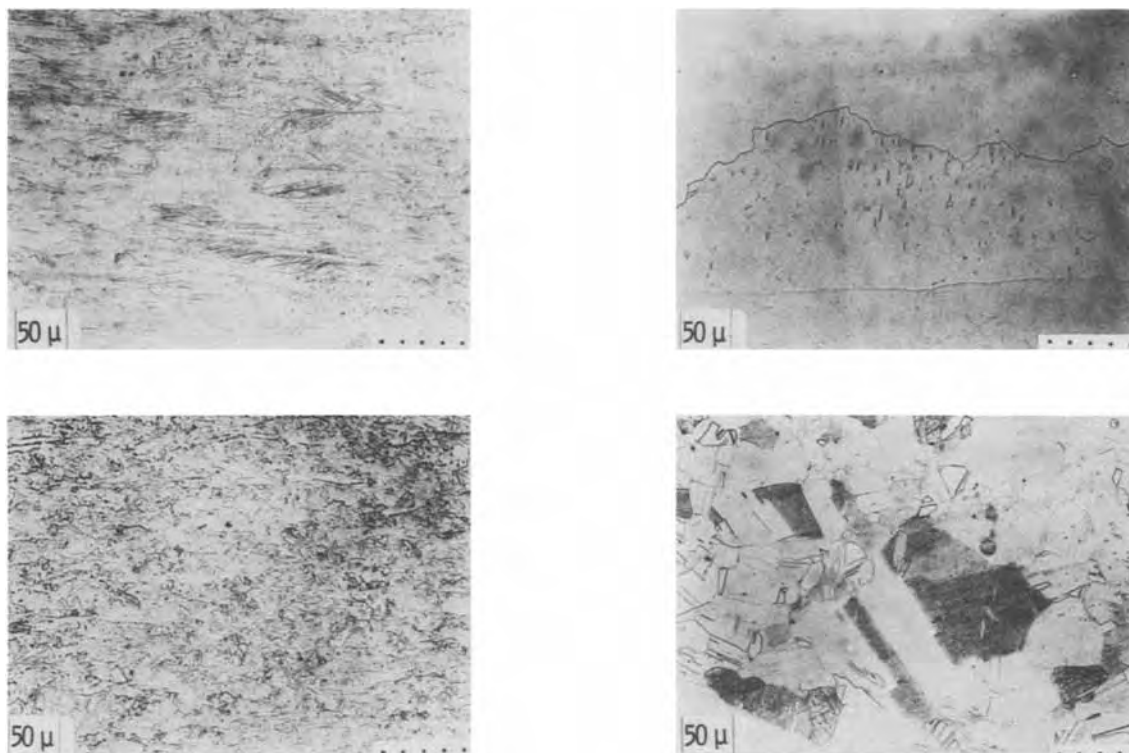


Fig. 6. Photomicrographs of the etched surfaces of the silver rods (a, upper left) JM2 as received; (b, upper right) JM1 as received; (c, lower left) JM2 after kinetic experiment at 220°C; (d, lower right) JM2 after annealing at 660°C for 100 hr. The dotted line in each photomicrograph indicates the rod axis.

(D2) of the type which had been used by Duffy (11) in his earlier experiments and which was similar with respect to impurity analysis to D1 were also annealed. The results of kinetic experiments using these pre-annealed samples are shown in Table II where it is evident in all cases that these specimens now exhibit higher values of k_0 and correspondingly lower values of E^θ . The effect of annealing is also shown in Fig. 5 where the overpotential *vs.* time traces for annealed and unannealed samples may be compared. Similar changes in the values of E^θ were observed for the annealed samples at all the other temperatures investigated. The similarity in behavior for the annealed samples D1 and D2 as shown in Table II is significant not only because it indicates just how reproducible these two batches, which were supplied at a four year interval, were, but also because it emphasizes the greater value of k_0 observed at any given temperature for the annealed JM2 samples. In no case, however, did preannealed samples reproduce the kinetic behavior of the unannealed JM1 silver and when the preannealed samples were examined metallurgically it was evident that although the grain size had increased in all cases it was never of the same order of magnitude as that found in the unannealed JM1. Etch patterns for annealed JM2 silver are shown in Fig. 6(d).

Table II. Experimental and calculated parabolic rate constants for preannealed silver samples

Temp (°C)	Sample	E^* (mV)	E^θ (mV)	k_0 (expt.) (10^{-5} cm ² sec ⁻¹)	k_0 (calc.) (10^{-6} cm ² sec ⁻¹)
220	D1	220	179	3.06	2.99
	D2	224	184	3.46	2.95
	JM2	223	159	4.53	4.62
260	D1	228	161	5.26	5.38
	D2	228	164	5.43	5.18
	JM2	228	126	7.25	8.18
300	D1	231	146	7.39	7.45
	D2	232	147	7.69	7.47
	JM2	231	101	11.6	11.4
340	D1	235	101	13.0	12.6
	D2	235	113	11.7	11.4
	JM2	235	80	14.3	14.5

This evidence might suggest that the grain size in bulk silver dictated the magnitude of the overpotential at the Ag/Ag₂S interface. However, it must be stated that since the grain sizes in annealed D1, D2, and JM2 were approximately the same and since the observed kinetics of sulfidation of JM2 were quite different from those of D1 and D2 samples, the differences in grain sizes, while obviously a factor, cannot fully account for the differences in behavior of the three types of silver used in this investigation.

The silver partial ionic conductivity.—The need for a new determination of σ_{Ag^+} at the temperatures of the kinetic experiments became apparent when use of the values available in the literature in Eq. [5] produced values for the parabolic rate constant which disagreed systematically with the experimental results. It also seemed important that measurements should be made on α -Ag₂S samples grown from each of the types of silver used in the present investigation. The values of σ_{Ag^+} were determined for cylindrical samples in the apparatus which has been described. Currents of both 5 and 10 mA were passed in each direction through the samples before averaging results to obtain the values shown in the last column of Table III. As well as the samples prepared from each kind of silver the ionic conductivities of sulfide specimens used by Duffy (11) were also measured but no significant differences were observed in any case. The activation energy for the process obtained by fitting to an Arrhenius equation is approximately 1200 cal mole⁻¹. The measurements

Table III. Comparison of values, at various temperatures, of the silver partial ionic conductivity of α -Ag₂S

Temp (°C)	σ_{Ag^+} (ohm ⁻¹ cm ⁻¹)				Present work
	Rickert Ref. (2)	Duffy Ref. (11)	Ozazaki Ref. (17)	Bartkowiez <i>et al.</i> Ref. (5)	
220	3.89	3.41	4.32	3.51	4.11
260	4.08	3.66	4.85	3.94	4.53
300	4.26	4.29	5.38	4.35	4.95
340	4.78	4.71	—	4.74	5.28

were made at the stoichiometry which corresponds to a potential of 100 mV at 220°C for a cell of type [3] but measurements were also made which showed that σ_{Ag+} was virtually independent (*i.e.*, varied <1% over the attainable range) of μ_{Ag} (Ag_2S) at all temperatures.

Other reported values of σ_{Ag+} are summarized in Table III. Miyatani (18) has also measured the silver partial ionic conductivity in α - Ag_2S at 183°C using a technique based on the rates of relaxation processes. He reported a value of $2.9 \text{ ohm}^{-1} \text{ cm}^{-1}$ for sulfide close to equilibrium with sulfur and a value of $4.1 \text{ ohm}^{-1} \text{ cm}^{-1}$ for sulfide in equilibrium with silver. Rickert (2) measured σ_{Ag+} at 200°, 300°, and 400°C but the scatter makes it impossible to deduce an activation energy for the ionic conduction process. Ozazaki (17) employed thin plates of α - Ag_2S in the range 180°-300°C and obtained values considerably higher than other workers. Duffy (11) reported that in the range 190°-350°C σ_{Ag+} did not vary with μ_{Ag} (Ag_2S) and his activation energy of $1500 \text{ cal mole}^{-1}$ is in agreement with that of Barkowicz *et al.* (4). If the values of σ_{Ag+} given in Table III for any temperature are averaged it will be seen that each value differs from the average by at most 15%. As four experimental parameters are needed to determine σ_{Ag+} and in view of the varying preparation and shapes of the sulfide samples used such disagreement may not be regarded as unreasonable. A likely source of error would be the presence of pores in the sulfide specimens but this is known not to be a problem with the samples grown as described above and used in the present work. The quality of the agreement between the experimental and calculated rate constants, which is evident in the data of Tables I and II, also lends credence to the values of σ_{Ag+} determined here.

Conclusions

The terminal stages of the one-dimensional sulfidation of bulk silver by liquid sulfur at 400°C when the rate determining step is diffusion under a near constant concentration gradient has been accepted as one of the best proofs for the correctness of the Wagner theory for such processes (19). It also affords a good example of a chemical reaction rate proportional to the affinity of the reaction. The present work confirms that at temperatures lower than 400°C the parabolic rate law is still obeyed. It is also seen that rate constants in excellent agreement with the experimental values may be calculated using the Wagner equation provided that allowance is made for the departure from equilibrium which now occurs at the bulk Ag/Ag_2S interface. New values for the silver partial ionic conductivity in α - Ag_2S which are necessary for these calculations have also been determined. Further, it has been shown that the extent of the departure from equilibrium at the Ag/α - Ag_2S interface depends on the particular sample of high purity silver being used. Specimens of three samples of high purity 6 mm silver rods have been shown to behave quite differently when exposed to identical experimental conditions. The order of increasing rate constant was found to correspond qualitatively with the order of decreasing impurity concentration but it was also shown that the rate constant could be influenced by preannealing the silver sample to increase the grain size though no clear-cut correlation was found. What is evident however is that some property of the bulk silver must be responsible, at least partly, for the observed differences

in behavior and it is obvious that a detailed examination of the Ag/Ag_2S interface is essential so that an attempt may be made to reveal the atomistic mechanism involved in the transfer of silver from bulk silver to α - Ag_2S during the sulfidation reaction. This is especially true in the light of the results of Corish and O'Briain for the transfer of silver from the vapor phase (20) and from silver whiskers (21) to α - Ag_2S . They found that once the silver atoms are free or readily available at active crystal positions they may dissolve readily in the solid without an overpotential. Their work together with the results of a controlled series of experiments involving the electrochemical transfer of silver from different samples of high purity bulk silver to α - Ag_2S will be discussed in Part II which is to follow.

Acknowledgments

We wish to thank Professor H. Rickert, University of Dortmund, for helpful discussions. The assistance of Dr. Eoin P. O'Neill is also gratefully acknowledged.

This work was carried out in partial fulfillment of requirements of the National University of Ireland for the award of the Ph.D. degree to C. J. Warde.

Manuscript submitted March 24, 1975; revised manuscript received July 12, 1975.

Any discussion of this paper will appear in a Discussion Section to be published in the June 1976 JOURNAL. All discussions for the June 1976 Discussion Section should be submitted by Feb. 1, 1976.

REFERENCES

1. C. Wagner, *Z. Physik. Chem.*, **B21**, 25 (1933).
2. H. Rickert, *Z. Physik. Chem. N.F.*, **23**, 355 (1960).
3. C. Wagner and H. Rickert, *ibid.*, **31**, 32 (1961).
4. J. Mizusaki, K. Fueki, and T. Mukaibo, *Bull. Chem. Soc. Japan*, **46**, 1663 (1973).
5. I. Barkowicz, S. Mrowec, and T. Werber, *Bull. Acad. Polon. Sci. Chim.*, **15**, 537 (1967); I. Barkowicz and S. Mrowec, *ibid.*, **20**, 145 (1972).
6. H. Reinhold and H. Seidal, *Z. Electrochem.*, **41**, 499 (1935).
7. W. Jost, "Diffusion und chemische Reaktion in festen Stoffen," p. 28, Steinkopff, Leipzig (1937).
8. K. Hauffe, *Oxidation von Metallen und Metalllegierungen*, Springer, Berlin (1956); also "Reaktionen in und an festen Stoffen," Springer, Berlin (1956).
9. C. D. O'Briain, Thesis, Nat. Univ. Ireland, Dublin (1963).
10. L. C. Brennan, Thesis, Nat. Univ. Ireland, Dublin (1965).
11. M. T. Duffy, Thesis, Nat. Univ. Ireland, Dublin (1965).
12. L. E. Price and G. J. Thomas, *J. Inst. Metals*, **63**, 21 (1938).
13. L. F. Fieser, *J. Am. Chem. Soc.*, **46**, 2639 (1924).
14. J. Darling, Private communication.
15. M. H. Hebb, *J. Chem. Phys.*, **20**, 185 (1952).
16. C. Wagner, Proc. Seventh Meeting International Committee of Electrochemical Thermodynamics and Kinetics, Lindau 1955, Butterworths, London (1957).
17. H. Ozazaki, *J. Phys. Soc. Japan*, **23**, 255 (1967).
18. S. Miyatani, *ibid.*, **10**, 786 (1955).
19. W. J. Moore, *J. Chem. Ed.*, **38**, 232 (1961).
20. J. Corish, M. T. Duffy, and C. D. O'Briain, *Trans. Faraday Soc.*, **67**, 1447 (1971).
21. J. Corish and C. D. O'Briain, *J. Mater. Sci.*, **6**, 252 (1971).

Electrochemical Studies at Silver/Alpha-Silver Sulfide Interfaces

II. Simulation of the Polarization Phenomena Occurring at the Ag/Alpha-Ag₂S Interface during the Sulfidation of Silver

C. J. Warde,^{*1} J. Corish, and C. D. O'Briain²

Department of Chemistry, University College, Belfield, Dublin 4, Ireland

ABSTRACT

Measurements have been made of the overpotentials at the bulk silver/ α -silver sulfide interface during the passage of neutral silver, silver ions, and electrons from three different samples of high purity silver across the interface. A semilogarithmic relationship between the overpotential and current density of silver was found in all cases in the temperature range 220°–340°C. In contrast with earlier results this relationship extended to the lowest current densities measured. A more detailed study of the three samples of silver was made at 260°C. The experimental method employed was designed to accentuate any differences between the specimens being used and the relative behavior of these samples has been characterized. A limited number of measurements were also made using preannealed silver samples. Possible reasons for the observed behavior are discussed, and the process is compared to that prevailing during the one-dimensional sulfidation of silver.

By using α -AgI as an auxiliary electrolyte it is possible to investigate fluxes of neutral silver, of silver ions, and of electrons across the phase boundary solid silver/ α -Ag₂S. Previous studies of this kind (1, 2) have sought to establish quantitative relationships between these three fluxes and the chemical potential difference of silver, the electrochemical potential difference of silver ions and of electrons across the interface, respectively. Even although silver and α -Ag₂S are both predominantly electronic conductors the inclusion of α -AgI tablets as electron blocks can ensure that the electric current measured during the passage of silver represents the rate of dissolution of silver at the interface and the process is thus analogous to that pertaining during the anodic dissolution of a metal in an electrolyte solution. The results which have been obtained with this system have shown that while no overpotential was observed during the transfer of electrons, fluxes of either silver ions alone or of equivalent quantities of silver ions and electrons (neutral silver) gave rise to measurable overpotentials which were found to be effectively equal. This overpotential, as might be expected, has therefore been assigned to an ionic polarization. Rickert and O'Briain (1) also reported that a minimum interface potential was required before any significant silver ion flux could occur while above this minimum a semilogarithmic relationship was found between the silver ion current density i_{Ag^+} and the observed overpotential. They represented these results by the following experimental equation

$$i_{Ag^+} = A \exp(BFE) \quad [1]$$

where A and B are dependent only on temperature, F is the Faraday constant, and E the relevant overpotential. The observed overpotentials have been used (3) to make quantitative calculations concerning the unidimensional growth of α -Ag₂S on silver and also the linear growth rate which is observed in the early stages of this reaction (4)

It is now known (5) that the extent of the departure from equilibrium which occurs at the silver/ α -Ag₂S interface during the terminal stages of the one-dimensional sulfidation reaction depends on the particular sample of high purity silver being used. Since

whatever process does occur at this interface during the reaction is of basic importance in determining the sulfidation rate it was felt that it would be worthwhile doing the electrochemical experiments necessary to re-investigate the various phase boundary processes but using now three different samples of high purity silver. These samples were chosen to be similar to those used in the sulfidation experiments (5). Since all previous phase-boundary work had employed only one kind of silver preliminary experiments were carried out which showed that the extent of polarization during the transfer of silver ions was, under otherwise identical conditions, dependent on the type of silver being used. This paper reports the results of a series of experiments designed to show clearly any differences in the behavior of these samples and also to seek to establish the effects of using preannealed samples in which the grain size had been increased. A detailed study was undertaken at 260°C and less extensive measurements made at 220°, 300°, and 340°C.

One of the features of the earlier experiments (1, 2) was the use made of the relaxation curves observed when the silver current being withdrawn from the α -Ag₂S in a steady state was switched off. As will be shown later, the fall in overpotential which is observed is due to silver crossing the interface from the silver sample under investigation and a dynamic current density $i_{Ag,dyn}$ may be calculated from the equation

$$i_{Ag,dyn} = \frac{V}{a} F \frac{dE}{dt} \frac{dc_{Ag}}{dE} \quad [2]$$

where V is the volume of the sulfide, a the area of the interface, dE/dt is the slope of the relaxation curve at the stage in question and dc_{Ag}/dE (where c_{Ag} is the number of equivalents of silver/cm³ of the sulfide) may be evaluated from the slope of a subsequent coulometric titration (6) of the sulfide tablet. The curves which result when these calculated dynamic current density values are shown as a function of the overpotential prove to be quite different from the corresponding curves observed under steady-state conditions.

The present reinvestigation includes a detailed study of relaxation curves. To this end the experimental arrangement was designed to allow the lightest sulfide tablets possible to be used and computer curve fitting routines were suitably adapted to calculate the dynamical current density curves. These curves are shown to vary with the particular sample of silver.

* Electrochemical Society Active Member.

¹ Present address: Westinghouse Research Laboratories, Pittsburgh, Pennsylvania 15235.

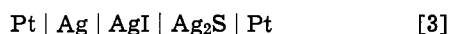
² Deceased.

Key words: silver iodide, anodic dissolution, overpotential, relaxation curves, annealing.

Experimental

Materials.—The three types of silver used for these experiments were supplied as rods of 3 mm diameter as follows: (i) Johnson-Matthey Chemicals Limited, major impurity, copper <5 ppm, over-all purity, 99.999%; (ii) Degussa Feinsilber, major impurity, copper <300 ppm, over-all purity 99.97%; (iii) Johnson-Matthey Chemicals Limited, major impurity, copper <50 ppm, over-all purity 99.99%. These samples will be referred to as JM1', D1', and JM2', respectively, since they are identical with the samples used in the sulfidation experiments reported in (5) except for their physical sizes. A precision lathe was used to reduce the diameter of each specimen to exactly 2.50 mm for a length of about 4-5 mm from the end to be used in the experiment and the specimens were then degreased as described previously. The silver iodide and silver sulfide used were of the same quality and from the same sources as those described in (5) and their fabrication into the various components utilized in the cell arrangement essential to the present work will be described in the following section. The experiments were again carried out in an atmosphere of oxygen-free nitrogen.

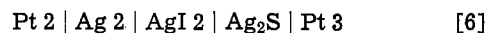
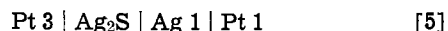
Circuitry.—The basic circuitry is shown diagrammatically in Fig. 1 and was as suggested by Rickert and O'Brian (1). The fundamental element of this system is a cell of the type



which may be studied under both equilibrium and dynamic conditions and which employs α -AgI as an auxiliary electrolyte. This compound is an almost pure ionic conductor, its silver partial ionic conductivity being several orders of magnitude greater than its electronic conductivity. Separate leads (Pt 4, Pt 5, and Pt 6) were used to pass current through the various parts of the cell and also (Pt 1, Pt 2, and Pt 3) to measure the resultant overpotentials at the silver/ α -silver sulfide interface. A small Ag/AgI probe pressed against the silver sulfide tablet near this interface and also the platinum probes ensured that the potential measurements were not invalidated by polarization phenomena. When a d-c current is passed between Pt 4 and Pt 6 (S1 left, S2 right) silver ions only cross the silver (Ag1)/ α -silver sulfide interface. If, instead, a small voltage is applied between Pt 5 and

Pt 4 (S1 right, S2 left) an electronic current only crosses the silver (Ag1)/ α -silver sulfide interface. Finally a potential applied between Pt 5 and Pt 6 and positive at Pt 5 (S1 right, S2 right) will cause silver to be withdrawn to Ag3 from the Ag₂S. As the chemical potential of silver in the silver sulfide decreases, silver from the silver sample Ag1 in contact with the sulfide will be found to cross the interface and steady state may be attained in which an equal flux of silver goes from Ag1 into the Ag₂S as leaves this phase through Ag1 and Pt 5 as silver ions and electrons, respectively. The establishment of the steady state can be assumed once the chemical potential of silver in the Ag₂S, as measured by the silver-silver iodide probe (Ag2/AgI2), remains constant.

Three different overpotentials E_{12} , E_{13} , and E_{32} may be measured when a current of ions, electrons, or neutral silver flows across the Ag/ α -Ag₂S phase boundary. These potential differences are the emf's, respectively, of the cells



The analysis of these cells has been discussed in detail previously (1) and these emf's are related to the differences in electrochemical potentials of silver ions and electrons and chemical potentials of silver across the interface by the following equations

$$-FE_{12} = \eta_{\text{Ag}^+}(\text{Ag}_2\text{S}) - \eta_{\text{Ag}^+}(\text{Ag}) \quad [7]$$

$$FE_{13} = \eta_{\text{e}^-}(\text{Ag}_2\text{S}) - \eta_{\text{e}^-}(\text{Ag}) \quad [8]$$

$$FE_{32} = \mu_{\text{Ag}}(\text{Ag}_2\text{S}) - \mu_{\text{Ag}}(\text{Ag}) \quad [9]$$

where μ and η are the chemical and electrochemical potentials, respectively, and the subscripts have their usual meanings. It is also evident from the analysis that the following relationship

$$E_{32} = E_{12} - E_{13} \quad [10]$$

should hold between the measured overpotentials.

Apparatus.—The experimental arrangement of the cells whose operation has been described in the previous section is shown in Fig. 2 (a) and (b). This design evolved after considerable experiment in an effort both to reduce the size of the sulfide tablet to facilitate investigation of the relaxation curves and to increase the reliability of the system over the lengthy time intervals necessitated by the comparative study of the silver samples. The upper AgI tablet shown was pressed under 100 kg cm⁻² in a specially constructed die with two platinum electrodes embedded in its upper surface. It was then drilled out in the shape shown and rested on a second AgI tablet which was also drilled and which was included to prevent short circuiting caused by dendritic growth of silver through this substance. The Ag₂S disks were 3.4 mm in diameter, 0.25 mm in thickness and each weighed 12.30 ± 0.05 mg. They were punched from a larger tablet which had been compacted at 6.1 × 10³ kg cm⁻². The silver block corresponding to Ag 1 of Fig. 1 and prepared as already described rested on the Ag₂S tablet. Its shape avoided experimental difficulties arising from the occasional failure to exactly center the sulfide wafer and the contact pressure was maintained at 6 kg cm⁻², (similar to that used in the sulfidation experiments) via a glass rod which passed outside the apparatus through a precision sliding gas tight seal. The Ag/AgI probe electrode was made from 6 mm glass tubing drawn into a tapering capillary which was cut and ground so that the narrower end could just reach through the drilled hole to the upper surface of the upper silver iodide tablet but no further. One of the consequences of this design was that this Ag/AgI probe was no longer on the same side of the

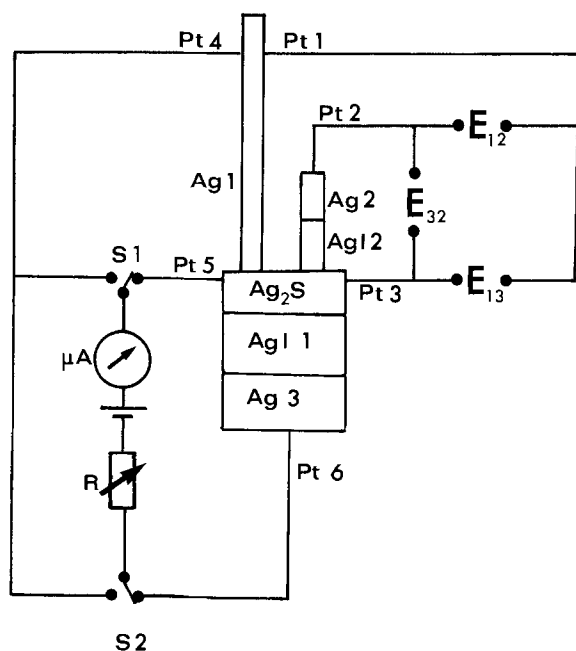


Fig. 1. Basic circuitry to study the transfer of silver across the Ag/ α -Ag₂S interface.

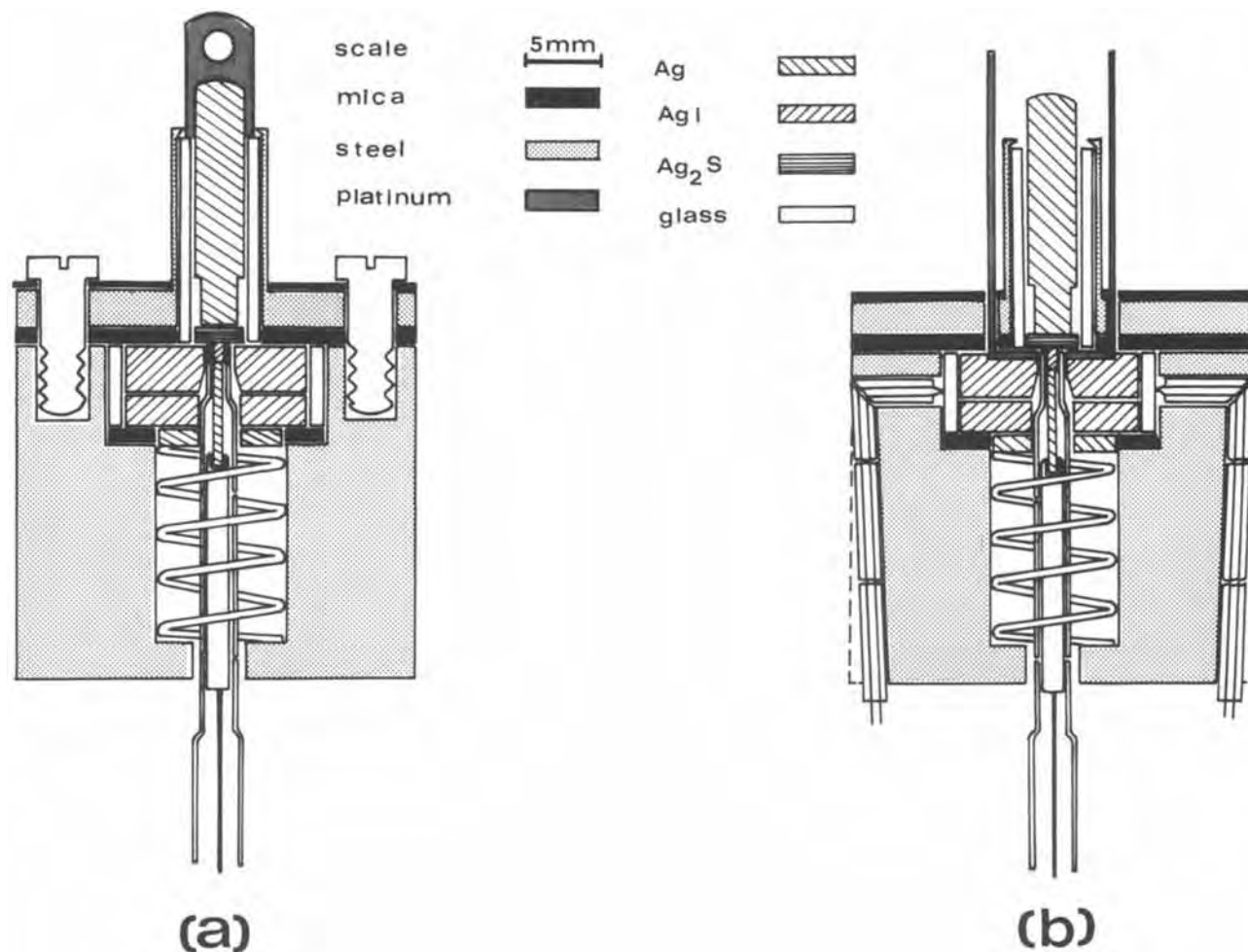


Fig. 2. Cell arrangement shown with the (a) and (b) cross sections at 90°C

α -silver sulfide tablet as was the silver block Ag 1. Fears that this might lead to incorrect measurements of the overpotentials E_{32} and E_{12} were allayed by the solution of the diffusion equation for the system which showed that any concentration gradient across this thickness of sulfide will fall to zero in ~ 50 msec because of the high value of the diffusion coefficient of silver in α - Ag_2S (6). As shown the cell assembly was held in a steel support unit and the necessary insulation was provided by mica strips. The temperature was measured using a pair of Chromel-Alumel thermocouples and the entire system was held in a 1 in. diameter Kovar joint at the center of an air-jacketed, nichrome wound furnace with temperature control to better than $\pm 1^\circ\text{C}$.

Procedure.—A number of procedures have been described previously (1, 2) to establish steady-state conditions at the $\text{Ag}/\alpha\text{-Ag}_2\text{S}$ interface in this type of experiment. Essentially these consisted of withdrawing a large current of silver from the sulfide thus causing silver to flow from the silver rod under investigation into the sulfide. Then when a steady state had been established the current was switched off and the relaxation process observed. These operations were repeated until the relaxation curves indicated that a suitable reproducible contact had been established. The current was then reduced successively thus obtaining new steady states. An alternative method was to commence at a low value of the current after reproducible contact was established and then to switch up the current in steps. These different procedures gave steady-state overpotentials which differed, at the same current density and temperature, by as much as 10-15 mV.

As the main objective of this work was to characterize the relative behavior of the different silver

samples, it was obviously desirable to adopt a standard procedure for every experiment. Consequently, it was decided (i) to operate each experiment at one fixed current of silver only and at a given temperature and (ii) to cause the same quantity of silver to be drawn across the $\text{Ag}/\alpha\text{-Ag}_2\text{S}$ interface in every experiment. The major disadvantage of (i) was that it greatly increased the number of experiments required. If there was a buildup of impurities at the phase boundary then (ii) ensured that for each sample of silver, the quantity of silver which had crossed the phase boundary when measurements of the overpotentials were made was the same in every experiment. Thus, at a current density of 0.75 A cm^{-2} , the system was operated for 1 hr, at 0.375 A cm^{-2} for 2 hr and so on to 64 hr at 0.0117 A cm^{-2} . The quantity of silver which crossed the interface in every experiment was then a length of 2.9 mm of the silver rod which corresponds to 1 unit in the overpotential traces shown later in Fig. 3. The experimental procedure followed was to withdraw a fixed current of silver from the silver sulfide while E_{32} was monitored continuously using a Honeywell Elektronik 19 recorder. When a steady state was eventually achieved the current density of silver crossing the interface was readily calculable. After the appropriate quantity of silver had crossed the interface, the steady-state values of E_{12} and E_{13} were measured. A relaxation curve of E_{32} vs. time was now observed by switching the current circuit off. By switching on again, the steady state could be regained, after an interval which was a function of the current density, and further relaxation curves were taken. The adequacy of the response time of the recorder (F.S.D. < 0.5 sec) for the purpose of observing these curves was checked by also using an oscillo-

Table I. Steady-state overpotentials observed when silver ions (E_{12}), electrons (E_{13}), and neutral silver (E_{32}) cross the Ag/ α -Ag₂S interface from three kinds of unannealed high-purity silver at 260°C. All overpotentials expressed in millivolts.

Current density (A/cm ²)	Sample JM1'			Sample JM2'			Sample D1'		
	E_{12}	E_{13}	E_{32}	E_{12}	E_{13}	E_{32}	E_{12}	E_{13}	E_{32}
0.375	128.0	-1.7	130.0	145.0	-3.6	150.5	190.0	-3.5	192.0
0.1875	121.0	-1.4	123.0	139.5	-0.8	142.0	180.0	-3.0	182.5
0.0938	103.0	-0.6	104.0	132.0	-0.5	133.0	173.5	-1.3	175.0
0.0468	87.0	-0.7	90.0	119.5	-0.7	122.0	167.0	-2.5	169.0
0.0234	82.0	-1.9	84.0	107.0	-0.9	110.5	158.5	-5.0	164.0
0.0117	69.5	-0.4	69.0	100.5	-0.5	104.0	151.0	-4.1	155.0

scope fitted with a Polaroid attachment to record transients.

Results and Discussion

The basic results with respect to the magnitudes of the observed overpotentials are summarized in Table I which gives data at 260°C for the three kinds of silver. The measurements of this kind made in this study show that: (i) when electrons alone crossed the Ag/ α -Ag₂S phase boundary E_{12} , E_{13} , and E_{32} were all less than 1 mV; (ii) when silver ions alone were transported, the measured values of E_{12} were approximately equal to those of E_{32} while E_{13} never exceeded 4% of the E_{32} value; (iii) the potential differences during the transfer of equivalent amounts of silver ions and electrons were the same as those observed during the transfer of silver ions alone; and (iv) Eq. [8] was, in general, obeyed. These observations are in agreement with the previous work on this system (1, 2) and also with the more recent results of Rickert *et al.* for the Ag/ α -Ag₂Se and Ag/ α -Ag₂Te interfaces (7). As we shall see later (Fig. 4) the semilogarithmic relationship between the silver current density, i_{Ag} , and the relevant overpotential, E_{32} , found previously is also confirmed but in contrast to the earlier work this relationship was now found to extend to the lowest current densities measured. The detailed results of the comparative study of the silver samples will be discussed in the following sections.

Unannealed silver.—The overpotential traces for the three silver samples at 260°C and at a current density of 0.375 A cm⁻² are shown in Fig. 3. In the interpretation of these traces it should be remembered that 1.0 units of silver consumed corresponds to 2.9 mm length of the silver rod. These curves are typical of those observed at other current densities and other temperatures and the following general conclusions could be drawn concerning the behavior of the various silver samples. JM1' was characterized by a short induction period at high overpotentials, followed by a rapid drop to near zero E_{32} values and finally, after ~0.25 units

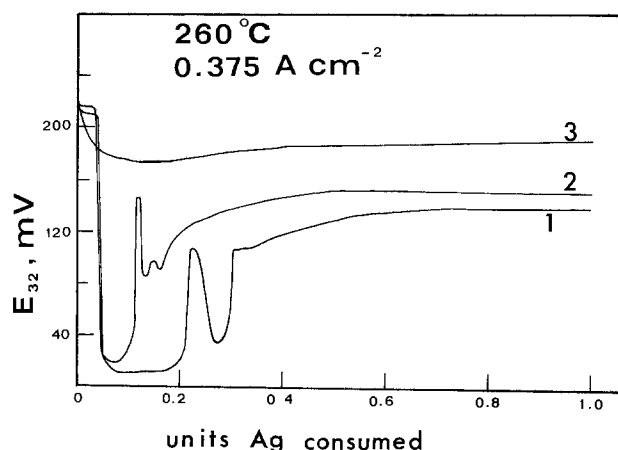


Fig. 3. Overpotential traces at 260°C and a current density of 0.375 A cm⁻². The traces shown are: curve 1, JM1'; curve 2, JM2'; and curve 3, D1' samples of silver.

of silver have crossed the interface, by a rapid rise to an overpotential ~20 mV below the steady-state value which was reached typically after 0.6 units had been consumed. The behavior of JM2' differed from that of JM1' in the following ways. Firstly, the overpotentials attained after the rapid drop were not quite so low; secondly, the rapid rise occurred after only about 0.1 units had passed; and thirdly, the steady-state overpotentials were ~20 mV higher than those observed from JM1' at every silver current density measured. The D1' silver was quite different in behavior to the two samples of Johnson-Matthey silver. Virtually no induction period was observed before E_{32} fell to a value which was, at most, 20 mV below the value observed after 1.0 units had crossed the interface. The minimum in E_{32} was observed after ~0.05 units had passed and this was followed by a slow rise until ~0.3 units which was followed in turn by an even slower rise. Even after 1.0 units of silver had been consumed no true steady state was observed, and E_{32} continued to rise slowly. Furthermore the values of E_{32} now measured were 40-50 mV higher than those observed for the JM2' silver at the same current densities.

The semilogarithmic relationships between the silver current densities, i_{Ag} , and the overpotentials, E_{32} , observed for each of the silver samples after 1.0 units had crossed the interface are shown in Fig. 4. The extent of the bars shown on some of the points represent the limit of any oscillations of E_{32} at the time the overpotential was read. It is most important to emphasize that in contrast to earlier work each point now represents a separate experiment thus confirming both the validity of the relationship shown and also the reproducibility of the differences between the overpotentials observed for each sample. Also in contrast to earlier results (1, 2), the semilogarithmic relationship was now shown to extend to the lowest current densities measured. As is evident from Fig. 4 the slopes of these plots for the various silver samples were almost identical despite the large differences in the magnitudes of the observed E_{32} values. These results are typical of those found at the other temperatures (220°, 300°, and 340°C) at which measurements were made while the effect of temperature on the semilogarithmic plots is shown for D1' silver in Fig. 5.

These results when considered with the fact that the impurity content of JM1' is less than that of JM2' which in turn is very much less than that of D1' lead to a postulate that the abrupt rise from near zero potentials, observed for the first two is due to the buildup of a critical quantity of impurities at the Ag/ α -Ag₂S interface. The passage of 0.25 units (i.e., a length of 0.7 mm) is required in the case of JM1' while 0.10 units of the more impure JM2' suffice for the same purpose. This effect is not, of course, observed for the D1' specimens. The major impurity in the three silver samples was copper in concentrations of 5, 50, and 300 ppm, respectively, but in the absence of data of detailed experiments using specifically doped samples no decision can be made as to whether the copper, or some other impurity, perhaps present in trace quantities, was responsible for the sudden rise to higher overpotentials. Since the magnitude of the overpotentials observed here correlate with those reported

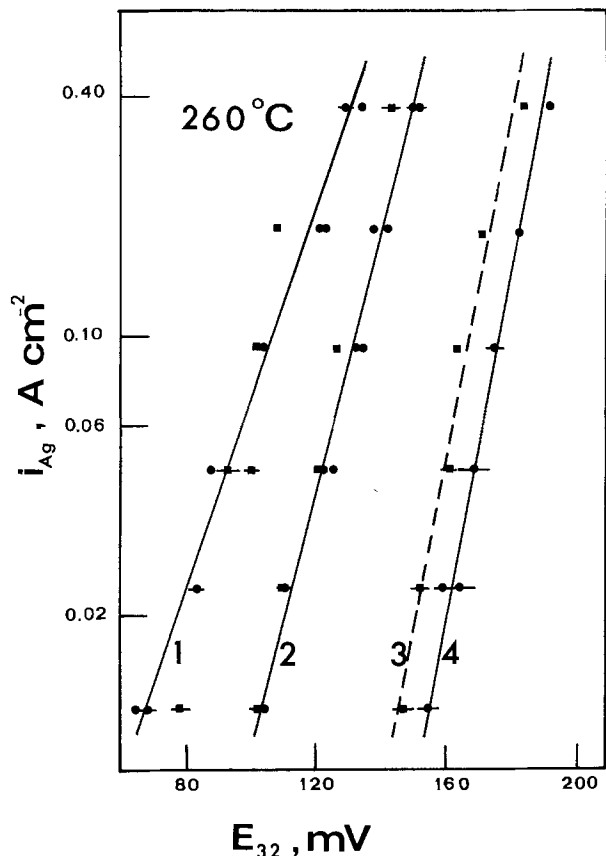


Fig. 4. Semilogarithmic plot of current density vs. steady-state overpotentials at 260°C. Data for unannealed silver (\bullet) and for annealed silver (\blacksquare) and the lines shown are fitted to the data as follows: line 1, JM1 unannealed; line 2, JM2' unannealed; line 3, D1' annealed; and line 4, D1' unannealed sample of silver.

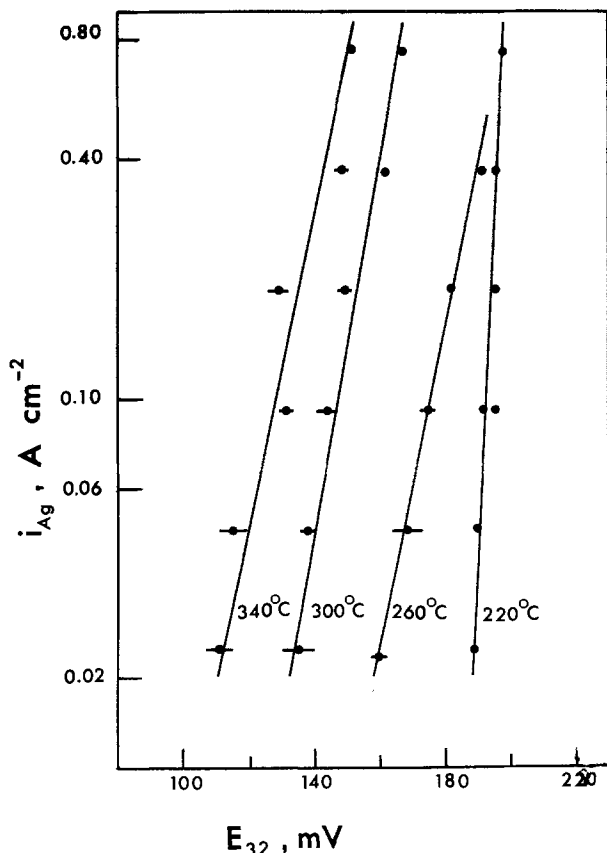


Fig. 5. Semilogarithmic plots of current density vs. steady-state overpotential at 220°, 260°, 300°, and 340°C for D1' silver.

during sulfidation of comparable silver samples (5) and since it has also been shown that changes in grain size effected by preannealing influence the sulfidation kinetics, a series of phase boundary experiments were now undertaken using annealed silver samples.

Annealed silver.—The annealing of the remaining samples of each type of silver was carried out at 660°C *in vacuo* for 100 hr. A metallurgical examination, as described in (5), followed and indicated that once again the grain sizes had been increased. Because of the limited supply of silver remaining the phase boundary experiments for the annealed samples were confined to measurements at 260°C only. It had been expected, bearing in mind the results of the sulfidation experiments with the annealed samples (5) that there would be a lowering of E_{32} for each of the annealed silver samples. In fact, only very small differences in behavior were observed between these samples and the unannealed specimens. The overpotential vs. time traces for JM1' and JM2' annealed samples were quite similar to those shown in Fig. 3 for the unannealed samples while the steady-state overpotentials attained were almost the same as those recorded previously. The pattern of behavior which emerged from these experiments is shown in Fig. 4 where the experimental results for annealed JM1' and JM2' are seen to fall close to the best-fit lines through the unannealed data. In contrast all data for annealed D1' lie consistently lower by ~ 7 mV and are fitted by the broken line. These results were therefore surprising in view of the sulfidation data (5). In this case it could not be claimed that increasing the grain size in the samples led, in general, to a lowering of the interface overpotential.

Relaxation curves.—The relaxation curves obtained when the current was switched off in the steady state corresponding to each current density measured at 260°C for JM2' silver are shown in Fig. 6. These curves are typical of those observed at all temperatures for both JM1' and JM2' silver. All were perfectly smooth with decreasing slope and the curves for these two kinds of silver were, in general, superposable for the initial 40–50 mV of the drop to zero. The relaxation curves for D1' silver were quite different and that obtained at 260°C from the steady state corresponding to a current density of 0.0117 A cm $^{-2}$ is compared with the curves obtained under identical circumstances for both the Johnson-Matthey samples in Fig. 7. As is evident the curve for D1' silver contained a point of inflection which was also a feature in all the curves for this sample except those originating from the steady states corresponding at each temperature to the

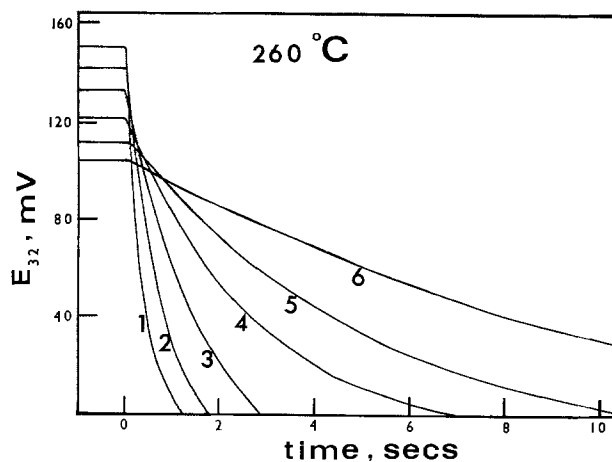


Fig. 6. Relaxation curves at 260°C for JM2' silver. The steady states from which the curves originate result from the following steady-state current densities in A cm $^{-2}$: curve 1, 0.375; curve 2, 0.1875; curve 3, 0.0938; curve 4, 0.0468; curve 5, 0.0234; and curve 6, 0.0117.

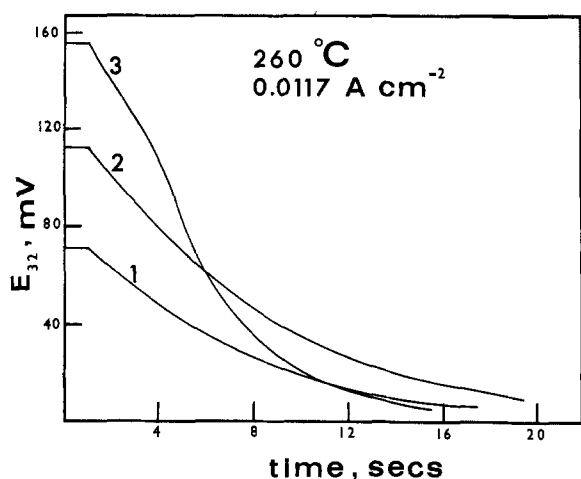


Fig. 7. Comparison of relaxation curves at 260°C from steady states resulting from a current density of 0.0117 A cm^{-2} ; curve 1, JM1'; curve 2, JM2'; and curve 3, D1' silver samples.

largest current density (0.375 A cm^{-2}) employed. As it was possible to again attain the same steady state by again switching on the appropriate current further relaxation curves could be observed. These subsequent curves for the Johnson-Matthey samples were found to be quite reproducible, *i.e.*, superposable, but those for the D1' silver were not. In the latter case repeated taking of relaxation curves caused an increase in the degree of inflection with the result that E_{32} fell more rapidly to zero. The relaxation curves of E_{12} for D1' silver also had a point of inflection, while those for E_{13} showed a step which occurred at a time corresponding to just before the onset of inflection in the E_{32} and E_{12} curves. This would suggest the operation of a two-stage relaxation process in the case of the D1' silver, and although there have been indications in earlier work also using Degussa Feinsilber (2) that this might be the case, we can, on the evidence currently available, offer no explanation as to the cause.

To calculate $i_{\text{Ag,dyn}}$, the dynamic silver current density across the $\text{Ag}/\alpha\text{-Ag}_2\text{S}$ interface at any value of E_{32} , coulometric titrations (6) were first carried out on tablets of the same weight as those used in all experiments. These curves were then computer fitted using a polynomial regression routine which also evaluated dE_{32}/dt . A similar program for the relaxation curves evaluated not only the slopes but also the $i_{\text{Ag,dyn}}$ at given values of E_{32} using data from the fit to the coulometric curve in Eq. [2]. The dynamic current density curves resulting from the relaxation curves of Fig. 6 are shown in semilogarithmic form in Fig. 8 and once again are typical of the curves obtained for JM1' and JM2' samples at all the temperatures at which measurements were made. Figure 9 shows the $i_{\text{Ag,dyn}}$ curves for the relaxation traces of Fig. 7 and the point of inflection for D1' silver now manifests itself as a maximum of current density. The curve itself from 100 mV down approximates to that observable for the relaxation current of a Johnson-Matthey sample from a steady state corresponding to approximately twice the current density. A comparison of Fig. 8 and 9 with Fig. 4 shows clearly that, as had been found previously, the relationship between $i_{\text{Ag,dyn}}$ and E_{32} during a relaxation process was quite different from that which existed between the current densities and overpotentials in the steady states. Since the dynamic current densities at the same stage (same value of E_{32}) of the different relaxation processes are quite different it is also evident that the dynamic current density also depends on the steady state from which the relaxation began. Furthermore the relaxation behavior is now also seen to depend on the particular sample of silver being used.

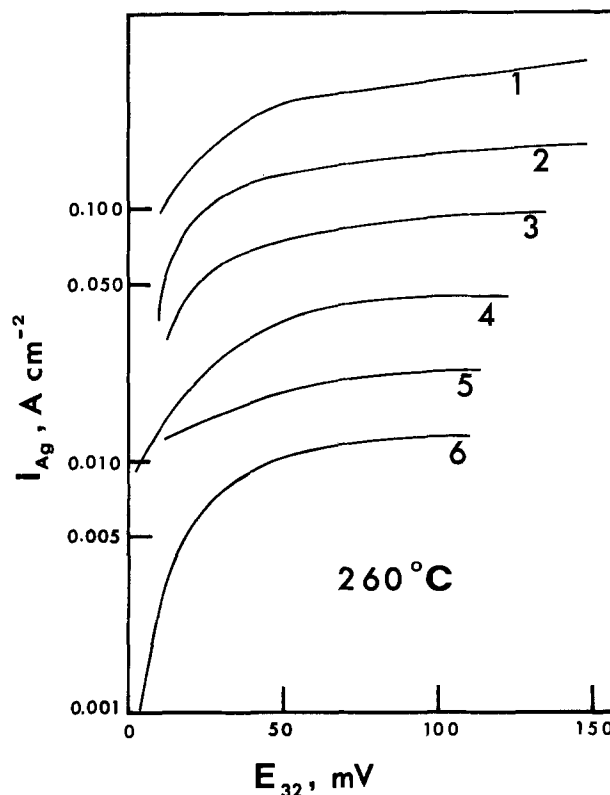


Fig. 8. Semilogarithmic plots of dynamic silver current density vs. overpotential at 260°C for JM2' silver calculated from relaxation curves of Fig. 6. The current densities, in A cm^{-2} , which produced the original steady states are as follows: curve 1, 0.375; curve 2, 0.1875; curve 3, 0.0938; curve 4, 0.0468; curve 5, 0.0234; and curve 6, 0.0117.

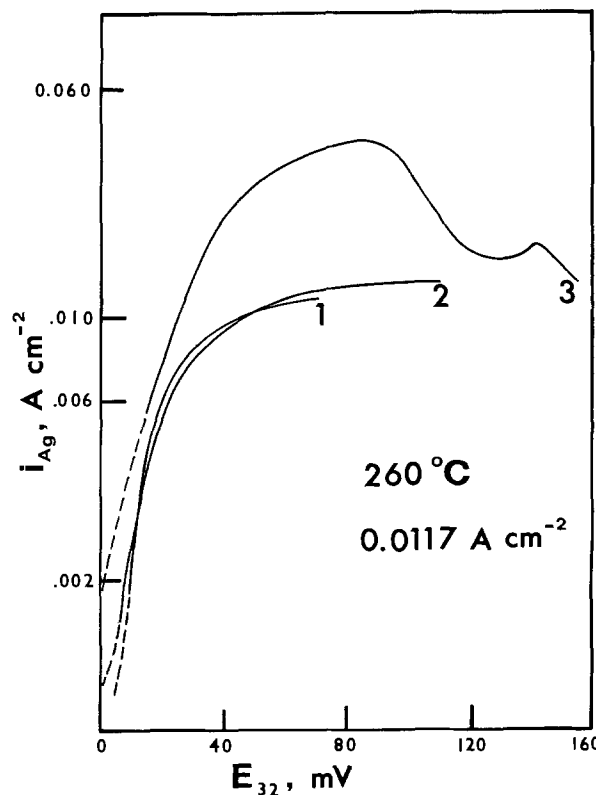


Fig. 9. Semilogarithmic plots of dynamic silver current density vs. overpotential at 260°C calculated from the relaxation curves of Fig. 7: curve 1, JM1'; curve 2, JM2'; and curve 3, D1' silver samples.

General Summary

The principal results from this investigation of the bulk silver/ α -silver sulfide interface show that the interface potentials are dependent, as might have been expected from the sulfidation results (4), on the type of high purity silver used. It has also been shown that the semilogarithmic relationship between the silver current density and the overpotential which had been thought to exist only above certain critical overpotentials (1) in fact extends over the entire current density range measured (i.e., 0.75 A cm⁻² to 0.0117 A cm⁻²). The previously observed critical overpotentials below which the overpotential became independent of the current density were used (1) to explain the steady overpotentials observed at the Ag/ α -Ag₂S interface during the sulfidation reaction. In view of the new results presented here these steady overpotentials may be explained as follows. The initial stages of the sulfidation reaction proceed rapidly so that by the time steady overpotentials are observed the sulfide layer is reasonably thick. It is obvious from inspection of the parabolic equation [Eq. [1] of Ref (5)] that for the silver flux to decrease by a factor of two, the sulfide layer thickness must have increased by the same factor. This may take a time of the order of hours as, in general, the supposed steady-state is reached after approximately 2-3 hr. When the current density is halved the overpotential, E_{32} , drops by no more than a few millivolts (e.g., at 260°C for D1' silver E_{32} is diminished by ~8 mV if i_{Ag} is halved). Counteracting this tendency of E_{32} to decrease is the fact, already commented upon, that at a fixed current density E_{32} for D1' silver continues to rise as more silver crosses the phase boundary. Thus a pseudo steady state may well be observed at the Ag/ α -Ag₂S interface during the formation of compact sulfide layers. Further efforts were made, by using preannealed silver samples in which grain size had been increased, to obtain results corresponding to those reported in recent sulfidation experiments (5). These attempts were somewhat surprising since only a small effect was found and that only in the case of D1' silver. A correlation was found to exist between a possible buildup of impurities at the interface and the magnitude of the observed overpotentials. However, it is felt that a series of experiments in which the impurity levels in the silver are systematically varied will be required before any definite conclusion may be reached as to the precise causes of these overpotentials.

The nature of the polarization is nonohmic while the relaxation behavior indicates that the exact condition of the interface is involved. O'Briain (2) proposed a polarization model based on an activated process, as suggested by Eq. [1], in which a silver ion on a surface site was assumed to have to surmount an energy barrier to reach a similar site on the α -Ag₂S. This model is, however, unacceptable if applied to the data for α -Ag₂S since it requires transfer coefficients appreciably larger than unity. Rickert *et al.* (7) also discussed this model but showed that it was similarly unacceptable for their observations of the Ag/ α -Ag₂Se and Ag/ α -Ag₂Te interfaces.

Since the net result of the process occurring at the block silver/ α -Ag₂S interface is the dissolution of one solid into another any attempt to elucidate the atomistic mechanism must consider the crystal structures of both substances. The α -Ag₂S structure (8) might be expected to be well suited to accept silver since the effective number of available silver sites per unit cell has been estimated at almost six with only four silver ions accommodated (9,10). As we have already mentioned the interdiffusion coefficient for silver (6) in this solid ($\sim 3 \times 10^{-2}$ cm² sec⁻¹ at 400°C) is sufficiently high to eliminate concentration gradients rapidly and so the dissolution process may well depend primarily on the particular form in which silver atoms are presented at the sulfide surface. In this respect two previous reports from this laboratory have con-

sidered the silver vapor/ α -Ag₂S and silver whisker/ α -Ag₂S interfaces. Silver vapor (11) impinging on the surface of an α -Ag₂S tablet was found to be incorporated readily into the solid. If the sulfide was made a part of a suitable electrochemical cell then it was found possible using very small overpotentials (<1 mV) to maintain a steady state in which the silver entering the tablet from the vapor phase was balanced by a corresponding electrochemical withdrawal of silver through the cell. The silver whiskers (12) were first grown electrochemically on preferentially nucleated sites on a sulfide tablet and the subsequent transfer of silver across the Ag(whisker)/ α -Ag₂S interface was found to occur with the application of very small overpotentials. Typically a current density of 0.5 A cm⁻² was achieved with overpotentials of ~2.9 mV and 2.2 mV at 220° and 300°C, respectively, which processes would be expected to require overpotentials well in excess of 100 mV for samples of block silver. The very small overpotentials observed at the Ag(whisker)/ α -Ag₂S interface, and similar observations have now been made at the Ag(whisker)/ α -Ag₂Se interface (13), were attributed to the presence of screw dislocations in the whiskers (14), the situation being analogous to that reported by Vermilyea (15) for the electrolytic growth and dissolution of copper whiskers in solution. It was also emphasized (12) that the special nature of the microcontact expected to be attained at the Ag(whisker)/ α -Ag₂S when the whiskers were actually grown *in situ* almost certainly significantly influenced the magnitude of the observed overpotentials. Unfortunately attempts to distinguish the part played in the silver transfer process by the presence of dislocations from that resulting from the nature of the microcontact were not successful. What is clear, however, from the vapor and whisker work is that silver atoms presented either free or at suitable active crystal positions may be very easily incorporated into α -Ag₂S.

The behavior of the bulk silver studied here at the chalcogenide interface is presumably much more complex. The attainment of an adequate microcontact is obviously difficult and since each sample has a different grain size and orientation, and most probably a different defect structure, the facility with which silver atoms are removed from the bulk silver may be expected to vary. These factors will then influence the exact nature of the interface and hence the magnitude of the overpotentials. Our results also indicate that any completely successful model must also take account of the possible influence of a buildup of impurity atoms at the interface, although the role of these impurities is at present less clear.

Acknowledgments

We are grateful to Professor H. Rickert, University of Dortmund, Dr. Eoin P. O'Neill, Westinghouse Research Laboratories, and Dr. Ronald F. Saunders, for many helpful discussions.

This work was in part fulfillment of the requirements for the award of the degree of Ph.D. by the National University of Ireland to C. J. Warde.

Manuscript submitted March 24, 1975; revised manuscript received July 12, 1975.

Any discussion of this paper will appear in a Discussion Section to be published in the June 1976 JOURNAL. All discussions for the June 1976 Discussion Section should be submitted by Feb. 1, 1976.

REFERENCES

1. H. Rickert and C. D. O'Briain, *Z. Physik. Chem. N. F.*, **31**, 71 (1962).
2. C. D. O'Briain, Thesis, Nat. Univ. of Ireland, Dublin (1963).
3. H. Rickert and C. Wagner, *Z. Physik. Chem. N.F.*, **31**, 32 (1962).
4. J. Czernski, S. Mrowec, K. Wallichow, and T. Werber, *Archiwum Hutnictwa*, **3**, 49 (1958).

5. C. J. Warde, J. Corish, and C. D. O'Briain, *This Journal*, **122**, 1421 (1975).
6. C. Wagner, *J. Chem. Phys.*, **21**, 1819 (1953).
7. L. Contreras and H. Rickert, in "Fast-Ion Transport in Solids," W. van Gool, Editor, p. 523, North Holland, Amsterdam, (1973).
8. P. Junod, *Helv. Physica Acta*, **32**, 567 (1959).
9. H. Rickert, *Z. Physik. Chem. N.F.*, **24**, 418 (1960).
10. H. Ozazaki, *J. Phys. Soc. Japan*, **23**, 355 (1967).
11. J. Corish, M. T. Duffy, and C. D. O'Briain, *Trans. Faraday Soc.*, **67**, 1447 (1971).
12. J. Corish and C. D. O'Briain, *J. Mater. Sci.*, **6**, 252 (1971).
13. D. C. A. Mulcahy and J. Corish, To be published.
14. H. Rickert, Private communication.
15. D. A. Vermilyea, *J. Chem. Phys.*, **27**, 814 (1957).

A State-of-Charge Test for Zinc-Mercuric Oxide Primary Cells

John J. Winter, James T. Breslin, Raymond L. Ross,
Herbert A. Leupold, and Frederick Rothwarf

U.S. Army Electronics Technology and Devices Laboratory (ECOM), Fort Monmouth, New Jersey 07703

ABSTRACT

A readily instrumented and conducted nondestructive technique to determine the state of charge of zinc-mercuric oxide primary cells has been developed and preliminary results obtained. Measurements of the current vs. voltage (I - V) characteristics, the a-c impedance, the electronically sampled derivative at different sampling currents and frequencies, and the discharge-time characteristics of the cells as a function of charge expended have been made and reported. The nearly constant slopes of the I - V curves above 75 mA were measured graphically. It was found that these slopes have a linear relation to charge expended and can be used as a basis for a simple state-of-charge indicator which determines remaining charge to about 12%. By combining this criterion with a-c resistance measurements the maximum experimental deviation was found to be less than 10% with 90% of the data points deviating less than 6% from the mean linear curve. These studies indicate that this technique constitutes a useful, easily applied state-of-charge test.

There has been a long standing need for a reliable, nondestructive state-of-charge test for many of the most commonly used primary cells. Attempts have been made in the past to link some output characteristic of a cell to its remaining charge, but invariably the resulting relationship was found to be either too insensitive, too internally inconsistent, or too variable from cell to cell. The results of one of the more interesting of these attempts were published by Sandia Laboratories in 1970 (1,2). This indicator was developed to improve the probability of selecting batteries having a state of charge exceeding 80% of capacity. The calibration curves obtained were extremely sensitive to discharge rates and temperatures as well as storage times and temperatures. In this technique, mercury cells were subjected to a series of large-current, pulsed discharges, each corresponding to a known remaining charge. Certain dimensions of the resulting pulse were measured graphically and combined mathematically to obtain a single parameter which was then plotted against the corresponding charge of the cell. Attempts to apply the Sandia technique to zinc-mercuric oxide primary cells were made at the U.S. Army Electronics Command, Fort Monmouth, New Jersey (3), and Mallory (4) without success, and the experiments were discontinued.

Accordingly, it was decided to investigate the possibility of utilizing the parameters of current vs. voltage (I - V) curves as state-of-charge indicators. Examples of such curves are shown in Fig. 1. The nearly constant slopes of the I - V curves at discharge currents above 75 mA show sufficient sensitivity to state of charge to suggest their utilization as an indicator. Accordingly, it was decided to investigate this possibility as well as the effect of the state of charge on both the cell a-c impedance and differential resistance.

Key words: zinc-mercuric oxide or mercury cells, current voltage (I - V) characteristics, state of charge, polarization resistance, internal resistance.

Experimental

Two different types of cell were used: seven RM4R cells denoted A1-A7 and four RM4H cells denoted B1-B4 with nominal voltages of 1.35 and 1.40V, respectively. All cells were discharged at room temperature ($22^\circ \pm 2^\circ\text{C}$). The A cells were stored for varying periods of time (2-7 months) at room temperature and the B cells were refrigerated at about 8°C for several months before being tested. A schematic representation of the experimental apparatus is shown in Fig. 2. Only the portion enclosed by the dotted line is needed to obtain the I - V curves. The latter are obtained by use of a forced discharge, that is, a discharge through a power supply in the constant current mode. When operated at constant current the power supply behaves as an active variable load to maintain a particular current which is set by manual adjustment of

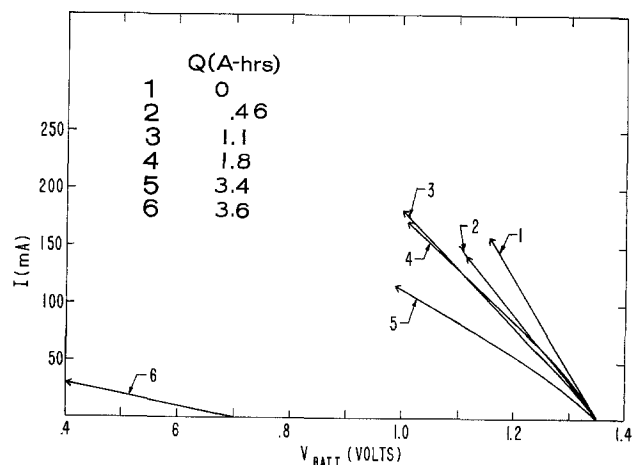


Fig. 1. The I vs. V curves of cell A6 at different states of charge.

5. C. J. Warde, J. Corish, and C. D. O'Briain, *This Journal*, **122**, 1421 (1975).
6. C. Wagner, *J. Chem. Phys.*, **21**, 1819 (1953).
7. L. Contreras and H. Rickert, in "Fast-Ion Transport in Solids," W. van Gool, Editor, p. 523, North Holland, Amsterdam, (1973).
8. P. Junod, *Helv. Physica Acta*, **32**, 567 (1959).
9. H. Rickert, *Z. Physik. Chem. N.F.*, **24**, 418 (1960).
10. H. Ozazaki, *J. Phys. Soc. Japan*, **23**, 355 (1967).
11. J. Corish, M. T. Duffy, and C. D. O'Briain, *Trans. Faraday Soc.*, **67**, 1447 (1971).
12. J. Corish and C. D. O'Briain, *J. Mater. Sci.*, **6**, 252 (1971).
13. D. C. A. Mulcahy and J. Corish, To be published.
14. H. Rickert, Private communication.
15. D. A. Vermilyea, *J. Chem. Phys.*, **27**, 814 (1957).

A State-of-Charge Test for Zinc-Mercuric Oxide Primary Cells

John J. Winter, James T. Breslin, Raymond L. Ross,
Herbert A. Leupold, and Frederick Rothwarf

U.S. Army Electronics Technology and Devices Laboratory (ECOM), Fort Monmouth, New Jersey 07703

ABSTRACT

A readily instrumented and conducted nondestructive technique to determine the state of charge of zinc-mercuric oxide primary cells has been developed and preliminary results obtained. Measurements of the current vs. voltage (I - V) characteristics, the a-c impedance, the electronically sampled derivative at different sampling currents and frequencies, and the discharge-time characteristics of the cells as a function of charge expended have been made and reported. The nearly constant slopes of the I - V curves above 75 mA were measured graphically. It was found that these slopes have a linear relation to charge expended and can be used as a basis for a simple state-of-charge indicator which determines remaining charge to about 12%. By combining this criterion with a-c resistance measurements the maximum experimental deviation was found to be less than 10% with 90% of the data points deviating less than 6% from the mean linear curve. These studies indicate that this technique constitutes a useful, easily applied state-of-charge test.

There has been a long standing need for a reliable, nondestructive state-of-charge test for many of the most commonly used primary cells. Attempts have been made in the past to link some output characteristic of a cell to its remaining charge, but invariably the resulting relationship was found to be either too insensitive, too internally inconsistent, or too variable from cell to cell. The results of one of the more interesting of these attempts were published by Sandia Laboratories in 1970 (1,2). This indicator was developed to improve the probability of selecting batteries having a state of charge exceeding 80% of capacity. The calibration curves obtained were extremely sensitive to discharge rates and temperatures as well as storage times and temperatures. In this technique, mercury cells were subjected to a series of large-current, pulsed discharges, each corresponding to a known remaining charge. Certain dimensions of the resulting pulse were measured graphically and combined mathematically to obtain a single parameter which was then plotted against the corresponding charge of the cell. Attempts to apply the Sandia technique to zinc-mercuric oxide primary cells were made at the U.S. Army Electronics Command, Fort Monmouth, New Jersey (3), and Mallory (4) without success, and the experiments were discontinued.

Accordingly, it was decided to investigate the possibility of utilizing the parameters of current vs. voltage (I - V) curves as state-of-charge indicators. Examples of such curves are shown in Fig. 1. The nearly constant slopes of the I - V curves at discharge currents above 75 mA show sufficient sensitivity to state of charge to suggest their utilization as an indicator. Accordingly, it was decided to investigate this possibility as well as the effect of the state of charge on both the cell a-c impedance and differential resistance.

Key words: zinc-mercuric oxide or mercury cells, current voltage (I - V) characteristics, state of charge, polarization resistance, internal resistance.

Experimental

Two different types of cell were used: seven RM4R cells denoted A1-A7 and four RM4H cells denoted B1-B4 with nominal voltages of 1.35 and 1.40V, respectively. All cells were discharged at room temperature ($22^\circ \pm 2^\circ\text{C}$). The A cells were stored for varying periods of time (2-7 months) at room temperature and the B cells were refrigerated at about 8°C for several months before being tested. A schematic representation of the experimental apparatus is shown in Fig. 2. Only the portion enclosed by the dotted line is needed to obtain the I - V curves. The latter are obtained by use of a forced discharge, that is, a discharge through a power supply in the constant current mode. When operated at constant current the power supply behaves as an active variable load to maintain a particular current which is set by manual adjustment of

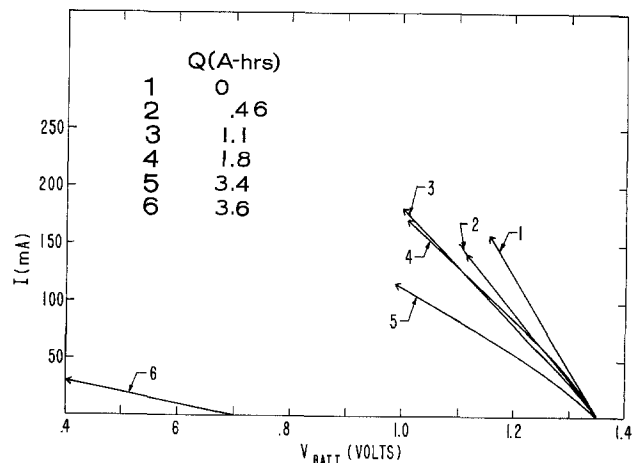


Fig. 1. The I vs. V curves of cell A6 at different states of charge.

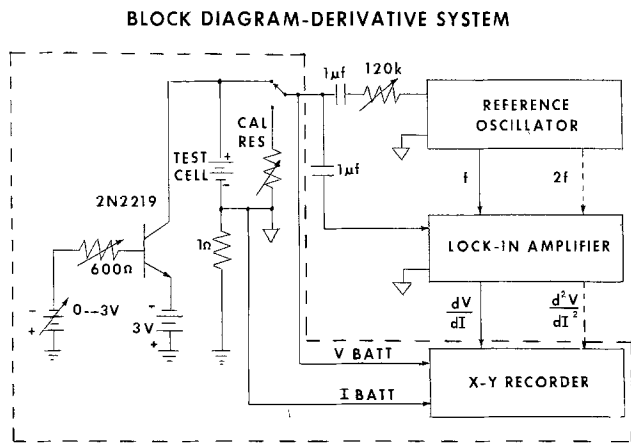


Fig. 2. The circuit employed in the I - V as well as the differential a-c resistance measurements.

the bias on the 2N2219 transistor. An I - V curve is traced on an X-Y recorder by increasing the current from 0 to 150 mA in 30-40 sec. Cycling times from 25 sec to 2 min yield essentially the same result. Significantly shorter cycling times were not possible due to the time constant of the recorder as well as the erratic response from rapid manual control of the current sweep. If the sweep is interrupted and the current is kept constant, the voltage of a cell having sustained major discharges will initially tend to drift downward. For example, if the sweep is halted at a current of 30 mA, the voltage drifts downward at a rate of about 2.5 mV/sec.

As Fig. 1 illustrates, the slope above 75 mA of the I - V curves decreases monotonically with the total charge expended. In general, the slope of each curve varies with current up to about 75 mA, above which it becomes nearly constant. Small local irregularities in the I - V curve due to the discrete nature of the electrochemical processes and the inevitable roughness of manual current control made consistent definition of a tangent at a point impracticable. It was, therefore, necessary to measure the slope not of a tangent but of a secant drawn through the curve over a small but finite voltage interval. This procedure effectively smoothed out local irregularities thus permitting definition of an effective d-c differential resistance. The voltage interval (ΔV) chosen was 0.1V and the low current boundary of the interval was taken at 75 mA as illustrated by the dashed triangle in Fig. 3.

The state of charge was usually obtained by starting with new cells and discharging them through fixed loads at currents ranging from 30 to 80 mA, since 80

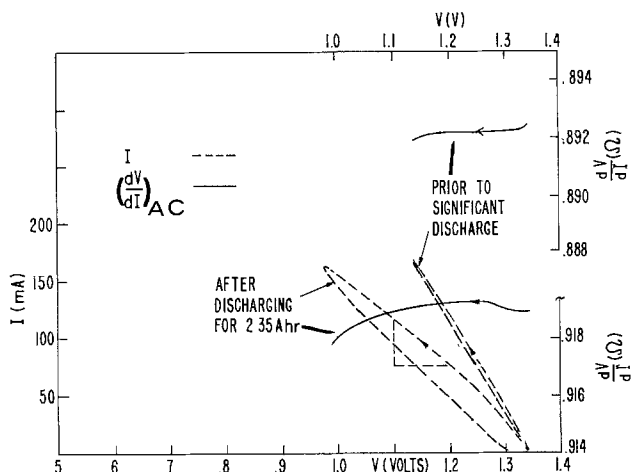


Fig. 3. Typical $(dV/dI)_{AC}$ vs. V and I vs. V curves of a cell at two different states of discharge.

mA is the upper rating of these cells for practical use. A graphical recording was kept of current vs. time so that the charge expended, ΔQ_i , was obtained from the area under the resulting curve. Typical discharges were of the order of 0.4 A-hr. The total charge expended, Q , was obtained by summing all discharges, i.e., $Q = \sum_i \Delta Q_i$. The I - V curves were obtained at least 16 hr subsequent to each discharge. This interval between discharge and state-of-charge measurement gave the cell time to reach chemical equilibrium and insured consistent results. The 16 hr period was convenient for our measurement schedule and could possibly be shortened to as little as an hour or less. The charge losses ($\sim 7 \times 10^{-4}$ A-hr) associated with the measurement of the I - V curves were less than 0.2% of a typical discharge and, therefore, negligibly small. For convenience several cells were sometimes discharged simultaneously by connecting them in series. The series combinations used were A1, A2, A3; B1, B2; and B3, B4.

Plots of slopes, $(\Delta V/\Delta I)_{75}$ vs. total discharge Q for several cells are shown in Fig. 4. Note that the relationship is invariant with the discharge rates indicated and between the two different types (A and B) of cells tested. The measurements for A4 and A5 are not included since they were discharged at the abnormally high average currents of 120 and 175 mA, respectively. At the beginning of each discharge of cell A5 the initial current was 250 mA. The current declined gradually to some cutoff value (ranging from 100 to 190 mA) after which the decrease became much more abrupt. As soon as this steep falloff commenced, the discharge was terminated. The average current drain over the discharge period was taken to be 175 mA and is referred to as such in the figures. The discharge current of cell A4 was held constant at 120 mA although maintenance of this value necessitated a slight load decrease in the course of the discharge.

To obtain the differential a-c resistance $(dV/dI)_{AC}$, all of the apparatus of Fig. 2 is employed. A small a-c signal is superimposed on the direct current for which $(dV/dI)_{AC}$ is desired (5). For greater sensitivity the resultant voltage is nulled and measured with a differential lock-in amplifier. The resistance scale was calibrated by substituting a precision wire-wound resistance decade box for the cell. That $(dV/dI)_{AC}$ cannot be used in lieu of the d-c differential resistance $(\Delta V/\Delta I)_{75}$ is clearly illustrated by the curves of Fig. 3 which show that while $(\Delta V/\Delta I)_{75}$ increases by about 50% after a 2.35 A-hr discharge, the corresponding change in $(dV/dI)_{AC}$ is only about 3%. The discrepancy between these measurements appears to be in accord with the literature. Vinal (6), for ex-

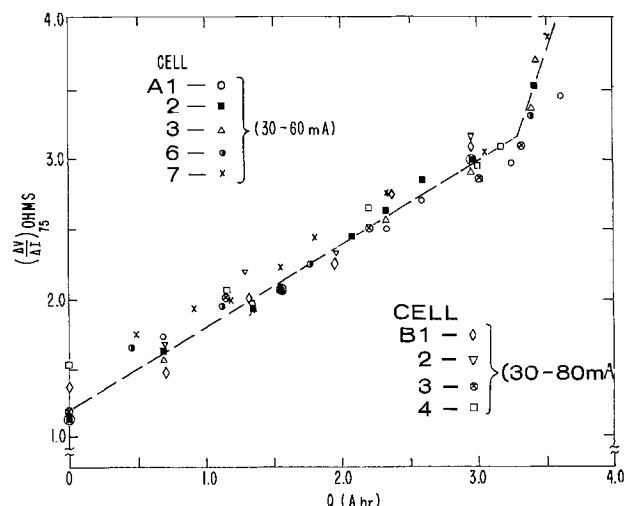


Fig. 4. The effective differential d-c resistance at 75 mA, $(\Delta V/\Delta I)_{75}$, vs. total prior discharge, Q .

Table I. Measurements made on cell A1 as a function of total discharge, Q . ΔT is the time elapsed from the end of a discharge to the start of the measurement.

ΔT (hr)	—	68	24	16	16	16	16	16	16	68	16	16
$(dV/dI)_{AC}^a$ (ohms)	0.893	0.940	0.858	0.837	0.893	0.906	0.950	0.988	1.23	1.49	1.74	1.59
$(\Delta V/\Delta I)_{75}^b$ (ohms)	1.15	1.72	1.96	2.06	2.44	2.44	2.50	2.7	2.99	3.17	3.51	3.44
R_B (ohms)	0.858	0.848	0.815	0.771	0.805	0.826	0.871	0.901	0.994	1.14	1.07	1.07
Q (A-hr)	0.689	1.35	1.56	1.80	2.08	2.32	2.59	2.95	3.25	3.42	3.61	—

^a $(dV/dI)_{AC}$ is sampled with an alternating current of 10 mA at 0.5 kHz.

^b $(\Delta V/\Delta I)_{75}$ is specified by a ΔV of 0.1V and a lower current value of 75 mA.

ample, reports his a-c measurements as lower than the lowest values obtained by any d-c measurement. The $(dV/dI)_{AC}$ measurements displayed in Fig. 3 were made at the relatively low frequency of 0.5 kHz. Even at this low frequency $(dV/dI)_{AC}$ is relatively small compared to $(\Delta V/\Delta I)_{75}$. $(dV/dI)_{AC}$ was typically found to vary irregularly from 0.8 to 1 ohm, whereas $(\Delta V/\Delta I)_{75}$ varied linearly with discharge from about 1.2 to 3 ohms up to 90% of capacity. Table I shows how these parameters vary with discharge for a typical cell. Nevertheless, as will be shown in results and discussion section, $(dV/dI)_{AC}$, taken at zero direct current, is a useful parameter when used in conjunction with $(\Delta V/\Delta I)_{75}$. However, $(dV/dI)_{AC}$ should be measured at frequencies above 6 kHz, since in that frequency region its value was found to be independent of current and frequency. Representative values of $(dV/dI)_{AC}$ at this frequency are shown in Table II. A similar observation has been made by others using a-c bridge measurements on dry cells (6) and storage cells (7) except that the minimum frequencies for constant results were lower, 3 and 2 kHz, respectively. In the present series of experiments, most of the a-c resistance measurements were made with a Wayne-Kerr B221 universal bridge and Q221 low-impedance adapter. These measurements were carried out with a sampling current of 2 mA at a frequency of 1592 Hz and are referred to as R_B . Above the cutoff frequency all a-c resistances measured by the authors, as well as those of Ref. (6) and (7), were independent of sampling current, and were, therefore, assumed to represent the true (6) internal resistance of the cell. The 0.5 kHz $(dV/dI)_{AC}$ measurements are useless but the 1.6 kHz R_B measurements are useful estimates of internal resistance.

Results and Discussion

It has already been stated that R_B essentially represents the internal resistance of the cell. The differential resistance $(\Delta V/\Delta I)_{75}$, which we consider to be a d-c measurement, is always larger than R_B , and can be analyzed as a series combination of the ohmic internal resistance of the cell and the current dependent polarization resistance at 75 mA (8-11). The polarization is associated both with exchanges of electrically charged particles between electrode and electrolyte and with changes in concentration of reacting molecules or ions in the vicinity of the electrode surfaces (8). The first component of polarization, which is known as the "transfer polarization," is dependent on the current density at the surface of an electrode and

therefore, for a given current, on the electrode's surface area. Since the area is usually related to the amount of active material present at a given time, it reflects the cell's state of charge. The second component or "concentration polarization" depends on the diffusion and reaction rates of the chemical constituents of the cell. Since these processes are also dependent on the amount of active material present, they must also reflect the state of charge of the cell. The internal ohmic resistance, however, may fail to reflect the state of charge of the cell due to offsetting changes in the resistance of the components of the cell (8).

Polarization occurs only when a current flows, and it increases with current. The sign of the polarization is such as to reduce the terminal voltage of a cell during discharge and, therefore, has the same effect as an added resistance. It would seem then, that since it is the polarization resistance, R_P , which varies most strongly with state of charge, it should be the best indicator. If R_B is approximately the internal ohmic resistance at all currents and $(\Delta V/\Delta I)_{75}$ is the d-c differential resistance, then $R_{PB} = (\Delta V/\Delta I)_{75} - R_B$ is an approximation to the polarization resistance at 75 mA. Since R_B is relatively insensitive to state of charge it might seem that its subtraction from $(\Delta V/\Delta I)_{75}$ is unnecessary. This is approximately correct for cells which have been drained at normal currents and have not been otherwise abused. For such cells $(\Delta V/\Delta I)_{75}$ varies linearly with total discharge Q throughout the life of the cell. This is illustrated in Fig. 4 where the nine normally used cells are seen to follow essentially the same relationship from which state of charge can be determined to within about 12%. The sharp change in slope at $Q \approx 3.3$ A-hr indicates the final stage of battery life by reflecting the dramatic increase in the internal resistance during that stage. Figure 5 contrasts the R_B 's for the two cells (A4 and A5) which had undergone abnormally high discharge currents with two of the cells which had been drained

Table II. Measurements made on cell B1 as a function of total discharge, Q . ΔT is the time elapsed from the end of a discharge to the start of the measurement.

ΔT (hr)	—	71	30	26	66	25	23
$(dV/dI)_{AC}^a$ (ohms)	0.869	0.811	0.775	0.714	0.833	0.796	0.777
$(\Delta V/\Delta I)_{75}^b$ (ohms)	1.39	1.48	2.00	2.25	2.77	3.07	3.08
R_B (ohms)	0.904	0.83	0.835	0.766	0.856	0.851	0.908
Q (A-hr)	0.711	1.30	1.95	2.34	2.95	3.28	—

^a $(dV/dI)_{AC}$ is sampled with an alternating current of 10 mA at 6.2 kHz.

^b $(\Delta V/\Delta I)_{75}$ is specified by a ΔV of 0.1V and a lower current value of 75 mA.

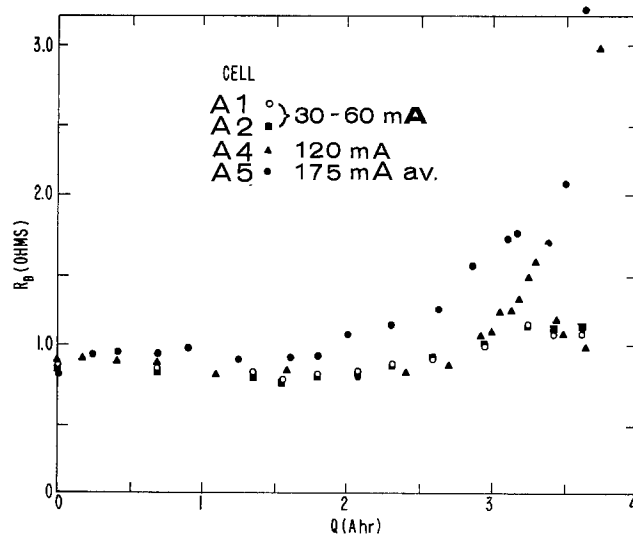


Fig. 5. A universal bridge measurement of the internal resistance of various cells vs. total prior discharge, Q .

normally. The difference is particularly striking for $Q > 1.5$ A-hr, the second half of cell life. Figure 6 illustrates how the plots of $(\Delta V/\Delta I)_{75}$ vs. Q for cells A4 and A5 differ from the dashed line which represents the average relationship followed by the other cells. That these differences are due to the aberrant behavior of R_B in cells A4 and A5 is easily corroborated by subtracting R_B from $(\Delta V/\Delta I)_{75}$ for all cells and replotting against Q as in Fig. 7. The loci of points representing cells A4 and A5 now merge with that obtained from the other cells and a single state-of-charge line valid for all cells results. This line is parallel to that defined in Fig. 4. Also, this revised curve shows a linear relationship that extends further into both the high and low Q regions. This is presumably because both the parametric dependence on discharge current and the small variations of R_B with lifetime have been subtracted from $(\Delta V/\Delta I)_{75}$. The simplicity and relative precision achieved by rendering the results in terms of the parameter $R_{PB} = (\Delta V/\Delta I)_{75} - R_B$ are manifest and justify the identification of R_{PB} with the polarization resistance of the cell at 75 mA. The discussion in the experimental section implies that $R_{Pd} = (\Delta V/\Delta I)_{75} - (dV/dI)_{AC}$ for an a-c frequency of 6 kHz would be a slightly better estimate of polarization resistance than R_{PB} . A comparison of the B cell scatter in Fig. 7 and 8 tends to confirm this, particularly at the upper values of Q . R_B must be

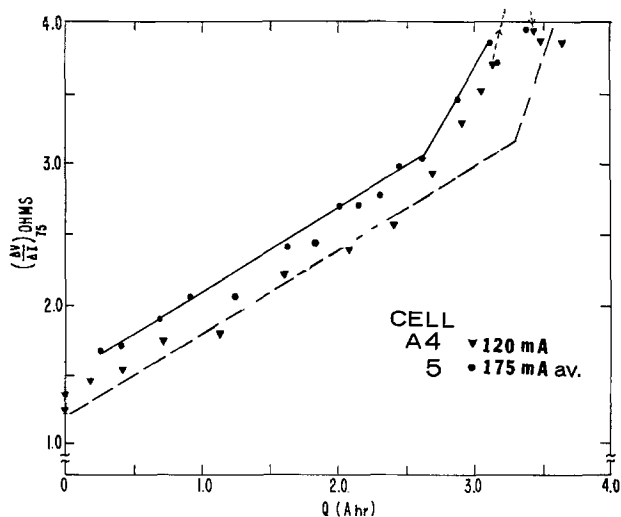


Fig. 6. Illustration of the deviation in $(\Delta V/\Delta I)_{75}$ for cells discharged at abnormally high currents from the dashed, normal state-of-charge graph defined in Fig. 4.

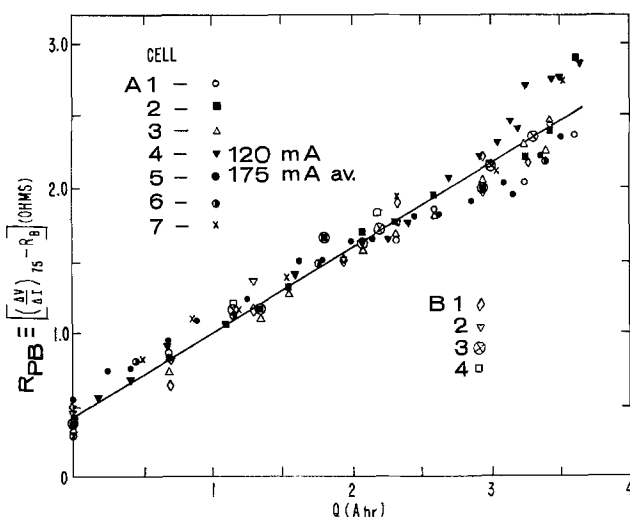


Fig. 7. An estimate of polarization resistance as a state-of-charge parameter which is valid even for abnormally high discharge rates.

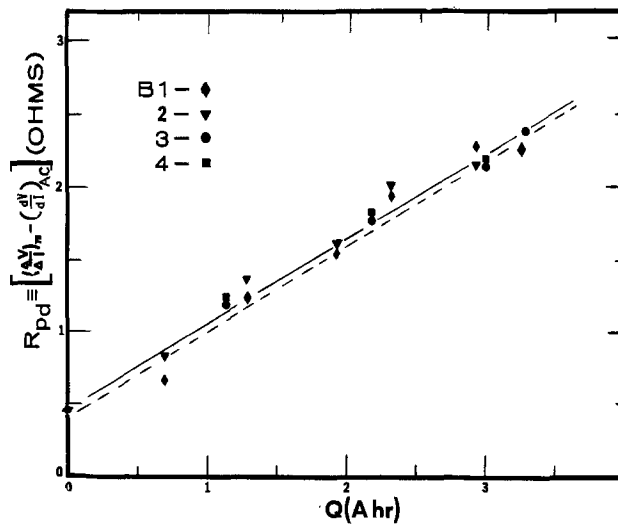


Fig. 8. A state-of-charge graph based on an improved estimate of polarization resistance.

relied upon as the estimate of the internal resistance of the A cells because in some cases no $(dV/dI)_{AC}$ measurements were made and in others the a-c frequency used was too low (0.5 kHz).

The B cells had been refrigerated at about 8°C for a few months then were left at room temperature for an hour before beginning the test sequence. These cells exhibited I-V curves which were unstable with respect to recycling of the test current. Successive cyclings (3 or 4) resulted in progressively steeper slopes (implying an increasing state of charge) until a stable value was reached. This stable value was then consistent with the $(\Delta V/\Delta I)_{75}$ of the other cells at full charge. This initial instability occurred only at full charge since the I-V curves showed good reproducibility upon recycling for all subsequent measurements. The result seems reminiscent of the gross effect that low temperature (0°C) storage had upon the calibration curves in the Sandia study. In our case, however, the problem is easily dealt with by running multiple I-V curves or by making provision for some preliminary cycling before $(\Delta V/\Delta I)_{75}$ is measured.

Conclusions and Recommendations

This report describes sensitive, readily instrumented and conducted state-of-charge measurements made on mercury cells. A linear relationship with a maximum experimental deviation of less than 10% of capacity was found to exist between the polarization resistance, R_P as approximated by $R_{Pd} = (\Delta V/\Delta I)_{75} - (dV/dI)_{AC}$ and the total expended charge, Q . For 90% of the data points the experimental deviation from the mean curve was less than 6%. When applying this procedure, it is advisable to make more than one cycle of the plot of the I-V curve to insure obtaining stabilized I-V curves of new cells when stored under possibly debilitating conditions. Successive cycling would also serve to eliminate irregularities which occasionally appear in the I-V curves, at least when the tracing is manually controlled. The adherence of all eleven cells tested to the same state-of-charge criteria despite having been subjected to a variety of discharges and storage environments suggests these criteria may have universal applicability. Further investigation of the limits of applicability by laboratories with the facilities and the need might be apropos.

Manuscript submitted April 23, 1975; revised manuscript received July 21, 1975.

Any discussion of this paper will appear in a Discussion Section to be published in the June 1976 JOURNAL. All discussions for the June 1976 Discussion Section should be submitted by Feb. 1, 1976.

Publication costs of this article were partially assisted by the U.S. Army.

LIST OF SYMBOLS

I or I_{BATT} current through the cell in mA
 V or V_{BATT} voltage across the cell in volts
 dV/dI or $(dV/dI)_{\text{AC}}$ the differential resistance of the cell as measured with a small a-c signal in the kHz range (in ohms)
 $(\Delta V/\Delta I)_{75}$ the slope of the I - V curve at 75 mA in ohms also referred to as effective differential d-c resistance
 R_{B} the internal resistance of the cell as measured with an impedance bridge (in ohms)
 Q the cumulative total number of A-hr of discharge
 R_{P} polarization resistance in ohms
 $R_{\text{PB}} \equiv (\Delta V/\Delta I)_{75} - R_{\text{B}}$ and $R_{\text{Pd}} \equiv (\Delta V/\Delta I)_{75} - (dV/dI)_{\text{AC}}$
 R_{PB} and R_{Pd} are experimental approximations to R_{P} and are in ohms.
 A cells are of type RM4R with a nominal EMF of 1.35V.
 B cells are of type RM4H with a nominal EMF of 1.40V.

REFERENCES

1. S. C. Levy and F. W. Reinhardt, SC-RR-70-332, Sandia Laboratories, Albuquerque, N.M., June 1970.
2. R. G. Easterling and S. C. Levy, SC-RR-70-33, Sandia Laboratories, Albuquerque, N.M., June 1970.
3. E. S. Brooks, Private communication.
4. M. Firshein, Private communication.
5. J. G. Adler and J. E. Jackson, *Rev. Sci. Instr.*, **37**, 1049 (1966).
6. G. W. Vinal, "Storage Batteries," 3rd ed., p. 328, John Wiley & Sons, New York (1940).
7. W. Willihnganz, *Trans. Electrochem. Soc.*, **79**, 253 (1941).
8. F. J. John, Paper 23, presented at Electrochemical Society Meeting, New York, N.Y., Sept. 29-Oct. 3, 1963.
9. F. Kornfeil, Private communication
10. J. J. McMullen and N. Hackerman, *J. Am. Chem. Soc.*, **106**, 328 (1959).
11. P. Delahay, "New Instrumental Methods in Electrochemistry," Interscience Publishers, Inc., New York (1954).

Diffusional Effects in Simulated Localized Corrosion

J. W. Tester¹*M.I.T. School of Chemical Engineering Practice, Oak Ridge National Laboratory, Oak Ridge, Tennessee 37830*and H. S. Isaacs*²*Metals and Ceramics Division, Oak Ridge National Laboratory, Oak Ridge, Tennessee 37830*

ABSTRACT

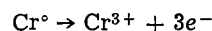
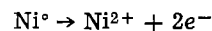
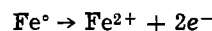
The importance of diffusion was investigated under potentiostatic dissolution conditions with wire electrodes contained in inert supports. The artificial cavities created simulated localized corrosion conditions. Current-time behavior at voltages in excess of the critical pitting potential [$>0.5V$ (SCE)] was examined for nickel and stainless steel specimens in concentrated chloride solutions. The effect of changing the concentration or activity gradient of the dissolving metal cations within the artificial cavity was studied by altering the composition of the bulk solution. Solutions of FeCl_2 , NiCl_2 , CrCl_3 , LiCl , NaCl , MgCl_2 , and CeCl_3 ranging from 0.5 to 10M were used. Mass transfer models were developed for the observed transient and quasi steady-state periods of dissolution.

Localized corrosion can be divided into various stages representing initiation and subsequent dissolution of a metal. Pitting corrosion has been divided into three stages: pit initiation, early growth, and the formation of a stable pit. In the third stage, when the pit becomes sufficiently large, conditions and processes taking place are closely related to those occurring in crevice corrosion. Earlier work (1-3) has suggested that the third stage of dissolution is controlled by diffusion within the occluded cell. Measurements of the rate of corrosion are usually complicated by changing surface areas. To overcome this difficulty, wire electrodes were used to simulate these conditions in the present study. The factors involved during diffusion-controlled stages within localized anodes were investigated and related to the properties and composition of the bulk electrolyte solution. Austenitic stainless steel, nickel, iron, and dilute nickel alloys were studied to emphasize various aspects of the diffusion process.

Mass Transfer Considerations

Localized corrosion is simulated under conditions where the geometry of the system is specified in order

that diffusional models can be tested. Basically, wire test specimens are mounted in an inert matrix with one cross-sectional surface exposed to the aqueous Cl^- environment (see Fig. 1). Anodic dissolution of the metal is studied under potentiostatic conditions above the critical pitting potential. The actual dissolution begins with pitting and undermining of the passive oxide film on the metal surface followed by pit growth until the entire cross-sectional area of the metal is dissolving. With an active surface developed each elemental constituent of the alloy undergoes oxidation to form a soluble ionic species, viz.



These ions dissolve under activation polarization control and are free to undergo hydration reactions with water (4) or form complexes with Cl^- ions, but in any case the concentration of each species will begin to increase because of a diffusional limitation between the metal-solution interface and the bulk solution (over distance $l + \Delta$ in Fig. 1). The ionic concentrations (Fe^{2+} , Ni^{2+} , or Cr^{3+}) will continue to increase until a saturation or slightly supersaturated condition exists with respect to the chloride or hydroxychloride complex of that cation. Isaacs (1) has shown that a

* Electrochemical Society Active Member.

¹ Present address: Q-22, Los Alamos Scientific Laboratory, Los Alamos, New Mexico 87544.² Present address: Brookhaven National Laboratory, Upton, New York 11973.

Key words: pitting, mass transfer, stainless steel, anodic dissolution, chloride layer, nickel.

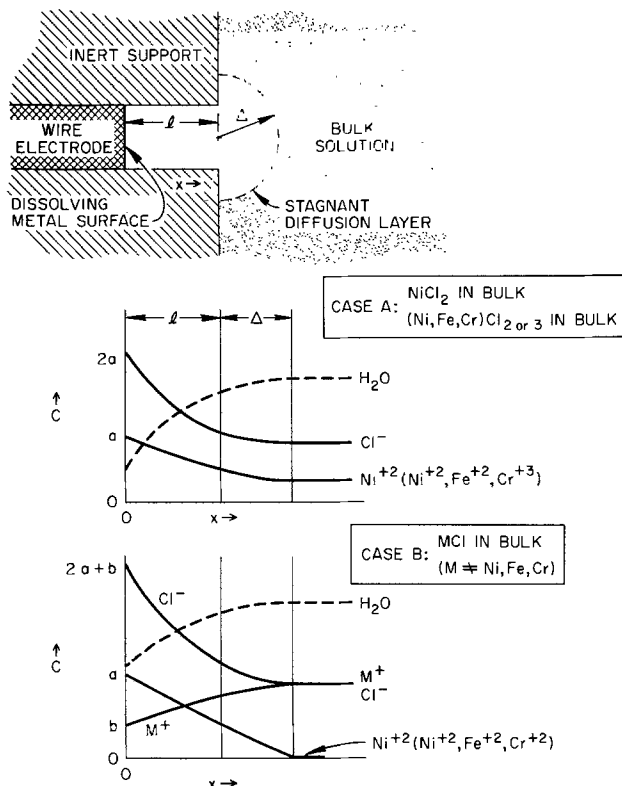


Fig. 1. Artificial pit model geometry (cross-sectional view) with qualitative concentration profiles illustrated schematically (scales arbitrary).

resistive layer (presumably metal chloride) then precipitates on the surface. The chloride layer displays ohmic resistance which is controlled by its thickness. During a steady dissolution period, a current equal to the diffusion flux in the solution passes through the layer. The current is determined by the ratio of the potential to resistance which is itself specified by the layer resistivity and thickness. A rapid increase in potential, for example, increases the potential across the layer and is followed by a transient increase in current. The increased flow of ions in the layer causes additional precipitation since the diffusion flux remains effectively independent of applied potential. As the thickness of the layer increases the potential gradient decreases along with the current. Once the chloride layer has formed, it displays a self-regulating effect in balancing the layer current with the diffusional flux in solution (1).

The presence of the layer and the diffusion control define the third stage of localized anodic dissolution, which may be described as a quasi steady state, whereby cations diffuse down a concentration gradient in an aqueous solution. The concentration difference is between the saturated value at the chloride film/solution interface ($x = 0$) and the bulk electrolyte, the distance between which ($x = l + \Delta$) is composed of the depth of the wire (l) in the case of a wire-type electrode and stagnant diffusion layer (Δ).

The diffusional limitations of two types of systems are illustrated by the concentration profiles presented in Fig. 1. Consider case A with a nickel wire dissolving and NiCl_2 in the bulk solution. The Ni^{2+} concentration decreases from the saturation concentration (a) at the metal surface ($x = 0$) to the bulk concentration at $x = l + \Delta$. A similar trend can be drawn for Cl^- by applying electroneutrality at any point in the solution. These same ideas can be applied to the localized corrosion of stainless steel, where three ions (Ni^{2+} , Fe^{2+} , and Cr^{3+}) will be diffusing away from the interface. An important example to note in case A is that by increasing only one component of the stainless steel dissolution product the

concentration gradient of this component may be decreased, while those of the other components remain the same. If, however, this component is one that predominates in the composition of the chloride film, this would lead to a decreased dissolution rate. If the component does not precipitate to form the chloride layer, increasing its concentration will have no direct effect on the dissolution rate.

Case B illustrates the concentration profiles for a second type of experiment. In this case, either stainless steel or nickel is anodically dissolved in an uncommon cation (M^+) Cl^- solution, e.g., LiCl or NaCl . The Ni^{2+} , Fe^{2+} , or Cr^{3+} ion concentration again varies from the saturation concentration at the metal surface ($x = 0$) to zero at $x = l + \Delta$. The Cl^- ion concentration profile can again be represented by electroneutrality with M^+ , Ni^{2+} , Fe^{2+} , and Cr^{3+} ions present. The slight decrease in M^+ from $x = l + \Delta$ to the interface at $x = 0$ is due to a resistance in diffusing toward the metal surface.

Mass transfer models were developed for the early or transient period and the quasi steady-state period of the corrosion process. In either case information concerning the transport properties of the electrolyte solution was required. Specifically, both the dependence of the diffusion coefficient and viscosity on the composition of the solution within the pit should be known. In addition, equilibrium properties, including the solubility and activity coefficient dependence of NiCl_2 , FeCl_2 , and CrCl_3 on the ionic strength of the solution, are important in determining suitable driving forces for the diffusional processes.

In our experiments, current measurements were made and can be used with Faraday's law to determine mass fluxes. For a constant cross section of wire, the cation mass flux \dot{N} from the interface can be represented as

$$\dot{N} = i/A_n\mathbf{F} \quad [1]$$

In addition, the length of wire dissolved during the course of the experiments is given by

$$l = \int_0^t \frac{M_w}{A_n\mathbf{F}\rho_0} i dt \quad [2]$$

The positive ion current produced in the oxidation reaction occurring at the metal surface will diffuse through the solution under the influence of two driving forces, namely, concentration gradient and potential gradient, as shown in the Nernst-Einstein equation

$$\frac{i}{A_n\mathbf{F}} = -D \left[\frac{\partial C}{\partial x} + \frac{C}{RT} \frac{\partial \Phi}{\partial x} \right] \quad [3]$$

The potential gradient in solution has been shown to be unimportant for the cases being considered (1, 2). In potentiostatic dissolution experiments at fixed voltages from 0.2 to 1V (SCE), Isaacs (1) has shown that almost all the potential drop is contained in a thin resistive layer adjacent to the anode. Frankenthal and Pickering (5) observed similar results showing negligible potentials in solution but attributed the large ohmic drop at the metal-solution interface to the presence of hydrogen bubbles. No bubbles were observed with any of the wire anode systems used in our studies. Therefore, Eq. [3] simplifies to

$$\frac{i}{A_n\mathbf{F}} = -D \frac{\partial C}{\partial x} \quad [4]$$

In the cases that follow, cation concentration (or activity) was used as the driving force for diffusion, and all transport properties including D and viscosity μ were assumed constant and uniform. The importance of these effects is discussed later in this paper.

Initial transient period.—During this early period of dissolution, the wire electrode surface is flush with the surface of the cavity ($l = 0$) and semi-infinite

geometries can be used to model the diffusional process that causes the electrolyte concentration to increase at the metal surface. Basically, the time required to reach saturation at the surface can be estimated from a transient model of this type. However, complex factors are operative. The nucleation of active dissolution sites on the wire surface is a microscopic phenomenon with respect to the total cross-sectional area of the wire. Many pits are nucleating and growing on the surface simultaneously. Since only the total current is measured, it would be misleading to assume that the actual current density (i/A) should be based on the total cross-sectional area during this early period when a significant fraction of the surface is not actively dissolving. The current increases as the actively dissolving area of the wire increases until the whole cross section is active and a decreasing current is observed as the system becomes diffusion controlled.

With the current density at the active site known, the mass flux can be specified (Eq. [1]) and used as a boundary condition to solve the transient diffusion equation, which expresses concentration as a function of time and distance into the liquid. Hemispherical and cylindrical geometries of semi-infinite extent were selected to approximate the stagnant liquid diffusion field surrounding the exposed wire surface (see Fig. 1). However, the analysis given in the Appendix closely approximated the observed periods taken to reach the maximum current.

Quasi steady-state period.—Once saturation of the dissolving cation species j occurs at the metal-solution interface (Fig. 2) after the initial period, a quasi steady-state period of diffusional control commences. The situation may be expected to be complex since the interface is actually moving as it recedes into the inert support. Assuming no potential dependence, a transient model involving unidirectional diffusion into a semi-infinite stagnant liquid with a moving boundary was solved and indicated that the measured current $i(t)$ should vary inversely with the square root of time, \sqrt{t} . Booth (6) and Danckwerts (7) suggest criteria that can be applied to decide if a quasi steady-state assumption is reasonable. By calculating l^2/D [$\approx (0.01 \text{ cm})^2/10^{-5} \text{ cm}^2/\text{sec} = 10 \text{ sec}$] and comparing it with typical experimental time periods of 1000 sec, the transient term can be eliminated without significant error. Under these conditions, the effect of a moving boundary on the diffusional flux is unimportant.

This simplified model was introduced earlier by Isaacs (1) and is reviewed briefly here. Essentially the current density i/A is specified by the Nernst-Einstein equation, Eq. [4], neglecting the mobility term and assuming a linear concentration gradient

$$\frac{i}{A} = \frac{nFD(C^S_j - C^B_j)}{l + \Delta} \quad [5]$$

where l , the length of dissolved wire, and Δ , the boundary layer thickness in the solution, constitute the total diffusion path. Substituting Faraday's law, Eq. [2], into Eq. [5] and integrating between $i = i_0$ at $t = \tau \approx 0$ and $i = i$ at $t > \tau \approx 0$ yields

$$\left(\frac{i}{A}\right)^{-2} = \left(\frac{i_0}{A}\right)^{-2} + \frac{2M_w t}{n^2 F^2 \rho_0 D (C^S_j - C^B_j)} \quad [6]$$

Equation [6] indicates that the current density varies inversely with \sqrt{t} , the identical result obtained for the moving boundary model. In addition, Eq. [6] can be used as a basis for interpreting our experimental current-time results. A plot of $(i/A)^{-2}$ vs. t should be linear, and the reciprocal slope $1/S$

$$S = \frac{d(i/A)^{-2}}{dt} \quad [7]$$

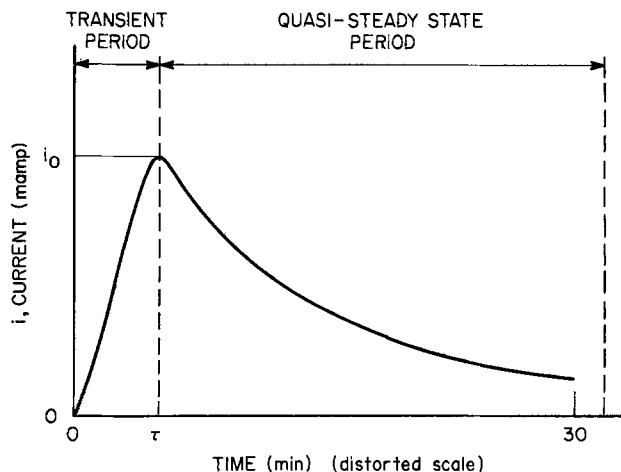


Fig. 2. Current-time plot showing periods of dissolution

should be directly related to the product of diffusivity D and the driving force $(C^S_j - C^B_j)$.

Apparatus and Procedure

Wire electrodes (~ 0.09 cm in diameter) were embedded in inert polytetrafluoroethylene supports to ensure that a constant cross-sectional area would be exposed to the Cl^- solution throughout the experiment. Initially the surface was mechanically polished with 600 grade emery to the outer surface of the inert support ($l = 0$, Fig. 1). A Wenking potentiostat was used to apply a fixed voltage between the wire test electrode and a saturated calomel reference electrode (SCE). The current was measured in another circuit with an auxiliary platinum electrode as the cathode and the test specimen as the anode. Applied potentials were 0.5-1V, far above the critical pitting potentials for any of the metal chloride systems examined. A Hewlett-Packard Model 700-4A recorder monitored the current as a function of time (Fig. 2) for 20-30 min.

Experiments were performed with aqueous metal chloride solutions at 22°C over concentrations from 0.5 to 10M. Both common-cation (FeCl_2 , NiCl_2 , and CrCl_3) and uncommon-cation (LiCl , NaCl , MgCl_2 , and CeCl_3) halide salts were used. In cases where viscosity data were not available a Brookfield synchroelectric viscometer was used to measure values over the solution concentrations studied.

The differences between the two kinds of experiments conducted with common and uncommon cations is illustrated by cases A and B in Fig. 1. In case A, the over-all driving force for mass transfer $(C^S_j - C^B_j)$ could be altered by changing C^B_j ($j = \text{Ni}$, Fe , or Cr) as a chloride in the bulk solution, and because all the ions are common to the metal dissolving, C^S_j will be a function of only temperature. Alternatively, in case B, C^B_j is always zero in the bulk solution and increases to a saturation value corresponding to the presence of uncommon cations (Li , Na , Ce , Mg), which alters the Cl^- activity by changing the Cl^- concentration and mean activity coefficient of the dissolving cation electrolyte.

Results and Discussion

Calculational procedures and data summary.—To evaluate the mass transfer model, the slope of reciprocal squared current density, $(i/A)^{-2}$, plotted vs. time t (Eq. [6] and [7]) must be determined from the raw data in the form of current i as a function of time t . A typical set of data is shown in Fig. 3, where the current density is plotted as a continuous function and $(i/A)^{-2}$ plotted from discretely selected points. During some runs, the data show abrupt changes in i over small time periods, especially during the early part of a run when microscopic pit growth is occurring. In most cases, two or three runs at the same set of conditions were sufficient for reproducible slopes; however, when sporadic i - t behavior was observed runs

Table I. Experimental results for Type 304 stainless steel
0.5V (SCE), 22°C, 0.076-cm-diam wire

Concentration (M)	$1/S \text{ (A}^2 \text{ sec/cm}^4) = \left[\frac{d(i/A)^{-2}}{dt} \right]^{-1}$					
	Chloride used					
	FeCl ₂	NiCl ₂	CrCl ₃	NaCl	LiCl	MgCl ₂
0.5	77 ± 4	100 ± 6	77 ± 5			
1.0	77 ± 4	77 ± 4	71 ± 4	100 ± 7	91 ± 5	
1.33			53 ± 3			
1.5		56 ± 5				
2.0	56 ± 3	40 ± 6				46 ± 2
2.5					71 ± 4	
3.75		6.7 ± 0.5				2.4 ± 0.2
4.0				77 ± 4	58 ± 3	
5.0					24 ± 1	
7.5					14.7 ± 0.1	
10.0					2.4 ± 0.1	

were repeated. For pure nickel wire in 1M LiCl solutions up to six runs were performed. For the low concentration chlorides, e.g., 0.5M NiCl₂, 0.5M FeCl₂, and 0.5M CrCl₃, up to six runs were also required.

Slopes were calculated by a least square regression applied to discrete values of $(i/A)^{-2}$ taken over the time interval of interest ($\tau < t \leq 20\text{-}30$ min, Fig. 2). Error bounds for the reciprocal slope are based on a 95% confidence level fit of the data averaged over the

runs used. The entire set of reciprocal slopes is summarized in Tables I and II for experiments with Type 304 stainless steel (nominal composition Fe 70%, Ni 9%, Cr 18.6%, and C + Mn + Si + Cu + S <3%) and nickel-rich alloy Ni-61 (nominal composition Ni 96%, Mg 0.3%, Fe 0.1%, Si 0.4%, Ti 3%).

Effect of applied voltage.—Earlier experiments on stainless steels demonstrated that the slope $S = d(i/A)^{-2}/dt$ was not affected by changing the applied voltage from 0.35 to 0.85V (SCE). Furthermore, the impedance characteristics of the wire surface strongly suggested that a thin (100Å) layer having a resistivity of approximately 10^8 ohm-cm exists throughout the quasi steady-state period. The potential drop across the resistive layer itself accounts for over 95% of the total voltage drop.

Additional measurements were made at fixed potentials of 0.5, 0.8, and 1V (SCE) for both Type 304 stainless steel and Ni-61 wire electrodes in solutions of identical electrolyte composition. In all cases, the variation of the slope S was within the statistical scatter of the data which again showed rates independent of potential for both stainless steel and nickel. It may also be mentioned that a few measurements with iron wires showed a similar behavior. In addition, step changes in voltage during a run indicated similar slopes after the transient perturbations had damped out. This effect also illustrates the importance of diffusion in controlling the self-regulating nature of the layer's thickness in which the layer adjusts its ohmic resistance to support the cation flux away from the interface (1).

Mass transfer effects during the quasi steady-state period.—The observed linear behavior of reciprocal squared current density, i/A^{-2} , as a function of time t supports the mass transfer model and is consistent with measurements by Novakovski and Sorokina (2) on a similar system. Equation [6] indicates that $1/S$ should vary as $D(C^S_j - C^B_j)$. If the diffusivity were constant, then for the runs with nickel wire in a NiCl₂ solution, $1/S$ should vary linearly with C^B_j since C^S_j is constant. In Fig. 4, the data from Table II are

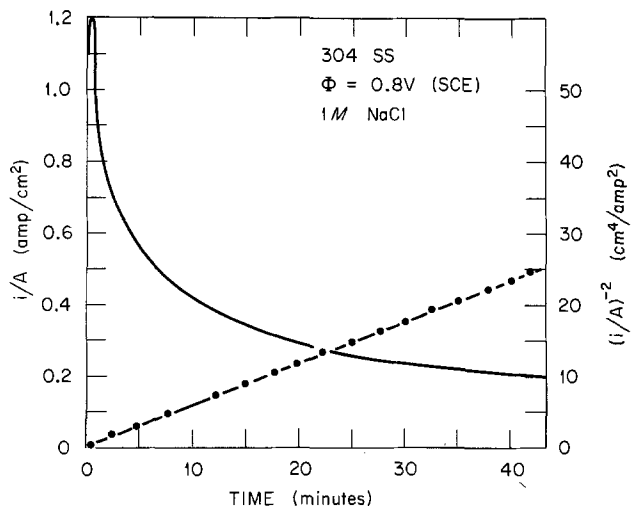


Fig. 3. Experimental current density as a function of time for a Type 304 stainless steel electrode in a 1M NaCl solution.

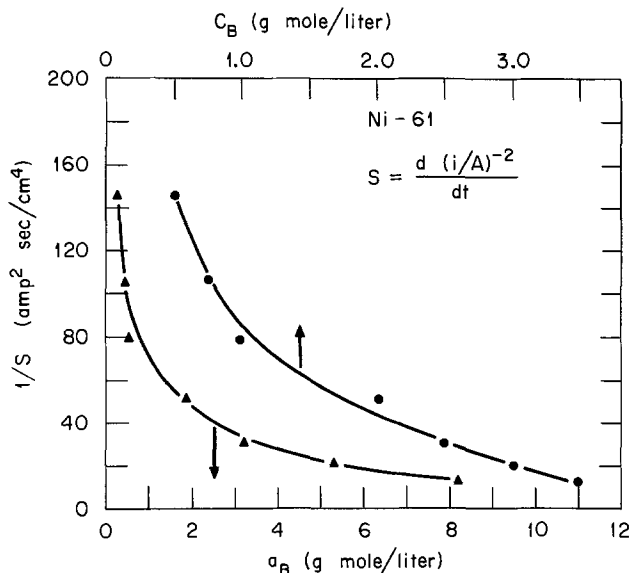


Fig. 4. Common metal cation effect: reciprocal slope $1/S = [d(i/A)^{-2}/dt]^{-1}$ as a function of bulk NiCl₂ concentration and activity for nickel dissolution.

Table II. Experimental results for nickel alloy Ni-61
0.5V (SCE), 22°C, 0.088-cm-diam wire

Concentration (M)	$1/S \text{ (A}^2 \text{ sec/cm}^4) = \left[\frac{d(i/A)^{-2}}{dt} \right]^{-1}$			
	Chloride used			
	NiCl ₂	LiCl	MgCl ₂	CeCl ₄
0.5	145 ± 9		134 ± 4	115 ± 4
0.75	106 ± 5			
1.0	79 ± 4	163 ± 24		62 ± 3
2.0	51 ± 2	80 ± 4		32 ± 3
2.25			57 ± 4	
2.5	30 ± 2	81 ± 3		
3.0	20 ± 1	63 ± 3	23.5 ± 1	
3.5	12.7 ± 0.6			
4.0		49 ± 1		
5.0		35 ± 1		
6.0		23.5 ± 0.9		

plotted over a concentration range from 0.5 to 3.5M NiCl₂ and are not linear. The nonlinear behavior shows that Eq. [6] is an approximation and variations not yet considered are brought about by the change in the bulk solution concentration. The first possible improvement incorporates activity rather than concentration as the driving force, where

$$a_{Ni^{2+}} = \gamma_{\pm} C_{Ni^{2+}} \quad [8]$$

The mean ionic activity coefficients, γ_{\pm} , were taken from experimental data tabulated by Harned and Owen (8) and extrapolated to higher concentrations by the techniques suggested by Meissner and Tester (9). Unfortunately, no further improvement was obtained (Fig. 4).

Viscosity effects on the diffusion coefficient were found to be significant. Although theoretical correlations for predicting D in concentrated electrolytes are limited (8,10) several empirical rules can easily be applied. The diffusivity can be expressed in terms of the solution's viscosity η_r relative to pure water at the same temperature and activity coefficient γ_{\pm} as (10)

$$D = \frac{D^{\circ}}{\eta_r} \left(1 + m \frac{d \ln \gamma_{\pm}}{dm} \right) \quad [9]$$

An integral diffusion coefficient can then be defined as

$$\frac{1}{C^{S_j} - C^{B_j}} \int_{C^{B_j}}^{C^{S_j}} D dC_j \quad [10]$$

such that the form of Eq. [5] is preserved with D' replacing D . By substituting Eq. [9] into Eq. [10] one can express D' as a function of D° , η_r , and γ_{\pm}

$$D' = \frac{D^{\circ}}{(C^{S_j} - C^{B_j})} \left[\int_{C^{B_j}}^{C^{S_j}} \left(1 + m \frac{d \ln \gamma_{\pm}}{dm} \right) \frac{dC_j}{\eta_r} \right] \quad [11]$$

To calculate D' requires knowledge of γ_{\pm} and η_r as functions of C . This information is usually known for pure aqueous solutions of a single electrolyte over a limited concentration range (8,11). In the preliminary analysis, the equation was simplified to permit integration using a linear expression for the viscosity and neglecting the γ_{\pm} term. For example, for a 4M solution of FeCl₂ at 25°C η_r is approximately 8. For a mixed electrolyte consisting of the dissolving cations (Ni²⁺, Fe²⁺, and/or Cr³⁺) and possibly uncommon cations (Li⁺, Na⁺, Mg²⁺, etc.) along with the Cl⁻ ions present, the relative viscosity can be approximated as a linear combination of all species present

$$\eta_r = 1 + \sum b_j C_j \quad [12]$$

where b_j is a constant dependent on the properties of component j . Simplifying the relationship further we assume the dissolving metal cation and uncommon cation can be divided into two terms

$$\eta_r \approx 1 + bC_j + b^*C^* \quad [13]$$

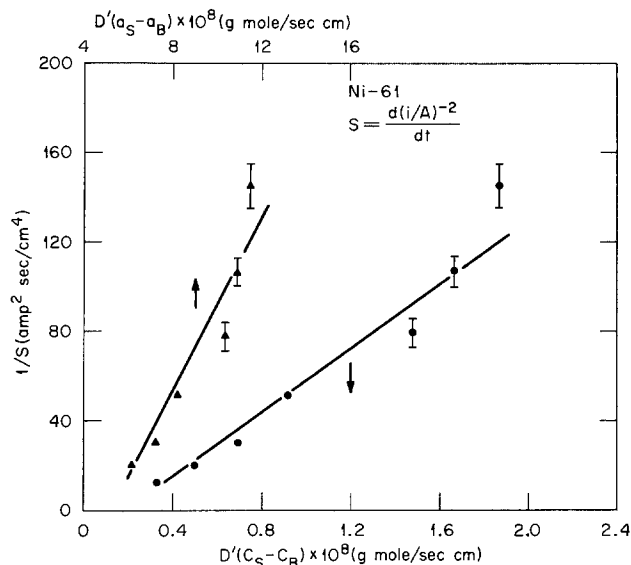


Fig. 5. Common metal cation effect: reciprocal slope $1/S = [d(i/A)^{-2}/dt]^{-1}$ as a function of the product of the integral diffusion coefficient, D' , and the concentration and activity driving forces ($C^S - C^B$) and $(a^S - a^B)$ for nickel dissolution.

where C_j is the total concentration of dissolving cations as chlorides and C^* is the concentration of the uncommon cations as chlorides. With these simplifications, Eq. [11] can be expressed as

$$D' = \frac{D^{\circ}}{(C^{S_j} - C^{B_j})} \int_{C^{B_j}}^{C^{S_j}} \frac{dC_j}{1 + bC_j + b^*C^*} \quad [14]$$

Integrating with C^* assumed constant gives

$$D' = \frac{D^{\circ}}{b(C^{S_j} - C^{B_j})} \ln \left(\frac{1 + bC^{S_j} + b^*C^*}{1 + bC^{B_j} + b^*C^*} \right) \quad [15]$$

which is essentially a log mean. By using Eq. [15] to replace D in Eq. [6], one can correct D for viscosity changes and then correlate $1/S$ with $D'(C^{S_j} - C^{B_j})$ or with $D'(a^{S_j} - a^{B_j})$ (see Fig. 5). For nickel wire in NiCl₂ solutions, the relationship is linear within the accuracy of the points given; however, no further improvement is apparent if activity rather than concentration is used as the driving force. For this case a value of $D^{\circ} = 1.29 \times 10^{-5}$ cm²/sec was used for the diffusivity of NiCl₂ in dilute solutions, and the viscosity coefficient $b = 0.86$ liter/mole was obtained from a plot of the viscosity data in Table III by using a linear approximation between concentrations C^{B_j} and C^{S_j} . In addition, the C^* term was zero since no uncommon cations were present.

The same improvement in the $1/S$ vs. $D(C^{S_j} - C^{B_j})$ correlation appeared when the Type 304 stainless steel data were used. However, several additional approxi-

Table III. Viscosity and density values of aqueous chlorides (22°C)

Concentration (M)	Relative viscosity, η_r				ρ , density, g/cm ³			
	LiCl ^(b)	NiCl ₂	MgCl ₂ ^(b)	CeCl ₃	LiCl	NiCl ₂	MgCl ₂	CeCl ₃
0.5		1.26	1.20	1.18		1.08	1.03	1.11
0.75		1.34				1.10 ^(c)		
1.0	1.14	1.49		1.69	1.02 ^(c)	1.12		1.22
2.0	1.29	2.31		3.88	1.05	1.23		1.42
2.25			7.49				1.13	
2.5	1.40	2.96			1.06 ^(c)	1.29 ^(c)		
3.0	1.48	3.84	3.35		1.07	1.35	1.20	
3.5		5.04				1.40 ^(c)		
4.0	1.72				1.09			
5.0	1.97				1.11 ^(c)			
6.0	2.33				1.14			

^(a) Relative to pure water at 22°C.

^(b) Ref. (13).

^(c) Estimated.

mations have to be made concerning the average valence n (Eq. [6]) and saturation concentration for the mixture of dissolving cations (Fe^{2+} , Ni^{2+} , and Cr^{3+}). In this case we assumed weighted average values for stoichiometric dissolution for the given alloy composition. Using FeCl_2 , CrCl_3 , and NiCl_2 from 0.5 to 2M showed no preferential effect for any one cation. This area does deserve further attention.

Because of a chloride common ion effect, saturation concentrations of NiCl_2 decrease as the bulk LiCl concentration increases. Figures 6 and 7 show these effects for nickel samples in LiCl solutions up to 6M. In this case the bulk concentration of Ni^{2+} was essentially zero. Values of C^S_j were tabulated by Linke and Seidell (12), and viscosity coefficients ($b^* = 0.20$ liter/mole and $b = 0.86$ liter/mole) were obtained from the data given in Table III. D° was specified as 1.29×10^{-5} cm^2/sec . As seen in Fig. 6 the curvature and uncertainty are quite pronounced at LiCl concentrations below 3M. Using the viscosity corrections as before and ne-

glecting the 1M LiCl point since pit initiation was sporadic for this case yielded an improved correlation between $1/S$ and $D'C^S_j$ (Fig. 7).

An attempt was made to correlate the LiCl runs for both 304 stainless steel and nickel. The Ni-61 data were plotted as before, and the stainless steel data were modified by incorporating the effects of LiCl on the solubility of the precipitated chloride as a weighted average based on the stoichiometry of the alloy and experimental data for NiCl_2 and FeCl_2 in the presence of LiCl . The resulting correlation is shown in Fig. 8 and is notably linear over a concentration range up to 10M.

Another verification of the mass transfer model is obtained by comparing the actual value of the reciprocal slope ($1/S$) with the theoretical value (Eq. [6])

$$\frac{1}{S'} = \frac{1}{S(C^S_j - C^{B_j})D'} = \frac{n^2 F^2 \rho_0}{2M_w} \quad [16]$$

For the nickel specimens: $\rho_0 = 8.9$ g/cm^3 , $n = 2$, $F = 96,500$ coulombs/equivalent, and $M_w = 58.7$ for Ni^{+2} . Therefore, $1/S' = 0.28 \times 10^{10}$ $\text{A}^2 \text{ sec}^2 \text{ cm}^{-3} \text{ mole}^{-1}$. An experimental $1/S'$ value for the case of NiCl_2 as the bulk electrolyte was 0.60×10^{10} $\text{A}^2 \text{ sec}^2 \text{ cm}^{-3} \text{ mole}^{-1}$ and with LiCl as the bulk electrolyte 0.34×10^{10} $\text{A}^2 \text{ sec}^2 \text{ cm}^{-3} \text{ mole}^{-1}$ at $D'(C^S_j - C^{B_j}) \approx 1.2 \times 10^{-8}$ $\text{mole sec}^{-1} \text{ cm}^{-1}$.

One further refinement was introduced by graphically evaluating the integral of Eq. [11] to approximate D' for effects of both viscosity and γ_{\pm} . Values of η_r were used from Table III, and the derivative $d \ln \gamma_{\pm}/dm$ was calculated at discrete points by use of experimental data (8) and the empirical charts of Meissner and Tester (9). Only minor improvement was obtained in the correlation.

In conclusion, it has been shown that the major premise of a quasi steady-state period of dissolution being mass transfer controlled is correct. The influence of the type and concentration of chloride salt used for localized corrosion tests of nickel-base and stainless steel alloys can be predicted on the basis of the diffusion model. At low concentrations (less than about 3M Cl^-) all chloride salts should behave similarly and show little concentration dependence. The high concentrations in the localized anode's anolyte itself will dominate the concentration differences and dissolution rates. At intermediate concentrations (around 5M Cl^-), the solubilities of the dissolving chloride layer will be markedly influenced by the chloride activity and its effect on reducing the solubility of the dissolv-

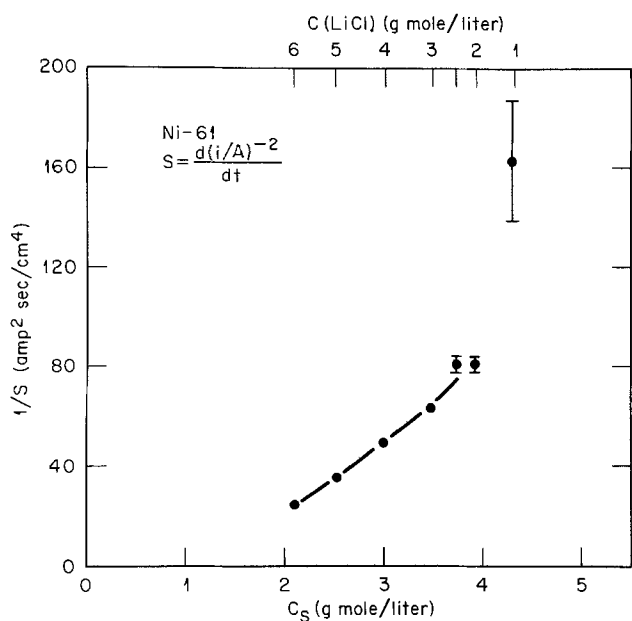


Fig. 6. Uncommon cation effect: reciprocal slope $1/S = [d(i/A)^{-2}/dt]^{-1}$ as a function of NiCl_2 saturation concentration C^S in the presence of LiCl solutions for nickel dissolution.

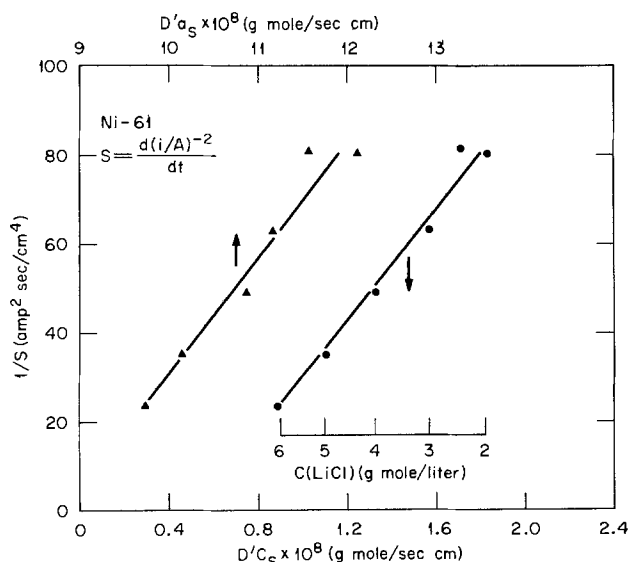


Fig. 7. Uncommon cation effect: reciprocal slope $1/S = [d(i/A)^{-2}/dt]^{-1}$ as a function of the product of the integral diffusion coefficient D' , and the saturation concentration or activity of NiCl_2 (C^S or α^S) for nickel dissolution.

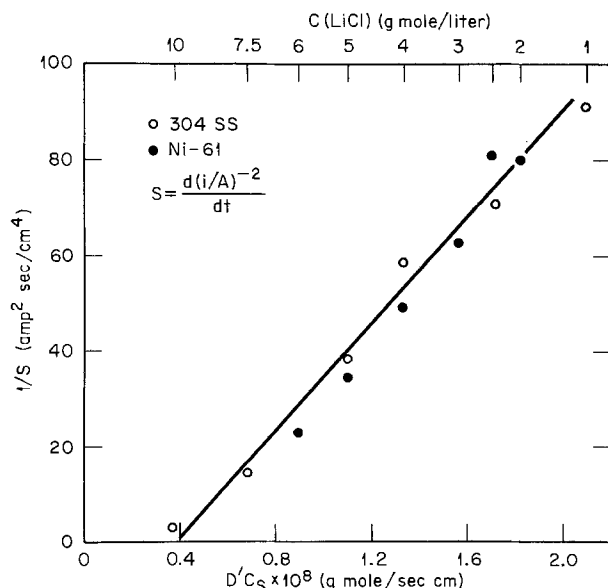


Fig. 8. Uncommon cation effect: reciprocal slope $1/S = [d(i/A)^{-2}/dt]^{-1}$ as a function of the product $D'C^S$ for Type 304 stainless steel and nickel dissolution.

ing metals. At high chloride concentrations the viscosity plays a major role in reducing the diffusion rates; hence the resulting dissolution rates will decrease with increased viscosity of the chloride solution.

Summary

1. Current-time behavior during the quasi steady-state period indicates that anodic dissolution during this period is controlled by diffusion with a concentration driving force ($C_j^S - C_j^B$).

2. Correcting the diffusion coefficient for viscosity was necessary for accurate interpretation of the mass-transfer model. For the solutions and metals studied, activity and concentration driving forces showed similar results when used in the diffusion model.

3. The chemistry at the metal-solution interface, in particular the effect of foreign ions in influencing C_j^S , is important in establishing the rate of dissolution.

Acknowledgments

The authors wish to thank the participants in the M.I.T. School of Chemical Engineering Practice for their assistance in collecting experimental data, especially S. A. Jones, J. J. Isenbeg, R. Blanchard, Y. N. Ganju, and A. M. Tschyrkow. Special thanks go to H. R. Greenberg and R. M. Mayer for their interest in the theoretical aspects of the paper. This research was sponsored by the U. S. Atomic Energy Commission under contract with Union Carbide Corporation.

Manuscript submitted Dec. 2, 1974; revised manuscript received June 9, 1975.

Any discussion of this paper will appear in a Discussion Section to be published in the June 1976 JOURNAL. All discussions for the June 1976 Discussion Section should be submitted by Feb. 1, 1976.

Publication costs of this article were partially assisted by Oak Ridge National Laboratory.

APPENDIX

Initial Transient Period Model

As a first approximation, the current density and diffusion coefficient during this induction period are assumed constant over the entire surface of the wire. The diffusion equations become

hemispherical geometry

$$D \left(\frac{\partial^2 \xi}{\partial r^2} + \frac{2}{r} \frac{\partial \xi}{\partial r} \right) = \frac{\partial \xi}{\partial t} \quad [\text{A-1}]$$

cylindrical geometry

$$D \left(\frac{\partial^2 \xi}{\partial x^2} \right) = \frac{\partial \xi}{\partial t} \quad [\text{A-2}]$$

where ξ_j is a dimensionless concentration

$$= \frac{C_j(x \text{ or } r, t) - C_j^B}{C_j^S} \quad [\text{A-3}]$$

For this system both initial and boundary conditions can be specified.

Initial condition

$$\left. \begin{array}{l} C_j(x \text{ or } r, t) = C_j^B \\ \xi_j = 0 \end{array} \right\} \text{at } t = 0 \\ \text{all } x \text{ or } r \quad [\text{A-4}]$$

Boundary conditions

$$\left. \begin{array}{l} 1. \text{ Prescribed flux} \\ -D \frac{\partial C_j}{\partial(x \text{ or } r)} = \frac{i(t)}{An_j F} \\ -D \frac{\partial \xi_j}{\partial(x \text{ or } r)} = \frac{i(t)}{An_j F} \frac{1}{C_j^S} = f \end{array} \right\} \begin{array}{l} x = 0, r = r_0 \\ t > 0 \end{array} \quad [\text{A-5}]$$

2. Semi-infinite approximation

$$\left. \begin{array}{l} C_j(x \text{ or } r, t) = C_j^B \\ \xi_j = 0 \end{array} \right\} \text{at } x \text{ or } r = \infty \\ t > 0 \quad [\text{A-6}]$$

Equations [A-1] and [A-2] with initial and boundary conditions specified by Eq. [A-4] through [A-6] have been solved previously by Carslaw and Jaeger (13). If $i(t)$ is assumed constant at some characteristic value ($f \rightarrow f_0$) during the early transient period (Fig. 2), then the solutions for ξ_j at the interface are

hemispherical model ($\tau = r_0$)

$$\xi_j(r_0, t) = \frac{r_0^2 f_0}{D} \left[1 - \exp \left[-\frac{Dt}{r_0^2} \right] \operatorname{erfc} \left[\frac{(Dt)^{1/2}}{r_0} \right] \right] \quad [\text{A-7}]$$

cylindrical model ($x = 0$)

$$\xi_j(0, t) = \frac{2f_0}{D} \left[\frac{Dt}{\pi} \right]^{1/2} \quad [\text{A-8}]$$

If f_0 can be approximated by measuring the current transient $i(t)$ and specifying the active dissolving area A , then the time required for ξ_j to reach a value corresponding to saturation of a given salt of cation j can be calculated. For example, with a 0.089 cm diameter $\approx 2r_0$ nickel wire potentiostatically dissolving into a 1M NiCl₂ solution assuming $D \approx 10^{-5}$ cm²/sec, Eq. [A-8] can be solved explicitly for t

$$t = \left(\frac{\xi_j}{2f_0} \right)^2 D \pi = \left(\frac{C_j - C_j^B}{2C_j^S f_0} \right)^2 D \pi \quad [\text{A-9}]$$

For this case $i_0 \approx 8$ mA (8×10^{-3} coulomb/sec), $n = 2$, and the time τ required to reach a saturation concentration of 4.65M NiCl₂ would be 2.4 sec assuming that the entire surface area is actively dissolving. Equation [A-7] can be solved by trial and error using Danckwerts (7) graphical solution to a similar problem and yields a value of $\tau = 3.9$ sec for the same set of parameters. At the other extreme, if only one small pit (1 μ m in diameter) was dissolving initially, the characteristic current density (i_0/A) would be greater than 10^6 times larger and the value for τ at saturation would be $\sim 10^{-12}$ sec.

Observed transient times were about 2 sec for this solution and type of wire electrode. According to both models τ should be independent of the initial depth l . Several experiments in which the wire electrode was initially withdrawn approximately 1 mm into the cavity resulted in similar values of τ .

All this evidence supports the hypothesis that the cation concentration is rapidly increasing at the surface and forming a thin resistive layer of a chloride or chloride complex as the solution becomes supersaturated. Using a transient diffusion model for this period is an approximation of real behavior. A refined treatment of this problem would apply an initiation and distribution function to describe microscopic pit growth and use this as a boundary condition of a specified time-dependent flux. The measured current $i(t)$ would be a sum over all active sites

$$\frac{i(t)}{A} = \frac{1}{A} \sum i(t)_i \quad [\text{A-10}]$$

where $i(t)_i$ would be specified by knowing the growth rate of a microscopic hemispherical pit

$$i(t)_i = nF\rho_0 \frac{dV_i}{dt} = nF\rho_0 4\pi r_i^2 \frac{dr_i}{dt} \quad [\text{A-11}]$$

Relevant analyses of these problems have been published (14).

LIST OF SYMBOLS

a_j	activity of species j , mole/liter
a_j^B	activity of species j in the bulk solution, mole/liter
a_j^S	activity of species j at saturation, mole/liter
A	area of artificial pit or wire cross section, cm ²
b_j	viscosity coefficient of species j , liter/mole
C_j	concentration of species j , mole/liter (M)
C_j^B	bulk concentration of species j , mole/liter (M)
C_j^S	saturation concentration of species j , mole/liter (M)
C^*	uncommon cation concentration, mole/liter (M)
D°	ionic diffusion coefficient at infinite dilution, cm ² /sec

D	ionic diffusion coefficient, cm^2/sec
D'	integral ionic diffusion coefficient, cm^2/sec
F	Faraday constant = 96,500 coulomb/equiv., A-sec/equiv.
f, f_0	specified flux during transient period, cm/sec
i	current, A
l	artificial pit depth, dissolution length, cm
m	molality, mole/1000g water
M	molarity, mole/liter
M_w	molecular weight, g/mole
n	charge (valance) of dissolving cation
\dot{N}	cation mass flux, equiv./ $\text{cm}^2\text{-sec}$
R	gas constant = $8.314 \text{ J/mole} - ^\circ\text{K}$
r	radial distance parameter, cm
r_i	radius of pit i , cm
r_0	radius of hemisphere centered at the dissolving metal surface such that $2\pi r_0^2 = A$, cm
S	slope of the plot $(i/A)^{-2} = f(t)$, $\text{cm}^4/\text{A}^2\text{-sec}$
t	time, sec or min
T	temperature, $^\circ\text{K}$
V_i	volume of pit i , cm^3
x	distance parameter, cm
Δ	boundary layer thickness, cm
γ_{\pm}	mean ionic activity coefficient
μ	solution viscosity, $\text{g}/\text{cm}\text{-sec}$
ξ	dimensionless concentration = $(C_i - C^B_j)/C^S_j$
ρ	solution density, g/cm^3
ρ_0	metal density, g/cm^3
η	solution viscosity relative to pure water at 22°C
Φ	potential, V
τ	time for initial current rise, sec

REFERENCES

1. H. S. Isaacs, *This Journal*, **120**, 1456 (1973).
2. V. M. Novakovski and A. N. Sorokina, *Corrosion Sci.*, **6**, 227 (1966).
3. H. S. Isaacs and G. Kissel, *This Journal*, **119**, 1628 (1972).
4. T. M. Suzuki, M. Yamabe, and Y. Kitamura, *Corrosion*, **29**, 18 (1973).
5. R. P. Frankenthal and H. W. Pickering, *This Journal*, **119**, 1297, 1304 (1972).
6. F. Booth, *Trans. Faraday Soc.*, **44**, 796 (1948).
7. P. V. Danckwerts, *ibid.*, **46**, 701 (1950).
8. H. S. Harned and B. B. Owen, "The Physical Chemistry of Electrolytic Solutions," 3rd ed., Reinhold Publishing Corp. New York (1958).
9. H. P. Meissner and J. W. Tester, *Ind. Eng. Chem. Proc. Design Develop.*, **2**(1), 128 (1972).
10. R. C. Reid and T. K. Sherwood, "The Properties of Gases and Liquids," McGraw-Hill Book Co., New York (1967).
11. E. W. Washburn, "International Critical Tables of Numerical Data," Vol. 5, 1st ed., McGraw-Hill Book Co., New York (1929).
12. W. F. Linke and A. Siedell, "Solubilities of Inorganic and Metal Organic Compounds," Vol. 2, American Chemical Society, Washington, D.C. (1965).
13. H. S. Carslaw and J. C. Jaeger, "Conduction of Heat in Solids," 2nd ed., Clarendon Press, Oxford (1959).
14. Z. Szklarska-Smialowska, *Corrosion*, **27**, 223 (1971).

The Influence of Cyclic Plastic Strain on the Transient Dissolution Behavior of 18/8 Stainless Steel in 3.7M H_2SO_4

T. Pyle, V. Rollins, and D. Howard

Department of Chemistry and Metallurgy, Lanchester Polytechnic, Coventry, England

ABSTRACT

Austenitic stainless steel specimens were subjected to strain cycling using a square strain wave while under potentiostatic control in aqueous 3.7M H_2SO_4 solution. Strains of ± 0.025 to ± 0.05 were employed at an average strain rate of 0.30 sec^{-1} . The transient dissolution behavior of the steel was investigated at active, passive, and intermediate potentials during both the tensile and compressive parts of the strain cycle. Enhanced dissolution of the metal surface was found to occur during the application of strain, the effect being much more pronounced for tensile strains. Subsequently, at constant strain, the enhanced activity decayed at varying rates depending on potential. The greatest dissolution transients were found to occur at potentials corresponding to the active/passive transition where substantial increases in surface activity were observed with each successive strain cycle.

In a study of the corrosion fatigue behavior of a high carbon steel, Rollins, Arnold, and Lardner (1) deduced that dissolution contributed to crack propagation and was, in the early stages of crack growth, the rate determining factor. Furthermore, they suggested that the anodic activity at the crack tip was enhanced by the plastic strain which occurred during the stress cycle. Recently, Uhlig and Duquette (2) have shown that for mild steel in aqueous solutions there is a critical value of corrosion rate which must be exceeded for the environment to have a deleterious effect on fatigue life.

Pyle, Rollins, and Howard (3) have suggested that such an effect could be explained if reverse slip occurred during cyclic deformation. During the application of stress, slip steps are generated on the surface

of the metal by dislocation movement. When the stress is reversed, it is possible that slip could occur in the opposite direction on or close to some of the original slip planes, which could return the steps completely or partially into the surface. If the atoms at the surface of the step were more active than the atoms occupying sites in the plane of the surface, then preferential dissolution at the step face could occur as soon as the deformation started to produce the step and could continue during the life of the step [Fig. 1(a)], until reversal of the load cycle caused the strain to drive the step back into the surface.

Howard and Pyle (4, 5) have shown that the activity of a step face depends upon slip step spacing. The amount of material which will dissolve from the step face is a function of the rate of dissolution and the time of exposure of the step face to the electrolyte.

Key words: corrosion, fatigue, passivity, reverse slip.

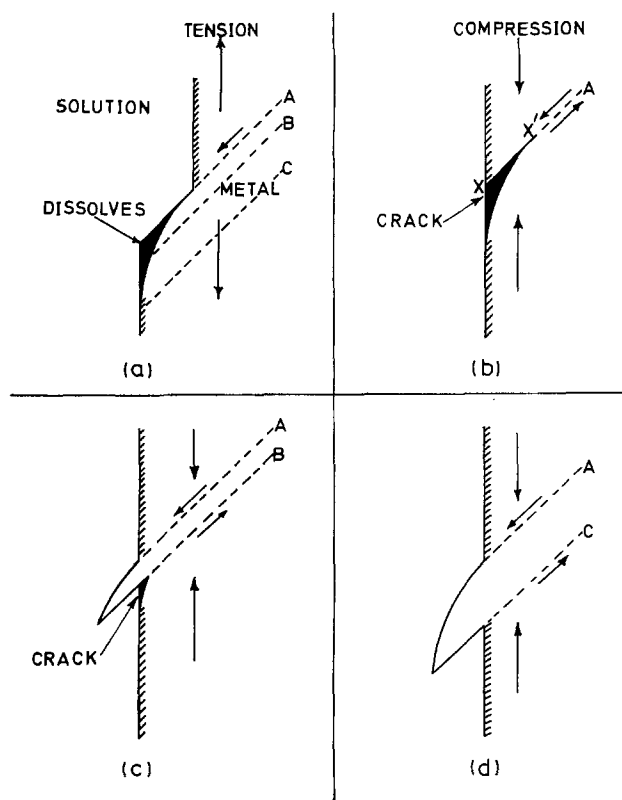


Fig. 1. Crack initiation in corrosion fatigue due to reverse slip

If reverse slip took place along the same slip plane, this would result in the formation of a wedge-shaped crack along the slip plane. The critical rate of dissolution would be that which would remove one atomic layer of atoms in the time that the step was exposed to the electrolyte. If the reverse slip occurred in a different place then it would be necessary for many atomic layers to be removed from the step face if a crack was to develop [Fig. 1(c) and (d)]. The extent of slip reversal and the contribution that this mechanism would make to crack development would depend on the crystal structure and stacking fault energy of the metal concerned. The idea that an increase in anodic activity (6) can be brought about for some metals by dynamic unidirectional strain while the metal is in contact with an electrolyte, has been demonstrated experimentally by several authors (7-11), although the precise mechanism by which it occurs may be open to debate. Smith and Staehle (12) have suggested that strain enhanced dissolution could be due simply to the rupture of surface films and that the speed with which the film repairs itself may play a major role in determining the susceptibility of metals to stress corrosion cracking. As the overpotential for film formation will influence the rate of film nucleation and growth, the potential dependence that is found for stress corrosion cracking behavior would thus be explained. Johansson and Staehle (13) have recently measured the dissolution transients that occur when a metal is suddenly deformed by a fixed amount of strain (0.02 at a high strain rate 2.2 sec^{-1}) and have shown that the magnitude of the charge which passes before dissolution ceases depends markedly upon potential.

However, the influence of cyclic plastic deformation on anodic activity has not been investigated. The results of preliminary tests by the authors on 18/8 stainless steel, mild steel, and aluminum under potentiostatically controlled conditions in 3% NaCl at pH 3 and subjected to a square wave cyclic total strain of ± 0.0375 are given in Fig. 2 and Fig. 3. In these tests the strain reversal took 0.25 sec giving an average strain rate of 0.3 sec^{-1} .

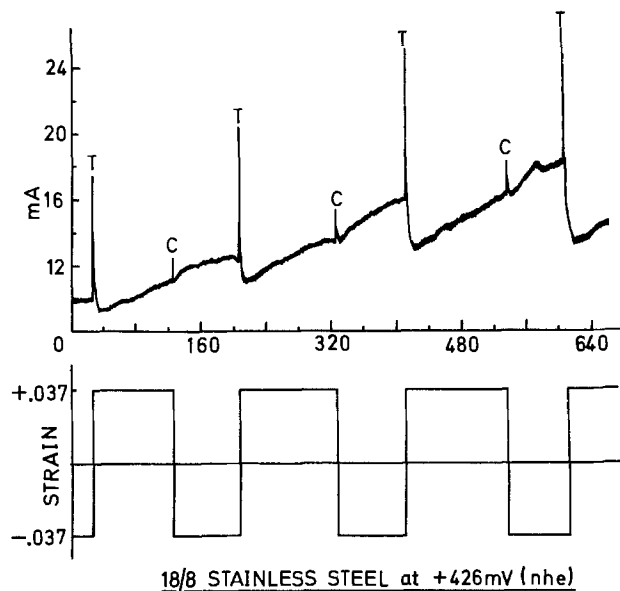


Fig. 2. Strain induced dissolution transients for 18/8 stainless steel in 3% NaCl (pH 3.0), ± 0.0375 total strain and 0.30 sec^{-1} strain rate.

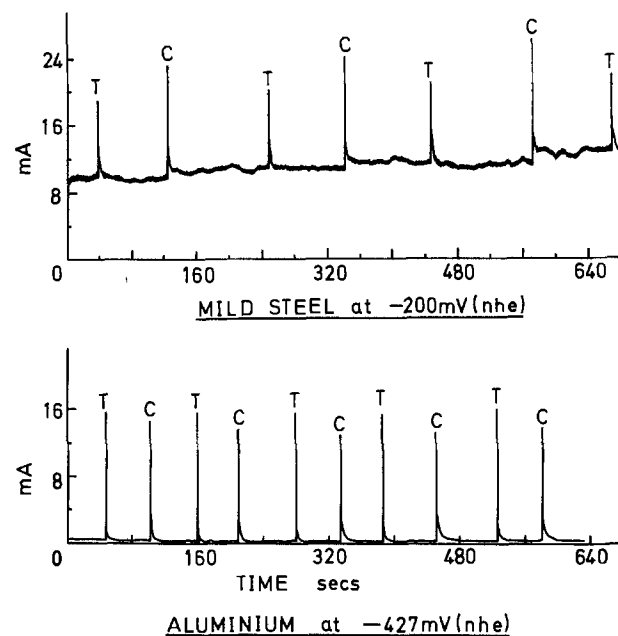


Fig. 3. Strain induced dissolution transients for mild steel and aluminum in 3% NaCl (pH 3.0), ± 0.0375 total strain and 0.30 sec^{-1} strain rate.

The potentials selected for mild steel and aluminum corresponded to the commencement of the active region. The 18/8 stainless steel was held at a potential where it would normally have been passive, but passive film formation was prevented by the presence of chloride ions. In Fig. 2 it is evident that very large increases in the dissolution rate of the stainless steel occurred during the 0.25 sec required to reverse the strain. Similar results were obtained for aluminum and mild steel and in each case the dissolution rate decayed during the constant strain portion of the square strain wave. These initial experiments showed clearly that reversed dynamic strain can greatly enhance dissolution rates in metals during both tension and compression half-cycles. They are important also in that they demonstrate that such effects can occur in conventional engineering materials subjected to reversed strain in a simple aqueous electrolyte at room temperature, i.e., under normal corrosion fatigue conditions.

The relative magnitudes of the transient currents produced in tension and compression for stainless steel were different from those for mild steel and aluminum. It was thought that this difference could be due to the strain characteristics of the metals. Interest was focused on stainless steel also because of the susceptibility of austenitic steels to transgranular stress corrosion cracking and because work by Spähn (14) had shown that the corrosion fatigue properties of 13% Cr stainless steel in solutions of sulfuric acid were markedly dependent on potential. Minimum fatigue life was found at potentials close to the active/passive transition.

It was decided, therefore, to make a more detailed examination of the transient dissolution behavior, under cyclic strain in the range ± 0.025 to ± 0.05 , of an austenitic stainless steel in an aqueous sulfuric acid solution. This paper describes the techniques used in these tests and the results obtained from strain cycling at different strains per cycle and at different potentials relative to the standard hydrogen electrode.

In practice, engineering structures are not subjected to plastic strains, but stress raisers such as notches, inclusions, and pits may locally raise the strain level above the average strain experienced by the structure as a whole. It is at these points that the dissolution effects described in this paper could occur.

Experimental Technique

Strain cycling experiments were carried out on En 58A stainless steel specimens using a Mand servo-hydraulic testing machine for controlled strain cycling and a Chemical Electronics 40V 10A potentiostat to control the specimen potential. The specimen was held in the jaws of the straining frame and surrounded by a glass chamber in which the sulfuric acid was held. Details of the cell are shown in Fig. 4. The electrolyte 3.7M H_2SO_4 was circulated through the cell by a peristaltic pump and was directed onto the exposed surface of the specimen along a tube concentric with the Luggin capillary at a rate of $\sim 0.1 \text{ msec}^{-1}$. The Luggin capillary was spring loaded so that a constant distance of 2.5 mm was maintained between the specimen surface and the end of the capillary despite the slight movement of the surface during the tension and compression cycles of strain. The reference cell for the potentiostat was a saturated calomel cell with a sintered glass base which stood in the 3.7M H_2SO_4 . The experiments were of short duration and it was found that the potential of the electrode did not change within this time.

Specimens.—Specimens were machined from a stainless steel having the composition shown in Table I after annealing at 1363°K and water quenching. The specimens which had a gauge length of 11.6 mm and a diameter of 12.5 mm were polished using 220 grade

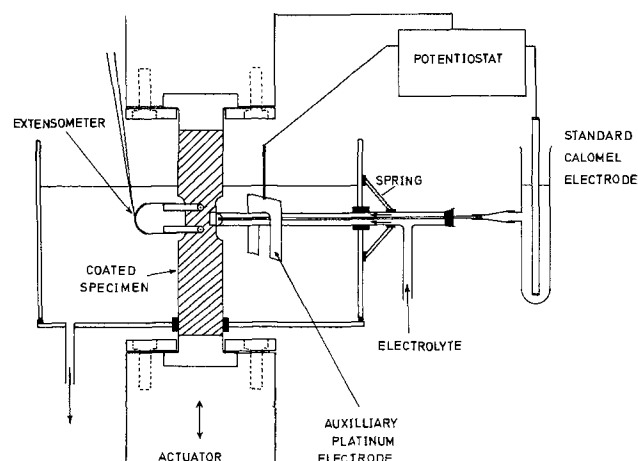


Fig. 4. The corrosion test cell and specimen

Table I. Chemical composition of the steel

	C	Si	Mn	P	Ni	Cr	Mo	Nb
Weight per cent (w/o)	0.12	0.40	1.17	0.02	9.10	17.90	0.80	Trace

emery paper, finished with crocus paper, washed with distilled water and industrial spirits, and dried in hot air. The specimen gauge length was coated with polythene, and the remainder of the specimen coated with synthetic rubber. The 100 mm² area to be exposed to the solution was coated with Lacomite prior to polythene coating. This facilitated the removal of the polythene coating from the center of the gauge length. The exposed surface was then polished with crocus paper to ensure that all traces of the Lacomite and polythene had been removed.

Electronic Equipment.—The potentiostat had a rise time of 0.5 μsec and was more than adequate to follow the changes in anodic activity due to straining which occurred over a time period of 0.25 sec. The strain was controlled from an extensometer, which consisted of strain gauges mounted on a high carbon steel U-spring which was located on four pop holes at the extremities of the gauge length *via* perspex pins. The whole of the extensometer was coated in synthetic rubber to protect it from the electrolyte. The strain, load, and current were recorded simultaneously on a Southern Electronics u.v. recorder. A Bryans 2000 X-Y plotter was used to record polarization curves and to provide a second independent recording of potentiostatic current variations with time. The recorders were calibrated against the potentiostat and the Mand extensometer after each run.

Procedure.—After polishing and coating, the specimens were set up in the machine and the electrodes and corrosion chamber arranged as in Fig. 4. The solution, nitrogen-saturated 3.7M sulfuric acid, was added and the pump started. The specimens were held at -460 mV (NHE) for 15 min to clean the surface. During this period, hydrogen was evolved and the current gradually decayed to a constant level. The specimen was then brought to the desired potential for the test at a rate of 1.04 mV sec^{-1} . The specimen potential was then maintained constant for 5 min before the strain was applied to ensure that equilibrium with the solution had been achieved.

In the tests reported, a square strain wave was applied and the first strain increment studied was in tension. The specimen was therefore strained very slowly into compression before switching on the automatic strain cycling control. Two types of tests were run. In the first series, after an increment of strain, the current was allowed to decay back to its original value before the next reverse strain increment was applied. In situations where the decay of the current was slow, a maximum period of 300 sec was allowed before the next half strain cycle. This time corresponded to the slowest cycling frequency that could be obtained with the equipment.

In a second series of tests, specimens were strain cycled using a square wave at 0.2 Hz, irrespective of the degree of decay of the current that had occurred between the reverse strain increments. A series of tests was conducted with the first strain increment in compression. The results obtained were similar to those where the first strain increment had been in tension, i.e., the transient current produced by the tensile strain reversal was larger than that produced by the compressive strain reversal. After each test the load was removed from the specimen and a polarization curve for the strained sample in the solution was determined.

Experimental Results

Tests were carried out at cyclic strains of ± 0.025 , 0.031, 0.0375, and 0.05 total strain about zero strain

and at different potentials in the range between -8 mV (NHE) and $+1042$ mV (NHE). References to strain values in the paper refer to total strain (elastic plus plastic). The positions of the chosen potentials relative to the polarization curve for the material in $3.7M$ H_2SO_4 , determined under precisely the same conditions, are shown in Fig. 5.

At the lower potential, -8 mV, the metal was in the active condition while at the higher potential, $+1042$ mV, the metal was in the passive range. A typical set of current transients obtained at potentials of -8 mV, $+262$ mV, and $+1042$ mV is shown in Fig. 6. In these tests the cycling frequency was adjusted to very low levels to ensure that during the initial strain cycles specimens held in the passive region were able to repassivate before the reverse strain half cycle was applied. Values of the peak currents for the transients produced by the tensile half cycles of strain at this low frequency and at 0.2 Hz are shown in Fig. 7-11 for different potentials and strains per half cycle. The results show that, as the metal was strained, a rapid increase occurred in the current required to maintain the specimen at a constant potential, indicating that an increased rate of metal dissolution had occurred. Immediately after dynamic tensile straining ceased, the current commenced to decay and continued to do so while the strain was maintained constant. Although all the current transients had the same general form, it can be seen from Fig. 6 that there were distinct differences both in the magnitude of peak currents and also in the rates of decay of the currents particularly after the application of the tensile half strain cycle. The following main points seem worthy of note:

1. At active potentials, the surface appeared to remain substantially more active for appreciable periods of time after dynamic straining ceased. The current supplied by the potentiostat at these potentials was several times greater than the starting cur-

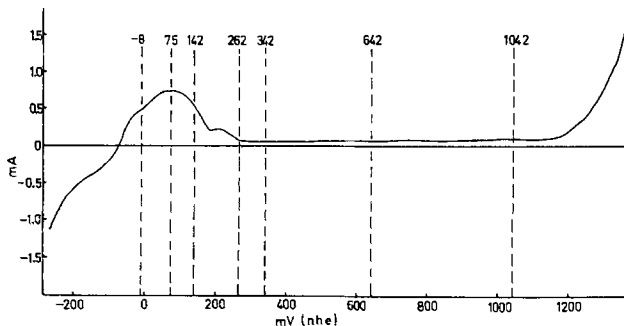


Fig. 5. The polarization curve for 18/8 stainless steel in $3.7M$ H_2SO_4 .

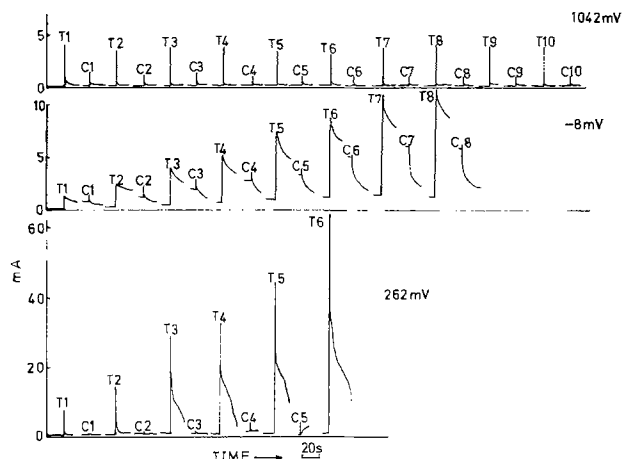


Fig. 6. Strain induced dissolution transients for 18/8 stainless steel in $3.7M$ H_2SO_4 at different potentials. Subjected to cyclic strain, ± 0.0375 total strain and 0.30 sec^{-1} strain rate.

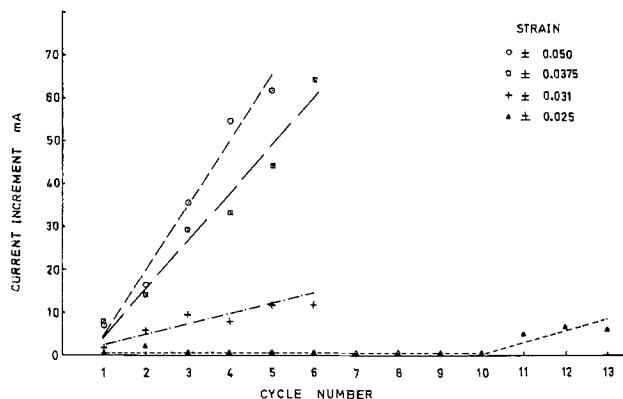


Fig. 7. Variation of dissolution transient peak with strain for 18/8 stainless steel in $3.7M$ H_2SO_4 at 262 mV, cycled after interval for repassivation, strain rate 0.30 sec^{-1} .

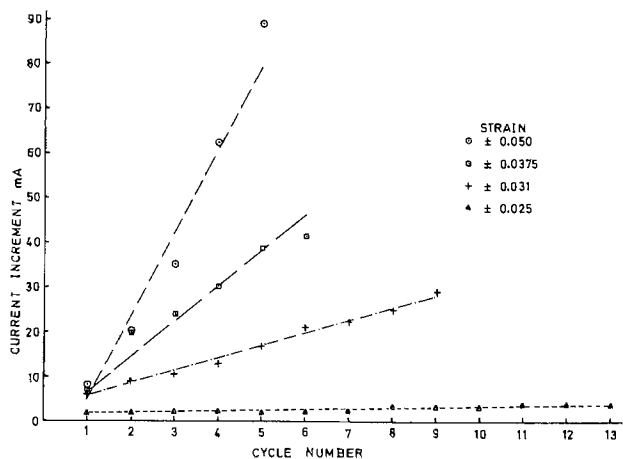


Fig. 8. Variation of dissolution transient peak with strain for 18/8 stainless steel in $3.7M$ H_2SO_4 at 262 mV, cycled at 0.2 Hz, strain rate 0.30 sec^{-1} .

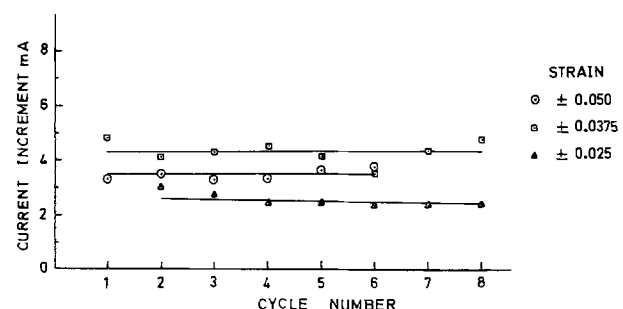


Fig. 9. Variation of dissolution transient peak with strain for 18/8 stainless steel in $3.7M$ H_2SO_4 at 1042 mV, cycled after interval for repassivation, strain rate 0.30 sec^{-1} .

rent. If it is assumed that strain occurred by slip at 45° to the surface, a tensile strain of 0.1 would produce an increase in surface area of $\sim 13 \text{ mm}^2$ equivalent to 0.13 of the original area. If the additional current was concentrated at this new area, it would correspond to a significant increase in the surface activity at these points compared to the normal surface.

2. At passive potentials ($+1042$ mV) the current transients did not vary with successive strain cycles whereas in the active and active/passive transition regions the transient peaks produced in tension increased rapidly with successive cycles.

3. At a potential ($+262$ mV) where the metal was just passive in the unstrained condition, the surface was able to repassivate within ~ 5 sec of the first and second tensile strain reversals. Gradually, however, it became increasingly difficult for repassivation to occur and large dissolution currents were found to

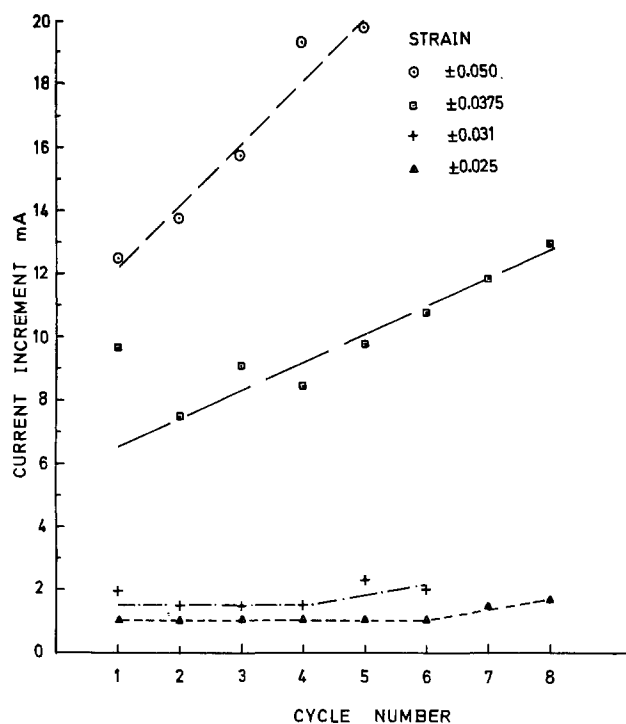


Fig. 10. Magnitude of dissolution transients for 18/8 stainless steel in 3.7M H_2SO_4 at 75 mV, cycled at ~ 0.0017 Hz, strain rate 0.30 sec^{-1} .

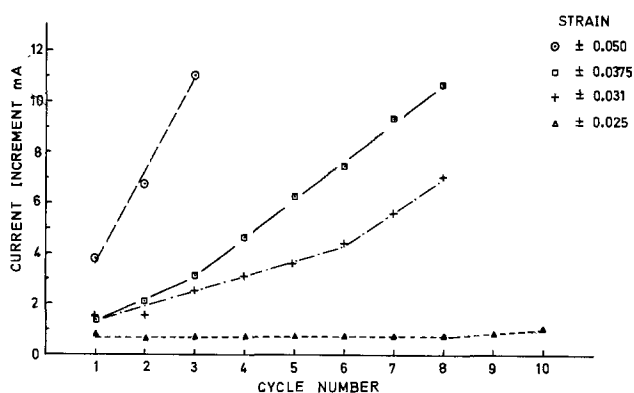


Fig. 11. Variation of dissolution transients peak with strain for 18/8 stainless steel in 3.7M H_2SO_4 at -8 mV, cycled at ~ 0.0017 Hz, strain rate 0.30 sec^{-1} .

be maintained for appreciable periods of time, e.g., > 60 sec after the tensile strain increment.

4. The current transients produced in compression were significantly smaller than those in tension. (Fig. 3 indicates that this is not so for mild steel in 3% NaCl.)

5. In the active region the peak produced during the compression half cycle diminished with successive cycles until the point was reached when the action of the compressive half cycle was mainly to remove the increased activity remaining after the tension half cycle.

6. At passive potentials the dissolution peaks occurred at approximately 50% of the applied tensile strain at a position corresponding to the maximum strain rate, whereas at active potentials the potentiostat current rose to a maximum close to the point of maximum strain. At potentials corresponding to the active/passive transition the peak position shifted gradually from the point of maximum strain rate to that of maximum strain as the cycle number increased.

In practice, most corrosion fatigue tests are run at a constant cycling speed. The tests at 0.2 Hz represent an initial attempt to examine the influence of

controlled frequency cycling on the dissolution transients. Although this speed was low compared to conventional tests it was sufficiently rapid for the second half cycle of strain to be applied before the surface had time to repassivate in the active/passive transition region. Figure 12 reveals that the compressive strain reversal at this frequency acts to remove the transient current produced by the tensile strain.

Discussion

The current transients observed are similar in shape to those shown by Johansson and Staehle (13) although in that work the peak currents occurred at the point of maximum strain. This was due presumably to the higher strain rate, 2.2 sec^{-1} , used by Johansson and Staehle compared with the value of 0.30 sec^{-1} used in these experiments. Johansson and Staehle characterize their transients by measuring the total charge passing in a fixed time. An alternative assessment used in this paper is to measure the peak current and the rate of decay of the peak current which is characterized by a half-life, $t_{1/2}$, which gives a measure of the ability of the surface to repassivate and limit dissolution effects, and may be an important parameter in determining cyclic frequency effects in corrosion fatigue failure.

The sudden increase in the potentiostatic current as the tensile strain was applied suggests that plastic deformation created areas from which dissolution of the atoms occurred more readily than from the unstrained surface. It is apparent that the precise manner in which deformation influenced dissolution depended upon whether the surface was or was not covered by an oxide film and by the ability of such films to reform if they were broken during straining. The results are most easily discussed, therefore, if the behavior of the specimens in the active and passive potential regions are considered before examining the active/

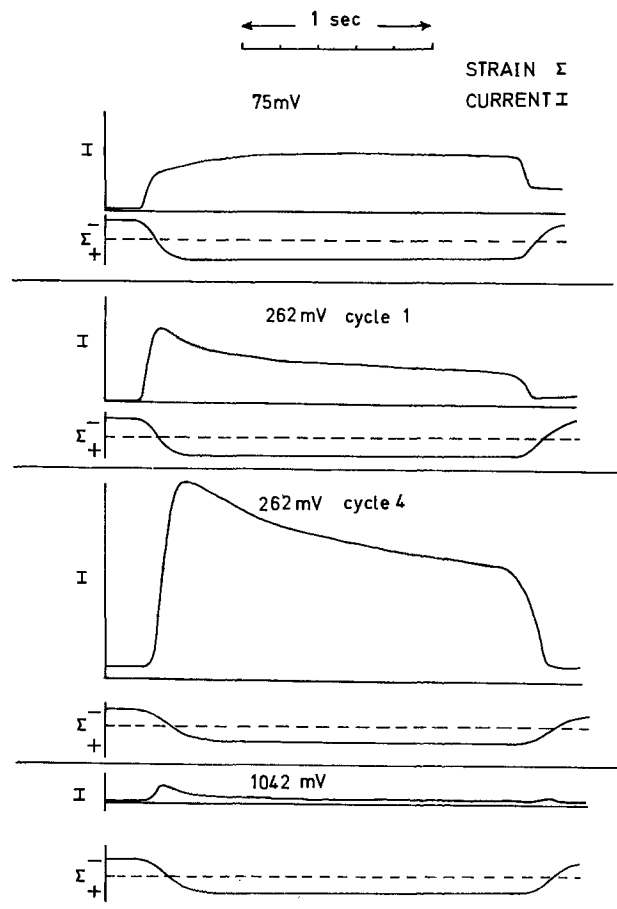


Fig. 12. Typical u.v. recordings of dissolution transients for 18/8 stainless steel in 3.7M H_2SO_4 .

passive transition where Fig. 6 indicates that significant changes take place either in the reactivity of the surface or the stability of films formed during repeated strain cycling at these potentials.

The active condition, potentials -8 mV, 75 mV.—At these potentials film formation appears unlikely and the current transients obtained in the first strain cycle varied with the magnitude of the imposed strain (Fig. 10 and 11). Furthermore, the transients showed a rate of increase of the peak current in successive cycles of strain which was dependent upon the applied strain (Fig. 10 and 11). From these results it seems probable that the function of strain was to produce more sites on the metal surface from which ions may dissolve.

Active site formation can occur when a slip step intersects the surface of the metal. Howard and Pyle (5) showed that the rate of dissolution of ions from steps on the surface of a metal was dependent upon the separation between successive steps and reached a maximum rate for steps $> \sim 10^{-4}$ mm. At spacings $> 10^{-4}$ mm, the instantaneous rate of dissolution of ions from a step was $\sim 2 \times 10^3$ ions/surface atom/sec for iron and $\sim 1.2 \times 10^3$ ions/surface atom/sec for nickel compared to rates of dissolution from a smooth surface calculated from Bass' model (4, 15) of 0.52 ions/surface atom/sec. For step sizes $< 10^{-4}$ mm the rate of dissolution will fall rapidly.

Electron microscopic measurement of slip step separation in this type of steel showed that a single tensile strain of 0.05 produced an average step separation of 2×10^{-4} mm. This figure covers a range of spacings, some smaller than 10^{-4} mm, while others were larger than 2×10^{-4} mm. This would give a range of dissolution rates from the different steps and the over-all dissolution rate would represent an average of these rates depending upon the frequency of step separations for a given strain. The effect of this distribution of slip step widths will be that on the initial strain cycle only a proportion of slip steps will be capable of providing sites for rapid dissolution. However, as strain cycling proceeds and the cyclic deformation concentrates slip on specific slip planes, the average slip step spacing will tend to increase, causing an increase in the rate of dissolution from the surface. Measurement of slip step spacings on specimens which had undergone ten cycles of a strain of ± 0.025 , i.e., a strain of 0.05 per half cycle, showed an average spacing of 4.5×10^{-4} mm.

The application of a 0.10 strain, moving from a strain of 0.05 in compression to a strain of 0.05 in tension, will produce $\sim 2 \times 10^{12}$ new sites per mm^2 of surface, assuming that the slip steps make an angle of 45° with the plane of the surface. This would produce an additional dissolution rate of $\sim 2 \times 10^{12}$ R ions mm^{-2} sec^{-1} where R is the rate of dissolution of ions per atomic site. If these sites are distributed in steps of $\sim 10^{-4}$ mm separation $R \approx R_{\text{max}}$, $\sim 2 \times 10^3$ ions/surface atom/sec for iron (5), and the new surface will dissolve at a rate of 4×10^{15} ions mm^{-2} sec^{-1} or ~ 1.2 mA mm^{-2} . The initial strain appears to produce only one-twentieth of the active sites due presumably to the formation of many finely spaced slip steps. However, as strain cycling proceeds, the progressive increase in the size of the transient current appears to indicate that there was an increase in the activity of the surface which is consistent with the observation that there was a progressive increase in separation of the planes on which slip was occurring. The production of active sites appears to be a reversible process in stainless steel. Figure 12 shows that the transient current was largely removed by the application of the compressive strain. It is possible that this effect was due to reversal of slip during compression along active slip planes produced in tension. There is evidence to suggest that reverse slip occurs in fatigue cycling of single crystals of copper (16, 17). If this did occur during the compressive strain cycle, then it would cause a decrease in the active current as observed and such a

process would then contribute to crack development in the manner suggested in Fig. 1. Although previous observations of reverse slip appear to be limited to single crystals of copper, reverse slip was observed in this polycrystalline 18 Cr-8Ni steel during strain cycling.

Figure 13 shows the surface of a stainless steel specimen at $1500\times$ magnification during the first half cycle of strain. Figure 13(a) shows the specimen at zero strain and load, Fig. 13(b) shows the specimen after 0.08 total tensile strain has been applied, and Fig. 13(c) shows the specimen after it has been compressed back to the zero strain position. It can be seen that the slip lines BB' and CC' lying on either side of the inclusion A in Fig. 13(b) have nearly disappeared in Fig. 13(c). A new slip line, DD' is visible and also some duplex slip has occurred towards the center of the field of view.

A slight difference in behavior during compression occurred between the specimen cycled at the low frequency and at 0.2 Hz.

In the latter tests, the application of the compressive strain caused a smooth and continuous decrease in dissolution current. However, in the low frequency tests, the application of the compressive strain always produced a small increase in current before the major decrease occurred. This effect could be due to excessive dissolution during the tensile cycle creating room for dissolution to start on the opposite face, XX', of the slip plane [Fig. 1(b)] once reverse slip occurs. Because free movement of the electrolyte could not

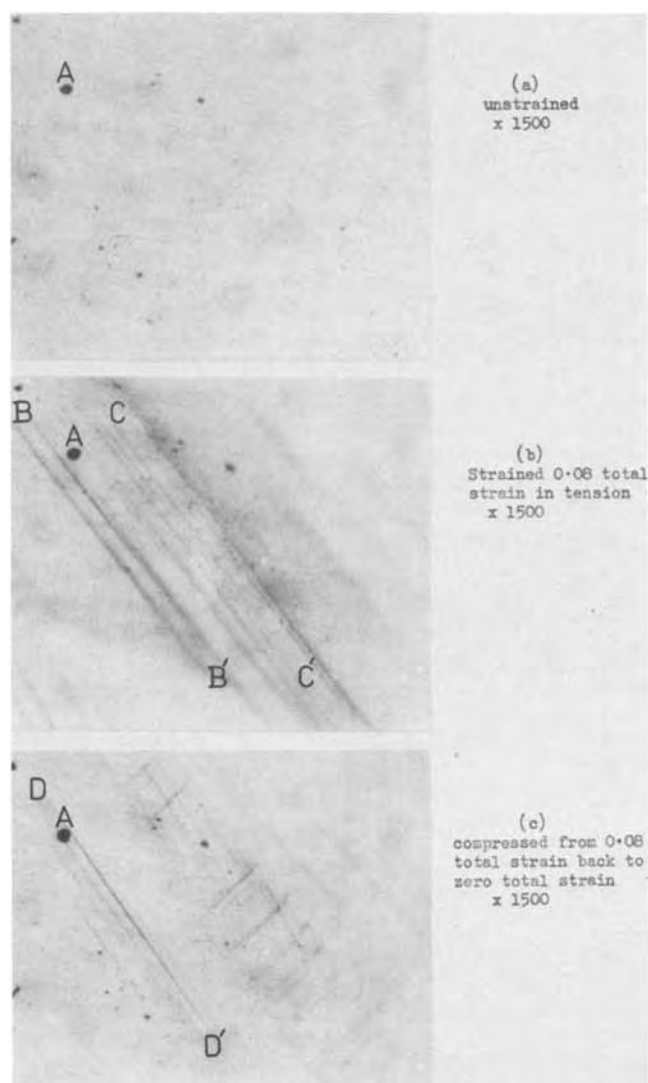


Fig. 13. Showing reversed slip during strain reversal of 18/8 stainless steel.

occur within such a microcrack, concentration polarization would rapidly prevent dissolution from proceeding throughout the compressive strain reversal. The effect of the compressive strain in reducing the dissolution current could alternatively be explained by the closing of cracks opened by the tensile strain. Microscopic examination of the specimens failed to reveal such cracks. It should be noted that the phenomenon was observed during the first strain cycle at a time when the formation of cracks sufficiently large to account for the increase in dissolution current would not be expected.

The passive condition, potentials 642-1042 mV.—In this potential region film formation apparently had an important effect on the current transient. The peak current occurred at the maximum strain rate where the balance between the strain rate and film formation exposed the maximum surface area to the electrolyte. Film formation occurred so rapidly that the surface was repassivated during the application of the tensile strain. Figure 14 shows a typical current transient produced at 1042 mV. The time, $t_{1/2}$, for the peak current to fall to half its peak value at different potentials is shown in Fig. 15 for the first strain cycle of ± 0.0375 .

At the active potentials the transient did not decay completely and in many cases the current reached a steady value greater than half the peak value. To obtain a comparison of the rate at which sites were removed at active potentials, a half-life based on the time for the current to fall to a value halfway between the peak current and the final value was taken and plotted in Fig. 15 for the potentials -8 mV and 75 mV. As would be expected, the half-life decreases with increasing potential presumably due to the increased over potential for film formation. At 1042 mV the half-life was found to be dependent also upon the strain per half cycle (Fig. 16). Strains of ± 0.005 produced peak transient currents of ~ 0.1 mA, while strains of ± 0.01 gave peaks of ~ 0.2 mA compared to values in the range 2-4 mA for strains between ± 0.02 and ± 0.05 (Fig. 9). This increase in peak current with strain combined with the reduction in half-life suggests that film formation was related to the amount of dissolution which occurred at the surface; a possible indication that film formation depends on the concentration of metal ions in solution at the interface. However, this effect could also be due to the degree of preferential dissolution of atomic species in the alloy which would change the effective surface composition and alter the repassivation kinetics. Although the precise mechanism of film formation cannot be deduced from these results

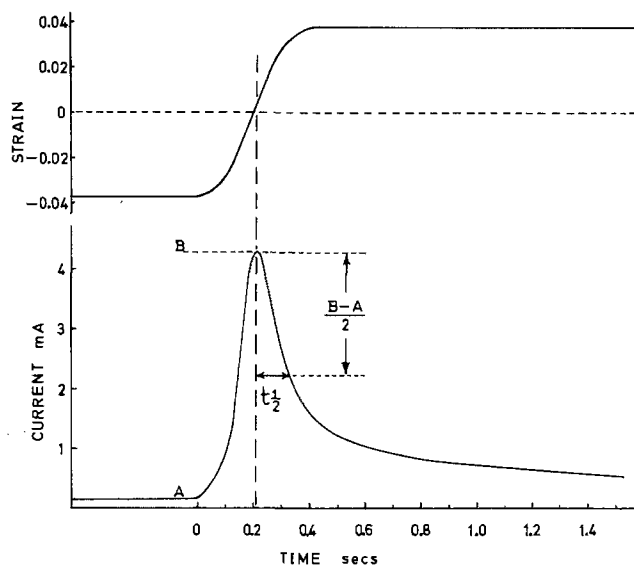


Fig. 14. The measurement of transient half-life, $t_{1/2}$, from a dissolution transient.

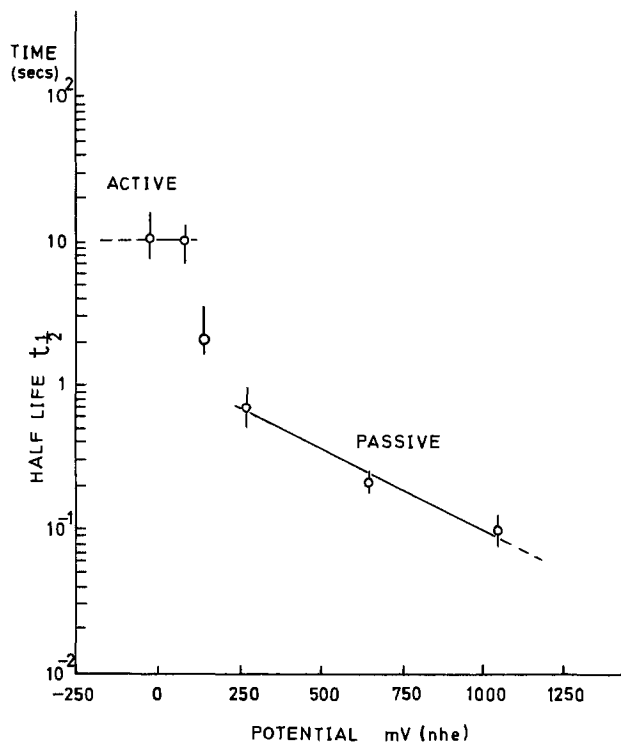


Fig. 15. The influence of potential on transient half-life. Tensile strain reversal from -0.0375 to $+0.0375$.

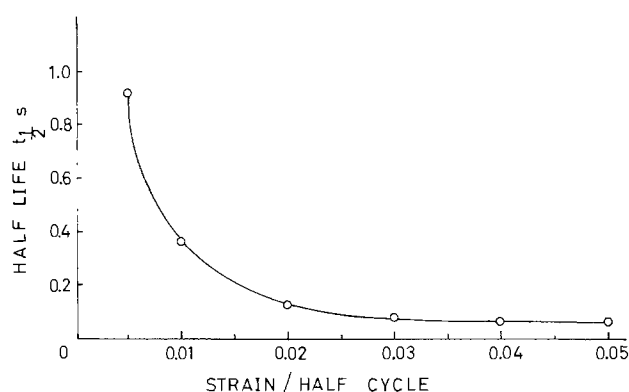


Fig. 16. The influence of strain on transient half-life. 18/8 stainless steel, $3.7M$ H_2SO_4 at $+1042$ mV (NHE).

as the half-life is determined by the strain rate as well as the film formation rate, it seems possible that the half-life of the transient taken in conjunction with the peak transient current could be a useful parameter in assessing the sensitivity of the alloy to corrosion fatigue. Furthermore, the half-life of the transient is of importance in considering the influence of frequency on the extent of dissolution per cycle and consequently on the contribution of dissolution to crack development per cycle in corrosion fatigue. Further strain cycles at these potentials did not cause an increase in the magnitude of the peak of the current transient, an indication that strain cycling did not increase the number of active sites. It is to be expected that strain cycling has the same effect on slip deformation as it has at the more active potentials and in this sense a widening of slip planes on which deformation takes place would occur. This would, on the basis of earlier arguments, lead to higher rates of dissolution from these slip step faces. However, it is suggested above that film formation occurs more rapidly at higher dissolution currents and it is possible that any changes in dissolution rate from the surface were compensated for by an equivalent change in the film formation rate. The small size of the current transients produced by compressive

strains indicates that the major proportion of slip produced in the tensile cycle was reversed along the original slip planes. The transient that did occur during compression was probably due either to disruption of the passive film formed on the exposed steps or to some slip along neighboring slip planes which produced fresh steps in contact with electrolyte. The magnitude of the transient peak indicates, however, that these effects were minimal.

The active/passive transitions, potentials 142 mV and 262 mV (NHE).—The most dramatic effects of strain cycling occurred at these potentials. The first current transients at these potentials were of a similar size to those at more noble potentials and occurred at the point of maximum strain rate in the tensile half cycle. In subsequent cycles there was a movement of the peak towards the position of maximum strain which showed the increasing difficulty encountered by the surface in re-passivating. The peak values of the tension current transients increased rapidly with cycle number (Fig. 7 and 8) and the surface behavior appeared more characteristic of the active condition although the current peaks were much larger. The increase in peak current/cycle, dI/dN , is shown for tensile strains of ± 0.0375 at different potentials in Fig. 17. A very rapid increase in dI/dN at potentials close to the active/passive transition is evident. If strain enhanced dissolution is a factor in corrosion fatigue failure, then minimum corrosion fatigue properties should occur at these transition potentials. Spähn (14) has demonstrated that this behavior occurs for a 13% Cr stainless steel tested in H_2SO_4 . It is clear from Fig. 7 and 8 that values of dI/dN are also sensitive to the magnitude of the applied strain as well as to potential.

From the data we are not able to explain why, after several strain cycles, the surface was unable to completely re-passivate or why the rate of formation of the films that were produced slowed sufficiently for the peak to occur at the maximum strain rather than the maximum strain rate. Two possibilities appear feasible. First, preferential dissolution during the first transients could have changed the surface composition removing chromium thus leaving a surface no longer able to form a passive film at these potentials. Changes were observed in the polarization curve where the small peak at 242 mV (NHE) had enlarged considerably after straining in comparison to the main active loop (Fig. 18). There is a peak in the polarization curve of nickel at this potential and it is possible that Fig. 18 is consistent with enrichment of the surface with nickel. The fact that nickel passivates at higher potentials would effectively explain why an increase in

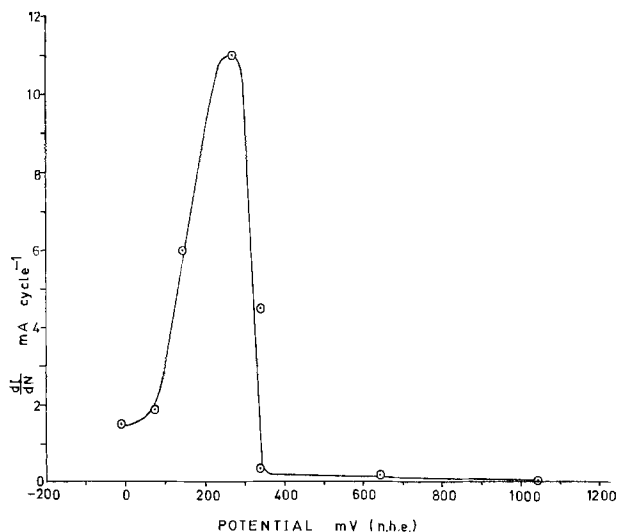


Fig. 17. The variation of the increase in tensile peak current per cycle, dI/dN , with potential. 18/8 stainless steel in 3.7M H_2SO_4 , strain cycled ± 0.0375 at a strain rate of 0.30 sec^{-1} .

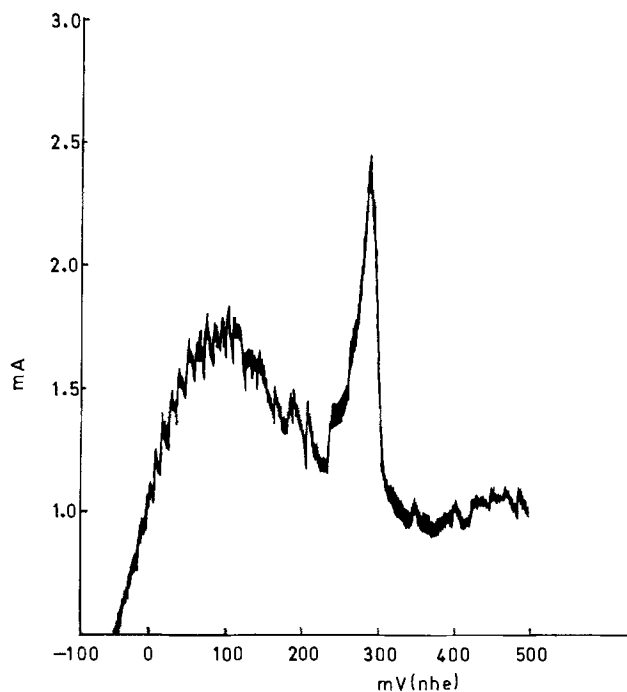


Fig. 18. A typical polarization curve obtained after strain cycling in the potential range -8 mV -242 mV.

the magnitude of the dissolution transient per strain cycle was not observed at more noble potentials. An alternative possibility is that at potentials close to the passivation potential the film is thinner and less stable than at higher potentials and the repeated rupture and reformation of the film during strain cycling makes it more susceptible to failure under tensile elastic strains in subsequent cycles. Rupture of the film in regions where it is not disturbed by slip of the underlying metal could occur and expose additional areas of the surface to the electrolyte which would account for the increase in peak current observed. Repeated fatigue cycling could then generate and extend microcracks in the film during the tensile half cycle and retard re-passivation. At a potential of 342 mV (NHE), *i.e.*, slightly further into the passive region, an intermediate type of behavior was observed where initial cycles produced the transition effects but with a smaller value of dI/dN . After three or four cycles, however, there was a sudden drop in the transient magnitude and subsequently the surface behaved as it did at noble potentials and showed only a small value of dI/dN (0.3 mA/cycle). The growth in peak transient then commenced once more as if the changes in the surface brought about by the dissolution caused the surface to oscillate between passive and active transition behavior. An X-Y recording of the transients produced at this potential at ± 0.0375 strain is shown in Fig. 19. This behavior was found to be reproducible and is probably worthy of further investigation.

Conclusion

The experimental work shows that cyclic plastic deformation can induce enhanced dissolution of a stainless steel in contact with sulfuric acid and that these effects are most pronounced during the tensile half of the strain cycle.

The fact that enhanced dissolution is mainly removed by the compressive strain is a possible indication that the slip deformation produced by the tensile strain is reversed along the same slip planes by the compressive strain. The probability that reverse slip occurs in this austenitic stainless steel is supported by micrographic examination of a specimen undergoing cyclic deformation. This suggests that the model of crack formation by slip-dissolution-reverse slip pro-

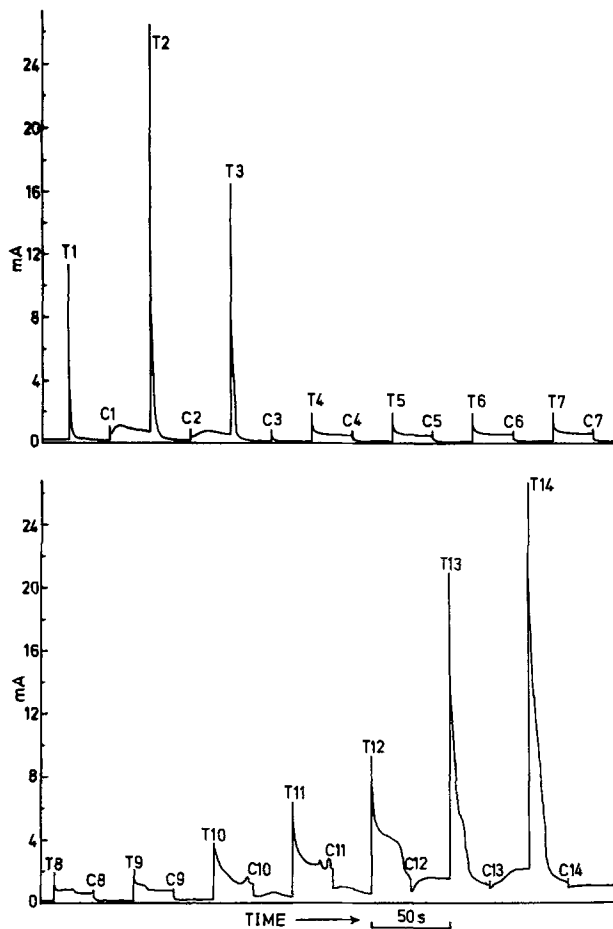


Fig. 19. Dissolution transients for 18/8 stainless steel in 3.7M H_2SO_4 at 342 mV subjected to cyclic strain, ± 0.0375 total strain and strain rate 0.30 sec^{-1} .

posed by Pyle, Rollins, and Howard (3) (Fig. 1) could occur in this steel.

The influence of cyclic strain on surface activity is shown to be dependent on the magnitude of the strain and on potential. The greatest effects occur at potentials close to the active/passive transition where substantial increases in surface activity occur with successive strain cycles.

The decay characteristics of strain generated dissolution transients are shown to depend on potential, strain magnitude, and the number of applied strain cycles and indicate that cyclic strain can significantly slow down the rate of film reformation.

Acknowledgment

Manuscript submitted Dec. 26, 1974; revised manuscript received July 14, 1975.

Any discussion of this paper will appear in a Discussion Section to be published in the June 1976 JOURNAL. All discussions for the June 1976 Discussion Section should be submitted by Feb. 1, 1976.

Publication costs of this article were partially assisted by Lanchester Polytechnic.

REFERENCES

1. V. Rollins, B. Arnold, and E. Lardner, *Brit. Corrosion J.*, **5**, 33 (1970).
2. H. H. Uhlig and D. J. Duquette, *Trans. Am. Soc. Metals.*, **62**, 839 (1969).
3. T. Pyle, V. Rollins, and D. Howard, "Corrosion Fatigue NACE-2," Proceedings of First International Conference of Corrosion Fatigue, p. 312 (1972).
4. D. Howard and T. Pyle, *Phil. Mag.*, **14**, 1179 (1966).
5. D. Howard and T. Pyle, *Brit. Corrosion J.*, **3**, 302 (1968).
6. T. P. Hoar and J. M. West, *Proc. Roy. Soc. (London), Ser. A.*, **268**, 304 (1962).
7. A. Windfeldt, *Electrochim. Acta*, **9**, 1139 (1964).
8. R. A. Raicneff, A. Damjanovic, and J. O'M. Bockris, *J. Chem. Phys.*, **47**, 2198 (1967).
9. T. Murata and R. W. Staehle, Ohio State Univ. Rep. No. COO-1319-71, 1968-06-03.
10. H. Leidheizer, and E. Kellerman, *Corrosion*, **26**, 99 (1970).
11. T. P. Hoar and R. W. Jones, *Corrosion Sci.*, **13**, 725 (1973).
12. T. J. Smith and R. W. Staehle, *Corrosion*, **23**, 117 (1967).
13. B. J. E. Johansson and R. W. Staehle, Corrosion Research Conference, Corrosion/74, Chicago, Illinois (1974).
14. H. Spähn, *Z. Physik. Chem. (Leipzig)*, **234**, 1 (1967).
15. L. Bass, *Proc. Roy. Soc. (London) Ser. A.*, **277**, 125 (1964).
16. C. Laird and D. J. Duquette, "Corrosion Fatigue NACE-2," Proceeding of First International Conference on Corrosion Fatigue, p. 88 (1972).
17. D. F. Watt, D. J. Embury, and R. K. Ham, *Phil. Mag.*, **17**, 199 (1968).

Polaromicrotribometry: A Friction Method for the Study of Polarized Metal Solution Interfaces

Application to the Gold Electrode

J. E. Dubois and P. C. Lacaze

Laboratoire de Chimie Organique Physique de l'Université de Paris VII, associé au C.N.R.S., 75005, Paris, France

and R. Courtel, C. C. Herrmann, and D. Maugis

Equipe de Recherche de Mécanique des Surfaces du C.N.R.S., 92190 Meudon Bellevue, France

ABSTRACT

A new adaptation of the technique of mechanical friction is proposed for the study of metal solution interfaces in electrochemistry. The coefficient of friction, especially sensitive to surface-state changes, is measured by means of a micro-slider, which does not disturb the i - v electrochemical curves. This method, called polaromicrotribometry, is easy to employ and of general application. It permits the measurement of electrochemical transient phenomena as well as stationary ones, in aqueous and organic electrolytes. The results obtained using different operating modes are described from the study of gold oxide formation and reduction. Different friction-potential behaviors were found for three different rubbing contacts, against gold in the same electrolyte. Gold/gold friction is elevated at cathodic potentials, indicating metal-metal bond formation, but at anodic potentials friction is reduced by chemisorbed oxygen: the friction-potential curve is in agreement with the current-potential curve. Teflon/gold friction is independent of potential, indicating that in this last case the slider is inert over the potential range studied. As opposed to gold/gold friction, silica/gold friction is low at cathodic potentials, but elevated at anodic potentials with appearance of stick-slip (high static friction). This high static friction is attributed to the electrochemical formation of bonds or bridges which require the presence of an adsorbed oxygen layer. When the electrode is covered by oxygen the friction variations depend only on the applied potential.

Measurement of friction for practical engineering applications is a classical technique of physics. The coefficient of friction is defined by $f = T/N$, where N is the normal force to the contact surface of two bodies, and T is the tangential force required to cause sliding. Two measures exist: the coefficient of static friction f_s is the force required to initiate sliding, while the coefficient of sliding friction f smaller than f_s , is the force required to keep the bodies sliding on each other. The friction coefficients are ordinarily independent of the force normal to the surface.

Friction and adhesion are phenomena which are very sensible to the physicochemical nature of the contact surface. One quarter of an oxygen monolayer on clean tungsten is sufficient to divide the coefficient of friction by half (1). Conversely any change of friction must be connected to a modification of the surface.

This sensitivity can be explained in the following way. Solids are sticking only on a small part of the apparent contact area (2), and it is on this real contact surface that adhesive forces are working. During the displacement of the slider, the junctions are stretched and broken and then built again; the stronger the adhesive forces the greater the frictional work dissipated. In the presence of adsorbed layers, the slider is always in contact with this superficial layer, and consequently it appears that friction measurement depends directly on the physico-chemical surface state, whatever the scratch behind the slider.

In the case of an electrode which is immersed in an electrolytic solution, adsorption depends on the applied potential and consequently adhesion and friction will depend on this potential.

Key words: friction, electrochemistry, gold electrode, oxidation, tribometry.

The first such friction measurements in electrolytes were those of Edison in 1877 (3) who observed the variation of the coefficient of friction of lead, thallium, and platinum against electrolyte-soaked paper in the presence of electrical current.

Koch (4) in 1879 notes an increase of the friction of platinum against glass (in acidified water) with the applied oxidizing potential. Waitz (5) in 1882 measured friction of gold, palladium, and nickel against glass in different electrolytic solutions, and observed also an increase of friction for anodic potentials and a decrease for cathodic potentials.

Krouchkoll in 1889 (6) reported quantitative measurements of the sliding friction of a platinum brush against glass in an acid electrolyte. The coefficient of friction increased from 0.10 to 0.30 with positive polarization and showed a local maximum at a potential of -120 mV with respect to the rest potential of platinum.

Clark (7) reported the sliding friction of tungsten and platinum wires on a perspex drum in various electrolytes.

Bowden and Young (8) measured the coefficient of static friction of platinum against platinum in 0.1M sulfuric acid. The method involved a small cylinder on a wire in a cell, with the apparatus being tilted at the angle required for the cylinder to slide on the wire at a chosen potential. They observed a maximum of static friction at the point of zero charge (accompanied by an increase in the damage to the surface) which they interpreted as a maximum of adhesion.

Staicopolus (9) measured the coefficient of sliding friction of glass against copper or stainless steel. The sample in the form of a cup was rotated against a spherical fulcrum coupled to a torque measuring de-

vice. He observed the electrocapillary maximum and detected specific adsorption and chemisorption of ionic species from the change in the friction potential characteristics.

Bockris, Argade, and Gileadi (10) applied the method of Bowden and Young, reporting data in the region of pzc for quartz against platinum, gold, silver, and platinum against platinum, silver against silver; they interpreted the variation of static friction in terms of double layer repulsion (11, 12).

In conclusion, it appears that two methods have been used: measurement of static friction with the inclined plane technique (8, 10), measurement of dynamic friction (5, 9).

The first method does not allow friction to be recorded with variation of electrochemical parameters whereas the latter does. However, in this last case the slider is always moving in the same friction track, a fact which is undesirable if the measurement periods are shorter than the time constants of the electrochemical phenomena.

Principle of Polaromicrotribometry

In order to interpret nonreproducible phenomena observed under certain conditions when using polarized platinum electrodes [servo-coulometry (13) and titrimetry (14)] we have attempted for the first time to apply the microtribometric technique (15), previously used for nonliquid environments, to the study of electrode surfaces in electrolytic media (16).

This microtribometric technique is based on continuous measurement of the frictional force between a small test contact and a sample, displaced slowly (a few microns per second). The apparent area of the contact, ca. $500\mu^2$, is quite small with respect to the electrode surface, so the perturbation of the electrochemical system is minimized.

Since the contact moves continuously on the new surface, the coefficient measured reflects the state reached by the surface, with any adsorbed layers, with at most a few seconds of response delay if the static friction is controlling, a fraction of a second for measurement of sliding friction. A choice of friction contacts may be made, including insulating materials, e.g., silica, or a metal contact, for study of metal-to-metal friction at controlled electrochemical potential.

It must be noticed, however, that friction causes surface distortion ahead of the slider (plastic deformation and work hardening). Consequently, the relation between friction and current-potential curves may be questionable. In fact, Bagotzki *et al.* (17) have shown that adsorption remains practically unaltered when structural defects are provoked. Moreover all the experiments we have performed confirm a close correlation between friction and intensity-potential curves.

The systematic exploratory work carried out in inorganic (18) and organic media confirmed by the analysis of the layers (19) has established the reliability of this technique. We have thus been able to demonstrate presence of a film, responsible for catalytic properties on electrodes during the Kolbe reaction (20) and the reduction of quaternary ammonium salts (21).

Using the study of gold oxides as a starting point, we hope to show below the possibilities offered by the use of this technique as well as its value for the study of slow transient phenomena whose time constants range from 1 to 3 sec.

Experimental

The polaromicrotribometer is composed of the following elements (Fig. 1). The cell, in the center of the diagram, is supported by an adapter on a microscope-type stage. This can be rotated to any chosen angle; it may be translated sideways by a micrometer screw, and it is translated longitudinally by a motor-driven lathe screw at velocities from 1 to $50\mu/\text{sec}$.

The friction contact, which presses on the exposed upper surface of the working electrode in the cell, is

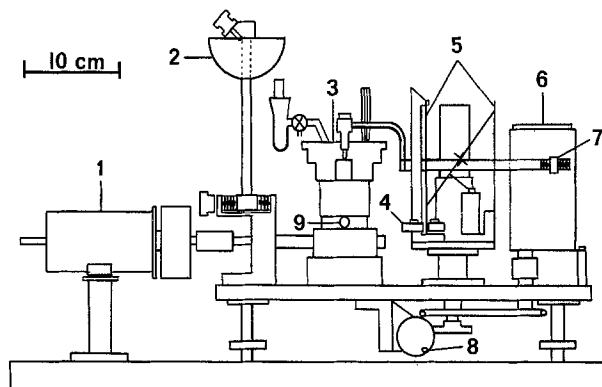


Fig. 1. Polaromicrotribometer. 1, Translation drive motor; 2, protractor for calibration; 3, cell; 4, displacement transducers; 5, spring blades; 6, friction measurement head lift motor; 7, counterbalance; 8, manual height adjustment for the friction contact; 9, micrometer screw for lateral positioning (displacement of the friction contact between successive passes).

connected to an arm supported at the virtual axis of an "N" shaped spring support, and is counterbalanced. A pair of inductive transducers is located symmetrically about the end of the first spring blade. Displacement of the friction contact restrained by the force constant of the springs is measured by these transducers, using a 5 kHz carrier-frequency amplifier. The output of this amplifier is displayed on one pen of an 'XYY' chart recorder *vs.* applied potential or *vs.* time. Pressure on the friction contact is supplied by weights on the platform above the contact. Hertz's theory shows that the radius of curvature of the slider would lead to elastic deformation for loads less than 2g. Actually the elastic range does not exist since the surface asperities always undergo plastic deformation, so the experiments have been conducted with loads from 5 to 10g which correspond to the best sensitivity of the apparatus. The sensitivity of the apparatus is calibrated by connecting a string, balancing the weights, at 45° upwards away from the detector. At this angle, a force exactly equal to the load is applied to the detector. The silica friction contact was a 2.5 mm rod, polished to a tip radius of 2.5 mm. Gold friction contacts used were (i) a 3 mm rod polished to a tip radius of 5 mm, and (ii) a brush 2.5 mm in diameter, made of 0.5 mm gold wire.

The electrochemical cell is drawn in detail in Fig. 2. A saturated calomel (or in some experiments a mercurous sulfate-saturated K_2SO_4) reference electrode is used, with a "stopcock" bridge. The reference electrode and nitrogen inlet tube are supported from the mobile stage. The cell cover is not tight-fitting, since a slot of about 3 cm^2 must be left for the friction-contact motion. It was found that continuous nitrogen bubbling in the cell does not disturb the measurements except at the lowest applied weights. The entire tribometer is inside a nitrogen-filled controlled-atmosphere chamber.

The potentiostat and galvanostat were constructed from $\pm 15\text{V}$ FET input operational amplifiers, with all components of the active feedback loop within the chamber, in order to maintain short leads (22).

Polarization of the working electrode was followed by a Tacussel "Minisis" digital electrometer-pH meter, which also drove the X axis of the chart recorder.

The working electrode was a gold disk, 6.22 mm in diameter, imbedded in a Teflon support machined to fit a 24/40 standard taper joint in the cell bottom. The electrode was polished either with diamond paste (to $\frac{1}{4}\mu$) or with alumina (to 24 hr sedimentation rate) before each experiment. The electrode was not electropolished, since it appeared that grain boundary development was more disturbing to the friction measurement than was the residual surface roughness after mechanical polishing.

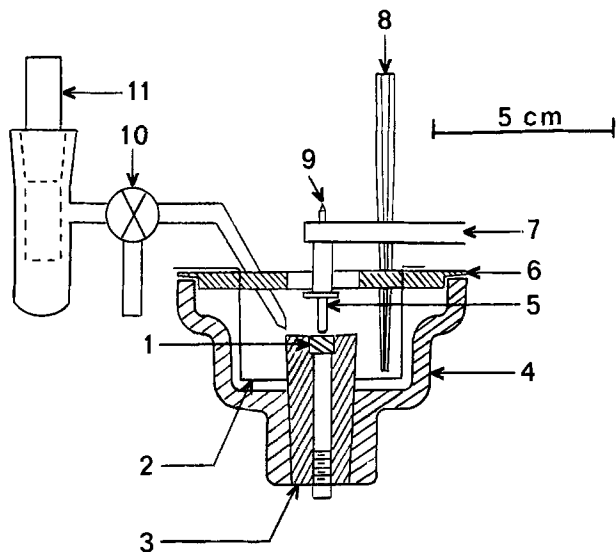


Fig. 2. Electrochemical cell. 1, Sample; 2, wire counterelectrode; 3, Teflon sample holder; 4, Pyrex cell; 5, rubbing contact (silica or gold, etc.); 6, cell cover; 7, arm to force measurement head; 8, nitrogen gas; 9, centering pin for weights; 10, stop-cockbridge; 11, reference electrode.

Electrolytes were, in general, prepared from Merck "Suprapur" reagents and double distilled water or water from a four-cartridge "Millipore" purification system. The studies reported here were conducted in N H_2SO_4 and in N KOH ; other studies have been made in H_2SO_4 of lower concentrations, $HClO_4$, H_3PO_4 , and NaF electrolytes.

Silica/Gold Friction

Triangular sweep.—When the interface potential is changed linearly with time a curve of friction vs. potential such as Fig. 3 results (in N sulfuric acid). The current voltage curve is conventional. The friction curve shows the following regions: a low coefficient at inert potentials, a rise in the coefficient at anodic potentials up to the onset of oxidation (1.35V), and then the violent variations called "stick-slip." In fact, in the "stick-slip" region one can resolve two curves, one for the static coefficient of friction (the peaks) and one for the dynamic coefficient of friction (the average of the peaks and the valleys) (2).

The frictional force measured is somewhat irregular. Deviations of 10% or more around the average value are normal, even with the most carefully cleaned and polished samples.¹ For this reason the friction curves are averaged and replotted pointwise. The curve of Fig. 3 has thus been replotted in Fig. 4, taking for one potential the average values of static and dynamic coefficients of friction of several experiments. The anodic and cathodic friction curves are quite close. We note particularly that, during the cathodic sweep, the coefficient of friction drops well before the electrochemical reduction peak, nearly at the same potential of oxide formation. These experiments show two unexpected results. First the coefficient of friction increases with oxide formation, and second its decrease is not synchronized with the oxide reduction, a fact which will be discussed below.

The hysteresis, or displacement in potential of the coefficient of friction curves between anodic and cathodic sweeps, seen in this series of experiments (Fig. 4) amounts to about 20 mV,² while the potential difference between corresponding oxygen coverage frac-

¹ Increase of friction at the point zero charge was not reliably above experimental deviations.

² The initial series (18) had shown a hysteresis of about 100 mV in the Pyrex/gold friction-potential curve.

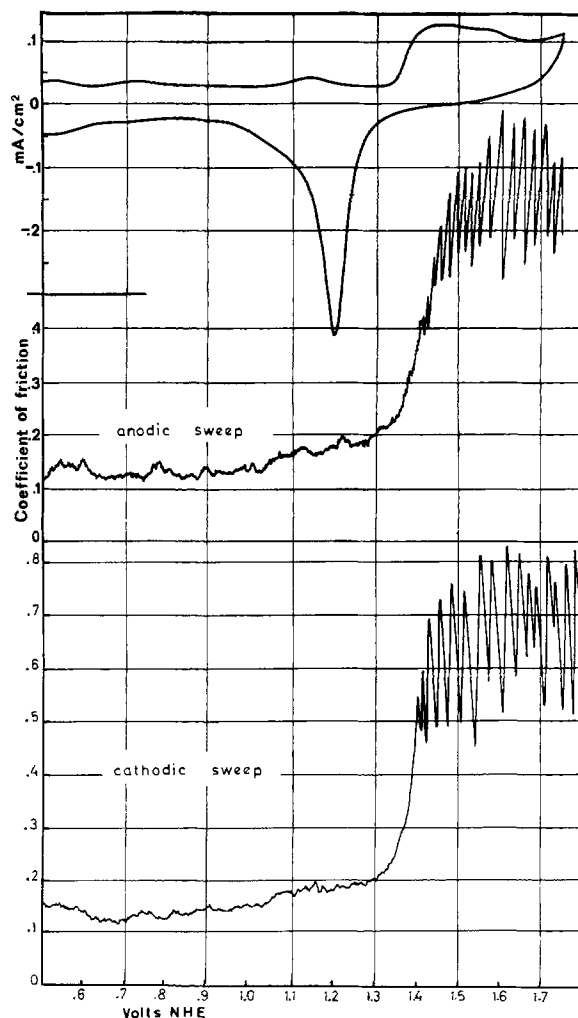


Fig. 3. Silica-gold friction in N sulfuric acid. Triangular sweep, 25 mV/sec, 3g load. Top, I-V curve; middle, coefficient of friction as a function of the interface potential: anodic sweep; and (bottom) cathodic sweep. The beginning of the friction rise is at the same potential as the beginning of oxidation.

tions on the anodic and cathodic triangular sweeps is about 200 mV.

In the note published previously (18) it was shown that the friction curve is displaced in potential by approximately 60 mV per pH unit (Fig. 5), as would be expected from the gold oxidation reaction (23).

Galvanostatic sweep.—For comparison with the galvanostatic studies of other authors (24) relating to the mechanism of oxidation at the gold surface, a set of experiments was conducted under galvanostatic control. Only low currents were employed (1-100 $\mu A/cm^2$) in order to resolve the friction curve adequately.

Several curves were run in which, after anodizing at constant current, the current was dropped to zero rather than being reversed. The polaromicrotribometric curves of Fig. 6 show the changes both of the potential and of the coefficient of friction with time, for a current of 20 μA . We see that the "stick-slip" appears at the beginning of oxidation, 1.35V, as under potentiostatic control.

The stick-slip continues after the current is dropped to zero, until the potential is relaxed to below 1.35V. The coefficient of friction increased with potential and oxygen coverage, but decreased with potential at constant coverage. We deduce that the change in coefficient of friction is a function of potential rather than of oxygen coverage. The data from several runs, at different anodic and cathodic currents, were replotted as a friction-potential graph (Fig. 7). Both zero current relaxation and cathodic (galvanostatic) sweep

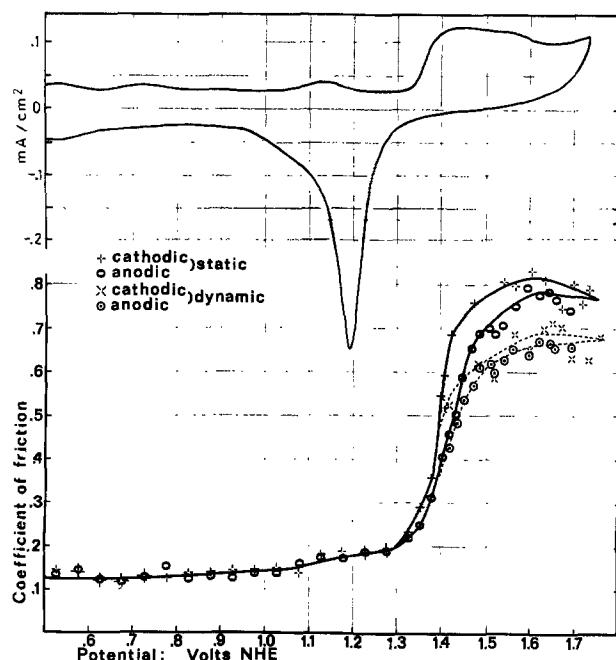


Fig. 4. Silica-gold friction. Triangular sweep, 25 mV/sec, 3g load. Data of Fig. 3 replotted with smoothing: static and dynamic coefficients separated. Top, I-V curve. The coefficients of friction during cathodic sweep decrease substantially before electrochemical reduction of the surface oxide.

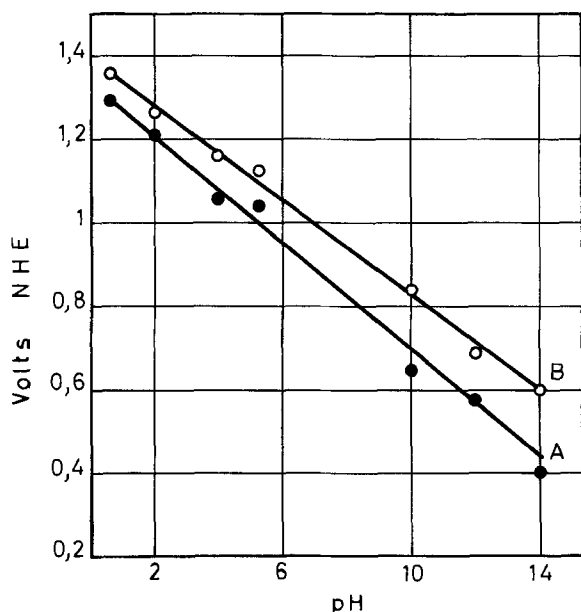


Fig. 5. Silica-gold friction. Curve displacement vs. pH. Curve A, potential of the beginning of friction increase on anodic sweep; curve B, potential of the beginning of friction decrease on cathodic sweep.

points fall on the same curve, vs. potential, as does the anodic branch.

Potential jump studies.—The previous results show that at constant oxygen coverage the silica/gold friction is a function of the potential only. This does not exclude *a priori* the possibility of a chemical reaction whose response time is shorter than the response time of the friction measurement apparatus (greater than 1 sec in the stick-slip region). Potentiometric curves obtained at sweep speeds from 40 to 150 mV/sec show no significant friction differences. We have therefore come to use a potential-jump method to test for the time constant of the change in friction

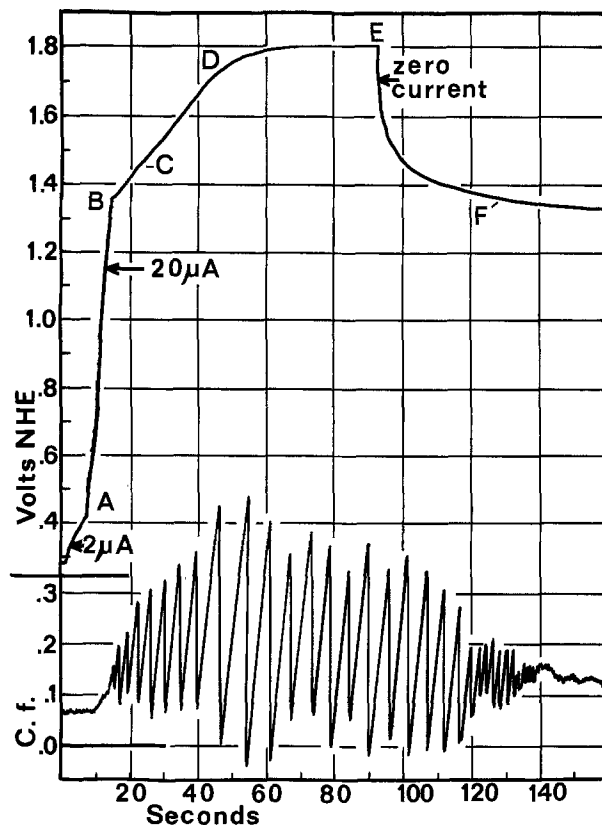


Fig. 6. Silica-gold friction. Galvanostatic control ($20 \mu\text{A} = 67 \mu\text{A}/\text{cm}^2$ apparent surface). Points A-F discussed in text. "Stick-slip" is visible at all potentials above 1.35V and absent below 1.35V.

with potential. The potential-jump method also helps to obtain more accurate friction measurements at a series of potentials, since one can hold a given potential for several minutes to obtain a better average.

In the anodic series the potential was stepped up, while the friction measurement was being recorded as a function of time, from a reference potential. One such curve is given in Fig. 8, from a series made as a function of polarization time.

It is observed, when the potential is stepped from 1.45 to 1.32V, that the static coefficient of friction decreases instantaneously from 0.40 to 0.25, in spite of the constant value ($\theta \sim 1$) of oxygen coverage fraction (25). The best average friction value, for a period of from 1 to 3 min, was determined, as well as the slope during that time and the instantaneous change observed when the potential was switched. The results are plotted in Fig. 9 and may be compared with the preceding figures. In general, no evidence of change of friction with time could be seen, except at potential extremes in which the relaxation time follows, as closely as can be inferred, the relaxation curve for the electrode current (*i.e.*, the friction may be influenced by the transient overpotentials).

Some difference in the measured values of coefficient of friction was found between the potential jump and the triangular series. The triangular series give higher coefficients of friction than the potential jump series; the cause of the difference has not yet been identified.

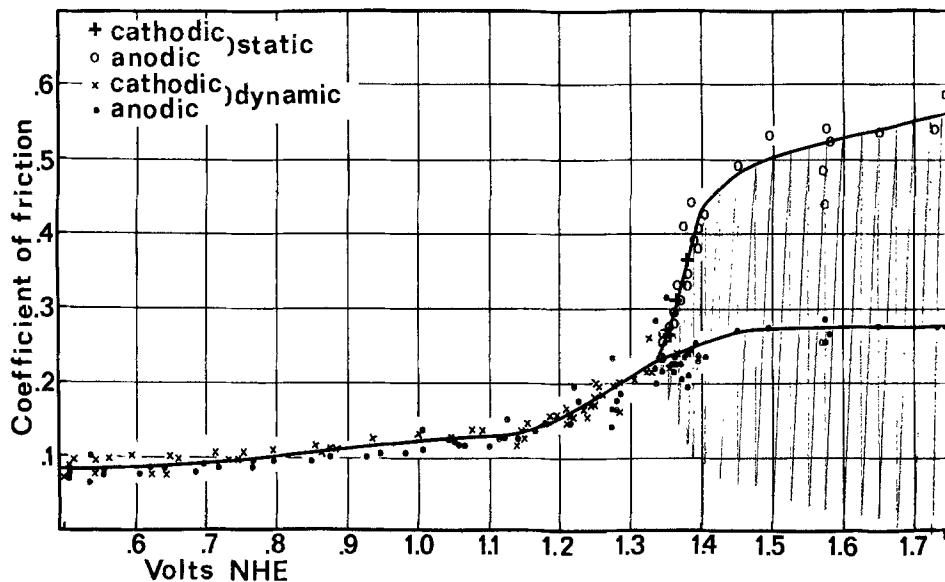
Teflon/Gold Friction

The friction of a Teflon rod against the gold surface was found to be independent of interface potential. Neither the oxidation nor reduction of the gold surface produced changes in the coefficient of friction against Teflon which remained at 0.11.

Gold/Gold Friction

Triangular sweep.—After the series of experiments reported above, we began to feel that the silica rubbing

Fig. 7. Silica-gold friction. Galvanostatic control. Average curves, static and dynamic coefficients separated.



contact was not a truly inert sensor, indicating the surface condition of the metallic or oxidized gold.

We found high silica/gold friction at oxidized gold potentials, and low friction at metallic potentials, whereas the *a priori* theoretical expectation (based on high vacuum studies) has been for high friction at a metallic surface, and lower friction at the oxygen-covered surface. The next best indicator to an inert body is a symmetrical system, containing only the gold interfaces. We mounted a gold ball in a Teflon support, to serve as the frictional contact against the gold electrode. Since the gold ball was insulated from the apparatus but was in contact with the electrode, it was supposed that its surface potential would remain the same as that of the working electrode (at

much lower contact pressures a noise resulting from irregular contact can be seen in the current response). The friction found for gold against gold was in fact lower in the potential region of oxidation than in the reduced interface region. The stick-slip phenomenon was observed at reducing potentials, as may be expected from metal-to-metal contact (Fig. 10). The cathodic friction curve is displaced with respect to the anodic curve by a potential similar to that between the observed oxidation and reduction peaks.

Potential jump.—The gold/gold friction was also studied using the potential-jump technique. The re-

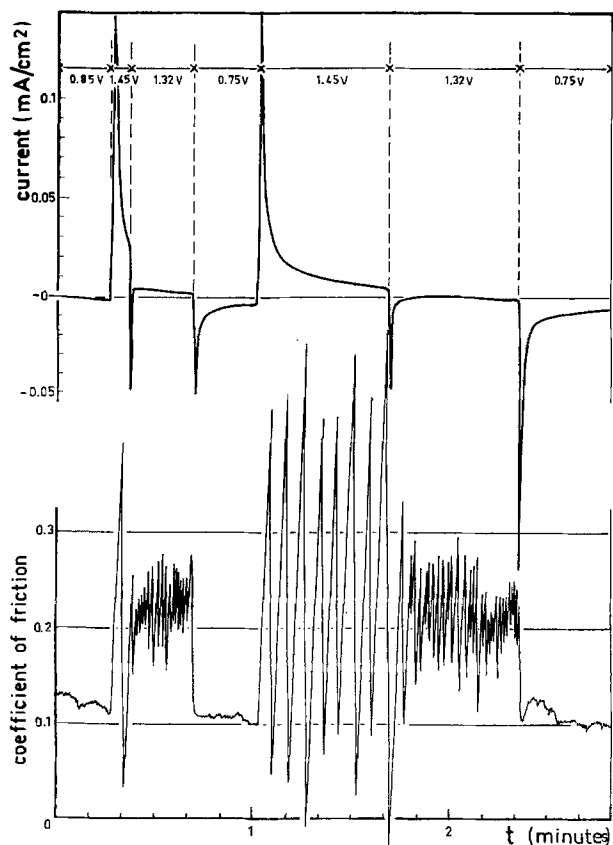


Fig. 8. Silica-gold friction. Typical potential jumps (potentials as indicated). The lower curve shows the immediate response of the coefficient of friction to the potential jump.

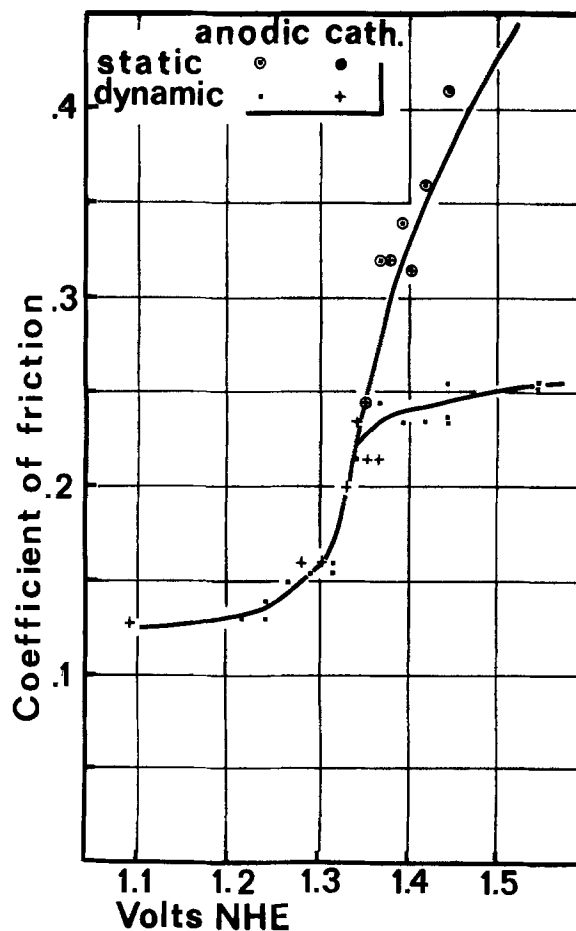


Fig. 9. Silica-gold friction. Averaged potential jump results. Anodic from 1.1V, cathodic from 1.45V.

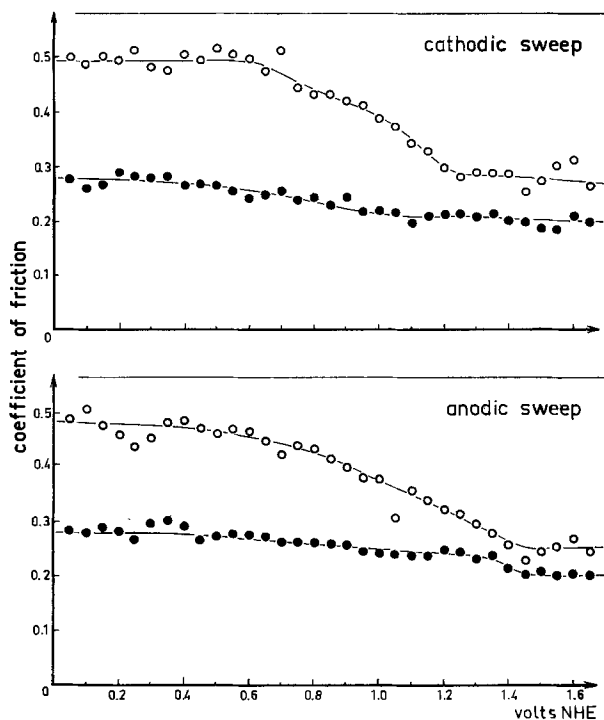


Fig. 10. Gold-gold friction. Triangular sweep, 25 mV/sec static (○) and dynamic (●) mean values. The coefficient of friction is lower at oxidizing potentials than at reducing potentials, the reverse of the gold/silica case.

sults were qualitatively similar, but substantially higher coefficients of friction were obtained than were found in the triangular-sweep experiment.

Discussion

Like previous investigators (4-6) we have seen an elevated coefficient of static silica/gold friction, a region of "stick-slip" at anodic potentials (Fig. 4), with lower friction at cathodic potentials. In contrast, an elevated coefficient of gold/gold friction was found at cathodic potentials (Fig. 10) with lower friction at anodic potentials.

This sticking of one material against another has many of the characteristics of chemical bonding between the materials. Formation of the metallic bond in high-vacuum metal-to-metal friction is classic. At anodic potentials on gold this "welding" is inhibited by chemisorbed oxygen. This results in hysteresis in the gold/gold friction-potential curve comparable to that in the electrochemical current-potential curve for gold.

At cathodic potentials silica does not adhere to gold, since no chemical bond is possible. At anodic potentials, however, silica/gold stick-slip begins at the oxidation potential of gold corresponding to an abrupt static coefficient increase. In the cathodic branch of the triangular sweep, the friction diminishes at nearly the same potential as the anodic increase well before the reduction current peak. In this zone oxygen coverage is constant, hence it follows that static friction only depends on potential.

We thus must propose an electrochemically induced reaction between silica and gold to account for this increase in friction related not to oxygen coverage but to electrode potential.

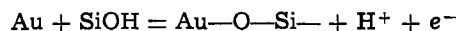
This hypothesis has been tested by the galvanostatic study (Fig. 6) in which the diminution of friction (point F) on potential relaxation after formation of the oxygen coverage, was found at the same potential (1.35V) as its initial increase (point B). That is, the friction changes at points B and F occurred at the same potential but at different oxygen coverages. In the region A-B in that figure the double-

layer is charged with little change in friction (0.3-1.35V). In the region B-C the oxygen coverage increases from 0 to 1 (25); in the region C-D the oxygen coverage ratio increases from 1 to nearly 2.³ Oxygen evolution characterizes the region D-E. During the region E-F the current imposed is zero, so the only change possible in oxygen coverage is due to the loss of 0.3 $\mu\text{A}/\text{cm}^2$ (23) which corresponds to 2% of the coverage during the time scale of the figure. We conclude from the galvanostatic study that for the high-friction (stick-slip) behavior, not just presence of oxygen coverage, but also a potential of at least 1.35V-0.06 pH is necessary.

It appears clearly from these measurements that adhesion is a function of applied potential. The adhesion forces stop at 1.35V, when the oxygen coverage is elevated and for a value which is practically the same as that corresponding to oxide formation.

The chemical bonding of this adhesion is not clear, and we must suppose that there are some bonds between silica and the gold oxide, which depend on potential, and which are stronger as the potential is higher.

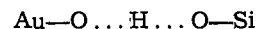
If there is a bond formed as a bridge between the two surfaces responsible for the sticking phenomenon, we might postulate that a superficial gold atom may react with the silica surface in a similar manner to its reaction with water



in comparison with



Here we write only the first electron of the process, without commitment as to the speed of following electron transfers. One may also postulate a weaker bond if a hydrogen-bond bridge is formed



We recognize that because of ion size the formation of gold silicate is not a favorable reaction and that this compound is not found in nature, but, as a surface reaction at independent sites, it is possible. A similar friction-potential study is in progress of the silica/platinum friction. The results are similar to those reported here for silica/gold friction.

Conclusions

The polaromicrotribometric technique, though used by only a few researchers, has been well established by the authors cited. We have attempted to improve the technique for use in this study (i) so that the rubbing contact always moves over a fresh surface, not deformed by previous passes and (ii) by using a contact sufficiently small with respect to the sample surface, to avoid serious shielding or surface disruption effects perturbing the simultaneous electrochemical characteristics correlated with the friction phenomena.

It appears that the coefficient of friction on the gold surface depends on the nature of the sliding contact. Silica-gold friction increases at the beginning of formation of the gold oxide, while gold-gold friction decreases.

In the first case, the friction-potential curves exhibit a greater reversibility than the intensity potential curves, in contrast with the gold-gold friction curves which follow the same variations as the current-potential curves.

At oxidizing potentials, an increase of the static coefficient of silica-gold friction is found. The revers-

³ Because of the considerable microscopic roughness remaining, we were unable to obtain values of quantity of charge per unit area comparable to the values of Brummer and Makrides (400 $\mu\text{C}/\text{cm}^2$ for oxygen coverage to $\theta = 1$ at 1.45V) (25). Anodic and cathodic charge densities, and the double-layer charging time all exceeded reported values for the flat gold surface by at least a factor of 2, and were not well reproducible between successive polishings of the sample.

ibility of friction curves show that at constant oxygen coverage the static friction only depends upon the applied potential. Other friction curves obtained under galvanostatic control or by the method of the potential jump confirm these results.

We suggest the formation of chemical bonds between silica and the gold oxide surface which depend on the potential.

Manuscript submitted Nov. 11, 1974; revised manuscript received July 1, 1975.

Any discussion of this paper will appear in a Discussion Section to be published in the June 1976 JOURNAL. All discussions for the June 1976 Discussion Section should be submitted by Feb. 1, 1976.

Publication costs of this article were partially assisted by Laboratoire de Chimie Organique Physique.

REFERENCES

1. D. H. Buckley, *J. Appl. Phys.*, **39**, 4224 (1968).
2. F. P. Bowden and D. Tabor, "The Friction and Lubrication of Solids," Vol. 1, Oxford Press (1954).
3. T. Edison, *Teleg. J.*, **5**, 189 (1877); *ibid.*, **7**, 332 (1879); *Compt. Rend. Acad. Sci.*, **87**, 270 (1879); *Nature (London)*, **19**, 471 (1879).
4. K. R. Koch, *Wiedemann's Ann.*, **7**, 92 (1879).
5. M. K. Waitz, *ibid.*, **20**, 285 (1882).
6. M. Krouchkoll, *Compt. Rend. Acad. Sci.*, **95**, 177 (1882); *Ann. Chim. Phys.*, **17**, 182 (1889).
7. R. E. D. Clark, *Trans. Faraday Soc.*, **42**, 449 (1946).
8. F. P. Bowden and L. Young, *Research*, **3**, 235 (1950).
9. D. N. Staicopolus, *This Journal*, **108**, 900 (1961).
10. J. O'M. Bockris, S. D. Argade, and E. Gileadi, *Electrochim. Acta*, **14**, 1259 (1969).
11. J. O'M. Bockris and S. D. Argade, *J. Chem. Phys.*, **50**, 1622 (1969).
12. J. O'M Bockris and R. K. Sen, *Surface Sci.*, **30**, 237 (1972).
13. J. E. Dubois and G. Mouvier, *Compt. Rend. Acad. Sci.*, **255**, 1104 (1962); *Tetrahedron Letters*, 1325 (1963).
14. J. E. Dubois, and P. C. Lacaze, *Anal. Chim. Acta*, **33**, 403 (1965).
15. M. Barquins, M. Kennel, and R. Courtel, *Wear*, **11**, 87 (1968).
16. J. M. Cesbron, R. Courtel, J. E. Dubois, M. Herlem, and P. C. Lacaze, *Compt. Rend. Acad. Sci.*, **266**, 1667 (1968).
17. V. S. Bagotzky, Yu B. Vassiliev, and I. I. Pyschnograeva, *Electrochim. Acta*, **16**, 2141 (1971).
18. J. M. Cesbron, R. Courtel, J. E. Dubois, and P. C. Lacaze, *Compt. Rend. Acad. Sci.*, **268**, 1985 (1969).
19. J. E. Dubois, A. Monvernay, and P. C. Lacaze, *J. Chim. Phys.*, **39** (1973).
20. J. E. Dubois, P. C. Lacaze, D. Massignon, and C. Le Gressus, International Congress on electron microscopy, Canberra, 1974.
21. F. Bruno and J. E. Dubois, *Electrochim. Acta*, **17**, 1161 (1972).
22. C. C. Herrmann, Thesis, University of Paris (1974).
23. K. J. Vetter and D. Berndt, *Z. Elektrochem.*, **62**, 378 (1958).
24. J. W. Schultze and K. J. Vetter, *Ber. Bunsen Ges.*, **75**, 470 (1971).
25. S. B. Brummer and A. C. Makrides, *This Journal*, **111**, 1122 (1964).

The Passive Film on Iron: An Application of Auger Electron Spectroscopy

R. W. Revie,^{*1} B. G. Baker, and J. O'M. Bockris*

School of Physical Sciences, The Flinders University of South Australia, Bedford Park, South Australia 5042

ABSTRACT

A method has been devised whereby the Auger spectra of films formed under electrochemical conditions can be examined without damage to the film in the transfer from the electrochemical situation. The conditions do not remove water molecules from the film at room temperatures. Application of the method to the passive film on iron shows that this film differs radically in its Auger spectra from that of an air-formed oxide film, or of the passive film after it has been heated to 150°. The change in spectrum from that of the air-formed oxide is associated with the presence of water molecules in the structure of the passive oxide. Examination of the relative intensities of the Auger spectra suggests one water molecule per two iron atoms. The change at 150° results from the removal of this water molecule. The results are consistent with a passive film which is a hydrated ferric oxide with a gel-like structure.

Much work has been done to elucidate the composition and structure of passive films (1). Electron diffraction results have led to the view that the chemical composition of the passive film on iron is γ -Fe₂O₃ (2), but because of the effect of vacuum environments to dehydrate passive films and the additional possible degrading effect of the electron beam, there is a possibility that such studies examined a decomposed passive film and not the passive film as it exists *in situ*.

The development of ellipsometry (3-10) has enabled the knowledge of passive film structure to be increased considerably. It is now known, for example,

that the passive film on iron is thick (tens of Å) (2, 11-13), and its refractive index and absorption coefficient have been computed (13, 14). The lattice-like nature of the film before the maximum of the i-V plot (13, 15), the critical thickness at the point of passivation (8, 9, 13, 15), the variation of the film thickness with potential (11, 13), and some aspects of the mechanism of film growth (16) have been established in the past 4-5 years by ellipsometric and transient ellipsometric work.

Although a number of the mechanistic aspects are now becoming established, the description of the passive oxide layer in terms of atomic structure is not clear. Ellipsometry gives the refractive index and absorption coefficient on the surface; however, the interpretation of this information depends on the relation at the surface between polarizability and struc-

* Electrochemical Society Active Member.

¹ Present address: Department of Engineering Physics, Research School of Physical Sciences, The Australian National University, P.O. Box 4, Canberra, A.C.T. 2600, Australia.

Key words: passivity, iron, Auger, spectroscopy, oxidation.

ture, which is insufficiently defined at present. A structural description of the passive layer is needed. Spectroscopic methods give information on surface energy states. Mössbauer spectroscopy has been applied to these films (17-19) and has detected chemical shifts which should be interpretable in terms of the structure of the film. Indeed, such interpretations have been made, but they retain some speculative character in the absence of reliable quantum mechanical calculations connecting such shifts to structure (18, 19).

Another method is Auger electron spectroscopy (20-26). Hubbard *et al.* (27, 28) have used Auger electron spectroscopy to monitor the elemental composition of a platinum surface after exposure to H₂O. These authors found that a layer of water, as shown by the oxygen Auger transition, remains on Pt(100) and Pt(111) surfaces in vacuum after room temperature exposure to water vapor or liquid water. Staehle *et al.* have used Auger electron spectroscopy to study the passive film on stainless steel (29) and on iron (30). The stainless steel studies showed that, with respect to the substrate, the passive film is enriched in Cr and depleted in Fe, Mo, Ni, and Si. The Auger electron spectra on iron passivated in a boric acid-sodium borate buffer, pH 8.4, were interpreted in support of previous work (31-34) which suggested that the passive film consists of two distinct structures: an inner Fe₃O₄ layer in contact with the metal and an outer γ -Fe₂O₃ layer.

This paper describes apparatus of a new design which enables Auger electron spectroscopy to be used in the examination of layers formed electrochemically with no intermediate atmospheric exposure. A novel feature of the spectroscope is the use of an analyzer (35, 36) that can be readily constructed in the laboratory using stainless steel mesh and nickel support rods and rings. This equipment has been used to apply Auger electron spectroscopy to the study of passive films formed in solution and unexposed thereafter to the atmosphere. Some initial results obtained using this approach are presented in this paper.

Experimental

Some requirements for the application of electron spectroscopy to the study of electrode processes in solution are that the initial specimen surface be atomically clean; the adsorption of carbon and other misleading contaminants be avoided, *i.e.*, the specimen should not be exposed to the atmosphere between the electrochemical experiment and spectroscopic analysis; the physically, but not the chemically, adsorbed water layer be desorbed during evacuation; and the passivated specimen not be in the spectroscope during bake-out.

It can be shown that during the evacuation, the physisorbed—but not the chemisorbed—water is lost, and therefore, the passive film is not likely to be decomposed. Using the Arrhenius equation

$$\text{rate of desorption} = Ae^{-E/RT} \text{ molecules/site-sec}$$

where A is the pre-exponential factor (10^{12} molecules/site-sec), E is the activation energy of desorption, and T is the temperature. Since $E < 15$ kcal/mole for physically adsorbed H₂O (37), the rate of desorption is >9.3 molecules/site-sec; *i.e.*, the time for 1 monolayer to desorb is <0.1 sec. Thus, the physically adsorbed water is desorbed during evacuation at room temperature. The activation energy for desorption of chemisorbed water from metal oxide surfaces is $\geq 20,000$ cal/mole and is not expected to desorb during room temperature evacuation in short times of the order of minutes (38-42). To preserve chemisorbed films formed electrochemically for longer times under high vacuum conditions, the specimen should be frozen, *e.g.*, using liquid nitrogen.

The electron beam intensity must be sufficiently small so that degradation of the film by thermal and

electron stimulated desorption does not occur. The increase in temperature caused by an electron beam impinging on a bulk metal specimen is negligible. Additional possible effects on an oxide film 50Å thick are also negligible, as may be shown by the temperature drop across the film, calculated, following de Graaf and Oosterkamp (43), from the equation

$$\Delta T = \frac{Wa}{\kappa}$$

where W is the power input per unit area, W/cm², a is the electron beam radius, cm, and κ is the thermal conductivity of the sample, W/cm²K. For the electron beam current used in these experiments, 2μA, the voltage, 2 kV, and the area 0.02 cm², $W = 0.20$ W/cm². Also, the beam radius a is ~ 0.08 cm and a typical value of the thermal conductivity, κ , for metal oxides (44) is ~ 0.2 W/cm²K. Then, ΔT is calculated to be $\sim 0.08^\circ\text{K}$.

The rate of electron induced desorption is given by (45)

$$-dN/dt = nQN$$

where n is the flux of electrons, electrons/cm² sec, Q is the total cross section for electron induced desorption, cm², and N is the total coverage of the adsorbed species/cm². The rate of desorption is determined mainly by Q , which is not known for H₂O adsorbed on Fe. Q for H₂O on W is $\sim 10^{-21}$ cm² and for O₂ on W varies from 10^{-19} to 10^{-21} cm² (45). It is assumed, therefore, that Q for H₂O on Fe $\sim 10^{-19}$ cm². Using the values $n = 0.62 \times 10^{15}$ electrons/sec cm² (corresponding to the electron current density of 1×10^{-4} A/cm²) and $N = 0.5 \times 10^{16}$ molecules/cm² (monolayer coverage of adsorbed H₂O), $-dN/dt \sim 0.3 \times 10^{12}$ molecules/sec, or 6×10^{-5} monolayer H₂O/sec; thus, the time to desorb a monolayer of chemisorbed H₂O is greater than 5 hr.

Figure 1 shows the apparatus used in the present studies. The high vacuum equipment is separated from the electrochemical cell by a straight-through valve, and a magnetically operated windlass enables the specimen to be transferred directly between the evacuated electrochemical cell and the electron spectroscope.

Figure 2 shows a block diagram of the vacuum system. The system is glass with metal Granville-Phillips valves that can be baked to 450°C. All glass blowing on the UHV side of the system was done using an argon-hydrogen mixture to prevent oxidation of metal parts and to avoid particulate contamination resulting from thermal decomposition of glass (46). When the argon-hydrogen mixture was not used, the sample was contaminated with boron.

In pumping the system from atmospheric pressure, a rotary pump and liquid nitrogen trap were used. During bake-out at 350°C, the system was pumped by a three-stage oil diffusion pump with a liquid nitrogen trap. After bake-out, the system was valved off and the ion pump used. Bake-out was carried out in two stages: a preliminary 1 hr bake-out, after which the iron filaments, the electron gun filament, the ion gauge, and the mass analyzer filaments were degassed, and a final 5 hr bake-out, after which degassing was again carried out. Pressures obtained in the Auger tube were $\sim 10^{-9}$ Torr or less.

The gas handling line, pumped by a two-stage oil diffusion pump with an associated cold trap, allows admission of gases into the UHV system via a break-seal. Gas bottles are connected using screw-on connectors.

The specimens were films of iron ($\sim 1000\text{\AA}$ thick) evaporated *in vacuo* from 99.998% iron wire (Koch-Light Laboratories) filaments 0.5 mm diameter. The filaments were degassed at 3A for 30 hr in a vacuum $\sim 10^{-8}$ Torr. Preparation of the electrodes was carried out by evaporation at 4.1A for 30 min on a 99.998%

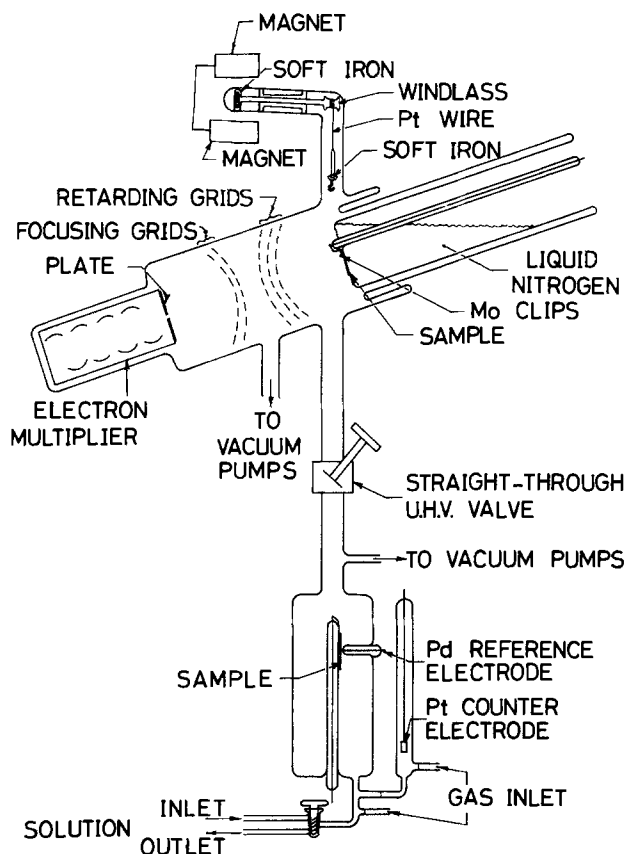


Fig. 1. Apparatus for combined electrochemical studies and Auger electron spectroscopy.

iron sheet substrate 1 mm thick, maintained at 0°C by an ice water mixture. This temperature was chosen to reduce the diffusion of impurities from the substrate into the evaporated film. The evaporation temperature was not lowered further because a rough surface would then develop (47).

The electron gun was a commercial television gun modified with a thoriated iridium filament (48, 49) to permit repeated atmospheric exposures. The iridium filament in the electron gun was coated with thoria by cataphoresis in a bath containing 5g of 200 mesh thoria and 0.075g of thorium nitrate to 100 ml of ethyl alcohol (48). The gun, after being prepared in this manner, is operated at 2 kV, and the electron beam impinging on the target has a current density of about 1.0×10^{-4} A/cm².

Electron energy analyzers currently used for Auger spectroscopy fall into two main categories (20): cylindrical mirror and retarding field. A cylindrical mirror analyzer (50) employs a pair of co-axial cylinders to focus electrons of a narrow energy band on an electron multiplier. The main disadvantage of the cylindrical mirror analyzer is the critical dependence of the resolution on the size and axial alignment of the incident electron beam on the specimen. The finely focused beam results in a high current density and may damage the surface being investigated.

In the present experiments, a retarding field analyzer was used because the sensitivity and resolution of this type of analyzer are relatively insensitive to the size of the emitting area. It is, therefore, possible to use defocused beams with low current density and still retain a large signal. This practice minimizes desorption and damage at the target surface. The analyzer used 100 mesh, 0.001 in. stainless steel wire retarding and focusing grids, and was based on the principle of Staib's design (35, 36).

Figure 3 shows the circuit used in the analyzer. The specimen, the electron gun, and grid (1) are grounded, so that the primary electrons move in a field-free re-

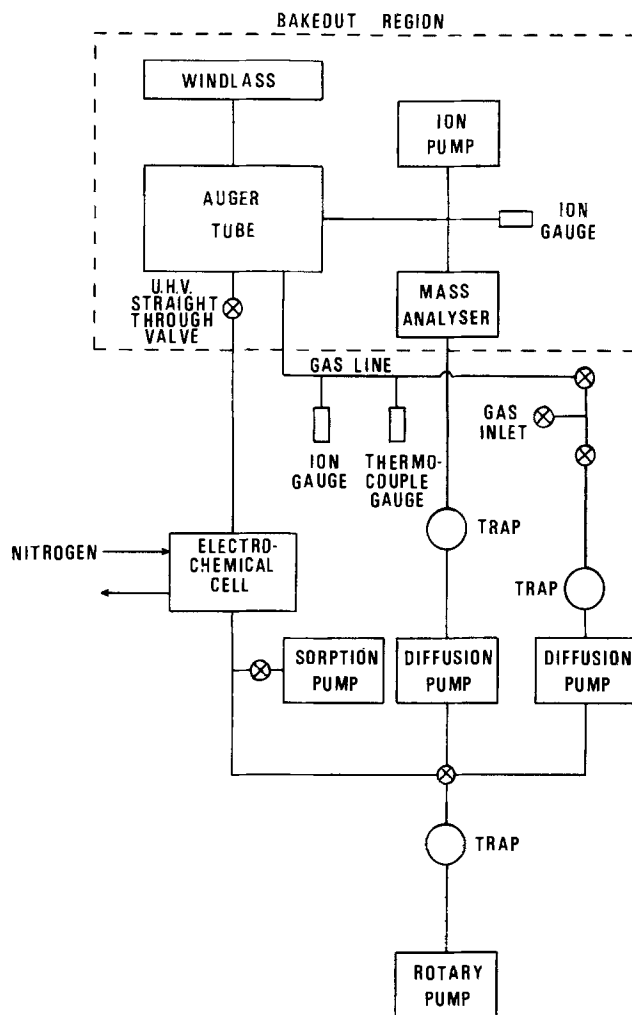


Fig. 2. Block diagram of vacuum system

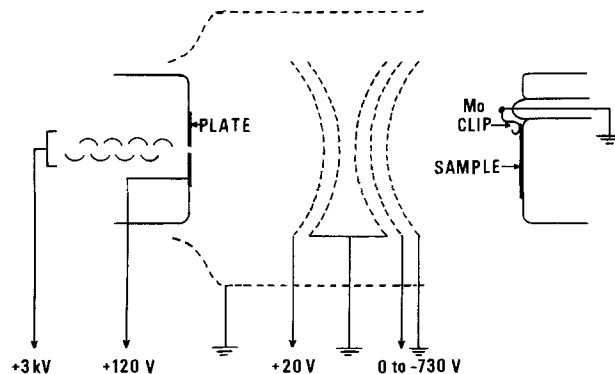


Fig. 3. Electrical circuit for analyzer of Auger electron spectroscopy.

gion. Grid (2), the retarding grid, is swept at 1 V/sec from -20 to -730V. Grids (3) and (4) are grounded, and grid (5), the focusing grid, has a potential of +20V. This grid focuses the retarded electrons on the electron multiplier, which amplifies the current of collected electrons. To improve the focusing further, the plate has a potential of +120V. The wall, which consumes the more energetic electrons that are not retarded, is grounded. To establish the optimum voltage values at which the signal/noise ratio was a maximum, these voltages were varied over large ranges and Auger spectra determined were compared. The multiplier designed for operation at -3000V, has 14 copper-beryllium dynodes and internally mounted resistors.

To obtain high noise rejection, the electronic detection scheme uses modulation and phase-sensitive

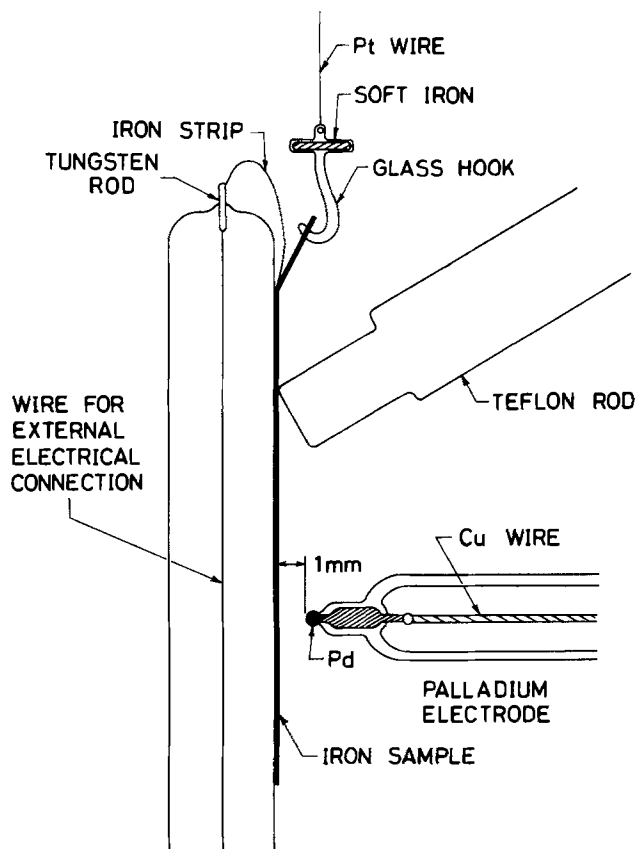


Fig. 4. Iron specimen in electrochemical cell showing palladium electrode (1 mm from specimen surface) and Teflon rod holding specimen on glass support.

detection techniques to modulate the analyzing energy and detect synchronously the current of collected electrons. The retarding grid is given a small amplitude modulating voltage, and the detector is tuned to the same frequency. The modulation voltage used was 3V rms for the low energy spectra and 8V rms for the high energy spectra. These voltages, at a frequency of 183 Hz, were found to give the optimum signal/noise ratio.

The electrochemical cell, located directly beneath the Auger tube, uses a palladium reference electrode (51-53), (Fig. 4), and a platinum auxiliary electrode. The main advantage of the palladium electrode is that it may be inserted directly into the electrolyte, i.e., no Luggin capillary is needed.

The solution used is 425 ml 0.1N KOH + 2500 ml 0.1M H_3BO_3 , diluted to 5000 ml, pH 8.1, which was kept in a storage bottle and transferred to the electrochemical cell as needed via a gas lift pump. The passivation experiments are carried out at +0.300V vs. SHE, a potential in the passive region (14). After a passivation experiment has been carried out, the electrolyte is drained from the cell and rinsed three times

with de-aerated distilled water. To remove excess water from the specimen surface, the cell is subjected to a preliminary evacuation, first with a rotary pump and then with a zeolite sorption pump. When a pressure of $\sim 10^{-4}$ Torr is reached, the valve between the Auger tube and the electrochemical cell is opened. The windlass is operated so that the hook contacts the specimen and transfers it into the Auger tube. After completing the transfer, the straight-through valve is closed, and the triode ion pump, acting on the Auger tube, regains a pressure $\sim 10^{-8}$ Torr within about 20 min.

The stage on which the specimen is mounted is cooled to -196°C with liquid nitrogen to prevent decomposition of hydrated films under high vacuum conditions. Using magnets the specimen is positioned on the stage and is then held in position with molybdenum clips, which also provide the electrical connection to the specimen. The Auger spectra are then measured and recorded on an X-Y recorder.

Results

Figure 5 shows the low energy spectra obtained (a) from an evaporated film of iron, (b) from a film exposed to O_2 at 10^{-3} Torr for 1 min, (c) from a film passivated for 10 min in a boric acid-potassium hydroxide buffer solution, pH = 8.1, at +0.300V vs. SHE, and (d) from a film passivated as in (c) and subsequently heated to 150°C . The iron film as evaporated, Fig. 5 (a), shows a low energy Auger $M_{2,3}M_{4,5}M_{4,5}^2$ transition at 46 eV, whereas the oxidized film, Fig. 5 (b), shows two transitions at 42 and 50 eV. The passivated specimen, Fig. 5 (c), shows one transition at 50 eV; and the passivated specimen after heating to 150°C , Fig. 5 (d), shows two transitions at 42 and 50 eV.

Figure 6 shows high energy spectra for films under the same conditions as Fig. 5. The oxygen KLL transition occurs at 508 eV, and the iron $L_3M_{2,3}M_{2,3}$, $L_3M_{2,3}M_{4,5}$, and $L_3M_{4,5}M_{4,5}$ transitions occur at 590, 645, and 695 eV, respectively. The passive film spectrum, Fig. 6 (c), shows some carbon contamination as evidenced by the carbon Auger transition at 270 eV.

Discussion

As shown in Fig. 5, oxidation of iron causes a splitting of the 46 eV iron Auger transition into two transitions at 42 and 50 eV. This doublet, characteristic of oxidized iron, has been observed previously by Suleman and Pattinson (54), Ueda and Shimizu (55), and Leygraf and Ekelund (56). The latter authors have suggested that the amplitudes of the 42 and 50 eV peaks are related to the surface concentrations of Fe^{2+} and Fe^{3+} , respectively. It would appear, then, from Fig. 5, that the passive film contains Fe^{3+} and no Fe^{2+} , at least in the first 10A. This conclusion agrees with the results from ellipsometric and electrochemical ex-

²K, L, M, . . . refer to the principal electronic quantum levels. The subscript 1 refers to s electrons; 2, 3 to p electrons; and 4, 5 to d electrons. It is customary to label Auger transitions in terms of the energy level first emptied, e.g., $M_{2,3}$; the level from which an electron drops to fill it, e.g., $M_{4,5}$; and the level from which the Auger electron is ejected, e.g., $M_{4,5}$, in that order; e.g., a $M_{2,3}M_{4,5}M_{4,5}^2$ transition.

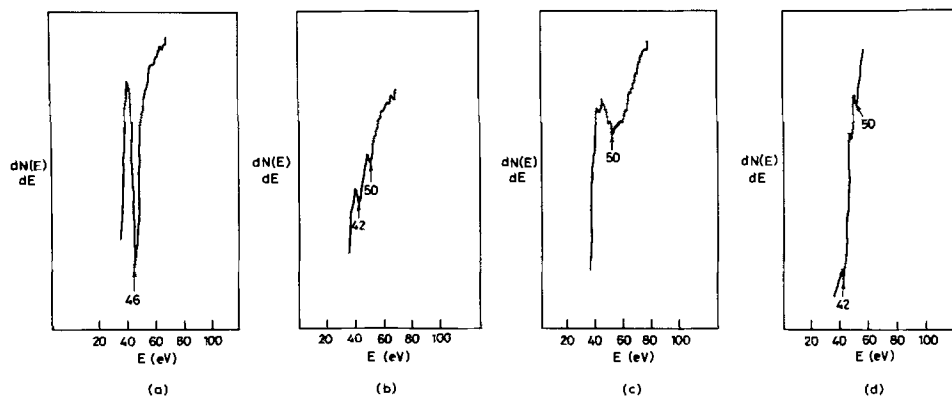


Fig. 5. Low energy Auger spectra of evaporated films of iron: (a) clean film as evaporated; (b) after exposure to O_2 at 10^{-3} Torr for 1 min; (c) passivated in boric acid-potassium hydroxide buffer solution, pH = 8.1, at 0.300V vs. SHE for 10 min; (d) passivated as in (c) and subsequently heated to 150°C .

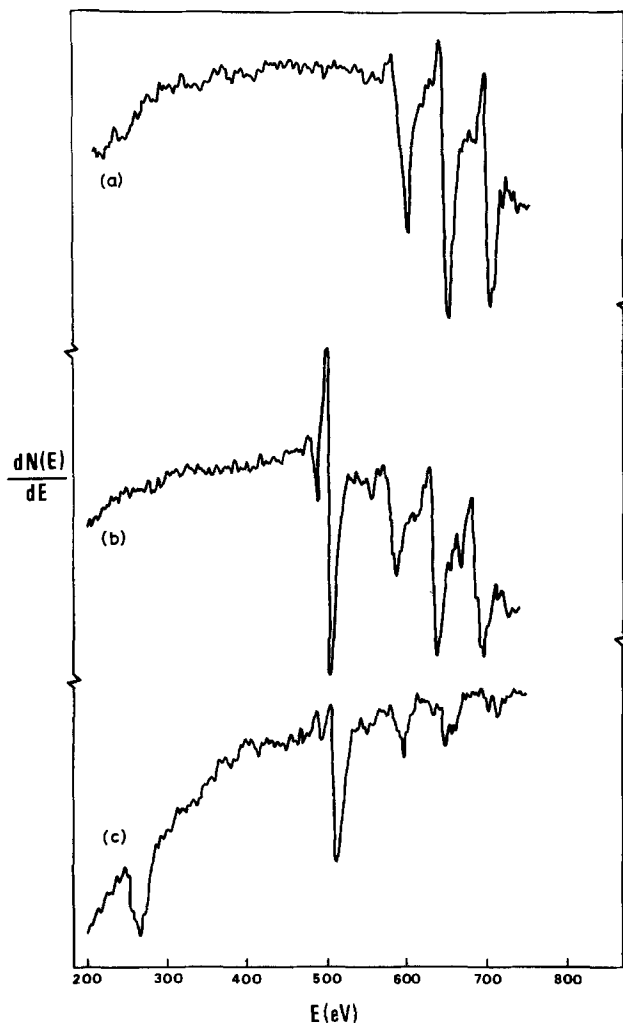


Fig. 6. High energy Auger spectra of evaporated films of iron: (a) clean film as evaporated; (b) after exposure to O_2 at 10^{-3} Torr for 1 min; (c) passivated in boric acid-potassium hydroxide buffer solution, $pH = 8.1$, at $0.300V$ vs. SHE for 10 min.

periments carried out by Bockris *et al.* (13, 15) and Sato *et al.* (57).

The carbon contamination shown in the spectrum for the passive film, Fig. 6(c), presumably occurred during exposure to the electrolyte and subsequent evacuation. Such carbon contamination did not occur on the iron during evaporation, Fig. 5(a), since the evaporation was carried out *in vacuo*. The possible effects of carbon contamination on shifts of the 46 eV iron transition were investigated by exposing evaporated films of iron to: (i) CO at 10^{-3} Torr in the Auger tube and (ii) the evacuated electrochemical cell at 10^{-4} Torr. In both experiments, the surface contamination resulted in no measurable change in the 46 eV transition energy.

The quantitative aspects of Auger electron spectroscopy, *i.e.*, the relation between Auger peak heights and concentration of surface species, have been reviewed in the literature (24, 26, 58-61). The production of Auger electrons depends on the ionization cross section of the inner level which is involved in the Auger process, and on the number and energy of the ionizing electrons. The Auger electron current, I_A , is given by (24, 59, 62)

$$I_A = I_p \sigma(E_p) \Omega n \theta_A \left\{ 1 - \exp\left(-\frac{d}{\lambda}\right) \right\}^{-1} (1 - \omega) \tau$$

where I_p = primary current on the crystal; $\sigma(E_p)$ = ionization cross section of the inner level at a primary energy E_p ; Ω = geometric factor that involves angles of incidence and emission, and the efficiency of collection and transmission of the analyzer, including rough-

ness factor; N = total number of atoms per unit area; θ_A = ratio of species A to the total number of atoms; d = interlayer spacing; λ = mean free path of Auger electron; ω = probability that an x-ray is emitted following ionization of the inner level; $(1 - \omega)$ = probability that an Auger process follows the ionization of the inner level; and τ = backscattering factor, due to the ionizing effect of secondary electrons.

The data presented by Vrakking and Meyer (63) show that the ionization cross section of the oxygen K level (containing 2 electrons) is $1.0 \times 10^{-19} \text{ cm}^2$ at a primary beam energy of 2 kV. A small extrapolation of their data for the ionization cross sections of $L_{2,3}$ shells (63) gives that for the iron $L_{2,3}$ level [8 electrons including Coster-Kronig transitions (64, 65)³] as $1.8 \times 10^{-19} \text{ cm}^2$. Hence, a stoichiometric oxide of FeO would have the sum of the amplitudes of the KLL oxygen Auger transitions, equal to $1.0/1.8 = 0.56$ times the sum of the amplitudes of the iron $L_{2,3}$ transitions. Similarly, Fe_2O_3 would have an oxygen transition with the sum of the peak heights $3 \times 1.0/2 \times 1.8 = 0.83$ times the sum of the amplitudes of iron $L_{2,3}$ transitions. Measurement of Auger spectra of the type presented in Fig. (6)b shows that, in fact, the ratio for iron oxidized at room temperature, *i.e.*, Fe_2O_3 (66), is 0.83 ± 0.04 (3 measurements) in excellent agreement with that predicted, 0.83.

These measurements are made with the assumption that the peak-peak height in the derivative spectrum is proportional to the Auger current, I_A , or to the area of the peak; *i.e.*, varying peak widths and modulation voltage distortion are neglected. The accuracy of the measurements may be inferred from the agreement of the theory with the results for the oxidized iron "standard."

Of a total of 6 measurements on the passive film as in Fig. 6(c), the average ratio of the amplitude of the oxygen transitions to the sum of the amplitudes of the iron $L_{2,3}$ transitions was 0.99 with a standard deviation of 0.11; these spectra, therefore, imply an oxygen/iron ratio in the passive film of $r = 0.99 \times 1.8/1.0 = 1.8$, with a standard deviation of 0.2. The oxygen/iron ratio of 1.8 ± 0.2 is higher than that of any known iron oxide.

A layer model may be used to estimate the amount of hydrated water in the passive film. The Auger electron current emerging at the sample surface from molecular layers below the surface is attenuated by the factor $e^{-nd/\lambda}$, where d is the interlayer spacing, λ is the mean-free path of the Auger electrons, and n is the number of layers through which the Auger electrons must pass to reach the surface. The relative contribution of oxygen and of iron to the total Auger current, I_A , may be calculated for a variety of assumed structures. For example, assuming that the passive film on iron consists of layers, each having the composition $Fe_2O_3 \cdot H_2O$, the ratio of the Auger currents due to oxygen and iron is

$$\frac{I_{\text{oxygen}}}{I_{\text{iron}}} = \frac{\frac{2}{3} (1 + e^{-d/\lambda} + e^{-2d/\lambda} + e^{-3d/\lambda} + \dots)}{1.8 \left(\frac{1}{3}\right) (1 + e^{-d/\lambda} + e^{-2d/\lambda} + e^{-3d/\lambda} + \dots)} = 1.1$$

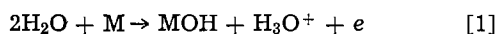
equal, within experimental error, to the ratio of the observed amplitudes of the Auger transitions. It would appear, therefore, that $Fe_2O_3 \cdot H_2O$ is a satisfactory representation of the passive film structure.

This conclusion is in essential agreement with the results of O'Grady and Bockris (18), who found that

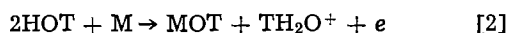
³ A Coster-Kronig transition involves 4 rather than 3 electrons. If the initial ionization occurs in the K shell, an electron from a higher energy level, such as the L shell, will drop to fill the vacant level. A third electron may then drop to fill this vacancy in the L shell, and the Auger electron is then emitted.

their Mössbauer spectroscopic results were consistent with a passive film on iron of a polymeric film of hydrated iron oxide. The Mössbauer parameters match values for the isomer shift and quadrupole splitting of iron-containing polymers, which have a structure containing di-oxy and di-hydroxy bridging bonds between the iron atoms.

Correspondingly, Kudo *et al.* (67) estimated from passivation experiments using tritiated solutions that the total content of water in the passive film on iron in the potential region of +0.04-+1.04V vs. SHE was equivalent to $\text{Fe}_2\text{O}_3 \cdot 1.99 \text{H}_2\text{O}$, except in the region of +0.24V vs. SHE, where inconsistent results were obtained. These authors (67) mention that the isotope effect was not considered in estimating the amount of bound water and that this would lower the reported values. Calculations based on the reactions



and



have been carried out to determine the ratio of the equilibrium constants, K_{H} and K_{T} , for reactions [1] and [2], respectively. The ratio $K_{\text{H}}/K_{\text{T}}$ was found to be ~ 0.01 , implying that equilibrium concentration of tritium in the passive film is much greater than that of hydrogen and that tritium measurements may greatly overestimate the amount of bound water in the passive film. Uncertainties in the relative rate constants of hydrogen and tritium (68, 69) place further doubt on the quantitative estimation of the H_2O content of the passive film using tritiated water. These considerations may explain the fact that the results of Kudo *et al.* (67) indicate a higher amount of H_2O than is consistent with the Auger results.

Heating the passivated specimen to 150°C caused the appearance [Fig. 5(d)] of the two Auger peaks, 42 and 50 eV, characteristic of oxidized iron. It may be assumed, then, that such heating causes decomposition of the passive film to iron oxide, perhaps $\gamma\text{-Fe}_2\text{O}_3$, the formation of which O'Grady (19) observed on drying passive iron.

Okamoto *et al.* (70-72) have studied the importance of hydrated water to the corrosion protection of the passive film. These studies indicated, in agreement with the work of O'Grady and Bockris (17-19), that the passive film is a hydrated oxide film having a gel-like structure. Between metal ions in the film, three different types of bridge exist: $-\text{M}-\text{H}_2\text{O}-\text{M}-$, $-\text{M}-\text{HO}-\text{M}-$, and $-\text{M}-\text{O}-\text{M}-$. Dehydration of the passive film, *e.g.*, by heating *in vacuo*, destroys bonds of the first two types, changing the passive film to a (less protective) perfect oxide.

Seo, Lumsden, and Staehle also studied the structure of the passive layer on iron (30). Their experimental technique involved a transfer of the sample through the atmosphere. Thereafter, they removed sections of the passive layer by sputtering it progressively and determining the spectrum as a function of depth. The Auger spectra registered by Seo, Lumsden, and Staehle were characteristic of the spectrum shown here [Fig. 5(b)] for air-formed oxide and showed the two peaks characteristic of this body rather than the single peak characteristic of the passive film [Fig. 5(c)]. Seo, Lumsden, and Staehle, however, interpreted their two peaks to be indicative of a duplex structure consisting of $\gamma\text{-Fe}_2\text{O}_3$ and Fe_3O_4 . Their interpretation must now be regarded as doubtful.

Conclusions

1. Auger electron spectroscopy may be used for electrochemical studies. It may be important that the films formed electrochemically be stabilized in vacuum by reduction to a low temperature.

2. The high energy Auger electron spectra are consistent with 1 water molecule per 2 iron molecules.

3. Heating the passive film in vacuum causes dehydration and the formation of an oxide.

4. The results are consistent with the model of the structure of the passive layer on iron arising from Mössbauer studies (17-19).

Acknowledgments

The authors express their appreciation to Mr. B. A. Sexton and Miss E. A. Chalmers for experimental assistance. The project was supported by the Australian Research Grants Committee and the Electricity Research Board, to whom the authors are most grateful.

Manuscript submitted Dec. 16, 1974; revised manuscript received July 11, 1975.

Any discussion of this paper will appear in a Discussion Section to be published in the June 1976 JOURNAL. All discussions for the June 1976 Discussion Section should be submitted by Feb. 1, 1976.

Publication costs of this article were partially assisted by The Flinders University of South Australia.

REFERENCES

- V. Brusic, *Oxides and Oxide Films*, **1**, 1 (1972).
- C. L. Foley, J. Kruger, and C. J. Bechtoldt, *This Journal*, **114**, 994 (1967).
- A. B. Winterbottom, *J. Sci. Instr.*, **14**, 203 (1937).
- A. B. Winterbottom, *Trans. Faraday Soc.*, **42**, 487 (1946).
- L. Tronstad, *ibid.*, **31**, 1151 (1935).
- A. K. N. Reddy and J. O'M. Bockris, in "Ellipsometry in the Measurement of Surfaces and Thin Films," p. 229 National Bureau of Standards, Misc. Pub. 256, Washington, D.C. (1964).
- J. Kruger, *ibid.*, p. 131.
- J. O'M. Bockris, A. K. N. Reddy, and B. Rao, *This Journal*, **113**, 1133 (1966).
- B. Rao, Ph.D. Thesis, University of Pennsylvania (1966).
- W. K. Paik and J. O'M. Bockris, *Surface Sci.*, **28**, 61 (1971).
- J. Kruger and J. P. Calvert, *This Journal*, **114**, 43 (1967).
- K. Kudo, T. Shibata, G. Okamoto, and N. Sato, *Corrosion Sci.*, **8**, 809 (1968).
- J. O'M. Bockris, M. Genshaw, and V. Brusic, *Symposia of the Faraday Society*, No. 4, 177 (1970).
- J. O'M. Bockris, M. A. Genshaw, V. Brusic, and H. Wroblowa, *Electrochim. Acta*, **16**, 1859 (1971).
- H. Wroblowa, V. Brusic, and J. O'M. Bockris, *J. Phys. Chem.*, **75**, 2823 (1971).
- V. Brusic, Ph.D. Thesis, University of Pennsylvania (1971).
- W. E. O'Grady and J. O'M. Bockris, *Chem. Phys. Letters*, **5**, 116 (1970).
- W. E. O'Grady and J. O'M. Bockris, *Surface Sci.*, **38**, 249 (1973).
- W. E. O'Grady, Ph.D. Thesis, University of Pennsylvania (1973).
- C. C. Chang, *Surface Sci.*, **25**, 53 (1971).
- N. J. Taylor, in "Techniques of Metals Research," Vol. 7, R. F. Bunshah, Editor, Interscience, New York (1971).
- P. W. Palmberg, *Anal. Chem.*, **45**, 549A (1973).
- A. M. Horgan and I. Dalins, *Surface Sci.*, **36**, 526 (1973).
- F. Meyer and J. J. Vrakking, *ibid.*, **33**, 271 (1972).
- M. P. Seah, *ibid.*, **40**, 595 (1973).
- C. C. Chang, in "Characterization of Solid Surfaces," P. F. Kane and G. B. Larrabee, Editors, Chap. 20, Plenum Press, New York (1974).
- A. T. Hubbard, *Crit. Rev. Anal. Chem.*, **3**, 201 (1973).
- A. T. Hubbard, R. M. Ishikawa, and J. A. Schoeffel, International Symposium on Characterization of Adsorbed Species in Catalytic Reactions, Ottawa, 1974.
- J. B. Lumsden and R. W. Staehle, *Scripta Met.*, **6**, 1205 (1972).
- M. Seo, J. B. Lumsden, and R. W. Staehle, *Surface Sci.*, **42**, 337 (1974).
- G. Gohr and E. Lange, *Naturwissenschaften*, **43**, 12 (1956).
- G. Gohr and E. Lange, *Z. Elektrochem.*, **61**, 1242 (1957).
- K. J. Vetter, *ibid.*, **62**, 642 (1958).
- K. J. Vetter, "Electrochemical Kinetics: Theoretical and Experimental Aspects" (Trans. by Scripta

- Technica), pp. 780-783, Academic Press, Inc., New York (1967).
35. P. Staib, *J. Phys. E: Sci. Instr.*, **5**, 484 (1972).
 36. P. Staib, *Vacuum*, **22**, 481 (1972).
 37. D. O. Hayward and B. M. W. Trapnell, "Chemisorption," 2nd ed., p. 3, Butterworths, London, (1964).
 38. J. L. Stakebake and L. M. Steward, *J. Colloid Interface Sci.*, **42**, 328 (1973).
 39. J. L. Stakebake, *J. Phys. Chem.*, **77**, 581 (1973).
 40. T. Morimoto, M. Nagao, and F. Tokuda, *ibid.*, **73**, 243 (1969).
 41. T. Morimoto, M. Nagao, and F. Tokuda, *Bull. Chem. Soc. Japan*, **40**, 2723 (1967).
 42. G. Blyholder and E. A. Richardson, *J. Phys. Chem.*, **66**, 2597 (1962).
 43. J. E. de Graaf and W. J. Oosterkamp, *J. Sci. Instr.*, **15**, 293 (1938).
 44. "Handbook of Chemistry and Physics," 52nd ed., p. E-5, Chemical Rubber Co., Cleveland, Ohio (1971).
 45. T. E. Madey and J. T. Yates, *J. Vacuum Sci. Technol.*, **8**, 525 (1971).
 46. E. E. Donaldson, *Vacuum*, **12**, 11 (1962).
 47. J. R. Anderson and B. G. Baker, in "Chemisorption and Reactions on Metallic Films," Vol. 2, J. R. Anderson, Editor, p. 1, Academic Press, Inc., London (1971).
 48. T. E. Hanley, *J. Appl. Phys.*, **19**, 583 (1948).
 49. O. A. Weinreich and H. Bleicher, *Rev. Sci. Instr.*, **23**, 56 (1952).
 50. P. W. Palmberg, G. K. Bohn, and J. C. Tracy, *Appl. Phys. Letters*, **15**, 254 (1969).
 51. S. Schuldiner, G. Castellán, and J. P. Hoare, *J. Chem. Phys.*, **28**, 16 (1958).
 52. M. J. Vasile and C. G. Enke, *This Journal*, **112**, 865 (1965).
 53. B. D. Cahan, Ph.D. Thesis, University of Pennsylvania (1968).
 54. M. Suleman and E. B. Pattinson, *Surface Sci.*, **35**, 75 (1973).
 55. K. Ueda and R. Shimizu, *Appl. Phys. Letters*, **22**, 393 (1973).
 56. C. Leygraf and S. Ekelund, *Surface Sci.*, **40**, 609 (1973).
 57. N. Sato, K. Kudo, and T. Noda, *Corrosion Sci.*, **10**, 785 (1970).
 58. M. P. Seah, *Surface Sci.*, **32**, 703 (1972).
 59. J. J. Vrakking and F. Meyer, *ibid.*, **35**, 34 (1973).
 60. B. G. Baker and B. A. Sexton, 2nd International Conference on Solid Surfaces, Kyoto, Japan, 1974.
 61. C. C. Chang, *Surface Sci.*, **48**, 9 (1975).
 62. B. G. Baker, *Mod. Aspects Electrochem.*, **10**, 93 (1975).
 63. J. J. Vrakking and F. Meyer, *Phys. Rev.*, **A9**, 1932 (1974).
 64. D. Coster and R. de L. Kronig, *Physica*, **2**, 13 (1935).
 65. E. J. McGuire, *Phys. Rev.*, **A3**, 587 (1971).
 66. U. R. Evans, "The Corrosion and Oxidation of Metals: First Supplementary Volume," p. 25, Edward Arnold, London (1968).
 67. K. Kudo, T. Shibata, G. Okamoto, and N. Sato, *Corrosion Sci.*, **8**, 809 (1968).
 68. J. Bigeleisen, *J. Chem. Phys.*, **17**, 675 (1949).
 69. M. Polanyi, *Nature*, **133**, 26 (1934).
 70. G. Okamoto and T. Shibata, *ibid.*, **206**, 1350 (1965).
 71. G. Okamoto and T. Shibata, "Proceedings of the Third International Congress on Metallurgy and Corrosion," Vol. 1, p. 396, MIR, Moscow (1969).
 72. G. Okamoto, *Corrosion Sci.*, **13**, 471 (1973).

Surface Brightening during High Rate Nickel Dissolution in Nitrate Electrolytes

Madhav Datta and Dieter Landolt*

Materials Department, Swiss Federal Institute of Technology, Lausanne, Switzerland

ABSTRACT

Conditions leading to surface brightening during ECM in passivating electrolytes were investigated by studying high rate transpassive nickel dissolution in acidified nitrate electrolytes under controlled hydrodynamic conditions. The experimental apparatus consisted of a flow channel cell in which constant electrolyte linear velocities between 100 and 1760 cm/sec could be reached. Dissolution experiments were performed galvanostatically at current densities ranging from 0.5 to 30 A/cm². Over-all current voltage behavior, current efficiency for metal dissolution and surface appearance were evaluated as a function of applied current density, flow rate, and electrolyte composition. Results indicate that the onset of surface brightening is mass transfer controlled and coincides with the formation of a salt precipitation layer at the anode.

The process of electrochemical machining (ECM) involves anodic dissolution of a workpiece at very high current density under conditions of high electrolyte flow rate and small electrode spacing. Dimensional accuracy and surface finish of the workpiece produced by ECM are intimately related to the nature of the electrolyte and to operating conditions. Passivating electrolytes such as sodium chlorate and sodium nitrate are well suited for electrochemical machining of iron and nickel base alloys because they give good dimensional control and good surface finish (1, 2). The relation between passivation behavior and dimensional control in ECM has been discussed by several authors (3-7) but little is known at present about the proc-

esses which determine surface finish in passivating ECM electrolytes.

In ECM practice, surface finish can frequently be improved by increasing current density. Cole and Hopenfeld explained this fact by an electrostatic model (8). According to this, a high potential gradient in the solution leads to preferred metal dissolution at peak sites of a rough surface and thus to leveling. The electrostatic model predicts that surface finish in ECM is independent of dissolution mechanism and of flow rate. This is in contradiction to the findings of Landolt, Muller, and Tobias who studied high rate dissolution of copper in different electrolytes (9, 10) and found that etched surfaces resulted from active dissolution while bright and pitted surfaces resulted from transpassive dissolution. The transition from one dissolution mode to the other depended not only on current den-

* Electrochemical Society Active Member.

Key words: electrochemical machining, transpassive dissolution, nickel, surface brightening.

sity but also on flow rate, indicating that the onset of surface brightening was controlled by mass transfer.

Surface brightening under conventional electro-polishing conditions is also controlled by mass transfer (11-15). Hoar and Rothwell (14), who studied copper dissolution in phosphoric acid in a flowing electrolyte, found that the onset of surface brightening coincided with the formation of a salt layer at the anode giving rise to well-defined limiting current plateaus. Their findings have recently been confirmed by Kojima and Tobias (16).

Very little is known about the mechanism of surface brightening of metals dissolving in the transpassive dissolution mode under ECM conditions. Mao and Chin (17) studying the dissolution of steel in sodium chlorate recently suggested that salt precipitation is responsible for the onset of surface brightening. However, they found no effect of flow rate on surface finish, therefore rendering the proposed mechanism questionable. The quantitative study of mass transport processes during transpassive dissolution under ECM conditions is rendered difficult not only by the fast metal dissolution rate which may affect cell geometry and therefore hydrodynamic conditions but also by the possibility of anodic oxygen evolution which can disturb the anodic diffusion layer. To minimize these effects, dissolution experiments have to be carried out at high electrolyte flow velocities using an electrolyte which gives high current efficiencies for metal dissolution. In addition a well-defined cell geometry has to be maintained during the experiments.

The aim of the present paper was to investigate the influence of mass transfer on surface brightening of metals dissolving at high rate at potentials more noble than those corresponding to anodic oxygen evolution. For that purpose, the anodic dissolution of nickel in concentrated acidified nitrate electrolytes was studied in a flow cell allowing for well-defined mass transfer conditions. The present investigation is part of our continuing effort to develop models for predicting the ECM behavior of passivating metals and alloys.

Experimental

All experiments were performed in a flow cell apparatus described in detail elsewhere (18). The electrochemical cell consisted of a rectangular flow channel 0.317 cm wide and 0.053 cm high. A hydrodynamic entrance length of 7 cm upstream from the electrode served for establishing fully developed velocity profiles at the electrodes. Anode and cathode made of Nickel 200 were positioned flush with the channel wall. The electrodes were 1.02 cm long and of the same width as the flow channel. The anode area was thus 0.32 cm². The electrolyte was forced through the cell by means of a single stroke piston pump at constant linear velocities ranging from 100 to 1760 cm/sec. Each experiment corresponded to one stroke of the piston after which the pump cylinder was refilled with electrolyte drawn from a 2 liter reservoir. Electrolyte temperature was maintained at 25°C by means of a thermostat. A saturated calomel electrode was used for potential measurements. It was connected to the flow channel by means of a back side capillary positioned upstream from the anode.

Before each experiment, the nickel anode was mechanically polished on 600 carborundum paper, degreased with benzene, and cleaned with soap solution and distilled water. It was subjected to cathodic pre-electrolysis in 1M NaOH solution at 20 mA/cm² for 30 sec followed by rinsing with distilled water. The anode was then immediately positioned in the cell. Electrolyte solutions were prepared from analytical grade chemicals and distilled water. Most data reported in this study were obtained in 5M NaNO₃ + 1M HNO₃. A strongly acidified solution was employed to reduce local pH changes at the anode due to oxygen evolution.

Except for preliminary experiments which were carried out potentiostatically, all experiments were

performed at constant current using a potentiostat (Amel Type 555) in the galvanostatic mode. Current densities applied ranged up to 30 A/cm². One series of experiments was aimed at the study of polarization behavior and surface finish. A constant charge was passed corresponding to a maximum depth of dissolution of 10 μ. After the experiments, the surface of the anode was observed visually and/or with the aid of a microscope. The surfaces of a few samples were also investigated by means of a scanning electron microscope. Current during the experiments was monitored on a conventional storage oscilloscope (Tektronix Type 5103N), while the anode potential was measured by means of a digital oscilloscope (Nicolet Type 109). In this instrument, the data are first stored in digital form in a memory. They can be displayed in analog or digital form on an oscilloscope screen or recorded on a pen recorder. In a second series of experiments, aimed at the study of the current efficiency for metal dissolution, the amount of charge passed corresponded to a maximum depth of dissolution of 20 μ. In these experiments, the current was monitored with the digital oscilloscope while the anode potential was measured with an electrometer (Keithly Type 615). The anode was carefully weighed before and after each experiment, using an analytical balance having a precision of 0.01 mg (Sartorius Model 2474). Before weighing, the samples were cleaned with acetone and dried with air.

Results

The anodic polarization behavior of nickel in 5M NaNO₃ + 1M HNO₃ solution is illustrated by the potentiodynamic data of Fig. 1 which were obtained at different electrolyte flow velocities by applying a potential scan rate of 500 mV/sec. The curves exhibit a typical active-passive behavior. The passivation potential is 0.250V vs. SCE, the critical current density for passivation is approximately 350 mA/cm². This cur-

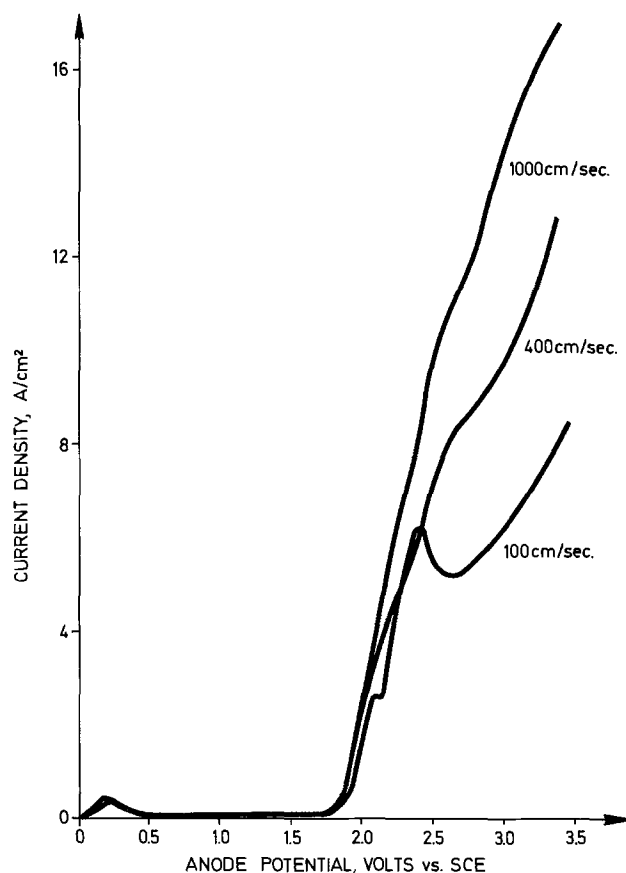


Fig. 1. Anodic potential sweep measurements on nickel in 5M NaNO₃ + 1M HNO₃ at different electrolyte flow velocities. Scan rate 500 mV/sec.

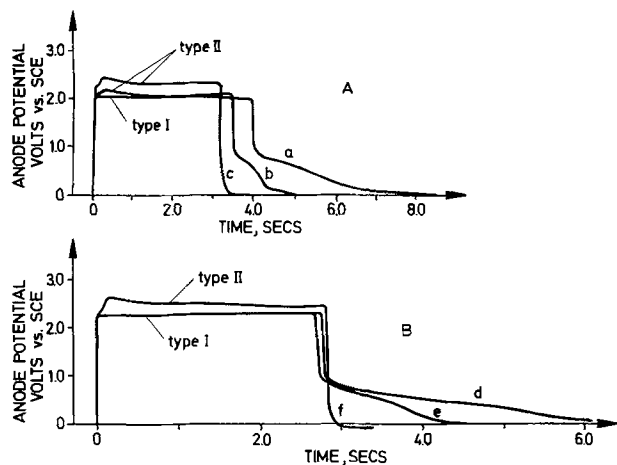


Fig. 2. Anode potential transients in 5M NaNO₃ + 1M HNO₃. A: Constant flow rate of 400 cm/sec, current density 7.0 A/cm² (a), 7.5 A/cm² (b), 9.0 A/cm² (c). B: Constant current density of 10 A/cm², flow rate 1760 cm/sec (d), 1000 cm/sec (e), 400 cm/sec (f).

rent density is smaller than those applied in subsequent dissolution experiments (0.5–30 A/cm²) which therefore refer exclusively to the transpassive potential region. The latter corresponds to potentials higher than 1.7V vs. SCE. Flow rate has no appreciable effect on the active-passive behavior of nickel in sodium nitrate but it affects the polarization curves in the transpassive potential region (Fig. 1). Because generally large IR drops between capillary and anode are present in high rate dissolution studies, current rather than potential was controlled in all subsequent experiments.

The application of a constant current pulse to the anode resulted in two distinct types of potential transients (Fig. 2). At low current densities, steady state was reached almost immediately and the potential stayed constant throughout the run (type I transient). At high current densities, on the other hand, the potential jumped to an initial value, then increased to a maximum before decaying to a more or less steady

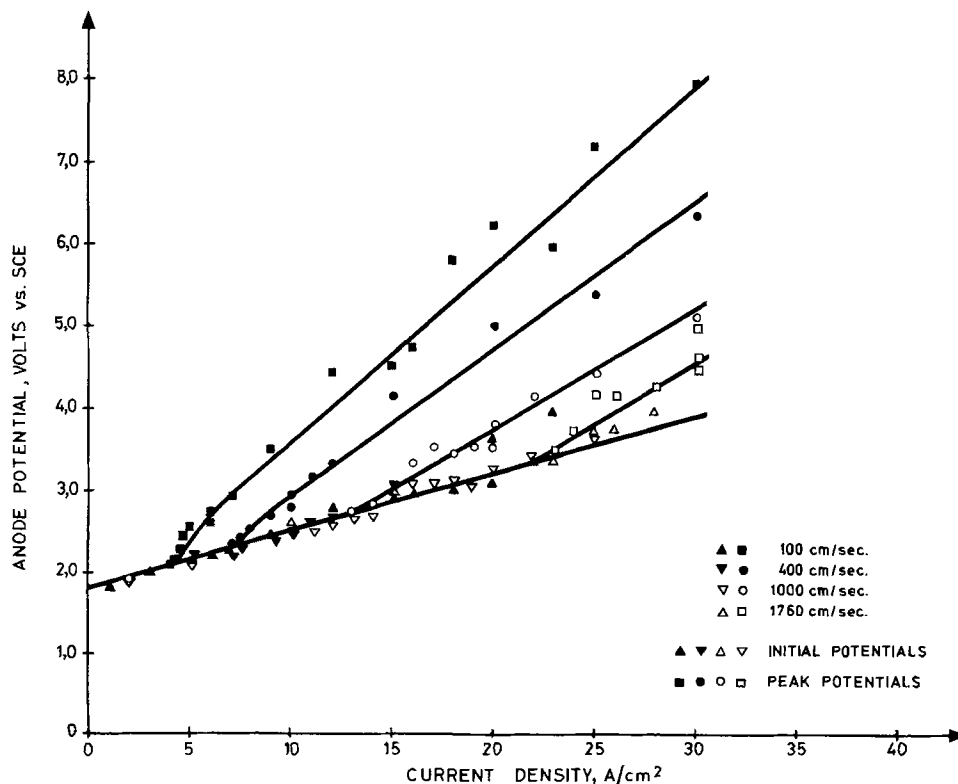
value (type II transients). Which type of potential transient occurred during an experiment depended not only on the magnitude of the applied current density but also on flow rate. For example, at a flow rate of 100 cm/sec, a type II transient was observed at a current density as low as 4.2 A/cm² while at a flow rate of 1760 cm/sec, a type I transient was observed up to current densities of 20 A/cm².

Upon current switch-off, a potential arrest at approximately 0.8V usually occurred before the original open-circuit potential of 0V vs. SCE was reached. The phenomenon is well known for passive electrodes undergoing self-activation, and a thorough discussion of the literature has been given by Vetter (19). The data of Fig. 2 indicate that upon current switch-off self-activation of the anode occurred faster the higher the applied current density and the lower the flow rate. The behavior has been discussed elsewhere (20).

In Fig. 3 initial values and peak values of measured potential transients are plotted as a function of current density for different flow rates. Steady-state potentials of type I transients and initial potentials of type II transients fall on the same straight line. Their value is governed mostly by the IR drop between reference electrode capillary and anode. Peak potential values of type II transients lie distinctly higher. The difference between peak potentials and initial potentials is due to the presence of an anodic layer which increases the effective resistance at the anode surface. This layer is different from the usual passive film present on nickel at lower current density because the passive film does not give rise to type II transients.

Two distinctly different types of surface texture resulted from anodic dissolution. One type of surface, typical for a type I transient, appeared grayish-black to the eye and gave the impression of a surface covered by a thick porous film. This impression was not consistent with reality, however. First of all, no deposits could be removed from the black-appearing surface by mechanical or chemical means. X-ray diffraction analysis of a black surface showed only the diffraction pattern characteristic for metallic nickel, but neither oxides nor salts could be identified on the surface. While this does not exclude the presence of a thin passive film [the thickness of passive films on nickel

Fig. 3. Over-all anode potential as a function of current density for nickel dissolution in 5M NaNO₃ + 1M HNO₃ derived from galvanostatic measurements.



is typically of the order of angströms (19)], it definitely excludes the presence of films of greater thickness. It is therefore concluded that the black surface appearance was due to a finely dispersed surface texture of the metal resulting from the anodic dissolution process. A scanning electron micrograph of a typical black-appearing surface is given in Fig. 4.

The second type of surface typical for type II transients appeared bright to the naked eye. Its average surface roughness determined with a mechanical surface tester (Talysurf Model 10) was $R_a = 0.1\mu$ compared to $R_a = 0.75\mu$ for a black-appearing surface.

A scanning electron micrograph of a bright surface is shown in Fig. 5. On a microscale, the surface appears almost perfectly flat, except for the presence of some grain boundary attack and of hemispherical pits. Several of the pits exhibit tails pointing in flow direction. It is interesting to note that no effect of flow direction was visible on black-appearing surfaces. On the other hand, bright surfaces not only exhibited pits tailing in flow direction but also so called flow streaks (1). A similar behavior has previously been observed during high rate anodic copper dissolution (10), where the surface texture of etched surfaces showed no discernible influence of flow direction, while bright and pitted surfaces frequently exhibited well pronounced flow streaks. It appears from this that the occurrence of

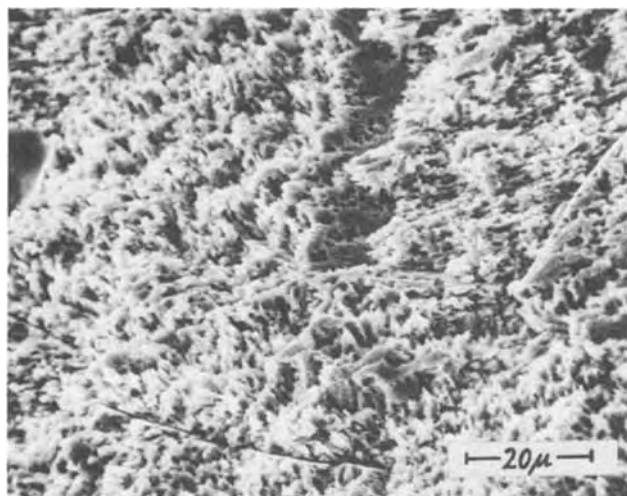


Fig. 4. Scanning electron micrograph of etched surface resulting from dissolution in $5M NaNO_3 + 1M HNO_3$ at a current density of $3 A/cm^2$ and a flow velocity of $400 cm/sec$.

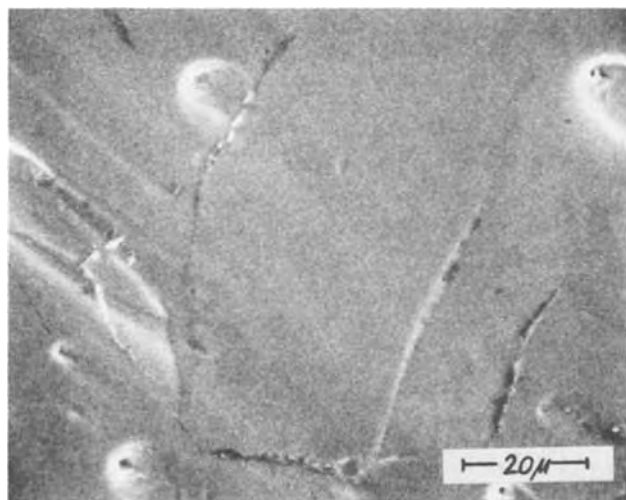


Fig. 5. Scanning electron micrograph of bright surface resulting from dissolution in $5M NaNO_3 + 1M HNO_3$ at a current density of $25.0 A/cm^2$ and a flow rate of $400 cm/sec$. Flow direction from upper left to lower right.

flow streaks in ECM is intimately related to pitting phenomena occurring under brightening conditions.

Surface brightening always started at the downstream end of the anode. Upon increasing current density, it gradually extended over the entire anode surface. The transition in appearance from a black to a bright surface was quite sharp as illustrated by Fig. 6. Because of the clear difference in surface appearance, the fraction of the anode surface that appeared bright could be estimated for each current density and flow rate. The results of such estimations are given in Fig. 7 where percentage brightening has been plotted as a function of current density for different flow rates. The data demonstrate that current density as well as flow rate have a strong influence on surface finish resulting from transpassive dissolution. The onset of surface brightening (Fig. 7) coincides with a change in the slope of the over-all current voltage curve (Fig. 3).

The current efficiency for metal dissolution was determined at various flow rates over a current density

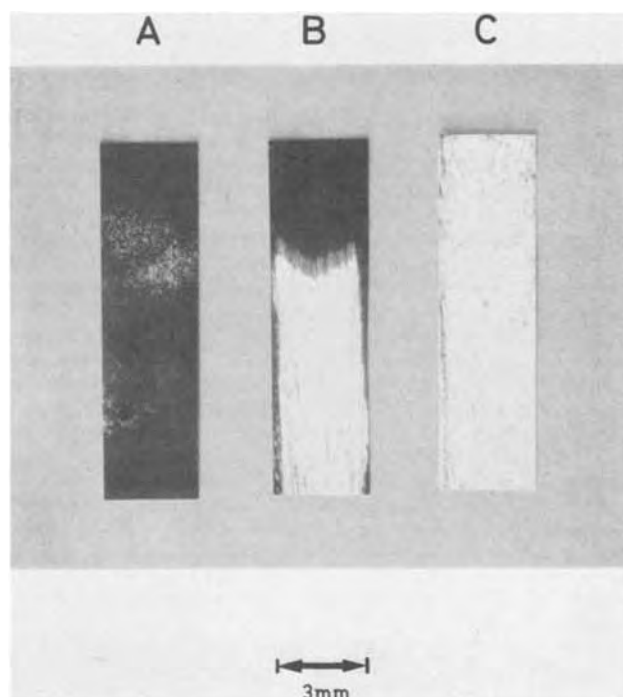


Fig. 6. Photomicrograph of typical nickel surfaces after anodic dissolution showing (A) black surface, (B) partially bright surface, (C) bright surface. Flow direction from top to bottom.

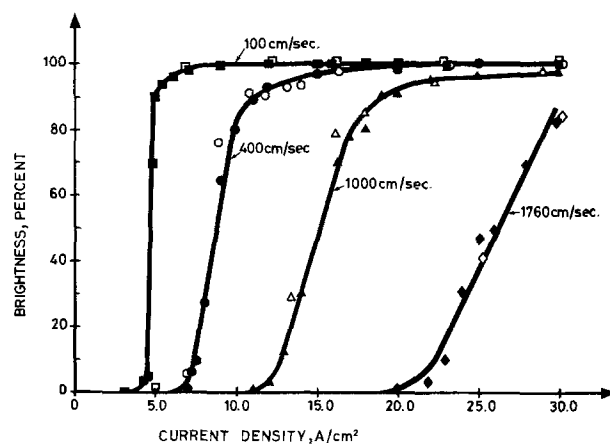


Fig. 7. Percentage of surface area of nickel anode appearing bright as a function of applied current density. Electrolyte $5M NaNO_3 + 1M HNO_3$. Charge passed: $30 coulombs/cm^2$ (■ ● ▲ ◆), $60 coulombs/cm^2$ (□ ○ △ ◇).

range from 0.5 A/cm² to 30 A/cm² by weight loss measurements. Current efficiency values calculated on the basis of Ni²⁺ formation are given as a function of current density in Fig. 8. The dissolution efficiency increases with increasing current density until a maximum of 90-95% is reached. The initial part of the current efficiency vs. current density curve is independent of flow conditions, but the current density at which maximum efficiency is attained increases with flow rate. After the maximum, the apparent current efficiency for dissolution decreases slightly and levels off at a constant value of 85-90%.

LaBoda *et al.* (21) recently investigated nickel dissolution in sodium chlorate under ECM conditions. The current efficiency for metal dissolution was measured while simultaneously the anodically evolved gas was collected and analyzed. The authors found that all the current passed could be accounted for by anodic oxygen evolution and divalent nickel ion formation. In the present flow channel system, anodically evolved gas could not be analyzed. However, a few preliminary experiments were performed in a cell without external convection in which the anode gas could be collected. These experiments performed at current densities up to 5 A/cm² indicated that divalent nickel ion formation and anodic oxygen evolution are the predominant reactions during transpassive nickel dissolution in sodium nitrate. It is therefore concluded that in the ascending part of the current efficiency vs. current density curves shown in Fig. 8 nickel dissolved to the bivalent state, the remainder of the current serving for oxygen evolution. Whether the same holds true for current densities above the current efficiency maximum cannot be decided from presently available data.

Discussion

Mass transport in the present flow channel cell can be described by Eq. [1] and [2] which apply to laminar (22) and turbulent (23) flow conditions, respectively¹

$$Nu = 1.85 (ReScD_h/L)^{1/3} \quad [1]$$

$$Nu = 0.022 Re^{7/8} Sc^{1/4} \quad [2]$$

The Nusselt number Nu is defined by: $i_l D_h / nF\Delta C D$. The Schmidt number Sc is defined by $Sc = \nu/D$ and the Reynolds number Re is defined by $Re = uD_h/\nu$. In the expressions i_l is the limiting current density, D_h is the hydraulic diameter of the flow channel, L is the length of the electrode, ΔC is the concentration difference between anode and bulk, D is the diffusion coefficient of the transport limiting species, ν is the kinematic viscosity, u is the linear flow velocity of the electrolyte.

¹Several different dimensionless relations describing heat and mass transport under turbulent flow conditions have been proposed in the literature (23-26). Most of them show Nu to be proportional to $Re^{7/8}$ and $Sc^{1/3}$ or $Sc^{1/4}$ but differ somewhat in the proportionality constant. Equation [2] is used here because previous limiting current measurements in the present apparatus (18) showed it to be in good agreement with experimental data.

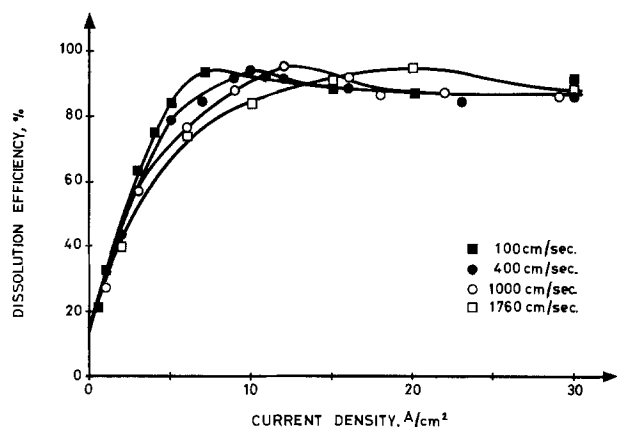


Fig. 8. Current efficiency for nickel dissolution (based on Ni²⁺ formation) in 5M NaNO₃ + 1M HNO₃ as a function of applied current density at different flow rates.

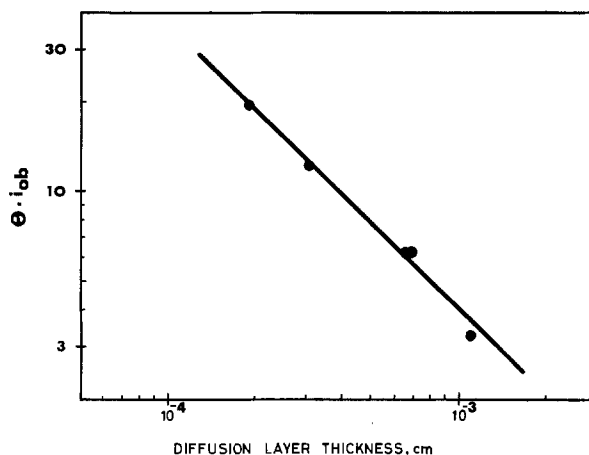


Fig. 9. Onset of brightening during nickel dissolution in 5M NaNO₃ + 1M HNO₃ as a function of diffusion layer thickness.

For a mass transport controlled surface brightening process Eq. [3] holds

$$\theta i_{ob} = nFD \frac{\Delta C}{\delta} \quad [3]$$

Here i_{ob} is the current density at the onset of brightening and θ is the current efficiency for metal dissolution at the onset of brightening. The diffusion layer thickness δ depends on flow conditions and is given by the relation

$$\delta = \frac{D_h}{Nu} \quad [4]$$

In Fig. 9 the product θi_{ob} derived from the data of Fig. 7 and 8 is plotted on a logarithmic scale as a function of δ evaluated from Eq. [1], [2], and [4]. The numerical value of i_{ob} corresponds to 5% of the surface being bright. The kinematic viscosity ν , needed for the calculation of Re and Sc , was determined experimentally (Table I). The numerical value of D needed for the calculation of Sc was assumed to be 9×10^{-6} cm²/sec. Since in Eq. [1] and [2] Sc appears with the exponent 1/3 and 1/4, respectively, the absolute value of D has relatively little influence on the data of Fig. 9. In particular it does not affect the slope of the straight line shown. The slope determined by regression analysis is -1.0 ± 0.06 . This is the same value as predicted by Eq. [3]. Therefore, the onset of surface brightening on nickel dissolving in sodium nitrate solution is mass transport controlled.²

According to Hoar (14) and others, electropolishing of metals proceeds in the presence of a precipitated salt layer on the anode surface and is mass transport controlled. The data given above suggest that a similar mechanism applies to high rate nickel dissolution under ECM conditions. To further test this hypothesis, dissolution experiments were performed in acidified nickel nitrate solution of different concentration. The composition of the three solutions employed is given

²In the above calculation of δ , it was assumed that anodic gas evolution has a negligible influence on mass transport at the onset of surface brightening. This assumption appears justifiable in view of the high electrolyte flow velocities employed and in view of the high value of metal dissolution current efficiency at the onset of brightening (Fig. 8).

Table I. Physical properties of nitrate electrolytes (25°C)

Electrolyte	Density, g/cm ³	Viscosity, c.p.	Kinematic viscosity, cm ² /sec
5M NaNO ₃ + 1M HNO ₃	1.288	1.868	1.45×10^{-2}
0.5M Ni(NO ₃) ₂ + 1M HNO ₃	1.103	1.181	1.07×10^{-2}
2.5M Ni(NO ₃) ₂ + 1M HNO ₃	1.387	2.758	1.99×10^{-2}
3.5M Ni(NO ₃) ₂ + 1M HNO ₃	1.517	2.169	3.40×10^{-2}

in Table I together with their physical properties which were determined experimentally. In principle, it would have been desirable to use binary nickel nitrate solutions because mass transport data can more easily be interpreted in binary solutions than in mixed electrolytes. However, preliminary experiments had shown that unless the nickel nitrate solutions employed were strongly acid, metal and hydroxide deposition processes at the cathode rendered results unreproducible. In the presence of 1M HNO₃, the cathode remained clean of deposits during the experiments. The solubility of nickel nitrate in 1M HNO₃ was determined experimentally to be 4.14 moles/liter. The concentration of the nickel nitrate solutions of Table I corresponds therefore to 12, 60, and 85% of saturation, respectively.

Figure 10 shows current voltage curves measured at a constant flow rate of 1000 cm/sec in nickel nitrate solutions of different concentration. The data were derived from galvanostatic transients in the same way as described above for sodium nitrate solution. As before, the change in slope in the current voltage curve corresponds to a change from type I to type II transients. The change occurred at a lower current density the higher the nickel nitrate concentration in the bulk and it coincided with the onset of surface brightening. The fraction of anode surface appearing bright is plotted as a function of current density for different nickel nitrate concentration in Fig. 11.

The data clearly show that at a given flow velocity, surface brightening sets in at lower current density the higher the bulk concentration of nickel nitrate. This is qualitatively consistent with a salt film precipitation mechanism of surface brightening. According to this model, the anode surface concentration of nickel nitrate at the onset of brightening corresponds to the saturation concentration and the driving force for diffusion (Eq. [3]) is the concentration difference of nickel ion between anode surface and bulk

$$\Delta C = C_s - C_b \quad [5]$$

The saturation concentration C_s is the same for the three nickel nitrate solutions employed. Therefore, by increasing the bulk concentration C_b , the current density for the onset of brightening becomes smaller.

A more quantitative test of the proposed model is provided by the data of Table II. Here, numerical values of ΔC and C_s for the experiments performed in nickel nitrate solution were evaluated by an iteration procedure. Different values of D were assumed and corresponding C_s values were calculated using the equations given above. The best numerical value for D was presumed to be the one giving identical C_s values for all different nickel nitrate solutions employed. The best value for D was thus found to be 9×10^{-6} cm²/sec. The ionic diffusion coefficient of Ni²⁺ at infinite dilution evaluated from mobility data (28) is 6×10^{-6}

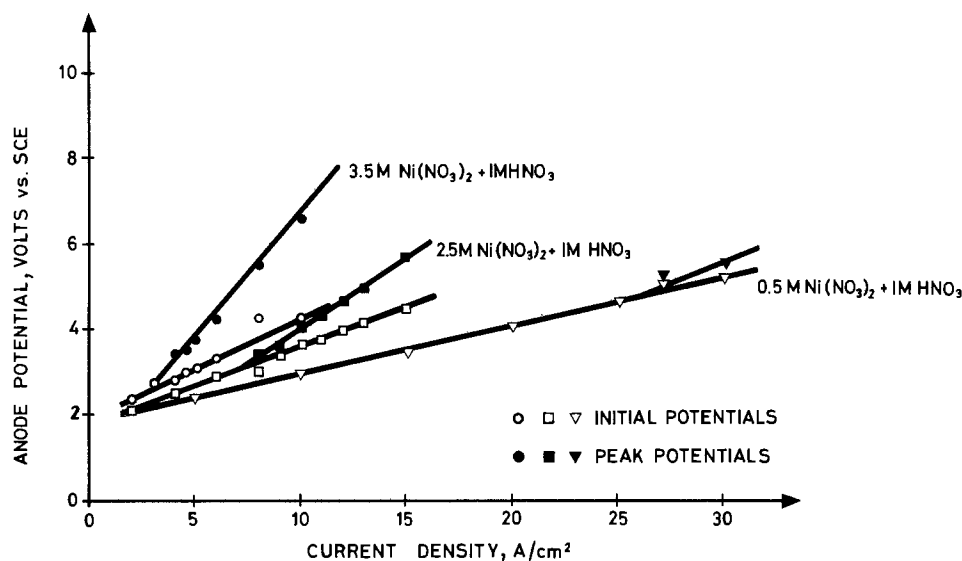


Fig. 10. Over-all anode potential as a function of current density for nickel dissolution in nickel nitrate solutions at a flow rate of 1000 cm/sec.

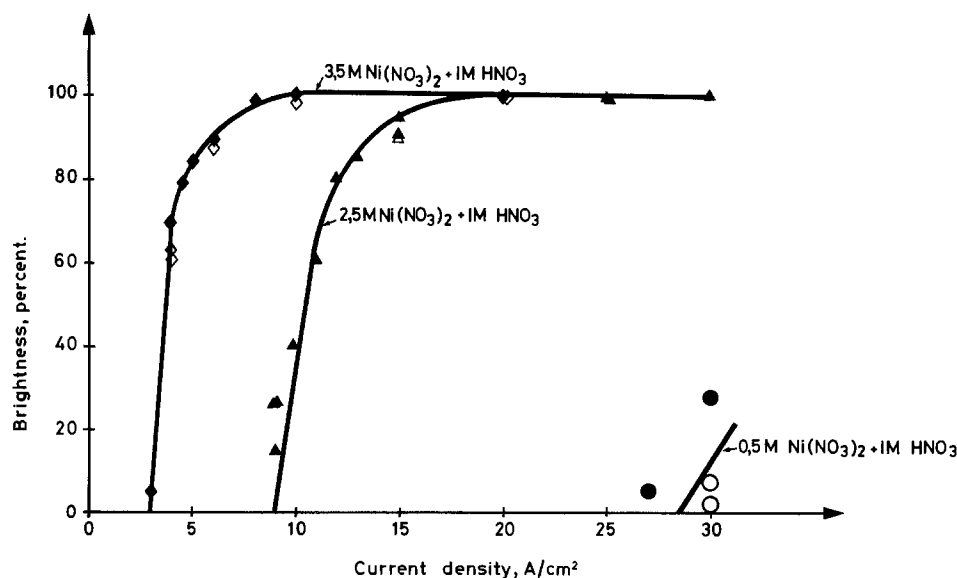


Fig. 11. Percentage of anode surface area appearing bright as a function of applied current density in nickel nitrate electrolytes of different concentration. Flow rate: 1000 cm/sec. Charge passed: 30 coulombs/cm² (◆ ▲ ●), 60 coulombs/cm² (◇ △ ○).

Table II. Estimation of surface concentration corresponding to onset of brightening in nickel nitrate solutions of different concentrations

Solution	Flow rate (cm/sec)	Reynolds number	Schmidt number	δ (μ)	i_{ob} (A/cm ²)	θ (%)	ΔC (moles/liter)	C_s (moles/liter)
3.5M Ni(NO ₃) ₂ + 1M HNO ₃	100	269	3378	11.4	1.0	93	0.6	4.1
	1000	2690		5.4	3.0	100	0.9	4.4
2.5M Ni(NO ₃) ₂ + 1M HNO ₃	100	460	2209	11.0	2.5	89	1.4	3.9
	1000	4600		3.7	9.0	97	1.9	4.4
0.5M Ni(NO ₃) ₂ + 1M HNO ₃	100	855	1189	11.0	9.0*	63	3.6	4.1
	1000	8550		2.5	29.0	88	3.7	4.2
							Average C_s = 4.2	

δ , Diffusion layer thickness.

i_{ob} , Current density corresponding to onset of brightening.

θ , Dissolution current efficiency corresponding to the onset of brightening.

ΔC , Concentration difference of nickel ion between anode and bulk.

C_s , Nickel nitrate concentration at anode surface.

* This value corresponds to that of the stoic iometric experiments in which a charge of 60 coulombs rather than 30 coulombs was passed. Contrary to the behavior in other electrolytes employed, the value of i_{ob} in 0.5M Ni(NO₃)₂ + 1M HNO₃ varied somewhat with the amount of charge passed during the experiments (cf. Fig. 11).

cm²/sec. The diffusion coefficient employed here is an effective diffusion coefficient which includes the contribution of migration to mass transfer and, therefore, its value has to be higher than that of the ionic diffusion coefficient. The numerical value of D found above, therefore, is very reasonable. It also compares favorably with effective diffusion coefficients reported recently for high rate iron dissolution in chloride media (27). According to the data of Table II, the surface concentration calculated with the given value of D not only is the same for the three nickel nitrate solutions studied but it also lies close to the experimentally determined saturation concentration. This fact provides additional support for the proposed salt film precipitation model.

Summary and Conclusions

Transpassive high rate dissolution of nickel occurs in the presence of two different types of anodic films. At relatively low current densities, the anode is covered by a thin oxide film, the passive film, which inhibits metal dissolution thus causing oxygen evolution to be the main reaction. With increasing current density, the passive film becomes less protective and the relative amount of metal dissolution increases. Dissolved metal ions accumulate at the anode surface to an extent which depends on mass transfer conditions. At a given point, the saturation concentration at the surface is exceeded and salt precipitation can occur. A salt layer, the brightening layer, is formed which manifests itself by an increase in anode potential and leads to surface brightening. The data of the present study suggest that surface brightening during ECM with passivating electrolytes is governed by a similar mechanism as conventional electropolishing.

Manuscript submitted Dec. 26, 1974; revised manuscript received July 10, 1975.

Any discussion of this paper will appear in a Discussion Section to be published in the June 1976 JOURNAL. All discussions for the June 1976 Discussion Section should be submitted by Feb. 1, 1976.

Publication costs of this article were partially assisted by the Swiss Federal Institute of Technology and by FERS.

REFERENCES

1. J. F. Wilson, "Practice and Theory of Electrochemical Machining," Wiley Interscience, New York (1971).
2. M. A. LaBoda and M. L. McMillan, *Electrochem. Technol.*, **5**, 340 (1967).
3. J. P. Hoare, *This Journal*, **117**, 142 (1970).
4. K. W. Mao, M. A. LaBoda, and J. P. Hoare, *ibid.*, **119**, 419 (1972).
5. D. Landolt, *ibid.*, **119**, 708 (1972).
6. D. T. Chin, *ibid.*, **119**, 1043 (1972).
7. M. Datta and D. Landolt, *Corrosion Sci.*, **13**, 181 (1973).
8. R. R. Cole and Y. Hopfenfeld, *J. Eng. Ind.*, **85**(B), 395 (1963).
9. D. Landolt, R. H. Muller, and C. W. Tobias, *This Journal*, **116**, 1384 (1969).
10. D. Landolt, R. H. Muller, and C. W. Tobias, *ibid.*, **118**, 36 (1971).
11. C. Wagner, *ibid.*, **101**, 225 (1954).
12. J. Edwards, *ibid.*, **100**, 189C (1953).
13. W. L. Elmore, *J. Appl. Phys.*, **10**, 724 (1939); **11**, 797 (1940).
14. J. P. Hoare and G. P. Rothwell, *Electrochim. Acta*, **10**, 403 (1965).
15. I. Epelboin and M. Keddam, *Compt. Rend.*, **259**, 137 (1964).
16. K. Kojima and C. W. Tobias, *This Journal*, **120**, 1026 (1973).
17. K. W. Mao and D. T. Chin, *ibid.*, **121**, 191 (1974).
18. D. Landolt, *Rev. Sci. Instr.*, **43**, 592 (1972).
19. K. J. Vetter, "Electrochemical Kinetics," Academic Press, New York (1967).
20. D. Landolt, *Chem. Ing. Tech.*, **45**, 188 (1973).
21. M. A. LaBoda, A. J. Chartrand, J. P. Hoare, C. R. Wiese, and K. W. Mao, *This Journal*, **120**, 643 (1973).
22. J. Newmann, *Ind. Eng. Chem.*, **60**, 12 (1968).
23. P. Van Shaw, L. P. Reiss, and T. J. Hanratty, *AIChE*, **9**, 362 (1963).
24. T. H. Chilton and A. P. Colburn, *Ind. Eng. Chem.*, **26**, 1183 (1934).
25. J. S. Son and T. J. Hanratty, *AIChE*, **13**, 689 (1967).
26. H. Bauer, "Stoffaustausch," p. 415 ff, Verlag Sauerländer, Aarau (1971).
27. H. C. Kuo and D. Landolt, *Electrochim. Acta*, **20**, 393 (1975).
28. Gmelin, "Handbuch der anorganischen Chemie 8." Aufl., Nr. 57, Teil A II, Lfrg 2, 1968, p. 410.

On the Electrodeposition of Copper Alloy Powders from Baths Containing Citrate/Tartrate Additives

R. K. Dube

Department of Metallurgy and Materials Technology, University College of Swansea, Swansea SA2 8PP, United Kingdom

and P. M. Prasad

Department of Metallurgical Engineering, Banaras Hindu University, Varanasi-5 (U.P.), India

ABSTRACT

The cathode polarization behavior of copper, zinc, cadmium, and tin in complex baths containing sodium citrate/sodium tartrate additives was investigated. Copper exhibited considerable polarization in baths containing sodium citrate or sodium tartrate. The polarization behavior of zinc, cadmium, and tin was not significantly affected by these additives. Codeposition of zinc, cadmium, or tin with copper was not possible from baths containing no complexing agents. However, studies on the cathode polarization characteristics from baths containing 40 g/liter sodium citrate/sodium tartrate and actual deposition trials revealed that whereas Cu-Sn powder can be codeposited, it was not possible to codeposit Cu-Zn or Cu-Cd powders.

Powder metallurgical alloy products are generally produced by compacting and sintering mixtures of the individual metal powders. Such products are often inhomogeneous, especially when one of the metals is in small proportion, e.g., 90% Cu-10% Sn. Hence there has been a consistent effort to produce alloy powders for the past few decades by several methods such as atomization, alloy disintegration, thermal decomposition, electrolytic deposition, etc. Of these, the electrolytic method is capable of giving homogeneous powders with the desired compacting and sintering characteristics. Surprisingly, codeposition from aqueous baths as a means of producing alloy powders has not received adequate attention. However, some studies have recently been reported on the preparation of Cu-Zn (1), Cu-Ni (2), Fe-Ni (3, 4), Fe-Co (5), and Co-Ni (6) powders by electrodeposition from suitable baths. In this context, cathode polarization studies are very helpful in predicting the possibility of codeposition of metals. The present work is concerned with studies on the cathode polarization characteristics of copper, zinc, cadmium, and tin in complex baths containing citrate/tartrate additives, enabling a prediction to be made of the possibility or otherwise of codeposition of zinc, cadmium, or tin with copper.

Experimental

Anodes.—Graphite plates.

Cathodes.—Plates of electrolytic copper, electrolytic zinc, electrolytic cadmium, and chemical purity tin. All cathodes were polished and degreased before use.

Chemicals.—A. R. Grade $\text{CuSO}_4 \cdot 5\text{H}_2\text{O}$, $\text{ZnSO}_4 \cdot 7\text{H}_2\text{O}$, $3\text{CdSO}_4 \cdot 8\text{H}_2\text{O}$, $\text{SnCl}_2 \cdot 2\text{H}_2\text{O}$, $\text{CuCl}_2 \cdot 2\text{H}_2\text{O}$, NH_4Cl , NaCl , and $\text{Na}_3\text{C}_6\text{H}_5\text{O}_7 \cdot 2\text{H}_2\text{O}$ (sodium citrate), and C.P. grade $\text{Na}_2\text{C}_4\text{H}_4\text{O}_8 \cdot 2\text{H}_2\text{O}$ (sodium tartrate).

The experimental setup for the measurement of cathode polarization, shown in Fig. 1, consisted of a cell having two graphite anodes (covered with anode bags of thick ordinary cloth) and a cathode of the required metal (copper, zinc, cadmium, or tin) dipped in the appropriate electrolyte (1.0N $\text{CuSO}_4 \cdot 5\text{H}_2\text{O}$ for copper, 1.0N $\text{ZnSO}_4 \cdot 7\text{H}_2\text{O}$ for zinc, 1.0N $3\text{CdSO}_4 \cdot 8\text{H}_2\text{O}$ for cadmium, and 1.0N $\text{SnCl}_2 \cdot \text{H}_2\text{O}$ for tin) contained in a tank made from methyl methacrylate sheet (trade name: Plexiglas or Lucite in U.S.A. and Perspex in U.K.). The metal electrode, whose cathode polariza-

tion was to be measured, was joined via a salt bridge against the standard and saturated calomel electrode. The calomel electrode was connected in series with a high-impedance micro-voltmeter and the cathode of the electrolytic cell via a key as shown in Fig. 1. The instantaneous emf developed was measured at current densities of 0, 1, 2, 4, 6, 8, 10, 12, 14, 16, and 18 ampere per square decimeter (asd).

Similar measurements were taken on all the above baths, but containing, respectively, 10, 20, and 40 g/liter sodium citrate. Experiments were also conducted in a similar way with sodium tartrate as an additive in place of sodium citrate.

The experimental setup used for the deposition of alloy powder was similar to the previous one, except that there was no provision for measurement of cathode polarization. Plates of copper and graphite (covered with thick ordinary cloth) were used as cathode and anode, respectively. The analysis of tin in the Cu-Sn alloy powder was done by the gravimetric method.

Results

Polarization behavior of copper.—The influence of concentration of sodium citrate and sodium tartrate on the cathode polarization of copper in 1.0N $\text{CuSO}_4 \cdot 5\text{H}_2\text{O}$ at 30°C is presented in Fig. 2 and 3, respectively. Copper exhibited considerable polarization

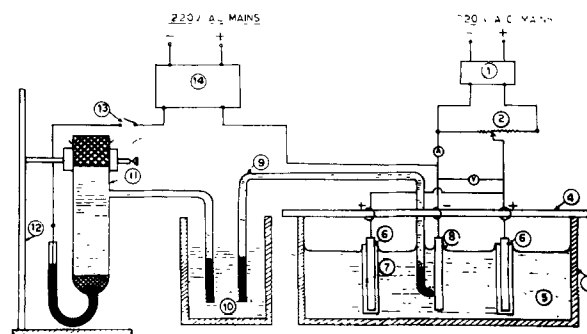


Fig. 1. Schematic diagram of experimental setup used for polarization measurements. 1, 12V battery eliminator; 2, rheostat; 3, Perspex tank; 4, silica rod; 5, electrolyte; 6, graphite anode; 7, anode bag; 8, metal cathode; 9, salt bridge; 10, saturated KCl solution; 11, saturated calomel electrode; 12, stand; 13, two way key; 14, high impedance micro-voltmeter.

Key words: cathode polarization, alloy powder, codeposition, sodium citrate, sodium tartrate, current density.

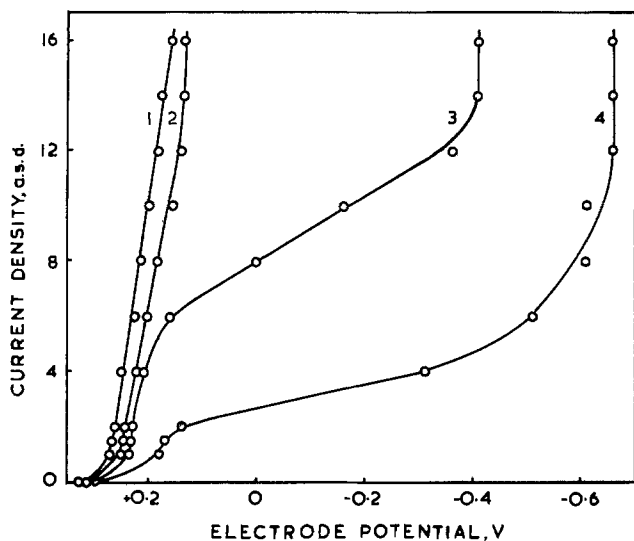


Fig. 2. Effect of concentration of sodium citrate on the cathode polarization of copper in $1.0N$ $\text{CuSO}_4 \cdot 5\text{H}_2\text{O}$ solution at 30°C . Curve 1, nil; curve 2, 10 g/liter; curve 3, 20 g/liter; and curve 4, 40 g/liter.

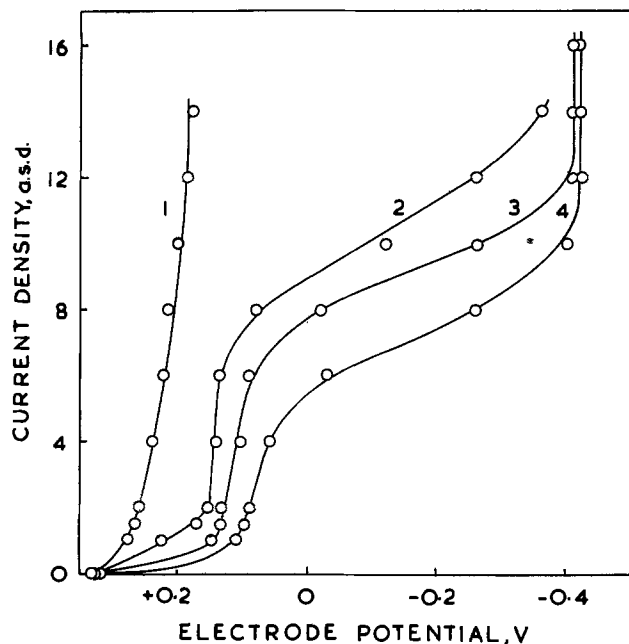


Fig. 3. Effect of concentration of sodium tartrate on the cathode polarization of copper in $1.0N$ $\text{CuSO}_4 \cdot 5\text{H}_2\text{O}$ solution at 30°C . Curve 1, nil; curve 2, 10 g/liter; curve 3, 20 g/liter; and curve 4, 40 g/liter.

in baths containing citrate or tartrate. In all cases, there was a significant amount of polarization at lower current densities. At lower current densities, plating of copper was observed, whereas at higher current densities copper powder was formed. The transition, plating \rightarrow powder was characterized by a large and sudden increase in the polarization with only a slight increase in current density. Current densities beyond a certain value had no significant effect on polarization and thus the electrode potential remained constant after a critical value of current density in each case.

Another interesting observation was that the addition of sodium citrate to the bath led to a more pronounced polarization than the addition of a corresponding amount of sodium tartrate, particularly at 40 g/liter concentration. Further, the increase in polarization with increasing addition of the complexing salts was also noteworthy. With both citrate as well as tartrate, addition of over 40 g/liter of the reagent did

not very much affect the polarization values. Thus greater additions than this amount were considered unnecessary.

Polarization behavior of cadmium.—The influence of concentration of sodium citrate and sodium tartrate on the cathode polarization of cadmium in $1.0N$ $3\text{CdSO}_4 \cdot 8\text{H}_2\text{O}$ solution at 30°C is presented in Fig. 4 and 5. As in the earlier case, lower current densities had a greater influence on the polarization behavior of cadmium than higher current densities. The critical current density for obtaining a fully nonadherent powdery deposit had been observed to be about 8 asd in all cases. Baths containing sodium citrate showed

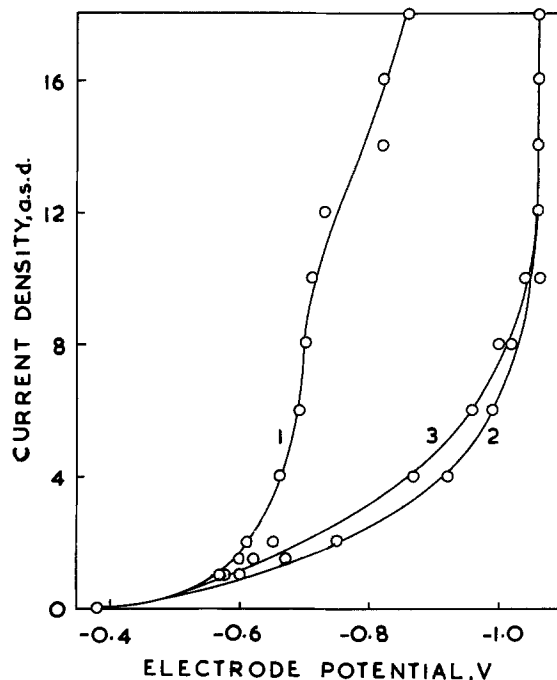


Fig. 4. Effect of concentration of sodium citrate on the cathode polarization of cadmium in $1.0N$ $3\text{CdSO}_4 \cdot 8\text{H}_2\text{O}$ solution at 30°C . Curve 1, nil; curve 2, 10 g/liter; and curve 3, 40 g/liter.

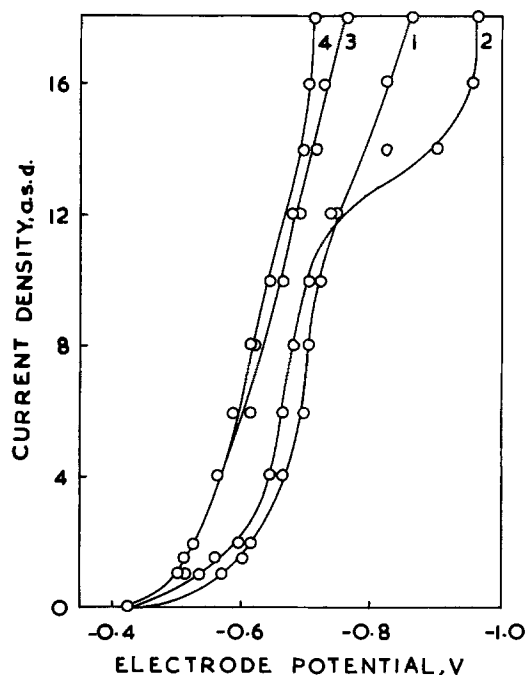


Fig. 5. Effect of concentration of sodium tartrate on the cathode polarization of cadmium in $1.0N$ $3\text{CdSO}_4 \cdot 8\text{H}_2\text{O}$ solution at 30°C . Curve 1, nil; curve 2, 10 g/liter; curve 3, 20 g/liter; and curve 4, 40 g/liter.

considerable polarization in cadmium. Addition of sodium citrate beyond 10 g/liter does not seem to have any significant effect on the polarization of cadmium.

In the case of sodium tartrate additions, some depolarization was observed up to about 12 asd. This was seen to persist even at higher current densities, when the amount of tartrate added was 20 g/liter or more. At low concentrations of tartrate (e.g., 10 g/liter) considerable polarization was observed beyond 12 asd.

Polarization behavior of zinc.—The effect of concentration of sodium citrate and sodium tartrate on the cathode polarization of zinc in 1.0N $ZnSO_4 \cdot 7H_2O$ at 30°C is presented in Fig. 6 and 7, respectively. The cathode potential of zinc was not significantly changed by the nature or amount of complexing salt. Nonad-

herent powdery deposits had been observed beyond a current density of about 8 asd.

Polarization behavior of tin.—The influence of concentration of sodium citrate and sodium tartrate on the cathode potential of tin in 1.0N $SnCl_2 \cdot 2H_2O$ at 30°C is represented in Fig. 8 and 9, respectively. In this case also, there was not much change in the cathode polarization of tin with addition of complexing agents. Powder formation had been observed at about 8 asd in all cases.

Discussion

Comparative assessment of polarization behavior.—The addition of complex salts had resulted in considerable polarization in the relatively noble metal copper, whereas in the case of the baser metals (i.e., those of zinc, cadmium, and tin) no significant polarization had been observed.

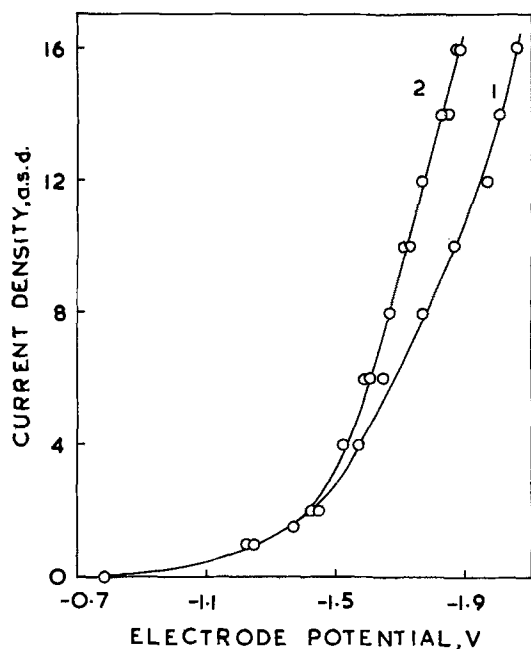


Fig. 6. Effect of concentration of sodium citrate on the cathode polarization of zinc in 1.0N $ZnSO_4 \cdot 7H_2O$ solution at 30°C. Curve 1, nil; and curve 2, for both 20 and 40 g/liter.

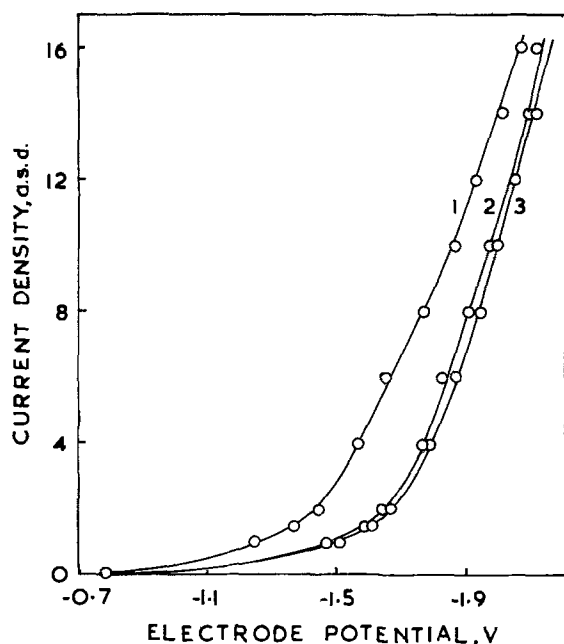


Fig. 7. Effect of concentration of sodium tartrate on the cathode polarization of zinc in 1.0N $ZnSO_4 \cdot 7H_2O$ solution at 30°C. Curve 1, nil; curve 2, 20 g/liter; and curve 3, 40 g/liter.

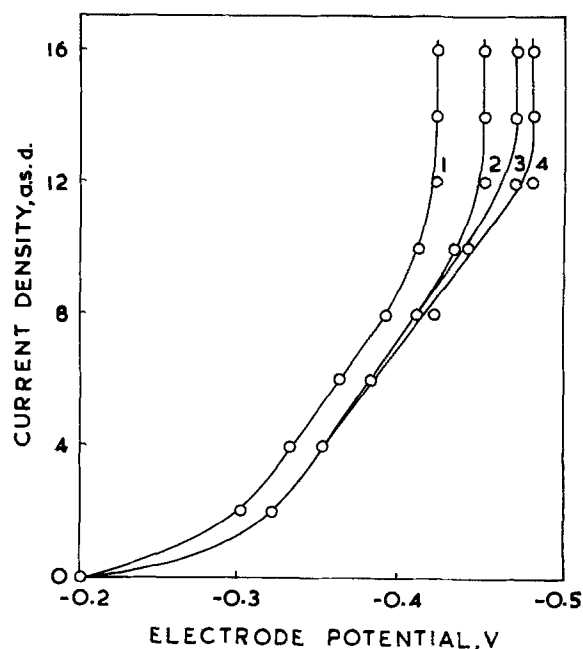


Fig. 8. Effect of concentration of sodium citrate on the cathode polarization of tin in 1.0N $SnCl_2 \cdot 2H_2O$ solution at 30°C. Curve 1, nil; curve 2, 10 g/liter; curve 3, 20 g/liter; and curve 4, 40 g/liter.

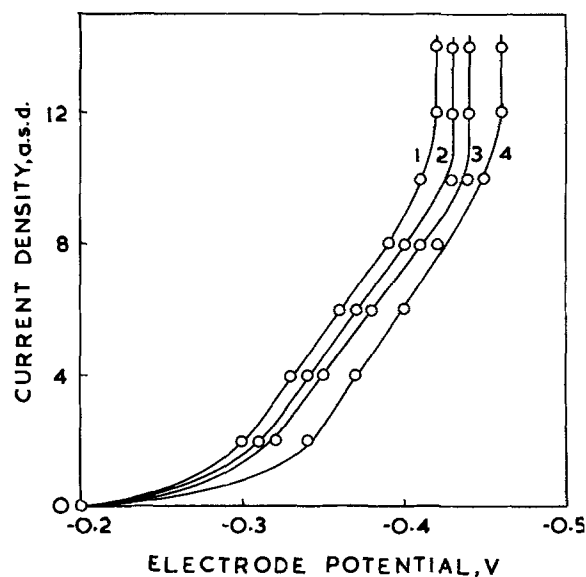


Fig. 9. Effect of concentration of sodium tartrate on the cathode polarization of tin in 1.0N $SnCl_2 \cdot 2H_2O$ solution at 30°C. Curve 1, nil; curve 2, 10 g/liter; curve 3, 20 g/liter; and curve 4, 40 g/liter.

Citrates and tartrates can form a variety of neutral, cationic, or anionic complexes, with the cations of common metals, depending on the concentration of the reagents, nature of the bath, its pH, and temperature, etc. (7, 8). Although it is difficult to obtain a quantitative idea of the exact nature of these complexes, a qualitative idea regarding the relative stabilities of complexes of interest in this study can be had from Table I. It can be seen that copper citrate is very much more stable than copper tartrate. This means that baths containing citrate additions will have smaller amounts of free copper ions than baths containing the tartrate additives. In other words, greater polarization is to be expected with copper baths containing citrate addition than with tartrate additions, a conclusion in good agreement with experimental observation.

Generally noble metal complexes are known to be more stable than base metal complexes (in the present case also, it is clear from Table I that copper citrate is more stable than the citrates of base metals cadmium and zinc). This leads to a tremendous decrease in the effective metal ion concentration in the case of the noble metal, whereas the ionic concentration of the base metal is not changed significantly. This is the reason why a more pronounced polarization was observed in the case of copper than in the case of cadmium, zinc, or tin.

Further, it may also be noted from Table I that the stability constants of the complexes of Cd and Zn are not substantially different from those of their sulfates. Hence, with the addition of sodium citrate/sodium tartrate no significant change should be expected in the polarization behavior of these base metals. Experimental observations discussed earlier are in conformity with expected behavior.

Possibility of codeposition of Zn, Cd, or Sn with Cu.—Figure 10 shows the effect of current density on the electrode potential of copper, tin, cadmium, and zinc in the normal solutions of their respective salts, as discussed earlier. It is clear from the above figure that the codeposition of zinc, cadmium, or tin with copper is not possible from baths containing no complexing agents as the curves are far removed from each other and there is no common current density or potential between copper and the others. Figure 11 shows the effect of current density on the electrode potential of copper, tin, cadmium, and zinc in their respective normal salt solutions, containing 40 g/liter sodium citrate at 30°C. The electrode potentials of copper, zinc, and cadmium are not close enough to permit codeposition of copper with either zinc or cadmium from the citrate bath at any current density. But the curve for tin crosses the curve for copper at a current density of 4.5 asd. Thus it may be possible to codeposit tin with copper from baths containing sodium citrate as the complexing agent. These theoretical predictions based on polarization measurements are in conformity with the actual deposition experiments from various baths, because it was possible to codeposit only tin with copper and not the others, as shown in Table II.

Figure 12 shows the effect of current density on the electrode potential of copper, tin, cadmium, and zinc in their respective normal salt solutions containing 40 g/liter sodium tartrate. Zinc and cadmium exhibited similar behavior as mentioned previously and their codeposition with copper was not possible. The curve for

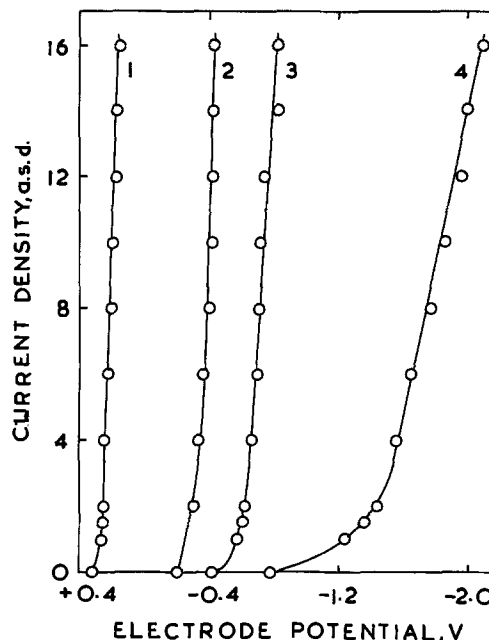


Fig. 10. Effect of current density on the electrode potential of copper (curve 1), tin (curve 2), cadmium (curve 3), and zinc (curve 4) in normal solutions of their respective salts at 30°C.

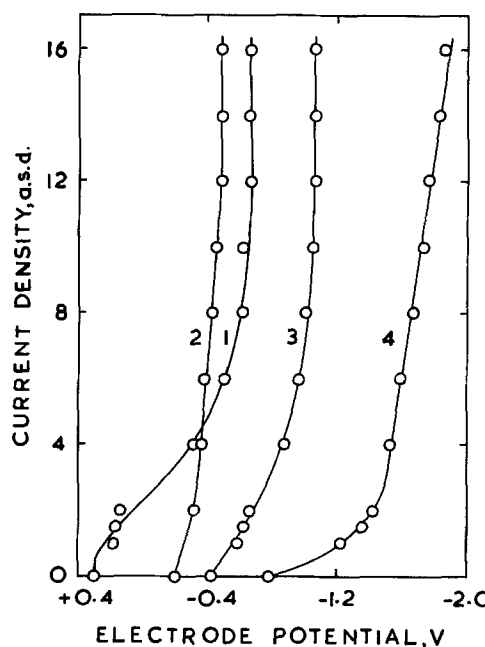


Fig. 11. Effect of current density on the electrode potential of copper (curve 1), tin (curve 2), cadmium (curve 3), and zinc (curve 4) in normal solutions of their respective salts containing 40 g/liter sodium citrate at 30°C.

tin also does not cross the curve for copper, but they are fairly close to each other above the current density of 12 asd. Thus, from polarization studies, it appears that there is no possibility of codeposition of copper and tin. Experimental observations are in accordance with above prediction in the case of Cu-Zn and Cu-Cd. However, in the case of Cu-Sn, the powder deposit was found to contain some tin, possibly because of the following reasons:

1. The cathode polarization values of copper and tin at high current densities are quite close.
2. What one measures in practice is the value of individual cathode polarization which may be different from the actual cathode polarization on the alloy deposit.

Table I. Stability constants of some simple salts and complexes

Name of complex	Stability constant	Reference
CuSO ₄	2.0×10^2	8
Cu citrate-	1.6×10^{14}	7
Cu tartrate-	1.1×10^3	7
CdSO ₄	2.0×10^2	8
Cd citrate-	1.7×10^4	7
Cd tartrate-	2.0×10^3	8
ZnSO ₄	1.9×10^2	8
Zn citrate	9.1×10^2	8
Zn tartrate	4.8×10^2	7

Table II. Studies on the possibility of codeposition of Cu-Zn, Cu-Cd, and Cu-Sn powders

Trials on codeposition of	Bath composition	Conditions employed			Results
		Anode	Cathode	CD, asd	
Copper and zinc	CuCl ₂ · 2H ₂ O 20, ZnSO ₄ · 7H ₂ O 30, NaCl 20, NH ₄ Cl 20, Na ₂ C ₆ H ₅ O ₇ · 2H ₂ O 40 g/liter	Graphite	Copper	12.0	No zinc was detected in the deposited powder
	CuCl ₂ · 2H ₂ O 20, ZnSO ₄ · 7H ₂ O 30, NaCl 20, NH ₄ Cl 20, Na ₂ C ₄ H ₄ O ₆ · 2H ₂ O 40 g/liter	Graphite	Copper	12.0	No zinc was detected in the deposited powder
Copper and cadmium	CuCl ₂ · 2H ₂ O 25, 3CdSO ₄ · 8H ₂ O 30, NaCl 20, NH ₄ Cl 20, Na ₂ C ₆ H ₅ O ₇ · 2H ₂ O 40 g/liter	Graphite	Copper	12.0	No cadmium was detected in the deposited powder
	CuCl ₂ · 2H ₂ O 25, 3CdSO ₄ · 8H ₂ O 30, NaCl 20, NH ₄ Cl 20, Na ₂ C ₄ H ₄ O ₆ · 2H ₂ O 40 g/liter	Graphite	Copper	12.0	No cadmium was detected in the deposited powder
Copper and tin	CuCl ₂ · 2H ₂ O 30, SnCl ₂ · 2H ₂ O 20, NaCl 20, NH ₄ Cl 20, Na ₂ C ₆ H ₅ O ₇ · 2H ₂ O 40 g/liter	Graphite	Copper	12.0	Tin was detected in the powder deposit
	CuCl ₂ · 2H ₂ O 30, SnCl ₂ · 2H ₂ O 20, NaCl 20, NH ₄ Cl 20, Na ₂ C ₄ H ₄ O ₆ · 2H ₂ O 40 g/liter	Graphite	Copper	15.0	Tin was detected in the powder deposit

3. As a consequence of the above, it may not be unreasonable to expect some depolarization effects in view of the good alloying ability of copper for tin, thus facilitating codeposition.

Conclusions

The addition of complexing salts (sodium citrate/sodium tartrate) to copper sulfate bath results in con-

siderable cathode polarization of copper. This beneficial effect is more pronounced with sodium citrate. The cathode polarization behavior of zinc, cadmium, and tin were not significantly affected by these additives.

Studies on the cathode polarization characteristics with baths containing 40 g/liter sodium citrate/sodium tartrate and actual deposition trials revealed that whereas Cu-Sn powder can be codeposited, it is not possible to codeposit Cu-Zn or Cu-Cd powder.

Acknowledgment

The authors thank Professor T. R. Anantharaman, Head of the Department of Metallurgical Engineering, Banaras Hindu University, Varanasi-5, India, for providing laboratory facilities and encouragement.

Manuscript submitted Jan. 13, 1975; revised manuscript received July 5, 1975.

Any discussion of this paper will appear in a Discussion Section to be published in the June 1976 JOURNAL. All discussions for the June 1976 Discussion Section should be submitted by Feb. 1, 1976.

REFERENCES

1. B. P. Yure'v and L. A. Aladzhalov, *Soviet Powder Metallurgy and Metal Ceramics*, 5 (77), 345 (1969).
2. V. Prithviraj, S. L. N. Acharyulu, and R. V. Tamhankar, *Trans. Indian Inst. Metals*, 23, 51 (1970).
3. A. V. Pomosov, I. B. Murashova, and V. P. Artamonov, *Soviet Powder Metallurgy and Metal Ceramics*, 5 (77), 341 (1969).
4. B. P. Yure'v and L. P. Sukhanova, *ibid*, 6 (78), 438 (1969).
5. B. P. Yure'v and S. A. Sviridova, *ibid*, 7 (79), 519 (1969).
6. B. P. Yure'v and L. A. Golubkov, *ibid*, 7(55), 525 (1967).
7. K. B. Yatsimirskii and V. P. Vasil'ev, "Instability Constants of Complex Compounds," D. Van Nostrand Co. Inc., Princeton, N. J. (1960).
8. "Stability Constants," Special Publication No. 17, The Chemical Society, London (1964).

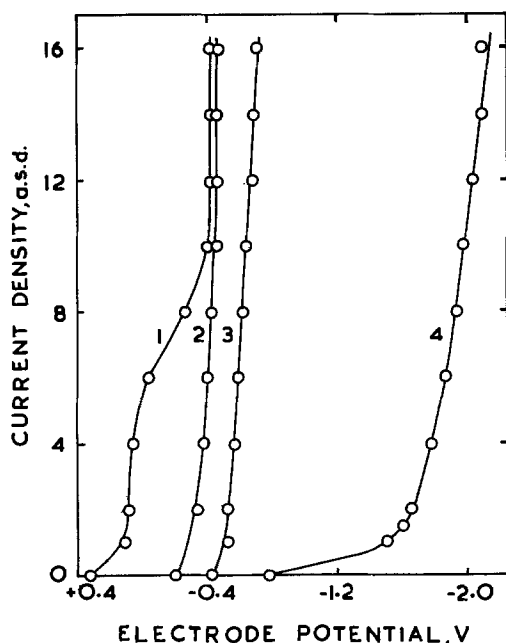


Fig. 12. Effect of current density on the electrode potential of copper (curve 1), tin (curve 2), cadmium (curve 3), and zinc (curve 4) in normal solutions of their respective salts containing 40 g/liter sodium tartrate at 30°C.

A Rutherford Scattering Study of Catalyst Systems for Electroless Cu Plating

II. SnCl₂ Sensitization and PdCl₂ Activation

R. L. Meek*

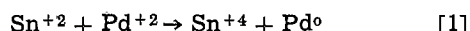
Bell Laboratories, Murray Hill, New Jersey 07974

ABSTRACT

High energy ion backscattering has been used to study the surface chemistry of the sensitization (SnCl₂) and activation (PdCl₂) processes used to prepare nonconductive substrates for electroless plating. This method of surface preparation is compared to catalysis using mixed Pd-Sn colloidal solutions. While the redox reaction between divalent Sn and Pd may occur during the activation of sensitized surfaces, it is suggested that any zero-valent Pd so produced only becomes catalytically active after a significant (~100 sec) immersion time in the electroless plating solution.

Electroless plating of insulating, i.e., plastic or epoxy glass composite, substrates is widely used in printed circuit and decorative plating technology. In a previous paper (1) referred to hereafter as (I), an ion scattering study of the surface chemistry of the mixed Pd-Sn colloidal system was described. Here, results of an ion scattering study of the older SnCl₂-sensitization, PdCl₂-activation process (2), which is still widely used, especially in applications where photoselective deposition (3) is desired, are reported.

A number of publications (3-14) which deal with various aspects of this process have recently appeared but there is still considerable controversy regarding interpretation. The Mossbauer spectroscopy work of Cohen *et al.*, (5,6) allows deduction of a fairly complete picture of the nature of the solutions and of the material deposited on sensitized and activated Kapton surfaces. The active species in the sensitizer which is deposited on the sensitized substrate is a complex Sn colloid consisting primarily of a Sn⁺⁴ complex core, stabilized by an outer layer of divalent Sn. The colloidal particle diameter is about 25-100Å, depending somewhat on the manner in which the sensitizing solution is prepared (4-6, 10, 11). The divalent Sn is oxidized to tetravalent Sn by exposure to oxygen, u.v. radiation or by dipping the sensitized substrate into the PdCl₂ activator solution (3, 5, 6), leading to the supposition that the reaction



takes place. It should be emphasized that the Mossbauer spectra (5, 6) show Sn⁺² and Sn⁺⁴ after sensitization but only Sn⁺⁴ after activation. Subsequent work by the author and Cohen on graphite substrates gives qualitatively the same results.

Although the Mossbauer results argue strongly in favor of the correctness of reaction [1], the ellipsometric measurements of de Minjer and v.d. Boom (12), using glass substrates, at first seem to preclude it. They show that no metallic Pd is present after the activation step. On the other hand, ESCA spectra do show the presence of metallic Pd after activation (15). However, it should be noted that Pd⁰ and Pd metal, or even catalytically active Pd, are not necessarily the same thing. For example, isolated, single neutral Pd atoms might not be expected to either have metallic optical properties or to be catalytically active for electroless deposition (16, 17). In fact, some of the present results strongly indicate that the sensitized and activated surface becomes active for deposition only after some

relatively long immersion time in the electroless bath. It is therefore proposed that some further change in the chemical state or structure of the material present on the sensitized and activated surface may take place during the early stages of electroless deposition.

Experimental Details

Solution preparation.—Three SnCl₂ sensitizing solutions, designated A, C, and W, were used. The A and C solutions were prepared by combining 16g SnCl₂·2H₂O with 30 ml HCl and 970 ml H₂O and differ due to the order of mixing (5, 6). For the A solution the SnCl₂ was dissolved in H₂O followed by addition of acid, while for the C solution, water and acid were combined followed by addition of SnCl₂. According to Ref. (5), the A solution will have the larger colloidal particle size. The W solution, one of the so-called wetting Sn solutions, was formed by adding (7.5g SnCl₄·5H₂O) then (20g SnCl₂·2H₂O) and finally (15g SnCl₂·2H₂O) to one liter of H₂O in the order given with thorough mixing after each addition. All solutions were used between 1 and 2 hr after preparation.

The activating solution was prepared by dissolving 0.2g PdCl₂ in 8 ml HCl and diluting to 1 liter with H₂O. The electroless Cu plating solution was the same as that used in (I) and standard H₂O rinse times of 30 sec were used after each process step.

Cleaved graphite substrates (~1 cm²) were chosen for the present study. [See(I).] The low mass of carbon eliminates substrate interference and, furthermore, graphite may be obtained in a very pure form. By using a freshly cleaved surface, unwanted surface impurities can be minimized. Substrates were prepared for analysis by immersing 1 cm² samples in 100 cm³ of the appropriate solution, or series of solutions, with gentle stirring. They were then carefully dried by placing the sample edge on filter paper and immediately (within 15 min) examined.

Surface analysis.—The high energy ion scattering technique was described in (I). A typical scattered ion spectrum from the surface layer produced by immersion in sensitizing solution C for 300 sec and rinsing is shown as Fig. 1. The peak positions (and yields) correspond to O[2.5(10)¹⁶ cm⁻²] Cl[2(10)¹⁵ cm⁻²] and Sn [2(10¹⁶) cm⁻²]. Si(10¹⁴ cm⁻²) is a frequently detected surface contaminant on control substrates (1).

The substrate area examined by the ion beam is 0.78 mm². The statistical error in a given measurement is typically 3% for heavy mass species (Cu, Pd, Sn) and 10% for light masses (O, Cl). During the experiments it became apparent that significant differences (a factor of three) can occur from point to point on a given

* Electrochemical Society Active Member.

Key words: catalysis, electroless plating, sensitization, activation, printed circuit processing.

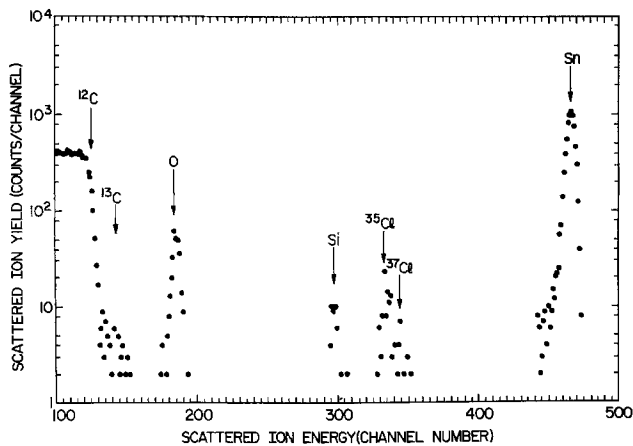


Fig. 1. Typical scattered ion spectrum (scattered ion yield as counts per channel vs. scattered ion energy as channel number) from sensitized ($t_{\text{SnCl}_2\text{-C}} = 300$ sec) substrate.

substrate. Thus 3-5 separate measurements were made at randomly selected points on a given sample. Throughout this paper, bars on data points indicate the point to point variation found, not an error bar. Of course, surface concentration variations on a smaller scale, smaller than the beam spot size, may be even greater. Two or more samples treated in the same way gave equivalent results within the point to point variations just mentioned.

Results and Discussion

Sensitization.—The Sn, Cl, and O surface concentrations found on sensitized surfaces are shown in Fig. 2, 3, and 4 for the A, C, and W solutions, respectively. The amount of each element found is fairly independent of the sensitizing solution used. The fact that the amount adsorbed goes roughly as the square root of immersion time implies diffusion controlled deposition (1) of the colloidal Sn particles; however, one must also expect some deposition due to hydrolysis during the rinse step. After sensitization, the O/Sn ratio is approximately 1.3, while the Cl/Sn ratio is approximately 0.1. The small amount of Cl found is in agreement with the observations of de Minjer and v.d. Boom (12). Experimentally, all of the sensitizer solutions used produced a wetting, hydrophilic, surface on graphite.

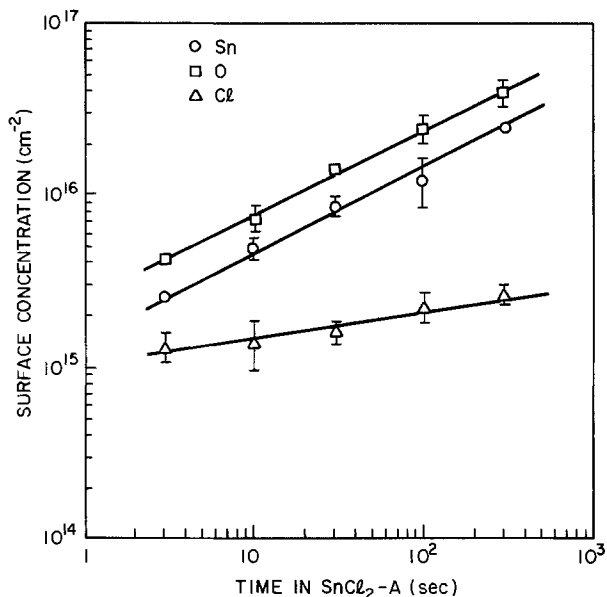


Fig. 2. Surface concentrations of Sn, O, and Cl vs. sensitization time for substrates sensitized in solution A.

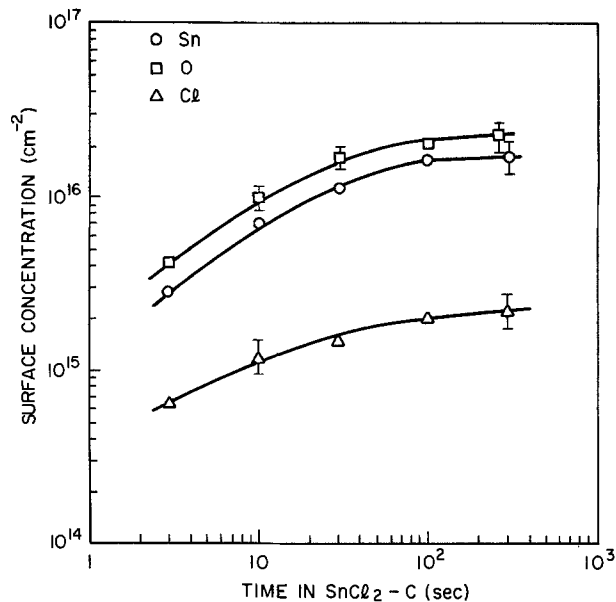


Fig. 3. Surface concentrations vs. sensitization time for sensitizer C.

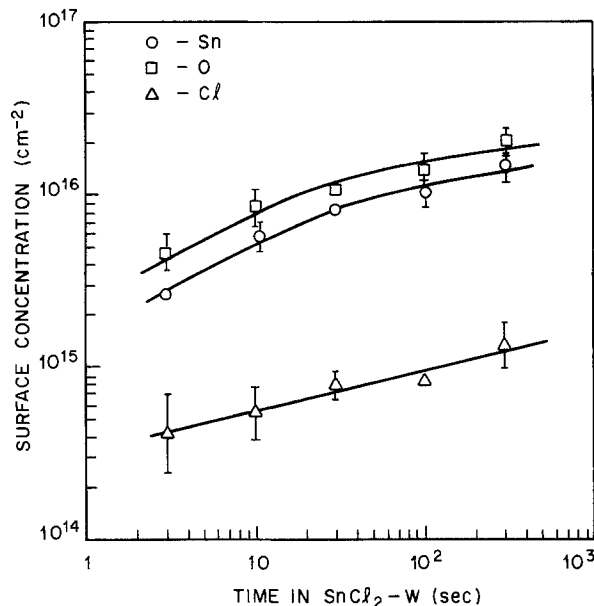


Fig. 4. Surface concentrations vs. sensitization time for sensitizer W.

Activation.—The Pd surface concentrations after immersion in the activator solution are given in Fig. 5 for the A solution. Similar results were obtained using the other solutions. Also shown are the remaining Sn concentrations; the dashed line represents the average Sn concentrations prior to the activation from Fig. 2. It is seen that the Sn concentration decreases slightly but probably not significantly, and that after activation the Pd/Sn ratio is about 0.2. The Mossbauer experiments (5, 6) would suggest that the Pd/Sn ratio should be 0.5 if reaction [1] takes place, if the $\text{Sn}^{+2}/\text{Sn}^{+4}$ ratio after sensitization is the same as in that work, and if the recoil-free fractions are the same for the Sn^{+4} and the Sn^{+2} species. However, the possibility of a considerable difference in $\text{Sn}^{+2}/\text{Sn}^{+4}$ ratio is rather likely, since it is known to depend sensitively on the quality of the chemicals used and the exact details of the solution preparation so that the present observations in no way contradict those of Cohen *et al.* (5, 6). Subsequent work by Cohen and the author has reproduced and extended the Mossbauer results using graphite substrates. Furthermore, it is seen that the Pd concentration is independent of time in the activator solution,

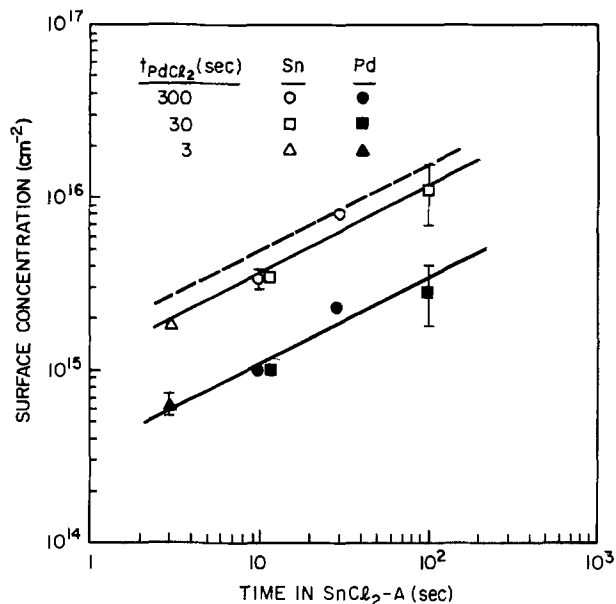


Fig. 5. Surface concentrations of Pd and Sn vs. sensitization time after various activator immersion times for substrates sensitized in solution A.

but rather depends on the time in the sensitizer solution; that is, the Sn concentration; and that the Pd concentration closely follows the Sn concentration. Note also the rapidity of the Pd deposition; it is found in general that 3 sec in the activator leads to the same amount of Pd as 300 sec in the activator. While the Pd concentration is about the same as that found after catalysis in mixed Pd-Sn colloids (1), the Sn concentration is larger or, equivalently, the Pd/Sn ratio is smaller.

After activation, the O/Sn ratio rises to 2 and the Cl/Sn ratio becomes approximately 0.2. The increase in O/Sn ratio is at least in accord with the existence of the redox reaction although it does not prove its existence. The small Cl/Sn ratio observed is not in agreement with the results of Ref. (12), where Cl/Sn ratios in the range 1-6 were found. We have observed such large Cl/Sn ratios, but only if the postactivator rinse is strongly acidic, and then a commensurate increase in Pd is also observed; but the results are very irreproducible (Pd and Cl vary by a factor of ten). It is noted that the possibility of a $Sn_4Pd_2Cl_{14}$ complex proposed in Ref. (12) and (18) is conclusively ruled out both by the present simple atom "counting" techniques and by the Mossbauer experiments which, while not quantitative, show the chemical state; that is, the electronic environment of the Sn atoms.

Electroless plating.—Figure 6 shows the Cu deposition vs. time in the electroless solution for the A sensitizer solution. Again similar results are obtained with the C or W solution. The line labeled 2.2 A/sec is the rate at which the bath used plates Cu on Cu (1). The Cu coverage is more or less independent of sensitizer used or time in activator solution, but depends strongly on time in the sensitizer; that is, original Sn concentration. The relatively long (> 100 sec) times for significant Cu deposition to take place are in distinction to the short (≤ 10 sec) initiation times observed when the mixed Pd-Sn colloid is used to catalyze the surface (1). In fact, for sensitization times ≤ 10 sec, the Cu plating initiation time is $> 10^4$ sec. These observations lend credence to the idea that, after activation, the Pd, while it may be zero-valent, is neither "metal" nor catalytically active. The significance of such long initiation times to processes where the total electroless plating time is only $\sim 10^3$ sec is obvious.

It is of considerable interest to determine the amount of Pd and Sn remaining after electroless deposition.

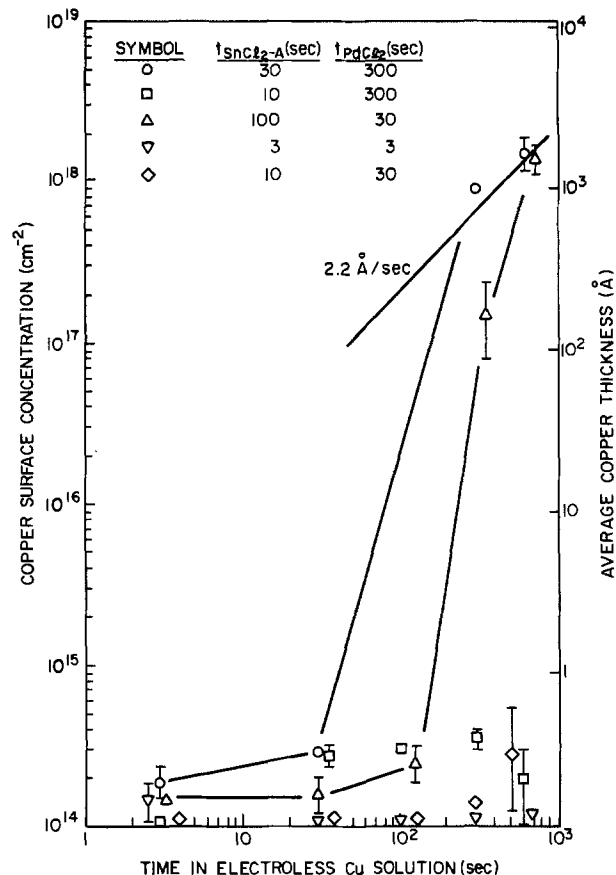


Fig. 6. Copper surface coverage vs. time of immersion in electroless bath for various sensitization (solution A) and activation times.

The data, normalized to initial concentration, for Pd and Sn, corresponding to Fig 6 is given in Fig. 7. While there is some scatter in the data, in general both the Pd and Sn concentrations decrease by about a factor of

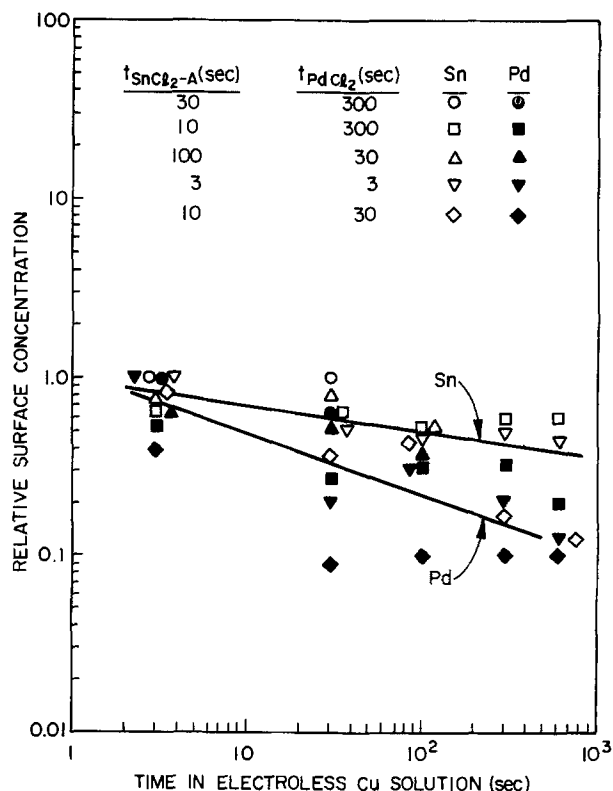


Fig. 7. Normalized Pd and Sn surface concentrations vs. time in electroless bath for samples sensitized in solution A.

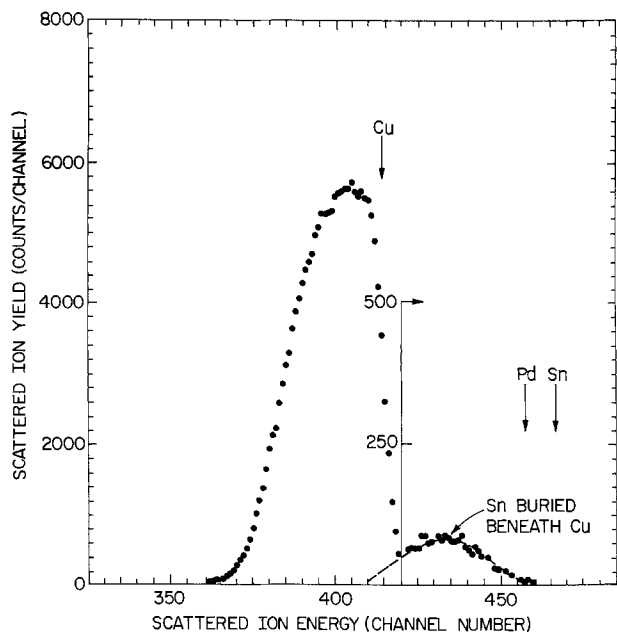


Fig. 8. Typical scattered ion spectrum from a sensitized ($t_{\text{SnCl}_2\text{-C}} = 30$ sec) activated ($t_{\text{PdCl}_2} = 30$ sec) plated ($t_{\text{Cu}} = 900$ sec) sample. The Sn and Pd peaks have been shifted to lower energy; scattering from Pd is completely obscured by scattering from overlying Cu at this stage.

two by the time complete Cu coverage occurs. For catalysis with mixed Pd-Sn colloid solutions, it was found that some Sn was lost into the electroless bath (1). For the present processing even more Sn is lost and also some Pd. It has been demonstrated (1) that Sn lost into the electroless bath may be codeposited; the concern with the possibility of Pd loss into the electroless bath is obvious. It is a general observation of our work that electroless Cu baths which have been used to process sensitized and activated samples are considerably less stable with respect to spontaneous Cu plate-out than are those used to process samples catalyzed by Pd-Sn colloid solutions.

The remaining Pd and Sn are, of course, buried beneath the deposited Cu layer. Figure 8 shows a typical scattered ion spectrum for $t_{\text{SnCl}_2\text{-C}} = 30$ sec, $t_{\text{PdCl}_2} = 30$ sec, $t_{\text{Cu}} = 900$ sec. As discussed in (I), the Sn peak has been shifted to lower energy due to the inelastic energy loss suffered by the scattered ions as they penetrate through and exit from the Cu layer. Again there is considerable difference between the present processing where $\sim 10^{16}$ Sn atoms cm^{-2} and $\sim 10^{15}$ Pd atoms cm^{-2} are found at the Cu-substrate interface and the Pd-Sn colloid catalyst process where $\sim 10^{15}$ Pd atoms cm^{-2} and $\sim 10^{14}$ Sn atoms cm^{-2} are found at the interface.

Some effort has been expended in preventing Pd and Sn loss into the electroless solution and in trying to change the Pd/Sn ratio and reduce the initiation time. Samples which had $t_{\text{SnCl}_2\text{-A}} = 100$ sec, $t_{\text{PdCl}_2} = 30$ sec were immersed in various 0.2M solutions of the so-called accelerators used after catalysis with Pd-Sn colloids. Results are given in Table I. It is seen that both the Pd and Sn concentrations are reduced, but that the Pd/Sn ratio is practically unchanged. It has also been found that after such treatments no further loss of Pd or Sn into the electroless solution results, but that the long initiation times are not reduced. However, as will be reported separately, a suitable treatment in a basic solution does achieve the desired result.

Conclusions

Sensitization (SnCl_2) and activation (PdCl_2) is basically different from catalysis by colloidal Pd-Sn solu-

Table I. Pd and Sn surface concentrations after postactivator immersion in various solutions

Solution	Atoms cm^{-2}		Pd/Sn
	Sn	Pd	
—	1.1(10) ¹⁶	2.8(10) ¹⁵	0.23
HCl	0.36(10) ¹⁶	0.80(10) ¹⁵	0.22
HF	0.53(10) ¹⁶	0.84(10) ¹⁵	0.16
NH ₄ F	0.62(10) ¹⁶	1.7(10) ¹⁵	0.27

tions. The Pd/Sn ratio is considerably less, more Pd and Sn are lost into the electroless plating solution, and longer times ($\geq 10^2$ sec) are required to initiate the electroless plating reaction than in the case of the mixed Pd-Sn colloid catalyst systems (1).

The present observations are consistent with, but not proof of, the correctness of the redox reaction involving divalent Sn and Pd during the activation treatment. It is suggested that while the Pd deposited during the activation step may be zero-valent, it has neither metallic properties nor catalytic activity. Rather, it is proposed that the sensitized and activated surface becomes catalytic only after some residence time in the electroless plating solution.

Acknowledgments

The author would like to thank R. L. Cohen for many stimulating and useful discussions and R. Sard for his enthusiastic support of this work.

Manuscript submitted Jan. 17, 1975; revised manuscript received July 16, 1975.

Any discussion of this paper will appear in a Discussion Section to be published in the June 1976 JOURNAL. All discussions for the June 1976 Discussion Section should be submitted by Feb. 1, 1976.

Publication costs of this article were partially assisted by Bell Laboratories.

REFERENCES

- R. L. Meek, *This Journal*, **122**, 1177 (1975).
- W. Goldie, "Metallic Coating of Plastics," Electrochemical Publications Ltd., Middlesex, England (1968).
- D. J. Sharp, J. Henrickson, J. D'Amico, and J. Kenney, Paper 136 presented at The Electrochemical Society Meeting, Detroit, Michigan, Oct. 5-9, 1969.
- R. Sard, *This Journal*, **117**, 864 (1970).
- R. L. Cohen and K. W. West, *ibid.*, **119**, 433 (1972).
- R. L. Cohen, J. F. D'Amico, and K. W. West, *ibid.*, **118**, 2042 (1971).
- N. Feldstein, J. A. Weiner, and G. L. Schnable, *ibid.*, **119**, 1486 (1972).
- J. T. Kenney, W. P. Townsend, and J. A. Emerson, *J. Coll. Interface Sci.*, **42**, 589 (1973).
- N. Feldstein and J. A. Weiner, *This Journal*, **120**, 475 (1973).
- N. Feldstein, S. L. Chow, and M. Schlesinger, *ibid.*, **120**, 875 (1973).
- M. Schlesinger, *ibid.*, **121**, 667 (1974).
- C. H. de Minjer and P. F. J. v.d. Boom, *ibid.*, **120**, 1644 (1973).
- R. L. Cohen and K. W. West, *Chem. Phys. Letters*, **16**, 128 (1972).
- R. L. Cohen and K. W. West, *This Journal*, **120**, 502 (1973).
- S. Huffner and R. L. Cohen, Unpublished data.
- A. L. Robinson, *Science*, **185**, 772 (1974).
- J. C. Slater and K. H. Johnson, *Physics Today*, **27**, 34 (1974).
- M. A. Khattak and R. J. Magee, *Chem. Commun.*, 400 (1965).

Maximum Effective Capacity in an Ohmically Limited Porous Electrode

William Tiedemann* and John Newman*¹

Globe-Union, Incorporated, Corporate Applied Research Group, Milwaukee, Wisconsin 53201

ABSTRACT

For large reaction rate constants and negligible change in solution composition, the performance of a porous electrode with solid reactants is governed by the ohmic potential drop within the matrix and solution phases. The cell potential changes with time, at constant current, as the reactants are consumed. Equations are developed which describe this time dependence as a function of electrode porosity and thickness, the electrolyte and solid phase conductivities, specific ampere-hour capacity, separator conductivity and thickness, and current density. These then yield the values of electrode porosity and electrode thickness so as to maximize the capacity for discharge to a given cutoff potential. Treatment of the porous LiAl electrode is presented as an example.

Many models have been proposed to predict the behavior of porous electrodes (1). Current distribution in porous electrodes has been examined in great detail. The correspondence between experiment and theory has been shown to be good for several different systems. The purpose of such models is to develop an understanding of the specific system, as well as to suggest directions for improved performance in the system. The ultimate objective of such investigations is the optimization of the electrochemical cell in question. However, relatively little information is available concerning the optimization of the performance of porous electrodes (1).

Let us consider here the constant-current discharge of an electrode where activation and concentration overpotential are small compared to the ohmic losses in the solution and solid phases. Under these conditions the reaction zone is very thin. The electrode potential changes during discharge because the positions of the reaction zones move as the solid reactant is consumed and also because the conductivities of the phases may be different in the discharged state.

We wish to maximize the capacity which can be utilized at a given current density before the discharge potential drops below a prescribed cutoff potential. An increase in the electrode thickness increases the theoretical electrode capacity, but it also increases the ohmic potential drop because of the increased distances that current must flow. The effective capacity is maximized at that electrode thickness where 100% utilization occurs at the moment that the potential drops to the prescribed cutoff.

Analysis

The system under investigation is a macrohomogeneous porous electrode [as originally proposed by Newman and Tobias (2)] in contact with a porous separator. The treatment presented here is one dimensional as shown in Fig. 1. Only the separator and porous electrode will be considered in this examination. The effects of the free electrolyte and metal backing plate can be dealt with separately.

In this treatment it is assumed that ohmic losses in the system are much larger than kinetic (activation overpotential) losses and losses due to concentration overpotential. This assumption simplifies the analysis. The behavior as well as the performance of the electrode can be determined by calculating the ohmic resistance of the system as a function of time.

The effective resistance of the system shown in Fig. 1, at time zero, can be expressed by (3)

$$R|_{t=0} = \frac{L_s}{\kappa_s} + \frac{L}{\kappa + \sigma} \quad [1]$$

where L_s and L are the thicknesses of the separator and porous electrode, respectively, and σ , κ , and κ_s are the effective conductivities (1) of the solid electrode matrix, electrolyte contained in the porous matrix, and the electrolyte contained in the porous separator, respectively. The current distribution in the porous electrode becomes nonuniform for large values of the exchange current density, the electrochemically active interfacial surface area, the electrode thickness, or the current density, or for small values of the electrolyte and solid phase conductivities.

As shown by Newman and Tobias (2), the ratio of the electrolyte and solid phase conductivities determines the shape of the current density distribution within a porous electrode. Depending on the value of κ/σ , the current density distribution can be displaced toward the electrode-separator interface, the electrode-backing plate interface, or portioned to these two interfaces, thereby producing a minimum value of the current density within the electrode. As the current distribution becomes highly nonuniform, it approaches a thin reaction zone in nature. We shall approximate the true current density distribution by a narrow reaction zone which can be envisioned to move through the electrode as the available material is consumed. The rate of the reaction and whether it is split between

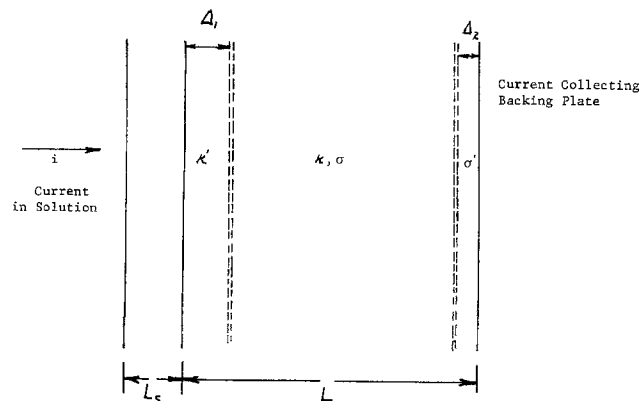


Fig. 1. Schematic representation of a separator and porous electrode of lengths L_s and L , respectively, with finite reaction zones indicated by dashed lines.

* Electrochemical Society Active Member.

¹ Present address: Department of Chemical Engineering, University of California, Berkeley, California 94720.

Key words: electrode thickness, electrode porosity, ohmic loss, optimization, nonuniform current distribution.

the front and back faces of the electrode will be governed by the conductivities of the electrolyte and solid phases.

As these reaction zones consume the available material and penetrate further into the electrode, a discharged region is left behind which may have different electrolyte and solid phase conductivities and thereby alter the over-all resistance of the electrode. We shall assume that concentration changes are small. The porosity of the electrode can change as a result of differences in the partial molar volumes of the reactants and products; also, the electrode can shrink and expand due to these volume changes. It is therefore necessary to alter the expression for the resistance of the system to account for these changes as follows

$$R_{(i,t)} = \frac{L_s}{\kappa_s} + \frac{L - \Delta_1 - \Delta_2}{\kappa + \sigma} + (1+f) \left(\frac{\Delta_1}{\kappa'} + \frac{\Delta_2}{\sigma'} \right) \quad [2]$$

where Δ_1 and Δ_2 are the thicknesses of the reacted zones of the electrode, κ' and σ' are the electrolyte and solid phase conductivities, respectively, of the reacted zone, and f is a constant equal to the fractional increase in electrode thickness resulting from volume changes within the electrode.

The thicknesses of the reacted zones can be expressed as

$$\Delta_1 = \frac{it}{q} \frac{\sigma}{\kappa + \sigma} \quad \Delta_2 = \frac{it}{q} \frac{\kappa}{\kappa + \sigma} \quad [3]$$

where i is the current density, t is time of discharge, and q is the specific electrode capacity. Substituting Eq. [3] into [2] and rearranging yields

$$R_{(i,t)} = \frac{L_s}{\kappa_s} + \frac{L}{\kappa + \sigma} + \frac{it}{q(\kappa + \sigma)} \left(\left(\frac{\sigma}{\kappa'} + \frac{\kappa}{\sigma'} \right) (1+f) - 1 \right) \quad [4]$$

The voltage loss in the composite system can be expressed as

$$\Delta V = iR_{(i,t)} \quad [5]$$

and the effective capacity of the electrode at time t as

$$Q = it \quad [6]$$

Using Eq. [5] and [6] to rearrange Eq. [4], we obtain

$$Q = (\kappa + \sigma) \left(\frac{\Delta V}{i} - \frac{L}{\kappa + \sigma} - \frac{L_s}{\kappa_s} \right) q \left| \left(\left(\frac{\sigma}{\kappa'} + \frac{\kappa}{\sigma'} \right) (1+f) - 1 \right) \right. \quad [7]$$

The total theoretical capacity of the electrode is given by

$$Q_T = qL \quad [8]$$

A qualitative plot of Eq. [7] and [8] is shown in Fig. 2. Dotted lines represent physically inaccessible situations. The effective capacity cannot lie above the value given by Eq. [8] because there is no more active material in the electrode. It cannot lie above the value indicated by Eq. [7] without exceeding the allowable potential loss. The intersection of these equations thus provides the condition at which the usable electrode capacity is maximized. Inspection of Fig. 2 shows that the maximum does not involve a zero derivative of capacity with respect to electrode thickness. Rather, it occurs when 100% of the theoretical capacity is utilized at the same time that the ohmic potential loss rises to the allowable value. The optimum L is given by

$$L_{opt.} = (\kappa + \sigma) \left(\frac{\Delta V}{i} - \frac{L_s}{\kappa_s} \right) \left| \left(\left(\frac{\sigma}{\kappa'} + \frac{\kappa}{\sigma'} \right) (1+f) \right) \right. \quad [9]$$

The thickness of the electrode has now been optimized to maximize the capacity. We now wish to maximize the electrode capacity with respect to porosity. The conductivities given in Eq. [7] can be expressed as

$$\kappa = \kappa_0 \epsilon^n, \quad \kappa' = \kappa_0 \epsilon_f^n \quad [10]$$

$$\sigma = \sigma_0 (1 - \epsilon)^n, \quad \sigma' = \sigma_0' (1 - \epsilon_f)^n \quad [11]$$

and

$$q = q_0 (1 - \epsilon) \quad [12]$$

where κ_0 and σ_0 are the bulk conductivities of the electrolyte and solid phases, respectively, ϵ and ϵ_f are the initial and final porosities of the electrode, respectively. The n is a factor lying between 1 and 3 which accounts for tortuosity effects (1). Since the solid product can be a different material from the reactant, the final conductivity σ_0' can be quite different from the initial conductivity σ_0 . The initial and final electrode porosities are related by

$$\epsilon_f = 1 - (1 - \epsilon)/B \quad [13]$$

where

$$B = (1+f)$$

$$\frac{(\text{volume of solid reactants}) + (\text{volume of solid inerts})}{(\text{volume of solid products}) + (\text{volume of solid inerts})}$$

Solid inerts should include product species present initially.

Substitution of Eq. [10] through [13] into the optimized form of Eq. [8] gives

$$Q = \frac{q_0 (1 - \epsilon) (\kappa_0 \epsilon^n + \sigma_0 (1 - \epsilon)^n) \left(\frac{\Delta V}{i} - \frac{L_s}{\kappa_s} \right)}{\left[\frac{\sigma_0 (1 - \epsilon)^n}{\kappa_0 \left(1 - \frac{(1 - \epsilon)}{B} \right)^n} + \frac{\kappa_0 \epsilon^n}{\sigma_0' \left(\frac{1 - \epsilon}{B} \right)^n} \right] (1+f)} \quad [14]$$

Differentiating Eq. [14] with respect to ϵ and setting the result equal to zero yields

$$\begin{aligned} \epsilon^n (1 - \epsilon)^{2n} \left(1 - \frac{(1 - \epsilon)^2}{B} - \frac{\epsilon}{n} \left(1 - \frac{(1 - \epsilon)}{B} \right) \right) \\ + (1 - \epsilon)^3 \epsilon \frac{\sigma_0}{\kappa_0} \left[\frac{1 - \epsilon}{B} - \frac{\left(1 - \frac{(1 - \epsilon)}{B} \right)}{n} \right] \\ - \frac{\kappa_0}{\sigma_0'} B^n \left(1 - \frac{(1 - \epsilon)}{B} \right)^{n+1} \left(\frac{\kappa_0}{\sigma_0'} \epsilon^{2n+1} \left(1 + \frac{1}{n} \right) \right. \\ \left. + \epsilon^n (1 - \epsilon)^n \left(1 + \epsilon + \frac{\epsilon}{n} \right) \right) = 0 \quad [15] \end{aligned}$$

The value of ϵ satisfying Eq. [15] is designated as the optimum porosity, $\epsilon_{opt.}$

Equation [15] gives the optimum porosity as a function of the relative conductivities of the electrolyte and solid phases and the system parameters B and n . In the case of $\sigma_0 \gg \kappa_0$, Eq. [15] reduces to

$$\epsilon_{opt.} = 1 - B/(1+n) \quad [16]$$

Discussion

Maximization of the available capacity, as given by Eq. [7] and [8], with respect to porosity yields an optimum porosity, as displayed in Fig. 1. Here we have taken the matrix conductivities σ_0 and σ_0' to be the same in the charged and discharged states, and we have displayed the dependence of the optimum porosity on the conductivity ratio of the bulk matrix and solution phases. The optimum electrode thickness is that for which 100% utilization occurs at the same moment that the ohmic potential loss reaches its allowable value. If concentration and kinetic effects begin to become important, we can expect that the actual curve

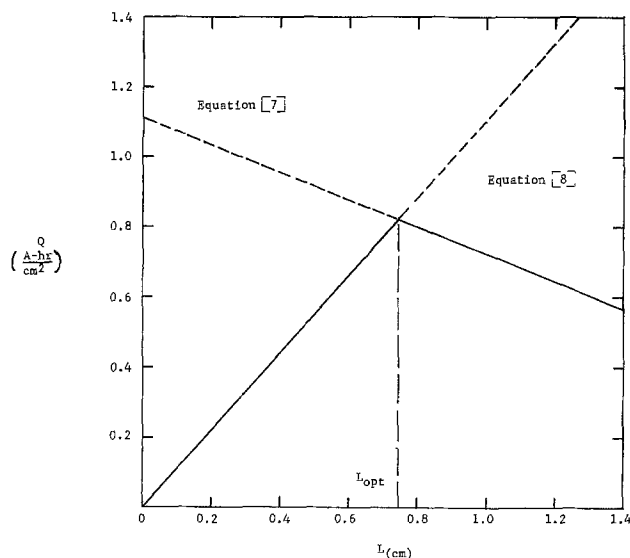


Fig. 2. Effective electrode capacity plotted as a function of electrode thickness, $\kappa = 0.138$ mho/cm, $\kappa' = 0.715$ mho/cm, $\sigma = \sigma' = 20K$, $q = 1.11$ A-hr/cm³, $\Delta V = 0.1V$, $i = 0.1$ A/cm², $f = 0$, $L_S/\kappa_S = 0$.

will lie below that of the solid curve generated from Eq. [7] and [8]. In other words, the maximum capacity should lie below that predicted, but the optimum electrode thickness could lie below or above the predicted value.

The optimum porosity curves shown in Fig. 3 are markedly different depending on whether the porosity increases ($B > 1$) or decreases ($B < 1$) during discharge. It is also apparent that the value of n can significantly alter the shape of the curve. Figure 4 shows the effect of different values of the conductivities for the initial and final states of the solid phases on the optimum porosity curves. These results indicate that it is very important to characterize the behavior of a given porous medium in terms of the porosity dependence of the conductivities, the conductivities of the bulk phases, and the volumetric expansion or contraction.

Note that the conditions of the specified discharge, current density and minimum allowable discharge potential in this case, influence the optimization of the electrode thickness. The optimum porosity is independent of these factors for the system treated here.

As an example of the applicability of the model to treat real systems, we select the porous LiAl electrode in molten LiCl + KCl. Since the concentration of Li⁺ ions is of the order of 20M, the assumption of minimal concentration gradients is reasonable. The operating temperature of 450°C further supports this assumption, since increased diffusion minimizes concentration gradients. The high temperature and large surface area couple to create very fast kinetics. The relative importance of diffusion in a particle compared with diffusion in the electrolyte phase of a porous electrode has been discussed by Johnson and Newman (3). A criterion to assess the importance of solid-state diffusion within a lithium-aluminum particle can be expressed as

$$S = \frac{3.87(1 - \epsilon)i}{nFCLa^2D} \quad [17]$$

where C is the concentration of lithium in the lithium-aluminum alloy (0.0517 equiv./cm³), D is the diffusion coefficient of lithium in the lithium-aluminum alloy ($2 \cdot 10^{-10}$ cm²/sec), a is the specific interfacial area ($2 \cdot 10^3$ cm²/cm³), L is the thickness of the porous electrode (1 cm), ϵ is the initial porosity of the electrode (0.2), i is the current density (0.1 A/cm²), n is the number of electrons transferred in the electrode reaction (1 electron), F is Faraday's constant (96,500

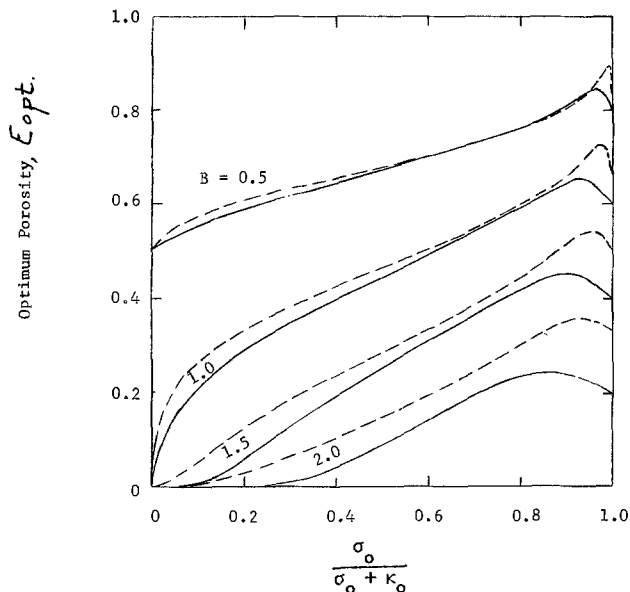


Fig. 3. Dependence of the optimum porosity on the relative conductivities of the bulk matrix and solution phases calculated by Eq. [15], $\sigma_0' = \sigma_0$. Solid curves are for $n = 1.5$; dashed curves are for $n = 2$.

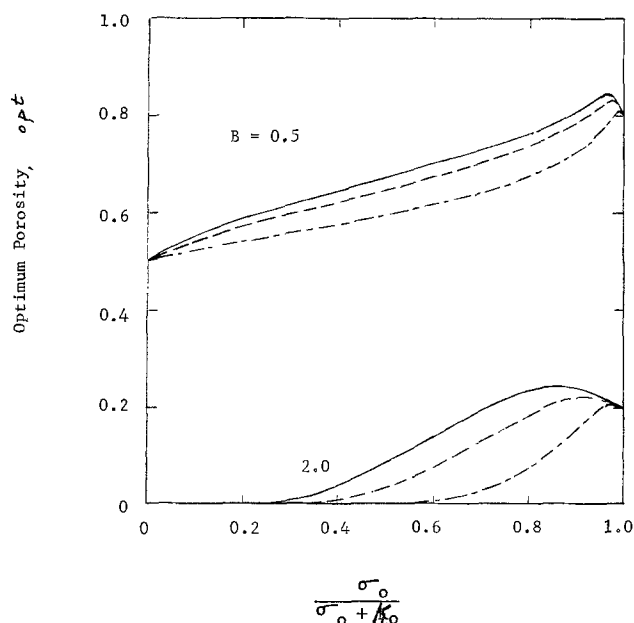


Fig. 4. Dependence of the optimum porosity on the relative conductivities of the bulk matrix and solution phase calculated by Eq. [15], $n = 1.5$. Solid curves are for $\sigma_0'/\sigma_0 = 1$; --- curves for $\sigma_0'/\sigma_0 = 0.5$; -·- curves for $\sigma_0'/\sigma_0 = 0.1$.

coulombs/equiv.). For $S < 1$ solid-state diffusion can be neglected. Using the parameters given above $S \approx 0.08$. For the example presently being treated solid-state diffusion can be neglected, however, one should note that decreasing the interfacial surface area (increasing particle size) and operating temperature (decreasing the diffusion coefficient) can greatly increase the value of S . Therefore, application of the model represented in this paper to the LiAl electrode is in harmony with its underlying assumptions.

One curve of Fig. 3 depicts the case of optimum porosity for the LiAl electrode, $B = 2$. For the condition that $\sigma_0 \gg \kappa_0$, the optimum porosity is equal to 0.2. This value can now be inserted into Eq. [9] to obtain the optimum electrode thickness provided values are assigned to the allowable voltage loss as well as the effect of separator resistance (L_S/κ_S). Using $\Delta V = 0.1V$, $i = 0.1$ A/cm², $L_S/\kappa_S = 0.0$, $\kappa_0 = 1.54$ mho/

cm, $\epsilon = 0.2$, $f = 0$, $n = 1.5$, and $\sigma_0 = \sigma_0' \gg \kappa_0$, we obtain $L_{opt.} \cong 0.713$ cm.

We have not presented results which show the effect of increasing or decreasing electrode thickness. However, one can expect that for electrodes which decrease in thickness as they are discharged the optimum electrode thicknesses will increase and that the opposite would be true for electrodes with increasing thicknesses. For the case of current collected from the front face (separator-electrode interface) instead of the backing plate, or for current collected from both faces, different equations will have to be developed, though their form will be similar. Should the entire cell (two porous electrodes plus a separator) be treated in a similar manner, the effects of changes of the parameters of one electrode will be seen to affect the optimum performance of the other electrode.

Acknowledgment

The authors wish to thank Globe-Union Incorporated for permission to publish this paper and for their cooperation and support that have made this research possible.

Manuscript submitted March 20, 1975; revised manuscript received June 25, 1975.

Any discussion of this paper will appear in a Discussion Section to be published in the June 1976 JOURNAL. All discussions for the June 1976 Discussion Section should be submitted by Feb. 1, 1976.

Publication costs of this article were partially assisted by Globe-Union Incorporated.

LIST OF SYMBOLS

a	specific interfacial area, cm^2/cm^3
B	a parameter given by Eq. [13] which accounts for volume changes within the electrode
C	concentration of the lithium in the lithium-aluminum alloy, equiv./cm^3
D	diffusion coefficient of lithium in the lithium-aluminum alloy, cm^2/sec
f	fraction increases in electrode thickness due to volume changes

F	Faraday's constant, A-sec/equiv.
i	current density, A/cm^2
L	electrode thickness, cm
L_s	separator thickness, cm
$L_{opt.}$	optimum electrode thickness as given by Eq. [9], cm
n	a parameter which accounts for tortuosity effects
q	effective electrode capacity equal to $q_0(1 - \epsilon)$, A-sec/ cm^3
q_0	specific electrode capacity, (A-sec)/(total solid volume), A-sec/ cm^3
Q	electrode capacity given by Eq. [14], A-sec/ cm^2
$R/t=0$	resistance given by Eq. [1], ohm/cm^2
$R_{(i,t)}$	resistance given by Eq. [2], ohm/cm^2
S	a parameter given by Eq. [17]
t	time, sec
ΔV	voltage loss, V
ϵ	electrode porosity in the charged state
ϵ_f	electrode porosity in the discharged state
$\epsilon_{ont.}$	optimum electrode porosity as given by Eq. [15]
κ	effective conductivity of solution in porous matrix in the charged state, mho/cm
κ'	effective conductivity of solution in porous matrix in the discharged state, mho/cm
κ_0	conductivity of the bulk solution, mho/cm
κ_s	conductivity of the separator, mho/cm
σ	effective conductivity of the solid phases in the porous matrix in the charged state, mho/cm
σ'	effective conductivity of the solid phases in the porous matrix in the discharged state, mho/cm
σ_0	conductivity of the bulk solid phases in the charged state, mho/cm
σ_0'	conductivity of the bulk solid phases in the discharged state, mho/cm

REFERENCES

1. John Newman and William Tiedemann, *Am. Inst. Chem. Engrs. J.*, **21**, 25 (1975).
2. John Newman and Charles Tobias, *This Journal*, **109**, 1183 (1962).
3. A. M. Johnson and John Newman, *ibid.*, **118**, 510 (1971).

Potential Differences Between the Alkali Metals and Their Amalgams

Jacob Jorné*

Department of Chemical Engineering and Material Sciences, Wayne State University, Detroit, Michigan 48202

and Charles W. Tobias*

Inorganic Materials Research Division, Lawrence Berkeley Laboratory and Department of Chemical Engineering, University of California, Berkeley, California 94720

ABSTRACT

Potential differences have been measured between the alkali metals and their dilute amalgams in propylene carbonate solutions. The general cell $M(s)|M^+, X^-(PC)|M(Hg)$ has been used where $M = Li, Na, K, Rb,$ and Cs , and $X^- = AlCl_4^-$ or PF_6^- . The emf values measured are in satisfactory agreement with those obtained earlier in other solvents.

In the course of our studies on the thermodynamic properties (1, 2) and the kinetic measurements (3) of the alkali metals in aluminum chloride-propylene carbonate (PC) solution, we have measured the poten-

tial difference between the alkali metals Li, Na, K, Rb, and Cs and their respective dilute amalgams.

This is a report of a fragmentary nature which establishes the feasibility for a complete thermodynamic study of the alkali metal amalgams using propylene carbonate as a nonaqueous solvent.

* Electrochemical Society Active Member.

Key words: lithium amalgam, sodium amalgam, potassium amalgam, rubidium amalgam, cesium amalgam, propylene carbonate.

In the present work we have confirmed some of the emf data of the early pioneering work of Lewis (4-7) and Bent (8-10) and their co-workers, and provided some additional emf data for different amalgam concentrations. We feel that the measurements on potassium, rubidium, and cesium should be especially useful because of the paucity of data for these experimentally difficult systems.

Experimental

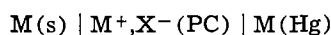
Alkali metal amalgams were prepared by weight from triple distilled mercury (Quicksilver Products Incorporated, San Francisco) and alkali metal ribbons (Li, Lithium Corporation of America, 99.9%; Na, Baker analyzed reagent; K, Mallinckrodt; Rb, Alfa Inorganic, m2N+; Cs, United Mineral & Chemical Corporation, New York, 99.8%). The amalgams were prepared inside a dry argon glove box (below 1 ppm water). The electrolytes were prepared from alkali metal chlorides (Mallinckrodt and Alfa Inorganic) and aluminum chloride (Baker, 99.2%) or sodium hexafluorophosphate (Alfa Inorganic, 99%) in propylene carbonate (Jefferson Chemical Corporation, Houston, Texas). The distillation, purification, and preparation of the solutions are discussed elsewhere. Special precautions were necessary for the K, Rb, and Cs cells (1, 2, 11).

Potentials were measured with a high impedance differential voltmeter (John Fluke, Model 887-A), accuracy ± 0.005 mV, which was calibrated against an Eppley Laboratory low temperature coefficient standard cell.

The six compartment cells and the electrodes were described previously (1, 11, 12). The potentials were measured between the alkali metals wires, or solidified pools of Rb and Cs in cup electrodes (1, 3, 11), and the corresponding alkali metal amalgams which were placed in cup electrodes. The measurements were repeated every 30 min for the first few hours. The potential drift during the first hour was less than 1 mV for most measurements. The potentials were extrapolated to zero time and represent average values of at least 2 electrodes for each cell. The temperature was maintained at $25^\circ \pm 0.01^\circ\text{C}$ for all experiments. In the case of potassium the measurements were repeated for various temperatures up to 50°C within $\pm 1^\circ\text{C}$.

Results

The potential differences of the general cell



(where X^- is AlCl_4^- or PF_6^-) were measured for $M = \text{Li, Na, K, Rb, and Cs}$. The results are summarized in Table I for various amalgam compositions.

Discussion

The results of the present work can be compared with early results. The value of 1.004V for $X_{\text{Li}} = 0.01907$ Li(Hg) agrees with a value of 1.0037V reported by Cogley and Butler (13). The first sodium amalgam measurement (0.843V) satisfactorily agrees with the

value of 0.8456V reported by Lewis and Kraus (5) for the identical amalgam composition ($X_{\text{Na}} = 0.01771$). The second value of 0.8319V agrees well with 0.830V calculated after Mussini, Maina, and Pagella (14). However the third value of 0.7347V for $X_{\text{Na}} = 0.02982$ is significantly lower than the calculated value of 0.822V (14). It is believed that the calculated value is the correct one because of the consistency of the data over the entire dilute range (14). It is quite possible that the present value is erroneous due to poisoning of the solid sodium in this particular measurement. The first two Na measurements agree well with the data reported by Hsueh and Bennion (15) and by Bent and Swift (9).

The emf of the potassium cell, 1.0523V, is slightly higher than the value of 1.0481V reported by Lewis and Keyes (6) for the same amalgam composition ($X_{\text{K}} = 0.01126$). The additional value of 1.0067V for $X_{\text{K}} = 0.02271$ agrees with 1.01036V calculated from the aqueous solution measurements of Bent and Gilfillan (10). The temperature coefficient of the emf of the $X_{\text{K}} = 0.02271$ amalgam cell was calculated from data obtained in the temperature range between 25° and 50°C , resulting in the average value of $dE/dT = 0.0022 \pm 0.001$ V/ $^\circ\text{K}$. The entropy of solution of potassium in $X_{\text{K}} = 0.02271$ amalgam is therefore

$$\Delta S = F(dE/dT) = (96,580/4.186)(0.0022)$$

$$= 50 \text{ cal/g-mole}^\circ\text{K}$$

The emf value of 1.0766V for Rb(Hg) ($X_{\text{Rb}} = 0.00539$) agrees reasonably with the corresponding value of 1.0745V reported by Lewis and Argo (7) for an identical amalgam composition, and with 1.077V calculated from the aqueous solution measurements of Longhi, Mussini, and Osimani (16).

The cesium amalgam mole fraction in the present work was 0.004551, higher than the composition of the cesium amalgam used by Bent *et al.* (8), $X_{\text{Cs}} = 0.002827$. The value of 1.107V obtained in the present work is indeed lower than the value of 1.121V measured by Bent *et al.* (8) for a more dilute amalgam, and agrees reasonably with the calculated value of 1.100V after Mussini, Longhi, and Riva (17).

The activity coefficient of cesium in its amalgams can now be calculated from the two measurements

$$\log \gamma_{\text{Cs}} = (F/2.303RT)E - \log X_{\text{Cs}}$$

where the pure cesium has been chosen as the reference state, and the activity coefficients are based on the mole fraction X of cesium in the amalgam. For both concentrations: $X_{\text{Cs}} = 0.002827$ and $X_{\text{Cs}} = 0.00454$, we obtained $\log \gamma_{\text{Cs}} = -16.4$.

The potentials were measured every 30 min for the first few hours and extrapolated to zero time. The time dependent potential drift is due to the reactivity of the alkali metal amalgams, especially lithium amalgam, toward PC. Dousek, Jansta, and Riha (18) report that active lithium reacts with PC freed from impurities with the formation of Li_2CO_3 and propylene. They prove that the Li_2CO_3 layer passivates the solid lithium surface. The decomposition of lithium amalgam in highly pure PC (water content was lower than 0.01 ppm) is even stronger due to surface renewal of the amalgam. The rate of PC decomposition by the alkali metal amalgams decreases sharply in the order $\text{Li} > \text{Na} > \text{K}$ (18). The presence of traces of water in the electrolytic solution (45 ppm) decreases the PC decomposition by the Li-Hg amalgam considerably as it is believed that the amalgam surface is blocked by LiOH (18). Dey (19) also speculates on the film formation in Li-PC systems, and Scarr (20) predicts PC decomposition by Li from thermodynamic considerations.

In the present investigation, the water content was mostly 10 ppm and in some cases up to 50 ppm, and therefore it is quite possible that the protective layer slowed down the chemical decomposition, especially in

Table I. Potential measurements of the alkali metal-alkali amalgam cells

Cell	X, mole fraction	Temp, $^\circ\text{C}$	E, volts
Li(s) LiAlCl ₄ (1M), PC Li(Hg)	0.01907	25	1.004
Na(s) NaAlCl ₄ (0.5M), PC Na(Hg)	0.01771	25	0.843
Na(s) NaPF ₆ (0.5M), PC Na(Hg)	0.02441	25	0.8319
Na(s) NaPF ₆ (0.5M), PC Na(Hg)	0.02982	25	(0.7347)*
K(s) KAlCl ₄ (0.5M), PC K(Hg)	0.01126	25	1.0523
K(s) KAlCl ₄ (0.5M), PC K(Hg)	0.02271	25	1.0067
		29	1.013
		30	1.016
		43	1.057
		50	1.067
Rb(s) RbAlCl ₄ (0.5M), PC Rb(Hg)	0.005395	25	1.0766
Cs(s) CsAlCl ₄ (0.5M), PC Cs(Hg)	0.004551	25	1.107

* Doubtful value, see discussion.

the Li amalgam case. Similar behavior of potential drift in nonaqueous cells was observed in PC (1, 21), DMSO (22, 23), DMF (24), and N-MF (25). True cell potentials were obtained by extrapolating to zero time in formamide (26, 27). The general agreement with the previous reliable data justifies the extrapolation procedure in the present work.

In conclusion, this fragmentary study establishes the feasibility of using propylene carbonate for thermodynamic measurements of the alkali metal amalgams.

Acknowledgment

This work was conducted under the auspices of the U.S. Atomic Energy Commission. The valuable comments of the reviewers are greatly appreciated.

Manuscript submitted March 24, 1975; revised manuscript received July 1, 1975.

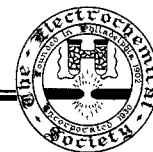
Any discussion of this paper will appear in a Discussion Section to be published in the June 1976 JOURNAL. All discussions for the June 1976 Discussion Section should be submitted by Feb. 1, 1976.

Publication costs of this article were partially assisted by the University of California.

REFERENCES

- Jacob Jorné and C. W. Tobias, *This Journal*, **122**, 624 (1975).
- Jacob Jorné and C. W. Tobias, *J. Phys. Chem.*, **78**, 2576 (1974).
- Jacob Jorné and C. W. Tobias, *This Journal*, **121**, 994 (1974).
- G. N. Lewis and F. G. Keyes, *J. Am. Chem. Soc.*, **35**, 340 (1913).
- G. N. Lewis and C. A. Kraus, *ibid.*, **32**, 1459 (1910).
- G. N. Lewis and F. G. Keyes, *ibid.*, **34**, 119 (1912).
- G. N. Lewis and W. L. Argo, *ibid.*, **37**, 1983 (1915).
- H. E. Bent, G. S. Forbes, and A. F. Forziati, *ibid.*, **61**, 709 (1939).
- H. E. Bent and E. Swift, Jr., *ibid.*, **58**, 2216 (1936).
- H. E. Bent and E. S. Gilfillan, *ibid.*, **55**, 3989 (1933).
- Jacob Jorné, PhD Thesis, LBL 1111, University of California, Berkeley, California (1972).
- W. H. Smyrl and C. W. Tobias, *This Journal*, **115**, 33 (1968).
- D. R. Cogley and J. N. Butler, *J. Phys. Chem.*, **72**, 1017 (1968).
- T. Mussini, A. Maina, and A. Pagella, *J. Chem. Thermodynamics*, **3**, 281 (1971).
- L. Hsueh and D. N. Bennion, *This Journal*, **118**, 1128 (1971).
- P. Longhi, T. Mussini, and C. Osimani, *J. Chem. Thermodynamics*, **6**, 227 (1974).
- T. Mussini, P. Longhi, and G. Riva, *ibid.*, **4**, 592 (1972).
- F. P. Dousek, J. Jansta, and J. Říha, *J. Electroanal. Chem.*, **46**, 281 (1973).
- A. N. Dey, Paper 62 presented at The Electrochemical Society Meeting, Atlantic City, N. J., Oct. 4-8, 1970.
- R. F. Scarr, *This Journal*, **117**, 295 (1970).
- M. Salomon, *J. Phys. Chem.*, **73**, 3299 (1969).
- W. H. Smyrl and C. W. Tobias, *Electrochim. Acta*, **13**, 1581 (1968).
- G. Holleck, D. R. Cogley, and J. N. Butler, *This Journal*, **116**, 952 (1969).
- J. N. Butler and J. C. Synnott, *J. Am. Chem. Soc.*, **92**, 2602 (1970).
- E. Luksha and C. M. Criss, *J. Phys. Chem.*, **70**, 1496 (1966).
- R. K. Agarwall and B. Nayak, *ibid.*, **70**, 2568 (1966); **71**, 2062 (1967).
- M. Mandel and P. Decroly, *Nature*, **182**, 794 (1958).

Technical Notes



Hydrogen Production under Sunlight with an Electrochemical Photocell

Akira Fujishima and Koichi Kohayakawa

Department of Applied Chemistry, Kanagawa University, Rokkakubashi, Kanagawa-ku, Yokohama, Japan

and Kenichi Honda

Institute of Industrial Science, the University of Tokyo, Roppongi, Minato-ku, Tokyo, Japan

An electrochemical photocell has been reported (1) which consists of titanium dioxide (rutile type) single crystal as an anode, and platinum as a cathode. The photocell works under irradiation with light, leading to oxygen evolution on the anode and hydrogen evolution on the cathode. Quantum efficiencies of the cell increases with an increase in the alkaline concentration in the titanium dioxide anode compartment and in the acidic concentration in the cathode compartment (2). However, the use of polycrystal or amorphous titanium dioxide in place of its single crystal is desired from the practical standpoint of realizing a large scale electrochemical photocell.

Key words: hydrogen production, electrochemical photocell, titanium oxide film.

Among the various methods of forming oxide film on metal, the following three methods were studied in the present work: (i) electrochemical formation of oxide film on metal; (ii) thermal formation of oxide film in an electric furnace; and (iii) thermal formation of oxide film by simple heating.

Electrochemical formation of oxide film on titanium metal.—Formation of anodic oxide film on titanium was carried out potentiostatically or galvanostatically. The electrolyte solutions used were basic (1.0M NaOH) or acidic (0.5M H₂SO₄). Photoelectrochemical behavior of the oxide film electrodes was investigated using a 500W xenon lamp. Maximum photocurrent under anodic polarization of the oxide electrodes was about one-tenth of that on the single crystal rutile

electrodes. Electric resistivity of the semiconductor is desired to be as low as possible in order to effectively separate electrons and holes formed by irradiation with light in the space charge layer of the semiconductor surface. Moreover, the thickness of a photosensitive layer necessary to absorb light quanta is about $1,000 \sim 10,000 \text{ \AA}$. Therefore these low quantum efficiencies may be attributed mainly to the high resistivity of the oxide film and partly to its thickness being insufficient to absorb all incident light quanta, since the thickness of the oxide film was estimated to be about $3000 \sim 5000 \text{ \AA}$ from its interference color.

Thermal formation of oxide film by means of an electric furnace.—Oxide films were thermally formed on the titanium metal plates at various temperatures

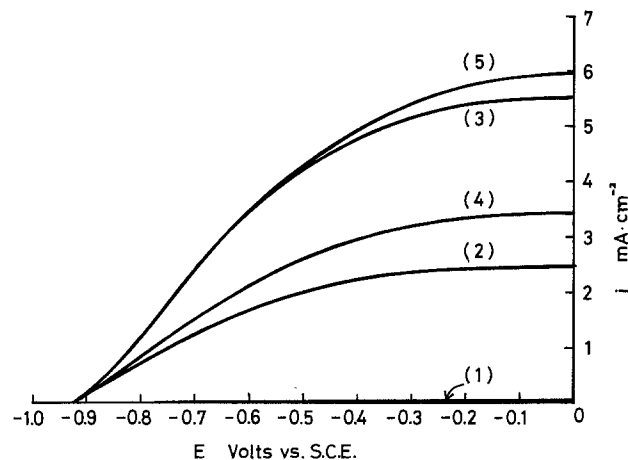


Fig. 1. Current-potential curves under irradiation in relation to the temperature of heating of 5 min. (1) Ti metal, (2) 1200°C , (3) 1300°C , (4) 1400°C , (5) rutile single crystal.

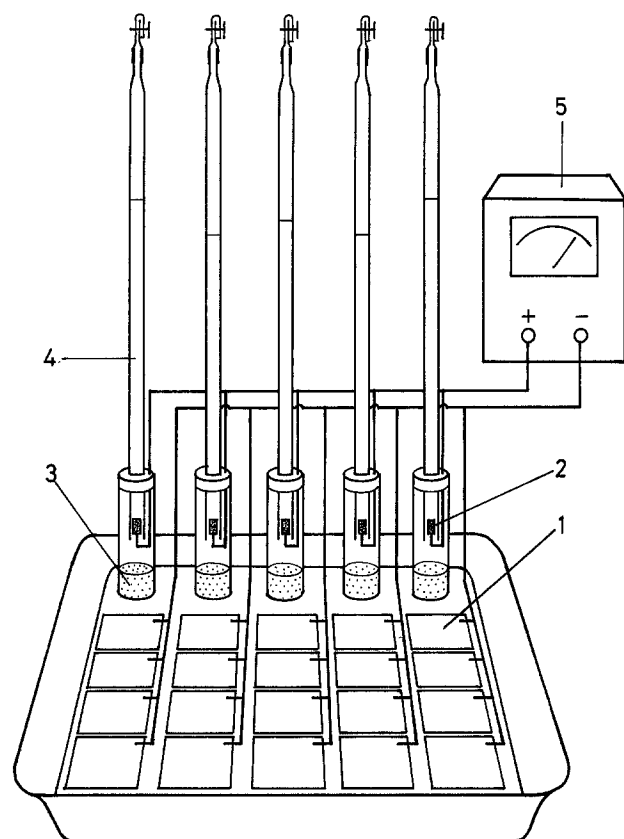


Fig. 2. The geometric arrangement of the electrochemical photocell. (1) Anodes coated with titanium dioxide film, (2) platinum black cathodes, (3) agar salt bridges, (4) gas burettes, (5) ammeter. Analyte: 1M NaOH , catholyte = $0.5\text{M H}_2\text{SO}_4$.

in an electric furnace to which oxygen was supplied. The anodic photocurrents obtained with these oxide film electrodes were nearly the same as those films formed electrochemically. On the other hand, when a reducing atmosphere was maintained during the oxide formation in the electric furnace, the anodic photocurrents slightly increased. In the case of TiO_2 single crystal, photoelectrochemical behavior depends on the degree of the reduction treatment, because its electric conductivity related to the amount of the oxygen vacancies in the crystal may govern the probability of the recombination between the electrons and holes created by the irradiation with light (3). Further detailed investigations will be reported elsewhere.

Thermal formation of oxide by a gas burner.—A plate of titanium was heated in a fire of town gas. Oxide could be easily formed on titanium metal. Temperature of fire on Meker burner or Bunsen burner was varied between 1100° and 1400°C . Thickness of the formed oxide film seemed greater than those formed by electrochemical oxidation or thermal oxidation in the electric furnace. Anodic photocurrents on these oxide electrodes were nearly as large as those obtained with the single crystal rutile electrode. Figure 1 shows current-potential curves in 1M NaOH in relation to the temperature of heating for 5 min. These high photocurrents might be due to both the thickness of the oxide being enough to absorb the incident light quanta and the low resistivity of films. The crystal structure of the oxide was found by x-ray diffraction analysis to be the rutile type. Observation of the surface by an electron microscope revealed that the oxide was not a perfect crystalline structure. In the present experiments, the titanium oxide films formed in a flame temperature between 1300° and 1350°C for several minutes showed good photoelectrochemical behavior.

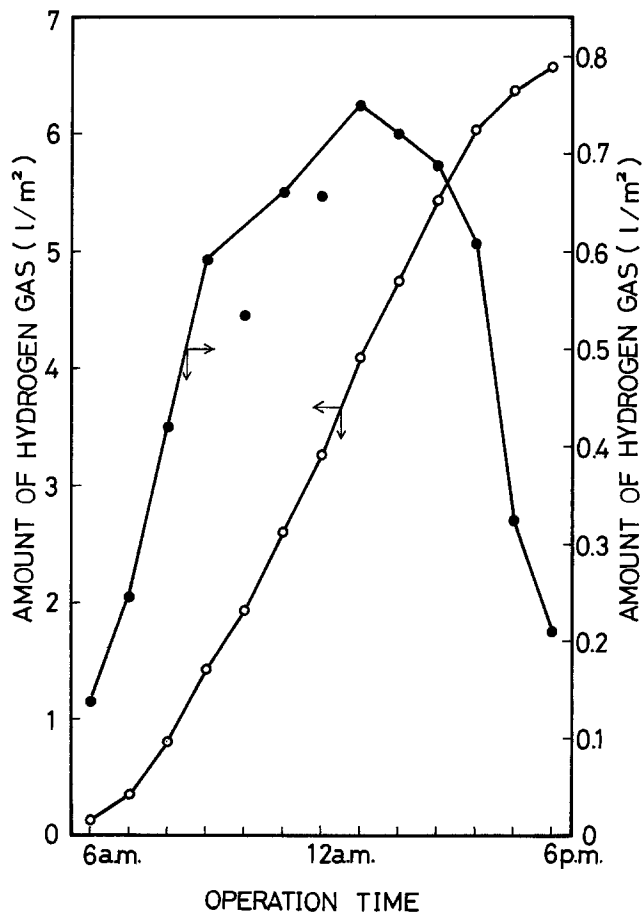


Fig. 3. Hydrogen evolution by the electrochemical photocell under the sunlight. \circ : Total amount of hydrogen evolution, \bullet : hourly evolution.

Hydrogen production under the sunlight.—As described above, the titanium oxide electrodes made by these three methods showed different photoelectrochemical behavior, even when they were irradiated with the light of the same intensity. These differences are probably due to the electric conductivity of the oxide films, and partly to the thickness of the films.

It is possible to prepare, by a simple heating, titanium dioxide film on titanium metal plate which shows pronounced photoelectrochemical activity. The anodes studied were prepared by heating the titanium metal with a surface area of 85×100 mm with nine Bunsen burners. Figure 2 shows the geometric arrangement of the electrochemical photocell using twenty anodes coated with titanium dioxide film. The cell consisted of five platinum cathode and titanium dioxide anode units in which four anode plates of the above dimension were connected in parallel. The cell contained alkaline solution in the anodic compartments and acidic solution in the cathodic compartments. Separation between the anodes and cathodes was made with an agar salt bridge saturated with potassium chloride. In this arrangement, a potential drop through the solution or the salt bridge was not found. The total anodic surface area (Fig. 2) was about 0.17 m^2 . Figure 3 shows the relationship between the operation time and the volume of the hydrogen collected under irradiation with the sunlight on a clear summer day. The intensity of the sunlight measured by means of Toshiba Photocell Illuminometer SPI-1 was about 110,000 lux from 11 A.M. to 2 P.M. We collected 1.1 liter per day using this photocell (6.6 liters of H_2 per m^2 of titanium dioxide).

The combustion heat of this hydrogen is calculated to be 20 kcal/m^2 per day. The mean incident energy of the sunlight at the surface of the earth in Japan was reported (4) to be about 3000 kcal/m^2 . As we measured the characteristics of the photocell in August, the incident energy of the sunlight might be larger than the mean one. The energy conversion efficiency of the photocell to the total sunlight energy is estimated to be more than 0.4%. As the energy ratio of the sensitive region of the titanium dioxide against the over-all spectral region of the sunlight may be below 10%, the quantum efficiency in the intrinsic absorption region becomes much larger.

Manuscript submitted April 28, 1975; revised manuscript received July 14, 1975.

Any discussion of this paper will appear in a Discussion Section to be published in the June 1976 JOURNAL. All discussions for the June 1976 Discussion Section should be submitted by Feb. 1, 1976.

Publication costs of this article were partially assisted by Kanagawa University.

REFERENCES

1. A. Fujishima and K. Honda, *Nature*, **238**, 37 (1972).
2. A. Fujishima, K. Kohayakawa, and K. Honda, *Bull. Chem. Soc. Japan*, **45**, 1041 (1975).
3. J. F. Dewald, *Bell System Tech. J.*, **39**, 615 (1960).
4. I. Oshida, "Taiyo Enerugi (Solar Energy)," p. 66, Nikkan Kogyo Shinbun, Tokyo (1958).

Intricate-Pattern ECM on Ferrous Alloys

Mitchell A. LaBoda* and James P. Hoare*

Electrochemistry Department, Research Laboratories, General Motors Corporation, Warren, Michigan 48090

In the electronics industry, the necessary circuit components are fabricated from various metals supported on a variety of substrates by generating the required, highly intricate patterns in the metal through a photomechanical method known as pattern etch machining (1-5). In a parallel development, another metal removing process known as electrochemical machining (ECM) (6, 7) has been investigated and evaluated which is based on controlled, high rate, anodic corrosion reactions. The ECM process can be used in a number of operations including plunge cutting, sizing, finishing, deburring and electrochemical grinding; but perhaps, the greatest advantage of this process is its speed in a replication application. This report describes the details of this ECM method and some of the underlying electrochemistry involved.

Experimental

The ECM fixture is composed of the cathode tool, the anode work piece, and all cell housing parts which are required to obtain a proper and uniform flow of electrolyte between the electrodes. In Fig. 1, the assembled fixture used in pattern ECM is shown; whereas in Fig. 2, a cross-sectional view of the fixture assembly is given. Essentially, the fixture consists of two machined blocks of brass separated from one another by an insulating layer of epoxy plastic. In operation, the two halves of the fixture were held together with insulated "C"-clamps and made leak-proof with an "O"-ring.

The cathode.—The top half of the fixture ($50 \text{ mm} \times 150 \text{ mm} \times 20 \text{ mm}$) serves as the cathode. Two cross-hatched patterns ($19 \text{ mm} \times 31.75 \text{ mm}$) of 12.6 lines/cm

(32 lines/in.) were etched to a depth of 0.13 mm in the flat ground face of the brass block by a photo-mechanical method. Next, a layer of epoxy (2 mm

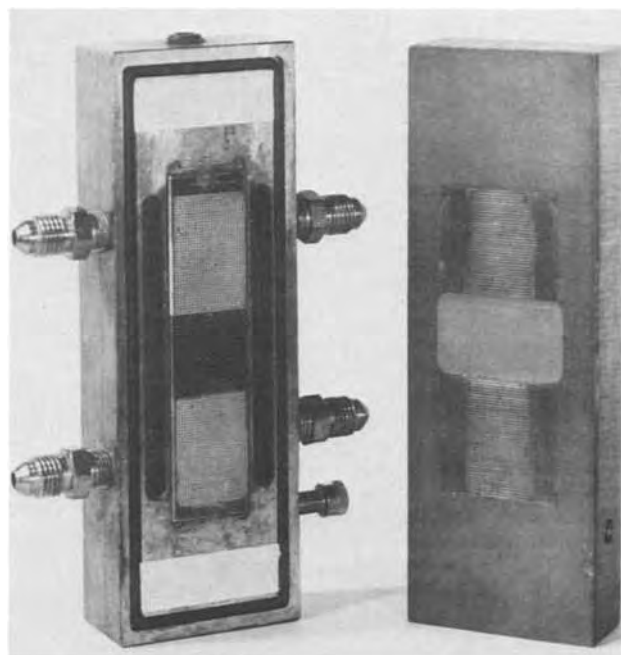


Fig. 1. The fixture for pattern ECM with anode holder and anode sample panel at left and machined cathode at right.

* Electrochemical Society Active Member.

Key words: ECM, ferrous alloys, pattern ECM, NaClO_3 electrolyte.

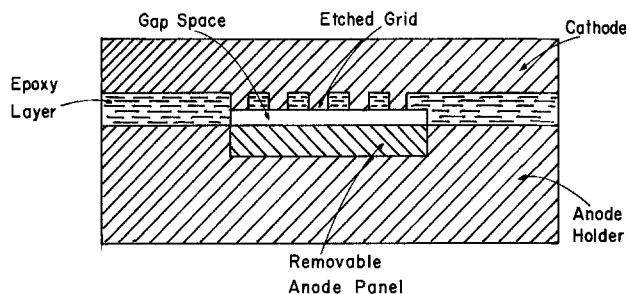


Fig. 2. Cross-sectional view of fixture for pattern ECM

thick) was applied to the etched face of the brass block; and after sufficient hardening of the plastic layer was achieved, the epoxy face was flat ground to within 0.45 mm of the cross-hatched face. A separate end mill machining operation was used to remove the plastic layer covering the two areas of the cross-hatched patterns. In this way, the exposed faces of a cross-hatched pattern of equally spaced lines are obtained and a gap space of 0.45 mm is formed between this cathode cutting face and the anode.

The anode.—The bottom half of the fixture (50 mm × 150 mm × 25 mm) serves as the anode holder. In the flat ground face of the holder, a cavity was machined which exactly accommodated the sample (20 mm × 90 mm × 1 mm); and on either side of this cavity, slots (5 mm × 80 mm × 10 mm) were machined as seen in Fig. 1 to provide a flow of electrolyte through the gap space between anode and cathode. Brass fittings were connected to the slots to serve as inlet and outlet ports for the electrolyte. A groove to hold the sealing "O"-ring was machined around the perimeter of the holder face.

The anode itself (the sample to be machined) was a mild steel panel (20 mm × 90 mm × 1 mm).

The ECM machining system.—The electrolyte required for the pattern ECM of steel was a solution of NaClO₃ (350 g/liter) which was pumped through the fixture by a turbine pump at flow rates ranging between 2 and 4 liters/min at a pressure of 1.4 atm and with the direction of flow perpendicular to the long axis of the sample. Direct current was supplied by a low voltage rectifier with a capacity of 0-3000A at 0-30V.

Procedure.—The sample panel was placed in the cavity of the anode holder and the cathode was clamped in place by an insulated "C"-clamp. After connecting the inlet parts to the pump and the outlet parts to the electrolyte reservoir, the NaClO₃ solution was pumped through the fixture. A preset voltage of 5V was applied between anode and cathode. Then ECM was carried out for up to 9 sec after which the current and solution flow was shut down so that the solution flow could be reversed by outside valving. Finally, ECM was continued with reverse electrolyte flow for the same length of time.

Results and Discussion

In the course of this work, it was found that the gap space between cathode and anode is a critical parameter. A steel panel blank is shown in Fig. 3A, and in Fig. 3B, the pattern machined in the panel by pattern ECM at a gap space of 0.45 mm shows washed out features. By flat grinding the plastic layer on the cathode, the gap space can be made narrower. At a gap space of 0.20 mm (Fig. 3C), an acceptably sharp pattern is obtained. The depth of this cut was 0.05 mm in Fig. 3C, but cuts of 0.1 mm can be obtained with only a small loss of resolution.

Dependency of the resolution of the pattern on gap space can be understood in terms of the passivation of steel in strongly oxidizing electrolytes. It was suggested (8-10) that the ECM process takes place in the

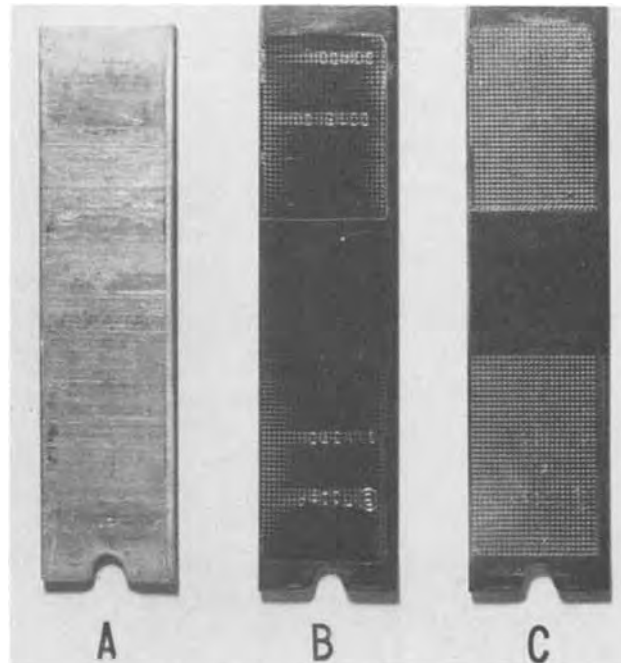


Fig. 3. The test panels of mild steel, 20 mm x 90 mm x 1 mm: (A) the blank; (B) a washed out pattern because of wide gap space or excessively high applied potential; (C) a sharp pattern obtained at a gap space of 0.20 mm, at a preset applied voltage of 5V, and a solution flow rate of 2 liters/min.

transpassive region where breakdown of the passive film on steel in NaClO₃ solution occurs and high rates of metal removal take place.

For a given applied voltage, V , across the anode and cathode, the potential, E , controlling the metal-removal process at the anode is determined by the relationship, $E = V - IR$, where I is the current passed and R is the ohmic resistance of the solution path. At sites on the anode directly opposite the exposed metal sites on the cathode, the current path is short, the IR is small, E is large so that the process occurs in the transpassive region (8) and high metal removal rates occur. For the high currents passed (of the order of 50 A/cm²), even a small value of R can result in a large value of IR . Consequently, at sites remote enough from the exposed cathode sites, the IR becomes so large that the value of E is shifted towards less noble values where the process enters the passive region (8). Under these conditions, metal removal virtually ceases.

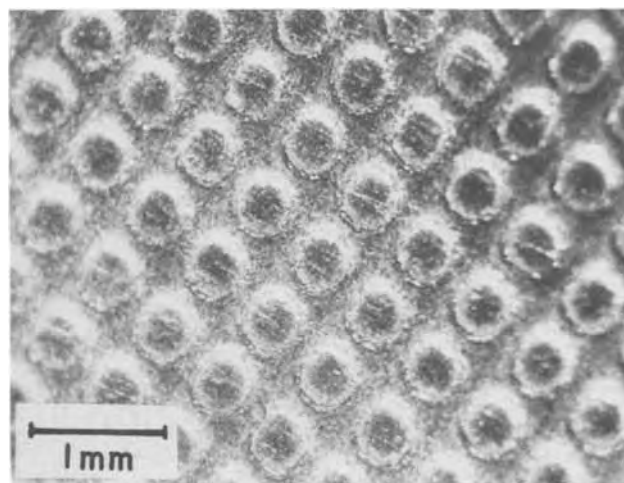


Fig. 4. Photomicrograph of pattern of 12.6 lines/cm (32 lines/in.) machined by pattern ECM in steel with NaClO₃ electrolyte.

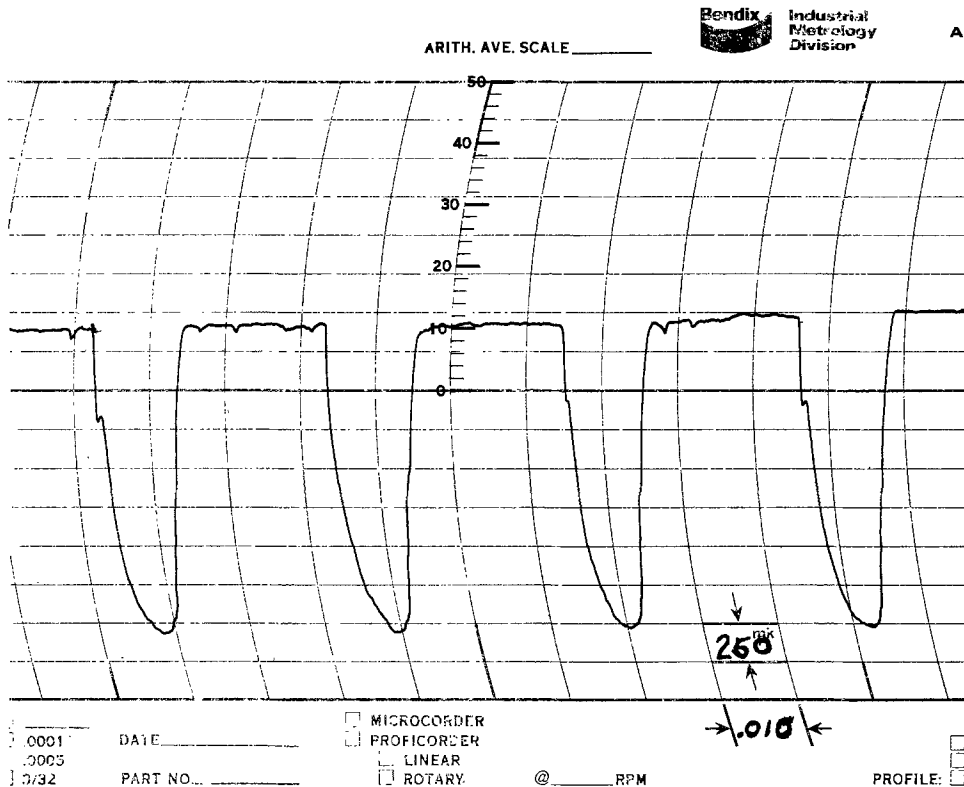


Fig. 5. Proficorder trace of a 12.6 lines/cm (32 lines/in.) pattern machined by ECM to a depth of 0.051 mm in mild steel in 18 sec; X-axis = 2.5×10^{-3} mm/div; Y-axis = 6.25×10^{-5} mm/div. The trace shows the uniformity of depth and land-to-groove ratio obtained on steel in NaClO_3 solution.

Conversely then, there may be some metal removal from anode sites which are only slightly removed. For this reason, the imprints of dots are rounded rather than square as noted in the photomicrograph of the machined pattern in Fig. 4. The proficorder trace in Fig. 5 shows that the tops of the dots are quite flat with tapering of the sides.

When the gap space is increased, V must be raised to maintain E at the same value if the same current density at the anode is desired since the current path has been lengthened. At this larger gap space, however, the percentage difference between the direct and remote current paths becomes less and the increase in IR may not be large enough for the remote current paths to cause a passivation of the remote anodic sites. Because some metal removal can take place at these remote sites, a washing out of the pattern can occur as in Fig. 3B.

Another sensitive parameter is the applied voltage, V . If V is too large, the IR of even the longest current paths may not be great enough to lower E into the passive region. Washing out of the pattern occurs in this case, also. One must operate at a value of V so that E is not too far removed from the point corresponding to the passive-transpassive transition of the polarization curve (8). The polarization curve for iron and steel in NaClO_3 solution has a relatively sharp transition from the passive to the transpassive region (8) which makes it possible (12) to obtain excellent control of dimensions at high metal removal rates and good surface finish.

The optimum operating values for V and the solution gap distance are found by trial and error. In general, as the pattern becomes finer V must be lowered and the gap space must be reduced because the difference between the direct and remote solution paths must be maintained as great as possible. Some modification of the solution flow rate may be required, but this parameter has less influence on the resolution of the pattern.

The pattern in Fig. 3C was produced in a total machining time of 18 sec at $V = 5V$ and a flow rate of 4 liters/min.

As can be seen from Fig. 5, the width of the ECM'd cut was 0.25 mm. The width of the cathodic grid line employed in the ECM cutting was 0.13 mm. Thus, in these experiments it appears that the overcut, the ratio of the ECM'd line width to the cathodic line width, is about 2. This ratio could be reduced to obtain finer patterns by either reducing the gap space or by reducing the cathodic line width, but each would present attendant difficulties.

Manuscript submitted May 9, 1975; revised manuscript received June 23, 1975. This was Paper 162 presented at the Dallas, Texas, Meeting of the Society, Oct. 5-9, 1975.

Any discussion of this paper will appear in a Discussion Section to be published in the June 1976 JOURNAL. All discussions for the June 1976 Discussion Section should be submitted by Feb. 1, 1976.

Publication costs of this article were partially assisted by General Motors Corporation.

REFERENCES

1. M. C. Cook, *Product Eng.*, **27**, 194 (1956).
2. R. C. Benton and G. D. Woodring, ASTM Paper No. 685 (1965).
3. T. H. P. Chang and B. A. Wallaman, *IEEE Trans. Electron Devices*, **ED-19**, 629 (1972).
4. C. R. Dix, J. P. Ballantyne, and W. C. Nixon, *ibid.*, **ED-19**, 641 (1972).
5. M. Hatzakis, *This Journal*, **116**, 1033 (1969).
6. A. E. DeBarr and D. A. Oliver, "Electrochemical Machining," Elsevier, New York (1968).
7. J. P. Hoare and M. A. LaBoda, *Scientific Am.*, **230**, 30 (1974).
8. J. P. Hoare, *Nature*, **219**, 1034 (1968); *This Journal*, **117**, 142 (1970).
9. K. Chikamori and S. Ito, *Denki Kagaku Oyobi Butsuri Kagaku*, **37**, 602 (1969).
10. D. Landolt, R. H. Muller, and C. W. Tobias, *This Journal*, **118**, 36 (1971).
11. A. D. Davydov, R. A. Mirzoev, V. D. Kashcheev, and B. N. Kabanov, *Elektrokhimiya*, **8**, 1468 (1972).
12. J. P. Hoare, M. A. LaBoda, M. L. McMillan, and A. J. Wallace, *This Journal*, **116**, 199 (1969).

On the Electrocatalytic Activity of Electrodeposited Palladium on Pyrolytic Graphite

Ikram Morcos*

Hydro-Quebec Institute of Research Varennes, Quebec, Canada

Data on the reduction of oxygen at the palladium electrode in both alkaline and acidic media have already been reported in the literature (1-5). In alkaline medium, Sobol *et al.* (1) obtained current-potential plots, which show limiting currents, that gradually deviate from theoretical Levich plots, with the increase in the rotation rate of the disk electrode. In acid medium, the reduction currents were found to decrease steadily with time until their values become significantly lower than the corresponding values in alkaline medium.

In the present communication experimental results are presented to show the difference between the electrocatalytic activity toward oxygen reduction of both bulk palladium electrodes and electrodes prepared by the electrodeposition of a palladium layer on pyrolytic graphite substrates. Current-potential curves were obtained as a function of the disk rotation speed on both types of electrodes by slow scanning voltammetry in acid and alkaline media.

The current-potential curves obtained in oxygen-saturated 0.1N KOH solution in the potential range between 0.2 and $-0.5V$ (Hg/HgO) show on both palladium surfaces linearly shaped limiting current at rotation speeds between 400 and 10,000 rpm. Plots of the limiting current *vs.* the square root of rotation speed are compared in Fig. 1 with the corresponding theoretical Levich plot for an over-all 4-electron oxygen reduction process. It is seen from Fig. 1 that the electrodeposited palladium has a higher electrocatalytic activity than the bulk palladium and that the difference in the activity increases with the increase in rotation speed.

The difference in the electrocatalytic activity was found to be even more significant in acid medium. Higher current densities (notice that the apparent area is not the same) and greater rotation dependence were observed on the electrodeposited surface. The difference in the electrocatalytic activity persisted regardless of the magnitude of the starting potential and the rate at which the potential was scanned. Figures 2 and 3 show the current-potential characteristics of both palladium electrodes in an oxygen-saturated 1.0N H_2SO_4 (ultra pure grade) at different rotation speeds, and a very slow scanning rate of 0.025 V/min to assure the attainment of steady state. Notice that the limiting currents which are under both diffusion and kinetic control are observed on the electrodeposited palladium but not on the bulk electrode.

The interpretation of these observations must take into account the dispersed nature of the palladium deposit on pyrolytic graphite. The present data, however, suggest that the deposited palladium may have different intrinsic electrocatalytic properties which are

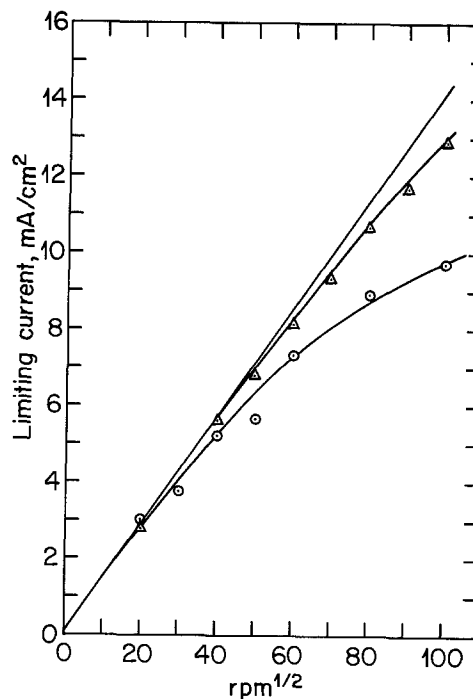


Fig. 1. Dependence of the limiting current density on the square root of rotation speed on palladium electrodes in O_2 -saturated 0.1N KOH solution. —, theoretical plot for a diffusion controlled process; Δ , electrodeposited palladium on pyrolytic graphite; \circ , mechanically polished bulk palladium electrode.

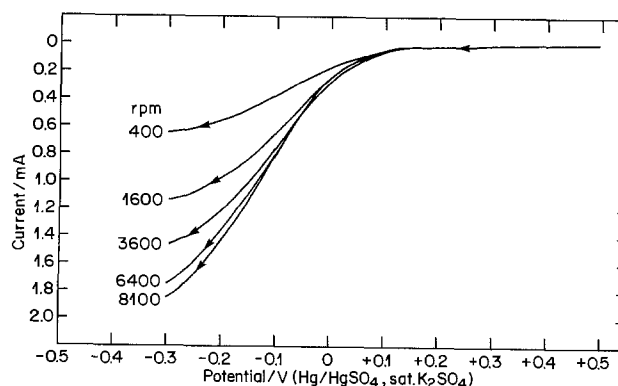


Fig. 2. Current-potential curves for O_2 reduction on a palladium surface electrodeposited on pyrolytic graphite at different rotation speeds in O_2 -saturated 1.0N H_2SO_4 solution. Potential scanned at a rate of 0.025 V/min in the cathodic direction. Electrode area is 0.338 cm^2 .

* Electrochemical Society Active Member.

Key words: oxygen reduction on palladium, electrocatalytic activity of electrodeposited palladium surface, oxygen reduction on electrodeposited palladium on pyrolytic graphite.

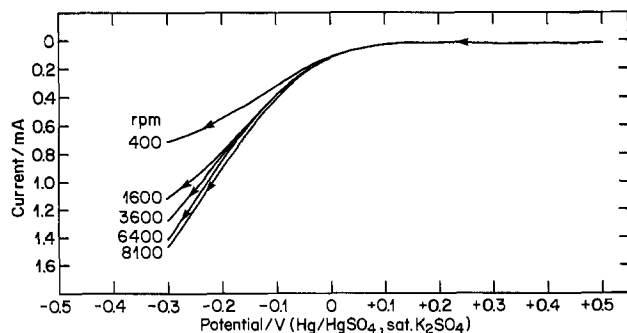


Fig. 3. Current-potential curves for O_2 reduction on a mechanically polished bulk palladium electrode at different rotation speeds in O_2 -saturated 1.0N H_2SO_4 solution. Potential scanned at a rate of 0.025 V/min in the cathodic direction. Electrode area is 0.478 cm^2 .

not accounted for by the mere increase in true surface area. Voltammetric experiments in helium-saturated solutions indicate a variation in the characteristics of oxygen adsorption on both palladium surfaces. An investigation of the actual mechanism of oxygen reduction on both palladium surfaces is presently being carried out with the aid of the rotating disk electrode with ring. Differential capacity and electron scanning

microscope techniques are used to detect variation in surface area and structure. A study of the electrochemical nucleation of palladium on pyrolytic graphite and possible correlation with the observed electrocatalytic aspects is also in progress.

Acknowledgment

The author thanks Mr. G. Larochelle for his assistance in the physical realization of the voltammetry curves.

Manuscript received June 24, 1975.

Any discussion of this paper will appear in a Discussion Section to be published in the June 1976 JOURNAL. All discussions for the June 1976 Discussion Section should be submitted by Feb. 1, 1976.

Publication costs of this article were partially assisted by Hydro-Quebec Institute of Research.

REFERENCES

1. V. V. Sobol, E. I. Khrushcheva, and V. A. Dagaeva, *Elektrokhimiya*, **1**, 1332 (1965).
2. A. J. Appleby, *This Journal*, **117**, 1373 (1970).
3. A. Damjanovic and V. Brusic, *Electrochim. Acta*, **12**, 1171 (1967).
4. N. D. Tomashov and L. P. Vershinina, *ibid.*, **15**, 501 (1970).
5. A. Damjanovic and Brusic, *J. Electroanal. Chem.*, **15**, 29 (1967).

Complex Ions and Corrosion

R. T. Foley*

Department of Chemistry, The American University, Washington, D.C. 20016

It is indeed remarkable the extent to which environmental effects are ignored in the development of corrosion mechanisms and concepts related to the passivity of metals and alloys. The specific anion effect in stress corrosion cracking has been well documented in the corrosion literature. Yet proposed mechanisms for stress corrosion cracking are put forth which incorporate purely mechanical phenomena. In the development of passivity mechanisms, including the formation of passive films, the composition of the electrolyte has been given virtually no consideration except in so far as it provides protons and hydroxyl ions. Yet the breakdown of passivity is often tied to specific ion adsorption and the chloride ion is attributed with unique properties that are evident for this ion in no other area of chemistry.

The purpose of this communication is to reexamine the role of environmental effects, specifically anion effects, with the view of establishing a concept that will be a useful and guiding principle describing the influence of anions in corrosion and passivity.

It is first desirable to characterize the actual environment in which a metal cation finds itself as it passes from the atomic to the ionic state. In most situations of concern to corrosion investigators the environment in which the metal cation finds itself at the instant of ionization is one of a concentrated aqueous electrolyte. This point has been well demonstrated experimentally, particularly during the last decade. A few of these observations wherein the composition of the environment at the actual corrosion site has been described may be cited.

Significant concentration gradients exist in the electrolyte resident in crevices formed on Fe-Cr alloys (1).

There is a build up of metal ions and a decrease in pH (to 1.7 from initially neutral solutions) in the

electrolyte in the advancing crack of the stress-corroding specimen (2).

In crevices formed on Type 304 stainless steel by the action of a differential aeration cell in seawater the pH falls to 1.2-2.0 and the ferrous ion concentration increases (3).

The chloride ion concentration builds up in the anolyte of a corrosion cell developed on the surface of steel corroding in dilute solutions of sodium salts of weak acids (4).

The wide-spread occurrence of such conditions in real corrosion situations has led to the concept of the "occluded corrosion cell" (5). The general finding is that in these real corrosion sites the electrolytic solution is quite concentrated and is often of very low pH.

The consequence of this real environment (the concentrated electrolytic solution) becomes immediately apparent. The metal atom, as it passes from the metallic lattice and is ionized is immediately surrounded by an ion atmosphere of negatively charged species located at relatively close distances. This is evident from the simplest calculation employing Avogadro's number to calculate the geometrical distribution of ions in a solution of a given molarity. For example, in a one molar solution of $FeCl_2$ the closest neighbor distance is 8.2 Å; for a two molar solution the distance is 6.5 Å. This distribution, of course, was specifically recognized in the development of the Debye Hückel theory (6) for ionic solutions as well as the Gouy-Chapman model (7) for the double layer. The assumption is made that the central (positive) ion is, on a time average basis, surrounded by a negatively charged atmosphere. The radius of this interionic atmosphere is calculated from the Debye-Hückel equation for a bi-uni aqueous electrolyte ($FeCl_2$) as 5.56 Å for a 0.1M solution and 1.76 Å for a 1M solution.

The existing theories dealing with the structure of concentrated solutions leave much to be desired but one of the most reasonable and most useful concepts

* Electrochemical Society Active Member.
Key words: corrosion, complex ions, passivity, concentrated solutions, electrolytes.

is that proposed by Bjerrum (8, 9) and extended by Kraus and Fuoss (10). The ion-pair theory would identify a minimum (distance) in the plot of the distribution of oppositely charged ions about a central ion. For a uni-univalent electrolyte this distance of separation is approximately 3.57Å, for a bi-uni electrolyte the distance is 7.14Å. According to Bjerrum, ions approaching closer to the central ion than this minimum distance are considered to be associated and to exist as "ion-pairs." These are species that are completely ionized but for symmetrical electrolytes have no net charge, i.e., would not migrate in an electric field. In dealing with concentrated solutions it is obvious that the statistical probability of a metal cation and an anion being within this critical distance is quite high. Ion pairing, according to the Bjerrum theory is favored by (i) higher valence cations and anions and (ii) a lower dielectric constant, two conditions that obtain adjacent to a metal strip immersed in a corrosive solution.

The net conclusion to be drawn from these considerations is that in the interfacial region, adjacent to the corroding metal, specific cation-anion species must exist. It might be argued that such close approach to the metal would make adsorption quite probable, but it is not necessary to postulate any adsorption process to draw the conclusion that anions must participate directly, in the chemical sense, in the dissolution reaction.

Any mechanism that is proposed for passivity or to describe the anodic dissolution process of a metal must start with a realistic count of the ions available for adsorption or interaction. Thus, the inhibition of the dissolution of iron by iodide ions has been correlated with the adsorption of iodide ions on iron as expressed by a Langmuir adsorption isotherm which established the concentration-dependency of the reaction (11). Such an experimental study recognized the need to take into account the available concentration of iodide ions. Further, such considerations must be prerequisite to the development of any corrosion mechanism. Consider, then, a solution of NaCl, one molar in concentration with a pH of 1. The concentrations of chloride ions and hydroxide ions are 1 molar and 10^{-13} molar, respectively. It would be very difficult to support a mechanism involving the competitive and preferential adsorption of hydroxide ion over chloride ion when the chloride/hydroxide ratio is 10^{13} .

From these rather basic considerations and from a consideration as well, of literature reports on iron corrosion and passivity one is led to the concept that the anions present in the environment must enter directly into the dissolution and passivation process. It is proposed that this is accomplished by the formation of specific metal-anion species, complexes, that are transitory in some cases, stable and insoluble in others, but in all cases are an essential part of the process.

Because of the transitory nature of these complexes it is difficult to obtain direct experimental evidence for their existence. However, there are a number of lines of evidence supporting this concept and these may be cited.

1. The direct spectrophotometric observation of iron-anion species produced by the dissolution of iron in acid solutions containing various anions (12). Under oxidizing conditions each anion yields a specific spectrum.

2. The feasibility of assigning specific ions to either the anodic or cathodic part of the corrosion process (13). Thus sulfate ion is involved in the cathodic process whereas chloride ion is involved in the anodic.

3. The effect that specific anions have on the functioning of inhibitors (13), e.g., chloride ion interferes with "anodic" inhibitors but not "cathodic."

4. The differences in activation energies observed for the corrosion of iron in acid solutions containing

different anions (14). The measurements were at constant pH (i.e., constant OH^- concentration). Not only the rate but the activation energies are different.

5. The observation that the adsorption of chloride ion and sulfate ion on iron is interdependent, may be competitive or synergistic (15).

6. The anodic corrosion current for iron in various electrolytes is a function of the anion in solution, perchlorate > sulfate > chloride > acetate > nitrate (16).

7. The inhibition of iron corrosion in very concentrated ferrous chloride solution (17).

8. A stoichiometric order of reaction existing with chloride ions in the pitting initiation reaction on passive iron (18) or stainless steel (19).

9. The dependence of electrochemical reaction order for the dissolution of iron in concentrated solutions on the chloride concentration (20).

Other lines of evidence may be cited. But the burden of evidence indicated that any mechanism of passivity, or any mechanism for metal dissolution, must include a consideration of the formation and existence of metal-anion complexes. Moreover, the rate of dissolution or degree of passivity must be correlated with the stability of these complexes.

Acknowledgment

The support of the Office of Naval Research under Contract N00014-68-A-0245-0009 is gratefully acknowledged. Some of this material was presented at the Joint USA-Japan Seminar on Passivity and Its Breakdown on Iron Base Alloys held in Honolulu, Hawaii, March 10-12, 1975.

Manuscript received June 9, 1975.

Any discussion of this paper will appear in a Discussion Section to be published in the June 1976 JOURNAL. All discussions for the June 1976 Discussion Section should be submitted by Feb. 1, 1976.

Publication costs of this article were partially assisted by The American University.

REFERENCES

1. F. D. Bogar and C. T. Fujii, Naval Research Laboratory Report 7690, March 21, 1974.
2. B. F. Brown, C. T. Fujii, and E. P. Dahlberg, *This Journal*, **116**, 218 (1969).
3. M. H. Peterson, T. J. Lennox, Jr., and R. E. Groover, *Mater. Protect.*, **9**, 23 (1970).
4. M. J. Pryor, *Corrosion*, **9**, 467 (1953).
5. B. F. Brown, *ibid.*, **26**, 249 (1970).
6. P. Debye and E. Hückel, *Physik. Z.*, **24**, 185 (1923).
7. D. L. Chapman, *Phil. Mag.*, **25**, 475 (1913).
8. R. A. Robinson and R. H. Stokes, "Electrolyte Solutions," Butterworths, London (1959).
9. J. F. Duncan and D. L. Kepert, in "The Structure of Electrolytic Solutions," W. J. Hamer, Editor, p. 380, John Wiley and Sons, New York (1959).
10. R. M. Fuoss and C. A. Kraus, *J. Am. Chem. Soc.*, **55**, 1019 (1933); *ibid.*, **80**, 5059 (1958).
11. K. E. Heusler and G. H. Cartledge, *This Journal*, **108**, 732 (1961).
12. B. J. Alexander and R. T. Foley, *Corrosion*, Submitted for publication.
13. S. E. Trautenberg and R. T. Foley, *This Journal*, **118**, 1066 (1971).
14. B. J. Alexander and R. T. Foley, *Corrosion*, **31**, 148 (1975).
15. N. Hackerman and S. J. Stephens, *J. Phys. Chem.*, **58**, 904 (1954).
16. J. O'M. Bockris, D. Drazic, and A. R. Despic, *Electrochim. Acta*, **4**, 325 (1961).
17. M. H. Jones and B. D. Oakes, *Mater. Protect.*, **7**, 38 (1968).
18. H. J. Engell and N. D. Stolica, *Arch. Eisenhüttenw.*, **30**, 239 (1959).
19. T. P. Hoar and W. R. Jacob, *Nature*, **216**, 1299 (1967).
20. N. A. Darwish, F. Hilbert, W. J. Lorenz, and H. Rosswag, *Electrochim. Acta*, **18**, 421 (1973).



1555

Growth and Structure of Nickel Oxide on Nickel Crystal Faces

N. N. Khoi,* W. W. Smeltzer,* and J. D. Embury

Department of Metallurgy and Materials Science, McMaster University, Hamilton, Ontario, Canada L8S 4M1

ABSTRACT

The structures of films of NiO 300Å-15μ thick formed on (100), (110), and (111)Ni crystal faces at temperatures in the range 500°-800°C were investigated by electron microscopy and x-ray diffraction. The oxide was initially polycrystalline but rearranged as the oxide thickened to major epitaxial relationships with the metal substrate. These relationships were characterized by coincidence between the close-packed directions of the metal and oxide; the number and type of oxide orientations were correlated with the number of close-packed directions in the metal faces. Oxide thicker than 1μ exhibited preferred {100} and {111} orientations. The oxide on (100) and (111)Ni exhibited the highest preferred orientation and a duplex layer structure consisting of equiaxed crystallites in the inner layer and columnar ones in the outer layer. These findings are rationalized in terms of a diffusional model for the growth of these oxide layers in which the reaction rate is determined by boundary and lattice diffusion of nickel through nickel oxide.

The growth kinetics of nickel oxide films and scales on nickel at temperatures less than 1000°C have been shown by several investigators to be related to the oxide morphologies developed (1-12). For both polycrystalline nickel and a variety of single-crystal orientations the rates of metal oxidation have been interpreted in terms of the character and number of easy diffusion paths such as dislocations and boundaries in the oxide. The oxidation rate is enhanced most in comparison to the rate expected solely from lattice diffusion when the easy diffusion paths in the oxide are high angle boundaries between crystallites of small diameter. This type of behavior extends to scales of the order 10μ in thickness due to the relatively small value of the nickel lattice diffusivity and the small size of the nickel oxide grains.

Herchl *et al.* (7) recently determined the oxidation kinetics of (100), (110), and (111)Ni faces at oxide thicknesses encompassing both the film and scale formation regions at temperatures in the range 500°-800°C. The kinetics were interpreted by a model wherein nickel transport occurred by boundary and lattice diffusion. In the present investigation, a structural study of the crystallite and grain sizes, orientations, and textures has been made of the films and scales formed on the (100), (110), and (111) faces in order to obtain a more complete understanding of these variables on the magnitudes of oxidation rates.

Experimental

Electropolished cylindrical specimens, 1 mm thick × 13 mm diameter, were prepared from 99.999 weight per cent (w/o) Ni crystals to within ±2° of a crystallographic plane by metallographic and electropolishing techniques (13). Four specimens were simultaneously exposed by means of winches using platinum wire and quartz rods in a quartz reaction tube suspended vertically in a furnace controlled to ±2°C. These specimens were subjected initially to a vacuum anneal at

3×10^{-6} Torr for 18 hr at 800°C whereupon they were raised from the furnace and exposed at room temperature to research grade oxygen containing <2 ppm H₂O. After setting the furnace at the reaction temperature, the specimens were lowered by means of the winches and exposed to oxygen at 400 Torr pressure for various time periods. Oxide thicknesses were determined by weight gains of the specimens to a precision of ±0.5 μg/cm² (1 μg O/cm² = 62Å NiO). Throughout this paper the thickness of an oxide film was deduced from the weight gain measurement assuming uniform thickness. For films >2000Å thick a considerable degree of nonuniformity was observed and the thinner regions of these films were examined by transmission electron microscopy (TEM) for films of average thickness up to 5000Å.

Films <5000Å thick were stripped from the metal using a saturated solution of iodine in methanol (5) and examined using bright field (BF), dark field (DF), and selected area diffraction (SAD) in the transmission electron microscope. Scanning electron microscopy (SEM) was used to study oxide cross sections >1μ thick prepared by mounting specimens in room setting epoxy resin with two strips of stainless steel arranged parallel to the oxide surface and polishing to 1μ diamond paste. The oxide structure became revealed upon anodic etching in a 1:1 HF-acetic acid solution at a potential of 3-5V for 1-5 min.

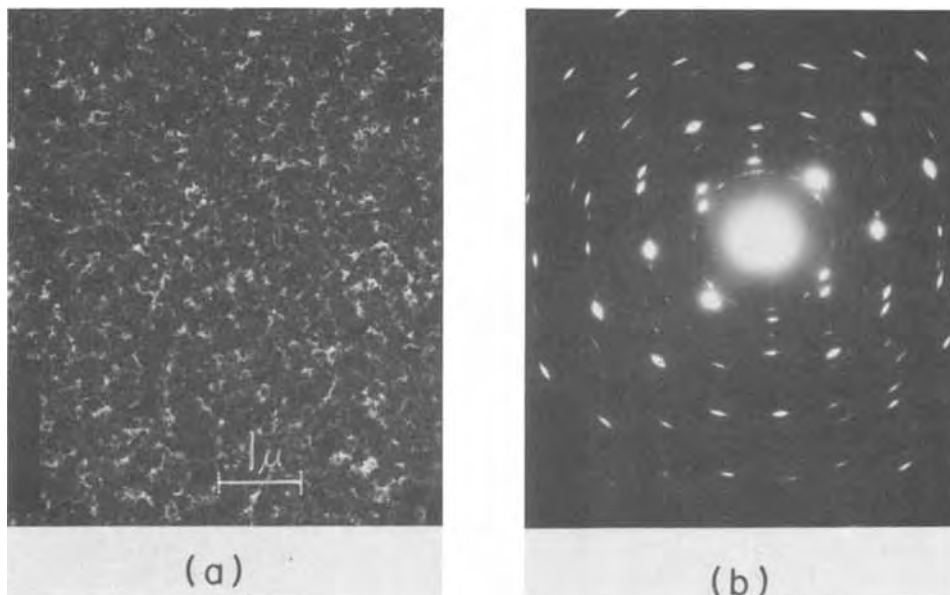
Preferred orientations of the oxide within scales were determined by reflection x-ray diffraction (XRD) using the inverse pole figure method proposed by Harris (14). This method consisted of a comparison of the integrated intensity of peaks from scales to those from randomly dispersed oxide obtained by counting the pulses from a rotating specimen at each peak maximum. The texture coefficient of a (hkl) plane then is

$$P_{hkl} = \frac{I_{hkl}/I_{r,hkl}}{\frac{1}{n} \sum I_{hkl}/I_{r,hkl}} \quad [1]$$

* Electrochemical Society Active Member.

Key words: NiO films and scales, NiO structures and growth.

Fig. 1. TEM micrographs of 350Å NiO film formed on (100)Ni. (a) BF, (b) SAD pattern.



where I_{hkl} and $I_{r,hkl}$ are integrated intensity from peaks of the textured and randomly oriented oxide, respectively, and n is the number of peaks examined.

The average size of the crystallites in films up to 3000Å thick were determined by TEM using the DF technique. The distribution of the crystallites was plotted as a fraction of crystallites *vs.* size and the average crystallite size calculated from this distribution for each film. A similar procedure was adopted to determine the average size of grains in scales $>1\mu$ thick by the SEM technique.

Results

TEM.—The structure of films in the range 300-3000Å was determined using BF, DF, and SAD methods. It was not possible to observe directly the orientation relationships between the film and the metal substrate or to know the relative position of the film once it was removed from the substrate. Thus any relationship between the film and the substrate must be deduced from the TEM and compared with models of oxide growth and previous experimental evidence in order to develop a consistent description of the oxide growth process. However, the TEM observations do permit observations of the relative frequency of various crystallographic orientations in the oxide film, the relationship between these structures, and the distribution of the crystallites within the film. In complex cases composed of mixed orientations it is difficult to describe the spatial distribution of crystallites due to the occurrence of double diffraction and the difficulties inherent in the use of intensity variations in the SAD patterns. Observations from 300-5000Å NiO films formed at 500°C are shown as BF, DF, SAD micrographs in order of increasing thickness.

(100)Ni: The uniformly thick films were composed of 300-400Å size crystallites in the early oxidation stages which gradually increased to 700-900Å size after 8 hr exposures. Some crystallites were randomly oriented as evidenced by weak polycrystalline SAD patterns but most were of the type (100), (110), and (111) with fewer cases of (211) and (233).

Figure 1 shows a 350Å film which consists of crystallites 300-400Å in size. Some randomly distributed crystallites contributed a faint ring pattern as illustrated in the SAD pattern. Most crystallites, nevertheless, exhibit (100), (110)NiO// (100)Ni. The DF micrographs from a variety of reflections from both SAD patterns showed that the (100) and (110) oriented crystallites are randomly distributed. The SAD pattern in Fig. 2 from another section of this film represents (111), (211), (233)NiO// (100)Ni. The structure of films up to 1000Å thick did not change appreciably

with the exception that (100)NiO became more pronounced.

(110)Ni: The most striking features of the films were the large number of structures accompanied with twins and dislocations. For example, within areas of an isolated film, diffraction patterns were obtained showing a mosaic structure, twins and crystallites exhibiting up to six different orientations. Eleven orientations were actually identified, ten of which can be divided into two sets. The first set was (100), (110), (111), (211), (311), (322), (411), (433)NiO|| (011)Ni and the second set was (210), (310)NiO|| (110)Ni. In addition some evidence was found for the (123)NiO orientation parallel to the (110)Ni face. These orientations changed with increasing film thickness and a trend similar to that for the oxide on (100)Ni was established since films up to 700Å thick exhibited a large number of oxide orientations including high index planes. These latter planes disappeared as the oxide thickened and in films exceeding 2000Å low index planes were predominantly observed.

For illustrative purpose, electron micrographs of a 500Å film are shown in Fig. 3 and 4. The BF and SAD

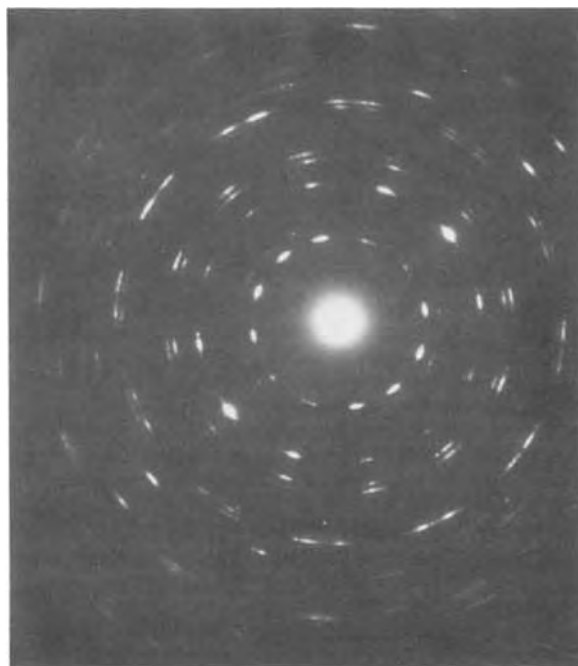


Fig. 2. SAD pattern of 350Å NiO film formed on (100) Ni

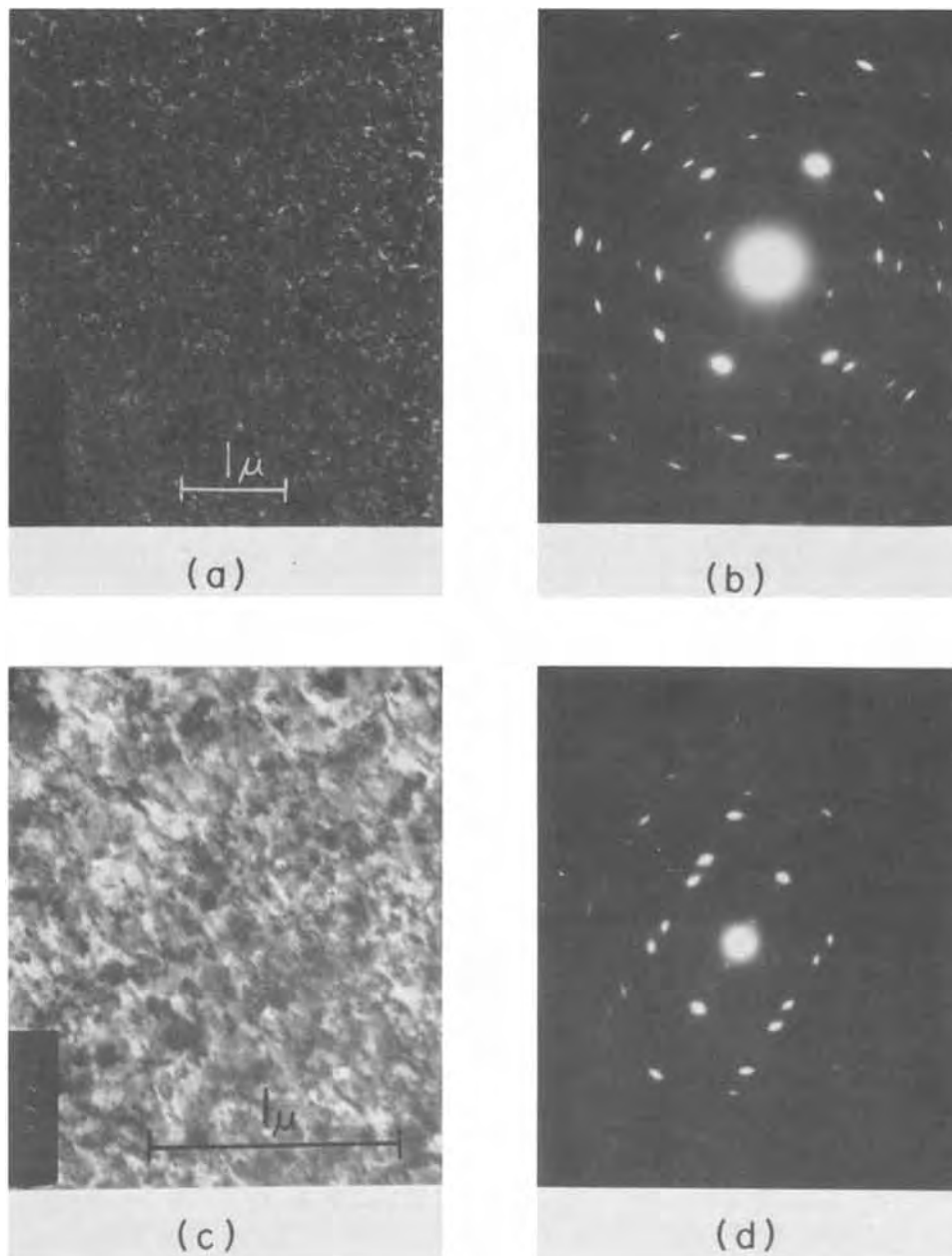


Fig. 3. TEM micrographs of 500 Å NiO film formed on (110)Ni. (a) BF, (b) SAD pattern, (c) BF, (d) SAD pattern.

micrographs in Fig. 3(a) and (b) reveal that the film is composed of relatively uniform sized crystallites which when indexed contain oxide with (111), (211), (311), (321), (322), (411), (433)NiO|| (110)Ni. In Fig. 3(c) and (d), the BF micrograph does not reveal twin plates, but the SAD pattern shows that twinning of crystallites has occurred as this composite pattern is obtained by rotating the (110) Relp 180° around the $[11\bar{1}]$ direction. Such rotation around a twin axis perpendicular to the electron beam shows, moreover, that the twin boundary lies perpendicular to the plane of the oxide film. The (100)NiO crystal pattern shown in Fig. 4 from another film section corresponds to a mosaic structure in which the crystallites are arranged to each other by very small misorientations. Films >1000 Å were irregular and contained dislocations.

(111)Ni: The structure of films on this surface were similar to those on (100)Ni. Five orientations were observed and the presence of a mosaic structure or twins was not detected. An interesting feature was the multiple occurrence of the same orientation including up to six (211) and (233)NiO planes in a single SAD pattern. The multiple orientations (111), (211), (233)NiO|| (111)Ni could be divided into two sets A

and B characterized by $[0\bar{1}1]$ NiO|| $[0\bar{1}1]$ Ni(A) and $[0\bar{1}1]$ NiO|| $[1\bar{1}2]$ Ni(B). The orientation (011)NiO|| (111)Ni satisfying $[0\bar{1}1]$ NiO|| $[0\bar{1}1]$ Ni was also observed. The B set disappeared in films >1000 Å and the (233) and (211) of the A set were seldom observed. 3000 Å films also evidenced some polycrystallinity.

These features are illustrated by the following micrographs. Properties of a 500 Å film are shown in Fig. 5(a) and (b); the crystallites are indexed as (011), (211)NiO|| (111)Ni with faint reflections arising from the (310) orientation. There are two (211) orientations: one shares a common close-packed direction (cpd) with (110) oxide and the other is rotated 30°. Figure 5(c) shows a 1300 Å film containing (011) and (211)NiO and dislocations. The 3500 Å film shown in Fig. 6 is irregular with evidence of both preferred orientation and polycrystallinity.

NiO crystallite size distribution: TEM was used to determine the size of crystallites in films up to 1000 Å thick formed at 500°C during exposures extending to 6 hr. The distributions and the average size of the crystallites as a function of exposure time are illustrated by the plots in Fig. 7 and 8. These parameters

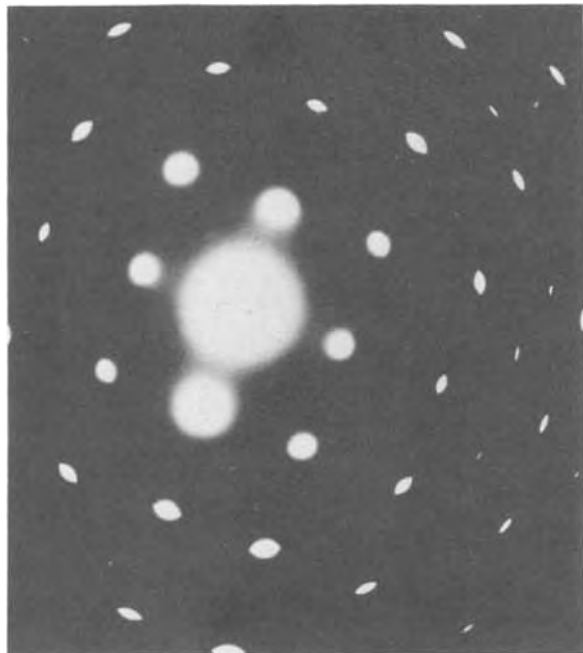


Fig. 4. SAD pattern of 500Å film formed on (110)Ni

did not appreciably change within 30 min. Subsequently the crystallites on each metal face grew at characteristic rates which decreased with time.

XRD.—The textures were determined of scales 1–15 μ thick formed at temperatures in the range 500°–800°C. Line broadening by strain and particle size was negligible in agreement with previous findings (6, 15). Accordingly Eq. [1] was used to determine the oxide texture based on the examination of seven reflection peaks. Typical results are shown in Table I and the resulting major oxide orientations are plotted vs. scale thickness in Fig. 9. The oxide on (100)Ni exhibited strong (100) and (111) orientations. The oxide on (110)Ni developed a (100) preferred orientation whilst the oxide on (111)Ni showed a (111) preferred orientation.

SEM.—A scale on (100) or (111)Ni exhibited a duplex morphology characterized by layers of equiaxed columnar grains as shown in Fig. 10, which was not found in the scale on (110)Ni. The inner layers of duplex scales exhibited a small degree of porosity. This duplex morphology revealed differences depending on whether the oxide was formed at high or low tem-

perature: at 800°C the boundary between the layers was diffuse since the size of grains in each layer was not much different; whereas, at 600°C a well-defined boundary occurred since the grains in the outer columnar layers were distinctly larger. Average grain sizes and the relative layer thicknesses are recorded in Table II. The grains grew during oxidation at rates increasing with temperature and the oxide grain size on the Ni faces tends to be in the order (110) > (111) > 100.

Discussion

NiO morphology.—The oxide formed on the three metal faces was composed of aggregates of crystallites exhibiting orientations which appear to be determined both by the orientation of the metal surface and by subsequent growth mechanisms since the orientations changed with thickness as summarized in Fig. 11. In order to rationalize the influence of the substrate a model is proposed based on the parallelism between cpd's in the film and substrate. In Fig. 11, lines drawn across the Ni and NiO symbols are close-packed directions and the angle between the lines represents the angle between these directions. The family of oxide crystallographic planes lying parallel to the metal surface is shown in a brace, the number before this brace representing the number of observed equivalent orientations.

(100)Ni can be characterized by two cpd's 90° apart. Five different oxide orientations were observed in thin films. Most crystallites with orientations (100), (011), (111), (211), (233)NiO|| (100)Ni can be rationalized by the relationship $[0\bar{1}1]\text{NiO}||[0\bar{1}1]\text{Ni}$. The (211) and (233) orientations, nevertheless, occur in multiples of six: two can be considered to have the directions $[0\bar{1}1]\text{NiO}||[011]\text{Ni}$ and the remaining four have $\langle 011 \rangle$ NiO at $\pm 30^\circ$ from the Ni cpd. The (111), (100)NiO-Ni epitaxial relations have been previously reported based on reflection electron diffraction from films retained on this metal face (13). The reported two (111) sets are equivalent. The most noticeable change is the disappearance of several orientations with increasing oxide thickness until only the (100) and (111) planes and polycrystallinity remain. These (100) and (111) preferred orientations in scales probably developed from the presence of these oriented crystallites in the films.

Eleven different oxide orientations were found in the films formed on (110)Ni which only contains one cpd. Ten of these orientations can be divided into two sets. The first set is (100), (011), (111), (211), (311), (322), (411), (433)NiO|| (110)Ni characterized by $[0\bar{1}1]\text{NiO}||[0\bar{1}1]\text{Ni}$ and the second set is (210), (310)NiO|| (110)Ni satisfying $[001]\text{NiO}||[001]\text{Ni}$. Fin-

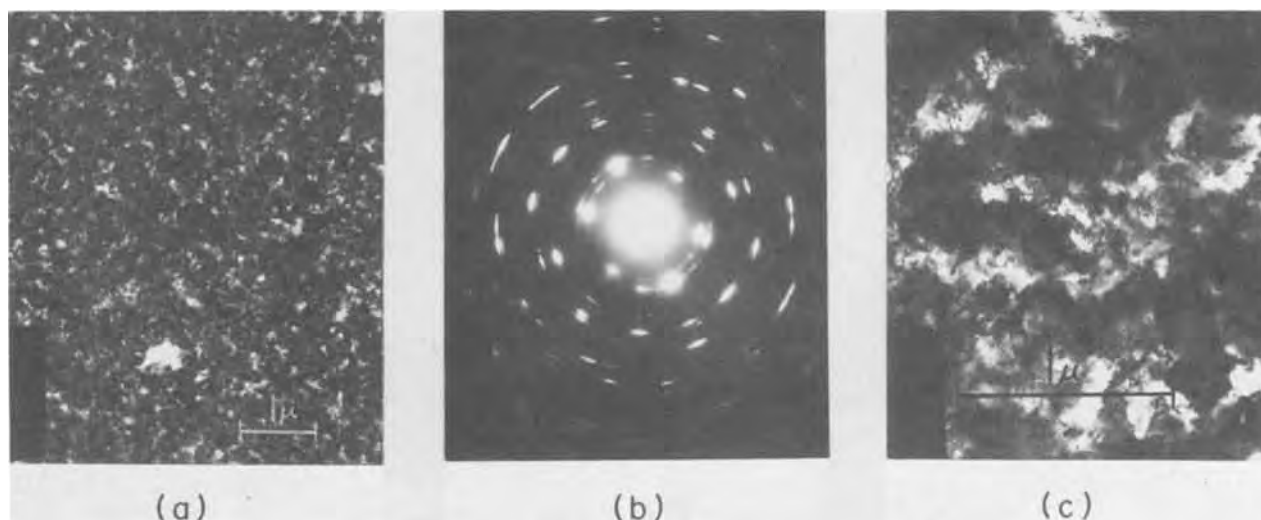


Fig. 5. TEM micrographs of 500 and 1300Å NiO films formed on (111)Ni. (a) 500Å, BF, (b) SAD pattern, (c) 1300Å, BF

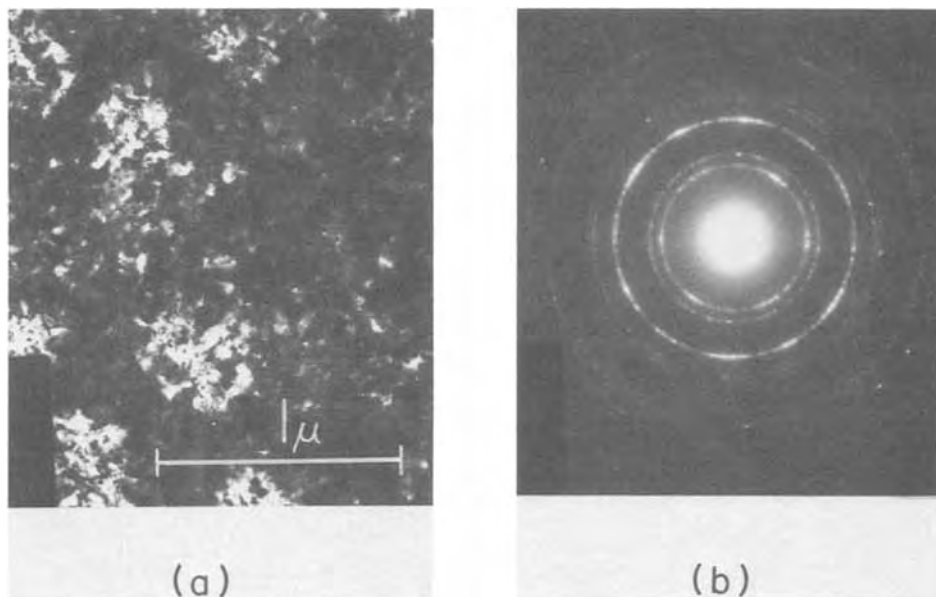


Fig. 6. TEM micrographs of 3500 Å NiO film formed on (111)Ni. (a) BF, (b) SAD pattern.

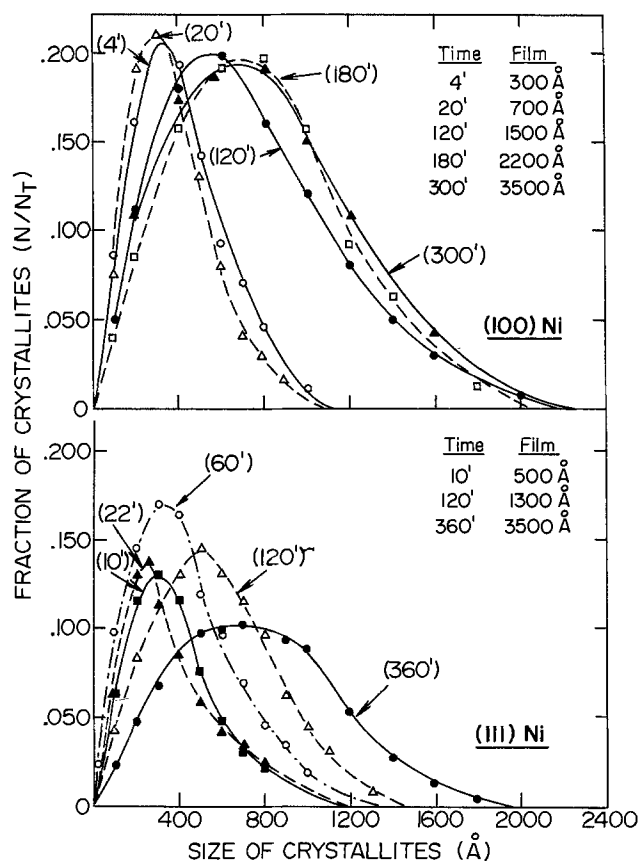


Fig. 7. Crystallite size distribution for films formed on (100) and (111)Ni at 500°C.

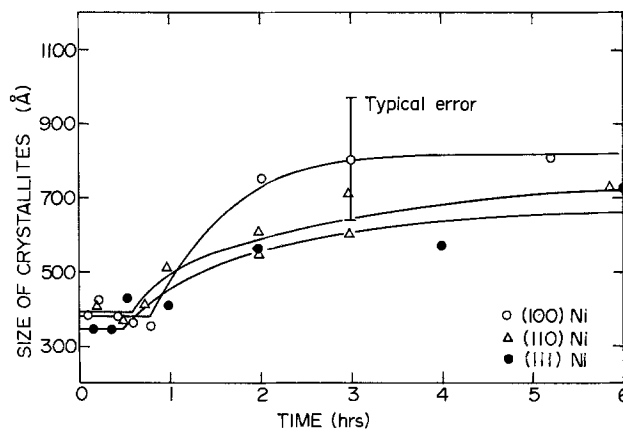


Fig. 8. Average crystallite size for films formed on (100), (110), and (111)Ni at 500°C.

ally (123)NiO|| (110)Ni satisfied $[\bar{1}1\bar{1}]NiO || [001]Ni$. The epitaxial relations for the (100), (011), and (211)

oxide planes have been previously reported (16). The (210), (310), and (123) orientations were seldom observed. The remaining eight orientations were frequently found and all contain at least one cpd which can lie parallel to the Ni cpd. Several of these orientations represent high index planes and of these only the (411) has been reported (16). Previous reflection x-ray diffraction work has indicated that the oxide on this face was polycrystalline (6). Also a 110 fibering-type structure has been reported (17) which probably refers to the series of planes including the high index planes found here sharing a common <110> direction. Gradual changes in orientation were only observed as the oxide thickened and the (100) orientation which finally dominated in a thick scale must have developed during oxide growth since it was not a major orientation in films.

Table I. Texture coefficients of NiO in scales on (100), (110), and (111) Ni

Ni face	Scale thickness (μ)	Texture coefficient of designated plane						
		(111)	(200)	(220)	(311)	(331)	(420)	(422)
(100)	1.5	4.85	0.76	0.03	0.09	<0.01	0.19	0.02
	6.8	3.11	3.40	0.05	0.16	0.09	0.03	0.16
	14	3.12	2.96	0.08	0.26	0.20	0.15	0.26
(110)	1.2	0.67	2.64	1.29	1.90	0.01	0.46	0.20
	3.3	0.38	3.55	0.76	1.14	0.56	0.60	<0.01
	7.2	0.35	4.5	0.69	0.59	0.28	0.17	0.16
(111)	1.5	3.07	1.50	0.43	0.90	0.95	0.31	0.25
	5.5	3.86	0.73	0.27	0.86	0.41	0.21	0.65
	10	4.10	0.43	0.34	0.83	0.54	0.24	0.43

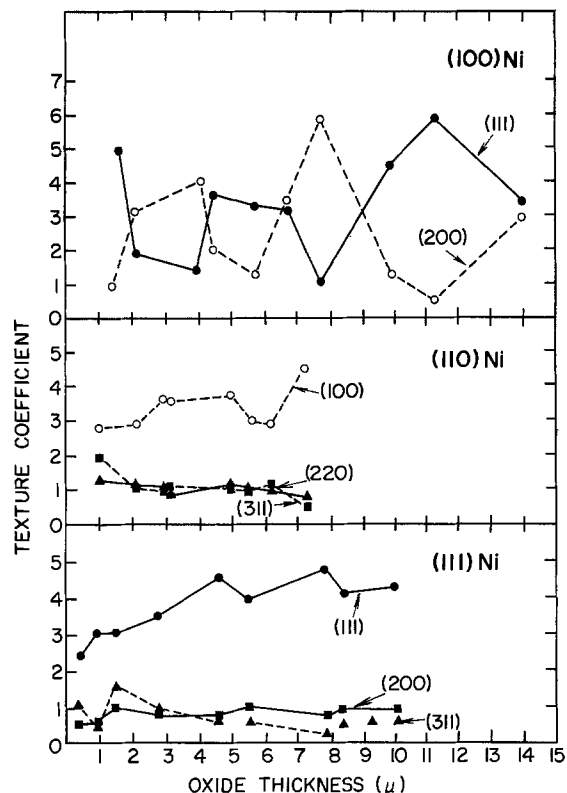


Fig. 9. Texture coefficients of NiO scales formed on (100), (110), and (111)Ni.

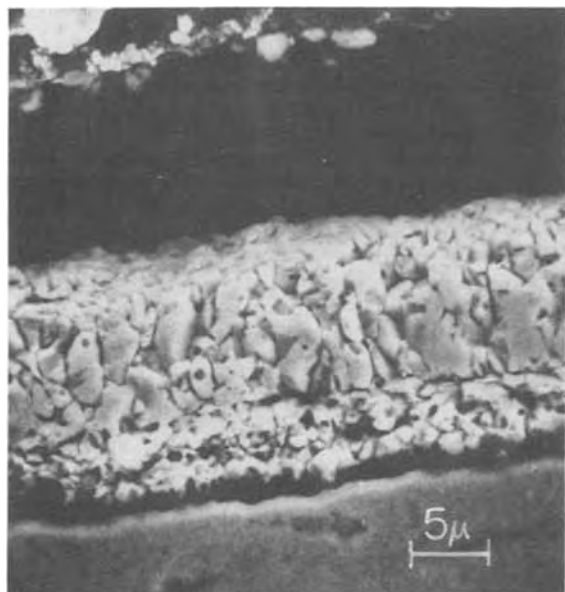


Fig. 10. SEM cross section of NiO scale formed on (100)Ni oxidized at 800°C for 120 hr.

(111)Ni is characterized by the maximum number of three cpd's 60° apart. Five different oxide orientations were observed and of these (111), (211), (233)NiO|| (111)Ni satisfy the epitaxial relations $[011]NiO|| [011]$ or $[112]Ni$ which have been previously established (2, 6, 12). An interesting feature was the occurrence of up to six equivalent orientations of (211) and (233) planes containing but one cpd which connotes the strong crystallographic influence of the metal. Three orientations lie with the cpd 60° apart and parallel to a (111)Ni cpd; the remaining three meet parallelism of the cpd with the $\langle 112 \rangle Ni$ directions (16). Since the oxide developed a (111) preferred orientation with increasing thickness, its growth corresponded to

Table II. Average NiO grain size and thickness ratio of layers in duplex scales

Ni face	Temperature (°C)	Time (hr)	Scale thickness (μ)	Average grain size* (μ)	Ratio outer/inner layer
(100)	800	16	4.7	1.13	0.8 ± 0.1
	800	25	7.8	1.28	1.0 ± 0.1
	800	48	11.4	1.76	1.2 ± 0.2
	800	120	14.2	1.87	2.1 ± 0.5
	700	50	6.8	0.92	3.0 ± 1.0
	700	110	10.7	0.78	3.2 ± 1.1
	600	50	3.5	0.63	1.2 ± 0.3
	600	115	5.9	1.03	1.9 ± 0.8
	500	104	2.1	0.25	1.2 ± 0.4
	(110)	800	67	6.4	1.90
800		100	7.0	2.48	Single layer
700		50	5.5	0.94	Single layer
700		100	5.3	1.62	Single layer
600		50	2.2	0.40†	—
(111)	600	100	2.7	0.71	—
	800	48	6.4	1.60	2.0 ± 0.2
	800	115	8.0	1.91	1.3 ± 0.3
	700	50	5.0	1.23	1.4 ± 0.5
	700	70	8.3	1.32	1.5 ± 0.3
	600	53	5.6	0.59	1.2 ± 0.2
	600	114	2.7	0.66	1.3 ± 0.4
	500	116	0.7	0.47†	—


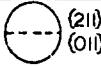
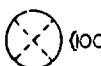



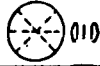

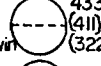


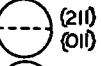
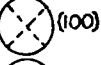
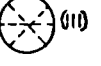
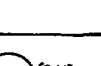


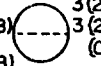


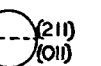
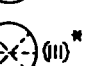
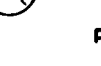


* The average grain size in a duplex scale was determined from outer layer.

† The average grain size determined from top view of specimen.

that of oxide on (100)Ni in that a major orientation observed in the film continued to develop as a preferred orientation during scale growth.

The average size of the oxide crystallites was 300–400 Å during an initial 30–40 min at 500°C and they subsequently grew to grains which were not of substantially different size on each metal face (Fig. 8 and Table II). The scale on (100)Ni exhibited the highest preferred orientation and most distinct columnar structure. This feature and the frequent observations of structural changes in less oriented oxide on (110) and (111)Ni accompanied with dislocations are common to findings of recrystallization and grain growth in solids (19).

These results lead to the consideration of general findings for overgrowth phases on solids. It is known that the degree of oxide polycrystallinity in films formed on Ni faces is dependent on the method of surface preparation and that the oxide formed at room temperature can rearrange upon heating the specimens in oxygen to 600°C (12). At the experimental pressure of 400 Torr, in this investigation, a nickel surface was subjected at room temperature to oxygen at least 10^{20} larger than the dissociation pressure of nickel oxide. Such large supersaturations as encountered here often lead to nucleation and growth of many, small, randomly oriented crystallites of the overgrowth phase on a substrate (20, 21). The films formed on the Ni faces exhibited some polycrystallinity upon raising the nickel specimens to the reaction temperature and allowing oxidation to proceed. Subsequently oxide rearrangement readily developed at the metal surface leading to epitaxial restraints since nickel diffuses outward during oxide growth. Because epitaxial relations in many film-substrate systems can often be correlated with the close-pack rule of parallel alignment of cpd's between the phases (22), one is led to inquire whether the number of cpd's in a Ni face influence the type and number of oxide orientations. (100) and (111)Ni possess two and three cpd's, respectively, and only five oxide orientations, all of them low index planes, were observed. The most dominant was the parallel orientation of cpd's. (110)Ni has only one cpd and eleven oxide orientations were observed. Thus the presence of only one cpd defined a less rigid condition for orienting oxide and to its relatively slow crystallographic change. Finally, the twinning which was frequently observed in this oxide with the twin boundary perpendicular to the plane of the oxide film may have arisen from the less rigid crystallographic restraints

MORPHOLOGICAL DEVELOPMENT OF THE STRUCTURE				
NICKEL	OXIDE		X-RAY Thickness (1-14 μ)	
	RESULTS FROM T.E.M.	Thickness (300-5000 Å)		
(100)	 6 (233) 6 (211) 1 (011)	 (211)  (011)	 (100)* polycrystalline  (100)* polycrystalline	 (100)*  (110)*
(011)	 433 (311) 411 (211) 322 (011) + Twin	 433 (311)  411 (211)  322 (011) + Twin	 (211)  (011)  (100)  (111)	 (100)*
(111)	 3(233)(A) + 3(233)(B) 3(211)(A) + 3(211)(B) 3(011)	 3(233) (A)  3(211) (A)  3(011)	 (211)  (011)  (111)*  (110)*	 (110)*

(*) major orientation
 (A) [011] NiO // [011] Ni ; (B) [011] NiO // [112] Ni

Fig. 11. Schematic diagram showing the development of textures in NiO formed on (100), (110), and (111)Ni.

leading to rapid growth of specific oriented crystallites.

Any influence of the metal substrate according to these considerations decreases with increasing oxide thickness. Consequently a stage is attained in which crystallite orientations become dependent on growth parameters. Some crystallites become randomly dispersed in films 1000Å thick and contributed to the commonly observed ring diffraction patterns. Since a growth mechanism now dominates a preferred orientation develops if the major orientations parallel to the metal surface in the films are the preferred growth planes. Such type of oxide growth occurs on (100) and (111)Ni. (110)Ni did not exhibit, however, a strong preference for a particular type of oxide orientation in thin films even though the scales showed a (100) preferred orientation. A (100) preferred orientation has also been observed to develop in scales on polycrystalline nickel (23-25). It would thus appear that (100) and (111) planes of nickel oxide lying parallel to the metal surface act as preferred growth planes due to preferential incorporation of adsorbed oxygen into nickel oxide resulting from the outward flux of nickel. The microstructures of the scales formed on (100) and (111)Ni exhibited the stronger preferred orientations and two distinct layers. These findings are also consistent with the development of a preferred orientation initially by epitaxial constraints and finally by growth parameters.

NiO growth kinetics.—Herchl *et al.* (7) found that the growth kinetics of the films and scales on these three Ni faces grew at a rate dependent on the metal crystallographic orientation. They therefore assumed a model wherein nickel migrated in nickel oxide by boundary and lattice diffusion to interpret the reaction kinetics. The present results on structural properties of the films and scales can be shown to substantiate these considerations.

Figure 12 demonstrates that the parabolic oxidation rate constants of both polycrystalline and single-crystal nickel at temperatures less than 900°C are much larger than values expected from calculations assuming lattice diffusion [the full lines in this graph represent the temperature coefficient of the parabolic rate constant

estimated from nickel tracer diffusion in NiO crystals using the Wagner theory (31)]. Caplan *et al.* (10) have shown for polycrystalline nickel, moreover, that the values for the parabolic rate constant and its activation energy at temperatures less than 900°C are larger and

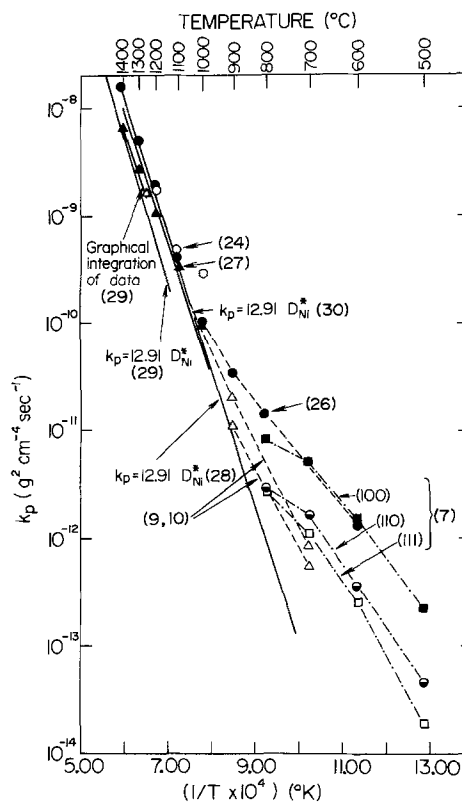


Fig. 12. The temperature coefficient of the parabolic oxidation constants for nickel oxide growth on nickel polycrystalline and crystal faces (>99.995% pure). The reference numbers correspond to those in the text. The solid lines represent calculated values using nickel tracer diffusion coefficients from Ref. (28-30) and the Wagner expression for the parabolic rate constant (31).

smaller, respectively, the finer the grain size of the oxide. We therefore express the effective diffusion coefficient for nickel in nickel oxide formed on a metal face as a weighted sum of the diffusivities for lattice and boundary diffusion (5)

$$D_{\text{eff}} = D_L(1 - f) + D_B f \quad [2]$$

where f is the fraction of diffusion sites in the boundaries. A modified parabolic rate equation

$$x^2 = 2\Omega D_L \Delta c \int_0^t (1 + f D_B/D_L) dt \quad [3]$$

represents the oxidation kinetics upon utilizing the approximation of a linear compositional gradient across the oxide. In this equation, x is the oxide thickness, Ω is the volume of oxide per metal ion, and Δc is the concentration difference across the oxide. NiO is of rock-salt structure so that anisotropy of oxidation with crystallographic orientation of a metal surface would be explained if the magnitude of the boundary diffusivity and/or the fraction of short-circuit sites depend on the NiO morphology on each crystal face. Assuming that the density of short-circuit diffusion paths decrease by the competitive growth of the oxide grains according to the following relations

$$f(t) = 2d/D_t; \quad D_t^2 - D_o^2 = Gt \quad [4]$$

Eq. [3] becomes

$$x^2 = 2\Omega D_L \Delta c \int_0^t \left\{ 1 + \frac{2D_B d}{D_L (D_o^2 + Gt)^{1/2}} \right\} dt \quad [5]$$

In these equations, D_t is the mean grain diameter after time t , D_o is the initial grain diameter, d is the boundary width, and G is the grain growth constant. Equation [5] was placed in the following form for graphical analysis of experimental results (7)

$$1/(dx^2/dt - k_p)^2 = (D_o^2/A) + (Gt/A) \quad [6]$$

where $A = [2k_p D_B d/D_L]^2$, $k_p = 2D_L \Omega \Delta c = 6D_{\text{Ni}}$ where D_{Ni} is the self-diffusion coefficient of nickel in NiO. The resulting good fit of Eq. [5] by this method to the oxidation kinetics of (100) and (111)Ni are shown in Fig. 13 and 14. Oxide growth on (110)Ni could not be interpreted by Eq. [6] as the oxidation curves for this metal face showed abrupt changes in

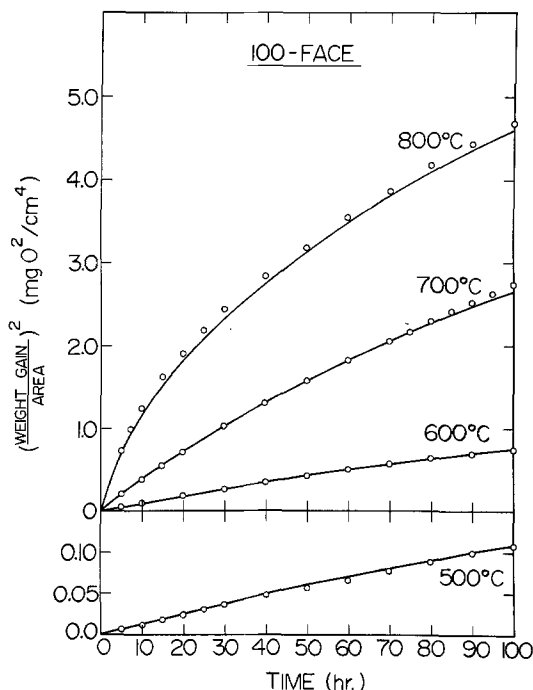


Fig. 13. The experimental results and the curves calculated by Eq. [5] for the growth of NiO on (100)Ni.

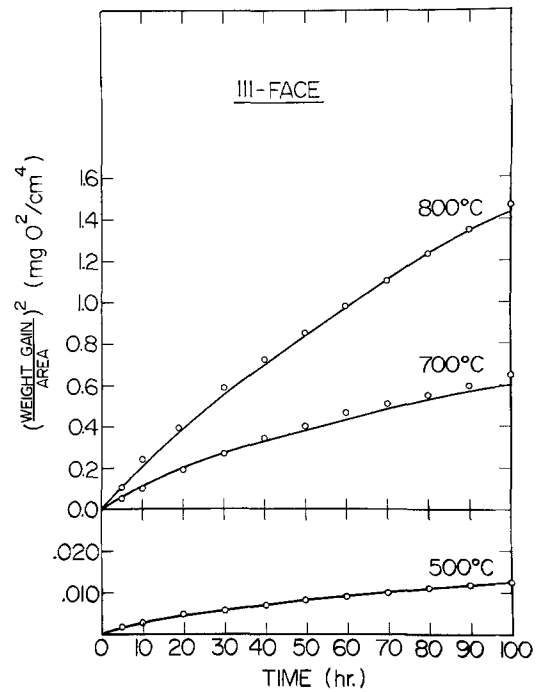


Fig. 14. The experimental results and the curves calculated by Eq. [5] for the growth of NiO on (111)Ni.

slope due to increased reaction rates resulting from oxide spalling and cracking (7).

Equation [3] can be expressed as

$$\frac{dx^2}{dt} = (k_p)_{\text{eff}} = k_p + (k_p)_B f(t) \quad [7]$$

where $(k_p)_{\text{eff}}$ is the rate constant determined from the tangents to the oxidation curves plotted x^2 vs. t and $(k_p)_B = 2\Omega D_B \Delta c$ is the parabolic constant for oxide growth by boundary diffusion. Thus, $(k_p)_B$ can be calculated using values of k_p and $f(t) = 2d/D_t$ obtained from the average crystallite and grain sizes determined by TEM and SEM assuming $d \sim 10\text{\AA}$. Values calculated for $(k_p)_B$ and the ratio of the diffusivities D_B/D_L by this method are recorded in Table III and the temperature coefficient of $(k_p)_B$ is given in Fig. 15.

Since the values of D_B/D_L are of the order 10^4 - 10^7 , rapid boundary diffusion of nickel led to a large enhancement in oxide growth compared to that expected from lattice diffusion only. This enhancement is so large that $(k_p)_B f(t)$ remains as the leading term determining the effective parabolic constants even in the scaling range where the oxide is 1-15 μ thick. The activation energies of 31 and 35 kcal/g-atom for oxide growth on (100) and (111)Ni by boundary diffusion, respectively, equal approximately one-half the activa-

Table III. Boundary diffusion oxidation constants for oxide growth on (100) and (111)Ni evaluated from $(k_p)_{\text{eff}}$, $f(t)$, and tangents to the oxidation curves x^2 vs. t

Ni face	Temperature (°C)	Time (hr)	$f(t)$	$(k_p)_B$ ($\text{g}^2 \text{cm}^{-4} \text{sec}^{-1}$)	$(k_p)_B/k_p = D_B/D_L$
(100)	500	4	2.9×10^{-2}	1.3×10^{-11}	8×10^7
		100	8.6×10^{-3}	3.0×10^{-11}	
	600	50	3.2×10^{-3}	4.8×10^{-10}	3×10^7
		100	2.0×10^{-3}	8.0×10^{-10}	
	700	50	2.2×10^{-3}	2.4×10^{-9}	2×10^6
		100	2.6×10^{-3}	2.0×10^{-9}	
800	50	1.1×10^{-3}	9.3×10^{-9}	5×10^5	
	100	1.1×10^{-3}	7.5×10^{-9}		
(111)	500	4	2.5×10^{-2}	2.4×10^{-12}	1×10^7
		100	4.3×10^{-3}	3.6×10^{-12}	
	700	50	1.6×10^{-3}	9.9×10^{-10}	9×10^5
		70	1.5×10^{-3}	7.4×10^{-10}	
800	48	1.3×10^{-3}	2.3×10^{-9}	1×10^5	
	115	1.2×10^{-3}	1.7×10^{-9}		

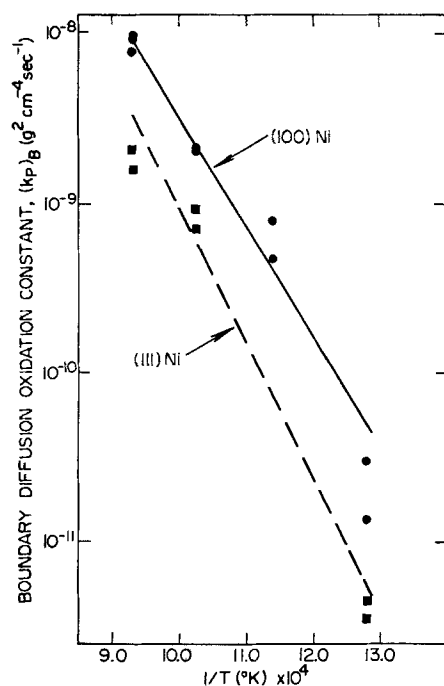


Fig. 15. Arrhenius plots of the parabolic constants for oxide growth by nickel boundary diffusion $(k_p)_B$ on (100) and (111)Ni.

tion energy of 61 kcal/g-atom for nickel lattice diffusion in nickel oxide (29). The values of grain size (Table II) and $(k_p)_B$ (Table III) for (100) and (111)Ni illustrate that differences in both of these quantities determine the degree of oxidation anisotropy with metal face. The differences in the magnitude of $(k_p)_B$, nevertheless, give rise to the most substantial effect. Hence, the influence of oxide orientation or texture on the value of the nickel boundary diffusivity largely accounted for the oxidation anisotropy of (100) and (111)Ni under the conditions of experimentation.

Conclusions

NiO up to 15μ thick formed on (100), (110), and (111)Ni at temperatures in the range 500° – 800°C consisted initially of small crystallites which grew to grains with increasing exposure. A number of oxide orientations were found; the most preferentially oriented film developed on (100) and (111)Ni consistent with the close-pack rule for parallel alignment of cpd's between the substrate and an overgrowth phase. (100) and (111) textured scales developed on the metal faces due initially to epitaxial constraints and finally by the mechanism of oxide growth. These findings substantiate a model for oxide growth and oxidation anisotropy with metal orientation in which boundary diffusion of nickel significantly accounts for reactant migration through the films and scales. The differences in the rate of nickel migration was determined most predominantly by the types rather than the different densities of boundaries in the textured oxide on the metal faces under the conditions of exposure.

Acknowledgments

This research was carried out by N. N. Khoi in partial fulfillment of the requirements for the award of

the Ph.D. degree, McMaster University. He wishes to acknowledge the award of an Ontario Graduate Fellowship. The work was carried out under the auspices of The National Research Council of Canada.

Manuscript submitted March 21, 1975; revised manuscript received June 30, 1975.

Any discussion of this paper will appear in a Discussion Section to be published in the June 1976 JOURNAL. All discussions for the June 1976 Discussion Section should be submitted by Feb. 1, 1976.

Publication costs of this article were partially assisted by McMaster University.

REFERENCES

1. E. A. Gulbransen and K. F. Andrew, *This Journal*, **161**, 129 (1954).
2. K. R. Lawless, F. W. Young, and A. T. Gwathmey, *J. Chim. Phys.*, **53**, 667 (1956).
3. J. M. Perrow, W. W. Smeltzer, and R. K. Ham, *Acta Met.*, **15**, 577 (1967).
4. J. J. Van der Broeck and J. L. Meijering, *ibid.*, **16**, 375 (1968).
5. J. M. Perrow, W. W. Smeltzer, and J. D. Embury, *ibid.*, **16**, 1209 (1968).
6. J. V. Cathcart, G. F. Petersen, and C. J. Sparks, Jr., *This Journal*, **116**, 664 (1969).
7. R. Herchl, N. N. Khoi, T. Homma, and W. W. Smeltzer, *Oxidation of Metals*, **4**, 35 (1972).
8. M. J. Graham and M. Cohen, *This Journal*, **119**, 879 (1972).
9. M. J. Graham, G. L. Sproule, D. Caplan, and M. Cohen, *ibid.*, **119**, 883 (1972).
10. D. Caplan, M. J. Graham, and M. Cohen, *ibid.*, **119**, 1205 (1972).
11. M. J. Graham, D. Caplan, and M. Cohen, *ibid.*, **119**, 1265 (1972).
12. M. J. Graham, R. J. Hussey, and M. Cohen, *ibid.*, **120**, 1523 (1973).
13. T. Homma, N. N. Khoi, W. W. Smeltzer, and J. D. Embury, *Oxidation of Metals*, **3**, 463 (1971).
14. G. B. Harris, *Phil. Mag.*, **43**, 113 (1952).
15. J. D. Sartell and C. H. Li, *J. Inst. Metals*, **90**, 92 (1961).
16. L. B. Garmon, Ph.D. Thesis, University of Virginia (1966).
17. H. Pu, C. Chien-ti, and K. Ke-hsin, *Sci. Sinica*, **14**, 632 (1965).
18. M. Otter, *Z. Naturforsch.*, **14a**, 355 (1959).
19. J. E. Burk and T. Turnbull, *Prog. Met. Phys.*, **3**, 220 (1961).
20. L. Lothe and G. M. Pound, *J. Chem. Phys.*, **36**, 2080 (1962).
21. J. L. Kenty and J. P. Hirth, *Surface Sci.*, **15**, 403 (1969).
22. R. J. Gerdes and R. A. Young, Tech. Rept. No. 6, Project A644, Office of Naval Research (1967).
23. J. P. Baur, R. W. Bartlett, J. N. Ong, Jr., and W. M. Fassel, Jr., *This Journal*, **110**, 185 (1963).
24. D. L. Douglass, *Corrosion Sci.*, **8**, 665 (1968).
25. R. Hales, *ibid.*, **12**, 555 (1972).
26. J. Paidassi and L. Berry, *Compt. Rend. Acad. Sci. Paris*, **262**, 1553 (1966).
27. K. Fueki and J. B. Wagner, Jr., *This Journal*, **112**, 384 (1965).
28. R. Lindner and A. Akerstom, *Discussions Faraday Soc.*, **23**, 133 (1957).
29. M. L. Volpe and J. Reddy, *J. Chem. Phys.*, **53**, 1117 (1970).
30. W. B. Crow, Report ARL-70-0090, Project No. 7021, Office of Aerospace Research, USAF, Wright-Patterson Air Force Base, Ohio (1970).
31. K. Hauffe, "Oxidation of Metals," p. 87, Plenum Press, New York (1965).

Oxidation of Titanium Thin Films

W. D. Sylwestrowicz

Fairleigh Dickinson University, Madison, New Jersey 07940

ABSTRACT

Titanium thin films were exposed to an oxidizing argon atmosphere in the temperature range from 30° to 400°C. In specimens exposed to the temperature above 300°C two stages were observed. Initially, resistance increased linearly with time and temperature coefficient values were positive. After prolonged exposure resistance increased exponentially with time, and negative temperature coefficients were observed. It is suggested that this behavior results from a progressive oxidation at grain boundaries. When oxidation is complete through grain boundaries to the substrate, conduction is then dependent on a tunneling process through the semiconducting titanium oxide leading to the observed exponential temperature and time of exposure dependence.

With progressive miniaturization of integrated and thin film circuits, the extremely small dimensions of the components introduce a number of new problems related to material stability and reliability. One of them is the effect of environment on the components of integrated circuits. Since the thickness of compounds may be of the order of a few hundreds atoms, environmental effects which might be negligible in bulk materials, can in such cases be of the utmost importance. In devices where thin films of gold are used as conductors on glass or ceramic substrates, titanium is often used as the bonding agent between gold and the substrate. It is well established that pure titanium is an efficient oxygen getter (1). Before undertaking an investigation of the effect of corrosive environments on gold-titanium metallization, it was thought desirable to conduct a study of the effect of temperature and humidity on the oxidation of titanium thin films and the results of this investigation are here described.

The theoretical aspects of growth and structure of the oxide films formed on the bulk metals were thoroughly discussed by Uhlig (2). Mindel and Pollack (3) investigated oxidation of the bulk titanium at room temperature.

Recently Smith published a paper (4) on oxidation of a titanium specimen exposed to different oxygen pressures at temperatures between 25° and 400°C. He expected to separate processes simultaneously occurring during oxidation of the titanium surface with the use of Auger spectroscopy, ellipsometry, and measurements of surface potential differences. It is not in-

tended to discuss here this interesting paper, but it will be of interest to indicate some fundamental differences between Smith's work and what has been presented here. The thin films used in this work were about 1000Å thick, while those in Smith's (4) work were about 0.8 mm thick. The exposure time was of the order of 800 hr against 2 hr in Smith's experiments. In Smith's experiments, tests started with a clean specimen surface (annealing at 600°C and 5×10^{-10} Torr vacuum). In the experiments described below, the specimen surfaces were covered with the initial oxide layer.

Essentially in the experiments described here, we are dealing with thin film samples while in the Smith experiments we are dealing with a bulk sample, and therefore a considerably longer exposure in the present tests produced effects which had no time to develop in the relatively short exposure of the bulk sample used by Smith.

It should be noted that the experiments described below are designed for investigations of the effects resulting from the long exposures and are not concerned with the initial layer of titanium oxides formed in the first few hours of exposure. Since the experiments are conducted on the thin films of titanium, the obtained results are not necessarily applicable to the bulk material.

Experimental Results

Experiments were conducted for the conditions shown in Table I. Titanium specimens which measured 3 cm in total length, 1.525×10^{-2} wide and 750Å thick,

Key words: titanium, oxidation, thin films.

Table I. Test conditions

Sp. lot	Sp. No.	h (Å)*	R ₀ (ohm)	$\rho \times 10^5$ (ohm · cm)	Initial tests		Final tests		Atmosphere
					T (°C)	t (hr)	T (°C)	t (hr)	
I	1	750	2770	10.5			300	520	Wet argon, water vapor 30 Torr
	2	750	2370	9			70	520	Wet argon, water vapor 30 Torr
	3	750	2450	9.5			325	840	Dry argon
	4	750	2810	10.5			170	840	Dry argon
	5	750	2500	9.5			75	840	Dry argon
II	6	770	4100	16			245	260	Dry argon
	7	770	4060	16			245	260	Wet argon, water vapor 70 Torr
	8	770	4160	16			180	260	Wet argon, water vapor 70 Torr
	9	770	4320	17			165	260	Dry argon
	10	770	3870	15			100	260	Dry argon
	11	770	4120	16			100	260	Wet argon, water vapor 70 Torr
III	12	730	3800	14	260	620	365	130	Dry argon, high oxygen content†
	13	730	3800	14	255	620	360	130	Dry argon, high oxygen content†
	14	730	3800	14	255	620	355	130	Dry argon, high oxygen content†
	15	730	4200	15.5	150	750	340	200	Dry argon, high oxygen content†
	16	730	4140	15	150	750	330	200	Dry argon, high oxygen content†
	17	730	3920	14.5	80	750	170	200	Dry argon, high oxygen content†
IV	18	7250	210	7.5	255	620	400	45	Dry argon, high oxygen content†
	19	7250	210	7.5	150	750	315	200	Dry argon, high oxygen content†
	20	7250	220	8.0	80	750	90	110	Dry argon, high oxygen content†

* h = thickness of titanium layer.

† Initial tests were conducted in wet argon with water vapor pressure 200 Torr.

were tested in the temperature range from 30° to 400°C in: (a) argon atmosphere (argon 99.9999% purity), (b) argon atmosphere with added water vapor, (c) argon atmosphere with added water vapor and oxygen, and (d) argon atmosphere with added oxygen.

Water vapor pressures in Table I refer to the pressures at the inlet to the furnace. High oxygen content indicates about 30% of oxygen by volume of oxygen. Specimens were prepared by electron beam gun deposition of titanium of 99.97% purity covered by a 5000Å thick gold layer. Sodium-free Corning 7059 glass (barium aluminum silicate) was used as a substrate. Specimens were obtained by etching with diluted solution of potassium iodine and iodine using the photoresist technique. The specimen's thickness was measured by the stylus-step method with the use of the Talysurf instrument made by Taylor Hobson. The accuracy of measurement is about 10Å for film up to 1000Å thick. Finally the gold layer was removed with the exception of the pads to which connecting gold wires were attached by compression bonding. Pressure after titanium evaporation was about 10^{-6} - 10^{-7} Torr and before evaporation, 10^{-8} Torr. The experimental setup was arranged in such a way that specimens could be tested simultaneously in six furnaces heated individually to different temperatures. These furnaces were inserted into a constant temperature chamber and this arrangement permitted close temperature control in tests of long duration, and control of water vapor pressure. Dry or wet argon, with or without addition of oxygen, was fed from a common source through each furnace. The argon used was of 99.9999% purity.

In tests with specimens of lots I and II (Table I) only one specimen was tested at each condition (temperature and atmosphere). In tests with specimens of lots III and IV three specimens were tested simultaneously at each temperature. Since observed changes for these specimens were similar, the data for only one specimen are given with the exception of specimens tested at higher temperatures. For most of these specimens experimental data are given. The resistance of the specimens was continuously recorded by drawing a current of 0.01 mA through the specimens and measuring the voltage change. In addition the resistance of specimens was periodically measured directly.

The following notations are used in this paper: R_0 = electrical resistance of a specimen at room temperature before the tests; R_r = electrical resistance of a specimen at room temperature after the test; R_t = electrical resistance of a specimen at test temperature T after time t of exposure; and R_T = electrical resistance of a specimen at test temperature T at the end of the test.

In the first series of tests, with specimens of lot I, specimens were exposed to two atmospheres: pure argon and pure argon with an addition of water vapor. These tests showed a marked difference between specimen No. 1 tested in wet argon and specimen No. 3 tested in dry argon at temperatures 300° and 325°C, respectively (Fig. 1). The second series of tests, with specimens of lot II, was supplementary to the first series and designed for the investigation of specimen behavior in the range of temperatures between 100° and 250°C (Fig. 2). At the end of these tests oxygen was added to specimens No. 6 and 9 exposed to dry argon atmosphere (Fig. 2). These specimens were tested at 245° and 165°C, respectively. The third series of tests, specimens of lot III and IV, was designed after taking into consideration the results of the previous tests and was intended to confirm conclusions drawn from these tests. An additional factor, the thickness of the specimens' layer, was also introduced (specimens of lot IV). The third series of tests was conducted in two stages. In the first stage, specimens were exposed to wet argon and oxygen (about 1/3 by volume) atmosphere at temperatures below 300°C (Table I). In the second stage, the same specimens were tested at temperatures above 300°C. The exceptions were specimens No. 20 and 17 tested at 90° and 170°C, re-

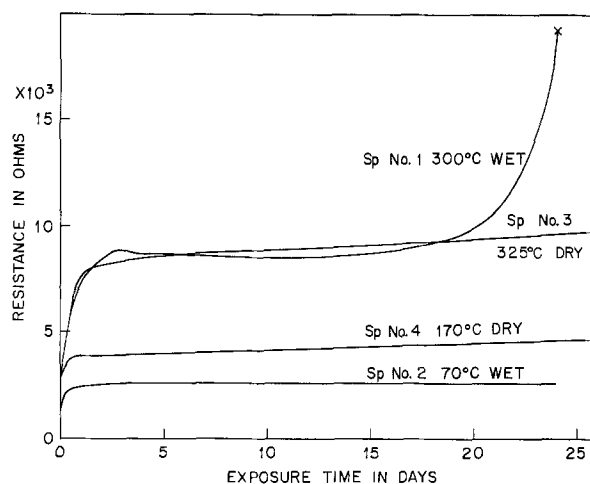


Fig. 1. Change of the electrical resistance with time of exposure time of specimens tested at different temperatures in dry or wet argon.

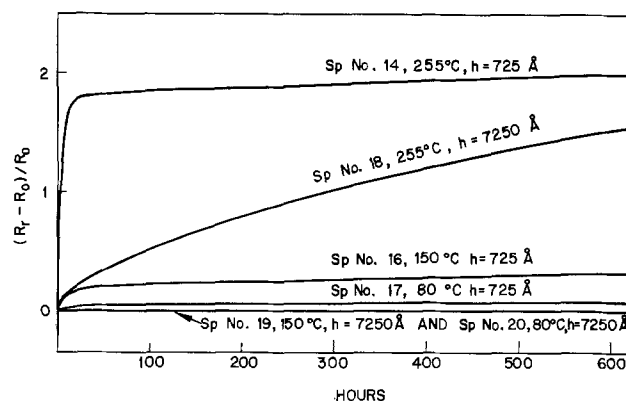


Fig. 2. Changes of electrical resistance ($R_t - R_0$) with time of exposure of specimens tested in two ranges of temperatures in dry and wet argon. Also the effect of oxygen addition to dry argon atmosphere is shown. The changes are normalized to the initial specimen resistances (R_0) at room temperature.

spectively. In this stage specimens were exposed initially to the same, wet, highly oxidizing argon atmosphere as in the first stage but after 106 hr of exposure water vapor was cut off from the system and the atmosphere was composed only of high purity argon and oxygen.

Discussion

In the thin film titanium specimens exposed to the highly oxidizing atmosphere (1/3 of oxygen by volume), even at a temperature as low as 80°C (specimen No. 17, Table II), some oxidation can be observed, but after the initial rise, resistance of the specimens becomes stable and continuous exposure (in the time of this study) does not further affect resistance of the specimens. This observation is valid for all specimens heated up to 255°C (specimens No. 14, 16, and 17, Fig. 3).

When specimens were exposed to the high purity argon atmosphere (dry or wet) at temperatures below 150°C, no noticeable change in resistance was observed (specimens No. 2, 5, 10, and 11, Table II).

In specimens exposed to the highly oxidizing atmosphere and at temperatures above 300°C, the resistance increases in two stages. Initially the increase is nearly linear (in what follows it will be linear), and then exponential. The time of exposure during which resistance increases linearly depends on temperature (Fig. 4). In this interval of exposure the resistance at room temperature (R_r) increases faster than resistance at the test temperature (R_t). Somewhere close to the end of the period of linear increase of resistance,

Table II. Experimental data

Sp. No.	T* (°C)	T (°C)	R ₀ (ohm)	R _r * (ohm)	R _r (ohm)	R _T (ohm)	R _r - R ₀		Atmosphere
							R ₀	R ₀	
1		300	2770		40,000	19,240	13.44	-7.49	Wet argon, water vapor 30 Torr
2		70	2370		2370	2670	0	0.13	Wet argon, water vapor 30 Torr
3		325	2450		11,030	10,800	3.50	-0.09	Dry argon
4		170	2810		3580	4740	0.27	0.41	Dry argon
5		75	2500		2420	2840	-0.03	0.17	Dry argon
6		245	4100		18,060	17,150	3.40	-0.22	Dry argon
7		245	4060		14,770	14,880	2.64	0.03	Wet argon, water vapor 70 Torr
8		180	4160		9590	10,330	1.16	0.17	Wet argon, water vapor 70 Torr
9		165	4320		11,460	11,560	1.63	0.02	Dry argon
10		100	3820		3800	4730	0	0.24	Dry argon
11		100	4120		4240	5220	0.29	0.24	Wet argon, water vapor 70 Torr
12	255	365	3800	11000	550,000	215,000	143.7	-88.168	Dry argon, high oxygen content
13	255	360	3800	—	76,900	45,500	19.24	-8.26	Dry argon, high oxygen content
14	255	355	3800	11400	30,200	29,300	6.95	-0.24	Dry argon, high oxygen content
15	150	340	4200	5100	125 × 10 ⁴	—	296.6	—	Dry argon, high oxygen content
16	150	330	4140	5500	113,000	—	26.29	-12.56	Dry argon, high oxygen content
17	80	170	3920	4240	4300	5500	0.31	0.31	Dry argon, high oxygen content
18	255	400	210	535	7,720	2970	35.76	-22.62	Dry argon, high oxygen content
19	150	315	210	210	465	655	1.21	0.90	Dry argon, high oxygen content
20	80	90	220	220	220	270	0	0.23	Dry argon, high oxygen content

* Initial tests with specimens from lots III and IV. Specimens were tested: in wet argon with 200 Torr water vapor pressure.

Table III. Temperature dependence of oxidized specimens.
Resistance in 10³ ohms

T (°C)	-70	-30	3	23	111	115	120	172	195	202
10 ⁻³ /T (°K ⁻¹)	4.93	4.12	3.66	3.38	2.60	2.58	2.54	2.25	2.14	2.02
Specimen No.	12	1.050	—	—	—	384	—	327	—	305
	16	160	—	—	—	—	88	81	81	—
	13	112	—	—	—	61.7	—	58.6	—	57.7
	18	14.7	10.92	9.17	7.72	5.77	—	—	—	—

the value of the resistance at room temperature (R_r) becomes equal to the resistance at test temperature (R_t). From this point the linear dependence of resistance changes to an exponential dependence (Fig. 4 and 5). In this range some tests were interrupted periodically, specimens cooled to the lower temperatures, and resistance measured. The results are shown in Table III and Fig. 6. It can be seen from Fig. 6 that the resistance depends exponentially on the reciprocal of temperature, and the specimen behaves as a semiconductor exhibiting a negative thermal coefficient of resistance $R_T - R_r < 0$ ¹ (Table II, Fig. 6). In the last stage, increases in the resistance were too fast to be accurately monitored.

As shown in Table II, the linear dependence of resistance ends when the resistance has increased by a factor of 3-4. This observation cannot be explained on the basis of a surface oxide layer gradually increasing in thickness. Since the resistivity of titanium oxides (5) is many orders of magnitude larger than that of

titanium, the major part of the current would flow through the titanium layer and be largely unaffected by the properties of the titanium oxide layer until oxidation was essentially completed.

However, the observed resistance change can be explained by assuming that oxidation occurs through the grain boundaries into the bulk of the grains.² The rate of oxygen diffusion through the grain boundaries in thin films is not known but it is expected to be much faster than through the bulk of the grains.

It can be proposed that diffusion of oxygen, through grain boundaries, is responsible for the formation of a network of titanium oxides along grain boundaries. This would result in a local reduction of the metallic cross section of the film and in an increase of resistance. When titanium oxide penetration to the sub-

² This mode of oxidation was proposed by P. A. Turner.

¹ This cause of the observed change of sign of the temperature coefficient of resistance was suggested by R. J. H. Voorhoeve.

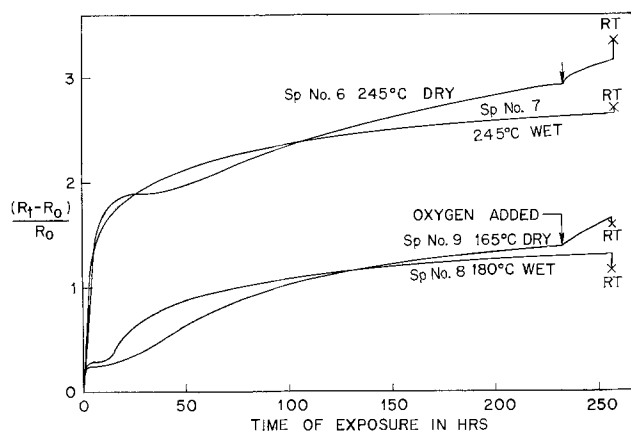


Fig. 3. Change of the electrical resistance with exposure time of specimens of lots III and IV in the initial tests. Specimens were tested in argon atmosphere of high oxygen concentration and 200 Torr water vapor pressure.

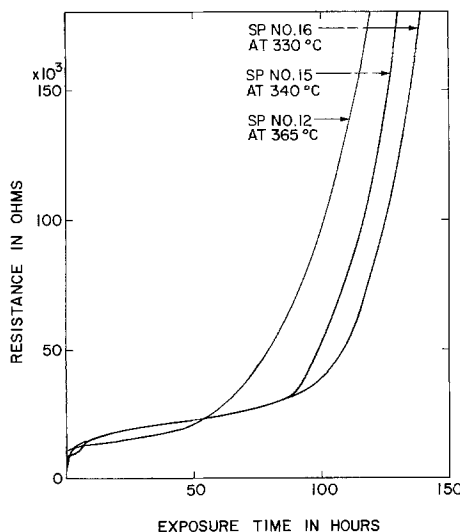


Fig. 4. Dependence of resistance on time of exposure of specimens No. 12, 15, and 16 exposed initially to a humid, highly oxidizing atmosphere then to a highly oxidizing but dry atmosphere. Test temperatures: 365°, 340°, and 330°C, respectively.

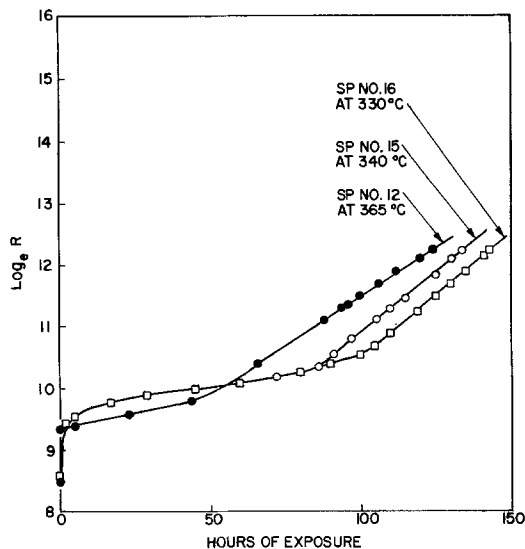


Fig. 5. Dependence in semilogarithmic scale of resistance on time of exposure of specimens No. 12, 15, and 16 exposed initially to a humid oxidizing atmosphere then to an oxidizing but dry atmosphere. Test temperatures: 365°, 340°, and 330°C, respectively.

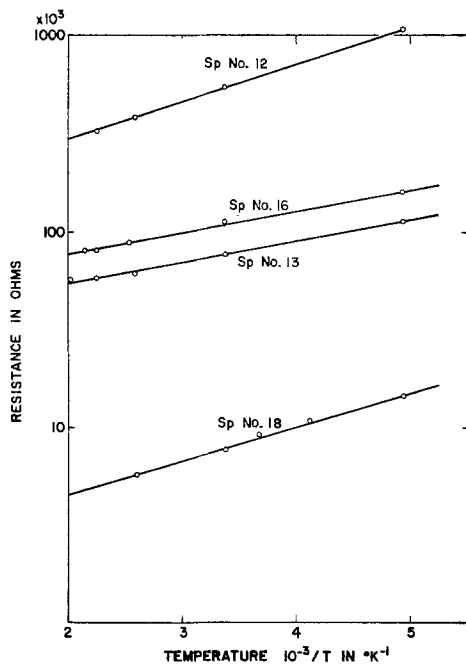


Fig. 6. Dependence of resistance on the reciprocal of temperature of specimens exposed at higher temperatures to oxidizing atmosphere.

strate is completed the linear dependence of resistance changes to the exponential

$$\rho = Ce^{E/KT} \quad [1]$$

The observed negative temperature coefficient of resistance is attributed to the formation of titanium oxides.

Once a titanium oxide network is formed around grains, the current must tunnel through the thin layers of titanium oxides at each boundary and the total specimen resistance consists of the sum of resistances of titanium oxide thin films at grain boundaries (of few interatomic spacings) in series with the sum of resistances of each titanium grain. A tunneling effect should be expected in such a configuration. In this model an exponential temperature dependence of resistance is expected, in agreement with the experiment (Fig. 6). Also the resistance should depend exponentially on the width of the barrier, in this case on the thickness of titanium oxide layers at the grain bound-

aries (6): i.e.

$$\rho = Ae^{ax} \quad [2]$$

where x is the width of the barrier. It is assumed here, that, since the thickness of the titanium layer is very small, diffusion of oxygen through grain boundaries to the substrate occurs fast especially at higher temperatures. Formation of titanium oxides, while occurring readily at temperatures above 700°C, at lower temperatures occurs much slower and at 150°C, even after 750 hr of exposure, no change in sign of temperature coefficient was observed. At temperatures below 400°C formation of titanium oxides and not diffusion of oxygen is, therefore, a rate-limiting process in the widening of the oxide layer at grain boundaries. It can be written, therefore, that $x = ct$, where c is a constant and t is the time of exposure counted from the moment at which the observed exponential dependence of resistance commences. By substituting x into [2] an exponential dependence of resistance on the time of exposure is obtained

$$\rho = Ae^{at} \quad [3]$$

The larger rate of increase of resistance, observed in the humid argon atmosphere at temperature 300°C (specimen No. 1), as compared with the dry argon atmosphere at 325°C (specimen No. 3, Fig. 1), seems to be related to the supply of additional oxygen derived from the water vapor. In the experiments with very high purity argon the amount of oxygen in the test was small, and during exposure the rise of electrical resistance was slow (specimen No. 3 and 4, Fig. 1). The introduction of additional oxygen produced a sharp increase of resistance (Fig. 2). In the tests in a highly oxidizing atmosphere humidity has no effect on the rate of increase of resistance (Fig. 7). All these observations indicate that the increase of resistance is caused by the oxidation of the titanium and water vapor is only one of the factors, probably an additional source of oxygen, in a test at temperature 300°C and in the atmosphere deficient in oxygen. Specimens of 7200Å thickness behave in the same manner as thinner specimens of 750Å thickness except that a longer time of exposure is needed for the process of oxidation. After about 45 hr of exposure at 400°C, specimen No. 18 of 7250Å thickness exhibited a negative temperature coefficient (Fig. 6). The ratio $(R_T - R_r)/R_0$ was -22.62 (Table II).

The exact composition of titanium oxides in the layer at the grain boundary was not investigated.

Conclusions

Exposure of titanium thin films, at temperatures above 300°C, to argon atmospheres containing oxygen results in the formation of titanium oxides at grain

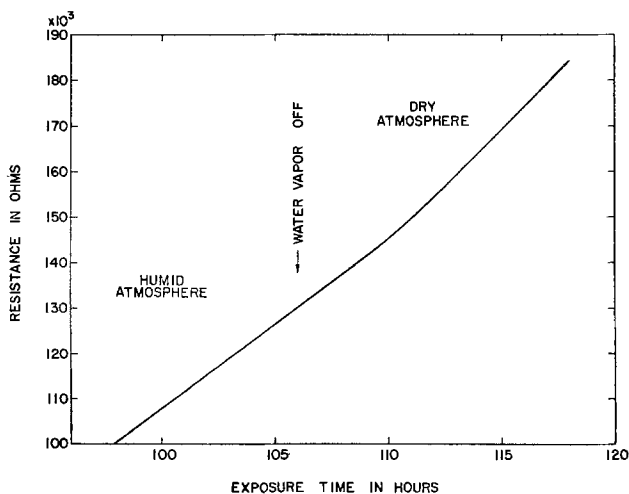


Fig. 7. Specimen No. 12 was tested at 365°C in highly oxidizing atmosphere with water vapor pressure 200 Torr. After 106 hr of exposure the supply of water vapor was cut off from the atmosphere.

boundaries and the formation of films which exhibit a negative temperature coefficient of resistance. Oxidation of specimens exposed to high purity argon proceeds very slowly, but addition of water vapor to the high purity argon accelerates the oxidation process. It is proposed that at temperatures above 300°C, oxidation of titanium along grain boundaries occurs, causing an increase in resistivity. After a nearly linear increase in resistivity an acceleration in the rate of resistance occurs due to the formation of a network of semiconductive titanium oxides along grain boundaries. This creates a tunneling effect with an exponential dependence of resistance on both temperature and also on the width of the titanium oxides layer, which in turn depends linearly on the time of exposure. It is assumed here that the rate-determining process is the formation of titanium oxides.

At temperatures below 300°C, oxidation does not penetrate through the whole cross section of the specimens. The resistance initially was increasing but became, after some time of exposure, constant. However, the film as a whole does not change to a semiconductor with a negative temperature coefficient.

Acknowledgments

The author would like to thank P. A. Turner and R. J. H. Voorhoeve for their numerous discussions and

suggestions. The author would like also to acknowledge the help of Miss L. V. Haller, L. J. Heilos, A. W. Koenig, and H. Kleest in preparation of the specimens and K. L. Tai and D. Bacon for help in setting up the equipment. This work was performed while the author was associated with Bell Laboratories, Murray Hill, New Jersey.

Manuscript submitted July 11, 1974; revised manuscript received July 2, 1975.

Any discussion of this paper will appear in a Discussion Section to be published in the June 1976 JOURNAL. All discussions for the June 1976 Discussion Section should be submitted by Feb. 1, 1976.

Publication costs of this article were partially assisted by Fairleigh Dickinson University.

REFERENCES

1. A. Klopfer and W. Ernrick, *Vakuum-Tech.*, **8**, 162 (1959).
2. H. H. Uhlig, *Corrosion Sci.*, **7**, 325 (1967).
3. M. J. Mindel and S. R. Pollack, *Acta Met.*, **17**, 1441 (1969).
4. T. Smith, *Surface Sci.*, **38**, 292 (1973).
5. A. E. Feuersanger, *Proc. IEEE*, **52**, 1463 (1964).
6. I. Giaever, "Tunneling Phenomena in Solids," p. 19, Plenum Press, New York (1967).

An Anodic Process for Forming Planar Interconnection Metallization for Multilevel LSI

G. C. Schwartz and V. Platter

IBM System Products Division, East Fishkill Facility, Hopewell Junction, New York 12533

ABSTRACT

Anodic processing has been extended to aluminum alloy metallurgy. A procedure for forming completely planar interconnection metallization has been described. The factors which control line profile and the electrical isolation of closely spaced conductors have been investigated, and the conclusions used to define the anodizing conditions. The planar structure and the increased cross-sectional area of the conductor which result from the use of this process make increased circuit density possible.

Large scale integration (LSI), with its high circuit density, has made the use of multilevel interconnection metallization a necessity. Conventionally, the interconnection pattern is formed by subtractive etching; the insulating layer may be either CVD SiO₂ or sputtered SiO₂. The resultant two-level structure is shown schematically in Fig. 1(a); the topography worsens as the number of levels increases. Photolithography becomes more difficult and the consequences of inadequate coverage of the metal edges by the insulator result in serious reliability problems. Tapering the metal edge has been suggested for improved coverage (1), but this is done at the expense of

Key words: multilevel metallization, planar metallization, large scale integrated circuits, anodic oxidation, aluminum alloy metallurgy.

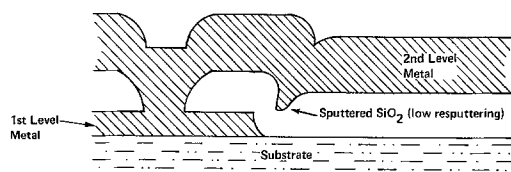


Fig. 1(a). Two level metal structure formed by conventional processing.

metal cross-sectional area which becomes increasingly important as the width of the conductor is decreased to increase circuit density. It is possible to compensate for the reduction of metal cross-sectional area by increasing initial line widths, but this decreases the possible circuit density. The SiO₂ can be deposited under high resputtering conditions which eliminates cusping (2), thus improving edge coverage, but this requires long sputtering runs. However, neither of these measures eliminates the unwieldy topography due to the etched metal. Earlier workers (3, 4) have shown that it is possible to eliminate subtractive etching for aluminum interconnection metallization systems; by anodic conversion of the unwanted metal to an insulating film of aluminum oxide, a substantial reduction in step height has been achieved, as indicated in Fig. 1(b).

This paper describes a process by which a completely planar structure can be made. Since the interconnec-

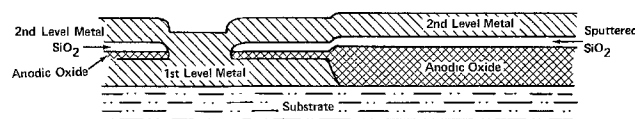


Fig. 1(b). Two level metal structure formed by anodic processing

tion metallurgy is not necessarily pure aluminum (copper may be added to aluminum to improve its electromigration resistance and small amounts of silicon are added to prevent junction penetration) we have extended the application of anodic planarization to aluminum alloys.

Anodization of Aluminum Alloys

The addition of copper and silicon to aluminum alters the anodizing process and the properties of the anodic oxide. For example, the anodizing efficiency decreases as the concentration of the alloying element increases (5).

Copper dissolves in the electrolytes used to form both barrier layer and porous anodic oxides. Consequently, it is not possible to form an impervious barrier layer on an aluminum-copper (AlCu) film. And it is not unexpected that the porous anodic oxide formed from an AlCu film contains voids superimposed upon the fine, fairly regular pore structure; this is seen in the scanning electron micrographs in Fig. 2(a) and (b). Therefore a composite structure is used for anodic planarization of aluminum alloy metallurgy: the bulk of the metal is the appropriate alloy, the top layer is pure aluminum. We refer to such a film as Al/AlCu or Al/AlCuSi. The porous anodic oxide formed from an Al/AlCu film is shown in Fig. 2(c).

Approaches to Planarization

In order to compensate for the expansion which usually accompanies the conversion to anodic oxide, one approach might be to etch a suitable fraction of the metal to be anodized before anodization; another, to dissolve some of the anodic oxide formed. The former requires precise control of the etching process

and leads, in any event, to undesirable surface roughness; the latter is impossible, since the time it takes to dissolve a porous anodic oxide film is independent of its thickness (6).

It is known that the thickness of porous anodic oxide formed from a given thickness of aluminum decreases with decreasing current density and increasing temperature; this is true for AlCu as well.¹ Therefore it is possible to find anodizing conditions such that the thickness of the oxide formed will be equal to the thickness of the metal converted. However, it will be shown that arbitrary adjustment of current density and elevated temperatures are not satisfactory means for realizing a planar structure.

The anodization of aluminum is 100% efficient under all conditions; therefore it is simple to anodize a precisely controlled thickness of aluminum. There is an etchant for anodic oxide which does not attack aluminum; it contains 35 ml/liter 85% H₃PO₄ and 20 g/liter CrO₃ and is used at 80°C and is referred to in this paper as P-C etch. Thus it is possible to reduce the aluminum thickness, in the areas in which complete conversion to aluminum oxide will occur ultimately, with precision and without surface roughening. It can be seen that the choice of this method of planarization makes the use of the composite film (Al/AlCu or Al/AlCuSi) necessary.

Experimental

The anodization cell is shown in Fig. 3. It provides electrical contact to the bare silicon side of the wafer; i.e., the bias is applied to the metal through the contact holes to silicon. The electrolyte is confined to the metallized top surface; the area exposed to the electro-

¹ Unpublished results; this laboratory.

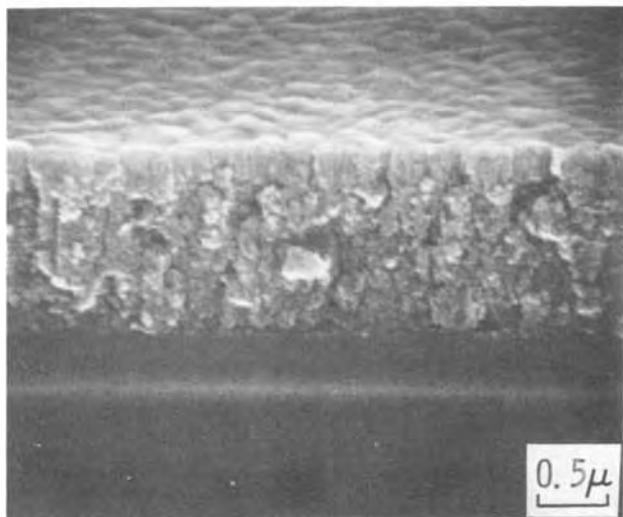
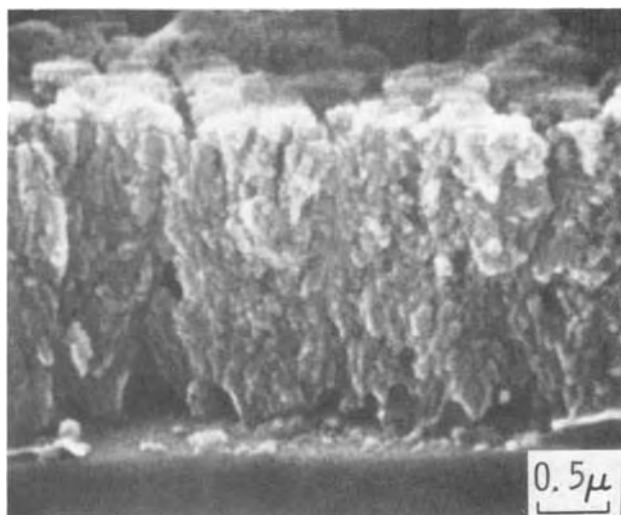
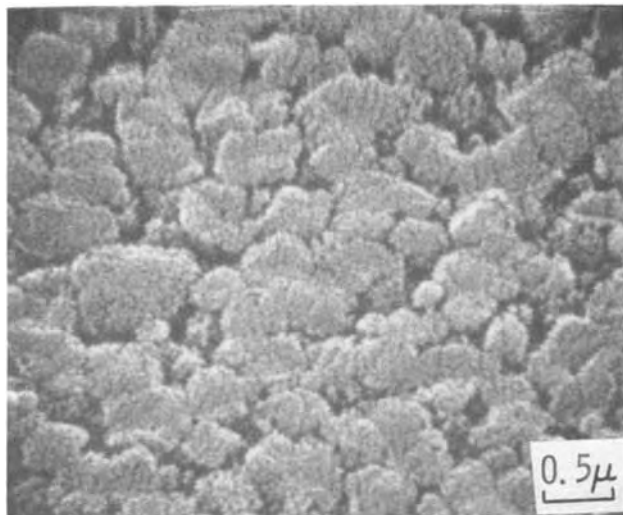
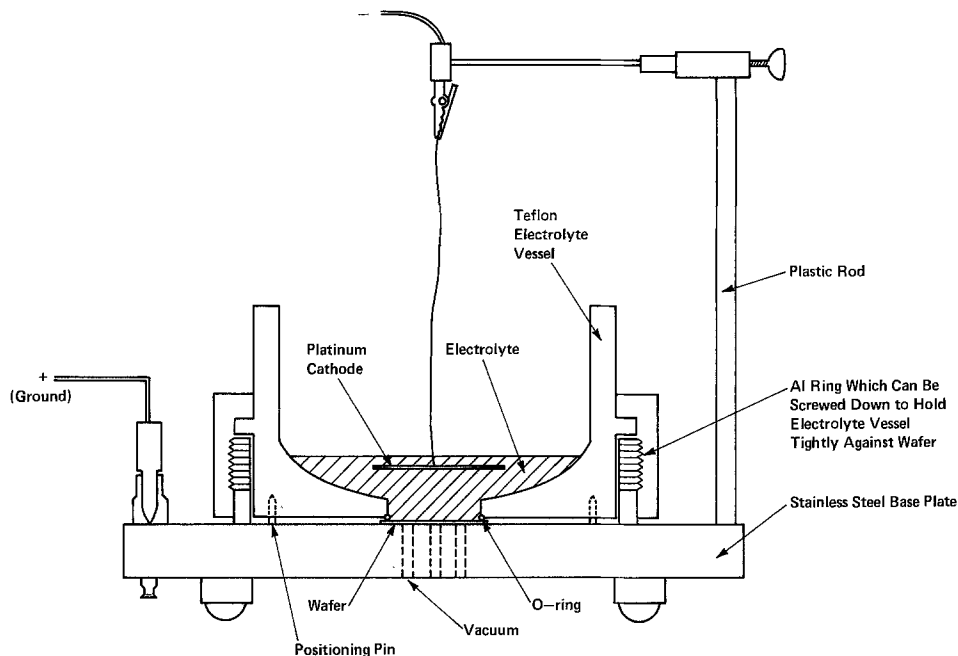
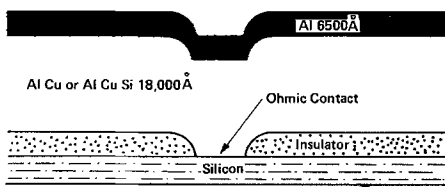


Fig. 2. Scanning electron micrographs of porous anodic oxides: (a, above left) AlCu: top view. (b, above right) AlCu: fractured edge. (c, left) Al/AlCu: fractured edge.

Fig. 3. Schematic cross section of the anodization cell.



1. For a final land thickness of $\sim 2\mu$, the starting structure is:



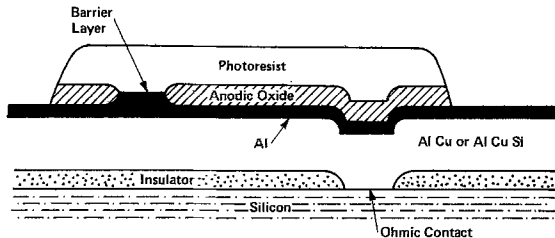
2. Anodize Al surface in oxalic acid to form $\sim 200 \text{ \AA}$ of anodic oxide
3. Using standard photoresist processing, form a mask which leaves free of resist those areas in which the interlevel metal connections will be made (via areas).



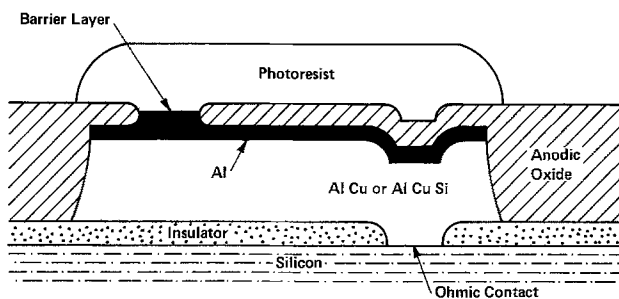
4. Form barrier layer in exposed via areas
5. Remove resist in dry asher
6. Anodize wafer in oxalic acid to a predetermined anodic oxide thickness



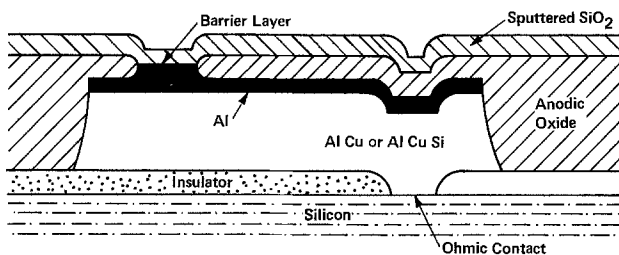
7. Using photoresist, define and protect the regions which will become the interconnection metallurgy. Remove exposed anodic oxide in P-C etch.



8. Anodize the exposed metal to completion



9. Remove photoresist in dry asher
10. Anneal wafer
11. Deposit sputtered SiO_2



12. Open via holes; deposit next level of metal

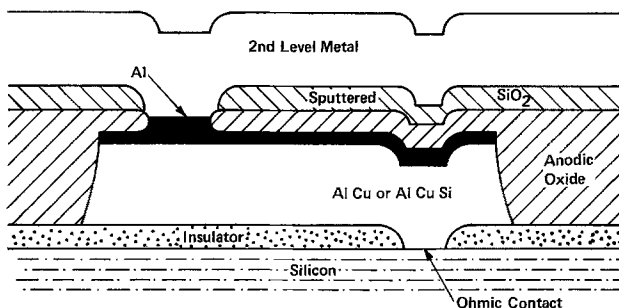


Fig. 4. Anodic planarization process

lyte is defined by the O-ring which seals the electrolyte vessel against the wafer. The cathode is a platinum disk slightly larger in diameter than the O-ring. The electrolyte is neither stirred nor kept at constant tem-

perature; the temperature rise during the longest anodization is only 0.5°C . The electrolyte for porous oxide formation is an 8% solution of oxalic acid in water. Oxalic acid is used because it is compatible

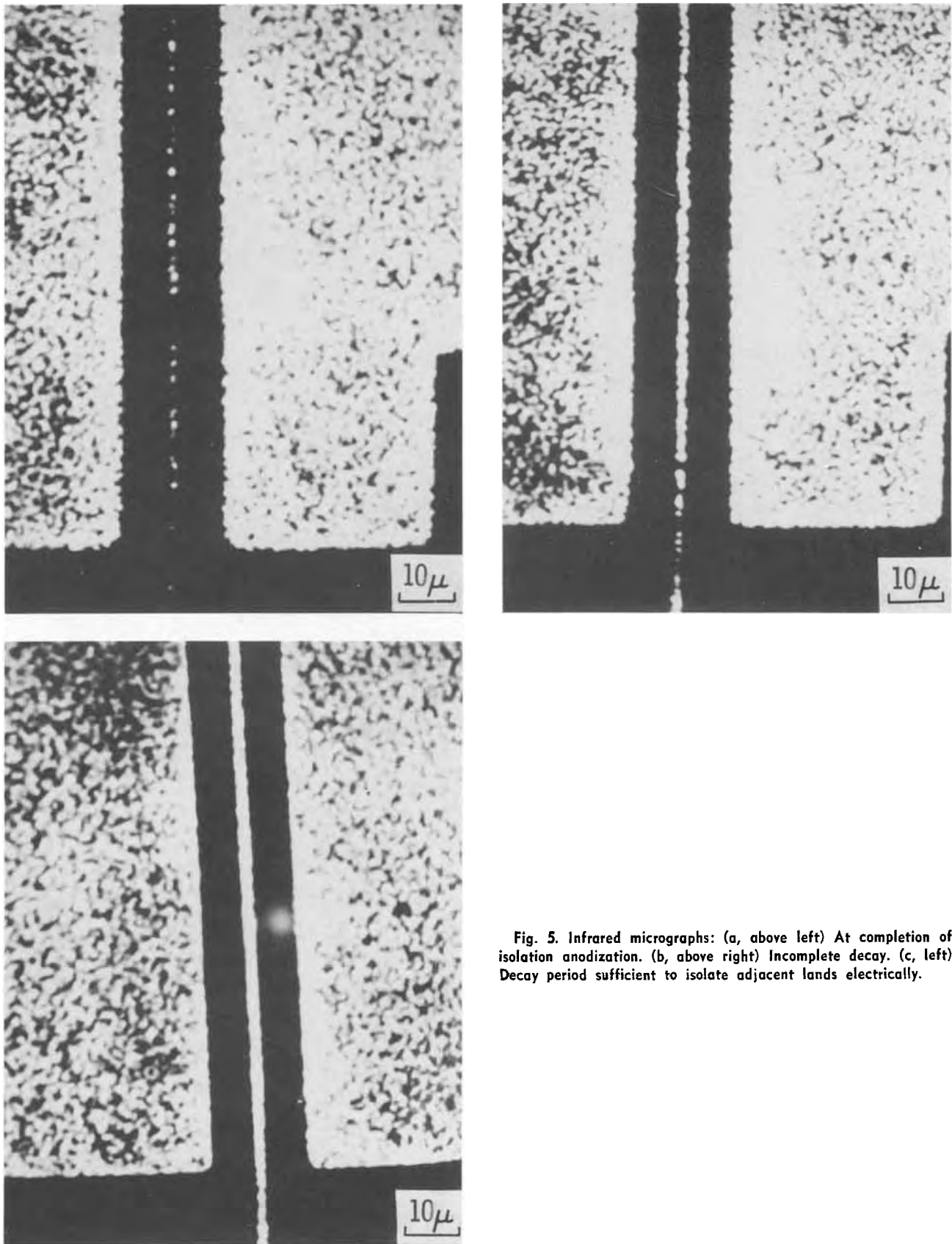


Fig. 5. Infrared micrographs: (a, above left) At completion of isolation anodization. (b, above right) Incomplete decay. (c, left) Decay period sufficient to isolate adjacent lands electrically.

with photoresist and is decomposed when the anodized film is dried. Also, at the appropriate current density, the voltage is suitable for device fabrication. Barrier layer is formed in a 30% solution of ammonium borate in ethylene glycol.

A constant current power supply is used. When a two-current mode of anodization is used, there is a control circuit which automatically reduces the current from its initial value to a preset value after any

predetermined time. There is another control circuit for automatic control of decay time. At the completion of anodization, the rising voltage is sensed and when it reaches a predetermined value, that voltage is maintained, as the current decays, for a preset length of time. At the end of the decay period, the anodization is stopped automatically and a buzzer is sounded to summon the operator to empty the cell.

Current and voltage are recorded on a strip chart throughout the anodization.

Process Description

The process is outlined, with the aid of diagrams, in Fig. 4.

Discussion.—To preserve the greatest possible thickness of metal in the areas in which the interlevel metal connection is to be made (*i.e.*, the via areas) such regions should not be anodized (4). However, we have observed that the adhesion of photoresist to an aluminum surface during anodization is too weak to prevent appreciable lateral anodization during porous oxide formation. Although the anodization time in step 6 is relatively short, the via diameter is quite small ($\sim 5\mu$). Therefore a thin barrier layer is formed in the via areas to prevent subsequent porous oxide growth (3).

The barrier layer is formed at low current density (1 mA/cm^2 is a typical value) and when the desired voltage is reached, the anodization is stopped since both high current density and prolonged maintenance of the film at constant voltage are reported to result in pore formation (7).

The initial anodization (step 2) improves resist adhesion during barrier layer growth but it is not essential.²

An alternate approach could be the formation of a somewhat thicker layer in step 2 (protection against porous oxide growth requires this), the use of the reverse mask in step 3, followed directly by step 6. While this eliminates one resist removal step, it does

² When barrier layer is grown within a resist mask to about 100V, the resist breaks down; providing a porous oxide underlay for the resist does not increase the voltage to which a barrier layer can be grown before resist breakdown.



Fig. 6. Scanning electron micrographs showing the effect of current decay. The anodic oxide has been removed in P-C etch to reveal the residual metal: (a, top left) Short decay: top view. (b, top right) Short decay: fractured edge. (c, bottom left) Long decay: top view. (d, bottom right) Long decay: fractured edge.

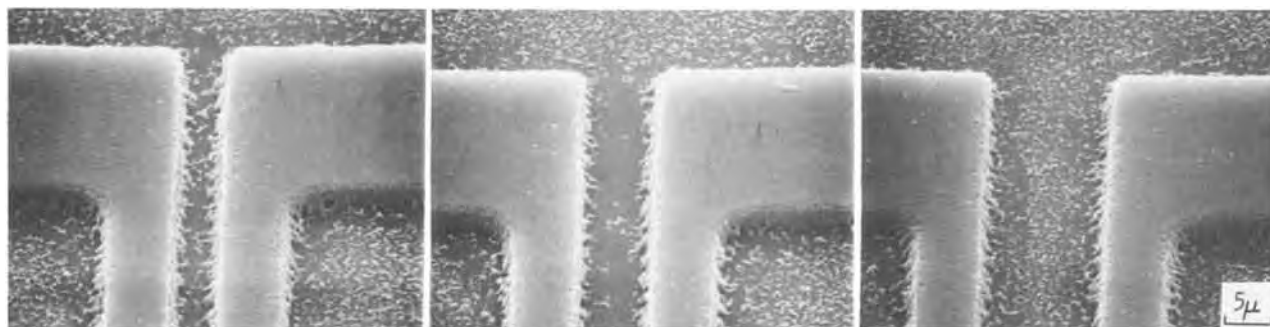


Fig. 7. Scanning electron micrograph showing the effect of line-to-line spacing on a single wafer; P-C etched

not eliminate a masking operation. More important, the structure of the via hole is better when the procedure given in Fig. 6 is followed, particularly if the mask used in step 3 protects an area slightly larger than that of the final via hole.

Photoresist is stripped in a dry asher because the usual chemical strippers (e.g., J-100) etch anodic oxide; there is also the risk of possible binding of some of the components of such strippers to the walls of the pores.

Step 6 is carried out at constant current since a known quantity of charge must be passed to anodize a given amount of aluminum. The area of aluminum to be anodized can be determined by measuring the rate of voltage rise during barrier layer formation at constant current since the rate is approximately proportional to current density (8). The current density used must be such that the voltage does not approach the final voltage in barrier layer formation in step 4 to insure that no further oxide growth occurs in the via areas.

When the bulk of the metal has been converted to anodic oxide, i.e., when the anodization voltage rises abruptly to its limiting value and the current decreases exponentially, closely spaced conductors are still shorted. The shorts are due to residual metal which clings to the edges of the lands and forms bridges between them. Only by continuing to supply current to the lands via the contact holes to the silicon can this residual metal be converted to an insulator. The interval during which this continually decreasing current is supplied to the lands we call the decay period. Residual metal within the isolation oxide, at some distance from the lands, is unaffected during the decay period. It cannot be emphasized too strongly that such residual particles do not form a conducting layer, they are merely a cosmetic defect. Indeed, after a sufficient

decay period, leakage between adjacent conductors is small. A test structure was designed so that it could be isolated from silicon after completion of the anodic processing. It consists of pairs of lines 9×10^{-2} cm long separated by 3, 6, and 15μ spaces. For the pairs which are 3μ apart, the leakage current at 10V is 10-20 picoA. One hundred chips, each containing one isolated test structure, were mounted on headers for stress testing under bias at 85°C and 85% R.H. The pairs of stripes separated by 6μ were biased at 20V. After 2000 hr, when the test was terminated, there had been no increase in leakage current on any chip, some of which had not been protected by sputtered SiO_2 .

During decay, the voltage must be limited to about 50V. R. C. Turnbull³ has shown that if the voltage is excessive, ridges are formed at the interface between the conducting stripe and the anodic oxide which abuts it.

The decay process may be monitored: the anodization is stopped, the wafer removed from the cell, rinsed, dried, then examined in the infrared microscope; if further decay is required the wafer is replaced in the cell and the bias reapplied. Infrared micrographs taken during a decay period are shown in Fig. 5. We have found that ordinary optical micrographs can be misleading, particularly when the anodic oxide is very thick.

The conversion of the residual metal clinging to the lands as well as the nonconversion of totally isolated residue during decay is seen very clearly in the scanning electron micrograph in Fig. 6. For examination in the scanning electron microscope, the anodic oxide must be removed in P-C etch to make the metal particles visible. In Fig. 7 scanning electron micrographs illustrate the efficacy of a fixed decay period in isolating pairs of lands with different spac-

³ R. C. Turnbull, this laboratory, private communication.

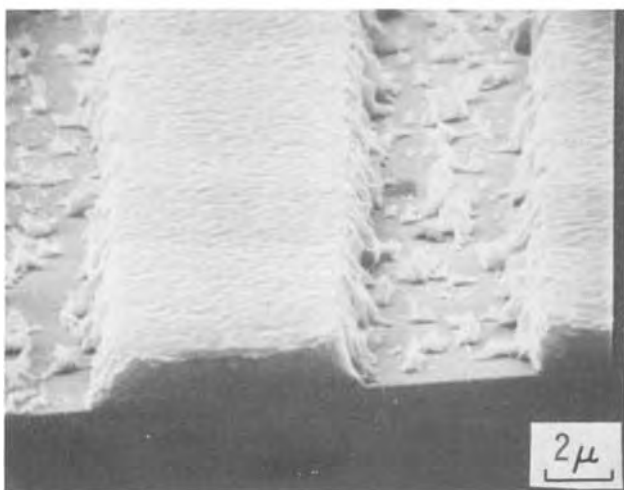
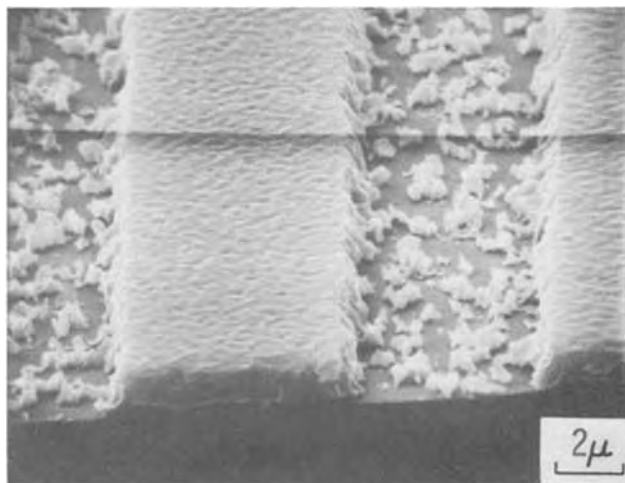
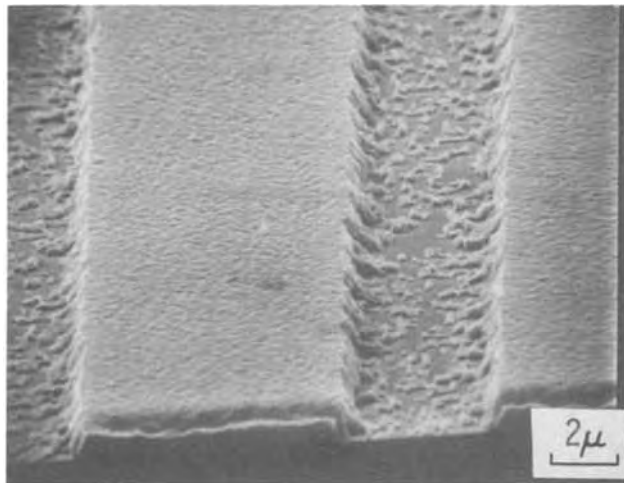


Fig. 8. Scanning electron micrograph showing the effect of metal thickness; P-C etched: (a, above left) 9000Å Al; isolation anodization 2.25 mA/cm^2 ; decay period 3.5 min. (b, above right) 12,900Å Al; isolation anodization 2.25 mA/cm^2 ; decay period 21 min. (c, left) 18,500Å Al; isolation anodization 2.25 mA/cm^2 ; decay period 61 min.

ings, while Fig. 8 shows that the thickness of metal which must be converted to isolation anodic oxide is an important factor in determining the length of the decay period.

Now it is clear why using elevated temperatures to reduce the ratio of anodic oxide formed to metal converted is not practical. The decay period has been shown to be necessary. If during the decay period the temperature were elevated, pore widening and pore shortening would proceed at an accelerated rate which is undesirable.

The current density during the isolation anodization influences the size and shape of the residual metal particles, which in turn determines the decay time required to achieve good electrical isolation, and thus ultimately determines the line profile and what may be called the anodization bias. The effect of current density is illustrated in Fig. 9. We have obtained the best line profile when two-thirds of the film is ano-

dized at 3.5 mA/cm^2 and the rest at 1 mA/cm^2 . The reduction in cross-sectional area after anodic processing can be substantially less than after standard chemical etching; using the two current density mode described above, the taper of the lines is about 70° . A rough estimate of the increase in cross-sectional area which results from this decreased taper can be made, assuming that a land is a trapezoid in cross section. For 5μ wide lands, 1μ thick, there is a 16% increase over conventionally etched lines (45°) and a 22% increase over deliberately tapered lines (30°). For 2.5μ wide lines, 1μ thick, there is a 42% increase over conventionally etched lines, while it is not possible to form usable lands with an exaggerated taper. Yet because the lands are encapsulated in the anodic oxide and the entire structure is planar, there are none of the edge coverage problems associated with insulating lands with such steep sides. In Fig. 10, the reduction in cross-sectional area is illustrated. In this case the proc-

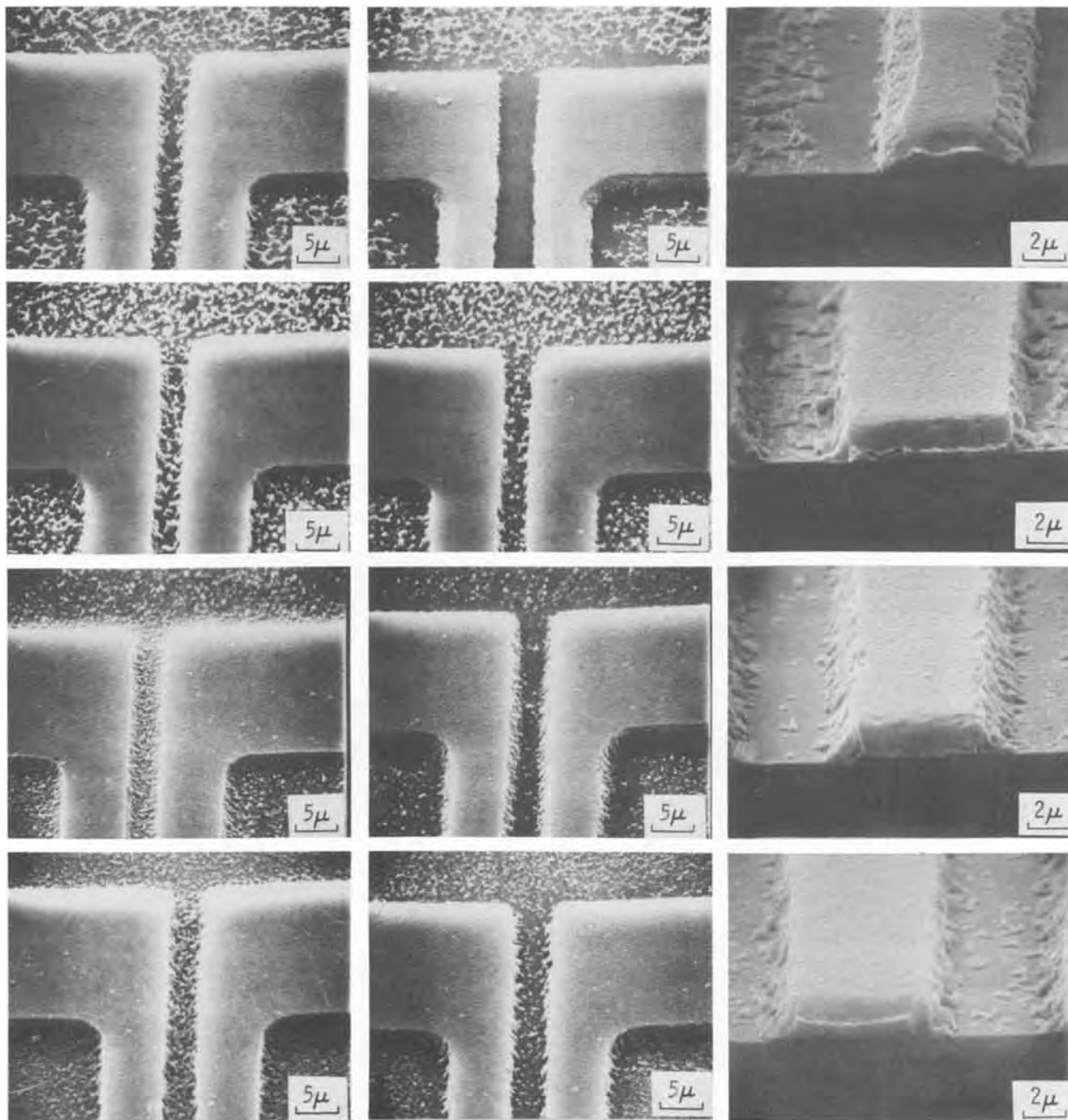


Fig. 9. Scanning electron micrographs showing the effect of current density during isolation anodization; P-C etched. (a, top row) Isolation anodization 1 mA/cm^2 . (b, second row) Isolation anodization 2.25 mA/cm^2 . (c, third row) Isolation anodization 3.5 mA/cm^2 . (d, bottom row) Two current density isolation anodization; i.e., two-thirds of film at 3.5 mA/cm^2 , finish at 1 mA/cm^2 .

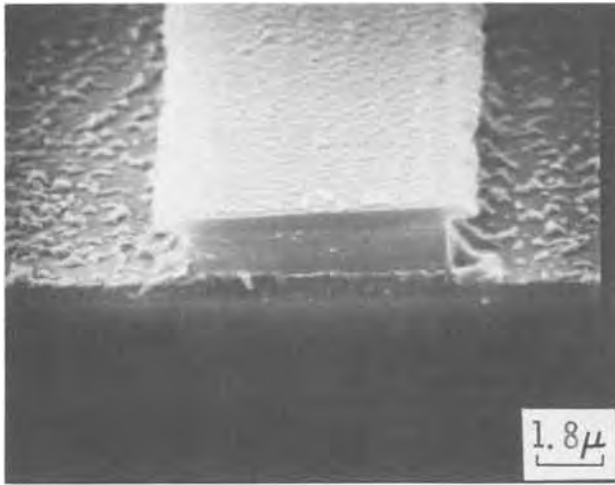


Fig. 10. Scanning electron micrograph showing the reduction of metal cross-sectional area after anodic processing. Metal 1.8μ Al/AlCu; isolation anodization $3.5 \text{ mA/cm}^2 \rightarrow 1 \text{ mA/cm}^2$; decay period 30 min; mask dimension defined by glass overlay; P-C etched.

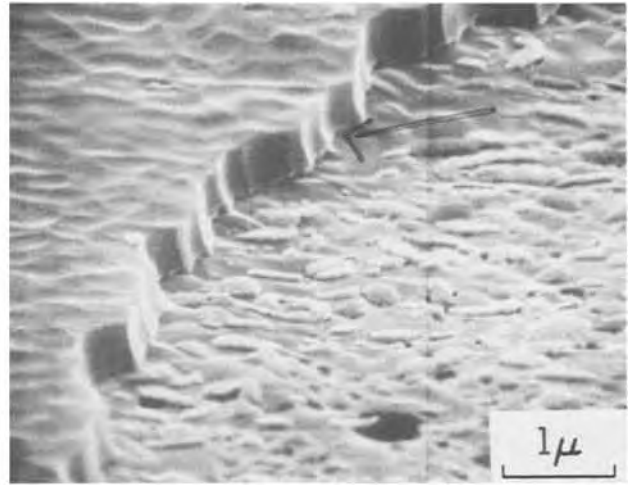


Fig. 11. Scanning electron micrograph of via hole

ess was altered somewhat⁴ to make it possible to see the final line profile together with the initial mask size which is replicated in the layer of SiO_2 at the top of the land.

Because of the importance of current density in determining line profile, it is apparent that arbitrary adjustment of current density is not a good approach to planarization.

Upon completion of the anodic processing, the wafer is stripped of photoresist and heated for about half an hour at 450°C to drive off the water and decompose the oxalic acid which is bound to the pores.

Anodic oxide is not suitable for interlevel insulation; it has a high dielectric constant and porous anodic oxide does not provide protection of a lower level during anodization of the next level.⁵ An additional dielectric layer (sputtered SiO_2) must therefore be deposited. Because of the planarity of the metallization structure, there are no edge coverage requirements; the thickness of the SiO_2 is determined only by the interlevel capacitance requirements and the need to insure a low defect level. The presence of the underlying anodic oxide reduces the hazard of pinholes that may be present in the thinner SiO_2 . Because the SiO_2 can be thinner than that required for conventional processing, via holes are easier to etch and the spacing between neighboring holes can be reduced. A typical via hole, etched through the SiO_2 and the barrier layer, is shown in Fig. 11.

The degree of planarity which has been achieved is illustrated in Fig. 12 which shows a scanning electron micrograph of a cross section of a land and the adjacent isolation anodic oxide. Figure 13(a) is a Talystep trace of such a structure. Figure 13(b) shows the Talystep trace of a planar structure which has a ridge between the land and the oxide because (as mentioned earlier) the voltage during decay was too high.

We have observed that the pattern definition (edges, line widths, and spacings) is superior when anodic

⁴The process used to produce this sample is as follows: A very thin layer of SiO_2 is sputtered on the surface of the aluminum. Using standard photoresist processing, the SiO_2 in the regions which are to become the interconnection pattern is protected. The unprotected SiO_2 is etched. Since the SiO_2 is very thin, there is little undercutting and the SiO_2 which remains approximates the dimensions of the mask which defines the interconnection pattern. The anodic processing is performed as usual; i.e., the initial anodization and P-C etch to compensate for the expansion and the isolation anodization and decay. While this variation eliminates some of the steps in the usual process, it involves an extra vacuum step. Under most circumstances the usual procedure is preferable.

⁵It is true that if the upper level were anodized at a voltage considerably lower than that used to anodize the layer beneath, the lower interconnection pattern would not be converted to oxide. However, it has been shown that the current density (and hence, voltage) cannot be changed in an arbitrary fashion if control of line profile is required.

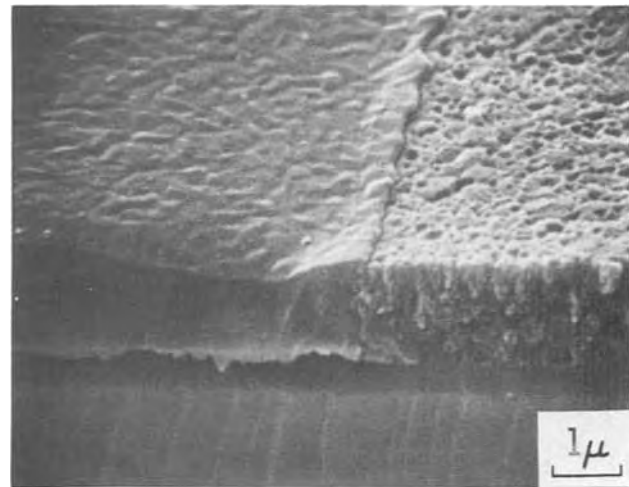


Fig. 12. Scanning electron micrograph on an anodically formed metal land with the adjacent anodic oxide in place.

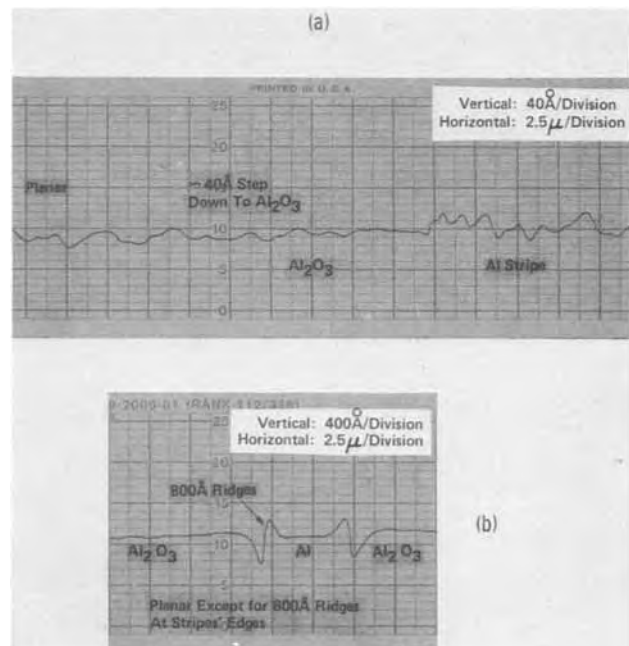


Fig. 13. Talystep traces: (a) Structure formed by the anodic planarization process. (b) Effect of excessive voltage during decay period.

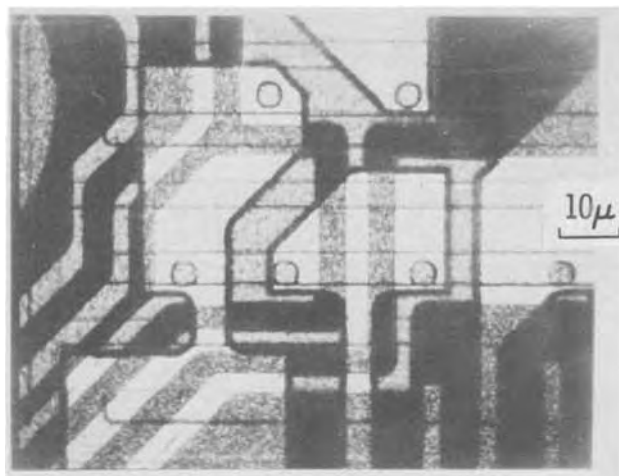


Fig. 14. Optical micrograph showing an enlarged section of a two-level device.

processing is substituted for conventional processing, using the same mask.

The electrical characteristics of both FET and bipolar transistors made by conventional and anodic processing are the same. A two-level device, made using anodic processing is shown in Fig. 14.

Summary

An anodic planarization process which is applicable to aluminum alloy metallurgy has been described. While anodic processing is more complex than conventional subtractive etching, the results justify the use of this technique. It has been shown that a completely planar structure is produced and the advantages of a planar structure have been discussed. The factors which affect the line profile have been discussed and illustrated; it has been shown that, with the proper choice of anodizing conditions, the cross-

sectional area of a conductor formed by this technique can be substantially greater than that formed by conventional subtractive etching. Therefore increased circuit density is possible without loss of performance or reliability. The factors which affect electrical isolation have also been discussed and low leakage levels have been obtained. Stress test results show that the residual aluminum is truly a cosmetic defect and is not a reliability hazard. Improved pattern definition is still another dividend of anodic processing.

Acknowledgment

The authors would like to thank F. Ordonez for the excellent scanning electron micrographs.

Manuscript submitted March 5, 1975; revised manuscript received June 25, 1975. This was Paper 3 presented at the San Francisco, California, Meeting of the Society, May 12-17, 1974.

Any discussion of this paper will appear in a Discussion Section to be published in the June 1976 JOURNAL. All discussions for the June 1976 Discussion Section should be submitted by Feb. 1, 1976.

Publication costs of this article were partially assisted by IBM Corporation.

REFERENCES

1. C. J. Santoro and D. L. Tolliver, *This Journal*, **118**, 66C (1971).
2. J. S. Logan, F. S. Maddocks, and P. D. Davidse, *IBM J. Res. Develop.*, **14**, 182 (1970).
3. H. Tsunemitsu and H. Shiba, *NEC Res. Develop.*, April 1972, p. 74.
4. W. R. McMahon, IEEE International Electron Devices Meeting, October 1970 (Abstract No. 7.1).
5. J. Hérenguel and P. Lelong, *Metal Finishing J.*, January 1958, p. 20.
6. M. Nagayama and K. Tamura, *Electrochim. Acta*, **12**, 1097 (1967).
7. J. S. L. Leach and P. Neufeld, *Corrosion Sci.*, **9**, 413 (1969).
8. L. Young, "Anodic Oxide Films," Academic Press, London (1961).

Electron Penetration and Power Dissipation in Thin Films of $Gd_2O_3:Eu$

J. S. Prener*

General Electric Company, Corporate Research and Development, Schenectady, New York 12301

ABSTRACT

The cathodoluminescent brightness as a function of electron energy was measured for thin films of $Gd_2O_3:Eu$. Proper account is taken of the power dissipation of the electron beam in the thin Al layers deposited on top of the phosphor films. These Al films were necessary to prevent charging during the measurements. From an analysis of the data we derive the power dissipation of the electron beam in the $Gd_2O_3:Eu$. We find that the results on power dissipation are in reasonably good agreement with theoretical calculations appearing in the literature.

There have been a number of investigations which have dealt with the problem of electron penetration in solids and the power dissipation of an electron beam as studied by cathodoluminescence. Feldman (1), using thin phosphor films, measured the brightness as a function of electron energy up to 20 keV and determined the electron range-energy relationship for a number of materials. He did not, however, utilize his data in determining the power dissipation of the electrons in

the phosphor films. Ehrenberg and King (2) studied optically the luminescence glow profiles produced by a narrow beam of electrons in a number of transparent phosphor crystals. They deduced electron ranges as well as power dissipation from their measurements. The accurate determination of contours of equal brightness from photomicrographs of the cathodoluminescent glow for high Z (average atomic number) materials is extremely difficult for primary electron energies below 30 keV since the total electron penetration depths are only a few microns. Bieringer (3)

* Electrochemical Society Active Member.

Key words: cathodoluminescence, electron range, electron energy.

again measured the brightness of thin phosphor films as a function of primary electron energies up to 30 keV. He compared his results with a model based on the density of energy dissipation per electron obtained by differentiation of the Thomson-Widdington law and the statistical loss in the number of electrons penetrating to a given depth in the solid. More recently Kingsley and Prener (4) showed that the luminescence efficiency as a function of electron beam power for powder ZnS:Cu phosphors having nonluminescent ZnS coatings of various thicknesses on each particle was compatible with Makhov's (5) formulation for the power dissipation of an electron beam in a solid. The analysis was, however, complicated by the necessity for making geometrical corrections since the phosphor layer was composed of small particles rather than being a continuous film of uniform thickness. A shortcoming of Makhov's formulation was his neglect of backscattered electrons. This can lead to significant errors in calculations of power dissipation for materials of high atomic number (6).

In this paper we analyze the relationship between the cathodoluminescence brightness and the energy of the primary electrons for thin phosphor films. We determine the power dissipation of the electron beam and show that the results are in agreement with theoretical calculations appearing in the literature. As far as we know no such comparison between theory and experimental data for thin phosphor films has been made previously. We measured the cathodoluminescent brightness of thin films of the $Gd_2O_3:Eu$ phosphor as a function of primary electron energies up to 20 keV. Proper account was taken of the power dissipation in the thin Al layers deposited on top of the phosphor films. These Al layers are necessary to prevent charging of the films during the measurements. The results were analyzed and shown to agree reasonably well with theoretical calculations of power dissipation of electrons in solids as given by Spencer (7) and by Kanaya and Okayama (8). $Gd_2O_3:Eu$ is a good choice of material for such studies. The diffusion of generated electrons and holes to the surface of the phosphor and their subsequent radiationless recombination lead to the phenomena of "dead-voltage" and diffusion layer thickness [see, for example, Gergeley (9)]. This greatly complicates the analysis of brightness-voltage data as we shall see later. The dead-voltage of $Gd_2O_3:Eu$ has been found to be about 0.5 kV which is quite small compared to many other phosphors (10). One can estimate from this a diffusion layer thickness of about 0.01μ which is much smaller than the thickness of our phosphor films and could be neglected in the analysis.

Preparation of $Gd_2O_3:Eu$ Phosphor Films by Spinning

The films were deposited on clear, fused quartz (CFQ) substrates which, after cleaning in boiling nitric acid, were prepared for film deposition by immersion for several minutes in a boiling 10% (V/V) solution of K-200 potassium silicate (du Pont) followed by a thorough rinse in distilled water. The silicate treatment was necessary since good continuous films could not otherwise be produced. A typical solution used for spinning consisted of 10g of $Gd_{0.95}Eu_{0.05}Cl_3 \cdot 6H_2O$, 5.7 ml H_2O , and 12.8 ml isopropanol. A few drops of the solution were placed on the substrate and allowed to spread on the surface. The substrate was then spun in a horizontal position, typically at 3000 rpm for about 30 sec until it was dry. It was then annealed for about 5 min in air. Depending on the annealing temperature $GdOCl:Eu$, $Gd_2O_3:Eu$, or a mixture of the two phases was obtained. Films of increasing thickness were obtained by repeating, a number of times, the spin-anneal cycle. With some care films of uniform thickness over an area of $\frac{1}{2} \times \frac{1}{2}$ in. could be produced as indicated by the interference colors. The films appeared to be thicker near the edges and for the purpose of measurement the outer edges of the films were dissolved in hot 1-1 H_2SO_4 leaving only the uniformly thick cen-

tral area. The film thickness was determined either by using a Sloan "Dektak" surface profile measuring instrument or chemically. For chemical analysis the oxide films of known area were dissolved in dilute HCl and the total rare earth content determined colorimetrically using sodium alizarinsulfonate (11). The thickness was calculated assuming bulk density.

Film Properties and Cathode-Ray Excitation

In Fig. 1 is shown the thickness of the $Gd_2O_3:Eu$ films as a function of the number of spin-anneal cycles. It is seen that about 0.07μ of film is deposited in each cycle. The emission spectra under 254 nm excitation for films annealed for a few minutes in air at various temperatures are shown in Fig. 2. At $200^\circ C$ only a weak broad-structured emission is seen indicating poor crystallinity of the film. At $300^\circ-500^\circ C$ the emission spectrum is characteristic of $GdOCl:Eu$; at $600^\circ C$ both $GdOCl:Eu$ and $Gd_2O_3:Eu$ spectra appear; and at $700^\circ C$ only the oxide spectrum remains. The formation of $GdOCl$ as an intermediate in the thermal decomposition of hydrated $GdCl_3$ in air has been well established (12, 13). X-ray diffraction indicated that the films annealed at $700^\circ C$ and higher consisted of polycrystalline Gd_2O_3 .

$Gd_2O_3:Eu$ films of various thicknesses deposited on polished CFQ substrates and overcoated with 800Å of Al were placed in a demountable cathode-ray tube and the radiated power measured as a function of electron energy (at constant current). The results are shown in Fig. 3. The lower portions of the curves are straight lines intercepting the abscissa near 2.5 keV. At some critical energy, depending on the film thickness, the curves deviate downward from a straight line.

Power Dissipation of an Electron Beam

The incident electron beam power density P is equal to the incident current density j multiplied by the in-

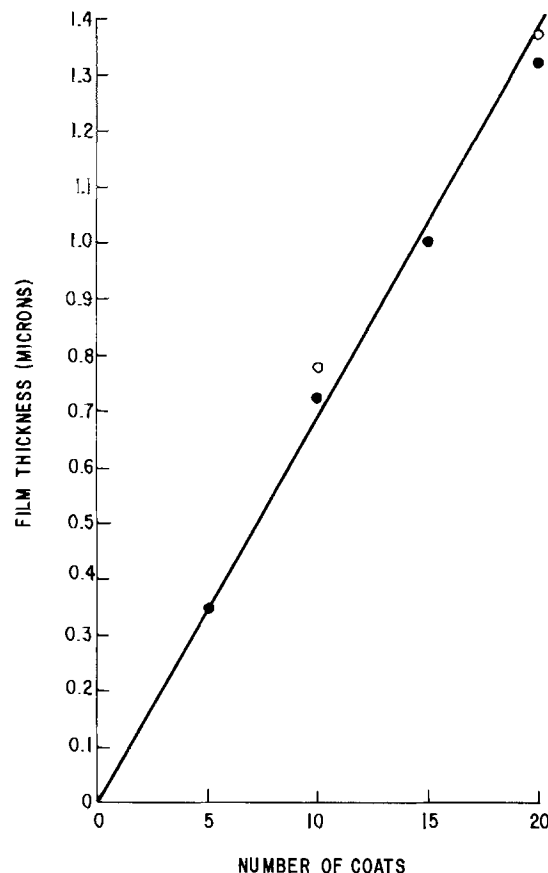


Fig. 1. Gd_2O_3 film thickness as a function of the number of spin-anneal cycles. ●, Thickness using Sloan "Dektak" surface profile measuring instrument; ○, thickness determined by chemical analysis.

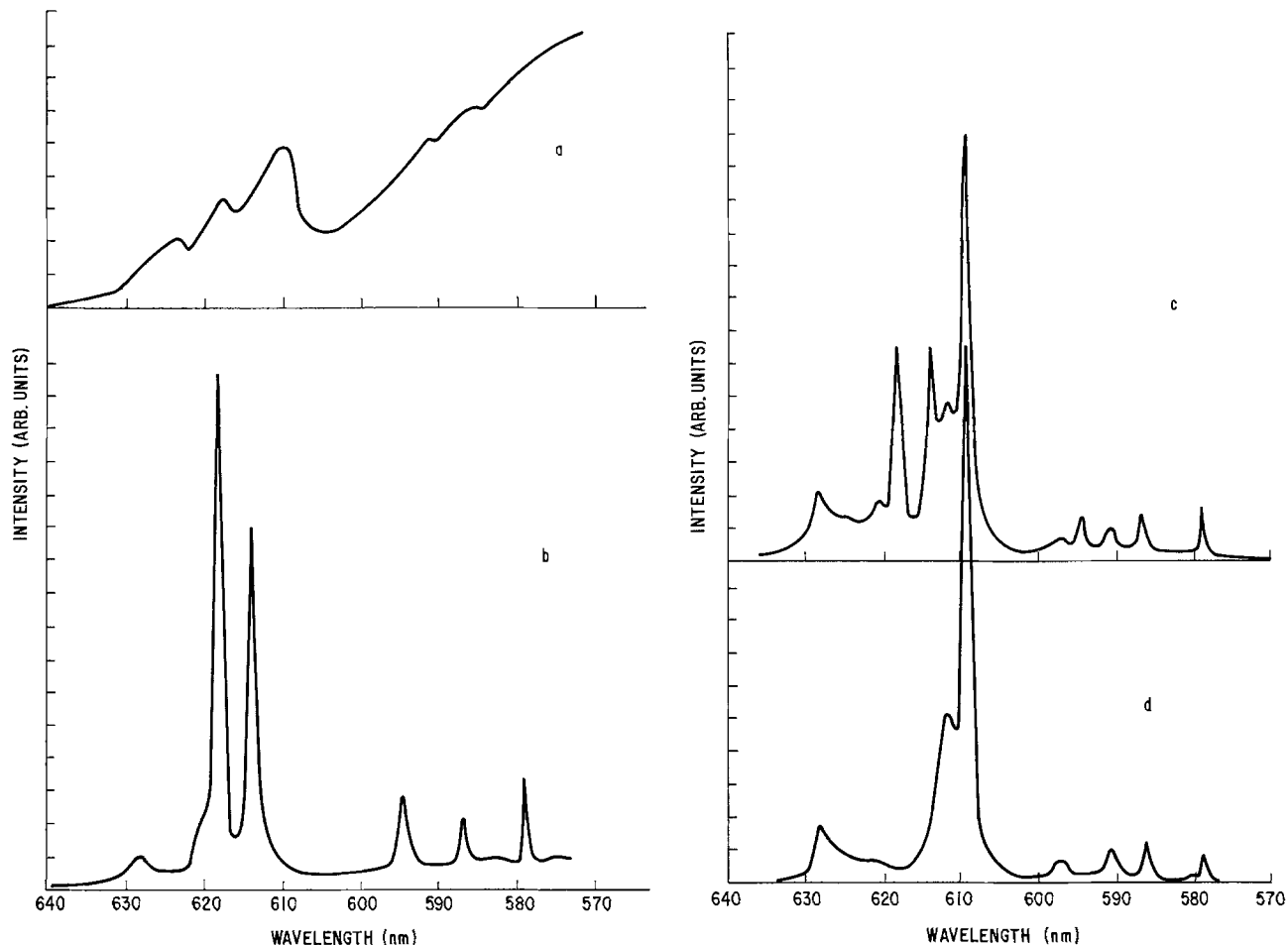


Fig. 2. Emission spectra of $Gd_2O_3:Eu$ films under 254 nm excitation. These were annealed at various temperatures. (a) 200°C; (b) 300°, 400°, 500°C; (c) 600°C; (d) 700°C.

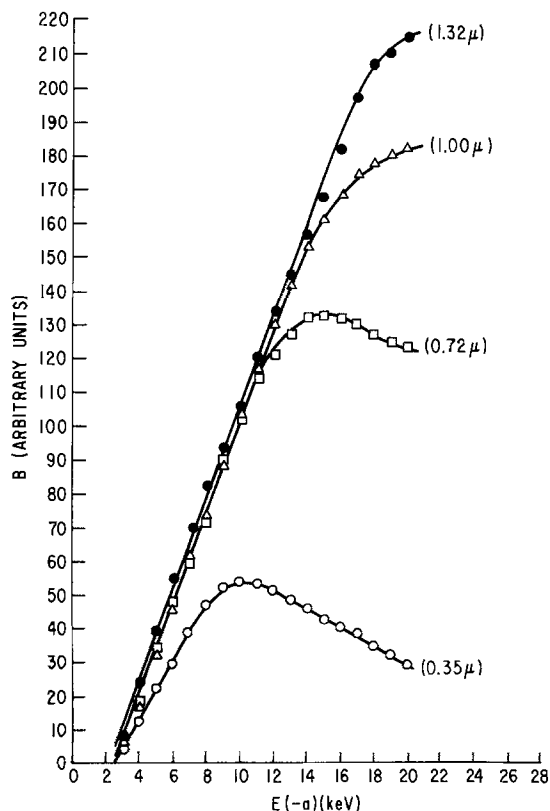


Fig. 3. Radiated power of $Gd_2O_3:Eu$ films overcoated with 800 Å of Al as a function of the electron beam energy. The thicknesses, s , of the films are marked on the curves.

cident electron energy E . If $P(x)$ is the mean power density at a depth x in the solid, then the power density lost by the electron beam in traversing a distance x in the solid is

$$\Delta P = P - P(x) - P_b \quad [1]$$

where P_b is the power density contained in the back-scattered electrons. The electrons in the solid will be distributed in space, energy, and direction of travel. If R is the mean distance in the solid where the electrons have lost all their initial kinetic energy, then the principle of scaling (2, 14) states that the shapes of the various distributions for a given distance x depend only on x/R , that is, on the fraction of the initial energy which has been lost. The mean values of the electron energy and current density in the solid are, of course, derivable from the various distributions. The quantity R is termed the electron range and there are in the literature a number of different definitions of electron range (15). However, from the scaling principle they should all be proportional to each other. Generally, over not too large an energy span, the range, however defined, has been found to depend on the initial electron energy through the equation

$$R = AE^n \quad [2]$$

where the constants A and n are material parameters (5, 15). Because of the proportionality of the various ranges they should differ only in the factor A .

It has, therefore, been common practice to express the mean values of the electron energy and current density at a depth x in the solid terms of a reduced distance y (3, 5, 8)

$$y = x/R = x/AE^n \quad [3]$$

The value of the reduced distance will vary depending

on the range definition used, but the quantity Δy should be independent of the choice of range. For our purposes we need not be concerned with any particular definition of range, but assume, as others have done, that at a distance x in the solid, the mean energy and current density and hence the mean power density, all of which are functions of E and x , can be written as functions of y . We write

$$\Delta P/P = g(y) \quad [4]$$

$$P^{-1}(d\Delta P/dx) = (dg/dy)/AE^n \quad [5]$$

The shape of the important functions $g(y)$ and dg/dy are shown schematically in Fig. 4b, c. [See, for example, Fig. 10 and 11 of Ref. (8).] Values of y_m and y_c are marked. At $y = y_c$, $dg/dy = 0$. The function $g(y)$ is a constant, $g_c = 1 - P_b/P$ for all $y > y_c$. The quantity y_m is some arbitrarily chosen value of $y < y_c$ and is discussed later.

Power Dissipation in Al Film

As indicated above, in order to prevent charging of our phosphor films they were coated, by evaporation, with 800Å of Al. The geometry of our Al-phosphor film layer is shown in Fig. 4a. The incident monoenergetic electrons have an energy $E(-a)$ and the current density of the beam is $j(-a)$. The electron beam suffers a power loss in passing through the Al layer and the transmitted electrons will be distributed in energy. For a thin, 800Å Al film ($\rho a = 22 \mu\text{g}/\text{cm}^2$) at incident energies larger than that required to penetrate the film (i.e., larger than 2.5 keV) the energy distribution of the transmitted electrons becomes sharply peaked so that the mean and most probable energies of the transmitted electrons differ very little from each other (15). Therefore, the electrons transmitted through the Al layer and impinging upon the phosphor layer may still be considered as being essentially monoenergetic with energy $E(0)$ where $E(0) < E(-a)$. At incident energies comparable to those required to penetrate the Al layer, $E(0)$ is the mean energy of the transmitted electrons.

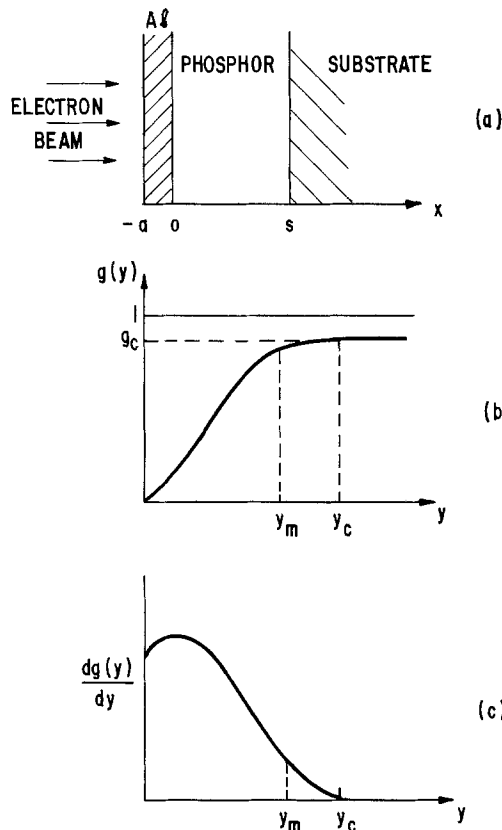


Fig. 4. (a) Geometry of Al-phosphor film; (b) shape of the function $g(y)$ (see text); (c) shape of the function dg/dy (see text).

Table I. Values of the mean energy, the transmission coefficient η_T , and the power density, for unit initial current density, of electrons transmitted through 800Å of Al

$E(-a)$ (keV)	$E(0)$ (keV)	$\eta_T(0)$	$P(0)$
1	0.01	1.0×10^{-14}	1.0×10^{-10}
2	0.44	0.043	0.02
3	1.33	0.448	0.60
4	2.36	0.737	1.74
5	3.42	0.865	2.96
6	4.50	0.925	4.16
7	5.58	0.954	5.32
8	6.64	0.971	6.45
9	7.70	0.980	7.56
10	8.76	0.986	8.64
11	9.81	0.990	9.71
12	10.85	0.992	10.76
13	11.89	0.994	11.82
14	12.93	0.995	12.87
15	13.96	0.996	13.90
16	14.99	0.997	14.95
17	16.02	0.998	15.99
18	17.05	0.998	17.02
19	18.07	0.998	18.03
20	19.09	0.999	19.07

We consider first the energy $E(0)$ and current density $j(0)$ of electrons transmitted through the 800Å Al film. For Al, Makhov (5) finds that the mean energy of the transmitted electrons is given by

$$E(0)/E(-a) = \exp(-0.9 y_a^{0.9}) \quad [6]$$

When the incident energy $E(-a)$ is measured in keV and the Al film thickness, a , is in angstroms, y_a is given by

$$y_a = a/1.41 \times 10^2 E(-a)^{1.68} \quad [7]$$

Values of $E(0)$ are given in Table I for values of $E(-a)$ from 1 to 20 keV with $a = 800\text{Å}$. Makhov also gives for the transmitted current density $j(0)$

$$j(0)/j(-a) = \eta_T = \exp(-y_a^2) \quad [8]$$

Values of η_T are also given in Table I. Finally, the mean power density of the transmitted beam $P(0) = j(0)E(0)$ for unit initial current density is tabulated in the last column of the table. We recall that for values of $E(-a) > 2.5$ keV, the transmitted electrons (i.e., those incident on the phosphor surface) are close to being monoenergetic.

We can replot, in Fig. 5, the experimental curves of Fig. 3, using as the abscissa not $E(-a)$ but $P(0)$. The lower portions of the curves are straight lines whose slopes and intercepts were determined by a least squares analysis (correlation coefficients were 0.999). The intercepts on the abscissa all lie close to the origin indicating a very small diffusion layer thickness for $\text{Gd}_2\text{O}_3:\text{Eu}$ (9). This is in accord with the results of Ludwig and Kingsley (10) who find a dead-voltage of about 0.5 keV for $\text{Gd}_2\text{O}_3:\text{Eu}$. As indicated earlier in this paper we will neglect the effect of the diffusion layers at the phosphor surfaces. At some critical value of $P(0) = P_c(0)$, depending on the thickness, the curves deviate downward from straight lines.

Analysis of Radiated Power: Beam Power Data

If we consider a phosphor film of thickness s , and if a fraction $\epsilon[x, E(0)]$ of the beam power density dissipated in a thickness dx at depth x generates fluorescence, then the total power density emitted as fluorescence radiation is given by

$$B = \int_0^s \epsilon[x, E(0)] (d\Delta P/dx) dx = P(0) \int_0^{y_s} \epsilon[y, E(0)] g'(y) dy \quad [9]$$

where $y_s = s/AE(0)^n$. We assume no diffusion of the excitation in the phosphor and take $\epsilon[y, E(0)]$ to be a constant ϵ_0 . Gergeley (9) treated the problem by including the diffusion of generated secondaries and radiationless recombination at the surface. In order to

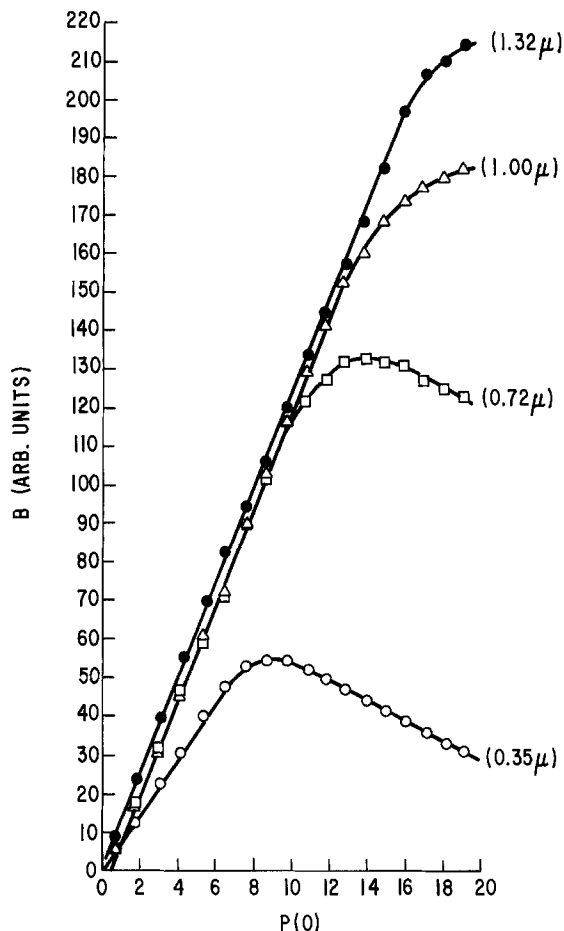


Fig. 5. Radiated power of $Gd_2O_3:Eu$ films overcoated with 800\AA of Al as a function of the electron beam power at the phosphor surface.

get a closed form solution to the diffusion equation he assumed a rather simple form for $g(y)$. He let $g(y) = y$ for $0 \leq y \leq 1$ and $g(y) = 1$ for $y \geq 1$. This is, of course, an unreasonable shape for the function and cannot generate the correct shape of $B - P(0)$ curves for $P(0) > P_c(0)$.

With ϵ a constant we get

$$B = P(0) \epsilon_0 g(y_s) \quad [10]$$

For values of $E(0) < (s/Ay_c)^{1/n}$ (i.e., $y_s > y_c$) Eq. [10] yields a linear relation between B and $P(0)$

$$B_1 = P(0) \epsilon_0 g_c = \text{constant} \cdot P(0) \quad [11]$$

The critical energy $E_c(0)$ is given by the condition that

$$y_s = y_c \\ E_c(0) = (s/Ay_c)^{1/n} \quad [12]$$

For values of $y_s < y_c$, the curves will deviate downward from a straight line. Since preparative conditions and the geometry used in measuring the radiated power might vary from sample to sample (for example, the thinnest film has a slope smaller than the other three samples), it is better to take the ratio of the radiated power values for $P(0) > P_c(0)$ and divide them by the ones obtained by extrapolation of the linear portion of the curves. We get

$$B/B_1 = g(y_s)/g_c \quad [13]$$

Range-Energy Relation

The values of $E_c(0)$ obtained from the observed values of $P_c(0)$ for the different film thickness enable us to determine the exponent n in the range-energy relation. Having this value, we can compare our experimental value of B/B_1 with the $g(y)$ functions derived from theory.

Table II. Values of $E_m(0)$ for $Gd_2O_3:Eu$ films of various thicknesses

s, μ	$\rho s, \text{mg/cm}^2$	$E_m(0), \text{keV}$
0.35	0.26	8.1
0.72	0.53	11.9
1.00	0.74	15.3
1.32	0.98	19.0

Since B/B_1 , particularly for the thicker samples, has a very small slope near $P_c(0)$, it is difficult to determine with precision the values of $P_c(0)$. We can, however, readily find the value of $P(0)$ at which B/B_1 has some arbitrary value less than unity. We have chosen the point at which $B/B_1 = 0.9$ and the corresponding values of electron energy and beam power we denote by $E_m(0)$ and $P_m(0)$.

The quantity y_m is defined by

$$y_m = s/AE_m(0)^n \quad [14]$$

so that

$$\log s = n \log E_m(0) + \log(y_m A) \quad [15]$$

In Table II are tabulated the values of $E_m(0)$ obtained from the experimental curves of Fig. 5 and Table I.

In Fig. 6 we plot $\log \rho s$ against $\log E_m(0)$. The slope of the line as determined by a least squares fit (correlation coefficient 0.995) gives $n = 1.53$. With ρs in mg/cm^2 we find $\rho A y_m = 0.011$. The value of n agrees very well with the results of Cosslett and Thomas for the extrapolated range (15). They find $n = 1.5$ for a number of elements (Al, Cu, Ag, Au) in the range 5-15 keV. We note that only the product $\rho A y_m$ is obtained from the data, the value of y_m being determined by the particular definition of electron range.

We can also compare our data with those obtained by Ehrenberg and King (2) who, as already mentioned, observed microscopically the extent of the luminous zone in single crystals of various phosphors. Their data for CsI ($Z_{\text{avg}} = 54$) can be used for comparison. They define an ultimate range, U , as the total length of the luminous zone. In Table III are tabulated Ehrenberg and King's values of U after correction, as they suggest, for errors in the optical observations.

The length of the luminous zone at any given value of the electron energy $E(0)$ is the distance in the solid at which $dg/dy = 0$. This distance is given by

$$\rho x_c = \rho A y_c E(0)^{1.53} \quad [16]$$

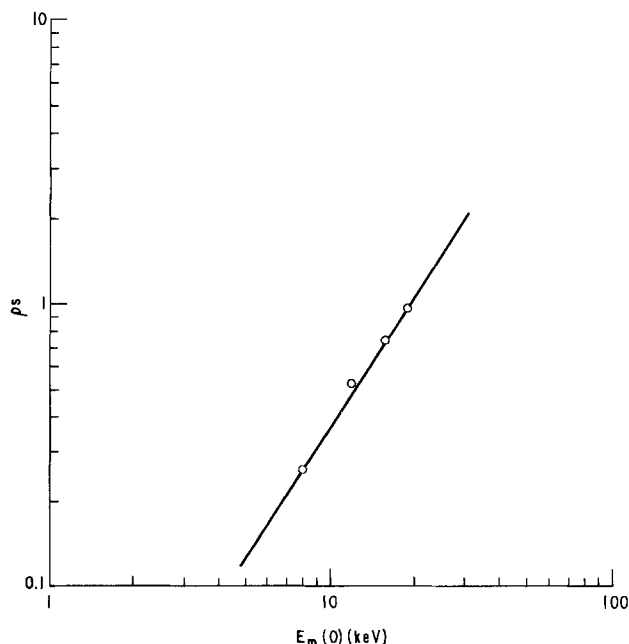


Fig. 6. $\log \rho s$ for the four $Gd_2O_3:Eu$ films plotted as a function of $\log E_m(0)$.

Table III. Comparison of various electron ranges

$E(0)$	ρU (mg/cm ²) ^(a) (CsI; $Z_{avg} = 54$)	ρx_c (mg/cm ²) (Gd ₂ O ₃ ; $Z_{avg} = 57$)	ρR_{max} (mg/cm ²) ^(b) (Ag; $Z = 47$)
5	0.48	0.18	0.15
10	0.72	0.50	0.42
15	1.06	0.95	0.85
20	1.48	1.47	—
25	1.98	2.07	—

^(a) Ref. (2).
^(b) Ref. (15).

From our data the quantity ρAy_c can be determined from

$$\rho Ay_c = \rho s / E_c(0)^{1.53} \quad [17]$$

Using the value of $E_c(0) = 6.5$ keV estimated from the data for our thinnest sample, we get $\rho Ay_c = 0.015$. Tabulated in Table III are our calculated values of the length of the luminous zone given by

$$\rho x_c = 0.015 E(0)^{1.53} \quad [18]$$

It can be seen that the results are in close agreement except at the lowest energies. Since our values of x_c should correspond to the maximum range R_{max} , of Cosslett and Thomas (15), we also compare in Table III the two ranges. R_{max} was measured for Ag ($Z = 47$) but the authors reported very little Z dependence in R_{max} . Again the agreement is seen to be reasonably good.

Electron Power Dissipation in Gd₂O₃:Eu

In accord with Eq. [13] when B/B_1 is plotted against $\rho s/E(0)^{1.53}$ ($= \rho Ay_s$) for the four Gd₂O₃ films, all the data points should fall on a common curve, this curve being the function

$$g(y)/g_c = [\Delta P/P(0)]/[1 - P_b/P(0)] \quad [19]$$

plotted against ρAy . Such a plot of the data is given in Fig. 7 and it is seen that the data do tend to cluster

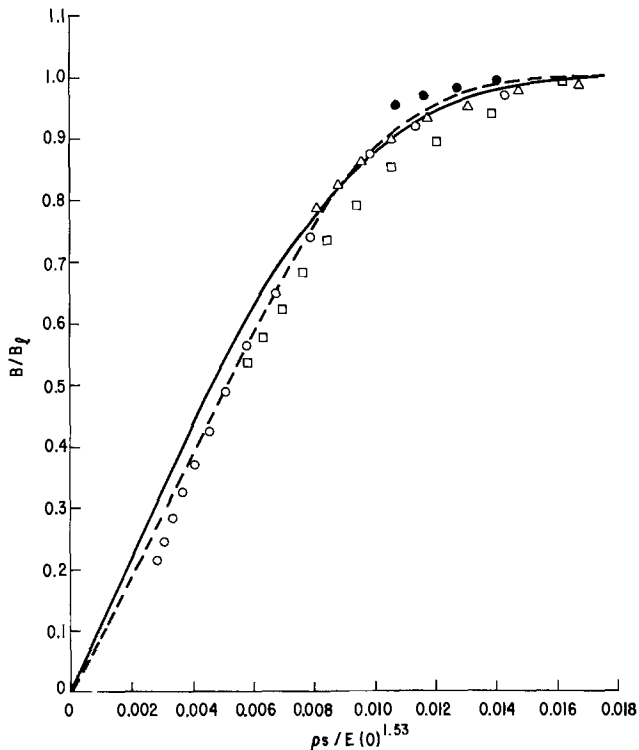


Fig. 7. Observed values of B/B_1 plotted against $\rho s/E(0)^{1.53}$ for the four Gd₂O₃:Eu films. Values of ρs in mg/cm² are: \circ , 0.26; \square , 0.53; \triangle , 0.74; \bullet , 0.98. The calculated curves $g(y)/g_c$ are from the data of Spencer (7) (—) and Kanaya and Okayama (8) (---).

about a single curve. It would have been advantageous to take data for the thicker films at electron energies, $E(-a)$, greater than 20 keV, but we were limited by the capabilities of our demountable cathode-ray tube.

We can compare our experimentally determined power dissipation with the theoretical calculations of Spencer (7) and of Kanaya and Okayama (8). In our notation, Spencer's tabulated values of $J(y)$ are related to the power loss by

$$J(y) = [d(\Delta P/dx)]/(dE/dr)_{E(0)} \quad [20]$$

where $(dE/dr)_{E(0)}$ is the stopping power for electrons of energy $E(0)$ and r is the distance measured along the path of the electron. From Eq. [5] and [20]

$$dg/dy = J(y)R[E(0)](dE/dr)_{E(0)}/P(0) \quad [21]$$

Upon integration we get

$$g(y)/g_c = \int_0^y J(y)dy / \int_0^\infty J(y)dy \quad [22]$$

Since the average atomic number of Gd₂O₃ is 57, we have used Spencer's computed values of $J(y)$ for Sn ($Z = 50$) at the lowest electron energy for which calculations were made: $E(0) = 50$ keV. This, of course, requires a rather large extrapolation in energy, but as Spencer points out, the shapes of the $J(y)$ curves change little with electron energy. This is in accord with the assumption that $g(y)$ is independent of energy. In order to compare the experimental data with theory, we must evaluate the constant ρA in the range-energy relation. In the previous section we found that $\rho Ay_m = 0.011$ where y_m is the particular value of y for which $g(y)/g_c = 0.9$. From Spencer's data we find that $y_m = 0.34$ so that $\rho A = 0.032$. Spencer's calculated curve of $g(y)/g_c$ vs. ρAy is shown by the solid line in Fig. 7. The agreement between theory and experiment is seen to be reasonably good.

Kanaya and Okayama, using the quasi elastic scattering theory of Lindhard *et al.* (16) applied to a semi-infinite medium, give an equation for evaluating $g(y)$ for any Z (Eq. [22] of Ref. (8) where E_A/E_0 is our $g(y)$). From their calculations $y_m = 0.47$ and, therefore, $\rho A = 0.023$. The calculated curve of Kanaya and Okayama is given by the dashed line in Fig. 7. The fit to the experimental points is again seen to be reasonably good.

From the experimental values of B/B_1 we can also evaluate the electron beam power dissipation in Gd₂O₃ as a function of depth, ρx , for various initial energies $E(0)$. Since $\rho Ay = \rho x/E(0)^{1.53}$, we can from Fig. 7 determine values of B/B_1 for a given $E(0)$ at various values of ρx . Using the data for our thinnest sample we plot in Fig. 8 the values of $B/B_1 = [\Delta P/P(0)]/[1 - P_b/P(0)]$ as a function of ρx for electron energies, $E(0)$ of 5, 10, 15, and 20 keV. The arrows at the top of the figure mark the values of ρx for which $B/B_1 = 0.9$. These values agree very well with those read from Fig. 6.

Summary

We have shown that brightness-electron energy data for thin films of Gd₂O₃:Eu are in reasonably good agreement with theoretical calculations of the power dissipation of an electron beam in a solid. Account was taken of the power loss of the electron beam in the Al film deposited on top of the phosphor layer. Since the dead-voltage of Gd₂O₃:Eu is about 0.5 keV, the diffusion layer is much smaller than the phosphor thicknesses being studied and was neglected. This made the relationship between the measured phosphor brightness as a function of electron energy and the power dissipation of the electron beam (Eq. [13]) a particularly simple one.

Manuscript submitted April 16, 1975; revised manuscript received June 18, 1975.

Any discussion of this paper will appear in a Discussion Section to be published in the June 1976

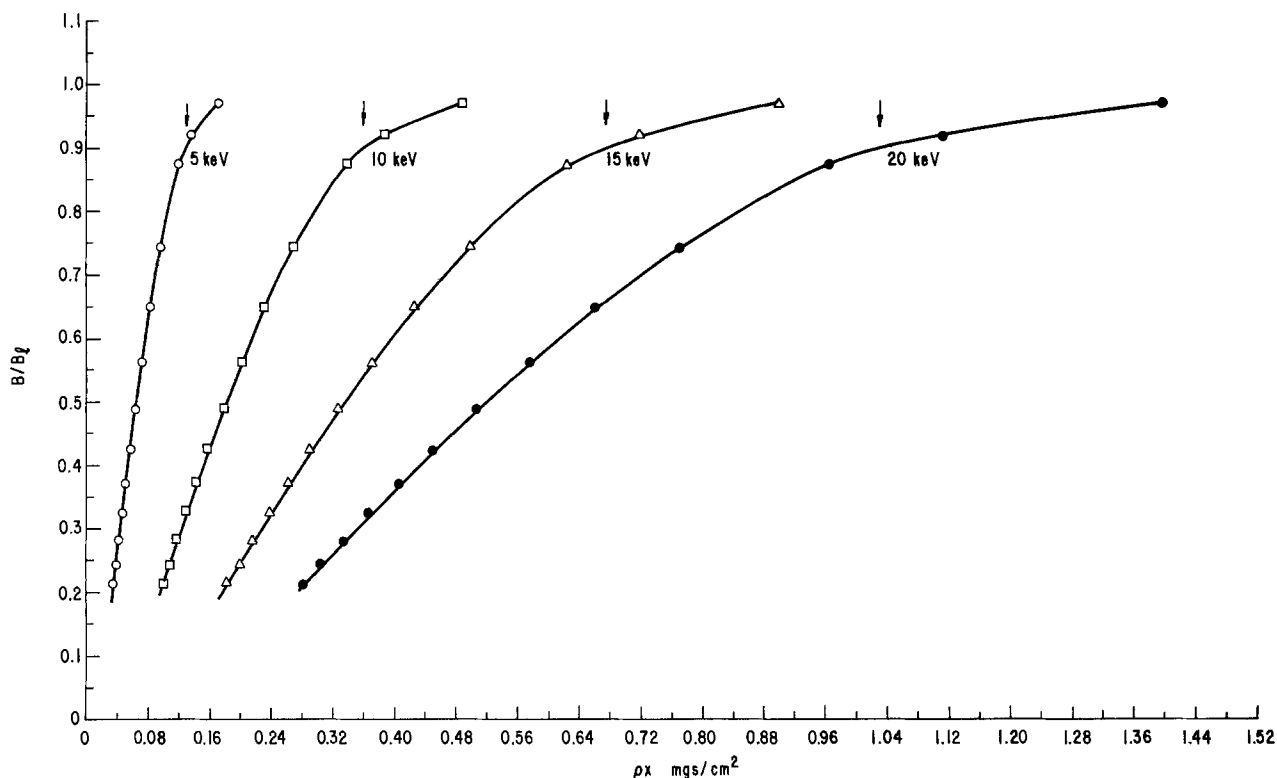


Fig. 8. Values of B/B_0 as a function of ρx for several values of the electron energy at the $Gd_2O_3:Eu$ phosphor surface. Values of $E(0)$ are: \circ , 5 keV; \square , 10 keV; \triangle , 15 keV; \bullet , 20 keV.

JOURNAL. All discussions for the June 1976 Discussion Section should be submitted by Feb. 1, 1976.

Publication costs of this article were partially assisted by General Electric Company.

REFERENCES

1. C. Feldman, *Phys. Rev.*, **117**, 455 (1960).
2. W. Ehrenberg and D. E. N. King, *Proc. Phys. Soc.*, **81**, 751 (1963).
3. R. J. Bieringer, *Phys. Rev.*, **142**, 550 (1966).
4. J. D. Kingsley and J. S. Prener, *J. Appl. Phys.*, **43**, 3073 (1972).
5. A. F. Makhov, *Soviet Physics Solid State*, **2**, 1934, 1942, 1945 (1960).
6. V. E. Cosslett and R. N. Thomas, *Brit. J. Appl. Phys.*, **16**, 779 (1965).
7. L. V. Spencer, *Nat. Bur. Std. Monograph 1*, National Bureau of Standards, Washington, D.C. (1959).
8. K. Kanaya and S. Okayama, *J. Phys. D: Appl. Phys.*, **5**, 43 (1972).
9. Gy. Gergeley, *J. Phys. Chem. Solids*, **17**, 112 (1960).
10. G. W. Ludwig and J. D. Kingsley, *This Journal*, **117**, 348 (1970).
11. E. B. Sandell, "Colorimetric Determination of Traces of Metals," p. 748, Interscience Publishers, Inc., New York (1959).
12. G. Haeseler and F. Matthes, *J. Less-Common Metals*, **9**, 133 (1965).
13. W. W. Wendlandt, *J. Inorg. Nucl. Chem.*, **5**, 18 (1957).
14. C. H. Blanchard, "Electron Physics," Nat. Bur. Std. Circular 527, p. 9, National Bureau of Standards, Washington, D. C. (1954).
15. V. E. Cosslett and R. N. Thomas, *Brit. J. Appl. Phys.*, **15**, 1283 (1964).
16. J. Lindhard, M. Scharff, and H. E. Schiott, *K. Danske Vidensk. Selskab., Mat.-Fys. Medd.*, **31**, 1 (1963).

Silicon Epitaxial Wafer with Abrupt Interface by Two-Step Epitaxial Growth Technique

T. Ishii, K. Takahashi, A. Kondo, and K. Shirahata

Mitsubishi Electric Corporation, Central Research Laboratories,
80 Nakano, Minamishimizu, Amagasaki, Hyogo 661, Japan

ABSTRACT

A new silicon epitaxial growth technique was developed to respond to the strong demand from higher frequency semiconductor devices. It includes a low temperature epitaxial growth technique by SiH_4 and a newly developed two-step epitaxial growth technique based upon a hydrodynamic analysis of crystal growth from vapor phase considering a stagnant gas layer. Autodoping and autodilution phenomena are both completely suppressed and a controlled abrupt impurity profile can be obtained between two regions of different doping level. Silicon Read Type IMPATT diodes made by this technique demonstrated a remarkable improvement of microwave characteristics over the ones made by the conventional technique, thus verifying the usefulness of this new technique.

A high quality silicon epitaxial wafer with an abrupt interface is required for high frequency, high efficiency, and high reliability operation of semiconductor devices. Such a wafer is especially required for high speed variable capacitors, bipolar IC's, high frequency transistors, and microwave diodes such as IMPATT diodes and PIN diodes. These devices are usually fabricated in a lightly doped epitaxial layer grown on a heavily doped substrate.

When the lightly doped epitaxial layer is formed on the heavily doped substrate, the so-called autodoping phenomenon occurs. It makes a graded impurity profile at the substrate-epitaxial layer interface. The presence of a region of graded impurity profile makes it difficult to design devices accurately because of the discrepancy between actual and apparent epitaxial layer thickness. It also increases an undesirable series and thermal resistance which results in the degradation of operation efficiency and device reliability. The restraint of the autodoping in an early stage of the epitaxial growth is therefore an important industrial problem.

Many papers have been published on this subject. The causes of the autodoping have so far been attributed as follows:

1. Solid-state diffusion of impurities: Impurities in the heavily doped substrate diffuse thermally into the lightly doped epitaxial layer (1).

2. Redeposition of vaporized impurities: Impurities vaporized from the substrate redeposit in the epitaxially growing layer at high concentration *via* gas phase (2, 3).

3. Etching by halides: Impurities etched off by halides and their halide by-products redeposit in the epitaxially growing layer *via* gas phase when silicon halides are used as source materials (4).

4. Acceleration of solid-state diffusion: The diffusion of impurities from the substrate into the epitaxial layer is accelerated by halides (5).

5. Contamination from the surroundings: Undesirable impurities vaporized from a heated susceptor, a

reactor tube, and so forth contaminate the epitaxial layer (6, 7).

6. Deviation from ideal, instantaneous injection of dopant gas at the steady-state composition.

Several techniques have been proposed to prevent the autodoping. They are:

1. Low temperature epitaxial growth: The silicon epitaxial growth is carried out at low temperature by use of silane (7, 8) or dichlorosilane (9, 10), by the high-low temperature cycle epitaxial growth method (11), or by the mole fraction coating epitaxial growth method (12).¹

2. Substrate sealing: The back surface of the substrate is sealed by highly pure polycrystalline silicon, silicon nitride, or silicon dioxide to suppress the vaporization of impurities (6, 7).

3. Susceptor sealing: The susceptor is sealed completely, usually by highly pure polycrystalline silicon to suppress the vaporization of undesirable contaminants (7).

4. Impurities of slow diffusion rate: Impurities of slow diffusion rate, such as antimony, are used as the substrate dopant to suppress a fast solid-state diffusion (3).

5. Silicon deposition without halides (7, 8).

These techniques are available to restrain the autodoping to some extent, but they are sometimes very troublesome industrially, and an essential solution has not so far been obtained. Low temperature epitaxial growth and accurate gas flow control are thought to be essential.

The widely used method for the silicon epitaxial growth is still the reduction of silicon halides, such as SiCl_4 or SiHCl_3 , by hydrogen. This method has merits of a high growth rate, easy handling, and low cost, but it has such demerits as a high growth temperature and an etching reaction by halides.

¹ The quality of an epitaxially grown layer is largely dependent on substrate conditions and it is more serious at low temperature. The mole fraction coating epitaxial method is a technique to obtain a good crystalline epitaxial layer grown at low temperature. It consists of an initial slight epitaxial growth from low mole fraction of a source gas (SiCl_4 , SiH_4 , etc.) in a carrier gas (H_2) and a succeeding normal epitaxial growth from higher mole fraction of source gas.

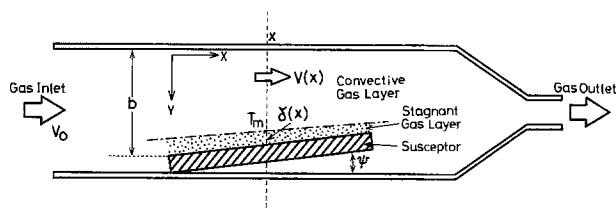


Fig. 1. Schematic cross section of the horizontal silicon epitaxial reactor (14).

Silane has become popular as a silicon source material in place of silicon halides because it does not have these disadvantages. The growth temperature is lowered to around 1000°C , even below 900°C (8, 13) from the common growth temperature of 1200°C in the case of silicon halides, and the etching reaction does not take place.

The gas flow control in the reactor tube is another important factor to restrain the autodoping. We investigated analytically the gas flow in the reactor tube and the autodoping mechanism based upon the stagnant gas layer model by Eversteyn *et al.* (14) and confirmed that the stagnant gas layer on the susceptor was supposed to be an essential reason for the autodoping. We developed a simple but very effective silicon epitaxial growth technique without the autodoping and named it "two-step epitaxial growth technique." The object of this paper is to show that the autodoping can be prevented by low temperature epitaxial growth through the pyrolysis of silane and by the controlled gas flow considering the stagnant gas layer.

We recognized that this new epitaxial growth technique was also available to restrain autodilution phenomenon, an inverse phenomenon which occurs when a highly doped epitaxial layer is formed on a lightly doped substrate.

Autodoping.—According to the stagnant gas layer model (14) or the boundary layer model (15), the gas flow in a horizontal reactor tube splits into two regions, a stagnant gas layer and a convective gas layer. The stagnant gas layer is formed on the heated susceptor by flow resistance and thermal force. The gas flow in it is negligible with respect to the main stream flow. It is so static and stable that a substantial transportation of gas molecules or atoms is performed only by diffusion. Figure 1 shows a schematic cross section of a horizontal reactor tube. Injected gases are carried in the convective gas layer. Molecules of silicon source gas and doping gas diffuse into and through the stagnant gas layer, reach the surface of the substrate, and then decompose to deposit silicon and impurity atoms epitaxially.

According to Eversteyn *et al.* (14), the thickness of the stagnant gas layer is expressed experimentally by

$$\delta(x) = \frac{A}{\sqrt{V_T(x)}} - B \quad [1]$$

where $\delta(x)$ is the thickness of the stagnant gas layer at

the distance of x from an entrance edge of the susceptor (cm); $V_T(x)$ is the gas velocity in the convective gas layer at x (cm/sec); and A and B are experimentally determined constants. $V_T(x)$ is expressed by

$$V_T(x) = \left(\frac{b}{b - x \tan \psi} \right) \left(\frac{T_m}{T_0} \right) V_0 \quad [2]$$

where b is the maximum distance between the wall of the reactor tube and the susceptor (cm); ψ is the tilted angle of the susceptor; T_m is the temperature of the convective gas layer depending upon the growth temperature and assumed to be constant throughout the convective gas layer ($^\circ\text{K}$); T_0 is the temperature at which a diffusion constant of the silicon source is given ($^\circ\text{K}$); and V_0 is the gas velocity of the injected gases at the entrance edge of the susceptor (cm/sec).

The thickness of the stagnant gas layer therefore depends upon the gas velocity and the growth temperature. The faster the gas velocity and the higher the growth temperature, the thinner the stagnant gas layer becomes.

Before the epitaxial growth starts, the heavily doped silicon substrate is exposed to high temperature and thereby vaporizes doped impurities up to high vapor pressure.

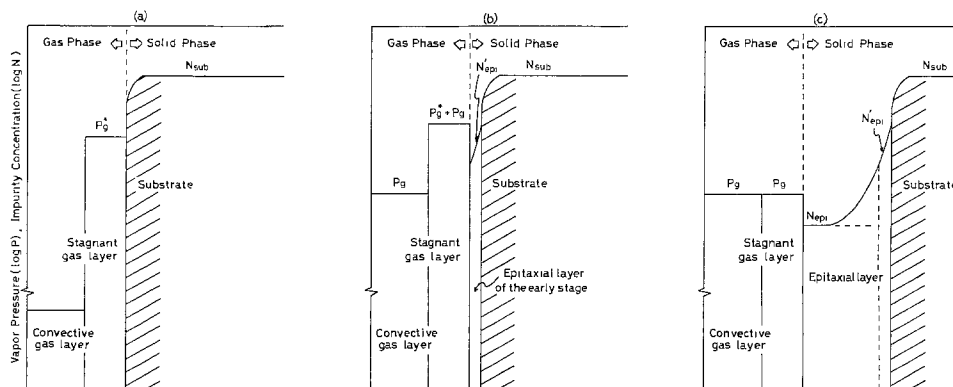
As the stagnant gas layer is stable and static enough, the vaporized impurities stay in the stagnant gas layer without flowing out promptly, and a steady state of the impurity concentration is established in the stagnant gas layer.

The vapor pressure of gaseous impurities in the stagnant gas layer is related to the impurity concentration of the substrate. The relation is expressed as follows [Fig. 2(a)]

$$N_{\text{sub}} = \eta \cdot k \cdot P_g^{*1/n} \quad [3]$$

where N_{sub} is the impurity concentration of the substrate (atoms/cm³); P_g^* is the vapor pressure of gaseous impurities in the stagnant gas layer vaporized from the substrate (atm); k is the distribution coefficient between the solid phase and the gas phase; η is a correction factor for the imperfect closing of the system; that is, while all impurity atoms vaporized from the substrate contribute to the gaseous pressure in the stagnant gas layer, some of the gaseous impurity atoms in the stagnant gas layer escape to the convective layer resulting in its imperfect contribution to its gaseous pressure. It depends on the gas velocity, process temperature, reactor dimensions, etc.; and n is an aggregation coefficient depending upon P_g . The gaseous impurities are composed of their various aggregates. The equilibria for arsenic, for instance, between the various aggregates' forms can be represented as (16): $\text{As}_4(\text{g}) \rightleftharpoons 2\text{As}_2(\text{g})$, $\text{As}_2(\text{g}) \rightleftharpoons 2\text{As}(\text{g})$. It depends on the process temperature and total pressure of impurities. Figure 3 shows our experimental result of the relation between the concentration of gaseous arsenic in the injected gases and the concentration of arsenic in the

Fig. 2. Schematic views of relation between vapor pressure of gaseous impurities in the stagnant gas layer and impurity concentration of the epitaxial layer or of the substrate: (a) before the epitaxial growth starts, (b) at a very early stage of the epitaxial growth, (c) after enough growth of the epitaxial layer.



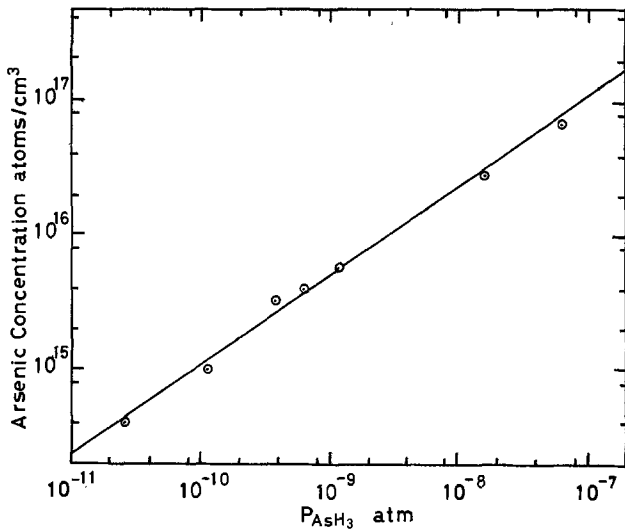


Fig. 3. Variation of arsenic concentration in the epitaxial layer grown at 1050°C with arsine partial pressure.

epitaxial layer after enough growth of the epitaxial layer (17). The subscript s-g means the vaporization from the solid phase (the substrate) to the gas phase (the stagnant gas layer).

When the doping gas of the predetermined vapor pressure P_g is supplied to form the epitaxial layer of the impurity concentration N_{epi} , the total vapor pressure of gaseous impurities in the stagnant gas layer becomes $P_g + P_g^*$ at the beginning of the epitaxial growth. In consequence, at a very early stage of the epitaxial growth the impurity concentration in the epitaxial layer N'_{epi} would be as follows [Fig. 2(b)]

$$N'_{epi} = \eta \cdot k \cdot (P_g^* + P_g)^{1/n} \quad [4]$$

where N'_{epi} is the impurity concentration in the epitaxial layer of the early stage (atoms/cm³) and P_g is the vapor pressure of the doping gas (atm). The subscript g-s means the deposition of impurities from the gas phase (the stagnant gas layer) to the solid phase (the epitaxial layer). As P_g^* is much greater than P_g in the case of interest, N'_{epi} becomes much higher than the expected N_{epi} . This means that the epitaxial layer at the beginning is doped more than the predetermined impurity concentration. This is the phenomenon of autodoping.

As the epitaxial growth proceeds, the vapor pressure of impurities vaporized from the substrate decreases and reaches the predetermined pressure P_g of the doping gas. The impurity concentration of the epitaxial layer in this case is expressed as follows [Fig. 2(c)]

$$N_{epi} = \eta \cdot k \cdot P_g^{1/n} \quad [5]$$

Figure 4 shows a typical impurity profile of the epitaxial layer grown by the conventional epitaxial growth method (18). The impurity concentration of the epitaxial layer N_{SS} is expressed by a sum of the solid-state diffusion of impurities from the substrate and the autodoping

$$N_{SS} = N_{sD} + N_{sA} \quad [6]$$

where N_{sD} is the term of the solid-state diffusion from the substrate; N_{sA} is the term of the autodoping; and the N_{sD} and the N_{sA} are expressed by

$$N_{sD} = \frac{N_{sub}}{2} \left(1 - \operatorname{erf} \frac{x}{\sqrt{2Dt}} \right) \quad [7]$$

$$N_{sA} = N_o^* \exp(-\phi x) \quad [8]$$

Here N_o^* is the impurity concentration of the epitaxially grown layer at a very early stage, coincides with N'_{epi} , and is expressed from Eq. [4] as follows

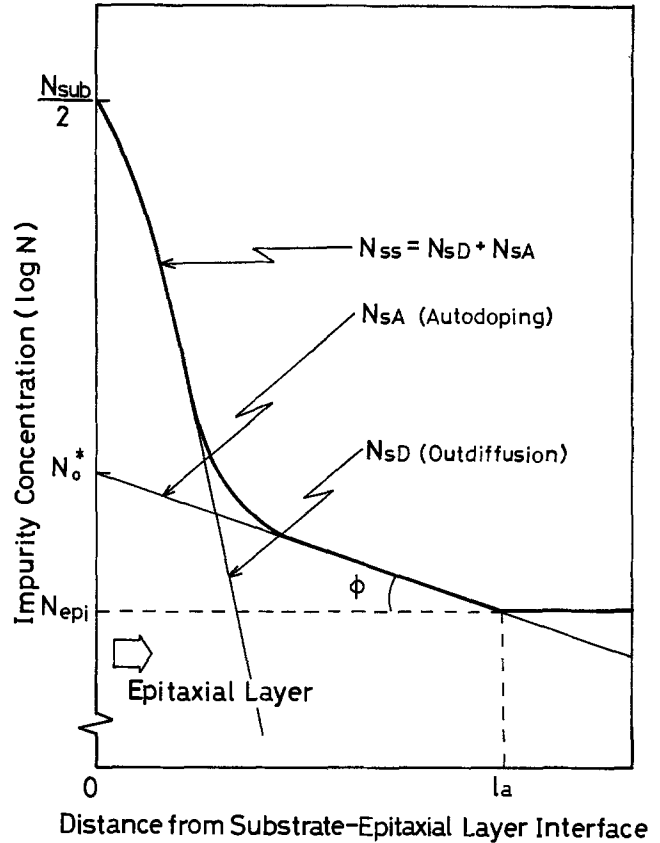


Fig. 4. Typical impurity profile of the epitaxial layer near the substrate grown by the conventional epitaxial growth method (18).

$$N_o^* = N'_{epi} = \eta \cdot k \cdot (P_g^* + P_g)^{1/n} \quad [9]$$

$$N_o^* = \eta \cdot k \cdot P_g^{*1/n} \quad [9a]$$

ϕ is defined as in Fig. 4. From Eq. [3] and [9a]

$$N_o^* = \frac{\eta}{\eta_{s-g}} \cdot N_{sub} = \eta \cdot N_{sub} \quad [10]$$

ϕ and η are determined experimentally and have been reported previously (18, 19).

In order to prevent the autodoping, it will therefore be understood as essential to suppress the vaporization of impurities from the heavily doped substrate at high vapor pressure and to clean up the excess impurities from the stagnant gas layer.

Two-step epitaxial growth technique (20).—Once the surface of the substrate is covered with a thin epitaxial layer, though it is doped excessively, it would effectively suppress the vaporization of impurities at a high vapor pressure from the heavily doped substrate. With the suppression of impurity vaporization, gaseous impurities in the stagnant gas layer decrease their vapor pressure, gradually approaching the predetermined value because some of them are taken into the epitaxially growing layer while others diffuse out into the convective gas layer. Figure 5 shows a schematic relation among the vapor pressure of gaseous impurities in the stagnant gas layer, the impurity concentration in the epitaxial layer, and the thickness of the epitaxial layer as a function of the growth time when the epitaxial growth is carried out conventionally. The lines A, B, and C represent the change of the vapor pressure, impurity concentration, and epitaxial layer thickness, respectively. Until the time t_a , the grown layer is doped excessively. In other words, autodoping is observed in a region within l_a of the substrate-epitaxial layer interface.

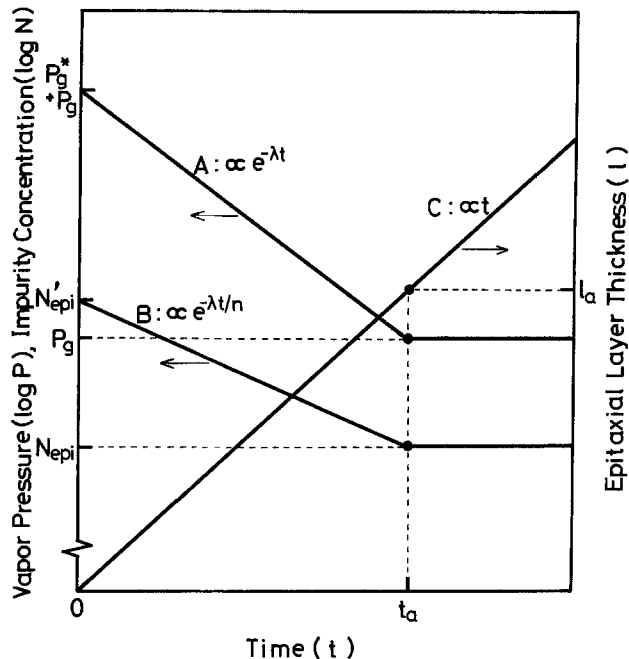


Fig. 5. Qualitative relation among the vapor pressure of impurities in the stagnant gas layer (A), the impurity concentration in the epitaxial layer (B), and the epitaxial layer thickness (C) as a function of time by the conventional epitaxial growth method concerning the autodoping. λ = decreasing coefficient of vapor pressure.

In the two-step epitaxial growth technique, the epitaxial growth process is divided into two growth steps. The first step is very short with only enough time to cover the substrate surface slightly. The second step is carried out conventionally until getting the required layer thickness. Between the two growth steps, purification of the stagnant gas layer is performed suppressing impurity vaporization from the substrate by the first thin epitaxial layer.

During the purification treatment of the stagnant gas layer, only the carrier gas is supplied; the source gas and the doping gas are stopped. So epitaxial growth does not occur and the vapor pressure of gaseous impurities in the stagnant gas layer decreases gradually. Figure 6 shows the principle of the two-step epitaxial growth technique. The vapor pressure of gaseous impurities changes along line A. At the time t_1 , the first growth step is over. Between the time t_1 and t_2 , the stagnant gas layer is purified and the vapor pressure of gaseous impurities decreases to reach the predetermined level P_g at the time t_2 .

The first epitaxial layer is doped excessively and the impurity concentration is shown by line B at first. During the purification treatment, as impurities vaporize from the surface of the first epitaxial layer and the vaporization rate is much faster than the solid-state diffusion of impurities from the substrate to the epitaxial layer, the impurity concentration in the first epitaxial layer will also fall down to the line B' at the end of the purification treatment. At the time t_2 , the second epitaxial growth starts. Now that the vapor pressure of gaseous impurities in the stagnant gas layer has reached the predetermined level, an epitaxial layer with the expected doping level N_{epi} can be obtained. The intermission of the epitaxial growth during the gas purification treatment shortcuts the autodoped region resulting in the abrupt impurity profile at the substrate interface.

These succeeding steps are carried out at the same temperature, and the supplied gas composition in the first and second epitaxial growth steps is kept the same. These facts make the two-step epitaxial growth technique quite simple and useful industrially in contrast with the so-called high-low temperature cycle

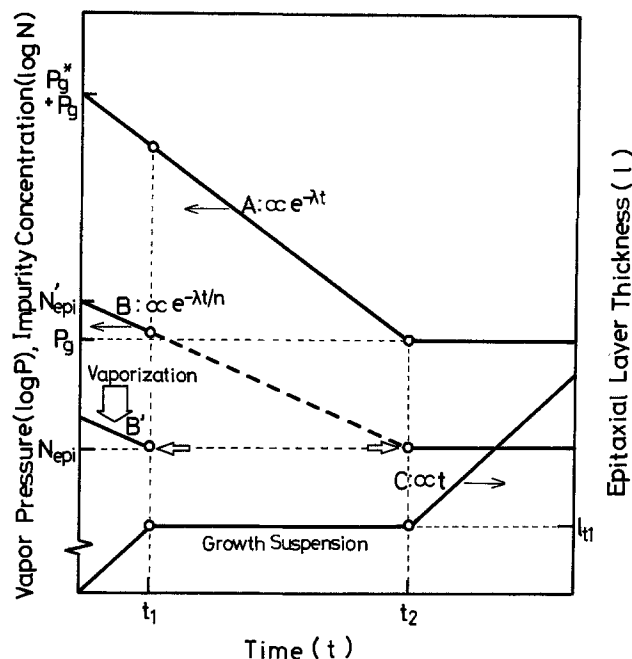


Fig. 6. Qualitative relation among the vapor pressure (A), the impurity concentration (B), and the epitaxial layer thickness (C) as a function of time by the two-step epitaxial growth technique. Between t_1 and t_2 , the stagnant gas layer is purified suspending the epitaxial growth.

epitaxial growth method or mole fraction coating epitaxial growth method.

Experimental Procedure

The silicon epitaxial growth apparatus used in the experiment was the conventional horizontal type and its flow diagram is shown in Fig. 7.

Silicon wafers were supported on a SiC-coated graphite susceptor which was 70 mm wide, 230 mm long, and 15 mm thick with a tilted angle of 2° . The susceptor was heated by a 15 kW, 450 kHz rf generator in a boron-free quartz reactor tube. In Table I, specifications of materials used in the experiments and the important experimental conditions are summarized. Highly purified H_2 was used as the carrier gas and its flow rate was 40 liter/min (26.7 cm/sec). Silane was used as the source material to allow low temperature epitaxial growth without halides. The silane concentration in the supplied gas was principally 0.13% and it set the epitaxial growth rate at $0.35 \mu\text{m}/\text{min}$. Arsine (AsH_3) and diborane (B_2H_6) were used as n- and p-type doping gases, respectively. AsH_3 and B_2H_6 concentration in the supplied gas was varied from 10^{-11} to 10^{-6} atm according to the doping level. The epitaxial

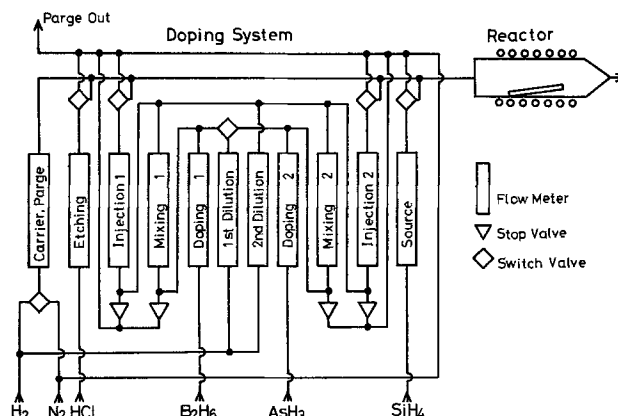


Fig. 7. Construction of the doping system of the silicon epitaxial growth apparatus.

Table 1. Specifications of materials used in the silicon epitaxial growth and the silicon epitaxial growth conditions

Si substrate	n-type	As doped Si (0.005 ohm-cm) Sb doped Si (0.015 ohm-cm) B doped Si (0.005 ohm-cm)
Supplied gas	p-type	99.9999% H ₂
	Carrier gas	100% HCl
	Etching gas	10% SiH ₄ (diluted by H ₂)
	Si source gas	50 ppm AsH ₃ (diluted by H ₂)
Growth condition	Doping gas	50 ppm B ₂ H ₆ (diluted by H ₂)
	Carrier gas flow rate	40 liters/min (26.7 cm/sec)
	Vapor etching	Temperature 1200°C
	Si deposition	Temperature 1050°C
		Gas composition HCl/H ₂ = 0.04
		SiH ₄ /H ₂ = 0.001-0.002 (0.0013 typical)
		AsH ₃ /H ₂ or B ₂ H ₆ /H ₂ = 10 ⁻¹¹ -10 ⁻⁹ (0.30-0.45 μm/min (0.35 μm/min typical)
	Growth rate	
	Doping level	10 ¹⁴ -10 ¹⁸ cm ⁻³

growth was mainly carried out on As-doped substrate and B-doped substrate at the growth temperature of 1050°C. As arsenic has the highest vapor pressure among commonly used impurities in silicon, autodoping occurs most easily with it. So it would be thought to be most suitable in the investigation of the autodoping phenomenon.

Figure 8 shows a typical temperature-time schedule of the silicon epitaxial growth process by the two-step epitaxial growth technique. Only a vapor etching process by HCl (process I in Fig. 8) was carried out at 1200°C. After the vapor etching, a gas cleaning-up (process II) was performed for enough time to purge etched materials and halides from the stagnant gas layer reducing the process temperature. At the growth temperature of 1050°C, the first epitaxial growth step (process III) provided a very thin epitaxial layer usually less than 0.5 μm, on the substrate surface. In the gas purification step between the first and the second epitaxial growth steps (process IV), excess impurities above the predetermined doping level were purged from the stagnant gas layer suspending the epitaxial growth. The second epitaxial growth step (process V) was carried out conventionally until the expected wafer characteristics were obtained. The duration of the gas purification treatment is very important in the two-step epitaxial growth technique and will be discussed later.

The impurity concentration distribution at the substrate-epitaxial layer interface was determined by capacitance measurement on mesa diodes with a shallow abrupt p-n junction fabricated from the epitaxial wafers.

Experimental Results

Figure 9 shows experimental results related to the cleaning-up effect of the stagnant gas layer contaminated by the HCl vapor etching. The epitaxial wafers A and B were both prepared in the same manner by the conventional epitaxial growth method except for the different cleaning-up time. The stagnant gas layer was cleaned up by 4 min after the HCl etching in sample A and by 16 min in sample B. The results show that a longer cleaning-up treatment is preferable to get an abrupt impurity profile at the substrate interface. This is proof that etched materials and halides stay in the stagnant gas layer without being carried away promptly and have a harmful effect on the abrupt impurity profile. By the conventional epitaxial growth method, a cleaning-up treatment in excess of 20 min was not so effective in improving the impurity profile at the substrate interface. So our sample B shows a technical limitation from the conventional epitaxial growth method.

Figure 10 shows impurity profiles made by three different epitaxial growth processes. Sample A was made by the conventional epitaxial growth method and was grown for 11 min. Samples B and C were both made by the two-step epitaxial growth technique, but the duration of the first epitaxial growth step was

different. Namely, it was 1 min long in sample B and was 30 sec long in sample C. The thickness of the first

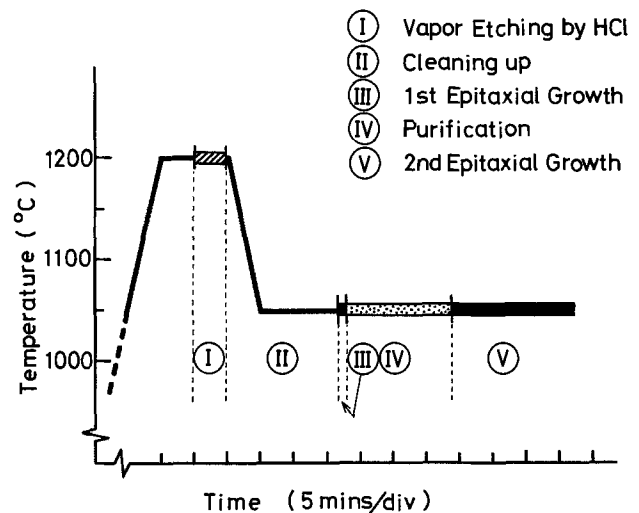


Fig. 8. Typical time-temperature schedule of the silicon epitaxial growth by the two-step epitaxial growth technique.

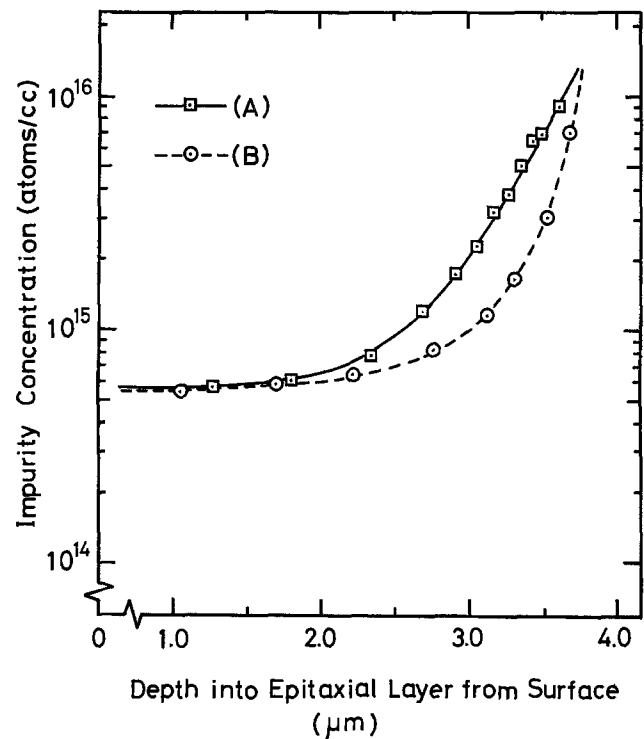


Fig. 9. Dependence of the impurity profile of the silicon epitaxial layer on the gas cleaning-up time after the HCl gas etching. Cleaning up time: (A) = 4 min, (B) = 16 min.

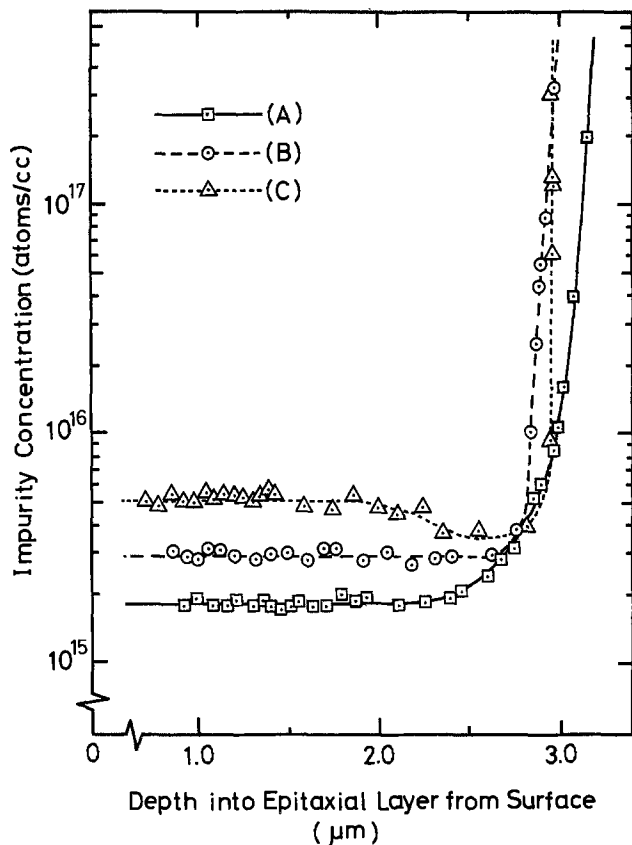


Fig. 10. Impurity profiles of the silicon epitaxial layers grown by the conventional epitaxial growth method (A) and by the two-step epitaxial growth technique (B, C). The first epitaxial layer thickness: (B) = $0.35 \mu\text{m}$, (C) = $0.2 \mu\text{m}$. The gas purification time: (B), (C) = 16 min.

epitaxial layer was $0.35 \mu\text{m}$ in sample B and $0.2 \mu\text{m}$ in sample C. Other growth conditions were the same, i.e., a 16 min gas purification after the first epitaxial growth, and a 10 min second epitaxial growth. The total epitaxial layer thickness was $4.0 \mu\text{m}$ in these three samples. Prior to the epitaxial growth, the surface of the substrates was etched by HCl for 5 min, then the gas cleaning-up was performed for 17 min. In sample A the impurity profile was rather gradual at the substrate interface, but it was abrupt enough in sample B or C. For convenience, we estimated the width in order to get a 10^2 increase of impurity concentration from the epitaxial layer with the predetermined impurity concentration to the substrate as an impurity gradient at the substrate interface. The impurity gradient was more than $1 \mu\text{m}$ in sample A, but it was $0.3 \mu\text{m}$ in sample B and less than $0.1 \mu\text{m}$ in sample C. The improved quantity of $0.3 \mu\text{m}$ or $0.1 \mu\text{m}$ is comparable to the theoretical solid-state diffusion of arsenic from the substrate. In spite of the high vapor pressure of As, the autodoping was completely suppressed in samples B and C. A slight dip in the impurity profile at the substrate interface observed in sample C will be discussed later.

Impurity profiles of three different epitaxial wafers are compared in Fig. 11. Arsenic-doped epitaxial layers were grown on As- and Sb-doped substrates in samples A and B, respectively, and a boron-doped epitaxial layer was grown on a B-doped substrate in sample C. Those were all prepared by the two-step epitaxial growth technique and the duration of the gas purification treatment after the first epitaxial growth was properly chosen. As antimony has the lowest vapor pressure and also the lowest diffusion rate in commonly used n-type impurities, the autodoping is minimized. But by use of the two-step epitaxial growth technique, an abrupt impurity profile without autodoping can be obtained even in the epitaxial growth

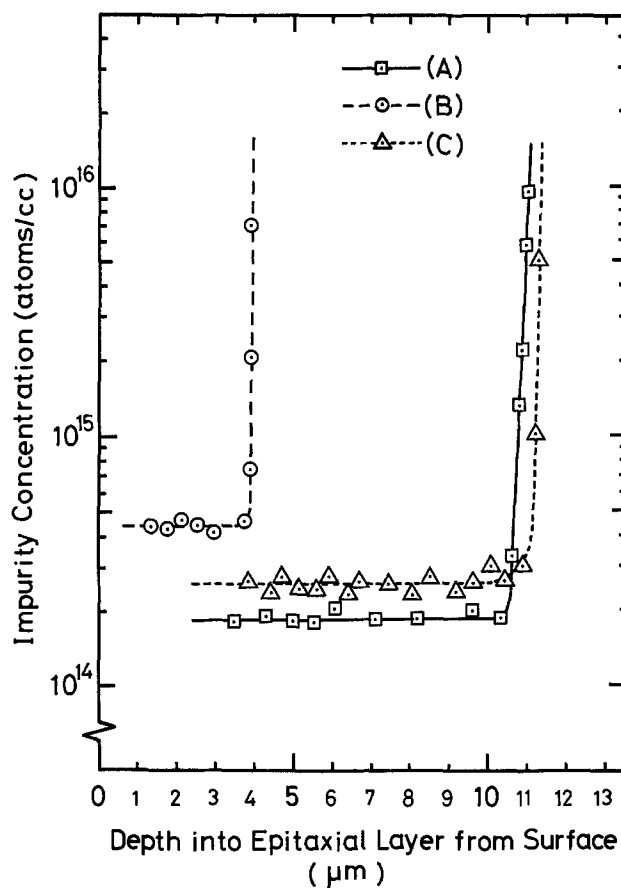


Fig. 11. Impurity profiles of the silicon epitaxial wafers of N on N^+ and P on P^+ structure prepared by the two-step epitaxial growth technique: (A) = N(As) on N^+ (As), (B) = N(As) on N^+ (Sb), and (C) = P(B) on P^+ (B).

on an As- or B-doped substrate as well as an Sb-doped substrate.

Application of the Two-Step Epitaxial Growth Technique

Restraint of autodilution (20).—Occasionally, the successive formation of a highly doped epitaxial layer on a lightly doped substrate or on a lightly doped epitaxial layer is required. In this case, just the opposite phenomenon from autodoping occurs in the early stage of the epitaxial growth; namely, the impurity concentration of the epitaxial layer is considerably lower than the predetermined beginning doping level. We call this phenomenon autodilution.

Before the epitaxial growth starts, the gaseous impurities in the stagnant gas layer practically equilibrate with the impurities in the lightly doped substrate or preceding epitaxial layer. The vapor pressure P_g^* in this case is lower than the P_g necessary to obtain the predetermined doping level $N_{\text{epi}} (P_g^* < P_g)$. When the source gas and the doping gas of appropriate composition are supplied to form the epitaxial layer of the predetermined doping level, the vapor pressure of the gaseous impurities in the stagnant gas layer does not respond quickly. According to the schematic illustration in Fig. 12, the vapor pressure increases gradually along line A and reaches the predetermined value P_g at the time t_d . Corresponding to this, the impurity concentration in the epitaxial layer changes along line B and the intended doping level is attained at t_d . Before that, the epitaxial layer of the thickness l_d has already grown and, therefore, the impurity profile becomes sluggish in this region.

Here we transform the two-step epitaxial growth technique a little and apply it to restrain the autodilution. At least until the time t_d in Fig. 12 is reached, the epitaxial growth is suspended by stopping the

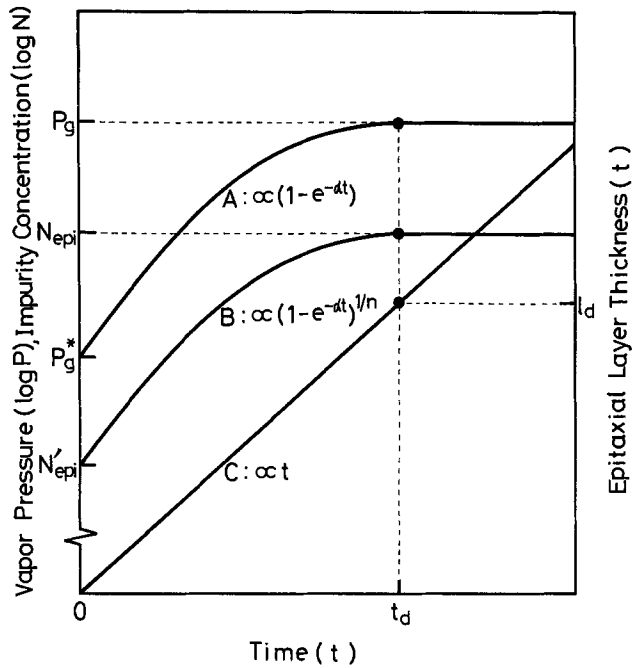


Fig. 12. Qualitative relation among the vapor pressure of impurities (A), the impurity concentration (B), and the epitaxial layer thickness (C) as a function of time concerning the autodilution. α = increasing coefficient of vapor pressure.

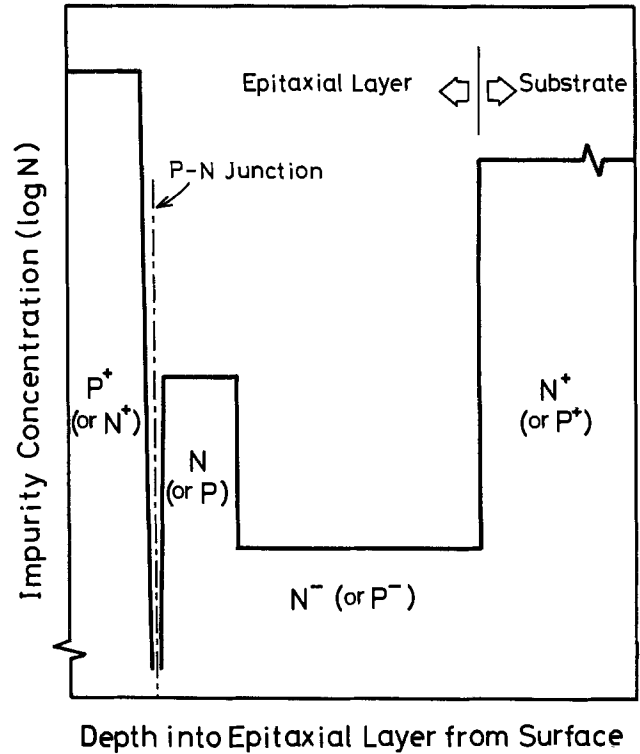


Fig. 13. Schematic hyperabrupt impurity profile of the Read Type IMPATT diode (21).

source gas (SiH₄). As the carrier gas and the doping gas are supplied continuously in this period, the vapor pressure of impurities in the stagnant gas layer is raised to the predetermined level P_g . The epitaxial growth starts only after the vapor pressure has reached P_g . The intermission of the epitaxial growth shortcuts the autodiluted region resulting in the abrupt impurity profile at the interface.

Hyperabrupt impurity profile.—Some microwave semiconductor devices, Read Type IMPATT diodes for example, require hyperabrupt impurity profiles such as P⁺NN⁻ on N⁺ or N⁺PP⁻ on P⁺ illustrated schematically in Fig. 13 (21). Such impurity profiles can be formed first by the epitaxial growth of a lightly doped layer (N⁻ or P⁻) on a heavily doped substrate (N⁺ or P⁺), then by the succeeding epitaxial growth of a highly doped layer (N or P) on the lightly doped epitaxial layer, and finally by the succeeding epitaxial growth or diffusion of a heavily doped layer (P⁺ or N⁺). The autodoping and the autodilution may occur at the N⁺N⁻ (or P⁺P⁻) and N⁻N (or P⁻P) interface, respectively.

Figure 14 shows the impurity profile of silicon epitaxial wafers with a hyperabrupt P⁺NN⁻N⁺ structure prepared for the Read Type IMPATT diodes of K band use (20,22). Sample A was made by the conventional epitaxial growth method and sample B was made by the two-step epitaxial growth technique. The two-step epitaxial growth technique was used twice in sample B to prevent autodoping at the N⁺N⁻ interface and to prevent autodilution at the N⁻N interface. Both samples were made by the same wafer parameters; namely, a $1 \times 10^{15} \text{ cm}^{-3}$ As-doped epitaxial layer (N⁻ layer) was first grown on a $3 \times 10^{19} \text{ cm}^{-3}$ As-doped substrate (N⁺ substrate) and then a $1 \times 10^{17} \text{ cm}^{-3}$ As-doped epitaxial layer (N layer) was grown successively. A P⁺ region was formed by boron diffusion at a high surface concentration from the surface of the N epitaxial layer.

In sample A, the autodoping occurred at the N⁺N⁻ interface. As a result, the impurity concentration in the N⁻ layer became higher than the expected doping level. In sample B, on the other hand, the impurity profile at the N⁺N⁻ interface was abrupt enough and the predetermined doping level was attained.

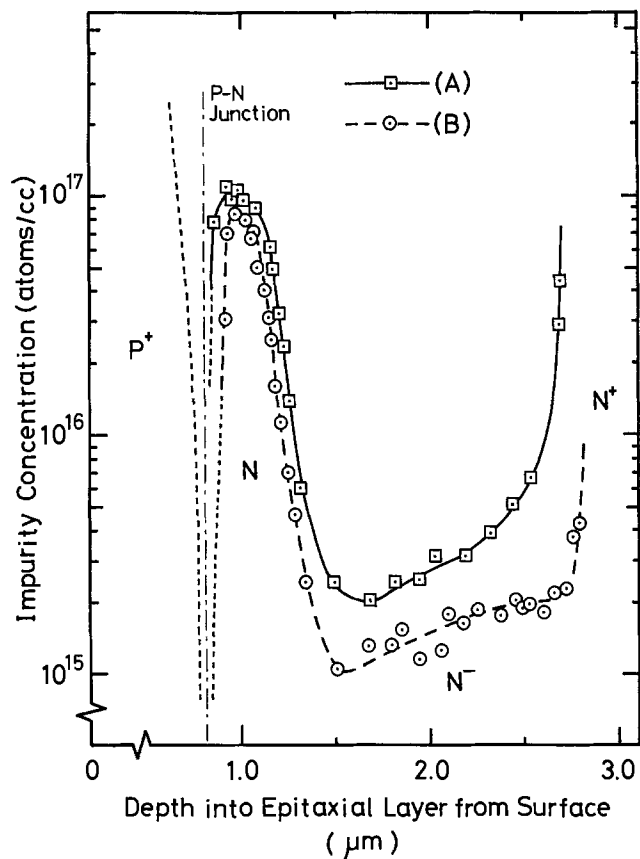


Fig. 14. Hyperabrupt impurity profiles of silicon epitaxial wafers for K band Read Type IMPATT diodes grown by the conventional epitaxial growth method (A) and by the two-step epitaxial growth technique (B).

The transition from N⁻ to N layer became steeper in sample B than in sample A. The Read Type IMPATT diode requires a narrow avalanche region for high efficiency and wide band operation and the narrow avalanche region corresponds to the abruptness of the

impurity profile at the N-N interface. The improvement of the impurity profile at the N-N interface in sample B narrows the avalanche region and therefore increases the operation efficiency of the Read Type IMPATT diodes. Figure 15 shows the comparison of typical operation characteristics of the Read Type IMPATT diodes. Diodes A and B were fabricated from the epitaxial wafers A and B as shown in Fig. 14, respectively. The CW output power and the operation efficiency were improved by 50% through the improvement of the avalanche region width.

Discussion

In the two-step epitaxial growth technique, the duration of the gas purification treatment after the first epitaxial growth is especially important. It depends upon the process temperature, the gas velocity, the thickness of the first epitaxial layer, and the impurity concentration of the second epitaxial layer. A higher temperature and a faster gas velocity make the stagnant gas layer thinner. The higher temperature also accelerates the vaporization of impurities from the first epitaxial layer and accelerates the diffusion of gaseous impurities in the stagnant gas layer. So the higher the process temperature and the faster the gas velocity become, the shorter the duration of purification treatment becomes. A thicker first epitaxial layer and a higher impurity concentration of the second epitaxial layer also shorten the duration.

An insufficient purification treatment accentuates the autodoped region and makes the impurity profile gradual at the substrate interface. An extreme purification treatment excessively lowers the impurity concentration at the surface of the first epitaxial layer by overvaporization. It also lowers the vapor pressure of gaseous impurities in the stagnant gas layer below the predetermined doping level. The shortage of impurities at the beginning of the second epitaxial growth results in a dip of the impurity profile at the substrate interface. Sample C in Fig. 10 is an example of this.

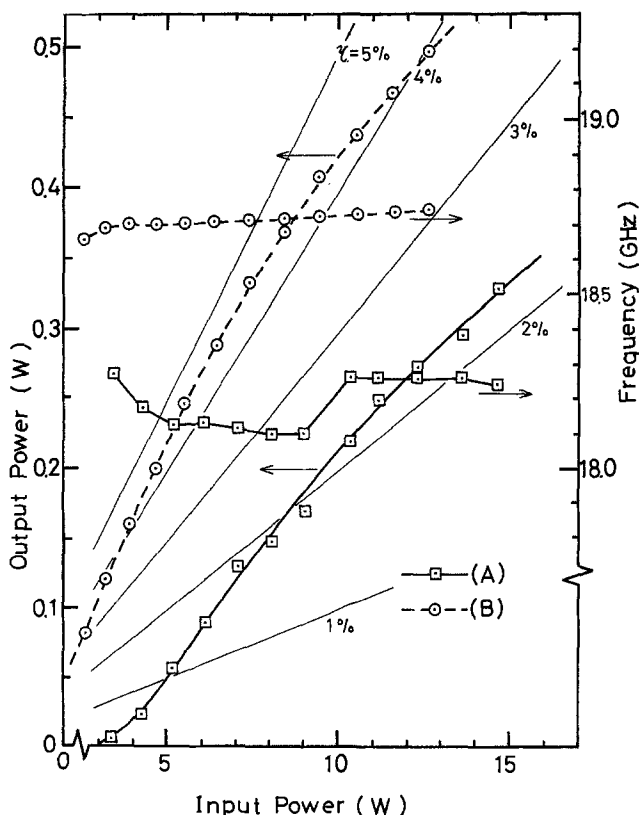


Fig. 15. Comparison of the oscillation characteristics of Read Type IMPATT diodes fabricated from silicon epitaxial wafers prepared by the conventional epitaxial growth method (A) and by the two-step epitaxial growth technique (B).

The slight dip means that the gas purification treatment was performed a little more than the appropriate duration required for the thickness of the first epitaxial layer and the impurity concentration of the second epitaxial layer.

The duration of the gas purification treatment is now determined experimentally, but it should be determined accurately by a rigid hydrodynamic analysis considering the diffusion of gaseous impurities in the stagnant gas layer and the vaporization of impurities from the wafer surface. The analysis is so complicated that a computer simulation is required.

The duration, however, can be roughly estimated by the following method. Referring again to Fig. 4, when the epitaxial layer of l_a thick has grown, the vapor pressure of gaseous impurities in the stagnant gas layer becomes P_g from the initial $P_g + P_g^*$ and the doped impurity concentration in the epitaxial layer N_{ss} becomes the predetermined value N_{epi} . The ratio of impurities being taken into the first epitaxial layer to gaseous impurities diffusing out into the convective gas layer is negligibly small during the gas purification treatment. The gas purification treatment should, therefore, be performed at least for the time necessary to get the epitaxial layer of l_a thick. That is, duration time = l_a (μm)/growth rate ($\mu\text{m}/\text{min}$). For our samples in Fig. 9, the autodoped region is about $2 \mu\text{m}$ for the epitaxial layer of doping level of about $6 \times 10^{14} \text{ cm}^{-3}$ grown by conventional technique. So in this case, the appropriate duration of heat-treatment is $2 \mu\text{m}/0.35 \mu\text{m}/\text{min} = 5.7 \text{ min}$. As for sample C in Fig. 10, the duration of heat-treatment was 16 min as already mentioned, and the slight dip in the doping level at substrate-epitaxial layer interface is quite reasonable for excess heat-treatment.

Conclusion

A silicon epitaxial wafer in which the impurity concentration and profile are rigidly controlled is required for microwave semiconductor devices. The low temperature epitaxial growth by SiH_4 and the newly developed two-step epitaxial growth technique based upon a controlled gas flow in the reactor tube make it possible to eliminate the autodoping and the autodilution phenomena. It has been confirmed by the two-step epitaxial growth technique that the epitaxial growth mechanism based upon the stagnant gas layer model is quite reasonable. The behavior of impurities in the stagnant gas layer is the essential phenomenon in autodoping and autodilution. The usefulness of the silicon epitaxial wafers with controlled abrupt impurity profile between two regions of different impurity concentration was proven concretely by the improved operation characteristics of Read Type IMPATT diodes. The problem left to be solved is the theoretical determination of the most appropriate duration of the gas purification treatment for attaining the best impurity profile at the substrate interface.

Acknowledgments

The authors would like to thank Dr. T. Hata and Mr. K. Fujibayashi for many helpful suggestions regarding this work and also for their encouragement.

Manuscript submitted Oct. 15, 1974; revised manuscript received June 15, 1975. This was Paper 179 presented at the Boston, Massachusetts, Meeting of the Society, Oct. 7-11, 1973.

Any discussion of this paper will appear in a Discussion Section to be published in the June 1976 JOURNAL. All discussions for the June 1976 Discussion Section should be submitted by Feb. 1, 1976.

Publication costs of this article were partially assisted by Mitsubishi Electric Corporation.

REFERENCES

1. A. S. Grove, A. Roder, and C. T. Sah, *J. Appl. Phys.*, **36**, 802 (1965).
2. B. A. Joyce, J. C. Weaver, and D. J. Maule, *This Journal*, **112**, 1100 (1965).

3. W. H. Shepherd, *ibid.*, **115**, 652 (1968).
4. S.R. Bhola and A. Mayer, *R C A Rev.*, **24**, 511 (1963).
5. T. Abe, T. Kato, Y. Nishi, and K. Sato, *Toshiba Rev.*, **19**, 1283 (1964).
6. T. Nishioka and M. Mizuno, Private communication.
7. D. C. Gupta and R. Yee, *This Journal*, **116**, 1561 (1969).
8. O. Richman, Y. S. Chiang, and P. H. Robinson, *R C A Rev.*, **31**, 613 (1970).
9. W. C. Benzing, A. E. Ozias, and I. M. Helmer, Abstract 75, p. 184, Electrochemical Society, Extended Abstracts, Spring Meeting, Washington, D. C., May 9-13, 1971.
10. A. Lekholm, *This Journal*, **119**, 1122 (1972).
11. S. Nakanuma, *IEEE Trans. Electron Devices*, **ED-13**, 578 (1966).
12. A. Ito, Y. Iwata, M. Nakajima, and T. Yamamoto, Abs. S-8-7 p. 151, IECE of Japan, Extended Abstracts, Fall Meeting, 1966.
13. W. G. Townsend and M. E. Uddin, *Solid-State Electron.*, **16**, 39 (1973).
14. F. C. Eversteyn, P. J. W. Severin, C. H. J. van den Brekel, and H. L. Peek, *This Journal*, **117**, 925 (1970).
15. H. Schlichting, "Boundary Layer Theory," 4th ed., Chapter 7, McGraw-Hill Book Co., New York (1970).
16. P. Rai-Choudhury and E. I. Salkovitz, *J. Cryst. Growth*, **7**, 353 (1970).
17. P. Rai-Choudhury and E. I. Salkovitz, *ibid.*, **7**, 301 (1970).
18. C. O. Thomas, K. Kahng, and R. C. Manz, *This Journal*, **109**, 1055 (1962).
19. T. Abe, T. Kato, and Y. Nishi, *Japan. J. Appl. Phys.*, **3**, 161 (1964).
20. A. Kondo, T. Ishii, K. Takahashi, and K. Fujibayashi, Abstract 179, p. 451, Electrochemical Society, Extended Abstracts, Fall Meeting, Boston, Oct. 7-11, 1973.
21. W. T. Read, Jr., *Bell System Tech. J.*, **37**, 401 (1958)
22. A. Kondo and T. Ishii, *IEEE Trans. Electron Devices*, **ED-19**, 695 (1972).

Studies of the Push-Out Effect in Silicon

I. Comparison of Sequential Boron-Phosphorus and Gallium-Phosphorus Diffusions

Christopher L. Jones and Arthur F. W. Willoughby

Engineering Materials Laboratories, The University, Southampton, SO9 5NH, England

ABSTRACT

The push-out effect in silicon has been investigated by comparing the effect of similar phosphorus emitter diffusions on previously diffused boron and gallium base diffusions, using junction depth and electrical measurements. The closely similar behavior of the two base dopants suggests that both diffuse by the same mechanism in silicon, despite their different covalent radii. For both dopants the amount of push-out increases with emitter diffusion time for constant base diffusion and emitter surface concentration, and decreases as base depth increases for constant emitter diffusion and base surface concentration, and it is concluded that push-out occurs during the emitter diffusion rather than during cooling. The results are discussed with reference to an approximate theory, and agreement between experiment and this theory strongly suggests that push-out is due to a uniform enhancement of the base diffusivity throughout the emitter diffusion period. This study, using junction depth and electrical profiling techniques only, is the first part of this investigation, the second of which will report results of a radiotracer study of push-out.

Diffusion is one of the most important processes in the manufacture of silicon bipolar transistors; yet diffusion mechanisms in silicon are still not well understood. Anomalous diffusion effects have been discussed in a review paper by one of the authors (1) and, more recently, by Hu (2). One of the most important effects is the push-out or emitter-dip effect which is the depression of a base-collector junction beneath a localized emitter diffusion. Since the original observation of this effect by Miller (3) it has become clear that push-out introduces considerable problems in the manufacture of microwave n-p-n transistors using phosphorus-diffused emitters. These problems arise chiefly because narrow base widths are difficult to achieve and control of the base doping level is poor. The influence of various process parameters (e.g., diffusion time, temperature, and surface concentration of the emitter; initial depth and surface concentration of the base) on the amount of push-out have not been definitely established and virtually no information is available concerning the base doping profile shape and how it changes with these parameters.

Most of the information about push-out has been obtained by the traditional method of junction depth measurement (4-8), but in order to understand the

diffusion processes much more information is required and this can only be obtained by determining the impurity profiles of the base and emitter through a complete transistor structure. Electrical profiling techniques, although useful, cannot give any information about the base profile within the emitter (5, 9, 10) and therefore a new approach has been adopted by the present authors, that is the radiotracer profiling of the complete base diffusion within and beyond the emitter, preliminary results of which were reported in Ref. (11). Unfortunately, boron does not have a radioisotope of sufficiently long half-life (⁸B and ¹²B half-lives are <1 sec) so the conventional boron base was replaced by gallium.

There is very little published information regarding gallium push-out (3, 12) so a necessary first step was to compare boron and gallium push-out by junction depth measurements. This comparison offers the interesting possibility of examining whether or not boron and gallium diffuse by the same mechanism, information which could be of great importance in resolving the current controversy on the diffusion mechanism of the Group III impurities in silicon [Seeger and Chik (13), Hu (2), Kendall and DeVries (14)]. These experiments were aimed also at obtaining more information on how the magnitude of push-out is affected by various parameters of the diffusions used. The results

Key words: diffusion, enhancement, emitter-push, junction depth, transistor.

of this work are described below and analyzed with reference to an approximate theoretical expression for the amount of push-out. A simple approach to estimating push-out in practical cases is also presented.

Further results and analysis of the radiotracer gallium profiling will be given in the second paper (which will be referred to as Part II) together with a discussion of possible causes of push-out in the light of the new evidence.

Experimental Techniques

Material.—All the silicon used was n-type, 1 ohm-cm. in (111) oriented wafer form, chemically polished on one side. Wafers were cleaned by boiling three times in 1-1-1 trichloroethane followed by a 15 min soak in a freshly prepared H_2SO_4/H_2O_2 , 1/1 mixture. They were then washed five times in deionized water and blown dry in dry N_2 .

Boron base diffusion.—A two-step boron diffusion was employed consisting of a deposition from BBr_3 for 40 min at $960^\circ C$ after which the boron glass was removed and the boron layer driven-in at $1200^\circ \pm 1^\circ C$ under oxidizing conditions for times in the range 18 to 30 min depending on the depth required.

Gallium base diffusion.—Gallium was diffused in an open tube system using Ga_2O_3 source powder over which was passed a mixture of H_2 and N_2 gases (15). Before entering the furnace the gas mixture passed through a temperature-regulated water bubbler in order to control the amount of water vapor in the gas stream. A diagram of the apparatus is given in Fig. 1. The source temperature was $1000^\circ C$ and silicon sample temperature was $1100^\circ \pm 2^\circ C$. Diffusion times ranged from 15 to 180 min depending on the depth required. A thin oxide is formed during the diffusion which can be used for masking subsequent emitter diffusions.

Phosphorus emitter diffusions.—Phosphorus diffusions at $1050^\circ \pm 1^\circ C$ from a $POCl_3$ source were used to form the emitter under the same conditions for both boron and gallium bases. The $POCl_3$ was held at $0^\circ C$ by crushed ice, and an O_2/N_2 mixture was bubbled through and into the furnace. The amount of dopant introduced was sufficient for the phosphorus concentration in the silicon to reach the solid solubility limit. Once the gas flow rates and the $POCl_3$ bubbler were set up conditions in the furnace tube were allowed to stabilize for 30 min before the silicon samples were introduced. A light weight furnace boat was used to keep wafer warm up time to a minimum and all samples were cooled rapidly following the diffusion.

Junction depth measurements.—P-N junctions were revealed by making a cylindrical groove in the silicon surface and staining the exposed p-type layers with an Hf/HNO_3 stain made by adding about one drop of conc HNO_3 to 25 ml of 48% Hf . The specimen was illuminated during staining. A photograph showing a stained transistor-type structure is given in Fig. 2(a). The junction depths shown diagrammatically in Fig. 2(b) were measured on the stained groove by sodium light interferometry.

Resistivity profiling.—The layer removal, sheet resistance measurement technique was used to obtain "electrical" profiles of the diffused layers. Sheet re-

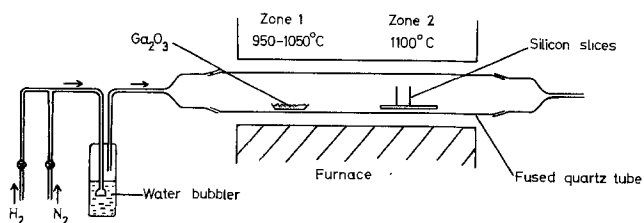


Fig. 1. Gallium diffusion apparatus

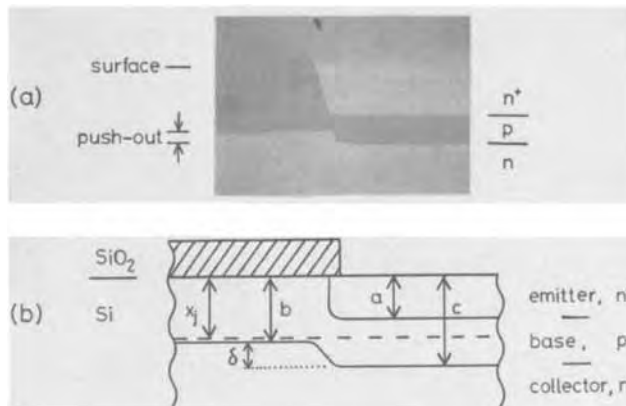


Fig. 2. a. Photograph of a stained transistor-type structure, dark regions are p-type. b. Section showing the depths measured: x_j is measured before the emitter diffusion; a , b , and c after the emitter diffusion; push-out $\delta = c - b$.

sistance was measured by a four-point probe having low tip pressure (60g) to avoid surface damage. Layers of silicon were removed either by a slow Hf/HNO_3 etch or anodization followed by an Hf etch. The thickness of silicon removed was determined from the oxide color (previously calibrated) when anodization was employed and by interference measurement of step heights when slow etching was used (steps were formed by masking part of the wafer during etching). The sheet resistance vs. depth data were converted to concentration vs. depth profiles by the method of Evans and Donovan (16) and using Irvin's (17) curves to convert resistivity to concentration. For profiling the emitter plus pushed-out base, and the nonpushed-out base the masking pattern shown in Fig. 3 was used. In this way the oxide formed during the base diffusion was used to prevent phosphorus in-diffusion in certain areas. The central striped area C (Fig. 3) allowed measurements of junction depths and push-out by grooving and staining, area A was used for resistivity profiling of the nonpushed-out base, while area B was used to profile the emitter and pushed-out base.

Results

Push-out of boron by phosphorus emitter diffusion.—A typical impurity profile through a transistor-type structure obtained by the resistivity method is shown in Fig. 4. The limitations of electrical profiling when investigating sequential diffusion processes are well illustrated in this example. These limitations are: (i) No information can be obtained about the boron profile within the emitter because the electrical properties in this region are completely dominated by the emitter dopant. (ii) Electrical profiling cannot give the true impurity concentration when compensation is heavy as in the vicinity of the emitter/base junction. For this reason the pushed-out base will always appear to have

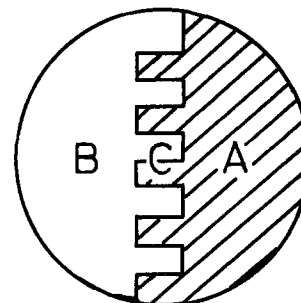


Fig. 3. Diagram showing masking pattern. Oxide is left behind in shaded areas after masking and etching. "A" is used for profiling the nonpushed-out base; "B" for profiling the emitter and pushed-out base; "C" for junction depth measurements by staining.

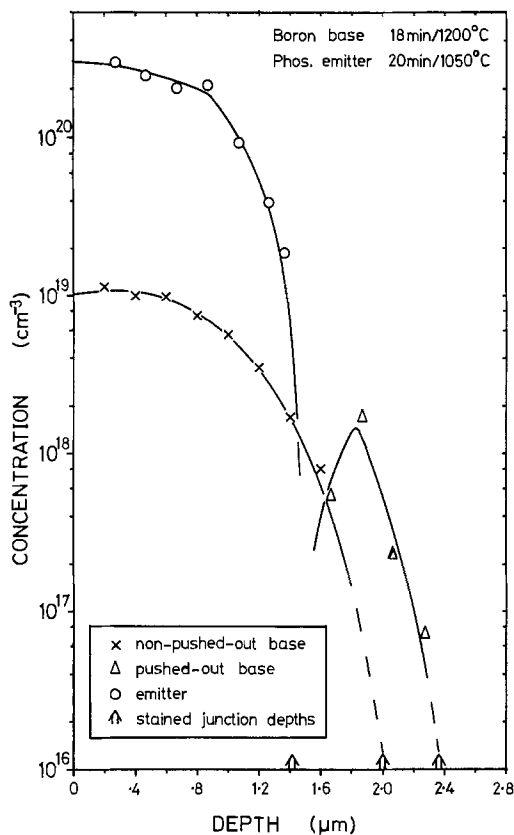


Fig. 4. A typical "electrical" impurity profile

a concentration peak even when the true boron profile is not peaked. (iii) It is necessary to assume that Irvin's (17) curves can be applied to convert resistivity to impurity concentration but this may lead to error, particularly when the impurity concentration is high ($> 10^{20}$ atoms cm^{-3}).

Clearly the full base profiles to be described in Part II can provide much more information than is obtainable from electrical measurements [see also Ref. (11)].

To examine the effect of varying the emitter diffusion time, t_e , a series of four samples were given the same base diffusion but different emitter diffusion times. Electrical profiling of these samples showed: (i) that the emitter and nonpushed-out base surface concentrations had been kept constant as required; (ii) that the amount of push-out, $\delta [= c - b]$, see Fig. 2(b), increased as t_e increased; and (iii) that the peak in the net p-type carrier concentration decreased as t_e increased. The junction depths were also measured by staining and are shown in Fig. 5. It can be seen from the figure that the nonpushed-out base depth was practically invariant as would be expected if the boron diffuses at its normal rate. (The 18 min/1200°C base drive-in diffusion is equivalent to 510 min at 1050°C and so the extra 15 to 35 min at 1050°C for the emitter should not noticeably deepen the base outside the emitter region.) Push-out, δ , is seen to increase with t_e . A straight line represents c vs t_e quite well and when extrapolated predicts almost zero push-out for $t_e = 0$.

The approximately linear increase of δ with t_e found here agrees with the recent results of Nakamura *et al.* (7) but is contrary to the early work on push-out by Gereth *et al.* (5). These last named authors apparently found no correlation of δ with t_e and suggested that push-out occurs during cooling following the emitter diffusion. Their cooling rate experiment is poorly designed, however, since no account was taken of the extra diffusion during the slow, 3°C/min, cool. This point has also been raised by Nakamura *et al.* (7) who could find no dependence on cooling rate them-

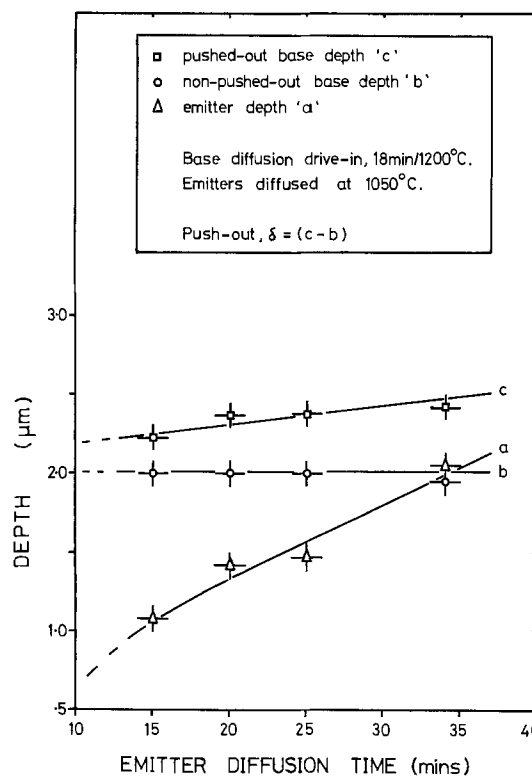


Fig. 5. Boron push-out vs. t_e

selves when they varied the cooling time from 1 to 180 sec following a 20 min/900°C phosphorus diffusion.

A linear increase of δ with t_e was predicted by Hu and Yeh (6) in their theoretical treatment of the push-out of an initially Gaussian base. The only assumptions they used to reach this result were that the base impurity diffusivity is uniformly enhanced throughout the emitter diffusion period and that the degree of enhancement is determined by the emitter diffusion and is independent of base diffusion parameters. The results of Fig. 5 can be used to estimate the magnitude, χ , of this enhancement following the method of Lee (8). Assuming both the pushed-out and nonpushed-out base profiles are Gaussian in shape and diffusion enhancement is constant throughout t_e , then

$$N_s = \frac{Q_b}{\sqrt{\pi D_b (t_e + t_b)}} \exp \left\{ -\frac{b^2}{4D_b (t_b + t_e)} \right\}$$

for the nonpushed-out base and

$$N_s = \frac{Q_b}{\sqrt{\pi D_b (t_b + \chi t_e)}} \exp \left\{ -\frac{c^2}{4D_b (t_b + \chi t_e)} \right\}$$

for the pushed-out base, where χ = enhancement factor; N_s = substrate doping concentration; t_e = emitter diffusion time; t_b = base diffusion time corrected to the equivalent at the emitter diffusion temperature; b = nonpushed-out base depth and c = pushed-out base depth, see Fig. 2(b); D_b = unenhanced base diffusivity at emitter diffusion temperature; and Q_b = base dopant atoms per cm^2 , considered constant.

Combining the two equations given above yields

$$\frac{t_b + \chi t_e}{t_b + t_e} = \exp \left\{ \frac{1}{2D_b} \left[\frac{b^2}{t_b + t_e} - \frac{c^2}{t_b + \chi t_e} \right] \right\} \quad [1]$$

Since the left-hand side of Eq. [1] is close to unity a good approximation for χ can be obtained from

$$\frac{b^2}{t_b + t_e} = \frac{c^2}{t_b + \chi t_e} \quad [2]$$

Table I gives the values of χ found using Eq. [2] which all lie in the range 9½-12 and there is apparently no systematic dependence of χ on t_e .

Table I. Enhancement factors for boron base. Emitter diffused at 1050°C

t_e , min	χ
15	9½
20	12
25	10
35	9½

Push-out of gallium by phosphorus emitter diffusion.—The shape of the gallium base profile prior to the emitter diffusion can be seen in Fig. 6. The set of three profiles was obtained by varying the ratio of H₂ to N₂ in the gas stream and shows clearly that the gallium concentration can be readily controlled in this system. The profiles are not complementary error functions but show a drop in concentration at the surface. An erfc can be fitted to part of the profile (see Fig. 6) yielding a diffusivity of 1.67×10^{-13} cm² sec⁻¹. In these diffusions the H₂ supply was turned off for about 1 min before removal of the sample but by reducing this flushing period the drop in concentration at the surface could be greatly reduced as shown in Fig. 7. This suggests that some out-diffusion is occurring during the flushing period and indeed Grove *et al.* (18) have shown that gallium out-diffuses very rapidly from oxidized silicon because diffusion through the oxide is so fast. The surface drop may also be due in part to compensation or electrical inactivity of the gallium as found by Okamura (19) for concentrations above 10¹⁸ cm⁻³.

The effect of emitter diffusion time, t_e , on the amount of gallium push-out was investigated as follows. A silicon wafer was gallium diffused for 120 min and cut into five pieces. The thin oxide grown during diffusion was etched into narrow stripes so that some areas of each piece were masked against phosphorus diffusion. Each piece was then phosphorus diffused at 1050°C for a different time and the junctions measured by grooving and staining. Figure 8 plots the depth of each junction [a, b, c, of Fig. 2(b)] as a function

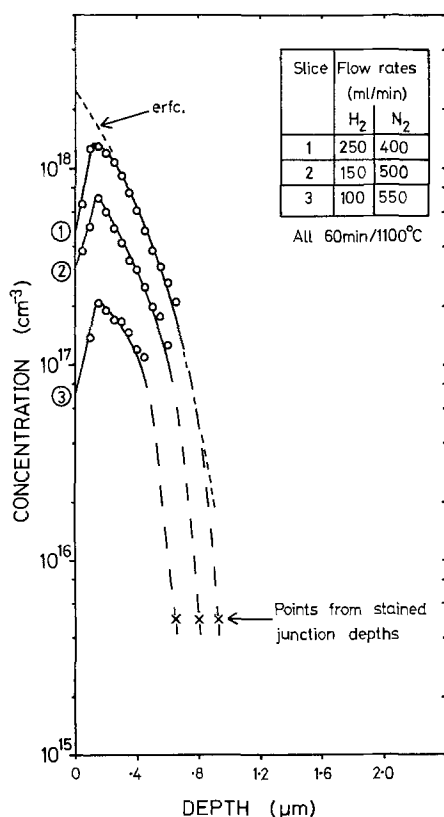


Fig. 6. Gallium profiles obtained for different gas compositions during diffusion, dashed line is complementary error function.

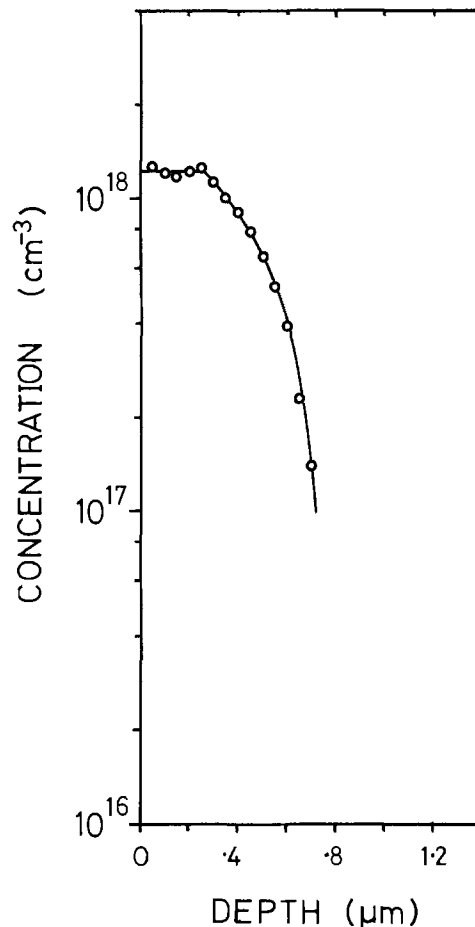


Fig. 7. Gallium diffusion for 30 min at 1100°C with short N₂ flush at the end.

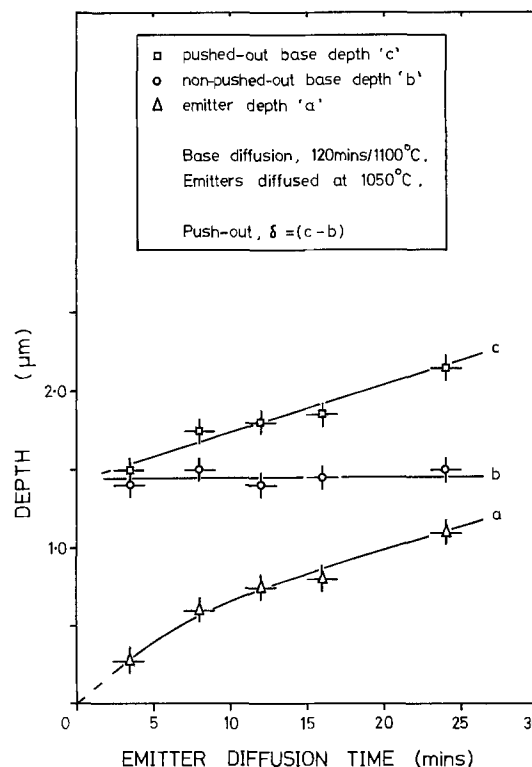


Fig. 8. Gallium push-out vs. t_e

of emitter diffusion time, t_e . It can be seen from the figure that gallium push-out ($c - b$) increases with t_e as for boron. A straight line represents c vs. t_e well and when extrapolated predicts zero push-out for $t_e = 0$.

Table II. Enhancement factors for gallium base. Emitter diffused at 1050°C

t_e , min	χ
3.5	16
8	17
12	21
16	15
24	17

The enhancement factors, χ , calculated using Eq. [2] are given in Table II. There is no systematic variation of χ with t_e for these gallium results nor for the boron results described above, but χ ranges from 15 to 21 for gallium as opposed to 9½-12 for boron. This apparent difference is discussed further at the end of this section.

The effect of varying the initial base depth, x_j , on the push-out of gallium was also investigated. Five pieces of silicon were gallium diffused for different times but under otherwise similar conditions to give layers of different depths (x_j) but equal surface concentration. All were then given the same phosphorus diffusion of 8 min at 1050°C, and their junction depths measured. Figure 9 shows push-out, $(c - b)$, plotted against x_j . It can be seen that push-out decreases as x_j increases in agreement with Nakamura *et al.*'s (7) and Lee's (8) results for boron. Lee's results are plotted in Fig. 9 for comparison (but note that his emitter conditions were not identical to those used for the gallium base experiment) and a further boron point has been obtained by extrapolating the results of Fig. 5 to $t_e = 8$ min (*i.e.*, emitter conditions identical to the gallium base experiment). The inverse relationship predicted by Hu and Yeh (6) assuming uniform enhancement throughout t_e and Gaussian base profiles is indicated by the dashed line in Fig. 9. An inverse relationship is also expected if the initial base is *erfc* (7).

The results described so far show that gallium behaves qualitatively exactly the same as boron but the χ values for gallium are higher than for boron for the same emitter diffusion. To test whether this discrepancy is real or whether it arises because the equation used to calculate χ (Eq. [2]) is derived assuming a Gaussian initial base profile, whereas the gallium base is initially *erfc* (apart from a drop in concentration at the surface), a further experiment was carried out. A gallium diffusion was performed in two parts: (i) 6 min at 1100°C with gallium depositing (H_2 on), (ii) 24 min drive-in in N_2 also at 1100°C. This schedule is

similar to the two-step boron process and should produce a more Gaussian base profile. The emitter was then diffused and the junction depths measured. The enhancement factor was calculated to be 12 which is comparable to the results for boron, and this indicates that there is no real discrepancy between the gallium and boron results.

Discussion

The results described above show that gallium is pushed-out in a very similar way to boron by a similar phosphorus emitter diffusion. Both dopants show (i) an increase in push-out with increasing emitter diffusion time for constant base diffusion and emitter surface concentration, and (ii) a decrease in push-out with increasing initial base depth for constant emitter diffusion and base surface concentration. The straight line representing pushed-out base depth, c , *vs.* t_e has a greater slope for the gallium base (Fig. 8) than for the boron base (Fig. 5) but this is as expected from the push-out *vs.* x_j results since the gallium base depths were shallower than those for boron, and for any particular t_e the shallower base should show the greater amount of push-out. The calculated enhancement factor, χ , is also the same for boron and gallium provided the initial base profile is Gaussian as is assumed in the calculation of χ .

The results also provide some valuable information both on the mechanism of push-out and on the diffusion mechanisms of boron and gallium. As pointed out by Hu (2) and Seeger and Chik (13), the mechanisms of diffusion of the Group III and Group V elements in silicon are still in considerable doubt. Mechanisms suggested for the Group III elements have been the vacancy (2) or interstitialcy (13) mechanisms and in view of this uncertainty it is not clear whether atoms like boron which have smaller covalent radii than the matrix silicon atoms, diffuse by the same mechanism as atoms like gallium, which have larger radii than the matrix atoms. The experiments reported above give direct evidence on the relation between these two elements, as reasoned in the following paragraph.

It is now well established from simultaneous marker layer and push-out studies (20) that push-out is caused by point defects rather than by direct interaction between base and emitter dopants: the main unresolved questions at present are how these point defects are generated and their identity. Most proposed generation mechanisms (6, 21, 22) would generate, however, one species of point defect only and it seems unlikely that even work-hardening generation mechanisms, which

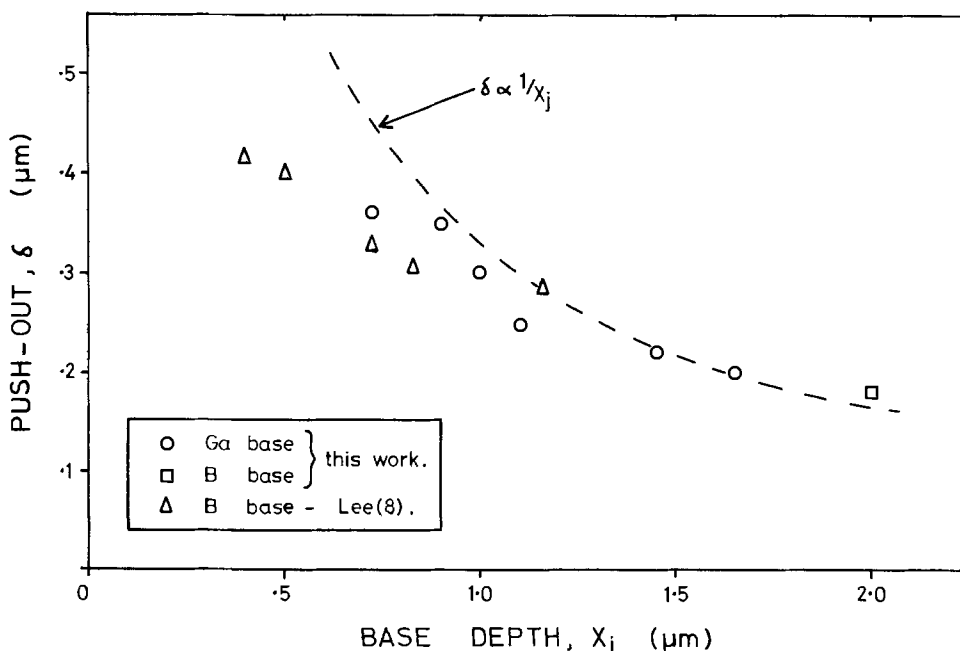


Fig. 9. Push-out vs. initial base depth. Dashed line is $\delta = \text{constant}/x_j$, as predicted by Hu and Yeh (6).

might generate both di-vacancies and di-interstitials, would always generate closely similar concentrations of both defect types. It thus follows from the observation in this work that boron and gallium are enhanced to such a closely similar extent that both diffuse by the same mechanism in silicon.

The agreement between experiment and Hu and Yeh's (6) theoretical predictions concerning the effects of t_e and x_j on δ suggest that push-out is due to a diffusion enhancement which is constant throughout the emitter diffusion period. This agreement cannot, however, be used to suggest that the enhancement is constant with depth, as Hu and Yeh assumed for mathematical convenience, for the following reason. The theory of sequential diffusion developed by Hu and Schmidt (23) shows that, when the base diffusion length during the emitter diffusion period is less than the initial base diffusion length, i.e.

$$\chi D_b t_e \lesssim D_b t_b \quad [3]$$

the base-collector junction movement is determined principally by the base diffusion coefficient beyond the emitter. In most practical cases of push-out condition [3] is met and the consequences are twofold.

(a) The agreement between experiment and theory mentioned above does not imply that χ is constant with depth and that push-out type enhancement is the only interaction between base and emitter dopants. In reality χ may fall off inside the emitter, and the electric field effect, Fermi-level effect, and ion-pairing may affect the base diffusion inside the emitter, but since these are all localized within the emitter they will have negligible influence on δ when condition [3] is satisfied. Agreement between experiment and theory does suggest, however, that χ is constant below the emitter to at least the base/collector junction. This conclusion has now been confirmed by the analysis of radiotracer profiles of pushed-out gallium bases, which will be reported in Part II of this paper.

(b) Although diffusion within the emitter region is complex, as will be shown in Part II, the simple theory assuming a uniform enhancement only can still be used to predict the amount of push-out. In other words, for the purposes of calculating δ the existence of the field effect, etc., within the emitter can be ignored.

Since the uniform enhancement model should be useful in predicting amounts of push-out it is worth discussing the theory and its predictions further. Without making any assumptions about the enhancement mechanism, except that χ is independent of t_e , and the base diffusion parameters, Hu and Yeh (6) obtained the following formula for the amount of push-out

$$\delta = \frac{2D_b(\chi - 1)t_e \ln(N_{b0}/N_s)}{\lambda^2 x_j} \quad [4]$$

where D_b = normal base diffusivity at emitter diffusion temperature; N_{b0} = base surface concentration before emitter diffusion; N_s = substrate doping concentration; and λ = a characteristic constant (≈ 0.73).

In deriving this formula Hu and Yeh make the approximation that $\Delta x_j \ll x_j$, where Δx_j is the increase in base depth as a result of the emitter diffusion. Since Δx_j outside the emitter (nonpushed-out base) is negligible, under the emitter $\Delta x_j \approx \delta$ [see Fig. 2(b)]. In the boron push-out work described above x_j was 2.0 μm and δ had a maximum value of 0.3 μm , while in the gallium push-out vs. t_e results x_j was 1.5 μm and δ had a maximum value of 0.6 μm so that the condition $\Delta x_j \ll x_j$ was barely met in these cases. The Hu and Yeh formula is thus likely to be a poor approximation when push-out becomes large. An alternative approach to the problem which also allows a better approximation for δ when push-out is large is given in the Appendix. The resulting formula for δ is

$$\delta = \frac{2D_b(\chi - 1)t_e \ln(N'_{b0}/N_s)}{b} \left\{ 1 - \frac{2D_b \chi t_e}{b^2} - \frac{2D_b t_b}{b^2} \right\} \quad [5]$$

where N'_{b0} = surface concentration of nonpushed-out base, and t_b = base drive-in time corrected to the equivalent at the emitter diffusion temperature.

Equation [5] is basically the same as Eq. [4] but with the following differences:

(i) Equation [5] contains N'_{b0} and b while Eq. [4] contains N_{b0} and x_j . In practice the differences between N'_{b0} and N_{b0} , x_j and b , are negligible because $D_b t_e \ll D_b t_b$. This has been pointed out above in the section on push-out of boron and was also noted by Hu and Yeh (6).

(ii) Equation [4] contains a characteristic constant λ . This is avoided in Eq. [5] by assuming that after drive-in and before the emitter diffusion the base is given by

$$N = N_{b0} \exp(-x^2/4D_b t_b)$$

an assumption which is valid when the diffusion length for the drive-in is much larger than for the deposition step.

(iii) Equation [5] contains additional terms in curly brackets. This is the most interesting difference and arises from the different approximation used to obtain Eq. [5], that is $\delta \ll 2b$ rather than $\delta \ll b$ (or $\Delta x_j \ll x_j$) used by Hu and Yeh; in other words Eq. [5] is applicable to larger amounts of push-out. The effect of these additional terms can be seen as follows. Firstly, when the base diffusion and χ are fixed but t_e varies, Eq. [5] can be rewritten as

$$\delta \propto t_e \cdot (m - q t_e)$$

where m and q are constants given by

$$m = 1 - \frac{2D_b t_b}{b^2} \quad \text{and} \quad q = \frac{2D_b \chi}{b^2}$$

In this case as t_e increases δ will drop below the straight line dependence on t_e predicted by Hu and Yeh and in fact some evidence of this can be seen in the results for boron, Fig. 5. The constants m and q can be estimated from the boron push-out parameters in the experimental section above and it is found, for this case, that $m \approx 1$ and $q = 6 \times 10^{-5} \text{ sec}^{-1}$. Then at $t_e = 35 \text{ min}$ δ is approximately 14% less than predicted by the simple linear relationship.

Secondly, when the emitter diffusion and base surface concentration are fixed but b varies, Eq. [5] can be rewritten as

$$\delta \propto \frac{1}{b} \left(m - \frac{\tau}{b^2} \right)$$

where τ is a constant given by $\tau = 2D_b \chi t_e$. It can be seen that as b decreases δ drops below the simple inverse relationship as was found for the gallium experimental results (Fig. 9). For example, using the gallium push-out data it turns out that at $b = 0.75 \mu\text{m}$, δ is approximately 22% less than predicted by the pure inverse relationship.

The analysis above indicates how Eq. [4] can be expected to break down when push-out is severe but because the additional terms of Eq. [5] involve D_b and χ the exact size of the corrections may be uncertain (D_b and χ are not usually known precisely) and therefore the approximation of Eq. [4] is generally more useful. Alternatively Eq. [5] can be used ignoring the bracketed terms. It should also be noted that for large amounts of push-out the assumption that D_b is enhanced uniformly with depth may begin to introduce other errors in δ because condition [3] is not satisfied.

To make the usefulness of the relations $\delta \propto t_e$ (for fixed base diffusion and emitter surface concentration) and $\delta \propto 1/x_j$ (for fixed emitter diffusion and base sur-

face concentration) clearer a graphical method for predicting push-out and base width in practical cases will now be described. First a curve of δ vs. x_j is established experimentally for the base surface concentration to be used and a particular emitter diffusion time $t_e = T$; see Fig. 10(a). This is best done with a few experimental points and fitting a curve $\delta = \text{constant}/x_j$ through these points. Next, for the required x_j and using Fig. 10(a), the expected push-out for $t_e = T$ is read off. On a graph of depth vs. t_e the points $(x_j + \delta, T)$ and $(x_j, 0)$ are plotted and a straight line drawn through them giving Fig. 10(b). This is the linear relationship between δ and t_e for given x_j . The emitter depth curve is then superimposed on Fig. 10(b) to give Fig. 10(c); the emitter curve is assumed to be independent of base parameters which is reasonable if the emitter profile has a steeply falling front. The push-out and base width for any t_e can now be obtained from Fig. 10(c). Base width vs. t_e curves have been calculated in this way for three base depths using the dashed line of Fig. 9 (Ga push-out vs. x_j results) together with the emitter depth curve of Fig. 8 (Ga push-out vs. t_e results) and are shown in Fig. 11 together with the experimental results for the 1.45 μm deep gallium base. The theory agrees well with experiment. In the figure solid lines end when the base is completely pushed-out, i.e., $a \cong b$ in Fig. 2(b). It is interesting to note that the base width does not always get narrower as the emitter is diffused deeper.

A final remark regarding the emitter diffusion period should be made. In all the theoretical analysis it is assumed that the whole of the emitter diffusion is at one temperature and that warm up and cool down are instantaneous. In a factory process large numbers of slices diffused together may make the warm up time a considerable fraction of the total emitter diffusion time and in this case the predictions discussed above may be difficult to apply.

Conclusions

(a) The push-out of a gallium base is very similar to that of a boron base under identical emitter diffusions, when observed by the junction depth method. This suggests that boron and gallium both diffuse by the same mechanism in silicon, despite their different covalent radii.

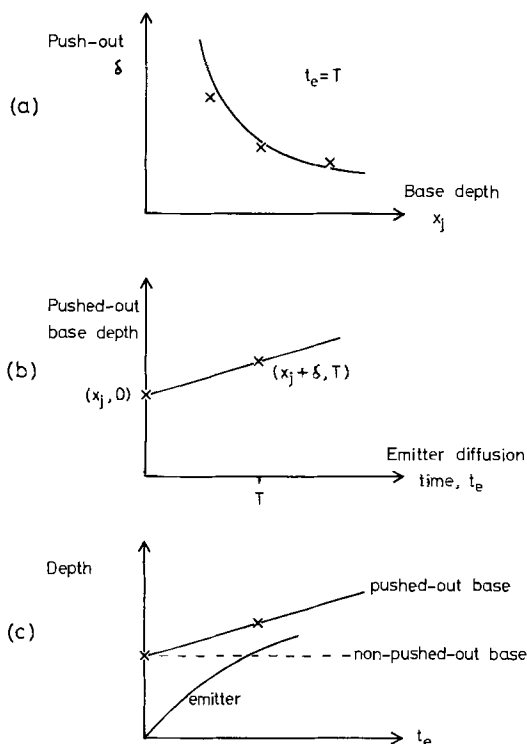


Fig. 10. Graphical method to predict push-out and base-width

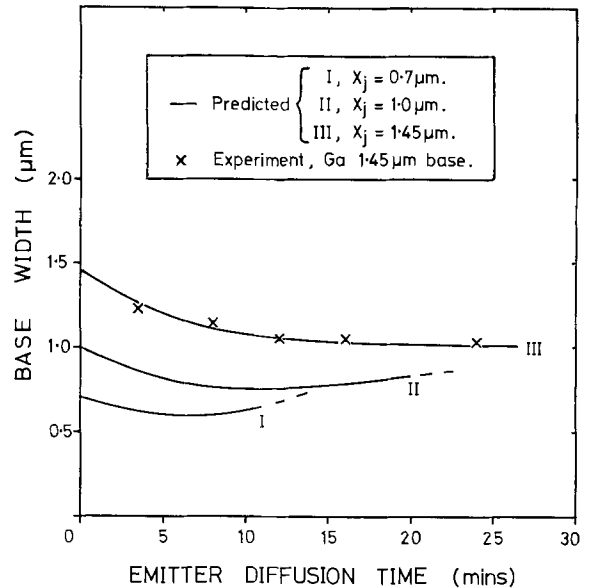


Fig. 11. Base width vs. t_e (1050°C emitter diffusion). Solid lines are predicted base widths. Points x are experimental values for the gallium 1.45 μm base.

(b) For both dopants push-out, δ , increases practically linearly with emitter diffusion time, t_e , when the base diffusion and emitter surface concentration are fixed. In common with Nakamura *et al.* (7) it is concluded that push-out occurs during the emitter diffusion rather than during cooling following the emitter diffusion.

(c) For both dopants δ decreases with increase in x_j , the initial base depth, when the emitter diffusion and base surface concentration are fixed.

(d) Push-out and base width can be predicted approximately by making use of conclusions (b) and (c) together with a few experimentally determined junction depths.

(e) Agreement between the experimental results and theory strongly suggests that push-out is due to an enhancement of the base diffusivity throughout the emitter diffusion period; the magnitude of enhancement being controlled by the emitter diffusion conditions.

(f) Junction depth measurements cannot tell how the diffusivity enhancement varies with depth except that it is probably constant below the emitter. The only means of determining diffusion processes within the emitter is by obtaining the complete chemical profile of the base as will be shown in Part II.

Acknowledgments

The authors wish to thank the Microelectronics Laboratory of Southampton University for providing phosphorus and boron diffusion facilities, Westinghouse Brake and Signal Company Limited (Chippenham) for advice on gallium diffusion, Mr. J. Keen of R.R.E. Malvern for useful discussions throughout this work, and Professor R. L. Bell for provision of laboratory facilities and discussions. This work has been carried out with the support of Procurement Executive, Ministry of Defense and sponsored by D.C.V.D.

Manuscript received March 24, 1975.

Any discussion of this paper will appear in a Discussion Section to be published in the June 1976 JOURNAL. All discussions for the June 1976 Discussion Section should be submitted by Feb. 1, 1976.

APPENDIX

Approximate Formula for δ

Suppose that before the emitter diffusion the base profile can be described by the Gaussian

$$N(x) = \frac{Q_b}{\sqrt{\pi D_b t_b}} \exp \left\{ -\frac{x^2}{4D_b t_b} \right\} \quad [\text{A-1}]$$

where $N(x)$ is the base dopant concentration at depth x ; Q_b is the quantity of base dopant per cm^2 surface; D_b is the normal base diffusivity at the emitter diffusion temperature; and t_b is the base diffusion time (drive-in) corrected to the equivalent time at the emitter diffusion temperature.

After the emitter diffusion and assuming uniform enhancement, χ , the nonpushed-out base is given by

$$N_1(x) = \frac{Q_b}{\sqrt{\pi D_b (t_b + t_e)}} \exp \left\{ -\frac{x^2}{4D_b (t_b + t_e)} \right\} \quad [\text{A-2}]$$

while the pushed-out base is

$$N_2(x) = \frac{Q_b}{\sqrt{\pi D_b (t_b + \chi t_e)}} \exp \left\{ -\frac{x^2}{4D_b (t_b + \chi t_e)} \right\} \quad [\text{A-3}]$$

where t_e is the emitter diffusion time. (It is assumed that no loss or gain of base dopant occurs during the emitter diffusion.)

At the base-collector junctions the base concentrations are equal to the substrate doping level N_s , i.e., $N_1(b) = N_2(c) = N_s$. Therefore, from Eq. [A-2] and [A-3]

$$\frac{t_b + \chi t_e}{t_b + t_e} = \exp \left\{ \frac{1}{2D_b} \left[\frac{b^2}{t_b + t_e} - \frac{c^2}{t_b + \chi t_e} \right] \right\} \quad [\text{A-4}]$$

The left-hand side of Eq. [A-4] can be rewritten as

$$1 + \frac{(\chi - 1)t_e}{t_b + t_e}$$

where the term $\frac{(\chi - 1)t_e}{t_b + t_e}$ is positive and generally less than unity. Taking logarithms of both sides of Eq. [A-4] and using the series expansion for $\ln(1 + x)$, i.e., $\ln(1 + x) = x - x^2/2 + x^3/3 \dots -1 \leq x < 1$, then

$$\frac{(\chi - 1)t_e}{t_b + t_e} \approx \frac{1}{2D_b} \left[\frac{b^2}{t_b + t_e} - \frac{c^2}{t_b + \chi t_e} \right] \quad [\text{A-5}]$$

where only the first term in the series has been retained because the other terms are small. Rearranging Eq. [A-5] gives

$$b - c = \frac{t_e}{(b + c)t_b} [2D_b \chi (\chi - 1)t_e + 2D_b (\chi - 1)t_b - \chi b^2 + c^2] \quad [\text{A-6}]$$

Now assume that $\delta \ll 2b$, where δ is the amount of push-out and equals $(c - b)$; this is a less restrictive approximation than that of Hu and Yeh (6). Then $b + c = 2b + \delta \approx 2b$ and terms in δ^2 can be ignored. Equation [A-6] then becomes

$$\delta = \frac{t_e(\chi - 1)}{2b(t_b + t_e)} [b^2 - 2D_b \chi t_e - 2D_b t_b] \quad [\text{A-7}]$$

Now

$$N_s = N'_{bo} \exp \left\{ -\frac{b^2}{4D_b(t_b + t_e)} \right\}$$

where N'_{bo} is the nonpushed-out base surface concentration. Therefore

$$\frac{b^2}{t_b + t_e} = 4D_b \ln(N'_{bo}/N_s)$$

and using this in Eq. [A-7] gives

$$\delta = \frac{2D_b(\chi - 1)t_e \ln(N'_{bo}/N_s)}{b} \left\{ 1 - \frac{2D_b \chi t_e}{b^2} - \frac{2D_b t_b}{b^2} \right\}$$

This formula gives the amount of push-out in terms of the base diffusion parameters D_b , N'_{bo} , b , t_b , and the emitter diffusion parameters χ and t_e .

REFERENCES

1. A. F. W. Willoughby, *J. Mat. Sci.*, **3**, 89 (1968).
2. S. M. Hu, in "Atomic Diffusion in Semiconductors," D. Shaw, Editor, Plenum Press, London (1973).
3. L. E. Miller, in "Properties of Elemental and Compound Semiconductors," H. Gatos, Editor, Interscience Publishers, Inc., New York (1960).
4. J. E. Lawrence, *J. Appl. Phys.*, **37**, 4106 (1966).
5. R. Gereth, P. G. G. Van Loon, and V. Williams, *This Journal*, **112**, 323 (1965).
6. S. M. Hu and T. H. Yeh, *J. Appl. Phys.*, **40**, 4615 (1969).
7. H. Nakamura, S. Ohyama, and C. Tadachi, *This Journal*, **121**, 1377 (1974).
8. D. B. Lee, *Philips Res. Rept. Suppl.* No. 5 (1974).
9. K. H. Nicholas, *Solid-State Electron.*, **9**, 35 (1966).
10. R. L. Kronquist, J. P. Soula, and M. E. Brillman, *ibid.*, **16**, 1159 (1973).
11. C. L. Jones and A. F. W. Willoughby, *Appl. Phys. Letters*, **25**, 114 (1974).
12. Y. Sato and H. Arata, *Japan. J. Appl. Phys.*, **3**, 511 (1964).
13. A. Seeger and K. P. Chik, *Phys. Status Solidi*, **29**, 455 (1968).
14. D. L. Kendall and D. DeVries, in "Semiconductor Silicon," R. R. Haberecht and E. L. Kern, Editors, The Electrochemical Society, Softbound Symposium Series, New York (1969).
15. C. J. Frosch and L. Derrick, *This Journal*, **104**, 547 (1957).
16. R. A. Evans and R. P. Donovan, *Solid-State Electron.*, **10**, 155 (1967).
17. J. C. Irvin, *Bell System Tech. J.*, **41**, 387 (1962).
18. A. S. Grove, O. J. Leistiko, and T. Sah, *J. Appl. Phys.*, **35**, 2695 (1964).
19. M. Okamura, *Japan. J. Appl. Phys.*, **10**, 434 (1971).
20. D. B. Lee and A. F. W. Willoughby, *J. Appl. Phys.*, **43**, 245 (1972).
21. R. F. Peart and R. C. Newman, in "Radiation Damage and Defects in Semiconductors," Institute of Physics, London (1972).
22. M. Yoshida, E. Arai, H. Nakamura, and Y. Terunuma, *J. Appl. Phys.*, **45**, 1498 (1974).
23. S. M. Hu and S. Schmidt, *ibid.*, **39**, 4272 (1968).

Ion Implanted Profiles from Two Point Spreading Resistance Measurements

T. E. Hendrickson

Solid State Electronics Center, Honeywell Incorporated, Plymouth, Minnesota 55441

ABSTRACT

A modified form of the Schumann and Gardner approach to correction of spreading resistance data, appropriate for a two point geometry, is given. Plotting the results of a numerical evaluation of "unilayer" theory yields a universal correction curve, useful for hand calculation. As an example of the use of this plot, consideration is given to the cases of 150 and 300 keV boron implants in (100) silicon.

Several authors have presented work based on numeric evaluation of three point spreading resistance data (1-3). More recently, however, the two point configuration (see the insert in Fig. 1) has become widely accepted. Owing to a fundamental difference in the quantities measured, modifications must be made to the basic three point formula. The formula thus obtained differs in form from that reported previously (1).

In contrast to other profiling techniques, spreading resistance data may be readily obtained from currently available commercial equipment.¹ The primary task is therefore one of accurately determining the appropriate correction factors (CF) to be applied. The work presently described represents the application of the simplest "unilayer" theory to the case of ion implanted layers. Correction factors determined in this fashion can be conveniently displayed in a "universal" plot suitable for hand calculation.

Correction Factors (CF)

In the three point geometry, current is forced through two probes while the voltage is measured between one of these points and a third probe "floating" with the body of the semiconductor. Detailed consideration of this geometry leads to the formula

$$V_{\text{measured}} = V_{\text{spreading}} + V_1(2s) - 2V_1(s)$$

where $V_1(r)$ is the surface potential, relative to the probe tip, at a distance r ; and s is the probe tip spacing. For the case of the two probe geometry, the measured voltage takes the simpler form

$$V_{\text{measured}} = 2(V_{\text{spreading}} - V_1(s))$$

Applying the general formula for $V_{\text{spreading}}$ and $V_1(r)$ developed by Schumann and Gardner (1) yields the form

$$R_{\text{spreading}} = \frac{V_{\text{measured}}}{2I_{\text{measured}}} = \frac{\rho_2}{2r_0} \left\{ \frac{4}{\pi} \int_0^\infty \left(\frac{1 + Ke^{-2hx}}{1 - Ke^{-2hx}} \right) \left(\frac{J_1(x)}{2X^2} - \frac{J_0(Sx)}{4X} \right) \sin(x) dx \right\}$$

where J_1 , J_0 = Bessel functions; $K = \rho_1 - \rho_2/\rho_1 + \rho_2$; $S = s/r_0$; r_0 = effective radius of the probe tip; s = probe spacing; $h = d/\tau_0$; d = thickness of the layer; and ρ_1 , ρ_2 = resistivities of the layers (see Fig. 1). The term in brackets is normally labeled the correction factor. Use is made of this quantity through the relationship

$$\rho_{\text{corrected}} = \rho_2 = (2r_0 R_{\text{spreading}}) / \text{CF}$$

Where the quantity $2r_0 R_{\text{spreading}}$ is obtained directly from a calibration chart (4) is hereafter referred to as ρ' .

Key words: unilayer theory, hand computations, channeling.

¹ The ASR-100 Mazur Automatic Spreading Resistance Probe purchasable from Solid State Measurements, Inc. was used in this work.

The form for the correction factor given here is that appropriate for two layers [referred to elsewhere as the unilayer theory (1)] of resistivity ρ_1 and ρ_2 and thicknesses ∞ and d , respectively. Since the background layer (ρ_1) is assumed to be of semi-infinite extent, its corrected resistivity is set equal to the measured resistivity taken from the calibration chart. Calculation of CF for a given value of ρ_2 then proceeds in the following manner:

1. Set ρ''_2 equal to ρ_2 and CF equal to 1.
2. Calculate CF' from the corresponding value of K (i.e., $K = \rho_1 - \rho''_2/\rho_1 + \rho''_2$).
3. If CF' is not within 0.5% of CF, set CF equal to CF' , ρ''_2 equal to ρ_2/CF' , and repeat step 2.
4. If CF' is within 0.5% of CF, set ρ_2 corrected = ρ_2'/CF' .

This procedure will yield values for CF self-consistent with the definition of K . Normally four to five iterations yield the desired accuracy.

Values for CF computed in the above-described fashion with s and r_0 set equal to 85 and 4μ ,² respectively, are plotted in Fig. 1. This plot has been made in a form convenient for hand calculation by plotting CF vs. the dimensionless parameter ρ defined as the ratio ρ_2/ρ_1 . The layer thickness (d) is used as a running parameter.

To use Fig. 1, correction is begun at the deepest portion of the profile and carried forward toward the surface. The general outline to be followed is (see Fig. 2):

1. Divide the profile into a set of equally spaced data points, beginning at the deepest point of the profile and continuing toward the surface.
2. Compute the ratios $\bar{\rho}'_1/\bar{\rho}'_0$, $\bar{\rho}'_2/\bar{\rho}'_1$, . . . , $\bar{\rho}'_n/\bar{\rho}'_{n-1}$, where $\bar{\rho}'_n$ represents the average of all data points contained in an interval of width d centered about the point ρ_n .
3. Find the appropriate values of CF from Fig. 1 and compute

$$\rho_n \text{ corrected} = \rho'_n / \text{CF} (\bar{\rho}'_n / \bar{\rho}'_{n-1})$$

The above outlined procedure is simple and direct, allowing for ease in hand computations. Use of this form of "tabular look-up with averaging" yields a rapidly executing alternative to the more lengthy multilayer approach (3). Averaging lengths can be readily varied according to the depth of the profile, however experience has shown the limits $0.75\mu \cong d \cong 0.15\mu$ to yield the best results.

Results

Corrected (dashed) and uncorrected (solid) resistivity curves are given in Fig. 2 for the case of a boron implanted layer in (100) p-type silicon. The implant was performed at an energy of 300 keV and dose of $10^{14}/\text{cm}^2$ through 680Å of thermally grown SiO_2 . An-

² This value for r_0 was obtained by finding the radius of the smallest circle entirely enclosing the probe markings on an SEM.

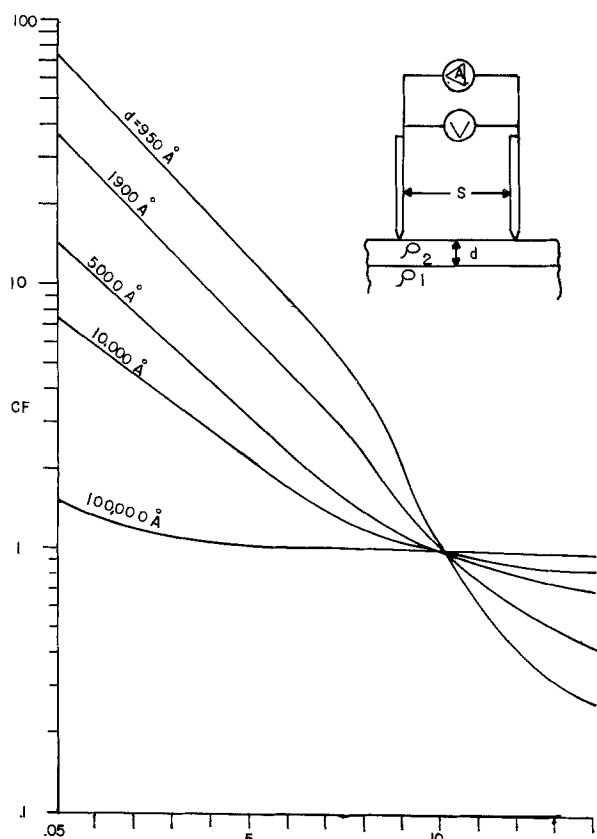


Fig. 1. Correction factor (CF) plotted as a function of the dimensionless parameter $\rho = \rho_2/\rho_1$ with thickness used as a running parameter. The curves are given for $s = 85$ and $r_0 = 4\mu$.

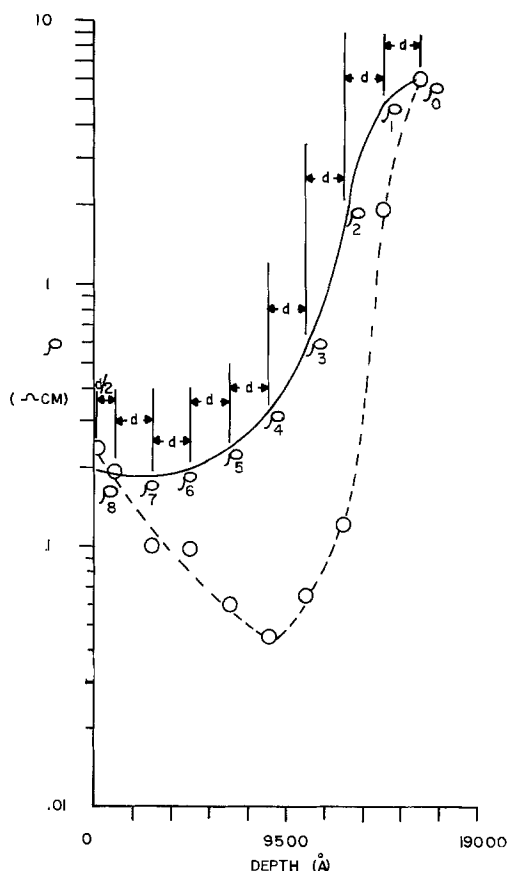


Fig. 2. Uncorrected (solid line) and corrected (dashed line) resistivity vs. depth curves for the case of boron implanted (energy = 300 keV; dose = $10^{14}/\text{cm}^2$) into (100) silicon through 680Å SiO_2 .

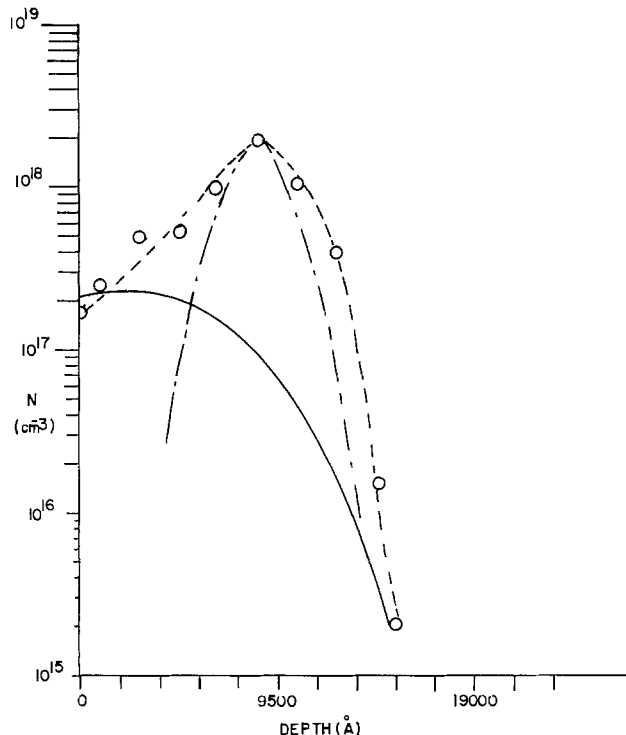


Fig. 3. Uncorrected (solid) and corrected (dashed) doping profiles obtained from Fig. 2. Also given is the shape predicted by the LSS theory (— · —).

nealing was performed at 950°C for 25 min in dry N_2 . Comparison of the two curves graphically demonstrates the "masking" of the implant peak by the uncorrected data.

Converting these curves into doping profiles results in the plot of Fig. 3. Also plotted here is the distribution predicted by the LSS theory.³ Notice that the measured range is in close agreement with theory, as is the peak concentration ($\sim 1.98 \times 10^{18}/\text{cm}^3$ empirical vs. $2.1 \times 10^{18}/\text{cm}^3$ theoretical). In contrast to this, the empirical curve displays a much larger value for the projected straggle (ΔR_p). A close fit to the data presented here is given by $\Delta R_p = 1460\text{Å}$ (curve not shown) which is in reasonable agreement with values observed by other authors (5) (typically 900-1300Å). The somewhat larger value found here is most likely ascribable to either an anomalously high diffusion rate during the post-implantation anneal, or errors introduced during correction of the profile [owing to the absence of an exponential tail normally observed in such implants (6), it seems reasonable to assume that the correction procedure has smeared this feature into the normal Gaussian shape thereby increasing ΔR_p measured]. The relatively high surface concentration ($\sim 2 \times 10^{17}/\text{cm}^3$) observed appears to represent a real phenomenon observable in all implants performed to date.

A second example of an ion implanted boron layer is given in Fig. 4. This implant was performed analogously to the first with an energy of 150 keV and dose of $10^{14}/\text{cm}^2$. Perhaps the most salient feature observable in this profile is the pronounced appearance of a channelled peak in the profile (note: though only one channelled point was chosen for correction, in all 8 actual data points were found to lie along this portion of the curve). This channelled peak was found to be present for all those implants performed at 200 keV or less, through $\sim 700\text{Å}$ SiO_2 . Agreement with the LSS theory (dashed curve) was found to be excellent for this implant.

Referring back to Fig. 3, notice that both the 150 and 300 keV implants show a definite surface inversion at

³ Allowance has been made for field-enhanced diffusion during the post-implantation anneal.

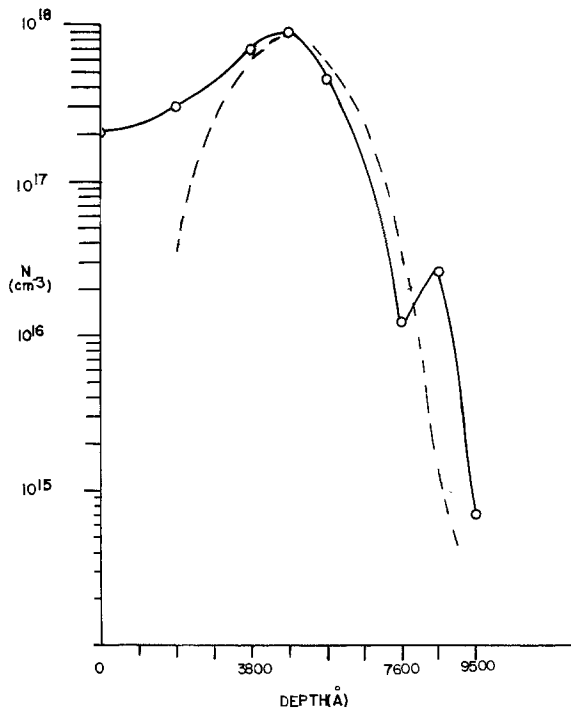


Fig. 4. Corrected profile for a 150 keV boron implant (solid) vs. that obtained from the LSS theory (dashed).

a doping level of approximately $2 \times 10^{17}/\text{cm}^3$. Speculation on the origin of this surface layer has led to the proposal that a p-type impurity normally present in the material has been getterd by the damage sites. Such an observation would appear consistent with results obtained by other authors (7).

Conclusion

Two point spreading resistance data have proven to be a reliable means of profiling ion implants when corrected by a modified form of the Schumann-Gardner approach. Correction factors computed from unilayer theory yield profiles consistent with work performed previously by other authors. Certain effects, most notably channeling and unexpected surface inversion, seem readily discernable by this technique.

Acknowledgments

The author would like to express gratitude to Dr. J. Huang for helpful discussions on the text and A. Ramde for preparation of samples used in this study.

Manuscript submitted April 7, 1975; revised manuscript received June 30, 1975.

Any discussion of this paper will appear in a Discussion Section to be published in the June 1976 JOURNAL. All discussions for the June 1976 Discussion Section should be submitted by Feb. 1, 1976.

Publication costs of this article were partially assisted by Honeywell Incorporated.

REFERENCES

1. P. A. Schumann, Jr. and E. E. Gardner, *Solid-State Electron.*, **12**, 371 (1969).
2. P. A. Schumann, Jr. and E. E. Gardner, *This Journal*, **116**, 87 (1969).
3. T. H. Yeh and K. H. Khokhani, *ibid.*, **116**, 1461 (1969).
4. R. G. Mazur and D. H. Dickey, *ibid.*, **113**, 255 (1966).
5. K. Wittmaack, J. Maul, and F. Schulz, in "Ion Implantation in Semiconductors and Other Materials," B. L. Crowder, Editor, pp. 119-131, Plenum Press, New York (1973).
6. W. K. Hofker, H. W. Werner, D. P. Oosthoek, and H. A. M. deGrefte, *ibid.*, pp. 133-145.
7. J. M. Poate and T. E. Seiden, *ibid.*, pp. 317-329.

Interface Demarcation during LPE Growth of GaAs

G. M. Blom,* J. J. Daniele,* and T. Kyros

Philips Laboratories, Briarcliff Manor, New York 10510

and A. F. Witt*

Massachusetts Institute of Technology, Department of Material Science, Cambridge, Massachusetts 02138

ABSTRACT

Liquid phase epitaxial growth is studied using interface demarcation during growth by transmitting current pulses across the substrate solution interface. This approach permits the investigation of the growth interface morphology and the determination of the instantaneous microscopic growth rate and epitaxial growth efficiency for any time of the cooling cycle. It is shown that the growth interface can be subject to significant transient morphological perturbations which are not necessarily reflected in the surface morphology of the epitaxial layers.

While liquid phase epitaxy (LPE) is recognized as one of the most important techniques for the production of high quality electronic materials and structures, many aspects of the basic growth process are as yet unexplained and subject to various interpretations. The microscopic growth rate variations associated with a particular cooling rate for any given system have to date only been approximated from layer thickness determinations (1-4). Reliable data on solute diffusivity, which are required to theoretically explain the micro-

scopic growth behavior, are as yet unavailable (5, 6). In addition, the nature of transient growth conditions during the initial part of the cooling cycle is as yet unresolved. Furthermore, incomplete knowledge of the growth and segregation controlling parameters is responsible for our inability to predict effective distribution coefficients, hence desired layer compositions are achieved on the basis of empirical growth procedures. Also unresolved to date is the mode of epitaxial solution growth on substrates of low-index surface orientation (2, 7). The experimental determination of the growth mode is of more than theoretical importance, since the segregation behavior and thus the composi-

* Electrochemical Society Active Member.

Key words: epitaxy, gallium arsenide, dopant segregation, growth rate.

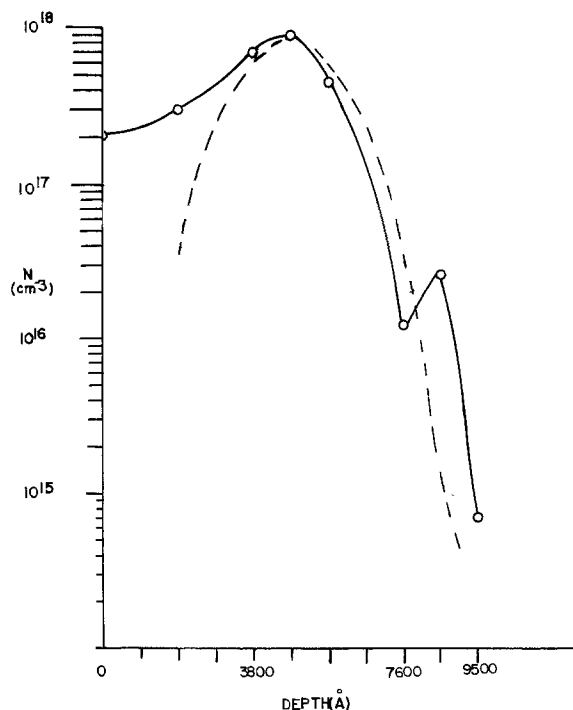


Fig. 4. Corrected profile for a 150 keV boron implant (solid) vs. that obtained from the LSS theory (dashed).

a doping level of approximately $2 \times 10^{17}/\text{cm}^3$. Speculation on the origin of this surface layer has led to the proposal that a p-type impurity normally present in the material has been getterd by the damage sites. Such an observation would appear consistent with results obtained by other authors (7).

Conclusion

Two point spreading resistance data have proven to be a reliable means of profiling ion implants when corrected by a modified form of the Schumann-Gardner approach. Correction factors computed from unilayer theory yield profiles consistent with work performed previously by other authors. Certain effects, most notably channeling and unexpected surface inversion, seem readily discernable by this technique.

Acknowledgments

The author would like to express gratitude to Dr. J. Huang for helpful discussions on the text and A. Ramde for preparation of samples used in this study.

Manuscript submitted April 7, 1975; revised manuscript received June 30, 1975.

Any discussion of this paper will appear in a Discussion Section to be published in the June 1976 JOURNAL. All discussions for the June 1976 Discussion Section should be submitted by Feb. 1, 1976.

Publication costs of this article were partially assisted by Honeywell Incorporated.

REFERENCES

1. P. A. Schumann, Jr. and E. E. Gardner, *Solid-State Electron.*, **12**, 371 (1969).
2. P. A. Schumann, Jr. and E. E. Gardner, *This Journal*, **116**, 87 (1969).
3. T. H. Yeh and K. H. Khokhani, *ibid.*, **116**, 1461 (1969).
4. R. G. Mazur and D. H. Dickey, *ibid.*, **113**, 255 (1966).
5. K. Wittmaack, J. Maul, and F. Schulz, in "Ion Implantation in Semiconductors and Other Materials," B. L. Crowder, Editor, pp. 119-131, Plenum Press, New York (1973).
6. W. K. Hofker, H. W. Werner, D. P. Oosthoek, and H. A. M. deGrefte, *ibid.*, pp. 133-145.
7. J. M. Poate and T. E. Seiden, *ibid.*, pp. 317-329.

Interface Demarcation during LPE Growth of GaAs

G. M. Blom,* J. J. Daniele,* and T. Kyros

Philips Laboratories, Briarcliff Manor, New York 10510

and A. F. Witt*

Massachusetts Institute of Technology, Department of Material Science, Cambridge, Massachusetts 02138

ABSTRACT

Liquid phase epitaxial growth is studied using interface demarcation during growth by transmitting current pulses across the substrate solution interface. This approach permits the investigation of the growth interface morphology and the determination of the instantaneous microscopic growth rate and epitaxial growth efficiency for any time of the cooling cycle. It is shown that the growth interface can be subject to significant transient morphological perturbations which are not necessarily reflected in the surface morphology of the epitaxial layers.

While liquid phase epitaxy (LPE) is recognized as one of the most important techniques for the production of high quality electronic materials and structures, many aspects of the basic growth process are as yet unexplained and subject to various interpretations. The microscopic growth rate variations associated with a particular cooling rate for any given system have to date only been approximated from layer thickness determinations (1-4). Reliable data on solute diffusivity, which are required to theoretically explain the micro-

scopic growth behavior, are as yet unavailable (5, 6). In addition, the nature of transient growth conditions during the initial part of the cooling cycle is as yet unresolved. Furthermore, incomplete knowledge of the growth and segregation controlling parameters is responsible for our inability to predict effective distribution coefficients, hence desired layer compositions are achieved on the basis of empirical growth procedures. Also unresolved to date is the mode of epitaxial solution growth on substrates of low-index surface orientation (2, 7). The experimental determination of the growth mode is of more than theoretical importance, since the segregation behavior and thus the composi-

* Electrochemical Society Active Member.

Key words: epitaxy, gallium arsenide, dopant segregation, growth rate.

tion of the epitaxial layer in the facet growth mode is controlled by the lateral growth rate rather than by the microscopic growth rate normal to the established growth interface (8-10). In this context it is important to realize that the functional dependence of the effective segregation coefficient on experimental variables for facet growth is still unknown (11).

The purpose of the present study was to investigate the microscopic growth behavior during LPE of GaAs (Te-doped) by means of interface demarcation. This technique, originally applied to the quantitative study of melt growth (12), was applied recently also to solution growth of InSb (13). Interface demarcation is achieved by transmitting periodic current pulses across the solid-liquid (S-L) interface. Each pulse, depending on the direction of current flow, leads to Peltier cooling or heating at the growth interface (14) (for the duration of the pulse) and thus to temporarily accelerated or decelerated growth (or even dissolution). The temporary growth rate change, which is uniform over all parts of the growing epitaxial layer if the current density is uniform across the interface, results in an alteration of effective dopant segregation. This yields a precise demarcation of the growth interface by producing dopant concentration striations that are readily revealed by cleaving the wafer and etching the exposed cleavage plane. Using current pulses of known repetition rate, it is thus possible to determine the microscopic growth rate from the spacing of the induced striations. It is furthermore possible to study the interface morphology from beginning to end of the growth experiment and to establish the relationship between growth and surface morphology of the epitaxial layer.

Experimental Procedure

The LPE experiments were carried out under flowing H_2 in a horizontal graphite boat (Fig. 1). The top part of the boat, containing a Te-doped Ga-As solution, was electrically isolated by a BN slider from the bottom part containing the GaAs substrate. Uniform electrical contact to the bottom surface of the substrate [(100) orientation, n-type, Si-doped to $10^{18}/cm^3$] was achieved by wetting the back side of the substrate with liquid Ga. The top and bottom sections of the boat were connected with stainless steel rods to a programmable d-c power supply. After the system was brought to the desired temperature (typically $850^\circ C$), substrate-solution contact was established by moving the slider into the appropriate position, and cooling was initiated at a rate of $0.25^\circ C/min$. During cooling, current pulses of up to 20A ($13.3 A/cm^2$) and of a duration ranging from 0.1 to 8 sec were transmitted at time intervals ranging from 1 to 10 min. After completion of a growth experiment, the solution was isolated from the epilayer by moving the slider into its original position. The wafer was subsequently cleaved along a (110) plane, and the cleaved face was etched for 30 sec in an AB etching solution (15) (8 mg $AgNO_3$, 1g CrO_3 , 1 ml HF, 2 ml H_2O) and then examined by interference contrast microscopy.

In preliminary experiments it was observed that the transmission of current pulses of either polarity, cor-

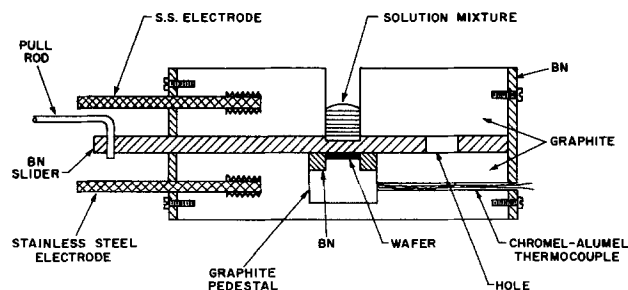


Fig. 1. Schematic diagram of boat used for LPE growth of GaAs with interface demarcation.

responding to current flow from seed to solution or the reverse, resulted in effective interface demarcation. The thermal effects associated with demarcation were measured with a Chromel-Alumel thermocouple (not shown in Fig. 1) located 1.2 mm from the edge of the S-L interface. To determine the sign of the Peltier coefficient and the relative contributions of Joule heating and of Peltier heating or cooling, four 2-sec current pulses of $+5.35$, -5.35 , $+2.67$, and $-2.67 A/cm^2$ were successively applied across the S-L interface (a + sign indicates that the solution has a positive polarity with respect to the substrate). The resulting temperature effects are shown in Fig. 2.

It is seen in Fig. 2 that the pulse of $+2.67 A/cm^2$ resulted in a temperature increase, while the pulse of $-2.67 A/cm^2$ caused a temperature decrease. The occurrence of the temperature decrease shows that at this current density Peltier cooling and heating ($=PI$) exceeded Joule heating ($=I^2R$), which tends to raise the temperature regardless of current polarity. From the observed relationship between the thermal effects and current direction, the Peltier coefficient is positive, according to the sign convention of Ref. (16). For pulses of $\pm 5.35 A/cm^2$, it is seen in Fig. 2 that the temperature increased for both current directions, although the increase was appreciably greater for the positive pulse. At this current density Joule heating had become dominant, because of its dependence on I^2 , although the relative magnitude of the Peltier effect was still large enough to have a significant influence on the temperature change. The dominance of Joule heating was observed for current densities exceeding about $3 A/cm^2$. In experiments of GaAlAs, however, it has been demonstrated that under certain conditions substantial net cooling can be achieved by the Peltier effect even at high current densities (17).

Results and Discussion

In the experiments described here the polarity of the current pulses was positive, so that both Peltier heating and Joule heating occurred at the growth interface. The resulting demarcation effects are visible in Fig. 3, which is a photomicrograph of a cleaved and etched GaAs LPE layer. During the growth of this layer, 25 current pulses of $13 A/cm^2$ and 0.5 sec duration were transmitted at 5 min intervals. The width of the observed demarcation bands is in all instances about $3 \mu m$, independent of the temperature, which decreased from 851° to $815^\circ C$ during the experiment. Since the solubility of As in liquid Ga decreases from approximately 3.8 to 2.6 atomic per cent over this temperature range (18), it must be concluded that the current-induced growth is not an equilibrium process. The formation of demarcation bands is attributed to temporary dissolution of a thin region of the LPE layer, due to the heat generated at

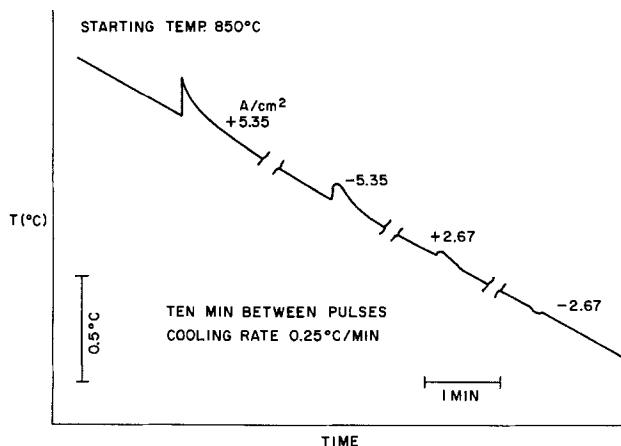


Fig. 2. Temperature-time profile for LPE experiment, showing the temperature changes associated with the transmission of current pulses across the solid-liquid interface.

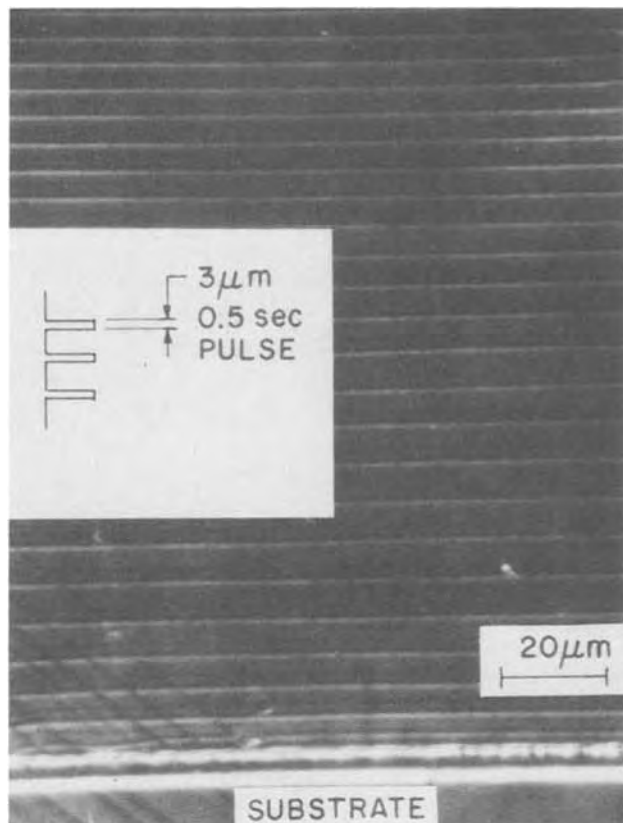


Fig. 3. Photomicrograph of a cleaved and etched GaAs layer grown by LPE with interface demarcation. During growth, 25 pulses of 0.5 sec duration were transmitted at 5 min intervals.

the S-L interface, followed by very rapid regrowth of this region after termination of current flow; The segregation varies with growth rate and the etching rate of the cleavage plane is a function of the Te concentration. (No demarcation lines could be observed in undoped GaAs.) This interpretation is consistent with the constant width of the demarcation bands, since the amount of heat generated per pulse was constant and the heat of fusion and heat capacity of GaAs can be assumed constant over the temperature range of the experiment. However, it does not explain the observations in other experiments where it was found that the width of the demarcation bands is not changed appreciably by variations of approximately one order of magnitude in pulse duration or pulse height.

Detailed information concerning LPE growth can be extracted from experimental results such as those in Fig. 3. The amount of material deposited over any temperature interval can readily be determined, since the demarcation bands delineate the S-L interface and each current pulse results in a signal on the recorded cooling curve (as illustrated in Fig. 2). Figure 4 is a plot of the epitaxial layer thickness as a function of growth temperature, obtained from the spacing of consecutive demarcation lines in Fig. 3. It can be seen in Fig. 4 that the experimental points very accurately follow the curve shown, which was obtained from the phase diagram (18). According to the phase diagram, a maximum layer thickness of 153 μm GaAs (on a 1.5 cm^2 substrate, from a solution containing 4.5g Ga and 0.383g GaAs) can be achieved by growth from solution over the temperature interval from 851° to 815°C. The measured average layer thickness was 149 μm , indicating that the growth efficiency in this particular case was close to 100%. A growth efficiency of 100% cannot be expected if growth is diffusion controlled, since this growth mode implies the existence of an arsenic concentration gradient perpendicular to the S-L interface. The results in Fig. 4 would suggest that growth occurs without the establishment

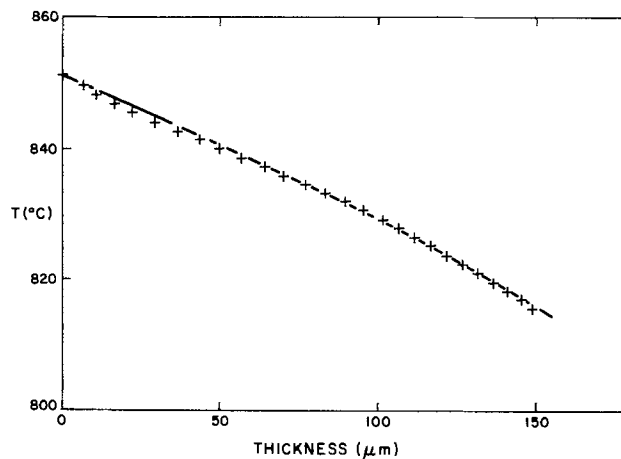


Fig. 4. Plot of LPE layer thickness vs. growth temperature. The data points, based on Fig. 3, follow the phase diagram, which is represented by the solid line.

of a substantial diffusion boundary layer. Etching experiments indicate the absence of random segregation inhomogeneities. It must therefore be concluded that thermal convection effects cannot readily account for the apparent decrease in the thickness of the diffusion boundary layer. On the other hand, it cannot be assumed that the equilibrium conditions prevailing during current-controlled LPE at the growth interface are identical with those encountered during conventional LPE.

It has been suggested (2, 7) that the surface morphology of an epitaxial layer corresponds to the morphology of its growth interface; thus, a flat surface is taken as indicative that growth proceeded with a flat interface. On the other hand, Ref. (19) has shown that the surface of the top layer in a GaAlAs/GaAs heterojunction laser is rather disturbed compared to the underlying interfaces. Figure 5 shows clearly that neither of these relationships can be assumed *a priori*, since here the top surface is flat while the underlying demarcation lines reveal a pronounced localized depression in the growth interface. In this case, the interface morphology remained basically unchanged over a growth period of 30 min (from 844° to 835°C), but there is a pronounced difference in morphology between the final surface and the last demarcation line. This observation suggests that surface morphology is significantly affected by growth during solution wiping. It was established that the solution was wiped off completely from the surface of the epitaxial layer. The surface morphology is therefore unrelated to

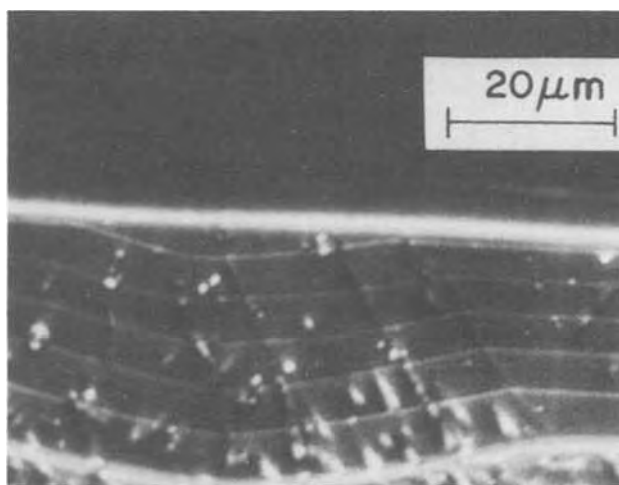


Fig. 5. Photomicrograph of a GaAs LPE layer. It can be seen that the surface flatness does not reflect the shape of the S-L interface (as depicted by demarcation lines) during growth.

residual solution left on the surface and cannot at this time be explained adequately. The presently observed wiping effects cannot be generalized, but they indicate potential complications arising from wiping in LPE systems.

Another application of interface demarcation to the study of LPE growth is illustrated in Fig. 6. In this experiment, a pit in the substrate surface created a local perturbation on a flat, possibly facet-type, growth interface. It took 18 μm of epitaxial growth (about 25 min) before the 2.5 μm deep pit was eliminated. In some other cases, however, the change from an irregular interface to a straight one took place within a short period.

Local retardation of the growth of an LPE layer is shown in Fig. 7. Of the nine demarcation lines observed, eight were formed by current pulses at intervals of 5 min, while the uppermost line was generated by interrupting the growth momentarily by separating and subsequently recontacting solution and wafer. Figure 7 indicates that locally no epitaxial growth had taken place over a distance of about 220 μm . This local retardation of growth persisted over a steadily decreasing area for a period in excess of 20 min. It is clear from Fig. 6 and 7 that during LPE growth a pit may result in the final surface if growth is restricted to thin layers (as is customary for certain devices). In the experiment shown in Fig. 7, it took 45 min of

growth before the retardation was overcome and a flat growth interface was formed. The area under the delineated pyramid was formed at an increased growth rate and can be expected to constitute a significant segregation discontinuity. In this area the average growth rate normal to the angle of inclination is calculated to be approximately 35% higher than that in the (100) direction. The orientation of the growth interface varies, and no specific set of low-index growth planes can be identified. The exact cause of the local inhibition of growth is unknown, but it is suggested that oxides or major defects in the substrate are responsible. While the present experiments are not exhaustive, they indicate clearly that smooth substrate-epilayer interfaces and smooth final layer surfaces are no assurance that LPE growth has proceeded in an unperturbed manner.

Summary

The presently reported experiments show that interface demarcation through current pulsing can be applied successfully to the quantitative study of liquid phase epitaxy. It has thus been shown that transient changes in the growth interface morphology, which are not necessarily reflected in the surface morphology of the epitaxial layer, may occur. Such transients may result in significant compositional inhomogeneities. While the experimental results were obtained on thick epitaxial layers, the observations should apply as well to thin layer growth.

Acknowledgment

The authors thank Dr. S. K. Kurtz for many stimulating discussions.

Manuscript submitted Oct. 4, 1974; revised manuscript received June 9, 1975.

Any discussion of this paper will appear in a Discussion Section to be published in the June 1976 JOURNAL. All discussions for the June 1976 Discussion Section should be submitted by Feb. 1, 1976.

Publication costs of this article were partially assisted by North American Philips Corporation.

REFERENCES

1. D. L. Rode, *J. Crystal Growth*, **20**, 13 (1973).
2. R. C. Peters, in "Symposium on Gallium Arsenide and Related Compounds," Conference Series No. 17, p. 55, Boulder, Colorado (1972).
3. J. J. Hsieh, *J. Crystal Growth*, **27**, 49 (1974).
4. R. L. Moon and J. Kinoshita, *ibid.*, **21**, 149 (1974).
5. I. Crossley and M. B. Small, *ibid.*, **11**, 157 (1971).
6. B. D. Lainer, V. V. Rakov, M. G. Mil'vidskii, and I. A. Magidson, *Dokl. Akad. Nauk SSR*, **185**, 142 (1969).
7. R. H. Saul and D. D. Roccasecca, *J. Appl. Phys.*, **44**, 1933 (1973).
8. J. C. Brice, "The Growth of Crystals from Liquids," p. 120, North-Holland, Amsterdam (1973).
9. K. F. Hulme and J. B. Mullin, *Phil. Mag.*, **4**, 1286 (1954).
10. J. A. M. Dickhoff, *Solid-State Electron.*, **1**, 202 (1960).
11. A. F. Witt, M. Lichtensteiger, and H. C. Gatos, *This Journal*, **121**, 787 (1974).
12. M. Lichtensteiger, A. F. Witt, and H. C. Gatos, *ibid.*, **118**, 1013 (1971).
13. M. Kumagawa, A. F. Witt, M. Lichtensteiger, and H. C. Gatos, *ibid.*, **120**, 583 (1973).
14. W. G. Pfann, K. E. Benson, and J. H. Wernick, *J. Electron. Control*, **2**, 597 (1957).
15. M. S. Abrahams and C. J. Buicchi, *J. Appl. Phys.*, **36**, 2855 (1965).
16. E. H. Putley, "The Hall Effect and Related Phenomena," p. 31, Butterworths, London (1960).
17. J. J. Daniele and C. Michel, *Vth Int. Conf. on GaAs and Related Compounds*, p. 155, British Institute of Physics, Deauville, France (1974).
18. R. N. Hall, *This Journal*, **110**, 385 (1963).
19. H. C. Casey Jr., M. B. Panish, W. O. Schlosser, and T. L. Paoli, *J. Appl. Phys.*, **45**, 322 (1974).

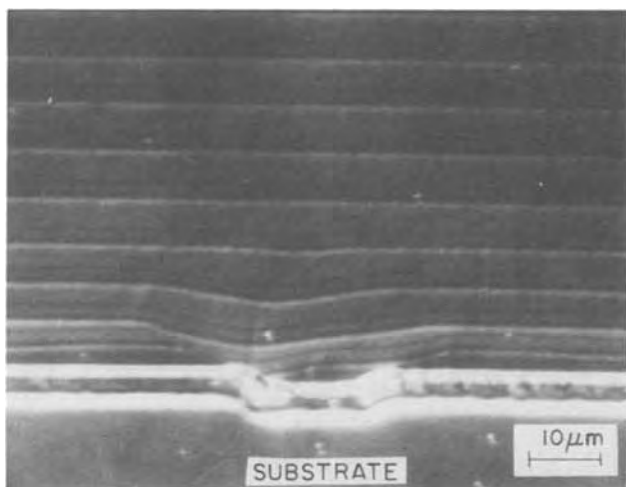


Fig. 6. Photomicrograph of a GaAs LPE layer, showing the development of a flat S-L interface from a pit in the surface of the substrate.

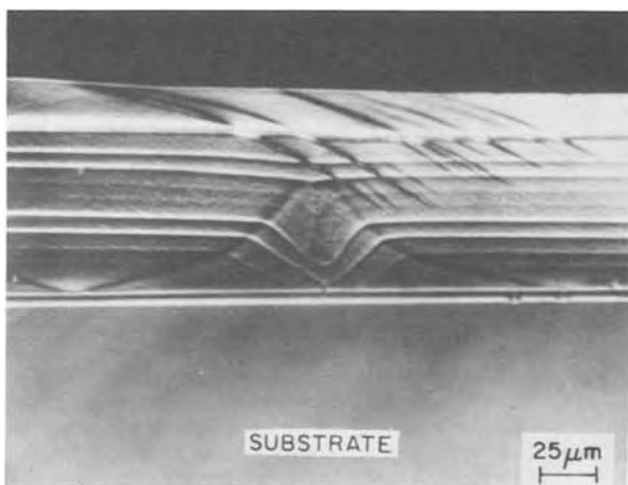


Fig. 7. Photomicrograph of a GaAs LPE layer, showing the development of a flat S-L interface after localized initial growth retardation.

Low Temperature Deposition of Metal Nitrides by Thermal Decomposition of Organometallic Compounds

Kozoh Sugiyama, Sangryul Pac, Yasutaka Takahashi, and Seiji Motojima

Department of Synthetic Chemistry, Faculty of Engineering, Gifu University, Kagamigahara, 504 Japan

ABSTRACT

Decomposition reaction of dialkylamides of boron, silicon, tin, titanium, zirconium, niobium, and tantalum was investigated. The amides of transition metals decomposed to the corresponding nitrides at 300°-500°C, whereas those of boron, silicon, and tin yielded elemental deposits at higher temperatures. In the deposition of titanium nitride from titanium tetrakis(dimethylamide), two optimum temperatures at 400° and at 800°C in nitrogen or hydrogen atmosphere were found, but in argon only low temperature deposition was possible. The low and high temperature processes are discussed in relation to mass spectral analysis of the exhaust gases formed at various decomposition temperatures of titanium amide.

Metal nitrides are well known to have outstanding physical and chemical properties and have been prepared by the reactions of metal halides or hydrides with nitrogen + hydrogen or ammonia, or of metals with nitrogen (1). These reactions usually require temperatures higher than 1000°C, which have limited the application of the nitrides as the useful coatings on many materials. Therefore, their preparation at lower temperature, where deformation of substrate materials can be avoided, should be important.

Recently, the use of organometallic compounds as the starting materials for the vapor deposition of some inorganic compounds such as oxides has been reported (2). Dialkylamides of metals are of particular interest with respect to the fact that they have direct metal-nitrogen σ -bonds, and controlled thermal decomposition of these organometallics could result in the deposition of the corresponding nitrides at temperatures much lower than the conventional preparation techniques mentioned above. With this in mind, the thermal decomposition of dialkylamides of various metals is investigated, and a detailed examination of the decomposition products including organic compounds was performed using titanium tetrakis(dimethylamide) as a representative compound.

Experimental

Materials—Metal dialkylamides used in this study were prepared according to the modified method of literature (3) from lithium dialkylamides and the corresponding metal chlorides and were supplied to be used for the decomposition reaction after identification with infrared, NMR, and mass spectra (4). Silicon tetrakis(dimethylamide) was found to include about 75% of chlorotris(dimethylamino)silane but was used without further isolation. Argon, hydrogen, and nitrogen were refined by passing over titanium sponge heated at ca. 800°C and phosphorus pentoxide, successively. Helium and other Guaranteed Grade reagents were used without further purification.

Decomposition reaction of the amides—An apparatus used for the decomposition reactions is shown in Fig. 1. An amide saturated in a carrier gas (argon, hydrogen, or nitrogen) at a suitable temperature, where it is thermally stable (in most cases below 100°C except for silicon amide; 140°C), was introduced onto a substrate [about 10 × 10 mm²: quartz, graphite, stainless steel (Ni 18, Cr 8), or copper plate] which was mounted on a SiC heater in a reaction tube (quartz; inside diameter 25 mm). The reactor was cooled by water flow from the outside in order to avoid the deposition on its inside surface. Temperature of the substrate was measured by an Alumel-Chromel

thermocouple (uncorrected) and was regulated using a regulator (Chino Electric Company, Model E-500). After the decomposition reaction, the furnace was cooled in an atmosphere of flowing carrier gas to room temperature. Most substrates were used after polishing with an emery paper. The surface of the copper plate was cleaned by heating in air and subsequent steeping in methanol. The films on the substrate were examined *in situ* on the substrate by x-ray diffraction (Rigaku Electric Company, Type 2040), scanning electron microscopy (JEOL, Model U3), and partly by x-ray microprobe analysis (JEOL, Model JAX-5 CHD).

Analysis of the exhaust gas—The exhaust gas formed in the decomposition of an amide was analyzed by gas chromatography (F.I.D.; Apiezon L column, 1.0m; 20°C) and by bubbling through a benzene solution of naphthylisocyanate which reacts to form urea derivatives of the corresponding amines. Detailed analysis was performed by a mass spectrometry. Helium gas, which was used because it does not interfere with detection of fragments with low molecular weights, was saturated with the vapor of titanium tetrakis(dimethylamide) or the silicon analogue and was passed through a quartz furnace (inside diameter 15 mm) heated from the outside at a given temperature. The gas formed was first collected in a gas reservoir, before it was introduced into the spectrometer (JEOL, JMS-01SG).

Evaluation of quantity of vapor transported of titanium tetrakis(dimethylamide)—Titanium amide is so sensitive to moisture and oxygen that it is difficult for us to determine the quantity transported by a

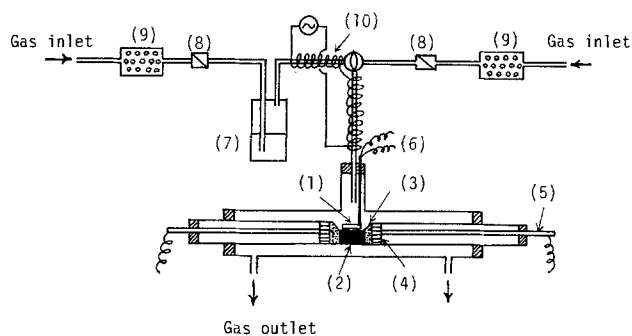


Fig. 1. Schematic diagram of the apparatus used for the decomposition of amides. 1, Substrate; 2, SiC heater; 3, carbon powder; 4, graphite; 5, iron rod; 6, a-c thermocouple; 7, amide saturator; 8, flow meter; 9, titanium sponge; 10, Nichrome heater.

Key words: metal-dialkylamides, nitrides, thermal decomposition.

carrier gas. However, this compound has been reported to react with carbon disulfide giving the stable complex, titanium tetrakis(N,N-dimethyldithiocarbamate) (5). Thus, by bubbling the carrier gas (nitrogen) saturated with the titanium amide at 90°C into a benzene solution of carbon disulfide and collecting the red precipitates by filtration, the quantity of the amide transported was calculated from the weight of the precipitates as 0.032 mg/ml (N₂).

Results

Decomposition products.—When the vapor of titanium tetrakis(dimethylamide) saturated in nitrogen gas was introduced onto a quartz substrate which was heated at 400°C, it decomposed resulting in brownish coatings. Their x-ray diffraction showed broad peaks, which are fully consistent with those of titanium nitride as shown in Fig. 2. The peaks became more pronounced when annealed in argon atmosphere at 800°C for 10 min. The high temperature decomposition products were yellow-colored and had sharper x-ray diffraction peaks (see Fig. 2). The low and high temperature products were inert to hydrochloric acid and sulfuric acid but were etched partly by nitric acid and soluble in aqua regia, being consistent with the chemical properties of titanium nitride. The x-ray microprobe analysis of the product obtained at 400°C shown in Fig. 3 suggests a homogeneous nitride which contains a small quantity of carbon, particularly in the grain boundaries. The lowest formation temperature was about 250°C.

The decomposition reaction was evident in hydrogen as well as in nitrogen. On the other hand, in argon atmosphere the nitride deposition was observed analogously at lower temperature reaction (about 400°C) but was very poor at temperatures higher than 700°C.

The decomposition reaction of other amides was investigated in a similar manner, and the products are listed in Table I, together with their lowest formation temperatures. The amides of transition metals such as titanium, zirconium, and niobium gave the corresponding nitrides. Their x-ray diffraction patterns are reproduced in Fig. 2. Tantalum amide gave the grayish deposits which had x-ray diffraction peaks Cu-K α $2\theta = 36.2^\circ$, 41.9° , and 61.0° (relative intensity 100:70:30) which were not consistent with available data of tantalum compounds. Therefore, we could not identify the products.

On the other hand, amides of boron and tin did not yield a nitride at any temperature in the range 300°-1000°C but gave the elements themselves. Boron was obtained above 700°C in the brown films and was identified by x-ray diffraction and the easy dissolution in nitric acid. Tin was formed at 300°-1000°C as gray coatings, which were clearly identified by the x-ray diffraction analysis (30.2° , 31.6° , 43.5° , and 44.5°). In the decomposition of silicon amide which was found to consist of both silicon tetrakis(dimethylamide) and monochloride (nearly 1:3, see experimental section), white powder and homogeneous yellowish or brownish coating were obtained at 800°C, below which no depositions occurred. The

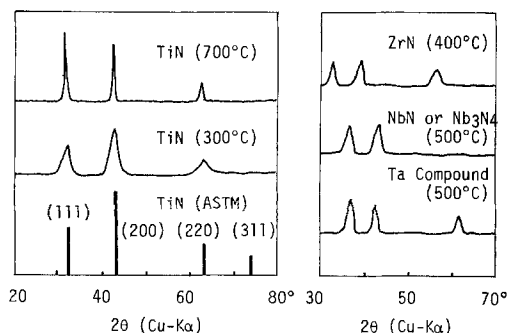


Fig. 2. X-ray diffractions of deposits formed on quartz

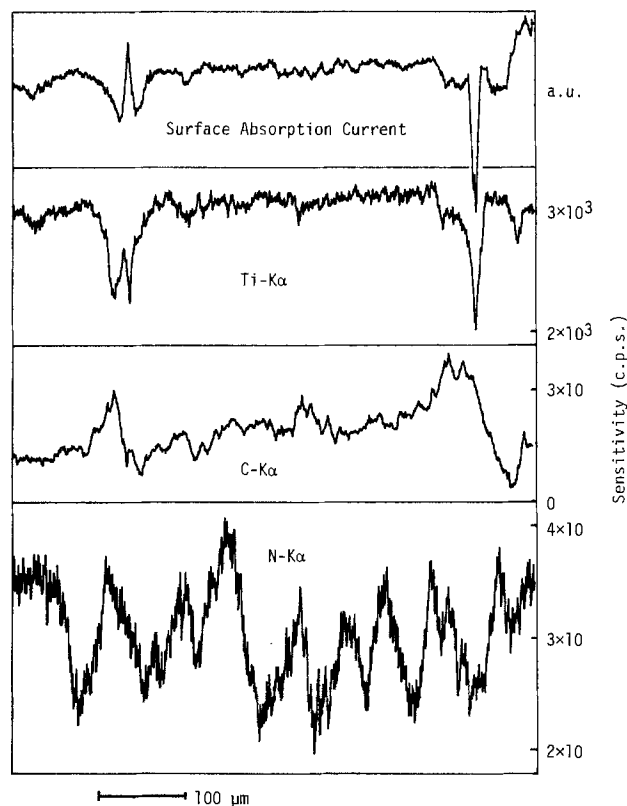


Fig. 3. X-ray microprobe analysis of the deposits obtained from Ti(NMe₂)₄ on quartz at 400°C in nitrogen.

former was identified as ammonium chloride by infrared spectrum and x-ray diffraction. The latter adhered tightly on the quartz substrate and exhibited no x-ray diffraction peaks, indicating an amorphous material. Its infrared spectrum showed the presence of an amino-group (ν_{N-H} 1400 cm^{-1}) (6). Its further heating at a higher temperature (1100°C) in argon released a small quantity of ammonia, suggesting that the deposit contained silicon amide. It was oxidized gradually in air at 1300°C to give a blue-colored product. In figuring the weight increase after the oxidation, silicon content in the product was estimated to be at least 80%. It was soluble partly in hydrofluoric acid, partly in 20% sodium hydroxide, and partly in hydrofluoric acid + nitric acid. Therefore, it can be assumed that the brownish product from silicon alkylamide contains a few compounds such as silicon, silicon nitride (or amide), and silicon carbide. But, the result of the oxidation reaction strongly suggests that silicon is a major product. Thus it is of great interest that the decomposition of the amides of the main group elements has a tendency to result in the corresponding elements themselves rather than the nitrides, being in striking contrast to that of transition metal amides.

Table I. Metal dialkylamides, decomposition products, and the lowest formation temperatures of nitrides

Amide	Product	Lowest formation temp (°C)	Remarks
Ti(NMe ₂) ₄	TiN	250	Reddish brown (low)
Ti(NEt ₂) ₄	TiN	350	or yellowish (high temperature) coatings
Ti(N-n-Pr ₂) ₄	TiN	500	
Ti(N-n-Bu ₂) ₄	TiN	600	
Zr(NMe ₂) ₄	ZrN	400	Pale brownish coatings
Zr(NEt ₂) ₄	ZrN	500	
Nb(NEt ₂) ₅	NbN or Nb ₃ N ₅	500	Black coatings
Ta(NEt ₂) ₅	Unidentified	(500)	Grayish coatings
Si(NMe ₂) ₄ *	Si, SiC and Si(NH ₂) _n	(800)	Brownish coatings
Sn(NMe ₂) ₄	Sn	(300)	Grayish coatings
B(NMe ₂) ₃	B	(600)	Dark brownish coatings

* It includes about 75% of ClSi(NMe₂)₃.

Temperature dependence of deposition.—The lowest formation temperatures of nitrides shown in Table I are remarkably low compared with those in the conventional chemical vapor depositions. The amides having a higher molecular weight or of heavier elements are apt to decompose at higher temperatures. The temperature dependence of the deposition was studied in more detail using titanium tetrakis(dimethylamide) and tetrakis(diethylamide) as representative compounds. The results in nitrogen are shown in Fig. 4 and 5, respectively. The maximum yields were found at about 400°–500°C and at a temperature above 800°C in either compounds, when hydrogen or nitrogen was used as a carrier gas. In the case of argon carrier, however, the nitride deposition occurred analogously at lower temperatures but was extremely suppressed at higher temperatures. The titanium nitride content in the deposits was evaluated from titanium oxide (TiO_2) formed by oxidation in air, and is shown also in Fig. 4 and 5. These results strongly suggest that the different mechanisms can take part in the low and high temperature decompositions. Table I indicates that the amides of the main group elements gave deposits at higher temperatures than those of transition metals.

Analysis of the exhaust gases.—In order to clarify the processes of deposition, the exhaust gas of the decomposition reaction was examined by gas chromatography, mass spectroscopy, and chemical analysis. When the exhaust gas formed by the decomposition of titanium tetrakis(dimethylamide) at the optimum condition (400°C) in nitrogen was bubbled into a benzene solution of naphthylisocyanate, white crystals which were identified as pure dimethylnaphthylurea by NMR and infrared spectra, m.p. and thin layer chromatography were separated, indicating a selective formation of dimethylamine. Its yield was found to decrease with the increasing decomposition temperature. The gas chromatographic analysis showed at least three peaks, one of which was identified as dimethylamine.

Detailed analysis of the gases obtained at the decomposition temperatures 300°, 600°, and 800°C in helium atmosphere was performed using a mass spectroscopy, and the results are shown in Fig. 6, in which the relative intensities of fragments to a fragment m/e 78 (unidentified) are shown. This figure indicates that at lower temperatures the elimination of dimethylamine was dominant and that at temperatures above 600°C further degradation could take

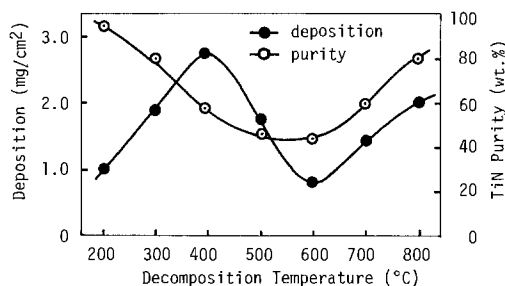


Fig. 4. Temperature dependence of deposition and purity from $\text{Ti}(\text{NMe}_2)_4$ on quartz in nitrogen.

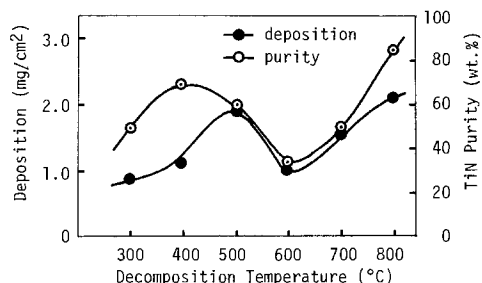


Fig. 5. Temperature dependence of deposition and purity from $\text{Ti}(\text{NEt}_2)_4$ on quartz in nitrogen.

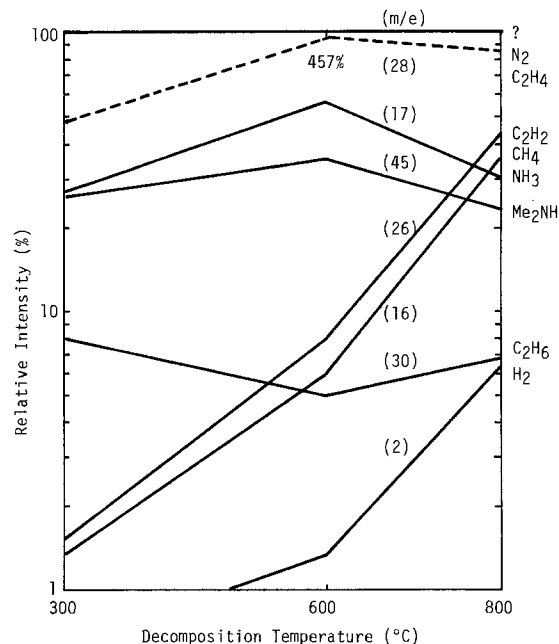


Fig. 6. Mass spectral analysis of the exhaust gases formed in the decomposition of $\text{Ti}(\text{NMe}_2)_4$ at different temperatures.

place. The formation of hydrogen and methane became significant at 800°C, which indicates an occurrence of a full decomposition of the complex. In contrast, the deposition yields of titanium nitride were maximum at about 400°C and at a temperature higher than 800°C, and a minimum of 600°C (see Fig. 4 and 5).

The temperature dependence of the composition of the exhaust gas of silicon dimethylamide was similar to that of titanium dimethylamide, as shown in Fig. 7. In the case of silicon amide, however, the deposition was found only at a temperature above 700°C. The difference between the behavior of silicon and titanium amides may be related to the stability of an intermediate of the reaction. The main fragments in the mass spectra of silicon and titanium complexes are summarized in Table II. In the case of the former, bis(dimethylamino)siliconium ion was observed at high abundance, but the analogous fragment ion of titanium was absent, suggesting the higher stability of low valent silicon species.

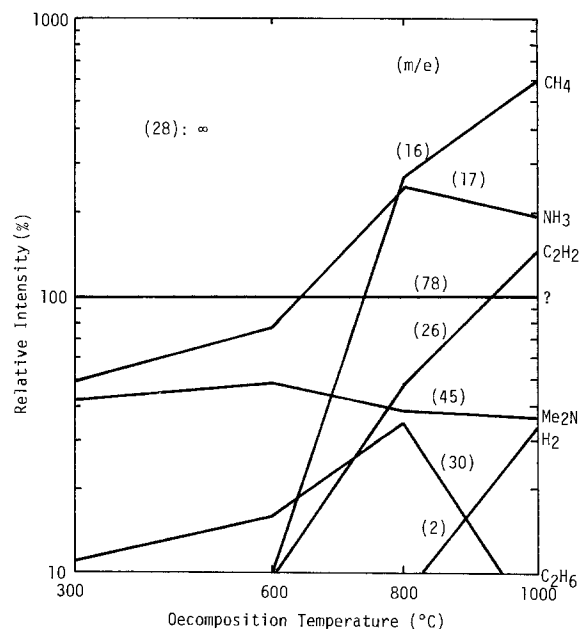


Fig. 7. Mass spectral analysis of the exhaust gases formed in the decomposition of $\text{Si}(\text{NMe}_2)_4$ [includes 75% of $\text{ClSi}(\text{NMe}_2)_3$] at different temperatures.

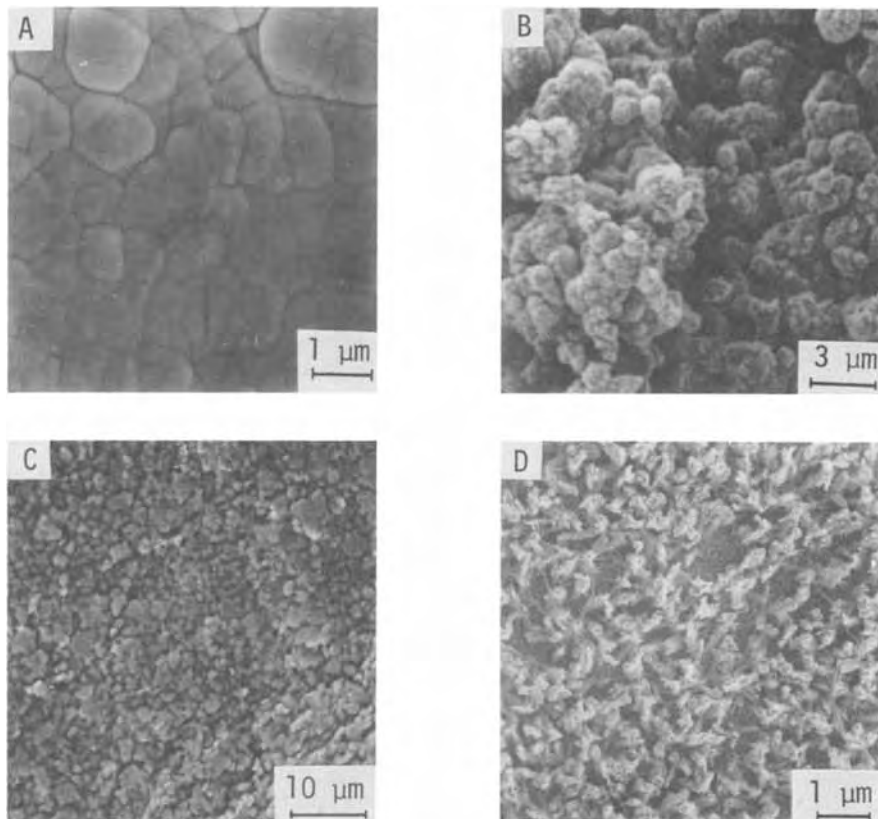


Fig. 8. TiN deposits formed on quartz. A, 300°C, low deposition; B, 300°C, high deposition; C, 800°C; D, 1000°C).

Properties of deposits.—In Fig. 8, the scanning electron micrographs of a typical titanium nitride deposited on a quartz substrate are shown. The grain sizes of the nitride obtained at a lower temperature were larger than those at a higher temperature. The x-ray diffraction pattern of low temperature deposits was quite similar to that of powdered titanium nitride except for considerable broadening, but the high temperature deposits had a larger intensity of (111) peak (see Fig. 2). Figure 8 demonstrates that the high temperature deposits are partly crystallized.

The deposition onto some other substrates such as graphite, copper, and stainless steel was also examined. The deposition rates on these substrates were found to be 0.25 mg/cm²·min (about 15% yield for the amide introduced), thus being faster than on the quartz substrate (0.15 mg/cm²·min). This difference might be due to the thermal conductivity of the substrates rather than their chemical nature such as a catalytic action of the surfaces. The adherence of the deposits to graphite and copper substrates seemed preferable to that of stainless steel and quartz. The deposits on the two latter substrates were often found to peel off. A cross section of the titanium nitride deposited on a quartz at 300°C is shown in Fig. 9. At the inter-

face between the nitride and the surface of the quartz, no other layers were found, suggesting that the nitride did not react with quartz at the deposition condition. The color of the nitride was brownish or dark yellowish at low temperature but became yellowish at a high temperature, being similar to the appearance of a typical titanium nitride.

A qualitative electrical conductivity measurement (four terminal method) showed that the nitride had a resistivity 10⁻² ohm·cm at room temperature, which is not in agreement with that of normal nitride (21.7 × 10⁻⁶ ohm·cm) (7), probably due to imperfect coatings, the contamination of some impurities (in particular at the grain boundaries), and the existence of fine cracks.

Discussion

The deposition processes of metal nitrides from the corresponding amides can be expected to vary with temperature. At low temperature, the deposition was independent of the atmosphere, but at high temperature, the process was affected by the atmospheric gas, and the deposition was suppressed in argon. Mass spectral results of the exhaust gas indicated that the

Table II. Mass spectra of M(NMe₂)₄ (M = Si and Ti)*

Fragment ion**	Intensity (%)	
	Si	Ti
M(NMe ₂) ₄	44.7	22.0
[M(NMe ₂) ₃ Cl]†	[66.0]	—
[M(NMe ₂) ₃]†	[55.3]	—
M(NMe ₂) ₃ NMeCH ₂	13.8	8.0
M(NMe ₂) ₃ NCH ₂	2.4	13.5
M(NMe ₂) ₂	20.2	—
Me ₂ NH	100.0	100.0

* Measured at 20 eV.

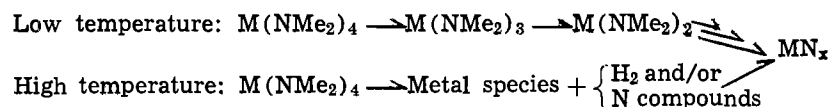
** These formulas were assigned from the high resolution analysis using perfluorokerosene as an internal standard (errors are within 5 mmass).

† Molecular ion of chlorotris(dimethylamino)silane involved and a fragment ion formed by its fragmentation.



Fig. 9. Cross section of TiN films deposited on quartz at 300°C

low temperature decomposition gave mainly amine, but the high temperature caused a full degradation of complexes. Therefore, the following decomposition schemes might be assumed



In the low temperature process, the amides may decompose through a successive elimination of amine fragments to give a low valent metal amide, followed by subsequent elimination of alkyl groups to yield the corresponding nitrides. A nitrogen atom originally bound to the metal may remain in the product without any separation through the reaction. Meanwhile, at high temperatures a complete degradation of the amides is preferable, followed by a recombination of metallic species formed with nitrogen compounds or by a further reduction with hydrogen, affording the nitrides. When argon is used in this reaction, it may dilute the concentration of nitrogen species or hydrogen to make the formation of the nitrides difficult. In a hydrogen atmosphere, splitting of the N-C bonds may be accelerated. These tentative schemes can explain the existence of two maxima in the temperature dependence of deposition. The optimum conditions were concluded to exist at approximately 400°C and at a temperature higher than 800°C in low and high temperature depositions, respectively.

At a medium temperature (about 600°C), the complete decomposition may take place, but this temperature is too low for nitride formation by subsequent recombination reactions. The amides of a main group elements may be so thermally stable that the successive reaction is difficult to occur. Therefore, they can decompose only at a high temperature to the elements. This selective element formation (the representative case was tin from tin dimethylamide) may be attributed to the easy reduction of the amides to zero valent species in comparison to the transition metals such as titanium.

In the case of titanium, zirconium, and niobium compounds, the corresponding nitrides which contain a small quantity of carbon were obtained. Although the product from the tantalum amide could not be identified, it is supposed that it is to be a kind of nitride. In spite of a larger ratio of carbon to nitrogen in the starting materials the selective formation of nitrides suggests that the nitrogen atoms originally linked are important for it, although the thermodynamic data also indicate the nitride formation to be easier than the carbide (8).

Unfortunately it was difficult to obtain a perfect homogeneous coating over the surface of the substrates even when the careful experiments were performed, probably due to very low thermal stability of the

amides. However, this defect may be corrected in a procedure of reduced reaction pressure.

Acknowledgment

We are indebted to Japan Electron Optics Laboratory (JEOL) Company for measuring mass spectra and to Messrs. Y. Ishikawa and K. Shima for the invaluable assistance during this study.

Manuscript submitted April 22, 1975; revised manuscript received June 23, 1975.

Any discussion of this paper will appear in a Discussion Section to be published in the June 1976 JOURNAL. All discussions for the June 1976 Discussion Section should be submitted by Feb. 1, 1976.

Publication costs of this article were partially assisted by Gifu University.

REFERENCES

1. C. F. Powell, J. H. Oxley, and J. M. Blocher, Jr., Editors, "Vapor Deposition," John Wiley & Sons Inc., New York (1966).
2. K. S. Mazdiasni, C. T. Lynch, and J. S. Smith, *J. Am. Ceram. Soc.*, **48**, 372 (1965); **49**, 286 (1966); M. Belog, M. Schieber, S. Patai, and M. Micham, *J. Crystal Growth*, **17**, 298 (1972); K. J. Sladek and W. W. Gibert, "Proceedings of Third CVD International Congress," p. 215 (1973); R. L. Hough, *ibid.*, p. 232
3. D. C. Bradley and I. M. Thomas, *J. Chem. Soc.*, **1960**, 3857.
4. K. Jones, in "Comprehensive Inorganic Chemistry," J. C. Bailar, H. J. Emeleus, R. Nyhold, and A. F. Trotman-Dickenson, Editors, Vol. 2, pp. 233-237; D. C. Bradley and P. Thornton, *ibid.*, Vol. 3, pp. 472-475.
5. D. C. Bradley and M. H. Gitlitz, *J. Chem. Soc. A*, **1969**, 1152.
6. S. Yamazaki, K. Wada, and I. Taniguchi, *Japan. J. Appl. Phys.*, **9**, 1467 (1970).
7. C. Agte and K. Moers, *Z. Anorg. Chem.*, **198**, 233 (1931).
8. G. V. Raynor, in "Metal Physics and Physical Metallurgy," O. Kubaschewski and E. L. Evans, Editors, Vol. 1, Pergamon Press, New York (1958).

Liquidus-Solidus Isotherms in the In-Ga-As System

M. A. Pollack, R. E. Nahory, and L. V. Deas¹
Bell Laboratories, Holmdel, New Jersey 07733

and D. R. Wonsidler
Bell Laboratories, Allentown, Pennsylvania 18103

ABSTRACT

Liquidus and solidus data are presented for the 800°, 850°, and 900°C isotherms in the In-rich corner of the In-Ga-As phase diagram. A simple solution model gives excellent agreement with the solidus data, but describes the liquidus more poorly than desired.

The $\text{In}_x\text{Ga}_{1-x}\text{As}$ mixed crystal system has attracted considerable interest for possible use in infrared optoelectronic devices. By choosing the appropriate InAs mole fraction x , a room temperature bandgap between 1.425 (0.87 μm) and 0.36 eV (3.4 μm) can be obtained. As part of a recent study of the liquid phase epitaxial (LPE) growth and characterization of this material (1), a number of liquidus and solidus measurements at 850°C in the In-rich corner of the In-Ga-As phase diagram were described. In the present work, we report liquidus and solidus data for the 800°, 850°, and 900°C isotherms extending all the way to the In-As binary cut.

Early work on the In-Ga-As phase diagram was reported by Stringfellow and Greene (2), who compared their calculations with some of Ewing's unpublished solidus data. Panish (3) measured liquidus temperatures between 700° and 1170°C for several solution compositions along the 0.25 and 0.55 atom fraction Ga concentration lines of the phase diagram. A number of liquidus and solidus points near 700°C were obtained by Antypas (3), who also derived a phase diagram for the system in fair agreement with his measurements. Additional liquidus and solidus points below 800°C in the In-rich corner were measured by Wu and Pearson (5). They obtained good agreement between their calculated phase diagram and measurements over a limited compositional range (1) by adopting a composition-dependent interaction parameter.

Panish and Ilegems (6) have compared the results of these workers and have suggested a new set of parameters in a phase diagram calculation for the In-Ga-As system. It was shown by Nahory *et al.* (1), that a small change in one of these parameters would permit excellent agreement between their own calculated and measured solidus isotherms at 850°C, although agreement for the liquidus was poorer than desired. As will be shown below, this conclusion holds true as well when the more extensive data reported here are included.

Experimental Procedure

The LPE apparatus consisted of a quartz reaction tube mounted in a horizontal furnace. The furnace temperature was electronically controlled to within $\pm 0.1^\circ\text{C}$. Liquidus measurements and layer growth were carried out in a palladium purified, flowing H_2 ambient, using a graphite boat and slider assembly. Solution temperature measurements were made by means of a thermocouple situated just below the solution well in the boat.

Accurately preweighed 99.999+ % pure Ga and In, and undoped polycrystalline InAs were used in order to obtain desired solution compositions. The Ga and In were cleaned in HCl, and the InAs in a 10% Br:

methanol solution before being weighed. Growth was obtained on 111B (As) faces of GaAs substrates which had been sawed, lapped, cleaned, and degreased and finally etched in a 10% Br:methanol solution immediately before being loaded into the boat.

Liquidus temperatures were determined *in situ* by the method of direct, visual observation of the solutions just prior to epitaxial growth. Briefly, the method consists of first heating to dissolve and mix all components thoroughly, and then cooling the solution sufficiently to form an $\text{In}_x\text{Ga}_{1-x}\text{As}$ crust. The liquidus temperature T_L is reached when, upon further heating, the last bit of this ternary solid crust is observed to dissolve in the ternary liquid. Details of the adaptation of the method to our apparatus have been described elsewhere (1).

The use of an open, flowing H_2 system resulted in a measurable loss of As by evaporation, which was observable by a reduction of T_L with time. The liquidus temperature of the original melt was readily determined, however, by measuring T_L as a function of time and extrapolating back to zero. The uncertainty in T_L introduced by this procedure was negligibly small at 800°C, but increased with T_L and arsenic concentration, becoming significant ($\sim 10^\circ$) at 900°C along the In-As cut. An absolute temperature calibration of the system was obtained at 960.8°C by observing the melting of silver in the same well usually used for the growth solutions.

After the determination of T_L for a particular solution, epitaxial growth of a layer several micrometers thick was carried out. The substrate was moved under the growth solution, cooled through several degrees at a rate between 0.25° and 1°C/min, and then slid out from under the solution again. It was possible to nucleate $\text{In}_x\text{Ga}_{1-x}\text{As}$ directly on the GaAs 111B substrates with x as large as 0.15, although for x larger than about 0.08, such layers exhibited many defects as a result of the large lattice mismatch with the substrate.

Solidus compositions were determined by electron microprobe analysis for most of the grown layers. An electron beam accelerating potential of 15 keV was used, producing x-ray fluorescence to an effective depth of approximately 1.3 μm . Indium L-alpha, gallium L-alpha, and arsenic K-alpha x-ray intensities were measured simultaneously using wavelength dispersive spectrometers. X-ray intensity ratios were determined by direct comparison with stoichiometric GaAs and InAs crystal standards and converted to chemical composition with the aid of a computer program (7). At least ten spots, approximately 5 μm in diameter, were probed on each layer, and in each case the lateral variation of x was less than 3% of its average value.

Results and Discussion

The liquidus temperatures T_L and solidus compositions x are summarized in Tables I, II, and III for solutions with T_L in the vicinity of 800°, 850°, and 900°C,

¹ Present address: Star Route 1, Box 89, Georgetown, South Carolina 29440.

Key words: liquid phase epitaxy, indium_x gallium_{1-x} arsenic, ternary phase diagrams.

Table I. Summary of liquidus and solidus data near 800°C. The liquidus compositions are given by the atom fractions X^l , the liquidus temperature by T_L , and the InAs mole fraction in the solid by x .

X^l_{In}	X^l_{Ga}	X^l_{As}	$T_L(^{\circ}C)$	x
0.525	0.410	0.065	810 ± 1	0.034
0.600	0.320	0.080	817 ± 1	0.051
0.650	0.270	0.080	811 ± 1	0.061
0.690	0.240	0.070	789 ± 1	0.065
0.680	0.240	0.080	802 ± 1	0.073
0.720	0.180	0.100	816 ± 1	0.097
0.748	0.150	0.102	800 ± 1	0.128
0.775	0.100	0.125	799 ± 1	•
0.795	0.050	0.155	791 ± 1	•
0.792	0.000	0.208	795 ± 1	•

Table II. Summary of liquidus and solidus data near 850°C. The liquidus compositions are given by the atom fractions X^l , the liquidus temperature by T_L , and the InAs mole fraction in the solid by x .

X^l_{In}	X^l_{Ga}	X^l_{As}	$T_L(^{\circ}C)$	x
0.460	0.452	0.088	852 ± 1	0.037
0.565	0.332	0.103	851 ± 1	0.053
0.580	0.312	0.108	852 ± 1	—
0.597	0.292	0.111	852 ± 1	0.065
0.615	0.272	0.113	851 ± 1	—
0.631	0.252	0.117	850 ± 1	—
0.651	0.222	0.127	852 ± 1	0.085
0.666	0.202	0.132	851 ± 1	0.098
0.681	0.177	0.142	853 ± 1	—
0.697	0.151	0.152	852 ± 2	0.141
0.707	0.131	0.162	849 ± 2	•
0.730	0.065	0.205	846 ± 2	•
0.732	0.000	0.268	847 ± 2	•

Table III. Summary of liquidus and solidus data near 900°C. The liquidus compositions are given by the atom fractions X^l , the liquidus temperature by T_L , and the InAs mole fraction in the solid by x .

X^l_{In}	X^l_{Ga}	X^l_{As}	$T_L(^{\circ}C)$	x
0.480	0.380	0.140	910 ± 2	0.043
0.550	0.300	0.150	904 ± 2	0.065
0.610	0.210	0.180	907 ± 2	0.109
0.640	0.160	0.200	903 ± 2	•
0.652	0.113	0.236	912 ± 2	•
0.647	0.110	0.243	915 ± 5	•
0.660	0.050	0.290	905 ± 5	•
0.655	0.000	0.345	900 ± 10	•

respectively. The compositions of these solutions are specified by the atom fractions X^l of In, Ga, and As, which were measured to better than 1 part per thousand. The estimated uncertainty in T_L , which is attributable to the procedure used in correcting for As evaporation, is given in the tables. The solidus compositions are not given for every solution because in some cases a layer could not be grown on the GaAs substrate (*), and in other cases no microprobe analysis was performed (—). A number of the solutions listed in Table II were previously reported (1).

The solution compositions of Tables I, II, and III are also shown on the phase diagram of Fig. 1, by open circles, closed circles, and open squares, respectively. The solid curves are the 800°, 850°, and 900° isotherms obtained by interpolation between the data points. The curves agree well with Panish's (3) data where they intersect the $X^l_{Ga} = 0.25$ and 0.55 cuts and with the two 795°C data points of Wu and Pearson (5). Agreement with the InAs data of Liu and Peretti (8) (along the $X^l_{Ga} = 0$ cut) is also well within the experimental error. The solidus compositions are plotted against X^l_{Ga} for the three temperatures in Fig. 2.

As described above, a small change of one of the interaction parameters in the model suggested by Panish and Ilegems (6) permitted Nahory *et al.* (1), to obtain theoretical results at 850°C in excellent agreement with their own solidus measurements, although in rather poor agreement with their liquidus data. This model treats the $In_xGa_{1-x}As$ solid as a strictly

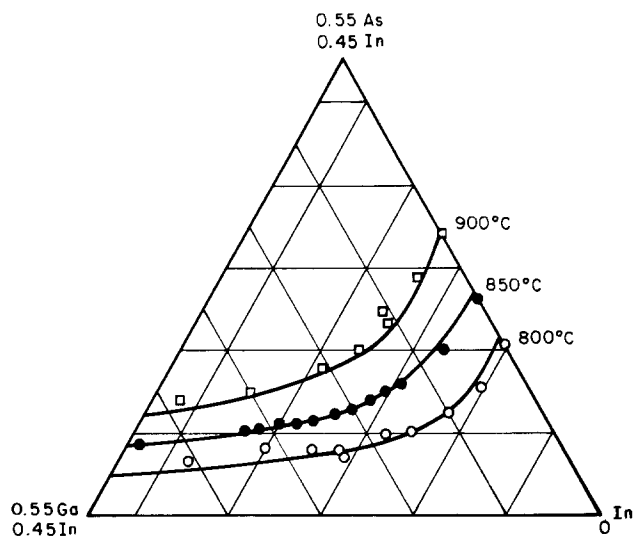


Fig. 1. Liquidus isotherms at 800° (open circles), 850° (solid circles), and 900° (open squares) in the In-rich corner of the In-Ga-As system. The points correspond to measured solutions and the curves are interpolated for the three temperatures.

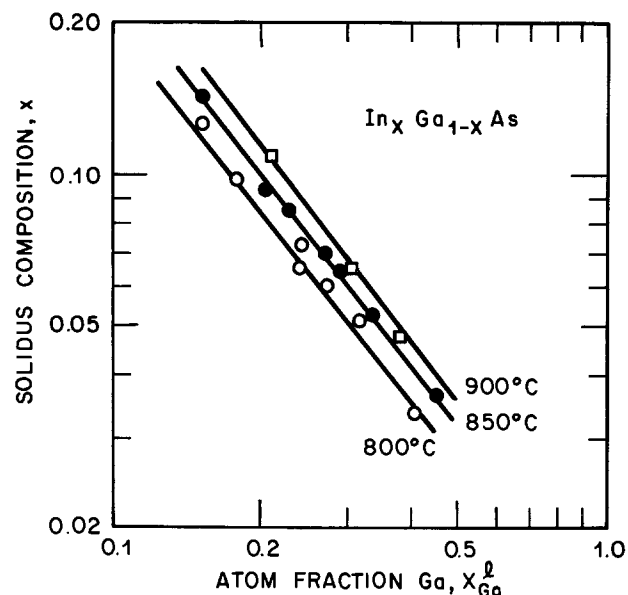


Fig. 2. Solidus isotherms at 800° (open circles), 850° (solid circles), and 900° (open squares) as functions of X^l_{Ga} in the In-Ga-As system. The solid curves have been calculated to fit the data points.

regular solution of the binary compounds InAs and GaAs, and the liquid as a simple solution of In, Ga, and As. Details of the calculation are given in the Appendix. Present attempts to optimize all the interaction parameters of this model to simultaneously fit the experimental liquidus and solidus isotherms of Fig. 1 and 2 were not successful, indicating that the model is a good approximation but not quite adequate. The best over-all fit was obtained using the parameters given in Table IV, which are the same as those used by Nahory *et al.* (1), and differ from those of Panish and Ilegems (6) only in the value of $\beta_{InAs-GaAs}$, which was increased from 3000 to 3450 cal/mole. The computed solidus curves, which are the nearly straight lines drawn in Fig. 2, are in excellent agreement with the data at all three temperatures, as can be readily seen from the figure.

For the liquidus data, a comparison of the measured curves (solid) with those calculated (dashed) using the parameters of Table IV is shown in Fig. 3. The solidus curves for $x = 0.05, 0.10,$ and 0.15 (coincident

Table IV. Parameters used in the phase diagram calculation, including the temperature of fusion T^F , entropy of fusion ΔS^F , and the interaction parameters α for the liquid and β for the solid

T_{In-As}^F (°K)	1215
ΔS_{In-As}^F (eu)	14.52
α_{In-As} (cal/mole)	$-10.0T + 3860$
T_{Ga-As}^F (°K)	1511
ΔS_{Ga-As}^F (eu)	16.64
α_{Ga-As} (cal/mole)	$-9.16T + 5160$
α_{In-Ga} (cal/mole)	1060
$\beta_{InAs-GaAs}$ (cal/mole)	3450

measured and calculated) have also been replotted in Fig. 3 from the solidus isotherms of Fig. 2. Agreement between experiment and theory for the liquidus is good along the In-As cut, but the curves differ by as much as 20°C elsewhere. It would appear that a more complex model than the present simple solution treatment is required.

Manuscript submitted Feb. 18, 1975; revised manuscript received June 12, 1975.

Any discussion of this paper will appear in a Discussion Section to be published in the June 1976 JOURNAL. All discussions for the June 1976 Discussion Section should be submitted by Feb. 1, 1976.

Publication costs of this article were partially assisted by Bell Laboratories.

APPENDIX

Phase Diagram Calculation

We follow Panish and Ilegems (6) in treating the In-Ga-As system. The $In_xGa_{1-x}As$ solid is considered to be a strictly regular solution of the binary compounds InAs and GaAs, and the liquid to be a simple solution containing In, Ga, and As mole fractions X_{In}^l , X_{Ga}^l , and X_{As}^l . Then

$$\gamma_{GaAs}^s(1-x) = \frac{4\gamma_{Ga}^l\gamma_{As}^l}{\gamma_{Ga}^{sl}\gamma_{As}^{sl}} X_{Ga}^l X_{As}^l \exp \left[\frac{\Delta S_{GaAs}^F}{RT} (T_{GaAs}^F - T) \right] \quad [A-1]$$

and

$$\gamma_{InAs}^s x = \frac{4\gamma_{In}^l\gamma_{As}^l}{\gamma_{In}^{sl}\gamma_{As}^{sl}} X_{In}^l X_{As}^l \exp \left[\frac{\Delta S_{InAs}^F}{RT} (T_{InAs}^F - T) \right] \quad [A-2]$$

where

$$X_{In}^l + X_{Ga}^l + X_{As}^l = 1 \quad [A-3]$$

The γ^l and γ^s are activity coefficients of the element in the liquid or the binary compound in the solid, respectively, the superscript sl signifies the stoichiometric liquid, ΔS^F is the entropy of fusion and T^F the fusion temperature of the binary solid.

The activity coefficients for the solid are related to the interaction parameter β by

$$RT \ln \gamma_{GaAs}^s = \beta_{InAs-GaAs} x^2 \quad [A-4]$$

and

$$RT \ln \gamma_{InAs}^s = \beta_{InAs-GaAs} (1-x)^2 \quad [A-5]$$

The activity coefficients for the liquid are related to the interaction parameters α by

$$RT \ln \gamma_{Ga}^l = \alpha_{Ga-As} (X_{As}^l)^2 + \alpha_{Ga-In} (X_{In}^l)^2 + (\alpha_{Ga-As} + \alpha_{Ga-In} - \alpha_{In-As}) X_{In}^l X_{As}^l \quad [A-6]$$

$$RT \ln \gamma_{In}^l = \alpha_{In-As} (X_{As}^l)^2 + \alpha_{Ga-In} (X_{Ga}^l)^2 + (\alpha_{In-As} + \alpha_{Ga-In} - \alpha_{Ga-As}) X_{Ga}^l X_{As}^l \quad [A-7]$$

$$RT \ln \gamma_{As}^l = \alpha_{Ga-As} (X_{Ga}^l)^2 + \alpha_{In-As} (X_{In}^l)^2 + (\alpha_{Ga-As} + \alpha_{In-As} - \alpha_{Ga-In}) X_{Ga}^l X_{In}^l \quad [A-8]$$

An iterative computer program is used to solve for the equilibrium liquid and solid compositions at a given temperature $T = T_L$ using Eq. [A-1]-[A-8]. The input parameters T^F , ΔS^F , α , and β used in the present work are given in Table IV. The simple solution approximation for the liquid requires that the α 's be independent of composition, although they are functions of temperature. The limitation that the solid be a strictly regular solution requires that the interaction parameter β be a constant.

REFERENCES

1. R. E. Nahory, M. A. Pollack, and J. C. DeWinter, *J. Appl. Phys.*, **46**, 775 (1975); R. E. Nahory, M. A. Pollack, and J. C. DeWinter, *Appl. Phys. Letters*, **25**, 146 (1974).
2. G. B. Stringfellow and P. E. Greene, *J. Phys. Chem. Solids*, **30**, 1779 (1969).
3. M. B. Panish, *This Journal*, **117**, 1202 (1970).
4. G. A. Antypas, *ibid.*, **117**, 1393 (1970).
5. T. Y. Wu and G. L. Pearson, *J. Phys. Chem. Solids*, **33**, 409 (1972).
6. M. B. Panish and M. Ilegems, in "Progress in Solid State Chemistry," Vol. 7, p. 39, H. Reiss and J. D. McCaldin, Editors, Pergamon Press, New York (1972).
7. J. W. Colby, "Proc. Sixth Nat. Conf. on Electron Probe Analysis," p. 17, 1971.
8. T. S. Liu and E. A. Peretti, *Trans. Am. Soc. Metals*, **45**, 677 (1953).

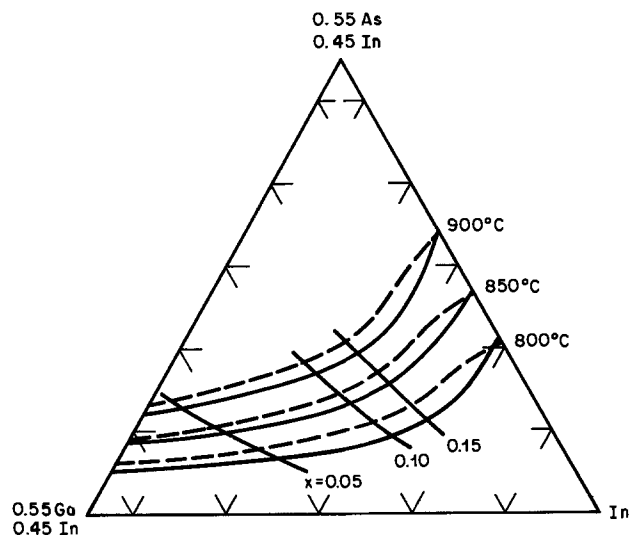


Fig. 3. Comparison of experimental liquidus isotherms from Fig. 1 (solid) with isotherms calculated using the model described in the text and the parameters of Table IV (dashed). The solidus curves for $x = 0.05, 0.10, \text{ and } 0.15$ are replotted from Fig. 2.

The Deformation of Anodic Films during the Plasma Anodization of Al-Si Structures

J. J. H. Reche¹ and D. L. Pulfrey

Electrical Engineering Department, The University of British Columbia, Vancouver V6T 1W5, Canada

Although the insulator/semiconductor combination of SiO_2/Si has proved very successful in semiconductor device technology, other combinations are of interest for particular applications. For example, Al_2O_3 on Si would appear to be of interest in devices requiring

¹ Present address: GTE-Lenkurt Electric (Canada) Ltd., 7018 Lougheed Highway, Burnaby, B.C. V5A 1W3, Canada.
Key words: thin-films, stress, oxidation.

good radiation resistance (1), low mobility of incorporated impurities, e.g., Na^+ (2), low surface state density (3), and increased oxide dielectric constant (~ 8 vs. ~ 4). Memory action in metal Al_2O_3 -Si FET's has also been observed (4). The Al_2O_3 film can be deposited in a variety of ways, e.g., pyrohydrolysis of AlCl_3 (4), decomposition of Al-alkoxides (5), pyrolytic deposition from AlB_3 (6), rf sputtering (7), and

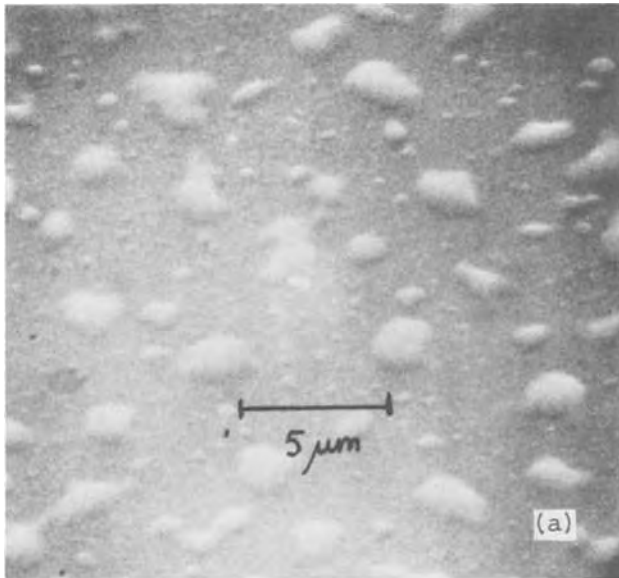
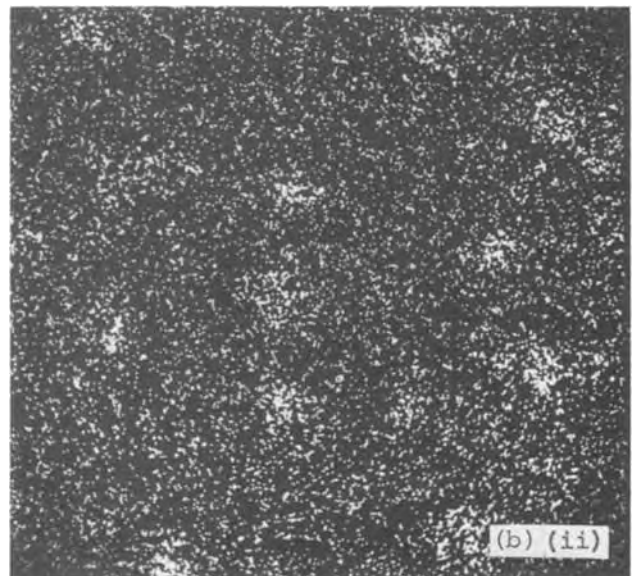
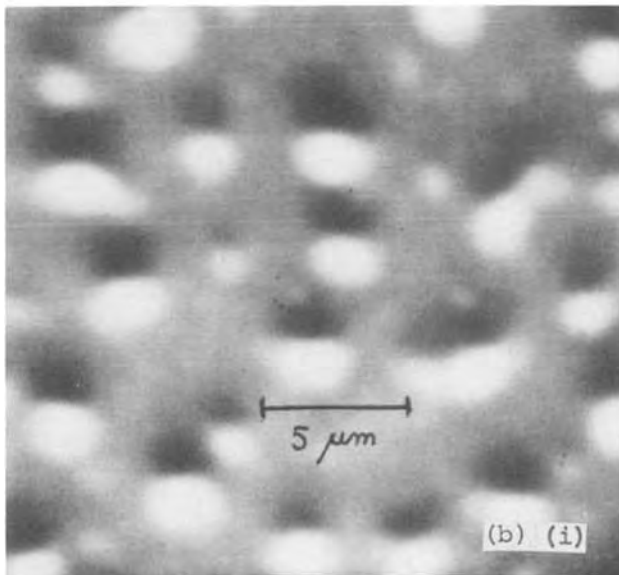


Fig. 1. Micrographs of sample A: (a) scanning electron microscope; (b) electron microprobe analysis (i) backscattered electron image (topography) (ii) aluminum x-ray image.



plasma anodization (1, 3). The latter method is considered here and results are presented indicating that severe deformation of the anodic oxide film can occur during anodization.

Anodization in an rf oxygen plasma was carried out utilizing the apparatus described in Ref. 8. The substrates used were (1-1-1) p-type silicon, 3-5 ohm-cm, and were etched in buffered HF and dried in nitrogen immediately prior to insertion in the vacuum chamber. The vacuum system had a liquid nitrogen trap and was operated at a base pressure of about 10^{-5} Torr. 99.999% grade aluminum was thermally evaporated from tungsten coil filaments onto the unheated substrates. The film deposition rate was approximately 100 \AA sec^{-1} and the mass deposited was monitored by a quartz crystal oscillator used as a microbalance. Film thicknesses were checked using a Sloan "angstrometer," Model M-100.

The data presented in this note refer to two samples anodized at a constant current of 16 mAcm^{-2} . Sample A had an aluminum film of initial thickness 450 \AA and was anodized to slightly past the point at which *in situ* reflectance measurements (9) indicated, assuming homogeneous anodization, all the metal had been converted to oxide. Sample B's initial aluminum film thickness was 1650 \AA and this was anodized until the Al_2O_3 was approximately 1000 \AA thick.

Figure 1 shows a scanning electron microscope (SEM) micrograph and electron microprobe results for a section of the anodic film on sample A. Small hillocks are clearly visible on the two topographical photographs and these can be identified in Fig. 1 b(ii) as aluminum-rich regions. The hillocks are not thought to be related to structure in the as-deposited aluminum

film as a SEM micrograph of an unanodized sample, deposited at the same time as sample A, revealed only very fine structure with any small visible features being spatially unrelated to the hillocks shown in Fig. 1.

Figure 2 shows SEM micrographs of a variety of hillocks and extrusions resulting from the anodization of sample B. Electron microprobe data from the same portion of sample B are shown in the four photos of Fig. 3. The four extrusions shown are clearly of a high aluminum content, yet possessing little or no oxygen or silicon. The dark vertical trails on the silicon x-ray image recording are the result of shadowing effects due to the low angle of the x-rays emitted by the silicon.

From the data presented it would appear that during anodization migration of aluminum in the metal film occurs and accumulation at sites of the order $10\text{-}20 \text{ \mu m}$ apart develops. If anodization is continued for a long enough time (which will only be permitted by a thick enough metal film) these accumulations or hillocks of aluminum actually rupture the overlying anodic film and extrude.

The cause of the mass transport is unlikely to be electromigration (10), a source of failure in some IC's using aluminum interconnects and current densities $>10^6 \text{ A-cm}^{-2}$, as the mass transport is in the direction of electron current flow (*i.e.*, opposite to that observed here) and, furthermore, the current densities are not high enough. *E.g.*, even if all the anodization current is assumed to flow through the hillocks, the current density would only be of the order of 10 A-cm^{-2} . A more probable cause is the presence of a film with high compressive stresses (the aluminum) under another film with lower diffusion rates (the aluminum oxide).

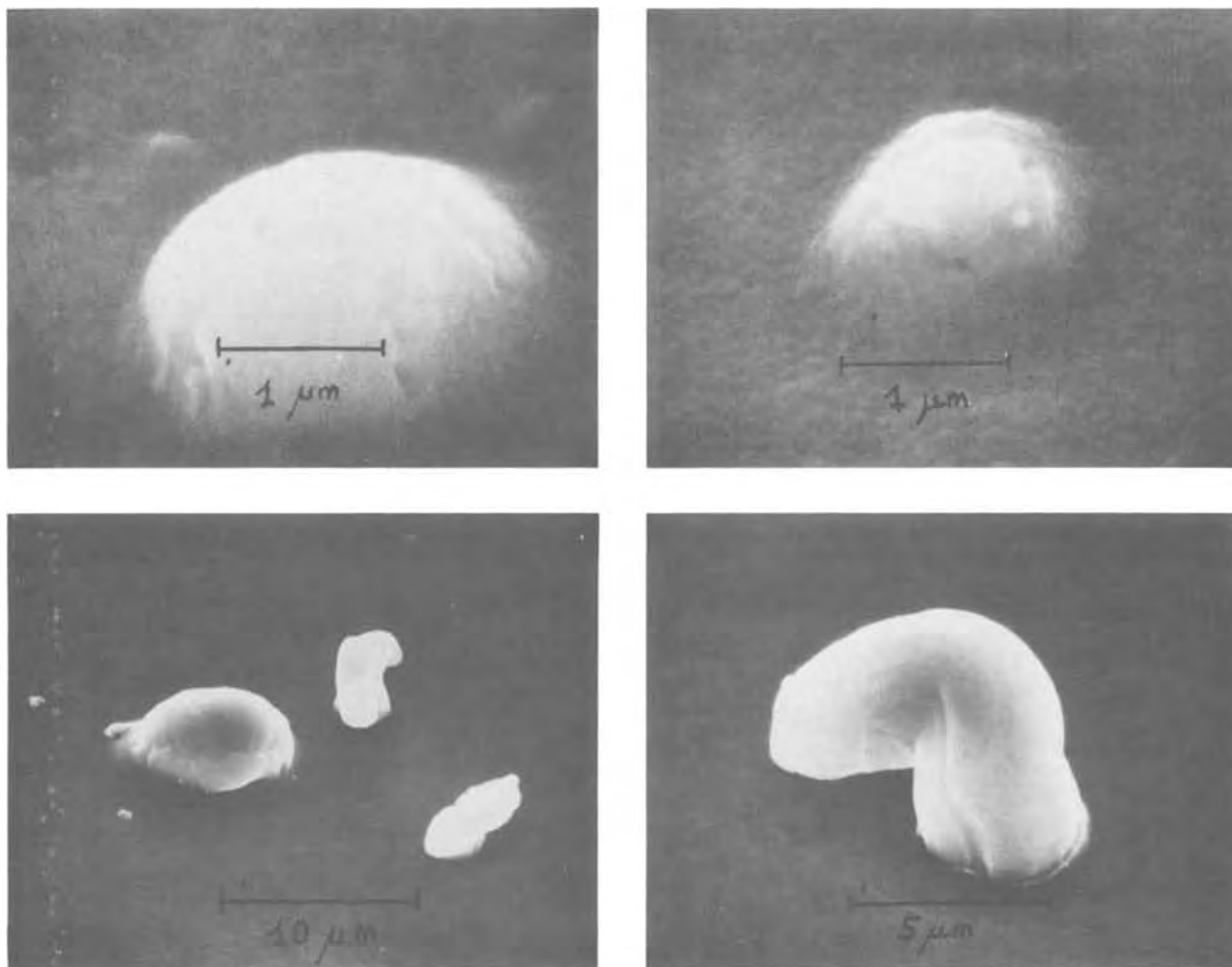


Fig. 2. Scanning electron microscope micrographs showing hillock formation and aluminum extrusions in sample B

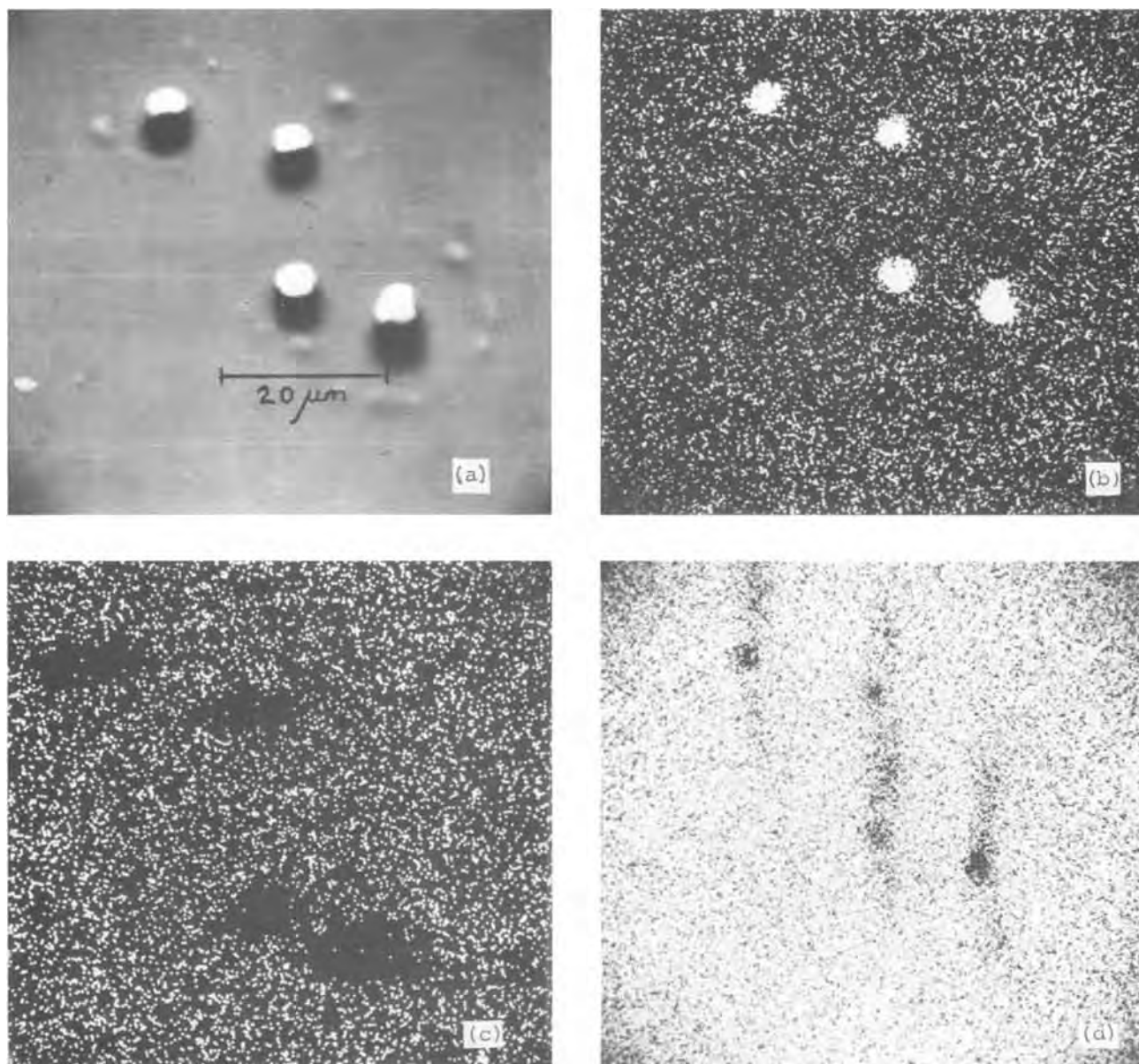


Fig. 3. Electron microprobe analysis of region of sample B: (a) backscattered electron image (topography); (b) aluminum x-ray image; (c) oxygen x-ray image; (d) silicon x-ray image.

The mechanism of stress relief is shown schematically in Fig. 4 and is similar to that treated theoretically by Chaudhari (11). In the case of compressive biaxial stress in the aluminum, the film will seek relief through the path of least resistance, *i.e.*, push the covering anodic film upwards. Although the oxide will accommodate some deformation by manifesting itself in hillocks, a crack will eventually occur, thus opening a path for stress relief by extrusion of the aluminum toward the free surface.

The presence of biaxial stress in the aluminum film could be due to growth defects, differential thermal expansion, temperature gradients, tensile stresses in the aluminum oxide film, and electrical stresses. In aluminum films internal stresses originating during vapor deposition have been shown (12) to cause hillocks, but this type of deformation does not seem relevant in the present case as SEM micrographs of unanodized aluminum films revealed no hillocks and, furthermore, annealing of the aluminum film prior to anodization did not prevent aluminum oxide film deformation on subsequent anodization. Stress analysis of d-c plasma-grown aluminum oxide (13) indicates the presence of stresses which are most probably tensile as the film

apparently contracts in the presence of an anodizing field. In the present case evidence of tensile stresses in the anodic film was provided by the almost complete removal of the film if the anodization field was suddenly removed when either the current was high or the oxide was thick. This can be contrasted to silicon oxide films which appear (8) to relieve stress by forming "bubbles." In the present work no film deformation was ever observed to develop after anodization.

In conclusion it would appear that the hillock and film rupture phenomena are well explained by Chaudhari's (11) model, and that the biaxial compressive forces in the aluminum film result from a combination of some of the factors discussed above, with the presence of an anodizing field being a necessary ingredient.

Acknowledgment

The authors wish to thank Mr. A. Lacis for obtaining the SEM and microprobe data and the National Research Council of Canada for financial support.

Manuscript submitted Feb. 10, 1975; revised manuscript received May 27, 1975.

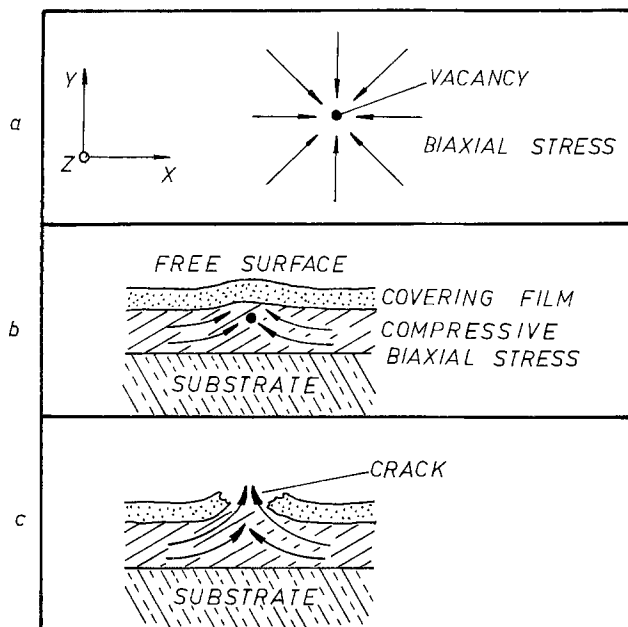


Fig. 4. Film on a substrate covered by another film with lower diffusion rate: (a) biaxial stress forces creating a vertical drift force component at a vacancy site; (b) mass flow under compressive biaxial stress; (c) mass flow toward free surface after rupture of the upper film.

Any discussion of this paper will appear in a Discussion Section to be published in the June 1976 JOURNAL. All discussions for the June 1976 Discussion Section should be submitted by Feb. 1, 1976.

Publication costs of this article were partially assisted by the National Research Council of Canada.

REFERENCES

1. K. H. Zaininger and A. S. Waxman, *IEEE Trans. Electron. Devices*, **ED-16**, 333 (1969).
2. S. K. Tung and R. E. Caffrey, *This Journal*, **115**, 239C (1968).
3. F. B. Micheletti, P. E. Norris, and K. H. Zaininger, *RCA Rev.*, **31**, 330 (1970).
4. S. Nakanuma, T. Tsujide, R. Tgarashi, K. Onoda, T. Wada, and M. Nakagiri, *IEEE J. Solid-State Circuits*, **SSC5**, 203 (1970).
5. J. A. Aboaf, *This Journal*, **114**, 948 (1967).
6. P. Balk and F. Stephany, *ibid.*, **118**, 1634 (1971).
7. C. A. T. Salama, *ibid.*, **118**, 1993 (1971).
8. D. L. Pulfrey and J. J. H. Reche, *Solid-State Electron.*, **17**, 627 (1974).
9. D. L. Pulfrey and J. J. H. Reche, *Appl. Opt.*, **12**, 1577 (1973).
10. I. A. Blech and E. S. Meiran, *Appl. Phys. Letters*, **11**, 263 (1967).
11. P. Chaudhari, *IBM J. Res. Develop.*, **13**, 197 (1969).
12. F. d'Heurle, L. Berenbaum, and R. Rosenberg, *Trans. AIME*, **242**, 502 (1968).
13. F. B. Micheletti and S. H. McFarlane, Abstract 22, Electrochemical Society, Extended Abstracts, Spring Meeting, Washington, D.C., May 9-13, 1971.

Microscopic Mechanisms of Growth of Dark Line Defects in Double Heterostructure Lasers

J. A. Van Vechten^{*1}

Bell Laboratories, Murray Hill, New Jersey 07974

Petroff and co-workers have studied the growth of dark line defects, DLD's, in GaAs-GaAlAs double heterostructure lasers (1). They claim to have established that the DLD dislocation network begins to grow in the p-alloy layer a variable distance from the active layer, grows only under recombination, and gradually propagates into the GaAs active layer via a climb mechanism. Although some still dispute these claims, the author accepts them. If one does accept them, then one must conclude that the more elementary defects which coalesce to form the DLD dislocation network must be nonradiative recombination centers, NRC's, acting via a configuration coordinate mechanism so as to exhibit recombination enhanced diffusion (2). One must further conclude either that the NRC's are much more prevalent in the alloy than in the binary, or that the concentration in the binary is not sufficient to degrade the device. The propagation of the NRC's toward the active layer should then result from a gradient in chemical composition. [If the rate of recombination in the p-alloy region within a diffusion length of the active layer is at least 0.1% that in the active layer in the devices studied, then the expected rate of enhanced diffusion is adequate. It seems reasonable that such a rate should obtain in this region as a result of the impurity absorption of light from spontaneous emission and the tail of the lasing mode, the passage of Auger electrons from the active region, and the imperfect reflection of electrons at the actual p-p junction. This hypothesis is supported by

the observation that the rate of degradation continues to increase above the lasing threshold (3).]

To test these conclusions the existence curve of GaAs, Fig. 1, and the concentration of the various native defects in GaAs and $\text{Ga}_{0.65}\text{Al}_{0.35}\text{As}$ were calculated using the author's prescription for estimating the energies of formation of vacancies and antisite defects in zincblende type semiconductors (4, 5). (See Table I.) The equilibrium concentrations of the various elementary native defects in the three layers of the p-p-n devices for 800°C growth in contact with the appropriate liquids (6-9) are listed in Table II. For the alloy layers, the dielectric theory of the electronic structure of alloys (10) and the defect parameters estimated previously (4, 5) were used. The defect ionization energies were assumed to be the same in the alloy

Table I. Theoretically predicted enthalpies and entropies of various reactions involved in the growth of the actual imperfect crystal (4, 5, 9). ΔH_{cv} and ΔS_{cv} denote the enthalpy and entropy of the fundamental bandgap and are fitted to the observed temperature dependence of that gap (5)

Reaction	ΔH , eV	ΔS , k
$\text{Ga}(I) = \text{Ga}_{\text{Ga}}^{\times} + \text{V}_{\text{As}}^{\times}$	1.827	-2.12
$\text{As}(I) = \text{V}_{\text{Ga}}^{\times} + \text{As}_{\text{As}}^{\times}$	1.632	-3.36
$\text{O} = \text{V}_{\text{Ga}}^{\times} + \text{V}_{\text{As}}^{\times}$	4.66	2.20
$\text{V}_{\text{Ga}}^{\times} = \text{V}_{\text{Ga}}^{-} + e^{+}$	$0.28 + \Delta H_{cv} - \Delta H_{cv}(T=0)$	ΔS_{cv}
$\text{V}_{\text{As}}^{-} = \text{V}_{\text{As}}^{-2} + e^{+}$	$1.1 + \Delta H_{cv} - \Delta H_{cv}(T=0)$	ΔS_{cv}
$\text{V}_{\text{As}}^{\times} = \text{V}_{\text{As}}^{+} + e^{-}$	$0.32 + \Delta H_{cv} - \Delta H_{cv}(T=0)$	ΔS_{cv}
$\text{Ga}(I) = \text{V}_{\text{Ga}}^{\times} + \text{Ga}_{\text{As}}^{\times}$	$1.827 + 0.35 + 2\Delta H_{cv}$	0
$\text{As}(I) = \text{As}_{\text{Ga}}^{\times} + \text{V}_{\text{As}}^{\times}$	$0.35 + 2\Delta H_{cv} + 1.632$	0
$\text{GaAs}^{\times} = \text{Ga}_{\text{As}}^{-2} + 2e^{+}$	0	$2\Delta S_{cv}$
$\text{AsGa}^{\times} = \text{As}_{\text{Ga}}^{+2} + 2e^{-}$	0	$2\Delta S_{cv}$

* Electrochemical Society Active Member.

¹ Present address: IBM Thomas J. Watson Research Center, Yorktown Heights, New York 10598.

Key words: GaAs, laser degradation, dark line defects, III-V nonstoichiometry.

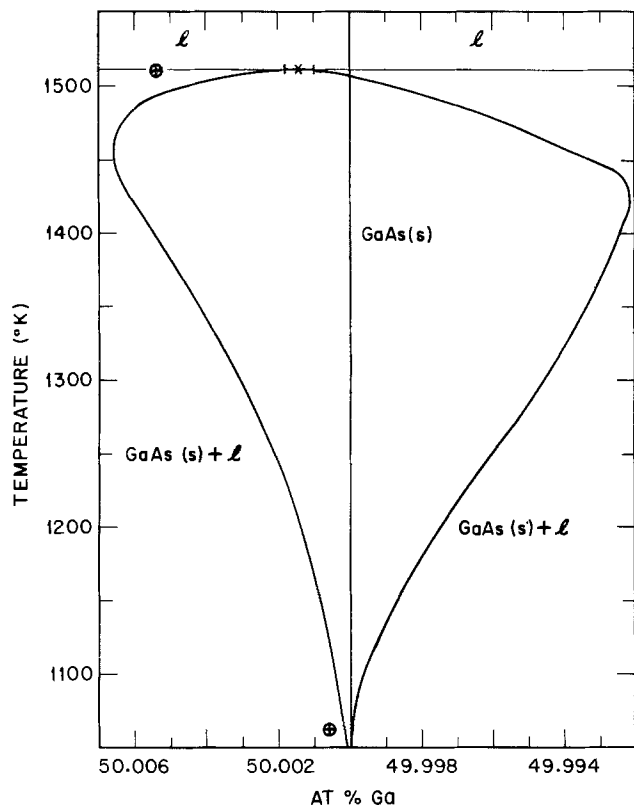


Fig. 1. Predicted existence curve for GaAs and one experimental datum due to Kim (14), x, at the congruent melting point. Also shown are the results of the stoichiometry calculation of Logan and Hurle (15) at the congruent melting point and at 800°C, ⊕.

and the binary and that for V_{As} in GaAs was taken to be the same fraction of the gap as was assumed for V_P in GaP (5). The ionization energies for V_{Ga} were slightly adjusted from the corresponding estimate to match the radiation-induced defect having levels denoted E3 and H1 by Lang and Kimerling (11).

The present theory was previously used (5) to calculate an existence curve for GaP which was in good agreement with experiment (12). It also offered an explanation for the observed dependence of the concentration of native NRC's on growth conditions (13). The theory indicated the dominant NRC to be a complex, $V_{Ga}^-P_{Ga}^{+2}V_{Ga}^-$, formed during cooling from the equilibrium distribution of point defects present during growth.

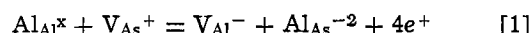
The existence curve for GaAs, Fig. 1, calculated here using the liquid phase activities of Thurmond (8) and heats of formation of Ilegems and Panish (9), may be compared against one reliable measurement at the congruent melting point (14). The calculated composition at that point is 50.0013% Ga in agreement with Kim's value of $50.0014 \pm 0.0005\%$ Ga for float zone material. Kim's one other measurement, on solution-grown (750°-950°C) material, indicates the material to be much more Ga-rich, 50.0077%, than the calculated

Table II. Calculated equilibrium concentrations of defects in the three layers of the double heterostructure layers studied by Petroff et al. (1). The parameters in Table I and 800°C LPE growth (7, 9) are assumed

	n-GaAlAs $\times 10^{16}/\text{cm}^3$	p-GaAs $\times 10^{16}/\text{cm}^3$	p-GaAlAs $\times 10^{16}/\text{cm}^3$
Ge_{As}^-	—	120	100
Ge_{Ga}^+	—	20	1
Te_{As}^+	1000	—	—
$V_{Ga,Al}^-$	0.2	0.01	0.01
V_{As}^+	0.8	2.2	19
AS_{Ga}^{+2}	2×10^{-5}	0.08	0.01
Ga_{As}^{-2}	257	9.4	0.46
Al_{As}^{-2}	235	—	0.42

equilibrium value. The author suspects that the material was not at its equilibrium composition due to the trapping of Ga-rich liquid inclusions during the growth of that material. The one other calculation of the existence curve of GaAs, that of Logan and Hurle (15), predicted the equilibrium composition at 800°C to be very close to that calculated here (Fig. 1). Indeed, it would be very difficult to construct any thermodynamic model for GaAs which predicts a large deviation from stoichiometry at such a low temperature. However, Logan and Hurle's calculation for the congruent melting point is substantially more Ga-rich than either the present calculation or Kim's experiment (see Fig. 1).

As the crystal cools, the reaction



and the corresponding Ga_{Ga} reaction will occur as the V_{As} 's migrate to the nearest neighbor sites. Therefore, the number of $V_{As}^+Al_{As}^{-2}V_{As}^+$ complexes which may form as the material cools is not limited by the number of Al_{As} present during growth but may be limited by the number of V_{As} present. Assuming, as in Ref. (5), that these complexes are the primary fate of the native defects formed at growth, we estimate their concentration for equilibrium growth to be $5 \times 10^{15} \text{ cm}^{-3}$ in the n-alloy, 1.1×10^{16} in the p-GaAs active region, and 7×10^{16} in the p-alloy, where they are about evenly divided between $V_{As}^+Al_{As}^{-2}V_{As}^+$ and $V_{As}^+Ga_{As}^{-2}V_{As}^+$.

Just as $V_{Ga}^-P_{Ga}^{+2}V_{Ga}^-$ and not $V_P^+GaP^{-2}V_P^+$ is the dominant NRC in GaP, the author believes $V_{As}^+Al_{As}^{-2}V_{As}^+$ and not $V_{As}^+Ga_{As}^{-2}V_{As}^+$ nor $V_{Ga}^-As_{Ga}^{+2}V_{Ga}^-$ will be the dominant NRC in this case, at least for recombination via the configuration coordinate mechanism. (They would seem about equally effective for an Auger mechanism, but this mechanism could not produce RED and so would not cause the DLD dislocation network to grow.) This follows from the fact that Al, like P, is much lighter than Ga and As and so should experience a larger attempt frequency, transition matrix element, and tunneling probability in the various recombination modes. The lighter mass should also lead to a lower barrier for migration.

Therefore, in the equilibrium growing condition model developed so far, the recombination enhanced diffusion of NRC's should begin in the p-alloy near the active region because that is where the requisite native defects will occur during growth. Assuming that the $V_{As}^+Al_{As}^{-2}V_{As}^+$ NRC's tend toward the threading dislocation due to its strain field, we see that the resulting dislocation network will propagate by climb (atomic diffusion) as the Al_{As}^{-2} atoms are injected into the dislocation and pipe-diffuse toward the active layer under the gradient in composition. This pipe-diffusion of Al will eventually produce $V_{As}^+Al_{As}^{-2}V_{As}^+$ NRC's in the active layer so that the DLD will propagate there.

The shortcoming of this equilibrium model is that the calculated concentration of mobile NRC's in the p-alloy layer, $3.5 \times 10^{16} \text{ cm}^{-3}$, is about two orders of magnitude smaller than the empirically estimated concentration (1). Indeed, transient capacitance spectroscopy measurements of similar alloy material show large concentrations of nonradiative deep traps which vary in a manner not easily describable in terms of equilibrium growth thermodynamics (16).

Two alternate explanations for the growth of DLD's are known to the author. Woolhouse (17) proposed that they are produced by electromigration of atoms along the dislocation in opposite directions in n- and p-type material. This explanation has the attraction of not requiring any large concentration of grown-in defects and does not address the problem of slow degradation in the absence of threading dislocations. This model would seem to require that the DLD grow at the p-n junction and not in the p-alloy layer some variable distance from the active layer, as is reported (1). The

other proposal made by Petroff and Hartman (1) is that nonradiative recombination at the threading dislocation produces vacancies which cause the DLD network to grow, and interstitials which pipe-diffuse away along the threading dislocation. This proposal does not explain the location of the DLD network or the slow degradation in the absence of a threading dislocation and seems to be inconsistent with the highly convoluted appearance of the network that does grow (18). Thus, both these alternate explanations seem to be irreconcilable with the reported observations (1).

The conclusion that alloy material of these layers is, in fact, not grown close to its equilibrium stoichiometry is supported by the observation of Kim (14) on material solution-grown at similar temperatures and rates. If the laser material is as metal-rich as the solution-grown samples Kim measured, the concentration of V_{As}^+ and Al_{As}^{-2} present could easily be large enough to produce sufficient NRC's to account for the subsequent growth of the DLD.

Added Note

Petroff and Hartman (1) concluded that the DLD were vacancy-type dislocation networks because they found small dislocation loops lying within the network to exhibit vacancy-type contrast in the electron microscope. After submission of this paper, Hutchinson *et al.* (19) published the results of a more extensive electron microscopy study of similar lasers and concluded that the dislocation loops of the DLD were mainly interstitial in character. The lasers observed in this latter study differed from those examined by Petroff *et al.* in that they contained 5% Al in the active layer while Petroff's were pure GaAs.

On the basis of the present model of the degradation, one might expect the DLD to originate in the active layer of the 5% Al lasers rather than in the p-alloy layer. Hutchinson *et al.* (19) tentatively concluded that this was the case with their samples. Reconsideration of pure GaAs lasers reaffirms the conclusion that the DLD's originate in the p-alloy layer (20).²

However, it now seems likely that the DLD dislocation loops are mainly interstitial in character in both types. Therefore, it is appropriate to point out that the NRC proposed here could cause either an interstitial or a vacancy-type network to grow depending upon whether As (*i.e.*, V_{As}^+) or Al pipe-diffuses more rapidly down the threading dislocation. This is easily seen if we assume the threading dislocation to be an edge dislocation of excess metal atoms. [The true nature of the threading dislocation has not yet been determined (20), but this simplifying assumption is consistent with Kim's observation of a gross excess of Ga in GaAs solution-grown at similar rates and temperatures (14).] If the Al atom from the $V_{As}Al_{As}V_{As}$ complex pipe-diffuses away, then, as assumed above, the remaining V_{As} 's cause a vacancy-type loop to grow by eating away at the extra plane of metal atoms. If the V_{As} pipe-diffuses away, *i.e.*, if As pipe-diffuses in, then

² G. M. Blom, in a private communication, has observed DLD networks originating in the n-alloy layer as well as in the p-alloy layer, but not in a pure GaAs active layer. As long as the material is not grown near equilibrium, this does not contradict the present conclusions about the equilibrium.

the remaining Al_{As} causes an interstitial loop to grow because these atoms would add to the extra plane of metal atoms. From the results of Hutchinson *et al.* (19), one may conclude that the latter is the dominant process.

The author would also like to note that Van der Sande and Peters have observed (21) defect clusters in LEC GaAs having the same length, width, orientation, and concentration as that here predicted for the $V_{As}Ga_{As}V_{As}$ complexes under LEC conditions, *i.e.*, at the congruent melting point.

Manuscript submitted Jan. 30, 1975; revised manuscript received June 27, 1975.

Any discussion of this paper will appear in a Discussion Section to be published in the June 1976 JOURNAL. All discussions for the June 1976 Discussion Section should be submitted by Feb. 1, 1976.

Publication costs of this article were partially assisted by Bell Laboratories.

REFERENCES

1. P. Petroff and R. L. Hartman, *Appl. Phys. Letters*, **23**, 469 (1973); P. Petroff, W. D. Johnston, and R. L. Hartman, *ibid.*, **25**, 226 (1974); P. Petroff, *J. Appl. Phys.*, **45**, 3899 (1974); P. Petroff, in "Proceedings of the International Conference on Lattice Defects in Semiconductors," A. Seeger, Editor, p. 73, Institute of Physics, London (1974).
2. D. V. Lang and L. C. Kimerling *Phys. Rev. Letters*, **33**, 489 (1974); J. D. Weeks, J. C. Tully, and L. C. Kimerling, *Bull. Am. Phys. Soc.*, **20**, 318 (1975), and to be published.
3. D. H. Newman and S. Ritchie, *IEEE J. Quantum Electron.*, **QE9**, 300 (1973).
4. J. A. Van Vechten, *This Journal*, **122**, 419 (1975).
5. J. A. Van Vechten, *ibid.*, **122**, 423 (1975).
6. R. L. Hartman, J. C. Dymont, C. J. Wang, and N. Kuhn, *Appl. Phys. Letters*, **23**, 181 (1973).
7. B. I. Miller, E. Pinkas, I. Hayashi, and R. J. Capik, *J. Appl. Phys.*, **43**, 2827 (1972).
8. C. D. Thurmond, *J. Phys. Chem. Solids*, **26**, 785 (1965).
9. M. Ilegems and M. P. Panish, *ibid.*, **35**, 409 (1974); M. Ilegems, Private communication.
10. J. A. Van Vechten and T. K. Bergstresser, *Phys. Rev.*, **B1**, 3351 (1970).
11. D. V. Lang and L. C. Kimerling, in "Proceedings of the International Conference on Lattice Defects in Semiconductors," A. Seeger, Editor, p. 589, Institute of Physics, London (1974).
12. A. S. Jordan, A. R. Von Neida, R. Caruso, and C. K. Kim, *This Journal*, **121**, 153 (1974).
13. A. S. Jordan, A. R. Von Neida, R. Caruso, and M. DiDomenico, *Appl. Phys. Letters*, **19**, 394 (1974).
14. C. K. Kim, *This Journal*, (In press).
15. R. M. Logan and D. T. J. Hurle, *J. Phys. Chem. Solids*, **32**, 1734 (1971).
16. D. V. Lang, Private communication.
17. G. R. Woolhouse, *IEEE J. Quantum Electron.*, **QE 11**, 556 (1975).
18. J. W. Matthews, Private communication.
19. P. W. Hutchinson, P. S. Dobson, S. O'Hara, and D. H. Newman, *Appl. Phys. Letters*, **26**, 250 (1975).
20. P. Petroff, Private communication.
21. J. B. Van der Sande and E. T. Peters, *J. Appl. Phys.*, **45**, 1298 (1974).

Correspondence between Nonradiative Dark Spots, Microplasma Emissions, and Dislocation Pits in GaP:N Light-Emitting Diodes

Takashi Kajimura, Kunio Aiki, and Jun-ichi Umeda

Central Research Laboratory, Hitachi, Limited, Kokubunji, Tokyo 185, Japan

Though many investigations have been carried out to relate the luminescence efficiency of light-emitting diodes (LED's) to crystal imperfections in melt-grown crystals and epitaxially grown wafers (1-5), little work has been done on completed LED's, which seems to give more direct information on the diode performance. In this paper, we report on a clear one to one correspondence between nonradiative dark spots under forward bias, microplasma emissions under reverse bias, and dislocation etch pits in GaP:N LED's.

Experimental

Diodes investigated in this experiment were fabricated from S- and N-doped liquid-phase epitaxial (LPE) wafers grown on LEC substrates. The p-n junctions were made both by Zn diffusion into the wafer and by LPE growth of a Zn- and N-doped layer upon the wafer. Electroluminescence in the forward biased diode was observed at a d-c current density of 8 A/cm². Light emission in the reverse biased diode was observed by applying current pulses in order to minimize the heating effect. The amplitude of each current pulse was 50 A/cm². The duration and repetition rate were $\sim 8 \mu\text{sec}$ and $\sim 25 \text{ kHz}$, respectively. Black wax was applied to each side face of the diode chip to avoid internal scattering of light which obscures the image. An etch pit study was performed using AB

Key words: dislocation, electroluminescence, microplasma, III-V compounds, LED, GaP.

etchant (6) for the {111}P surface. For the {100} surface, thermal etching was used.

Results

A light emission image in the forward biased diode, which was made by Zn diffusion into n-LPE layer grown on {111}P LEC substrate, is shown in Fig. 1(a). Nonradiative dark spots with a radius of 2-3 μ , which is the same order of magnitude as the diffusion lengths of carriers in the GaP LPE layer, and with a density of $\sim 5 \times 10^5/\text{cm}^2$ are seen in the picture. In the case of reverse bias, emission spots originating from the microplasma were observed. Figure 1(b) shows the reverse biased image of the diode. The microplasma emissions appear at positions where the nonradiative dark spots did (see a-e in Fig. 1). The etch pit pattern of the surface of the diode is shown in Fig. 1(c). The etch pits observed are D-pits (2) which are caused by dislocations in the crystal. In Fig. 1(c) D-pits appear where the dark spots (and microplasma emissions) did. These results show that the nonradiative dark spots were caused by the dislocations in the LPE layer, and the emission spots due to microplasma appear at positions where the dislocations cross the p-n junction. Dark spots appeared at the positions where D-pits did without exception in diodes investigated. There are a few positions where microplasma emissions did not appear in Fig. 1. This shows that the breakdown voltages

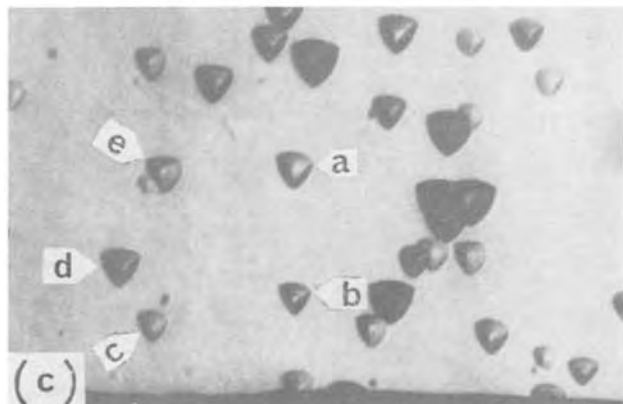
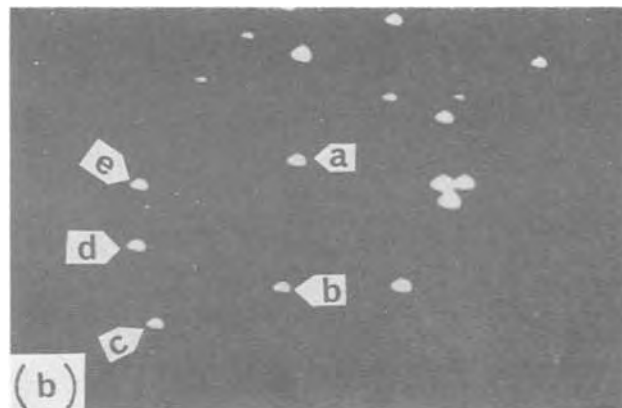
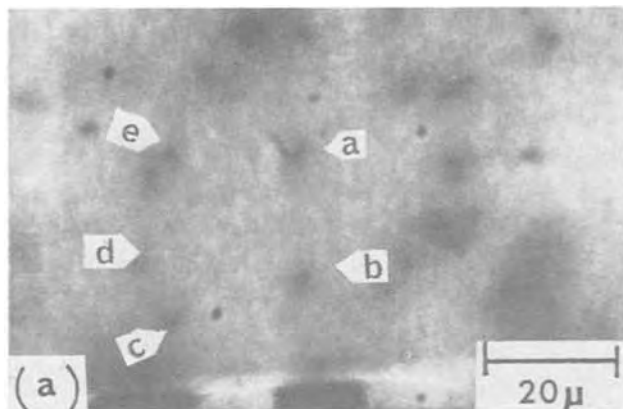


Fig. 1. (a). An electroluminescence image of a GaP:N LED in the forward bias. The density of the nonradiative dark spots is $5 \times 10^5/\text{cm}^2$. Typical nonradiative dark spots are shown by a \sim e. (Comparatively small and black spots in the figure are due to dusts in the optical system and should be distinguished from the inherent nonradiative spots.) (b). A reverse biased image of the diode. Microplasma emissions appear at the positions of the dark spots. (c) The etch pit pattern of the diode surface.

at the positions are higher than the ones at the other positions.

Rozgonyi *et al.* (1, 3) reported that dislocations, by themselves, are of secondary importance to the luminescence efficiency and decorated dislocations, which only occur when there is a high density of S-pits (2, 3), can be a significant factor in GaP. However, Fig. 1 shows that dislocations are important to the luminescence efficiency of GaP LED's, even if there is a low density of S-pits.

Similar results were obtained in diodes made by double layer growth. There were, however, some positions where dark spots (and emission spots due to microplasma) appeared, but no etch pits appeared in these diodes. This shows that some of the dislocations in the n-layer do not propagate into the p-LPE layer in LPE growth. From the photoluminescence image of the {110} cleavage face of a LPE layer made by the double layer growth, it was found that some of the dark lines which are caused by dislocations and extend from the substrate towards the LPE surface stopped at the p-n junction and did not propagate into the p-LPE layer. These dislocations may be pinned by some kinds of crystal imperfections (for example, precipitates).

The density of the dislocation in the LPE layer varied 2×10^4 – 7×10^5 /cm² from wafer to wafer. From the radius and the density of the nonradiative dark

spots, it was found that the dislocations lower the luminescence efficiency of the diode by 0.3–20%. The same results were also obtained for the {100} wafers.

Acknowledgments

The authors are indebted to Messrs. M. Hirao, M. Ogirima, K. Hunakoshi, M. Nakamura, and S. Kishino of this laboratory for their helpful discussions.

Manuscript submitted April 3, 1975; revised manuscript received June 18, 1975.

Any discussion of the paper will appear in a Discussion Section to be published in the June 1976 JOURNAL. All discussions for the June 1976 Discussion Section should be submitted by Feb. 1, 1976.

Publication costs of this article were partially assisted by Hitachi, Limited.

REFERENCES

1. G. A. Rozgonyi and M. A. Afromowitz, *Appl. Phys. Letters*, **19**, 153 (1971).
2. T. Iizuka, *This Journal*, **118**, 1190 (1971).
3. G. A. Rozgonyi and T. Iizuka, *ibid.*, **120**, 673 (1973).
4. S. Kishino, M. Ogirima, T. Kajimura, and K. Kurata, *J. Crystal Growth*, **24/25**, 266 (1974).
5. G. B. Stringfellow and P. E. Greene, *J. Appl. Phys.*, **40**, 502 (1969).
6. M. S. Abrahams and C. J. Buiocchi, *ibid.*, **36**, 2855 (1965).

Fabrication Techniques for Tungsten Cat Whisker Infrared Antennas

Bor-long Twu

Department of Electrical Engineering and Computer Sciences, Electronics Research Laboratory, University of California, Berkeley, California 94720

Metal-insulator-metal tungsten cat whisker point-contact diodes have been used as mixers in the far infrared, infrared, and near infrared regions (1). At 10.6 μ wavelength the ability of the device to detect radiation arises from the diode's nonlinear current-voltage characteristic (2). In work to be reported elsewhere, we have described the antenna properties at 10.6 μ wavelength in some detail (3). A particularly interesting finding is that the effective antenna length is not determined by the over-all length of the tungsten wire, but rather by the length of the etched away portion which is produced in the electrochemical etching process. In general, the antenna length affects the number of lobes, the positions of maxima and minima, and the directivity in the antenna pattern. In this note we report a technique by means of which conical antennas with different lengths in the range between ~ 40 and $\sim 170\mu$ can be fabricated in a reproducible way.

The electrochemical etching technique that we have used is already known to many workers in the field, but to our knowledge it has not been published, and therefore it will be summarized here. A 25 μ diameter tungsten wire, after being soldered to a BNC connector, is dipped into NaOH solution to a depth of approximately 0.5 cm to act as anode. A sheet of pure platinum is used as cathode. The etching process occurs when a direct current is passed between the tungsten wire and the platinum sheet. The tungsten wire is continuously etched away near the solution surface until the weight of the immersed part causes it to break and drop off, leaving a sharp conical tip. An electrical cir-

cuit is designed to turn off the etching current as soon as the immersed wire drops off, in order to prevent further etching and consequent dulling of the tip. Typically, it takes from ~ 30 sec to a few minutes to etch 25 μ tungsten wires. A similar technique involving alternating current and KOH solution is also known (4).

The etching apparatus consists of the etching cell, controlling circuit and power supply, tungsten wire holder mounted on a vertical micropositioner for controlling the tungsten wire position as it is dipped into the etching solution, an inclining stereomicroscope of 90X magnification for viewing the etching process, and a compound microscope of 40X, 100X, 400X, and 1000X different magnifications for examining etched conical tips.

Micrographs of 25 μ tungsten wires with tips ranging in length l from 40 to 170 μ are shown in Fig. 1 and Fig. 2. These tips were produced by using etching solutions with different concentrations ranging from 0.75 to 0.1875N. It is interesting that the final length of the conical tip can be controlled effectively within $\pm 15\%$ accuracy by varying the concentration. To etch 75, 100, and 125 μ wires, more concentrated solutions are needed. We have not attempted to produce tips with controllable lengths on these thicker wires, although it appears to be possible.

Especially for shorter tips, unexpected irregular shapes do occur occasionally. By watching the process through the stereomicroscope, the reason can be determined. During the first few seconds, initial oxidation of the tungsten wire is rapid. This causes gas bubbles to be formed. The bubbles are then attracted to the tungsten wire surface. The result is the appearance of ir-

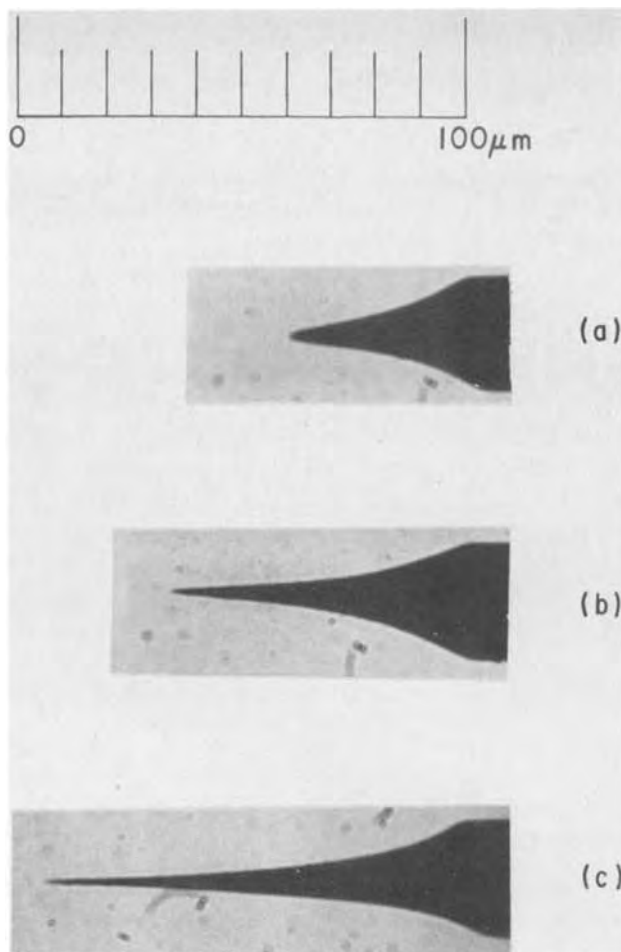


Fig. 1. Micrographs of direct current, electrochemically etched tips of 25μ diameter tungsten wires by using NaOH with different concentrations. (a) $0.75N$ NaOH, $l = 40\mu$. (b) $0.5N$ NaOH, $l = 67\mu$. (c) $0.375N$ NaOH, $l = 93\mu$.

regular bumps on the tips, since places covered by bubbles are protected from the etching solution. An easy way to get rid of bubbles is to divide the etching process into steps. First, the tungsten wire is dipped into the solution and direct current passed as usual for ~ 15 sec. Bubbles are formed and attached to the wire. Then the wire is raised out of the solution to interrupt the etching process. The bubbles are left at the surface of the solution and dissipate. The etched wire is then dipped into the solution again to approximately the same depth as in the first step by means of the micro-positioner. Current is passed again and the etching process resumed. No more bubbles are observed to form. Without bubbles attached to the tungsten wire surface, the tip etching processes were always reproducible.

In conclusion, we report a fairly easy method to fabricate tungsten cat whisker antennas with controllable lengths in the range from 40 to 170μ . Similar techniques may also find applications in field emission microscopy.

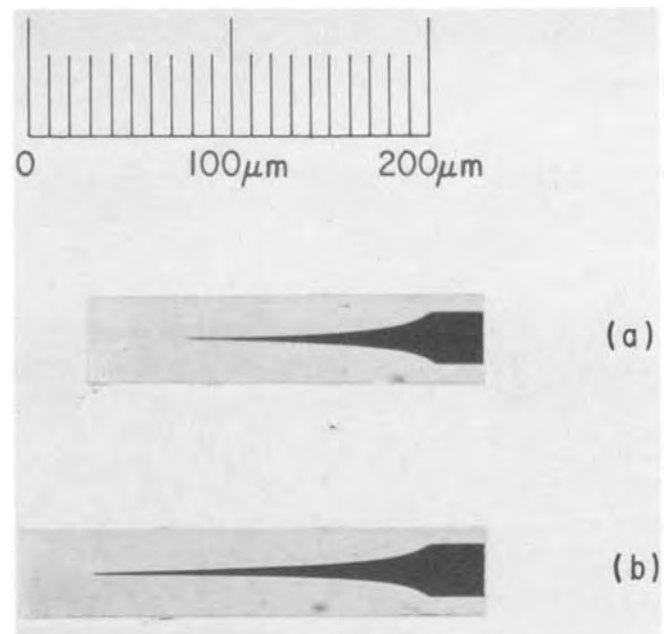


Fig. 2. Micrographs of longer tips of 25μ diameter tungsten wires. (a) $0.25N$ NaOH, $l = 125\mu$. (b) $0.1875N$ NaOH, $l = 170\mu$.

The availability of tips with different lengths and cone angles allows one to vary these parameters in situations when they can be expected to influence the antenna behavior or other useful characteristics.

Acknowledgments

The author wishes to thank Professor S. E. Schwarz for discussions and reviewing the manuscript, Dr. John C. Wiesner for designing the controlling circuit and many useful comments, and Professor J. R. Whinnery, Professor T. K. Gustafson, and Professor T. Van Duzer for encouraging the author to publish the material. This research was supported by the U.S. Army Research Office Contract DAHCO4-73-C-0026, National Science Foundation Grant GK-42721, and Joint Services Electronics Program Contract AFOSR-F44620-71-C-0087.

Manuscript received March 17, 1975.

Any discussion of this paper will appear in a Discussion Section to be published in the June 1976 JOURNAL. All discussions for the June 1976 Discussion Section should be submitted by Feb. 1, 1976.

Publication costs of this article were partially assisted by the University of California at Berkeley.

REFERENCES

1. K. M. Evenson, J. S. Wells, F. R. Peterson, B. L. Danielson, and G. W. Day, *Appl. Phys. Letters*, **22**, 912 (1973).
2. B. Twu and S. E. Schwarz, *ibid.*, **25**, 595 (1974).
3. B. Twu and S. E. Schwarz, Submitted to *Appl. Phys. Letters*.
4. K. M. Evenson, Private communication.

Semi-Empirical Calculation of Depletion Region Width in n^+ -p Silicon Solar Cells

E. Y. Wang and R. N. Legge

Department of Electrical Engineering, Wayne State University, Detroit, Michigan 48202

In recent calculations (1) of the short-circuit current contributed by the n^+ diffused region in n^+ -p silicon solar cells, we have found that the results are extremely sensitive to the depletion region width occurring in the n^+ -region. To obtain the depletion region width in usual treatments of a solar cell junction, assumptions of either abrupt or one-sided step, or linear approximations (2, 3) are used. More recently an exponential charge density approximation (4) was used to obtain the width. In this note we extend the width calculation for impurity distributions of complementary error function and the Gaussian function, in addition to the exponential function. In combination with experimental width values deduced from capacitance measurements at zero bias, we can determine numerically the width occurring in both n^+ and p regions. It should be emphasized here that diffusion anomalies observed in the shallow n^+ -p junction of a solar cell may result in an impurity profile which is a mixture of the aforementioned distributions (5).

Results

Depletion region width measurements.—The capacitance measurement circuit used to determine the depletion width is shown in Fig. 1. The a-c source and the current-sensitive pre-amplifier are part of a PAR 124 lock-in amplifier. The output of the lock-in signal is related to the conductance at zero bias. The junction capacitance at zero bias can be obtained by simply measuring the current 90° out of phase. Table I summarizes the capacitance results for various silicon solar cells.

Calculations.—The basic assumptions used in the calculations are: (i) one dimensional analysis using the

Key words: depletion region width, solar cell, capacitance measurement.

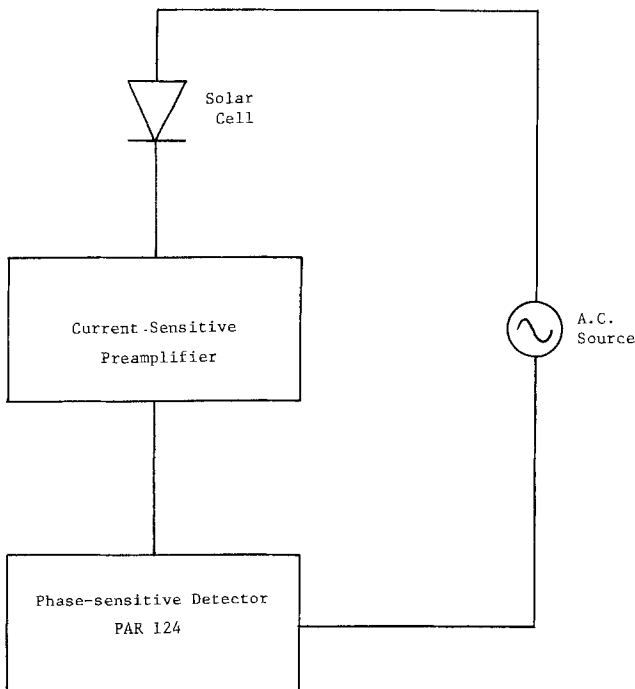


Fig. 1. Schematic circuit diagram for capacitance measurement

Table I. Junction capacitance and corresponding widths of silicon solar cells

Base material resistivity	Junction capacitance in μf per cm^2	Depletion region width (W) in μm
10 ohm-cm	0.0145	0.75
1 ohm-cm	0.038	0.28
0.1 ohm-cm	0.106	0.098

abrupt space-charge edge approximation, (ii) charge neutrality condition in whole depletion region, and (iii) fully ionized impurity atoms in both n^+ and p regions.

Under the above conditions we have charge neutrality in the whole depletion region

$$\int_{d_n}^{x_j} [N_D^+(x) - N_A^-(x)] dx = \int_{x_j}^{d_p} [N_A^-(x) - N_D^+(x)] dx \quad [1]$$

where x_j is the metallurgical junction depth where the space-charge density is zero. The depletion region widths occurring in the n^+ and p regions, respectively, are $x_j - d_n$, $d_p - x_j$. $N_D^+(x)$ is the positive donor ion density and $N_A^-(x)$ is the negative acceptor ion density. Notations are illustrated in Fig. 2.

In a conventional n^+ -p silicon solar cell, $N_A^-(x)$ is constant, and the value of the constant depends on the doping level of the base material. For 10 ohm-cm solar cells $N_A^-(x)$ is about $1.3 \times 10^{15}/\text{cm}^3$. $N_D^+(x)$ depends on the type of diffusion profile and is given as $N_D^+(x) = N_D^+(0)f(x)$ where $N_D^+(0)$, the surface concentration, is taken as 10^{20} cm^{-3} and $f(x)$ is the functional form of the impurity profile (erfc, Gaussian, or exponential). Table II lists $N_D^+(x)$ functions for the three impurity profiles used in our calculations. The constant argument in the functional form is directly related to the surface concentration we choose.

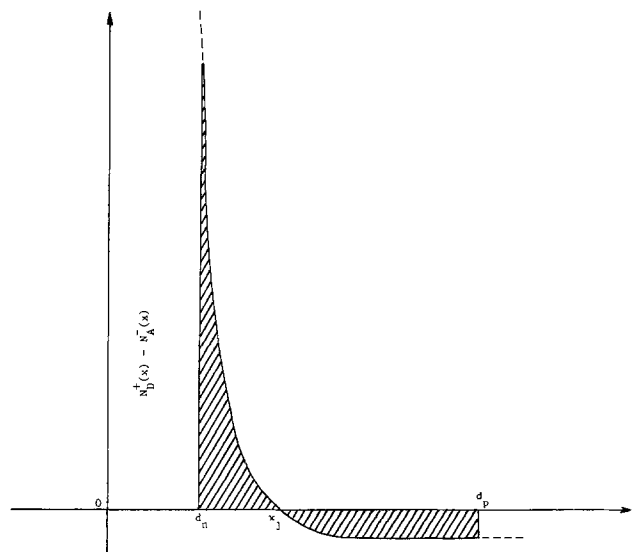


Fig. 2. Illustration of impurity distribution in n^+ -p silicon solar cell.

Table II. Functional form for three impurity profiles

	10 ohm-cm	1 ohm-cm	0.1 ohm-cm
Complementary error function	$\operatorname{erfc}\left(3.07 \frac{x}{x_j}\right)$	$\operatorname{erfc}\left(2.68 \frac{x}{x_j}\right)$	$\operatorname{erfc}\left(1.986 \frac{x}{x_j}\right)$
Gaussian	$\exp\left(-3.34 \frac{x}{x_j}\right)^2$	$\exp\left(-2.97 \frac{x}{x_j}\right)^2$	$\exp\left(-2.3 \frac{x}{x_j}\right)^2$
Exponential	$\exp\left(-11.178 \frac{x}{x_j}\right)$	$\exp\left(-8.806 \frac{x}{x_j}\right)$	$\exp\left(-5.298 \frac{x}{x_j}\right)$

Table III. Summary of results for 10 ohm-cm cells with $N_D^+(O) = 10^{20} \text{ cm}^{-3}$, $N_A = 1.3 \times 10^{15} \text{ cm}^{-3}$, and $w = 0.75 \mu\text{m}$

	Complementary error function				Gaussian function				Exponential function			
$x_j (\mu\text{m})$	0.2	0.3	0.4	0.5	0.2	0.3	0.4	0.5	0.2	0.3	0.4	0.5
$x_j - d_n (\mu\text{m})$	0.0467	0.0631	0.0777	0.0907	0.0427	0.0577	0.0711	0.0833	0.0673	0.0903	0.1105	0.1287
$d_p - x_j (\mu\text{m})$	0.7033	0.6869	0.6723	0.6593	0.7073	0.6923	0.6789	0.6667	0.6527	0.6597	0.6395	0.6213
$N_D^+(d_n) \times 10^{16} \text{ cm}^{-3}$	8.3	5.7	4.4	3.5	10.0	6.9	5.3	4.3	6.1	4.1	3.1	2.5
$V_B (V)$	0.698	0.689	0.682	0.676	0.705	0.695	0.689	0.683	0.692	0.682	0.675	0.669

Table IV. Summary of results for 1 ohm-cm cell with $N_D^+(O) = 10^{20} \text{ cm}^{-3}$, $N_A = 1.6 \times 10^{16} \text{ cm}^{-3}$, and $w = 0.276 \mu\text{m}$

	Complementary error function				Gaussian function				Exponential function			
$x_j (\mu\text{m})$	0.15	0.2	0.3	0.4	0.15	0.2	0.3	0.4	0.15	0.2	0.3	0.4
$x_j - d_n (\mu\text{m})$	0.0355	0.0431	0.0561	0.0669	0.0321	0.0391	0.0511	0.0611	0.0487	0.0589	0.0757	0.0893
$d_p - x_j (\mu\text{m})$	0.2405	0.2331	0.2203	0.2091	0.2439	0.2369	0.2251	0.2153	0.2275	0.2175	0.2003	0.1863
$N_D^+(d_n) \times 10^{17} \text{ cm}^{-3}$	4.0	3.1	2.2	1.7	4.5	3.5	2.5	1.9	2.8	2.1	1.5	1.1
$V_B (V)$	0.804	0.797	0.788	0.782	0.807	0.800	0.791	0.785	0.794	0.788	0.778	0.771

Table V. Summary of results for 0.1 ohm-cm cells with $N_D^+(O) = 10^{20} \text{ cm}^{-3}$, $N_A = 4.6 \times 10^{17} \text{ cm}^{-3}$, and $w = 0.098 \mu\text{m}$

	Complementary error function				Gaussian function				Exponential function			
$x_j (\mu\text{m})$	0.1	0.2	0.3	0.4	0.1	0.2	0.3	0.4	0.1	0.2	0.3	0.4
$x_j - d_n (\mu\text{m})$	0.0271	0.0391	0.0471	0.0533	0.0243	0.0355	0.0431	0.0491	0.0341	0.0479	0.0565	0.0627
$d_p - x_j (\mu\text{m})$	0.0709	0.0587	0.0505	0.0451	0.0739	0.0621	0.0547	0.0493	0.0637	0.0497	0.0411	0.0357
$N_D^+(d_n) \times 10^{18} \text{ cm}^{-3}$	3.9	2.2	1.7	1.4	4.5	2.6	1.9	1.6	2.9	1.7	1.3	1.1
$V_B (V)$	0.950	0.936	0.928	0.923	0.954	0.940	0.932	0.927	0.942	0.928	0.921	0.917

The total space-charge width, W , obtained from the capacitance measurements is given as

$$d_p - d_n = W \tag{2}$$

By solving Eq. [1] and [2] simultaneously, d_n and d_p values can be obtained. The value of $N_D(d_n)$ thus obtained can then be used to find the built-in potential

$$V_B = \frac{kT}{q} \ln \frac{N_A N_D(d_n)}{n_i^2}$$

The results for three different values of base material resistivity and a range of x_j values are presented in Tables III to V.

Discussion

The calculated width values are within $\pm 1\%$ error. This is because we are numerically balancing the charge neutrality in Eq. [1] within $\pm 1\%$. The experimental determination of the width used for Eq. [2] is well within $\pm 2\%$. Therefore the total possible error in this semi-empirical calculation is less than $\pm 3\%$. The results show that depletion region widths in the Gaussian and complementary error function impurity distribution in the n^+ -region for 10 ohm-cm cells is about 10% or less of the total width, depending on x_j values. For an exponential impurity distribution, the percentage of the total width occurring in the n^+ -region is even higher (up to about 20%). In the usual one-sided step approximation, it is assumed that the entire width occurs in the p -region. For 1 ohm-cm and 0.1 ohm-cm base material cells, the $x_j - d_n$ values can be comparable with the $d_p - x_j$ values. In fact, the $x_j - d_n$ value will dominate for some x_j values.

In conclusion, the results have shown that the $x_j - d_n$ and $d_p - x_j$ values have quite a variation for different impurity profiles. Therefore caution should be exercised in choosing a proper impurity profile for determining some of the device parameters in shallow junction devices such as solar cells and high frequency transistors, where accurate values of $x_j - d_n$ and $d_p - x_j$ are needed.

Acknowledgments

This work was partially supported by NASA Grant NGR 23-066-057 and NSF Eng. 75-14104.

Manuscript submitted Aug. 26, 1974; revised manuscript received June 20, 1975.

Any discussion of this paper will appear in a Discussion Section to be published in the June 1976 JOURNAL. All discussions for the June 1976 Discussion Section should be submitted by Feb. 1, 1976.

Publication costs of this article were partially assisted by Wayne State University.

REFERENCES

1. E. Y. Wang, *et al.*, Proceedings of International Conference on Photovoltaic Power Generation, Hamburg, Germany (1974).
2. M. Wolf, *Energy Conversion*, **11**, 63, (1971).
3. A. S. Grove, "Physics and Technology of Semiconductor Devices," p. 159, John Wiley and Sons, New York (1967).
4. E. H. Stevens, *IEEE Trans. Electron Devices*, **659** (1973).
5. P. A. Iles and B. Leibenhaut, *Solid State Electron.*, **5**, 331 (1962).



Identification of the U.V. Irradiation Product in Nematic Chlorostilbene Imaging Processes

K. F. Nelson, W. E. Haas,* and J. E. Adams

Research Laboratories, Xerox Corporation, Webster, New York 14580

In a previous article (1), we described an imaging process based on the photochemical degradation of the nematic *trans*-chlorostilbenes. In that process, the nematic-isotropic transition temperature (T_{n-i}) was selectively lowered in those regions exposed to u.v. irradiation. The depression of T_{n-i} was attributed to a u.v. generated impurity tentatively identified as the *cis* isomer of the parent compound.

In order to positively identify the impurity element, liquid column chromatography was employed to first separate the u.v. generated impurity from the host material. A 20 mm diameter column was packed to a height of 400 mm with silica gel slurred in reagent grade hexane. Nematic *trans*-4-butyl- α -chloro-4'-ethoxystilbene (BCES), which had been irradiated in spectroscopic grade hexane at a wavelength of 300 nm, was then passed through the column. The first-eluted material, the u.v. generated impurity, crystallized at room temperature following solvent evaporation (mp = 46°-50°C) and did not have a mesomorphic phase. The second-eluted material was pure *trans*-BCES having the same nematic temperature range as the non-

* Electrochemical Society Active Member.
Key words: liquid crystals, stilbenes, ultraviolet, imaging.

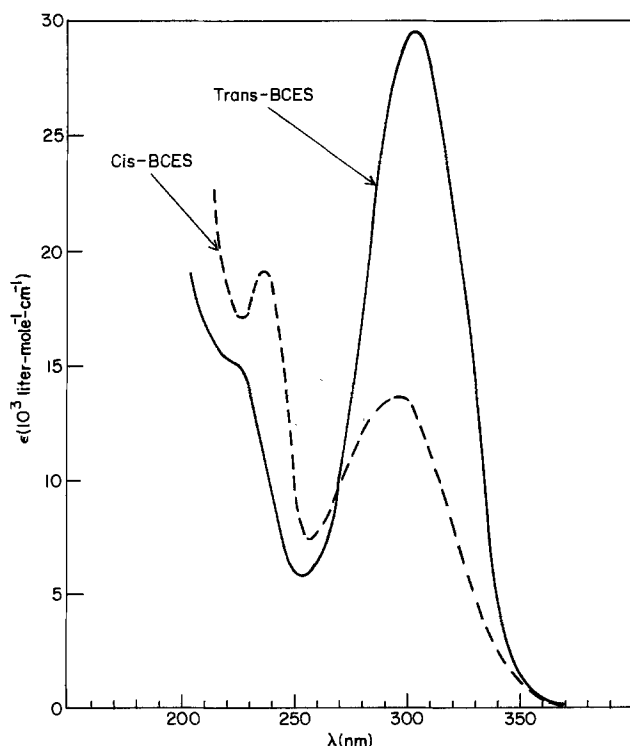


Fig. 1. The u.v. absorption spectra of *trans*-BCES and the separated impurity, *cis*-BCES, in cyclohexane.

Table I.

Material	%C	%H	%Cl	%O	Molecular weight
<i>trans</i> -BCES*	76.29	7.36	11.26	5.08	314.861
<i>trans</i> -BCES**	76.10	6.89	11.79	5.20	340
impurity**	75.85	6.95	11.91	5.29	330

* Calculated values.
** Determined by Galbraith Laboratories, Incorporated, Knoxville, Tennessee.

irradiated, original BCES. Following several irradiation/separation sequences, several hundred milligrams of a single impurity (verified by thin layer chromatography) had been separated for analyses.

Figure 1 shows the absorption spectra of *trans*-BCES and the separated impurity. A comparison with similar spectra, Fig. 2, of *trans*- and *cis*- α -chloro-4-methylstilbene (2) indicates that the isolated impurity is indeed *cis*-BCES. Table I shows the results of elemental analysis and molecular weight determinations of *trans*-BCES and of the impurity material compared with the calculated values for *trans*-BCES. The composition and molecular weight of the impurity molecule is, again, indicative of the *cis* isomer of BCES.

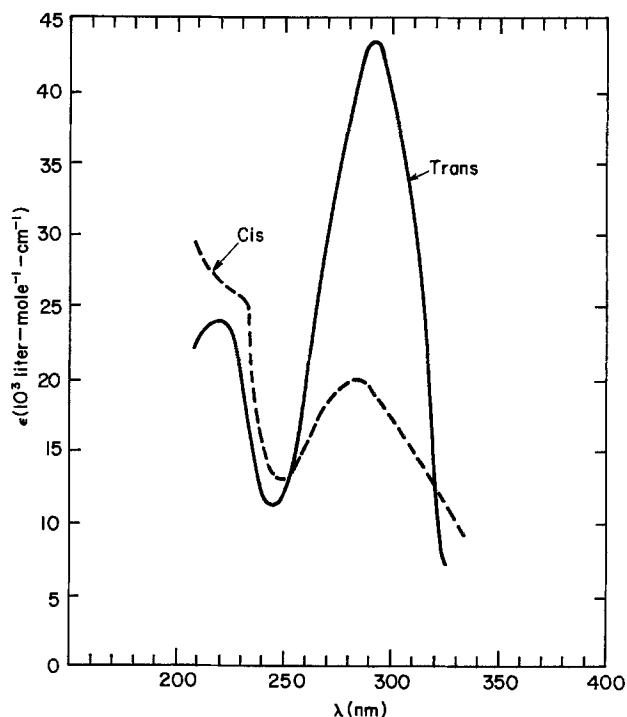


Fig. 2. The u.v. absorption spectra of *trans*- and *cis*- α -chloro-4-methylstilbene [after McDonald and Schwab, Ref. (2)].

Finally, proton nmr spectra showed a down-field shift in the resonance of the vinyl hydrogen of the impurity molecule compared to the vinyl hydrogen resonance in *trans*-BCES. A similar shift is observed in *cis*-stilbene compared to *trans*-stilbene. We conclude that the impurity generated by u.v. irradiation of *trans*-BCES is the isomer, *cis*-BCES.

Acknowledgments

We wish to thank Dr. Henry K. Hall, Jr., of the University of Arizona for suggestions and stimulating discussions, and Dr. David J. Williams of our laboratory for his help with the nmr spectra.

Manuscript received June 20, 1975.

Any discussion of this paper will appear in a Discussion Section to be published in the June 1976 JOURNAL. All discussions for the June 1976 Discussion Section should be submitted by Feb. 1, 1976.

Publication costs of this article were partially assisted by Xerox Corporation.

REFERENCES

1. W. E. Haas, K. F. Nelson, J. E. Adams, and G. A. Dir, *This Journal*, **121**, 1667 (1974).
2. R. N. McDonald and P. A. Schwab, *J. Am. Chem. Soc.*, **85**, 4004 (1963).

Simple Method for Separating Completed Diodes from Semiconductor Wafers

J. Klatskin and A. Rosen

RCA Laboratories, David Sarnoff Research Center, Princeton, New Jersey 08540

Finding ways of cutting processed semiconductors into individual diodes or transistors is a major time-consuming activity for process designers. One problem, for instance, has been the separation of completed Trapatt diodes so they could be packaged. Many designers use techniques such as wire sawing, diamond sawing, etching, laser cutting, and scribe and break separation.

Problems associated with these methods, excluding the cost of the equipment involved in cutting, include low yields due to damage along the edges of the completed devices, as well as inadvertent fractures of the device itself.

Wire sawing requires a cutting medium such as oil, or a tenacious diamond mixture which retains the shavings on or near the device. In addition to metal contamination, the substance used presents cleaning problems.

Diamond sawing requires a large capital investment, without solving fine-line requirements (< 1 mil).

Etching introduces contaminants, which can ruin an otherwise good device. Etching is a lengthy process, often up to 2 hr, and the masking material seldom holds that long.

Scribe and break separation often causes damage due to breaks along lines not defined by the scribe. Unintentional breaks come about because the natural cleavage line to scribe line angle is too large.

An analysis of the methods and the review of their associated problems have led to an improved process

Key words: diodes, Trapatt, heat sink.

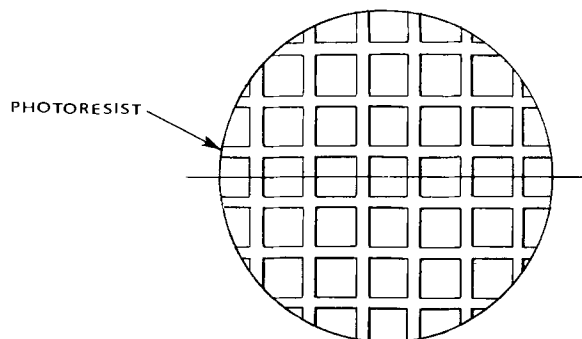


Fig. 1. Photoresist defining the device regions. The type of photoresist used is dictated by the design requirement. AZ111 has been used successfully and, for forming a thick base, dynachem thick film resist has been utilized.

for cutting a semiconductor wafer into individual devices of desired geometrical configuration.

A metal film is deposited on the support side of a semiconductor material. Photoresist is applied and processed, forming the device regions by a pattern of

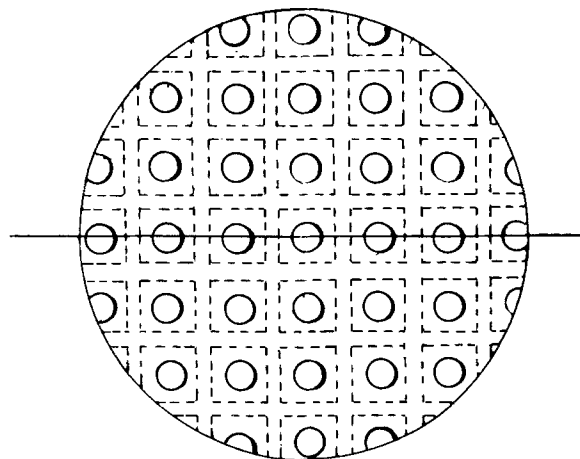


Fig. 2. Alignment of each device within the defined regions

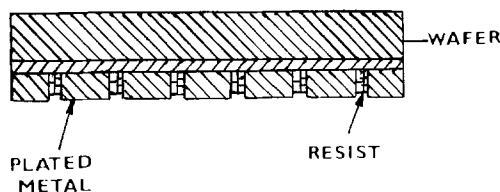


Fig. 3. Plated heat sink with photoresist separators

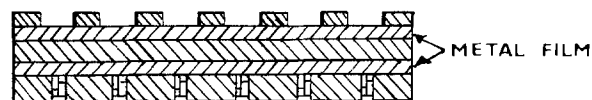


Fig. 4. Wafer prior to etching for diode fabrication

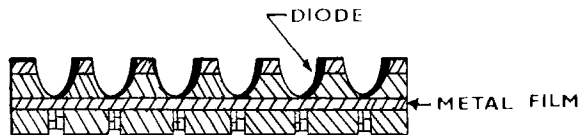


Fig. 5. Completed wafer with diode formed above each heat sink ready for separation.

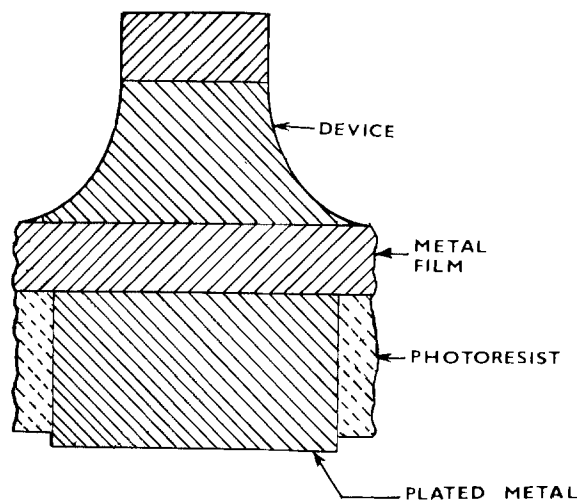


Fig. 6. The separated device, in this example a diode

intersecting strips (Fig. 1). A layer of metal, such as copper or gold, is plated within each device region (Fig. 2). This forms a base for mounting or bonding in a package. The opposite side of the semiconductor

wafer is selectively etched down to the metal film. The mechanics of etching diodes completes both the structure formation of the diode and material removal in one step. Different device structures could require a masking procedure.

Separation of each device takes place by fracturing the thin metal film along the strips of photoresist (Fig. 3-6). The presence of photoresist at this point is not required, and removal is possible prior to separation.

This process has increased device yields while saving the manhours normally required in the dicing operation.

Acknowledgment

This work was supported in part by the U.S. Army Electronics Command under Contract No. DAAB07-74-C-0180.

Manuscript received May 2, 1975.

Any discussion of this paper will appear in a Discussion Section to be published in the June 1976 JOURNAL. All discussions for the June 1976 Discussion Section should be submitted by Feb. 1, 1976.

Publication costs of this article were partially assisted by the RCA Corporation.

Electrochemically Etched Tunnels in Gallium Arsenide

M. M. Faktor, D. G. Fiddym, and M. R. Taylor

Post Office Research Department, Dollis Hill, London, NW2 7DT, England

The purpose of this communication is to convey information about the deep and extensive tunneling of n-type gallium arsenide which can occur under certain, well-defined conditions of anodic dissolution. Tunnel formation in gallium arsenide was first reported by Krumme and Straumanis (1), and similar features have more recently been observed by Chase and Holt (2) on jet-etched gallium phosphide.

Anodic dissolution of (100), (110), and (111) faces of n-type GaAs slices in flowing 10% aqueous KOH solution was carried out as described previously (3, 4). The slices were obtained from various sources and possessed lapped or sawn surfaces which, before use, were mechano-chemically polished in bromine-methanol (5). The material examined was doped with either Si or S giving carrier concentrations in the range $10^{16} - 10^{18} \text{ n cm}^{-3}$.

The principal result was that tunnel formation occurred only when anodic dissolution was carried out in the dark, or at high anode potentials in the light where the current is in excess of its "saturation" value. Under the latter condition, the "light" current closely approaches the "dark" current (Fig 1).

The polarization behavior shown in Fig. 1 has previously been reported and discussed by Ambridge *et al.* (3, 4). The existence and magnitude of the "dark" current and the "light" current above saturation at high potentials are not adequately understood, though explanations have been advanced (7, 8). No simple correlation was found between the "dark" current level and either the doping level or structural defects in the material. The latter were investigated by etching studies (9), x-ray topography, and transmission electron microscopy. In all cases the tunnels were found to run in $\langle 111 \rangle$ directions, as demonstrated by angle measurements on cleaved surfaces and on tunnel entrances using optical and scanning electron microscopy, and confirmed by infrared transmission microscopy. On

(110) specimens, some tunnels intersected the surface forming channels. Typically, tunnels were some $150 \mu\text{m}$ long, and of equilateral triangular section with a width of $5 \mu\text{m}$ (after anodization for 2 min at 2 mA cm^{-2} and at a potential of 0.7V with respect to a saturated calomel electrode). The tunnel directions were such that they terminated in (111)B (arsenic) planes (1). Order of magnitude calculations showed that anodic dissolution was confined to tunnels with little general leveling of the exposed surface occurring.

Examination of anodically etched (100) specimens by optical and scanning electron microscopy indicated the general evolution of the surface morphology; the first sign of tunnel formation being the appearance of single triangular pits, or adjacent pairs of triangular pits extended parallel to $\langle 110 \rangle$ directions. Yamamoto and Yano (6) have recently observed similar surface features. We would like to emphasize that such features are in fact the entrances to the deep and narrow $\langle 111 \rangle$ tunnels mentioned earlier. Subsequent anodic etching enlarges these surface features. In the case of triangular pit pairs, rectangular features are formed. Coalescence and further enlargement leads eventually to large square pits [Fig. 10 of Ref. (5)]. The underlying complex of tunnels, frequently accompanied by branching, is dramatically revealed by infrared transmission microscopy, as demonstrated in Fig. 2 on a (111)A sample.

Although occasionally tunnels intersect the surface along impurity bands or other defects, this was by no means the general rule. In fact tunnels were generated in dislocation-free material, which on a macroscale at least, was uniformly doped. Furthermore transmission electron microscopy of dislocation free material did not reveal either columnar precipitates or any defects which could be construed as tunnel guides (10). Apparently bulk heterogeneities are not responsible for tunnel formation or their guidance.

Preferential adsorption on (111)B faces was strongly indicated by measurements of the band bending poten-

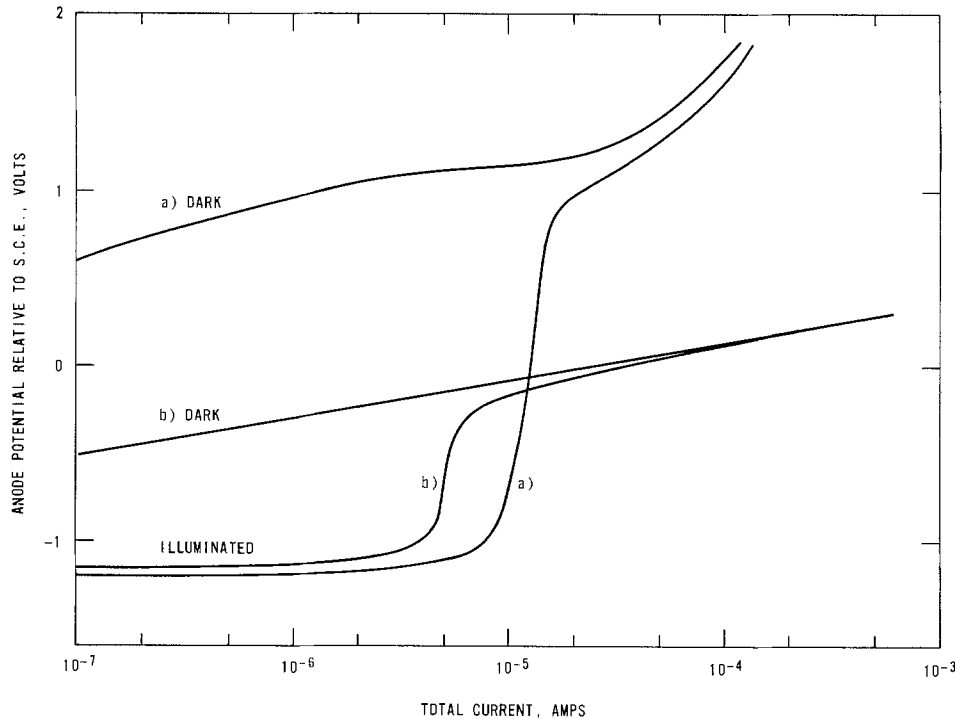


Fig. 1. Typical polarization plots for n-type GaAs of doping level $3.8 \times 10^{16} \text{ n cm}^{-3}$ (a) and $1.9 \times 10^{18} \text{ n cm}^{-3}$ (b). The curves tend to merge when the current exceeds its saturation value.

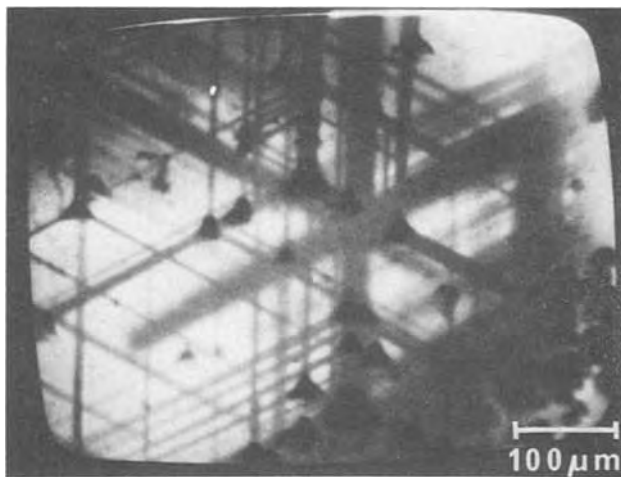


Fig. 2. Combined transmission and reflection infrared micrograph of an anodically etched (111)A (Ga) surface showing tunnels (gray) and tunnel entrances and surface details (black). The $\langle 111 \rangle$ tunnels are projected on to the (111)A surface in $\langle 211 \rangle$ directions. (Doping level $2 \times 10^{17} \text{ n cm}^{-3}$)

tial (11) on surfaces of different orientation (see Table I). The Schottky-Mott expression (4) was used to determine the band bending potential. Such adsorption may well lead to the appearance of surface states of energies suitable for communication with electrons in solution, and resultant preferential attack in these re-

Table I. Band bending potential as a function of orientation for n-type Si doped GaAs (carrier concentration $2 \times 10^{17} \text{ n cm}^{-3}$)

Orientation	Band bending potential (V)	
	In the dark	In the light
(111)A	1.83 ± 0.05	1.67 ± 0.05
(111)B	2.41 ± 0.05	2.07 ± 0.05
	2.38 ± 0.05	2.13 ± 0.05
(110)	2.06 ± 0.05	1.82 ± 0.05
(100)	2.04 ± 0.05	1.82 ± 0.05

gions. The dark current would then be mainly due to the catalytic action of the adsorbent.

Finally it is worth mentioning that if current values are kept beneath saturation, then smooth surfaces result from anodic dissolution under illumination with light of frequency greater than $3.46 \times 10^{14} \text{ sec}^{-1}$ (4). This corresponds to a bandgap energy of 1.43 eV at 300°K. Using light of energy which spans the bandgap, it is possible to reveal banding due to doping variations and if one confines the current to below saturation, no pits appear. It is a useful, as yet qualitative technique, for looking at doping inhomogeneities in n-type GaAs (3, 4).

Acknowledgment

Acknowledgment is made to the Director of Research of the Post Office for permission to publish this paper.

Manuscript submitted Jan. 28, 1975; revised manuscript received July 15, 1975.

Any discussion of this paper will appear in a Discussion Section to be published in the June 1976 JOURNAL. All discussions for the June 1976 Discussion Section should be submitted by Feb. 1, 1976.

Publication costs of this article were partially assisted by the Post Office Research Department.

REFERENCES

1. J. P. Krumme and M. E. Straumanis, *Trans. Met. Soc. AIME*, **239**, 395 (1967).
2. B. D. Chase and D. B. Holt, *This Journal*, **119**, 314 (1972).
3. T. Ambridge, C. R. Elliott, and M. M. Faktor, *J. Appl. Electrochem.*, **3**, 1 (1973).
4. T. Ambridge and M. M. Faktor, *ibid.*, **4**, 135 (1974).
5. M. V. Sullivan and G. A. Kolb, *This Journal*, **110**, 585 (1963).
6. A. Yamamoto and S. Yano, *ibid.*, **122**, 260 (1975).
7. V. A. Myamlin and Yu. V. Pleskov, "Electrochemistry of Semiconductors," p. 253, Plenum Press, New York (1967).
8. Yu. V. Pleskov, *Dokl. Akad. Nauk USSR*, **143**, 1399 (1962).
9. M. S. Abrahams and C. J. Buiocchi, *J. Appl. Phys.*, **36**, 2855 (1965).
10. J. B. Smith, Private communication.
11. R. M. Redstall, Private communication.

Doping of Silicon by Neutron Irradiation

H. A. Herrmann and H. Herzer

Wacker-Chemitronic, Burghausen, Germany

In the manufacture of high power devices such as thyristors and special diodes, there is a great demand for homogeneously doped n-type silicon. In our efforts to reduce striations in dislocation-free float-zone silicon (1), we rediscovered a quite interesting method which was used in the field of nuclear particle detectors.

In nuclear physics experiments for the detection of high energy particles, the application of silicon junction counters has become a standard way of measurement. Due to the range of high energy particles, deep depletion layers are necessary that are dependent on the concentration of free charge carriers and the applied voltage. For that reason, only ultrapure silicon with a very high resistivity can be used for the production of high quality silicon radiation detectors.

Besides using ultrapure silicon, two methods are known to increase the resistivity of the bulk material: (i) compensation by lithium drift technique (2) and (ii) compensation by doping of silicon with neutron irradiation, called transmutation doping (3-5).

Contrary to the lithium drift which is a well-known technique for production of highly compensated silicon, transmutation doping has not been so successful. In this case compensation is achieved by use of the nuclear reaction $^{30}\text{Si} + n \rightarrow ^{31}\text{Si} + \gamma \rightarrow ^{31}\text{P} + \beta$. The reason for this technique has never become significant

Key words: dislocation-free silicon, striations, transmutation doping, thermal neutrons.

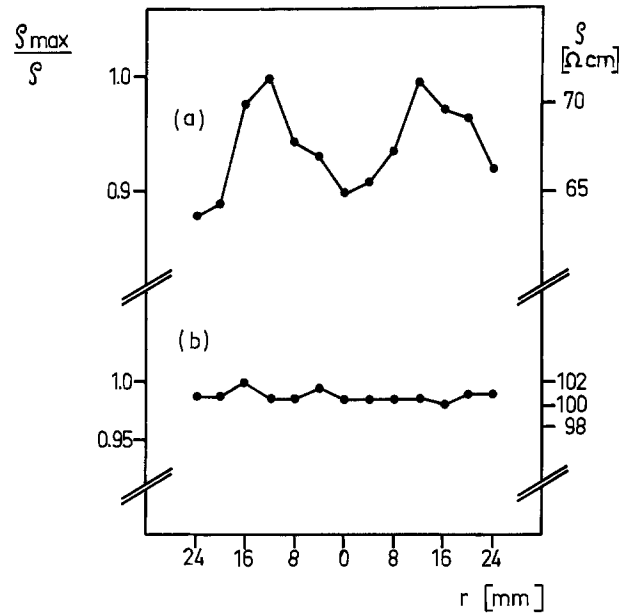


Fig. 1. Radial resistivity variations: (a) standard material (b) neutron transmutation doped.

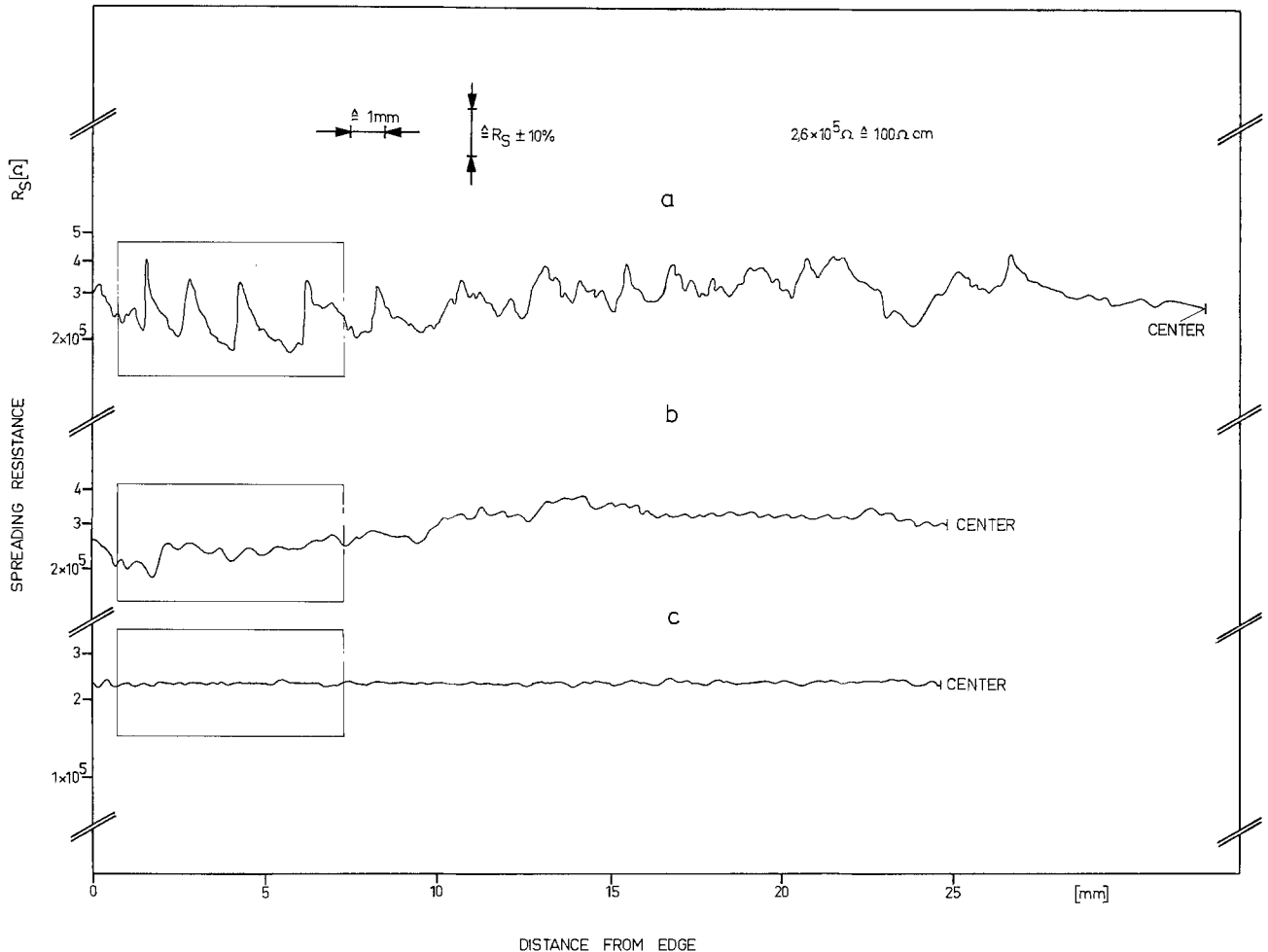


Fig. 2. Spreading resistance profiles: (a) conventional technique, (b) improved growth technique, and (c) neutron transmutation doping

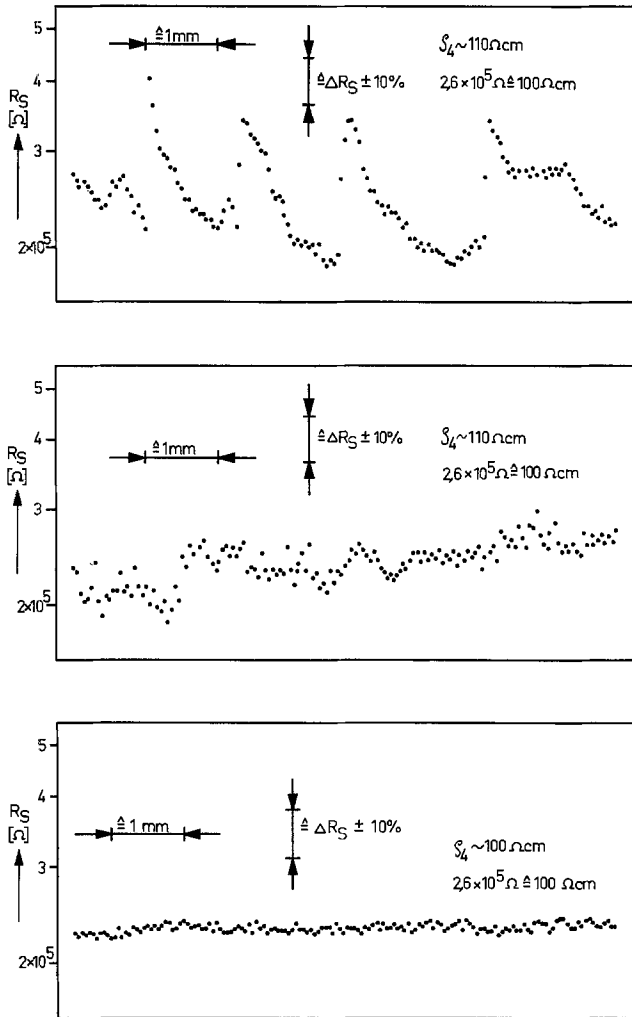


Fig. 3. Sections of Fig. 2

has to be seen in the lack of uniformly doped p-type silicon as the starting material.

We have now recognized that for the application in the lower ohmic range, i.e., between 100 and 500 ohm-cm, the nuclear reaction is an excellent method to dope silicon homogeneously. Starting with undoped polycrystalline silicon which is purified by several vacuum passes, the influence of grown-in dopants can be neglected. The final resistivity is represented by the number N of transmuted ^{30}Si isotopes which can be calculated from the equation

$$N = N_0 \cdot \sigma \cdot \phi \cdot t$$

where $N_0 = 0.15 \times 10^{22} \text{ cm}^{-3}$ gives the number of ^{30}Si isotopes, $\sigma = 110 \text{ mbarn}$ is the neutron capture

cross section, ϕ is the thermal neutron flux, and t is the irradiation time. The irradiation is performed in the core of a nuclear reactor where $\phi \approx 5 \times 10^{13} \text{ cm}^{-2}\cdot\text{sec}$. To achieve resistivities between 100 and 500 ohm-cm, typical irradiation times are between 20 and 100 min.

After the neutron bombardment, the silicon lattice is damaged due to the different interactions between silicon nuclei and neutrons, recoil atoms after neutron capture, high energy heavy particles created by fast neutron induced transfer reactions, high energy β and γ radiation, etc. The damage requires subsequent annealing treatments as it is known from ion implantation (6, 7). At a temperature of about 700°C , full electrical conductivity can be obtained. Figure 1 shows the four point probe measurement of a neutron transmutation doped silicon compared to conventionally grown standard material. The radial resistivity variation is markedly reduced to about 2%. Figure 2 represents the spreading resistance profiles of samples grown by (a) conventional technique, (b) improved growth technique, and (c) neutron transmutation doping. Figure 3 shows sections of Fig. 2 which demonstrate most clearly the advantage of constant resistivity in the microscopic range.

The results indicate that transmutation doping may be a rather good technique for production of homogeneously doped silicon material. Up to now, the influence of fast neutrons and high energy β and γ radiation seems to be negligible. Further work must be undertaken to establish whether transmutation doping will play a dominant role in addition to the standard methods for growing silicon crystals.

Manuscript submitted Aug. 8, 1974; revised manuscript received June 27, 1975.

Any discussion of this paper will appear in a Discussion Section to be published in the June 1976 JOURNAL. All discussions for the June 1976 Discussion Section should be submitted by Feb. 1, 1976.

Publication costs of this article were partially assisted by Wacker-Chemitronic.

REFERENCES

1. H. A. Herrmann and E. Mücke. 2. DFG Colloquium on Power Devices, Freiburg (1973).
2. E. M. Pell, *J. Appl. Phys.*, **31**, 291 (1960).
3. M. Tannenbaum and A. D. Mills, *This Journal*, **108**, 171 (1961).
4. J. Messier, Y. Le Coroller, and J. Merlo Flores, Proceedings of 9th Scintillation and Semiconductor Counter Symposium, Washington, D.C. (1964).
5. G. Dearnaley and D. C. Northrop, "Semiconductor Counters for Nuclear Radiations," Spon Limited, London (1966).
6. W. Stumpf, Dissertation, MPI für Kernphysik, Heidelberg (1970).
7. W. Stumpf and S. Kalbitzer, *Radiat. Effects*, **6**, 205 (1970).



EST

Effects of Temperature on the Kinetics of Passive Film Growth on Iron

C. Lukac,¹ J. B. Lumsden, S. Smialowska,² and R. W. Staehle*

Department of Metallurgical Engineering, The Ohio State University, Columbus, Ohio 43210

ABSTRACT

Ellipsometry was used to investigate the effects of temperature and potential on the growth kinetics of passive films on iron exposed to a pH 8.6 borate buffer solution. It was found that over the temperature range of 0°–80°C the growth kinetics could be described with an equal degree of confidence by either logarithmic, inverse logarithmic, or a modified form of inverse logarithmic kinetics. None of the existing models for film growth were found to be completely consistent with the temperature and potential dependencies of the growth constants.

There have been several ellipsometric studies (1-8) of the passive film formed on iron in near-neutral solutions. These investigations have shown that the film thickness is directly proportional to the applied potential and that film growth can be described equally well by either inverse logarithmic or logarithmic kinetics. Thus, it has not been possible to identify the model which represents the growth of this film from existing results. This investigation was undertaken to assess possible distinguishing features which might corroborate one of the proposed models for film growth. This was approached by measuring the temperature dependence of film thickening.

In order to correlate with the experimental data we review briefly here the four major models for interpreting film growth on metal surfaces. The first of these is the inverse logarithmic model proposed by Mott and Cabrera (9). This model assumes field assisted cation diffusion according to which the potential drop, V , across the film remains constant while the field, V/X , decreases as the film thickens. The rate-determining step is assumed to be the surmounting of the potential barrier, W , between the metal-oxide interface. The rate of film growth is given by the expression

$$\frac{dx}{dt} = u_0 \exp(qaV - W)/kT \quad [1]$$

where

$$u_0 = Na^{\nu} \quad [2]$$

N is the number of mobile ions per unit volume of oxide; a is the jump distance; q is the charge on the ion; W is the activation energy; ν is the phonon frequency. If the absolute reaction rate theory is used, $\nu = (kT/h)$. Mott and Cabrera give an approximate integration of Eq. [1] as

$$1/x = \frac{kT}{qaV} \ln \frac{x_0^2 kT}{qaVu_0} + \frac{W}{qaV} - \frac{kT}{qaV} \ln t \quad [3a]$$

or

$$1/x = A - B \ln t \quad [3b]$$

The quantity, x_0 , is the average film thickness over the range considered.

Recently, Ghez (10) has examined the integration of Eq. [1]. According to his results the inverse logarithmic kinetic expression derived by Mott and Cabrera is not an asymptotic solution to this equation. His basic objection is the approximation of X by X_0 . He obtains as a solution the expression

$$1/x = \frac{kT}{qaV} \ln \frac{kT}{qaVu_0} + \frac{W'}{qaV} - \frac{kT}{qaV} \ln \frac{t + t_0}{x^2} \quad [4a]$$

or

$$1/x = A' - B' \ln \frac{t + t_0}{x^2} \quad [4b]$$

Sato and Cohen (11) have proposed a model which rationalizes logarithmic kinetics. According to their suggestion, film growth proceeds by the field assisted place-exchange of metal-oxygen pairs. All such pairs in a given row normal to the surface are assumed to exchange places simultaneously. This model gives a growth rate

$$\frac{dx}{dt} = 2 \alpha(T) \exp \frac{FV}{2RT} - \frac{xW_0}{a\nu RT} \quad [5]$$

which integrates to

$$x = \frac{a\nu RT}{W_0} \ln \frac{W_0 \alpha}{a\nu RT} + \frac{a\nu FV}{2W_0} + \frac{a\nu RT}{W_0} \ln(t_0 + t) \quad [6a]$$

or

$$x = C + D \ln(t + t_0) \quad [6b]$$

where a is the lattice constant, ν the stoichiometric number, W_0 the chemical potential between a cation in the activated state and the normal state in any lattice layer, and

$$\alpha(T) = \beta T \exp \delta/T \quad [7]$$

Here β and δ are constants independent of potential and temperature.

* Electrochemical Society Active Member.

¹ Present address: Cerro de Pasco Corporation, La Oroya, Peru.

² On leave from Institute of Physical Chemistry, Polish Academy of Science, Warsaw, Kasprzaka 44, Poland.

Key words: iron, passivity, film, ellipsometry, corrosion.

Fehlner and Mott (12) have described logarithmic growth differently. They suggest that the structure of the film changes with thickness so that the potential drop across the film increases as the film thickens in such a way that the field remains constant. With this assumption the activation energy is of the form $W_0 + \mu x$; therefore

$$\frac{dx}{dt} = A \exp [-(W_0 + \mu x)/kT] \quad [8]$$

and

$$x = kT/\mu \ln \mu A/kT - W_0/\mu + kT/\mu \ln (t + t_0) \quad [9a]$$

$$x = C + D \ln (t + t_0) \quad [9b]$$

In the results reported here we have determined the thickness of the passive films on iron as a function of time, potential, and temperature using ellipsometry. The results have been analyzed in terms of the above three models of film growth.

Experimental

A schematic diagram of the cell used is shown in Fig. 1. This was a double-walled glass vessel having optically flat Pyrex windows and a capacity of 500 ml. The cell consisted of a Luggin capillary leading through a wetted, closed stop-cock to a saturated calomel reference electrode. The temperature of the solution was measured by a thermometer positioned 2 cm from the sample. Temperature control was maintained by circulating ethylene glycol through the jacket. The cell was connected to a double-walled 2 liter reservoir where the electrolyte was deaerated by bubbling with prepurified helium; the temperature of the solution was raised or lowered as desired before it was admitted to the cell.

The iron specimen was a 99.99% zone-refined rod with a threaded hole for the electrical connection. It was mounted in a Teflon holder and had an exposed area of 0.32 cm².

The solution used was an equivolume mixture of 0.15N H₃BO₃ and 0.15N Na₂B₄O₇ (pH 8.7). Measurements were made at 0°, 20°, 35°, 50°, and 80°C. The solutions were deaerated by bubbling prepurified helium for at least 24 hr.

The ellipsometer was a Rudolph & Sons, Type 43603-200E. A Keithley Model 4145 picoammeter was used to measure the output from the photomultiplier tube (RCA 1P21). All measurements were made using the 5461Å mercury green line.

Before placing the sample in the cell, it was mechanically polished to a ¼ μm finish using diamond

paste. The specimen was then cleaned, degreased, and electropolished in a solution consisting of 20 parts glacial acetic acid to one part 20% perchloric acid. Next the sample was washed with double-distilled water and then with reagent grade methanol, dried, and placed in the cell.

The specimen was first cathodically reduced at a constant current density of 40 μA/cm². Cathodic reduction was continued until the optical constants of the film-free surface were obtained. The passive film was then formed potentiostatically by switching directly from the cathodic potential (approximately -1.0V SCE) to the desired potential in the passive region. The sample was polarized approximately 1 hr at each potential; measurements of the ellipsometric parameters were made at 10 min intervals. This procedure was repeated 3-5 times at each potential.

The optical constants obtained for the film-free surface are in satisfactory agreement with those found by others as shown in Table I. These values also compare favorably with those measured by Yolken and Kruger (13) for a film-free surface in an ultra-high vacuum.

A cathodic current density of 40 μA/cm² was used to reduce the film since at this current density it could be removed within 10-15 min. The final potential attained was close to that established by others (6-8) for this system as "the optical reference state."

It was found to be unnecessary to change the solution after cathodic reduction in order to avoid the effects of ferrous ions. Several measurements were made following the procedure of replacing the solution after reduction, excluding oxygen, while maintaining the surface at the reduction potential. The steady-state results were the same as those for the unrefreshed solution.

Results

The current-potential curves for iron exposed to the borate buffer solution with the range of temperatures 0°-80°C are shown in Fig. 2. These curves were obtained by scanning at a rate of 20 mV/min. There was no measurable change in pH over this temperature range.

The optical constants of the film were determined using the first-order approximation of the ratio of the Fresnel reflection coefficients (16). Thus, if the film thickness is less than 50-100Å, the change in both of the ellipsometric parameters $\delta\Delta$ and $\delta\psi$ is directly proportional to the thickness. This implies that $\delta\Delta$ and $\delta\psi$ are related linearly. The $\delta\Delta$ vs. $\delta\psi$ curve for films formed at 20°C is given in Fig. 3. This is the least squares curve and was found to be linear at the 95% confidence level by the F ratio test. The standard deviation of the slope was 4.6%. It is not possible to obtain unique values for the optical constants using this curve. This is one of the inherent problems associated with the ellipsometric technique when working with semiconducting films of unknown thicknesses. The difficulty arises since there are three unknowns (the

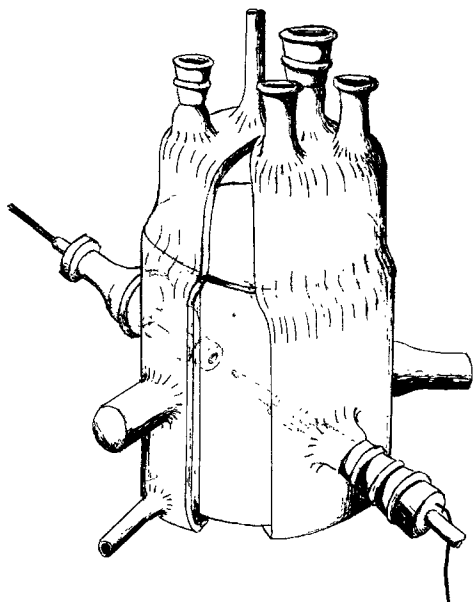


Fig. 1. Schematic of the ellipsometric-electrochemical cell

Table I. Optical constants of iron and iron oxides

$n_2 = n(1 - ik)$		Room temperature	
Source	Material	n	k
Kruger and Yolren (1)	Fe	3.35	1.15
Ord and Desmet (2)	Fe	3.50	1.05
Sato and Kudo (3)	Fe	3.18	1.21
Present work	Fe	3.21 ± 0.02	1.26 ± 0.02
Winterbottom (14)	Fe ₃ O ₄	2.50	0.12
Bockris et al. (15)	Fe ₃ O ₄	2.39	0.104
Winterbottom (14)	α-Fe ₂ O ₃	3.42	0.309
Bockris et al. (15)	-Fe ₂ O ₃	2.88	0.131
Kruger and Calvert (1)	Anodic film on Fe (room temperature)	2.50	0.12
Ord and Desmet (2)	Anodic film on Fe (room temperature)	2.60	0.15
Sato and Kudo (3)	Anodic film on Fe (room temperature)	2.55	0.137

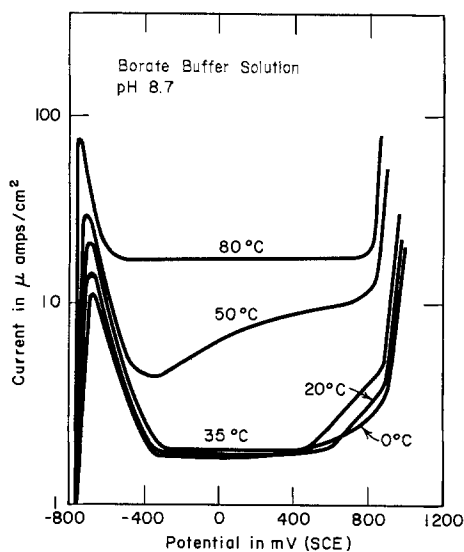


Fig. 2. The current density-voltage curves for Fe exposed to a pH 8.7 borate buffer solution at 0°, 20°, 35°, 50°, and 80°C.

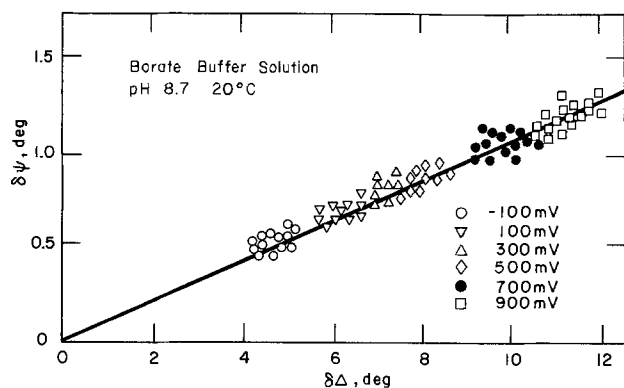


Fig. 3. The $\delta\psi$ and $\delta\Delta$ values for the anodic oxidation of Fe in a pH 8.7 borate buffer solution at 20°C.

thickness, the index of refraction, and the absorption coefficient), and only two experimental parameters, Δ and ψ . Accordingly, the real part of the refractive index was assumed to be 2.6 and the imaginary part was determined by fitting a theoretical curve, which was calculated using the exact equations (17), to the least squares curve. The curve which gave the best fit corresponded to the optical constants 2.6 (1-0.19i). As shown in Table I these optical constants are in good agreement with those rationalized by others at room temperature.

The same procedure was used to find the optical constants at each temperature. A minimum of seventy points was used to obtain each curve. The standard deviations in the slope of the $\delta\psi$ vs. $\delta\Delta$ curves ranged from 2.2% for 35° to 7.8% for 80°. The values of the optical constants for each temperature are given in Table II. All are the same within error except those determined for films formed at 0° and 35°C. The imaginary parts of the optical constants for these films are substantially smaller than those formed at other temperatures.

Table II. Optical constants of anodic film

Temperature, °C	$n_2 = n(1 - ik)$	
	n	k
0	2.60	0.04
20	2.60	0.19
35	2.60	0.07
50	2.60	0.20
80	2.60	0.20

The least squares curves of the reciprocal of the film thickness vs. $\log t$ and $\log t/x^2$ and the film thickness vs. $\log t$ are shown in Fig. 4, 5, and 6. Plots are given as a function of potential for films formed in solutions at 0°, 35°, 50°, and 80°C. Results were also obtained at 20°C but are not shown. Each of these curves were found to be linear well within the 95% confidence level using the F ratio test. The confidence level of the fit was approximately the same for all three models.

Table III gives the values of the constants A , B , A' , B' , C , and D where

$$1/x = A - B \ln t \quad [8]$$

$$1/x = A' - B' \ln t/x^2 \quad [9]$$

and

$$x = C + D \ln t \quad [10]$$

The quantity $1/B$ vs. potential is plotted in Fig. 7 and $1/B'$ vs. potential in Fig. 8. These show that B and B' are directly proportional to potential and that the proportionality constant, m (the slope), is temperature dependent. There is some scatter in these results; nevertheless, the least squares analysis indicates that the correlation for the set of data for each temperature is linear at the 95% confidence level.

The results of Fig. 9 show the slopes of the curves in Fig. 7 and 8, m_1 . A least squares analysis of the data gives a linear relationship. This is in accordance with Eq. [3] and [4], i.e.

$$B = B' = kT/qaV \quad [10]$$

These correlations show that B and B' are inversely proportional to V and directly proportional to T in agreement with the Mott-Cabrera model.

It should be pointed out that the applied electrochemical potential, which is that given in Fig. 7 and 8, is not the potential drop, V , across the film. However, it differs from V only by an additive constant. Thus, the only effect of plotting the electrochemical potential instead of V is a shift in the axis. This assumes

Table III. Constants for the film growth models

mV (SCE)	$A (A^{-1})$	$B \times 10^3 (A^{-1})$	$A' (A^{-1})$	$B' (A^{-1})$	$C(A)$	$D(A)$	
							0°C
-100	0.0668	2.96	0.0492	3.24	11.8	0.82	$D_{av} = 1.04A$
100	0.0508	1.70	0.0399	1.84	19.5	0.78	
300	0.0426	1.38	0.0292	1.81	25.4	1.39	
500	0.0325	0.92	0.0265	0.981	30.7	0.89	
700	0.0321	1.07	0.0243	1.12	31.0	1.20	
900	0.0280	0.826	0.0226	0.895	35.5	1.22	
							20°C
-100	0.0611	4.12	0.0531	3.31	15.8	1.56	$D_{av} = 1.04A$
100	0.0450	1.73	0.0334	1.89	22.0	1.00	
300	0.0383	1.15	0.0306	1.19	26.1	0.82	
500	0.0382	1.21	0.0297	1.30	26.0	0.95	
700	0.0271	0.817	0.0210	0.844	37.7	1.26	
900	0.0243	0.743	0.0187	0.746	41.0	1.30	
							35°C
-100	0.0537	2.93	0.0347	3.15	18.3	1.32	$D_{av} = 1.04A$
100	0.0405	1.57	0.0298	1.62	24.6	1.10	
300	0.0340	1.22	0.0252	1.28	28.2	1.25	
500	0.0326	1.38	0.0223	1.50	30.3	1.60	
700	0.0281	1.01	0.0199	1.20	34.9	1.63	
900	0.0249	0.839	0.0183	0.903	39.8	1.60	
							50°C
-100	0.0514	2.45	0.0352	2.70	19.2	1.16	$D_{av} = 1.04A$
100	0.0434	2.13	0.0282	2.37	22.8	1.44	
300	0.0349	1.51	0.0239	1.63	28.4	1.50	
500	0.0302	1.24	0.0206	1.37	32.8	1.68	
700	0.0276	1.36	0.0163	1.59	35.9	2.26	
900	0.0259	1.15	0.0162	1.34	38.0	2.27	
							80°C
-100	0.0452	2.86	0.0223	3.17	21.4	2.22	$D_{av} = 1.04A$
100	0.0373	1.20	0.0294	1.15	26.8	0.93	
300	0.0320	1.50	0.0229	1.55	31.0	1.81	
500	0.0278	1.47	0.0171	1.45	35.5	2.45	
700	0.0270	1.23	0.0178	1.25	36.5	2.13	
900	0.0251	1.25	0.0148	1.27	1.26	2.52	

Fig. 4. The reciprocal of film thickness vs. log of time as a function of temperature and potential.

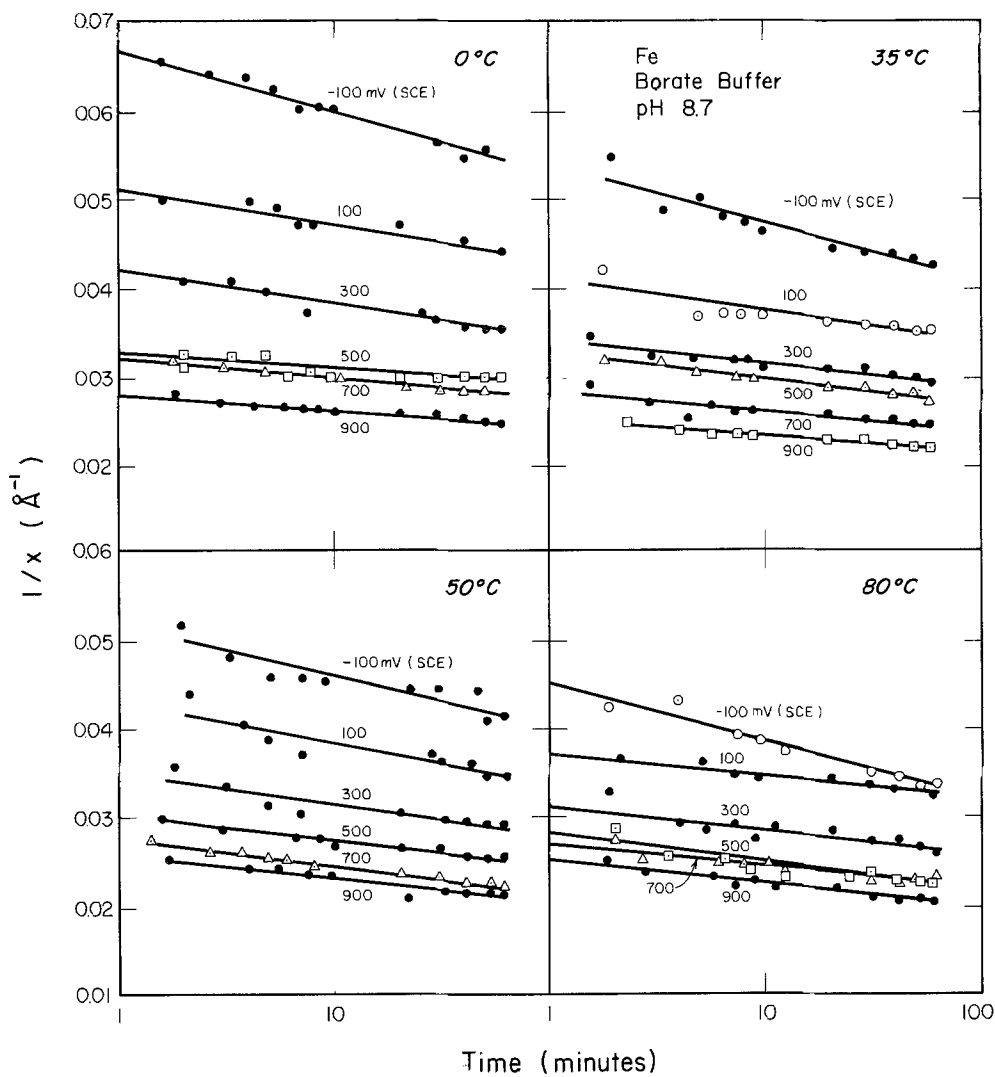
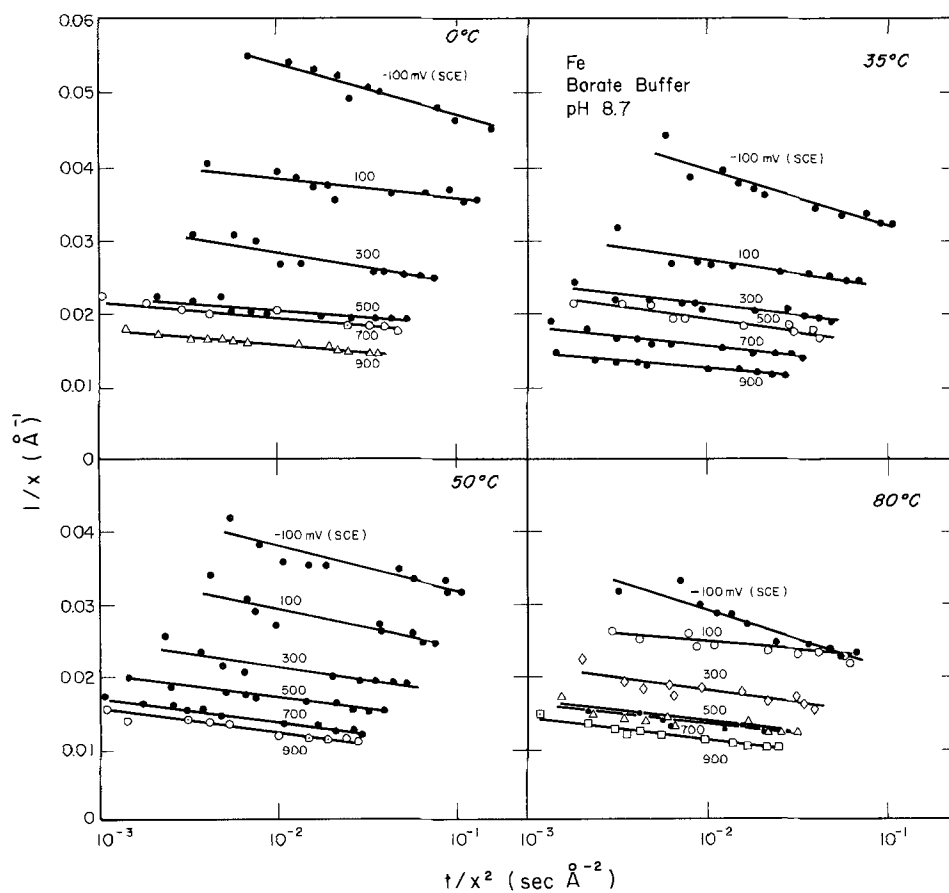


Fig. 5. The reciprocal of film thickness vs. log of time divided by the film thickness squared.



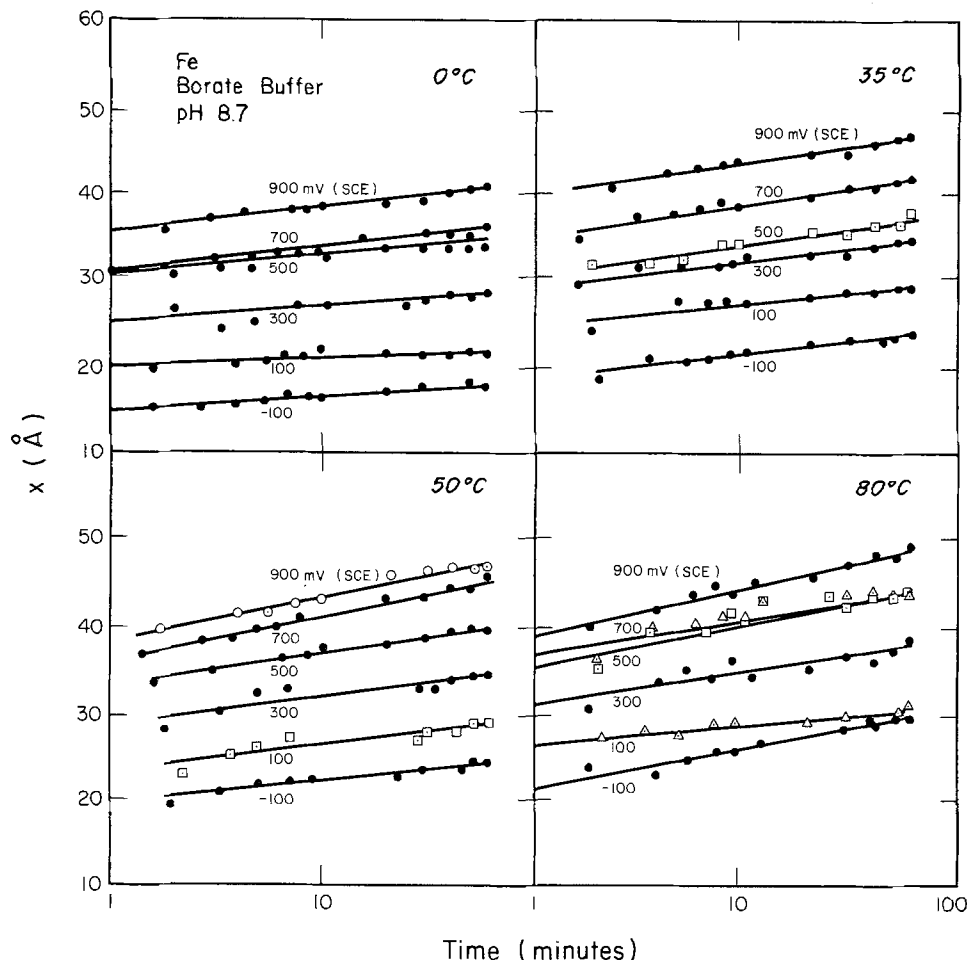


Fig. 6. Logarithmic plot showing the changes in the thickness of the passive film on iron with time.

that the potential across the double layer remains constant.

The jump distance, a , was calculated using the slopes in Fig. 7 and 8 since $m_1 = kT/qa$. These values are given in Table IV. Figure 10 shows the the jump distance as determined using inverse logarithmic kinetics as well as a' from the modified inverse logarithmic kinetic model decreases linearly with temperature.

Figures 11 and 12 show that A and A' are linearly related to the inverse of the potential with a temperature dependent slope, m_2 . This potential dependence is in accordance with Eq. [3a] and [4a] since $\ln x_1^2 kT/qaVu_0$ is a slowly varying function of T and V over the ranges considered. The temperature dependence of the slopes, m_2 , is shown to be linearly related to the tem-

perature in Fig. 13. This indicates that A and A' are directly proportional to the temperature.

The constant D appears to behave in a random fashion with potential; therefore, it was assumed to be potential independent. The average values are given in Table III. Figure 14 indicates that D_{av} gives a good linear correlation with temperature. This is in accordance with the constant field model. From the slope the value 9.42×10^8 is obtained for μ .

The Sato-Cohen model gives D as

$$D = \frac{a\nu RT}{W_0} \tag{11}$$

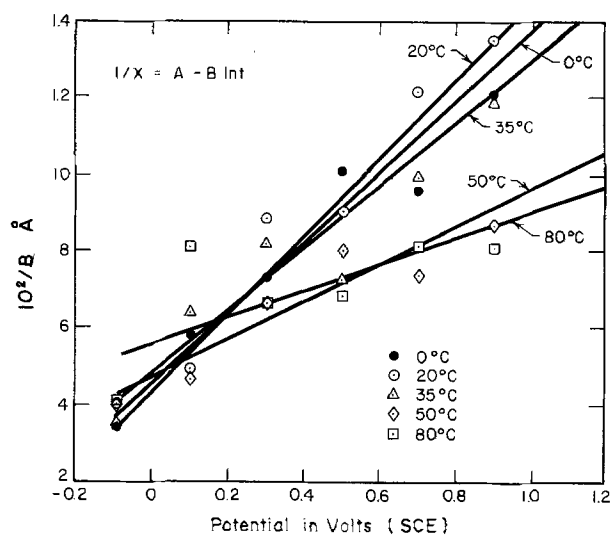


Fig. 7. The reciprocal of the rate constant B vs. applied potential.

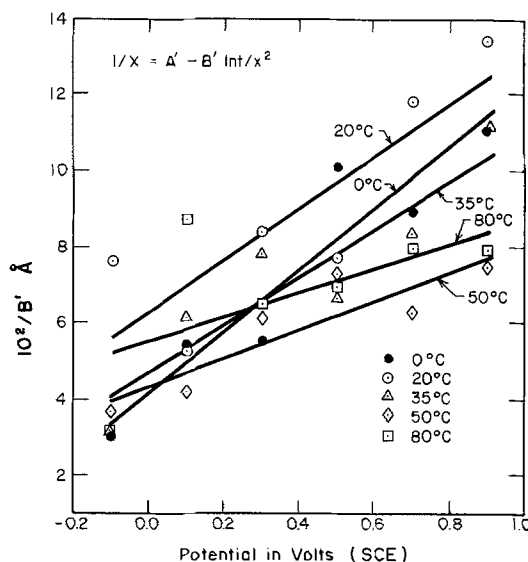


Fig. 8. The reciprocal of the rate constant B' vs. applied potential

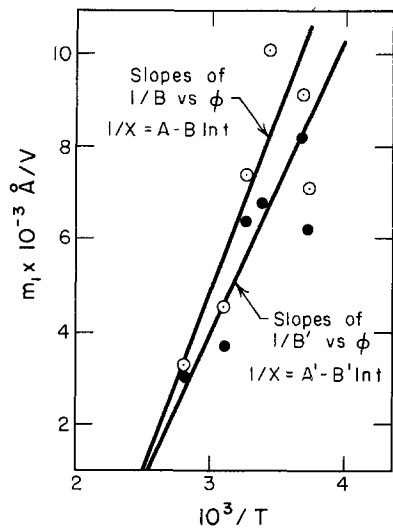


Fig. 9. The relationship between the reciprocal of temperature and the slopes of the 1/B and 1/B' vs. applied potential curves.

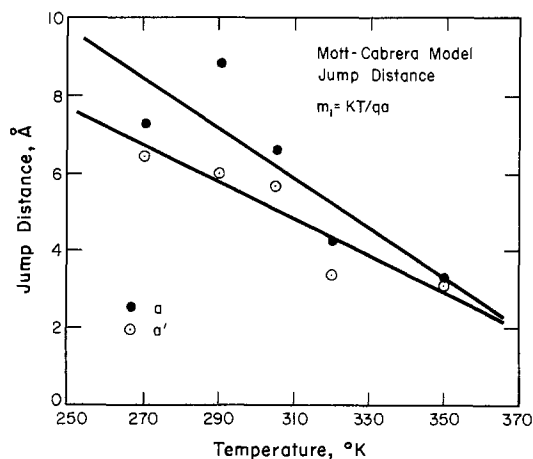


Fig. 10. The values of the jump distance as a function of temperature.

where W_0 , the activation energy, is split into an enthalpy ΔH_0 and an entropy ΔS_0 term (8, 18). Thus

$$D = \frac{a\nu RT}{\Delta H_0 - T\Delta S_0} \quad [12a]$$

or

$$1/D = \frac{\Delta H_0}{a\nu RT} - \frac{\Delta S_0}{a\nu R} \quad [12b]$$

Figure 15 shows that $1/D$ is proportional to $1/T$.

The constant C is proportional to the potential as shown in Fig. 16. From Eq. [6a] and [6b] the slopes of Fig. 16 are given by

$$m_3 = \frac{a\nu F}{W_0} \quad [13a]$$

or

$$1/m_3 = \frac{\Delta H_0}{a\nu F} - \frac{T\Delta S_0}{a\nu F} \quad [13b]$$

Table IV. The jump distances a and a' , the activation energies W and W' of the Mott-Cabrera and the modified Mott-Cabrera models

Temperature, °K	a , A	a' , A	W , eV	W' , eV
273	7.2	6.4	2.16	1.68
293	8.9	6.04	2.11	1.68
308	6.6	5.65	1.84	1.68
323	4.3	3.4	1.80	1.68
353	3.3	3.18	2.50	1.68

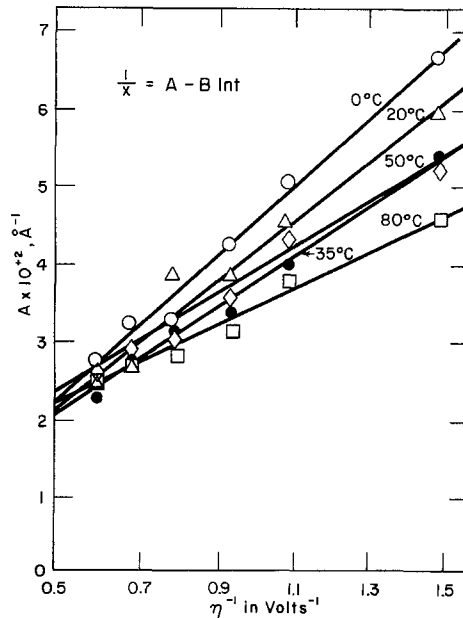


Fig. 11. Plots of the rate constant A vs. the reciprocal of the overpotential.

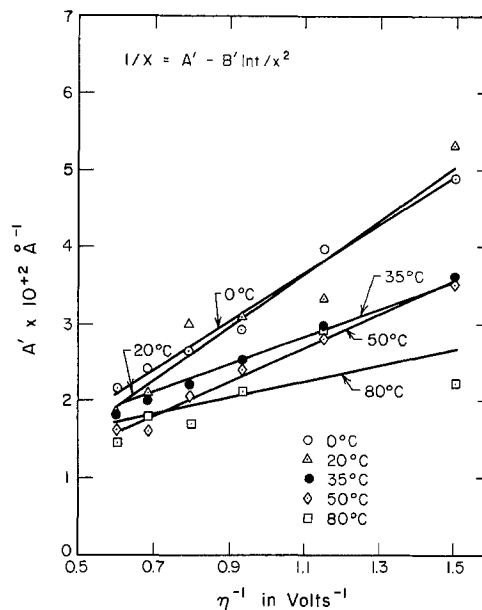


Fig. 12. Plots of the rate constant A' vs. the reciprocal of the overpotential.

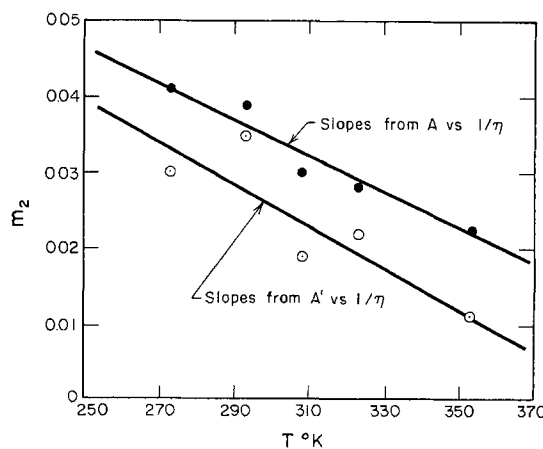


Fig. 13. The change in slope with temperature of the A and A' vs. $1/T$ curves.

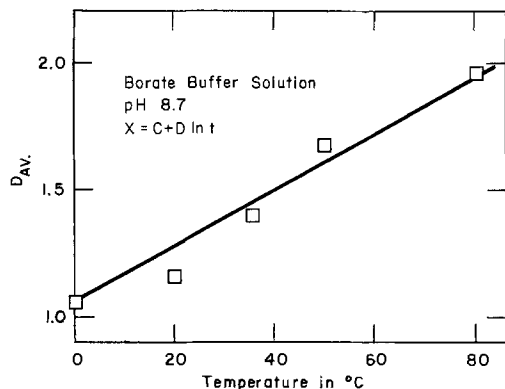


Fig. 14. The change in the rate constant D_{AV} with temperature

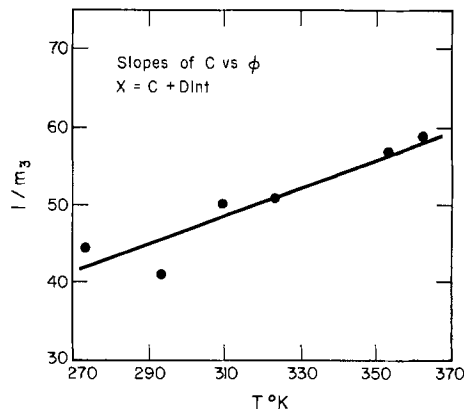


Fig. 17. The relationship between the reciprocal of the slopes of the C vs. applied potential curves and temperature.

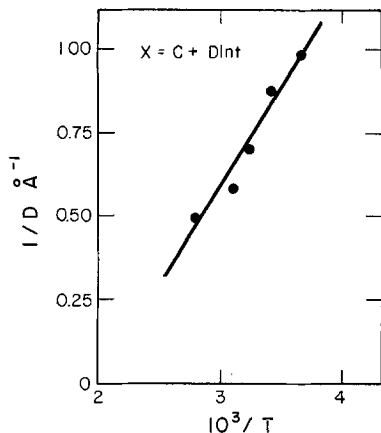


Fig. 15. The relationship between the reciprocal of D_{AV} and the reciprocal of temperature.

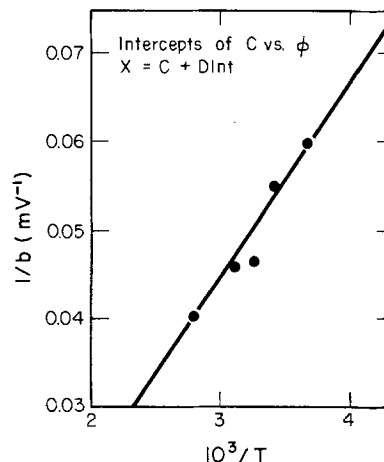


Fig. 18. Plot of the intercepts of the curves in Fig. 16 vs. the reciprocal of temperature.

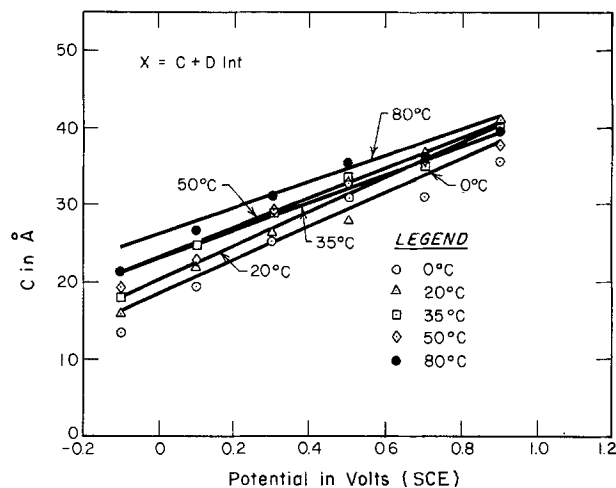


Fig. 16. The values of the rate constant C at various applied potentials.

Figure 17 shows that $1/m_3$ is proportional to T in accordance with the Sato-Cohen model. Also from Eq. [6a] and [6b] the intercepts of Fig. 16 are a function of temperature

$$b = \frac{2a_v RT}{W_o} K \quad [14a]$$

or

$$1/b = \frac{\Delta H_o}{2s_x R k} \frac{1}{T} - \frac{\Delta S_o}{2a R k} \quad [14b]$$

The intercepts $1/b$ are linearly related to $1/T$ as shown in Fig. 18. This assumes that K is a slowly varying function of T .

Discussion

These results have shown that the dual nature of the growth kinetics of passive films on iron observed

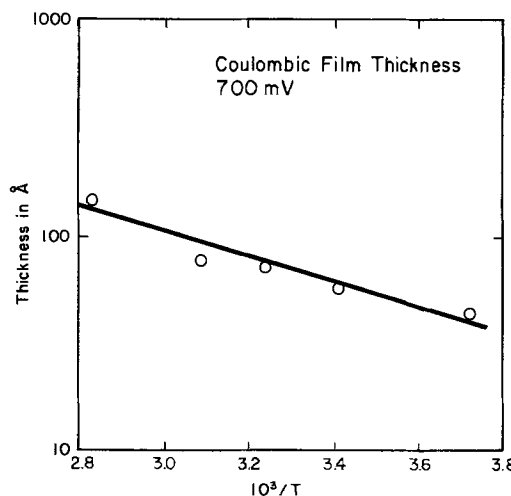


Fig. 19. The activation energy determined from the ellipsometric film thickness vs. the applied potential.

by others at room temperature (1, 4) in borate solutions also apply over the temperature range from the near freezing point to the near boiling point of the solution. In addition, plots of the inverse thickness vs. $\log t/x^2$ also give straight lines over the potential and temperature ranges considered. However, it should be pointed out that it is not possible to determine which type of kinetics is applicable by merely plotting a graph when the film thickness varies over a small range of values. This can be illustrated by eliminating the logarithmic terms of Eq. [3b] and [6b] giving

$$\frac{1/A - X}{BX/A} = \frac{C - D}{D} \quad [15]$$

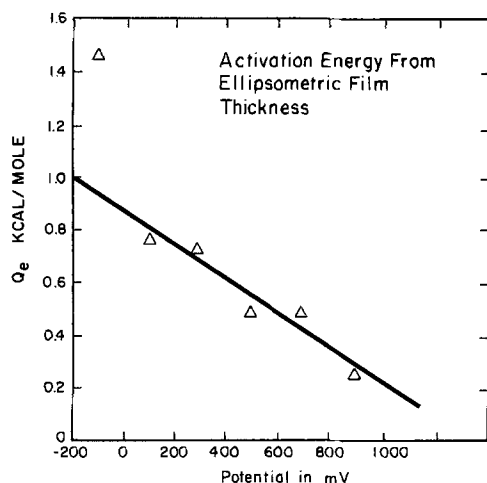


Fig. 20. The coulombic film thickness vs. $1/T$

Thus

$$1/A = C \quad [16]$$

and

$$BX/A = D \quad [17]$$

if the change in X is small. In the same manner it can be shown that

$$B = B' \quad [18]$$

and

$$A = A' - \frac{B}{X} \ln X^2 \quad [19]$$

for small changes in X .

The temperature and potential dependencies of the time-independent constants B and B' were found to be consistent with the Mott-Cabrera and modified Mott-Cabrera kinetics, respectively, i.e., directly proportional to temperature and inversely proportional to potential. In addition, the jump distance, a , was found to vary linearly with temperature such that

$$a = 25.7 - 0.0633T \quad [20a]$$

in the case of the Mott-Cabrera model and

$$a' = 19.2 - 0.0462T \quad [20b]$$

for the modified Mott-Cabrera model. Thus, expressing a as $a_0 - pT$, the constants B and B' take the form

$$B = B' = \frac{kT}{qaV} = \frac{kT}{8(a_0 - pT)V} + C_1(T) \quad [21]$$

The values for the jump distance, a , are quite large below 100°C . It is difficult to explain these large values within the framework of the assumptions of Mott and Cabrera. Kruger and Calvert have obtained similar values for the jump distance at room temperature (1). They rationalized their results within the Mott-Cabrera model by assuming the film to be composed of two layers with only the outer layer capable of supporting fields of sufficient strength to pull cations across the film. They assumed that the actual value of the jump distance was the product of the apparent value and the fraction of the film which was nonconducting; they estimated that this fraction was approximately $1/3$. This assumption and Eq. [20] lead to the conclusion that the thickness of the dielectric outer layer increases with increase in temperature. However, there still exists an inconsistency since there is a critical temperature at which the jump distance becomes zero. These temperatures are 406° and 457°K for Eq. [20a] and [20b], respectively.

Both the Mott-Cabrera and the modified Mott-Cabrera models give additive constants A and A' , respectively, which are inversely proportional to potential across the film and directly proportional to temperature. However, experimentally

$$A = \frac{1}{\eta} (10.86 \times 10^{-2} - 2.46T \times 10^{-4}) + C_2(T) \quad [22a]$$

$$A' = \frac{1}{\eta} (11.05 \times 10^{-2} - 2.81T \times 10^{-4}) + C_2'(T) \quad [22b]$$

where the overpotential η has been defined relative to the corrosion potential, -770 mV (SCE). Such a dependence on temperature is not in agreement with the above models. It is interesting to note that there exists a temperature at which A and A' become independent of potential. The temperatures are 441° and 393°K for A and A' , respectively. These temperatures are not far from the critical values found for a and a' .

One can explain the temperature dependent constants in Eq. [21] and [22], which are the ordinate intercepts in Fig. 7, 8, 11, and 12, as resulting from the potential drop across the film being temperature dependent. However, an examination of the intercepts on the potential axis of the $1/B$ vs. ϕ curves suggests that this may not be the complete explanation. These are the potentials at which field dependent growth begins. The values of the intercepts were found to be -498 , -403 , -660 , -1037 , and -1743 mV for 0° , 20° , 35° , 50° , and 80°C , respectively. Similar values were obtained for the $1/B'$ vs. ϕ curves. It is difficult to rationalize the low values obtained for 50° and 80° since the corrosion potential is -770 mV and independent of temperature.

The constant D was found to have a temperature dependence which is consistent with the Sato-Cohen model for film growth. From Eq. [12b] and the least squares equation for the curve in Fig. 15, it was found that $\Delta S_0 = 14.8$ cal/deg mole and $\Delta H_0 = 7.19$ kcal/mole; where the lattice constant, a , has been assumed to be $2A$ and ν to be 3.

In Fig. 16 the constant C was shown to be proportional to the applied potential with a temperature-dependent slope, m_3 , in accordance with Sato-Cohen model. The reciprocal of the slopes is proportional to the temperature and related to the enthalpy and entropy as given by Eq. [13b]. Figure 17 shows that $1/m_3$ is proportional to the temperature. The least squares line is

$$1/m_3 = 0.181T - 7.44 \quad [23]$$

The signs are the reverse of those in Eq. [13b]; further, ignoring the signs, the calculated value for the enthalpy is 4310 kcal/mole and that for the entropy is 104 kcal/mole, which are unrealistic numbers.

The activation energies have been determined using the Mott-Cabrera model and are shown in Table IV. The energy W has been determined from the expression given by Mott and Cabrera for the limiting thickness X_L

$$X_L = Va'q/(W - 39kT) \quad [24]$$

where X_L is the film thickness when the growth rate is 10^{-5} Å/sec. This quantity was calculated by differentiating the expression giving the film growth as a function of time and solving for X when $dX/dt = 10^{-5}$ Å/sec. The other quantities in this expression are the same as those in Eq. [1]. The values of W were determined for each temperature using

$$W = 1/p + 39kT \quad [25]$$

where p is the slope of the X_L vs. qaV curve; qaV was determined from the expression

$$qaV = kT/B \quad [26]$$

The values of W , given in Table IV, are approximately the same as those obtained by Kruger and Calvert (1) at room temperature.

From expression [24] there exists a temperature, T_c , such that

$$39T_c = W \quad [27]$$

above which rapid growth will occur. Using the mean value of W , 2.08 eV, T_c was found to be 620°K.

The activation energy, W' , was determined using (from Eq. [4a])

$$A' = \frac{kT}{qaV} \ln \frac{kT}{qaVu} = B' \ln B'/u \quad [28]$$

where

$$u = u_0 \exp - (W/kT) \quad [29]$$

therefore, W' can be determined from the slope of the $\ln u$ vs. $1/T$ curve. The value of W' was found to be 1.74 eV for 900 mV and 1.63 eV for 300 mV. The average of these two values is 1.68 eV as shown in Table IV.

The activation energy, Q_e , was also calculated using Arrhenius plots of the ellipsometric film thickness after 1 hr of polarization vs. $1/T$. The values obtained for Q_e at each potential have been plotted against potential in Fig. 17. This plot illustrates that Q_e decreases linearly as the potential is increased or

$$Q_e = W' - mV \quad [19]$$

where V is the potential drop across the film.

Likewise, an activation energy, Q_c , can be determined from an Arrhenius plot of the coulombic film thickness after 1 hr of polarization vs. $1/T$. This was done for 700 mV by assuming that the passive film was Fe_2O_3 with a density of 5 g/cm³ and a roughness factor of one. A value of 2500 cal/mole was obtained whereas, a value of 500 cal was obtained for Q_e at the same potential. If it is assumed that the difference between the coulombic film thickness and the ellipsometric film thickness is due to film dissolution, then

$$Q_c - Q_e = Q_{diss}$$

where Q_{diss} is the activation energy for film dissolution. This gives a value of 2 kcal/mole for Q_{diss} .

In essence it was found that none of the proposed models for passive film growth are completely consistent with the observed temperature and potential effects. The time-independent constants A and A' of the two expressions for inverse logarithmic kinetics are inversely proportional to potential in accordance with Eq. [3a] and [4a]; however, the temperature dependence is not in accordance with these equations. The constants B and B' of the same kinetic expressions have temperature and potential dependences which are consistent with Eq. [3a] and [4a]; but assumptions have to be made in explaining the large value of the

jump distances a and a' obtained from these constants. Also, the values obtained for the potentials corresponding to the onset of field-dependent growth are difficult to rationalize. The effects of temperature on D of Eq. [6b] were found to be exactly those of the Sato-Cohen model; yet although temperature and potential dependences C are in accordance with the Sato-Cohen model proportionally, the signs in the functional relationship are not correct physically. Thus either the existing models do not postulate the correct mechanism, or they are in need of modification.

Manuscript submitted Jan. 20, 1975; revised manuscript received July 23, 1975.

Any discussion of this paper will appear in a Discussion Section to be published in the June 1976 JOURNAL. All discussions for the June 1976 Discussion Section should be submitted by Feb. 1, 1976.

Publication costs of this article were partially assisted by The Ohio State University.

REFERENCES

1. J. Kruger and J. P. Calvert, *This Journal*, **110**, 670 (1963).
2. J. L. Ord and D. J. DeSmet, *ibid.*, **113**, 1258 (1966).
3. N. Sato and K. Kudo, *Electrochim. Acta*, **16**, 447 (1971).
4. K. N. Goswami and R. W. Staehle, *ibid.*, **16**, 1895 (1971).
5. F. C. Ho and J. L. Ord, *This Journal*, **119**, 139 (1972).
6. J. O'M. Bockris, M. Genshaw, and V. Brusic, *Symp. Faraday Soc.*, **4**, 177 (1970).
7. H. Wroblowa, V. Brusic, and J. O'M. Bockris, *J. Phys. Chem.*, **75**, 2823 (1971).
8. J. O'M. Bockris, M. A. Gensaw, V. Brusic, and H. Wroblowa, *Electrochim. Acta*, **16**, 1859 (1971).
9. N. Cabrera and N. F. Mott, *Rep. Prog. Phys.*, **12**, 163 (1948).
10. Richard Ghez, *J. Chem. Phys.*, **58**, 1838 (1973).
11. N. Sato and M. Cohen, *This Journal*, **111**, 512 (1964).
12. F. P. Fehlner and N. F. Mott, *Oxidation of Metals*, **2**, 59 (1970).
13. H. T. Yolken and J. Kruger, *J. Opt. Soc. Am.*, **55**, 842 (1965).
14. A. B. Winterbottom, *J. Iron Steel Inst.*, **165**, 9 (1950).
15. J. O'M. Bockris, M. A. Genshaw, V. Brusic, and W. Wroblowa, *Electrochim. Acta*, **16**, 1859 (1971).
16. G. Bootsma and F. Meyer, *Surface Sci.*, **14**, 52 (1969).
17. F. L. McCrackin and J. P. Colson, *Nat. Bur. Std. Tech. Note 242* (1964).
18. N. Sato, *Electrochim. Acta*, **16**, 659 (1971).

A Limitation to the Mixed Potential Concept of Metal Corrosion

Copper in Oxygenated Sulfuric Acid Solutions

T. N. Andersen,¹ M. H. Ghandehari,² and H. Eyring

Department of Chemistry, University of Utah, Salt Lake City, Utah 84112

ABSTRACT

The corrosion of copper in oxygenated sulfuric acid solutions was studied by means of weight-loss and polarization curves. At a given potential, the rate of copper dissolution is greater in the presence than in the absence of oxygen reduction, which is contrary to the conventional theory of mixed potentials. An explanation of this phenomena is proposed on the basis of chemical attack by dissolved oxygen on the Cu^+ ions which are intermediates in the electrochemical copper oxidation scheme. The model is further verified by results of varying the solution agitation rate, acid strength, and oxygen partial pressure.

In 1938 Wagner and Traud (1) put forth the principle of superposition of electrochemical partial processes and applied it to mixed potentials. According to this principle, the rate of a faradaic process is independent of other faradaic processes occurring simultaneously at the electrode and thus depends only on the electrode potential. Thereby the polarization curves for independent oxidation and reduction processes may be added to predict the over-all rates and potentials which exist when more than one reaction occurs simultaneously at an electrode. Several studies have been reported which verify the above superposition (or mixed potential) principle. Wagner and Traud (1) showed the independence of dissolution of Zn amalgam of the simultaneous H_2 evolution process. They also found H_2 oxidation and reduction of several oxidants on Pt to be mutually independent. Glassner and Kimball (2) found the rate of Cd dissolution in dilute acid to be dependent on the Cd potential but independent of the rate of simultaneous H^+ -ion reduction. Petrocelli (3) verified the independence of Al dissolution, at given potential, on the simultaneous reduction of ceric (Ce^{+4}) ions.

From such findings as referenced above, the independence of partial electrode reactions has been generally assumed in most recent discussions of metal corrosion in electrolyte solutions [e.g., see Ref. (4-6)]. Application of the mixed potential theory to corrosion is valuable in clarifying the rate-determining processes and thus in suggesting solutions to the corrosion. It is also valuable in predicting corrosion phenomena from the polarization curves for the partial processes. These polarization curves may be obtained in the potential region of the corrosion by one or more of the following methods: (i) by measuring the rate of metal dissolution directly from electrode weight-loss or ion concentration changes in the solution; (ii) by removal of the depolarizer (e.g., O_2) and measuring the rate of metal dissolution directly as the electric current; (iii) by measuring the rate of cathodic reduction on a nonreactive metal such as Pt, to approximate the reduction on the active metal [see Ref. (3)]; or (iv) by measuring the polarization curve for depolarizer reduction at potentials so negative of the corrosion potential that metal oxidation can be neglected; the resultant Tafel line is then extrapolated to the corrosion region to yield the desired polarization curve.

Certain limitations are recognized in developing polarization curves by each of the above methods. Weight-loss measurements require more time than is desirable, and changes in the surface as well as metal loss through spalling is possible. The kinetics of O_2 or H^+ -ion reduction differs for different metals, so it is desirable to directly study the metal of interest. Therefore, determination of polarization curves directly and extrapolation to the corrosion potential appear to be a desirable approach. This approach is not valid if the catalytic properties of the surface change with potential over the range of interest. It is also not valid if the rate-determining step and hence the Tafel slope for any process changes in the potential range through which the polarization curve is extrapolated.

In the present work we have found a further limitation to the extrapolation of polarization curves (and to the theory of mixed potentials in general) which does not appear to have been stressed previously; i.e., the opposing partial processes are not independent, if the intermediates of one process react with the reactants of the opposing partial process to produce new reaction paths with lower reaction barriers than those of the isolated processes.

This limitation was discovered during the course of attempting to quantitatively apply the theory of mixed potentials to the corrosion of Cu in oxygenated H_2SO_4 solutions. Thus, extrapolation of the polarization curve for Cu dissolution in N_2 -saturated solution to the corrosion potential in O_2 -saturated solution yielded a corrosion rate which is less than 0.1 of the observed value. Further study of this phenomena revealed that oxygen attacked the intermediate of the copper dissolution (i.e., Cu^+ ions) and thus short-circuited the electrochemical dissolution path.

Experimental

Corrosion studies.—Because of differences in the kinetics and rates in the published literature (7-12), it was necessary to develop corrosion data to support the polarization tests. For this purpose samples of high purity copper sheets, 1 cm^2 in area, were covered on one side and on the edges with silicone rubber (Dow-Corning Silastic); these were placed in a 600 ml cell containing 200 ml of 2M H_2SO_4 . The solution was stirred at a constant rate and O_2 , air, or high-purity N_2 was purged through the solution during each experiment. The sample was removed at different time intervals, washed with doubly distilled water and acetone, dried in an oven, and then weighed to deter-

¹ Present address: Kennecott Research Center, Salt Lake City, Utah 84100.

² On leave of absence from Arya-Mehr University of Technology, Tehran, Iran.

Key words: copper, corrosion, mixed potential.

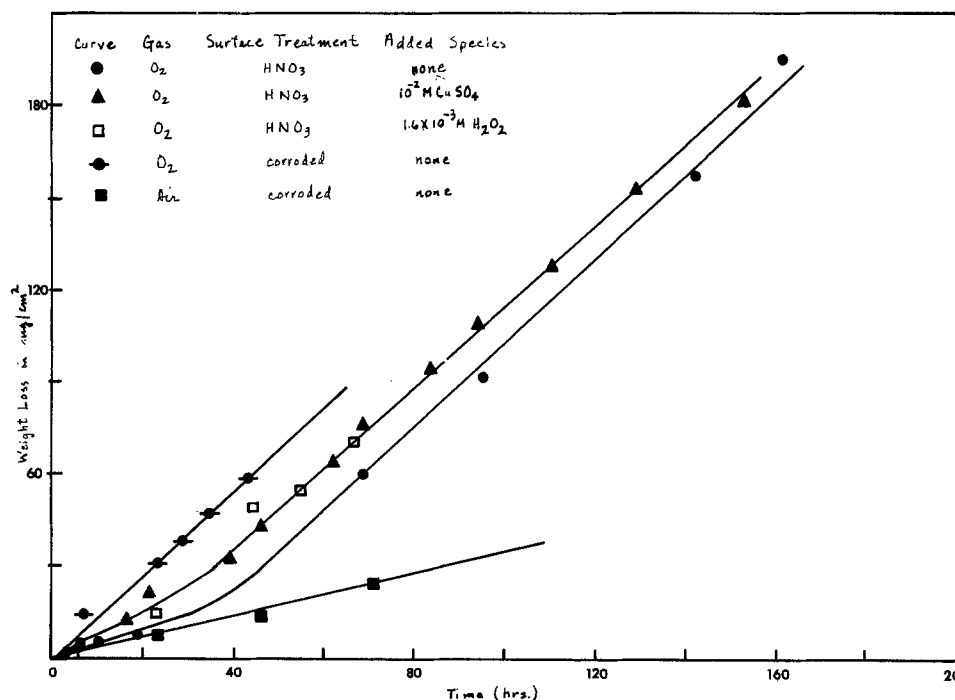


Fig. 1. Copper corrosion in stirred, 2M H₂SO₄ under various conditions.

mine the amount of Cu dissolved. For many of the tests the same sample was then put back in the cell and the corrosion continued. Each weight-loss measurement required approximately ½ hr and an entire corrosion test lasted from 6 to 160 hr. The concentration of H₂O₂ was measured at various corrosion times by means of the titanium sulfate colorimetric method (13) in the following manner: 2 to 4 ml of 0.008M titanium sulfate was added to the same amount of corrosion solution, and the maximum absorption peak at about 410 nm was compared to that of standard H₂O₂ solutions in 2M H₂SO₄. The Cu surface was prepared, prior to each test, in one of two ways: (i) leaching it with a few drops of HNO₃ or (ii) by corroding it for 40 hr in O₂-saturated 2M H₂SO₄. Corrosion tests were performed on Cu at open-circuit and at potentiostatically polarized conditions.

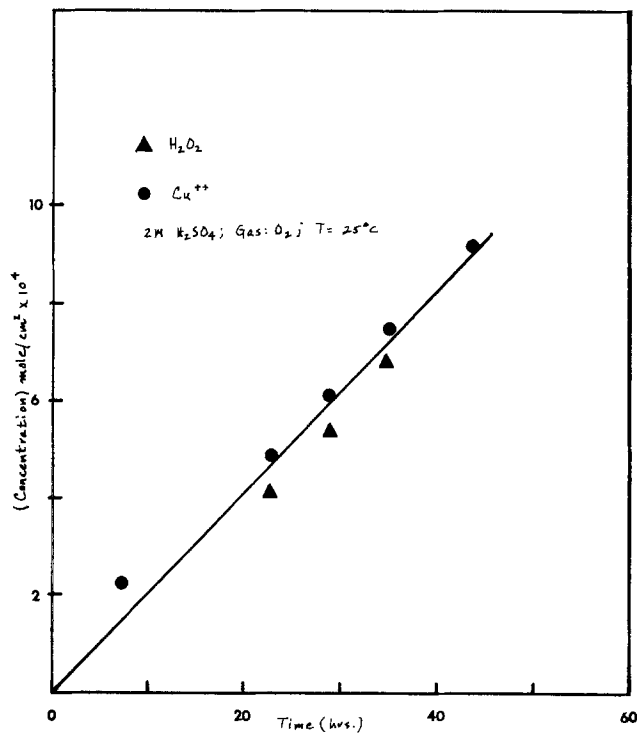


Fig. 2. Rate of copper dissolution and simultaneous hydrogen peroxide buildup during Cu corrosion at open circuit.

Polarization curves.—Cathodic and anodic polarization curves were determined by manual potentiostatic means. These curves were obtained by stepping the potential every few minutes and recording the resultant current. Also for anodic polarization the electrode was potentiostated for times from 4 to 24 hr and the current was recorded continuously and integrated. For this same period the copper weight loss was measured. Electric currents were checked for accuracy by inserting a standard resistor in the circuit and measuring the potential across it.

Results

Open-circuit corrosion tests.—Copper weight loss vs. time curves under various conditions in 2M H₂SO₄ are shown in Fig. 1. For the HNO₃-pretreated surface the corrosion rate increased with time until approximately 40 hr, after which the rate was approximately constant. When an already corroded sample was placed in a fresh corroding medium, the rate was constant from the beginning of the experiment and corresponded to the rate after 40 hr on the HNO₃-pretreated electrode (cf. Fig. 1).

The stable products of corrosion were H₂O₂ and Cu⁺² ions which formed in equimolar amounts at times less than 40 hr (cf. Fig. 2). At longer times, the rate of Cu weight-loss continued at the same rate but the rate of H₂O₂ production decreased. This indicates that further reduction of H₂O₂ to H₂O or catalytic decomposition of the H₂O₂ occurs. These results contrast with those from previous corrosion studies of Cu in oxygenated H₂SO₄, in which it was generally assumed that H₂O is the final product (7, 10-12). In most such studies no direct tests for H₂O₂ formation were conducted.

To further investigate the effects of the products on the rate of corrosion, measurements were conducted in solutions which initially contained H₂O₂ and Cu⁺² ions at concentrations observed toward the end of a typical test. From the results of these tests (see Fig. 1) it also is concluded that product Cu⁺² ions at C ≤ 0.01M and H₂O₂ at C ≤ 1.6 × 10⁻³M have no effect on the corrosion.

The corrosion curves for Cu in O₂- and air-saturated solutions are both shown in Fig. 1; weight loss in N₂-saturated solutions was negligible. The corrosion currents are 1.15 and 0.29 mA/cm² in O₂ and air, respectively, which indicates that the rate is approximately first order with respect to oxygen concentra-

tion. Corrosion potentials of 0–10 mV (*vs.* SCE) were noted in O₂- and air-saturated solutions, whereas the open-circuit potential in N₂-saturated solution (with no added Cu²⁺ ions) was approximately –50 mV. The addition of Cu²⁺ ions shifted the open-circuit potentials in N₂ or O₂ in a positive direction.

Corrosion tests were carried out in both O₂-saturated 2M H₂SO₄ and 0.2M H₂SO₄. The rate in the 2M H₂SO₄ was 1.15 mA/cm² and that in the 0.2M H₂SO₄ was 0.82 mA/cm². In both cases the Cu²⁺ ions and H₂O₂ were formed in nearly equimolar amounts.

To test the role of agitation in the mechanism, tests were run in O₂-saturated 2M H₂SO₄ without stirring and at a faster rate than the "standard" stirring rate employed in most of the tests. The corrosion current densities obtained were 0.5 mA/cm² for no stirring, 1.15 mA/cm² for the standard stirring rate, and 1.43 mA/cm² for the rapid stirring rate. This indicates that at the standard conditions the corrosion is either partially or wholly controlled by diffusion. Inasmuch as the limiting diffusion current for O₂ reduction at the standard stirring rate was 1.6 mA/cm², which is substantially more than the corrosion rate of 1.15 mA/cm², the corrosion is only partially diffusion controlled and is hence partially reaction controlled. The positive effect of acid strength on the corrosion rate also indicates that the corrosion is partially reaction controlled.

Polarization tests.—Polarization curves were measured from open-circuit to potential regions substantially positive and negative of the open-circuit potential region. This was done to produce Tafel curves for Cu oxidation alone and O₂ reduction alone; these curves then could be extrapolated to the same potential (*i.e.*, to the corrosion potential in O₂-saturated solution) as a test of the mixed potential theory. If the curves extrapolated to the observed corrosion potential (0–10 mV) and at the current density observed in the corrosion tests, then the mixed potential theory would be considered applicable.

Figure 3 shows the cathodic Tafel plot for Cu in O₂-saturated 2M H₂SO₄ and the anodic plot for Cu in N₂-saturated 2M H₂SO₄. The copper surface was precorroded and hence corresponded to that in the linear corrosion region of Fig. 1. The plots were obtained by manual potentiostatic means with an allowance of approximately 5 min per point. The solutions were stirred at the same standard rate as in the case of the corrosion studies represented by Fig. 1 and 2. Both of the curves in Fig. 3 were repeatable in position and shape.

The anodic curve which corresponds solely to Cu oxidation consists of a Tafel line similar to those obtained in previous investigations (14–17). The cathodic curve is atypical of conventional O₂-reduction curves as the current increases to a maximum and then decreases to a minimum before increasing to the O₂ limiting diffusion current, $i_{O_2,l}$, and to the region of H₂ evolution. From the open-circuit potential to the current minimum on the negative side of the hump, both O₂ reduction and Cu dissolution occur. From the current minimum to $i_{O_2,l}$, O₂ reduction is the only significant reaction and thus equals the measured current. In a previous study (18) the region of the current maximum (hump) was investigated and the hump was identified as the result of cathodic passivation. The surface at the hump allows O₂ to be reduced with a greater rate constant than that at more negative potentials. Accordingly, the curve at current densities just less than $i_{O_2,l}$ cannot be extrapolated to the corrosion potential, E_{cor} (10 mV), to yield the corrosion current, i_{cor} , as the resulting current is too small. Rather the O₂ reduction characteristics at potentials positive of the hump would need to be extrapolated to predict i_{cor} .

Apart from problems on the cathodic side of E_{cor} , the anodic polarization curve in N₂-saturated solution fails to yield i_{cor} at E_{cor} but rather yields a value of i_{cor} which is only approximately 0.1 the value of 1.15 mA/cm² obtained from copper weight-loss measurements. Therefore the anodic polarization curve in N₂-saturated solution cannot be used to deduce the corrosion rate in oxygenated solutions.

Copper dissolution rates in N₂ vs. O₂ saturated solutions.—To further clarify this phenomena four different kinetic currents were obtained at various potentials: (i) The weight loss of Cu in N₂-saturated solution was obtained and converted to the corresponding 2 electron current, $i(Cu, N_2)$; (ii) the meter-derived current corresponding to the above test, $i_a(N_2)$, was obtained, (iii) the weight loss of Cu in O₂-saturated solution was obtained and converted to the current $i(Cu, O_2)$; and (iv) the meter-derived current in test (iii), $i_a(O_2)$, was obtained.

To obtain each current, at a given potential, the Cu was potentiostated for 4–24 hr. Inasmuch as the electric currents at the higher overvoltages ($\eta \geq 40$ mV) increased with time, the current was recorded and averaged to yield the effective meter values. Current densities corresponding to weight-loss results were based on 2 electrons per dissolved Cu atom because

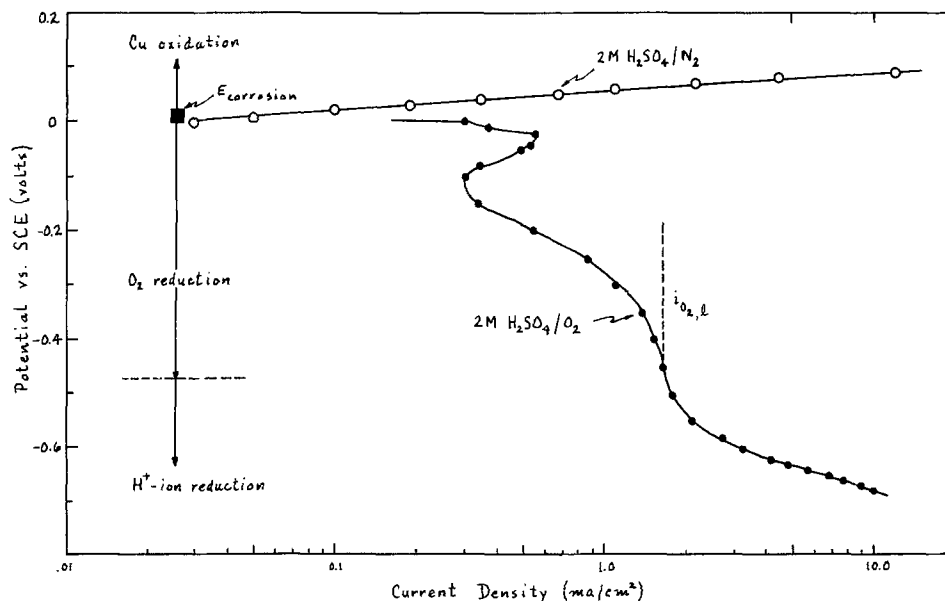


Fig. 3. Steady-state polarization curves obtained potentiostatically for Cu electrode in stirred 2M H₂SO₄. Anodic curve: N₂-saturated. Cathodic curve: O₂-saturated. Temperature: 25°C.

Table I. Experimental kinetic currents at various potentials for Cu electrode in stirred 2M H₂SO₄. Temperature: 25°C.

E (mV vs. SCE)	N ₂ -saturated		O ₂ -saturated	
	Recorded, <i>i_a</i> (N ₂) (mA/cm ²)	Weight loss, <i>i</i> (Cu,N ₂) (mA/cm ²)	Recorded, <i>i_a</i> (O ₂) (mA/cm ²)	Weight loss, <i>i</i> (Cu,O ₂) (mA/cm ²)
+10 (open circuit in O ₂ -saturated solution)	~0.07		0	1.16, 1.06, 1.15, 1.1 (1.15) ^(a)
+20	0.12, 0.26 (0.19)	0.18, 0.24 (0.21)		
+30	0.50, 0.48 (0.49)	0.56, 0.67 (0.61)	0.59, 0.62, 0.48 (0.57)	2.04, 2.09, 2.29 (2.14)
+40	1.0, 0.9, 0.7 (0.87)	1.06, 1.01, 0.88 (0.98)	2.05, 1.61, 0.94, 0.94 (1.37)	3.59, 2.92, 2.72, 2.17 (2.85)
+50	1.64, 1.66, 2.02 (1.77)	2.61, 1.88, 2.09 (2.19)	3.43, 2.34, 2.36 (2.71)	4.83, 3.72, 3.51 (4.02)
+80	12.6, 8.7, 10.9, 9.2 (10.4)	13.4, 9.1, 12.8, 9.3 (11.1)	15.9, 11.8, 13.4, 15.8 (14.2)	17.6, 13.2, 14.7, 17.0 (15.6)

(^a) Average of all tests at given potential.

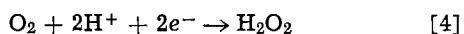
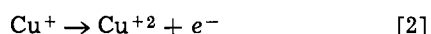
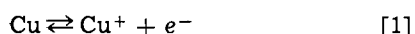
+2 is the only oxidation state for Cu in sulfate solutions in significant concentration [e.g., cf. Ref. (19) and (20)]. The results of tests (*i*) = (*iv*) are given in Table I. Each test was repeated up to four times; both the individual and average values are listed. The values are arranged such as to show paired values from the same test of *i_a*(N₂) vs. *i*(Cu,N₂) and *i_a*(O₂) vs. *i*(Cu,O₂); i.e., the first values listed at a given potential are from the same test [e.g., 0.12 for *i_a*(N₂) and 0.18 for *i*(Cu,N₂)], the second are from the same test, etc.

The following trends are evident: (a) *i*(Cu,O₂) > *i_a*(O₂); the difference is substantial. (b) *i*(Cu,N₂) > *i_a*(N₂); the difference is small. (c) *i_a*(O₂) is slightly less than *i_a*(N₂) and *i*(Cu,N₂) at 10 mV; *i_a*(O₂) becomes indistinguishable from the currents in N₂ at slightly more positive potentials; at the most positive potentials studied, *i_a*(O₂) is larger than the currents in N₂.

The effects of varied stirring and acid strength are shown in Table II. It is apparent that both the rate of Cu weight loss, *i*(Cu,O₂), and the anodic current density, *i_a*(O₂), increase with increases in stirring and acid strength. The anodic polarization results in N₂-saturated solution were shown in a previous study (14) to be independent of stirring rate.

Discussion

That Cu dissolution is faster in O₂- than in N₂-saturated solution at a given potential is an anomaly compared to the previously described systems (1-3) and to the conventional theory of mixed potentials (1). To explain the present results we propose the following simultaneous reactions



The Cu⁺ ions in Eq. [1]-[3] are transient intermediates which exist in significant concentrations only in the adsorbed state or very near the electrode surface.

Steps [1] and [2] alone constitute the mechanism for anodic Cu oxidation in N₂-saturated solutions, as

manifest by test data in Table I and Fig. 3. A well-defined Tafel line is noted with values given by

$$b_a = dE/d \log i = 35-40 \text{ mV} \quad [5]$$

Previous investigators [see Ref. (14-17)] have obtained similar results which are interpreted in terms of Eq. [1] being in quasi-equilibrium followed by the rate-determining charge-transfer step, Eq. [2].

The faster rate of Cu dissolution, at a given potential, in the presence of O₂ rather than N₂ follows from step [3]. This step represents the attack by O₂ and H⁺ ions on the intermediate Cu⁺ ions. Thereby Cu is dissolved while exchanging only one electron with the electrode, although the final product is still the Cu⁺² ion. Equation [4] is the electrochemical reduction of O₂ at the Cu surface.

The measured reactions of Table I are related to the proposed mechanism as follows:

$$i(\text{Cu,N}_2) \simeq i_a(\text{N}_2) = 2i_2^3 \quad [6]$$

$$i_a(\text{O}_2) = i_1 + i_2 - i_4 = 2i_2 + i_3 - i_4 \quad [7]$$

$$i(\text{Cu,O}_2) = 2i_2 + 2i_3 \quad [8]$$

The total O₂ utilization or H₂O₂ production current is given as

$$i_{\text{H}_2\text{O}_2} = i_3 + i_4 \quad [9]$$

From Eq. [6]-[9] and the results given in Table I the values for the reactions [2], [3], and [4] were calculated. The values for 2*i₂* and 2*i₃* (the components of Cu dissolution), *i₃* + *i₄* (the total O₂ consumption current), and *i₄* are shown in Table III at various potentials. The value for 2*i₂* was taken as the average of *i*(Cu,N₂) and *i_a*(N₂). Average values for *i_a*(O₂) and for *i*(Cu,O₂) were used in Eq. [7] and [8].

The calculated value for *i₃* increases with a positive increase in potential as the theory predicts. This is because the concentration of Cu⁺ ions is increased as the

* Although *i*(Cu,N₂) is slightly larger than *i_a*(N₂), we consider them to be identical in this treatment. The reason for this difference was not established but may be expected to arise from a combination of phenomena which includes dissolution of Cu⁺ ions (20), mechanical loss from the electrode, and errors of up to 3% in the measured current. Inasmuch as the differences in *i*(Cu,O₂) and *i_a*(N₂) [or *i*(Cu,O₂) and *i*(Cu,N₂)] are much larger than those between *i*(Cu,N₂) and *i_a*(N₂), the latter differences are of no consequence with regard to the qualitative conclusions of this paper.

Table II. Effects of varied stirring and sulfuric acid strength on results

E (mV)	[H ₂ SO ₄] (M)	Rate of stirring	<i>i_a</i> (O ₂) (mA/cm ²)	<i>i</i> (Cu,O ₂) (mA/cm ²)
+50	2.0	"Standard" rate used throughout Table I (moderately rapid)	3.43, 2.34, 2.36	4.83, 3.72, 3.51
+50	2.0	More rapid than "standard" rate	3.88	5.08
+50	0.2	"Standard" rate	1.76, 1.76	3.06, 3.12

Table III. Kinetic currents calculated from experimental results (Table I) and proposed model

E vs. SCE	2 <i>i₂</i> (mA/cm ²)	2 <i>i₃</i> (mA/cm ²)	<i>i₄</i> (mA/cm ²)	<i>i₃</i> + <i>i₄</i> (mA/cm ²)
10	0.20	0.95	0.67	1.14
30	0.55	1.59	0.78	1.58
40	0.92	1.93	0.51	1.47
50	2.0	2.02	0.29	1.27
80	10.7	4.9	-1.1	1.35

equilibrium of reaction [1] is shifted with a positive increase in potential. Although the data are not adequate to produce a reliable Tafel slope, it is observed that i_3 yields a slope between 60 and 100 mV which is reasonable for partial rate control by O_2 diffusion and part by chemical reaction. The value of i_4 decreases with a positive shift in potential, but the Tafel slope is much less well defined than that for i_3 . The apparent negative value of i_4 at 80 mV is further indication of the limitation in data precision.

The total oxygen consumption, $i_3 + i_4$, is approximately constant for $E \geq 30$ mV, at a value equal to or slightly less than the O_2 limiting diffusion current (which is measured as 1.6 mA/cm² at the rate of stirring employed in Table III). From Table III it is observed that i_3 is the predominant path for Cu dissolution at and near open-circuit potentials while the purely electrochemical path, i_2 , is predominant at the more positive overpotentials. The path i_3 is the predominant reaction for O_2 consumption or H_2O_2 production at the more positive potentials; at and near open circuit i_4 is as large or larger than i_3 .

The effects of stirring and acid strength on $i_a(O_2)$ and $i(Cu, O_2)$ (see Table II) are clarified by Eq. [7] and [8] and the fact that $i_3 \gg i_4$.

The present model explains not only the differences in Cu dissolution rates in O_2 - and N_2 -saturated solutions, but also the effects on the corrosion rate of stirring rate, acid strength, and O_2 partial pressure, and the lack of effect of Cu^{+2} ions. This model also correlates anodic electrochemical results with corrosion data.

The present results and interpretation are in accord with the kinetics of corrosion of Cu by oxygenated HCl solutions (10, 21) and with the kinetics of anodic oxidation of Cu in HCl solutions (22, 23). In these cases the product is Cu^+ . The rate constant of the reaction $Cu \rightarrow Cu^+$ is so rapid that the rate-determining step during anodic dissolution is the diffusion of Cu^+ products away from the electrode (24, 25). In sulfate solutions the Cu^+ ions are not stable in solution and must be removed mainly by further oxidation steps (Eq. [2] and [3]) which become rate determining. In weakly acidic sulfate solutions the Cu^+ ions are removed by precipitation of Cu_2O (24).

Although the present model does not specifically take anions into account, it is not inconsistent with the observation of Robertson *et al.* (10) that the corrosion rate of Cu is different in the presence of Cl^- than of $SO_4^{=}$ ions and that the relative anion effects change with pH. In the present work, corrosion tests were made in 2M HCl at open circuit. The corrosion rate was 0.25 mA/cm² (compared to 1.15 mA/cm² at 2M H_2SO_4); the corrosion potential was -260 mV (SCE) compared to +10 mV in the case of 2M H_2SO_4 . This difference in corrosion rates is qualitatively explicable on the basis of potential, but may also depend on effects of anionic specific adsorption on the reaction rates for the given mechanism.

Although the partial processes for Cu oxidation and O_2 reduction in H_2SO_4 solutions are interdependent, the present model does not indicate such interdependence of reactions for Cu in oxygenated HCl. This is because Cu^+ is the final product and thus there is no vulnerable intermediate. Data obtained by Miller and Bellavance (21) indicate that this is indeed the case. The rate of Cu dissolution from either N_2 - or O_2 -saturated 0.1M HCl-1M NaCl was the same at a given potential [data from Fig. 4 and 5 in Ref. (21) were compared].

From the present results one would suspect that some other multivalent metals would behave similarly to Cu. In dissolving via the route of consecutive electron transfer, such that the mixed potential theory does not apply to corrosion of them. Although the pertinent potentiostatic data has not been located, dissolution of metals via ions of suboxidation states is

supported by test results of Epelboin and co-workers and Davidson and co-workers [e.g., cf. Ref. (25-29) and others listed in the review by Garreau (30)]. These investigators observed that various metals are anodically dissolved in certain solutions with an electron loss per atom less than the conventional one [e.g., Al was found to dissolve with the withdrawal of only 2-2.7 electrons per atom in aqueous solutions containing halide, nitrate, chlorate, bromate, and perchlorate ions (25)]. Although the above phenomena is believed by some authors to be due to metal disintegration [cf. work of Straumanis and co-workers in Ref. (31-33) and in other works referenced in the above-mentioned review article (30)], the suboxidation state finds support in numerous test results (25-30).

Acknowledgments

The authors gratefully acknowledge the Army Research Office-Durham, Contract DAHCO4-75-G-0019 and the Paint Research Institute for financial support of this work. M.H.G. would also like to thank Arya-Mehr University of Technology for the leave of absence.

Manuscript submitted May 6, 1975; revised manuscript received Aug. 4, 1975.

Any discussion of this paper will appear in a Discussion Section to be published in the June 1976 JOURNAL. All discussions for the June 1976 Discussion Section should be submitted by Feb. 1, 1976.

Publication costs of this article were partially assisted by the University of Utah.

REFERENCES

1. C. Wagner and W. Traud, *Z. Elektrochem.*, **44**, 391 (1938).
2. G. E. Kimball and A. Glassner, *J. Chem. Phys.*, **8**, 820 (1940).
3. J. V. Petrocelli, *This Journal*, **97**, 10 (1950).
4. K. J. Vetter, "Electrochemical Kinetics," chap. 5, Academic Press, New York (1967).
5. M. Henthorne, *Chem. Eng.* (1971), 99.
6. M. Stern and A. L. Geary, *This Journal*, **104**, 56 (1957).
7. B. C. Y. Lu and W. F. Graydon, *Can. J. Chem.*, **32**, 153 (1954).
8. A. I. Kinevskii, *Zh. Prikl. Khim.*, **28**, 1088, 1113 (1955); C.A. 50: 6161 f.g.
9. N. L. Jensen, Ph.D. Thesis, University of Utah, Salt Lake City, Utah (1956).
10. W. D. Robertson, V. F. Nole, W. H. Davenport, and F. P. Talboom Jr., *This Journal*, **105**, 569 (1958).
11. I. Cornet, E. A. Barrington, and G. U. Behrsing, *ibid.*, **108**, 947 (1961).
12. Z. Zembura, *Corrosion Sci.*, **8**, 703 (1968).
13. F. D. Snell and C. T. Snell, "Colorimetric Methods of Analysis," Vol. 2, p. 882, Van Nostrand Publishing Co., New York (1959).
14. T. Hurlen, *Acta Chem. Scand.*, **15**, 630 (1961).
15. E. Mattsson and J. O'M. Bockris, *Trans. Faraday Soc.*, **55**, 1586 (1959).
16. J. O'M. Bockris and V. Enyo, *ibid.*, **58**, 1187 (1962).
17. Q. J. M. Slaiman and W. J. Lorenz, *Electrochim. Acta*, **19**, 791 (1974).
18. M. H. Ghandehari, T. N. Andersen, and H. Eyring, Paper submitted to *Corrosion Sci.*
19. M. C. Petit, *Electrochim. Acta*, **10**, 291 (1965).
20. G. V. Makarov, O. A. Songina, and E. A. Buketov, *Zh. Prikl. Khim.*, **45**, 310 (1972).
21. B. Miller and M. I. Bellavance, *This Journal*, **119**, 1510 (1972).
22. C. H. Bonfiglio, H. C. Albaya, and O. A. Cobo, *Corrosion Sci.*, **13**, 717 (1973).
23. T. Hurlen, *Acta Chem. Scand.*, **15**, 1231 (1961).
24. G. T. Miller, Jr. and K. R. Lawless, *This Journal*, **106**, 854 (1959).
25. I. Epelboin, *Z. Elektrochem.*, **59**, 689 (1955).
26. I. Epelboin and M. Froment, *J. Chim. Phys.*, (1963), 1301.
27. E. Rajola and A. W. Davidson, *J. Am. Chem. Soc.*, **78**, 556 (1956).
28. R. L. Petty, A. W. Davidson, and J. Kleinberg, *ibid.*, **76**, 363 (1954).

29. A. W. Davidson and F. Jirik, *ibid.*, **72**, 1700 (1950).
 30. M. Garreau, *Métaux*, No. 541, p. 291 (1970).
 31. M. E. Straumanis, J. L. Reed, and W. J. James, *This Journal*, **114**, 885 (1967).
 32. W. J. James, M. E. Straumanis, and J. W. Johnson, *Corrosion*, **23**, 15 (1967).
 33. M. E. Straumanis and K. Poush, *This Journal*, **113**, 1345 (1966).

An Ellipsometric Investigation of the Underpotential Deposition of Lead on Gold

Jean Horkans,^{*1} B. D. Cahan,^{*} and Ernest Yeager^{*}

Department of Chemistry, Case Western Reserve University, Cleveland, Ohio 44106

ABSTRACT

Potential scanning ellipsometry has been used to examine the wavelength and potential dependence of the optical constants of the lead layer formed on Au by underpotential deposition from Pb^{2+} solution. The two main current peaks in the voltammetry curves of the system can be identified with two different states of the surface film. Neither state has optical constants resembling those of bulk Pb. Both films have an ellipsometrically determined thickness of 1.5Å. The large wavelength dependence of the optical constants of the films indicates a strong interaction of the lead adlayer with the surface layer of the Au substrate. The ellipsometric data are consistent with a model in which the layer formed on the surface at less cathodic potentials is primarily ionic and at cathodic potentials undergoes a transition to a metal-like lead adlayer.

Optical reflectance techniques have given useful information about the phenomenon of underpotential deposition² (UPD) and the nature of the surface lead layers formed on gold at potentials anodic to the reversible potential of lead (2-4). The use of modulated specular reflectance techniques, in conjunction with electrochemical and surface-specific methods, to investigate UPD is discussed in an earlier paper (4). The information obtained by these specular reflectance methods, although important to a better understanding of the electrode-electrolyte interface, is largely of a qualitative nature. More quantitative information may be gained by the use of ellipsometric techniques, which are capable of determining the optical dielectric constant of a surface or a surface film.

Ellipsometry has not previously been applied to the study of the UPD phenomenon, in part because of the slowness of manual ellipsometry and the expense of automation. Recently, a potential scanning ellipsometric technique has been developed (5-7) in order to allow changes in the ellipsometric parameters to be rapidly measured. Three ellipsometric parameters Δ_o , Ψ_o , and reflectivity are determined, thus allowing the determination of the complex refractive index and thickness of an absorbing film using a three layer model [i.e., the substrate, film, and solution of the interface as discussed in Ref. (5)]. This method has been applied in the investigation of the UPD of lead on gold. The dependence of the optical constants of the lead film on both electrode potential and wavelength has been investigated. In addition, the effective optical film thickness was determined.

Experimental

The ellipsometric system and cylindrical optical electrochemical cell are the same as used by the authors in earlier studies with potential scanning ellipsometry (5-7). The light intensity is recorded during three identical linear voltage scans with a given offset from null of the polarizer of the ellipsometer and three different settings of the analyzer. Since the

functional dependence of the light intensity on the three surface parameters, Δ_o , Ψ_o , and reflectivity R , is known, the voltage dependence of $\delta\Delta_o$, $\delta\Psi_o$, and $\delta R/R$ can be determined from the three light intensity transients, as described earlier (5-7). The parameters Δ_o and Ψ_o are related in a straight-forward manner to p_o and a_o , the characteristic null polarizer and analyzer settings, which will be used here. The relationships between p_o and a_o and Δ_o and Ψ_o are given in Ref. (6) or (8). The method is described in detail in Ref. (5).

The complex refractive index $\hat{n} = n - ik$ and the thickness of the surface film have been determined by a modified form of the unconstrained minimization techniques used in earlier studies of oxide layers on Pt (7), using a simple, three layer model of the interface (i.e., assuming a film with sharp boundaries with the substrate and the solution both having bulk optical constants). For each of a series of film thicknesses, chosen by the user, the unconstrained minimum is found for the function F

$$F = (\delta\Delta_{om} - \delta\Delta_{oc})^2 + (\delta\Psi_{om} - \delta\Psi_{oc})^2 \quad [1]$$

where the subscript m denotes the measured value of each parameter and c denotes the value calculated from the assumed dependence of Δ_o and Ψ_o on the film optical constants and thickness. At each thickness, the n and k determined in this manner are used to calculate $\delta R/R$ (using the Fresnel equations). The thickness at which this calculated $\delta R/R$ is equal to that determined experimentally is taken to be the film thickness and the n and k determined from Eq. [1] at this thickness are taken as the film optical constants.

The electrodes were Au films of 0.5-1 μ thickness evaporated on glass microscope slides with a thin sputtered Nb undercoat to give adhesion. The preparation of the electrodes has been described elsewhere (5, 9). The Nb undercoat was found not to interfere with the optical or electrochemical measurements (9). Although all measurements reported here were done with evaporated Au electrodes, Adzic, Cahan, and Yeager (4) have found that evaporated Au prepared in this manner and the 111 orientation of single-crystal Au give similar results in electrochemical and reflectance studies of the UPD of Pb.

* Electrochemical Society Active Member.

¹ Present address: IBM Thomas J. Watson Research Center, Yorktown Heights, New York 10598.

Key words: underpotential deposition, monolayer metal films, ellipsometry, lead on gold.

² Lorentz et al. (1) have recently published a review of the various techniques for the study of UPD and discussed the structure and kinetics of the formation of UPD layers.

The Au vapor deposited films behave similarly to a highly oriented bulk Au.

The electrolyte was 1M HClO₄ prepared from reagent grade acid and triply distilled H₂O, the second distillation being from basic permanganate solution. The Pb²⁺ solution was prepared from Johnson Matthey Specpure Pb(NO₃)₂. All solutions were deaerated with N₂ gas from which CO₂ and O₂ had been removed by passing through molecular sieves. A N₂ atmosphere was maintained in the cell at all times. The squareness of the voltammetry curve in the double layer region, before the addition of Pb²⁺, was taken as an indication of cleanliness.

An α -Pd hydrogen bead reference electrode was placed near the surface of the working electrode. A stable reference potential was maintained even in the presence of Pb²⁺ in solution. (All potentials will be quoted vs. NHE). The counterelectrode was a thin-walled (0.005 in.) tube of Pd-Ag alloy, sealed at one end, with H₂ gas at 1 atm inside the tube.

Results and Discussion

The linear sweep voltammetry curve for Au in 1M HClO₄ + 5.0 × 10⁻³M Pb²⁺ is shown in Fig. 1. The entire potential range shown is anodic to the reversible potential of bulk lead metal. Two distinct peaks I and II are observed with shoulders and smaller peaks also evident. The shape of the pronounced cathodic peak II differs from that reported by Adzic, Yeager, and Cahan (4) using similar electrodes, probably as a result of differences in the voltage range over which the potential was swept. In any event, this peak is surprisingly narrow in both studies. There is evidence of fine structure, including the extraordinarily sharp spike in the cathodic sweep.

The shape of these voltammetry peaks has been discussed by Adzic *et al.* (4). The more anodic peak I is broad and undoubtedly due to the adsorption of lead species on the gold surface. The remarkably narrow peak II has been explained (4) on the basis of a surface phase transition in which lead adions condense into patches to form a predominantly metallic layer. Evidence that this peak does not involve the direct adsorption of lead from solution is to be found in the observation that this peak is not under diffusion control under conditions where peak I is under pure diffusion control. With this explanation, the charge under the peak II must then correspond to the release of compensating negative charge in the ionic double layer attending the change of the adsorbed layer from ionic to predominantly metallic character.

This explanation has been challenged by Schmidt and Wüthrich (10) on the basis that their data for lead adsorption on gold obtained with the twin electrode-thin layer technique (11) did not reveal any deviation from a linear relation between the amount of lead adsorbed and charge passed through the electrode at the potential corresponding to the narrow

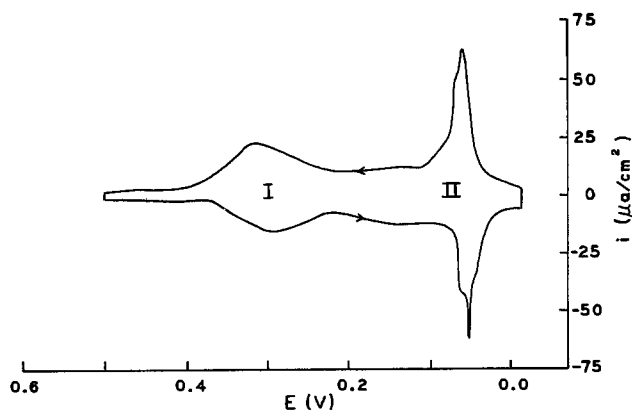


Fig. 1. Linear sweep voltammetry of Au in 1M HClO₄ with 5 × 10⁻³M Pb²⁺. Sweep speed 20 mV/sec.

peak. Adzic *et al.* (12), however, question whether Schmidt and Wüthrich would have necessarily been able to see the small deviation from linearity in view of the small amount of charge observed under the corresponding peak in their voltammetry curves, which was much smaller than in the work of Adzic *et al.* (4) or in the present work. The use of an acetic acid-acetate buffer system in their thin layer cell experiments may also have caused complications.

The UPD of Pb on Au has also been studied by Vicente and Bruckenstein (13) using rotating ring-disk methods. Although most of their investigations were done in Cl⁻ solutions, they claim qualitatively similar results in ClO₄⁻ solution. These authors suggest that peak II is only observed after all the available sites associated with peak I have been filled, and observe that bulk Pb is not deposited until a monolayer of lead species is deposited at underpotentials, an observation in agreement with the results of Adzic *et al.* (4).

The optical changes caused by the UPD of lead on Au are highly dependent on wavelength. The potential dependences of $\delta R/R$, δp_o , and δa_o at 456 and 652 nm are shown in Fig. 2 and 3, respectively. The zeros of the ordinates for these curves have been adjusted to correspond to the values at 0.45V. At 456 nm (Fig. 2) on the blue side of the adsorption edge of Au (which occurs at 500 nm), both voltammetry peaks are attended by large increments in reflectivity. The δp_o curve shows a shape similar to $\delta R/R$. At this wavelength, δa_o is small and is positive for the more anodic current peak but negative for the more cathodic peak. At 652 nm (Fig. 3), on the red side of the adsorption edge of Au, a decrease in reflectivity is observed for both peaks. The shape δp_o does not vary drastically as a function of wavelength, although the magnitude

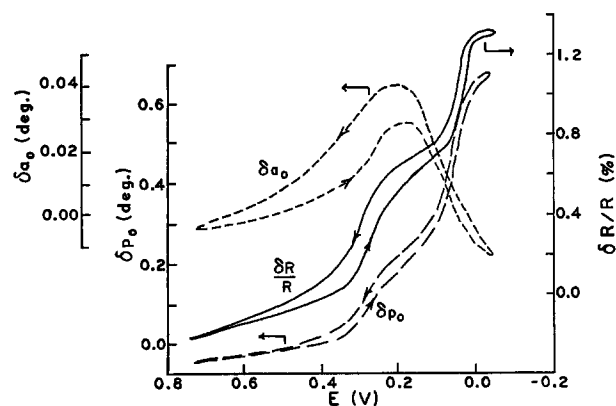


Fig. 2. Potential dependence of $\delta R/R$ at $\alpha = \pi/4$ (—), δp_o (—), and δa_o (---) for Au in 1M HClO₄ with 5 × 10⁻³M Pb²⁺. Wavelength 456 nm, angle of incidence 65°, sweep speed 20 mV/sec.

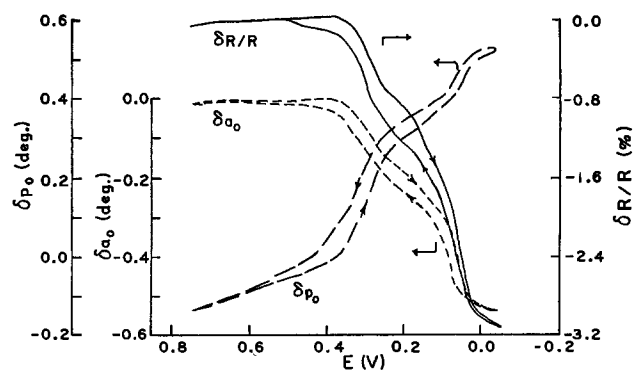


Fig. 3. Potential dependence of $\delta R/R$ at $\alpha = \pi/4$ (—), δp_o (—), and δa_o (---) for Au in 1M HClO₄ with 5 × 10⁻³M Pb²⁺. Wavelength 652 nm; other conditions same as for Fig. 2.

of the change differs. At this wavelength δa_o is large and is negative at all potentials.

The apparently large hysteresis in the δa_o vs. E curve at 456 nm (Fig. 2) is actually no larger than that of the other two parameters; the scale for δa_o is much expanded. However, any hysteresis at potentials anodic to 0.4V is rather surprising. At such anodic potentials, the voltammetry curves indicate that most of the lead has been desorbed. The adsorption-desorption process would not be expected to be under diffusion control in this section of the voltammetry curves at a sweep rate of 20 mV/sec in $5 \times 10^{-3}M$ Pb^{2+} . Vicente and Bruckenstein (13) have observed a similar result, in that their ring currents showed desorption of species from the disk in potential regions where the disk current indicated no faradaic processes. They suggest that this current is caused by desorption of Pb(II) adsorbed during the oxidation of underpotential lead. Possible alternative explanations are that the process is under kinetic control or that some type of aging process occurs.

The calculation of the optical properties of the adsorbed lead layer using a three-layer model requires the determination of the changes in p_o , a_o , and R relative to a film-free, two-layer reference state. The problems associated with the selection of such a reference state have been discussed elsewhere (7). In the present study, the changes in p_o , a_o , and R upon formation of the lead layer were taken to be the difference between the value of each parameter at the electrode potential of interest and its value extrapolated from the portion of the curve (scanning in the cathodic direction) in which no lead is adsorbed (anodic to 0.4V). This is essentially equivalent to taking the difference between the value of the parameter at a given potential in the presence and absence of Pb^{2+} ions in solution.

The wavelength dependence of $\delta R/R$, δp_o , and δa_o for the lead layers formed by the more anodic and more cathodic peaks are shown in Fig. 4 and 5, respectively. The reflectivity change shows the wavelength dependence observed by Adzic *et al.* (4). The measured $\delta R/R$ curve crosses zero at 505 nm in Fig. 4 and 492 nm in Fig. 5. The difference is significant; measurements at 502 nm show that the first peak causes an increase in reflectivity and the second peak causes a decrease. For both films, δp_o is everywhere positive and shows a peak at ~ 470 -500 nm, which is rather near the absorption edge of Au at ~ 500 nm. The value of δa_o is small and positive in the blue, becoming large and negative in the red.

The thickness and optical constants of the UPD lead layers were determined by the procedure described in the experimental section. The function F of Eq. [1] is minimized and the calculated value of $\delta R/R$ is matched to the experimentally measured value. The

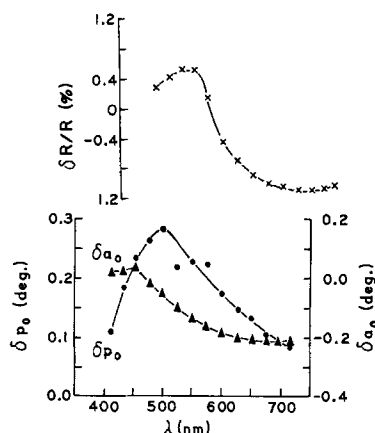


Fig. 4. Wavelength dependence of $\delta R/R$, δp_o , and δa_o for Au in $1M$ $HClO_4$ with $5 \times 10^{-3}M$ Pb^{2+} . Layer formed by more anodic current peak (0.15V in cathodic sweep). Angle of incidence 65° .

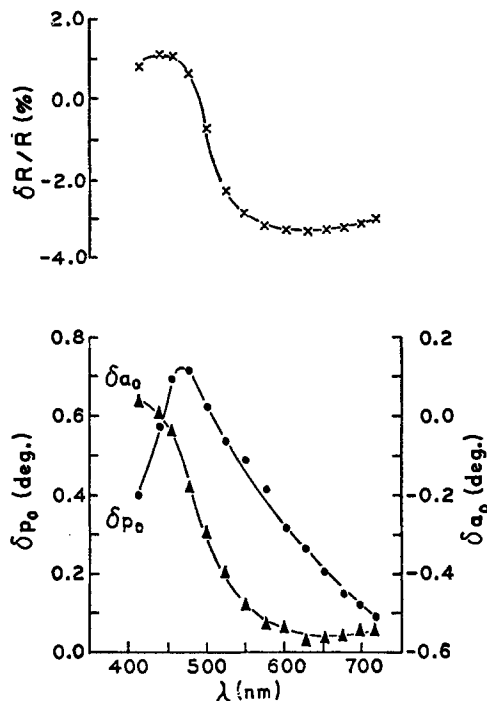


Fig. 5. Wavelength dependence of $\delta R/R$, δp_o , and δa_o for Au in $1M$ $HClO_4$ with $5 \times 10^{-3}M$ Pb^{2+} . Layer formed by more cathodic current peak ($-0.05V$ in cathodic sweep). Angle of incidence 65° .

two potentials at which these calculations were done were 0.15 and $-0.05V$ in the cathodic sweep; these potentials were chosen to be after the completion of the voltammetric peaks I and II, respectively. At both potentials, the film thickness t of 1.5\AA minimized the difference between calculated and measured $\delta R/R$ values over the entire wavelength range studied. The measured and calculated values of $\delta R/R$ are in good agreement, within the precision with which the changes in a_o , p_o , and R are known from the experimental measurements, at all wavelengths examined for the film at $+0.15V$ and at wavelengths shorter than 500 nm at $-0.05V$. At longer wavelengths than 500 nm at $-0.05V$, the difference between the observed and calculated $\delta R/R$ values was somewhat greater (5% of the measured $\delta R/R$ values). This may be due to some inadequacy of the three-layer model in this wavelength region, where the film formation probably substantially affects the optical properties of the surface of the Au substrate. Such failures of the three-layer model have previously been encountered with Au in this wavelength region (7) due to the presence of the adsorption edge of Au at 500 nm. Consequently, the values of the optical constants above 500 nm in Fig. 7 may be somewhat in error.

The precision with which the t values could be determined at each wavelength is estimated to be $\pm 0.3\text{\AA}$ with the precision of the measured values of $\delta R/R$ being the limiting experimental measurement in the present work. While the precision with which any one value of t could be determined is rather limited, the average of the values at 14 wavelengths at each potential is expected to have a standard deviation of 0.1\AA . Consequently no appreciable change in the ellipsometric thickness occurs between $+0.15$ and $-0.05V$ despite the fact that the total charge associated with the film formation almost doubles.

The wavelength dependences of the optical constants of the film are shown in Fig. 6 and 7 for $+0.15$ and $-0.05V$, respectively. In both cases, very large dependences of n and k on wavelength and very high values of k are observed for the film, results that would not be expected if the film resembles Pb metal. Since the optical constants of Pb are not available in

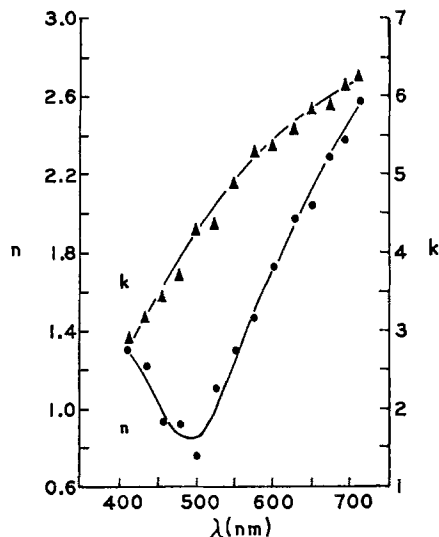


Fig. 6. Optical constants of lead film deposited by more anodic current peak (0.15V in cathodic sweep) on Au in 1M HClO₄ with 5×10^{-3} M Pb²⁺. ($t = 1.5\text{\AA}$.)

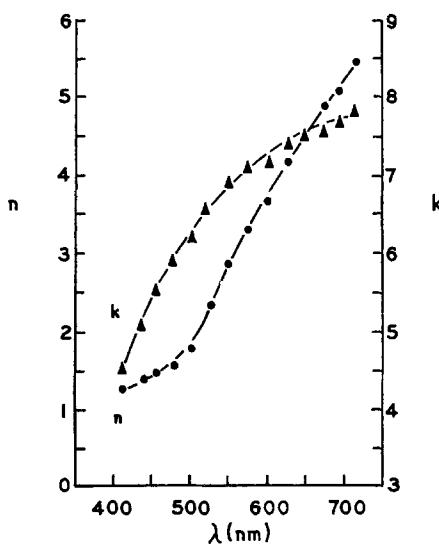


Fig. 7. Optical constants of lead film deposited by more cathodic current peak (-0.05V in anodic sweep) on Au in 1M HClO₄ with 5×10^{-3} M Pb²⁺ ($t = 1.5\text{\AA}$.)

the literature, a rough determination of the optical constants of bulk Pb metal has been made in this wavelength region using conventional null balance ellipsometry (Fig. 8). Although the Pb surface used undoubtedly had an oxide film and lacked the desired flatness, neither the absolute values of n and k nor their wavelength dependence should be grossly in error. None of the conclusions presented here is directly dependent on the data of Fig. 8, which are presented only for purpose of comparison with Fig. 6 and 7.

The absolute significance of the n , k , and t values of the film is not clear in view of the strong interaction of the adsorbed lead species with the gold substrate and also complications associated with surface roughness. Nonetheless, there is no question that a very pronounced change has occurred in the optical constants and hence the structure of the surface layer between +0.15 and -0.05V. The real and imaginary components of the refractive index are much higher at -0.05V and the minimum in the real component has disappeared. The imaginary component of the dielectric constant, given by $\epsilon'' = 2nk$ is far higher over the entire wavelength range, indicating much higher surface conductivity. This supports the view that the pro-

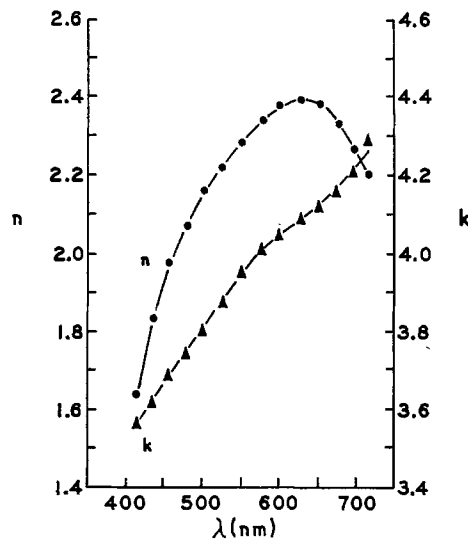


Fig. 8. Optical constants of Pb metal in air

nounced voltammetry peak II at +0.05V corresponds to a change of the film to a more metallic-like layer, with strong interaction of the lead orbitals with the band structure of the gold, as was proposed by Adzic, Cahan, and Yeager (4) on the basis that peak II is too sharp for an adsorption process and is not under diffusion control. It is difficult to reconcile such changes in the optical constants as evident between Fig. 6 and 7 and the constancy of the thickness t with the proposal of Schmidt and Stucki (14) that peak II corresponds to the formation of a metal layer more distant from and less strongly bound to the substrate.

Even at +0.15V, the values of the optical constants of the film and their wavelength dependence in Fig. 6 are indicative of a gross modification of the surface electronic properties of the gold electrode and hence of very strong interaction of the adsorbed species with the gold surface. This is at variance with the view of Schmidt and Wüthrich [see, e.g., Ref. (10)] that only simple ionic adsorption of Pb²⁺ ions is involved but in accord with the proposal of Adzic *et al.* (4) that partial charge transfer occurs with voltammetry peak I. Kolb, Przasnyski, and Gerischer (15) have also recently expressed the view that underpotential deposition involves partially charged adatoms and present arguments for such based on the correlation of the underpotentials with the difference in work functions of substrate and deposit.

The sharpness of the voltammetry peak II, its insensitivity to diffusion control, the constancy of the effective ellipsometric thickness, and the pronounced change in the optical constants together support the explanation that the lead ions are first adsorbed with partial charge transfer but still primarily as ions at relatively anodic potentials and then at a more cathodic potential the layer undergoes a phase transition corresponding to a condensation into patches of predominantly metallic character.

Acknowledgments

The authors are pleased to acknowledge the support of this research by the Office of Naval Research and the National Steel Corporation through a fellowship to one of the authors (JH). The research has also benefitted through discussions with Dr. R. Adzic of the Institute for Chemistry, Technology and Metallurgy of Belgrade.

Manuscript submitted Jan. 30, 1975; revised manuscript received July 25, 1975.

Any discussion of this paper will appear in a Discussion Section to be published in the June 1976 JOURNAL. All discussions for the June 1976 Discussion Section should be submitted by Feb. 1, 1976.

REFERENCES

1. W. Lorentz, H. Hermann, N. Würthrich, and F. Hilbert, *This Journal*, **121**, 1167 (1974).
2. T. Takamura, K. Takamura, W. Nippe, and E. Yeager, *ibid.*, **117**, 626 (1970).
3. T. Takamura, Y. Sato, and K. Takamura, *J. Electroanal. Chem.*, **41**, 31 (1973).
4. R. Adzic, B. D. Cahan, and E. Yeager, *This Journal*, **121**, 474 (1974).
5. J. Horkans, Ph.D. Thesis, Case Western Reserve University, 1973.
6. B. D. Cahan, J. Horkans, and E. Yeager, *Surface Sci.*, **37**, 559 (1973).
7. J. Horkans, B. D. Cahan, and E. Yeager, *ibid.*, **46**, 1 (1974).
8. A. B. Winterbottom, *Kgl. Norske Videnskab. Selskabs Skrifter*, p. 57 (1955).
9. R. Adzic, J. Horkans, B. D. Cahan, and E. Yeager, *This Journal*, **120**, 1219 (1973).
10. E. Schmidt and N. Würthrich, *ibid.*, **121**, 1611 (1974).
11. E. Schmidt and N. Würthrich, *J. Electroanal. Chem.*, **34**, 377 (1972).
12. R. Adzic, E. Yeager, and B. D. Cahan, *This Journal*, **121**, 1611 (1974).
13. V. A. Vicente and S. Bruckenstein, *Anal. Chem.*, **45**, 2036 (1973).
14. E. Schmidt and S. Stucki, *Ber. Bunsenges*, **77**, 915 (1973).
15. D. Kolb, M. Przasnyski, and H. Gerischer, *J. Electroanal. Chem.*, **54**, 25 (1974).

The Effect of Oxide Dissolution on the Electrodepositing of Dispersion-Hardened Co and Ni-Al₂O₃ Alloys

G. R. Lakshminarayanan, E. S. Chen, and F. K. Sautter

Watervliet Arsenal, Watervliet, New York 12189

ABSTRACT

The solubilities of γ - and α -Al₂O₃ particles have been investigated in dilute H₂SO₄ and in watts-type plating electrolytes of cobalt and nickel. The effects of the presence of Al³⁺ ions in the plating solutions on the properties of electrodeposits of cobalt and nickel have also been studied. The results show that γ -oxide is more soluble than α -oxide, the solubility increases with decreasing solution pH and increasing temperature. Aluminum contents of up to 0.04 weight per cent (w/o) in cobalt and 0.02 w/o in nickel were found and the room temperature yield strength values increased to about 40% for cobalt and 20% for nickel deposits. The effects on the yield strength values of Co-Al₂O₃ and Ni-Al₂O₃ alloys due to the presence of Al³⁺ ions in their respective plating electrolyte-oxide suspensions are also discussed.

The preparation of dispersion-hardened alloys by electrodeposition is attaining increasing importance in view of the many advantages this method offers for a variety of applications. In this method, submicron oxide particles are suspended in a conventional plating electrolyte and during plating the particles are codeposited with the metal matrix. A number of investigations dealing with the preparation and properties of these alloys have been reported from this (1-6) and other laboratories (7-12). The submicron oxide particles suspended in the plating solution are generally assumed to be inert although some of them do undergo dissolution in the plating solution over a period of time. In our experience with cobalt electrolytes in which γ -Al₂O₃ was suspended over a period of time, we have observed through spectrographic analysis that an appreciable amount of aluminum was present in the solution. The primary way aluminum could have been introduced in the solution was by the partial dissolution of oxide. The contribution of this or the effect of it in the electroforming of alloys would be of interest particularly if the dissolved aluminum is incorporated in the deposit as a basic metal hydroxide. The present investigation deals with studies relative to the solubility characteristics of γ -Al₂O₃ and α -Al₂O₃ in different electrolytes, the possibility of incorporation of aluminum in the electrodeposited cobalt and nickel and its effect on the strength properties of the deposits. In addition the effects of the presence of aluminum ions in the plating electrolyte-Al₂O₃ suspension on the strength properties of electrodeposited cobalt-Al₂O₃ and nickel-Al₂O₃ alloys were also studied.

Experimental

Materials.—All chemicals were of reagent quality grade and were used without further purification. Two

different aluminum oxides, γ -Al₂O₃ (0.03 μ , Cabot Corporation) and α -Al₂O₃ (0.3 μ Adolf Meller Company) were used to prepare the suspensions. The γ -oxide suspensions were dispersed with ultrasonic agitation to break up the agglomeration in the electrolyte.

Equipment.—pH measurements were made using both a Beckman Electroscan 30 in the pH mode of operation and a Digital pH meter (Leeds and Northrup) and dilute H₂SO₄ was used to adjust the solution pH. The surface area of the oxides was obtained by a Micromeritics Surface Area Analyzer (13) using nitrogen as an adsorbate. The design of this instrument is such that one can obtain the surface area of the samples directly and rapidly. The analyses of Al in solutions were carried out using both an atomic absorption spectrophotometer (Perkin-Elmer) and a Beckman Model Du spectrophotometer. For the atomic absorption spectrophotometer nitrous oxide-acetylene was used as an oxidizer (14) and the absorption of solution containing aluminum ions was measured at 390 m μ . When using a Beckman Du spectrophotometer, the method (15) selected was based on the extraction of aluminum 8-hydroxy quinolate by chloroform and measuring the optical density of the resultant yellow extract at 395 m μ . The oxide content in the Co-Al₂O₃ and Ni-Al₂O₃ deposits was obtained by dissolving the deposits in 50% HNO₃ and separating the oxide with Millipore filters. The oxides were then dried for an hour at 95°C and weighed on a microbalance.

Preparation and measurement of properties of the deposits.—Cobalt, nickel, Co-Al₂O₃, and Ni-Al₂O₃ alloys were deposited from their respective plating baths on a brass shim stock (0.003 in.) and the brass substrate was anodically dissolved in a KOH-K₂CO₃ solution. These deposits were cut into tensile specimens and their yield strength (0.2% offset) at room temperature was measured using an Instron tensile

Key words: electrolyte-oxide suspension, solubility of oxide, yield strength.

testing machine. A Leitz metallograph microscope was used to examine microstructural features of the deposits. Hardness values were also obtained from the above instrument fitted with the Leitz hardness tester operated at 50 and 100g load capacity.

Results and Discussion

Solubility of oxides in suspensions.—The addition of oxides to the electrolyte influences the solution pH to a different degree depending on the initial pH of the electrolyte. From Fig. 1 it is seen that the pH of electrolytes is raised significantly within minutes after the addition of γ - Al_2O_3 followed by a slow variation of pH with time. Several investigators (16, 17) have observed this type of behavior and from the kinetic studies of oxide-solution interface it has been suggested that the initial rapid change of pH is due to the establishment of primary equilibrium of the surface with the potential determining ions (H^+ , OH^-) and that the slow variation of pH was partly due to the solubility of the oxide leading to various secondary reactions such as hydrolysis, complex formation, dissociation of complexes, and so on.

In the plating solutions where oxide particles are suspended the partial dissolution of oxide introduces aluminum ions in the solution. Periodic adjustment of the plating solution pH through the addition of acid would further contribute to increase the dissolution of oxide. The concentrations of Al obtained as a function of time in different solution pH are shown in Fig. 2-4, for dilute H_2SO_4 - γ - Al_2O_3 , dilute H_2SO_4 - α - Al_2O_3 , Ni watts- γ - Al_2O_3 , and Co watts- γ - Al_2O_3 suspensions, respectively. In Fig. 2, in order to make proper comparison of the solubility of γ - Al_2O_3 and α - Al_2O_3 whose surface areas are different (γ - Al_2O_3 , $98.2 \text{ m}^2/\text{g}$; α - Al_2O_3 , $20.6 \text{ m}^2/\text{g}$) and whose concentrations in dilute H_2SO_4 suspensions are different (γ - Al_2O_3 , 25 g/liter and α - Al_2O_3 , 100 g/liter) the concentration of Al is represented based on the amount of oxide dissolved per square meter surface area of the respective oxide.

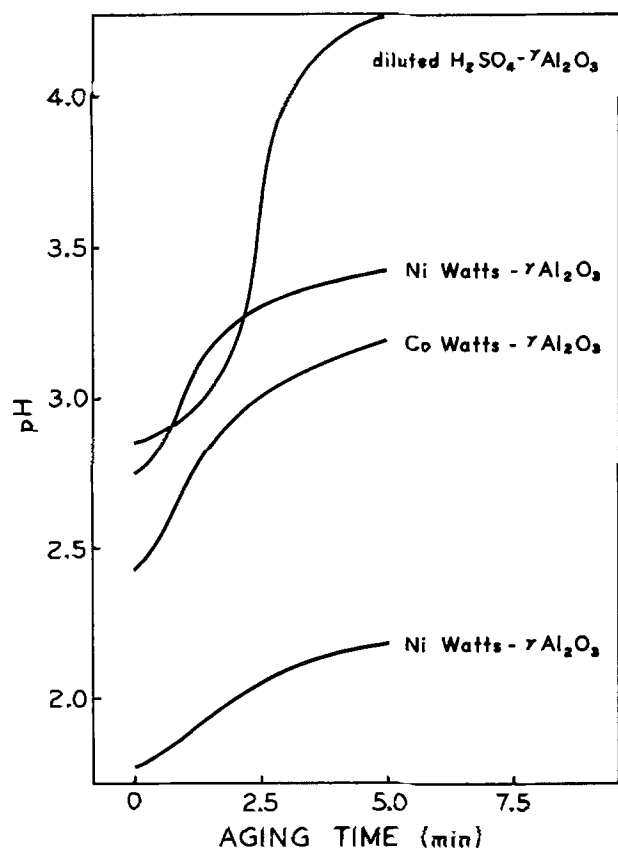


Fig. 1. Variation of pH at 25°C due to the addition of γ - Al_2O_3 (25 g/liter) in different electrolytes with time. A Beckman Electrascan 30 was used to scan the variation of pH with time.

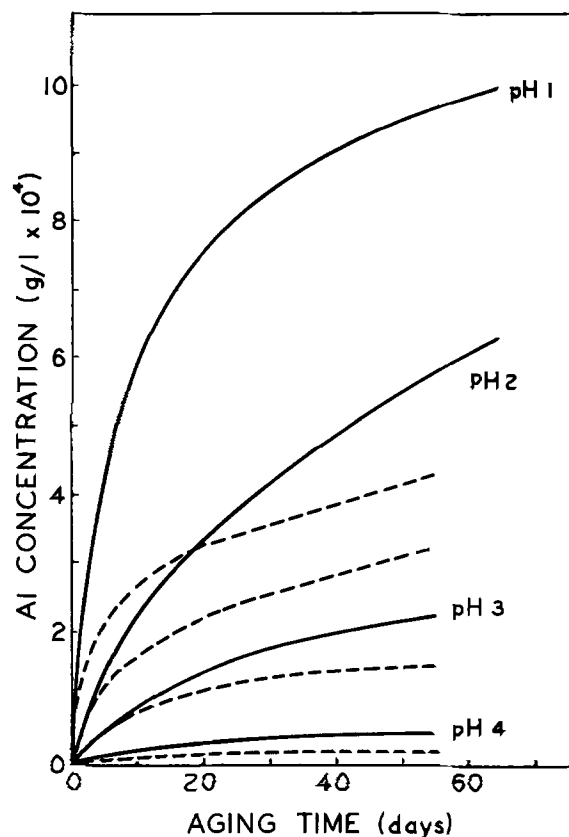


Fig. 2. Concentration of Al in solution of different pH due to the solubility of oxide at room temperature as a function of solution aging. Solid lines correspond to γ -oxide and dashed lines correspond to α -oxide. Since the surface areas of the oxides are different and different amounts of oxides in solution were used, the concentration of Al represented is per square meter of the surface area of the respective oxide.

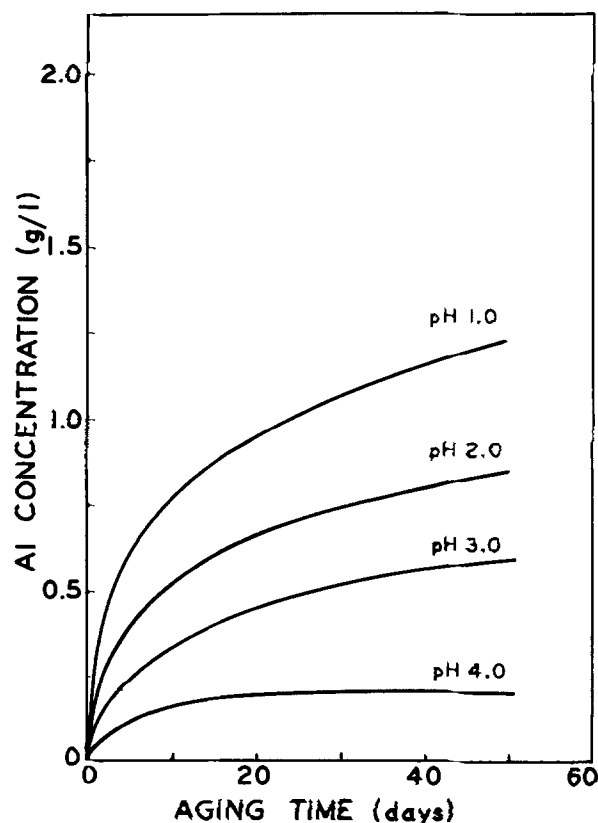


Fig. 3. Concentration of Al in nickel watts- γ - Al_2O_3 (25 g/liter) suspensions of different pH due to the solubility of oxide at room temperature as a function of solution aging.

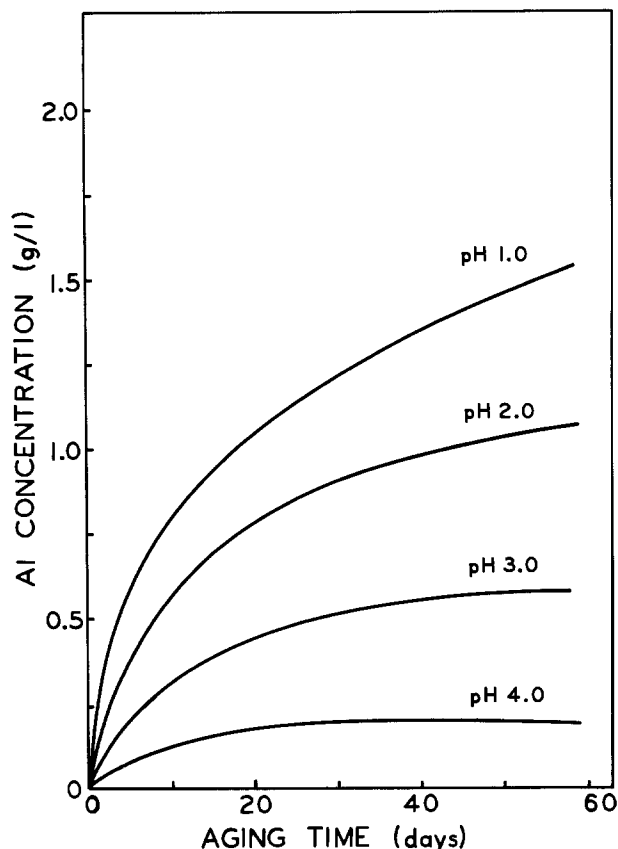


Fig. 4. Concentration of Al in cobalt watts- γ -Al₂O₃ (25 g/liter) suspensions of different pH due to the solubility of oxide at room temperature as a function of solution aging.

From Fig. 2. it is apparent that the rate of dissolution of both γ - and α -oxides is initially high and decreases with aging time especially at pH 1.0 and 2.0. The amount of oxide dissolution is also strongly dependent on the solution pH and is large at pH 1.0. At a high pH value the solubility is low and is possibly limited by the solubility product of aluminum hydroxide. The crystalline nature and the size of the oxide have a definite influence on the dissolution characteristics, in that α -Al₂O₃ is much less soluble at comparable pH values than γ -Al₂O₃. The solubility characteristics of γ -Al₂O₃ in nickel watts and cobalt watts solutions as a function of pH and solution aging (Fig. 3 and 4) are very similar to those observed in dilute H₂SO₄- γ -Al₂O₃ suspensions in that greater solubility at low pH and lower solubility at high pH values were observed.

An increase of solution temperature increases the solubility of the oxides in suspensions. For example, the concentrations of aluminum in NiSO₄- γ -Al₂O₃ suspensions (pH 2.0) at room temperature and at 53°C were found to be, respectively: 0.008 and 0.30 g/liter after 1 hr; 0.013 and 0.36 g/liter after 2 hr; 0.035 and 0.46 g/liter after 6 hr. Since cobalt and nickel plating are usually carried out at higher temperatures (40°-50°C), the concentration of aluminum ions due to the dissolution of γ -oxide in the plating solutions can be expected to be considerably higher over a period of time.

Cobalt watts and nickel watts plating solutions.—In order to investigate the effects of presence of aluminum ions in a watts-type cobalt or nickel plating bath on the properties of the Co or Ni electrodeposits, a series of deposits were obtained under different plating conditions as shown in Table I. It has to be pointed out that only small amounts of Al [max 0.04 weight per cent (w/o)] were found in the deposits. Since Al cannot be cathodically discharged, it has to be incorporated in the deposits as a basic metal hydroxide (18). It has been observed that in nickel plating (19) the cathode film has a pH value as high as 6 or 7 and at

Table I. Effect of variation of aluminum ion concentration in the plating solutions on the inclusion of aluminum with cobalt and nickel deposits

	Al content in deposits	
	Cobalt	Nickel
Concentration of Al ³⁺ ions in plating solutions:		
0.5 g/liter	No Al	
1.0 g/liter	Traces	
1.5-4.5 g/liter	Al (0.002-0.04 w/o)	Al (0.002-0.022 w/o)

* Plating solutions: Cobalt watts solution contains 310 g/liter of CoSO₄ · 7H₂O, 31 g/liter of CoCl₂ · 6H₂O, and 25 g/liter of boric acid; nickel watts plating solution contains 330 g/liter of NiSO₄ · 6H₂O, 45 g/liter of NiCl₂ · 6H₂O, and boric acid 37.5 g/liter. Aluminum ions were introduced in the plating solutions as Al₂(SO₄)₃ · 18H₂O. Plating conditions: pH 1.0-4.0; current density 4ASD; temperature 40°C for Co and 50°C for Ni.

this high pH region aluminum ion can become hydrolyzed to Al(OH)₃ and subsequently included in the deposit. There is no definite trend between the Al inclusion in the deposit and the aluminum ion concentration in the plating solution except deposits from baths containing less than 1.0 g/liter Al ions showed no or only trace inclusion of Al while from baths containing larger amounts of Al ions (1.5, 2.5, 4.5 g/liter) the Al content in the deposits varied up to about 0.04 w/o. No definite trend was observed for Al inclusion in the deposits with respect to variations of the pH of the plating solution.

An examination of microstructures of electrodeposited cobalt and nickel (Fig. 5 and 6) with Al revealed interesting features. It is seen from Fig. 5 that the coarse grained columnar structure of cobalt is modified and a finer grain structure results when Al is included. A similar trend was observed for nickel containing Al (Fig. 6). As a result of the fine grained structure the Knoop hardness values obtained using a 100g load showed an increase from 270 for pure Co to 403 for Co with 0.04 w/o Al while for nickel it varied from 250 to 290 with 0.02 w/o Al. One possible explanation for the finer structure could be that the reaction product at the cathode layer, Al(OH)₃, may be preferentially adsorbed at the active sites (edges, corners, half-crystal position) and thus inhibits normal growth (repeatable step process). The metal atoms are forced to enter the crystal lattice at less active sites on the cathode. Thus formation of new crystallization nuclei is more frequent, the number of nuclei consequently leading to a fine grained structure.

The effects due to the presence of aluminum in cobalt and nickel deposits on their respective strength values are illustrated in Fig. 7 and 8. The yield strength values of both the as-plated and hydrogen-annealed (800°C, 1 hr) samples of cobalt and nickel increased with an increase in aluminum content. For example, an inclusion of about 0.04 w/o of Al in cobalt deposits has increased the yield strength value of the as-plated sample to about 40% over that of pure cobalt and an inclusion of about 0.02 w/o of Al in nickel deposit increased the yield strength value by almost 20% over that of pure nickel. The higher strength of the deposits with aluminum is thus seen associated with finer grained structures (Fig. 5 and 6).

Cobalt watts- γ -Al₂O₃ and nickel watts- γ -Al₂O₃ plating solutions.—To assess the effects of presence of aluminum ions in the plating solutions of cobalt or nickel with oxides on the yield strength values of their respective deposits, a series of deposits were prepared with varying amounts of aluminum sulfate in the bath and the yield strength values of both the as-plated deposits and deposits annealed in hydrogen (800°C, 1 hr) are reported in Table II. It can be seen that the codeposition of oxide with cobalt increases the yield strength values of the as-plated sample from 34.8 to 48.3 kg/mm² while no significant change was observed for nickel deposits with the codeposition of oxide. Annealed Co-Al₂O₃ and Ni-Al₂O₃ deposits, however, re-

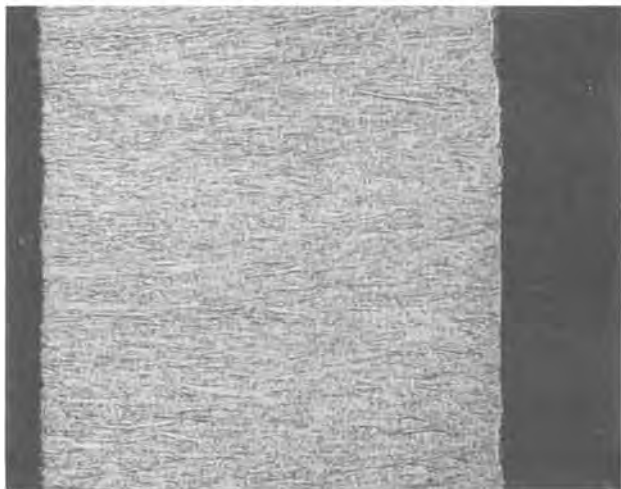


Fig. 5. Microstructures showing the effect Al inclusion in cobalt. Deposits produced at 40°C, 4 ASD. (a, top) Pure Co, (b, center), 0.02 w/o Al inclusion, (c, bottom), 0.04 w/o Al inclusion. 740X magnification.

tained higher strength values over that of pure metals annealed under identical conditions due to dispersion strengthening effects of oxide particles. In fact it is interesting to note that high temperature annealing of the Co-Al₂O₃ deposits increased the yield strength value while a decrease in yield strength value was observed for Ni-Al₂O₃ deposits. The presence of aluminum ions in the plating solution increased the yield strength values of the as-plated Co-Al₂O₃ alloys slightly while somewhat of a decrease in yield strength values was observed for nickel deposits in the presence of aluminum ions in the plating solution.



Fig. 6. Microstructures showing the effect of Al inclusion in nickel. Deposits produced at 50°C, 4 ASD. (a, top) Pure Ni, (b, bottom) 0.02 w/o Al inclusion. 740X magnification.

Analyses of oxide content in these deposits revealed some interesting features. As seen in Table II a general decrease in oxide content was observed for both Co-Al₂O₃ and Ni-Al₂O₃ deposits with increases in aluminum ion concentration in their plating baths. It is well known that the strength of dispersion-hardened alloys increases with oxide content in the deposits. It has been noted earlier by Sadak and Sautter (5) that a decrease of about 33% in oxide content in Co-Al₂O₃ deposits (prepared from a plating bath containing no added aluminum ions) resulted in 10-12% decrease in yield strength. In the present study, the Co-Al₂O₃ alloys obtained from the plating bath containing added aluminum ions have a slightly higher yield strength than those obtained from the plating solution without added aluminum ions. The fact that a slightly higher yield strength was obtained for Co-Al₂O₃ deposits in spite of a decrease in oxide content (up to about 33%) can be attributed only to the presence of aluminum ions in the plating solution. The increase in yield strength of Co-Al₂O₃ deposits due to the presence of aluminum ions in the plating bath is very similar but only smaller than those observed for cobalt deposits prepared from plating baths with added aluminum ions (Fig. 7). Unlike Co-Al₂O₃ deposits, a decrease in yield strength was observed for Ni-Al₂O₃ deposits that were obtained from plating baths containing added aluminum ions (Table II), the oxide content in these deposits decreased up to 37%. The effect of added aluminum ions in the nickel watts-Al₂O₃ bath on the yield strength of the deposits is quite different than those observed for deposits from nickel watts bath

Table II. Yield strength data for deposits from watts-type plating solutions of cobalt and nickel containing gamma Al₂O₃ and aluminum sulfate

Plating solution	Yield strength values (0.2% offset), kg/mm ²					
	Oxide v/o	Cobalt		Oxide v/o	Nickel	
		As plated	Annealed (800°C 1 hr)		As plated	Annealed (800°C 1 hr)
Watts plating solution		34.8	26.7		32.0	9.6
Watts-Al ₂ O ₃	1.8	48.3	50.3	0.8	31.7	25.4
Watts-Al ₂ O ₃ -1.5 g/liter Al ³⁺	1.6	53.2	51.0	0.6	31.2	23.3
Watts-Al ₂ O ₃ -2.5 g/liter Al ³⁺	1.3	51.9	55.3	0.5	28.8	20.7
Watts-Al ₂ O ₃ -4.5 g/liter Al ³⁺	1.2	50.9	51.8	0.5	28.0	22.2

Plating parameters: current density 4 ASD, pH 2.0, temperature 40°C for cobalt and current density 4 ASD, pH 2.0, temperature 50°C for nickel.

Concentration of γ -Al₂O₃ for cobalt bath, 25 g/liter and for nickel bath, 25 g/liter; aluminum ions were introduced in the plating solutions as Al₂(SO₄)₃, 18H₂O. Deposits were annealed in hydrogen atmosphere and the yield strength values are the average of 4-6 specimens.

(Fig. 8) where an increase in yield strength was observed. Apparently, the presence of added aluminum ions to the plating solutions of cobalt and nickel containing Al₂O₃ and no oxide has different effects on the deposits and their respective yield strength values.

Summary

The solubility of aluminum oxide in electrolytes and the effects of the presence of aluminum ions in cobalt and nickel plating solutions on the properties of electrodeposits have been investigated and the results are summarized as follows:

1. Both γ and α aluminum oxide show definite solubility in aqueous electrolytes of low pH, the dissolution being more pronounced for γ -oxide. The oxide dissolution increases with decreasing solution pH and increasing temperature.

2. Trace amounts of Al (up to 0.04 w/o) included with cobalt and nickel refine the structure of cobalt and nickel and increase the yield strength and hardness of the deposits; the effect is more pronounced for cobalt than for nickel deposits.

3. The presence of aluminum ions in the plating bath used for the electroforming of dispersion hardened Co-Al₂O₃ alloys contributes to an increase in the yield strength of the as-plated deposits while a decrease in yield strength is observed for Ni-Al₂O₃ deposits.

Acknowledgment

The authors appreciate the assistance of Mr. Richard Carter in performing the many mechanical tests required.

Manuscript submitted June 9, 1975; revised manuscript received July 28, 1975. This was Paper 139 presented at the Boston, Massachusetts, Meeting of the Society, Oct. 7-11, 1973.

Any discussion of this paper will appear in a Discussion Section to be published in the June 1976 JOURNAL. All discussions for the June 1976 Discussion Section should be submitted by Feb. 1, 1976.

Publication costs of this article were partially assisted by Watervliet Arsenal.

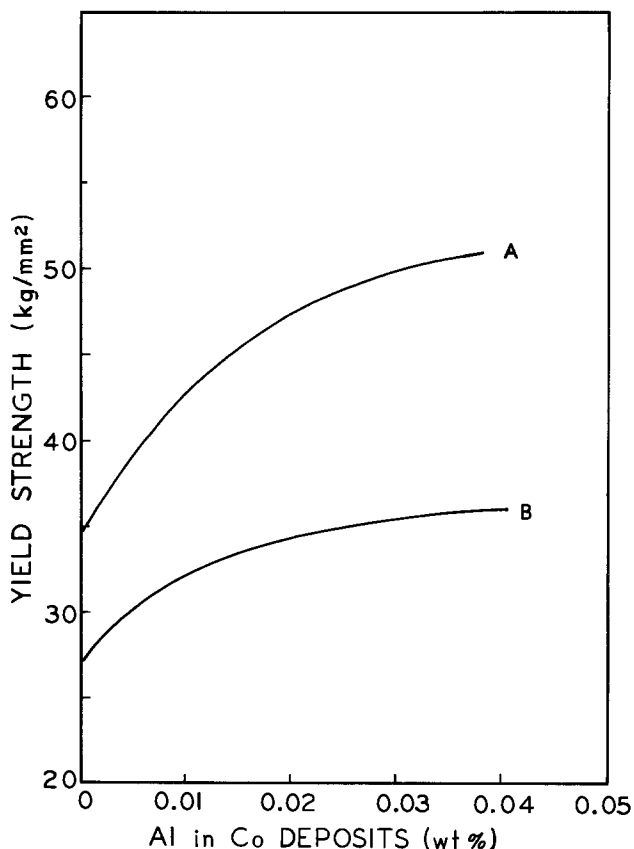


Fig. 7. Variation of yield strength with Al inclusion in cobalt deposits. Curve A, as plated; curve B, hydrogen annealed (800°C, 1 hr).

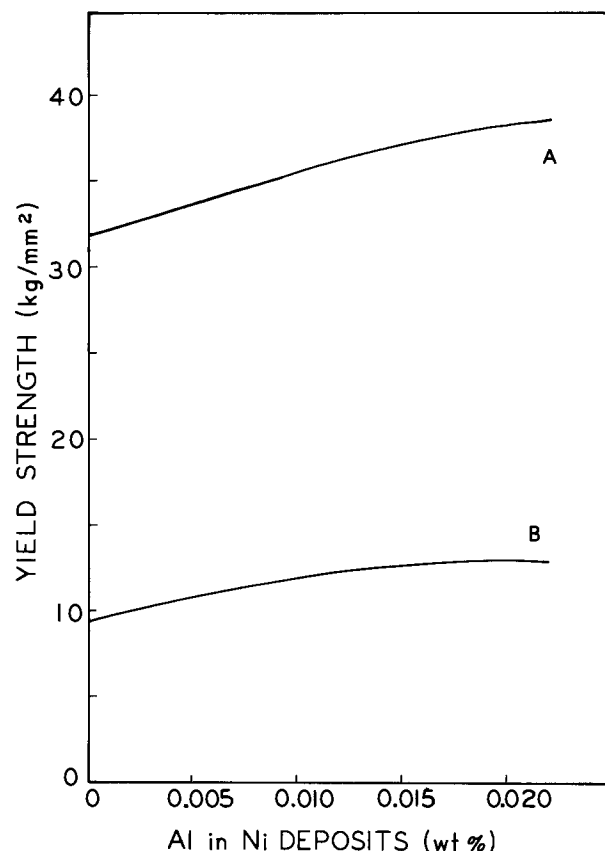


Fig. 8. Variation of yield strength with Al inclusion in nickel deposits. Curve A, as plated; curve B, hydrogen annealed (800°C, 1 hr).

REFERENCES

1. F. K. Sautter, *This Journal*, **110**, 557 (1963).
2. G. R. Lakshminarayanan and F. K. Sautter, *Water-vliet Arsenal Tech Rept.*, WVT-7024 (1970).
3. F. K. Sautter and E. S. Chen, *Oxide Dispersion Strengthening*, *Met. Soc. Conf.*, Vol. 47, p. 495 (1968).
4. E. S. Chen, G. R. Lakshminarayanan, and F. K. Sautter, *Met. Trans.*, **2**, 937 (1971).
5. J. Sadak and F. K. Sautter, *Metals Eng. Quart.*, **14**, 44 (1974).
6. V. P. Greco and W. Baldauf, *Plating*, **35**, 250 (1968).
7. T. W. Tomaszewski, L. C. Tomaszewski, and H. Brown, *ibid.*, **56**, 1234 (1969).
8. F. J. Dunkerley, H. W. Leavenworth, and G. E. Eichelman, *Oxide Dispersion Strengthening*, *Met. Soc. Conf.*, Vol. 47, p. 695 (1968).
9. J. E. Hoffmann and C. L. Mantell, *Trans. TMS-AIME*, **236**, 1015 (1966).
10. M. Viswanath, *Metal Finishing*, **71**, 38 (1973).
11. M. E. Browning and F. J. Dunkerley, *ASME Publ. No. 64-MD-53* (1964).
12. G. A. Malone, *Proceedings of Symposium on Electrodeposited Metals for Selected Applications*, MC1C Report-74-17, p. 49.
13. *Instruction Manual for High Speed Surface Area Analyzer (Model 2200)* Micromeritics Instruments Corp. (1972).
14. *Instruction Manual: Analytical Methods for Atomic Absorption Spectrophotometry*, Perkin-Elmer Corp. (1968).
15. E. B. Sandell, "Colorimetric Determination of Trace Metals," Interscience Inc., New York (1959).
16. S. M. Ahmed and D. Maksimov, *J. Colloid Interface Sci.*, **29**, 97 (1969); S. M. Ahmed and D. Maksimov, *Can. J. Chem.*, **46**, 3841 (1968).
17. I. H. Warren and E. A. Devuyt, *Proceedings of Second International Symposium On Hydrometallurgy*, Metallurgical Society 102nd AIME Annual Meeting (1973), p. 229.
18. P. K. Frolich, *Trans. Am. Electrochem. Soc.*, **49**, 395 (1926).
19. O. O. Schaus, R. J. Gale, and W. H. Garvin, *Plating*, **58**, 801 (1971).

Flow-Through Porous Electrodes

Richard Alkire* and Brian Gracon**

Department of Chemical Engineering, University of Illinois, Urbana, Illinois 61801

ABSTRACT

Experimental limiting current data obtained on two systems of known configuration clarify conditions under which internal mass transfer restrictions control the current distribution and collection efficiency of flow-through porous electrodes. At sufficiently low flow rates, the limiting current is controlled by the rate of reactant supply to the electrode. A theoretical model is developed which includes mass transfer, ohmic, kinetic, and geometric parameters. The model succeeds in predicting limiting current behavior over a wide range of operating conditions. A simple algebraic criterion is suggested for estimating the limiting current and collection effectiveness of flow-through porous electrodes.

Because electrochemical reactions are heterogeneous, porous electrodes have come into widespread usage in order to provide large reaction rates per unit volume. Although the interior surface area of porous electrodes can be exceedingly large, dilemmas nevertheless arise which can restrict the effectiveness of the large interior surface area. For example, limitations may be encountered owing to the ohmic resistance of the electrolyte or to mass transfer limitations on the supply of reactants.

In recent years, the need for improved reactor designs to accomplish high rate electrolysis has led to the development of new reactor configurations as well as methods for scale-up and prediction of performance. Several recent publications discuss promising configurations which provide for enhanced mass transfer rates (1, 2, 3). A few of these configurations have also been recommended for the development of new electro-organic synthesis routes (4, 5). The following investigation directs attention toward one particular electrode configuration, namely, flow-through porous electrodes in which the current flows along the same spatial direction as the flowing electrolyte.

The literature on porous electrode investigations up to mid-1974 has been reviewed quite thoroughly (6). In the recent past, a number of investigators have focused attention on mass transfer limitations which arise within the porous electrodes under certain operating conditions. The extensive publications of Sioda (7) are especially noteworthy since they establish

experimental procedures as well as theoretical methods for data analysis. Additional studies have appeared which account for mass transfer effects in specific electrochemical systems such as electro-organic synthesis reactions (8), metal deposition (9, 10, 11), and dissolution systems (12). These electrochemical studies provide the framework upon which the present investigation rests.

Correlations of mass transfer rates within packed beds have been investigated by traditional chemical engineering methods as noted in Ref. (6). In addition to works cited therein, the studies of Satterfield and Cortez (13), and Mandelbaum and Böhm (14) are also noteworthy since they reported correlations at low flow rates as found in most porous electrode systems. In addition, McMaster and Gilliland (15) have recently examined the influence of porosity variations which may lead to channeling and thereby cause loss of effectiveness.

The purpose of the present investigation is, on the one hand, to investigate experimentally the region of operating conditions where mass transfer restrictions affect behavior and, on the other hand, to develop a general mathematical model for flow-through porous electrodes which is applicable over wider ranges of parameter space than previous theories.

Apparatus

The flow circuit shown in Fig. 1 was used. The anode, located in a side chamber upstream from the porous electrode compartment, was a platinum sheet of approximately 20 cm². Saturated calomel reference electrodes were placed in side chambers on either side

* Electrochemical Society Active Member.

** Electrochemical Society Student Member.

Key words: current distribution, mathematical model, mass transfer, reactor design, electrochemical engineering.

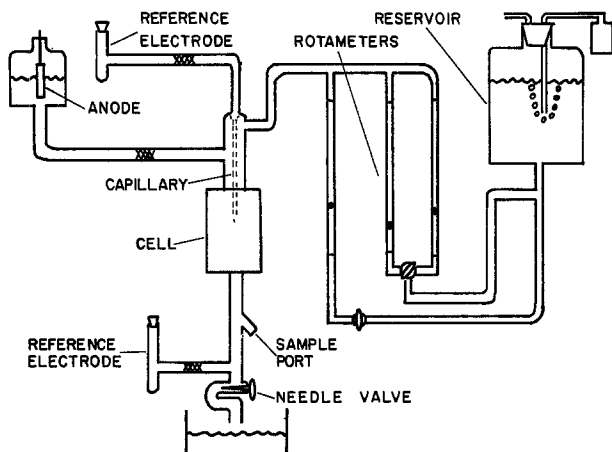


Fig. 1. Flow circuit

of the porous electrode; a glass capillary extended from the upstream SCE compartment to within 1 mm of the upstream face of the porous electrode. Downstream from the porous electrode, samples of electrolyte were withdrawn through plastic tubing to avoid galvanic displacement reactions.

The porous cathode electrode was fabricated from disks of 100-mesh platinum screen (wire diam 0.003 in.) stacked in the electrode holder (Ref. 7) as indicated in Fig. 2. The stack of disks (12 mm diam) was supported around the edge by a piston which pressed the stack against a 26-gauge platinum contact wire on the lip in the cell block. The electrical resistance of the contact was less than 0.05 ohm. The Lucite cell block was connected to the glass flow system through standard taper joints with seamless Teflon sleeves.

In order to assure that the flow within the porous electrode was uniform over the entire cross section, auxiliary experiments were conducted by depositing copper (from acidified sulfate solution) onto the screens. Observation of the deposit distribution indicated that the deposits were uniform over the cross section provided that a porous glass disk was placed downstream from the working electrode.

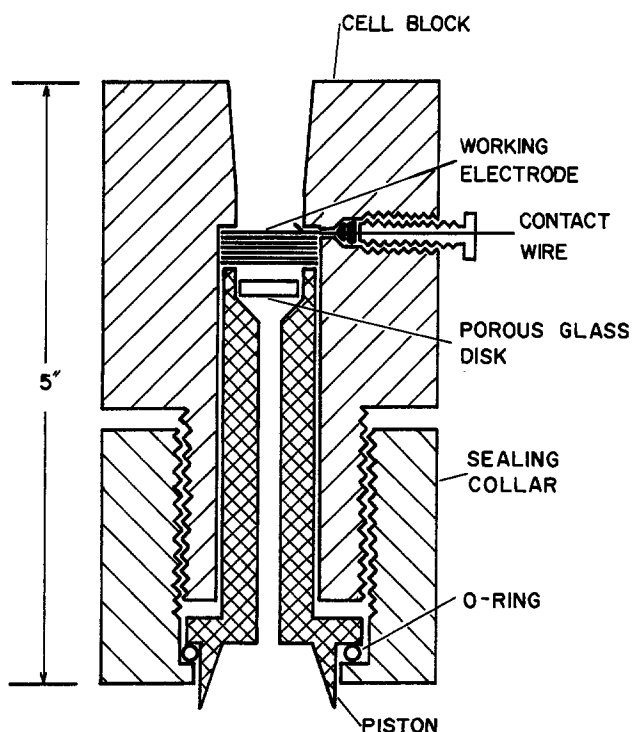


Fig. 2. Diagram of porous electrode cell holder

Current to the porous electrode was supplied by a potentiostatic source (Wenking 68TS3) with use of the upstream reference electrode. Potentials throughout the system were measured with a high impedance multipoint recorder (Leeds and Northrup Speedomax).

Two electrolytic solutions were employed, both of which used deionized, distilled water (conductivity 4×10^{-6} mho/cm). The first solution consisted of 1.0M KCl with equimolar concentrations of potassium ferricyanide and potassium ferrocyanide. Owing to the light sensitivity, nearly all parts of the flow system were shielded from light. The potassium ferricyanide concentration was determined by an iodometric titration method which was found to be accurate to within 1%. The second solution consisted of 0.002M CuSO_4 in 1.5M H_2SO_4 . The copper concentration was determined by colorimetric determination with neocuproine (16).

Procedure

Electrolytic solution was prepared from AR chemicals and deaerated by nitrogen flow for one hour prior to use. The metal disks were punched from screen (Unique Wire Weaving Company), soaked in trichloroethylene, air-dried, soaked in NaOH (25 g/liter), rinsed, soaked in warm concentrated nitric acid, and rinsed. The electrode was assembled under water to eliminate bubbles, placed in the flow circuit, and rinsed with copious amounts of electrolytic solution.

The flow rate was measured both with rotameters and by collecting measured volumes. The needle valve permitted flow rate control to within 2% of the mean value reported.

Steady-state polarization curves were determined by current measurement at various applied potentials. The steady-state current was attained within three residence times. In some cases, but not all, while operating at the limiting current condition, electrolyte samples were withdrawn from both sides of the porous cathode and were subsequently analyzed to determine reactant concentration.

The measured potential difference between the working and upstream reference electrodes was corrected in order to remove the ohmic contribution external to the porous electrode. For this purpose, the distance between the upstream reference capillary tip and the porous electrode face was measured optically. It was found that the potential gradient in the upstream solution, determined by varying the capillary position, corresponded to a value of electrolyte conductivity which agreed to within 5% of that value determined independently in a conductivity cell. The capillary tip was positioned 1 mm from the upstream face of the porous electrode in order to avoid interference with the fluid flow.

The current distribution within the porous electrode was determined from the deposit distribution obtained with the acid copper system. Electrolysis was conducted under limiting current conditions for a measured period of time. Subsequently, the electrode was disassembled. The amount of copper stripping followed by copper-ion measurement using the neocuproine method (16).

Results and Discussion: Experimental

The properties of the electrochemical systems investigated are compiled in Table I. Table II contains the geometric properties of the porous electrodes. The electrode porosity was determined by weighing. The electrode length, determined by measurement through the transparent cell wall, was accurate to within 0.1 mm. The specific surface area given in column four of Table II was estimated by a method which is known to predict values which are somewhat high (27). As will be discussed later, it was found that agreement between experimental data and theoretical predictions could be obtained if the specific surface area was

Table I. Physical properties of systems under study

Property	Ferricyanide system	(Ref)	Copper system	(Ref.)
n , g-eq/g-mol	1		2	
k_s (ohm-cm) ⁻¹	0.108		0.55	
D , cm ² /sec	0.76×10^{-5}	(17)	0.76×10^{-5}	(22)
μ , g/cm sec	9.9×10^{-3}	(18)	1.18×10^{-2}	(23)
ρ , g/cm ³	1.0445	(19)	1.065	(24)
i_0 , A/cm ²	10^{-2}	(20)	1.94×10^{-4}	(25)
d_p , cm	0.018		0.018	
a , cm ²	1.13		1.13	
k , cm/sec	$(6.35 \times 10^{-3})\text{Re}^{1/3}$	(21)	$(7.05 \times 10^{-3})\text{Re}^{1/3}$	(21)

Table II. Electrode properties

Electrode length l , mm	Number of screens	Pors-ity, %	Estimated specific surface area a , cm ⁻¹	Adjusted specific surface area a , cm ⁻¹
0.3	3	64	260	210
0.5	5	64	260	210
1.0	10	64	260	210
2.5	20	80	208	168
4.0	40	64	260	210
7.0	60	72	223	180

reduced by a multiplier of 0.81; the "adjusted value" of the specific surface area is given in the last column in Table II.

Figure 3 illustrates a typical set of polarization curves; all voltages reported are vs. SCE and have been corrected for ohmic drop external to the porous electrode. In subsequent discussion, attention will focus solely on the limiting current plateau region. The dependence of limiting current upon velocity, given in Fig. 3, is shown in Fig. 4 along with similar data obtained at two other reactant concentrations. It is seen that when the limiting current for each sys-

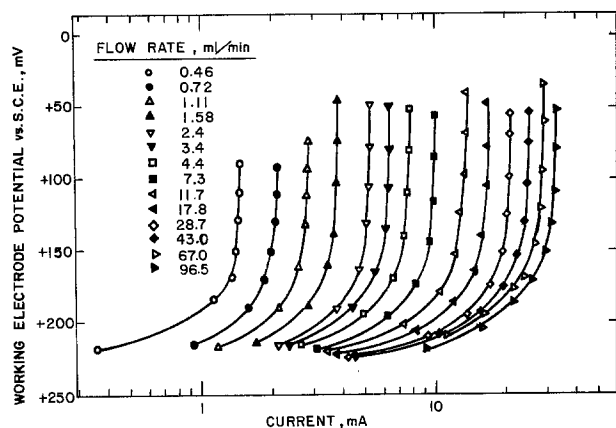


Fig. 3. Polarization curves for 0.002M potassium ferricyanide reduction, $l = 1.0$ mm.

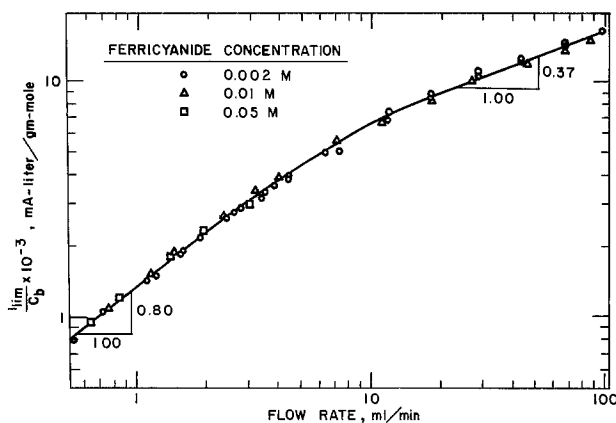


Fig. 4. Dependence of limiting current upon flow rate for three reactant concentrations, $l = 1.0$ mm.

tem is normalized by the corresponding reactant concentration, the data fall on a single curve which assures that mass transport processes control electrode behavior.

The effect of electrode thickness on limiting current is shown for a range of velocities in Fig. 5. At low flow rates, all the data for a given chemical system converge to a single curve which corresponds to the equation

$$i_{lim} = nF c_1^0 v \quad [1]$$

The solid lines in Fig. 5 correspond to Eq. [1] for the two systems studied. At high flow rates, all curves approach similar slopes but the value of limiting current depends upon electrode length. For flow rates between about 40-1200 ml/min, the slope is about one-third; for still higher flow rates, the slope increases to approximately one-half. These data indicate that for low flow rates, the limiting current depends upon the rate of reactant supply in accord with Eq. [1]. At higher flow rates, on the other hand, the limiting current depends upon another type of mass transfer process occurring within the interior of the porous electrode; that is, reactants entering the porous region experience difficulty in reaching the interior surface. As a consequence, the limiting current depends upon reactor length.

The effectiveness of the porous electrode in removing reactant species may be defined as

$$\text{collection effectiveness} \equiv CE = \frac{c_1^0 - c_1^x}{c_1^0} \quad [2]$$

It was determined experimentally that the reactions under investigation proceeded with a current efficiency of 100%. Therefore, by a materials balance, Eq. [2] can also be written as (7)

$$CE = \frac{i_{lim}}{nF c_1^0 v} \quad [3]$$

By direct experimental measurement of c_1^x , the downstream electrolyte concentration, it was found that determination of the collection effectiveness, or limiting degree of conversion, by Eq. [2] agreed to within 1% of that value determined independently by Eq. [3]. Referring again to Fig. 5, it is seen that those data which lie below the solution line, Eq. [1], correspond to conditions where the collection effectiveness is less than unity. Under these conditions, owing to internal mass transfer resistance, there exists a plume of reactants which cannot reach the interior surface and which therefore escape from the reactor.

Figure 6 provides current distribution data from the copper deposition system operated at several solution velocities and electrode lengths. The data are normalized by the total deposit weight so that a uni-

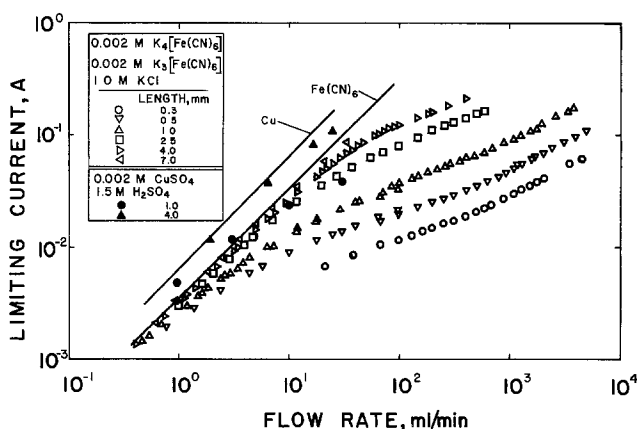


Fig. 5. Dependence of limiting current upon flow rate and electrode length.

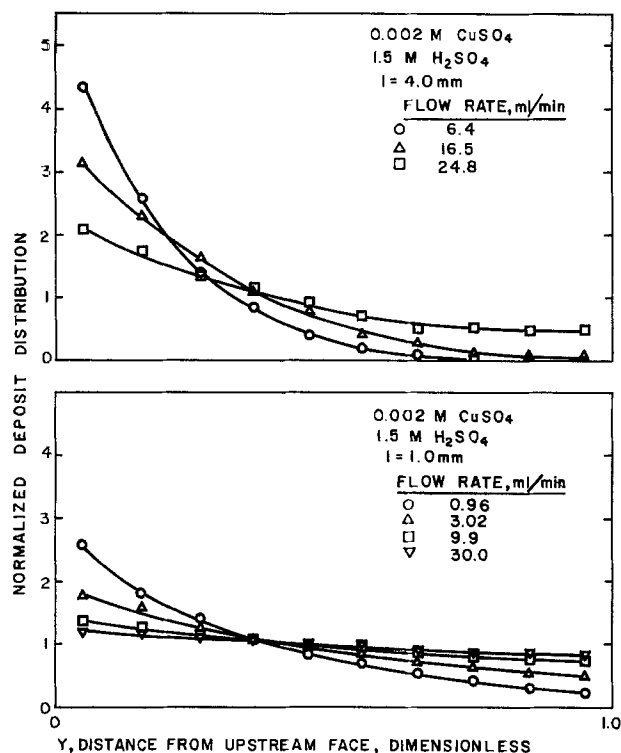


Fig. 6. Dependence of current distribution upon flow rate and electrode length.

form distribution corresponds to an ordinate value of unity. At low flow rates, the limiting current distribution is quite nonuniform and indicates that there is little reaction in the downstream portions of the electrode; these data indicate that the reactant is consumed within the electrode to such extent that there is very little reactant remaining in the electrolyte on the downstream regions. At high flow rates, the limiting current distribution is nearly uniform, indicating that mass transfer from the flowing electrolyte to the solid interior surface controls behavior, and that the mass transfer coefficient is independent of position within the porous electrode.

Theoretical

The foregoing experimental program has provided a firm basis upon which to develop a theoretical model for predicting the behavior of flow-through porous electrode systems. As indicated in the literature survey section, several models have been proposed which are valid over limited ranges of operating conditions. In what follows, a more general model will be developed which is capable of predicting behavior over wide ranges of operating conditions and which includes charge transfer, ohmic resistance, convection, and diffusion (dispersion) in addition to internal mass transfer limitations. Only behavior at the limiting current condition will be investigated below. A more extensive theoretical investigation will be the subject of future papers.

The porous electrode to be modeled is of uniform thickness, l , and is of uniform specific surface area throughout. The counterelectrode is upstream; solution enters the porous electrode at position $y = 0$ and exits at position $y = l$. These conditions correspond to the experimental configuration shown in Fig. 1 and 2.

Since rigorous calculations are cumbersome, several assumptions have been adopted which conform closely to the foregoing experimental systems: (i) electrolysis proceeds in the steady-state without structural changes or insulation effects occurring at the electrode; (ii) only one electrochemical reaction occurs; (iii) conduction within the electrolytic solution obeys Ohm's law, and migration effects are negligible; (iv)

the porous electrode is of uniform potential throughout; (v) convection through the porous electrode takes place by forced plug flow without channeling effects, and there are no diffusion limitations exterior to the porous electrode; (vi) internal mass transfer processes, localized near the solid interior surface of the porous electrode, may be characterized by a mass transfer coefficient which is independent of location; and (vii) the pores of the electrode are sufficiently small that the model may be written in one-dimensional form wherein heterogeneous electrode reactions appear as pseudohomogeneous source terms. Although these assumptions limit the model, most of them may be altered to suit particular applications.

The stoichiometry of the electrode reaction is defined by

$$\sum_i \nu_i M_i z_i = ne^- \quad [4]$$

For the redox system of ferro- and ferricyanide, the reaction rate expression is assumed to be

$$j(y) = i_0 \left\{ \left(\frac{c_1^s(y)}{c_1^0} \right) \exp \left(\frac{\alpha_a n F \phi(y)}{RT} \right) - \left(\frac{c_2^s(y)}{c_2^0} \right) \exp \left(\frac{-\alpha_c n F \phi(y)}{RT} \right) \right\} \quad [5]$$

Owing to mass transfer processes occurring near the interior solid surface, however, the surface concentrations which appear in Eq. [5] may be substantially different from reactant concentration in the "core" of the flowing electrolyte filament. The local concentration difference between surface and "core" are related through the mass transfer coefficient

$$j(y) = \frac{nk_s F}{\nu_i} (c_i - c_i^s) \quad [6]$$

In this work, the mass transfer correlation of Wilson and Geankoplis (21) will be used over the range of low flow rates for which it is valid

$$k_i = \frac{1.09}{\epsilon} \frac{1}{Sc^{2/3}} \left(\frac{\mu}{d_p} \right)^{2/3} L^{1/3} \quad [7]$$

The internal mass transfer process is assumed to be localized near the solid surface; the species balance which incorporates diffusion, convection, and reaction is therefore

$$D_1 \frac{d^2 c_1}{dy^2} - v \frac{dc_1}{dy} = k_1 a [c_1(y) - c_1^s(y)] \quad [8]$$

In the electrolyte phase, the potential field obeys Ohm's law

$$i(y) = -\kappa \frac{d\phi}{dy} \quad [9]$$

The current in the solution, $i(y)$, varies with position owing to electrochemical reaction

$$\frac{di}{dy} = -a j(y) \quad [10]$$

Combination of Eq. [9] and [10] gives

$$\frac{d^2 \phi}{dy^2} = \frac{a}{\kappa} j(y) \quad [11]$$

The model is completed by specification of the boundary conditions.

At $y = 0$

$$\phi = \phi_a \quad [12]$$

$$c_1 = c_1^0$$

At $y = l$

$$\frac{d\phi}{dy} = \frac{dc_1}{dy} = 0 \quad [13]$$

In order to reduce the number of independent parameters, the following dimensionless quantities are defined

$$Y = \frac{y}{l} \quad C_1^s = \frac{c_1^s}{c_r} \quad [14]$$

$$C_1 = \frac{c_1}{c_r} \quad \Phi = \frac{F\phi}{RT}$$

With these groupings, the equations of the model yield the dimensionless system parameters

$$\xi = \frac{i_0 a l^2 n F}{\kappa R T} \quad \gamma_1 = \frac{c_1^0}{c_r} \quad \chi = \frac{i_0 a l^2}{n F c_r D_r} \quad [15]$$

$$\zeta = \frac{v l}{D_r} \quad \Gamma = \frac{k_1 a n^2 F^2 l^2 c_r}{\kappa R T} \quad \pi_1 = \frac{D_i}{D_r}$$

In the discussion section below, attention will turn to a physical interpretation of each of these parameters and the role they play in determining the behavior of the system.

In the foregoing dimensionless notation, the equations which define the model are

$$\Phi'' = \xi \left\{ \frac{C_1^s}{\gamma_1} \exp(\alpha_a n \Phi) - \frac{C_2^s}{\gamma_2} \exp(-\alpha_c n \Phi) \right\}$$

$$\pi_1 C_1'' - \zeta C_1' = \frac{\chi \Gamma}{\xi} (C_1 - C_1^s) \quad [16]$$

$$\Gamma (C_1 - C_1^s) = \nu_1 \xi \left\{ \frac{C_1^s}{\gamma_1} \exp(\alpha_a n \Phi) - \frac{C_2^s}{\gamma_2} \exp(-\alpha_c n \Phi) \right\}$$

Each "prime" superscript denotes differentiation with respect to the dimensionless spatial variable Y . The boundary conditions become

$$\Phi(0) = \Phi_a$$

$$\frac{d\Phi(1)}{dY} = \frac{dC_1(1)}{dY} = 0 \quad [17]$$

$$C_1(0) = \gamma_1$$

Once the potential and concentration distributions are found by solving the model equations, the current distribution within the porous electrode may be found from the dimensionless form of either Eq. [5] or Eq. [6] which are, respectively

$$\beta J = \xi \left\{ \frac{C_1^s}{\gamma_1} \exp(\alpha_a n \Phi) - \frac{C_2^s}{\gamma_2} \exp(-\alpha_c n \Phi) \right\} \quad [18]$$

$$\beta J = \Gamma (C_2^s - C_2) \quad [19]$$

The above equations have been derived for a redox system. The same general approach may be used to develop a model for metal deposition reactions by replacing Eq. [5] with the reaction rate equation

$$j(y) = i_0 \left\{ \exp\left(\frac{\alpha_a n F \phi}{RT}\right) - \frac{c_2^s}{c_2^0} \exp\left(\frac{-\alpha_c n F \phi}{RT}\right) \right\} \quad [20]$$

Models have been developed which use both Eq. [5] and [20] in order to analyze the experimental data reported above.

Method of Solution

The solution of the model equations was carried out on a digital computer with a finite difference numerical procedure. The equations were first linearized about a trial solution and then written in finite difference form. The resulting set of simultaneous tridiagonal matrices was then inverted with use of an IBM 360 computer (28). Solutions of the nonlinear equations were obtained by iteration on the approximate linear solution;

Table III. Dimensionless parameters of systems under study

Parameter	Ferricyanide	Copper
Re	0.0431 V	0.0369 V
Sc	1245	1460
ξ	0.0426 $a l^2$	0.0273 $a l^2$
χ	1.62 $a l^2$	1.323 $a l^2$
Γ	0.222 $a l^2 \text{ Re}^{1/3}$	0.185 $a l^2 \text{ Re}^{1/3}$
ζ	7000 l Re	8220 l Re

convergence was usually achieved within seven iterations.

Comparison of Theory with Experiment

The foregoing theoretical model was tested over the range of limiting current conditions for which experimental data have been reported above. It was found that excellent agreement was obtained by arbitrarily adjusting the specific surface area by a multiplier of 0.81. This adjustment is not large in comparison with the accuracy of the method employed in estimating the original values (27). With this single minor adjustment, the values of dimensionless system parameters which correspond to the experimental systems are given in Table III. Calculations with these values were compared by three different methods with experimental data as follows.

Figure 7 provides the comparison for limiting current vs. flow rate for several reactor lengths. The agreement is excellent over the entire flow range for which the mass transfer correlation is valid ($\text{Re} < 55$). At the highest flow rates investigated, the slope changes from one-third to one-half; the Reynolds number at which this change occurs corresponds to the upper limit of validity of the mass transfer correlation used. At such flow rates, a different mass transfer correlation could be used (29); however, the range of high flow rate and low collection effectiveness is perhaps of scant interest for most industrial applications.

A second method of comparison was made by using Eq. [3] to determine collection effectivenesses as shown in Fig. 8. Direct experimental measurement of collec-

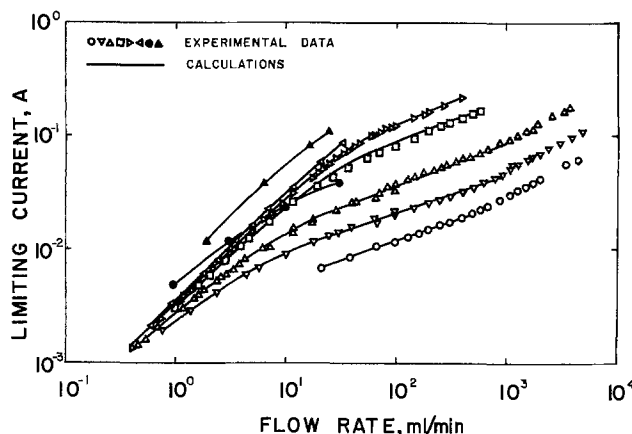


Fig. 7. Comparison of experimental limiting current data (Fig. 5) with theoretical calculations.

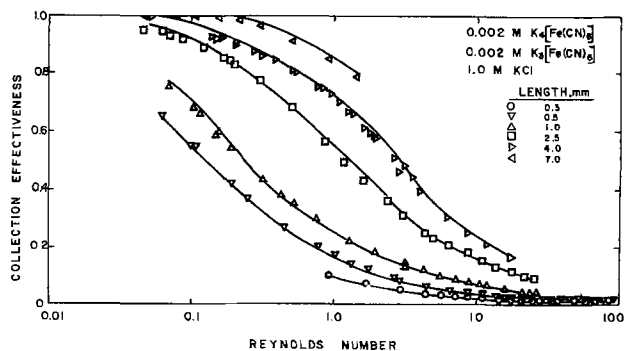


Fig. 8. Comparison of measured collection effectiveness with theoretical calculations.

tion effectiveness, by concentration determinations, was found to agree within 1% of the values calculated from the limiting current with Eq. [3]. These data indicate that the collection effectiveness falls from unity to zero in about three orders of magnitude of flow rate. An approximate method for estimating the maximum flow rate for which all reactants are collected is provided in the discussion section which follows.

Current distributions predicted for the acid copper system are given in Fig. 9; these calculations may be compared with experimental data under the same conditions in Fig. 6. The general trends of the calculated distributions agree with the trends of the experimental data: at low flow rates the upstream portions of the porous electrodes are more reactive, but, at high flow rates the current distribution is more nearly uniform. However, the experimental distributions are more non-uniform than those predicted on a theoretical basis. Since operation at the limiting current is purely mass transport controlled, the factors which may contribute to the discrepancy would include only those associated with the mass transport phenomena, namely, diffusion, convection, and internal mass transfer. Although the diffusion process may be influenced by dispersion of fluid packets within the bed, or nonplug type flow, the effect of such a process would be opposite to that observed; that is, the experimental distributions would be more uniform than theoretically expected. The accuracy with which the concentrations and velocities are measured is sufficient to assure that the discrepancy is not due to errors in estimating the system parameters. It is suggested that the mass transfer coefficient is not constant, as assumed, but varies with position within the bed.

Errors regarding the form of the mass transfer coefficient are critical only insofar as the internal mass transfer process dominates electrode behavior. For example, predictions of behavior below the limiting current would not be expected to depend upon the mass transfer coefficient. Because the experimental data at high flow rates ($Re \gg Re_{cr}$) are in excellent agreement with calculations, it is clear that the value of the average mass transfer coefficient is correctly modeled. The disparity between Fig. 6 and 9 indicates the need

for additional studies on local mass transfer processes within packed beds operated at low flow rates.

Discussion: Theoretical Model

In this study, calculations with the theoretical model have been reported only under limiting current conditions. The model is also capable of predicting behavior below the limiting current insofar as its parameters contain information about charge-transfer, ohmic resistance, diffusion, electrolyte flow, internal mass transfer resistance, and geometric properties. The agreement obtained in this study between experiment and theory, however, justifies further discussion of several qualitative aspects of the model. In the following paragraphs, a physical interpretation of the dimensionless parameters is provided. In addition, several examples are given to illustrate how the model can be employed to define regions of parameter space within which previously published limiting cases can be used to predict system behavior.

The parameter ξ contains the ratio i_0/κ and thereby indicates the relative importance of electrolyte resistance and charge-transfer resistance. In the absence of other phenomena, a value of ξ greater than unity corresponds to conditions under which the current distribution within the porous electrode is nonuniform owing to low solution conductivity. The parameter χ contains the ratio i_0/D and thus indicates the relative importance of diffusion *vs.* charge-transfer resistance; in the absence of other effects, a value of χ greater than unity indicates that the current distribution will be nonuniform owing to slow diffusive transport of reactants to the interior regions. The parameter ζ indicates the relative importance of electrolyte convection (by plug flow) with respect to diffusional transport; if ζ is sufficiently large, limitations on reactant supply depend upon convection processes, not diffusion. The parameter Γ is a dimensionless mass transfer coefficient and describes the ease with which reactants are transported to the solid surface once they have entered the porous region; a small value of Γ indicates the situation wherein reactants experience great difficulty in moving from the "core" of the flowing electrolyte filaments to the solid surface where reaction occurs.

Each of these dimensionless parameters indicates the relative importance of two effects. In general, however, more than two effects may be important in controlling electrode behavior. However, the relative magnitude of the parameters with respect to each other can be employed to estimate which particular effects are the most important for any particular electrode design. The following paragraphs provide four examples. It is worthwhile to note that the following discussion does not require solutions of the differential equations which define the model; that is, algebraic knowledge of the parameters alone is sufficient to provide a great deal of intuitive insight into the behavior of complex electrochemical systems.

(i) *Role of electrolyte conductivity.*—Concentration variations within the porous electrode are negligible under conditions of rapid diffusion, high flow rates, and large mass transfer coefficients ($\chi \ll 1$, $\zeta \gg 1$, and $\Gamma \gg 1$). Under these conditions, the parameter ξ controls the uniformity of reaction within the porous electrode. When ξ is large, the conductivity is sufficiently low that the potential distribution, and thereby the current distribution, is nonuniform (30). Many of these special cases have been applied to battery systems (6); the same approach also applies to resistive electrodes (31).

(ii) *Role of diffusion.*—Reactants may experience difficulty in penetrating into interior regions of an electrode when convection rates are low ($\zeta < 1$), even though the potential distribution would otherwise be uniform ($\xi < 1$). For steady-state behavior under these conditions, the parameter χ controls the current distribution. Large values of χ indicate that diffusion from

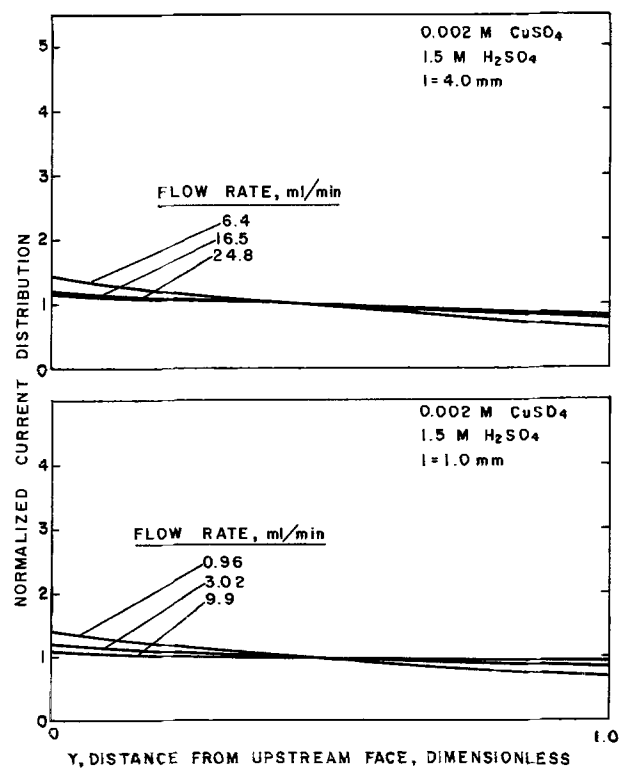


Fig. 9. Theoretical current distribution calculations to be compared with experimental data in Fig. 6.

the electrode face is insufficient to supply interior regions, thus leading to a nonuniform current distribution. Many specific cases have been applied to battery systems (30-34) as reviewed in Ref. (6).

The relative importance of solution conductivity *vs.* diffusional limitations is given by the ratio ξ/χ .

(iii) *Role of convection.*—By flowing electrolyte through the porous electrode, high rates of reaction can be sustained provided that ohmic resistances do not limit behavior. Calculations conducted with the above model (35) have indicated that for $\xi < 10^{-1}$, pure diffusion controls and the situation under (ii) above obtains; for $\xi > 10^4$, the convection is sufficiently rapid that the electrolyte is of uniform concentration so that comments under (i) above pertain. For intermediate values $10^{-1} < \xi < 10^4$, more complex behavior is obtained (6, 30, 36, 37).

All convection models published to date assume plug flow within the pores. In the absence of internal mass transfer limitations, the maximum current which can be obtained with a flow-through porous electrode is given by Eq. [1] which, in dimensionless notation is

$$\beta_L = \frac{\gamma\xi}{\chi} \xi \quad [21]$$

Equation [21] indicates that, under these operating conditions, the limiting current is linearly proportional to the convective velocity and is independent of the electrode length. In addition, the collection effectiveness is unity at the limiting current for all flow rates.

(iv) *Role of mass transfer.*—It may not be possible to attain the maximum current predicted by Eq. [21] if mass transfer processes within the pores are sluggish (small Γ) (6-10), in which case the limiting current is given by

$$i_{lim} = nF\Gamma akc_1^0 \quad [22]$$

or

$$\beta_L = \gamma\Gamma \quad [23]$$

By combining Eq. [21] and [23], the collection effectiveness under mass transfer control is

$$CE = \frac{\Gamma\chi}{\xi\xi} \quad [24]$$

Equations [21] and [23] correspond to the low flow and high flow asymptotes shown in Fig. 7. By combination of Eq. [7], [21], and [23], the Reynolds number at which the asymptotes intersect is found to be

$$Re_{cr} = \left[\frac{\Gamma^* \chi d_p}{Sc \xi l} \right]^{3/2} \quad [25]$$

For $Re \ll Re_{cr}$ the discussion given in (iii) above applies. For $Re \gg Re_{cr}$, the discussion given in (iv) can be used to predict behavior. For Reynolds numbers in the range $0.10 Re_{cr} < Re < 10 Re_{cr}$, the algebraic relations given above are not suitable for accurate predictions.

Conclusions

The experimental data reported above have led to clarification of different regimes of mass transport phenomena which control the limiting current density of flow-through porous electrodes. At low flow rates, the limiting current is controlled by the rate of reactant supply to the upstream face of the electrode and the current distribution is rather nonuniform within the electrode. At high flow rates, the limiting current is controlled by the rate at which reactants are transported to the reactive surface once they have entered the electrode pores, and the current distribution is uniform provided that secondary reactions do not occur. Whereas data on limiting current and collection effectiveness are in excellent agreement with theoretical predictions, the measured current distributions at low flow rates are more nonuniform than predicted by the theoretical model. In order to investigate the dis-

crepancy, experiments with the use of sectioned porous electrodes are suggested for more convenient current distribution data acquisition.

A qualitative discussion of the theoretical model illustrates the important point that, without solving any mathematical equations whatsoever, a great deal of intuitive insight can be gained from knowledge of the dimensionless parameters characteristic of the system. With the dimensionless parameters, one can determine what physical phenomena are most likely to control electrode behavior: charge-transfer, diffusion, convection, mass transfer, or conduction phenomena. The dimensionless parameters provide scale-up criteria by which data from different experimental systems may be correlated. In addition, knowledge of the relative magnitude of the parameters aids in determining under what conditions simpler models of limiting cases can be employed instead of the foregoing general model.

The model described herein is based on assumptions which naturally affect its applicability. However, in order to apply the model to other systems, a significant number of the assumptions may be removed or substantially altered without major complication of the calculational procedure. In particular, the model may be expanded to investigation of multiple electrode reactions, heterogeneous plus homogeneous scavenger reaction systems, and channeling effects owing to porosity variations.

The investigation reported here has served both to unify diverse previous efforts at predicting porous electrode behavior and also to establish a firm basis for further investigations of more complex electrochemical systems.

Acknowledgments

The assistance of Mr. Ronald M. Gould in conducting some of the computer calculations is gratefully acknowledged. Portions of this study constituted partial fulfillment of requirements for a Master of Science degree in the Department of Chemical Engineering, University of Illinois, Urbana-Champaign. The junior author (Brian Gracon) received support as a NSF Fellow. Additional costs were borne by a du Pont Grant-in-Aid, and NSF Grants GK-36623 and ENG 72-04168.

Manuscript submitted May 16, 1975; revised manuscript received Aug. 14, 1975.

Any discussion of this paper will appear in a Discussion Section to be published in the June 1976 JOURNAL. All discussions for the June 1976 Discussion Section should be submitted by Feb. 1, 1976.

Publication costs of this article were partially assisted by the University of Illinois.

LIST OF SYMBOLS

English characters:

a	specific surface area, cm^2/cm^3 void
c_i	concentration of species i , $\text{g-mole}/\text{cm}^3$
C_i	concentration of species i , c_i/c_1^0 , dimensionless
c_r	reference concentration, $\text{g-mole}/\text{cm}^3$
d_p	diameter of packed bed particle, cm
D_i	diffusion coefficient of species i , cm^2/sec
D_r	reference diffusion coefficient, cm^2/sec
F	Faraday's constant, 96,500 coulomb/g-equiv
i_{lim}	limiting current density, A/cm^2
I_{lim}	limiting current, A
i_o	exchange current density, A/cm^2
j	local reaction rate, A/cm^2
J	local reaction rate, jal/i_o , dimensionless
k	mass transfer coefficient, cm/sec
l	electrode length in flow direction, cm
L	mass flow rate, $\text{g}/\text{cm}^2\text{-sec}$
M_i	chemical symbol of species i
n	number of electrons taking part in reaction
R	gas constant
Re	Reynolds number, vd_p/ν
Sc	Schmidt number, ν/D_i
T	temperature, $^\circ\text{K}$
v	electrolyte velocity within porous electrode, cm/sec

V	electrolyte flow rate, ml/min
y	spatial variable, cm
Y	spatial variable, y/l, dimensionless
z _i	valence of species i

Greek characters:

α_a, α_c	transfer coefficient
β	current at $Y = 0$, $i_0 \ln F / \kappa RT$
γ	upstream concentration of species i, c_i^0 / c_r , dimensionless
Γ	mass transfer coefficient, $\kappa n^2 F^2 c_r a l^2 / \kappa RT$, dimensionless
Γ^*	value of Γ when $Re = 1.0$
ϵ	void fraction of packed bed electrode
ζ	flow rate, $v l / D$, dimensionless
κ	electrolyte conductivity, (ohm-cm) ⁻¹
ν	electrolyte kinematic viscosity, cm ² /sec
ν_i	stoichiometric coefficient of species i
ξ	reaction rate constant, $i_0 a l^2 n F / \kappa RT$, dimensionless
π_i	diffusion coefficient, D_i / D_r , dimensionless
ϕ	potential in electrolyte, V
Φ	potential, $F\phi / R T$, dimensionless
χ	diffusion coefficient, $i_0 a l^2 / n F C_r D_r$, dimensionless

Superscripts:

o	denotes upstream position
x	denotes downstream position
s	denotes surface position

REFERENCES

- R. B. MacMullin, *This Journal*, **120**, 135C (1973).
- C. W. Tobias, *ibid.*, **120**, 65C (1973).
- R. W. Houghton and A. T. Kuhn, *J. Appl. Electrochem.*, **4**, 173 (1974).
- M. Fleischmann and D. Pletcher, *Chem. Britain*, **11**, 50 (1975).
- J. L. Fitzjohn, *Chem. Eng. Progr.*, **71**, 85 (1975).
- J. Newman and W. Tiedemann, *Am. Inst. Chem. J.*, **21**, 25 (1975).
- R. E. Sioda, *Electrochim. Acta*, **13**, 375, 1559 (1968); *ibid.*, **15**, 783 (1970); *ibid.*, **16**, 1569 (1971); *ibid.*, **17**, 1171, 1939 (1972); *ibid.*, **19**, 57 (1974); *J. Electroanal. Chem. Interfacial Electrochem.*, **34**, 399, 411 (1972); *Anal. Chem.*, **46**, 964 (1974).
- A. S. Gendron, H. P. Meissner, and M. C. Diebert, Paper 12b presented at Am. Inst. Chem. Engrs. 64th Annual Meeting, San Francisco, California, 1971.
- D. N. Bennion and J. Newman, *J. Appl. Electrochem.*, **2**, 113 (1972).
- A. K. P. Chu, M. Fleischmann, and G. J. Hills, *ibid.*, **4**, 323 (1974).
- A. T. Kuhn and R. W. Houghton, *ibid.*, **4**, 69 (1974).
- A. K. P. Chu and G. J. Hills, *ibid.*, **4**, 331 (1974).
- C. N. Satterfield and D. H. Cortez, *Ind. Eng. Chem., Fundamentals*, **9**, 613 (1970).
- J. A. Mandelbaum and U. Böhm, *Chem. Eng. Sci.*, **28**, 569 (1973).
- L. P. McMaster and E. R. Gilliland, *ibid.*, **27**, 2265 (1972).
- A. R. Gahler, *Anal. Chem.*, **26**, 577 (1954).
- M. Eisenberg, C. W. Tobias, and C. R. Wilke, *This Journal*, **103**, 413 (1956).
- "Handbook of Chemistry," N. A. Lange, Editor, p. 1665, McGraw-Hill Book Co., New York, (1961).
- "Handbook of Chemistry and Physics," R. C. Weast, Editor, 50th ed., p. 193, Chemical Rubber Company, Cleveland, Ohio (1969).
- K. J. Vetter, "Electrochemical Kinetics," p. 494, Academic Press, New York (1967).
- E. J. Wilson and C. J. Geankoplis, *Ind. Eng. Chem., Fundamentals*, **5**, 9 (1966).
- H. K. Richardson and F. D. Taylor, *Trans. Am. Electrochem. Soc.*, **20**, 179 (1911).
- W. G. Eversole, H. M. Kindsvater, and J. D. Peterson, *J. Phys. Chem.*, **46**, 370 (1942).
- G. W. Vinal and D. N. Craig, *Bur. Std. J. Res.*, **10**, 781 (1933).
- F. H. Rhodes and C. B. Barbour, *Ind. Eng. Chem.*, **15**, 850 (1923).
- J. S. Newman, "Electrochemical Systems," p. 177, Prentice-Hall, Englewood Cliffs, N. J. (1973).
- J. L. Bomben, M.S. Thesis, University of California, Berkeley, Calif. (1963).
- J. Newman, *Ind. Eng. Chem., Fundamentals*, **7**, 514 (1968).
- R. B. Bird, W. E. Stewart, and E. N. Lightfoot, "Transport Phenomena," John Wiley & Sons, Inc., New York (1960).
- R. de Levie, *Advan. Electrochem. Electrochem. Eng.*, **6**, 329 (1967).
- R. Alkire, *This Journal*, **118**, 1935 (1971); R. Alkire and A. Tvarusko, *ibid.*, **119**, 340 (1972); R. Alkire, *ibid.*, **120**, 900 (1973); R. Alkire and R. Varjian, *ibid.*, **121**, 622 (1974).
- J. S. Newman and C. W. Tobias, *ibid.*, **109**, 1183 (1962).
- I. G. Gurevich and V. S. Bagotskii, *Electrochim. Acta*, **9**, 1151 (1964).
- L. G. Austin and H. Lerner, *Electrochim. Acta*, **9**, 1469 (1964); L. G. Austin, *Trans. Faraday Soc.*, **60**, 1319 (1964).
- A. A. Mirarefi, Ph.D. Thesis, University of Illinois, Urbana-Champaign, Illinois (In progress).
- L. G. Austin, P. Palasi, and R. R. Klimpel, "Fuel Cell Systems," Advanced Chemistry Series, No. 47, p. 35, American Chemical Society, Washington, D.C. (1965).
- R. Alkire and R. Plichta, *This Journal*, **120**, 1060 (1973).

The Gibbs-Helmholtz Equation and the EMF of Galvanic Cells

I. Inapplicability to Liquid-Liquid Junction Potentials

Abner Brenner*

N-Q Electrochemical Research Corporation, Reston, Virginia 22070

ABSTRACT

Measurements were made of the temperature coefficient of the emf of a type of concentration cell in which the emf was generated solely by liquid-liquid junctions. The data fit the Henderson equation very well but not the Gibbs-Helmholtz equation. The discrepancy between the values of ΔH , computed from the Gibbs-Helmholtz equation, and the values measured calorimetrically is shown to be calculable from ionic mobilities. In addition, data are presented showing that the sum of the thermoelectric powers of the three junctions (including a liquid-liquid junction) is equal to the isothermal temperature coefficient of the emf of the cell.

This is the first of three papers dealing with the precision of the Gibbs-Helmholtz equation when applied to the emf of galvanic cells.

This paper deals with the measurement of the isothermal temperature coefficient of liquid-liquid junction potentials. To my knowledge this is the first time that such measurements have been reported and, therefore, the data should be of interest for that reason alone. (Incidentally, the data reported in the literature for the temperature coefficients of liquid-liquid junctions are actually thermoelectric powers.) A matter of even greater interest is that of Gibbs-Helmholtz equation did not fit the data.

In the second paper, several sets of data dealing with the emf of various types of galvanic cells, with and without liquid-liquid junctions, were taken from the literature and examined with respect to the Gibbs-Helmholtz equation. I found that the discrepancy of the Gibbs-Helmholtz equation was in many instances greater than the expected experimental error.

In the third paper the cause of the discrepancy between the value of ΔH obtained via the Gibbs-Helmholtz equation and the value obtained calorimetrically was investigated for various types of cells.

My interest in investigating the precision of the Gibbs-Helmholtz equation came about indirectly. We had been measuring by thermal means the reversible heat effects at liquid-liquid junctions (1), during the passage of direct current, with the rather naive idea of thereby obtaining a knowledge of the liquid junction potential (which idea, however, did not materialize). In addition, we measured the thermoelectric power, dE'/dT , of the junctions. According to an accepted thermodynamic relation, the value of $j \cdot T \cdot dE'/dT$ (where j is 23,050 cal/V) should equal the calorimetrically determined heat Q_{rev} , but we found a large discrepancy. This suggested to me that the Gibbs-Helmholtz equation might not apply to liquid-liquid junctions. After a different kind of measurement (to be described herein) had shown this indeed to be the case, I became interested in studying the precision of the Gibbs-Helmholtz equation when applied to galvanic cells in general.

In my study of the literature of the Gibbs-Helmholtz equation, I found that the equation had been accepted as precise by the early electrochemists on the basis of scanty, imprecise measurements, mostly made before 1900. In no textbook or even in the treatise of Helmholtz (2) himself did I find any limitation to the appli-

cation of the equation other than the customary statement that certain variables of the system must be held constant. I believed that a study of the precision of the equation, when applied to more recent data, would be useful in the application of the equation.

Background

In the early development of the thermodynamics of galvanic cells, the emf of the cell was considered to be determined entirely by the enthalpy of the chemical reaction. This was known as Thomsen's rule and, indeed, it held rather well for some of the simple cells, such as the Daniel cell. Subsequently, between 1860 and 1880 various investigators showed experimentally that the emf of a cell was sometimes greater and sometimes less than that calculated from the enthalpy change of the reaction, as measured in a calorimeter.

Nearly all textbooks on electrochemistry make a point of sharply exposing the fallacy of Thomsen's rule. The texts, however, are unjust in being so critical of Thomsen, because the great Helmholtz, himself, originally also subscribed to Thomsen's rule, until the researches mentioned above led him to change his view. Helmholtz, thus, became aware that the entropy change of the reaction was also involved in determining the emf of the cell and in 1882 published a paper (2) dealing with the relation, which was discovered at about the same time by Gibbs (3), now known as the Gibbs-Helmholtz equation.

The Gibbs-Helmholtz equation is a combined statement of the first and second laws of thermodynamics. It is derived from the equation

$$\Delta F = \Delta H - T \cdot \Delta S \quad [1]$$

and when applied to a galvanic cell has the form

$$E = \frac{-\Delta H}{nj} + T \cdot dE/dT \quad [2]$$

dE/dT being the isothermal temperature coefficient.

A galvanic cell which is operated reversibly at constant temperature evolves or absorbs heat from the surroundings. This reversible heat Q_{rev} is given by the expression

$$Q_{rev} = T \cdot \Delta S = nj \cdot T \cdot dE/dT \quad [3]$$

in calories per mole of reaction. If the cell absorbs heat, which represents an increase of entropy ΔS (in this case the cell tends to become colder on adiabatic operation), this absorbed heat is given out in the form of electrical energy. Consequently, the cell delivers more energy than corresponds to the enthalpy change. The reverse is true if the cell evolves heat.

* Electrochemical Society Active Member.

Key words: Gibbs-Helmholtz equation, concentration cells, liquid junction potentials, Henderson's equation, temperature coefficient of emf of liquid junctions, thermoelectric power of liquid junctions, heat of dilution of liquid junctions.

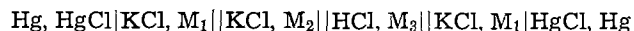
In checking the validity of Eq. [2], it is advantageous to use cells in which the ΔH term is small compared to the $T \cdot dE/dT$ term, which latter is the one of interest. It is expedient, therefore, to use concentration cells, since their enthalpy change is relatively small being derived from heats of dilution compared to that of cells involving a chemical reaction.

Experimental Measurements of Liquid-Liquid Junction Potentials and Their Temperature Coefficients

Procedure for Measuring Isothermal Temperature Coefficients

The measurement of the isothermal temperature coefficient of the emf of a liquid junction potential requires that the emf itself be capable of measurement and at two different temperatures. However, except for a certain special situation—in which a concentration cell with transference can be set up in two different ways: (i) with electrodes reversible with respect to the anion and, (ii) with electrodes reversible with respect to the cation—the liquid junction potential cannot be measured because in a cell it is always accompanied by the two emf's arising from the two electrode-electrolyte interfaces of the cell.

To eliminate the uncertainty occasioned by the electrode-electrolyte interface, a novel type of concentration cell was used containing three liquid-liquid junctions and two equal and opposite electrode-electrolyte systems. The emf's of the latter cancelled each other and, consequently, the emf of the cell came entirely from the liquid-liquid junctions. A typical cell is the following



Concentration cells in which the emf was produced only by the liquid-liquid junctions were first used by Müller (4) about 100 years ago. Nernst (5) also used them, except that his cells had four liquid-liquid junctions, instead of three.

A schematic diagram of the concentration cell which I used for measuring the temperature coefficient of the emf of liquid-liquid junctions is shown in Fig. 1. These cells will hereafter be referred to as the "tri-junction" cells. The tri-junction cell consisted of two identical reference electrodes A and A' which were calomel or mercury-mercurous sulfate electrodes. The same electrolyte was used in A, A', B, and B'. The other two electrolytes were C and D. The three junc-

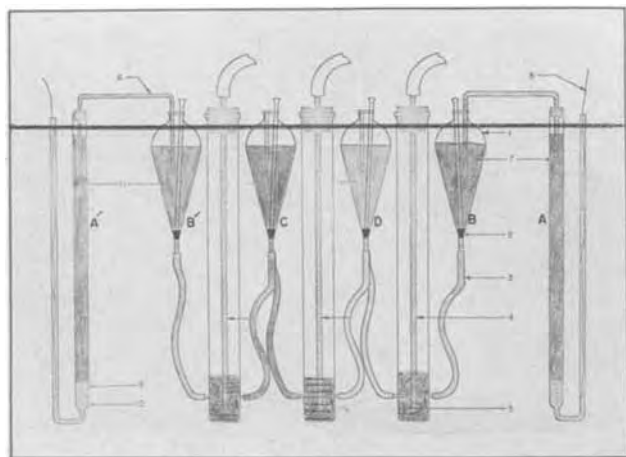


Fig. 1. Apparatus for measuring the isothermal temperature coefficient of liquid junction potentials. Entire apparatus at uniform temperature T_1 and then at T_2 in separate experiments. 1. separatory funnel; 2. rubber plug acting as valve; 3. flexible tubing; 4. glass tube for withdrawing waste liquid at conclusion of experiment by means of a water aspirator; 5. mixed liquids; 6. bridge (agar gel); 7. potassium chloride solution; 8. wire lead to potentiometer; 9. mercurous salt; 10. mercury; 11. potassium chloride solution, same as 7.

tions were formed in the long tubes by the pairs of electrolytes flowing together from B' and C, C and D, and D and B. The method of forming the flowing junctions is discussed in a subsequent paragraph. The entire cell was maintained at a uniform temperature. Consequently, the emf's produced by the reference electrodes A and A' annulled each other since they were equal and opposite. The emf of the cell was produced entirely by the aforementioned three liquid-liquid junctions. Furthermore, dilute solutions were used so that the heats of dilution of the liquids would be small.

The temperature coefficient of the emf of the three liquid junctions, collectively, was obtained by measuring the emf of the cell at temperature intervals of 10°C , mostly in the range between 15° and 55°C , although a few measurements were made at 0°C . If the individual liquid-liquid junction potentials followed the relation of Eq. [2], then the sum of the emf's of the three junctions (which was the quantity actually measured) should also follow the relation.

Since the temperature coefficients of these cells were small, a high precision was required in measuring the emf of the cells. Therefore, the emf had to be both constant and reproducible. The production of constant and reproducible liquid junction potentials is a familiar problem in electrochemistry. Initially, I tried a method devised by Lakhani (6) in which the junction of two electrolytes was formed by the mutual impingement of jets (about 1 mm in diameter) of each electrolyte. This method did not result in adequate constancy of the liquid junction potential, as the fluctuations amounted to tenths of a millivolt. However, when the discharged electrolytes in the mixing chamber (see Fig. 1) rose to a height sufficient to cover the impinging jets, the emf became constant and reproducible to a few hundredths of a millivolt.

The entire cell shown in Fig. 1 was immersed in a thermostat, constant to about 0.1° , to a depth such that the electrolytes were below the level (indicated by a line in Fig. 1) of liquid in the thermostat. Deep vessels insured that the electrolyte in the jets remained at the same temperature as the bulk of electrolyte in the tap funnels. Oil was used in the thermostat, because the conductivity of water resulted in parasitic voltages being picked up by the electronic galvanometer.

In performing an experiment, the closures (consisting of a rubber stopper at the end of a glass rod) were removed from the throats of the tap funnels, thus allowing the electrolyte to flow and form jets in the mixing chambers. The rate of flow of solution was about 25 ml/min. The emf was not sensitive to the rate of flow. As soon as the jets became covered with electrolyte, emf measurements of the cell were made. Measurements could be made for about two minutes before the supply of electrolyte in the tap funnels was exhausted. Voltages were measured on a microvolt potentiometer with an electronic voltmeter, sensitive to $1 \mu\text{V}$, serving as null instrument. At the conclusion of the experiment, the electrolyte which had collected in the mixing chambers was removed by a water aspirator.

To prevent the liquid in the reference electrodes A and A' from being drawn into the tap funnels B and B' as the solution in the latter was lowered, the electrolyte bridges contained an agar-agar gel. In an actual experiment only two flowing junctions were used instead of three, as three such junctions were difficult to manage and required too much space in the thermostat. Therefore, instead of a flowing junction, the connection between the two electrolytes B' and C was made by a bridge containing an agar-agar gel. Since the two electrolytes B' and C were different concentrations of the same electrolyte (either potassium chloride or magnesium sulfate), the liquid junction potentials were smaller than those of the other junctions; furthermore, the agar-agar bridge, by independent experiments, was found to afford adequate con-

stancy and reproducibility. In these experiments the reproducibility of measurements on cells which had a small emf of 10 mV or less was about 0.02 mV. The reproducibility of measurement on the cells with an emf of about 25 mV was about 0.1 mV. Since measurements were made at temperatures 10° apart, this made the precision of measurement of the temperature coefficient of the emf about 1×10^{-5} V/°C. This precision is equivalent to a possible error of about 3 mV in the calculated emf or to an error of about 70 cal/mole for univalent salts.

Results of Measurements of the Temperature Coefficients of Liquid Junction Potentials

The results of the measurements on the tri-junction cells are given in Table I. To make a check of the validity of the Gibbs-Helmholtz equation, it is customary to compare the value of the enthalpy ΔH_{emf} calculated via the Gibbs-Helmholtz equation

$$-\Delta H_{emf} = nj \left(E - T \cdot \frac{dE}{dT} \right) \quad [4]$$

with the calorimetrically measured value ΔH_{cal} . In these experiments with the tri-junction cells the enthalpy change is a heat of dilution, and at present there is no method in the literature for calculating the heat of dilution at a liquid-liquid junction. Therefore, it is necessary to digress at this point for the purpose of developing a formula for calculating the heat of dilution.

Calculation of the heat of dilution at a liquid-liquid junction.—The derivation of a relation for calculating the heat of dilution between two solutions S and S' is patterned after the derivation of the Henderson equation (7) for liquid-liquid junction potentials. Note that the Henderson equation involves only the Nernst equation and does not involve the energy derivable from the heat of dilution.

As is the case with the Henderson derivation, the energy derived from the heat of dilution depends on the net transfer of solute across the boundary of the two solutions under the influence of the current, and this in turn depends on the transference number of the ions. Between two solutions S and S' there must be a region in which the composition of the solution varies from that of S to that of S' and, consequently, the transference number of all of the ions must change continuously throughout this region. In the special case that all the cations and anions had the same transference number, the movement of solute to the left would be exactly cancelled by movement to the right; consequently, there would be no net contribution of energy. For example, in a potassium chloride solution the K ion and the Cl ion have about the same mobility and the liquid junction potential between two solutions of differing concentration is small.

The basic relation for the heat of dilution at a liquid-liquid junction is

$$\Delta H_{cal} = \sum [t_i \cdot d(\Delta H) + t'_i \cdot d(\Delta H')] \quad [5]$$

where t_i and t'_i are the varying transference numbers of the ions of MX and M'X', respectively; ΔH is the partial molal heat of dilution resulting from the transfer of one mole of MX from solution S into solution S'; and $\Delta H'$ is the partial molal heat of dilution resulting from the transfer of one mole of M'X' from solution S' into solution S. The summation is for the four ions M, X, M', and X', having the mobilities U, V, U', and V', respectively.

All of the intermediate compositions of solutions between S and S' can be considered to be obtainable by making up a unit volume of solution consisting of a fraction (x) of S' with the fraction $1 - x$ of solution S. Solution S has the concentration C of MX, and solution S' has the concentration C' of M'X'.

The method of the derivation is to express the transport number of each ion as a function of the mixing fraction x . For a given x , the generalizer concentration of the salt MX is represented by C_1 where

$$C_1 = C(1 - x) \quad [6]$$

This is also the concentration of the ions M^+ and X^- . Similarly, for the salt M'X', the generalized concentration C'_1 is

$$C'_1 = C'x \quad [7]$$

The current-carrying ability of each ion is equal to the product of mobility and concentration, and the total current-carrying capacity of the solution at x is

$$CU(1 - x) + CV(1 - x) + C'U'x + C'V'x \quad [8]$$

or

$$C(U + V) + x[C'(U' + V') - C(U + V)] \quad [9]$$

or

$$a + bx \quad [10]$$

where

$$a = C(U + V); \quad b = C'(U' + V') - C(U + V); \quad a + b = C'(U' + V') \quad [11]$$

The transference numbers of the ions U, V, U', and V' at x are, respectively

$$\frac{CU(1 - x)}{a + bx}; \quad \frac{CV(1 - x)}{a + bx}; \quad \frac{C'U'x}{a + bx}; \quad \text{and} \quad \frac{C'V'x}{a + bx} \quad [12]$$

Consider now that the heat of dilution, ΔH_m , due only to the ion M^+ :

$$\Delta H_m = \Delta H \int_{x=0}^{x=1} \frac{CU(1 - x)dx}{a + bx} = UC \cdot \Delta H \left[\int_{x=0}^{x=1} \frac{dx}{a + bx} - \int_{x=0}^{x=1} \frac{x \cdot dx}{a + bx} \right] \quad [13]$$

Table I. Emf and temperature coefficients of emf for tri-junction concentration cells

Cell No.	Structure of the cells					$\frac{dE}{dT} \times 10^5$	emf mV	$T \cdot \frac{dE}{dT}$ mV	$-\Delta H_{emf}$ cal	
	J_a	J_b	J_c^{**}							
1	Hg,HgCl	KCl 0.30N	KCl 0.03N	HCl 0.20N	KCl 0.30N	Hg,HgCl	-0.3	27.4	-0.9	652
2	Hg,Hg ₂ SO ₄	MgSO ₄ 0.30N	MgSO ₄ 0.03N	H ₂ SO ₄ 0.20N	MgSO ₄ 0.30N	Hg,Hg ₂ SO ₄	-5.2	28.0	-15.6	2009
3	Hg,Hg ₂ SO ₄	MgSO ₄ 0.30N	MgSO ₄ 0.03N	LiCl 0.30N	MgSO ₄ 0.30N	Hg,Hg ₂ SO ₄	0.4	10.0	1.2	406
4	Hg,Hg ₂ SO ₄	MgSO ₄ 0.30N	MgSO ₄ 0.03N	Li ₂ SO ₄ 0.30N	MgSO ₄ 0.30N	Hg,Hg ₂ SO ₄	3.6	5.3	10.8	-245

* Arrow gives the direction of the conventional flow of current through the cell when the electrodes are shorted.

** J_a , J_b , and J_c designate the three liquid-liquid junctions.

† $-\Delta H_{emf}$ designates the enthalpy obtained via the Gibbs-Helmholtz equation (see Eq. [4]). The cell emf's are for 30°.

Integration of Eq. [13] and substituting in the limits gives

$$\Delta H_m = \frac{C \cdot U \cdot \Delta H}{b^2} \left[(a+b) \cdot \ln \frac{a}{a+b} + b \right] \quad [14]$$

The heat of dilution due to the ion X having the mobility V would be similar to Eq. [14] with V substituted for U. The net heat of dilution for MX would be the difference due to the two ions M and X

$$\Delta H_{mx} = \frac{C \cdot (U - V) \cdot \Delta H}{b^2} \left[(a+b) \cdot \ln \frac{a}{a+b} + b \right] \quad [15]$$

The net heat of dilution, $\Delta H_{m,x}$, for the transfer of a mole of salt M'X' from solution S' to S is similarly computed

$$\Delta H_{m,x} = C'(U' - V') \cdot \Delta H' \int_{x=0}^{x=1} \frac{x \cdot dx}{a+bx} \quad [16]$$

Integration of Eq. [16] and substituting in the limits gives

$$\Delta H_{m,x} = \frac{C'(U' - V') \cdot \Delta H'}{b^2} \left[a \cdot \ln \frac{a}{a+b} + b \right] \quad [17]$$

For conciseness in writing, let

$$\alpha = C(U + V) \cdot \Delta H \quad [18]$$

$$\beta = C'(U' + V') \Delta H' \quad [19]$$

$$\delta = \ln \frac{a}{a+b} \quad [20]$$

The net heat of dilution of the four ions is the difference of Eq. [15] and [17]

$$\Delta H_{mx} - \Delta H_{m,x} = \frac{\alpha - \beta}{b^2} [b + a \cdot \delta] + \frac{\alpha \cdot \delta}{b} \quad [21]$$

Ion mobilities are the important quantities which are required for making the calculations both of the heats of dilution, as just described, and of liquid junction potentials (by means of the Henderson equation) as described in the following section. However, it is not necessary to know the true mobility of an ion; it is sufficient to know what MacInnes (8) calls the "mobility of an ion constituent" given by the relation

$$U_i = t_i \cdot \Lambda_i / F \quad [22]$$

where Λ_i is the equivalent conductivity of the compound at the concentration in question. Furthermore, since Eq. [21] is homogenous with respect to ion mobilities, it is not necessary to deal with F in Eq. [22], and the quantity actually substituted for the mobility of the ion constituent in Eq. [21] is

$$U_i = t_i \cdot \Lambda_i \quad [23]$$

The values of the equivalent conductivities and transference numbers required for the calculation of the heats of dilution and for the calculation of liquid junction potentials (in the next section by means of the Henderson equation) were obtained from the Landolt-Börnstein tables (9).

In calculating the heats of dilution for the liquid junctions, it was necessary to know the net partial molal heat of solution ΔH involved in transferring a mole of compound MX from solution S into solution S', which contains compound M'X'; and similarly, one must know $\Delta H'$ for the transfer of a mole of M'X' from solution S' into S, which latter contains MX.

Since data on the partial molal heats of dilution of compounds in solutions containing other salts are not available, some approximations had to be made. First of all, in the dilute solutions used in these experiments, the difference between two partial molal heats of dilution does not differ much from the difference between two integral heats of solution for which much data are available. Also, another approximation had to be made with regard to the range of concentration of the dilution, inasmuch as the compound MX was transferred from solution S (where its concentration was C) into solution S' in which its concentration was zero, although the concentration of M'X' was C'. It was assumed that the heat effect was the same as if MX had been transferred from a solution of concentration C into a solution of concentration C' (the same as the concentration of M'X').

The heats of dilution (10) used in the calculations of the data in Table II and the ranges of concentration are as follows

HCl	0.20-0.01N	170 cal
KCl	0.30-0.01N	4 cal
H ₂ SO ₄	0.20-0.01N	2160 cal
MgSO ₄	0.30-0.03N	372 cal
Li ₂ SO ₄	0.30-0.03N	285 cal
LiCl	0.30-0.03N	103 cal

Presentation of the data.—Table I gives the data for the four tri-junction cells. The quantity of most interest in the table is the enthalpy ΔH_{emf} calculated via the Gibbs-Helmholtz equation (Eq. [4]). These values (in the last column of the table) are to be compared with the calorimetric values given in Table II.

In Table II are given the heats of dilution which were calculated for each of the three junctions, J_a, J_b, and J_c. The net heat of dilution for the cell (ΔH_{cal}) is given in column five. Although the heat of dilution at most of the junctions is appreciable, the net heat of dilution for a cell is smaller than might be expected, because the heat of dilution at one of the junctions opposes the heat effects at the other two. In column six of Table II the values of ΔH_{emf} (from the last column of Table I) are reproduced for comparison with ΔH_{cal} in the preceding column five. In column seven the difference between the two values of the enthalpy are given. This difference will be referred to as the "discrepancy" of

Table II. Heat of dilution in tri-junction cells (derived from calorimetric data) compared with ΔH_{emf} obtained via the Gibbs-Helmholtz equation. Also, comparison of the Gibbs-Helmholtz discrepancy in ΔH with the discrepancy calculated via the Henderson equation.

Cell No.	Heat of dilution, ΔH_{cal} *				$-\Delta H_{emf}$ ** (cal)	Discrepancy (experimental) $-\Delta H_{emf} + \Delta H_{cal}$ (cal)	Discrepancy (calculated) (cal)
	J _a	J _b	J _c	Summation J _a + J _b + J _c			
1	<1	103	73	30	652	622	800
2	101	1231	993	339	2009	1670	1535
3	101	35	57	123	406	283	323
4	101	126	133	108	-254	-353	-124

* Calculated from calorimetric data. See Eq. [21].

** Derived from Gibbs-Helmholtz equation. See Eq. [4].

† Discrepancy calculated via the Henderson equation. See Eq. [31].

the Gibbs-Helmholtz equation and has the form

$$\text{Discrepancy} = -\Delta H_{\text{emf}} + \Delta H_{\text{cal}} \quad [24]$$

It is apparent that the discrepancies given in column seven of Table II are large, much too large to be attributed to experimental errors or to uncertainties in the approximations used in the calculation of the values of ΔH_{cal} .

Calculation of the Gibbs-Helmholtz discrepancy from ionic mobilities.—To add weight to the view that the Gibbs-Helmholtz discrepancy is *bona fide* and not a result of experimental error, I shall now show that the discrepancy can be calculated with a fair degree of precision from simple electrochemical data obtained from the literature (9).

The first step in the demonstration is to show that the experimental data closely follows the Henderson equation (7), which is

$$E_L = \frac{RT}{F} \cdot \frac{C(U - V) - (U' - V')C'}{C(Uw_c + Vw_a) - C'(U'w_c' + V'w_a')} \cdot \ln \frac{C(Uw_c + Vw_a)}{C'(U'w_c' + V'w_a')} \quad [25]$$

where E_L is the liquid junction potential, w_c and w_a are the valences of the cation and anion in one salt, w_c' and w_a' are the valences of the ions of the other salt, and the other symbols have the same meanings as in Eq. [8] and those following.

The calculated emf's and their temperature coefficients for the three junctions of each of the four cells are given in Table III. It is seen that the calculated emf for a cell, given in column D, agrees well with the experimental emf given in column G. Also, the calculated temperature coefficients given in column K agree reasonably well with the experimental values in column L.

A refinement may now be introduced. Since the Henderson equation does not include the energy derived from the heat of dilution, it is reasonable to add this energy (see column five of Table II) in the form of its voltage equivalent, as given in column E of Table III, to the Henderson liquid junction potentials in column D of Table III. This gives the more nearly correct calculated values of emf listed in column F, which are the sum of the emf's in columns D and E. On an average, the calculated emf's in column F are about 2.5 mV higher than the experimental values in column G, which is a discrepancy within experimental error.

The second step in the demonstration is to set up an equation for the emf of the tri-junction cells which is experimentally valid. This is done simply by adding to the usual equation for the emf of a cell the Henderson equation, which will be represented by RTZ

$$E = -\Delta H_{\text{cal}} + T \cdot \int \frac{\Delta C_p}{T} dT + RTZ \quad [26]$$

In this discussion we do not know the value of the heat capacity term, but in view of the reasonable agreement between the experimental and calculated values of emf it would appear that the contribution to the emf might be a few millivolts.

The third step in the demonstration is to derive an expression for the Gibbs-Helmholtz discrepancy, as follows. Equation [26] is differentiated and a substitution made, as in the derivation of the Gibbs-Helmholtz equation, to yield the following

$$E = -\Delta H_{\text{cal}} + T \cdot \frac{dE}{dT} - RT^2 \cdot \frac{dZ}{dT} \quad [27]$$

The Gibbs-Helmholtz equation is

$$E = -\Delta H_{\text{emf}} + T \cdot \frac{dE}{dT} \quad [28]$$

The Gibbs-Helmholtz discrepancy is obtained by subtracting one equation from the other and rearranging terms

$$\text{discrepancy} = -\Delta H_{\text{emf}} + \Delta H_{\text{cal}} = -RT^2 \cdot \frac{dZ}{dT} \quad [29]$$

Since Z is the part of the Henderson equation that contains the ionic mobilities, it is seen that the discrepancy is due to the variation of the ionic mobilities with temperature.

The expression $RT^2 \cdot dZ/dT$ can be simplified by utilizing the Henderson equation for the liquid junction potential, E_L , in the abbreviated form

$$E_L = RTZ \quad [30]$$

On differentiating Eq. [30], one obtains

$$RT^2 \cdot \frac{dZ}{dT} = T \cdot \frac{dE_L}{dT} - E_L \quad [31]$$

where E_L is the emf calculated from the Henderson equation and given in column D of Table III, and dE_L/dT is the temperature coefficient, based on the Henderson equation for two different temperatures, and given in column K of Table III.

The last column of Table II gives the values of the Gibbs-Helmholtz discrepancy calculated according to Eq. [31]. These values agree reasonably well with the experimental values of the discrepancy given in the next to the last column of Table II.

Discussion of the Gibbs-Helmholtz discrepancy.—Scarpa (11) was the first to suggest that the Gibbs-Helmholtz equation is not accurate when applied to concentration cells. He did no experimental work but

Table III. Comparison of experimentally determined emf's and temperature coefficients of emf's of tri-junction concentration cells at 30° with values calculated from Henderson's equation for 25°C. (See Table I for composition of cells.)

Cell No.	Emf of cell by calculation				ΔH_{cal}^* mj mV	Cell emf		Temperature coefficients, $\times 10^5$				
	J_a mV	J_b mV	J_c mV	Summation $J_a + J_b + J_c$ mV		Calc** mV	Exp mV	J_a^\dagger mV/°C	J_b^\dagger mV/°C	J_c^\dagger mV/°C	$J_a + J_b + J_c^\dagger$ mV/°C	Exp mV/°C
1	1.0	53.7	24.8	29.9	1	31	27.4	+0.6	-9.0	-7.0	-1.6	-0.3
2	7.0	39.5	22.2	24.3	7	31	28.0	+3.0	-8.6	-3.0	-2.6	-5.2
3	7.0	21.4	6.4	7.9	3	11	10.0	+3.0	+5.7	+2.4	+0.3	+0.4
4	7.0	19.9	6.6	6.3	2	8	5.3	+3.0	+10.0	+4.0	+3.0	+3.6
Column	A	B	C	D	E	F	G	H	I	J	K	L

Arrows give the direction of the spontaneous flow of conventional current across the junction that is determined by the phenomena at the junction itself.

The + and - signs in columns H through L indicate, respectively, that the voltage increases or decreases with elevation in temperature.

* ΔH_{cal} is from column 5 of Table II. (Summation: $J_a + J_b + J_c$).

** Sum of columns D and E.

† Calculated by means of Henderson's equation.

based his belief on the following theoretical considerations. If the solutions in a concentration cell were so dilute that there was no entropy change on operation, then the Gibbs-Helmholtz equation simplifies to

$$E = KT \tag{32}$$

where K is a constant. This result, however, is inconsistent with the Nernst equation for the emf of concentration cells because the Nernst equation involves the product of T and a transport number, and the latter is not a constant but varies with temperature.

The fact that the Gibbs-Helmholtz discrepancy can be very simply calculated, as shown in the last column of Table II, in my opinion, leaves little doubt that the equation is not exact when applied to liquid junction potentials. The examples in this paper are not unique, as in the second paper of this series, a similar calculation is made for a more conventional type of concentration cell with transport.

Since the Gibbs-Helmholtz equation is not exact, this means that the equation from which it was derived

$$E = -\frac{\Delta H}{nF} + T \cdot \Delta S \tag{33}$$

is not exact. More specifically, the source of error is in the term $T \cdot \Delta S$ which does not adequately describe the reversible heat generated in the operation of a galvanic cell. Or stating the matter in a different way, there does not exist in nature a quantity ΔS with the mathematical properties that thermodynamicists have associated with it.

The Nernst Equation and the Thermoelectric Power of Liquid-Liquid Junctions

Since in the past the thermoelectric power of a liquid-liquid junction has been confused with the isothermal temperature coefficient, I have considered it worthwhile to extend this paper a little, both to resolve this confusion and to include some of our measurements of thermoelectric power.

Nernst (5) in 1889 had shown a remarkable analytical insight, not only in satisfactorily explaining the complex phenomenon of liquid junction potentials, but also in deriving a formula for calculating them. Nernst's equation was improved by Henderson (7).

It is both ironic and paradoxical that Nernst, himself, was not successful in validating his equation with respect to the temperature coefficient of the emf of liquid-liquid junction potentials, although he made a try at it. The reason for the failure was that his student, Duane (12), measured the thermoelectric power of the junctions instead of the isothermal temperature coefficient of the emf of the junction. But perhaps he should be forgiven for this error, since there is no way to measure the isothermal coefficient of a single junc-

tion. Needless to say, the agreement of the experimental results of Duane with the Nernst equation was very poor and a fair proportion of the lengthy publication was used in an effort to explain the cause of the discrepancy.

The difference between the measurement of an isothermal temperature coefficient of emf for a cell and the measurement of a thermoelectric power can be seen by comparing Fig. 1 with Fig. 2 which shows an idealized apparatus for measuring the thermoelectric power of a liquid-liquid junction. The two similar reference electrodes A and A' were at the same temperature T_1 , hence their emf's annulled each other and did not enter in the emf of the concentration cell. The electrolyte in B and B' was the same as that in A and A' . The electrolytes C and C' were the same. Two similar

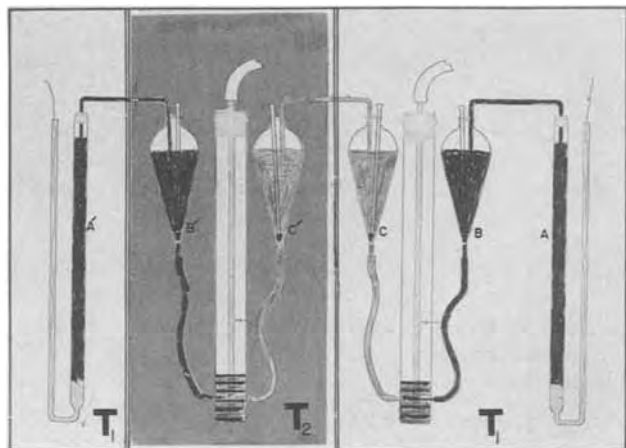


Fig. 2. Apparatus for measuring the thermoelectric power (false temperature coefficient) of liquid junction potentials.

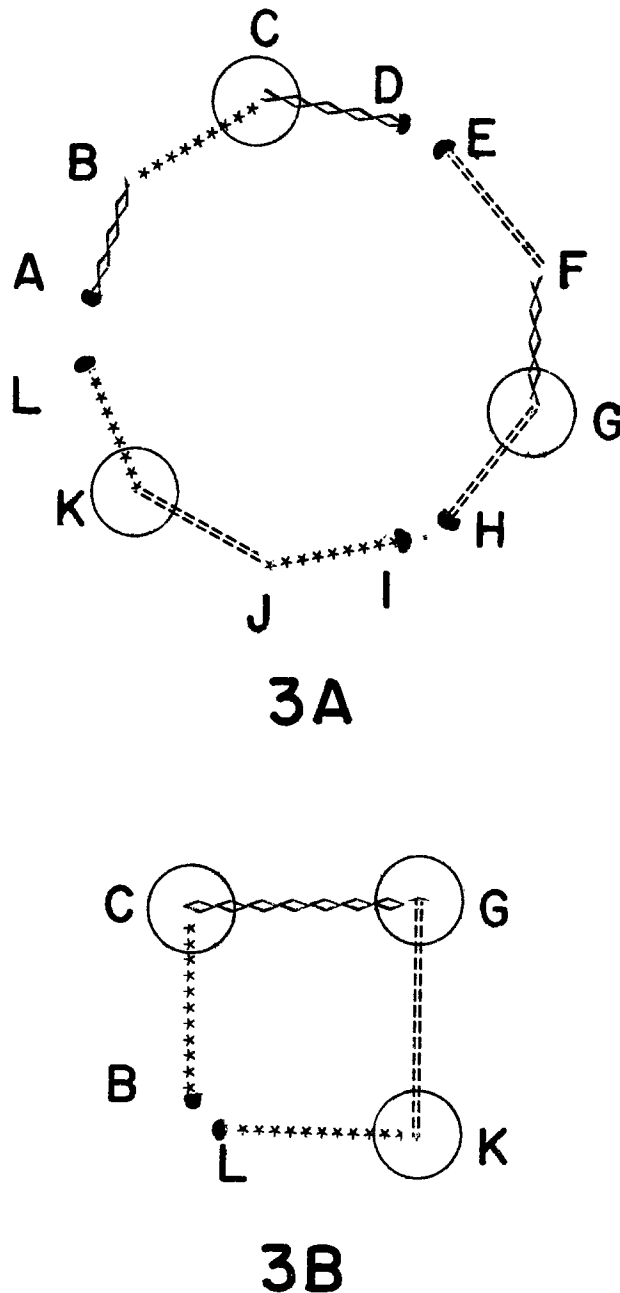
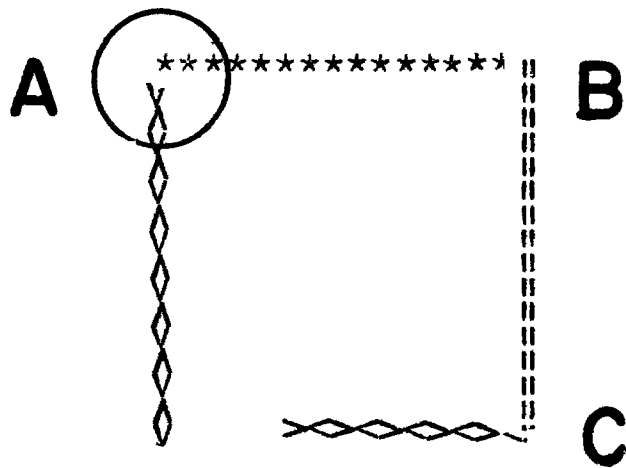
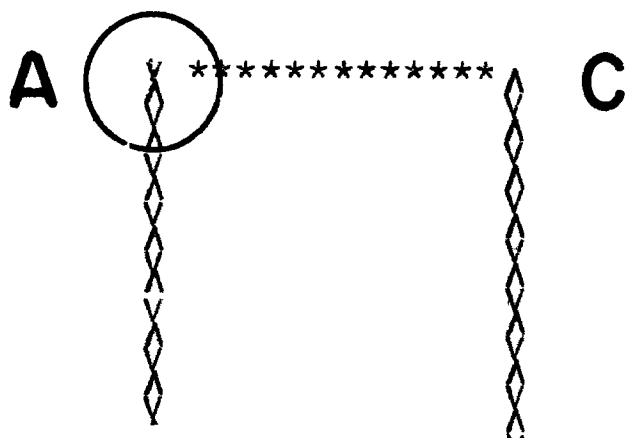


Fig. 3. Demonstration that three different thermocouples formed from three different materials, taken two at a time, when connected into a complete circuit with one set of junctions at T_1 and the other set at T_2 do not generate an emf. KL , AB , and BC represent the three different materials. The area encompassed by the circles represents temperature T_2 and the rest of the material outside the circle represents T_1 . The three thermocouples are AD , EH , and IL in 3A. The circuit in A is equivalent to the circuit in 3B in which the junctions C , G , and K are all at the same temperature.



4A



4B

Fig. 4. Demonstration that a circuit (4A) composed of three materials connected to yield three junctions, A, B, and C, with only one junction at temperature T_2 , is equivalent to a simple thermocouple (4B) with two junctions, A and C.

liquid-liquid junctions were formed between electrolytes B and C at temperature T_1 and between electrolytes B' and C' at temperature T_2 . The emf of the cell was due to the difference in temperature between the two junctions B'C' and BC. The cell constituted a thermocouple and the laws of thermocouples are applicable to it. The setup used by Nernst and his students was similar to the arrangement in Fig. 2, except that no means were provided for flowing junctions. It may be noted that the thermoelectric power of the junction could be determined with a cell having only one liquid-liquid junction by operating it at two different temperatures, for if a reversible electrode were put into C or C', the system then could be considered as two identical cells, A' - C' and C'A. The sum of the voltages of the two cells divided by the temperature

difference is the same as the thermoelectric power of the liquid-liquid junction.

To complete this discussion of temperature coefficients, I shall show that there is a simple relation between the isothermal temperature coefficient of the emf of a cell and the thermoelectric power of a junction. Brenner (13) has suggested that the thermoelectric power of a junction of a reversible electrode in an electrolyte is the sum of two terms, one representing the thermocouple effect and related to the Peltier coefficient Π by the equation

$$\frac{\Pi}{T} = \frac{dE_1}{dT} \quad [34]$$

the other representing the entropy change associated with the change of state

$$\Delta S = \frac{dE}{dT} \quad [35]$$

It is a law of thermocouples that in a complete circuit at constant temperature the sum of the thermoelectric powers due to the Peltier coefficient must vanish. Hence, in the summation of the thermoelectric powers of all of the junctions in a cell, that portion which is related to the Peltier coefficient vanishes for a complete cell, and the remainder of the sum is equal to the isothermal temperature coefficient of the emf of the cell

$$\sum \frac{dE'}{dT} = \frac{dE}{dT} \quad [36]$$

isothermal for the cell.

The summation is for every junction in the cell and dE'/dT is the thermoelectric power of a junction.

Since I have not seen Eq. [36] in the literature, in Table IV, I have given some data to demonstrate its validity. The cells contain two electrode-electrolyte junctions and one liquid-liquid junction. The data on the thermoelectric powers and on the isothermal temperature coefficients were obtained in my laboratory, with the assistance of Jean Berkeley, by methods similar to those described in the earlier parts of this paper. The data have not been published previously.

The sum of the thermoelectric powers of three junctions, including the liquid-liquid junction, is given in column D of Table IV. The sum is to be compared with the experimentally measured isothermal temperature coefficient of the cell given in column E. The difference between the values in the two columns averages about 1.3×10^{-5} V/°C, which is within experimental error.

Acknowledgments

This investigation was one of the author's "extracurricular" interests and as such did not require specific support. However, the ideas involved were a spin-off from the author's program of Electrochemical Calorimetry which the Research Division of the Atomic Energy Commission sponsored at the National Bureau of Standards from about 1958 to 1964. For this support the author wishes to express appreciation to A. R. Van Dyken of the Chemistry Branch, Division of Research of AEC. Also, the author wishes to acknowledge the laboratory assistance of Jean J. Berkeley in the initial phases of the laboratory work with the concentration cells.

Manuscript submitted Dec. 18, 1973; revised manuscript received June 9, 1975.

Any discussion of this paper will appear in a Discussion Section to be published in the June 1976 JOURNAL. All discussions for the June 1976 Discussion Section should be submitted by Feb. 1, 1976. A portion of this paper was Paper 188 presented at the Cleveland, Ohio, Meeting of the Society, May 1-6, 1966.

Publication costs of this article were partially assisted by the N-Q Electrochemical Research Corporation.

Table IV. Comparison of the sum of the thermoelectric power of the three junctions of a cell with the isothermal temperature coefficient of the voltage of the cell

	Concentration cell			Volt per degree $\times 10^5$ Electrode-electrolyte and electrolyte-electrolyte Thermoelectric power				Isothermal temp coef of cell	Column E - D	
	J _a	J _b	J _c	J _a	J _b	J _c	J _a + J _b + J _c			
A-1	Hg,HgCl	HCl 0.040N	HCl 0.40N	Hg,HgCl	52.3	2	35.8	18.5	17.7	-0.8
A-2	H ₂ Pt	HCl 0.040N	HCl 0.40N	H ₂ Pt	47.2	2	32	13.2	15.5	2.3
B-1	Ag,AgCl	CdCl ₂ 0.10M	CdCl ₂ 1.0M	Ag,AgCl	42	4	34	4.0	4.5	0.5
B-2	Cd	CdCl ₂ 1.0M	CdCl ₂ 0.10M	Cd	58.5	4	59.0	3.5	3.8	0.3
C-1	Hg,HgCl	LiCl 1.21N	HCl 1.15N	Hg,HgCl	57	31	26	0	2.0	2.0
C-2	Ag,AgCl	LiCl 1.21N	HCl 1.15N	Ag,AgCl	28	31	5	2	0	-2.0
D-1	Hg,HgCl	LiCl 0.30N	LiCl 3.0N	Hg,HgCl	69	0	50	19	18	-1.0
				A	B	C	D	E		Avg = 1.3

REFERENCES

1. A. Brenner and S. L. Catey, *This Journal*, **111**, 1225 (1964).
2. H. Helmholtz, *Sitzber. Königlich Akad. Wiss. Berlin*, **22**, (1882).
3. The Collected Works of J. Willard Gibbs, Vol. 1, "Thermodynamics," pp. 338-349, Longmans, Green and Co., London (1928).
4. J. W. Müller, *Ann. Physik*, **216**, 114 (1870).
5. Walther Nernst, *Z. Physik. Chem.*, **4**, 129 (1852).
6. Jamiat V. Lakhani, *J. Chem. Soc.*, 179 (1932).
7. P. Henderson, *Z. Physik. Chem.*, **59**, 118 (1907); *ibid.*, **63**, 325 (1908).
8. D. A. MacInnes, "The Principles of Electrochemistry," p. 60, Dover Publications, Inc., New York (1961).
9. Sechste Auflage, "Landolt-Börnstein Zahlenwerte und Funktionen aus Physik, Chemie, Astronomie, Geophysik und Technik," Springer-Verlag, Germany (1960) Band II, Teil 7, Elektrische Eigenschaften II.
10. F. D. Rossini, Donald D. Wagman, W. H. Evans, S. Levine, and I. Jaffe, "Selected Values of Chemical Thermodynamic Properties," Circular 500, Part I, National Bureau of Standards, Washington, D.C. (1961); V. B. Parker, "Thermal Properties of Aqueous Uni-univalent Electrolytes," National Standard Reference Data Series, National Bureau of Standards, Washington, D.C. (1965).
11. Oscar Scarpa, *Atti Accad. Naz. Lincei, Rend., Classe Sci. Fis., Mat. Nat.*, **8**, 226 (1948).
12. W. Duane, *Ann. Physik*, **301**, 374 (1898).
13. J. M. Sherfey, *This Journal*, **110**, 213 (1963).

The Gibbs-Helmholtz Equation and the EMF of Galvanic Cells

II. Precision of its Application to Concentration Cells

Abner Brenner*

N-Q Electrochemical Research Corporation, Reston, Virginia 22070

ABSTRACT

The Gibbs-Helmholtz equation is usually tested by comparing the enthalpy, ΔH_{emf} , of the cell reaction obtained by means of the equation with the calorimetrically determined enthalpy, ΔH_{cal} . A survey was made of three such tests in the literature. An examination of the precision of the correspondence between ΔH_{emf} and ΔH_{cal} was made using concentration cells without transference, containing either hydrochloric or sulfuric acid. The enthalpy change was a partial molal heat of dilution. With dilute solutions of hydrochloric acid the agreement was satisfactory. With strong solutions of hydrochloric and of sulfuric acid the differences amounted to a hundred calories or more. In sulfuric acid concentration cells with transference the difference amounted to several hundred calories. The differences for these cells are shown to be due mainly to the variation of the transference number of the hydrogen ion with temperature. On this basis, the discrepancy of the Gibbs-Helmholtz equation is easily calculated.

In Part I of this series of papers it was shown that the emf of liquid-liquid junctions did not follow the Gibbs-Helmholtz equation, although it followed the Henderson equation within experimental error. The cells used in this investigation were an unusual type in which the emf was derived solely from liquid-liquid junctions. The results of Part I raised the issue of the precision of the Gibbs-Helmholtz equation when applied to conventional types of galvanic cells.

The data in this paper is in two parts. The first part is a brief survey of some of the tests of the Gibbs-

Helmholtz equation reported in the literature. In the second part and main treatment of data, the precision of the Gibbs-Helmholtz equation was investigated with respect to concentration cells containing either hydrochloric or sulfuric acid. The raw data were taken from the published results on simple galvanic cells. These were combined so as to form concentration cells. The reason for investigating concentration cells is that the precision of the tests was improved, as shown in the subsequent discussion.

The Gibbs-Helmholtz equation was discussed in Part I, however, a little reiteration is necessary. The second law applied to galvanic cells can be stated in the form

* Electrochemical Society Active Member.

Key words: Gibbs-Helmholtz equation, concentration cells.

$$E = -\Delta H/nj + Q_{rev}/nj \quad [1]$$

where j is approximately 23,050 (cal/V-F) and Q_{rev} is the quantity of heat either absorbed or evolved when a cell operates reversibly.

The Gibbs-Helmholtz equation is

$$E = -\Delta H/nj + T \cdot dE/dT \quad [2]$$

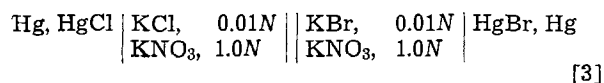
Comparison of the two equations shows that $T \cdot dE/dT$ should be equal to the voltage equivalent of the reversible heat, that is Q_{rev}/nj .

The usual manner in which the Gibbs-Helmholtz equation is checked is to calculate ΔH from Eq. [2] using the experimentally obtained values of E and its temperature coefficient. This particular ΔH will henceforth be referred to as ΔH_{emf} . Then, ΔH_{emf} is compared with the value of ΔH (henceforth referred to as ΔH_{cal}) obtained by calorimetry.

The most direct check of the Gibbs-Helmholtz equation would be to measure calorimetrically the reversible heat absorbed or evolved in the working of a cell and to compare this with $T \cdot dE/dT \times nj$. Unfortunately, this kind of calorimetric measurement is difficult and has been done on only a few occasions.

Survey of the Tests of the Gibbs-Helmholtz Equation in the Literature

Typical of the early investigations of the Gibbs-Helmholtz equation is that of Bugarszky (1) whose paper was published in 1897. He measured the emf of cells having mercury-mercurous salt electrodes, such as the following



Although the cells had a liquid-liquid junction, the potential of the latter was presumably suppressed by the use of potassium nitrate in both sides of the cell at a 100-fold higher concentration than the working electrolyte.

The following is a summary of the results obtained with ten different cells. The discrepancy between the value of ΔH_{cal} and ΔH_{emf} (calculated from the Gibbs-Helmholtz relation) ranged between 40 and 2300 cal with an average of about 660 cal.

In 1909 Mellencamp (2) published the results of an investigation of the Gibbs-Helmholtz relation. His work is of special interest and unique in that it is the

only investigation in the literature specifically directed toward demonstrating that the Gibbs-Helmholtz equation held for concentration cells in which the emf was partly derived from the heat of dilution of the electrolyte. His cells all had liquid-liquid junctions, and since he did not mention them in his calculations, it is apparent that he assumed that the law held for such cells.

Mellencamp's original data are presented in Table I. Three out of the four experiments show a deviation of 20 cal or less between the heat of dilution derived from the use of the Gibbs-Helmholtz relation and that measured calorimetrically. The percentages of error (for the three experiments) based on $2j \cdot T \cdot dE/dT$ are 1% or less. These results, taken at their face value, show as precise an agreement of the Gibbs-Helmholtz relation as can be expected on the basis of the experimental errors involved.

However, I have made a careful examination of Mellencamp's experimental procedures and calculations and have come to the conclusion that the excellent agreements that he found were fortuitous and must have resulted from the canceling of various errors.

Although Mellencamp measured voltages with a precision of 10^{-5} V, the accuracy of his measurements of emf could not have been that high because of three experimental faults: (i) he did not use flowing liquid-liquid junctions; (ii) the liquid junctions were not at the same temperature as the electrolytes in the cells; and (iii) the emf measurements were made after a period of hours or even days, during which time considerable diffusion must have occurred across the liquid-liquid junction, thus altering the emf of the cell with time.

Another reason that the close agreements found by Mellencamp cannot be valid is that the calorimetric data that he used in his comparisons were not of high accuracy. The data that he used, given in column A of Table I, differ significantly from more recent data, given in column A of Table II. For example, for experiments 1 and 4 the values of ΔH_{cal} differ by 190 and 160 cal, respectively.

Mellencamp should not be criticized for the inaccuracy of the calorimetric data available at that time. However, he is culpable in neglecting two important details in the calculations. First of all, Mellencamp used the integral heats of dilution instead of partial molal heats (partial molal quantities were not even mentioned). Second and most serious, he did not take into

Table I. Mellencamp's original data (2) on the comparison of the heat of dilution computed from emf of cells with that obtained calorimetrically. The electrodes of all cells were amalgams.

No.	Cell	Heat of dilution, cal			$2j \cdot T \cdot dE/dT$, cal	Error, %
		Calorim	emf	Diff		
1	Zn ZnSO ₄ · 50H ₂ O ZnSO ₄ · 400H ₂ O Zn	82	80	2	707	0.3
2	Cd CdSO ₄ · 30.6H ₂ O CdSO ₄ · 400H ₂ O Cd	722	701	21	320	0.7
3	Zn ZnCl ₂ · 18.8H ₂ O ZnCl ₂ · 180H ₂ O Zn	4530	4435	95	-1338	7.0
4	Pb Pb(NO ₃) ₂ · 100H ₂ O Pb(NO ₃) ₂ · 400H ₂ O Pb	-1270	-1250	20	1998	1.0

Table II. Adjustment of Table I using corrected values of the calorimetrically measured heat of dilution. This consists in multiplying the value obtained from the National Bureau of Standards tables² by the transference number of the anion.

Cell No.	Heat of dilution per mole ² (A)	Transference number of anion (B)	Heat of dilution, calories in cell			$2j \cdot T \cdot dE/dT$	Error, %
			(A × B) calorimetric	From Mellencamp emf data	Diff		
1	272	0.7	190	80	-110	707	16
2	760	0.7	532	701	169	320	53
3	4550	0.9	4095	4435	340	-1338	25
4	-1100	0.5	-550	-1250	-700	1998	35
				Avg	330		Avg 32%

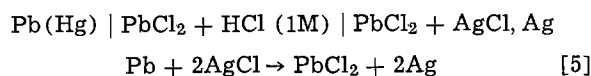
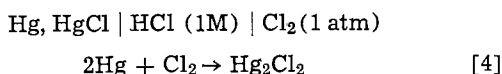
¹ From Mellencamp's data.

² D. D. Wagman, W. H. Evans, V. B. Parker, I. Halow, S. M. Baily, and R. H. Schumm, Editors, "Selected Values of Chemical Thermodynamic Properties," Technical Note 270-3, National Bureau of Standards, Washington, D. C. (1968).

consideration the electrical migration of ions across the liquid-liquid junction. This migration reduced the amount of salt transported per Faraday from one compartment of the cell to the other.

In Table II this latter omission has been rectified by multiplying the heat of dilution by the transference number of the anion to give a more nearly correct value for the calorimetrically derived heat of dilution resulting from the passage of current. Comparisons of these corrected values of ΔH_{cal} with Mellencamp's values of ΔH_{emf} derived from his emf measurements on the cells show an average discrepancy of 330 cal and an average percentage error of 32% based on the value of $2j \cdot T \cdot dE/dT$.

The third and last example of a test of the Gibbs-Helmholtz equation that I have taken from the literature utilizes the data of Gerke (3). Gerke measured the emf and the temperature coefficient of the emf of cells of which the following two are typical

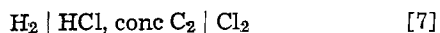
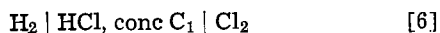


Gerke did not examine the relation of his data to the Gibbs-Helmholtz equation but was concerned with testing the third law of thermodynamics. However, his data was used by MacInnes (4) to illustrate the Gibbs-Helmholtz equation. The five examples cited show discrepancies ranging from 30 to 2600 cal with an average discrepancy of 870 cal. If the large discrepancy of 2600 cal is omitted, the average discrepancy was about 440 cal.

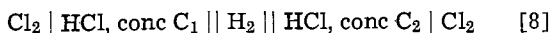
In contrast to these discrepancies, Gerke's results (based on the temperature coefficient of the emf of the cells) agreed with the third law within 30 cal. This indicates that his measurements of the temperature coefficients of emf were accurate. If such measurements are generally accurate, it would throw the onus of the large discrepancies of hundreds of calories observed in the tests of the Gibbs-Helmholtz equation (as shown by the data of Bugarszky, Mellencamp, and Gerke) on either the inaccuracy of conventional calorimetric measurements or on the imprecision of the equation, or on both.

Gibbs-Helmholtz Equation Applied to Concentration Cells without Transference

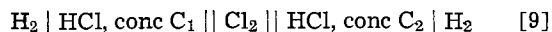
The simplest and most accurate way in which to check the precision of the Gibbs-Helmholtz equation is to use concentration cells having no liquid-liquid junctions. These cells are formed by connecting together two of the same kind of simple cells, similar in all respects except for a difference in the concentration of the electrolyte, with the added specification that one electrode be reversible with respect to the cation, the other reversible with respect to the anion. For example, the two cells



can be connected together to give the concentration cells

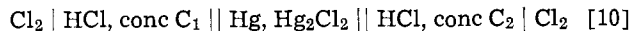


or



It makes no difference as to the order in which the simple cells are connected. Cells [8] and [9] yield the same reaction and the same emf.

The simple cells of the type used by Gerke would not yield a concentration cell because the composition of the electrolyte does not change on operation of the cell. For example, the cell formed by connecting two cells of the type of Eq. [4]



appears similar to Eq. [8], above. However, passage of current through this cell simply results in the transfer of chlorine from one end of the cell to the other. This involves no energy, hence this cell should have no emf.

The passage of 1F of current through the concentration cells [8] or [9] results in the transfer of one equivalent of HCl from the solution at higher concentration to the solution at the lower concentration. The enthalpy change, ΔH_{cal} , involved in the working of the cell is equal to the difference between the partial molal heats of solution of HCl in solutions of concentration C_1 and C_2 . The electrical energy developed by the cell comes from two sources: the aforementioned enthalpy change, ΔH_{cal} , and the heat, Q_{rev} , reversibly absorbed from the surroundings. This latter portion of energy is the quantity with which this paper is essentially concerned, and the matter to be decided is whether Q_{rev} is exactly equal to $nj \cdot T \cdot dE/dT$ as required by the Gibbs-Helmholtz equation.

In dealing with concentration cells without transference, it is unnecessary to actually electrically connect two simple cells such as Eq. [6] and Eq. [7] for the purpose of making measurements. It is sufficient to simply subtract the emf's of the temperature coefficients, or the ΔH_{cal} of the simple cells (for which data are reported in the literature) to arrive at the corresponding data of emf etc. for the concentration cells such as Eq. [8] or Eq [9].

It is now necessary to justify the expedient of using concentration cells to explore the precision of the Gibbs-Helmholtz equation, as is done in this paper, instead of dealing with simple cells, as used by Bugarszky and others. As noted above, the quantity of importance in this quest is the reversible heat, Q_{rev} , and it is the more accurately determined (*via* Eq. [1]) the larger it is relative to ΔH_{cal} . In simple cells Q_{rev} may range widely in magnitude, but in many instances it amounts to only from one-third to one-tenth of the magnitude of ΔH_{cal} . In concentration cells the enthalpy change, ΔH_{cal} , is of course much smaller than in simple cells, but this is not the matter of importance. The improvement of the precision of the test using concentration cells results from the situation that the magnitude of Q_{rev} is closer to that of ΔH_{cal} than in the case of simple cells. Although in the concentration cells, also, the ratio of Q_{rev} to ΔH_{cal} may vary over a wide range, in many instances Q_{rev} is of the same magnitude as ΔH_{cal} and may be larger; it seldom is smaller than one-third the size of ΔH_{cal} .

Another important source of the improved precision of the test, using concentration cells, is that in the subtraction of the values of emf and ΔH_{cal} obtained for simple cells (to derive the values for concentration cells) some errors cancel out. For example, if only the difference of two voltages was to be determined, the zero point of the instrument would be of no consequence. As a concrete example of the manner in which taking differences improves precision, I have compared the data of Sturtevant (5) with that of Rossini (6) for the partial molal heats of dilution of hydrochloric acid over the range 0.01 to 3.24M. The values for 12 concentrations of HCl differed by an average of 53 cal. However, if for each investigator's data, the 0.25M solution were taken as the reference value from which the values of the other concentrations of solutions were subtracted (which would be done with concentration cells as discussed above), then the two sets of data differed only by an average of 17 cal. This is a three-fold improvement in precision. Going a step farther, if the comparison were made over the more limited range of 9 concentrations between 0.16 and 3.24M, the average difference between the two sets of data was only 10 cal.

The comparison of ΔH_{cal} with ΔH_{emf} to obtain a measure of the precision of the Gibbs-Helmholtz equation (or a comparison of Q_{rev} with $nj \cdot T \cdot dE/dT$) does not involve any judgment as to whether or not the equa-

tion is an exact law of nature. To make such a judgment would require an exact knowledge of the experimental error so as to be able to determine whether the discrepancies were within or greater than the experimental error.

It is my opinion that not enough information is available to determine the experimental error. Nevertheless, even a rough estimate is of value as a guide, even though no conclusions should be based on it.

The experimental error has two sources: the measurement of emf and the calorimetric measurements. The emf of a cell is generally measured with a precision of 10^{-5} V or better. The heat equivalent of this error per mole ($nj \cdot 10^{-5}$) would be less than a calorie, hence not significant. A larger error is involved in the determination of the term $nj \cdot T \cdot dE/dT$. The temperature coefficient of emf is usually determined by measurement of emf's ten degrees apart and the precision of dE/dT might be 10^{-6} V. Since T is usually about 300, the value of $j \cdot T \cdot dE/dT$ might be in error by about 7 cal.

With regard to calorimetric measurements, the above comparison of the data of Sturtevant with that of Rossini gave a precision of about 17 cal on a relative basis for the partial molal heat of dilution of hydrochloric acid. The sum of the errors involved in the test of the precision of the Gibbs-Helmholtz equation *via* HCl concentration cells would thus be about 24 cal ($17 + 7$). This amount is not far from the precision of 30 cal that Gerke found in his test of the third law, which involved measurements of both temperature coefficients of emf and heat capacities of elements. As an estimate of the experimental error in the tests involving the HCl concentration cells, a value of 30 cal seems reasonable.

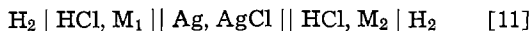
A measure of the calorimetric error involved in the determination of the heats of dilution of sulfuric acid is not available, as in the case of HCl, because there are not two different sets of data covering a wide range of concentration. The papers of Kunzler and Giauque (7) and of Giauque, Hornung, Kunzler, and Rubin (8) do not give an estimate of the precision of measurement of the partial molal heat of dilution of sulfuric acid. A statement in the latter paper implies that the precision should be better than 100 cal. Data, however, are given to the nearest calorie. Without more data to go on, I suggest 100 cal as the total experimental error involved in the test of the Gibbs-Helmholtz equation *via* sulfuric acid concentration cells. This is equivalent to considering that the error in the measurement of the relative partial molal heats of dilution of sulfuric acid is not greater than 1%.

Concentration Cells without Transference Containing Either Hydrochloric or Sulfuric Acid

In this section I have investigated the precision of the Gibbs-Helmholtz equation with respect to concentration cells constructed from simple cells for which data were reported in the literature. I have combined the simple cells in many different fashions to form concentration cells in which the ratios of the concentrations varied widely.

The data on the hydrochloric acid cells were taken from four sources. The concentration of acid covered the range from 0.001 to about 15M.

Table III contains data on concentration cells constructed from the simple cells measured by Bates and Bower (9)



These concentration cells had electrolytes in the dilute range of 0.0001-0.1M. The comparisons are based on the partial molal heats of dilution of both Rossini (6) and Sturtevant (5). The difference between the calorimetric ΔH_{cal} and the value of ΔH_{emf} (derived from the Gibbs-Helmholtz relation) is about 9 cal on the average, based on Rossini's data and about 30 cal, based on Sturtevant's data. These differences are within the ex-

Table III. Survey of the precision of the Gibbs-Helmholtz equation based on hydrochloric acid concentration cells without transport constructed from the data of Bates and Bowers (9).

$$\text{H}_2 | \text{HCl}, M_1 || \text{Ag}, \text{AgCl} || \text{HCl}, M_2 | \text{H}_2$$

Molality of HCl	$-\Delta H_{\text{cal}}, ^\circ\text{cal}$		Difference		Reversible heat, cal $j \cdot T \cdot dE/dT$	
	$-\Delta H_{\text{emf}}, ^\circ\text{cal}$	Rossini (6)	Sturtevant (5)	$-\Delta H_{\text{emf}} + \Delta H_{\text{cal}}$ Rossini Sturtevant		
0.1/0.07	46	36	28	10	18	350
0.1/0.05	71	66	51	5	20	701
0.1/0.02	140	127	100	13	40	1655
0.1/0.01	159	155	123	4	36	2420
0.1/0.005	181	178	142	3	39	3183
0.1/0.002	218	196	155	22	63	4205
0.1/0.001	221	209	167	12	54	5008
0.001/0.002	0	10	10	-10	-10	805
0.001/0.005	27	31	26	-4	1	1822
0.001/0.01	60	52	45	8	15	2590
				Avg	9	30

¹ ΔH_{emf} = Partial molal heat of dilution computed from the emf of the cell and dE/dT .

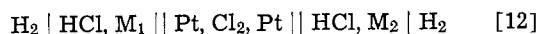
² ΔH_{cal} = Partial molal heat of dilution obtained by calorimetry.

perimental error of 30 cal which I had suggested. Quite apart from their use *vis-à-vis* the Gibbs-Helmholtz equation, these cells have an interest in themselves. In contrast to the other concentration cells examined, their reversible heat (given by $j \cdot T \cdot dE/dT$) is 10 or 20 times greater than the enthalpy change due to heat of dilution. Thus these cells function mainly as heat engines.

The HCl concentration cells presented in Tables IV, V, and VI differ from those in Table III in possessing a more concentrated electrolyte. At least one compartment of the cell had an HCl concentration of 3.0M or higher.

The data in Table IV are based on the simple cell data of Harned and Ehlers (10) and those in Table V are based on the data of Akerlof and Teare (11). The concentration cells were of the same type as in Table III (see Eq. [11]). The average difference between ΔH_{cal} and ΔH_{emf} in Table IV is about 40 cal and in Table V about 76 cal. The data in Table V covers a higher range of HCl concentration (3-15M) than the data in Table IV (0.001-4M).

The results in Table VI are based on the data of Cerquetti, Longhi, and Mussini (12). Their simple cells differ from those on which Tables III-V are based in that the positive electrode was a chlorine electrode instead of a silver-silver chloride electrode. The concentration cell constructed from the simple cells is



The data of Table VI gives an average difference of 250 cal between ΔH_{cal} and ΔH_{emf} . This large difference may be partly due to a lack of precision in drawing a

Table IV. Survey of the precision of the Gibbs-Helmholtz equation based on hydrochloric acid concentration cells without transport constructed from the data of Harned and Ehlers (10)

$$\text{H}_2 | \text{HCl}, M_1 || \text{Ag}, \text{AgCl} || \text{HCl}, M_2 | \text{H}_2$$

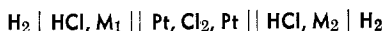
Molality of HCl	$-\Delta H_{\text{cal}}, \text{cal}$		Difference		Reversible heat, cal $j \cdot T \cdot dE/dT$	
	$-\Delta H_{\text{emf}}, \text{cal}$	Rossini (6)	Sturtevant (5)	$-\Delta H_{\text{emf}} + \Delta H_{\text{cal}}$ Rossini Sturtevant		
3.0-2.0	473	436	426	37	47	323
3.0-1.0	881	847	842	34	39	996
3.0-0.5	1116	1067	1056	49	60	1662
3.0-0.1	1356	1318	1286	48	70	3270
3.0-0.01	1463	1526	1455	-63	8	5735
4.0-0.001	1958	1980	—	-22	—	858
4.0-0.01	1917	1926	—	-9	—	596
4.0-0.10	1823	1771	—	52	—	349
4.0-1.00	1353	1300	—	53	—	1208
4.0-2.00	946	890	—	56	—	535
4.0-3.00	473	460	—	13	—	216
				Avg	40	45

Table V. Survey of the precision of the Gibbs-Helmholtz equation based on hydrochloric acid concentration cells without transport constructed from the data of Akerlof and Teare (11). Calorimetric values all obtained from data of Rossini (6).



Molality of HCl	$-\Delta H_{\text{emf}}, \text{cal}$	$-\Delta H_{\text{cal}}, \text{cal}$	Difference $-\Delta H_{\text{emf}} + \Delta H_{\text{cal}}$	Reversible heat, cal $j \cdot T \cdot dE/dT$
3.0-4.0	450	460	-10	247
3.0-6.0	1409	1390	16	481
3.0-7.0	1970	1865	105	515
3.0-8.0	2443	2370	73	542
3.0-9.0	2966	2870	96	516
3.0-10.0	3460	3363	97	481
3.0-12.0	4340	4285	55	433
3.0-14.0	5303	5180	123	165
4.0-5.0	520	470	50	125
4.0-6.0	1012	930	82	199
4.0-7.0	1525	1405	120	261
4.0-8.0	2002	1910	92	275
4.0-9.0	2508	2410	98	282
4.0-10.0	3010	2903	107	234
4.0-12.0	3916	3825	91	131
6.0-8.0	995	980	15	69
6.0-10.0	2018	1973	45	9
6.0-12.0	2906	2895	11	70
14.0-4.0	4842	4720	122	76
14.0-5.0	4302	4250	52	158
14.0-6.0	3837	3790	47	289
14.0-7.0	3294	3315	-21	288
14.0-8.0	2833	2810	23	344
14.0-9.0	2334	2310	24	350
14.0-10.0	1846	1817	29	337
14.0-12.0	964	895	69	282
15.0-14.0	438	410	28	152
15.0-13.0	1100	835	265	392
15.0-11.0	1964	1730	234	508
			Avg 76	

Table VI. Survey of the precision of the Gibbs-Helmholtz equation based on hydrochloric acid concentration cells without transport constructed from the data of Cerquetti, Longhi, and Mussini (12). Calorimetric values all obtained from data of Rossini (6).



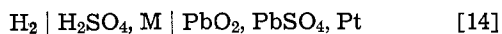
Molality of HCl	$-\Delta H_{\text{emf}}, \text{cal}$	$-\Delta H_{\text{cal}}, \text{cal}$	Difference $-\Delta H_{\text{emf}} + \Delta H_{\text{cal}}$	Reversible heat, cal $j \cdot T \cdot dE/dT$
1.000-3.084	1127	890	237	826
1.000-3.701	1415	1150	265	941
1.000-4.626	1800	1590	210	1141
1.000-5.551	2280	2015	265	1216
1.000-6.938	3110	2665	445	1168
1.000-7.930	3220	3175	45	1580
1.000-9.251	3887	3825	62	1554
1.000-10.092	4585	4245	340	1236
1.000-11.102	5040	4700	340	1202
11.102-10.092	699	455	244	275
11.102-9.251	1215	900	315	412
			Avg 251	

tangent to the curve of emf vs. temperature at a temperature of 25°, since the authors' data did not have values below this temperature.

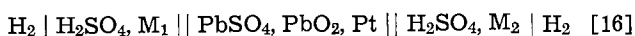
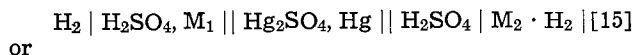
The researches of Harned and Hamer (13) on the thermodynamics of aqueous sulfuric acid solutions yield another large amount of accurate data for examining the precision of the Gibbs-Helmholtz equation. Their data cover the range of concentration from 0.005 to 17.5M. Cells of the type



were used for concentrations of acid above 0.05M and cells of the type



for acid concentrations below 0.05M. With their data for the simple cells it was possible to obtain similar data for the following concentration cells



In Table VII the difference between the partial molal heats of dilution of sulfuric acid at two concentrations

Table VII. Survey of the precision of the Gibbs-Helmholtz equation based on sulfuric acid concentration cells without transport constructed from the data of Harned and Hamer (13). Calorimetric values of partial molal heats of dilution, ΔH_{cal} , obtained from data of Giauque *et al.* (8) for acid concentrations above 1.0M and from Young (14) for lower acid concentrations. Temperature 25°.

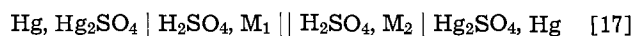
Molality of H ₂ SO ₄ (M)	$-\Delta H_{\text{emf}}, \text{cal}$	$-\Delta H_{\text{cal}}, \text{cal}$	Difference $-\Delta H_{\text{emf}} + \Delta H_{\text{cal}}$	Reversible heat, cal $2 \cdot j \cdot T \cdot dE/dT$
Cell $\text{H}_2 \text{H}_2\text{SO}_4 (0.05M) \text{Hg}_2\text{SO}_4, \text{Hg} \text{H}_2\text{SO}_4 (M) \text{H}_2$ was used for concentrations above 0.05M.				
Cell $\text{H}_2 \text{H}_2\text{SO}_4 (0.05M) \text{PbSO}_4, \text{PbO}_2, \text{Pt} \text{H}_2\text{SO}_4 (M) \text{H}_2$ was used for concentrations below 0.05M.				
17.5	10,884	10,312	572	2140
16.0	10,266	9851	415	2280
14.0	9447	9181	266	2430
12.0	8532	8396	136	2600
10.0	7535	7487	48	2750
8.0	6379	6354	25	2910
6.0	5009	4857	152	3050
4.0	3397	3013	384	3170
3.0	2530	2119	411	3190
2.0	1679	1367	312	3090
1.0	1197	889	308	2420
0.5	900	707	193	1790
0.2	734	500	233	870
0.1	496	285	211	300
0.05	0	0	0	0
0.02	456	625	-169	660
0.01	938	1205	-267	1070
0.005	1693	1875	-182	1280
0.002	2713	2883	-170	1580
0.001	3322	3530	-208	2030
0.0005	3792	3965	-173	2690
			Avg 225	
Cell $\text{H}_2 \text{H}_2\text{SO}_4 (1.0M) \text{Hg}_2\text{SO}_4, \text{Hg} \text{H}_2\text{SO}_4 (M) \text{H}_2$				
2.0	482	478	4	670
3.0	1333	1230	103	770
4.0	2200	2124	76	750
6.0	3812	3968	-156	630
8.0	5182	5465	-283	490
10.0	6338	6598	-260	330
12.0	7335	7507	-172	180
14.0	8250	8292	-42	10
16.0	9069	8962	107	-140
17.5	9687	9423	264	-280
			Avg 147	

has been calculated from the data of Harned and Hamer (13), via the Gibbs-Helmholtz equation. This quantity, ΔH_{emf} , is compared with the similar quantity, ΔH_{cal} , obtained from the calorimetric data of Giauque and co-workers (8) for the range of acid concentration from 1.0 to 17.5M and from the data of Young (14) for the lower range of concentration.

In Table VII data are given for two sets of concentration cells: one set of cells with a compartment containing 0.05M sulfuric acid and the other set with a compartment containing 1.0M sulfuric acid. The average deviation of the ΔH_{cal} values from the ΔH_{emf} values (derived via the Gibbs-Helmholtz equation) is about 225 cal for the first set of concentration cells and 147 cal for the second set of concentration cells. Some of the differences were larger than 300 cal.

Sulfuric Acid Concentration Cells with Transference

Hamer (15) measured the emf and the temperature coefficient of the emf of the following cell in which there is transference of sulfuric acid from one compartment to the other during the working of the cell



The objective of Hamer's research was to determine the transference number of the ions of sulfuric acid as a function of concentration and temperature, and he did not use his data to check the precision of the Gibbs-Helmholtz equation.

For testing the precision, the calorimetric value of the partial molal heat of dilution of sulfuric acid, ΔH_{cal} , must be known for comparison with ΔH_{emf} . This requires a measurement that was not needed for the concentration cells without transference, namely the transference number, t_+ , of the hydrogen ion. The rea-

son for this is that in the working of a cell with liquid-liquid junctions and with electrodes reversible with respect to the anion, the passage of $1F$ of electricity through the cell results in the transport of only t_+ equivalents of sulfuric acid from one compartment to the other. To obtain the heat effect resulting from the passage of $2F$ through the cell, the difference between the partial molal heats of dilution for concentrations M_1 and M_2 must be multiplied by t_+ . This has been done, using Hamer's values for t_+ , to yield the values of ΔH_{cal} given in Table VIII.

In this table the values of ΔH_{emf} obtained by applying the Gibbs-Helmholtz equation to Hamer's data are compared with ΔH_{cal} derived as mentioned in the preceding paragraph. The average discrepancy is about 600 cal, which is considerably larger than that for cells without transference.

Calculation of the Gibbs-Helmholtz Discrepancy from the Transference Number of the Hydrogen Ion

In Part I of this series, I showed that the Gibbs-Helmholtz discrepancy could be calculated from data on the variation of ionic mobilities with temperature, by using Henderson's equation. A similar treatment of the data on sulfuric acid concentration cells with transference permits the Gibbs-Helmholtz discrepancy to be easily calculated from the variation of the transference number of the hydrogen ion with temperature, which, of course, in the final analysis means that the discrepancy is due to variation of ionic mobilities with temperature.

The calculation in the case of the sulfuric acid concentration cells is more straightforward and convincing than that with the liquid-liquid, tri-junction cells, because the calorimetric effects (partial molal heats of dilution of sulfuric acid) are accurately known and did not have to be calculated as was done with the tri-junction cells. Furthermore, the data on the variation of transference number of the hydrogen ion with temperature were directly available from Hamer's (15) publication.

The derivation of the Gibbs-Helmholtz discrepancy is as follows: The passage of $1F$ of electricity through the cell with transport results in the transfer of t_+

Table VIII. Survey of the precision of the Gibbs-Helmholtz equation based on sulfuric acid concentration cells with transport constructed from the data of Hamer (15) on the cells



Calorimetric values of partial molal heats of dilution, ΔH_{cal} , obtained from data of Giauque et al. (8).¹

Molality of H ₂ SO ₄		$-\Delta H_{emf}$, cal	$-\Delta H_{cal} \times t_+$, cal	Difference $-\Delta H_{emf} + \Delta H_{cal}$	Reversible heat, cal $2 \cdot j \cdot T \cdot \frac{dE}{dT}$
M_1	M_2				
0.05	0.1	830	495	335	+880
0.1	0.2				
0.2	0.3				
0.3	0.5	1795	615	1180	+385
0.5	1.0				
1.0	2.0				
2.0	3.0	2970	1990	980	-992
3.0	4.0				
4.0	5.0				
5.0	6.0	2300	1720	580	-908
6.0	7.0				
7.0	8.0				
8.0	9.0	1620	1070	550	-673
9.0	10.0				
10.0	11.0				
11.0	12.0	1165	735	430	-467
12.0	13.0				
13.0	14.0				
14.0	15.0	920	530	390	-385
15.0	16.0				
16.0	17.0				

Avg 635

¹ Each of the 7 sections in the above Table represents the results for 3 concentration cells, as noted under M_1 and M_2 , considered connected in series.

equivalents of sulfuric acid from one side to the other. Consequently, the emf, E_t , of the cell is considered as equal to that of the cell without transport, E , multiplied by t_+ , which is the transport number of the hydrogen ion

$$njE_t = njE \cdot t_+ = t_+ \left(-\Delta H_{cal} + T \int \frac{C_p}{T} d\tau + KT \cdot \ln \cdot f_c \right) \quad [18]$$

where j is approximately 23,050 cal/V-F. The last term represents some form of the Nernst relation for emf with f_c representing some function of concentration of sulfuric acid in the two sides of the cell.

Differentiation of Eq. [18] gives

$$nj \cdot \frac{dE_t}{dT} = \frac{dt_+}{dT} \left(-\Delta H_{cal} + T \int \frac{C_p}{T} dT + KT \cdot \ln \cdot f_c \right) + t_+ \left(-\frac{d(\Delta H_{cal})}{dT} + T \cdot \frac{C_p}{T} + \int \frac{C_p}{T} dT + K \cdot \ln \cdot f_c \right) \quad [19]$$

Note that

$$-\frac{d(\Delta H_{cal})}{dT} + T \cdot \frac{C_p}{T} = 0 \quad [20]$$

Multiplying both sides of Eq. [19] by T gives

$$njT \cdot \frac{dE_t}{dT} = T \cdot \frac{dt_+}{dT} \left(-\Delta H_{cal} + T \int \frac{C_p}{T} dT + dT + KT \cdot \ln \cdot f_c \right) + t_+ \left(T \cdot \int \frac{C_p}{T} dT + KT \cdot \ln \cdot f_c \right) \quad [21]$$

Rewrite Eq. [21] so as to place the t_+ () term on the left

$$t_+ \left(T \int \frac{C_p}{T} dT + KT \cdot \ln \cdot f_c \right) = njT \cdot \frac{dE_t}{dT} - T \cdot \frac{dt_+}{dT} \left(-\Delta H_{cal} + T \int \frac{C_p}{T} dT + KT \cdot \ln \cdot f_c \right) \quad [22]$$

Substitute the left side of Eq. [22] into Eq. [18] for E_t using the values on the right side of Eq. [22] and at the same time substitute the terms in the parenthesis on the right side of Eq. [22] for their value given by Eq. [18] which is njE_t/t_+ . This yields a simple equation for E_t in terms of temperature coefficients

$$njE_t = -t_+ \cdot \Delta H_{cal} + T \cdot \frac{dE}{dT} nj - T \cdot \frac{dt_+}{dT} \cdot \frac{E_t}{t_+} \cdot nj \quad [23]$$

Note that in the cell with transport, the heat effect for the passage of $2F$ is $t_+ \cdot \Delta H_{cal}$, hence the Gibbs-Helmholtz discrepancy is given by the equation

$$\text{discrepancy} = -\Delta H_{emf} + t_+ \cdot \Delta H_{cal} \quad [24]$$

To derive the expression for the discrepancy, subtract the Gibbs-Helmholtz equation, Eq. [25] from Eq. [23] and rearrange terms to yield Eq. [26] for the discrepancy

$$njE_t = -\Delta H_{emf} + njT \cdot \frac{dE_t}{dT} \quad [25]$$

$$\text{discrepancy} = -T \cdot \frac{dt_+}{dT} \cdot \frac{E_t}{t_+} \cdot nj \quad [26]$$

Table IX gives the values of the discrepancies, which have been calculated from Eq. [26] using data for E_t , t_+ , and dt_+/dT obtained from Hamer's publication (15). In my opinion, the agreement is satisfactory except for the first entry in the table.

Table IX. Gibbs-Helmholtz discrepancy calculated from the variation of the transference number, t_+ , of the hydrogen ion with temperature (see Eq. [26]) with data obtained from Hamer (15).

Conc range of H_2SO_4 (M)	$-\Delta H_{\text{cal}}$, cal	E_t , V	t_+	dt_+/dT	Discrepancy	
					Calc, cal	Exp, cal
0.05-0.30	605	0.03704	0.819	0.00113	813	335
0.30-2.0	762	0.04731	0.806	0.00121	969	1180
2.0-5.0	2593	0.04292	0.768	0.00125	966	980
5.0-8.0	2394	0.03015	0.716	0.00130	757	580
8.0-11.0	1588	0.02057	0.663	0.00120	515	550
11.0-14.0	1239	0.01513	0.605	0.00095	329	430
14.0-17.0	988	0.01160	0.537	0.00060	179	390

Summary and Discussion

1. The absolute value of ΔH_{emf} was generally larger than that of ΔH_{cal} .

2. In dilute solutions of HCl the discrepancies were small and within experimental error.

3. The discrepancies for the concentrated solutions of HCl and most of the sulfuric acid concentration cells were more than 100 cal and in some instances a few hundred calories, which, in my opinion, is greater than the experimental error.

4. The largest discrepancies occurred with sulfuric acid concentration cells with transference.

5. The discrepancies for the sulfuric acid cells with transference were readily calculated on the basis of the variation of the transference number of the hydrogen ion with temperature.

The discrepancies of the Gibbs-Helmholtz equation have been calculated for two different types of concentration cells. In Part I of this series it was calculated for tri-junction cells in which the emf was generated entirely by liquid-liquid junctions. In this paper, Part II of the series, it was calculated for a conventional type of concentration cell with transport. The importance of these calculations is that they show that for at least two types of cells, the discrepancy is a genuine phenomenon and not an experimental error.

To preserve the sanctity of the Gibbs-Helmholtz equation (which is a laudable crusade, since so much has been based on it), the theorists can prohibit application of the equation to any cell with a liquid-liquid junction. However, this seems a bit *ex post facto*, because at least up to this moment, the data derived from the sulfuric acid concentration cells with transference have been considered as thermodynamically acceptable. In treating of the use of such cells for obtaining transference numbers, MacInnes (16) stated that, "Although thermodynamically sound this method for obtaining transference numbers has not attained the accuracy of the recent moving boundary or Hittorf methods." The general acceptability of the data from such cells is further illustrated by the inclusion of Hamer's data on the transference numbers of the hydrogen ion in sulfuric acid (derived from the cells with transference) in the standard reference works, such as the Landolt-Börnstein (17).

If the sulfuric acid cells with transference are accepted as thermodynamically correct, there seems to be no reason why the tri-junction cells with three liquid-liquid junctions should not also be acceptable. Furthermore since the Gibbs-Helmholtz discrepancy could be calculated for them, this would seem to put them in the

same thermodynamically acceptable class as the sulfuric acid concentration cells with transference.

However, even if the cells with a liquid-liquid junction are excluded from participation in the Gibbs-Helmholtz equation, the theorist must still face the situation that the discrepancies of many of the cells without transference are rather large. These might be dismissed on the basis of a large experimental error. However, even this crutch is swept away, because in Part III of this series I shall show that the discrepancies for the sulfuric acid cells without transference can be explained or even roughly calculated on the basis of a shift of equilibrium with temperature. In the final analysis, the variation of ionic mobilities and of transference numbers with temperature is caused by a shift of equilibrium.

In view of the foregoing discussion, it seems to me simpler to deal with the Gibbs-Helmholtz discrepancies by accepting the situation that the equation for the emf of a galvanic cell

$$njE = -\Delta H + T \cdot \Delta S \quad [27]$$

is not accurate and that it must be specifically modified or supplemented as required for each individual cell.

Acknowledgments

I wish to thank Donald D. Wagman for suggesting sources of data.

Manuscript submitted May 3, 1974; revised manuscript received July 21, 1975.

Any discussion of this paper will appear in a Discussion Section to be published in the June 1976 JOURNAL. All discussions for the June 1976 Discussion Section should be submitted by Feb. 1, 1976.

Publication costs of this article were partially assisted by the N-Q Electrochemical Research Corporation.

REFERENCES

1. S. Bugarszky, *Z. Anorg. Chem.*, **14**, 145 (1897).
2. F. J. Mellencamp, *Phys. Rev.*, **29**, 329 (1909).
3. R. H. Gerke, *J. Am. Chem. Soc.*, **44**, 1684 (1922).
4. D. A. MacInnes, "The Principles of Electrochemistry," p. 113, Dover Publications, Inc., New York (1961).
5. J. M. Sturtevant, *J. Am. Chem. Soc.*, **62**, 584 (1940).
6. F. D. Rossini, *J. Res. Nat. Bur. Std.*, **9**, 677 (1932).
7. J. E. Kunzler and W. F. Giauque, *J. Am. Chem. Soc.*, **74**, 3472 (1952).
8. W. F. Giauque, E. W. Hornung, J. E. Kunzler, and T. R. Rubin, *ibid.*, **82**, 62 (1960).
9. R. G. Bates and V. E. Bower, *J. Res. Nat. Bur. Std.*, **53**, 283 (1954).
10. H. S. Harned and R. W. Ehlers, *J. Am. Chem. Soc.*, **54**, 1350 (1932); *ibid.*, **55**, 2179 (1933).
11. G. Åkerlöf and J. W. Teare, *ibid.*, **59**, 1855 (1937).
12. A. Cerquetti, P. Longhi, and T. Mussini, *J. Chem. Eng. Data*, **13**, 458 (1968).
13. H. S. Harned and W. J. Hamer, *J. Am. Chem. Soc.*, **57**, 27 (1935).
14. T. F. Young, Private communication to Donald Wagman at U.S. National Bureau of Standards.
15. W. J. Hamer, *J. Am. Chem. Soc.*, **57**, 662 (1935).
16. D. A. MacInnes, "The Principles of Electrochemistry," p. 169, Dover Publications, Inc., New York (1961).
17. Sechste Auflage, "Landolt-Börnstein Zahlenwerte und Funktionen aus Physik, Chemie, Astronomie, Geophysik und Technik," p. 241, Springer-Verlag, Germany (1960).

Electrochemical Reduction of Molybdate in the Presence of Zinc Chloride in Molten Lithium Chloride-Potassium Chloride Eutectic

R. Cvetković and B. N. Popov

Faculty of Technology and Metallurgy, University Kiril and Metodij, Skopje 91000, Yugoslavia

and H. A. Laitinen*

Department of Chemistry, University of Florida, Gainesville, Florida 32611

ABSTRACT

Two chronopotentiometric waves were observed for the electrochemical reduction of molybdate in the presence of zinc chloride, with quarter-wave potentials of -1.5V and -1.75V vs. the Pt(II)/Pt reference electrode, respectively. It was observed that an increase in the molybdate concentration causes a decrease of the first transition time indicating a chemical reaction between ZnCl_2 (which is reduced at -1.5V) and Li_2MoO_4 in the melt forming ZnMoO_4 which is sparingly dissociated in LiCl-KCl eutectic. The equilibrium constant for the observed reaction was calculated. X-ray powder diffraction patterns of the reduction product of ZnMoO_4 have been obtained.

Laitinen and Propp (1) have shown that the electrochemical reduction product of K_2CrO_4 in LiCl-KCl eutectic containing dissolved MgCl_2 is a single compound of formula $\text{Li}_x\text{Mg}_y\text{CrO}_4$, where $x + 2y = 5$. Laitinen and Hanck (2) observed that the reduction of chromate in the presence of Zn(II) was shifted from -1.0V vs. Pt(II)/Pt reference to -0.5V . Analysis of the deposit indicated the composition to be $\text{LiZn}_2\text{CrO}_4$. Laitinen and Popov (3) also observed that when chromate is reduced in the presence of NiCl_2 at 500°C the deposit approaches the composition $\text{LiNi}_2\text{CrO}_4$.

The purpose of the present research is to characterize the insoluble electrode deposit formed when Li_2MoO_4 is reduced in the presence of ZnCl_2 in LiCl-KCl eutectic. The knowledge gained through this study will contribute to the over-all understanding of molybdate electrochemistry (4, 5) and should aid the interpretation of the mechanism of the electrochemical reduction of Li_2MoO_4 in LiCl-KCl eutectic.

Experimental

Solvent.—The eutectic mixture of potassium chloride [41 mole per cent (m/o)] and lithium chloride (59 m/o) at 450°C was used as a solvent system. The LiCl-KCl eutectic was obtained from Anderson Physics Laboratories, Incorporated, Champaign, Illinois. The method of purification has been described (1).

Apparatus.—The instrumentation and equipment used in this study have been previously described (1-5).

Electrolytic cell.—The cell used in this experiment has been previously described (6). Within this cell and under an atmosphere of dry, oxygen-free argon, the solvent was allowed to collect into the fritted compartments which were used as experimental cells. At the end of the experiment the volume of each compartment was determined by titrating its chloride content, and making calculations from the known density of the melt at 450°C .

Electrodes.—The reference electrode was a platinum foil in contact with platinum(II) solution. This reference electrode has been shown to be reproducible and nonpolarizable over a long period of time (7). The Pt indicator electrode used in this study has been pre-

viously described (1-5). The electrode had a geometric area of 0.5 cm^2 and was constructed so that the glass-metal seal was always kept above the level of the melt. The platinum gauze electrodes used to prepare samples of the film, as well as the carbon electrode which served as counterelectrode in all electrochemical investigations in the melt, were constructed as described by Propp (1).

Chemicals.—All chemicals used in this study were reagent grade. ZnMoO_4 was prepared by fusion of ZnO and MoO_3 at 700°C (8) as well as by the methods described by Schultze (9), Carriere (10), and Jander (11). The product was light rose in color and has been identified by x-ray and chemical analysis as ZnMoO_4 . Those chemicals containing water of hydration were vacuum dried at 110°C before being added to the melt. Solid chemicals were added to the melt by means of a small glass spoon. A blanket of argon was kept over the melt at all times to exclude oxygen and water vapor. The purification train used in purifying the argon has been described (1-5).

Experimental techniques.—Samples of the electrode deposit resulting from the reduction were obtained by constant current electrolysis using platinum gauze electrodes. Before their insertion in the melt solution, the gauze electrodes were cleaned in boiling, concentrated HNO_3 , rinsed with distilled water, and dried at 130°C for 20 hr. After the material had been deposited on the electrode, the electrode was allowed to cool, washed with deionized water, and dried at 120°C . The deposits were then dissolved in 5 ml of concentrated nitric acid by heating on a hot plate. The zinc content of the solution was conveniently determined by a simple EDTA titration with Eriochrome Black T as the indicator. The molybdenum content of the deposit was determined by addition of an excess of Pb^{2+} which was backtitrated with EDTA using xylenol orange as the indicator. The total molybdenum was also obtained by amperometric titration with lead, a procedure developed by Aylward (12). The lithium content was determined using flame photometry, observing the Li emission at 670.8 nm . X-ray powder diffraction patterns were obtained using an 11.47-cm camera loaded with Ilford Type G x-ray film and exposed to Ni filtered $\text{CuK}\alpha$ radiation. The Cu tube was mounted in a Nolco generator. Chloride was determined by the Volhard method.

* Electrochemical Society Active Member.

Key words: fused salts, zinc molybdate, chronopotentiometry.

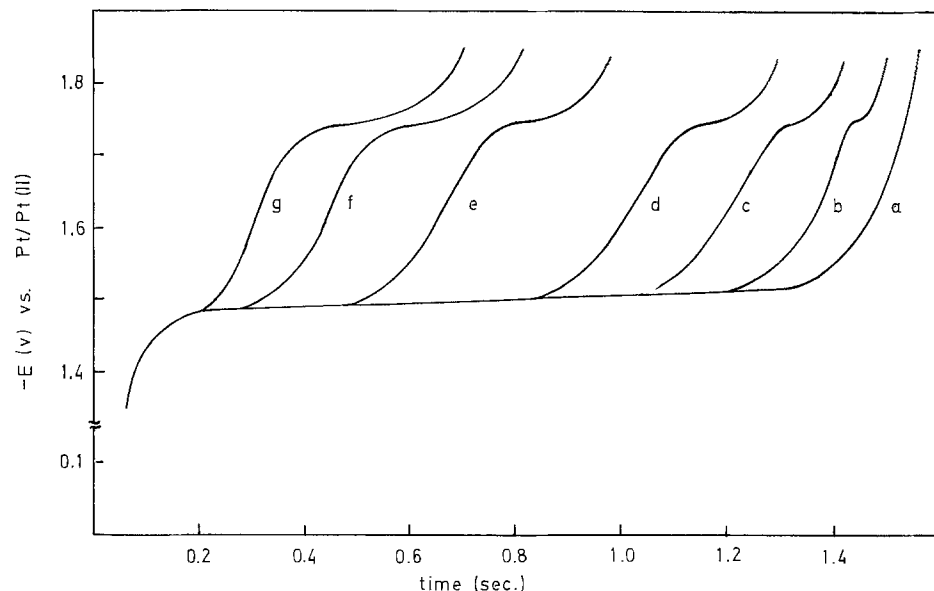


Fig. 1. Potential-time curves for chronopotentiometric reduction of mixture $\text{ZnCl}_2\text{-Li}_2\text{MoO}_4$. Current density = 50.4 mA/cm^2 .

	Concentration of ZnCl_2 , mm	Concentration of Li_2MoO_4 , mm
a.	74	0
b.	74	7.55
c.	74	19.3
d.	74	32.7
e.	74	51.8
f.	74	87.8
g.	74	118.5

Results and Discussion

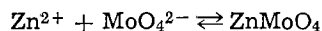
$\text{ZnCl}_2\text{-Li}_2\text{MoO}_4\text{-LiCl-KCl}$ system.—Under certain conditions one chronopotentiometric wave is observed for the reduction of Li_2MoO_4 at -1.75V vs. the Pt(II)/Pt reference electrode. This reduction was found to be diffusion controlled over the time interval investigated. Chronopotentiograms were obtained over the concentration range ($5.3 \times 10^{-3}\text{M}$ $\text{Li}_2\text{MoO}_4\text{-}153.3 \times 10^{-3}\text{M}$). The average value of $I\tau^{1/2}/C$ calculated from the chronopotentiometric results is $175 \text{ A sec}^{1/2} \text{ mole}^{-1} \text{ cm}^3$, which agrees with the results obtained earlier (4, 5).

Chronopotentiometry of ZnCl_2 in the absence of Li_2MoO_4 revealed a wave with a quarter-wave potential of -1.5V vs. the Pt(II)/Pt reference electrode. Diffusion control was shown by the constancy of $I\tau^{1/2}/C$ at $800 \pm 4 \text{ A sec}^{1/2} \text{ mole}^{-1} \text{ cm}$ for four different concentrations ranging from $8.34 \times 10^{-3}\text{M}$ to $125 \times 10^{-3}\text{M}$ at three different current densities. The above value of $I\tau^{1/2}/C$ was used as a calibration factor for evaluating Zn(II) concentration in calculating the formation constant of ZnMoO_4 .

The effect of Zn(II) on the reduction of Li_2MoO_4 was demonstrated by successively increasing the concentration of Li_2MoO_4 at constant Zn(II) concentration as shown in Fig. 1. Two chronopotentiometric waves were observed. The first wave has a quarter-wave potential at -1.5V vs. the Pt(II)/Pt reference electrode corresponding to the reduction of Zn(II) and the other at -1.75V corresponding to the reduction of molybdate. It was observed that an increase on the molybdate concentration in the melt causes a decrease of the first transition time and at the same time an increase of the second transition time. The quantitative variation of the transition time constant was tested by running duplicates of three current densities at different Li_2MoO_4 concentrations. The decrease of $I_0\tau^{1/2}$, for the reduction step at -1.5V , with increasing Li_2MoO_4 concentration, is demonstrated in Table I.

The chronopotentiometric data for the second reduction are presented in Table II.

The data in Tables I and II can be quantitatively interpreted in terms of an equilibrium



$$K = \frac{[\text{ZnMoO}_4]}{[\text{Zn}^{2+}][\text{MoO}_4^{2-}]} = \frac{X}{(C_{\text{ZnCl}_2} - X)(C_{\text{Li}_2\text{MoO}_4} - X)}$$

The results, given in Table III indicate that $K = 30.1 \pm 2.9$, as calculated from the data in Table I.

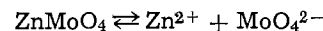
$\text{ZnMoO}_4\text{-LiCl-KCl}$ system.—In order to examine further the electrochemical reduction of Li_2MoO_4 in the

presence of ZnCl_2 , chronopotentiograms of ZnMoO_4 in molten LiCl-KCl were obtained.

Qualitatively, two chronopotentiometric waves occur in the case of ZnMoO_4 reduction with quarter-wave potentials at -1.5V and at -1.75V vs. the Pt(II)/Pt reference electrode.

The Sand equation was tested by running duplicates of four current densities at five different ZnMoO_4 concentrations. The dependence of $I_0\tau^{1/2}$ on C is demonstrated in Table IV for the first wave and in Table V for the second reduction.

The data in Tables IV and V can be quantitatively interpreted in terms of an equilibrium



In order to compare the results given in Table IV for the system ZnMoO_4 with those obtained for the system $\text{Li}_2\text{MoO}_4\text{-ZnCl}_2$ one can write for the above equilibrium

$$K = \frac{[\text{ZnMoO}_4]}{[\text{Zn}^{2+}][\text{MoO}_4^{2-}]} = \frac{(C_{\text{ZnMoO}_4} - X)}{X^2}$$

Table I. Chronopotentiometric data for the first reduction step of ZnCl_2 and Li_2MoO_4 mixtures

$$C_{\text{ZnCl}_2} = 74 \cdot 10^{-3} \text{ (M)}$$

$C_{\text{Li}_2\text{MoO}_4}$ (M)	I_0 , $\text{mA} \cdot \text{cm}^{-2}$	τ , sec	$I_0\tau^{1/2}$ ($\text{A} \cdot \text{sec}^{1/2}$ cm^{-2})
$7.55 \cdot 10^{-3}$	50.4	1.20	$55.2 \cdot 10^{-3}$
	57.8	0.90	$54.9 \cdot 10^{-3}$
	69.8	0.65	$56.3 \cdot 10^{-3}$
	Avg		$55.4 \cdot 10^{-3}$
$19.30 \cdot 10^{-3}$	50.4	1.00	$50.4 \cdot 10^{-3}$
	57.8	0.70	48.4
	69.8	0.55	$51.7 \cdot 10^{-3}$
	Avg		$50.2 \cdot 10^{-3}$
$32.7 \cdot 10^{-3}$	50.4	0.75	$43.6 \cdot 10^{-3}$
	57.8	0.55	$42.8 \cdot 10^{-3}$
	69.8	0.40	$44.1 \cdot 10^{-3}$
	Avg		$43.5 \cdot 10^{-3}$
$51.8 \cdot 10^{-3}$	50.4	0.45	$33.8 \cdot 10^{-3}$
	57.8	0.40	36.6
	69.8	0.25	$34.9 \cdot 10^{-3}$
	Avg		$35.1 \cdot 10^{-3}$
$87.8 \cdot 10^{-3}$	40.4	0.40	$25.6 \cdot 10^{-3}$
	50.4	0.25	$25.2 \cdot 10^{-3}$
	57.8	0.15	$22.4 \cdot 10^{-3}$
	Avg		$24.4 \cdot 10^{-3}$
$118.5 \cdot 10^{-3}$	36.2	0.25	$18.1 \cdot 10^{-3}$
	40.4	0.20	$18.1 \cdot 10^{-3}$
	50.4	0.15	$19.5 \cdot 10^{-3}$
	Avg		$18.6 \cdot 10^{-3}$

Table II. Chronopotentiometric data for the second reduction step of $ZnCl_2$ and Li_2MoO_4 mixtures

$$C_{ZnCl_2} = 74 \cdot 10^{-3} (M)$$

$C_{Li_2MoO_4}$ (M)	I_0 , mA · cm ⁻²	τ_2 , sec	$\tau^{1/2}$, sec ^{1/2}	$I_0 \tau^{1/2}$ (A · sec ^{1/2} cm ⁻²)
7.55 · 10 ⁻³	50.4	—	—	—
18.30 · 10 ⁻³	50.4	0.05	0.025	1.26 · 10 ⁻³
	57.8	—	—	—
	69.8	—	—	—
32.7 · 10 ⁻³	50.4	0.10	0.056	2.80 · 10 ⁻³
	57.8	0.05	0.033	1.91 · 10 ⁻³
	69.8	—	—	—
			Avg	2.36 · 10 ⁻³
51.8 · 10 ⁻³	50.4	0.12	0.084	4.23 · 10 ⁻³
	57.8	0.08	0.060	3.47 · 10 ⁻³
	69.8	—	—	—
			Avg	3.85 · 10 ⁻³
87.8 · 10 ⁻³	40.4	0.30	0.204	8.24 · 10 ⁻³
	50.4	0.18	0.156	7.86 · 10 ⁻³
	57.8	0.10	0.112	6.47 · 10 ⁻³
			Avg	7.52 · 10 ⁻³
118.5 · 10 ⁻³	36.2	0.45	0.422	15.2 · 10 ⁻³
	40.4	0.35	0.294	11.9 · 10 ⁻³
	50.4	0.25	0.245	12.3 · 10 ⁻³
			Avg	13.1 · 10 ⁻³

Table III. Evaluation of equilibrium constant from Table I*

$C_{Li_2MoO_4}$ (M)	[Zn ²⁺] (M)	[MoO ₄ ²⁻] (M)	X (M)	K (M ⁻¹)
7.55 · 10 ⁻³	68.8 · 10 ⁻³	2.35 · 10 ⁻³	5.2 · 10 ⁻³	32.1
18.30 · 10 ⁻³	62.5 · 10 ⁻³	7.80 · 10 ⁻³	11.5 · 10 ⁻³	24.0
32.70 · 10 ⁻³	54.0 · 10 ⁻³	12.7 · 10 ⁻³	20.0 · 10 ⁻³	29.2
51.80 · 10 ⁻³	44.0 · 10 ⁻³	21.8 · 10 ⁻³	30.0 · 10 ⁻³	31.3
87.80 · 10 ⁻³	30.5 · 10 ⁻³	44.3 · 10 ⁻³	43.5 · 10 ⁻³	32.2
118.50 · 10 ⁻³	23.3 · 10 ⁻³	67.8 · 10 ⁻³	50.7 · 10 ⁻³	32.1
			Avg	30.2

* Standard deviation is ±2.94.

Table IV. Chronopotentiometric data for the first reduction step of $ZnMoO_4$

C_{ZnMoO_4} (M)	I_0 , mA · cm ⁻²	τ , sec	$I_0 \tau^{1/2}$ (A · sec ^{1/2} cm ⁻²)	
29.05 · 10 ⁻³	14.4	1.05	14.8 · 10 ⁻³	
	20.0	0.50	14.1 · 10 ⁻³	
	24.4	0.38	15.1 · 10 ⁻³	
	30.2	0.24	14.8 · 10 ⁻³	
			Avg	14.7 · 10 ⁻³
44.3 · 10 ⁻³	14.4	1.80	19.3 · 10 ⁻³	
	20.0	0.95	19.5 · 10 ⁻³	
	30.2	0.46	20.4 · 10 ⁻³	
	36.2	0.32	20.4 · 10 ⁻³	
			Avg	20.0 · 10 ⁻³
87.9 · 10 ⁻³	30.2	1.00	30.2 · 10 ⁻³	
	36.2	0.78	32.0 · 10 ⁻³	
	40.4	0.60	31.3 · 10 ⁻³	
	50.4	0.40	32.0 · 10 ⁻³	
			Avg	31.4 · 10 ⁻³
107.0 · 10 ⁻³	30.2	1.45	36.4 · 10 ⁻³	
	36.2	0.94	35.3 · 10 ⁻³	
	40.4	0.74	34.7 · 10 ⁻³	
	50.4	0.50	35.7 · 10 ⁻³	
			Avg	35.5 · 10 ⁻³
142.7 · 10 ⁻³	30.2	1.90	41.7 · 10 ⁻³	
	36.2	1.42	43.2 · 10 ⁻³	
	40.4	1.10	42.4 · 10 ⁻³	
	50.4	0.70	42.2 · 10 ⁻³	
			Avg	42.4 · 10 ⁻³

The results given in Table VI for the equilibrium constant have been obtained using the data from Table IV.

Characterization of electrode deposit.—Samples of electrode deposit were prepared by constant current electrolysis. The cathode was immersed into 3.7 ml 0.035M $ZnMoO_4$ and attempts were made to prepare coulometrically the reduction product at -1.5V. It was

Table V. Chronopotentiometric data for the second reduction step of $ZnMoO_4$

C_{ZnMoO_4} (M)	I_0 , mA · 10 ⁻³	τ_2 , sec	$\tau^{1/2}$, sec ^{1/2}	$I_0 \tau^{1/2}$ (A · sec ^{1/2} cm ⁻²)
29.05 · 10 ⁻³	14.4	0.50	0.216	3.76 · 10 ⁻³
	20.0	0.30	0.188	3.11 · 10 ⁻³
	24.4	0.20	0.143	3.49 · 10 ⁻³
	30.2	0.14	0.129	3.89 · 10 ⁻³
			Avg	3.56 · 10 ⁻³
44.3 · 10 ⁻³	14.4	0.85	0.290	4.18 · 10 ⁻³
	20.0	0.50	0.231	4.62 · 10 ⁻³
	30.2	0.20	0.136	4.11 · 10 ⁻³
	36.2	0.14	0.117	4.24 · 10 ⁻³
			Avg	4.29 · 10 ⁻³
87.9 · 10 ⁻³	30.2	0.55	0.245	7.24 · 10 ⁻³
	36.2	0.40	0.203	7.35 · 10 ⁻³
	40.4	0.30	0.176	7.11 · 10 ⁻³
	50.4	0.20	0.141	7.10 · 10 ⁻³
			Avg	7.24 · 10 ⁻³
107.0 · 10 ⁻³	30.2	0.80	0.295	8.91 · 10 ⁻³
	36.2	0.50	0.231	8.36 · 10 ⁻³
	40.4	0.40	0.203	8.40 · 10 ⁻³
	50.4	0.30	0.187	9.40 · 10 ⁻³
			Avg	8.77 · 10 ⁻³
142.7 · 10 ⁻³	30.2	1.05	0.338	10.21 · 10 ⁻³
	36.2	0.70	0.263	9.52 · 10 ⁻³
	40.4	0.60	0.256	10.34 · 10 ⁻³
	50.4	0.40	0.213	10.74 · 10 ⁻³
			Avg	10.20 · 10 ⁻³

Table VI. Evaluation of equilibrium constant from Table IV*

C_{ZnMoO_4} (M)	X	($C_{ZnMoO_4} - X$)	K, M ⁻¹	
29.05 · 10 ⁻³	18.38 · 10 ⁻³	10.67 · 10 ⁻³	31.6	
44.30 · 10 ⁻³	24.88 · 10 ⁻³	19.42 · 10 ⁻³	31.4	
87.90 · 10 ⁻³	39.20 · 10 ⁻³	48.70 · 10 ⁻³	31.7	
107.0 · 10 ⁻³	44.40 · 10 ⁻³	62.60 · 10 ⁻³	31.7	
142.7 · 10 ⁻³	52.90 · 10 ⁻³	89.80 · 10 ⁻³	32.1	
			Avg	31.7

* Standard deviation is ±0.23.

possible to monitor the electrode potential only at -1.65V vs. Pt(II)/Pt reference electrode using current densities of 10, 20, 30, and 40 mA/cm². Examination of the cathode showed only one type of solid product, a dark brown solid which adhered to the surface of the electrode. Following electrolysis, the samples were washed with distilled water and dried at 130°C.

Qualitatively, the electrode deposit was found to contain Li, Zn, and Mo. Samples of the deposit were analyzed by the methods described. Table VII summarizes the composition of four samples of deposit prepared under identical conditions. If it is assumed that the deposit contains only Li, Mo, Zn, and O, one obtains the empirical formula $Li_2Zn_{0.5}MoO_4$ or $Li_4ZnMo_2O_8$. On the other hand it is not possible from the data given in Table VII to obtain the exact oxidation state of Mo, both because it was supposed that O⁼ weight percentages add up to 100% of the sample weight and because some $ZnMoO_4$ may be incorporated into the deposit during the electrolysis. $ZnMoO_4$ is not soluble in water or any other suitable solvent. X-ray diffraction studies were therefore carried out on the dried sample.

Table VII. Typical analysis of $ZnMoO_4$ deposit prepared at constant current

	A	B	C	D
Sample weight, mg	32	35.3	43.5	61.4
Li, per cent weight	6.68	6.80	6.75	6.70
Zn, per cent weight	15.84	15.65	15.60	15.79
Mo, per cent weight	46.65	46.95	47.12	47.02
Per cent weight O = to 100	30.83	30.60	30.53	30.49
Empirical formula				
(A)	$Li_{1.98}Zn_{0.5}MoO_{3.98}$	(B)	$Li_2Zn_{0.49}MoO_{3.91}$	
(C)	$Li_{1.98}Zn_{0.49}MoO_{3.89}$	(D)	$Li_{1.97}Zn_{0.49}MoO_{3.89}$	

Table VIII. X-ray powder diffraction pattern of $ZnMoO_4$ deposit prepared at constant current

d (Å)	I/I ₀
4.770	20
4.085	20
2.9595	30
2.4815	80
2.380	10
2.0805	100
1.8924	5
1.8464	5
1.6848	20
1.5876	50
1.4904	40
1.4576	40

The "d" spacings and relative intensities of the diffraction pattern are presented in Table VIII. The "d" spacings were not comparable with any known Mo or Zn compound listed in the ASTM files.

From the preceding study of molybdate reduction in which the product $Li_5Mo_2O_8$ was identified (4), the simplest reduction mechanism for the formation of $Li_4ZnMo_2O_8$ would involve the reduction of MoO_4^{2-} to MoO_4^{3-} , which is then incorporated into a crystal lattice with Li^+ and Zn^{2+} , in the appropriate ratio. In the absence of Zn^{2+} , both MoO_4^{2-} and MoO_4^{3-} are involved in the final product.

Acknowledgment

Financial support of this research was provided by the Army Research Office, Durham, North Carolina.

Manuscript submitted April 14, 1975; revised manuscript received July 17, 1975.

Any discussion of this paper will appear in a Discussion Section to be published in the June 1976 JOURNAL. All discussions for the June 1976 Discussion Section should be submitted by Feb. 1, 1976.

Publication costs of this article were partially assisted by the University of Florida.

REFERENCES

- H. A. Laitinen and J. H. Propp, *Anal. Chem.*, **41**, 645 (1969).
- H. A. Laitinen and K. W. Hanck, *This Journal*, **118**, 9 (1971).
- H. A. Laitinen and B. N. Popov, *ibid.*, **117**, 644 (1970).
- H. A. Laitinen and B. N. Popov, *ibid.*, **120**, 1346 (1973).
- B. N. Popov, Ph.D. Thesis, University of Zagreb (1972).
- H. A. Laitinen and H. C. Gaur, *Anal. Chim. Acta*, **18**, 1 (1958).
- H. A. Laitinen and W. S. Ferguson, *Anal. Chem.*, **38**, 644 (1957).
- A. N. Zelikman, C. A., **51**, 10287i (1957), Bulletin Cdb-4 Climax Molybdenum Chemicals, Oct. (1962).
- H. Schultze, *Lieb. Ann.*, **126**, 50 (1963), Bulletin Cdb-4 Climax Molybdenum Chemicals, Oct. (1962).
- E. Carriere, H. Guiter, and M. Annour, *Bull. Soc. Chim. France*, **261** (1948), Bull. Cdb-4 Climax Molybdenum Chemicals, Oct. (1962).
- W. Jander, *Z. Anorg. Allgem. Chem.*, **190**, 399 (1930), Bull. Cdb-4 Climax Molybdenum Chemicals, Oct. (1962).
- G. H. Aylward, *Anal. Chim. Acta*, **14**, 386 (1956).

Kinetics of Electrogenative Hydrogenation over Platinum Black Electrocatalyst

Stanley H. Langer* and George P. Sakellaropoulos*

Department of Chemical Engineering, University of Wisconsin, Madison, Wisconsin 53706

ABSTRACT

The kinetics of the electrocatalytic hydrogenation of ethylene at positive potentials has been studied over polytetrafluoroethylene-bonded, porous platinum black electrodes in perchloric acid electrolyte. Pore diffusion was generally not a significant factor except at low concentrations of reactants. Steady-state kinetic parameters and deuterium exchange results suggest that surface reaction of hydrogen with ethyl radicals is rate limiting. A mechanistic model is proposed and examined in terms of Temkin adsorption of hydrogen atoms in the low potential region ($<0.18V$). Strong Langmuir adsorption of ethylene appears to take place for all mechanisms considered. The energy production of the electrogenerative reactor is favored by high electrolyte concentration, high alkene partial pressure, elevated temperatures, and increased catalytic loading.

Few electrocatalytic reactions have been well characterized; the frequent referral to hydrogen and oxygen electrode reactions, and not many others, in the context of "electrocatalysis" is symptomatic of this situation. The electrocatalytic nature of electrogenerative hydrogenation and the availability of significant amounts of information on the process from earlier investigations (1-6) stimulated a study of the kinetics of the hydrogenation reaction at an ethylene electrode

with porous platinum black electrocatalyst. Such kinetic information should provide an additional basis for comparison with conventional catalytic hydrogenation (7-10) and with other reactions, which utilize these and similar electrodes for generation of current.

This electrogenerative process involves the operation of a hydrogen electrode against a hydrogenating olefinic electrode separated by an aqueous, acidic, barrier electrolyte phase (1-3). The external circuit between the electrodes is regulated to allow operation at varying voltages and currents generated by the reacting species. The olefinic electrode operates at positive po-

* Electrochemical Society Active Member.

Key words: ethylene, catalysis, porous electrodes, deuterium exchange.

tentials relative to the hydrogen electrode. The study here differs from a number of others [some of which we mentioned earlier (1-3)] in that hydrogen *per se* is not placed in the olefin chamber during the electrochemical reaction. Davitt and Albright (11) and Fujikawa *et al.* (12) carried out some related studies using sulfuric acid electrolyte in which ethylene is more soluble than in the perchloric acid of our system. The open-circuit voltage of the present system differs significantly from that of other workers using sulfuric acid electrolyte (11, 12) and from systems where gaseous hydrogen is present (4-6, 12). We chose perchloric acid because it is a strongly ionized electrolyte which tends not to be adsorbed. Furthermore, there is the advantage of dealing with a univalent acid.

The electrogenerative reactor allows a relatively reproducible, controlled steady-state investigation of the catalytic process with a constant composition electrolyte. The use of porous electrodes calls for caution in the interpretation of the kinetics, but makes the results applicable to macro current operation.

Experimental

Cell.—The free electrolyte cell is shown in Fig. 1. The electrolyte chamber of polytrifluorochloroethylene, with a capacity of about 4.5 ml of electrolyte, had two small $\frac{1}{8}$ in. ports to allow filling and removal of electrolyte. A groove at the upper end of this chamber minimized the accumulation of gas bubbles between the two electrodes. Polytetrafluoroethylene sheet gaskets were found to effectively prevent electrolyte leakage during prolonged cell operation. The assembly was held together with four $\frac{3}{16}$ in. diameter stainless steel bolts. Polypropylene screen spacers were used to press the electrodes uniformly against platinum screen current collectors. No stainless steel parts came in contact with the electrolyte. Excess gas was fed continuously at the back of each electrode at a rate that would not affect the cell polarization.

Electrodes.—American Cyanamid polytetrafluoroethylene-backed, polytetrafluoroethylene-bonded, platinum black, commercial porous electrodes were used (13, 14). These electrodes are supported on tantalum screen and are gas permeable, liquid impermeable. LAA-2 electrodes contain 9 mg Pt/cm² electrode area (13). Type LAA-25 carry a catalyst load of 25 mg Pt/cm². The LAA electrodes were used in direct con-

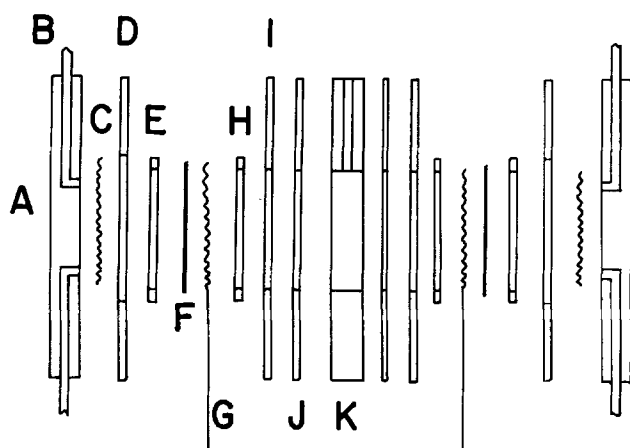


Fig. 1. Exploded view of static free electrolyte cell. A, Lucite face plate, 2.5 in. square, 0.25 in. thickness; B, stainless steel tubing, $\frac{1}{8}$ in. diameter; C, polypropylene screen spacer, 1 in. diameter; D, I, Viton-A gaskets, $\frac{1}{16}$ in. thickness; E, polytetrafluoroethylene ring gasket, 1.25×1 in. diameter, $\frac{1}{16}$ in. thickness; F, porous platinum-polytetrafluoroethylene electrode, 1.25 in. diameter; G, current collector, platinum screen 45 \times 45 mesh, 1.25 in. diameter; H, Viton-A ring gasket, 1.25×1 in. diameter, $\frac{1}{16}$ in. thickness; J, polytetrafluoroethylene film gasket, 0.002 in. thickness; K, electrolyte chamber, KEL-F, 0.25 in. thickness, with ports.

tact with free electrolyte with an exposed geometric area of 5.07 cm². The platinum black had a surface area of 20-25 m²/g (3, 15).

Flow system.—An all-glass and Teflon auxiliary gas system was used, Fig. 2. Both sides of the cell could be purged with nitrogen or hydrogen, and ethylene could be introduced to the cathode without exposing the electrodes to the atmosphere. Nitrogen and ethylene were prepurified by being passed through alkaline pyrogallol solution and over packed beds of calcium sulfate and Molecular Sieves 13X or 4A. All gases were saturated with water before entering the cell to minimize electrolyte evaporation. Gas samples were collected at the cell exit and analyzed by gas chromatography (Carle 8000, Basic Gas Chromatograph with a Porapak QS aluminum column, 6 ft long, $\frac{1}{8}$ in. diameter). Sampling bulbs and handling techniques were similar to those used earlier (3).

Materials.—Commercial prepurified nitrogen and hydrogen were employed. Ethylene, C.P. grade, and an ethylene standard mixture, 10.27%, in prepurified nitrogen were obtained from the Matheson Company. The ionic strength of all perchloric acid (A.R., Baker Chemical Company) electrolyte solutions were made up to 2N, assuming complete ionization, by adding lithium perchlorate (A.R., Alfa Inorganics-Ventron).

Electrical system.—A load box (with 1-1000 ohm variable resistors) was used to control the cell current. The current was occasionally stabilized with a constant current supply (Quan Tech, Model 151B). Currents were measured with an accurate ammeter (Sensitive Research Instrument Corporation, Polyrange S). Cell voltage was measured with a calibrated digital voltmeter (United Systems Corporation, Digitek 201). The cell internal resistance was measured before each run, with hydrogen flowing over both electrodes, with a milliohmeter (Keithley Instruments, Model 503).

Procedure.—Elimination of oxygen and impurities from the cell and good electrocatalyst pretreatment were essential for reproducible results. The following procedure allowed repeated reproducible results to within 5%. After cell assembly, the electrolyte compartment was filled slowly through one of the electrolyte compartment ports to avoid air bubble formation. The ports were stoppered with polyethylene plugs to eliminate oxygen diffusion into the cell. The anodic and cathodic gas compartments were purged with nitrogen for 20 min. Hydrogen was then passed through both electrode compartments for at least 15 min while shorting the cell. During this time period, the current from the cell was normally less than 1 μ A and the open-circuit voltage (OCV) effectively zero. At the end of the hydrogen pretreatment of the electrocata-

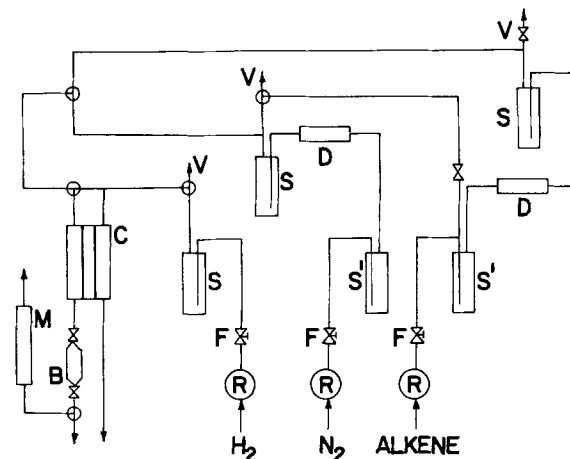


Fig. 2. Gas flow system. C, cell; S, gas saturator; S', pyrogallol solution; D, drier and adsorbing molecular sieves; F, fine control valve; R, gas regulator; B, sampling bulb; M, flow meter; V, vent.

lysts, the internal resistance of the cell was measured and was found constant for at least 5 min. Other experiments showed that the cell internal resistance, R_{int} , remained constant throughout each experiment; IR-correction using the measured R_{int} or a Kordes-Marko bridge agreed within 2-3 mV. The cathode compartment was flushed with nitrogen for 10 min before ethylene was allowed to contact the cathode. The flow rate of all gases was normally about 8 ml/min at atmospheric pressure. For ethylene mixtures other than 1.0 and 0.10 atm, additional nitrogen was introduced continuously into the ethylene stream. By bubbling the gas mixture through two gas-washing bottles in series, complete mixing was achieved. Gas chromatographic (GC) analysis of samples, before and after each run, ensured the constant composition of the mixture to within ± 0.002 atm. Open-circuit voltage was stabilized within 20-30 min as indicated by a change of less than 2 mV/5 min. Preliminary polarization runs removed any remaining traces of oxygen or impurities. All data represent steady-state values, normally achieved after about 3 min at any specified current, and after at least two preliminary polarization runs. Results obtained with a variable resistor load or a constant current supply were practically identical. Gas samples were obtained after 10 min operation at steady state and they were analyzed by GC immediately. The hydrogen electrode did not polarize more than 8 mV/decade, measured against a hydrogen reference electrode in the same electrolyte. The IR-free cell voltage was corrected for the anode polarization and the ethylene electrode potential is given with reference to the NHE. All current densities are based on exposed electrode area.

Results

In the course of operation of the ethylene-hydrogen cell in the region of 0.52-0.25V, high polarization is observed which does not obey either a linear or logarithmic current relationship. At lower potentials, Tafel behavior with a slope of 0.035V is found at the cathode as shown in Fig. 3. As the concentration of H^+ or C_2H_4 is decreased, some change in the Tafel slope occurs before a limiting current is attained. After correction for concentration overpotential associated with the limiting current, the Tafel slope attains its intrinsic value of 0.035V except for acid concentrations below 0.2N for which a slope of 0.055V is observed (Fig. 4). At ethylene partial pressures below about 0.10 atm, Nernstian hydrogen transport and evolution (2) becomes significant after a limiting current seemingly is observed, as shown in Fig. 5. In our earlier studies (1-3) we did not report results for the concentrations at which limiting currents might be observed.

If nitrogen flow is substituted for ethylene in the cathode compartment, some hydrogen ions can discharge at positive potentials relative to the normal

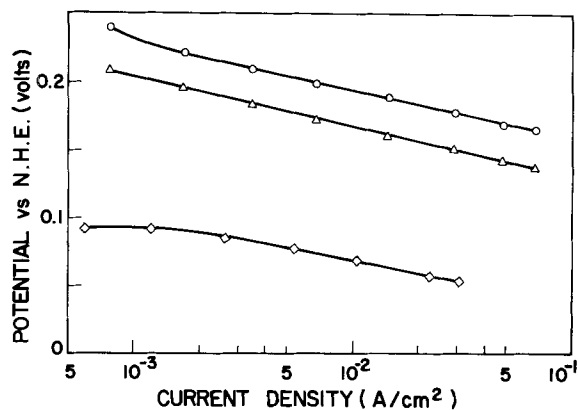


Fig. 3. Effect of catalytic load on ethylene electrode potential. Electrolyte, 2N $HClO_4$. Temperature, 25°C. \circ , Platinum 25 mg/cm²; Δ , platinum 9 mg/cm²; \diamond , platinum 9 mg/cm², the hydrogen evolution reaction.

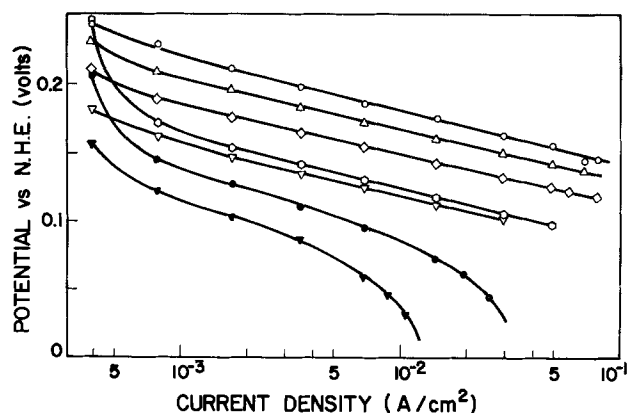


Fig. 4. Effect of electrolyte concentration on cathode potential. Electrolyte, aqueous $HClO_4$ - $LiClO_4$. Temperature, 25°C. LAA-2 electrode. \circ , 3N $HClO_4$; Δ , 2N; \diamond , 1N; \square , 0.5N; ∇ , 0.4N; \bullet , 0.2N; \blacktriangledown , 0.1N $HClO_4$.

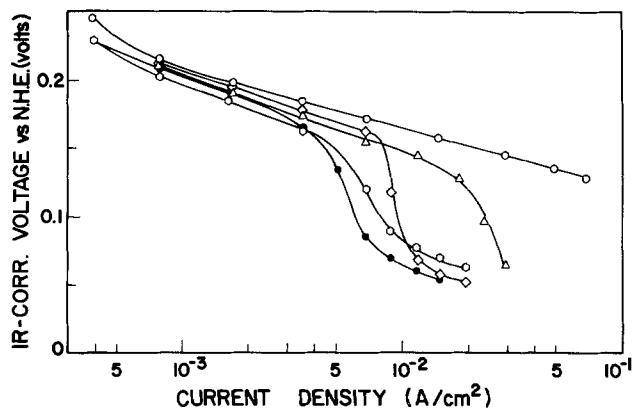


Fig. 5. Effect of ethylene partial pressure on cathode potential. Electrolyte, 2N $HClO_4$. Temperature, 26°C. LAA-2 electrode. \circ , $P_{C_2H_4} = 1$ atm; Δ , 0.1 atm; \diamond , 0.06 atm; \bullet , 0.04 atm; \circ , 0.03 atm.

hydrogen electrode (NHE) because of the Nernst or concentration driving force (2). For reference purposes here, a hydrogen-nitrogen cell was run under our experimental conditions with results shown in Fig. 3. For a given cathode potential, the current of the H_2/N_2 cell is about two orders of magnitude less than the current of the H_2/C_2H_4 cell, for comparable electrolyte concentrations. Therefore, the hydrogen evolution reaction (HER) normally can be neglected in the Tafel region of ethylene hydrogenation.

Using the data reported in Fig. 4 and 5, it is possible to estimate a reaction order with respect to either reactant with the assumption of a simple exponential rate expression

$$\left[\frac{\partial \log i}{\partial \log C_J} \right]_{T,E,C_{K \neq J}} = j \quad [1]$$

Here i represents current density, C bulk concentration of a specific reactant, and j is the order of the reaction with respect to reactant J . The straight lines of Fig. 6 support the applicability of Eq. [1] for H_3O^+ concentrations higher than 0.2N in each potential region studied. Tafel plot deviations do not allow determination of reaction orders at potentials corresponding to current densities below 0.5 mA/cm². Use of electrodes with higher catalytic loads (25 mg Pt/cm²) results in a significant decrease in cell polarization with parallel shift in Tafel lines as shown in Fig. 3.

The temperature effect on the reaction rate has been determined in our laboratories by Feiz (16). From these results, an apparent activation energy can be calculated for the temperature range of 25°-70°C using data at three temperatures. This as well as other ki-

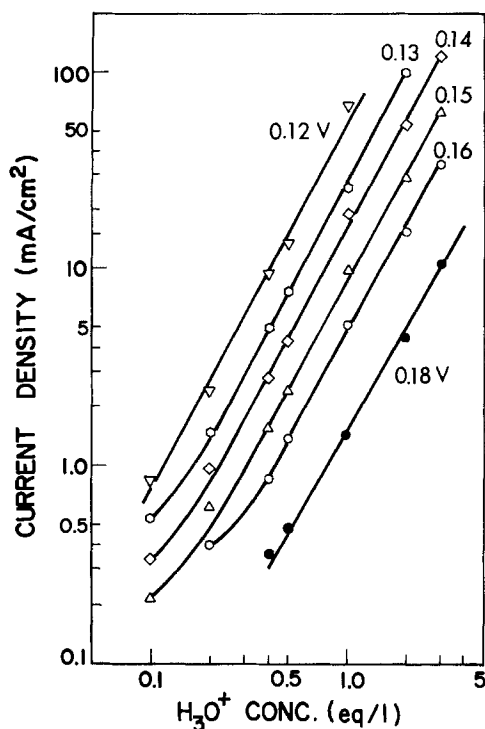


Fig. 6. Rate dependence on electrolyte concentration and electrode potential. Platinum electrode, 9 mg/cm²; $P_{C_2H_4}$, 1 atm. Temperature, 25°C.

netic data related to our system are presented in Table I for the ethylene electrode. The surface rate constant for zero potential referred to NHE, k_0 , and the calculated standard exchange current density at unit concentrations are based on the exposed geometric surface area of the electrode of 5.07 cm². The data of Table I given for the HER are based on the hydrogen concentration cell for which some experimental data are represented in Fig. 3.

Discussion

Catalyst utilization.—Heterogeneous catalytic studies over porous catalysts are often complicated by the superimposition of pore diffusion effects on the reaction kinetics. The direct measurement of reaction rate as current in an electrochemical cell, however, presents a distinct advantage over conventional catalytic investigations. Comparative analysis of the results from the electrochemical cell for systems with well-established mechanisms might, in simple cases, resolve some ambiguities regarding pore diffusion. The HER was chosen for this purpose.

The Volmer-Tafel mechanism is generally accepted for the HER, where either hydrogen atom recombination on the surface or diffusion of molecular hydrogen away from the electrode are believed to be rate limiting with platinum electrodes (17-20). The Tafel slope and reaction order observed here with respect to H^+

Table I. Kinetic parameters for ethylene hydrogenation and hydrogen evolution over platinum black at positive potentials and 25°C

Parameter	Ethylene	Hydrogen (23)
Tafel slope (V)	0.035	0.033
Reaction order in H^+	1.9	1.9
Reaction order in C_2H_4	0.1	—
Catalyst load exponent	1.5	-1.5
Apparent E_a (at 0.17V), (kcal/mole)	2.5	—
Rate constant, k_0 , (cm ² mole ⁻¹ sec ⁻¹)	8.0×10^{-4}	2.8×10^{-6}
Standard exchange current density, i_0 , (A/cm ²) ^a	1.9×10^{-13}	5.4×10^{-1}

^a Based on unit concentrations of reactants. $i_0 = nFk_0 \exp(-\alpha E^0 F/RT)$.

or H_3O^+ differ only slightly from those expected on theoretical grounds from planar electrodes. Since ethylene molecules would reach the catalytic sites from the gaseous side of the pore, diffusion of H_3O^+ to the same catalytic site is expected to be fast for the ethylene-hydrogen system as well. All observations (reaction orders, Tafel slopes) indicate that the observed kinetics have not been complicated by pore diffusion at electrolyte concentrations higher than 0.2N. This is reasonable, given the very open porosity and the short pore length of the electrodes (13, 15). Increase of the Tafel slope (Fig. 4) and straight line deviations (Fig. 6) at low acid concentrations are probably a result of hydronium ion pore diffusion limitations. At high electrolyte concentrations and intermediate currents, it is expected that the active electrocatalytic area would remain approximately constant. With careful use, the activity of our electrodes remained unchanged even after 100 hr of use under varying experimental conditions.

Catalysis enhances the rate of reaction according to the relation

$$\left[\frac{i_1}{i_2} \right]_{E,T,C,J} = \left[\frac{W_1}{W_2} \right]_{E,T,C,J}^{1.5} \quad [2]$$

for our two catalytic loadings where i_1 , i_2 are current densities corresponding to catalytic loads W_1 and W_2 , respectively. Energy recovery from the cell is significantly improved at high catalytic loads, since the operation potential is higher at any given current density.

Maintaining a constant ionic strength in the electrolyte regardless of H_3O^+ concentration should make it possible to neglect any potential drop across the diffuse layer supported by the observed relation $(\partial E/\partial \ln C_{H^+})_i = RT/F$ at constant temperature and ethylene partial pressure (21). Use of strong electrolytes $HClO_4$ and $LiClO_4$ is further advantageous, since lithium and perchlorate ions tend to adsorb less than many other ions on electrodes and catalyst poisoning is minimized. The solubility of C_2H_4 in the electrolyte is low thus avoiding "chemical shorting" of the cell. Attempting to use a similar procedure for maintaining ionic strength with sulfuric acid is more complicated since the ionization constants of the first and second hydrogens are significantly different as is well known but not always appreciated.

Limiting currents.—The slight solubility of ethylene has little effect on its mass transport to active catalytic sites because of the nature of the polytetrafluoroethylene-treated electrodes. The ethylene limiting currents, which are observed only at lower partial pressures, are enhanced by the porous electrode structure (22). Electrolyte limiting currents, i_L , are observed for hydronium ion concentrations less than 0.4N in acid. The dependence of i_L on each reactant bulk concentration $C_{J,z}$ is not linear but it is given by

$$i_{L,J} \propto C_{J,z}^\gamma \quad [3]$$

where γ varies between 1.4 and 1.5. This behavior will be discussed further in the future, in view of similar results with other electrocatalysts.

Open-circuit voltage.—The open-circuit voltage seems to follow Nernstian behavior with respect to H_3O^+ , while ethylene partial pressure has little if any effect (Fig. 7). The value of 0.52V at atmospheric pressures agrees with that observed earlier by us (3) and Fujikawa *et al.* (12). It appears that ethylene adsorbs strongly at OCV with almost full surface coverage even at relatively low ethylene partial pressures. This is further supported by the rapid approach to OCV at the end of each run (0-0.3V in about 1 min). Hydrogen is removed from the surface in the low voltage region readily by chemical reaction and desorption of the ethane formed.

Kinetic model.—The kinetic rate equation at intermediate current densities (> 0.5 mA/cm²) is of the

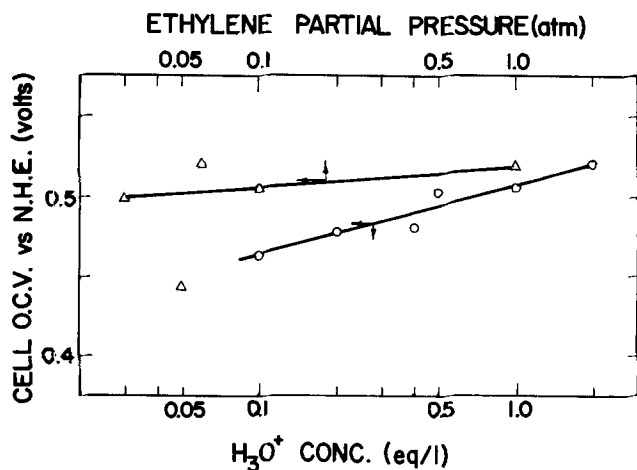


Fig. 7. Dependence of cell open-circuit voltage on acid concentration and ethylene partial pressure. Δ , 2N HClO₄; \circ , $P_{C_2H_4} = 1$ atm.

form

$$i = nFk_0P_{C_2H_4}^{0.1}C_{H^+} \exp(-2EF/RT) \quad [4]$$

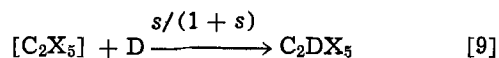
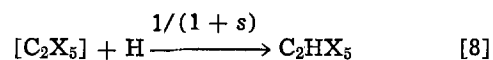
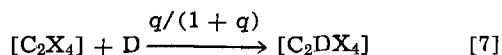
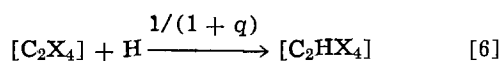
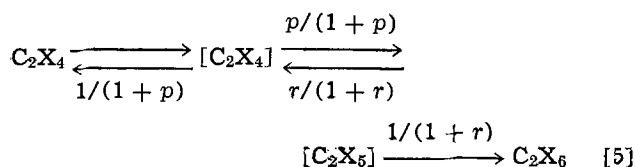
This is a close approximation of the experimental kinetic equation

$$i = nFk_0P_{C_2H_4}^{0.1}C_{H^+} \exp(-1.7EF/RT) \quad [4a]$$

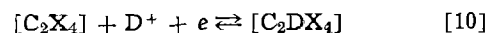
after neglecting the small differences in reaction orders. The rate constant at zero potential vs. NHE, k_0 , would depend only on temperature in an Arrhenius-type relation.

The approximation of 2 for the exact transfer coefficient determined from the Tafel slope of Table I is justified in view of the results for the simpler well characterized HER (Table I). The 20% discrepancy between Tafel slopes obtained from using Eq. [4] and [4a] is about what one can expect in comparing actual kinetic results with an idealized model. Equation [4a] reproduces the electrode polarization of Fig. 4 and 5 in the Tafel region quite satisfactorily (within 10%). If k_0 , obtained by extrapolation using Eq. [4a], is used with the approximate Eq. [4] to predict current densities, somewhat lower reaction rates result than observed experimentally, with Tafel curves shifted to lower potentials by 10-15 mV. This is expected, since the approximation for the transfer coefficient can change the extrapolated value of k_0 by about an order of magnitude.

In interpreting the kinetic results, it must be remembered that it is unlikely that two hydrogen atoms would add to the ethylene molecule simultaneously. Therefore the Tafel slope and the reaction order in H_3O^+ (Table I) are consistent with a rate-limiting step involving the addition of the second hydrogen, qualitatively in agreement with an earlier deuterium study of the addition reaction to ethylene (3). Those data recently have been reevaluated with only one partial change (value of q) in the qualitative picture of the course of the reaction on the electrocatalyst (23). Normally such information is not available from simple kinetic studies. The analysis is based on Kemball's model (24), according to the following scheme where X represents either hydrogen isotope



Brackets indicate an adsorbed species and p , q , r , and s are the model parameters representing probability ratios: p is the probability of adsorbed ethylene forming ethyl radicals, relative to the probability of ethylene desorbing; q is the probability of adsorbed ethylene acquiring a D-atom, relative to the probability of acquiring an H-atom; r is the probability of an ethyl radical reverting to ethylene, relative to the probability of reacting to form ethane; and s is the probability of an ethyl radical acquiring a D-atom, relative to the probability of acquiring an H-atom. The values of the parameters p , q , r , and s can be estimated, from the isotopic product distribution, using nonlinear regression analysis (3, 16, 23). Results are presented in Table II. A rough estimate of the rate of some steps can be made using the relations of Eq. [5]-[9]. These results are given in Table III. The monotonic increase of p with decreasing potential reflects the increase in ethylene conversion with increasing current. However, the first addition step is about an order of magnitude faster than the second one, while formation and reversal of ethyl radicals is in quasi-equilibrium. Parameters q and s are indicative of the selectivity of each step for D- or H-atom addition. If a statistically probable addition occurred on the surface, based on total hydrogen isotopes present, both parameters would have a value of 0.5. High values of q indicate a preference for deuterium over hydrogen in the first addition. At high positive potentials surface coverage by a hydrogen isotope is expected to be low. Since this model does not specify the origin of D or H, a predominant direct addition of D^+ from the deuterated electrolyte seems probable. As potential decreases, D-addition becomes less selective, but it tends to remain higher than H-addition. The model cannot distinguish between a concerted electron transfer such as



or a preceding electron transfer

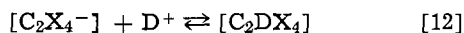
Table II. Statistical parameters for Kemball model

Sample	Current (mA)	Conversion (%)	Potential (V)	p	q	r	s
A	5.3	1.04	0.220	3.79	3.15	10.44	0.90
B	46.0	9.17	0.155	6.21	2.48	6.40	0.28
C	118.0	23.82	0.130	14.53	1.63	7.16	0.15
D	180.0	34.26	0.117	22.76	1.05	8.20	0.12
E	265.0	49.38	0.110	31.92	0.89	8.40	0.10
F	330.0	54.94	0.114	51.76	1.04	6.89	0.11
Catalytic*	—	~50.00	—	45.2	0.66	10.57	0.20

* As recalculated by nonlinear regression analysis for deuteration (8).

Table III. Relative probabilities of individual steps in the Kemball hydrogenation model

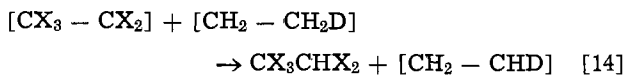
Step	A	B	C	D	E	F
$[C_2X_4] \rightarrow C_2X_4$	0.208	0.139	0.064	0.042	0.030	0.019
$[C_2X_4] \xrightarrow{+X} [C_2X_5]$	0.792	0.861	0.936	0.958	0.970	0.981
$[C_2X_5] \xrightarrow{-X} [C_2X_4]$	0.913	0.865	0.877	0.891	0.896	0.873
$[C_2X_5] \xrightarrow{+X} C_2X_6$	0.087	0.135	0.123	0.109	0.104	0.127
$[C_2X_4] \xrightarrow{+H} [C_2X_4H]$	0.241	0.287	0.380	0.488	0.530	0.490
$[C_2X_4] \xrightarrow{+D} [C_2X_4D]$	0.759	0.713	0.620	0.512	0.470	0.510
$[C_2X_5] \xrightarrow{+H} C_2X_5H$	0.528	0.780	0.869	0.892	0.908	0.900
$[C_2X_5] \xrightarrow{+D} C_2X_5D$	0.472	0.220	0.131	0.108	0.092	0.100



The selectivity of the second addition step (parameter s) varies with the potential at which addition occurs. At 0.22V (sample A), ethyl radicals seem to acquire D atoms preferentially which presumably originate from the electrolyte. The selectivity changes radically at lower potentials to favor H-addition over D-addition. For a deuterated electrolyte this can be explained by a surface reaction, such as

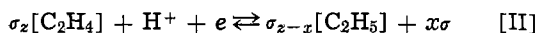


or



or surface reorganization involving a reaction of a labeled ethyl radical with an impinging ethylene molecule (3).

Based on the observed kinetics and the deuterium study under similar operating conditions, the following mechanistic model is proposed for reaction at platinum black porous electrodes at potentials less than 0.18V



where σ represents an active catalytic site, z the number of catalytic sites for adsorption of ethylene, and x the sites released by ethyl formation.

For examining this general mechanism, kinetic expressions are derived below assuming: (i) σ adsorption of ethylene, $z = 2, x = 1$ (3, 25), and (ii) π adsorption, $z = 1, x = 0$ (8, 25). The problem in testing the mechanism further is in choosing a model for the adsorption isotherms of the reactants and intermediates with appropriate assumptions.

Hydrogen adsorption on platinum in acidic electrolytes has been studied by Breiter and co-workers (26, 27). The heat of adsorption of hydrogen from 1N HClO₄ varies significantly and approximately linearly with surface coverage, θ_H , for $\theta_H > 0.2$ (26). This, and logarithmic dependence of θ_H on hydrogen pressure suggest that at intermediate coverages Temkin hydrogen adsorption on platinum could be operative. The observed relative invariance of the free energy of adsorption with surface coverage was apparently a result of a compensation effect between the enthalpy and entropy of adsorption (26).

Adsorption of ethylene on platinum from an HClO₄ solution has also been found to be strong by Gilman (28) and independent of temperature or potential. However, we as well as Fujikawa *et al.* (3, 12) find no evidence for a significant acetylene surface intermediate for the experimental conditions. No data are available on the free energy and heat of adsorption from HClO₄. Small variation of these parameters with potential has been reported for sulfuric acid (29). We have expressed our reservations regarding this electrolyte (3). But, if this result is accepted in contrast to hydrogen adsorption, then hydrogen would impose its potential-surface coverage characteristics on the system. Then, a Temkin isotherm for hydrogen adsorption would be appropriate, with a potential dependence of surface coverage by hydrogen atoms. Such an isotherm should be applicable for potentials at which $0.2 \leq \theta_T \leq 0.8$, where θ_T is the total surface coverage of the electrocatalyst (30).

For Temkin adsorption a total surface interaction energy $f(\theta)$, can be defined

$$f(\theta) = \sum_J \tau_J \theta_J \quad [15]$$

where θ_J is the surface coverage of species J with a free energy of adsorption τ_J (30). The free energy of activation for adsorption of species J will then be

$$\Delta G^{\neq}_J = \Delta G^{\neq}_{o,J} + \lambda_J x_J f(\theta) \quad [16]$$

where $\Delta G^{\neq}_{o,J}$ is the free energy of activation for adsorption at zero coverage, x_J is the number of surface sites required for adsorption, and λ_J an interaction parameter similar to a transfer coefficient. In general, $0 \leq \lambda_J \leq 1$ with $\lambda_J \simeq 0.5$ for activated adsorption with a symmetric potential energy barrier, and $\lambda_J = 0$ for nonactivated adsorption.

Assuming quasi-equilibrium for all other steps except the rate-limiting one, we can write for σ adsorption of ethylene, $z = 2, x = 1$ (step I)

$$C_E(1 - \theta_T)^2 \exp\{-[\Delta G^{\neq}_{o,I} + \lambda_I 2f(\theta)]/RT\} = \theta_E \exp\{-[\Delta G^{\neq}_{o,-I} - (1 - \lambda_I)2f(\theta)]/RT\} \quad [17]$$

$$K_I C_E(1 - \theta_T)^2 \exp[-2f(\theta)/RT] = \theta_E \quad [18]$$

where C_E is the bulk concentration of ethylene, K_I an equilibrium constant for step I, at zero coverage, and θ_T is total fractional coverage by all species. Similar expressions can be written for steps II and III

$$K_{II} \theta_E C_{H^+} \exp(-EF/RT) \exp[f(\theta)/RT] = \theta_{EH}(1 - \theta_T) \quad [19]$$

$$K_{III} C_{H^+} (1 - \theta_T) \exp(-EF/RT) \exp[-f(\theta)/RT] = \theta_H \quad [20]$$

where θ_H and θ_{EH} represent the fractional surface coverage of H-atoms and ethyl radicals, respectively. With step IV as rate limiting, the rate of reaction will be

$$i = nF r_{IV} = nF k^{\circ}_{IV} \theta_H \theta_{EH} \exp[(1 - \lambda_{IV})2f(\theta)/RT] \quad [21]$$

where r_{IV} is the rate of step IV. Since the chance of ethyl radical reversal is high (large parameter τ), the steady-state surface concentration of ethyl radicals is expected to be small compared to surface H-atoms in the low potential region. Variations in surface coverage by H-atoms (Eq. [20]) is much more dependent on the exponential terms than on θ_H, θ_T . Therefore, Eq. [20] can be simplified (30) to

$$\exp[f(\theta)/RT] \simeq K_{III} C_{H^+} \exp(-EF/RT) \quad [22]$$

Similarly θ_H and θ_{EH} can be neglected in Eq. [21]. By substituting Eq. [22] into Eq. [21], the final expression for the rate equation is obtained

$$i = nF k^{\circ}_{IV} [K_{III} C_{H^+} \exp(-EF/RT)]^{2(1-\lambda_{IV})} \quad [23]$$

A similar result is obtained for $z = 1, x = 0$ assuming π adsorption of ethylene (25). Nondissociative adsorption of ethane would be expected to be nonactivated or possibly not take place. Then Eq. [23] becomes

$$i = nF k^{\circ}_{IV} K^2_{III} C^2_{H^+} \exp(-2EF/RT) \quad [24]$$

Equations [24] and [4] are identical, if

$$k_0 = k^{\circ}_{IV} K^2_{III} \quad [25]$$

This is a result of the assumption of Temkin adsorption for hydrogen and significant adsorption of ethylene which may be governed by a Langmuir adsorption isotherm.

Langmuir adsorption for both ethylene and hydrogen with the assumption of strong ethylene adsorption and less strongly held hydrogen can also explain the observed kinetics. Equations [18]-[20] will still hold with $f(\theta) = 0$. For θ_E close to unity, then, the unoccupied fractional surface is

$$1 - \theta_T \simeq (K_I C_E)^{-1/2} \quad [26]$$

The rate equation takes the form

$$i = nF r_{IV} = nF k^{\circ}_{IV} K_I K_{II} K_{III} C_E C^2_{H^+} (1 - \theta_T)^2 \exp(-2EF/RT) \quad [27]$$

or

$$i = nFk_{IV}^{\circ}K_I K_{II} K_{III} C_E C_{H+}^2 + (K_I C_E)^{-1} \exp(-2EF/RT) \quad [28]$$

or

$$i = nFk_{IV}^{\circ}K_{II} K_{III} C_{H+}^2 \exp(-2EF/RT) \quad [29]$$

Low values of parameter s indicate that ethyl radical disproportionation (Eq. [14]) could be important. The rate equation would be for Langmuir adsorption of ethylene and $z = 1$, $x = 0$

$$i = 2nFk_{D}^{\circ} \theta_{EH}^2 = 2nFk_{D}^{\circ} [K_I K_{II} C_E C_{H+} \exp(-EF/RT)]^2 (1 - \theta_T)^2 \quad [30]$$

where k_D is the rate constant for Eq. [14]. For strong ethylene adsorption then

$$1 - \theta_T \approx (K_I C_E)^{-1} \quad [31]$$

$$i = 2nFk_{D}^{\circ} K_{II}^2 C_{H+}^2 \exp(-2EF/RT) \quad [32]$$

Kinetic experiments do not make it possible to discriminate from among Eq. [24], [29], and [32], all consistent with experimental results. It is possible that two of these mechanisms operate concurrently or at different potentials.

The three rate expressions developed here all involve some type of prior equilibrium before the rate-determining step. Two expressions involve hydrogen adsorption and all involve the ethylene \leftrightarrow ethyl interconversion. The relatively small activation energy for the over-all hydrogenation reaction then is a result of the interaction of the energy of activation of a rate step, k_{IV}° or k_D° , and heats for prior equilibria, hydrogen adsorption, and/or ethyl formation. The latter are presumably negative.

The hydrogenation kinetics found here (Eq. [4]) are in agreement with those obtained in a number of studies of platinum in heterogeneous catalysis (7, 10) but not others (9). Despite the fact that surface reaction rate is limiting under standard atmospheric operating conditions in the electrogenerative reactor heretofore (1-3), reactant concentrations may be decreased to determine order or so that mass transport of either may be rate limiting. The potential of operation is generally oxidizing for hydrogen so that the equilibrium surface concentration of hydrogen atoms must be considerably less than that found with conventional catalysis on a platinum surface. The mechanism proposed involves two different types of hydrogen addition: one electrochemical (a proton and an electron) and one essentially chemical (involving a preceding electrochemical step). If this mechanism is valid, it would seem possible that a similar mechanism may operate in heterogeneous catalysis under some conditions. The net addition of two hydrogen atoms would be involved. The mechanism of the first addition essentially could involve a proton and an electron, while the second addition would result from addition of an adsorbed hydrogen atom.

Competitive adsorption of ethylene and hydrogen, absence of electrolyte and of electric fields in gas-phase catalytic hydrogenation do make comparison with electrogenerative hydrogenation difficult. The reported kinetic parameters (7) vary widely from system to system. However, it is interesting to note that recalculated results of Bond *et al.* (8) for ethylene deuteration over Pt-on-alumina are in good agreement with our results (3, 23) at low potentials where conditions are most comparable. It has been stated (8) that the Kemball model parameters, obtained by trial and error, give only an approximate fit with the experimental product distribution so that the further application of nonlinear regression analysis (Table II) seemed appropriate. The agreement with samples D-F is surprisingly close.

Heat of activation.—By differentiating Eq. [4] and [24] with respect to temperature at constant potential, the heat of activation of step IV at zero potential,

ΔH°_{IV} , can be related more quantitatively to the apparent activation energy, E_a , for the Temkin adsorption

$$\Delta H^{\circ}_{IV} = E_a - 2\Delta H_{o,III} - 2FE \quad [33]$$

Similarly, for Langmuir adsorption the heat of activation is

$$\Delta H^{\circ}_{IV} = E_a - \Delta H_{o,II} - \Delta H_{o,III} - 2FE \quad [34]$$

and for ethyl radical disproportionation

$$\Delta H^{\circ}_{D} = E_a - 2\Delta H_{o,II} - 2FE \quad [35]$$

$\Delta H_{o,II}$ is not known for platinum electrodes. Twigg (31) has estimated that the enthalpy change is 1-10 kcal/mole for the first H-addition over nickel in the gas phase. Although these values have been based on different heats of adsorption of C_2H_4 and H_2 , they can be used for a rough approximation to estimate ΔH°_{IV} . Obviously, for $\Delta H_{o,II} = -1$ kcal/mole, the activation enthalpy calculated from Eq. [34] or [35] is too low for a surface reaction limiting step. Using $\Delta H_{o,II} = -10$ kcal/mole and $2\Delta H_{o,III} = -23$ kcal/mole (26) the activation enthalpy has been estimated for both adsorption types, Table IV.

The change in E_a and ΔH°_{IV} is expected since the Tafel plots were not linear above 0.16V for these experiments (16). Very low E_a at high potentials is indicative of strong ethylene adsorption in this region [see also Gilman (28)]. Since surface coverage by hydrogen should be low, ethyl radical disproportionation possibly could contribute to ethane formation above 0.2V. Below this potential, hydrogen adsorption increases and a transition region is observed before adsorption of hydrogen atoms prevails.

It is important to realize that electrogenerative hydrogenation takes place on catalytic electrodes under conditions less drastic than those encountered in conventional fuel cell operation with hydrocarbons. Nevertheless, knowledge on the utilization of catalysts in electrogenerative hydrogenation might be applicable to fuel cell operation. This is particularly true if it is remembered that the addition of the second hydrogen is the reverse of the probable rate-determining step in hydrocarbon combustion in a fuel cell.

Conclusions

Kinetic results can be obtained for some reactions on porous electrocatalysts *in situ*, for mechanistic investigations. By studying results for well-characterized reactions, such as those for hydrogen evolution, some questions regarding pore diffusion can be resolved. In the investigated electrogenerative hydrogenation of ethylene on platinum black, pore diffusion apparently did not affect the kinetics except at low reactant concentrations. Further catalysis at the electrode surface decreased cell polarization and increased energy output of the cell.

The over-all electrochemical reaction rate was essentially independent of ethylene partial pressure and second order in hydrogen ion concentration. Isotopic exchange provided additional insight into the reaction mechanism, particularly on steps preceding the rate-limiting one. A general mechanism can be proposed for electrogenerative hydrogenation on platinum black electrocatalyst, involving simultaneous electrochemical addition of electrons and protons to adsorbed ethylene

Table IV. Estimated heat of activation of limiting step for Temkin and Langmuir adsorption (25°-70°C). (See text)

Potential (V) vs. NHE	E_a (kcal/ mole)	ΔH°_{IV} (kcal/mole)		
		Temkin adsorption	Langmuir adsorption	
			H-addi- tion	Dispro- portion- ation
0.200	1.5	15.3	13.8	12.3
0.170	2.5	17.6	16.1	14.6
0.145	4.9	21.2	19.7	18.2

molecules, followed by the rate-limiting, surface reaction of ethyl radicals and hydrogen atoms. Temkin hydrogen adsorption can determine the kinetic and electrochemical behavior of this system below 0.18V. At higher potentials, where hydrogen atom surface coverage is low, strong Langmuir adsorption of ethylene and ethyl radical disproportionation probably control the reaction. The similarity between conventional catalytic and electrogenerative hydrogenation deserves further investigation. The nature of the results obtained for electrogenerative hydrogenation indicates the reaction to be suitable for characterizing platinum black electrodes.

Acknowledgment

We are grateful to the National Science Foundation and the University of Wisconsin for support of this work.

Manuscript submitted May 2, 1975; revised manuscript received Aug. 6, 1975. This was Paper 242 presented at the New York, New York, Meeting of the Society, Oct. 13-17, 1974.

Any discussion of this paper will appear in a Discussion Section to be published in the June 1976 JOURNAL. All discussions for the June 1976 Discussion Section should be submitted by Feb. 1, 1976.

Publication costs of this article were partially assisted by the National Science Foundation.

LIST OF SYMBOLS

C_J	concentration of species J (mole/ml)
E	cathode potential vs. NHE (V)
E_a	apparent activation energy (kcal/mole)
E°	standard reversible electrode potential referred to NHE (V)
$f(\theta)$	total surface interaction energy for all species (kcal/mole)
ΔG^\ddagger_J	free energy of activation for adsorption (kcal/mole)
ΔH_0	change in enthalpy of designated reaction step at zero potential vs. NHE (kcal/mole)
$\Delta H^\circ \neq_{IV}$	activation enthalpy of the rate-limiting step (kcal/mole)
i	current density for geometric electrode area (A/cm^2)
$i_{L,J}$	limiting current density of species J (A/cm^2)
i_0	standard exchange current density for unit concentrations (A/cm^2). $i_0 = nFk_0 \exp(-\alpha E^\circ F/RT)$
j	reaction order of species J
K	equilibrium constant of indicated reaction step
k_0	experimental rate constant at zero potential vs. NHE ($cm^4 \text{ mole}^{-1} \text{ sec}^{-1}$)
k°_{IV}	rate constant of rate-determining step ($cm^4 \text{ mole}^{-1} \text{ sec}^{-1}$)
n	number of electrons in reaction
p, q, r, s	Kemball model parameters, see text
r_J	free energy of adsorption of species J (kcal/mole)
x_J	number of sites required for adsorption (Eq [16])
x	number of sites released in first reaction step (Eq. [II])
W	catalytic load (mg/cm^2)

γ	concentration exponent for limiting current density
θ_J	surface coverage of species J
θ_T	total surface coverage for all species
λ_J	adsorption interaction parameter for species J
σ	active catalytic site (Eq. [I]-[IV])

REFERENCES

- S. H. Langer and H. P. Landi, *J. Am. Chem. Soc.*, **85**, 3043 (1963).
- S. H. Langer and H. P. Landi, *ibid.*, **86**, 4694 (1964).
- S. H. Langer, I. Feiz, and C. P. Quinn, *ibid.*, **93**, 1092 (1971).
- D. V. Sokol'skii and A. B. Fasman, *Dokl. Akad. Nauk SSSR*, **117**, 845 (1957).
- A. B. Fasman, G. V. Taneeva, and D. V. Sokol'skii, *Elektrokhim.*, **1**(8), 900 (1965).
- F. Beck and H. Gerischer, *Z. Elektrochem.*, **65**, 504 (1961).
- G. C. Bond, "Catalysis by Metals," pp. 239-256, Academic Press, New York (1962).
- G. C. Bond, J. J. Phillipson, P. B. Wells, and J. M. Winterbottom, *Trans. Faraday Soc.*, **60**, 1847 (1964).
- J. H. Sinfelt, *J. Phys. Chem.*, **68**, 856 (1964).
- A. S. Hussey, G. W. Keulks, G. P. Nowack, and R. H. Baker, *J. Org. Chem.*, **33**, 610 (1968).
- H. J. Davitt and L. F. Albright, *This Journal*, **118**, 236 (1971).
- K. Fujikawa, H. Kita, and K. Miyahara, *J. C. S. Faraday Trans. I*, **69**, 481 (1973).
- Brochure of Commercial Development Division, American Cyanamid Co., Wayne, N.J.
- H. P. Landi, U.S. Pat. 3,407,096 (Oct. 22, 1968); U.S. Pat. 3,527,616 (Sept. 8, 1970).
- R. G. Haldeman, W. P. Colman, S. H. Langer, and W. A. Barber, *Advan. Chem. Ser.*, **47**, 116 (1965).
- I. Feiz, Ph.D. Thesis, Department of Chem. Engrg., University of Wisconsin-Madison (1968).
- R. Parsons, *Trans. Faraday Soc.*, **56**, 1340 (1960).
- B. E. Conway, *Proc. Roy. Soc., (London) Ser. A*, **256**, 128 (1960).
- M. Breiter, H. Kammermaier, and C. A. Knorr, *Z. Elektrochem.*, **60**, 37 (1965).
- H. A. Liebhafsky and E. J. Cairns, "Fuel Cells and Fuel Batteries," pp. 139-152, John Wiley & Sons, New York (1968).
- K. J. Vetter, "Electrochemical Kinetics, Theoretical and Experimental Aspects," p. 725, Academic Press, New York (1967).
- J. O'M. Bockris and S. Srinivasan, "Fuel Cells: Their Electrochemistry," pp. 231-238, McGraw-Hill Book Co., New York (1969).
- G. P. Sakellaropoulos, Ph.D. Thesis, Dept. of Chem. Engrg., University of Wisconsin-Madison (1974).
- C. Kemball, *J. Chem. Soc.*, **146**, 735 (1956).
- R. L. Burwell, Jr., *Chem. Eng. News*, **44**, 56 (Aug. 22, 1966).
- M. Breiter, *Electrochim. Acta*, **7**, 25 (1962).
- M. Breiter and B. Kennel, *Z. Elektrochem.*, **64**, 1180 (1960).
- S. Gilman, *Trans. Faraday Soc.*, **62**, 466, 480 (1966).
- E. Gileadi, B. T. Rubin, and J. O'M. Bockris, *J. Phys. Chem.*, **69**, 3335 (1965).
- B. E. Conway and E. Gileadi, *Trans. Faraday Soc.*, **58**, 2493 (1962).
- G. H. Twigg, *Discussions Faraday Soc.*, **8**, 152 (1950).

Electrochemistry of Potassium Chromate in Molten Zinc Chloride-Potassium Chloride Eutectic

M. L. Deanhardt¹ and K. W. Hanck*

Department of Chemistry, North Carolina State University, Raleigh, North Carolina 27607

ABSTRACT

The electrochemistry of K_2CrO_4 in an equimolar $ZnCl_2$ - KCl eutectic at $300^\circ C$ was investigated by chronopotentiometric, chronoamperometric, and neovoltammetric techniques. The reduction occurs as a single, irreversible, diffusion-controlled step yielding an insoluble electrode deposit that would not undergo electrochemical oxidation. The value of $nD_{ox}^{1/2}$ at $300^\circ C$ was found to be $(3.46 \pm 0.10) \times 10^{-3}$ eq-cm/mole-sec^{1/2}. The charge transfer step was found to be totally irreversible; $\alpha = 0.57$ and $k_{h,f}$ (at 1.2V) = 4.46×10^{-4} cm/sec. Chemical analyses were performed to determine the composition of the electrode deposit. The deposit appears to be an unstoichiometric compound of the general form $K_xZn_yCrO_z$ where x , y , and z depend upon the conditions of the electrolysis. A mechanism consistent with the observed results is proposed.

The electroreduction of chromate has been the subject of extensive investigation by Laitinen and co-workers because of its use as a depolarizer in thermal batteries (1-5). Their studies were carried out in $LiCl$ - KCl , a neutral, nonoxidizing solvent. With the addition of acidic $ZnCl_2$ to the $LiCl$ - KCl solvent, the reduction of chromate is shifted to more positive potentials (4). A mechanism involving the formation of a $Zn(II)$ - $Cr(IV)$ adduct as a reaction intermediate was proposed to account for the positive shift in potential.

Recently acidic solvents such as the chloroaluminate melts have gained popularity as solvents for electrochemical studies (6-8). Low oxidation states of metals are usually more basic than the higher oxidation states and are stabilized through formation of an acid-base adduct with strongly acidic solvents. Several such states have been observed in chloroaluminates.

In attempting to further characterize the $Cr(IV)$ species proposed by Hanck and Laitinen we sought a solvent acidic enough to stabilize $Cr(IV)$ yet not so acidic as to introduce complications from $Cr_2O_7^{2-}$. Consequently we have elected $ZnCl_2$ - KCl as a solvent over the more acidic chloroaluminate melts. The reduction of chromate in $LiCl$ - KCl containing $ZnCl_2$ is free of side reactions and yields a stoichiometric reduction product, $LiZn_2CrO_4$, over a wide range of preparative conditions (4); the influence of $AlCl_3$ on the reduction of chromate in $LiCl$ - KCl , on the other hand, has not been fully explored.

Experimental

Reagents and solvent preparation.—Anhydrous K_2CrO_4 was obtained by drying reagent grade K_2CrO_4 (J. T. Baker) at $110^\circ C$ for 1 hr and storing over $Mg(ClO_4)_2$ a few days before use.

The $ZnCl_2$ - KCl eutectic was prepared by vacuum drying reagent grade $ZnCl_2$ (J. T. Baker) and reagent grade KCl at $150^\circ C$ for 48 hr. The two dried salts were mixed in a 1:1 mole ratio under a nitrogen atmosphere and stored over $Mg(ClO_4)_2$ in a vacuum desiccator. To prevent hydrolytic decomposition of $ZnCl_2$, anhydrous HCl (Air Products electronic grade) was slowly passed through the salt mixture for 30 min during which the temperature was raised from room temperature to $450^\circ C$; fusion occurred at $230^\circ C$. The temperature was maintained at $450^\circ C$ for 1 hr in order to rapidly decompose any organic matter present, then the temperature was lowered to $300^\circ C$. Argon was passed through the melt for 4 hr to expel excess HCl . Finally the melt was filtered through a medium porosity,

sintered glass frit directly into the electrochemical cell and maintained under vacuum for 4 hr.

The purity of the $ZnCl_2$ - KCl solvent was carefully examined using chronopotentiometry. Both anodic and cathodic residuals were sharp; at an applied current of 5 mA/cm², 150 msec were typically required for the potential to shift from the rest potential to the cathodic limit of the solvent. The anodic limit of the solvent is due to the oxidation of chloride; the cathodic limit is due to the reduction of $Zn(II)$; the useful potential range of the solvent is 1.5V.

Apparatus.—The molten salt furnace, temperature controller, and cell assembly have been previously described (9).

Current-time and voltage-time curves were obtained with a Princeton Applied Research Corporation Model 173 potentiostat/galvanostat. A triangle wave generator constructed using the circuit of Bull and Bull (10) was interfaced with the Model 173 to obtain linear sweep voltammograms.

Data were digitized with an IBM system/7 data acquisition computer which was linked to the IBM 370/165 computer located at the Triangle Universities Computation Center. The laboratory instruments were interfaced to the computer by means of logic circuits constructed on a Heath Schlumberger Model EU-801 analog/digital designer. In some cases data were collected with a Tektronix 502-A oscilloscope equipped with a Model C-12 oscilloscope camera.

Controlled current depositions of the reduction product were obtained with the PAR 173 galvanostat.

Electrodes.—A zinc rod (0.125 in. in diameter; Alfa Inorganics, 99.95% Zn) in equilibrium with the equimolar $ZnCl_2$ - KCl solvent was used as the reference electrode. The counterelectrode was a rod of spectroscopic grade graphite (0.125 in. in diameter; Ultra Carbon Corporation).

Platinum flag electrodes (area approximately 0.5 cm²) were used as working electrodes. Construction and area determination of these electrodes have been previously described (4). Platinum gauze electrodes (52 mesh) served as working electrodes in the electrode deposit analysis.

Analytical procedures.—The following analytical procedures were used in the preparation and analysis of the electrode deposits.

Platinum gauze electrodes were cleaned in boiling $HClO_4$, rinsed with deionized H_2O , dried, and weighed to the nearest microgram. After deposition the deposits were reweighed and dissolved in $HClO_4$ according to the procedure described by Propp (11).

* Electrochemical Society Active Member.

¹ Present address: Department of Chemistry, George Mason University, Fairfax, Virginia 22030.

Key words: molten salt, chromite, chromium(IV).

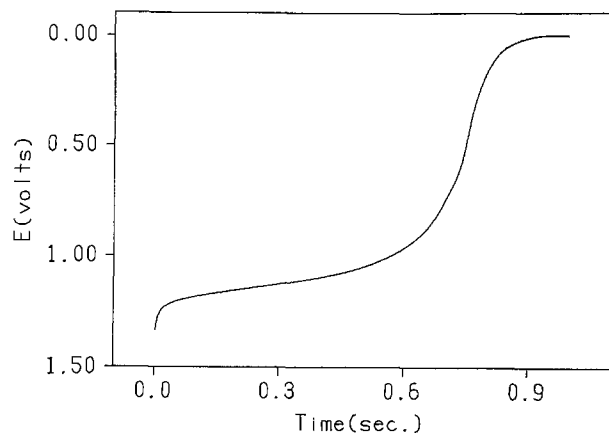


Fig. 1. Potential-time curve for the chronopotentiometric reduction of K_2CrO_4 . Current density = 14.98 mA/cm^2 . $[K_2CrO_4] = 29.93 \text{ mM}$.

The deposits were found to contain chromium, zinc, and potassium. Chromium was determined by a coulometric titration with electrogenerated Cu(I) using a biamperometric endpoint as described by Meier, Myers, and Swift (12).

Zinc was determined by a spectrophotometric titration (750 nm) with EDTA using Eriochrome Black T as an indicator.

The potassium content was determined by flame photometry.

The deposits were analyzed for chloride by oxidizing the deposits with ammonium hexanitratocerate(IV) and coulometrically titrating with electrogenerated Ag(I) (13).

Results and Discussion

Electrochemical measurements.—The reduction of K_2CrO_4 in the $ZnCl_2$ -KCl solvent involves a single reduction step with the formation of an insoluble product which adheres to the electrode. This insoluble product was not oxidizable in the observable potential range, therefore double step techniques could not be used to deduce the reduction mechanism. Three single step techniques, chronopotentiometry, chronoamperometry, and neovoltammetry were chosen to study the electrochemical reduction. Cyclic voltammetric experiments were attempted but very little useful information could be obtained because the i - E curves were extremely broad with poorly defined maxima. All electrochemical measurements were made at 300°C .

Digitized chronopotentiograms of K_2CrO_4 in the $ZnCl_2$ -KCl solvent were taken at several different concentrations and current densities using a 2 msec sampling interval. Transition times were limited to a range of 0.2-2.0 sec in order to minimize double layer effects and convection. A typical chronopotentiogram of the reduction is shown in Fig. 1. A fresh electrode was used for each chronopotentiogram. Transition times were measured using the method of Delahay and Berzins (15) and corrected for double layer effects by the method of Bard (16).

The range of concentrations and current densities studied are shown in Table I. The reduction was found to obey the Sand equation; a linear regression analysis of $I_0\tau^{1/2}$ vs. $[K_2CrO_4]$ indicates a diffusion controlled process with $I_0\tau^{1/2}/C$ being $0.295 \pm 0.009 \text{ mA}\cdot\text{sec}^{1/2}/$

Table I. Chronopotentiometric data

$[K_2CrO_4]$ (mM)	$I_0\tau^{1/2}$ (mA·sec ^{1/2} /cm ²)	Range of I_0 (mA/cm ²)
10.45	3.21	4.69-9.29
28.66	8.61	11.55-18.33
44.20	13.73	19.08-24.32
78.90	24.38	28.63-38.61
116.90	34.27	39.53-49.50

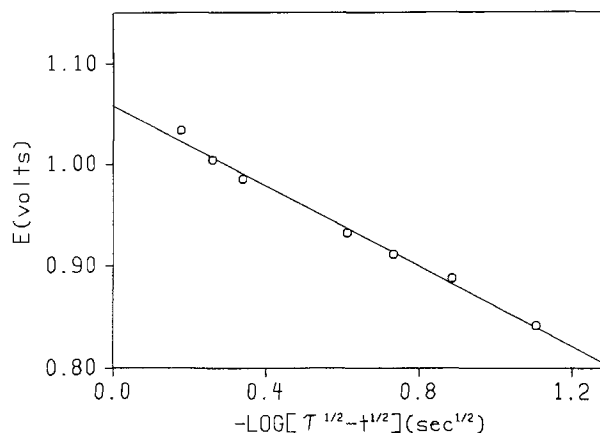


Fig. 2. Potential time analysis. $[K_2CrO_4] = 30.59 \text{ mM}$. Current density = 10.14 mA/cm^2 .

$\text{cm}^2\cdot\text{mM}$. From this slope $nD_{ox}^{1/2}$ was calculated to be $(3.46 \pm 0.10) \times 10^{-3} \text{ equiv}\cdot\text{cm}/\text{mole}\cdot\text{sec}^{1/2}$.

We have also investigated the reduction of $K_2Cr_2O_7$ in the $ZnCl_2$ -KCl solvent. The results indicate that the diffusion coefficient of dichromate, as expected, is slightly smaller than that of chromate. The rest potential of solutions of dichromate was significantly higher than that observed for chromate and very close to the oxidation limit of the solvent. Similar results were observed in molten LiCl-KCl (11). The reduction of dichromate was not pursued further but the differences in electrochemical behavior between CrO_4^{2-} and $Cr_2O_7^{2-}$ indicate that dichromate is not formed when chromate is added to the acidic solvent.

Plots of E vs. $\log(\tau^{1/2} - t^{1/2})$ were found to be linear indicating a totally irreversible charge transfer step. An example of such a plot is shown in Fig. 2. From the average slope of these plots we calculate $\alpha = 0.57$. From the average intercept, the forward heterogeneous charge transfer rate constant $k_{h,f}^0$ was calculated to be 327 cm/sec , referred to the zero of the potential scale (Zn^0 /equimolar $ZnCl_2$ -KCl). The reduction of K_2CrO_4 occurs at $\sim 1.2V$ vs. the zinc reference electrode; at $E = 1.2V$, $k_{h,f} = 3.27 \times 10^{-4} \text{ cm/sec}$.

Chronoamperograms of the reduction of K_2CrO_4 provided an independent method for the determination of $nD_{ox}^{1/2}$. The electrode potential was stepped from the rest potential to $0.5V$; plots of I vs. $t^{-1/2}$ were found to be linear as predicted by the Cottrell equation. Using a linear regression analysis, values of $nD_{ox}^{1/2}$ were obtained from the slopes of the regression lines as shown in Table II. The chronoamperometric values of $nD_{ox}^{1/2}$ agree within experimental error with the value obtained from the chronopotentiometric data.

Recently, the "semi-integral" technique has been applied to linear sweep voltammetry (17-21). Plots of the semi-integrated current vs. potential have two basic advantages over the normal voltammetric plots. First the semi-integral technique provides an easier method for obtaining quantitative data from the voltammetric measurements. Second the semi-integral technique provides a convenient way of removing effects of solution resistance from the analytical data.

Digitized linear sweep voltammograms of K_2CrO_4 were taken at several different sweep rates from ~ 1 to $\sim 10 \text{ V/sec}$; the potential was scanned from the rest

Table II. Chronoamperometric data^a

$[K_2CrO_4]$ (mM)	$nD_{ox}^{1/2}$ (equiv·cm/ mole·sec ^{1/2})
9.81	$(3.50 \pm 0.08) \times 10^{-3}$
78.90	$(3.45 \pm 0.08) \times 10^{-3}$
116.90	$(3.42 \pm 0.12) \times 10^{-3}$

^a Uncertainties quoted in this paper are 95% confidence intervals.

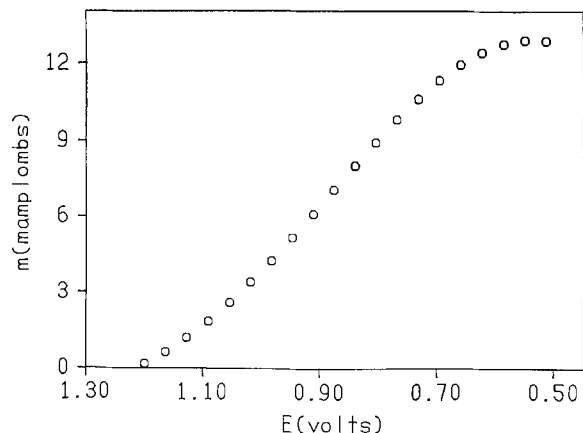


Fig. 3. Neovoltammogram for the reduction of K_2CrO_4 . $[K_2CrO_4] = 78.90$ mM. Sweep rate = 3.61 V/sec. Electrode area = 0.488 cm^2 .

potential to 0.5V. The semi-integrated currents, $m(t)$ were calculated using the algorithm described by Grenness and Oldham (18). Blank neovoltammograms were taken of the pure solvent to correct for nonfaradaic effects. Effects of uncompensated solution resistance were corrected using positive feedback resistance compensation provided on the PAR 173 potentiostat.

One of the neovoltammograms is shown in Fig. 3. At a sufficiently negative potential the semi-integrated current reaches a limiting value, $m(\infty)$ given by

$$m(\infty) = nFACD_{ox}^{1/2} \quad [1]$$

Using several neovoltammograms and Eq. [1] the average value of $nD_{ox}^{1/2}$ was calculated to be $(3.45 \pm 0.19) \times 10^{-3}$ equiv.-cm/mole-sec $^{1/2}$, which is in good agreement with the chronopotentiometric and chronoamperometric values (Table III).

Plots of E vs. $\log [(m_\infty - m)/i]$ were found to be linear indicating a totally irreversible charge transfer step (20). An example of such a plot is shown in Fig. 4. A transfer coefficient of 0.57 was obtained from the slope. From the intercept, the heterogeneous charge transfer rate constant $k_{h,f}$ was calculated to be 4.46×10^{-4} cm/sec at $E = 1.2$ V. As can be seen in Table III, the $k_{h,f}$ obtained from the chronopotentiometric data is lower than that obtained from neovoltammetry. This discrepancy is probably due to the effects of uncompensated solution resistance on the chronopotentiograms where positive feedback resistance compensation was not possible.

Characterization of the electrode deposit.—Electrode deposits were prepared by constant current electrolysis using the method outlined by Propp (2) and analyzed for chromium, zinc, and potassium as previously described. The potential was never allowed to become more negative than 0.5V during the deposition process; the concentration of chromate was 0.15M. Approximately 100 μ equiv. of deposit was formed on each electrode using five current densities ranging from 0.5 to 10 mA/cm 2 . The area of the platinum gauze electrodes was determined by a chronoamperometric technique using a standard $K_3Fe(CN)_6$ solution. The results of the deposit analysis are shown in Table IV.

The effective number of electrons transferred was determined by

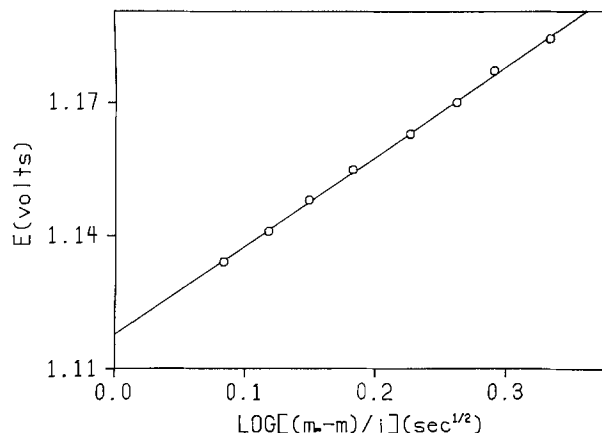


Fig. 4. Relationship between potential and semi-integrated current. $[K_2CrO_4] = 78.90$ mM. Sweep rate = 3.61 V/sec. Electrode area = 0.488 cm^2 .

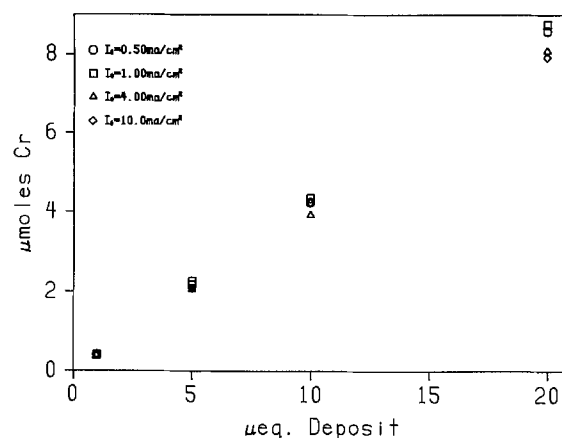


Fig. 5. Relationship between micromoles of chromium and microequivalents of deposit.

$$n_{eff} = \frac{\mu\text{equiv. deposit}}{\mu\text{moles Cr found}} \quad [2]$$

The oxygen to chromium ratio in each deposit was calculated using a charge balance and assuming the oxidation states of potassium, zinc, and chromium to be I, II, and VI — n_{eff} , respectively.

Deposits formed with high current densities were found to be hygroscopic, green in color, and not strongly attached to the gauze electrodes. The per cent of sample weight accounted for by the empirical formulas in Table IV was ~92-100%, where the remaining weight is assumed to be H_2O . Chloride could not be detected in any deposit. The low current depositions were very stable when exposed to the atmosphere, black in color, and adhered strongly to the gauze electrodes.

Additional experiments were performed to determine if the deposit composition varied with the amount of deposit formed on the electrode. Deposits ranging from 1 to 20 μ equiv. were formed at several current densities and analyzed for Cr and Zn by atomic absorption. The results are shown in Fig. 5 and 6. A straight line passing through the origin was obtained for each current

Table III. Comparison of data obtained from the various electrochemical techniques

Technique	$nD_{ox}^{1/2}$ (equiv.-cm/ mole-sec $^{1/2}$)	α	$k_{h,f}$ (at $E = 1.2$ V) (cm/sec)
Chronopotentiometry	$(3.46 \pm 0.10) \times 10^{-3}$	0.57	3.27×10^{-4}
Chronoamperometry	$(3.46 \pm 0.05) \times 10^{-3}$	—	—
Neovoltammetry	$(3.45 \pm 0.19) \times 10^{-3}$	0.57	4.46×10^{-4}

Table IV. Deposit analysis

Current density (mA/cm 2)	n_{eff}	Empirical formula	Formula wt
0.5	2.39	$K_{0.07}Zn_{1.18}CrO_{3.02}$	180
1.0	2.39	$K_{0.11}Zn_{1.36}CrO_{3.42}$	213
2.0	2.33	$K_{0.12}Zn_{1.71}CrO_{3.60}$	226
4.0	2.50	$K_{0.17}Zn_{2.38}CrO_{4.03}$	265
10.0	2.79	$K_{0.32}Zn_{2.15}CrO_{3.92}$	268

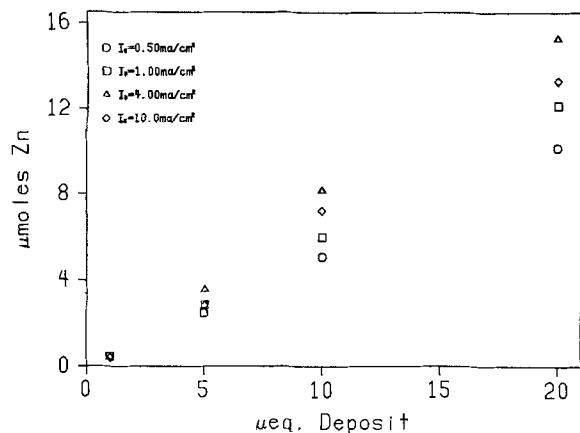


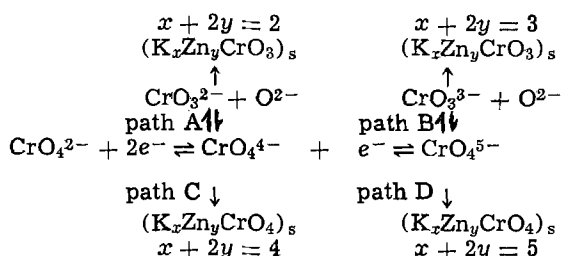
Fig. 6. Relationship between micromoles of zinc and microequivalents of deposit.

density. The excellent linearity of these plots strongly suggests that neither Cr nor Zn is being trapped by the deposit. These results are consistent with the n_{eff} and Zn/Cr ratios shown in Table IV.

ESR and magnetic measurements have been made on several of the deposits (22). The ESR measurements clearly indicate the presence of Cr(III) in the deposits. Specific magnetization and thermomagnetic analysis indicate that the deposits are ferromagnetic; the saturation magnetization and Curie temperature vary with deposit composition. Similar results have been reported for oxides formed by the thermal decomposition of chromium trioxide (23, 24).

X-ray powder diffraction studies indicate that the deposits have a diamond cubic lattice (DC) with a unit cell edge of 8.43Å. This phase is slightly larger than the DC phase of pure Cr_2O_3 which has a unit cell edge of 8.36Å.

Reduction mechanism.—The composition of the electrode deposit depends on the current density applied during the electrolysis. A reduction mechanism consistent with the results of Table V is shown below



At high current densities the total time of the electrolysis is small. This would tend to limit the decomposition reactions of paths A and B and favor the depositions of paths C and D. Due to the large overvoltage at very high current densities, path D would be favored over path C. At low current densities the total time of electrolysis is very large providing more time for the chemical reactions of paths A and B to occur. Due to the small overvoltage at very low current densities, path A would be favored over path B. Table V summarizes the changes in deposit composition predicted to occur as preparative current density is changed; these predictions are experimentally verified in Table IV.

Table V. Compositional changes with electrolysis current

Current density	(x + 2y)	n_{eff}	O/Cr
Very low	2	2	3.0
Low	2 to 3	2 to 3	3.0
High	4 to 5	2 to 3	4.0
Very high	5	3	4.0

The mechanism for the reduction of K_2CrO_4 in the presence of Zn(II) in molten LiCl-KCl involves a three electron process with CrO_4^{4-} formed as a transitory intermediate (4). Our data indicate that Cr(IV) is sufficiently stable in ZnCl_2 -KCl to prevent complete reduction to Cr(III) unless high current densities are used. This infers the presence of a stronger Cr(IV)-Zn(II) interaction than in LiCl-KCl containing ZnCl_2 . The source of this increased interaction is undoubtedly the high acidity of the ZnCl_2 -KCl solvent. Weakly basic solutes display more alkaline properties in acidic than in neutral solvents, consequently the acid-base adduct Zn(II)-Cr(IV) is more stable in ZnCl_2 -KCl than in LiCl-KCl containing ZnCl_2 .

The loss of oxide at low current density (path A) is also a consequence of the acidity of ZnCl_2 -KCl. Acidic Zn(II) species would be expected to rapidly react with oxide to produce zinc oxychloride. This may, in fact, divert significant quantities of CrO_4^{4-} from the second electron transfer to path A.

This mechanism is consistent with the results obtained from the electrochemical measurements. Due to the high current densities and short time intervals of the chronopotentiometric analysis, the value of n_{eff} is approximately 3 as indicated in Table V. The small uncertainty in the value of $nD_{\text{ox}}^{1/2}$ also indicates a constant value of n . Using $n = 3$, the value of D_{ox} is $(1.33 \pm 0.08) \times 10^{-6} \text{ cm}^2/\text{sec}$.

The kinetic data suggest an irreversible charge transfer step in the reduction sequence. The oxygen coordination remains tetrahedral in the first reduction step and changes from tetrahedral to octahedral in the second reduction step (4). Therefore the second step is slower than the first and is considered to be the irreversible, rate-determining step. It should be pointed out that due to the chemical reactions involved in the reduction mechanism, it may be possible that the irreversible shape of the chronopotentiograms and neovoltammograms is due to a reversible electron transfer reaction with a rapid following chemical reaction. Using only single step techniques as described here, it was virtually impossible to distinguish between these two cases.

Conclusions

Molten ZnCl_2 -KCl is a useful moderately acidic solvent for electrochemical investigations. The electroreduction of K_2CrO_4 in ZnCl_2 -KCl involves a moderately stable Cr(IV) intermediate and produces an insoluble electrode deposit which is ferromagnetic at room temperature.

Acknowledgment

We thank Donald Martin, Robert Fornaro, Richard Kistler, Sam Warren, and the N. C. State University Systems Analysis and Control Center for assistance in interfacing our laboratory to the System/7 computer.

Manuscript submitted May 27, 1975; revised manuscript received Aug. 20, 1975.

Any discussion of this paper will appear in a Discussion Section to be published in the June 1976 JOURNAL. All discussions for the June 1976 Discussion Section should be submitted by Feb. 1, 1976.

REFERENCES

- H. A. Laitinen and R. D. Bankert, *Anal. Chem.*, **39**, 1790 (1967).
- J. H. Propp and H. A. Laitinen, *ibid.*, **41**, 644 (1969).
- B. Popov and H. A. Laitinen, *This Journal*, **117**, 482 (1970).
- K. W. Hanck and H. A. Laitinen, *ibid.*, **118**, 1123 (1971).
- S. M. Selis and L. P. McGinnis, *ibid.*, **106**, 900 (1959).
- D. A. Hames and J. A. Plambeck, *Can. J. Chem.*, **46**, 1727 (1968).
- U. Andres and J. A. Plambeck, *ibid.*, **47**, 3055 (1969).
- K. W. Fung and G. Mamantov, *J. Electroanal. Chem.*, **35**, 27 (1972).

9. K. W. Hanck and M. L. Deanhardt, *Anal. Chem.*, **45**, 176 (1973).
10. R. H. Bull and G. C. Bull, *ibid.*, **43**, 1342 (1971).
11. J. H. Propp, Ph.D. Thesis, University of Illinois (1968).
12. D. J. Meier, R. J. Myers, and E. H. Swift, *J. Am. Chem. Soc.*, **71**, 2340 (1949).
13. J. J. Lingane, *Anal. Chem.*, **26**, 622 (1954).
14. H. A. Laitinen and W. S. Ferguson, *ibid.*, **29**, 4 (1957).
15. P. Delahay and T. Berzins, *J. Am. Chem. Soc.*, **75**, 2486 (1953).
16. A. J. Bard, *Anal. Chem.*, **35**, 340 (1963).
17. K. B. Oldham, *ibid.*, **44**, 196 (1972).
18. M. Grenness and K. B. Oldham, *ibid.*, **44**, 1121 (1972).
19. P. E. Whitson, H. W. VanderBorn, and D. H. Evans, *ibid.*, **45**, 1298 (1973).
20. M. Goto and K. B. Oldham, *ibid.*, **45**, 2043 (1973).
21. H. W. VandenBorn and D. H. Evans, *ibid.*, **46**, 643 (1974).
22. M. L. Deanhardt and K. W. Hanck, North Carolina State University, Raleigh, N. C., work to be published, 1975.
23. T. V. Rode, V. B. Kazanskii, and Y. I. Pecherskaya, *Russ. J. Phys. Chem.*, **35**, 1170 (1961).
24. T. V. Rode and V. E. Rode, *ibid.*, **35**, 1225 (1961).

Technical Note



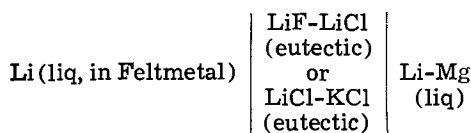
Electromotive Force Measurements in Molten Lithium-Magnesium Alloys

Marie-Louise Saboungi* and Milton Blander

Chemical Engineering Division, Argonne National Laboratory, Argonne, Illinois 60439

In the development of high-energy lithium alloy/metal sulfide cells, investigations of lithium alloys as the active material in the negative electrode appear to be desirable. The aim of such investigations is to identify those lithium alloys that perform better than the Li-Al electrode presently used (1). The choice of an optimum alkali metal alloy electrode for new battery systems requires the availability of data on the thermodynamic behavior of a large number of systems. The paucity of such data led us to start measurements in order to fill this gap and to gain fundamental insights into the thermodynamic properties of alkali metal alloys.

We report here electromotive force measurements of molten lithium-magnesium alloys using the cell



The results of our measurements may be combined with data from the measured Li-Mg phase diagram (2) to calculate the thermodynamic properties of solid Li-Mg alloys at the solidus. Earlier, magnesium vapor pressure measurements over Li-Mg melts were made by Mashovets and Puchkov (3) at only five compositions. The concentration dependence of their deduced excess chemical potential is quite unusual; consequently, more detailed investigations appeared to be needed to check their conclusions.

Experimental

Materials.—Lithium metal (99.97% purity) was obtained from the Foote Mineral Company, Philadelphia, Pennsylvania, in the form of 1 lb ingots sealed in cans under an argon atmosphere. Bright metal pieces were melted and floating impurities were skimmed off at about 200°C under a purified helium atmosphere; part of the remainder was passed through a pinhole at the

bottom of a heated tantalum vessel. Small drops (0.1–0.3g) of lithium were obtained and only those with the brightest surfaces were used in this study.

Magnesium metal (99.98% purity) was obtained from Brooks and Perkins, Livonia, Michigan, in the form of cylindrical rods. The oxide coating was removed by dipping the rods in a dilute solution of HCl.

Anhydrous purified LiCl-KCl eutectic mixture was supplied in 200g ampuls by the Anderson Physics Laboratory, Champaign, Illinois. The LiF-LiCl eutectic mixture was prepared by weighing the appropriate amounts of predried reagent grade solids [30 mole per cent (m/o) LiF and 70 m/o LiCl], placing them into a fused silica vessel and melting the mixture. Chlorine gas was passed through the molten eutectic, after which the excess chlorine was removed by bubbling helium through the melt.

Apparatus and procedure.—The experimental arrangement of a typical cell is indicated in Fig. 1. A porous beryllia crucible (high purity grade) from National Beryllia Corporation, North Bergen, New Jersey, contained the molten electrolyte in which was immersed the pure lithium anode. This crucible, which served as a barrier to separate the two electrodes, was 20 mm in diameter and 2.4 mm in thickness; its pore size was about 50 μm . The BeO cup was presoaked in the molten electrolyte to wet it so as to minimize possible chemical attack by molten lithium. Cairns *et al.* (4) noted that the purity and manner of preparation of beryllia have a strong influence on its resistance to attack by lithium.

The molten lithium-magnesium electrode (positive electrode) was contained in a 100 mm diameter tantalum crucible. The reference electrode consisted of porous stainless steel Feltmetal (Type 347 SS, approximate area 1 cm^2) soaked in pure lithium at 500°C. At this temperature, the lithium wets the metal with such tenacity that no loss of lithium due to dewetting occurs when the lithium reference electrode is submerged in the electrolyte. The porosity (the pore size is about 35 μm) of the Feltmetal from Brunswick Corporation, Milford, Connecticut, was quoted as approximately 80%. Tantalum leads were used to connect

* Electrochemical Society Active Member.

Key words: lithium, magnesium, alloys, activity, electromotive force, alkali-metals.

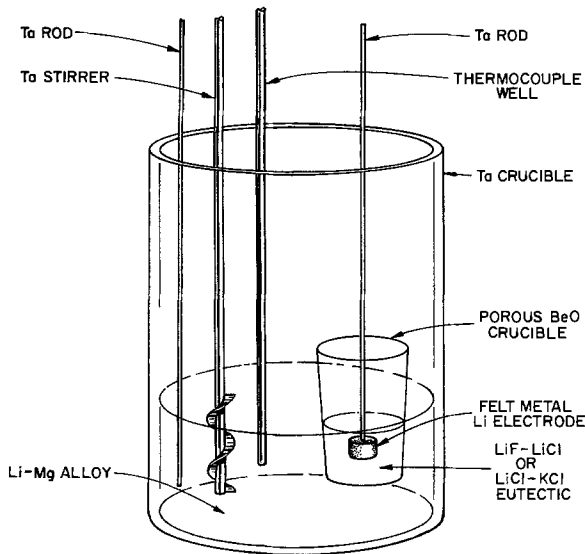


Fig. 1. Schematic of the cell

both electrodes to a digital voltmeter (Dana Model 5000, input resistance greater than 10^{10} ohms). The entire assembly was set in a furnace well which was attached to a helium-filled glove box; all operations were carried out completely inside the glove box. The procedure for purifying the helium is described elsewhere (5); the impurities in this atmosphere consisted of 0.1-0.5 ppm of water while oxygen was undetected (limit of detection 1 ppm).

The temperature was measured with a calibrated (Pt-Pt10%Rh) thermocouple protected by a tantalum well. For each run, the temperature was held constant within a three degree range. The composition of the alloy was kept homogeneous (and the temperature uniform) by vigorous stirring with a tantalum stirrer. Because of the small amount of the electrolyte, the salts in the BeO crucible were not stirred; no significant loss of lithium from the reference electrode was apparent. The emf of the cell with two pure lithium electrodes was measured first. The bias potential was always less than 0.2 mV and when checked remained constant for several hours. The composition of the melt in the tantalum crucible was then changed by adding successive weighed amounts of magnesium. The dissolution of the magnesium in the alloy was immediate, and the emf of the cell became stable (to within 0.2 mV) for as long as the composition and the temperature were held constant, often for hours and sometimes overnight. After temperature cycling, the emf generally returned to within 0.1 mV of the initial value.

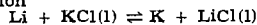
The choice of electrolyte in collecting these data depended on the temperature of the cell. For temperatures lower than 773°K, the LiCl-KCl eutectic mixture (mp 625°K) was used. For temperatures greater than 773°K, the LiF-LiCl eutectic mixture (mp 774°K) was used in order to ensure the stability of the cell.¹

The use of a large amount of alloy (40-50g of lithium) appears to be significant in minimizing the effects of self-discharge, i.e., the transfer of lithium from the reference electrode to the alloy. Finally, it should be pointed out that at these temperatures, the solubility of metallic Li in the electrolytes is less than 1 m/o (8).

Results and Discussion

Compositions of molten alloys, emf data, and activities of lithium, at four temperatures, are given in

¹ At temperatures greater than 773°K, it was observed experimentally by us and by others (1, 6) that the lithium metal reduces KCl to potassium metal, which condenses mainly on the cooler sections of the well and the electrode leads. This effect can be understood from simple thermodynamic considerations. The standard free energy of the reaction



is about 3 kcal mol⁻¹ at 800°K according to JANAF Tables (7). Even at 723°K, the vapor pressure of potassium in this mixture is noticeable (about 1 Torr).

Table I. Emf results at four temperatures

T = 670°K			T = 735°K		
X _{Li}	E (mV)	a _{Li}	X _{Li}	E (mV)	a _{Li}
0.958	2.62	0.956	0.908	6.81	0.898
0.891	6.89	0.888	0.792	16.66	0.769
0.813	13.38	0.793	0.684	30.15	0.621
0.749	19.75	0.710			
0.685	25.95	0.638			

T = 830°K			T = 887°K		
X _{Li}	E (mV)	a _{Li}	X _{Li}	E (mV)	a _{Li}
0.928	5.79	0.922	0.899	8.39	0.896
0.855	12.82	0.836	0.836	14.59	0.826
0.816	17.26	0.786	0.762	23.52	0.736
0.782	21.19	0.744	0.699	32.42	0.656
0.755	24.90	0.707	0.643	41.76	0.579
0.725	29.06	0.666	0.589	51.91	0.507
0.683	35.65	0.606	0.534	61.41	0.448
0.648	41.61	0.560	0.506	67.87	0.412
0.627	45.70	0.528	0.480	77.00	0.365
0.594	52.12	0.482	0.459	82.57	0.339
0.566	57.84	0.445	0.429	90.77	0.305
0.541	63.41	0.413	0.406	98.62	0.277
0.522	67.96	0.387	0.381	105.10	0.253
0.507	71.36	0.369	0.354	114.00	0.225
0.487	76.05	0.346	0.330	122.37	0.203
0.475	78.84	0.333	0.298	134.22	0.172

Table I. The emf values, *E*, are corrected for the bias potential.

The activities of lithium, *a*_{Li}, in the alloys calculated from the relation

$$E = - \frac{RT}{F} \ln a_{\text{Li}} \quad [1]$$

(*R* is the gas constant, and *F* is the Faraday constant) are plotted in Fig. 2. In the molten alloys, deviations from ideality are small and negative. The activities of lithium in solid alloys at the solidus can be calculated by combining these results with the phase diagram. The data for the solidus are somewhat uncertain, which lends uncertainty to our values of the activities of Li in solid alloys. We chose for our calculations the phase diagram as given by Hultgren *et al.* (2) (Fig. 3). The ratio of the activities of lithium in the molten alloy (liquid lithium is the standard state) to the activity of lithium in the solid alloy (hypothetical solid lithium is the standard state) in equilibrium with the liquid is given by

$$\ln \frac{a_{\text{Li}}}{a'_{\text{Li}}} = \frac{\Delta H_f}{R} \left(\frac{1}{T_m} - \frac{1}{T} \right) \quad [2]$$

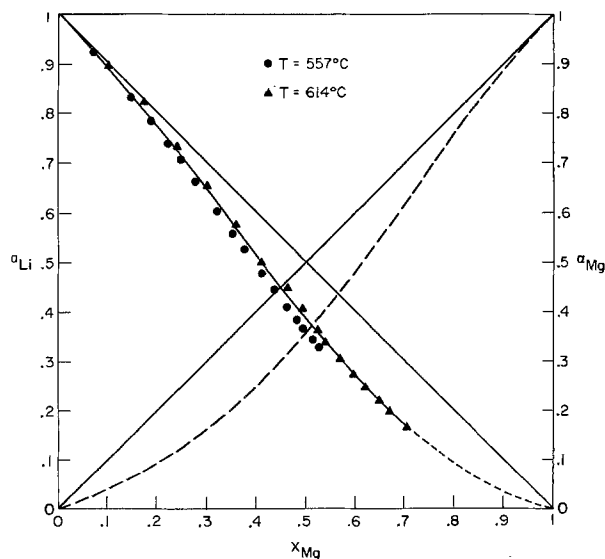


Fig. 2. Activities of Li and Mg in the Li-Mg system. ● *a*_{Li} measured at 557°C; ▲ *a*_{Li} measured at 614°C; --- *a*_{Mg} calculated at 614°C.

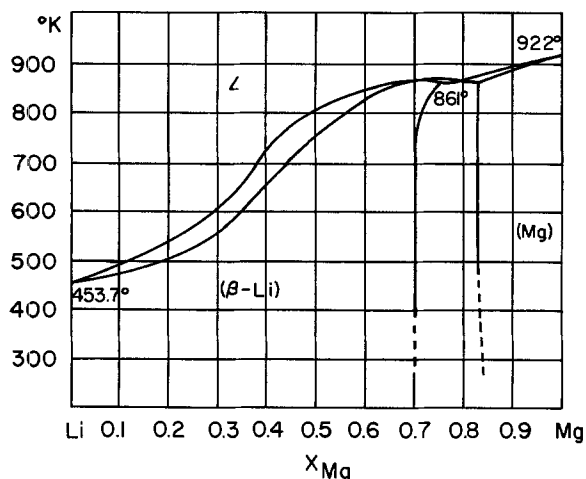


Fig. 3. Phase diagram of the Li-Mg system (2)

The prime denotes solid lithium as standard state, ΔH_f is the enthalpy of fusion of lithium ($0.7171 \text{ kcal mol}^{-1}$), and T_m is the melting point of lithium (453.69°K) (7). The excess chemical potential of lithium in the molten alloys ($\mu_{\text{Li}}^{\text{xs}}$) is

$$\mu_{\text{Li}}^{\text{xs}} = RT \ln \gamma_{\text{Li}} = -FE - RT \ln X_{\text{Li}} \quad [3]$$

where γ_{Li} is the activity coefficient and X_{Li} is the atom fraction of lithium. By assuming that $\mu_{\text{Li}}^{\text{xs}}$ is independent of temperature, the activities of lithium at the liquidus may then be calculated. Values of $\mu_{\text{Li}}^{\text{xs}}$ at 830° and 887°K differ somewhat. However, this small difference is about the size of the combined uncertainties; it is, therefore, reasonable to assume that $\mu_{\text{Li}}^{\text{xs}}$ is independent of temperature. The composition of the solid alloy in equilibrium with the liquid is given in column 2 of Table II. The values of the activities of solid and liquid lithium at the solidus and liquidus (2), respectively, at temperatures ranging from 500° to 870°K , are given in columns 3 and 4 of Table II.

As with the liquids, deviations from ideality at the solidus are relatively small and negative. At higher temperatures and lower atom fractions of lithium, activity coefficients of lithium in the solid alloy are lower than in the liquid. This is a necessary consequence of the reported maximum in the liquidus and solidus curves in the phase diagram (Fig. 3). At this maximum, we have $\gamma_{\text{Li}} > \gamma'_{\text{Li}}$ but $\gamma_{\text{Mg}} > \gamma'_{\text{Mg}}$ where the prime denotes the solid alloy. Thus, if the reported phase diagram is correct, the differences in activity coefficients (and activities) of each component in the liquid and solid have opposite signs at the maximum.

The data at 887°K (Table I) were utilized to calculate the activity coefficients of magnesium from the Gibbs-Duhem relation

$$\ln \gamma_1 = \frac{-X_2}{X_1} \ln \gamma_2(X_2) - \int_{X_1=1}^{X_1=X_1} \frac{\ln \gamma_2}{X_1^2} dX_1 \quad [4]$$

where component 1 is Mg and component 2 is Li. Ex-

Table II. Estimated values of the activity of Li* in solid Li-Mg alloys at the solidus

T(K)	X'_{Li}	a'_{Li}	a_{Li}
500	0.80	0.80	0.87
600	0.65	0.54	0.66
700	0.56	0.40	0.53
800	0.44	0.28	0.40
850	0.36	0.18	0.27
870	0.30	0.12	0.17

* The concentrations, X'_{Li} , are atom fractions at the solidus. Activities in column 3 are relative to a hypothetical solid lithium as standard state and activities in column 4 are relative to liquid lithium.

Table III. Excess chemical potentials of magnesium and lithium (cal mol^{-1})

X_{Mg}	This work		Reference 3	
	$\mu_{\text{Li}}^{\text{xs}}(887^\circ\text{K})$	$\mu_{\text{Mg}}^{\text{xs}}(887^\circ\text{K})$	$\mu_{\text{Li}}^{\text{xs}}(887^\circ\text{K})$	$\mu_{\text{Mg}}^{\text{xs}}(887^\circ\text{K})$
0	0	-1450	(0)	(-5406)
0.1	-4	-1390	(-66)	(-4129)
0.2	-30	-1230	-258	-3041
0.3	-110	-1010	-561	-2130
0.4	-230	-780	-958	-1390
0.5	-420	-550	-1442	-799
0.6	-670	-350	-1986	-351
0.7	-960	-190	-2470	-87
0.8	(-1290)	(-80)	-2776	19
0.9	(-1640)	(-20)	-2759	20
1.0	(-1970)	(0)	-2285	0

() Extrapolated.

perimental values of $\ln \gamma_2$ were fit by a least-squares method to an equation of the form $\ln \gamma_2 = A X_1^2 + B X_1^3 + C X_1^4$. The coefficients A, B, and C were then used to numerically calculate the integral in Eq. [4]. The calculated activities of magnesium for $T = 887^\circ\text{K}$ are plotted in Fig. 2. As with Li, the deviations from ideal solution behavior of Mg appear to be relatively small.

Our calculations for the excess chemical potentials of Li and Mg at 887°K , given in columns 2 and 3 of Table III, respectively, differ considerably from those of Mashovets and Puchkov (2, 3) at 887°K given in columns 4 and 5 of Table III. The results of these experiments were derived from magnesium vapor pressure measurements at only five concentrations, and no information was given on the reproducibility of their results. We believe that the large asymmetry and the unusual concentration dependence of the excess chemical potentials of Mashovets and Puchkov, as well as the small number of measurements, place their results in some doubt. The small deviations from ideality of our results at all concentrations are consistent with the small difference in electronegativities and the small difference in molar volumes between Li and Mg.

Acknowledgments

We would like to acknowledge the help of F. J. Martino and R. M. Yonco in preparing the lithium, and Dr. J. R. Selman for valuable discussions.

This work was performed under the auspices of the U.S. Energy Research and Development Administration.

Manuscript submitted May 22, 1975; revised manuscript received Aug. 15, 1975. This was Paper 36 presented at the Toronto, Canada, Meeting of the Society, May 11-16, 1975.

Any discussion of this paper will appear in a Discussion Section to be published in the June 1976 JOURNAL. All discussions for the June 1976 Discussion Section should be submitted by Feb. 1, 1976.

Publication costs of this article were partially assisted by Argonne National Laboratory.

REFERENCES

- P. A. Nelson *et al.*, USAEC Report ANL-8109 (1974).
- R. Hultgren *et al.*, "Selected Values of the Thermodynamic Properties of Binary Alloys," American Society for Metals, Metals Park, Ohio 44073 (1973).
- V. P. Mashovets and L. V. Puchkov, *Zh. Prikl. Khim.*, **38**, 1875 (1965).
- E. J. Cairns *et al.*, USAEC Report ANL-7888 (1971).
- M. S. Foster, C. E. Johnson, and C. E. Crouthamel, USAEC Report ANL-6652 (1962).
- M. S. Foster, S. E. Wood, and C. E. Crouthamel, *Inorg. Chem.*, **3**, 1428 (1964).

7. "JANAF Thermochemical Tables," 2nd Edition, N.B.S. 37, Superintendent of Documents, U. S. Government Printing Office, Washington, D. C. (1971).

8. a. M. V. Smirnov and N. P. Podlesnyak, *Zh. Prikl. Khim.*, **43**, 1463 (1970).
 b. A. Dworkin, H. R. Bronstein, and M. A. Bredig, *J. Phys. Chem.*, **66**, 572 (1962).

DISCUSSION SECTION



This Discussion Section includes discussion of papers appearing in the *Journal of The Electrochemical Society*, Vol. 121, No. 11 and 12; November and December 1974; and Vol. 122, No. 1, 2, 3, 4, and 5; January, February, March, April, and May 1975.

A Palladium Hydride pH Electrode for Use in Buffered Fluoride Etch Solutions

R. Jasinski (pp. 1579-1584, Vol. 121, No. 12)

J. V. Dobson, B. R. Chapman, and D. Start:¹ There is some ambiguity in the Jasinski paper concerning the effect of purging the electrolyte with air. The sentence "no distinguishable effect of purging with air" may mean to the uninformed that no difference was observed between bubbling (purging) or stirring the electrolyte. Alternatively, it may suggest that no effect was found with purging the electrolyte at all. The results shown in Fig. 1 from our own more extensive studies show that some significant "bubbling effect" is obtained with the palladium hydride electrode in addition to a stirring effect. Thus in Fig. 1 a change in cell emf is found for bubbling with nitrogen or air and also with stirring.

The use of a 20 mV criterion for determination of composition and lifetime of the electrode may result in errors of 2-3 days for some electrodes, e.g., Fig. 3 in the paper under discussion. There are two ways of overcoming the difficulty in accurately determining the lifetimes (and composition) of palladium hydrogen electrodes of long lifetimes. First, the use of long lengths of very thin palladium wire supported on a former enables the relative resistance to be determined.² For long wires the desorption rate of hydrogen or lifetime is inversely proportional to the radius and is independent of the length.³ Second, if large rods of wire are employed, the general Eq. [1] derived in an earlier paper²

$$T = \frac{0.766 \frac{dr}{dt} (t + S) a}{i_a} \quad [1]$$

may be used to determine the lifetime and predict the charging conditions for an electrode. T and i_a are the charging time (hr) and current density (A/cm^{-2}); t , the lifetime in the $\alpha + \beta$ phase; S , the $[H]/[Pd]$ α -max composition; and dr/dt the desorption rate (hr^{-1}). Further details are given in our paper.³

We find it difficult to understand why the pH of the electrolyte should have any effect at all on the lifetime let alone a trend to increase with increasing pH. The data in Table III in the paper under consideration show a decrease in lifetime above pH 3. An increase in lifetime by decreasing the surface area exposed to the electrolyte by sleeving, for example, has been shown dramatically in several recent papers.⁴

The minimum dependence of "stirring effect" on $[H]/[Pd]$ (stated incorrectly throughout the paper as $[Pd]/[H]$) composition is only partly true from the given data. For example, Jasinski's Table IV suggests that there is an optimum composition of 0.49 at least for pH 8, though not pointed out in the paper. A decided optimum composition is clearly shown from the results of some of our studies which are shown in Fig. 2. We have converted and replotted the data obtained for the Jasinski paper. It is seen that for our system, a wire-wound coil of 0.025 in. (8-10 ohm) diameter wire whose electrical resistance was monitored, an optimum value would be $r = R/R_0 = 1.23$, while the Jasinski data would give a value of r around 1.48.

The profound discrepancy thus detected may be partly reconciled by Jasinski's uncontrolled arbitrary choice to make measurements of stirring effect after

¹ School of Chemistry, The University of Newcastle upon Tyne, Newcastle upon Tyne NE1 7RU, England.

² F. A. Lewis, "The Palladium Hydrogen System," Academic Press, New York (1967).

³ J. V. Dobson, B. R. Chapman, and H. R. Thirsk, in "Electrochemistry in Aqueous Solutions," International Conference on High Temperature and High Pressure, NACE Publications (1975).

⁴ J. V. Dobson, M. N. Dagless, and H. R. Thirsk, *Trans. Faraday Soc.*, **68**, 764 (1972); *ibid.*, **68**, 749 (1972).

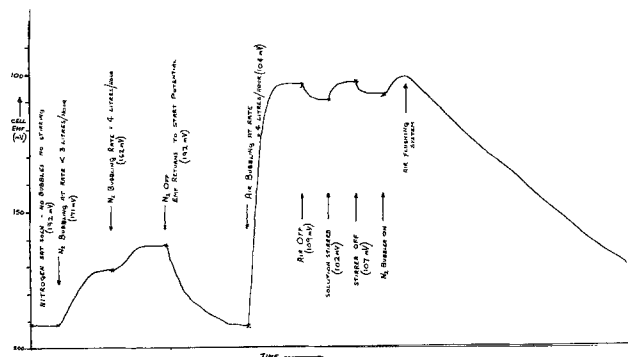


Fig. 1. Variation of emf levels (in constant electrolyte) with N_2 and air, showing stirring effect.

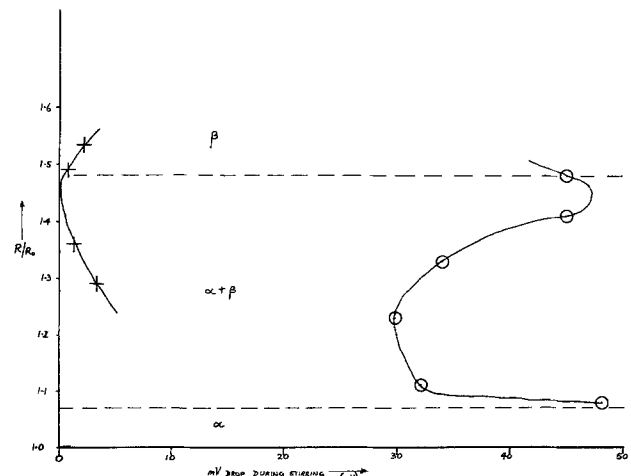


Fig. 2. Variation of stirring effect (mV drop) with R/R_0 .

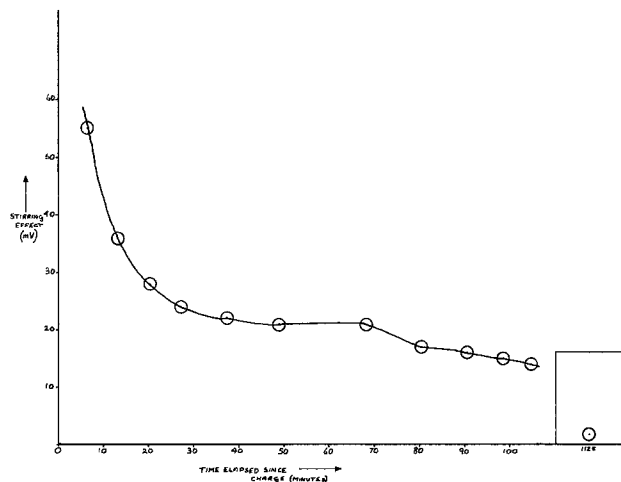


Fig. 3. Variation of stirring effect (mV drop) with time elapsed since charge. $R/R_0 = 1.48$; pH constant.

10 min. We have found, Fig. 3, a considerable change or lowering in stirring effect with time after charge.

Finally, we get the impression from the discussion that there is a suggestion of a loss of a Pd H species from the electrode surface into the bulk electrolyte. It may be instructive to recall that Troost and Hautefeuille⁵ oversimplified the problem of structure by suggesting the formation of discrete Pd₂H. Later work⁶ has made it clear that the $\alpha + \beta$ -phase is a mixed phase system of variable H/Pd composition. It would appear, therefore, that a discrete Pd-H compound dissolving into the electrolyte would be contrary to the formation of a nonstoichiometric mixed phase system. Desorbed hydrogen on the electrode surface could of course be dissolving into the bulk electrolyte, thereby reducing the electrode composition.

R. Jasinski:⁷ Constructive criticism is always appreciated, and I wish to apologize for any difficulty Dobson *et al.* have had in understanding my paper. The point of my work, as stated in the introduction, was to develop a practical pH electrode which was usable in a corrosive, commercially important silica etchant. This was done by maximizing the content of palladium hydride in the electrode structure and by minimizing the rate at which it was lost to the surroundings.

Now to the specific criticisms. On the "ambiguity ... concerning the effect of purging ...," the complete sentence in the Experimental Section reads: "There was no distinguishable effect of purging the test solutions with air *vs.* stirring in an open beaker after first saturating with air." This still seems to me to be a relatively unambiguous description of the general electrode behavior that I observed under the experimental conditions I described. It is possible to devise a situation where stirring will be less effective than bubbling in maintaining the bulk dissolved air concentration at the electrode surface. Also, if bubbles of air are delivered to the electrode surface to increase the availability of oxygen "depolarizer" at the surface, greater shifts in potential will be observed. Such potential shifts would also be particularly large if the hydride concentration of the electrode were particularly low, as with Dobson's wires.

Next, I stated in my paper, that the 20 mV criterion used to define electrode life was indeed arbitrary, but was nevertheless adequate for comparing electrode lifetimes of minutes with electrode lifetimes of days. Dobson *et al.* are perfectly entitled to desire a more rigorous criterion for electrode life. Thin wires do not give long electrode lifetimes (days) as I have shown. Accurate measurements of electrical resistance for

large rods of metal are difficult, and would indicate an average hydride concentration, at best, rather than the operative surface concentration. I did find it difficult to correlate my data published in 1974 with Dobson's equations published in 1975 (Dobson's Eq. [1] and Ftn⁸). It is instructive to note, however, that our two correlation equations are of the same sense, i.e., the electrode life in the $\alpha + \beta$ phase (a) is proportional to the total charge put into the electrode (in the $\alpha + \beta$ phase), minus that left in the α -phase, and (b) is inversely proportional to a desorption rate (dr/dt). I have, in effect, attempted to establish a proportionality between this desorption rate of Dobson and the surface area of the electrode exposed to the solution. Some proportionality is to be expected since one mechanism for the loss of palladium hydride phase is chemical reaction with dissolved oxygen.

One possible "why" for the pH effect is postulated (not proved) at the end of the paper and so labeled: "that this process is the acid catalyzed recombination of palladium hydride to yield H₂." The possibility of different oxygen solubilities according to electrolyte is also raised in the final paragraph of the paper.

The use of the "sleeve" in the work of Dobson, Dagless, and Thirsk, was to retard the rate of absorption of H₂ by palladium once sufficient hydride has been formed to generate the potential of the palladium $\alpha + \beta$ phase. Indeed this technique is analogous to the reverse situation described in my paper that of increasing the life of the electrochemically formed $\alpha + \beta$ phase, in the absence of H₂, by restricting the surface area of the palladium electrode presented to the solution for reaction. Unfortunately I did not have the reference at the time of preparing my paper.

I do stand corrected on the use of {Pd}/{H}, rather than {H}/{Pd}.

Considering the complicated chemistry and poorly defined mass transport conditions in the solution and in the palladium phase during these stirring experiments, I fail to appreciate the profound significance based on such results of an enhanced stability for an intermediate {H}/{Pd} composition.

The time of stirring in my paper was 1 min, not 10 min. The stability of potentials with the palladium rods was such that little change in potential was noted after longer periods of time. The data presented in the paper unambiguously demonstrated the point (Table IV in the paper under discussion) stated clearly as "stirring dependence is dependent upon PdH content of the electrode." Such a dependence is entirely reasonable in view of reaction between PdH at the electrode surface with dissolved oxygen, followed by diffusion of hydride from the bulk of the electrode to the surface to replace the hydride removed. A low PdH content in the electrode must yield a low diffusion gradient and hence a low rate of transport of hydride from the bulk to the surface. As indicated in the references quoted in my paper, this diffusion coefficient is also about an order of magnitude slower in palladium than for ions in solution.

Finally I must apologize for giving Dobson *et al.* the impression that I have suggested the dissolution of Pd or PdH species from the electrode into the electrolyte. This was not my intent and is not stated. The work of Troost and Hautefeuille (Dobson Ftn⁸) was published in 1874 not in 1974; Ftn^{8b} is page 1229 not page 1220.

I do wish to thank Dobson *et al.* for their interest in my paper.

Supersaturated Zincate Solutions

W. Van Doorne and T. P. Dirkse, pp. 1-4, Vol. 122, No. 1)

A. G. Briggs, N. A. Hampson, and A. Marshall:⁸ We wish to point out in connection with the above-mentioned paper that the constitutions of the supersaturated potassium zincate solutions are dependent upon

⁵ L. Troost and P. Hautefeuille, *Ann. Chim. Phys.*, **2**, 273 (1974).
⁶ J. W. Simons and T. B. Flanagan, *J. Phys. Chem.*, **69**, 3773 (1965); W. T. Lindsay and F. W. Pement, *ibid.*, **36**, 1220 (1962).
⁷ Texas Instruments Incorporated, Dallas, Texas 75222.

⁸ Department of Chemistry, University of Technology, Loughborough, LE11 3TU, England.

the time which has elapsed between the preparation of the saturated solution and the structure determination.⁹ This point appears to have been omitted from a number of past investigations in this area. However, we have recently been able to show that some of the anomalies observed from time to time have a satisfactory explanation when the above time dependence is taken into account.¹⁰

The Effect of Solvent on the Electrochemistry of Iron

A. L. Bacarella and A. L. Sutton (pp. 11-18, Vol. 122, No. 1)

K. Schwabe:¹¹ It is well known that the acidity of inorganic acids measured by the thermodynamic values pH or pWH increases strongly with respect to the solutions in water of equal concentration at high contents of organic solvents especially ethanol.¹² Therefore it is not surprising that Bacarella and Sutton receive an increasing corrosion current of iron at constant concentration of H_2SO_4 with rising content of ethanol. The dependence of the potential of the iron electrode on the ethanol content can also be explained by the increasing acidity. But it is quite impossible to found an absolute acidity scale on these measurements and to define the absolute acidity as proposed by the authors.

This definition is based on the assumption of Grunwald *et al.*¹³ who postulated the same medium effect for similar solutes (degenerate coefficient). As proved by Wynne-Jones¹⁴ this postulate is not right. Surely it cannot be used for H_2SO_4 , and therefore the degenerate coefficients, calculated by Bacarella and Sutton for ethanol and mixtures of ethanol-water are not correct. That means that the "diffusion potential E_L^S " cannot be calculated with the help of these coefficients. The cell used by Bacarella and Sutton gives no possibility to estimate the diffusion and phase boundary potentials. But it is quite improbable¹⁵ that they are 0 mV with 0.5M H_2SO_4 in water, and 140 mV in ethanol as shown in Fig. 1 of the paper being discussed. So the proposal of Bacarella and Sutton cannot be accepted as a new absolute measure for acidity.

A. L. Bacarella and A. L. Sutton:¹⁶ In our publication, we have shown that using the junction potentials E_L^S estimated by Gutbezahl and Grunwald,¹⁷ a very satisfactory interpretation of the iron dissolution and hydrogen evolution reactions on zone-refined iron in hydrogen saturated acidic ethanol-water media was obtained. It was also shown that by using the junction potentials provided by Popovych and Dill,¹⁸ a satisfactory fit to the data was not obtained.

Schwabe suggests that the junction potentials in EtOH-HOH solvents are not larger than those between similar electrolytes in water. We interpret this to mean that the junction potentials are therefore small for all

⁹ A. G. Briggs, N. A. Hampson, and A. Marshall, *Trans. Faraday Soc.*, **70**, 1978 (1974).

¹⁰ See, for example: T. P. Dirkse, *This Journal*, **101**, 328 (1954); T. P. Dirkse, *ibid.*, **102**, 497 (1955); J. S. Fordyce and R. L. Baum, *J. Chem. Phys.*, **43**, 843 (1965); G. H. Newman and G. E. Blomgren, *ibid.*, **43**, 2794 (1965); N. A. Hampson, G. A. Herdman, and R. Taylor, *Electroanal. Chem.*, **25**, 9 (1970); J. F. Jackovitz and A. Langer, in "Zinc-Silver Oxide Batteries," J. J. Lander and A. Fleischer, Editors, p. 29, John Wiley & Sons, Inc., New York (1971).

¹¹ Meinsberg Nr. 70, Postschlossfach 30, Post DDR-7305, Waldheim, Germany.

¹² See, for example: K. Schwabe and M. Kunz, *Z. Elektrochem.*, **64**, 1188 (1960); K. Schwabe, R. Ullrich, and A. Ferse, *ibid.*, **68**, 46 (1964); K. Schwabe and R. Müller, *Ber. Bunsenges. Phys. Chem.*, **73**, 178 (1969).

¹³ E. Grunwald *et al.*, *J. Am. Chem. Soc.*, **70**, 846 (1948); *ibid.*, **73**, 4939 (1951); *ibid.*, **75**, 565 (1953).

¹⁴ Professor Lord Wynne-Jones, in "Hydrogen Bonded Solvent Systems," A. K. Covington and P. Jones, Editors, p. 245, Taylor and Francis Limited, London (1968).

¹⁵ It could be shown that the phase boundary potentials between water and organic solvents are probably not larger than the diffusion potentials between different electrolytes in water. See, for example: K. Schwabe, *Novo Acta Leopoldina*, **36**, 103 (1971); K. Schwabe and Ch. Queck, *Sitzber. Südsch. Akad. Wiss.*, To be published; R. Parsons and B. T. Rubin, *Trans. Faraday Soc.*, **70**, 1636 (1974).

¹⁶ Oak Ridge National Laboratory, Oak Ridge, Tennessee 37830.

¹⁷ B. Gutbezahl and E. Grunwald, *J. Am. Chem. Soc.*, **75**, 565 (1953).

¹⁸ O. Popovych and A. J. Dill, *Anal. Chem.*, **41**, 456 (1969).

EtOH-HOH solvents, and can be neglected. Again, with such an assumption a satisfactory interpretation of the experimental data cannot be made.

It was also stated that it is not surprising that the corrosion current of iron at constant H_2SO_4 concentration increased with increasing ethanol content of the solvent. Unfortunately, our observation was that the corrosion current decreased with increasing ethanol content, as shown in Fig. 2 and 3 of our paper. Also, Fig. 7 shows a very satisfactory fit to the data for the corrosion current, $\log i^S_{(corr)}$ (corrected for coverage), as a function of pA . Here, the pA of the solution was determined from the potential of the Pt/ H_2 electrode, and using the junction potentials provided by Gutbezahl and Grunwald.¹⁷

It is also stated that Wynne-Jones¹⁴ has proved that the basic assumption (the activity postulate) upon which the estimation of the junction potentials is made is not right. This is, of course, not so and suggests that the "activity postulate"¹⁹ is not understood. Indeed, if such ratios of the acid dissociation constants of the anilinium, toluidinium, and ammonium salts are made with respect to anilinium as the reference acid, it is observed that the curves are not necessarily parallel; some increase, some decrease, and some remain essentially unchanged with increasing ethanol content of the solvent. For these acids, however, a quantitative correlation of the dissociation constants was made using the activity postulate.

Light-Deflection Errors in the Interferometry of Electrochemical Mass Transfer Boundary Layers

F. R. McLarnon, R. H. Muller, and C. W. Tobias
(pp. 59-64, Vol. 122, No. 1)

T. Z. Fahidy:²⁰ In computing light-deflection errors, the authors postulate for basis the convection-free diffusion equation

$$\frac{\partial c}{\partial t} = D \frac{\partial^2 c}{\partial y^2} \quad [1]$$

in the boundary layer of a "convectionless" metal deposition cell in electrolysis. Much evidence has been shown lately²¹ for the existence of local convective currents in such cells using parallel plane electrodes and one wonders if Eq. [1] has as wide an applicability as inferred from the paper. It appears that if local Peclet numbers are large and convective "loci" are numerous, the more realistic, but still unrigorous, mass balance

$$\frac{\partial c}{\partial t} = D \frac{\partial^2 c}{\partial y^2} + v_y \frac{\partial c}{\partial y} \quad [2]$$

would have to be taken as basis for the analysis of errors. The solution to Eq. [2], employing an arbitrary

velocity profile $v_y = P(y) = \sum_{k=1}^N a_k y^k$ of polynomial

form is $c = c_1 + c_2$, where c_1 is the well-known error function solution to Eq. [1] (Eq. [6] in the authors' paper) and c_2 is computed as

$$c_2/c_b = \sum_{k=0}^N D^{k-1/2} P^{(2k)}(y) \frac{t^{k+1/2}}{\Gamma(k+3/2)} - \frac{y}{2\pi^{1/2}} \sum_{k=1}^N D^{k-1} a_{2k} (2k)! \int_0^t \frac{(t-u)^{k+1/2}}{\Gamma(k+3/2)} \times \frac{1}{u^{3/2}} \exp\left(-\frac{y^2}{4Du}\right) du \quad [3]$$

¹⁹ E. Grunwald and S. Winstein, *J. Am. Chem. Soc.*, **70**, 846 (1948).

²⁰ Department of Chemical Engineering, University of Waterloo, Waterloo, Ontario, Canada N2L 3G1.

²¹ A. A. Wragg and M. A. Patrick, *Electrochim. Acta*, **19**, 929 (1974).

for times less than the so-called transition time in the theory of unsteady-state convective diffusion. Thus, the authors' analysis seems to apply only to very short times and at very low current densities, *i.e.*, when the condition for the thickness of the boundary layer

$$\delta P(\delta) \ll D \quad [4]$$

is satisfied. Do interferometric studies of electrochemical mass transfer boundary layers really satisfy this criterion? It seems logical that one should know, at least approximately, the velocity field in the boundary layer and if it is assumed *a priori* to be zero, a firm base for the analysis of deflection errors will be missing.

F. R. McLarnon,²² R. H. Muller,²³ and C. W. Tobias:²⁴

It is well known that, in the absence of forced convection, transport of an ionic species which is consumed at a horizontal electrode facing downward is only by diffusion and migration, because the density gradient established by the electrode reaction is stable. The role of free convection in ionic mass transport with other electrode configurations has already been described and analyzed by the authors 20 years ago. Free convection velocity and concentration fields have been measured by dark field photography and interferometry,²⁵ and limiting current studies on the same models²⁶⁻²⁸ have confirmed the interpretation of optical data.

As stated in the paper under discussion, "Diffusion boundary layers free of convection effects offer a useful model for optical investigation since the concentration profiles are easily derived and experimental results can serve to test the optical calculations." In no way has it been suggested that optical corrections derived for concentration profiles in the absence of convection could serve to accurately predict concentration fields in the presence of various velocity boundary layers.

Clearly, if we had assumed any particular velocity profile, the validity of the computed light deflection errors would be just as restricted as those for the chosen profile. The concentration field in the pure diffusion model in fact can be predicted on theoretical grounds with higher accuracy, and less ambiguity than in the case of forced or free convection. We have reported elsewhere on the excellent agreement between theoretical concentration fields in unsteady-state diffusion and those obtained from corrected interferograms.²⁹

Details of the computer-implemented numerical solution of the equations involved in the correction procedure for an arbitrary concentration profile have been published in a journal devoted to physical optics.³⁰ These calculations showed that the errors incurred are not very sensitive to the exact shape of the entire concentration profile, but depend strongly on the inner regions of the boundary layer, where the concentration changes are large. Therefore, the error estimates derived for the convection-free profiles are useful for obtaining good first estimates of corrections in the presence of flow as well. Results of analysis of interferograms in the presence of flow, performed in this laboratory, are to be published in the near future.

²² Western Electric Engineering Research Center, P.O. Box 900, Princeton, New Jersey 08540.

²³ Lawrence Berkeley Laboratory, University of California, Berkeley, California 94720.

²⁴ Department of Chemical Engineering, University of California, Berkeley, California 94720.

²⁵ N. Ibl and R. Muller, *Z. Elektrochem.*, **59**, 671 (1955).

²⁶ C. R. Wilke, M. Eisenberg, and C. W. Tobias, *This Journal*, **100**, 513 (1953).

²⁷ E. J. Fenech and C. W. Tobias, *Electrochim. Acta*, **2**, 311 (1960).

²⁸ C. W. Tobias and R. G. Hickman, *Z. Physik. Chem. (Leipzig)*, **229**, 145 (1965).

²⁹ F. R. McLarnon, R. H. Muller, and C. W. Tobias, *Electrochim. Acta*, in press.

³⁰ F. R. McLarnon, R. H. Muller, and C. W. Tobias, *J. Opt. Soc. Am.*, **65**, 1011 (1975).

Unified Approach to Cell EMF Calculations

D. Gray (pp. 75-76, Vol. 122, No. 1)

C. P. Keszthelyi:³¹ In the paper under discussion, the author provides an important service to the scientific community in general, and electrochemistry (and analytical chemistry) in particular, by pointing out an error in Laitinen's well known text.³² This is made all the more urgent by the latest edition of the book,³³ which not only leaves the error uncorrected, but further degrades the treatment by using cell potentials given to only two decimal places, whereas the previous edition gave three decimals. It is nevertheless an unwarranted conclusion to suggest that a correct unified approach to cell EMF calculations is something we are lacking at present. What we are faced with is a correct ("unified") approach augmented by some errors published—errors which clearly contradict the correct method.

We are in disagreement with a comment in the paper under discussion, that "Laitinen's is the only major textbook which discusses the problem at length;" perhaps "length" is a subjective term, but we cite the following from three major texts to document that the correct approach is available in published works.

In Ref. (2) given by the paper under discussion,³⁴ we find the following:

However, in addition or subtraction of two half-reactions to give a third half-reaction, the free energies, *i.e.*, volt equivalents of the two half-reactions, must be added or subtracted to give the free energies of the third half-reactions.

Example	E°	volt equivalents
$\text{Cl}^- + 3\text{H}_2\text{O} = \text{ClO}_3^- + 6\text{H}^+ + 6e^-$	-1.45	-8.70
$\text{Cl}^- = \frac{1}{2}\text{Cl}_2 + e^-$	-1.36	-1.36
$\frac{1}{2}\text{Cl}_2 + 3\text{H}_2\text{O} = \text{ClO}_3^- + 6\text{H}^+ + 5e^-$	-1.47	-7.34

Thus the volt equivalents for the new half-reaction are -7.34, and since there are 5 electrons for this reaction E° is -7.34/5, or -1.47.

In a major text dealing with quantitative chemical analysis³⁵ we find:

By application of certain thermodynamic concepts it can be shown that for a redox couple

$$RT \ln K = nFE^\circ_{\text{cell}} = -\Delta G^\circ$$

where G° is the standard free energy change, and the other symbols represent the usual terms in the Nernst equation. By the IUPAC conventions, E° assumes that the given half-cell is the right-hand electrode in a cell having the standard hydrogen electrode on the left; therefore, E°_{cell} is numerically equal to E° associated with the half-reaction in question. Half-reactions may be combined, by addition or subtraction, and the E° of the resulting half-reaction can be calculated by adding or subtracting the free energy changes (nFE°) associated with the half-reactions. Because F , the Faraday number, is common to all the free energy changes, the calculations are simplified by the use of nE° , the dimensions of which are electron volts.

This paragraph is augmented by two examples which we do not reproduce here to conserve paper.

In a major freshman textbook,³⁶ the authors unmistakably stir their students in the correct direction:

³¹ Department of Chemistry, Louisiana State University, Baton Rouge, Louisiana 70803.

³² H. A. Laitinen, "Chemical Analysis," p. 286, McGraw-Hill Book Co., New York (1960).

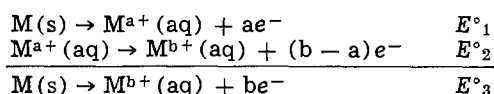
³³ H. A. Laitinen and W. E. Harris, "Chemical Analysis: An Advanced Text and Reference," 2nd ed., p. 224, McGraw-Hill Book Co., New York (1975).

³⁴ W. M. Latimer, "Oxidation Potentials," 2nd ed., pp. 4-5, Prentice-Hall Inc., Englewood Cliffs, N.J. (1952).

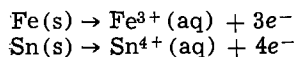
³⁵ G. H. Ayres, "Quantitative Chemical Analysis," 2nd ed., p. 385, Harper and Row, New York (1968).

³⁶ W. L. Masterton and E. J. Slowinski, "Chemical Principles," p. 594, W. B. Saunders Co., Philadelphia (1973).

°21.43 Consider the half-reactions



- Write expressions for ΔG° for each of the three half-reactions in terms of E° .
- Knowing that $\Delta G^\circ_3 = \Delta G^\circ_1 + \Delta G^\circ_2$, derive a relationship that would enable you to calculate E°_3 given E°_1 and E°_2 .
- Use the relationship in (b) to obtain E° for the half-reactions below, using Table 21.1.



All it takes at this stage is a competent freshman instructor to assure that any encounter by the student with erroneous suggestions^{32,33} in later years will be identified by him as such.

We have no intention to belittle the contribution made by the paper under discussion by the above comments; it is indeed cause for concern³⁷ when a new breed of Ph.D. analytical chemist is surfacing who is aware of the merits of interfacing, automation, computerization, and analog to digital conversion, but is alien to basic freshman-sophomore chemistry.

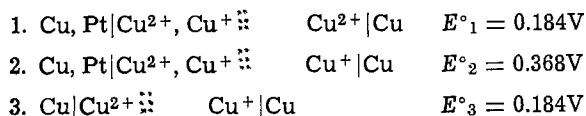
D. Gray:³⁸ I did not mean to imply that my development of forming new half-cells from other half-cells is in any way original and it was an oversight on my part not to reference it properly with at least one of the numerous appropriate sources. As I noted in the paper under discussion: "For completeness, the method of combining half-cell reactions to form a new half-cell reaction will be included in the discussion." This trivial case was only inserted in the paper under discussion to avoid any possible confusion of it with the (incorrect) method of combining half-cell reactions to form new cell (not half-cell) reactions. Keszthelyi has apparently confused the two cases and as a consequence he has misunderstood the purpose and the point of the paper under discussion.

Unified Approach to Cell EMF Calculations

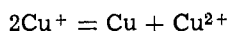
D. Gray (pp. 75-76, Vol. 122, No. 1)

R. Parsons:³⁹ The argument of this article is incorrect because of an erroneous identification of n_{cell} which is, in fact, always equal to $n_r n_{\text{ox}}$ (using the notation of the paper under discussion). If n_{cell} were correctly defined as "the number of electrons sent round the external circuit in the completion of unit cell reaction in the form written," then the error should become clear. In fact the definition of n_{cell} given by Gray (the net cell electron change) is vague and misleading.

The standard emf's of the three copper cells used as examples should be as follows:



and although the cell reaction in each case is



the completion of this reaction in cells 1 and 3 involves the passage of two electrons round the external circuit, whereas in cell 2 it involves the passage of one electron round the external circuit. Thus the standard free energy change in the disproportionation reaction is $-35.5 \text{ kJ mole}^{-1}$ whichever way it is calculated from these data.

³⁷ P. W. West, "Picasso the Chemist—Fischer Award Address in Analytical Chemistry," *Anal. Chem.*, **46**, 784-A (1974).

³⁸ Golden West College, Huntington Beach, California 92647.

³⁹ School of Chemistry, University of Bristol, Bristol BS8 1TS, England.

Thus Eq. [1] is correct and leads to no anomaly, if it is correctly applied. In contrast, the article by Gray would lead to the result that the standard emf's of the three cells 1, 2, and 3 were all 0.368V which would be contrary to experiment.

D. Gray:³⁸ The primary difficulty here is not what is n_{cell} , but rather what is the thermodynamic nature of $E(\text{rev})$. It is generally conceded, when explaining the different possible cell potentials calculated for the same disproportionation cell reaction involving different half-cell combinations, that E° is not a state (or thermodynamic) function.⁴⁰ This is, of course, incorrect. $E(\text{rev})$ is a thermodynamic function which can be simply shown by letting $E(\text{rev}) = f(T, P)$, assuming ideality, and evaluating the second derivatives.

$$\begin{aligned} \left[\frac{\delta}{\delta P} \left(\frac{\delta E}{\delta T} \right)_P \right]_T &= \frac{1}{nF} \left(\frac{\delta \Delta S}{\delta P} \right)_T = -\frac{1}{nF} \left(\frac{\delta \Delta V}{\delta T} \right)_P \\ \left[\frac{\delta}{\delta T} \left(\frac{\delta E}{\delta P} \right)_T \right]_P &= \frac{\delta}{\delta T} \left(-\frac{\Delta V}{nF} \right)_P = -\frac{1}{nF} \left(\frac{\delta \Delta V}{\delta T} \right)_P \end{aligned}$$

Since the second derivatives are equivalent, $E(\text{rev})$ is shown to be a thermodynamic function. One should note that a similar thermodynamic treatment for $E(\text{irrev})$ does not yield equivalent second derivatives (due to the overvoltage) and it is not a thermodynamic function.

Since $E(\text{rev})$ is a thermodynamic function, it is path independent and must yield the same value for a cell reaction regardless of the manner of half-cell construction. Calculating $E_{\text{cell}}(\text{rev})$ by assuming that in all cases $n_{\text{cell}} = n_{\text{ox}} n_r$ leads to nonunique E_{cell} values in certain disproportionation reactions, *i.e.*, Cu^+ . In order to maintain the necessary uniqueness of $E_{\text{cell}}(\text{rev})$ it is necessary that $n_{\text{cell}} \neq n_{\text{ox}} n_r$ in these particular disproportionation reactions. This is why I defined n_{cell} in the paper under discussion as "the net cell electron change" which can be easily determined by inspection of the over-all balanced cell reaction, and not as Parsons has done as "the number of electrons sent round the external circuit in the completion of unit cell reaction in the form written." It is intriguing to note that in the paper under discussion a mathematical impasse is reached in these same disproportionation systems (cases II and III) of interest and one cannot show mathematically how n_{cell} is related much less equal to $n_{\text{ox}} n_r$.

By evaluating n_{cell} from the over-all cell reaction, one is essentially equating n_{cell} to the "number of equivalents of electricity flowing per mole of reaction as written."⁴¹ This may be a better and less ambiguous way to define n_{cell} . The significant point here is that regardless how n_{cell} is defined, it cannot in general be determined from the contrived half-cell reactions. A trivial consequence of this is that n_{cell} is uniquely defined for a cell reaction.

The Free Energy of Formation of Iridium Oxide by Solid Electrolyte Galvanic Cell

E. S. Ramakrishnan, O. M. Sreedharan, and
M. S. Chandrasekharaiah
(pp. 328-331, Vol. 122, No. 3)

H. Kleykamp:⁴² Ramakrishnan *et al.* have criticized and called into question the results of our paper "Gibbs Energy of Formation of Iridium Dioxide."⁴³ The objections are baseless. It has escaped their attention that we have used zirconia as the electrolyte and a closed cell arrangement instead of thoria and an open cell as Ramakrishnan *et al.* imputed. Further, we applied both

⁴⁰ T. Ree, *J. Chem. Educ.*, **48**, 467 (1971).

⁴¹ G. N. Lewis and M. Randall, "Thermodynamics," 2nd ed., Revised by K. S. Pitzer and L. Brewer, Chap. 24, McGraw-Hill Book Co., New York (1961).

⁴² Kernforschungszentrum Karlsruhe, Institut für Material und Festkörperforschung, 7500 Karlsruhe, Germany.

⁴³ H. Kleykamp and L. J. Paneth, *J. Inorg. Nucl. Chem.*, **35**, 477 (1973).

Fe, FeO and Ni, NiO as reference electrodes and $ZrO_2 \cdot Y_2O_3$ and $ZrO_2 \cdot CaO$ as the electrolyte as we have discussed in quoted previous investigations. No differences resulted in the Gibbs energy values. Ramakrishnan *et al.* cited our experimentally determined Gibbs energy of formation in Eq. [21] of their paper to be

$$\Delta G_f^\circ <IrO_2> = (-61.66 \pm 0.741) + (43.26 \pm 0.956) F \times 10^{-3} T \text{ kcal/mole}$$

in comparison to their own value to be

$$\Delta G_f^\circ <IrO_2> = -56.76 + 40.41 \times 10^{-3} T \text{ kcal/mole}$$

The presupposed disagreement should not be a pretense for their redetermination of this system. A mistake might have been committed by the authors in copying our results which are given correctly as

$$\Delta G_f^\circ <IrO_2> = -59.42 + 43.26 \times 10^{-3} T \text{ kcal/mole}$$

between 900° and 1200°K (1 cal = 4.184 J). Consequently, their work should be regarded as a confirmation of our results and lays no claim to a higher reliability.

Two objections should be made regarding the validity of their data: (i) the cells mentioned in Eq. [7] and [14] of the paper under discussion are not symmetric. The conducting leads on the right and the left hand sides of the cells consist of Pt/Ir and Pt, respectively, which results in an additional thermal emf and (ii) it might be possible that the system has not attained equilibrium below 1000°K, but this could have been checked easily by polarizing the cells.

E. S. Ramakrishnan, O. M. Sreedharan, and M. S. Chandrasekhariah:⁴⁴ We regret the inadvertent arithmetical error in converting the $\Delta G^\circ <IrO_2, f>$ expression of Kleykamp and Paneth.⁴³ Our Eq. [21] should read

$$\begin{aligned} {}^f\Delta G_T^\circ (IrO_2)/\text{kcal mole}^{-1} &= (-59.42 \pm 0.741) \\ &+ (43.26 \pm 0.956) T \quad [1] \end{aligned}$$

Our contention that if the oxygen potential difference between the reference electrode and the electrode of interest is very large (as it was the case with the measurement of Kleykamp and Paneth who have employed Fe, FeO_x reference resulting in the emf of 800-870 mV), the oxygen permeation rates through the electrolyte increases resulting in a possible systematic error in the measured emf. This point has been reiterated recently by Giddings and Gordon.⁴⁵ This effect is less in the case of biphasic mixture than in case of single phase. Nevertheless it is there. Therefore in the paper under discussion we have employed Cu, Cu₂O and Ni, NiO as the references.

That there exists a higher systematic error in the reported ${}^f\Delta G^\circ$ for IrO₂ by Kleykamp and Paneth compared to our data will become obvious when one compares the third law enthalpy of formation values calculated using the same free energy functions. Kleykamp and Paneth's Table IV⁴³ presents an estimated change in free energy function, $T\Phi^\circ$ for the reaction



at various temperatures. ${}^f\Delta H^\circ_{298}$ calculated from their ${}^f\Delta G^\circ$ data shows a systematic increase from -241.9 kcal mole⁻¹ at 900°K to -236.3 kcal mole⁻¹ at 1200°K. They have attributed this variation entirely to the uncertainties in the estimated specific heat of IrO₂. We have recalculated the ${}^f\Delta H^\circ_{298}$ of IrO₂ employing their estimated $T\Phi^\circ$ and our ${}^f\Delta G^\circ$ data and it is shown in Table I.

As can be seen, the spread is from -241.4 kcal mole⁻¹ at 900°K to -239.1° at 1200°K, a maximum variation of 2.3 kcal mole⁻¹ compared to their 5.6 kcal

Table I. ${}^f\Delta H^\circ (IrO_2, 298^\circ K)$ calculated from the third law

T/°K	$T\Phi^\circ /$ kj mole ^{-1 43}	$-{}^f\Delta G^\circ /$ kj mole ^{-1 43}	$-{}^f\Delta H^\circ_{298} /$ kj mole ^{-1 43}	$-{}^f\Delta G^\circ /$ kj mole ⁻¹	$-{}^f\Delta H^\circ_{298} /$ kj mole ⁻¹
900	156.1	85.8	241.9	85.3 ₂	241.4 ₂
1000	172.6	67.4	240.0	68.4 ₁	240.9 ₇
1100	188.8	49.5	238.3	51.5 ₀	240.2 ₆
1200	204.5	31.8	236.3	34.5 ₆	239.1 ₃

mole⁻¹. Since the same $T\Phi^\circ$ values are used in both cases, this disagreement cannot be due to the errors of the estimated heat capacity alone but also due to much smaller systematic errors in our measurements. This variation in the calculated ${}^f\Delta H^\circ_{298}$ would be smaller in our case if we had limited our evaluation to the temperature range 950°-1170°K to which our expression for ${}^f\Delta G^\circ (IrO_2)$ (our abstract) was considered valid. Thus, our conclusion in the paper under discussion that the results of our work for the ${}^f\Delta G^\circ (IrO_2)$ is more reliable stands to reason.

In view of the above-mentioned reasons, we take strong objection to Kleykamp's statement, "The presupposed disagreement should not be a pretense for their redetermination of this system." Besides, when we began our galvanic cell investigations in 1972,⁴⁶ there was no other galvanic cell results available in the literature for IrO₂ and hence the question of redetermination did not arise.

In their communication,⁴³ Kleykamp and Paneth describe only their experiments employing Fe, wustite electrode, and yttria-zirconia electrolyte cup in which the sample was sealed. No results obtained with Ni, NiO as the reference with Ir, IrO₂ system are given as claimed in the above comments while we have measured the IrO₂ system with two separate reference electrodes. Hence it is not at all clear what they mean by the statement, "No differences resulted in the Gibbs energy values." In their measurements, the sample was sealed inside the electrolyte cup with glass. There is a possibility that the sealing glass can act as the path for the oxygen permeation between the reference electrode outside and the system sealed inside. Giddings and Gordon⁴⁵ have discussed this mechanism at length. This may also add to the systematic error.

In cells [7] and [14] of our paper, there is no asymmetry of the kind indicated by Kleykamp. In both cases, the lead wires were Pt wires on both sides. Only an iridium foil was interposed between Ni and Pt (as also between Cu and Pt) so as to minimize the thermal effects. To check this, the positions of the reference and the Ir, IrO₂ electrode pellets were interchanged and the emf measured did not show any appreciable (<0.1 mV) variation indicating insignificant contributions from the thermal emf.

Their other objection that our measurements below 1000°K were nonequilibrium ones is also incorrect. As described in our experimental procedure, we did subject the emf readings to micropolarizations even for those below 1000°K readings. The time independent emf at any one temperature setting was reproducible within ± 0.5 mV. But the scatter from the results of one temperature cycle to another was larger than this. As described in our paper, the change in the slope of emf vs. temperature was observed with both references and hence we felt it as real and not due to not attaining equilibrium.

Thus the difference in the results of the two measurements are real and we have to refute the claim made by Kleykamp that our work boils down to nothing but the confirmation of their results and lays no claim to a higher reliability. The results we have reported have much smaller systematic errors and hence are more reliable.

⁴⁴ Chemistry Division, Bhabha Atomic Research Centre, Bombay 400085, India.

⁴⁶ R. A. Giddings and R. S. Gordon, *This Journal*, 121, 793 (1974).

⁴⁵ E. S. Ramakrishnan, *Proceedings Indo-Soviet Symposium on Solid-State Studies*, Bangalore, India (1972).

Structural Transformations of the PbO₂ Active Material during Cycling

A. C. Simon, S. M. Caulder, and J. T. Stemmler
(pp. 461-466, Vol. 122, No. 4)

B. Burrows and H. Giess:⁴⁷ It was observed by the authors of the paper under discussion that, after formation, PbO₂ had a uniform tightly packed structure which was transformed during cycling into a coralloid structure characterized by large voids and a dense network of PbO₂. It is claimed that this coralloid structure should be ideal for a porous electrode since the dense convolutions of the coralloid structure should provide maximum strength and electrical conductivity and the surfaces of these convolutions should present an enormous surface area while the large voids should enable a free flow of electrolyte. With cycling, however, the capacity of positives in the lead-acid battery decreases rather than increases. To account for this contrary trend three explanations were offered.

The first explanation is in terms of the structure of the PbSO₄ formed during discharge. With increase in cycle number it was observed that the PbSO₄ deposits in a progressively more closely packed and dense layer on the surface of the dense PbO₂ network thereby passivating the PbO₂. This is not surprising and simply shows that the coralloid structure is, contrary to the authors' claims, not ideal for a porous positive electrode.

The second explanation offered is that the coralloid structure itself is the cause of capacity loss which contradicts the claim that the coralloid structure is ideal.

The third proposed explanation is that an increase in the proportion of "inactive" PbO₂ causes the capacity loss. The existence of this "inactive" PbO₂ has not, however, been unequivocally established. Rather the existence of an electrochemically inert form of PbO₂ in the active mass has been inferred from the authors' NMR⁴⁸ and DTA⁴⁹ measurements and, even if one admits the existence of "inactive" PbO₂, it has not yet been demonstrated that its concentration can be quantified (either absolutely or relatively) and related to cycle number of a positive electrode.

The observations and conclusions of Simon *et al.*, which we have briefly summarized and commented upon above, indicate the difficulties of interpreting optical and scanning electron micrographs. This is particularly so when one is attempting to understand the nature of the complex changes taking place in a porous battery plate which is subjected to periodical transformations during charge and discharge of the electrodes. Therefore, it is extremely important that any conjectures arising from the examination of micrographs be corroborated with quantitative physical measurements.

In some of our own work, which we have not yet been able to publish, we have systematically investigated the influence of deep cycling on the structure of PbO₂ active mass. Apart from optical and scanning electron microscope observations we have used x-ray diffraction analysis, BET surface area measurements, and porosity and pore size distribution measurements in order to monitor the structural changes during cycling of the active material.

Our measurements show that the BET surface area characteristically decreases from values of $\sim 8 \text{ m}^2 \text{ g}^{-1}$ after formation to values of $\sim 2 \text{ m}^2 \text{ g}^{-1}$ after 130 cycles. Accompanying this considerable decrease in surface area we have observed small decreases in total porosity and a marked change in the pore size distribution with large pores becoming predominant with increase in cycle number. These quantitative trends were also qualitatively evident in the optical and SEM

micrographs and we have observed active mass structures similar to those reported by the authors.

Also if one examines the coralloid structure with a higher magnification than that used in the paper under discussion one can clearly see a crystalline structure. Our own x-ray diffraction work and that of others⁵⁰⁻⁵² also provides evidence that PbO₂ is recrystallized during cycling. It is this recrystallization and densification accompanied by a decrease in surface area and an increase in the proportion of large pores which we think is the likely explanation for the gradual loss in capacity of positives with deep cycling. In other words the coralloid structure is definitely not an ideal morphology if one is to avoid loss of capacity in positives.

A. C. Simon, S. M. Caulder, and J. T. Stemmler:⁵³ The remarks by Burrows and Giess in general appear to confirm our observations concerning the changes that take place in the positive active material during cycling. Although we have, unfortunately, no means of judging their work, since it remains unpublished, we can assume from their remarks that they have observed a decrease in surface area, a marked change in pore size toward much larger pores, and also have obtained optical and SEM micrographs of the same structures as we observed and described.

They are not the first to confirm our observations. Mention should be made of the excellent work of Dr. S. Hattori, Dr. M. Yamaura, and their associates at Yuasa Battery Company, Limited in Japan. These investigators have done considerable work in this area of investigation that has not yet appeared in a journal publication although progress reports can be obtained from the International Lead Zinc Research Organization (ILZRO) by reference to project LE-197.

Burrows and Giess are in error in stating that we claimed the coralloid structure to be ideal. The statement made by us was that on the basis of theoretical considerations the structure would appear to be ideal for a porous electrode, but we then went on to state that our experience had demonstrated that it was not.

We suggested three possibilities as reasons why this structure was not as ideal as appearances suggested it should be. The first was that, in the presence of such a structure, the PbSO₄, upon repeated cycling, appeared to form a progressively more closely packed and dense layer on the surface of the coralloid structure that effectively passivated the surface before all of the PbO₂ could react. In view of the fact that this was offered as a reason why the coralloid structure was not ideal, the remark by Burrows and Giess are irrelevant. It is not irrelevant, however, that further study since publication of the paper under discussion has led us to the belief that this explanation is incorrect and a passivation by the PbSO₄ occurs no more readily with the coralloid microstructure than with any other.

The remarks by Burrows and Giess regarding our suggested second reason why the coralloid structure is not ideal are as irrelevant as those regarding our first statement, and for the same reason, that we have not claimed the coralloid structure is ideal. However the observations made by us regarding the presence of a hard dense core in each coralloid branch are correct and the observation by Burrows and Giess that there is a considerable decrease in surface area following cycling would seem to confirm it. Since they do not give details of their cycling procedure we cannot correlate this decrease exactly with the onset of the growth of the coralloid structure but a correlation certainly seems likely.

As to the remarks by Burrows and Giess concerning inactive positive active material, we consider that we have conclusive evidence that such material does exist. The NMR and DTA evidence that we found,

⁴⁷ Battelle, Geneva Research Center, 1227 Carouge-Geneva, Switzerland.

⁴⁸ S. M. Caulder, J. S. Murday, and A. C. Simon, *This Journal*, 120, 1515 (1973).

⁴⁹ S. M. Caulder and A. C. Simon, *ibid.*, 121, 1546 (1974).

⁵⁰ J. Burbank and E. Ritchie, *ibid.*, 117, 300 (1970).

⁵¹ J. Burbank, "Power Sources 3," p. 13, Oriol Press (1971).

⁵² D. Korde, *Chem. Ingr.-Tech.*, 38, 638 (1966).

⁵³ Naval Research Laboratory, Washington, D.C. 20375.

referenced by Burrows and Giess, is in itself fairly convincing evidence for the existence of an inactive form of PbO_2 but, in addition, studies made of the formation of tetrabasic lead sulfate have shown that a layer of PbO_2 is formed at the surfaces of these crystals that can be clearly demonstrated to be unreactive, since it remains visible as a reticulate structure in both the charged and discharged states of the electrode, indicating that this material takes no part in the reduction process.⁵⁴ Only after ten or more capacity discharge cycles does this reticulate structure break up. Moreover, its breakup is accompanied by a large increase in the amount of PbO_2 found as discrete particles in the PbSO_4 crystals, indicating that, despite the breakup of the reticulate structure, the inactive PbO_2 has not disappeared but merely has been segregated into smaller, discrete particles that now appear within the lead sulfate crystals.

We do not agree with the final paragraph of the remarks by Burrows and Giess. In the first place, the coralloid structure is in all its transformations still crystalline. It is not clear what they mean by recrystallization, since clearly PbO_2 is regenerated from PbSO_4 at each charge portion of a cycle. It is true, however, that the PbO_2 lattice is disordered and may depend on this disorder for its electrochemical activity. If this is true, a more ordered crystal becomes an inactive crystal and this is the mechanism that we have proposed for the loss of capacity. In this process the presence or absence of the coralloid structure is immaterial and we do not see how this can be used to argue that the coralloid morphology should be avoided.

We certainly agree that conclusions arising from examination by microscope should be corroborated with quantitative physical measurements, but it is equally true that erroneous conclusions can be derived from physical measurements in the absence of microscopic examination. In the present case, we see nothing in the physical measurements reported by Burrows and Giess that would necessitate a change in the conclusions that we have reported.

Their concluding statement, "It is this recrystallization . . ." is merely another way of stating what we have previously reported, *i.e.*, inactive material and coralloid structure increase during the loss of life and capacity that accompanies cycling. But neither their results nor ours have yet shown whether the one is caused by the other, or whether the coralloid structure is necessarily undesirable even though it is self-evident that an increase in inactive PbO_2 would be detrimental.

Conduction Characteristics of Polycrystalline Lead Fluoride

C. C. Liang and A. V. Joshi (pp. 466-470, Vol. 122, No. 4)

J. H. Kennedy:⁵⁵ The paper by Liang and Joshi presents a substantial amount of data concerning the conductivity of lead fluoride using doping techniques. Several important parameters of the system can be calculated using their data; however, these calculations present some basic inconsistencies which should be considered.

First, one could ask if the nominally pure $\beta\text{-PbF}_2$ was acting intrinsically. If so, then $n_v = n_i$ and $\sigma_{\text{total}} = \sigma_v + \sigma_i = n_v e \mu_v + n_i e \mu_i$. Since the Arrhenius slope gave an activation energy the same as +3-doped PbF_2 (resulting in interstitials), $\sigma_i \gg \sigma_v$ and $\mu_i \gg \mu_v$. However, at high doping levels assuming Frenkel equilibrium

$$\begin{aligned}\sigma_i &= (D_i + n_v) e \mu_i \cong D_i e \mu_i \quad (D_i = \text{conc of } +3 \text{ doping}) \\ \sigma_v &= (D_v + n_i) e \mu_v \cong D_v e \mu_v \quad (D_v = \text{conc of } +1 \text{ doping})\end{aligned}$$

Data from the paper give the following results at 25°C

$$e \mu_v = \frac{\sigma_v}{D_v} = \frac{5.5 \times 10^{-4}}{0.01} = 5.5 \times 10^{-2} \quad (\text{slope of line in Fig. 3})$$

$$e \mu_i = \frac{\sigma_i}{D_i} = \frac{2 \times 10^{-7}}{0.003} = 6.7 \times 10^{-5} \quad (\text{conductivity from Fig. 7})$$

and thus it is seen that $\mu_i \ll \mu_v$. Therefore the conductivity of nominally pure PbF_2 is not intrinsic and must be due to impurities (D_o) leading to a preponderance of interstitials to explain the Arrhenius slope.

If we now assume a Frenkel equilibrium we can write several expressions for the Frenkel equilibrium constant

$$\begin{aligned}\text{pure} & K = [n_i^o] [n_v^o] \\ \text{nominally pure} & K = [D_o + n_v] [n_v] \\ +3 \text{ doping (interstitials)} & K = [D_o + D_i + n_v] [n_v] \\ +1 \text{ doping (vacancies)} & K = [n_i] [D_v - D_o + n_i] \\ & \text{if } D_v > D_o\end{aligned}$$

For nominally pure PbF_2

$$\frac{\sigma_i}{\sigma_v} = \frac{(D_o + n_v) e \mu_i}{n_v e \mu_v} = \frac{6.7 \times 10^{-5} (D_o + n_v)}{5.5 \times 10^{-2} n_v} \gg 1$$

For comparing D_o and n_v let us assume $\sigma_i/\sigma_v \sim 10$ so that Arrhenius slope only shows Δh_i . Then

$$\frac{D_o + n_v}{n_v} = \frac{5.5 \times 10^{-2}}{6.7 \times 10^{-5}} \times 10 = 8.2 \times 10^3 \quad \text{and } D_o \gg n_v$$

We can now calculate D_o from data in the paper without making any assumptions concerning σ_i/σ_v

$$\begin{aligned}\text{nominally pure: } e \mu_i &= \frac{\sigma}{D_o} = \frac{10^{-7}}{D_o} \\ +3 \text{ doping: } e \mu_i &= \frac{\sigma}{D_i + D_o} = \frac{2 \times 10^{-7}}{0.003 + D_o}\end{aligned}$$

Solving these two equations for D_o gives a value of 0.003. That is, the nominally pure PbF_2 contains 0.3 mole per cent (m/o) of interstitials from impurities. A recalculation for $e \mu_i = \sigma_i/D_o + D_i$ gives the value of 3.3×10^{-5} , but this does not change the situation regarding $D_o \gg n_v$. We are now faced with a basic inconsistency. If Frenkel equilibrium is established, these interstitials should react with doped-in vacancies (doping with KF) up to 0.3%. The conductivity should fall with addition of KF until this level is reached and the activation energy should become Δh_v only when $D_v > D_o$. One possible explanation is that equilibrium is not reached and that the product $[n_i][n_v] > K$. This explanation, however, contains its own inconsistencies since the conductivity lines for nominally pure PbF_2 and KF-doped PbF_2 then could not cross as shown in Fig. 5 in the paper under discussion. That is, at high temperatures the mobility of interstitials becomes predominant, and curves b-f in Fig. 5 should begin to track curve a. One could argue that at high temperature reaction occurs between vacancies and interstitials to reach Frenkel equilibrium, but upon cooling the pellets the conductivity and Arrhenius slope for 0.1 and 0.3 m/o KF-doped PbF_2 should now be considerably different than before heating. No mention of such a change was made in the paper and in view of the preparation procedure would not be expected.

Additional calculations can be made but are not meaningful until the question of whether or not Frenkel equilibrium is established. The comments above refer to $\beta\text{-PbF}_2$, but the results for $\alpha\text{-PbF}_2$ are similar except that D_o is much smaller (*ca.* 0.0004). The arguments presented depend critically on the +3-doping of PbF_2 and these studies should be expanded to cover a larger concentration range and possibly another MF_3 compound. Work in our laboratories has shown a decrease in conductivity when BiF_3 was the dopant with an increase in electronic conductivity. We

⁵⁴ Abstract 34, p. 85, Extended Abstracts, Electrochemical Society Fall Meeting, New York, New York, October 13-17, 1974.

⁵⁵ Department of Chemistry, University of California, Santa Barbara, California 93106.

also observed a gradual change in Arrhenius slope which might indicate that at low doping levels σ_i and σ_v are nearly equal, because doped-in vacancies are reacting with interstitials present in the nominally pure material. Other explanations are, of course, also possible.

C. C. Liang and A. V. Joshi:⁵⁶ Dr. Kennedy calculated the M^{3+} impurity concentration in the nominally pure PbF_2 as being 0.3 m/o and thereby raised the question of basic inconsistencies in the conduction behavior. We shall show in the following that the M^{3+} impurity concentration in the nominally pure PbF_2 is very much lower than 0.3 m/o (in fact, it is much lower than 0.1 m/o) and our interpretation of the PbF_2 conduction behavior is indeed consistent with the experimental data.

In the Kennedy calculation of the M^{3+} impurity concentration, an assumption was made that the 0.3 m/o YF_3 added to PbF_2 was completely dissolved in the β - PbF_2 lattice. In fact, we found that under our experimental conditions the solubility of YF_3 in β - PbF_2 is very much less than 0.3 m/o as shown by the fact that the same value of $1.6 \pm 0.3 \times 10^{-7}$ (ohm-cm)⁻¹ was obtained from the room temperature conductivity of β - PbF_2 containing 0.1, 0.3, 0.5, 0.8, or 1.0 m/o YF_3 . We did not report these results nor did we attempt to determine the solubility of YF_3 in PbF_2 inasmuch as they were not pertinent to our principal objective which was to determine the defect structures. It was important, however, to recognize that some YF_3 was dissolved in β - PbF_2 as shown by the slight increase in conductivity and that the YF_3 doping did not result in a change in activation energy for β - PbF_2 .

The principal objective of our paper was to investigate the defect structures and the results of our investigation clearly demonstrated a Frenkel defect structure in β - PbF_2 as well as α - PbF_2 . The defect concentration was not computed inasmuch as we had not obtained enough quantitative information from our YF_3 doping experiments for such a computation. Nonetheless, in view of the question of basic inconsistencies we shall estimate the M^{3+} impurity concentration in the nominally pure PbF_2 .

The spectrographic analysis showed that the effective M^{3+} impurity concentration in the commercial PbF_2 was about 150 ppm (0.015 m/o). Even if we took into consideration that such an analysis could be semi-quantitative and the results could be off by $\pm 100\%$, the maximum concentration for the M^{3+} impurities would be 300 ppm (0.03 m/o).

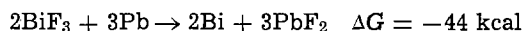
If one were to carry out the Kennedy calculation using the YF_3 -doped α - PbF_2 results (Fig. 6 in the original paper) and assuming a complete solubility of YF_3 in α - PbF_2 , one would obtain a M^{3+} impurity concentration of about 400 ppm (0.04 m/o) in the nominally pure α - PbF_2 . It is extremely unlikely that the M^{3+} impurity concentration in β - PbF_2 would be much higher than that in α - PbF_2 .

Accordingly, the decrease in conductivity with addition of KF as argued by Kennedy would occur up to 0.04 m/o KF. On the other hand, the conductivity of the 0.1 m/o or higher KF-doped β - PbF_2 is expected to be higher than that of the nominally pure β - PbF_2 . Furthermore, the activation energy determined from the Arrhenius plots of the 0.1, 0.3, 0.5, 0.8, or 1 m/o KF-doped β - PbF_2 is for the mobility of fluoride ion vacancies in β - PbF_2 .

Bismuth fluoride was also one of the MF_3 used in our studies. We found that the conduction behavior of BiF_3 -doped PbF_2 appeared to depend on the electrode material in the conductivity cell. When Pb electrodes were used the total conductivity was much lower and the electronic conductivity appeared to be very high compared to the total conductivity. On the other hand,

when graphite electrodes were used we observed a rather normal increase in conductivity.

There are, of course, many explanations for such a behavior. Nonetheless, we do not rule out the simple explanation that Pb reacts with BiF_3 even though the concentration of the added BiF_3 was only 1 m/o or less in our experiments



$$\Delta G_f(PbF_2) \text{ at } 25^\circ C = -148 \text{ kcal/mole}$$

$$\Delta G_f(PbF_2) \text{ at } 325^\circ C = -138 \text{ kcal/mole}$$

$$\Delta G_f(BiF_3) \text{ at } 25^\circ C = -200 \text{ kcal/mole}$$

$$\Delta G_f(BiF_3) \text{ at } 325^\circ C = -185 \text{ kcal/mole}$$

Electrogenerated Chemiluminescence. XXIII. On the Operation and Lifetime of ECL Devices

D. Laser and A. J. Bard (pp. 632-640, Vol. 122, No. 5)

C. P. Keszthelyi:⁵⁷ In the above-mentioned paper, the authors report that in electrogenerated chemiluminescence (ECL) under the usual potential program (cyclic double potential steps to the diffusion plateau) only

$\sim 1\%$ of the ions $R^{\cdot -}$ and $R^{\cdot +}$ are quenched by the

electrode due to $R^{\cdot -} \rightarrow R^{\cdot +} + 2e^-$ and $R^{\cdot +} + 2e^- \rightarrow R^{\cdot -}$, i.e., only about 2% of the total current is consumed by these processes, a result in good agreement with the present writer's previous result,⁵⁸ hence the following discussion raises no critical questions whatsoever in that regard. Although the paper is adequately documented in general (30 literature references plus three "private communications"), it omits one of the prestigious published works in the field. The missing reference⁵⁹ states that 34.4% of the Faradaic current is consumed by the two-electron oxidation and reduction processes, and this same value had also been used by Pighin⁶⁰ in rubrene electrogenerated chemiluminescence calculations. As both the paper under discussion

and the work of Schwartz *et al.*⁵⁹ assume stable $R^{\cdot +}$ and $R^{\cdot -}$, the maximum possible efficiency, expressed as Φ_{ecl} , should be the same;⁶¹ yet the former gives $\sim 98\%$, and the latter, 82.8%. Consequently, the general scientific community is faced with some difficulty in selecting a proper value of $\Phi_{\text{ecl,max}}$ (or, $\Phi_{\text{coul,max}}^{\text{ss}}$) due to a conflict in reported values. It is the purpose of the present discussion to settle that $\sim 98\%$, given by Laser and Bard, is the correct value (or $1.0 \times 100\%$ ⁵⁸), and the related work^{59,60} should be recalculated.

Improved documentation and careful evaluation of published works in ECL⁶² can be both revealing and

rewarding; for example, the fate of $R^{\cdot +}$ and $R^{\cdot -}$ in typical ECL experiments has been published some time ago,⁶³ leading to the unmistakable conclusion that "destruction of the ions [is] virtually negligible . . .,"⁶⁴ a conclusion which, for the record, well predates the relevant sections of both the present writer's related publication⁵⁸ and the paper under discussion.

⁵⁷ Department of Chemistry, Louisiana State University, Baton Rouge, Louisiana 70803.

⁵⁸ C. P. Keszthelyi, *Bull. Chem. Soc. Japan*, **48**, 1083 (1975).

⁵⁹ P. M. Schwartz, R. A. Blakeley, and B. B. Robinson, *J. Phys. Chem.*, **76**, 1868 (1972).

⁶⁰ A. Pighin, *Can. J. Chem.*, **51**, 3567 (1973).

⁶¹ It appears unnecessary to develop this point at length here, as the authors of the paper under discussion have done so already. Yet the authors' contention in the original paper is misleading, for $\Phi_{\text{coul}}^{\text{ss}}$ does not approach 98% when two electrodes of equal size are used, unless one counts photons at both electrodes, while counts electrons at only one.

⁶² C. P. Keszthelyi, *Appl. Optics*, **14**, 1710 (1975).

⁶³ R. Bezman and L. R. Faulkner, *J. Am. Chem. Soc.*, **94**, 6317 (1972).

⁶⁴ L. R. Faulkner, Private communication (1973).

A Correlation Between the Quantum Efficiency of Electrogenerated Chemiluminescence and the Redox Potentials of Rubrene in Various Solvents

A. Pighin and B. E. Conway (pp. 619-624, Vol. 122, No. 5)

C. P. Keszthelyi:⁶⁵ In the above-mentioned paper, the authors report electrogenerated chemiluminescence (ECL) efficiency of rubrene in several solvents. In view of the close agreement between some of our rubrene ECL efficiency results⁶⁶ and the ones reported in the paper under discussion, the following comments do not attempt to question the direct measurements; however, there are still some disturbing aspects that should be cleared up in as brief a space as possible.

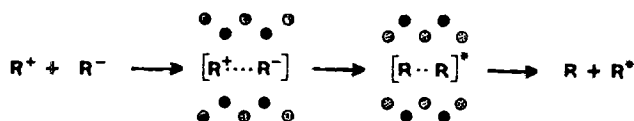
(1) The authors define "quantum efficiency" in ECL in a manner which is inconsistent with previous as well as current "mainstream" usage.⁶⁶⁻⁷¹ We should probably stay with $\phi_{\text{ecl}} \equiv \text{ECL quantum efficiency} \equiv \text{number of photons emitted/radical ion annihilation (usually)}$,⁷² if for no other reason, to avoid needless confusion due to redefinition of common terms by every newcomer to the field.

(2) In Fig. 1 in the paper under discussion the Faradaic current should merge into the capacitive current with a smooth line, following the Nernst equation. The implication of Fig. 1 is that the Faradaic current component drops to zero at $\sim 2.3\text{V}$, whereas the Nernst equation tells us otherwise, together with "underpotential electrodeposition" experiments.

(3) Based on our experience in the same general area,⁷³ point No. 11 in Fig. 4 should have been augmented by a few additional measurements. With 1 mM solute concentration the 0.020M TBAP-100 Hz combination is apt to lead to dubious results. It would have been imperative to decrease the rubrene concentration, or the Hz, or preferably systematically vary both. Also, with solutions of this type a potentiostat employing positive IR feedback and a three-electrode configuration is a virtual necessity.⁷³

(4) On p. 623-624 the authors make a perplexing statement: "... the solvent component (benzene) which tends to produce relatively high ($E_{\text{p,ox}} - E_{\text{p,red}}$) will also then tend to solvate the radical ions." Benzene is definitely unlikely to preferentially solvate radical ions when other solvent components are also present such as propylene carbonate or acetonitrile. It seems proper to call to the authors' attention the figure reproduced from the 1973 issue of *This Journal*⁷⁴

it is possible to have preferential solvent interaction as shown in the inset (solid circles represent the more polar component in the heteropolar solvent



mixture). It has been experimentally observed that use of a heteropolar mixed solvent having the same over-all dielectric constant as a given single solvent leads to higher efficiency than use of said single solvent in ECL.

Whereas a number of important aspects of the creation

⁶⁵ Department of Chemistry, Analytical Division, Louisiana State University, Baton Rouge, Louisiana 70803.

⁶⁶ C. P. Keszthelyi, N. E. Tokel-Takvoryan, and A. J. Bard, *Anal. Chem.*, **47**, 249 (1975).

⁶⁷ A. J. Bard, C. P. Keszthelyi, H. Tachikawa, and N. E. Tokel, "Chemiluminescence and Bioluminescence," M. J. Cormier, D. M. Hercules, and J. Lee, Editors, Plenum Press, New York-London (1973).

⁶⁸ D. M. Hercules, *Accounts Chem. Res.*, **2**, 301 (1969).

⁶⁹ R. Bezman and L. R. Faulkner, *J. Am. Chem. Soc.*, **94**, 6317, 6324, 6331 (1972).

⁷⁰ C. P. Keszthelyi, *J. Am. Chem. Soc.*, **96**, 1243 (1974).

⁷¹ C. P. Keszthelyi, *Bull. Chem. Soc. Japan*, **48**, 1083 (1975).

⁷² Compounds like DPACl₂ present some difficulties, since the light producing reaction path remains to be elucidated. See C. P. Keszthelyi and A. J. Bard, *J. Org. Chem.*, **39**, 2936 (1974).

⁷³ C. P. Keszthelyi, N. E. Tokel-Takvoryan, and A. J. Bard, *Chem. Phys. Letters*, **23**, 219 (1973).

⁷⁴ C. P. Keszthelyi, *This Journal*, **120**, 39C (1973).

of electronically excited states by electron transfer and preferential solvation in mixed heteropolar solvents remain open for discussion,⁷⁵ one should make certain that we are moving forward with the passage of time, instead of proposing preferential ion solvation by the benzene solvent component.

A. Pighin⁷⁶ and **B. E. Conway**:⁷⁷ We regret that our paper disturbed Keszthelyi. However, had he read our paper more carefully and been less dogmatic about his work most of his comments would not have been necessary. Our replies to his comments are, point by point:

(1) Since we have led a 15-man-year investigation of EGCL⁷⁸ over 4 years for display applications,⁷⁷⁻⁸¹ we should hardly be called newcomers.

The so-called "mainstream" definition of quantum efficiency of EGCL has at least the following difficulties: (a) it does not consider electrogenerated ions, which do not partake in radical ion annihilation, as contributing to the inefficiency of the EGCL process, e.g., losses due to diffusion, side reactions, potential cycling, etc.; (b) it would consider EGCL produced from the di-ion radicals to be as efficient as that produced from mono-ion radicals, although the former consumes twice as much current; (c) it requires a knowledge of the light-producing mechanism; and (d) for various reasons, e.g., (a) and (b) above, it tends to overestimate the over-all quantum efficiency.

Our definition of EGCL quantum efficiency is free from these difficulties and is more inclusive and more pragmatic. It also gives a more realistic basis for evaluation of quantum efficiency which minimizes corrections.

(2) Experimental points taken at ca. 2.3V did follow the Nernst equation and we were not surprised by this. The delineation of the Faradaic current line in Fig. 1 of our paper into the capacitive current line was drawn simply to demonstrate the potential of onset of appreciable Faradaic current. More closely spaced experimental points would have been required to demonstrate the role of the back reaction. However, the purpose of Fig. 1 was, of course, not to demonstrate this well-known, but trivial, effect.

(3) It only takes two precise points to determine a difference. Since the TBAP concentration was varied fivefold and no significant change in ϕ_{coul} , measured over a wide frequency range,⁷⁹ was observed, we considered that to be sufficient proof that ϕ_{coul} was independent of electrolyte concentration.

In the paper referred to,⁷³ Keszthelyi *et al.* equate the relative EGCL intensity to ϕ_{egcl} . ϕ_{egcl} requires knowledge of the Faradaic current (or number of radical ion annihilations). Without this knowledge, it is dangerous for them to conclude by implication that their results show a variation in ϕ_{egcl} with electrolyte concentration. Therefore, this question appears to have been based on a premise which has no substance. Furthermore, he has been wrong previously⁸² on the interpretation of quantum efficiency.

The recommendation that we ought to have measured ϕ_{coul} as a function of rubrene concentration and frequency is baffling because such information is given (Fig. 3) in the paper under discussion and our previous paper⁷⁹ (Fig. 4) which was referenced, respectively.

As for the need for IR compensation, other methods for measuring ϕ_{coul} may require IR compensation but

⁷⁵ C. P. Keszthelyi, *Appl. Optics*, **14**, 1710 (1975).

⁷⁶ Labor Canada, Ottawa, Ontario, Canada.

⁷⁷ Department of Chemistry, University of Ottawa, Ottawa, Ontario, Canada.

⁷⁸ We prefer to use EGCL rather than ECL as the abbreviation for electrogenerated chemiluminescence to avoid confusion with ECL used in the electronics industry for emitter-coupled logic.

⁷⁹ A. Pighin, *Can. J. Chem.*, **51**, 3567 (1973).

⁸⁰ M. A. Kabayama, A. Pighin, and W. M. Coderre, Paper presented at Symposium of Soc. for Info. Display, New York, May 1975. See also p. 169 of 1974 Symposium Digest.

⁸¹ A. Pighin *et al.*, U.S. Patent 3,868,534 (1972). Two other EGCL patents have been allowed.

⁸² E. A. Chandross and D. J. Freed, *J. Am. Chem. Soc.*, **97**, 1274 (1975).

our technique is relatively insensitive to IR effects. In our procedure for measuring ϕ_{coul} , IR effects will decrease the slope of the extrapolation of the capacitive current line in the current *vs.* voltage plots (Fig. 1) but this effect is obviously small because the change in slope is small and the length of the extrapolation is short. It was observed that both the EGCL and Faradaic current commenced together. Thus, although the redox potentials of rubrene are asymmetrical about the SCE, they were symmetrical about the ground of the driving circuitry. This, together with the fact that EGCL was generated at two equal-area electrodes, resulted in equal quantities of oppositely charged radical ions being produced alternately at both electrodes.

(4) We are fully aware of the paper by Keszthelyi which discusses preferential solvation in EGCL and would like to refer him to our patent⁸¹ in this area which was filed during the previous year.

The charge on rubrene radical ions is well diffused due to delocalization. Its radical ions may be regarded

as a large aromatic structure with a small charge density over its central π -bond network which contains 18 carbon atoms. Because of the large space over which the single charge is distributed, the force which will attract and orient polar solvent molecules will be weak. Furthermore, since the radical ions retain some aromatic character, it is reasonable to assume that with an increasing aromatic fraction in the solvent the solvation shell may accommodate some aromatic solvent. It is to be noted that this does not exclude, in this case, some solvation also by the polar component, as recognized in our paper. Keszthelyi appears to insist on an all-or-nothing model of preferential solvation but we do not feel bound by his view.

We feel that our interpretation of preferential solvation is reasonable and thus contributes to the understanding of EGCL. We hold a flexible opinion on this and are prepared to alter our thinking if new evidence should warrant it.



Barrier-Type Aluminum Oxide Films Formed under Prolonged Anodizing

I. Influence of Anodizing Parameters on Film Morphology

Yoon H. Choo* and Owen F. Devereux*

Department of Metallurgy and Institute of Materials Science, University of Connecticut, Storrs, Connecticut 06268

ABSTRACT

The morphology of anodic aluminum oxide films formed in neutral aqueous 3% ammonium tartrate was investigated using transmission and replica electron microscopy and transmission stereoscopy. After an initiation period of approximately 90 min, corresponding to the appearance of a minimum in the potentiostatic anodic current, development of a porous structure was observed. The film structure was comparable to that formed in conventional pore-forming electrolytes at shorter times, with approximately polygonal oxide cells, each containing a central pore. Pore depth and diameter both increased in a systematic manner with anodizing time; a hypothetical model relying on field-assisted dissolution of oxide, with local field enhancement due to the pore geometry, is used to explain this dependence. At longer times, the pore depth increases linearly with anodizing time, also consistent with this model and with the observed establishment of a stable pore structure. The stable pore size and oxide cell size are proportional to formation voltage in accord with the geometric argument forwarded to explain pore coalescence and the formation of stable terminal pores.

Anodic aluminum oxide films are commonly classified as porous or barrier-type (i.e., nonporous) according to the electrolyte in which they are formed. Barrier-type films are formed by anodically polarizing aluminum in an electrolyte which exerts little solvent action on the oxide film, e.g., aqueous borate or tartrate, and grow to a limiting thickness in proportion to the applied potential. Porous films, on the other hand, are formed by anodic polarization of aluminum in an electrolyte which exerts appreciable solvent action on the film, e.g., aqueous sulfuric, chromic, oxalic, or phosphoric acids, and tend to thicken indefinitely under constant potential in proportion to the charge passed. The structure of porous films has been characterized by Keller, Hunter, and Robinson (1), and later by O'Sullivan and Wood (2), as a close-packed array of columnar hexagonal cells, each containing a central pore normal to the substrate surface and separated from it by a layer of barrier-type film. The dimensions of these structural features are dependent on the formation potential as well as the electrolyte (2). The barrier film beneath the porous structure is proportional in thickness to the applied potential, the proportionality constant being of the order of 10 \AA-V^{-1} in contrast to the value of approximately 13 \AA-V^{-1} seen in typically barrier-forming electrolytes (3-5).

A number of authors have studied the mechanism of pore formation and growth in anodic films. Keller, Hunter, and Robinson (1) proposed that pore growth occurs by simultaneous formation and dissolution of oxide. This occurs initially at regions experiencing a locally high dissolution rate; Joule heating in the adjacent electrolyte then enhances the process at these

sites. While Hunter and Fowle (6) explained pore formation simply in terms of chemical dissolution, Hoar and Mott (7) postulated that the dissolution was field-assisted and, thus, that both formation and dissolution of oxide were enhanced by the locally high field at the pore bases. This mechanism appears most generally accepted at present (2). To explain the observation that pores do not initiate until a barrier-type layer of at least a critical thickness has formed, Hoar and Yahalom (8) have suggested that proton entry into the oxide film is necessary to pore formation and that this is possible, against the anodic field, only when the field has decreased to a value characteristic of the critical thickness. Random local defects in the initial barrier film are seen as important to pore nucleation by Arrowsmith, Culpan, and Smith (9) who studied pore nucleation in films formed on aluminum substrates of varying purities.

Hoar and Yahalom (8) have reported that barrier-type films (formed in 3% ammonium tartrate at pH 7.3, 25°C, 14.4V) and porous films (formed in 15% sulfuric acid, 25°C, 14.4V) both develop their structures after only seconds of anodizing. Several investigators have reported formation of porous-like cellular structures in films formed in borate or tartrate solutions at high formation voltages or prolonged anodizing times. Franklin (10) observed an irregular polygonal cell structure in films formed at 500V in aqueous 3% boric acid-0.05% borax, with the cell diameter proportional to the formation voltage and the cells bulging out into both the electrolyte and the substrate. Stirland and Bicknell (11) confirmed this observation and, through electron diffraction by thinned films, demonstrated that the centers of the cells were amorphous while the edges were $\gamma\text{-Al}_2\text{O}_3$. Hoar and Yahalom (8) reported

* Electrochemical Society Active Member.

Key words: aluminum, anodic oxidation, impedance, porosity.

1975

pore formation in films formed in 3% ammonium tartrate, pH 7.3 at 14.4V for 10 min. Hunter and Towner (12) found a porous layer formed above the barrier layer on aluminum anodized in 3% ammonium tartrate, pH 5.5, for times up to 900 min. The substrate surface after anodizing was seen to have a cellular pattern similar to that seen in the case of porous films. They observed that the barrier layer reached a limiting thickness after 12 min, after which the porous layer formed at a linear rate of about $175 \text{ \AA}\cdot\text{hr}^{-1}$. Leach and Neufeld (13) observed pore formation in films formed in aqueous borate at pH 9.7 subsequent to attainment of a steady leakage current under constant applied potential. Pore growth was affected both by formation rate and electrolyte temperature.

The present study was undertaken specifically to investigate more fully the porous structure of anodic aluminum oxide formed in barrier-forming electrolytes, and to characterize the effects of the anodizing time and formation potential on this structure. Attention was restricted to aluminum anodized in aqueous 3% ammonium tartrate at pH 7.

Experimental Procedures

High purity aluminum (99.99%) sheet of 2.5 mm thickness was cut into rectangular specimens, 12 x 50 mm, annealed in air at 350°C for 1 hr, and furnace cooled. Specimens were then chemically polished in a solution comprised of 80 volume per cent (v/o) phosphoric acid and 3 v/o nitric acid in water for 20 min, followed by electropolishing in a conventional bath of 20 v/o perchloric acid in ethanol. All anodizing was done in a solution of 3 weight per cent (w/o) ammonium tartrate, reagent grade, in double distilled water; the solution was adjusted to pH 7 by titration with dilute aqueous ammonium hydroxide. Anodizing was performed in a simple cell employing a cylindrical platinum gauze surrounding the anode as cathode; the anodizing time and formation potential employed in this study ranged from 15 min to 48 hr, and from 25 to 100V, respectively. Anodizing was conducted at a constant current density of $1 \text{ mA}\cdot\text{cm}^{-2}$ until the desired formation potential was obtained; at this point the current was allowed to decay under constant potential for the balance of the experiment. Anodic current was recorded directly with a strip chart recorder.

Upon removal from the anodizing cell, anodized specimens were gently washed, first with absolute methanol and then with double distilled water, then allowed to dry in a gentle air stream. For transmission electron microscopy oxide films were scribed into grid size (2.5 x 2.5 mm) while on the substrate, then removed by the amalgamation method (1). For replica electron microscopy carbon-platinum replicas were prepared from the oxide surface that had been adjacent to the electrolyte, and from the substrate surface. The latter surface was prepared by dissolution of the oxide film by immersing the specimen in a mixture of phosphoric and chromic acids (35 cm³ 85% phosphoric acid and 20g chromic acid per liter of solution) at 90°C for 10 min. Surface features of the aluminum were unattacked by this treatment (1).

Most electron micrographs were taken at the same magnification to facilitate measurement of pore and cell sizes and also to eliminate comparative errors possibly inherent in different magnification settings. Stereopair electron micrographs were taken of given areas of films by tilting the specimen holder $\pm 5^\circ$; this technique enabled measurement of pore depth and barrier layer thickness and permitted clear three-dimensional viewing of the film morphology. Stereopair micrographs, typically at $92,200\times$, were viewed with a Hilger and Watts SB 185 mirror stereoscope; barrier layer thickness and pore depth measurements were made using a parallax bar, accurate to 0.01 mm.

Results

Current/time transient behavior.—Anderson and Devereux (14) have reported that, on potentiostatic

formation of anodic aluminum oxide films in neutral aqueous tartrate solutions, the leakage current decreases continuously to a minimum value characteristic of the formation voltage in 45–90 min. This value is not stable, however, as the leakage current increases beyond this time at nearly an exponential rate for 10–15 hr before attaining a terminal stable value. That report is confirmed by data from this study, shown in Fig. 1, in which anodic current is plotted vs. anodizing time for several different formation potentials. Each curve represents a single experiment; therefore, these are typical, rather than average, results. Similar curves are seen for aluminum anodized in pore-forming electrolytes; however, the current minimum may occur after as little as 2 sec anodizing time and the steady-state value after as little as 10 sec (8). The current minimum in pore-forming environments is seen to correspond to pore initiation in accord with the postulate that initiation does not occur until the field has dropped to a level that permits proton entry into the film; the subsequent increase in leakage current reflects thinning of the barrier layer at the pore bases as pore growth proceeds; the steady-state current reflects stability of the barrier film ($\sim 10 \text{ \AA}\cdot\text{V}^{-1}$) and pore growth occurring by addition to the film rather than by subtraction. A similar mechanism is proposed in the present study, with transmission electron microscopy demonstrating pore initiation approximately coincident with the current minimum.

Influence of anodizing time on pore size.—A time sequence of transmission electron micrographs of anodic oxide films formed at 50V is shown in Fig. 2. At 15 min the oxide is seen to be virtually featureless, while at 2 hr definitive pores are seen, the dark edge surrounding each pore indicating diffraction by the pore wall and/or oblique transmission of electrons through the barrier film comprising the pore wall. At 2 hr, pore diameter ranges to 120 \AA ; as anodizing time is increased pore size increases until approximately 32 hr, when it approaches a stable value. It is apparent, especially in the photomicrograph for 8 hr, that as pores grow and coalesce new pores form. Thus, there is a distribution of sizes and shapes at any given anodizing time; for purposes of comparison pore size has been defined herein as the average diameter of the most frequently appearing and fully developed pores. Prior to attainment of a stable value, the pore diameter is seen in Fig. 3 to follow the relation

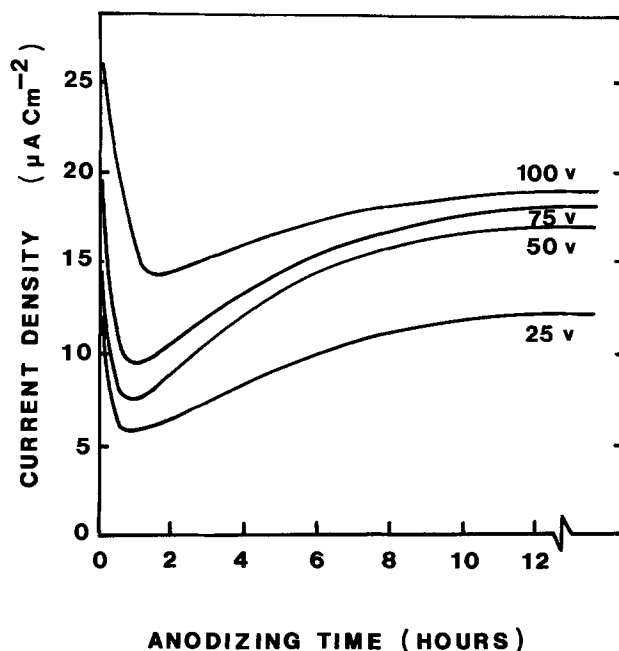


Fig. 1. Current density vs. anodizing time for various formation voltages.

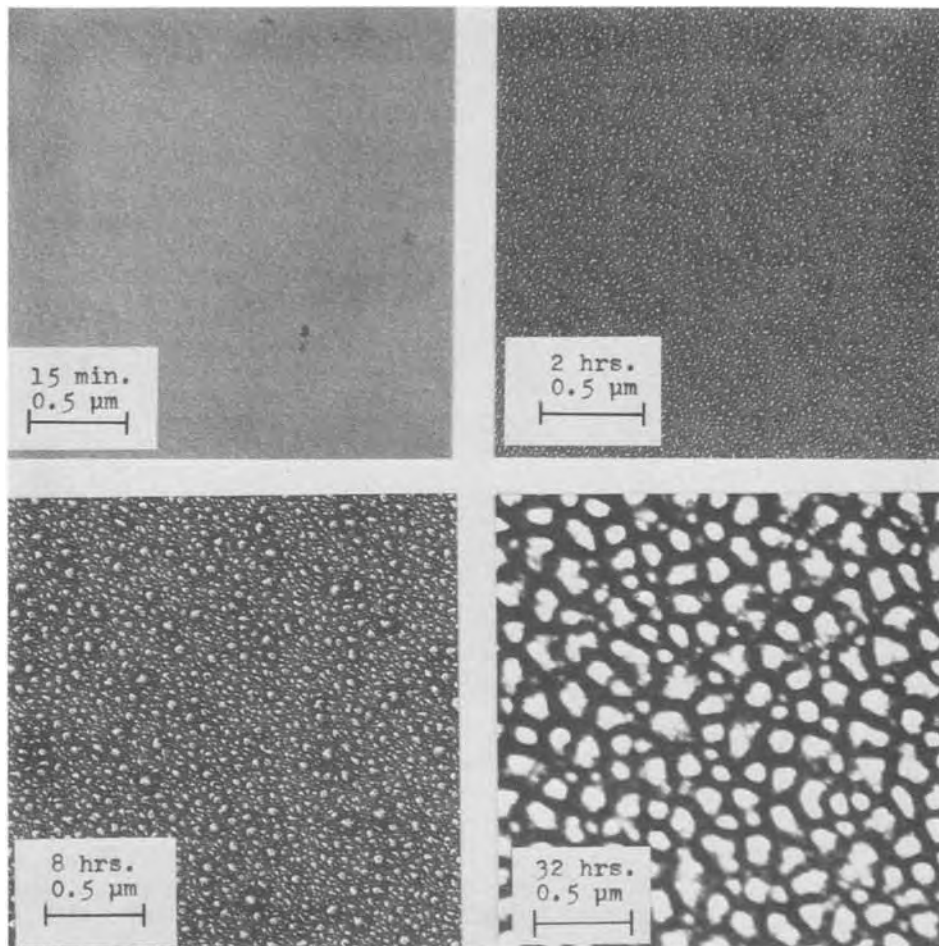


Fig. 2. Transmission electron micrographs of anodic oxide films formed at 50V for various anodizing times.

$$\frac{D}{1.31} - d \ln \left(\frac{D/1.31 + d}{d} \right) = K (t - t_0)$$

to be derived in the Discussion section, where D is the

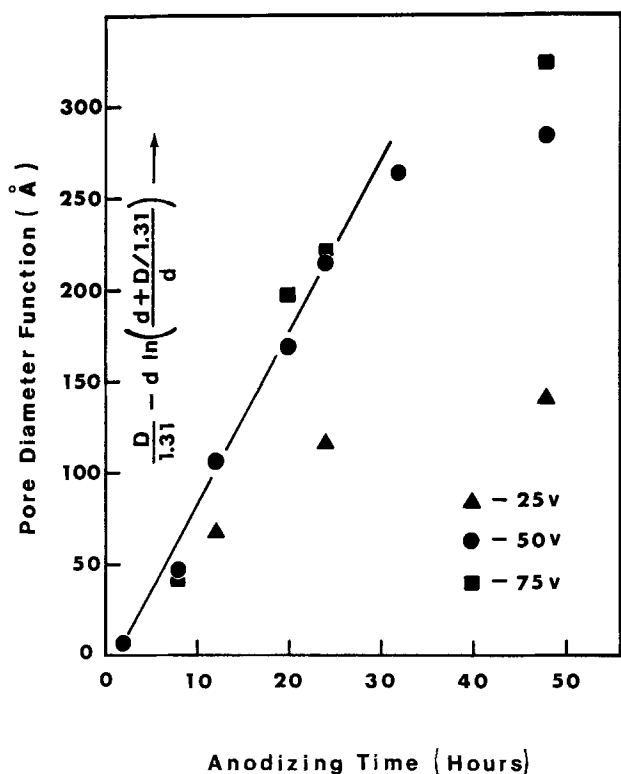


Fig. 3. Pore diameter function vs. anodizing time for various formation voltages.

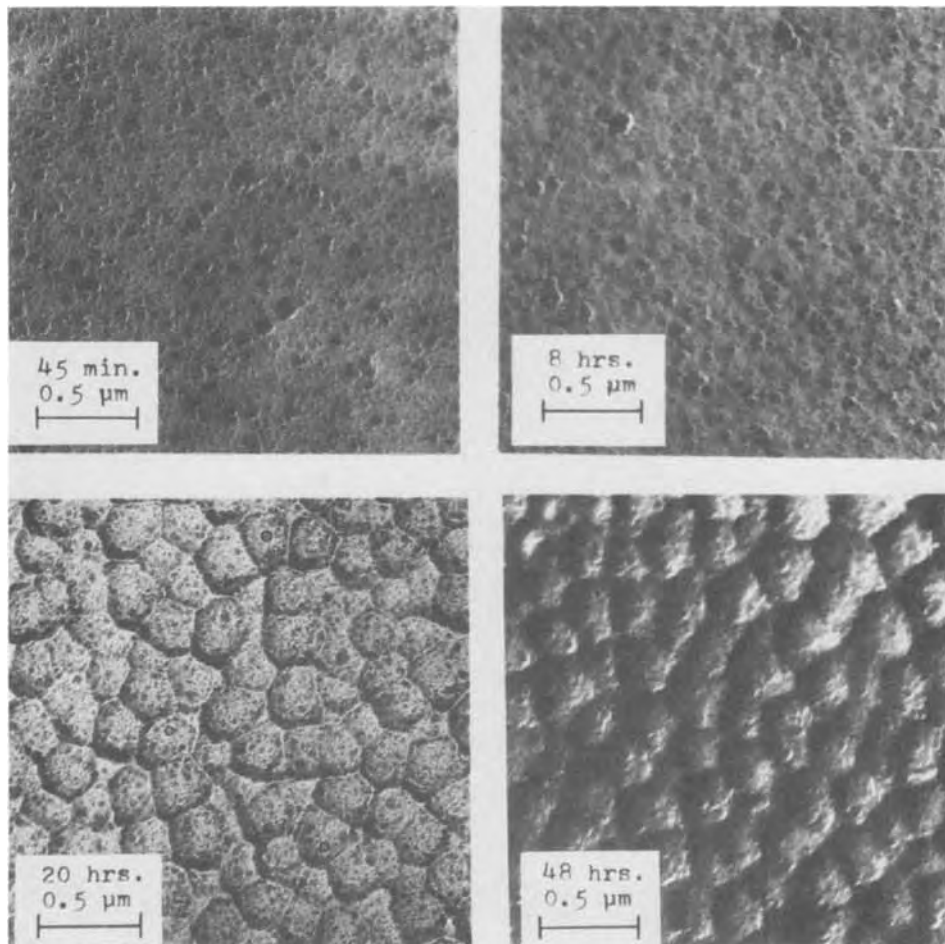
measured pore diameter, d is the barrier layer thickness, t is anodizing time, and t_0 is the time required for pore initiation. This expression is closely followed at 50 and 75V, with $K = 9.5 \text{ \AA-hr}^{-1}$. Data taken at 25V deviate from this behavior, possibly due to earlier establishment of a stable pore size. Pore initiation time is of the order of 90 min as noted above.

Influence of anodizing time on oxide cell size.—Replica electron micrographs of the aluminum substrate subsequent to anodizing at 75V for various times are shown in Fig. 4; these replicas clearly depict the basal structure of oxide cells comprising the anodic film. There is an initial cell structure which does not change significantly during the first 8 hr of anodizing. It then undergoes rather rapid growth, but attains a maximum size representative of the final structure after 20 hr. This behavior is typical of that seen at other formation potentials.

Determination of the density (i.e., number per unit area) of cells and pores from photomicrographs of comparable specimens indicated a one-to-one correspondence, i.e., to each cell corresponds a pore. Consequently, $(\text{pore density})^{-1/2}$ is approximately equal to the cell diameter. A time sequence of such values is shown in Fig. 5 for films formed at 50V. Clearly, these data lack the simple time dependence of the pore diameter; the cell sizes as computed from pore density represent the average of all cells, whereas the plotted pore diameters are only for fully developed pores. Cell size shows a slow initial growth, but a very marked transition after about 16 hr of anodizing; this may be interpreted as a disappearance of a large number of small cells leaving a relatively stable film structure of large cells only.

Influence of formation potential on terminal pore and cell sizes.—Figure 6 shows transmission electron micrographs of films formed after 48 hr of anodizing at

Fig. 4. Replica electron micrographs of substrate surfaces after anodizing at 75V for various times, showing oxide cell formation.



various formation potentials, illustrating the dependence of terminal pore size on formation potential. Figure 7 depicts replica electron micrographs of the corresponding substrates, showing cell size dependence on formation potential. Pore and cell diameters are plotted in Fig. 8, showing a linear dependence of each on formation potential: terminal pore diameter (\AA) =

$18.5 \times$ formation voltage and terminal cell diameter (\AA) = $35 \times$ formation voltage. Directly measured average cell diameters and values computed from pore density are both shown and are comparable. Inasmuch as these are "terminal" there is no significant contribution to the average size from small undeveloped cells.

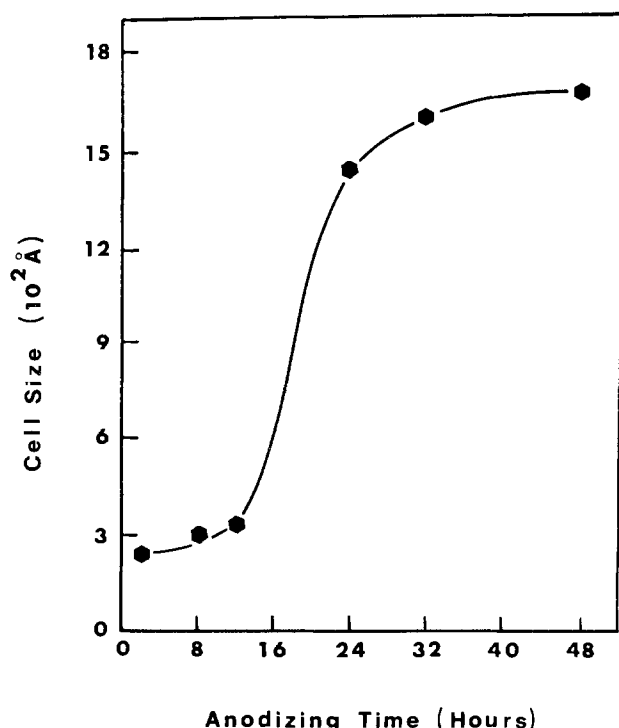


Fig. 5. Cell diameter vs. anodizing time at 50V

Barrier thickness and pore depth measurements.—The barrier layer thickness and the pore depth were determined by use of electron stereomicroscopy. Vertical distances were determined from the equation (15, 16)

$$T = \frac{x}{2M \sin \theta}$$

where T is the vertical distance; x , the measured parallax; M , the over-all magnification; and 2θ , the angle through which the specimen is tilted between exposures. Pore depth was evaluated by measuring the change in distance between features at the pore opening and at the pore bottom; similarly, the barrier layer thickness was determined by examination of features on opposite sides of a nonporous region of film. The relative (vertical) position of such features is readily apparent in stereo viewing. A typical pair of stereo electron micrographs, from a film formed at 50V for 24 hr, is shown in Fig. 9. With use of an appropriate viewer it may be seen that there is a considerable variation in pore depth; this is also evident in Fig. 10. Figure 10 is a cross-sectional view of a film formed under the same conditions employed for Fig. 9; while wet the film was folded over the edge of a specimen grid for viewing through the folded edge. Figure 11 shows average pore depth for several specimens as a function of anodizing time. It is apparent that there is no dependence of the pore depth growth rate on formation potential. As with the pore diameter, the behavior is nonlinear at short times with an abscissa

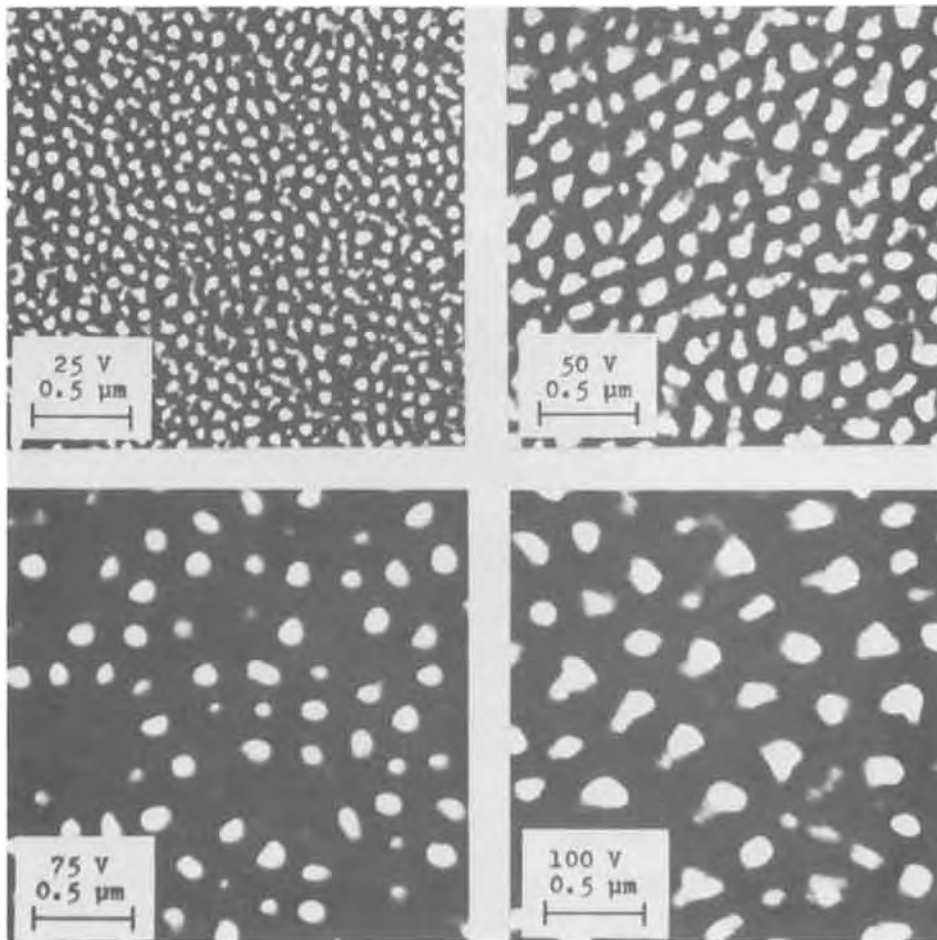


Fig. 6. Transmission electron micrographs of anodic oxide films formed for 48 hr at various voltages.

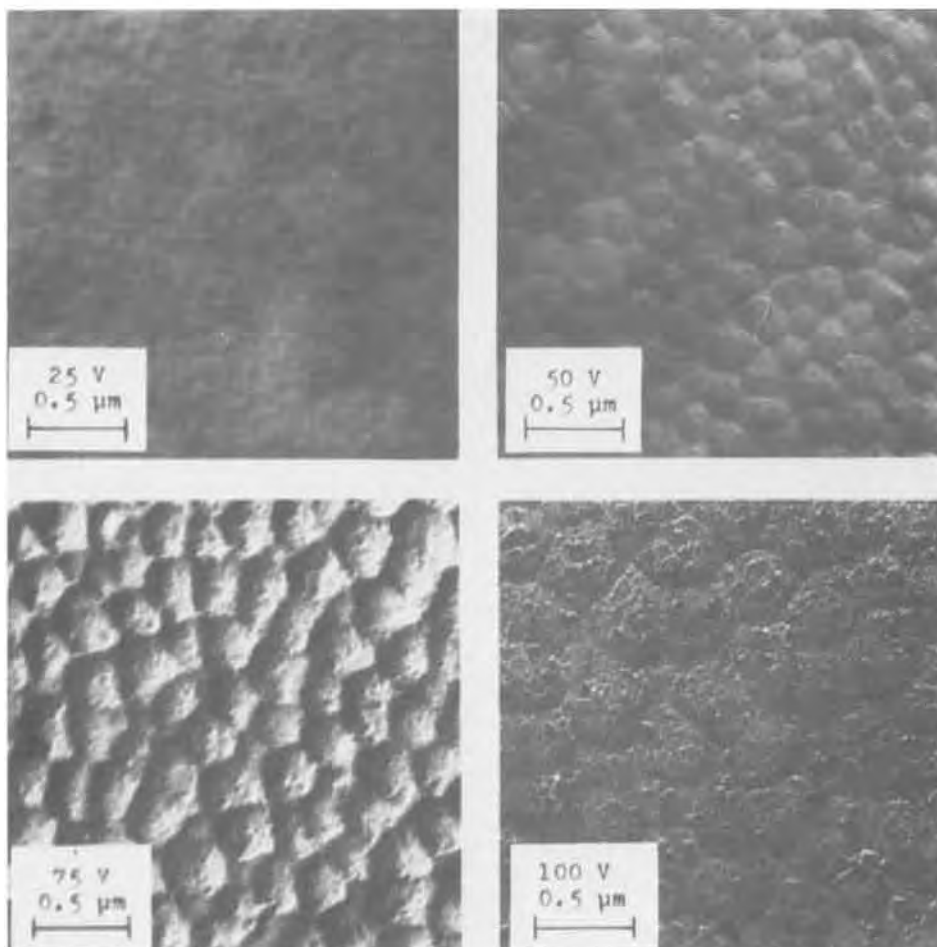


Fig. 7. Replica electron micrographs of substrate surfaces after anodizing for 48 hr at various voltages, showing oxide cell formation.

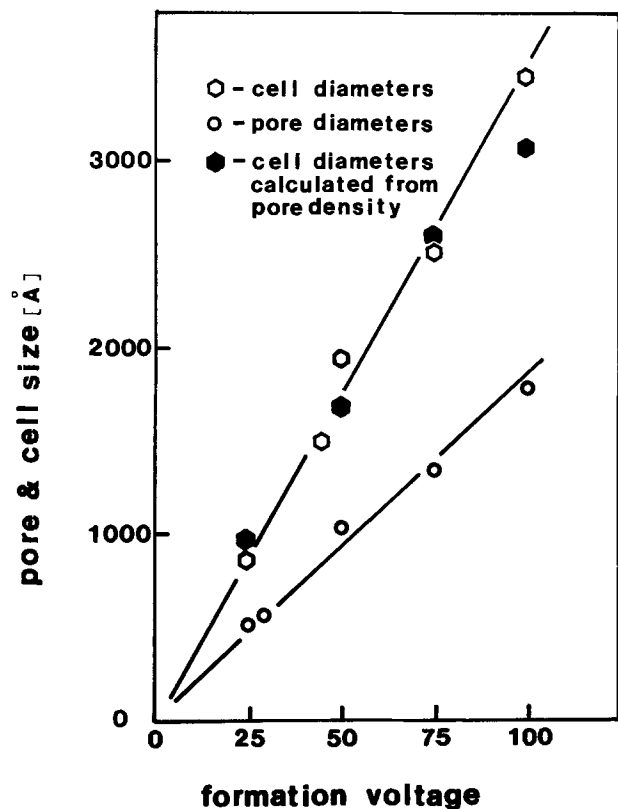


Fig. 8. Terminal pore and cell sizes vs. formation voltage

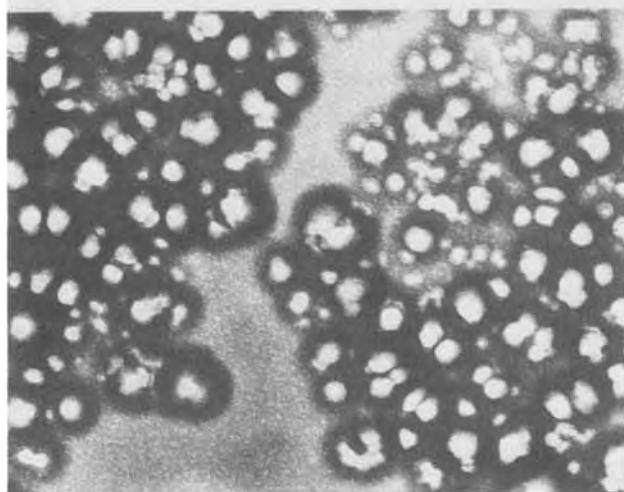
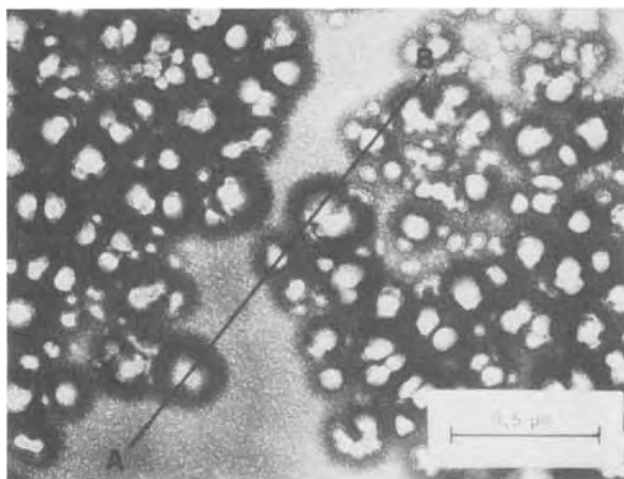


Fig. 9. Stereo transmission electron micrographs of anodic oxide film formed at 50V for 24 hr. Tilting angle $\pm 5^\circ$.

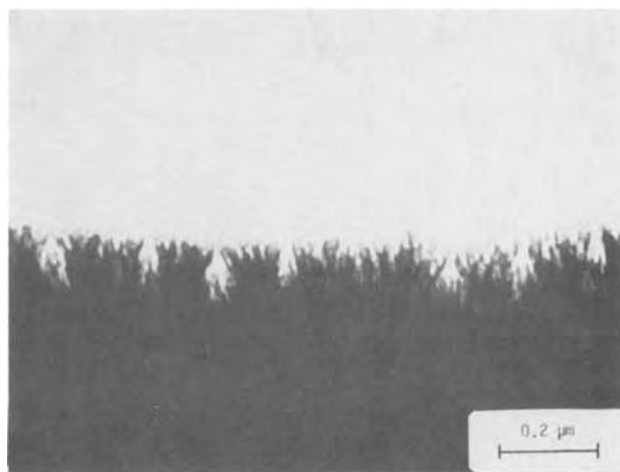


Fig. 10. Transmission electron micrograph of cross section of anodic oxide film formed at 50V for 24 hr.

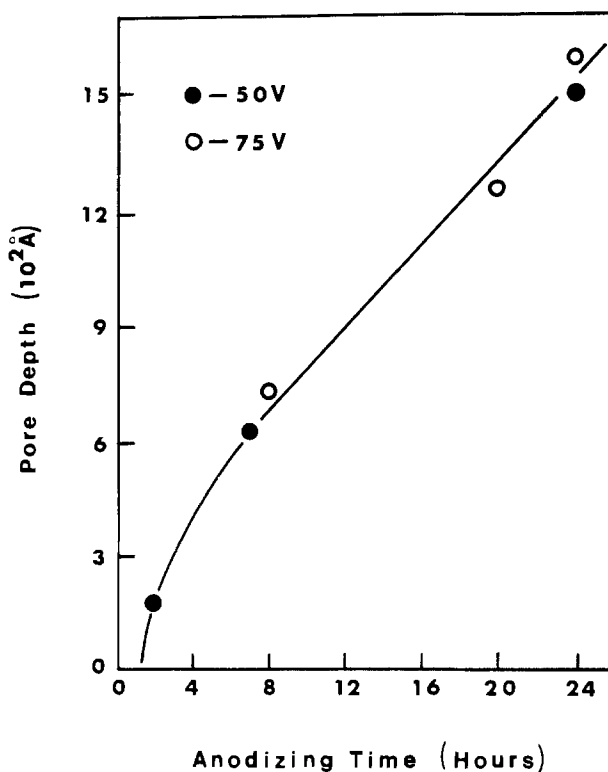


Fig. 11. Pore depth vs. anodizing time at 50 and 75V

intercept of the order of 90 min. The pore depth approaches linearity with time after about 8 hr of anodizing with a growth rate of 54 Å-hr^{-1} . Barrier layer thickness was determined for the pore-free regions of the film shown in Fig. 9; the value measured was $633 \pm 45 \text{ Å}$ or $12.6 \pm 0.9 \text{ Å-V}^{-1}$. Due to lack of suitable markers it was not possible to obtain reliable measurements for the thickness at the pore bases.

The power of electron stereomicroscopy is not evident in Fig. 9 unless viewed with a stereo viewer. The film appears as a transparent overlay on the opaque substrate surface. It can be seen that the oxide/electrolyte interface is virtually planar and that to each pore corresponds a pit in the substrate metal. The pore itself is separated from the substrate on all sides by a relatively uniform barrier layer. This layer appears to be somewhat thinner at the pore bases than on the pore walls or in the nonporous region. Furthermore, pores are consistently wider toward the base than at the pore opening. Figure 12 is a schematic representation of the section A-B indicated in Fig. 9, illustrating these points. Especially deep substrate pitting, with corre-

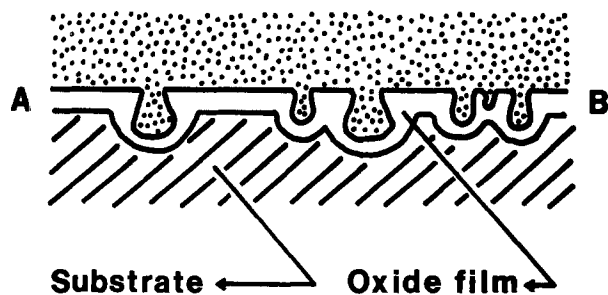


Fig. 12. Schematic representation of cross-section A-B marked on Fig. 9. Approximately to scale.

sponding thick porous layer formation, was observed over grain boundary junctions in the substrate. Such a site is shown in Fig. 13. These structures are, in fact, the "pore colonies" described in detail by Renshaw (17), constituting radial arrays of pores growing outward from a central site. This phenomenon occurs beneath the barrier layer; the two very light spots in the center of the pore colony shown in Fig. 13 are holes in the barrier layer, necessary to continued dissolution of oxide within the colony. Except for these holes the barrier layer over this region is planar and intact.

Discussion

O'Sullivan and Wood (2) have examined in considerable detail the structure of porous aluminum oxide films formed in acidic media and the effect of various anodizing parameters on this structure. Although as noted above other investigators have observed porous structure in films grown in barrier-forming media (8, 10-13) and, indeed, the similarity between films grown in barrier-forming electrolytes and those grown in pore-forming electrolytes (8, 13, 18, 19), no detailed

study has previously been performed on the porous structure developed in such media as neutral aqueous ammonium tartrate. The most striking feature of the present study is the degree of similarity between anodic films formed in this electrolyte and those formed in conventional pore-forming environments.

Figures 1, 3, and 11 suggest that a period of the order of 90 min elapses prior to initiation of visible pores. According to the mechanism postulated by Hoar and Yahalom (8) the film gradually thickens during this time, the average field finally decreasing to a value that will permit diffusion of protons into the film and initiation of pores. O'Sullivan and Wood (2) do not evoke a critical field for proton diffusion, but suggest that local regions of high current density thicken and spread during this initiation period, leaving relatively thinner sites between them that become pore nuclei. The significance of field-assisted dissolution as the primary mechanism of pore growth is well established (2, 7). It is thus proposed that the field is intensified by a pseudo-spherical geometry of the pore base, causing penetration of the pore and enlargement of its base diameter. The pore wall, being further from the substrate than is the base, experiences only a weak field and dissolves at a proportionately slower rate. Thus the pore base widens as it progresses, creating a pore that may be idealized as a truncated cone whose base is a spherical segment. Similar pore shapes were noted by O'Sullivan and Wood (2), but only under constant current conditions. They attributed this to the increase in voltage with anodizing time and the observation that pore diameter was proportional to voltage. Under constant voltage conditions they observed cylindrical pores terminating in spherical caps. The authors do not believe their findings to be in contradiction to those of O'Sullivan and Wood, but, instead, to represent the drastic difference in time scale of events in barrier-forming *vs.* pore-forming electrolytes, *i.e.*, that the pores depicted in Fig. 9 and 12 are yet in an early stage and that once the pore diameter stabilizes (~ 32 hr) and the pore depth assumes a linear rate of increase in time the pores will assume a cylindrical shape as indicated by the pore wall uniformity shown in Fig. 2 (32 hr).

O'Sullivan and Wood (2) indicated that rapidly growing pores would alter the field in their vicinity such that adjacent shallower pores would virtually cease to grow. Although these shallow pores would remain, they would become increasingly difficult to resolve optically as the over-all film thickness increased. With both pore diameter and wall thickness proportional to voltage, it followed that the density of pores (per unit area) would also be directly related to voltage. Although the authors do not disagree with the above, they also believe that there is evidence for pore coalescence in Fig. 2 and 9. It is clear that a large pore with the O'Sullivan and Wood "peardrop" shape can undermine a smaller adjacent pore, with eventual collapse of the pore wall separating them. On the other hand, adjacent pores of comparable size may remain essentially stable once oxidation of the substrate metal separating them at the base terminates field-assisted dissolution. Several stages in both the annihilation and stabilizing of pore walls are shown schematically in Fig. 14. Inasmuch as the terminal oxide cell size is 35 \AA-V^{-1} and the terminal pore diameter is 18.5 \AA-V^{-1} , the terminal thickness of oxide separating adjacent pores is 16.5 or 8.25 \AA-V^{-1} per cell. Assuming, for want of direct measurement, that the barrier layer at the pore base is comparable to the measured barrier layer exterior to the pores, 12.6 \AA-V^{-1} , the cell wall/barrier layer is 0.655 , not greatly different from O'Sullivan and Wood's figure of 0.71 for pore-forming media.

Using some simplifying assumptions an estimate of the time-dependence of field-assisted dissolution at the pore base may be calculated. Assuming that the electrolyte is a conductor and the oxide in the basal region of the pore is a portion of a spherical shell, the field

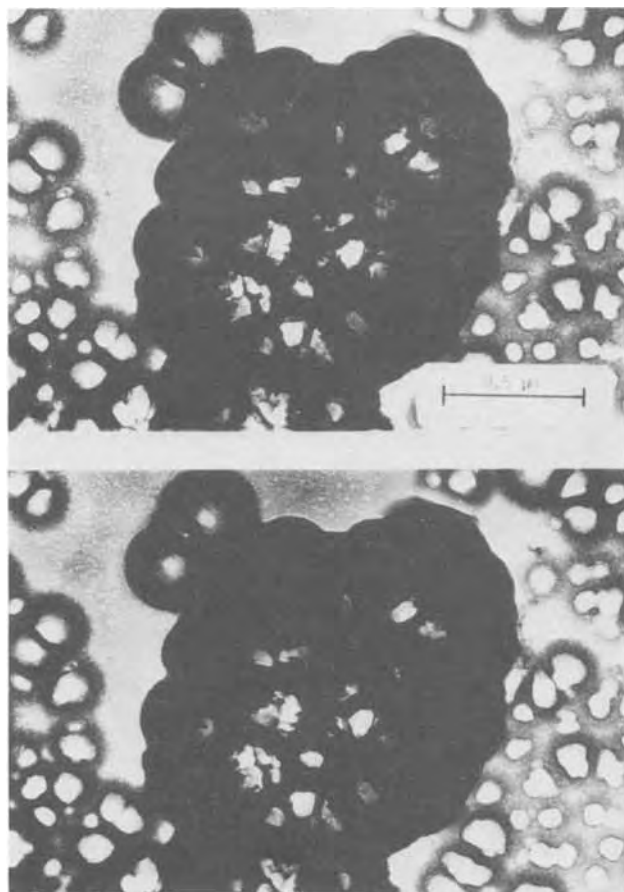


Fig. 13. Stereo transmission electron micrographs of anodic oxide film formed at 50V for 24 hr, showing deep pitting at substrate grain boundary junctions. Tilting angle $\pm 5^\circ$.

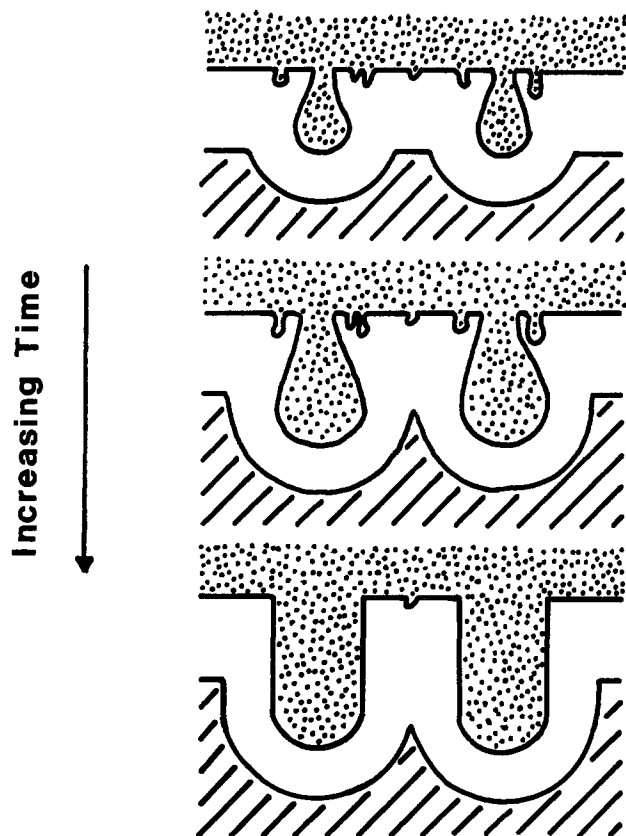


Fig. 14. Schematic representation of pore progression during anodizing, showing coalescence and formation of stable pore walls.

at the oxide/electrolyte interface is

$$E_i = \frac{V}{d} \left(1 + \frac{d}{R_i} \right)$$

where V is the potential drop across the oxide (and thus assumed equal to the formation voltage), R_i is the radius of curvature of the oxide/electrolyte interface, and d is the oxide thickness. The radius R_i is not necessarily the basal pore radius; under steady growth conditions (attainment of terminal pore size) O'Sullivan and Wood (2) demonstrated that normals to the pore axis and pore base defined a minimum angle of

$$\begin{aligned} \theta &= \cos^{-1} \left(\frac{\text{pore radius}}{\text{pore base radius of curvature}} \right) \\ &= \cos^{-1} \left(\frac{\text{cell wall thickness}}{\text{barrier layer thickness}} \right) \end{aligned}$$

which, in their case, was 45° . The authors found this value to be $\theta = \cos^{-1} 0.655 = 49^\circ$ in the present system. Assuming this ratio to be valid during pore enlargement the radius R_i is related to the basal pore diameter D by

$$R_i = \frac{0.5D}{0.655} = \frac{D}{1.31}$$

and the field may be written

$$E_i = \frac{V}{d} \left(1 + \frac{1.31d}{D} \right)$$

Although O'Sullivan and Wood (2) discussed in detail possible mechanisms for field-assisted dissolution, the actual mechanism is unknown as is any empirical dependency on system parameters. Due to this lack, a simple linear dependence of dissolution on field is assumed

$$\frac{dR_i}{dt} = CE_i$$

or

$$\frac{dD}{dt} = 1.31 C \frac{V}{d} \left(1 + \frac{1.31d}{D} \right)$$

This expression may be integrated to yield

$$\frac{D}{1.31} - d \ln \left(\frac{d + D/1.31}{d} \right) = \frac{CV}{d} (t - t_0)$$

As seen in Fig. 3, this expression is closely followed at 50 and 75V with $CV/d = 9.5 \text{ A}\cdot\text{hr}^{-1}$ or $C = 119.7 \text{ A}^2\cdot\text{hr}^{-1}\cdot\text{V}^{-1}$.

During the period of pore diametral growth the pore depth should be increasing by dissolution at a rate

$$\frac{dh}{dt} = \frac{dR_i}{dt} = \frac{1}{1.31} \frac{dD}{dt}$$

or

$$\frac{h}{D} = \frac{1}{1.31} = 0.764$$

This is readily checked using data from Fig. 3 and 11. The experimental values of the ratio h/D are given in Table I. Thus, the pore depth is seen to increase approximately 108% faster than expected in this simple model. This could be attributed to precipitation of aluminum oxide, dissolved within the pore, on the outer oxide surface. That is, material dissolved from the pore base may simply be transported out of the pore and be deposited on the exterior surface (12, 18, 20), either in hydrous or anhydrous form. The extent to which this occurs is not established; however, the data of Smith (20) show that after the first half-hour of anodizing the aluminum content of the electrolyte ceases to increase, suggesting that despite the continued occurrence of field-enhanced dissolution further aluminum is not removed from the oxide film, but is simply redistributed. Clearly the degree to which this occurs must depend on many factors, among them the pore geometry, relative volume of electrolyte, convective parameters, and solubility parameters. As a rough estimate of the possible magnitude of the effect, the area of the pore base may be compared to the available exterior area. Regarding, for convenience, the pore base as a hemisphere $18.5 \text{ A}\cdot\text{V}^{-1}$ in diameter, it has an area of $538 \text{ A}^2\cdot\text{V}^{-1}$. The exterior surface corresponding to each pore is approximately a ring of inner diameter $18.5 \text{ A}\cdot\text{V}^{-1}$ and an outer diameter larger by twice the pore wall thickness, or $35 \text{ A}\cdot\text{V}^{-1}$, having an area of $693 \text{ A}^2\cdot\text{V}^{-1}$. Assuming a constant molar volume for the oxide during dissolution and precipitation, the depth increase due to precipitation could be of the order of $538/693 = 0.77$, that due to dissolution, or the total depth increase, could be 1.77 of that due to dissolution alone.

An additional estimate of C may be obtained from the observed linear rate of pore depth increase that occurs following stabilization of the pore structure. As above

$$\frac{dh}{dt} = C E_i = \frac{CV}{d} \left(1 + \frac{1.31d}{D} \right)$$

Using the empirical values for 50V: $d = 630 \text{ A}$, $D = 1050 \text{ A}$, $dh/dt = 54 \text{ A}\cdot\text{hr}^{-1}$, C is calculated as $381 \text{ A}^2\cdot\text{hr}^{-1}\cdot\text{V}^{-1}$.

Table I. Experimentally determined values of h/D

V	t	h	D	h/D
50	2	175	120	1.458
	8	620*	360	>1.722
	24	1500	880	1.704
75	8	730	400	1.825
	20	1250	950	1.316
	24	1590	1050	1.514
				Avg = 1.59

* Measured at 7 hr.

$V^{-1}\text{-hr}^{-1}$, of the same order as the value calculated from the change of pore diameter with time.

It is not easy to be even hypothetically quantitative about the proportionality between terminal pore diameter and formation voltage. The argument regarding the annihilation of small pores, or at least termination of their growth, and the establishment of a stable pore size is qualitative and geometric in nature. For this reason the authors regard the linear relation between formation voltage and pore size as a manifestation of that between formation voltage and steady-state barrier layer thickness. That is, the state at which adjacent pores stabilize diametrically by dissolution of the web of substrate separating them and, hence, do not further enlarge other than in depth is presumably geometrically similar at different formation voltages. Thus, the structural dimensions of the porous oxide would be proportional to the only dimension which is independently controlled, the steady-state barrier layer thickness.

Conclusions

After a detailed electron microscopic examination of anodic films formed on highly pure aluminum in neutral aqueous 3% ammonium tartrate during anodizing times up to 48 hr, it is clear that these films may be distinguished from those formed in conventional pore-forming electrolytes such as sulfuric acid only by the rate at which the porous structure develops, in agreement with previous investigators (8, 18, 19). The mechanism by which pores form in such electrolytes that has appeared most plausible, simultaneous field-assisted dissolution of the oxide and reoxidation (7, 18), offers an equally likely explanation of observations pertaining to pore formation in barrier-forming electrolytes. Indeed, a pore growth rate with time is observed which may, in a semiquantitative way, be explained by the decay of the field at the inner surface of a spherical segment pore base as the pore enlarges, leading to a field-assisted dissolution constant of the order of $120 \text{ \AA}^2\text{-hr}^{-1}\text{-V}^{-1}$. A similar order of magnitude, $381 \text{ \AA}^2\text{-hr}^{-1}\text{-V}^{-1}$, is estimated from the linear rate of pore depth increase once a stable pore structure is developed. Coalescence of pores during growth is observed and explained by a purely geometrical argument, the undermining of small pores by adjacent, larger pores, and by their decreasing optical significance as the oxide thickens. Similarly, adjacent pores of similar size may form a stable shared pore wall when the substrate separating them has been consumed. Stable pore size and oxide cell size are seen to be proportional to formation voltage and, thus, to the barrier layer thickness as it is customarily defined. This is interpreted as supportive of the concept that the establishment of a stable pore structure is geometrically controlled and, thus, independent of actual dimensions.

The authors found the use of electron stereomicroscopy to provide a powerful tool for structure analysis of thin oxide films. Not only did it provide an accurate means for measuring local film thicknesses and individual pore depths, but provided a clear three-dimensional view of the complex film morphology.

Acknowledgments

The authors express their appreciation to the National Science Foundation for its generous support through Grants No. GK 20017 and No. GH 35580.

Manuscript submitted March 5, 1975; revised manuscript received July 25, 1975.

Any discussion of this paper will appear in a Discussion Section to be published in the June 1976 JOURNAL. All discussions for the June 1976 Discussion Section should be submitted by Feb. 1, 1976.

Publication costs of this article were partially assisted by the University of Connecticut.

REFERENCES

1. F. Keller, M. S. Hunter, and D. L. Robinson, *This Journal*, **100**, 411 (1953).
2. J. P. O'Sullivan and G. C. Wood, *Proc. Roy. Soc.*, **A317**, 511 (1970).
3. G. Haas, *J. Opt. Soc. Am.*, **39**, 532 (1949).
4. M. S. Hunter and P. Fowle, *This Journal*, **101**, 481 (1954).
5. R. C. Plumb, *ibid.*, **105**, 498 (1958).
6. M. S. Hunter and P. Fowle, *ibid.*, **101**, 515 (1954).
7. T. P. Hoar and J. F. Mott, *J. Phys. Chem. Solids*, **9**, 97 (1959).
8. T. P. Hoar and J. Yahalom, *This Journal*, **110**, 614 (1963).
9. D. T. Arrowsmith, E. A. Culpan, and R. J. Smith, *Proc. Intern. Symp. on Anodizing*, Birmingham, 1967, p. 17, Aluminum Federation, London (1967).
10. R. W. Franklin, *Nature*, **180**, 1470 (1957).
11. D. J. Stirland and R. W. Bicknell, *This Journal*, **106**, 481 (1959).
12. M. S. Hunter and P. F. Towner, *ibid.*, **108**, 139 (1961).
13. J. S. L. Leach and P. Neufeld, *Corrosion Sci.*, **9**, 413 (1969).
14. P. G. Anderson and O. F. Devereux, *This Journal*, **122**, 267 (1975).
15. P. B. Hirsch, A. Howie, R. B. Nicholson, D. W. Pashley, and M. J. Whelan, "Electron Microscopy of Thin Crystals," Butterworths, London (1965).
16. J. F. Nankivell, *Brit. J. Appl. Phys.*, **13**, 126 (1962).
17. T. A. Renshaw, *This Journal*, **108**, 185 (1961).
18. G. C. Wood, in *Oxides and Oxide Films*, J. W. Diggle, Editor, Vol. 2, p. 167, Marcel Dekker, Inc., New York (1973).
19. J. W. Diggle, T. C. Downie, and C. W. Goulding, *Chem. Rev.*, **69**, 365 (1969).
20. R. D. Smith, M.S. Thesis, University of Connecticut, 1974.

Barrier-Type Aluminum Oxide Films Formed under Prolonged Anodizing

II. Dielectric Characteristics

T. A. Libsch* and O. F. Devereux*

Department of Metallurgy and Institute of Materials Science, University of Connecticut, Storrs, Connecticut 06268

ABSTRACT

Nonporous anodic aluminum oxide films were potentiostatically formed at 30V and subsequently exposed to neutral aqueous ammonium tartrate for 3000 min at 30V, 10V, and at rest potential. Porous film growth was observed at the formation potential in accordance with Part I. Some factors responsible for the observed stability of the film capacitance and resistance at 30V have been determined by modeling the porous film as a parallel combination of two parallel RC circuits. Films tested at 10V thinned slowly by the development of a large number of fine pores at the oxide/electrolyte interface; in addition, pore colonies were observed in the metallic substrate below the thinning film. At rest potential the film developed a nonporous cellular topography, presumably an artifact of a selective dissolution process. The film capacitance at 10V and rest potential has been expressed as film thickness *vs.* time profiles under the assumption of uniform thinning.

A brief survey of the salient contributions to the literature concerning anodic aluminum oxide films is given in the first paper of this two part series (1). While the development of structure in anodic aluminum oxide films at the formation potential, both in pore-forming and barrier-forming electrolytes, is now reasonably well characterized, very little work has been done on the structural changes in such films resulting from reduced potentials. The phrase reduced potential is used here to indicate a film tested for some time at a potential below its formation potential.

O'Sullivan and Wood (2) formed porous aluminum oxide films at a constant potential of 115V for 30 min in 0.4M phosphoric acid at 25°C. Upon reducing the potential to 85V, they observed the following structural changes: (i) the barrier layer at the pore bases started to thin immediately, (ii) new pores were nucleated in this thinning barrier layer, and (iii) these pores increased in diameter until a new steady-state pore population density characteristic of the lower voltage was reached. Renshaw (3) formed 340Å thick nonporous films by anodizing aluminum in 3% ammonium tartrate (pH 5.5) at a constant potential of 25V for 1 min. These films were subsequently tested at a reduced potential of 15V in a 10% chromic acid electrolyte. The nonporous layer was observed to impede the formation of the porous film which normally would be formed in the chromic acid electrolyte. Hemispherical pore colonies, however, the pores of which developed radially from flaws or low resistance pathways present in the nonporous layer, were found to undermine the nonporous film. Edwards and Keller (4) had previously reported pore colony formation beneath barrier-layer anodic aluminum oxide films. These investigators, however, created artificial linear pores by intentionally cracking the nonporous anodic oxide film.

The purpose of the current investigation was to determine what structural alterations occur in preformed nonporous anodic aluminum oxide films upon exposure to neutral aqueous ammonium tartrate for a prolonged period (3000 min) at potentials equivalent to and less than the formation potential and to relate these alterations to changes in the film capacitance and resistance.

Experimental Procedure

Cylindrical specimens were machined from aluminum rod of 99.999% purity, mechanically polished

using 240, 320, 400, and 600 grit metallographic papers, and chemically polished (5) by immersion in: (i) a 3 weight per cent (w/o) sodium hydroxide solution at 75°C for 1 min and (ii) a 50 w/o nitric acid solution at 75°C for 2 min. Specimens were ultrasonically rinsed in double distilled water for 10 min following exposure to each chemical polishing solution. Electrolytes were prepared from reagent grade chemicals and double distilled water. The anodizing electrolyte was an aqueous 0.17M¹ ammonium tartrate solution with pH adjusted to 7 by the addition of several drops of dilute ammonium hydroxide. The testing electrolyte was either the anodizing electrolyte or a neutral 1M ammonium tartrate solution.

The electrode assembly, comprised of two Teflon gaskets compressed against the parallel faces of a prepared specimen, and the electrochemical cell used for anodizing and testing have been described previously (6). The cells were maintained at a constant temperature of 30.0° ± 0.3°C during both anodizing and testing by a conventional water bath. Anodic films were formed by gradually increasing the potential between the specimen and platinum gauze counterelectrode in such a manner that the current remained constant at 0.75 mA/cm² until the desired potential of 30V was obtained. This potential was maintained for 45 min, during which time the leakage current normally decayed to less than 20 μA/cm²; specimens exhibiting leakage currents in excess of this value were discarded. Based on the anodizing constant of 12.0 Å/V reported by McMullen and Pryor (7) for anodic aluminum oxide films formed in neutral ammonium tartrate, this procedure created nonporous films 360Å thick.

These films were tested at 30V, 10V, and at rest potential for a period of 3000 min. In the case of cells tested at 30V, anodizing blended into testing in that the anodizing electrolyte was not changed and the potential was continuous with time. In the case of cells tested at 10V and rest potential, the 30V potential was removed at the conclusion of the anodizing period and the electrolyte changed from 0.17M to 1M. This change was made to correct a problem discovered during testing at 30V wherein the procedure for calculating film dielectric data from cell data, described below, yielded erroneous values at high frequencies in the more dilute electrolyte. At the conclusion of a test, the film was rinsed with double distilled water, air dried, and scribed into small squares which were detached from the aluminum substrate by immersion in a saturated

* Electrochemical Society Active Member.

Key words: aluminum, anodic oxidation, impedance, porosity.

¹ 0.17M ammonium tartrate is equivalent to 3 w/o.

aqueous mercuric chloride solution. Stripped film sections were rinsed twice in double distilled water, mounted on 200 mesh copper grids, and examined in the transmission electron microscope. At 10V, several specimens were tested for times shorter than the 3000 min period in order to construct a sequence of transmission electron micrographs.

During the test period, the dielectric properties of the electrochemical cells were recorded at 0.5, 1, 5, 10, 20, and 50 kHz utilizing a capacitance measuring assembly comprised of a General Radio Type 1310-B oscillator, a Type 1615-A capacitance bridge, a Type 1232-A null detector, and a Sorenson Model QHS 100-.2 power supply. The dielectric properties of cells subjected to 30 and 10V were also monitored for 150 min after the potential was removed at the end of the 3000 min test period.

Results

Calculation of the series resistance of the electrolyte and subsequent correction of the cell data involve the following steps: (i) calculation of the series resistance of the cell (R_{s3}) at several frequencies from²: $R_{s3} = D_3/\omega C_{s3}$, where ω represents the angular frequency in rad/sec; (ii) determination of the series resistance of the electrolyte (R_{s2}) from a plot of R_{s3} vs. ω^{-1} at the point where the reciprocal frequency equals zero (8); (iii) calculation of the series resistance of the film (R_{s1}) by subtraction of R_{s2} from R_{s3} at any frequency; and (iv) calculation of the parallel capacitance (C_{p1}) and resistance (R_{p1}) of the film from the expressions: $C_{p1} = C_{s1}/[1 + (\omega R_{s1} C_{s1})^2]$ and $R_{p1} = [1/(\omega C_{s1})^2 R_{s1}] + R_{s1}$, where the series capacitance of the film (C_{s1}) and that of the electrochemical cell are equivalent.

The dielectric data employed to determine the electrolyte resistance comprised the initial measurements recorded after the application of the testing potential since, at this time, the film may be regarded as having an essentially parallel plate configuration inasmuch as pore development does not commence immediately (1). At longer exposure times such structural alterations may result in nonlinearity of the plots mentioned in (ii) above (9).

Figure 1 illustrates the average initial series resistance of electrochemical cells vs. reciprocal frequency at each test potential. These plots were constructed from data points (not shown) having reciprocal frequency values of 200×10^{-5} , 100×10^{-5} , 20×10^{-5} , 10×10^{-5} , 5×10^{-5} , and 2×10^{-5} Hz⁻¹. The data points shown in this and subsequent figures are only for the purpose of illustrating typical scatter. Note the high value of electrolyte resistance (y-intercept) and the curvature of the plot at 30V, to be discussed later. The average plots at 10V and rest potential are virtually identical and have not been distinguished. While the error bars on this line encompass the data from both potentials, the data scatter at 10V is significantly greater than that at rest potential for the higher values of reciprocal frequency.

Figure 2 illustrates the average parallel capacitance and resistance of films tested at 30V. As defined here, zero exposure time corresponds to the end of the 45 min anodization; the 30V potential was removed after 3000 min exposure. In this and subsequent figures of film data, the time scale has been expanded by a factor of five at the conclusion of the 3000 min test period. The dashed curve in Fig. 2 shows typical anomalous behavior arising from the correction procedure described above at high frequencies for cells having a low concentration electrolyte. The important characteristics in Fig. 2 are the negligible data scatter, the time stability of the data, and the frequency dependent, but essentially time independent, change in capacitance and resistance upon removal of the potential. Figure 3 shows typical transmission electron micrographs of the anodic oxide film as-anodized and after 3000 min at

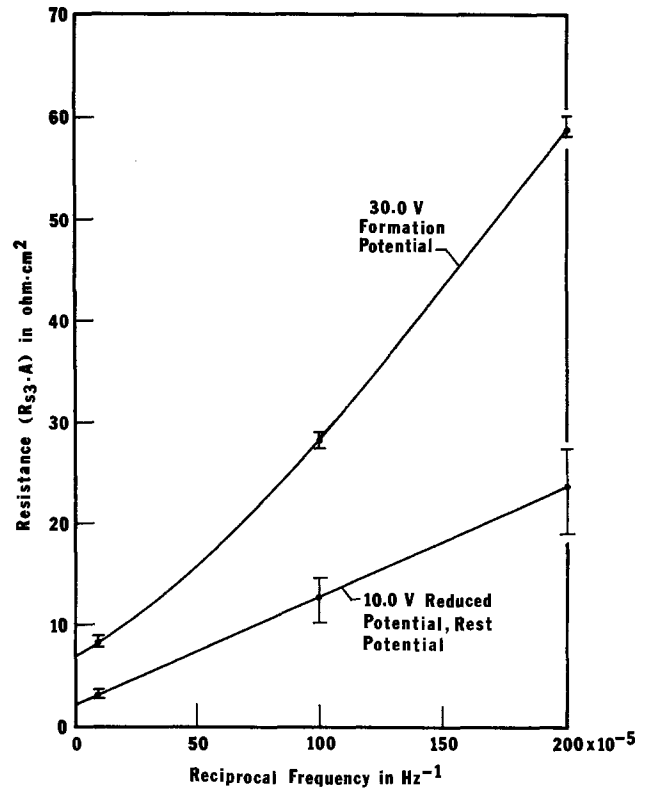


Fig. 1. Average initial series resistance of electrochemical cells tested at 30V, 10V, and rest potential vs. reciprocal frequency. Error bars typical.

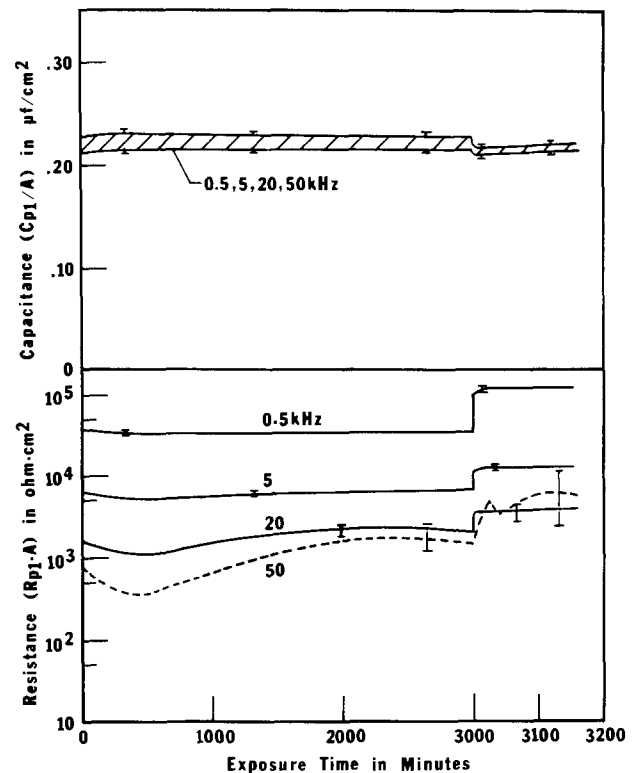


Fig. 2. Average parallel capacitance and resistance of anodic oxide films tested at 30V as a function of exposure time and frequency. The applied potential was removed at 3000 min. Error bars typical.

30V, illustrating porous film growth in accordance with Part I.

Figure 4 portrays the average parallel capacitance and resistance of films tested at 10V. The important characteristics of this figure are the large data scatter,

²The series capacitance (C_{s3}) and dissipation factor (D_3) of the cells were recorded from the bridge readouts.

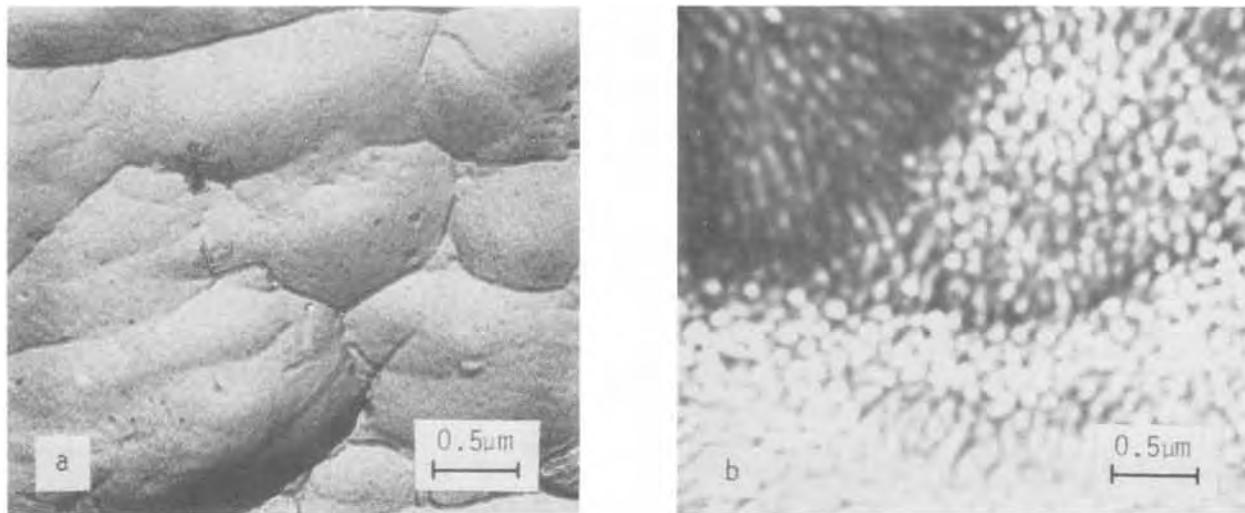


Fig. 3. Transmission electron micrographs of the anodic oxide films: (a) as-anodized, and (b) tested for 3000 min at 30V.

a time dependent increase in capacitance and associated decrease in resistance, and a frequency dependent, but essentially time independent, change in the capacitance and resistance upon removal of the potential that is less than that of cells tested at 30V. As mentioned previously, several specimens were tested at 10V for times shorter than the 3000 min test period in order to obtain a set of transmission electron micrographs illustrating the progressive change in the film structure. Due to the large variation in dielectric data in cells tested at this potential, the micrographs, shown in Fig. 5, have been placed in a capacitance sequence rather than in a time sequence. Figure 3a, which is the as-anodized film, may be considered as the initial micrograph in this capacitance sequence, having a capacitance of $0.202 \mu\text{f}/\text{cm}^2$ at 0.5 kHz.

Figure 6 illustrates the average parallel capacitance and resistance of the anodic films tested with no ap-

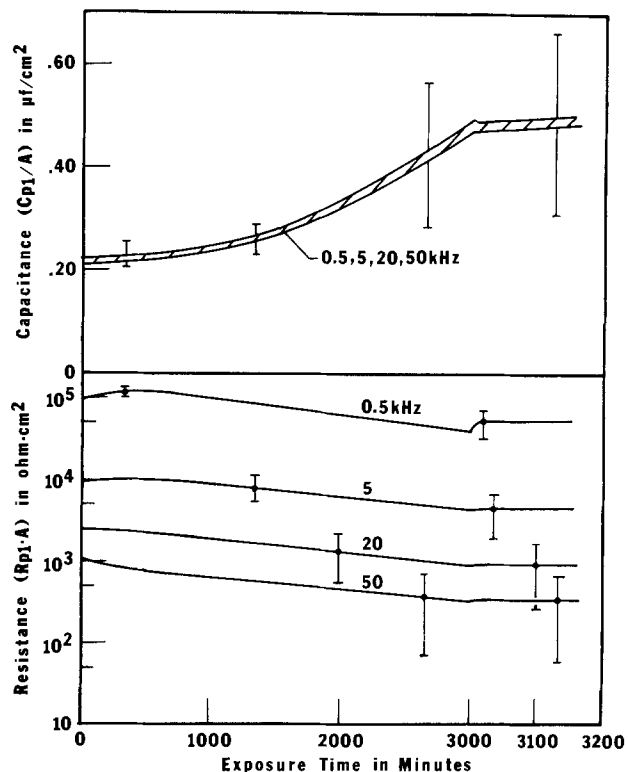


Fig. 4. Average parallel capacitance and resistance of anodic oxide films tested at 10V as a function of exposure time and frequency. The applied potential was removed at 3000 min. Error bars typical.

plied potential. The important characteristics in this figure are the negligible data scatter and an increase in capacitance and decrease in resistance which are less than those observed in the film data at 10V (Fig. 4). Figure 7 is a typical transmission electron micrograph of the film after 3150 min of testing at rest potential illustrating a different topography and a lack of the dark circular spots which were observed in films tested at 10V (Fig. 5).

Discussion

Films tested at the 30V formation potential.—Cell resistance during 30V tests showed a nonlinear dependence on reciprocal frequency, in contrast to measurements at the lower potentials. The linear dependence seen at 10V and at the rest potential is reported as an indication of good cell geometry (9); however, cell geometry per se was a constant parameter in these tests. The curvilinear behavior at 30V may be due to (i) field-induced changes in the dielectric properties of the oxide film (10), (ii) nonuniformity of the dielectric properties of the oxide with respect to position on the substrate surface, or (iii) a significant capacitive contribution from the lower concentration electrolyte used at 30V. (The series resistance of the electrolyte, determined as the infinite frequency intercept in Fig. 1, is $6.89 \text{ ohm} \cdot \text{cm}^2$ for the 0.17M electrolyte and $2.08 \text{ ohm} \cdot \text{cm}^2$ for the 1M electrolyte.) The data on hand do not permit meaningful comment on the contributions attributable to these factors.

The low concentration electrolyte also caused large frequency dispersions of capacitance and resistance in cell measurements involving freshly anodized films. The previously outlined procedure for correcting for the presence of the electrolyte reduced these dispersions, but proved somewhat inadequate above frequencies of approximately 20 kHz, as shown by the anomalous behavior of the dashed curve in Fig. 2. Similar problems have been encountered using alternate correction methods (6). These problems did not occur with the 1M electrolyte.

Films tested at 30V for 3000 min (Fig. 3b) are observed to possess a high degree of porosity in agreement with previous workers (1, 11, 12). The linear appearance of some pores is due to the irregular substrate features, created by the sodium hydroxide-nitric acid chemical polish. Richardson, Wood, and Breen (13) have examined the surface of 99.99% aluminum at various stages during a similar surface treatment and reported that individual cells or "saucers" were created in the aluminum by the sodium hydroxide solution, with the nitric acid solution removing much of the ridges separating these saucers.

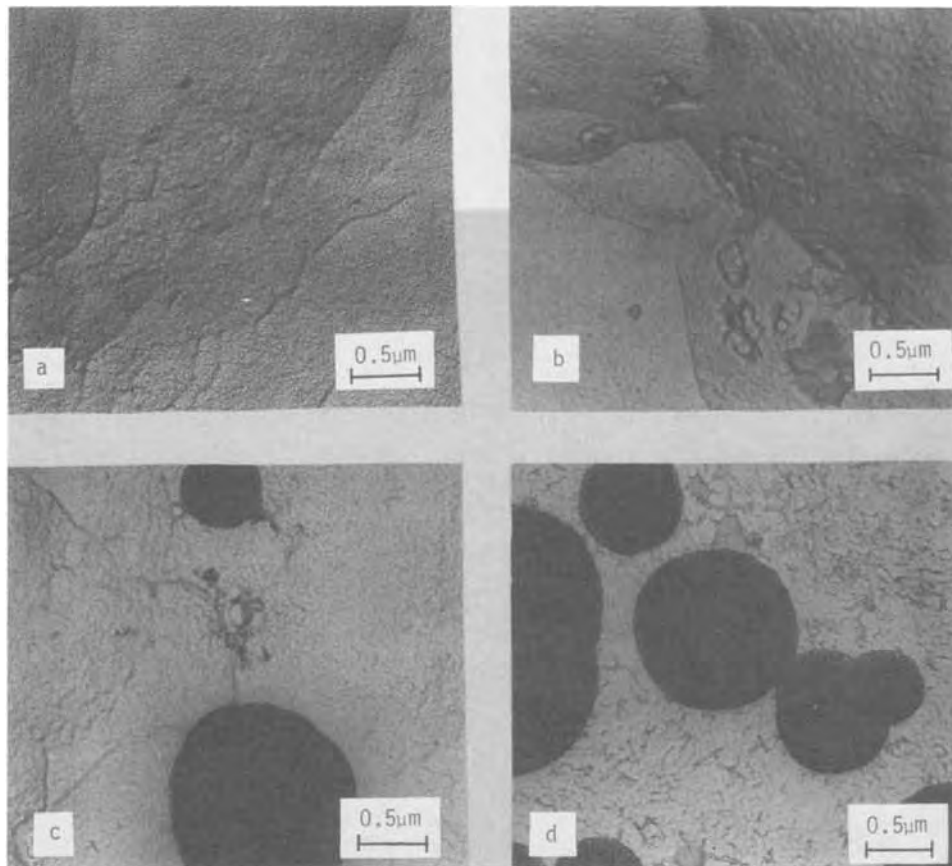


Fig. 5. Capacitance sequence of transmission electron micrographs for anodic oxide films tested at 10V. The parallel capacitance (C_{p1}/A), measured at 0.5 kHz, of the film for each micrograph is: (a) 0.227, (b) 0.272, (c) 0.300, and (d) 0.661.

The initial average series dielectric constant (κ_s) and resistivity (ρ_s) of the anodic film at 30V and rest potential were calculated from the initial average series film capacitance and resistance by the expressions: $\kappa_s = C_{s1}d_o/\epsilon_o A$ and $\rho_s = R_{s1}A/d_o$, where d_o , A , and ϵ_o represent the initial film thickness, the film area,

and the permittivity constant, respectively. The dielectric constant and resistivity are often reported in the parallel configuration; κ_p and ρ_p were, therefore, transformed to the parallel dielectric constant (κ_p) and resistivity (ρ_p) by the expressions: $\kappa_p = \kappa_s/[1 + (\omega\rho_s\kappa_s\epsilon_o)^2]$ and $\rho_p = [1/(\omega\kappa_s\epsilon_o)^2\rho_s] + \rho_s$. These values are tabulated vs. frequency in Table I. It is noted that Ord, Hopper, and Wang (14) have reported the low frequency dielectric constant of tantalum, niobium, and tungsten oxides to decrease linearly with increasing field, i.e., opposite to the trend for aluminum oxide in Table I. There is, however, no *a priori* reason to expect a decrease.

The authors believe that the potential dependent changes in dielectric data (Fig. 2 and 4) can be explained by the presence of a transitory population of ionic defects. While a significant anodic potential is

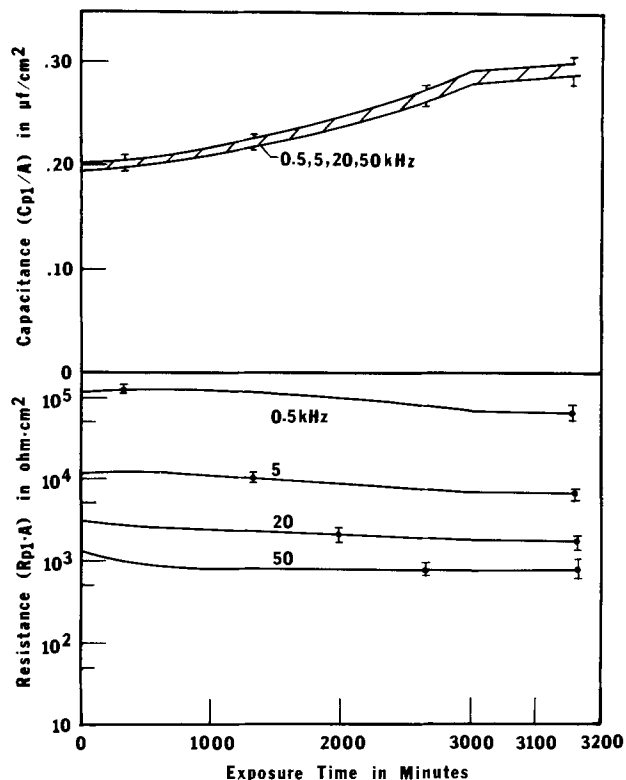


Fig. 6. Average parallel capacitance and resistance of anodic oxide films tested at rest potential. Note that the time scale has been expanded by a factor of five at 3000 min. Error bars typical.

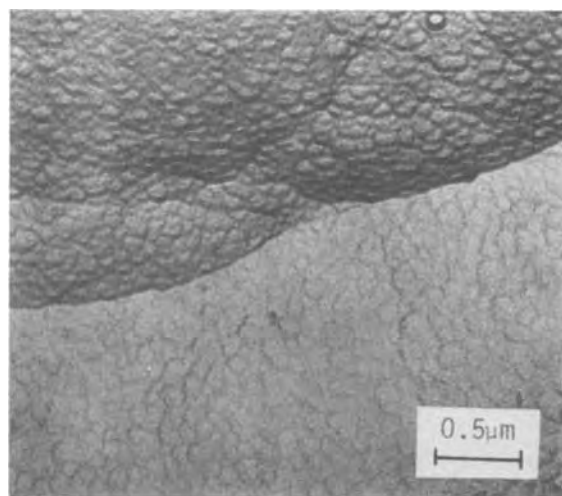


Fig. 7. Typical transmission electron micrograph of anodic oxide film tested at the rest potential for 3150 min.

Table I. Initial values of the dielectric constant and resistivity of the anodic film

f (kHz)	κ_s (unitless)	ρ_s (ohm · m)	κ_p (unitless)	ρ_p (ohm · m)
Values at the 30V formation potential				
0.5	9.29	1.45×10^5	9.28	1.04×10^8
5	8.93	9.49×10^3	8.93	1.71×10^7
20	8.73	2.33×10^3	8.72	4.57×10^6
50	8.69	8.71×10^2	8.68	1.97×10^6
Values at rest potential				
0.5	8.23	5.91×10^4	8.22	3.24×10^8
5	8.08	6.11×10^3	8.07	3.25×10^7
20	7.98	1.51×10^3	7.98	8.40×10^6
50	8.00	5.43×10^2	8.00	3.72×10^6
Changes in parallel film capacitance and resistance upon removal of the 30V potential				
f (kHz)	$\Delta C_{p1}/A$ ($\mu\text{f}/\text{cm}^2$)		$\Delta R_{p1}A$ (ohm · cm ²)	
	Actual	Initial	Actual	Initial
0.5	-0.008	-0.026	63,900	79,200
5	-0.006	-0.021	4,460	5,530
20	-0.005	-0.018	1,285	1,380
50	-0.004	-0.017	—	630

applied, there is a finite population of Al^{+3} ions in the oxide, contributing to the a-c as well as d-c conductance. Assuming a constant field across the thickness, it is reasonable to presume that the population density is also independent of position in the film. This population is not stable, however, since under the very high field ($\sim 10^7$ V/cm) the Poisson-Boltzmann space charge would be of negligible thickness. Hence when the potential is removed, the Al^{+3} ion population in the film will be quickly drained to the oxide/electrolyte interface, drastically reducing the a-c and d-c conductance. A similar argument would hold for electronic defects in the film produced by the anodic reaction. The changes in parallel film capacitance and resistance upon removal of the 30V potential (Fig. 2) are listed vs. frequency in Table I. These changes have been compared with those which would occur if the potential were removed immediately after its application, i.e., at the time when the film has an essentially parallel plate configuration (compare Fig. 2 and 6). Alterations in the film's structure and distribution of dielectric constant and resistivity account for the minor differences observed.

Dekker and Urquhart (15) have previously determined that the 60 Hz capacitance of porous anodic aluminum oxide films formed by anodizing at a constant current of 8 mA/cm² in a 5.4 volume per cent (v/o) sulfuric acid solution are independent of time after 1 min of anodizing; the final film capacitance, however, was reported to be a function of current density and solution concentration and composition. No analysis of these results was attempted, however. In the current investigation, the authors have represented the thickening anodic film by a parallel combination of two parallel RC circuits; one circuit representing the porous area of the film, the other the thicker film adjacent to the pores. An a-c circuit analysis (16) for this analog yields for the series film capacitance and resistance: $C_{s1} = -a/bc\omega \sin \theta_1$ and $R_{s1} = bc \cos \theta_1/a$ where

$$a = [(b \cos \theta_2 + c \cos \theta_3)^2 + (b \sin \theta_2 + c \sin \theta_3)^2]^{1/2}$$

$$\theta_1 = -\theta_2 - \theta_3 + \tan^{-1} \left[\frac{(b \sin \theta_2 + c \sin \theta_3)}{(b \cos \theta_2 + c \cos \theta_3)} \right]$$

$$b = \frac{d_0 [1 + (\omega \kappa_s \epsilon_0 \rho_s)^2]^{1/2}}{\omega \kappa_s \epsilon_0 A_1}$$

$$c = \frac{d [1 + (\omega \kappa_s \epsilon_0 \rho_s)^2]^{1/2}}{\omega \kappa_s \epsilon_0 (A - A_1)}$$

$$\theta_2 = \tan^{-1} (1/\omega \epsilon_0 \kappa_s \rho_s)$$

$$\theta_3 = \tan^{-1} (1/\omega \epsilon_0 \kappa_s \rho_s)$$

The parallel film capacitance and resistance were subsequently calculated from equations previously presented. The parameters d and A_1 represent the film thickness and the area of the pores within the area A .

In this model, the fractional area of pores (A_1/A), determined from Fig. 3b to be 0.42, was assumed constant.

The analog presented is not an exact model of the thickening film due to lack of a definitive relation between film thickness and time and the unknown distribution of dielectric constant and resistivity within the oxide. In respect to the former deficiency, the parallel film capacitance and resistance were evaluated as a function of the thickness of the outer porous layer, i.e., $d - d_0$, in lieu of time as an independent parameter. In respect to the latter deficiency, three cases were evaluated: case I, the film has the dielectric constant and resistivity values at rest potential (Table I); case II, the film has the dielectric constant and resistivity values at 30V (Table I); and case III, the film below the pores has the dielectric constant and resistivity values at 30V, while the remainder of the film has the values at rest potential. In case III, κ_s and ρ_s in the expressions for b and θ_2 are those at 30V; κ_s and ρ_s in c and θ_3 are those at rest potential.

Figure 8 illustrates the results of this model; the parallel film capacitance, being virtually identical in each case, has been illustrated only for case III. The parallel film capacitance and resistance of the model are observed to approach a stable value rapidly as the film thickens. The changes in capacitance and resistance of the model at low $d - d_0$ values, which are not present in the film data in Fig. 2, may reasonably be credited to the initial growth and coalescence of pores as reported in Part I (1). Four conclusions concerning the stability of the film data in Fig. 2 can be drawn from the model: (i) the film at the pore bases has a thickness controlled by the anodizing constant reported previously, (ii) the porous film area dominates the over-all dielectric properties, (iii) the uneven distribution of dielectric constant and resistivity contributes significantly to the stability of the data,

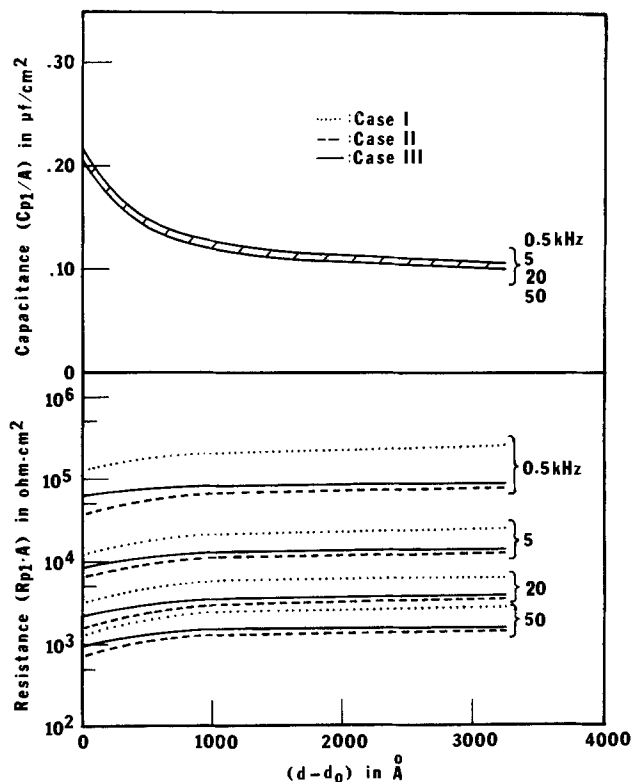


Fig. 8. Results of electrical analog used to represent anodic oxide films tested at 30V. Case I: The film has the dielectric constant and resistivity values determined at rest potential. Case II: The film has the dielectric constant and resistivity values determined at 30V. Case III: The porous film area has dielectric constant and resistivity values determined at 30V, while the thicker film outside the pores has the dielectric constant and resistivity values determined at rest potential.

and (iv) a negligible frequency dispersion of capacitance accompanies porous film growth of this type. The minor frequency dispersion of capacitance observed in Fig. 2 is in sharp contrast to that previously reported by Libsch and Devereux (6). In that investigation, nonporous anodic aluminum oxide films tested in acidic electrolytes developed a porous film structure by the radial growth of pores without film thickening. This manner of porous film development creates a significant increase in and a broad frequency dispersion of capacitance.

Films tested at the 10V potential.—The topographical features noted in the films tested at 10V (Fig. 5) are: (i) the scalloped form of the film, discussed previously, (ii) the development of a large number of small pores at the oxide/electrolyte interface believed to be created by a decrease in the local pH value of the electrolyte, caused by the applied field as suggested by Plumb (17), and (iii) the development of pore colonies at the substrate/oxide interface (dark circular spots). The pore colonies often, although not always, form below the film at the network of ridges created by the juncture of the saucer shapes on the aluminum surface. These sites in the film may be more defective than average due to impurity concentrations in the substrate or thinner than average due to enhanced oxide dissolution at the small radius of curvature of the ridge peak, resulting in higher anodic current in these regions, effectively lowering the pH of the electrolyte adjacent to the film in comparison to the bulk solution. These pore colonies are identical to those observed by Renshaw (3) and similar to those reported by Edwards and Keller (4).

A film thickness *vs.* time profile (Fig. 9) was determined under the assumptions that the film thins uniformly in a parallel plate configuration and that the film dielectric constant is independent of film thickness. The former assumption is expected to be reasonably accurate since the pores at the oxide/electrolyte interface are numerous, *i.e.*, a negligible amount of pore wall material exists at this interface, and the pore colonies at the substrate/oxide interface encompass a negligible area of the film during the majority of the test period. The validity of the latter assumption is clearly difficult to ascertain. The data points in Fig. 9

were calculated from the average 0.5 kHz series film capacitance by the expression $d = \kappa_{se}A/C_{s1}$, the average initial 0.5 kHz series dielectric constant having a value of 9.12. Figure 9 shows that the data obtained at 10V are consistent with an essentially constant rate of thinning of 1.42×10^{-13} m/sec (5.1 Å/hr) following an induction period of approximately 1000 min.

Each of the specimens tested at 10V was examined microscopically to determine the cause of poor reproducibility in the dielectric data (Fig. 4). The two specimens with greater changes were observed to have a greater area encompassed by pore colonies. While the presence of pore colonies is not expected to significantly alter the dielectric behavior, it is indicative of greater film thinning, to which the anomalous dielectric behavior is attributed.

Films tested at rest potential.—The films tested at rest potential (Fig. 7) are observed to have the scalloped shape as in the 30 and 10V cases, to be composed of an array of small apparently nonporous cells, and to be entirely free of pore colonies. The cellular pattern is presumed an artifact of a selective dissolution process rather than a genuine cellular structure as reported by Franklin (18) and Stirland and Bicknell (19) in films formed at high voltage in a boric acid-borax electrolyte. The time-dependent nature of the film data (Fig. 6) contradicts Plumb's (17) statement that neither ammonium tartrate nor potassium sulfate electrolytes will dissolve aluminum oxide by simple contact without current flow.

A thickness *vs.* time profile (Fig. 9) determined under the assumptions and in the manner previously described, shows the average rate of thinning after a 1000 min induction period to be constant at 6.94×10^{-14} m/sec, *i.e.*, approximately one-half the average rate of films tested at 10V.

Summary and Conclusions

Anodic films tested at the 30V formation potential thickened into a porous structure similar to that of porous films formed in aggressive electrolytes; the rate of pore formation, however, being markedly less in accordance with the results of Part I. Films tested at 10V thinned slowly by the development of a large number of fine pores at the oxide/electrolyte interface; in addition, pore colonies were observed to develop at the substrate/oxide interface, primarily at surface irregularities created by substrate preparation. Films tested at rest potential were observed to have a nonporous cellular topography, this topography resulting from a slow thinning process.

The time independent nature of the film capacitance and resistance observed at 30V was examined by modeling the porous film as a parallel combination of two parallel RC circuits. The results of this model show that: (i) the film at the pore bases has a thickness governed by the anodizing constant, (ii) the porous film area dominates the over-all dielectric properties, (iii) an uneven distribution of dielectric constant and resistivity contributes significantly to the stability, and (iv) a negligible frequency dispersion of capacitance accompanies this type of porous film growth. The capacitance increases and resistance decreases of films tested at 10V and rest potential are consistent with uniform thinning. The thinning rate in both cases was found essentially linear following an induction period of approximately 1000 min, the average rate at 10V (1.42×10^{-13} m/sec) being approximately twice the average rate at rest potential. Potential dependent changes in the capacitance and resistance of the film at 30 and 10V have been explained by the flow of a transitory population of ionic defects to the oxide/electrolyte interface.

Acknowledgments

The authors express their appreciation to the National Science Foundation for its support through Grants No. GK 20017 and No. GH 35580. Computations

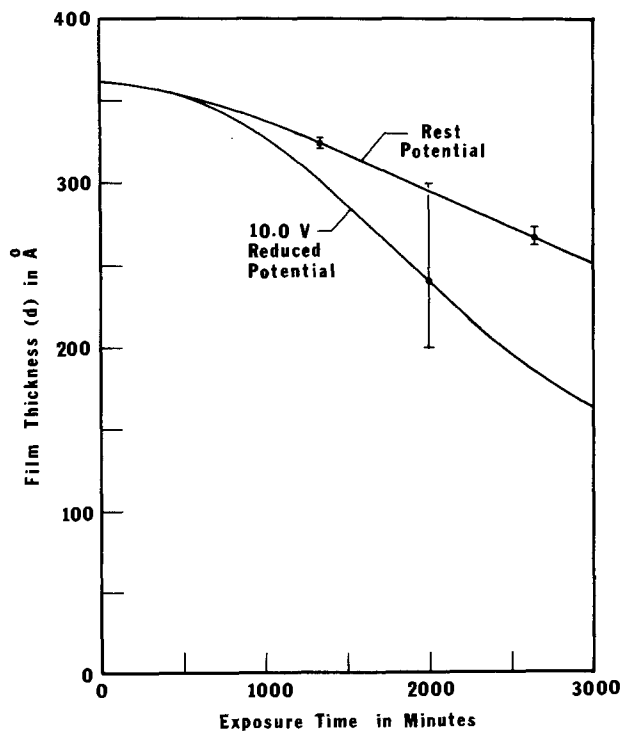


Fig. 9. Average film thickness as a function of exposure time for cells tested at 10V and at rest potential. Error bars typical.

were carried out using the facilities of the University of Connecticut Computer Center. The authors also gratefully acknowledge the assistance of Mr. Larry McCurdy in operation of the electron microscope.

Manuscript submitted March 5, 1975; revised manuscript received July 25, 1975.

Any discussion of this paper will appear in a Discussion Section to be published in the June 1976 JOURNAL. All discussions for the June 1976 Discussion Section should be submitted by Feb. 1, 1976.

Publication costs of this article were partially assisted by the University of Connecticut.

LIST OF SYMBOLS

A	total area of the film, m^2
A_1	porous area of the film, m^2
C_{p1}	calculated parallel capacitance of the anodic film, f
C_{s1}	calculated series capacitance of the anodic film, f
C_{s3}	uncorrected series capacitance of the electrochemical cell, f
d	thickness of the film, m
d_0	initial thickness of the film, m
D_3	uncorrected dissipation factor of the electrochemical cell, unitless
f	frequency, kHz
R_{p1}	calculated parallel resistance of the anodic film, ohm
R_{s1}	calculated series resistance of the anodic film, ohm
R_{s2}	series resistance of the electrolyte, ohm
R_{s3}	uncorrected series resistance of the electrochemical cell, ohm
ϵ_0	permittivity constant, f/m
κ_p	initial parallel dielectric constant of the film, unitless
κ_s	initial series dielectric constant of the film, unitless
ρ_p	initial parallel resistivity of the film, ohm·m

ρ_s	initial series resistivity of the film, ohm·m
ω	angular frequency, rad/sec

REFERENCES

- Y. H. Choo and O. F. Devereux, *This Journal*, **122**, 1645 (1975).
- J. P. O'Sullivan and G. C. Wood, *Proc. Roy. Soc.*, **A317**, 511 (1970).
- T. A. Renshaw, *This Journal*, **108**, 185 (1961).
- J. D. Edwards and F. Keller, *Trans. AIME*, Tech. Publ. 1710 (1944).
- P. M. Deeley, "Electrolytic Capacitors," Recorder Press, Plainfield, N. J. (1938).
- T. A. Libsch and O. F. Devereux, *This Journal*, **121**, 400 (1974).
- J. J. McMullen and M. J. Pryor, in "Proc. 1st International Congress on Metallic Corrosion," p. 52, Butterworths, London (1961).
- L. Young, "Anodic Oxide Films," Academic Press, New York (1961).
- D. M. Smyth, in "Oxides and Oxide Films," J. W. Diggle, Editor, Vol. 2, Marcel Dekker, Inc., New York (1973).
- T. A. Libsch, Ph.D. Thesis, University of Connecticut, 1975.
- T. P. Hoar and J. Yahalom, *This Journal*, **110**, 614 (1963).
- M. S. Hunter and P. F. Towner, *ibid.*, **108**, 139 (1961).
- J. A. Richardson, G. C. Wood, and A. J. Breen, *Thin Solid Films*, **16**, 81 (1973).
- J. L. Ord, M. A. Hopper, and W. P. Wang, *This Journal*, **119**, 439 (1972).
- A. J. Dekker and H. M. A. Urquhart, *Can. J. Res.*, **B28**, 541 (1950).
- V. Del Toro, "Principles of Electrical Engineering," Prentice-Hall, Inc., Englewood Cliffs, N. J. (1965).
- R. C. Plumb, *This Journal*, **105**, 498 (1958).
- R. W. Franklin, *Nature*, **180**, 1470 (1957).
- D. J. Stirland and R. W. Bicknell, *This Journal*, **106**, 481 (1959).

Dielectric Anisotropy in Amorphous Ta₂O₅ Films

Peter W. Wyatt

Bell Laboratories, Incorporated, Allentown, Pennsylvania 18103

ABSTRACT

The capacitance of Ta-Ta₂O₅ thin-film capacitors changes by the order of 1% when an electric field is applied across the dielectric. The dependence of capacitance on field is a potentially useful tool for studying the fundamental properties of this device. The capacitance-field curve is asymmetric which suggests that an interface effect might be involved. In this paper it is shown that the C-E curve at liquid nitrogen temperature is independent of oxide thickness. This independence holds whether the oxide was produced by simple anodization or by anodization followed by chemical thinning. It is argued that interface effects cannot account for these experimental results, so therefore the C-E dependence must result from bulk effects. It is suggested that local structural anisotropy, produced by the ionic current responsible for anodization and frozen in when the field is removed, is responsible for the asymmetry of the C-E curve.

Hybrid integrated circuits based on Ta thin films are becoming increasingly important in the Bell System. The Ta film capacitor is one of the major components in many of these circuits. It has long been known that these capacitors are voltage dependent (1), but the dependence is small enough that it would not seriously affect circuit operation in any but the most critical applications. It is, for example, many times smaller in its working voltage range than that of a solid Ta capacitor. Perhaps for this reason the voltage dependence has received little attention. The present study was made in order to use the voltage dependence as a

source of information about the physical processes which are active in the capacitor and which determine its performance.

The small-signal capacitance was measured as a function of slowly varying bias voltage for a range of measurement parameters using capacitors made with several variations on the basic process. These experiments clearly indicate that the capacitor responds in several different ways simultaneously when a d-c voltage is applied, which leads to considerable confusion in data analysis. The results are somewhat simplified at low temperature, so this paper is limited to work at liquid nitrogen temperature, 77°K.

Key words: capacitors, anodization, interface, ellipsometry.

This study divides naturally into two segments. The first, presented in this paper, is the question of whether the voltage dependence is produced by effects involving one of the metal-insulator interfaces or alternatively by effects distributed throughout the insulator. We will find that an interface model cannot account for the observed behavior and therefore will conclude that the voltage dependence must arise from bulk processes. Because the capacitance is not symmetric about zero voltage, we will conclude that the anodic oxide is anisotropic despite its amorphous structure. The second segment of the study, to be presented in a later paper (2), considers how many bulk processes are involved and what their properties are.

The next two sections describe sample preparation and measurement. Then a general interface model is introduced, and predictions are derived from it. The pertinent experiments to test these predictions are summarized, and in the last section the disagreement between prediction and experiment is discussed. It is concluded that interface effects cannot account for the data, and a qualitative explanation for the apparent bulk anisotropy is suggested.

Sample Fabrication

A typical sample is shown in cross section in Fig. 1. A Ta film 500Å thick is deposited by d-c sputtering in argon on a glass substrate and oxidized thermally to produce a protective layer of Ta₂O₅. A second Ta film, 5000Å thick, is then d-c sputtered onto this underlay. The Ta contains about 1 atomic per cent (a/o) nitrogen, an impurity which is conventionally added as a dopant in the sputtering gas to improve capacitor performance (3). Sputtering conditions are such as to produce the β (tetragonal) crystal structure (4). The Ta film forms one electrode of the capacitor and is oxidized to produce the dielectric.

The oxidation is done anodically in dilute citric acid [0.01 weight per cent (w/o) in water] at room temperature using a Ta sheet cathode. A constant current of 0.16 mA/cm² is applied until the desired anodization voltage, V_A, is reached, and this voltage is then held constant for a soak period, t_s. Standard values, assumed in Fig. 1, are 230V and 1 hr, but these parameters were varied in the present experiments as discussed below. It is well known that this procedure produces an amorphous stoichiometric film of Ta₂O₅ (5). The nitrogen contained in the Ta is distributed nonuniformly in the oxide (6),¹ but these experiments show that its presence does not affect the C(V) characteristic (2).

The counterelectrode is a round dot of NiCr backed by Au which is evaporated through a metal mask by electron beam heating. The area is 0.1 cm². The resulting capacitor, for V_A = 230V and t_s = 1 hr, has capacitance and dissipation factor at 1 kHz of 5.8 nF,

¹ Auger analysis by J. M. Morabito indicated about 1 a/o N in the Ta, with the N in the oxide film confined to the 70-80% of the oxide nearer the Ta. This subject is discussed for samples with higher N concentration in Ref. (6).

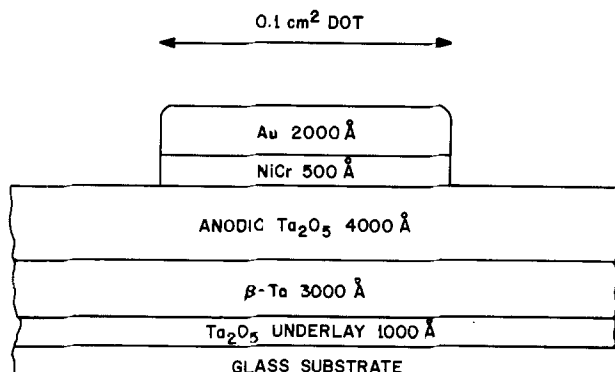


Fig. 1. Cross section of a Ta film dot capacitor

and 0.0025, respectively, at room temperature, and 5.5 nF, 0.0012 at 77°K.

In this study it was necessary to prepare samples of various oxide thicknesses by two different techniques. The first experiment used the usual technique of varying the anodization voltage. The anodization conditions and oxide thicknesses for this experiment are summarized in Table I. Six voltages were used, 50-300V in 50V steps. The current density was the same for all six samples, 0.16 mA/cm². The soak period was varied in proportion to the voltage, with t_s in minutes equal to ¼ the anodization voltage in volts. This is important because the asymmetry of the C(V) characteristic, discussed below, depends on the soak time (2). It means that the fraction of oxide grown at reduced current density is the same for the different thicknesses.

Oxide thickness was measured with an ellipsometer (O. C. Rudolph and Sons, Type 43603-200E) using light with 5461Å wavelength. Polarizer and analyzer readings were taken in zones 1 and 3 (7) and averaged. An optically uniform, nonabsorbing oxide was assumed, and this assumption was confirmed by the observation that the points fall on the same curve for different cycles of the ellipsometric parameters. Fitting the data for six thicknesses to calculated curves gives thicknesses of 900-5400Å with an oxide index of refraction of 2.24 ± 0.02. The Ta film index of refraction is not accurately determined, since many values fit equally well. The value 2.98 - i 3.29 has been taken in this work, since it leads to a calculated thickness which is directly proportional to the anodization voltage, d = KV_A, with K = 18.02 ± 0.02 Å/V. Choosing other values of the Ta index does not significantly affect the results discussed here. The index values (8) and K value (6) determined here are consistent with earlier work.

In the second experiment the Ta was anodized as usual, but the oxide was then thinned by chemical etching to produce the desired thickness. The Ta was anodized to 230V with a 1 hr soak period. In order to reduce weak spots, the films were anodically back-etched at room temperature in a solution of 0.02% NH₄Cl in methanol for ~ 15 sec, reaching a voltage of ~ 90V. This treatment does not affect the vast majority of the oxide area, but it penetrates through weak spots and etches the Ta underneath, thus reducing the number of flaws in the finished capacitor (9). The films were then anodized in the citric acid for a second hour at 230V. Thus the total soak period was twice the usual one.

Oxide thinning was done at room temperature in a vigorously stirred solution of 470g of 49% HF plus 190g of NH₄F (nearly saturated) (10). The etchant attacks the glass substrate as well as the Ta₂O₅ and Ta, so it became contaminated with numerous impurities as the experiment progressed, but this had no apparent effect. The etch time for each sample is given in Table II. After thinning and a long rinse in deionized water the samples were anodically back-etched again for ~ 10 sec.

This thinning procedure results in a very uniform oxide thickness, as judged by interference color, over the vast majority of the area. However, the HF-NH₄F etchant attacks flaws in the oxide at a much higher rate, creating pinholes, and then etches some of the Ta underneath. The NH₄Cl backetch is intended to reduce this problem, but it cannot be eliminated. The result is capacitors with very low breakdown voltages.

Table I. Anodization conditions for the first experiment

Anodization voltage (V)	Soak time (min)	Thickness (Å)
50	12.5	900
100	25	1800
150	37.5	2700
200	50	3600
250	62.5	4500
300	75	5400

Table II. Properties of the thinned samples

Dielectric etch time (min)	Dielectric thickness (Å)	Reanodization voltage (V)
0	4130	180
20	3430	150
30	2980	130
40	2370	105
45	2010	90

In order to reach the high voltages needed for this experiment, it was necessary to reanodize in citric acid after thinning. Each sample was reanodized for 10 min at a field of 4.4 MV/cm, which is 80% of the 5.5 MV/cm field which exists at the end of the soak period in a standard anodization. (During the constant-current part of the anodization the field is about 6 MV/cm). The reanodization grows new oxide in the weak spots, allowing the measurement to be made, but the field is not high enough to significantly affect the good oxide. This point is considered further in the Discussion section. The good oxide makes up nearly all the area, and hence dominates the capacitance measurement.

The oxide thickness after thinning was measured with the ellipsometer. The points fell on the same calculated curve as the previous samples, indicating that the oxide index of refraction is uniform within ± 0.04 despite the nonuniform nitrogen distribution. The thickness and reanodization voltage of each sample are given in Table II.

Measurements

Contact to the counterelectrode is made with a gold-plated, blunt-tipped spring probe which exerts very little force. There is no evidence of any damage by this probe, and measurements made on samples with etched patterns, which do not require such a probe, give essentially the same results. The probes are mounted in a Teflon block and connected via coaxial cable to the measurement system. The sample assembly is immersed in liquid nitrogen.

The measurement system is shown schematically in Fig. 2. The General Radio 1654 impedance comparator measures the magnitude and phase of the impedance difference, ΔZ , between the unknown capacitor and a variable RC standard using a small a-c signal. The signal was $1V_{rms}$ at 1 kHz for all samples except for the thinnest oxide ones, where it was $0.3V_{rms}$. The magnitude of the impedance difference is expressed as a percentage of the standard impedance, Z_0 . The phase

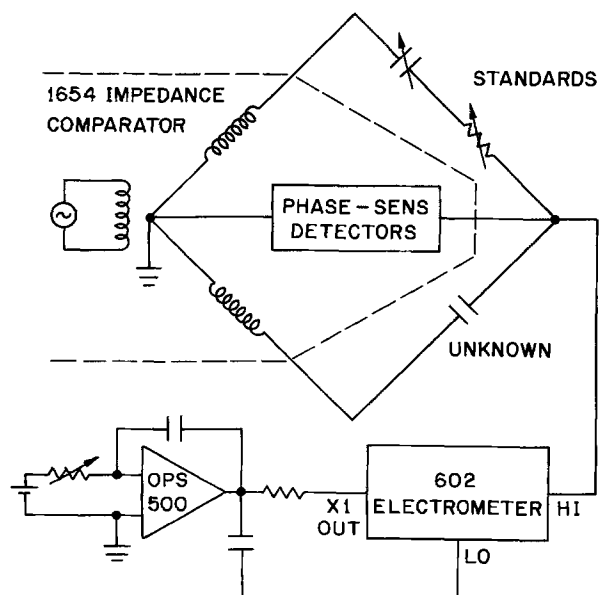


Fig. 2. Schematic diagram of the system used for $C(V)$ measurements.

angle is small enough ($\lesssim 0.002$) that $|\Delta Z/Z_0|$ is essentially equal to $|\Delta C/C_0|$, the normalized change in capacitance. A pair of Kepco OPS 500 power supplies, connected as a bipolar integrator, provide a variable-rate linear ramp voltage from -200 to $+200V$. The voltage rise rate was adjusted to give an approximately constant rate of increase of electric field for samples of all thicknesses. The rise rate has only a very small effect on the $C(V)$ curve (2) so precise adjustment is not necessary. The bias is applied across both the unknown and standard capacitors, but the air and mica standards have such a small voltage coefficient that it need not be considered.

The bias supply is also connected across the 1654 detector input. A large resistance in series with the supply is required to avoid shorting out the a-c signal. This resistance is provided by the Keithley 602 battery powered electrometer, with the bonus that the d-c current flowing to the capacitors is measured simultaneously. The 602 is connected in such a way that while its a-c impedance is high, producing negligible distortion of the capacitance measurements, the d-c voltage drop across it is very low.

To record a $C(V)$ curve the bias voltage is set to zero, and the impedance comparator is balanced by adjusting the standards. The voltage ramp is then started and the change in impedance recorded as a function of voltage on an X-Y recorder. In addition to the analog recording, the voltage and change in capacitance are also digitized and printed for later computer analysis. It is estimated that the over-all accuracy of the ΔC measurement is on the order of 0.01% of C_0 .

Application of a high voltage to a Ta film capacitor produces polarization, part of which decays only very slowly, with time constants the order of hours or even days. Thus it is not practical to measure the full voltage range on one capacitor. Rather, one capacitor is used for positive voltage and another for negative. In each case the measurement starts either at zero voltage or at a small voltage of the opposite polarity.

Typical data at 77°K are given in Fig. 3, traced directly from a pair (one + and one -) of X-Y recorder plots. The curve shows the change in capacitance from zero voltage, ΔC , normalized by the zero voltage capacitance, C_0 . The x-coordinate is voltage, with Ta positive to the right. These were typical capacitors with $V_A = 230V$ and $t_s = 1$ hr, measured at liquid nitrogen temperature with a 1 kHz, $1V_{rms}$ test signal and a 1V/sec bias rise rate. One sees that the change in capacitance is the order of $\pm 1\%$, and that it is highly asymmetric about zero voltage, with the asymmetry apparent even at very low voltage.

Interface Model

The asymmetry in the $C(V)$ curve shown in Fig. 3 suggests an interface effect. The MOS capacitor, for example, is highly asymmetric about the flatband point

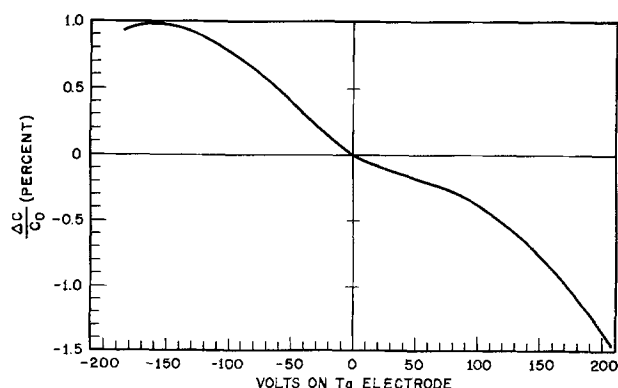


Fig. 3. Typical capacitance-voltage curve for a pair of capacitors anodized at 230V for 1 hr and measured at 77°K with a 1 kHz test signal and 1V/sec bias rise rate.

because the interface between conductive material and the depletion layer, which forms part of the insulator, moves in response to the d-c field. A similar situation has been reported by Smyth and co-workers in the case of Ta-Ta₂O₅ capacitors which have been heated at 300°-500°C and then measured at room temperature (11). Their observations are explained by noting that at the high temperature the Ta tends to extract oxygen from its oxide, leaving behind vacancies which can act as donors, doping the oxide in the region close to the Ta interface. If the partially localized states associated with these defects are occupied by electrons, the oxide in that region is conductive and it behaves as part of the Ta electrode. If the Ta is biased positively, electrons are removed from these states, and the oxide becomes insulating. Thus the insulating thickness increases when positive bias is applied, and the capacitance decreases.

This effect involves thermal activation of carriers from the defect states, and it disappears below about -40°C (11). Since the present measurements are at much lower temperature and the samples have not been heat-treated, we are definitely not seeing the same effect. However, one can imagine similar effects involving a different type of defect state, perhaps shallower in energy or with substantially higher density, such that thermal activation is not required. In the remainder of this section a general interface model is proposed, and predictions are derived from it which can be tested against experiment. We find a contradiction and thus are forced to conclude that the C(V) characteristic results from bulk, not interface, processes.

The model is shown schematically in Fig. 4. We assume that there exist defect states in the oxide near the Ta interface such that when they are occupied by electrons the oxide in that region is conductive. We define a conductive thickness, d_c , which is the order of 1% of the oxide thickness, d . This is an idealization, since in reality the conductivity must change gradually with position. To be specific one can, following Smyth *et al.* (11), define the interface as the plane at which the local capacitive admittance and local conductance are equal. The conductive thickness will in general depend on the temperature and test frequency, but these parameters are held constant during the present measurements.

The conductive layer thickness is determined by the density of electrons in the interfacial region and the density of defect states which can accommodate them. The density of electrons depends on the electric field, E , in the oxide, so d_c is a function of E , increasing when the Ta electrode is made more negative. For such a structure the capacitance per unit area is

$$C = \epsilon / (d - d_c) \approx (\epsilon/d) [1 + (d_c(E)/d)] \quad [1]$$

where ϵ is the dielectric constant. Changing the field from E_2 to E_1 causes a change in capacitance

$$\Delta C = C(E_1) - C(E_2) \approx (\epsilon/d^2) [d_c(E_1) - d_c(E_2)] \quad [2]$$

The normalized change in capacitance, which is the measured quantity, is thus

$$\frac{\Delta C}{C_0} \approx [d_c(E_1) - d_c(E_2)]/d = \Delta d_c/d \quad [3]$$

This equation is accurate for $d_c \ll d$.

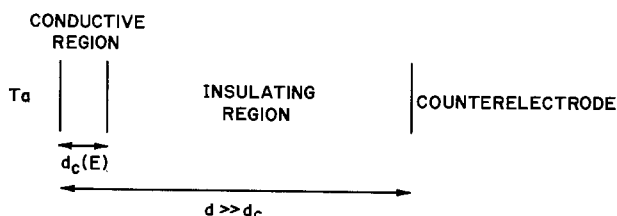


Fig. 4. Interfacial model for the capacitance-field dependence

The measured quantity is thus directly proportional to the change in d_c , with ΔC negative for an increase in field in the positive (parallel to anodization) direction. To account for the observed magnitude of change of C , d_c must be 2 or 3% of d for large negative (opposite to anodization) field, which is easily small enough to make Eq. [3] accurate. The change in d_c is determined by the change in field and by the local density of defect states, which is a function of energy and position. These are the only parameters which explicitly influence Δd_c . In particular, Δd_c does not explicitly depend on d . Thus Eq. [3] seems to indicate an inverse dependence on oxide thickness. However, the density of states is determined by conditions near the Ta interface during anodization and could conceivably vary with the time of anodization, and therefore with d . So to check the validity of Eq. [3] we must first determine the dependence of $\Delta C/C_0$ for a given change in field on d , and then establish whether or not the pertinent properties of the interfacial region change with oxide thickness. These experiments are discussed in the next section.

It has been assumed that the conductive layer is next to the Ta electrode. One could alternatively place it next to the counterelectrode. All the same arguments would apply except that conduction would have to be by positive holes instead of by electrons.

The model thus far is restricted to an infinitely conductive layer whose thickness is modulated by the field. It can be made completely general by allowing both the conductivity and the local dielectric constant near the interface to be modulated by the field. This general model is discussed in the Appendix. The result is, for our present purpose, the same as the simple model above, so reference will be made in the following to Eq. [3] rather than the more general Eq. [A-5].

Experimental Results

The first experiment described in the Sample Fabrication section serves to establish the dependence of $\Delta C/C_0$ on the oxide thickness, d . Six different values of d were produced by varying the anodization voltage. Using the thicknesses determined by ellipsometry the voltage scale of $C(V)$ curves was converted to an average field scale, using $E = V/d$ as the average field. For each thickness and each voltage polarity data from two capacitors were averaged to reduce the effect of sample-to-sample variation. Thus four capacitors were used for each $C(E)$ curve. The curves from all six anodization voltages are given in Fig. 5. They are essentially identical for positive field (parallel to anodization). The two thinnest ones exhibit $\Delta C/C_0$'s for negative field (opposite to anodization) which are $\sim 10\%$ greater than the thicker ones.

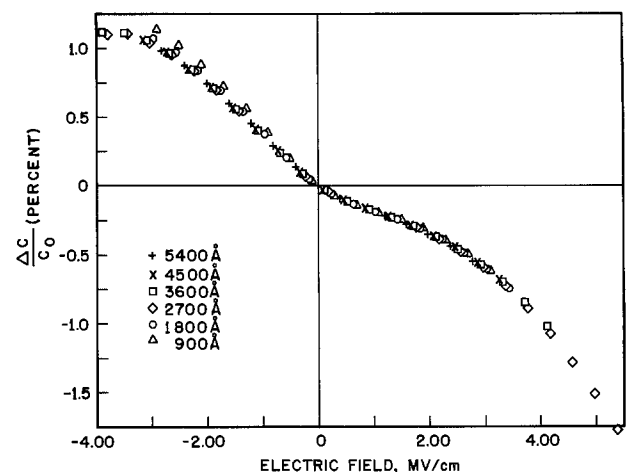


Fig. 5. Capacitance-field dependence for the capacitors of Table I, made with six different anodization voltages.

The inverse dependence on d indicated by Eq. [3] would predict a factor of six difference between the curves for the thinnest and thickest oxides. The observed difference is negligible compared with this factor, so one can for present purposes conclude that the $C(E)$ characteristic is independent of oxide thickness. Recalling Eq. [3], this result indicates that if an interface effect is involved in the $C(E)$ characteristic, then $d_c(E_1) - d_c(E_2)$ must be proportional to d , and hence to the anodization voltage. So in order for the interface hypothesis to be correct, one must assume this proportionality as a second hypothesis.

It was argued before that d_c is determined by local conditions near the interface. These conditions are themselves established during anodization, specifically near the end of the soak period. Once the capacitor is completed these conditions do not change, so d_c for a given field is fixed. One can determine whether d_c depends on anodization voltage by changing d using a method which does not change these local conditions. This was accomplished in the second experiment described in the Fabrication section using chemical thinning of the oxide.

Equation [3] requires that if interface effects influence the $C(E)$ characteristics, then $\Delta C/C_0$ for a given field should be larger than in Fig. 5 in inverse proportion to the fraction of the original oxide thickness remaining. Figure 6 shows that this is definitely not the case. The curves for four different degrees of thinning, up to removal of more than half the initial thickness, are essentially the same as the curve for a sample which was not thinned. Thus the second hypothesis is not obeyed, Eq. [3] does not agree with the true behavior, and the interface model is not correct. Using the general model expressed by Eq. [A-5] leads to the same result. One is therefore forced to conclude that the variation of capacitance with d-c field is produced by bulk effects, that is, physical processes which are distributed at least approximately uniformly through the oxide thickness. The significance of this conclusion is discussed further in the next section.

Discussion

The necessity of reanodization in the thinning experiment casts some doubt on the result. One can imagine that during the reanodization the atoms near the Ta interface might rearrange themselves sufficiently to make the conductive thickness, d_c , the same as it would be for a sample anodized to the smaller thickness and not thinned. That this is extremely unlikely can be shown by several different arguments, some of which are given here.

First, the ionic motion which allows anodization depends exponentially on the field, so a small reduction

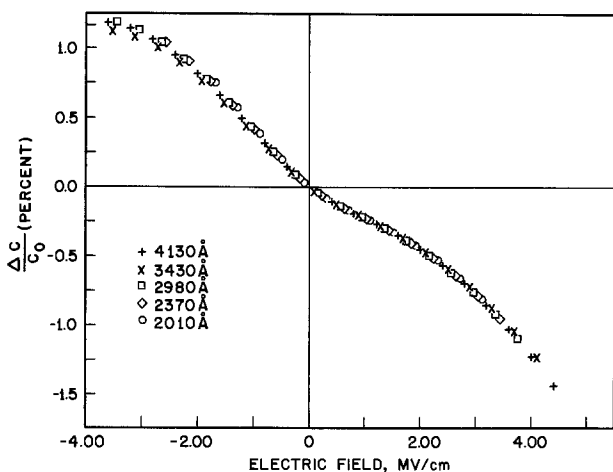


Fig. 6. Capacitance-field dependence for the capacitors of Table II. All oxides were initially 4130Å thick and four of them were chemically etched to the thicknesses shown.

in the field causes a large reduction in the current density. At 80% of the final anodization field the current is very small, so not much rearrangement of atoms is expected. A check of this assertion is provided by a second thinning experiment in which the sample was reanodized at only 50% of the usual, final anodization field. The result was the same: the $C(V)$ characteristic was the same as that of a sample from the same batch which was anodized to the smaller thickness and not thinned.

A similar argument can be given from a different point of view. The current during reanodization was recorded, so the total charge transferred, and hence an upper bound on the total oxide grown, is known. If we suppose for the moment that the current flowed uniformly over the oxide surface, then the amount of new oxide grown was less than about 11Å. But the current could not have been uniform. Most of it must have gone to the pinholes; otherwise they would not have been repaired and the measurement could not have been made. So a realistic upper bound on the amount of new oxide grown in the "good" oxide area would be perhaps 1Å average thickness. To destroy the effect in question, a layer of $\sim 2\%$ of the total thickness, 40-70Å, would have to be rearranged, a highly unlikely result.

As a third argument, we note that if the interface model (Eq. [3]) were correct the slope at zero field of the $C(E)$ curve should be greater for a thinned sample than for one not thinned. The reanodization could reasonably be considered as an extension of the usual anodization soak period. But increasing the soak time causes the slope of $C(E)$ to increase (2), not decrease. So reanodization should tend to amplify the difference between a thinned capacitor and one not thinned, not eliminate it.

It is thus highly unlikely that reanodization would significantly affect the local conditions near the interface. Moreover, if it did, the effect would be the opposite of what is required to destroy the meaning of the experiment. So the conclusion stands: the $C(E)$ characteristic is produced by bulk oxide effects.

The detailed nature of these effects is not clear, but the fact that the $C(E)$ characteristic is asymmetric requires that they be anisotropic. This is somewhat surprising, since the oxide is known to be crystallographically amorphous. Asymmetry in d-c current-voltage curves has been reported by many investigators (12), but there is considerable disagreement as to the cause of this asymmetry. Indeed, some authors deny that it exists at all in properly prepared samples (1, 13). The d-c conduction experiments surely do not demonstrate conclusively that the bulk oxide is anisotropic. Thus, to the author's knowledge, the present capacitance data is the first strong evidence of such anisotropy. Ord, Hopper, and Wang (14) reported from ellipsometric work a linear dependence of oxide thickness on field over a narrow range of field, with the proper sign to account for these results. However Cornish and Young (15), using a similar technique, showed that the dependence is actually quadratic. Both studies used H_2SO_4 as the counterelectrode, which precludes applying negative bias, but it is reasonable to assume that the quadratic dependence is symmetric. Those measurements were at room temperature.

Ord, Hopper, and Wang (14) also reported a large negative dependence of 1 kHz dielectric constant on field (-2.4% per MV/cm). Capacitance-voltage curves taken at room temperature with the samples of the present study indicate that $\Delta C/C_0$ does indeed approach linearity at high field ($\gtrsim 4$ MV/cm), with a slope approaching the above value. This slope, however, does not extrapolate to low fields, and it does not appear to be directly related to the much smaller ($\sim 0.3\%$ per MV/cm) slope observed at low temperature (2). The latter slope, as previously noted, exists even at very low field.

Cornish and Young (15) demonstrated that the index of refraction with an applied field is uniaxially aniso-

tropic, with the index perpendicular to the field (n_o) larger than the index parallel to the field (n_e). The present work indicates a very different kind of anisotropy, namely that the low frequency dielectric constant with a d-c field parallel to the forming direction is less than with a d-c field antiparallel to it. No such effect was observed in the ellipsometric work (15), so it is probable that the modes which are responsible involve ionic motion, which is too slow to affect the index of refraction at visible light frequencies.

In the amorphous oxide the surroundings of some of the ions are asymmetric. When a field is applied the displacement of a given ion depends on the shape of the barrier on the downfield side. If the potential in that direction rises rapidly (a high barrier), the displacement is less than if it rises slowly (a low barrier). Hence an ion in an asymmetric site makes a smaller contribution to the polarization if the barrier downfield is high than if it is low.

The motion of ions during anodization is exceedingly complex and is not understood (16, 17). If the dynamics are such that there is a preference for ions to be located in sites with a high barrier on the downfield side, then asymmetry of $C(E)$ in the observed direction would result. There is no independent evidence that such a preferred orientation exists, but the following arguments suggest a way in which it might develop.

An ion in an asymmetric site will stay there longer during anodization if the barrier downfield is high than if it is low. Pringle (16) has suggested as a result of work with radioactive markers that the charge transfer event does not consist simply of one ion jumping between adjacent sites, but rather involves simultaneous motion of a small group of both Ta and O ions. In this view, when an ion leaves its site the surrounding ions are rearranged and the symmetry of the site is likely to be changed. A site with a low barrier downfield is more likely to lose its ion and therefore is more likely to be rearranged. Thus its lifetime is shorter and, in equilibrium, the density of such sites is expected to be less than that of sites with a high barrier downfield. So, based on this simple physical picture of ionic current flow, one expects to find a preferred orientation in the direction required to explain the observed asymmetry.

Summary

It has been shown that the low temperature capacitance-field characteristic of Ta film capacitors is independent of oxide thickness and of chemical thinning of the oxide. The characteristic is asymmetric, suggesting that an interface mechanism is likely. A general interface model, however, cannot account for the experimental results. One is therefore forced to conclude that a bulk mechanism is responsible. That is, the variation of the capacitance must result from processes which are distributed throughout the oxide, not localized near the metal interfaces. It is suggested that structural anisotropy resulting from the dynamics of ionic conduction during oxide growth produces the observed asymmetry. To the author's knowledge, this is the first strong evidence of such anisotropy in amorphous Ta₂O₅.

Acknowledgments

Thanks are due to O. J. Duff and R. G. Fekula for their assistance with the $C(V)$ equipment and measurements, to J. M. Morabito for the Auger analysis, and to R. C. Fulton for the use of her ellipsometry program.

Manuscript received May 21, 1975. This was Paper 2 presented at the San Francisco, California, Meeting of the Society, May 12-17, 1974.

Any discussion of this paper will appear in a Discussion Section to be published in the June 1976 JOURNAL. All discussions for the June 1976 Discussion Section should be submitted by Feb. 1, 1976.

Publication costs of this article were partially assisted by Bell Laboratories.

APPENDIX

Referring again to Fig. 4, the conductive layer has thickness d_c , dielectric constant ϵ_c , and conductivity σ_c . All of these depend on the field, E , as well as local variables including but not limited to the density of defect states. We retain the idealized sharp interface between $\sigma > \omega\epsilon$ (conductive) and $\sigma < \omega\epsilon$ (insulating). The insulating layer has parameters d_i , ϵ_i , and σ_i . The total thickness is constant, $d = d_i(E) + d_c(E)$, and we neglect any field dependence of ϵ_i and σ_i .

The model thus consists of two capacitors in series, each with admittance per unit area

$$Y_j = (j\omega\epsilon_j + \sigma_j)/d_j \quad [\text{A-1}]$$

The total admittance is

$$Y \equiv Y_c Y_i / (Y_c + Y_i) \quad [\text{A-2}]$$

and the normalized change in admittance on changing the field from 0 to E is

$$\begin{aligned} \Delta Y/Y_0 &= [Y(E) - Y(0)]/Y(0) \\ &= \frac{Y_i(E)}{Y_i(0)} \cdot \frac{1 + Y_i(0)/Y_c(0)}{1 + Y_i(E)/Y_c(E)} - 1 \quad [\text{A-3}] \end{aligned}$$

We know that $d_c \ll d_i$, $\sigma_c \cong \sigma_i$, and $\epsilon_c \ll \epsilon_i$. So $Y_c \gg Y_i$, and we find

$$\begin{aligned} \frac{\Delta Y}{Y_0} &\approx \frac{Y_i(E)}{Y_i(0)} \left[1 + \frac{Y_i(0)}{Y_c(0)} - \frac{Y_i(E)}{Y_c(E)} \right] - 1 \\ &= \frac{Y_i(E) - Y_i(0)}{Y_i(0)} \\ &\quad + Y_i(E) \left[\frac{1}{Y_c(0)} - \frac{Y_i(E)}{Y_i(0)} \frac{1}{Y_c(E)} \right] \quad [\text{A-4}] \end{aligned}$$

Putting in the definition of Y_j yields

$$\Delta Y/Y_0 \approx [d_c(E)f_1(E) - d_c(0)f_2(0)]/d_i(E) \quad [\text{A-5}]$$

where

$$f_1(E) = 1 - [d_i(0)/d_i(E)][j\omega\epsilon_i + \sigma_i]/[j\omega\epsilon_c(E) + \sigma_c(E)]$$

and

$$f_2(0) = 1 - [j\omega\epsilon_i + \sigma_i]/[j\omega\epsilon_c(0) + \sigma_c(0)]$$

If $\sigma_c \rightarrow \infty$ we recover Eq. [3] for the simplified model. Note that within the accuracy of this discussion $d_i = d$, making f_1 and f_2 the same function. This function, f , is dependent on the constants ω , ϵ_i , and σ_i , and the functions ϵ_c and σ_c . These functions and d_c are determined by the applied field and by local structural and chemical conditions. Neither f nor d_c is explicitly a function of the oxide thickness. Thus just as in the simple model we apparently have an inverse dependence on oxide thickness, which might be modified if local properties (including but now not limited to the density of defect states) near the interface are dependent on how much oxide has been grown.

REFERENCES

1. M. Nakamura, J. Yamazaki, W. Endou, and Y. Nishimura, *Electronics and Communications in Japan*, **55C**, 107 (1972).
2. Peter W. Wyatt, Paper 77 presented at the Electrochemical Society Meeting, Toronto, Canada, May 11-16, 1975.
3. Robert D. Huttemann, J. M. Morabito, and D. Gerstenberg, *IEEE Trans., PHP*, **11**, 67 (1975).
4. P. N. Baker, *Thin Solid Films*, **14**, 3 (1972).
5. L. Young, "Anodic Oxide Films," Academic Press, New York (1961).
6. R. T. Simmons, P. T. Morzenti, D. M. Smyth, and D. Gerstenberg, *Thin Solid Films*, **23**, 75 (1974).
7. F. L. McCrackin, E. Passaglia, R. R. Stromberg, and H. L. Steinberg, *J. Res. Natl. Bur. Std.*, **67A**, 363 (1963).
8. D. G. Muth, *J. Vacuum Sci. Technol.*, **6**, 749 (1969).
9. R. W. Berry, P. M. Hall, and M. T. Harris, "Thin Film Technology," p. 278, Van Nostrand Reinhold Co., New York (1968).

10. J. P. S. Pringle, *This Journal*, **119**, 482 (1972).
11. D. M. Smyth, G. A. Shirn, and T. B. Tripp, *ibid.*, **110**, 1264 (1963).
12. See, for example, M. W. Jones and D. M. Hughes, *J. Phys. D*, **7**, 112 (1974), and the many references given therein.
13. J. P. Sitarik, Paper 27, presented at Electrochemical Society Meeting, New York, May 4-9, 1969, Ext. Abstr., p. 66; J. P. Sitarik, PhD thesis, Lehigh University, 1970. These reports concern capacitors made on Ta-Al alloy films. Similar results were found by Sitarik with β -Ta in unpublished work.
14. J. L. Ord, M. A. Hopper, and W. P. Wang, *This Journal*, **119**, 439 (1972).
15. W. D. Cornish and L. Young, *Proc. Roy. Soc. London*, **A335**, 39 (1973).
16. J. P. S. Pringle, *This Journal*, **120**, 398 (1973).
17. J. P. S. Pringle, *ibid.*, **120**, 1391 (1973).

Epitaxial Deposition of Silicon in Deep Grooves

R. K. Smeltzer*¹

Texas Instruments, Inc., Semiconductor Research and Development Laboratories, Dallas, Texas 75222

ABSTRACT

An epitaxial silicon growth technique to preferentially deposit into and refill deep, vertically walled, orientation-dependent etched grooves in (110) silicon was developed. All of the common silicon chlorides can be used with the addition of HCl to the deposition system. A mask on the top surface of the substrate is not needed with this selective deposition technique. After refill of the deep grooves, even with variable depths, a planar surface is created. A thermodynamic analysis of the experimental conditions was carried out, and it shows that all of the various experimental conditions successfully used are about equally shifted from equilibrium.

Selective deposition into depressions or onto a surface to create protrusions has been investigated because of its application to devices and circuits. Also, selective epitaxy studies have been useful in efforts to understand deposition processes. In general, chemically vapor deposited layers tend to contour the surface of a bare substrate, although other factors, such as the orientation dependence of deposition rate may produce a deposited surface contour altered from the original surface contour. The only selective silicon deposition technique which is in use requires a mask on the substrate to prevent growth except on the substrate within mask openings. Selective growth occurs at low supersaturations of the desired material, and for the case of silicon deposited from a chloride source, the addition of HCl to the system has been used (1, 2).

The basic purpose of this paper is to show that well-controlled preferential deposition into deep surface depressions can be achieved, at least for certain geometrical configurations and a particular substrate orientation, without use of a mask on the substrate. A maskless epitaxial technique has been developed to preferentially deposit defect-free silicon into very deep, narrow, orientation-dependent etched grooves in a (110) silicon substrate with very little deposition on the top surface of the slice. The present purpose for the development of this technique is the fabrication of vertical p-n junction solar cells (3).

A previous investigation (4) had demonstrated that preferential epitaxial deposition into shallow surface depressions in a bare substrate could be achieved by a particular choice of gas phase composition in the reactor. It was shown that with concentrations of SiCl₄ in H₂ higher than the composition at which the maximum growth rate occurs on a flat surface, wide shallow depressions will tend to fill to produce a flat surface. A basic limitation of the high SiCl₄ concentration approach to preferential deposition is that the Si/Cl ratio is fixed. The work discussed in this paper shows that the use of low silicon halide concentrations with the addition of HCl to the reactor offers a high degree of

control for preferential deposition into deep surface depressions in (110) silicon wafers.

Experimental Details

The epitaxial deposition experiments described in this paper were carried out with 1 ohm-cm (110) silicon substrates, which had 2 cm long, vertically walled, orientation-dependent etched grooves. To produce the substrates, conventional photolithographic methods were used to open lines in thermally grown oxide on the slices, and the silicon was etched in a nominal 42.5% KOH:H₂O solution. The oxide etch mask was removed after the orientation-dependent etch. The grooves were oriented approximately parallel to the set of intersections between one set of (111) planes, which intersect the surface vertically, and the (110) surface of the slice. An important factor in the achievement of reproducible epitaxial depositions is the accurate control of the groove width. Since it has been recently shown (5) that the undercutting etch rate of the nominal (111) walls of grooves in (110) silicon is a very sensitive function of the misorientation of the walls, accurate mask alignment to about $\pm 0.2^\circ$ was required. The etched grooves occupied a 4 cm² area in the center of 1½ in. diameter slices with a packing density of 500 grooves/cm. Typically, the grooves were 100 μ m deep and 10 μ m wide, although other dimensions were also used to characterize the effects of groove geometry on the epitaxial deposition process. For a later discussion, it is important to note that the ends of the grooves are terminated by one of the (111) planes which makes a 35° angle with the (110) surface. Consequently, near the ends of the grooves, the groove depth linearly decreases to zero.

The depositions discussed in this paper were done in an rf heated reactor operated at atmospheric pressure. The vertical deposition chamber is a 9.5 cm diameter fused silica tube. The gas inlet is at the top and the outlet is at the bottom. A bottom plate, which seals to the reaction tube, has a feedthrough for rotation of the graphite susceptors. Two different susceptor arrangements were used with similar results. In one case, the substrates were located on the top of small cylindrical susceptors, which rotated around their own axis and around the axis of the reaction tube. Three susceptors,

* Electrochemical Society Active Member.

¹ Present address: Department of Electrical Engineering, Princeton University, Princeton, New Jersey 08540.

Key words: silicon deposition, selective epitaxy, preferential deposition.

whose total cross-sectional area occupied 60% of the cross-sectional area of the reaction tube, were used. With this arrangement, the substrates directly faced the incoming gas flow. In the other susceptor arrangement, the substrates were located on the side of a solid susceptor such that the wafers were tilted about 15° from the vertical. The cross section of the bottom of the solid susceptor occupied 87% of the cross-sectional area of the reaction tube. This latter susceptor design was more convenient, and it was used for most of the deposition experiments.

The adjustment of the Si/Cl ratio, which was done by the addition of HCl to the H_2 -silicon chloride systems, is the key factor which produces preferential deposition in deep grooves. Although the epitaxial refill process was demonstrated with $SiCl_4$, $SiHCl_3$, and SiH_2Cl_2 , the H_2 - $SiHCl_3$ -HCl system was more extensively investigated. Prior to deposition, the substrates were heated in H_2 at $1220^\circ C$ for 5 min. This prebake, rather than a HCl vapor etch, was used because a vapor etch preferentially removed silicon from the top corners of the grooves and produced nonvertical groove walls. Since the groove walls are etched surfaces, the absence of the vapor etch should not be detrimental to the deposition of defect-free material. After the H_2 bake, the substrate temperature was adjusted and deposition started by the simultaneous introduction of metered amounts of $SiHCl_3$ and HCl. The effect of substrate temperature, which was measured with an optical pyrometer and corrected for the emissivity of silicon and a $10^\circ C$ error due to the reactor wall, and gas flow rates are discussed in the next section.

Experimental Results

Depositions from the H_2 - $SiHCl_3$ -HCl system onto deep grooved slices were investigated with a variety of gas flow conditions. For comparison purposes, a few depositions were also carried out with no HCl in the reactor, and Fig. 1 shows a slice cross section from a 4 min epitaxial deposition done near $1140^\circ C$ with 0.45% $SiHCl_3$ in H_2 . The cross section shown in Fig. 1 and the cross sections in other photomicrographs except Fig. 2b are from slices with grooves with a $20\ \mu m$ center-to-center spacing. The photomicrographs show (111) cleavage planes which are about 19.5° from the perpendicular to the grooves. The cross sections were briefly etched to reveal the boundary between the p-type substrate and the n-type deposit. Not surprisingly, conventional deposition conditions with a deep grooved slice yielded a faster growth rate on and near the top of the silicon columns than on the side walls of the grooves away from the top. With a longer deposition

time, the silicon deposit bridged the grooves at the top and left large voids in the deposit. Note, however, that significant deposition did occur on the groove bottoms,

In contrast to the result illustrated by Fig. 1, it was demonstrated that preferential deposition into deep grooves in (110) silicon can be done with the addition of HCl to the common silicon halide systems. With HCl added, etching or a reduced growth rate occurred near the top of the grooves as in conventional silicon depositions onto a flat substrate with HCl added to the system. However, the addition of HCl to the system did not produce a reduced growth rate near the groove bottoms. Near the critical conditions for which no net deposition occurs on a flat substrate, it was possible to completely refill deep grooves without voids. The photomicrographs in Fig. 2 show two stained cross sections from refilled slices. Neither defect-sensitive etches nor x-ray topographical studies revealed defects in refilled epitaxial silicon deposited with the critical gas concentrations discussed below.

A particularly important characteristic of refilled slices is the planar top surface of the deposit, as shown by both examples in Fig. 2. A surface perturbation does not occur even near a shallow groove such as shown in Fig. 2a. A planar surface occurs because of the very small amount of silicon deposited on the top of the silicon columns during the refill. In addition, cross sections from slices with grooves only partially refilled show facets at the top corners of the grooves

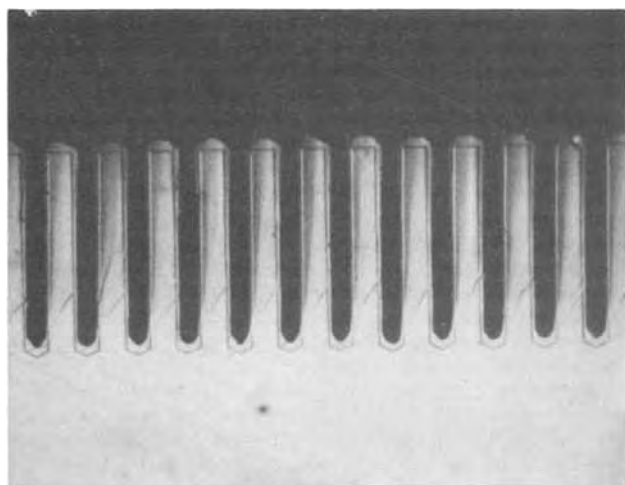


Fig. 1. Stained cross section from a p-type (110) deep grooved substrate with a 4 min, n-type epitaxial layer deposited at $1140^\circ C$ from 0.45% $SiHCl_3$ in H_2 . The groove center-to-center spacing is $20\ \mu m$.

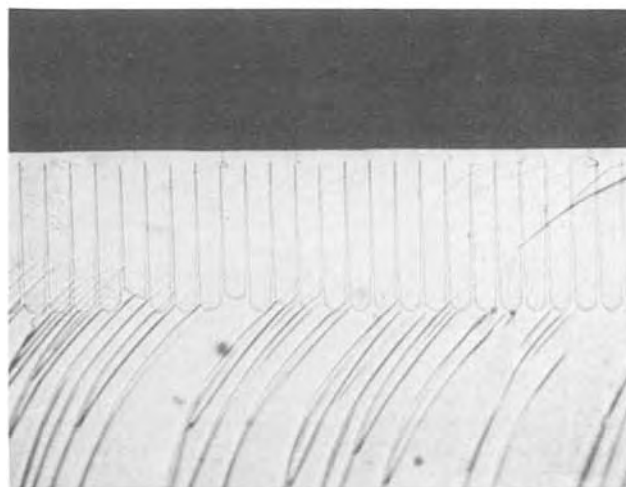
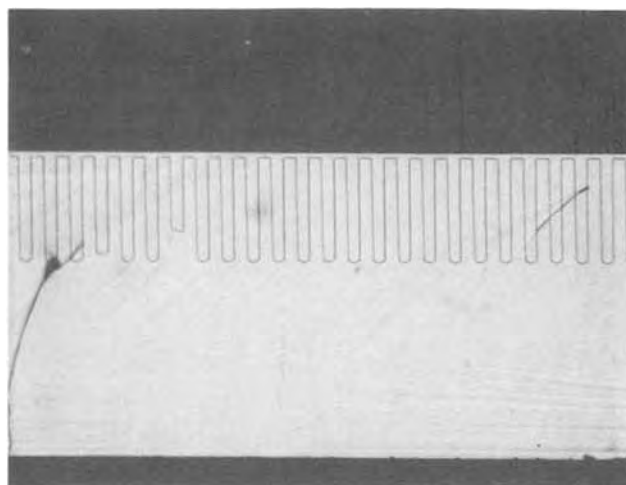


Fig. 2. Stained cross sections from two epitaxially refilled silicon slices. Deposition conditions were: (a, top) 45 liters/min H_2 , 0.2 liter/min $SiHCl_3$, 1.0 liter/min HCl, $1140^\circ C$ substrate temperature and (b, bottom) 45 liters/min H_2 , 0.3 liter/min $SiHCl_3$, 1.2 liters/min HCl, $1140^\circ C$ substrate temperature. Groove center-to-center spacings are: (a) $20\ \mu m$ and (b) $10\ \mu m$.

similar to those in Fig. 1; with HCl added to the system, however, the facets terminate very near the top corners of the silicon columns during most of the deposition. After deposition has completely filled the grooves, growth predominately occurs to fill in the volume between these facets. The result is a planar top surface about 5 μm above the original substrate surface. This tendency to produce a planar (110) surface after refill may also be related to a previous observation (6), which indicated that (110) planes yield a more planar surface in selective epitaxy than other common planes.

The refill of vertically walled grooves without voids suggests either that the deposition rate on the walls increases with depth into the grooves or that growth on the groove bottom is much faster than growth on the walls. To investigate the growth characteristics within the grooves, depositions during which the dopant was cycled on and off were done. Figure 3, which is a photomicrograph of a stained cross section from a deposition during which the dopant was cycled on and off every 6 min, shows that, in fact, the deposition rate on the groove walls does increase with depth. Figure 3 shows six distinct regions, and the growth rate within the grooves, except near the bottoms and the tops, appears to increase approximately linearly with depth. A planar top surface occurred during the fifth 6-min interval of growth. To determine the effect of small temperature variations on the growth within grooves, one deposition with cycled doping was done with a temperature gradient across the substrate. Experimentally, the temperature gradient was obtained by slightly elevating the substrate from the susceptor at one point. It was observed that the slope of the growth profiles was strongly temperature dependent, and consequently, as discussed below, the refill process itself is very temperature sensitive.

The deposition characteristics of the epitaxial refill process were also investigated with regard to the effect of different groove dimensions. A few substrates with 90 μm deep grooves were found to contain grooves with widths in the range from 9 to 30 μm . From photomicrographic measurements, it was estimated that the deposition time required to completely fill variable width grooves is approximately proportional to the width.

In contrast to the variable width case, it was found that for grooves of equal width, the time needed to completely fill grooves of variable depth is approximately independent of the depth. It was observed, for example, that substrates with 200 μm deep grooves require at most a 10% longer deposition time to fill the

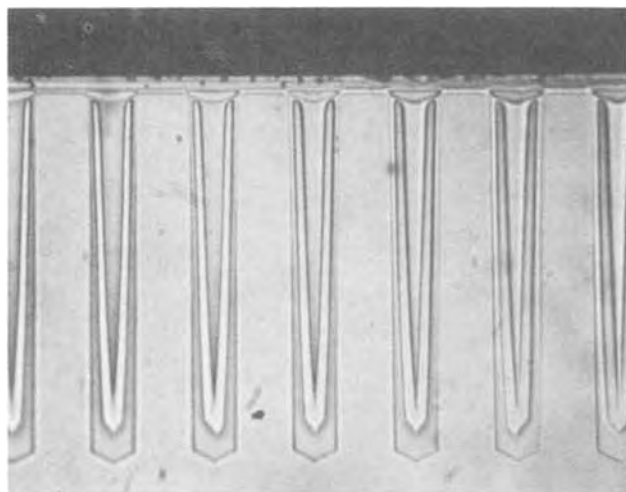


Fig. 3. Cross section from a refilled silicon slice with deposition profiles obtained by dopant alternation every 6 min and subsequent staining of the cross section. The groove center-to-center spacing is 20 μm .

grooves than substrates with 100 μm deep grooves. It was also found that for substrates with 100 μm deep grooves, no top surface perturbation results from the presence of a few shallow grooves. Additionally, with dopant alternation, it was observed that the deposition rate was faster on the walls near the bottom of deep grooves compared with shallow grooves, and by the time the grooves were almost filled, an equal volume of silicon was needed to fill the remaining volume in both deep and shallow grooves. Figure 4 illustrates the observed depth independence of the epitaxial refill process more dramatically. This photomicrograph is from a cross section near the edge of a 2 cm \times 2 cm array of grooves, where the groove ends are terminated by one of the (111) planes which make a 35° angle from the (110) surface. The grooves shown in Fig. 4 are therefore not uniformly shallow for any distance. Side wall growth rate measurements taken from this refilled slice are, however, consistent with measurements taken from other slices with shallow grooves extending over long distances. Figure 4 also shows that the initial growth rate on the bottom of terminated grooves was the same as the initial growth rate on the side walls near the bottom; this is understandable since both surfaces are (111)-type planes. In contrast, the growth rate in nonterminated, double faceted grooves was initially faster on the bottom than on the side walls. The depth independence of the epitaxial refill process is important because top surface planarity can be achieved even with variable depth grooves within one substrate.

The epitaxial depositions discussed above were done with the H_2 - SiHCl_3 -HCl system at 1140°C. Various concentrations of SiHCl_3 up to 2.4% were used, and, in all cases, a critical HCl concentration was found which produced defect-free refill. Figure 5, which gives the HCl/ SiHCl_3 concentration ratio as a function of the SiHCl_3 concentration, summarizes the experimental conditions which were used. The solid circles represent the conditions which yielded good refilled silicon; these gas concentrations were routinely used for refill depositions. The open circles represent deposition conditions which did not produce good refill. With excessive HCl the deep groove deposition was very slow and etching of the top surface of the substrate occurred. With too little HCl, the deposition rate near the top of the grooves was too fast and voids were left in the refilled silicon. It was not possible to define a critical range for the HCl/ SiHCl_3 parameter at any SiHCl_3 concentration, and this suggests that, if a critical range exists, it is within the reproducibility of flow meter settings. From the depositions with the various SiHCl_3 concentrations, it was found that the adjustment of the Si/Cl ratio by the addition of HCl to produce defect-free silicon, always resulted in the same deposition time. About 40 min was needed with each of the four, well-established deposition conditions given in Fig. 5. On this basis it was concluded that no increase in epitaxial refill rate can be obtained with higher silicon chloride concentrations. The effect of the total H_2 gas flow on the refill process was also determined from a few ex-

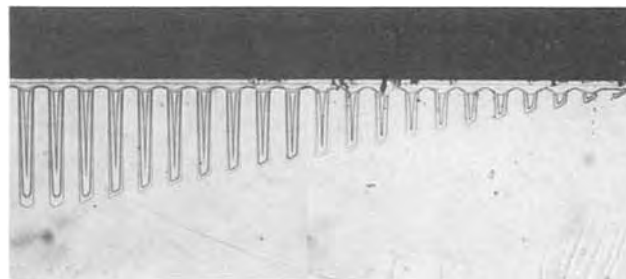


Fig. 4. Cross section from a refilled slice near the groove end terminations to illustrate the groove depth independence of the epitaxial refill process.

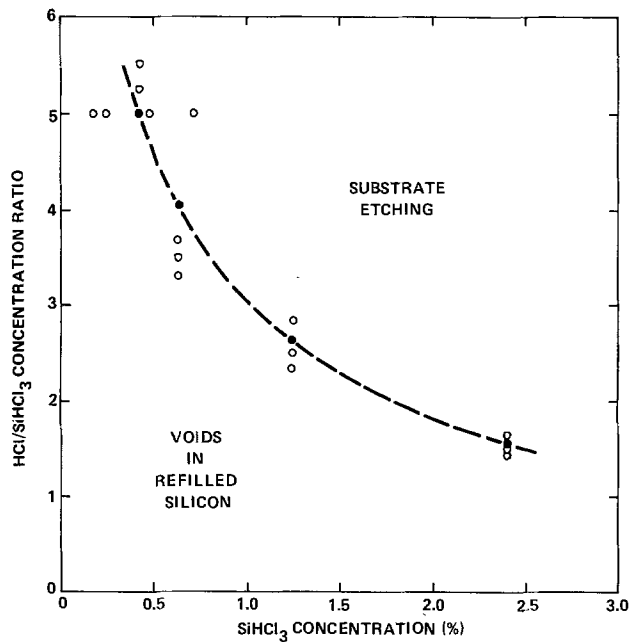


Fig. 5. Deposition conditions used for epitaxial refill experiments at 1140°C with 45 liters/min H₂. Four critical gas concentrations, defined by ●, refilled grooves without producing voids in the deposited silicon or etching of the substrate. The grooves were 2 cm long, 10 μm wide, and 90 μm deep.

periments. Total H₂ flow rates greater than or less than about 45 liter/min reduced the refill deposition rate.

The cross sections shown in Fig. 6 are representative of the effect of deposition temperature variations on the epitaxial refill process. For a particular set of gas concentrations which produced defect-free silicon at a particular deposition temperature, a higher temperature produced a faster deposition rate near the top of the substrate and left voids in the refilled silicon. Conversely, a lower temperature tended to produce an etching condition and the refill rate was slow. From examinations of slice cross sections it appeared that a low substrate temperature was equivalent to an excess of HCl and that a high temperature was equivalent to a deficiency of HCl.

In addition to the use of SiHCl₃, SiCl₄ and SiH₂Cl₂ were evaluated for epitaxial refill depositions. The H₂-SiCl₄-HCl system near 1200°C yielded results similar to the H₂-SiHCl₃-HCl system at about 1140°C. Similar deposition times and characteristics were obtained. In an effort to reduce the deposition temperature, H₂-SiH₂Cl₂-HCl was also investigated for refill depositions. Deep grooves can be filled without voids near 1080°C; however, a planar top surface was not obtained, at least for depositions terminated with a 10 μm, average film thickness above the original substrate surface. Deposition times are about the same with SiH₂Cl₂ as with the other halides. The deposition temperature is much less critical with SiH₂Cl₂, and a 10°C variation does not appear to affect the refill characteristics. The usefulness of SiH₂Cl₂ for refill depositions may be limited, however, by the nonplanar surface obtained after the grooves are filled.

Discussion

From the experimental observations, which are summarized in the previous section, insight into certain features of the epitaxial refill process and an understanding of the role of some parameters have been obtained. There is evidence that the thermal conditions in the substrate are important from two viewpoints. First, as in any silicon halide deposition system, the Si/Cl ratio near the substrate is a very sensitive function of the substrate temperature. As a consequence, the epitaxial refill process is very temperature sensitive, especially with the use of SiCl₄ and SiHCl₃. In

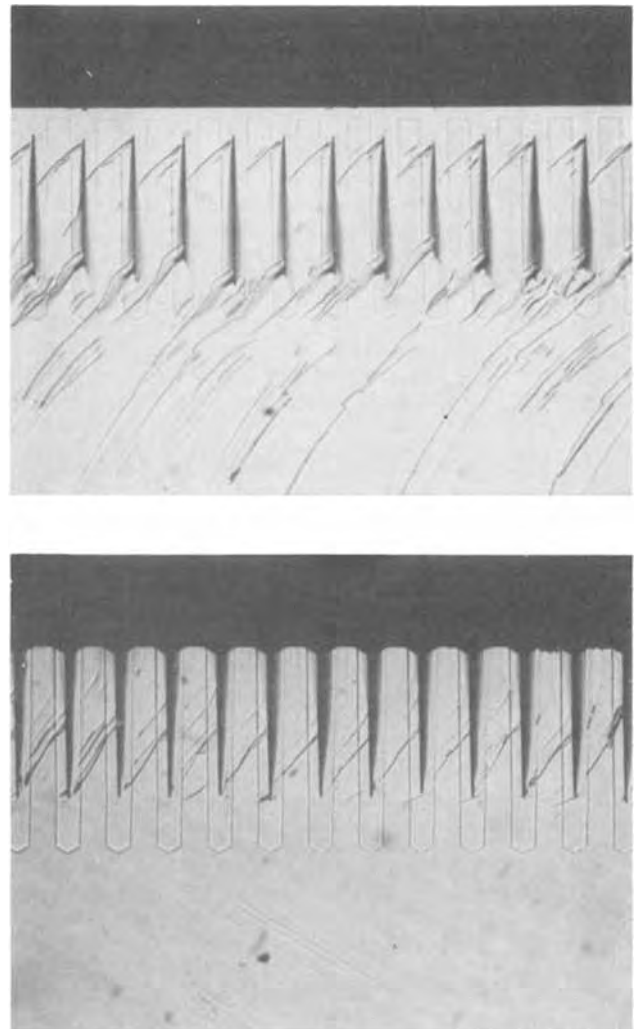


Fig. 6. Cross sections from silicon slices after deposition at two different temperatures with critical gas concentrations for 1140°C (a, top) 1150°C and (b, bottom) 1130°C.

agreement with previous observations (7, 8) from conventional epitaxial studies, however, refill from SiH₂Cl₂ is much less temperature dependent than refill with the other chlorides. Second, there is evidence which suggests that the temperature gradient within the substrate is important in the refill technique. Refill deposition experiments in both a horizontal reactor and a vertical domed reactor with the gas inlet at the bottom did not produce deposited silicon without voids. Groove wall deposition profiles observed on samples from experiments done in a horizontal and a domed reactor showed that the growth rate on the groove walls did not measurably increase with depth into the grooves. It is hypothesized that the reactor used for the successful refill experiments produces a larger temperature gradient in the groove walls than the other two reactors, since the incoming gas impinges directly, although not perpendicularly for one of the susceptor arrangements, onto the substrates. It is concluded, therefore, that the temperature distribution within the deep grooved substrate is critical to the epitaxial refill process, and that a large temperature gradient such that the groove bottoms are at the highest temperature is required to produce defect-free refilled silicon.

The adjustment of the Si/Cl ratio by the addition of HCl to the reactor is the key factor in the epitaxial refill technique. Based simply on the observations, it appears that the HCl tends to preferentially attack corners. More significant, however, may be that the growth conditions used for the refill depositions should produce silicon transport from the top of the substrate down into the grooves. From an analysis (9) which

gives the silicon content in the gas phase as a function of the Cl/H ratio and from the data in Fig. 5, the transport direction, which is the direction to lower the Si/Cl ratio, is from low temperature to high temperature for the deposition conditions used in this work. If the gas conditions are stagnant within the deep grooves, then deposition at the bottoms would act as a driving force for silicon-bearing species to enter the grooves.

The thermodynamic analysis of the Si-Cl-H system (9) has been used to analyze in more detail the critical epitaxial refill gas concentrations. Table I gives both experimental and equilibrium Si/Cl ratios as a function of the Cl/H ratio for the four critical deposition conditions given in Fig. 5 and for two well-established deposition conditions with the H_2 - SiH_2Cl_2 -HCl system. Of particular interest is that the critical epitaxial conditions are all about equally shifted from equilibrium. For defect-free epitaxial refill, the value of the difference between the experimental and equilibrium Si/Cl ratios is about 0.075. Based on the analysis, critical deposition conditions to refill grooves can probably be predicted for a variety of silicon systems and temperatures.

The experimental observations which indicated that a low substrate temperature is equivalent to an excess of HCl and that a high substrate temperature is equivalent to a deficiency of HCl are consistent with the above analysis. With the low Cl/H ratios used for the refill depositions, both an excess of HCl and a low substrate temperature result in a difference between the experimental and equilibrium Si/Cl ratios less than the critical value. Since a smaller difference between the two ratios means that the system is closer to equilibrium, a slow growth rate or etching of the substrate occurs. Conversely, a deficiency of HCl and a high substrate temperature result in a difference between the experimental and equilibrium Si/Cl ratios greater than the critical value. Therefore, deposition is too fast and the deposit tends to bridge the grooves at the top of the substrate. From the experimental observations, the analysis given here is applicable only to the growth near the top of the substrate. Deposition in the groove bottoms was less sensitive to the small temperature and HCl concentration changes.

The groove depth independence of the epitaxial refill rate is another important aspect of this process. A very simple phenomenological model, illustrated in Fig. 7, explains the observations. Growth profiles are shown in three equal width grooves based on four assumptions: (i) a zero growth rate at the top corner, (ii) a linearly increasing growth rate with depth, (iii) an equal growth rate at any depth independent of the total groove depth, and (iv) a bottom growth rate equal to the growth rate on the walls at the bottom. Under these conditions, Fig. 7 shows that growth profiles in deep grooves eventually correspond to the profiles in shallow grooves. Consequently, all of the grooves will be completely filled in the same time interval. The four assumptions used to derive the growth profiles in Fig. 7 are very reasonable in view of the experimental observations. The first three agree with observations and measurements from slice cross sections. Figures 3 and 4 show that the fourth assumption is only correct for grooves with a single (111) plane termination on the bottom. However, the results

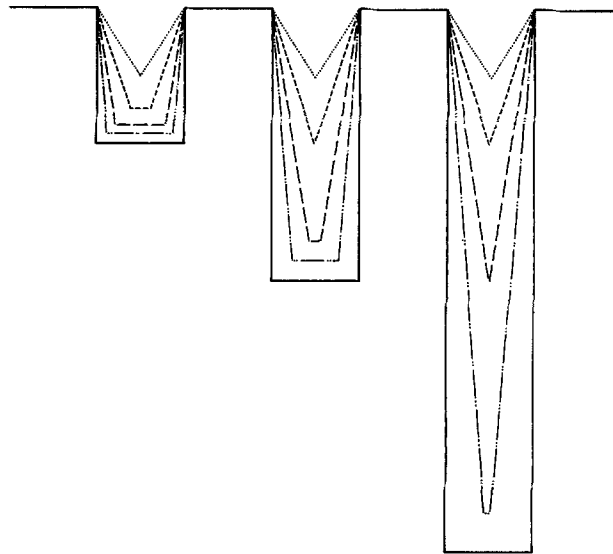


Fig. 7. Model to illustrate the groove depth independence of the epitaxial refill process for equal width grooves. Growth profiles are derived from assumptions given in the text.

obtained in Fig. 7 are only slightly influenced by the bottom growth rate assumption, since, as the grooves fill, side wall growth dominates over bottom growth. Similarly, the exact shape of the groove bottoms is also not important in the model. It is likely that this model for deep groove refill does not apply to grooves with depths less than the width. For grooves with depths greater than the width, however, the growth rate model illustrated by Fig. 7 is appropriate. Exactly why the deposition conditions produce the particular growth profiles remains to be determined.

Conclusion

An epitaxial growth process which produces preferential deposition of silicon in deep, vertically walled, orientation-dependent etched grooves in (110) silicon without a mask on the top of the substrate was developed. With the optimum deposition conditions, the growth rate on the groove walls increases with depth into the grooves so that the grooves are completely filled without voids or defects in the deposited silicon. Even with variable groove depths within a substrate, a planar top surface is produced after the grooves are filled. The key factor in this chemical vapor deposition technique is the adjustment of the Si/Cl ratio, which is conveniently done by the addition of HCl to the reactor. All of the deposition conditions successfully used are shifted about equally from equilibrium, since the difference between the experimental and equilibrium Si/Cl ratios is about the same for all of the depositions. It was also concluded that a temperature gradient within the substrate is critical to the epitaxial refill process.

This silicon deposition technique, which preferentially deposits into and fills orientation-dependent etched grooves in a substrate, may be useful in a number of ways. In essence, it is a method to reconstruct a silicon slice with alternate regions with different properties. Some new structures with unique characteristics are possible.

Acknowledgments

This work was supported by the United States Air Force, Aero Propulsion Laboratory under Contract No. F33615-73-C-2019. Discussions with K. E. Bean and D. L. Kendall with regard to the experimental work were helpful. G. F. Wakefield made useful suggestions during the manuscript preparation, especially with regard to the thermodynamic analysis. The technical assistance of Jim Anderson and Max Evans made possible the experimental work.

Table I. Analysis of critical refill deposition conditions from Fig. 5 and from two established deposition conditions with SiH_2Cl_2 . Equilibrium (Si/Cl) values are taken from Ref. (9).

Cl/H	Experimental Si/Cl	Equilibrium Si/Cl	Experimental Si/Cl - Equilibrium Si/Cl
0.017	0.13	0.06	0.07
0.023	0.14	0.08	0.06
0.036	0.18	0.11	0.07
0.056	0.22	0.14	0.08
0.025	0.19	0.10	0.09
0.043	0.22	0.14	0.08

Manuscript submitted May 12, 1975; revised manuscript received July 28, 1975. This was Paper 224 presented at the New York, New York, Meeting of the Society, Oct. 13-17, 1974.

Any discussion of this paper will appear in a Discussion Section to be published in the June 1976 JOURNAL. All discussions for the June 1976 Discussion Section should be submitted by Feb. 1, 1976.

REFERENCES

1. E. G. Alexander and W. R. Runyan, *Trans. Met. Soc. AIME*, **236**, 284 (1966).
2. P. Rai-Choudhury and D. K. Schroder, *This Journal*, **118**, 107 (1971).
3. R. K. Smeltzer, D. L. Kendall, and G. L. Varnell, "Conference Record of the Tenth IEEE Photo-voltaic Specialists Conference," November 1973, p. 194.
4. W. R. Runyan, E. G. Alexander, and S. E. Craig, *This Journal*, **114**, 1154 (1967).
5. D. L. Kendall, *Appl. Phys. Letters*, **26**, 195 (1975).
6. P. Rai-Choudhury and D. K. Schroder, *This Journal*, **120**, 664 (1973).
7. W. C. Benzing, A. E. Ozias, and H. B. Bradley, Paper 75, presented at Electrochemical Society Meeting, Washington, D.C., May 9-13, 1971.
8. A. Lekholm, *This Journal*, **119**, 1122 (1972).
9. L. P. Hunt and E. Sirtl, *ibid.*, **119**, 1941 (1972).

CVD-BN for Boron Diffusion in Si and Its Application to Si Devices

Makoto Hirayama and Katsufusa Shohno

Department of Electronics, Sophia University, Chiyoda-ku, Tokyo, 102 Japan

ABSTRACT

Amorphous and polycrystalline boron nitride (BN) films were deposited on n-type Si substrates using a $B_2H_6-NH_3-H_2$ system. During deposition of the BN film, boron diffuses into the Si; a BN film deposited at temperatures below about $1000^\circ C$ acts as an infinite diffusion source of boron in Si. The maximum values of boron surface concentration give solid solubility of boron in Si at each temperature. A thin layer of BN (below 80\AA) gives a surface concentration of boron in the range between 10^{16} and 10^{20} cm^{-3} , by varying the heat-treatment conditions. Amorphous BN decomposes easily when heated in a nitrogen atmosphere. This can be used for planar diode processes using only one photomask. An MIS-memory diode with Al-BN-SiO₂-Si structure, shows an anomalous C-V shift due to the formation of borosilicate glass between BN and SiO₂.

Boron is the most common doping element for p-type Si in the present semiconductor technology. For boron diffusion in Si, many kinds of diffusion sources are used: boron trioxide (1), boron trichloride (2), boron tribromide (2), borosilicate glass (3), and boron nitride disks (4). A large number of experimental and theoretical works have already been published. Rand and Roberts (5) used CVD-BN as an insulator thin film for a varistor device, and also showed that a boron diffusion layer was formed in the Si substrate. In this paper, physical and chemical properties of CVD-BN thin films and methods to obtain boron diffusion layers with high and low surface concentrations are described. As examples of the use of CVD-BN in present planar technology, a Si planar diode process and an MIS-memory diode are shown.

Experimental Procedure

The experimental apparatus is schematically shown in Fig. 1. Deposition is carried out in a quartz reaction chamber with dimensions of $25 \times 40 \times 400$ mm. Diborane (B_2H_6) diluted to 5% in hydrogen and ammonia (NH_3) are used as reactant gases and high purity hydrogen is a carrier gas. The flow rates of reactant gases are kept at $30\text{ cm}^3/\text{min}$ and that of hydrogen is $2000\text{ cm}^3/\text{min}$ throughout the experiments. Deposition temperatures of the Si substrate are changed in the range of $700^\circ-1250^\circ C$. The growth rate of the film at $700^\circ C$ is about $500\text{ \AA}/\text{min}$. Mirror-polished n-type Si wafers (P-doped) with resistivities of $3 \sim 5\text{ ohm-cm}$ are used.

The surface of a deposited film is observed by an optical microscope. Reflection electron diffraction is used for an investigation of crystalline properties of

the films. The deposited films are also studied by infrared absorption before and after heat-treatment in an appropriate ambient gas.

In order to measure pinhole density of the deposited films, Si wafers are etched to make pits through any pinholes that may exist in the film. Wafers are boiled at $110^\circ C$ in APW solution, which has 17 cm^3 of ethylenediamine, 3g of pyrocatechol, and 8 cm^3 of deionized water. Then the samples are boiled for 30 min in a hot solution ($\sim 130^\circ C$) with equal volumes of phosphoric acid and deionized water for complete removal of the deposited films. The pinhole density of the film is measured by counting the number of etch pits in the Si wafer under an optical microscope.

Although boron diffusion layers are formed during deposition of the film, the total diffusion time was varied from 10 to 3000 min to get diffusion depth from

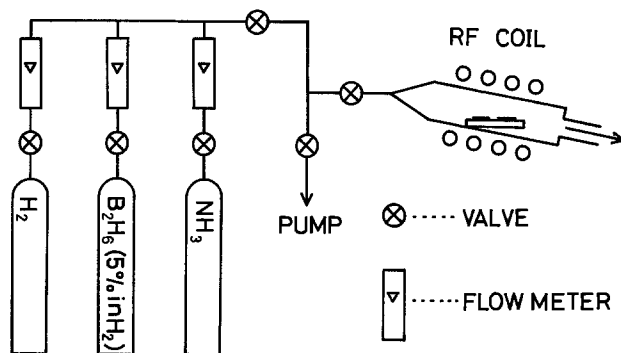


Fig. 1. Schematic diagram of experimental apparatus for deposition of a BN film on a Si substrate.

Key words: CVD-BN, boron diffusion, planar diode, memory diode.

about 0.2 to 5 μm . The diffusion depth is measured by spherical drilling and staining (6). To obtain the boron surface concentration in Si, an average resistivity of the boron diffusion layer is measured by four-point probe and Irvin's plots (7) of resistivity vs. impurity concentration. To determine the boron profile, the change of the sheet resistivity is measured by repeated anodic growth and removal of silicon dioxide layers (8). Anodic oxidation is carried out in a solution with 3 parts propylene glycol and 2 parts phosphoric acid at a d-c applied voltage of 100V. The thin silicon dioxide layer ($\sim 200\text{\AA}$) is removed with HF. After every fourth anodization-HF cycle, a measurement is made of the sheet resistivity. The thickness of silicon removed was determined by an interference microscope.

Results and Discussion

Properties of boron nitride.—Typical reflection electron diffraction patterns are shown in Fig. 2. These faint ring patterns are obtained from films which were deposited at temperatures near 1000°C . The film is polycrystalline boron nitride, with hexagonal structure, whose lattice parameters are measured as $a = 2.51\text{\AA}$ and $c = 6.68\text{\AA}$. These values are in good agreement with those given by Pease (9). On the other hand, the faint ring patterns changed to hollow ring patterns as the deposition temperature was decreased below about 1000°C . This means that the films obtained below 1000°C are amorphous. Films obtained in this experiment are identified as boron nitride (BN).

An infrared absorption spectrum of the film also shows that it is boron nitride. For infrared spectroscopy, the back side of a Si substrate was chemically etched smooth to prevent diffuse reflection. The absorption peak from the film appears at $7.3\ \mu\text{m}$, as shown in Fig. 3. This agrees well with the value of the B-N stretching vibration previously reported by Brame *et al.* (10). This value of the B-N vibration is independent of deposition temperature. For films of the same thickness, the magnitude of absorption band changes according to the deposition temperature. This is due to the number of the B-N stretching vibrations and also depends on a crystallization of the films.

The surface of the film is quite smooth and no structural features can be observed on films deposited in the temperature range of 700°C - 1250°C . The BN film is transparent and shows interference colors.

The BN film is chemically stable and cannot be attacked by any etching solution except hot phosphoric acid. A solution of equal volumes of deionized water and phosphoric acid is heated to its boiling point ($\sim 130^\circ\text{C}$). The etch rate of a film deposited at 700°C is about $80\ \text{\AA}/\text{min}$. Although the etch rate becomes small for a film deposited at high temperatures, BN films 2000\AA thick, which we usually use, can be completely removed when boiled for 30 min in the solution.

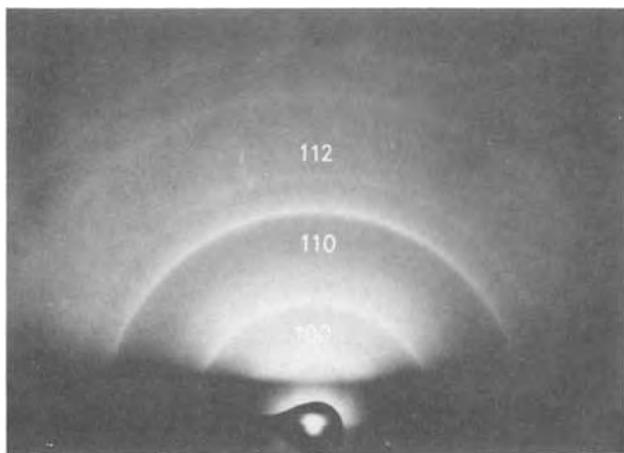


Fig. 2. Typical electron reflection diffraction patterns from a BN film deposited at 1200°C .

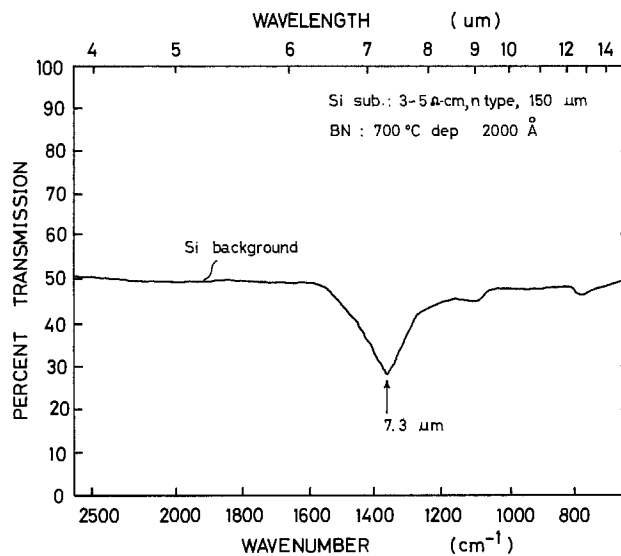


Fig. 3. Infrared absorption spectrum of a BN film deposited at 1000°C on a Si substrate.

Plasma dry etching is also useful, especially for selective removal of BN films by the use of well-known photoresist processes. Experimental results are shown in Fig. 4. The rf power (at 13.7 MHz) was set as small as possible to avoid attack of the Si substrate. Deposition temperatures over about 1000°C , where the etch rate of the film decreases with increasing deposition temperature, correspond to the temperature range where a polycrystalline BN film is obtained.

Pinhole density was below $10\ \text{cm}^{-2}$ for 500\AA films deposited at 700°C . When the film was thicker than 500\AA , defects could not be found on the Si substrate.

Polycrystalline BN films deposited at temperatures over about 1000°C are thermally stable. Changes in the polycrystalline patterns were not observed even after long heat-treatment in hydrogen or nitrogen for several tens of hours at 1250°C . However, amorphous BN films deposited below about 1000°C are unstable and easily decompose during heat-treatment in nitrogen or hydrogen. For example, a 500\AA BN film deposited at 700°C completely decomposes after heat-treatment in nitrogen at 1100°C for 3 hr, after which the bare Si surface appears. The change from an amorphous to a polycrystalline form due to heat-treatment was not observed on the patterns by reflection electron diffraction.

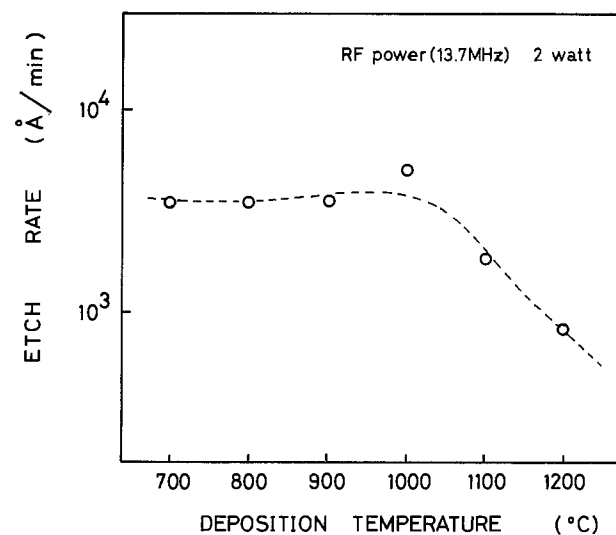


Fig. 4. Plasma etch rate vs. deposition temperature of a BN film.

Al-BN-Si structures with 1000Å of BN were prepared for measurements of dielectric constant, resistivity, and dielectric strength of the BN film. An a-c bridge at 1 MHz was used for measurement of diode capacitance to determine the dielectric constant of a film. The dielectric constant of a BN film has a value that depends on the deposition temperatures. For an amorphous film deposited at a temperature below about 1000°C, the dielectric constant is 3.3 ~ 3.5, while for a polycrystalline film deposited at temperatures over about 1000°C it is 4 ~ 6. From the ohmic region in the V-I characteristics of a diode, resistivity of the film was determined to be in the range $10^9 \sim 10^{10}$ ohm-cm. Breakdown voltages of 80 ~ 150V give a dielectric strength of $0.8 \sim 1.5 \times 10^7$ V/cm for the films. The values of resistivity and dielectric strength do not depend on the deposition conditions of the film.

Boron diffusion in Si.—During the deposition of a BN film on an n-type Si substrate, a boron diffusion layer can be formed. The boron surface concentration vs. deposition temperature is shown in Fig. 5. When deposition temperatures are below about 1000°C, the boron surface concentration C_s is about 10^{20} cm⁻³. C_s increases with deposition temperature, and does not depend on deposition time of the BN film. This means that an amorphous BN film deposited below about 1000°C acts as an infinite diffusion source of boron. However, as the deposition temperature is increased over about 1000°C, the boron surface concentration decreases to about $10^{18} \sim 10^{19}$ cm⁻³. In this temperature range, the film has a polycrystalline form.

A BN film deposited below about 1000°C can be used to obtain the highest value of boron surface concentration at each temperature. After the films were deposited on n-type Si substrates at 700°C, the samples were heated in a hydrogen atmosphere. Values of boron surface concentrations are plotted in Fig. 6 for various heat-treatment temperatures. The curve in this figure seems to give the solid solubility of boron in Si

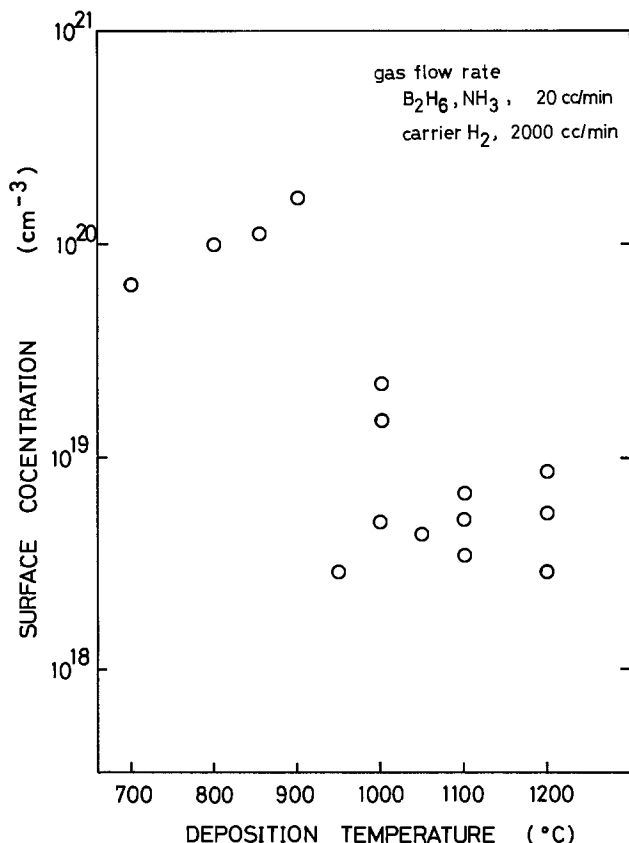


Fig. 5. Boron surface concentration vs. deposition temperature of a BN film.

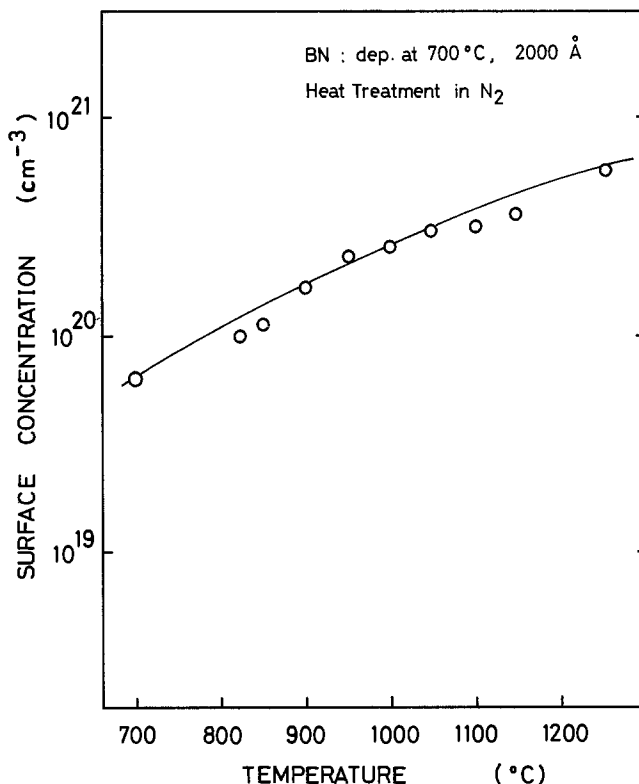


Fig. 6. Maximum values of boron surface concentration at each temperature of heat-treatment (boron solid solubility in Si).

at each temperature. It corresponds to that reported by Vick *et al.* (8).

Assuming a complementary error function profile, the boron diffusion coefficient was calculated from the measured values of boron surface concentration, diffusion depth, and diffusion time. Figure 7 shows values of the diffusion coefficient obtained vs. the reciprocal of

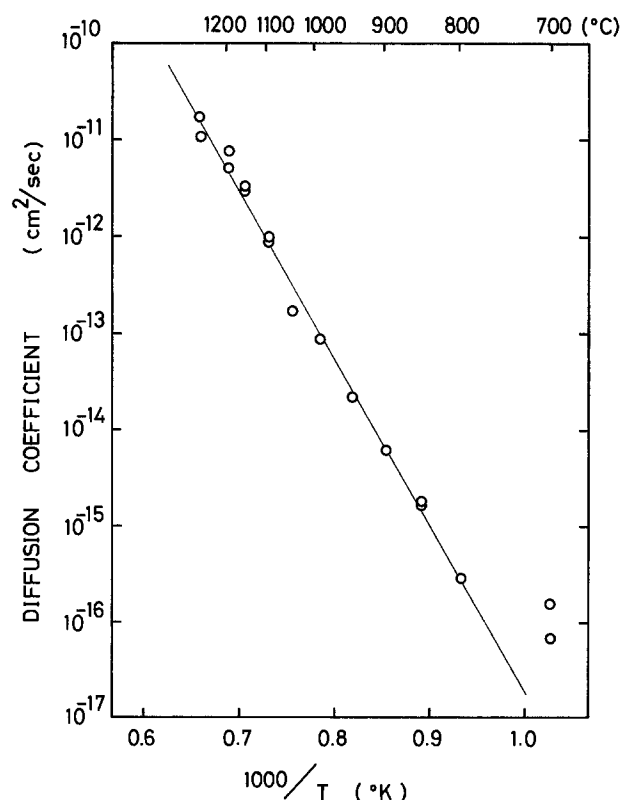


Fig. 7. Diffusion coefficient of boron in Si vs. reciprocal absolute temperature.

absolute temperature. The straight line is represented by $D = 26.5 \times \exp(-88,900/RT)$. The activation energy of 88.9 kcal compares to that of 85 kcal reported by Fuller *et al.* (11) and 81 kcal reported by Kurtz *et al.* (1). When the boron surface concentration is over 10^{19} cm^{-3} , it was pointed out by Vick *et al.* (8) that the boron profile deviates from a complementary error function. Our experiments do not show a measurable deviation from a complementary error function.

In order to obtain a lower boron surface concentration than that of solid solubility in Si, a thin layer of BN can be used. As a thin diffusion source, the BN film was deposited at 700°C for 10 sec. The film thickness was estimated to be about 80\AA , and the boron diffusion layer which was formed during the deposition was less than 25\AA . Heat-treatment for the boron diffusion was carried out in hydrogen or nitrogen. Relationships between diffusion depth, boron surface concentration, and heat-treatment time are shown in Fig. 8. During heat-treatment for 20–800 min at a temperature of 1100°C , the BN decomposed and the bare Si surface appeared. In Fig. 8 the diffusion depth is proportional to the square root of the heat-treatment time, and the boron surface concentration is inversely proportional to the square root of the heat-treatment time. This means that diffusion conditions with a finite amount of impurity on the Si surface are satisfied.

There is another way to obtain a low boron surface concentration. After the BN film was deposited (for 10 sec at a temperature of 700°C), the samples were heated in steam for 3 min at a temperature of 1100°C . The BN film changed to a borosilicate glass. In the next step heat-treatment for boron diffusion was carried out in a nitrogen atmosphere. Relationships between diffusion depth, boron surface concentration, and heat-treatment time are shown in Fig. 9. Diffusion depth is proportional to the square root of the heat-treatment time. On the other hand, boron surface concentration decreases more slowly than the inverse square root of the heat-treatment time. This means that the boron is still supplied from the borosilicate glass during the heat-treatment in nitrogen.

Formation of a borosilicate glass by rapid thermal oxidation in steam was confirmed with infrared absorption. Results are shown in Fig. 10. The absorption peak due to B-N stretching vibration is at $7.3 \mu\text{m}$, as shown in Fig. 3. After rapid thermal oxidation in steam, absorption peaks appeared at 7.2 , 9.2 , and $12.5 \mu\text{m}$. The last two peaks at 9.2 and $12.5 \mu\text{m}$ correspond to those established for silicon dioxide (12, 13). The broadening of the adsorption peak at $7.3 \mu\text{m}$ due to thermal oxidation is apparent. The small change of the peak from 7.3 to $7.2 \mu\text{m}$ means that the peak at $7.2 \mu\text{m}$ is due to a new vibrational mode. The new peak at $7.2 \mu\text{m}$

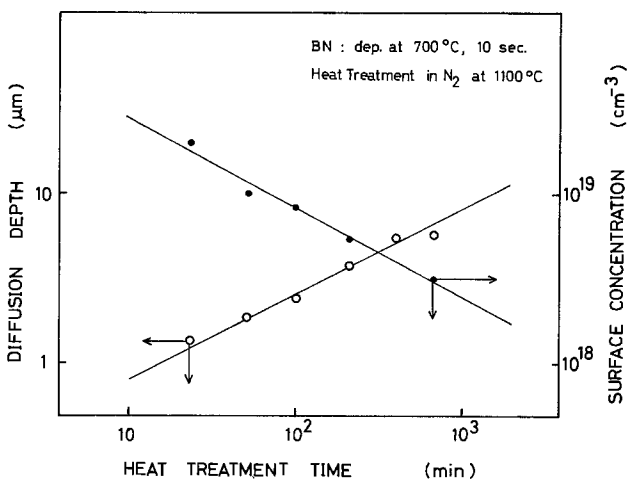


Fig. 8. Diffusion depth and boron surface concentration vs. heat-treatment time when the BN film was deposited for 10 sec at 700°C .

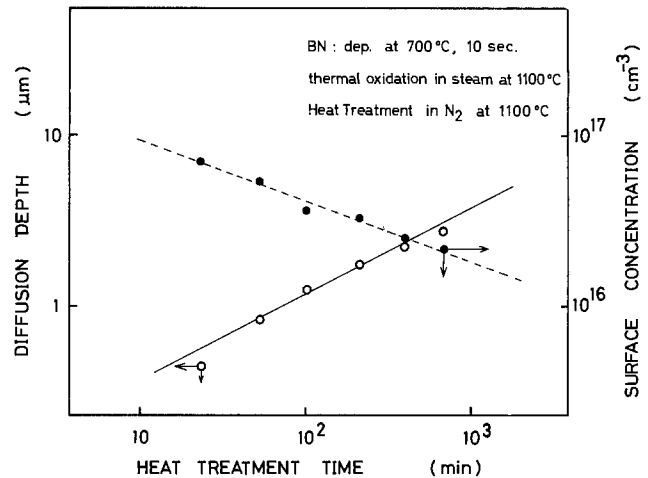


Fig. 9. Diffusion depth and boron surface concentration vs. heat-treatment time when the sample was rapidly oxidized in steam before diffusion.



Fig. 10. Infrared absorption spectrum of the borosilicate glass formed by rapid thermal oxidation of a thin BN film on silicon.

agrees with that due to the B-O stretching vibration (14, 15).

Simple planar diode.—A BN film deposited at 700°C as a diffusion source decomposes easily when heated in a nitrogen atmosphere. This can be used for a planar diode. Schematic diagrams of the processes are shown in Fig. 11. N-type 5 ohm-cm Si wafers are thermally oxidized to about 3000\AA , and windows of 1 mm diameter opened in the silicon dioxide. Next, a BN film is deposited for 10 sec at 700°C . To diffuse the boron and decompose the BN in the windows, the samples were heated in a nitrogen atmosphere at 1100°C for 120 min. Boron diffused into the Si through the windows, and a bare Si surface appears in the windows. The diffusion depth of boron is about $3 \mu\text{m}$, and the boron surface concentration is about $8 \times 10^{18} \text{ cm}^{-3}$. Nickel can be deposited directly by electroless plating on the bare Si surfaces of the windows. Nickel was also plated on the back face of the Si wafers to make an ohmic contact. Thus, we can simply make planar diodes by the use of only one photomask. A sharp avalanche breakdown is observed in the reverse direction. The breakdown voltages are in the range of $115 \sim 120\text{V}$, which are expected values from the diffusion depth and the resistivity of Si substrates (16).

MIS-memory diode.—An interesting application of the BN film is as an insulator in an MIS-memory diode. In studying this application, it was found that the

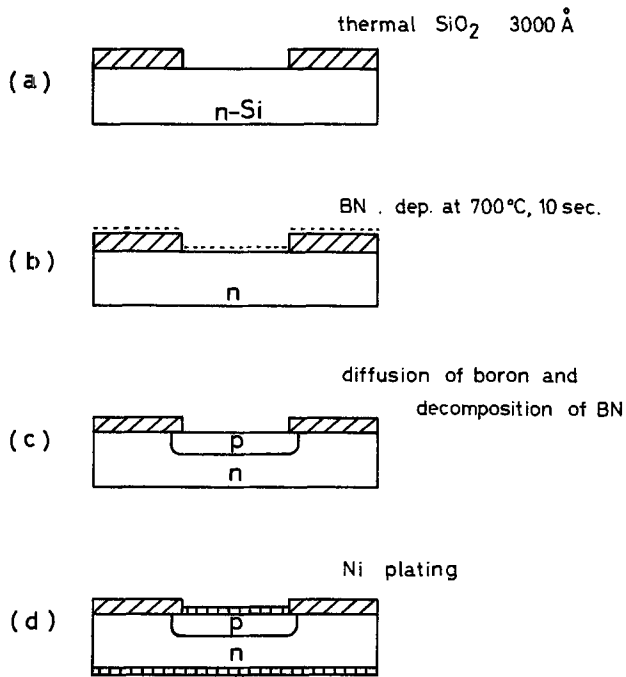


Fig. 11. Schematic diagram of the processes of a simple planar diode using a BN film as a diffusion source.

Al-BN-SiO₂-Si structure, shown in Fig. 12(a), exhibited an anomalous shift in C-V characteristics. An experimental device was fabricated as follows. An n-type 5 ohm-cm (100) Si wafer was thermally oxidized in a pure dry oxygen for 3 min at 1050°C. The thickness of silicon dioxide obtained was about 170Å. A BN film of about 500Å was then deposited at a temperature of 700°C. Finally, Al was evaporated to make an electrode on the BN film, using a metal mask with windows of 0.3 mm diam. No additional heat-treatment was necessary to observe a shift in C-V characteristics.

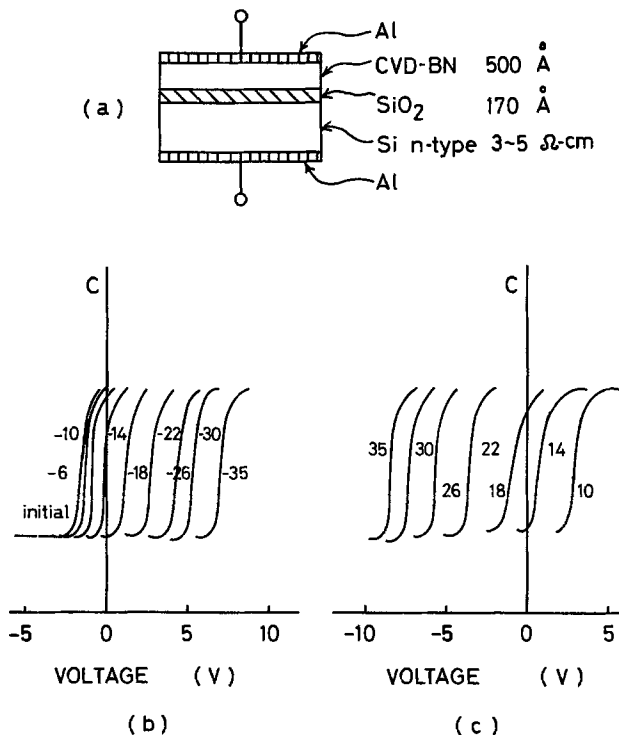


Fig. 12. (a) Schematic diagram of Al-BN-SiO₂-Si structure, (b) typical C-V curves when a negative voltage is applied to the Al electrode, (c) typical C-V curves when a positive voltage is applied to the Al electrode.

Typical C-V characteristics are shown in Fig. 12(b) and (c). When a negative voltage of more than 10V is applied to the Al electrode, the C-V curve begins to shift in the positive direction. The length of the applied voltage pulse was kept at 1 sec throughout this experiment. The C-V shift saturates at an applied voltage of about -35V. Next, we applied a positive voltage to the Al electrode. The C-V curve then begins to shift in the negative direction. The C-V shift saturates again when the voltage applied to the Al electrode is more than 35V.

The direction of these shifts is opposite to those observed for well-known MNOS (17) and MAOS (18) devices. These C-V shifts might be due to polarization of the borosilicate glass which would be formed between the BN film and silicon dioxide layers during deposition of the BN film. Formation of the borosilicate glass is confirmed by the infrared absorption spectrum.

Conclusion

BN films can be deposited on Si substrates by thermal reaction in a B₂H₆-NH₃-H₂ system. When the deposition temperature is below about 1000°C, the film is amorphous. When the deposition temperature is over about 1000°C, the film is polycrystalline with a hexagonal structure. The surface of the BN film is smooth, with a pinhole density below 10 cm⁻² for a 500Å thick film deposited at 700°C. Boiling phosphoric acid can remove the BN film from a Si substrate; gas plasma dry etching is also useful for removal of the BN film.

BN deposited at a temperature of 700°C easily decomposes when heated in a nitrogen atmosphere. This can be used to fabricate a simple planar diode using only one photomask. The formation of borosilicate glass was confirmed by observing its characteristic infrared absorption spectrum for samples where the BN film was deposited on a thermally grown SiO₂ layer. This can be used for an MIS-memory diode with an Al-BN-SiO₂-Si structure. Such a structure shows an anomalous shift of its C-V curve with applied voltage.

During deposition of BN films, boron diffuses into the Si substrates. BN films thicker than 500Å deposited below about 1000°C act as infinite diffusion sources of boron. When these films are used as diffusion sources, the maximum values of boron surface concentration correspond to the solid solubility of boron in Si at each temperature. A thin BN film (about 80Å deposited at 700°C) gives a surface concentration of boron in the range between 10¹⁶ and 10²⁰ cm⁻³ by varying the pre-diffusion heat-treatment conditions.

Acknowledgment

The authors would like to express their sincere thanks to Prof. J. F. Gibbons of Stanford University for his kind suggestions, valuable discussions, and final critical reading of the manuscript. The authors wish to acknowledge Mr. M. Takigawa, Mr. Y. Hirai, and Mr. M. Ozaki for their technical assistances and advice in performing the experiments.

Manuscript submitted Sept. 12, 1974; revised manuscript received July 7, 1975. This was Paper 59 presented at the San Francisco, California, Meeting of the Society, May 12-17, 1974.

Any discussion of this paper will appear in a Discussion Section to be published in the June 1976 JOURNAL. All discussions for the June 1976 Discussion Section should be submitted by Feb. 1, 1976.

Publication costs of this article were partially assisted by Sophia University.

REFERENCES

1. A. D. Kurtz and R. Yee, *J. Appl. Phys.*, **31**, 303 (1960).
2. J. Yamaguchi, S. Horiuchi, K. Matsumura, and Y. Ogino, *J. Phys. Soc. Japan*, **15**, 1541 (1960).
3. D. M. Brown and P. R. Kennicott, *This Journal*, **118**, 293 (1971).

4. D. Rupprecht and J. Stach, *ibid.*, **120**, 1266 (1973).
5. M. J. Rand and J. F. Roberts, *ibid.*, **115**, 423 (1968).
6. T. Kinoshita and K. Shohno, *Oyo Butsuri*, **39**, 788 (1970) (in Japanese).
7. J. C. Irvin, *Bell System Tech. J.*, **41**, 387 (1962).
8. G. L. Vick and K. M. Whittle, *This Journal*, **116**, 1142 (1969).
9. R. S. Pease, *Acta Cryst.*, **5**, 356 (1952).
10. E. G. Brame, Jr., J. L. Margrave, and V. W. Meloche, *J. Inorg. Nucl. Chem.*, **5**, 48 (1957).
11. C. S. Fuller and J. A. Ditzenberger, *J. Appl. Phys.*, **27**, 544 (1956).
12. H. J. Hrostowski and R. H. Kaiser, *Phys. Rev.*, **107**, 966 (1957).
13. J. W. Corbett, G. D. Watkins, R. M. Chrenko, and R. S. McDonald, *ibid.*, **121**, 1015 (1961).
14. W. Kern and R. C. Heim, *This Journal*, **117**, 568 (1970).
15. E. Arai, H. Nakamura, and T. Terunuma, *ibid.*, **120**, 980 (1973).
16. D. P. Kennedy and R. R. O'Brien, *IBM J. Res. Develop.*, **10**, 213 (1966).
17. J. T. Wallmark and J. H. Scott, Jr., *RCA Rev.*, **30**, 335 (1969).
18. N. J. Chou and P. J. Tsang, *Met. Trans.*, **2**, 659 (1971).

{332} Ga Habit Planes Formed on GaAs during Br₂:CH₃OH Etching

L. A. Koszi and D. L. Rode

Bell Laboratories, Murray Hill, New Jersey 07974

ABSTRACT

This paper describes the different habit (stop) planes formed when GaAs substrates are etched in various concentrations of a Br₂:CH₃OH etching solution. It was previously found that concentrations less than 1% Br₂ in methanol yielded {111}Ga habit planes. Concentrations in excess of this amount were investigated and it was discovered that a different set of planes was preferred. Changes in etch pit shapes and mask orientation preference show that these new planes are the {332}Ga planes. The change from {111}Ga to {332}Ga habit planes is a result of increased Br₂ concentration. Initial results of the electrochemical etching properties of Br₂:CH₃OH solutions are also presented. These initial results show that with proper biasing of the sample and solution, the Br₂:CH₃OH etch becomes isotropic.

Dilute mixtures of bromine in methanol are commonly used for free chemical etching and chemical/mechanical polishing of GaAs to achieve smooth, defect-free surfaces. The dependence of etch rate on crystallographic orientation, among other factors, has been studied by Gatos (1) and Moest (2) who find {111}Ga¹ habit planes for this solution with bromine concentrations less than 1% by volume. Similar results were obtained by Tarui, Komiya, and Harada (3) who used this property to chemically etch vee-shaped trenches in (100)GaAs through long rectangular windows formed in an Al₂O₃ mask. In this case, the long axis of the window must be aligned parallel to the [011] to expose the (111) and (111) planes as sides of the vee. These workers pointed out the expected linear dependence of the vee depth (*d*) on mask window width (*w*), i.e., $d = w/\sqrt{2}$.

The above work utilized bromine concentrations of less than 1.3% by volume of bromine in methanol. We have obtained similar results at these concentrations. However, during experiments with bromine concentrations above this amount, up to and including 20% Br₂:CH₃OH, we have noted enhanced undercutting of our etching mask window (SiO₂) and the formation of facets along the side of the vee trench leading to a scalloped appearance of the walls which form the trench.

Further experiments are described below which show that the habit planes at bromine concentrations of 5% Br₂:CH₃OH and higher are {332}Ga planes. With the higher concentration etchant, unafaceted vee-shaped trenches on (100)GaAs are obtained if the long axis of the window mask is aligned parallel to the [023] or

[032]. The apex of the vee is then inclined away from the normal to the (011) cleavage plane by 11.31° and the walls of the vee subtend an angle of 79.52°.

Results

Br₂:CH₃OH etching was performed at room temperature on polished wafers of boat-grown, Si-doped GaAs with $n = 2 \times 10^{18} \text{ cm}^{-3}$. The substrates were subsequently coated with a 5000Å vapor deposited SiO₂ film into which the etching mask pattern was photolithographically defined. Using the "pinhole alignment method" described earlier by Tarui *et al.* (3) the desired mask orientation with respect to the [011] was determined. The SiO₂ etching mask consisted of a fan-shaped pattern shown in Fig. 1. Each leg of the fan, where the SiO₂ had been removed, was 25.4 μm wide and the legs were arranged in 10° increments over a 90° field. A centrally located leg of the pattern was aligned normal to the (011) cleavage plane.

A fan etched in a 0.1 volume per cent (v/o) Br₂ in CH₃OH mixture for 25 min confirmed the Tarui *et al.* results (3). Our results are shown in Fig. 2. Note, in the scanning electron micrograph of the surface, the formation of a vee-shaped trench occurs along the center [011] leg only. The other legs form reverse mesa structures discussed by Tarui *et al.* (3). The formation of rectangular etch pits in oxide pinholes was also noted and expected.

A sample was also etched in 5% Br₂:CH₃OH for 15 min. Scanning electron micrographs of the results are shown in Fig. 3. The formation of a vee-shaped trench was noted not only in the center leg of the fan, aligned normal to the (011), but also in the legs oriented at ±10° to this normal. Note the formation of scalloped walls in the center leg. Other legs were observed to be "reverse-mesa" geometries.

* Key words: chemical etchants, selective etching, gallium arsenide.

¹ The [111] direction is taken to be a positive normal to a (111)Ga surface in agreement with the convention which denotes (111) and (111) as Ga and As surfaces, respectively.

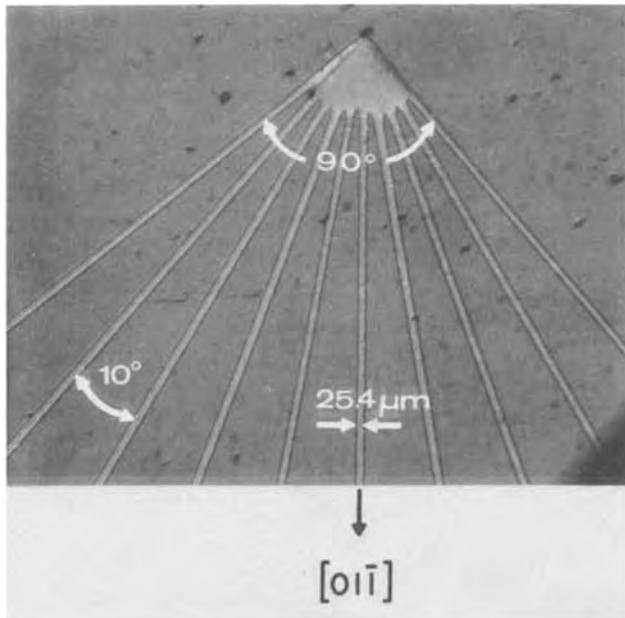


Fig. 1. The alignment and geometric sizes are shown in this photograph of the fan pattern delineated on the (100) surface of a GaAs substrate.

Another important difference between the two concentrations can be seen in the resultant geometries of the etch pits formed in the oxide pinholes. Two micrographs of these etch pits formed by the 0.1% (a) and 5.0% (b) $\text{Br}_2:\text{CH}_3\text{OH}$ solutions are shown in Fig. 4. The long sides of the diamond-shaped pit, produced by the 5% solution, form an 11° angle with a line bisecting the two acute angles of the diamond. This line lies perpendicular to the $(01\bar{1})$ cleavage plane. This difference in etch pit geometry is due to the delineation of a set of habit planes other than the $\{111\}$ Ga planes. The planes forming the sides of the diamond-shaped etch pits were found to be the $\{332\}$ Ga planes.

To confirm the results mentioned above, two slices were etched in a 5% $\text{Br}_2:\text{CH}_3\text{OH}$ solution. The first slice had windows ($125\ \mu\text{m}$ wide on $508\ \mu\text{m}$ centers) aligned perpendicular to the $(01\bar{1})$ and the second slice had windows aligned 11.3° off the normal to the $(01\bar{1})$. To reiterate, the 11.3° angle is the angle of intersection between the apex of the vee trench, formed by

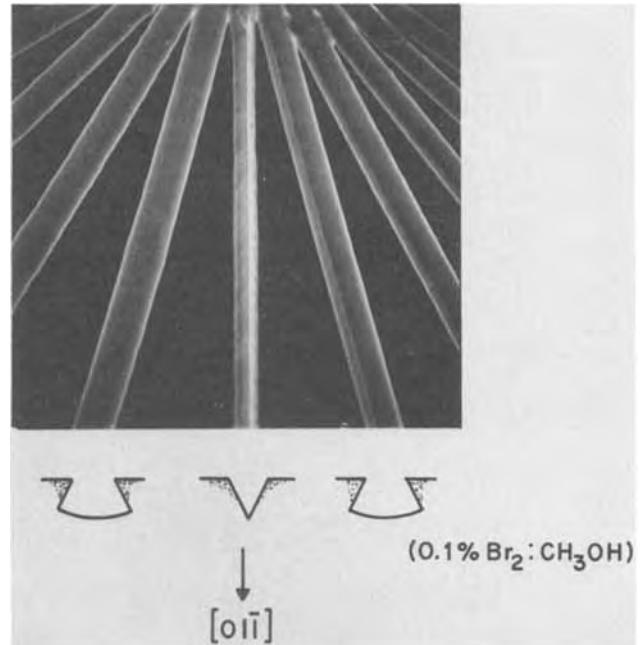


Fig. 2. This photograph shows the results of etching the fan pattern in a 0.1% $\text{Br}_2:\text{CH}_3\text{OH}$ solution. Trench cross sections are also shown.

$\{332\}$ Ga planes, and the normal to the $(01\bar{1})$ cleavage plane. The walls of the resultant vee in the second slice would then be the $\{332\}$ Ga planes. If these walls are smooth as opposed to the scalloped walls of the vee trench of the first slice, then one can infer that the higher concentration solution prefers the $\{332\}$ Ga planes.

The micrographs in Fig. 5 show the results of the etching of the two slices in the 5% $\text{Br}_2:\text{CH}_3\text{OH}$ solution. Micrograph (a) depicts the resultant trench produced in a window aligned perpendicular to the $(01\bar{1})$ while micrograph (b) shows the trench formed in the window aligned parallel to the $[02\bar{3}]$ direction which is 11.3° off the $[01\bar{1}]$ axis. The scalloped walls of the top figure show the delineation of planes which are not perpendicular to the $(01\bar{1})$. The smooth walls of the lower figure show the resultant and preferred $\{332\}$ Ga habit planes.

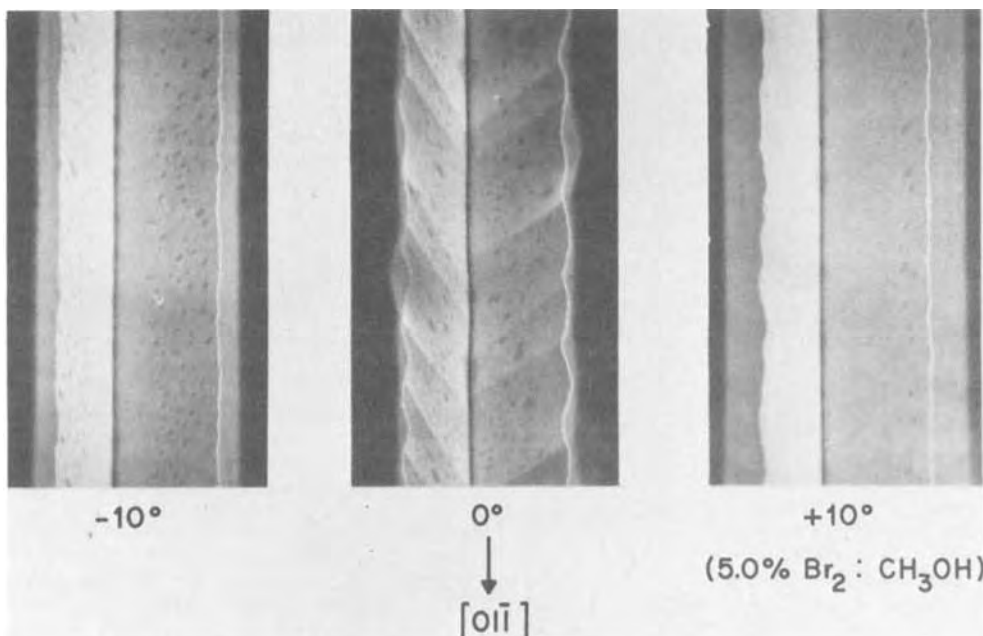


Fig. 3. These three scanning electron micrographs show the shape of the three legs of the fan pattern etched in 5% $\text{Br}_2:\text{CH}_3\text{OH}$. Note the center leg which is aligned parallel to the $[01\bar{1}]$ has serrated walls while the two trenches aligned $\pm 10^\circ$ to it are smooth.

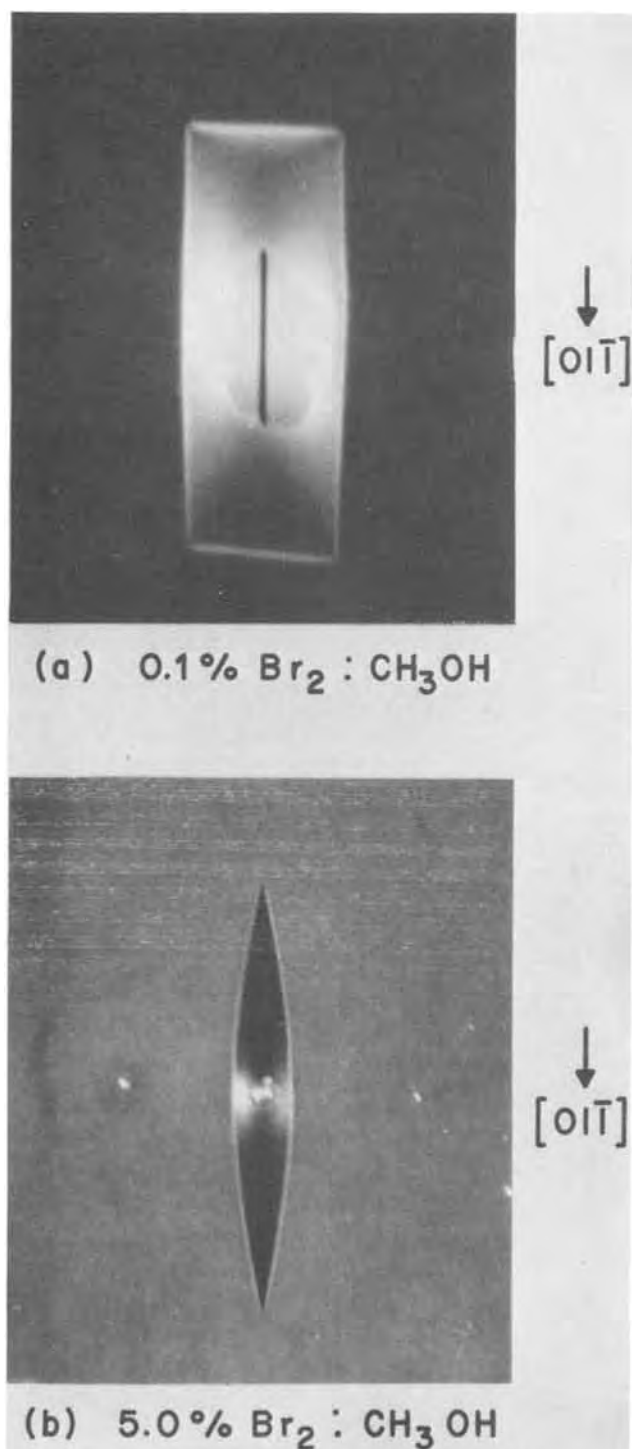


Fig. 4. Pinholes etched by a 0.1% (a) and 5.0% (b) $\text{Br}_2:\text{CH}_3\text{OH}$ solution are shown in these scanning electron micrographs.

A cleave through the $[02\bar{3}]$ aligned windows and subsequent measurement of the angle formed between the intersecting walls should give a result relating to the angle of intersection of the $\{332\}$ Ga planes. However, since the cleave does not pass through the vee perpendicularly, the projected angle of the apex onto the $(01\bar{1})$ cleavage plane is calculated to be 80.6° instead of the angle 79.52° between $(3\bar{3}2)$ and (332) . The measured angle was found to be $79^\circ \pm 2$. Had the planes been (111) Ga the corresponding angle is calculated to be 70.53° . This evidence confirms the interpretation that $\{332\}$ Ga habit planes appear with etching in 5% $\text{Br}_2:\text{CH}_3\text{OH}$.

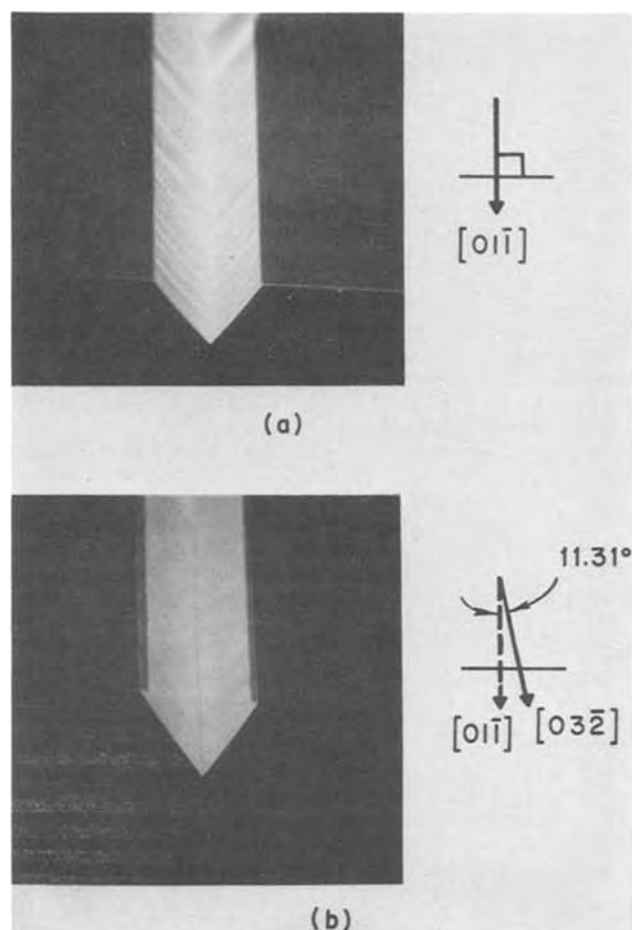


Fig. 5. The formations of vee trenches by a 5% $\text{Br}_2:\text{CH}_3\text{OH}$ are shown in these scanning electron micrographs. The windows were aligned (a) perpendicular to the $(01\bar{1})$ and (b) 11.3° off the normal to the $(01\bar{1})$ plane. Note the serrulated walls of the top photograph.

The shifting of habit planes due to concentration changes is felt to be related to chemical potentials. Etching with concentrations up to 20% were tried in hopes of shifting the habit planes to the $\{110\}$ planes. These experiments all yielded the same results as the 5% solution. However, it was found that above 1% the solution is reasonably conductive. Hence, experiments with electrical bias applied to the slice during etching with a 5% solution of $\text{Br}_2:\text{CH}_3\text{OH}$ were performed. The procedure and initial results of etching the fan-shaped pattern are presented below. An ability to shift to other planes by means of an applied bias proved fruitless. However, the $\text{Br}_2:\text{CH}_3\text{OH}$ etch was made isotropic with the application of a positive bias to the slice.

Electrical experiments were conducted using GaAs substrates (n-type) which had a fan mask delineated in an SiO_2 layer on the substrate. Electrical access to the sample was made via a spark contacted Sn-Au wire to an area near the edge of the slice. After the unmasked surface was mounted to a glass slide, a liberal coating of wax was applied to cover the wire contacted area to prevent electrical shorting to the etching solution. The samples were then negatively or positively biased during etching in a 5% solution of $\text{Br}_2:\text{CH}_3\text{OH}$.

Figure 6(a) shows the results obtained with negative bias (-6V). The photograph on the left shows the control slice etched in the same solution, but without bias. Although no difference in the crystallographic properties of the etching solution were noted, a decrease in etching rate resulted with the negative bias. The photograph on the right shows the results of the biased sample. Both samples were etched for 20 min.

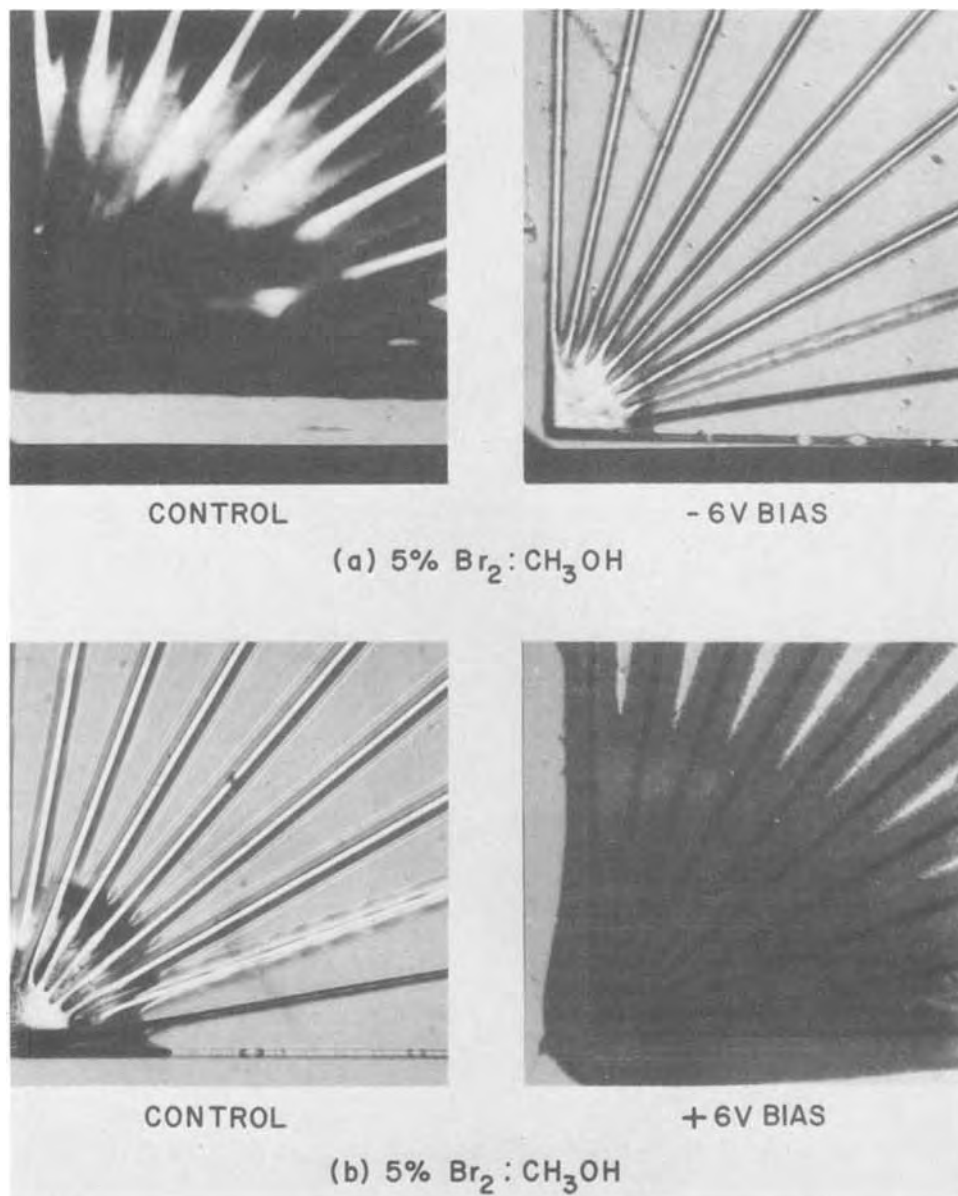


Fig. 6. These photographs show the results of electrically biasing samples during a 5% $\text{Br}_2:\text{CH}_3\text{OH}$ etch of fan shaped patterns.

Figure 6(b) shows photographs of a control (left) and a sample etched for 2 min in a 5% solution with a positive (+6V) bias applied. Note the exaggerated undercutting and increased etch rate of the biased sample. The results were expected. However, note the change in trench shape due to the etchant with the sample biased at a positive potential. Figure 7 shows the etched fan (a) and a photograph of a cleave through the legs to show the trench geometries (b). Figure 7(c) shows the type of etch pits formed with a positive bias applied to the sample during etching. Note that they are circular! These facts suggest that the etch has become isotropic. The application of a higher potential (+40V) produced crystallographically shaped vee trenches with reverse-mesa shaped dendrites superimposed over isotropic trenches.

Conclusion

Using fan-shaped windows delineated into an etching mask and etching with various concentrations of $\text{Br}_2:\text{CH}_3\text{OH}$, we were able to observe the characteristics of the resultant trenches along different orientations. At concentrations greater than 1% by volume, a change was noted in the number of legs which formed vee trenches, and the wall smoothness of these trenches. Legs oriented at $\pm 10^\circ$ (to the original vee formed at lower concentrations) flipped from reverse mesas to vee trenches. A change in the characteristic

shapes of etched pinholes was also noted as the concentration of Br_2 was increased. Lower concentrations formed predicted rectangular pits while pits at higher concentrations were diamond shaped.

Angular measurements from the fan pattern and diamond-shaped etch pits suggested that the habit planes for the higher concentrations were $\{332\}\text{Ga}$ planes. The etching of smooth walled vee trenches, 11.3° off the normal to the $(01\bar{1})$ cleavage plane, supported this assumption. Measurements of various angles formed by these offset trenches confirmed the observation that $\text{Br}_2:\text{CH}_3\text{OH}$ concentrations greater than 1-2% by volume prefer the $\{332\}\text{Ga}$ planes as principal habit planes. At concentrations greater than 1-2%, the $\text{Br}_2:\text{CH}_3\text{OH}$ etching solution was found to be conductive. It was also found that the application of an electrical bias to the sample during etching produced interesting results. A negative bias reduced the etching rate without changing the crystallographic properties of the $\text{Br}_2:\text{CH}_3\text{OH}$ etch. The use of a positive bias produced two changes in the etchant's properties: (i) increased etching rate, and (ii) a change in the shape of the resultant etch pits and trench geometries suggesting that the $\text{Br}_2:\text{CH}_3\text{OH}$ is isotropic in this case.

Acknowledgment

We would like to acknowledge R. W. Dixon for his informative discussions and encouragement, and R. A.

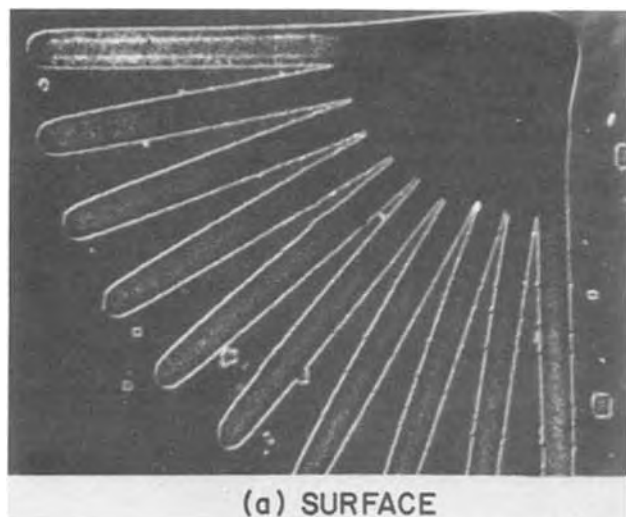
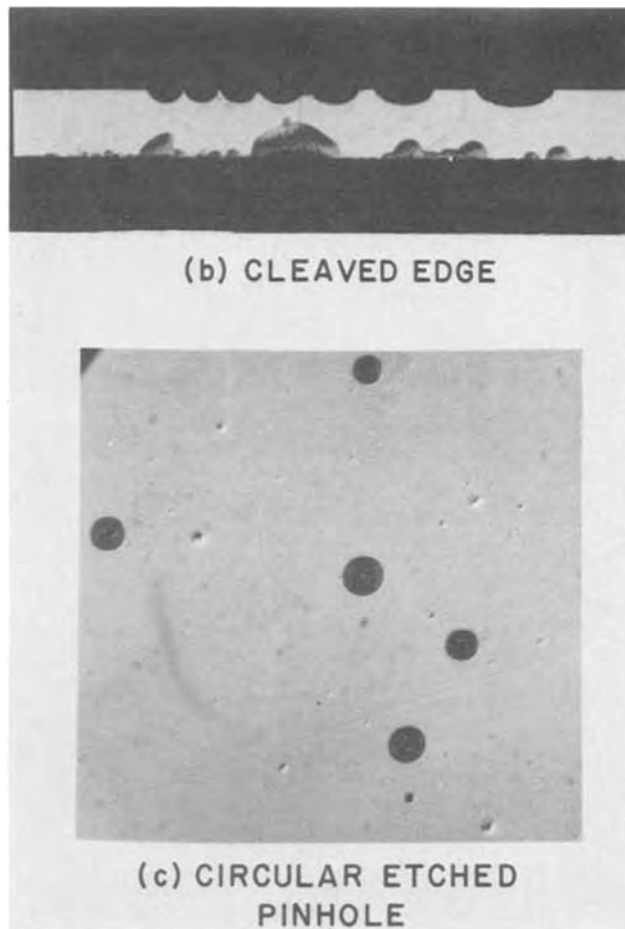


Fig. 7. The results of etching with a +6V bias in a 5% Br₂:CH₃OH solution are shown in these photographs. Of interest is the formation of circularly etched pinholes and isotropic trenches.



Linnell for providing the scanning electron micrographs.

Manuscript received April 29, 1975.

Any discussion of this paper will appear in a Discussion Section to be published in the June 1976 JOURNAL. All discussions for the June 1976 Discussion Section should be submitted by Feb. 1, 1976.

Publication costs of this article were partially assisted by Bell Laboratories.

REFERENCES

1. H. C. Gatos, "The Surface Chemistry of Metals and Semiconductors," p. 381, John Wiley & Sons, Inc., New York (1960).
2. R. R. Moest, *This Journal*, **113**, 141 (1966).
3. Y. Tarui, Y. Komiya, and Y. Harada, *ibid.*, **118**, 118 (1971).

Polycrystalline Silicon on Coated Steel Substrates

T. L. Chu,* H. C. Mollenkopf, and Shirley S. Chu

Institute of Technology, Southern Methodist University, Dallas, Texas 75275

ABSTRACT

Steel is the most economical substrate for the deposition of silicon. At temperatures used for the chemical vapor deposition of silicon, however, a barrier layer must be used to prevent the diffusion of iron from the substrate into the silicon layer. Tungsten was found to be ineffective as a diffusion barrier when silicon was deposited by the thermal decomposition of silane at 900°C and above. Borosilicate deposited by the oxidation of a silane-diborane mixture was found to be an effective barrier at temperatures up to 1150°C. Silicon deposited on borosilicate/steel substrates is polycrystalline. The microstructure and crystallographic properties of silicon depend strongly on the substrate temperature, deposition rate, and extent of doping. Silicon layers deposited at low temperatures and high rates consist of small crystallites with a strong preferred {110} orientation, while those deposited at high temperatures and low rates consist of larger crystallites with more random orientation. Silicon p-n junctions deposited on borosilicate/steel substrates show poor electrical characteristics because of the high concentration of grain boundaries, and solar cells have low conversion efficiencies.

Polycrystalline silicon has found increasing applications in device technology during the past few years. For example, polycrystalline silicon film deposited on an oxidized single crystalline silicon substrate has been used for the fabrication of p-channel field-effect transistors, and the characteristics of these transistors were very similar to those of control devices fabricated from single-crystalline silicon (1). The deposition of polycrystalline silicon on silicon dioxide-silicon structures is also an important process in the fabrication of silicon-gate MOS structures and for dielectric isolation in single-crystalline silicon devices (2, 3). The structural and crystallographic properties of polycrystalline silicon for the silicon-gate and dielectric isolation are not as critical as those for the field-effect transistor since polycrystalline silicon is not in the active region of the devices in the former case.

The recent interest in the utilization of solar energy by photovoltaic converters, under the impetus of the energy crisis, has stimulated considerable research and development on the fabrication of solar cells for terrestrial applications. The use of polycrystalline silicon layers on suitable substrates appears to be a promising approach for the fabrication of low-cost solar cells. Ideally, these substrates should be of low cost, light weight, high electrical conductivity, high heat capacity, and low chemical reactivity toward silicon at high temperatures, and they should have a thermal expansion coefficient similar to that of silicon. Such substrates have not been found. In this work, steel was selected as the substrate for the deposition of silicon since it is readily available in sheet form at low cost, \$0.10-0.15/lb. The thermal decomposition of silane in a gas flow system was used for the deposition of silicon. The experimental procedure used for the deposition process and the properties of deposited silicon layers are summarized in this paper.

Necessity for Diffusion Barrier in the Silicon-Steel System

The deposition of silicon by the thermal decomposition of silane in a gas flow system should be carried out at substrate temperatures above 700°C to obtain reasonable deposition rates, 1 $\mu\text{m}/\text{min}$ or higher. However, the use of high temperatures is not compatible with the silicon-steel system. A major difficulty is that the thermal expansion coefficients of most low-cost steels are 3-4 times higher than that of silicon. Also, silicon and iron diffuse rapidly into each other at high

temperatures. The phase diagram of the iron-silicon system indicates the existence of four silicides, Fe_3Si , Fe_5Si_3 , FeSi , and FeSi_2 , which have metallic properties (4). The deposition of silicon on steel at temperatures above 800°C was found to produce a solid solution of iron disilicide in silicon. To minimize the diffusion of iron, a diffusion barrier must therefore be applied to the surface of steel substrates before the deposition of silicon. The diffusion barrier may also be used to buffer the effects of the large difference in the thermal expansion coefficients of silicon and steel.

A metallic diffusion barrier is preferred for solar cells so that the substrate can serve as an ohmic contact. On the basis of various metal-silicon and metal-iron phase diagrams (4) tungsten was selected. Tungsten is readily deposited by the hydrogen reduction of tungsten hexafluoride (5), and its thermal expansion coefficient ($4.2 \times 10^{-6} \text{ }^\circ\text{C}^{-1}$) is very similar to that of silicon ($3.6 \times 10^{-6} \text{ }^\circ\text{C}^{-1}$). In addition, the usefulness of silica (amorphous silicon dioxide) as a diffusion barrier was investigated, as silica is known to be capable of preventing the diffusion of many impurities into silicon (6). Since the thermal expansion coefficient of silicon is several times smaller than those of silicon and iron but can be increased by the addition of boron oxide, the use of borosilicate as a diffusion barrier was also studied. Both silica and borosilicate are readily deposited by chemical reactions, silica by the oxidation of silane (7) and borosilicate by the oxidation of a silane-diborane mixture (8). The composition of borosilicate can be adjusted to have a thermal expansion coefficient similar to that of silicon.

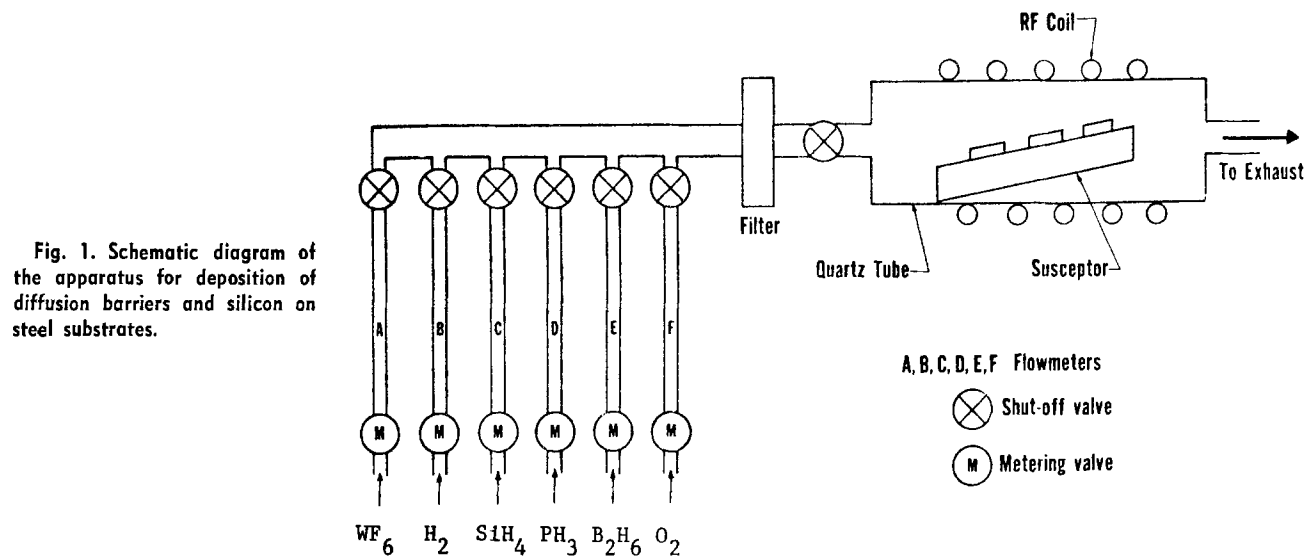
Deposition of Silicon on Coated Steel Substrates

U.S. Steel Vitrenamel I, a low carbon steel sheet used for porcelain enameling applications, and Armco silicon steel, with a large grain structure for use in transformers, were selected as substrate materials. The deposition apparatus is shown schematically in Fig. 1. The flow of various gases was controlled by appropriate valves and measured by flow meters. Hydrogen purified by diffusion through a palladium-silver alloy was used as a diluent in all deposition reactions. The reaction tube was made of fused silica and had an ID of 55 mm. The substrates were supported on a silicon-carbide-coated graphite susceptor, which was heated externally by an rf generator. Prior to the deposition process, the substrates were heated in hydrogen at 900°-1000°C to remove the iron oxide film from the surface.

The deposition of tungsten was carried out at 750°-900°C using hydrogen and tungsten hexafluoride flow rates of 20 liters/min and 8-20 ml/min, respectively.

* Electrochemical Society Active Member.

Key words: borosilicate, diffusion barrier, silicon, steel, substrate, vapor deposition.



Tightly adherent layers of tungsten were obtained at deposition rates of 0.3-0.8 $\mu\text{m}/\text{min}$. When the deposition of tungsten was followed by the deposition of silicon at 900°C or above using hydrogen containing 0.1-0.5% silane at a flow rate of 20 liters/min (9), the deposit always exhibited a grain structure similar to that of the substrate, and centimeter-size crystallites were obtained on silicon steel substrates. However, the silicon was always n-type with very low electrical resistivity, less than 10^{-3} ohm-cm by spreading resistance measurements, and chemical analysis also showed the presence of iron. Thus, the deposit consisted of a solid solution of iron disilicide in silicon, showing that tungsten was not able to prevent the diffusion of iron at 900°C and above. This is due presumably to the polycrystalline nature of deposited tungsten, where the diffusion rate of iron along the grain boundaries is considerably higher than that through the bulk. As the temperature of silicon deposition was decreased, the electrical resistivity of the silicon increased. The silicon deposited at 800°C, for example, was n-type with a resistivity of about 1 ohm-cm, indicating that the diffusion of iron was considerably reduced. Figure 2 shows the vertical cross section of a silicon/tungsten/USS Vitrenamel I specimen prepared at 800°C, where the columnar structure of tungsten is apparent.

The deposition of silica in steel substrates was carried out at 800°-900°C using hydrogen, silane, and oxygen flow rates of 20 liters/min, 25 ml/min, and 250 ml/min, respectively. Silica films of 3-5 μm thickness were adherent to the substrate and served as a good barrier

against the diffusion of iron, as indicated by the high electrical resistivity of silicon subsequently deposited at 1100°C. However, cracks were sometimes observed in the silica film, due presumably to the large difference between the thermal expansion coefficients of silica and steel. This difficulty was overcome by adding diborane to the reactant mixture to deposit borosilicate as the diffusion barrier. At temperatures above 450°C, the B₂O₃/SiO₂ molar ratio in borosilicate is very similar to the B₂H₆/SiH₄ molar ratio in the reactant mixture (8). To obtain borosilicate with a thermal expansion coefficient similar to that of silicon, the B₂H₆/SiH₄ molar ratio should be approximately 1:5. Using hydrogen, silane, diborane, and oxygen flow rates of 20 liters/min, 25 ml/min, 5 ml/min, and 250 ml/min, respectively, the deposition rate of borosilicate was approximately 0.25 $\mu\text{m}/\text{min}$ at 900°C. At lower flow rates of silane and diborane, the deposition rate was directly proportional to the flow rates of the hydrides.

Following the deposition of borosilicate on steel substrates, silicon was deposited at 900°-1150°C at rates of 0.2-2 $\mu\text{m}/\text{min}$. Tightly adherent layers were obtained in all cases. Figure 3 shows the mechanically polished and chemically etched (Sirtl etch, 10 sec) vertical cross section of a silicon/borosilicate/USS Vitrenamel I specimen prepared at 900°C, where the thicknesses of borosilicate and silicon are approximately 5 μm and 55 μm , respectively. The grain structure in silicon is revealed by etching. Silicon deposited without intentional doping was n-type with an elec-

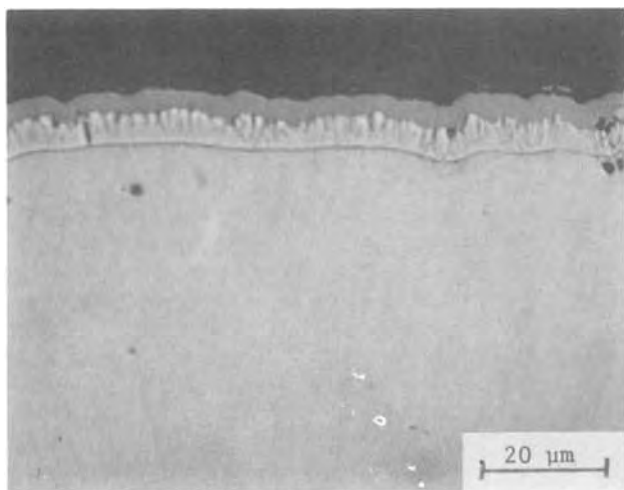


Fig. 2. Vertical cross section of a silicon/tungsten/USS Vitrenamel I specimen prepared at 800°C.

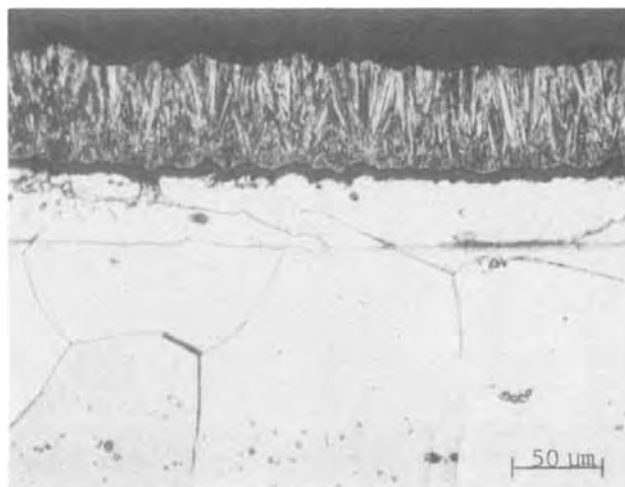


Fig. 3. Mechanically polished and chemically etched vertical cross section of a silicon/borosilicate/USS Vitrenamel I specimen prepared at 900°C.

trical resistivity of several hundred ohm-centimeters; this high electrical resistivity could be due to grain boundaries and may not be a good measure of the dopant concentration.

Silicon specimens deposited on borosilicate/steel substrates at 900°-1150°C were analyzed by the ion-probe mass spectrometric technique using an O_2^+ beam to sputter-etch the surface of the specimen. The concentration of iron was found to be below the detection limit, about 1 ppm. Although the ion beam removed only the surface layer of silicon, any iron present should have been uniformly distributed due to the high diffusion coefficient of iron in silicon at the deposition temperatures used.

Properties of Polycrystalline Silicon on Borosilicate/Steel

Since borosilicate deposited on steel is amorphous, silicon deposited on borosilicate/steel substrates is similar in properties to silicon deposited on silicon dioxide or silicon nitride (10-12). Its microstructure was found to depend strongly on the substrate temperature, deposition rate, and extent of boron doping. In general, silicon deposited at low temperatures and high rates without intentional doping consists of small crystallites. The size of crystallites increases with increasing deposition temperature, decreasing deposition rate, or the incorporation of high concentrations of boron (10^{20} cm^{-3} , for example). Figure 4 shows the micrographs of mechanically polished and chemically etched surfaces of four silicon films of about 20 μm thickness deposited under various conditions. Undoped silicon deposited at 900°C at a rate of 2 $\mu\text{m}/\text{min}$ showed a fiber-like structure (Fig. 4A). When the deposition rate was reduced to 0.2 $\mu\text{m}/\text{min}$, small crystallites of less than 1 μm size dominated (Fig. 4B). The size of the crystallites was increased appreciably by doping with a high concentration of boron (Fig. 4C) and was further increased by increasing the deposition temperature to 1000°C (Fig. 4D). The largest crystallite was about 5 μm in size, and the crystallite size also

increased with increasing thickness of the silicon layer. Furthermore, diborane was found to enhance the deposition rate of polycrystalline silicon as reported by others (13).

The crystallographic properties of many silicon layers deposited on borosilicate/USS Vitrenamel I substrates at 900°-1150°C and at 0.2-2 $\mu\text{m}/\text{min}$ containing various concentrations of dopants were examined by the x-ray diffraction technique using $\text{CuK}\alpha$ radiation. Polycrystalline silicon powder of random orientations is known to show three strong diffraction peaks associated with {111}, {220}, and {311} reflections, with 2θ values of 28.4°, 47.3°, and 56.1°, and relative intensities of 100, 60, and 35, respectively (14). The {220}/{111} intensity ratio in the diffraction spectra of the silicon layers was found to vary considerably with deposition conditions. In general, very large {220}/{111} intensity ratios were observed in layers deposited at low substrate temperatures, high deposition rates, and low concentrations of dopants. This ratio decreases with increasing substrate temperature, decreasing deposition rate, or the introduction of a high concentration of dopants (boron or phosphorus). Two extreme cases are shown in Fig. 5. Figure 5A shows the diffraction spectrum of an undoped silicon film deposited at 900°C at a rate of 2 $\mu\text{m}/\text{min}$; the {220}/{111} intensity ratio is approximately 1000, indicating that the crystallites show a strong {110} preferred orientation. Figure 5B shows the spectrum of a 0.002 ohm-cm boron-doped silicon film deposited at 1100°C at a rate of 0.2 $\mu\text{m}/\text{min}$; the {220}/{111} intensity ratio is approximately 2.5, indicating that the crystallites are more randomly oriented.

The conductivity type and electrical resistivity of silicon films on borosilicate/USS Vitrenamel I substrates were readily controlled by using diborane and phosphine as dopants in the reactant mixture (9). Many p-n junctions were prepared by varying the dopant concentrations during deposition. An example of the resistivity profile of such a structure, obtained by using a spreading resistance probe along the angle-

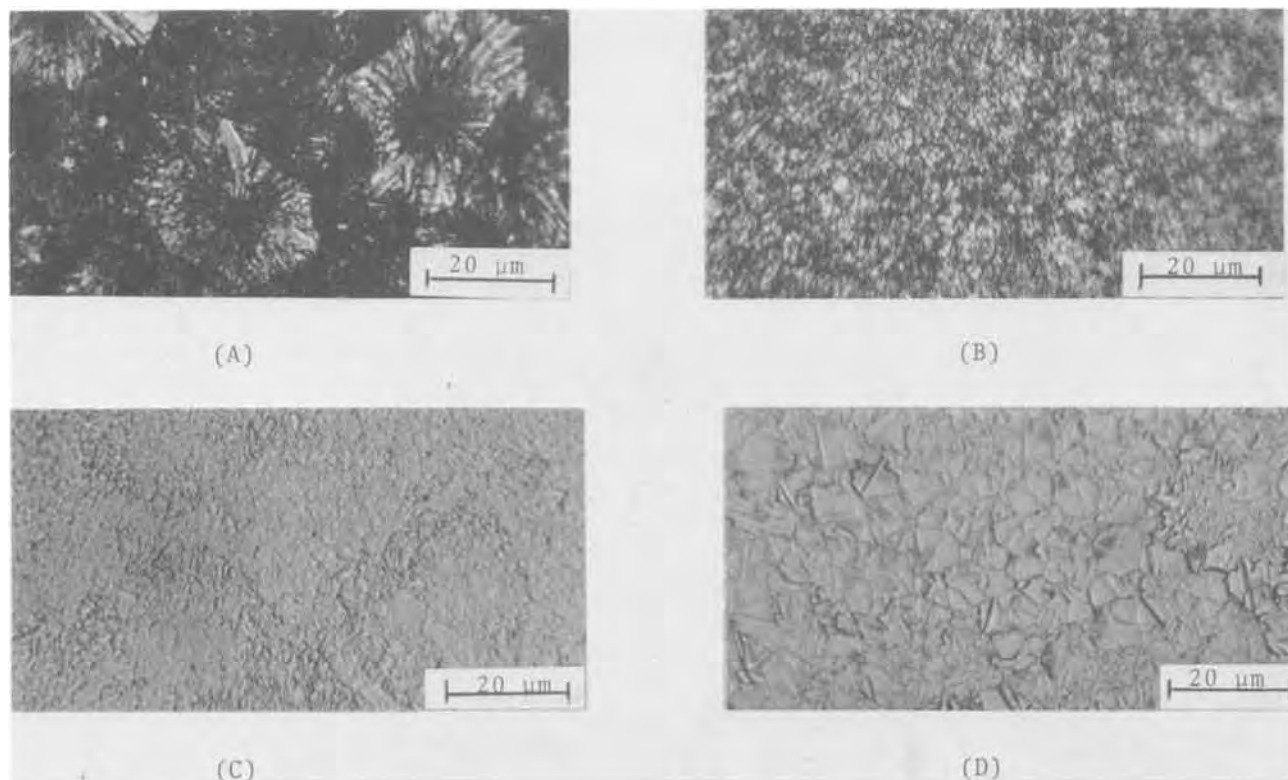


Fig. 4. Mechanically polished and chemically etched surfaces of silicon layers of 20 μm thickness deposited on borosilicate/USS Vitrenamel I substrates. (A) Undoped silicon deposited at 900°C at 2 $\mu\text{m}/\text{min}$, (B) undoped silicon deposited at 900°C at 0.2 $\mu\text{m}/\text{min}$, (C) boron-doped silicon deposited at 900°C at 0.2 $\mu\text{m}/\text{min}$, and (D) boron-doped silicon deposited at 1000°C at 0.2 $\mu\text{m}/\text{min}$.

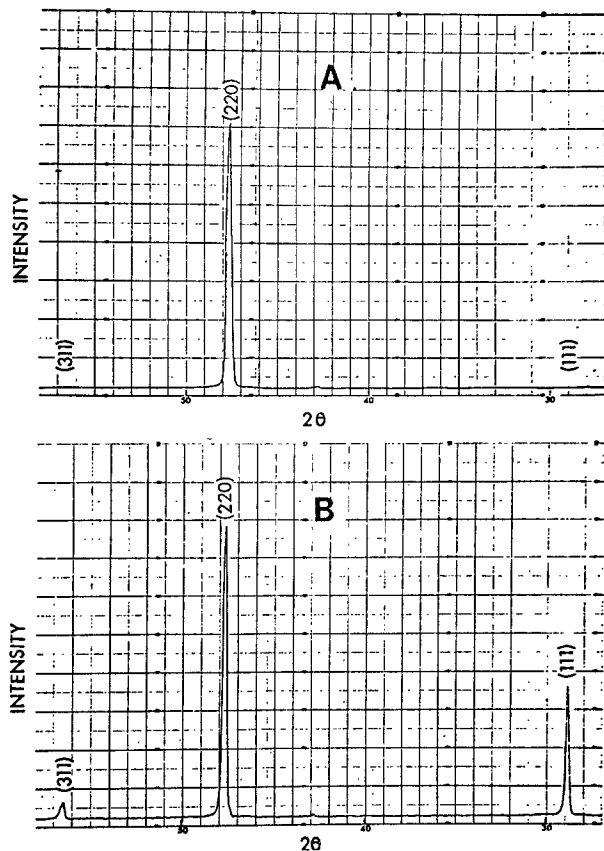


Fig. 5. X-ray diffraction spectra of silicon layers deposited on borosilicate/USS Vitrenamel I substrates. (A) Undoped silicon deposited at 900°C at 2 $\mu\text{m}/\text{min}$, and (B) 0.002 ohm-cm boron-doped silicon deposited at 1100°C at 0.2 $\mu\text{m}/\text{min}$.

lapped surface of a specimen (15), is shown in Fig. 6, where the specimen was prepared by successively depositing 5 μm of borosilicate (not shown), 35 μm of 0.002 ohm-cm p-type silicon, 5 μm of undoped silicon, and 10 μm of 0.3 ohm-cm n-type silicon on an USS Vitrenamel I substrate. The initial, relatively thick, boron-doped silicon layer was used to improve the microstructure of silicon in the junction region. Using masking and etching techniques, mesa diodes of 0.5 mm diameter were isolated. The electrical characteristics of a typical diode are shown in Fig. 7. The "n" value calculated from the forward characteristics is about 3.9 as compared with 1.5-1.9 for single-crystalline silicon p-n junctions at low voltages; this high "n" value is presumably related to the carrier recombination at grain boundaries. The grain boundaries also contribute to the relatively high reverse current. Because of the poor junction characteristics, solar cells fabricated from the structure n⁺-silicon/p-silicon/p⁺-silicon/borosilicate/USS Vitrenamel I were found to have low conversion efficiencies, less than 0.5%.

Summary

Borosilicate has been found to be an effective barrier against the diffusion of iron into silicon at temperatures up to 1150°C. Silicon has been deposited on borosilicate/steel substrates at 900°-1150°C by the thermal decomposition of silane. The deposited silicon is polycrystalline, and its microstructure and crystallographic properties are affected by the substrate temperature, deposition rate, and extent of doping. Silicon layers deposited at low temperatures and high rates consist of small crystallites with a strong preferred {110} orientation, while those deposited at high temperatures and low rates consist of larger crystallites with more random orientations. Silicon p-n junctions deposited on borosilicate/steel substrates exhibit poor electrical characteristics, and solar cells have low conversion efficiencies.

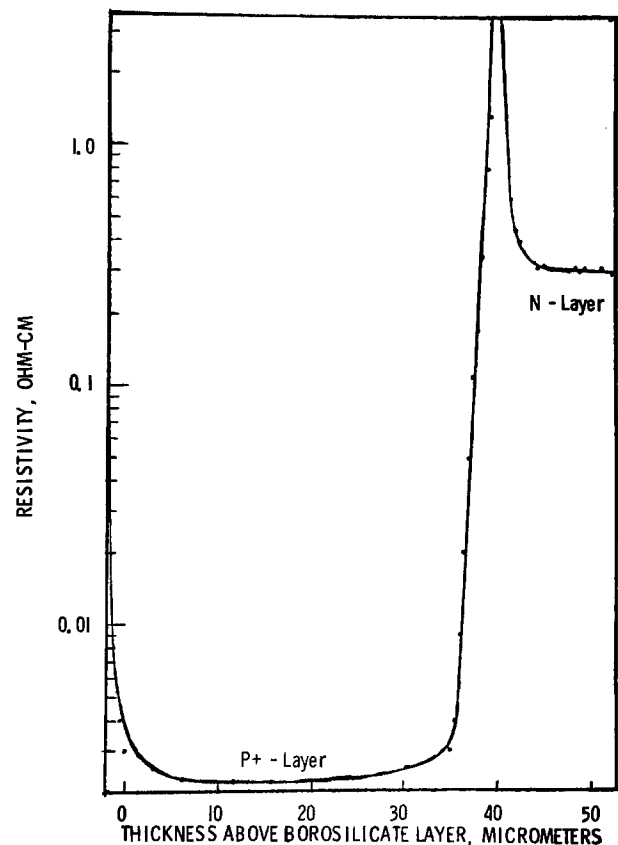


Fig. 6. Resistivity profile of polycrystalline silicon in an n-silicon/p⁺-silicon/borosilicate/USS Vitrenamel I structure.

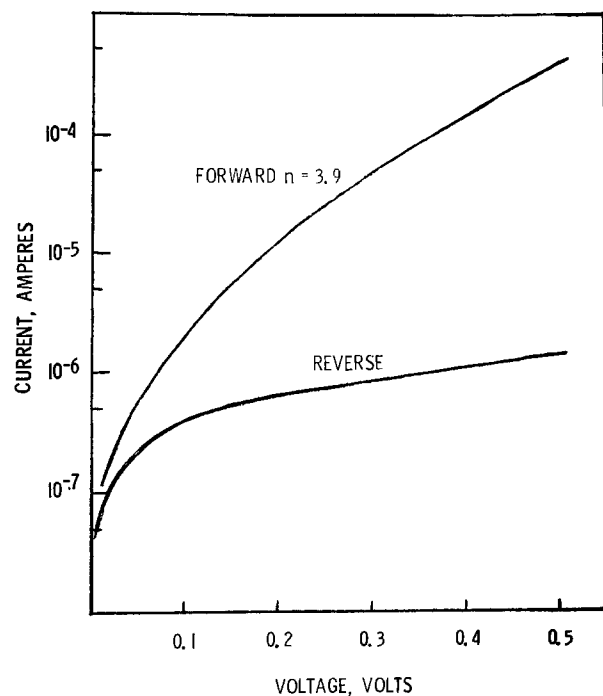


Fig. 7. Current-voltage characteristics of a polycrystalline silicon p-n junction.

Acknowledgments

The authors wish to thank Dr. James W. Flowers of Armco Steel Corporation and Dr. Don Toland of U.S. Steel Research Laboratory for their generous supply of steel samples, and Drs. Robert D. Dobrott and Gene F. Wakefield of Texas Instruments Incorporated for the ion-probe mass spectrometric analysis of silicon deposited on borosilicate/steel substrates.

This work was supported by the National Science Foundation, Research Applied to National Needs (RANN), under grant GI-38981.

Manuscript submitted Aug. 29, 1974; revised manuscript received Aug. 8, 1975. This was Paper 22 presented at the San Francisco, California, Meeting of the Society, May 12-17, 1974.

Any discussion of this paper will appear in a Discussion Section to be published in the June 1976 JOURNAL. All discussions for the June 1976 Discussion Section should be submitted by Feb. 1, 1976.

Publication costs of this article were partially assisted by Southern Methodist University.

REFERENCES

1. C. H. Fa and T. T. Jew, *IEEE Trans. Electron Devices*, **ED-13**, 290 (1966).
2. F. Fagin and T. Klein, *Solid-State Electron.*, **13**, 1125 (1970).
3. D. McWilliams, C. H. Fa, G. A. Larchian, and O. Maxwell, Jr., *This Journal*, **111**, 153C (1964).
4. M. Hansen, "Constitution of Binary Alloys," p. 713, McGraw-Hill Book Co., New York (1958).
5. W. A. Bryant, in "Chemical Vapor Deposition, Second International Conference," John M. Blocher, Jr. and James C. Withers, Editors, p. 409, The Electrochemical Society Softbound Symposium Series, New York (1970).
6. C. J. Frosch and L. Derick, *This Journal*, **104**, 547 (1957).
7. T. L. Chu, J. R. Szedon, and G. A. Gruber, *Trans. Met. Soc. AIME*, **242**, 538 (1968).
8. W. Kern and R. C. Heim, *This Journal*, **117**, 562 (1970).
9. T. L. Chu and G. A. Gruber, *ibid.*, **114**, 522 (1967).
10. A. L. Frupp and R. L. Stermer, *ibid.*, **117**, 1569 (1970).
11. C. C. Mai, T. S. Whitehouse, R. C. Thomas, and D. R. Goldstein, *ibid.*, **118**, 331 (1971).
12. M. E. Cowher and T. O. Sedgwick, *ibid.*, **119**, 1565 (1972).
13. F. C. Eversteyn and B. H. Put, *ibid.*, **120**, 106 (1973).
14. H. E. Swanson and R. K. Fuyat, NBS Circular **539**, p. 8 (1953).
15. R. G. Mazur and D. H. Dickey, *This Journal*, **113**, 255 (1966).

Low Surface Concentration of Boron in Silicon by Diffusion Through Silicon Dioxide

W. von Muench and C. Gessert

Institut A fuer Werkstoffkunde, Technische Universitaet, D-3000 Hannover, Germany

ABSTRACT

It is shown that the diffusion of boron through a thin silicon dioxide layer can be used to control the surface acceptor concentration in silicon within the range from 5×10^{15} to 2×10^{20} cm^{-3} , with the junction depth varying from 0 to 15 μm . The diffusion constant of boron in SiO_2 was determined to be $D_1 = 3.4 \times 10^{-6} \exp(-2.60 \text{ eV}/kT)$ cm^2/sec , for a boron surface concentration of about 2×10^{19} cm^{-3} . Examples for the technical application of this method are briefly discussed.

Silicon dioxide is extensively used for masking purposes in the silicon planar technology. Consequently, the main objective of the early work on impurity diffusion in silicon dioxide was an examination of those experimental conditions for which the limit of complete masking is reached (1, 2). In the technology of III-V compounds, on the other hand, the method of diffusion through a thin protective layer has served mainly to eliminate surface erosion problems (3, 4). It was pointed out also that diffusion through a solid layer into a semiconductor body can facilitate the generation of specific impurity concentration profiles (5). More recently, it was observed that a thin ($\sim 100\text{\AA}$) layer of silicon dioxide grown by hot nitric acid cleaning of silicon wafers may have a significant influence on the impurity surface concentration obtained by subsequent diffusion from a solid source layer (6, 7). The diffusion of gallium through silicon dioxide films into silicon was studied recently by MOS techniques (8). It is the purpose of this contribution to demonstrate the possibility of achieving surface concentrations in the 5×10^{15} to 2×10^{20} cm^{-3} range with good reproducibility by diffusion of boron through a silicon dioxide layer of appropriate thickness. This technique is useful especially for devices comprising regions with low and high surface concentrations of the same conductivity type (or shallow and deep p-n junctions).

There are numerous experiments on boron diffusion reported in the literature. A survey on these results has been published recently by Ghezzi and Brown (9).

Key words: boron diffusion, silicon dioxide, junction depth, sheet resistivity.

The resulting figures for the diffusion coefficient of boron in silicon dioxide are covering a very large range (e.g., activation energy from 2.38 to 3.58 eV). While some of the discrepancies may be properly explained in terms of a concentration dependent diffusivity, it is felt that the various experimental conditions (e.g., type of source) must also be taken into account in an assessment of the diffusivity data. In view of the particular nature of the source material employed by the authors (boron-doped silicon powder), a redetermination of the diffusion constant of boron in silicon dioxide and a comparison with published data seemed to be useful.

Theory

The one-dimensional theory for the diffusion of impurities from a semi-infinite high-diffusivity source (gas phase) through a partially masking layer into a semiconductor body has been developed previously (2). With notations according to Fig. 1a one obtains the following expression for the diffused impurity concentration in silicon

$$C_2(x,t) = m(1-a)C_0 \sum_{n=0}^{\infty} a^n \operatorname{erfc} \left[\frac{(2n+1)x_0}{L_1} + \frac{x}{L_2} \right] \quad [1]$$

where m is the distribution coefficient, D_1 the diffusion coefficient in silicon dioxide, D_2 the diffusion coefficient in silicon, and $L_1 = 2\sqrt{D_1 t}$, $L_2 = 2\sqrt{D_2 t}$, $a = (m-r)/(m+r)$, $r = \sqrt{D_1/D_2}$ ($t =$ diffusion time).

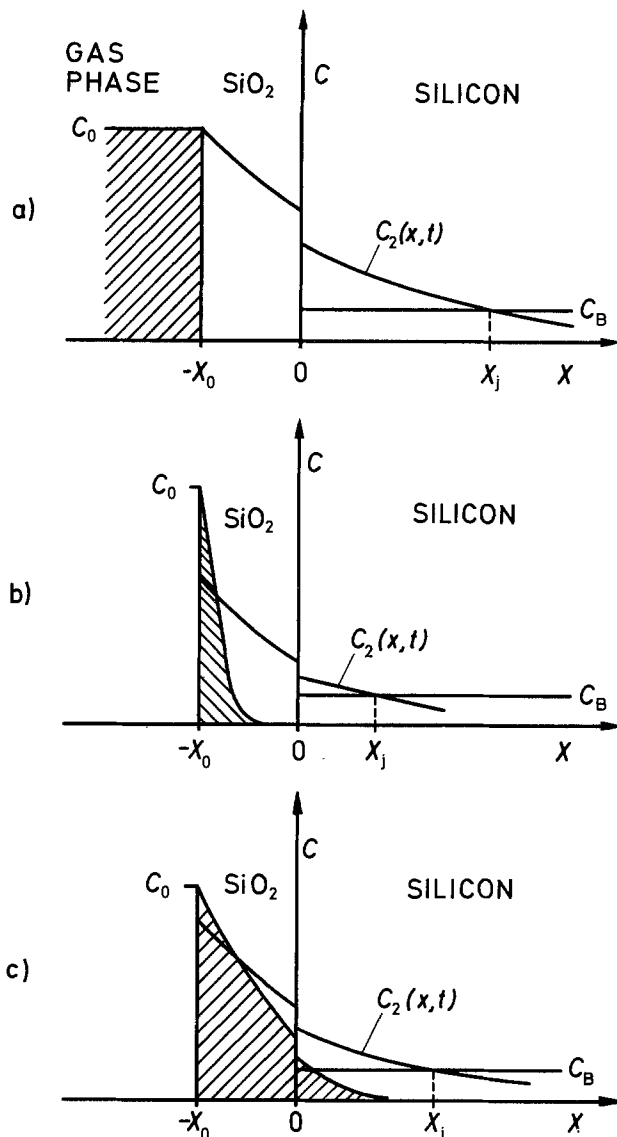


Fig. 1. Impurity concentration profile to be obtained by diffusion through silicon dioxide. (a) Diffusion from gas phase. (b) Diffusion with shallow predeposition. (c) Diffusion with deep predeposition.

If the bulk contains a uniform impurity concentration C_B of opposite conductivity type than the diffusant, a p-n junction will result at a depth x_j which is determined by setting $C_2(x,t) = C_B$ in Eq. [1]. For the condition of almost complete masking, i.e., $x_0/L_1 > x_j/L_2$, $x_0/L_1 > 0.7$, only the zero order term needs to be retained in the summation. This yields a simple relationship between the junction depth and the oxide thickness

$$x_j = -\frac{1}{r} x_0 + L_2 \arg \operatorname{erfc} \frac{C_B}{m(1-a)C_0} \quad [2]$$

from which r may be deduced. Plotting x_j vs. x_0 for a series of diffusion experiments with varying temperature, one obtains the difference of the activation energies of the diffusion in silicon dioxide (E_1) and in silicon (E_2)

$$E_1 - E_2 = \left(\frac{1}{kT_2} - \frac{1}{kT_1} \right)^{-1} \ln \frac{r^2(T_1)}{r^2(T_2)} \quad [3]$$

In practice, the diffusion from an infinite gaseous source is often employed during the initial stage of the diffusion process only. In this case, a thin solid source is formed within the top layer during the predeposition step; a redistribution of impurities then takes place during the main diffusion cycle (Fig. 1b). Due to the limited amount of impurity atoms available in this case, the concentration C_2 will be lower than predicted by Eq. [1]. Alternatively, a prolonged predeposition may produce an impurity distribution according to the hatched area of Fig. 1c. The main diffusion will then yield a final distribution which is close to that of Eq. [1] if the total diffusion time is of the same order of magnitude as the predeposition time.

Experimental

N-type silicon wafers of (111) orientation were carefully cleaned in organic solvents, boiling nitric acid, and distilled water. These wafers were oxidized at 1050°C in a dry oxygen stream with a flow rate of 12 liters/hr. The oxidation time was varied between 20 and 180 min in order to produce oxide layers in the 500-1800Å range. The oxide thickness was measured with a "Dektak" surface profile measuring instrument (Sloan Corporation) with an estimated accuracy of $\pm 10\text{Å}$ for SiO_2 layers up to 1000Å and $\pm 25\text{Å}$ for thicker SiO_2 layers. The boron predeposition step was performed in a sealed quartz system with a powdered silicon/boron source ($N_A = 2 \times 10^{20} \text{cm}^{-3}$). Experiments for the reevaluation of the boron diffusion coefficient in SiO_2 were carried out in the 1000°-1200°C temperature range, the diffusion time (1-20 hr) being adjusted to yield a junction depth sufficiently large for evaluation. The bulk donor concentration was $5 \times 10^{14} \text{cm}^{-3}$.

The generation of low-concentration boron diffused layers in silicon requires a two-step process. The electrical data of the bulk silicon and the predeposition conditions pertaining to the four series of experiments (A-D) described in this paper are summarized in Table I. The main diffusion (drive-in step without external source) was performed in an open-flow system at 1150°C with a slightly oxidizing ambient (50 liters/hr nitrogen plus 0.5 liter/hr oxygen). The diffusion time ranged from 1 to 128 hr. Standard four-point probe and beveling techniques were employed to determine the sheet resistivity and the junction depth.

Results and Discussion

The experimental relation between the normalized junction depth, x_j/\sqrt{t} , and the normalized oxide thickness, x_0/\sqrt{t} , is plotted in Fig. 2. From the straight lines fitting the experimental data one obtains the boron diffusion constant D_1 and the activation energy E_1 according to Eq. [2] and [3]. Using recently published data for the boron diffusion in silicon by Fair (10) it is concluded that the diffusion constant of boron in silicon dioxide is

$$D_1 = 3.4 \times 10^{-6} \exp(-2.60 \text{ eV}/kT) \text{ cm}^2/\text{sec}$$

with a boron/silicon source (2×10^{20} boron atoms/ cm^3). This result is compared in Table II with literature data, taken from the summary compiled by Ghezzi and Brown (9). In Table II the diffusion constants are

Table I. Electrical data of bulk silicon and diffusion conditions for experimental series A-D

	A	B	C	D
Bulk resistivity ρ_B (ohm-cm)		6.7-8.7		0.48-0.8
Bulk donor concentration C_B (cm^{-3})	5.2×10^{14} - 7×10^{14}		6.4×10^{15} - 1.3×10^{16}	
Predeposition temperature (°C)	1000	1150	1000	1150
Predeposition time (min)		60		60
Main diffusion temperature (°C)		1150		1150
Main diffusion time (hr)		1-128		1-128

Table II. Summary of boron diffusion constants in silicon dioxide $D_1 = D_0 \exp - E_1/kT$

Source	D_0 (cm ² /sec)	E_1 (eV)	Surface boron concentration, C_s (cm ⁻³)	Researched by author(s)
Borosilicate	7.4×10^{-4}	3.58	$4-8 \times 10^{19}$	Barry and Olofsen (1969)
Borosilicate	3.0×10^{-2}	3.56	2×10^{20}	Schwenker (1971)
Borosilicate	3.2×10^{-4}	3.53	$<3 \times 10^{20}$	Brown and Kennicott (1971)
B ₂ O ₃ vapor	1.2×10^{-4}	3.39	6×10^{18}	Horifuchi and Yamaguchi (1962)
Borosilicate	1.6×10^{-5}	2.82	7×10^{19}	Schwenker (1971)
B/Si	3.4×10^{-6}	2.60	$\sim 2 \times 10^{19}$	This work
B ₂ O ₃ vapor	7.2×10^{-6}	2.38	$10^{18}-10^{20}$	Thurston et al. (1961)

listed in the order of decreasing activation energy. It is obvious that the activation energy increases with increasing boron concentration. The surface concentration C_s of this work was estimated from the extrap-

Table III. Approximate limits of junction depth and sheet resistivity obtained with diffusion conditions according to Table I

Diffusion condition	x_j (μ m)	ρ_{\square} (ohm)
A	0-8	$2 \times 10^8-10^5$
B	0.5-12	10^2-10^4
C	0-4	$2 \times 10^8-5 \times 10^4$
D	0.5-10	10^2-10^4

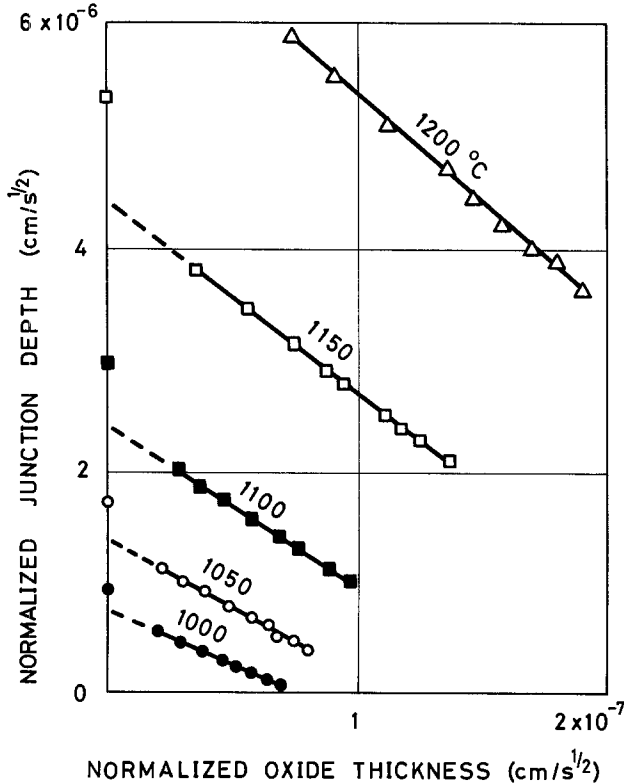


Fig. 2. Normalized junction depth vs. normalized oxide thickness, obtained by boron diffusion through SiO₂ (bulk concentration $C_B = 5 \times 10^{14}$ cm⁻³).

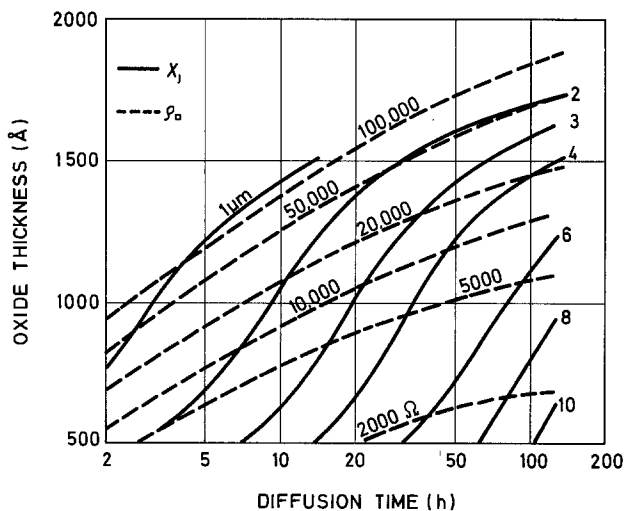


Fig. 3. Relation between oxide thickness, diffusion time, junction depth, and sheet resistivity (predeposition at 1000°C, $C_B = 5 \times 10^{14}$ cm⁻³, series A).

lation of the $x_j(x_0)$ lines (Fig. 2) compared with the junction depth obtained by diffusion without an intermediate SiO₂ layer.

The results of two-step diffusion experiments, with parameters according to Table I, are shown in Fig. 3-6. A wide range of diffusion depths and sheet resistivities can be accomplished by properly selecting the experimental conditions. For an arbitrary pair of x_j and ρ_{\square} (within some limits compiled in Table III) one can find the appropriate diffusion procedure from one of the figures (Fig. 3-6). This includes the fabrication of closely compensated layers in the 10⁵ ohm/□ range.

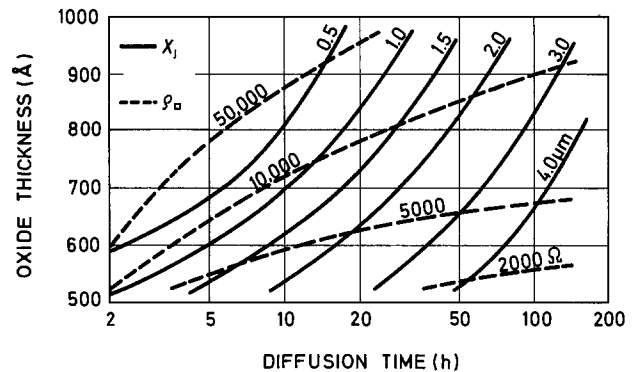


Fig. 4. Relation between oxide thickness, diffusion time, junction depth, and sheet resistivity (predeposition at 1000°C, $C_B = 7 \times 10^{15}$ cm⁻³, series C).

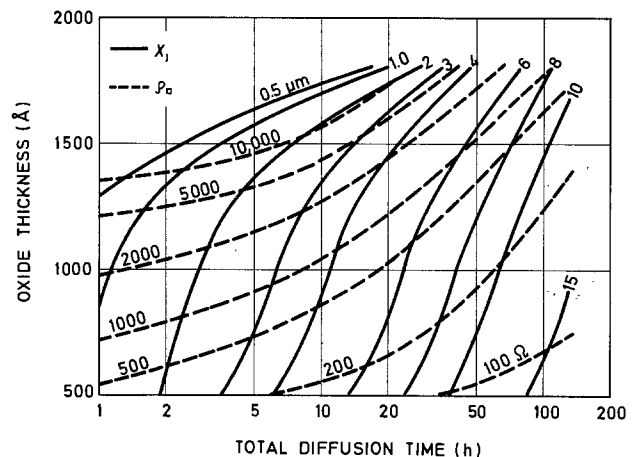


Fig. 5. Relation between oxide thickness, diffusion time, junction depth, and sheet resistivity (predeposition at 1150°C, $C_B = 5 \times 10^{14}$ cm⁻³, series B).

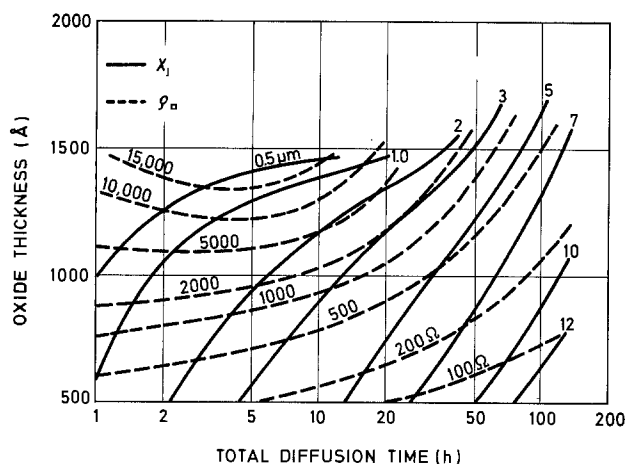


Fig. 6. Relation between oxide thickness, diffusion time, junction depth, and sheet resistivity (predeposition at 1150°C , $C_B = 7 \times 10^{15} \text{ cm}^{-3}$, series D).

The low resistivity limit is set by the source impurity concentration.

The experiments on which Fig. 3 and 4 are based (series A and C) were performed with a low-temperature (1000°C) predeposition step, yielding an impurity profile according to Fig. 1b. This type of predeposition is appropriate for the generation of very shallow, low impurity concentration p-layers. Series B and D (Fig. 5 and 6), on the other hand, involve a high-temperature (1150°C) predeposition step. A shallow junction is formed during the predeposition, which moves farther into the bulk silicon during the drive-in step (Fig. 1c). This type of diffusion can produce sheet resistivities in the 200-400 ohm/ \square range, as required for the base region of junction transistors.

Applications

The technique of boron diffusion through a partially masking silicon dioxide layer is most useful for those devices which require a low concentration p-type region or two regions with different doping levels (or a shallow and a deep p-n junction). A reduction of fabrication costs for integrated circuits may be achieved by the simultaneous generation of the base regions, diodes, and resistors (with partially masking oxide) and the isolation frames (without oxide). Figure 7 describes the sequence of fabrication steps for the transistor region of an integrated circuit.

Exploratory logic circuits have been produced by the above described technique, with diffusion parameters according to Table IV. Figure 8 shows an angle lap through a transistor region, including the isolation frame which was produced in the same diffusion step as the base. A current amplification of 100 at $I_c = 5 \text{ mA}$ was obtained with boron diffusion through SiO_2 and standard (POCl_3) emitter diffusion techniques.

High-sensitivity photodetectors for ultraviolet radiation require a very shallow junction and a diffused impurity surface concentration which slightly exceeds

Table IV. Technological data for the fabrication of integrated circuits by simultaneous diffusion of base and isolation regions

Diffusion parameters	
Substrate carrier concentration (cm^{-3})	1.5×10^{16} (p)
Epitaxial layer carrier concentration (cm^{-3})	2.5×10^{16} (n)
Totally masking oxide (\AA)	3400
Partially masking oxide (\AA)	950
Predeposition	
Main diffusion	1150°C , 1 hr
Junction depth (μm)	7.1
Sheet resistivity without oxide (ohm)	20
Junction depth (μm)	2.5
Sheet resistivity with partially masking oxide (ohm)	980
Emitter junction depth (μm)	1.2
	} isolation
	} base

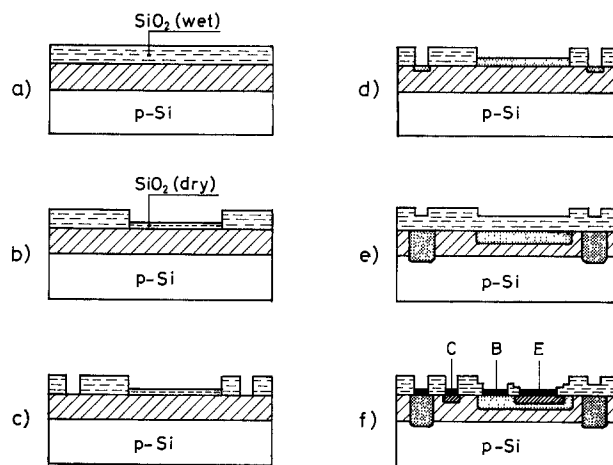


Fig. 7. Sequence of fabrication steps for integrated circuits (transistor section). (a) Epitaxy and wet oxidation. (b) Dry oxidation. (c) Opening of isolation frames. (d) Predeposition. (e) Drive-in diffusion. (f) Complete device.

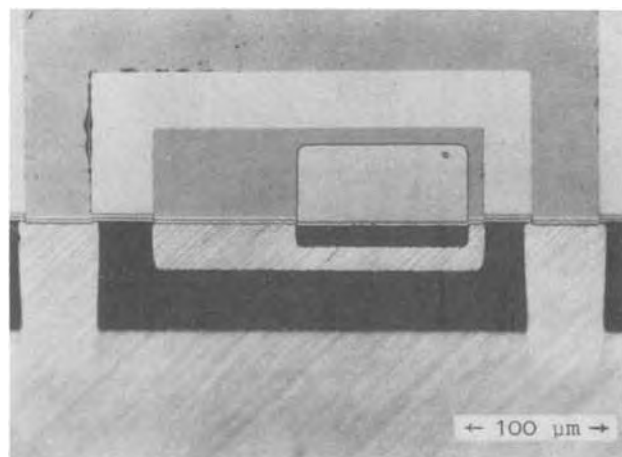


Fig. 8. Photomicrograph of angle lap through an integrated circuit (transistor section), produced by simultaneous diffusion of base and isolation regions.

the bulk doping level. Devices of this kind have been successfully produced, the quantum efficiency exceeding 90% at a wavelength of 366 nm (11).

Other applications of the technique described in this paper may include uhf-(pedestal-)transistors, guarding diodes, and the tailoring of the channel region of MOS structures.

Manuscript submitted Feb. 4, 1975; revised manuscript received Aug. 5, 1975.

Any discussion of this paper will appear in a Discussion Section to be published in the June 1976 JOURNAL. All discussions for the June 1976 Discussion Section should be submitted by Feb. 1, 1976.

Publication costs of this article were partially assisted by the Technische Universitaet, Hannover.

REFERENCES

1. R. B. Allen, H. Bernstein, and A. D. Kurtz, *J. Appl. Phys.*, **31**, 334 (1960).
2. S. Horiuchi and J. Yamaguchi, *Japan J. Appl. Phys.*, **1**, 314 (1962).
3. T. H. Yeh, *This Journal*, **111**, 253 (1964).
4. S. R. Shortes, J. A. Kanz, and E. C. Wurst, *Trans. Met. Soc. AIME*, **230**, 300 (1964).
5. W. von Muench, Proc. Second Intern. Symposium on Gallium Arsenide, Dallas, 1968, p. 77.
6. J. Middelhoeck and J. Holleman, *This Journal*, **121**, 132 (1974).

7. J. Middelhoek and J. Holleman, Report Technische Hogeschool Twente, Kenmerk 1213.1156 (1973).
8. S. Wagner and E. I. Povilonis, *This Journal*, **121**, 1487 (1974).
9. M. Ghezzeo and D. M. Brown, *ibid.*, **120**, 146 (1973).
10. R. B. Fair, *ibid.*, **122**, 800 (1975).
11. C. Gessert, M. Königer, and W. v. Münch, To be published.

The Diffusion of Ion-Implanted Arsenic in Silicon

Richard B. Fair* and Joseph C. C. Tsai

Bell Laboratories, Reading, Pennsylvania 19603

ABSTRACT

In order to characterize implanted-diffused As layers in Si and to develop general processing information, impurity profiles were determined by secondary ion mass spectrometry (SIMS) and differential conductivity measurements. An analysis of these profiles is given which has yielded information regarding the diffusion of As and the electrical quality of these implanted-diffused layers. It is shown that implanted-diffused As profiles with $C_{TO} \geq 1 \times 10^{20} \text{ cm}^{-3}$ can be described by a Chebyshev polynomial approximation to the diffusion equation with concentration-dependent diffusivity. The diffusion of As is not dependent upon the furnace ambient, but As pile-up within 200-400Å of the Si surface does occur during diffusion in an oxidizing atmosphere. It is also shown that implanted-diffused As layers show higher electrical activity for diffusion temperatures below 1100°C than layers diffused from chemical sources. For implanted As layers in which the peak concentration is greater than the solubility limit, the fraction of electrically active As increases at a rate proportional to $t^{1/3}$.

When As is diffused into Si from chemical sources such as doped oxides or solid As in evacuated ampuls, chemical reactions occur in the Si which create inactive As complexes, thus limiting the solubility of the electrically active As (1). It has been suggested that vacancies are involved in these complexes (1, 2) because of the strong cooperative diffusion effects that exist between sequentially diffused As and B layers in Si (3). However, it was recently pointed out that cooperative diffusion effects between As and B are reduced to an electric-field interaction when the source of As is an ion-implanted As layer in the Si (4). The results of that study suggested that As complexes appear to be formed very rapidly during implantation or annealing, and the existence of such complexes is dose dependent.

Since these initial studies were performed, a large amount of ion-implanted-diffused As profile data have been measured in an attempt to study the characteristics of As ion predepositions as diffusion sources. These data in conjunction with Hall mobility measurements have also aided in the construction of a resistivity vs. electron concentration curve for As in Si that is more accurate than Irvin's curve (5) at concentrations $> 10^{20} \text{ cm}^{-3}$. In addition, general relationships describing the important profile parameters have been derived (6).

In the next section the experimental details of this study will be described. An analysis of the experimental results will follow which will cover total As profile shapes, As diffusivity, and electrical activity.

Experimental

Profile determination.—Silicon of $\langle 100 \rangle$ orientation, p-type, 0.2 ohm-cm bulk slices and As-doped n-type epitaxial Si, 0.6 ohm-cm (8-11 μm thick) on p-type 8 ohm-cm substrates was used in the present study. All As implantations were performed at 50 keV in the dose range 1×10^{15} to $2 \times 10^{16} \text{ cm}^{-2}$. The implantations were directed in a random orientation (slices tilted $\sim 8^\circ$ toward the ion beam). All diffusions of the as-implanted samples were performed in N_2 or O_2 over the temperature range 900°-1200°C and in wet O_2

at 1050°C. After diffusion, the slices were divided, one-half for differential conductivity profile measurements and the other half for profile measurements by secondary ion mass spectrometry (SIMS).

Details of the differential conductivity measurements have been given elsewhere (7, 8). Anodizations were generally performed at 100V in a mixture of tetrahydrofurfuryl alcohol and potassium nitrite (9). 200 $\pm 20\text{Å}$ of Si was removed for each oxidation step as measured on an ellipsometer.

The in-depth total As profiles were determined by mass analysis of secondary ions ejected from the samples by 15 keV oxygen ion (predominantly O_2^+) bombardment using the Cameca IMS 300 Ion Analyzer (8). AsO^- secondary ions were selected and counted using an AS-200 multichannel analyzer. The analyzer data was converted to As concentration vs. depth by a method previously described (8). Calibration was achieved by knowing the total implanted dose in the Si.

Resistivity vs. electron concentration.—In order to convert the differential conductivity data into concentration of electrons (electrically active As concentration), Hall mobility measurements were obtained on samples that had been profiled. In addition, the data of Müller *et al.* (10) (Hall measurements on As-implanted samples) and the data of Fistul' (11) and Logan (12) (Hall measurements of As-doped samples) were converted to resistivity vs. electron concentration, where it was assumed that μ_H (Hall mobility) equals μ_c (conductivity mobility). This assumption should be valid under conditions of degeneracy (11). These data are shown in Fig. 1. Also shown are direct resistivity measurements taken on well-annealed As-implanted samples that had been profiled by SIMS as well as by the differential conductivity method on profiles which gave 100% electrical activity. The concentration values associated with these data are the total local As concentration. Thus, none of the data in Fig. 1 have been determined by Irvin's curve (5), which is shown plotted for comparison. It can be seen that Irvin's curve underestimates the free-electron concentration in As-doped Si layers by as much as 30% over the range $10^{20} < n < 4 \times 10^{20} \text{ cm}^{-3}$. This is probably due to the fact that Irvin used total phosphorus con-

* Electrochemical Society Active Member.
Key words: ion implantation, arsenic diffusion, solubility, electrical activity.

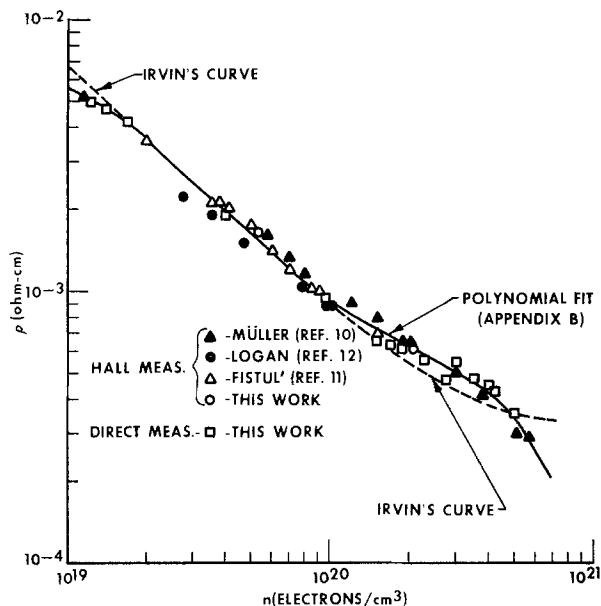


Fig. 1. Resistivity vs. electron concentration for arsenic-doped silicon.

centration vs. resistivity data in order to establish this portion of his curve (5). A polynomial fit for the As data is given in Appendix B.

Analysis of Results

Total As profiles.—Implanted-diffused As.—The results of the experimental determination of total As profiles in Si are shown in Fig. 2 where concentration data normalized to total As surface concentration, C_{TO} , are plotted vs. normalized junction depth (x_J was selected as the depth at which C falls to $0.01 C_{TO}$). These data represent implantations at 50 keV (dose range 2×10^{15} to 2×10^{16} cm^{-2}) which were diffused at 1000°C – 1200°C for various times. It can be seen that most of the data can be described in total concentration, C (cm^{-3}), and depth, x (cm), by the simple equation (13)

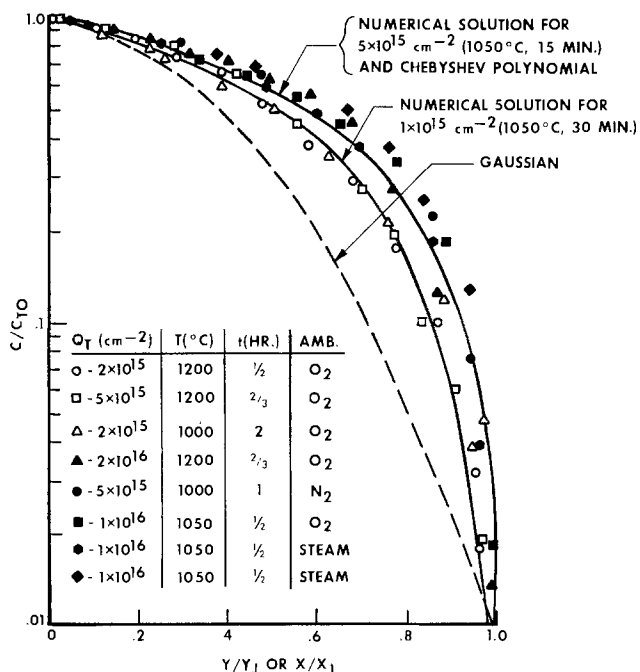


Fig. 2. Normalized total As profiles of implanted-diffused layers in Si. The numerical solutions to the diffusion equation are compared to the polynomial approximation for two different implant doses.

$$\frac{C}{C_{TO}} = 1 - 0.87Y - 0.45Y^2 \quad [1]$$

where

$$Y = x(8C_{TO}D_1t/n_i)^{-1/2} \quad [2]$$

D_1 and n_i are the intrinsic As diffusivity and intrinsic electron concentration at the diffusion temperature, respectively. Equation [1] was originally used as a Chebyshev polynomial approximation to the solution of the diffusion equation with linear concentration-dependent diffusivity and constant surface concentration (14). For the diffusion conditions studied the arsenic surface concentration is a slow varying function of diffusion temperature and time, hence, a constant surface concentration of arsenic can be assumed as a first order approximation.

When Eq. [1] is compared to high accuracy numerical solutions of the diffusion equation describing the relaxation of an implanted gaussian impurity distribution, it is found that if the diffusivity is expressed as (assuming 100% electrical activity)

$$\frac{D}{D_i} = \frac{2C}{n_i}, \text{ for } C \gg n_i \quad [3]$$

then Eq. [1] agrees exactly with the numerical results. Equation [1] was derived using the D vs. C expression of Eq. [3].

A more exact expression for As diffusivity in the absence of As complexing is (15)

$$\frac{D}{D_i} = h \left(\frac{1 + \beta f}{1 + \beta} \right) \quad [4]$$

where

$$h = 1 + \frac{C}{2n_i} \left[\left(\frac{C}{2n_i} \right)^2 + 1 \right]^{-1/2} \quad [5]$$

is the self electric-field enhancement factor (2 factor in Eq. [3])

$$f = \frac{C}{2n_i} + \left[\left(\frac{C}{2n_i} \right)^2 + 1 \right]^{1/2} \quad [6]$$

and $\beta \approx 100$ for positively charged donor impurities (15). The factor f is approximately linearly proportional to the ionized donor concentration, C_A , when $C_A = C \gg n_i$, and Eq. [4] reduces to Eq. [3] at high concentrations.

The result of using Eq. [4], [5], and [6] in the numerical solutions is that the As profile shape is not uniquely described by Eq. [1], but is a function of the surface concentration (or implant dose and diffusion time and temperature). The normalized solution of the diffusion equation for a $5 \times 10^{15} \text{ cm}^{-2}$, 50 keV As implant diffused at 1050°C for 15 min ($C_{TO} = 2.5 \times 10^{20} \text{ cm}^{-3}$) is shown plotted in Fig. 2. This solution agrees almost exactly with Eq. [1]. However, the normalized solution for a $1 \times 10^{15} \text{ cm}^{-2}$, 50 keV As implant diffused at 1050°C for 30 min ($C_{TO} = 7.4 \times 10^{19} \text{ cm}^{-3}$) deviates from Eq. [1], but it describes those data of the first 3 sets of points in the insert of Fig. 2, with C_{TO} of 4×10^{19} to $1 \times 10^{20} \text{ cm}^{-3}$. In Fig. 2, the remaining data were taken from profiles for which $C_{TO} > 1 \times 10^{20} \text{ cm}^{-3}$ and they are represented by the polynomial approximation. As C_{TO} approaches n_i , the diffusion coefficient becomes independent of concentration and the As profile approaches a gaussian distribution.

Chemical source As diffusion.—In contrast to the well-behaved, reproducible As profile from ion implanted-diffused samples, the normalized total concentration profiles from constant As surface concentration chemical sources (doped oxides and ampuls) are shown in Fig. 3 for comparison. The difficulty in obtaining a general profile shape for a given C_{TO} for these profiles lies in the complicated properties of the As diffusion coefficients which are affected by the formation of As complexes and by the background substrate con-

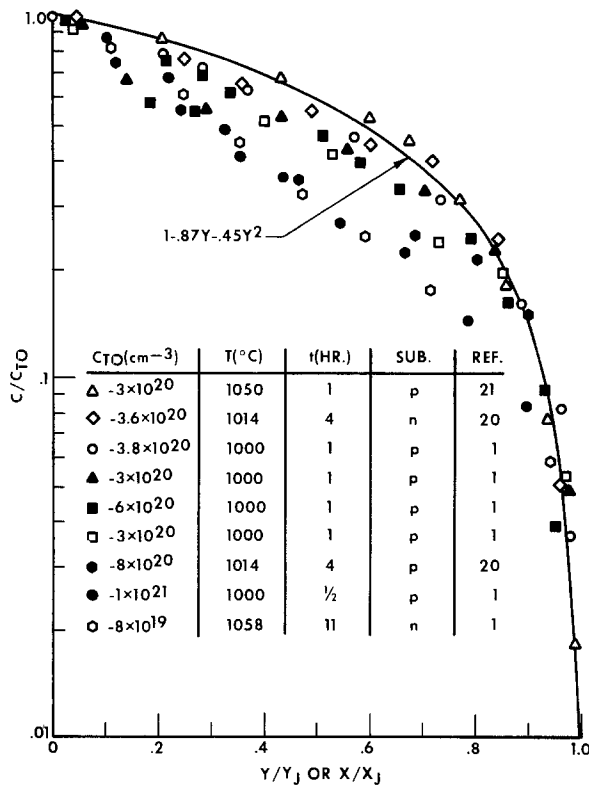


Fig. 3. Normalized total As profiles of diffused layers from chemical sources.

ductivity type (1). It has been reported previously (4) that rapid annealing of As complexes of high dose ion-implanted As layers occurs, and the As diffusion from such layers is, therefore, better behaved.

Diffusion coefficient.—The intrinsic arsenic diffusivity, D_i .—In order to determine the concentration-dependent diffusion coefficients from the measured As profiles and, thus, check the validity of Eq. [4], it was necessary to develop an expression for diffusivity that was applicable to a redistributing impurity of fixed total concentration, Q_T . Since the Boltzmann-Matano analysis requires diffusion from a constant surface concentration, it cannot be applied to diffusion from an ion-implanted source. As shown in Appendix A for diffusion from a predeposited source (i.e., a delta function)

$$D = \frac{-C(x_0, t)(x_0 + x_{ox})}{2t \left. \frac{dC}{dx} \right|_{x_0}} \quad [A-16]$$

where D is the diffusivity at a depth x_0 from the surface, and x_{ox} is the thickness of the SiO_2 that is grown during the As diffusion process.

Equation [A-16] has been applied to determine D vs. the concentration of total As from the measured ion-implanted-diffused profiles, and these results are shown in Fig. 4 for the diffusion temperature range 1000°-1200°C. For diffusions performed in O_2 and wet O_2 , the oxide thicknesses were measured following diffusion, and these values were used in the calculations of D . It can be seen that the As diffusivity in Si does not depend on the diffusion ambient.

From Eq. [4] values of D_i were obtained which best described the data in Fig. 4. These results are shown as a function of diffusion temperature in Fig. 5. Also shown are the diffusivity data from Chan and Mai (16) obtained by driving-in low concentration As predeposited layers, and the D_i value at 900°C of Baldo *et al.* (17) from As ion-implanted layers. It can be seen that the temperature dependence of these data is given by the expression

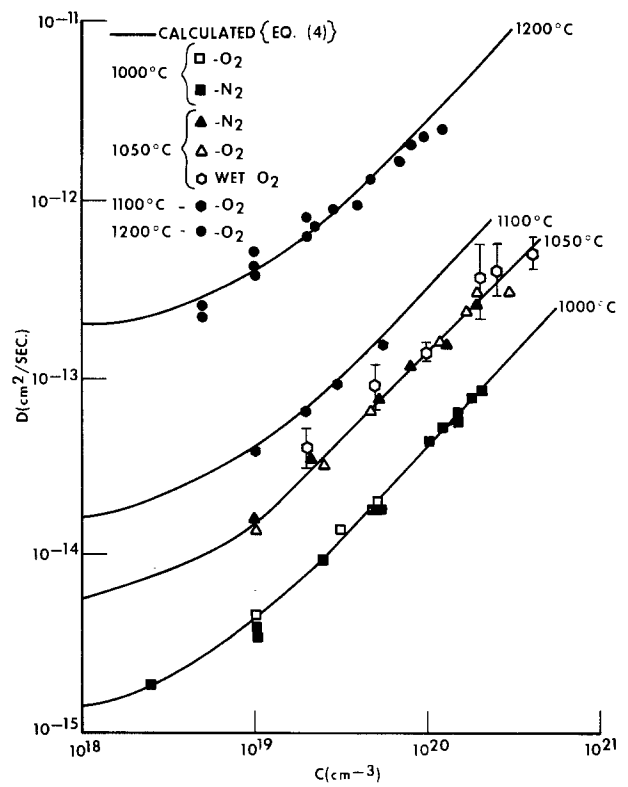


Fig. 4. Arsenic diffusivity vs. total As concentration for several diffusion temperatures.

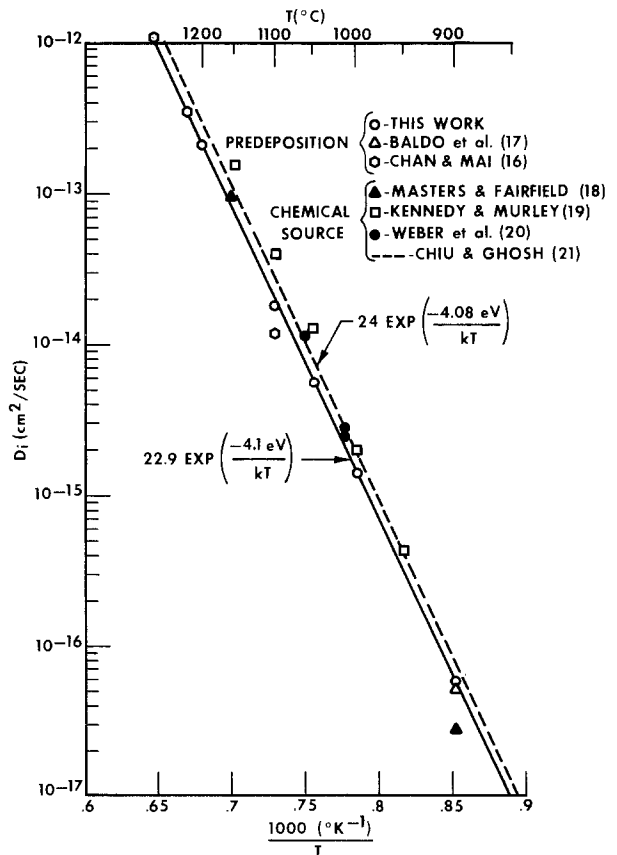


Fig. 5. Intrinsic diffusion coefficient of As as a function of temperature.

$$D_i \Big|_{PD} = 22.9 \exp \left(\frac{-4.1 \text{ eV}}{kT} \right) \quad [7]$$

where the subscript PD refers to "predeposition." Dif-

fusion coefficient data (18-20) from studies on As chemical sources are also shown in Fig. 5. These data can be compared with the expression for D_1 obtained by Chiu and Ghosh (21)

$$D_1 \Big|_{CS} = 24 \exp \left(\frac{-4.08 \text{ eV}}{kT} \right) \quad [8]$$

where the subscript CS refers to "chemical source." It is not clear at this point whether the differences between $D_1|_{PD}$ and $D_1|_{CS}$ are significant or not.

Diffusion ambient effects.—Comparisons among the measured total As profiles for samples which have been diffused in wet O_2 , O_2 , and N_2 are shown in Fig. 6. In order to show the As profiles near the surface clearly, normalized coordinates with linear scales have been used. The complete profiles in Si and SiO_2 for the two samples of $1 \times 10^{16} \text{ cm}^{-2}$ dose (50 keV) which were diffused in oxidizing ambients are shown in Fig. 7 (22). The following observations can be made from Fig. 6 and 7:

1. Arsenic atoms "pile-up" within 200-400 Å of the Si surface during diffusion in an oxidizing ambient. 4000 Å of SiO_2 were grown in the wet O_2 ambient, and $5.9 \times 10^{14} \text{ cm}^{-2}$ As was nonuniformly segregated into the SiO_2 [SIMS measurement (22)]. 500 Å of SiO_2 were grown in the O_2 ambient and only $1.4 \times 10^{13} \text{ cm}^{-2}$ As was segregated into the SiO_2 . A segregation coefficient of $m = 800$ for both oxidation ambients at 1050°C was observed which agrees well with the thermodynamic calculations (23). Consequently, the segregation of As into the SiO_2 does not significantly reduce the As doping in the Si. However, As pile-up is significant since the integrated concentration in the surface pile-up region is $\sim 1.5 \times 10^{15} \text{ cm}^{-2}$ for both O_2 and wet O_2 oxidations of the $1 \times 10^{16} \text{ cm}^{-2}$ implanted samples.

2. The junction depth of the wet O_2 diffused As profile is $\sim 10\%$ shallower ($x_J = 0.43 \mu\text{m}$) than the junction depth of the dry O_2 diffused As ($x_J = 0.48 \mu\text{m}$) at $C = 10^{18} \text{ cm}^{-3}$. However, from Fig. 4 it can be seen that the diffusion coefficient is independent of the diffusion ambient. Additional data are presented in Fig. 8 where the junction depths of measured As profiles are plotted vs. an expression which contains implant dose,

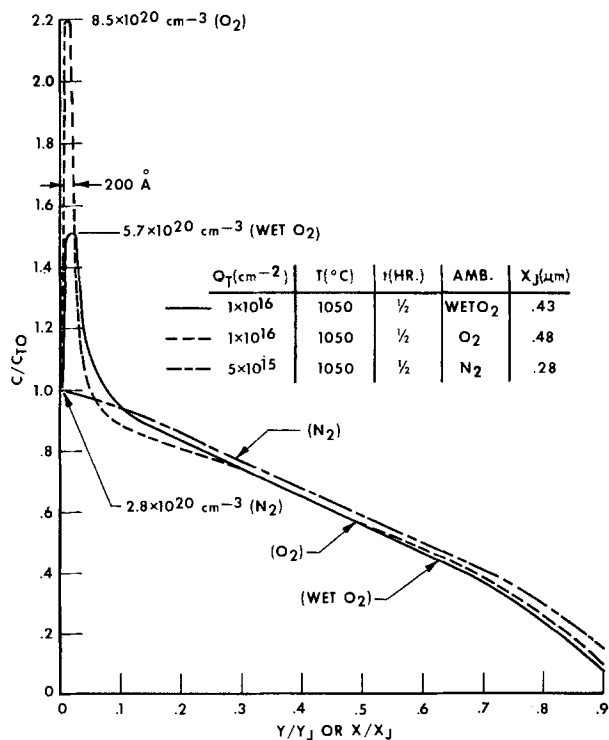


Fig. 6. Normalized implanted-diffused As profiles diffused in wet O_2 , O_2 , and N_2 .

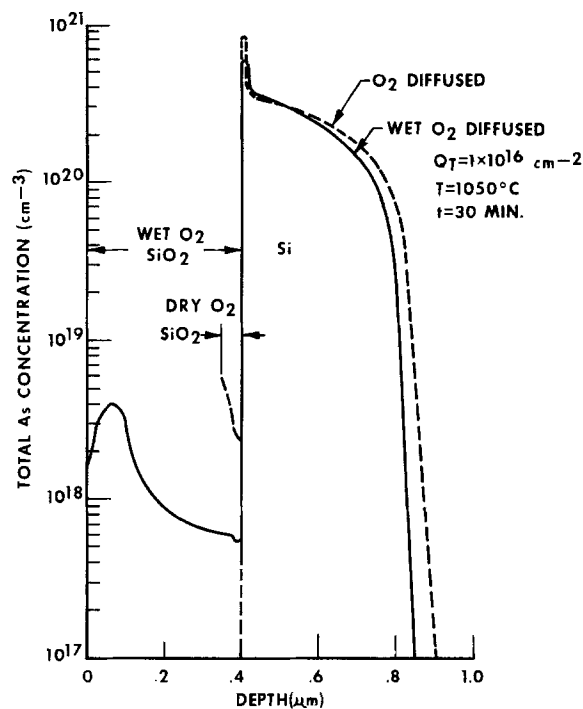


Fig. 7. Total implanted As profiles diffused in O_2 and wet O_2

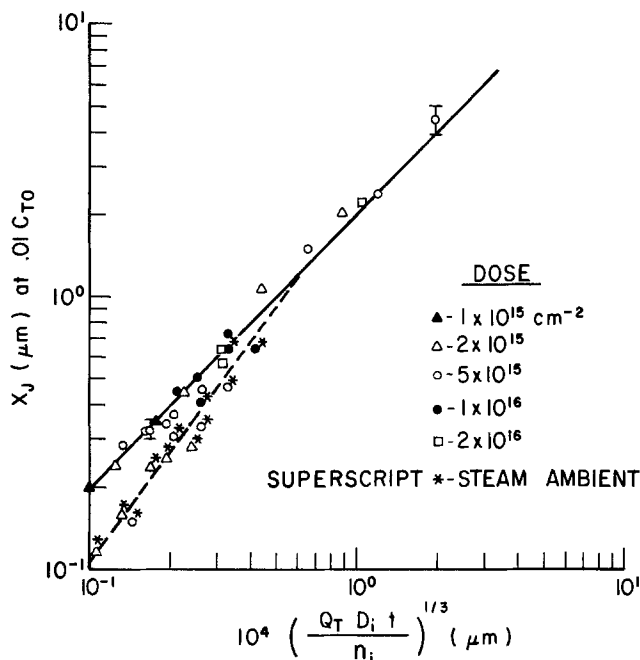


Fig. 8. Time, temperature and implant dose dependence of junction depth of implant-diffused As layers in Si. The effect of As diffusion in a wet O_2 ambient is illustrated.

diffusion time, and temperature (13). The data represent diffusions in the temperature range of 1000°C in N_2 , O_2 , and steam (wet O_2). It can be seen that shallower junction depths are obtained for diffusions performed in wet O_2 up to $\sim 1 \mu\text{m}$ from the Si surface. For the case of dry O_2 , the influence of the moving, oxidizing surface boundary on the junction depth can be neglected.

Electrical Activity

It has been pointed out previously that the fraction of As that is electrically active in an implanted-diffused layer in Si is greater than in a layer diffused from a chemical source (4). This is due to the fact that in a well-annealed implanted layer, As complexes ap-

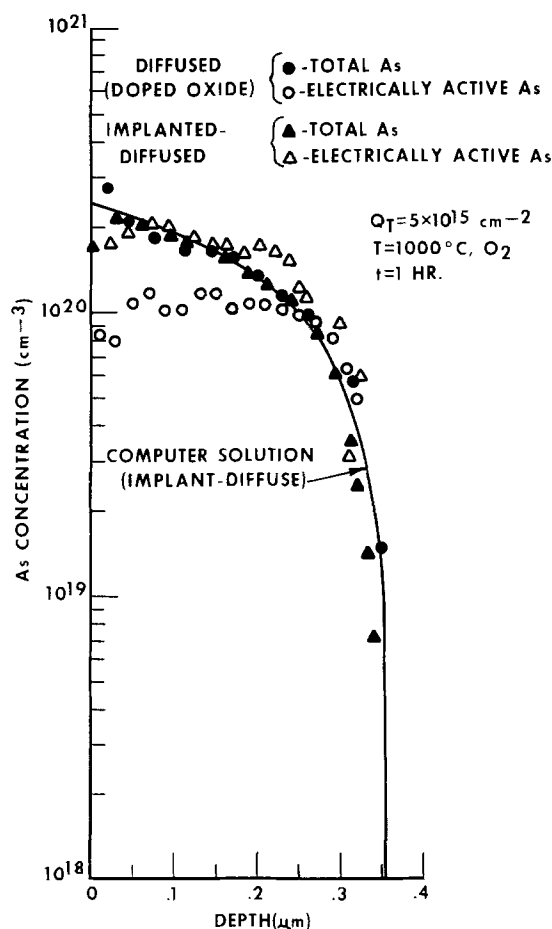


Fig. 9. Comparison between diffused and implanted-diffused As profiles in Si. The numerical solution to the diffusion of an implanted layer is also shown.

parently are not formed. An example is shown in Fig. 9 where a diffused As layer (doped oxide source) with a total concentration of $5.06 \times 10^{15} \text{ cm}^{-2}$ As is compared with an implanted As layer ($5 \times 10^{15} \text{ cm}^{-2}$) which was diffused to the same junction depth as the doped oxide-diffused layer (1000°C , 60 min in O_2 ambient). It can be seen that the total As data practically coincide except near the surface. These data were determined by neutron activation and anodic stripping (\bullet), and SIMS (\blacktriangle). In addition, the theoretical solution of the redistribution of the implanted As layer is shown to agree very well with these data. However, the concentration data obtained from these diffusions by the differential conductivity method and Fig. 1 show a large disparity, reflecting differences in electrical activity between the diffusion from a chemical source and an implanted source. For the chemical-source diffused layer, $Q_A/Q_T \approx 0.65$, while $Q_A/Q_T \approx 1$ for the implanted-diffused layer.

A general conclusion that As^+ is more soluble in implanted-diffused layers than in chemical-source diffused layers in Si is illustrated in Fig. 10. $C_{A,\text{SOL}}$ values determined from diffused As implants for which complete activation had not yet been achieved are plotted vs. diffusion temperature (\bullet and \blacksquare data). Also shown are the calculated As^+ solubility curves and data for As diffused layers from Ref. (1). These curves and data have been adjusted in accordance with the revised resistivity vs. concentration curve in Fig. 1 (Δ and \square data correspond to diffusion into p- and n-type Si substrates, respectively). It can be seen that below 1100°C , As^+ is more soluble in implanted-source layers than in a chemical source layer. This result is further evidence of the absence of As complexes in implanted-diffused layers. However, as it will be shown below,

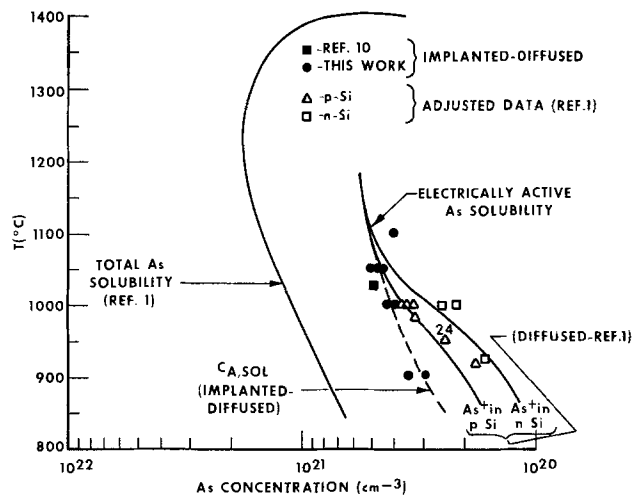


Fig. 10. Solid solubilities of As in Si for diffusion from chemical sources and non-implanted sources. The solid lines denoting solubility of electrically active As are calculated from Ref. (1).

complete activity only occurs in high dose implants after diffusion for some period.

Time behavior of electrically active As.—For the case of diffusion of an As-layer in Si, the integrated As concentration is related to the surface concentration, C_{10} , and the depth by the equation (13)

$$Q_i = K_i C_{10} x_j \quad [11]$$

where K_i is a numerical constant ($0.5 \lesssim K_A \lesssim 1$ for electrically active As and $K_T \approx 0.53$ for total As profiles). The ratio of Q_A (active As) to Q_T (total As) is

$$\begin{aligned} \frac{Q_A}{Q_T} &= \frac{K_A C_{A0}}{K_T C_{T0}} \\ &= K' \frac{C_{A,\text{SOL}}}{C_{T0}} \end{aligned} \quad [12]$$

where it is assumed that C_{A0} is limited to the solubility limit $C_{A,\text{SOL}}$, and $K' = K_A/K_T$.

It can be shown that

$$C_{T0} = 0.94 \left(\frac{Q_T^2 n_i}{D_i t} \right)^{1/3} \quad [13]$$

hence, Eq. [12] becomes

$$\frac{Q_A}{Q_T} = 1.06 K' C_{A,\text{SOL}} \left(\frac{D_i t}{Q_T^2 n_i} \right)^{1/3} \quad [14]$$

for $Q_A/Q_T \leq 1$. Equation [14] indicates that complete electrical activity will be achieved initially for a redistributing As layer when $C_{T0} \leq C_{A,\text{SOL}}$. The increase of Q_A/Q_T from some initial value less than one is $\propto t^{1/3}$, where t is the diffusion time. The use of Eq. [14] is restricted to As layers for which, initially, $C_{T0} > C_{A,\text{SOL}}$.

Using the revised resistivity vs. concentration curves shown in Fig. 1, electrically active As profiles were obtained on implanted layers that had been diffused at various times. The Q_A/Q_T data as a function of time are shown in Fig. 11 where Q_A/Q_T is plotted vs. $C_{A,\text{SOL}} \cdot (D_i t / Q_T^2 n_i)^{1/3}$ for $K' = 1$. Values of $C_{A,\text{SOL}}$ were obtained from Fig. 10. Reasonable agreement with the measured data is obtained.

The $t^{1/3}$ relationship for Q_A/Q_T can also be obtained from the results of Ohkawa *et al.* (24). The experimental conditions for their data were an ampule pre-diffusion at 950°C for 30 min into 1 ohm-cm p-type Si to a total As concentration of $9.5 \times 10^{15} \text{ cm}^{-2}$, and drive-in diffusions without the presence of the source at 950°C in N_2 for 1.5 to 31.5 hr.

The $C_{A,\text{SOL}}$ was $1.9 \times 10^{20} \text{ cm}^{-3}$ which agrees with a previously reported result (1). In order to calculate

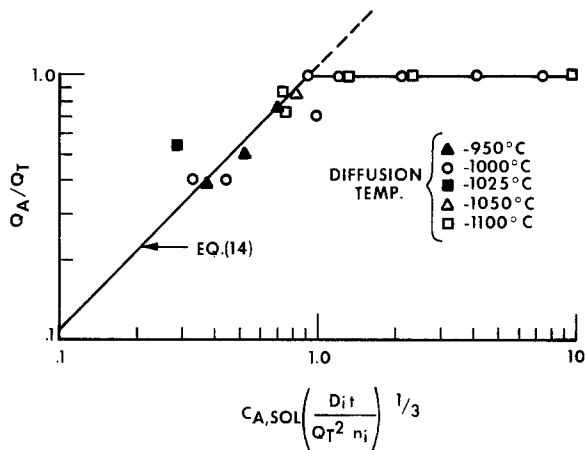


Fig. 11. Fraction of activated As as a function of diffusion time, temperature, and solubility.

the increase of Q_A/Q_T with time for a 950°C drive-in with $D_i = 3.2 \times 10^{-16}$ cm²/sec, Eq. [14] becomes

$$\frac{Q_A}{Q_T} = 2.1 \times 10^{-2} t^{1/3} \quad [17]$$

Ohkawa's data and the calculated values from Eq. [17] are shown in Table I, and good agreement is observed.

Electrically active As profiles.—The distribution of electrically active As in Si will have the same shape as the total As profile (Fig. 2) when all of the As in the diffusing layer is active ($C_{A,SOL} \cong C_{TO}$). However, when $Q_A/Q_T < 1$, the active As concentration is limited to the $C_{A,SOL}$ value, and the active As profile will be quite flat. This effect is shown in Fig. 12, where the data shown were obtained from differential conductivity measurements and the resistivity vs. concentration curve of Fig. 1. Nevertheless, the majority of electrically active As profiles that are formed by the diffusion of an implanted layer have a shape that can be approximately represented by Eq. [1], as shown in Fig. 2 and Fig. 12 (▲-data represents a completely activated As layer).

Discussion

In spite of the fact that an ion-implanted layer of As in Si diffuses in a well-behaved, predictable manner, there still remain some unanswered basic questions. Why does a solubility limit exist for electrically active As, $C_{A,SOL}$ (Fig. 10) that is ~30% of the solubility of total As, and in what form is the inactive As? Also, during oxidation why does As tend to pile up within a few hundred angstroms of the Si/SiO₂ interface. These questions are briefly considered below.

Solubility of the electrically active arsenic.—The solubility of an impurity in silicon is dependent primarily upon the impurity bonding energy in the Si lattice, provided that the strain energy associated with the impurity in the host crystal is small (as it is for As in Si) (25, 26). Arsenic diffused from a chemical source is known to be highly substitutional in Si (27, 28). For such diffusions, As may be tied up in inactive complexes, or exist as ionized As⁺. The fact that definite solubility limits exist for both total As and electrically active As (1, 29) suggests that the inactive As may be more tightly bound in the lattice as was assumed in Ref. (1).

Table I. Rate of change of Q_A/Q_T with time

Q_A/Q_T		t (hr)
Meas.	Calc. (Eq. [17])	
0.23	0.23 [Ref. (1)]	initial
0.43	0.37	1.5
0.63	0.63	7.5
1	1	31.5

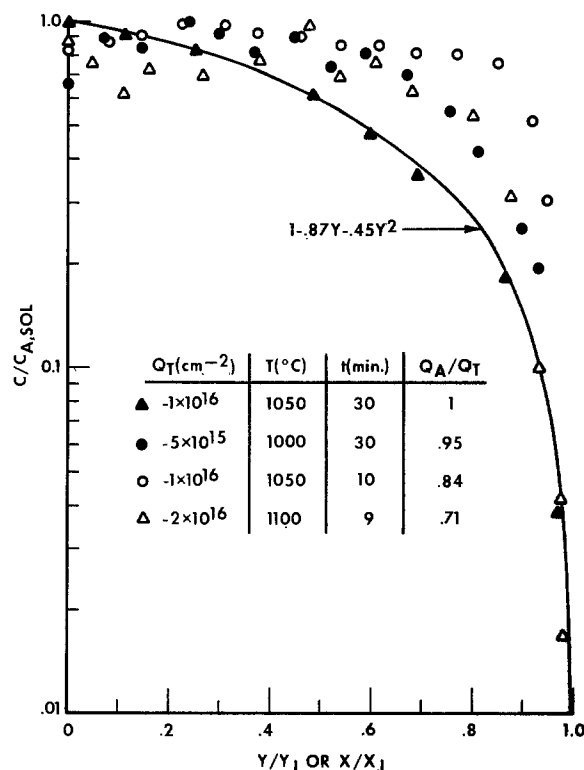


Fig. 12. Electrically active As profiles normalized to $C_{A,SOL}$ for several values of Q_A/Q_T .

For the high-dose ion-implanted As diffusion sources, the implantation of the As creates an amorphous layer in the Si surface region, and epitaxial reordering appears to aid in establishing a high degree of electrical activity, even at low anneal temperatures (550°–650°C). As a result, the solubility of active As⁺ is higher in implanted-diffused layers than in comparable layers diffused from chemical sources (see Fig. 9 and 10) for diffusion temperatures <1100°C. Nevertheless, a definite solubility limit, $C_{A,SOL}$, does exist for implanted As⁺ in Si that is not dependent upon the presence of complexes, but is related to the solubility considerations discussed above. The structure and nature of the inactive As in As implanted-diffused layers is still not known (4, 10, 17).

Effect of oxidation on As diffusion and pile-up.—Dash and Joshi (30) reported the surface pile-up of redistributing As layers in (111) Si during oxidation. Coincident with As pile-up was the formation of extrinsic stacking faults. Hu (31) has proposed that during oxidation excess interstitial Si atoms are generated which contribute to surface regrowth, nucleate around precipitates to cause stacking fault growth, or displace substitutional impurities near the surface whose enthalpy of interstitial formation is low (Group I, II, and III impurities) (32).

Channeling measurements on As-implanted layers that show pile-up at the surface indicate that some of these atoms are not on lattice sites (10). One possible, but unsupported, explanation for pile-up is that As atoms are absorbed by the growing stacking faults, a process that would effectively remove As from solution in the Si lattice and reduce As diffusivity near the Si surface. On the other hand, it has been observed in this study that much of the As in the surface region is electrically active. The active concentration has not been observed to exceed the solubility limit $C_{A,SOL}$.

It was pointed out earlier that the diffusion of As in Si is independent of the furnace ambient (see Fig. 4). Thus, Si interstitials which may be generated during oxidation (31) do not affect As diffusion, which further supports the vacancy diffusion model for As in Si.

Conclusions

The diffusion of ion-implanted As in Si has been studied by generating As profile data from differential conductivity measurements and secondary ion mass spectrometry. It has been shown that:

1. Implanted-diffused As profiles all have a very similar shape provided $C_{T0} \geq 1 \times 10^{20} \text{ cm}^{-3}$ (surface concentration after diffusion), which can be described by a Chebyshev polynomial approximation to the diffusion equation (Eq. [1]) with concentration-dependent diffusivity (Eq. [3]). For the general case of the diffusion of any implanted As layer, numerical solutions of the diffusion equation with diffusivity expressed by Eq. [4] give excellent profile calculations.

2. The diffusion of As is independent of the diffusion ambient. Shallower junction depths as measured from the Si/SiO₂ interface are obtained for diffusions in wet O₂ when x_j is less than $\sim 1 \mu\text{m}$. This result is not caused by segregation of As into SiO₂ ($m = 800$ at 1050°C), but is due to the moving boundary condition.

3. Implanted-diffused As layers show higher electrical activity for diffusions below 1100°C than comparable layers diffused from chemical sources. For doses sufficiently large so that $C_{\text{peak}} > C_{A,\text{SOL}}$, rapid activation of As⁺ to the solubility limit of $C_{A,\text{SOL}}$ has been observed at diffusion temperatures. During diffusion the fraction of electrically active As increases at a rate proportional to $t^{1/3}$, until complete activation occurs when $C_{T0} \simeq C_{A,\text{SOL}}$.

Manuscript received May 15, 1975.

Any discussion of this paper will appear in a Discussion Section to be published in the June 1976 JOURNAL. All discussions for the June 1976 Discussion Section should be submitted by Feb. 1, 1976.

Publication costs of this article were partially assisted by Bell Laboratories.

APPENDIX A

Diffusion Coefficient Analysis for a Redistributing Layer with Concentration-Dependent Diffusivity

The Boltzmann-Matano analysis (33) is the most suitable method for extracting diffusion coefficients from measured diffusion profiles, provided that the surface concentration of the indiffused species is invariant with time. When the diffusing substance is subject to redistribution, the Boltzmann-Matano analysis may not be used because the time dependence of the concentration is not a function of x/\sqrt{t} .

In the case of ion-implantation of impurities into Si, the redistribution of a fixed total amount of impurities is of interest. Thus, the relationship

$$Q_T = \int_0^\infty C(x,t) dx \quad [\text{A-1}]$$

implies a time independence on Q_T which is achieved by the transformation (34)

$$C(x,t) = F(x/\sqrt{t})/\sqrt{t} \quad [\text{A-2}]$$

where F satisfies the diffusion equation and the boundary conditions

$$C(x,t) = 0 \text{ for } x \rightarrow \infty \quad [\text{A-3}]$$

$$C(x,t) = 0 \text{ for } x = 0, t = 0 \quad [\text{A-4}]$$

$$C(x,t) = 0 \text{ for } x > 0, t = 0 \quad [\text{A-5}]$$

Conditions [A-4] and [A-5] indicate the initial profile is represented as a delta function.

The one-dimensional diffusion equation with concentration-dependent diffusion coefficient is

$$\frac{\partial C}{\partial t} = \frac{\partial}{\partial x} \left(D(C) \frac{\partial C}{\partial x} \right) \quad [\text{A-6}]$$

Defining a new variable, η as

$$\eta = x/\sqrt{t} \quad [\text{A-7}]$$

and replacing C in Eq. [A-6] with Eq. [A-2] yields an expression in η , $F(\eta)$ and t (34). Adding the limitative hypothesis that D be a function of the ratio $C(x, t)/C_{T0}$ (C_{T0} is surface concentration), where

$$C_{T0} = F(0)/\sqrt{t} \quad [\text{A-8}]$$

gives rise to the expression

$$-\frac{\eta}{2} F(\eta) = D \left[\frac{F(\eta)}{F(0)} \right] \frac{dF(\eta)}{d\eta} \quad [\text{A-9}]$$

or

$$-\frac{Cx}{2} = D \left(\frac{C}{C_{T0}} \right) t \frac{dC}{dx} \quad [\text{A-10}]$$

Thus, the local diffusion coefficient at $x = x_0$ for a diffusion that took t sec is

$$D \left(\frac{C(x_0, t)}{C_{T0}} \right) = \frac{-C(x_0, t) x_0}{2t \frac{dC}{dx} \Big|_{x_0}} \quad [\text{A-11}]$$

As an example, consider the case where the redistributed impurity has a profile shape described by

$$C(x, t) = C_{T0} \exp \left(\frac{-x^2}{4Dt} \right) \quad [\text{A-12}]$$

Substitution of Eq. [A-12] into Eq. [A-11] yields

$$D = D_i, \text{ for all } x \quad [\text{A-13}]$$

It is well known that a redistributing impurity with constant diffusion coefficient will assume a gaussian shape.

For the case of diffusion in an oxidizing ambient where the movement of the Si surface must be considered, the continuity equation becomes

$$\frac{\partial C}{\partial t} = \frac{\partial}{\partial x} \left(D(C) \frac{\partial C}{\partial x} + vC \right) \quad [\text{A-14}]$$

where v is the inward velocity of the oxidizing Si surface. Transforming v according to the expression

$$v = \frac{\eta}{\sqrt{t}} \quad [\text{A-15}]$$

it can be shown in a similar way that the diffusivity becomes

$$D \left(\frac{C(x_0, t)}{C_{T0}} \right) = \frac{-C(x_0, t) (x_0 + x_{ox})}{2t \frac{dC}{dx} \Big|_{x_0}} \quad [\text{A-16}]$$

where $x_{ox} \simeq 2vt$ is the SiO₂ thickness.

APPENDIX B

Polynomial Fit for Resistivity vs. Electron Concentration in As-Doped Si

In order to provide an analytical description of the resistivity vs. electron concentration data in the range $1 \times 10^{19} \leq n \leq 7 \times 10^{20} \text{ cm}^{-3}$ shown in Fig. 1, a tenth order polynomial was generated. Thus

$$\log \rho = \sum_{i=0}^{10} a_i k^i \quad [\text{B-1}]$$

where $k = \log n$, $a_0 = -6.633667 \times 10^3$, $a_1 = 7.682531 \times 10^2$, $a_2 = -2.577373 \times 10^1$, $a_3 = 9.658177 \times 10^{-1}$, $a_4 = -5.643443 \times 10^{-2}$, $a_5 = -8.008543 \times 10^{-4}$, $a_6 = 9.055838 \times 10^{-5}$, $a_7 = -1.776701 \times 10^{-6}$, $a_8 = 1.953279 \times 10^{-7}$, $a_9 = -5.754599 \times 10^{-9}$, $a_{10} = -1.316567 \times 10^{-11}$. The fit of this polynomial to the data in Fig. 1 is shown drawn in Fig. 1. The agreement is much better than the fifth order polynomial generated previously by Lee (35).

REFERENCES

1. R. B. Fair and G. R. Weber, *J. Appl. Phys.*, **44**, 273 (1973).
2. R. O. Schwenker, E. S. Pan, and R. F. Lever, *ibid.*, **42**, 3195 (1971).

3. R. B. Fair, *ibid.*, **44**, 283 (1973).
4. R. B. Fair, *Solid-State Electron.*, **17**, 17 (1974).
5. J. C. Irvin, *Bell Syst. Tech. J.*, **41**, 387 (1962).
6. R. B. Fair and J. C. C. Tsai, Unpublished.
7. E. Tannebaum, *Solid-State Electron.*, **2**, 123 (1962).
8. J. C. C. Tsai, J. M. Morabito, and R. K. Lew, in "Ion Implantation in Semiconductors and Other Materials," B. L. Crowder, Editor, p. 87, Plenum Press, New York (1973).
9. P. F. Schmidt and A. E. Owens, *This Journal*, **111**, 683 (1964).
10. H. Müller, H. Kranz, H. Ryssel, and K. Schmid, *Appl. Phys.*, **4**, 115 (1974).
11. V. I. Fistul, "Heavily Doped Semiconductors," p. 129, Plenum Press, New York (1969).
12. R. A. Logan, J. F. Gilbert, and F. A. Trumbore, *J. Appl. Phys.*, **32**, 131 (1961).
13. R. B. Fair, *ibid.*, **43**, 1278 (1972).
14. Y. Nakajima, S. Ohkawa, and Y. Fukukawa, *Japan J. Appl. Phys.*, **10**, 162 (1971).
15. S. M. Hu and S. Schmidt, *J. Appl. Phys.*, **39**, 4272 (1968).
16. T. C. Chan and C. C. Mai, *Proc. IEEE*, **58**, 588 (1970).
17. E. Baldo, F. Cappellani, and G. Restelli, *Radiation Effects*, **19**, 271 (1973).
18. B. J. Masters and J. M. Fairfield, *J. Appl. Phys.*, **40**, 2390 (1969).
19. D. P. Kennedy and P. C. Murley, *Proc. IEEE Letters*, **59**, 335 (1971).
20. G. R. Weber, J. A. Heilig, E. I. Pavilonis, and C. F. Gibbon, Unpublished.
21. T. L. Chiu and H. N. Ghosh, *IBM J. Res. Develop.*, **15**, 472 (1971).
22. These profiles were measured by B. Blanchard, Centre D'Etudes Nucléaires De Grenoble using a CAMECA IMS-300. Calibration was achieved from radio active As-doped samples.
23. C. D. Thurmond, in "Properties of Elemental and Compound Semiconductors," H. C. Gatos, Editor, p. 121, Interscience, New York (1960).
24. S. Ohkawa, Y. Nakajima, T. Sakurai, H. Nishi, and Y. Fukukawa, *Japan J. Appl. Phys.*, **13**, 361 (1974).
25. R. A. Swalin, "Thermodynamics of Solids," pp. 149-155, John Wiley and Sons, Inc., New York (1962).
26. K. Weiser, *J. Phys. Chem. Solids*, **7**, 118 (1958).
27. E. Dimini, J. Haskell, and J. W. Mayer, *Appl. Phys. Letters*, **20**, 237 (1972).
28. J. A. Golovchenko, B. W. Batterman, and W. L. Brown, Unpublished.
29. F. A. Trumbore, *Bell Syst. Tech. J.*, **39**, 205 (1960).
30. S. Dash and M. L. Joshi, *IBM J. Res. Develop.*, **14**, 453 (1970).
31. S. M. Hu, *J. Appl. Phys.*, **45**, 1567 (1974).
32. J. A. Van Vechten, *Phys. Rev. B*, **10**, 1482 (1974).
33. J. Crank, "The Mathematics of Diffusion," p. 148ff, Oxford University Press, Clarendon, England (1956).
34. M. Ghezzi, *This Journal*, **119**, 977 (1972).
35. T. P. Lee, *Trans. Electron Dev.*, **ED-13**, 881 (1966).

Kinetics of the Initial Stage of Si Transport Through Pd-Silicide for Epitaxial Growth

Z. L. Liou, S. U. Campisano,¹ C. Canali,² S. S. Lau, and J. W. Mayer*

California Institute of Technology, Pasadena, California 91125

ABSTRACT

Backscattering spectrometry and scanning electron microscopy (SEM) have been used to study the transport of Si from an amorphous Si layer ($\lesssim 1 \mu\text{m}$) through a Pd-silicide layer ($\lesssim 0.2 \mu\text{m}$) onto $\langle 100 \rangle$ oriented Si. For a given annealing temperature, two distinct stages of this process have been observed. The initial transient stage starts with island growth of Si and ends with a uniform layer of Si on the substrate. The thickness of the initial transient stage is found to be equal to the thickness of the Pd-silicide layer.

Silicon and Ge can migrate through thin metal films at temperatures below the melting point of any of the components of the system (1, 2). During isothermal heat-treatment of amorphous or fine-grain polycrystalline Si films in contact with metal films, it is observed that the Si dissolves into the metal film and precipitates in crystallite form in the metal film. It has been suggested (1) that the driving force for the amorphous to crystalline transition is due to the higher free energy of the amorphous material as compared to the crystalline form. For the polycrystalline case, Nakamura *et al.* (3) propose that the solid-phase dissolution of small crystallites and reformation of larger crystallites is caused by the tendency to reduce grain boundary areas. In both cases the heights of the crystallites are governed by the thickness of the metal solvent matrix.

As an alternate growth mode involving migration through a metal film, it is possible to form epitaxial layers on a single crystal substrate rather than crystallites in a metal film. It has been pointed out (4) that

the conditions of the interface between crystal-substrate and metal-film play a crucial role. For epitaxial growth, the transport of the semiconductors through metal layers is not a sufficient condition; it is necessary to provide a proper interface for nucleation and growth.

Recently, it has been demonstrated (5) that a uniform Si epitaxial layer can be grown on a single crystal Si substrate by solid-state diffusion of Si from an amorphous Si layer through a Pd-silicide layer. During anneal at about 300°C, the deposited Pd layer reacts with both single crystal and amorphous Si on both sides to form a Pd₂Si layer. Then, when annealed at about 500°C, the top layer of amorphous Si is transported through the Pd₂Si layer and grows epitaxially onto the underlying single crystal substrate. Uniform grown Si layers of about 1 μm thickness have been formed this way. X-ray diffraction and channeling techniques have been used to demonstrate that this grown Si is a single crystal layer grown epitaxially on the substrate.

For a given annealing temperature, two distinct stages of this process have been observed; an initial transient stage of rapid transport of Si followed by a

* Electrochemical Society Active Member.

¹ Present address: Istituto di Struttura della Materia, 95129 Catania, Italy.

² Present address: Istituto di Fisica, Università de Modena, 41100 Modena, Italy.

Key words: silicon transport in epitaxy, Pd-silicide.

slower steady-state stage. In the steady-state stage, the transport of Si is linear in time.

In the present work, we have been concerned with the initial transient stages of growth. This aspect of the transport and growth of Si layers has been investigated in this work by 2 MeV $^4\text{He}^+$ backscattering spectrometry and scanning electron microscopy.

Experimental Procedures

Commercially available Si single crystal wafers with polished surfaces and $\langle 100 \rangle$ orientation were used. The wafers were first cleaned by the R C A process (6), etched in HF, rinsed in high purity water, and then were immediately placed into the vacuum system. The electron-gun evaporation of Pd was performed at a vacuum of approximately 5×10^{-7} Torr at a rate of approximately 5 Å/sec. The source to sample distance was about 25 cm. Typical thickness of Pd evaporated ranged from 300 to 1200 Å. Immediately following the evaporation of Pd, a layer of amorphous Si ($\lesssim 1 \mu\text{m}$) was deposited by electron-gun evaporation at a rate of ~ 100 Å/sec.

Anneals were performed in a vacuum quartz-tube furnace. The typical vacuum during anneals was 1×10^{-6} Torr. The precision of the annealing temperatures was $\pm 1^\circ\text{C}$ and the precision of the annealing times was ± 3 min. The samples were first annealed at 280°C for 0.5 hr for the Pd layer to react with Si to form a uniform Pd_2Si layer (7). After silicide formation, a higher temperature (ranging between 450° and 550°C) anneal was used for the transport and epitaxial growth of Si.

To study this process quantitatively, 2 MeV $^4\text{He}^+$ backscattering spectrometry was used. This technique has been described in detail elsewhere (8). Briefly, a 2 MeV $^4\text{He}^+$ ion beam is incident on a sample placed in a vacuum chamber. By energy analyzing the He atoms backscattered from the specimen, one can determine the atomic concentration profiles in the sample. The depth resolution is about 200 Å for layer thickness ranging between 300-5000 Å. The beam size is usually 1-2 mm² therefore a lateral uniformity of at least this dimension is required. In the present study, a solid-state detector of energy resolution of about 20 keV was used to detect the energy of the particles at a backscattered angle of 168° . The layer thicknesses can be calculated from energy loss data and bulk densities as described in the Appendix.

Results

Backscattering spectra of a sample annealed at 280°C for 0.5 hr (formation of Pd_2Si) and the same sample (cut into separate pieces) annealed further at 475°C for 7 different annealing times are shown in Fig. 1. The transport of Si through the Pd-silicide layer can be seen from the spectra of the samples annealed at 475°C . In these spectra the signals of the top amorphous Si layers become thinner and the Pd signals shift to higher energies as compared to the upper spectrum in Fig. 1. This indicates that the Pd-silicide layer moves toward the surface of the sample as the Si migrates through the silicide layer. From the difference in the energy width of the amorphous Si layer in the samples before and after Si transport, one can determine the amount of Si that has been transported. This same information can also be obtained from the shift in the Pd signal to higher energies.

The time dependence of the amount of Si transported is obtained by plotting the amount of Si that has migrated away from the top amorphous layer vs. annealing time. Such a transport curve is shown in Fig. 2 for heat-treatment at 475°C of the same samples as those of Fig. 1.

There are two distinct regions in the curve. In the initial stages, the rate is fast, then after a certain transported amount (1800 Å in the example shown in Fig. 2) the transport changes abruptly into a slower rate and maintains this rate until the end of the whole process.

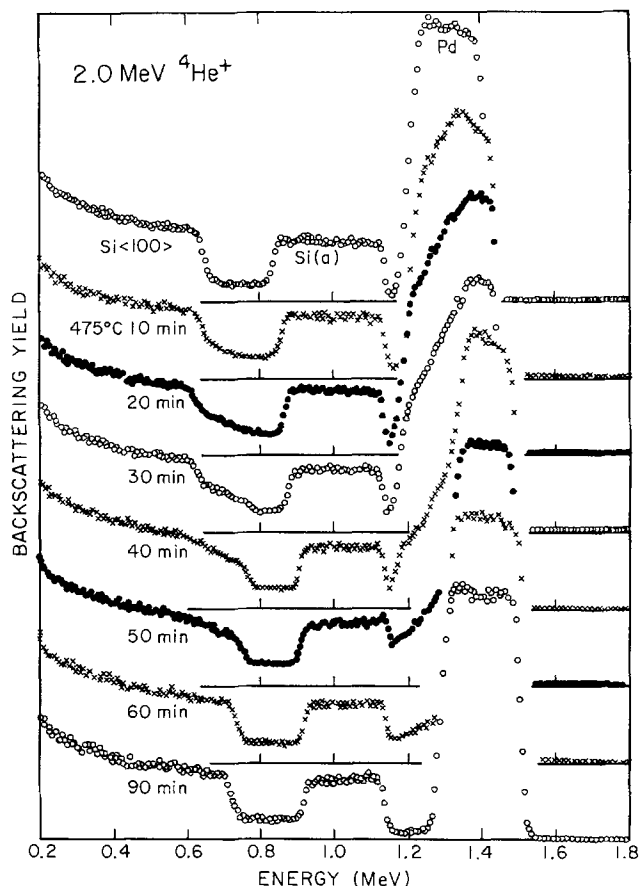


Fig. 1. Backscattering spectra of a sample for different annealing times in the initial transient stage and the beginning of the steady-state stage. The backscattering yield is in a linear scale. The thickness of the Pd_2Si layer is $0.18 \mu\text{m}$ and that of the amorphous Si layer before transport is $0.63 \mu\text{m}$ (upper curve).

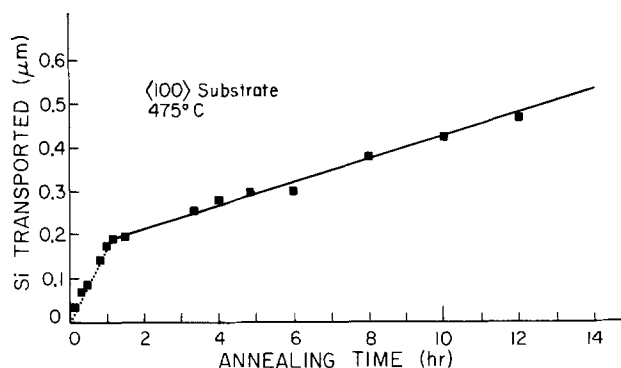


Fig. 2. An isothermal transport curve which shows the time dependence of the transport of Si for the same sample as that of Fig. 1.

The beginning fast period and the subsequent slower period are referred to as the initial transient stage and the steady-state stage, respectively. In the steady-state stage the transport of Si is found to be linear with time. In the initial transient stage the transport rate of Si can also be estimated by a straight line as shown by a dashed line in Fig. 2. From the two slopes of these two straight lines, the transport rate of the initial transient stage is about 8 times faster than that of the steady-state stage. This same ratio is also found for other annealing temperatures.

Similar results have been observed on other samples made at different times and annealed at various temperatures, i.e., the initial transient transport rate is five to ten times faster than that of the steady-state.

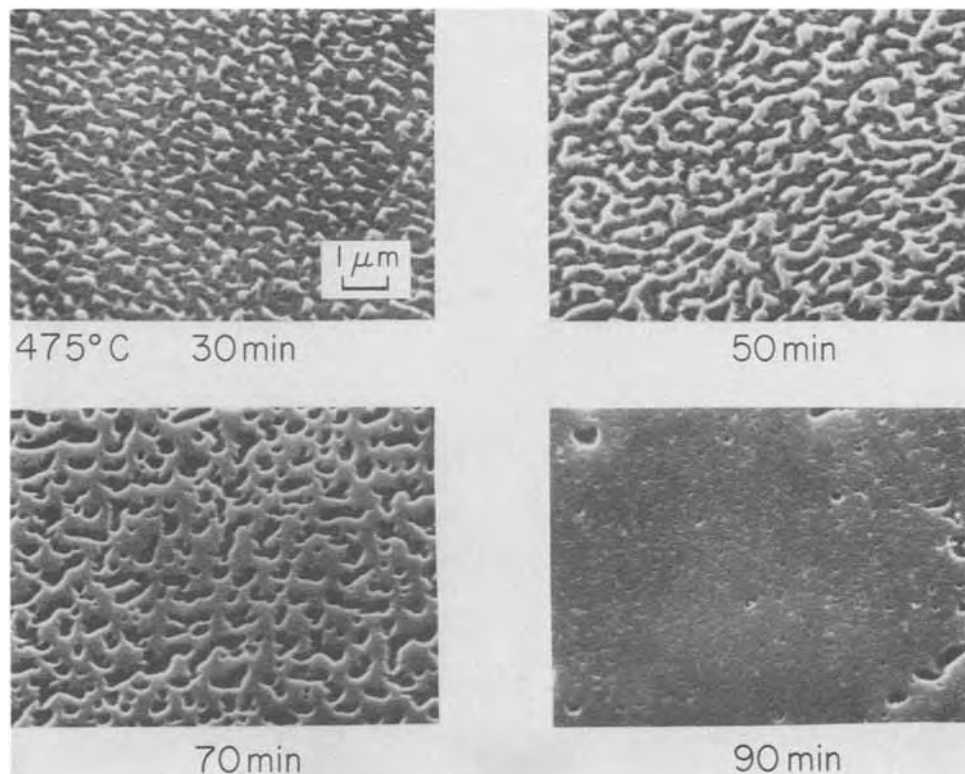


Fig. 3. SEM photos showing Si islands grown on the substrate surface in the initial transient stage and a uniform Si grown layer that is formed just after the completion of the initial transient stage.

The backscattering spectra of samples in the initial transient stage (475°C 10-60 min of Fig. 1) show that the grown Si layers are nonuniform as indicated by the graded slopes of the signal edges corresponding to the interfaces between the grown Si layers and the corresponding Pd-silicide layers. On the other hand, the spectrum of the sample annealed for a longer time (90 min of Fig. 1 which is just in the beginning of the steady-state stage) shows that the surface of the grown Si layer is uniform. The nonuniformity of layer in the transient stage is a general phenomenon observed for Pd₂Si thickness between 0.04 and 0.2 μm and anneal temperature between 440° and 550°C.

To examine the surface nonuniformity in the initial transient stage of the sample used for backscattering measurements in Fig. 1, we put the samples in HF for ~ 10 min for the Pd-silicide and the remaining top layer of amorphous Si to peel off. Thus the grown Si layers on the substrate surfaces were exposed for SEM observations. Figure 3 shows the SEM pictures of the surface view of a time sequence (30, 50, and 70 min) of samples in the initial transient stage and a sample (90 min) just in the beginning of the steady-state stage. These figures show that the growth of the Si starts with islands of dimensions of about 0.2 μm (both in height and in width) and then these islands grow laterally and join themselves. Toward the end of the initial transient stage a uniform Si grown layer is gradually formed. This picture of island growth in the initial transient stage and the transition to a uniform Si grown layer in the beginning of the steady-state stage is consistent with backscattering spectra. Further, the island structures of the grown Si layer have also been confirmed by SEM observations of the cleavage of the samples before being put in HF. This same island growth and transition to a more uniform layer is common to other samples and other annealing temperatures. It should be pointed out that throughout this process the remaining top layer of amorphous Si always remains flat and uniform.

A study of the correlation between the thickness of the initial transient stage of a sample and the thickness of the Pd₂Si layer of that sample has been performed on samples with Pd₂Si thicknesses ranging from 440 to 1820 Å. (In all these samples, the thicknesses of the original amorphous Si layer are always about 1 μm.)

A correlation between these two thicknesses has been found as shown in Fig. 4. The thicknesses of the Pd₂Si layers of all samples presented in Fig. 4 are also measured from backscattering spectra. The experimental points can be well fitted by a straight line passing through the origin with a slope equal to 1. This shows that for each sample the thickness of its initial transient growth is equal to the thickness of its Pd₂Si layer.

Discussion and Conclusion

In the present study of the transport of amorphous Si through Pd-silicide layers, two distinct regions (initial transient region and steady-state region) have been observed. The initial transient stage has a fast transport rate and is characterized by the island growth structure. At the end of the initial transient stage, the island structure develops into a more uniform grown layer. This process can be described schematically (according to the experimental data of Fig. 1 and 3) as shown in Fig. 5. The thickness of this layer is equal to that of the Pd₂Si layer. The migration rate of Si also changes rather abruptly into a slower rate. In this slower rate region (steady-state stage), the transport of Si is linear with time.

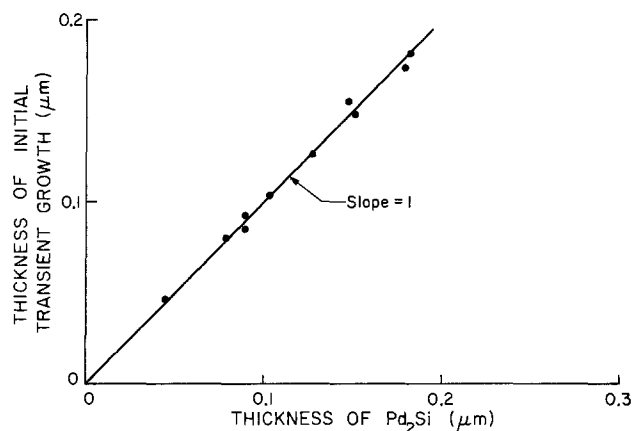


Fig. 4. The linear relation between the thickness of Pd₂Si layer and the thickness of the corresponding initial transient growth.

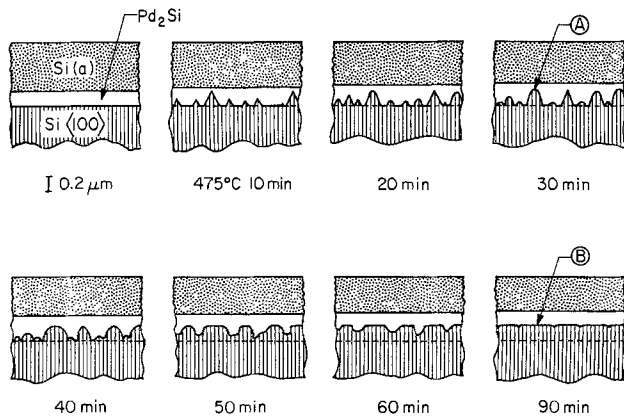


Fig. 5. A schematic picture which describes the growth of islands and the formation of a uniform layer for the sample of Fig. 1.

The Si transport in the initial transient stage can also be approximated by a linear rate which is about eight times faster than that of the steady-state stage. This difference in transport rates is probably due to the island structure in the initial transient stage, which effectively provides many more growth sites.

The equality of the thickness of the initial transient layer and that of the Pd₂Si layer can, perhaps, be rationalized by the following considerations. Initially, small nuclei are nucleated on the substrate surface either randomly or more likely on preferential sites such as defect sites. These nuclei, then grow in size and develop into islands. The height of these islands cannot exceed the thickness of the Pd-silicide layer which is the transport medium. Presumably, the growth of the islands required the incorporation of free Si atoms dissolved in the transport medium. Once these islands (with their height equal to Pd₂Si thickness) are formed, they start to grow laterally and join themselves. During this time, there is no further increase in the height of islands, otherwise there would be an increase of the interfacial energy between the islands and Pd-silicide due to increased interfacial area. In this way, a uniform grown layer of the same thickness as the original Pd₂Si layer can finally be formed. A rather similar phenomenon has been observed recently by Nakamura *et al.* (3) in a study of the dissolution and growth process of polycrystalline Si in contact of Al films. The height of the regrown Si crystals is found to be the same as the thickness of the original Al layer which acts as the transport medium in this case.

The Si transport changes to the steady-state region after the formation of the initial transient layer. As pointed out earlier, this initial transient Si grown layer is uniform and flat. However, there should be some significant differences between the original substrate surface and this uniformly flat surface after the transient stage. Otherwise, instead of changing to the steady-state region, another "initial transient stage" should have been developed on this surface similar to that observed on the original substrate surface. Differences in dislocation densities between the initial transient grown layer and the original crystal substrate, surface morphology, and microstructures are the possible candidates for the difference in growth behavior. In addition, surface conditions caused by polishing, etching, and Pd-silicide formation on the substrate surface are also among the possibilities. Further experimentation to distinguish between these possibilities is now in progress. For example, experiments with substrates of various orientations, different ways of Pd₂Si formation (*e.g.*, evaporation of Pd on a heated Si substrate), metals other than Pd, or even substrates other than Si single crystals may further provide valuable information.

Acknowledgments

The authors acknowledge helpful discussions with M.-A. Nicolet, and the financial support of Gulf Oil (A.

Lewis), The Ford Foundation (T. Cole), and NSF (T. Mukherjee).

Manuscript submitted May 22, 1975; revised manuscript received Aug. 12, 1975.

Any discussion of this paper will appear in a Discussion Section to be published in the June 1976 JOURNAL. All discussions for the June 1976 Discussion Section should be submitted by Feb. 1, 1976

Publication costs of this article were partially assisted by the California Institute of Technology.

APPENDIX

Depth Scales

From the energy loss studies of ⁴He⁺ through materials (9), the thickness of a layer (ΔX) is related to its backscattering spectrum width (ΔE) by

$$\Delta X = \frac{\Delta E}{[S]}$$

where $[S]$ is a depth-scale factor which is determined by the stopping power and the density of the material and the kinematics of the scattering. For convenience, we have assumed bulk densities even for the thin film case (8). Use of a depth scale in atoms/cm² would lead to the same features shown in Fig. 2 and 4. The factor $[S]$ is a slowly varying function of ΔX and, for a practical purpose, can be approximated as a constant. For example, when a 2.0 MeV ⁴He⁺ beam is incident on a Si layer with a backscattering angle of 168°, $[S] = 46.9$ eV/Å at a depth of 1000 Å and 48.9 at 4000 Å. For the $[S]$ factor of Pd₂Si layers, the calculation was made from the stopping powers of Si and Pd using Bragg's rule (9). The calculated values are $[S] = 103$ eV/Å when the spectrum width ΔE is measured from the Si signal of Pd₂Si, and $[S] = 115$ eV/Å when ΔE is measured from the Pd signal width. From these values, the thickness of the top layer of amorphous Si of the sample before transport shown in Fig. 1 is determined to be 0.63 μm and thickness of its Pd₂Si layer is 0.18 μm. The thickness of Si that has been transported for the sample annealed 475°C for 90 min shown in Fig. 1 is 0.19 μm.

A careful comparison of the backscattering spectrum of the 475°C for 30 min sample and that of the 90 min sample in Fig. 1, would suggest that the heights of the mountain-shaped islands of the 30 min sample are more than 500 Å higher than the thickness of the uniform grown Si layer of the 90 min sample. But actually the height of the islands is very close to (if not exactly equal to) the thickness of the uniform grown layer. The apparent big difference in heights is due to the fact that Pd-silicide and Si have rather different stopping powers for the incident helium particles. (The stopping power of Pd₂Si is about twice as great as that of Si.) This can be easily seen from Fig. 5. If the height of islands is equal to the thickness of the uniform layer, then points A and B are of the same depth from the sample surfaces. But in the backscattering spectra the signal of the point A will appear at a higher energy than that of the point B, because the point A has essentially only Si in front of it, but point B has a thick layer of Pd-silicide displacing a layer of Si of the same thickness.

REFERENCES

- G. Ottaviani, D. Sigurd, V. Marrello, J. W. Mayer, and J. O. McCaldin, *J. Appl. Phys.*, **45**, 1730 (1974).
- D. Sigurd, G. Ottaviani, H. J. Arnal, and J. W. Mayer, *ibid.*, **45**, 1740 (1974).
- K. Nakamura, M.-A. Nicolet, J. W. Mayer, R. J. Blattner, and C. A. Evans, Jr., To be published.
- C. Canali, J. W. Mayer, G. Ottaviani, D. Sigurd, and W. van der Weg, *Appl. Phys. Letters*, **25**, 3 (1974).
- C. Canali, S. U. Campisano, S. S. Lau, Z. L. Liao, and J. W. Mayer, *J. Appl. Phys.*, **46**, 2831 (1975).
- W. Kern and D. A. Puotinen, *R C A Rev.*, **31**, 187 (1970).
- R. W. Bower, D. Sigurd, and R. E. Scott, *Solid State Electron.*, **16**, 1461 (1973).
- W. K. Chu, J. W. Mayer, M.-A. Nicolet, T. M. Buck, G. Amsel, and F. Eisen, *Thin Solid Films*, **17**, 1 (1973).
- J. F. Ziegler and W. K. Chu, *At. Data Nucl. Data Tables*, **13**, 463 (1974).

Ultrahigh Purification of Silane for Semiconductor Silicon

A. Yusa and Y. Yatsurugi

Komatsu Electronic Metals Company, Shinomiya 2612, Hiratsuka, Japan 254

and T. Takaishi

Institute for Atomic Energy, Rikkyo (St. Paul's) University, Yokosuka, Japan 240-01

ABSTRACT

Monosilane was purified with a newly developed ion-exchanged zeolite A, which sorbs phosphine in silane. The phosphine content of silane was determined from electrical resistivity of silicon which was obtained by decomposing silane. Two kinds of silicon samples were used for analysis, i.e., epitaxial films on silicon substrate, and single crystal rods. The electrical resistivity of the silicon rods of p-type ranged between 1×10^4 and 8×10^4 ohm-cm at room temperature, depending on conditions of purification. A surface barrier type solid-state detector, fabricated from this silicon, was evaluated with x-rays and conversion electrons from ^{207}Bi , and showed satisfactory characteristics. Characteristics of the adsorption column were studied with a simulation column by the aid of gas-chromatographic techniques. Optimum conditions were deduced for the operation of the adsorption column.

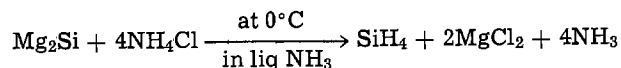
High purity silicon is used in the fabrication of various elements such as a rectifier for high voltage use and a solid-state detector for x-rays and β -particles. In recent years the demand for it is continuously increasing. Furthermore, a much higher degree of purity is required with increasing needs for elements of higher qualities. The present industrial processes do not meet these requirements.

Usually, semiconductor silicon is obtained by decomposing hydride or by reducing silicon halides. Two processes, i.e., monosilane and trichlorosilane processes, have been industrialized. In order to obtain high purity silicon, the monosilane process is superior to the trichlorosilane one, as can be seen from the following technical considerations:

(i) Silane decomposes at $700^\circ\text{--}800^\circ\text{C}$ to silicon and hydrogen, which do not cause any corrosion troubles. This is a significant merit in semiconductor technology, since it is possible that silicon is easily contaminated through chemical transport processes of corrosion products.

(ii) In a generation process of monosilane, boron hydrides are completely removed from silane by the chemical reaction, $\equiv\text{B} + :\text{NH}_3 \rightarrow \equiv\text{B}:\text{NH}_3$. Hence, the main residual impurity, which is electrically active, is phosphine, but phosphine is rather easily removed by zone refining. According to our experience, boron content in silicon, prepared from silane, ranges between 0.02–0.01 ppb in atomic ratio, which is very low in comparison with that from trichlorosilane. Phosphorus content in silicon is mentioned in the next paragraph. However, the monosilane process is slightly inferior to the trichlorosilane process in the area of production cost, as far as the present process is concerned.

In the present industrial process, silane is generated by reacting magnesium silicide with ammonium chloride in liquid ammonia solution as



Impurities generally contained in the evolved gas are highly volatile hydrides (diborane, arsine, phosphine, and methane), carbon monoxide, and nitrogen. Diborane is easily eliminated in the generation step as already mentioned. Arsine is rather unstable and, in our experience, has not caused any problem. It is un-

avoidable that silane contains traces of CH_4 , CO , and N_2 . When these gases are decomposed to elements, they give electrically less inactive impurity centers. Hence, the existence of these impurities is not a serious matter, as long as their amounts do not exceed 1 ppm. Phosphine is removed by distillation under reduced pressure at temperatures below the boiling point of silane (-112°C). Phosphine impurity is reduced from about 10 ppm in raw silane to about 0.05 ppb after distillation. This process has some disadvantages. The apparatus for the distillation is complicated and expensive, since liquefied silane, which forms a spontaneously explosive mixture with air, is processed. Fine distillation with a high number of plates is necessary in order to remove phosphine thoroughly from silane. Purified silane is thermally decomposed on a heated substrate of single crystal silicon to yield polycrystalline silicon. Polycrystalline silicon is further purified and single crystallized by means of the floating-zone melting techniques. Resistivity of n-type silicon prepared in this manner ranges from 2000 to 3000 ohm-cm at room temperature. This value is considerably lower than that of the ideally pure silicon, say, 230,000 ohm-cm. Many investigators (1, 2) reported properties of nearly intrinsic silicon which was prepared by techniques of automatically repeated zone-melt refining. The techniques, however, are not suitable to mass production of high purity silicon.

The aim of the present work is to establish the process of the production of high purity silicon, especially, by adsorptive purification of silane. Caswell (3) purified silane with some zeolites, and obtained the p-type silicon with a resistivity of 40–75 ohm-cm. We have developed an improved adsorbent (4). This is an ion-exchanged modification of molecular sieve A, having a composition of $(\text{Zn}_x\text{K}_{12-2x})\text{-A}$ with $2 < x < 4$. The commercially available molecular sieves A are 3A, 4A, and 5A. Adsorptive properties of these zeolites for silane and phosphine are shown in Table I, along with those of a newly developed 4.5A and the concerned zeolite. As can be seen from Table I, 3A and 4A sorb neither silane nor phosphine, while 4.5A and 5A sorb both of them. $(\text{Zn}_x, \text{K}_{12-2x})\text{-A}$ zeolite with $2 < x < 4$, may be classified as 3A as far as its sieving actions for nonpolar and saturated compounds are concerned (5). However, it can sorb polar molecules with diameters slightly larger than its window size. Equilibrium properties of this adsorbent were thoroughly investigated in the preceding paper (5), but the sorption kinetics were only briefly reported. In the present paper we report, in detail, results of the purification

Key words: surface barrier type SSD of silicon, fabrication of ultrahigh purity silicon, analysis of phosphine in silane.

Table I. Adsorptive abilities of 3A, 4A, 5A, and 4.5A and the concerned zeolite for silane, phosphine, arsine, and diborane. The signs + and - indicate active and nonactive, respectively.

Adsorbate gas	Adsorbent zeolite				The concerned zeolite
	3A	4A	5A	4.5A	
Phosphine	-	-	+	+	+
Silane	-	-	+	+	-
Diborane	-	-	+	-	-
Arsine	-	-	+	-	-

of silane conducted for the purpose of the production of high purity silicon.

Experimental

Adsorbent.—The (M^{II} , K)-A zeolites were prepared by ion-exchanging potassium ion in molecular sieve 3A with divalent cations M^{II} , such as Zn^{2+} , Mg^{2+} , Mn^{2+} . The ion exchange was carried out at 80°C with solutions of $M^{II}Cl_2 + KCl$ in 0.2 total metal ion normality. Figure 1 shows adsorptive properties of powdered (M^{II} , K)-A for SiH_4 , PH_3 , B_2H_6 , and AsH_3 as a function of the zeolite composition. One can conclude from this figure that the A-zeolites, having a composition of ($M^{II}_xK_{12-2x}$)-A with $2 < x < 4$, are useful for the selective adsorption of phosphine from silane. The rates of adsorption of phosphine by these zeolites were measured with a McBain type quartz spring balance. As can be seen in Fig. 2, (Zn, K)-A zeolite surpasses (Mg, K)-A and (Mn, K)-A in the rate of adsorption of phosphine. For these properties, (Zn, K)-A was adopted as the adsorbent for purification in the succeeding experiments.

Experimental apparatus.—Figure 3 shows the flow sheet of the present experiment, i.e., purification of silane by adsorption and decomposition to elemental silicon and hydrogen. The liquefied crude silane, stored in a storage tank T, was evaporated by warming and the silane gas passed through a dehydration column C and the silane gas passed through a dehydration column C (2½ in. diameter × 5 ft long) packed with molecular sieve 3A. Adsorption columns A and B are stainless steel tubes 5 ft long and 2½ in. diameter packed with the concerned adsorbent (1/16 in. pellet form) weighing about 2.1 kg. Prior to adsorption measurements, the adsorbent was baked out under a flow of hydrogen (purified through palladium diaphragm) at 400°C for 24 hr. The columns were cooled by standing in air to room temperature, and further to -20° to -30°C by circulating coolant (methanol) through jackets wound on the wall of the column. Silane passed through the

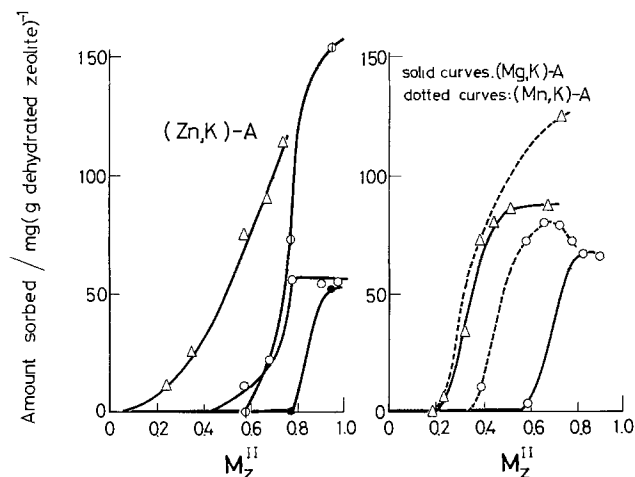


Fig. 1. Adsorptive capacities of (M^{II} , K)-A zeolites as a function of the composition. $M_z^{II} = 2[M^{II}]/\{2[M^{II}] + [K]\}$; ○, silane at 150 Torr, 0°C; △, phosphine at 150 Torr for (Mn, K)- and (Mg, K)-A, and 21 Torr for (Zn, K)-A, 0°C; □, arsine, 10 Torr, 0°C; ◆, diborane, 50 Torr, 0°C.

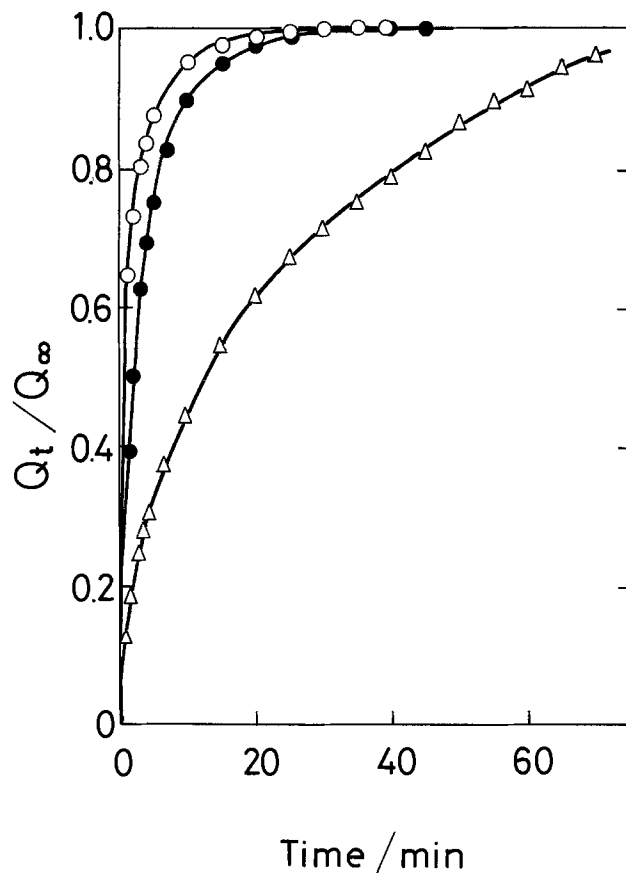


Fig. 2. The rate of sorption of phosphine with several (M^{II} , K)-A zeolites. (At 85 Torr and 0°C). Q_t and Q_∞ are amount sorbed at time t and ∞ , respectively. ○, ($Zn_{2.2}K_{7.8}$)-A, $Q_\infty = 54.5$ mg/g; △, ($Mg_{2.2}K_{7.8}$)-A, $Q_\infty = 55$ mg/g; ◆, ($Mn_{2.5}K_7$)-A, $Q_\infty = 81.0$ mg/g.

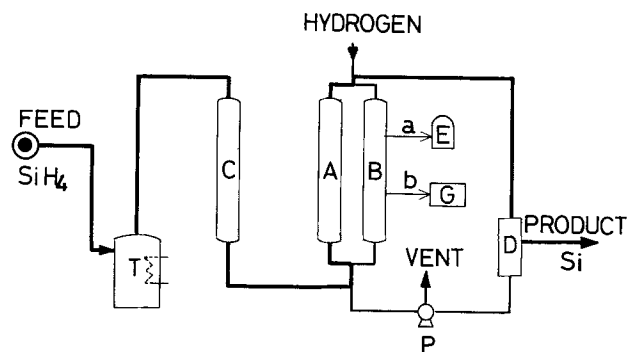


Fig. 3. Process flow chart for the production of ultrahigh purity silicon. T, storage tank for silane; C, dehydration column; A and B, purification columns; D, furnace for the decomposition of silane; E, furnace for epitaxial growth of silicon layer; G, gas chromatograph; a and b, sampling pipes; P, pump.

column C to A or B at a flow rate of 4 liters \cdot min $^{-1}$ and a pressure of 2.0 atm. The purified silane was introduced into a decomposition furnace, D, and thermally decomposed to polycrystalline silicon onto a silicon wire heated to 820°-880°C. A furnace, E, is used to analyze the sampling gas, and a and b are sampling pipes connected to E and a gas chromatograph G, respectively. The zeolite, which had lost the sorptive ability for phosphine, was regenerated by the same procedure as the activation carried out at the starting step.

The polycrystalline rod obtained was single crystallized in a floating-zone chamber. The rod, before loading, was shaped by mechanical grinding, and its surface was etched with $HF-HNO_3$ soln. Only one zoning was made under an atmosphere of argon at a positive gauge pressure. Single crystals for the seed had resis-

tivities ranging between 800-2000 ohm-cm at room temperature of n-type, and were held by stainless steel chuck.

Analyses of phosphine in silane.—The concentration of phosphine was measured by two methods. The first was a gas-chromatographic analysis having a sensitivity of 10 vol. ppm. A separation column packed with chromosorb 104 (Johns-Manville) was 3 mm in diameter and 1 m in length, and controlled at 70°C. The second was resistivity measurements of a silicon epitaxial layer deposited from the silane in the furnace E. The apparatus consisted of a stainless steel chamber (30 cm in diameter \times 40 cm in height), an oil-free vacuum pumping system, and a gas doser. A vacuum better than 10^{-7} Torr was easily attained after baking-out of the apparatus. The substrate for the epitaxial film was a p-type silicon bar of 0.7 ohm-cm ($5 \times 5 \times 200$ mm) with the rod axis parallel to [111]. All faces of the bar were polished with emery, ultrasonically cleaned successively in trichloroethylene, methanol, and acetone, chemically etched, and washed. The rod was held vertically by stainless steel clips and electrically heated. After cleaning the substrate silicon in hydrogen at 10 Torr and 1200°C or so, silane was admitted to the chamber at a pressure between 10^{-1} and 10^{-3} Torr. Most of the epitaxial growth was carried out at 10^{-1} Torr and 1070°C. Under this condition, the growth rate (the thickness of deposited silicon divided by growth time) was about $0.2 \mu\text{m} \cdot \text{min}^{-1}$.

The epitaxial layer is of n-type while the substrate of p-type, and the thickness of the layer is about $40 \mu\text{m}$, so that we are obliged to measure a very high resistance. This limits the measurable range of the specific resistivity, by the four-point probe method, to a value lower than 1×10^3 ohm-cm. To measure the high resistance of a very thin epitaxial layer, we must use the spreading resistance microprobe techniques (6). Then, we can measure the resistivity of the epitaxial layer in a range between 1×10^{-3} and 6×10^4 ohm-cm. The concentration of phosphine in silane is calculated from observed resistivity data, under the assumptions that $([\text{PH}_3]/[\text{SiH}_4])_g = ([\text{P}]/[\text{Si}])_s$, and further that the main impurity in solid is phosphorus. These assumptions might be open to some ambiguity, but the impurity concentration thus deduced has a useful meaning in production processes.

Concentration of impurities in single crystal rod.—The concentration of excess donors or acceptors was obtained from the temperature dependence of Hall coefficient, R_H . Furthermore, the concentrations of boron and phosphorus were determined by the frozen-drop method (7) with a sensitivity of 0.01 ppb and an accuracy of 10%. In the present experiments, contents of carbon and oxygen in silicon were not investigated in detail, because both of them cannot be deduced from electric properties. According to infrared spectroscopic analysis, the high purity silicon prepared by the floating-zone refining techniques had impurity oxygen at a lower concentration than 10^{16} atoms/(cm³ of Si) and carbon ranging from 0.5 to 1.1×10^{16} atoms/(cm³ of Si).

Results and Discussion

Concentration of impurities in the purified silane.—The resistivity of the silicon layer, which is a decomposition product of the purified silane, is shown in Fig. 4 as a function of the depth from the surface. The vertical arrow in the figure shows the position of the p-n junction which is determined by the stain-etching method. If the experiment could have been conducted ideally, the dotted curve would have been obtained. Several reasons are considered for the discrepancy between the observed and dotted curves. Out-dopings from the substrate may reduce the steepness of the slope in the p-n transition region. The exact shape of the peak cannot be obtained owing to a limited positional resolution of the present microprobe, $1 \mu\text{m}$. We cannot claim that contamination from the apparatus

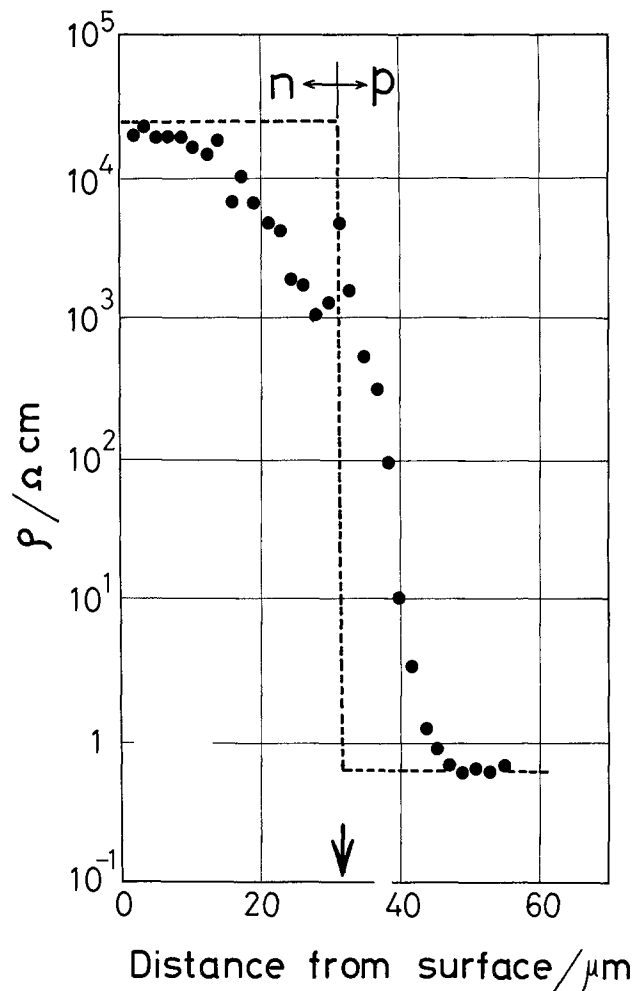


Fig. 4. Profile of the resistivity of the silicon layer deposited onto p-type substrate silicon crystal. Material silane gas was purified with the zeolite at a column temperature of -10°C .

wall is completely excluded. In spite of these shortcomings, the ρ -value at the plateau region becomes a measure of the concentration of phosphine. Applying Irvin's equation (8), we have

$$(\text{donor concentration}) \approx (\text{concentration of P}) = 5 \times 10^{11} \text{ atoms}/(\text{cm}^3 \text{ of Si})$$

Single crystal rods obtained from the polycrystalline silicon were 20-33 mm in diameter and 300 mm in length, and their resistivities at room temperature were greater than 10^4 ohm-cm of p-type without exception. Figure 5 shows a representative curve for the resistivity vs. position along the axis of the rod. The part near the seed crystal had a much lower resistivity than that of the middle part. This is attributed to the contamination from the low resistivity seed (600 ohm-cm of n-type). The single crystal silicon rods were of p-type in contrast with the result, obtained in the preceding paragraph, that the epitaxial layer was of n-type. It is considered that phosphorus was efficiently removed but boron was not in the process of the floating-zone melt.

Hall coefficient, R_H , was measured as a function of temperature. The excess donor or acceptor concentration, ΔN , is given by the relation $\Delta N = |N_A - N_D| = 1/R_H \cdot e$, where N_A and N_D are the concentration of acceptor and donor, respectively, and e is the elementary charge. The value for ΔN was 1.9×10^{11} atoms/(cm³ of Si), as estimated from R_H value in the extrinsic region.

Intrinsic resistivities of the samples ranged between 3×10^4 and 8×10^4 ohm-cm at room temperature. Three measuring techniques—the spreading resistance microprobe, the four-point probe and the bulk

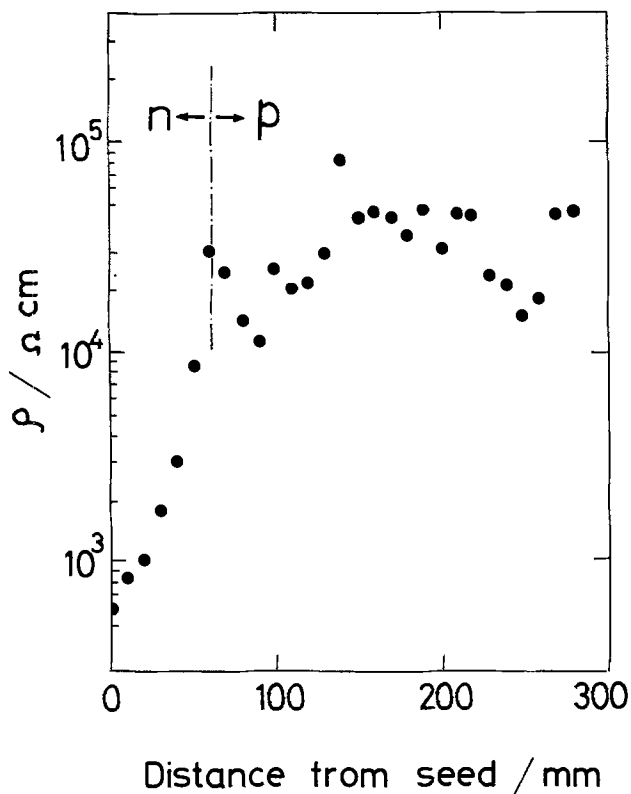


Fig. 5. Profile of the resistivity of silicon along the rod axis at room temperature. Dimension of crystal, 21 mmϕ × 300 mm; the seed crystal, of n-type with a resistivity of 600 ohm-cm at room temperature.

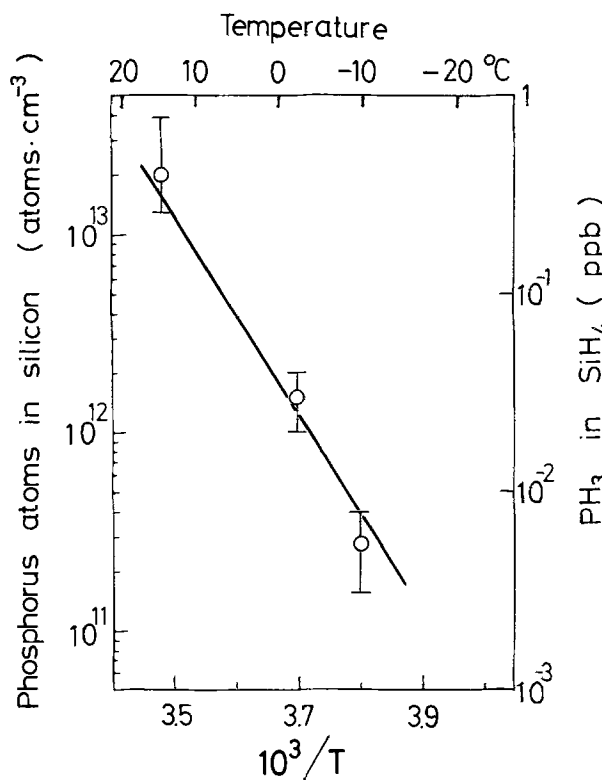


Fig. 6. Concentration of PH₃ in SiH₄ as a function of the temperature of the purification column. ○, values deduced from the resistivity of the epitaxial layer.

resistance methods—were used for comparison. These results are tabulated in Table II, and the agreement among these results was satisfactory.

Characteristics of the adsorption column.—The concentration of phosphine in the effluent silane is shown as a function of the column temperature in Fig. 6, where the phosphine concentration was obtained from the resistivity of the deposited silicon layer. If the rate of adsorption is so high that the local equilibrium is attained along the column, the effective isosteric heat of adsorption of phosphine by the adsorbent, q_{st} , can be deduced from this figure with the Clausius-Clapeyron equation as

$$q_{st} = 23 \pm 2 \text{ kcal} \cdot \text{mole}^{-1}$$

This heat is slightly smaller than those of ammonia and water (9). The higher purity of the effluent silane is obtained with the decreasing column temperature, up to the point where the assumption of the adsorption equilibrium breaks.

Further studies were carried out by using a simulation column to obtain detailed knowledge in a wider temperature range. The simulation column had a diameter of 4.2 mm and a length of 450 mm, containing 5g of the adsorbent (40-60 mesh particles). A gas mixture of phosphine and silane was passed through the column, and an effluent was directly introduced into a gas chromatograph and analyzed. Since the sensitivity

of the detector was 10 ppm for phosphine, the test gas used contained about 350 ppm of phosphine. This composition differs considerably from that used in other experiments at our plant, but we can expect that results of the simulation experiments elucidate the characteristic properties of the adsorbent. The breakthrough curve of the column was measured at temperatures between -78°C and 50°C and at flow rates ranging from 60 to 600 mliter · min⁻¹. Results are shown in Fig. 7. In this figure, the concentration of phosphine in the effluent is expressed in a normalized unit (conc of phosphine in the outlet gas/conc of phosphine in the inlet gas). The breakthrough point is defined as the total volume of gas effused before phosphine in the effluent can be detected by the gas chromatography. The breakthrough point increases first with the decreasing column temperature, reaches the maximum value at about -30°C , and then drops steeply, as shown in Fig. 8. Two possible reasons are considered for this drop. The first is concerned with an inherent property of phosphine, that its adsorption may

Table II. Resistivity of high purity Si

Measurement techniques	$\rho / (10^4 \text{ ohm-cm})$	$ N_D - N_A / 10^{12} / \text{cm}^3 \text{ Si}$	Type
Four-point probe	5 ~ 7	(2 ~ 3)*	—
Spreading resistance	8.5	(1.5)*	—
Hall effect	8.9	1.9 (1.5)*	p
Bulk resistance	8.2	(1.5)*	—

* Values in parentheses obtained from Irvin's table, Ref. (8).

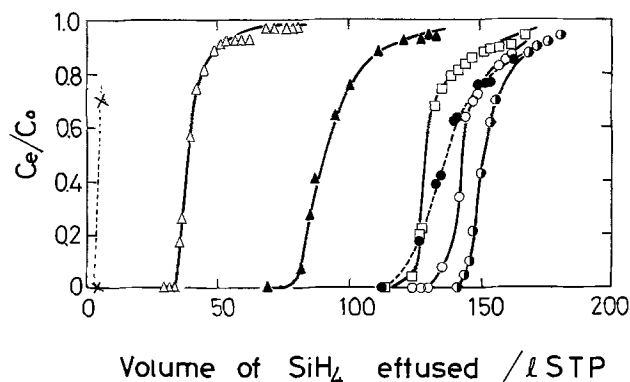


Fig. 7. Breakthrough curves of the simulation column—Effect of the column temperature. ×, -78°C ; ○, -45°C ; ○, -30°C ; ○, -21°C ; □, 0°C ; ▲, 30°C ; △, 50°C .

require some activation energy and become very slow at lower temperatures. The second is that the adsorption of phosphine is reasonably rapid but seriously hindered by coexisting silane at lower temperatures. To make a choice between these two, the breakthrough curve of a mixture of argon and phosphine was studied, and the results are shown by a dotted curve in Fig. 8. In this case, the breakthrough point monotonically increases with decreasing temperatures and is always higher than that in the phosphine-silane system. Consequently, it is concluded that silane hinders the adsorption of phosphine and that its effect becomes serious below -40°C . The effect of the flow rate of the gas was also investigated, with results shown in Fig. 9.

The column, when saturated with phosphine, was regenerated by warming gradually up to 400°C under

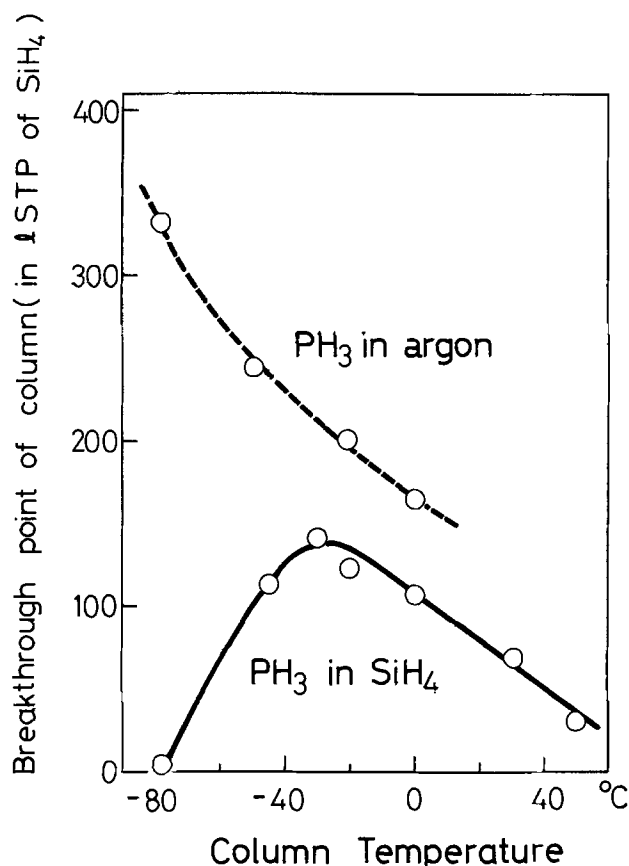


Fig. 8. Breakthrough point of the simulation column expressed as a function of the column temperature. The solid curve is referred to PH_3/SiH_4 system, with a molar concentration of PH_3 of 360 ppm, at a flow rate of $167 \text{ ml} \cdot \text{min}^{-1}$; the dotted curve is referred to PH_3/Ar system, with a molar concentration of PH_3 of 370 ppm, at a flow rate of $300 \text{ ml} \cdot \text{min}^{-1}$.

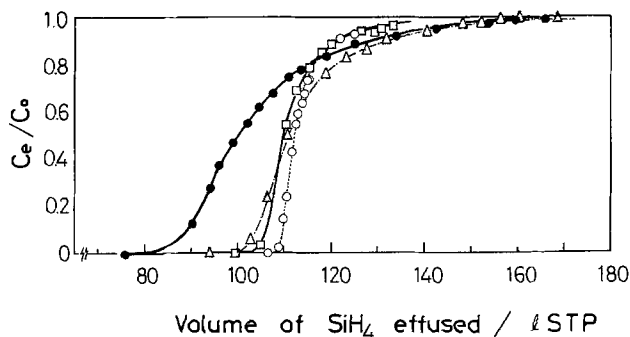


Fig. 9. Effect of the flow rate of the effluent to the breakthrough curve at 0°C . \circ , $69 \text{ ml} \cdot \text{min}^{-1}$; \square , $220 \text{ ml} \cdot \text{min}^{-1}$; \triangle , $418 \text{ ml} \cdot \text{min}^{-1}$; \bullet , $582 \text{ ml} \cdot \text{min}^{-1}$.

a flow of hydrogen. The adsorption activity of the column was reduced to one-third of its initial value by the first regeneration treatments, and almost lost after three cycles. In contrast with the phosphine-silane system there was no hysteresis on regeneration of the adsorbent in the phosphine-argon system. One possible conclusion is that silane decomposition impairs the adsorption activity of the zeolite in the regeneration process. This means that silane may be sorbed to some extent, and decompose and block the pores on heating. The adsorbed amount of gas in Fig. 1 was obtained by waiting 2 hr for equilibration. Hence, more careful measurements were carried out by waiting 100 hr for equilibration, and it was found that a measurable amount of silane was sorbed very slowly. After pumping out residual silane in a dead space, the zeolite adsorbent was heated to 400°C , hydrogen being evolved in that course. Thus it is concluded that silane competes, though weakly, with phosphine in adsorption, and that the sorbed silane decomposes to hydrogen and silicon by heat-treatments. The product silicon blocks the window to the cavity of the zeolite and hinders the regeneration. It is a considerable demerit that the adsorbent cannot be regenerated. Still, the present process is economical for the following reasons: (i) The ratio of weight of zeolite consumed to that of treated silane is very large, that is, the purified silane weighing 200 kg can be obtained from 2 kg of zeolite in one bed; (ii) zeolite is far less expensive than a silicon rod; (iii) in the adsorption purification process, losses of silane are negligibly small; and (iv) adsorption purification is carried out at temperatures between -30° and -20°C , attained by a one-stage refrigerator.

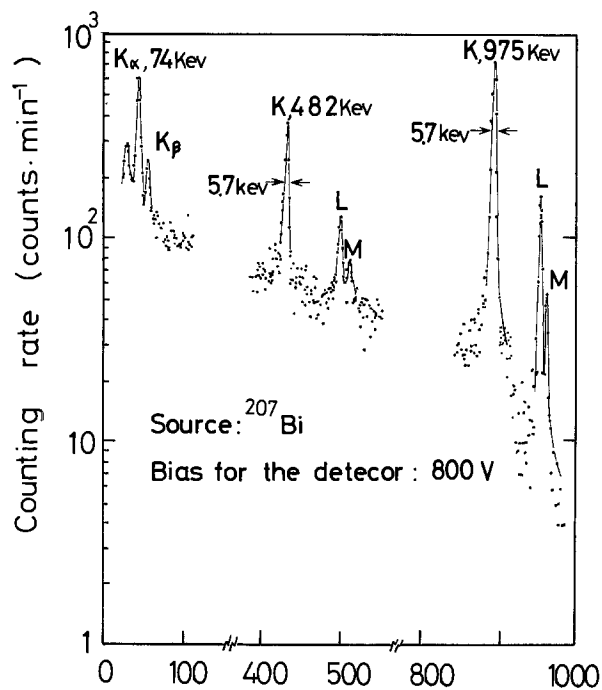
To seek a better adsorbent, we measured adsorption properties of $(\text{Mg}, \text{K})\text{-A}$, $(\text{Mn}, \text{K})\text{-A}$, and $(\text{Zn}_x\text{K}_{12-2x})\text{-A}$ with $1 < x < 2$, but all of them are inferior to the one discussed herein. With these zeolites, phosphine was sorbed rather slowly, so that an unreasonably long adsorption column may be required to purify silane to the desired degree. Other kinds of zeolites such as $(\text{Cd}, \text{K})\text{-A}$, $(\text{Ca}, \text{K})\text{-A}$, and $(\text{Ni}, \text{K})\text{-A}$, did not satisfy the required conditions.

Characteristics of the high purity silicon.—A surface barrier type detector with a depletion layer thickness of 1 mm was fabricated from high purity silicon (of p-type with a resistivity of $1 \times 10^4 \text{ ohm-cm}$ at room temperature). Figure 10 shows a representative spectrum and the full widths at half maximum, measured with the detector at 77°K , for x-rays and conversion electrons from ^{207}Bi . The total system resolution was 5.7 keV at 0.975 MeV with 800V bias on this detector. The same resolution was obtained for a signal from a test pulser, so that the resolution was limited by the electronic circuit used. Consequently, we can say that the intrinsic resolution of the detector is better than the above value.

Conclusion

In the present work, use was made of a conventional floating-zone apparatus and deposition furnace for routine production, so that the apparatus unavoidably caused contamination of the silicon rod. Therefore, the observed purity in the present work gives the lowest limit to the true purity of the treated gas. Ultrahigh purity silicon ($\rho > 10^5 \text{ ohm-cm}$ at room temperature) can be fabricated from silane purified by adsorption on modified zeolite, if use is made of a very clean apparatus specially designed for the purpose.

The high purity silane gas is valuable not only for the production of silicon rods, but also for chemical vapor deposition process. The epitaxial silicon layer with a very high resistivity is useful for some purposes, and the high resistivity polycrystalline silicon layer is required for isolation of electrodes on IC chips. Commercially available silane for CVD, usually, contains n-type impurities (probably, phosphine) and the epitaxial silicon obtained from it has a resistivity of about 200 ohm-cm or lower at room temperature. High



Channel number of a pulse height analyzer

Fig. 10. Spectrum of x-rays and conversion electrons from ^{207}Bi , measured at 77°K with a surface barrier type Si detector having a depression layer of 1 mm thickness.

resistivity layers can easily be obtained by passing such a gas through a small adsorption column of (Zn, K)-A zeolite. This application of zeolite is promising in

the production of some types of IC, and is now under investigation.

Acknowledgment

The present authors thank F. Shiraishi of Rikkyo University who fabricated and evaluated the solid-state detector, Y. Chujo, N. Takahashi, and T. Ikeda, of the Komatsu Electronic Metals, for their skillful assistance in the experiments, and Y. Takami of Rikkyo University who kindly read the manuscript and gave valuable comments.

Manuscript submitted June 9, 1975; revised manuscript received Aug. 8, 1975.

Any discussion of this paper will appear in a Discussion Section to be published in the June 1976 JOURNAL. All discussions for the June 1976 Discussion Section should be submitted by Feb. 1, 1976.

Publication costs of this article were partially assisted by the Komatsu Electronic Metals Company.

REFERENCES

1. E. H. Putley and W. H. Mitchell, *Proc. Phys. Soc. (London)*, **72**, 193 (1952).
2. A. Hoffmann, K. Reuschel, and H. Rupprecht, *J. Phys. Chem. Solids*, **11**, 284 (1959).
3. E. G. Caswell, U.S. Pat. 2,971,607 (1961).
4. T. Takaishi, A. Yusa, and Y. Yatsurugi, *Proc. 3rd Int. Conf. Molecular Sieves*, p. 246, Leuven University Press (1973).
5. T. Takaishi, Y. Yatsurugi, A. Yusa, and T. Kuratomi, *JCS Faraday Trans. I*, **71**, 97 (1975).
6. E. E. Gardner, P. A. Schuman, and E. F. Gorey, in "Measurement Techniques for Thin Films," B. Schwartz and N. Schwartz, Editors, p. 258, The Electrochemical Society Softbound Symposium Series, New York (1967).
7. F. H. Horn, *This Journal*, **114**, 1307 (1967).
8. J. C. Irvin, *Bell System Tech. J.*, **41**, 387 (1962).
9. D. W. Breck, "Zeolite Molecular Sieves," p. 654, Wiley-Interscience, New York (1974).

Reduction of Autodoping

Carl O. Bozler*¹

Sperry Rand Corporation, Gainesville, Florida 32601

ABSTRACT

Silicon epitaxial layers are grown on silicon substrates highly doped with arsenic using the pyrolysis of silane. A special technique is used to reduce the autodoping by minimizing impurity evaporation from the back side of the wafer. A comparison of impurity profiles obtained from layers grown under a number of different conditions reveals that autodoping can be reduced still further by increasing the flow rate, decreasing the volume around the susceptor, and decreasing the growth rate. The formulation of a mathematical model helps to describe the interrelation of those three variables. By optimizing the growth conditions, it is shown that the autodoping can be essentially eliminated.

For many silicon devices, especially microwave diodes and transistors, it is desirable to have very abrupt transitions between doping levels. In some cases it is required to have a heavily doped substrate with light doping in an epitaxial layer. Fabrication of such an epitaxial layer where the transition in doping level must occur in less than a micron can be difficult because of dopants coming from the substrate during growth.

Impurities can move from the substrate into the epitaxial layer in two ways. First, they can simply diffuse through the bulk silicon into the layer, and according to Fick's law the impurities will assume a

complementary error function distribution (1). Second, impurities can leave the substrate via the gas phase adding to dopants already in the gas. Some of these impurities will then be incorporated into the growing layer. This second impurity transport mechanism, via the gas phase, is generally termed autodoping.

To clarify the events which lead to autodoping, one can divide the growth sequence into two time periods. Before growth begins, there is a period where the substrate is at growth temperature with dopant evaporating from the substrate surfaces reaching some steady-state concentration in the gas phase. The second time period begins with the initiation of growth. The exposed surfaces of highly doped silicon become sealed with a layer of silicon within a few seconds and can no longer contribute to autodoping. No growth occurs

* Electrochemical Society Active Member.

¹ Present address: Lincoln Laboratory, Massachusetts Institute of Technology, Lexington, Massachusetts 02173.

Key words: silicon, epitaxy, autodoping.

on the back surface of the substrate, however, which is more or less in contact with the susceptor, and consequently the back surface continues to contribute to autodoping. There are then two sources for autodoping: the impurities in the gas before growth begins and the impurities evaporating from the back surface during growth.

A number of authors (2-4) have demonstrated that a dramatic decrease in autodoping occurs when the back side of the wafer is coated with SiO_2 prior to epitaxial growth. With the back side of the wafer sealed, the entire wafer becomes sealed after growth begins. The only impurities contributing to autodoping in this case are those which have evaporated from the front surface of the substrate in the period before growth began. It is the pregrowth contribution to autodoping that is investigated in this paper.

Experimental

The system used to grow the epitaxial layers is an Applied Materials Technology AMV 500. The cross section of the reactor chamber in Fig. 1 shows the rotating susceptor which is made of high purity graphite with an over-layer of silicon carbide. The susceptor has a 12.5 cm diameter and is inductively heated. The silicon layers are grown by the pyrolysis of silane at a corrected temperature of 1050°C. Before each growth run, the susceptor is first stripped with hydrogen chloride in hydrogen (1200°C) and then recoated with a fresh layer of undoped silicon.

The substrates are highly doped with arsenic having a resistivity of 0.001 ohm-cm and (111) orientation. They are 3.1 cm in diameter, 0.017 cm thick, and have dislocation counts less than 500/cm². They are chem-mechanically polished on one side and chemically etched on the back side to remove lapping strain. The substrates are prepared for epitaxial growth by degreasing in organic solvents followed by 5 min in hot 1:1, $\text{NH}_4\text{OH}:\text{H}_2\text{O}_2$, then 5 min in hot H_2SO_4 saturated with CrO_3 , and 5 min in hot 18 megohm water. The wafers are then vapor-etched in the epitaxial reactor with 2% hydrogen chloride in hydrogen (20 liters/min) for 4 min at a corrected temperature of 1200°C. The etch is done immediately prior to film growth and removes about 2 μ of silicon.

A very important discovery was made when examining the wafers after etching. During the vapor etch a layer of silicon grows on the back side of the wafer. The layer is 1-2 μm thick and the carrier concentration is approximately $10^{17}/\text{cm}^3$ at the surface. The reason for this growth during etching is illustrated in Fig. 2. The substrate is 20°C cooler than the susceptor and with the presence of HCl, transport of silicon occurs from the susceptor to the substrate. This layer of silicon seals the back side of the highly doped ($5 \times 10^{19}/\text{cm}^3$) substrate. The effectiveness of the seal was verified by comparing epitaxial layers grown on wafers

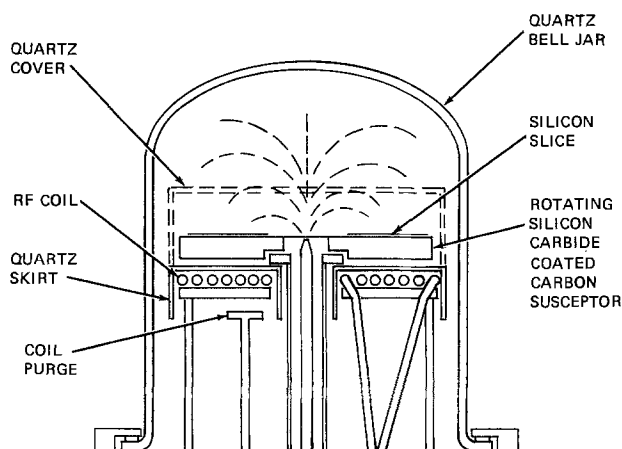


Fig. 1. Silicon epitaxial reactor

ATMOSPHERE: HYDROGEN 98%
HYDROGEN CHLORIDE 2%

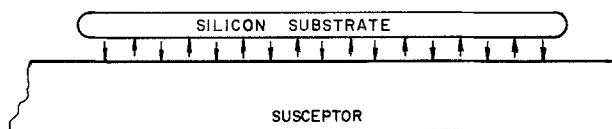


Fig. 2. Transport of silicon from susceptor to substrate

with and without a steam-grown oxide, 10,000Å thick, over the silicon layer on the back side. No detectable reduction in autodoping was observed due to the extra oxide film. This convenient method of sealing the back side of the wafers was used on all of the runs reported here.

After the vapor etch the system is purged for 10 min (various purge times in the range 5-30 min had no effect on the impurity profile) and then epitaxial growth is begun. The hydrogen flow rate was constant throughout the run and except where noted was 20 liters/min.

The silane concentration was varied from 0.01 to 0.1% with the growth rate varying linearly. For the layers grown with a slow growth rate of 0.03 $\mu\text{m}/\text{min}$, a special two-step procedure was used to decrease total growth time. The slow growth rate was maintained for 30 min; then, the silane concentration was increased to give a growth rate of 0.3 $\mu\text{m}/\text{min}$ for 7 min. This procedure provided the 3 μm thick film required by the electrical evaluation technique.

Generally, only one substrate was used per experiment except where noted. To reduce the volume around the susceptor from 3 liters to 1 liter, a quartz cover (dotted line in Fig. 1) was added to the reactor for several of the experiments.

The quality of the layers was evaluated with Sirtl etch and they were found free of stacking faults. The film thickness uniformity over each wafer was better than $\pm 2\%$.

The impurity profile measurements were made using the voltage-capacitance technique (5). Two different procedures were used to form the barrier. One technique was to use a boron predeposition to form a 0.1 μm thick p-layer. Mesas were etched and contact made. The second technique made use of the mercury probe (6). Calibration of the mercury probe was made very accurate by measuring a known standard before each profile measurement. There was excellent correlation between these two techniques.

Results and Discussion

The effect of flow rate and volume around the susceptor on autodoping is illustrated in Fig. 3. The dotted line is the complementary error function determined by time and diffusion constant at growth temperature and represents the part of the doping which would remain if the autodoping were eliminated. The solid curve is the measured impurity profile. Due to the nature of the voltage-capacitance measurement, the position of the impurity profile along the x-axis relative to the interface between substrate and layer was initially unknown. The correct position has been determined by noting that for all the experimental curves the slope above a carrier concentration of $10^{17}/\text{cm}^3$ is essentially the same as the corresponding complementary error function curve. This implies that autodoping becomes negligible above $10^{17}/\text{cm}^3$ and that in this range the experimental and complementary error function curves can be matched by shifting the experimental curve in the x-direction. The three experimental curves in Fig. 3 have been matched, and it is evident that by either increasing the hydrogen flow or decreasing the volume, the autodoping is reduced.

It has been found by some (7) that this result could be explained by impurities stored in a stagnant bound-

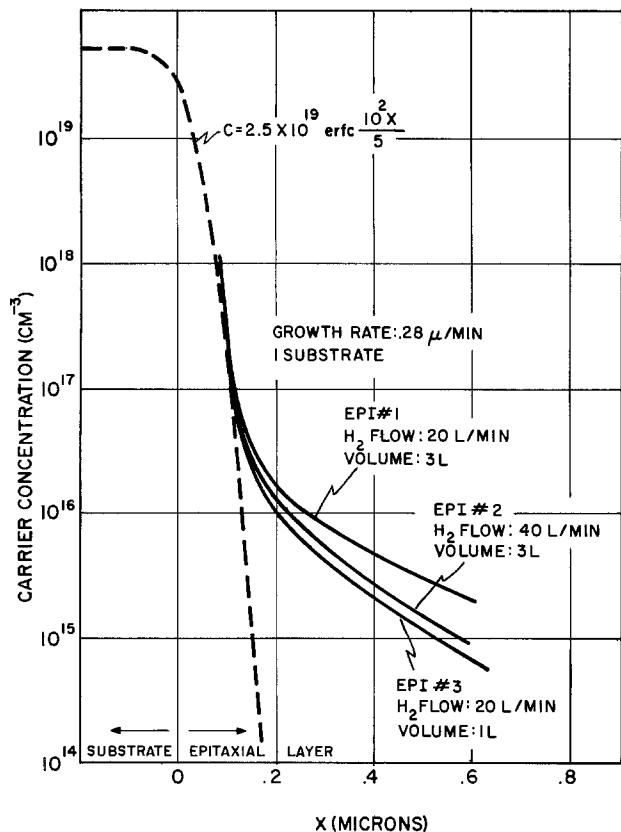


Fig. 3. Impurity profiles showing the effect of volume around the susceptor and flow rate.

ary layer. A special experiment was made to determine the effect of the boundary layer. A fixed quartz wiper was placed over the susceptor in a radial direction so that, with the susceptor rotating, the wiping action would disturb the boundary layer releasing the stored impurities. The clearance between the bottom of the wiper and the top surface of the wafer was 1/2 mm. The height of the wiper was 1 cm. A layer was grown using the wiper under conditions identical to Epi No. 1 and the profile obtained was indistinguishable from that given for Epi No. 1 in Fig. 3. Therefore for the vertical system used in these experiments the boundary layer is not a major cause of the autodoping.

A second possible explanation of the results in Fig. 3 is that both smaller volume and higher flow cause more rapid impurity dilution. The relation of the growth variables to impurity concentration can be clarified with a model. Consider V to be the volume above the susceptor of Fig. 1 and assume, because of turbulence, that gas entering at flow rate f is completely mixed immediately upon entering. One can describe the impurity concentration in the gas as a function of time with the differential equation

$$C = -\frac{V}{f} \frac{dC}{dt} \quad [1]$$

$$C(0) = C_0$$

It is easy to visualize in the reactor of Fig. 1 that large vortices may exist inside the bell jar above the susceptor. Even though the gas inside a vortex is well mixed a large percentage of pure gas may pass around the outside of the vortex and past the skirt without mixing. To account for this, a mixing factor k less than one is factored into the flow term of Eq. [1]

$$C = \frac{-V}{kf} \frac{dC}{dt} \quad C(0) = C_0 \quad [2]$$

A solution to this equation is

$$C = C_0 e^{-\frac{kf}{V}t} \quad [3]$$

Because of the nearly linear relationship between gas impurity concentration and layer impurity concentration, let

$$N_1 = hC \quad [4]$$

where N_1 is that part of the impurity concentration in the silicon which comes from the pregrowth gas impurities and h is the proportionality constant. With the change of variables

$$x = Gt \quad [5]$$

where G is the growth rate. The impurity concentration in the layer as a function of distance is

$$N_1 = hC_0 e^{-\frac{kf}{GV}x} \quad [6]$$

In Fig. 4, the impurity profile of epitaxial run No. 1 given in Fig. 3 has been replotted on a contracted x -scale in order to show the impurity level further from the layer-substrate interface. Equation [6] has been plotted also with $k = 0.2$, and one can see that there is some contribution to autodoping in addition to the pregrowth gas impurities. A possible source for this additional autodoping is the walls of the reactor which are relatively cool (300°-700°C). Impurities could condense on the walls in the pregrowth period; then, after growth begins and the impurity concentration in the gas decreases, the impurities on the walls could be released. In Fig. 4 the line having the equation

$$N_2 = B_0 \frac{V}{f} e^{-\frac{\eta}{G}x} \quad [7]$$

has been included to represent these released impurities. η does not depend on the volume around the

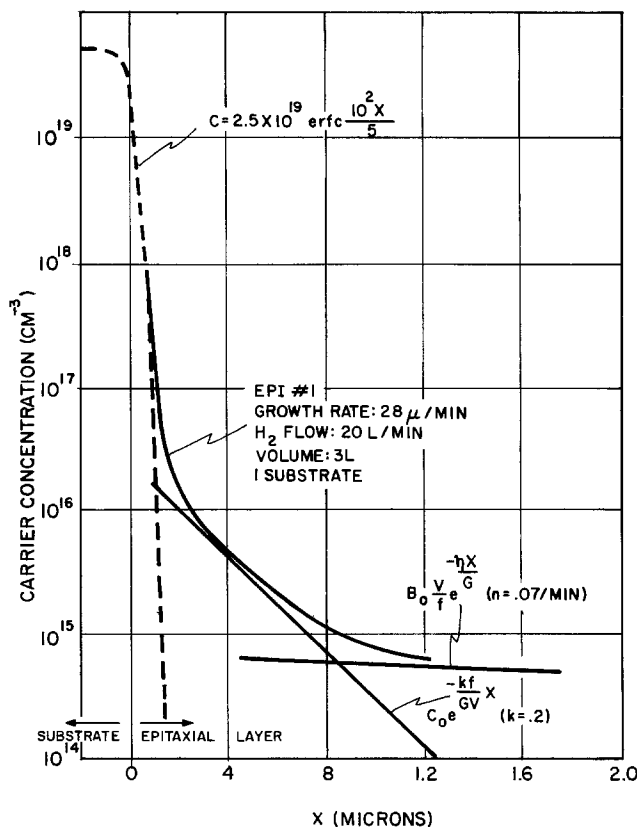


Fig. 4. A comparison of the mathematical model to the measured profile Epi No. 1.

susceptor or the flow rate, but is probably a complicated function of wall temperature and impurity vapor pressure. B_0 is determined by the initial rate of impurity release, and the V/f term represents the effect of flow rate and volume. The total concentration in the film is the sum of Eq [6] and [7]

$$N = hC_0 e^{-\frac{kf}{VG}x} + B_0 \frac{V}{f} e^{-\frac{\eta}{G}x} \quad [8]$$

Even though Eq. [8] is a rather crude model which ignores the effects of diffusion during growth, it has a very good qualitative agreement with several experimental results which follow and is able to predict the requirements for minimum autodoping.

Equation [8] predicts that decreasing the growth rate should have a strong influence in reducing the autodoping. This was indeed found to be the case, as illustrated in Fig. 5. The effect of the low growth rate is to maintain a sealed substrate with a minimal thickness of silicon while allowing time for the impurity level in the gas to decrease. The lower growth rate requires a longer growth time, however, and consequently the impurity diffusion from the substrate into the layer is larger (dotted lines). A comparison of the impurity profile of the 0.03 $\mu\text{m}/\text{min}$ layer (Epi No. 5) and Eq. [8] is made in Fig. 6. The values of C_0 , B_0 , f , η , and V are the same as those used in Fig. 4. The agreement is good with the realization that the increased out-diffusion of impurities from the substrate in Epi No. 5 has covered over the autodoping contributed by pregrowth gas impurities. The impurities designated as coming from the reactor walls now play the most important part.

In addition to growth rate, the one other variable in the system which was found to influence autodoping was the number of substrates on the susceptor, as illustrated in Fig. 7. Increasing the number of substrates increases the autodoping, which is at least in qualitative agreement with the model. The increased surface area of highly doped silicon has the effect of increasing

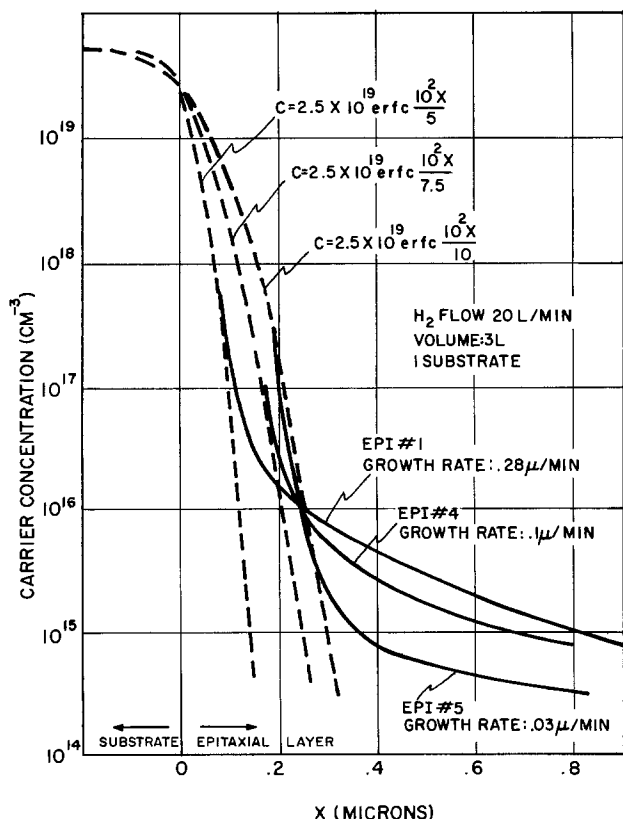


Fig. 5. Impurity profiles showing the effect of growth rate

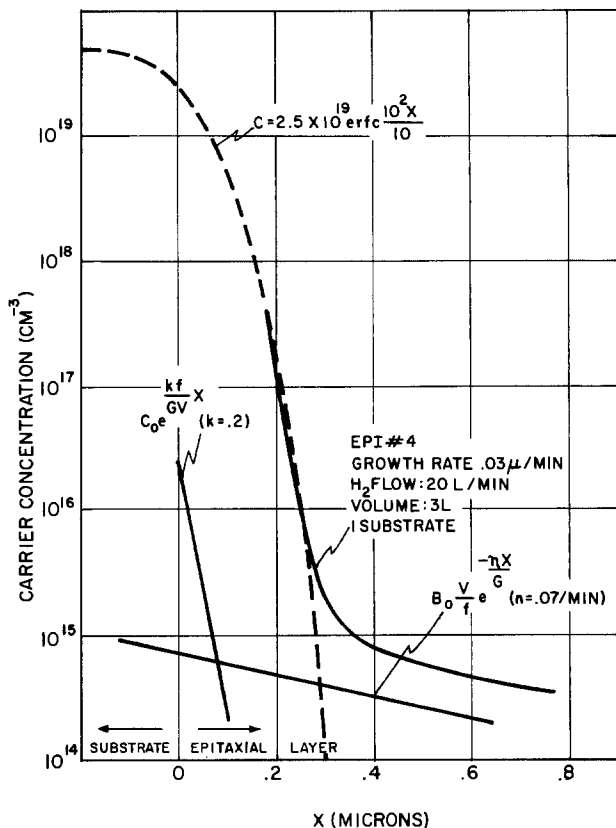


Fig. 6. A comparison of the mathematical model to the measured profile Epi No. 5.

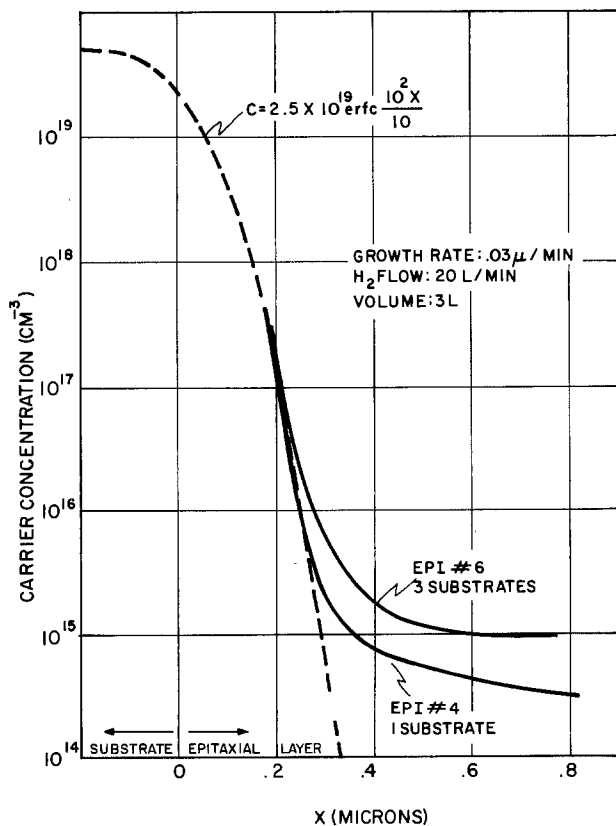


Fig. 7. Impurity profiles showing the effect of number of substrates.

the gas concentration of impurities before growth, which increases the value of C_0 and B_0 in Eq. [8].

Using the model as a guide, an attempt was made to reduce the autodoping as much as possible. A layer

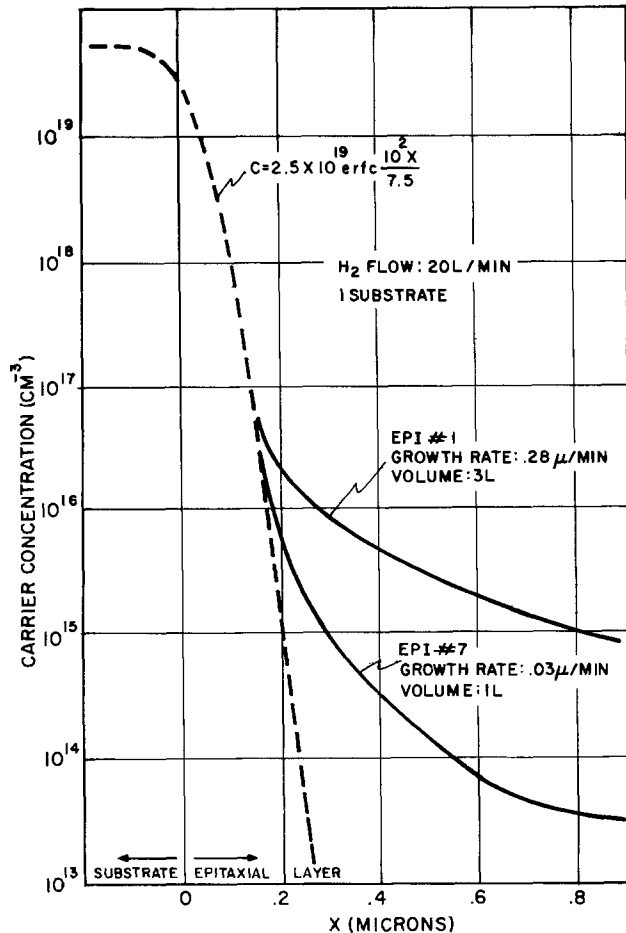


Fig. 8. Impurity profiles showing the result of minimizing autodoping.

was grown using a single substrate, a low growth rate of 0.03 $\mu\text{m}/\text{min}$, and a small volume around the susceptor (1 liter). The result is given in Fig. 8 and compared with Epi No. 1 (the complementary error function for Epi No. 1 has been omitted for clarity). The amount of autodoping has been greatly reduced and has made the transition in doping level very abrupt. The transition is so abrupt that when using the voltage-capacitance technique to measure impurity concentration, there can be appreciable measurement error due to electron redistribution. Using the theoretical data presented by Kennedy (5) on distribution of car-

riers around hi-low junctions, the remaining autodoping in Epi No. 7 can be accounted for by measurement error.

Although only seven impurity profiles have been given here to describe the results in Fig. 3-8, actually many additional profiles were made of epitaxial layers grown under conditions identical with layers 1-7. Each layer was repeated at least twice and Epi No. 1 has been repeated over twenty-five times. In every case when growth conditions were identical the profile differences were insignificant.

Conclusions

For a specific epitaxial crystal growth system using substrates doped with arsenic, the causes of autodoping have been studied. A mathematical model has been established to help organize the experimental results. With the elimination of autodoping from the back side of the wafer, the important requirements to reduce the remaining autodoping are increased flow rate, decreased volume around the susceptor, decreased growth rate, and decreased number of substrates. It was found possible to meet a combination of these requirements which resulted essentially in the elimination of the autodoping.

Acknowledgment

This work was sponsored in part by the Naval Electronic Systems Command under Contract No. N00039-72-C-0207.

Manuscript submitted Aug. 15, 1974; revised manuscript received July 21, 1975.

Any discussion of this paper will appear in a Discussion Section to be published in the June 1976 JOURNAL. All discussions for the June 1976 Discussion Section should be submitted by Feb. 1, 1976.

REFERENCES

1. A. S. Grove, A. Rader, and C. T. Sah, *J. Appl. Phys.*, **36**, 802 (1965).
2. B. A. Joyce, J. C. Weaver, and D. J. Maule, *This Journal*, **112**, 1100 (1965).
3. D. C. Gupta and Roy Yee, *ibid.*, **116**, 1561 (1969).
4. G. Skelly and A. C. Adams, *ibid.*, **120**, 116 (1973).
5. D. P. Kennedy, P. C. Murley, and W. Kleinfelder, *IBM J. Res. Dev.*, **12**, 399 (1968).
6. P. J. Severin and G. J. Poodt, *This Journal*, **119**, 1384 (1972).
7. H. B. Pogge, D. W. Bass, and E. Ebert, in "Chemical Vapor Deposition, Second International Conference," J. M. Blocher, Jr. and J. C. Withers, Editors, p. 767, The Electrochemical Society, Softbound Symposium Series, New York (1970).

Fluoride Ion Contamination and TiO Film Migration in the Ti-Pt-Au Metallization

A. Christou* and H. M. Day*

Naval Research Laboratory, Washington, D.C. 20375

ABSTRACT

F⁻ ions exist as probable sources of contamination from the contact etchant and from the platinum etchant during the processing of the Ti-Pt-Au metallization contact system. Annealing up to 200°C has resulted in the formation and migration of a TiO layer as identified in the Si-Ti-Pt-Au structure. Sputter profiles using Auger electron spectroscopy (AES) indicate that the Ti layer has been transformed into a Ti, TiO, O₂ composition. It is shown that the thin oxide film (TiO) passivates the titanium layer. Interdiffusion failures observed were found to be directly dependent on the migration and chemical dissolution of the passivation (TiO) film. These specimens were characterized by random pinhole formation and microcracking as identified with the SEM. Migration of the thin oxide film resulted in the titanium becoming active in a contaminated ion environment. F⁻ ion contamination was found to provide a more active corrosive environment for pinhole formation. Interdiffusion of gold through the barrier layers increased as F⁻ ion concentration increased.

A number of investigations on the reliability of semiconductor devices as affected by diffusion controlled processes which take place at metal-silicon contacts have been reported in the literature (1-3). These investigations indicate that halogen ions at silicon and silicide contacts can degrade the low temperature stability of gold/refractory thin film structures. In the present investigation we report (i) the effect of F⁻ ion contamination on the reliability of the Ti-Pt-Au metallization, (ii) the effect of oxygen gettered by the titanium on the stability of Ti-Pt-Au test structures, and (iii) the pinhole and interdiffusion (Au ⇌ Si) failure mode. F⁻ ions exist as probable sources of contamination from the contact etchant. In addition to contact contamination, a number of intermetallic compounds are formed in the diffusion couples of the Ti-Pt-Au system (4, 5). These compounds include Ti₃Pt which has been postulated to be the high temperature diffusion barrier to gold-silicon interdiffusion (6). If pinhole formation is accelerated in the presence of a corrosive environment, pinhole formation in the barrier layers can result in a low temperature gold-silicon interdiffusion.

Experimental Techniques

In LSI and microwave transistor metallization applications, an oxide-nitride-oxide sandwich is deposited before the initial emitter diffusion. The upper oxide is photoetched in contact areas and is used as a mask for etching the nitride layer. Contact windows in the silicon are subsequently opened, and after removal of the photoresist, platinum is evaporated for platinum silicide formation. The PtSi is followed by a titanium (for adhesion) and a platinum (gold diffusion barrier) deposition. The gold is then plated onto the beam areas and the titanium is etched resulting in the cross section shown in Fig. 1. Figure 1 also summarizes the various processing steps. The F⁻ and Cl⁻ ions are probable sources of contamination from an HF etchant, from the platinum etchant (HNO₃ and HCl), and from the SiO₂ etchant. Test structures with contacts shown in Fig. 1 and with known amounts of F⁻ ion surface concentration were annealed in a vacuum (1 × 10⁻⁵ Torr) at temperatures up to 350°C in order to investigate gold migration, pinhole formation, and microcracking.

A second set of test structures consisting of Ti-Pt-Au deposited on F⁻ pretreated (100) silicon wafers was used to determine the low temperature 150°-350°C

thermal stability of the Ti-Pt-Au system. Radioactive ¹⁸F was prepared according to the reaction ¹⁸O(α, pn)¹⁸F from Li₂O by α-particle irradiation in the Naval Research Laboratory cyclotron (1). The fluorine was extracted in the form of H₂¹⁸F and added directly to the etch solution. Prior to metallization the silicon wafers were dipped in the etch solution for 10 sec, rinsed, and then monitored at various intervals for verification of fluorine concentration and the absence of other radioactive contaminants such as Na. The variation of the fluorine ion concentration as a function of rinse duration is shown in Fig. 2. Figure 2 shows that wafers pretreated by an additional 1200°C thermal quench also fall on the same curve.

INVESTIGATION OF THE EFFECT OF ION CONTAMINATION ON THE Ti/Pt/Au INTERDIFFUSION CHARACTERISTICS.

VARIOUS ETCH STEPS:

- | | |
|------------------------|--|
| 1. DEPOSIT PASSIVATION | SiH ₄ , CO ₂ H ₂ /SiH ₄
NH ₃ , H ₂ AT 350°C |
| 2. CONTACT ETCH | HF, H ₃ PO ₄ , HF |
| 3. Pt ETCH | HNO ₃ AND HCl |
| 4. Ti ETCH | H ₂ SO ₄ |
| 5. GLASS ETCH | SATURATED SOLUTION OF AMMONIUM
BIFLOURIDE BUFFERED TO pH 4.7 |

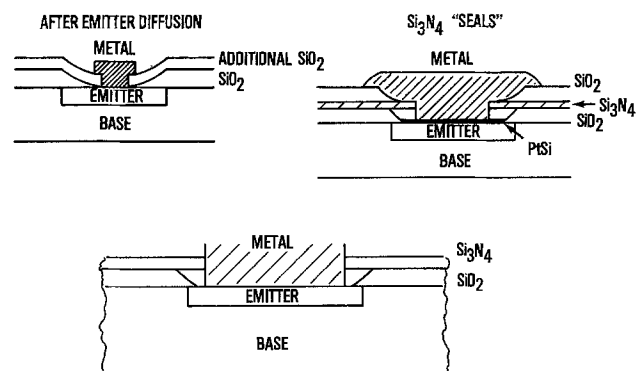


Fig. 1. Cross section and summary of etching steps in the Ti-Pt-Au metallization scheme.

* Electrochemical Society Active Member.

Key words: Auger spectroscopy, surfaces, interdiffusion, interfaces.

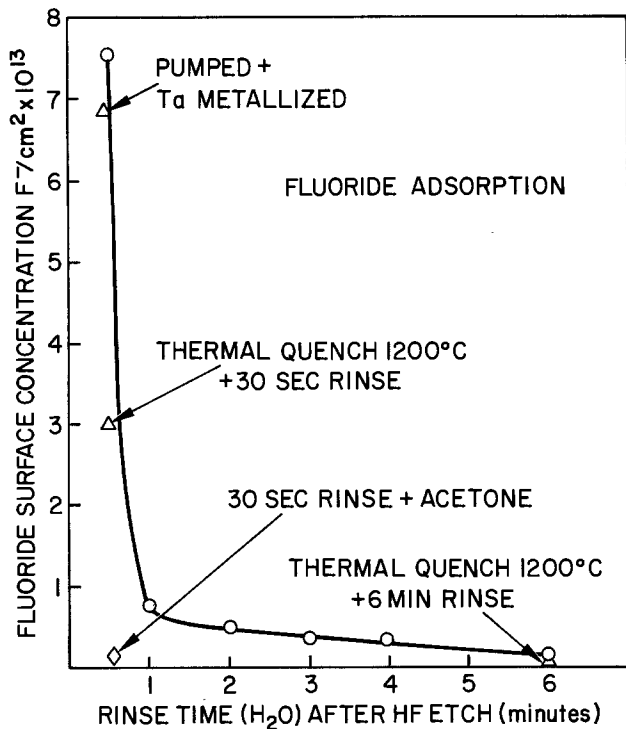


Fig. 2. Variation of F^- concentration as a function of rinse duration.

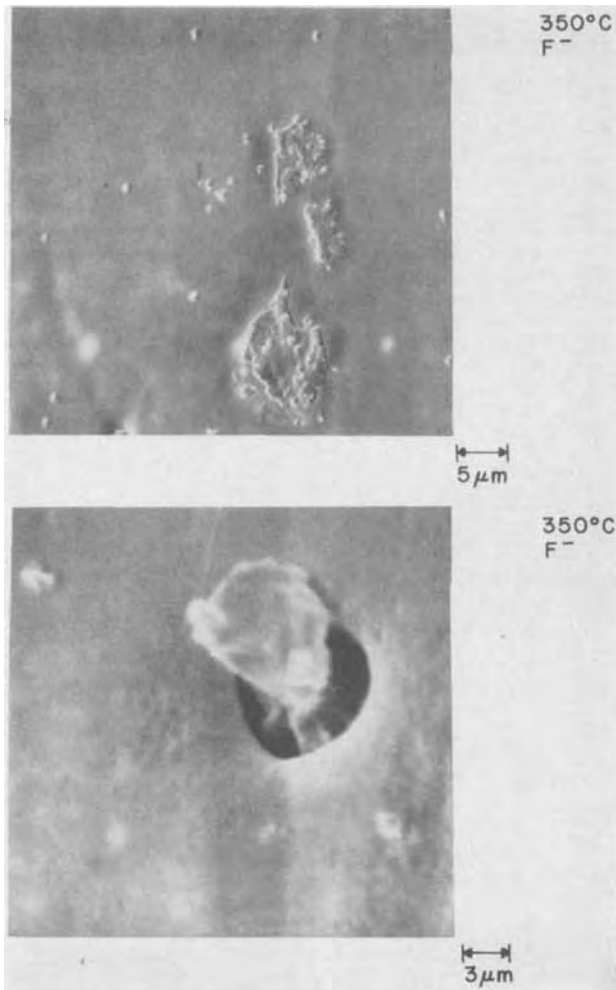


Fig. 3. Pinhole and hillock formation in Ti-Pt-Au test structures as a result of F^- contamination.

The metallizations were sputter-deposited using the techniques reported earlier (7, 8). The titanium, platinum, and gold layers were 1000, 1500, and 3000 Å thick, respectively. The metallization structure after heat-treatment was analyzed using scanning electron microscopy and AES. A third set of test structures of Ti-Pt-Au was deposited on oxidized silicon and unoxidized silicon (no F^- contamination) and annealed in vacuum at temperatures between 150° and 350°C.

Results and Discussion

Fluorine contaminated Ti-Pt-Au contacts.—Annealing at 200° and 350°C of the Ti-Pt-Au contact test structures has resulted in pinhole and hillock formation as shown in Fig. 3. The level of F^- contamination of the Ti-Pt-Au contact shown in Fig. 3 was measured to be approximately $1 \times 10^{13} F^-/cm^2$. The areal density of etch pits was measured to be approximately $20/cm^2 \times 10^3$, while the hillock density was approximately $10/cm^2 \times 10^3$. Pinhole density as well as hillock density increased as F^- concentration at the contacts increased. From the present investigation, it is believed that fluoride species precipitate at silicon surface defects and subsequent annealing between 200° and 350°C results in enhanced diffusion at silicon defects (1) and the subsequent hillock and pinhole formation in the metallization.

Additional problems identified on the Ti-Pt-Au contact test structure as a result of the F^- ion contamination and annealing at 150°C for 24 hr include: (i) pinholes and cracking at contact points between Ti/ Si_3N_4 as shown in Fig. 4, and (ii) cracks in the Pt layer at the Si_3N_4 shelf and pinholes in the Pt layer as shown in Fig. 5. The pinholes and microcracks can result in diffusion paths between gold and silicon and may initiate a Pt- Si_3N_4 reaction. In addition, titanium and platinum have been found to spread into voids beneath the Si_3N_4 shelf as a result of film discontinuities and compressive loads on these layers. Gold when

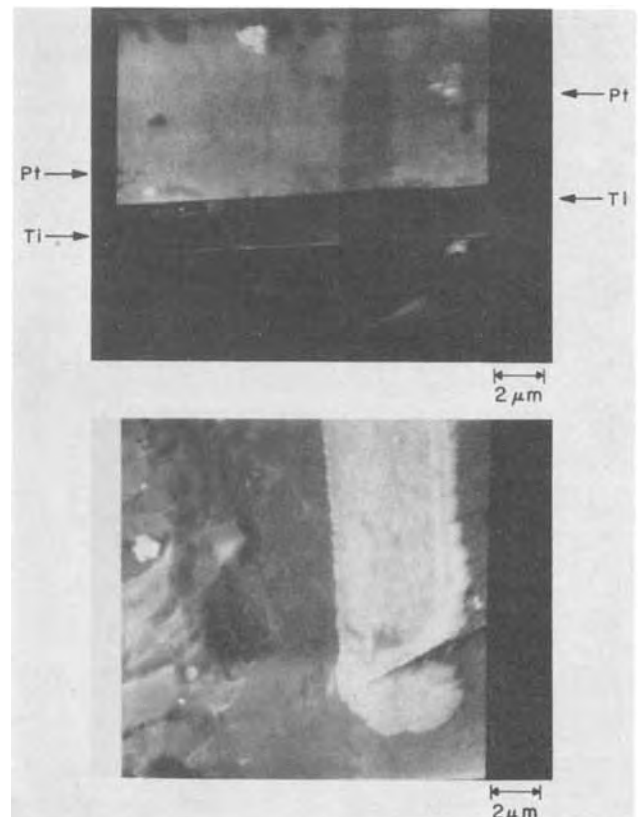


Fig. 4. Pinholes and microcracks found at contact points between Ti/ Si_3N_4 .

plated into the voids results in gold-silicon interdiffusion at temperatures as low as 150°C.

Migration of titanium and oxygen.—The migration of titanium, oxygen, and TiO was studied as a function of F^- ion concentration and anneal temperature using the sputter profiling technique. The location of the TiO layer was monitored by observing the splitting of the Ti, 387 eV LMM transition. In the as-deposited state, titanium combines with gettered oxygen to form a stable TiO film. Although Ti is a very active metal (10), the thin TiO film passivated the titanium so that it essentially functions as an inert adhesion layer. The initial location of the TiO layer was isolated after 200 min of sputtering. Annealing Ti-Pt-Au (Si substrate) specimens with a $2 \times 10^{12} F^-/cm^2$ absorbed layer up to 200°C for 24 hr has resulted in the migration of the TiO layer toward the metal-vacuum interface. The migration of the TiO layer was accompanied by the out-diffusion of titanium and oxygen. Maintaining the anneal temperature at 200°C but increasing the F^- ion concentration to $1 \times 10^{13} F^-/cm^2$ has resulted in an increase in the activity of the titanium and a further migration of TiO toward the free surface. The TiO layer was located after 80 min of sputtering. A further increase of the F^- concentration to $5 \times 10^{13} F^-/cm^2$ and annealing at 200°C has resulted in the migration of the TiO layer so that it was detected after 40 min of sputtering. The migration of TiO at 200°C is summarized in Fig. 6. Annealing at 350°C for 24 hr has re-

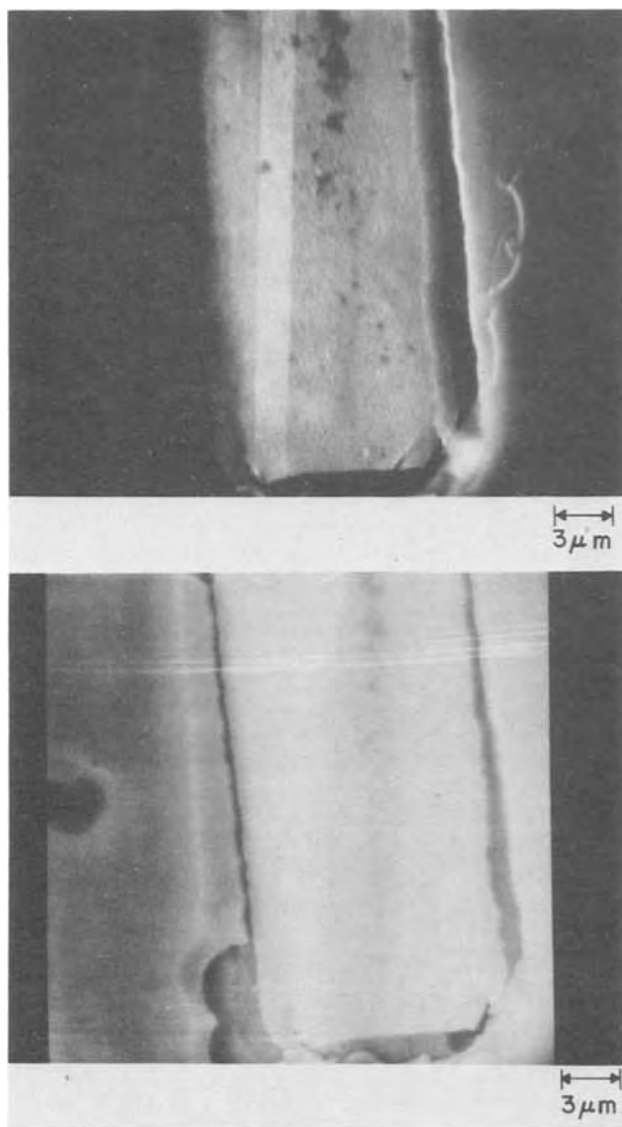


Fig. 5. Microcracking in the Pt layer at the Si_3N_4 shelf

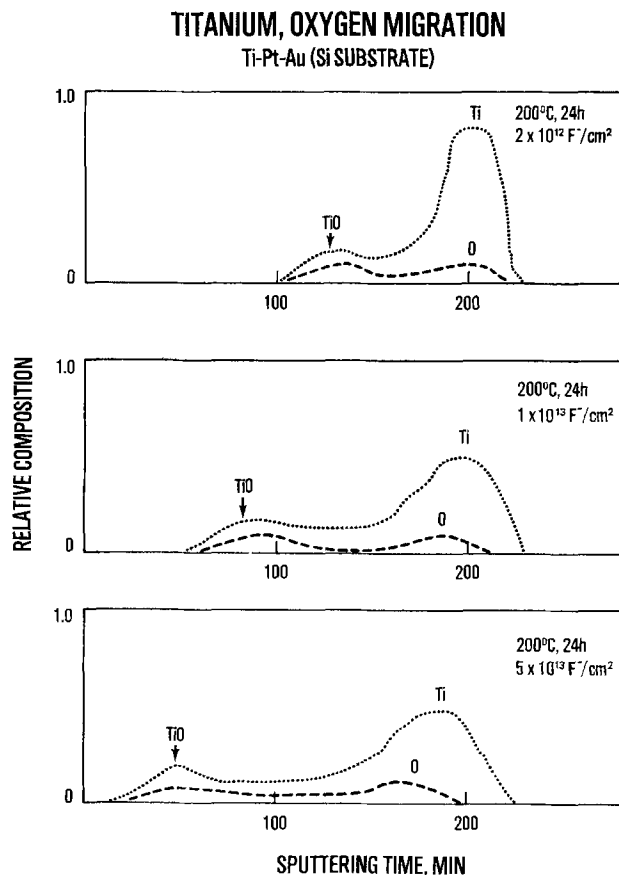


Fig. 6. Migration of TiO at 200°C as a result of F^- ion contamination.

sulted in an accelerated migration of the TiO layer toward the free surface as shown in Fig. 7.

At $2 \times 10^{12} F^-/cm^2$ the TiO layer was detected after 80 min of sputtering for the specimens annealed at 200°C, while for specimens annealed at 350°C, the TiO layer was detected after 40 min. At $5 \times 10^{13} F^-/cm^2$ and anneal temperature of 350°C, no TiO layer was detected. However, by decreasing the anneal temperature from 350° to 200°C, the TiO layer was detected after 45 min of sputtering for specimens with $5 \times 10^{13} F^-/cm^2$ surface concentration. The specimens with no detectable TiO layer, as a result of annealing at 350°C, were characterized by pinhole formation and in some instances by gold-silicon interdiffusion. Therefore the migration of the thin TiO film has resulted in the titanium becoming active and behaving as the anode in a contaminated ion environment. The dissolution of the TiO film leaves the titanium in direct contact with the Au (where Pt is defective) resulting in excessive pinhole formation since Au is not an effective oxygen reducer and cannot maintain the anodic passivation of the titanium.

In the present investigation with ion contaminated Ti-Pt-Au structures, a galvanic cell has been established with F^- ion concentrations as low as $10^{12} F^-/cm^2$. The Ti has been attacked preferentially by the Au in the vicinity of either deposited defects in the Pt layer or microcracks in Pt induced by interdiffusion between Pt and Au. Since the reaction occurred with no electrical biasing, the environmental conditions can also be postulated to contain water vapor. Similar multimetallic systems including Ti-Au and Ti-Pd-Au have been investigated using an environmental condition containing chloride ions (9). The corrosion of Ti was found to begin at pinholes in the noble Au coating. Intermediate layers such as Pd were found to effectively improve the corrosion resistance of the bimetallic metallizations.

TITANIUM, OXYGEN MIGRATION Ti-Pt-Au (Si SUBSTRATE)

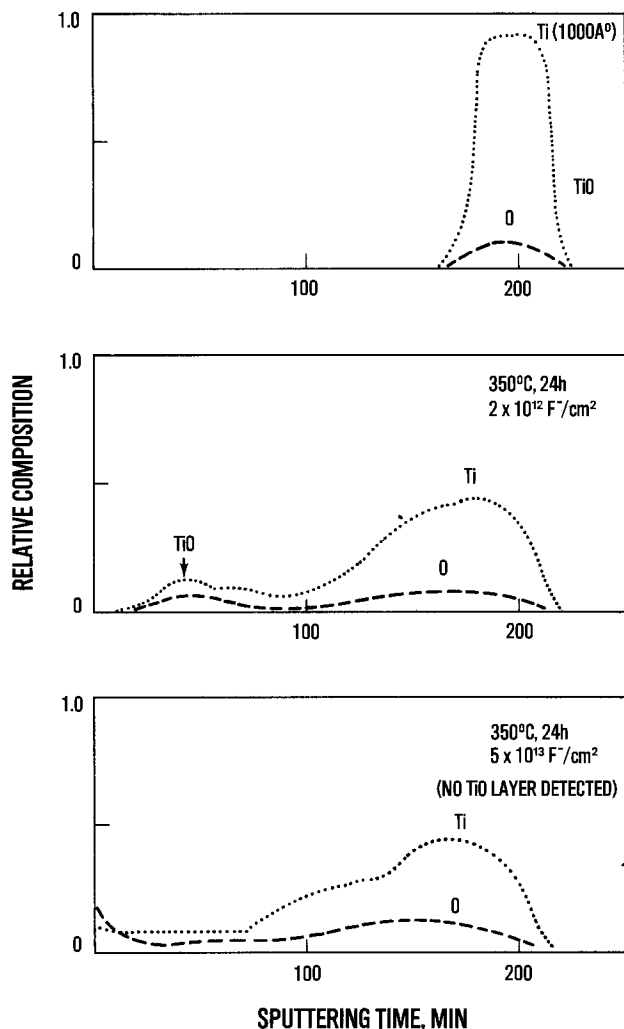


Fig. 7. Migration of TiO at 350°C as a result of F^- ion contamination.

In discussing kinetics, the present investigation has shown that the phenomenon of passivity greatly affects the rate of the reaction. In the case of Ti, the passivity is due to the formation of a thin adherent oxide film which has been identified to be TiO. The oxide film acts as a barrier between the metal and environment and effectively decreases the rate of dissolution involving metal ions. It has been shown that when the passivating film breaks down as a result of increasing fluoride ion concentration, the reaction proceeds rapidly and pinhole formation results. Figure 8 summarizes the kinetics results for $1 \times 10^{13} F^-/cm^2$ and $5 \times 10^{13} F^-/cm^2$ samples heat-treated at 350°C. The time to sputter to the TiO layer decreased approximately as the square root of the anneal time, thus indicating that the migration of TiO is governed by a diffusion process. The F^- ions can then be assumed to provide sites for the acceleration of the diffusion process. The sputtering time in Fig. 8 was converted directly to film thickness using a separately measured sputtering rate of 22.5 Å/min. The slope of the solid line of Fig. 8 yields a diffusion constant of $D = (\Delta x)^2/4(\Delta t_a) \approx 3.6 \times 10^{-13} cm^2/sec$. The activation energy for the processes at $T = 200^\circ$ and $350^\circ C$ was measured to be 1.5 eV. This energy agrees with energy required for the $Ti = Ti^{++} + 2e^-$ reaction (1.63 eV) (10). Therefore, the kinetics

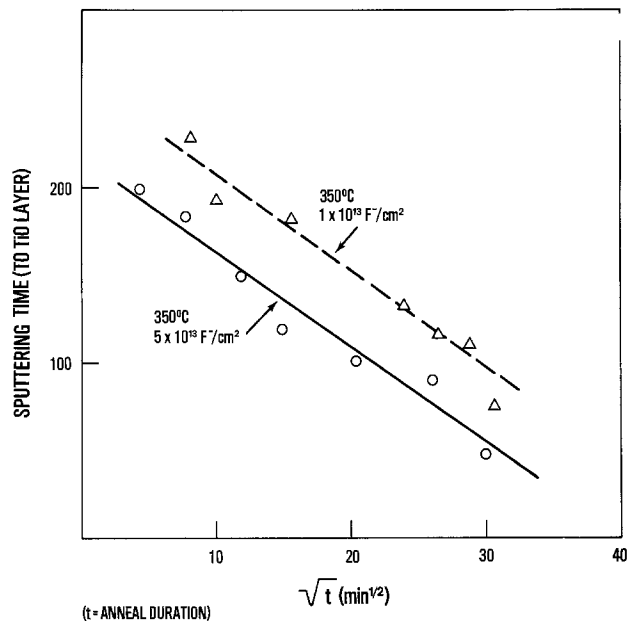


Fig. 8. Summary of migration kinetics for $1 \times 10^{13} F^-/cm^2$ and $5 \times 10^{13} F^-/cm^2$ samples heat-treated at 350°C.

data indicate that the migration and dissolution of the TiO layer corresponds to a simultaneous Ti corrosion reaction.

Conclusions

The present investigation shows that pinhole failures in Ti-Pt-Au film test structures are directly dependent on the chemical dissolution or migration of the TiO layer. Annealing at 200° and 350°C has resulted in the migration of the TiO layer toward the free surface for ion concentrations between 1×10^{12} and $5 \times 10^{13} F^-/cm^2$. Interdiffusion of gold through the barrier layers increased as the F^- concentration increased. The F^- ion contamination has been found to provide a more active corrosive environment for pinhole formation.

Manuscript submitted May 23, 1975; revised manuscript received Aug. 4, 1975. This was Paper 192 presented at the Toronto, Canada, Meeting of the Society, May 11-16, 1975.

Any discussion of this paper will appear in a Discussion Section to be published in the June 1976 JOURNAL. All discussions for the June 1976 Discussion Section should be submitted by Feb. 1, 1976.

Publication costs of this article were partially assisted by the Naval Research Laboratory.

REFERENCES

1. A. Hiraki, M. A. Nicolet, and J. W. Mayer, *Appl. Phys. Letters*, **18**, 178 (1971).
2. H. Sankur and J. O. McCaldin, *This Journal*, **122**, 565 (1975).
3. H. Day, A. Christou, and D. J. Bressan, *ibid.*, **121**, 790 (1974).
4. J. Drobek, R. C. Sun, and T. C. Tisone, *Phys. Status Solidi*, **8**, 243 (1971).
5. T. C. Tisone and J. Drobek, *J. Vac. Sci. Technol.*, **1**, 271 (1972).
6. J. A. Eisele, R. E. Larson, and P. E. Wilkins, *Intern. J. Appl. Radiation Isotopes*, **21**, 219 (1970).
7. A. Christou and H. M. Day, *J. Appl. Phys.*, **44**, 3386 (1973).
8. A. Christou and H. M. Day, *J. Elec. Mat.*, **3**, 25 (1974).
9. A. T. English and P. A. Turner, *ibid.*, **1**, 1 (1972).
10. W. M. Latimer, "Oxidation Potentials," 2nd ed., Prentice-Hall, Englewood Cliffs, N.J. (1952).

Thermal Stability of PtSi Films on Polysilicon Layers

A. K. Sinha, S. E. Haszko, and T. T. Sheng

Bell Laboratories, Murray Hill, New Jersey 07974

ABSTRACT

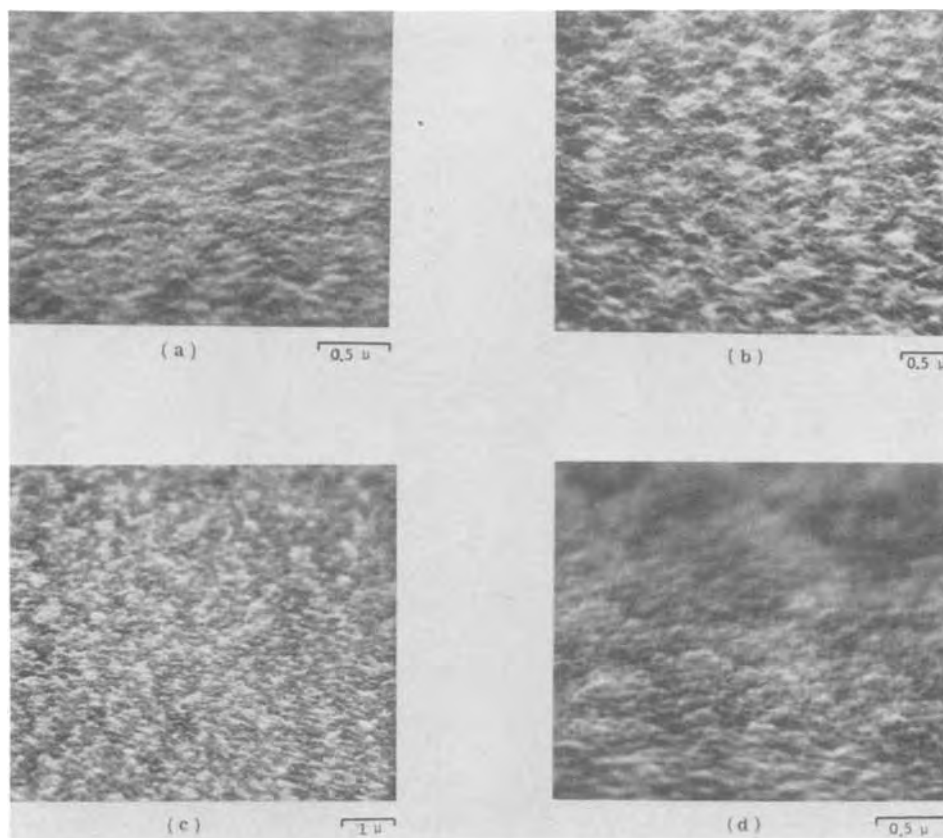
A thin-film combination containing PtSi (2000Å)/poly-Si (1000Å) has been considered for application as first-level metallization in large scale silicon integrated circuit devices. The present investigation was made to ascertain the thermal stability of this structure as reflected by changes in microstructure, resistivity, and stresses of these films upon heat-treatment up to 1000°C. The PtSi films (2000Å thick) were formed by sintering Pt on poly-Si at 700°C (15 min) in vacuo or forming gas; the wafers were then coated with 5000Å of Silox SiO₂ and heat-treated at various temperatures. No agglomeration was observed at up to 900°C, although a moderate amount of grain growth did take place. The sheet resistance of these films decreased from ~4 ohm/□ to ~2 ohm/□ after the 750°C anneal, it then increased with increasing annealing temperature to ~16 ohm/□ (900°C anneal). The resistivity increase is tentatively attributed to the accumulation of Si at the grain boundaries of PtSi. At 1000°C, a liquid-eutectic phase was formed. However, the liquid did not "ball-up," i.e., it wetted PtSi and poly-Si, and on cooling, it precipitated relatively large areas of variously oriented single crystals of Si. This recrystallization process led to a sharp decrease in the sheet resistance of PtSi.

With continuing growth of the LSI (large scale integration) technology, several two-level metallization schemes have been investigated for use on SIC's (silicon integrated circuits). A particularly successful scheme, for unipolar devices, involves the application of P- or B-doped poly-Si on the first level (Si-gate technology) (1). In addition to its excellent MOS compatibility, poly-Si can be used to provide low-resistance contacts to doped Si areas on the device. However, doped poly-Si suffers from one major drawback. Its electrical conductivity is rather poor; it has a sheet resistance 10-100 ohm/□ for 5000Å thick lines (2), and this is undesirable for many bipolar LSI circuits and also certain

Key words: heat-treatment, LSI metallization, thin films.

high-speed (e.g., n-channel) unipolar LSI devices. A potential solution to this problem, proposed by Lepselet and others (3), is to utilize a structure containing metal-silicide/poly-Si where the more conducting silicide is formed over previously defined poly-Si lines; the unreacted metal is chemically etched away, generally without the use of a second photoresist step. An attractive system of this type is PtSi on poly-Si, and the present investigation has been concerned with the thermal stability of this structure at temperatures (750°-1000°C) commonly employed to deposit intermediate oxide/nitride layers using chemical vapor deposition. A nearly analogous system comprising thinner PtSi films on single crystal Si was previously

Fig. 1. Scanning electron micrographs of PtSi (2000Å) on poly-Si (1000Å) after various heat-treatments: (a) sintered at 700°C, 15 min, (b) annealed at 750°C, ½ hr, (c) annealed at 800°C, ½ hr, (d) annealed at 900°C, ½ hr.



characterized (4) and it was shown that thin PtSi films (900 and 200Å) agglomerate above 800°C.

Experimental

The substrates for Pt deposition consisted of oxidized Si wafers coated with a 3000Å thick layer of poly-Si which was produced at 700°C in a "Nitrox" reactor (manufactured by Applied Materials Technology, Inc.) using pyrolysis of SiH₄ in Ar/N₂. The poly-Si was lightly doped with B (sheet resistance ~1000 ohm/□) in most cases, but similar results on the thermal stability of PtSi were obtained with poly-Si doped with P to a sheet resistance of 50-100 ohm/□. Immediately prior to metallizing, the poly-Si layer was cleaned by a dip in 50:1 mixture of H₂O:HF for ~1 min (or until its surface turned hydrophobic) followed by DI water rinse and spin-dry. A 1000Å thick film of Pt was deposited using a conventional rf-diode sputtering apparatus (0.2 W/cm²). The PtSi (~2000Å thick) was produced by sintering the Pt/poly-Si combination at 700°C *in vacuo*, or in a reducing ambient such as forming gas. Such ambients were preferred over oxidizing ones in order to minimize any subsequent harmful effects of excessive SiO₂ buildup (5, 6) on or under the PtSi surface. Complete formation of PtSi in these samples was ascertained through x-ray diffraction (7). In order to facilitate subsequent high-temperature annealing studies and also to simulate device structures, the PtSi/poly-Si films were coated with 5000Å of Silox SiO₂ produced at 480°C by reacting SiH₄ and O₂ in Ar/N₂ carrier gas. All the annealing experiments were done in air at temperatures ranging from 750° to 1000°C for ½ hr each. Next, the Silox SiO₂ protective layer

was removed by etching in buffered HF and changes in the PtSi layer were evaluated through measurements of sheet resistance (using four-point probe measurements), and stresses [using radius of curvature measurements with an optically levered laser beam (8)], and examination of the microstructure (using scanning and transmission electron microscopy).

Results and Discussion

Wide-film x-ray diffraction patterns showed that the sintered PtSi films were single phase with an (020) type of preferred orientation. The PtSi films were found to be under a relatively large tensile stress of 1.6×10^{10} dyne-cm⁻². A tensile stress would be expected on the basis of 10% volume contraction associated with PtSi formation. Subsequent thermal treatments up to 900°C reduced the stress somewhat to 1.1×10^{10} dyne-cm⁻².

Figures 1(a) through (d) show scanning electron micrographs of PtSi films (2000Å) on poly-Si after various heat-treatments, namely, (a) sintering at 700°C *in vacuo* for 15 min, (b) annealing at 750°C ½ hr, (c) annealing at 800°C, ½ hr, and (d) annealing at 900°C, ½ hr. In all cases, the PtSi films are continuous and there appears to be no evidence of any agglomeration even at 900°C. By contrast, thinner films of PtSi (900 and 200Å) on single crystal Si show clear evidence of agglomeration at 900°C (4). Although in the latter case, it was shown that the as-sintered PtSi films are associated with surface irregularities of the order of 100Å, the present PtSi films on poly-Si show a much more pronounced degree of granularity and surface roughness (of the order of 1000Å). This increased

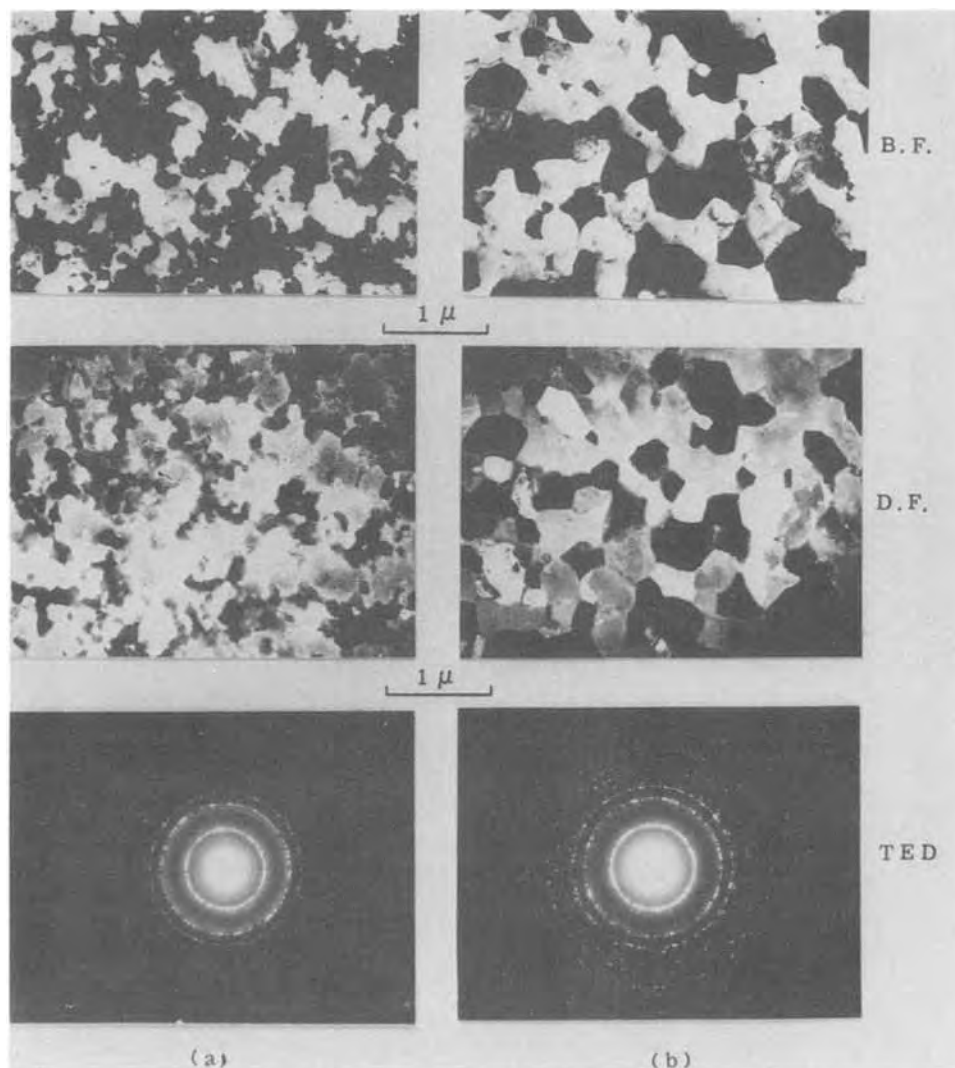


Fig. 2. Transmission electron microscopy results on PtSi films on poly-Si: (a) as-sintered, (b) annealed at 900°C, ½ hr. BF-bright field micrograph, DF-dark field, TED-selected area transmission electron diffraction pattern.

roughness can be partly ascribed to the texture of the underlying poly-Si layer; however, it appears that sintering enhances any surface roughness originally present in the poly-Si and initially replicated by the sputtered Pt film.

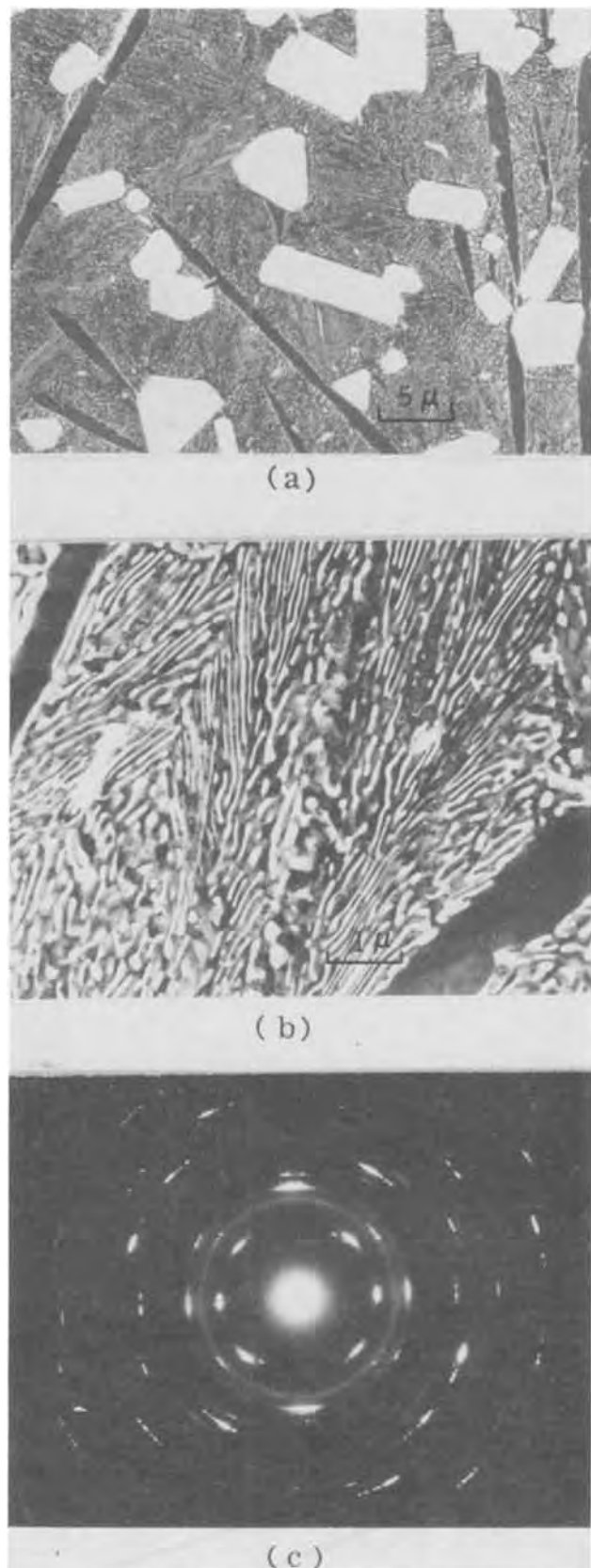


Fig. 3. (a) and (b) Bright-field TEM photos of PtSi on poly-Si annealed at 1000°C, 1/2 hr. (c) TED pattern from lamellar regions of above micrographs.

Detailed information on the microstructure of the films was obtained through examination of the transmission electron micrographs (TEM) of PtSi films (thinned by ion-milling from the poly-Si side), taken in the bright- and dark-field mode, and of the transmission electron diffraction (TED) patterns. Figures 2(a) and (b) show the data for PtSi in the as-sintered state and after annealing at 900°C (1/2 hr). The grain size of as-sintered PtSi on poly-Si ranged from 1000 to 3000Å whereas after annealing at 900°C, it increased to the 1500-9000Å range. This is also manifested in in-

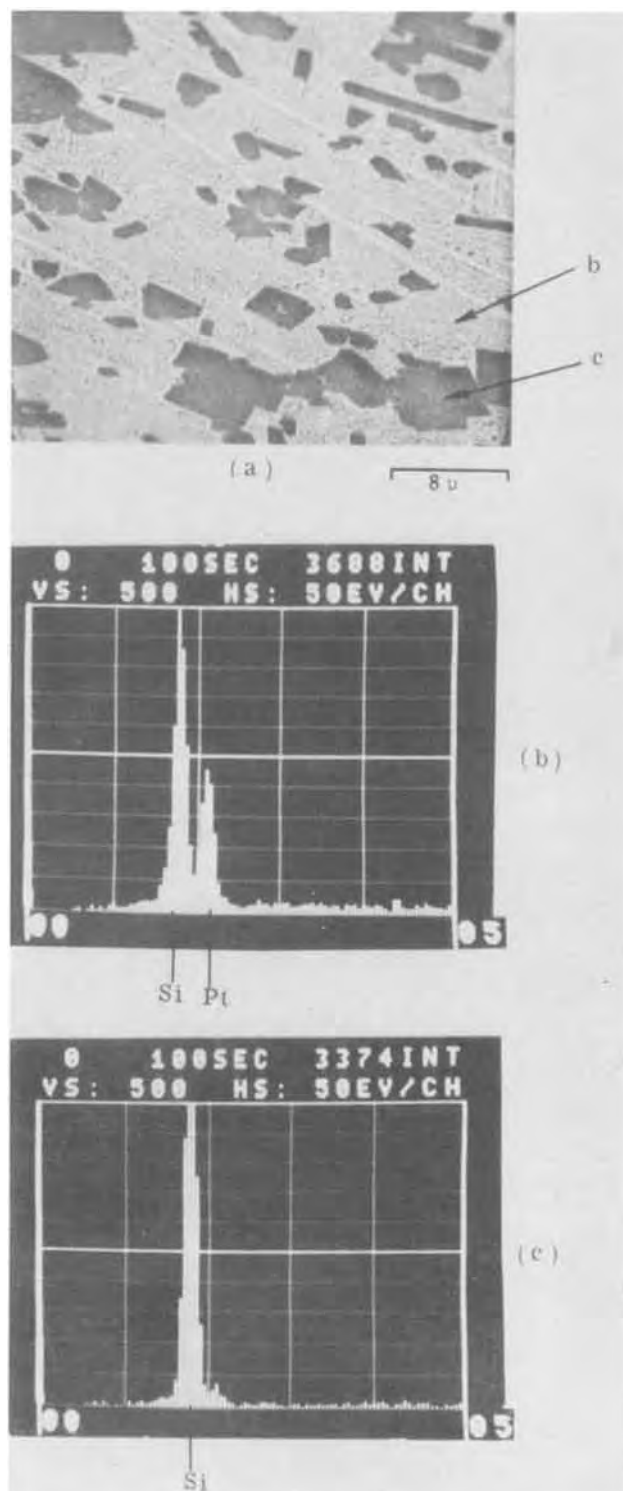


Fig. 4. (a) Scanning electron micrograph of PtSi on poly-Si annealed at 1000°C, 1/2 hr. (b) and (c) Energy dispersive x-ray analysis of dark and light areas, respectively, of Fig. 3(a).

creased spottiness of the TED pattern for annealed PtSi. The sample annealed at 1000°C showed a two-phase microstructure in the bright-field micrographs [Fig. 3(a) and (b)] consisting of large crystals of Si and a lamellar distribution of PtSi in a Si-matrix. This complex microstructure, which was not apparent in micrographs of the surface replica (because of similar surface texture of PtSi and crystallized Si), is clearly revealed in transmission electron micrographs because of contrast differences between PtSi and Si due to diffraction effects. The selected area TED pattern [Fig. 3(c)] taken from the lamellar regions confirmed the presence of PtSi in these areas.

The unusual microstructure of PtSi/poly-Si samples heat-treated at 1000°C was further investigated using the SEM in conjunction with the energy dispersive x-ray analyzer (EDAX). Figure 4(a) shows the SEM photo where the contrast arises from differences in secondary electron emission coefficients of PtSi (light) and Si (dark) areas. Positive identification of these light and dark areas was made by EDAX analysis

whose results are shown in Fig. 4(b) and (c), respectively. The silicon areas in Fig. 4(a) have large geometrical shapes with dimensions of the order of 10 μ . The single crystal nature of these areas was ascertained through TED. Figures 5(a) through (d) show the bright-field TEM and selected area TED patterns for various silicon areas. The orientation of Si in the four cases is [001], [111], [110], and [112] which is generally consistent with the macroscopic shapes of these areas.

The formation of relatively large areas of single crystal Si upon annealing PtSi/poly-Si at 1000°C is clearly associated with recrystallization from the liquid eutectic phase (9), and is not due to any grain growth of the poly-Si which would be relatively small at 1000°C (2). The facts that several orientations of Si were observed and that the original PtSi/poly-Si combination was deposited on SiO₂/Si would rule out a simple liquid-phase epitaxial growth of the single crystal Si areas. It is interesting to observe that even liquid formation did not cause significant "balling up"

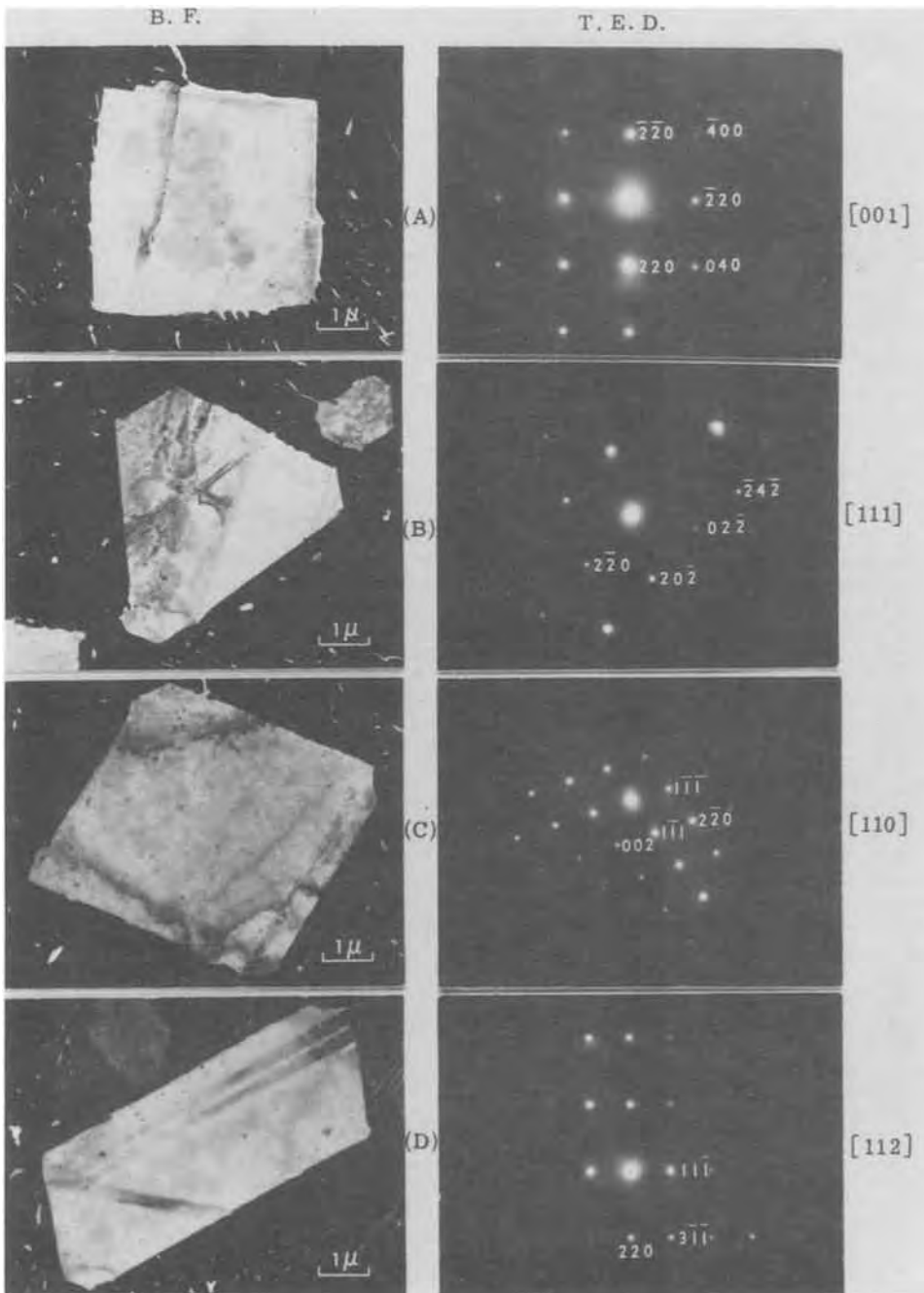


Fig. 5. Bright-field TEM and selected area TED from variously oriented single crystal Si-areas recrystallized from PtSi/Si eutectic: (a) [001] orientation, (b) [111] orientation, (c) [110] orientation, (d) [112] orientation.

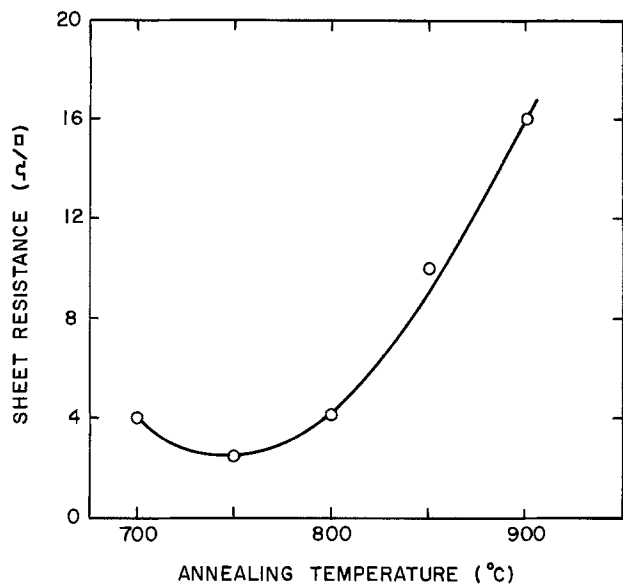


Fig. 6. Sheet resistance of PtSi (2000Å) on poly-Si vs. annealing temperature.

effects; this indicates a very effective wetting action between the liquid eutectic and the PtSi or poly-Si.

The resistivity behavior of PtSi on poly-Si is shown in Fig. 6. The resistivity of as-sintered PtSi on poly-Si is rather high at $\sim 80 \mu\text{ohm-cm}$ (sheet resistance 4 ohm/□) as compared to $17.5 \mu\text{ohm-cm}$ for 900Å thick PtSi on single crystal Si. The sheet resistance decreased by a factor of 2 upon annealing at 750°C; however, with further increase in the annealing temperatures up to 900°C, there was a progressive increase in the sheet resistance to 16 ohm/□. The sheet resistance again dropped sharply to 4.5 ohm/□ for the sample annealed to 1000°C which contained recrystallized PtSi/Si. Since no agglomeration or even grain boundary voids were observed in the samples annealed at 900°C, the observed resistivity increase is somewhat unexpected. We tentatively ascribe this increase to the diffusion and accumulation of small amounts of Si at the grain boundaries of PtSi (10). Further detailed work on the microstructure as well as temperature dependence of resistivity will be desirable to better understand this effect. The sharp drop in sheet resistance following the 1000°C treatment is probably due to the fact that upon recrystallization from the melt, the PtSi grain boundaries are relatively "clean" and free of excessive silicon.

Conclusions

1. Single-phase PtSi films (020 orientation), $\sim 2000\text{Å}$ thick with a sheet resistance of $\lesssim 4 \text{ ohm}/\square$ and tensile

stress of $1.6 \times 10^{10} \text{ dyne-cm}^{-2}$ were formed by sintering 1000Å Pt on 3000Å poly-Si.

2. These films can sustain thermal treatment up to 900°C which causes no agglomeration and leads to only moderate grain growth.

3. At 1000°C, a liquid eutectic phase is formed which wets PtSi and poly-Si and, on cooling, precipitates relatively large areas of single crystal Si.

4. The sheet resistance of the PtSi/poly-Si films decreases from ~ 4 to ~ 2 ohm/□ after the 750°C anneal; it then increases with increasing annealing temperature to ~ 16 ohm/□ after the 900°C anneal. Recrystallization upon cooling from 1000°C leads to a sharp decrease in the sheet resistance back to 4 ohm/□.

Acknowledgments

The authors would like to thank A. C. Adams and C. D. Capio for the CVD poly-Si and SiO₂-film depositions, T. E. Smith for the Pt-film deposition, G. Quintana for the heat-treatments, Mildred H. Read for x-ray diffraction work, J. Bindell for his cooperation, and W. R. Dawes, H. J. Levinstein, and R. S. Wagner for valuable discussions.

Manuscript submitted April 9, 1975; revised manuscript received July 21, 1975.

Any discussion of this paper will appear in a Discussion Section to be published in the June 1976 JOURNAL. All discussions for the June 1976 Discussion Section should be submitted by Feb. 1, 1976.

Publication costs of this article were partially assisted by Bell Laboratories.

REFERENCES

1. L. L. Vadasz, A. S. Grove, T. A. Rowe, and G. F. Moore, *IEEE Spectrum*, **6**, 28 (1969).
2. A. P. Gnadinger and B. B. Kosicki, Abstract 25, p. 74, Electrochemical Society Extended Abstracts, Spring Meeting, San Francisco, California, May 12-17, 1974.
3. M. P. Lepselter and W. Van Gelder, Bell Laboratories, Private communication (March 1972); V. L. Rideout, *IBM Tech. Disclosure Bull.*, **17**, No. 6, p. 1831 (Nov. 1974).
4. A. K. Sinha, R. B. Marcus, T. T. Sheng, and S. E. Haszko, *J. Appl. Phys.*, **43**, 3637 (1972).
5. M. J. Rand and J. F. Roberts, *Appl. Phys. Letters*, **24**, 49 (1974).
6. C. Ladas and T. Kingjett, *This Journal*, **121**, 288C (1974).
7. M. H. Read and D. H. Hensler, *Thin Solid Films*, **10**, 123 (1972).
8. N. N. Axelrod, H. J. Levinstein, and W. Royer, Unpublished work.
9. M. Hansen, "Constitution of Binary Alloys," McGraw-Hill Book Co., New York (1958).
10. R. M. Anderson, in "Proceedings of the 30th Annual Meeting, Electron Microscopy Society of America," C. J. Arcineaux, Editor, p. 518, Claytor's Publishing Division, Baton Rouge, La. (1972).

Properties of Sn-Doped In_2O_3 Films Prepared by RF Sputtering

John C. C. Fan and Frank J. Bachner

Lincoln Laboratory, Massachusetts Institute of Technology, Lexington, Massachusetts 02173

ABSTRACT

An rf sputtering process has been used without postdeposition annealing to prepare Sn-doped In_2O_3 films with low electrical resistivity (down to 2×10^{-4} ohm-cm), high visible transmission, and high infrared reflectivity (up to 93% at $10 \mu\text{m}$) for applications as transparent conductors and heat mirrors. Substrate heating is accomplished entirely by the electron bombardment intrinsic to rf sputtering, rather than by using an auxiliary resistance heater. The film properties improve with increasing substrate temperature up to 650°C , the maximum employed, and are relatively independent of other sputtering parameters. The electrical and optical properties of the films do not depend significantly on the crystallographic orientation, degree of texturing, or substrate material (glass, fused silica, and single crystal Al_2O_3 and CaF_2).

Transparent heat-mirror films that transmit in the visible and reflect in the infrared are becoming important for radiation insulation and solar energy collection (1-3). Two types of materials have been used for these films: metals with very high infrared reflectivity (approaching 100%) and low enough visible absorption for thin films to be transparent [for example, Au (2) and Ag (4)], and semiconductors with a sufficiently wide bandgap to be transparent in the visible and a high enough free-carrier concentration to have high infrared reflectivity [for example, Sb-doped SnO_2 (1, 5, 6) and Sn-doped In_2O_3 (1, 5, 8)]. To obtain improved films of Sn-doped In_2O_3 for heat-mirror applications, we have studied films prepared by rf sputtering to determine the dependence of film properties on preparation conditions.

The techniques that have been used to prepare Sn-doped In_2O_3 films include chemical spray deposition (1), d-c sputtering (7, 8), and rf sputtering (5-7). In order to obtain satisfactory electrical and optical properties by any of these techniques, it has generally been necessary either to heat the substrate during deposition or to anneal the film after deposition. Either procedure requires fairly high temperatures, typically over 500°C . Our rf sputtering method employs substrate heating rather than post deposition annealing. The main feature of the method is that, by operating at sufficiently high forward power levels, heating is accomplished entirely by the electron bombardment intrinsic to rf sputtering, rather than by using an auxiliary resistance heater in the conventional manner. [Fraser and Cook (8) have produced good films by using the intrinsic heating associated with d-c sputtering, but they did not correlate film properties with substrate temperatures.]

Preparation

Films of Sn-doped In_2O_3 were deposited on a variety of substrates, including Corning CG 7059 glass, fused silica, and single crystals of Al_2O_3 and CaF_2 , by sputtering in Ar gas from a 12.7 cm diameter, hot-pressed target of nominal composition In_2O_3 -9 mole per cent (m/o) SnO_2 . (Targets obtained from Materials Research Corporation, Orangeburg, New York, and from Haselden Company, San Jose, California, gave similar results.) The sputtering apparatus is a commercial rf diode unit with a liquid- N_2 cold-trapped, 15 cm diffusion pump, which is easily capable of achieving a base pressure of 7×10^{-7} Torr.

Figure 1 is a schematic diagram of the target and substrate configuration. The substrate was insulated from the water-cooled, stainless steel substrate plat-

form by means of a Pyrex spacer about 1.6 mm thick. The substrate surface temperature, T_s , was measured with a Chromel-Alumel thermocouple that was mounted on the substrate surface with kaolin-sodium silicate paste, and the assembly was vacuum-baked at 150°C for several hours before being placed in the sputtering system. For CG 7059 glass substrates about 0.5 mm thick, the value of T_s increased reproducibly with increasing rf power, as shown in Fig. 2, reaching over 600°C for 650W, the maximum power used. For a given rf power level, T_s was about 100°C higher with the Pyrex spacer than without it.

Before being used for film deposition, a newly received target was usually sputtered at 200W for more than 10 hr to remove contaminants and to eliminate any differential sputtering effects. After this initial preparation, the target usually yielded reproducible films. The substrates were ultrasonically cleaned in a heated detergent solution, rinsed in ultrasonically agitated, flowing deionized water, and blown dry in N_2 gas. A typical set of sputtering conditions was as follows: target-to-substrate distance = 5.7 cm, Ar pressure = 10^{-2} Torr, Ar flow rate = $0.5 \text{ cm}^3/\text{min}$, presputtering at 500W for 15 min, deposition at 500W (deposition rate = $250 \text{ \AA}/\text{min}$ for 15 min).

We have also used other sputtering conditions, including different Ar pressures (5×10^{-3} to 1×10^{-2} Torr), different Ar flow rates (0.25 - $10 \text{ cm}^3/\text{min}$), and different presputtering powers (200-650W). The quality of the films was insensitive to variations in these parameters. Apparently the deposition rate was not critical either. At a sputtering power of 500W, the deposition rate increased to $500 \text{ \AA}/\text{min}$ when the Ar flow rate was changed from 0.5 to $10 \text{ cm}^3/\text{min}$, but the properties of the films were similar to those of films grown

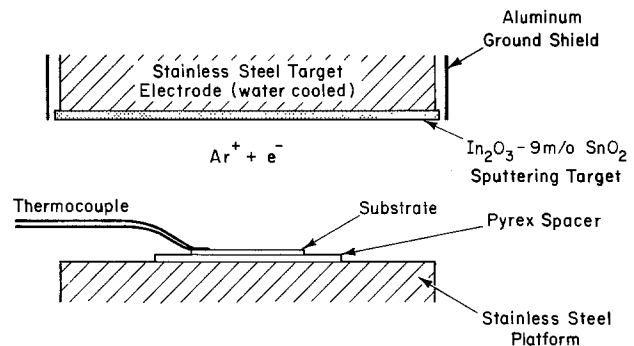


Fig. 1. Schematic diagram of target and substrate configuration in rf sputtering apparatus.

Key words: transparent conductors, solar-energy collection, heat mirrors, thin films.

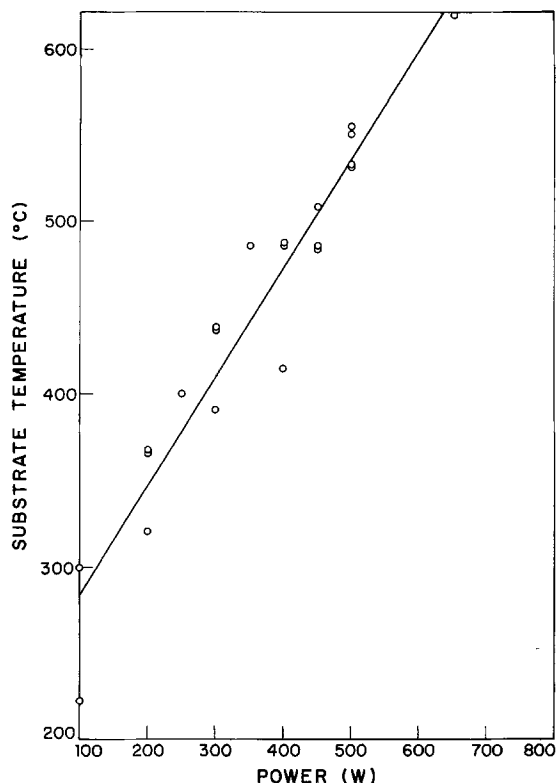


Fig. 2. Substrate temperature with a Pyrex spacer as a function of sputtering power.

at a flow rate of $0.5 \text{ cm}^3/\text{min}$. However, as we shall discuss below, film quality was sensitive to changes in the sputtering power. These changes caused changes in deposition rate (e.g., from $150 \text{ \AA}/\text{min}$ at 100 W to $300 \text{ \AA}/\text{min}$ at 650 W , for the set of conditions listed above) as well as in substrate temperature (Fig. 2). In view of the apparent insensitivity of film properties to deposition rate, we attribute the effect of changes in sputtering power to the resulting changes in substrate temperature. This is confirmed by the fact that several films grown at a sputtering power of only 100 W and a substrate temperature of about 500°C (obtained by using an auxiliary heater) are comparable to those grown at 500 W with no auxiliary heating.

Characterization Techniques

The individual film-on-substrate samples were generally broken into several pieces so that the films could be characterized in several different ways. A photolithographic technique was used in measuring film thickness. A Cr layer 1000 \AA thick was sputter-deposited on the film, and stripes were opened in the Cr by applying photoresist, producing a stripe pattern by photolithography, and removing the unprotected Cr by using an etchant consisting of 1000 cm^3 water, 50 cm^3 perchloric acid, and 100 g ceric ammonium nitrate. The sample was then immersed in concentrated H_2SO_4 at $50^\circ\text{--}60^\circ\text{C}$ to remove the In_2O_3 film (etching rate $\sim 0.5 \text{ \mu m}/\text{hr}$) wherever it was not masked by Cr. Finally the Cr masking stripes were etched away to expose the In_2O_3 film stripes underneath, and the height of these stripes was measured by microtopography. Most films were from 0.3 to 5 \mu m thick.

The electrical resistance of the samples was determined by four-point probe measurements, and in many instances confirmed by the van der Pauw technique, which was also used for Hall coefficient measurements. Optical transmission and reflectivity measurements were made from 0.35 to 2.5 \mu m wavelength with a laboratory-built, normal-incidence spectrophotometer (9) and from 2.5 to 10 \mu m with a commercial spectrophotometer in which the angle of incidence for reflectivity measurements is about 20° . The crystal structure of

the films was examined by x-ray diffractometry. Auger electron spectroscopy was performed on several films, and the compositions of some films were determined by electron microprobe analysis of In and Sn.

Results

Unless stated otherwise, the results described here were obtained for films on CG 7059 glass, and similar results were obtained from measurements made on films deposited on other substrates.

Electrical properties.—Figure 3 shows the resistivity, ρ , measured at room temperature by the van der Pauw method, as a function of sputtering power and substrate temperature. (The substrate temperatures were obtained from the measured power values by using the straight line shown in Fig. 2, which is a least squares fit to the data.) The resistivity measurements were made on films more than 0.20 \mu m thick, for which resistivity was essentially independent of thickness. The resistivity decreases from about $8 \times 10^{-4} \text{ ohm-cm}$ for a substrate temperature of 300°C to about $2 \times 10^{-4} \text{ ohm-cm}$ for 650°C . The curve indicates that even lower resistivities could be obtained for higher temperatures, but our sputtering apparatus does not operate effectively at higher power levels. Moreover, the glass substrates would soften above 650°C .

The van der Pauw method was also used to measure the room temperature Hall coefficient (R_H) of the samples. The conductivity is n-type. As shown in Fig. 4 and 5, both the carrier concentration (from the single-carrier expression $N = -1/R_H e$) and Hall mobility ($\mu_H = R_H/\rho$) increase with increasing substrate temperature, although the rate of increase becomes smaller above $400^\circ\text{--}500^\circ\text{C}$. For 650°C , $N \approx 7 \times 10^{20} \text{ cm}^{-3}$ and $\mu_H \approx 40 \text{ cm}^2/\text{V-sec}$.

Optical properties.—Figure 6 shows the transmission and reflectivity measured over the wavelength range from 0.35 to 2.5 \mu m for a typical film, 0.36 \mu m thick, that was deposited at a sputtering power of 500 W (substrate temperature of about 550°C). In the visible region of the spectrum the transmission is very high

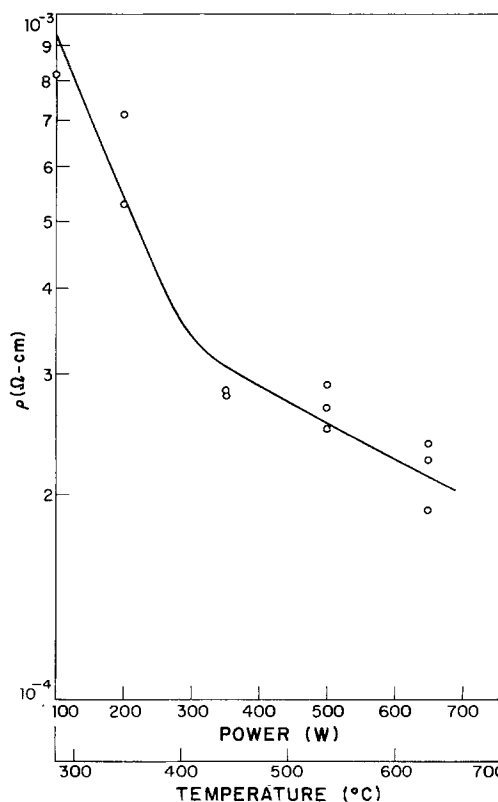


Fig. 3. Resistivity ρ as a function of sputtering power and substrate temperature.

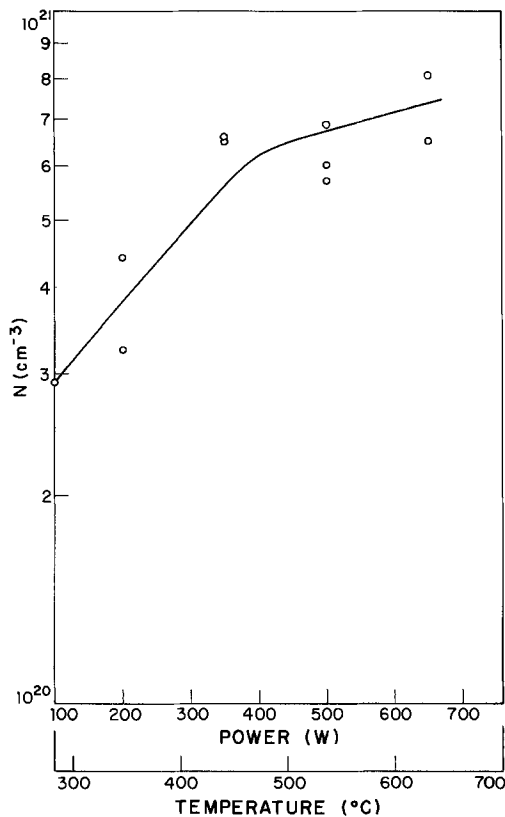


Fig. 4. Carrier concentration as a function of sputtering power and substrate temperature.

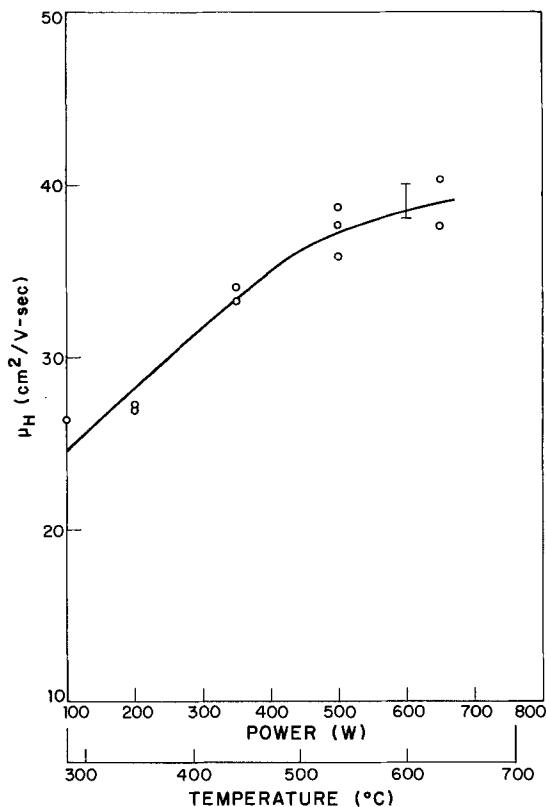


Fig. 5. Hall mobility μ_H as a function of sputtering power and substrate temperature.

(high enough for interference fringes to be observed) because the reflectivity is low and there is no absorption due to valence-to-conduction-band transitions. At about $1.5 \mu\text{m}$ the reflectivity increases abruptly (caus-

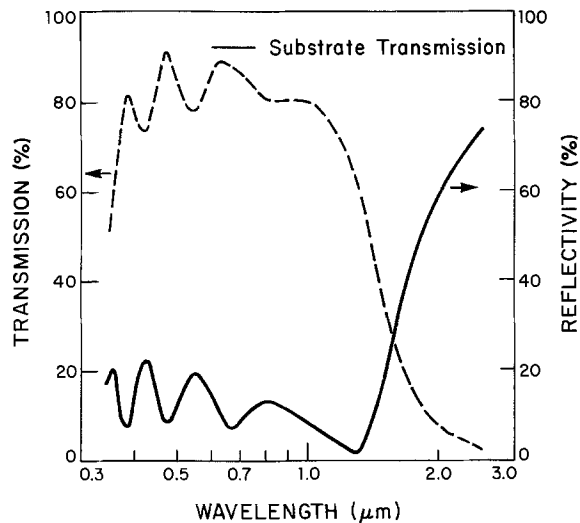


Fig. 6. Transmission and reflectivity as a function of wavelength for a film deposited on CG 7059 glass at sputtering power of 500W. The transmission of the bare substrate is indicated.

ing a corresponding reduction in transmission) because of the plasma effect resulting from the high concentration of mobile carriers. As shown in Fig. 7, as the wavelength increases to $10 \mu\text{m}$ the reflectivity of this film increases to more than 90%, while the transmission becomes negligible at about $3 \mu\text{m}$.

Before the theoretical treatment of these results is presented, it should be noted that the reflectivity of the Sn-doped In_2O_3 films in the infrared increases significantly with increasing sputtering power (i.e., substrate temperature), as shown by the experimental curves for reflectivities at 5 and $10 \mu\text{m}$ plotted in Fig. 8. In addition, the absorption of the films in the visible appears to decrease with increasing sputtering power, although this is less clear because analysis of the data is complicated by the interference fringes and also by the effect of the substrate in this spectral region.

To a good approximation the reflectivity and transmission curves plotted in Fig. 7 can be fitted by using a simple free-carrier model for the photon-energy dependence of the complex dielectric constant, $\epsilon(E)$, which determines the refractive index and extinction coefficient of the film (10). According to this model, in the spectral region of interest $\epsilon(E)$ is the sum of two terms: a constant, ϵ'_1 and an energy-dependent free-carrier term that depends on the carrier concentration (N), effective mass (m^*), and optical mobility (μ_{opt}) (12). The expression for $\epsilon(E)$ is

$$\epsilon(E) = \epsilon'_1 - \frac{E_n^2}{E^2 + iE_cE} \quad [1]$$

where E_n and E_c are energy parameters given by

$$E_n = \hbar \left(\frac{4\pi N e^2}{m^*} \right) \quad [2]$$

and

$$E_c = \frac{\hbar e}{m^* \mu_{\text{opt}}} \quad [3]$$

In using this model to fit the curves of Fig. 7, a multi-layer matrix formulation (10) was employed to take account of the fact that the observed reflectivity and transmission values are those of a film-on-glass composite, and a nonlinear minimization routine (13) was

¹ In some recent literature, e.g., Verleur (11), the symbol ϵ_{∞} has been used not only in the conventional manner, to represent the high-frequency (optical) dielectric constant, but also to represent an adjustable parameter that is the sum of all contributions to the complex dielectric constant other than those that vary within the spectral region of interest. For clarity, we have adopted ϵ'_1 rather than ϵ_{∞} as the symbol for the adjustable parameter.

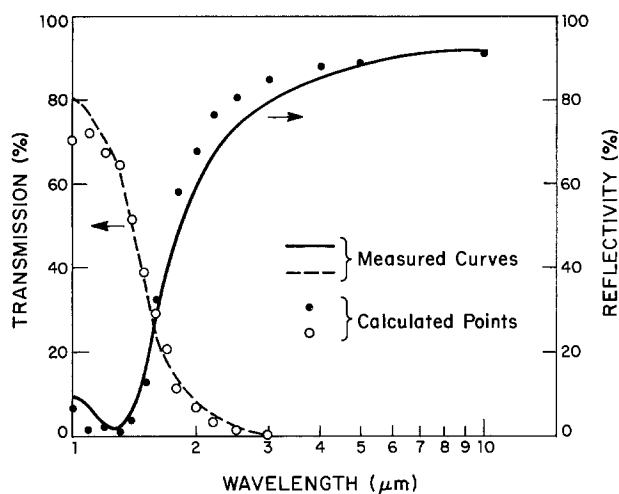


Fig. 7. Measured transmission and reflectivity curves with calculated points. (See text.)

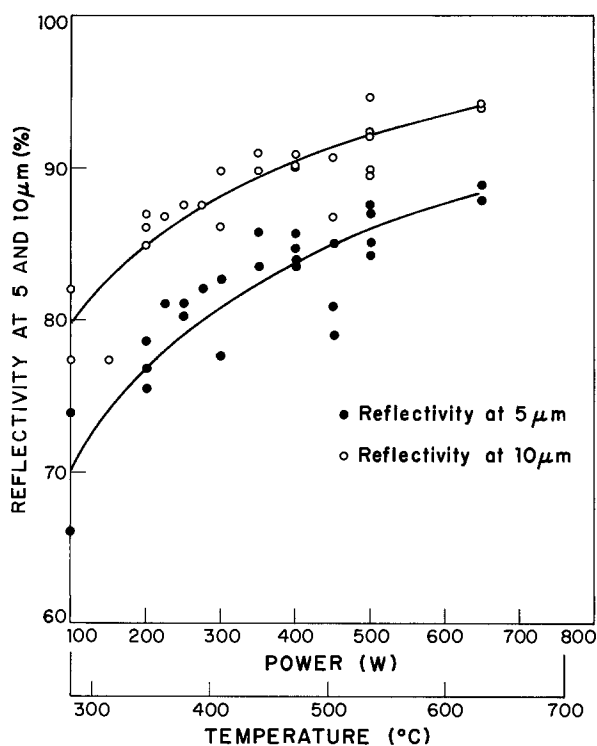


Fig. 8. Reflectivity at 5 and 10 μm as a function of sputtering power and substrate temperature.

utilized to determine the values of the adjustable parameters ϵ' , E_n , and E_c that would yield the best fit to the experimental data. The best fit that we achieved by using this procedure is represented by the calculated points that are plotted in Fig. 7. The agreement is quite good, except that in the 2-4 μm region the calculated reflectivity increases somewhat more steeply than the observed.

The values of the adjustable parameters used to obtain the calculated points of Fig. 7 were $\epsilon' = 4.45$, $E_n = 1.64$ eV, and $E_c = 0.075$ eV. Taking the square root of ϵ' gives $n = 2.1$ as the refractive index for wavelengths between the interband absorption edge (~ 0.35 μm) and the onset of free-carrier contribution, in good agreement with the value of 2.2 found by analysis of the transmission interference fringes shown in Fig. 6. From the value adopted for E_n , together with the concentration $N = 7 \times 10^{20}$ cm^{-3} determined by measuring the Hall coefficient, Eq. [2] gives $m^* = 0.2 m_0$, where m_0 is the free-electron mass. This effective mass is fairly close to the values of 0.3 and 0.55 m_0 , respec-

tively, obtained from transport data for films (14) and single crystal samples (15) of undoped In_2O_3 . For the effective mass of 0.2 m_0 and the value adopted for E_c , Eq. [3] gives an optical mobility of 75 $\text{cm}^2/\text{V}\text{-sec}$, which agrees to within a factor of two with the Hall mobility of 40 $\text{cm}^2/\text{V}\text{-sec}$ measured for the same film.

The values for ϵ' , E_n , and E_c can be used to calculate the dependence of infrared reflectivity on film thickness. The results obtained for wavelengths of 5 and 10 μm are shown in Fig. 9. The reflectivity initially increases with increasing thickness, but becomes essentially constant when the thickness reaches about 0.3 μm . Since the visible transmission and the electrical resistance also depend on thickness for specific applications it is necessary to select the optimum thickness for best performance.

Vossen and Poliniak (6) have reported that Sn-doped In_2O_3 films less than 0.1 μm thick are unstable, but we have prepared films as thin as 0.06 μm (resistance of 150 ohm/sq) that have not shown significant changes in optical and electrical measurements made over a period of several weeks in a laboratory ambient. Figure 10 shows the transmission of a film about 0.12 μm thick (resistance about 55 ohm/sq) that was deposited at a power of 500W.

X-ray diffraction results.—X-ray diffraction measurements were made on films deposited at power levels from 100 to 650W. All the diffraction patterns contain only In_2O_3 peaks, except for one that also contains weak Sn_3O_4 peaks. The film with the two-phase pattern has very poor electrical and optical properties ($\rho \sim 0.5$ ohm-cm, reflectivity $\sim 20\%$ at 10 μm). Because of the presence of the second phase, the properties of this film are not plotted in any of the figures.

The diffraction results are summarized in Table I. The $\langle 400 \rangle$ peak is the strongest one observed for the films deposited on glass at 100W (substrate temperature below 300°C). For all films deposited on glass at higher powers (except one at 400W), the $\langle 222 \rangle$ peak is the most prominent, as it is in the ASTM powder

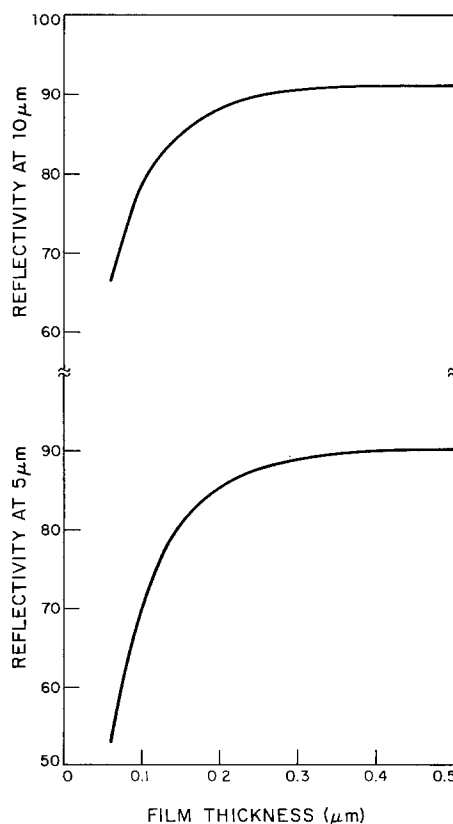


Fig. 9. Infrared reflectivity at 5 and 10 μm calculated as a function of film thickness.

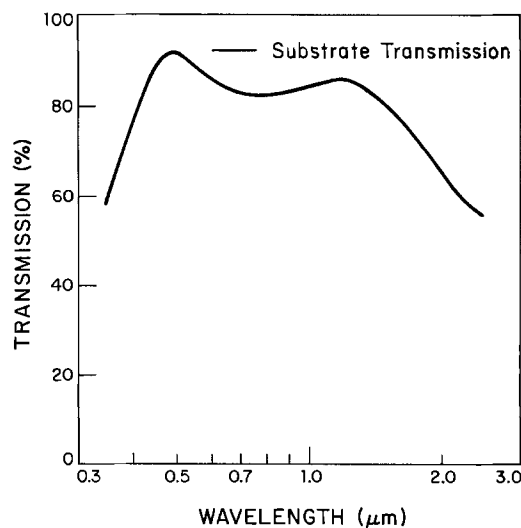


Fig. 10. Optical transmission as a function of wavelength for a film 0.12 μm thick.

pattern for In_2O_3 . In fact, for some of the films deposited on glass at 500 or 650W, all peaks other than the $\langle 222 \rangle$ are either weak or absent, indicating that these films have a strong $\langle 111 \rangle$ texture. For films deposited at 650W on other substrates, only the $\langle 222 \rangle$ peak is observed for the film on (111)-face CaF_2 , while the strongest peaks for the films on fused silica and (0001)-face Al_2O_3 are the $\langle 400 \rangle$ and $\langle 332 \rangle$, respectively. According to our measurements, the electrical and optical properties of the films are not significantly affected by either their principal orientation, their degree of texturing, or their substrate material.

The values of the cubic lattice constant measured for the films range from 10.17 to 10.27Å, compared with the ASTM value of 10.118Å for bulk In_2O_3 . There appears to be no systematic dependence of lattice constant on substrate temperature. Since two films of undoped In_2O_3 deposited on CG 7059 glass at 500W have lattice constants of 10.11Å, close to that of the bulk material, the observed lattice expansion is due to the incorporation of Sn. This suggests that the n-type conductivity of the films is not due to the replacement of In^{3+} ions by Sn^{4+} ions, which are smaller and would be expected to cause a contraction. The observed expansion is consistent with the replacement of In^{3+} ions by the larger Sn^{2+} ions and also with the incorporation of Sn

Table I. X-ray diffraction results for Sn-doped In_2O_3 films

Sputtering power (W)	Substrate	Lattice constant a (Å)	Strongest peak	Second strongest peak	
				Orientation	Intensity relative to strongest peak (%)
100	7059	10.22*	$\langle 400 \rangle$	$\langle 222 \rangle$	16
		10.27	$\langle 400 \rangle$	$\langle 222 \rangle$	22
		10.27	$\langle 400 \rangle$	$\langle 211 \rangle$	15
200	7059	10.20	$\langle 222 \rangle$	$\langle 211 \rangle$	5
		10.23	$\langle 222 \rangle$	$\langle 211 \rangle$	35
		10.17	$\langle 222 \rangle$	$\langle 440 \rangle$	18
350	7059	10.19	$\langle 222 \rangle$	$\langle 211 \rangle$	7
400	7059	10.22	$\langle 400 \rangle$	$\langle 211 \rangle$	18
450	7059	10.22	$\langle 222 \rangle$	$\langle 400 \rangle$	33
500	7059	10.22	$\langle 222 \rangle$	$\langle 211 \rangle$	2
		10.19	$\langle 222 \rangle$	$\langle 440 \rangle$	10
		10.23	$\langle 222 \rangle$	$\langle 211 \rangle$	8
650	7059	10.25	$\langle 222 \rangle$	$\langle 400 \rangle$	38
		10.18	$\langle 400 \rangle$	$\langle 211 \rangle$	70
		10.20	$\langle 332 \rangle$	$\langle 400 \rangle$	33
		10.22	$\langle 222 \rangle$	—	—
	Fused silica	10.18	$\langle 400 \rangle$	$\langle 211 \rangle$	70
	(0001) Al_2O_3	10.20	$\langle 332 \rangle$	$\langle 400 \rangle$	33
	(111) CaF_2	10.22	$\langle 222 \rangle$	—	—

Experimental uncertainty in a is about $\pm 0.02\text{Å}$.

In the ASTM powder pattern for In_2O_3 , the strongest peak is $\langle 222 \rangle$, and the second strongest is $\langle 440 \rangle$, with a relative intensity of 34%.

* Small SnO_4 peaks also observed.

ions in interstitial positions. In the latter case, the observed n-type conductivity could result from the excess electrons supplied by the interstitial Sn, without a change in the O/In ratio. (Of the eight available sites around each In^{3+} ion in the cubic In_2O_3 structure, only six are occupied by O^{2-} ions, leaving two positions available for incorporation of interstitial Sn.) Substitution of Sn^{2+} for In^{3+} ions, on the other hand, would decrease the electron concentration so that a stoichiometric deficiency of O would be necessary to explain the n-type conductivity. In this case, the film composition would be represented by the formula $(\text{In}_{1-x}\text{Sn}_x)_2\text{O}_{3-y}$, and the carrier concentration would be proportional to $(y-x)$, since O vacancies should act as donor centers. An accurate chemical analysis of the films could probably help to determine which of the three alternative modes of Sn incorporation actually occurs.

X-ray diffractometer measurements were also made on powdered samples taken from a sputtering target before and after sputtering. As-received targets are yellowish-white in color, but after some hours of sputtering the surface becomes grayish and is speckled with many, small dark areas. The diffraction results show that an as-received target is a two-phase mixture of In_2O_3 and SnO_2 , but the diffraction patterns for samples scraped from a sputtered surface contain only In_2O_3 peaks. The decrease in SnO_2 content below the limit of a few weight per cent detectable by diffractometer measurements may be due in part to preferential removal of SnO_2 from the surface by differential sputtering. Electron microprobe analysis of the powder removed after sputtering shows that the darkest regions contain Sn rather than In. This indicates that the darkening of the surface results from the chemical reduction of the SnO_2 phase by loss of O during sputtering, a process that could also contribute to the disappearance of the SnO_2 diffraction peaks.

Electron microprobe and Auger spectrometer studies.—Electron microprobe analysis was used to determine the composition of films deposited at power levels from 100 to 500W. For each film, the weight percentages of In and Sn were measured directly, the weight percentage of O was found by difference (assuming that the concentration of all other elements was negligible), and the atomic percentages were then calculated. The results are given in Table II. With increasing sputtering power the weight percentage of Sn decreased from 4.2 weight per cent (w/o) at 100W to 2.1 ± 0.1 at 450 and 500W, while that of In, 81 ± 1 w/o, was constant within the experimental uncertainty of the microprobe (estimated as $\pm 3\%$ of the measured values). The atomic percentage of Sn and In derived from these results both decreased with increasing sputtering power, while the percentage found for O increased from 54 to 61 atomic per cent (a/o).

The atomic compositions listed in Table II clearly do not have a straight-forward relationship to the carrier concentrations measured for the films as a function of sputtering power. Since O vacancies are expected to act as donor centers, the increase of 7 a/o in the atomic percentage of O found with increasing power should cause a large decrease in carrier concentration,

Table II. Composition of Sn-doped In_2O_3 films prepared by rf sputtering

Sputtering powder (W)	Estimated substrate temperature, T_s ($^{\circ}\text{C}$)	Weight per cent			Atomic per cent		
		Sn	In	O*	Sn	In	O
100	280	4.2	81.6	14.2	2.2	43.6	54.2
200	350	3.3	80.1	16.6	1.6	39.5	58.9
450	500	2.0	81.6	16.4	1.0	40.5	58.5
500	550	2.2	79.9	17.9	1.0	37.9	61.1

* Obtained by difference.

but the opposite is observed (Fig. 4). Furthermore, since the O content found for the film deposited at 500W is 1 a/o higher than the stoichiometric composition of 60 a/o, such a film should be either p-type (if the 1 a/o Sn is incorporated as Sn^{2+} ions) or closely compensated (if the Sn is interstitial or incorporated as Sn^{4+} ions), whereas films deposited at 500W are actually n-type with carrier concentrations of about $7 \times 10^{20} \text{ cm}^{-3}$. To a considerable extent these inconsistencies are probably due to the uncertainty in the atomic percentages found for O. For the film deposited at 500W, for example, an increase in the weight percentage measured for In from 79.9 to only 81.0 w/o would cause a reduction in the O content from 61.1 to 59.2 a/o. We conclude that the microprobe measurements are not sufficiently accurate to elucidate the source of current carriers in Sn-doped In_2O_3 films, even though they do give a good measurement of the Sn content. Thus we are unable to determine the significance of the fact that the Sn content decreases with increasing substrate temperature, while the carrier concentration increases.

Auger spectrometer measurements were performed on several films deposited on glass at either 100 or 450W. In these studies, a profile of each film was obtained by recording the Auger spectrum, removing a thin layer from the surface of the film by sputter-etching with 500 eV Ar ions, repeating the Auger measurement, removing another surface layer, and so forth. The heights of characteristic Auger peaks for In, Sn, and O were then read off the spectra and ratios between them calculated. Since the escape depth for Auger electrons is generally less than 20Å, each spectrum reflects the composition of a layer of this depth.

The Auger peak-height ratios obtained for a film deposited at 450W are plotted as a function of the total sputter-etching time in Fig. 11, where they are compared with data obtained in the same manner for a disk prepared by cold-pressing undoped In_2O_3 powder. Similar results were obtained for films deposited at 100W. Since the strongest Auger peak for Sn could not be resolved from the In peak at 424 eV, the variation of the Sn/In ratio is indicated by plotting the ratio of the

height of the combined peak at 424 eV to the height of the In peak at 403 eV.

As shown in Fig. 11, with increasing sputter-etching time the Auger signals for Sn and O in the film, relative to those for In, initially decreased and then became constant. Comparison of the data for the film and the In_2O_3 disk indicates that the Sn/In ratio in the surface layer of the film changed by a factor of about 2, while the O/In ratio decreased by only about 10%, if it is assumed that the composition ratios are proportional to the peak-height ratios. We attribute the observed changes to differential sputtering that occurred during Ar-ion bombardment, as it did during bombardment of the sputtering targets, rather than to compositional inhomogeneities in the as-deposited films.

Conclusions

A one-step rf sputtering process has been used without postdeposition annealing to prepare Sn-doped In_2O_3 films with excellent properties for applications as transparent conductors and as transparent heat mirrors for radiation insulation and solar energy collection. The substrate temperature is the critical preparation parameter: The electrical conductivity, visible transmission, and infrared reflectivity all increase with increasing substrate temperature, as a result of the increases in carrier concentration and mobility. The electrical and optical properties of the films do not depend significantly on the crystallographic orientation, degree of texturing, or substrate material.

There is no reason to believe that the films described here have the best properties that can be achieved when Sn-doped In_2O_3 is deposited by rf sputtering. If films with still higher carrier concentration and/or mobility can be prepared, their properties could be even better. The present results suggest that deposition at higher substrate temperature is one possible means for obtaining improved films. In addition, the Sn/In and O/In ratios in the sputtering target should be changed in order to determine the effects of such changes on the composition and therefore the properties of the films.

Acknowledgments

The authors acknowledge the technical assistance of G. H. Foley, P. M. Zavracky, and W. L. McGilvary. M. C. Finn performed the electron microprobe analysis and Auger electron spectroscopy. We also appreciate many helpful discussions with J. B. Goodenough and A. J. Strauss. This work was sponsored by the Department of the Air Force.

Manuscript submitted March 10, 1975; revised manuscript received Aug. 1, 1975.

Any discussion of this paper will appear in a Discussion Section to be published in the June 1976 JOURNAL. All discussions for the June 1976 Discussion Section should be submitted by Feb. 1, 1976.

Publication costs of this article were partially assisted by Massachusetts Institute of Technology.

REFERENCES

1. R. Groth and E. Kauer, *Philips Tech. Rev.*, **26**, 105 (1965); R. Groth, *Phys. Status Solidi*, **14**, 69 (1966).
2. T. B. Reed, Solid State Research Report, Lincoln Lab., MIT (1969:1), p. 21.
3. J. C. C. Fan, T. B. Reed, and J. B. Goodenough, "Proceedings of 9th Intersociety Energy Conversion Engineering Conference, San Francisco, California," p. 341, Society of Automotive Engineering Inc., New York (1974).
4. J. C. C. Fan, F. J. Bachner, G. H. Foley, and P. M. Zavracky, *Appl. Phys. Letters*, **25**, 693 (1974).
5. J. L. Vossen, *RCA Rev.*, **32**, 289 (1971).
6. J. L. Vossen and E. S. Poliniak, *Thin Solid Films*, **13**, 281 (1972).
7. R. R. Mehta and S. F. Vogel, *This Journal*, **119**, 752 (1972).
8. D. B. Fraser and H. D. Cook, *ibid.*, **119**, 1368 (1972).
9. J. C. C. Fan and P. M. Zavracky, Solid State Research Report, Lincoln Lab., MIT (1975:1), p. 45.
10. O. S. Heavens, "Optical Properties of Thin Solid Films," chap. 4, Dover, New York (1965).

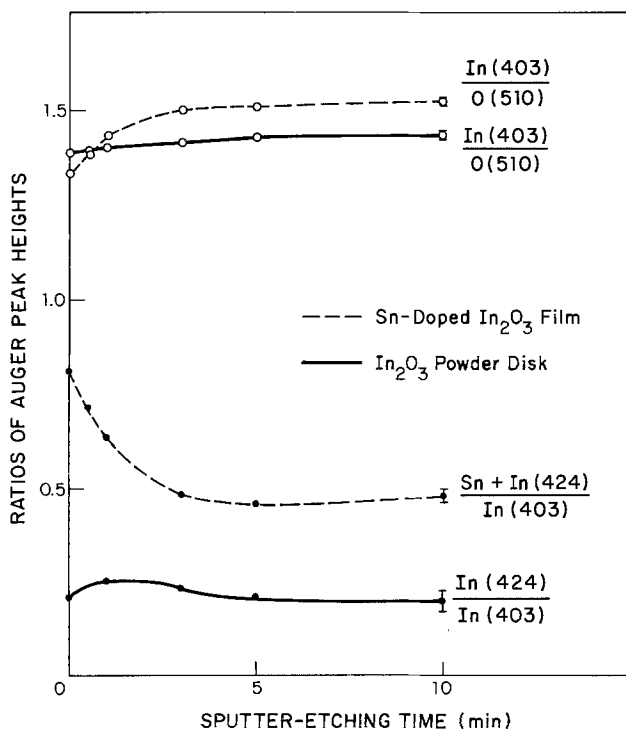


Fig. 11. Auger profiles obtained by sputter-etching a Sn-doped In_2O_3 film and a cold-pressed In_2O_3 disk. The numbers in parentheses are the energies of the Auger peaks in eV.

11. H. W. Verleur, *J. Opt. Soc. Am.*, **58**, 1356 (1968).
12. R. A. Smith, "Semiconductors," chap. 5 and 7, Cambridge University Press, Cambridge, England (1959).
13. J. C. C. Fan, PhD Thesis, HR-28, Gordon McKay Lab., Harvard University, 1972 (unpublished).
14. H. K. Müller, *Phys. Status Solidi*, **27**, 733 (1968).
15. R. L. Wehner, *J. Appl. Phys.*, **33**, 2834 (1962).

Elimination of Oxidation-Induced Stacking Faults by Preoxidation Gettering of Silicon Wafers

I. Phosphorus Diffusion-Induced Misfit Dislocations

G. A. Rozgonyi,* P. M. Petroff,* and M. H. Read

Bell Laboratories, Murray Hill, New Jersey 07974

ABSTRACT

In the present paper a preoxidation gettering procedure (called POGO) is described which prevents the formation and/or activation of stacking fault nucleation sites during oxidation. In this way the stacking faults and their possible device degrading influences are eliminated at the start of a processing schedule. In addition, the gettering medium is retained through all subsequent high temperature processing, thereby continuing to suppress the formation of stacking faults. The gettering of the nucleation sites, whether they be process induced, such as impurity precipitation, or native to the original crystal growth, such as vacancies or impurities, is achieved by the controlled introduction of interfacial misfit dislocations on the back side of the wafer. The dislocations interact with the stacking fault nucleation sites such that the nuclei diffuse from the active device side of the wafer to the line defects which are confined to within a few microns of the back surface.

The presence of stacking faults introduced during the processing of silicon devices is known to have a deleterious effect on device performance. For example, localized microplasma breakdown (1), increased p/n junction leakage (2), and reduced storage time of CCD devices (3) have all been correlated with stacking fault defects. The stacking faults are most frequently generated during steam oxidation (4, 5). The nucleation sites for these defects have been shown to be related to residual mechanical damage (6), local impurity precipitation (7), and the so-called "swirl" defects (8). The latter two may be either process induced or native to the original crystal growth. Although adequate removal of surface damage is easily achieved with proper etching before polishing, it has not been a simple matter to remove process-induced precipitation or native defects from device wafers. However, progress has been made in reducing the electrical activity of stacking faults once they are formed (2), particularly if the electrical activity is related to precipitation on the stacking fault (9).

In the present paper we describe a process whereby stacking fault nuclei are gettered from the active device side of the wafer by the deliberate introduction of an array of misfit dislocations on the back side of the wafer. The driving force for the generation of the dislocations is the misfit strain gradient introduced into the silicon lattice during an extended phosphorus diffusion (10, 11). The depth and density of the dislocation array can be adjusted by varying the diffusion time and temperature (12). Since the dislocations are interfacial in character they lie parallel to the wafer surface and are confined to within a few microns of the back surface. It is well known that line defects will act as sinks for a variety of point defects such as impurities and vacancies. This gettering action of one type of defect, an interfacial misfit dislocation, for point defects or impurities which act as stacking fault nucleation sites, is the basis for our approach to the elimination of oxidation-induced stacking faults.

The above process has been given the acronym POGO for preoxidation gettering of the other side in order to distinguish it from the commonly used phosphorus gettering (13), back side abrasion (14), and ion implantation damage gettering techniques (15). It is important to point out that there are two essential differences in the POGO procedure. First, the gettering misfit dislocations are generated in the as-received wafers before any device processing is initiated and are intended initially as sinks for native defects which were incorporated during crystal growth or inadvertently introduced during wafer preparation and cleaning. Second, the misfit dislocations are expected to continue to act as sinks for impurities introduced during subsequent high temperature processing. The total effect of these gettering actions is expected to be the gross reduction or elimination of defects near active device regions with a resulting improvement in device properties (MOS storage time, junction leakage, and breakdown).

Experimental Procedures

The gettering results to be described below were obtained on n-type {100} oriented dislocation-free wafers with a nominal resistivity of 5 ohm-cm. The wafers, which were purchased from the Monsanto and Wacker Corporations, were received with a Syton polished front side and chemically etched back side. The Monsanto wafers were from Czochralski ingots while the Wacker were float zone.

Because of wafer-to-wafer variations within a given batch it was necessary to process each wafer such that only half of the back side was gettered before the entire wafer was oxidized. In this way a control was built into each sample. This was accomplished as follows. A thick (1.2-1.5 μm) masking oxide layer was deposited at 480°C on the front and then the back side of each wafer. A low temperature silane process was chosen to insure that no stacking faults were generated. Conventional photolithography was used to strip the oxide from half of the back side while a uniform oxide coating was retained on the front. Phos-

* Electrochemical Society Active Member.

Key words: stacking faults, gettering, defects.

phorus was then diffused into the unmasked half of the wafer at temperatures from 1070° to 1150°C for times of 1-7 hr. Within this temperature range a dense array of misfit dislocations is introduced to a depth of 2μ or more below the P-diffused surface. A POCl_3 process with an oxygen flow rate of 110 cm^3/min was used. After stripping of the phosphorus and masking oxides those wafers which were to be evaluated for stacking faults were then oxidized in steam at 1050°C for 110 min to grow about 7500Å of SiO_2 .

The various etch pits were delineated in an $\text{HF-K}_2\text{Cr}_2\text{O}_7$ preferential etch as described by Secco D'Aragona (16), hereafter referred to as the Secco etch. During etching the wafers were mechanically rotated for 10 min in an ultrasonically agitated bath to remove about 15 μm from each side of the wafer. Observation of the pits was performed in a Zeiss Ultra-phot microscope using Nomarski interference contrast optics.

Three types of each pits are distinguished in oxidized $\{100\}$ wafers as illustrated in Fig. 1. Emerging dislocations give rise to deep, black pits (D-pits) with a pointed bottom, see arrows D in Fig. 1. Unless a wafer has deliberately had misfit dislocations introduced D-pits are only found near the perimeter of a wafer and are of the slip type, generally attributed to thermal asymmetries during high temperature processing. Saucer pits, see arrows S, are shallow and flat bottomed and are generally associated with stacking fault nucleation sites if they are distributed in a swirl pattern (4, 5, 8). Stacking faults, see arrows SF in Fig. 1, are always aligned along perpendicular $\langle 110 \rangle$ directions, horizontal or vertical in all our photomicrographs, and when fully developed often appear like orthogonal arrays of beads.

Experimental Results

Oxidized POGO wafers.—A photomicrograph of the boundary between the phosphorus gettered (PG) plus misfit dislocation (MD) half and the nongettered (NG) half of the back side of a wafer after oxidation and Secco etching is shown in Fig. 2a. The front side of the same wafer, which is shown in Fig. 2b, is discussed below. Enlarged views of the regions surrounding the slip dislocations D_3 and D_1 are shown in Fig. 3a and b.

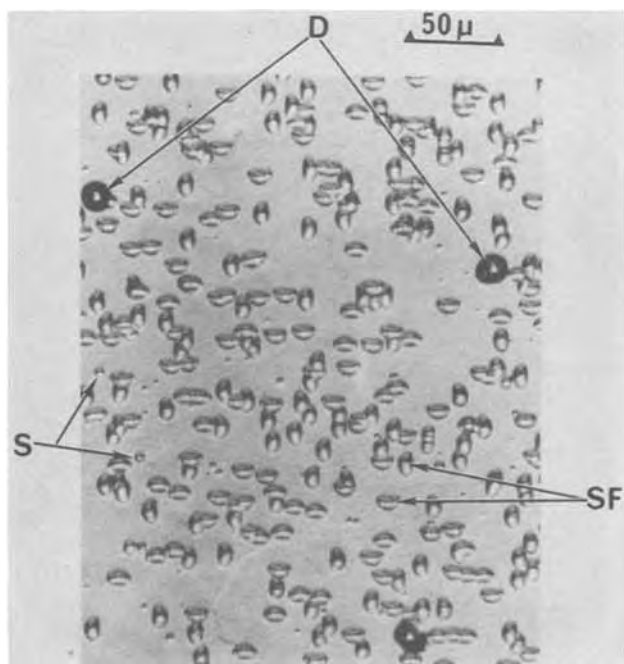


Fig. 1. Optical photomicrograph of etched $\{100\}$ surface illustrating morphology of dislocations, D, saucer pits, S, and stacking faults, SF.

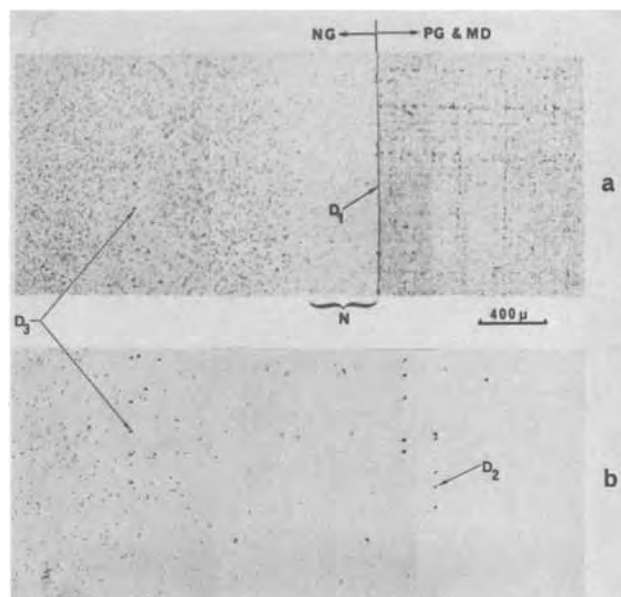


Fig. 2. Back (a) and front (b) etched surfaces of an oxidized Czochralski wafer half of whose back surface was phosphorus gettered (PG) to produce misfit dislocations (MD) while the other half and the front were not gettered (NG). The region N was denuded of stacking faults.

Since the lattice contraction in the PG half of the sample, which was treated for 1 hr at 1150°C, exceeded the threshold strain for generation of misfit dislocations the trace of a cross grid of misfit dislocation is evident to the right of D_1 , which is right on the PG/NG boundary line. Only a trace of the misfit dislocation array remains since the removal of 15 μm of silicon during the Secco etch has also removed most of the interfacial MD network from the sample. It has been found that no stacking fault etch pits (SF) exist on that half of the wafer which was gettered, see Fig. 3b; whereas, several millimeters to the left of the PG/NG boundary the SF pit density is $\sim 10^5 \text{ cm}^{-2}$, see Fig. 3a. We conclude that the phosphorus diffusion plus misfit dislocation process provides a very effective gettering action for those nucleation sites which promote the formation of stacking faults during oxidation.

The range of misfit dislocation gettering action is believed to be at least as large as the region N in Fig. 2a, which is denuded of all SF pits for a distance of $\geq 400 \mu\text{m}$ from the PG/NG boundary. Since the wafer thicknesses were $\sim 300 \mu\text{m}$ for Monsanto and $\sim 450 \mu\text{m}$ for Wacker material SF gettering effects were also expected on the front side of the phosphorus-treated wafers. This was checked as follows. The same D-pits were located on the front of the wafer under discussion, see arrow D_3 in Fig. 2b, in order to accurately align the PG/NG boundary. Note Fig. 2a and 2b are mirror imaged about a horizontal axis with D_3 the third D-pit in a row of five. It was necessary to use the slip type D-pits for alignment because the misfit dislocations are truly interfacial in character and are confined to the back side of the wafer. Higher magnification photos of front surface regions around the dislocations D_3 and D_2 are presented in Fig. 3c and d. The density of SF pits in the vicinity of D_2 is zero and is representative of the entire volume of the wafer below the misfit dislocation array. This volume has been further checked using transmission x-ray topography to confirm that stacking faults are only present in the NG half of the wafer. The higher density of SF in the back of the wafer, compare Fig. 3a with Fig. 3c, appeared to be related to a local difference in contamination of the back of the wafer.

In addition to the pits, there are also etch hillocks observed, see arrows H_1 and H_2 in Fig. 3c and d, which

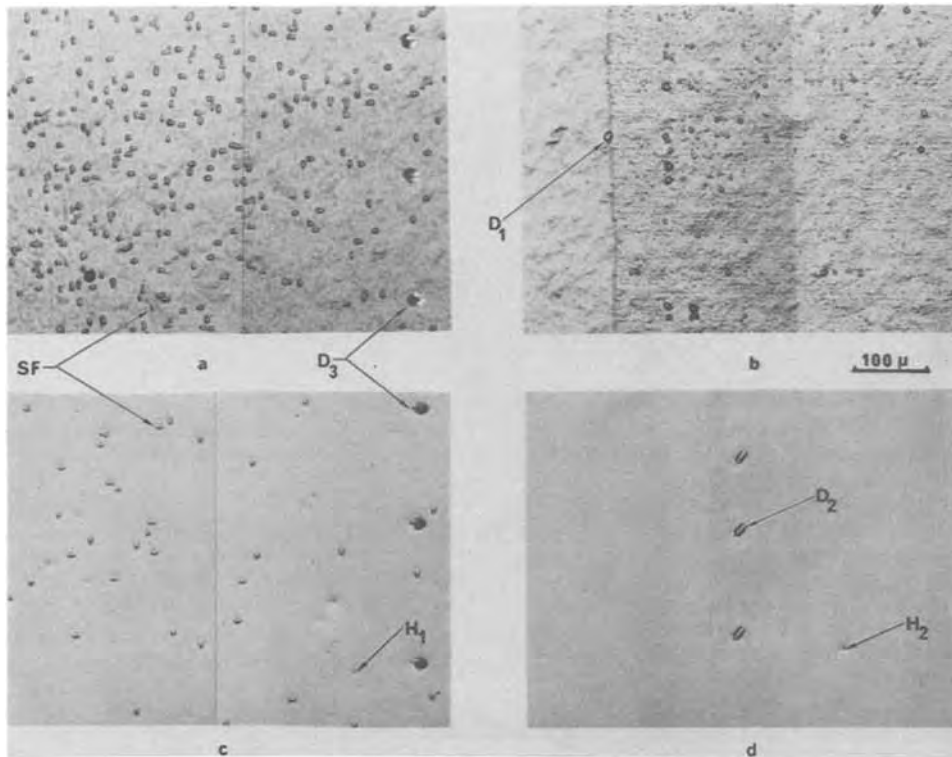


Fig. 3. Higher magnification micrograph of those regions of Fig. 2 surrounding the slip dislocations D_1 , D_2 , and D_3 . H are unidentified hillock defects while the arrows SF point to two separate stacking faults.

may also be associated with a microdefect, perhaps a small dislocation loop, for example. Further etching transforms the hillocks into shallow pits which are similar, but not identical to the S-pits. The hillocks are not observed using x-ray topography, however, transmission electron microscopy studies are under way to help identify the source of the hillocks. Although there is a large reduction in the hillock density across the PG/NG boundary it is nowhere near the 10^4 - 10^5 cm^{-2} difference observed with the SF pits. However, samples which have been POGO treated for 4 and 7 hr do show a further reduction in hillock density indicating that the gettering action, although slower, is also effective for the hillock defects. Results on a 4 hr POGO sample before oxidation are presented in the next section.

Nonoxidized POGO wafers.—Stacking faults were not generated during the POGO treatment unless there was residual surface damage or localized chemical contamination. Prior to oxidation the gettering action was evident for both S-pits and hillocks. This is illustrated in Fig. 4a, which is the Secco etched PG/NG boundary of the polished side of a Wacker float zone wafer which was phosphorus gettered on half of the back side for 4 hr at 1150° , as described above. The S-pit and hillock densities are both about 10^5 cm^{-2} in the NG region, see the arrows S and H in Fig. 4b, which is an enlarged view of the area marked (b) in Fig. 4a. On the front surface of the wafer directly opposite the POGO treated back side, see Fig. 4c, no hillocks were observed at all and the S-pit density was reduced to $\sim 5 \times 10^3$ cm^{-2} . The ability to eliminate the hillocks completely varied from sample to sample but was always more effective for gettering times longer than 1 hr.

Float zone vs. Czochralski.—Because of the well-documented differences in the oxygen content of float zone and Czochralski material and the possibility that oxygen plays a role in the formation of SF nuclei, a group of five float zone and five Czochralski wafers were gettered simultaneously. However, it was found that the variations in pit density, and other factors such as the occurrence of a swirl pattern, varied just as much within the separate groups of five as they did from group to group. The only consistent observation in the large batch studies was that on the gettered half of any wafer stacking faults, S-pits, and hillocks

were either eliminated or reduced in number by several orders of magnitude. It therefore appears that the oxygen concentration is not the predominant factor in the gettering of nucleation sites. This does not mean, however, that oxygen is not important when the stacking faults are actually generated.

Discussion and Conclusions

The experiments and etch pit data presented above demonstrate the existence of a very favorable inter-

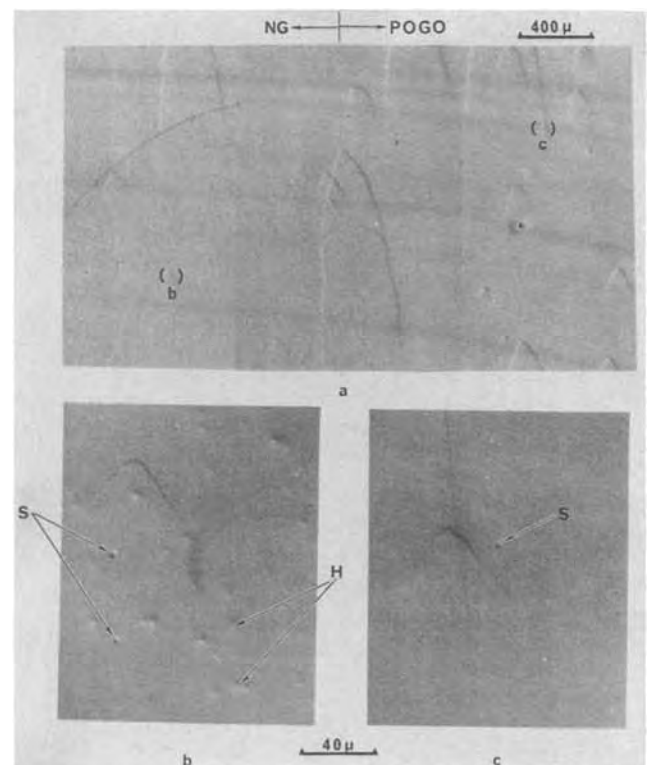


Fig. 4. Etched front surface of an unoxidized float zone wafer preoxidation gettered on half of the other side (POGO). Arrows S and H are saucer pits and hillocks.

action between a phosphorus gettering plus misfit dislocation procedure and the nuclei responsible for oxidation-induced stacking faults. The presence of misfit dislocation was indeed found necessary to achieve the stacking fault elimination. Those samples subjected to a phosphorus diffusion treatment which did not introduce misfit dislocations ($T < 1050^\circ\text{C}$) did form stacking faults during oxidation. The role of misfit dislocations is consistent with the extensive literature on line defects acting as sinks for mobile point defects, such as impurities and vacancies. Unfortunately, the precise nature of those point defects (or clusters and complexes thereof) which create an environment for stacking fault formation is not fully understood at this stage of our work. We have, however, schematically outlined the problem as shown in Fig. 5, which is based, in part, on recent work of Pomerantz (17) and de Kock (8, 18, 19).

These workers have demonstrated that interactions which exist between grown-in and process-induced microdefects, whose macroscopic distribution is in the form of a swirl pattern, can be traced back to variations in the microscopic growth rate of the original crystal. Figure 5 identifies two groups of grown-in defects according to whether or not a swirl pattern can be delineated by etching or x-ray topography of Cu or Li decorated samples. Following de Kock we attribute the swirl of S-pits in as-received wafers, stage I in Fig. 5, to a point defect/impurity (PD/i) complex (8), or to collapsed vacancy (8, 20, 23), or interstitial (22) clusters in the form of dislocation loops. If no swirl is delineated we still assume that isolated point defects are distributed in the crystal in a nonhomogeneous fashion. This is based on the observation that swirl defects can be formed by a suitable heat-treatment (24), see process IIB in Fig. 5, of swirl-free wafers. Also, a swirl distribution of stacking faults is observed after steam oxidation, process IIA, in Fig. 5, even if no stage I swirl is delineated by etching (21).

It is well established (8, 17) that metallic impurities introduced during stage II processing can become associated with stage I defects to form stacking faults during oxidation or epitaxial growth. This type of process-induced defect is most certainly gettered by the POGO misfit dislocation and/or phosphorus diffusion treatment itself. Process IIC in Fig. 5 illustrates how swirl and stacking faults can be suppressed in as-received material and, we would expect, in any material which has not previously nucleated stacking faults during processing, e.g., process IIB. However, since stacking faults can be formed under very clean oxidizing conditions the question arises as to whether our gettering procedure is also effective in eliminating stage I defects. e.g., vacancies, copper, or small dislocation loops. The complete suppression of stacking faults in the various material supplied to us indicates that native defect gettering may, in fact, be taking

place. In addition, the elimination of the etch hillocks and large reduction in S-pit density discussed above with reference to Fig. 4 is interpreted as a dissolution of stacking fault nuclei. These etch features, although not distributed in a swirl pattern, are very similar in appearance to the A- and B-type native swirl defects recently characterized by Petroff and de Kock (22). Also, preliminary results on POGO treated wafers from the same ingot used by Petroff and de Kock (22) indicates that stacking faults are not formed during subsequent oxidation. It should also be noted that the temperature of these treatments is more than 100°C lower than the recent high temperature argon annealing gettering work done by Shiraki (25). Finally, besides the dissolution or deactivation of native defects, the continued capture of process-induced stacking fault nuclei during subsequent processing cannot be overstated because of the many oxidations and high temperature treatments required in silicon integrated circuit fabrication.

It is hoped that the outline provided by Fig. 5 will serve as a guide to help identify those defects and processes vital to the nucleation of stacking faults. For example, it is occasionally found that swirl and stacking faults are not generated during oxidation of wafers from a specific ingot. Further analysis of these special crystals and their growth history would be most useful in enhancing our understanding of the stacking fault problem. Meanwhile, we believe the POGO gettering process described in this paper, although somewhat empirical, is quite viable and could readily be adapted to several device processing lines.

Acknowledgments

The authors would like to thank V. Morris for carrying out the phosphorus diffusions and oxidations described in this report. Comments on the manuscript and several very enlightening discussions with A. J. R. de Kock, T. E. Seidel, and R. B. Marcus are also appreciated.

Manuscript submitted May 19, 1975; revised manuscript received July 16, 1975. This was Paper 172 presented at the Toronto, Canada, Meeting of the Society, May 11-16, 1975.

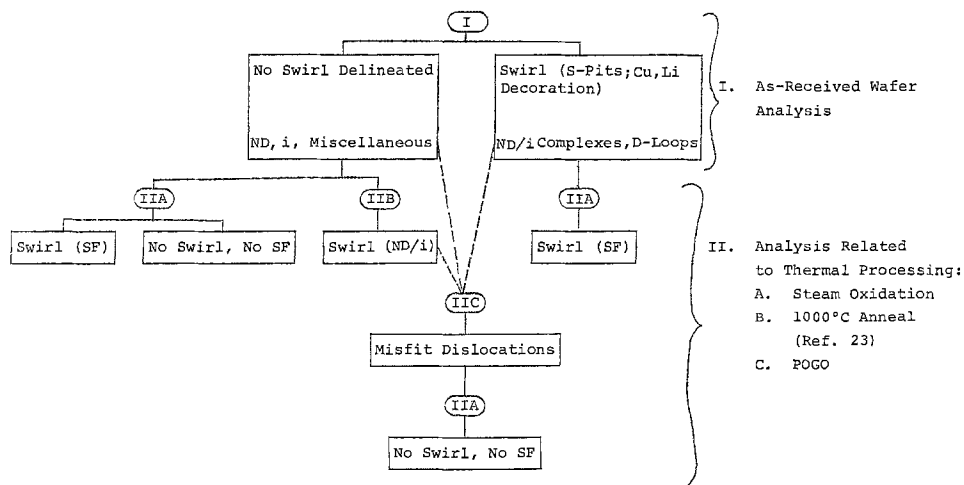
Any discussion of this paper will appear in a Discussion Section to be published in the June 1976 JOURNAL. All discussions for the June 1976 Discussion Section should be submitted by Feb. 1, 1976.

Publication costs of this article were partially assisted by Bell Laboratories.

REFERENCES

1. H. J. Quiesser and A. Goetzberger, *Phil. Mag.*, **8**, 1063 (1963).
2. C. J. Varker and K. Ravi, *J. Appl. Phys.*, **45**, 272 (1974).
3. G. A. Rozgonyi, F. J. Morris, and T. A. Shankoff, Unpublished data.
4. J. Matsui and T. Kawamura, *Japan. J. Appl. Phys.*,

Fig. 5. Schematic outline of interrelations between swirl, native defects, process-induced defects, and the suppression of oxidation-induced stacking faults. ND and i represent native defect and impurity, while SF and S correspond to stacking fault and saucer-type defects.



- 11, 197 (1972).
5. K. Ravi and C. J. Varker, *J. Appl. Phys.*, **45**, 263 (1974).
 6. W. A. Fischer and J. A. Amick, *This Journal*, **113**, 1054 (1966).
 7. C. M. Drum and W. van Gelder, *J. Appl. Phys.*, **43**, 4465 (1972).
 8. A. J. R. de Kock, *Philips Res. Rept.*, Suppl. 1 (1973).
 9. A. G. Cullis and L. Katz, *Phil. Mag.*, **30**, 1419 (1974).
 10. H. J. Quiesser, *J. Appl. Phys.*, **32**, 1776 (1961).
 11. S. Prussin, *ibid.*, **32**, 1876 (1961).
 12. P. M. Petroff, T. T. Sheng, and G. A. Rozgonyi, Unpublished data.
 13. J. E. Lawrence, in "Semiconductor Silicon," R. R. Haberecht and E. L. Kern, Editors, p. 596, the Electrochemical Society Softbound Symposium Series, New York (1969).
 14. E. J. Metz, *This Journal*, **112**, 420 (1965).
 15. C. M. Hsieh, J. R. Mathews, H. D. Seidel, K. A. Pickar, and C. M. Drum, *Appl. Phys. Letters*, **22**, 238 (1973); T. E. Seidel and R. L. Meek, in "Ion Implantation in Semiconductors," B. L. Crowder, Editor, Plenum Press, New York (1973); R. L. Meek, T. E. Seidel, and A. G. Cullis, *This Journal*, **122**, 786 (1975).
 16. F. Secco D'Aragona, *This Journal*, **119**, 948 (1972).
 17. D. I. Pomerantz, *ibid.*, **119**, 255 (1972).
 18. A. J. R. de Kock, *J. Appl. Phys.*, **44**, 2816 (1974).
 19. A. J. R. de Kock, *This Journal*, **119**, 1241 (1972).
 20. L. I. Bernewitz, B. O. Kolbesen, K. R. Mayer, and G. E. Schuh, *Appl. Phys. Letters*, **25**, 277 (1974), also Proc. Freiberg Conf. on Lattice Defects in Semiconductors, August 1974.
 21. G. A. Rozgonyi and S. P. Murarka, Unpublished data.
 22. P. M. Petroff and A. J. R. de Kock, *J. Cryst. Growth*, **30**, 117 (1975).
 23. A. J. R. de Kock, P. J. Roksnoer, and P. G. T. Boonen, *ibid.*, **22**, 311 (1974).
 24. A. J. R. de Kock, P. J. Roksnoer, and P. G. T. Boonen, in "Semiconductor Silicon," H. R. Huff and R. R. Burgess, Editors, p. 83, The Electrochemical Society Softbound Symposium Series, New York (1973).
 25. H. Shiraki, *Japan. J. Appl. Phys.*, **13**, 1514 (1974).

Effect of Oxidizing Ambients on Platinum Silicide Formation

I. Electron Microprobe Analysis

T. J. Kingzett and C. A. Ladas*

Motorola Incorporated, Semiconductor Products Division, Mesa, Arizona 85201

ABSTRACT

The effect of oxidizing and inert ambients on the formation and oxidation of PtSi films from 450° to 650°C has been investigated. The presence of O₂ in the annealing furnace ambient during PtSi formation results in the growth of an SiO₂ layer which separates the underlying PtSi from a surface layer of unreacted Pt. The SiO₂ layer acts as a barrier to further silicide formation. In inert ambients, PtSi formation proceeds to completion, and subsequent exposure to O₂ results in the formation of a surface SiO₂ layer. Electron microprobe analysis was used to analyze the composition of the films.

Platinum silicide (PtSi) is commonly used for ohmic or rectifying contacts to silicon (1-3). PtSi is formed from Pt films on silicon substrates at temperatures above 300°C (4) and is reportedly stable up to 800°C (5). Although PtSi formation has been extensively studied (6), certain questions relating to the mechanism of the termination of the reaction as well as the oxidation of PtSi remain unresolved.

Hiraki *et al.* (7) reported that Pt on Si is completely converted to PtSi by annealing at 400°C. Poate and Tisone (8) reported that silicide formation is initiated by diffusion of Si atoms into the Pt film, forming an intermediate Pt₂Si phase which is converted, along with all of the remaining Pt, to PtSi. Rand and Roberts (3) reported that Si diffuses through the Pt along grain boundaries to form a thin SiO₂ layer (~100Å) on the surface of the PtSi film. The oxide formation was attributed to impurities in the annealing furnace ambient.

Several authors (10, 11) have reported the existence of a layer of unreacted platinum on the surface of annealed PtSi films, but do not explain the reason for incomplete silicide formation. Danyluk and McGuire (12) reported that a layer of PtSiO₄ is formed between the PtSi and a surface Pt film, and that a native SiO₂ layer on the silicon substrate may interact with the metal in order to form this silicate layer.

In this paper, we report a study of the effect of various ambients on PtSi formation, and of the oxidation of

PtSi, both during and subsequent to the annealing process. PtSi was formed by annealing Pt films on Si in oxidizing and inert ambients at temperatures from 450° to 650°C. Oxygen was found to react at the surface of PtSi to form SiO₂. If the Pt film is completely annealed (in an inert ambient) prior to exposure to O₂, then a layer of SiO₂ forms on the surface. If, however, the film is annealed in O₂ or air, then O migrates through the Pt, a layer of SiO₂ is formed at the advancing PtSi-Pt interface, and a layer of unreacted Pt remains on the surface. Analysis of the PtSi films was performed by the electron microprobe method.

Experimental

Thin Pt films were deposited on silicon by RF sputtering in argon at 5μ (Hg) pressure and 200W. The silicon substrates were etched in HF and then sputter etched with Ar for 30 sec prior to deposition in order to ensure atomically clean Si surfaces. Two-inch n-type <100> silicon wafers with a resistivity of 0.3 ± 0.05 ohm-cm were used throughout. Pt films of 1300 or 2400Å (±10%) thickness were deposited, and the samples were then annealed in air, nitrogen, oxygen, or argon at temperatures of 450°, 550°, and 650°C.

Electron microprobe analysis was performed with an ETEC scanning electron microscope equipped with a dispersive x-ray spectrometer (13). Quantitative analysis was performed using single crystal Si, sputter-deposited Pt and SiO₂ on silicon as primary standards for silicon, platinum, and oxygen, respectively. A primary electron beam energy of 5 kV was used, and

* Electrochemical Society Active Member.

Key words: platinum silicide, oxidation, ohmic contacts, electron microprobe analysis.

SiK α , PtM α , and OK α x-ray intensities were used to determine the relative mass concentration of each element in the surface film. The standard correction factor method (14) was employed.

Film thickness measurements were made by DEK-TAK (Sloan Instrument Company), CARIS (15), and ellipsometer (16) techniques.

Aqua regia etching of Pt and PtSi was done at 60°C with a 3:1:4 by volume mixture of 37% HCL:70% HNO $_3$:H $_2$ O. HF etching of all samples was done at room temperature using a 6:1 mixture of 40% NH $_4$ F:49% HF. Infrared reflectance spectra of SiO $_2$ films were obtained using a Perkin-Elmer 331 spectrophotometer.

Results

Table I lists the relative mass concentrations [weight per cent (w/o) relative to a standard without normalizing] of Pt, Si, and oxygen in the films produced by annealing samples of 1300 or 2400Å thick Pt on Si in air or oxygen at 650°C for 15 min. The effective electron penetration, or maximum depth of x-ray production, depends upon the energy of the incident electrons, the density of the surface film, and the energy of the electronic transition which results in x-ray emission (17). This depth is approximately 900Å for PtM α , 1000Å for SiK α , and 1300Å for OK α x-rays in PtSi.

The data in Table I show that after annealing in air or oxygen, higher Pt and lower Si concentrations are found in the films than for PtSi, which is 87.45% Pt and 12.55% Si. The presence of a high concentration of oxygen indicates that an oxide layer may have formed. After the samples have been etched in HF, the films display composition closely approximating that of PtSi, and the oxide layer appears to have been removed.

Table I also lists the relative mass concentration of Pt, Si, and O for films annealed in N $_2$ or Ar for 15 min at 650°C. In this case the Pt concentrations are lower, and Si concentrations are higher than expected for PtSi. A high level of oxygen is also found, again indicating that an oxide formation has occurred. The results of HF etching of each sample are that a film which approximates PtSi remains, and that the oxide layer is removed.

Inspection of the samples following the annealing cycles shows that those samples annealed in O $_2$ or air appear identical to the original Pt films, but that the films annealed in N $_2$ or Ar have the darker appearance characteristic of PtSi. By etching the samples annealed in air or O $_2$ in the HF, a thin metal film, which was insoluble in the etch solution, was removed from the surface. The underlying material then exposed was the darker shade of PtSi. Analysis of the thin metal film recovered from the etch solution established it to be pure platinum in each case. The thickness of the platinum film removed in this manner was found to be ~10-15% of the original sputtered platinum film thickness. HF etching of the samples annealed in N $_2$ or Ar resulted only in a slight darkening of the surface appearance.

The relative mass concentrations of the Pt, Si, and O in the films annealed at 550° and 450°C for 30 and 45 min, respectively, are listed in Tables II and III. The compositions of the films before and after etching in HF

Table I. Weight per cent (w/o) of platinum, silicon, and oxygen found in platinum silicide films annealed at 650°C

Sample identification		Before HF etch			After HF etch		
Pt film	Ambient	Pt	Si	O	Pt	Si	O
1300A	O $_2$	94.0	7.5	3.2	87.7	13.4	<1.0
2400A	O $_2$	95.4	5.4	2.5	85.0	13.8	<1.0
1300A	Air	92.1	7.3	3.6	87.3	12.9	<1.0
2400A	Air	93.4	4.9	3.2	86.7	13.0	<1.0
1300A	N $_2$	84.9	16.3	2.1	87.5	12.2	<1.0
2400A	N $_2$	83.6	16.2	2.5	88.8	12.3	<1.0
1300A	Ar	78.4	14.7	1.7	89.1	12.4	<1.0
2400A	Ar	81.3	14.8	1.8	84.0	11.5	<1.0

Table II. Weight per cent (w/o) of platinum, silicon, and oxygen found in platinum silicide films annealed at 550°C

Sample identification		Before HF etch			After HF etch		
Pt film	Ambient	Pt	Si	O	Pt	Si	O
1300A	O $_2$	93.1	5.1	2.1	88.9	13.3	<1.0
2400A	O $_2$	96.4	4.7	1.5	84.7	13.2	<1.0
1300A	Air	90.2	8.0	3.7	86.2	13.5	<1.0
2400A	Air	92.3	5.1	2.8	84.6	12.7	<1.0
1300A	N $_2$	86.1	15.2	1.4	88.6	12.8	<1.0
2400A	N $_2$	84.2	14.6	1.2	85.9	12.7	<1.0
1300A	Ar	83.5	15.0	1.8	83.7	13.3	<1.0
2400A	Ar	79.5	14.6	1.5	85.1	12.7	<1.0

Table III. Weight per cent (w/o) of platinum, silicon, and oxygen found in platinum silicide films annealed at 450°C

Sample identification		Before HF etch			After HF etch		
Pt film	Ambient	Pt	Si	O	Pt	Si	O
1300A	O $_2$	93.7	4.4	3.9	88.7	12.7	<1.0
2400A	O $_2$	98.9	3.9	2.8	84.9	12.6	<1.0
1300A	Air	94.2	4.5	2.7	82.1	12.7	<1.0
2400A	Air	94.4	3.7	3.1	83.7	12.2	<1.0
1300A	N $_2$	83.8	16.4	2.7	83.7	13.7	<1.0
2400A	N $_2$	83.8	17.0	1.5	85.6	12.7	<1.0
1300A	Ar	88.8	16.4	1.7	83.4	12.7	<1.0
2400A	Ar	87.1	14.7	1.9	84.2	12.6	<1.0

were found to be essentially the same as for the samples annealed at 650°C, i.e., provided that the annealing time is sufficient, the effect of the various ambients on PtSi formation is unchanged throughout the temperature range studied. In each case, a thin layer of Pt is removed from the surface of the samples annealed in air or O $_2$, while only a slight darkening of the surface is noted after etching samples which were annealed in Ar or N $_2$.

The oxide layer on the surface of the samples annealed in N $_2$ or Ar is probably formed as the hot wafers contact air upon removal from the annealing furnace. This oxide layer, presumed to be SiO $_2$ is about 100Å thick, and is sufficient to protect the underlying PtSi from attack by aqua regia. If the film is first etched in HF, however, removing the protective SiO $_2$ film, then aqua regia etches away the PtSi very rapidly. This result is in agreement with previously reported data on the reactivity of PtSi (18, 19).

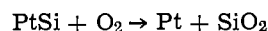
The oxide layer which is formed on the samples annealed in O $_2$ or air is also presumed to be SiO $_2$, but this layer is formed beneath the surface of the Pt film. This is due to the migration of O through the Pt, and its subsequent reaction at the surface of the forming PtSi layer to give SiO $_2$. Extended annealing of the samples does not result in completion of silicide formation, which indicates that the SiO $_2$ is a sufficient barrier to completion of the reaction.

Figures 1 and 2 are electron micrographs of the unreacted Pt film which is removed from the surface of the sample annealed at 650°C in O $_2$ (2400Å Pt). The film is resting on the surface of the PtSi following HF etching of the interlayer SiO $_2$.

Discussion

The model which we propose is that O $_2$ will react at the surface of a PtSi film to form SiO $_2$. The thickness of the SiO $_2$ layer depends upon the time and temperature of exposure to the oxidizing ambient. A 1000Å thick oxide film was grown on the surface of PtSi formed in N $_2$ by subsequent annealing in O $_2$ at 650°C. The film was determined to be SiO $_2$ by IR reflectance spectrophotometry.

The SiO $_2$ layer may result from oxidation of the PtSi or from the reaction of Si atoms which diffuse to the surface of the PtSi film. At this point, either mechanism seems quite reasonable. ΔH_F 298 for the reaction



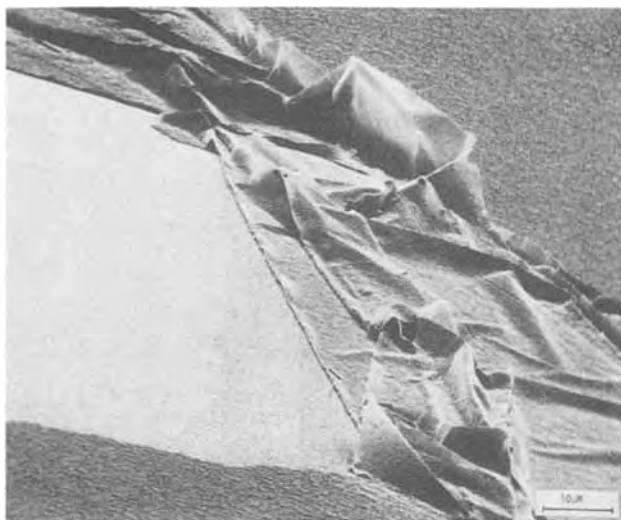


Fig. 1. SEM of Pt film lying on PtSi surface following HF etch

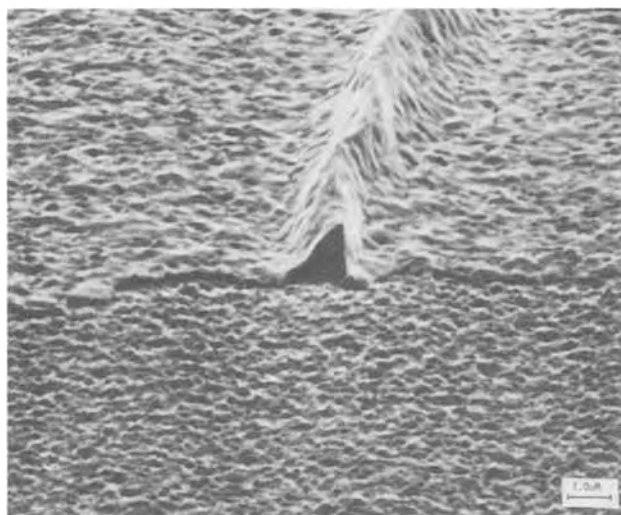


Fig. 2. SEM of Pt film lying on PtSi surface following HF etch

is -211.8 ± 5.5 kcal/mole as calculated from the data of Searcy and Finnie (20, 21). That this reaction does occur at 650°C was verified by forming a PtSi film on a silicon nitride (Si_3N_4) substrate and annealing in O_2 . The PtSi was formed by depositing 1000\AA each of polysilicon and Pt on the Si_3N_4 , then annealing for 15 min in N_2 . Silicide formation was verified by electron microprobe analysis. The sample was then annealed in O_2 at 650°C , and an SiO_2 layer formed on the PtSi surface. Etching of the sample in HF removed the SiO_2 film, and 1000\AA of Pt remained on the Si_3N_4 substrate.

If the reaction of PtSi with O_2 is the mechanism by which the surface SiO_2 layer is formed, then the free Pt which is a product of the reaction must immediately react with silicon atoms which diffuse through the silicide to reform PtSi. This is shown by the fact that repeated oxidation and HF etching of the resultant SiO_2 produces neither free detectable Pt on the surface of the PtSi nor depletion of the PtSi layer, the silicon substrate being an "infinite source" of the Si atoms.

The formation of the SiO_2 layer below the surface of the Pt on the samples annealed in O_2 or air is due to the migration of O through the Pt as the silicide formation occurs. Although diffusion of O through bulk Pt has not been firmly established, surface absorption and migration of O on Pt surfaces has been reported by many authors (22, 23). Annealing in O_2 or air produces the same result because O_2 is preferentially ad-

sorbed upon and not displaced from Pt by nitrogen (24).

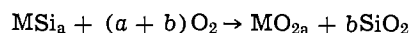
The SiO_2 layer which is formed below the Pt surface is an effective barrier to further silicide formation because it blocks the diffusion of silicon atoms. Oxide layers have been shown to impede silicide formation in other metal films on Si (25). Extended annealing merely results in the formation of a thicker oxide layer. Although the ratio of unreacted Pt to the original sputtered Pt film thickness was relatively constant throughout the range of thicknesses and temperatures studied, this value may vary depending upon the permeability of Pt films prepared by other methods.

In order to confirm that migration of O does occur in the sputtered Pt films, bilayer films of Pt over W (1000\AA each) on Si_3N_4 substrates were annealed at 450° , 550° , and 650°C in O_2 . In each case, the bilayer films disintegrated upon oxidation of the tungsten. Microprobe analysis of fragments of the films confirmed the formation of tungsten oxide. No oxidation or disintegration of the bilayer films was observed when identical samples were annealed in N_2 over the same temperature range.

It does not appear likely that impurities in the annealing furnace ambient are the cause of the surface oxidation of the PtSi films formed in N_2 or Ar. When Pt films on Si were annealed in Ar contaminated with 1-2% O_2 , then incomplete silicide formation resulted, and a layer of unreacted Pt remained on the surface. As in the case of samples annealed in air or O_2 , a layer of SiO_2 formed between the PtSi and Pt, which blocked further silicide formation. It is also improbable that a native oxide on the Si substrates is the source of O which forms the oxide layer between the Pt and PtSi. We have observed the formation of this oxide interlayer only if O_2 is contained in the annealing furnace ambient, or if the Pt films are in contact with O_2 for a period of ~ 150 hr or more prior to annealing in an inert ambient. In the latter case, O_2 which is absorbed by the Pt film prior to annealing is the likely oxygen source.

Hiraki *et al.* (26) report that the amount of SiO_2 grown on the surface of Au films on Si at low temperature is limited due to the diffusion of gold into the silicon. The silicon atoms which are oxidized at the surface of the Au film originate at the Au-Si interface, from which they easily diffuse through the Au film. After all of the Au has interdiffused with the silicon, however, the Au-Si interface no longer exists, and Si diffusion and thus the oxide formation is terminated. In the case of SiO_2 formation on PtSi films on Si, the amount of SiO_2 which may be grown on the surface is not limited in this manner. This is due to the stability of the PtSi film and the preservation of the PtSi-Si interface during oxidation. As much as $10,000\text{\AA}$ of SiO_2 has been grown on the surface of a 2500\AA film of PtSi by successive oxidation and HF etch cycles in order to remove the SiO_2 .

The formation of protective layers of silica on the surface of metal silicides has been frequently cited as the reason for the high oxidation resistance of these materials (18, 19, 27, 28). Reactions of the type



are commonly accepted as the origin of the silica layer, which may also contain the metal oxide. This was found to be true in the case of the oxidation of titanium disilicide (29).

Summary

PtSi is formed by annealing films of Pt on Si. A layer of SiO_2 is formed on the surface of the PtSi by subsequent exposure to O_2 . The thickness of this SiO_2 layer depends upon the time and temperature of formation. The formation of this oxide layer does not result in the formation of a layer of Pt on the surface of the PtSi.

If the Pt films on Si are annealed in air or O_2 , then a layer of SiO_2 is formed at the PtSi-Pt interface prior to completion of the reaction. The O migrates through

the Pt and reacts at the advancing PtSi-Pt interface, and a layer of unreacted Pt remains on the surface. The SiO₂ layer is a sufficient barrier to prevent further silicide formation up to 650°C.

Acknowledgment

The authors wish to acknowledge discussions with J. W. Mayer, and the superior technical assistance of L. Damme and L. Nichols. We also thank L. Garten and L. Fleschner for the micrographs.

Manuscript submitted May 9, 1975; revised manuscript received July 24, 1975. This was Paper 177 presented at the New York, New York, Meeting of the Society, Oct. 13-17, 1974.

Any discussion of this paper will appear in a Discussion Section to be published in the June 1976 JOURNAL. All discussions for the June 1976 Discussion Section should be submitted by Feb. 1, 1976.

Publication costs of this article were partially assisted by Motorola Incorporated.

REFERENCES

- M. P. Lepselter and J. M. Andrews, in "Ohmic Contacts to Semiconductors," B. Schwartz, Editor, p. 159, The Electrochemical Society Softbound Symposium Series, New York (1969).
- M. P. Lepselter and S. M. Sze, *Bell System Tech. J.*, **47**, 195 (1968).
- A. K. Hochberg, in "Transactions: Electronic Materials Processing Conference," p. 81, Materials Research Corp., Orangeburg, N.Y. (1973).
- T. Kawamura, D. Shinoda, and H. Muta, *Appl. Phys. Letters*, **11**, 101 (1967).
- A. K. Sinha, R. B. Marcus, T. T. Sheng, and S. E. Haszko, *J. Appl. Phys.*, **43**, 3637 (1972).
- H. Muta and D. Shinoda, *ibid.*, **43**, 2913 (1972).
- A. Hiraki, M-A. Nicolet, and J. W. Mayer, *Appl. Phys. Letters*, **18**, 178 (1971).
- J. M. Poate and T. C. Tisone, *ibid.*, **24**, 391 (1974).
- M. J. Rand and J. F. Roberts, *ibid.*, **24**, 49 (1974).
- G. A. Walker, R. C. Wnuk, and J. E. Woods, *J. Vacuum Sci. Technol.*, **7**, 543 (1970).
- J. G. Christ and J. N. Ramsey, *IEEE Spectrum*, **69**, 109 (1969).
- S. Danyluk and G. E. McGuire, *J. Appl. Phys.*, **45**, 5141 (1974).
- D. R. Beaman and J. A. Isasi, "Electron Beam Microanalysis," ASTM Publication STP506, Philadelphia Pennsylvania (1972).
- K. F. J. Heinrich, Editor, "Quantitative Electron Probe Microanalysis," National Bureau of Standards Special Publication 298, Washington, D.C. (1968).
- R. A. Wesson, R. P. Phillips, and W. A. Pliskin, *J. Appl. Phys.*, **38**, 2455 (1967).
- A. N. Saxena, *J. Opt. Soc. Am.*, **55**, 1061 (1965).
- J. W. Colby, in "Advances in X-Ray Analysis," Vol. 11, J. Newkirk, G. Mallett, and H. Pfeiffer, Editors, p. 287, Plenum Press, New York (1968).
- R. Wehrmann, in "High Temperature Materials and Technology," I. E. Campbell and E. M. Sherwood, Editors, p. 399, The Electrochemical Society Softbound Symposium Series, New York (1967).
- A. S. Berezhnoi, "Silicon and Its Binary Systems," p. 224, Consultants Bureau, New York (1960).
- A. W. Searcy and L. N. Finnie, *J. Am. Ceram. Soc.*, **45**, 268 (1962).
- JANAF Thermochemical Tables, Dow Chemical Co., Midland, Mich.
- R. Lewis and R. Gomer, *Surface Sci.*, **12**, 157 (1968).
- C. W. Tucker, *J. Appl. Phys.*, **35**, 1897 (1964).
- Y. L. Sandler and D. D. Durigon, *J. Phys. Chem.*, **72**, 1051 (1968).
- J. W. Mayer and K. N. Tu, *J. Vacuum Sci. Technol.*, **11**, 86 (1974).
- A. Hiraki, E. Lugujo, and J. W. Mayer, *J. Appl. Phys.*, **43**, 3643 (1972).
- B. Aronsson, T. Lundstrom, and S. Rund, "Borides, Silicides and Phosphides," p. 10, John Wiley & Sons, Inc., New York (1965).
- J. H. Westbrook, in "High Temperature Technology," p. 113, McGraw-Hill, New York (1960).
- F. N. Schwettman, R. A. Graff, and M. Kolodny, *This Journal*, **118**, 1973 (1971).

Effect of Oxidizing Ambients on Platinum Silicide Formation

II. Auger and Backscattering Analyses

R. J. Blattner and C. A. Evans, Jr.

Materials Research Laboratory, University of Illinois, Urbana, Illinois 61801

and S. S. Lau, J. W. Mayer,* and B. M. Ullrich

California Institute of Technology, Pasadena, California 91125

ABSTRACT

Auger electron spectroscopy combined with ion sputtering for layer removal and MeV ⁴He⁺ ion backscattering spectrometry were used to analyze the depth profile of Pt, Si, and O in platinum silicide layers. Layers formed during heat-treatment at 600°C in an O₂ ambient consisted of an outer layer of Pt on an SiO₂ layer on PtSi. The structure formed in an N₂ ambient followed by heat-treatment in an O₂ ambient consisted of PtSi. In both cases there was a thin SiO₂ layer on the outer surface; in the latter case the SiO₂ layer was appreciably thicker.

The formation of silicide layers has been studied in detail because of their importance in integrated circuit technology. The process steps of evaporation of a metal layer on Si and subsequent heat-treatment to form the

metal-silicide layers are easily adapted to device production. A number of analytical techniques have been used to determine the elemental composition as a function of depth, for phase identification, and to provide structural information. For example, Auger electron spectroscopy (AES) combined with layer removal by ion sputtering provides in-depth composition profiles

* Electrochemical Society Active Member.

Key words: Auger electron spectrometry, MeV ion backscattering spectrometry, silicon and thin films.

(1-3). Similar data, but without recourse to ion sputtering, are provided by MeV $^4\text{He}^+$ ion backscattering spectrometry (BS) (4-6). Glancing angle x-ray diffraction is used for phase identification and structural information (7) and is often employed (8, 9) with AES or BS techniques for composition analysis.

In most studies of silicide formation, heat-treatments are carried out in vacuum or in inert ambients. Under these conditions silicide layers of uniform thickness and composition can be formed (5, 8, 10). For example, low temperature annealing (200°C) of Pt layers on Si produces a Pt_2Si compound (11). Upon further annealing of this Pt_2Si structure for either longer times or at higher temperatures, additional Si is consumed to produce a PtSi compound (6).

In the preceding paper, Kingzett and Ladas (12) studied the influence of oxidizing ambients on platinum silicide formation using the electron microprobe for analysis. This method provides an average analysis over depths of 1000Å or more in PtSi. The purpose of the present study was to utilize Auger electron spectroscopy and MeV $^4\text{He}^+$ ion backscattering to directly measure in-depth composition profiles as suggested by the study of Behrisch *et al.* (13). Backscattering analysis gives absolute depth scales and quantitative compositional data without the requirement of standards. Auger electron spectroscopy provides surface layer analysis and relative concentration of the elemental constituents *vs.* sputtering time. In the present case, Auger analysis is more sensitive to oxygen than backscattering.

Experimental

Sample preparation.—The samples were prepared by Kingzett and Ladas as described in the preceding paper (12).

Auger electron spectroscopy and backscattering spectrometry were used to evaluate the structures resulting from two different annealing procedures for silicon single crystal wafers having a 2000Å surface layer of evaporated platinum. The first procedure was to anneal the as-evaporated samples for 20 min in N_2 at 600°C followed by a 10 min postanneal in O_2 at 600°C. The second procedure was a 30 min anneal of the as-evaporated samples in O_2 at 600°C. Four 3 in. wafers were simultaneously prepared for each annealing procedure. After heat-treatment, two wafers of each type were provided to the AES and BS laboratories, respec-

tively. Duplicate analyses for the redundant wafers provided to each laboratory gave similar results. Therefore, it was assumed that similarly prepared samples were identical and no interchange of samples was made between laboratories.

Backscattering spectrometry.—The experimental setup at the California Institute of Technology and analytical method for backscattering spectrometry have been reviewed elsewhere (14). In brief, the technique consists of placing a sample in a beam of mono-energetic helium ions and energy analyzing the particles backscattered out of the sample. Backscattering spectrometry with MeV $^4\text{He}^+$ ions provides information on concentration profiles with a depth resolution of about 200Å for layers as thick as 5000Å. With thicker films the depth resolution degrades due to energy straggling of the probing particles in the film. The beam spot is typically 1-2 mm², and hence backscattering requires lateral sample homogeneity of at least such dimensions.

Auger electron spectroscopy.—A Physical Electronics Model 545 scanning Auger microprobe at the University of Illinois was used for all Auger electron spectroscopic measurements. The samples were mounted on the standard carousel at 30° grazing incidence to the primary electron beam. The sample chamber residual vacuum was $<1 \times 10^{-9}$ Torr prior to all analyses. Primary electron energies of 6 keV were employed in both the depth profiling and imaging modes. Depth profiles were made by repetitively monitoring the Pt, O, and Si Auger transitions with simultaneous 2 keV Ar^+ ion sputtering for removal of successive atomic layers.

Results and Discussion

Platinum silicide (PtSi) postannealed in O_2 atmosphere.—A sample of PtSi/Si previously formed in N_2 at 600°C for 20 min was postannealed in O_2 at 600°C for 10 min. Surface AES spectra taken prior to ion etching and the AES depth profile of Fig. 1A both indicate Pt depletion at the film surface and the presence of a substantial amount of O and Si. Using the AES data and a sputtering rate determined from the known PtSi thickness, this Pt depleted region is calculated to have a thickness of about 140Å.

Scanning Auger electron micrographs of the surface (Fig. 2) show that there are islands of PtSi surrounded by SiO_2 . The fact that the Si is actually present as SiO_2

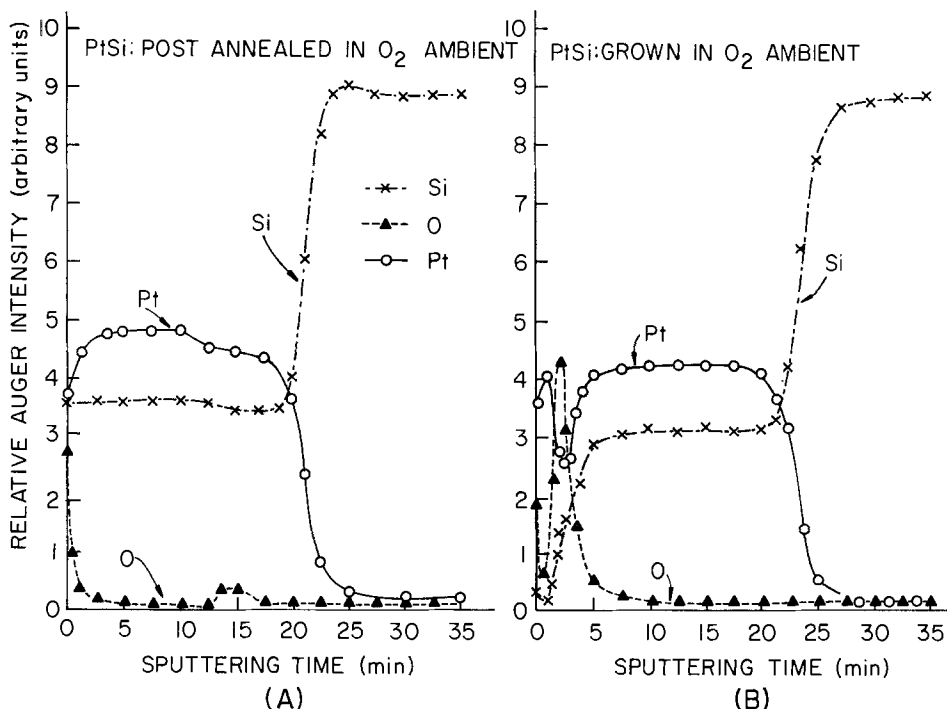


Fig. 1. (A) Pt, Si, and O Auger intensities vs. sputtering time from PtSi grown for 20 min in N_2 at 600°C followed by 10 min anneal in O_2 at 600°C. (B) Pt, Si, and O Auger intensities vs. sputtering time from PtSi grown for 30 min in O_2 at 600°C. (Note that for both Auger depth profiles data points were taken about 1 min apart. Only representative points are shown on the graphs for clarity.)

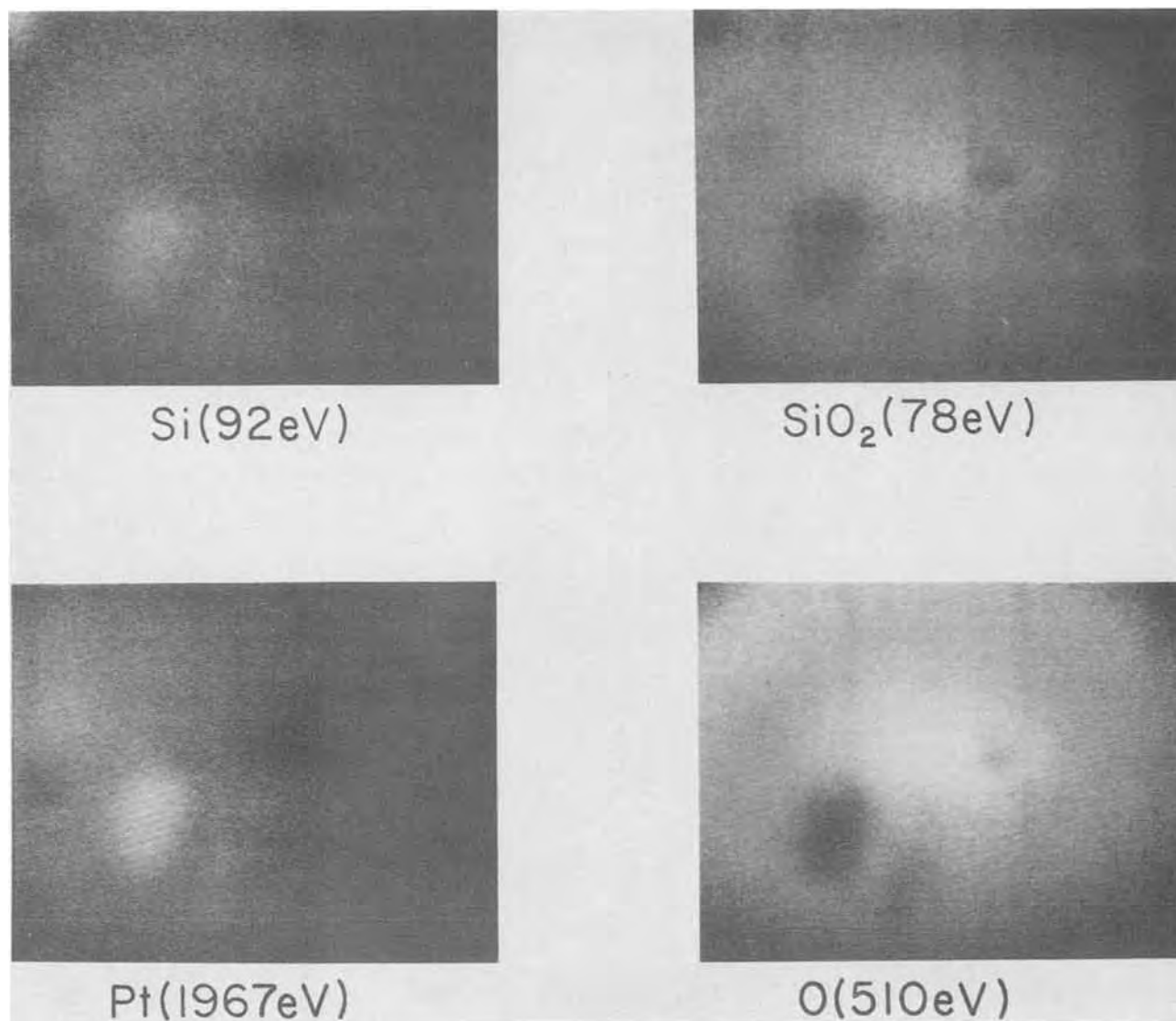


Fig. 2. Scanning Auger micrographs of Si (92 eV), Si (78 eV from SiO₂), Pt (1967 eV), and O (510 eV) taken at 300X for surface of PtSi postannealed in O₂ ambient (same sample as Fig. 1a).

is confirmed by using the Si 78 eV transition which has been shown to arise from a "chemical" spectral energy shift when Si is present as SiO₂ (15).

The backscattering data for similar samples are shown in Fig. 3. The broad peak at high energies centered around 1.7 MeV represents the Pt signal and the broad plateau centered at 1 MeV represents the Si signal from the PtSi layer. The increase in the Pt signal with decreasing energy reflects the change in scattering and stopping cross sections experienced by the analyzing particles (14). Using the measured backscattering yields for Pt and Si, the atomic ratio of Pt to Si is determined to be 1 ± 0.1 across the entire film indicating that the compound PtSi is formed. The data of Fig. 3 show that the silicide layer is uniform in composition with a thickness (assuming bulk density) of 3000 Å. For the energy-to-depth conversion, (14), the compilation of Ziegler and Chu was used (16).

Backscattering data in Fig. 3 do not directly indicate the presence of a thin SiO₂ layer at the surface. However, having determined the existence of the thin SiO₂ layer by AES, very careful scrutiny of the BS spectrum suggests a barely perceptible rounding of the high energy edge of the Pt signal. This would indicate the presence of nonuniform surface layers of an energy-absorbing nature (presumably SiO₂). Tilting the sample by 60° with respect to the beam and hence doubling the effective thickness of the silicide layer produces an even more pronounced rounding of the high energy

edge. This observation may have been overlooked had the Auger data not been available. From the backscattering data alone, we cannot assign a layer thickness to the SiO₂.

The BS data in Fig. 3 show that the changes in the absolute level of the Pt and Si Auger intensities (see Fig. 1A) are probably due to an instrumental artifact since the Pt and Si intensity ratio as determined by BS and AES is constant within experimental error ($\pm 5\%$) throughout the PtSi layer. The Auger data indicate a small but real oxygen contamination in the PtSi layer. Sensitivity limitations prevent backscattering spectrometry from confirming or denying this observation.

Platinum silicide (PtSi) reacted in O₂ atmosphere.—A sample with 2000 Å of Pt on single crystal Si was reacted at 600°C in an O₂ atmosphere for 30 min. The resultant structure was characterized by AES depth profiling and backscattering spectrometry. AES surface spectra and the complete depth profile (Fig. 1B) revealed a very thin (< 50 Å) layer of Si and O, presumably SiO₂. Scanning Auger micrographs of this surface oxide region showed no lateral compositional inhomogeneities within the resolution limits of the instrument (5–10 μm). Below this superficial layer, there is a 120 Å thick platinum-rich layer calculated using a sputtering rate determined from the known PtSi thickness. Below this Pt-rich region AES data indicated a Pt-depleted, Si- and O-rich layer, pre-

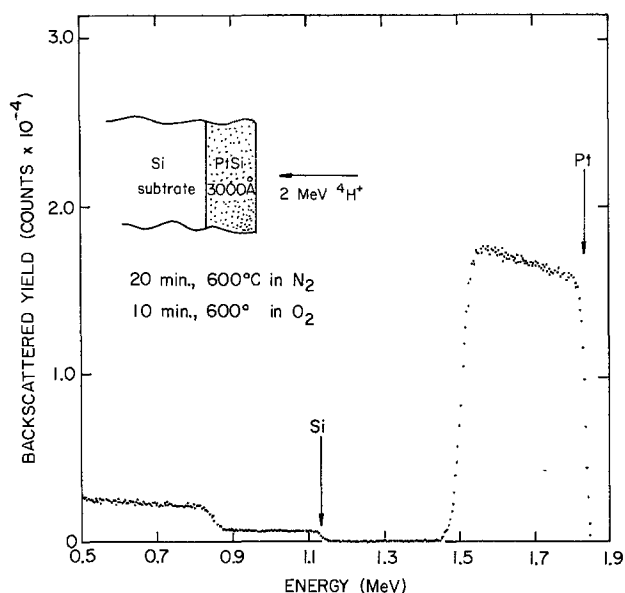


Fig. 3. Backscattering energy spectrum for a sample of Pt/Si annealed at 600°C in N₂ for 20 min and then in O₂ for 10 min.

sumably containing some SiO₂. The Pt intensities did not go to background levels, suggesting this region contains a mixture of PtSi and SiO₂. In a similar manner as before, this region is calculated to be about 200Å thick. The bulk of the reacted film consists of a uniform distribution of Pt and Si. The Pt/Si Auger intensity ratio is the same as for the PtSi film discussed above within $\pm 5\%$. It was not possible to use the chemically shifted 78 eV SiO₂ peak to determine that the Si and O present in this sample occurred in this chemical form because of a spectral interference from the very intense and broad Pt peak at 64 eV. As shown in Fig. 1B, a large amount of Pt was present throughout the layer.

The backscattering spectrum for a similar sample as that analyzed in Fig. 1B, is shown in Fig. 4. The thin peak at the high energy edge of the Pt signal indicates the presence of unreacted Pt. The width of this peak corresponds to a thickness of 160Å. The leading edge of the Si signal is shifted to a lower energy indicating that the outer surface is essentially Si-free. The valley

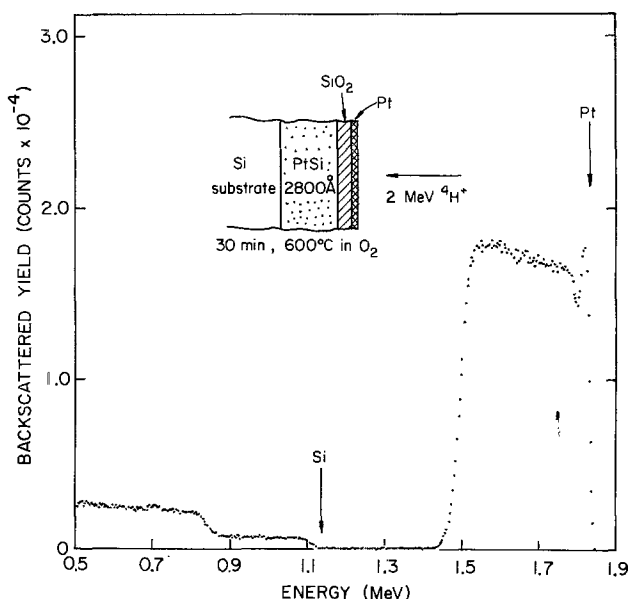


Fig. 4. Backscattering energy spectrum for a sample of Pt/Si grown for 30 min in O₂ at 600°C.

PtSi POST-ANNEALED IN O₂ AMBIENT

PtSi FORMED IN O₂ AMBIENT

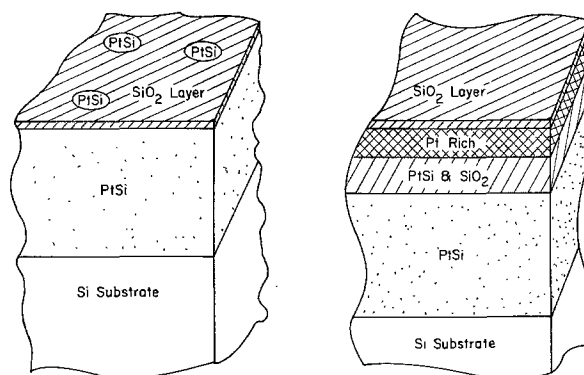


Fig. 5. Schematic representation of the influence of annealing ambients on the composition of PtSi layers. (Not to scale.)

between the thin peak and the broad plateau of the Pt signal represents the presence of an energy-absorbing layer. If the layer is SiO₂, as indicated by Fig. 1B, it would have an average thickness of 400Å. Under tilting conditions which double the effective layer thickness, the valley signal did not drop to the background level, indicating that the SiO₂ layer is nonuniform in thickness. Underneath the surface layers, there is a uniform layer with a Pt to Si ratio of 1 ± 0.1 . The thickness of the PtSi layer is 2800Å.

Backscattering analysis of samples annealed in O₂ at temperatures between 400° and 700°C all revealed essentially the same features as that shown in Fig. 4. There is a thin layer of Pt ($\lesssim 200\text{Å}$ thick) separated from the PtSi by a thin layer of SiO₂. Although the thickness of the unreacted Pt layer is relatively unchanged, the oxide layer increases in thickness with increasing annealing temperature.

Summary

The results of this work confirm the general composition features deduced by Kingzett and Ladas in the preceding paper. The results of the analysis are shown schematically in Fig. 5. The most pronounced difference between annealing in N₂ and in O₂ ambients is the formation in the latter case of a layer of SiO₂ between PtSi and unreacted Pt.

The comparison of Auger electron spectrometry and backscattering spectrometry points out the merits of using both techniques for the analysis of layered structures. Although backscattering provides a depth scale and composition ratio, it is not sensitive to the presence of oxygen. Auger data requires calibration with samples of known thickness and composition for quantitative depth profiling. Layer erosion rates, for example, are sensitive to the ion beam parameters as well as the target composition itself.

Acknowledgment

The work at Materials Research Laboratory is supported in part by the National Science Foundation Grants MPS 74-05745 and DMR 72-03026, and that at Caltech is supported by Air Force Cambridge Research Laboratories (D. E. Davies). We take pleasure in acknowledging discussions with our colleagues M-A. Nicolet, T. Kingzett, and C. Ladas.

Manuscript submitted May 9, 1975; revised manuscript received Aug. 12, 1975.

Any discussion of this paper will appear in a Discussion Section to be published in the June 1976 JOURNAL. All discussions for the June 1976 Discussion Section should be submitted by Feb. 1, 1976.

Publication costs of this article were partially assisted by the University of Illinois.

REFERENCES

1. G. Y. Robinson, *Appl. Phys. Letters*, **25**, 158 (1974).
2. J. M. Morabito and M. J. Rand, *Thin Solid Films*, **22**, 293 (1974).
3. S. Danyluk and G. E. McGuire, *J. Appl. Phys.*, **45**, 5141 (1974).
4. J. F. Ziegler, J. W. Mayer, C. J. Kircher, and K. N. Tu, *ibid.*, **44**, 3851 (1973).
5. K. E. Sundstrom, S. Petersson, and P. A. Tove, *Phys. Status Solidi (a)*, **20**, 653 (1973).
6. J. M. Poate and T. C. Tisone, *Appl. Phys. Letters*, **24**, 391 (1974).
7. R. Feder and B. S. Berry, *J. Appl. Cryst.*, **3**, 372 (1970).
8. J. W. Mayer and K. N. Tu, *J. Vacuum Sci. Technol.*, **11**, 86 (1974).
9. S. S. Lau, W. K. Chu, J. W. Mayer, and K. N. Tu, *Thin Solid Films*, **23**, 205 (1974).
10. J. A. Borders and S. T. Picraux, *Proc. IEEE*, **62**, 1224 (1974).
11. H. Muta and D. Shinoda, *J. Appl. Phys.*, **43**, 2913 (1972).
12. T. Kingzett and C. Ladas, *This Journal*, **122**, 1729 (1975).
13. R. Behrisch, B. M. U. Scherzer, and P. Staib, *Thin Solid Films*, **19**, 57 (1973).
14. W. K. Chu, J. W. Mayer, M-A. Nicolet, T. M. Buck, G. Amsel, and F. Eisen, *ibid.*, **17**, 1 (1973).
15. C. C. Chang, in "Characterization of Solid Surfaces," P. F. Kane and G. R. Larrabee, Editors, Plenum Press, New York (1974).
16. J. F. Ziegler and W. K. Chu, *At. Nucl. Data Tables*, **13**, 463 (1974).

Technical Notes



Silicon Nitride Ledge Removal Techniques for Integrated Circuit Devices

V. D. Wohlheiter*

Western Electric Company, Allentown, Pennsylvania 18103

In order to reduce the silicon area of integrated circuit chips and potentially improve device yield, a non-reoxidized emitter (1) can be utilized. Specifically, a silicon dioxide layer is not grown on the emitter window after the emitter diffusion. However, the combination of this design procedure and the dual dielectric sealed junction technology (2) causes an undesirable silicon nitride overhang to be created. These ledges, if not removed, can manifest reliability problems for all metallization techniques. The scope of this paper is confined to the effects of the dielectric ledges on the titanium-platinum-gold metallization system. This particular overhang was associated with device failures which occurred during the life testing at 325°C. The purpose of this paper is to discuss both the successful and unsuccessful techniques investigated for removing the overhanging dielectric thereby eliminating the resulting integrated circuit failure mode and making the nonreoxidized emitter a reliable design and manufacturable process.

Creation of the Overhanging Dielectric

The mask for the device contact window was formed in the silicon nitride by conventional etching in boiling phosphoric acid using a pattern generated in a layer of CVD silicon dioxide or photoresist on the silicon nitride. The silicon nitride was deposited at 910°C in a diffusion furnace and meets the requirement previously reported (3). However, due to the relative chemical inertness of the silicon nitride film to the fluoride etching solution used to remove the underlying thermal silicon dioxide layers during the contact window opening, a ledge is created as illustrated in Fig. 1 and the actual SEM in Fig. 2. If these ledges are not removed, this structure combined with the gold metallization system can allow a gold-silicon alloy under elevated temperature to form which causes a shorted p-n junction. The dotted lines on Fig. 3 indicate the

extent of the gold migration in the contact window. The typical failures appear as gold discolorations in the contact areas.

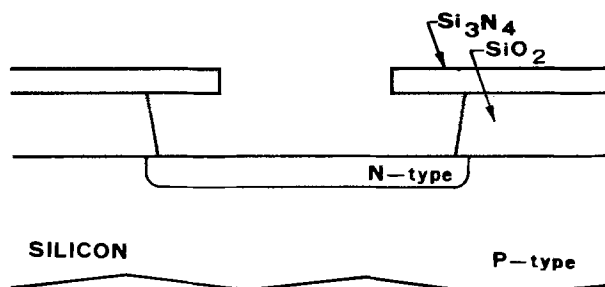


Fig. 1. Silicon nitride ledge in a device structure

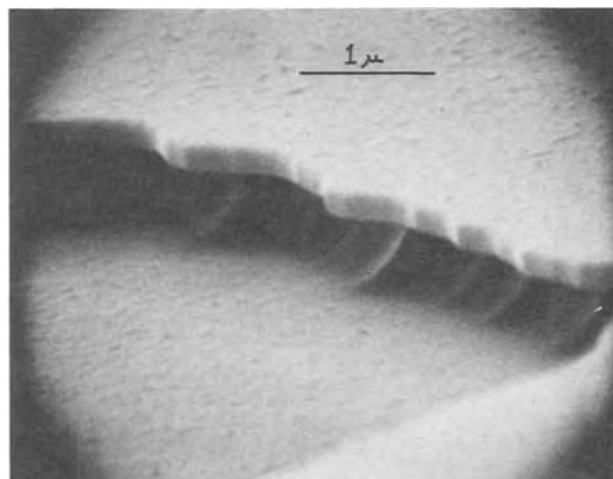


Fig. 2. SEM micrograph illustrating the ledge

* Electrochemical Society Active Member.

Key words: silicon nitride, ledges, reliability, etching, dielectric, nonreoxidized emitter.

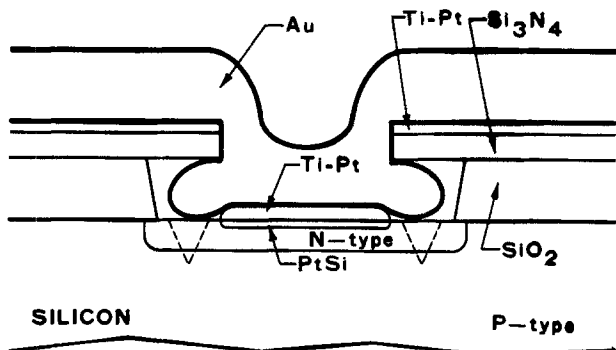


Fig. 3. Cross section of a contact illustrating the potential for gold alloying.

Experimental Methods to Remove the Ledge

In this study, three basic methods were investigated to reduce or eliminate the dielectric overhang. They were metal masking, thin dielectric with mechanical abrasion, and dielectric thinning. The following paragraphs describe these processes.

Metal masking for ledge removal.—An inert metal was used to mask the top of the dielectric and permit the removal of the overhang by etching from beneath (4). Since the deposition of the inert metal is rather unidirectional, the underside portion of the ledge remains unprotected by metal. By prolonged etching in phosphoric acid, the underside silicon nitride overhang will be attacked and the ledge removed. This method also permits the original thickness of dielectric to be maintained. Since platinum was compatible with the beam lead technology, it was chosen as the masking metal.

However, the results were somewhat unexpected. During the sputtering of platinum, some platinum silicide began to form in the contact window before any other heat-treatment. Upon subjecting the wafers to a sufficient amount of time in boiling $180^{\circ}\text{C} \pm 3^{\circ}\text{C}$ phosphoric acid to remove the overhang, it was noted that some undermining of silicon occurred. This has been illustrated in Fig. 4, and the actual contact structure is shown in Fig. 5. Upon further investigation, it appeared that this attack of the silicon is occurring at the platinum silicide-silicon interface. Since any metal masking technique requires several extra and elaborate processing steps to be added in the device fabrication, this technique was abandoned as a method to remove dielectric ledges for a more cost feasible method. Other inert metals were not investigated for the latter reason.

Thin dielectrics.—Since a 500Å silicon nitride film remains a significant barrier to sodium and also possesses junction sealing capability, it was used in place of the standard 2000Å thick layer. It was expected that the ledge would be abraded away by processing with a mechanically applied force. However, the 500Å silicon nitride film remained intact even after an agitation

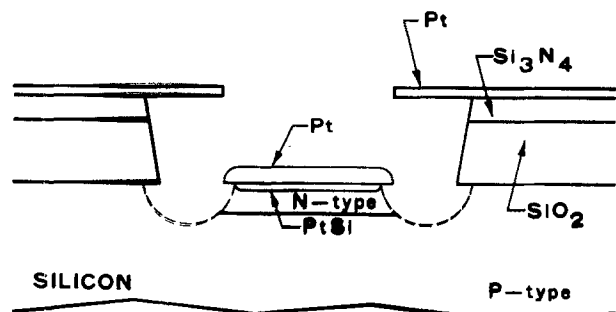


Fig. 4. Preferential etch of silicon-platinum silicide interface

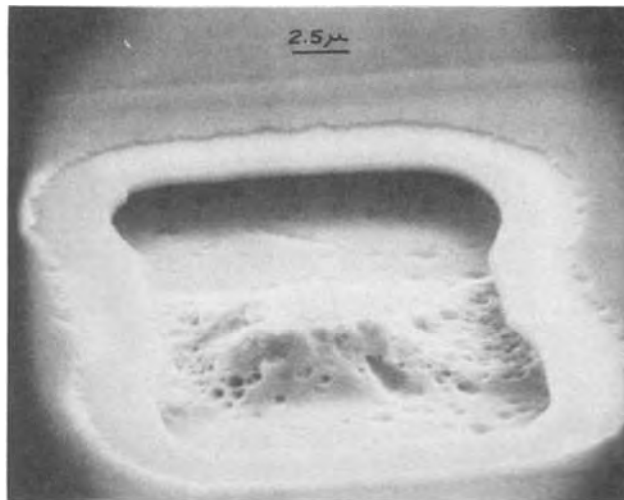


Fig. 5. SEM micrograph illustrating the etched interface

in the etching solution (BHF) for the underlying layer of silicon dioxide. The overhanging ledge was clearly able to withstand the further stresses of water rinsing and spin drying. The condition of the film remained unchanged even after ultrasonic agitation in water and nonionic detergent mixture to insure proper wetting of the sample.

Mechanical abrasion of silicon nitride.—This technique suggested the use of the 500Å thick silicon nitride and removing it by processing it through an automatic silicon wafer scrubbing machine. Figure 6 shows silicon nitride debris clinging to the walls or edges of the contact holes. Ultrasonic cleaning was not normally successful in removing this debris but etching in phosphoric acid after scrubbing produced a clean ledge-free edge as shown in Fig. 7. This method was successful in removing the silicon nitride ledge in some areas, however, variation of breakage across the wafer and lot to lot variables inhibited full adoption as a manufacturable technique.

Dielectric thinning.—A ledge approximately 2000Å thick is created as outlined above. It was then intended to sacrifice one-half of this layer in order to eliminate this ledge (5). The overhang is eliminated by etching since it is attacked from both the top and bottom surfaces. The high temperature phosphoric acid utilized to etch the silicon nitride did cause localized plating of copper or antimony on the heavily doped n-type silicon in the emitter contact windows (6). Attempts were made to passivate the exposed silicon by regrow-

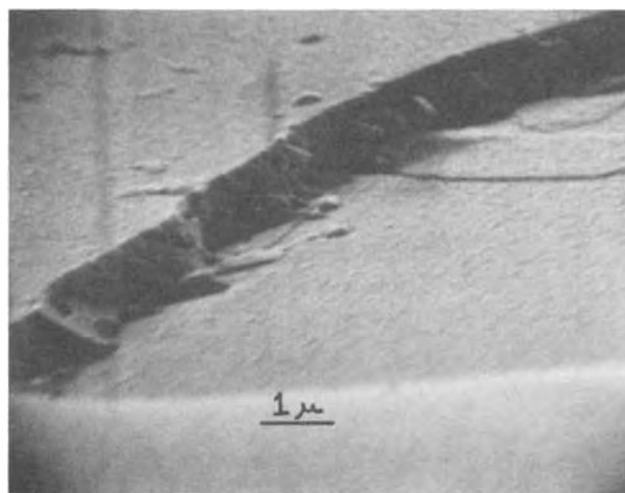


Fig. 6. SEM micrograph of silicon nitride (500Å) ledge after mechanical scrubbing.

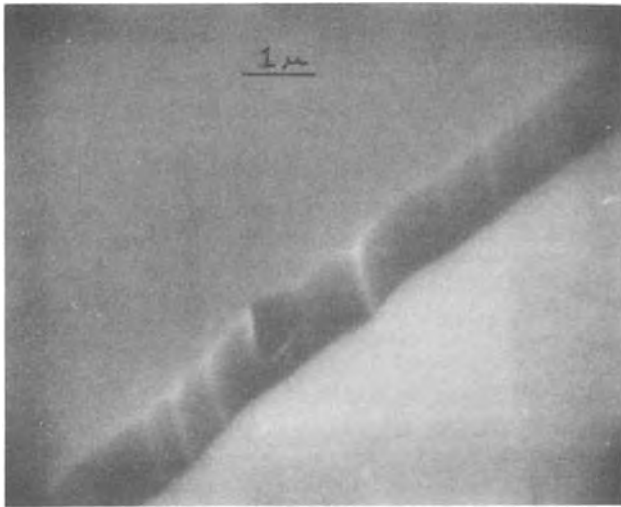


Fig. 7. SEM micrograph of scrubbing debris removed by phosphoric acid.

ing a thin steam oxide in the contact windows. It was found that although the n^+ silicon areas could be protected by reoxidation, the silicon nitride ledge was not always removed during an appropriate time in the phosphoric acid. The silicon nitride etching after the thermal oxidation heat-treatment was erratic, and several minutes were sometimes required in the etchant before the attack would commence. It was presumed that the steam reoxidation treatment converted a thin layer of silicon nitride to silicon dioxide or to an oxynitride that has a significantly reduced etching rate in the phosphoric acid. A similar reaction has been reported by Appels (7) who observed the conversion of approximately 500Å of silicon nitride to silicon dioxide during a 9 hr steam oxidation at 1000°C.

A chemical mixture (8) of concentrated sulfuric acid and phosphoric acid was suggested for etching the silicon nitride that would also, at the same time, effectively passivate the exposed n^+ silicon surfaces. This method oxidized the silicon surface and prevented attack by the phosphoric acid. This etchant mixture was found to be more successful in preventing the selective plating on n^+ silicon and exhibited the same etching rate on silicon nitride as 100% phosphoric acid. While phosphoric acid without the sulfuric acid additive also does reduce plating of n^+ silicon to a significant extent in 160°C, the addition of sulfuric acid is recommended. No plating is apparent on the silicon as can be seen in Fig. 8, and the silicon nitride ledge has been completely removed. The structure shown in Fig. 8 has



Fig. 8. SEM micrograph of a contact window with ledge removed

been etched in a 10% sulfuric acid mixture in phosphoric acid boiling at 160°C. Reliable ledge removal is achieved with a furnace silicon nitride system and the proper control of the temperature of the phosphoric acid.

Testing of Thinned Dielectric

To investigate the adverse effect, if any, on the thinned silicon nitride properties, test samples of silicon nitride were deposited on chemically clean, 10 ohm-cm, $\langle 111 \rangle$ oriented, polished silicon wafers to thicknesses of $2000\text{Å} \pm 200\text{Å}$ and $1000\text{Å} \pm 100\text{Å}$. The thicknesses were measured with a spectrophotometer. The 1000Å group of silicon nitride was used as the control. The half of the lot with 2000Å of silicon nitride was etched in phosphoric acid to one-half the original thickness while the control remained unetched. Forty-eight aluminum dots, 20 mil in diameter, were evaporated on the surface of the test wafers to form capacitors with silicon nitride as a dielectric. The wafers were subjected to electrical testing which consisted of ramping the voltage and observing the point at which the capacitor exhibited excessive current exceeding $10\ \mu\text{A}$ and below 50V indicating premature breakdown. A calculated value of breakdown voltage for a silicon nitride film of 1000Å is 50-100V. Silicon nitride is reported to have a dielectric field strength of $0.5-1 \times 10^7\ \text{V/cm}$ (9). The voltage distributions are plotted in Fig. 9 for etched and unetched silicon nitride. The over-all conclusion which can be drawn from these data is that the etched film does remain pinhole-free with adequate dielectric properties for use in beam lead sealed junction integrated circuits. The 10% difference at the 90% point between the etched and unetched can be explained by some variation of the etch rate used for the silicon nitride. Based upon these results, the thinning of silicon nitride can be utilized without fear for loss of film quality. In addition to these breakdown voltage tests, radioactive sodium penetration tests (10) were conducted to evaluate the integrity of the etched film. The results indicated that the thinned silicon nitride continued to act as a sufficient barrier to Na^{++} .

Conclusion

In order to minimize the use of silicon area in device layout and to improve performance, a nonreoxidized emitter structure can be utilized. However, to couple this technique with the dual dielectric, sealed junction technology, it is necessary to eliminate an overhanging dielectric created during processing. The ledge com-

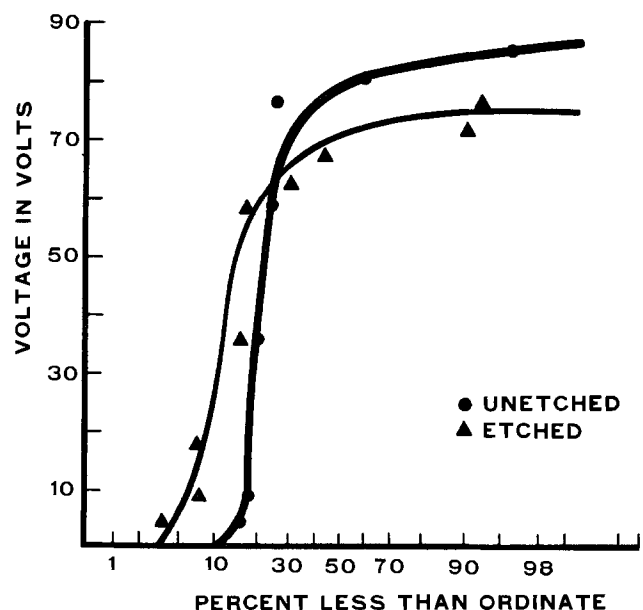


Fig. 9. Breakdown voltage distribution of etched and unetched silicon nitride.

bined with the described metallization can manifest itself as the cause of failures during accelerated aging.

Several types of ledge removal techniques, both successful and unsuccessful, were discussed, which included metal masking, mechanical abrasion, and dielectric thinning.

The most successful method for the removal of silicon nitride was by dielectric thinning. By thinning the dielectric to one-half its original thickness, the ledge is completely eliminated since the etchant, which is a mixture of phosphoric and sulfuric acids, attacks both the top and the bottom of the overhang. Additionally, mechanical damaging of the ledge with a wafer scrubber followed by a short phosphoric acid dip can result in removal of the ledge in certain areas. However, the repeatability of the process was less than adequate.

Acknowledgment

The author is grateful for the technical discussions with H. J. Patterson and H. A. Tooker of Western Electric; also with V. E. Hauser and P. T. Panousis of Bell Laboratories. The SEM micrographs were provided by J. A. Radosevich.

Manuscript submitted Oct. 4, 1974; revised manuscript received Aug. 6, 1975. This was Paper 72 presented at the Chicago, Illinois, Meeting of the Society, May 13-18, 1973.

Any discussion of this paper will appear in a Discussion Section to be published in the June 1976 JOURNAL. All discussions for the June 1976 Discussion Section should be submitted by Feb. 1, 1976.

Publication costs of this article were partially assisted by the Western Electric Company.

REFERENCES

1. L. Stern, "Fundamentals of Integrated Circuits," p. 65, Hayden Book Company, Inc., New York (1968).
2. M. P. Lepselter, *Bell System Tech. J.*, **45**, 233 (1966).
3. V. D. Wohlheiter and R. A. Whitner, *This Journal*, **119**, 7 (1972).
4. R. E. Caffrey, A. C. Dumbri, and R. N. Tauber, U.S. Pat. 3,808,069 (1974).
5. J. A. Appels and M. M. Paffen, *Phillips Res. Rept.*, **26**, 164 (1971).
6. V. C. Garbarini, V. E. Hauser, M. J. Rand, and B. Leon, Paper 19RNP presented at Electrochemical Society Meeting, San Francisco, California, May 12-17, 1974.
7. J. A. Appels *et al.*, *Phillips Res. Rept.*, **25**, 119 (1970).
8. P. T. Panousis and H. A. Waggener, U.S. Pat. 3,715,249 (1973).
9. J. T. Milek, "Silicon Nitride for Microelectronics Applications," Part 1, IFI/Plenum Data Corp., New York (1971).
10. J. V. Dalton and J. Drobek, *This Journal*, **115**, 865 (1968).

Calculations of the S_2 and Se_2 Partial Pressure and the ZnS-CdS and ZnSe-CdSe Sublimation Point Diagrams

Warren P. Heim¹ and Kenneth A. Jones

Thayer School of Engineering, Dartmouth College, Hanover, New Hampshire 03755

It is frequently assumed that the only sulfur and selenium molecular specie in the vapor in equilibrium with their II-VI compounds is the dimer. We wanted to determine the temperature range for stoichiometric CdS, ZnS, CdSe, and ZnSe, and their composition range at different temperatures for which the assumption is valid. We did this by plotting curves of the total pressure for a given dimer pressure as a function of temperature, and superimposing the partial dimer pressures in equilibrium with stoichiometric CdS, ZnS, CdSe, and ZnSe that were calculated assuming that the vapor was composed only of dimers.

These plots are shown in Fig. 1 (sulfur) and 2 (selenium). The integers (-5 to 2) on the right-hand side are the powers of the fixed dimer pressures, e.g., $2 = 10^2$ Torr. Since in the regions where the $\log P$ vs. T curves are horizontal the total pressure equals the dimer pressure, it can be seen that the assumption is valid for CdS up to $\sim 1400^\circ\text{K}$, for all temperatures that are shown for ZnS, for CdSe up to $\sim 1200^\circ\text{K}$, and for ZnSe up to $\sim 1700^\circ\text{K}$. In all instances the limitation is due to the formation of molecules containing more than two atoms at the higher pressures. A significant contribution to the total pressure from the monomers occurs only at the highest temperatures and lowest pressures. It can also be seen that if the assumption is valid for the stoichiometric composition it is valid for all practical excess cation concentrations and is valid over a larger excess anion range at lower temperatures.

The P vs. T curves for a fixed dimer pressure, P_2 , were calculated using the equations

¹ Present address: Gulf Oil Company, P.O. Box 199, Dupont, Washington 98327.

Key words: sulfur, selenium, wurtzite, II-VI compounds.

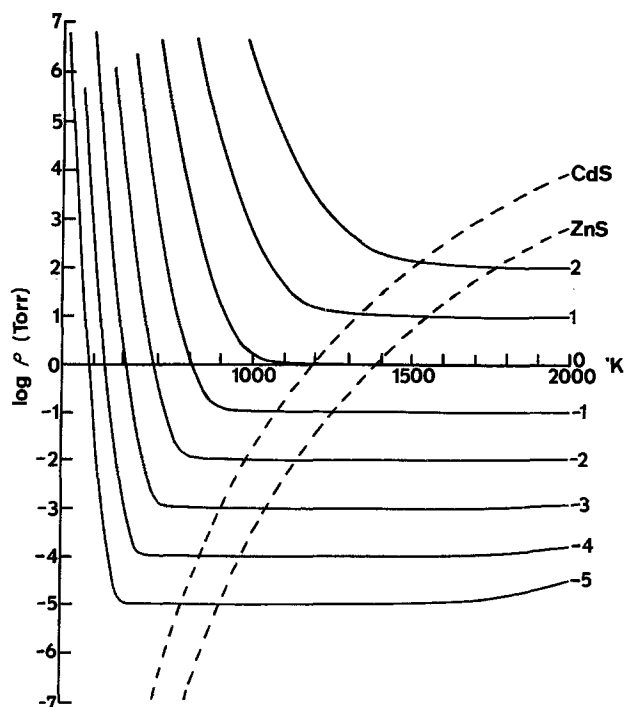


Fig. 1. The S_2 sulfur partial pressures in equilibrium with stoichiometric CdS and ZnS superimposed on a diagram of the log of the total sulfur pressures for different S_2 pressures plotted as a function of the temperature ($^\circ\text{K}$).

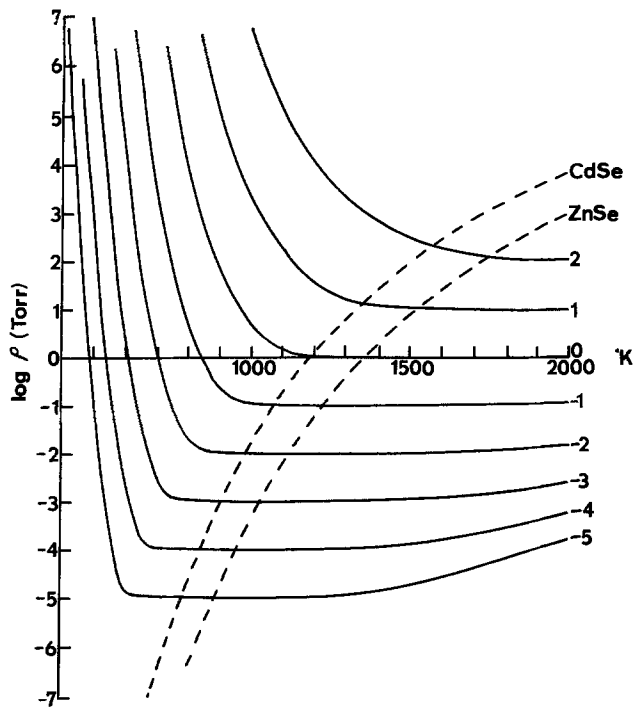


Fig. 2. The Se_2 selenium partial pressures in equilibrium with stoichiometric CdSe and ZnSe superimposed on a diagram of the log of the total selenium pressures for different Se_2 pressures plotted as a function of the temperature ($^{\circ}K$).

$$\ln K_n = -\frac{\Delta H_n}{RT} + C_n$$

$$P_n = (K_n P_2)^{n/2}$$

$$P = \sum P_n$$

where $n = 1-8$ is the number of atoms in the molecule. The sulfur data listed in Table I are from Berkowitz and Marquart (1) and the selenium data are from Berkowitz and Chupka (2). The heat of formation of Se_4 and the corresponding constant, C_4 , were not experimentally determined by them so we estimated their values from a plot of ΔH vs. n as was suggested by them. The partial pressures of S_2 and Se_2 in equi-

Table I. The heats of reaction, ΔH_n , and the integration constants, C_n , for the reactions $S_2 \rightarrow \frac{2}{n} S_n$ and $Se_2 \rightarrow \frac{2}{n} Se_n$ where n is an integer from 1 through 8

n	Sulfur		Selenium	
	ΔH_n kcal/ mole S_2	C_n (atm) $\frac{2-n}{n}$	ΔH_n kcal/ mole Se_2	C_n (atm) $\frac{2-n}{n}$
1	101.0	15.5	71.6	11.90
2				
3	-8.5	-6.0	-8.6	-6.27
4	-13.3	-7.52	-13.3	-7.42
5	-17.8	-9.46	-18.0	-8.57
6	-21.4	-11.36	-21.7	-11.40
7	-21.9	-11.82	-22.4	-11.81
8	-23.5	-12.97	-23.1	-12.50

Table II. The heats of sublimation, ΔH_s , and the integration constants, C_s , for the compounds CdS, CdSe, ZnS, and ZnSe

Compound	ΔH_s kcal/mole	C_s (atm)
CdS	78.0	16.5
CdSe	76.3	16.0
ZnS	87.5	15.7
ZnSe	86.6	15.8

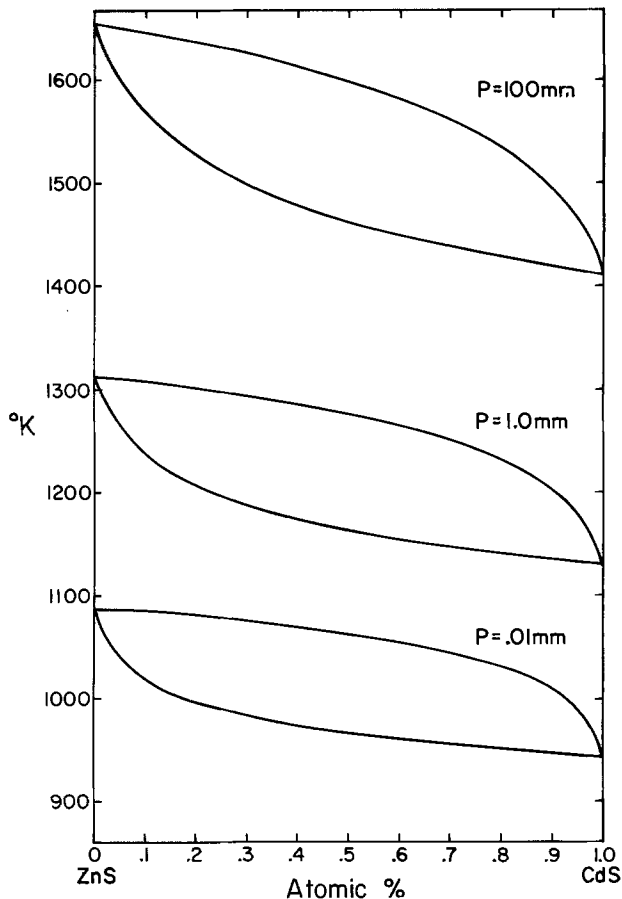


Fig. 3. The calculated sublimation point diagram for an ideal CdS-ZnS solid solution at total pressures of 10^2 , 1, and 10^{-2} Torr.

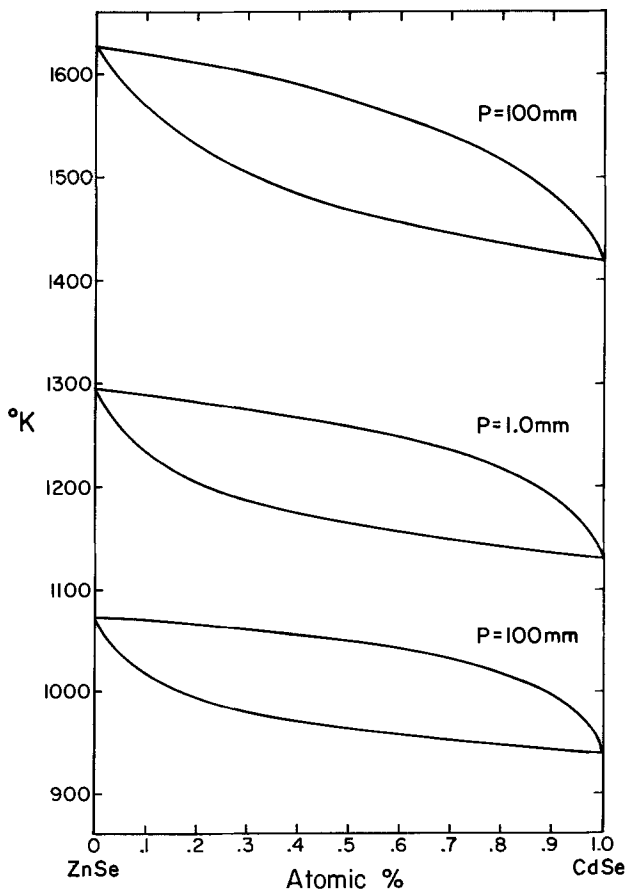


Fig. 4. The calculated sublimation point diagram for an ideal CdSe-ZnSe solid solution at total pressures of 10^2 , 1, and 10^{-2} Torr.

librium with stoichiometric CdS, ZnS, CdSe, and ZnSe were calculated using the equations

$$\ln P = -\frac{2}{3} \frac{\Delta H_s}{RT} + C_s$$

$$P_2 = \frac{1}{3} P$$

using the data of Shiozawa and Jost (3) which are listed in Table II.

In order to know the composition of the vapor of ternary mixtures to aid us in analyzing platelet growth (4) for the ternary platelets used in our solar cell research, we also calculated the ideal sublimation point diagrams for ZnS-CdS and ZnSe-CdSe at pressures of 10², 1, and 10⁻² Torr. They are shown in Fig. 3 and 4. The diagrams are ideal in that Raoult's law was used, it was assumed that only anion dimers were present, and it was assumed that the constituents form complete solid solutions even though the room temperature structure of the zinc compounds is zinc blende and not wurtzite. The calculations were made by computing the vapor pressures, P₁⁰ and P₂⁰, of the constituents at a number of temperatures between the sublimation tem-

peratures of the pure constituents and calculating the solid mole fractions, X, from the equation

$$X_1 = (P - P_2^0)/(P_1^0 - P_2^0)$$

and the vapor mole fractions, Y, from the equation

$$Y_1 = X_1 P_1^0 / P$$

Manuscript submitted June 10, 1975; revised manuscript received Aug. 11, 1975.

Any discussion of this paper will appear in a Discussion Section to be published in the June 1976 JOURNAL. All discussions for the June 1976 Discussion Section should be submitted by Feb. 1, 1976.

Publication costs of this article were partially assisted by Dartmouth College.

REFERENCES

1. J. Berkowitz and J. L. Marquart, *J. Chem. Phys.*, **39**, 275 (1963).
2. J. Berkowitz and W. A. Chupka, *ibid.*, **45**, 4289 (1966).
3. L. R. Shiozawa and J. M. Jost, *U.S. Govt. Res. Rept. AD-660 874* (1968).
4. K. A. Jones, *J. Cryst. Growth*, **19**, 33 (1973).

Brief Communication



Liquid-Phase Epitaxial Growth of 6H-SiC by Vertical Dipping Technique

A. Suzuki,* M. Ikeda,* H. Matsunami, and T. Tanaka

Department of Electronics, Faculty of Engineering, Kyoto University, Kyoto 606, Japan

As a method to prepare SiC single crystals for semiconductor devices, liquid-phase epitaxial growth from a Si melt will be more useful than the conventional sublimation method because the growth temperature is lower and the growth process, impurity level, and polytypes may be controlled more easily.

Brander *et al.* obtained epitaxial layers of 6H-SiC up to 100 μm thick at a growth temperature of 1650°C by supporting a substrate crystal on a stock in the Si melt (1, 2). After the growth, they took out the grown crystal from the solidified silicon by cutting the crucible and etching the silicon. However, grown crystals tended to be damaged by stresses induced when the Si melt solidified. In order to solve this problem, we have attempted liquid-phase epitaxial growth of 6H-SiC by vertical dipping technique.

The arrangement for the growth is shown in Fig. 1. The crucible was made of dense and high purity graphite (apparent density 1.60 g/cm³, ash content 0.02%). Its size was 53 mm in height and 35 mm in outer diameter. In order to avoid evaporation of silicon, we used a graphite lid which had a center hole of 8 mm in diameter. The crucible was filled with a 26g charge of silicon and heated inductively. The gas ambient was Ar flowing at ~200 cm³/min.

A single crystal of 6H-SiC prepared by the Acheson method was used to make a substrate. The substrate

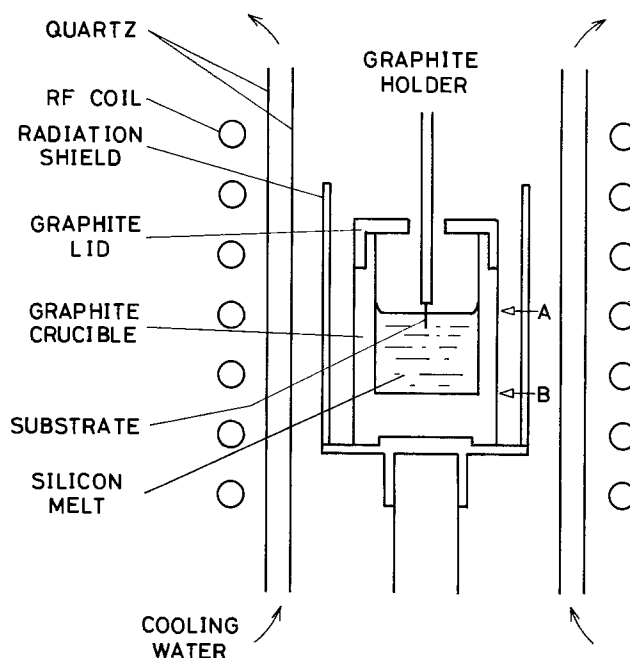


Fig. 1. Arrangement for liquid-phase epitaxial growth by the vertical dipping technique with a Si melt.

* Electrochemical Society Student Member.

Key words: solution growth, Si melt, polytype, x-ray diffraction, photoluminescence.

was prepared by lapping and polishing the {0001} faces of the crystal with diamond paste, and cutting it into pieces of $1 \times 1 \times 8 \text{ mm}^3$. Then it was rinsed with de-ionized water. The surface polarity was examined by etch pits with H_2 gas etching at 1550°C for 20 min. The substrate was tied to a graphite holder with molybdenum or tantalum wire. The $\langle 0001 \rangle$ direction was set perpendicular to the holder axis. After the silicon was melted, the substrate was dipped to a depth of 2 ~ 3 mm and maintained for 5 hr at a growth temperature between 1550° and 1750°C . The temperature at point A in Fig. 1 was kept $10^\circ \sim 40^\circ\text{C}$ lower than that at point B. After the growth, the substrate was pulled up from the crucible before the Si melt solidified. Residual silicon on the grown layers was removed with a 1:1 mixture of HF and HNO_3 . By this dipping technique, the crucible and silicon could be used several times.

Layers 20 ~ 140 μm thick were grown on the {0001} faces after 5 hr growth at $1550^\circ \sim 1750^\circ\text{C}$. The layer on the Si face was thinner than on the C face with every growth. Each layer was thick near the surface of the Si melt. Figure 2 shows the average thickness as a function of growth temperature. It increased with increasing growth temperature, which may be due to the increase of the solubility of carbon into the Si melt. But above 1750°C etching effects appeared. Fairly even layers were grown at lower growth temperature and with less temperature difference of the crucible.

The appearance of the grown layers was quite different between the Si face and the C face as shown in Fig. 3. The former was relatively smooth and showed a wavy pattern, whereas the latter was composed of small islands.

By taking x-ray oscillation photograph about the $\langle 0001 \rangle$ axis of the layer grown at 1700°C , it was found to be a 6H-type single crystal grown epitaxially on the {0001} face of the substrate.

Previously we reported that aluminum and boron impurities were introduced unintentionally from the graphite crucible in our experiments and that they acted as strong luminescent centers at 77K and 300K, respectively (3, 4). We have observed photoluminescence of the grown layers at 77K and 300K. By comparing the spectra with those due to aluminum and boron in various polytypes of SiC reported by other

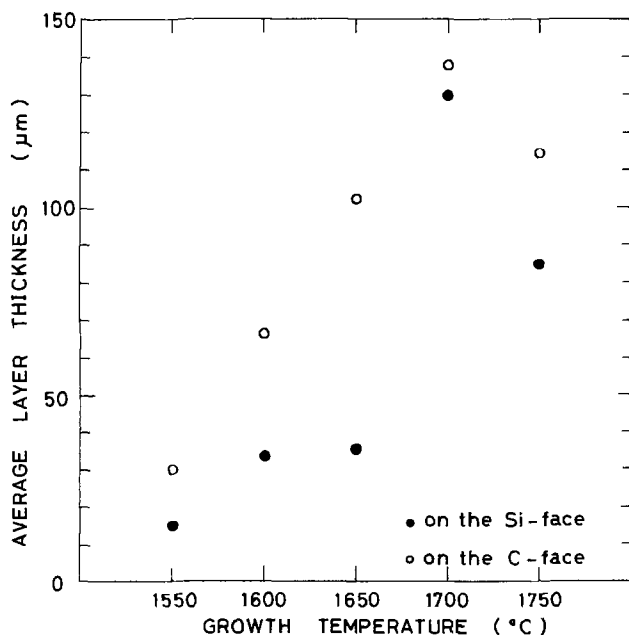


Fig. 2. Average thickness of grown layers on the {0001} faces as a function of growth temperature (5 hr growth).

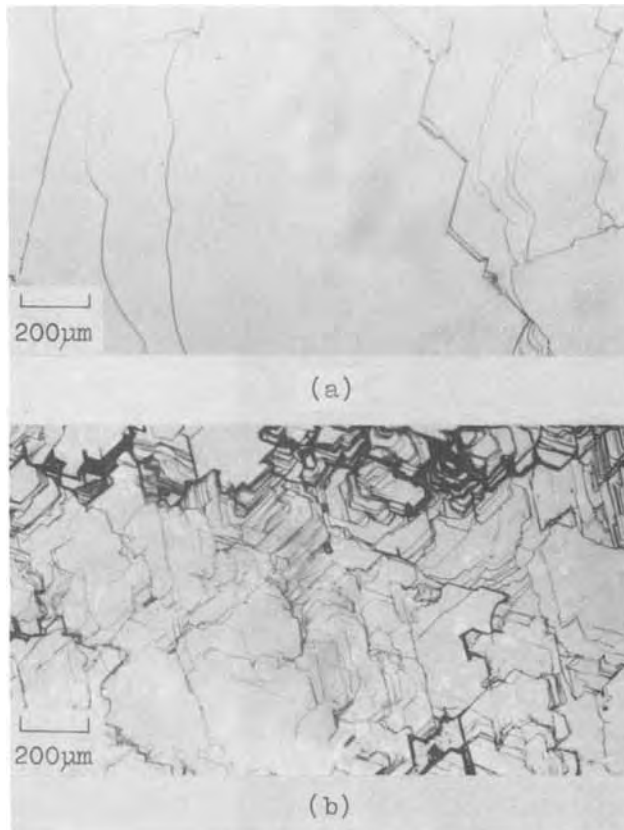


Fig. 3. Grown layers on the {0001} faces after 5 hr growth at 1550°C , (a) Si face, (b) C face.

researchers (5, 6), all grown layers were found to be 6H-type.

Pellegrini *et al.* reported liquid-phase epitaxial growth by a similar technique to ours, using the melt of Ti-Si alloy instead of Si (7). They utilized the high solubility of carbon into Ti melt and the low vapor pressure of Ti to obtain thick layers. But thickness of 35 ~ 140 μm at $1600^\circ \sim 1700^\circ\text{C}$ for 5 hr in our experiments is much the same as 120 ~ 150 μm at $1600^\circ \sim 1700^\circ\text{C}$ for 8 hr in their experiments. Moreover, evaporation of silicon was little even in our long run for 120 hr at 1700°C . By using only silicon as a solvent, grown layers may not suffer from undesired impurities.

Acknowledgment

This work was partially supported by the Kurata Research Grant.

Manuscript submitted July 9, 1975; revised manuscript received Aug. 18, 1975.

Any discussion of this paper will appear in a Discussion Section to be published in the June 1976 JOURNAL. All discussions for the June 1976 Discussion Section should be submitted by Feb. 1, 1976.

REFERENCES

1. R. W. Brander and R. P. Sutton, *Brit. J. Appl. Phys.*, (J. Phys. D), **2**, 309 (1969).
2. R. W. Brander, *Mater. Res. Bull.*, **4**, 187 (1969).
3. A. Suzuki, H. Matsunami, and T. Tanaka, *Japan. J. Appl. Phys.*, **12**, 1083 (1973).
4. H. Matsunami, A. Suzuki, and T. Tanaka, in "Silicon Carbide-1973," p. 618, University of South Carolina Press, Columbia (1974).
5. A. Addamiano, *This Journal*, **111**, 1294 (1964).
6. S. H. Hagen, A. W. C. van Kemenade, and J. A. W. van der Does de Bye, *J. Luminescence*, **8**, 18 (1973).
7. P. W. Pellegrini and J. M. Feldman, in "Silicon Carbide-1973," p. 161, University of South Carolina Press, Columbia (1974).



This Discussion Section includes discussion of papers appearing in the *Journal of Electrochemical Society*, Vol. 121, No. 11; November 1974; and Vol. 122, No. 2 and 3; February and March 1975.

The Oxidation of Thin Single Crystals of Iron

P. L. Fan and L. O. Brockway (pp. 1534-1537, Vol. 121, No. 11)

J. Manenc:¹ In this very interesting work about oxidation of single crystals of iron, Fan and Brockway give electron diffraction results. They found reflections they were unable to index as Fe, FeO, or Fe₃O₄. Using A.S.T.M. file they chose the compound Fe₄N as the best fitting phase.

I think this interpretation is not valid in view of the results we obtained earlier at IRSID.²⁻⁹ Briefly, we showed that wustite has different structures depending on its departure from stoichiometry and on the heat-treatment. These structures probably correspond to cation vacancy ordering²⁻⁴ resulting in the building of a supercell which gives extra selective spots. The number and the repartition of these spots are a function of the vacancy concentration.

The order can exist in certain circumstances at high temperature as we^{8,9} and other people¹⁰ have showed.

It is particularly interesting to compare Fig. 2 of the paper under discussion to Fig. 5 of our paper.⁴

Thus, it is most probable that the reflections attributed to Fe₄N by Fan and Brockway are order spots of oxygen-rich wustite formed at the top of the largest crystals. Moreover, the extra spots always accompany the normal wustite reflections.

Effect of the Rate of Cooling on the Emission of CaS:Ce Phosphor

D. R. Vij and V. K. Mathur (pp. 310-311, Vol. 122, No. 2)

W. Lehmann:¹¹ The article by Vij and Mathur describes preparation of CaS:Ce³⁺ phosphor at relatively low temperature (900°C) with Na₂SO₄ serving as fluxing agent and without the use of any halide. Since presence of Na and absence of a halide in our own work^{12,13} was observed to be just about the worst possible condition under which to prepare this phosphor, we tested once again following the procedure described by Vij and Mathur as closely as possible. The result was a discolored and strongly sintered material with only very weak luminescence (less than 10% of what routinely is available by the halide method) essentially confirming our previous experiences.

At this point, Dr. Mathur kindly supplied a sample of his material (A) for inspection and for comparison to a sample (B) made in our laboratory. Sample A was made with Na₂SO₄ as described, sample B was made with iodine as described in our paper¹² (there is little or no difference between the actions of F, Cl, Br, and

I in CaS:Ce³⁺). Both samples contain about 0.03-0.05% of Ce. The following are the most interesting results of this comparison.

1. Routine x-ray analysis indicates no other phase, besides CaS, to be present in either material (limit of detectability: ~ 1-2%).

2. Sample A consists mainly (not only) of remarkably well-developed particles in the size range of about 10 μm despite the low preparation temperature (particles of similar size prepared by the halide method would require at least 1200°C). It is also somewhat more stable in water slurry (pH ≈ 8.5) than material B (pH ≈ 10).

3. The efficiencies of photoluminescence (254 nm u.v.) and of cathodoluminescence (10 kV, low current) of A are approximately 30% of B.

4. The emission spectra of A and B are slightly different; A is shifted by about 0.05-0.06 eV to higher energies (Fig. 1).

We emphasize at this point that the statement "The two peak positions (of CaS:Ce³⁺ made by the halide process) vary only very little with the cerium concentration. . .,"¹² still is correct. Some measured data are shown in Fig. 2. Comparing the low efficiency of A and the spectral positions of the peaks of its emission bands to Fig. 2 shows a fair agreement with CaS:Ce³⁺, halide containing only 0.001% Ce or slightly more. We interpret this that, probably, less than 10% of all added Ce atoms in A are optically active, i.e., in lattice sites and under conditions where they contribute to luminescence.

An undisputed merit of the preparation procedure used by Vij and Mathur is its simplicity and the lower required firing temperature made possible by the presence of a large amount of Na₂SO₄ flux. However, we still believe Na⁺ ions to be detrimental to Ce³⁺ luminescence in CaS. One might wonder whether a

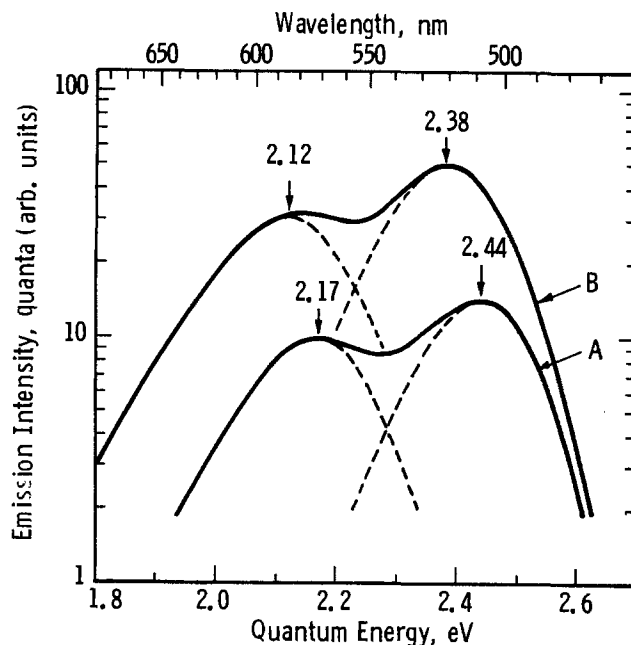


Fig. 1. Emission spectra of photoluminescence (excitation by 254 nm u.v.) of (A) CaS:Ce³⁺, Na₂SO₄ and (B) CaS:Ce³⁺, I at room temperature.

¹ Institut de Recherches de la Sidérurgie Française (IRSID), 185 rue President Roosevelt, 78104 Saint-Germain-en-Laye, France.

² J. Manenc, J. Bourgeot, and J. Benard, *Compt. Rend. Acad. Sci.*, 256, 931 (1963).

³ J. Manenc, J. Bourgeot, and T. Herai, *ibid.*, 258, 4263 (1964).

⁴ T. Herai, B. Thomas, J. Manenc, and J. Benard, *ibid.*, 258, 4528 (1964).

⁵ T. Herai and J. Manenc, *Mem. Sci. Rev. Met.*, 61, 677 (1964).

⁶ J. Manenc, T. Herai, and G. Vagnard, *Bull. Soc. Chim. France*, 1154 (1965).

⁷ T. Herai, B. Thomas, and J. Manenc, *Mem. Sci. Rev. Met.*, 63, 397 (1966).

⁸ J. Manenc, *ibid.*, 64, 692 (1967).

⁹ J. Manenc, *Bull. Soc. Mineral. Crist.*, 91, 594 (1968).

¹⁰ F. Koch and J. B. Cohen, *Acta Cryst.*, B25, 275 (1969).

¹¹ Westinghouse Electric Corporation, Research and Development Center, Beulah Road, Pittsburgh, Pennsylvania 15235.

¹² W. Lehmann and F. M. Ryan, *This Journal*, 118, 477 (1971).

¹³ W. Lehmann, *J. Luminescence*, 5, 87 (1972).

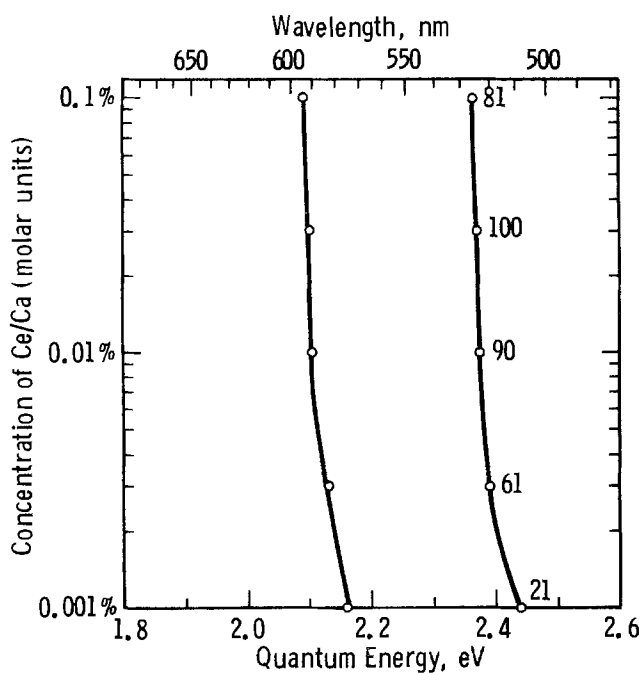


Fig. 2. Peak positions of the two emission bands of $\text{CaS}:\text{Ce}^{3+}$, I as function of the Ce concentration. Added numbers are relative efficiencies of photoluminescence.

suitable flux could be found containing no alkaline ions.

It is a pleasure to the writer to thank Dr. Mathur for supplying his phosphor sample and for discussion and ready cooperation in this matter.

D. R. Vij and V. K. Mathur:¹⁴ We acknowledge that the efficiency of photoluminescence and cathodoluminescence of $\text{CaS}:\text{Ce}$ phosphor B (prepared by Lehmann's method) is more than the phosphor A (prepared by our procedure). Under u.v. excitation we found that the efficiency of our phosphor is approximately 40% of that of the sample kindly supplied to us by Dr. Lehmann. However, it is difficult to agree at least in the first instance with his assertion that it is due to the addition of halide in his phosphors. According to spectrochemical analysis of A and B (available to us by the courtesy of Dr. Lehmann), the concentration of Fe is eight times more in A than B. It is well known that Fe is a killer impurity of luminescence. Hence we suggest that the lower efficiency in our case may be due to the presence of higher concentration of Fe. We have tried to eliminate this impurity but without any success so far. It may be mentioned here that we have tried CaCl_2 as flux but the samples were found to be of very low efficiency.

The Origin of the Cubic Rate Law in Zirconium Alloy Oxidation

G. P. Sabol and S. B. Dalgaard (pp. 316-317, Vol. 122, No. 2)

B. Cox and R. A. Ploc:¹⁵ The relationship between changes in the crystallite size in the oxide film during growth and the kinetics of oxidation is one of the most important factors yet to be established for zirconium alloy oxidation. It is unfortunate, therefore, that Sabol and Dalgaard present an oversimplified picture which may be misleading to readers.

That the pretransition oxidation kinetics of zirconium alloys are close to cubic is only well established for specimens oxidizing at relatively high tempera-

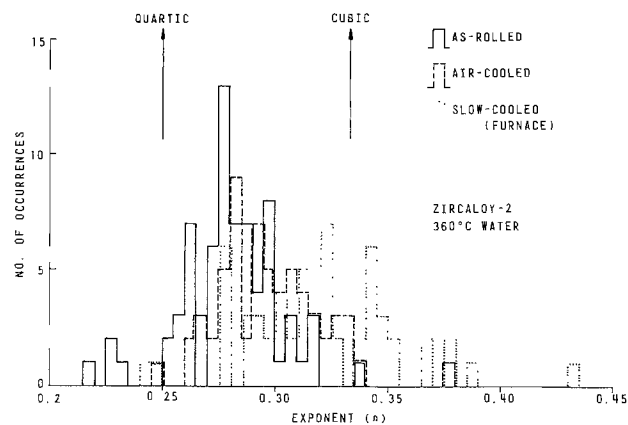


Fig. 1. Histogram of oxidation rate exponents (n).²¹ Note that slow-cooling results in poor oxidation resistance.

tures.^{16,17} In water at low temperatures ($\sim 300^\circ\text{C}$), the pretransition kinetics are often close to quartic for a large fraction of the time prior to the principal transition in the kinetics at $\sim 30 \text{ mg}/\text{dm}^2$. If the authors study the reference they cited to Kass' work,¹⁸ they will see that many of the exponents quoted in his Table 1 are less than 0.33, even when averaged over the whole oxidation curve. When the data beyond the minor inflection, which occurs in the weight gain curve at $\sim 10 \text{ mg}/\text{dm}^2$, are fitted independently to a curve of the form $\Delta w/kt^n$ the exponents (n) are usually < 0.33 , for Zircaloy-2 or Zircaloy-4 in their normal metallurgical condition.¹⁹⁻²¹ Thus the majority of the pretransition oxidation kinetics in water are usually between a cubic and a quartic, with considerable variation from specimen to specimen (Fig. 1). Similar results have been reported elsewhere.¹⁹⁻²¹

A quartic kinetic law could be explained by crystallite sizes increasing proportional to the film thickness squared, a dependence to which Sabol and Dalgaard's results show better agreement than the linear dependence they propose to force a fit to cubic oxidation kinetics. In the light of the observed variation in kinetic exponents, however, it is even more important, if an acceptable correlation of crystallite size and kinetics is to be made, that both the crystallite size and the applicable kinetics be derived from the same set of specimens; a correlation which is absent here.

Another factor which Sabol and Dalgaard ignore completely is the influence of the electronic component of the oxidation process on the oxidation kinetics. Theoretically, even for a constant oxide crystallite size (and oxygen ion mobility) as a function of oxide thickness, the rate law will only be parabolic if the electric field across the oxide is constant. This is probably not the case.²²⁻²⁴ The previously mentioned inflection in the kinetics may be caused by an increase in electronic conductivity (manifested as a sudden drop in the field across the oxide and an increase in the instantaneous oxidation rate) similar to that causing the inflection at $\sim 1 \text{ mg}/\text{dm}^2$ during oxidation in other environments.^{22,23} Beyond this inflection in the oxidation curve the field across the oxide is relatively constant and decreases only slowly. Thus, to a first approximation we can consider only the effect of crystallite size and shape on the kinetic law in this region; however, any perturbation caused by changes in elec-

¹⁶ R. D. Misch, USAEC Conference on Zirconium Alloy Development, GEAP-4089, Vol. II, Castletwood, California (1962).

¹⁷ E. Hillner, *Electrochem. Technol.*, 4, 132 (1966).

¹⁸ S. Kass, *J. Nucl. Mater.*, 28, 315 (1969).

¹⁹ B. Cox, *ibid.*, 25, 310 (1968); *ibid.*, 29, 50 (1969).

²⁰ B. Cox, *ibid.*, 30, 351 (1969).

²¹ L. S. Rubenstein, J. G. Goodwin, and F. L. Shubert, *Corrosion*, 18, 456 (1962).

²² P. J. Shirvington and B. Cox, *J. Nucl. Mater.*, 35, 211 (1970).

²³ P. J. Shirvington, *ibid.*, 37, 177 (1970).

²⁴ B. Cox, International Conference on "High Pressure Electrochemistry of Aqueous Solutions," Guildford, England (1973).

¹⁴ Department of Physics, Kurukshetra University, Kurukshetra, India.

¹⁵ Atomic Energy of Canada Limited, Chalk River Nuclear Laboratories, Chalk River, Ontario, Canada.

tronic conduction (indicated by changes in the field) will be in the direction of increasing the exponent in the rate law. Thus, the measured oxidation kinetic exponents during a period of decreasing field across the oxide will be higher than would be determined under a constant-field condition.

Sabol and Dalgaard conclude further that the initially formed crystallites of ZrO_2 did not change in size during continued oxidation. Our results^{25,26} and those of Roy *et al.*²⁷ cast doubt on this conclusion. Though complicated by several factors such as non-identical conditions, our results suggest that at about a film thickness of 500-900Å the oxide crystallites over many prior metal grains change in appearance. Electron diffraction data²⁶ and transmission electron micrographs²⁵ strongly support the idea that recrystallization, growth, and re-orientation (possibly caused by grown-in stresses) of the crystallites occur in the early stages of oxidation. The work of Roy *et al.*,²⁷ which shows that some orientations of crystallites disappear, i.e., that the absolute x-ray intensity of that orientation passes through a maximum as the oxide thickens, rather than merely the relative intensity being reduced, as the oxide continues to thicken, suggests that these processes continue at greater oxide thicknesses. These results require a more extensive exposition than is possible here, or in the reference cited, and further details are currently being prepared for publication.

Let us make it clear in conclusion that we are basically in agreement with the hypothesis for oxygen transport in growing oxide films adopted by Sabol and Dalgaard, having long espoused such an hypothesis ourselves. However, demonstrable proof of the relation between crystallite size in the oxide film and the kinetics of the process requires considerably more care than was shown by these authors in this paper.

G. P. Sabol²⁸ and S. B. Dalgaard²⁹ The purpose of publishing the original technical note was to call to the attention of the scientific community the correlation between the structural aspects of oxide film growth and the observed deviation in kinetics from parabolic towards cubic. It was not the intent of the manuscript to fully explain the details of the corrosion process, but rather to stimulate additional work directed specifically toward the behavior of zirconium in aqueous environments. While we acknowledge that other factors of perhaps equal importance are also involved, it is believed that the structure of the diffusion barrier significantly affects the corrosion kinetics in the pretransition regime.

Rebuttal to specific comments made by Cox and Ploc are the following:

The exponent n in our work was 0.37. This is sufficiently close to the values reported by others [Ref. (1-3) of original paper] that repetition of the kinetic data would have been redundant.

We are well aware that the pretransition corrosion rate is a function of the ionic and electronic resistances of the barrier layer. Furthermore, we believe that these resistances are unique functions of the corrodent as well as the chemical and metallurgical condition of the alloy. Thus, models^{22,26,27} based upon observations in electrolytes other than water do not necessarily apply to corrosion in aqueous media.

The disappearance of reflections in transmission electron diffraction patterns with increasing oxide film thickness was taken to indicate either recrystallization or preferential growth by Ploc and Arnal.²⁶ Our data

[Ref. (9) of original paper] strongly indicate preferential growth rather than recrystallization.

Although Ftn²⁷, private communication, is difficult to assess, the results referred to were obtained after oxidation in 500° and 650°C oxygen at 30 Torr. These temperatures are significantly greater than those considered in the paper and recrystallization at these higher temperatures is not unexpected.³⁰ However, the applicability of these results to corrosion in aqueous media at < 400°C is highly questionable.

Oxide Growth on Etched Silicon in Air at Room Temperature

S. I. Raider, R. Flitsch, and M. J. Palmer
(pp. 413-418, Vol. 122, No. 3)

F. P. Fehlner³¹ The paper of Raider *et al.* points up the role of impurities in the oxidation process. They find that at low temperatures an adsorbed layer of impurities can block the attack of oxygen on silicon. Conversely, in the presence of ultraviolet irradiation and impurities, Fehlner has shown that the growth of a dielectric film on silicon can be enhanced.³²

Another manifestation of the combined effect of ultraviolet light and impurities can be seen during the etching of SiO_2 on Si by dilute HF.³³ This may be relevant to the impurity film observed by Raider *et al.*

Figure 1 shows the thickness of dielectric film present on silicon [6-9 ohm-cm, n-type, (111)] after incremental etching in the dark and under u.v. illumination (medium pressure mercury arc). In the dark, the original SiO_2 film is etched completely away, leaving the silicon surface covered with a film 5-8Å thick. However, under illumination, a surprising event occurs. After the original SiO_2 has been etched away, a new film of unknown composition grows on the silicon. Part of this film can be subsequently removed by further etching in the dark. The results in Fig. 1 argue for carefully controlled etching in the dark of SiO_2 on Si.

³⁰ C. W. Hughes, G. P. Sabol, and G. P. Airey, *Microstructural Sci.*, 1, 199 (1974).

³¹ Corning Glass Works, Research and Development Laboratories, Corning, New York 14830.

³² F. P. Fehlner, *This Journal*, 119, 1723 (1972).

³³ Experimental work performed at Signetics Corporation, Sunnyvale, California.

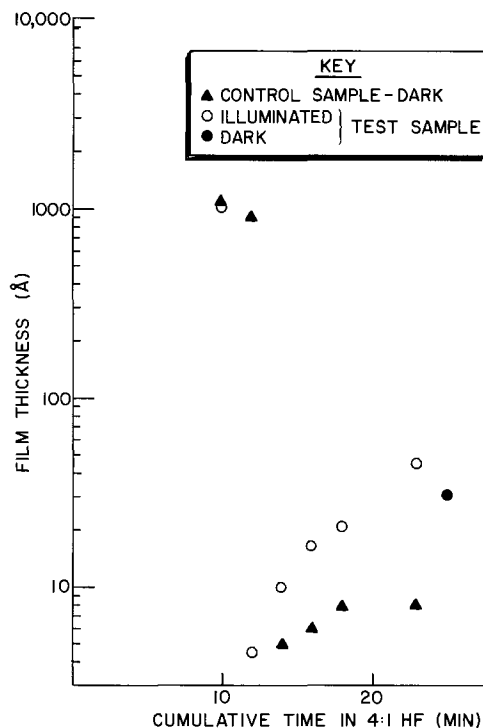


Fig. 1. Dielectric film thickness on silicon originally covered with 8700Å of thermally grown SiO_2 after etching with 4:1 HF. Ellipsometric measurements carried out as described.³²

²⁵ R. A. Ploc, *Septième Congrès International de Microscopie Electronique*, p. 373, Grenoble, France (1970).

²⁶ R. A. Ploc and H. J. Arnal, *Atomic Energy of Canada Limited Report, AECL-3997* pp. 64-67 (1971).

²⁷ C. Roy, Private communication.

²⁸ Westinghouse Electric Corporation, Research Laboratories, Pittsburgh, Pennsylvania 15235.

²⁹ Westinghouse Electric Corporation, Nuclear Fuel Division, Box 355, Pittsburgh, Pennsylvania 15230.

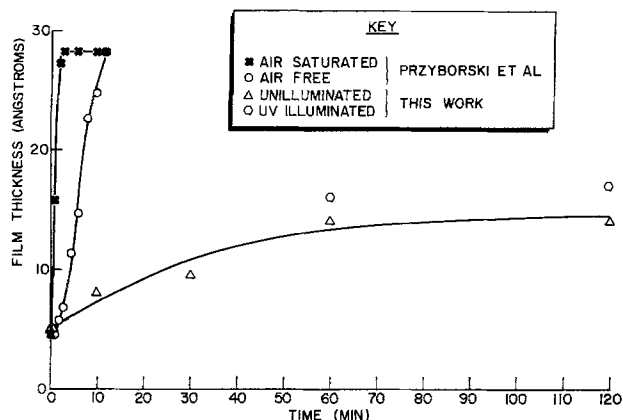


Fig. 2. Thickness of film formed on silicon as a function of time in boiling deionized water.

A second point of interest, which bears on the thickness of film left on etched silicon, concerns the oxide grown on silicon in boiling, deionized water. Etched silicon wafers were exposed to boiling water in equilibrium with the atmosphere for increasing lengths of time. The thickness of film formed on the silicon was then measured. The results are compared with those of Przyborski *et al.*³⁴ in Fig. 2. The thickness measurements in the present work were made with an ellipsometer, while those of Przyborski *et al.* were done by neutron activation analysis. The difference between the two sets of results is thought to be due to the purity level of the water. In this case also, illumination of the silicon with a high pressure mercury arc led to an increase in film thickness.

These observations, along with those of Raider *et al.* aid in confirming the hypothesis that oxidation is an impurity controlled process.

Simple Theoretical Estimates of the Schottky Constants and Virtual-Enthalpies of Single Vacancy Formation in Zinc-Blende and Wurtzite Type Semiconductors

J. A. Van Vechten (pp. 419-422, Vol. 122, No. 3)

J. Jacobs:³⁵ J. A. Van Vechten has proposed a theory which predicts, seemingly without exception, the charge carrier type of pure semiconductor compounds in the zinc-blende and wurtzite structure from the quotient of the covalent tetrahedral radii (p-type for quotients <1, n-type for quotients >1). Is this the case for zinc sulfide, too? The quotient here is 1.09.

Blount, Sanderson, and Bube³⁶ treated zinc sulfide crystals at high temperatures in zinc vapor and in sul-

fur vapor. According to the discussion of the authors and also that of Morozova and Nikitenko³⁷ is zinc sulfide after sulfur treatment high ohmic p-type with the position of the Fermi level at $E_v + 1.2$ eV. Probably, the intrinsic disorder situation in zinc sulfide is similar to that in zinc selenide. In this material the activation energy of the carrier concentration in the partial equilibrium corresponds to the distance between the corresponding band and the Fermi level in the high temperature equilibrium under extreme metal or nonmetal conditions. From this we conclude the ionization energies of the isolated doubly ionized intrinsic defects.³⁸ With this note I would also refer to this possibility to determine the ionization energies of the isolated defects, when experiments were carefully analyzed. The formation of complexes and other phenomena, which disturb this determination, apparently does not occur.

J. A. Van Vechten:³⁹ Of course, it is true that the position of the Fermi level, E_f , in an undoped semiconductor can be influenced by deviations from stoichiometry induced by heat-treatments in an excess of either the metal or the nonmetal component of the compound. Thus, Blount *et al.*³⁶ reported that they could drive E_f to about 1.3 eV above the valence band maximum, E_v , by annealing "pure" ZnS in S vapor for 8 days at 891°C. (The starting material contained 1×10^{18} Cu/cm³, 1×10^{18} Si/cm³, and 5×10^{17} Mg/cm³.) E_f was then slightly above a defect level at $E_v + 1.2$ eV, which they associated with the zinc vacancy, V_{Zn} . There is no evidence whether or not the V_{Zn} is present in a complex when observed at, or below, room temperature. This material was then very highly resistive ($\sim 10^{10}$ ohm-cm) p-type.

To the author's knowledge, reasonably highly conductive p-type ZnS has never been produced by any means, although conductive n-type ZnS is common. One may conclude that vacancy self-compensation does prevent the attainment of low resistivity conduction only on the p-type side in Zn. Thus, the correlation between the covalent radius ratio and the side on which vacancy self-compensation restricts conductivity is as predicted in the case of ZnS as well as the other II-VI's. No further inference was intended.

It is further noted that in wider gap materials, such as the alkali halides, vacancy self-compensation restricts conduction on both the n- and p-type sides, although deviations from stoichiometry may be obtained, while in smaller gap semiconductors, like GaSb and GaP, the intrinsic conductivity type (p- and n-type, respectively) may be reversed by doping because self-compensation does not occur until after E_f has reached one band edge or another.

³⁴ W. Przyborski, J. Roed, J. Kippert, and L. Sarholt-Kristensen, *Radiation Effects*, 1, 33 (1969).

³⁵ Technische Hochschule, 63 Ilmenau, GDR.

³⁶ G. H. Blount, A. C. Sanderson, and R. H. Bube, *J. Appl. Phys.*, 38, 4409 (1967).

³⁷ Morozova and Nikitenko, *Izv. Akad. Nauk SSSR, Neorg. Mater.*, 9, 1555 (1973).

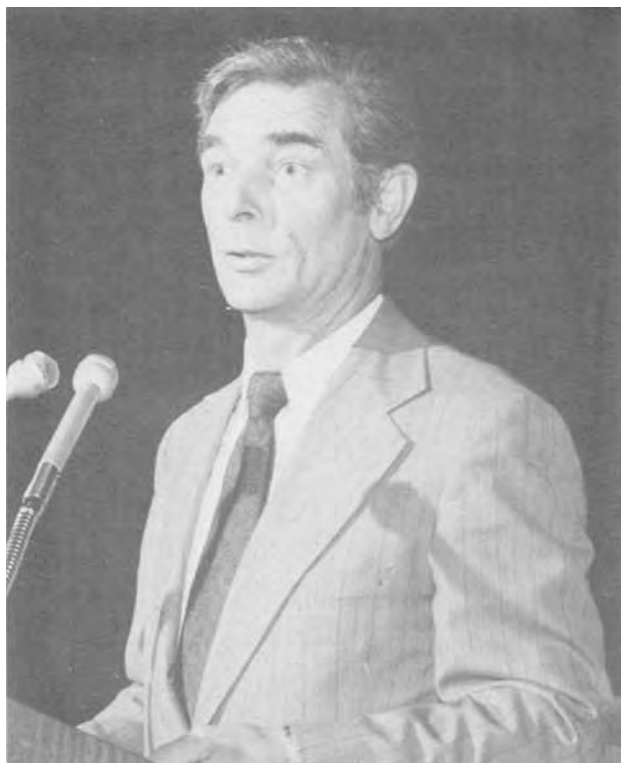
³⁸ J. Jacobs and H. Arnold, *Kristall und Technik*, 10, 71K (1975).

³⁹ IBM Thomas J. Watson Research Center, P.O. Box 218, Yorktown Heights, New York 10598.



Harry C. Gatos—Solid State Science and Technology Award Medalist

August F. Witt¹



August F. Witt delivers introductory remarks about the Solid State Science and Technology Award Medalist.

Shortly, Harry Gatos will be the second recipient of The Electrochemical Society Award in Solid State Science and Technology. On the occasion of the award presentation I have the great honor to reflect for a few minutes on Harry's background and technical accomplishments.

To convey to you a real image of his truly outstanding personality I would now have to talk not only about his scientific achievements but also about Harry the poet, the flutist, the violinist, the conductor, the educator and, last but not least, about Harry the personal friend. I would have to talk about musical soirees at his home during which he conducted professional musicians performing Mozart and about endless nights spent over the twelfth draft of a publication. I would also have to talk about his family: his son who, at the age of seven, asked me at the beach to do arithmetic with him when I wanted to play ball, and about his

daughters who, besides being intelligent, are great young ladies.

Time does not permit me to dwell on this side of Harry's life, so let us look at his biography: Harry was born in Amphissa, Greece, and began his studies in chemistry at the University of Athens where, still an undergraduate student, he functioned as instructor, lecturer, and tutor and wrote his first book on inorganic chemistry at the ripe old age of 22, his second on analytical chemistry at 24, and his third on organic chemistry at 25. In 1946 he was awarded a one-year fellowship for graduate studies in the United States, enrolled at Indiana University and received his M.A. after only 18 months. In 1948 he was admitted to M.I.T., enrolled in the Chemistry Department, and did his graduate work on the passivation of iron in the Metallurgy Department. Only one year after graduation, as research associate at M.I.T., he already did pioneering work on self-diffusion in iron which today is considered one of the classical works on the use of radio-tracers for self-diffusion studies.

In 1952 he joined the Engineering Research Laboratory of du Pont where he worked for three years on corrosion and corrosion inhibition of metallic systems. Harry then came back to M.I.T., accepting the position of leader of the chemistry section in the Solid State Group of the Lincoln Laboratory. When the Electronic Materials Group was established, largely on his initiative in 1957, he became its first leader. Besides coordinating and supervising research involving both materials and device oriented groups, initiating new research activities and taking care of administrative details, he found the time to assume the personal responsibility for the growth of a Cr-doped K-cobalt-cyanide single crystal which was used in the first operational three-level MASER. It was at this time also that he first focused his attention on semiconductor surfaces, semiconductor growth and microsegregation effects, superconductors and high-pressure phase transformation. In 1959 he became Associate Head and in 1964 Head of the Solid State Division of the Lincoln Laboratory. In 1961 he accepted a professorship at M.I.T. which he still holds.

What are his research accomplishments? They are truly outstanding in both quality and quantity, and I can only enumerate. While his leadership abilities forced his attention to the coordination and direction of major research projects and made him devote much of his time to national issues associated with solid-state science and technology, his personal research accomplishments are well documented in over 170 technical publications. During his tenure as Leader of the Electronic Materials Group at the Lincoln Laboratory, the first operation three-level MASER crystal was produced. Soon thereafter his efforts led to an explanation of the polarity effect in III-V and II-VI semiconductor compounds and to a clarification of its implications on the growth characteristics of so-called A and B sur-

¹ Introductory remarks by August F. Witt, Massachusetts Institute of Technology, Cambridge, Massachusetts, on the occasion of the presentation of the Solid State Science and Technology Medal Award to Harry C. Gatos on May 13, 1975, at the Toronto, Canada, Meeting of the Society.

faces which led to a drastic improvement in the growth of defect-free compound semiconductor materials. On the basis of extensive, systematic etching experiments his group identified for the first time α and β dislocations in InSb. He then published the first comprehensive treatise concerned with the etching characteristics of elemental and compound semiconductors. His efforts to bridge the gap between the rigorous formalism used by theoretical physicists and the chemical concepts used by materials scientists in the treatment of semiconductor surfaces led him to the extremely useful concept of "dangling bonds" now generally adopted in the international literature. His research on high pressure phases of compound semiconductors resulted in the discovery of several previously unknown structures, among those the superconducting tetragonal high pressure structure of InSb. He and his collaborators discovered for the first time the existence of nonrotational segregation inhomogeneities in Czochralski-type semiconductors and in a series of publications they subsequently elucidated the microscopic growth and segregation behavior associated with this industrially most important crystal pulling process. Of major impact on the study of semiconductor surfaces was his research effort which led to the development of surface photovoltage spectroscopy and the discovery of a surface piezoelectric effect in noncentrosymmetric semiconductor systems. His most recent accomplishment as head of the Electronic Materials Group at M.I.T. is the development of a quantitative approach to the analysis of crystal growth and segregation on the microscale which is based on the use of growth interface demarcation in combination with high resolution spreading resistance measurements. This work for the first time clarifies previously unexplained discrepancies between theoretical treatments of segregation and experimental results. It also gives direct evidence of convective interference on microsegregation, a phenomenon which had been expected but could only now be unambiguously proven and quantitatively studied.

His current research is concerned with the application of thermo-electric cooling at crystal-solution interfaces for the production of epitaxial layers with controlled composition obtained under constant temperature conditions.

Harry's attitude toward his research is best summarized in a Shakespeare quote:

And now remains
that we find out the cause of this effect
or rather say, the cause of this defect
for this effect defective comes by cause.

Let us now consider the impact of Harry's efforts to advance solid-state science and technology. Harry's internationally recognized outstanding contributions to the advancement of solid-state science and technology are not only his many accomplishments in research. His unique contributions come also from his early realization of the existence of a communications gap between solid-state physicists using rigorous formalism and materials oriented scientists such as metallurgists and chemists operating to a large extent with empirical concepts. This communications gap, in his opinion, relegated electronic materials research for too long to a service function which strongly impeded progress in solid-state technology. Harry's unrelenting efforts to bridge this gap were multifaceted. In his position as leader of the Electronic Materials Group at the Lincoln Laboratory, for which he eminently qualified with his background in chemistry and materials science, he attracted in the mid-1950's outstanding scientists with recognized experimental and theoretical background to electronic materials research and within a few years established an internationally recognized, leading Electronic Materials Research Center. The unique accomplishments of his group in the areas of semiconductor, superconductor, and laser materials and amorphous semiconductors were largely responsi-

ble for stimulating similar approaches in other research centers of the United States and the rest of the world.

In his function as chairman of the Electronic Materials Committee of the A.I.M.E. he was instrumental in removing materials research from its isolation by establishing a forum in which electronic materials scientists communicated closely with theoretical physicists and electrical engineers. His efforts led ultimately to the publication of the *Journal of Electronic Materials*. As a member of the Board of The Electrochemical Society he fought for the recognition of the importance of electronic materials research within the realm of the Society's activities. As its elected president in 1967 he strongly supported reorganization of the structure of the *Journal of The Electrochemical Society* which soon thereafter led to the introduction of the subdivision of Solid-State Science and Technology and made the *Journal* one of the most important outlets for publications on solid-state research. Recognizing the importance of surface effects in solid-state research and technology he focused his attention toward surface chemistry and physics and in 1964 founded the journal *Surface Science*. This journal, with strong emphasis on electronic materials, gained within a few years international recognition and constitutes today the most important publication in this field.

In his efforts to advance materials research in solid-state science, Harry recognized significant deficiencies in the educational background of young scientists who had just graduated from outstanding academic institutions. Conspicuous to him was the lack of adequate appreciation for materials on the part of physics and chemistry majors on the one hand and the inadequate solid-state physics background of most majors in metallurgy on the other hand. He resigned as Head of the Solid State Division at the Lincoln Laboratory and assumed a faculty position at M.I.T. with a joint appointment in Metallurgy and Electrical Engineering. He subsequently became instrumental in bringing about changes in the basic curriculum of both departments, changes which have in the meantime been adopted by major academic institutions throughout the United States. He provided, furthermore, the stimulus for the establishment of materials science as a discipline, a concept which is now adopted nationally and internationally.

The Electronic Materials Group at M.I.T., which he founded in 1962, developed into a mecca for scientists in electronic materials from all over the world. (Four of them are currently there doing advanced research and broadening the horizon of his graduate students—needless to say, many of his former graduate students are now actively contributing to the advancement of solid-state science and technology.)

Most recently Harry focused his attention on the potential of zero gravity environment for electronic materials research. He is at this time instrumental in establishing and coordinating a comprehensive exploratory research program aimed at a realistic assessment of the beneficial aspects of outer space conditions on electronic materials processing.

About three years ago Harry told me: "Gus, I'm tired; it is time for me to relax, to lie in the sun and write a book or two." Since then he got deeply involved in space processing, initiated new research activities at M.I.T. concerned with: photo-voltage inversion, the photo-mechanical effect, materials for solar energy conversion, current controlled liquid phase epitaxy, and he is now thinking about a major new involvement in research on the catalytic activity of semiconductor surfaces. Harry, I'm sorry your program for the next ten years is on record—your books must wait.

What else can be said about a man who in twenty years shaped the advancement of solid-state science with forcefulness and determination? I could talk about his accomplishments as chairman and member

on numerous committees, about his national and international awards, about his membership of several academies, about his books and patents—I do not have the time. But I will finally say a word about Harry's great accomplishment which now dates back some 25 years and made all the other accomplishments pos-

sible. It was at that time that he succeeded in persuading Dawn to become his wife. It was she who made it possible and still makes it possible for him to operate with efficiency and success, day by day, on a 20 hour work schedule. Congratulations, Harry.

Thank you.

Structure Property Relationships: Key to Solid-State Science and Technology²

Harry C. Gatos



Harry C. Gatos presents the Solid State Science and Technology Medal Award Address.

I am deeply honored to be the recipient of the Solid State Science and Technology Award. Having lived the excitement of the explosive and frantic development of solid-state science and technology through the fifties and early sixties, this award, beyond its high status, has special overtones for me. It relates to that electrifying environment in which researchers in the field around the world lived and moved, like fiercely competing athletes bound by the spirit of classical sportsmanship. The field was boiling over: being first to publish on a new result rather than second or third was often a matter of days.

In my research over the years I have been very privileged to work with outstanding colleagues, associates, students, and technical assistants. I am grateful to every one of them. Without their contributions I would not be addressing you today.

In this address I would like first to sketch a historical framework to help view solid-state science and technology in perspective and discuss some of the dominant patterns underlying its growth. Then I will outline the evolution of two of the research themes we

have pursued for a number of years. Finally, I would like to share with you some of my views on the future.

Historical Perspective

The discovery of the transistor has changed the course of science and technology at large more sharply than any other single discovery in history. Semiconductor (solid-state) electronics, an offspring of the transistor, brought into sharp focus the necessity for interdisciplinary research and development on materials. The needs for ultrahigh purity; for large single crystals with high crystalline perfection; for incorporating selected impurity elements at controlled concentration levels in the part per million range; the necessity to know the concentration, mobility, and lifetime of charge carriers; to prepare and understand p-n junctions; to understand and control the surface properties brought together physicists, chemists, metallurgists, and electrical engineers at an unprecedented level of close collaboration. It was this collaboration that proved the striking nonlinear effects of multidisciplinary interactions.

The consequences reached far beyond the rapid development of solid-state electronics and its revolutionary impact on technology. Semiconductors, such as germanium and silicon, familiar only to physicists up to that time, turned out to be a blessed class of materials. They were prepared at purity levels never approached in other material and in single crystal form with nearly theoretical perfection. Consequently, experimental studies became possible at extraordinary stages of refinement. The covalent nature of semiconductors, their well-defined four-nearest neighbor coordination, and their highly directional bonds, made possible elegant theoretical studies. Experiment and theory reinforced each other with an unparalleled effectiveness. The detailed structure of the electron energy bands, the effective masses of the electrical carriers, their transport and scattering characteristics, their interaction with impurity atoms and crystalline defects, and their response to electric and magnetic fields became well-understood realities. Striking experimental developments occurred far more frequently and consistently on semiconductors than in metals or insulators.

Interdisciplinary studies on semiconductor surfaces were intimately interwoven with the study of the bulk. It is perhaps not fully recognized that the discovery of surface states in semiconductors (1947) led directly to the discovery of the transistor. For the first time the study of the electronic and crystalline structure of solid surfaces could be pursued on a quantitative basis.

Semiconductor research led to a situation never before encountered in science and engineering: basic understanding of material overtook materials development and engineering. That is, new fundamental phenomena, properties, and new devices were predicted rather than discovered directly on available materials. For example, basic phenomena such as the cyclotron resonance (which permitted the determination of the

² Solid State Science and Technology Medal Award Address delivered May 13, 1975 at the Toronto, Canada, Meeting of the Society.

effective mass of the electrical carriers) and numerous devices (including the field-effect transistor) were theoretically described in the context of materials requirements; they reached the experimental stage as the materials requirements were met. In other words, soon after the discovery of the transistor, materials development, rather than basic understanding of materials or device principles, became the slow step in the progress of solid-state electronics. Unfortunately, this situation is still prevalent today.

The contribution of disciplines such as chemistry and metallurgy were certainly basic to the development of solid-state electronics; however, the benefits derived by these disciplines, in return, are not often appreciated. Germanium and silicon (by far the best understood solids) proved unique among all materials for chemical and metallurgical studies and for materials understanding. Purification methods (zone refining) and crystal growth techniques developed for semiconductors were extended to metals, bringing research and development on these materials to a new plateau of refinement. The dislocation theory developed in the early thirties to account for the mechanical behavior of metals was first experimentally verified when edge dislocations in a low-angle boundary configuration were observed in germanium crystals. Screw dislocations and their characteristics were first observed and studied, by infrared microscopy, in copper-decorated silicon crystals; the operation of the Frank-Read source was visually demonstrated in these crystals. Giant strides were made in the understanding of nucleation and growth, solid-state diffusion, segregation phenomena through research on semiconductors. Experimental methods developed for the study of the electronic and crystalline structure, the composition, the stoichiometry and the surfaces of semiconductors were invariably extended to other materials. Finally, the theoretical framework of the energy band structure, electronic transitions, and carrier transport in semiconductors has served as the basis for theoretical advances on metals insulators and other materials.

Through tractable reality, rather than foresight, it was realized that the science and technology of any class of materials (metals, ceramics, glasses, polymers) cannot be fostered within the confines of individual classical disciplines. Materials science and engineering emerged from solid-state electronics as a discipline in itself but linked effectively to the classical disciplines. Solid-state science and technology, rooted also in semiconductor electronics, now encompasses the study and applications of a broad spectrum of materials and phenomena. It interacts intimately and to some extent overlaps with materials science and engineering, with physics and with electrical engineering (Fig. 1).

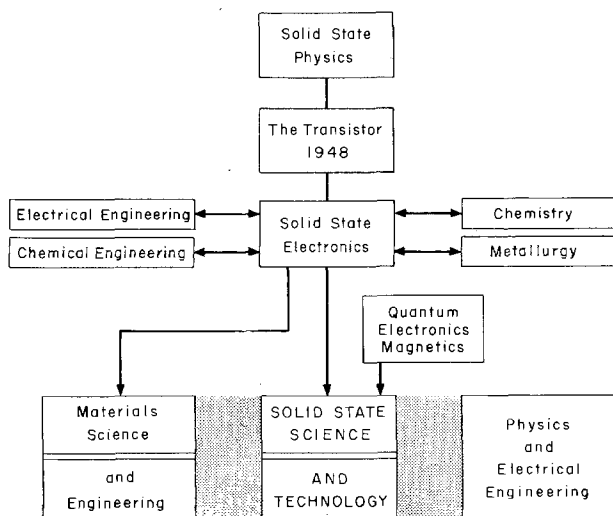


Fig. 1. Solid-state science and technology in perspective

Structure-Property Relationship

Structure-property relationships have been useful for some time in accounting qualitatively for the behavior of solids and in pointing to new directions for the search for materials with improved properties. But they became the driving force of progress in semiconductor and solid-state electronics. Electronic properties are strongly dependent on "structure," i.e., on composition, crystalline structure, lattice defects, and interatomic forces. Because of the unique nature of semiconductors, this dependence can usually be pursued on a quantitative basis: The properties can be experimentally measured reliably and accurately. The "structure" cannot only be experimentally determined, but it can be controlled and varied at will often with high precision; the composition (level of desired impurities) can be controlled in the part per million range; nearly perfect single crystals can be prepared (with zero dislocation density); interatomic forces (strength and nature of bonding) vary in a known way from one semiconductor to another or can be carried at will by controlled alloying.

At the same time, semiconductors lend themselves better than any other solids to the development of theoretical treatments and theoretical calculations. Thus, feedback between theory and experiment has led to an avalanche of new experiments and basic understanding. Device development is also interwoven in the fabric of structure-property relationships. The identification of the "structural" parameter related to specific effects has been the way to device development, to prediction of new devices and new device-functions.

A comprehensive illustration of the interplay between structure-property relationships and progress in the evolution of solid-state science and technology, would certainly make a fascinating and most instructive document. I hope someone undertakes this task some day. I will only touch on it here.

One could start with the studies just preceding the discovery of the transistor. A group, now famous, at the Bell Laboratories was studying metal-semiconductor rectifying contacts; according to theory, the potential barrier in a given semiconductor should be greater (and the rectifying characteristics better), the greater the work function of the contacting metal. But using germanium as the semiconductor the height of the potential barrier was found to be independent of the contacting metal. Through a stroke of genius, this behavior was related to a "structural parameter" of the semiconductor: surface states within the forbidden energy gap; these states trap charge carriers and lead to a surface barrier, characteristic of the semiconductor rather than of the metal-semiconductor contact. Thus, a structure-property relationship was formulated; it set things into motion; the existence of surface states had to be verified. The ingenious field-effect experiment was conceived which not only verified the existence of surface states, but revealed their detailed characteristics. Experiment reinforced theory, and new structure-property relationships with device implications evolved. The transistor was discovered. In turn, its function and improved performance was related to "structural" parameters, i.e., to types, concentration levels, and configurations of dopant impurities and to crystalline perfection. These parameters were identified and studied; their control was improved. Better devices were obtained and new devices were conceived; further refinements in materials were indicated. The study of processing parameters for improving the quality of materials entered the feedback loop. Planar diffusion and epitaxial growth methods, developed for improving the control of dopant concentration, opened the way to integrated circuitry. In parallel experimental techniques for materials characterization were developed to keep pace with the advancing level of materials refinement. Such self-feeding progress through structure-property relationships has no precedent in the history of science and technology. Originally germanium, and subsequently silicon, have

been the materials in this evolution, but certainly not the only ones. Behind the recent precipitous entry of the light-emitting devices (based on III-V semiconductor compounds) into solid-state electronics there is a similar pattern of development (Fig. 2).

Through the evolution of solid-state science, theory has made enormous advances. For example, band-structure theories can determine with remarkable precision the electronic properties of some solids. Theory, however, has not as yet predictive powers in relating the electronic properties to the composition or defect structure of the crystals. Empirical, intuitive and semi-quantitative structure-property relationships will continue to be at least for the foreseeable future, the key to solid-state science and technology.

Tracing the Evolution of Two Research Themes

As I reviewed the structure-property and structure-processing programs I have worked on in the last twenty years, I decided to discuss two of them. I chose them not necessarily because of their greater importance, but because, all these years, they have survived the changes in fashion and the points of diminishing return. The one was initiated to investigate the "structural" parameters responsible for the chemical behavior of semiconductor compound surfaces; the other was initiated to study the processing variables responsible for the composition (dopant distribution) and the defect structure of semiconductors. In the interest of time I will attempt to convey a general impression rather than present a rigorous account of our findings.

Semiconductor Compounds

In 1956, together with Mary Cretella-Lavine, I became involved in the study of the chemical behavior of the A^{III}B^V compounds (e.g., InSb), then a relatively new class of semiconductors. Because these compounds have the noncentrosymmetric (crystallographically polar) zinc-blende structure their {111} surfaces must terminate with Group III or A atoms, e.g., In atoms; on the other hand, the $\bar{1}\bar{1}\bar{1}$ surfaces must terminate with Group V or B atoms, e.g., Sb atoms (Fig. 3). These two types of surfaces are referred to as A and B surfaces, respectively. We observed, as others had, that the etching behavior of the A surfaces is strikingly different than that of the B surfaces (Fig. 4) and that edge dislocation can be revealed, as etch pits, only on the A surfaces (Fig. 5); this behavior was particularly puzzling because the observed etch pits were associated with only one type of edge dislocations, namely, those whose dislocation line consisted of A atoms (α dislocation); dislocations with their line consisting of B atoms (β dislocations) should also be present in these compounds; furthermore, edge dislocations must intersect both A and B surfaces (Fig. 6).

In germanium, Walter Harvey had found that the dissolution rates of the various crystallographic planes,

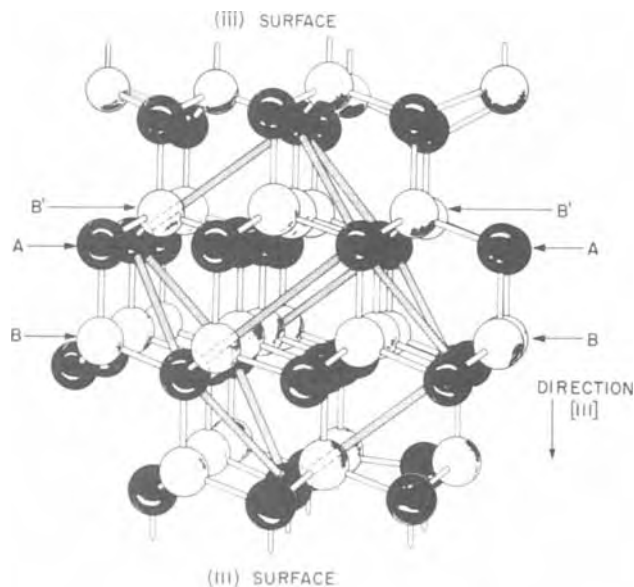


Fig. 3. Model of the structure of the A^{III}B^V compounds (zinc-blende structure); the unit cell is indicated. ●, Group III or A atoms; ○, Group V or B atoms.

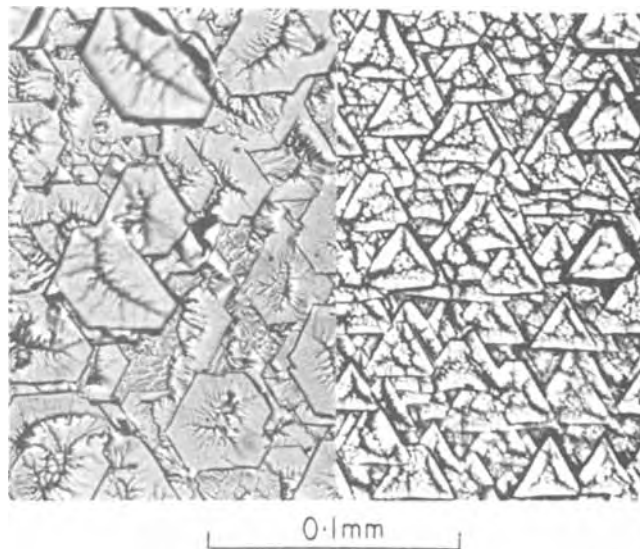


Fig. 4. The A (left-hand side) and B (right-hand side) surface of an InSb wafer etched in Fe⁺⁺⁺ etchant.

in oxidizing solutions, were related to the density of their dangling bonds. But the density of dangling bonds is the same on the A and on B surfaces. We turned our attention to the nature of the dangling bonds and arrived at the following model: The Group III atoms on the A surfaces cannot have dangling electrons, as they must share their three electrons in forming three bonds with the lattice; on the other hand, each Group V atom on the B surfaces contributes three of its five electrons to the three bonds with the lattice, and thus, must have two (paired) dangling electrons (Fig. 7).

We proceeded to test the obvious implication of this simple model. The B surfaces, whose outermost atoms have two unshared electrons, must react much faster in oxidizing media than the A surfaces whose atoms have no available unshared electrons. From single crystals of InSb we prepared two types of tetrahedral samples, one bounded by A surfaces and the other bounded by B surfaces (Fig. 8). Using such samples we found that indeed the dissolution rate of the B surfaces in oxidizing solutions was an order of magnitude greater than that of the A surfaces. On the basis of this finding, i.e., that the triply bonded B atoms are much more reac-

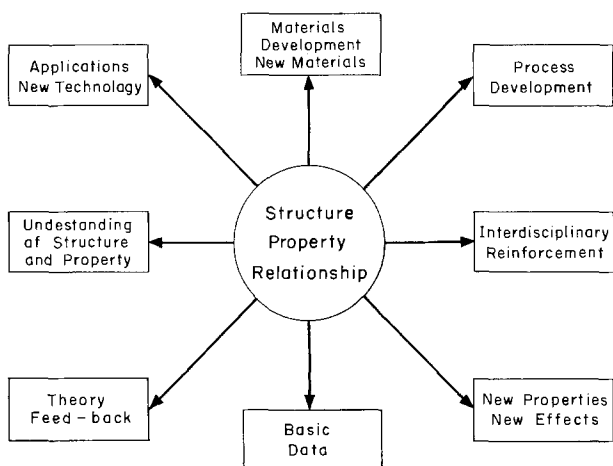


Fig. 2. Dynamics of structure-property relationships

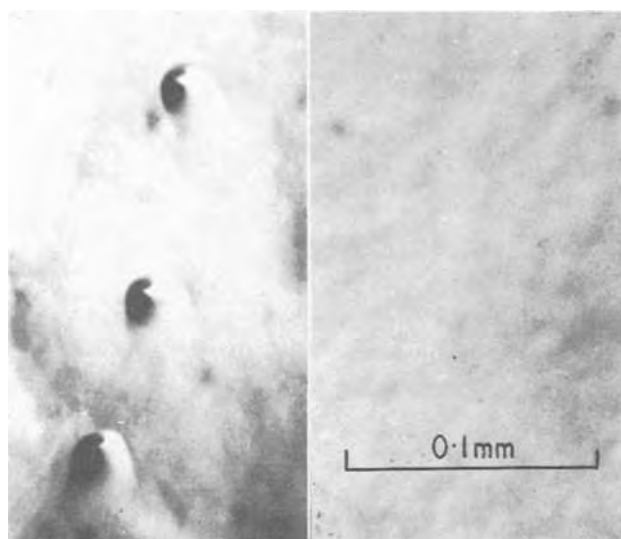


Fig. 5. The A (left-hand side) and B (right-hand side) surface of an InSb wafer etched in a modified CP4 etchant.

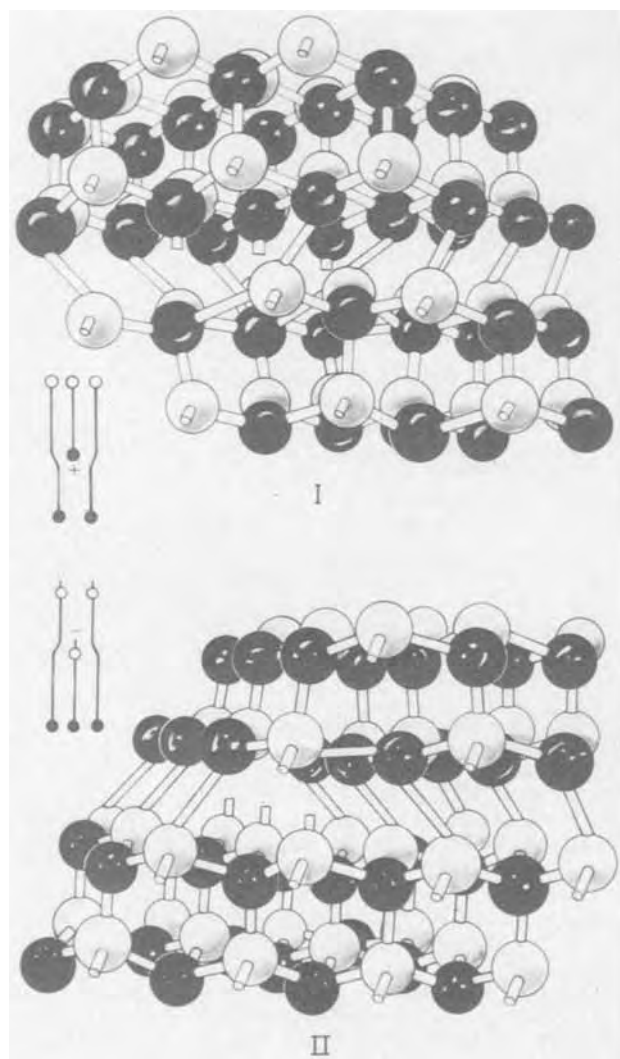


Fig. 6. Atom models showing (I) an edge dislocation terminating in A atoms (black atoms) and (II) an edge dislocation terminating in B atoms (white atoms) intersecting the B surface defined in the models by the atoms with protruding bonds.

tive than the triply bonded A atoms, it was relatively straightforward to explain why only α dislocations and

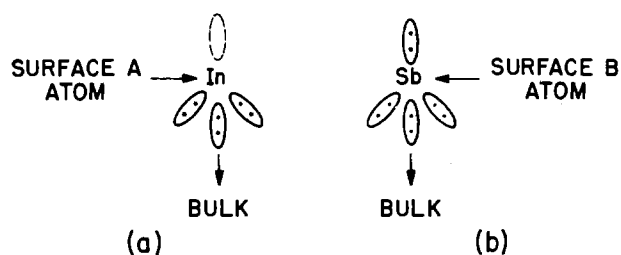


Fig. 7. Atomic model of the A and B {111} surfaces of the $A^{III}B^V$ compounds (e.g., InSb). The A surface atoms have no dangling electrons, (a), whereas each B surface atom has two dangling electrons (b).

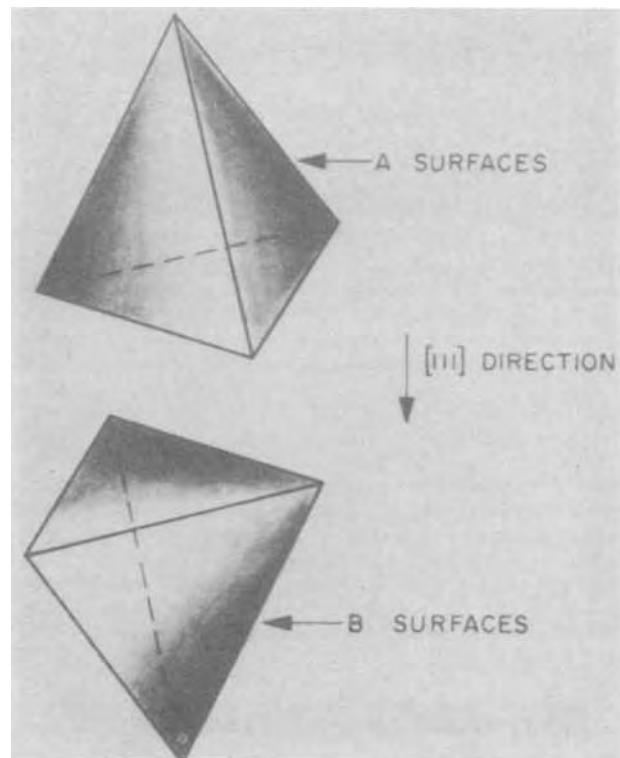


Fig. 8. Two types of tetrahedra of an $A^{III}B^V$ compound; one has only A surfaces and the other only B surfaces. Both types are obtained from the same single crystal. Compare geometric relationship of the tetrahedra with Fig. 1.

only on the A surfaces can lead to the formation of etch pits. Our structure-property relationship had survived its first test. But if the presence of unshared electrons was responsible for the high reactivity of the B surfaces in oxidizing media then this reactivity should decrease in the presence of electrophilic chemical compounds which attach themselves to unshared electrons. When we added small amounts of electrophilic organic compounds to oxidizing etchants the reactivity of the B surfaces of InSb decreased and approached that of the A surfaces. Under these conditions, α as well as β dislocations were revealed, through etch pit formation, on both types of surfaces (Fig. 9).

Thus, the presence of two types of dislocations in the $A^{III}B^V$ compounds (see Fig. 6) was confirmed by chemical etching. Furthermore, these results provided direct evidence that the formation of dislocation etch pits is controlled by the chemical reactivity of the dislocation and surface atoms; until that time it was generally believed that the strain fields associated with edge dislocations are responsible for the formation of dislocation etch pits.

This early success pointed to a closer examination of the model. The atoms in the III-V compounds are tetrahedrally bonded (diamond structure); can the

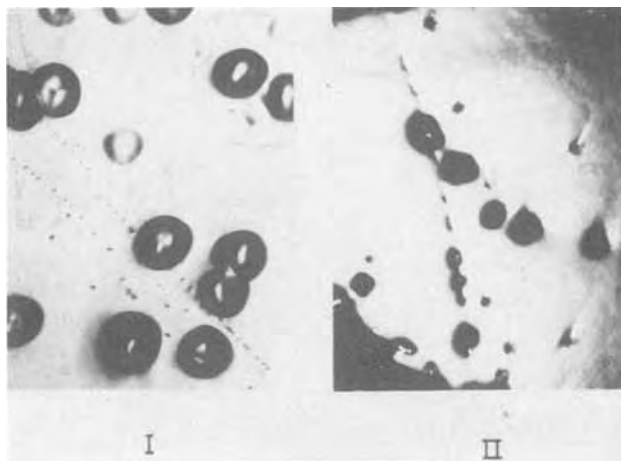


Fig. 9. Dislocation etch pits on the A (I) and B (II) surfaces of an (111) InSb wafer. Two types of pits (small and large) are clearly seen on the A surfaces. A modified CP4 etchant was saturated with stearic acid. 90X.

bonds of the surface atoms maintain this angular configuration? In the case of the B atoms with a pair of electrons occupying the unshared (dangling) tetrahedral orbital, no significant distortion would be expected. However, tetrahedral configuration should not be possible in the case of A surface atoms where there are no electrons in the dangling orbital (see Fig. 7); accordingly, the triply bonded A atoms should exhibit a strong tendency to acquire planar (sp^2) bonding, characteristic of the Group III elements in their compounds with nonmetals. Thus, the A surface atoms should arrive at a distorted configuration, in between tetrahedral and planar; assuming no major surface reconstruction, this distorted bonding configuration must introduce significant strain in the A surfaces in the form of stored elastic energy. The implications of this aspect of the model were pursued.

X-ray diffraction techniques showed indeed that the A surface of a single crystal sample (*i.e.*, InSb) exhibited significant strain in contrast to the B surface. This result was confirmed by much simpler means. After abrading both surfaces in the same way it was found that the depth of damage was much greater in the B surface than in the A surface; clearly, the A surfaces with their stored elastic energy are more resistant to abrasion than the B surface (Fig. 10).

Crystal growth has always been (and still is) basic to semiconductor research and development. In the fifties, the growth of single crystals presented far greater difficulties in the case of compounds than in

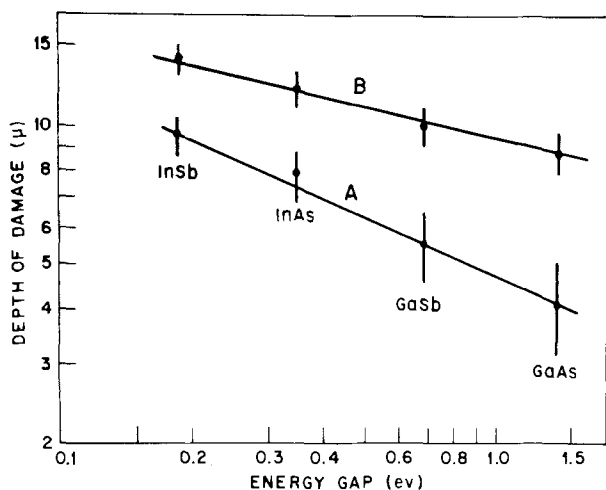


Fig. 10. Depth of damage of the A and B surfaces of $A^{III}B^V$ compounds. A 20μ particle-size abrasive was used.

the case of elemental semiconductors; could the surface structure implications of our bonding model be related to crystal growth? If the A surface was inherently strained, then the B surface of a $\langle 111 \rangle$ seed should be more suitable for crystal growth than the A surface. We tested this prediction on the growth of both InSb and GaAs crystals. Single crystals could be obtained only when the B surface of the seed was used. When the A side of the seed was used twinning or polycrystallinity could not be avoided. Paul Moody, who did the experiments, had been growing InSb crystals in the $\langle 111 \rangle$ direction for the entire solid-state group at the Lincoln Laboratory. In checking his laboratory notebooks he found that among numerous InSb crystals he had grown before these experiments, only one-half of them were single; he, thus, proved that the probability of using the proper end of a seed coincided with the probability of obtaining single crystals. Since the time of this finding, the B surface of the seed is being used for growing III-V compounds from the melt in the $\langle 111 \rangle$ direction. In epitaxial growth also, the B surface is the preferred substrate surface. Furthermore, the elastic stored energy in the A surfaces of III-V compounds is now implicitly taken into consideration in III-V semiconductor layer device structures.

The stored elastic energy on the A surfaces manifested itself directly in thin (111) wafers; such thin (about 10μ m) wafers prepared from single crystals of several $A^{III}B^V$ compounds were spontaneously bent (Fig. 11); the elastic strain on the A surfaces overcame the cohesive energy of the wafers. From the radius of curvature of the spontaneously bent InSb wafers, their dimensions and elastic parameters, Rodney Hanneman calculated the elastic stored energy ($\sim 1 \times 10^{-6}$ ergs/g-surface atom) using the classical theory of elasticity; this result was in good agreement with the elastic stored energy he calculated from x-ray diffraction data.

Turning to the electronic properties, the A surface atoms having no dangling electrons should be electron acceptor-type, whereas the B surface atoms should be electron donor-type. The implications of the bonding model on the electronic characteristics of the A and B surface are schematically illustrated in Fig. 12. A direct electronic characterization of III-V semiconductor compound surfaces presented severe experi-

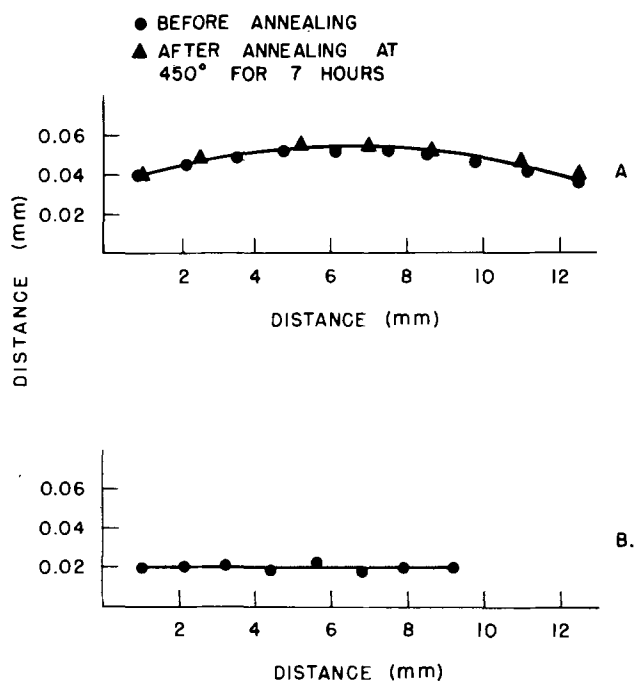


Fig. 11. Spontaneous bending of an InSb (111) wafer 8μ m thick (A); a germanium wafer of the same orientation and thickness exhibited no spontaneous bending.

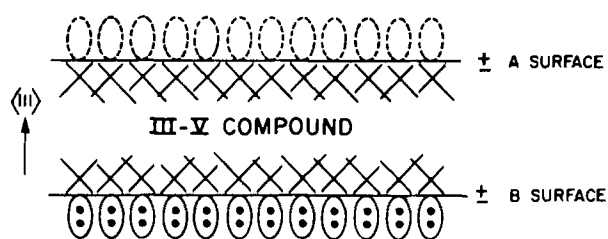


Fig. 12. Schematic representation of the dangling bonds on the A and B surfaces of III-V compounds and the associated surface dipole moments.

mental difficulties. We arrived, however, at the electronic characterization of the triply bonded A and B atoms through a relatively simple approach: the dislocation lines of the α dislocations consist of triply bonded A atoms and those of the β dislocations consist of triply bonded B atoms (see Fig. 6); accordingly, n-type InSb single crystal samples were deformed so as to introduce either excess In dislocations or excess Sb dislocations; as predicted, the samples with excess In dislocations became less n-type, i.e., the triply bonded In atoms introduced acceptor levels; the samples with excess Sb dislocations became more n-type, i.e., the triply bonded Sb atoms introduced n-type levels.

The class of $A^{II}B^{VI}$ semiconductor compounds (e.g., CdS) had not received nearly as much attention as the III-V compounds in the late fifties. These compounds have the noncentrosymmetric wurtzite or zinc-blende structures; like the III-V compounds, they are characterized by sp^3 (tetrahedral) bonding. The absolute identification of the A and B surfaces had not been carried out. Edward Warekois achieved this identification by x-ray diffraction techniques, on eight II-VI compounds.

As in the case of the III-V compounds, in all II-VI compounds also pronounced differences in etching behavior were observed between the A and B surfaces. These differences were correlated with the x-ray results so that the identification of the A and B surfaces was reduced to simple etching tests. The surface properties of these compounds were also successfully related to the bonding characteristics of the A and B atoms. The stored strain energy due to bonding distortion in the A surfaces was confirmed by the spontaneous bending of thin (00.1) wafers. Most recently the nature of this distortion was theoretically calculated for the Zn surfaces of ZnO from LEED intensity data by other investigators.

In the early sixties Shinji Kawaji undertook to study, in our new electronic materials group at M.I.T., the electronic characteristics of the A and B surfaces of InSb employing field-effect techniques. He and Howard

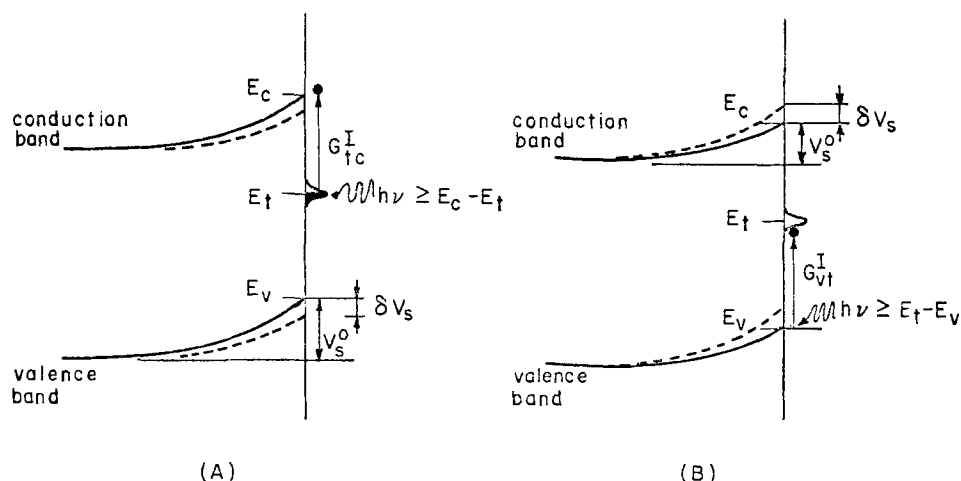
Huff found that surface states present on the A surfaces were characteristic of the triply bonded In atoms and surface states of the B surfaces were characteristic of the Sb atoms consistent with the bonding model. This work clearly showed the significant influence of crystallographic polarity on the electronic behavior of semiconductor compounds. The implications of the bonding model on the electronic characteristics of the A and B surfaces as illustrated in Fig. 12 were directly confirmed later on by other investigators on cleaved (00.1) surfaces of ZnO. In the course of his studies Shinji Kawaji observed quantization of the motion of electrons in the surface region in the presence of electric and magnetic fields; this phenomenon became of significant interest in understanding carrier transport phenomena in semiconductors.

Extensive efforts in our group to study the electronic characteristics of surfaces of high energy gap semiconductor compounds, i.e., GaAs and CdS, led us to the conclusion that the field-effect technique was not applicable to the detailed study of surface characteristics of such semiconductors and that no experimental method was available for the purpose. The experimental approach in this instance, as is often the case, became an end itself rather than a means to an end.

Jacek Lagowski joined the group in the early seventies as Chester Balestra was investigating the electronic characteristics of CdS surfaces by a photovoltage approach employing a method he developed for linear off-null measurements of the contact potential difference (cpd). In exploring the effects of illumination on the height of the surface barrier, they observed that discreet electron transitions from the surface states to the conduction band (surface-state depopulation) and from the valence band to the surface states (surface-state population) could be identified when illumination energies less than those corresponding to the energy gap were employed (Fig. 13). From the values of the surface photovoltage (changes in the surface barrier) as a function of the energy of the monochromatic sub-bandgap illumination, spectra were obtained from which the energy levels of the surface states could be directly determined. Surface photovoltage spectroscopy was born. The transients of the surface photovoltage provided the means for determining the dynamic parameters of the surface states such as occupancy, capture cross section and others. A detailed characterization of the electric configuration of CdS and GaAs surfaces was achieved. A surface photovoltage spectrum of the prismatic surfaces of CdS is shown in Fig. 14, and the data obtained from this spectrum are summarized in Fig. 15.

Jacek Lagowski became interested in reexamining the bonding model on thin (00.1) wafers of CdS. Like the thin wafers of other noncentrosymmetric compounds the CdS wafers were also spontaneously bent.

Fig. 13. Schematic representation of the origin of surface photovoltage (change in surface barrier V_s) in an n-type semiconductor. (A) Surface-state depopulation, (B) surface-state population.



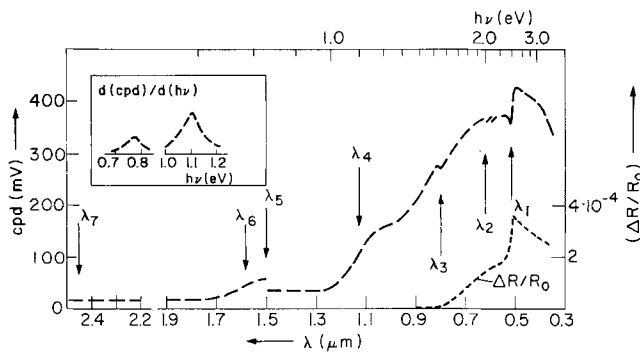


Fig. 14. Surface photovoltage spectrum and photoconductivity of the prismatic surfaces of CdS. The insert shows the derivative of surface photovoltage (cpd) with respect to the photon energy at two typical step-like increases in the photovoltage; each peak gives the energy position of a surface state.

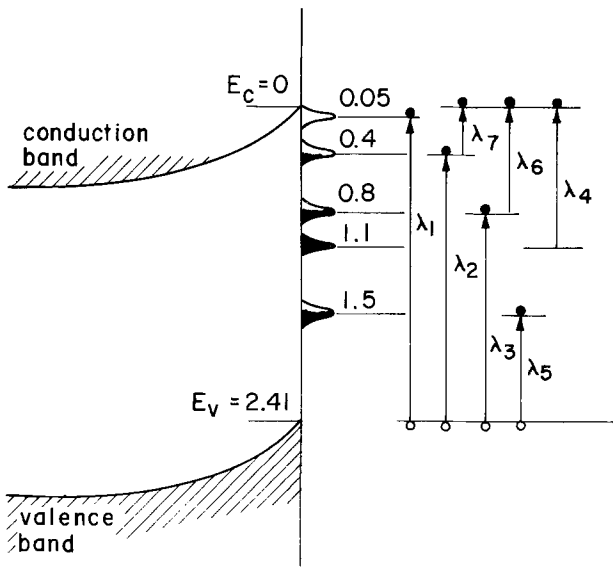


Fig. 15. Energy positions of the surface states in the prismatic surfaces of CdS and the associated electron transitions.

In studying these wafers he observed that illumination with white light led to far greater bending than that caused by stored elastic energy. This behavior represented a new effect associated with light-induced changes in the electric field at the surface (*i.e.*, changes in the surface barrier) and thus, with light-induced surface strains, since CdS is a piezoelectric material. The electric field (and thus the strain components) in the basal surfaces is in opposite directions because a depletion layer is present at both parallel surfaces. Consequently, upon illumination, one surface is under compression and the other under tension, and the wafer undergoes bending. We called this phenomenon the photopiezoelectric effect. The wafers, anchored at one end, were excited to their fundamental-frequency vibration when the electric field was modulated at that characteristic frequency by chopped light (Fig. 16).

It was subsequently found that, under sub-bandgap illumination, the amplitude of the photo-induced vibration underwent changes at illumination energies corresponding to electron transitions from or to the surface states. In fact, the spectra of the amplitude of the vibration as a function of the wavelength of the illumination were virtually identical to the surface photovoltage spectra (Fig. 17). The amplitude of the vibration was found to be very sensitive to the in-

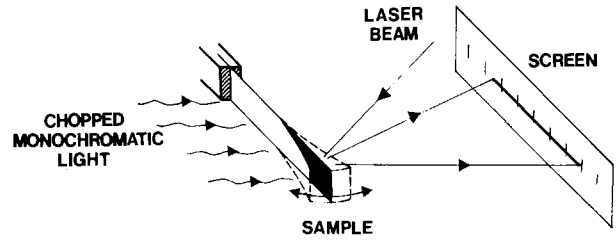


Fig. 16. Experimental arrangement employed in observing and studying light-induced mechanical vibration.

tensity of illumination; light intensities of the order of 10^{11} photons/cm²/sec could readily be detected. Furthermore, the amplitude of the vibrations was found to be sensitive to very small amounts of ambient gases causing changes in the surface state configuration. Thus, the photopiezoelectric effect constitutes a very sensitive means for photodetection and for the detection of trace amounts of ambient gases.

The normal mode of vibration of (111) GaAs wafers with a thickness below 15 μm was found to depend on the surface preparation and the ambient atmosphere. This dependence was attributed to effects directly related to surface stress; accordingly, a new method was developed for determining the surface stress in solids from the natural frequency vibration.

The photopiezoelectric effect should have its reverse counterpart, and it does. Mechanical bending of

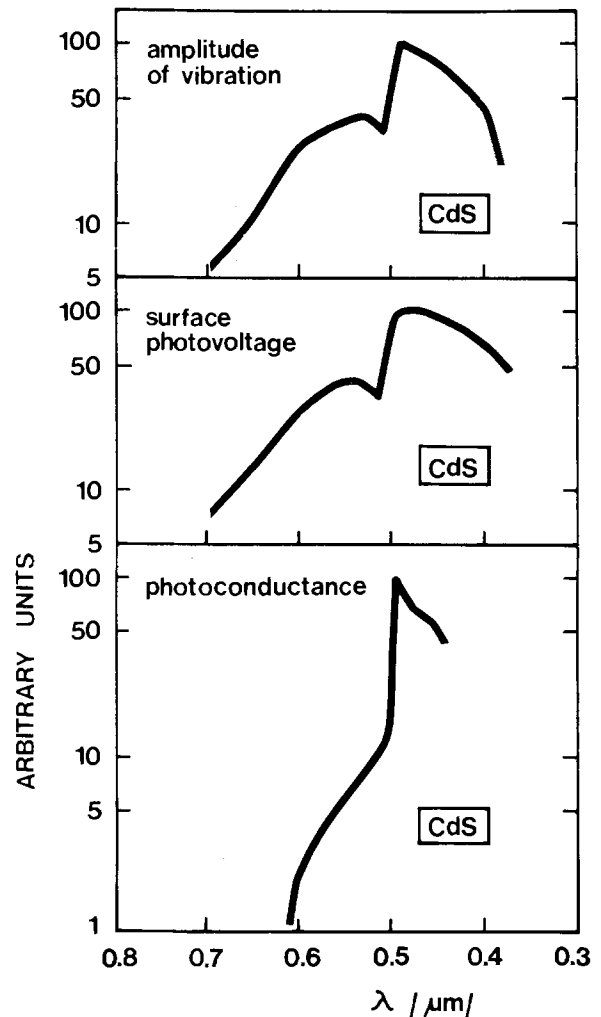


Fig. 17. Typical spectra of the amplitude of the light-induced vibration, surface photovoltage and photoconductance of (00.1) CdS wafers; frequency of light-chopping ≈ 104 Hz.

thin (00.1) wafers of CdS and other crystallographically polar semiconductors was found to cause pronounced changes on the surface barrier. This new effect we called the surface piezoelectric effect: strain due to bending leads to changes of the electric field in the space charge region. Accordingly, the surface piezoelectric effect provides the means for changing the electric field at the surface; it permits field-effect experiments, without an external electrode, and the determination of the surface potential employing a cpd probe for monitoring changes in the height of the surface barrier. Thus, this effect is a powerful complement to surface photovoltage spectroscopy for the electronic characterization of surfaces.

Since in thin wafers of semiconductor compounds the surface barrier is a sensitive function of the radius of bending (or stresses in general) the surface piezoelectric effect is a powerful tool for determining the curvature or changes in curvature of solids or for determining very small stresses.

Surface photovoltage spectroscopy as outlined above or with some modifications is now widely used for the study of surfaces and interfaces in semiconductors or semiconductor device structures.

With the new surge of interest in chemisorption and catalysis, the importance of the surface barrier and surface states of semiconductor catalysts in these processes (recognized about twenty-five years ago) have been brought into sharp focus. At the present, surface photovoltage spectroscopy in conjunction with the surface piezoelectric effect, represent the only direct experimental approach to this problem. The interaction of gaseous species with semiconductor surfaces via surface states and the study of the associated charge transfer can be directly studied with surface photovoltage spectroscopy. The surface piezoelectric effect is uniquely suited for varying at will the height of the surface barrier on a given sample without altering the surface-state configuration. Our preliminary results on the interaction of oxygen and carbon monoxide with ZnO are extremely promising. They could represent the first step towards advancing our understanding of catalytic processes involving semiconductor catalysts.

Relating chemical bonding to chemical, mechanical, structural, and electronic properties of compound semiconductors has led us, for about twenty years, to many directions for fruitful research and applications. Still our original bonding model has not outlived its usefulness.

Crystal Growth and Dopant Segregation

From the very start of solid-state electronics, it was found that the dopant elements were not homogeneously distributed in the single crystals. About twenty-five years later we are still confronted with the same problem. This problem is as acute today as it was then, not because progress has not been made in crystal growth and dopant segregation, but rather because much greater progress has been made in decreasing the size and extending the functions and complexity of semiconductor devices.

Like many solid-state groups around the world our group at the Lincoln Laboratory became involved in investigating the origin of dopant inhomogeneities. Periodic inhomogeneities always present in Czochralski-pulled crystals had been found to be associated with the seed rotation, and in fact their period had been shown to be the same as the period of rotation. In the late fifties, with my colleagues at the Lincoln Laboratory, we performed a simple experiment; we pulled a segment of an InSb crystal without rotating the seed. The normal rotational inhomogeneities were not present in this segment but inhomogeneities were there (Fig. 18). Their presence indicated temperature fluctuations at the growth interface, but the origin of such fluctuations was quite puzzling.

While a number of groups were theoretically and

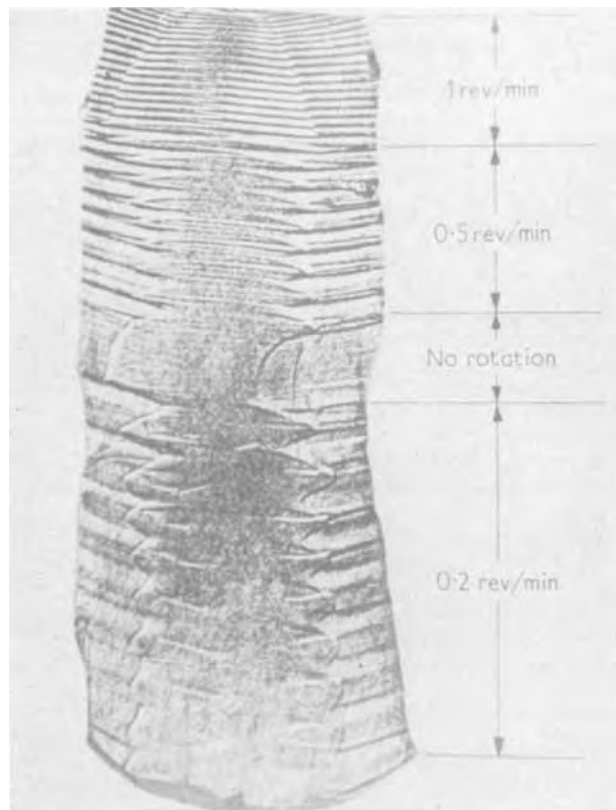


Fig. 18. Longitudinal etched section of a Se-doped InSb crystal. Dopant striations are present in both the rotated and unrotated segments of the crystal. 5X.

experimentally demonstrating temperature fluctuations in melts under thermal gradients, we set out in our new electronic materials group at M.I.T. (1962) to study the nature and origin of dopant inhomogeneities in semiconductor single crystals. We began with InSb primarily because its low melting point minimized experimental complexities. Professor Witt joined the group three years later, was fascinated by the problem, and became a partner in the work and a prime mover.

The main tools for studying dopant inhomogeneities were then, and still are, chemical etching and optical microscopy. Professor Witt began to sharpen these tools and has sharpened them to their limit. With every increase in the resolution of etching and optical microscopy new types of dopant inhomogeneities were being revealed (Fig. 19).

Kenji Morizane devoted his post-graduate years to the study of dopant inhomogeneities in InSb. He developed the first quantitative model showing that, in Czochralski-pulled crystals, grown under seed rotation, the microscopic rate of growth cannot be the same as the pulling rate. It must vary sinusoidally when the thermal axis of the isotherm at the growth interface does not coincide with the axis of rotation, i.e., due to thermal asymmetry in the melt, the microscopic growth rate must gradually increase from a minimum to a maximum and then decrease again to a minimum within each rotational cycle. Thus, the portion of the crystal grown under increased rate is larger than the corresponding portion grown under decreased rate within a given cycle. Consequently, a greater dopant concentration (for a distribution coefficient smaller than one) is expected in the portion grown at an increased rate than in the portion grown at a decreased rate. Thus, a crystal grown under rotation should exhibit impurity inhomogeneities consisting of alternating broad and narrow bands. The narrow bands whose width becomes very small, depending on

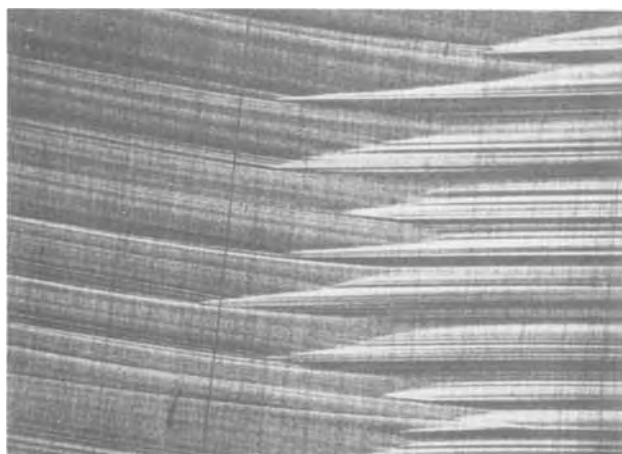


Fig. 19. Etched (211) section of a Te-doped InSb crystal showing the presence of rotational and other types of dopant inhomogeneities. 190X.

the extent of thermal asymmetry, constitute the rotational striations (Fig. 20). The model further predicted that under pronounced thermal asymmetry the microscopic growth rate should assume negative values, *i.e.*, backmelting should take place within each rotational cycle. Indeed, rotational backmelt striations were identified in InSb crystals (Fig. 21).

The Morizane model brought us to an impasse. To pursue the study of dopant inhomogeneities in semiconductor crystals, it was now essential to determine the microscopic growth rate since the pulling rate was shown to be of little relevance; it was also essential to know the dopant concentration on a microscale. At that time there was no method available for determining microscopic growth rates; dopant microprofiling could only be achieved by radio-tracer or other equally complex techniques.

Unexpectedly, we observed in an InSb crystal a type of pronounced dopant striations which had not been observed previously. They were superimposed on the normally observed striations, persisted throughout the crystal and were rather evenly spaced. We suspected that a mechanical vibration of constant frequency was present during the growth of the crystal; its origin was unknown. From the pulling rate and the average spacing of these striations we determined the frequency of the undesirable vibration and traced its origin to a poorly mounted mechanical vacuum pump. This incident turned into an important discovery: We introduced a mechanical vibration of known frequency into the melt (by coupling a vi-



Fig. 20. Rotational striations (narrow lines) in a Te-doped crystal of InSb. Although the pulling rate and the rotation rate were maintained constant during growth, the distance between rotational striations is not constant, indicating that the actual growth rate is not the same as the pulling rate. 150X.

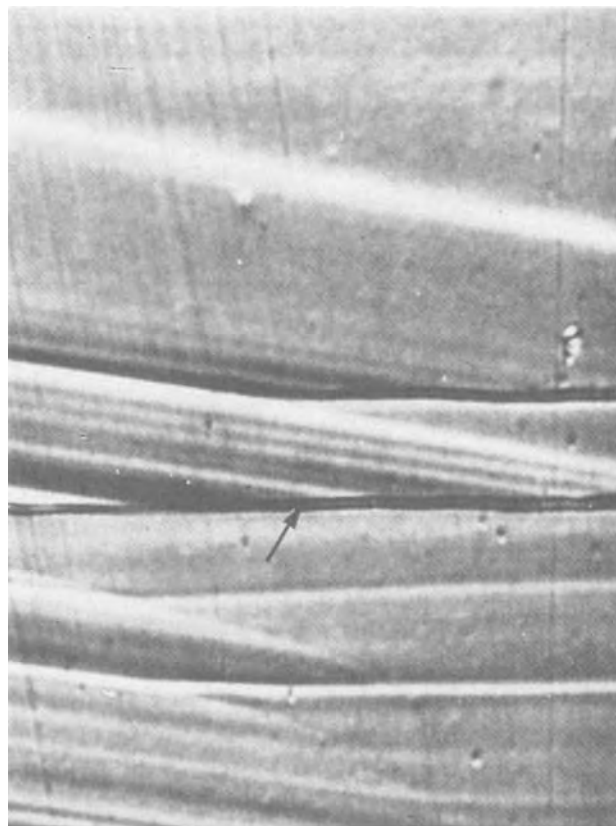


Fig. 21. Rotational backmelt striations (one is indicated by arrow) in a Te-doped InSb crystal. The abrupt termination of non-rotational striations at the rotational striations is caused by the backmelting associated with the formation of the rotational striations. 600X.

brator to the crucible) and found that each individual vibration could be identified into the grown crystal as a dopant striation; the normal growth process was not affected. An experimental method for determining microscopic growth rates was now at hand. From the known frequency of the vibration and the separation of the resulting striations in the crystal we could determine the microscopic growth rate throughout the crystal growth process. We called these intentionally introduced striations "rate striations."

We demonstrated that the microscopic growth rate is not the same as the pulling rate and that in fact it varies significantly depending on the thermal conditions prevailing during growth (Fig. 22, 23). The model of Kenji Morizane was proven to be correct. Soon after Ranjit Singh discovered that rate striations could be introduced into the growing crystals, far more advantageously, by transmitting current pulses of known frequency across the growth interface. Each current pulse, depending on its polarity, causes Peltier cooling or heating at the growth interface. The growth rate is thus suddenly increased or decreased for the duration of the pulse (of the order of 30 msec), and a striation is formed in the crystal. Ranjit Singh went on to accomplish experimentally the quantitative study of oscillatory interface instability associated with constitutional supercooling (in germanium crystals grown from heavily doped melts). He determined for the first time the wavelength and phase velocity of this instability and provided a testing ground for theoretical treatments.

Manfred Lichtensteiger refined the technique and showed that the characteristics of the pulse (rise time, duration, and shape) are precisely reflected in the induced striations (Fig. 24). The delineation of the growth interface into the crystal by current pulses provided a new basis for pursuing crystal growth and segregation. We called this technique interface demar-

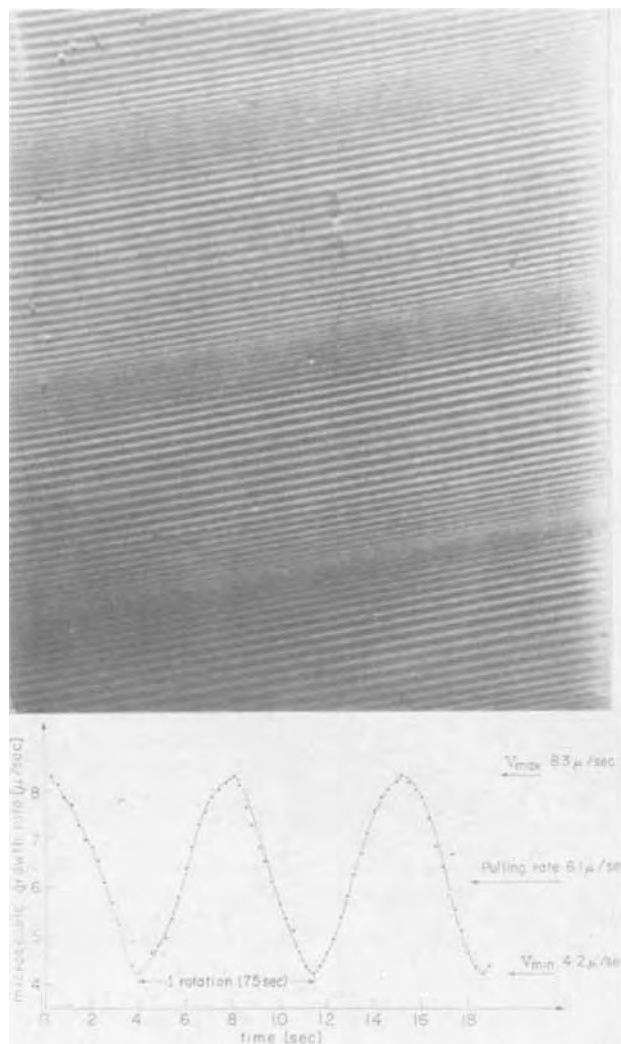


Fig. 22. Cross-section of a Te-doped InSb crystal grown with seed rotation. Rate striations were introduced by a vibration of constant frequency. The variations in the spacing of the rate striations reflect fluctuations in the microscopic growth rate. Rotational fluctuations appear as areas of decreased growth rate (close spacing of rate striations). 550X. The microscopic growth rates of this section are shown in the lower part of the figure.

Without interfering with the over-all growth process, the current-induced striations permit not only the determination of the microscopic growth rates, but also they delineate into the crystal the exact morphology of the growth interface at precisely known instances in time. They serve, thus, as time markers for establishing directly cause and effect relationships, in absolute time, between the prevailing growth conditions and the characteristics of the resulting crystal.

Kyongmin Kim established such cause and effect relationships in his InSb growth experiments under destabilizing thermal gradients. He introduced thermocouples into various parts of the melt and recorded continuously the thermal characteristics of the melt during growth. Current pulses, transmitted at known time intervals, delineated the interface into the growing crystal; simultaneously, through electrical induction, the pulses were sensed by the thermocouples and registered on the temperature recording. Thus, after the experiment, the characteristics of any microscopic segment of the crystal could be related to the thermohydrodynamic characteristics of the melt in absolute time. With continuing growth the melt exhibited successively turbulent convection, oscillatory thermal instability, and finally, thermal stability. During turbulent convection the crystal underwent pronounced transient backmelting and the average microscopic

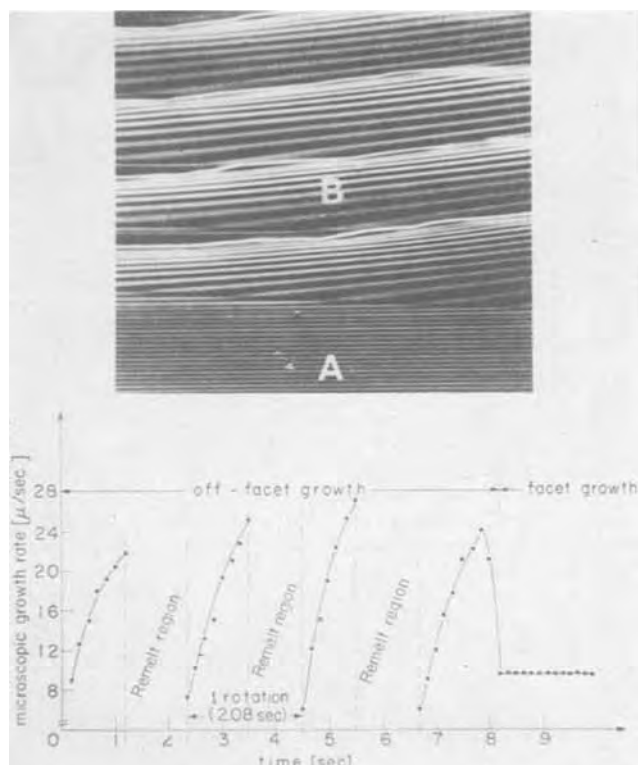


Fig. 23. Cross-section of a Te-doped InSb crystal grown under pronounced thermal asymmetry. The upper part of the crystal segment shown was grown with seed rotation; rotational backmelt striations are visible. The lower part of the segment was grown without rotation; the constant spacing of the rate striations in this part show that thermal asymmetry does not affect the microscopic growth rate in the absence of rotation. 750X. The microscopic growth rates (determined from the rate striations) are shown in the lower part of the figure.

growth rate was independent of and up to twenty times greater than the average macroscopic growth rate. In the region of oscillatory instability in the melt the crystal exhibited fluctuations in dopant concentration with a periodicity identical to that of the thermal oscillations in the melt (Fig. 25). Under stabilizing thermal gradients (no temperature fluctuations in the melt), the microscopic and macroscopic growth rates were identical and fluctuations in dopant concentration could not be detected (Fig. 26). A cause and effect relationship between the thermohydrodynamics of the melt and crystal growth was established.

As high resolution etching, interference contrast microscopy and interface demarcation brought us to a new plateau for investigating growth and segregation phenomena, the quantitative determination of compositional variations in the crystals on a micro-scale became a necessity for further studies. In assessing possible approaches to the problem Ashok Murgai concluded that suitable compositional microprofiling in semiconductors could be achieved by spreading resistance measurements. It had been demonstrated by a number of investigators that the measured resistance by pressing a fine metal probe against a semiconductor could be reduced to the dopant (carrier) concentration of a small volume element in the semiconductor. By traversing the probe (or the semiconductor sample) composition microprofiles, with a resolution of the order of 20 μm , had been obtained.

Manfred Lichtensteiger modified a commercial spreading resistance probe and developed surface preparation techniques so that microprofiling, with a resolution of less than 5 μm , could be obtained on the identical surface on which rate striations were revealed for the simultaneous determination of the

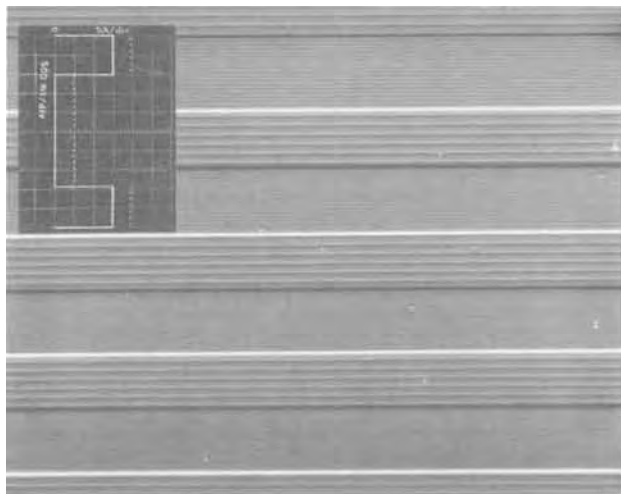


Fig. 24. Cross-section of a Te-doped InSb crystal grown without rotation. As seen from the insert, for 1 sec the crystal was grown with current passing through the interface and for 3 sec without current. Current pulses were of 15 msec duration and a frequency of 6/sec. Each current pulse introduces a well-defined rate striation. It is seen that the separation of the rate striations is much greater in the regions grown with current (they contain six rate striations) showing that the current accelerates crystal growth significantly. The regions grown without current contain eighteen rate striations (the 15 msec current pulses do not perturb the over-all crystal growth process). 800X.

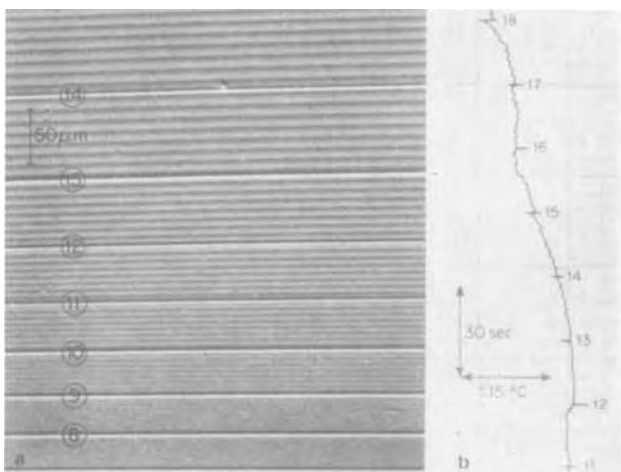


Fig. 25. InSb crystal segment grown in the presence of thermal oscillations in the melt. The time markers introduced by current pulses (at 21 sec intervals) are numbered on the photomicrograph and also on the temperature recording. It is seen that each temperature oscillation in the melt (see temperature recording) causes a dopant striation in the melt; the number of temperature oscillations between two time markers on the temperature recording is identical to the number of dopant striations between the same two markers in the crystal.

microscopic growth rates. Thus, the first quantitative microsegregation analysis, relating the dopant concentration to the microscopic growth rates was carried out on germanium crystals (Fig. 27). Theoretical models on microsegregation, available for more than twenty years, could now be tested against experimental results, and conversely crystal growth and segregation could be examined with some confidence in the light of scientific principles. A start was made in bridging the gap between theory and experiment.

Up to that time (about three years ago) we had worked with semiconductors having relatively low melting points (*i.e.*, first with InSb, mp 525°C and then with germanium, mp 938°C), since the experimental

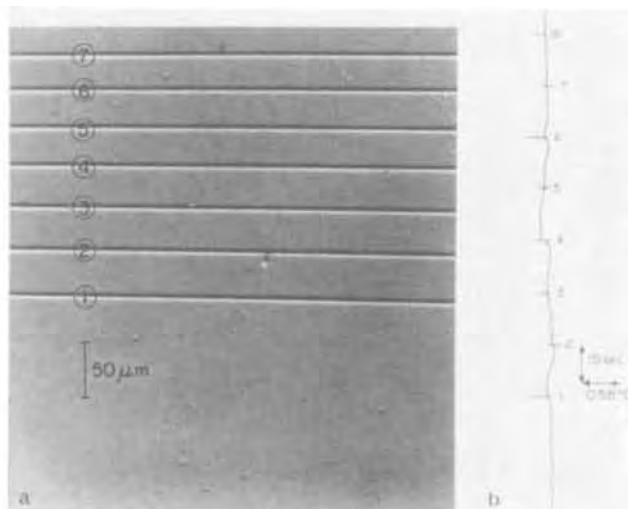


Fig. 26. InSb crystal section grown under thermal stability. No dopant inhomogeneities can be seen. The time markers (indicated by numbers) were introduced by current pulses applied at 21 sec intervals. No temperature fluctuations are indicated in the corresponding temperature recording.

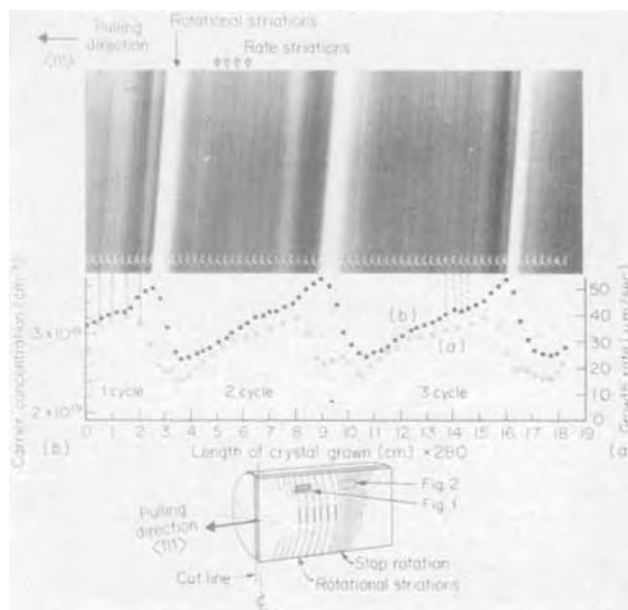


Fig. 27. Segment of a Ga-doped Ge crystal pulled with seed rotation. The microscopic growth rate as determined by the current-induced rate striations are shown in curve (a); the dopant distribution as obtained by spreading resistance measurements at spacings of 10 μm is shown in curve (b); the impact tracing of the spreading resistance probe is visible at the lower part of the photomicrograph.

complexities increase exponentially with increasing melting point. The study of silicon, the key semiconductor material in solid-state electronics, was the next step. Turbulent convection invariably present in the silicon melt, leading to uncontrolled random dopant fluctuations, was found to interfere with the interface demarcation and, thus, the quantitative study of segregation phenomena in silicon. Very recently, however, Ashok Murgai, by introducing severe thermal asymmetry in the melt, obtained thermal conditions under which forced laminar convection rather than turbulent convection, prevailed at the growth interface (Fig. 28). A quantitative segregation analysis in silicon was completed a few weeks ago (Fig. 29); the results are in good agreement with existing theories and provide a new basis for further theoretical developments. In addition, they elucidate certain aspects of segregation

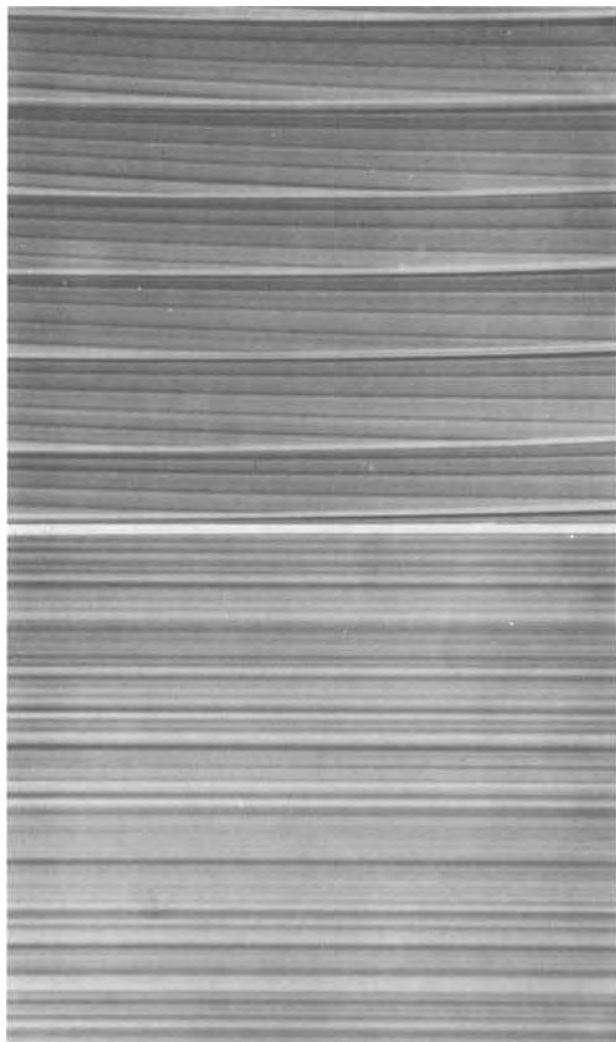


Fig. 28. Microsegregation in Sb-doped silicon grown with 5 rpm seed rotation. Upper photomicrograph shows the normal segregation behavior characterized by random nonrotational striations caused by convection. Lower photomicrograph shows the segregation behavior in silicon grown under laminar flow conditions at the growth interface; periodic rotational striations now become well defined and random striations are eliminated. The rate striations introduced at 1 sec intervals are clearly visible. 100X.

under turbulent convection invariably present in industrial silicon growth processes.

At this point I would like to outline an application to which interface demarcation has led. Manfred Lichtensteiger's finding, that crystal growth and segregation could be precisely modulated by electric current, indicated that controlled crystal growth could be achieved by passing electric current through the growth interface (Peltier cooling) while the over-all temperature in the growth system (except at the growth interface) was retained constant. This approach appeared particularly attractive for liquid phase epitaxy where the objective is the preparation of thin semiconductor layers with controlled compositional characteristics. It was successfully applied to the growth of III-V compound epitaxial layers. Since the microscopic growth rate responds instantaneously to current density changes and is functionally dependent on the current density, desired compositional profiles can be conveniently achieved.

Outer Space a Unique Dimension in Materials Processing

As I review our work, I see no end to the challenging problems in segregation and crystal growth. We have reduced the reference scale from macro to micro, but we are still in the "macro" end of the microscale.

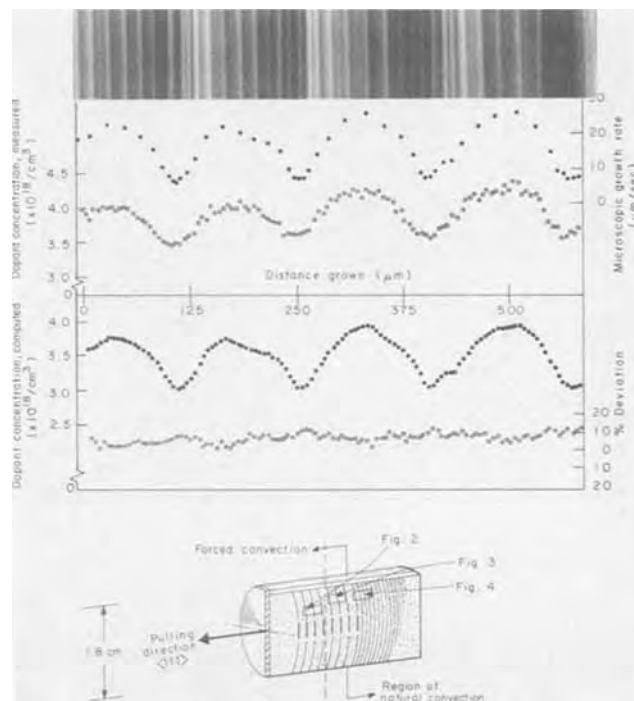


Fig. 29. Microsegregation analysis of an Sb-doped silicon segment pulled with a seed rotation of 5 rpm; rate striations and the impact of the spreading resistance measurements are visible; the uppermost curve (black dots) is the microscopic growth rate plot as a function of distance grown; the second curve from the top is the corresponding dopant concentration. The theoretical dopant concentration computed on the basis of the Burton, Prim, and Slichter model (black dots) and the deviation between the experimental and the theoretical concentration are shown in the lower part of the figure.

We and others will be working, on earth, refining our understanding of segregation and growth for many years to come. However, gravity-induced convection will never permit us to investigate growth and segregation under ideal, strictly diffusion-controlled steady-state conditions. Thus, theoretical predictions on the properties of homogeneous materials on an atomic scale, will essentially remain predictions.

It is incomprehensible to me that experimentation in space has captivated workers in astronomy, spectroscopy, communications, meteorology, and other fields, but has hardly penetrated the skepticism or excited the imagination of the materials community. Experiments in the Skylab mission have provided astronomers, earth scientists, and others with a plethora of original information to keep them challenged for many years. The materials experiments in that mission were almost an afterthought, limited in number and scope of instrumentation. We were fortunate to participate and the results of our simple solidification experiment were beyond our expectations.

We used single crystals of InSb (about 1 cm in diameter and 11 cm long). In space, one-half of each crystal was backmelted and regrown, with the unmelted part of the crystal serving as seed. In this way, the earth-grown seed and the space-grown crystal could be directly compared. As seen in Fig. 30, the compositional inhomogeneities present in the earth-grown seed are eliminated in the crystal segment grown in the absence of gravity; thermal convection was not present in the melt. Growth took place under ideal diffusion-controlled, steady-state conditions, resulting in homogeneous dopant distribution on a macro- and micro-scale, following a dopant concentration transient as predicted from theory (Fig. 31 and 32). No such homogeneity has ever been achieved on earth, either by nature or by man. In addition, we observed some unexpected new effects associated with solidification

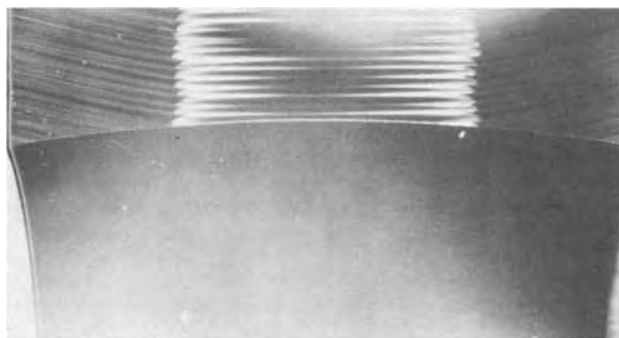


Fig. 30. Etched cross-section of crystal grown in Skylab; space-grown region (bottom) in contrast to earth-grown region (top) exhibits no compositional inhomogeneities. 13X.

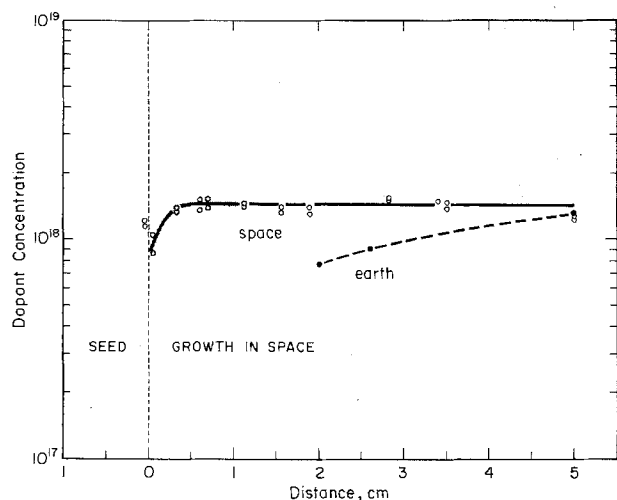


Fig. 31. Dopant concentration profile obtained from Hall-effect measurements for a Te-doped InSb crystal grown in Skylab (the shaded area represents the dopant concentration results obtained with an ion microprobe); the dopant distribution in an InSb crystal grown during ground-based testing is also shown (due to the presence of twin and grain boundaries in this crystal no meaningful Hall-effect measurements could be carried out in the vicinity of the regrowth interface). Note that ideal steady-state, diffusion-controlled, segregation takes place in space.

and segregation which we have discussed in a recent publication in *The Journal of the Electrochemical Society*.

On the basis of the first results we have designed a more refined growth experiment, using germanium, for the space mission in July of 1975, which will be carried out jointly by the U.S. and the Soviet Union. Unfortunately, there are no other space missions planned for materials processing until the Shuttle missions, five to six years from now. With intensive participation of the materials community, experiments can perhaps be designed for the Shuttle missions which could represent a turning point in advancing materials and materials processing into new levels of understanding and raise structure-property relationships to a refined, quantitative framework.

Looking into the Future

Solid-state electronics has had a brilliant recent past. It has revolutionized our technology within two decades. It has brought to focus semiconductors, model materials for testing structure-property relationships, for discovering new effects, for breeding theoretical concepts, for discovering new materials and for showing the way to progress in all other classes of materials. It broke the barrier among classical science and engineering disciplines and demonstrated the striking resonance energy of multidisciplinary interactions. It

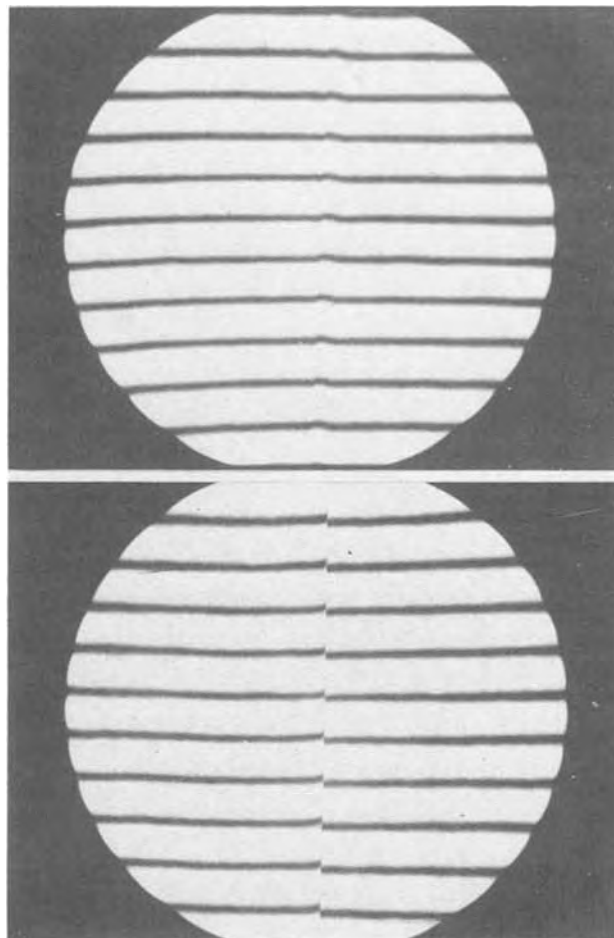


Fig. 32. Double beam interferogram of an InSb crystal grown in Skylab. The interference fringes are straight lines and parallel to each other indicating uniform dopant distribution on a microscale. The segregation discontinuity on the upper interferogram was caused by an intentional mechanical shock during growth; the discontinuity on the lower interferogram was caused by regrowth after an intentional cooling arrest during the growth experiment.

gave birth to materials science, an ideal intermediary for multidisciplinary interactions.

With such a brilliant past, in principle, we cannot expect any less brilliant future for solid-state electronics and for solid-state science. I certainly cannot be specific about the future, but I would like to share with you my views.

Three questions come to mind. (i) Will solid-state science and technology progress through improvements and refinements of known materials and through advances in materials processing? (ii) Will progress be based on the discovery of new materials and new phenomena? (iii) How can the promise of solid-state science and technology be fostered?

At present the limiting step to progress in solid-state science and technology is materials preparation, materials characterization, and materials processing. Future progress then hinges on improvements of known materials and processes. Even in the case of silicon, on which more than 90% of the electronics industry is based, fundamental materials problems still confront us. Compositional homogeneity on a microscale, lattice defects (particularly point defects) and their role in device processing and performance, control and understanding of the electronic properties of surfaces and interfaces in device structures; there are others. Improved capacity, speed, reliability, and cost reduction of integrated and hybrid circuits in the future is intimately related to advances in materials processing.

Light emitting diodes have in the last two to three years made a grand entry into solid-state electronics,

as sophisticated materials technology developed for silicon (for example, crystal growth and p-n junction formation by planar diffusion) was expanded to III-V compounds. Progress in light emitting efficiency throughout the visible spectrum and improvements in cost will broaden immensely the applications of LED's as light sources. But, processing of high energy gap semiconductors and controlled p-n junctions will be the critical steps.

Optical communication of information, voice and pictures, now feasible on a laboratory scale, represent a major quantum jump over present technology in terms of capacity and cost. Here again the existing needs: efficient lasers, modulators, detectors, and low loss glass fibers, are all materials related.

New means for energy generation, an issue of major concern, have been in principle demonstrated: solar energy conversion, new batteries, fuel cells, magneto-hydrodynamics, nuclear fusion; their large-scale implementation will certainly be based on improvements in processing electronic and other types of materials.

These are just a few typical instances where future progress is linked to improvements of known materials and processes.

Assessing progress through new phenomena, new materials, and new technologies is not a linear extrapolation process; fundamental or empirical knowledge can be of little help in planning "breakthroughs." On the other hand, it will be naive, at best, to rely for our future on serendipity. New discoveries that have changed the course of civilizations, emerged invariably although unpredictably in well planned, intellectually ripe and stimulating environments. In a recent article³ it was stated that, "The significance of the wartime semiconductor developments in setting the stage for the invention of the transistor cannot be overemphasized." Another recent article⁴ points out that, "It would be well to bear in mind when we begin our attempts to divine the future that the invention of the transistor was not a random event."

In this context I would like to quote from an internal Bell Laboratories document written in the summer of 1945: "Authorization for work. Subject: Solid State Physics—the fundamental investigation of conductors, semiconductors, detectors, insulators, piezoelectrics and magnetic materials. Statement: Communication apparatus is dependent upon these materials for most of its functional properties. The research carried out under this case has as its purpose the obtaining of new knowledge that can be used in the development of completely new and improved components and apparatus elements of communication systems. . . . The modern conception of the constitution of solids that has resulted indicates that there are great possibilities of producing new and useful properties by finding

physical and chemical methods of controlling the arrangement and behavior of the atoms and electrons which compose solids." An area of research with great potential on promising materials was selected. A competent group representing the appropriate disciplines was established. Two and one-half years later the transistor was invented. This is a model approach to the discovery of new phenomena, materials and devices. I do not even remotely intend to underplay a major ingredient in this as in other discoveries: the flash of genius. But a flash of genius can only be triggered in the right environment.

The development of solid-state science and technology is linked with structure-property relationships, with the drawing of general principles from specific facts. But the facts have not been and will not be better than the materials; the generalizations, whether they represent predictions, relationships, or theories will always be as good as the facts.

I would like to conclude with a quotation from Thomas Edison, which could be entitled: setting the stage for progress. "My own ambition is to be able to work without regard to the expense. What I mean is that if I want to give up a whole month of my life and that of my establishment to finding out why one form of carbon filament is slightly better than another, I want to do it without thinking of the cost. That galls me. I want none of the rich man's usual toys. I want no horses or yachts—I have no time for them. What I want is a perfect workshop."

Acknowledgments

Since in this address I have only sketched the evolution of two research areas and did not even touch on our research on high pressure transformations, superconductors, and amorphous semiconductors, I have omitted the names and contributions of a large number of my associates and students. This omission in no way reflects a value judgment. In my collaboration with every one of my associates and students I have not only been stimulated and rewarded, but also enriched by their friendship. How can I thank them enough?

I wish to take this opportunity to express my gratitude to the sponsors of our work: The National Aeronautics and Space Administration, the National Science Foundation, the Office of Naval Research, and the M.I.T. Lincoln Laboratory (supported jointly by the U.S. Army, Navy and Air Force).

References

I have chosen not to include references to our work reviewed here, since it has been published principally in readily available journals: *The Journal of the Electrochemical Society*, *Surface Science*, and the *Journal of Applied Physics*. Regarding the work of other investigators mentioned in this address, it is either very well known or it has appeared in the above journals.

³ C. Weiner, "How the Transistor Emerged," *I.E.E.E. Spectrum*, p. 24, January 1973.

⁴ R. A. Laudise and K. Nassau, "Electronic Materials of the Future: Predicting the Unpredictable," *M.I.T. Technology Review*, p. 61, October/November 1974.

Report of the Electrolytic Industries for the Year 1974¹

R. S. Karpiuk*

The Dow Chemical Company, Midland, Michigan 48640

and S. D. Argade*

BASF Wyandotte Corporation, Wyandotte, Michigan 48192

Chlorine—Caustic Soda

I. Production.—Chlorine production in the U.S. reached a new record level in 1974 (1, 2). The U.S. 1974 output was 10,872,000 short tons of chlorine and increased 4.3% from 10.42 million tons in 1973. This represents a 10.5% increase over the 1972 production level. Canadian production was 1.07 million tons in 1974 compared with that in 1973 of 1.01 million tons, which is an increase of 6.3% (1, 2).

U.S. chlorine production capacity rose 11.1% in 1974 to 33,300 tons/day on December 1, 1974, compared with 29,982 tons/day a year earlier (2). Canadian capacity increased 6.7% during the year to 3250 tons/day compared with 3045 tons/day in December 1973 (2). During most of the year chlorine producers operated close to an average of 95% of the capacity (4). Three major new brine electrolysis plants came on stream during the year and a total of 13 locations underwent modest expansions, modernizations or replacement of facilities (1, 3) (see Table 1). A plant based on nonelectrolytic oxidation of HCl also came on stream (3). The Chlorine Institute estimates that by January 1, 1976, new plant constructions and expansions of operating facilities at nine locations will boost U.S. chlorine capacity from the 1974 level of 33,300 tons/day to about 35,800 tons/day, an increase of about 7.5% (1). Two projects should raise the present Canadian chlorine capacity of 3250 tons/day by 13.2% during 1975 (1).

In 1974, 69.9% of U.S. chlorine production capacity was in diaphragm cells, 24.8% in the mercury cells, and miscellaneous production from all other sources accounted for the remaining 5.3% (3). In Canada, 64.5% of chlorine production capacity in 1974 was in the diaphragm cell route and the rest in mercury cells (3).

Demand for chlorine in the U.S. was somewhere between 100 and 110% of ability to produce with certain geographic and industrial dislocations. The major hurdles were the availability of power and fuel (1). The national economic downturn first affected chlorine production in December of this year (1).

Due to severe shortages of chlorine and caustic soda and high energy costs, the price of each product increased to the \$90/ton level by midyear (5-8) and shortly thereafter to the \$100/ton level (9, 10). Toward the end of the year the prices for chlorine were at \$120-140/ton (11). Shortage of chlorine appeared to be easing in December (11); however, demand for caustic soda has remained strong with prices in the range of \$140-165/ton (4).

The market breakdown for chlorine is as follows (11):

Vinyl chloride (VCM)	20%
Other chlorinated organics	30%
Inorganic chemicals	11%
Pulp and paper	15%
Miscellaneous	17%
Water purification	7%

¹ This report is sponsored by the Industrial Electrolytic Division of The Electrochemical Society. While it is primarily a summary of production and developments in the chlor-alkali industry, reports of other electrolytic industries are included.

The material presented herein has been gathered from many sources, as noted in the References, and does not necessarily represent the opinions of the authors.

* Electrochemical Society Active Member.

Vinyl chloride is the largest single product that uses chlorine and factors that affect this industry affect in turn the chlorine industry. Polyvinyl chloride (PVC) output and use stayed at the 400 \bar{M} lb/month level during the first ten months of 1974; however, in November the consumption slipped 10%, and 22% further in December to 281 million lb (4). This decline in the PVC market late last year was a delayed reaction to trouble in the auto and housing industries (4, 11). After much controversy (14), O.S.H.A. has set strict standards on worker exposure to vinyl chloride (12). The new standard, covering vinyl chloride, polyvinyl chloride, and PVC fabricating facilities, will be implemented in steps (12). After January 1, 1975, vinyl chloride in work-place air must be reduced to 1 ppm averaged over an 8 hr period. Workers may not be exposed to more than 5 ppm averaged over any period for longer than 15 min (12). If these levels cannot be met, employees must be provided respirators. The plastic industry has challenged these standards in courts (12). The effect of these standards on the chlorine industry is unknown. A number of new vinyl chloride monitors have come on the market (13).

The sharp downturn in automotive markets also affected the demand for chlorinated organic products used as degreasing solvents for metals in late 1974 (4). Other markets for chlorine have been less weak than those for organics.

The chlorine shortages in the summer of 1974 for sewage and water treatment were worse than 1973; however, shortages were to ease in early 1975 when new capacity would be on stream (15).

Production of caustic soda reached a record level of 11,400,000 tons in 1974 (16). Demand for caustic soda remained strong throughout the year and markets for caustic soda such as soap and detergent continued to grow at 4-5% per year (4). Mining and metallurgical markets held up well in almost all of 1974 (4). Caustic markets were reacting more slowly and less violently to the economic slowdown in late 1974 compared to chlorine (4). The cutbacks in chlorine production, which are bound to occur, would aggravate the caustic shortage further (4).

II. Developments.—A. Chlorine cells and components.—A number of new cells are available on the market for chlorine producers, many of which were presented at the joint Electrochemical Society and Chlorine Institute meeting held in San Francisco in May 1974, to commemorate the 200th anniversary of the discovery of chlorine by Scheele. Metal anode conversions of chlorine cells continue, as seen in Tables 1 and 2.

Diamond Shamrock's plant at Battleground, Texas, uses cells that have a new expandable dimensionally stable anode and a modified asbestos diaphragm. These cells operate at 40,000-80,000A and have a narrower brine gap between the electrodes which reduces electrical energy consumption to 2300-2500 kW-hr/short ton of chlorine (18). The expandable metal anode is made in a contracted configuration, then expanded against the cathode with the modified diaphragm during assembly of the cell. The modified asbestos diaphragm has given voltage savings of 150 mV and has

Table I. Current changes in chlorine operations (3)

Company and location	Type of cell	Capacity tons/day	Completion date
A. Production Started			
Diamond Shamrock Corp. LaPorte, Texas	Diamond MDC29 (diaphragm)	1200	November 1974
The Dow Chemical Co. Freeport, Texas	Dow (diaphragm) expansion	1000	September 1974- March 1975
E. I. du Pont de Nemours Corpus Christi, Texas	Kelchlor process	600	June 1974
Hooker Chemical and Plastics Corp. Taft, La.	Hooker H4 (diaphragm)	815	September 1974
Allied Chemical Corp. Moundsville, W. Va.	Conversion to DSA and expansion	—	November 1974
Aluminum Co. of America Point Comfort, Texas	Conversion to DSA completed	—	August 1974
Dow Chemical of Canada, Ltd. Fort Saskatchewan, Alberta	50% expansion completed	—	June 1974
Hercules, Inc. Hopewell, Va.	Conversion and expansion completed	—	—
Hooker Chemical and Plastics Corp. Niagara Falls, N.Y.	Phase 1 Conversion to DSA completed	—	—
Hooker Sobin Corp. Niagara Falls, N.Y.	Conversion to DSA completed	—	September 1974
Kaiser Aluminum and Chemical Corp. Gramercy, La.	Conversion and expansion	535	November 1974
Occidental Petroleum Canada Vancouver, B.C.	10+ % expansion and conversion to DSA	—	December 1974
Olin Corp. McIntosh, Ala.	Expansion completed	—	—
Olin Corp. Charleston, Tenn.	Conversion to Marstolin anodes and expansion	—	August 1974
Pennwalt Corp. Calvert City, Ky.	Conversion to DSA completed	—	—
Shell Chemical Co. Deer Park, Texas	Conversion to DSA and 50% expansion completed	—	August 1974
Sobin Chlor-Alkali Orrington, Me.	Expansion completed	—	December 1974
B. Plant Shutdowns Scheduled			
Dryden Chemical Ltd. Dryden, Ontario	Krebs (mercury)	45	When new facility will be completed
Hooker Chemical and Plastics Corp. Niagara Falls, N.Y.	Gibbs and Hooker S cells (diaphragm)	—	—
Pennwalt Corp. Tacoma, Wash	Gibbs (diaphragm)	—	When new facility completed
Weyerhaeuser Co. Longview, Wash.	de Nora (mercury)	265	June 1975

Table 2. New or expanded plants planned or under construction (3)

Company and location	Type of cell and capacity	Status	Completion date
Brunswick Chemical Co. Brunswick, Ga.	Conversion S4B to HC4B, modest expansion	Engineering	1st Quarter 1975
Vulcan Materials Co. Wichita, Kan.	25% expansion Hooker (diaphragm)	Engineering	4th Quarter 1976
BASF Wyandotte Corp. Geismar, La.	Modest expansion (diaphragm cells)	Engineering	2nd Quarter 1976
The Dow Chemical Co. Plaquemine, La.	Expansion	Planning	1976
Georgia Pacific Corp. Plaquemine, La.	Hooker H4 (diaphragm) 800 tons/day	Building	2nd Quarter 1975
PPG Industries Inc. Lake Charles, La.	Glanor 1144 bipolar (diaphragm) 1500 tons/day	Engineering	1977
Vulcan Materials Co. Geismar, La.	Diamond MDC55 (diaphragm) 600 tons/day	Engineering	3rd Quarter 1977
BASF Wyandotte Corp. Wyandotte, Mich.	Conversion to DSA modest expansion	Engineering	1st Quarter 1975
Hooker Chemical and Plastics Corp. Niagara Falls, N.Y.	Additional Hooker H4	Engineering	1977
Sobin Chemicals, Inc. Ashtabula, Ohio	Conversion to DSA Conversion to KOH	—	3rd Quarter 1975 1st Quarter 1975
Pennwalt Corp. Portland, Ore.	Diamond (diaphragm) expansion, 200 tons/day	Engineering	2nd Quarter 1976
Aluminum Co. of America Point Comfort, Texas	de Nora (mercury) expansion 80 tons/day	Engineering	4th Quarter 1976
Diamond Shamrock Chemical Co. Deer Park, Texas	Conversion DS34 to MDC22 (modified diaphragm)	Underway	2nd Quarter 1975
E. I. du Pont de Nemours Corpus Christi, Texas	Diamond MDC55 (diaphragm) 1000 tons/day	Engineering	1st Quarter 1977
Mobay Chemical Co. Baytown, Texas	Uhde HCl electrolyzers expansion by 100 tons/day	Engineering	4th Quarter 1975
NL Industries Inc. Magnesium Div. Rowley, Ut.	MgCl ₂ electrolysis 45,000 tons/yr Mg 80,000 tons/yr Cl ₂	Building	4th Quarter 1974
Georgia Pacific Corp. Bellingham, Wash.	Conversion to DSA 20% expansion	Engineering	—
Hooker Chemical and Plastics Corp. Tacoma, Wash.	Hooker (diaphragm) expansion 400-675 tons/day	Engineering	1977
Pennwalt Corp.* Tacoma, Wash.	Glanor Bipolar 1144 (diaphragm) 200 tons/day	Engineering	3rd Quarter 1975
Weyerhaeuser Corp.* Longview, Wash.	Diamond MDC29 (diaphragm) 385 tons/day	Engineering	2nd Quarter 1975
PPG Industries Inc. New Martinsville, W. Va.	Conversion to DSA Columbia N3 and N6 (diaphragm)	Underway	3rd Quarter 1975
BASF Wyandotte Port Edwards, Wisc.	de Nora (mercury) modest expansion	Engineering	1977
Dryden Chemicals, Ltd.* Dryden, Ontario	Hooker MX (membrane) 45 tons/day	Engineering	3rd Quarter 1975
Canadian Industries Ltd. Beauport, Quebec	Hooker H2A (diaphragm) 385 tons/day	Engineering	1st Quarter 1975

* See also Table IB

demonstrated life of over 500 days (17). The combination of expandable metal anode and the modified diaphragm is said to save the cell voltage by a total of 300 mV at 1.5 kA/m² compared to DSA and asbestos diaphragm (17).

PPG's Glanor bipolar electrolyzers will be used in a 1500 tons/day plant to be built at Lake Charles, Louisiana, by 1977. About 6000 tons/day capacity using this technology has already been licensed (18).

Hooker's 150,000A version of a diaphragm cell has been used at Hooker's 900 tons/day plant at Taft, Louisiana (18). This cell is supposed to have a labor cost advantage over smaller versions (18).

Diamond Shamrock Corporation and du Pont reported on a joint project for demonstration and application of "Nafion" perfluorosulfonic acid membranes for chlorine cells (19-22). Diamond Shamrock is already operating a commercially sized chlorine cell using "Nafion" membranes and is planning to operate a large facility to demonstrate its commercial practice (20, 22, 23). Hooker Chemical has also developed chlorine cells based on "Nafion"-type ion exchange membranes. A 45 tons/day plant has been installed by Hooker for a pulp mill (18, 20) and Hooker plans a 250 ton/day plant for itself (20). At The Electrochemical Society meeting in San Francisco in May 1974, both Hooker and Diamond Shamrock presented papers concerning their development of new cells in which "Nafion" membranes are used (22, 24).

du Pont is also reported (22) to be working with Ionics, Inc., Watertown, Massachusetts, on "Nafion" membranes for chlorine cells for units with less than 100 tons/day capacity (19, 20). Ionics has a system using "Nafion" membranes for on-site chlorine, caustic soda, and hypochlorite generation (19).

Asahi Chemical, Tokuyama Soda, and Maruzen Oil have independently developed a membrane cell process for chlorine production (25, 27). The membrane process is said to produce caustic soda product with less than 100 ppm NaCl and the size of the caustic evaporators is a third the size necessary in the existing diaphragm cell process. The life of the ion-exchange membrane is 4-5 times that of the conventional diaphragms (25). Asahi is reported to be constructing a semipilot plant of 25,000 tons/year caustic soda capacity to be completed in early 1975 (25). The technical data on the Japanese membrane processes are not available as yet (25). The Ministry of International Trade and Industry of Japan which has sponsored the work of Asahi is recommending the membrane process technology for the first phase of the conversion program, away from the mercury cells, which ends in March 1976 (26).

B. Other developments.—Mobay Chemical Company is doubling its HCl electrolysis facility of 200 tons/day at Baytown, Texas, using F. Uhde cells (28).

Kellogg has continued design studies on the recovery of chlorine from HCl by the Kelchlor process, which has resulted in the development of an economic low pressure design (27). This reportedly permits the use of brick-lined towers and Inconel 600 for the oxidizer unit (27). Kellogg has also announced that it has a new variant of the process under development, named Kelchlor II, which can handle either anhydrous or aqueous hydrogen chloride feed (27).

A new quadruple-effect evaporator in the NaOH concentration system requires only 5000-6000 lb of steam/ton of NaOH (18, 29). The steam requirement for the quadruple effect unit is about half the amount required for the double effect units and 20% less than the triple effect units (18, 29).

An absorption-distillation method to liquefy chlorine is ready for licensing by Akzo Zout Chemie Nederland (Hengelo, Netherlands) (23, 30). Chlorine is absorbed in carbon tetrachloride and the solution is distilled. The process presumably consumes less energy than compression and condensation, producing liquid chlorine containing 99.9% chlorine, with a yield of 99.8% (23, 30).

EPA is proposing amendments to the emission standards for asbestos for certain field fabrication operations in new construction. The amended regulations would prohibit the installation of asbestos containing molded insulating materials which are friable, and wet applied insulating materials which are friable after drying (31). Friable asbestos material is defined as any material that contains more than 1% asbestos by weight and can be crumbled, pulverized, or reduced to powder when dry by hand pressure (31).

Asbestos fibers in water can be identified, counted, and measured with a transmission electron microscope equipped with selected area electron diffraction and an energy dispersive spectrometer, according to The Dow Chemical Company (32). The technique was developed to measure asbestos levels, typically 0.001 ppm, in diaphragm cell chlor-alkali plant streams. Almost all of the asbestos fibers from these streams average under 6 μ in length and could be filtered out (32).

Employees at an asbestos mine aim to buy the mine from GAF Corporation for \$1.25 million (33). The employees of Vermont Asbestos Group, Inc. have won a one year extension of EPA's deadline to install pollution control equipment. Additional equipment and worker safety devices would cost another \$1.25 million (33).

Capital expenditures required for environmental controls for the water and air quality standards have boosted the total plant investment by 20% for new plant construction (18). Typical investment for 1000 tons/day diaphragm cell and mercury cell chlorine plants is compared below (17). The direct investment costs are comparable (17). See Table 3.

C. Mercury cells.—No new mercury cell plants were built in 1974 in the U.S. (34). There were a few planned expansions and modernizations, e.g., conversion of Olin's plant at Charleston, Tennessee, from graphite to Marstolin metal anodes (3). One mercury cell plant has been slated for conversion to a diaphragm cell plant in the U.S. and another to a membrane cell process in Canada (3). In the foreseeable future, all new chlorine production capacity will be in the diaphragm cell plants.

The first phase of Japan's conversion program of mercury cells to other cells ending in March 1976, involves 65% of the total capacity, amounting to 3,051,000 tons NaOH/year (26). The second phase ends in March 1978, when facilities for 5,579,000 tons NaOH/year or 100% of the capacity will be converted to diaphragm or membrane process plants from the present mercury cell process (26).

The initial capital investment costs for conversion of mercury cell facilities in Japan have now more than doubled to 800,000 million yen (\$2,016 million) due to the dramatic rise in construction costs because of inflation (27). Besides inflation, financial and market factors are also affecting the conversion away from mercury cells and the increase in capacity of the Japanese chlor-alkali industry (27).

Table 3. Capital cost of 1000 short tons/day chlorine plant* (17)

Process item	Capital cost \$ millions	
	Diaphragm cell	Mercury cell
Brine area	3.5	5.0
Cell room, excluding license or anode fees	13.0	19.0
Chlorine processing	8.0	8.0
Cell liquor storage	1.5	—
Caustic evaporation	15.0	2.0
Caustic purification	3.0	—
Caustic storage-loading	4.0	4.0
Hydrogen system	1.0	1.0
Utilities	10.0	7.0
General facilities	6.0	6.0
Mercury	—	4.0
Mercury recovery	—	7.0
Total direct investment	65.0	63.0

* U.S. Gulf Coast, 1974-1975 costs.

The formation of mercury butter in mercury cells used in brine electrolysis may be prevented or reduced by using a technique developed by de Nora of Italy (35). Magnets placed in the mercury amalgam circuit retain ferromagnetic particles, *e.g.*, Fe, Ni, suspended in the amalgam (35). The magnets are cleaned periodically (35).

Georgia-Pacific Corp. has completed testing its new process for the recovery of mercury traces from liquid and solid wastes from the chlorine plant at Bellingham, Washington (36, 37). The project was supported partly by EPA. The removal of mercury from the brine sludge by roasting in a six hearth furnace at 1000°-1400°F is said to be 98.3-99.8% efficient and the residual mercury in solids is 0.5-0.7 ppm (37). The waste water is treated with sodium sulfide and filtered; the HgS filter cake containing 15-30% Hg is roasted in the furnace (37). This process is said to be meeting EPA's 0.1 lb/day limit for discharge of mercury (37).

According to USDA's northern regional laboratories, a highly efficient method has been developed for recovering heavy metals from water or up to 10% salt solutions by using a crosslinked starch xanthate in the pH range of 3-11. The metal and starch are recovered by treating with nitric acid. Mercury concentrations are reduced from 100,000 to 3 ppb (42).

Mercury consumption increased by 10% from 54,283 flasks in 1973 to 59,600 flasks in 1974, according to U.S. Bureau of Mines (38, 39). The chlor-alkali producers purchased 16,813 flasks of mercury in 1974 compared to 12,780 flasks in 1973 (39, 41). The domestic production of mercury was 1700 flasks from ten mines in California (65%), Nevada, and Alaska. Secondary production amounted to 9000 flasks. Imports of mercury totaled 51,400 flasks, a 10% increase over 1973 and were received from Canada (30%), Mexico (22%), Algeria (20%), Yugoslavia (11%), and Spain (10%). The seven mercury exporting countries (representing 95% of mercury exports) were planning a base price of \$350/flask (40). The mid-year free market mercury price ranged at \$270-275 per flask (40).

Other Alkalis and Electrolytic Processes

Caustic Potash.—Caustic potash production in 1974 was 206,252 short tons as 88-92% liquid; this represents an increase of 9% over 1973 production of 188,454 short tons (43, 44).

U.S. production of marketable natural potassium chloride, sulfate, magnesium sulfate, and manure salts was 2.5 million tons of K₂O equivalent, a decrease of 2% in quantity and increase in value by 30% compared with that of 1973 (43).

The government of Saskatchewan removed production controls and the price floor on potash during 1974, and subsequently put into effect a policy of higher taxation and majority participation in future capacity expansions (43, 45). This has resulted in deferral of added capacity by six potash producers amounting to a total of \$200 million investment (45).

The price of potassium muriate in bulk f.o.b. Carlsbad, New Mexico, and Saskatchewan, Canada, freight equalized, was quoted in early 1974 at \$0.38-0.44/lb; in late 1974 prices were quoted at \$0.54-0.65/lb. The caustic potash price after the government controls were lifted was quoted at \$4.60/100 lb lots on a 45% basis (46), and in late 1974 it was quoted at \$6.00 (47).

Allied Chemical Corporation is planning to shut down its caustic potash production at Solvay, New York (48).

Soda Ash.—Demand for soda ash continued strong in 1974, but total production declined 1.5% to 7.53 million tons. Synthetic (Solvay) soda ash continued its 8 year slump by dropping 9.5% below the 1973 production level to 3.48 million tons. Part of this decrease was the shut-down of PPG Industries 600,000 ton/year synthetic soda ash plant in Barberton, Ohio, in 1973. Existing synthetic plants could manage only an 87% operating rate in the face of strong demand. Natural soda ash production did increase 9.3% to 4.05 million tons,

topping the output from synthetic plants for the first time, but this was the smallest annual increase in several years and was not nearly up to the predictions of the producers who were all striving to enlarge their capacities (49, 50).

The main drawback to the construction of additional natural soda ash capacity seemed to be the lack of skilled labor in the relatively undeveloped area. The synthetic soda ash plants are plagued with operating and environmental problems.

The soda ash demand was high, but the producers could not supply about 500,000 tons. There was also a world-wide caustic shortage. Soda ash exports jumped 20% to 530,000 tons in 1974. With the high demand, customers were put on allocation and inventories decreased (50).

The Allied Chemical natural soda ash plant with an annual capacity of 1,100,000 tons came on stream in late 1974 at Green River, Wyoming. In 1975, the FMC Corp. and Allied Chemical natural soda ash plant expansions will bring an additional 1.85 million tons to the industry's capacity, increasing the total to 6.4 million tons.

In March, 1974, the Kerr-McGee Chemical Company announced the selection of a contractor to build their new 1.3 million ton-per-year soda ash plant at Trona, California, at a cost of more than \$100 million. Target date for operation has been set as 1977 (51). Kerr-McGee also purchased Stauffer Chemical's plant in West End, California (49).

Texasgulf is expecting to have its one million ton/year natural soda ash plant operating at Grunger, Wyoming, by the third quarter of 1976 (50).

A consortium of five Japanese companies announced intention to develop the natural soda ash resources at Lake Natron in Tanzania (49). Japan's Asahi Glass, Central Glass, Toya Soda Manufacturing, and Tokuyama Soda are planning to build a 1000 ton/day soda ash plant in Australia.

In the face of ever increasing demand and rising costs, the soda ash industry gradually raised its unit costs (52, 53). The average unit value of soda ash, as evaluated by the producers, was about 30% higher in 1974 than the average 1973 price (49). In December, PPG raised soda ash prices to \$60/ton in bulk and \$74 in bags, f.o.b. Corpus Christi, Texas, from the previous prices of \$44 and \$58/ton, respectively (54).

A new method of separating sodium minerals from oil shale has been patented by Industrial Resources (U.S. 3,806,044). Nahcolite and dawsonite are separated from shale by froth flotation before the minerals are sent to a shale retort (55).

Sodium Chlorate.—According to the U.S. Department of Commerce data (56), sodium chlorate production in the U.S. in 1974 amounted to 201,453 short tons with a production capacity totaling 235,500 tons (57). Canadian sodium chlorate production was estimated at 138,000 tons for 1974 (58).

In early 1974 the sodium chlorate price was fixed at \$135/ton because of government price controls (57). The mid-year price for sodium chlorate was \$165/ton (59), and quotes at the end of the year for sodium chlorate were about the same (60).

Engelhard Mineral and Chemical Corp. has developed a line of metal anodes for the production of sodium chlorate (61). The anodes are reportedly a titanium structure with a conductive coating. They demonstrate a lower cell voltage and offer cell design flexibility.

Standard Chemical Limited, a Canadian subsidiary of PPG Industries, will expand its sodium chlorate plant at Beauharnois, Quebec (62, 63). The multimillion dollar expansion in two phases would almost double the production capacity at this location, making it Canada's largest sodium chlorate plant (64). The first phase is expected to be in production by January 1977. The new facilities will include metal anodes using cell technology developed by Standard Chemical and PPG (64). PPG purchased a license for the U.S.

and Canada for using Kema Nord's bipolar electrode technology for sodium chlorate cells last year (57).

Aluminum.—The U.S. aluminum industry sustained another record production year in 1974, with 4,903,000 short tons of the primary metal produced. This represents an 8% increase over the 1973 production level (65). The General Services Administration shipped 509,000 short tons of aluminum in 1974, virtually depleting government inventories (66, 67). The total aluminum supply which includes primary production, secondary recovery, imports and GSA shipments amounted to 7,214,000 short tons in 1974 compared to that of 7,062,000 short tons in 1973 (65).

U.S. shipments of aluminum started to slip midway in the second quarter of 1974 and the demand situation worsened in the third and fourth quarters as the housing and transportation markets, representing 45-50% of the domestic aluminum market, were affected by the national economic slowdown (67). The containers and packaging markets, which account for 30-35% of the total, were strong throughout the year (67). The supply-demand balance was maintained by aluminum production cutbacks (67-69), for which the aluminum industry came under fire from the Council on Wage and Price Stability (67).

The domestic price for aluminum from large producers remained at \$0.29/lb through March 29 when controls were lifted and the price was raised to \$0.315/lb. The price was raised in successive amounts to \$0.39/lb by September 5, 1974, where it remained for the rest of the year (66). The price of aluminum on an average was about \$0.34/lb in 1974 (67). Prices on the major world markets approached \$0.46/lb at mid-year but softened to a level of \$0.35-0.45/lb at the end of the year (66).

Aluminum Company of America (Alcoa) is planning to increase its primary aluminum capacity at Badin, North Carolina, from 120,000 tons/year to 180,000 tons/year by the addition of a third potline. Completion is projected in 1976 at a cost of \$50 million (70).

Amax Aluminum Company, owned equally by Amax, Incorporated and Mitsui and Company, will be adding a second potline with a capacity of 87,400 tons/year of primary aluminum at Howmet's Eastalco plant in Frederick, Maryland, at a cost of \$85 million (71). The facility will be operated jointly between Howmet and Amax Aluminum. Amax Aluminum is also planning a 287,300 ton/year aluminum plant at Warrenton, Oregon, at a cost of \$200 million. The Government approval was sought for the project (71).

In a joint venture, Revere Copper and Brass, Incorporated, and six Japanese firms are studying the possibility of investing \$160 million at Revere's aluminum plant at Scottsboro, Alabama, to increase the capacity from 112,000 to 232,000 tons/year, and possibly later to 360,000 tons/year. The Japanese companies will take the increased output (72).

Aluminum Company of Canada and Nippon Light Metals KK of Japan (Alcan's 50% subsidiary) are planning a new subsidiary to produce 100,000 tons/year aluminum in Kitimat, B.C., Canada. Each company will receive half of the output of the plant which will be operated by Alcan (73). Alcan will also add 48,000 tons/year aluminum capacity by 1975 at Arvida, Quebec (74).

Noranda Mines, Limited, of Canada is planning to double the aluminum capacity of the Noranda Aluminum Incorporated, plant at New Madrid, Missouri, from 70,000 to 140,000 tons/year aluminum by mid-1976 (75).

In March 1974, Australia, Guinea, Guyana, Jamaica, Sierra Leone, Surinam, and Yugoslavia formed the International Bauxite Association for the purposes of achieving higher revenues for bauxite and alumina, and maximum vertical integration of their own industries. The United States is traditionally dependent on these countries for greater than 90% of alumina and bauxite requirements (66, 76). Jamaica levied higher taxes on bauxite (76); Guyana, Surinam, and Haiti

followed with similar actions (77, 78). These countries are demanding active participation in the bauxite operations of the North American companies (79). Many of the aluminum producers, for this reason, have been looking into alternative materials for bauxite, such as alunite, kaolinite, and laterite (80).

Reynolds Metals Company carried out a full scale test on laterite ore (35% aluminum content) at Hurricane Creek, Arkansas, proving that this ore can be processed in the Bayer process plants without major equipment changes (80).

Pechiney Ugine Kuhlman and Alcan Aluminum, Limited, of Canada have joined efforts in a new venture for the development of a new method for processing nonbauxite ores into alumina (81). The venture will invest \$25 million for constructing a pilot plant of 20 tons/day of alumina based on Pechiney's H-Plus technology. PUK has been operating a 1 ton/day alumina laboratory unit since 1971 which can use shale, clays, and sandstone (81). In this process, ores are treated with concentrated sulfuric and hydrochloric acids to produce a crystalline aluminum chloride which is subsequently processed to yield alumina (82).

Alcoa has been operating a pilot plant converting coal wastes into alumina. Coal wastes which contain 28% alumina offer attractive commercial possibilities. Although the process is undisclosed, it is said to be based on conventional chemistry and ready equipment (83). Alcoa and Anaconda have signed an agreement for exchanging information on the alumina extraction technology from sources other than bauxite. Anaconda has operated a pilot plant for producing alumina from clay with a hydrochloric acid process (84).

The Bureau of Mines' Research Laboratory in Nevada is converting 70 lb/hr of domestic alumina clay into 25 lb/hr of alumina, based on a nitric acid leaching process. The project is being sponsored by eight industrial firms and is planned to process alunite, anorthosite, and dawsonite (85).

Another patented method reacts the ore with chlorine at high temperatures to produce aluminum chloride gas which is decomposed on cooling into molten metal (86).

Beryllium.—The over-all production and consumption of beryllium ores in 1974 was relatively unchanged from that of 1973 (87), about 7650 and 9000 short tons, respectively. Bertrandite was produced in Millard County, Utah, by Brush-Wellman, Incorporated. There was no report of any domestic beryl production. Imports of beryl in 1974 were estimated at 1350 short tons, valued at \$392,000. Imports were primarily from Brazil and the Republic of South Africa. The other and larger supplier of beryllium products is Kawecki Berylco Industries.

Beryllium is used as the metal, as an alloying agent, and as an oxide. Major uses for the metal are for military and aerospace applications, utilizing light weight and high strength and rigidity, and for nuclear applications where its low thermal-neutron absorption and high-neutron-scatter cross section are required. More than half of the beryllium is used as a beryllium-copper alloy, to which it imparts qualities of strength and resistance to fatigue and corrosion that are superior to those of copper. Molds fabricated from beryllium copper are used to give plastic furniture the appearance of wood-grain surface (87). Beryllium-copper is a substitute for gold in certain contact applications in the electronic and computer fields. Strong growth in consumption also occurred in auto safety devices where beryllium-copper is used for buzzers and relays for seat belts and air-bags (88).

As of November 30, 1974, government stockpile inventories contained 17,986 short tons of beryl (11% BeO equivalent), 7387 tons of beryllium-copper master alloy (approximately 4% Be), and 229 tons of beryllium metal. The stockpile of both beryl and the master alloy was declared surplus. The stockpile objective for beryllium metal is 88 short tons, leaving 141 tons surplus.

As the 1974 boom accelerated, the price of beryllium rod and beryllium-copper alloys increased. The increases were necessary because of higher costs for copper, raw materials, labor, and supplies (89). With the increase in price of aluminum, beryllium-aluminum alloy price also increased per pound of contained aluminum (90). As the boom cooled, prices were also cut, reflecting lower material prices (91). At the end of the year, alloy 25 was quoted at \$3.89/lb and beryllium metal rod at \$106.05/lb.

The Environmental Protection Agency under the Clean Air Act amendments of 1970 has limited beryllium emissions from stationary sources to 10 grams/day (93).

Chromium.—As in earlier years, the U.S. continues to rely solely on imports and purchases from the government stockpiles for chromium requirements. The strong demand that initiated in early 1973 continued throughout 1974. Domestic consumption of chromite was 1,438,400 tons, 4% higher than that in 1973. In the refractory industry, the consumption in 1974 was 12% higher than that in 1973. Chromite usage in the metallurgical industry decreased nearly 3% from the level in 1973 (94).

Imports of chromite totaled 1,170,000 tons, an increase of nearly 26% compared with that of 1973. Imports of chromite from the U.S.S.R. and the Philippines were significantly higher in 1974 than in 1973, while imports from South Africa, Turkey, and Southern Rhodesia exceeded their 1973 levels (95).

The demand for chromium alloys was strong since stainless steel production exceeded two million tons for the first time. Imports of ferrochromium set a yearly record high of 162,000 tons, an increase of 4% over 1973 (94). During the year GSA sold 571,000 tons of refractory grade chromite, 323,000 tons of chemical grade, and 900,000 tons of metallurgical grade. GSA also sold 3182 tons of chromium metal (95).

The strong demand world-wide for chromium and the inflationary pressures raised the chromite and primary chromium product prices (95). South African chromite (44% Cr₂O₃) began the year at \$33-34/long ton delivered in the U.S. Atlantic ports; by June 1, prices quoted were \$47-52/long ton. The Turkish chromite (48% Cr₂O₃), quoted at \$37/long ton early in the year, increased to \$65/long ton in September 1974. The ferrochromium similarly was quoted at \$0.22-0.23/lb chromium at the first of the year and increased to \$0.50/lb by year's end (95). Sodium bichromate was priced at \$0.1725/lb in January 1974, and rose to \$0.2125 by the end of the year (2).

A year-long battle to repeal the Byrd Amendment was terminated when the backers of a Congressional bill withdrew the measure prior to the end of the 93rd Congress (95, 96). The Byrd Amendment is part of a 1971 military procurement law and states that, if the U.S. imports a strategic material from a communist country, it may not refuse to import the material from a noncommunist country. Under this part of the law, chromite ore and ferrochromium have been imported from Southern Rhodesia since early 1972 (95).

Copper.—Preliminary 1974 data indicated that the U.S. mine, smelter, and refinery production and consumption of refined copper were all substantially smaller than in 1973. Strikes at most producing units during portions of July and August and reduced demand for copper in the latter half of the year were factors that adversely affected the level of activity. Imports of copper were an increased supply component as imports of unmanufactured copper increased significantly while exports declined. An additional component of supply in 1974 resulted from the sale or commitment during the months of February through May of all 252,000 tons of refined copper remaining in the national stockpile (97).

Mine production was 1.59 million tons, an 8.4% decline from the preceding year and the smallest quantity since 1971 (98). Principal copper producing states

were Arizona with 53% of the total, Utah (15%), New Mexico (13%), Montana (9%), Nevada (5%), and Michigan (4%) (99). Increased operating costs and a drop in copper prices were factors cited in an October announcement by the Anaconda Company of its decision to terminate underground mining at Butte, Montana. In response to the reduced demand for copper, several Arizona producers also made announcements in November and December of decisions to curtail operations (97).

Smelter production from primary materials decreased 10% from the 1973 record high to 1.57 million tons. Refinery production from primary materials was projected to decline 13% to 1.65 million tons. However, production of refined copper from scrap was approximately 495,000 tons compared with 465,000 tons in 1973 (98).

Consumption of refined copper was down 12% to 2.14 million tons from the 1973 record high of 2.44 million tons (98). The first half of the year had a relatively high level of consumption, whereas the second half was significantly lower, reflecting the slump in construction, automobile production, and the general economy.

Stocks of refined copper at primary producers fluctuated around 40,000 tons during the first five months, were drawn down to 23,500 tons during June, increased rapidly to 71,000 in November and 101,300 tons in December, the largest end-of-month level since March 1971 (98, 99). Stocks of copper at brass plants and wire mills were drawn down from 73,000 to 52,000 tons during the first quarter, moved up to 121,000 tons by the end of July, declined to 99,000 tons by the end of September, and closed the year with 144,000 tons (98).

Imports of copper were an increased supply component as imports of unmanufactured copper were 608,000 tons compared with 417,000 tons in 1973, while exports declined from 263,000 to 170,000 tons. The largest trade category, refined copper, had a 55% increase in imports to 310,000 tons and a 33% decrease in exports to 126,500 tons. Imports of blister were indicated to be 207,800 tons compared with 154,100 tons in 1973 (98).

The domestic delivered price for cathode copper was restricted to \$0.687/lb until the removal of price controls at the end of April. The monthly average price then advanced to \$0.812 on May 1 and to \$0.861 on June 1, then, reflecting changing market conditions, was reduced to \$0.83 in September, to \$0.782 in October, and to \$0.758 in November, and \$0.73 in December. The yearly average was \$0.77/lb. Prices on the London Metal Exchange escalated from a monthly average of \$0.921/lb for January to \$1.38/lb for April, followed by an equally rapid descent to around \$0.584 in December. The yearly average on the London Metal Exchange was \$0.931/lb (98).

According to Dravo Corporation, copper smelting costs can be cut by using a top-blown rotary converter process. Test data from an Inco nickel refinery show that energy requirements are only one quarter of those for electric or reverberatory furnaces, or electrowinning (100).

Hydrometallurgical extraction of copper from ores by the Marconaflor process was being carried out by Kaiser Industries and Marcona Corporation. The metal values are extracted in a leaching solution (101).

Anaconda, which is starting up the first commercial plant using its Arbiter fumeless extraction process in Anaconda, Montana, will run pilot plant tests on copper ore from Poland. Results of the tests could lead to licensing negotiations (102).

A flash-oxidation system that continuously produces copper, nickel, and lead from sulfide concentrates will be pilot-planted by American Air Liquide (New York) and other partners. The multistage converting operation is carried out in a single reactor, with continuous feeds of oxygen, concentrates, and flux. The advantages are that energy requirements, slag losses, and

cost of sulfur fixation are each about half as much as in standard processes (103).

A process by cyanide-free copper electroplating is offered by R. O. Hull. The major constituent is copper pyrophosphate with proprietary brightening and leveling agents. It is mildly alkaline and noncorrosive, and does not need any special plating equipment (104). A new electrochemical process that recovers 99% of the copper from leach liquor has been developed by Douglas Bennion and John Newman at UCLA. They believe that the process could be competitive with General Mills' LTX system (105).

Considerable activity was shown during 1974 in the mining of ocean nodules for the copper, nickel, cobalt, and molybdenum values. In January, Kennecott Copper announced a large-scale program aimed at commercial mining of some three million tons of nodules a year by 1980-1981. To achieve this goal, a five-year, \$50 million R and D program will be carried out by a five-company consortium of major metal producers, including Rio Tinto-Zinc, Consolidated Gold Fields, Mitsubishi, and Noranda Mines. Key objectives are to build and test a full-scale prototype nodule recovery system capable of handling 10,000 tons/day of nodules, and a demonstration-scale process plant, to handle a minimum of 10 tons and a maximum range of 100 to 150 tons of nodules/day (106).

Likewise, Tenneco's subsidiary Deepsea Ventures has joined forces with a Japanese group of companies, Nichimen, C. Itoh, and Kanematsu-Gosho, U.S. Steel and Union Miniere (Belgium) for the purpose of carrying out a three-year, \$20 million program for the development of the deep ocean manganese nodule resource. A 5 ton/day pilot plant will be built in Gloucester, Virginia. Further development will be continued at the Pacific mine site, and Deepsea's hydraulic system will be tested aboard its vessel R/V Prospector (107).

The other American firm interested in the nodules, Summa Corporation of Houston, owned by Howard Hughes has slated tests for its prototype nodule recovery system in 1975 (106). The movements of Howard Hughes "mystery barge" and its activities in the Pacific have made the news media.

An up-to-date account of the activity and organizations interested in deep sea mining was published recently (108). A brief review article on the process technology of extracting copper, nickel, and cobalt from the manganese nodules also appeared (109).

Poland plans to become the world's largest copper exporter, eventually shipping 400,000 million tons/year. Poland's government has approved a \$1-billion investment program to enlarge the copper industry. Refined copper production in Poland is expected to reach 206,000 mt in 1974, a 26% gain over 1973 (110).

After suspending initial work in May, Texasgulf has decided to resume building the copper complex planned for Kidd Creek (Timmins), Ontario (111).

Three Finnish companies will build a \$575 million extraction and smelting complex for nickel and copper for the Soviet Union in Norilsk, Siberia. The project is due on stream in 1976 and 1977 (112).

Hudson Bay Mining and Smelting Company and Anglo American Corporation of Canada agreed to purchase Lytton Minerals, Limited, interest in the Minas del Otono, S.A., Mexico, which owns the La Verde copper deposit 200 miles west of Mexico City (113).

As 1974 ended, the economic, political, and social factors affecting the world copper trade pointed to a poor year in 1975, with production cutbacks, continuation of price declines, and no viable answers to those problems. In the U.S., several mines cut back production in December in response to depressed copper markets and increasing inventories. Fabricators have also cut production by furloughing mill workers. The CIPEC have agreed to reduce shipments by 10% over the first six months of 1975. They will not cut back production, but will stockpile the copper. Japan is also planning to stockpile copper, but not as much as cop-

per ore contractual commitment would indicate. France was drawing up plans to stockpile copper in 1975 for the first time in history (114).

Lithium.—Lithium carbonate consumption in the aluminum industry in 1974 continued the strong growth trend started in 1972 (115). This growth, combined with a strong demand by other lithium consumers, created a tight supply situation for lithium products last year. In the aluminum industry, the addition of lithium compounds to the potlines lowers the internal resistance of the electrolytic cells, thereby reducing the energy consumption requirements. Lithium also reduces the fluoride emissions. Since both of these factors are important to the aluminum industry, this end use for lithium compounds is expected to grow (115).

In 1974, lithium compounds were produced by Foote Mineral Company, Lithium Corporation of America, and Kerr-McGee in the U.S. (115). Foote Mineral added to the lithium carbonate capacity in 1974 at its Silver Peak, Nevada, operation with the total capacity at 14 million lb/year of lithium carbonate (116) and it is anticipated that output will increase further in 1975 (115). In 1974, Foote Mineral announced the construction of a 12-15 million lb/year lithium carbonate plant at Kings Mountain, North Carolina (117). The project was on schedule for production in 1976 (115). Lithium Corporation of America also inaugurated expansion of production capacity by 12% over 1973 in lithium chemicals at its Bessemer City, North Carolina, operation (118). Lithium Corporation of America also acquired Spartan Minerals Company, a major feldspar processor (119). The tight supply situation of lithium chemicals will ease when Foote Mineral's new plant comes on stream in 1976. Another 8-10 million pounds of lithium carbonate per year operation will be on stream in 1976 at Bernic Lake, Manitoba, Canada.

The total U.S. consumption of lithium chemicals was estimated at 32 million pounds of Li_2CO_3 equivalent in 1974 compared to 30.5 million pounds in 1973. World-wide estimated consumption went up from 49.5 million pounds Li_2CO_3 in 1973 to 53.4 million pounds in 1974 (115).

In early 1974, the quotes for lithium hydroxide were \$0.63/lb in bulk quantities (120). In late 1974, the lithium hydroxide price was quoted at \$0.87/lb (121). The price for butyl lithium in cyclohexane in early 1974 was \$4.80/lb (120), and in late 1974 it was quoted at \$7.32/lb (121). Lithium carbonate in early 1974 was quoted at \$0.55/lb (119) and by late 1974 the price was quoted at \$0.75/lb (121). In late 1974, lithium metal was quoted at \$9.38/lb (121).

According to the Bureau of Mines, the U.S. Government has 5.9 million pounds of lithium hydroxide monohydrate in the U.S. General Services Administration stockpile, which was turned over to GSA by the former Atomic Energy Commission (122).

Foote Mineral Company is investing \$600,000 for exploration in the Atacama desert for lithium in an agreement with the Chilean Government (123).

In other developments, many research groups are continuing investigations with lithium as an anode material for batteries, since these systems would potentially yield very high energy density (124). Primary organic lithium cells, which are already on the market, are said to be operational from -40° to 160°F , with a shelf life of 10 years and 95 W-hr/lb of energy density. These batteries are finding military applications (124).

Molten salt lithium-sulfur cells, being investigated at ESB, Atomics International, and Argonne National Laboratory, are expected to find applications in "load leveling" or energy storage at power plants and vehicle propulsion (124, 125). Atomics International reported (125) that with a copper sulfide cathode the loss of sulfur from such cells is minimized and over 700 charge-discharge cycles have already been attained. This system indicates an energy density of 60-80

W-hr/lb and would have a cycle life of 2000-3000 cycles.

Magnesium.—Magnesium had a banner year in 1974. Apparent demand far outstripped primary production, even though the plant of the major producer, The Dow Chemical Company, was operating at 105% of capacity at mid-year (126). To ensure an adequate supply of the metal to consumers and to improve inventory levels, The Dow Chemical Company purchased 21,410 tons of magnesium in the latter part of 1973 from the General Services Administration for monthly delivery in 1974 and 1975 (127). The GSA also sold about 4,000 tons of magnesium monthly to other companies (127), until the stockpile was depleted in the second quarter (130).

The American Magnesium Company, Snyder, Texas, with a capacity of 10,000 tons/year, resumed production in the second quarter of 1974 (129). NL Industries, Inc., Rowley, Utah, also produced and shipped a small quantity of magnesium during the first quarter (130).

Northwest Alloys, Inc., a subsidiary of the Aluminum Company of America, is constructing a new magnesium facility at Addy, Washington, for the production of the metal. Startup of this plant is now scheduled for 1976 (178). Norsk Hydro has announced its intention to build a 50,000 tons/year magnesium plant in Mongstad, Norway. Operation of this plant is slated for the early 1980's (131).

According to Nils Hoy-Petersen, Norsk Hydro director and president of the International Magnesium Association, the free world magnesium production should rise to 220,000 tons and consumption to 280,000 tons in 1974 (126).

The Dow Chemical Company has been exploring new technology which is expected to use 50% less power, to be less polluting, and to have lower operating costs than the present technology (126). However, the projected shortages of magnesium encouraged Dow to consider a major new plant on modified present technology rather than wait for new techniques to be proven. Both domestic and foreign sites are being evaluated for a 100 million lb/year magnesium plant to go on stream by 1978 or 1979 (132).

The price of 99.8% purity magnesium ingot in lots of 10,000 pounds or more was progressively raised in five steps from \$0.42/lb at the beginning of the year to \$0.47 on March 11 (132), \$0.55 on May 1 (134), \$0.65 on July 1 (126), \$0.75 on August 1 (126), and \$0.82 on January 1, 1975 (135).

The price of AZ91B alloy, used in die casting and general alloys, also increased correspondingly, and developed a differential of \$0.05/lb, with the end-of-year price of \$0.87/lb. The increases reflected the large increased costs of electrical energy, increased demand, competitive export markets, and the need to widen depressed profit margins of the materials.

Imports of magnesium metal in all forms in 1974 totaled 5307 tons, while exports of magnesium metal and alloys totaled 46,399 tons (135). American primary production approached 130,000 tons, and consumption 120,000 tons (126).

Manganese.—According to the Bureau of Mines, there was no 1974 U.S. production of manganese ore, concentrate, or nodules, containing 35% or more manganese, and this was the first year since 1880 that no producer shipments were recorded. Ferruginous manganese ore or concentrate, containing 10-35% manganese, was produced and shipped from New Mexico, and the Cuyuna Range of Minnesota (136). The manganese requirements were met by imports and sales from the government stockpile (137).

Consumption of manganese ore was again down from that of 1973 in the U.S. and amounted to 1,645,000 short tons in 1974. Imports of manganese ore this year containing 35% or more manganese were 1,188,000 short tons. Brazil and Gabon continued to supply more than half of this manganese ore and Australia became a significant third (137).

Domestic 1974 production of ferromanganese (high carbon, medium carbon, and low carbon grades) amounted to 582,500 short tons, appreciably lower than that in 1973 (137). The imports of ferromanganese totaling 421,000 tons (327,600 tons Mn content) established a new record. As in 1973, the major ferromanganese suppliers were France and the Republic of South Africa, supplying more than two-thirds of the total. Manganese metal imports for the year amounted to 2507 short tons and originated from South Africa (137).

The General Services Administration released for sale from its stockpile manganese ore, synthetic dioxide, and high carbon ferromanganese (136, 137).

Prices for metallurgical manganese ore containing a minimum of 48% manganese was \$1.05-1.15/long ton for the first half of the year and \$1.10-1.18/long ton in the second half of 1974 until December when the quote was increased to \$1.18-1.38 for the same unit. Prices for ferromanganese after removal of the controls in March were quoted at \$270/long ton and by November three subsequent increases brought the price to \$400/long ton (136). Prices for the imported ferromanganese went up from \$190 at the beginning of the year to \$450-460/long ton toward the end of the year. At the end of December 1974, Union Carbide raised the price for ferromanganese to \$440/long ton (137). The price for the electrolytic manganese metal went up from \$0.3325-0.3725/lb to that of \$0.54/lb by mid-November (136). The new South African source of electrolytic manganese metal, Delta Manganese (Pty) Ltd., started production about the middle of the year in Nelspruit in the Transvaal (136). Foote Mineral Company is the distributor for the United States and Mexico, but the initial output was destined for Canada and Europe (136).

Tenneco, Inc., has joined a group of Japanese trading firms, C. Itoh and Company, Nichimen Company, and Kanematsu-Gosho Ltd., in a three-year project to develop and evaluate metal recovery from Pacific Ocean manganese nodules. Tenneco's mining subsidiary, Deepsea Ventures, Inc., will have the responsibility for processing and marketing recoverable manganese. The initial goal is to produce and market 280,000 tons/year of manganese. The assessment program is supposed to cost \$20 million over a three-year period. Commercialization would involve \$200 million and eventually the group hopes to capture half of the U.S. manganese market. Other recoverable minerals are copper, nickel, and cobalt (136, 138, 139).

Kennecott Copper, as the head of the international group of companies, will continue its research and development program to determine the feasibility of mining sea floor nodules, but with its primary interest on the nickel and copper values. An expenditure of \$50 million over a five year period is programmed (136).

The Chemetals Division of the Diamond Shamrock Chemical Company is planning to double, in 1975, its manganese capacity to 17,000 tons/year at Kingwood, West Virginia, at an investment of \$6 million (136, 140).

Australia's producer of ferromanganese, Tasmania Electro Metallurgical Company, was reported planning an expansion that would include a new furnace and a sinter machine for feed. Completion was scheduled for late 1975 (136).

A Japanese survey team found substantial deposits of manganese ore, more than 10 million tons, (Tambora Mines) in the Upper Volta. The ore contains 56% manganese (141).

Nickel.—The U.S. consumption of nickel in 1974 exceeded the high level reached in 1973 and resulted in a tight supply of nickel that lasted throughout most of 1974 according to the U.S. Bureau of Mines (142). The limited availability of nickel was also compounded by delays in the scheduled start-ups at several nickel producing facilities (142). The 1974 U.S. consumption of nickel was 208,107 short tons compared to that in 1973

of 198,461 short tons, according to Bureau of Mines data (143), which represents an increase of about 5%.

The U.S. nickel supply base that began changing in 1973 continued to shift in 1974. Imports of Russian nickel in 1974 continued to increase, doubling the 1973 level. Import data for the year 1974 indicate that the Dominican Republic replaced Norway as the second leading U.S. nickel source behind Canada, and New Caledonia (the French Pacific Islands) took over third place (142, 143).

Bureau of Mines data indicate that the level of activity in the domestic nickel production changed little from that in 1973 (142). Hanna Mining produced about 17,000 tons of nickel from laterite ore, the same as in 1973 (142, 143). The only domestic smelter recovered 12,500 tons of Ni as ferronickel (142). By-product plants recovered 950 tons of nickel in various forms. Other refiners and manufacturing plants recovered 34,000 tons of nickel from scrap (142). Canadian nickel production through the first ten months of 1974 was 10% greater than that for the same period in 1973 and totaled 242,089 short tons (142).

The price of pure nickel increased several times during 1974. The 1973 price of \$1.53/lb was raised in early January to \$1.62/lb. Falconbridge Nickel Mines, Ltd., and N.C. Trading Company increased the prices on May 16 to \$1.85/lb of nickel. International Nickel raised their price to \$1.85/lb effective June 28. Falconbridge again on December 1 increased the nickel price to \$2.05/lb. The ferronickel prices were raised about 10% in October 1974, to about \$2.00/lb of nickel content (142).

Ferronickel increased its market share in 1974 due to record stainless steel production at the expense of pure nickel, while nickel oxide maintained its 1973 market share. The over-all pattern of consumption of nickel remained at about the same levels, with approximately 48% consumed in steels, 22% in other nickel alloys and nickel, and 13% for electroplating (142).

Major exploration and development projects were underway in 1974 in the Philippines, Indonesia, Africa, Guatemala, and Australia. Interest in the United States centers around the possibility of exploitation of copper-nickel deposits located in the Duluth gabbro of Minnesota (142).

Amamax Nickel Refining Company has started its nickel refinery at Port Nickel, Louisiana. Full capacity of 80 million lb/year of nickel is now expected to be reached in 1976. Besides nickel, the facility will produce 47 million lb of copper/year, 1.2 million lb of cobalt/year and 100,000 tons/year of ammonium sulfate (144).

Marinduque Mining & Industrial Corporation has started the operation of its \$250 million nickel mine and refinery in the Philippines. The designed capacity is for 68.4 million lb/year of nickel with sulfide concentrates and 6.6 million lb/year of nickel and 3.3 million lb/year of cobalt (145).

The Greenvale nickel-cobalt project in Queensland, Australia, is near completion, according to Metals Exploration, Queensland (Pty) Ltd. The facility will have an output of 46 million lb/year of nickel oxide (90%), 7.5 million lb/year of nickel and 2.75 million lb/year of cobalt in the form of mixed sulfides (146).

Agnew Mining Company (Pty) Ltd. and the Australian government are near an agreement for a new large nickel project in Western Australia. The new firm was formed by Western Seleast (Pty) Ltd. and Mount Isa Mines Ltd. (147). Endeavour Oil Company has found a major nickel sulfide deposit at Digger Rocks, in Western Australia, estimated at 520,000 tons of nickel (148).

Societe Metallurgique-Le Nickel Sln. Aquitaine, a joint company formed by Societe Le Nickel and Societe Nationale des Petroles d'Aquitaine, will invest \$230 million for a 50% interest in the venture. The new company will take over Societe Le Nickel's mining and other assets in New Caledonia and the refining plant

at Le Havre. Production at Doniambo, New Caledonia, will be increased to 75,000 tons/year of nickel (149). Amamax, Inc. has acquired a 10% interest in Le Nickel, SA, Paris (147).

The Cie Francaise d'Entreprises Miniers, Metallurgiques et d'Investissements, a subsidiary of Patino, N.V., has received approval from the French government for a nickel mining and processing facility to be completed in 1976, which will produce 18,000 tons/year of nickel as ferronickel (149).

A high recovery nickel extraction (90% extraction efficiency) process is being piloted by Universal Oil Products (UOP) Company's Mineral Sciences Division. The \$1.6 million pilot plant will process 5 tons/day of nickel laterite ore, by roasting at 1000°-1800°F with a reducing gas in the presence of SO₂, H₂S, or HCl (150, 151).

The Commonwealth of Puerto Rico and UOP are planning a joint nickel mining and processing venture, based on UOP's extraction technology. UOP will begin a two year evaluation of the project including the pilot plant. The project investment is pegged at \$75 million (152, 153).

A process developed by Dartmouth College and Purdue University, called QS Oxygen Process, is being piloted by American Air Liquide of New York with other partners. The process consists of a single reactor with continuous feeds of oxygen, concentrates, and flux and can be used with copper, nickel, and lead sulfide concentrates. The cost for energy, slag, and sulfur fixation are claimed to be 50% of the costs of conventional converters (154).

The U.S.S.R. is operating a metals mining complex on the Taimyr Peninsula, Northern Siberia, where sulfide ores of nickel and other metals are obtained (155). Three Finnish companies will build copper and nickel smelters worth \$300 million with annual capacity to handle 550,000 tons of nickel concentrate and 650,000 tons of copper concentrate. The plants will be located at Norilsk in Western Siberia. The project is due on stream in 1976 and 1977 (156, 157).

Sodium.—Metallic sodium production was down an estimated 2.3% in 1974 as compared to the 176,903 tons of metal in 1973. The historic growth rate in production of metallic sodium was 2%/year. About 80% of the metallic sodium went into the manufacture of the gasoline additives, tetramethyl and tetraethyl lead. The shortage of gasoline at the beginning of 1974, the requirement of no-lead gasoline for 1975 model cars equipped with catalytic exhaust systems, and the EPA ruling that most service stations must sell at least one grade of unleaded gasoline were contributing factors in reducing the usage of metallic sodium (158).

The regulations of the Environmental Protection Agency required a reduction in the average lead content of gasoline to 2.00 g/gallon in 1975, 1.70 by 1976, 1.5 by 1977, and 1.25 by 1978. Thus, the regulations could have a direct effect on sodium production over the next four years.

However, PPG, a leading tetraethyl lead producer, filed a petition with the District of Columbia Court of Appeals to invalidate or review EPA's decision to phase down the use of lead in gasoline (159). Ethyl Corporation, also a large producer of tetraethyl lead, appealed the EPA ruling in August, charging that the agency had failed to prove its health case against lead in gasoline and that it had overstepped its bounds in issuing a final phasedown of lead (160). In December, the Federal District Court in Washington, in response to the plaintiffs, the National Petroleum Refiners Association, Ethyl Corporation, PPG Industries, du Pont, and Nalco, overturned EPA's regulation on the phasedown of lead in gasoline, ruling that EPA did not prove that lead emitted from automobiles is a health hazard to humans (161).

Like most industrial items, the prices of antiknock compounds also increased in 1974. Demand for the compounds was strong, despite opposition to its continued use on the part of environmental groups and

government timetables for reduction of lead in gasoline (162).

Titanium.—Industrial demand for titanium metal, which began to strengthen in the last quarter of 1973, continued through 1974 (163). This strong demand and sharply escalating prices featured the titanium markets during 1974.

Production of titanium sponge was 18% greater in 1974 than in 1973 (163). Final deliveries of sponge to the stockpile under GSA contracts were made during the third quarter of 1974. Consumption of sponge and scrap was about 27,000 tons and 10,500 tons, respectively. Production of ingot was about 36,500 tons. Imports of sponge for consumption were about 6800 tons, 30% more than in 1973. Of these imports, 62% came from the U.S.S.R., 30% from Japan, and 8% from the United Kingdom (163). Japanese production was expected not to exceed 9000 tons, 40% gain over 1973 (164). The titanium production rate was limited by shortages of power, labor, replacement parts, and raw materials.

A healthy demand for titanium metal was evident from both the industrial and aerospace sectors (163). Producers of chlorine and caustic soda are increasingly replacing graphite anodes in diaphragm cells with dimensionally stable titanium anodes and switching from the mercury cell process to diaphragm cells. Increased interest was shown by utilities in using titanium for condensers because of resistance to corrosion, erosion-corrosion and fouling, and good heat transfer characteristics. The first all titanium tube condenser for a steam boiler in the U.S. is scheduled to go into operation in June 1975, at New Haven Harbor, Connecticut (165). A major east coast refinery was replacing all of its heat exchanger tubing with titanium tubes (166). Titanium as a specialized construction material was also engineered into desalination plants (164).

The SR-71 prototype aircraft, which crossed the Atlantic Ocean in two hours, was an all titanium plane. The Navy's Grumman F-14 fighter plane was designed with about 25% titanium in its airframe (167).

Gould, Incorporated, has reached agreement with Energy Development Associates (a research and development partnership of Gulf and Western and Hooker Chemical's Oxy Energy Development Company subsidiary) to cooperate in the development of rechargeable zinc-chlorine batteries. Gould will use its powder metallurgy technology to develop a porous titanium electrode, which is not attacked by chlorine. Energy Development has been operating 1-kW-hr, zinc-chlorine batteries, which rely on storing chlorine in the hydrate form. The battery system, with an energy density five times greater than best-available lead-storage batteries, is envisioned for use in peak-load power generation at utilities and in electric cars (168).

The price of domestic sponge increased from \$1.42/lb to \$1.90/lb in mid-year, to \$2.25/lb at the end of the year. The price of rutile increased from \$310.00/short ton as the year began to \$330.00 in March, \$520.00 in June, and \$710.00 in November. Ilmenite similarly rose in price from \$38.00 to \$55.00/long ton. The price of Sorel slag remained at \$60.00/long ton throughout the year (163). It was reported that Japanese sponge will be priced at \$2.85/lb in the first half of 1975 and \$3.05 for the second half (169). The price increases for titanium sponge reflect higher energy and raw material costs.

Because sponge production requires 15-18 kW-hr of electric power to produce a pound of sponge (compared with 6-9 kW-hr for a pound of aluminum), production costs increased with utility rate increases. Freight rates and raw material prices for rutile, chlorine, magnesium, sodium, and argon have also risen sharply (170).

An excellent review on the direct reduction processes for the production of titanium metal was published in 1974 by the National Research Council (171).

Mine production of titanium minerals was about 764,000 tons, a decline of about 1.6% from the 1973 level. The mine of the American Smelting and Refining Company in New Jersey had its first full year of production. Mechanical difficulties at one mine and exhaustion of another property accounted for the decrease. In western Tennessee, Ethyl Corporation conducted an extensive pilot program in anticipation of mining and processing sands of the McNairy formation for their titanium mineral content (163).

Imports of ilmenite increased to 96,000 tons, as heavy shipments from Western Australia began in June. Imports of rutile, both natural and synthetic, decreased to 181,000 tons, off 13% from 1973. Imports of slag were 252,000 tons, 6% more than in 1973. The General Services Administration released 3700 tons of rutile from the stockpile (163).

The demand for titanium pigment, while strong throughout the year, came more nearly into balance with supply than was the case in 1973. Production in 1974 was estimated at 808,000 tons, a 4.7% increase over 1973. E. I. du Pont de Nemours and Company neared completion of its chloride-process facility at Edge Moor, Delaware. du Pont abandoned plans for a pigment plant New Brunswick, Georgia, and took preliminary action toward a similar plant in Mississippi (163).

Kerr-McGee Chemical Company announced plans for 110,000 tons/year of synthetic rutile capacity and a smaller pigment plant at Mobile, Alabama. Sherwin-Williams Company sold its 27,000 ton/year chloride-process pigment plant at Ashtabula, Ohio, to New Jersey Zinc Company in October (163).

Imports of pigment were about 38,000 tons, a decrease of 37% from 1973 levels. Exports during the same period reached 34,500 tons, 63% greater than in 1973. Domestic prices, decontrolled by the Cost of Living Council at the end of May, rose from about \$0.38/lb to about \$0.43 for the highest grade, with similar increases of about \$0.05/lb for lower grades (163).

Australian production of rutile was estimated at 340,000 tons, continuing the decline from the peak year of 1970. Australian ilmenite production, however, was estimated at 775,000 tons, about equal to 1973 production. Current activity in Western Australia may result in increased production of ilmenite in 1975 (163).

Zinc.—The slackening demand for zinc that began in late 1973 continued through 1974. This slackening was principally a result of the turndown in automobile production (1972).

Mine production in 1974 was approximately 494,446 tons, up 3.3% over that of 1973. New York, Missouri, and Tennessee were the principal producing states, accounting for 54% of domestic production. The new Elmwood mine in central Tennessee near Carthage was ready for production. About 25,000 feet of lateral development had been completed. This development confirmed earlier estimates that the deposit consists of approximately 20 million tons of zinc ore grading 4.5-5% zinc. A new mill constructed near the mine site was approaching completion. The concentrator has a capacity for processing 2000-3000 tons/day and will produce a 63% zinc concentrate. A new mine in Utah, developed as a joint venture by two major producers, will be ready for production in 1975 (172, 173).

Smelter production of slab zinc from ore was 546,140 tons in 1974, nearly 15.1% less than 1973 (174).

The decline in domestic zinc smelting capacity was reversed with the announcement of plans to erect two electrolytic zinc smelters, the first in thirty years. Upon completion of the plants, possibly in 1977, domestic capacity will be increased by 340,000 tons annually to over 1 million tons.

National Zinc announced that construction will begin on March 1 on a 50,000 tons/year electrolytic plant in Bartlesville, Oklahoma, replacing a horizontal retort smelter. The \$27 million facility is scheduled for completion by May 31, 1975 (175, 176). The Oklahoma Air Control Board extended permission to operate the

other remaining horizontal retort smelter beyond May 31, 1975, the date now scheduled for closure.

Engelhard Minerals and Chemicals acquired the assets of National Zinc, including the horizontal retort smelter. Engelhard will carry out the zinc producer's previously announced plans to construct an electrolytic zinc facility at Bartlesville (177, 178).

New Jersey Zinc announced the construction of a new electrolytic zinc refinery, with an initial capacity of 80,000 tons/year in 1977 and planned expansion to 160,000 tons/year by 1979, to be built near Clarksville, Tennessee. The company is also planning an extensive modernization program at its vertical retort zinc plant at Palmerton, Pennsylvania (179).

No new primary zinc facilities have been constructed in the U.S. since 1942. The closing of seven outdated smelters has decreased domestic zinc production from a peak of 1.3 million tons in 1968 to approximately 840,000 tons/year at present. Further shutdown scheduled for outdated smelters will reduce domestic primary capacity to about 655,000 tons/year, resulting in increasing dependence on zinc imports (179).

Canadian Electrolytic Zinc is planning to expand its Valleyfield zinc plant from 400 to 620 tons/day (180). Cominco began construction on the Rubiales lead-zinc mine in northern Spain. It is expected to come on stream in 1977, with an annual output of 115,000 metric tons/year of zinc concentrates (181).

General imports of zinc in ores and concentrates increased 20.6% over those of 1973 to 240,043 tons. Receipts from Canada were up, but from other countries—Mexico, Nicaragua, Honduras, Peru, and Australia—were substantially less. Imports for consumption of zinc in ores and concentrates declined approximately 13.1% to 133,728 tons. In 1974, both general imports and imports for consumption of slab zinc were nearly the same at 538,585 and 543,805 tons, respectively, representing decreases of 9.1 and 7.4%, respectively, from 1973. Canada provided about 50% of the slab zinc imports, West Germany 8%, and Australia and Peru each 7% (182).

Consumption of slab zinc decreased almost 14% from that of last year to 1,293,921 tons. Zinc used for galvanizing was down 12.3%, zinc base alloy down 29%, brass and bronze down 10.4%, zinc oxide up 6.6%, and other uses up 4% (182).

The General Services Administration continued to release zinc from the national stockpile as authorized by Public Law 92-283. On December 28, 1973, the President signed Public Law 93-212, which authorized an additional 357,300 tons of zinc for release, thus adding to the previous balance and creating a balance of approximately 415,000 tons of zinc available for commercial disposal. Early in the year, GSA started a new set-aside program by offering 150,000 tons over a period of 1 year with 75,000 tons available for the second quarter of 1974 and 25,000 tons each quarter thereafter. The offers were oversubscribed for the first two quarters in the program, but a turn-around occurred in the fourth quarter of 1974 when only 8360 tons was purchased from the 25,000 tons available. GSA sales of stockpile zinc in 1974 amounted to approximately 270,000 tons, leaving a balance of 166,000 tons authorized for release (172).

Legislation to suspend the duty on imports of zinc concentrates, H.R. 6191, was passed by the House of Representatives and the Senate, but was vetoed by the President because it contained a nongermane tax rider. The bill would have suspended through June 30, 1977, the \$0.67/lb import tariff on zinc ores, concentrates, and certain other zinc-bearing materials (172).

The monthly average price of domestic Prime Western zinc ranged from \$0.31168/lb for January to a high of \$0.39334/lb for October and decreasing to a December average price of \$0.3924/lb. The European producer price was raised during the year from \$0.3026/lb in January to \$0.381/lb in October and \$0.3804/lb in December. The London Metal Exchange (LME) price rose from \$0.602 to \$0.806/lb from January to May, then de-

clined sharply to the average December quotation of \$0.3495/lb (173, 174, 183).

These prices are substantially higher than the 1973 prices, when the monthly average price of Prime Western zinc ranged from \$0.1866 to \$0.2737/lb. The European producer price ranged from \$0.1849 to \$0.3154/lb, with an average for the year of \$0.24/lb. The LME price fluctuated from a low of \$0.1753/lb in January to a high of \$0.7331/lb in November, with an average for the year of \$0.3855/lb (173, 174, 183).

At the end of the year, the U.S. and foreign zinc markets were seriously affected by the world economic doldrums, resulting in lower demand, oversupply, and decreasing prices. To counteract these adverse conditions, zinc producers have gradually cut production to get supply and demand into balance. European producers have reduced output from 10% to a "significant percentage." Japanese producers cut production 20% from 1973 levels. U.S. producers have not announced any cuts, but some facilities were not running at full capacity (184).

The Bureau of Mines issued a significant document in "The U.S. Zinc Industry: A Historical Perspective," in which the changes in world mine and smelter supply sources of zinc and changes in zinc supply patterns in the U.S. during the last three years are described. The result has been a growing reliance on foreign sources of zinc to furnish an ever increasing portion of expanding domestic requirements. The document also reviews the developments, properties, uses, reserves, technology, production, consumption, imports, and government actions (185).

The Electrical Industry

In 1974, the electric utility industry was swamped with many problems: the flattening of the load growth rate of the use of energy, the high cost of money, lack of adequate return, skyrocketing capital costs of building, high fuel costs, restrictions on western coal, legal delays by environmental intervenors, construction delays, material problems, and new plant cancellations. Because of the conservation program and the recession, for the first time in many years there was a small decline in the total production of electricity. The only segment of the industry which showed an improvement was nuclear generating plants. In contrast to last year, water conditions substantially improved hydroelectric resources particularly in the Pacific Northwest.

In the fall of 1974, President Ford signed into law the bill that formed a federal Energy Research and Development Agency (ERDA) and a Nuclear Regulatory Commission to replace the AEC and the various energy research activities scattered throughout the governmental departments. The President was given the power to appoint the regulatory commissioners, the ERDA administrator, his deputy, and six assistants—one each for fossil energy; nuclear; environment and safety; conservation; solar, geothermal, and advanced energy systems; and national security. The ERDA objective is to guide the energy policies of the nation to attain Project Independence.

In a proclamation which appeared in many major newspapers, a group of 34 scientists, headed by Dr. H. Bethe and including 10 Nobel Prize Laureates, called for oil exploration on the continental shelf and greatly increased use of coal and nuclear energy. They hold that the energy shortage is the most serious problem in the U.S. since World War II, and the U.S. choice is not between coal and uranium, but both.

Howard Drew, of the Texas Electric Service Company, is pessimistic that the U.S. can achieve the goal of self-sufficiency by 1980 (186). He believes that the earliest the nation could possibly reach the goal is 1985, assuming several things that may be difficult to achieve. The assumptions are (i) that the nation can cut its growth in energy demand in half (to 2% per year); (ii) that the U.S. will be able to double the use of coal as an energy resource (opening 100 new strip mines in the next 11 years); (iii) that gas and oil pro-

duction be increased by 25% (drilling hundreds of new offshore oil wells by 1985); and (iv) that construction of nuclear power plants be started at the rate of two or three new plants each month for the next 11 years. One of the big problems in reaching the 1985 goal will be the raising of nearly \$600 billion in capital needed for new construction.

In the first eight months of 1974, indefinite postponements, cancellations, and scheduled stretchouts in the construction of power plants involved some 65,000 MW through the 1980's, according to a survey of 74 utilities by National Economic Research Associates (187). Of this capacity, some 35,000 MW was nuclear and the balance fossil-fired. This delay of the nuclear power plants could mean the equivalent annual consumption of 400 million bbl of fuel oil, at a cost of \$4 billion.

Two recent conferences, one at the Ninth Intersociety Energy Conversion Conference in San Francisco, and the other at the World Energy Conference in Detroit, brought together the recent advances in energy and power R&D, the hydrogen economy, and energy economics. Last March, the first major international conference devoted to the hydrogen economy of the future was held in Miami Beach. Eighteen sessions covered many aspects of the hydrogen economy, from production, storage, transmission, uses, the environment, to legal considerations. In October, the New York meeting of The Electrochemical Society also held sessions on the hydrogen economy.

The interest of power utilities in fuel cells is for baseload, standby generation, or backup power in an environmentally acceptable way. A major advance in the application of fuel cells was made when nine utilities joined with Pratt and Whitney in a financial arrangement to develop a 26 MW fuel cell to generate power. One demonstrator unit will be fabricated and tested by 1975, and, if successful, 56 provisional initial orders by the utilities could be firmed up (188, 189).

A commercial sodium-sulfur battery for load leveling and peaking that could meet a mid-1980 market estimated at 50,000 MW-hr/year was viewed with optimism at a recent Intersociety Energy Conversion Conference meeting (190). Problem areas include extension of cell life by a factor of ten and suitable low-cost, corrosion-resistant materials for containers and current collectors.

U.S. Power Generation.—The following tables give a preliminary summary of the production, installed generating capacity, fuel consumption, and consumption of electrical energy for the twelve-month period, January through December, 1974. For comparison purposes, revised final figures are also given for 1973. The Edison Electrical Institute expects the kW-hr use to rise by 4.5% in 1975 and to average about 7% annual growth during the 1975-1980 period (197).

Power prices are of prime concern to the electrolytic industry. Quadrupled prices of foreign oil and strong demand for low-sulfur coal have forced full escalation clauses in utility contracts. Power that cost 6-8 mills/kW-hr a few years ago now costs 30-60% more. Hydro-power prices are also climbing; Bonneville Power Ad-

Table 4. Production of electrical energy in 1974 (191-193)
(Billions-kW-hr)

Electric utility	1973	1974	% Change
Coal-fired	848.9	828.3	-2.43
Oil-fired	312.4	292.3	-6.43
Gas-fired	340.2	320.4	-5.82
Nuclear	83.3	106.7	+28.09
Total	1584.8	1547.7	-2.34
Hydroelectric	271.6	260.9	-3.94
Total	1856.4	1808.6	-2.57
Other*	2.7	2.7	0
Total	1859.1	1811.3	-2.57
Private industry	105.7	105.7*	0
Grand total	1964.8	1917.0	-2.43

* Includes geothermal, wood, and other sources.
* Estimated.

Table 5. Installed generating capacity* (194, 195)
(Millions-kW)

Investor owned	1973	1974	% Change
Hydro	21.5	22.1	+2.8
Steam**	305.8	325.6	+7.5
Nuclear	17.8	26.4	+48.3
Internal Combustion	1.4	1.4	0
Total	345.4	375.5	+8.7
Public owned			
Hydro	39.8	40.3	+1.3
Steam**	48.5	51.1	+5.4
Nuclear	1.3	4.2	+22.3
Internal combustion	3.5	3.5	0
Total	93.1	99.1	+6.4
Industry total	438.5	474.6	+8.2
Fuel type			
Hydro	53.7	54.3	1.2
Pumped storage	7.6	8.8	15.8
Fossil fuel	318.3	336.9	5.1
Nuclear	21.1	30.3	43.6
Internal combustion	4.9	5.0	1.9
Combustion turbine	32.9	39.3	19.5
Total industry	438.5	474.6	+8.2

* As of December 31, 1974.

** Includes generation by combustion turbine.

Table 6. Fuel consumption by electric utilities (191)

Fuel	1973	1974	% Change
Coal, million tons	386.6	389.3	-0.08
Oil, million barrels	560.0	527.1	-5.88
Gas, billion of cu ft	3635.8	3413.5	-6.11
Coal equivalent,* million tons	728.6	728.7	0

* Includes equivalent for nuclear, geothermal, wood, and waste.

Table 7. Electric utility sales to ultimate consumers in
1974 (196)
(Billions-kW-hr)

Consumer	1973	1974	% Change
Residential	554.2	548.9	-0.96
Commercial	396.9	389.1	-1.97
Industrial	687.2	692.3	+0.74
Other	64.9	63.3	-2.47
Total	1703.2	1693.6	-0.56

ministration is seeking a 39% increase in its present 2.3 mills/kW-hr rate (198, 199). TVA, with more fossil fuel generating plants, is increasing its rates by 53% over 1973 rates.

An updated analysis of power costs by Arthur D. Little gives nuclear power a 5 mill/kW-hr edge over fossil-fueled plants. In a 1150 MW plant, the annual savings would be nearly \$40 million in power generating costs (200).

TVA's fuel expense summary for September 1974, shows that nuclear fuel costs were 1.588 mills/kW-hr and coal fuel costs were 4.632 mills/kW-hr (201). Nuclear fuel costs were equivalent to \$3/ton of coal, but coal prices were at \$10/ton. The two TVA nuclear plants produce electricity equivalent to burning 20,000 tons of coal/day, three large trainloads (202).

Energy from fossil fuels.—Even before Arab oil embargo in the fall of 1973, it was apparent that current domestic sources of petroleum could not fulfill the requirements demanded by consumers. Petroleum imports steadily increased until the OPEC nations lowered the boom.

In the pre-embargo period, natural gas and oil increased to 65-75% of the total energy, and the contribution of coal gradually decreased, being first displaced in the residential and commercial heating markets. Following World War II, the coal industry lost a large market when the railroads converted to diesel engines. The remaining coal markets were for the production of coke as a fuel, for the rapidly growing utility market, and for large industrial users, such as the cement mills. By 1974, the electric utility industry

consumed 70% of all the coal used in the U.S., while the cement industry consumed 18%.

Prices of coal remained relatively inexpensive and static, about \$5/ton up to the end of 1973. Starting in 1973, inflation increased, the field price for natural gas escalated, steep rises in price of imported oil were imposed by OPEC nations, and coal mine productivity declined. As a result of these developments, the price of eastern bituminous coal increased to about \$8.50/ton in 1973 and \$10/ton in 1974.

The increased price of coal also indicates an increased demand by the utility industry for low-sulfur coal, as well as other industrial uses and exports of coal. At the same time, considerable governmental and industrial interest was shown in converting coal into liquid and gas products for chemicals and heating as substitutes for petroleum products. There are numerous articles in the literature describing the conversion techniques, such as pyrolysis, solvation, hydrogenation, and production of synthesis gas. Excellent reviews of coal conversion technology and coal gasification (203) have been published (204).

A comprehensive survey of established coal-gasification processes as well as new ones was reported by Chohey (205).

The Office of Coal Research is putting emphasis on converting coal into liquefied, clean, storable, transportable fuel that can be burned by central power stations or other big industrial users with minor environmental effects. Energy conversion efficiency is higher for liquefaction than it is for gasification, about 78% vs. approximately 60%, respectively. The liquids are more easily stored than gas, big plants could be built to run at optimized output, and production would not have to be synchronized to the demand of a power plant or other big user. Moreover, liquids are more concentrated and can be pumped more economically for greater distance than gas. Liquefaction does not have the heavy demand for water that gasification does, and liquid fuel is more easily pressurized to fire industrial power turbines than gas (206).

During the year, new projects for making gas and oil from coal were started. However, before they go commercial, many economic, equipment, and other problems have to be solved. Despite availability of processes, no construction work had begun and it appeared unlikely that any plant could be completed by 1978. Government approvals, plant sitings, and economics are factors which affect the slow progress toward commercialization (207).

Exxon, El Paso Natural Gas, Texas Eastern Transmission, Northern Natural Gas, Cities Service Gas, and Michigan-Wisconsin Pipeline are among the companies who have announced their intention to build commercial coal gasification plants (207).

Consumers in County Fife, Scotland, are getting synthetic natural gas made from coal. Up to 2.5 million cu ft/day are supplied from a demonstration plant in nearby Westfield. The project is being sponsored by Continental Oil Company and more than a dozen U.S. companies, working in collaboration with British Gas and Woodall-Dickham. The aim of the project is to demonstrate the feasibility of the gasification process developed by Lurgi Mineralotechnik, West Germany, for producing high Btu gas (208).

The effects of electric fields on plants, animals, and soils near and under high voltage transmission lines will be studied by Westinghouse and Pennsylvania State University under contract from the Electric Power Research Institute (209).

The question of the efficacy of installed stack-gas scrubbers was unresolved in the first part of the year. Louisville Gas and Electric was caught in the middle of the dispute between EPA, who issued a directive to install scrubbers, and Federal Power Commission (FPC), who ordered all work stopped on scrubbers (210).

Scrubbing efficiency was claimed to be increased by 2.3 times with thiosorbic lime than with conventional

lime. Thiosorbic lime has a balanced amount of magnesium oxide to promote high alkalinity in solution (211).

To cope with energy shortages, chemical companies are trying to become at least partially self-sufficient. Dow, Grace, Union Carbide, du Pont, and others are moving into oil and gas exploration by the acquisition of, or joint ventures with, independent exploration companies (212), as well as acquiring coal companies. Grace merged with Blue Diamond Coal (213), Cleary Petroleum, Magness Petroleum, and Amini Oil (214); Ethyl acquired Elk Horn Coal (213); Dow obtained a stake in Magma's geothermal technology and tracts, leased 12 producing wells owned by Quitana Production (215), and bought a 20% interest in McMoRan Exploration (213); and Gulf Resources and Chemical acquired coal reserves in Cambria County, Pennsylvania, and two small oil companies (216). Dow will also participate in a Gulf Coast superport, is planning a fuels and feedstock refinery for Brazosport, Texas, and is lining up ventures in energy-rich western Canada and the Mideast (212).

Connected indirectly to electrical energy is the recovery of the fuel value of oil shale or oil sands. The influence of the oil embargo and the price of Arab oil made the bidding for oil shale leases in western Colorado competitive and the price high (217). The chemical extraction of oil from sands will undergo pilot plant tests at Edmonton, Alberta. The process has shown evidence of higher yield and utility than steam or water (218). The *in situ* combustion to recover oil from tar sands will undergo field testing for feasibility by the Bureau of Mines (219). A one-year study on the feasibility of petrochemicals from the Alberta oil sands will also be made (220).

Project Independence placed reliance on the future energy needs on domestic sources of energy, especially on the vast coal reserves. Estimates indicated that coal production will have to be doubled by 1985 to fulfill its assigned role. One of the many problems in doubling production involves moving that much more coal, since the present transportation system is already strained. Modern technology is making progress to solve the transportation bottleneck.

Overland conveyor systems for transporting coal up to 15-20 miles with capacities of up to 5000 tons/hr are becoming common in the industry (221).

A coal slurry pipeline is operated by Peabody in northern Arizona. The coal is crushed, rod-milled, and wet-ground to 8-mesh. The slurry is formed in the rod mills, from where it is pumped to large storage tanks equipped with mechanical agitators. The 273 mile, 18 in. pipeline is capable of moving 660 tons of coal/hr in a 50% by weight slurry at a flow rate of 4200 gallons/min. Transit time from mine to destination is three days, and the line holds 45,000 tons of coal. Four pumping stations operate at between 1000 and 1500 psi, and require up to 1750 hp (221).

An 800 mile slurry pipeline system from the coal fields in Montana, Wyoming, Colorado, and Utah to the Pacific Northwest is being considered by Northwest Pipeline Corporation. The coal would be slurried with water, which would be recycled to the coal fields. Ultimately, the slurry would be composed of coal and methanol (222).

Consolidation Coal Company has announced a new hydraulic system of moving coal via pipeline from underground mine faces to above-ground preparation plants. Coal from a continuous miner is put through a mobile crusher to obtain a maximum 4 in. size, fed into a mixer where water is added to form a slurry, and sent under pressure through a 10 in. pipeline to the surface. The water is removed from the coal in the preparation plant and returned to the closed-circuit system. Consolidation Coal claims greater productivity, increased tonnage, and many safety advantages (223).

Energy from nuclear sources.—Coal and uranium are in much more abundant supply than oil and gas in the U.S. In view of this, many experts are advocating

that all our power generation should be geared to coal and nuclear energy to conserve oil and gas for other uses. Even the Shah of Iran advocated petroleum uses other than energy. Over the long term, nuclear power should be the base-load, so that coal can be used for synthetic oil and gas, thus augmenting the scarcer supplies of petroleum crude and natural gas. This postulate practically dictates that the breeder reactor be in large-scale commercial operation by 1990 (224).

According to Atomic Industrial Forum, 56 reactors are now operable in the U.S., with a capacity to generate 37,536 MW, nearly 8% of the U.S. total. In 1974, U.S. reactors generated 121 billion kW-hr, saving 183 million barrels of oil or 42 million tons of coal, equivalent to \$1.8 billion in foreign trade (225).

However, a mid-year report by the FPC listed 27 nuclear units, originally scheduled for operation in the summer of 1974, that have been delayed. The missing 26,120 MW of power is equivalent to 17 million barrels of oil/month (226).

The Atomic Energy Commission proposed legislation to change the nuclear power plant licensing process. The objective is to decrease the time required for approval and construction of nuclear power facilities from ten to six years, while providing for more effective state and public participation in planning these facilities. To reach the six year period, AEC is requesting authority to approve standardized power plant designs and to establish a list of approved plant sites (227).

For comparison, Sweden has built a nuclear plant in just over four years. Construction of Ringhals 2, an 820 MW pressure water reactor (PWR), began in February 1970, and went critical on June 19, 1974 (228).

Critics and intervenors questioned the availability of existing nuclear-fueled power plants. Three factors should be considered: cost of construction, cost of fuel, and availability. Coal-burning plants are cheaper to build by 30%. The other two factors appear to favor nuclear plants.

The Atomic Industrial Forum reported a 10% drop in nuclear-fuel costs in 1974, while fossil-fuel costs rose by 85%. Fossil fuels, on the average, now cost 11.6 mills/kW-hr, nearly six times the cost of nuclear fuel at 2.0 mill/kW-hr. Average nuclear power plant availability was 68.6% as the year drew to a close, compared to 58.4% for similar-sized fossil plants (229).

In the TVA system, Brown's Ferry Nuclear Unit 1 generated 1.9 billion kW-hr in the third quarter of 1974, equivalent to 650,000 tons of coal. The 1065 MW boiling water reactor (BWR) was available 87% of the time during the quarter, which compares to the average availability for large coal-burning units last year of 72% (230).

Commonwealth Edison reported that the availability of its four large nuclear units averaged 82% in 1974, against 69% for five new 500-800 MW coal-fired units (231).

The Connecticut Yankee 575-MW PWR plant had a capacity factor of 73%, including 88% for the first eleven months of 1974. Compared to equivalent oil-fired generation, the reactor saved its customers over \$96 million in 1974 (232).

The average cost of 1 kW-hr from nuclear plants at the end of 1974 was 10.52 mills, compared to 17.03 mills from fossil-fuel plants. The figures included amortized capital allocations. The big savings was in fuel, 2.15 mills in a nuclear plant and 11.25 mills in a fossil-fuel unit (233).

The U.S. uranium enrichment capacity has already been obligated. The projected U.S. and world demand for enriched uranium mandates that the present capacity be enlarged to guarantee a long-term supply for the expanding nuclear power plant market (234, 235). Two groups, CENGEX Associates (236) and Center Associates (237, 238), have shown interest in developing private capacity for enriching uranium by gas centrifuge technology with probable start-up in 1979-1980. Another group, Uranium Enrichment Asso-

ciates, was studying the current diffusion technology, but initial estimates indicate high capital requirements (234).

A European uranium enrichment plant, involving France, Belgium, Italy, and Spain, is scheduled for completion in 1979. The \$1.5 billion plant, based on gaseous diffusion separation, being built at Tricastin in the Rhone Valley, has been increased by an unspecified amount beyond the original level of 9 million separative work units (239).

The U.K.'s fast-breeder reactor prototype went critical in the first quarter of the year. The unit, at Dunrea, Scotland, feeds about 250 MW into the national grid, but its main purpose is to provide practical implications of building a commercial-size unit. Two other prototypes already are operating in Europe, a 150 MW unit in the U.S.S.R. and a 250 MW unit in France (240).

France has built a 250 MW unit and operated an experimental liquid metal, fast-breeder reactor, LMFBR, named Phenix, which produces more plutonium than it consumes as part of the fuel. The U.S. breeder reactor program is mired in red tape. The construction of the reactor, slated to be along the Clinch River near Oak Ridge, Tennessee, and to be operational in the early 1980's, has not started, more than two years behind schedule (241).

The U.S.S.R. also has a BN 350 (350 MW) breeder reactor at Shevchenko. However, this plant was forced to shut down due to tube leaks in three of the steam generators. The plant was operating at 30% of full power at the time of shutdown (242).

Dr. David J. Rose of MIT claimed that burning coal to produce electricity is 100 times more deadly than using nuclear power plants to produce the same amount of energy (243). Health risks from nuclear plants were also called minimal by Dr. Roger E. Lenzenman. Radiation levels from nuclear power plants are small compared to normal risks tolerated by society (244). The accidental potential of fission reactors has been exhaustively surveyed recently, and found to be below the risk potential of many industrial processes and natural phenomena (245).

Roughly one-third of Chicago and northern Illinois electricity is now provided by nuclear energy, and the oldest atomic unit has been operating safely for almost 14 years. The state monopoly in France has decided that all new power stations will be nuclear. Twenty nations other than the U.S., including all major industrial powers, are moving ahead on the nuclear power front (246).

In May, Electricite de France ordered 16 Westinghouse PWR's from Frametome (owned 45% by Westinghouse), the largest order ever placed in the history of the nuclear industry. The plants are to go into operation between 1979 and 1982 (247).

Other energy sources.—A number of other energy sources are being developed, including waste combustion, geothermal steam, solar radiation, wave energy, wind power, magnetohydrodynamics, and controlled fusion. Commercial development of these sources require long lead times (except the first two which are already producing energy on a limited scale), and it seems unlikely that any of these sources will contribute materially to the U.S. energy pool before 1985. Controlled fusion is not expected to contribute materially before the year 2000 (248). However, research and development efforts are proceeding in attempts to advance the technology of these methods to generate power economically on an industrial scale.

The energy crisis, the activity of environmentalists for cycling, and the price of fuel have led to the concept of utilizing domestic, agricultural, and industrial wastes as a source of fuel, recovery of ferrous materials, and decrease in weight and volume of the wastes for landfill in the form of ash (249). Many cities, especially St. Louis (244-251) which has been in the forefront in waste combustion for power, and others such as Boston (249, 251), Montreal (249), Chicago (250, 252), San Diego (244), New Jersey (253), New York

(251), Oakland (254), Nashville (255), El Cajon, California (256), etc., have already installed or are committed to the concept of energy from waste. The TVA is also considering production of power from garbage by the "separation process" (257).

One ton of solid waste can provide the same amount of energy as one-third ton of coal, or 65 gal of No. 2 fuel oil, or 8000 cu ft of natural gas. One pound of coal has about 12,000 Btu heating value, whereas wastes average about 4600 Btu (249).

Industrially, Weyerhaeuser has set a goal of becoming energy self-sufficient by 1980 using wastes from their operations. At present, 66% of its energy requirements are obtained from burning black liquor and hogged fuel.

Of the other potential sources of energy, geothermal steam is also producing electrical energy on a limited basis. With the energy crunch and the federal energy research budget including geothermal projects, the activity in geothermal utilization is expanding (259).

The Pacific Gas and Electric Company, which supplies San Francisco, is operating a geothermal field commercially, and is expanding its capacity. In 1976, it will have a capacity of 847,000 kW, far exceeding Italy's 380,000 kW facility (260).

A conceptual design for a 10 MW geothermal electric power plant in Mono County, California, will use the Magnamax power process, an advanced binary cycle for converting thermal energy to electrical energy (261).

An AEC sponsored Geothermal Power Development Conference held in June in Berkeley, California, included papers from AEC and industry (262).

The Dow Chemical Company purchased an interest in the Magma Power Company. Dow will assist in exploration and development of geothermal properties under Magma control and will use Magma's technology to obtain geothermal steam for its chemical plants (263).

The radiant energy received continuously by this planet from the sun far exceeds our present energy needs, or that of the immediate future. A variety of ways have been suggested in which this energy could be used to heat and cool buildings or to generate electricity and synthetic fuels.

NASA is developing an experimental solar collector system to heat and cool a structure that will be built in Hampton, Virginia. Water-filled tubes inside the solar collectors would absorb the solar heat, using it for direct hot-water heating and to operate an absorption refrigeration unit (264). NASA has also applied for a patent on a special absorptive coating for aluminum panels that are used in building a solar energy collector. The coating absorbs about 93% of the total solar heat, but reradiates only 6% of the infrared heat (265).

Continental Oil is testing solar panels as a supplemental power source on a Gulf of Mexico oil production platform. Banks of solar panels absorb sun energy and convert it to electricity for storage batteries that operate warning devices (266).

A photovoltaic solar cell demonstration system was being set up in McLean, Virginia, by Metro Corporation to convert solar energy directly into 1500 kW-hr of electricity annually (267). The system is the first step in a continuing evaluation program. Sandia Laboratories are exploring the possibility of developing photovoltaic cells to produce power at cost equivalent to fossil fuel conversion cells (268). They are also studying the concept for a community powered mostly by solar energy.

The NSF is sponsoring the experimental augmentation of regular heating systems of four schools with solar heating systems (269). A Harvard University-Tyco Laboratories team, also sponsored by NSF, has developed a process for the continuous production of silicon-crystal solar cells. This breakthrough in technology is supposed to cut the cost of a solar array unit

capable of producing 1 kW by a factor of 100, to about \$350 (265).

PPG is now producing solar energy collector cells, designed for hot water and heating systems of multi-story buildings and homes (270). A new Japanese solar battery uses thin film of ultrapure chlorophyll extracted from spinach to generate electricity (271).

In other novel energy schemes, an ocean wave-driven air pump consists of a cylinder submerged in the ocean, through which water rises and falls, pumping air that can power a generator (272).

In a workshop conference, it was concluded that there were no insurmountable obstacles in collecting a part of the energy from Gulf stream currents off the coast of Florida (273).

The University of Edinburgh received a grant to harness ocean wave power to generate electricity. It is claimed that better than 80% of the wave energy could be collected by using the rolling motion of the waves to rotate vanes in partially submerged containers (274).

Methods to recover the energy in tidal waves have been periodically suggested, particularly in the Bay of Fundy and in France. The construction of a dam for a tidal power project is being planned for Mezan Bay in the White Sea in the U.S.S.R. Plans are to install 600 capsule and turbine units, each with 10 MW capacity. The construction method will be similar to that of the first Soviet tidal power unit at Kislaya Guba, on the Barents Sea (275).

The cost of the French 240 MW plant on the Rance estuary was three times as much as a conventional hydropower station (275).

A wind energy conversion system, a series of windmills, could be constructed in the Texas Panhandle by 1985, to produce 500 MW of electrical energy. The windmills could be operating with 20 mph winds 40% of the time in most areas and 50% of the time in some areas of the Panhandle, the windiest region of the U.S. (276).

Both NASA and NSF are funding projects for wind energy conversion systems. Michigan State University, General Electric, and Kaman Aerospace will study the feasibility and design of wind conversion systems (277-279).

Canada's B.C. Hydro, Vancouver, has ordered two small wind-driven power plants from Par Industrial Contractors. The 2000W units, costing \$8210 each, will be used in an evaluation study in the spring of 1975 (280).

Windpower systems can generate electricity directly or produce hydrogen by electrolysis of water, and with a storage system the hydrogen can be later used in a fuel cell to produce electricity. Using a computer model to analyze windpower for the New England area, it was found that incremental demand from 1976 to 1990 could be satisfied at a cost of \$0.119-0.201/kW-hr. The system would have 173 wind stations with three identical 2 MW generators per station (281).

Magnetohydrodynamic (MHD) power got another boost with an \$8 million contract to the University of Tennessee Space Institute to build an intermediate-size MHD plant. The plant, funded by the Office of Coal Research will integrate all components of a direct coal-fired MHD plant and will operate continuously for 100 hr or more (282). Avco also received funding from the same source for development of MHD power systems operating on coal or fuel derived from coal (283).

General Electric reported a breakthrough in MHD efficiency. It converted 20% of the heat produced in a closed-cycle MHD setup into 1800 kW of electricity in a hundredths-of-a-second bursts in a 60 ft shock tube (284).

Manuscript received June 16, 1975. This report was presented at the Industrial Electrolytic Division Luncheon at the Toronto, Canada, Meeting of the Society, May 11-16, 1975.

Any discussion of this paper will appear in a Discussion Section to be published in the June 1976 JOURNAL. All discussions for the June 1976 Discussion Section should be submitted by Feb. 1, 1976.

REFERENCES

- Chlorine Institute News Release, Feb. 5, 1975.
- Chemical Week*, p. 31, Feb. 12, 1975.
- Chlorine Institute, Pamphlet 10, North American Chlor-Alkali Industry Plants and Production Data Book, Jan. 1975.
- Chemical Week*, p. 35, March 12, 1975.
- Ibid.*, p. 25, March 6, 1974.
- Ibid.*, p. 25, April 17, 1974.
- Ibid.*, p. 23, April 24, 1974.
- Electrochemical Progress*, p. 3, April 1974.
- Chemical and Engineering News*, p. 8, April 29, 1974.
- Chemical Week*, June 12, 1974.
- Chemical and Engineering News*, p. 9, Dec. 16, 1974.
- Ibid.*, p. 5, Oct. 7, 1974.
- Ibid.*, p. 24, Dec. 16, 1974.
- Ibid.*, p. 9, July 22, 1974.
- Chemical Week*, p. 35, April 17, 1974.
- Chemical Marketing Reporter*, p. 44, Jan. 6, 1975.
- European Chemical News*, p. 32, Oct. 18, 1974.
- Chemical Week*, p. 45, Nov. 27, 1974.
- Electrochemical Progress*, p. 11, June 1974.
- European Chemical News*, p. 30, June 21, 1974.
- Chemical and Engineering News*, p. 17, May 20, 1974.
- Chem. Tech.*, p. 708, Dec. 1974.
- Chemical Engineering*, p. 54, Feb. 3, 1975.
- The Electrochemical Society, Extended Abstracts, San Francisco, California, Meeting, May 12-17, 1974.
- European Chemical News*, p. 31, Oct. 11, 1974.
- Chemical Economy and Engineering Review (Japan)*, Vol. 6, p. 65, Nov. 1974; *Electrochemical Progress*, p. 3, Nov. 1974.
- European Chemical News*, p. 21, Jan. 31, 1975.
- Electrochemical Progress*, p. 9, May 1974.
- Ibid.*, p. 3, Dec. 1974.
- Chemical Week*, p. 31, May 8, 1974; *Electrochemical Progress*, p. 11, July 1974.
- Chemical Marketing Reporter*, Nov. 4, 1974.
- Chemical Week*, p. 27, Feb. 12, 1975.
- Chemical Engineering*, p. 18, Feb. 3, 1975.
- Chemical Engineering Progress*, p. 59, March 1974.
- Electrochemical Progress*, p. 11, June 1974.
- Ibid.*, p. 11, Jan. 1975.
- Chemical Week*, p. 32, March 5, 1975.
- Electrochemical Progress*, p. 5, Feb. 1975.
- Mineral Industry Surveys, U.S. Dept. of the Interior, Bureau of Mines, Mercury in 1974, Annual Preliminary.
- Electrochemical Progress*, p. 5, July 1974.
- Chlorine Institute letter, Mercury Material Balance Task Force, dated March 4, 1975.
- Electrochemical Progress*, p. 13, Oct. 1974.
- Current Industrial Reports, Inorganic Chemicals, U.S. Dept. of Commerce, Bureau of the Census, January-December, 1974.
- Report of the Electrolytic Industries for the Year 1973.
- Chemical Age*, p. 15, Jan. 24, 1975.
- Chemical Marketing Reporter*, May 27, 1974.
- Ibid.*, Dec. 30, 1974.
- Electrochemical Progress*, p. 8, Jan. 1975.
- Mineral Industry Surveys, U.S. Dept. of the Interior, Bureau of Mines, Annual Preliminary, "Soda Ash," Dec. 26, 1974.
- Chemical and Engineering News*, p. 11, Feb. 24, 1975.
- Chemical Week*, p. 18, March 27, 1974.
- Ibid.*, p. 33, Jan. 9, 1974.
- Wall Street Journal*, April 8, 1974.
- Chemical Week*, p. 29, Dec. 4, 1974.
- Ibid.*, p. 31, May 8, 1974.
- Current Industrial Reports, Inorganic Chemicals, Bureau of the Census, U.S. Dept. of Commerce, January-December 1974.
- Report of the Electrolytic Industries for the Year 1973.
- Canadian Chemical Processing*, p. 20, Aug. 1974.
- Chemical Marketing Reporter*, p. 35, May 27, 1974.
- Ibid.*, p. 36, Dec. 23, 1974.
- Electrochemical Progress*, p. 11, July-August 1974.
- Chemical Week*, p. 22, Nov. 27, 1974; *CPI Management*, p. 1, Nov. 25, 1974.
- Chemical Marketing Reporter*, p. 3, Nov. 25, 1974.
- European Chemical News*, p. 14, Dec. 13, 1974.
- Mineral Industry Surveys, Dept. of the Interior, Bureau of Mines, Aluminum Monthly, Aluminum Industry in December 1974, March 5, 1975.
- Mineral Industry Surveys, Dept. of the Interior, Bureau of Mines, Annual Preliminary, Aluminum and Bauxite in 1974, Dec. 24, 1974; *Chemical Week*, p. 17, April 10, 1974.
- Chemical Week*, p. 33, Feb. 12, 1975.
- Electrochemical Progress*, p. 8, Jan. 1975.
- Ibid.*, p. 9, Jan. 1975.
- Ibid.*, p. 11, Sept. 1974.
- Ibid.*, p. 5, Sept. 1974.
- Ibid.*, p. 6, May 1974.
- Ibid.*, p. 4, June 1974.
- Ibid.*, p. 8, April 1974.
- Ibid.*, p. 9, July-August 1974.
- U.S. Industrial Outlook, 1975, with Projections to 1980, U.S. Dept. of Commerce.
- Electrochemical Progress*, p. 5, Dec. 1974.
- Ibid.*, p. 4, Jan. 1975.
- Chemical Week*, p. 15, Oct. 9, 1974.
- Chemical Engineering*, p. 98, April 29, 1974.
- Electrochemical Progress*, p. 5, Jan. 1975.
- Ibid.*, p. 9, April 1974.
- Ibid.*, p. 11, May 1974.
- Chemical Engineering*, p. 57, May 27, 1974.
- Electrochemical Progress*, p. 11, Jan. 1975.
- Chemical Week*, p. 25, Jan. 1, 1975.
- Mineral Industry Surveys, U.S. Dept. of Interior, Bureau of Mines, Annual Preliminary, Dec. 17, 1974, "Beryllium in 1974."
- Metals Week*, p. 7, May 20, 1974.
- Ibid.*, p. 7, May 6, 1974.
- Ibid.*, p. 9, Aug. 26, 1974.
- Ibid.*, p. 3, Sept. 30, 1974; p. 3, Oct. 28, 1974.
- Ibid.*, p. 5, Dec. 20, 1974.
- Chemical and Engineering News*, p. 11, April 9, 1974.
- Mineral Industry Surveys, Bureau of Mines, Chromium Monthly, Chromium in December 1974.
- Ibid.*, Chromium Annual 1974, Dec. 26, 1974.
- Metallurgical Bulletin (London)*, p. 26, Dec. 24, 1974.
- Mineral Industry Surveys, U.S. Dept. of the Interior, Bureau of Mines, Preliminary; Dec. 24, 1974, "Copper in 1974."
- Ibid.*, "Copper Industry in December 1974," Feb. 26, 1975.
- Ibid.*, "Copper Production in December 1974," Feb. 26, 1975.
- Chemical Week*, p. 39, March 6, 1974.
- Ibid.*, p. 39, March 27, 1974.
- Chemical and Engineering News*, p. 14, Sept. 30, 1974.
- Chemical Week*, p. 38, Feb. 20, 1974.
- Ibid.*, p. 40, Jan. 23, 1974.
- Ibid.*, p. 31, May 8, 1974.
- Chemical and Engineering News*, p. 19, Feb. 11, 1974.
- Metals Week*, p. 2, May 13, 1974.
- Chemical and Engineering News*, p. 6, May 13, 1974.
- Chemical Engineering*, p. 35, Nov. 25, 1974.
- Metals Week*, p. 2, Aug. 26, 1974.
- Ibid.*, p. 2, Dec. 16, 1974.
- Chemical Week*, p. 51, April 10, 1974.
- Wall Street Journal*, p. 35, May 1, 1974.
- Metals Week*, p. 2, Dec. 9, 1974; *Chemical Week*, p. 20, Nov. 27, 1974.
- Engineering and Mining Journal*, p. 155, March 1975.
- American Metals Market*, p. 8, March 28, 1975.
- Chemical Week*, p. 20, March 6, 1974.
- Mineral Industry Surveys, U.S. Dept. of the Interior, Bureau of Mines, Annual Preliminary, "Lithium in 1974."
- Electrochemical Progress*, p. 8, May 1974.
- Chemical Marketing Reporter*, p. 34, Feb. 24, 1974; *Chemical Week*, p. 16, Jan. 23, 1974.
- Chemical Marketing Reporter*, Dec. 23, 1974.

122. *Journal of Commerce*, p. 8, Feb. 23, 1975.
123. *American Metals Market*, p. 8, Jan. 23, 1975.
124. *Chemical Week*, p. 27, Aug. 28, 1974.
125. *Electrochemical Progress*, p. 12, Sept. 1974.
126. *Metals Week*, p. 10, June 24, 1974.
127. *Ibid.*, p. 7, Jan. 7, 1974.
128. Mineral Industry Surveys, U.S. Dept. of the Interior, Bureau of Mines, Annual Preliminary, Dec. 20, 1974, "Magnesium in 1974."
129. *Metals Sourcebook*, p. 4, Jan. 28, 1974.
130. *Metals Week*, p. 7, May 20, 1974.
131. *Ibid.*, p. 7, Jan. 21, 1974.
132. *Chemical Week*, p. 17, Oct. 23, 1974.
133. *Metals Week*, p. 7, March 18, 1974; *Chemical Week*, p. 25, March 20, 1974.
134. *Metals Week*, p. 7, May 6, 1974; *Wall Street Journal*, p. 13, April 30, 1974.
135. Mineral Industry Surveys, U.S. Dept. of the Interior, Bureau of Mines, Fourth Quarter, Feb. 13, 1975, "Magnesium."
136. Mineral Industry Surveys, U.S. Dept. of the Interior, Bureau of Mines, Manganese, Annual Preliminary, 1974.
137. *Ibid.*, Manganese, Dec. 1974.
138. *Chemical Week*, p. 47, May 15, 1974.
139. *Electrochemical Progress*, p. 6, June 1974.
140. *Ibid.*, p. 11, Sept. 1974.
141. *Ibid.*, p. 5, April 1974.
142. Mineral Industry Surveys, U.S. Dept. of the Interior, Bureau of Mines, Annual Preliminary, Nickel in 1974, Dec. 26, 1974.
143. *Ibid.*, Nickel Monthly, Dec. 1974, Feb. 27, 1975.
144. *Electrochemical Progress*, p. 10, June 1974; p. 8, Jan. 1975.
145. *Ibid.*, p. 8, Nov. 1974.
146. *Ibid.*, p. 10, Dec. 1974.
147. *Ibid.*, p. 5, Nov. 1974.
148. *Ibid.*, p. 5, Jan. 1975.
149. *Ibid.*, p. 4, April 1974.
150. *Chemical Engineering*, p. 49, Oct. 14, 1974.
151. *Chemical and Engineering News*, p. 14, Oct. 7, 1974.
152. *Chemical Week*, p. 26, May 29, 1974.
153. *Electrochemical Progress*, p. 5, Feb. 1975.
154. *Ibid.*, p. 11, May 1974.
155. *Ibid.*, p. 6, May 1974.
156. *Chemical Engineering*, p. 51, Sept. 16, 1974.
157. *Chemical Week*, p. 51, April 10, 1974.
158. Mineral Industry Survey, U.S. Dept. of the Interior, Bureau of Mines, Annual Preliminary, Dec. 26, 1974, Revised, Sodium.
159. *Metals Week*, p. 1, March 18, 1974.
160. *Ibid.*, p. 1, Sept. 2, 1974.
161. *Ibid.*, p. 3, Dec. 23, 1974; *Chemical and Engineering News*, p. 13, Feb. 10, 1975.
162. *Chemical Week*, p. 23, Feb. 13, 1974.
163. Mineral Industry Surveys, U.S. Dept. of the Interior, Bureau of Mines, Annual Preliminary, Dec. 27, 1974, Titanium in 1974.
164. *Ibid.*, Quarterly, March 20, 1975, Titanium.
165. *Electrical World*, pp. 44-46, Feb. 15, 1974.
166. Mineral Industry Surveys, U.S. Dept. of Interior, Bureau of Mines, Quarterly, Aug. 22, 1974, Titanium.
167. *Ibid.*, Quarterly, Dec. 2, 1974, Titanium.
168. *Chemical Week*, p. 35, March 20, 1974.
169. *Metals Week*, p. 7, Oct. 14, 1974.
170. *Ibid.*, p. 9, March 11, 1974.
171. Direct Reduction Processes for the Production of Titanium Metal, Report NMAB-304, March 1973; National Materials Advisory Board, National Research Council, National Academy of Science and Engineering, Washington, D.C.
172. Mineral Industry Surveys, U.S. Dept. of the Interior, Bureau of Mines, Annual Preliminary, Dec. 31, 1974, Zinc in 1974.
173. *Ibid.*, Zinc, Production in December 1974, Feb. 21, 1975.
174. *Ibid.*, Zinc Production in November 1974, Jan. 21, 1975.
175. *Chemical Week*, p. 14, Jan. 23, 1974.
176. *Metals Week*, p. 1, Jan. 14, 1974.
177. *Ibid.*, p. 1, Jan. 21, 1974.
178. *Chemical and Engineering News*, p. 6, July 15, 1974.
179. *Metals Week*, p. 1, July 15, 1974.
180. *Ibid.*, p. 3, May 6, 1974.
181. *Ibid.*, p. 6, Sept. 30, 1974.
182. Mineral Industry, Surveys, U.S. Dept. of the Interior, Bureau of Mines, "Zinc Industry in December 1974," March 5, 1975.
183. *Metals Week*, Monthly Price Index.
184. *Ibid.*, p. 1, Dec. 16, 1974.
185. A. D. Mahon *et al.*, "The U.S. Zinc Industry: A Historical Perspective," Bureau of Mines Information Circular, IC 8629, 1974.
186. *Electrical World*, p. 26, July 15, 1974.
187. *Ibid.*, p. 25, Sept. 1, 1974.
188. *Chemical and Engineering News*, pp. 31, 32, Jan. 7, 1974.
189. *Chemical Engineering*, pp. 62, 64, May 27, 1974.
190. *Electrical World*, p. 28, Oct. 1, 1974.
191. *Ibid.*, p. 58, March 15, 1975.
192. Edison Electric Institute, Statistical Year Book of the Electric Utility Industry for 1973.
193. *Federal Power Commission News*, p. 4, Jan. 28, 1975.
194. *Electrical World*, p. 51, March 15, 1974.
195. *Ibid.*, p. 59, March 15, 1975.
196. *Ibid.*, p. 66, March 15, 1975.
197. *Ibid.*, p. 19, Feb. 15, 1975.
198. *Chemical Week*, p. 52, Oct. 23, 1974.
199. *Metals Week*, p. 9, Aug. 26, 1974; p. 6, Sept. 2, 1974.
200. *Electrical World*, p. 33, Oct. 15, 1974.
201. *Ibid.*, p. 30, Nov. 15, 1974.
202. *Ibid.*, p. 34, Feb. 1, 1975.
203. H. Perry, *Scientific American*, pp. 19-25, March 1974.
204. H. Perry, *Chemical Engineering*, pp. 88-102, July 22, 1974.
205. N. P. Chohey, *Chemical Engineering*, p. 70, March 4, 1974.
206. *Chemical Week*, pp. 38-43, Sept. 11, 1974.
207. *Ibid.*, p. 35, Jan. 9, 1974.
208. *Chemical and Engineering News*, p. 18, Aug. 26, 1974; and p. 22, Aug. 19, 1974; *Chemical Week*, p. 39, Aug. 21, 1974.
209. *Electrical World*, p. 57, Jan. 1, 1975.
210. *Ibid.*, p. 19, May 15, 1974.
211. *Ibid.*, p. 107, Oct. 15, 1974.
212. *Chemical Week*, p. 52, Oct. 23, 1974.
213. *Ibid.*, p. 4, Jan. 2, 1974.
214. *Ibid.*, p. 17, March 27, 1974.
215. *Ibid.*, p. 15, March 6, 1974.
216. *Ibid.*, p. 9, April 10, 1974.
217. *Ibid.*, p. 13, Jan. 16, 1974.
218. *Chemical and Engineering News*, p. 13, March 18, 1974.
219. *Ibid.*, p. 14, Sept. 30, 1974.
220. *Ibid.*, p. 13, Dec. 23, 1974.
221. *Chemical and Engineering News*, p. 17, April 15, 1974.
222. *Chemical Week*, p. 22, May 29, 1974; *Chemical Engineering*, p. 33, June 10, 1974; *Chemical and Engineering News*, p. 17, May 30, 1974.
223. *Electrical World*, p. 51, June 15, 1974.
224. *Ibid.*, p. 94, June 1, 1974.
225. *Ibid.*, p. 33, Feb. 15, 1975.
226. *Ibid.*, p. 25, June 15, 1974.
227. *Chemical and Engineering News*, p. 12, March 18, 1974.
228. *Electrical World*, p. 33, Aug. 1, 1974.
229. *Chemical Week*, p. 35, Nov. 6, 1974.
230. *Electrical World*, p. 34, Dec. 15, 1974.
231. *Ibid.*, p. 30, Jan. 1, 1975.
232. *Ibid.*, p. 34, Jan. 1, 1975.
233. *Chemical Week*, p. 57, Dec. 11, 1974.
234. *Electrical World*, p. 25, July 15, 1974; p. 33, Sept. 1, 1974.
235. *Chemical and Engineering News*, p. 14, Aug. 12, 1974.
236. *Ibid.*, p. 6, May 27, 1974.
237. *Chemical Week*, p. 39, Nov. 13, 1974.
238. *Ibid.*, p. 45, Dec. 1, 1974.
239. *Ibid.*, p. 12, July 29, 1974.
240. *Chemical and Engineering News*, p. 13, March 18, 1974.
241. *Wall Street Journal*, p. 30, Jan. 28, 1975.
242. *Power*, p. 136, May 1974.
243. *Chemical Engineering*, p. 63, Dec. 9, 1974.
244. *Electrical World*, pp. 42-45, Dec. 1, 1974.
245. Rasmussen's Report, Document WASH 1400, Atomic Energy Commission.
246. Comments by J. Harris Ward, Commonwealth Edison Company, "Exploring Energy Choices," p. 56, The Ford Foundation, 1974.

247. *Electrical World*, p. 34, May 1, 1974; *Power*, p. 136, May 1974.
248. *Chemical Week*, p. 24, May 29, 1974.
249. *Chemical and Engineering News*, p. 21, Feb. 19, 1974.
250. *Ibid.*, p. 13, June 10 1974; *Power*, p. 134, May 1974.
251. *Electrical World*, p. 27, May 15, 1974.
252. *Ibid.*, p. 19, May 1, 1974.
253. *Chemical and Engineering News*, p. 16, Aug. 26, 1974; *Chemical Engineering*, p. 69, March 4, 1974.
254. *Chemical Engineering*, p. 73, Jan. 21, 1974.
255. *Power*, p. 18, Dec. 1974.
256. *Chemical Engineering*, p. 35, Nov. 25, 1974.
257. *Ibid.*, p. 71, Nov. 11, 1974; *Electrical World*, p. 26, Nov. 1, 1974.
258. *Chemical Week*, p. 24, May 29, 1974.
259. *Wall Street Journal*, Feb. 21, 1974.
260. *Evening Baltimore Sun*, 5 Star Edition, p. 14, March 13, 1974.
261. *Chemical and Engineering News*, p. 29, April 22, 1974.
262. Report LBL-3099 Atomic Energy Commission, or from NTIS, U.S. Dept. of Commerce, Springfield, Virginia, 22161.
263. *Chemical Week*, p. 17, March 27, 1974; *Chemical Week*, p. 50, March 6, 1974.
264. *Chemical Engineering*, p. 73, June 10, 1974.
265. *Ibid.*, p. 39, June 10, 1974.
266. *Times-Union*, Rochester, New York, p. 7D, Feb. 5, 1974.
267. *Chemical and Engineering News*, p. 13, May 10, 1974.
268. *Power*, p. 136, May 1974.
269. *Chemical and Engineering News*, p. 13, March 18, 1974.
270. *Ibid.*, p. 15, Sept. 9, 1974.
271. *Democrat and Chronicle*, Rochester, New York, p. 7A, Jan. 7, 1974.
272. *San Diego Tribune*, p. 3x, March 15, 1974.
273. *Electrical World*, p. 27, Oct. 1, 1974; *Science Trens*, p. 4, Sept. 30, 1974.
274. *Chemical and Engineering News*, p. 16, Oct. 10, 1974.
275. *New Scientist*, p. 514, Feb. 27, 1975.
276. *Times-Union*, Rochester, New York, p. 44, Jan. 2, 1975.
277. *Chemical and Engineering News*, p. 23, March 25, 1974.
278. *Ibid.*, p. 19, Jan. 27, 1975.
279. *Ibid.*, p. 16, Dec. 2, 1974.
280. *Chemical Engineering*, p. 27, Dec. 23, 1974.
281. *Electrical World*, p. 27, Oct. 1, 1974.
282. *Chemical and Engineering News*, p. 12, Jan. 6, 1974.
283. *Ibid.*, p. 16, Feb. 3, 1975.
284. *Chemical Week*, p. 64, Oct. 9, 1974; *Electrical World*, p. 40, Nov. 1, 1974.



Science and Technology—The New Challenges¹

W. G. Schneider

National Research Council Canada, Ottawa, Ontario, Canada



Science and technology today have attained a fairly high degree of maturity and scientific research has become highly institutionalized. These developments have evolved largely during the decades following World War II. During this period we have seen unprecedented advances in both science and technology. However, as we look to the future there are serious concerns whether the new challenges now facing the nations of the world can be adequately dealt with by simple linear extrapolations. Both the nature and the longer term implications of the new challenges will demand greater R&D initiatives and much greater adaptability by the scientific community than it has been accustomed to in the past.

The new realities.—As we approached the 70's a number of problem areas, which had been formerly of only minor concern, rapidly developed to a degree where they have now become of major concern both nationally and internationally. Some of these areas have reached near crisis proportions. What is equally clear is that many of these problems are closely inter-related and that they have serious long-term implications for man's well-being on this planet.

That having been said, I should make clear at the outset that I do not share most of the "doom and gloom" prophecies with respect to man's survival. Recognizing the problems and their implications, man also has the necessary intelligence, capability, and

adaptability to act rationally and to manage his affairs so as to ensure his future well-being. As a result of the broad advances in science and technology over the past few decades, we are in a much stronger position to face up to these challenges, to devise new solutions, and to develop optional technologies for new strategic approaches. This is not to suggest that national and world problems will be solved by science and technology alone, but rather that science and technology will be needed as essential aids in the alleviation of and solutions to such problems.

Because the new challenges I refer to also imply possible serious consequences in the long term as well as in the short term, I prefer to call them the new realities. To be realist rather than alarmist, it is nevertheless appropriate to raise the question whether, in view of past inertia, the nations of the world, as well as the scientific community, have the conviction and the will to respond actively and comprehensively to the new realities.

To be more explicit, I would like to start with the following list of topics which have been identified as problem areas in many countries and which relate directly to our major concerns: (i) energy, (ii) food, (iii) housing and urban problems, (iv) industrial development (goods and services, employment), (v) environment, (vi) materials (resources) and materials recycling, (vii) transportation and communications, (viii) health, (ix) disarmament and peace, (x) economic, scientific, and technical aid to less developed countries, (xi) oceans, (xii) space.

This list is not intended to be in any particular order of importance or priority nor is it necessarily complete. Others might be added, such as economic stability (including trade, monetary problems, inflation, etc.), social justice, public safety and security. These are indeed explicit areas of concern. To some degree also they are implicit in the above list.²

In recent years much of the rhetoric on science policies has been concerned with relating scientific research to national goals. In the first instance, that is, without further elaboration, such goals are generally stated in very broad terms, as follows: food, shelter, prosperity, health, peace and security, justice and social welfare.

These could equally well be a statement of international goals. In essence, they reflect basic human needs and no country could long survive if such needs were not met to some minimum standard. When we compare these basic needs with the longer list of topics above, there is a striking overlap and resemblance.

There are several other distinguishing features of the longer list of twelve topics:

(i) Most of these areas have become more important or critical in recent years and are likely to be of on-

¹This is the Electrochemical Society Lecture delivered at the Toronto, Canada, Meeting of the Society, May 12, 1975.

²The problem of population should properly be considered as part of the new reality. However, it would seem to belong more in the social or moral domain than in the domain of science and technology.

going concern in future. Frequently a particular topic forms the unique mission of a ministry of national governments.

(ii) There is a high degree of inter-connection between these problem areas.

(iii) Most of these problem areas are now also of international concern.

(iv) All depend heavily on applications of science and technology and will require considerably more R&D investment in future.

To this audience, there is no need to elaborate in detail on each of these topics but certain features are worth mentioning.

Energy.—Although the finite supply of fossil fuels had been frequently pointed out, it took the recent oil embargo to bring home to us an awareness of this fact, as well as of our excessive dependence (and therefore also vulnerability) on this form of energy. Past R&D investments in nuclear energy have provided an alternative form of energy. Other sources of energy will also have to be developed especially from renewable resources.

Food.—Ultimate shortages of food, especially cereals and protein had also been foreseen. The green revolution gave hope of buying time but made heavy demands on fertilizer supplies. Increased food demands were due in part to population increase and in part due to nutritional upgrading of substandard diets. The world now faces the double challenge of increasing food supply while conserving energy, including fertilizers.

Housing and urban problems.—The concerns relating to low-cost housing and a complex of urban problems are well known. The need for energy conservation, for environmental preservation, and for waste and materials recycling are added dimensions.

Industrial development.—In the past, economic viability of a private enterprise could be virtually assured if it had an efficient technology, good management and adequate market access. The ground rules are rapidly altering. Future enterprises will also be required to take into account and be accountable for social costs, environmental costs, energy costs, and material costs. It is doubtful whether many of today's technologies will be able to meet all criteria, and these technologies may have to be modified or alternate technologies may have to be developed. Such new technologies may not necessarily be large-scale technologies. Employment opportunity is an additional factor of growing importance.

Environment.—With today's numerous environmental concerns and risks, it is clear much more basic knowledge and understanding will be required to make environmental impact analyses with confidence. Indeed many environmental risks now of concern were detected only recently as a result of highly sensitive analytical techniques made possible by recent scientific advances.

Materials (resources) and materials recycling.—This is an area which will obviously continue to be science and technology intensive. The new parameters are likely to be energy conservation, materials conservation, substitution, and recycling.

Transportation and communications.—These are the essential service networks required by any nation (and among nations) to move people, goods, and information. Their importance to modern societies has grown enormously with a strong demand for new technologies. Future transportation systems will be required to meet stringent energy consumption standards, environmental acceptability, and urban standards. Electronic communications systems will be required with greater load handling capabilities and as a partial substitute for paper communications.

Health.—With R&D in the health sciences already at a substantial level, new emphasis is likely to be directed toward preventive medicine and health delivery systems.

Disarmament and peace.—This is a topic which requires special comment. At one time referred to as the War Department of national governments, it is currently called the Defense Department. In the new realities, it might better be called the Disarmament and Peace Department. On the one hand we need to question whether present defense theories and postures are becoming outmoded, and on the other hand whether the nations of the world can continue to condone the high wastage of capital, energy, and materials under the guise of defense. Accepting that every nation has a right to defend itself, and that what is regarded as an adequate defense bears an international relativity, the only feasible way to de-escalate mounting defense costs is through mutual and collective agreements among nations. A first goal in this direction must be a total ban on nuclear weapons together with verifiable and enforceable safeguards. The failure to contain the so-called nuclear club and the failure of the Nuclear Non-Proliferation Treaty should now be ample warning that we are drifting along a dangerous course and that a whole new positive approach is needed.

What does all this have to do with science and technology? Today's highly sophisticated defense systems are, of course, heavily dependent on science and technology. It is sometimes suggested that scientists in all countries should refuse to work on weapons technology. Unless a total moratorium could be guaranteed and enforced, such a tactic would be impractical and totally unacceptable, since it would place scientists in an untenable situation of having their motives questioned as unpatriotic. A much more positive approach has a better chance to succeed. An example of this was the contribution made by scientists in developing sensitive detection systems for nuclear explosions anywhere in the world, which led to the acceptance of the partial ban on nuclear tests. Obviously, rather sophisticated safeguard systems would have to be devised to achieve a high level of confidence and an acceptable agreement to ban nuclear weapons. This could be an area of active international collaboration and, if scientists of many countries worked together toward such a common purpose, the chances of success would be greatly enhanced. Such a combined effort could also help to influence attitudes and foster a better climate of understanding and trust. There would appear to be little hope of general disarmament until the problem of nuclear weapons and their delivery systems is resolved on a world scale.

I am not sure whether this is a practical suggestion or not. But I think the scientific community in all countries must seriously ask itself whether there is not some positive role or some new approach which could contribute to the ultimate resolution of this problem. Progress made in the other problem areas I have mentioned may well be negated or diverted unless there is also much more rapid progress toward disarmament and peace.

Economic, scientific, and technical aid to less developed countries.—This is an enormous problem, and in spite of a great deal of discussion and good intentions relatively little progress has been made in reducing the wide disparities between have and have-not countries. It is now widely recognized that to achieve a more stable world community, this gap must be narrowed substantially and more rapidly than has been achieved until now. The difficulties are well known. More effective action programs, together with possible new approaches, are now urgently needed.

Oceans and space.—These are both areas of growing importance. Here, too, the international and political problems are well known and remain to be resolved. It is also clear that the exploitation of the world's

oceans and outer space for the benefit of mankind will require substantial R&D investments.

Implications for science and technology.—How can the scientific community play a more active role in seeking solutions to the above list of problem areas? These are formidable and highly complex problems. Ultimate solutions must of course seek to resolve simultaneously the socio-economic and political aspects. However, with better technological solutions and more technological options available these aspects become much more tractable.

A related question frequently posed is: How can I as an individual scientist or engineer contribute? What research should I do? What research is needed? This points up a major difficulty. Before we can start looking for answers and solutions by doing research, it is necessary to be clear what the question is. Has the question related to a problem been adequately defined and validated? Who should frame the questions and who is best able to do so?

Such uncertainties, of course, do not arise when we are talking about basic research, but for the major problem areas of concern, they are highly relevant. The fact that these difficulties persist could mean that we lack a sufficient understanding of the problem areas to be able to define the significant questions amenable to research, or that in relation to the questions, we lack promising ideas worth researching, or simply that we have not yet developed adequate ways and means to focus our best talents and capabilities on these problems. Each of these possibilities is no doubt pertinent in particular instances.

Central to these issues is the role of government and its interface modes with the scientific research community. Research and development activities organized on a national scale largely grew out of government initiatives during the last war to mobilize scientific resources for the war effort. A cadre of peer scientists worked closely with various government departments and agencies to evaluate key problems and to formulate significant research requirements. A system for funding research projects through grants and contracts was devised. This system, with but minor modifications, was carried over into peacetime and continues today. Accordingly, government had taken on a major central role not only in funding mission research, but also basic research.

It is also worth noting that during the last war many scientists set aside their own research programs and became primarily problem solvers. What was especially impressive was the effective way in which basic scientists, given strong motivation, successfully became applied scientists and engineers. After the war most of these researchers went back to their prewar pursuits.

During the past thirty years government-funded R&D expanded very substantially. During this period of high affluence and expectation, we have lacked the same strong sense of focus, and the clear articulation of urgent problem areas that was so evident during the war. In this situation and with the rapid buildup of universities and academic research, science tended to become more inward-looking. However, as I mentioned earlier, during this period there had also been very impressive advances in science and technology, and in research capability, which require no defense, and which constitute essential and strategic resources for our future endeavors.

If scientists are to be in a position to respond more effectively to contribute toward the solution of key problem areas, there will need to be a more articulate identification of needs and longer-term objectives by governments. Science policy studies in recent years have attempted to deal with these issues. However, many of these attempts became more preoccupied with structures, budgets, and methodologies, that is, the "how" rather than with matters of substance such as what we should be doing, and why, and relative prior-

ities. It should now be clear that dealing with the latter cannot be accomplished by an external group of planners working in isolation and out of contact with the real world. Action programs of the kind we are considering here can only be developed by having knowledgeable and well-informed scientists working in close consultation and collaboration with government policymakers and decisionmakers.

I am encouraged that we are now beginning to move more positively in this direction and that some of the results of these efforts will soon become apparent. As an example of this approach, many countries, including Canada, are well on the way to developing an integrated national energy R&D program. A similar articulation of objectives and R&D needs and opportunities in other major problem areas is in prospect and is needed to focus our R&D efforts and to permit the scientific community to contribute more effectively to these efforts.

On the other hand, there are also impediments arising from science itself which may inhibit more effective R&D participation on the part of individual scientists. These are matters scientists themselves must take under their purview for they are in the best position to effect changes that are deemed necessary or desirable. These matters touch on the structure and functioning of science as it has evolved over the years.

The strong discipline-orientation of science is usually seen as a handicap because of the apparent mismatch between discipline-oriented research and problem-oriented research. Historically, the development of science took place largely in universities, where it was closely coupled with academic programs. Scientific disciplines were simply a convenience to delineate manageable fields of study. As such, they also became the basis of organizational structures. Our university departments, our scientific societies, and our scientific publications all have a strong discipline basis.

I do not mean to imply that this discipline orientation is now outmoded. In fact, I believe it has served us extremely well and there is at present no obviously superior system to replace it. However, we now also recognize it is not self-sufficient and that other systems, in parallel or in series, will be needed to complement it.

It may be noted that even in basic science as knowledge advanced there has been a considerable blurring of disciplinary boundaries. Modern electrochemistry is an example of this. So are also disciplines such as biology and earth sciences. Numerous hybrid disciplines have also come into being, with their own scientific societies and their own research journals. This fragmentation, particularly of the scientific literature, has been a matter of some concern. On the other hand, there have also been some recent countervailing developments where a related number of scientific societies have joined together in a federation to pursue their common purposes. Examples are the Canadian Federation of Biological Societies and the Canadian Geoscience Council.

As scientific research has become more institutionalized over the years it has also tended to institutionalize its own system of incentives and rewards. Younger scientists sometimes assert that they would like to engage in problem-oriented research, but are concerned whether this might jeopardize their future scientific career. They contend that obtaining research grants and job promotions based on peer review virtually demand a continuous flow of published papers. This is easier to achieve by continuing to research the researchable in a particular specialty than by attempting to pioneer a new field which has as yet no recognized peers and where a research investment of several years may be required before publishable results emerge. There is no doubt that these concerns exist and a better system of incentives and merit recognition will need to be developed.

Looking to the future, what is the R&D picture likely

to be ten or twenty years from now? Because of the gravity of a number of the problems of ongoing national concern, and because of the potential contribution science and technology are capable of making toward alleviating these problems, it is likely that substantially increased R&D expenditures will be made in these areas. This, of course, must be conditional on the availability of competent research manpower in each of these areas as well as promising research ideas. The mounting of significant programs will also require more integrated and cooperative projects with closer collaboration between the government, industry, and university sectors.

In the government and industry sectors the problem of discipline mismatch is a minor one since research teams built around competent specialists required for particular research projects are readily formed. It does, however, pose serious problems in universities where research projects tend to follow disciplinary lines. Indeed, the extent to which universities should engage in mission or problem-oriented research remains a matter of active debate. In view of the many other pressures now being exerted on universities, this is a further question the universities will have to resolve for themselves.

If there are to be substantial new research expenditures in the major problem areas it is likely that a large proportion of new Ph.D. graduates emerging from universities will be required in these areas. This further underscores current discussions as to the most appropriate Ph.D. programs for the future. This is also a matter for which universities have primary responsibility.

In speculating about the future it also seems reasonable to assume there will be no cutback on the present level of effort in basic research to offset in part an increased level of effort in problem-oriented research. But such comparisons may well amount to a somewhat meaningless kind of bookkeeping. In the first place, the value of basic research is no longer in question and the need to support basic research is well recognized

by government. The question is only "how much" is needed. New programs in problem-oriented research are very likely to create a demand for more basic research in particular areas. However, this may not necessarily amount to added effort in basic research since the new earmarked research dollars will also be competing for the talents and time of existing researchers in basic research. Accordingly, we may expect the future course of basic research to be strongly influenced by increased R&D effort in the major problem areas. Whether this is beneficial or not in the long term we can only speculate since there is no way of predicting in advance where new opportunities or knowledge gaps are likely to arise.

Finally, I would like to emphasize again the international dimensions of some of the major problem areas. These will demand a more active international cooperation than we have had in the past. Science, because of its universality and the many common links it has already established, provides us with a favorable and strategic base on which to build. Successful cooperation at this level can also serve to foster better mutual understanding, trust, and confidence, thereby facilitating ultimate resolution of the more difficult social and political problem areas.

In summary, the challenges which now face the nations of the world will demand new initiatives and responses from the scientific research community as well as from governments. Both government and the scientific community will need to develop better collaborative interfaces and new approaches in their respective roles. Present day science and technology are in a strong position to contribute significantly to the alleviation of the major problem areas of growing national and international concern. These will demand greater leadership and the focused efforts of highly competent scientists and engineers. In such endeavors we truly serve to further the common ideals and promise of science, namely, the betterment of human life on earth and of all mankind.